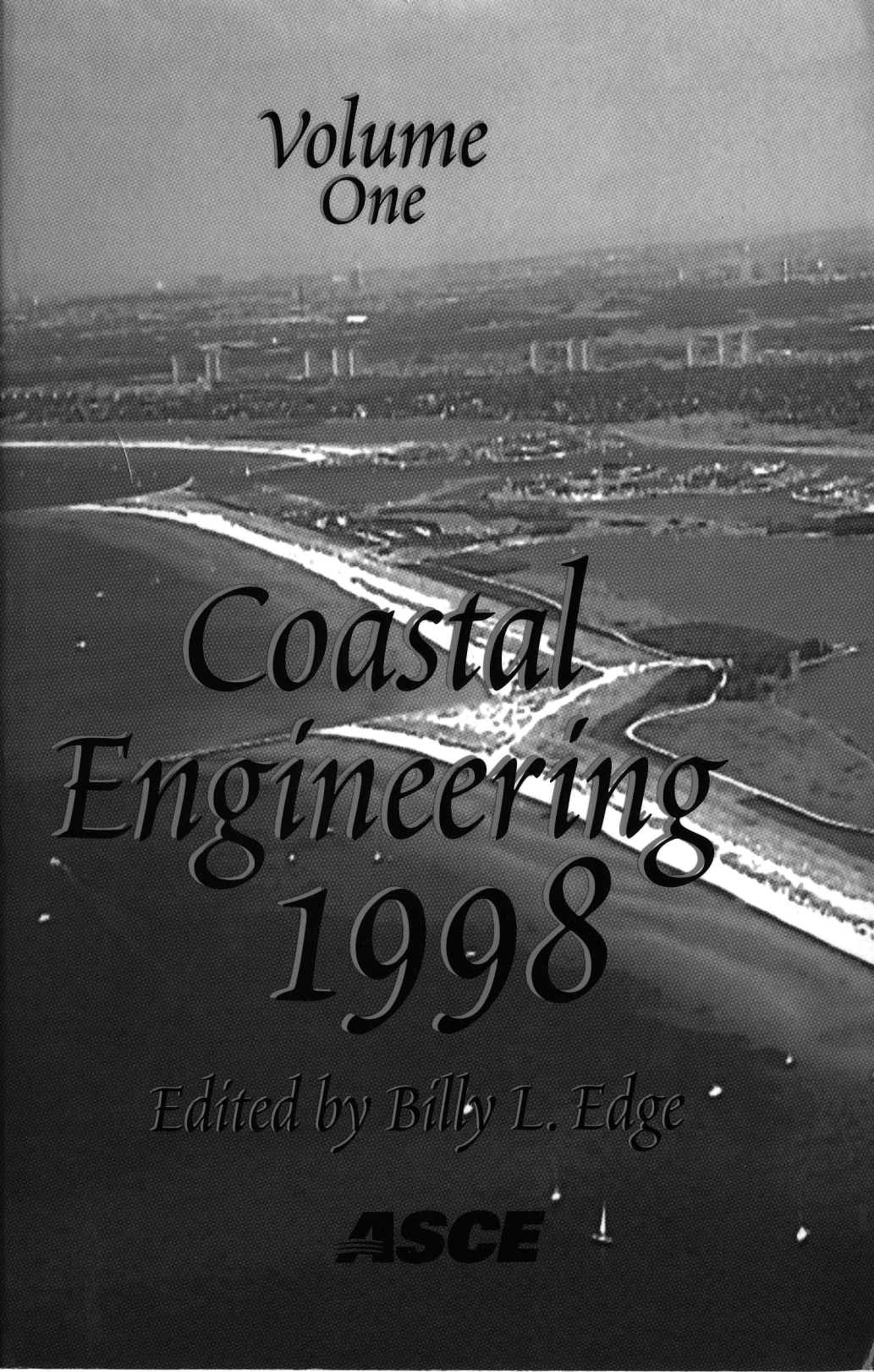
Volume One
Coastal Engineering 1998
Edited by Billy L. Edge
ASCE

COASTAL ENGINEERING 1998

Volume 1

CONFERENCE PROCEEDINGS

June 22-26, 1998
Falconer Hotel
Copenhagen, Denmark

EDITED BY
Billy L. Edge

ASCE American Society of Civil Engineers
1801 ALEXANDER BELL DRIVE
RESTON, VIRGINIA 20191-4400

Abstract: This proceedings, *Coastal Engineering 1998*, contains over 270 papers presented at the 26th International Conference on Coastal Engineering which was held in Copenhagen, Denmark, June 22-26, 1998. The proceedings is divided into five parts: 1) characteristics of coastal waves and currents; 2) long waves and storm surges; 3) coastal structures; 4) coastal processes and sediment transport; and 5) coastal, estuarine, and environmental problems. The individual papers include such topics as the effects of wind, waves, storms, and currents as well as the study of sedimentation, erosion, and beach nourishment. Special emphasis is given to case studies of completed engineering projects. With the inclusion of both theoretical and practical information, these papers provide the civil engineer and professionals in related fields with a broad range of information on coastal engineering and coastal processes affecting design and operations in the coastal zone.

Cover photo and all photos on section breaker pages 71, 1153, 1393, 2263, and 3373 provided by Danish Hydraulic Institute.

Library of Congress Cataloging-in-Publication Data

Coastal engineering 1998: proceedings of the twenty-sixth international conference: 22-26 June 1998, Falconer Hotel, Copenhagen, Denmark / edited by Billy L. Edge.
p. cm.
"Held under the auspices of the Coastal Engineering Research Council of the American Society of Civil Engineers."
Includes bibliographical references and index.
ISBN 0-7844-0411-9
1. Coastal engineering–Congresses. 2. Ocean waves–Congresses. 3. Shore protection –Congresses. I. Edge, Billy L. II. Coastal Engineering Research Council (U.S.) III. International Conference on Coastal Engineering (26th: 1998: Copenhagen, Denmark)
TC203.5.C6184 1999 98-55126
627'.58–dc21 CIP

Any statements expressed in these materials are those of the individual authors and do not necessarily represent the views of ASCE, which takes no responsibility for any statement made herein. No reference made in this publication to any specific method, product, process or service constitutes or implies an endorsement, recommendation, or warranty thereof by ASCE. The materials are for general information only and do not represent a standard of ASCE, nor are they intended as a reference in purchase specifications, contracts, regulations, statutes, or any other legal document.
ASCE makes no representation or warranty of any kind, whether express or implied, concerning the accuracy, completeness, suitability, or utility of any information, apparatus, product, or process discussed in this publication, and assumes no liability therefore. This information should not be used without first securing competent advice with respect to its suitability for any general or specific application. Anyone utilizing this information assumes all liability arising from such use, including but not limited to infringement of any patent or patents.
Photocopies. Authorization to photocopy material for internal or personal use under circumstances not falling within the fair use provisions of the Copyright Act is granted by ASCE to libraries and other users registered with the Copyright Clearance Center (CCC) Transactional Reporting Service, provided that the base fee of $8.00 per chapter plus $.50 per page is paid directly to CCC, 222 Rosewood Drive, Danvers, MA 01923. The identification for ASCE Books is 0-7844-0411-9/99/ $8.00 + $.50 per page. Requests for special permission or bulk copying should be addressed to Permissions & Copyright Dept., ASCE.

Copyright © 1999 by the American Society of Civil Engineers, All Rights Reserved.
Library of Congress Catalog Card No: 98-55126 ISBN 0-7844-0411-9
Manufactured in the United States of America.

Foreword

The Editor would like to acknowledge the work of the Local Organizing Committee in developing a very successful conference. Being a member of the LOC brings the amount of work required to develop and conduct a successful conference into sharp focus. Nevertheless the members of the LOC worked tirelessly to ensure the success of the ICCE98. In addition to the Local Organizing Committee, the work of the eight members of the technical review panel were critical to selecting the highest quality papers to be presented. Each reviewer was responsible for a critical review of 310 abstracts, of the total 640 abstracts submitted, in a very brief period of time.

The ICCE's are very special in bringing together people from around the world concerned with coastal engineering. Through this conference many special relationships and friendships have been developed. With the addition of the internet to our communication it is very easy to stay in touch with friends developed at the conferences. One very special friend of the ICCE and the many people from around the world who attended these conferences was Professor Yoshito Tsuchiya. He became seriously ill immediately before the 26th ICCE, preventing him from presenting his paper, and he passed away on October 14, 1998. Because of his long and dedicated service to the leadership in the coastal engineering community, the Proceedings of the Twenty-sixth Conference is dedicated to Professor Tsuchiya.

The next ICCE will be held in Sydney, Australia, 16-21 July 2000. ICCE 2000 promises to be a unique opportunity to see Australia including the Great Barrier reef, Uluru (Ayers Rock) and Kakadu National Park, three natural wonders of the world. The 28th ICCE will be held in Cardiff, Wales, 7-12 July, 2002. The 29th ICCE will be held in Lisbon, Portugal, in 2004, and it will be followed by the 30th ICCE in San Diego, California in 2006. Updated information can be obtained from the ICCE web page at http://www.coastal.udel.edu/coastal/icce/.Two special people deserving of recognition are Joyce Hyden and Becky Edge. They continue to support the conference and the preparation of the *Proceedings* and communicate with authors. They both have unselfishly given time and energy to producing the databases from which the conference and Proceedings are maintained and over the years have developed a network among those who contribute papers to the Conference. To the above and to the many others who have helped to produce these Proceedings, I again say "Thanks."

Billy L. Edge
b-edge@tamu.edu
Ocean Engineering Program
Department of Civil Engineering
Texas A&M University

Dedication

Professor Yoshito Tsuchiya

Professor Yoshito Tsuchiya was a leader in Coastal Engineering in Japan and Asia for many years before becoming involved in the International Conference on Coastal Engineering and the IAHR conferences. He has worked with numerous researchers from outside Japan including Ole Madsen, Richard Sylvester, James Tarrent, John Herbich and David Basco. Although many of his contributions during his thirty-year career were related to wave dynamics, his made contributions in the areas of storm surge, tsunami, beach processes and shoreline restoration. Professor Tsuchiya was born in Nagano Prefecture, Japan, in 1930 and studied at Nagoya Institute of

Technology and Kyoto University where he served from 1961 until his retirement in 1994. In 1968 he became affiliated with the Disaster Prevention Research Institute (DPRI) at Kyoto University and became its director in 1991. While at the DPRI he designed and constructed the offshore research tower at Shirahama and the field research pier at Ogata which are both in continuing service.

After his retirement in 1994 from the DPRI, which still carries forth largely in the directions he established, he became a Professor of Meijo University in Nagoya. While at Kyoto University he supervised 29 doctoral students. He was also well noted as an expert at a card game named "Koi-Koi" which his students and colleagues such as Dr. Ole Madsen at MIT came to respect. In spite of his dedication to his work, he found time to enjoy golf at least once a month with his wife Shoko. We will miss his contributions in coastal engineering research and most importantly his friendship and motivation. Prof. Tsuchiya passed away on October 14, 1998 and left a long list of accomplishments and an equally long list of assignments for his colleagues to continue.

Acknowledgements

Local Organizing Committee

Conference Chairman:

Torben Sørensen, Danish Hydraulic Institute (Chair)

Organizing Committee:

Jens Kirkegaard, Danish Hydraulic Institute (Secretary)
Hans F Burcharth, Aalborg University
Jørgen Fredsøe, Technical University of Denmark
Helge Gravesen, Carl Bro as
Per Roed Jakobsen, Danish Coastal Authority
Kaj Holm Jørgensen, Port of Copenhagen
V V Leisner, State Ports Authority

ICCE '98 Secretariat:

Dis Congress Service Copenhagen A/S, 2 C
Herlev Ringvej
DK-2730 Herlev
Denmark

Coastal Engineering Research Council (ASCE)

Chairman:
Robert G. Dean
Vice-Chairman
Orville T. Magoon
Secretary:
Billy L. Edge
Members:
Kees d'Angremond
Robert A. Dalrymple
Kyoshi Horikawa
J. William Kamphuis
Nobuhisa Kobayashi
Ronald M. Noble

Financial Support

The Conference Organizing Committee expresses sincere gratitude to the exhibitors for their financial support of the conference.

Supporting Organizations

Danish Ministry of Public Works
Danish Coastal Authority
State Port Authorities
Danish International Development Agency
City of Copenhagen
Danish Society of Civil Engineering
Danish Society of Hydraulic Engineering
Port of Copenhagen
Øresunds konsortiet
Øresund Marine Joint Venture
Rohde Nielsen A/S
Scandinavian Airlines
Danish Hydraulic Institute
International Association of Navigation Congresses (PIANC)
International Association for Hydraulic Research (IAHR)

Contents

VOLUME 1

Keynote Presentations

The Art of Coastal Engineering 1
Torben Sorensen

The European Research Programmes in Coastal Engineering 15
Hans-Werner Partenscky

Beach Nourishment: A Limited Review and Some Recent Results 45
Robert G. Dean

Part I: Characteristics of Coastal Waves and Currents

The Modelling of a Spilling Breaker: Strong Turbulence at a Free Surface 72
M. Brocchini and D.H. Peregrine

Time-Dependent Depth-Integrated Turbulence Modeling of Breaking Waves 86
Kazuo Nadaoka and Osafumi Ono

Wave Crest Interaction in Water of Intermediate Depth 98
C.C. Bird and D.H. Peregrine

Energy Dissipation Model for Irregular Breaking Waves 112
Winyu Rattanapitikon and Tomoya Shibayama

Stochastic Modelling of Nonlinear Waves in Shallow Water 126
Henrik Kofoed-Hansen and Jørgen H. Rasmussen

Comparing First, Second, and Third Generation Coastal Wave Modelling 140
L.H. Holthuijsen, N. Booij, and I.J.G. Haagsma

Wave Transformation near a Quasi-1D Coast 150
J.H. Andorka Gal, L.H. Holthuijsen, J.C.M. de Jong, and
A.T.M.M. Kieftenburg

A New Formulation of Deterministic and Stochastic Evolution Equations for Three-Wave Interactions Involving Fully Dispersive Waves 161
Per A. Madsen and Yasser Eldeberky

The Horizontal Eddies in the Offshore Zone 175
Li Li and Robert A. Dalrymple

Nonlinear Distribution of Nearshore Free Surface and Velocity 189
Nobuhito Mori and Nobuhisa Kobayashi

Evolution Equations for Edge Waves and Shear Waves on Longshore Uniform Beaches 203
James T. Kirby, Uday Putrevu, and H. Tuba Özkan-Haller

On the Viscous Destabilization of Longshore Currents 217
Uday Putrevu, James T. Kirby, Joan Oltman-Shay, and H. Tuba Özkan-Haller

Shear Waves over Longshore Nonuniform Barred Beaches 230
F.E. Sancho and I.A. Svendsen

Trapped and Free-Wave Propagation in Channels and Harbours 244
João A. Santos and D.H. Peregrine

A Boussinesq Model for Breaking Waves: Comparisons with Experiments 258
Jayaram Veeramony and Ib A. Svendsen

Nearshore Wave Dynamics Simulated by Boussincsq Type Models 272
Ole R. Sørensen, Per A. Madsen, and Hemming A. Schäffer

A 2D Model of Waves and Undertow in the Surf Zone 286
Brian A. O'Connor, Shunqi Pan, John Nicholson, Neil MacDonald, and David A. Huntley

Field Measurements of Undertow on Longshore Bars 297
Yoshiaki Kuriyama

Application of an Undertow Model to Irregular Waves on Barred Beaches 311
Douglas L. Kennedy, Daniel T. Cox, and Nobuhisa Kobayashi

Wake Wash of High-Speed Craft in Coastal Areas 325
Jens Kirkegaard, Henrik Kofoed-Hansen, and Berry Elfrink

Wave Propagation Directions under Real Sea State Conditions 338
Joachim Grüne

On the Accuracy of Parabolic Wave Models 352
Hakeem K. Johnson and Sanne Poulin

A Refraction-Diffraction Model for Irregular Waves 366
Q. Gao and A.C. Radder

Calculation of Velocity Field in 3-D Random Waves 380
Yu-xiu Yu and Ning-chuan Zhang

On the Reflection of Short-Crested Waves in Numerical Models 394
Michael Brorsen and Jacob Helm-Petersen

Breaking Waves and Induced Currents on Coastal Structures 408
Entin A. Karjadi and Nobuhisa Kobayashi

ALES Shallow-Water Flow Solver with Non-Hydrostatic Pressure: Wave Applications 422
J.G. Zhou and P.K. Stansby

Linear and Nonlinear Modeling of Long Waves Propagating around Channel Bends 433
Aimin Shi and Michelle H. Teng

Mass Transport of Progressive Edge Waves: A Comparison between the Full and Shallow-Water Wave Theories 443
K.M. Mok and Harry Yeh

Coherent Motions in the Bottom Boundary Layer under Shoaling and Breaking Waves 457
Daniel T. Cox and Nobuhisa Kobayashi

Experimental Study on Non-Linear Wave Boundary Layers 471
Hitoshi Tanaka, Hiroto Yamaji, and Ahmad Sana

A 2-DV Numerical Solution for the Turbulent Wave Boundary Layer under Breaking Waves 484
Nguyen The Duy, Tomoya Shibayama, and Akio Okayasu

Wave Modelling in the WISE Group 498
L. Cavaleri and L.H. Holthuijsen

A Long Term Wave Hindcast System Using ECMWF Winds 509
Yoshio Hatada and Masataka Yamaguchi

Numerical Simulations of Directionally Spread Shoaling Surface Gravity Waves 523
Françoise Becq, Michel Benoit, and Philippe Forget

Effects of Wave Reflection and Dissipation on Wave-Induced Second Order Magnitudes 537
Fernando J. Méndez, Iñigo J. Losada, Robert A. Dalrymple, and M.A. Losada

Green-Function Analysis of a Wave Field over Arbitrary Bathymetry 551
Hitoshi Nishimura and Moon-Su Kwak

Wave Propagation over a Bar and Wave Induced Bed Pressure Gradients 562
Øivind A. Arntsen

A Multi-Level Model for Nonlinear Dispersive Water Waves 576
Susumu Kanayama, Hitoshi Tanaka, and Nobuo Shuto

Recent Extensions to Local Polynomial Approximation Models 589
Andrew B. Kennedy

Depth Inversion for Nonlinear Waves Shoaling over a Barred-Beach 603
Stéphan T. Grilli and Jesper Skourup

Numerical Model of Fully-Nonlinear Wave Refraction and Diffraction 617
Masahiko Isobe and Samir Abohadima

A Comparison of Higher-Order Boussinesq and Local Polynomial Approximation Models 631
Maurício F. Gobbi, Andrew B. Kennedy, and James T. Kirby

Experiments on Nonlinear Wave Groups Shoaling in a Tank 645
L. Shemer, Haiying Jiao, and E. Kit

Modulation of Bichromatic Wave Train in a Wave Tank 656
Motohiko Umeyama

Simulation of Nonlinear Wave Deformation by a Shoal in 3D 670
Paul de Haas and Maarten Dingemans

Variations in Nonlinearly Evolved Nearshore Spectra and Their Significance in the Estimation of Wave Forces 682
Serdar Beji and Kazuo Nadaoka

Wave Refraction across a Current with Strong Horizontal Shearing 692
Richard R. Simons and Ruairi D. Maciver

Random Waves on a Vertically-Sheared Current 706
C. Swan and R.L. James

Wave Setup and Other Tidal Anomalies in Coastal Rivers 720
Eko Santoso, David Hanslow, Peter Nielsen, and Kevin Hibbert

3D Wave-Current Interactions in Wave-Current Channels 732
Jacco Groeneweg and Jurjen A. Battjes

Vorticity and Surf Zone Currents 745
D.H. Peregrine and O. Bokhove

Experimental Study of Wave Breaking and Blocking on Opposing Currents 759
Arun Chawla and James T. Kirby

Tidal Ellipses in the Nearshore Zone (-3 to -10m): Modelling and Observations 773
Klaas T. Houwman and Piet Hoekstra

ADCP Observation of Nearshore Current Structure in the Surf Zone 787
Takao Yamashita, Hiroshi Yoshioka, Shigeru Kato, Lu Ming, and Chikara Shimoda

Numerical Modeling of Nearshore Circulation on a Barred Beach with Rip Channels 801
K.A. Haas, I. A. Svendsen, and M.C. Haller

Applicability of a Quasi-Three Dimensional Numerical Model to Nearshore Currents 815
Masamitsu Kuroiwa, Hideaki Noda, and Yuhei Matsubara

Three-Dimensional Nearshore Currents Model Based on Vertical Distribution of Radiation Stress 829
Hisamachi Nobuoka, Nobuo Mimura, and Hajime Kato

Numerical Simulation of Wave Fields around the Submerged Breakwater with SOLA-SURF Method 843
Norio Hayakawa, Tokuzo Hosoyamada, Shigeru Yoshida, Gozo Tsujimoto

Numerical Analysis of Wave Breaking Due to Submerged Breakwater in a Three-Dimensional Wave Field 853
Koji Kawasaki and Koichiro Iwata

Classification of Wave Loading on Monolithic Coastal Structures 867
Andreas Kortenhaus and Hocine Oumeraci

Lagrangian Measurements of Accelerations in the Crests of Breaking and Broken Waves 881
Søren Peter Kjeldsen, Pierre Bonmarin, Michael G. Skafel, and William M. Drennan

Numerical Simulation of Breaking Waves by Large Eddy Simulation and VOF Method 892
Qun Zhao and Katsutoshi Tanimoto

Influence of Steep Seabed Slopes on Breaking Waves for Structure Design 906
N.W.H. Allsop, N. Durand, and D.P. Hurdle

Influence of False Waves on Wave Records Statistics 920
Marcos H. Giménez, Carlos R. Sánchez-Carratalá, and Josep R. Medina

Changing of Local Wave Climate Due to Ebb Delta Migration 934
Ralf Kaiser and Hanz D. Niemeyer

Sensitivity of Wind Wave Simulation to Coupling with a Tide/Surge Model with Application to the Southern North Sea 945
J. Monbaliu, C.S. Yu, and P. Osuna

Probability Distribution of Wave Height in Finite Water Depth 958
Michel K. Ochi

Increase of Wave Height in the North Pacific Ocean 972
Kozo Okada, Yasushi Suzuki, Yoshihiro Utsunomiya, and Yoshihiro Watanabe

Analysis of Wave Data at Sines 985
Carlos Pita and Fernando Abecasis

On the Statistical Variability of Wave Height and Period Parameters 999
Carlos R. Sánchez-Carratalá and Marcos H. Giménez

Duration in Wave Climate Analysis 1013
Rodney J. Sobey and Leah S. Orloff

Encounter Probability of Individual Wave Height 1027
Zhou Liu and Hans F. Burcharth

Wave Run-up and Overtopping: Prototype Versus Scale Models 1039
Julien De Rouck, Raf Verdonck, Peter Troch, Luc Van Damme, Flemming Schlütter, and John De Ronde

Wave Run-up and Reflection on Coastal Structures in Depth-Limited Conditions 1053
Joel R. Rathbun, Daniel T. Cox, and Billy L. Edge

Wind Effects on Run-up and Breakwater Crest Design 1068
Josep R. Medina

Some Design Aspects of an Absorbing 3D Wavemaker 1082
Hemming A. Schäffer

Generation of Double Peak Directional Wave by Dual Mode Snake-Type Wave Maker 1096
Tetsuya Hiraishi and Katsuya Hirayama

Extreme Multi-Directional Waves 1110
T.B. Johannessen and C. Swan

Low Frequency Surf Zone Response to Wave Groups 1124
Merrick C. Haller, Uday Putrevu, Joan Oltman-Shay, and Robert A. Dalrymple

Wave Dynamics and Revetment Design on a Natural Reef 1138
Thomas Jensen, Peter Sloth, and Vagner Jacobsen

VOLUME 2

Part II: Long Period Waves, Storm Surges, and Wave Groups

Long Waves in Flume Experiments 1154
J. William Kamphuis

Probabilistic Model for Tsunami-Wave Elevation along the Alborán Seacoast 1168
M. González and R. Medina

Long-Period Wave Responses in a Harbor with a Narrow Mouth 1182
Weon Mu Jeong, Kil Seong Lee, and Woo Sun Park

Application of Computer Modeling for Harbor Resonance Studies of Long Beach and Los Angeles Harbor Basins 1196
Jiin-Jen Lee, Ching-Piau Lai, and Yigong Li

Attenuation of Very Long Waves by a Large Resonator as an Outer Harbor 1210
Takayuki Nakamura and Satoshi Morita

Application of Physical Model in Long Wave Studies for the Port of Long Beach 1222
Ying-Keung Poon, Frederic Raichlen, and James (Kimo) Walker

Nautical Design Studies: Haifa Port Extensions 1236
J.A. Zwamborn, F. Di Castro, M. Radomir, and J.T.M. van Doorn

Wave Propagation Modeling for Pusan New Harbor 1250
Jang-Won Chae and Weon Mu Jeong

The Studies for the Resonance of Hwa-Lian Harbour Agitated by Typhoon Waves 1263
Chien-Kee Chang, Chung-Ching Chien, and Hsiang-Maw Tzeng

Application of Mathematical Modeling in Optimizing Layout of a Large Industrial Fishery Harbour 1276
P.P. Gunaratna, P. Justesen, D.S. Abeysirigunawardena, and H.-J. Scheffer

Characteristics of Long-Period Flow Velocity Fluctuations around Tomakomai Harbor 1290
Hiroya Kinoshita, Hideki Hoshi, Youichi Atsumi, Shin-ichiro Sekiguchi, and Toshihiko Yamashita

Transformation of Wave Groups and Accompanying Long Waves in Shallow Water 1299
M. Mizuguchi and H. Matsutate

Observation and Simulation of Low-Frequency Waves on Two Natural Beaches 1313
Satoshi Nakamura and Nicholas Dodd

Quasi 3-D Effects in Infragravity Waves 1323
A.R. Van Dongeren, I.A. Svendsen, and U. Putrevu

Numerical Modelling of Long Wave Ship Motions 1337
John R. Headland and Ying-Keung Poon

Response of Moored Vessels in Buffington Harbour 1350
E.P.D. Mansard, T. Faure, and K. MacIntosh

Statistical Wave Forecasting through Kalman Filtering Combined with Principal Component Analysis 1364
Noriaki Hashimoto, Toshihiko Nagai, and Masanobu Kudaka

Data Assimilation and Nested Hydrodynamic Modelling in Storm Surge Forecasting 1378
Rafael Cañizares and Henrik Madsen

Part III: Coastal Structures

Berm Breakwaters: Influence of Stone Gradation, Permeability, and Armouring 1394
Jørgen Juhl and Peter Sloth

Berm Breakwaters: Fifteen Years Experience 1407
Sigurdur Sigurdarson, Gisli Viggosson, Sigtryggur Benediktssson, Sigurdur Einarsson, and Omar Bjarki Smarason

The First Berm Breakwater in Hong Kong 1421
K.C. Ander Chow, Charles P. Fournier, P.F. Ma, and W.Y. Shiu

On the Stability of Berm Breakwaters in Shallow and Deep Water 1435
Alf Tørum

The Economic Analysis of "Soft" Versus "Hard" Solutions for Shore Protection: An Example 1449
David R. Basco

Uncertainty Analysis of Coastal Projects 1461
Jim W. Hall, John P. Davis, and David I. Blockley

Preventing Natural Breaching of the Major Sand Spit Protecting the Port of Walvis Bay 1475
J.S. Schoonees, L. Lenhoff, and A.J. Raw

Phenomena in Standing Wave Impact on a Horizontal Plate 1489
Piotr Wilde, Kazimierz Szmidt, and Eugeniusz Sobierajski

Two and Three-Dimensional Pressure-Impulse Models of Wave Impact on Structures 1502
Deborah J. Wood and D. Howell Peregrine

Thyborøn Barriers: A Master Case of Coastal Engineering 1516
Per Roed Jakobsen, Ida Brøker, Jesper Holt Jensen, Ann Skou, and Sanne Poulin

Application of Shore Protection Schemes in Hornbæk 1530
Mads Peder Jørgensen, Peer Skaarup, Karsten Mangor, and Jørgen Juhl

Design and Construction of Seawater Exchange Breakwaters 1539
Sadamitsu Akeda, Yasushi Yamamoto, Katsutoshi Kimura, and Kenji Yano

Application of Overtopping Models to Vertical Walls against Storm Surges 1553
Holger Schüttrumpf, Andreas Kortenhaus, and Hocine Oumeraci

Advanced Assessing of the Stability of Existing Placed Block Revetments 1567
Adam Bezuijen and Gerard A.M. Kruse

Design of Revetments in the Öresund Link: Reclaimed Artificial Island and Peninsula 1576
Jeppe Blak-Nielsen, Helge Gravesen, and Niels Lykkeberg

Design of Alternative Revetments 1587
M. Klein Breteler, K.W. Pilarczyk, and T. Stoutjesdijk

Inventory of the Stability of Existing Placed Block Revetments in the Netherlands 1601
Theo Stoutjesdijk, Mark Klein Breteler, and Hans Johanson

Second Order Wave Interaction with a Large Structure 1613
Bjarne Büchmann, Jesper Skourup, and David L. Kriebel

On the Effect of Two-Layer Thickness by High-Specific Gravity Armor Blocks on Wave Reflection 1625
Masahiro Ito, Yuitch Iwagaki, Hiroshi Murakami, Kenji Nemoto, Masato Yamamoto, and Minoru Hanzawa

Development of Two-Dimensional Numerical Wave Flume for Wave Interaction with Rubble Mound Breakwaters 1638
Peter Troch and Julien De Rouck

Nonlinear Wave Forces on a Rubble Covered Pipeline 1650
William G. McDougal, Norimi Mizutani, and Ayman M. Mostafa

Sea Level Set-up Behind Detached Breakwaters 1665
J.H. Loveless, D. Debski, and A.B. MacLeod

Coastal Erosion Caused by Construction of an Artificial Island and Performance of Beach Nourishment 1679
Ryuichiro Nishi, Takaaki Uda, Michio Sato, Masakazu Wakita, Yasuro Ohtani, and Takahiro Horiguchi

On the Design of Shore-Parallel Breakwaters 1693
J.A. Zyserman, I. Brøker, H.K. Johnson, K. Mangor, and K. Jørgensen

Shore Parallel Breakwaters and Beach Nourishments 1706
Jan van de Graaff, Henk Steetzel, Bram Bliek, and Hans de Vroeg

Sediment Transport around a Mound Breakwater: The Toe Erosion Problem 1720
Asunción Baquerizo and Miguel A. Losada

Stability of Near-Bed Rubble-Mound Structures 1730
César Vidal, Íñigo J. Losada, and Francisco L. Martín

Coastal Defense Structures in NSW, Australia 1744
S.J. Wyllie, D.B. Lord, I.F.W. Jayewardene, and T. Young

Alderney Breakwater: Scheme Evolution 1758
Paul B. Sayers, N. William H. Allsop, and Alan A. Hill

Breakwater Repair: Monitoring, Modelling, and Construction 1775
S. Pillay, D. Phelp, and A. Bartels

Digital Imaging Processing Techniques for the Aerial Field Monitoring of Harbour Breakwaters 1789
Gavin Hough and David Phelp

Design of Rock Armoured Single Layer Rubble Mound Breakwaters 1800
T. Hald, A. Tørum , and T. Holm-Karlsen

The Form of the Mound of Rubble Dumped by a Barge 1814
J.K. Vrijling and G. van Oord

Hydraulic Model Test of Stability of Amenity-Oriented Breakwater 1824
Shoji Kunitomi, Hajime Mase, and Tomotsuka Takayama

Stability of Mound Breakwaters: Dependence on Wave Reflection 1833
Cristina López, Miguel A. Losada, and Nobuhisa Kobayashi

Impact Structural Response of Core-Loc 1846
George F. Turk and Jeffrey A. Melby

Results of Field Monitoring of the New Core-Loc Breakwater at Port St. Frances, South Africa 1857
D. Phelp, A. Holtzhausen, and J. Melby

The First Core-Loc Breakwater 1871
Anton H. Holtzhausen

Damage Progression on Breakwaters 1884
J. A. Melby and N. Kobayashi

The Influence of Pressure Fluctuations on the Flow between Armour Elements 1898
Robert Booij, Wim S.J. Uijttewaal, Patrick van Os, Harry L. Fontijn, and Jurjen A. Battjes

Wave Kinematics on Breakwater Heads and Stability of Armour Layers under Multidirectional Waves 1906
Yoshiharu Matsumi, Akira Kimura, and Kenichi Ohno

A Statistical Tool for Breakwater Design 1920
Rodolfo Silva, Georges Govaere, and Francisco Martin

Cost Comparison of Breakwater Types 1934
W.H. Tutuarima and K. d'Angremond

Wave Forces on Solid and Perforated Caisson Breakwaters: Comparison of Field and Laboratory Measurements 1945
L. Franco, M. de Gerloni, G. Passoni, and D. Zacconi

Wave Impacts on Caisson Breakwaters Situated in Multidirectionally Breaking Seas 1959
P. Frigaard, H.F. Burcharth, and J.P. Kofoed

Prototype Measurements of the Dynamic Response of Caisson Breakwaters 1972
Alberto Lamberti and Luca Martinelli

Experimental and FEM Simulation of the Dynamic Response of a Caisson Wall against Breaking Wave Impulsive Pressures 1986
Shigeo Takahashi, Muneo Tsuda, Kojiro Suzuki, and Ken-ichiro Shimosako

Wave Transmission at Submerged Rubblemound Breakwaters 2000
Stuart R. Seabrook and Kevin R. Hall

Vertical Circulation Induced by a Submerged Breakwater 2014
A. Sánchez-Arcilla, F. Rivero, X. Gironella, D. Vergés, and M. Tomé

2DH Morphological Modelling of Submerged Breakwaters 2028
S.C. van der Biezen, J.A. Roelvink, J. van de Graaff, J. Schaap, and L. Torrini

Wave Pressure Distribution on Permeable Vertical Walls 2042
Hendrik Bergmann and Hocine Oumeraci

Impact Loadings on Vertical Walls in Directional Seas 2056
N.W.H. Allsop and M. Calabrese

Wave Forces on a Vertical Wave Barrier 2069
David Kriebel, Charles Sollitt, and William Gerken

Statistical Distribution of Horizontal Wave Forces on Vertical Breakwaters 2082
Janice McKenna and William Allsop

Neural Network Modelling of Forces on Vertical Structures 2096
Marcel R. A. van Gent, and Henk F. P. van den Boogaard

Pore Pressures in Vertical Breakwater Foundations 2110
C. Zwanenburg, M.B. de Groot, T. J. Kvalstad, and A. van Hoven

Economic Optimal Design of Vertical Breakwaters 2124
H. G. Voortman, H.K.T. Kuijper, and J.K. Vrijling

Design of Vertical Wall Caisson Breakwaters Using Partial Safety Factors 2138
Hans F. Burcharth and John Dalsgaard Sørensen

Lateral Versus Longitudinal Artificial Reef Systems 2152
Yoshimi Goda and Hiroshi Takagi

Development of a New Type of Reef Breakwater: Theoretical and Experimental Study 2166
Shohachi Kakuno, Masao Endoh, Yiming Zhong, Takaaki Shigematsu, and Kazuki Oda

Performance of Submerged Active Breakwaters in a Hydraulic Model 2179
K.R. Hall and M.P. Fischer

Wave Force and Stability of Armor Units for Composite Breakwaters 2193
Katsutoshi Kimura, Yuzo Mizuno, and Michifumi Hayashi

Hydraulic Performance of a High Mound Composite Breakwater 2207
M. Muttray, H. Oumeraci, K. Shimosako, and S. Takahashi

Double Walled, Low Reflection Wave Barriers 2221
R.J. Cox, P.R. Horton, and S.H. Bettington

Wave Overtopping of Rubble Mound Breakwaters 2235
Mogens Hebsgaard, Peter Sloth, and Jørgen Juhl

Directional Wave Overtopping Estimation Model and Experimental Verification 2249
Tetsuya Hiraishi and Haruhiro Maruyama

Part IV: Coastal Processes and Sediment Transport

The Morphological Changes along the Northern Coast of the Nile Delta 2264
John B. Herbich, Abdel-Fattah Elfiky, and Gamal H. Elsaeed

Modelling the Morphological Sensitivity of Large Nontidal Coastal Areas to Climatological Changes 2269
H. Weilbeer and W. Zielke

North-Coast of Texel: A Comparison between Reality and Prediction 2281
Rob Steijn, Dano Roelvink, Dick Rakhorst, Jan Ribberink, and Jan van Overeem

Littoral Processes in a Prograding Coast: The Case Study of the Atlantic Ocean Coast of Uruguay 2294
Luis Teixeira, Juan Montaña, and Miguel Losada

Turbidimetric Measuring of Suspended Sediment Concentration in the Coastal Zone 2303
Ruben D. Kos'yan, Igor S. Podymov, and Sergey Yu. Kuznetsov

Characteristics of Suspended Sediment Transport in the Surf Zone of Irregular Waves and Their Reproduction by a Cross-Shore Beach Deformation Model 2317
M. Ikeno and T. Shimizu

Cross-Shore Sediment Transport: A Field Test of the Bailard Energetics Model 2331
Troels Aagaard, Brian Greenwood, and Jørgen Nielsen

Field Observations of Small Scale Sedimentation Processes 2344
Daniel M. Hanes, Eric D. Thosteson, Yeon-Sihk Chang, Craig Conner, and Chris E. Vincent

Littoral Transport under Complex Wave Fields: Pecém, Northeast Brazil 2353
Berry Elfrink, Domenico Accetta, Berenice Motta Vargas, and Wagner Santos Scisinio Dias

Morphological Modelling Using a Modified Multi-Layer Approach 2368
Henk J. Steetzel, Hans de Vroeg, Leo C. van Rijn, and Jean-Marie Stam

Parameterizing Beach Erosion/Accretion Conditions 2382
John P. Ahrens and Edward B. Hands

Determining Depth from Remotely-Sensed Images 2395
Robert A. Dalrymple, Andrew B. Kennedy, James T. Kirby, and Qin Chen

VOLUME 3

On the Predictability of Nearshore Bar Behaviour 2409
Stefan Aarninkhof, Claire Hinton, and Kathelijne Wijnberg

Laboratory Evaluation of Instrumentation Used in Field Studies of Wave-Sediment Interactions 2423
J.J. Williams, P. Bell, L.E. Coates, A.E. Davies, P.J. Hardcastle, J.D. Humphery, S.P. Moores, L.C. van Rijn, P.D. Thorne, and K. Trouw

Size Gradation Effects in Sediment Transport 2435
Y. Chatelus, I. Katopodi, M. Dohmen-Janssen, J.S. Ribberink, P. Samothrakis, B. Cloin, J.C. Savioli, J. Bosboom, B.A. O'Connor, R. Hein, and L. Hamm

Phase-Lag Effects in Oscillatory Sheet Flow 2449
C. Marjolein Dohmen-Janssen, Gizella van der Hout, and Jan S. Ribberink

Cross-Shore Graded Sediment Transport: Grain Size and Density Effects 2463
R.L. Koomans, R.J. de Meijer, and L.B. Venema

Cross-Shore Sediment Transports on a Cut Profile for Large Scale Land Reclamations 2475
Martijn Onderwater, Dano Roelvink, and Jan van de Graaff

Optimum Size of Distorted Ripple Train for the Control of Cross-Shore Sediment Transport 2489
Satoshi Takewaka, Isao Irie, Masahiro Uchida, Hirokazu Sakamoto, and Nobuyuki Ono

The Effect of Sediment Composition on Cross-Shore Bed Profiles 2495
Leo C. van Rijn

The Breaching of Sand Investigated in Large-Scale Model Tests 2509
Cees van Rhee and Adam Bezuijen

A Dimensionless Parameter Describing Sea Cliff Erosion 2520
Akira Mano and Shigenori Suzuki

The Sand Trapping Trench as a Countermeasure To Control Wind-Blown Sand on Beaches 2534
Shintaro Hotta, Katsumori Hatanaka, Hiroyoshi Tanaka, and Kiyoshi Horikawa

Coastal Sediment Transport: The COAST3D Project 2548
R.L. Soulsby

Modelling of a Three-Layer Sediment Transport System in Oscillatory Flow 2559
Leszek M. Kaczmarek and Rafal Ostrowski

Analytical Model for Wave-Related Transport 2573
Judith Bosboom, Gert Klopman, Ad Reniers, and Marcel J.F. Stive

Vertical Length Scales of Nearshore Suspension Events 2587
D.L. Foster, A.J. Bowen, and A.E. Hay

Sediment Resuspension under Non-Breaking Waves: Predicting Sediment "Pulses" as a Function of Groupiness 2595
José A. Jiménez, Agustín Sánchez-Arcilla, and German Rodríguez

Coherent Doppler Sonar: Sediment Flux and Turbulent Velocities in a Wave Flume 2607
Len Zedel and Alex Hay

Eddy Viscosity Models for Wave Boundary Layers 2615
Ole Secher Madsen and Paulo Salles

Measurement of Shear Stress on a Moveable Bed 2628
Kelly L. Rankin, Michael S. Bruno, and Richard I. Hires

Evaluation of Longshore Sediment Transport Models on Coarse Grained Beaches Using Field Data: A Preliminary Investigation 2640
Erik van Wellen, Andrew J. Chadwick, Mark Lee, Brian Baily, and John Morfett

Motions of Pebbles on Pebble Beach 2654
Ichiro Deguchi, Masanobu Ono, Susumu Araki, and Toru Sawaragi

ONELINE: A Numerical Model for Shoreline Change 2668
Mohamed Dabees and J. William Kamphuis

Seasonal Shoreline Variations by Cross-Shore Transport in a One-Line Model under Random Waves 2682
Hans Hanson and Magnus Larson

Coastline Evolution in Response to a Major Mine Sediment Discharge on the Namibian Coastline 2696
G.G. Smith and G.P. Mocke

Longshore Patterns of the Sea Bottom Morphology 2710
Giovanna Vittori, Huib de Swart, and Paolo Blondeaux

Simple Models for Equilibrium Profiles under Breaking and Non-Breaking Waves 2722
Magnus Larson and Randall A. Wise

Equilibrium Terraced and Barred Beaches 2736
Mark D. Orzech and Nobuhisa Kobayashi

Breaker Bar Formation and Migration 2750
Bart T. Grasmeijer and Leo C. van Rijn

Beach Evolution on the Southern North Sea Coast 2759
Daniel J. Leggett, Jeremy P. Lowe, and Nicholas J. Cooper

Extracting Morphologic Information from Field Data 2773
Nathaniel G. Plant and Rob A. Holman

Nonlinear Time-Averaged Model in Surf and Swash Zones 2785
Bradley D. Johnson and Nobuhisa Kobayashi

Swash Zone Morphodynamics and Sediment Transport Processes 2799
K. Todd Holland, Asbury H. Sallenger, Britt Raubenheimer, and Steve Elgar

Field Measurements of Swash Induced Pressures within a Sandy Beach 2812
D.P. Horn, T.E. Baldock, A.J. Baird, and T.E. Mason

Flow Structures in Swash Zone 2826
H.H. Hwung, K.S. Hwang, W.S. Chiang, and C.F. Lai

Modelling Large-Scale Dynamics of Hel Peninsula, Poland 2837
Marek Szmytkiewicz, Ryszard B. Zeidler, Grzegorz Różyński, and Marek Skaja

Morphodynamics of Shoreface-Connected Ridges 2851
A. Falques, D. Calvete, H.E. de Swart, and N. Dodd

The Spatial Variability of Large Scale Sand Bars 2865
C.R. Worley, T.C. Lippmann, J.W. Haines, and A.H. Sallenger

Modeling the Dynamics of a Bar System at Duck, North Carolina, USA 2877
B. Boczar-Karakiewicz, W. Romańczyk, J.L. Bona, and E.B. Thornton

Depth of Closure: Improving Understanding and Prediction 2888
Robert J. Nicholls, Magnus Larson, Michele Capobianco, and William A. Birkemeier

Short-Term Relatively Deep Sedimentation on the Ebro Delta Coast: Opening the Closure Depth 2902
Vicente Gracia, José A. Jiménez, Agustín Sánchez-Arcilla, Jorge Guillén, and Albert Palanques

Spatial and Temporal Behavior of Depth of Closure along the Holland Coast 2913
Claire Hinton and Robert J. Nicholls

Depth of Closure and Seabed Variability Patterns 2926
Grzegorz Różyński, Zbigniew Pruszak, Tomasz Okrój, and Ryszard Zeidler

2DH Non-Linear Dispersive Wave Modelling and Sediment Transport in the Nearshore Zone 2940
Theofanis V. Karambas

Comparison of Storm Longshore Transport Rates to Predictions 2954
Herman C. Miller

Depth of Erosion under Storm Conditions 2968
John F.A. Sleath

Numerical Investigation of Sediment Transport for Combined Waves and Currents 2980
Juan Savioli

A Morphodynamic Model for River and Estuary Management 2992
Volker Barthel and Ulrich Zanke

Random Wave Modelling Approach Included in a Beach Deformation Model 3008
Ioan Nistor and Tomoya Shibayama

Geomorphological Modelling in Coastal Waters 3022
Morteza Kolahdoozan, Roger A. Falconer, and Yiping Chen

Beach Recharge Design and Bi-Modal Wave Spectra 3036
T.T. Coates and P.J. Hawkes

Management of Beach Nourishment in an Open Sand System 3046
Hans H. Dette

Beach Fills in Europe: Projects, Practices, and Objectives 3060
L. Hamm, H. Hanson, M. Capobianco, H.H. Dette, A. Lechuga, and R. Spanhoff

Evaluation of the Effect of 20 Years of Nourishment 3074
Christian Laustrup and Holger Toxvig Madsen

Zurriola Beach Evolution Two Years after Nourishment 3086
José C. Santas, José M. Medina, Alejandro Caballero, Adolfo Uriarte, and Vicente Esteban

Model Tests for Evaluating Beach Nourishment Performance 3096
Massimo Tondello, Piero Ruol, Mauro Sclavo, and Michele Capobianco

Assessmcnt of Depth of Closure on a Nourished Beach: Terschelling, The Netherlands 3110
S.W. Marsh, R.J. Nicholls, A. Kroon, and P. Hoekstra

Post-Stabilization Morphology of Oregon Inlet, North Carolina 3124
Brian P. Joyner, Margery F. Overton, and John S.Fisher

Predictive Model of Three-Dimensional Development and Deformation of a River Mouth Delta by Applying Contour Line Change Model 3138
Takaaki Uda, Hiroshi Yamagata, Ken-ichi Katoh, and Naohiro Akamatsu

Field Investigation on Sediment Transport into the Submarine Canyon in the Fuji Coast with the New Type Tracers 3151
Shigenobu Tanaka, Koji Yamamoto, Hitoshi Ito, Toshiharu Arisawa, and Toshimitsu Takagi

Sea Breeze Climatology and Nearshore Processes along the Perth Metropolitan Coastline, Western Australia 3165
G. Masselink and C.B. Pattiaratchi

Field Observation of Erosion and Accretion Waves on Shizuoka and Shimizu Coasts in Suruga Bay in Japan 3178
Naoki Itabashi and Takaaki Uda

Coastal Erosion at Keta Lagoon, Ghana: Large Scale Solution to a Large Scale Problem 3192
R.B. Nairn, K.J. MacIntosh, M.O. Hayes, G. Nai, S.L. Anthonio, and W.S. Valley

Morphological Vulncrability Index: A Simple Way of Determining Beach Behavior 3206
Óscar Ferreira, Rui Taborda, and J. Alveirinho Dias

Homogeneity Aspects in Statistical Analysis of Coastal Engineering Data 3215
P.H.A.J.M. van Gelder and J.K. Vrijling

A Simple Method To Predict Long-Term Morphological Changes 3224
Dano Roelvink, Alain Boutmy, and Jean-Marie Stam

Coastal Morphologic Variability of High Energy Dissipative Beaches 3238
Peter Ruggiero, George Kaminsky, and Nathaniel Plant

Effect Resonance on Morphology of Tidal Channels 3252
Willem T. Bakker

Inlet Cross-Sectional Area Calculated by Process-Based Model 3265
Nicholas C. Kraus

Stabilisation of the Tidal Entrance at Hornafjordur, Iceland 3279
Gisli Viggosson, Sigurdur Sigurdarson, and Bjorn Kristjansson

Application of a Long-Term Evolution Model of Tidal Inlets to the Design of a Navigation Channel, The Navia Inlet Case 3293
R. Medina, M.A. Losada, P. Lomónaco, and A. Baquerizo

Change of Mean Tidal Peaks and Range Due to Estuarine Waterway Deepening 3307
Hanz D. Niemeyer

Inlet Dynamics from Semi-Annual Surveys 3318
Owen W. Callard, William R. Dally, and Kathy FitzPatrick

Nearshore Coastal Processes Adjacent to a Tidal Inlet 3331
Thomas O. Herrington, Michael S. Bruno, Majid Yavary, and Kelly L. Rankin

Inlet Impacts on Local Coastal Processes 3345
Rajesh Srinivas and R. Bruce Taylor

Long-Term Morphological Development of the Accumer Ee Tidal Inlet and Its Impact on Island Beaches and Engineering Responses 3359
U. Abels, H. Kunz, G. Ragutzki, and H.-J. Stephan

Part V: Coastal, Estuarine, and Environmental Problems

Integrated Design Optimization for a Tropical Land Reclamation: Bali Turtle Island Development 3374
Andrew M. Driscoll, Tom Foster, Claus Pedersen, Palle Mikkelsen, and Yukimitsu Tateishi

The Influence of Marina Construction in Beach Stability: El Milagro Case Study 3388
J. Galofré, F.J. Montoya, and R. Medina

Man Made Beaches Balancing Nature and Recreation 3401
Ulf Anderskouv, Hanne Bach, Dan B Hasløv, and Karsten Mangor

Environmentally Friendly Coastal Protection: The ECOPRO Project 3412
Brendan Dollard

Coastal Restoration Considerations 3425
Karsten Mangor

Integrated Approach on the Safety of Dikes along the Great Dutch Lakes 3439
Jentsje van der Meer, Harry de Looff, and Peter C.G. Glas

Maintenance Dredging Required after Port Extensions at Walvis Bay 3453
R.C. Coppoolse and J.S. Schoonees

Accuracy in Spill Monitoring: Turbidity Distribution and Conversion Factors 3466
Klavs Høgh, Iris Buxbom, and Trine Borum Bojsen

Defining an Unusual Littoral Regime To Optimize Dredging at East London 3479
A.K. Theron and J.S. Schoonees

The Development of Sand Waves and the Maintenance of Navigation Channels in the Bisanseto Sea 3490
Kazumasa Katoh, Hidetoshi Kume, Keiji Kuroki, and Junzo Hasegawa

Coastal Disaster Prevention Works in Japan 3503
Ichio Motono and Susumu Naruse

Breach Erosion in Sand-Dikes 3516
Paul J. Visser

Bayesian Estimation of Quantiles for the Purpose of Flood Prevention 3529
J.M. van Noortwijk, and P.H.A.J.M. van Gelder

Flood Protection in the Danish Wadden Sea Area 3542
Jens Otto Andersen

Dispersion of Wave Action 3553
James M. Buick and Tariq S. Durrani

Predicting and Evaluating Turbidity Caused by Dredging in the Environmentally Sensitive Saldanha Bay 3561
S.A. Luger, J.S. Schoonees, G.P. Mocke, and F. Smit

Simulation of the Behavior of Oxygen-Deficit Water in Tokyo Bay by Three-Dimensional Water Quality Model 3575
Nobuo Mimura, Mitsuhiro Tsukada, and Masaharu Suzuki

Watertable Fluctuations in a Sandy Ocean Beach 3588
B. Raubenheimer, R.T. Guza, and Steve Elgar

Seepage Effects on Sediment Transport by Waves and Currents 3601
T.E. Baldock and P. Holmes

The Settlement, Hardness and Liquefaction of Sand Beds Due to Fluctuating Water Pressure 3615
Takaaki Minamimura, Masaki Niiyama, Takao Akutu, Kenji Yano, and Toshihiko Yamashita

A Method for Estimating the Bed Velocities Produced by a Ship's Propeller Wash Influenced by a Rudder 3624
G.A. Hamill, J.A. McGarvey, and P.A. Mackinnon

Design of Scour Protection for the Bridge Piers of the Øresund Link 3634
Lars Kirkegaard, Mogens Hebsgaard, and Ole Juul Jensen

Experimental Analysis of Wave-Induced Liquefaction in a Fine Sandbed 3643
Kojiro Suzuki, Shigeo Takahashi, and Yoon-Koo Kang

Long-Period Oscillations in a Harbor with a Fluid Mud Bottom **3655**
Wataru Kioka, M. Akter Hossain, and Kenji Kashihara

Non-Uniformity in the Wind Generated Gravity Waves Phase Distribution **3668**
Germán Rodríguez, C. Guedes Soares, E. Pérez Martell, and J.C. Nieto

Subject Index **3681**

Author Index **3691**

The Art of Coastal Engineering

by
Torben Sorensen[1]

Introduction

A Coastal Engineering Conference is a forum for exchange of technical and scientific ideas and progress in our professional field of activities. How can it make sense in this context to talk about the Art of Coastal Engineering?

I believe it does. Sedimentary coastlines exposed to the dynamic and ever varied effects of waves and currents constitute such an intricate interaction between land and sea that understanding and describing this environment in predictive terms require almost an artistic approach that starts with observation of nature, intuition and imagination before one can proceed to scientific analysis and description.

Through the last 50 years our capability to subject this environment to scientific analysis has increased tremendously, helped by the development in technology, especially the hydraulic laboratories, the computers and sensors, and by the impressive advances in the knowledge of sediment transport under the action of currents and waves as well as in the description of the hydrodynamics of the coastal environment. While the importance of an artistic approach to the problems and tasks of coastal engineering is still significant, one may well say that today coastal engineering is much more a science than an art.

This was not the case 100 years ago. At that time the most important elements of coastal engineering were experience, visual observation of nature, and intuitive understanding and inspiration developed from previous works and features of nature. Of course the engineers of that period strove to express their understanding and ideas in mathematical and scientific terms, and sometimes with remarkable success, as we shall see, but experience and the artistic elements were still of dominating importance.

[1] *Danish Hydraulic Institute, Agern Allé 5, DK-2970 Hørsholm, Denmark, Fax: +45 45 179 200, e-mail: ts@dhi.dk*

Except for the most southern part of the North Sea coast the tidal range of astronomical tides is virtually negligible, being in the order of 10 to 30 cm. Extreme water levels are therefore dominated by storm surges, which may reach levels of 1,5 to 2 m above MSL, and are strongly correlated with strong winds from certain directions. The directions causing high water, respectively low water, are of course site specific, and most often - but not always - high water levels occur simultaneously with severe wave action.

The absence of large tidal ranges made it quite simple for Danish engineers of more than 100 years ago to realise that littoral drift - coastal erosion and sedimentation - was totally dominated by the wave action. In contrast to many other places in the world they were not confused by the presence of strong tidal currents running parallel to the coast, and the storm surges - except for the cases of straits connecting large water basins - generally generate only relatively weak currents parallel to the coast.

These conditions, in combination, made Denmark a very good "laboratory" for studying coastal sediment transport in full scale as generated by waves. In those days the technology of physical scale modelling for engineering purposes and research had not been developed. The engineers had only one possibility: To go out in nature and observe before, during and after severe wave action. And this they did, sometimes at an impressive scale, with the advantage that they understood that what had happened was caused by the waves and the currents generated by the waves in and shoreward of the breaker zone.

Denmark - a Full Scale Laboratory for Coastal Hydraulics

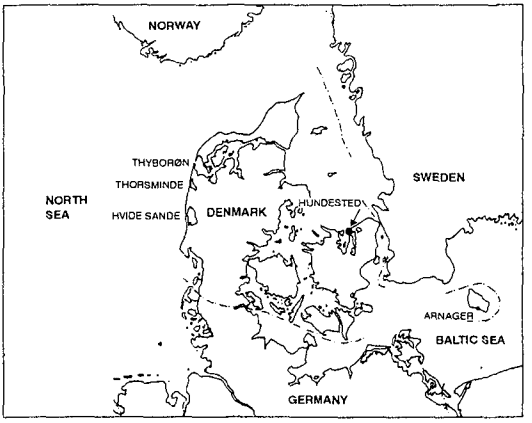

Figure 1: Denmark – between the North Sea and the Baltic Sea.

To understand why coastal engineering is and has been such an important and exciting challenge to Danish engineers a glance at the map of Denmark, Fig. 1, would suffice.

Nowhere in the country you are more than about 60 km from the nearest seacoast. Moreover, virtually the entire country is made up of sedimentary soils of marine, fluvial or glacial origin, and as such prone to littoral drift along its coasts to a variety of scales.

The country is located around the centre line of the varying locations of the polar front separating the polar air masses from those of the sub-tropic region giving rise to the development and passage of numerous low-pressure weather systems. These are particularly strong during autumn and winter, but can occur at any time of the year, and they generate predominantly westerly winds. This, together with the fact that Denmark is located at the eastern side of the North Sea, causes the Danish North Sea coast to be in the class of the most dynamic coastlines on an international scale in terms of littoral drift - up to 1 million cu. m. per year.

On the Danish coastlines in the regions East of Jutland the wave climates are less severe because of fetch limitations (up to 200 km). Even so the littoral drift on many parts of these coastlines is in the range of 10.000 to 100.000 cu. m. per year.

The Danish Coasts

The North Sea coast of Jutland offers good illustration of the challenges met and taken up by Danish coastal engineers towards the end of the last century and in the beginning of the present century.

The two first examples from the North Sea coast are of a similar nature. They represent schemes to prevent flooding of low-lying farmland in the coastal fiords - or rather lagoons - Ringkobing Fiord and Nissum Fiord, and at the same time stabilise the entrances to these lagoons and provide road connection across the stabilised entrances. In both cases the entrances were stabilised by means of breakwaters, and the entrances were provided with sluices for discharging the water supplied to the lagoons by rivers, as well as sluices allowing the passage of relatively small vessels.

The works are illustrated by Figs 2 and 3, which are photos taken in recent years. The dramatic coastal development in terms of accretion and erosion caused by these works is clearly visible and has led to the construction of additional breakwaters and groynes, and to nearshore breakwaters for erosion protection, as well as in recent years to substantial sand bypassing and beach nourishment.

Therefore, I have chosen to illustrate the Art of Coastal Engineering by giving examples of the achievements of Danish coastal engineers of 100 years ago. This presentation thus could also have been given a more modest title to reflect this content, but I thought that since, in my opinion, the element of art continues to be important for good coastal engineering and should not be forgotten, I chose the more ambitious title for the presentation.

Figure 2: Hvide Sande Inlet.

Figure 3: Thorsminde Inlet.

The works at Hvide Sande at Ringkøbing Fiord became the first hydraulic engineering works in Denmark to be studied in a small physical model built at the Technical University of Denmark in the 1930ies.

Another dramatic situation controlled by engineering works for more than a century is the case of the Thyboron inlet, Fig. 4, which has been described and discussed at various Coastal Engineering Conferences over the last 40 years. The extensive documentation of the development of the coastal profiles provided by annual soundings carried out over more than 100 years has formed the basis for several engineering studies, including

Professor Per Bruun's doctor's thesis of 1954, and studies carried out under the auspices of various committees established by the Danish government.

Figure 4: Thyborøn. The inlet is to the left.

All three cases initially constituted experimenting in nature, and all three of them, but especially the case of Thyborøn, have generated observations and documentation providing much food for thought for contemporary and later coastal engineers.

To the East of Jutland the most severely exposed coastline in the country is that of the North coast of Zealand, on which a number of fishing harbours/marinas and beach landing places protected by offshore breakwaters were built around the beginning of this century. One of these, the port of Hundested, will be the subject of a more detailed discussion below.

The Concept of Island Harbours

Building harbours on open coasts with sediment transport has been known for centuries to give rise to problems of sediment accumulation and erosion around the works. Already in Roman times this was realised, and Roman harbours, such as Ostia, Tarentum and Antium, were built with openings in the breakwaters running crosswise to the coastline in an attempt to let the littoral drift bypass the harbour behind the main breakwater, albeit without much success.

In an attempt to radically solve these problems, engineers, especially in the UK and France, in the middle of the 19th century, developed ideas for proper island harbours, i.e. harbours in the form of a "hollow" island connected to the shore by an open bridge providing minimal obstruction to the littoral drift. Several projects of this nature were

developed and presented by imaginative engineers, but few of them ever built, and some of those that were built had breakwaters parallel to the coastline that were so long in relation to the distance from the coast that the harbour basins were completely filled up, such as the port of Ceara in Brazil, built in 1887, Figs 5 and 6.

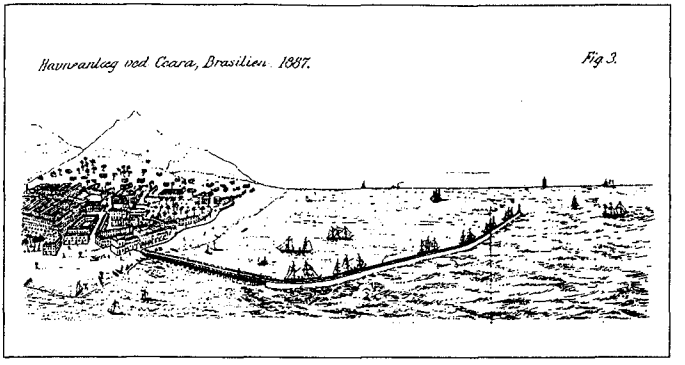

Figure 5: Port of Fortaleza, Ceara, Brazil, 1887.

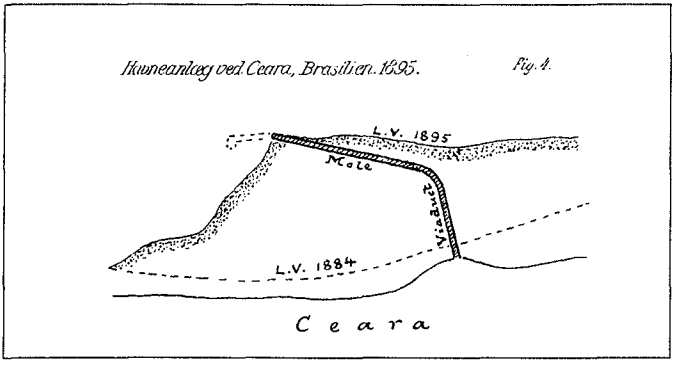

Figure 6: Sand accumulation around Port of Fortaleza, 1895.

Quite naturally, the concept of island harbours caught the interest of Danish coastal engineers because of the need in our country to build harbours on coastlines with littoral drift. In the second half of the 19th century several such harbours were constructed, one of them being the port of Arnager built in 1884 on the South coast of the island of Bornholm in the Baltic Sea, Fig. 7. This harbour is a good illustration of the understanding,

developed at the time, of the importance of placing the harbour at a relatively large distance from the shoreline to avoid the formation of a tombolo that would eliminate the character of an island harbour. This harbour still exists, and is still an island harbour.

Figure 7: Arnager Harbour, Bornholm.

However, heated discussions went on in the Society of Engineers of Denmark between the believers and the non-believers in island harbours, and these discussions were extensively reported in the Society's monthly journal. To try to get to the bottom of this the Ministry of Public Works in July 1902 appointed an expert commission of three engineers with the task of considering whether and under what circumstances island harbours would be a suitable solution in lieu of harbours protruding from the coastline.

The commission submitted its deliberations in a hand written report to the Ministry in November 1903, which was published in lithographed form in view of the general interest in the subject. A printed version was published in 1909.

The 1903 Commission Report

The report starts with a remarkable overview of projects and ideas for island breakwaters and island harbours from many countries, including the UK, France, Belgium, Canada, Italy, USA, South Africa and Brazil. In this way the commission demonstrated that it realised the need to look beyond national experience in search of knowledge and inspiration, just as we are doing today through the International Conferences on Coastal Engineering. It came, however, to the conclusion that on the international scene proper island harbours (not island breakwaters) were all proposed to be placed so far offshore

that they were located outside of the zone of coastal sediment transport, for which reason they became so expensive that none of them were ever built.

The question facing the commission with regard to the suitability of island harbours for Danish conditions was therefore whether such harbours could be built inside the zone of coastal sediment transport and yet not be blocked by accumulating sand, and the commission states as its first observation that it considers it to be self-evident that this can be achieved, provided that the width of the harbour in the direction parallel to the coastline is not too large and the connecting bridge is sufficiently open.

The commission then proceeds to describe the Danish experience with island harbours as illustrated by three case histories described in considerable detail. One of these is that of Arnager, Fig. 7, which clearly satisfies the condition for success formulated by the commission.

In the report the commission presents a general description of sediment transport as caused by currents and waves, respectively, in the course of which they make some - for the time - remarkable observations. For instance, they distinguish clearly between bed load transport and suspended load transport, and in the case of transport by currents alone they observe that for clay or mud a current velocity of ¼ ft. per sec. will move the material, while for small pebbles a current velocity of 3 ft. per sec. is required for transport to commence.

In the case of waves they observe that waves do not transport material as long as their motion is of an oscillating character only, while the breaking waves do cause sediment to be transported, especially, as they state in so many words, due to the longshore currents generated by the breaking of the waves.

They then proceeded to develop a formula describing the littoral drift capacity of waves represented by a littoral drift vector, or - as they more appropriately call it - a "wave-effect rose". Although the reasoning behind this theory is, of course, open to criticism, the result is nevertheless remarkable. They conclude that the littoral drift is proportional to the square of the wind velocity times the square root of the fetch (provided that the fetch is less than 300 nautical miles) times the frequency of occurrence of the wind (velocity and direction) considered, and they represent this wave effect in a vectorial form, Fig. 12. This is not very different from what was developed some 40 years later by engineers in other countries.

The commission's studies of the concept of island harbours located inside the zone of coastal sediment transport is also remarkable. It concentrates on the case history of the port of Hundested, which was - and probably still is today - by far the most well-documented such case history.

The Island Harbour of Hundested

Hundested is located on the coast of North Zealand at the eastern side of the entrance to the Isefiord, see the map of Denmark, Fig. 1, and the map of the Isefiord entrance, Fig. 8. The coast at the site of the port is actually facing West, and the littoral drift on this coast is southward, probably in the order of a few thousand cu. m. per year.

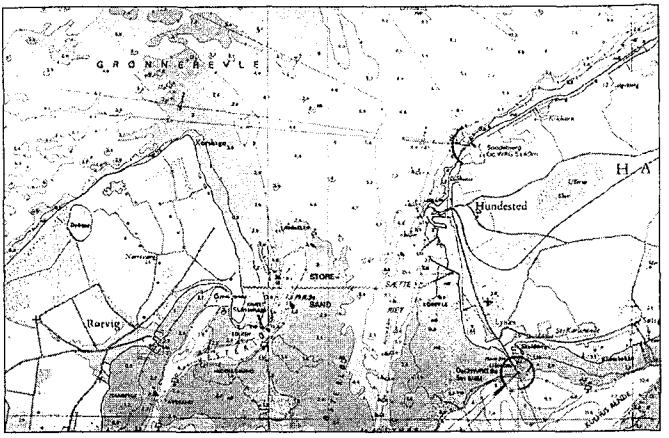

Figure 8: Isefiord entrance and approaches to Hundested.

The site has the special feature of being located at the relatively narrow strait between the sea North of Zealand named Kattegat and the large basin of the Isefiord. The winds in the sector West to North, which cause the southward littoral drift, are strongly correlated with storm surge high waters in the Kattegat resulting in strong southgoing currents in the strait, while the return flow from the fiord to the sea takes place after the wind has abated or turned towards easterly directions. Thus there is a strong correlation between severe wave action and strong currents in the southgoing direction.

The bathymetry of the entrance to the Isefiord, Fig. 8, clearly reflects these conditions. It may be added that the southgoing currents are generally stronger along the western part of the entrance, while the northgoing currents are stronger towards the eastern side near the location of Hundested.

The first harbour facility was built in 1868 as a 60 m long stone breakwater with a quay on the South side. It quickly got virtually buried in sand, Fig. 9. In 1886 a small octagonal harbour basin was built at the end of this breakwater, but sand accumulation quickly occurred around the harbour and in front of the entrance, Fig. 10. Even in the harbour basin sand accumulated, chiefly by passing through and over the stone breakwaters, to such an extent, that rumour has it, you could grow potatoes in the harbour!

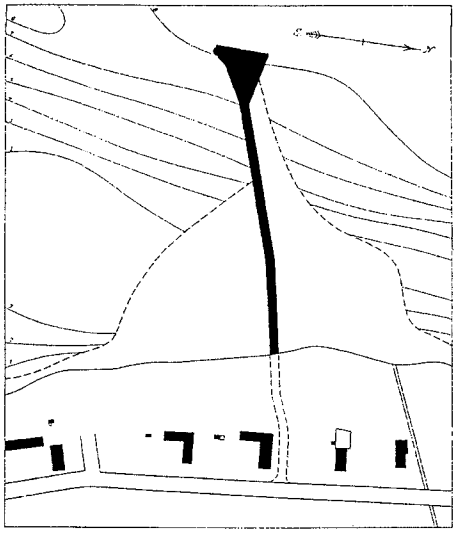

Figure 9: Hundested Breakwater, built in 1862. Subsequent sand accumulation indicated.

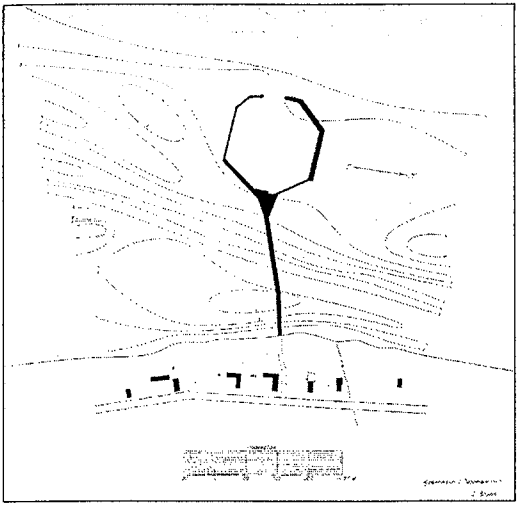

Figure 10: Hundested Harbour, 1886. (Bathymetry from before 1862).

After these frustrating experiences and costly futile efforts to develop a usable harbour at Hundested the leading proponent of island harbours in Denmark, engineer Hans Zahrtmann, was commissioned to design the conversion of the port into an island harbour, Fig 11, in the hope and expectation that this would solve the problems of sedimentation around and in the harbour. This conversion into an island harbour was completed in 1892 by replacing the connecting stone breakwater with a wooden bridge, and at the same time the harbour breakwaters were reconstructed so as to prevent sand from passing through the breakwaters.

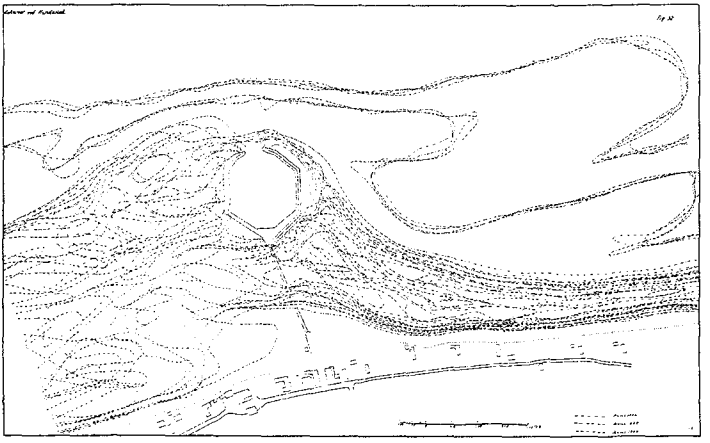

Figure 11: Hundested Island Harbour and depth soundings 1893-1896.

During the years 1893 through 1896 the bathymetry in a considerable zone around the harbour was surveyed every spring and every autumn, clearly for no other purpose than to study the effect of the harbour's conversion into an island harbour. Such soundings were also made in the autumn of 1898, the spring and autumn of 1902 and in January 1903. An example of results from these soundings is shown on Fig.11.

Between the harbour and the original coastline a tombolo shaped formation remained, and the commission, in addition to calculating the "wave-effect rose", also attempted to calculate the shape of the tombolo based upon diffraction calculations!

The studies demonstrated that the island harbour concept was indeed in this case effective. The sand accumulation between the harbour basin and the original coastline was quickly broken through, and the accumulation of sand at the harbour entrance was substantially reduced.

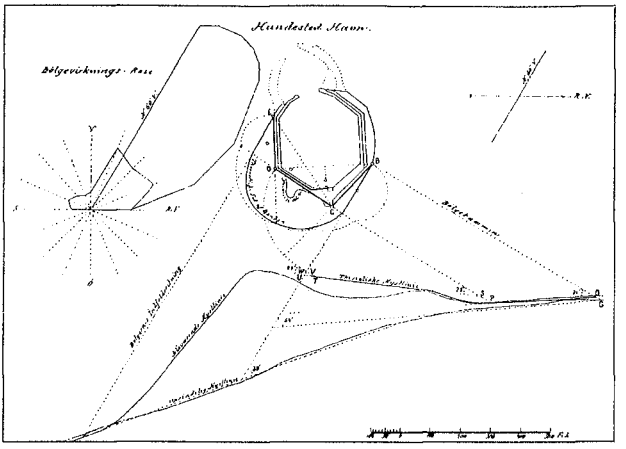

Figure 12: Wave-effect rose and tombolo formation at Hundested, Report of 1903.

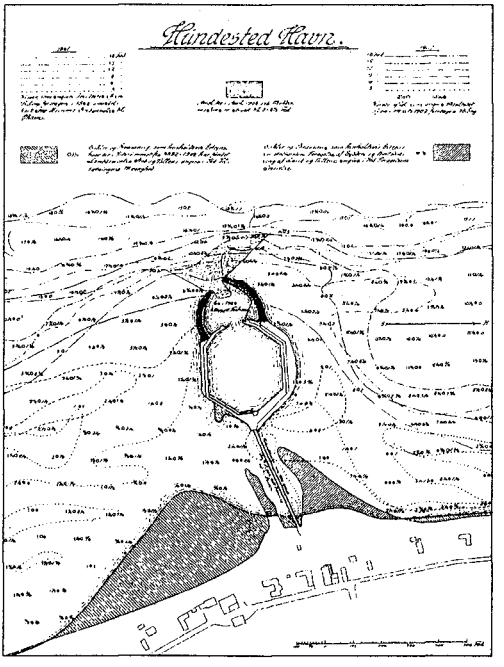

Figure 13: Hundested Harbour, 1900.

In 1900 a small outer harbour was constructed, Fig. 13, probably chiefly to provide better shelter for the fishing boats in the harbour basin, but possibly also in the hope of further reducing sand accumulation at the harbour entrance, and in 1907 the wooden access bridge was replaced by a reinforced-concrete structure, Fig. 14.

Figure 14: Access bridge to Hundested Harbour.

Detailed study of the numerous soundings - at a larger and more readable scale - shows interesting features observed by the 1902 commission, including the fact that between the harbour and the coast, sand tended to accumulate during the calmer summer season, and to be eroded during the winter, as well as various other interesting features. In the context of the present presentation the most interesting point, however, is the extent to which engineer Zahrtmann and others used observations and measurements in nature in a much similar way as today where we use a hydraulic scale model test.

The development of the port of Hundested did not by any means stop in 1907. During the First World War a large outer basin was constructed as a general cargo and ferry traffic port, and in the 30ies further expansions were implemented, Fig. 15. On this figure careful scrutiny can identify the remaining portions of the breakwaters of 1886 and 1900. Already the expansion made during the First World War caused the tombolo to connect the harbour to the shoreline and to bury the concrete bridge in sand, such as was indeed predictable on the basis of the analysis of the 1902 commission. However, this tombolo did not have any negative effect because by this expansion the new outer breakwaters reached out so far that the strong outgoing currents after severe storms were capable of keeping the entrance region free of sand deposits so that after this expansion virtually no maintenance dredging has been required.

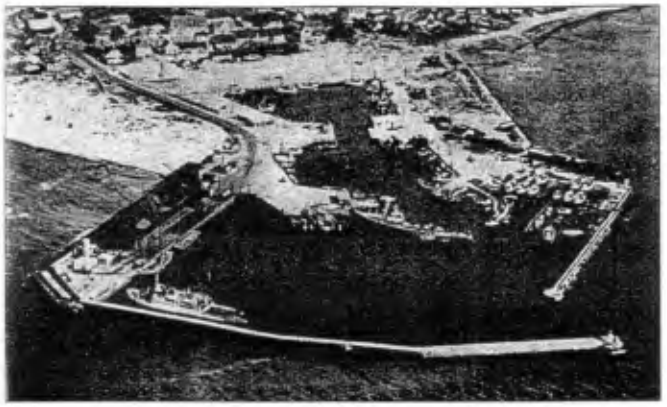

Figure 15: Hundested Harbour, 1938.

Further expansions have followed after the Second World War, and it is quite possible that all of these expansions and the associated economic development might never had materialised if imaginative and courageous engineers of the turn of the century had not exercised to the best of their ability, and with success, the Art of Coastal Engineering.

The European Research Programmes in Coastal Engineering

by
Hans-Werner Partenscky*)

1. General Introduction

Since 1989, the European Union has established a number of scientific programmes to promote and coordinate a wide range of activities such as transport, fisheries, environment, tourism, etc. which also have an impact on the coastal zone.

The efforts of the European Commission to promote an overall concept of Integrated Coastal Zone Management (ICZM) encompass activities from the research carried out under the Marine Science and Technology programme (MAST) to the Environment and Climate programme (ENV).

2. The MAST-programme

The MAST-programme (Marine Science and Technology) has grown in three stages: first as a pilot programme (1989-92, budget ECU 50 million), then as MAST-II (1991-94, budget ECU 118 million), and finally as MAST-III (1994-98, 244 million ECU). From the start, coastal zone science and engineering has played an important part among the areas covered by the programme, absorbing about 20% of the budget. In the on-going MAST-III, coastal zone research will receive about 50 million ECU.

According to the detailed contents of the first pilot programme, the objectives of coastal zone research were: "to strengthen European research in coastal processes, thereby allowing for better management of resources and for engineering designs; to provide the information and data required for application of modern tools in coastal management, such as mathematical numerical modelling; to advance and harmonise design of coastal

*) *Former Director of the Franzius-Institut, University of Hannover/GERMANY*

engineering works and to help prepare for the consequences of the currently predicted rise in sea level in the next century" /1/.

Up to now, the MAST-programme has focussed on two areas of coastal zone research: morphodynamics and coastal structures.

Coastal morphodynamics refers to the fact that the state of a sandy coast is a manifestation of the dynamic system which is formed by the water motion (waves, currents), the sediment motion and the bed topography. These elements mutually interact in a highly dynamic, non-linear way. As a result, the behaviour of a coast is not a straightforward response to the inputs (storms, tides, etc.), but includes the effects of complex forms of autonomous behaviour at a variety of length and time scales. Examples of such autonomous behaviour are the formation of beach cusps, nearshore bars, sand waves, channel/shoal systems, etc. This makes the predictive modelling of coastal morphodynamics a complicated task /2/.

In coastal engineering, MAST supports work both on hard structures (rubble mound breakwaters, berm breakwaters, monolithic vertical walls, etc.) and on soft options (beach nourishment techniques, maintenance of intertidal flats, salt marshes and other defence mechanisms where Nature performs the actual work). The aim is to improve criteria and guidelines for the design of structures or schemes in a manner, which ensures reliability, economy and environmental compatibility. Here, research again covers a wide range of issues, such as overtopping, scouring, wave impact forces on caissons, the role of biological factors in the consolidation of cohesive sediments, etc. /3/.

Under the MAST-umbrella, leading European hydraulic institutes have set up, for the first time, systematic cooperation projects on issues that are too complex to be tackled individually.

At the beginning, there were, of course, some difficulties in bringing the scientific ideas and basic approaches of University laboratories together with the more mission-oriented research aspects of commercial and governmental institutes. However, very soon an excellent cooperation was established between the partners from universities and government research institutes, with the common aim of promoting European research and knowledge in coastal engineering.

Six European institutes participated in the project on coastal morphodynamics as the main contractors: Delft Hydraulics, HR Wallingford, Danish Hydraulic Institute, Sogreah Electricité de France and the Technical University of Braunschweig. In addition, 26 associated contractors from European universities, state laboratories and consulting companies participated from Italy, Great Britain, Ireland, Spain, Denmark, France, The Netherlands, Belgium, Norway and Portugal.

Five European institutes participated as the main partners in the programme on coastal structures: The Franzius and Leichtweiss Institute, HR Wallingford, Delft Geotechnics, University of Sheffield and Delft University of Technology. The research work was in addition supported by 18 associated partners from Denmark, Great Britain, Spain, The Netherlands, Italy, Germany, France and Norway.

3. Scientific Results of the Morphodynamics-Project

The morphodynamics-project was subdivided into several sub-projects dealing with waves, currents, non-cohesive sediment transport, cohesive sediments and morphodynamics, respectively. The project also had a structure of working groups addressing cross-discipline problems such as wave-current-sediment interaction.

The morphodynamics-project had the following focal points:

(1) medium-term coastal profile modelling,

(2) medium-term-coastal area modelling,

(3) rhythmic features ("bars and banks"), and

(4) long-term modelling.

Fundamentally different approaches were used: process-based simulation models for the medium-term applications, mathematical stability analyses for the rhythmic features and a range of more or less empirical large-scale modelling techniques for the long-term modelling.

3.1 Medium-term coastal profile models

The work on medium-term profile modelling concerned the evolution of the coastal profile in the case of longshore uniformity. These PC-based models are based on state-of-the-art knowledge of waves, current and sediment transport and their interactions with the changing bed topography.

Special attention was paid to bar formation, taking into account phenomena such as non-linear wave kinematics, low-frequency waves, the wave breaking process, undertow and induced streaming, bottom boundary layer effects, sloping-bed effects, sediment transport mechanisms and sediment sorting effects. A range of profile models was intercompared and tested against laboratory data, mainly from the Large-Wave-Flume-facility in Hannover. These models were extended, improved and validated against data from other laboratory and field experiments /4/. Figure 1 shows an example of measured and computed beach profile evolution /5/.

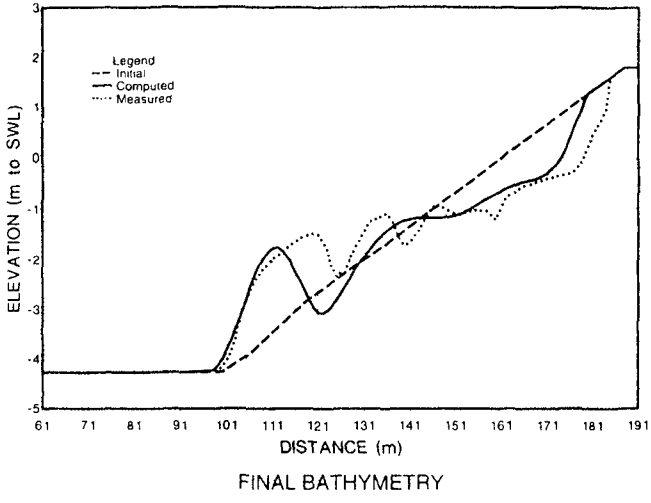

Figure 1: Measured and computed beach profile /5/.

The availability of comprehensive data sets for validation of the profile evolution is an prerequisite for morphodynamic modelling. Therefore a significant effort was spent on getting access to new data. For field data, a link was made with the MAST-project NOURTEC, which concerns the coastal response to underwater nourishment /5/. Other field data were obtained from the German coast and from El Saler Beach, near Valencia, Spain. A valuable set of laboratory data for model validation was obtained from a series of experiments in Delft Hydraulics' Delta Flume.

3.2 Medium-term coastal area models

There are many situations in which the assumption of longshore uniformity does not work and the coastal profile modelling approach is an over-simplification of reality. In such cases, a coastal area model is needed. Process-knowledge, modelling know-how and software implementation of this type of model is much less advanced than in the profile case, because of the extra complexity due to the second horizontal dimension. Also, there is a need for field and laboratory data to help develop and validate coastal area morphodynamic models. The effort, which this requires, is beyond the capacity of most research projects. This is why the validation of coastal area models was based, so far, on model intercomparisons for hypothetical cases and on comparisons with small-scale laboratory experiments /7, 8/.

Although the necessity to include 3-D effects is obvious, the morphodynamic modelling is still far from operational. Instead, some 2-D depth-integrated models have reached a level of operational use.

Figure 2 shows, as an example, the results of a coastal area model with the morphological response of the shore-line due to a shore-parallel breakwater for different angles of wave approach /5, 6/.

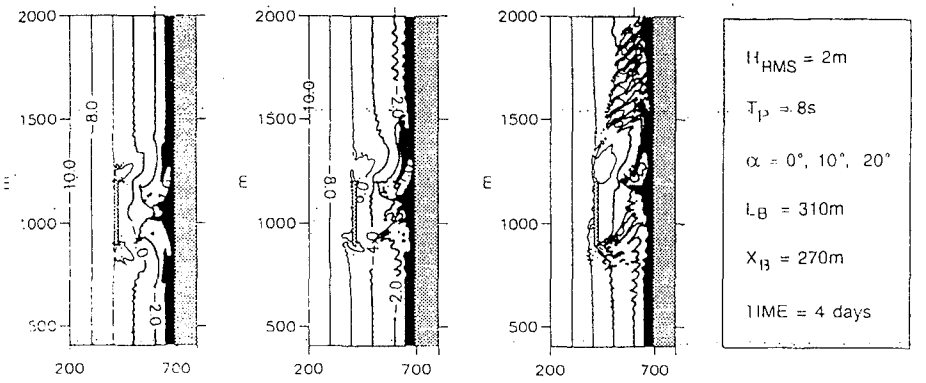

Figure 2: Morphological changes behind a shore parallel breakwater for different angles of wave approach. Results of a morphological model of DHI /5, 6/.

3.3 Rhythmic features

The main focus in the domain of rhythmic features was the analysis of free instabilities of the morphodynamic system. This involved non-linear analyses of wave-induced bed-ripple patterns, formed by turbulent boundary layers and effected by grain sorting and steady drift, but also much larger features, such as tidal sand banks, sand waves and shore face ridges. Such an analysis, including the 3-D velocity field, revealed the essential mechanisms of the formation of large-scale rhythmic features on a horizontal seabed (sand banks, sand waves or tide-parallel ridges).

One example concerns sand waves on the seabed which can influence the effective depth of navigation channels. Here the deepening of the channel might lead to higher sand waves and to a smaller effective depth.

3.4 Long-term modelling

The driving factor behind the work on long-term modelling is the need for knowledge and model concepts with the scales of long-term/large-scale phenomena. There are practical as well as theoretical arguments for not relying exclusively on medium-term models to bridge the gap between the scales of the existing process knowledge and the scales of interest.

Large-scale modelling must be considered as being in an early stage of development. Only recently, new data-abundant monitoring techniques have been developed which enable us to study phenomena at time-scales up to a decade with a resolution of hours. These techniques are now being deployed all over the world and they are producing results, which offer perspectives to the use of advanced analysis techniques from other disciplines. For the time being, long-term modelling is still a matter of a number of ad-hoc models for specific applications /9, 10/.

3.5 Present and future projects on morphodynamic modelling

At present, research on morphodynamic modelling is being carried out in projects on large scale modelling (PACE), shore nourishment techniques (SAFE), tidal inlets (INDIA) and nearshore dynamics (SASME). Underlying processes are further investigated in several sub-projects /2/.

In a large field programme field data are gathered to support and validate the morphodynamic models.

The results of the research work carried out so far in the MAST-programme on morphodynamics have been published in over 460 papers, in reports, theses, congress proceedings and papers in journals. In addition, a special volume on the project was issued in 1993 in Coastal Engineering /9/ and the scientific results obtained are summarised in a book in preparation from De Vriend /10/.

Some of the software for the morphodynamics model concepts is commercially available through the big hydraulic laboratories, which participated in the projects (Delft Hydraulics, Danish Hydraulic Institute, HR Wallingford, etc.).

4. Results of the MAST-project on coastal structures

The first large European project on Coastal Structures was co-ordinated by HR Wallingford in 1990 - 1992. This project created strong links between European research groups and formed the basis for the following MAST-projects /11/:

- Monolithic coastal structures,
  coordinated by H. Oumeraci, Techn. Univ. of Braunschweig/Germany.

- Rubble mound breakwater failure modes,
  coordinated by H.F. Burcharth, Aalborg University/Denmark.

- Full-scale dynamic load monitoring of rubble mound breakwaters,
  coordinated by J. De Rouck, Univ. of Ghent/Belgium.

- Berm breakwater structures,
  coordinated by J. Juhl, Danish Hydraulic Institute/Denmark.

- Reflection of waves from natural man-made coastal structures,
  coordinated by M. Losada, Cantabria Univ./Spain.

The following MAST 3 projects are ongoing as a continuation of two of the above mentioned projects /12/:

- Probabilistic design tools for vertical breakwaters,
  coordinated by H. Oumeraci, Techn. Univ. of Braunschweig/Germany.

- The optimisation of crest level design of sloping coastal structures through prototype monitoring and modelling,
  coordinated by J. De Rouck, Univ. of Ghent/Belgium.

4.1 Monolithic coastal structures

For the stability calculation of monolithic structures the wave loading must be known. Although the front face geometry of a caisson is very simple, the wave pressures are very complicated functions of the sea state.

The character of the force histories and the pressure distributions due to breaking waves have therefore been intensively studied in the Hannover Large Wave Flume of the Universities of Hannover and Braunschweig /11/ (Figure 3).

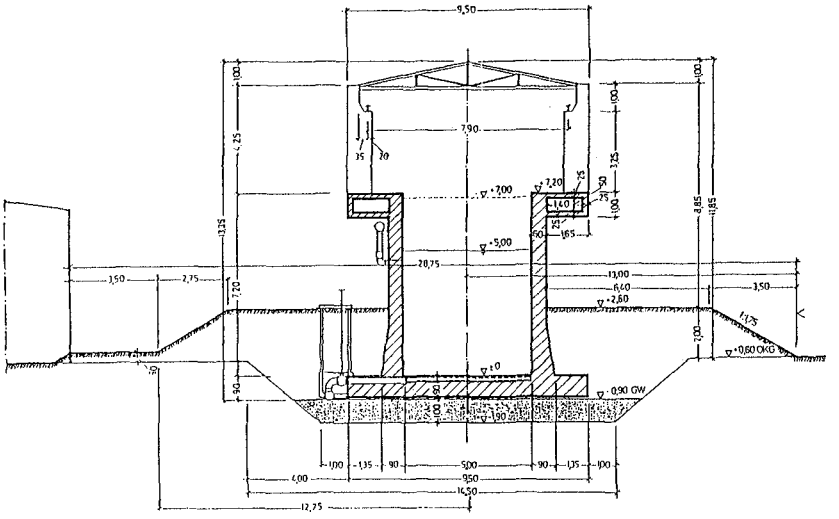

Figure 3: Cross-section of the Large Wave Channel in Hannover /11/.

In the tests, four principal breaker types could be distinguished (Figure 4) /13/. The highest wave impact as well as horizontal force at the structure occurs when waves are breaking against the breakwater.

LOADING CASE 1	LOADING CASE 2	LOADING CASE 3	LOADING CASE 4
turbulent bore	well-developed plunging breaker	plunging breaker	upward deflected breaker
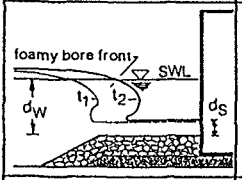	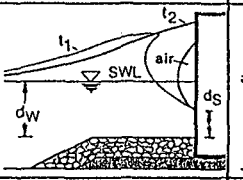	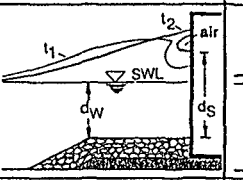	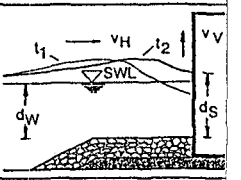
$d_S < d_W$	$d_S < d_W$	$d_S > d_W$	$d_S > d_W$
$v_H >> v_V$	$v_H > v_V$	$v_H \geq v_V$	$v_V >> v_H$

Figure 4: Classification of breaker types and loading cases /13/.

Here, two cases must be distinguished: Waves with an almost vertical front hit the breakwater (Figure 5), and breaking waves with an entrapped air pocket under the overturning tongue (Figure 6).

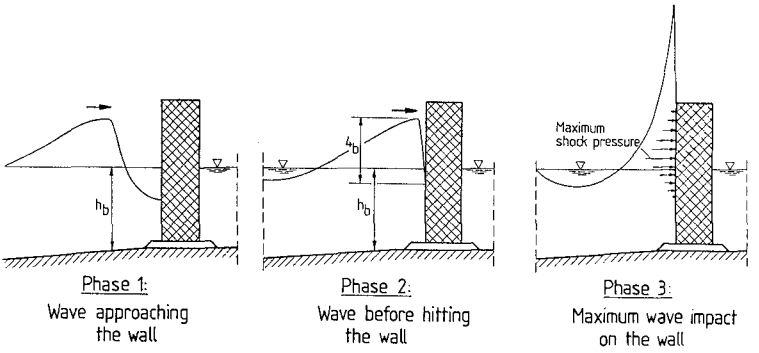

Figure 5: Breaking of wave without an enclosed air pocket /15/.

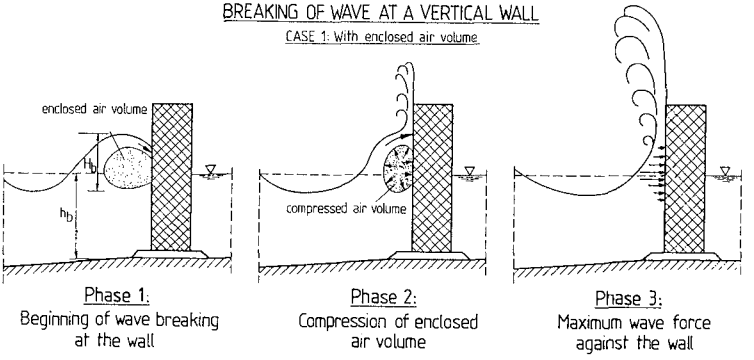

Figure 6: Breaking of wave with an enclosed air volume /15/.

The first case has up to now been considered the most unfavourable condition with the highest impact force at the structure. Figure 7 shows the development of the dynamic pressure distribution at the structure during the wave impact. The maximum pressure occurs slightly above the mean water level. The impact duration, however, is very short ($t \leq 0{,}02$ s) and in general not long enough to displace the structure (Figure 8).

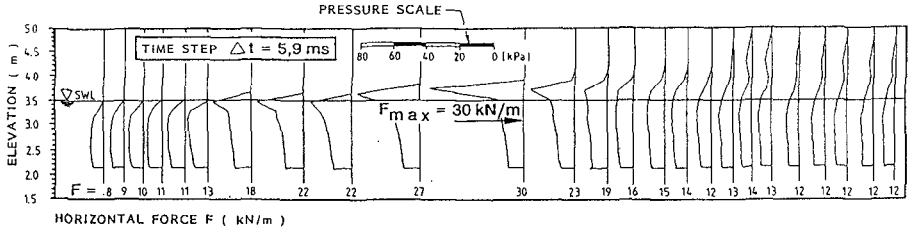

Figure 7: Development of the dynamic pressure distribution at the structure during the wave impact /15/.

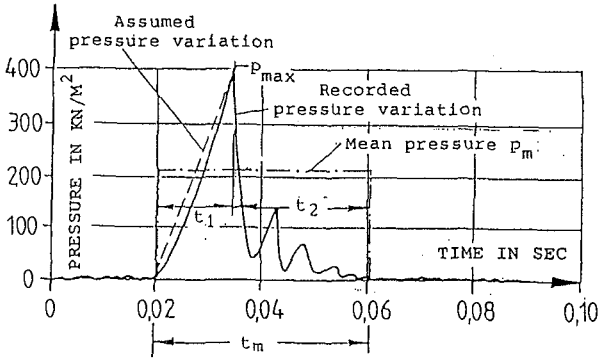

Figure 8: Duration of impact pressure /15/.

A theoretical distribution of the impact pressure is shown in Figure 9 /14/. However, this pressure distribution is only valid for a completely rigid structure without structural elasticity. In case of a displacement of the breakwater under the wave impact the resulting horizontal wave force will be considerably dampened.

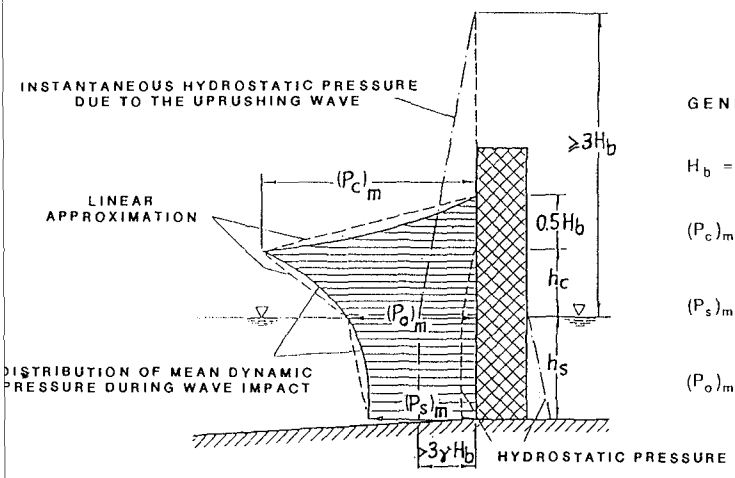

Figure 9: Dynamic pressure distribution at an unelastic rigid structure /15/.

The displacement or reaction of a caisson-like structure under the wave impact is dependent on the kind of foundation, its structure and on the duration of the wave impact. Figure 10 shows some types of vertical and composite breakwaters.

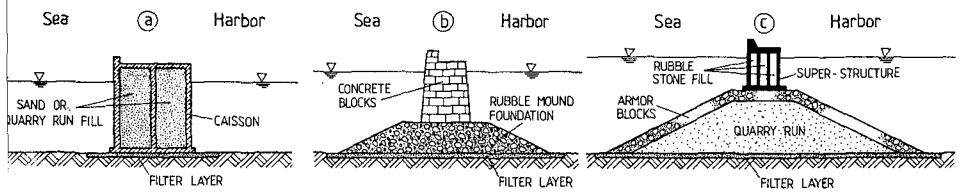

Figure 10: Types of vertical and composite breakwaters /15/.

In order to determine the reaction of a caisson under wave impact, some systematic tests were carried out in the Large Wave Flume in Hannover with an instrumentated caisson that has accelerometers for vertical and horizontal motions, pressure cells for impact and uplift pressures as well as pore pressure cells in the foundation (Figure 11) /14). The tests

showed only small displacements of the caisson due to the wave impact. However, depending on the breaker characteristics, the caisson oscillated with periods of 0.06 to 0.08 s, leading to structure oscillation amplitudes of 0.5 to 1.0 mm /13/.

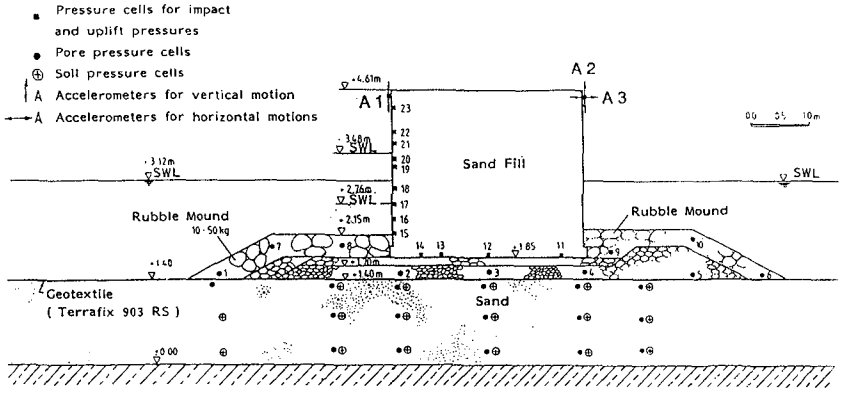

Figure 11: Cross-section of the caisson model with installed instrumentation /14/.

In another series of tests, the second case of a breaking wave with an entrapped air volume was investigated. Here, the pressure and force diagram generally showed two peaks with a time interval of approximately 0.02 to 0.03 s (Figure 12). The second peak was in this case caused by the compressed air volume. Depending upon the amount of air enclosed, the second peak pressure was in some cases higher than the first.

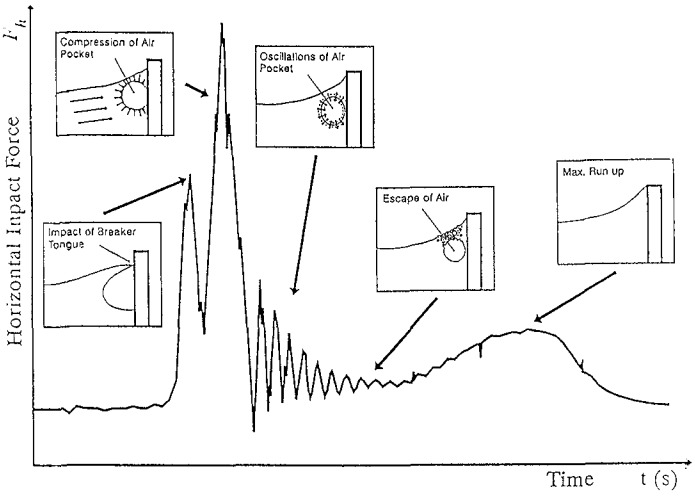

Figure 12: Horizontal impact force due to a breaking wave with an enclosed air pocket /11/.

This means that the wave impact with an entrapped air volume can under certain conditions be the most unfavourable case for the structure. When the time lapse between the two peak forces is in the same order of magnitude as the natural period of the structure itself, the consecutive wave impact could initiate a structural oscillation. The same applies for the low-frequency force oscillations following the peak values (Figure 12). The test results showed that the force oscillations have a period in the range of 0.3 to 0.7 s (Figure 13) /13, 14/.

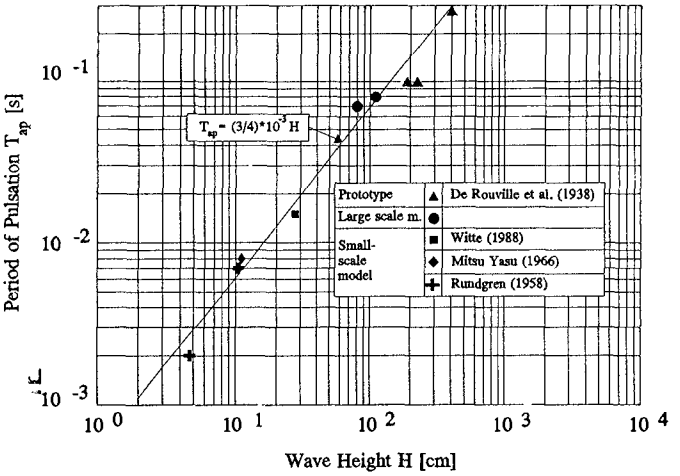

Figure 13: Pulsation Period of an entrapped air pocket versus height of breaking wave /14/.

Figure 14 shows the natural periods of some vertical structures which have been determined by means of a dying-out test /15/. As can be seen, the natural periods of vertical coastal structures lie partly in the same order of magnitude as the force oscillations due to the wave impact.

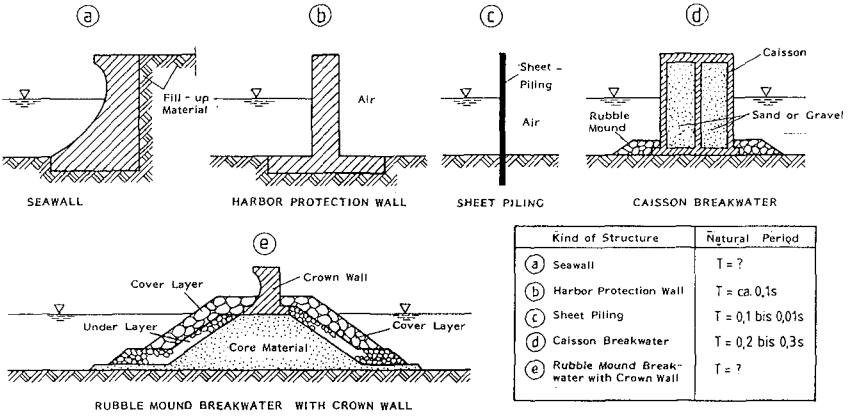

Kind of Structure	Natural Period
ⓐ Seawall	T = ?
ⓑ Harbor Protection Wall	T = ca. 0,1s
ⓒ Sheet Piling	T = 0,1 bis 0,01s
ⓓ Caisson Breakwater	T = 0,2 bis 0,3s
ⓔ Rubble Mound Breakwater with Crown Wall	T = ?

Figure 14: Natural periods of some vertical structures /15/.

In addition, wave loads on crown walls were investigated. For the crown wall stability, the simultaneous wave induced pressures on the front face and the uplift pressures had to be analysed. A first systematic study of wave forces on crown walls of different heights including the influence of water level, berm height and width is presented by Pedersen /16/. The results comprise the statistics of the horizontal force, the tilting moment and the wall base pressure, providing the basis for stability calculations of the crown wall.

Based on experience from offshore platform designs and on extensive advanced laboratory soil tests, some guidelines for the design of foundation under caisson structures have been presented. The work continues and will probably result in sets of constitutive equations necessary for numerical stability calculations.

4.2 Rubble mound breakwaters

In a world-wide survey of existing breakwaters carried out in 1992 by an International Working Group of PIANC, some 150 rubble-mound and composite structures were investigated and the observed damage was analysed. The results showed that damage varied from slight to about 100% and occurred to more than 25% of all breakwaters under investigation. The most spectacular cases within the last 15 years, with high damage or complete failure, were those at Sines/Portugal in 1978. Arzew/Algeria and San Ciprian and Bilbao/Spain /17/.

This damage and these failures show clearly that the existing design criteria for these structures are still inadequate and must be replaced by new approaches in which not only the hydraulic stability of the cover layer, which is generally composed of artificial armour units (Figure 15), is considered, but also the structural resistance of the individual armour unit against breaking due to rocking and displacement under wave impact as well as the geo-technical stability of the foundation. Figure 16 shows a typical cross-section of a rubble-mound breakwater with a crown wall.

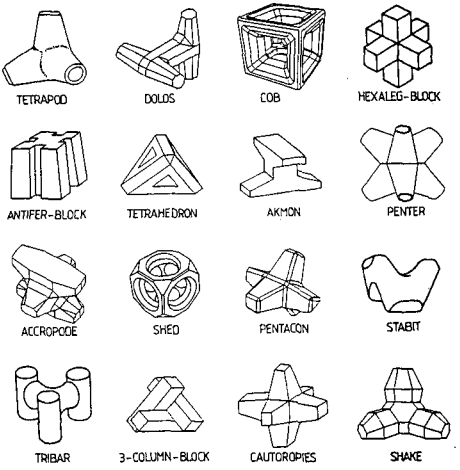

Figure 15: Artificial armour units for the cover layer of rubble-mound breakwaters.

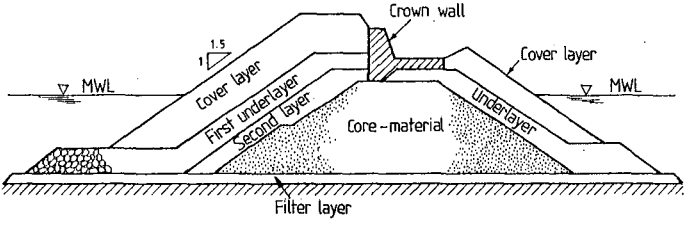

Figure 16: Typical Cross-section of a rubble-mound breakwater.

The MAST-projects of the European Union were closely coordinated with the activities of the PIANC-working groups /12/. In particular wave overtopping, wave run-up, wave reflection, internal porous flow and pore pressure distributions have been tested in different laboratories. Special attention was payed to the displacement of armour units (Accropodes, Tetrapods, Cubes, hollowed Antifer cubes, etc.) and the breakage of slender concrete armour units (Dolosses, etc.). Corporation between Aalborg University, Techn. University of Delft, Franzius-Institut and WES/USA resulted in formulae for a number of broken units /12/.

The breakage of slender units depends on the wave height, the interlocking effect between the unit blocs and on the strength of the concrete. For this reason prototype measurements of concrete strength in Tetrapods and Dolos units were carried out in Italy /18/. In addition, the effects of thermal stresses, solar stress and fatigue on the strength of the concrete in the armour units were investigated /12/.

The structural resistance of Tetrapod-blocs was investigated in the Franzius-Institute / University of Hannover. Static tests, pendulum tests and drop tests were carried out with Tetrapods of different sizes (Figure 17 and 18). Figure 19 shows a summary of the investigations performed. The results showed that for increasing wave heights the structural resistance of the armour units required bloc weights higher than those determined by the HUDSON-formulae. These investigations must be continued for other kinds of slender armour units (Dolos, etc.).

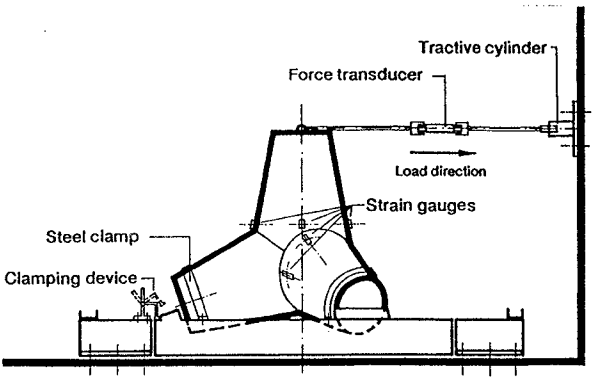

Figure 17: Set-up for static tests with tetrapods of 250 kg and 1.8 t.

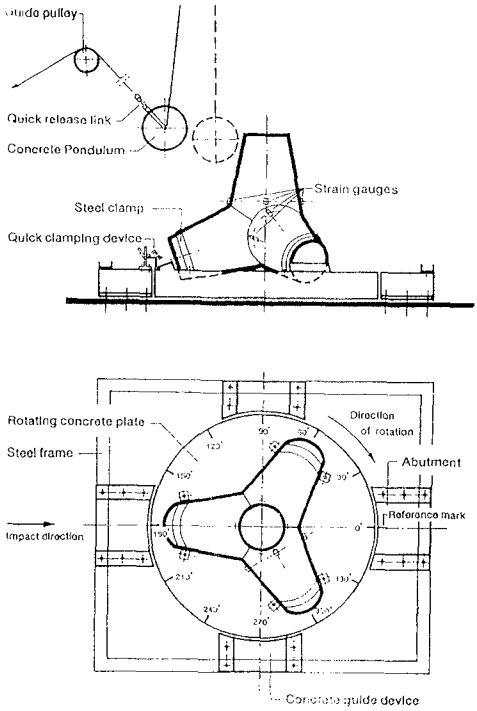

Figure 18: Set-up for pendulum tests with tetrapods of 250 kg and 1.8 t.

4.3 Berm breakwaters

A Berm breakwaters is a rubble-mound breakwater with a berm above the still water level on the seaward side. During exposure to wave action of a certain intensity and duration, the berm reshapes until a final equilibrium profile on the seaward face of the breakwater is reached (Figure 20). The advantage of this type of breakwater is that the average armour rock size required for the structure is in general smaller than for a traditional rubble-mound breakwater /19/.

In order to study the physics of berm breakwaters, their profile development as well as the stone transport at the trunk and the roundhead stability, eight European institutes from Denmark, The Netherlands, United Kingdom, Norway, Italy and Iceland participated in a joint research project co-sponsored by the European Commission under the second research and development programme MAST II (1994-1997). In addition, physical processes involved in the hydraulic and structural response of berm breakwaters under wave attack were examined, and a predictive numerical model for wave interaction with

berm breakwaters developed. The results obtained were in good agreement with prototype measurements (Figure 20).

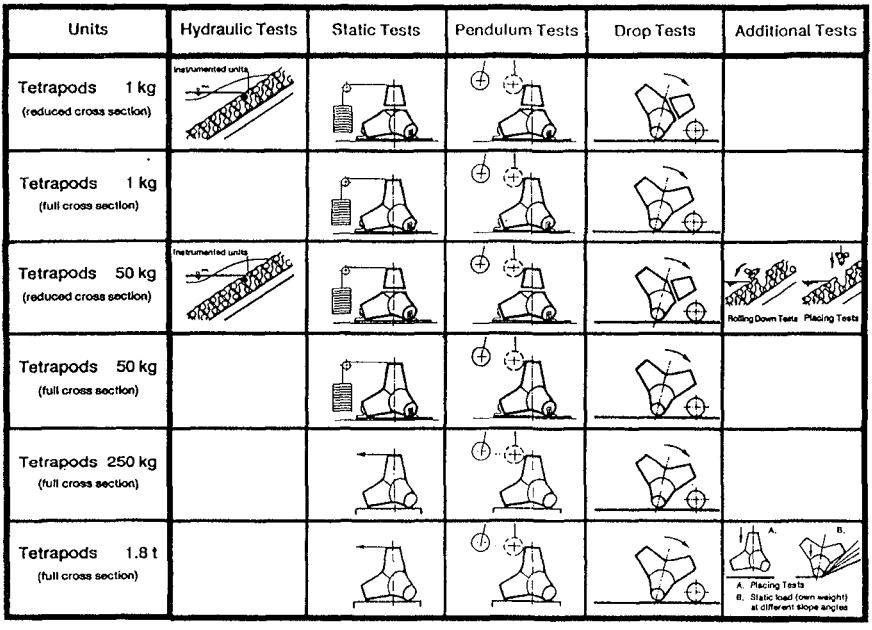

Figure 19: Summary of the laboratory tests performed with tetrapods.

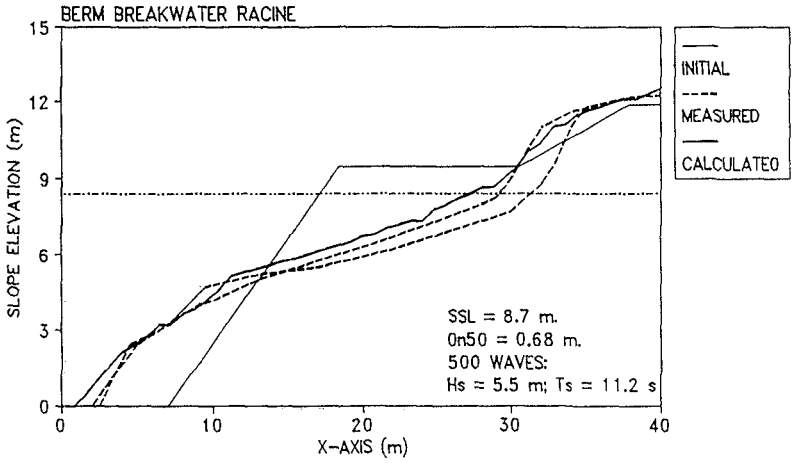

Figure 20: Comparison between measured and computed reshaped profiles of a berm breakwater /19/.

A summary of all the results obtained in the MAST-project can be found in the final report of JUHL, J. et al. on "Berm Breakwater Structures" of May 1997 /19/ as well as in a number of individual papers /12, 20, 21, 22, 23/.

4.4 Probabilistic failure mode analysis

The basic principle in reliability analyses is that the probability of damage is assessed for each failure mode. On this basis it is possible to estimate the safety or reliability of the whole structure by system analysis.

In each failure mode analysis all the load and resistance parameters are treated as stochastic variables. Consequently, it is necessary to introduce the uncertainty of these parameters, e.g. on the sea-state parameters (load) and the soil/strength parameters (resistance). The uncertainties with the parameters are given by their probability distributions. For most parameters a normal distribution with a certain standard deviation is used. The same holds for uncertainties concerning formulae. Most often a safety-index method is used for the estimation of the damage probability related to each failure mode /24/.

On the basis of extensive numerical simulations the PIANC working group developed a system of safety factors for most of the rubble mound breakwater failure modes and for the overall stability failure modes related to caisson breakwaters. Verification of the use of the coefficients in a fully dynamic analysis will be checked in a MAST-project and the system will be extended to include important local structure failure modes for caisson breakwaters.

4.5 Publications on breakwater research programmes

The results of the research work carried out in the MAST-projects on breakwaters and coastal structures have been published in a great number of papers in congress proceedings, scientific journals, internal reports and in theses. A summary of the findings on wave impact on vertical structures is found in the report of H. Oumeraci et al. on "Coastal structures - overview of MAST2-projects" /11/ and on rubble mound breakwaters in the book of H.F. Burchardt on "Reliability-based design of coastal structures" /24/.

5. Future research required in coastal engineering

The results of the different MAST-programmes have certainly essentially contributed to the solution and understanding of coastal problems and to the safer construction of coastal structures.

However, there are at least some main problems which must be dealt with in coastal engineering in the next decades /25/:

1. The effect of the predicted rises of the sea water level on existing and future coast protection works as well as on the human community. (According to the latest predictions the water level rise in the next 100 years will be approximately 0.60 m/100 years, Figure 21).

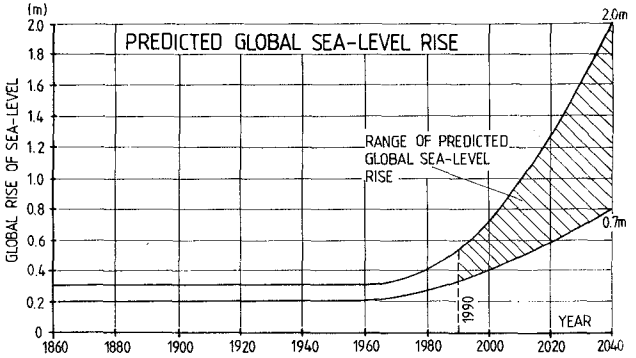

Figure 21: Predicted rise of mean sea level /25/.

2. The deposit of contaminated dredging material from harbours and navigation channels.

3. The increasing thermal and waste water pollution of tidal rivers, estuaries and near-shore coastal regions.

The predicted global sea level rises up to the year 2050 vary considerably, they have nevertheless sent alarming signals to all countries bordering the oceans /26/. Here more investigations are needed, based on reliable prototype data, in order to narrow the gap between the results of statistical approaches and interdisciplinary studies by means of mathematical models.

This opens a wide field of new activities for the coastal engineer in the future. All problems to be solved are more or less linked to the adaptation of coast protection measures to the rising mean sea level. Examples in this respect are the development and construction of new harbours and access channels to them, the modification of existing jetties, the exploration and exploitation of marine resources as well as the reduction of pollution in estuaries and near shore regions, - to name a few.

The deposit of contaminated dredging material from navigation channels and harbours represents a world-wide problem for all countries bordering the sea. Here, methods must be developed to process the contaminated material in order to make it usable for reclamation purposes.

On the other hand, hydraulic measures must be investigated to reduce the annual maintenance dredging quantities in existing navigation channels as well as in the access channels to seaports.

The tendency of new industrial plants to be constructed on the coast as well as on tidal rivers and estuaries leads to a steady increase of thermal and wastewater pollution in these areas. The cooling water systems of industrial factories and conventional as well as nuclear power plants, when designed as fresh water systems, cause increasing thermal pollution in these coastal regions due to the discharge of heated cooling water into the ambient bodies of fresh or sea water.

In addition, the continuous wastewater discharge from communities, harbours and industrial factories into coastal waters must be considered a very serious problem in environmental engineering. Therefore, intensive further research on pollution problems must be carried out in estuaries as well as on the interaction of rivers and ocean regions /25, 26/.

In addition, international standards of permissible loads should be elaborated and measures to reduce the environmental impact must be developed.

However, there is still another problem in which coastal engineering and environmental engineering is closely related. Our present population on Earth amounts to approximately 6 billion, but shows a steady increase of some 300,000 people per day /27/. Our present population will therefore double in about 50 years, i.e. in the year 2050 a total of approximately 12 billion people must be expected on Earth (Figure 22).

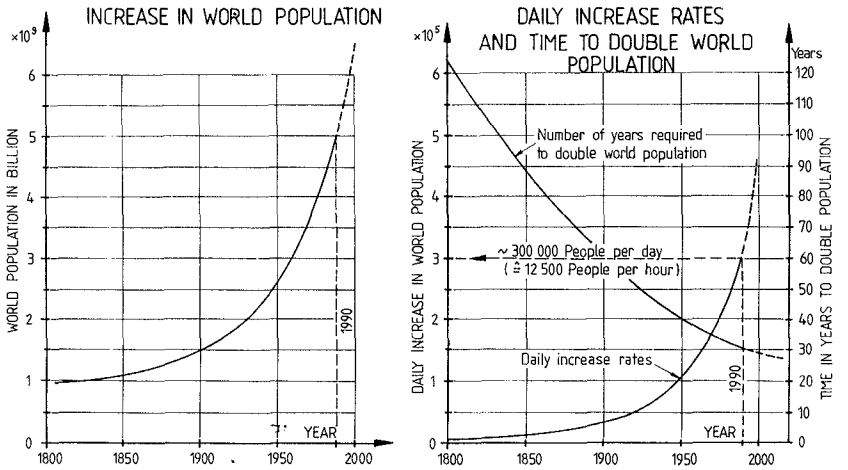

Figure 22: Increase in world population and rates of daily increase /25, 26, 27/.

This enormous increase in population in the near future has produced alarming signs for the whole of mankind, since the available food and water resources as well as the limited resources for the production of energy are not sufficient and will be used up at a steadily increasing rate.

This certainly involves a great number of future problems in which also the coastal engineer has a world-wide task.

In addition, the increasing demand of our population for leisure and recreation requires the urgent preservation of existing natural beaches as well as the creation of new, artificial resorts. This means that new methods must be developed and tested to sustain and protect our sandy coasts from erosion by means of artificial beach nourishment, stabilisation of the bar-systems as well as by use of tombolo-effects (Figures 23, 24, 25)

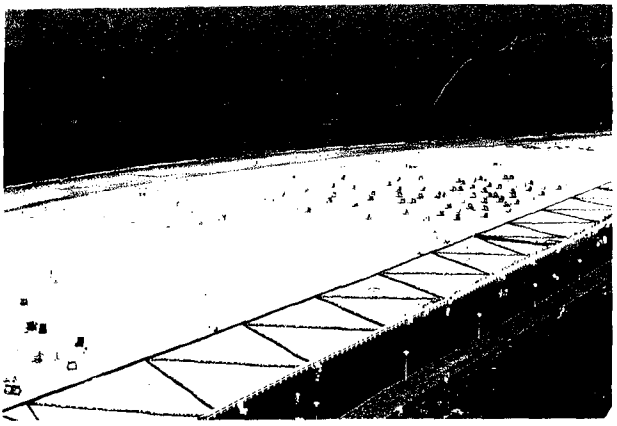

Figure 23: Beach nourishment on the Island of Sylt / Germany /25/.

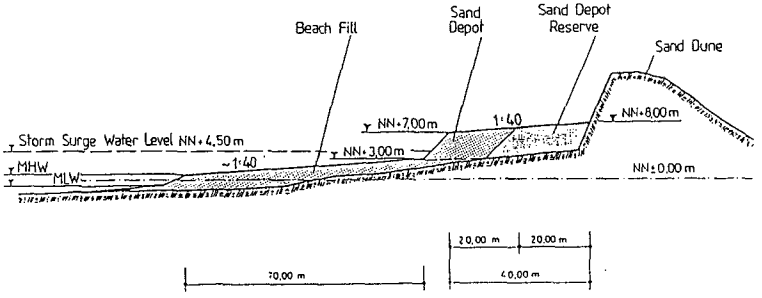

Figure 24: Principle of beach nourishment on the Island of Sylt /25/.

Figure 25: Effect of detached breakwaters at the Spanish Meditarranian coast (tombolo effect) /25/.

Ladies and Gentlemen, the time is certainly not sufficient to discuss all aspects of future research required in coastal engineering.

However, the presentation of the present European Research Programmes already shows that international cooperation is required to solve a few urgent problems in our field. It is hoped that the already existing connections of our European research laboratories with scientists of overseas countries such as Japan, USA, Canada, Australian, etc. will be intensified in the years to come because the solution of the before mentioned world-wide problems, I have mentioned, need the international collaboration of all scientists and research institutes in the world.

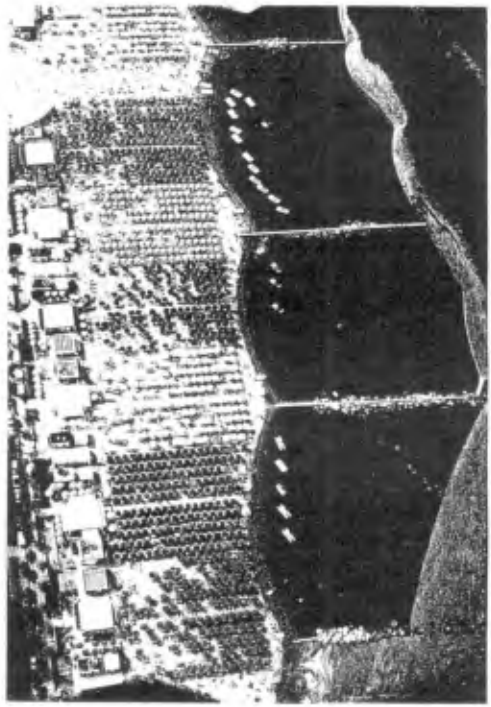

Figure 26: Densely occupied beach at Rimini/Italy

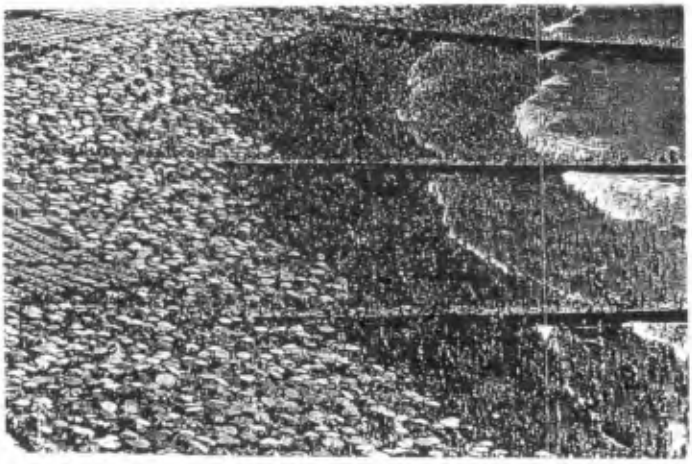

Figure 27: Overcrowded beach at Mar Del Plata (near Buenos Aires) Argentina.

6. Bibliography

/1/ BOISSONNAS, J.: Background, Philosophy and Objectives of MAST. Proceedings of the HTG-Congress 1997, Bremen, Sept. 1997

/2/ DE VRIEND, H.: State of the Art in Modelling Coastal Morphodynamics Practical Implications. Proceedings of the HTG-Congress 1997, Bremen, Sept. 1997

/3/ BURCHARDT, H.F.: State of the Art in the Design of Coastal Structures. Proceedings of the HTG-Congress 1997, Bremen, Sept. 1997

/4/ DE VRIEND, H.: State of the Art in Modelling Coastal Morphodynamics. HANSA-Zeitschrift, 135 Jahrgang, No. 1, 1998, Hamburg

/5/ STIVE, M.J.F. et al.: Advances in Coastal Morphodynamics. G8-MAST II-Project, Delft Hydraulics, Delft 1995

/6/ BROKER, I. et al.: Coastal Profile and Coastal Area Modelling at DHI. Paper in Advances in Coastal Morphodynamics /5/. Delft Hydraulics, Delft 1995

/7/ DE VRIEND, H. et al.: Medium-Term 2-DH Coastal Area Modelling. Coastal Engineering, 21, 1993

/8/ NICHOLSON, J. et al.: Intercomparison of Coastal Area Morphodynamic Models. Coastal Engineering 31, 1997

/9/ DE VRIEND, H. et al.: Approaches to Long-term Modelling of Coastal Morphology: A Review. Coastal Engineering, Vol. 21, 1993

/10/ DE VRIEND, H.: Mathematical Modelling of Coastal Morpholodynamics. Advanced Series on Ocean Engineering (in preparation). World Scientific, Singapore, 1997

/11/ OUMERACI, H. et al.: Coastal Structures - Overview of MAST 2 -Projects. XXVIth IAHR-Congress Hydra 2000, Proceedings, 1995

/12/ BURCHARDT, H.F.: State of Art in the Design of Coastal Structures. Proceedings of the HTG-Congress 1997, Bremen, Sept. 1997

/13/ OUMERACI, H. et al.: Impact Loading and Dynamic Response of Vertical Breakwaters. Proceedings of MAST-G6-S Final Project, Workshop, Lisbon, 1993

/14/ OUMERACI, H.: Multi-disciplinary Research Experience in Europe on Vertical Breakwaters. Proceedings of International Workshop on Wave Barriers in Deep Water, Yukosoko / Japan, 1994

/15/ PARTENSCKY, H.W.: New Investigations on Impact Pressures on Vertical Coastal Structures. Proceedings of the 3rd European Workshop on Coastal Zones, University of Athens / Greece, 1990

/16/ PEDERSEN, J.: Wave forces and Overtopping on Crown Walls of Rubble Mound Breakwaters. Series paper 12, Hydraulic and Coastal Engineering Laboratory, Aalborg University, Denmark, 1996

/17/ PIANC: Analysis of Rubble Mound Breakwaters. Report of Working Group 12 of PTC II, Supplement to PIANC-Bulletin 78/79, 1992

/18/ FRANCO, L. et al.: Concrete Strength and Durability of Prototype Tetrapods and Dolosse. Results of Field and Laboratory Tests. Proceedings of the Final Workshop, MAST 2-Project: Rubble-mound Breakwater Failure Modes, Sorrento / Italy, 1995

/19/JUHL, J. et al.: Berm Breakwater Structures. Final Report of MAST II-Contract. Commission of the European Communities, Brussels, 1997

/20/ VAN DER MEER et al.: Conceptual Design of Berm Breakwaters. Int. Conference on Coastal and Port Engineering in Developing Countries, Rio de Janeiro, 1995

/21/ HALD, T. et al.: Berm Breakwater Design. Influence Movements on Stone Durability.
Proceedings Final Workshop, MAST 2, Reykjavic / Iceland, 1996

/22/ JUHL, J. et al.: Roundhead Stability of Berm Breakwater.
Proceedings of 25th Int. Conference on Coastal Engineering, Orlando / USA, 1996

/23/ ALIKHANI, A. et al.: Berm Breakwater Trunk Exposed to Oblique Waves.
Proceedings of 25th Int. Conference on Coastal Engineering, Orlando / USA, 1996

/24/ BURCHARDT, H.F.: Reliability-based Design of Coastal Structures.
Ed. Philip L.-F. Liu, World Scientific, Vol. 3, 1997

/25/ PARTENSCKY, H.W.: Future Research Activities Required in Coastal and Environmental Engineering (Key-note lecture).
Proceedings of the Third European Workshop on Coastal Zones, Paralimni / Cyprus, Sept. 1990

/26/ PARTENSCKY, H.W.: Propositions pour les activités de recherches en génie maritime et dans l'environnement pour l'an 2000.
Comptes-rendus du Colloque International de la Société. Hydrotechnique de France, Paris, Sept. 1990

/27/ PARTENSCKY, H.W.: Quo Vadimus - Zukunftsperspektiven für die Erdbevölkerung.
Jahresbericht 1997 der Hafenbautechnischen Gesellschaft, Hamburg, p 1998

BEACH NOURISHMENT: A LIMITED REVIEW AND SOME RECENT RESULTS

Robert G. Dean[1], M. ASCE

Abstract

A limited review of methodologies for design and prediction of beach nourishment performance is presented and some recent results of the evolution of the total plan area of a nourishment project on a long straight beach are examined. The emphasis is on rather simple approaches which may be more applicable for preliminary design and screening of candidate designs rather than final design. Most beach nourishment projects are placed at slopes that are steeper than equilibrium. Thus the project is initially out of equilibrium both in the planform and profile. The simple approaches represent the planform evolution and cross-shore processes separately. Planform evolution can be represented by the Pelnard Considère equation, which in addition to providing a basis for representing the performance of a particular design, also provides a good overall basis for understanding the behavior of beach nourishment projects. Several solutions of the Pelnard Considère equation are examined and some of the general results obtainable from this equation are presented and discussed. Particular results include the insensitivity of evolution to storm sequence, the reduction of spreading "losses" due to refraction around a planform anomaly, relative insensitivity of planform evolution to wave direction for nourishment sand that is compatible with the native, and the effects of nourishing on beaches with sand coarser and finer than the native. Profile evolution is best modeled over short time scales when the profile is significantly out of equilibrium. Limited observations indicate that profile equilibration time scales associated with oversteepened nourished profiles are on the order of 5 years. Application of equilibrium beach profile methodology demonstrates the sensitivity of additional dry beach width to sand size. Recent results of the evolution of the total plan area of a beach nourishment project are presented. It is found that nourishment with sands coarser and finer than the native, results in total plan areas that increase and decrease, respectively, with time.

---

[1] Professor, Coastal and Oceanographic Engineering Department, University of Florida, PO Box 116580, Gainesville, Florida 32611-6580

Because the results obtained considering nourishment sands of a single size are unrealistic, a method is applied in which the nourishment sands are characterized by two sizes of different proportions. The results for this approach are more reasonable and consistent with expectations.

Introduction

Beach nourishment comprises the placement of large quantities of good quality sand on the beach to advance the shoreline seaward. In most cases, beach nourishment is applied in areas where erosion exists and thus the effect of the nourishment is to restore the beach to a position which it occupied at some previous time. The erosion compensated by the nourishment can be due to natural causes or may be due to a littoral obstruction placed updrift of the area of concern or other human-induced causes. In such cases, in addition to beach nourishment, it is important to attempt to minimize any human causes of erosion. This most likely action would be bypassing of sand around a constructed obstruction or removal of the obstruction.

The earliest beach nourishment projects in the U.S. were placed in the 1930's along fairly short stretches of beaches as "projects of opportunity." These projects of opportunity usually occurred at locations where substantial volumes of good quality sand were available from some other project, such as the excavation of a harbor. For many years starting in the 1950s, the recommended approach to addressing beach erosion was structures usually in the form of groins to trap sand from the littoral system. With greater development of the shoreline, the adverse impacts of structures built in one area became more apparent in another and there was a transition from the use of structures to softer approaches, namely beach nourishment. Often there are only two options for stabilization of areas facing beach erosion. One option is armoring such that the erosion is limited by the armoring. The second is beach nourishment which has the potential to both advance the shoreline seaward and to restore the natural characteristics of the eroded beach.

With the increasing value of the shoreline and its popularity for both residential and commercial development and recreational purposes, and the loss of the beach as an environmental resource if armoring is carried out, beach nourishment becomes a much more attractive option. However, the future of beach nourishment faces serious challenges. One of these challenges is the availability of large quantities of good quality sand within a proximity that will allow the economic placement of these sediments on the eroded beaches. The second challenge which has emerged is in the environmental arena and includes concerns regarding the potential adverse impacts of beach nourishment. Although a significant number of beach nourishment projects have been monitored to quantify both their physical and biological performances, questions remain. Undoubtedly, these will only be resolved through careful monitoring and interpretation of many future beach nourishment projects.

A Limited Review of Beach Nourishment

When a beach nourishment project is placed, the initial profile slopes are usually steeper than those of the equilibrium profile and the nourishment planform represents a perturbation which is out of equilibrium. Thus the beach nourishment induces both cross-shore and longshore sediment transport, see Figure 1. One of the principal challenges facing the coastal engineer in the design of such projects is the reasonable prediction of the time scales associated with both the profile and planform equilibrations. This paper considers the evolution in the longshore and cross-shore directions separately although, of course, in actuality the evolution of these two components proceeds simultaneously and may be interrelated.

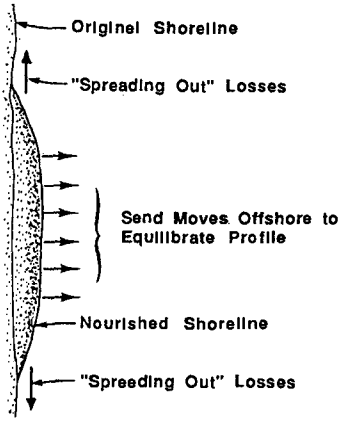

a) Plan View Showing "Spreading Out" Losses and Sand Moving Offshore to Equilibrate Profile

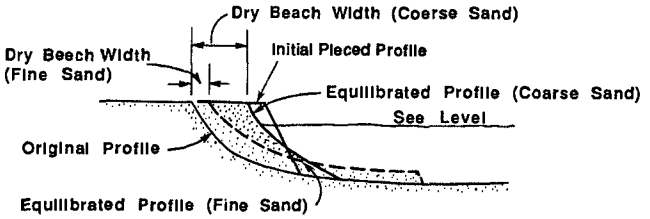

b) Elevation View Showing Original Profile, Initial Placed Profile and Adjusted Profiles That Would Result by Nourishment with Coarse and Fine Sands

Figure 1. Sand transport "losses" and beach profiles associated with a beach nourishment project.

In general, there are two approaches to the design and performance prediction of beach nourishment projects. The first which will be the main subject of this paper is through the use of relatively simple models that readily allow estimation of the physical performance of such projects. The second, which will be discussed only briefly, involves the application of much more complicated numerical models in which the particular wave climate can be introduced as well as any specific initial planform and complicated boundary conditions. Of course, in the application of either level of model, it is important to ensure that the proper boundary conditions and forcing functions are applied. In the following paragraphs, we will address a number of planform models and describe their applications to various situations.

Simple Models of Planform Evolution

The simple models of planform evolution are based on the so-called Pelnard Considère Equation which is the result of combining the linearized sediment transport equation with the continuity equation, resulting in

$$\frac{\partial y}{\partial t} = G \frac{\partial^2 y}{\partial x^2} \tag{1}$$

in which y is the displacement of the shoreline from some reference baseline, x is the longshore coordinate of that baseline defined as positive to the right of a seaward looking observer, t is time and G is the so-called "longshore diffusivity" defined as

$$G = \frac{K H_b^{5/2} \sqrt{\frac{g}{\kappa}}}{8(s-1)(1-p)(h_* + B)} \tag{2}$$

In Eq. (2), K is the sediment transport coefficient (usually taken as 0.77, but more likely a function of sediment size), H_b is the representative breaking wave height, g is gravity, κ is the ratio of breaking wave height to water depth (≈ 0.78), s is the ratio of specific weight of the sediment to that of the water in which it is immersed and p is the in-place porosity. The quantities h_* and B are the depth to which the sediment is mobilized and the berm height, respectively. Eq. (1) is the classical heat conduction equation for which many solutions exist. Several useful solutions are reviewed in the following paragraphs.

Initially Rectangular Beach Planform

The solution representing placement of an initially rectangular beach nourishment project on an infinitely long beach is useful both for preliminary design and pedagogical purposes. The solution for this case is

$$y(x,t) = \frac{Y}{2}\left\{\operatorname{erf}\left[\frac{\ell}{4\sqrt{Gt}}\left(\frac{2x}{\ell}+1\right)\right] - \operatorname{erf}\left[\frac{\ell}{4\sqrt{Gt}}\left(\frac{2x}{\ell}-1\right)\right]\right\} \tag{3}$$

in which Y is the initial beach width and ℓ is the project length. It can be shown that the portion of material remaining in the area placed, M(t), is related to the parameter, $\sqrt{Gt}/\ell$, as follows

$$M(t) = \frac{\sqrt{4Gt}}{\ell\sqrt{\pi}} \left(e^{-(\ell/\sqrt{4Gt})^2} - 1\right) + \text{erf}(\ell/\sqrt{4Gt}) \tag{4}$$

This equation is plotted in Figure 2 where it is seen that the volume remaining within the region placed decreases rapidly at first and then decreases much more slowly. Eq. (3) or (4) can be used to investigate the longevity of a project in terms of the variables

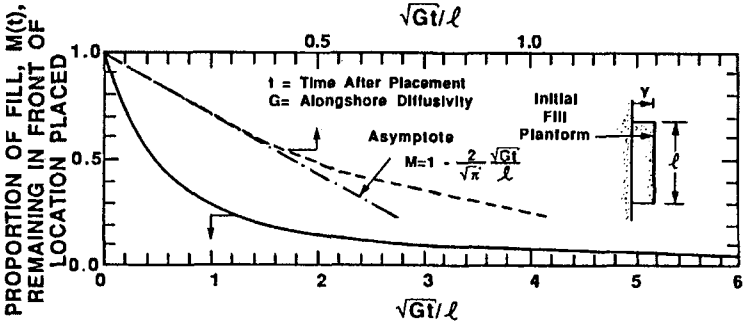

Figure 2. Proportion of material remaining in region placed vs. the parameter $\sqrt{Gt}/\ell$.

causing changes. Examining Eqs. (3) and (4), it is seen that the proportion of material remaining at any time, t, is dependent on the variable $\sqrt{Gt}/\ell$. We can select any proportion remaining and determine the life of that project in terms of the relevant variables. As an example, if we select a proportion equal to 50% of the material placed, then the associated time is the so-called "half-life" of the project. We see that the value of $\sqrt{Gt}/\ell$ associated with an M value of 0.5 is 0.46. Solving for the half-life, $t_{50\%}$, we find that

$$t_{50\%} = \frac{(0.46)^2 \ell^2}{G} \tag{5}$$

Using reasonable values for all variables but leaving breaking wave height, H_b, and project length, ℓ, arbitrary, Eq. (5) can be simplified to the following

$$t_{50\%} = K'' \frac{\ell^2}{H_b^{5/2}} \tag{6}$$

where $K'' = 0.179$ years $-m^{5/2}/km^2$ for ℓ in kilometers, $t_{50\%}$ in years and H_b in meters. For purposes here, the values of K, h_*, B, S, p, and g were taken as 0.77, 7 m, 2 m, 2.56, 0.35 and 9.81 m/s^2, respectively. As an example of the application of Eq. (6), if the project length, ℓ, is 1 kilometer and the associated wave height, H_b, is 1 meter, the half-life is 0.18 years, i.e., slightly in excess of 2 months. However, if the project length is 10 kilometers and the wave height is 1 meter, the project life is 17.9 years.

Other Initial Planforms

Due to the linearity of Eq. (1), solutions exist for many initial planforms. Walton (1994) has developed the solution for a trapezoidal planform. Larson, et al. (1997) have developed solutions for many additional initial planforms.

Nourishment on a Barrier Island

An example of interest is that of an initially rectangular nourishment on a barrier island in which the nourishment can extend to the limits of the barrier island at an inlet or the nourishment can be set back from the inlet. In this case, approximating the shoreline displacement as zero at the inlet is the most logical boundary condition. The results for an initial nourishment extending along an entire barrier island are presented in Figure 3 in which the results are compared with a shoreline of infinite length. The advantages

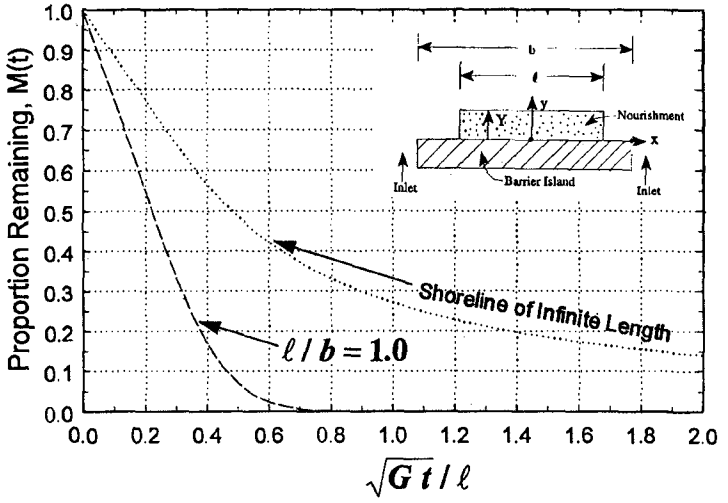

Figure 3. Proportion remaining, M(t), for nourishment along full length of barrier island compared to nourishment on an infinitely long beach, "ℓ" = nourishment project length.

of nourishment on a long beach are clearly evident since the effect of an inlet is to cause the sand to be drained off much more rapidly. Figure 4 shows the proportion remaining for different lengths of the nourishment relative to the length of the barrier island.

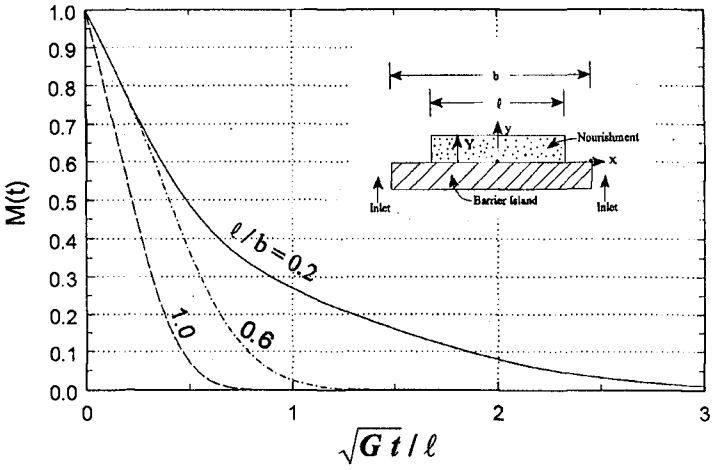

Figure 4. Proportion remaining, M(t), for nourishment ends sent back from ends of a barrier island.

Additional Characteristics of the Pelnard Considère Approach

There are several additional characteristics associated with or results obtained from application of the Pelnard Considère approach that are worthy of note.

Wave Refraction Effect. It can be shown that because the placement of a beach nourishment project on a long straight shoreline results in a planform anomaly that causes wave refraction, the effect of the waves "wrapping around" the planform anomaly is to reduce the value of the longshore diffusivity, G, by the ratio C_b/C_* where C_b is the wave celerity at breaking and C_* is the celerity at the depth to which the nourishment extends. In some locations, this effect can increase the longevity of the project by 40%.

Sequencing of Storms. Our previous discussions have considered the wave height appearing in the longshore diffusivity term to be constant. However, it is seen that it is the product of the longshore diffusivity and time that is relevant to the project evolution (cf., Eqs. (3) and (4)). It is readily shown that on a long straight beach the sequencing of storms is irrelevant to the evolution of a nourishment project. Rather it

is $\int_0^t G(t)dt$ that governs the evolution of a project. Stated differently, it is the general cumulative energy loading due to the waves affecting the project that causes the project evolution. Appealing to the same fundamental property of the Pelnard Considère Equation, it can be shown that it is possible to quantify an "effective wave height" H_{eff} to represent any sequence of waves (Dean and Yoo, 1992).

Insensitivity to Wave Direction. For the case of beach nourishment with compatible sand on a long, straight beach, the planform evolution is very insensitive to reasonable ranges of wave direction. This can be seen by noting that Eqs. (1) and (3) do not include any effect of wave direction. Dean and Yoo (1992) have carried out detailed numerical modeling and compared these results with the simple method applied here. It was shown that the simple approaches provided a good approximation to the more detailed and complex approaches which include the effect of wave direction.

Nourishment with Sands that are Finer or Coarser than the Native. Dean and Yoo (1994) have shown that nourishments with sands that are finer or coarser than the native result in centroid migrations of the nourishment planform in the downdrift and updrift directions, respectively.

Nourishment on a Seawalled Coast. Beach nourishment along a coast that does not have any sand available for transport will migrate in the downdrift direction and the planform length and centroid migrational speed will increase with time (Dean and Yoo 1994).

Multiple Nourishments

In the case of multiple nourishments and in the absence of background erosion, renourishment intervals required to maintain a particular minimum volume within the nourishment area will increase with successive renourishments. The interpretation is that after the first nourishment has spread out to some degree and renourishment occurs, the subsequent evolution is the superposition of the continued spreading out of the first nourishment and the spreading out of the second nourishment. Because the first nourishment is now an effectively longer project, it will lose material much more slowly, see Figures 2 and 5. Thus the aggregate rate of loss is less than it was for the first nourishment and the duration before the next required renourishment is increased. Thus, the periods between subsequent renourishments increase with the renourishment number. However, it can be shown that in the presence of background erosion, the periods between successive renourishments can increase for low renourishment numbers, then decrease for successive nourishments. The explanation, though rational, is complicated.

Effect of Background Erosion

Beach nourishment projects usually take place in locations where a substantial background erosion has been operative. In evaluating the evolution of a nourishment

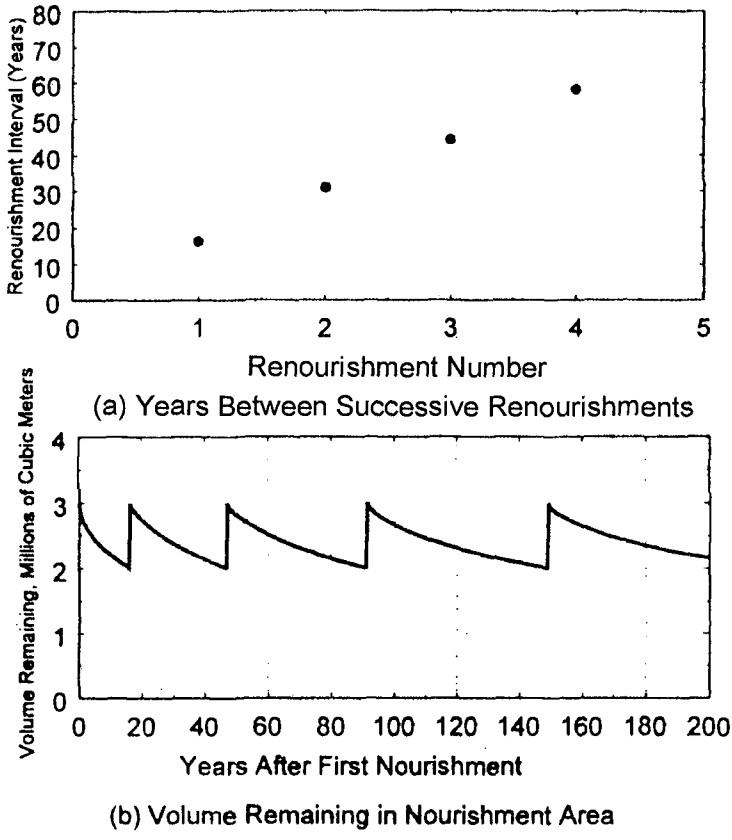

Figure 5. Renourishment characteristics. No background erosion. Breaking wave height = 0.5m, project length = 6 km, $h_* + B = 9$ m, $V_{max} = 3{,}000{,}000$ m^3, $V_{min} = 2{,}000{,}000$ m^3. (From Dean, 1985).

project it is important to account for the background erosion, usually by superimposing the losses due to planform spreading and those due to background erosion. The background erosion is usually due to gradients in the longshore sediment transport. The reasons for these gradients are poorly known and in general it is difficult to calculate the background erosion unless it is due to a major perturbation such as construction of a littoral barrier. Figure 6 shows the effect of background erosion for an initially rectangular nourishment project on a long straight beach. The vertical axis is the product of the background erosion rate, e, and time, t, divided by the initial uniform additional beach

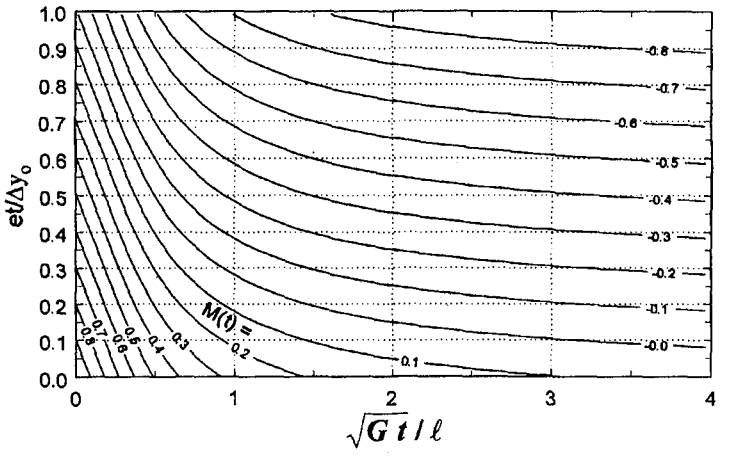

Figure 6. Isolines of M(t) vs spreading and background erosion parameters, e = erosion rate, Δy_0 = initial equilibrium shoreline displacement, G = longshore diffusivity and t = time. Long straight beach.

width, Δy_0. The proportion of sand remaining in the nourishment area, M(t) is a function of time (represented on the horizontal axis) and different amounts of background erosion relative to the initial planform width (represented on the vertical axis). For a background erosion rate of 0, the values of M(t) along the horizontal axis correspond to Figure 2. It is noted that for non-dimensional erosion values greater than 0.2, the portion of material remaining in the project area, M(t), becomes negative after a non-dimensional time (horizontal axis) of approximately 1.5.

Detailed Numerical Models of Planform Evolution

As noted previously, the main advantages of numerical planform models over the simple models described earlier is their ability to represent time varying forcing functions, arbitrary initial planforms, and background erosion distribution and to represent complex boundary and internal conditions as might be associated with a field of groins. Another very significant advantage is the capability to incorporate all available knowledge of mechanisms and detail into the numerical model.

There are two predominant levels of detail of numerical models of planform evolution. For these models, it is not necessary to linearize the transport equation as was done for the simple models. The most direct is the one-line model in which it is assumed that the beach profile responds by moving seaward or landward without change of form in response to gradients in the longshore sediment transport. The next level of complexity includes the cross-shore transport through a so-called "n line model" in

which a number of contours is represented or a model that represents the area of interest by a series of cells. The advantage of representation by a series of cells is that bars are readily represented whereas this is quite complicated with an n-line model. An example of a one-line model is GENESIS (Hanson, 1989; Hanson and Kraus, 1989) and an example of an n-line model has been presented by Perlin and Dean (1985).

Models of Profile Characteristics

There are two issues that will be discussed in relation to the evolution and form of nourished profiles: equilibration time and equilibrium dry beach width.

Equilibration Time

The first issue is the time required for equilibration and will be treated only briefly here. Profile equilibration time is significant because an observer may interpret the results of this equilibration (narrower beach) as a loss of material and a consequent poor performance of the project. Thus it is incumbent on the engineer to inform and educate the client and the general public of the expected equilibration and associated narrowing of the dry beach width due to this process which can be especially rapid due to major storms. It has been our experience that the equilibration times for beach profiles placed steeper than normal are on the order of 5 years to achieve approximately 50% of the equilibration. This is based in part on our 7 year monitoring program of the beach nourishment project at Perdido Key, Florida in which approximately 4.5 million cubic meters of compatible sand were placed along the beach.

Equilibrium Dry Beach Width

The second issue related to profile considerations is the equilibrium effect of using sands which are of different sizes than the native. For this purpose, methodology developed for equilibrium beach profiles (EBP) is especially useful. The simple form of the EBP is that found initially by Bruun (1954) and later explored by Dean (1977, 1991)

$$h(y) = Ay^{2/3} \tag{7}$$

in which h is the water depth at a distance, y, from the mean sea level shoreline and A is the so-called "sediment scale parameter" which depends on the median sand size, D. Moore (1982) examined many profiles from nature and laboratory tests and developed the relationship between median sediment size, D, and the sediment scale parameter, A, as shown in Figure 7. For ease of application, the A values in Figure 7 have been tabulated for 0.01 mm increments of the usual beach sand size range in Table 1.

It is well known that consistent with Eq. (7) and Figure 7 beach profiles associated with coarse sands are steeper than those associated with fine sands. Applying the concepts of equilibrium beach profiles, (Dean 1991) has shown that 3 types of equilibrated nourished profiles are possible as shown in Figure 8. Commencing with the upper

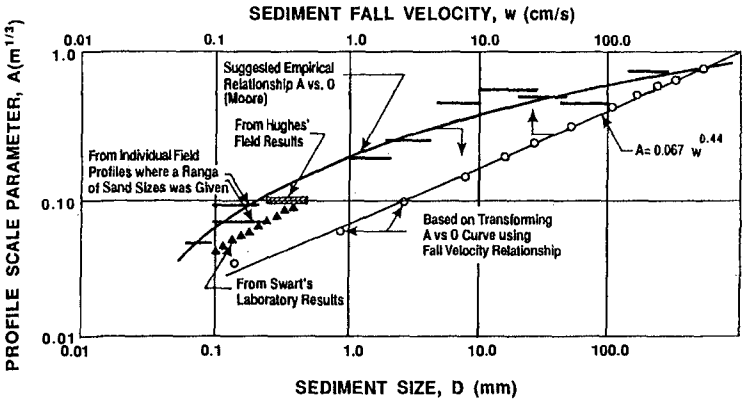

Figure 7. Variation of sediment scale parameter, A, with sediment size and fall velocity (Dean 1987 modified from Moore, 1982).

panel in Figure 8 and proceeding toward the lower, these types are intersecting, non-intersecting and submerged. Intersecting profiles require sand that is coarser than the native, although this is not a sufficient condition for intersecting profiles to occur. If the sand is of the same size as the native, then non-intersecting profiles will occur as shown in the middle panel. Non-intersecting profiles can also occur with nourishment sands that are coarser or finer than the native. A third type of profile, submerged profiles, can

Table 1 Summary of Recommended A Values ($m^{1/3}$)

D(mm)	0.00	0.01	0.02	0.03	0.04	0.05	0.06	0.07	0.08	0.09
0.1	0.063	0.0672	0.0714	0.0756	0.0798	0.084	0.0872	0.0904	0.0936	0.0968
0.2	0.100	0.103	0.106	0.109	0.112	0.115	0.117	0.119	0.121	0.123
0.3	0.125	0.127	0.129	0.131	0.133	0.135	0.137	0.139	0.141	0.143
0.4	0.145	0.1466	0.1482	0.1498	0.1514	0.153	0.1546	0.1562	0.1578	0.1594
0.5	0.161	0.1622	0.1634	0.1646	0.1658	0.167	0.1682	0.1694	0.1706	0.1718
0.6	0.173	0.1742	0.1754	0.1766	0.1778	0.179	0.1802	0.1814	0.1826	0.1838
0.7	0.185	0.1859	0.1868	0.1877	0.1886	0.1895	0.1904	0.1913	0.1922	0.1931
0.8	0.194	0.1948	0.1956	0.1964	0.1972	0.198	0.1988	0.1996	0.2004	0.2012
0.9	0.202	0.2028	0.2036	0.2044	0.2052	0.206	0.2068	0.2076	0.2084	0.2092
1.0	0.210	0.2108	0.2116	0.2124	0.2132	0.2140	0.2148	0.2156	0.2164	0.2172

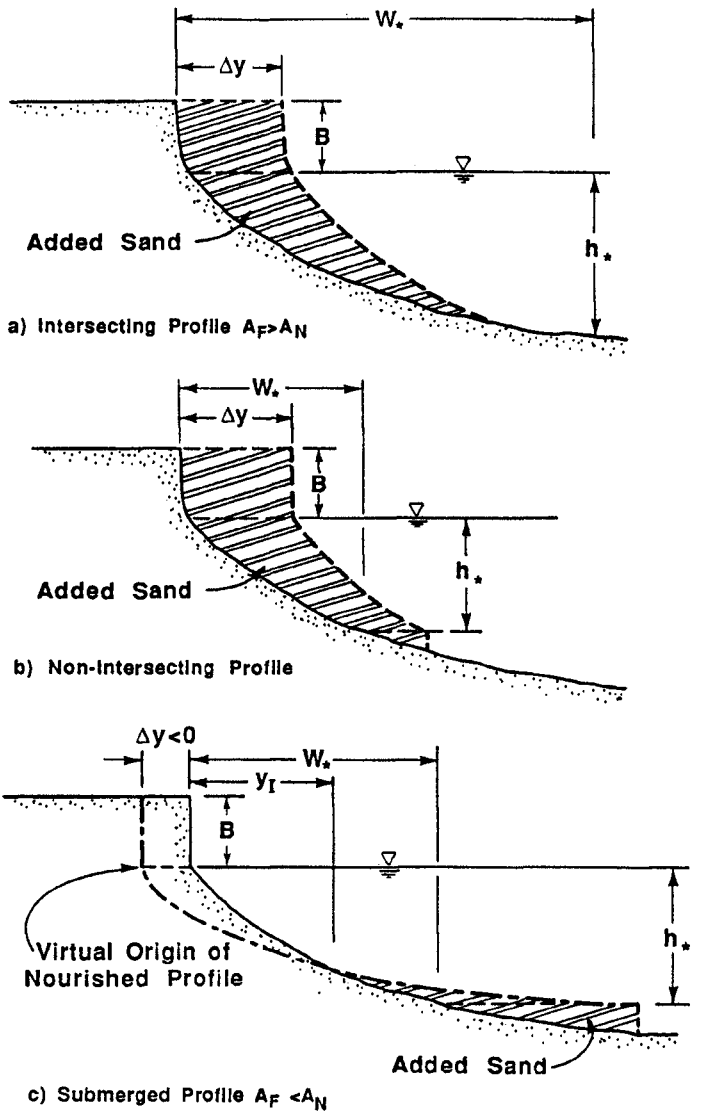

Figure 8. Three generic types of nourished profiles. (Dean, 1991)

only occur if the nourishment sand is finer than the native. Figure 9 shows the effect of nourishing with equal volumes of sands that are coarser than, equal to, and finer than the native. Progressing from the upper to lower panel, it is clear that sediment size is a critical parameter in terms of the volumes required to obtain a particular additional dry beach width.

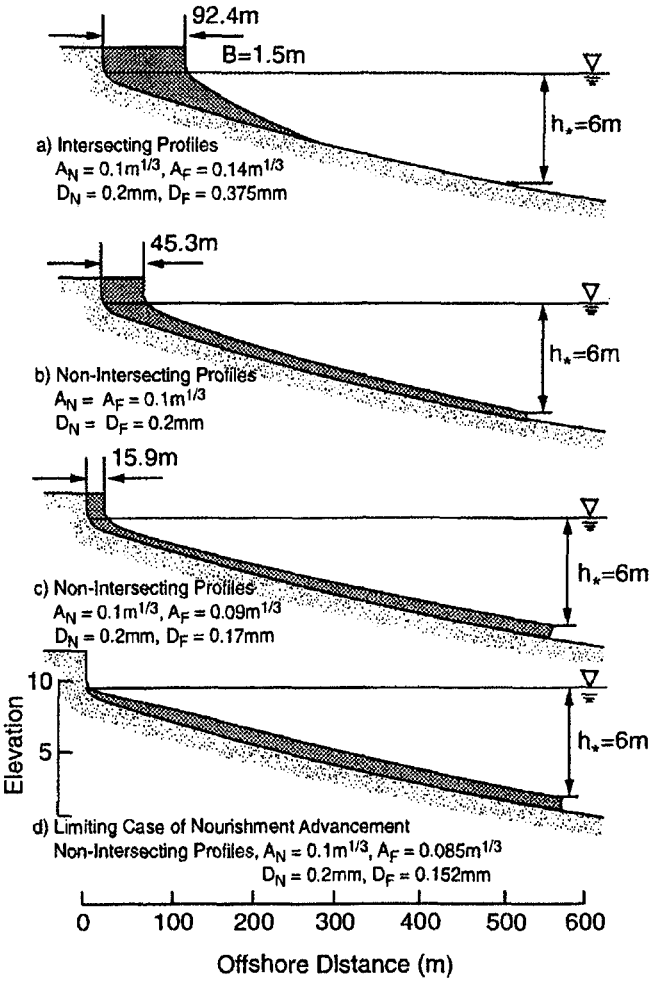

Figure 9. Effect of nourishment scale parameter, A_F, on width of resulting dry beach. Four examples of decreasing A_F with same added volume per unit beach length (Dean, 1991).

Foregoing detailed discussion and development, it can be shown that the non-dimensional additional dry beach width, $\Delta y_o/W_*$, is a function of three non-dimensional variables: non-dimensional volume, V/W_*B, the ratio of sediment scale parameters A_F/A_N and h_*/B.

$$\frac{\Delta y_o}{W_*} = f\left(\frac{V}{W_* B}, \frac{A_F}{A_N}, \frac{h_*}{B}\right) \tag{8}$$

In the above, A_F and A_N are the sediment scale parameters for the "fill" and "native" sands, respectively and W_* is the cross-shore distance to h_* on the native profile, i.e., $W_* = (h_*/A_N)^{3/2}$. There are three equations of the form of Eq. 8, one for each of the profile types described earlier. The solution for a particular value of $h_*/B = 4$ is presented in Figure 10. For a particular case and three grain sizes, the additional dry beach width as a function of nourishment volume is presented in Figure 11. It is again evident that sediment size is very important to the performance of a project.

Models of Profile Evolution

Cross-shore sediment transport processes are so complex that practically all models of profile evolution require numerical solution. Two types of profile evolution exist which can be termed as "open loop" and "closed loop." All such models employ a transport equation and the conservation of sand equation.

Open Loop Profile Evolution Models

Open loop profile evolution models require detailed or idealized representation of the hydrodynamics and sediment transport processes. As an example, the suspended sediment distribution and mean velocity may be a component of, or the dominant transport mechanism. Some models include bed load transport as a principal component. Most, if not all, of these open loop models if allowed to run indefinitely under the action of steady forcing will become unstable unless some artificial "smoothing" of the results is introduced. Examples of open loop models include: Bailard and Inman (1981), Dally and Dean (1984), Watanabe (1988), Southgate and Nairn (1993) and Nairn and Southgate (1993). Roelvink and Hedegaard (1993) have presented a review of several open-loop models.

Closed Loop Models

Closed loop profile models are characterized by the specification of a particular "target profile," to which the computed profile will converge if the forcing mechanisms are held constant indefinitely. Thus, computational stability is ensured by this approach. As noted previously, Eq. (7) has been used as the target profile in at least two of these models. Since Eq. (7) is consistent with uniform wave energy dissipation per unit water volume, D_*, within the surf zone, (where the subscript "$_*$" denotes the value for equilib-

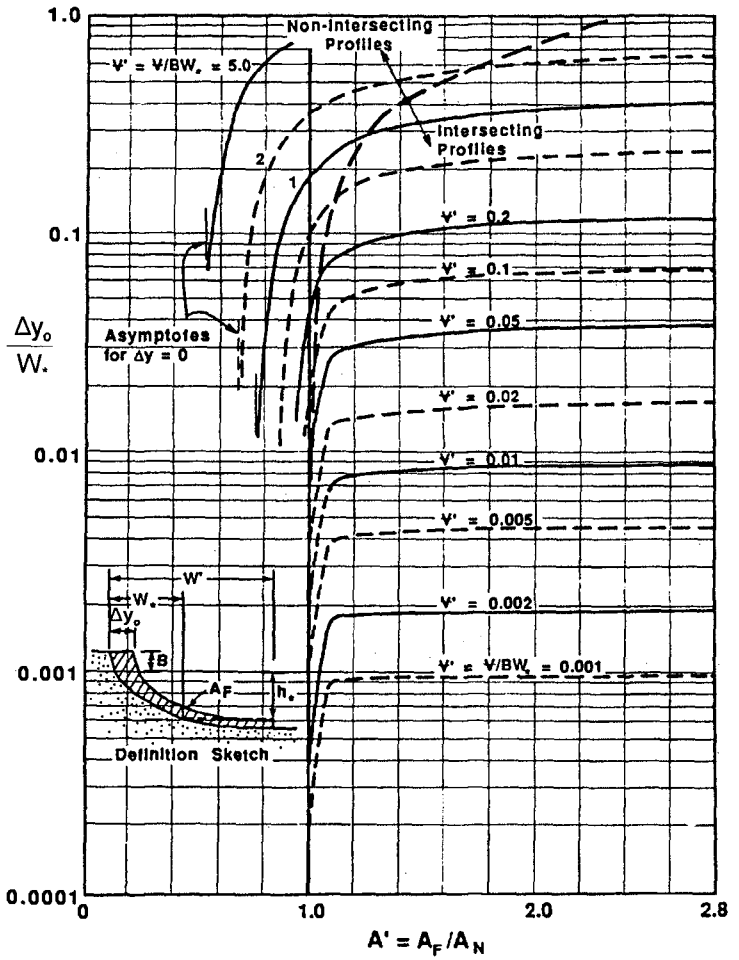

Figure 10. Variation of non-dimensional shoreline advancement $\Delta y_0 / W_*$, with A′ and Ψ. Results shown for $h_*/B = 4.0$. (Dean, 1991)

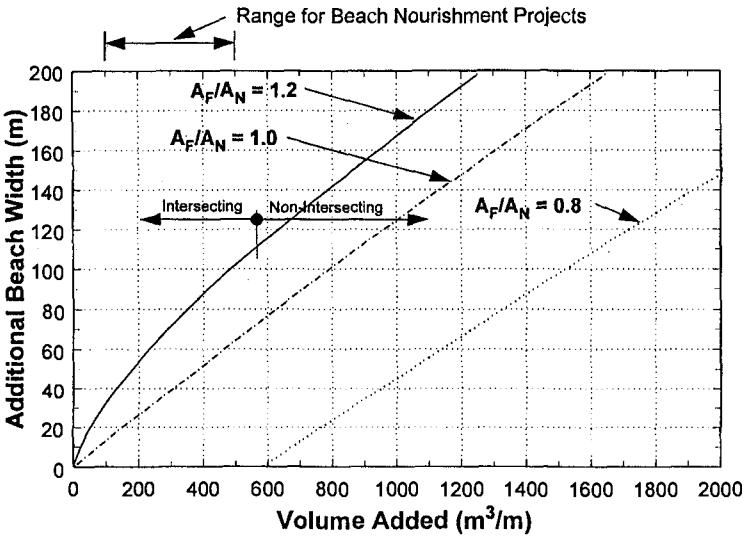

Figure 11. Additional dry beach width versus volume of sand added per unit length of beach. $h_* = 6$ m, B = 1.5 m.

rium conditions), the seaward transport, q, is related to the actual (non-equilibrium) wave energy dissipation per unit volume by

$$q = K'(D - D_*)^m$$

where K′ and m are constants and in two of the models, m = 1. Examples of closed loop profiles include: EDUNE (Kriebel and Dean, 1985), and SBEACH (Larson and Kraus, 1989). In EDUNE, the cross-shore positions of the contours are specified and it is thus not efficient to represent non-monotonic profiles. SBEACH represents the offshore distance as a series of grids which readily allows representation of offshore bars. The closed loop models are much more effective and reliable for the beach and dune erosion phase than for the recovery phase which occurs on a longer time scale and can be characterized by the sediment moving onshore in "pulses."

Closed loop models are considered much more in the engineering applications arena as compared to the open loop models which are more in the research and development arena.

Some Recent Results: Planform Area Evolution

The contributions to be described here relate to the evolution of the additional total plan area associated with a beach nourishment project. In addressing this problem it will be assumed for convenience that the profile equilibration occurs instantaneously such that the additional dry beach at any particular location can be determined from one of the three equations of the type of Eq. 8.

Starting with sand that is compatible, which is the most simple case, the relationship between the additional dry beach width and the volume density per unit beach length, V, at any location is given by $\Delta y(x) = V(x)/(h_* + B)$. Integrating this additional dry beach width we obtain the following result which, since the total volume, V_{TOT}, does not vary with time, neither does the plan area, PA. That is, the total plan area PA is constant

$$PA(t) = \int_{-\infty}^{\infty} \Delta y(x)\, dx = \int_{-\infty}^{\infty} \frac{V(x)}{(h_* + B)}\, dx = \frac{V_{TOT}}{(h_* + B)} \qquad (9)$$

Consider next nourishment sand sizes which differ from the native sand. For a sand which is coarser than the native, reference to Figures 8 and 9, will demonstrate that as the volume density decreases as the planform spreads out, the intersection point will occur closer and closer to the shoreline and the ratio of additional dry beach width to volume density of sand will increase. In the limit, as the volume density of sand approaches zero, the vertical dimension of the active profile approaches the berm height, B, and the relationship between Δy and V will be

$$\Delta y(x, t \rightarrow \infty) = \frac{V(x)}{B} \qquad (10)$$

Thus it can be shown that with time the total planform area will increase for sands that are coarser than the native and in the limit will achieve the asymptotic total plan area

$$PA(t \rightarrow \infty) = \frac{V_{TOT}}{B} \qquad (11)$$

The same procedure as demonstrated for sands which are coarser than the native also applies for sands that are finer than the native. In this case, as the volume density becomes smaller and smaller due to spreading out of the beach nourishment project, the dry beach width becomes smaller and smaller (see Figure 11) and in the limit the plan area associated with the finer sands approaches zero. An example of total plan area evolution results for single sized sands which are coarser, finer and the same size as the native is presented in Figure 12 for non-dimensional time.

The previous treatment of nourishment with sands composed of only one diameter results in asymptotes at large time that are not realistic, particularly for sands that are finer than the native. We now consider the nourishment sand to be composed of

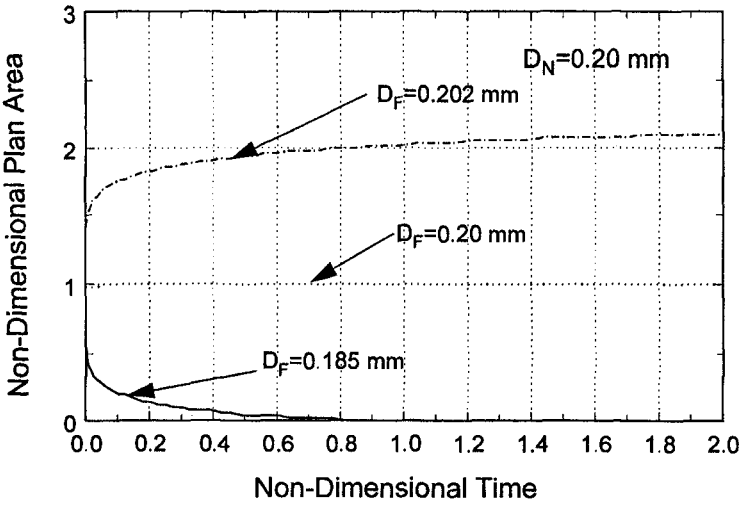

Figure 12. Non-dimensional plan area vs. non-dimensional time for various sizes of fill material. Single nourishment size sand.

sands of two sizes which can vary in proportion from 100% of the finer sands to 100% of the coarser sands. Consistent with findings in nature it will be assumed that the coarser sands always remain in the landward portion of the nourished profile, see Figure 13. In Figure 13, since the nourishment material is generally coarser than the native, the sands of the same size as the native are located in the seaward portion of the profile. Also, one of the sand sizes will be chosen to be the same size as the native; the remaining fraction can be coarser or finer than the native. This involves a procedure for size characterization of the nourishment sediment which will not be discussed here. In this case, the evolution of the beach nourishment planform can be determined using a somewhat more complicated numerical model. Figure 14 shows the results for a case in which the native sand is 0.20 mm and nourishment sands are generally coarser than the native. The proportion of coarser (0.23 mm) sands ranges from 0.0 to 0.9 of the total volume placed. Figure 15 illustrates the planform evolution for cases in which the nourishment sands are generally coarser than the native with equal proportions of nourishment sand equal to and coarser than the native. In this example the size of the coarser friction varies. Again, the sensitivity of both initial and asymptotic plan areas on sand size are substantial. Figures 16 and 17 are the counterparts of Figures 14 and 15, respectively, for the case in which the nourishment sand is generally finer than the native.

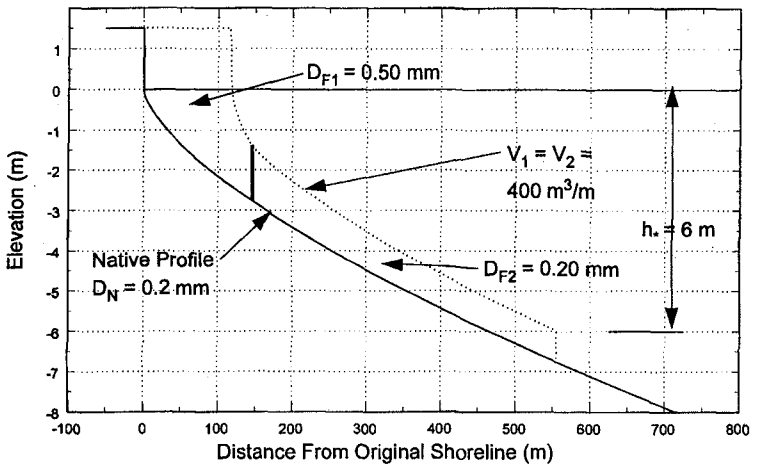

Figure 13. Example of $V_1 = V_2$ with $D_N = 0.20$ mm, $D_{F1} = 0.50$ mm, $D_{F2} = 0.20$ mm.$h_* = 6$ m, B = 1.5 m.

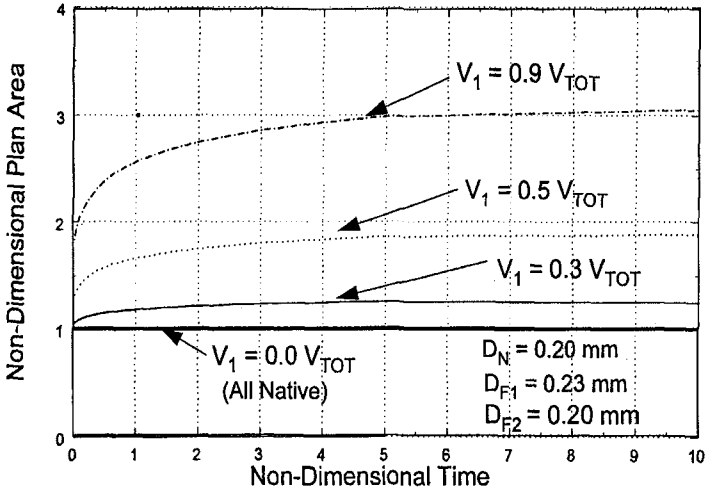

Figure 14. Example calculation for nourishment sand coarser than the native. Effect of proportions of coarser sand. Two nourishment sizes considered.

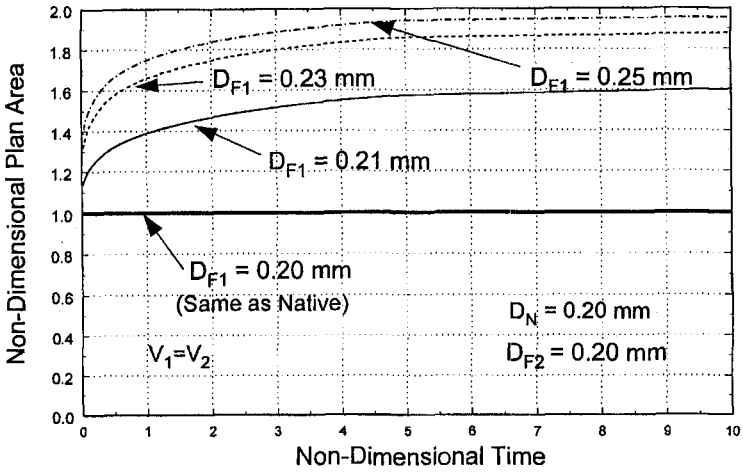

Figure 15. Example calculation for nourishment sand coarser than the native. Effect of sand size. Two nourishment sizes considered.

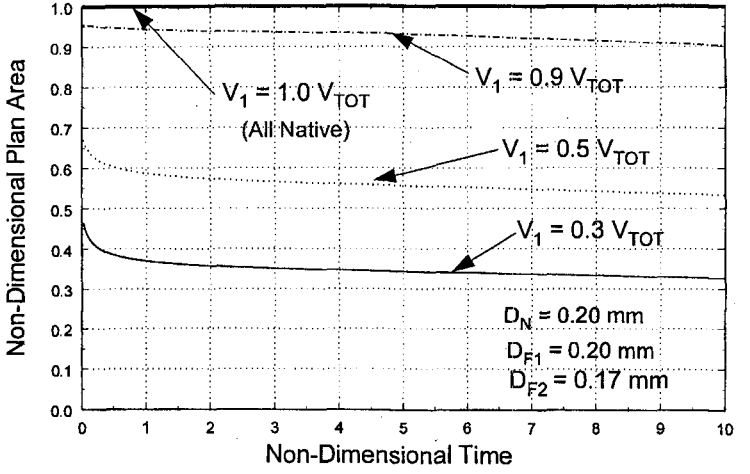

Figure 16. Example calculation for nourishment sand coarser than the native. Effect of proportions of finer sand. Two nourishment sizes considered.

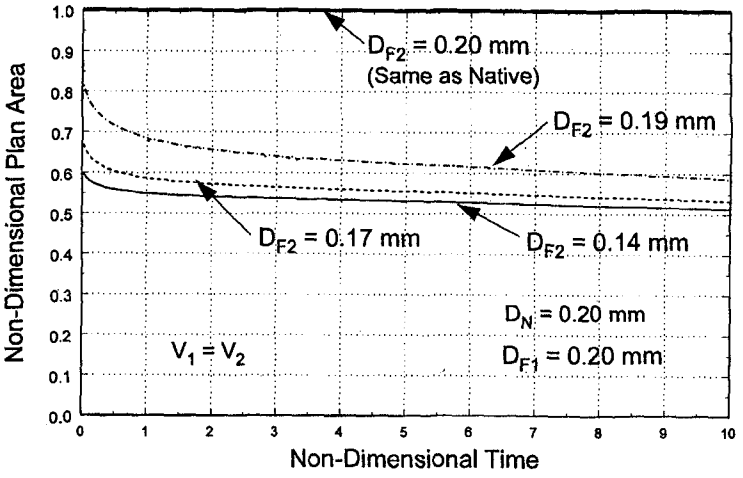

Figure 17. Example calculation for nourishment sand finer than the native. Effect of sand size. Two nourishment sizes considered.

As a summary statement, the effects of nourishment sand size on the initial and asymptotic total additional plan area for a project constructed on an infinitely long beach are substantial. For projects constructed in other settings, the effects of sand size on plan area evolution are also expected to be significant.

Summary

This paper has presented a limited review of the available methodology for simple calculations of prediction of beach nourishment performance. Additionally, recent results describing the importance of sediment size on beach planform evolution are provided.

The predicted performance of beach nourishment projects can be aided by considering the planform and profile evolution separately. Although these two processes occur simultaneously, it is reasonable to separate them for preliminary design and performance prediction purposes. The Pelnard Considère Equation, the heat conduction equation, can be applied with confidence to a number of significant problems if the boundary conditions and initial planforms are satisfied reasonably well. Solutions are available for nourishment with initially rectangular or trapezoidal planforms on a long, straight beach or nourishment on a beach with one or both lateral boundaries located at inlets. Many solutions for other initial planforms and boundary conditions exist. Simple relationships for the longevity as affected by the project length and wave height can be developed and

applied readily. Other useful results relate to refraction due to the perturbation associated with the beach nourishment planform, the insensitivity of the planform evolution to wave sequencing, the planform effects of nourishing with sands which are finer or coarser than the native, nourishment along a coastline for which no other sand is available for transport, multiple nourishments, and the effects of background erosion.

Two issues are examined with respect to profile equilibration. Response time has been found through monitoring of full scale projects to be on the order of five years. The second issue, and probably the more important, relates to the effect of nourishment sand size on the equilibrated dry beach width. It is shown that three profile types occur depending on the relative sizes of the nourishment and native beach sands. Due to the steeper profiles associated with coarser grain sizes, the additional dry beach width can be substantially greater than for the case of finer nourishment sediments. The sensitivity of equilibrated dry beach width to sediment size is significant.

The results of recent investigations of the evolution of the total additional beach planform area are presented in which it is shown that the effects of nourishment sand size are again significant. For single size nourishment sands that are coarser than the native a simple model is developed which allows determination of the asymptotic (at large times) beach planform area. For sands that are finer than the native the asymptotic planform area due to the nourishment project is zero. Due to the unrealistic results for single size nourishment sands, especially for sands finer than the native, a more representative model is investigated in which the nourishment sands are composed of two sizes which can vary in their proportions. The coarser sand fraction is assumed to occupy the landward portion of the profile, one size is the same as the native and the remaining component can be coarser or finer than the native. Results based on this model appear to be much more realistic and to allow the computation of reasonable total additional plan area evolution.

Acknowledgments

The author is indebted to the Florida Sea Grant Program and the Bureau of Beaches and Coastal Systems of the Florida Department of Environmental Protection which have provided funding over the years for the work which he and his students have conducted on nearshore processes and the related engineering applications.

Appendix-References

Bailard, J.A. and D.L. Inman (1981) "An Energetics Bed Load Model for a Plane Sloping Beach: Local Transport," Journal of Geophysical Research, Vol. 86, No. C3, pp. 2035-2043.

Bruun, P. (1954) "Coast Erosion and the Development of Beach Profiles," U.S. Army Corps of Engineers, Beach Erosion Board, Tech Memo No. 44.

Dally, W.R. and R.G. Dean (1984) "Suspended Sediment Transport and Beach Profile Evolution," Journal, Waterway, Port, Coastal and Ocean Engineering, American Society of Civil Engineers, Vol. 110, No. 1, pp. 15-33.

Dean, R.G. (1977) "Equilibrium Beach Profiles: U.S. Atlantic and Gulf Coasts," Department of Civil Engineering, Ocean Engineering Report No. 12, University of Delaware, January.

Dean, R.G. (1987) "Coastal Sediment Processes: Toward Engineering Solutions." In: Coastal Sediments '87, Specialty Conference on Advances in Understanding of Coastal Sediment Processes, New Orleans, LA, ASCE, pp. 1-24.

Dean, R.G. (1991) "Equilibrium Beach Profiles: Principles and Applications," *J. Coastal Res.*, 7, 1, 53-84.

Dean, R.G. and C.-H. Yoo (1992) "Beach Nourishment Performance Predictions," *J. Waterway, Port, Coastal, and Ocean Engrg.*, ASCE, 118, 6, 567-586.

Dean, R.G. and C.-H. Yoo (1994) "Beach Nourishment in Presence of Seawall," *J. Waterway, Port, Coastal, and Ocean Engrg.*, 120, 3, 302-316, 1994.

Dean, R.G. (1995) "Beach Nourishment: Planform Considerations," Proceedings, Coastal Dynamics '95, American Society of Civil Engineers, pp. 533-546.

Hanson, H. (1989) "GENESIS - A Generalized Shoreline Change Numerical Model," Journal of Coastal Research, Vol. 5, No. 2, pp. 1-28.

Hanson, H. and N.C. Kraus (1989) "GENESIS: Generalized Model for Simulating Shoreline Change, Report 1, Technical Reference," Technical Report No. 89-19, Coastal Engineering Research Center, Waterways Experiment Station, Vicksburg, MS.

Kriebel, D.L. (1982) "Beach and Dune Response to Hurricanes," MSc Thesis, University of Delaware, 349 pp.

Kriebel, D.L. and R.G. Dean (1985) "Numerical Simulation of Time-dependent Beach and Dune Erosion," *Coastal Engrg.*, pp. 9, 3, 221-245.

Larson, M., H. Hanson and N.C. Kraus (1997) "Analytical Solutions of One-Line Model for Shoreline Change Near Coastal Structures," Journal Waterway, Port, Coastal and Ocean Engineering, Vol. 123, No. 4, pp. 180-191.

Larson, M. and N.C. Kraus (1989) "SBEACH: Numerical Model for Simulating Storm-induced Beach Change, Report 1: Empirical Foundation and Model Development." U.S. Army Coastal Engineering Research Center, Waterways Experiment Station, *Technical Report CERC-89-9.*

Moore, B.D. (1982) "Beach Profile Evolution in Response to Changes in Water Level and Wave Height," MCE Thesis, Department of Civil Engineering, University of Delaware, 164 pp.

Nairn, R.B. and H.N. Southgate (1993) "Deterministic Profile Modelling of Nearshore Processes. Part 2. Sediment Transport and Beach Profile Development," Coastal Engineering, Vol. 19, No. 1, 2, pp. 57-96.

Perlin, M. and R.G. Dean (1985) "3-D Model of Bathymetric Response to Structures," ASCE, *Journal of Waterway, Port, Coastal, and Ocean Engineering*, Vol. 111, No. 2, March, pp. 153-170.

Roelvink, J.A. and I.B. Hedegaard (1993) "Cross-Shore Profile Models," Coastal Engineering, Special Issue No. 21, Part 1/3, pp. 163-192.

Southgate, H.N. and R.B. Nairn (1993) "Deterministic Modelling of Nearshore Processes, Part 1." Waves and Currents, Coastal Engineering, Vol. 19, No. 1, 2, pp. 27-56.

Walton, T.L. (1994) "Shoreline Solution for Tapered Beach Fill," *Journal of Waterway, Port, Coastal, and Ocean Engineering*, Technical Note, ASCE, Vol. 120, No. 6, pp. 651-655.

Watanabe, A. (1988) "Modeling of Sediment Transport and Beach Evolution," In: Nearshore Dynamics and Coastal Processes; Theory, Measurement and Predictive Models, K. Horikawa, (ed), University of Tokyo Press, pp. 292-302.

Part I: Characteristics of Coastal Waves and Currents

Wave Diffraction E of Hornbæk Harbour, Zealand

North Sea Waves at Groin Protected Danish West Coast

The modelling of a spilling breaker: strong turbulence at a free surface.

M. Brocchini [†] and D.H. Peregrine [‡]

Abstract

A brief review is given of the initial development of a model for the turbulence generated by a spilling breaker riding on an unsteady wave. The turbulent volume of water in a spiller is modelled as a thin layer. The basis for such a model comes from the analysis of the interaction between an air-water interface with patche of turbulence. Hence, the behaviour of a free surface which is affected by strong turbulence is being studied. We summarise some of the salient points of our work. These include a derivation of averaged boundary conditions which include mass and momenturn flows in the surface layer and the transfer to the bulk liquid. A brief account is also given of the type of equations needed to represent the motion of the front edge of the breaker. Illustration of the method is only given in terms of the equations derived by integration from the equation of mass conservation. Finally, there is description of the various free surface regimes that occur and need to be considered in order to determine suitable closures for the averaged terms.

Motivation and Methodology

This study is motivated by a wish to model the spilling breakers that arise from the crests of steep water waves (e.g. see figure 1). Spilling breakers are classified in a wider class of types of breaking where the wave form changes relatively slowly. Together with the bore (or turbulent bore) they form the class of the quasi-steady breakers. If the turbulence is confined to a region near the crest of the wave the wave is a spilling breaker but if the whole face of the wave is turbulent it is a bore.

In their analysis of spilling breakers, bores and hydraulic jumps Peregrine & Svendsen (1978) suggested that the volume of turbulent flow in a spilling breaker resembles a turbulent mixing layer. The roller model in which the turbulent

[†]Assistant Professor, Istituto di Idraulica, Universitá di Genova, Via Montallegro 1, 16145 Genova, Italy, (*brocchin@idra.unige.it*)

[‡]Professor of Applied Mathematics, School of Mathematics, University of Bristol, (*D.H.Peregrine@bristol.ac.uk*)

region is modeled as a separate flow region passively riding the wave crest is seen to be only a partial solution as it is evident that the fluid content of the roller itself is continually mixing with the rest of the turbulent fluid in the wave.

Peregrine (1992) also suggests that a spilling breaker may be considered as a quasi-steady system in a frame of reference moving with the wave where deformations of the spiller shape occur at longer time scales than those typical of the motion of water through the turbulent region. The structure of such a quasi-steady breaker is thus an initial mixing layer region, followed by a region beneath the crest of the wave where gravity influences and restrains the turbulent motions near the surface.

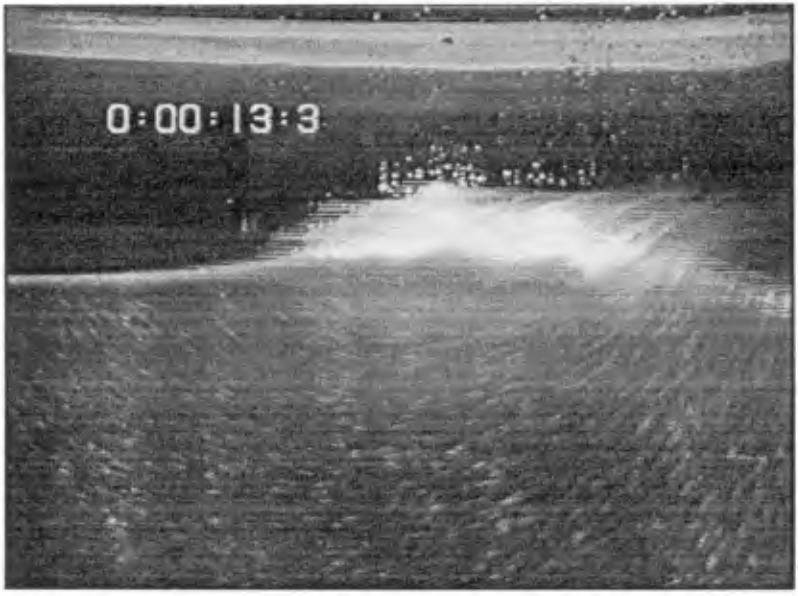

Figure 1: Example of a spilling breaker. Photograph taken at the Fluid Dynamics unit of the University of Edinburgh. (Courtesy of T.C.D. Barnes.)

Developing some of the ideas suggested in Peregrine & Svendsen (1978) and Peregrine (1992) we are trying to build a model which is:

1. as *reliable* and *accurate* as possible in terms of numerical solver $\Longrightarrow$ use a boundary integral solver for the irrotational flow of the bulk of the breaking wave (for a detailed description please refer to Dold & Peregrine, (1984) and Cooker *et al* (1990);

2. as *complete* as possible in terms of physical phenomena $\Longrightarrow$ take into account: two-phase flow, turbulence, flow unsteadiness and curvature, response of turbulence to curvature ...;

3. as *simple* as possible $\Longrightarrow$ lump the effects of two-phase and turbulent flow into Boundary Conditions for the solver used to model the bulk of the propagating wave.

[for more details on this model we refer the reader to Brocchini (1996).]

As a result we are working at a 'three-layer-model' a sketch of which is reported in figure 2. Note that in this model three different time scales are of relevance. They are respectively the time scale for the water particles to cross the layer, the time scale for the evolution of the layer shape and the time scale for the evolution of the shape of the underlying wave. Even if the spilling breaker is said to be quasi-steady because its evolution occurs at a larger time scale than that for a particle to cross the layer, it can be considered unsteady when referring to the motion of the wave because the evolution of the wave shape occurs at a larger time scale than the evolution of the thin layer.

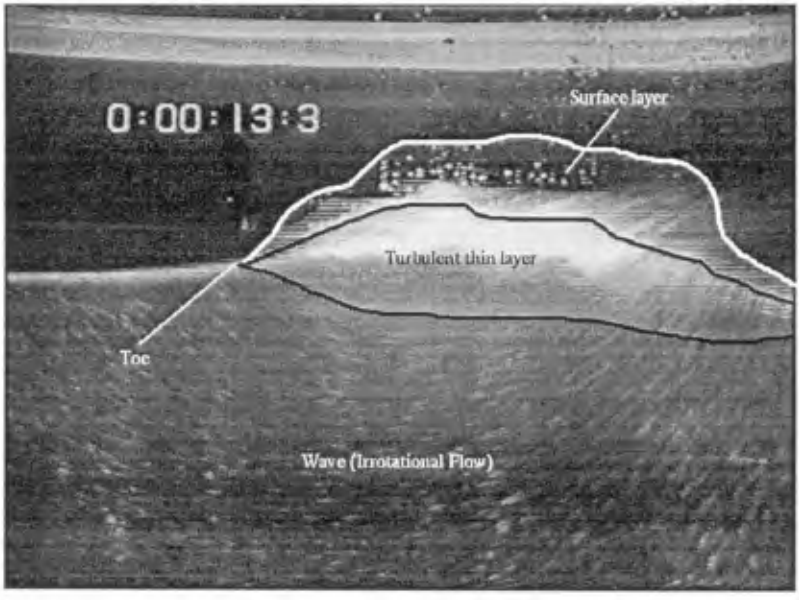

Figure 2: Global geometry adopted in the model for the system wave - turbulent thin layer - surface layer.

One of the main difficulties in modelling a spilling breaker is that at present

there is no good description of free surface boundary conditions for a turbulent flow. The most interesting, and difficult, flows are those breakers which are strongly nonlinear and splashing, but even the much smoother flows occurring in small "micro-scale" breakers, that are restrained by surface tension, require special attention. Hasselmann (1971) is the only paper we know that describes similar surface flows in the context of both wave and turbulent averaging.

In that paper a perturbation is made about the undisturbed free surface, assuming Taylor series make good approximations. This may be a good approximation for irrotational motions but is clearly more limited for turbulence. An interaction stress tensor and a surface mass transfer must be introduced to take proper account of interactions between short and long period motions. However this particular analysis is no longer appropriate when turbulent eddies cause the interface to develop sharply curved features or to disintegrate into splashes. In this case the problem to be faced is of a twofold nature as both turbulence and two-phase flow must be taken into account (e.g. see top layer of figure 2). The interface between the air and water can be extremely complex.

Here we only analyse the problems of modelling the top layer ('surface layer'). At first we illustrate the physical/mathematical framework which concerns both the avaraging within the two-phase layer and the subsequent definition of suitable model equations and boundary conditions. Then, a brief account is given on the equations which are needed to represent the motion of the front edge of the breaker ('toe of the breaker'). Finally, in recognition of the need for closures which depend on specific flow regimes, we describe the main features of such regimes leaving open (for moment) the question of quantifying closures.

The boundary conditions for the 'surface layer'.

The top region of the spilling breaker is studied as a layer consisting of an air-water mixture ('surface layer' of figure 3). The analysis of the flow of two fluids, one dispersed throughout the other, is most often carried out by solving equations which arise from averaging over each phase. In recent research this is achieved by introducing a 'phase function' or 'intermittency function', which is essentially a step function, and then averaging (e.g. Drew, 1983). The properties of the phase function are such that a number of conservation equations are obtained for each dispersed phase.

Within the layer flow properties (e.g. velocities) are not continuous functions of time and space hence we introduce a 'phase function' or 'intermittency function' such that:

$$I(s,n,t) = \begin{cases} 1 & \text{if } (s,n) \text{ is in the water at time } t \\ 0 & \text{if } (s,n) \text{ is in the air at time } t. \end{cases} \quad (1)$$

The we introduce an averaging process $\langle\cdot\rangle$ such that if $\mathcal{G}(s,n,t)$ is a generic flow variable then $\langle\mathcal{G}(s,n,t)\rangle = G(s,n,t)$ is the corresponding average. The most appropriate averaging process is the 'ensemble average' however many of the flows studied in the laboratory are statistically stationary with respect to time. If this is so, the ergodic hypothesis asserts that the time average is equivalent to the ensemble average and $\langle\cdot\rangle$ can simply be regarded as a time average.

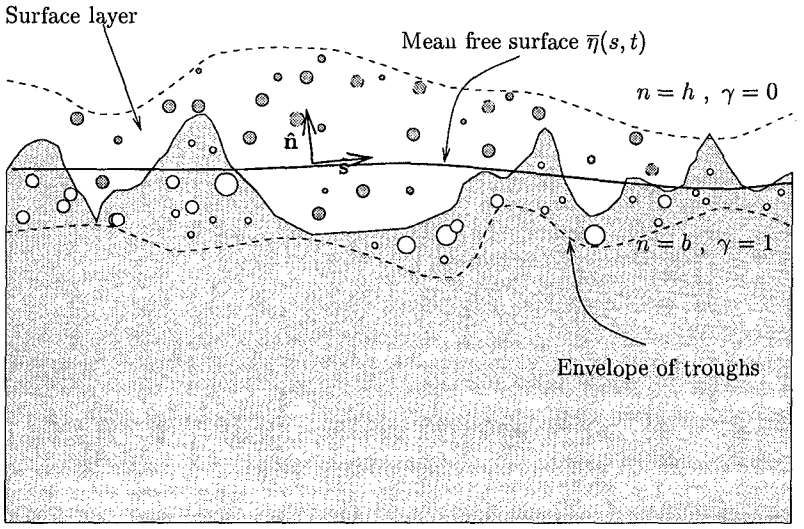

Figure 3: Global geometry adopted in the model for the surface layer.

After averaging the intermittency function becomes an average volume fraction $\gamma(s,n,t)$ also called 'intermittency factor' such that

$$\gamma(s,n,t) = \langle I(s,n,t) \rangle = \begin{cases} 1 & \text{below trough level } n = b \\ 0 & \text{above crest level } n = h. \end{cases} \quad (2)$$

Within the surface layer there can be regions in which only the air, or only the water, or both, are connected. Whether connected or not there is a range of γ from 0 to 1. Somewhere within the layer a mean interface can be defined. Several possible definitions are available, e.g. the surface $\gamma = 0.5$, or the surface corresponding to an equi-distribution, within the surface layer, of the two phases on each side of the chosen surface (see figure 3). In principle this interface can be regarded as a local reference for defining the origin of a local curvilinear coordinate set (s,n), where s follows the mean surface and n is normal to it. However, following experience developed in defining mean shorelines for waves on a beach (Brocchini & Peregrine, 1996) we choose to avoid any specific definition of the mean surface since it seems more meaningful to deal with the surface layer as a whole. For interaction with the water below, the lower boundary of the layer is most relevant, this we denote as b.

Since the intermittency factor γ is a continuous function of time and space it is most useful to characterize different flow conditions. For example three cases are here reported of a wavy surface (figure 4a), a 'scarified' surface (figure4b) and a splashing surface. This has been modelled by considering a Normal distribution

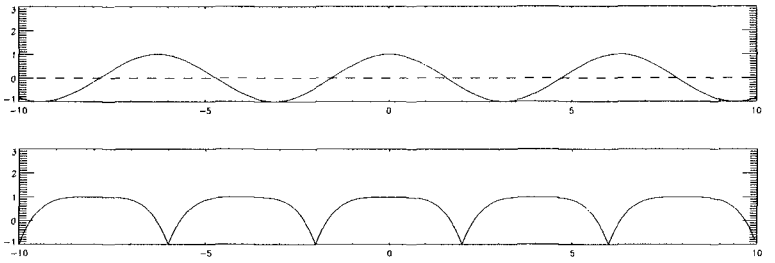

Figure 4: Free surface profile for: (a) sinusoidal wavy interface, (b) periodic scarified interface.

for η such that a simple result is obtained for γ:

$$\gamma(s,n,t) = \tfrac{1}{2}\left[1 - \mathrm{erf}\left(\frac{n - \overline{\eta}(s,t)}{\sqrt{2}\sigma(s,t)}\right)\right]. \tag{3}$$

[In this model σ is a measure of the lateral extent of the surface layer].

For each of the three types of surfaces we have a different γ factor which is reported in figure 5.

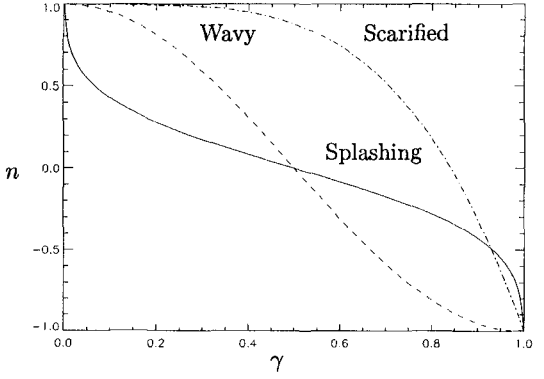

Figure 5: The intermittency factor (or residence time) γ for: (a) wavy air-water interface (dashed line), (b) periodically scarified interface (dot-dashed line) and (c) turbulent splashing interface (solid line).

It is evident that for wavy regimes water is present at the top of the surface layer ($n = 1$) for a longer time than for a splashing regime in which water drops are present for a shorter time near the top of the layer. This behaviour is reversed at the bottom of the layer where large values of γ ($\gamma \approx 1$) are reached faster while

approaching the base of the layer ($n = -1$) in a splashing regime. The relative residence time is nearly 1 for most of a periodic scarified air-water interface.

In order to obtain the boundary conditions use the following steps:

1. obtain conservation equations using integral equations within a control volume V (for more details see Brocchini & Peregrine, (1998b)). With this method there is no need to rely on the usual assumption that each phase can be considered as a continuum;

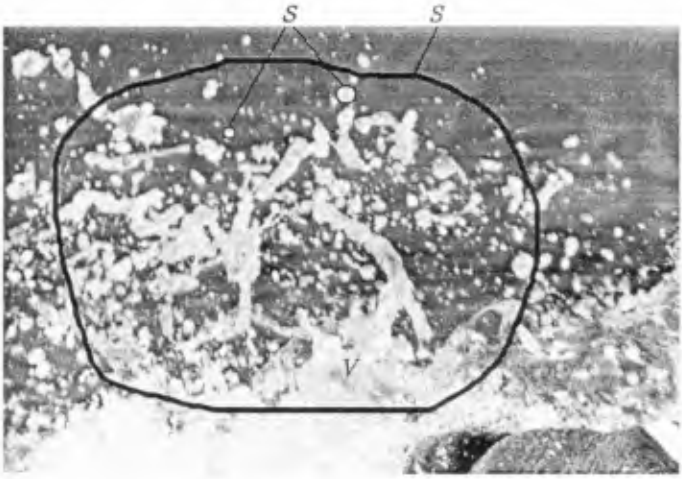

Figure 6: The air-water continuum. The thick closed curve represents the boundary S of the fixed control volume V. An example of the discontinuity interface $\mathcal{S}$ between the two phases is drawn around two water droplets.

2. for simplicity in initial studies assume air flow has negligible effect and no phase change occurs;

3. integrate conservation equations across the 'surface layer' i.e. from the base level $n = b(s,t)$ to crest level $n = h(s,t)$;

4. define the amount of water contained in the layer as:

$$d(s,t) \equiv \int_b^h \gamma \, dn. \tag{4}$$

To get the required boundary conditions we apply the above procedure to each conservation equation (i.e. conservation of mass, linear momentum ...).

For example application to the conservation of mass gives the following kinematic boundary condition:

$$\frac{\partial b}{\partial t} + U|_b \frac{\partial b}{\partial s} - V|_b = W = -\left(\frac{\partial d}{\partial t} + \frac{\partial}{\partial s}\int_b^h \gamma U_w \, dn\right). \quad (5)$$

where U_w is the mean flow velocity in the water (i.e. *phase average* in the liquid phase) and W represents an extra normal-to-surface velocity which would be zero if there were no surface layer. [Note that $U_w(n = b) = U$ and $V_w(n = b) = V$].

Formally, this is very similar to that of Hasselmann (1971) valid for a continuous interface [see surface flow term], but it is applied at base of the layer rather than at a mean surface $\overline{\eta}$.

Note that the equation can be regarded as:
either the kinematic B.C. for the flow below $n = b$ for which W must be given,
or as an equation for the conservation of mass inside the layer.

To use the equation as a boundary condition it is necessary to find a suitable closure for the surface flow term

$$\frac{\partial}{\partial s}\int_b^h \gamma U_w \, dn.$$

Closures are required for even more complicated contributions which appear in the dynamic boundary conditions (e.g. terms corresponding to momentum flow in and into the surface layer giving effective stresses).

The toe (2D) or the foot (3D) of the breaker.

For a physically sound representation of the spilling breaker a crucial point is the modelling of the region where turbulence is generated at the free surface. In a 2D description of the flow this is called the 'toe of the breaker'.

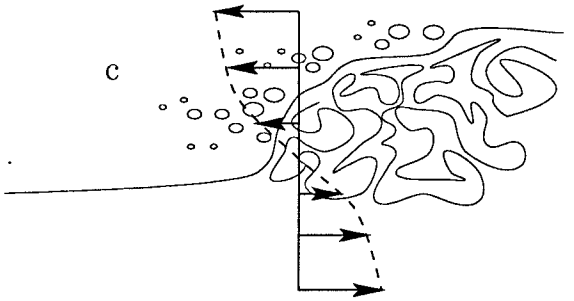

Figure 7: Sketch of the flow and of the velocity profile at the toe of a breaker propagating with celerity c.

According to Peregrine & Svendsen (1978) at the inception point (line) there's meeting of two layers of water travelling in opposite direction. More recently, this

scenario has been also reported by Lin & Rockwell, (1995) in their experimental investigation of the early stages of generation of a quasi-steady spilling breaker. In that case, however, since turbulent blobs spill down the wave face (figure 7) generation of turbulence is greater than in a normal mixing layer (where the velocities are in the same direction).

A quantitative description of the inception region has been obtained following the method used by Brocchini & Peregrine (1996) for averaging the flow at the swash zone. Notice that:

- averaging over the turbulence is inadequate in the region right in front of a spiller which the turbulent water only reaches rarely;
- there is little dynamical significance in such a thin intermittent layer of turbulent water;

As a consequence of the above, the whole region which the turbulence only meets intermittently is taken as a 'Boundary Region' (see figure 8) such that there is a non-zero mean depth at the front edge of the layer.

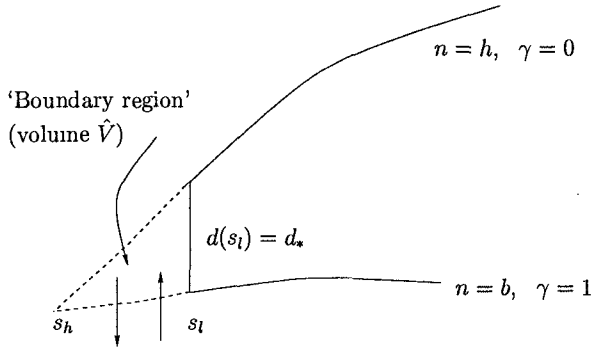

Figure 8: Sketch of the flow properties used in the modelling of the toe of the breaker.

In more detail first introduce the following definitions:

$$d(s_l) = d_* \; ; \qquad d(s_h) = 0 \; ; \qquad h(s_h) = b(s_h) \; ; \qquad \hat{V} = \int_{s_l}^{s_h} d \; ds. \tag{6}$$

Within our model the toe of the breaker is the mathematical boundary characterized by the coordinate s_l and by a non-zero mean depth d_*.

Following on our illustration based on the equation for the conservation of mass (see Brocchini & Peregrine, 1998b for more details) we integrate the kinematic boundary condition in the streamwise direction from s_l to s_h to get:

$$\frac{\partial \hat{V}}{\partial t} + d_* \frac{\partial s_l}{\partial t} = \left[\int_b^h \gamma U_w \; dn \right]_{s=s_l} - \int_{s_l}^{s_h} \left[\frac{\partial b}{\partial t} + U|_b \; \frac{\partial b}{\partial s} - V|_b \right] ds. \tag{7}$$

This equation is formally very similar to one of the shoreline boundary conditions of Brocchini & Peregrine (1996) and it can be regarded as an equation for the motion of the front edge of the layer (s_l) when rewritten as:

$$\frac{\partial s_l}{\partial t} = \frac{1}{d_*}\left\{\left[\int_b^h \gamma U_w \, dn\right]_{s=s_l} - \frac{\partial \hat{V}}{\partial t} - \int_{s_l}^{s_h}\left[\frac{\partial b}{\partial t} + U|_b\frac{\partial b}{\partial s} - V|_b\right] ds\right\} \tag{8}$$

Closure is now needed not only for the surface flow term but also for the volume of water in the 'Boundary Region' $\hat{V}$ and for the mean depth d_*.

Analysis and description of the flow regimes.

In is clear that an in depth analysis of the flow regimes is needed to determine the closures both for the boundary conditions and for the equations relative to the motion of the toe of the breaker. However, analysis of the interaction of turbulence with an air-water interface is interesting *per se* as a large number of natural flows are characterized by strong turbulence at a free surface and they fall in two main classes:

- **turbulence generated at the free surface** (breaking waves, sprays...),
- **turbulence generated far from the surface** (steep rivers, artificial spillways...).

In our description of the flow regimes we assume it is possible to characterize different flow regimes in terms of two flow properties only (Brocchini, 1996; Brocchini & Peregrine, 1997 and Brocchini & Peregrine, 1998a). These are:

1. the turbulence intensity
$$q = \sqrt{2k} \tag{9}$$
where k =turbulent kinetic energy;
2. the length scale L of the most energetic flow feature (wavelength, eddy size, water blob size, ...)

Considering the two stabilising factors of the water surface (gravity and surface tension) four main regions can be found in the (L, q) plane (see figure 9).

For gravity we compare the specific potential energy gL with the specific kinetic energy of turbulence $k = \frac{1}{2}q^2$ and find the Froude number

$$Fr = \frac{q}{\sqrt{gL}}, \tag{10}$$

while for surface tension we compare the specific surface energy $S = T/\rho$ with $\frac{1}{2}q^2L$ to get the Weber number:

$$We = \frac{q^2 L}{2S}. \tag{11}$$

Fr_c and We_c have been obtained working on literature data dealing with wave generation, bubble and drop formation... Here we only summarize some of the results which can be found with more detail in Brocchini & Peregrine (1998a).

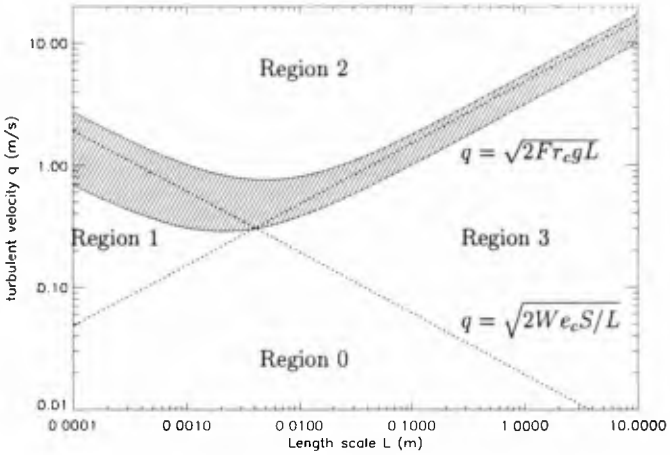

Figure 9: Diagram of the (L, q) plane. The shaded area represents the region of marginal breaking and has been obtained two values for both the critical Weber number ($0.3 < We_c < 5$) and the critical Froude number ($0.5 < Fr_c < 1.5$).

Region 0: $Fr \ll Fr_c$ **and** $We \ll We_c$

In this region the stabilizing effects are dominant leading to a nearly flat surface. Hence, the free surface behaviour in this quadrant may be described as either *flat* or *wavy* (see figure 10).

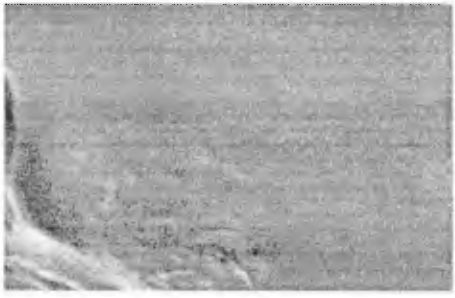

Figure 10: Illustration of a *flat* or *wavy* surface.

Region 1: $Fr > Fr_c$ **and** $We < We_c$

For large Froude number and small Weber number we are concerned with relatively small scale turbulence: of the order 1 cm and less for water, region

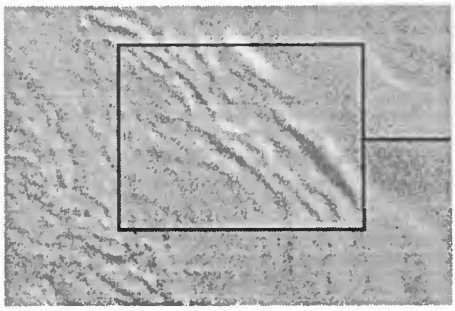

Figure 11: Illustration of a *knobbly* or *microbreaking* surface.

1 of figure 9. Here surface tension is well able to maintain the cohesion of the liquid but gravity fails to keep the surface flat. The result is smooth rounded surfaces. If the turbulence is below the critical region then there is not much wave generation and we describe the surface as *knobbly* or *microbreaking.*

Region 2: $Fr \gg Fr_c$ **and** $We \gg We_c$

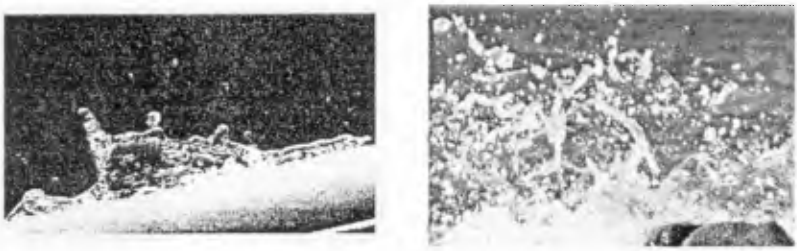

Figure 12: Illustration of a *weakly splashing* surface (left) and of a *violently splashing* surface (right).

When turbulence is so strong that neither surface tension nor gravity can maintain surface cohesion the flow breaks up into drops and bubbles, region 2 of the (L, q) plane. This is an essentially two-phase flow region. At a free surface there is the growth and decay of the strong turbulence to consider as well as the structure of the transition between gas and liquid. When strong turbulence, generated elsewhere, meets a free surface it 'erupts' as the fluctuating eddies form blobs of liquid that are no longer restrained by the inertia of surrounding non-turbulent liquid. This eruption may be exemplified by the 'rooster tail' seen at the rear of high speed vessels as the turbulent flow from their driving mechanism meets the free surface. Sometimes the flow is sufficiently well organised that some of the 'tail' is due to a discrete splash.

We can contrast this case with the weak turbulence case of an almost flat surface. For weak turbulence the vertical velocity fluctuations v approach zero at the free surface, on the other hand for strong turbulence v can be expected to be larger than u and w since the horizontal fluctuations are more constrained by the inertia of the surrounding liquid. This complete contrast in the variation of v gives the clearest indication that different surface regimes need different approaches in developing turbulent models. At the very least different closures are needed for averaged terms.

Region 3: $Fr < Fr_c$ **and** $We > We_c$

Region 3 of our (L, q) diagram has gravity dominating the turbulence, $Fr \gg 1$, with weak surface tension, $We \ll 1$. It is by far the commonest state since it applies to almost all terrestrial water bodies with flow: stream, rivers, seas and oceans. The free surface is essentially flat or nearly so. Linearised boundary conditions are generally satisfactory. However, there are a range of interesting flow properties in this regime as the turbulent energy is increased towards the splashing case. These are local effects and their significance in various applications is not well determined.

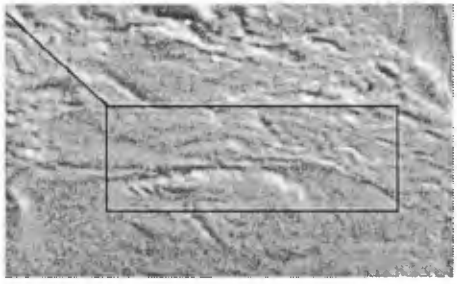

Figure 13: Illustration of a *scarified* surface.

These phenomena arise since the turbulence has more than adequate energy to disturb the free surface, but only at length scales which are smaller than the main turbulent eddies. At the edge of the eddies, where strong shear develops, or where the eddy boundary is moving or there is a strong surface convergence shorter length scales, $L/10$ or $L/100$ or even less becomes important. The surface develops linear features, or scars, which may be a sharp downward trough as shown in figures 4 and 13, or else involve localised breaking.

Acknowledgements

Support from the European Commission Research Grant MAS3-CT97-0081 (SASME) and the Office of Naval Research NICOP Grant N00014-97-1-0791 is gratefully acknowledged.

References

BROCCHINI, M. (1996). *Flows with freely moving boundaries: the swash zone and turbulence at a free surface.* Ph.D Dissertation. University of Bristol, Bristol.

BROCCHINI, M. & PEREGRINE, D.H. (1996). Integral flow properties of the swash zone and averaging. *Jour. Fluid Mech.* **317**, 241-273.

BROCCHINI, M. & PEREGRINE, D.H. (1997). Strong turbulence at a free surface. *Proc. Conf. on Wind-over-Wave Couplings: Perspectives and Prospects*, Inst. Maths. & its Applic. Salford, eds. S.G.Sajjadi & N.Thomas, Oxford Univ. Press. (To appear). Salford.

BROCCHINI, M. & PEREGRINE, D.H. (1998a). The dynamics of turbulent free surfaces. Part 1. Description of strong turbulence at a free surface. *to be submitted.*

BROCCHINI, M. & PEREGRINE, D.H. (1998b). The dynamics of turbulent free surfaces. Part 2. The boundary conditions. *to be submitted.*

COOKER, M.J., PEREGRINE, D.H., VIDAL, C. & DOLD, J.W. (1990). The interaction between a solitary wave and a submerged semicircular cylinder. *Jour. Fluid Mech.* **215**, 1-22.

DREW, D. (1983). Mathematical modelling of two-phase flow. *Ann. Rev. Fluid Mech.* **15**, 261–291.

HASSELMANN, K. (1971). On the mass and momentum transfer between short gravity waves and larger-scale motions. *Jour. Fluid Mech.* **50**, 189–205.

LIN, J.C. & ROCKWELL, D. (1995). Evolution of a quasi-steady breaking wave. *Jour. Fluid Mech.* **302**, 29–44.

PEREGRINE, D.H. (1992). Mechanisms of water-wave breaking. In *Breaking waves. IUTAM Symposium, Sydney.* (ed. M.L. Banner & R.H.J. Grimshaw), 39–53.

PEREGRINE, D.H. & SVENDSEN, I.A. (1978). Spilling breakers, bores and hydraulic jumps. *Proc. 16th Int. Conf. Coastal Eng.* , ASCE, **1**, 540–550.

Time-Dependent Depth-Integrated Turbulence Modeling of Breaking Waves

Kazuo Nadaoka[1] and Osafumi Ono[2]

Abstract

A breaking wave model is presented to simulate non-equilibrium evolution of turbulence with a time-dependent depth-integrated equation of turbulence intensity, which is to be coupled with nonlinear wave. As the crucial part of the modeling, a method to estimate the production rate of turbulent kinetic energy is developed. This method is based on the experimental observation of the pseudo-periodic generation of large-scale eddies near the wave crest of turbulent bore. As a demonstration to show the performance of the present model, numerical examples are given for regular and irregular waves on a slope and regular waves on a double step, indicating that this model can give favorable features of evolution of regular and irregular breaking waves and the production and diffusion of turbulent kinetic energy.

Introduction

Although the recent progress in the developments of nonlinear-dispersive wave equations enables us to precisely describe even nonlinear evolution of irregular waves up to breaking, the broken wave simulation is still limited mainly because of the lack of proper turbulence model with wide applicability and sound physical background.

In the previous studies, many efforts have been made to incorporate the effect of wave breaking by introducing damping terms in a time-dependent wave model. Among these, e.g., Karambas and Koutitas (1992) presented a breaking wave model based on Boussinesq equations with a diffusion-type term, in which the damping factor is determined by time-averaged equation of the turbulence energy. However their model has a difficulty in further extension to unsteady wave field.

Schäffer et al. (1992) and Madsen et al. (1997) developed a breaking wave

[1] Prof., Department of Mechanical and Environmental Informatics, Graduate School of Information Science and Engineering, Tokyo Institute of Technology, 2-12-1 O-okayama, Meguro-ku, Tokyo 152-8552, Japan. (Email: nadaoka@mei.titech.ac.jp, Fax: +81-3-5734-2650)

[2] Graduate student, Department of Mechanical and Environmental Informatics, Graduate School of Information Science and Engineering, Tokyo Institute of Technology, 2-12-1 O-okayama, Meguro-ku, Tokyo 152-8552, Japan.

model based on a surface roller concept and a time domain formulation of Boussinesq-type equations. As the wave breaking criterion they assumed the presence of a critical value in the local water surface slope according to Deigaard (1989). However Nadaoka et al. (1997a) indicated through a laboratory experiment of irregular breaking waves that the front surface slope at the breaking exhibits appreciable scatter. Besides there is no experimental evidence to support the validity of the surface roller concept as the physical process, although it has been one of useful concepts for the breaking wave modeling. For example Nadaoka et al. (1989) found experimentally that the actual process of turbulence production is governed by a *pseudo-periodic* generation of large-scale eddies near the wave crest.

In the present paper, a new breaking wave model is presented to simulate non-equilibrium evolution of the turbulence with a time-dependent depth-integrated equation of turbulence intensity, which is to be coupled with nonlinear wave equations. As the crucial part of the modeling, a method is developed to estimate the production rate of turbulent kinetic energy, which governs the non-equilibrium development of turbulence and hence the breaking wave evolution. This method is based on the experimental observation of the pseudo-periodic generation of large-scale eddies near the wave crest as mentioned above. As the wave breaking criterion the free-fall condition by Nadaoka et al. (1997a), which is based on the vertical pressure gradient near the wave crest, is adopted for the simulation. Numerical examples as a demonstration to show the performance of the present model are given for regular and irregular waves on a slope and regular waves on a double step.

Depth-Integrated Turbulence Modeling

Since the turbulence production of breaking waves is closely related with the instantaneous wave profile, the turbulence model developed in the present study is in a form to be *simultaneously* solved with the wave equations. In general, the existing equations to describe evolution of water waves such as Boussinesq equations are those of the depth-integrated type. Therefore, as a consistent way of formulation, the present turbulence model is to be of a depth-integrated type.

For the subject of suspended sediment transport in the surf zone, as one of important applications of the turbulence model, one needs to know the variation of turbulence intensity within a wave cycle for the evaluation of the sediment pick-up from the sea bottom. For such a purpose a time-dependent formulation is required for the turbulence modeling.

Besides in the turbulence development on a beach with an arbitrary profile like a stepped beach, the non-equilibrium aspect becomes crucial. Therefore both the turbulence production and dissipation must be properly estimated in the turbulence model.

For these requirements, the depth-integrated equation of the turbulent kinetic energy transport may be used, which is

$$\frac{\partial k}{\partial t} + \bar{u}\frac{\partial k}{\partial x} = P_k - \varepsilon + D_k, \tag{1}$$

where k denotes the depth-averaged turbulent kinetic energy, $\bar{u}$ the depth-averaged velocity, ε the energy dissipation rate, D_k the diffusion term and P_k the production rate of the turbulent kinetic energy. The energy dissipation rate, ε, may be evaluated with k and the turbulence length scale l according to the usual k-equation model,

$$\varepsilon = c^* \frac{k^{3/2}}{l}, \tag{2}$$

The length scale l may be estimated according to Svendsen (1987),

$$l = 0.2h, \tag{3}$$

where h is the local water depth. The energy diffusion term is simply evaluated with the turbulent eddy viscosity, ν_t, as

$$D_k = \frac{\partial}{\partial x}\left(\frac{\nu_t}{\sigma_k}\frac{\partial k}{\partial x}\right). \tag{4}$$

For the model parameters, c^* and σ_k, in eqs.(2) and (4), the standard values, c^*=0.17, σ_k=1.0 are adopted. The eddy viscosity, ν_t, is estimated as

$$\nu_t = k^{1/2} l. \tag{5}$$

Although eqs.(1) to (5) constitute a depth-integrated one-equation model*, one may employ a two-equation model such as k-ε model as the turbulence equations to be vertically integrated.

One of the crucial points for the present turbulence modeling is the estimation of the turbulence production near the bore crest, which governs the non-equilibrium development of the turbulence. The local production rate of the turbulent kinetic energy is usually estimated with the product of the local shear stress, τ, and the shear rate, $\partial u/\partial z$. Hnece the depth-averaged form of the turbulent enery production rate, P_k, may be obtained by the vertical integration of $\tau \partial u/\partial z$. However this idea, as described below in detail, may not be applicable directly to the modeling of the surf zone turbulence, in which the the large-scale eddy generation near the wave crest is the dominant turbulence source.

* Recently Nwogu (1996) proposed a time-dependent breaking wave model based on Boussinesq-type equations, in which a one-equation type model is adopted to estimate turbulence development. The evaluation of the turbulence production is made by the assumption that it is proportional to the vertical gradient of the horizontal velocity at the wave crest and that the breaking process is of spilling-type.

Turbulence-Energy Production Modeling

In the initial development of turbulence at the breaking point, the entire process is governed by the generation of a large-scale eddy due to the water masss impingement at the front surface. This process, as illustrated in Fig.1, is a conversion from an irrotational motion in a simply connected region to the rotational flow in the doubly connected region with a circulation, Γ, at the moment when the water jet reaches the front surface. This circulating flow motion, in other words, the horizontal large-scale vortex involves ample vorticity and air bubbles in the water, providing subsequently smaller scale turbulence. In this process the initial turbulence generation may not be evaluated simply by $\tau \partial u/\partial z$. Our question is then what about in the inner region of the surf zone?

In the conventional modeling of the breaking waves, a concept of steady vortex attached at the bore front such as "surface roller" (Svendsen, 1984) as illustrated in Fig. 2 has been employed. However the actual process of the eddy formation at the bore front exhibits *pseudo-periodic* generation of large-scale eddies, which are advected behind the bore crest with appreciable diffusion (Fig. 3; Nadaoka et al., 1989). The essential feature of the development of each eddy is the same with that for the initial vortex development in terms of the generation of the circulation and associated supply of the vorticity and air bubbles.

Based on this observation, in the present model, the turbulent energy production rate, P_k, is estimated with the kinetic energy of a large-scale eddy, e_L, and its generation frequency per unit time, n; both of which may be evaluated with the circulation of the large-scale eddy, Γ_0 as described below.

The kinetic energy of a large-scale eddy, e_L, is estimated here with the Rankine eddy model,

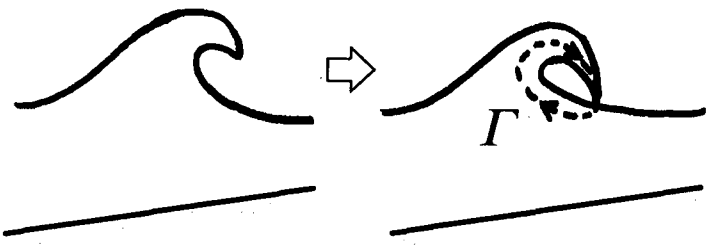

(a) a simply connected region (b) a doublly connected region with Γ

Fig.1 Illustration of initial development of a large-scale eddy with the circulation Γ, which involves ample vorticity and air bubbles into the water.

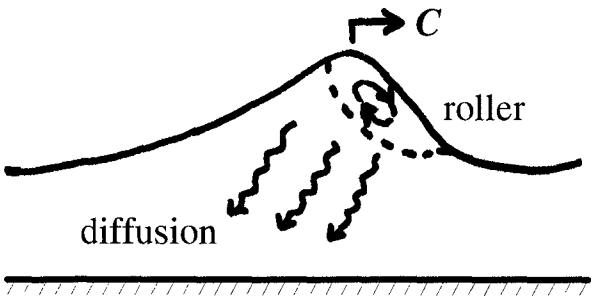

Fig. 2 Illustration of the surface roller model.

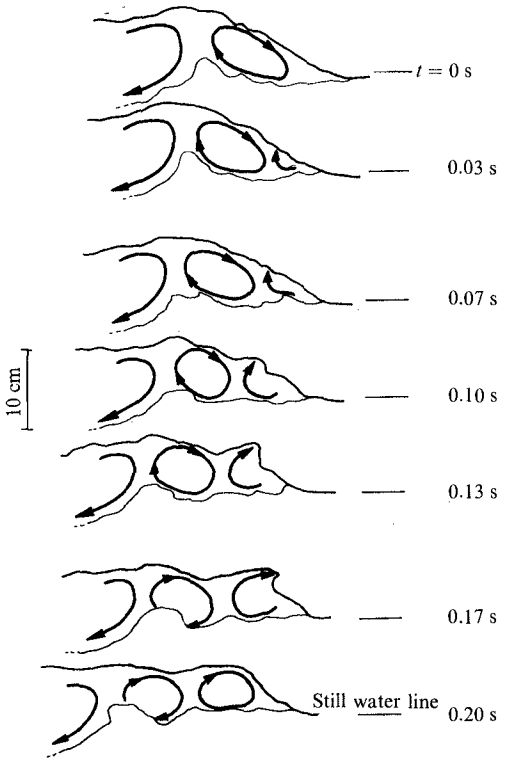

Fig.3 *Pseudo-periodic* generation of large-scale eddies at the bore front (Nadaoka et al., 1989).

$$e_L \cong \frac{\rho}{8}\Gamma_0^2, \tag{6}$$

where r_0 denotes the eddy radius. On the other hand, the number of eddies generated per unit time, n, may be evaluated simply as

$$n \cong \frac{\Gamma_0}{2(\pi r_0)^2}. \tag{7}$$

Therefore, with the assumption that all the kinetic energy of the large-scale eddies is supplied to the turbulence, the production of kinetic turbulent enegy within a wave length per unit time, E_L, is

$$E_L = ne_L \cong \frac{\rho|\Gamma_0|^3}{16(\pi r_0)^2}. \tag{8}$$

The circulation, Γ_0, itself is estimated by equating the vorticity production rate associated with the eddy generation, $n\Gamma_0$, with the mean production rate of the vorticity at the singular point of the bore front, A, as indicated in Fig. 4. The latter may be evaluated as

$$\Omega = \frac{(u_w - c)^2}{2} \tag{9}$$

where c denotes the bore celerity and u_w represents the velocity of orbital motion at A. Equating this with $\Omega = n\Gamma_0$, we obtain

$$\Gamma_0 = \pi r_0(u_w - c). \tag{10}$$

Therefore the turbulence production rate, P_k, is estimated as,

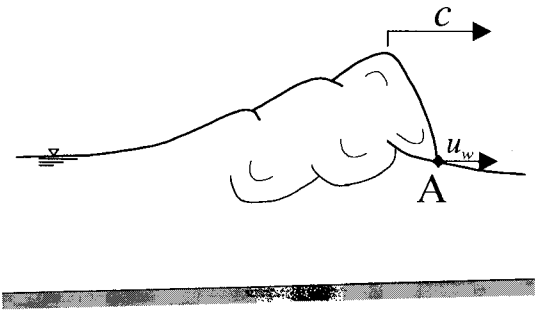

Fig.4 Definition sketch of u_w in a turbulent bore.

$$P_k = \frac{\pi r_0 |(u_w - c)|^3}{16(h+\eta)L_1} \tag{11}$$

where L_1 represents the horizontal length of the vorticity supply region in a wave and is assumed here to be the horizontal length between the zero-up crossing point and the wave crest. Besides the eddy radius, r_0, and the horizontal velocity, u_w, are simply assumed here to be the half of the crest height and zero, respectively. For further improvement of the evaluaiton of P_k, one should develop more reasonable way to specify the location of A and the corresponding values of L_1, r_0 and u_w.

Depth-Integrated Wave Equation

Although the turbulence model described above may be coupled with any depth-integrated time-dependent wave equations including Boussinesq-type equations. In the present study, the new wave model developed by Nadaoka et al.(1994, 1997b) has been used. This wave model can describe nonlinear dispersive waves under general conditions, such as nonlinear random waves with a broad-banded spectrum at an arbitrary depth. Among the various versions of the model, the following multi-component equations are adopted here.

$$\frac{\partial \eta}{\partial t} + \sum_{m=1}^{N} \nabla \cdot \left[\left(\frac{\omega_m^2}{g k_m^2} + \eta \right) \boldsymbol{U}_m \right] = 0, \tag{12}$$

$$\sum_{m=1}^{N} A_{nm} \frac{\partial \boldsymbol{U}_m}{\partial t} + B_n \nabla \left[g\eta + \eta \frac{\partial w_0}{\partial t} + \frac{1}{2} \left(\boldsymbol{u}_0 \cdot \boldsymbol{u}_0 + w_0^2 \right) \right] =$$

$$\frac{\partial}{\partial t} \sum_{m=1}^{N} \left[C_{nm} \nabla (\nabla \cdot \boldsymbol{U}_m) + \boldsymbol{D}_{nm} (\nabla \cdot \boldsymbol{U}_m) \right] + \sum_{m=1}^{M} A_{nm} \nu_t \nabla^2 \boldsymbol{U}_m$$

$$(n = 1,2,\cdots,N) \tag{13}$$

where,

$$\omega_m^2 = g k_m \tanh k_m h, \quad A_{nm} = \frac{\omega_n^2 - \omega_m^2}{k_n^2 - k_m^2}, \quad A_{nn} = \frac{g\omega_n^2 + h\left(g^2 k_n^2 - \omega_n^4\right)}{2g k_n^2},$$

$$B_n = \frac{\omega_n^2}{k_n^2}, \quad C_{nm} = \frac{B_n - A_{nm}}{k_m^2}, \quad \boldsymbol{D}_{nn} = \nabla C_{nn},$$

$$\boldsymbol{D}_{nm} = \frac{2}{k_m^2 - k_n^2} \left[\frac{2\nabla k_m}{k_m} \left\{ A_{nm} - \left(k_m^2 - k_n^2 \right) C_{nm} \right\} + \frac{\nabla h \sqrt{\left(g^2 k_n^2 - \omega_n^4 \right) \left(g^2 k_m^2 - \omega_m^4 \right)}}{g k_n k_m} \right]. \tag{14}$$

$\boldsymbol{u}_0$ and w_0 in eq.(12) are the velocities at z=0 and may be evaluated as

$$\boldsymbol{u}_0 = \sum_{m=1}^{N} \boldsymbol{U}_m, \quad w_0 = -\sum_{m=1}^{N} \nabla \cdot \left(\frac{B_m}{g} \boldsymbol{U}_m \right). \tag{15}$$

The last term in eq.(13) represents the damping effect due to wave breaking.

Wave Breaking Criterion

By developing a method to experimentally evaluate pressure field of irregular waves with a time sequence of the wave profile data, Nadaoka et al. (1997a) found out that at the wave breaking the vertical pressure gradient near the wave crest becomes nearly zero even for irregular waves. This fact may be used as a general wave-breaking criterion which is applicable to regular or irregular and progressive or standing waves. Nadaoka, et al. (1997a) called this criterion "free-fall condition" and showed that the breaker depths computed by eqns. (12) and (13) with this breaking condition give good agreements with those by the Goda (1970)'s empirical breaking criterion. Therefore, in the present study, this free-fall condition has been used to detect the breaking point and to impose the production rate of turbulent kinetic energy, P_k, according to the occurrence of the wave breaking; i.e.,

$$\text{if } -\frac{1}{\rho g}\frac{\partial p}{\partial z}\bigg|_{crest} \le 0, \quad \text{then } P_k \neq 0,$$
$$\text{if } -\frac{1}{\rho g}\frac{\partial p}{\partial z}\bigg|_{crest} > 0, \quad \text{then } P_k = 0. \tag{16}$$

Numerical Examples and Discussion

To demonstrate the fundamental performance of the present model, numerical simulations for various conditions of regular and irregular waves were made both for uniform slope and stepped bottom.

As the most fundamental case, Fig.5 shows the evolution of the spatial distribution of the water surface elevation η and the turbulent kinetic energy k in case of regular waves with T=8s, H_0/L_0=0.02 on a uniform slope of 1:50. At the shore-side end of the slope a shallow horizontal section was connected for better computational performance in the treatment of outgoing waves. The generation of turbulence near the wave crest and its subsequent decay behind the wave crest are reasonably simulated. Figure 6 represents the results for the irregular waves with the Bretschneider spectrum having the significant wave height of 8s. The irregular feature of the occurrence of the wave breaking can be observed with the subsequent development and decay of the turbulence energy. Figure7 shows the results for regular waves with T=8s, H_0/L_0=0.02 on a double step. This is a typical case in which the non-equilibrium feature of the wave evolution becomes appreciable due to the imbalance between the turbulence production and dissipation rates. After the first breaking of waves the turbulence intensity attenuates with the corresponding reform of waves on the step, which is followed by another breaking on the second slope.

Conclusion

With the time-dependent depth-integrated formulation of turbulence, which is to be coupled with nonlinear wave equations, and the development of a method to estimate the turbulence production due to wave breaking, a new model for the breaking wave simulation is presented in this study. As a governing factor to describe

non-equilibrium turbulence evolution of breaking waves on a beach with arbitrary profile, the turbulence production is modeled based on *pseudo-periodic* generation of large-scale eddies at the bore front. Through numerical simulations, the present model has been demonstrated to give favorable features of evolution of regular and irregular breaking waves and the production and diffusion of turbulent kinetic energy.

References

Deigaard, R. (1989): Mathematical modelling of waves in the surf zone, *Prog. Rep.* 69, ISVA, Technical Univ., Lyngby, pp.47-59.

Goda, Y. (1970): A synthesis of breaker indices, *Trans. Japan Soc. Civil Eng.*, No.180, pp.39-49. (in Japanese)

Karambas, T.V. and Houtitas, C. (1992): A breaking wave propagation model based on the Boussinesq equations, *Coastal Eng.*, Vol. 18, pp.1-19.

Madsen, P.A., Sørensen, O.R. and Schäffer, H.A. (1997): Surf zone dynamics simulated by a Boussinesq type model. Part I. Model description and cross-shore motion of regular waves, *Coastal Eng.*, Vol. 32, pp.255-287.

Nadaoka, K., Hino, M. and Koyano, Y. (1989): Structure of the turbulent flow field under breaking waves in the surf zone, *J. Fluid Mech.*, vol.204, pp.359-387.

Nadaoka, K., Beji, S. and Nakagawa, Y. (1994): A fully-dispersive nonlinear wave model and its numerical simulations, *Proc. 24th Int. Conf. on Coastal Eng.*, ASCE, pp.427-441.

Nadaoka, K., Ono, O. and Kurihara, H. (1997a): Near-crest pressure gradient of irregular water waves approaching to break, *Proc. Coastal Dynamics '97*. pp.255-264.

Nadaoka, K., Beji, S. and Nakagawa, Y. (1997b): A fully dispersive weakly nonlinear model for water waves, *Proc. Royal Society of London A*, Vol.453, pp.303-318.

Nwogu, O.K. (1996): Numerical prediction of breaking waves and currents with a Boussinesq model, *Proc. 25th Int. Conf. on Coastal Eng.*, ASCE, pp.4807-4820.

Schäffer, H.A., Deigaard, R. and Madsen, P.A. (1992): A two-dimensional surf zone model based on Boussinesq equations, *Proc. 24th Int. Conf. on Coastal Eng.*, ASCE, pp.576-589.

Svendsen, I.A. (1984):Wave heights and setup in a surf zone, *Coastal Eng.*, Vol.8, pp.303-329.

Svendsen, I.A. (1987): Analysis of surf zone turbulence, *J. Geophys. Res.*, 92, pp.5115-5124.

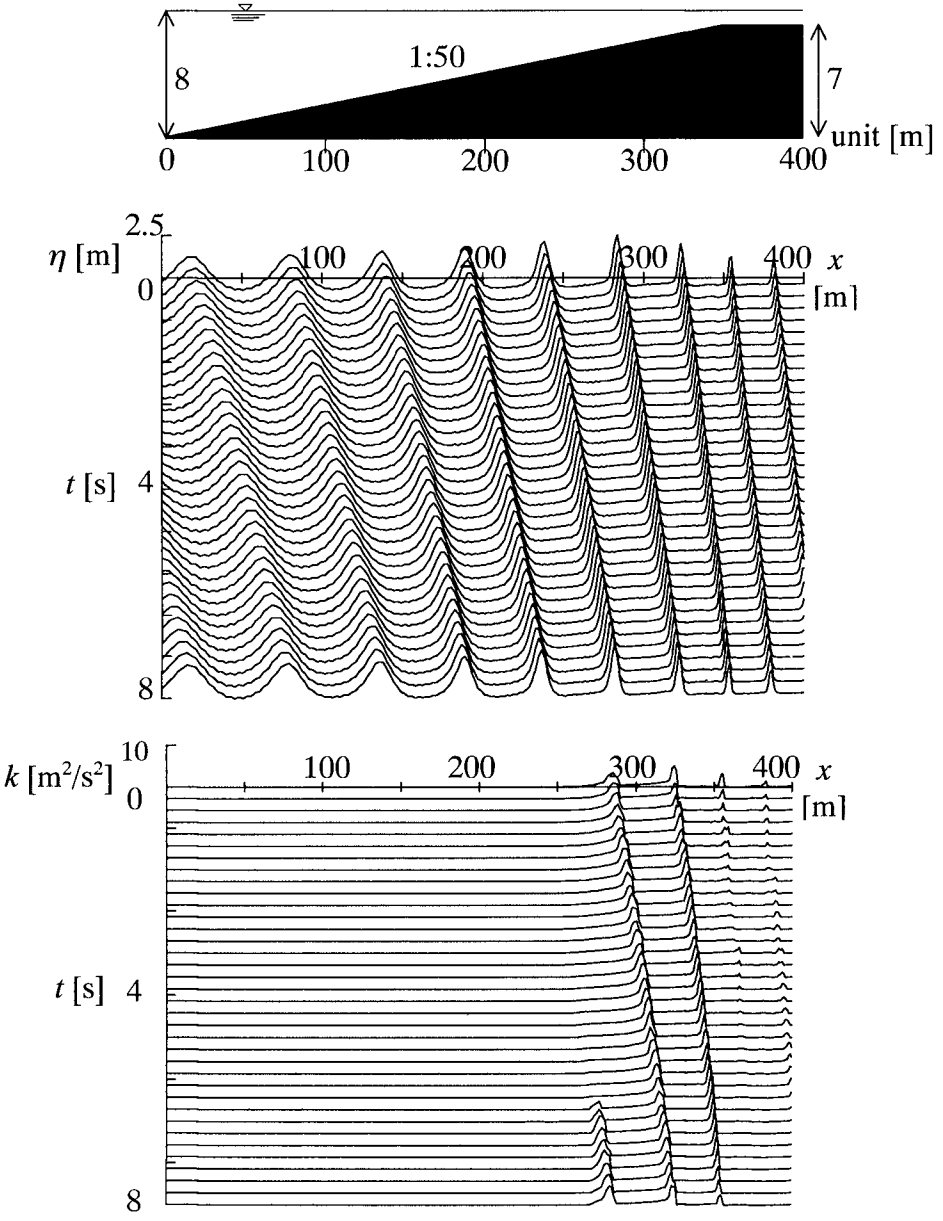

Fig. 4 Regular waves breaking on a uniform slope.

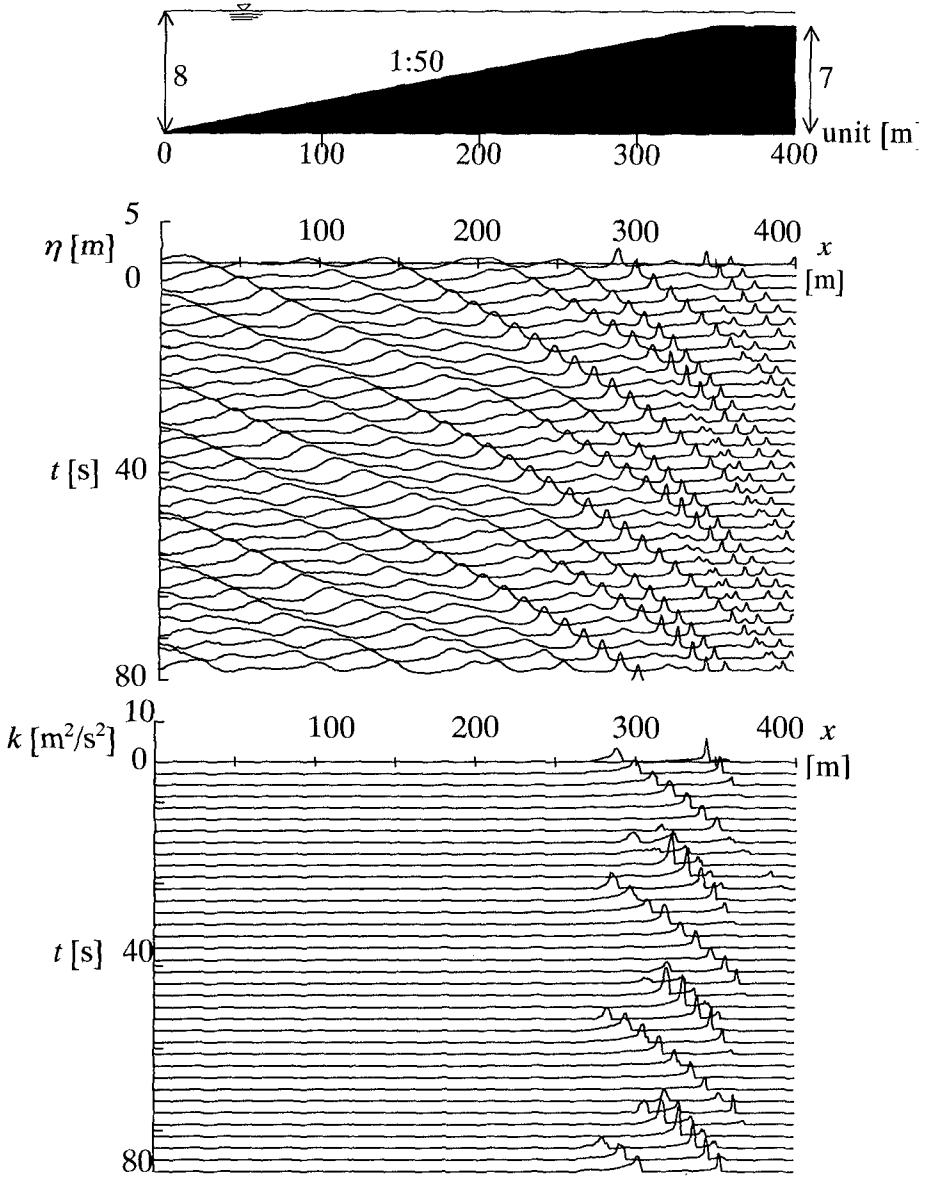

Fig. 5 Irregular waves breaking on a uniform slope.

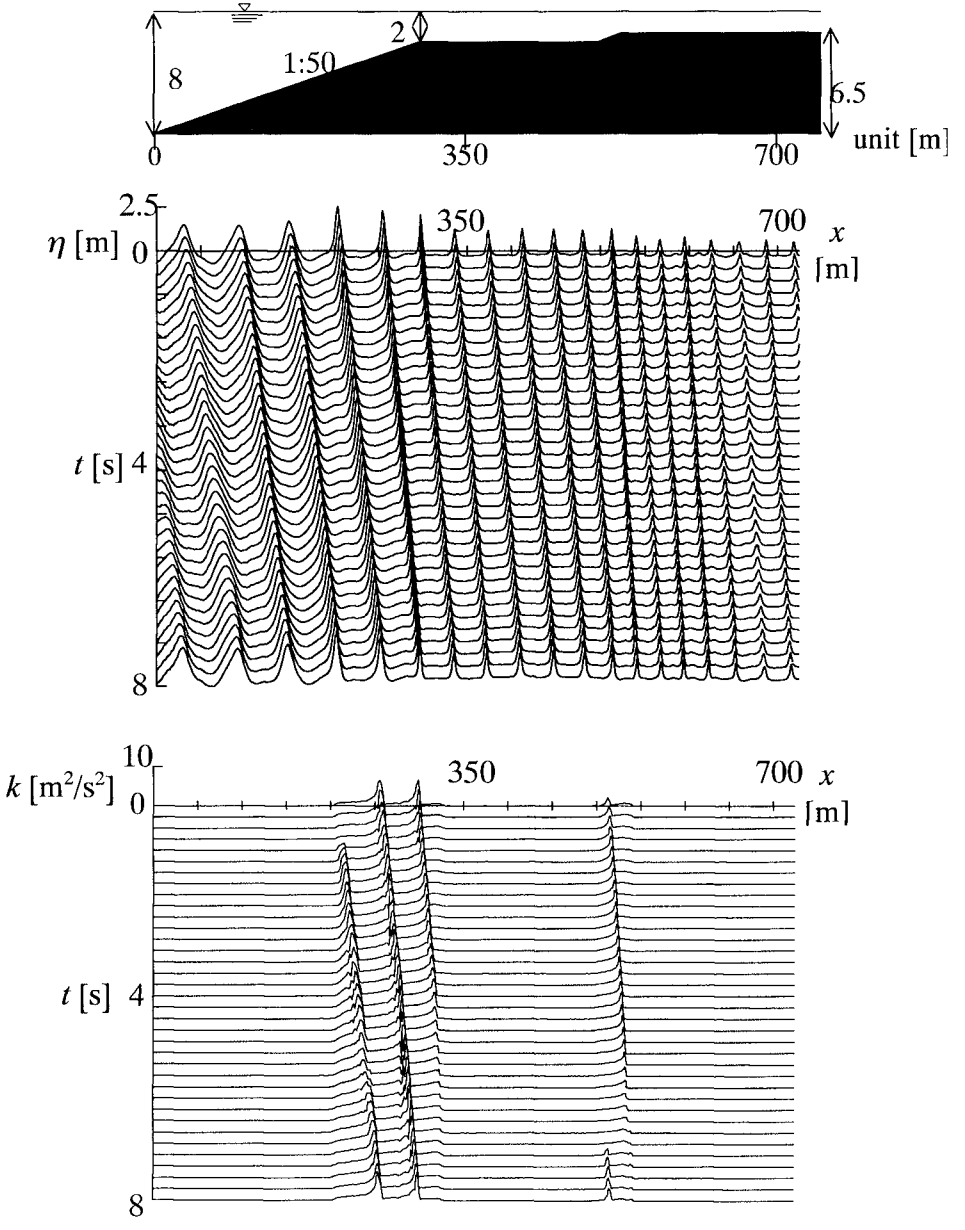

Fig. 6 Regular waves breaking on a stepped beach.

Wave Crest Interaction in Water of Intermediate Depth

C.C.Bird [†] and D.H.Peregrine [‡]

Abstract

Numerical computations using a fully nonlinear potential flow solver are carried out on water of intermediate depth. Properties of single and multiple wave groups are examined on horizontal and sloping beaches. Comparisons are made with linear and weakly nonlinear theories. An important result is that the increase in wave amplitude due to wave shoaling is likely to be much less than the linear theory result for short steep wave groups because of the tendency for the group to spread.

Introduction

This paper is part of a series of studies of waves on a beach, which aims to learn more of finite amplitude effects on irregular waves. It follows Bird & Peregrine (1997) where attention is directed towards the long waves associated with and generated by a single wave group. Here the waves within one or more wave groups are studied in water of intermediate depth, that is for $1.36 > kh > \approx 0.7$, where h is the water depth and k is the wavenumber.

The characteristic behaviour of wave groups on deep water differs greatly from that on shallow water. On deep water the waves are dispersive, and thus their energy travels at a speed different from that of the individual waves. Typically the group and its energy travel at half the speed of the individual waves in that group (the group velocity concept). In wave groups where the wave number is constant, the individual waves do not meet, and their interaction is in the form of energy 'slipping' back through the group relative to the wave crests.

[†]Research Student, School of Mathematics, University of Bristol, University Walk, Bristol, BS8 1TW, UK *(C.C.Bird@bristol.ac.uk)*

[‡]Professor of Applied Mathematics, School of Mathematics, University of Bristol *(D.H.Peregrine@bristol.ac.uk)*

In shallow water, energy flows with the wave crests. In the Boussinesq region, which often occurs before the waves break, the waves are typically solitary type waves, and as is described by two-soliton solutions of the Korteweg-de-Vries equation, they may merge temporarily if a wave of high amplitude catches up a smaller one ahead of it. However, unless the waves break at the point at which they merge, they separate again, suffering only a change of phase. The case of two waves of almost equal amplitude is slightly different; the solution of the KdV equation indicates if such waves are close, then they do not merge, but exchange amplitudes and shift phases as if they had. Figure 1 shows an example of the first case, computed using a fully nonlinear potential flow solver (described in a later section). Successive surface elevation profiles are plotted, shifted with time. The initial conditions consist of a single group of 5 modulated solitary waves, a large central one and much smaller outer waves. A small amount of set down is added, but not enough to balance the mass of the waves. They are propagated on a beach of slope 1:60. It is clear to see that the largest wave merges with the one ahead of it. The waves have almost passed through each other when the largest one breaks.

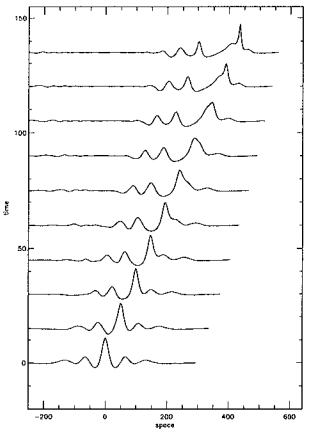

Figure 1: Surface elevation profiles of a single wave group progressing up a 1:60 beach.

After breaking, waves can be modelled by bores (discontinuites of the shallow water equations). Bores frequently catch up one another and merge. This has been observed in the field study carried out by Packwood and Peregrine in 1980; some details are given in Peregrine (1998). Unlike solitary waves however, a merged bore retains its unity. Peregrine (1974) uses invariants of the nonlinear shallow water equations to show that in this situation, a small backward travelling wave of depression is formed

at the merger.

However, the present topic of interest is the region between deep water and the Boussinesq regime, ie. intermediate depth water. Barnes & Peregrine (1995) used a fully nonlinear potential flow model to study the progress of individual wave groups travelling up a plane beach in the context of low frequency waves. Instead of the converging type behaviour seen in figure 1, they noted that the group and its energy appeared to spread significantly, and also that the waves shoaled far less than is predicted by (regular wave) linear theory. We address these last points by carrying out computations using the same nonlinear potential flow solver. Both single and multiple wave groups are considered, on horizontal and sloping beaches. It is useful to examine the behaviour of groups over a horizontal bed in order to clarify the processes at work since then the effect of the slope is separated out. But first we briefly review the relevant theory for wave groups.

Brief review of applicable linear and weakly nonlinear theory

To model modulated waves it is useful to consider the wave elevation to be described by

$$\eta(x,t) = A(X,T)e^{i(kx-\omega t)} \quad + \quad complex\ conjugate \tag{1}$$

(eg. see Mei, 1983). Here X and T represent the 'slow' space and time coordinates, and ω and k are related by the dispersion equation

$$\omega^2 = gk\tanh(kh) \tag{2}$$

The water depth h is a function of the slow space variable, ie. $h(X)$, and g is the gravitational acceleration.

From the assumption of slow variations of the wave amplitude A, linear theory gives a first approximation:

$$\frac{\partial A}{\partial T} + c_g\frac{\partial A}{\partial X} = 0; \qquad c_g = \frac{\partial \omega}{\partial k} \tag{3}$$

This result corresponds to geometrical ray theory if extended to two dimensions. It gives the usual linear shoaling theory for varying depth, and indicates that a wave group simply translates with the group velocity c_g. As already noted, unless kh is small, the wave speed $c = \omega/k \neq c_g$.

Including the next linear terms in the slow modulation approximation gives

$$\frac{\partial A}{\partial T} + c_g\frac{\partial A}{\partial X} = \frac{i}{2}\omega''\frac{\partial^2 A}{\partial X^2}; \qquad \omega'' = \frac{\partial^2 \omega}{\partial k^2} \tag{4}$$

which is a Schrödinger equation, or a linear parabolic wave equation. The extra term on the right hand side gives an extra dispersion to the wave groups.

Including weakly nonlinear terms in the above approximation gives

$$i\frac{\partial A}{\partial T} + ic_g\frac{\partial A}{\partial X} + \frac{1}{2}\omega''\frac{\partial^2 A}{\partial X^2} = \lambda|A|^2 A \tag{5}$$

a nonlinear Schrödinger (NLS) equation. Here λ is a function of kh. In deep water, $\omega'' < 0$ and the equation has soliton solutions corresponding to special groups that propagate unchanged. This equation then gives the Benjamin-Feir modulational instability, which can also be described as 'self-focussing' of the waves. However for intermediate water depths, $kh < 1.36$, ω'' has the opposite sign, and the equation has a more stable 'defocussing' character. This aspect of wave modulations can be seen in the following computations with an accurate flow solver.

The numerical model

The computations were carried out using an accurate fully nonlinear irrotational flow solver. This is able to solve from deep water up to the first occurrence of wave breaking. The spatial domain is of finite length, bounded by uniform conditions.

The fluid is considered to be two-dimensional, inviscid, incompressible and irrotational, and surface tension is neglected. Defining points (x, y) on the free surface by $(X(s,t), Y(s,t)) = \mathbf{R}(s,t)$, where s is a particle-following (Lagrangian) coordinate, we have:

$$\nabla^2\phi = 0 \quad \text{in fluid body} \tag{6}$$

$$\frac{D\mathbf{R}}{Dt} = \nabla\phi \quad \text{on free surface} \tag{7}$$

$$\frac{D\phi}{Dt} = \frac{1}{2}|\nabla\phi|^2 - gY \quad \text{on free surface} \tag{8}$$

with the appropriate bed boundary conditions. The velocity potential is represented by $\phi(x, y, t)$.

If the spatial domain is a plane sloping beach, then the model first transforms this into a horizontal plane using a conformal mapping. The above system of equations is solved using a Cauchy theorem boundary integral, and hence the velocity at the free surface is computed. The surface is then stepped in time using a Taylor series truncated at the sixth order. Further details may be found in Tanaka *et al.* (1987) and Cooker (1990).

A single wave group propagated on a horizontal bed

Once one departs from considering a regular periodic wave train there is a huge range of incident waves that may be considered. For simplicity and uniformity we have

chosen initial conditions in the form of a wave group with the surface properties of the deep water soliton of the same steepness, ie. to linear approximation

$$\eta(x,0) = \frac{1}{2}\left(a \operatorname{sech}\left(\sqrt{2}ak^2x\right) e^{ikx} + c.c.\right) \quad (9)$$

$$\phi(x,0) = -\frac{g}{2\omega}\left(ia \operatorname{sech}\left(\sqrt{2}ak^2x\right) e^{ikx} + c.c.\right). \quad (10)$$

The subsurface velocities adjust appropriately in the computation when the frequency ω comes from the linear dispersion relation given above (equation 2), chosen to be appropriate to the depth.

In the initial conditions the higher order corrections to equations (9) and (10) were not fully included. Usually only the second harmonic terms were added, thus generation of associated long waves occurs. See Bird & Peregrine (1997) for discussion of this feature.

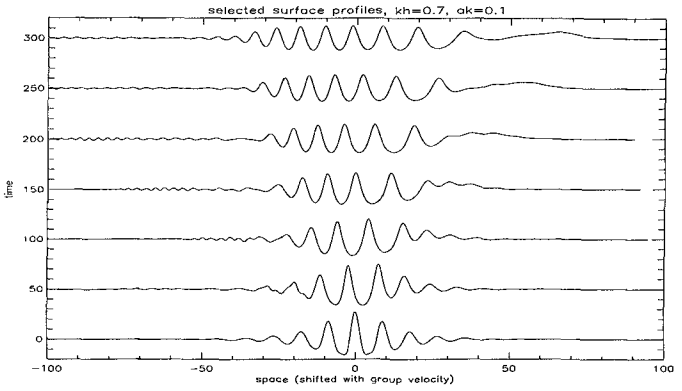

Figure 2: Selected surface profiles for single wave group progressing over a horizontal bed, in a frame of reference moving with the group velocity.

Results from a typical computation over a horizontal bed are given in figure 2. Selected surface profiles illustrate the progress of the free surface with time. Time in non-dimensionalised units ($t^* = t/\sqrt{h/g}$) is shown on the relevant axes. We summarize results from several such computations.

In every case the expected defocussing, or spreading out of the group is evident. Such behaviour might be expected to scale with the Ursell number, $Ur = a/k^2h^3$, but it depends most strongly on wave steepness ak, and less so on Ur or kh. As Peregrine (1983) notes, all NLS equations can be transformed to the same canonical form, with either a + or − sign for the nonlinear terms. The canonical equation can then have any solution transformed in the wave amplitude, space and time to give a

whole family of solutions, depending on amplitude as a parameter. Here, because of the dependence of ω'' and λ on kh such transformations do not give any particularly simple result. However, they do show that if the waves are not too steep or long, e.g. $Ur < 0.3$ then this defocussing behaviour is to be expected from our knowledge of solutions of NLS equations.

Linear theory is appropriate for small waves at the margins of a wave group, and hence, as we can expect, for a lengthening group the waves at the front of each group are longer than those at the rear. The additional trailing group of very short waves comes from the waves' requirement for bound high harmonics that were not included in the initial conditions. Corresponding short free waves are emitted. Similarly, the long set-down wave was not included and a free long wave can be seen emerging from the front of the group, see Bird & Peregrine (1997) for more details.

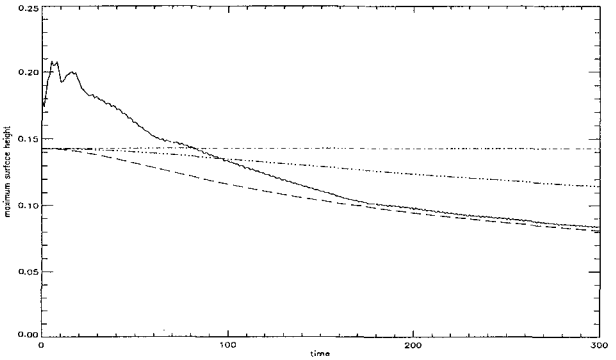

Figure 3: Maximum wave amplitude of a single wave group progressing over a horizontal bed; solid = fully nonlinear method, dash dot = basic linear theory, dash dot dot dot = linear theory including higher order dispersion, dash = weakly nonlinear theory (NLS).

The maximum surface height as computed by the fully nonlinear potential flow solver, is compared with the the theories described in the previous section (linear, linear with higher order dispersion, weakly nonlinear) in figure 3. A method by Taha & Ablowitz (1984) is used to compute solutions of the nonlinear Schrödinger equation; this is easily adjusted to compute the solutions to the linear equations. Since no higher order correction terms were added to the initial conditions when computing the solutions to the approximate theories, there is a difference in the initial heights of the surfaces.

A more accurate description of the value plotted for the fully nonlinear method is that it is of the highest grid point, and since no interpolation is carried out, this differs slightly from the maximum height of the surface. This results in the small

oscillations evident on this plot. The larger oscillations are due to the difference in the phase and group velocities of the waves. Individual waves still pass through the group in the manner described above for deep water (although they no longer travel at twice the speed of the group), and thus the largest wave persists only for a limited time, marked by the length of these oscillations. These oscillations are not seen in the solutions to the theories since these give only details of the wave envelope rather than the individual waves.

We can see that the NLS equation gives a good approximation after the initial transients whereas the linear theories are poor. From consideration of other examples we find that the basic linear theory is adequate only for very gentle waves which, because of our special choice of initial conditions, also corresponds to very long groups. The linear theory with higher-order dispersion is noticeably better, and in a number of cases is almost as good as the NLS.

Three wave groups propagated on a horizontal bed

Here the initial conditions consist of three envelope soliton groups alongside each other, centred a distance of 6 or more wavelengths apart. These distances were chosen to ensure that the groups were sufficiently far enough apart to have initial identities, but not so far apart as to prevent significant interaction between them. The example presented has the same initial wave steepness and depth as that in the section on single groups above. Again terms of the second harmonics are added. This example is illustrated in figures 4 and 5.

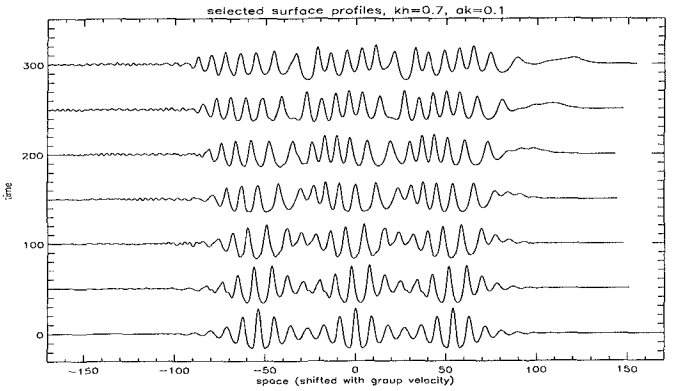

Figure 4: Selected surface profiles for three wave groups progressing over a horizontal bed in a reference frame moving with the group velocity.

Selected profiles illustrating the progression of the surface elevation in time are given in figure 4. Again the groups spread to varying degrees depending on their initial

steepnesses, but the interactions between the waves slightly limit this effect. The individual waves interact with each other. Initially waves in each group are in phase, but the phase changes involved in the spreading out of the groups lead to significant irregularities as the groups overlap.

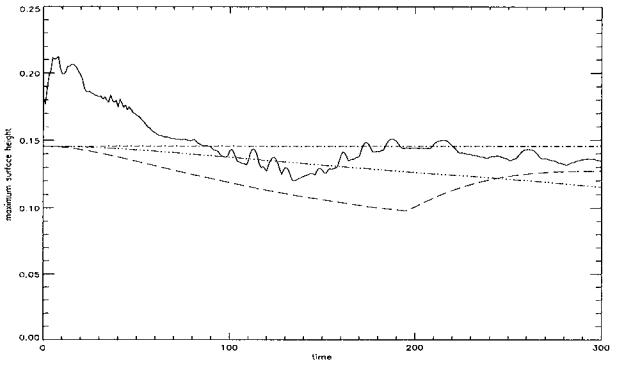

Figure 5: Maximum wave amplitude of three wave groups progressing over a horizontal bed; solid = fully nonlinear method, dash dot = basic linear theory, dash dot dot dot = linear theory including higher order dispersion, dash = weakly nonlinear theory (NLS).

The maximum surface height of the wave group as computed by the fully nonlinear potential flow solver is compared with the basic linear, linear with higher order dispersion and weakly nonlinear theories in figure 5. In the fully nonlinear plots we observe additional oscillations on different (and varying) lengthscales from the short and long ones discussed above for single wave groups. These are due to both the forward travelling free long waves passing through the groups and elevating individual waves for short periods of time, wave interference, and differing modulations giving the highest wave. This latter behaviour is the source of the large kink in each of the nonlinear curves in figure 5.

The basic linear theory is slightly more successful in predicting the maximum wave amplitude, as it is generally slightly higher than for an isolated group. However, the envelopes of the steeper groups do not progress without change of form, thus basic linear theory is still not appropriate for changes on these length scales. Again the weakly nonlinear theory and the linear higher order dispersion theory perform better. One of the reasons for this is the inability of the theories to model the free long waves and harmonics which emerge from the group. We have already noted that the long waves computed in the fully nonlinear computation pass through the group and elevate individual waves, thus effectively increasing the maximum surface elevation. The long waves are higher for the steeper groups, and so it is for these groups that we see the greater difference in maximum amplitude. However, modulation equations

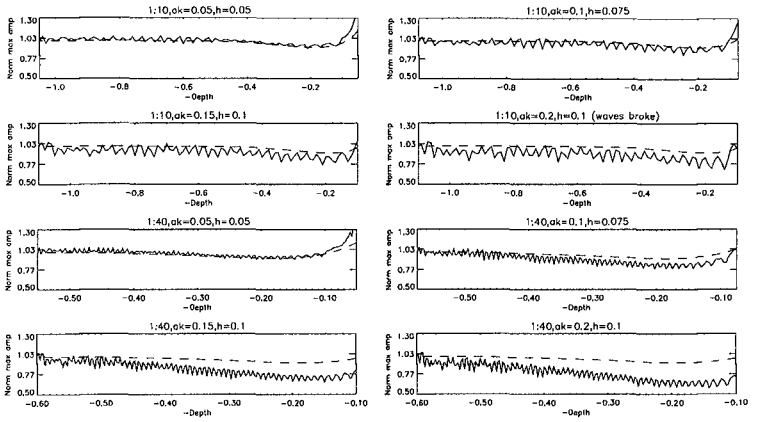

Figure 6: Normalised maximum amplitude of single wave groups progressing on a plane beach (solid line), shoaling coefficient (dashed line).

corresponding to the NLS level of approximation can model the long waves. Such free long waves and very short waves are also generated in real situations of depth variation.

So in summary, the multiple groups spread out slightly less than isolated groups of the same steepness on the same depth. The maximum surface elevation is higher, due to the interactions between the waves. Basic linear theory is again the least appropriate for the steeper groups. Both linear theory which includes higher order dispersion and the weakly nonlinear theory are more successful, but the free long waves formed by the group are important.

A single wave group propagated on a plane sloping beach

In this section we repeat and extend some of the computations of Barnes & Peregrine (1985). The bed topography is a sloping beach leading onto a shelf of constant depth. The initial condition is a single deep water envelope soliton, with no added higher order terms. Beach slopes of 1:10 and 1:40 are used. The beach corners are located at $x = 10$ for the 1:10 beach and $x = 20$ for the 1:40 beach. The depth of the water at the centre of the group's initial position may be computed by adding the shelf depth h (indicated in figures 6 and 9) to either 1.0 for the 1:10 beaches or 0.5 for the 1:40 beaches. This means that the groups start in a water depth of at least half a wavelength.

Figure 6 shows a comparison between the linear shoaling coefficient (dashed line) and the shoaling of the computed wave groups (solid line), calculated as the maximum surface elevation at each depth. The irregularity of the computational results is due both to the irregularities explained earlier, and to the finite intervals at which the computation is sampled. We note that the maximum surface elevation increases quite suddenly and significantly as the waves propagate on the constant depth shelf. It is easy to verify the conclusions of Barnes & Peregrine (1995), that shorter, steeper groups spread out and thus shoal much less than longer, less steep groups, and that this effect is more marked on gentle beaches. After considering the horizontal bed case, this conclusion is not surprising. The group does not encounter other waves around it as it spreads and thus cannot interact with any other waves. On a gentler beach the group spreads more since it has more time in which to spread.

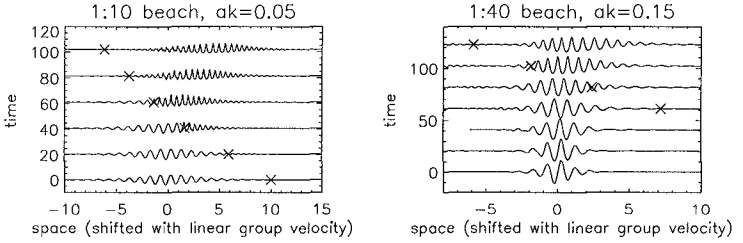

Figure 7: Selected surface profiles for single wave groups progressing on a plane beach. 'x' marks the beach corner position.

Selected surface profiles from two of the examples are shown in figure 7. The space coordinate has been shifted with linear group velocity, and thus we mark the beach corner position (ie. that point where the slope changes to constant depth shelf) by crosses. It is easy to see the transformation of the sinusoidal waves to near solitary type waves in the shallowest water.

Many of the features of the groups observed on the horizontal bed topography may be seen here too in our full range of examples. The steeper groups spread more than the shallower ones; again the wave groups formed of waves of steepness $ak = 0.05$ barely spread at all. Higher-order harmonic corrections are emitted from the back of the group, as before, but there is no easily visible evidence of free long waves until the group passes onto the shelf. Longer waves are towards the front and shorter waves towards the back of the group while it is on the sloping section, and the envelope becomes asymmetric. However as the waves pass onto the shelf, their wavelength reduces (in addition to their amplitude suddenly increasing). This is quite dramatic in the cases of the wave groups of steepness $ak = 0.05$, due to particularly shallow depth chosen for those shelves. On a plane beach without a shelf, breaking would occur just after the point where the corner is placed.

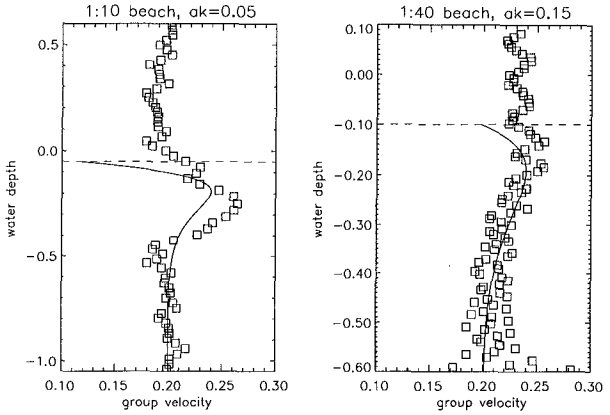

Figure 8: Speed of single wave group progressing on a plane beach (squares), linear group velocity (solid line).

It is easy to observe that the group does not always travel with the linear group velocity. The trend is for the group to travel a little slower than c_g shortly before it reaches the shelf, and faster as it passes onto and travels along the shelf. This may be observed more clearly in figure 8, which compares the speed of the computed groups (squares) with the linear group velocity (solid line). The dotted line represents the start of the shelf; above it the depth is constant (the markings on the vertical axis are inappropriate there).

The speed of the computed groups is estimated as follows: at each time, a Hilbert transform of the surface elevation is taken to give the group envelope. Since the waves are nonlinear, this envelope is very 'noisy', and so we use a Fourier filter to remove the higher harmonics. We denote the position at which this smoothed envelope has a maximum to be the centre of the group. Numerically differentiating the positions of the group centres with respect to time gives the group velocity.

It is not very surprising that the comparison is poor at the shallower depths; with the waves being more nonlinear there (behaving more as individual solitary-type waves) we can expect the linear group velocity concept to fail.

In summary, the maximum amplitude of a single wave group propagated up a sloping beach is almost always less than that predicted by the linear shoaling coefficient. This effect is most marked for steep groups on gentle beaches, but is not surprising, since the regular wave theory is least appropriate for short isolated wave groups. Many of the features of the groups observed on the horizontal beach are also seen on the

sloping beach. The group travels with the linear group velocity in deeper water, but not in shallower water where we may expect the group velocity concept to fail.

Three wave groups propagated on a plane sloping beach

Here the initial conditions were formed of 3 adjacent envelope soliton groups, again with no higher harmonic corrections added, spaced by either 10 wavelengths ($ak = 0.05$) or 6 wavelengths (other steepnesses). We choose the same combinations of beach slopes and wave steepnesses as for the single groups, except that for the case of beach slope 1:10, initial wave steepness $ak = 0.05$, the beach corner is now located at $x = 15.0$.

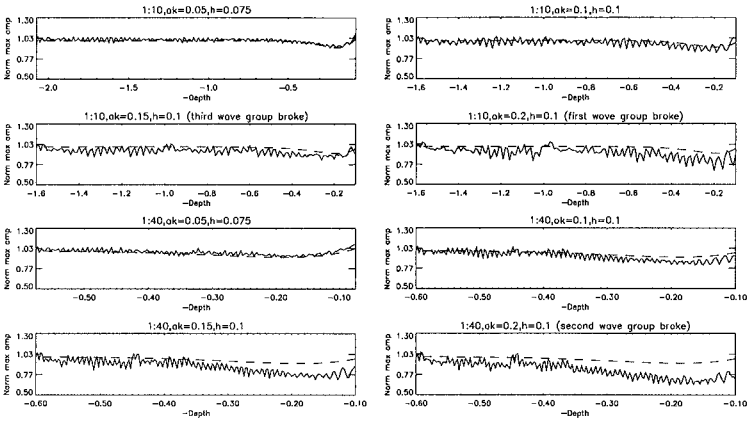

Figure 9: Normalised maximum amplitude of three wave groups progressing on a plane beach (solid line), shoaling coefficient (dashed line).

A comparison between the shoaling coefficient and the maximum height of the computed surface is shown in figure 9. The results are very similar to those for the isolated groups (see figure 6); the computed maximum amplitudes are generally slightly higher for 3 groups than for one, but the differences are quite small.

Examining the surface profiles shown in figure 10, it is not difficult to see why the changes are small: there is not enough time for any significant interactions between the waves to occur, unlike the horizontal bed case. Also there are no significant long waves to raise the individual waves of the group, as there was on the horizontal bed. The tendency of the very short steep groups to spread is very strong, with the maximum amplitude below the shoaling coefficient, as before.

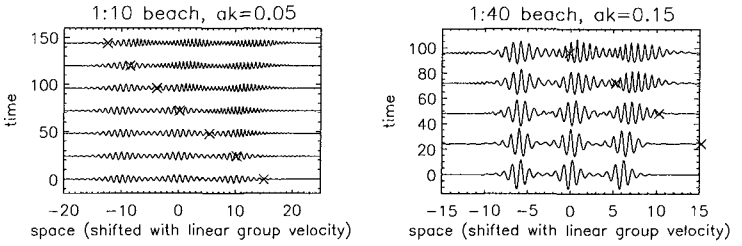

Figure 10: Selected surface profiles for three wave groups progressing on a plane beach. 'x' marks the beach corner position.

Conclusions

We have examined the behaviours of wave groups in water of intermediate depth. Features of both the deep water and Boussinesq type behaviours were evident; however the primary area of concern was the differences between the linear shoaling coefficient and the shoaling of the computed groups. It was noted that basic linear theory is the least appropriate for short, steep isolated groups and that on a horizontal bed, both linear theory including higher order dispersion and the weakly nonlinear theory give better results. The differences with the linear shoaling theory were explained by the tendency of the groups to spread and the lack of interaction with other waves; the differences are smaller when the initial conditions consisted of three wave groups instead of just one. An important result is that the increase in wave amplitude due to wave shoaling is likely to be much less than the linear theory result for short steep wave groups because of the tendency for the group to spread.

Acknowledgements

We are grateful for support from an EPSRC studentship, from the U.S Office of Naval Research, NICOP Grant N00014-97-1-0791 and European Commission research grant MAS3-CT97-0081 (SASME).

References

T.C.D. BARNES and D.H. PEREGRINE. Wave groups approaching a beach: Full irrotational flow computations. *Proc. of Coastal Dynamics, 116-127,* (1995).

C.C. BIRD and D.H. PEREGRINE Wave groups from Deep to Shallow water. *Proc. of Coastal Dynamics, 1013-1022,* (1997).

M.J. COOKER. A boundary integral method for water wave motion over irregular beds. *Engineering Analysis with Boundary Elements,* **7(4):** *178-195,* (1990).

C.C. MEI. The Applied Dynamics of Ocean Surface Waves. John Wiley & Sons, (1983).

D.H. PEREGRINE. Water-wave interaction in the surf zone. *Proc. 14th Coastal Eng. Conf.,* **1:** *500-517,* (1974).

D.H. PEREGRINE. Water waves, nonlinear Schrödinger equations and their solutions. *J. Austral. Math. Soc. Ser. B,* **25:** *16-43,* (1983).

D.H. PEREGRINE. Surf Zone Currents. *Theoretical and Computational Fluid Dynamics,* **10:** *295-309,* (1998).

T.R. TAHA and M.J. ABLOWITZ. Analytical and numerical aspects of certain nonlinear evolution equations II: Numerical, nonlinear Schrödinger equation. *J. Comp. Phys.,* **55:** *203-230,* (1984).

M. TANAKA, J.W. DOLD, M. LEWY and D.H. PEREGRINE. Instability and breaking of a solitary wave. *J. Fluid Mech.,* **185:** *235-248,* (1987).

Energy Dissipation Model for Irregular Breaking Waves

Winyu Rattanapitikon[1] and Tomoya Shibayama[2]

Abstract

A simple model is presented to compute the average rate of energy dissipation in irregular breaking waves. The average rate of energy dissipation rate is assumed to be proportional to the difference between the local mean energy flux and stable energy flux. The local fraction of breaking waves is determine from the derivation of Battjes and Janssen (1978). Root mean square wave height deformation is computed from the energy flux conservation. The model is validated using root mean square wave height data from small and large scale laboratory and field experiments. Total 144 wave height profiles are used in the calibration and verification of the model. Reasonable good agreement is obtained between the measured and computed root mean square wave heights. The root mean square relative error of the model is 10.2 %.

1. Introduction

In studying many coastal engineering problems it is essential to have accurate information on wave conditions. When waves propagate to the shore, they increase in height and decrease in length wave and eventually waves break. Once the waves start to break, energy flux from offshore is dissipated to turbulence and heat and causes the decreasing of wave height towards the shore in the surf zone. Irregular wave breaking is more complex than regular wave breaking. In contrast to regular waves there is no well-defined breaking point for irregular waves. The highest waves tend to break at greatest distances from the shore. Thus, the energy dissipation of irregular waves occurs over a considerably greater area than that of regular waves.

---

[1] Asst. Prof., Dept. of Civil Engineering, Sirindhorn International Institute of Technology, Thammasat University, Klong Luang, Phatum Thani 12121, Thailand.
[2] Prof., Dept. of Civil Engineering, Yokohama National University, 79-5 Tokiwadai, Hodogaya-ku, Yokahama 240-8501, Japan.

For computing beach transformation, the wave model should be kept as simple as possible because of the frequent updating of wave field for accounting the variability of mean water surface and the change of bottom profiles. In the present study, wave height transformation is computed from the energy flux conservation:

$$\frac{\partial\left(Ec_g \cos\theta\right)}{\partial x} = -\overline{D}_B \tag{1}$$

where E is the wave energy density, c_g is the group velocity, θ is the mean wave angle, x is the distance in cross-shore direction, and $\overline{D}_B$ is the average energy dissipation rate of the breaking waves. Snell's law is employed to describe wave refraction.

The wave height transformation can be computed from the energy flux balance equation (Eq. 1) by substituting the formula of the average energy dissipation rate, $\overline{D}_B$, and numerical integrating from offshore to shoreline. The main difficulty of energy flux conservation approach is how to determine the average energy dissipation rate, $\overline{D}_B$. Owing to the complexity of wave breaking mechanism, an empirical approach based on measured data is the only feasible way of describing the energy dissipation rate.

In order to make the empirical formula reliable, it is necessary to calibrate or verify that formula with wide range of experimental results. Since many energy dissipation models were developed based on data with the limited experimental conditions, there is still a need for more data to confirm the underlying assumptions and to make the model more reliable. The main target of this study is to develop the energy dissipation model based on wide range of experimental conditions. Small and large scale laboratory and field experiments have been collected for calibration and verification of the present models. A summary of the collected experimental results is given in Table 1.

Table 1. Summary of collected experimental data used to validate the present models.

Sources	Total No. of cases	Bed condition	Apparatus
SUPERTANK project (Kraus and Smith, 1994)	128	sandy beach	large-scale
Smith and Kraus (1990)	12	plane and barred beach	small-scale
Thornton and Guza (1986)	4	sandy beach	field
Total	144		

The energy dissipation model of irregular breaking wave will be developed based on a similar concept as regular breaking wave model of the authors. The summaries of related regular wave models are as follows.

a) Dally et al. (1985) assumed D_B is proportional to the difference between the local energy flux and the stable energy flux of breaking wave:

$$D_B = \frac{K_d c_g \rho g}{8h}\left[H^2 - (\Gamma h)^2\right] \tag{2}$$

where all variables are computed based on linear wave theory, K_d is the wave decay factor (=0.15), H is the local wave height, h is the local water depth, Γ is the stable wave factor (=0.4).

b) Rattanapitikon and Shibayama (1996) modified the model of Dally et al. (1985) and proposed to compute the stable wave factor, Γ:

$$\Gamma = \exp\left[-0.36 - 1.25\frac{h}{\sqrt{LH}}\right] \tag{3}$$

where L is the wavelength.

Nine sources of published laboratory results, totally 332 wave profiles, were used to verify the formula.

2. Model Development

Dally (1992) used the regular wave model of Dally et al. (1985) to simulate transformation of irregular wave by using wave-by-wave approach. This means that Dally assumed that D_B is proportional to the difference between local energy flux of a breaking wave and stable energy flux. Also wave-by-wave approach requires much computation time. Therefor it may not suitable to use in a beach deformation model.

However, the model becomes simple if we consider the macro-features by set an assumption that the average rate of energy dissipation in irregular breaking waves is proportional to the difference between local mean energy flux and stable energy flux. After incorporating the fraction of breaking, the average rate of energy dissipation in irregular wave breaking, $\overline{D}_B$, can be expressed as

$$\overline{D}_B = \frac{K_1 Q_b c_g}{h}\left[E_m - E_s\right] \tag{4}$$

where

$$E_m = \frac{1}{8}\rho g H_{rms}^2 \tag{5}$$

$$E_s = \frac{1}{8}\rho g H_s^2 = \frac{1}{8}\rho g(\Gamma_{ir} h)^2 \tag{6}$$

in which all variables are computed based on the linear wave theory, K_1 is the proportional constant, Q_b is the fraction of breaking waves, c_g is the group velocity related to the peak spectral wave period T_p, E_m is the local mean energy density, E_s is the stable energy flux, H_{rms} is the root mean square wave height, H_s is the stable wave height and Γ_{ir} is the stable wave factor of irregular wave.

Rewriting Eq. (4) in term of wave height:

$$\overline{D}_B = \frac{K_1 Q_b c_g \rho g}{8h}\left[H_{rms}^2 - (\Gamma_{ir} h)^2\right] \tag{7}$$

The stable wave factor, Γ_{ir}, is determined by applying Eq. (3) as

$$\Gamma_{ir} = \exp\left[K_2(-0.36 - 1.25\frac{h}{\sqrt{L_p H_{rms}}})\right] \tag{8}$$

where K_2 is the coefficient, L_p is the wavelength related to the peak spectral wave period.

The local fraction of breaking waves, Q_b, is the ratio of the number of breaking waves to the total number of waves. To determine the fraction of breaking waves, Battjes and Janssen (1978) assumed that the probability density function of wave heights is the Rayleigh-type. The fraction of breaking waves is derive based on the assumption of truncated Rayleigh distribution at the breaking wave height:

$$\frac{1-Q_b}{-\ln Q_b} = \left(\frac{H_{rms}}{H_b}\right)^2 \tag{9}$$

where H_b is the breaking wave height.

Various empirical formulas have been proposed to compute the breaking wave height, e.g., Goda (1970), Weggel (1972), Singamsetti and Wind (1980), and Hansen 1990. However there is no conclusion that which one is the best. Since the breaking criterion of Goda (1970) was developed from wide range of experimental results, it is selected for inclusion into the present model. The breaking criteria of Goda (1970) is

$$H_b = K_3 L_o\left\{1 - \exp\left[-1.5\frac{\pi h}{L_o}\left(1 + 15m^{4/3}\right)\right]\right\} \tag{10}$$

where K_3 is the coefficient, L_o is the deep-water wavelength, and m is the bottom slope. The published value of K_3 is 0.17 for regular breaking waves. For the present study, K_3 is the adjustable coefficient to allow for effect of the transformation to irregular waves.

Since Eq. (9) is an implicit equation, the iteration process is necessary to compute the fraction of breaking waves, Q_b. It will be more convenient if we can compute Q_b from the explicit form of Eq. (9). From the multi-regression analysis, the explicit form of Q_b can be expressed as the following (with R^2 =0.999):

$$Q_b = \begin{cases} 0 & for \dfrac{H_{rms}}{H_b} \le 0.43 \\ -0.738\left(\dfrac{H_{rms}}{H_b}\right) - 0.280\left(\dfrac{H_{rms}}{H_b}\right)^2 + 1.785\left(\dfrac{H_{rms}}{H_b}\right)^3 + 0.235 & for \dfrac{H_{rms}}{H_b} > 0.43 \end{cases} \quad (11)$$

The energy dissipation model (Eqs.7, 8 and 10) contains 3 coefficients, $K_1 - K_3$, that can be found from model calibration.

3. Model Calibration

The model is calibrated for determining the optimal values of the coefficients $K_1 - K_3$ in Eqs. (7), (8) and (10). The calibration is carried out with the large-scale experimental data from the SUPERTANK Laboratory Data Collection Project (Kraus and Smith, 1994). The SUPERTANK project was conducted to investigate cross-shore hydrodynamic and sediment transport processes, during the period August 5 to September 13, 1992, at Oregon State University, Corvallis, Oregon, USA. A 76-m-long sandy beach was constructed in a large wave tank of 104 m long, 3.7 m wide, and 4.6 m deep. Wave conditions involved regular and irregular waves. The 20 major tests were performed and each major test consisted of several cases (see Table 2). Most of the major tests were performed under the irregular wave actions, except the test No. STBO, STEO, STFO, STGO, STHO, and STIO. The collected experiments for irregular waves include 128 cases of *rms* wave height profiles, covering incident *rms* wave heights from 13.9 cm to 60.1 cm, peak wave periods from 2.8 sec to 9.8 sec. Sixteen resistance wave gages were deployed at 3.66 m intervals from the mid surf zone to the wave paddle. Ten capacitance wave gage were placed at 0.61-to 1.83-m intervals in the vicinity of the shoreline and on the beach face to measure runup properties. The measured data from 18 wave gages (16 from resistance wave gage and 2 from capacitance wave gages) are used in this study.

In order to evaluate the accuracy of the prediction, the verification results are presented in term of root mean square (*rms*) relative error, *ER*, which is defined as

$$ER = 100\sqrt{\frac{\sum_{i=1}^{tn}(H_{ci} - H_{mi})^2}{\sum_{i=1}^{tn} H_{mi}^{\ 2}}} \tag{12}$$

where i is the wave height number, H_{ci} is the computed wave height of number i, H_{mi} is the measured wave height of number i, and tn is the total number of measured wave height. Smaller values of ER correspond to a better prediction.

The *rms* wave height transformation is computed by the numerical integration of energy flux balance equation (Eq. 1) with the energy dissipation rate $\overline{D}_B$ of Eq. (7):

$$\frac{\partial\left(H_{rms}^2 c_g \cos\theta\right)}{\partial x} = -\frac{K_1 Q_b c_g}{h}\left[H_{rms}^2 - \left(h\exp(-0.36K_2 - 1.25K_2\frac{h}{\sqrt{L_p H_{rms}}})\right)^2\right] \tag{13}$$

where Q_b is computed from Eq. (11), and H_b is computed from Eq. (10).

The measured water depth and wave height and wave period at the most seaward wave gage are used as input to the model. Eq. (13) is solved by backward finite difference scheme. Trial simulations indicated that $K_1 = 0.10$, $K_2 = 1.60$, and $K_3 = 0.10$ give good agreement between measured and computed *rms* wave heights. Finally, the energy dissipation rate of irregular wave breaking can be written as

$$\overline{D}_B = \frac{0.1 Q_b c_g \rho g}{8h}\left[H_{rms}^2 - \left(h\exp(-0.58 - 2.00\frac{h}{\sqrt{L_p H_{rms}}})\right)^2\right] \tag{14}$$

where Q_b is computed from Eq. (11) and

$$H_b = 0.1 L_o\left\{1 - \exp\left[-1.5\frac{\pi h}{L_o}\left(1 + 15m^{4/3}\right)\right]\right\} \tag{15}$$

Comparison between measured and computed *rms* wave heights for all 128 cases are shown in Fig. 1. Table 2 shows the *rms* relative error, ER, of the present model for each major tests. The average *rms* relative error, ER, for all 128 cases is 10.0 % which indicates very well prediction. Typical examples of computed *rms* wave height transformation for each major test are shown in Figs. 2 and 3. From Table 2 and Figs. 2-3, it can be seen that the model results generally show very well prediction, except the test no. STKO (broad-crested offshore mound). Furthermore, for some cases, the model tends to under-predict the wave heights very close to the shore.

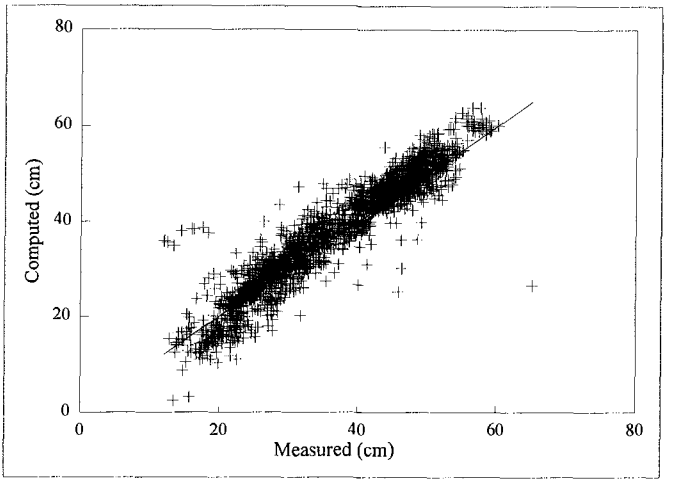

Figure 1 Comparison between computed and measured *rms* wave height for 128 cases of large-scale experiments (measured data from SUPERTANK project).

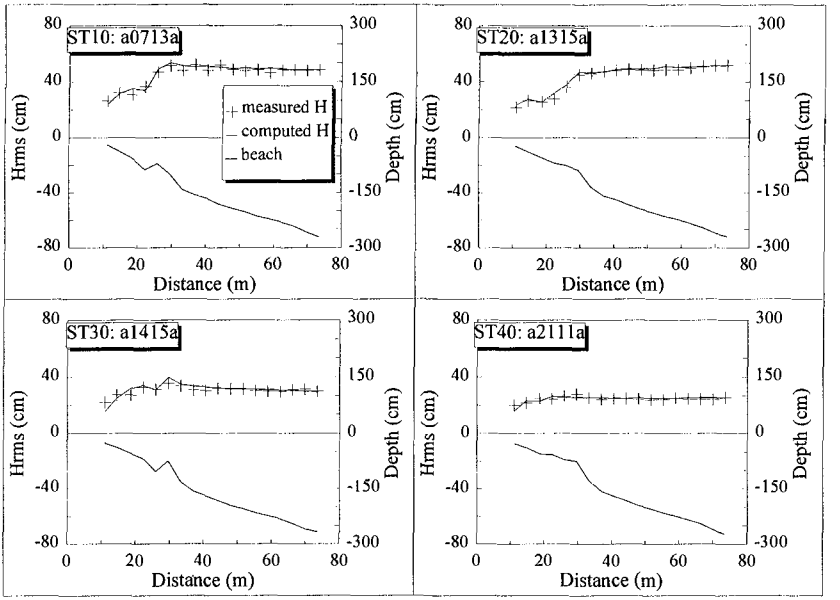

Figure 2 Examples of computed and measured *rms* wave height transformation for Test No. ST10-ST40 (measured data from SUPERTANK project).

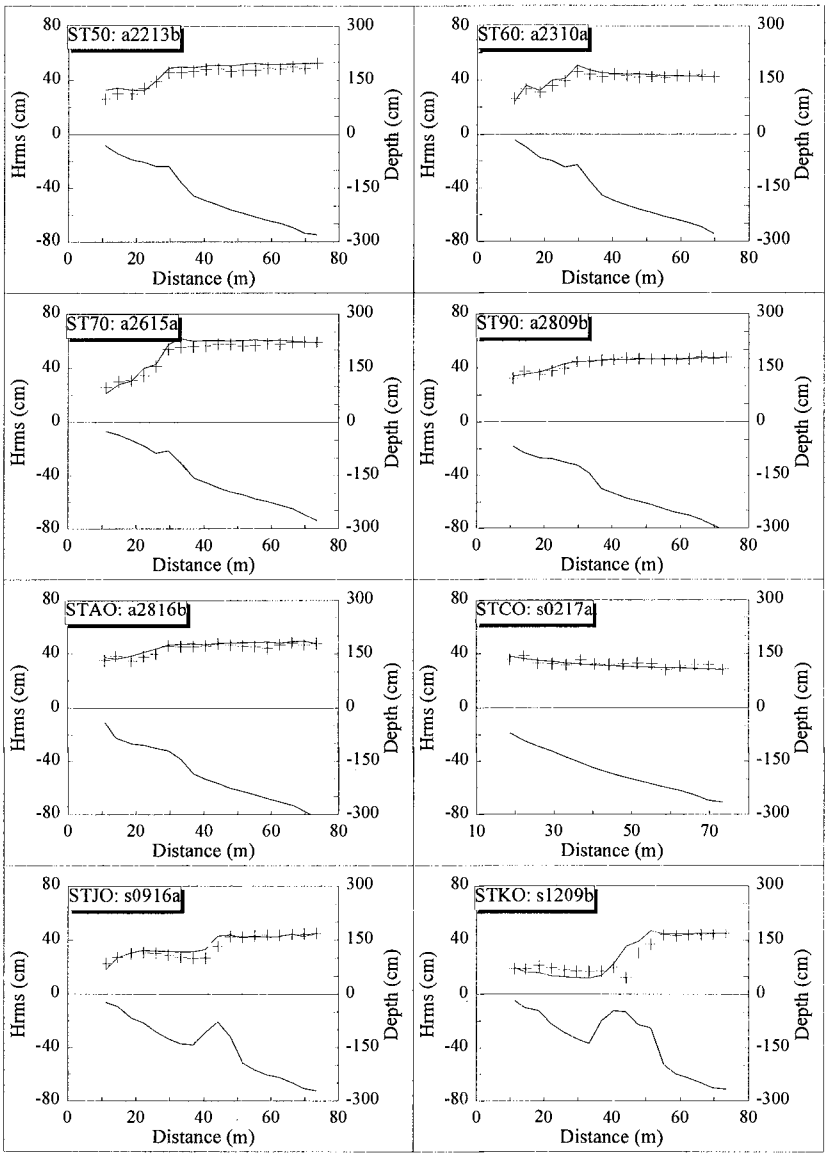

Figure 3 Examples of computed and measured *rms* wave height transformation for Test No. ST50-STKO (measured data from SUPERTANK project).

Table 2. Root mean square relative error (*ER*) of the present model comparing with irregular wave data from SUPERTANK project (Kraus and Smith, 1994).

Test No.	Description	Total No. of cases	ER. of Present study
ST10	Erosion toward equilibrium, irregular waves	26	5.82
ST20	Acoustic profiler tests, regular and irregular waves	8	6.96
ST30	Accretion toward equilibrium, irregular waves	19	9.99
ST40	Dedicated hydrodynamics, irregular waves	12	10.28
ST50	Dune erosion, Test 1 of 2, irregular waves	8	12.26
ST60	Dune erosion, Test 2 of 2, irregular waves	9	10.03
ST70	Seawall, Test 1 of 3, irregular waves	9	8.21
ST80	Seawall, Test 2 of 3, irregular waves	3	11.03
ST90	Berm flooding, Test 1 of 2, irregular waves	3	4.99
STAO	Foredune erosion, irregular waves	1	5.83
STBO	Dedicated suspended sediment, regular waves	0	-
STCO	Seawall, Test 3 of 3, irregular waves	8	10.21
STDO	Berm flooding, Test 2 of 2, irregular waves	3	13.96
STEO	Laser Doppler velocimeter, Test 1/2, regular waves	0	-
STFO	Laser Doppler velocimeter, Test 2/2, regular waves	0	-
STGO	Erosion toward equilibrium, regular waves	0	-
STHO	Erosion, transition toward accretion, regular waves	0	-
STIO	Accretion toward equilibrium, regular waves	0	-
STJO	Narrow-crested offshore mound, regular and irregular waves	10	11.03
STKO	Broad-crested offshore mound, regular and irregular waves	9	23.15
	Total	128	9.99

4. Model Verification

Since the present model is calibrated with only the data from the large-scale experiments, there is still a need of data from small-scale and field experiments for confirming ability of the present model. Two sources of experimental results are collected to verify the model, i.e., small-scale experimental data of Smith and Kraus (1990), and field data of Thornton and Guza (1986).

The wave height transformation is computed from the energy flux balance equation (Eq. 1) using $\overline{D}_B$ from Eq. (14) and numerical integration, using backward finite difference scheme, from offshore to shoreline. All coefficients in the model are kept to be constant for all cases in the verification.

4.1 Comparison with small-scale laboratory data

The small-scale laboratory data of Smith and Kraus (1990) is used in this subsection. The experiment was conducted to investigate the macro-features of wave breaking over bars and artificial reefs using small wave tank of 45.70-m-long, 0.46-m-wide, and 0.91-m-deep. Submerged triangular-shaped obstacles representing bars and reefs were installed on a 1/30 concrete slope to cause wave breaking. Both regular and irregular waves were employed in this experiment. Total 12 cases were performed for irregular wave tests. Three irregular wave conditions were generated for three bar configurations each, as well as for the control case of plane beach. The wave conditions were developed from input JONSWAP spectrum for spectral peak periods of 1.0, 1.5. and 1.75 sec, with significant wave heights of 11.3, 14.3, and 13.7 cm, respectively. Eight resistance wave gages were installed in the wave tank, 3 gages were placed in the offshore zone, 1 gage was place at the incipient break point, and 4 gages were placed in the surf zone.

Comparison between measured and computed *rms* wave heights for all cases are shown in Fig. 4. The average *rms* relative error, ER, for all cases is 11.2 % which indicates a good prediction of the model. Fig. 5 shows the typical examples of computed *rms* wave height transformation for incident *rms* wave height of 10 cm, peak period of 1.75 s and four bottom conditions. The model results generally show good agreement with the measured data. However, the model could not predict the rapid increase and decrease in wave heights near the narrow-crested bar.

4.2 Comparison with field data

The field data from Thornton and Guza (1986) are used in this subsection. The experiment was conducted on a beach with nearly straight and parallel depth contours at Leadbetter Beach, Santa Barbara, California, USA, to measure longshore currents, waves, and beach profiles, during the period January 30 to February 23, 1980.

Comparison between computed and measured *rms* wave height for all four cases are shown in Fig. 6. The average *rms* relative error, ER, is 14.5%. Fig. 7 shows the typical examples of computed and measured *rms* wave height transformation for the cases of Thornton and Guza (1986). The model results also generally show good agreement with the measured data.

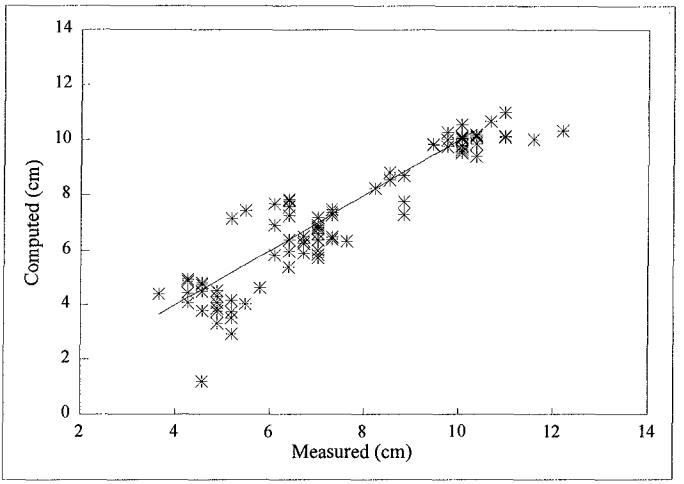

Figure 4 Comparison between computed and measured *rms* wave height for 12 cases of small-scale experiments (measured data from Smith and Kraus, 1990).

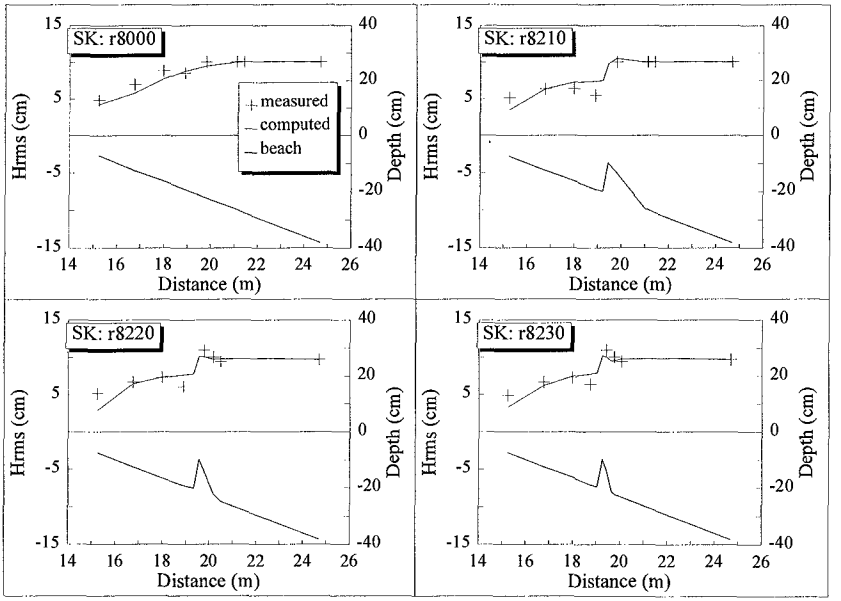

Figure 5 Examples of computed and measured *rms* wave height for incident *rms* wave height of 10 cm, and peak period of 1.75 s (measured data from Smith and Kraus 1990).

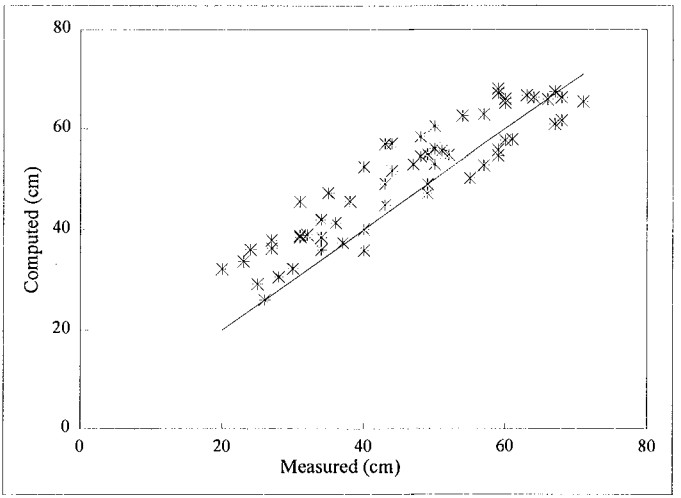

Figure 6 Comparison between computed and measured *rms* wave height for 4 cases of field experiments (measured data from Thornton and Guza, 1986).

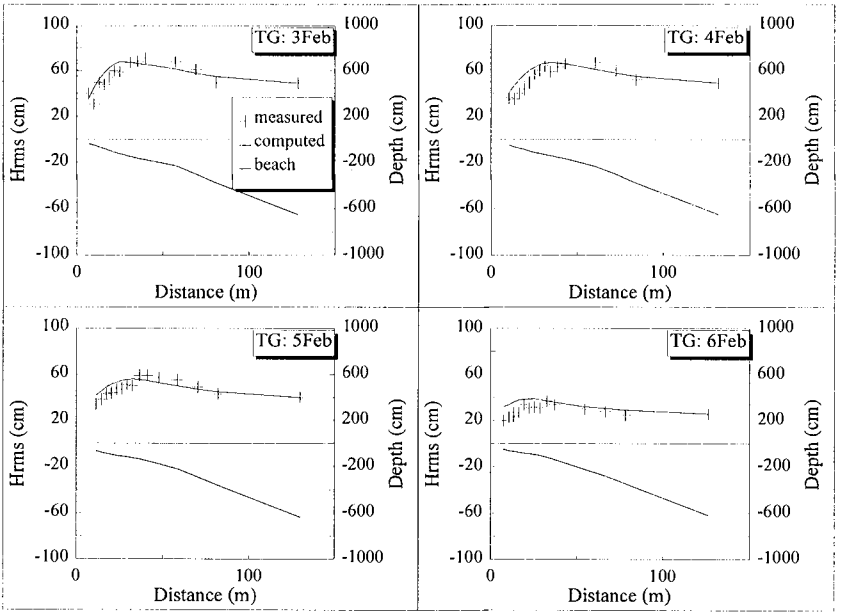

Figure 7 Examples of computed and measured *rms* wave height transformation for cases 3Feb - 6Feb (measured data from Thornton and Guza, 1986).

5. Conclusions

The energy dissipation model for irregular breaking waves is developed and applied to compute *rms* wave heights by using energy flux conservation law. The model is developed based on the modified regular breaking waves model of Dally et al. (1985) and on the local fraction of breaking waves of Battjes and Janssen (1978). The computed *rms* wave heights agreed well with the measured data for general cases, except the case of broad-crested offshore mound which is shown only fairly well prediction. The model is capable of simulating the increase in *rms* wave height due to shoaling and subsequent decrease due to wave breaking over wide range of wave conditions and various shape of beach profiles. The validity of model is confirmed by small scale laboratory data from Smith and Kraus (1990), large scale laboratory data from SUPERTANK project and field data from Thornton and Guza (1986). Table 3 shows the average *rms* relative error, ER, of the present model for each data sources. The average *rms* relative error, ER, of the model is 10.2 %.

Table 3. Root mean square relative error (ER) of the present model.

No.	Sources	No. of data sets	No. of data points	ER of Present study
1	SUPERTANK project (Kraus and Smith, 1994)	128	2223	9.99
2	Smith and Kraus (1990)	12	96	11.23
3	Thornton and Guza (1986)	4	60	14.50
	Total	144	2379	10.21

Acknowledgments

This research was sponsored by the Thailand Research Fund. The authors wish to express their gratitude to Prof. Yoshimi Goda of the Yokohama National University for his comments and fruitful discussions. Thanks and sincere appreciation are expressed to Dr. Nicholas C. Kraus, Dr. Jane McKee Smith, Dr. Edward B. Thornton and Dr. R.T. Guza for providing the experimental data used in this work.

References

Battjes, J. A., and Janssen, J.P.E.M. (1978). Energy loss and set-up due to breaking of random waves, Proc. 16th Coastal Engineering Conf., ASCE, pp. 569-587.

Dally, W.R., Dean, R.G., and Dalrymple, R.A. (1985). Wave height variation across beach of arbitrary profile, J. of Geo. Res., Vol. 90, No. C6, pp. 11917-11927.

Dally, W.R. (1992). Random breaking waves: Field verification of a wave-by-wave algorithm for engineering application, Coastal Engineering, Vol. 16, pp. 369-397.

Goda, Y. (1970). A synthesis of breaking indices, Trans. Japan Soc. Civil Eng., Vol. 2, Part 2, pp. 227-230.

Hansen, J.B. (1990). Periodic waves in the surf zone: Analysis of experimental data, Coastal Engineering, Vol. 14, pp. 19-41.

Kraus, N.C., and Smith, J.M. (1994). SUPERTANK Laboratory Data Collection Project, Technical Report CERC-94-3, U.S. Army Corps of Engineers, Waterways Experiment Station, Vol. 1-2.

Rattanapitikon, W. and Shibayama, T. (1996), Cross-shore sediment transport and beach deformation model, Proc. 25th Coastal Eng. Conf., ASCE, pp. 3062-3075.

Singamsetti, S.R. and Wind, H.G. (1980), Breaking waves: Characteristics of shoaling and breaking periodic waves normally incident to plane beaches of constant slope, Delf Hydraulic Lab., Rep. M1371, 142 pp.

Smith, J.M. and Kraus, N.C., (1990). Laboratory study on macro-features of wave breaking over bars and artificial reefs, Technical Report CERC-90-12, U.S. Army Corps of Engineers, Waterways Experiment Station.

Thornton, E.B. and Guza, R.T. (1986). Surf zone longshore currents and random waves: field data and model, J. of Physical Oceanography, Vol. 16, pp. 1165-1178.

Weggel, R.J. (1972). Maximum breaker height, J. of the waterways, Harbors, and Coastal Engineering Division, Vol. 98, No. ww4, pp. 529-548.

STOCHASTIC MODELLING OF NONLINEAR WAVES IN SHALLOW WATER

Henrik Kofoed-Hansen[1] and Jørgen H. Rasmussen[2]

Abstract

In this paper we shall study and model the nonlinear transformation of frequency wave spectra using two different types of stochastic models. The nonlinear processes considered include triad wave interaction and dissipation due to depth-induced wave breaking. The two stochastic models are the two-equation model proposed by Kofoed-Hansen and Rasmussen (1998) and the one-equation Lumped Triad Approximation (LTA) originally proposed by Eldeberky and Battjes (1995). Model results are compared with laboratory experiments and results obtained by the underlying deterministic time-domain Boussinesq model. The two stochastic models are found in good agreement with measurements of wave height (H_{m0}) and wave period (T_{01}). In case of wave transformation on a horizontal bottom, the LTA model fails as the rapid oscillations are neglected. The two-equation model predicts the energy transfer to sub-harmonics and non-resonant interaction excellently. In the inner surf zone and where the nonlinearity is strong, only the underlying deterministic model predicts the spectra and higher order wave statistics accurately.

Introduction

In recent years, considerable effort has been put on modelling of shallow water phenomena such as quadratic nonlinear wave interaction and depth-induced wave breaking using stochastic models. One of the major objective is to extend third generation wind-wave models, like the well-known WAM model developed for oceanic waters and shelf seas, to coastal waters where triad interaction and wave breaking are the dominating phenomena, see eg Cavaleri and Holthuijsen (1998). The starting point is typically

[1]*Research Engineer, International Research Centre for Computational Hydrodynamics (ICCH), Agern Allé 5, DK-2970 Hørsholm, Denmark, Fax: +45 45 76 25 67, e-mail: hkh@dhi.dk*

[2]*PhD student, ICCH and Department of Hydrodynamics and Water Resources (ISVA), Technical University of Denmark, Building 115, DK-2800 Lyngby, Denmark, Fax: +45 45 93 28 60, e-mail: jhr@dhi.dk*

deterministic evolution equations for the complex amplitudes of a weakly nonlinear wave field using either Boussinesq type equations (eg Freilich and Guza, 1984; Madsen and Sørensen, 1993) or the Laplace equation with leading order nonlinearity in the surface boundary conditions (eg Agnon and Sheremet, 1997; Madsen and Eldeberky, 1998).

In this study we have adopted the Boussinesq type equations with enhanced linear dispersion characteristics derived by Madsen and Sørensen (1993). Eldeberky and Battjes (1996) extended their equations by including energy dissipation due to depth-induced wave breaking. Based on these deterministic formulations, coupled stochastic evolution equations for the power spectrum and bispectrum have been derived recently by Eldeberky (1996) and Kofoed-Hansen and Rasmussen (1998) assuming that the trispectrum may be formulated as products of the power spectrum. The stochastic evolution equations suggested by Herbers and Burton (1997) are derived on basis of an extension of Freilich and Guza's (1984) deterministic model with lowest order dispersion and nonlinearity. Kofoed-Hansen and Rasmussen (1998) solved numerically the coupled evolution equations in order to calculate the wave spectrum and higher order nonlinear measures such as skewness and asymmetry (integral measures of the wave shape). For application in coastal energy-based wave models, Eldeberky and Battjes (1995) introduced a series of simplifications in order to avoid solving the evolution equation for the bispectrum. This resulted in a simple source function accounting for the effect of triad wave interaction, which can be used in conventional phase-averaged transport equations for the wave energy spectrum.

Stochastic Nonlinear Models

Time-domain Boussinesq type equations

The stochastic models considered in this paper are based on Boussinesq type equations derived by Madsen et al (1991) and Madsen and Sørensen (1992). These equations incorporate enhanced linear dispersion characteristics and shoaling properties, which are important for an accurate representation of the nonlinear energy transfer. This paper considers unidirectional waves propagating normally to the bottom contours (one horizontal dimension). The depth-integrated equations of continuity and momentum can then be formulated as

$$\frac{\partial \eta}{\partial t} + \frac{\partial P}{\partial x} = 0 \tag{1}$$

$$\frac{\partial P}{\partial t} + \frac{\partial}{\partial x}\left(\frac{P^2}{d}\right) + gd\frac{\partial \eta}{\partial x} - Bgh^3\frac{\partial^3 \eta}{\partial x^3} - \left(B + \frac{1}{3}\right)h^2\frac{\partial^3 P}{\partial x^2 \partial t} - \frac{\partial h}{\partial x}\left(2Bgh^2\frac{\partial^2 \eta}{\partial x^2} + \frac{1}{3}h\frac{\partial^2 P}{\partial x \partial t}\right) + R_{xx} = 0 \tag{2}$$

where η is the surface elevation, P the depth-integrated horizontal velocity, h the still water depth, g the acceleration due to gravity, d the instantaneous total water depth, and B the dispersion coefficient. Variable x is the horizontal space coordinate and t denotes time. The inclusion of wave breaking is based on the surface roller concept, see Madsen et al (1997). The effect of the roller on the wave motion is taken into account by the excess momentum term (term R_{xx} in Eq. 2) originating from a non-uniform velocity profile due to the presence of the roller. The equations have lowest order nonlinearity as the classical Boussinesq equations. For a dispersion coefficient of B=1/15, accurate dispersion characteristics are obtained for kh less than about 3.2.

Deterministic evolution equations

Now the surface elevation is represented as a Fourier series

$$\eta(x,t)=\sum_{p=-\infty}^{\infty} A_p(x)e^{i(\omega_p t-\psi_p(x))} \tag{3}$$

where A_p is a complex amplitude, ω_p is the angular frequency, $\psi_p(x)$ is a phase function and i denotes the imaginary unit. Following Madsen and Sørensen (1993), the spatial evolution of the complex amplitude, A_p, is to leading order given by the differential equation

$$\frac{dA_p}{dx}=(L_p\frac{dh}{dx}+\gamma_p)A_p+i\sum_{m=-\infty}^{\infty} J_{m,p-m}A_m A_{p-m}e^{-i\delta\psi(x)} \tag{4}$$

which describes the spatial evolution of a weakly nonlinear wave field on a mildly sloping bottom. In the derivation it has been assumed that the amplitudes are slowly varying in space. The first term on the right-hand side of Eq. (4) represents the linear shoaling and the dissipation due to wave breaking (γ_p), whereas the second term describes the nonlinear triad wave interaction (bound waves as well modulated free waves). Here $\delta\psi(x)=\int(k_{m+p}-k_m-k_p)dx$ is the phase-mismatch and may be considered as a measure of the departure from exact resonance. Variable k_p denotes the wave number. The detailed expression for L_p and $J_{m,m-p}$ is given in Kofoed-Hansen and Rasmussen (1998). Eq. (4) is identical to Eq. (7.1) in Madsen and Sørensen (1993) when γ_p= 0, and is the starting point for the derivation of the stochastic models suggested by Eldeberky and Battjes (1995), Eldeberky (1996) and Kofoed-Hansen and Rasmussen (1998).

Two-equation stochastic model

Stochastic evolution equations for the various order of spectra are derived by manipulating the deterministic evolution equations for the complex amplitude followed by ensemble-averaging. At lowest order, this procedure leads to an evolution equation for the power or wave energy spectrum including terms involving the next order spectrum, ie the bispectrum. An evolution equation for the bispectrum is derived at the following order, where terms including the trispectrum appear. In order to close the system of equations we

write the trispectrum as products of the power spectrum, the well-known Gaussian closure approximation. Hence, the evolution equation for the power spectrum and bispectrum constitutes the two-equation stochastic model describing the spatial evolution of a weakly nonlinear unidirectional wave field propagating on a mildly sloping bottom, see Kofoed-Hansen and Rasmussen (1998) for a thorough derivation. The coupled evolution equations are written as

$$\frac{dF_p}{dx} = 2\left(L_p \frac{dh}{dx} - \gamma_p \right) F_p - 2 \sum_{m=-\infty}^{\infty} J_{m,p-m} \Im\left(B_{m,p-m}\right) \tag{5}$$

$$\frac{d\,B_{m,p-m}}{dx} = \left(\left(L_m + L_{p-m} + L_p\right)\frac{dh}{dx} - \left(\gamma_m + \gamma_{p-m} + \gamma_p\right) - i\delta k(x) \right) B_{m,p-m}$$

$$+ 2i\, J_{m,p-m} \left(\frac{k_m}{k_p} F_p F_{p-m} + \frac{k_{p-m}}{k_p} F_p F_m - \frac{k_p}{k_p} F_m F_{p-m} \right) \tag{6}$$

where F_p and $B_{m,p-m}$ denote the discrete power and bispectrum, respectively. The bispectrum describes the degree of coupling and phase relationship in triads of nonlinearly interacting wave components. It describes statistically the shape of shoaling waves, ie skewness ~ $\Re(B_{m,p-m})$ and asymmetry ~ $\Im(B_{m,p-m})$, see Elgar and Guza (1985). $\Re$ and $\Im$ denote the real and imaginary part, respectively. The discrete spectrum is converted into a continuous spectrum by dividing the power spectrum by the frequency resolution and the bispectrum by the frequency resolution squared, respectively.

One-equation model

Based on the evolution Equations (5) and (6), Eldeberky and Battjes (1995) derived a parameterised model for application in conventional phase-averaged models, the Lumped Triad Approximation, LTA. They introduced a series of simplifying assumptions in order to avoid the computation of the evolution equation for the bispectrum. First, they integrated this equation, then they neglected the rapid oscillations involving the wave number mismatch. Finally, they restricted the formulation to self-self interaction and parameterised the biphase in terms of the local Ursell number as originally suggested by Doering and Bowen (1995). The evolution equation for a continuous wave spectrum can be written as

$$\frac{dF_p}{dx} = 2\left(L_p \frac{dh}{dx} - \gamma_p \right) F_p + S_p - S_{2p} \tag{7}$$

where the quadratic term, S_p, is expressed by

$$S_p = \alpha\, c_p J^2_{p/2,p/2} \sin\left|\beta_{p/2,p/2}\right| \left[F^2_{p/2} - 2F_p F_{p/2}\right] \tag{8}$$

The relation between the biphase, $\beta_{p,p}$, and the Ursell number is given by

$$\beta_{p,p} = -\frac{\pi}{2} + \frac{\pi}{2} tanh\left(\frac{0.2}{Ur}\right), \quad Ur = \frac{g}{8\sqrt{2}\pi^2} \frac{H_{m0} T_{01}^2}{h^2} \tag{9-10}$$

where $H_{m0} = 4\sqrt{m_0}$ and $T_{01} = m_0/m_1$. The moments are calculated as $m_n = \int_0^\infty f^n F df$ and the tuning parameter α appearing in Eq. (8) is of order 1. The variable, c_p, denotes the phase speed.

Dissipation due to wave breaking

The dissipation rate, γ_p, incorporated in the stochastic models is either taken as frequency independent as suggested by Eldeberky and Battjes (1996) or as a frequency squared dependent dissipation term as suggested by Chen et al (1997). In general the dissipation rate, γ_p, should be treated as a complex quantity. Here we restrict ourselves to consider the dissipation as purely real.

The coupled set of stochastic evolution equations for the power spectrum and bispectrum are solved numerically using standard numerical integration techniques and with linear upwind boundary conditions, ie $B_{m,p-m} \equiv 0$.

Numerical Results and Comparison with Experimental Data

Results of numerical simulations using the two stochastic models are compared with experimental data and results obtained by the underlying phase-resolving time-domain deterministic model.

Submerged bar

The measurements of Beji and Battjes (1993) are used to evaluate the two stochastic models for propagation of non-breaking waves over a trapezoidal submerged bar. Figure 1 illustrates their experimental setup. We consider the case with a very narrow-banded target spectrum. At WG1 this spectrum has a peak frequency of $f_p = 0.4$ Hz and a significant wave height of $H_{m0} = 0.023$ m, see Figure 2. A spatial resolution of 0.1 m is used and the frequency resolution is 0.03906 Hz. The tuning parameter α used in LTA is set to 1.

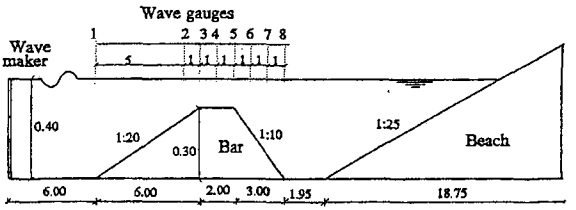

Figure 1. Layout of experiment of Beji and Battjes (1993). All lengths are given in meter.

Figure 2 presents a comparison of simulated and measured frequency spectra at locations WG1 and WG5. It has previously been shown (eg Kofoed-Hansen and Rasmussen, 1998 and Eldeberky, 1996) that the power spectrum is very accurately modelled on the uphill slope of the bar using the two stochastic models. On the top of the bar (see Figure 2) the two-equation model shows too much energy transfer to particularly the second harmonic components. The reason for the discrepancies is due to violation of the basic assumption of quasi-Gaussianity. At the crest section of the bar, the medium is almost non-dispersive for the primary waves ($k_p h$ ~ 0.26). The LTA model underestimates the energy transfer towards higher harmonics ($f > 2f_p$) as well as to lower frequencies ($f < \frac{1}{2} f_p$) as a consequence of the introduced simplifications.

The spatial evolution of quantities such as the significant wave height, H_{m0}, and the characteristic mean wave period, T_{01}, determined by the two stochastic models is compared measured data and the results obtained with the time-domain Boussinesq model in Figure 3.

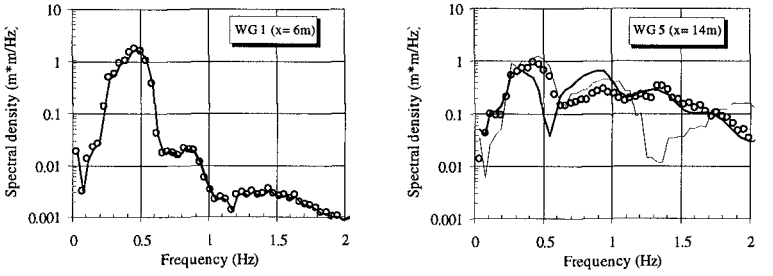

Figure 2. Comparison of frequency spectra from numerical simulations and measurements. (—) two-equation stochastic model, (—) LTA model and (ooo) experimental data by Beji and Battjes (1993).

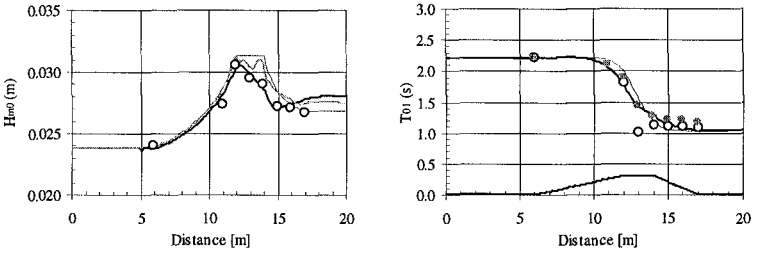

Figure 3. Spatial evolution of characteristic integral measures. (— and •) Deterministic model, (—) two-equation stochastic model, (—) LTA model and (ooo) experimental data by Beji and Battjes (1993). The bathymetry is sketched on the right panel.

From Figure 3 it appears that all three types of model result in similar growth of the wave height up-slope. Here the generated bound waves are phase-locked to the primary free waves and thus having almost the same group velocity. On the horizontal bar crest, two-way exchange of energy between free and bound waves takes place, which results in spatial inhomogeneity. This phenomena is only included in the deterministic as well as in the two-equation stochastic model. As LTA model neglects the rapid oscillations involving the wave number mismatch, the significant wave height will here remain constant. The reduction of the mean wave period over the bar is well predicted by all three types of model. Kofoed-Hansen and Rasmussen (1998) have shown that higher order statistical quantities (ie skewness and asymmetry) can be predicted reasonably well using the two-equation model for this non-breaking bar test. The results will not be shown here.

Barred beach

In this case, we consider the spatial evolution of an incident Pierson-Moskowitz type spectrum over a barred sandy beach (test no LIP 11D, Case C, Arcilla et al, 1994) as illustrated in Figure 4. This figure also indicates the location of the wave gauges. The power spectrum of the measured surface elevation at WG1 yields a significant wave height of H_{m0}= 0.58 m and a peak frequency of f_p= 0.125 Hz. This spectrum is applied as boundary condition for the stochastic models at the boundary 20 m seawards of WG1. The most energetic waves are characterised by having very weak dispersion as $k_p h$= 0.53. The spatial resolution is again set to 0.1 m and the frequency resolution is 0.0097 Hz. The tuning parameter used in LTA is set to α= 0.5, which results in best agreement with the measured data.

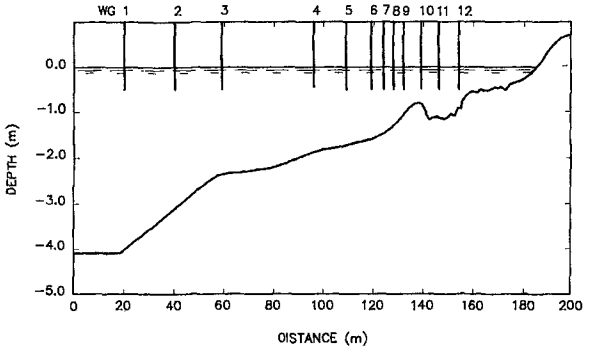

Figure 4. Layout of the large-scale laboratory flume experiment of Arcilla et al (1994).

In Figure 5 the predicted frequency spectrum is compared to the measured spectrum at the four locations WG1, WG3, WG6 and WG11. In this case, the frequency-independent wave breaking dissipation model (suggested by Eldeberky and Battjes, 1996) is used. At WG3 is seen that the two stochastic models predict accurately the measured spectrum until a frequency of approximately $3f_p$. Here mainly one way of energy transfer

occurs (as was the case for the bar test). At WG6 and WG11 there is an increasing tendency of too strong transfer rates in both models, which is probably due to violation of the basic assumption of a quasi-Gaussian sea state. Although some discrepancies appear between the model results and measurements, the overall performance is reasonable. Particularly the energy transfer towards low-frequency wave components is excellently predicted by the two-equation model.

The spatial evolution of the significant wave height, the mean wave period, skewness and asymmetry determined by the stochastic models are compared to the measured data and the results obtained with the time-domain Boussinesq model in Figure 6. It is seen that the three models predict almost the same significant wave height and mean wave period in reasonably good agreement with measurements. The LTA model shows a slightly better agreement with the measured mean wave period than the deterministic and two-equation model at a distance of 100-130 m. The mean wave period decreases as the higher order spectral moments increase during the nonlinear shoaling. In a linear model the wave period will be almost constant. Figure 6 also shows that the skewness and asymmetry are in good agreement with the measurements for distances less than, say, 100 m. For larger distances both measures deviate significantly from the measurements most likely as a consequence of too strong nonlinearity.

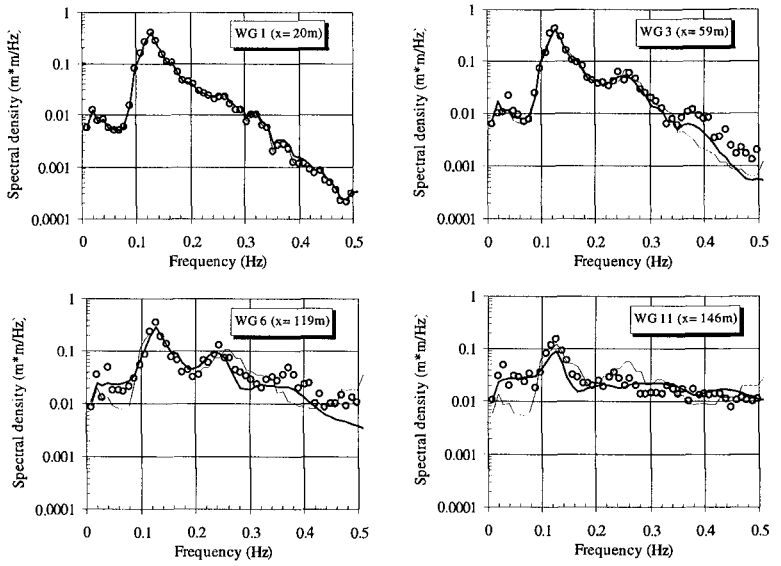

Figure 5. Comparison of frequency spectra from numerical simulations and measurements. (—) two-equation stochastic model, (—) LTA model and (ooo) experimental data by Arcilla et al (1994).

The assumption of using a wave breaking dissipation rate in proportion to the spectral density (ie independent of the frequency) is not found to be the major reason for the discrepancy between measured and simulated (by the two-equation stochastic model) skewness and asymmetry as suggested by Chen et al (1997). The results of simulations using a frequency-independent and frequency-dependent (f^2) formulation are depicted in Figure 7. As seen from the figure the skewness and asymmetry were not improved by weighting the dissipation towards higher frequencies in this case. It is also seen that by setting F= 1 (frequency-independent formulation) in the model by Kaihatu and Kirby (1996), the third-order statistical quantities are almost identical to the results obtained using the model Eldeberky and Battjes (1996). As the basic assumption of Gaussianity is highly violated in the inner surf zone and the statistical closure is highly questionable, only a phase-resolving model (including an advanced wave breaking formulation) is applicable there.

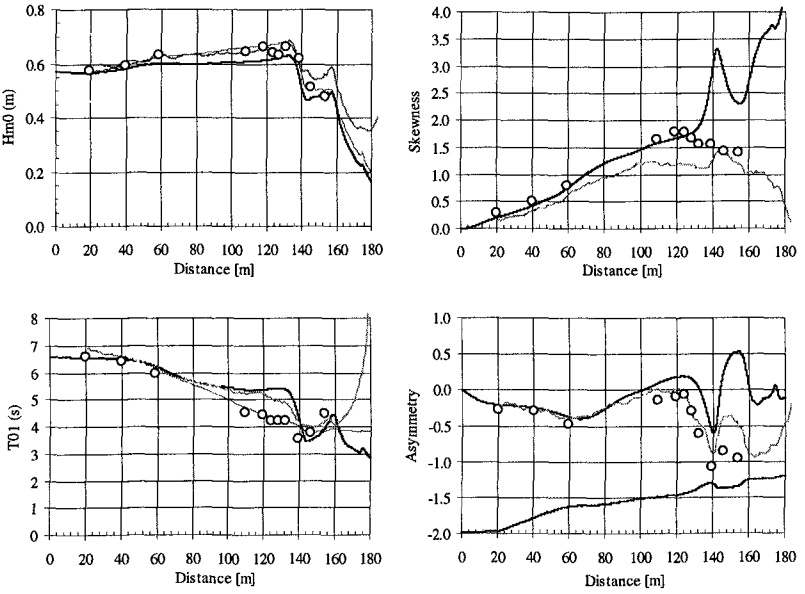

Figure 6. Spatial evolution of characteristic integral measures. (—) Deterministic model, (—) two-equation stochastic model, (–) LTA model and (ooo) experimental data by Arcilla et al (1994). The bathymetry is sketched at the lower right panel.

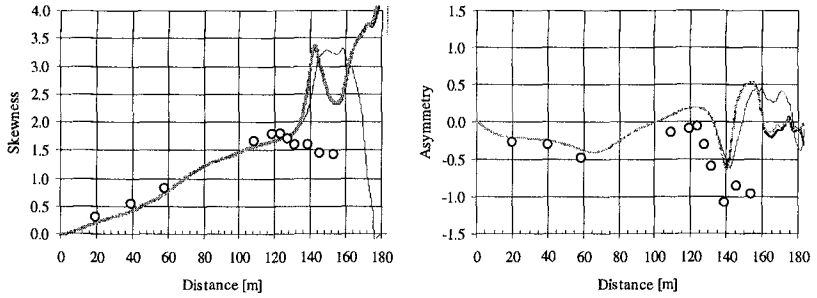

Figure 7. Spatial evolution of skewness and asymmetry simulated by the two-equation model using different wave breaking dissipation models. (—) Kaihatu and Kirby (1996), F=0, (▬) Kaihatu and Kirby (1996) model, F=1, (▬) Eldeberky and Battjes (1996) model and (○○○) experimental data by Arcilla et al (1994). When F= 1 the dissipation is frequency-independent and for F=0 the dissipation has a frequency squared dependency.

Horizontal bottom

The numerical results for the bar test show that the LTA model predicts no spatial variation of the total wave energy on the horizontal crest contrary to the measured data and the results of the two-equation stochastic model. In the following, we shall examine the long-term evolution of a narrow-banded spectrum at a constant depth a bit more using the two stochastic models. The simulations have been performed using similar parameters as used in Elgar et al (1990), see their Figure 6 p. 11552. The initial spectrum (x=0) consists of a single large primary peak at f_p= 0.0625 Hz as illustrated in Figure 8. The water depth is 2.0 m. As the significant wave height is H_{m0}= 0.169 m, the Ursell number Ur= $(½H_{m0}/h)/(k_ph)^2$= 1.33, k_ph= 0.18. The frequency resolution is 0.0625 Hz, and the tuning parameter α used in the LTA model is set to 1.

The spatial evolution of the primary spectrum is presented in Figure 8 at x= 0, x= $7L_p$, x= 30 L_p, and x= $70L_p$, where L_p denotes the wave length corresponding to the initial peak frequency. The results obtained by the two-equation model shows that harmonics of the primary wave components grow during the initial stages of evolution. As the wave field evolves further, spectral valleys are filled in at the expense of spectral peaks. After about 70 wave lengths, the frequency spectrum is essentially featureless, and almost all traces of the initial spectrum and its harmonics are gone. In this case the beat length for the super-harmonie interaction between the primary peak and its second harmonic is 31-$32L_p$, but as the nonlinear transfer is very strong no clear evidence of recurrence is found in this particular case. Test cases with recurrence is presented and discussed in Rasmussen (1998). The simulated results presented in Figure 8 are in quite good agreement with the results presented by Elgar et al (1990) based on integration of Freilich and Guza's (1984) evolution equations.

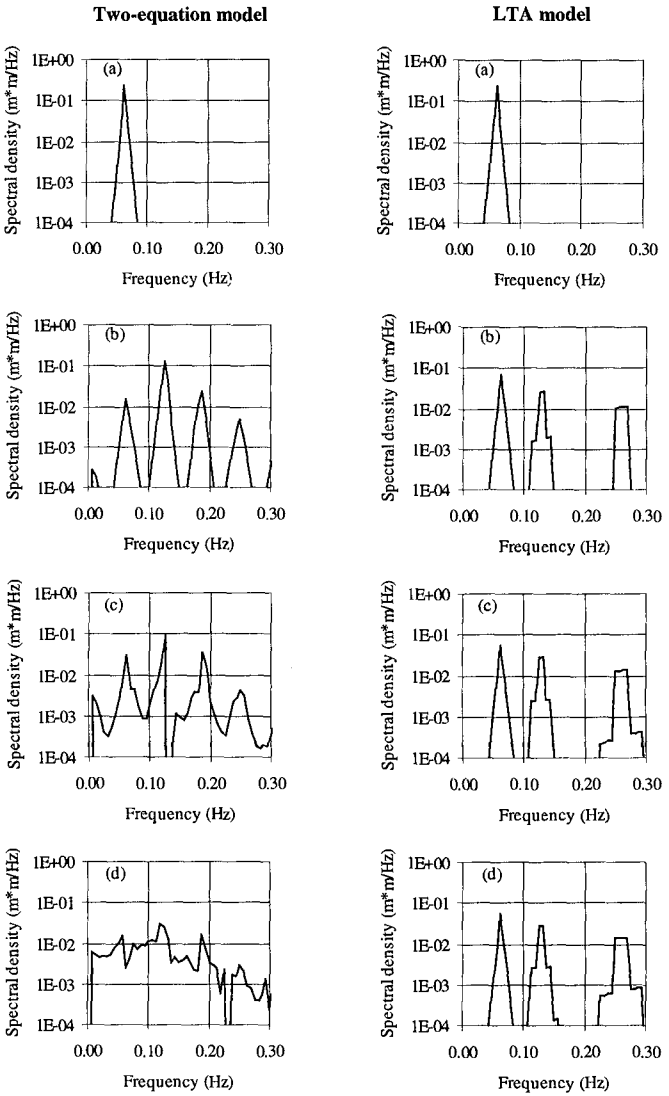

Figure 8. Evolution of a narrow-banded frequency spectrum on a horizontal bottom simulated by the two-equation model (left) and the LTA model (right). The power spectrum is presented at different distances a) x= 0, b) x= $7L_p$, c) x= $30L_p$ and d) x= $70L_p$, where L_p= 70.5 m is the wave length corresponding to the initial (x=0) peak frequency of f_p= 0.0625 Hz. The water depth is h= 2.0 m.

The spectral evolution simulated with the LTA model (see Figure 8), shows initially energy transfer to the second and fourth harmonics. After a few wave lengths (< 10), the wave spectrum remains almost unaltered. From Eq. (8), it is seen that an 'equilibrium' spectrum is obtained, where $F_p = \frac{1}{2}F_{p/2}$, ie the spectral density at the second harmonic is half of the spectral density at the primary peak and so on. Thus, the LTA model is not applicable for simulation of recurrence and white-noise type spectra on constant or nearly constant water depth. This is a result of neglecting the phase-mismatch between free and bound wave components.

Discussion

Having examined the performance of the two stochastic models, we may define the area of model application. As discussed in Kofoed-Hansen and Rasmussen (1998) the two-equation model can be used to predict the evolution of the frequency spectrum and bispectrum and associated characteristic integral measures in shallow water when the Ursell number (based on the peak frequency of the primary waves) is less than 1-2. Beyond that limit, the basic assumption of a quasi-Gaussian sea state is highly violated and the underlying phase-resolving model (including a proper description of the wave breaking process) is more accurate. In cases with a high degree of frequency dispersion, say, $k_p h > 2$, a more accurate description of the dispersion is required as shown in Madsen and Eldeberky (1998).

The LTA model, which is presently used in the public domain third-generation wind-wave model SWAN, see eg Cavaleri and Holthuijsen (1998), shows excellent agreement with the measurement of the significant wave height, H_{m0}, and mean wave period, T_{01}, for the two cases considered in this paper. The tuning parameter α is set to 1.0 for the bar test and 0.5 for the barred beach test. In case of a constant water depth the model predicts an unphysical long-term spectral evolution of the frequency spectrum, which is different from the expected featureless white-noise type spectrum. As a consequence of the introduced simplifications, the LTA model is mainly appropriate for relatively short evolution distances on sloping bathymetries, where the generation of bound super-harmonics is substantial.

Further, as the LTA model only includes self-self interactions the approach can in general only be applied for uni-modal (and unidirectional) frequency spectra. In cases of sea states involving swells and wind-waves, the LTA model is not expected to model accurately the nonlinear energy exchange between the two frequency regimes.

Although both types of stochastic models are of phase-averaged type, the required spatial resolution is different. Using the two-equation model, the wave number mismatch has to be resolved. Therefore the resolution is typically of the same order as for the underlying deterministic model. The spatial resolution used for solving the conventional phase-averaged energy transport equation including the LTA model (as source function for triad wave interaction) is usually at least 100 times larger.

Summary and Conclusions

This paper compared results of numerical calculations obtained from phase-averaged one- and two-equation stochastic models as well as the underlying deterministic (phase-resolving) model with laboratory experiments in case of a submerged bar (Beji and Battjes, 1993) and on a barred beach (Arcilla et al, 1994). Also the long-term evolution of a narrow-banded frequency spectrum on a horizontal bottom has been examined. The sensitivity of wave breaking formulations on third-order wave statistics derived from the two-equation model has been studied as well.

The simplified one-equation stochastic model (LTA) represents an average effect of triad wave interaction, transferring energy from lower to higher frequencies through self-self interaction. The model is in excellent agreement with measurements of H_{m0} and T_{01} in the two cases considered. The two-equation model also takes into account the energy transfer to sub-harmonics as well as the non-resonant wave interaction and provides third-order statistics too. In general, the agreement between the simulated results and measurements is found to be acceptable, even beyond the domain where Gaussianity may be justified. However, in the inner part of the surf zone, the stochastic model underestimate significantly the skewness and asymmetry. Results of simulations using frequency-dependent formulations did not improved the accuracy. As the basic assumption of Gaussianity is highly violated in the inner surf zone and the statistical closure is highly questionable, only a phase-resolving model is applicable there.

The results of the simulations performed on a horizontal bottom indicate that the LTA model is not applicable for prediction of long-term evolution on a nearly horizontal bottom in shallow water. As the two-equation model retains the phase-mismatch between free and bound waves, the frequency spectrum considered here tends to evolve towards a white-noise type spectrum after several wave lengths.

Acknowledgements

We would like to thank Yasser Eldeberky for providing the subroutine for the LTA model. Thanks are also due to Per A. Madsen and Hemming A. Schäffer for drawing our attention to the limitations of the LTA model for spectral evolution on a horizontal bottom. The present work was financed by the Danish National Research Foundation. Their support is greatly appreciated.

References

Agnon, Y. and A. Sheremet (1997), "Stochastic nonlinear shoaling of directional spectra", *J. Fluid Mech.*, 345, 79 -99.

Arcilla, A.S., J.A. Roelvink, B.A. O'Connor, A. Reniers and J.A. Jimenez (1994), "The Delta Flume'93 experiment", *Proc. Coastal Dynamics '94*, ASCE, 488-502.

Beji, S. and J.A. Battjes (1993), "Experimental investigation of wave propagation over a bar", *Coastal Eng.*, 19, 151-162.

Cavaleri, L. and L.H. Holthuijsen (1998), "Wave modelling in the WISE Group", *Proc. 26th International Coastal Engineering Conference, Copenhagen, Denmark*, ASCE.

Chen, Y., R.T. Guza and S. Elgar (1997), "Modeling spectra of breaking surface waves in shallow water", *J. Geophys. Res.*, 102, C11, 25035-25046.

Doering, J.C. and A.J. Bowen (1995), "Parameterisation of orbital velocity asymmetries of shoaling waves using bispectral analysis", *Coastal Eng.*, 26, 15-23.

Eldeberky, Y. (1996), "Nonlinear transformation of wave spectra in the nearshore zone", *PhD. thesis*, Delft University of Technology, The Netherlands, 203 pp.

Eldeberky, Y. and J.A. Battjes, (1995), "Parameterisation of triad interaction in wave energy models", *Proc. Coastal Dynamics '95*, Gdansk, Poland, ASCE, 140-148.

Eldeberky, Y. and J.A. Battjes (1996), "Spectral modelling of wave breaking. Applications to Boussinesq equations", *J. Geophys. Res.*, 101, C1, 1253-1264.

Elgar, S. and R.T. Guza (1985), "Observations of bispectra of shoaling surface gravity waves", *J. Fluid Mech.*, 161, 425-448.

Elgar, S., M.H. Freilich and R.T. Guza (1990), "Recurrence in truncated Boussinesq models for nonlinear waves in shallow water", *J. Geophys. Res.*, 98, C7, 11547-11556.

Freilich, M.H. and R.T. Guza (1984),"Nonlinear effects on shoaling surface gravity waves", *Phil. Trans R. Soc. London*, A311, 1-41.

Herbers, T.H.C. and M.C. Burton (1997), "Nonlinear shoaling of directionally spread waves on a beach", *J. Geophys. Res., 102, C9, 21101-21114.*

Kaihatu, J.M. and J.T. Kirby (1996), "Effects of mode truncation and dissipation on predictions of higher order statistics", *Proc. 25th International Coastal Engineering Conference*, Orlando, FL, USA, ASCE, 123-135.

Kofoed-Hansen, H. and J.H. Rasmussen, (1998), "Modelling of nonlinear shoaling based on stochastic evolution equations", *Coastal Eng.*, 33, 203-232.

Madsen, P.A. and Y. Eldeberky (1998), "A new formulation of deterministic and stochastic evolution equations for three-wave interactions involving fully dispersive waves", *Proc. 26th International Coastal Engineering Conference*, Copenhagen, Denmark, ASCE.

Madsen, P.A., R. Murray and O.R. Sørensen (1991), "A new form of the Boussinesq equations with improved dispersion characteristics", *Coastal Eng.*, 371-388.

Madsen, P.A. and O.R. Sørensen, (1992), "A new form of the Boussinesq equations with improved dispersion characteristics, Part 2. A slowly-varying bathymetry", *Coastal Eng.*,18, 183-204.

Madsen, P.A. and O.R. Sørensen, (1993), "Bound waves and triad interactions in shallow water", *Ocean Eng.*, 20, 359-388.

Madsen, P.A., H.A. Schäffer and O.R. Sørensen (1997), "Surf zone dynamics simulated by a Boussinesq type model. Part I: Model description and cross-shore motion of regular waves", *Coastal Eng., 32,* 255-288.

Sørensen, O.R., P.A. Madsen and H.A. Schäffer (1998), "Nearshore wave dynamics simulated by Boussinesq type models", *Proc. 26th International Coastal Engineering Conference*, Copenhagen, Denmark, ASCE.

Rasmussen, J.H. (1998), "Deterministic and stochastic modelling of surface gravity waves in finite depth", *PhD. thesis*, Technical University of Denmark.

COMPARING 1st-, 2nd - AND 3rd-GENERATION COASTAL WAVE MODELLING

L.H. Holthuijsen[1], N. Booij[1] and IJ.G. Haagsma[1]

ABSTRACT

The SWAN wave model for shallow water is used in three generation modes to show the differences in results between these modes and with observations in two real, rather field situations. These are situations of waves approaching two different sites in the Netherlands and Germany: one closed part of an estuary and one region between and beyond barrier islands with channels and tidal flats. The differences between the modes are significant (more than 25% locally) in terms of significant wave height and mean wave period. These differences are ascribed, at least partially to the indirect effects of triad wave-wave interactions which shorten the wave period. The observations are located at positions where the differences between the modes are hardly significant.

INTRODUCTION

Over the last decade, the traditional wave ray models to compute waves in coastal regions are being replaced by models that compute the waves on a regular grid. In analogy with ocean wave models, three generations of such grid models can be distinguished. The differences between these generations are essentially in the approximation of the physical processes, in particular in the representation of the nonlinear wave-wave interactions. Here we compare computational results of all three generations against each other and against observations in two real, rather complex field cases.

THE WAVE MODEL

In the present study the three modes of the spectral wave model SWAN of Booij et al. (1996) are used. The 1st- and 2nd-generation mode are essentially those of the DOLPHIN model of Holthuijsen and de Boer (1988; see also Holthuijsen et al., 1993) in which wave generation and dissipation are formulated with fairly simple expressions. In the 3rd-generation mode all processes are represented explicitly as in the WAM Cycle 3 model (WAMDI group, 1988), supplemented with depth-induced wave breaking and triad

[1]) Delft University of Technology, Department of Civil Engineering and Geosciences, Stevinweg 1, 2628 CN Delft, the Netherlands

wave-wave interactions. The formulations of these three modes that are used in the present study are briefly described next without the effects of currents.

Basic equation

In the absence of ambient currents, the basic equation of SWAN is the discrete spectral energy balance which can be written as (e.g. Hasselmann et al., 1973):

$$\frac{\partial}{\partial t}E + \frac{\partial}{\partial x}c_x E + \frac{\partial}{\partial y}c_y E + \frac{\partial}{\partial \theta}c_\theta E + \frac{\partial}{\partial \sigma}c_\sigma E = S$$

where E is the energy density as function of intrinsic frequency, spectral direction, spatial coordinates and time $E=E(\sigma,\theta;x,y,t)$. The first term in the left-hand side of this equation represents the local rate of change of energy density, the second and third term represent wave propagation in geographical space. The fourth term represents propagation is the spectral domain (refraction and frequency shifting due to (time) variations in depth). The expressions for the propagation speeds in these terms are taken from linear wave theory. The term S $(=S(\sigma,\theta;x,y,t))$ at the right hand side of the action balance equation is the source term representing the effects of generation, dissipation and nonlinear wave-wave interactions (to be addressed below).

Generation

Transfer of wind energy to the waves is described in SWAN with a resonance mechanism (linear growth in time) and a feed-back mechanism (exponential growth). In the 1st- and 2nd-generation mode of this model, the expression for the linear growth is due to Cavaleri and Malanotte-Rizzoli (1981). In the 3rd-generation mode it is ignored. In all three generation modes the expression for the exponential growth is due to Snyder et al. (1981) with different coefficients in the three modes: for the 1st- and 2nd-generation mode they have been obtained from fitting results to standard, fetch-limited deep water growth curves and for the 3rd-generation mode they are taken from WAM Cycle 3.

Dissipation

The formulations for bottom friction and depth-induced wave breaking are the same for all three modes of SWAN. Bottom friction is represented with the JONSWAP expression of Hasselmann et al. (1973) with the bottom friction coefficient of Bouws and Komen (1983). Depth-induced wave breaking has been modelled with a spectral version of the random-bore model of Battjes and Janssen (1978) that retains the shape of the spectrum during breaking. The remaining dissipation due to whitecapping is simulated in 1st- and 2nd-generation mode by terminating the wave growth per spectral component when an upper limit in energy density is achieved. This upper limit is a shallow-water version of the Pierson-Moskowitz (PM) spectrum formulated in terms of wave number and with a $\cos^2(\theta - \theta_{wind})$ directional distribution. Its peak frequency is taken from the SPM (1973; with deep water obviously as a special case). The energy scale coefficient α of this limit spectrum is an increasing function of decreasing depth that is tuned to standard shallow-water growth curves (it has the conventional value of $\alpha = 0.0081$ in deep water). If the energy density is larger than this limit spectrum (e.g. due to a change in wind speed or direction), whitecapping is simulated with a relaxation model with a frequency-dependent time scale that is small for high frequencies and very long for low frequencies. In 3rd-

generation mode, the whitecapping formulation is based on the pulse-based model of Hasselmann (1974), as adapted by the WAMDI group (1988) for the WAM model.

Nonlinear wave-wave interactions

The effects of quadruplet wave-wave interactions on wave growth in 1st- and 2nd-generation mode is simulated by enhancing the above described wind input term with a factor five. In 2nd-generation mode, the overshoot effect of these interactions is additionally simulated: the energy scale parameter α of the assumed limit spectrum is taken to be a decreasing function (obtained by tuning to standard deep-water growth curves) of the dimensionless energy of the wind sea part of the spectrum. The actual spectrum thus obtained with 1st- and 2nd-generation mode in standard, deep-water, fetch-limited situations is very similar to the JONSWAP spectrum, slowly changing into the PM spectrum with $\alpha = 0.0081$ for the fully developed situation. In 3rd-generation mode the quadruplet interactions are computed explicitly with the Discrete Interaction Approximation (DIA) of Hasselmann et al. (1985).

Triad wave-wave interactions are computed explicitly only in 3rd-generation mode with the Lumped Triad Approximation (LTA) of Eldeberky (1996).

APPLICATIONS

The three modes of modelling are applied to two real field cases in the Netherlands with complex bathymetry, 95% reduction in the observed wave energy due to depth-induced wave breaking with subsequent local generation by wind. These cases will first be shown here with the results of the 3rd-generation mode of SWAN. In the next section the results of the other modes will be addressed in terms of differences with these 3rd-generation results.

Haringvliet

The Haringvliet is a branch of the Rhine estuary in the south-west of the Netherlands that is separated from the main estuary by sluices. The bathymetry of the area and the locations of the (eight) observation stations are shown in Fig. 1. A local storm generated on October 14, 1982 waves from north-westerly directions and the SWAN computations are carried out for 23:00 UTC on this day. The incident wave conditions and the wind are given in Table 1 (significant wave height H_s and the mean wave period $\overline{T}$ defined as $H_s = 4\sqrt{m_0}$ and $\overline{T} = 2\pi (m_1 / m_0)$ where $m_m = \int \sigma^n E(\sigma,\theta))$. Figures 2 and 3 show the 3rd-generation results for the significant wave height and the mean wave period The waves approach the estuary from deep water and break over a shoal with a reduction of significant wave height from about 3.6 m in deep water to 2.5 m just in front of the shoal to about 0.6 m just behind the shoal. The local wind regenerates the waves behind the shoal to about 1.1 m significant wave height at station 8.

Norderneyer Seegat

The Norderneyer Seegat (Fig. 4) is a tidal gap between the barrier islands of Juist and Norderney in the northern part of Germany. The region behind this gap is an inter-tidal area with shoals and channels over a distance of 7.5 km to the main land. A high-tide case (November 17, 1995, 04:00 UTC) has been selected (no currents, Table 1). Figures 5 and 6 show the computed pattern of the significant wave and mean wave period. As the

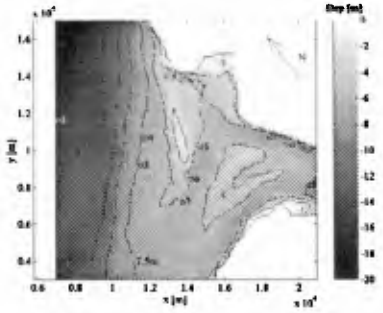

Fig. 1 The bathymetry of the Haringvliet with the eight observation stations.

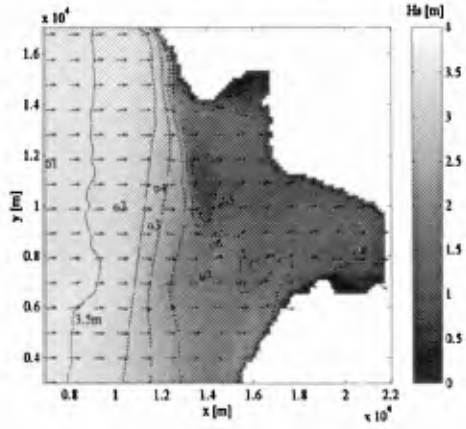

Fig. 2 The computed pattern (3rd-generation) of the significant wave height and mean wave direction (unit vectors; Haringvliet)

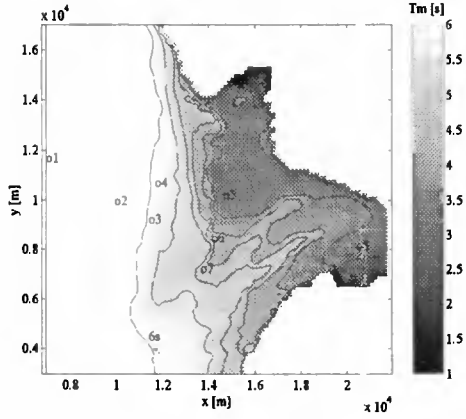

Fig. 3 The computed pattern (3rd-generation) of the mean wave period (Haringvliet).

	$H_{s,i}$ (m)	$\overline{T}$ (s)	$\overline{\theta}_{wave,i}$ (°)	$\sigma_{\theta,i}$ (°)	U_{10} (ms^{-1})	θ_{wind} (°)
Haringvliet	3.56	6.7	306	31	14	300
Norderneyer Seegat	2.98	6.8	375	45	8	338

Table 1 The incident significant wave height, mean wave period, mean wave direction, directional spreading and wind speed and direction for the two cases of this study.

waves propagate from deep water to the barrier islands the wave height gradually decreases from about 3 m to about 2.5 m at station 2. As the waves propagate through the gap they refract out of the channels to the shallower parts where wave energy is dissipated rapidly and local wind regenerates high-frequency waves.

MODEL INTERCOMPARISON

The results of the 1st- and 2nd-generation modes are qualitatively very similar to those of the 3rd-generation mode shown above. Therefore only the differences will be shown. These are presented as relative differences, defined as $\Delta H_s = [\, H_{s,3} - H_{s,i} \,] / H_{s,3}$ and $\Delta \overline{T} = [\, \overline{T}_3 - \overline{T}_i \,] / \overline{T}_3$ where the subscript $_3$ refers to the 3rd-generation results and the subscript $_i$ to either the 1st-generation or 2nd-generation results. The differences for the Haringvliet for the 1st-generation mode are given in Fig. 7 where it is obvious that the differences are relatively large over and behind the shoal, north of the shoal and in the sheltered area deep in the bay (south of station 8). Beyond the shoal the significant wave height is typically 15% lower in the 1st-generation results than in the 3rd-generation results and the mean wave period is some 20% longer (50% over the shoal). In the 2nd-generation results the differences are qualitatively very similar but they are quantitatively considerably smaller, as shown in Fig. 8. The differences in significant wave height in the areas lateral of the shoal (seen in the direction of wave propagation) seem to be due to differences in refraction (not shown here). These in turn seem to be induced by the differences in mean wave period up-wave from these locations (to be addressed later). The differences in the sheltered area south of station 8 may well be due to differences in short-fetch wave growth.

For the Norderneyer Seegat, the differences for 1st-generation mode are given in Fig. 9. Again it is obvious that the differences are relatively large, particularly in the channels and in the short-fetch areas behind the islands. The differences for 2nd-generation mode are again qualitatively equal to those in 1st-generation mode but quantitatively smaller as shown in Fig. 10. As in the Haringvliet case, the differences seem to be related to differences in refraction (due to differences in period) and short-fetch wave growth.

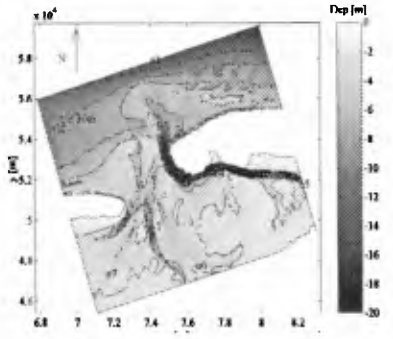

Fig. 4 The bathymetry of the Norderneyer Seegat with the locations of nine observation stations.

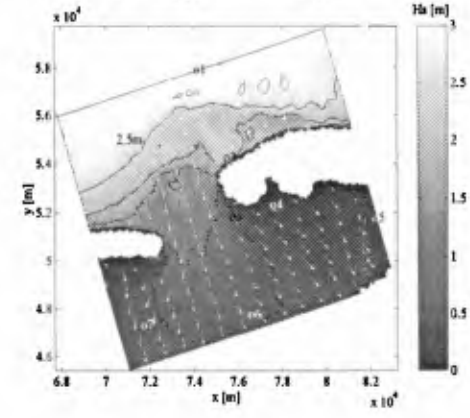

Fig. 5 The computed pattern of the significant wave height and mean wave direction (unit vectors; Norderneyer Seegat).

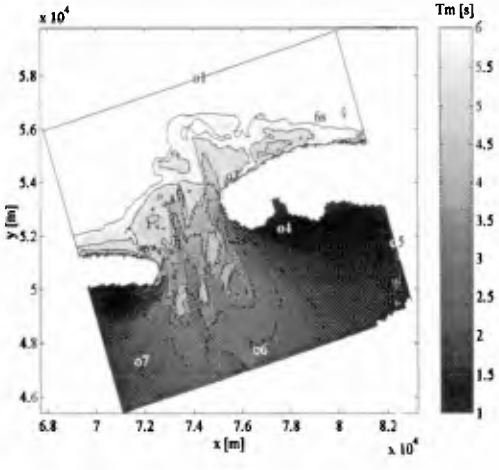

Fig. 6 The computed pattern of the mean wave period (Norderneyer Seegat).

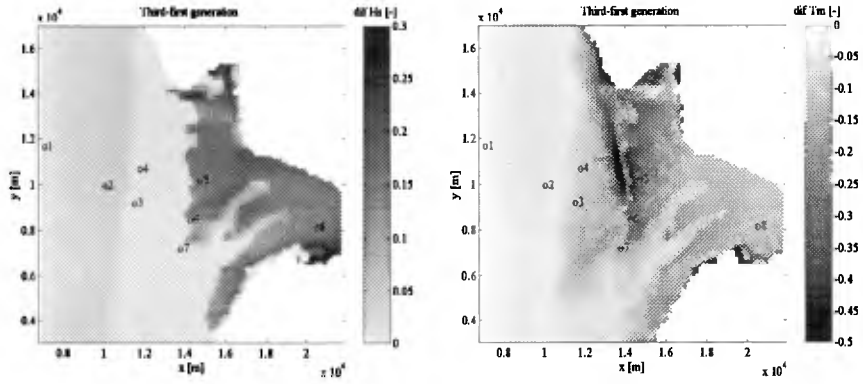

Fig. 7 The relative differences in significant wave height and mean wave period for the Haringvliet (1st-generation compared to 3rd-generation).

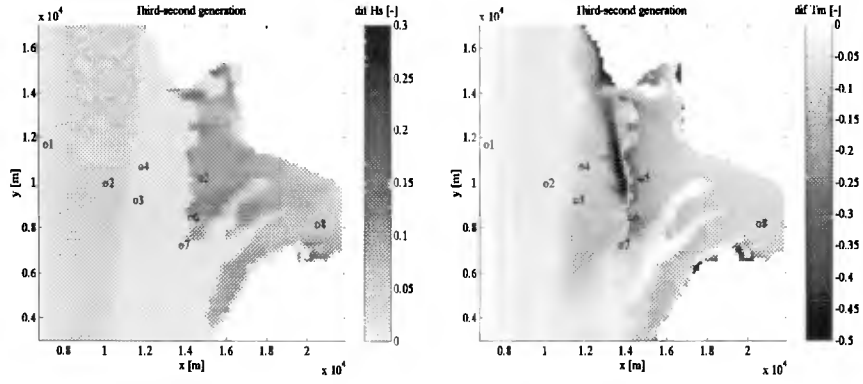

Fig. 8 The relative differences in significant wave height and mean wave period for the Haringvliet (2nd-generation compared to 3rd-generation).

DISCUSSION

The above differences are attributed (partly) to differences in refraction which in turn would be due to differences in wave periods due to the absence of triad wave-wave interactions in the 1st-generation and 2nd-generation mode. This is inferred from the stronger refraction in 1st-generation and 2nd-generation results than in the 3rd-generation results (not shown). The computations were therefore repeated for the Norderneyer Seegat

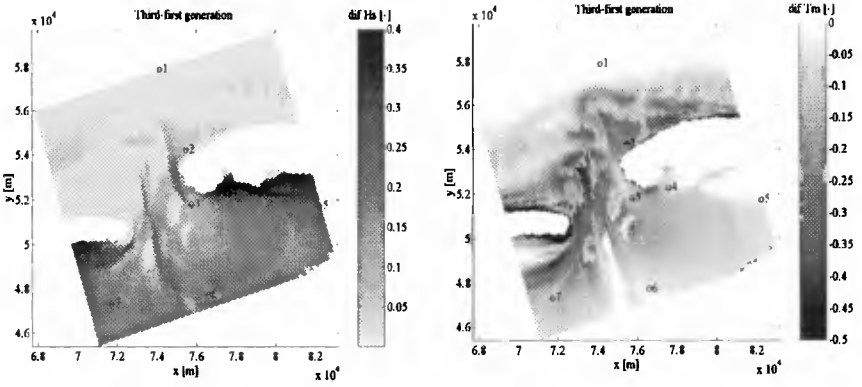

Fig. 9 The relative differences in significant wave height and mean wave period for the Norderneyer Seegat (1st-generation compared to 3rd-generation).

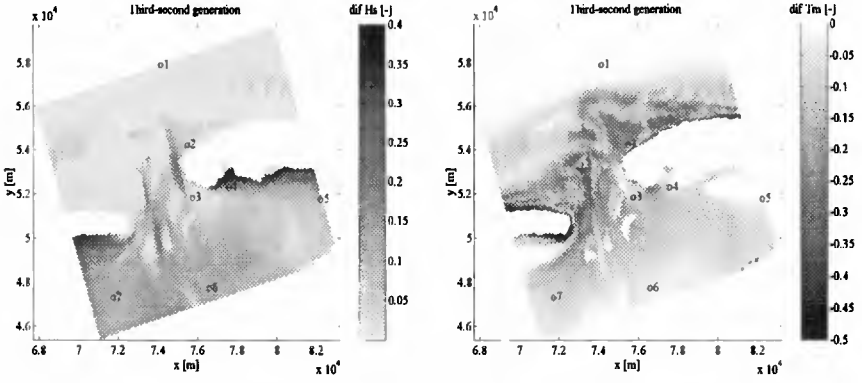

Fig. 10 The relative differences in significant wave height and mean wave period for the Norderneyer Seegat (2nd-generation compared to 3rd-generation).

where the refraction effect seems to be particularly clear, with the 3rd-generation mode without triad wave-wave interactions. These results seem to confirm that indeed refraction is affected by these interactions (through the difference in wave periods). To show that other effects can be ignored, these computations have been repeated without refraction (by de-activating the refraction term in the basic equation). The results are shown in Fig. 11 and they confirm the speculation about the indirect effect of the triad wave-wave interactions on refraction.

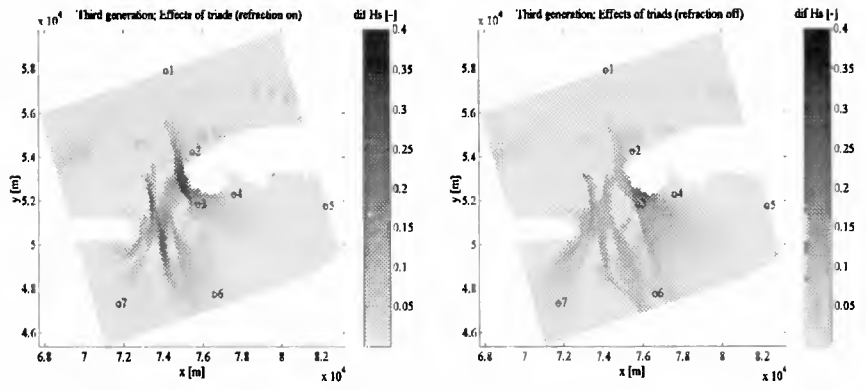

Fig. 11 The effect of triad wave-wave interactions on the refraction in the Norderneyer Seegat. Left panel: relative difference in significant wave height in 3rd generation mode due to disabling refraction with triad wave-wave interactions active, right panel: relative difference in significant wave height due to disabling refraction in 3rd generation mode without triad wave-wave interactions.

	Haringvliet		Norderneyer Seegat	
	rms H_s (m)	rms $\overline{T}$ (s)	rms H_s (m)	rms $\overline{T}$ (s)
1st-generation	0.33	0.45	0.23	0.84
2nd-generation	0.33	0.28	0.24	0.88
3rd-generation	0.39	0.43	0.23	1.03

Table 2 The root-mean-square errors (model results *vs* observations) for the 1st-, 2rd and 3rd-generation mode for the Haringvliet and Nordeneyer Seegat cases of this study.

The observations (see Figs. 3 and 6 for locations) should tell which of the three modes of SWAN provide the best wave estimates. Unfortunately, most of the observations have been taken in regions where the differences between the three modes are rather small (less than 10%). This is also obvious from the small differences between the errors in the three modes (see Table 2).

CONCLUSIONS

In the rather complex coastal field conditions of this study, the triad wave-wave interactions in the SWAN model (3rd-generation mode) generate a shorter wave period in very shallow water than in either the 1st- or 2nd-generation mode of SWAN. This affects the refraction pattern of the waves wich in turn affects the pattern of significant wave height. Moreover, the short-fetch wave growth is very different between the three modes.

Although a fair amount of observations is available, the locations of these observations are not well suited to discriminate between the three modes.

ACKNOWLEDGEMENTS

We are very grateful to John de Ronde, Joska Andorka Gal and their co-workers at the Ministry of Transport, Public Works and Water Management (the Netherlands) for providing us with the data of the Haringvliet. We are equally indebted to Hanz Niemeyer and Ralf Kaiser of the Niedersächsisches Landesamt für Ökologie - Forschungsstelle Küste - (Germany) for providing us with the data of the Norderneyer Seegat.

REFERENCES

Battjes, J.A. and J.P.F.M. Janssen, 1978: Energy loss and set-up due to breaking of random waves, *Proc. 16th Int. Conf. Coastal Engineering*, ASCE, 569-587

Booij, N., L.H. Holthuijsen and R.C. Ris, 1996, The "SWAN" wave model for shallow water, *Proc. 25th Int. Conf. Coastal Engineering*, 668-676

Bouws, E. and G.J. Komen, 1983: On the balance between growth and dissipation in an extreme, depth-limited wind-sea in the southern North Sea, *J. Phys. Oceanogr.*, **13**, 1653-1658

Cavaleri, L. and P. Malanotte-Rizzoli, 1981: Wind wave prediction in shallow water: Theory and applications. *J. Geophys. Res.*, **86**, No. C11, 10,961-10,973

Eldeberky, Y., 1996: Nonlinear transformation of wave spectra in the nearshore zone, Ph.D. thesis, Delft University of Technology, The Netherlands, 203 p.

Hasselmann, K., et al., 1973: Measurements of wind-wave growth and swell decay during the Joint North Sea Wave Project (JONSWAP), *Dtsch. Hydrogr. Z. Suppl.*, **12**, A8

Hasselmann, K., 1974: On the spectral dissipation of ocean waves due to whitecapping, *Bound.-layer Meteor.*, **6**, 1-2, 107-127

Hasselmann, S., K. Hasselmann, J.H. Allender and T.P. Barnett, 1985: Computations and parameterizations of the linear energy transfer in a gravity wave spectrum. Part II: Parameterizations of the nonlinear transfer for application in wave models, *J. Phys. Oceanogr.*, **15**, 11, 1378-139

Holthuijsen, L.H. and S. De Boer, 1988: Wave forecasting for moving and stationary targets, *Computer modelling in Ocean Engineering*, Eds. B.Y. Schrefler and O.C. Zienkiewicz, Balkema, Rotterdam, The Netherlands, 231-234

Holthuijsen, L.H., N. Booij and L. Bertotti, 1993, The effect of wind errors on ocean wave hindcasts, In: Proc. 12th Int. Conf. OMAE, ASME, Vol. 2, pp. 117-124

Snyder, R.L., Dobson, F.W., Elliott, J.A. and R.B. Long, 1981: Array measurement of atmospheric pressure fluctuations above surface gravity waves, *J. Fluid Mech.*, **102**, 1-59

SPM, Shore Protection Manual, 1973, U.S. Army Coastal Eng. Res. Center, Corps of Engineers, 1145 p.

WAMDI group, 1988: The WAM model - a third generation ocean wave prediction model, *J. Phys. Oceanogr.*, **18**, 1775-1810

WAVE TRANSFORMATION NEAR A QUASI-1D COAST

J.H. Andorka Gal[1], L.H. Holthuijsen[2],
J.C.M. de Jong[1,2] and A.T.M.M. Kieftenburg[2]

ABSTRACT

Two sets of observations of wave transformation near two quasi one-dimensional coasts, from deep water (22 m) to shallow water (0.5 m) have been simulated with the third-generation spectral wave model SWAN. The first set of observations contains wind waves that are generated by a local storm off the North Sea coast of the Netherlands. The second set contains a mix of swell and local wind waves at the Pacific coast of Japan. Repeated computations without triad wave-wave interactions show that the inclusion of this process in the model is essential. A f^{2}-dependency of the depth-induced dissipation (rather than the conventional frequency independence in SWAN), causes too much energy dissipation in the high frequencies, shifting the mean frequency to too low values.

INTRODUCTION

As waves approach a gently sloping coast, both the significant wave height and the mean wave period are reduced. The former is mostly due to depth-induced breaking. The latter can be ascribed to a transfer of energy from lower frequencies to higher frequencies (triad wave-wave interactions; e.g. Beji and Battjes, 1994) which is often evident from the generation of a secondary high-frequency peak in the observed spectra. To properly describe and understand such evolution, field observations and models that take into account the relevant physical processes are required. In the present study, observations of such waves approaching two, quasi-1D coasts (one in the Netherlands and one in Japan) are modelled with a third-generation spectral wave model. The computational results are compared with observations.

THE OBSERVATIONS

The waves that are considered in this study have been observed off the beach near the town of Petten in the Netherlands (waves from the southern North Sea; courtesy Ministry

---

1) Ministry of Transport, Public Works and Water Management, Kortenaerkade 1, 2500 EX The Hague, the Netherlands

2) Delft University of Technology, Stevinweg 1, 2628 CN Delft, the Netherlands

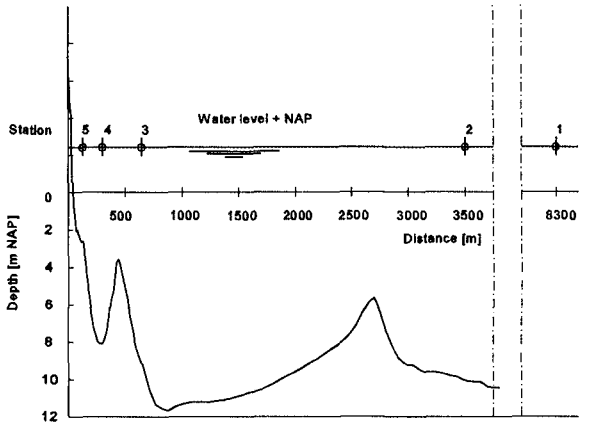

Fig. 1 The bathymetry and observation locations off the Petten coast.

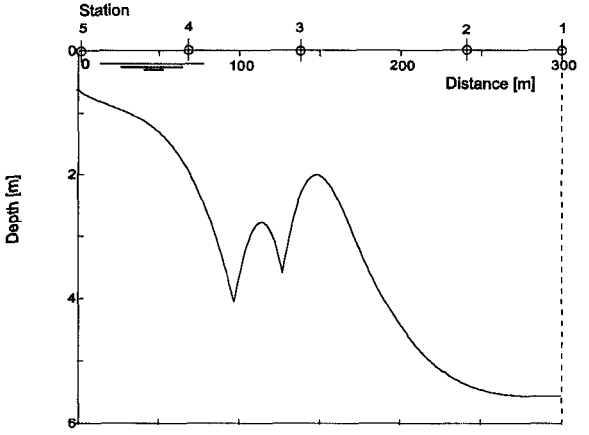

Fig. 2 The bathymetry and observation locations off the Kashimanada coast

of Transport, Public Works and Water Management, the Netherlands) and off the beach at the Kashimanada coast in Japan (waves from the Pacific Ocean; courtesy Hazaki Oceanographical Research Facility, Port and Harbour Research Institute, Japan; Nakamura and Katoh, 1992). In both cases the coast is rather straight with two sand bars (Figs. 1 and 2).

The observations are made from deep water to the shore, along a line normal to the beach over a distance of about 8.3 km in the Petten case (from 22.0 m to 4.2 m water depth). The data set from Kashima overlaps this range on the shallow water with the observations starting at about 300 m from shore, from 5.4 m to 0.5 m water depth. Several

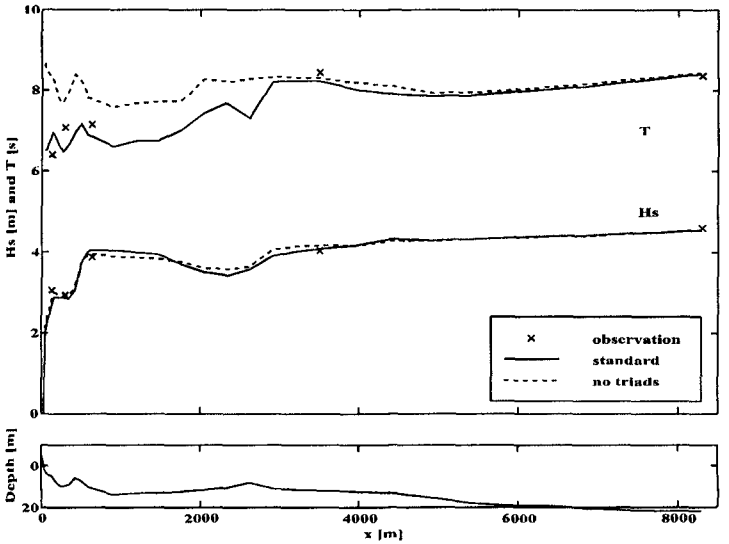

Fig. 3 The observed and computed significant wave height and mean wave period for the Petten case, with and without triad wave-wave interactions.

techniques were used to measure the waves along these transects: buoys (directional and omni-directional), wave gauges and a pressure transducer (Petten) and ultra-sonic wave gauges (Kashima). From the Petten data set, a storm situation is selected with a uni-modal, deep-water spectrum (characteristic for a local storm in a sheltered sea). It has been described by Eldeberky et al. (1997). From the Kashima data set a situation is available with a bi-modal, deep-water spectrum (characteristic for the mix of wind sea and swell along an open oceanic coast). It has been described by Beji and Nadaoka (1998).In the Petten case, the wind speed was 18.6 m/s, the deep-water significant wave height was 4.61 m and the mean wave period was 8.4 s (peak period 10.0 s). In this case the (uni-modal) spectrum shows qualitatively the above described characteristic behaviour as the waves propagate along the transect. In the measurements the significant wave height reduces to 3.07 m at the shallowest station. Remarkably the observed significant wave height-to-depth ratio remains well above the value of 0.4 which is often used in engineering practice. The mean wave period reduces to about 6.4 s while the peak period remains constant. In the Kashima case, the wind is ignored, the deep-water significant wave height was 1.68 m and the mean wave period was 5.7 s (peak period 14.9 s). Here the observed wave height reduces to 0.32 m at the shallowest station (0.5 m water depth so that the observed ratio of significant wave height-to-depth ratio equals 0.64). The evolution of the observed spectra and of the significant wave height H_s and the mean wave period $\overline{T}$ defined as $H_s = 4\sqrt{m_0}$ and $\overline{T} = 2\pi(m_1/m_0)^{-1}$ where $m_n = \int\int \sigma^n E(\sigma,\theta)d\sigma d\theta$, are given in Figs. 3 through 6.

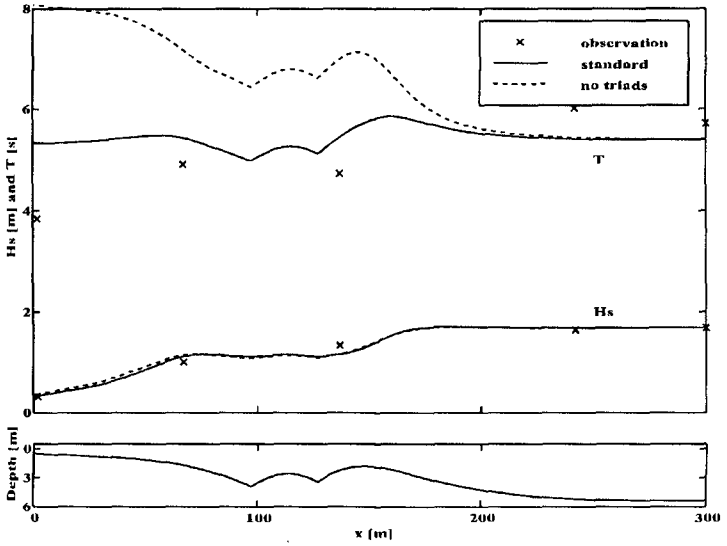

Fig. 4 The observed and computed significant wave height and mean wave period for the Kashima case, with and without triad wave-wave interactions.

THE WAVE MODEL

The wave model is a discrete spectral model which is based on the action balance equation of random, short-crested waves (the SWAN wave model; e.g. Booij et al., 1996). It is a discrete spectral model based on the action balance equation which for Cartesian coordinates is

$$\frac{\partial}{\partial t}N + \frac{\partial}{\partial x}c_x N + \frac{\partial}{\partial y}c_y N + \frac{\partial}{\partial \sigma}c_\sigma N + \frac{\partial}{\partial \theta}c_\theta N = \frac{S}{\sigma} \qquad (1)$$

in which $N(\sigma, \theta, x, y, t)$ is the action density as a function of intrinsic frequency σ, direction θ, horizontal coordinates x and y and time t. The first term in the left-hand side of this equation represents the local rate of change of action density in time, the second and third term represent propagation of action in geographical space (with propagation velocities in x- and y-space, c_x and c_y respectively). The fourth term represents shifting of the intrinsic frequency due to variations in depths and currents (with propagation velocity in σ-space, c_σ). The fifth term represents depth- and current-induced refraction (with propagation velocity in θ-space, c_θ). The expressions for these propagation speeds are taken from linear wave theory. The source terms are taken from the WAM model (WAM Cycle 3; WAMDI, 1988: exponential growth by wind, quadruplet wave-wave interactions, whitecapping and bottom friction). They are supplemented with a spectral version of the dissipation model for depth-induced breaking of Battjes and Janssen (1978)and a discrete interaction approximation for the triad wave-wave interactions (Eldeberky 1996). It was verified that the processes of depth-induced wave breaking and

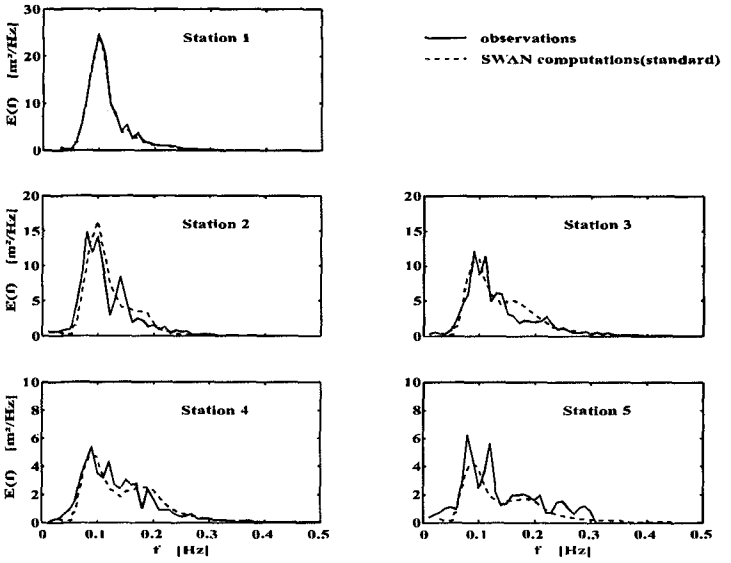

Fig. 5 The observed and computed spectra for the Petten case.

triad wave-wave interactions dominate the evolution of the waves in the present study. The formulations of these processes is therefore briefly addressed here.

Laboratory observations (e.g., Battjes and Beji, 1992; Vincent et al. 1994; Arcilla et al., 1994 and Eldeberky and Battjes, 1996) have shown that the shape of initially uni-modal spectra propagating across simple (barred) beach profiles, is fairly insensitive to depth-induced breaking. This has led Eldeberky and Battjes (1995) to formulate a spectral version of the bore model of Battjes and Janssen (1978) which conserves the spectral shape. Expanding their expression to include directions, the expression that is used in SWAN is:

$$S_{ds,br}(\sigma,\theta) = -\frac{D_{tot}}{E_{tot}} E(\sigma,\theta) \tag{2}$$

in which E_{tot} is the total wave energy and D_{tot} is the rate of dissipation of the total energy due to wave breaking according to Battjes and Janssen (1978). The value of D_{tot} depends critically on the breaking parameter $\gamma = H_{max}/d$ (in which H_{max} is the maximum possible individual wave height in the local water depth d). The value in the SWAN computations is $\gamma = 0.73$ (the mean value of the data set of Battjes and Stive, 1985).

A first attempt to describe triad wave-wave interactions in terms of a spectral energy source term was made by Abreu et al. (1992). However, their expression is restricted to non-dispersive shallow water waves and is therefore not suitable in many practical applications of wind waves. The breakthrough in the development came with the work of Eldeberky and Battjes (1995) who transformed the amplitude part of the Boussinesq model of Madsen and Sørensen (1993) into an energy density formulation and who parameterized the biphase of the waves on the basis of laboratory observations (Battjes and Beji, 1992; Arcilla et al., 1994). A discrete triad approximation (DTA) for co-linear waves was

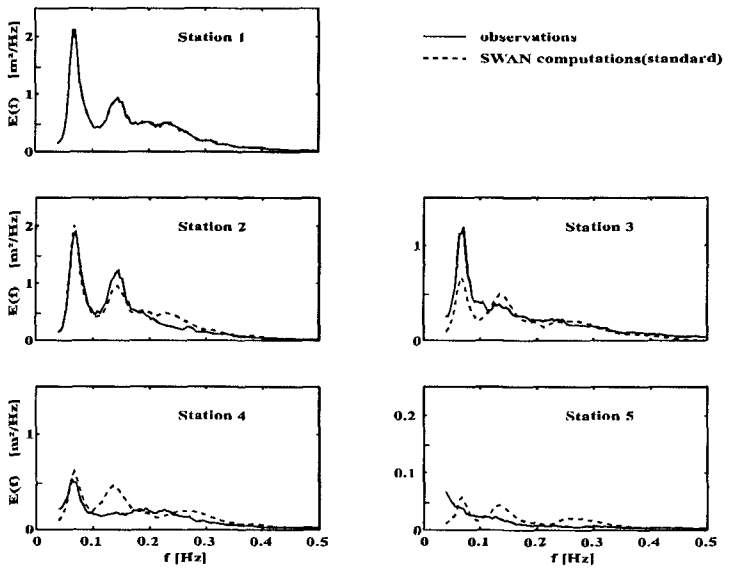

Fig. 6 The observed and computed spectra for the Kashima case.

subsequently obtained by considering only the dominant self-self interactions. Their model has been verified with flume observations of long-crested, random waves breaking over a submerged bar (Beji and Battjes, 1993) and over a barred beach (Arcilla et al., 1994). The model appeared to be fairly successful in describing the essential features of the energy transfer from the primary peak of the spectrum to the super harmonics. The slightly different version of Eldeberky (1996) is used in SWAN (the lumped triad approximation).

COMPUTATIONS AND RESULTS

The Petten case has been computed as a two-dimensional case (although the coast is fairly straight) with the two-dimensional spectrum at deep-water taken from the observations (a directional buoy at station 1, Figs.1 and 5). The Kashima case has been computed as a one-dimensional case (see Beji and Nadaoka, 1998) with the two-dimensional, deep-water spectrum constructed from the observed one-dimensional spectrum with the assumption that the mean wave direction is normal to the shore and that the directional spreading is relatively narrow for the swell part of the spectrum ($\sigma_\theta = 5°$ for $f < 0.1$ Hz) and typical for wind sea for the higher frequencies ($\sigma_\theta = 30°$ for $f > 0.1$ Hz). For both cases the model results in terms of the significant wave height and the mean wave period are shown in Figs. 3 and 4, respectively. The agreement with the observations is fairly good with a slightly better model performance in the Petten case than in the Kashima case: the rms-error in the significant wave height and mean wave period are about 7 % and 5 % of the deep water values respectively in the Petten case, *versus* 7 % and 16 % in the Kashima case. The difference in performance is also illustrated with the computed spectra in Fig. 5 and 6 where it is obvious that the amount of energy at the peak frequency for the shallowest stations is slightly better predicted in the Petten case.

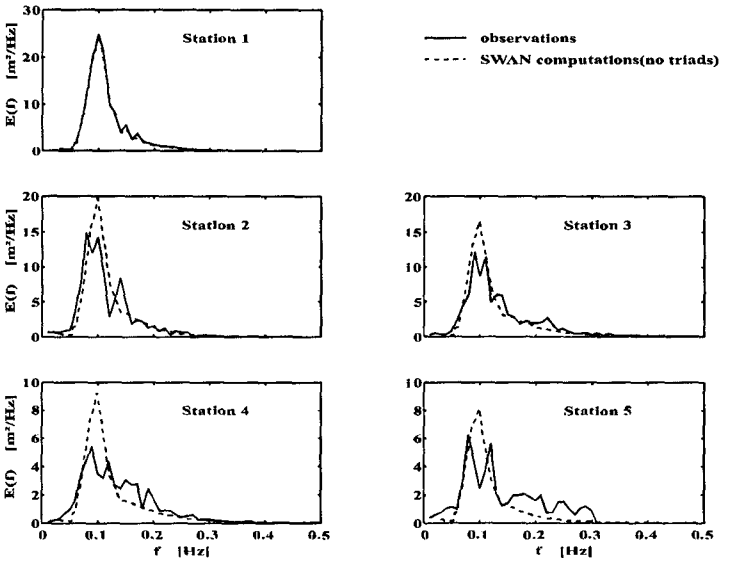

Fig. 7 The computed spectra for the Petten case without triad wave-wave interactions, compared with measured data (compare with Fig. 5).

DISCUSSION

As noted above, the computations were carried out with triad wave-wave interactions active. To illustrate the effect of these triad wave-wave interactions, the computations have been repeated without these interactions. The results in terms of significant wave height and mean wave period are shown in Figs. 3 and 4 and in terms of the spectra in Figs. 7 and 8. It is evident that the significant wave height is only marginally affected but that the mean wave period is greatly affected, especially in the shallowest region. The inclusion of these interactions also gives a much better agreement with the observations of the spectra (notably near the low-frequency peak).

In the above computations, the spectral distribution of the depth-induced wave breaking is proportional to the energy density and independent of frequency. This is based on observations of initially unimodal spectra. However, Mase and Kirby (1992, supported by Elgar et al., 1997) found a f^2-dependency in many observations, although Chen et al. (1997) inferred from observations and simulations with a Boussinesq model that the high-frequency (i.e. above the lowest peak frequency) levels in the spectra are insensitive to such frequency dependency. This is due the approximate compensation of the increased dissipation at high frequencies by increased nonlinear energy transfer (but they did find the frequency dependency to be relevant in time domain). To investigate this for the Kashima case, the computations have been repeated for this case with such f^2-dependency ($F = 0$ in the notation of Chen et al., 1997). The results are shown in Figs. 9 and 10. The significant wave height is only marginally affected but the mean wave period is significantly affected in the shallowest region. The spectra at stations 4 and 5 show that this

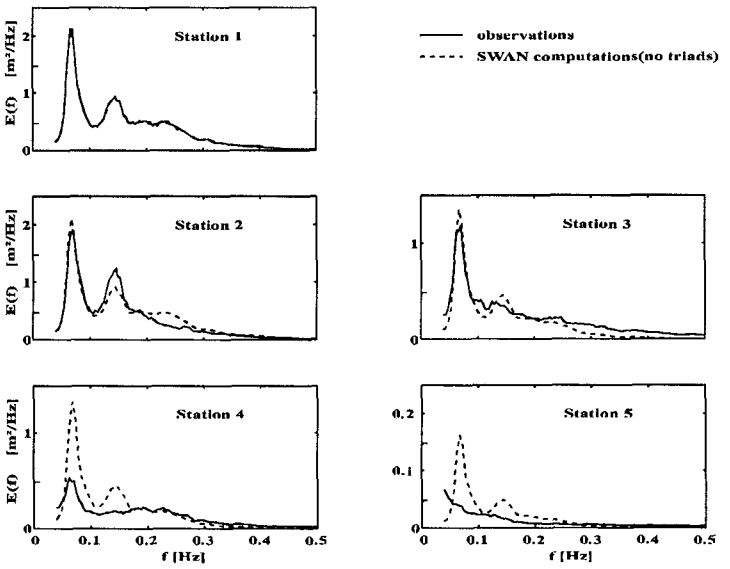

Fig. 8 The computed spectra for the Kashima case without triad wave-wave interactions (with $\sigma_\theta = 5°$ for $f < 0.1$ Hz and $\sigma_\theta = 30°$ for $f > 0.1$ Hz), compared with measured data (compare with Fig. 6).

is due the overestimation of the amount of energy at the lower frequencies.

Separate computations with individual processes of generation, dissipation and wave-wave interactions de-activated show the relatively minor importance of wind generation, bottom friction, whitecapping and quadruplet wave-wave interactions and the dominant effect of depth-induced wave breaking and triad wave-wave interactions.

CONCLUSIONS

The observed evolutions of a uni-modal spectrum and of a bi-modal spectrum, approaching a gently sloping, barred coast of a shelf sea (North Sea) and an oceanic coast (Pacific Ocean) respectively have been numerically simulated with the third-generation SWAN wave model. The agreement between the observed and computed evolution, both in terms of integral wave parameters and spectra is rather good. Repeated computations without triad wave-wave interactions show that the inclusion of this process in the model is essential. A f^2-dependency of the depth-induced dissipation (rather than the conventional frequency independence in SWAN), causes too much energy dissipation in the high frequencies, shifting the mean frequency to too low values.

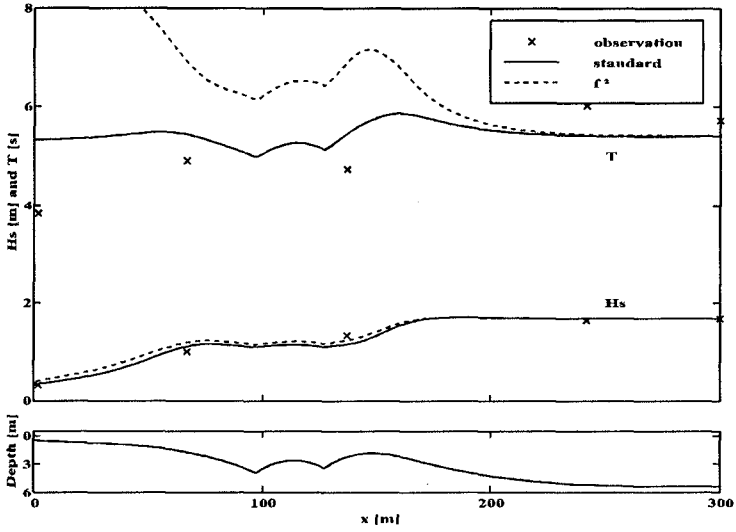

Fig. 9 The observed and computed significant wave height and mean wave period for the Kashima case, with and without f^2-dependency of depth-induced breaking (F=0).

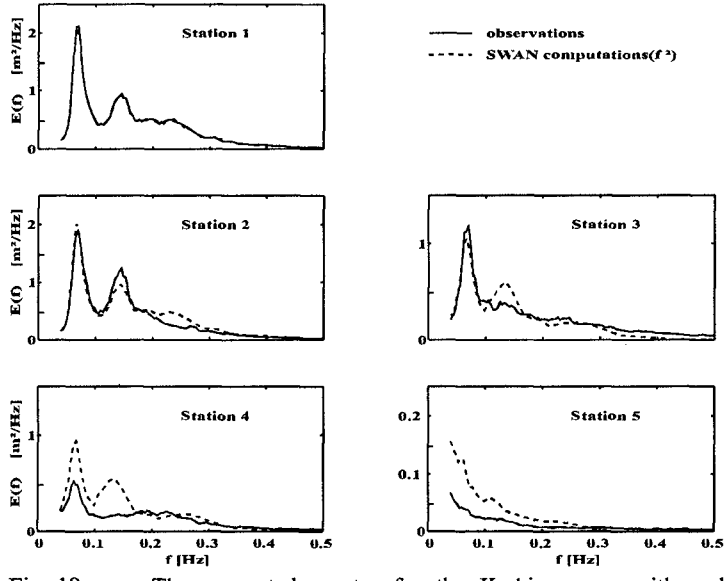

Fig. 10 The computed spectra for the Kashima case with and without f^2-dependency of depth-induced breaking (F=0).

ACKNOWLEDGEMENTS

We are very grateful to S. Nakamura and K. Katoh of the Port and Harbour Research Institute of Japan who gave us a unique opportunity to work with data from the Hazaki Oceanographical Research Facility by providing us with the observations and giving us permission to publish. We received the data through the good office of K. Nadaoka of the Tokyo Institute of Technology and S. Beji (on leave at the Tokyo Institute of Technology from the Istanbul University of Technology) who we hereby thank for their support and assistance.

REFERENCES

Abreu, M., Larraza, A. and E. Thornton, 1992: Nonlinear transformation of directional wave spectra in shallow water, *J. Geophys. Res.*, **97**, 15579-15589

Arcilla, A.S., J.A. Roelvink, B.A. O'Connor, A.J.H.M. Reniers and J.A. Jimenez, 1994: The Delta flume '93 experiment, *Proc. Coastal Dynamics Conf. '94*, 488-502

Battjes, J.A. and J.P.F.M. Janssen, 1978: Energy loss and set-up due to breaking of random waves, *Proc. 16th Int. Conf. Coastal Engineering*, ASCE, 569-587

Battjes, J.A. and S. Beji, 1992: Breaking waves propagating over a shoal, *Proc. 23rd Int. Conf. Coastal Engineering*, ASCE, 42-50

Battjes, J.A. and M.J.F. Stive, 1985: Calibration and verification of a dissipation model for random breaking waves, *J. Geophys. Res.*, **90**, No. C5, 9159-9167

Beji, S. and J.A. Battjes 1993: Experimental investigation of wave propagation over a bar, *Coastal Engineering*, **19**, 151-162

Beji, S and J.A. Battjes, 1994: Numerical simulation of nonlinear waves propagating over a bar, Coastal Engineering, 23, 1-16

Beji, S. and K. Nadaoka, 1998: Spectral modelling of nonlinear wave shoaling and breaking over arbitrary depths, Coastal Dynamics'97, Ed. E.B. Thornton, ASCE, Plymouth, 285-294

Booij, N., L.H. Holthuijsen and R.C. Ris, 1996: The "SWAN" wave model for shallow water, 25th Int. Conf. Coastal Engng., Orlando, pp. 668-676

Chen, Y., R.T. Guza and S. Elgar, 1997: Modelling of breaking surface waves in shallow water, *J. Geophys. Res.*, 102, C11, 25035-25046

Eldeberky, Y., 1996: Nonlinear transformation of wave spectra in the nearshore zone, Ph.D. thesis, Delft University of Technology, Department of Civil Engineering, The Netherlands

Eldeberky, Y. and J.A. Battjes, 1995: Parameterization of triad interactions in wave energy models, *Proc. Coastal Dynamics Conf. '95*, Gdansk, Poland, 140-148

Eldeberky, Y. and J.A. Battjes, 1996: Spectral modelling of wave breaking: Application to Boussinesq equations, *J. Geophys. Res.*, **101**, No. C1, 1253-1264

Eldeberky, Y., O.R. Sørensen and J.A. Battjes, 1997: Numerical simulation of wave transformation in the nearshore zone, *Proc. Coastal Dynamics Conf. '97*, ASCE, 147-156

Elgar, S., R.T. Guza, B. Raubenheimer, T.H.C. Herbers and E.L. Gallagher, 1997: Spectral evolution of shoaling and breaking waves on a barred beach, *J. Geophys. Res.*, 102,C7, 15797-15805

Madsen, P.A. and O.R. Sørensen, 1993: Bound waves and triad interactions in shallow water, *Ocean Engineering*, **20**, 4, 359-388

Mase, H. and J.T. Kirby, 1992: Hybrid frequency-domain KdV equation for random wave transformation, *Proc. 23th Int. Conf. Coastal Engineering*, ASCE, 474-487

Nakamura, S. and K. Katoh, 1992: Generation of infra-gravity waves in breaking process of wave groups, *Proc. 23th Int. Conf. Coastal Engineering*, ASCE, 990-1003

Vincent, C.L., J.M. Smith and J. Davis, 1994: Parameterization of wave breaking in models, *Proc. of Int. Symp.: Waves - Physical and Numerical Modelling*, Univ. of British Columbia, Vancouver, Canada, M. Isaacson and M. Quick (Eds.), Vol. II, 753-762

WAMDI group, 1988: The WAM model - a third generation ocean wave prediction model, *J. Phys. Oceanogr.*, **18**, 1775-1810

A new formulation of deterministic and stochastic evolution equations for three-wave interactions involving fully dispersive waves

Per A. Madsen[1] and Yasser Eldeberky[1]

Abstract

This paper presents a new and more accurate set of deterministic evolution equations for three-wave interactions involving fully dispersive, weakly nonlinear, irregular, unidirectional waves. The equations are derived directly from the Laplace equation with leading order nonlinearity in the surface boundary conditions. It is demonstrated that previous fully dispersive formulations from the literature have used an inconsistent linear relation between the velocity potential and the surface elevation. As a consequence these formulations are accurate only in shallow water, while nonlinear transfer of energy is significantly underestimated for larger wave numbers. In the present work we correct this inconsistency. In addition to the improved deterministic formulation, we present improved stochastic evolution equations in terms of the energy spectrum and the bispectrum for unidirectional waves.

1. Introduction

Three-wave interactions (or triad interactions) generally play an important role in the nonlinear transformation of irregular waves in shallow or intermediate depth waters. Very often these phenomena can be described quite accurately by Boussinesq-type formulations either in terms of time-domain equations (see e.g. Madsen & Sørensen, 1993) or in terms of evolution equations for the spatial variation of the complex amplitudes at discrete frequencies (see e.g. Freilich & Guza, 1984; Madsen & Sørensen, 1993). In both cases the phase information is retained and we talk about deterministic formulations.

Recently, Herbers & Burton (1997) and Kofoed-Hansen & Rasmussen (1998) presented stochastic formulations derived from deterministic Boussinesq-type evolution equations. In their formulations the second- and third-order statistics of random, shoaling waves are described by a coupled set of evolution equations for the energy spectrum and the bispectrum.

[1] International Research Centre for Computational Hydrodynamics (ICCH), Agern Allé 5, DK-2970 Hørsholm, Denmark.

While Boussinesq-type formulations are generally more or less restricted by weak dispersion, the approach by Agnon et al. (1993) and Kaihatu & Kirby (1995) retains full dispersion. They presented deterministic evolution equations derived directly from the Laplace equation with leading order nonlinearity in the surface boundary conditions. On this basis Agnon & Sheremet (1997) derived stochastic evolution equations for the energy spectrum and the bispectrum.

One of the key arguments by Agnon et al. (1993) and Kaihatu & Kirby (1995) for deriving equations with full dispersion was the need for a nonlinear evolution equation describing the interaction processes all the way from deep to shallow water. Indeed, triad interaction models based on fully dispersive equations can be expected to be superior to those based on Boussinesq-type formulations for large wave numbers not only in terms of improved dispersion but also in terms of a higher accuracy in nonlinear transfer functions. This should generally result in more accurate estimates of higher-order statistics such as skewness and asymmetry.

On the other hand, this expectation of a superior accuracy relative to existing Boussinesq formulations, has not yet been demonstrated in the literature. In fact, Kaihatu & Kirby (1995, 1996) concluded that "the lowest order Boussinesq model, despite its shallow water formalism, yields skewness and asymmetry values closer to those of the experimental data than those of the fully dispersive model". This conclusion was indeed disappointing.

In the present work we shall demonstrate that while the previous formulations by Agnon et al. (1993), Kaihatu & Kirby (1995, 1996), and Agnon & Sheremet (1997) presented consistent nonlinear equations for the velocity potential, they invoked an inconsistent linear relation to obtain the corresponding equations for the surface elevation. We shall show that high accuracy for larger wave numbers is achieved only if a nonlinear transformation is invoked, and we shall derive a new set of fully dispersive evolution equations for the surface elevation. Section 2 contains a brief review of the derivation of deterministic evolution equations in terms of the velocity potential. In Section 3 these equations are converted into equations for the surface elevation using: 1) a linear transformation; 2) a second order transformation. In section 4, a coupled set of stochastic evolution equations for the energy spectrum and the bispectrum is presented. Model validation is given in Section 5, while summary and conclusions can be found in Section 6.

2. Deterministic evolution equations in terms of the velocity potential

In this section we give a brief outline of the derivation of deterministic evolution equations in terms of the velocity potential at the still water level. The equations include leading order nonlinearity and full dispersion. The derivation follows the work by Agnon et al. (1993) and Kaihatu & Kirby (1995).

We adopt a Cartesian co-ordinate system (x, z) with z measured upwards from the still water level. The fluid domain is bounded by the sea bed at $z = -h(x)$ and the free surface $z = \eta(x,t)$. The fluid is assumed incompressible and inviscid, and the flow is assumed to be irrotational. Dimensional quantities are retained with the understanding that leading order nonlinearity is $O(\varepsilon^2)$, where the nonlinearity parameter ε is defined by kA (k being the wave number and A the wave amplitude). After expanding the nonlinear free surface boundary conditions in Taylor series about $z=0$ and retaining terms to $O(\varepsilon^2)$, the truncated boundary value problem in terms of the velocity potential Φ reads,

$$\nabla^2\Phi+\Phi_{zz}=0; \quad -h\le z\le 0, \tag{1}$$

$$\Phi_z+\nabla h\cdot\nabla\Phi=0; \quad z=-h, \tag{2}$$

$$\eta_t-\Phi_z+\nabla\cdot(\eta\nabla\Phi)=O(\varepsilon^3); \quad z=0, \tag{3}$$

$$\Phi_t+g\eta+\eta\Phi_{tz}+\tfrac{1}{2}(\nabla\Phi)^2+\tfrac{1}{2}(\Phi_z)^2=O(\varepsilon^3); \qquad z=0, \tag{4}$$

where ∇ is the horizontal gradient operator. We note that the linearized dynamic free surface boundary condition, i.e.,

$$\Phi_t+g\eta=O(\varepsilon^2); \qquad z=0, \tag{5}$$

can consistently be applied to eliminate η in the nonlinear terms in (3) and (4) by which we get

$$\eta_t-\Phi_z-\frac{1}{g}\nabla\cdot(\Phi_t\nabla\Phi)=O(\varepsilon^3); \quad z=0, \tag{6}$$

$$\Phi_t+g\eta-\frac{1}{g}\Phi_t\Phi_{tz}+\tfrac{1}{2}(\nabla\Phi)^2+\tfrac{1}{2}(\Phi_z)^2=O(\varepsilon^3); \quad z=0. \tag{7}$$

Substituting (7) into (6) yields

$$\Phi_{tt}+g\Phi_z-\left[\frac{1}{g}\Phi_t\Phi_{tz}-\tfrac{1}{2}(\nabla\Phi)^2-\tfrac{1}{2}(\Phi_z)^2\right]_t+\nabla\cdot(\Phi_t\nabla\Phi)=O(\varepsilon^3); \quad z=0 \tag{8}$$

The system of equations (1), (2) and (8) is the starting point for the derivation of evolution equations for weakly nonlinear and fully dispersive water waves.

First, we express the surface elevation and the velocity potential as a linear superposition of unidirectional waves,

$$\eta(x,t)=\frac{1}{2}\sum_{p=1}^{\infty}A_p(x)\exp\left[i\left(\omega_p t-\int k_p dx\right)\right]+\quad c.c. \tag{9a}$$

$$\Phi(x,z,t)=\frac{1}{2}\sum_{p=1}^{\infty}f_p(z)\,\tilde{\Phi}_p(x)\exp\left[i\left(\omega_p t-\int k_p dx\right)\right]+\quad c.c. \tag{9b}$$

where $\omega_p=p\Delta\omega$ is the frequency, $\Delta\omega$ is the band-width in the Fourier representation, k_p is the wave-number satisfying the linear dispersion relation, A_p and $\tilde{\Phi}_p$ are the complex spatially varying Fourier amplitudes, f_p represents the vertical structure of the velocity potential and c.c. indicates the complex conjugate.

The specification of the vertical structure f_p is one of the key elements in the derivation of evolution equations for fully dispersive waves. Agnon et al. (1993) initially considered the influence of bound waves as well as free waves on the vertical structure of the potential, but eventually they ignored the effect of the bound wave structure on their equations. Here we simply adopt the procedure of Kaihatu & Kirby (1995) and assume a vertical structure dictated by linear theory, i.e.

$$f_p(z) = \frac{\cosh k_p(h+z)}{\cosh k_p h} \tag{10}$$

where k_p is obtained from

$$\omega_p^{\,2} = g k_p \tanh k_p h \tag{11}$$

The spatial variations of water depth, wave numbers and complex amplitudes are assumed to be weak, and consequently the formulation will include only first derivatives of these quantities, while no derivatives will be included in connection with nonlinear terms. The resulting evolution equations derived by Agnon et al. (1993) and by Kaihatu & Kirby (1995) can be expressed by

$$\frac{d\widetilde{\Phi}_p}{dx} = -\frac{\widetilde{\Phi}_p}{2c_{g,p}}\frac{dc_{g,p}}{dx} + \left(\sum_{m=1}^{p-1} \beta^{+} \widetilde{\Phi}_m \widetilde{\Phi}_{p-m} e^{i\Delta\psi^{+}} + 2\sum_{m=1}^{N-p} \beta^{-} \widetilde{\Phi}_m^{*} \widetilde{\Phi}_{p+m} e^{i\Delta\psi^{-}} \right) \tag{12a}$$

where

$$\beta^{\pm} \equiv \frac{1}{8g^2 c_{g,p}} \left(\frac{g^2}{\omega_p} \left(\omega_{p\mp m} k_m^2 \pm \omega_m k_{p\mp m}^2 \right) \pm 2g^2 k_m k_{p\mp m} + \omega_m^2 \omega_{p\mp m}^2 \mp \omega_p^2 \omega_m \omega_{p\mp m} \right) \tag{12b}$$

$$\Delta\psi^{\pm} = \int \delta^{\pm} dx \quad , \qquad \delta^{\pm} \equiv \left(k_p \mp k_m - k_{p\mp m} \right) \tag{12c}$$

and where c_g is the group velocity. The first term in the right-hand-side of (12a) represents linear shoaling, while the second/third terms represent the nonlinear super/sub-harmonic interactions.

3. Deterministic evolution equations in terms of the surface elevation

In comparison with the evolution equations derived from Boussinesq-type equations (e.g., Freilich and Guza, 1984; Madsen and Sørensen, 1993), the set given by (12a-c) has the potential of being applicable to a wider range of wave numbers as it incorporates full dispersion. However, in order to utilise this potential, it is important to make a consistent transformation from the velocity potential to the surface elevation. In the following we convert (12a-c) into evolution equations for the amplitudes of the surface elevation using two different approaches: a) A linear transformation (Section 3.1); b) A second order transformation (Section 3.2).

3.1 Using the linear relation between the velocity potential and the surface elevation

In this section we follow Kaihatu & Kirby (1995) and apply the linear approximation (5) in combination with the Fourier representation (9), which yields

$$\widetilde{\Phi}_p = \frac{ig}{\omega_p} A_p \tag{13}$$

By substituting (13) into (12a) we obtain

$$\frac{dA_p}{dx} = -\frac{A_p}{2c_{g,p}}\frac{dc_{g,p}}{dx} + i\left(\sum_{m=1}^{p-1}\tilde{\alpha}^{+}A_m A_{p-m}e^{i\Delta\psi^{+}} + 2\sum_{m=1}^{N-p}\tilde{\alpha}^{-}A_m^{*}A_{p+m}e^{i\Delta\psi^{-}}\right) \tag{14a}$$

with

$$\tilde{\alpha}^{\pm} \equiv \pm\frac{g\,\omega_p}{\omega_m\,\omega_{p\mp m}}\beta^{\pm} \tag{14b}$$

where $\beta^{\pm}$ is given by (12b). These are the deterministic evolution equations derived by Agnon et al. (1993), and Kaihatu & Kirby (1995). Also Agnon & Sheremet (1997) used these equations as the basis for their stochastic formulation.

It turns out that the use of the linear approximation (5) results in inaccuracies in the nonlinear transfer functions. This can easily be demonstrated by the following example: Let us consider a velocity potential (at z=0) determined from Stokes second-order theory for regular waves, i.e.,

$$\tilde{\Phi}(x,t) = \tilde{\Phi}_1 sin(kx-\omega t) + \tilde{\Phi}_2 sin(2kx-2\omega t) \tag{15}$$

If we apply the linear approximation (5) on (15) we obtain as a consequence the second order surface elevation

$$\eta(x,t) = A_1 cos(kx-\omega t) + G_L\frac{A_1^2}{h}cos(2kx-2\omega t) \tag{16}$$

where

$$G_L \equiv \frac{3}{4}kh\frac{cosh2kh}{coshkh\,sinh^3 kh} \tag{17}$$

This obviously deviates from Stokes reference solution, which reads

$$G_{Stokes} \equiv \frac{1}{4}kh\frac{coshkh}{sinh^3 kh}(2+cosh2kh) \tag{18}$$

A Taylor expansion of (17) and (18) yields

$$G_L \rightarrow \frac{3}{4k^2h^2}\left(1+k^2h^2-\frac{11}{15}k^4h^4+O(k^6h^6)\right)$$

$$G_{Stokes} \rightarrow \frac{3}{4k^2h^2}\left(1+\frac{2}{3}k^2h^2+\frac{7}{45}k^4h^4+O(k^6h^6)\right) \tag{19}$$

which shows that the two expressions converge in shallow water. For comparison we may also consider the transfer function corresponding to the Boussinesq formulation of Madsen & Sørensen (1993) i.e.

$$G_{Bous} = \frac{3}{4k^2h^2}\left(1+\frac{8}{45}k^2h^2\right) \tag{20}$$

Fig. 1 shows the variation with kh of G_L and G_{Bous} relative to the target solution G_{Stokes}. In both cases the nonlinearity is significantly underestimated for larger kh values. This lack of accuracy in nonlinear transfer shows up in the numerical calculations in Section 5.

3.2 Using the nonlinear relation between the potential and the surface elevation

In the following we shall use (7) to establish the second-order relation between the surface elevation and the velocity potential. To a first approximation (9b) and (10) yield

$$\nabla\Phi = -ik\Phi, \qquad \Phi_t = i\omega\Phi, \qquad \Phi_z = \frac{\omega^2}{g}\Phi, \qquad z = 0 \tag{21}$$

Hence by the use of (21), the Fourier transformation of (7) now yields

$$A_p = \frac{-i\omega_p}{g}\widetilde{\Phi}_p + 2\left(\sum_{m=1}^{p-1}\widetilde{\gamma}^{+}\widetilde{\Phi}_m\widetilde{\Phi}_{p-m}e^{i\Delta\psi^{+}} + 2\sum_{m=1}^{N-p}\widetilde{\gamma}^{-}\widetilde{\Phi}_m^{*}\widetilde{\Phi}_{p+m}e^{i\Delta\psi^{-}}\right) \tag{22a}$$

where

$$\widetilde{\gamma}^{\pm} \equiv \frac{1}{8g^3}\left[\pm g^2 k_m k_{p\mp m} + \omega_m^2\omega_{p\mp m}^2 \mp \omega_p^2\omega_m\omega_{p\mp m}\right] \tag{22b}$$

One possibility is to solve (22) along with the evolution equation (12) in order to calculate the local variation of the surface elevation (see e.g. Chen et al., 1997). A better option is, however, to invert (22a) by the use of successive approximations and to eliminate the velocity potential from the evolution equations. Thus, we apply the linear approximation (13) in the nonlinear terms of (22a) and obtain

$$\widetilde{\Phi}_p = \frac{ig}{\omega_p}A_p + 2i\left(\sum_{m=1}^{p-1}\gamma^{+}A_m A_{p-m}e^{i\Delta\psi^{+}} + 2\sum_{m=1}^{N-p}\gamma^{-}A_m^{*}A_{p+m}e^{i\Delta\psi^{-}}\right) \tag{23a}$$

where

$$\gamma^{\pm} \equiv \pm\frac{g^3}{\omega_p\omega_m\omega_{p\mp m}}\widetilde{\gamma}^{\pm} \tag{23b}$$

The next step is to differentiate (23a) with respect to x while retaining terms to $O(\varepsilon^2)$. Consistent with the derivation of (12a-c), we ignore, in connection with the nonlinear terms, spatial derivatives of the slowly varying amplitudes and of the group velocity. With this assumption the differentiation of (23a) yields

$$\frac{d\widetilde{\Phi}_p}{dx} = \frac{ig}{\omega_p}\frac{dA_p}{dx} - 2\left(\sum_{m=1}^{p-1}\delta^{+}\gamma^{+}A_m A_{p-m}e^{i\Delta\psi^{+}} + 2\sum_{m=1}^{N-p}\delta^{-}\gamma^{-}A_m^{*}A_{p+m}e^{i\Delta\psi^{-}}\right) \tag{24}$$

where $\delta^{\pm}$ is defined by (12c). Finally after substituting (23a-b) and (24) into (12a), we get

$$\frac{dA_p}{dx} = -\frac{A_p}{2c_{g,p}}\frac{dc_{g,p}}{dx} + i\left(\sum_{m=1}^{p-1}\alpha^{+}A_m A_{p-m}e^{i\Delta\psi^{+}} + 2\sum_{m=1}^{N-p}\alpha^{-}A_m^{*}A_{p+m}e^{i\Delta\psi^{-}}\right) \tag{25a}$$

with

$$\alpha^{\pm} \equiv \pm\frac{g\omega_p}{\omega_m\omega_{p\mp m}}\left(\beta^{\pm} - \frac{g\tilde{\gamma}^{\pm}}{c_{g,p}}\Gamma^{\pm}\right), \qquad \Gamma^{\pm} \equiv \frac{2\delta^{\pm}c_{g,p}}{\omega_p} \tag{25b}$$

which, by inserting $\beta^{\pm}$ and $\tilde{\gamma}^{\pm}$ from (12b) and (22b), can be expressed as

$$\begin{aligned}\alpha^{\pm} = \pm\frac{\omega_p}{8g\,c_{g,p}\omega_m\omega_{p\mp m}}\Big[&g^2\omega_p^{-1}\left(\omega_{p\mp m}k_m^2 \pm \omega_m k_{p\mp m}^2\right)\\ &\pm\left(2-\Gamma^{\pm}\right)g^2k_m k_{p\mp m} + \left(1-\Gamma^{\pm}\right)\left(\omega_m^2\omega_{p\mp m}^2 \mp \omega_p^2\omega_m\omega_{p\mp m}\right)\Big]\end{aligned} \tag{25c}$$

The new deterministic evolution equation (25) is the main result of this work. The dispersion characteristics of the model are dictated by fully-dispersive linear theory. The present evolution equation insures, through the new complex interaction coefficient $\alpha^{\pm}$, a higher accuracy in the nonlinear transfer function. We emphasize that the nonlinear transformation between the velocity potential and the surface elevation is retained in the parameter Γ. The formulation (14a-b), as used by Agnon et al (1993), Kaihatu & Kirby (1995), and Agnon & Sheremet (1997), corresponds to setting $\Gamma = 0$ in (25).

The importance of including the Γ-terms in (25) is illustrated in Fig. 2, which shows the ratio of $\alpha^{\pm}_{\Gamma=0}$ to $\alpha^{\pm}$ as a function of ω_m and $\omega_{p\mp m}$. The upper triangle in Fig. 2 illustrates the super-harmonic interactions while the lower triangle illustrates the sub-harmonic interactions. The second-harmonic interaction is represented by the diagonal line and this result agrees with Fig. 1. It can be concluded that neglecting Γ has a major effect on super-harmonics which are consequently significantly underestimated, while the sub-harmonics are less sensitive.

4. Stochastic evolution equations for the energy spectrum and the bispectrum

Stochastic evolution equations for the energy spectrum and for the complex bispectrum can be derived on the basis of the deterministic evolution equations given by (25). We follow the procedure as outlined e.g. by Agnon and Sheremet (1997), Herbers & Burton (1997), and Kofoed-Hansen & Rasmussen (1998): Firstly, we multiply equation (25a) by the conjugate of A_p; secondly, the conjugate of equation (25a) is multiplied by A_p; thirdly, the former is added to the latter and finally the result is ensemble averaged. This leads to

$$\frac{dE_p}{dx} = -\frac{E_p}{c_{g,p}}\frac{dc_{g,p}}{dx} - 2\left[\sum_{m=1}^{p-1}\alpha^{+}\Im\left(B^{+}_{m,p-m}\right) - 2\sum_{m=1}^{N-p}\alpha^{-}\Im\left(B^{-}_{m,p+m}\right)\right] \tag{26}$$

where

$$E_p \equiv \left\langle A_p A_p^{*}\right\rangle, \qquad B^{+}_{m,p-m} \equiv \left\langle A_p^{*}A_m A_{p-m}e^{i\Delta\psi^{+}}\right\rangle, \qquad B^{-}_{m,p+m} \equiv \left\langle A_p^{*}A_m^{*}A_{p+m}e^{i\Delta\psi^{-}}\right\rangle \tag{27}$$

and where $\Im$ denotes the imaginary part and $\langle \ldots. \rangle$ is the ensemble average operator. The right-hand-side contains the average of the third-order moment, the so-called bispectrum, B. In order to obtain a stochastic description of the effect of the nonlinear interactions one needs to go to higher-order moments, and evaluate the bispectrum. An evolution equation for the bispectrum is derived and the terms including the trispectrum, i.e., fourth-order statistical average, appear. In order to close this system of equations, the trispectrum is expressed as products of second-order averages (the socalled Gaussian closure), and we retain only products of terms with opposite-signed phases. The resulting evolution equations of the bispectrum can be written as follows

$$\frac{dB^{+}_{m,p-m}}{dx} = (i\delta^{+} + F^{+})\, B^{+}_{m,p-m} - 2i\left[\alpha^{+}_{p,m,p-m} E_m E_{p-m} + \alpha^{-}_{m,p-m,p} E_p E_{p-m} + \alpha^{-}_{p-m,m,p} E_p E_m\right] \tag{28}$$

$$\frac{dB^{-}_{m,p+m}}{dx} = (i\delta^{-} + F^{-})\, B^{-}_{m,p+m} - 2i\left[\alpha^{-}_{p,m,p+m} E_m E_{p+m} + \alpha^{-}_{m,p,p+m} E_p E_{p+m} + \alpha^{+}_{p+m,m,p} E_p E_m\right] \tag{29}$$

where we emphasise that the $\alpha^{\pm}$ defined by (25c) is actually a short hand notation for $\alpha^{\pm}_{p,m,p\mp m}$, while $F^{\pm}$ denotes the shoaling term defined by

$$F^{\pm} \equiv -\frac{1}{2}\left(\frac{1}{c_{g,p}}\frac{dc_{g,p}}{dx} + \frac{1}{c_{g,m}}\frac{dc_{g,m}}{dx} + \frac{1}{c_{g,p\mp m}}\frac{dc_{g,p\mp m}}{dx}\right) \tag{30}$$

We note that (26), (28) and (29) comprise a coupled set of stochastic evolution equations for the energy spectrum and the bispectrum. The formulation is identical to Agnon and Sheremet (1997) except for the inclusion of the Γ-terms in $\alpha^{\pm}$.

The stochastic model explicitly takes into account, via the bispectrum, the development of the phase correlation between wave triads due to nonlinearity. In this model, the bispectrum is required to calculate the effects of triad wave interactions on the wave spectrum evolution. It can also be used to calculate the overall third-order statistical parameters such as the skewness and asymmetry.

5. Model verification

In order to validate the models from Sections 3 and 4, we concentrate on the experimental data from Cox et al. (1991). This test case considers the shoaling (and breaking) of irregular waves on a plane beach. The water depth at the offshore boundary is 47 cm and the beach slope is 1:20. The surface elevations are measured at eleven locations (denoted WG1 to WG11) in still water depths of 47, 35, 30, 25, 20, 17.5, 15, 12.5, 10, 7.5, and 5 cm. The target spectrum is a Pierson-Moskowitz type with a peak frequency of 1.0 Hz and with a significant wave height of 6.5 cm. At the incoming boundary the peak frequency corresponds to fairly large wave numbers (kh=1.9), and in combination with the broad-banded spectral shape this allows significant energy on frequencies that are well into the deep water range. Hence this test is quite demanding for models incorporating only weak dispersion and it is well suited for checking the applicability of fully dispersive models.

First we apply the stochastic formulation (26)-(30) with $\Gamma = 0$, which is basically the model of Agnon & Sheremet (1997). We note that similar results (not shown here) can be obtained by using the deterministic evolution equations of Agnon et al. (1993) and Kaihatu & Kirby (1995). Fig. 3a shows the computed and measured values of the skewness, while the asymmetry is shown in Fig 4a. Two different simulations are shown corresponding to offshore boundary conditions based on the measured bispectrum and a zero bispectrum, respectively. With the zero bispectrum, the skewness starts off with a zero and stays at that level on most of the shoal. The computed skewness is clearly significantly underestimated in most of the model area. This is in agreement with the analysis shown in Figs. 1 and 2. On the other hand, using the measured bispectrum as input does not really improve the simulation. Although the skewness is now correct right at the boundary, the mismatch between this value and the nonlinearity sustained by the model equations introduces a local recurrence phenomenon with a sudden decrease in the skewness and an increase in the asymmetry. Further inshore the skewness values computed by the two different boundary conditions are not very different. The large discrepancies between the computed and measured values of the asymmetry (Fig 4a) further inshore are due the mechanism of wave breaking, which is absent in the models considered here. It is emphasised that it requires a rather sophisticated breaking formulation in order to capture the variation of the asymmetry in the surf zone. A few examples of frequency domain formulations of wave breaking are discussed by Chen et al. (1997). This topic is, however, outside the scope of the present work.

For reference we have included the result of using the stochastic Boussinesq model of Kofoed-Hansen & Rasmussen (1998). As seen in Figs. 3b and 4b the computed skewness and asymmetry are quite similar to the ones obtained in Figs. 3a and 4a, and again the significant underestimate of the skewness is in agreement with the analysis in Fig. 1.

Figs. 3c and 4c show the result of including the new Γ-terms in the stochastic formulation. From Fig. 3c we notice that the computed skewness is significantly improved. The best result is now obtained by using the measured bispectrum as input, but even with a zero initial bispectrum the skewness and asymmetry values quickly fall in line with the measurements after a short distance dominated by recurrence.

Finally, Fig. 5 shows the energy spectra of the surface elevation computed by the stochastic model (26)-(30) including and excluding the new Γ-terms. In both cases the measured bispectrum is applied at the offshore boundary. The spectra are shown at three locations: WG2 (h=0.35m), WG5 (h=0.20m), and WG8 (h=0.125m). With Γ=0 we notice that the lack of nonlinearity in the model results in an artificial release of higher harmonics and an overestimation of the high-frequency tail of the spectrum. On the other hand, the model results obtained with the new Γ-terms are generally in good agreement with the measured spectra.

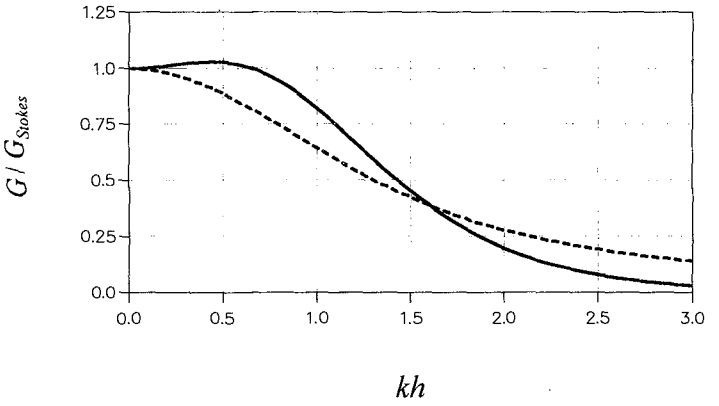

Figure 1. Transfer function for second harmonics. —— G_L / G_{Stokes} ; ----- G_{Bouss} / G_{Stokes}.

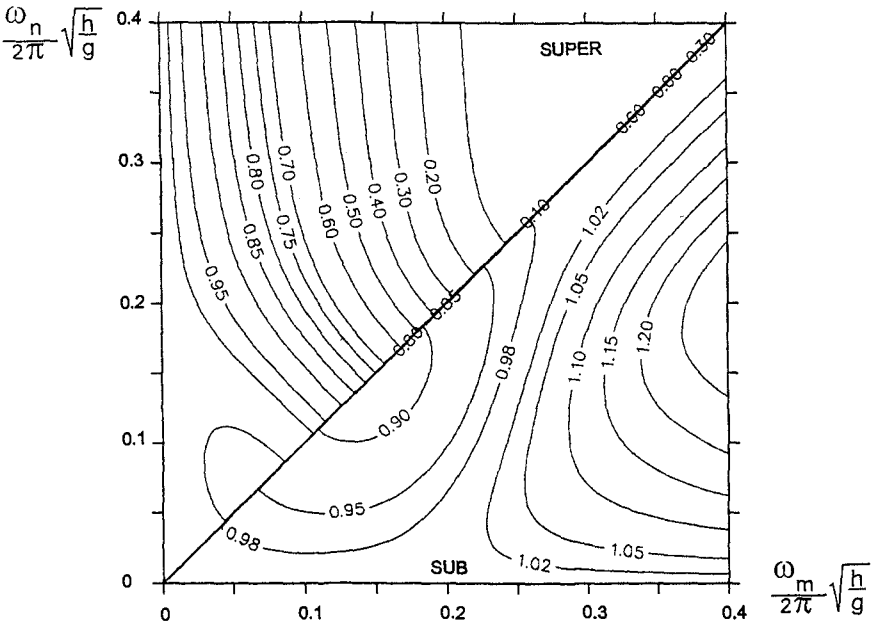

Figure 2. Isoline map of the ratio of $\alpha^{\pm}_{\Gamma=0}$ to $\alpha^{\pm}$ (from eq. 25c) as a function of the interacting frequencies ω_m and $\omega_n \equiv \omega_{p\mp m}$. Super-harmonic results shown above the diagonal; sub-harmonic results shown below it.

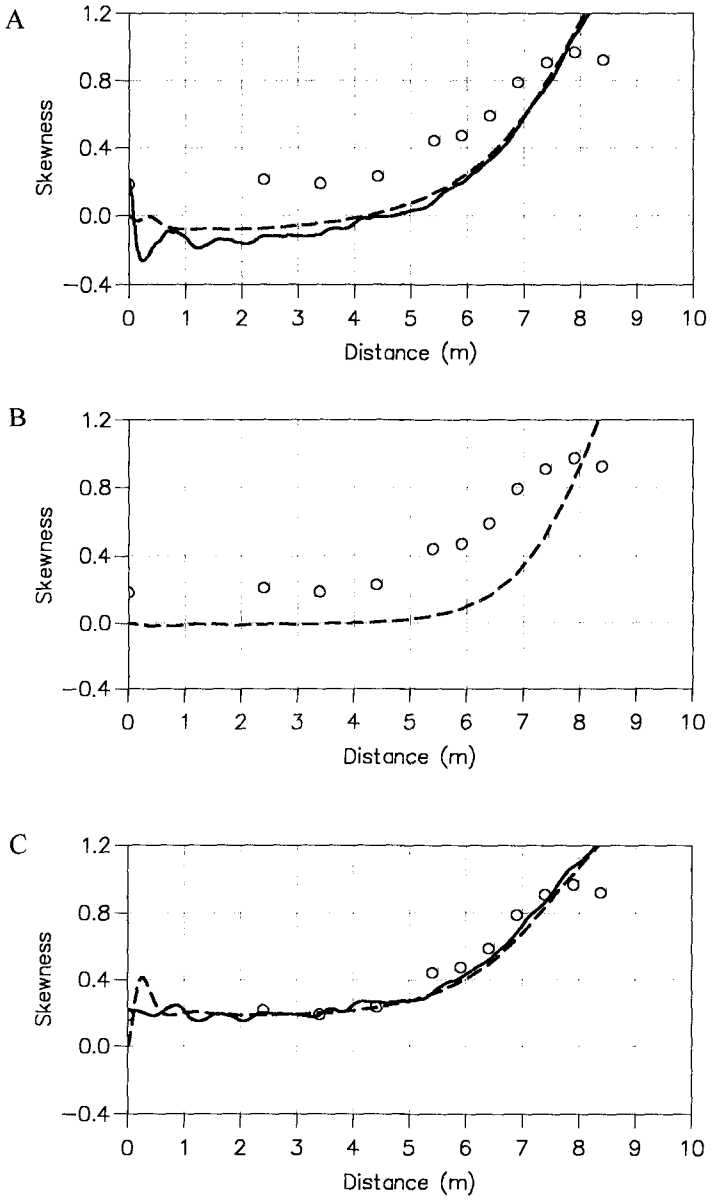

Figure 3. Spatial variations of the skewness during shoaling. Markers are measurements of Cox et al., 1991; ----- Computed with zero bispectrum at the boundary; —— Computed with measured bispectrum at the boundary. A) Stochastic model of Agnon & Sheremet (1997); B) Stochastic Boussinesq model of Kofoed-Hansen & Rasmussen (1998); C) Stochastic model based on the present formulation i.e. eqs (26)-(30) incl. the new Γ-terms.

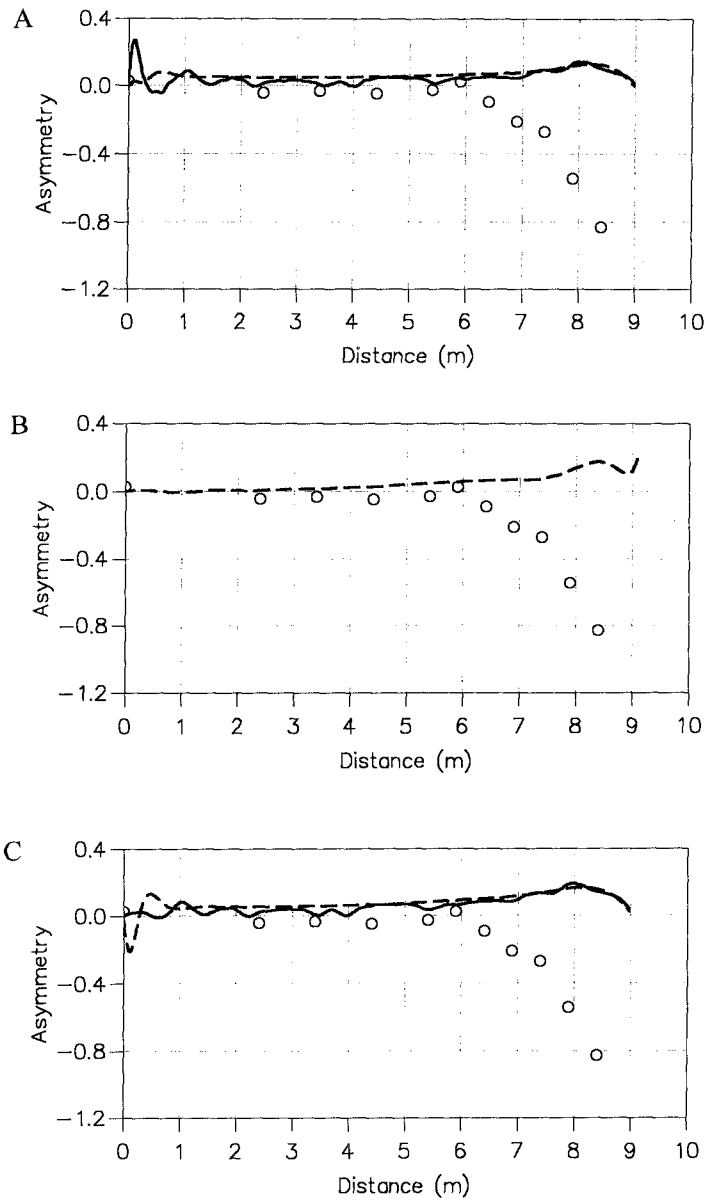

Figure 4. As Fig. 3, but for asymmetry instead of skewness.

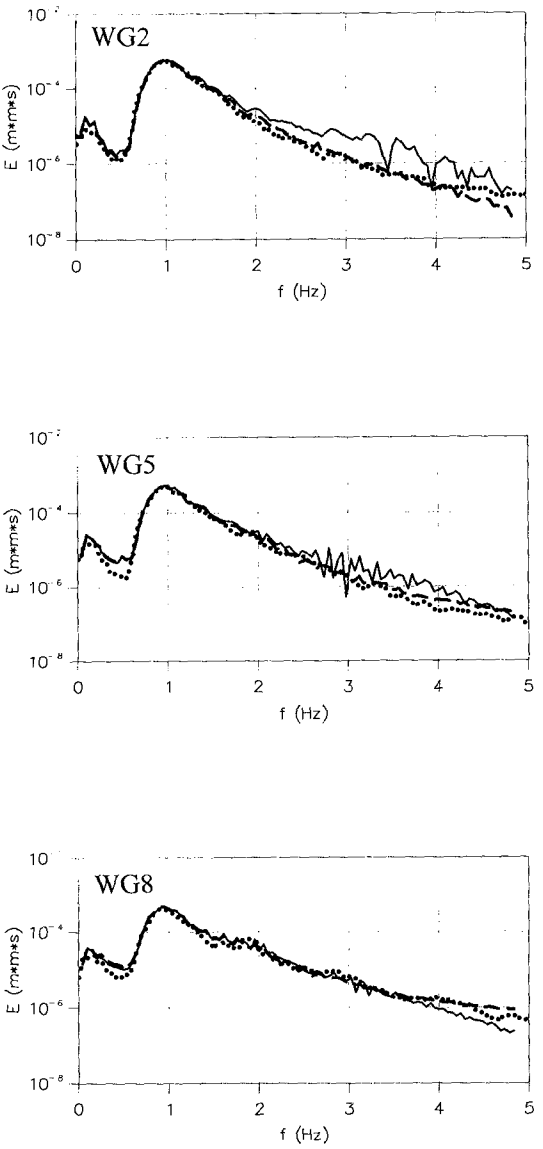

Figure 5. Energy spectra of the sea surface elevation at three locations WG2, WG5 and WG8. Computations made with the measured bispectrum at the boundary. —— Stochastic model of Agnon & Sheremet (1997); ----- Stochastic model based on the present formulation i.e. eqs (26)-(30) incl. the new Γ-terms; Dotted line indicates measurements of Cox et al. (1991).

6. Summary and conclusions

This paper presents a new and more accurate set of deterministic evolution equations for triad interactions involving fully dispersive, weakly nonlinear, irregular waves. Previous formulations from the literature have included consistent nonlinear evolution equations for the velocity potential, while an inconsistent linear relation has been invoked to obtain the corresponding surface elevation. This approximation is only valid in shallow water and as a result, the previous formulations significantly underestimate nonlinear energy transfer for larger wave numbers. As a consequence bound higher harmonics and nonlinear statistical measures such as the skewness are typically underestimated in these formulations.

In the present work we have corrected this inconsistency. Furthermore, in addition to the improved fully dispersive deterministic equations, we present a set of coupled stochastic evolution equations in terms of the energy spectrum and the bispectrum.

The influence of the new terms is demonstrated on a test case involving irregular waves in intermediate water depths. This case requires a combination of dispersion and nonlinearity and it is shown that existing formulations from the literature fail to predict the evolution of the energy spectrum and of the third-order statistics. A considerable improvement is found by including the new terms presented in this work. Further details and results can be found in Eldeberky & Madsen (1998).

Acknowledgements
The present work is financed by the Danish National Research Foundation. Their support is greatly appreciated.

References

Agnon, Y., A. Sheremet, J. Gonsalves, and M. Stianssnie, 1993, Nonlinear evolution of a unidirectional shoaling wave field, Coastal Eng., 20, pp. 29-58.

Agnon, Y., and A. Sheremet, 1997, Stochastic nonlinear shoaling of directional spectra, J. Fluid Mechanics, 345, pp. 79-100.

Chen, Y., R.T. Guza, S. Elgar, 1997, Modeling spectra of breaking surface waves in shallow water, J. Geophys. Res., Vol 102, No C11, pp 25,035-25,046.

Cox, D.T., H. Mase and T. Sakai (1991), An experimental on the effect of fluid acceleration on seabed stability, Report No. 91-HY-01, Kyoto University, Japan.

Eldeberky, Y., and P.A. Madsen, 1998, Deterministic and stochastic evolution equations for fully dispersive and weakly nonlinear waves, Submitted to Coastal Engineering.

Freilich, M.H., and R.T. Guza, 1984, Nonlinear effects on shoaling surface gravity waves, Philos. Trans. R. Soc. London., A 311, pp. 1-41.

Herbers, T.H.C, and M.C. Burton, 1997, Nonlinear shoaling of directionally spread waves on a beach, *J. Geophys. Res.*, 102(C9), pp. 21,101- 21,114.

Kaihatu, J.M., and J.T. Kirby, 1995, Nonlinear transformation of waves in finite water depth. *Physics of Fluids* 7 (8), pp. 1903-1914.

Kaihatu, J.M., and J.T. Kirby, 1996, Effects of mode truncation and dissipation on predictions of higher order statistics. In *Proc. of the 25th Coastal Eng. Conf., ch. 10,* pp. 123-136.

Kofoed-Hansen, H. and J.H. Rasmussen, 1998, Modelling of nonlinear shoaling based on stochastic evolution equations. *Coastal Engineering,* Vol. 33, pp 203-232.

Madsen, P.A., and O.R. Sørensen, 1993, Bound waves and triad interactions in shallow water, *J. Ocean Engng.*, 20(4), pp. 359-388.

The Horizontal Eddies in the Offshore Zone

Li Li[1], Robert A. Dalrymple[2]

Abstract:

The mean flow outside the surf zone can be unstable and form a train of submerged vortices, which migrate slowly in the offshore direction, as discovered by Matsunaga , Takehara & Awaya (1988, 1994). Li and Dalrymple (1998) conducted large scale experiments and a numerical study. They showed that two layers of vortices could exist over the water depth. Eddies near the water surface rotated in the opposite direction of eddies at mid-depth. For example, for the surface wave propagating to the right, the rotation direction of eddies near mid-depth was counterclockwise, while the rotation direction of eddies near surface was clockwise. The vortices decay offshore where there was no shear layers over water depth. Experimental and numerical studies show the velocity of long time scale vortical motion is uniform over water depth and is much slower than the undertow. A theoretical analysis showes that the stresses due to turbulence and wave serve as the source of the vorticity and this vortex train is formed by the shear instabilities of the mean flow in the cross-shore direction.

1 Introduction

The nearshore circulation system induced by wave breaking plays an important role in sediment transport. This circulation system (longshore, rip and cross-shore currents) has been studied for years to develop predictive models. The theory of longshore currents changed abruptly with the introduction of radiation stresses, which codified the momentum input to the surf zone by the waves; and lateral mixing, which is

[1]Graduate Student, Center for Applied Coastal Research, Department of Civil and Environment Engineering, University of Delaware, Newark, DE 19716, USA.

[2]Professor, Department of Civil and Environment Engineering, Center for Applied Coastal Research, University of Delaware, Newark, DE 19716, USA

necessary to create a smooth transition of longshore current from onshore to offshore of the breaker line.

In addition to the longshore currents, there are cross-shore currents flowing perpendicularly to the shoreline. The cross-shore currents consist of the mass transport to the shoreline carried by waves and return flow known as undertow. The undertow inside the surf zone has drawn much attention in the literature (e.g. Nadaoka et al. (1982), Svendsen et al. (1992), Okayasu et al. (1992) and Cox et al. (1995)).

Matsunaga et al. (1988, 1994) conducted a experiment on the flow outside the surf zone in a small wave tank (12 m long, 0.4 m deep, 0.15 m wide and equipped with a sloping planar bed). They discovered that the mean flow in the cross-shore direction outside the surf zone could be unstable and formed a single layer vortex train. The vortices rotate at the direction opposite the direction of the wave-induced water particle trajectories. They also found that these offshore migrating vortices would decay when it reached the region with deeper water depth. The formation of eddies is independent of the breaker type. Li and Dalrymple (1998) studied this offshore vortex train and concluded that the vortices formed due to the instability of undertow seaward of the breaker line. They also found that the vortices decayed when the velocity profile of the undertow becomes linear over the water depth.

Bagnold (1947) studied mass transport outside the surf zone by experiments. He discovered that there were a fast shoreward current along the bed and a slow seaward current under the water surface when two-dimensional surface wave propagating over a horizontal smooth bed. This phenomenon is due to the existence of Stokes layer and viscosity (Longuet-Higgins (1953)). Dore (1970) studied the mass transport outside the surf zone theoretically by taking into account the air-water interface. He concluded that on a clean interface the surface viscosity greatly affected the drift velocity of short waves and the air boundary layer greatly affected the long waves. The mean Eulerian velocity near the surface which is in the onshore direction had a greater onshore velocity than the Stokes drift. On the study of clean and contaminated fluid, Craik (1982) obtained similar results. Through a experimental study, Nadaoka et al. (1982) obtained linear velocity profile outside of the breaker line: a weak seaward velocity at the bed and a strong seaward velocity under the trough level. Cox et al. (1995) obtained similar velocity profile on the experiment of regular waves spilling on a 1 : 35 impermeable slope. Okayasu et al. (1992) conducted detailed laboratory measurements of the undertow due to regular and random waves on a 1 : 20 smooth uniform slope. Rather than a straight-line distribution over the depth outside the surf zone, their measured undertow velocity profiles are curved; it has a shoreward directed velocity at the bed and a seaward oriented velocity under the trough level. In the present study, we obtained the velocity profiles experimetally at the place where the vortices can be observed and at the place that the vortices decayed. This paper also investigate the offshore vortices experimentally and numerically.

2 Experimental Set-up

The wave experiments were conducted in a Precision Wave Tank (PWT) at the Center of Applied Coastal Research at the University of Delaware. This section describes the experimental setup and data acquisition procedure.

The experimental wave tank was 35 m long, 0.6 m deep and 0.6 m wide. It was 3 times longer, 4 times wider and 1.5 times deeper than the wave tank used by Matsunaga *et al.* (1988, 1994). Figure 1 shows a schematic of the experimental setup. The region at the wavemaker had constant depth, and the region at the other end had a sloping planar bed with 1 : 35 slope. A piston wavemaker was used to generate the two-dimensional periodic surface waves. As shown in Figure 1, three 3-D Acoustic Doppler Velocimetries (ADV) were used to obtain the Eulerian velocity outside of the surf zone. Two capacitance wave gages were used to measure the local wave height H and wave period T. The local phase velocity C was calculated from the time lag of signals from two wave gages that were located 20 cm apart. The local wavelength L was then determined from the product of the celerity and wave period.

The vortex train offshore of the breaker point was observed by flow visualization. Granules of water-soluble aniline blue dye was used as a tracer. Flow patterns were photographed through the glass sidewall of the tank using a 35 mm camera.

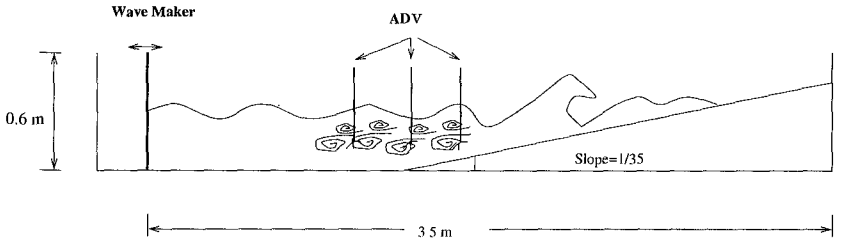

Figure 1: Schematic of experiment set-up.

Based on Matsunaga et al. (1994) (Figure 2), eight tests were designed to explore the effects of varying local water depth h and wave frequencies on the offshore vortex train (Table 1). Tests 1 through 4 were designed in the formation region: the combinations of the dimensionless wave height (H/L) and dimensionless water depth (h/L) would always generate vortices. Test 5 and Test 6 were in the region where the occurrence of vortex varies. Test 7 and Test 8 were designed in the region that no vortices were observed.

Table 1: List of Experiments

Test	Wave Period (s)	Water Depth (m)	h/L	H/L	Existence of Vortices
1	2.0	0.303	0.0925	0.0272	yes
2	2.0	0.310	0.0946	0.0267	yes
3	2.0	0.275	0.0878	0.0301	yes
4	2.0	0.313	0.0942	0.0285	yes
5	1.4	0.270	0.1306	0.0676	yes
6	1.4	0.381	0.1619	0.0594	yes
7	1.1	0.310	0.2057	0.0970	no
8	1.1	0.418	0.2580	0.0900	no

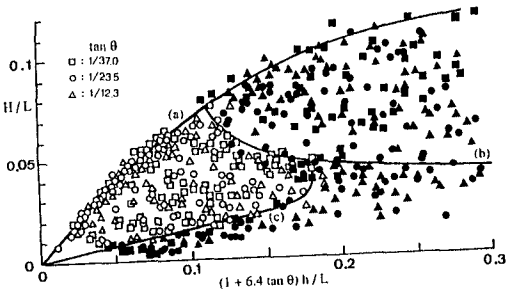

Figure 2: Formation regions of offshore vortices from Matsunaga, Takehara & Awaya (1994): open symbols, formation of offshore vortex; solid symbols, non-formation. Lines (a) and (b) indicate the limit of wave steepness and $H_0/L_0 = 4.2 \times 10^{-2}$, respectively. Line (c) is the offshore border of vortex formation.

3 Experimental Results and Discussion

3.1 Flow Pattern

Figures 3 through 5, are a sequence of photos taken at a fixed location for a typical flow pattern: a $2.0s$ wave train propagates in the wave tank with still water depth $h = 0.297m$ in the constant depth region. The direction of wave propagation was from left to right in all the photos presented below. They show the vortices migrating in the offshore direction (left) as reflected by the movement of the dye. The pictures were taken 2 m offshore from the injection point five seconds apart. They clearly show that there are two layers of vortices: one layer with small vortices exists near the water surface (approximately 0.05 m below water surface), and the other near the mid-depth (approximately 0.1 m below water surface). Vortices near the water surface rotate in the opposite direction of vortices at mid-depth. For example, for the surface wave propagating to the right, the rotation direction of vortices near mid-depth was observed to be counterclockwise as shown by Matsunaga et al. (1994), while the rotation direction of vortices upper in the water column was observed to be clockwise. The upper layer vortices migrate in the same offshore direction as the lower layer vortices, propagate at the same slow speed as the lower layer vortices, and have the same separation distance as those in the lower layer.

Figure 3: Dye pattern of vortices, 150 wave periods after dye injection. The water wave propagates from left to right.

The velocity of the vortex migrating offshore V_{vm} was obtained by determining the time taken for a vortex to move a given distance. For example, the surface wave phase speed for Test 2 is $C = 1.33m/s$, average instabilities speed is $V_{vm} = 0.0072m/s$. The average rotating time of vortices T_{rot} is 21.5 s, about 10 times of the surface wave period. These vortices in the offshore direction migrate with the speed slower than the undertow. They rotate with longer time than the water particle orbital motions.

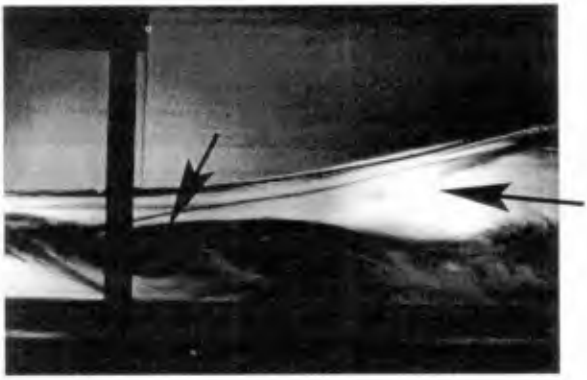

Figure 4: Dye pattern of vortices, 155 wave periods after dye injection.

Figure 5: Dye pattern of vortices, 160.9 wave periods after dye injection.

3.2 Mean Velocity Profile

The measured velocity u, w can be split into 4 components: a steady wave-induced current component U, longer time scale components u_{vor}, w_{vor} due to the vortices, the orbital wave motions components u_w, w_w and turbulent components u_t, w_t. The velocity due to the vortices is defined as angular frequencies less than 1.25 Hz for test 1 through 8. The $\overline{u_t w_t}$ represents the turbulent contribution to the momentum transfer, whereas the $\overline{u_w w_w}$ and the $\overline{u_{vor} w_{vor}}$ represent the wave contribution and the vortices contribution, respectively. The average $\overline{u_{vor} w_{vor}} / \overline{u_w w_w}$ is less than 10%, implying that the vortices contribution to the momentum transfer is insignificant compare to the wave contribution.

The mean velocity profiles measured by the ADV for the eight experiments are shown in figure 6. When we filtered the high frequency components, the mean velocity was obtained from low frequency component which includes the mean current and the longer time scale component. From figure 6, the velocity profiles are curved over the depth. Changes in the curvature of these profiles correspond to the presence of shear layers, there are two shear layers existing over the depth. Tests 7 and 8 show linear distribution over the depth.

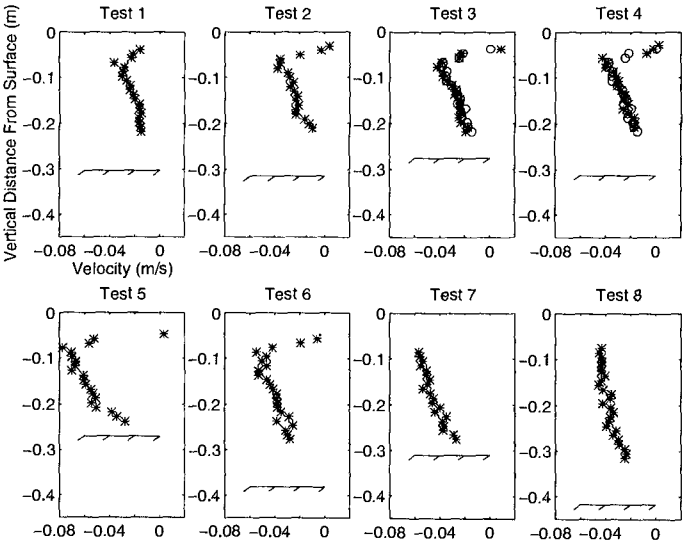

Figure 6: Undertow profile for each test versus depth.

3.3 Long Time Scale Component Velocity Profile

Figure 7 shows the distribution of horizontal velocity of the low frequency component due to vortices for Test 1 and 2. The root-mean-square value $u_{vor_{rms}}$ were obtained by using the low pass filter. The cutoff frequency is 0.2 Hz, while the sampling frequency is 50 Hz. The velocity profile for longer time component is uniformly distributed. The

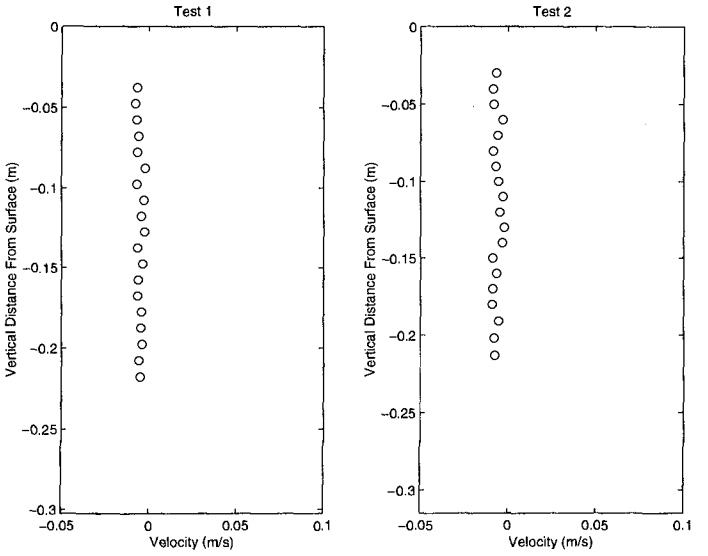

Figure 7: Undertow profile for each test versus depth.

speed of vortices with long time scale is much slower than the undertow. It indicate that upper layer vortices migrate in the same offshore direction as the lower layer vortices and propagate at the same slow speed as the lower layer vortices, which was shown by the dye pattern.

3.4 Nonlinearity

In figure 2, line (c) is the boundary of nonlinearity. Ursell number Ur represents the ratio of wave nonlinearity to frequency dispersion. The importance of nonlinearity of the surface wave to the presence of the vortices is discussed here. The value of Ur for all eight tests are shown in Table 2. For the tests that vortices were observed (tests 1 through 6), Ursell numbers are higher, and lower Ursell numbers exist for the tests that no vortices were noticed (tests 7 through 8). Thus the nonlinearity of the surface wave is important for the presence of vortices.

Table 2: Ursell Number

Test	1	2	3	4	5	6	7	8
Ur	0.4357	0.4000	0.5652	0.4319	0.3844	0.1773	0.1413	0.0664

4 Theoretical Analysis

4.1 Stability Equation

The experimental study shows that the vortices are embedded in orbital wave motion, have longer time scales and shorter length scales than the incident waves. Therefore, the velocity u, w consist of a steady wave-induced current component U, longer time scale components u_{vor}, w_{vor} due to the vortices, the orbital wave motions components u_w, w_w, and turbulent components u_t, w_t.

For the study of fluid motion outside of the surf zone when surface wave runs up at the beach, viscosity should be considered. The governing equations for the homogeneous and incompressible flow is the Navier-Stokes equations and continuity equation. As shown in Li and Dalrymple (1998), the nondimentional equation for the longer time scale motion can be obtained by averaging first over the high frequency turbulence scale, and then over the orbital wave period.

$$\frac{\partial \vec{u_R}}{\partial t} + (\vec{u_R} \cdot \nabla)\vec{u_R} = -\nabla p + \frac{1}{Re}\nabla^2 \vec{u_R} - \vec{R_t} - \vec{R_w} \tag{1}$$

where $\vec{u_R} = \{U + u_{vor}, w_{vor}\}$. Re is Reynolds number $U_{ref}L_{ref}/\nu >> 1$. ν denotes the kinematic viscosity. L_{ref} is the water depth. U_{ref} is the maximum velocity of the undertow. The turbulent stresses $R_{t_x} = \frac{\partial \overline{u_t^2}}{\partial x} + \frac{\partial \overline{u_t w_t}}{\partial z}$, $R_{t_z} = \frac{\partial \overline{u_t w_t}}{\partial x} + \frac{\partial \overline{w_t^2}}{\partial z}$. R_w denotes the time-averaged Reynolds stress resulting from the wave field (Radiation stress): $R_{w_x} = \frac{\partial \overline{u_w^2}}{\partial x} + \frac{\partial \overline{u_w w_w}}{\partial z}$, $R_{w_z} = \frac{\partial \overline{u_w w_w}}{\partial x} + \frac{\partial \overline{w_w^2}}{\partial z}$.

As shown in Li and Dalrymple (1998), through a perturbation analysis of equation 1, at the zeroth order the governing equations for the mean flow are obtained, and at the first order the equations of the interaction between disturbances and mean flow are generated. The equation of the interaction between disturbances and mean flow is the Orr-Sommerfeld equation which governs the stability of fluid motion:

$$\frac{1}{i\alpha Re}(D^2 - \alpha^2)^2\phi = (U - c)(D^2 - \alpha^2)\phi - U''\phi \tag{2}$$

where $D\phi = \phi'$. $\psi(x, z, t) = \phi(z)e^{i\alpha(x-ct)}$, ψ is a stream function, α is the wave number and c is the wave phase speed.

The wave number α is real. Solutions of the Orr-Sommerfeld equation are progressive disturbance waves with phase speed equal to the real part of c. If c has a negative imaginary component, the solution has an exponentially growing amplitude

which indicates that mean velocity profile, $U(z)$, is unstable to perturbations of the velocity field with that wavenumber. In cases where more than one such c are present, it is assumed that the one with the largest imaginary component will dominate the instability of that wavenumber. This correspond to the point of maximum αc_{im}, where c_{im} is the imaginary part of c. If c has zero imaginary component, the solution is neutrally stable to disturbance of the velocity field with that wavenumber.

The boundary conditions are that the normal and shear stresses are zero at the free surface, and the rigid boundary condition applies at the bottom.

Equation 2 is difficult to solve analytically for a general velocity distribution U(z). Therefore, a numerical approach was attempted, which was discussed in Li and Dalrymple (1998).

4.2 Vorticity Equation

The vorticity equation derived from the momentum equations 1 is:

$$\frac{\partial \omega}{\partial t} + (\vec{u_R} \cdot \nabla)\omega = \frac{1}{Re} \nabla^2 \omega + \omega \nabla \cdot \vec{u_R} - \nabla \times \vec{R_t} - \nabla \times \vec{R_w} \tag{3}$$

The first term on the right hand side represents the diffusion of vorticity due to the action of viscosity. $\omega \nabla \cdot \vec{u_R}$ provides the mechanism of vortex stretching. The stress terms due to turbulence and radiation stress serve as the source of vorticity. The vortices that we observed are due to instabilities of the undertow.

5 Numerical Results and Discussions

Since we do not have a theoretical profile of mean velocity with shear layers, the measured undertow profiles will be used in our numerical calculations that follow. The smooth velocity profile was obtained by fitting a 5-th order polynomial to the measured wave-averaged data, Li and Dalrymple (1998). Tests 7 and 8 are neutrally stable to any disturbance to the corresponding mean flow.

Numerical approach was used to predict the vortices generation under the flow conditions similar to the cases in the experimental study. The numerical predictions are then compared with the results measured in the experimental study.

5.1 Numerical Predicted Vortices

As stated in Li and Dalrymple (1998), the numerical instability model successfully obtained single layer vortex, by using the assumed velocity profile based on the deformation of dye lines shown in Matsunaga et al. (1988, 1994). Figure 8 shows the numerically predicted flow for one surface wave wavelength using the undertow velocity profile and water depths of Tests 1 and 2. The stream lines are gained by summing the mean flow and the fasted growing unstable wave. Figure 9 show velocity field and the spatial patterns of the streamlines for a quarter surface wave for Test 2. More

figures of predicted instabilities are shown in Li and Dalrymple (1998). These figures show similar results as the observations in the experiments: there are two layers of unstable waves exist over depth. The rotation direction of vortices near surface was the same as the wave-induced water particle trajectories, while the rotation direction of vortices near mid-depth was in opposite direction. The unstable wavelength is much shorter than the surface wave length.

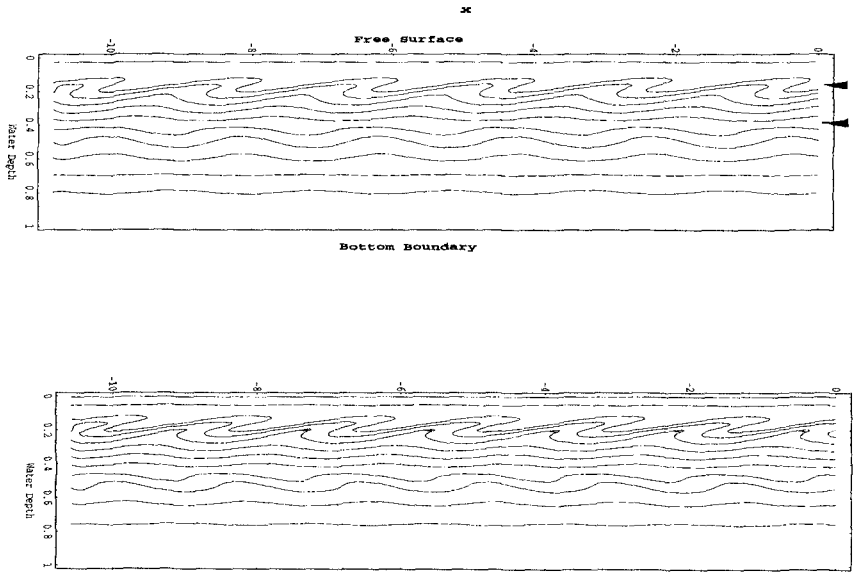

Figure 8: Streamline of the instabilities over one surface wavelength. The surface wave propagates to the left, top: test 1, bottom: test 2.

5.2 Velocity of Vortical Motion

Li and Dalrymple (1998) also showed the good agreement of horizontal length scales and vertical positions between the numerical instabilities and the corresponding experimental results. The experimental and numerical results of the speed of the instabilities are shown in Table 3. Good agreement between the experiment and numerical model is observed. As stated in the experimental study, the instabilities move offshore

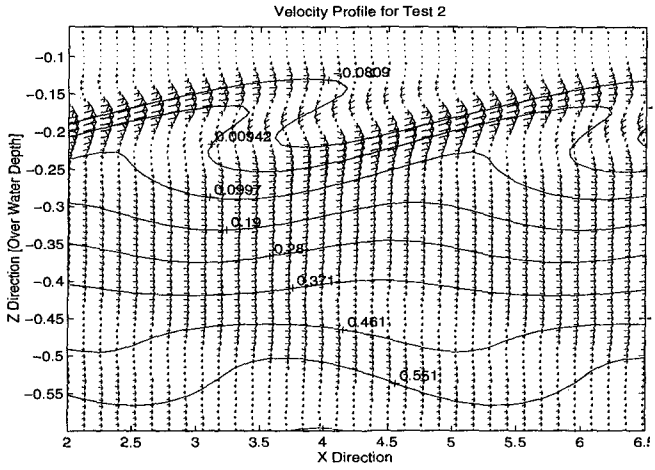

Figure 9: The velocity field for test 2 over a quarter surface wavelength. The surface wave propagates to the left.

Table 3: Comparison between the numerical solution and experimental results

	Speed of Vortices in Offshore Direction (m/s)		
Test	Experiment	Numerical Result	Matsunaga et al. (1994)
1	0.0063	0.0077	0.0112
2	0.0072	0.0070	0.0119
3	0.0069	0.0072	0.0124
4	0.0070	0.0079	0.0133
5	0.0102	0.0140	0.0341
6	0.0056	0.0089	0.0272

slower than the undertow do. Clearly, the linear perturbation model can predict the speed, the position, length scale of the vortices and the existence of the vortex.

6 Conclusions

In this paper, both experimental and numerical studies on the offshore vortex train were conducted. The following conclusions can be drawn.

It has been shown that an undertow seaward of the surf zone can cause oscillations that are different from regular surface waves. These oscillations are below water surface with shorter length scale and longer time scale. Two vortex layers exist over the water depth, because of the existence of two shear layers. The resulting vortices near the water surface rotate in the opposite direction as one at mid-depth. Vortices near the water surface migrate in the same offshore direction as the vortices at mid-depth, propagate at the same speed which is slower than undertow as vortices at mid-depth.

Using the flow conditions similar to those in the experiments, the speed for the instabilities calculated from the numerical model is compared with the corresponding experimental results. Good agreement between the experiment and numerical model is observed. It may be concluded that the linear stability model can predict the occurrence of the vortices from the velocity profile.

The stresses due to turbulence and wave serve as the source of the vorticity. The nonlinearity of the surface wave may play an important role in the presence of vortices.

Reference

Bowen, A.J., 1969 "The Generation of Longshore Currents on a Plane Beach." *J. Marine Res.* , 27, no. 2, 206–215.

Cox, Daniel T., N. Kobayashi & A. Okayasu, 1995 "Vertical Variations of Fluid Velocities and Shear Stress in Surf Zones. " *Proc. 24th Intl. Coastal Engineering Conference*, 1, 98-112.

Craik, A.D.D., 1982 "The Drift Velocity of Water Waves." *J. Fluid Mechanics* , 116, 187–205.

Drazin, P.G. & W.H. Reid, 1981 "Hydrodynamic Stability." Cambridge University Press.

Li, L. & R.A. Dalrymple, 1998 "Instabilities of the Undertow." *J. Fluid Mechanics*, 369, 175-190.

Lin, C.C., 1955 "The Theory of Hydrodynamic Stability." Cambridge University Press.

Longuet-Higgins, M.S., 1953 "Mass Transport in Water Waves." *Phil. Trans. R. Soc. Lond.*, A 245, 535–581.

Matsunaga, N., K. Takehara & Y. Awaya, 1988 " Coherent Eddies Induced by Breakers on a Sloping Bed." *Proc. 21st Intl. Coastal Engineering Conference,* 234–245.

Matsunaga, N., K. Takehara & Y. Awaya, 1994 "The Offshore Vortex Train." *J. Fluid Mechanics*, 276, 113–124.

Nadaoka, K. & T. Kondoh, 1982 "Laboratory Measurements of Velocity Field Structure in the Surf Zone." *Coastal Eng. Jpn.*, 25, 125–145.

Okayasu, A. & H. Katayama, 1992 " Distribution of Undertow and Long-wave Component Velocity Due to Random Waves. " *Proc. 23rd Intl. Coastal Engineering Conference, Venice, Italy, October, 1992*, Chapter 66, 883-893.

Svendsen, I.A. & U. Putrevu, 1992 "A Mixing Mechanism in the Nearshore Region." *Proc. 23rd Intl. Coastal Engineering Conference, Venice, Italy, October, 1992*, Chapter 211, 2758-2771.

Nonlinear Distribution of Neashore Free Surface and Velocity

Nobuhito MORI * and Nobuhisa KOBAYASHI †

ABSTRACT

The Edgeworth expansion with the measured skewness and kurtosis is shown to be capable to describe the measured nonlinear distributions of the surface elevation and horizontal velocity in the shoaling and surf zones. The moments involved in the energetics-based model are expressed in terms of the skewness and kurtosis and shown to be in agreement with available data. Stokes wave theory is applied to obtain a relationship between skewness and kurtosis. The relationship is adjusted empirically because of the limitation of Stokes wave theory in the shoaling and surf zones. The relative simple relationship for the higher moments obtained here may be applied for cross-shore sediment transport analysis.

INTRODUCTION

Nonlinear waves in nearshore regions are important in estimating sediment transport and designing coastal structures. The estimation of an extreme wave crest is an important factor in predicting the deck elevation of an offshore structure. The wave profile in the surf zone is significantly skewed because of wave breaking and bottom topography effects. Time dependent numerical models based on extended Boussinesq equations have been shown to be capable of predicting the nonlinear profile of the surface elevation outside the surf zone(*e.g.*, Nwogu 1993). Time dependent numerical models, however, require large computation time to calculate the wave profiles.

On the other hand, time-averaged models for random waves are more efficient computationally at the expense of the loss of the detailed temporal information(*e.g.*, Battjes and Janssen 1978; Thornton and Guza 1983; Mase and

*Hydraulics Dept., Abiko Research Laboratory, Central Research Institute of Electric Power Industry(CRIEPI), Abiko 1646, Chiba 270-11, JAPAN (mori@criepi.denken.or.jp)

†Center for Applied Coastal Research, University of Delaware, Newark, DE, 19716, USA (nk@coastal.udel.edu)

Kobayashi 1991). However, time-averaged models may not be accurate enough, because random wave are expressed as the superposition of regular waves or by a representative wave. Guza and Thornton (1985) has pointed out that both randomness and nonlinearity are necessary to predict the moments of the cross-shore fluid velocity on a beach. Hence, the purpose of this study is to develop a probabilistic model of the surface elevation and cross-shore velocity in the nearshore including both random and nonlinear effects.

Many studies have were performed to describe the nonlinear distribution of the free surface elevation. Ochi and Ahn (1994) and Kobayashi et al. (1998) used Siegert solution and the exponential gamma distribution, respectively, to describe the distribution of the surface elevation and velocity. These distributions agree fairly with the measured skewed distributions. However, it is difficult to obtain the relationships among the various moments of the distribution analytically. In contrast, attempts were made to describe the nonlinear distribution of the free surface elevation using perturbations of the Gaussian distribution(Longuet-Higgins 1963; Haung and Long 1980; Bitner 1980). These methods based the Gram-Charlier or Edgeworth approximation can be expanded as a function of skewness and kurtosis. Then, it is much easier express the various moments in terms of the skewness and kurtosis, although these approximations give negative density values for certain skewed distributions.

In the following, the probability density distributions and moments of the measured free surface elevation and horizontal velocity in a large wave flume are compared with the Edgeworth expansion and the measured skewness and kurtosis. Stokes wave theory is applied to derive a relationship between the skewness and kurtosis.

EXPERIMENTS

The experimental data used here was reported in Japanese by Shimizu *et al.*(1996). The experiment was conducted in a large wave flume that was 205m long, 3.4m wide, 6m high. The water depth in the flume was 4m. A sand beach of a 1:30 slope was installed at the end of the wave tank. Water surface displacements at 17 locations in Fig.1 were measured using capacitance type wave gages located in the still water depth range of 0.1-4.0m. Fluid velocities were measured with six electro-magnetic current meters. The current meters were set 15cm above the bottom. The current meters $C_1 - C_6$ in Fig.1 were located in the still water depths 2.25, 1.92, 1.58, 1.25, 0.92 and 0.48m, respectively. The measurements with a sampling frequency of 20Hz were performed for the duration of 819s.

Random waves based on the JONSWAP spectrum and random phases were generated using linear wave theory with a computer-controlled piston-type wave paddle. Two cases were reported by Shimizu *et al.*(1996) as summarized in Table 1 where $H_{1/3}$ and $T_{1/3}$ are the significant wave height and period above the horizontal bottom. In Table 1, the wave amplitude a_0=$H_{1/3}/2$, the water

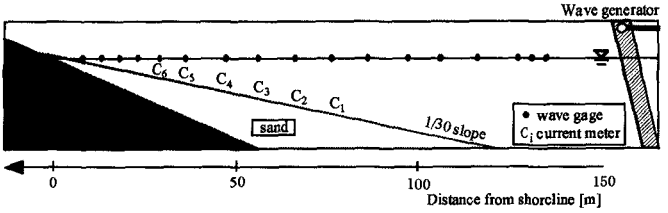

Figure 1 Experimental setup and locations of wave gages and current meters.

Table 1 Experimental conditions for two cases.

case No.	$H_{1/3}$	$T_{1/3}$	ka_0	kh_0
case1	0.43m	4.93s	0.049	0.91
case2	1.12m	3.06s	0.262	1.87

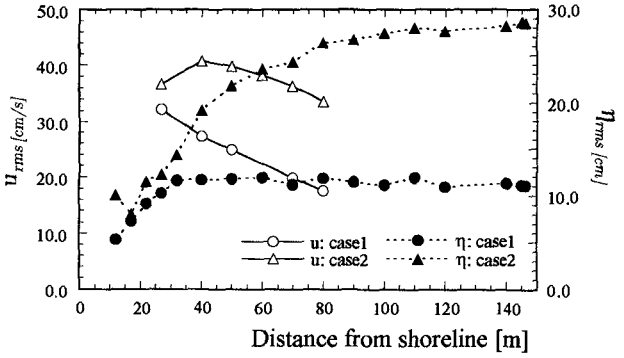

Figure 2 Measured cross-shore variations of *rms* values of horizontal fluid velocity u and surface elevation η.

depth h_0=4.0m on the horizontal bottom, and k is the linear wave number based on $T_{1/3}$ and h_0. The value of ka_0 and kh_0 in Table 1 indicate wave steepness and nondimensional water depth at the wave paddle. Case 2 was more nonlinear than case 1.

The surface displacement η and the horizontal fluid velocity u near the bottom are analyzed in the following. Fig.2 shows the spatial distributions of the root-mean-square(*rms*) values of the horizontal fluid velocity u and the surface elevation η. Solid lines with open symbols indicate the *rms* values of u and dashed lines with filled symbols indicate the *rms* values of η. Circles ○ are

for case 1 and triangles △ are for case 2. Fig.2 illustrates the difference in the width of the surf zone for case 1 and 2. The *rms* values of u increased landward, whereas the *rms* values of η decreased monotonically landward.

The moments μ_3, μ_4, μ_3^* and $\mu_4^\bullet$ for f=η or u are defined as follows:

$$\mu_n = \frac{1}{N}\sum_{i=1}^{N}\left(\frac{f_i-\bar{f}}{f_{rms}}\right)^n \tag{1}$$

$$\mu_n^* = \frac{1}{N}\sum_{i=1}^{N}\left|\frac{f_i-\bar{f}}{f_{rms}}\right|^n \tag{2}$$

$$\mu_n^\bullet = \frac{1}{N}\sum_{i=1}^{N}\left(\frac{f_i-\bar{f}}{f_{rms}}\right)\left|\frac{f_i-\bar{f}}{f_{rms}}\right|^{n-1} \tag{3}$$

where $\bar{f}$ is the mean value of f, f_{rms} is the *rms* value of f, and N is the number of data point. Eq.(1) with n=3 and 4 gives μ_3=skewness and μ_4=kurtosis. The moments are calculated after removing the high-frequency components with frequency larger than 4 times of the peak frequency to reduce the statistical sensitivity. The third order absolute moment μ_3^* and the fourth order signed moment $\mu_4^\bullet$ for the velocity are related to the energetics-based sediment transport model(Bailard 1981). The measured third and fourth moments are shown in Fig.3. The measured moments of η show systematic trends. The values of the moments of η are close to the Gaussian values, μ_3=0, μ_4=3, μ_3^*=1.6 and $\mu_4^\bullet$=0, offshore. These values then increase landward before their decrease toward the shoreline. On the contrary, the measured moments of u are below the values of the Gaussian offshore. μ_4 and μ_3^* are reduced first and then increase landward, whereas μ_3 and $\mu_4^\bullet$ increase monotonically.

In summary, the spatial variations of the moments of the horizontal fluid velocity u and the surface elevation η deviate from the Gaussian values near and inside the surf zone. The measured moments of u are close to the Gaussian values but the moments of η exceed the Gaussian values significantly inside the surf zone. These results are consistent with the small scale tests on a 1:16 slope by Kobayashi et al. (1998).

STATISTICAL MODELING OF SURFACE AND VELOCITY MOMENTS

The data shown in Fig.3 indicates strong nonlinearity of η in the shoaling and surf zones. The horizontal velocities near the bottom have weaker nonlinearity. Hence, the Edgeworth expansion(Kendall and A.Stuart 1963) is applied to describe the probability density function(PDF) of the surface elevation and horizontal velocity. The Edgeworth expansion is adequate to describe random and weak nonlinear stochastic processes. The Edgeworth expansion is derived in the same manner as the Gram-Charlier expansion but the terms of the series are expressed in terms of cumulants.

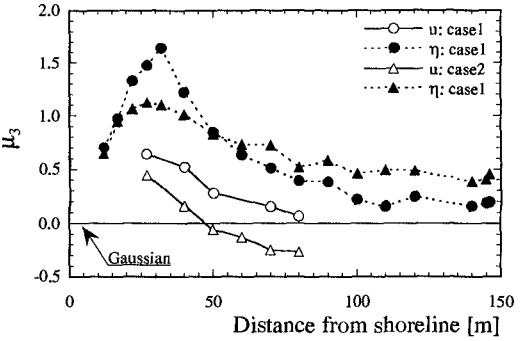

(a) Measured cross-shore variations of skewness μ_3

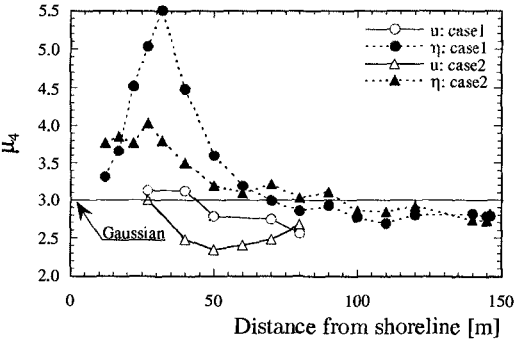

(b) Measured cross-shore variations of kurtosis μ_4

Figure 3 Measured cross-shore variations of third and fourth of moments of horizontal fluid velocity u and surface elevation η.

The PDF $p(x)dx$ of the normalized statistical variables x with zero mean and its standard deviation of unity can be described as(Kendall and A.Stuart 1963)

$$p(x)dx = \sum_{r=0}^{\infty} c_r H_r(x) G(x)\, dx \tag{4}$$

with

$$G(x) = \frac{1}{\sqrt{2\pi}} \exp\left(-\frac{x^2}{2}\right) \tag{5}$$

where $G(x)$ is the Gaussian distribution, $H_r(x)$ is the Chebyshev-Hermite poly-

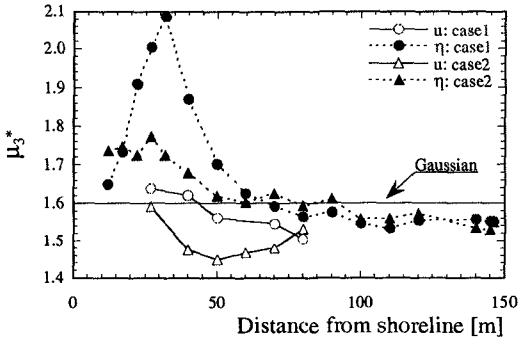

(c) Measured cross-shore variations of third order absolute moment μ_3^*

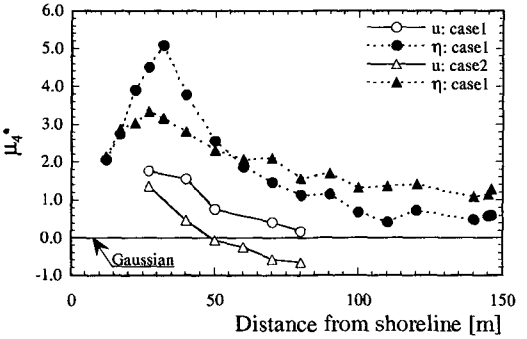

(d) Measured cross-shore variations of fourth order signed moment $\mu_4^\bullet$

Figure 3 Continued

nomial and c_r is the rth order coefficient of the Gram-Charlier expansion. Introducing the characteristic function, the Edgeworth expansion of type A is given by (*e.g.*, Longuet-Higgins 1963)

$$p(x)dx = G(x)\left\{1 + \frac{\kappa_3}{6}H_3(x) + \left[\frac{\kappa_4}{24}H_4(x) + \frac{\kappa_3^2}{72}H_6(x)\right] + \left[\frac{\kappa_5}{120}H_5(x) + \frac{\kappa_3\kappa_4}{144}H_7(x)\right] + \cdots\right\}dx \qquad (6)$$

where κ_r is the rth order cumulant. The cumulants with r=3-6 are related to

the rth order moments μ_r as follows:

$$\left.\begin{aligned}\kappa_3 &= \mu_3 \\ \kappa_4 &= \mu_4 - 3 \\ \kappa_5 &= \mu_5 - 10\mu_3 \\ \kappa_6 &= \mu_6 - 15\mu_4 - 10\mu_3^2 + 30\end{aligned}\right\} \tag{7}$$

where the mean value μ_1 of x is equal to zero(κ_1=0) and the standard deviation of x is unity(κ_2=1). Therefore, μ_3 is skewness and μ_4 is kurtosis.

It must be noted that an asymptotic expansion does not have monotonic convergence for high order corrections. There are many studies about the truncation of (6)(Longuet-Higgins 1963; Haung and Long 1980; Ochi and Wang 1984; Mori and Yasuda 1996). They have shown that the first three terms of (6) are sufficient for describing the nonlinear property of the PDF of the surface elevation. Hence, the first three terms in (6) are used to represent the PDF of x denoting the normalized the surface elevation and horizontal velocity

$$p(x)dx = G(x)\left\{1 + \frac{\kappa_3}{6}H_3(x) + \left[\frac{\kappa_4}{24}H_4(x) + \frac{\kappa_3^2}{72}H_6(x)\right]\right\}dx \tag{8}$$

which requires κ_3=μ_3=skewness and κ_4=(μ_4-3) with μ_4=kurtosis . The truncation of high order terms in (6) gives the following relationships based on κ_5=0 and κ_6=0 for the high order moments:

$$\mu_5 = 10\mu_3 \tag{9}$$

$$\mu_6 = 10\mu_3^2 + 15\mu_4 - 30 \tag{10}$$

The other higher moments related to the energetics-based sediment transport model(Bailard 1981) can be calculated using (8)

$$\mu_3^* = \int_{-\infty}^{\infty} |x|^3 p(x)dx = \frac{1}{6\sqrt{2\pi}}(3\mu_4 - \mu_3^2 + 15) \tag{11}$$

$$\mu_5^* = \int_{-\infty}^{\infty} |x|^5 p(x)dx = \frac{2}{3\sqrt{2\pi}}(15\mu_4 + 5\mu_3^2 - 21) \tag{12}$$

$$\mu_4^\bullet = \int_{-\infty}^{\infty} x|x|^3 p(x)dx = \frac{8}{\sqrt{2\pi}}\mu_3 \tag{13}$$

Fig.4 show the comparisons of the measured PDF of u and η with (8) for case 2 where the measured values of μ_3 and μ_4 are used in (8). The PDF of u is skewed negatively offshore but positively in the surf zone. The measured spatial variation of μ_3 shown in Fig.3a indicates the corresponding sign shift. This may be important for the cross-shore sediment transport. On the other hand, the PDF of η is always skewed positively as expected from nonlinear wave theory. The nonlinear PDF given by (8) agrees better with the data than the linear Gaussian distribution partly because of the additional input of μ_3 and μ_4.

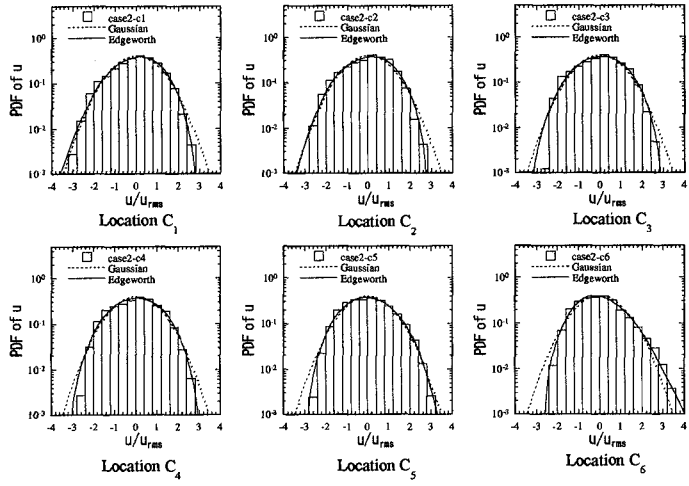

(a) PDF of horizontal velocity u.

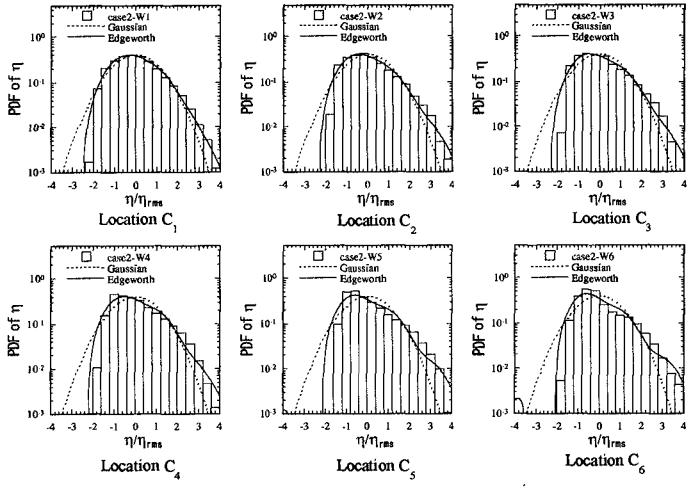

(b) PDF of surface elevation η.

Figure 4 Measured PDF of u and η for case 2 in comparison with the theory.

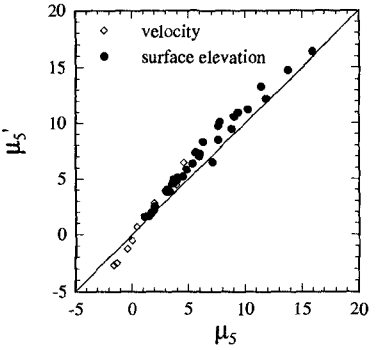

(a) measured μ_5 vs. calculated μ_5'

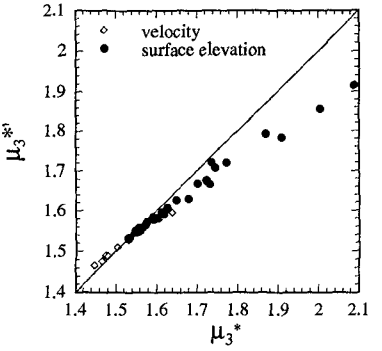

(b) measured μ_3^* vs. calculated $\mu_3^{*\prime}$

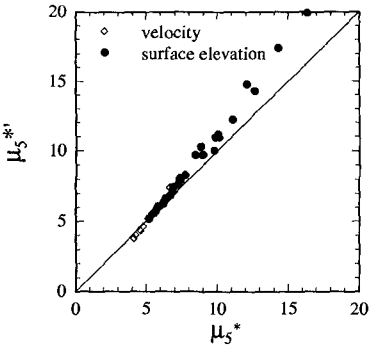

(c) measured μ_5^* vs. calculated $\mu_5^{*\prime}$

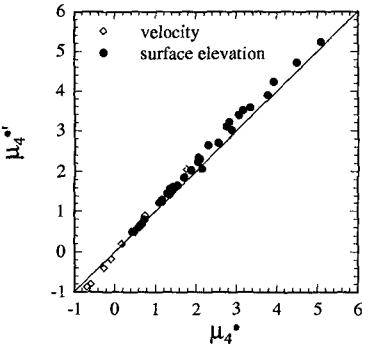

(d) measured $\mu_4^\bullet$ vs. calculated $\mu_4^{\bullet\prime}$

Figure 5 Comparison between measured μ_5, μ_3^*, μ_5^* and $\mu_4^\bullet$, and calculated μ_5', $\mu_3^{*\prime}$, $\mu_5^{*\prime}$ and $\mu_4^{\bullet\prime}$ for measured μ_3 and μ_4.

To check the validity of (9)-(13), the comparisons between the measured moments μ_n and the calculated moments μ_n' indicated by the prime are shown in Fig.5. Eq.(9) gives a simple relationship between μ_3 and μ_5. The correlation coefficient of in Fig.5a is 0.98, indicating good agreement between the measured μ_5 and the calculated μ_5' . The sixth moments μ_6 given by (10) for u and η show similar results(not shown). Fig.5b-d also show good agreement between the measured moments(μ_3^*, μ_5^* and $\mu_4^\bullet$) and the calculated moments($\mu_3^{*\prime}$, $\mu_5^{*\prime}$ and $\mu_4^{\bullet\prime}$) using (11)-(13). The PDF of u and η in the shoaling and surf zones can be described by the Edgeworth expansion given by (8). As a consequence, the associated moments can be estimated by (9)-(13).

Eq.(8) requires both skewness μ_3 and kurtosis μ_4 as input. An attempt is made to express μ_4 in terms of μ_3.

RELATIONSHIP BETWEEN SKEWNESS AND KURTOSIS

Tayfun (1980), Srokosz and Longuet-Higgins (1986) and Winterstein et al. (1991) derived the PDF of the surface elevation based on the assumption that random waves can be expressed as a summation of Stokes 2nd or 3rd waves. This assumption considers only the self wave interaction components, although there are random wave-wave interaction components. This approach is easy to apply and calculate the moments in comparison with the fully nonlinear random interaction method(*e.g.*, Sharma and Dean 1979). Admittedly, Stokes wave theory may not be valid in shallow water and the derived relationship will be interpreted in view of this limitation. The 3rd order Stokes wave in finite water depth h is given by:

$$k\eta = \frac{1}{2}(ak)^2 D_1 + ak\cos\theta + \frac{1}{2}(ak)^2 D_2 \cos 2\theta + \frac{3}{8}(ak)^3 D_3 \cos 3\theta \qquad (14)$$

where a is the amplitude, k is the wave number, θ is the phase with θ=($kx-\omega t+\varepsilon$) in which ω is the angular frequency, and the phase ε is assumed to random. Eq.(14) neglects the phase shift of the second and third harmonics which may be important for the wave profile pitched landward in the surf zone. D_i is the function of the nondimensional water depth kh:

$$\begin{aligned} D_1 &= \coth kh \\ D_2 &= \coth kh \left(1 + \frac{3}{2\sinh^2 kh}\right) \\ D_3 &= 1 + \frac{1}{\sinh^2 kh}\left(3 + \frac{3}{\sinh^2 kh} + \frac{9}{8\sinh^4 kh}\right) \end{aligned} \qquad (15)$$

It is assumed that the PDF of the first order component $a\cos\theta$ is the Gaussian and that the amplitude a and the phase ε are independent of each other with ε being distributed uniformally between 0 to 2π. These assumptions yields the joint PDF of a and θ as

$$f(a,\theta) = \frac{a}{2\pi\sigma^2}\exp\left(-\frac{a^2}{2\sigma^2}\right), \qquad (16)$$

where σ is the rms value of the first order component($a\cos\theta$). The moments λ with n=0, 1, $\cdots$ can be calculated using (14) and (16):

$$\lambda_n = \int_{a=0}^{\infty}\int_0^{2\pi} [\eta(a,\theta)]^n f(a,\theta)\, da\, d\theta \qquad (17)$$

which yields

$$\lambda_0 = \sigma D_1 \alpha \qquad (18)$$

$$\lambda_2 = \sigma^2\left[1 + (D_1^2 + D_2^2)\alpha^2 + O(\alpha^4)\right] \qquad (19)$$

$$\lambda_3 = \sigma^3\left[3(D_1 + D_2)\alpha + \frac{1}{2}(4D_1^3 + 12D_1D_2^2 + 27D_2D_3)\alpha^3 + O(\alpha^4)\right] \qquad (20)$$

$$\lambda_4 = \sigma^4\left[3 + 3(6D_1^2 + 6D_2^2 + 8D_1D_2 + 3D_3)\alpha^2 + O(\alpha^4)\right] \qquad (21)$$

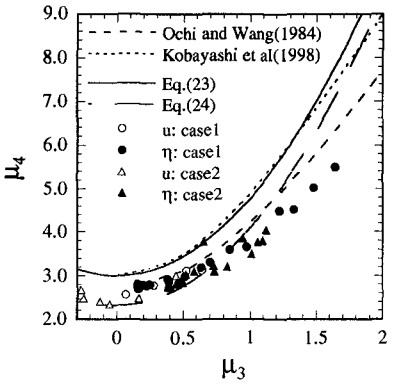

(a) Comparison with laboratory data

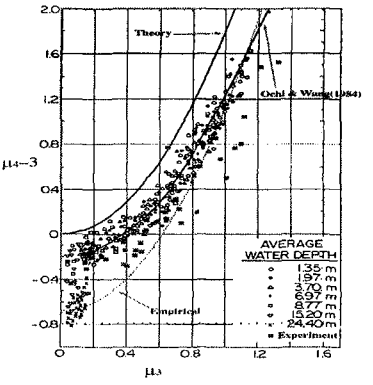

(b) Comparison with field data[Ochi and Wang, 1984]

Figure 6 Measured and predicted μ_4 as a function of measured μ_3.

where α is the wave steepness ak of the linear component. Dividing λ_3 by $\lambda_2^{3/2}$, the leading skewness contribution is given by

$$\mu_3 = 3\alpha(D_1 + D_2) \tag{22}$$

The low frequency component involving D_1 in (14) was retained by Vinje (1989) but was neglected by Tayfun (1980) and Winterstein *et al.*(1991). Dividing λ_4 by λ_2^2, neglecting D_1 and D_3 and substituting (22), the leading kurtosis contribution obtained

$$\mu_4 = 3 + \left(\frac{4}{3}\mu_3\right)^2 \tag{23}$$

The effect of the water depth D_2 on μ_4 is included in (23) through μ_3 given by (22) with D_1=1.

To examine the validity of (23), Fig.6a shows the comparison between the measured and calculated μ_4 as a function of the measured μ_3. Eq.(23)(solid line) follows the trend of the data point but overpredicts the kurtosis μ_4. The measured μ_4 corresponding to $\mu_3 \simeq 0$ is smaller than 3. It means that for zero skewness the kurtosis is smaller kurtosis than linear random wave theory. The field data of Ochi and Wang (1984) also showed similar tendency. Therefore, (23) is adjusted empirically as follows:

$$\mu_4 = \beta + \left(\frac{4}{3}\mu_3\right)^2 \tag{24}$$

where β is the empirical constant. Eq.(24) reduces to (23) for β=3. Eq.(24) with β=2.3 is shown as a dashed line in Fig.6. The value of β=2.3 is determined by a

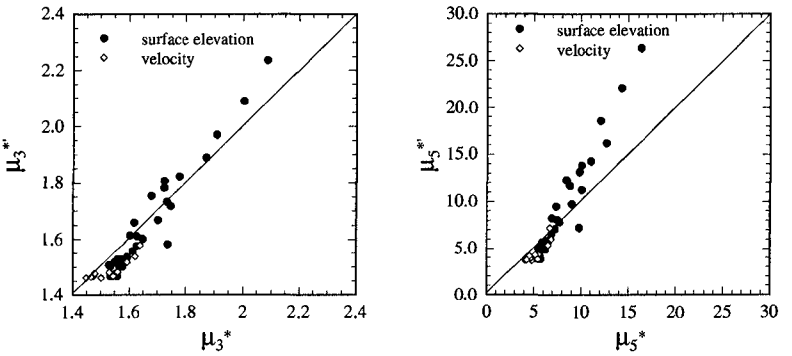

(a) measured μ_3^* vs. calculated $\mu_3^{*\prime}$ **(b)** measured μ_5^* vs. calculated $\mu_5^{*\prime}$

Figure 7 Comparisons between measured μ_3^* and μ_5^* and calculated $\mu_3^{*\prime}$ and $\mu_5^{*\prime}$ for measured μ_3.

least-square method using the laboratory data in Fig.6a. Additional two lines are plotted in Fig.6a. One is derived by Kobayashi *et al.*(1998) using the exponential gamma distribution and another is the empirical relationship obtained by Ochi and Wang (1984) using extensive field data on the free surface elevation. The exponential gamma distribution tend to overpredict μ_4 and is almost the same as (23). The empirical equation (24) and that by Ochi and Wang (1984) give better agreement with the data. Fig.6b shows the comparisons among (23), (24), the laboratory data, the empirical relation and the field data by Ochi and Wang (1984). Eq.(24) with the measured μ_3 underpredicts the field data but (23) overestimates the field data.

Substituting (24) into (11) and (12) gives μ_3^* and μ_5^* as a function of μ_3 only:

$$\mu_3^* = \frac{1}{18\sqrt{2\pi}}\left[13\mu_3^2 + 9(\beta+5)\right], \tag{25}$$

$$\mu_5^* = \frac{2}{9\sqrt{2\pi}}\left[95\mu_3^2 + 9(5\beta-7)\right]. \tag{26}$$

The measured μ_3^* and μ_5^* are compared with (25) and (26) in Fig.7. The predicted μ_3^* and μ_5^* as a function of the measured μ_3 are reasonable and the agreement is similar to Fig.5b and 5c.

COMPARISON WITH FIELD DATA

Finally, (9), (11) and (12) using the measured μ_3 and μ_4 are compared with the field data on cross-shore(c) and longshore(l) velocities measured by Guza and Thornton (1985) at Torreys Pines Beach, San Diego, California, during

November 1978. The observed moments in Table 2 are spatially-averaged values. Table 2 also includes the predicted moments using (23), (25) and (26) with β=3 for the measured μ_3 only. Guza and Thornton (1985) analyzed their velocity data to estimate the sediment transport rates using the energetics model by Bailard (1981).

For the cross-shore velocities, the calculated moments μ_5, μ_3^* and μ_5^* using the measured μ_3 and μ_4 are in good agreement with the data on Nov.20th but the agreement is worse for Nov.17th. This is due to the unexpected combination of μ_3 and μ_4 for the Nov.17th data(high skewness and low kurtosis). For the alongshore velocities, the measured skewness was almost zero and the Gaussian distribution with μ_3=0 appears to be acceptable except for μ_5^*.

Table 2 Comparison between velocity moments field data by Guza and Thornton(1985) and theory with β=3.

moment	Data		Model				
	Nov.17th	Nov.20th	Nov.17th		Nov.20th		Gaussian
			μ_3&μ_4	μ_3	μ_3&μ_4	μ_3	μ_3=0
μ_3-c	0.55	0.50	–	–	–	–	0
μ_3-l	-0.04	0.01	–	–	–	–	0
μ_4-c	2.86	3.50	–	3.54	–	3.44	3.0
μ_4-l	3.41	3.44	–	3.00	–	3.00	3.0
μ_5-c	4.95	5.39	5.5	5.5	5.0	5.0	0
μ_5-l	-0.05	-0.52	-0.4	-0.4	0.1	0.1	0
μ_3^*-c	1.60	1.69	1.55	1.68	1.68	1.67	1.6
μ_3^*-l	1.68	1.67	1.68	1.60	1.68	1.60	1.6
μ_5^*-c	7.77	8.58	6.23	8.93	8.71	8.49	6.38
μ_5^*-l	8.06	8.56	8.02	6.40	8.14	6.38	6.38

c for cross-shore velocities; l for longshore velocities

CONCLUSION

Nonlinear wave statistics of irregular waves are examined in the shoaling and surf zones on a beach. First, the probability density function of the surface elevation and velocity can be represented by the Edgeworth expansion. Second, the analytical relationships among the order odd and even moments involved in the energetics-based sediment transport model are derived and verified using laboratory and field data. Third, semi-empirical relationship between the skewness and kurtosis is proposed to facilitate future applications.

REFERENCES

Bailard, J. A. (1981). An energetics total load sedment transport model for a plane sloping beach. *J. Geophys. Res., 86*(C11), 10938–10954.

Battjes, J. and J. Janssen (1978). Energy loss and set-up due to breaking wave. In *Proc., 16th Int. Conf. on Coastal Eng.*, Volume 1, pp. 596–587. ASCE.

Bitner, E. (1980). Non-linear effects of the statistical model of shallow-water wind waves. *Applied Ocean Res., 2*(2), 63–73.

Guza, R. and E. Thornton (1985). Velocity moments in nearshore. *J. Waterway, Port, Coast. and Ocean Eng., 111*(2), 235–256.

Haung, N. and S. Long (1980). An experimantal study of the surface elevation probaibility distribution and statistics of wind-generated waves. *J. Fluid Mech., 101*, 179–200.

Kendall, M. and A.Stuart (1963). *The advanced theory of statistics* (4th ed.)., Chapter 3.12-15 and 6.17-20. London: Charles Griffin.

Kobayashi, N., M. N. Herrmann, B. D. Johnson, and M. D. Orzech (1998). Probability distribution of surface elevation in surf and swash zones. *J. Waterway, Port, Coast. and Ocean Eng., 124*(3), 99–107.

Longuet-Higgins, M. (1963). The effect of non-linearities on statistical distirbutions in the theory of sea waves. *J. Fluid Mech., 17*, 459–480.

Mase, H. and N. Kobayashi (1991). Transformation of random breaking waves and its empirical numerical model considering surf beat. In *Proc., Coastal Sediments'91*, Volume 1, pp. 688–702. ASCE.

Mori, N. and T. Yasuda (1996). Weakly non-gaussian model of wave height distribution for random waves. In *Proc., 25th Int. Conf. on Coastal Eng.*, Volume 1, Orlando, pp. 412–426. ASCE.

Nwogu, O. (1993). An alternative form of the Boussinesq equations for nearshore wave propagation. *J. Waterway, Port, Coast. and Ocean Eng., 119*(6), 618–638.

Ochi, M. and K. Ahn (1994). Non-Gaussian probability distribution of coastal waves. In *Proc., 24th Int. Conf. on Coastal Eng.*, Volume 1, pp. 482–496. ASCE.

Ochi, M. and W. C. Wang (1984). Non-Gaussian characteristics of coastal waves. In *Proc., 19th Int. Conf. on Coastal Eng.*, Volume 1, pp. 516–531. ASCE.

Sharma, J. and R. Dean (1979). Developement and evaluation of a procedure for simulating a random derectional second order sea surface and associated wave forces. Technical Report 20, Dept. of Civil Eng., Univ. of Delaware, Newark, DE.

Shimizu, T. *et al.* (1996). Simutaneous measurements of wave field above sand beach in large wave flume. In *Proc., 43th Coastal Eng. Conf. in Japan*, Volume 1, pp. 491–495(in Japanese).

Srokosz, M. and M. Longuet-Higgins (1986). On the skewness of sea-surface elevation. *J. Fluid Mech., 164*, 487–497.

Tayfun, M. (1980). Narrow band nonlinear sea waves. *J. Geophys. Res., 85*(C3), 1548–1552.

Thornton, E. and R. Guza (1983). Energy saturation and phase speeds measured on a natural beach. *J. Geophys. Res., 87*(C12), 9499–9508.

Vinje, T. (1989). The statistical distribution of wave heights in a random seaway. *Appl. Ocean Research, 11(3)*, 143–152.

Winterstein, S., E. Bitner-Gregersen, and K. Ronold (1991). Statistical and physical models of nonlinear random waves. In *Proc., OMAE*, Volume 2, pp. 23–31. ASME.

Evolution Equations for Edge Waves and Shear Waves on Longshore Uniform Beaches

James T. Kirby, M.ASCE[1], Uday Putrevu, A.M.ASCE[2] and H. Tuba Özkan-Haller[3]

Abstract

A general formalism for computing the nonlinear interactions between triads of coastally-trapped gravity and vorticity waves is developed. An analysis of the linearized problem reveals that gravity (or edge) waves and vorticity (or shear) waves exist as members of the same non-Sturm-Liouville eigenvalue problem, with unstable shear waves representing the complex eigenvalue portion of the resulting spectrum. Interaction equations derived here cover resonant interactions between three edge waves, three shear waves, or a shear vave and two edge waves. Numerical examples are shown for the case of three edge waves on a planar beach in the absence of a longshore current. It is found that edge waves can exchange significant amounts of energy over time scales on the order of ten wave periods, for realistic choices of edge wave parameters.

Introduction

The low frequency wave climate on an open coastal beach contains a complex mix of trapped gravity wave motions (edge waves) as well as vorticity (or shear) waves associated with the instability of the longshore current. To date, there has been a tendancy in the literature to treat both classes of motion as isolated systems in which the principle effect of nonlinearity is through amplitude dispersion. Formulations of this type typically treat the wave field in terms of a wave envelope modulated by cubic nonlinearity, leading to the cubic Schrödinger equation for conservative edge wave systems (Yeh, 1985) or Ginzburg-Landau equation for marginally unstable shear waves (Feddersen, 1998). However, in field conditions, all of these motions occur in a relatively dense spectral environment, and the existence of combinations of waves satisfying three-wave resonance conditions makes it likely that the dominant nonlinear mechanism affecting edge or shear waves would be through resonant interactions at second order.

Direct numerical simulations (Allen et al, 1997; Özkan-Haller and Kirby, 1998)

[1]Professor, Center for Applied Coastal Research, University of Delaware, Newark, DE 19716 USA.
[2]Research Scientist, NorthWest Research Associates, Inc., PO Box 3027, Bellevue, WA 98009-3027 USA.
[3]Assistant Professor, Department of Naval Architecture and Marine Engineering, University of Michigan, Ann Arbor, MI 48109 USA.

suggest that the growth to finite amplitude of the shear wave climate involves strong nonlinear interaction between the various length scales in the motion. It is likely that there are also opportunities for edge waves to undergo strong interactions, although this pathway has not been heavily investigated to date. All of these interactions contribute to the final evolution of the low frequency climate on a beach, which may or may not have some sort of equilibrium configuration.

The goals of present study are to:

1. Derive evolution equations describing the nonlinearly-coupled evolution of the discrete modes of the low frequency wave climate.
2. Use these equations to investigate the full range of edge wave - edge wave, shear wave - shear wave, and edge wave - shear wave interactions.
3. Couple the resulting system to incident wave conditions.
4. Investigate the equilibrium statistics of the resulting low-frequency wave climate, and compare to field measurements.

The core of our approach to this problem is the development of a spectral model describing nonlinear interactions between the free waves of the system by means of resonant interactions at second order. To date, the literature has identified the possibility of these resonances for the case of three edge waves (Kenyon, 1970; Bowen, 1976) or three shear waves (Shrira et al, 1997). We wish to add to this list the possibility of a triad involving a single shear wave and two edge waves, either of which can be propagating with or against the shear wave. Figure 1 illustrates such a case with all three waves propagating in the same direction as the longshore current. A general framework for computing these interactions is outlined below, and then specialized to the case of edge waves on a planar beach with no current in order to obtain analytical results.

Formulation of the Problem

For simplicity, our attention here is restricted to the case of unforced, undamped nonlinear long wave motions on a longshore uniform beach. The inclusion of forcing would lead to a coupling of the low-frequency motion to the incoming short wave climate (Lippmann et al, 1997). The introduction of longshore variability would extend the present analysis to include both the slow variation of model parameters in the longshore direction as well as the direct scattering of wave modes by wavelength-scale bottom features (Chen and Guza, 1998). These topics will be addressed in extensions of the present work.

The dependent variables in the present analysis are the surface displacement $\eta(x,y,t)$, cross-shore velocity $u(x,y,t)$ and longshore current $v(x,y,t)+V(x)$, where a distinction is made between the mean current profile $V(x)$ and the wave-induced fluctuations $v(x,y,t)$. The governing equations are given by

$$\frac{d\eta}{dt} + (hu)_x + hv_y = -(\eta u)_x - (\eta v)_y \equiv {}^{\eta}N \tag{1}$$

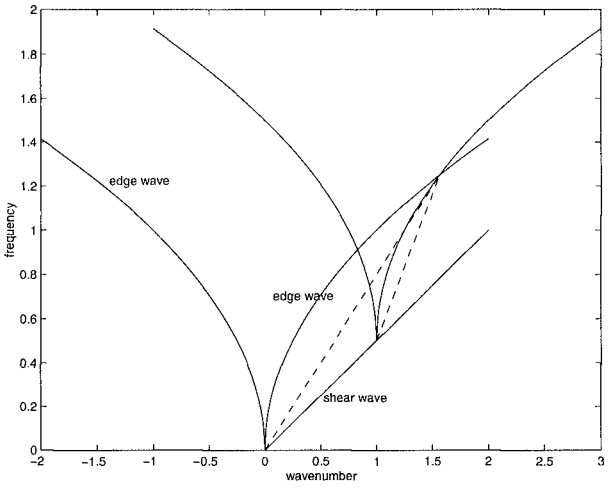

Figure 1: Diagram illustrating hypothetical resonant triad interaction involving a shear wave and two edge waves. Identifying the shear wave as the first wave in the triad, the origin of the edge wave dispersion curve is translated up the shear wave dispersion curve to the locus of shear wave frequency and wavenumber. Resonances involving two edge waves are then indicated by the intersections of the original and the translated edge wave dispersion curves. The two dashed lines here indicate two edge waves with the same mode number and propagating downstream with the longshore current.

$$\frac{d\,(hu)}{dt} + gh\eta_x = -huu_x - hvu_y \equiv {}^{u}N \tag{2}$$

$$\frac{d\,(hv)}{dt} + V'\,(hu) + gh\eta_y = -huv_x - hvv_y \equiv {}^{v}N \tag{3}$$

where a prime denotes differentiation with respect to x, and where

$$\frac{d}{dt} \equiv \frac{\partial}{\partial t} + V(x)\frac{\partial}{\partial y} \tag{4}$$

is a time derivative following the local mean current. Eliminating u and v from linear terms gives

$$\frac{d}{dt}\left\{\frac{d^2\eta}{dt^2} - g(h\eta_x)_x - gh\eta_{yy}\right\} + 2ghV'\eta_{xy} = (\epsilon)\text{N.L.T.} \tag{5}$$

where

$$\text{N.L.T.} = \frac{d}{dt}\left\{\frac{d\,{}^{\eta}N}{dt} - ({}^{u}N)_x - ({}^{v}N)_y\right\} + 2V'({}^{u}N)_y \tag{6}$$

and where ϵ denotes a small parameter characterizing the weakness of the wave motions.

The Linearized Problem

We first seek solutions to the linearized problem, obtained by taking the limit $\epsilon = 0$ in (5). Solutions will be of the form

$$\eta = F(x)e^{i(\lambda y - \omega t)} \tag{7}$$

$$u = G(x)e^{i(\lambda y - \omega t)}; \quad G(x) = \frac{-ig}{\sigma}F'(x) \tag{8}$$

$$v = H(x)e^{i(\lambda y - \omega t)}; \quad H(x) = \frac{g}{\sigma}\left\{\lambda F - \left(\frac{V'}{\sigma}\right)F'\right\} \tag{9}$$

where

$$\sigma \equiv \omega - \lambda V(x) \tag{10}$$

is the local intrinsic frequency of the wave with respect to the local longshore current velocity. Substituting (7)-(9) in (5) gives an eigenvalue problem which may be written in self-adjoint form (Howd et al, 1992) as

$$\left(1 - \frac{g\lambda^2 h}{\sigma^2}F\right) + \left(\frac{ghF'}{\sigma^2}\right)' = 0 \qquad 0 \le x \le \infty \tag{11}$$

$$F \text{ bounded at } x = 0\,, \quad F \downarrow 0 \text{ as } x \to \infty \tag{12}$$

which is not convenient for solution of the eigenvalue problem but which serves as a basis for establishing solvability conditions in the nonlinear problem. The resulting eigenvalue problem is a non-Sturm-Liouville eigenvalue problem for $\{F^r(x), \omega^r\}$ given λ and $h(x)$. There are possible singularities at $\sigma^r = \omega^r - \lambda V_c = 0$, where V_c denotes the critical longshore current velocity. Possible types of solutions include:

1. Gravity motions without a critical level in the current profile $\rightarrow$ Distorted "regular" edge waves (Howd et al, 1992)

2. Gravity motions in the presence of a double set of critical levels, including:

   (a) Waves trapped against the shore by the faster offshore velocity (Falqués and Iranzo, 1992).

   (b) Waves trapped between the critical levels, propagating upstream relative to the current (Bryan and Bowen, 1998)

   (c) Waves trapped between the offshore critical level and deep water (hypothetical).

3. Vorticity motions representing the unstable growth of meanders in the longshore current (where ω^r is complex; Bowen and Holman, 1989) or the stable propagation of similar meanders (Falqués and Iranzo, 1992; Bowen and Holman, 1989).

For a given λ, the orthogonality condition for two modes with distinct mode numbers n, m and frequencies ω^n, ω^m is easily established,

$$\int_0^\infty \frac{gh(\sigma^n + \sigma^m)}{(\sigma^n)^2(\sigma^m)^2} \left\{ F^{n\prime} F^{m\prime} + \lambda^2 F^n F^m \right\} dx = 0$$

but we do not have a theorem for the completeness of the F^n basis. Since the system is of non-Sturm-Liouville form, we expect to obtain a complex spectrum of eigenvalues, of which the components containing positive imaginary parts will correspond to unstable and growing vorticity modes, or shear waves. We wish to emphasize here that the edge waves and shear waves are members of the same basis of eigenfunctions.

The Nonlinear Problem

Returning to the full problem, we follow the usual approach for obtaining evolution equations for variation of modal amplitudes on slow time and longshore space scales. We introduce multiple scales in order to identify slow changes of modal amplitudes in time and in longshore distance.

$$t \to t + \epsilon t = t + T \tag{13}$$

$$y \to y + \epsilon y = y + Y \tag{14}$$

We then introduce an expansion for η,

$$\eta = \eta^{(1)} + \epsilon \eta^{(2)} \tag{15}$$

The solution for $\eta^{(1)}$ corresponds to a superposition of all eigenmodes of the linearized system,

$$\eta^{(1)} = \sum_n \sum_r \frac{1}{2} A_n^r(Y,T) F_n^r(x) E_n^r + \text{complex conjugate} \tag{16}$$

where

$$E_n^r = e^{i(\lambda_n y - \omega_n^r t)} \tag{17}$$

is the oscillatory dependence on fast time and longshore distance, and the F_n^r are the eigenmodes of the linear eigenvalue problem. At $O(\epsilon)$, we get a forced problem for each n, r combination. We require the forcing for each component to be orthogonal to the solution of the adjoint of the original eigenvalue problem. Nonlinear terms in the system may be simplified by imposing resonance conditions, given by

$$\pm\lambda_l \pm \lambda_m - \lambda_n = 0 \tag{18}$$

$$Re\left\{ \pm\omega_\ell^p \pm \omega_m^q - \omega_n^r \right\} = 0 \tag{19}$$

The final evolution equation for each discrete mode in the system has the form

$$\begin{aligned} A_{nT}^r + C_{gn}^r A_{nY}^r = i \sum_l \sum_m \sum_p \sum_q \{ & + T_{lmn}^{pqr} A_l^p A_m^q \delta(l + m - n) \delta(\omega_l^p + \omega_m^q - \omega_n^r) \\ & + {}_- T_{lmn}^{pqr} A_l^p A_m^{q\,*} \delta(l - m - n) \delta(\omega_l^p - \omega_m^q - \omega_n^r) \\ & + {}_- T_{mln}^{qpr} A_l^{p*} A_m^q \delta(m - l - n) \delta(\omega_m^q - \omega_l^p - \omega_n^r) \} \end{aligned} \tag{20}$$

where ${}_+T$ and ${}_-T$ are complicated interaction coefficients for sum and difference interactions respectively. The group velocity C^r_{gn} for each mode is given by

$$C^r_{gn} = \frac{\int_0^\infty \left[\frac{2g\lambda_n}{(\sigma^r_n)^2}h(F^r_n)^2 + \frac{2V}{\sigma^r_n}(F^r_n)^2 - \frac{2g\lambda_n VV'hF^r_nF^{r\prime}}{(\sigma^r_n)^4} - \frac{2gV'hF^r_nF^{r\prime}}{(\sigma^r_n)^3}\right]dx}{\int_0^\infty \left[\frac{2}{\sigma^r_n}(F^r_n)^2 - \frac{2g\lambda_n h}{(\sigma^r_n)^4}V'F^r_nF^r_n\right]dx} \tag{21}$$

In the no-current limit, the corresponding group velocity for edge waves on an arbitrary profile reduces to

$$C^r_{gn} = g\left(\frac{\lambda_n}{\omega^r_n}\right)\frac{\int_0^\infty h(F^r_n)^2dx}{\int_0^\infty (F^r_n)^2dx} \tag{22}$$

given originally by Pearce & Knobloch (1994).

In order to proceed beyond this point to a numerical determination of a solution, a number of steps need to be carried out. First, a reliable method of determining solutions for the linear eigenvalue problem must be established. Then, given eigenvalue pairs $\{\lambda_n, \omega^r_n\}$, we require an algorithm to reliably search for solutions to resonance conditions. Finally, an accurate means for evaluating integrals in expressions for C_g and the nonlinear coupling coefficients must be developed.

Edge Wave Interactions

In this section, we consider the special case of interaction between triads of edge waves on a planar beach in the absence of currents. In this case, the mode structure and wave dispersion relation is known, and model interaction coefficients may be evaluated analytically.

The possibility of triad interactions between progressive edge waves has been mentioned many times but not often addressed in a direct way. Kenyon (1970) provides a version of the Hasselmann interaction equations for random edge wave interactions, but provided no calculations. Kochergin and Pelinovsky (1989) consider the case of a colinear triad (all waves propagating the same direction) and show results for a single interacting triad. We will establish below that their results are wrong.

For the case of no currents, the interaction coefficients reduce to:

$$\begin{aligned}
{}_\pm T^{pqr}_{lmn} &= \omega^p_l(\pm\omega^q_m)[8\omega^r_n\int_0^\infty (F^r_n)^2dx]^{-1}\cdot \\
&\int_0^\infty \Big\{2(\omega^p_l \pm \omega^q_m)F^{p\prime}_l F^{q\prime}_m F^r_n + \omega^p_l F^p_l F^{q\prime\prime}_m F^r_n \pm \omega^q_m F^{p\prime\prime}_l F^q_m F^r_n \\
&+ [2(\omega^p_l \pm \omega^q_m)\lambda^p_l(\mp\lambda^q_m) - \omega^p_l(\lambda^q_m)^2 \mp \omega^q_m(\lambda^p_l)^2]F^p_l F^q_m F^r_n\Big\}dx
\end{aligned} \tag{23}$$

For a planar beach, the F^r_n are given in terms of Laguerre polynomials by

$$F^r_n(x) = \mathrm{e}^{-|\lambda_n|x}L_r(2|\lambda_n|x) \tag{24}$$

Solutions for isolated triads are obtained in terms of Jacobi elliptic functions. In the cases we have investigated, we have found that cases involving counterpropagating

Wave	Mode	Frequency	Wave number
1	0	ω_1	λ_1
2	0	$\omega_2 = \frac{1}{2}\omega_1$	$\lambda_2 = -\frac{1}{4}\lambda_1$
3	1	$\omega_3 = \frac{3}{2}\omega_1$	$\lambda_3 = \frac{3}{4}\lambda_1$

Table 1: Case 1. Parameters for lowest-order edge wave triad involving counter-propagating zero-mode waves.

waves show strong interactions with energy exchange time scales on the order of 10 wave periods. In contrast, cases involving colinear waves have interaction coefficients of zero, indicating an absence of interaction, contrary to the results of Kochergin and Pelinovsky (1989). Because this result is at odds with the existing literature, we verify it using a direct numerical simulation. The spectral-collocation method of Özkan-Haller and Kirby (1997) is used to obtain direct numerical solutions of the nonlinear shallow water equations with shoreline runup.

Results and Numerical Verification

As a first example, we consider the lowest-order triad involving two counter-propagating zero-mode edge waves, with the relation between frequencies, wavenumbers and mode numbers as indicated in Table 1. The geometry of the triad in wavenumber-frequency space is indicated in Figure 2. The resulting interaction equations are given by

$$A_{1T} = \frac{i\omega_1^3}{8gs^2} A_2^* A_3 \tag{25}$$

$$A_{2T} = \frac{i\omega_1^3}{64gs^2} A_1^* A_3 \tag{26}$$

$$A_{3T} = \frac{9i\omega_1^3}{64gs^2} A_1 A_2 \tag{27}$$

$$|A_1|^2 + |A_2|^2 + |A_3|^2 = \text{constant} \tag{28}$$

In this case, the parameters are chosen such that ω_1 corresponds to a wave with a period of $20s$ on a beach with a slope of $1:10$. In the results illustrated in Figure 3, we have initialized the triad by giving waves 1 and 2 amplitudes of $10cm$, with wave three having no amplitude to start. The resulting solution for the triad interaction is shown in Figure 3 by the smooth curves. The results indicate a complete exchange of energy between one of the Mode 0 waves and the Mode 1 wave propagating the same direction. The exchange occurs in somewhat less than 20 periods of the Mode 0 wave. The counterpropagating Mode 0 wave is crucial to the interaction but exchanges only a small amount of energy with the other modes. This non-reactivity of the counterpropagating wave has been noted for a wide range of initial conditions.

The analytic results shown in Figure 3 have been verified using direct numerical

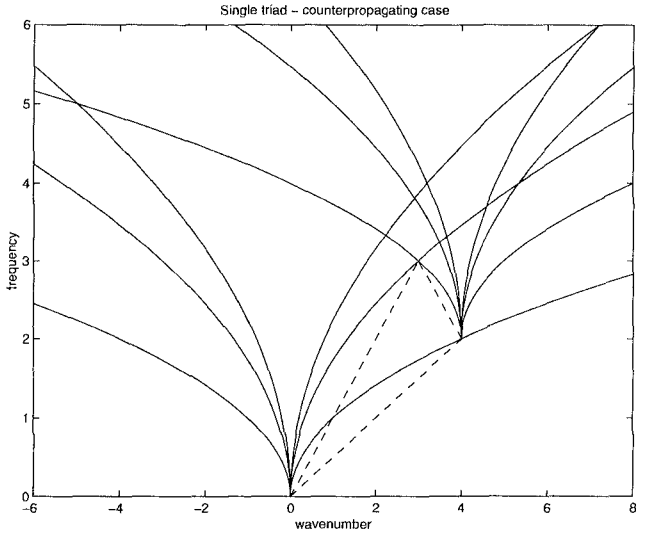

Figure 2: Resonant triad edge-wave interaction with counterpropagating components.

simulation with the pseudospectral model of Özkan-Haller and Kirby (1997). Results from that model were obtained by Fourier transforming the longshore dependence of the runup tip. Results are shown in Figure 3 as the curves with smaller-scale jitter in time. (This jitter occurs at wave-period or sub-wave-period scales, and is probably associated with the fact that the linear edge waves input as initial conditions differ from fully nonlinear solutions to the problem.) Agreement between analytical triad results and numerical solutions are close, with the numerical solutions indicating a slightly slower energy exchange time and a tendency for energy to leak out of the three components making up the triad.

The fate of the missing energy can be seen in the plot of the frequency-wavenumber spectrum computed from the numerical solution, shown in Figure 4. The spectrum is dominated by the three waves making up the resonant triad, but there are clear contributions at forced, non-resonant peaks representing sum and difference interactions lying off the edge wave dispersion curves. There has also been an excitation of the Mode 0 edge wave at twice the wavenumber of Wave 1, and at a frequency that is not commensurate with any sum or difference combination in the original triad. The mechanism for exciting this free wave is not clear and may be associated with start-up transients in the initial value problem.

Figure 5 shows one longshore period of the numerically computed wave field at two instances in time. The top panel shows the situation at 20 wave periods into the simulation, where the wave field is dominated by the higher-frequency Mode 1

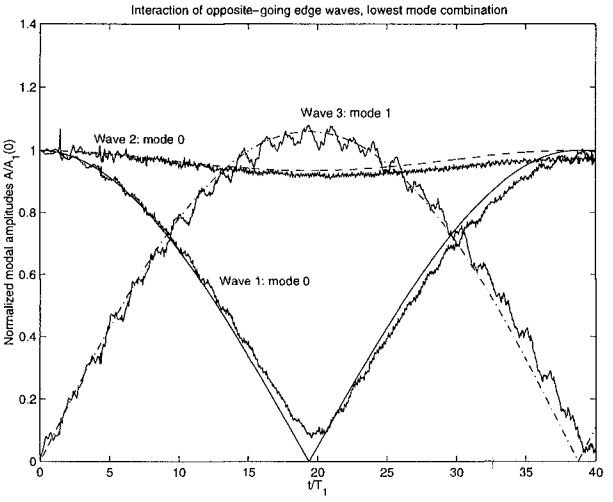

Figure 3: Comparison of time series of modal wave amplitudes: analytic and numerical results.

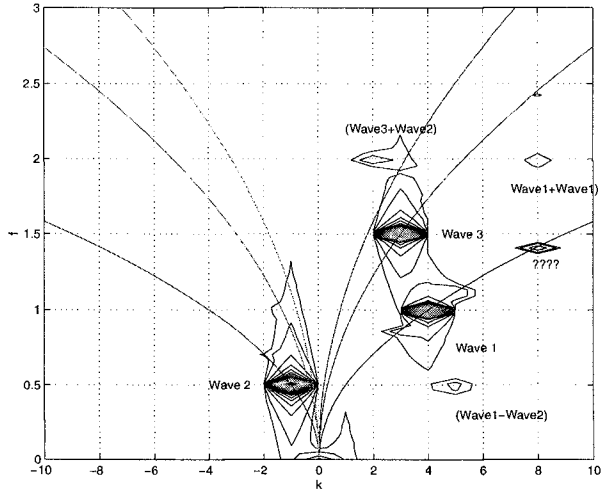

Figure 4: Frequency-wavenumber spectrum for case of counterpropagating waves. Direct numerical simulation.

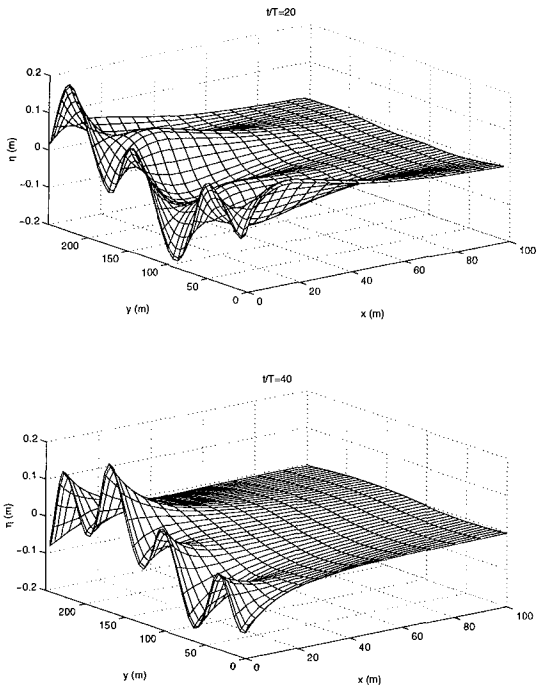

Figure 5: Snapshot of numerically computed instantaneous wave field showing conditions dominated by Mode 1 wave (top panel) and Mode 0 wave (lower panel).

wave riding on the longer, counterpropagating Mode 0 wave. The lower panel shows the situation at 40 periods (close to the end of the recurrence cycle), where the two counterpropagating Mode 0 waves dominate the wavefield.

As a second example, we consider the case elaborated by Kochergin and Pelinovsky (1989) with all waves travelling the same direction, illustrated in Figure 6. The parameters for the lowest-order case are indicated in Table 2. The present theory indicates that nonlinear interaction coefficients reduce to zero, giving solutions $A_1, A_2, A_3 =$ constant. Figure 7 shows time histories for the first twelve Fourier modes of the longshore runup in a direct numerical simulation, with modes $k = 1$ and $k = 3$ corresponding to the initialized low-frequency modes in the triad. The numerical results indicate no interaction between the initialized modes and an absence of growth of the third member of the possible triad. This result is also clear in the resulting frequency-wavenumber spectrum shown in Figure 7, which shows an almost complete lack of energy appearing at the third component, which would appear at scaled wavenumber $k = 4$ and frequency $f = 2$.

Wave	Mode	Frequency	Wave number
1	0	ω_1	λ_1
2	1	$\omega_2 = \omega_1$	$\lambda_2 = \frac{1}{3}\lambda_1$
3	1	$\omega_3 = 2\omega_1$	$\lambda_3 = \frac{4}{3}\lambda_1$

Table 2: Parameters for lowest order triad with waves propagating in the same direction, as in Kochergin and Pelinovsky (1989).

Conclusions

In this paper, we have described a framework for deriving coupled-mode equations for a sea of edge waves and shear waves. Interaction coefficients have been obtained for the special case of edge waves on a plane beach in the absence of currents. For this system, interactions have been shown to exist and to be fairly rapid for triads involving counterpropagating waves. Triads involving unidirectional propagation have been found to not lead to interaction, in contradiction to the existing literature. We do not yet have a conclusive proof that this result holds for all colinear edge wave triads on a planar beach, but it has been found to hold for all combinations tested so far. Results for both cases have been verified by direct numerical simulation. The close agreement between numerical and analytic results also indicates that a weakly nonlinear formulation is appropriate for examining edge wave interactions. This result is to be expected due to the strongly dispersive nature of the edge wave motions.

The work on edge wave interactions is presently being extended to look at more complicated systems involving multiple coupled triads, leading up to an evaluation of equilibrium distribution of energy in a random sea of edge waves. In order to further this goal, we need to:

1. Automate the process of identifying resonances.
2. Extend calculations to a large number of components, in order to investigate the assumptions to be made in going over to a stochastic version of the equations.
3. Implement the stochastic version and couple it to the incident wave climate.

In addition, the limitation of the present analytical theory to the case of waves on planar beach topographies is restrictive, and needs to be extended to the case of non-planar topographies such as the exponential profile of Ball (1967). It is also possible that the non-interaction of edge wave triads involving waves propagating the same direction, found here for waves on a planar beach, is an anomalous result that will not hold for arbitrary topographies.

For the case with a net longshore current added to the system, we need to elaborate the process for numerically determining the eigenmodes for an arbitrary topography and longshore current distribution, and then repeat the steps outlined above.

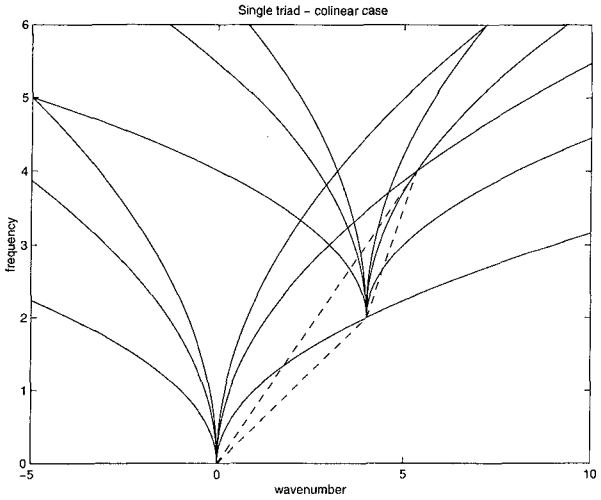

Figure 6: Single triad with colinear components. No resulting interaction.

Acknowledgements: This work has been supported by the Office of Naval Research, Coastal Dynamics Program.

Appendix: References

Allen, J. S., Newberger, P. A. and Holman, R. A., 1996, "Nonlinear shear instabilities of alongshore currents on plane beaches", *J. Fluid Mech.*, **310**, 181-213.

Ball, F. K., 1967, "Edge waves in an ocean of finite depth", *Deep Sea Res.*, **14**, 79-88.

Bowen, A. J., 1976, "Wave-wave interactions near the shore", in *Waves on Water of Variable Depth*, D. G. Provis and R. Radok (eds), Lecture Notes in Physics **64**, 102-113.

Bowen, A. J. and Holman, R. A., 1989, "Shear instabilities in the mean longshore current. 1: Theory", *J. Geophys. Res.*, **94**, 18,023-18,030.

Bryan, K. R. and Bowen, A. J., 1998, "Bar-trapped edge waves and longshore currents", *J. Geophys. Res.*, submitted.

Chen, Y. and Guza, R. T., 1998, "Resonant scattering of edge waves by longshore periodic topography", *J. Fluid Mech.*, in press.

Falqués, A. and Iranzo, V., 1992, "Edge waves on a longshore shear flow", *Phys. Fluids A*, **4**, 2169-2190.

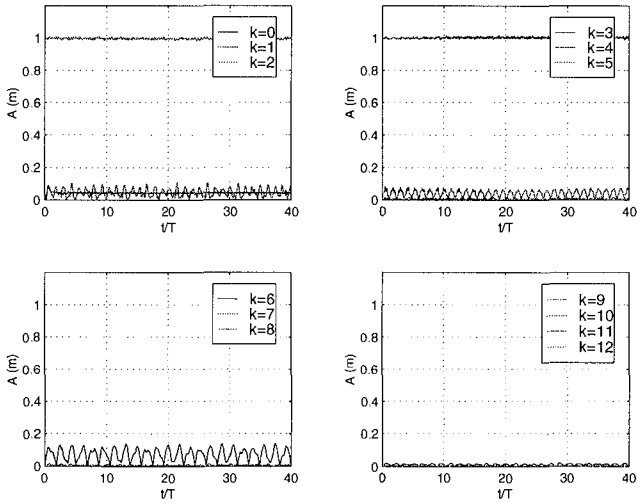

Figure 7: Time series of modal wave amplitudes for colinear case: Direct numerical simulation.

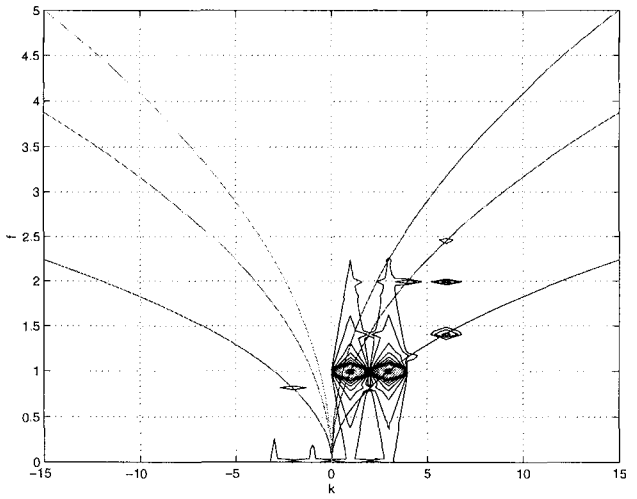

Figure 8: Wavenumber-frequency spectra for colinear case: Direct numerical simulation.

Feddersen, F., 1998, "Weakly nonlinear shear waves", *J. Fluid Mech.*, in press.

Howd, P. A., Bowen, A. J. and Holman, R. A., 1992, "Edge waves in the presence of strong longshore currents", *J. Geophys. Res.*, **97**, 11357-11371.

Kenyon, K. E., 1970, "A note on conservative edge wave interactions", *Deep-Sea Res.*, **17**, 197-201.

Kochergin, I. Ye. and Pelinovsky, Ye. N., 1989, "Nonlinear interaction in an edge wave triad", *Oceanology*, **29**, 669-672.

Lippmann, T. C., Holman, R. A. and Bowen, A. J., 1997, "Generation of edge waves in shallow water", *J. Geophys. Res.*, **102**, 8663-8679.

Özkan-Haller, H. T. and Kirby, J. T., 1997, "A Fourier-Chebyshev collocation method for the shallow water equations including shoreline runup", *Applied Ocean Res.*, **19**, 21-34.

Özkan-Haller, H. T. and Kirby, J. T., 1998, "Nonlinear evolution of shear instabilities of the longshore current: A comparison of observations and computations", submitted to *J. Geophys. Res.*

Pearce, R. D. and Knobloch, E., 1994, "Evolution equations for counterpropagating edge waves", *J. Fluid Mech.*, **264**, 137-163.

Shrira, V. I., Voronovich, V. V. and Kozhelupova, N. G., 1997, "Explosive instabilities of vorticity waves", *J. Phys. Oceanogr.*, **27**, 542-554.

Yeh, H. H., 1985, "Nonlinear progressive edge waves: their instability and evolution", *J. Fluid Mech.*, **152**, 479-499.

On the viscous destabilization of longshore currents

Uday Putrevu[1] A.M.ASCE, James T. Kirby[2] M.ASCE, Joan Oltman-Shay[3], and H. Tuba Özkan-Haller[4] A.M.ASCE

ABSTRACT: *The effects of lateral mixing on the stability of longshore currents are examined. For the model problem originally considered by Bowen and Holman (1989), it is shown that the inclusion of lateral mixing changes the stability characteristics of the longshore current. In particular, it eliminates the low wavenumber cutoff predicted by the inviscid theory.*

INTRODUCTION

In this paper we investigate how lateral mixing affects the stability of longshore currents. Bowen and Holman (1989; BH89 hereafter) showed that longshore currents in the surf zone are frequently unstable and that these instabilities manifest themselves as wavelike oscillations of the longshore current of the kind found by Oltman-Shay *et al.* (1989).

BH89 derived the equations governing the linear stability of the longshore current in the absence of bottom friction and lateral mixing. They showed that the stability of the longshore current is governed by a modified Rayleigh equation. BH89 solved the stability equation for a model problem in which a longshore current of the form sketched in figure 1 flows over a horizontal bottom. They demonstrated that the longshore current is unstable for wavenumbers in a certain range and that many properties of the waves generated due to the instability of the longshore current are consistent with the observations of shear waves reported by Oltman-Shay *et al.* (1989).

Since the pioneering work of Bowen and Holman, several contributions have been made that have clarified many aspects of the shear wave generation problem [see Özkan-Haller and Kirby (1998) for a brief review]. Here we consider how the inclusion of lateral mixing affects the stability of longshore currents.

[1]Research Scientist, NorthWest Research Associates, Inc., 14508 NE 20th Street, Bellevue, WA 98007, USA.

[2]Professor, Center for Applied Coastal Research, University of Delaware, Newark, DE 19716, USA.

[3]Senior Research Scientist, NorthWest Research Associates, Inc., 14508 NE 20th Street, Bellevue, WA 98007, USA.

[4]Assistant Professor, Department of Naval Architecture and Marine Engineering, University of Michigan, Ann Arbor, MI 48109, USA.

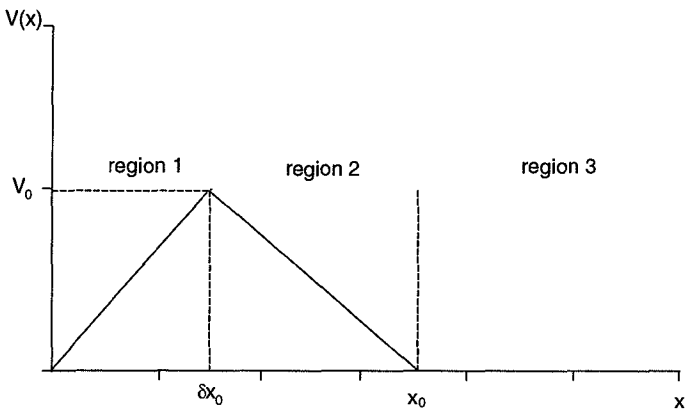

Figure 1: Velocity profile used by BH89. This same velocity profile is also used in our model problem. In all of the calculations below, we use $x_0 = 100$ m and $V_0 = 1$ m/s.

Falqués and Iranzo (1994) and Falqués *et al.* (1994) have already included lateral mixing in the calculations of the stability of longshore currents. Our work differs from that of Falqués *et al.* in that here we consider how the inclusion of lateral mixing changes the stability of a simple longshore current profile of the type considered by BH89. The simplicity of the current profile allows us to perform analytical calculations of how the addition of the lateral mixing changes the stability characteristics of the longshore current. This, in turn, makes the interpretation of the results easier.

The outline of the rest of the paper is as follows. We first derive the equation that governs the stability of the longshore current in the presence of lateral mixing. We then solve the resulting equation for the model problem considered by BH89. Example results are then presented that demonstrate that the inclusion of lateral mixing can destabilize the longshore current. A discussion of the mechanism by which lateral mixing can destabilize the longshore current follows the example results. The paper concludes with a summary.

MATHEMATICAL FORMULATION

We start with the depth-integrated equations of continuity and momentum

$$\frac{\partial \zeta}{\partial t} + \frac{\partial (h+\zeta) u_i}{\partial x_i} = 0 \tag{1}$$

$$\frac{\partial u_i}{\partial t} + u_j \frac{\partial u_i}{\partial x_j} = -g \frac{\partial \zeta}{\partial x_i} + \frac{1}{\rho h} \frac{\partial S_{ij}}{\partial x_j} + \frac{\partial}{\partial x_j} \left[\nu h \left(\frac{\partial u_i}{\partial x_j} + \frac{\partial u_j}{\partial x_i} \right) \right] - \frac{\tau_{b,i}}{\rho h} \tag{2}$$

where ζ is the surface elevation, h is the water depth, u_i is the depth-integrated horizontal velocity, S_{ij} is the radiation stress, ν is a lateral mixing coefficient, and

$\tau_{b,i}$ is the bottom shear stress. The lateral mixing represented by the ν terms in (2) could be either due to turbulent lateral mixing (generated by breaking waves) or due to dispersive mixing generated by the interaction of the cross-shore and longshore currents (Svendsen and Putrevu 1994; Smith 1997). Since these lateral mixing terms have the same form as viscous terms, the terms *viscosity* and *lateral mixing* will be used interchangeably in the rest of this paper.

We now assume that the total flow consists of a steady longshore current $V(x)$ and a shear wave with surface elevation $\eta(x,y,t)$ and depth-averaged horizontal velocities $u(x,y,t)$ and $v(x,y,t)$ in the cross-shore (x) and longshore (y) directions. We further assume that u and v are much smaller than V. Under these assumptions the momentum equations governing the shear wave reduce to (neglecting the forcing and the bottom shear stress)

$$\frac{\partial u}{\partial t}+V\frac{\partial u}{\partial y}=-g\frac{\partial \eta}{\partial x}+\frac{2}{h}\frac{\partial}{\partial x}\left(\nu h\frac{\partial u}{\partial x}\right)+\frac{1}{h}\frac{\partial}{\partial y}\left[\nu h\left(\frac{\partial u}{\partial y}+\frac{\partial v}{\partial x}\right)\right] \tag{3}$$

$$\frac{\partial v}{\partial t}+u\frac{dV}{dx}+V\frac{\partial v}{\partial y}=-g\frac{\partial \eta}{\partial y}+\frac{2}{h}\frac{\partial}{\partial y}\left(\nu h\frac{\partial v}{\partial y}\right)+\frac{1}{h}\frac{\partial}{\partial x}\left[\nu h\left(\frac{\partial u}{\partial y}+\frac{\partial v}{\partial x}\right)\right] \tag{4}$$

The continuity equation under the rigid lid assumption [see BH89 or Dodd and Thornton (1990) for a justification of the rigid lid assumption] reduces to

$$\frac{\partial}{\partial x}(hu)+\frac{\partial}{\partial y}(hv)=0 \tag{5}$$

The nondivergence of the continuity equation allows us to introduce a stream function Ψ such that

$$\Psi_x=hv \qquad \Psi_y=-hu \tag{6}$$

Since we are seeking wavelike solutions, we assume that

$$\Psi(x,y,t)=\phi(x)\exp i(ky-\omega t) \tag{7}$$

where k is the wavenumber and ω is the frequency. The stream function can be used to combine (3) and (4) [by cross-differentiation followed by subtraction] into a single equation in ϕ:

$$\begin{aligned}(V-c)\left[\left(\frac{\phi_x}{h}\right)_x-\frac{k^2\phi}{h}\right]-\phi\left(\frac{V_x}{h}\right)_x&=\frac{\nu}{ik}\left(\frac{\partial^2}{\partial x^2}-k^2\right)\left[\left(\frac{\phi_x}{h}\right)_x-\frac{k^2\phi}{h}\right]\\ +\frac{1}{ik}\left\{\nu_x\left[\left(\frac{\phi_x}{h}\right)_{xx}-\frac{k^2\phi_x}{h}-\frac{k^2\phi h_x}{h^2}\right]+\left[\frac{(\nu h)_x}{h}\left(\frac{\phi_x}{h}\right)_x\right]_x-\frac{k^2(\nu h)_x}{h}\left(\frac{\phi}{h}\right)_x\right\}&\end{aligned} \tag{8}$$

where $c=\omega/k$ is the wave speed. The boundary conditions corresponding to (8) are

$$\phi,\frac{d\phi}{dx}=0 \quad x=0,x\to\infty \tag{9}$$

(8) subject to (9) forms an eigenvalue problem. As is usual in stability calculations, we assume that the wavenumber k is known and treat the frequency ω as the eigenvalue.

If ω has a positive imaginary component for a given k it implies that the longshore current is unstable to disturbances of that wavenumber.

The terms on the RHS of (8) are terms that arise due to the inclusion of the lateral mixing. For $\nu = 0$, (8) reduces to the equation derived by BH89. [The appropriate boundary conditions for the reduced equation are $\phi = 0$ at $x = 0, x \to \infty$.] For small values of ν the RHS of (8) is small and unimportant except at the shoreline and the singular points of the inviscid equation. At the shoreline, the necessity of satisfying an additional boundary condition leads to the generation of a boundary layer. At the locations where $V = c$, the inviscid equation is, in general, singular whereas the full equation is not. Therefore, at these locations, internal boundary layers will develop when lateral mixing is included.

MODEL PROBLEM

We consider the stability of the longshore current sketched in Figure 1. The bottom is assumed to be horizontal. The inviscid stability of this current profile was calculated by BH89. Here we modify their solution to account for lateral mixing. For a horizontal bottom (8) reduces to the Orr-Sommerfeld equation

$$(V-c)\left(\frac{d^2}{dx^2}-k^2\right)\phi - V_{xx}\phi = \frac{\nu}{ik}\left(\frac{d^2}{dx^2}-k^2\right)^2\phi \tag{10}$$

We assume that the strength of the lateral mixing is such that a typical term on the RHS of (10) is much smaller than a typical term on the LHS. Formally, this requires that

$$\frac{k_t \nu_t}{V_0} \ll 1 \tag{11}$$

where k_t is a typical wavenumber, ν_t is a typical value of the lateral mixing coefficient, and V_0 is the maximum longshore current. Note that since $k_t \sim 0.01$ m^{-1}, $\nu_t \sim 0.1$ m^2/s, $V_0 \sim 1$ m/s, (11) is easily satisfied.

For the longshore current sketched in figure 1, (10) reduces to

$$(V-c)\left(\frac{d^2}{dx^2}-k^2\right)\phi = \frac{\nu}{ik}\left(\frac{d^2}{dx^2}-k^2\right)^2\phi \tag{12}$$

in each of the three regions. In this case, the singular points of the inviscid equation are the points $x = \delta x_0$ and $x = x_0$ and internal boundary layers develop at these points to smooth out the discontinuities predicted by the inviscid theory.

At $x = 0$ and $x = x_0$, the boundary layer correction to the inviscid solution is governed approximately by

$$-c\frac{d^2\phi_{BL}}{dx^2} \approx \frac{\nu}{ik}\frac{d^4\phi_{BL}}{dx^4} \tag{13}$$

which implies that at these locations

$$\phi_{BL} \propto \exp\left[\pm(1-i)\beta_1 x\right] \tag{14}$$

where $\beta_1 = \sqrt{\omega/2\nu} \gg k$. At $x = \delta x_0$ the boundary layer correction is approximately governed by

$$(V_0-c)\frac{d^2\phi_{BL}}{dx^2} \approx \frac{\nu}{ik}\frac{d^4\phi_{BL}}{dx^4} \tag{15}$$

which leads to

$$\phi_{BL} \propto \exp\left[\pm(1+i)\beta_2 x\right] \tag{16}$$

where $\beta_2 = \sqrt{(kV_0 - \omega)/2\nu} \gg k$.

The solution to (12) can therefore be written as

$$\phi = \begin{cases} \sinh(kx) + B_1\cosh(kx) + F_1\exp[-(1-i)\beta_1 x] \\ \quad +G_1\exp[(1+i)\beta_2(x-\delta x_0)] & x < \delta x_0 \\ \\ A_2\sinh[k(x-\delta x_0)] + B_2\cosh[k(x-\delta x_0)] \\ \quad +F_2\exp[-(1+i)\beta_2(x-\delta x_0)] + G_2\exp[(1-i)\beta_1(x-x_0)] & \delta x_0 < x < x_0 \\ \\ A_3\exp[-k(x-x_0)] + F_3\exp[-(1-i)\beta_1(x-x_0)] & x > x_0 \end{cases} \tag{17}$$

The unknown coefficients (the A's, B's, F's, and G's) and the eigenvalue (ω) have to be determined by imposing the boundary conditions at $x = 0$ and the matching conditions at $x = \delta x_0$ and $x = x_0$. [The boundary conditions at infinity have already been imposed in (17).] The appropriate matching conditions are:

1. hu continuous $\Rightarrow$ ϕ continuous
2. hv continuous $\Rightarrow$ ϕ_x continuous
3. η continuous $\Rightarrow$ $ik\phi dV/dx + \nu d^3\phi/dx^3$ continuous
4. $-g\partial\eta/\partial x + \nu\partial^2 u/\partial x^2$ continuous $\Rightarrow$ $(V-c)d^2\phi/dx^2 + (\nu/ik)[2k^2 d^2\phi/dx^2 - d^4\phi/dx^4]$ continuous

The last of these conditions follows from the cross-shore momentum equation (3).

Applying the boundary and matching conditions leads to (after a fair amount of algebra)

$$\omega^2 + F(\delta, kx_0)\omega + G(\delta, kx_0) + \left(\frac{k}{\beta_1}\right) T(\omega, kx_0, \delta, \beta_1/\beta_2) = O\left(\frac{k}{\beta}\right)^2 \tag{18}$$

where

$$F = -kV_0\left[1 - \frac{S_0}{(S_0+C_0)}\frac{V_{x2}}{kV_0} - \frac{(S_{1-\delta}+C_{1-\delta})S_\delta}{(S_0+C_0)}\frac{\Delta V_x}{kV_0}\right] \tag{19}$$

$$G = (kV_0)^2\left[\frac{V_{x2}\Delta V_x}{(kV_0)^2}\frac{S_\delta S_{1-\delta}}{(S_0+C_0)} - \frac{S_0}{(S_0+C_0)}\frac{V_{x2}}{kV_0}\right] \tag{20}$$

$$\begin{aligned} T = {} & \left\{2(1+i)\left\{\sigma\left[C_0 + \frac{\omega}{V_{x2}}(S_0+C_0)\right] + \Delta V_x C_\delta\left[S_{1-\delta} + \frac{\omega}{V_{x2}}(S_{1-\delta}+C_{1-\delta})\right]\right\}\right. \\ & +\sigma(1+i)\left[(S_0+C_0) + S_\delta\frac{\Delta V_x}{\sigma}(S_{1-\delta}+C_{1-\delta})\right] \\ & \left.-\frac{\beta_1}{\beta_2}\frac{(\Delta V_x)^2}{\sigma}(1-i)S_\delta\left[S_{1-\delta} + \frac{\omega}{V_{x2}}(S_{1-\delta}+C_{1-\delta})\right]\right\}\frac{V_{x2}}{4(S_0+C_0)} \end{aligned} \tag{21}$$

In the above, $S_0 = \sinh(kx_0)$, $S_\delta = \sinh(k\delta x_0)$, $S_{1-\delta} = \sinh[kx_0(1-\delta)]$ and the C's are short forms for the corresponding cosh functions. Additionally, V_{x1} and V_{x2} represent dV/dx in regions 1 and 2 respectively, $\Delta V_x = V_{x1} - V_{x2}$, and $\sigma = \omega - kV_0$.

In the limit of $\nu \to 0$ ($\beta_1, \beta_2 \to \infty$), F and G reduce to the expressions given by BH89's (16), and we then recover Bowen and Holman's solution. The term denoted by T represents the effects of including the lateral mixing.

For $\nu = 0$, (18) has two solutions for ω for a given value of k – these are the solutions found by BH89. For small ν, the T-term modifies these solutions. These modifications can be calculated in a straightforward manner. In addition to modifying the BH89 solution, the T-term also introduces new roots to (18). The significance of these new roots is, at present, unknown. In the following, we discuss only the roots that can be interpreted as modifications of the BH89 solution.

RESULTS

Figure 2 shows the variation of the growth rate ω_{im} as a function of the wave number. For comparison, we also show Bowen and Holman's inviscid solution. It is clear from this figure that including lateral mixing in the calculations significantly alters the stability characteristics. In particular, the range of wavenumbers over which the instability occurs is significantly enhanced, the location of the most unstable wave is changed, and the low wavenumber cutoff predicted by the inviscid theory is removed.

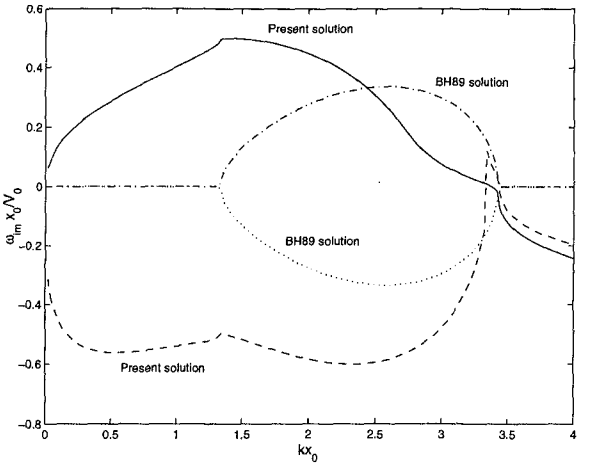

Figure 2: Plot of growth rate, ω_{im}, vs wavenumber for the model problem. The parameters used in this calculation are $\delta = 0.5$, $\nu = 5 \times 10^{-3}$ m^2/s, $x_0 = 100$ m, and $V_0 = 1$ m/s.

In a recent paper, Shrira *et al.* (1997) solved the weakly nonlinear version of the model problem considered by BH89. They showed that the triad interactions between individual shear wave modes could remove the low wavenumber cutoff predicted by the linear inviscid theory. Our results show that including the lateral mixing leads to

the same result. Thus, a plausible scenario is that the low wavenumber oscillations are initially generated by the present mechanism and grow to finite amplitude by the mechanism discussed by Shrira *et al.*

Figure 3 shows the variation of the real part of the frequency as a function of the wavenumber for the branches of the solution that have a positive growth rate. We see from this figure that the addition of lateral mixing does not alter the dispersion relationship significantly in the region where the inviscid theory predicts an instability.

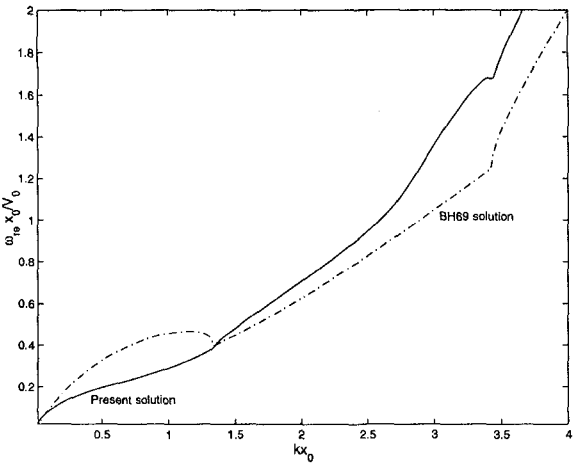

Figure 3: Plot of the real part of the frequency, ω_{re}, vs wavenumber for the model problem. The parameters used in this calculation are $\delta = 0.5$, $\nu = 5 \times 10^{-3}$ m^2/s, $x_0 = 100$ m, and $V_0 = 1$ m/s. Note that only the branches that have a positive growth rates are shown.

Figure 2 showed the growth rate as a function of wavenumber for a particular choice of the lateral mixing coefficient ν. It is also of interest to examine the sensitivity of the growth rate at a fixed wavenumber to the choice of the mixing coefficient. This is done in figure 4 which shows the variation of the growth rate as a function of ν. Realistic values of ν for the nearshore are expected to be in the range 10^{-3} to 0.1 m^2/s. The lower end of the range would apply if the lateral mixing were due to the turbulence generated by breaking waves (Svendsen 1987; George *et al.* 1994). The higher end would apply if, as is more likely, the lateral mixing were due to dispersive mixing generated by the interaction of the cross-shore and longshore currents (Svendsen and Putrevu 1994). We see from figure 4 that the growth rate increases with ν for ν in the range that is normally expected.

BH89 found that the backshear parameter δ controls the strength of the instability in

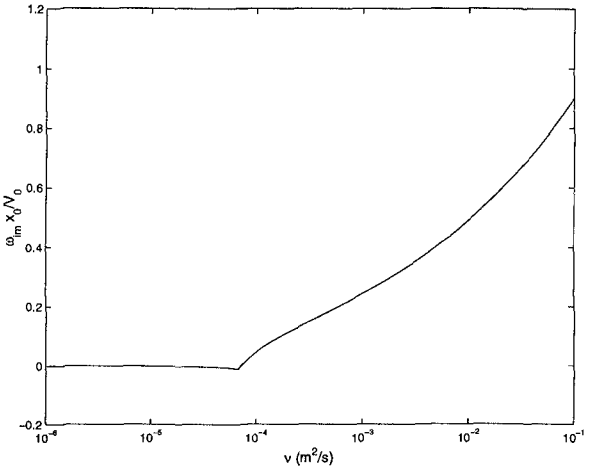

Figure 4: Variation of growth rate with the lateral mixing coefficient. The parameters used in this calculation are $\delta = 0.5$, $kx_0 = 1$, $x_0 = 100$ m, and $V_0 = 1$ m/s.

the inviscid problem – the stronger the backshear, the stronger is the instability. It is therefore of interest to see whether this behavior carries over to the case where lateral mixing is included. Figure 5 shows the variation of the growth rate with δ. For this calculation we have chosen the parameters such that the inviscid calculations predict stability. This figure clearly shows that the backshear δ also controls the stability of the viscous problem.

MECHANISM

The calculations presented so far have shown that including the lateral mixing can destabilize an otherwise stable longshore current. Since this result is somewhat counter-intuitive, it is useful to examine it in more detail. Therefore, we discuss below the mechanism by which lateral mixing (or viscosity) can destabilize a longshore current. The discussion here largely follows Lin's (1967) discussion (see pp. 60-63 of Lin's book).

For h = constant, the equations governing the stability of the longshore current reduce to

$$\frac{\partial u}{\partial x} + \frac{\partial v}{\partial y} = 0 \tag{22}$$

$$\frac{\partial u}{\partial t} + V\frac{\partial u}{\partial y} = -g\frac{\partial \eta}{\partial x} + \nu\left(\frac{\partial^2 u}{\partial x^2} + \frac{\partial^2 u}{\partial y^2}\right) \tag{23}$$

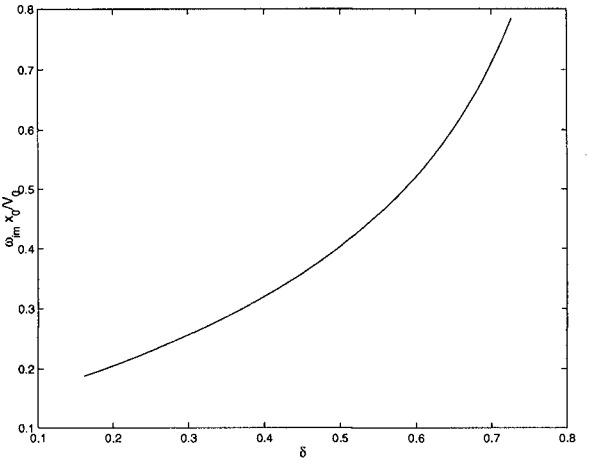

Figure 5: Variation of the growth rate as a function of the backshear parameter. The values used in the calculations are $\nu = 5 \times 10^{-3}$, m^2/s and $kx_0 = 1$, $x_0 = 100$ m, and $V_0 = 1$ m/s. The inviscid solution is stable for this choice of parameter values.

$$\frac{\partial v}{\partial t} + u\frac{dV}{dx} + V\frac{\partial v}{\partial y} = -g\frac{\partial \eta}{\partial y} + \nu\left(\frac{\partial^2 v}{\partial x^2} + \frac{\partial^2 v}{\partial y^2}\right) \tag{24}$$

From these equations, it is straightforward to derive the following energy equation

$$\begin{aligned}\frac{dE}{dt} &= -\int_0^\infty h\overline{uv}(dV/dx)dx \\ &\quad -\nu\int_0^\infty h\left[(\partial u/\partial x)^2 + (\partial u/\partial y)^2 + (\partial v/\partial x)^2 + (\partial v/\partial y)^2\right]dx\end{aligned} \tag{25}$$

where an overbar denotes averaging over a shear wave period and E is the total kinetic energy defined by

$$E = \frac{h}{2}\int_0^\infty \overline{(u^2+v^2)}dx \tag{26}$$

(Because of the rigid-lid assumption, the potential energy does not enter the energy equation.)

The first term in (25) represents the energy transfer from the longshore current to the shear wave and the second term represents the dissipation of the shear wave energy by the viscosity-like terms. Now the introduction of viscosity changes the phase between the cross-shore and longshore velocities so that the first term on the RHS of (25) is

changed relative to the inviscid solution. Thus, viscous terms modify the inviscid solution in two important ways: 1) they change the phase between the velocity components of the shear wave which leads to an extraction of energy from the longshore current and 2) they lead to direct dissipation of the shear wave energy. Therefore, viscous terms can destabilize an otherwise stable longshore current profile if the energy extracted from the longshore current exceeds the direct dissipation.

To explore the changes caused by the inclusion of viscosity-like terms further, we show in figures 6, 7, and 8 the cross-shore variations of ϕ (which is proportional to u), ϕ_x (proportional to v), and $-\overline{uv}(dV/dx)$ respectively. (The parameter values are chosen such that the inviscid calculation predicts stability whereas the viscous calculation predicts instability.) It is clear from figures 6 and 7 that the introduction of lateral mixing terms changes the phase of u and v. Figure 8 shows that this change in phase results in an extraction of energy from the longshore current. Figure 8 further demonstrates that most of the energy extraction takes place on the seaward face of the longshore current, thereby explaining the importance of the backshear on the stability found in figure 5.

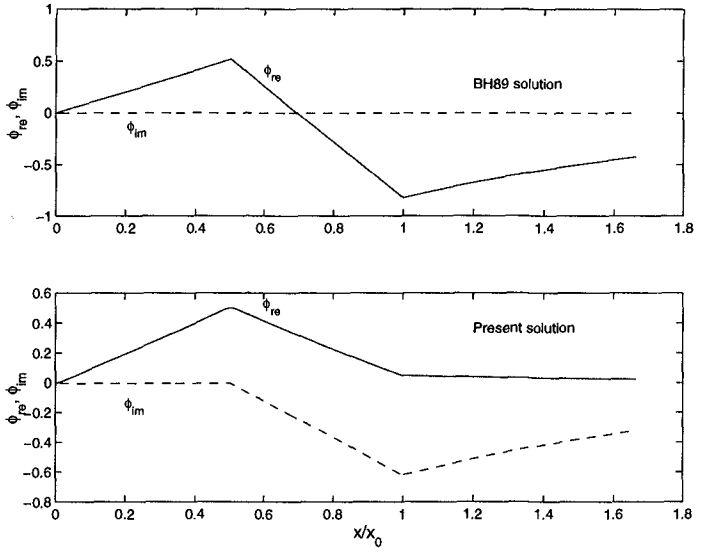

Figure 6: Cross-shore variation of $\phi \propto u$. Top panel inviscid (BH89) solution. Bottom panel calculation including lateral mixing terms. Note that the scale of the y axis is arbitrary. The parameter values used in the calculations are $kx_0 = 1$, $x_0 = 100$ m, $\delta = 0.5$, $V_0 = 1$ m/s, and $\nu = 5 \times 10^{-3}$ m^2/s.

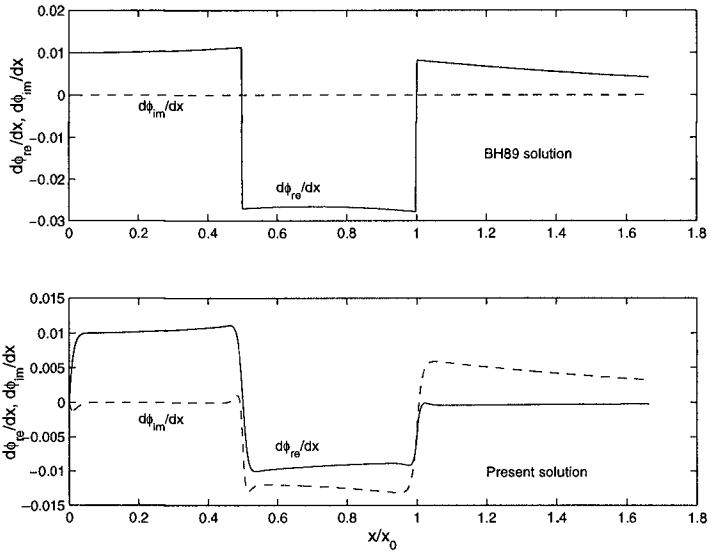

Figure 7: Cross-shore variation of $\phi_x \propto v$. Top panel inviscid (BH89) solution. Bottom panel calculation including lateral mixing terms. Note that the scale of the y axis is arbitrary. The parameter values used in the calculations are $kx_0 = 1$, $x_0 = 100$ m, $\delta = 0.5$, $V_0 = 1$ m/s, and $\nu = 5 \times 10^{-3}$ m^2/s.

SUMMARY

In this paper we considered how the addition of lateral mixing affects the stability of longshore currents. We showed that the inclusion of lateral mixing can destabilize an otherwise stable longshore current. The instability induced by the lateral mixing is such that it removes the low-wavenumber, low-frequency cutoff predicted by the inviscid theory. As in the inviscid case, the parameter that controls the stability of the longshore current is the shear on the seaward face of the longshore current.

The inclusion of lateral mixing destabilizes the longshore current as follows: it provides a Reynolds' stress that enables the shear wave to extract energy from the longshore current. We showed that this extraction of energy takes place mainly on the seaward face of the longshore current.

Finally, note that Falqués and Iranzo (1994) and Falqués *et al.* (1994) have already investigated the effects of lateral mixing on the stability of longshore currents using a numerical model. While Falqués *et al.* did find that the inclusion of lateral mixing increased the instability in certain cases, they did not find the instability at low

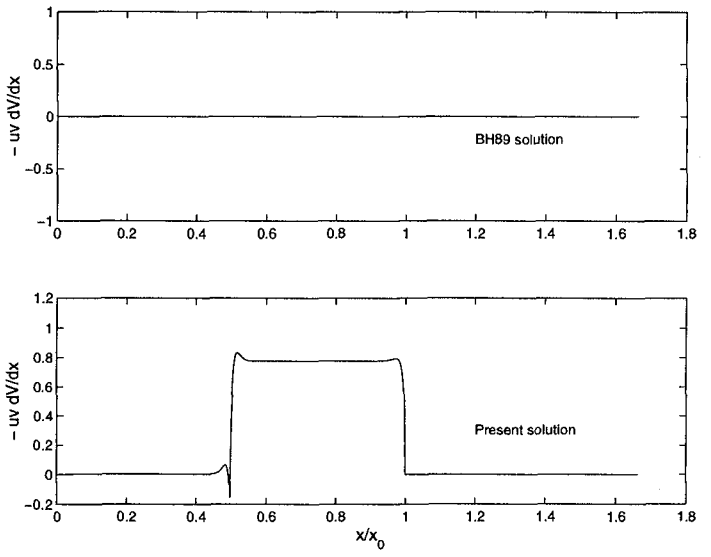

Figure 8: Cross-shore variation of $-\overline{uv}dV/dx$. Top panel inviscid (BH89) solution. [The inviscid solution is stable for the choice of parameter values used in this calculation (see below). This is the reason why $\overline{uv}$ is zero for the BH89 solution.] Bottom panel calculation including lateral mixing terms. Note that the scale of the y axis is arbitrary. The parameter values used in the calculations are $kx_0 = 1$, $x_0 = 100$ m, $\delta = 0.5$, $V_0 = 1$ m/s, and $\nu = 5 \times 10^{-3}$ m^2/s.

wavenumbers found here. At present we do not know whether this discrepancy is due to the artificial nature of our model problem or due to the boundary conditions used by Falqués *et al.* Therefore, it is necessary to extend the present analysis to more realistic longshore current variations.

ACKNOWLEDGEMENTS

This work was sponsored by the U.S. Office of Naval Research, Coastal Dynamics Program under contracts N00014-97-C-0075 (UP and JOS), N00014-94-1-0214 and N00014-98-1-0521 (JTK and TOH).

REFERENCES

Bowen, A. J. and R. A. Holman, 1989. Shear instabilities in the mean longshore current 1: Theory. *J. Geophys. Res.*, **94**: 18,023-030.

Dodd, N. and E. B. Thorntón, 1990. Growth and energetics of shear waves in the nearshore. *J. Geophys. Res.*, **95**, 16,075-083.

Falqués, A. and V. Iranzo, 1994. Numerical simulation of vorticity waves in the nearshore. *J. Geophys. Res.*, **99**, 825-841.

Falqués, A., V. Iranzo and M. Caballeria, 1994. Shear instability of longshore current: Effects of dissipation and nonlinearity. *Proc. Intl. Conf. Coastal Eng.*, **24**, 1983-1997.

George, R., R. E. Flick and R. T. Guza, 1994. Observations of turbulence in the surf-zone. *J. Geophys. Res.*, **99**, 801-810.

Lin, C. C., 1967. *Theory of hydrodynamic stability.* Cambridge University Press, 155 pp.

Oltman-Shay, J., P. A. Howd and W. A. Berkemeier, 1989. Shear instabilities of the mean longshore current 2: Field observations. *J. Geophys. Res.*, **94**, 18031-18042.

Özkan-Haller, H. T. and J. T. Kirby, 1998. Nonlinear evolution of shear instabilities of the longshore current: A comparison of observations and computations *J. Geophys. Res.*, in press.

Shrira, V. I., V. V. Vornovich, and N. G. Kozhelupova, 1997. Explosive instability of vorticity waves. *J. Phys. Oceanogr.*, **27**, 542-554.

Smith, R., 1997. Multi-mode models of flow and of solute dispersion in shallow water. Part 3. Horizontal dispersion tensor for the velocity, *J. Fluid Mech.*, **352**, 331-340.

Svendsen, I. A. 1987. Analysis of surf zone turbulence. *J. Geophys. Res.*, **92**, pp. 5115-24.

Svendsen, I.A. and U. Putrevu, 1994. Nearshore mixing and dispersion. *Proc. Roy. Soc. Lond. A.*, **445**, 561-576.

Shear waves over longshore nonuniform barred beaches

F.E. Sancho[1] and I.A. Svendsen[2]

Abstract

In the present paper we address the far-infragravity motion (0.001–0.01 Hz) associated with shear (or vorticity) waves over a fixed-bed, longshore nonuniform beach. The model equations are simplified forms of the fully nonlinear, depth-integrated, wave-averaged Reynolds equations, which are solved by the SHORECIRC numerical model. The currents are forced by stationary, monochromatic, incident short waves. The formation of flow instabilities depends on physical model parameters (e.g., bottom friction), the incident wave field, and the beach topography. The latter two effects are analysed here in the prediction of shear waves and unsteady rip-currents.

1 - Introduction

Shear waves were first observed in the field by Oltman-Shay *et al.* (1989), and were recognized by Bowen and Holman (1989) as instabilities of the longshore currents. The latter authors analysed the dynamics of these motions over a simple geometry for the linear and frictionless system of equations governing the perturbed velocities. Other analytical and numerical studies included the effect of bottom shear stresses and lateral turbulent mixing, and extended the analysis to planar and barred longshore uniform beaches (Putrevu and Svendsen, 1992b; Dodd *et al.*, 1992; Allen *et al.*, 1996; Özkan-Haller and Kirby, 1996). These studies gave insight into the shear wave dynamics, and comparisons with field data (collected during the SUPERDUCK experiment) showed a good agreement of the predicted versus the observed range of frequencies and wavelengths at which these motions were strong.

[1]Laboratório Nacional de Engenharia Civil, Av. do Brasil, 101, 1799 Lisbon, Portugal. E-mail: fsancho@lnec.pt

[2]Center for Applied Coastal Research, University of Delaware, Newark, DE 19716, USA. E-mail: ias@coastal.udel.edu

The studies mentioned above, however, only considered a longshore uniform beach. The problem studied here deals with the effect that the longshore variation of the topography has on the development of shear waves. Sinusoidally longshore varying topographies have been considered in the analysis of shear waves by Deigaard *et al.* (1994) and Slinn *et al.* (1996). The results of the former suggest that growing amplitudes of the longshore bottom disturbances act to suppress the shear instabilities of the background flow. In another example, Sancho *et al.* (1997) showed model predictions of shear instabilities over a surveyed bathymetry at Duck, North Carolina. The beach was characterized by the presence of an almost uniform longshore bar.

In the present paper we isolate and study the effect of well-defined longshore bottom variations on the characteristics of the shear instabilities. The goal is to analyze the nonlinear evolution of shear (vorticity) instabilities over canonical longshore varying, fixed bed, beach configurations. Hence, we look at the influence of rip-channels in the mean and time-varying (unstable) flow field.

2 - Model equations and numerical method

In this study we make use of the depth-integrated, short-wave averaged Reynolds equations. We assume turbulent flow, but neglect the turbulent normal stresses, and we also assume zero surface shear stress. For depth-varying currents the governing equations for conservation of mass and momentum can be written in Cartesian coordinates ($(x, y, z) \equiv (x_\alpha, z)$ in tensor notation) as (e.g., Van Dongeren *et al.*, 1994):

$$\frac{\partial \bar{\zeta}}{\partial t} + \frac{\partial \bar{Q}_\alpha}{\partial x_\alpha} = 0\,, \tag{1}$$

$$\frac{\partial \bar{Q}_\beta}{\partial t} + \frac{\partial}{\partial x_\alpha}\int_{-h_o}^{\bar{\zeta}} V_\alpha V_\beta \, dz + \frac{\partial}{\partial x_\alpha}\overline{\int_{\zeta_t}^{\zeta} (u_{w\alpha} V_\beta + u_{w\beta} V_\alpha)\, dz} =$$

$$-g\,(h_o + \bar{\zeta})\frac{\partial \bar{\zeta}}{\partial x_\beta} - \frac{1}{\rho}\frac{\partial}{\partial x_\alpha}\left[S_{\alpha\beta} - \overline{\int_{-h_o}^{\zeta} \tau_{\alpha\beta}\, dz}\right] - \frac{\tau_\beta^B}{\rho}\,. \tag{2}$$

In these equations $\bar{\zeta}$ is the mean surface elevation, h_o is the still water depth, and ρ is the fluid density. $\tau_{\alpha\beta}$ represents the turbulent shear stress tensor, V_α is the horizontal current velocity and $\bar{Q}_\alpha$ is the depth-integrated volume flux, defined as

$$\bar{Q}_\alpha = \int_{-h_o}^{\bar{\zeta}} V_\alpha \, dz + Q_{w\alpha}\,, \tag{3}$$

where $Q_{w\alpha}$ is the shortwave-induced mean volume flux. In equation (2), $u_{w\alpha}$ is the short-wave velocity component, $S_{\alpha\beta}$ is the radiation stress tensor (defined according to Mei, 1989), and the bottom shear stress is represented by τ_α^B.

The system of equations above constitute the basis of the Quasi-3D numerical model SHORECIRC (Van Dongeren *et al.*, 1994). A somewhat simplified version of that model is used here.

The turbulent shear stress (the turbulent lateral mixing) is modeled according to the eddy viscosity closure, assuming that

$$\tau_{\alpha\beta} = \rho \nu_t \left(\frac{\partial V_\alpha}{\partial x_\beta} + \frac{\partial V_\beta}{\partial x_\alpha} \right) , \tag{4}$$

where the eddy viscosity ν_t is calculated by (Sancho and Svendsen, 1997)

$$\nu_t = C_1 \kappa \sqrt{\frac{f_w}{2}} u_0 h + M h (\frac{D}{\rho})^{1/3} . \tag{5}$$

The first term of equation (5) represents the bottom-induced turbulence and it is always present (Coffey and Nielsen, 1984), whereas the second term accounts for the turbulence generated by the breaking waves (Battjes, 1975), and it is only active in the surf region. In the above, D is the energy dissipation rate per unit area, M and C_1 are constants, κ represents the von Karman constant, f_w is the bottom friction coefficient, and u_0 is the amplitude of the short-wave orbital velocity at the bottom. We choose $M = 0.1$, which is one order of magnitude smaller than the value suggested by Battjes (1975), because it gives estimates of ν_t in agreement with those estimated by Svendsen (1987). Similary we choose $C_1 = 0.75$, which yields values of ν_t outside the surf region of the same order as the experimental results of Cox *et al.* (1995).

The shortwave-averaged bottom shear stress is computed according to the nonlinear wave-current formulation of Putrevu and Svendsen (1992a),

$$\tau_\alpha^B = \frac{1}{2} \rho f_w u_0 (\beta_1 V_\alpha + \beta_2 u_{0\alpha}) , \tag{6}$$

where β_1 and β_2 depend on the short-wave phase angle, and the current and short-wave orbital velocity magnitude and direction. The friction factor is chosen as $f_w = 0.006$. The orbital velocity amplitude u_0 is calculated according to linear wave theory, and the energy dissipation rate D is given by Dally *et al.* (1985), with the wave field obtained from REF/DIF1 (Kirby and Dalrymple, 1994) model applications. The results from this model (wave height and direction) are also used to estimate the radiation stress $S_{\alpha\beta}$, and the wave-induced volume flux $Q_{w\alpha}$, using linear wave theory. Inside the surfzone, an extra term has been added to $Q_{w\alpha}$ in order to account for the effect of the mass of water transported shorewards by the roller (Svendsen, 1984).

The system of equations above is solved numerically by a third-order ($\mathcal{O}(\Delta t^3)$) predictor-corrector finite difference method. Spatial derivatives are 4th-order accurate (Sancho and Svendsen, 1997). The (horizontal) domain of integration is discretized by a rectangular grid with open boundaries everywhere, except at the shoreline. At the seaward boundary, a generating-absorbing condition is used (Van Dongeren and Svendsen, 1997), and at the shore-normal boundaries a periodicity condition is implemented. At the landward boundary, the shoreline (horizontal) position is held fixed with the boundary condition $V_\alpha = 0$ at a small water depth ($\sim 0.005 - 0.05$ times the water depth at breaking, h_b). We note that a similar treatment of the shoreline is utilized by Özkan-Haller and Kirby (1997), as those authors found minor differences between the results obtained by including the shoreline runup and those from calculations with a zero-velocity condition at the shore.

3 - Applications

3.1 - Longshore uniform plane beach

Although most natural beaches can exhibit complicated bottom contours, it is interesting to analyze the development and propagation of shear waves on a longshore uniform plane beach. We choose to first investigate the nonlinear shear instabilities on a 1/20 sloping beach with the same characteristics as that studied by Allen *et al.* (1996) and Özkan-Haller and Kirby (1995, 1997). We also use this example to test the numerical accuracy of our model versus the accuracy of the different numerical schemes of those other models.

Hence for the purpose of the comparison, we assume the currents are depth uniform. We also consider a longshore uniform beach and assume the short-wave forcing in the cross-shore direction to be in balance with the setup gradient, and in the longshore direction it balances the bottom shear stress associated with the steady (time-averaged over the infragravity oscillations) longshore current V_S and the lateral mixing (see above references and Sancho and Svendsen, 1997, for details). This implies that the lateral mixing from turbulence and the mixing effects of the nonlinear intergrals in (2) are included for the V_S-part of the total velocity. However, we neglect turbulent and dispersive mixing effects generated by the deviations in the velocity from V_S. Similarly (6) is linearized so that the bottom shear stresses are linear functions of U and V

$$\tau_x^B = \rho\,\mu\,U\,, \tag{7}$$

$$\tau_y^B = \rho\,\mu\,(V - V_S)\,, \tag{8}$$

with a constant friction coefficient $\mu = 0.006$. This essentially reduces the complete equations to the model equations of Özkan-Haller and Kirby (1997). Those are a slightly modified set of the equations solved by Allen *et al.* (1996), who further introduced the rigid lid approximation. Initial and boundary conditions are also similar to those of the authors above.

The longshore domain length l_y equals that of the most unstable wavelength calculated from linear instability theory, $l_y = 5x_b'$, where $x_b' = 90$ m is the distance from the shoreline to the position of the maximum of the longshore current. In the cross-shore direction the domain length is $l_x = 4x_b'$. The grid spacings are the same as those used by Allen *et al.*, namely $\triangle x = \triangle y = \frac{x_b'}{18} = 5$ m.

Fig. 1 shows the time series of $\eta, \tilde{U}$ and $\tilde{V}$ at $\frac{x}{l_x} = 0.75$ and $\frac{y}{l_y} = 0.5$, predicted both by the present model (upper three panels) and the numerical model of Özkan-Haller and Kirby (1997) (lower three panels). The landward-oriented cross-shore direction with origin at the seaward domain boundary is denoted by x. For both model results, we see that the amplitude of the shear waves grows quasi-exponentially for $2-3.5$ hr, and then remains quasi-steady, oscillating around a mean value. It is also visible that the higher amplitude disturbances have larger periods, which confirms previous observations on the weakly dispersive properties of shear waves (Oltman-Shay *et al.*, 1989). Although they differ in some details, the similarity between our results and

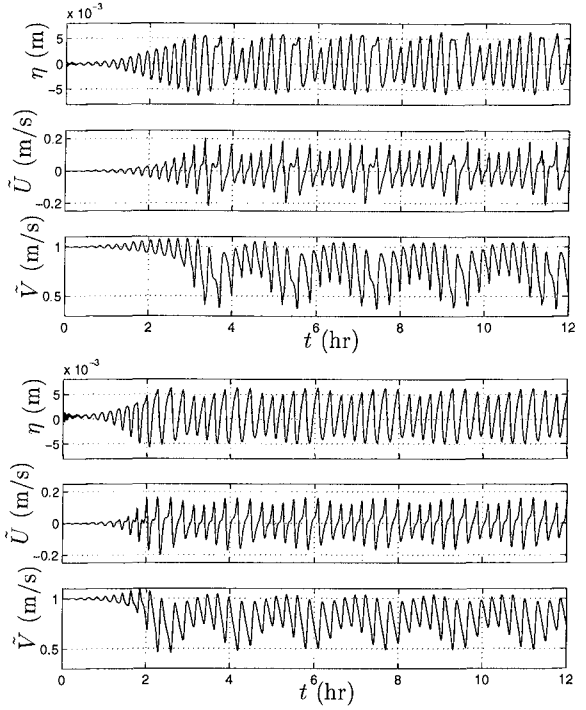

Figure 1: Time series of $\eta, \tilde{U}$ and $\tilde{V}$ at $\frac{x}{l_x} = 0.75$ and $\frac{y}{l_y} = 0.5$ from the present model simulations (upper three plots) and Özkan-Haller and Kirby (1997) model simulations (lower three plots).

those of Özkan-Haller and Kirby is evident. We have also compared the present solution with that of Allen *et al.* (1996), and the agreement is not quite as good, which may be due to the rigid-lid assumption of Allen *et al.*. For brevity the results are omitted here.

Analysis of the results also shows that the shear wave propagation velocity c_S is within the interval $0.5 < \frac{c_S}{V_M} < 0.54$, where V_M is the maximum of the initial longshore current profile. The low-frequency oscillations ($T \simeq 2$ hr) are the same in ours and Özkan-Haller and Kirby's results.

It is interesting to analyze the effect the shear wave motion produces on the mean longshore current. The initial current forms a quasi longshore uniform flow with the longshore current profile as plotted in Fig. 2. However, the shear waves cause a dispersion of momentum, which will modify the background time-mean longshore current profile relative to the profile maintained by the forcing and turbulent mixing. This is illustrated in Fig. 2, where we plot the initial cross-shore profile of the longshore current at $\frac{y}{l_y} = 0.5$ (solid line), versus the current profile obtained by time-averaging V over the entire period of simulation ($t = 12$ hr), (dashed line). The maximum of

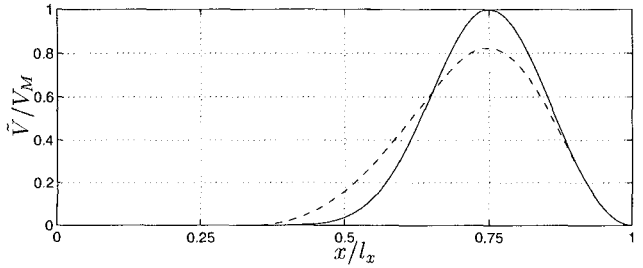

Figure 2: Cross shore distribution of the initial (——) and time-averaged (- -) longshore current over a longshore uniform plane beach.

the time-averaged longshore current is approximately 20% smaller than that of the initial distribution. this result is similar to the results of Özkan-Haller and Kirby (1997).

3.2 - Longshore varying barred beach

Weak longshore forcing gradient

As a second example we analyze the nearshore currents over a periodically longshore varying barred beach. The longshore bottom perturbation is characterized by a slight depression in the bar crest, similar to the formation of a rip-channel (Fig. 3), located at the centerline of the computational domain. The bottom topography used in the present example is similar to the barred beach often encountered at the FRF experimental station in Duck, NC (e.g., Thornton and Kim, 1993). Details of the analytical expression for the bathymetry are given by Sancho and Svendsen (1997). The governing equations, closure submodels, and relevant parameters are given by equations (1)–(6). For simplicity and brevity, we again consider (below-trough) depth-uniform currents only. It turns out that the dispersive mixing caused by depth varying currents will somewhat reduce the development of the shear waves. This more complex situation was analysed in Sancho and Svendsen (1997). The initial condition for the simulations is a "cold start", and the short-wave forcing is "ramped" smoothly until it reaches a steady forcing.

The relevant parameters that define the bathymetry and domain size are the crest to shoreline distance $l_c = 120$ m, and the domain lengths in the cross-shore and longshore directions, $l_x = 4\,l_c$, and $l_y = 16\,l_c$, respectively. The depth at the crest of the longshore uniform section of the bar is $h_c \simeq 1.18$ m, and at the rip-channel is just 10% deeper. The width of the rip-channel is $w_r = 0.84\,l_c$ (100 m), and the numerical grid spacings are $\triangle x \simeq 4.24 h_c$ (5 m) and $\triangle y \simeq 8.48 h_c$ (10 m).

First, we choose the incident wave conditions so that intense wave breaking occurs

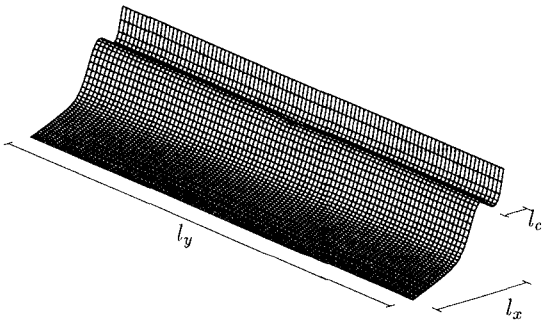

Figure 3: Perspective view of the barred beach for the example in section 3.2.

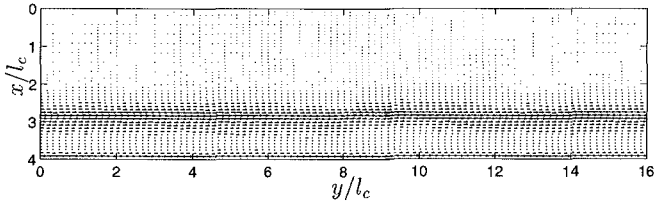

Figure 4: Time-averaged (over 4 hr), depth-averaged, current velocity vectors for the case of weak longshore forcing gradient.

along the entire bar, including over the rip channel, starting just before the bar crest, (at $x/l_c = 2.75$). The waves then propagate over the bar-trough without breaking before a second breaking occurs nearer the shoreline. This results in a nearly longshore uniform wave forcing. In numbers, the wave height at the seaward boundary ($x = 0$) is $H_o = 0.9\,h_c$ (1.06 m), the incident wave angle is $\alpha_{w0} = 7.5°$ with the shore normal direction x, the wave period is $T = 14.4\sqrt{h_c/g}$ (5 s), and the breaking criterion $H_b/h_b = 0.78$ is used.

Time-averaged velocity vectors of the current field are shown in Fig. 4. The time-averaging is performed over a period of approximately 4 hr, after the flow reached near stationarity. The time-averaged velocity vectors show a slight variation of the flow at the region of the rip-channel ($y = 8\,l_c$). The largest variations are observed, as expected, around the rip-channel, but are more pronounced slightly downstream of it due to the inertia of the flow. In fact, examination of the magnitude of the terms in the longshore momentum equation shows that it is a combination of a steady and a fluctuating component of the advective accelerations that are responsible for the divergence the flow around the rip-channel, and the existence of currents in the

trough, respectively. Away from the rip-channel it turns out that the wave-induced shoreward mass flux is locally balanced by the return current (undertow).

The results show that even a small rip-channel is able to disturb the otherwise longshore uniform flow, although, the existence of a rip-channel does not necessarily induce the formation of a rip-current. This turns out to be due to the fact that the wave field, as well as the mean surface elevation, are very homogeneous in the longshore direction. The (time-averaged) longshore current profile at any section exhibits the "classical" double-peaked distribution caused by the breaking over the bar and at the foreshore. There is, however, a significant current in the trough driven largely by the mixing generated by the shear waves.

The instantaneous nearshore current fields are, however, quite different from the time-averaged situation. Fig. 5 shows the instantaneous depth-averaged velocity vectors at four different times during the simulation. The first three pictures are at early stages of the computation, and show how the growth of shear waves starts at the rip-channel location. Looking consecutively at plots (a), (b) and (c) shear instabilities develop continuously at $y = 8\,l_c$, where the small channel is, and propagate downstream with the longshore current. In general, the shear wave celerity is equal to 0.45–0.65 of the maximum (time-averaged) longshore current, which is comparable to that suggested by field measurements (Dodd *et al.*, 1992). Between subplots (c) and (d) there is a significant time lapse (3.6 hr), during which the predicted predominant wavelength (and period) of the shear waves increased considerably. This frequency downshift is similar to that observed by Özkan-Haller and Kirby (1997). Closer inspection of the dynamics of these motions indicates that the shear waves are more intense seaward and over the bar-crest.

Clearly the rip channel acts as a strong disturbance that instantly initiates almost fully grown shear waves. Similar computations over a longshore uniform barred beach (not shown) indicate that shear waves develop much slower in the absence of the rip-channel. The longterm properties of the shear waves are, however, identical to those of the results just presented, indicating that once shear instabilities have formed they are relatively independent of small topographic perturbations.

Large longshore forcing gradient

The previous example illustrated that a nearly longshore uniform mean flow can occur over a longshore varying beach. In order to further analyse the conditions for generation of rip currents we consider an incident wave field that is slightly different from the previous example, over the same bottom topography of Fig. 3. The initial wave height is chosen so that outside the rip channel wave breaking occurs over the bar crest, whereas no breaking occurs in the rip-channel ($y = 8\,l_c$), (Fig. 6). The wave height is about 30% smaller at the seaward boundary than in the previous example. The incident wave angle and period are the same as before. The substantial differences in wave conditions over the rip-channel and the bar, induce strong longshore longshore variations of the forcing, in particular the pressure gradients. Note that although the wave model predictions may not be accurate, a similar trend in the wave height

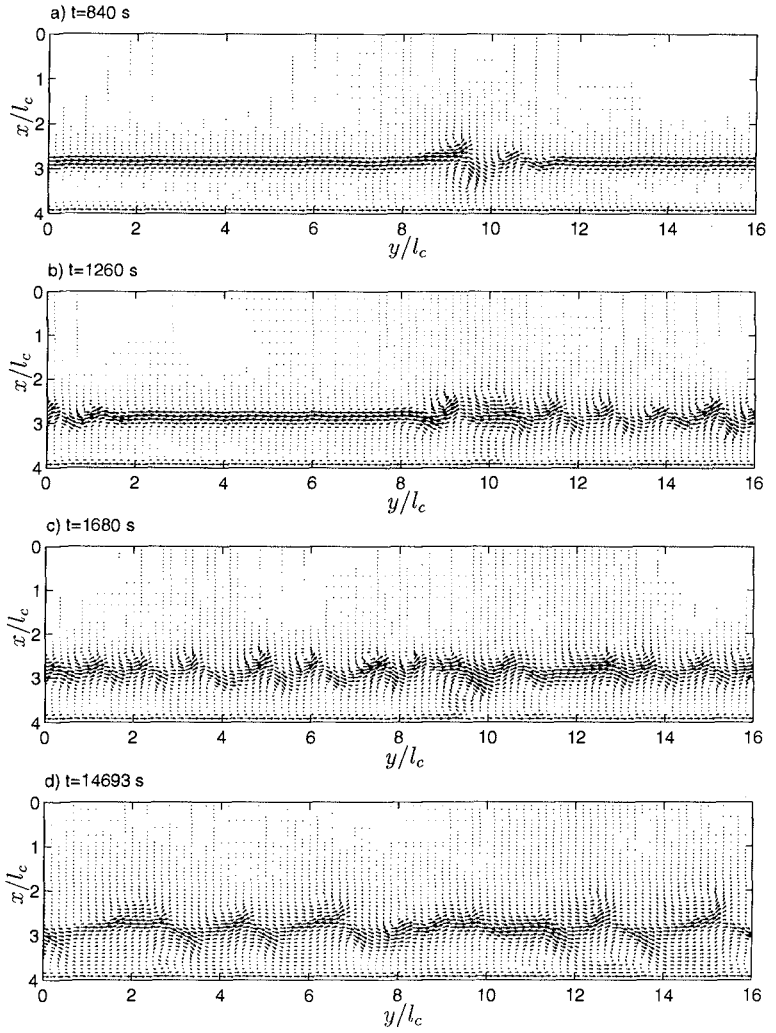

Figure 5: Depth-averaged current vectors at four instants of the simulation for the case of weak longshore forcing gradient.

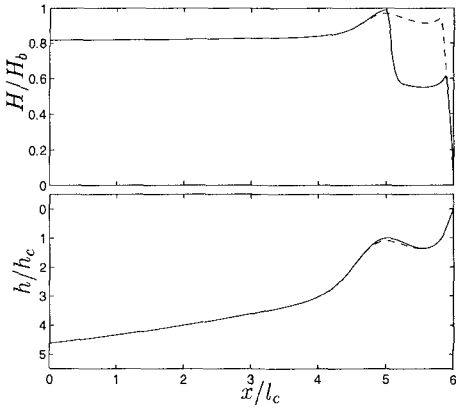

Figure 6: Wave height and bottom cross-shore variations over the barred beach at two longshore positions: $y = 0$ (solid line) and $y = 8\,l_c$ (dashed line) for the case of large longshore forcing gradient.

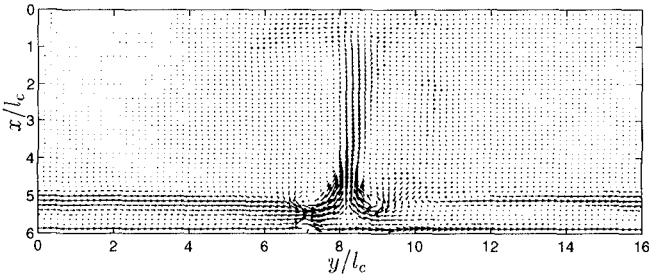

Figure 7: Time-averaged (over 2.1 hr), depth-averaged, current velocity vectors for the case of large longshore forcing gradient.

variation over the channel and the bar has been observed in laboratory experiments (Haller *et al.*, 1997).

The resulting time-averaged (over a period of 2.1 hr) and depth-averaged currents are illustrated in Fig. 7, which shows that a rip-current has formed, with two circulation cells around it, centered at the bar-crest. (The domain has been extended offshore to $l_x = 6\,l_c$). The width of the rip increases slowly towards offshore, as the result of a small turbulent dispersion as well as the dispersion caused by fluctuations of the rip (explained below). Bottom friction is also responsible for the widening of the rip. Longshore currents flow towards the rip-channel at both sides of the rip, mainly driven by local longshore gradients of the mean surface elevation. The maximum velocity in the rip-current is $0.2\sqrt{g\,h_c}$ (0.70 m/s), which is about twice as large as the maximum longshore current.

The results in Fig. 7 contrast with those of Fig. 4. Nearly longshore uniform currents are, however, found at a distance $10l_c$ (1200 m) from the channel axis.

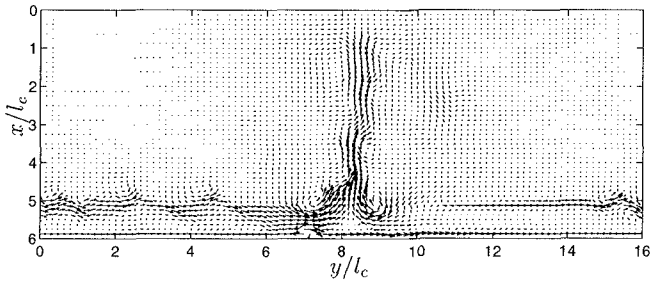

Figure 8: Instantaneous depth-averaged current vectors for the case of large longshore forcing gradient.

Larger differences from longshore uniformity mainly occur near and downstream of the rip-channel. Through inspection of the magnitude of the terms in the momentum equations, we find that the longshore pressure gradient and nonlinear advective accelerations are quite important in the longshore momentum balance, whereas in the cross-shore direction, the radiation stress gradient is mostly balanced by the surface elevation gradient.

The flow for the present simulation is, however, also unsteady. In fact, the current velocities are very dynamic, as can be seen in one "snapshot" of the depth-averaged current velocities, shown in Fig. 8. We find that in the rip-current vortices are generated at each side (note the similarity between the patterns predicted here and those observed in Fig. 7 of Shepard *et al.*, 1941). Initiation of shear wave motion is delayed. The motion is steady downstream of the rip-channel until $y = 14\,l_c$ and then shear waves start to form very rapidly over the longshore uniform section of the beach. Both the cross-shore and longshore velocities vary dramatically with the position, depending on whether this is located upstream or downstream of the rip-channel. We also see that shear waves approaching the rip channel from upstream are washed out to the sea by the rip current.

Inspection of the time series of the predicted velocities along the rip-channel indicates that the rip-currents are periodically unsteady. The most energetic periods of oscillation are seen to range between $400 < T < 450$ s, but there are also appreciable variations in the time series at a much lower frequency. The higher frequency oscillations are associated with a meandering motion of the rip-currents, whereas the longer period variations are related to a "side-to-side" shift of the rip-current, and with the passage of vortices released by the unstable rip over a certain location. Similarly, at locations where shear instabilities have formed, the period of the shear waves is initially ~ 440 s, and later a frequency downshift occurs and the period becomes ~ 800 s.

We find that the rip-current exhibits several features common with the shear waves. In fact, a hydrodynamic instability mechanism is common to the two flow types: shear waves are an instability mechanism of the longshore currents (Bowen and Holman, 1989), and rip-currents can be considered an unstable jet (whose me-

chanics are given by, e.g., Drazin and Reid, 1982). Both mechanisms have been observed in field and laboratory conditions, either isolated or simultaneously (e.g., Sonu, 1972). For the present conditions, the formation of the rip-current over the rip-channel destroys the structure and shear waves do not pass it.

Multiple rip-channels

Lastly, we investigated the effect of the domain size by performing calculations in a longshore periodic domain of size $l_y = \frac{10}{3} l_c$ (400 m) and $l_y = \frac{20}{3} l_c$ (800 m). Rip channels were 400 m apart, and the short-wave input lead to flow conditions similar to those of Figs. 4 and 5. This gave exactly the same longshore periodicity, and the results from these computations were identical, thus, meaning that the predicted shear waves were not dependent of the computational domain size. However, computations with different distance between the rip channels gave different patterns of the shear waves, with different period and wavelength, though their speed of propagation remained the same. Hence, the local signature of the shear waves appears to depend on the distance between rip-channels.

In a final example we chose a larger periodic domain size, of length $l_y = 1600$ m. Within this computational domain, we placed four rip-channels with different distances apart. The results from this computation showed the prediction of very irregular shear waves. In fact, time series of the predicted motions indicated a wide spectrum of energetic frequencies, which is in closer resemblance with those observed under field conditions (Oltman-Shay *et al.*, 1989). This suggests that the shear waves observed in nature may come from many different sources of disturbance.

4 - Conclusions

In this study we addressed the development of flow instabilities over longshore nonuniform barred beaches. It was found that shear waves can be triggered by small bottom perturbations (in the form of rip-channels) in an otherwise longshore uniform coast, but the shear wave average properties are nearly independent of these. Those properties are found to depend mainly of the background longshore current. Similarly, the distance between rip-channels also affects the shear waves dynamics.

A second important conclusion is that rip-currents not always form in the presence of rip-channels. Rip-currents may occur when short-wave conditions give rise to large longshore forcing gradients around the rip-channel such as changes in breaking conditions. In that situation, unstable rip-currents were predicted. Conversely, shear waves can be suppressed by the existence of rip-currents, and will then form far downstream of the rip-channel, seemingly away from the influence of the rip.

The results suggest that the longshore variability of a beach, over a considerable domain length, can play an important role in the prediction of the dynamics of steady and unsteady currents. Hence, care should be taken in the comparison of model to field results, when assuming longshore uniform conditions, or using too small model domains.

Acknowledgments

Funding was provided by the Office of Naval Research, Coastal Sciences, (contract no. N00014-95-C-0075). The first author held a scholarship from the Portuguese Research Council (PRAXIS XXI, contract no. BD/3656/94). The U.S. Government is authorized to produce and distribute reprints for government purposes notwithstanding any copyright notation that may appear herein.

References

Allen, J., P. A. Newberber, and R. A. Holman (1996). Nonlinear shear instabilities of alongshore currents on plane beaches. *J. Fluid Mech.* (310), 181–213.

Battjes, J. A. (1975). Modeling of turbulence in the surf zone. In *Proc. Symp. on Modelling Techniques*, San Francisco, 1050–1061.

Bowen, A. J. and R. A. Holman (1989). Shear instahilities in the mean longshore current: 1-theory. *J. Geophys. Res. 94*(C12), 18023–18030.

Coffey, F. C. and P. Nielsen (1984). Aspects of wave current boundary layer flows. In *Proc. 19th Int. Conf. Coastal Engng.*, Vol. 3, Houston, 2232–2245. ASCE.

Cox, D. T., N. Kobayashi, and A. Okayasu (1995). Experimental and numerical modeling of surf zone hydrodynamics. (Ph. D. Dissertation) Res. Report CACR-95-07, Center for Applied Coastal Research, Univ. of Delaware.

Dally, W. R., R. G. Dean, and R. A. Dalrymple (1985). Wave height variation across beaches of arbitrary profile. *J. Geophys. Res. 90*(C6), 11917–11927.

Deigaard, R., E. D. Christensen, J. S. Damgaard, and J. Fredsœ(1994). Numerical simulation of finite amplitude shear waves and sediment transport. In *Proc. 24th Int. Conf. Coastal Engng.*, Vol. 2, Kobe, 1919–1933. ASCE.

Dodd, N., J. Oltman-Shay, and E. B. Thornton (1992). Shear instahilities in the longshore current: A comparison of observation and theory. *J. Phys. Oceanogr. 22*(1), 62–82.

Drazin, P. G. and W. H. Reid (1982). *Hydrodynamic stability.* Cambridge: Cambridge University Press. pp. 527.

Haller, M. C., R. A. Dalrymple, and I. A. Svendsen (1997). Rip channels and nearshore circulation. In *Coastal Dynamics'97*, Plymouth, 594–603. ASCE.

Kirby, J. T. and R. A. Dalrymple (1994). Combined refraction/diffraction model REF/DIF1, Version 2.5. Res. Report CACR-94-22, Center for Applied Coastal Research, Univ. of Delaware.

Mei, C. C. (1989). *The Applied Dynamics of Ocean Surface Waves.* Singapore: World Scientific. pp. 740.

Oltman-Shay, J., P. A. Howd, and W. A. Birkemeier (1989). Shear instabilities in the mean longshore current: 2-field observations. *J. Geophys. Res. 94*(C12), 18031–18042.

Özkan-Haller, H. T. and J. T. Kirby (1995). Finite amplitnde shear wave instabilities. In *Coastal Dynamics'95*, Gdansk, 465–476. ASCE.

Özkan-Haller, H. T. and J. T. Kirby (1996). Numerical study of low frequency surf zone motions. In *Proc. 25th Int. Conf. Coastal Engng.*, Vol. 2, Orlando, 1361–1374. ASCE.

Özkan-Haller, H. T. and J. T. Kirby (1997). Nonlinear evolution of shear instabilities of the longshore current. (Ph. D. Dissertation), Res. Report CACR-97-08, Center for Applied Coastal Research, Univ. of Delaware.

Putrevu, U. and I. A. Svendsen (1992a). A mixing mechanism in the nearshore region. In *Proc. 23rd Int. Conf. Coastal Engng.*, Vol. 3, Venice, 2758–2771. ASCE.

Putrevu, U. and I. A. Svendsen (1992b). Shear instability of longshore currents: A numerical study. *J. Geophys. Res. 97*(C5), 7283–7303.

Sancho, F. E., I. A. Svendsen, J. Oltman-Shay, and E. B. Thornton (1997). Modelling nearshore circulation under field conditions. In *Proc. 3rd Int. Symp. WAVES97, Ocean Wave Measurement and Analysis*, Virginia Beach, 765–776. ASCE.

Sancho, F. E. P. and I. A. Svendsen (1997). Unsteady nearshore currents on longshore varying topographies. (Ph. D. Dissertation), Res. Report CACR-97-10, Center for Applied Coastal Research, Univ. of Delaware.

Shepard, F. P., K. O. Emery, and E. C. La Fond (1941). Rip currents: A process of geological importance. *J. Geology XLIX*(4), 337–369.

Slinn, D. N., J. S. Allen, P. A. Newberger, and R. A. Holman (1996). Nonlinear dynamics of alongshore currents over beaches with irregular topography. In *Proc. Amer. Geophys. Union, Fall Meeting*, S. Francisco, F388. AGU.

Sonu, C. J. (1972). Field observation of nearshore circulation and meandering currents. *J. Geophys. Res. 77*(18), 3232–3246.

Svendsen, I. A. (1984). Mass flux and undertow in a surf zone. *Coastal Engng. 8*, 347–365.

Svendsen, I. A. (1987). Analysis of surf zone turbulence. *J. Geophys. Res. 92*(C5), 5115–5124.

Thornton, E. B. and C. S. Kim (1993). Longshore current and wave height modulation at tidal frequency inside the surf zone. *J. Geophys. Res. 98*(C9), 16509–16519.

Van Dongeren, A. R., F. E. P. Sancho, I. A. Svendsen, and U. Putrevu (1994). Shorecirc: A quasi-3d nearshore model. In *Proc. 24th Int. Conf. Coastal Engng.*, Vol. 3, Kobe, 2741–2754. ASCE.

Van Dongeren, A. R. and I. A. Svendsen (1997). An absorbing-generating boundary condition for shallow water models. *J. of Waterway, Port, Coastal and Ocean Engng. 123*(6), 303–313.

Trapped and Free-Wave Propagation in Channels and Harbours

João A. Santos[1] and D. H. Peregrine[2]

Abstract

Most of the literature on edge waves is only concerned with edge-wave propagation over a bottom that is uniform in the propagation direction. There is still little knowledge of what happens when the bottom topography changes suddenly, as in the presence of a cape, submarine valley or harbour.

This paper presents some results of our study on the wave motion in such places, where edge waves may be transmitted, reflected or radiated as free waves and thus may have an important role in determining the wave conditions in otherwise sheltered regions.

We send an edge wave along a coast with an alongshore uniform bottom profile and, at a given section change suddenly for another bottom profile. This study is carried out with a very simple model. The linearised shallow water equations are used in a wide channel with the simplest bottom profile that enables the existence of edge waves: a ledge close to the coast and a uniform depth offshore.

Introduction

Edge waves are common in the spectrum of waves at the surf zone, Huntley et. al. (1981) showed that these waves could be responsible for up to 30 % of the energy in the longshore current spectrum measured at Torrey Pines beach, California, and are believed to be responsible by the formation of beach cuspate patterns, (Guza and Inman 1975), and so they can play an important role in coastal morphology.

However, most of the references in the literature on this subject are only concerned with edge-wave propagation over bottom configurations that are uniform

[1] Research Assistant, Laboratório Nacional de Engenharia Civil, Av. do Brasil, 101, 1799 Lisboa Codex, Portugal, JASantos@lnec.pt. Currently Research Student, School of Mathematics, University of Bristol.

[2] Professor, School of Mathematics, University of Bristol, University Walk, Bristol, BS8 1TW, United Kingdom, D.H.Peregrine@bris.ac.uk

alongshore. To our knowledge the only exceptions are Smith (1974), where an asymptotic technique is used study the propagation of high frequency edge waves along coasts whose bottom geometry varies gradually, and Evans & Fernyhough (1995), where edge waves are found for a vertical coast with periodic bays at the boundary of a flat ocean.

When the longshore uniformity in the bottom geometry that enables the occurrence of edge waves disappears suddenly, due to the presence of a cape, a submarine valley or a harbour, this obstacle may cause the reflection of that energy, its transmission to the region after the obstacle, if edge waves can propagate there, or its release as free long waves. This is the objective of our study: to understand what happens when such discontinuities appear. We send an edge wave along a coast with an alongshore uniform bottom profile and, at a given section change suddenly for another bottom profile.

We solve these problems by using a very simple model: we have a wide channel, instead of the semi-infinite ocean, and use the simplest bottom profile that enables the occurrence of edge waves, a ledge close to one of the channel walls. The linearised shallow water equations are employed to evaluate the modes (trapped, freely-propagating and evanescent) in each of the regions into which the domain under study can be divided.

In spite of its simplicity the results produced by this model allow us to draw some conclusions on the energy distribution between trapped and free waves when those longshore discontinuities occur and to explain some difficulties in using physical models to model long waves reported by Dodd & Bowers (1995).

Methodology

To study the influence of a sudden variation of the longshore bottom profile on edge wave propagation, we send an edge wave along a straight coast formed by two or more stretches with uniform longshore profile. At a given section, where two stretches meet, a sudden change in the longitudinal bottom profile occurs.

Although the number of edge-wave modes for a given frequency and bottom geometry is limited, the number of the freely-propagating and evanescent modes that can be excited by such a discontinuity is not. For both there is a continuous spectrum in frequency. So, to make analysis easier we use a wide channel instead of the semi-infinite ocean, as shown in figure 1. This gives a discrete spectrum but implies that we must choose a sufficiently wide channel and, as we will show later, special care must be used when interpreting the results so obtained.

Many cross-shore bottom profiles support the existence of edge wave modes. We choose the simplest such bottom profile: a ledge close to the coast. This profile, unlike the plane beach profile of Eckart (1951) or Ursell (1952), makes the establishment of the dispersion relation a straightforward task. In addition to that, it is always possible, by adjusting the ledge dimensions, to get an edge wave mode in this geometry with similar behaviour to a similar mode propagating over other bottom profiles.

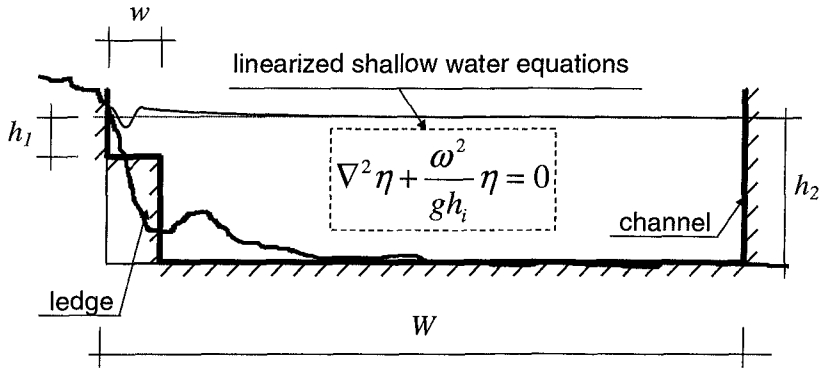

Figure 1. Scheme of an edge wave with the simplifications adopted in this study

Because the region we are interested in is quite close to the shoreline and the waves long enough to have negligible vertical variation of the horizontal velocity, we use the linearised shallow water equations. Assuming a time harmonic variation of the free--surface elevation, η, gives the following equation:

$$\nabla^2\eta+\frac{\omega^2}{gh}\eta=0 \qquad (1)$$

where h is the water depth, ω the angular frequency of the wave and g the acceleration of gravity. Using this equation the dispersion relations for both the propagating (either trapped or free) and the evanescent modes in the channel with the ledge, figure 2, are evaluated.

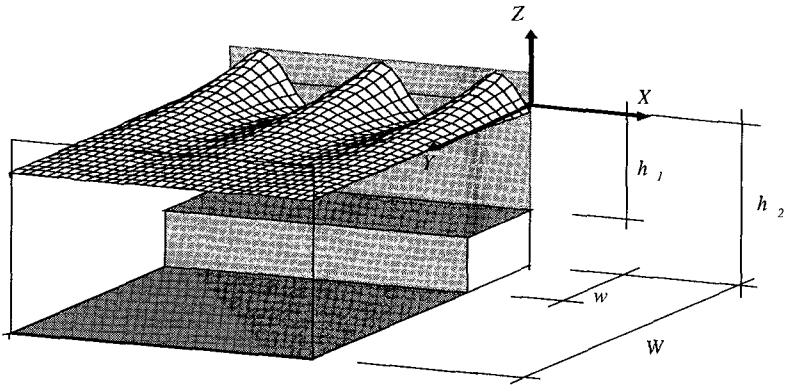

Figure 2. Channel with ledge

We scale the space quantities by the maximum channel depth, h_2, and the time quantities by $\sqrt{h_2/g}$ and the following dispersion relation is obtained:

$$\gamma\sqrt{\frac{\Omega^2}{\gamma}-K^2}\tan\left(\alpha\sqrt{\frac{\Omega^2}{\gamma}-K^2}\right)=\sqrt{\Omega^2-K^2}\tan\left[(\alpha-\beta)\sqrt{\Omega^2-K^2}\right] \qquad (2)$$

where $\alpha = w/h_2$ is the ledge width ratio, $\beta = W/h_2$ is the channel width ratio, γ is the depth ratio, $\Omega = \omega\sqrt{h_2/g}$ is the dimensionless frequency (can be interpreted also as the ratio between the total water depth and the free-wave wavelength) and $K = kh_2$ is the dimensionless longshore wavenumber (or the ratio between the total water depth and the longshore wavelength). See figure 2 for definitions of depths and widths.

Each mode is defined by the number of zero-crossings in the y-variation of its free-surface profile. For a given frequency, the character of the modes produced by equation (2) depends on their dimensionless longshore wavenumbers, K. For $K^2 < 0$ we have evanescent modes or, being more precise, we have non-propagating modes with an alongshore exponential variation of the free-surface elevation. We chose the sign of that variation such that it decays exponentially inside our domain. For $0 \le K^2 \le \Omega^2$ we have freely propagating modes and for $\Omega^2 \le K^2 \le \Omega^2/\gamma$ we have trapped or edge-wave modes.

If the ledge occupies the whole width of the channel then $\alpha = \beta$, $\gamma = 1$ and equation (2) gives the dispersion relation for a flat channel. In this case no trapped modes are possible in the channel.

In what follows, we are going to designate by "leaky modes" the free-propagating modes in the channel with ledge. Although this does not make sense for a ledge along a channel wall, since no energy can escape the channel walls, these freely propagating modes do constitute a sample (albeit not a evenly spaced one) of the leaky modes continuum that would be obtained for the same ledge at the coast of a semi-infinite ocean.

For a given mode, as the dimensionless frequency increases, its character changes from evanescent to freely-propagating and then to trapped. In the channel with ledge this change in character implies the concentration over the ledge of the zero crossings in that y-variation. So, the sinusoidal variation over both the ledge and the deep part of the channel, when the mode is evanescent, changes to sinusoidal both across and along the channel, for the "leaky" modes, and ends up as a sinusoidal variation over the ledge with an exponential decay away for the ledge in the deep part of the channel, when the mode is trapped.

The transition between the "leaky" and the trapped character occurs when $K = \Omega$, or when the dimensionless frequency is such that

$$\Omega = n\pi\sqrt{\gamma}/\left(\alpha\sqrt{1-\gamma}\right) \qquad (3)$$

where n is the mode number. Since this expression is independent of the channel width it is also valid for a ledge along the cost of a semi-infinite ocean. In fact, when a mode becomes trapped the y-variation of the free-surface profile after the ledge is horizontal,

this can be seen at Ω = 5.236 in figure 3 which shows how mode 2 changes with frequency. In this case we have a ledge with $\alpha = 0.4$ and $\gamma = 0.1$, in a channel with $\alpha / \beta = 0.05$, but it is clear that, for Ω = 5.236, the shape of this mode, and the associated value of K, does not change when other channel widths, or even a semi-infinite ocean, are considered.

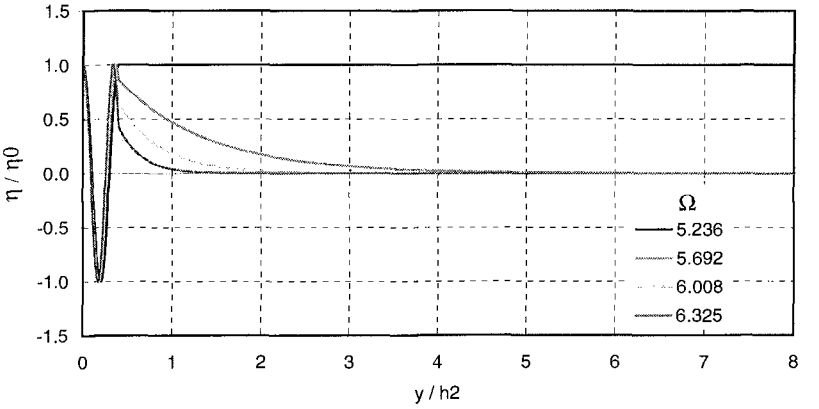

Figure 3. Free-surface elevation for mode 2 trapped waves in channel with ledge. $\alpha = 0.4$, $\alpha / \beta = 0.05$ and $\gamma = 0.1$.

The figure also indicates that for larger values of Ω the same insensitivity to channel width is likely. In this case the free surface after the ledge approaches the undisturbed mean water level and the y-coordinate of this coincidence varies with Ω.

The superposition of all the modes in each of the uniform regions into which we can divide our domain and the enforcement of the continuity of both the free-surface elevation and of the mass flux across the boundaries between those regions allow us to define a set of equations whose solution provides the amplitudes for all the modes considered. This mode-matching technique is used to get all the results presented here.

The number of modes in each region into which the domain of the problem was divided was always 200. Since this is the total number of modes (trapped + "leaky" + evanescent, in channel with ledge, or freely-propagating + evanescent, in flat channel) and the number of propagating modes increases with the frequency, this means that high frequencies have less evanescent modes than low frequencies. However, in the frequency range considered, the number of evanescent modes was always larger than 100.

The Beginning of the Ledge

We started by studying the excitation of trapped waves by external incident waves at the beginning of the ledge. Our domain is made of a flat channel, for $x > 0$, and a

channel with ledge, for $x < 0$. A flat channel mode comes from $+\infty$ and meets the beginning of the ledge at $x = 0$.

Since the incident energy is uniformly spread across the channel and the ledge occupies only a small fraction of the channel width, one would expect no significant influence of the ledge on the wave propagation in this problem, being most of the energy transmitted to $-\infty$ in the "leaky" modes of the channel with ledge.

However, figure 4 shows that this is not true when the incident wave is a zero "flat channel" mode. In that figure the energy transmitted in the trapped modes of a channel with ledge, $\alpha = 0.4$, $\gamma = 0.1$ and $\alpha / \beta = 0.05$ (the same used in figure 3), is plotted for several values of the dimensionless parameter $\Omega\ \alpha$ and for three different "flat channel" modes meeting the beginning of the ledge: zero, five and ten. The curve for mode zero has jumps at some frequencies and the transmitted energy in trapped modes reaches, at those frequencies, quite high values. In fact, the important property is how close the "channel with ledge" modes are to the incident "flat channel" modes.

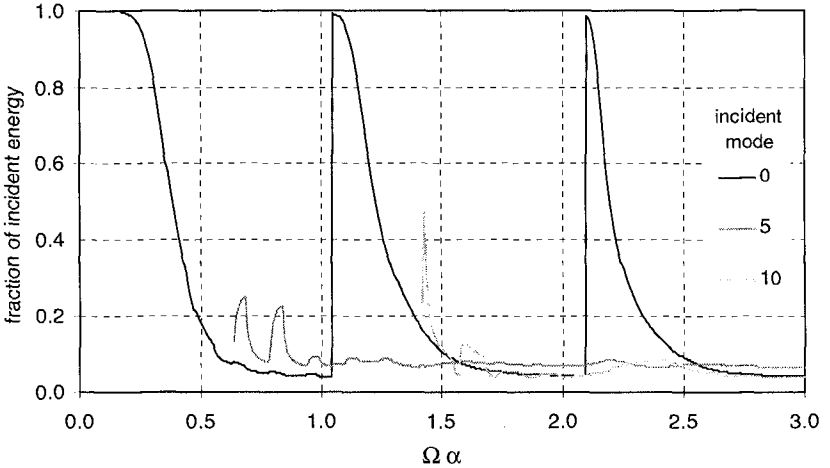

Figure 4. Total energy transmitted in trapped modes for different incident modes meeting the beginning of ledge in channel. $\alpha = 0.4$, $\alpha / \beta = 0.05$ and $\gamma = 0.1$.

We saw before, figure 3, that whenever a new trapped mode appears, the free surface elevation in the deep part of the channel is horizontal. For this frequency the free-surface elevation of the trapped mode almost coincides with the zero-mode incident wave over the deep part of the channel and so most of the incident energy is transmitted in it towards $-\infty$. Then a jump appears in the associated curve for the transmitted energy in trapped modes.

Figure 3 shows also that, as frequency increases, the slope of the free-surface elevation in the deep part of the channel becomes more pronounced and the disturbance in the free-surface elevation narrows down to the region close to the ledge. Then the free-

-surface elevation of this mode is quite different from the zero-mode incident wave and the amount of energy transmitted in trapped modes decreases.

If, instead of trapped modes only, we look to all of the propagating modes in the "channel with ledge" domain, we observe a more gradual variation in the transmitted energy, figure 5. In fact, the sudden increase in the energy in the energy in trapped modes happens because the "leaky" mode that was carrying most energy becomes a trapped mode at the frequency where the jump occurs. As the frequency increases the energy in this trapped mode goes to zero (the only exception occurs for the zero mode) and the energy carried in the next leaky mode increases. Another interesting feature in figure 5 is the absence of energy transported in the other leaky modes when a leaky mode becomes trapped.

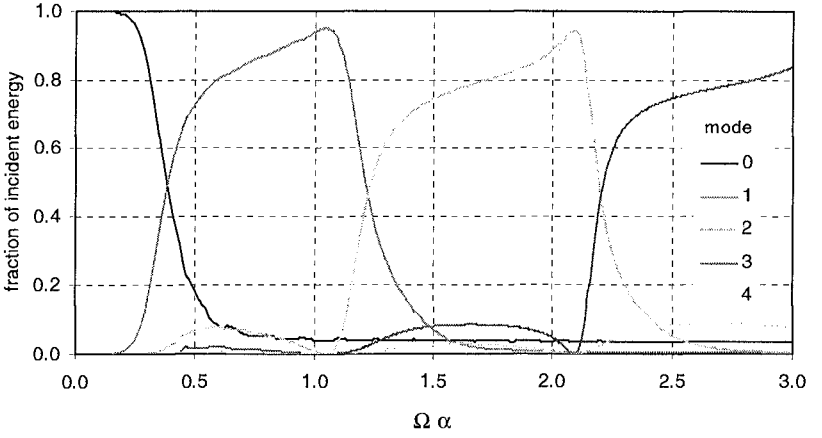

Figure 5. Distribution of transmitted energy by several modes when zero-mode incident wave meets the beginning of ledge in channel. $\alpha = 0.4$, $\alpha / \beta = 0.05$ and $\gamma = 0.1$.

A similar behaviour is observed when the incident wave is a flat channel mode different from zero. In this case the energy is transmitted mainly in "leaky" modes, because no trapped mode has a free-surface elevation that oscillates in the deep part of the channel. Assuming that the ledge does not occupy a significant fraction of the channel width, the mode that carries most energy is the one that has the same number of zero-crossings in the deep part of the channel as the incident mode. When the frequency increases, the zero-crossings of any given mode tend to concentrate over the ledge. This phenomenon makes the "leaky" mode that was carrying most energy increasingly different from the incident wave and the next "leaky" mode more similar to it. Then, even before becoming a trapped mode, the "leaky" mode that was carrying most energy loses it to the next leaky mode.

The End of the Ledge

We now look at what happens when a trapped wave meets the abrupt end of the cross-shore depth variation that enabled its existence. This problem is also used to illustrate the influence of the channel width on the results obtained.

We use the same geometry, i.e. a channel with ledge for $x < 0$ and no ledge for $x > 0$, to study what happens when a zero-mode trapped wave coming from $-\infty$ meets a discontinuity in the ledge at $x = 0$.

Plotting the total energy reflected back in trapped modes for several values of the parameter $\Omega\,\alpha$ we get figure 6. In all the curves there, each corresponding to a given value of the depth ratio, γ, three regions with distinct behaviour can always be identified: a region in the low frequency range where most of the incident energy is transmitted to the flat channel; a region in the high frequency range where the reflected energy in trapped modes tends to the value that would be obtained in a channel where the ledge occupies the whole channel width, this means that at $x = 0$ we would have a depth discontinuity of γ; and an intermediate region of high oscillations.

In the low frequency range the free surface elevation of the zero mode trapped wave, the incident wave, is almost horizontal and the phase velocity of this wave is quite close to the phase velocity of the zero mode in the "flat channel" part of the domain. Then all the energy can be transmitted to the region after the end of the ledge.

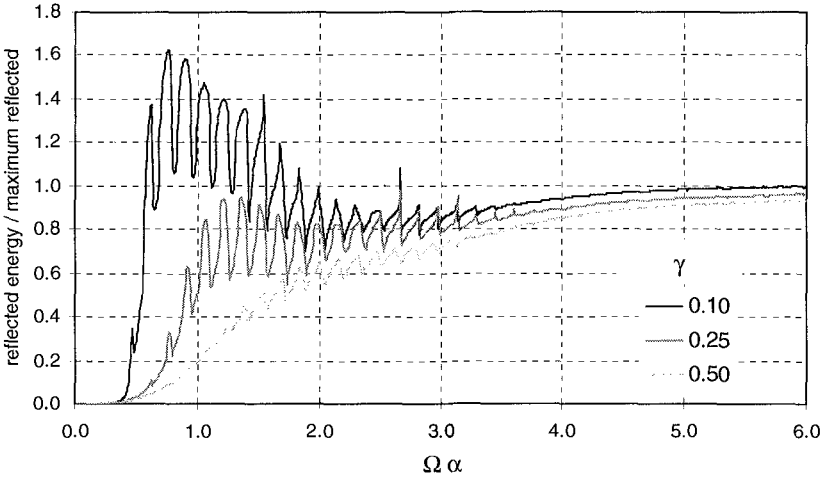

Figure 6. Influence of ledge depth ratio on reflected energy carried in trapped modes when zero-mode incident wave meets the end of ledge in channel. $\alpha = 0.4$, $\alpha / \beta = 0.05$.

In the high frequency range the free-surface elevation of the incident wave is concentrated over the ledge, being its phase velocity similar to the phase velocity of a zero mode wave in a flat channel whose the water depth equals the water depth over the

ledge. Since most of the energy in the "flat channel" part of the domain is transmitted in the zero mode, when the incident wave meets the end of the ledge this is similar to a free zero mode in a flat channel meeting a depth discontinuity γ in such a channel. So, in the high frequency range, the amount of reflected energy in trapped modes depends on γ only.

In the intermediate frequency range, where the response varies rapidly with frequency, the oscillations in the curves are found to be dependent on the channel width. This dependence is illustrated figure 7 where the reflected energy in trapped modes is presented for two different values of channel width, $\alpha / \beta = 0.05$ and $\alpha / \beta = 0.1$, for a channel with ledge with $\alpha = 0.4$ and $\gamma = 0.1$. When the channel width increases, for the same frequency range, more "leaky" modes appear in the channel and so more oscillations in the reflected energy curve can be observed. Actually whenever a "leaky" mode appears a sudden increase in that curve occurs while a new mode in the "flat channel" part of the domain is responsible for a sudden decrease in that curve. The reduction in the amplitude of those oscillations can be explained by wave radiation from the end of the ledge: the farther the channel wall the lower the amplitude of the radiated waves when reaching the far channel wall and so the smaller their influence on the reflected energy.

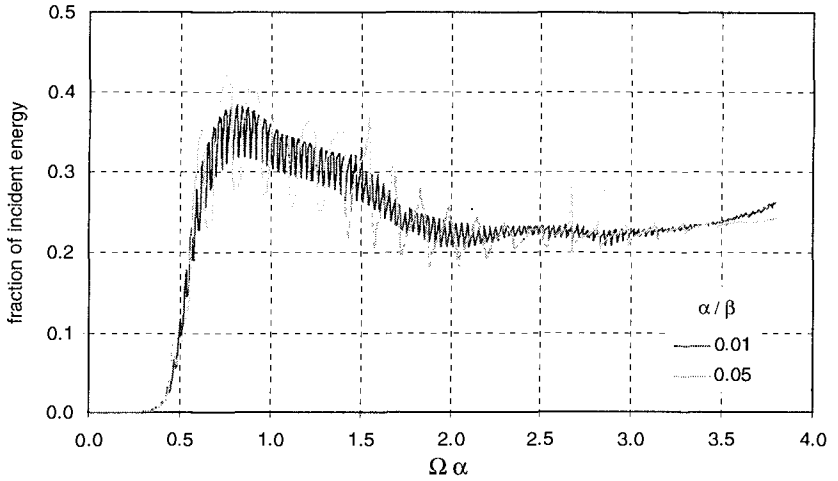

Figure 7. Influence of channel width on reflected energy carried in trapped modes when zero-mode incident wave meets the end of ledge in channel. $\alpha = 0.4$, $\gamma = 0.1$.

This strong dependence of the results on the channel width, in this frequency range, is not the best result for our initial assumption that a semi-infinite ocean could be replaced by a wide channel.

However, this does show how careful one must be when interpreting results from scale model tests where long waves are to be produced. Since long waves are difficult to

attenuate at the boundaries of the model, results from this kind of model may have a strong variability with the frequency of the incident wave.

In addition to that, this geometry is also appropriate for modelling wave propagation in narrow or enclosed seas.

A Square Bay

The last geometry presented is an interruption in the ledge produced by a square bay that opens perpendicularly to the coast and whose bottom is at the same level of the deep part of the channel. The channel has a ledge along the whole length except in the bay region.

We investigate what happens when a zero-mode incident trapped wave coming from $-\infty$ meets that discontinuity. It is expected that part of the energy shall be reflected back, part shall be radiated through the gap, part shall be transmitted to the region after the gap and that waves are excited in the bay.

The behaviour of the whole system is controlled by the ratio between the bay dimensions (width, a, and length, b) and the wavelength of the zero mode in the "flat channel" part of the domain since resonance may occur in the bay. So, the relevant non--dimensional parameters are $\Omega\mu$ and $\Omega\nu$, where μ is the non-dimensional bay width, $\mu = a / h_2$ and ν is the non-dimensional bay length, $\nu = b / h_2$.

Of course the dimensionless parameter $\Omega\ \alpha$ also plays a role in this behaviour because it controls the energy spreading across the channel and this does influence energy transmission across the interruption in the ledge.

This was clearly seen in one special case of the bay geometry we studied: a gap in the ledge (the bay length, b, is nil). We looked at the transmitted energy for several values of the gap width, μ, for two values of the parameter $\Omega\ \alpha$, 5.06 and 0.63.

For $\Omega\ \alpha = 5.06$ the incident energy is concentrated over the ledge and the curve with the transmitted energy in trapped modes versus the gap width oscillates as if the ledge occupied the whole channel width. The amplitude of those oscillations decreases slightly as the gap width increases.

Figure 8 shows the contour lines of the free surface elevation for $\Omega\ \alpha = 5.06$ when the gap width equals 4.5 times the wavelength of the zero mode in the "flat channel" part of the domain. There we can see the oscillating mode excited inside the gap region and the energy being radiated from the end of the ledge. Some of this energy misses the ledge after the gap and is transferred into "leaky" modes at that part of the domain.

Something different happens for $\Omega\mu = 0.63$. Then the incident energy is not concentrated over the ledge and the amount of energy transmitted to the region after the gap decreases sharply with the gap width. It is difficult to identify any pattern in the oscillations of that curve.

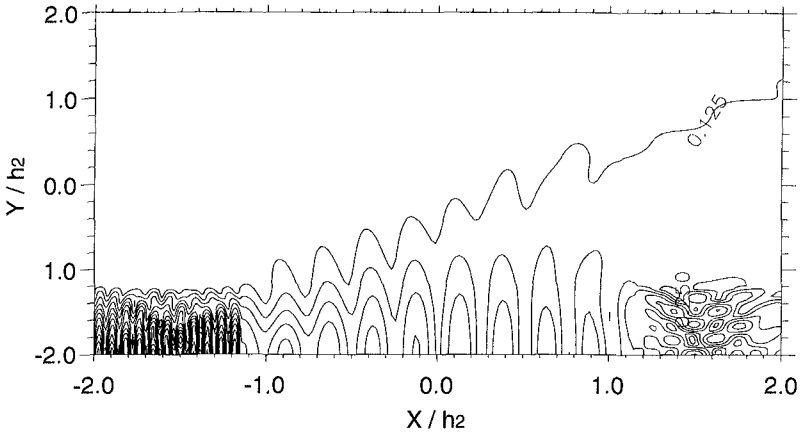

Figure 8. Amplitude of free surface elevation when zero-mode incident wave, with $\Omega\ \alpha = 5.06$, in channel with ledge, $\alpha = 0.4$, $\gamma = 0.1$ and $\alpha / \beta = 0.05$, meets gap in the ledge, $\mu = 2.28$.

For the square bay we keep the dimensions of the domain constant, $\alpha = 0.4$, $\gamma = 0.1$, $\alpha / \beta = 0.05$, $\mu = \nu = 1.0$, and vary the dimensionless frequency of the incident wave, Ω, such that the ratio between the bay width and wavelength of the zero mode in the "flat channel" part of the domain varied between zero and 1.2.

This variation of the incident wave frequency implies that $\Omega\ \alpha$ varies with the dimensionless parameter $\Omega\ \mu$ and so does the concentration over the ledge of the incident energy. The evolution, with the dimensionless parameter $\Omega\ \mu$, of the fraction of the incident energy transmitted in all the modes as well as the fraction transmitted in trapped modes is not smooth. There are many jumps and depressions related to the appearance of the several trapped and freely-propagating modes, as the frequency increases. That is why we focus only at the evolution, with $\Omega\ \mu$, of the free-surface elevation amplitude at three points at the far end of the bay:

- left : at the bay corner close to the end of the ledge, $x / h_2 = -0.5$ and $y / h_2 = -1.0$;
- center: at the middle at bay far end, $x / h_2 = 0.0$ and $y / h_2 = -1.0$;
- right: at the bay corner close to the beginning of the ledge, $x / h_2 = 0.5$ and $y / h_2 = -1.0$.

Figure 9, shows the amplitude of the free surface elevation at those points, with jumps and depressions due to the appearance of new modes in the channel. However, they cannot be mistaken for the sharp peaks on the same curves around $\Omega\ \mu = \pi$ and $\Omega\ \mu = 2\pi$ that are related to the occurrence of resonance at the bay.

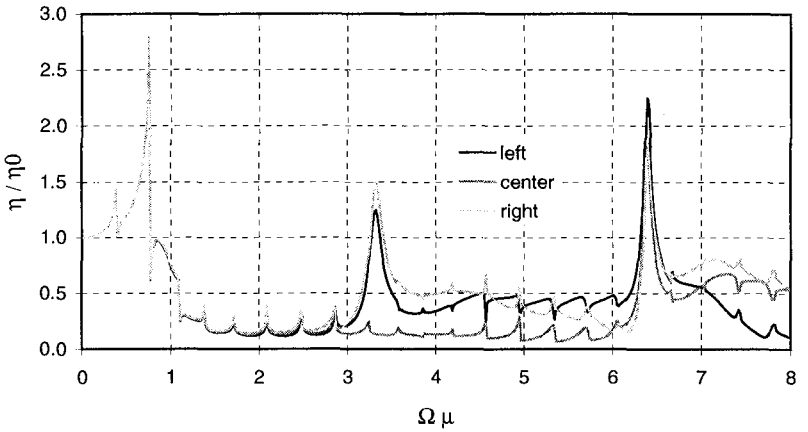

Figure 9. Channel with ledge, $\alpha = 0.4$, $\gamma = 0.1$ and $\alpha / \beta = 0.05$, that is interrupted by square bay, $\mu = \nu = 1.0$. Amplitude of free surface elevation inside bay for zero-mode incident wave.

The oscillation modes excited at those frequencies have nodal lines perpendicular to the channel boundary and is shown in figure 10 a). These peaks do not coincide with an integer number of half wavelengths across the bay width (the natural frequencies of the bay) but are slightly above it.

Next to each of those sharp peaks, at a higher frequency, a broad peak can always be noticed in figure 9. It corresponds to the excitation of an oscillation mode that has nodal lines parallel to the channel axis, in addition to the nodal lines perpendicular to the channel axis, figure 10 b).

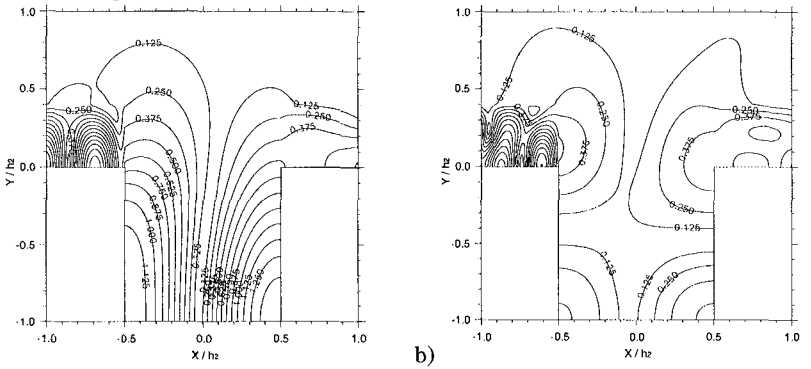

Figure 10. Amplitude of free surface elevation when zero-mode incident wave in channel with ledge, $\alpha = 0.4$, $\gamma = 0.1$ and $\alpha / \beta = 0.05$, meets gap in the ledge created by square bay, $\mu = \nu = 1.0$. a) $\Omega \mu = 3.320$ and b) $\Omega \mu = 4.206$

All these peaks imply an oscillation that involves the bay only. However, since the domain considered here is not semi-infinite but a wide channel, some of the energy radiated from the bay entrance is reflected at the far channel wall and may contribute to the build-up of the oscillation at the region in front of the bay. This could be the cause for the oscillation involving the whole channel around the bay area, shown in figure 11, associated to the sharp peak at $\Omega\mu$ = 0.759. Further investigation of this case is continuing.

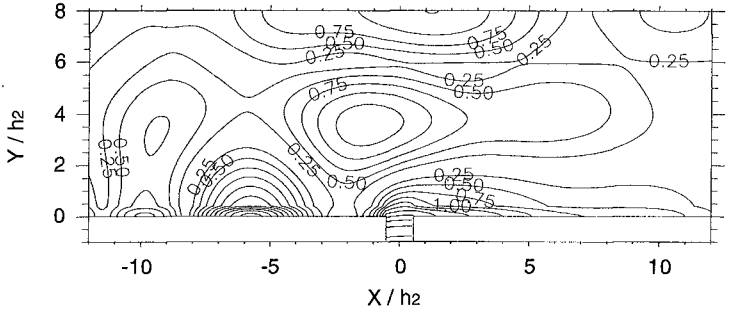

Figure 11. Amplitude of free surface elevation when zero-mode incident wave, with $\Omega\mu$ = 0.759, in channel with ledge, α = 0.4, γ = 0.1 and α/β = 0.05, meets gap in the ledge created by square bay, $\mu = \nu$ = 1.0.

Conclusions

We use a channel with a ledge along one of its walls to investigate the effects of a sudden change in the bottom geometry that enables the presence of trapped waves on the propagation of those waves.

The results obtained in this channel allow us to infer on the general trend of the response to similar problems in a semi-infinite ocean. However, in some parameter ranges they show a strong dependence on the channel width. The variability of the results with the dimensionless frequency Ω, show how careful one must be when interpreting results from scale model tests where long waves are to be produced. Since long waves are difficult to attenuate at the boundaries of the model, the effect of the wave tank walls is similar to the far channel wall in our model.

Acknowledgement

The support of the Portuguese Research Council (PRAXIS XXI BD 2770 / 94) and of the European Commission Research Grant MAS3-CT97-0081 (SASME) is gratefully acknowledged.

References

Dodd, N. and E. Bowers (1995). Low-frequency waves: wave basin experiments and numerical modelling. *Advances in Coastal Morphodynamics*, edited by H. J. De Vriend et al., Delft Hydraulics, Delft, 3.21-3.24.

Evans, D. V. and M. Fernyhough (1995). Edge waves along periodic coastlines. Part 2. *J. Fluid Mech.* **297**: 307-325.

Guza, R. T. and D. L. Inman (1975). Edge Waves and beach cusps. *J. Geophys. Res.* **80**: 2997-3012.

Huntley, D. A., R. T. Guza and E. B. Thornton (1981). Field observation of surf beat. 1. Progressive edge waves. *J. Geophys. Res.* **86**: 6451-6466.

Smith, R. (1974). Asymptotic solutions for high-frequency trapped wave propagation. *Proc. R. Soc. Lond. A* **1189**: 289-324.

Ursell, F. (1952). Edge waves on a sloping beach. *Proc. R. Soc. Lond. A* **214**: 79-97.

A Boussinesq Model for Breaking Waves: Comparisons with Experiments

Jayaram Veeramony[1] and Ib A. Svendsen[2]

ABSTRACT: *The paper describes results with a breaking wave model based on an extended set of Boussinesq equations. The wave breaking is described by accounting for the effect of vorticity generated by the breaking process. The vorticity field in the domain is obtained by solving the vorticity transport equation, which is based entirely on the Reynold's equations. In addition to the wave height decay and profile deformation predicted by earlier breaker models, the present model also provides information about the velocity profiles. The model results give good agreement with experimental data for wave height, setup and the velocity profiles. The cross-shore variation of the radiation stress calculated from the model results gives a good representation of the results from experimental data.*

1. Introduction.

Recently, there has been an increased need for time-domain modelling of breaking waves. This stems from a need to accurately model the nearshore wave motion and circulation. Simulations of breaking waves have been performed by Lin and Liu (1998a, 1998b). They solved the Reynolds equations for the mean flow and the $k - \epsilon$ equation for turbulent kinetic energy using the VOF method. The model results and experimental data were found to be in good agreement. The advantage of this type of modelling is that the flow details such as the turbulent intensities and the shear stresses can be directly evaluated from the model results. However, it takes about 48 hours of CPU time on a supercomputer to simulate one minute of real time for a two-dimensional case. As a

[1]Center for Applied Coastal Research, University of Delaware, Newark, DE. 19716 USA. email: jay@coastal.udel.edu

[2]Center for Applied Coastal Research, University of Delaware, Newark, DE. 19716 USA. email: ias@coastal.udel.edu

result, applications to practical cases are limited.

Hence, modelling of breaking waves using shallow water theories such as the nonlinear shallow water equations or the Boussinesq equations remain of practical importance. To incorporate breaking in such models, a wave breaking criterion and an energy dissipation mechanism is necessary. The wave breaking criteria used in all models are semi-empirical in nature, as there are no general theoretical bases on which a wave can be assumed to start breaking.

There are several ways in which the energy dissipation can be included in the models. One method is based on the concept of an artificial eddy viscosity term which is introduced in the momentum equations (see for example Zelt 1991; Karambas and Koutitas 1992; Wei and Kirby 1995). The value of the eddy viscosity is calibrated with experimental data. With suitable choices for the eddy viscosity, very good approximations to the wave height data is obtained. The problem with this approach is that the velocity profile is not changed from the standard quadratic profile (or a higher order polynomial depending upon the order of the terms retained in the Boussinesq theory) because the flow is modelled as a potential flow. The eddy viscosity term is also not physically justified.

Another method uses the concept of a roller model first used by Svendsen (1984a, 1984b). In these breaking models, the roller rides on the front face of the wave at the speed of the wave (Brocchini et al. 1991; Schäffer et al. 1992; Schäffer et al. 1993). This introduces a change in the velocity profile once the waves break. The velocity is assumed to have a constant value in the roller region equal to about 1.3 times the wave speed. Associated with this change in velocity profile is an excess momentum flux, which simulates wave breaking. As before, comparisons with experimental data show that the results for the wave heights and setup can be modeled quite accurately although the flow is essentially modelled as a potential flow. However, physically, the velocity profile assumed in such models is unrealistic.

Svendsen et al. (1996) presented a model for surf zone waves by accounting for the vorticity present in the breaking waves. The vertical distribution of the vorticity was obtained by solving the vorticity transport equation. The boundary condition was prescribed at the mean water level and a finite-difference scheme was used to solve the vorticity equation. However, though consistent with classical Boussinesq theory, this approach misses the significant contributions of the vorticity generated in the roller region. Also, by using a finite-difference scheme, it turns out that the small water depths in the surf zone resulted in significant numerical errors while resolving the vorticity distribution. The model used in

this paper is based on the same general principles. However, the boundary condition for vorticity is prescribed at the lower edge of the roller which is physically much more accurate. Furthermore, the vorticity equation is solved analytically, thus avoiding the problems associated with numerical modelling. Also, enhanced dispersion characteristics have been used.

2. Governing Equations.

The governing equations are derived from the basic equations for conservation of mass and momentum. The derivation, which is an extension of the classical Boussinesq theory with the Ursell number $U = O(1)$, was given in Svendsen et al. (1996). The Ursell number is defined as the ratio between the two parameters $\delta = a_0/h_0$ and $\mu = k_0 h_0$ where a_0, h_0 and k_0 are the characteristic wave amplitude, water depth and wave number respectively.

Then, the nondimensional depth integrated countinuity equation is

$$\frac{\partial \zeta}{\partial t} + \frac{\partial Q}{\partial x} = 0 \tag{1}$$

where ζ is the instantaneous water surface elevation and Q is the volume flux.

The model uses the direct depth integrated version of the momentum equations, with the enhancement of the frequency dispersion suggested by Madsen et al. (1991), which is

$$\frac{\partial Q}{\partial t} + (h+\delta\zeta)\frac{\partial \zeta}{\partial x} + \delta\left(\frac{Q^2}{h+\delta\zeta}\right)_x - \mu^2\left(B+\frac{1}{3}\right)h^2(Q)_{xxt} - Bgh^3\zeta_{xxx} + \delta(\Delta M)_x + \mu^2(\Delta P)_{xxt} = 0 \tag{2}$$

where

$$\Delta M \equiv \int_{-h}^{\delta\zeta}(u_r^2 - \overline{u}_r{}^2)\,dz, \tag{3}$$

$$\Delta P \equiv \int_{-h}^{\delta\zeta}\frac{\partial^2}{\partial x \partial t}\int_z^{\delta\zeta}\frac{\partial}{\partial x}\int_{-h}^{z}(u_r - \overline{u}_r)\,dz\,dz\,dz \tag{4}$$

are the momentum signatures of breaking. In (3) and (4), the velocities are given by

$$u = \overline{u}_p + \mu^2\left(\frac{h}{2} - z\right)(h\overline{u}_p)_{xx} + \frac{\mu^2}{2}\left(\frac{h^2}{3} - z^2\right)\overline{u}_{p_{xx}} + u_r + O(\mu^4) \tag{5}$$

$$u_r \equiv \int_{-h}^{z}\omega\,dz - \mu^2\int_{-h}^{z}\int_{-h}^{z}\int_{-h}^{z}\omega_{xx}\,dz\,dz\,dz \tag{6}$$

where $\overline{u}_p$ is the depth-averaged velocity corresponding to the potential part of the flow (i.e. terms that do not include the vorticity) and u_r is the rotational

part of the velocity which essentially represents the effect of breaking. ω is the vorticity.

Assuming a constant eddy viscosity, the vorticity transport equation and the boundary conditions read

$$\frac{\partial \omega}{\partial t} = \nu_t \frac{\partial^2 \omega}{\partial z^2} + O(\delta, \mu^2) \tag{7}$$

$$\omega(z = \zeta_e, t) = \omega_s(x, t) \tag{8}$$

$$\omega(z = -h, t) = 0 \tag{9}$$

$$\omega(z, t = 0) = 0 \tag{10}$$

where ζ_e is the lower edge of the roller and $\omega_s(x,t)$ is as yet unspecified. Noting that the terms involving breaking in (2) are $O(\delta)$ and $O(\mu^2)$, we keep only terms of $O(1)$ in the vorticity transport equation.

The bottom boundary condition of zero vorticity is consistent with the assumption that breaking is the most important source of vorticity. At the free surface we can expect zero vorticity along the part of the surface which does not include the roller region. In the roller region, measurements from hydraulic jumps (Svendsen et al. 1998) show that the free surface vorticity will also be close to zero. However, strong vorticity is generated inside the roller region with a maximum occuring near the lower limit of the roller. We approximate the vorticity generated in this region by the vorticity between the surface roller and the region beneath.

In the Svendsen et al. (1996) version of of the model, ω_s was specified along the mean water level rather than the lower limit of the roller. Though this is consistent with the Boussinesq assumptions, this turns out to be a major source of inaccuracy. Also, in the previous version of the model, the vorticity equations were solved using a Crank-Nicholson method. With the small water depths in the surf-zone, the numerical error due to the finite difference methods were also very large due to the necessity of a very fine discretization in z, unless a very fine discretization in x and t was also used. These deficiencies have been eliminated in the present version by introducing the coordinate transformation $\sigma = (h + z)/(h + \zeta_e)$ where ζ_e is $O(\delta)$. To $O(\delta, \mu^2)$ this gives (7) with σ instead of z. Solving (7)-(10) analytically gives

$$\omega = \sigma \omega_s - 2 \sum_{n=1}^{\infty} G_n \sin n\pi\sigma, \tag{11}$$

where

$$G_n \equiv \frac{(-1)^{n+1}}{n\pi} \int_0^t \frac{\partial \omega_s}{\partial t} e^{n^2\pi^2\kappa(t-\tau)}\, d\tau. \tag{12}$$

Using (11), the expressions for ΔM and ΔP are obtained.

3. Boundary conditions for vorticity.

Measurements of velocity in the roller region for breaking waves are not yet available inside the surf-zone. However, velocity measurements are available for hydraulic jumps with for the range of Froude numbers $1 \simeq Fr < 2$ (Svendsen et al. 1998; Lin and Rockwell 1994; Bakunin 1995) which is similar to Froude numbers for breaking waves. Breaking waves viewed in a coordinate system which moves at the wave speed have flow patterns around the roller region that are very similar to that observed in hydraulic jumps. The absolute velocities and the bottom boundary layer would of course be different under this coordinate transformation but the turbulent stresses, the surface profile and especially the vorticity are the same in a moving coordinate system.

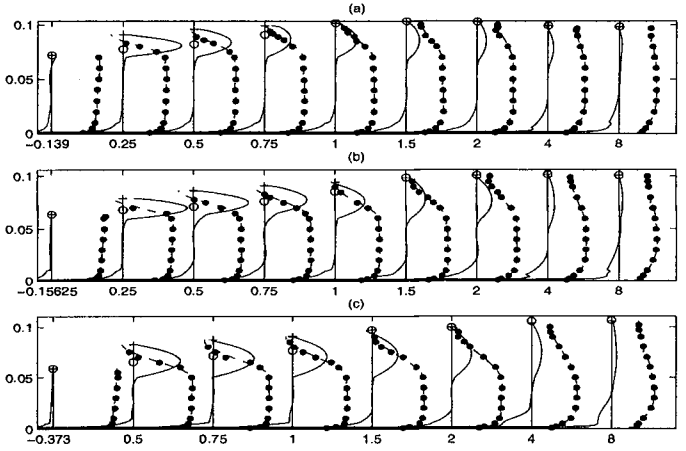

Figure 1: Velocity profiles in three hydraulic jumps with Froude numbers 1.38, 1.46 and 1.56. Data is '•', vorticity is '———' and the fit to the velocity is '– – –'. The total water depth at each location is '+' and the location of the lower edge of the streamline is 'o'(from Svendsen et al. 1998)

Velocity measurements by Bakunin (1995) were available for Froude numbers of 1.38, 1.46 and 1.56, from which the vorticity distribution could be calculated. The details of the analysis of the data can be found in Veeramony and Svendsen

(1997) and Svendsen et al. (1998). Figure 1 shows the variation of the horizontal velocity and the vorticity in the three jumps. The volume flux is also known for each jump condition from which the thickness of the roller is calculated, since the net volume flux through the roller region is zero. Figure 2a shows that the non-dimensional roller thickness is similar for all three cases. Therefore, the dimensionless roller thickness can be represented by the curve, obtained using a least squares fit to the data, shown in figure 2a.

$$\zeta_e = 0.78e^{x/l_r}\left(\frac{x}{l_r} - \frac{x^2}{l_r^2}\right) \tag{13}$$

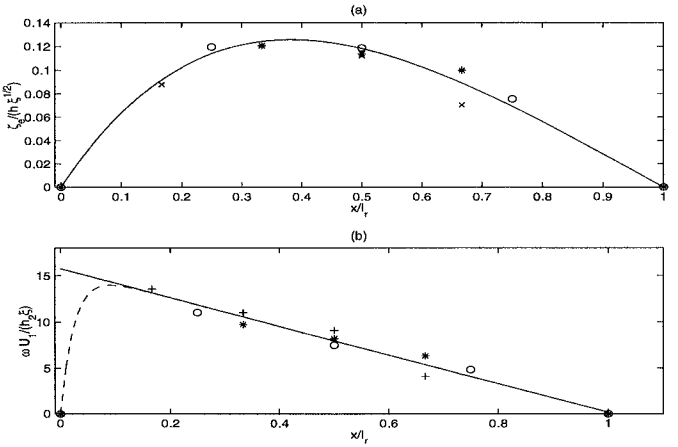

Figure 2: (a) The non-dimensional thickness of the roller for the hydraulic jumps: Data for Froude numbers 1.38 (o), 1.46 (x), 1.56(*) and least-squares fit (13). (b) Non-dimensional vorticity at the lower edge of the roller with the linear fit (———) and according to (14) (– – –).

Figure 2(b) shows the vorticity at the lower edge of the roller. Again, the non-dimensional values for all three cases are very similar, and the dimensionless ω_s can be represented by

$$\omega_s = 15.75\left(1 - \frac{x}{l_r}\right)$$

which is shown as the solid line in the figure. However, though physically realistic, the step discontinuity at $x/l_r = 0$ causes instabilities during the numerical evaluation of (12). To avoid this, we represent the vorticity by the expression

which is shown as the dashed line in figure 2b.

$$\omega_s = 15.75\left(1 - e^{40x/l_r}\right)\left(1 - \frac{x}{l_r}\right) \tag{14}$$

The expressions of ζ_e and ω_s from (13) and (14) are used in the solution (11) to the vorticity equation.

4 Comparison between model results and data.

The results from the model described in the previous section was compared to two sets of experiments with monochromatic waves. Wave heights and setup measurements for monochromatic waves are available from set of experiments by Hansen and Svendsen (1979). Wave shape and the velocity profiles below the wave trough are available from the measurements by Cox et al. (1995). Both experiments were conducted in wave flumes with plane beaches. The computational domain, shown in figure 3, is similar to the experimental domain. A

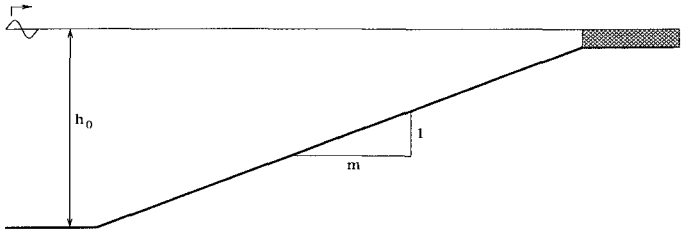

Figure 3: Schematic figure showing the computational domain. The shaded area represents the sponge layer and and the slope is $1{:}m$.

fourth-order ABM method is used to solve the equations numerically. Permanent form waves corresponding to (2) is used as input to the model. At the offshore boundary, an absorbing-generating boundary condition similar to that developed by Van Dongeren and Svendsen (1997) is used. A sponge layer is used to absorb the waves in the constant depth section which represents the shoreline. The wave is assumed to start breaking once the steepness at any point on the wave front is larger than 20°. Once the waves start breaking on a plane beach, it does not stop until it reaches the shoreline. The value of the eddy viscosity (ν_t) used in the model is $0.05h\sqrt{gh}$ for all comparisons.

4.1 Wave height and set-up comparisons.

The first set of comparisons is to the data from Hansen and Svendsen (1979). The experiments were conducted in a wave flume with a plain beach of slope 1:34.26. The water depth at the start of the slope was $h_0 = 0.36\ m$. Seven tests

Case No.	T $(secs)$	H (cm)	$T\sqrt{g/h}$
1	3.3333	4.3	17.4
2	2.5	3.9	13.0
3	2.0	3.6	10.44

Table 1: Wave parameters from (Hansen and Svendsen 1979) at the toe of the beach.

were conducted in all. The wave heights and set-up for each case was measured at a number of locations. In this paper, comparisons will only be shown for three cases. Table 1 presents the wave period and the wave height at the start of the slope for each of the cases.

Figure 4 shows the comparison between the model results and the data for Case 1. The wave heights in the initial part of the shoaling region is represented well. As the waves get closer to breaking, the agreement between the model and data deteriorates. At the point of wave breaking, the difference between the two is very obvious. The reason for this discrepancy is that the present version of the potential part of the model is based on weakly nonlinear theory as in Madsen et al. (1997a, 1997b)

Though that can be improved, the emphasis of this study, however, is the modelling of the phenomena after breaking. A short while after the breaking has been initiated in the model, it is seen that the agreement is very good.

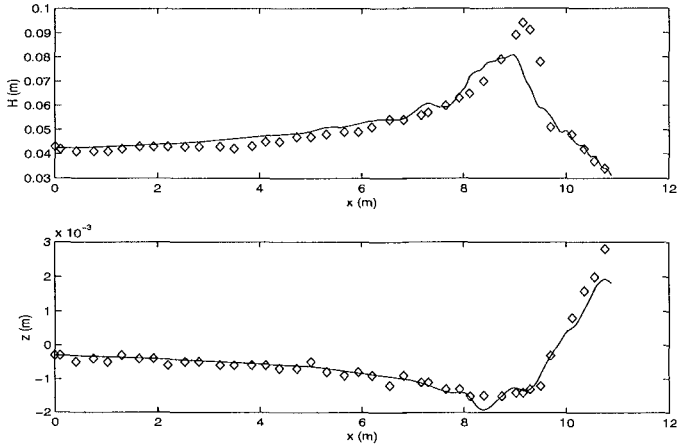

Figure 4: Comparison between model results (———) and data (o) from (Hansen and Svendsen 1979) of wave heights (a) and setup (b) for Case 1 in table 1.

An important gauge of the model performance is obtained from looking at the prediction of the set-up (figure 4b), which show good agreement between the model results and the experimental data. This suggests that the evaluation of such terms as the radiation stresses will also be accurate.

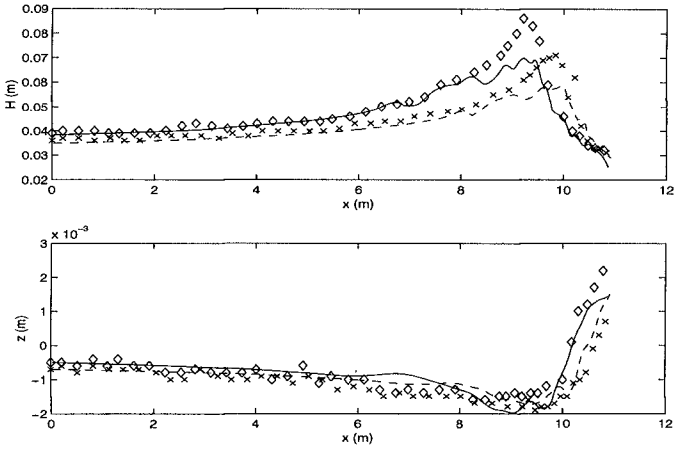

Figure 5: Comparison between model results and data from (Hansen and Svendsen 1979) of wave heights (a) and setup (b) for Case 2 (———is model, ◇ is data) and Case 3 (– – –is model, × is data) in table 1.

Figure 5 shows the comparisons for Cases 2 and 3. Again, the model underestimates the wave height near the breaking region. On the other hand, the prediction of the set-up is consistently good. All this indicates that the flow properties in the surf-zone are being modelled correctly. To illustrate this further, the results from the model are compared to velocity data from breaking waves in the next section.

4.2 Velocity and surface elevation comparisons to data.

Velocity and surface elevation data were gathered by Cox et al. (1995). The experiments were conducted in a wave flume with a plain beach slope of 1:35. The wave height at the wavemaker was $H_0 = 11.5\ cm$ and the water depth at the start of the beach was $h_0 = 0.40\ m$. The wave period was $T_0 = 2.2\ secs$. Measurements of velocity in the vertical were taken at six locations given in table 2.

The first measuring line was outside the breaking region, the second was close to the breaking point and the last four were inside the surf zone. Comparisons

Line No.	L1	L2	L3	L4	L5	L6
h (cm)	28.0	21.14	17.71	14.29	10.86	7.43

Table 2: Location of measuring lines for the data of (Cox, Kobayashi, and Okayasu 1995)

will be shown again for three cases inside the surf-zone.

Figure 6 show the comparisons at the still water depths of $h = 17.71 cm$ (6a), $h = 14.29\ cm$ (6b) and $h = 10.86\ cm$ (6c). The x-axis in the figure is normalized by the wave period. The wave shape according to the model (– – –) does not have the saw-tooth shape seen in the data (———) at any location in the surf zone. To obtain a saw-tooth profile for the wave in the surf-zone it is necessary to have full non-linearity at least up to the order of dispersion that is retained. As a result, the weakly non-linear Boussinesq model will perform significantly worse in this regard than, say, the non-linear shallow water (NSW) model, although the NSW equations retain less terms than the Boussinesq equations. The comparison between the velocity profiles predicted by the model (–·–·–) and that obtained from measurements (o) are also shown in figure 6. For the most part, the agreement between the two are excellent. An exception is near the toe of the wave face ($t/T = 0.2$) where the model tends to predict a positive velocity whereas the data shows negative velocities. The differences are clearly due to the differences in the predicted and measured surface profiles.

Figure 7 shows the vorticity field in a breaking wave. The contour lines of vorticity (7a) show that the vorticity produced in the roller region is convected downward and towards the back of the wave. The maximum value of the vorticity in the wave is close to the toe of the roller as is expected. On the other hand, along each vertical cross-section, it is only in the initial region of the roller that the maximum of the vorticity is close to the lower edge of the roller. Behind approximately the halfway point between the start of the roller and the end, the maximum of the voriticty is below the lower limit of the roller. This result is similar to that observed in the hydraulic jumps (Figure 1). Thus, this important feature of the vorticity distribution is captured by the model, even though only terms upto $O(1)$ are retained in (7)-(10).

The results of the model for u and ζ are used to compute the radiation stress. The radiation stress in the cross shore direction is defined as

$$S_{xx} = \overline{\int_{-h}^{\zeta} (\rho u^2 - p_D)\, dz} + \frac{1}{2}\rho\overline{(\zeta - \bar{\zeta})^2} \tag{15}$$

where the $\overline{()}$ denotes averaging over a wave period and p_D is the dynamic pressure. To the lowest order of approximation that has been retained so far,

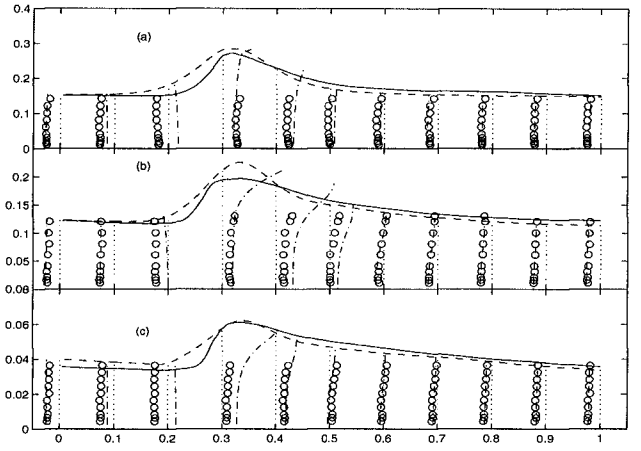

Figure 6: Comparison between model predictions and data from Cox et al. 1995 at $h = 17.71\,cm$ (a), $h = 14.29\,cm$ (b) and $h = 10.86\,cm$ (c) showing water surface elevations from model (– – –) and data (———) and velocity profiles from model (–·–·–) and data (o). The vertical lines (·····) show the locations at which the velocities are compared.

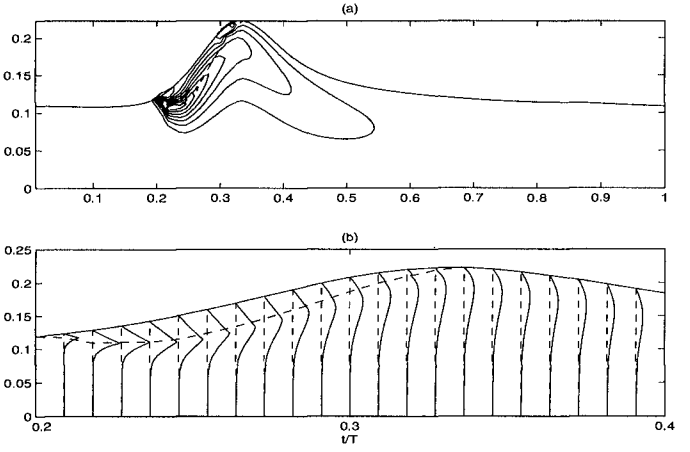

Figure 7: (a) Contours of vorticity at $L4$. (b) Vertical profiles of vorticity under the roller and behind the crest.

$p_D \simeq \rho w^2$ where w is the vertical velocity.

Figure 8 shows the spatial variation of the dimensionless radiation stress defined as

$$P \equiv \frac{S_{xx}}{\rho g H^2}.$$

Linear theory predicts a constant value of $P = 0.1875$. Wave breaking in the model starts at $x \simeq 9.6\,m$. The value of P at the start of breaking is relatively low due to the peaky shape of the waves (see Svendsen 1984b for a detailed discussion). Svendsen and Putrevu (1993) presented results from experimental data for the normalized radiation stress, which shows considerable variation from one data set to another. However, all results have the same feature that the value of P starts at the breaker point with fairly low values, increases to a maximum and then decreases towards the shoreline. Although the results of the model do not show that P quite reaches the value predicted by linear wave theory, the same trend is observed.

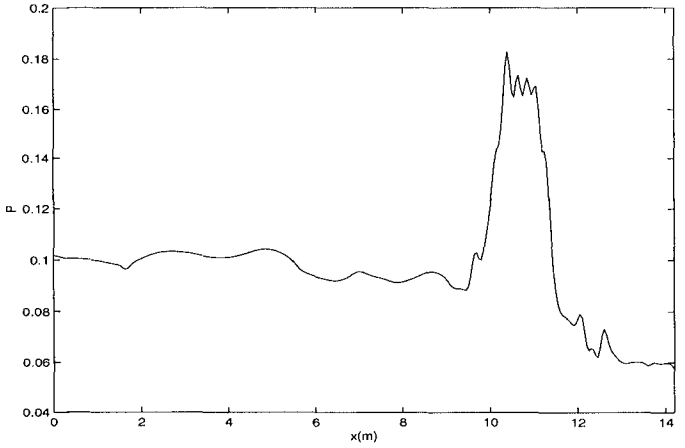

Figure 8: Spatial variation of the dimensionless radiation stress $P = S_{xx}/(\rho g H^2)$. Wave breaking starts at $x = 9.6\,m$. The sponge layer starts at $x = 15\,m$.

5 Conclusions.

The breaking model is an extension of the classical Boussinesq equations. The vorticity field in the domain is obtained by solving the lowest order vorticity transport equation, which is based entirely on the Reynold's equations. The boundary conditions for the solution for vorticity is parameterized using measurements from hydraulic jump. Comparisons with experimental data for

monochromatic waves show that the model performs well in the surf-zone. The wave heights are predicted reasonably accurately within the limitations of the form of the Boussinesq equations. The comparisons to the velocity profiles are especially good. The vorticity distribution calculated by the model agrees qualitatively with the results shown for hydraulic jump. The radiation stress in the cross-shore direction is calculated directly from the velocity field given by the model. The result is seen to agree qualitatively with that observed from other experiments.

Acknowledgements.

This study was sponsored by the National Science Foundation under the grant OCE-9203277 and by the Office of Naval Research under contract No. 98PRO5167-00. The United States Government is authorized to produce and distribute reprints for government purposes notwithstanding any copyright notation that may appear herein.

References

Bakunin, J. (1995). Experimental study of hydraulic jumps in low froude number range. Master's thesis, Center for Applied Coastal Research, University of Delaware, Newark, DE19711.

Brocchini, M., P. Cherubini, and L. Iovenitti (1991). An extension of boussinesq type model to the surf zone. *Computer Modelling in Ocean Engineering 91, Rotterdam, The Netherlands*, pp. 349–359.

Cox, D. T., N. Kobayashi, and A. Okayasu (1995). Experimental and numerical modeling of surf zone hydrodynamics. Technical Report CACR-95-07, Center for App. Coastal Res., University of Delaware.

Hansen, J. B. and I. A. Svendsen (1979). Regular waves in shoaling water: Experimental data. Technical report, ISVA Series Paper 21.

Karambas, T. K. and C. Koutitas (1992). A breaking wave propagation model based on the boussinesq equations. *Coastal Engineering 18*, pp. 1–19.

Lin, J. C. and D. Rockwell (1994). Instantaneous structure of a breaking wave. *Physics of Fluids 6(9)*, pp. 2877–2879.

Lin, P. and P. L. F. Liu (1998a). A numerical study of breaking waves in the surf zone. *Journal of Fluid Mechanics 359*, pp. 239–264.

Lin, P. and P. L. F. Liu (1998b). Turbulence transport, vorticity dynamics, and solute mixing under plunging breaking waves in surf zone. *Journal of*

Geophysical Research 103, pp. 15677–15694.

Madsen, P. A., R. Murray, and O. R. Sørensen (1991). A new form of boussinesq equations with improved dispersion characteristics. *Coastal Engineering 15*, pp. 371–388.

Madsen, P. A., O. R. Sørensen, and H. A. Schäffer (1997a). Surf zone dynamics simulated by a boussinesq type model. part i. model description and cross-shore motion of regular waves. *Coastal Engineering 32*, pp. 255–287.

Madsen, P. A., O. R. Sørensen, and H. A. Schäffer (1997b). Surf zone dynamics simulated by a boussinesq type model. part ii. surf beat and swash oscillations for wave groups and irregular waves. *Coastal Engineering 32*, pp. 289–319.

Schäffer, H. A., R. Deigaard, and P. A. Madsen (1992). A two-dimensional surf zone model based on the boussinesq equations. *Proceedings of the 23rd ICCE*, pp. 576–589.

Schäffer, H. A., P. A. Madsen, and R. Deigaard (1993). A boussinesq model for wave breaking in shallow water. *Coastal Engineering 20*, pp. 185–202.

Svendsen, I. A. (1984a). Mass flux and undertow in a surf-zone. *Coastal Engineering 8*, pp. 347–365.

Svendsen, I. A. (1984b). Wave heights and set-up in a surf-zone. *Coastal Engineering 8*, pp. 303–329.

Svendsen, I. A. and U. Putrevu (1993). Surfzone wave paramters from experimental data. *Coastal Engineering 19*, pp. 283–310.

Svendsen, I. A., J. Veeramony, J. Bakunin, and J. T. Kirby (1998). The flow in weak turbulent hydraulic jumps. *Submitted to the Journal of Fluid Mechanics*.

Svendsen, I. A., K. Yu, and J. Veeramony (1996). A boussinesq breaking wave model with vorticity. *Proceedings of the 25rd ICCE*, pp. 1192–1204.

Van Dongeren, A. R. and I. A. Svendsen (1997). Absorbing-generating boundary condition for shallow water models. *ASCE Journal of Waterway, Port, Coastal and Ocean Engineering 123*(6), pp. 303–313.

Veeramony, J. and I. A. Svendsen (1997). Analysis of the roller in hydraulic jumps. *To appear in the proceedings of Coastal Dynamics*.

Wei, G. and J. T. Kirby (1995). A coastal processes model based on time-domain boussinesq equations. *Coastal Dynamics*.

Zelt, J. A. (1991). The run-up of nonbreaking and breaking solitary waves. *Coastal Engineering 15*, pp. 205–246.

NEARSHORE WAVE DYNAMICS SIMULATED BY BOUSSINESQ TYPE MODELS

Ole R. Sørensen[1], Per A. Madsen[1], and Hemming A. Schäffer[1]

Abstract

This paper presents a numerical study of nearshore wave dynamics including the surf zone. Two different time-domain Boussinesq type formulations are applied for this purpose. The first model incoporates Padé [2,2] dispersion characteristics and lowest order nonlinearity. The second and more sophisticated model incorporates Padé [4,4] characteristics and higher-order nonlinearity in the dispersive terms. The models are validated on the shoaling and breaking of regular and irregular waves with and without an ambient current.

1. INTRODUCTION

Numerical models of nearshore wave hydrodynamics have developed rapidly in complexity over the last decade. Today, the most advanced Boussinesq type models offer an accurate representation of complicated processes such as triad wave interactions and wave-current interaction, while wave breaking of irregular waves and the resulting dissipation processes can be approximated by fairly simple but reasonably accurate descriptions. This allows for a study of a variety of complicated phenomena in the surf zone and in the swash zone.

In previous publications (e.g. Schäffer et al., 1993; Madsen et al., 1997a,b; Sørensen et al., 1998) we have studied and modelled surf zone dynamics such as the shoaling, breaking and runup of regular and irregular waves, the generation and release of low frequency waves, wave-induced rip-currents and circulation cells behind detached breakwaters. For this purpose we have until recently applied a time-domain Boussinesq model (I) in terms of the depth-integrated velocity and including lowest order nonlinearity and Padé [2,2] dispersion characteristics. The results obtained with this model have been satisfactory with a few exceptions. However, it has been clear for some time that this model underestimates the nonlinear shoaling

[1]International Research Centre for Computational Hydrodynamics (ICCH), Danish Hydraulic Institute, Agern Allé 5, DK-2970, Hørsholm, Denmark

near the break point. This shortcoming shows up in the wave height or wave crest variations and even more clearly in the evolution of nonlinear measures such as the skewness and asymmetry.

In this work we introduce a more sophisticated Boussinesq model (II) which includes higher-order nonlinearity in the dispersive terms as well as more accurate linear dispersion characteristics (Padé [4,4]-type). Both models (I and II) are applied in this study to investigate shoaling and breaking of regular and irregular waves on different bathymetries. The emphasis is on the evolution of higher-order statistics in terms of the skewness and asymmetry. Comparisons with physical experiments are presented for three cases. The effect of an opposing current on the shoaling and breaking of regular waves on a sloping plane beach is also investigated. Here we concentrate on validating the ability of the breaking model to predict the breaker depth and breaker height.

2. MODEL DESCRIPTION

The two different time-domain Boussinesq formulations considered in this work are described below. For simplicity we shall list the equations for a constant depth althrough the variable-depth terms were included in all computations. Both models are extended into the surf zone by the use of the so-called roller concept as summarized in Section 2.2.

2.1 Boussinesq formulations

Model I is formulated in terms of the depth-integrated horizontal velocity and it retains terms of order $O(\mu^2,\epsilon)$, where ϵ is a measure of the nonlinearity and μ is a measure of linear dispersion. The general two-dimensional equations valid on a sloping bottom were originally derived by Madsen & Sørensen (1992) and later extended to the surf zone by Madsen et al. (1997a,b). In one dimension and on a constant depth the equations read

$$\frac{\partial \eta}{\partial t} + \frac{\partial Q}{\partial x} = 0 \tag{1a}$$

$$Q_t + \epsilon \frac{\partial}{\partial x}\left(\frac{Q^2}{h+\epsilon\eta}\right) + \epsilon R_x + (h+\epsilon\eta)\eta_x + \mu^2\left(\left(v_1 - \frac{1}{3}\right)h^2 Q_{xxt} + v_1 h^3 \eta_{xxx}\right) = O(\epsilon\mu^2, \mu^4) \tag{1b}$$

where Q is the depth integrated velocity, h is the still water depth, η is the surface elevation and v_1=-1/15. This formulation is superior to the classical Boussinesq equations as it incorporates Padé [2,2] dispersion characteristics for pure waves, i.e. in the absence of current. We note that the R-term in (1b) represents the roller dynamics as described in Section 2.2.

Model II is formulated in terms of the horizontal velocity at a certain z/h-location and it retains terms of order $O(\mu^2,\epsilon^3\mu^2)$. The general two-dimensional equations valid on a sloping bottom can be found in Madsen & Schäffer (1998a), and they have previously been solved in one-dimension by Madsen et al. (1996). In one dimension and on a constant depth the equations read

$$\eta_t + h\acute{u}_x + \mu^2\left(\left(\alpha+\frac{1}{3}-\beta_1\right)h^3\acute{u}_{xxx} - \beta_1 h^2\eta_{xxt}\right) + \epsilon(\eta\acute{u})_x +$$

$$\epsilon\mu^2 h^2\frac{\partial}{\partial x}\left(\alpha\eta\acute{u}_{xx} - \beta_1(\eta\acute{u})_{xx}\right) - \epsilon^2\mu^2\frac{h}{2}\frac{\partial}{\partial x}\left(\eta^2\acute{u}_{xx}\right) - \tag{2a}$$

$$\epsilon^3\mu^2\frac{\partial}{\partial x}\left(\frac{1}{6}\eta^3\acute{u}_{xx}\right) = O(\mu^4)$$

$$\acute{u}_t + \eta_x + \mu^2\left((\alpha-\alpha_1)h^2\acute{u}_{xxt} - \alpha_1 h^2\eta_{xxx}\right) + \epsilon\left(\acute{u}\acute{u}_x + \frac{R_x}{h+\epsilon\eta}\right) +$$

$$\epsilon\mu^2\frac{\partial}{\partial x}\left(\alpha h^2\acute{u}\acute{u}_{xx} - \frac{\alpha_1}{2}h^2(\acute{u}^2)_{xx} + \frac{1}{2}h^2(\acute{u}_x)^2 - h\eta\acute{u}_{xt}\right) +$$

$$\epsilon^2\mu^2\frac{\partial}{\partial x}\left(-\frac{1}{2}\eta^2\acute{u}_{xt} + h\eta\left(\acute{u}_x^2 - \acute{u}\acute{u}_{xx}\right)\right) + \tag{2b}$$

$$\epsilon^3\mu^2\frac{\partial}{\partial x}\left(-\frac{1}{2}\eta^2\acute{u}\acute{u}_{xx} + \frac{1}{2}(\eta\acute{u}_x)^2\right) = O(\mu^4)$$

where ú is the velocity in a specific z/h-location and

$$(\alpha,\beta_1,\alpha_1) = \left(\frac{-3-\sqrt{23/35}-2\sqrt{19/7}}{18}\ ,\ \frac{28-2\sqrt{133}}{126}\ ,\ \frac{105-3\sqrt{805}}{1890}\right) \tag{3}$$

Again the R-term in (2b) represents the roller dynamics as described in Section 2.2. Madsen & Schäffer (1998a,b) demonstrated that (2a-b) is Galilean invariant and that it incorporates Padé [4,4] dispersion characteristics for pure waves as well as for waves in currents. Furthermore, the characteristics for shoaling and wave-wave interaction are generally superior to the ones obtained by Model I.

Fig. 1 shows the accuracy of the second order transfer functions derived from the two different Boussinesq formulations. The individual transfer functions are scaled with the target solution of Stokes. We notice that Model II obviously contains the best nonlinear performance, while Model I significantly underestimates the transfer function for larger kh-values.

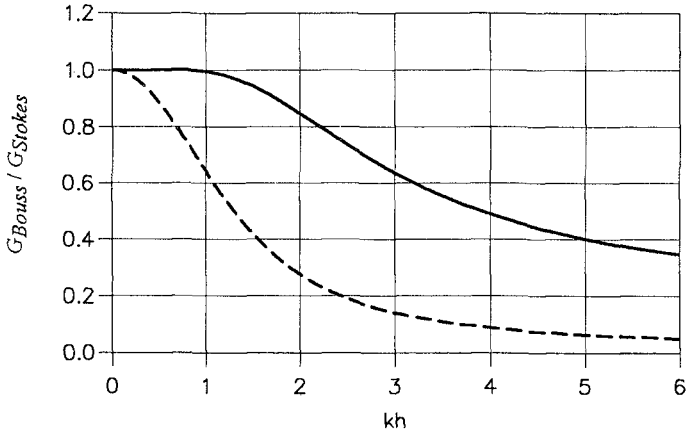

Figure 1 Transfer function for the second harmonic as function of kh for the two Boussinesq-type models. Results scaled by Stokes solution. (- - -) Model I and (——) Model II.

2.2 Breaker model based on the roller concept

Wave breaking is introduced in the Boussinesq equations on the basis of the surface roller concept for spilling breakers as described by Schäffer et al. (1993) and Madsen et al. (1997a, 1997b). The basic principle is that the surface roller is considered as a volume of water carried by the wave with the wave celerity. The influence of breaking on the governing equations is modelled by an additional momentum term orginating from a non-uniform velocity profile due to the presence of the roller. This momentum term can be expressed as

$$R = \frac{\delta}{1 - \delta/d}(c - u) \tag{4}$$

Here d is the total water depth, δ is the roller thickness, c is the roller celerity, while u is the depth-averaged velocity (Q/d) in eq. (1b) and the velocity at a specific z/h-location in eq. (2b).

The instantaneous roller thickness at each point is determined based on a heuristic geometrical approach. Incipent breaking is assumed to occur when the local slope of the surface elevation exceeds an initial critical value, $\tan\phi_B$. During the

transition from initial breaking to a bore-like stage in the inner surf zone the critical angle is assumed to gradually change from ϕ_B to a smaller terminal angle ϕ_0. Hence the instantaneous value of ϕ defining the toe of the roller depends on the age of the roller and is assumed to follow an exponential time-variation with a half time $t_{1/2}$. Locally, the roller is defined as the water above the tangent of slope tanϕ. Prior to inclusion in the governing equations the roller thickness is multiplied by a shape factor. In Model I a constant factor of 1.5 is applied, while a shape factor which has a linear variation from 2 at the toe of the roller to zero at the back of the roller is applied in Model II. The latter modification of the shape factor was introduced because the previous formulation had a tendency to give small spurious oscillations near the back of the roller, when applied to the peaked wave profiles appearing with Model II.

For Model I all test cases in the present paper are modelled with a default set of breaking parameters (ϕ_B, ϕ_0, $t_{1/2}$) = (20 deg, 10 deg, T/5), where T is a characteristic wave period. These parameters were given by Madsen et al. (1997a). However, the calibration of ϕ_B and to some extent $t_{1/2}$ is related to the accuracy of the computed surface elevation before the breaking occurs. As Model II incorporates more nonlinearity, the wave profiles computed by this model will generally contain a higher level of skewness and this will show up in particular near the breaking point. Therefore, the breaking parameters, which have been calibrated on the basis of Model I, have to be revised. In the present paper all simulations with Model II are performed with (ϕ_B, ϕ_0, $t_{1/2}$) = (32 deg, 10 deg, T/10).

The wave celerity, which is an important part of (4), is determined interactively from the instantaneous wave field using

$$c = -\frac{\eta_t}{\eta_x} \tag{5}$$

determined at the steepest point of each wave front.

3. Shoaling and breaking of regular and irregular waves

3.1 Regular waves on a plane sloping beach

Ting and Kirby (1994) presented measurements for spilling breakers on a plane sloping beach with a slope of 1/35 starting in a depth of 0.40 m. As input they generated regular waves with a wave period of 2.0 s and a wave height of 0.125 m. Fig. 2 shows the spatial variation of the crest and trough elevations and of the mean water level computed by the two different Boussinesq models. It is obvious that model II, which contains higher-order nonlinear terms, significantly improves the nonlinear shoaling up to the vicinity of the breaking point. This result is in accordance with the analysis from Fig. 1. The difference between the two model results is emphasized in Fig. 3, which shows the spatial variation of the skewness and asymmetry, and in Fig 4, which shows the computed wave profiles at the point of wave breaking. Again model II is seen to predict a much higher level of nonlinearity.

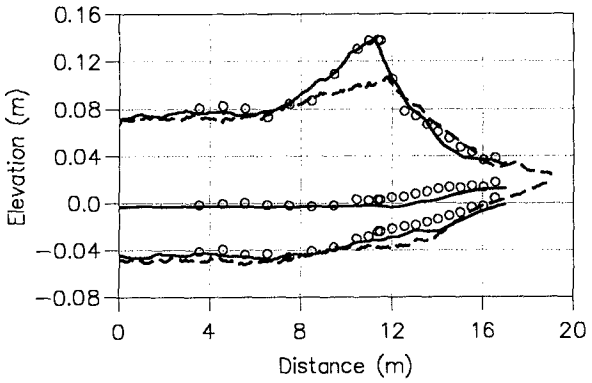

Figure 2 Spatial variation of wave crest elevation, wave trough elevation and mean water level for the test of Ting and Kirby (1994). (- - -) Model I; (——) Model II; (o) experimental data.

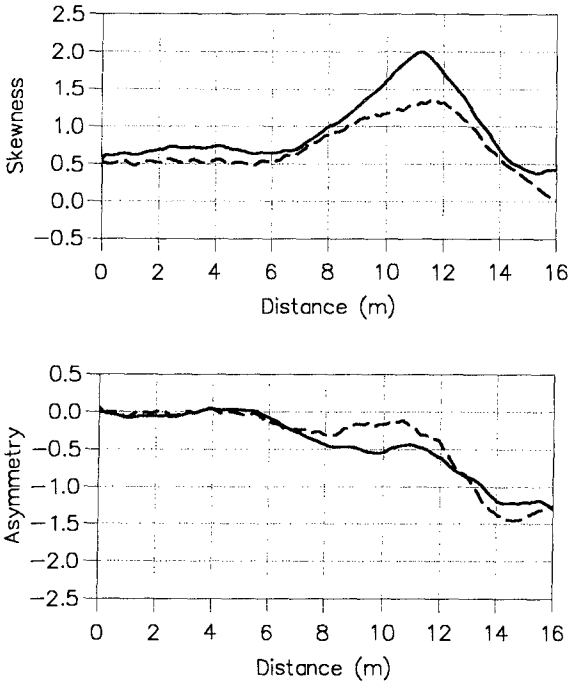

Figure 3 Spatial variation of the skewness and asymmetry for the test of Ting and Kirby (1994), (- - -) Model I and (——) Model II.

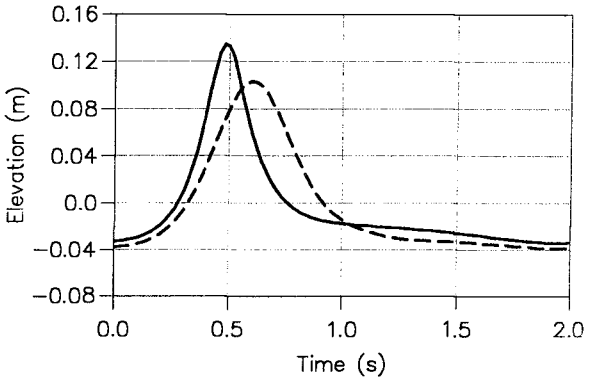

Figure 4 Timeseries of surface elevations at a location near the break point (x=11 m). (- - -) Model I and (——) Model II.

3.2 Irregular waves on a plane sloping beach

This test case is based on the laboratory measurements reported by Cox et al. (1991). Fig. 5 illustrates the experimental setup. The flume consists of a 10 m horizontal section with a water depth of 0.47 m and a 12 m section with a constant slope of 1/20. Measurements of the surface elevation are available at eleven locations (denoted WG1 to WG11) in still water depths of 47, 35, 30, 25, 20, 17.5, 15, 12.5, 10, 7.5 and 5 cm. The input waves are generated on the basis of a target spectrum of Pierson-Moskowitz type with a peak frequency of 1.0 Hz and a significant wave height of 6.45 cm.

Based on the peak frequency we find that $h/L_0=0.30$ (L_0 being the deep water wave length) at the offshore boundary and this makes the test very demanding for weakly dispersive Boussinesq models. Model I, which incorporates Padé [2,2] dispersion characteristics, is resticted to h/L_0 values less than approximately 0.5 and beyond this limit errors in the linear dispersion relation will exceed 5% (see Madsen et al., 1991). Hence an accurate representation of free waves at 2.0 Hz (two times

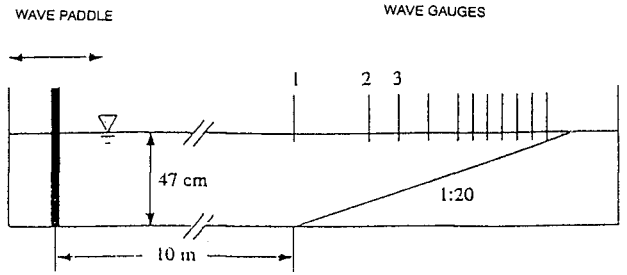

Figure 5 Sketch of physical wave flume (Cox et al. (1991).

the peak frequency) requires the water depth to be less than 0.25 m. For this reason model I does not cover the full domain of the experimental flume, but it is started at station WG4 in a depth of 0.25 m. Model II, on the other hand, incorporates Padé [4,4] dispersion characteristics, which are accurate for h/L_0 as high as 1.0. Hence this model is started at WG1 at a depth of 0.47 m. In both cases the following procedure is used to obtain the incoming wave conditions: First, the measured surface elevation at WG4 (model I) and WG1 (model II) is analysed by FFT. Second, a bandpass filter is applied to remove the energy on frequencies lower than f=0.4 Hz, and higher than f=3.0 Hz. Third, the remaining energy is synthesized back into a flux or a velocity boundary condition by the use of a second order pertubation theory corresponding to each of the model equations.

Fig. 6a-c show the measured and computed spatial variations of the significant wave height, the skewness and the asymmetry. For both models the predicted wave heights are in fairly good agreement with the measurements. From Fig. 6b we notice that the skewness computed by model I is seen to be significantly underestimated everywhere in the flume, while model II picks up the correct variation of this quantity. The skewness is a measure of the nonlinearity in the wave profile and we notice that the results obtained in Fig. 6b confirm the analysis of the transfer function to second harmonics as shown in Fig. 1. Fig. 6c shows the spatial variation of the measured and computed asymmetry. This quantity, which measures the forward pitching of the wave profiles, is almost zero up to the break point beyond which the value decreases drastically. The results obtained by model II are seen to be in almost perfect agreement with the measurements. This result is remarkable and it confirms that the time-domain surf zone Boussinesq model can provide an accurate prediction of the statistics of the wave shape under the combined influence of triad interactions and wave breaking.

Fig 7 shows the measured and computed energy spectra at three locations (WG7, WG9, WG11). Model II is seen to be in very good agreement with the measurements, while model I tends to underestimate the high frequency tail of the spectrum. As mentioned above, the input spectrum used for model I, did not contain energy for frequencies higher than 3.0 Hz. Hence, whatever is present beyond this frequency limit in more shallow water is generated by triad interactions. It is therefore not surprising that the high frequency tail is underestimated by model I.

3.3 Irregular waves on a barred beach

This case is based on the Delta Flume '93 laboratory experiment (Arcilla et al., 1994) which was conducted on a barred beach (Fig. 8d) using a Pierson-Moskowitz spectrum with peak frequency of 0.122 Hz and a significant wave height of 0.58 m. The procedure described in section 3.2 to obtain the incoming wave conditions is also applied here. Fig. 8a-c shows the computed spatial variation of the significant wave height, skewness and asymmetry for the two Boussinesq models. Again the two models predict almost the same variation of the wave heights while significant differences appear in the measures of the nonlinearity: Model I clearly underpredicts the skewness (as well as the asymmetry) while model II is in very good agreement with the measurements.

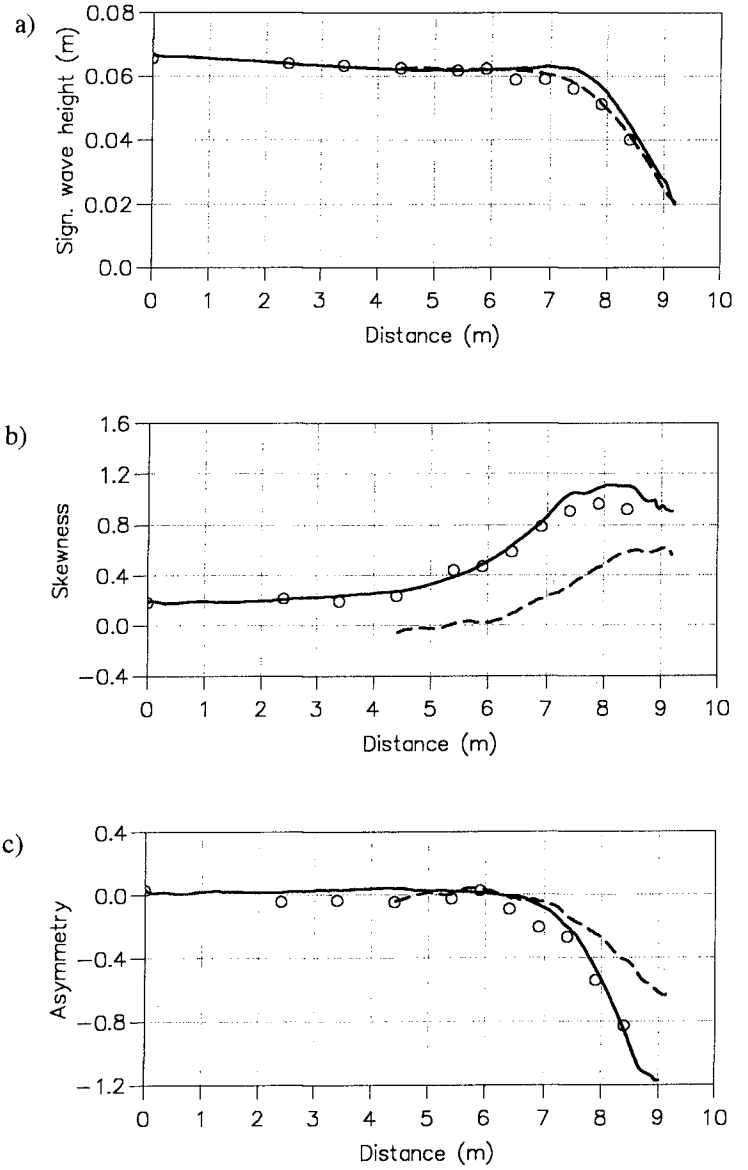

Figure 6 Irregular wave on a plane beach. Spatial variation of (a) the significant wave height, (b) skewness, (c) asymmetry. (- - -) Model I; (——) Model II; (o) Experimental data by Cox et al. (1991).

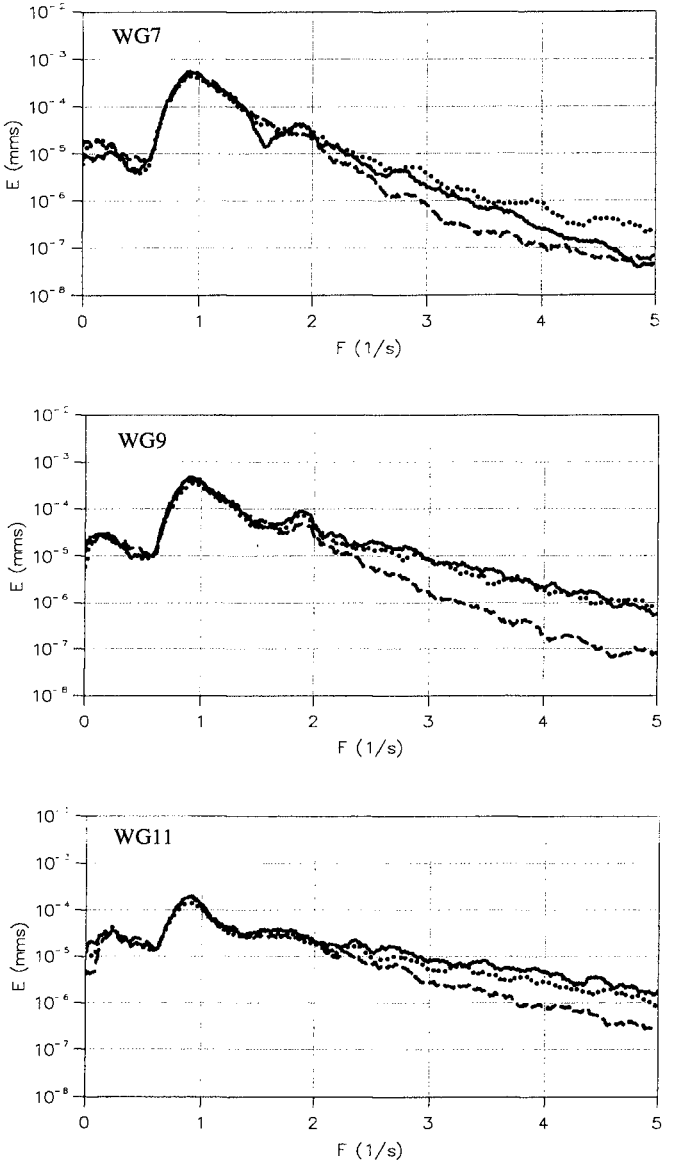

Figure 7 Surface elevation spectra at three locations. (- - -) Model I; (——) Model II; (.....) Experimental data by Cox et al. (1991).

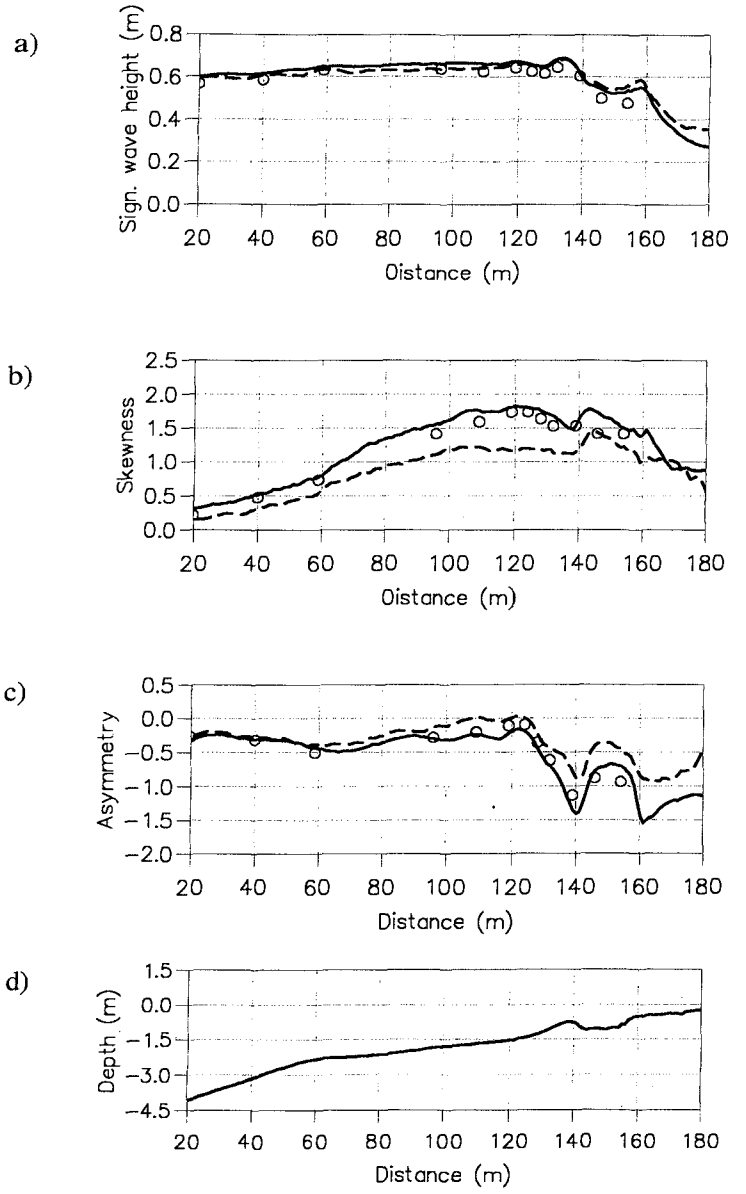

Figure 8 Irregular waves on a barred beach. Spatial variation of (a) the significant wave height, (b) skewness, (c) asymmetry and (d) bathymetry. (- - -) Model I; (——) Model II; (o) Experimental data by Arcilla et al. (1994).

4. Waves in an opposing current

Boussinesq model II is Galilean invariant in contrast to model I, and it provides Padé [4,4] dispersion characteristics with the correct Doppler shift in connection with ambient uniform currents (see e.g. Madsen & Schäffer, 1998a,b). In this work we have applied model II to study the phenomenon of wave breaking in adverse currents. We have focused on the experiments by Sakai et al.(1981) who investigated breaker types and breaker depth indices for a variety of opposing currents, beach slopes and deep water wave stepnesses. The experiments were performed in a 24 m long, 0.36 m wide and 0.80 m deep wave flume as shown in Fig. 9. In this paper we present results for the following cases: A beach slope of s = 1/30, regular waves with wave period of T = 1.2 s, wave heights in the interval between 0.009 m and 0.180 m and the current discharges of q = 0, 0.0169 m^2/s and 0.0297 m^2/s.

Fig. 10 shows the calculated breaker depth index h_B/L_0 as a function of the deep water wave steepness H_0/L_0. Here h_B is the still water depth at the break point, H_0 is the wave height in deep water and L_0 is the deep water wave length. We notice that the breaker depth clearly increases for increasing currents and that the model results are in good agreement with the measurements.

Sakai et al. (1988) presented emperical formulas for breaking conditions of shoaling waves on opposing currents. These were based on the extensive flume experiments by Sakai et al. (1981, 1984) and they give the ratio of the breaker depth, R_h, with and without current and likewise for the breaker height, R_H. Both ratios are given as function of a new parameter γ which accounts for the combined effect of the discharge, the incident wave steepness and the slope of the bed

$$\gamma = q^* s^{1/4} (H_0/L_0)^{-1} \tag{6}$$

where

$$q^* = q g^{-2} T^{-3} \tag{7}$$

In Fig. 11 the calculated values of R_h and R_H are compared with the emperical formulas by Sakai et al. (1988). It is seen that for the relative breaker depth the

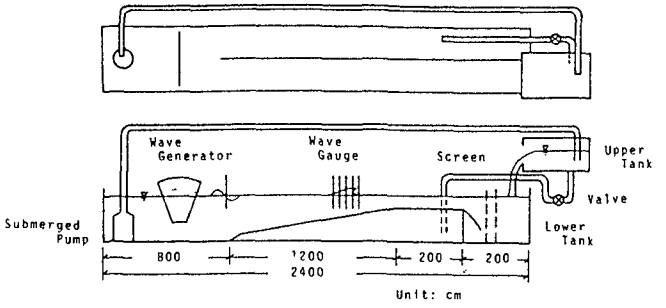

Figure 9 Experiment setup by Sakai et al. (1981).

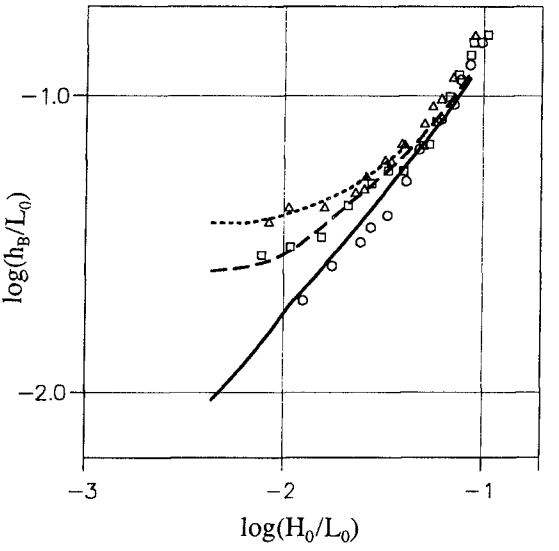

Figure 10 Breaker depth index, h_b/L_0 as funtion of the deep water wave steepness H_0/L_0. Lines show calculations with Model II (——) q=0, (- - -) q=0.0169 m^2/s, (....) q=0.0297 m^2/s; Markers show measurements by Sakai et al. (1981), (o) q=0, (□) q=0.0169 m^2/s, (Δ) q=0.0297 m^2/s.

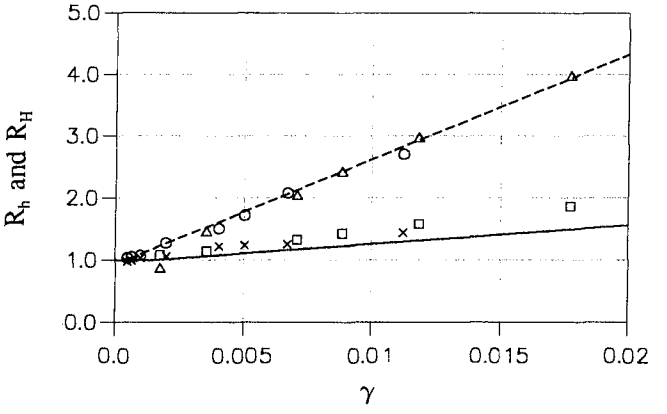

Figure 11 Relative breaker depth and relative breaker height as function of the parameter γ. Lines show formulas by Sakai et al. (1988), (- - -) R_h and (——) R_H; Markers show calculation with Model II, (○) R_h for q=0.0169 m^2/s, (Δ) R_h for q=0.0297 m^2/s; (×) R_H for q=0.0169 m^2/s and (□) R_H for q=0.0297 m^2/s.

agreement with measurements are quite good, while the relative breaker height seems to be overestimated.

Acknowledgements

This research was funded by the Danish National Research Foundation and their support is greatly appreciated. Many thanks to Peter Kjeldsen who contributed to the work concerning waves in an opposing current.

REFERENCES

Arcilla, A.S., Roelvink, J.A., Connor, B.A., Reiners, A. and Jimenez, J.A. (1994), The Delta flume '93 experiment", Proc. Coastal Dynamics Conf., UPC, Barcelona, pp. 488-502.

Cox, D.T., Mase, H. and Sakai,T. (1991), An experiment on the effect of fluid acceleration on seabed stability. Report no. 91-HY-01, Kyoto University, Japan.

Madsen, P.A. and Schäffer, H.A. (1998a). Higher order Boussinesq-type equations for surface gravity waves - Derivation and analysis. Phil. Trans. Roy. Soc., Series A, London, Vol 356,1-59.

Madsen, P.A. and Schäffer, H.A. (1998b), A Review of Boussinesq-type equations for surface gravity waves. In Advances in Coastal and Ocean Engineering, Vol 5., World Scientific.

Madsen, P.A., Sørensen , O.R. and Schäffer H.A. (1997a), Surf zone dynamics by a Boussinesq type model. Part I. Model description and cross-shore motion of regular waves, Coastal Eng., 32, 255-287.

Madsen, P.A., Sørensen , O.R. and Schäffer H.A. (1997b), Surf zone dynamics by a Boussinesq type model. Part II. Surf beat and swash oscillations for wave groups and irregular waves, Coastal Eng., 32, 289-319.

Madsen, P.A., Banijamali, B., Schäffer, H.A. and Sørensen, O.R. (1996), Higher Order Boussinesq Type Equations with Improved Dispersion and Nonlinearity, Proc. 25nd Int. Conf. Coastal Eng., Florida, USA, pp. 95-108.

Madsen, P.A., and Sørensen, O.R (1992), A new form of the Boussinesq equations with improved linear dispersion characteristics. Part II. Coastal Eng., Vol 18, 183-204.

Sakai, S. Hirayama, K. and Saeki, H. (1988), A new parameter for wave breaking with opposing current on a sloping sea bed, Proc. 21st Conf. Coastal Eng., Spain, pp. 1035-1044.

Sakai S. and Saeki H., Effects of opposing current on wave transformation on sloping sea bed, Proc. 19th Conf. Coastal Eng., Texas, USA, pp. 1132-1148.

Sakai S., Otsuka, Saeki H. and Ozaki A. (1981), Interaction between finite amplitude waves and opposing currents on sloping sea bed, Proc. International Symposium on Hydrodynamics, Norwegain Institute of Technology, Tronheim, Norway.

Schäffer, H.A., Madsen, P.A. and Deigaard, R. (1993), A Boussinesq model for waves breaking in shallow water, Coastal Eng., 20, 185-202.

Sørensen , O.R., Schäffer H.A. and Madsen, P.A. (1998), Surf zone dynamics by a Boussinesq type model. Part III. Wave induced horizontal nearshore circulations, Coastal Eng., 33, 155-176.

Ting, F.C.K and Kirby, J.T. (1994), Observation of undertow and turbulence in a laboratory surf zone. Coastal Eng., 24, 51-80.

A 2D MODEL OF WAVES AND UNDERTOW IN THE SURF ZONE

Brian A. O'Connor[1], Shunqi Pan[1], John Nicholson[1], Neil MacDonald[1] and David A. Huntley[2]

Abstract

This paper describes the details of a 2D model of waves and undertow in the surf zone. The model uses an assumed shape of the undertow velocity profile together with the wave energy equation, surface and near-bed shear stresses and the mass flux balance due to the wave drift, surface roller and undertow velocity to compute the cross-shore wave development, surface set-up/set-down and the vertical distribution of the undertow velocity at cross-shore sections. The numerical model has been tested against both laboratory and field data and produces good agreements.

INTRODUCTION

The wave period-averaged horizontal cross-shore velocity in the surf zone (known as the *undertow*) is of great importance to hydrodynamic and morphodynamic studies in this area, as it controls the on-off shore sediment transport. The undertow structure is characterized by a two-dimensional circulation in the vertical plane, which has an offshore component near the bed. This flow, which is driven by the shear stresses induced by the waves and water surface slope (set-up/down), and also by the roller in the breaker zone, contributes to the flux balance in conjunction with the wave drift and the roller in the breaker zone. Aspects of the undertow flow have been studied by many researchers, such as Stive and Wind (1982) for radiation stress and surface elevation; Svendsen (1984a) for wave height predictions; Svendsen (1984b) for mass flux and the undertow pattern; Deigaard et al (1991), Fredsøe & Deigaard (1992), Deigaard (1993) for the shear stress and turbulence distributions in the surf zone and Cox and Kobayashi (1997) and Dean (1998) for the undertow velocity profile. However, difficulty has been experienced in computing wave heights, shear stresses, water surface slope and undertow velocity

[1] Department of Civil Engineering, The University of Liverpool, Liverpool, L69 3BX, UK
[2] Institute of Marine Studies, University of Plymouth, Plymouth, PL4 8AA, UK

together using a single simple model. It was also found that the determination of the water surface slope was particularly difficult due to its significant effect on the computation of the undertow velocity profile and the mass flux balance at each cross-shore section.

During project CSTAB (O'Connor, 1996), which was a Liverpool University co-ordinated multi-disciplinary research project involving 10 institutes under the European Community MAST 2 Programme for examining the coastal processes on the Flemish Banks near Middelkerke and the adjacent coastline at Nieuwpoort, a 2D hydrodynamic and sediment transport model was developed to compute the wave decay, undertow flow and sediment transport in the surf zone. The hydrodynamics in the model was based on the solution of the wave energy equation, the force balance due to the shear stresses and the mass flux balance in the water column with an assumed shape of the undertow velocity profile. This paper describes details of the hydrodynamic model as well as the results of model tests against laboratory data (Stive and Wind, 1982; Kraus and Smith, 1994; Dette et al, 1994) and field data (O'Connor, 1996).

THEORY AND METHODOLOGY

Figure 1 shows the hydrodynamics associated with a typical beach profile with incident wave characteristics ($\mathbf{H_0}$ and $\mathbf{T}$) and initial bed level information ($\mathbf{Zb}$), where $\mathbf{x}$ =

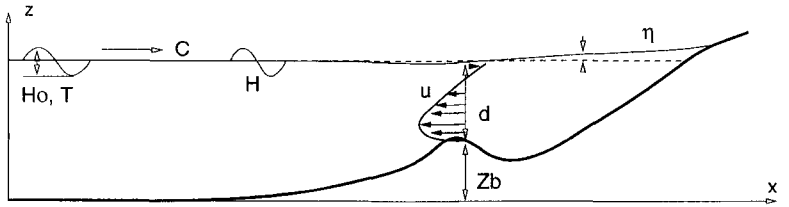

Figure 1 Schematic diagram of cross-shore hydrodynamics

shorewards coordinate; $\mathbf{z}$ = vertical coordinate and η = water surface elevation relative to the mean water level. The computation of the wave height in the cross-shore direction can be carried out using a one-dimensional wave energy equation together with an energy dissipation equation. However, the computed wave height is not correct unless the correct water surface slope is used. Therefore, additional conditions are needed in computing the surface elevation. It was found that by assuming a particular undertow velocity distribution over the flow depth, use could be made of the relations between the undertow

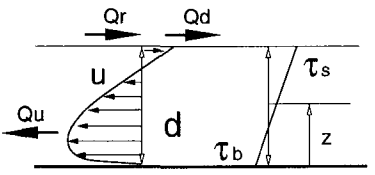

Figure 2 Undertow velocity and shear stress distributions in the water column

velocity profile, the surface and near-bed shear stresses and the mass flux balance through the water column due to the wave drift, surface roller and undertow velocity to solve the problem (see Figure 2). The following sections describe details of the new approach.

1) Wave energy equation

To compute the wave height distribution in the cross-shore direction (see Figure 1), the following one-dimensional wave energy equation (Fredsøe & Deigaard, 1992) was used:

$$\frac{dE_f}{dx} = -\breve{D} \tag{1}$$

where $\mathbf{E_f}$ = wave energy flux; $\mathbf{x}$ = cross-shore distance and $\breve{\mathbf{D}}$ = energy dissipation rate. In the breaker zone, the energy dissipation rate is calculated based on the energy loss in a hydraulic bore, which can be expressed as follows:

$$\breve{D} = \frac{1}{T}\rho g d\left(\frac{H^3}{4d^2 - H^2}\right) \tag{2}$$

where $\mathbf{d}$ = water depth; ρ = water density; $\mathbf{g}$ = acceleration of the gravity; $\mathbf{H}$ = wave height; $\mathbf{T}$ = wave period. For non-breaking waves, the wave energy dissipation due to the bed shear was taken into consideration. However the energy dissipation for non-breaking waves is rather small by comparison with the conditions produced by breaking waves.

2) Surface and near-bed shear stresses

The wave period-averaged shear stresses at the water surface and near the sea bed in the surf zone contain contributions from the wave motion, the surface roller and the water surface slope. In the present model, expressions for the surface and near-bed shear stresses given by Deigaard (1993) were used:

$$\frac{\tau_s}{\rho} = -\frac{g}{8C}\frac{\partial(H^2C)}{\partial x} - \frac{\partial}{\partial x}\left[\frac{AC}{T}\right] \tag{3}$$

$$\frac{\tau_b}{\rho} = -\frac{3g}{16}\frac{\partial(H^2)}{\partial x} - \frac{\partial}{\partial x}\left[\frac{AC}{T}\right] - gds \tag{4}$$

where τ_s = wave period-averaged shear stress at the water surface; τ_b = wave period-averaged shear stress near the sea bed; s = wave period-averaged surface slope; A = roller area given by $A = 0.9H^2$.

3) Mass fluxes

In the surf zone, mass transport occurs due to the wave drift, streaming and the surface roller if the waves are broken. By neglecting the flux due to the streaming, the fluxes due to wave drift and the surface roller can be expressed respectively as follows (Fredsøe & Deigaard, 1992):

$$Q_d = \frac{\pi H^2}{4T} \frac{1}{\tanh(kd)} \tag{5}$$

$$Q_r = \frac{A}{T} \tag{6}$$

where **k** = wave number.

4) The vertical distribution of undertow velocity

Theoretical and experimental results suggest that the undertow velocity profile in the vertical direction can be described by the following equation:

$$u = a\left(\frac{z - z_0}{d}\right)^2 + b\ln\left(\frac{z}{z_0}\right) \tag{7}$$

where u = horizontal undertow velocity; z = vertical coordinate measured upwards from the bed; z_0 = height where the velocity is zero; a and b are arbitrary constants. It can be seen that the undertow velocity consists of two parts: a parabolic distribution representing the upper part of the flow and a logarithmic distribution representing the lower part of the flow. The assumed undertow profile was also confirmed by recent laboratory work of Cox and Kobayashi (1997).

By relating the assumed undertow velocity profile (Eq. 7) gradient to the surface and near-bed shear stresses and balancing the mass flux due to undertow with the mass fluxes due to the wave drift and the surface roller, the following expressions can be obtained:

$$\tau_s / \rho = \nu_s \frac{\partial u}{\partial z}\Big|_{z=d} \quad \Rightarrow f_1(a,b,s)=0 \tag{8}$$

$$\tau_b / \rho = \nu_b \frac{\partial u}{\partial z}\Big|_{z=z_0} \quad \Rightarrow f_2(a,b,s)=0 \tag{9}$$

$$Q_u = \int_{z_0}^{d} u\,dz = Q_d + Q_r \quad \Rightarrow f_3(a,b,s)=0 \tag{10}$$

Solving Equations 8, 9 and 10 gives the constants a and b and the water surface slope **s**. The mean water depth determined by the surface slope is then returned to the wave energy equation (Eq. 1) to give a better estimate of the wave height. The whole process is then repeated until a converged water surface is obtained. The flow diagram of the model is shown in Figure 3.

NUMERICAL MODELLING

A finite difference method was used to solve wave energy equation (Eq. 1). The wave height was computed at each node point in the cross-shore direction, while the undertow velocity profile was computed mid-way between the node points (in the cell). Saturation wave breaking criteria were used in the computation without considering the wave breaking transition length. In order to increase the resolution of the undertow velocity near the bed, a non-uniform vertical grid system was adopted with a finer grid size near the bed and a coarser grid size near the water surface.

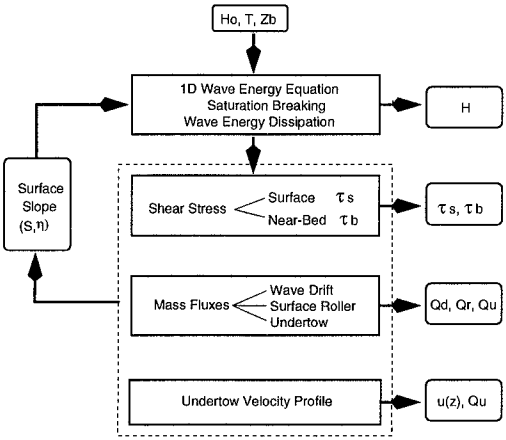

Figure 3 Flow diagram of the model

The eddy viscosities at the water surface and near the sea bed, which are needed in Eq. 8 and Eq. 9 were computed by a mixing length approach so that:

$$\nu = l_{mix} u_* \tag{11}$$

where, l_{mix} = mixing length; u_* = shear velocity ($u_* = \sqrt{\tau/\rho}$). The mixing length increases linearly from zero at the bed up a maximum value of 0.19d at a particular level and remains constant at the higher level (Fredsøe & Deigaard, 1992).

RESULTS

The model was tested against prototype-scale laboratory and field data for the water surface set-up/down, wave height and undertow velocity. The test results involved laboratory data collected by Stive and Wind (1982), Kraus and Smith (1994) in Supertank and Dette et al (1992) in the Large Wave Flume at Hannover University, as well as field data measured at Nieuwpoort beach on Belgian coast (O'Connor, 1996). It should be noted that the laboratory test cases involved monochromatic waves with normal incidence.

1) Stive and Wind (1982) data

The experimental data used in the model were obtained from tests conducted in a wave flume at the Delft Hydraulics Laboratory. The wave flume was 55 m long, 1 m wide and 1 m deep. The bed slope was 1:40 and the water surface elevation was measured by conductivity-type wave gauges. The wave height was 0.159 m with 1.79 s period and the offshore water depth was 0.7 m.

Figure 4 shows a comparison of the computed and measured surface elevations with an exaggerated scale of the water depth for the purpose of clarity. The model results agree well with measurements and the breaking point was also predicted satisfactorily.

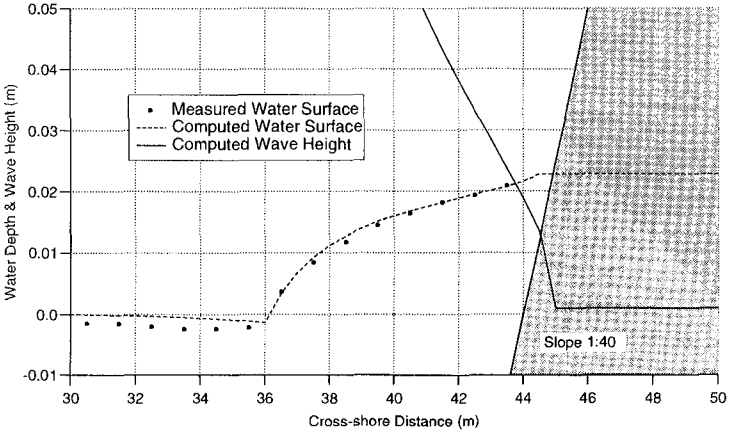

Figure 4 Computed and measured surface elevation for Stive and Wind (1982) data

2) Supertank data (Kraus and Smith, 1994)

The Supertank Data Collection Project (Kraus and Smith, 1994) was conducted in a large wave flume 104 m long, 3.7 m wide and 4.6 m deep at Oregon State University. Among 20 major data collection runs, ST_G0 was a case with monochromatic waves (normal incidence). The incident wave height was 0.8 m, the wave period was 3.0 s and offshore water depth was 4.0 m.

The numerical model was run with 146 grid points and a step size of 0.61 m (2 feet), which covered a total length of 91.38 m (300 feet). Five data sets measured at various stages of this run were used to validate the model, two of which are presented in this paper; the other data sets are in similar accuracy to those presented herein.

Figures 5 and 6 show comparisons between computed and measured wave heights and undertow velocities respectively for Case S0414a. In this case, a nearshore bar was in an early stage of its development. The results given in Figure 5 show that the model produces good agreement for the wave height; the breaking point is also well predicted. However, only few measurement points were available for use in the comparison of the undertow velocity. Figure 6 shows general agreement of the computed undertow with the

measurements, but discrepancies can be seen, particularly in the areas near the bar and break point.

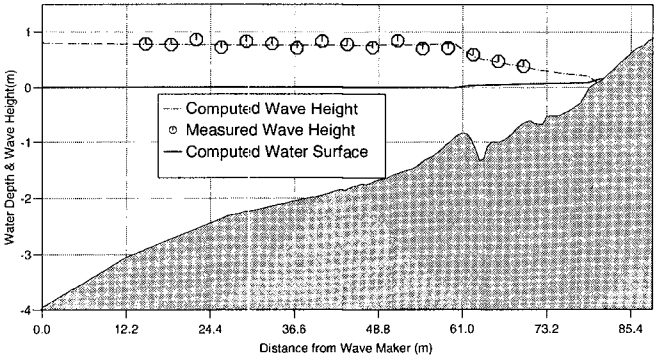

Figure 5 Computed and measured wave heights for Supertank data (Case S0414a)

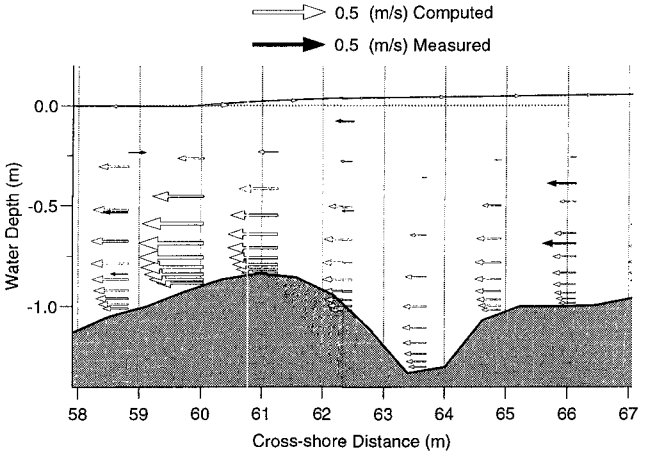

Figure 6 Computed and measured undertow velocities for Supertank data (Case S0414a)

Figures 7 and 8 show comparisons between the computed and measured wave heights and undertow velocities respectively for Case S0418a. In this case, the bar was further developed compared with Case S0414a. Again, the computed wave heights shown in Figure 7 are in good agreement with the measurements and the position of the break point

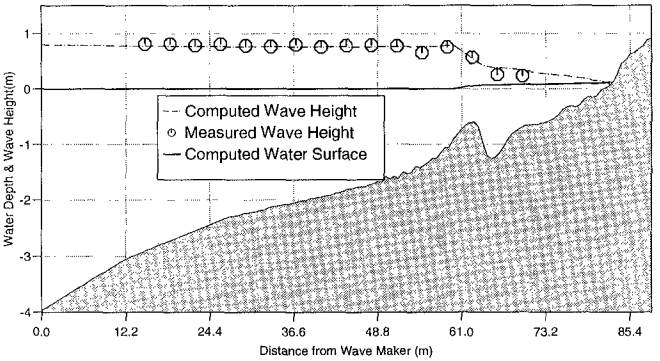

Figure 7 Computed and measured wave heights for Supertank data (Case S0418a)

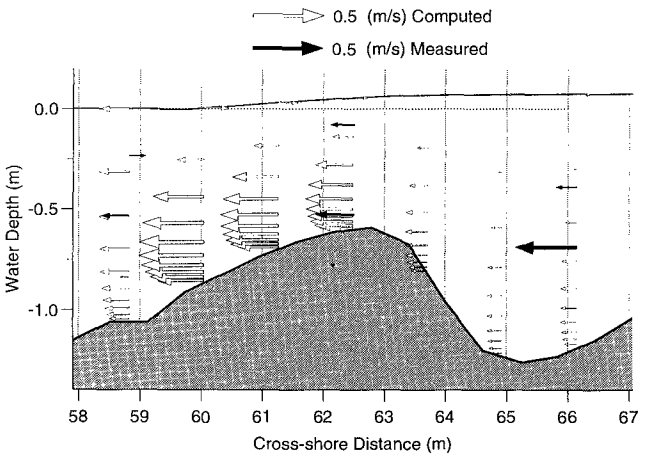

Figure 8 Computed and measured undertow velocities for Supertank data (Case S0418a)

was predicted well. Similarly to the previously mentioned case, the undertow velocity computed by the model shown in Figure 8 agrees reasonably with the experimental data. Discrepancies between the computed and measured undertow velocities for both cases landwards of the bar are believed to be due to a vortex generated by plunging breakers. The present model is not capable of predicting undertow velocities in such detail. In Figures 6 and 8, the computed undertow is found to be in the opposite direction from that of the measurements at the measuring points near the surface offshore of the bar. This may be due to these measuring points being partially exposed to the air within the wave period leading to spurious wave period-averaged velocity measurements.

3) Large Wave Flume data (Dette et al, 1992)

Prototype-scale experiments were carried out in the Large Wave Flume in Hannover University in 1990 (Test series I) and 1991 (Test series II) (Dette et al, 1992) in a flume 320 m long, 5 m wide and 7m deep. One case (16109001) in Test Series I (1990) with monochromatic waves was used in the model test. The incident wave height was 0.7 m with a 4.0 s wave period. The offshore water depth was 2.0 m. The computations were carried out with 1 m grid size.

Figure 9 shows comparisons of the computed and measured wave heights and surface elevations. Good agreement is obtained for the surface elevation and the wave break point is also well predicted. The computed wave heights also agree well with the measured results, except the wave height at the point nearest to the shore. The reason for this discrepancy is unclear, but it could be due to downwash effects. It may also be due to long wave effects as described in recent investigations by Kamphuis (1998).

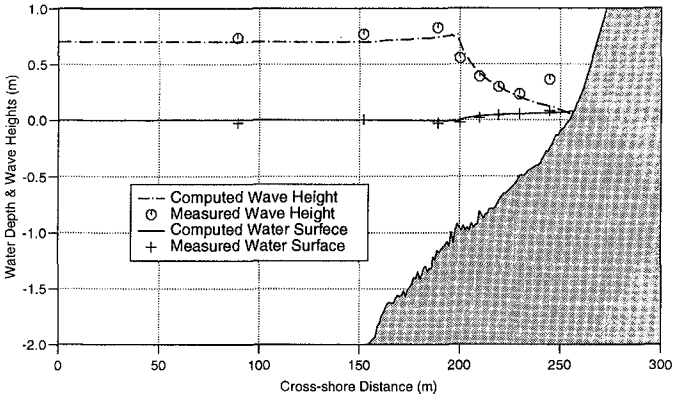

Figure 9 Computed and measured wave heights and surface elevations for Large Wave Flume data (16109001)

4) Field data - Nieuwpoort Beach (O'Connor, 1996)

Field data had been obtained during the CSTAB Project which took place on Nieuwpoort Beach, off the Belgian coast (O'Connor, 1996). As the present model is limited to dealing with monochromatic waves, the root-mean square value of wave height was used as a first approximation to the random waves measured on site. The following wave parameters were used in the model test for the field data: root-mean square wave height was 0.7 m, mean wave period was 4. 0 s and offshore wave depth was 4.33 m. The computation was carried out with 1.0 m grid size.

Figure 10 shows a comparison of computed and measured wave heights. The results once again demonstrate that the model predicts the wave height satisfactorily. Realistic undertow velocities have also been obtained, but are not shown here, see O'Connor (1996).

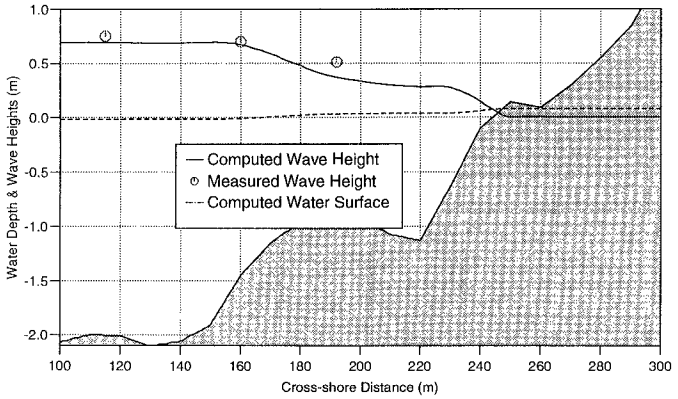

Figure 10 Computed and measured wave heights at Nieuwpoort beach

CONCLUSIONS

A 2D wave and current model has been developed to compute the wave decay, water surface slope and the undertow velocity distribution in the surf zone. Results produced by the model show good agreement as regards both wave height and water surface elevation against the laboratory and field data. The undertow flow structure was also reasonably reproduced by the model. This model provides a simple and practical method for engineers to predict the wave characteristics and hydrodynamics in the surf zone.

ACKNOWLEDGEMENTS

This work was undertaken as a part of the MAST2 CSTAB and MAST3 INDIA research projects funded by European Commission's Directorate General for Science, Research and Development under Contracts MAS2-CT92-0024 and MAS3-CT97-0106

APPENDIX. REFERENCES

Cox, D. T. and Kobayashi, N. (1997), "Kinematic undertow model with logarithmic boundary layer", J. of Waterway, Port, Coastal, and Ocean Engineering, Vol. 123, No 6, pp. 354-360

Dean, R. G. (1998), "Cross-shore sediment transport processes" in "*Coastal processes with engineering applications*" by R. G. Dean and R. A. Dalrymple (Draft), pp. 159-220

Deigaard, R. (1993), "A note on the three-dimensional shear stress distribution in surf zone", Coastal Eng., Vol 20, pp.157-171

Deigaard, R., Justeen, P. and Fredsøe, J. (1991), "Modelling of undertow by a one-equation turbulence model", Coastal Eng., Vol. 15, pp.431-459

Dette, H. H., Rahlf, H., Wu, Y. and Peters, K. (1992), "Wave measurements across the surf zone at equilibrium beach profile", LWI Report No. 762, Technical University Braunschweig.

Fredsøe, J. and Deigaard, R. (1992) "Mechanics of coastal sediment transport", World Scientific, Singapore

Kamphuis, J. W. (1998), "The effect of long waves on flume experiments", Paper No. 32, Book of Abstracts, 26th ICCE, Copenhagen, Denmark, pp. 64-65

Kraus, N. C. and Smith, J. M., (1994), SUPERTANK Laboratory Data Collection Project, Technical Report CERC-94-3, Coastal Engineering Research Centre, WES, US Army Corp. of Engineers

O'Connor, B. A. (1996), "CSTAB Handbook and Final Report", Report No. CE/05/96, Dept. of Civil Engineering, The University of Liverpool

Stive, M. J. F. and Wind, H. G., (1982), "A study of radiation stress and set-up in the nearshore region", Coastal Eng., Vol 6, pp. 1-25

Svendsen, I. A. (1984a), "Wave heights and set-up in a surf zone", Coastal Eng., Vol. 8 (4), pp.303-330

Svendsen, I. A. (1984b), "Mass flux and undertow in a surf zone", Coastal Eng., Vol. 8 (4), pp.331-346

Field Measurements of Undertow on Longshore Bars

Yoshiaki KURIYAMA[1]

Abstract

Field measurements of undertow over longshore bars were conducted at Hazaki Oceanographical Research Station (HORS) on the Kashima coast of Japan facing the Pacific Ocean. The field measurements, other field measurements and large-scale experiments were compared with one-dimensional models for undertow; one of them was developed in this study. The comparisons showed that the present model well predicted the undertow velocities over longshore bars in the field, while a previous model calibrated with small-scale experiment data underestimated the velocities.

1. Introduction

The prediction of undertow velocity over a longshore bar is required for predicting the deformation of the bar, which breaks waves and reduces the wave energy to protect the beach as a submerged breakwater. The undertow velocity prediction over a bar is also required for designing offshore nourishment, which has been recently developed in the United States, Australia and Europe (e.g., McLellan and Kraus, 1991); nourished sediment forms an artificial bar and the prediction of the bar movement is essential for the offshore nourishment project.

Although many models for undertow have been developed and verified with experiment data on planar beaches (e.g., Svendsen, 1984; Stive and Wind, 1986; Svendsen and Hansen, 1988; Okayasu et al. 1988; Deigaard et al., 1991; Dally and Brown, 1995), only a few models have been verified with data on barred beaches in experiments (Okayasu and Katayama, 1992; Rakha et al., 1996) and in the field (Smith et al., 1992; Haines and Sallenger, 1994). In this study, hence, field measurements of undertow were conducted over longshore bars at Hazaki Oceanographical Research Station (HORS) and compared with one-dimensional models for undertow, which predict the depth-averaged undertow velocity below the wave trough level; one of the models was developed in this

[1] Head, Littoral Drift Laboratory, Marine Environment Division, Port and Harbour Res. Inst. Ministry of Transport, Nagase 3-1-1, Yokosuka, Kanagawa 239-0826, JAPAN
E-mail: kuriyama@cc.phri.go.jp

study. The models were also compared with other data obtained over longshore bars in large-scale experiments and in the field. The purposes of this paper are to describe the field measurements at HORS and to show the comparisons of undertow velocities measured and predicted.

2. Field Measurements

Field measurements were conducted from January 29 to February 3, 1997 at HORS, which is a field observation pier of 427 m in length on the Kashima coast of Japan facing the Pacific Ocean; the location of HORS is shown in Figure 1. Cross-shore and longshore current velocities were measured with electro-magnetic current meters for thirty minutes every two hours at a sampling frequency of 5 Hz, and water surface elevations were measured with ultrasonic wave gages. Wave breaking positions and types, and the locations of rip currents were visually observed several times a day, and the beach profile along HORS has been measured daily every 5 m.

The locations of the measurement points are shown in Figure 2 with the beach profiles on January 31 and February 1; the reference level is the Hasaki datum level, which is equal to the low water level, and the tidal rage is 1.4 m. Seaward bar migration occurred on January 31, and the bar crest moved seaward about 50 m. Except for the bar migration, no significant beach profile changes occurred during the measurements. The measurement point where the seaward distance is 230 m (referred to as P230m) was located shoreward of the bar crest, while the measurement point of P290m was located seaward of the bar crest. The measurement point of P260m was located just seaward of the bar crest before the bar migration and shoreward of the bar crest after the bar migration.

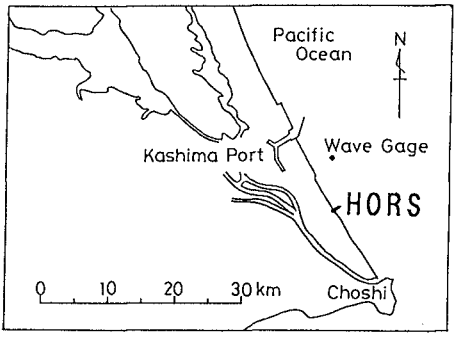

Figure 1 Location of HORS.

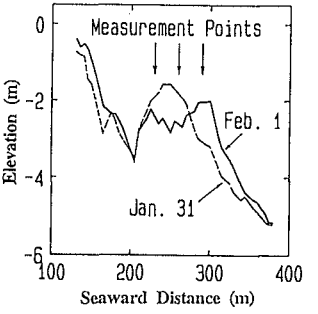

Figure 2 Locations of current meters and beach profiles on Jan. 31 and Feb. 1.

The seaward bar migration on January 31 damaged the supporting systems of the current meters at all measurement points, and current velocities were not measured temporarily. At P260m, two current meters were installed on January 29 at D.L. -0.87 m and D.L. -1.37 m, and were reinstalled on February 1 after the damage at D.L. -1.09 m and D.L. -1.59 m. At P230m, one current meter was installed at D.L. -1.99 m and reinstalled at D.L. -1.90 m. Although at P290m, a current meter was installed at D.L. -1.72 m, the supporting system of the current meter was completely destroyed at 7 a.m. on January 31, and then current velocities were not measured any more.

Figure 3 shows the time series of significant wave height $H_{1/3}$, significant wave period $T_{1/3}$ and undertow velocity V measured. The significant wave heights at the tip of HORS, where the water depth was approximately 6m, increased from 11 p.m. on January 30, reached about 2.6m at 8 a.m. on January 31, and then gradually decreased. Undertow velocities increased as the wave heights increased, and from February 1 fluctuated regardless of the wave height changes.

Nearshore currents during the measurements are considered to be uniform alongshore owing to two reasons mentioned below. First, in the visual observations conducted several times a day during the measurements, no rip currents were observed, and the breaker lines were linear alongshore. Second, the low-frequency components of cross-shore current velocities $v_{rms,l}$ (<0.04 Hz) were not related to the undertow velocities as shown in Figure

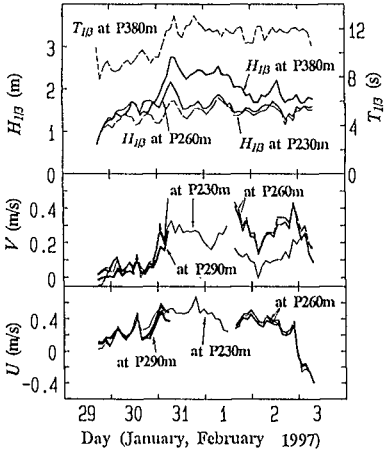

Figure 3 Time series of significant wave height $H_{1/3}$ and period $T_{1/3}$, and undertow velocity V.

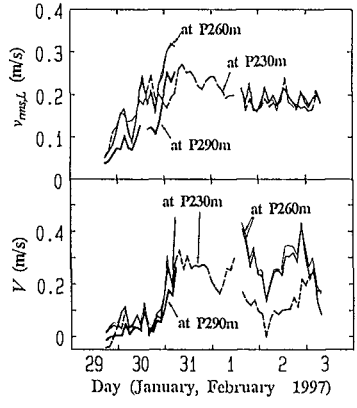

Figure 4 Time series of low-frequency component of cross-shore current velocity $v_{rms,l}$ and V.

4; the low-frequency components were relatively constant although the undertow velocities significantly changed. Some field measurements showed that rip currents were intermittent events (Wright and Short, 1983; Short, 1985, Smith and Largier, 1995), and hence the low-frequency component of cross-shore current in or near a rip current is expected to be large. The constant low-frequency components of the cross-shore currents in Figure 4 suggest that the possibility of rip current during the measurements is low.

3. Numerical Model

The one-dimensional model of undertow developed here consists of a wave transformation model and an undertow model, and adopts a wave-by-wave approach, in which wave heights and undertow velocities are calculated for individual waves. The time-averaged undertow velocity for an irregular wave group is estimated with averaging the undertow velocities of individual waves weighted according to the wave periods.

3-1 Wave transformation model

The wave transformation model is based on the model developed by Kuriyama (1996). The shoaling of a wave is estimated with a shoaling coefficient proposed by Shuto (1974) with the consideration of wave nonlinearity.

The criterion on wave breaking is based on a formula proposed by Seyama and Kimura (1988). Because Seyama and Kimura (1988) proposed the formula on the basis of experimental data, Kuriyama (1996) introduced a dimensionless coefficient C_{br} to adjust the formula to field data. The criterion is expressed by the following equation with the wave height-water depth ratio at wave breaking H_b/h_b, wavelength in deep water L_0, and beach slope $\tan\beta$, which is defined here as the average slope in the area from 15 m shoreward of the definition point to 15 m seaward of the point.

$$\frac{H_b}{h_b} = C_{br}\left[0.16\frac{L_0}{h_b}\left[1-\exp\left\{-0.8\pi\frac{h_b}{L_0}(1+15\tan^{4/3}\beta)\right\}\right]-0.96\tan\beta+0.2\right]. \quad (1)$$

Energy dissipation of a wave in the surf zone is estimated with a periodic bore model used by Thornton and Guza (1983); the model is expressed by

$$\frac{\partial E_w C_g}{\partial y} = \frac{1}{4}\rho g\frac{1}{T}\frac{(BH)^3}{h}, \quad (2)$$

where E_w is the energy of wave motion, C_g is the group velocity, ρ is the sea water density, T is the wave period, H is the wave height, h is the water depth, and B is a dimensionless coefficient determining the amount of energy dissipation. Kuriyama and Ozaki (1996) investigated the coefficient B with the experiment data of Seyama and Kimura (1988), and

proposed the following equation:

$$B = C_B\left\{1.6 - 0.12\ln(H_0 / L_0) + 0.28\ln(\tan\beta)\right\}, \tag{3}$$

where H_0 is the wave height in deep water, and C_B is a nondimensional coefficient introduced with the consideration of scale effect.

The wave height-water depth ratio at wave reforming H_r/h_r is set to be 0.35 based on field data obtained by Kuriyama and Ozaki (1996).

When a significant wave height and a period are given at an offshore boundary, a time series of water surface elevation for ten minutes having the JONSWAP type spectrum at the offshore boundary is numerically simulated with the given wave height and period. Then, with the zero-down crossing method, the time series is divided into individual waves, which are used in the calculation.

The incident directions of individual waves at the offshore boundary are determined with the given principal wave direction, the directional spreading function of Mitsuyasu-type and the spreading parameter estimated with the method of Goda and Suzuki (1975). When the spreading parameter exceeds 100, the individual waves are treated as uni-directional waves.

The root-mean-square wave height H_{rms} and the wave height H_{m0}, which are defined with the root-mean-square of water surface elevation η_{rms} by

$$H_{rms} = 2\sqrt{2}\,\eta_{rms}, \tag{4}$$

$$H_{m0} = 4.004\,\eta_{rms}, \tag{5}$$

are not directly estimated in the wave-by-wave approach. The values of H_{rms} and H_{m0}, thus, are obtained with the relationship between $H_{1/3}/\eta_{rms}$ and a dimensionless parameter $\Pi_{1/3}$, which has been propose by Goda (1983) for expressing wave nonlinearity. The parameter $\Pi_{1/3}$ is expressed by Eq.(6), and the relationship between $H_{1/3}/\eta_{rms}$ and $\Pi_{1/3}$, which has been obtained by Kuriyama (1996), is expressed by Eq.(7).

$$\Pi_{1/3} = H_{1/3} / L_{1/3}\coth^3(2\pi h / L_{1/3}). \tag{6}$$

$$\begin{aligned} H_{1/3} / \eta_{rms} &= 0.349\ln\Pi_{1/3} + 4.648, \quad \Pi_{1/3} \geq 0.1, \\ H_{1/3} / \eta_{rms} &= 3.8, \qquad\qquad\qquad\quad \Pi_{1/3} < 0.1. \end{aligned} \tag{7}$$

In all calculations in this study, to minimize the error in the prediction of undertow velocity caused by the error in the prediction of wave height, coefficients C_{br} and C_B in Eqs. (1) and (3) were determined so that the predicted significant wave heights fit the measured values.

3-2 Undertow model

Undertow velocity of an individual wave V_{ind} is estimated with the mass flux due to wave motion Q_w and that due to surface roller Q_r.

$$V_{ind} = (Q_w + Q_r) / d_{tr}, \tag{8}$$

where d_{tr} is the distance between the wave trough level and the bottom, and is obtained as $d_{tr} = h - H/2$.

The mass flux due to wave motion Q_w is calculated with the wave celerity C, the water depth h, and the root-mean-square of water surface elevation of an individual wave ζ_{rms} by the following equation proposed by Svendsen (1984).

$$Q_w = (C / h)\, \zeta_{rms}^2. \tag{9}$$

The value of ζ_{rms} is estimated with the consideration of wave nonlinearity. With the parameter Π expressing nonlinearity of an individual wave and data shown by Goda (1983), the relationship between ζ_{rms} and H was obtained; the parameter Π and the relationship obtained are expresses by

$$\Pi = H / L \coth^3(2\pi h / L), \tag{10}$$

$$\begin{aligned} \zeta_{rms} &= 1/8 H^2, && \Pi < 0.15, \\ \zeta_{rms} &= (1.668 \log \Pi + 4.204)^{-2} H^2, && 0.15 \le \Pi < 3, \\ \zeta_{rms} &= 1/25 H^2, && \Pi \ge 3. \end{aligned} \tag{11}$$

In the estimation of Q_r, the vertical distribution of the time-averaged velocity shown in the middle of Figure 5 is assumed. In previously proposed models (e.g., Svendsen, 1984), the vertical distribution shown in the left of Figure 5 is assumed; the time-average velocity in the roller is equal to C. Although just behind the front of the roller, the cross-shore velocity near the wave trough level sharply changes from shoreward velocity equal to C to

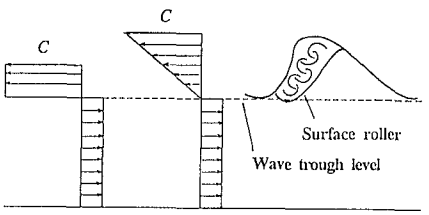

Figure 5 Vertical distribution of time-averaged cross-shore current velocity assumed.

seaward undertow velocity, the cross-shore velocity in the middle of the roller is considered to change gradually from the top to the wave trough level. Hence, the vertical distribution shown in the middle of Figure 5 is assumed in the present model, and accordingly the mass flux due to the roller is obtained from

$$Q_r = A_r C / (2L), \tag{12}$$

where A_r is the area of the roller.

The area of the surface roller is estimated on the basis of two assumptions mentioned below.

1. The area of the surface roller fully developed is proportional to H^2.
2. Up to the point where the roller is fully developed, the roller develops without energy dissipation.

When the values of A_{r1} and A_{r2} are defined to be the roller areas obtained on the basis of the assumptions No.1 and No.2, respectively, the smaller value between A_{r1} and A_{r2} is assumed to be the area of the surface roller.

Even in the developing roller, some energy is dissipated. However, the amount of energy dissipation in the developing roller is considered to be smaller than that in the developed roller because turbulence in the developing roller is not fully developed. The amount of energy dissipation in the developing roller, hence, is assumed to be zero.

The area A_{r1} is estimated with a dimensionless coefficient C_A from

$$A_{r1} = C_A H^2. \tag{13}$$

The area A_{r2} is obtained from the following energy balance equation as Okayasu et al. (1990) and Dally and Brown (1995). In Eq.(14), however, the rate of energy dissipation is set to be zero.

$$\frac{\partial (E_w C_g)}{\partial y} + \frac{\partial (E_r C)}{\partial y} = 0, \qquad E_r = \frac{1}{8}\rho C^2 \frac{A_{r2}}{L}, \tag{14}$$

where E_r is the energy of the roller having the triangle-shaped distribution of the time-averaged velocity above the wave trough level.

4. Calibration

In the present model, C_A in Eq.(13) is a key coefficient for estimating the area of the surface roller. Hence, the model was calibrated with the field data of fourteen cases

obtained at HORS from 11 p.m. on January 30 to 10 a.m. on February 2 in 1997, when the wave heights were large.

The offshore boundary was set at P600m. The beach profiles measured every day were used for those shoreward of the tip of HORS, and the beach profile surveyed on January 16, 1997 shown in Figure 6 was used for that seaward of the tip of HORS; according to Kuriyama (1996), the amount of beach profile changes seaward of the tip of HORS is considered to be small.

The wave heights at the offshore boundary were estimated from the wave data obtained at a water depth of about 23m offshore of Kashima Port; the location of the wave gage is shown in Figure 1. The wave directions at the boundary were calculated with the Snell's law from the principal wave directions at P260m.

The value of C_A optimal for all cases was 7. The value of C_A optimal in each case, on the other hand, was related to the surf similarity parameter at the wave breaking position ξ_b. The parameter ξ_b is estimated by

$$\xi_b = \tan\beta / (H_{1/3,b} / L_{1/3,0})^{1/2}, \tag{15}$$

where $H_{1/3,b}$ is the significant wave height at wave breaking position and $L_{1/3,0}$ is the offshore wavelength corresponding to the significant wave period. The value of $H_{1/3,b}$ was defined to be the maximum of the significant wave heights over a longshore bar, and was obtained from the calculation result of wave transformation. The beach slope used in Eq.(15) was the value at the point where $H_{1/3,b}$ was defined.

Figure 7 shows the relationship between C_A optimal in each case and ξ_b. There is a positive correlation between them as Deigaard et al. (1991) and Dibajnia et al. (1994) reported; the correlation coefficient is 0.61. The value of C_A increased as ξ_b increased, that is, the coefficient increased as the ratio of the plunging breaker increased.

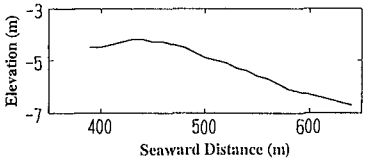

Figure 6 Beach profile seaward of the tip of HORS surveyed on Jan. 16, 1997.

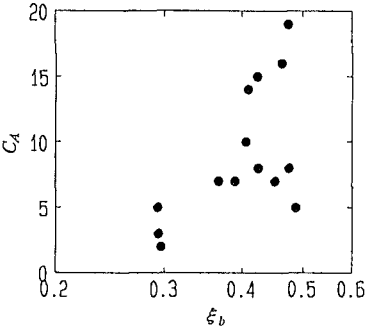

Figure 7 Relationship between C_A and ξ_b.

The relationship between C_A and ξ_b obtained with the least square method is given by

$$C_A = 17.0 \log \xi_b + 24.7. \tag{16}$$

5. Comparisons of Models with Measurements

Undertow velocities predicted with C_A give by Eq.(16) and with C_A=7 were compared with the values measured in the field. Because ξ_b in the measurements ranged from 0.3 to 0.5, the values of C_A larger than 12 and those smaller than 4 were set to be 12 and 4, respectively. The values predicted with a model that has been proposed by Stive and De Vriend (1994) and calibrated by Reneirs and Battjes (1997) were also compared with the measurements; the model will be referred to as the previous model.

Figure 8 shows comparisons for four cases of the fourteen cases used in the calibration. The significant wave heights, periods, principal wave directions θ, water depths and mean water levels $\overline{\eta}$ at the offshore boundary, and ξ_b in the four cases are listed in Table 1; the values of s_{max} at the offshore boundary exceeded 100. As shown in Figure 8, the previous model, which has been calibrated with experiment data, underestimated the undertow velocities. Both models with C_A agreed with the measurements, while the performance of the model with C_A give by Eq.(16) was better than that of the model with the constant C_A.

The root-mean-square errors defined by

$$\varepsilon = \left(\frac{\sum (V_{meas} - V_{pred})^2}{\sum (V_{meas})^2} \right)^{1/2}, \tag{17}$$

where V_{meas} and V_{pred} are the undertow velocities measured and predicted, for the fourteen cases used in the calibration were calculated for the three models. The values of ε for the previous model and the present models with C_A =7 and C_A give by Eq.(16) were 52%, 41% and 35%.

The models with C_A give by Eq.(16) and with C_A =7, and the previous model were also compared with the filed measurement of DELILAH (Smith et al., 1992) and the large-scale experiments of Delta Flume '93 (Rakha et al., 1996). The data on October 19, 1990 in DELILAH and of the cases 1-b and 1-c in Delta Flume '93 were used for the comparisons. The wave heights, periods, principal wave directions and water depths at the offshore boundaries are listed in Table 2, where T_p is the wave period at the spectral peak. The value of s_{max} exceeded 100 on October 19 in DELILAH.

Figure 9 shows a comparison of the models and the measurement DELILAH. Although the previous model underestimated the velocities, both of the models with C_A

Table 1 Offshore boundary conditions and ξ_b in measurements at HORS.

Case	$H_{1/3}$ (m)	$T_{1/3}$ (s)	θ	h (m)	$\overline{\eta}$ (m)	ξ_b
2	2.11	9.63	16.5	6.58	0.58	0.293
4	2.91	11.81	19.0	6.98	0.98	0.367
5	2.50	11.56	7.0	6.50	0.50	0.463
7	2.37	12.16	6.0	6.65	0.65	0.475

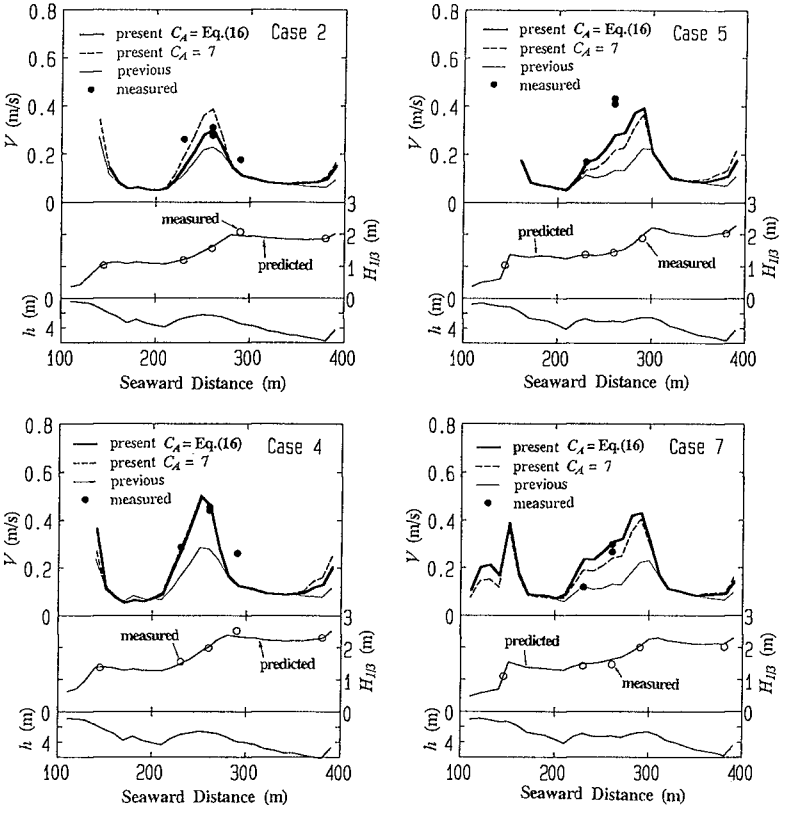

Figure 8 Comparisons of models with measurements at HORS.

Table 2 Offshore boundary conditions in DELILAH and Delta Flume '93.

Case	H_{rms} (m)	T_p (s)	θ	H (m)
Oct. 19	0.75	7	15.1	2.63

Case	H_{m0} (m)	T_p (s)	h (m)
1b	1.40	5	4.1
1c	0.60	8	4.1

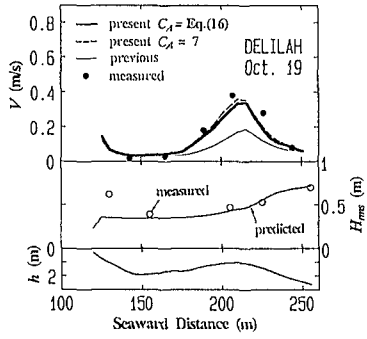

Figure 9 Comparisons of models with DELILAH measurement.

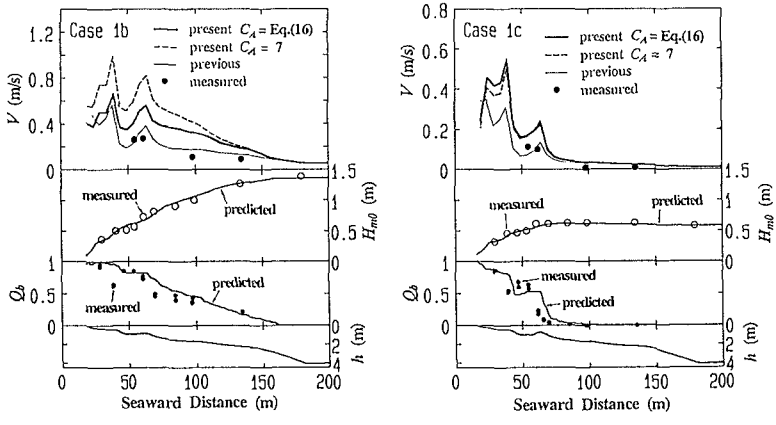

Figure 10 Comparisons of models with Delta Flume '93 experiments.

agreed with field data. Comparisons between the models and the measurements in Delta Flume '93 are shown in Figure 10. The previous model agreed with the measurements, while both models with C_A overestimated the undertow velocities. However, the performance of the model with C_A give by Eq.(16) was better than that of the model with the constant C_A.

6. Discussion

In the calibration of the present model of undertow, the time-averaged cross-shore

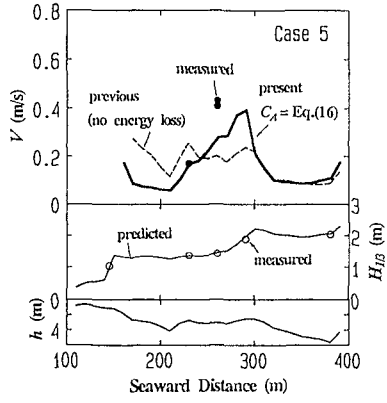

Figure 11 Comparisons of models with the measurement in Case 5 at HORS.

velocity was assumed to be vertically uniform below the wave trough level, and the undertow velocities measured with one current meter at P230m and those at P290m were used. As shown in Figures 3 and 8, differences of the undertow velocities measured with two current meters at P260m were small, and this suggests that the assumption is appropriate.

Through the comparisons between the models and the measurements, it is concluded that for predicting undertow velocities over a longshore bar in the field where water depth ranges from 1 m to 3 m, the model with C_A give by Eq.(16) was better than that with C_A=7. The previous model, on the other hand, sometimes underestimated the undertow velocities in the field. Figure 11 shows a comparison between the undertow velocities measured in case 5 at HORS and those predicted with the present model having C_A give by Eq.(16) and with a modified previous model that assumes no energy dissipation. The previous model with no energy dissipation still underestimated the undertow velocities, and this result seems to suggest that the assumption of the rectangular-shaped distribution of time-averaged velocity above the wave trough level, shown in the left of Figure 5, is inappropriate. The previous model, however, has good agreements against experiment data (e.g., Dally and Brown, 1995). The discrepancy seems to be attributed to scale effect; size of vortex and the development of the surface roller in the field are considered to be different from those in small-scale experiments. For developing a model applicable to a wide range of conditions, from a small-scale experiment to the field, further improvement of the models and calibrations with a wide range of data would be required.

7. Conclusion

Field measurements of undertow were conducted over longshore bars at Hazaki Oceanographical Research Station (HORS), and the field data were used for the calibration of the one-dimensional model developed in this study. The calibration showed that the parameter C_A, which is the ratio of the area of the surface roller fully developed to the square of the wave height, had a positive correlation with the surf similarity parameter at the wave breaking position; the correlation is expressed by Eq.(16).

The field measurements, other field measurements and large-scale experiments were compared with one-dimensional models for undertow. The comparisons showed that the present model with C_A given by Eq.(16) well predicted the undertow velocities over the longshore bars, while a previous model calibrated with small-scale experiment data underestimated the velocities.

Acknowledgement

The author would like to thank Mr. Toshiyuki Nakatsukasa for helping the field measurements at HORS.

References

Deigaard, R., Justesen, P. and Fresoe J. (1991): Modelling of undertow by a one-equation turbulence model, *Coastal Eng.*, 15, pp.431-458.

Dibajnia, M., Shimizu, T. and Watanabe, A. (1994): Profile change of a sheet flow dominated beach, *Proc. 24th Coastal Eng. Conf.*, ASCE, pp.1946-1960.

Dally, W.R. and Brown, C.A. (1995): A modeling investigation of the breaking wave roller with application to cross-shore currents, *J. Geophys. Res.*, Vol.100, No.C12, pp.24873-24883.

Goda, Y. and Suzuki, Y. (1975): Computation of refraction and diffraction of sea waves with Mitsuyasu's directional spectrum, *Tech. Note Port and Harbour Res. Inst.*, No.230, 45p. (*in Japanese*)

Goda, Y. (1983): A unified nonlinearity parameter of water waves, *Rep. Port and Harbour Res. Inst.*, Vol.22, No.3, pp.3-30.

Haines, J.W. and Sallenger, A.H., Jr. (1994): Vertical structure of mean cross-shore currents across a barred surf zone, , *J. Geophys. Res.*, Vol.99, No.C7, pp.14223-14242.

Kuriyama, Y. and Ozaki, Y. (1996): Wave height and fraction of breaking waves on a bar-trough beach -Field measurements at HORS and modeling-, *Rep. Port and Harbour Res. Inst.*, Vol.35, No.1, pp.1-38.

Kuriyama, Y. (1996): Models of wave height and fraction of breaking waves on a barred beach, *Proc. 25th Coastal Eng. Conf.*, ASCE, pp.247-260.

Kuriyama, Y. (1996): Short-term cross-shore movements of longshore bars, *Proc. Coastal Eng.*, JSCE,

Vol.43, pp.576-580. (*in Japanese*)

McLellan, T.N. and Kraus N.C. (1991): Design guidance for nearshore berm construction, *Coastal Sediments* '91, ASCE, pp.2000-2011.

Okayasu, A., Shibayama, T., and Horikawa, K. (1988): Vertical variation of undertow in the surf zone, *Proc. 21st Coastal Eng. Conf.*, ASCE, pp.478-491.

Okayasu, A., Watanabe, A. and Isobe, M. (1990): Modeling of energy transfer and undertow in the surf zone, *Proc. 22nd Coastal Eng. Conf.*, ASCE, pp.123-135.

Okayasu, A. and Katayama, H. (1992): Distribution of undertow and long-wave component velocity due to random waves, *Proc. 23rd4 Coastal Eng. Conf.*, ASCE, pp.883-893.

Rakha, K.A., Deigaard, R., Madsen, P.A., Brøker, I. and Rønberg, J.K. (1996): Simulation of coastal profile development using a Boussinesq wave model, *Proc. 25th Coastal Eng. Conf.*, ASCE, pp.3048-3061.

Reniers, A.J.H.M. and Battjes, J.A. (1997): A laboratory study of longshore currents over barred and non-barred beaches, *Coastal Eng.*, 30, pp. 1-22,

Seyama, A. and Kimura, A. (1988): The measured properties of irregular wave breaking and wave height change after breaking on the slope, *Proc. 21st Coastal Eng. Conf.*, ASCE, pp.419-432.

Short, A.D. (1985): Rip-current type, spacing and persistence, Narrabeen Beach, Australia, *Marine Geology*, 65, pp.47-71.

Shuto, N. (1974): Nonlinear long waves in a channel of variable section, *Coastal Eng. Japan*, Vol.17, pp.1-12.

Smith, J.A. and Largier, J.L. (1995): Observations of nearshore circulation: Rip currents, *J. Geophys. Res.*, Vol.100, No.C6, pp.10967-10975.

Smith, J.M., Svendsen, I.A. and Putrevu, U. (1992): Vertical structure of the nearshore current at DELILAH: Measured and modeled, *Proc. 23rd Coastal Eng. Conf.*, ASCE, pp.2825-2838.

Stive, M.J.F. and Wind, H.G. (1986) : Cross-shore mean flow in the surf zone, *Coastal Eng.*, 10, pp.325-340.

Stive, M.J.F. and De Vriend, H.J. (1994): Shear stresses and mean flow in shoaling and breaking waves, *Proc. 24th Coastal Eng. Conf.*, ASCE, pp.594-607.

Svendsen, I.A. (1984): Mass flux and undertow in a surf zone, *Coastal Eng.*, 8, pp.347-365.

Svendsen, I.A. and Hansen, J.B. (1988) : Cross-shore currents in surf-zone modelling, *Coastal Eng.*, 12, pp.23-42.

Thornton, E.B. and Guza, R.T. (1983): Transformation of wave height distribution, *J. Geophys. Res.*, Vol.88, No.C10, pp.5925-5938.

Wright, L.D. and Short, A.D. (1983): Morphodynamics of beaches and surf zones in Australia, *CRC Handbook of Coastal Processes and Erosion*, edited by Komar, D., CRC Press Inc., pp.35-64.

Application of an Undertow Model to Irregular Waves on Barred Beaches

Douglas L. Kennedy[1], Daniel T. Cox[2] and Nobuhisa Kobayashi[3]

ABSTRACT: An undertow model calibrated for regular waves on plane beaches is applied to predict the irregular wave induced undertow for both plane and barred beaches and for both laboratory and field data sets. The model combines a logarithmic profile in the bottom boundary layer with a conventional parabolic profile in the interior. The height and period of the irregular waves are represented by the local root-mean-square wave height and spectral peak period, and the measured mean volume flux below trough level is used as input to the model. The model is capable of predicting the undertow profiles both inside and outside the surf zone, provided that the empirical coefficient associated with the mean bottom shear stress is adjusted at each measuring line. The model appears to give reasonable predictions of the bottom boundary layer thickness and shear velocity, although these predictions could not be verified due to a lack of data. To develop a predictive undertow model, a simple relationship with an adjustable coefficient is applied to predict the measured volume flux below trough level using the local wave height and water depth. The calibration coefficients involved in the predictive model are not universal among the lab and field conditions possibly due to the effects of wave directionality and longshore currents in the field measurements which are neglected in this paper.

INTRODUCTION

Detailed sediment transport models require accurate prediction of the cross-shore currents or undertow. Most undertow models are based on the time-averaged, cross-shore momentum equation and are verified primarily with laboratory measurements of the undertow induced by regular waves breaking on smooth, plane slopes. Cox and Kobayashi (1996) showed the difficulties inherent in standard undertow models, including the difficulties in obtaining reliable estimates of all the terms in the time-averaged, cross-shore momentum equation. Furthermore, some of these models give no estimate of the undertow in the bottom boundary layer or the mean bottom shear stress. Recently, Cox

[1]Graduate Student, Div. of Coastal and Ocean Engrg., Dept. of Civil Engrg., Texas A&M Univ., College Station, TX 77843-3136.

[2]Asst. Prof., Div. of Coastal and Ocean Engrg., Dept. of Civil Engrg., Texas A&M Univ., College Station, TX 77843-3136; Email: dtc@arlo.tamu.edu

[3]Prof. and Assoc. Dir., Center for Applied Coastal Res., Univ. of Delaware, Newark, DE 19716.

and Kobayashi (1997) developed a new undertow model without relying on the time-averaged momentum equation. They calibrated and verified the model using laboratory data of regular waves breaking on rough and smooth plane slopes. The model was found to give accurate predictions of the undertow profiles inside and outside the surf zone, provided that the empirical coefficient associated with the mean bottom shear stress was calibrated at each measuring line.

This paper extends their work by applying the model to predict undertow induced by irregular waves breaking over plane and barred beaches using both laboratory and field data. Additionally, this paper shows how the mean volume flux below trough level, which is an input to the model, may be predicted from the local root-mean-square wave height and water depth. This paper is organized as follows. The model is briefly summarized, and the data sets used for comparison are discussed. Comparisons are then presented for undertow profiles and the mean volume flux below trough level along with a discussion of the calibration coefficients and model sensitivity. The performance of the model is summarized at the end with a discussion of the implications of the coefficients.

UNDERTOW MODEL

The undertow model was presented in detail in Cox and Kobayashi (1997) and is summarized herein to facilitate the comprehension of the subsequent comparisons. The model combines a conventional parabolic profile in the interior with a logarithmic profile in the bottom boundary layer. The undertow $\overline{u}$ from the bottom to trough level is expressed as

$$\overline{u} = \frac{\overline{u_*}}{\kappa} \ln\left(\frac{z_b}{z_0}\right) \quad \text{for} \quad z_0 \le z_b \le \delta \tag{1}$$

and

$$\overline{u} = \overline{u}_b + \alpha {z_b}^2 \quad \text{for} \quad \delta < z_b \le d_t \tag{2}$$

where $\overline{u_*}$ = mean shear velocity; κ = von Kármán constant, taken as $\kappa = 0.4$ in this paper; z_0 = bottom roughness height; z_b = vertical coordinate above the bottom, positive upward with $z_b = 0$ on the bottom; $\overline{u}_b$ = hypothetical undertow velocity in the absence of the boundary layer; δ = boundary layer thickness; d_t = water depth below trough level; and α = dimensional coefficient to be expressed in terms of the physical variables.

For smooth slopes typical of laboratory experiments, the roughness height is specified as $z_0 = \nu/(9\,\overline{u_*})$ based on unidirectional flow where ν is the kinematic viscosity. For rough slopes in the absence of bed forms, $z_0 = 2\,d_{50}/30$ based on the analysis of regular waves breaking on a plane, rough slope where d_{50} is the median grain diameter. Estimates of z_0 for the field data are more difficult due to the presence of ripples and megaripples and are explained later.

An expression for the mean shear velocity $\overline{u_*}$ in (1) is developed using the quadratic friction equation for the temporal variation of the bottom shear stress τ_b given by

$$\tau_b = \frac{1}{2}\rho f_b |u_b| u_b \tag{3}$$

where ρ = fluid density; f_b = constant bottom friction factor; and u_b = instantaneous horizontal velocity at the bottom in the absence of the boundary layer. For normally

incident regular waves, u_b may be expressed as a sum of the sinusoidal wave component and the mean component $\overline{u}_b$ and is given as

$$u_b = U_b \cos(kx - \omega t) + \overline{u}_b \tag{4}$$

where k = local wave number; x = horizontal coordinate, positive onshore; ω = angular wave frequency; and t = time. The amplitude U_b of the wave component in (4) is based on linear wave theory and is given as (e.g., Jonsson, 1966)

$$U_b = \frac{H\,\omega}{2\,\sinh(k\overline{h})} \tag{5}$$

where H = local wave height, and $\overline{h}$ = local water depth including the setup. Substituting (4) into (3) and taking the time-average with the assumption of a small current $(\overline{u}_b/U_b)^2 << 1$, the mean bottom shear stress $\overline{\tau}_b$ may be given as

$$\overline{\tau}_b \simeq \frac{2}{\pi}\,\rho\, f_b\, U_b\, \overline{u}_b \tag{6}$$

Defining the mean shear velocity by $|\overline{u_*}|\,\overline{u_*} = \overline{\tau}_b/\rho$ together with (6) yields

$$\overline{u_*} = (C_*\, f_b\, U_b\, |\overline{u}_b|)^{1/2}\, \frac{\overline{u}_b}{|\overline{u}_b|} \tag{7}$$

in which C_* = empirical coefficient calibrated later. It is noted that $C_* \simeq 2/\pi$ if (3) and linear wave theory are accurate enough to estimate the relatively small value of $\overline{u_*}$, and it is further noted that the time-averaged bottom boundary layer is much less understood than the oscillatory bottom boundary layer.

The bottom friction factor f_b in (7) may be estimated for rough slopes as (Jonsson, 1966)

$$\frac{1}{4\sqrt{f_b}} + \log\frac{1}{4\sqrt{f_b}} = \log\left(\frac{A_b}{k_s}\right) - 0.08 \tag{8}$$

and for smooth slopes as (Kamphuis, 1975)

$$\frac{1}{8.1\sqrt{f_b}} + \log\frac{1}{\sqrt{f_b}} = \log\sqrt{Re} - 0.135 \tag{9}$$

where A_b = excursion amplitude given by $A_b = U_b/\omega$; k_s = equivalent roughness taken as $k_s = 30\,z_0$; and Re = Reynolds number defined as $Re = U_b\,A_b/\nu$.

Assuming that the thickness of the undertow boundary layer is approximately equal to the thickness of the wave boundary layer, the boundary layer thickness δ in (1) and (2) may be approximated by (Grant and Madsen, 1979)

$$\delta = C_\delta\,\frac{\kappa\,(u_*)_{max}}{\omega} \tag{10}$$

where $(u_*)_{max}$ = maximum shear velocity over the wave period; and C_δ = empirical constant in the range $1 \le C_\delta \le 2$ and is taken as $C_\delta = 1.5$ in this paper because the predicted results have been found to be insensitive to C_δ in this range. The maximum shear velocity $(u_*)_{max}$ in (10) is estimated by taking the maximum of (3) using (4)

and employing the small current assumption used to derive (7). Substitution of this expression into (10) yields

$$\delta = C_\delta \left(\frac{\kappa}{\omega}\right) \left[\frac{1}{2} f_b U_b \left(U_b + 2\left|\overline{u}_b\right|\right)\right]^{1/2} \tag{11}$$

The coefficient α in (2) can be obtained by matching (1) and (2) at $z_b = \delta$ which yields

$$\alpha = \frac{1}{\delta^2}\left[\frac{\overline{u_*}}{\kappa} \ln\left(\frac{\delta}{z_0}\right) - \overline{u}_b\right] \tag{12}$$

To close the problem, the mean volume flux below trough level, Q_t, is specified and is estimated from the measured undertow profile in this paper. The prediction of Q_t will be addressed separately at the end of this section. The volume flux is defined as

$$Q_t = \int_{z_0}^{d_t} \overline{u}\, dz_b \tag{13}$$

where Q_t is negative for the undertow $\overline{u}$. Substituting (1) and (2) into (13) and solving for $\overline{u}_b$ gives

$$\overline{u}_b = \frac{1}{d_t}\left[Q_t + \frac{\overline{u_*}}{\kappa}\delta - \frac{\alpha}{3}\left(d_t{}^3 + 2\delta^3\right)\right] \tag{14}$$

The solution of (1), (2), (7), (11), and (12) with (14) is termed Method 1.

In light of the uncertainty in estimating the relatively small $\overline{u_*}$ using the time-averaging of the quadratic equation (3), a second method is proposed to estimate $\overline{u_*}$ directly from $\overline{u}_b$ without regard to the oscillatory wave velocity. Instead of (7), $\overline{u_*}$ is assumed to be expressed as

$$\left|\overline{u_*}\right| \overline{u_*} = \frac{1}{2} \overline{f}\, \left|\overline{u}_b\right| \overline{u}_b \tag{15}$$

in which $\overline{f}$ = empirical friction factor for the undertow assumed to be given by $\overline{f} = C_f f_b$ where C_f is an empirical coefficient. It is noted that $C_f = 1$ if the friction factors $\overline{f}$ and f_b for the undertow and wave induced velocity are the same. From (15), the mean shear velocity is given by

$$\overline{u_*} = \sqrt{0.5\, C_f f_b}\ \ \overline{u}_b \tag{16}$$

Since (16) does not require the small current assumption used in (7), $(\tau_b)_{max}$ is derived from (3) without this assumption and is given as

$$(\tau_b)_{max} = \rho\left[(u_*)_{max}\right]^2 = \frac{1}{2}\rho f_b \left(U_b + \left|\overline{u}_b\right|\right)^2 \tag{17}$$

Substitution of (17) into (10) for the boundary layer thickness gives

$$\delta = C_\delta \left(\frac{\kappa}{\omega}\right) \sqrt{\frac{f_b}{2}}\ \left(U_b + \left|\overline{u}_b\right|\right) \tag{18}$$

In short, $\overline{u_*}$ and δ estimated by (7) and (11) in Method 1 are replaced by (16) and (18) in Method 2. Since C_δ is fixed, each method has only one primary calibration coefficient: C_* for Method 1 and C_f for Method 2. These methods may not be satisfactory

physically, but they are necessary to estimate the mean shear velocity $\overline{u_*}$ whose data appears to be limited, especially inside the surf zone.

The above undertow model developed originally for normally-incident regular waves may also be applied to normally-incident irregular waves by approximating the irregular waves by the equivalent regular waves based on the local root-mean-square wave height, H_{rms}, and the spectral peak period, T_p. The use of H_{rms} may be appropriate because the mean volume flux Q_t given by (13) is approximately proportional to the square of the local wave height as explained below. The choice of the spectral peak period is somewhat arbitrary, but this period is typically reported for irregular wave data. For field data, the cross-shore fluid motion under directional random waves may be approximated by that under normally-incident random waves if $\theta_c^2 << 1$ where θ_c is the characteristic incident angle in radians. The assumption of $\theta_c^2 << 1$ is usually satisfied in the surf zone because of wave refraction. However, longshore currents may not be negligible even if $\theta_c^2 << 1$ and may affect the mean cross-shore bottom shear stress in view of the cross-shore sediment transport analysis using field data by Thornton *et al.* (1996). Consequently, the subsequent comparisons with field data will need to be interpreted bearing this limitation in mind.

The use of the measured volume flux Q_t below trough level implies that this undertow model predicts the undertow profile but can not be used to predict the magnitude of the undertow. To address this shortcoming, an attempt is made to estimate Q_t from the local root-mean-square wave height, H_{rms}, and local water depth, $\overline{h} = (d + \overline{\eta})$, where d = still water depth and $\overline{\eta}$ = setup. The volume flux below trough level is approximated as

$$Q_t \simeq \overline{U}\, d_t \tag{19}$$

where $\overline{U}$ = depth-averaged velocity estimated by

$$\overline{U} \simeq -\frac{C_u \sqrt{g\overline{h}}}{8} \left(\frac{H_{rms}}{\overline{h}}\right)^2 \tag{20}$$

where g = gravitational acceleration, and C_u = empirical coefficient introduced herein to account for the roller effect. The roller effect is expected to increase the magnitude of $\overline{U}$ inside the surf zone. Equation (20) with $C_u = 1$ can be derived from the time-averaged continuity equation together with the assumption of linear progressive long waves where H_{rms} is defined as $H_{rms} = \sqrt{8}\sigma$ with σ = standard deviation of the free surface elevation. It is further noted that cross-shore variation in wave height and setup could be predicted using the time-averaged equations for momentum and energy.

SUMMARY OF DATA SETS

Table 1 summarizes the data sets used for comparison with the undertow model, indicating the literature cited, the data set name from each paper, and the abbreviation used in this paper. The data are comprised of both laboratory and field conditions, and the undertow is induced by irregular waves for all cases. The fifth through eighth columns indicate the quantities used to compute the surf similarity parameter given by

$$\xi = \frac{\tan\alpha}{\sqrt{H_{rms}/L_p}} \tag{21}$$

where α = local beach slope, and L_p = local wavelength computed using linear wave theory with the peak period, T_p. For the first five cases, ξ is estimated at the most seaward measuring line as shown in the subsequent figures. For the last two cases, ξ is estimated at the fifth measuring line since the first four seaward measuring lines had a very gentle slope. The range of the surf similarity parameter for the seven cases listed in Table 1 is $0.22 \leq \xi \leq 0.44$, indicating spilling and plunging waves with little reflection of wind waves. It is noted that the definition of H_{rms} for these data sets was not clearly stated in all cases. As a result, the values of H_{rms} based on the standard deviation σ, the spectral method, and the zero-crossing method are assumed to be the same.

Table 1: Summary of irregular wave induced undertow data for comparison with the undertow model.

Literature Cited	Abbr.	Lab or Field	Bathy.	$\tan\alpha$	H_{rms} (cm)	T_p (s)	$\overline{h}$ (cm)	ξ
Sultan (1995)	S95	Lab	P, S	1:35	7.1	3.0	28.9	0.24
Okayasu and Katayama (1992)	OK92	Lab	B, S	1:20	7.6	1.14	20.0	0.22
Smith *et al.* (1992)	SSP92-A	Field	B, R	1:22	59	9.7	230	0.38
Smith *et al.* (1992)	SSP92-B	Field	B, R	1:23	61	5.6	190	0.26
Smith *et al.* (1992)	SSP92-C	Field	B, R	1:28	65	7.0	221	0.25
Haines and Sallenger (1994)	HS94-A	Field	B, R	1:22	99	13.3	145	0.32
Haines and Sallenger (1994)	HS94-B	Field	B, R	1:18	101	14.4	200	0.44

Note: P=Plane, B=Barred; S=Smooth, R=Rough

Cox and Kobayashi (1997) compared the undertow model to the measured undertow induced by regular waves on plane slopes in the laboratory. The first extension of this paper is to compare the model to laboratory undertow data for irregular waves on a plane slope (Sultan, 1995), and then for irregular waves on a triangular barred profile (Okayasu and Katayama, 1992). These laboratory tests were for normally incident irregular waves with no longshore current. The next extension is to compare the model to the field data of Smith *et al.* (1992) and Haines and Sallenger (1994). The field measurements were collected on a barred beach at the USACE Field Research Facility in Duck, North Carolina, under a fairly uniform bathymetry in the longshore direction (e.g., Smith *et al.*, 1992). Although the longshore current was not reported in Smith *et al.* (1992), the peak incident wave angle measured counter-clockwise from shore normal was given as $\theta = -15$, -43, and $+24$ degrees at 8 m depth for SSP92-A, SSP92-B, and SSP92-C. Nevertheless, Smith *et al.* (1992) compared their undertow model for essentially normally-incident waves with these data sets apart from an empirical correction of $\cos\theta$ in (20) with $C_u = 2.4$.

Haines and Sallenger (1994) reported the magnitude and direction of the longshore current for HS94-A and HS94-B. For HS94-A, the magnitude of the longshore current was generally less than the cross-shore current, but the longshore current was not uni-directional. For HS94-B, the magnitude of the longshore current was approximately on

the same order as the cross-shore current and was unidirectional. Haines and Sallenger (1994) compared their undertow model for normally-incident waves with their data sets, excluding one data set with vigorous longshore currents. It is noted that none of the data sets mentioned above included detailed measurements of the undertow and shear stress in the bottom boundary layer.

UNDERTOW PROFILES

The undertow model is compared with the seven data sets listed in Table 1 using the measured volume flux below trough level to close the system of equations as described above. The volume flux is estimated by integrating a cubic spline fitted through the measured points. For both Method 1 and Method 2, the calibration coefficients are adjusted at each measuring line to give a best fit "by eye" to the data.

Table 2 lists the input parameters to the model at each measuring line for the data of Sultan (1995) where η_{tr} = negative trough elevation relative to the still water level which is used to calculate $d_t = (d + \eta_{tr})$. Since the trough level η_{tr} was not given in Sultan (1995), η_{tr} was taken as the elevation where the undertow changed sign from negative to positive below the still water level. This elevation corresponds roughly to $0.3\,H_{rms}$; and it is noted that the ratio of $|\eta_{tr}/H| \simeq 0.3$ was found for the regular wave data of Cox and Kobayashi (1996), Nadaoka and Kondoh (1982), and Hansen and Svendsen (1984). Column 8 indicates the amplitude of the orbital velocity U_b based on linear wave theory; and for the cases presented here, the small current assumption $(\overline{u}_b/U_b)^2 << 1$ used in (6) is reasonable. Column 9 gives the Reynolds number used to estimate the friction factor f_b in Column 10 using (9) for the smooth slope, which are in the range $0.8 \times 10^4 \leq Re \leq 4.1 \times 10^4$ and $0.011 \leq f_b \leq 0.017$.

Table 2: Model input and calibration coefficients for S95.

Line	d	H_{rms}	$\overline{\eta}$	η_{tr}	Q_t	$k\bar{h}$	U_b	Re	f_b	C_*	C_f	C_u
No.	(cm)	(cm)	(cm)	(cm)	(cm^2/s)		(cm/s)	$\times 10^{-4}$	$\times 10^{-2}$			
S1	29.0	7.1	-0.11	-3.2	-49	0.367	19.8	1.6	1.4	0.060	1.2	1.5
S2	23.3	8.1	-0.15	-2.6	-44	0.327	25.5	2.7	1.2	0.060	1.3	0.9
S3	20.8	8.6	-0.17	-1.8	-45	0.308	28.8	3.4	1.1	0.060	1.3	0.8
S4	17.7	8.6	-0.16	-1.9	-39	0.283	31.4	4.1	1.1	0.060	1.3	0.6
S5	16.1	8.1	-0.14	-2.1	-46	0.271	31.0	4.0	1.1	0.060	1.2	0.8
S6	14.4	7.2	-0.13	-2.1	-36	0.256	29.2	3.5	1.1	0.070	1.1	0.8
S7	13.1	6.5	-0.09	-1.5	-44	0.243	27.8	3.2	1.2	0.080	1.0	1.1
S8	12.1	6.1	-0.01	-1.2	-41	0.229	27.6	3.2	1.2	0.090	1.0	1.1
S9	9.7	5.3	0.09	-1.3	-45	0.209	26.3	2.9	1.2	0.110	1.8	1.5
S10	7.7	4.2	0.23	-1.0	-29	0.186	23.5	2.3	1.3	0.120	1.8	1.5
S11	5.6	3.3	0.40	-1.1	-25	0.164	21.0	1.8	1.4	0.130	1.7	1.9
S12	3.1	1.7	0.66	0.0	-16	0.128	13.8	0.8	1.7	0.170	1.6	3.4

Columns 11 and 12 give the calibration coefficients C_* for Method 1 and C_f for Method 2. C_* increases shoreward as was found in Cox and Kobayashi (1997) for the regular wave comparisons, but the variation in C_* from outside the surf zone to inside the surf zone is less pronounced for the irregular wave case. The magnitude of

C_* is 0.1 which is much less than $(2/\pi) = 0.64$, indicating that (6) overpredicts the mean bottom shear stress as was found by Cox and Kobayashi (1997). C_f generally decreases shoreward as was also noted in Cox and Kobayashi (1997); however, C_f increases unexpectedly in the inner surf zone. Overall, the magnitude of C_f is on the order of 1.0, indicating that $\overline{f} \simeq f_b$. Column 13 gives the values of C_u in (20) which are discussed later in relation to the prediction of the volume flux below trough level.

Figure 1 compares the model predictions with the measurements of Sultan (1995). Trough level is indicated in the figure by the vertical extent of the model predictions. The horizontal extent from S1 to S12 is approximately 9 m. The figure indicates that the model predicts the measured undertow profile below trough level both outside and inside the surf zone for both methods with the coefficients adjusted at each measuring line. The boundary layer thickness is estimated by the model to be in the range $0.5 \leq \delta \leq 0.7$ cm, and the mean shear velocity is estimated to be in the range $-0.5 \leq \overline{u_*} \leq -0.2$ cm/s over the 12 measuring lines for Methods 1 and 2. These ranges indicate the difficulty in measuring the undertow and mean shear velocity in the bottom boundary layer in the laboratory. Figure 2 shows the model sensitivity to a 20% variation in C_*. In this figure, the adopted C_* at each measuring line is shown by a solid line whereas $0.8\,C_*$ and $1.2\,C_*$ are shown by dashed and dash-dot lines, respectively. A similar variation in the undertow profiles is achieved for only a 5% variation in C_f, and the figure is not shown for brevity.

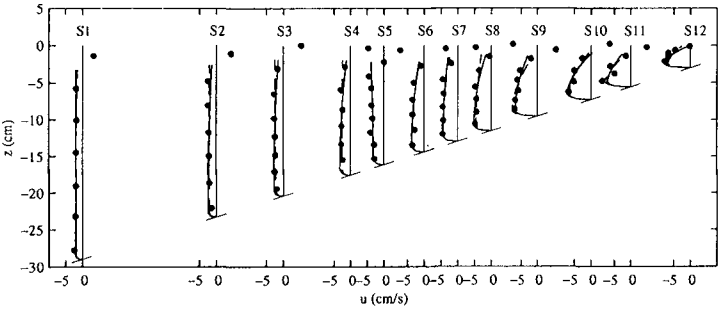

Figure 1: Model predictions for S95: Measured $\overline{u}$ (•); Predicted, Method 1 (——); and Predicted, Method 2 (– –).

For the data of Okayasu and Katayama (1992), the local H_{rms} is estimated by $H_s = \sqrt{2}\,H_{rms}$ where the significant wave height H_s is taken from the significant crest and trough elevations, $(\eta_{cr})_s$ and $(\eta_{tr})_s$, reported in their paper. Figure 3 compares the model and data for both methods. In this figure, the horizontal extent from O1 to O6 is approximately 5 m, and the triangular bar consists of three linear segments. Figure 3 indicates that the model predicts the undertow profile over a barred bathymetry as well, apart from the scatter of data points at O6, provided that the coefficients are adjusted at each measuring line. For this case, the boundary thickness is estimated to be in the range $0.2 \leq \delta \leq 0.4$ cm, and the mean shear velocity is estimated to be in the range $-0.4 \leq \overline{u_*} \leq -0.05$ cm/s.

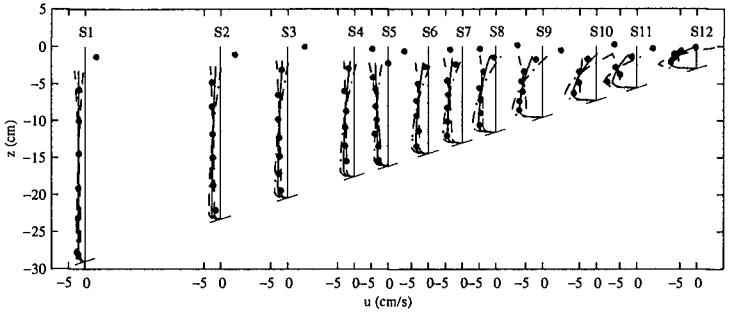

Figure 2: Model sensitivity for S95: Measured $\overline{u}$ (•); Predicted, Method 1 with adopted C_* (——); Predicted, Method 1 with $0.8\,C_*$ (– –); and Predicted, Method 1 with $1.2\,C_*$ (– · –).

For comparisons with the data of Smith *et al.* (1992), the local H_{rms} for each of the six measuring lines is obtained by a linear interpolation of the measured values in their paper. Although the local setup $\overline{\eta}$ was not measured, $\overline{\eta}$ was estimated in Smith *et al.* (1992); and the ratio of this estimated setup to the minimum local water depth was approximately 0.03 for the three cases. Therefore, $\overline{\eta}$ is neglected here, and the approximation $\overline{h} \simeq d$ is assumed for input in the undertow model. The trough level was also not reported, and the crude approximation of $\eta_{tr} \simeq 0.3\,H_{rms}$ is used here. The relative roughness in (8) is found to be in the range $29 \leq A_b/k_s \leq 73$ for the three cases where the roughness height is assumed as $z_0 = 0.05$ cm and $k_s = 30\,z_0 = 1.5$ cm for lack of data on bed forms. The Reynolds number is found to be in the range $2.1 \times 10^5 \leq Re \leq 7.8 \times 10^5$ for the field data. This range of relative roughness and Reynolds number indicates that the flow in the bottom boundary layer is rough turbulent even without the turbulence generated by wave breaking (Jonsson, 1966). The friction factor was found to be in the range $0.025 \leq f_b \leq 0.038$ which is larger than $f_b = 0.01$ specified in Smith *et al.* (1992) for their model comparisons. However, the use of a much smaller value for z_0 would reduce f_b. For example, $z_0 = 0.007$ cm would yield the range $0.012 \leq f_b \leq 0.016$.

For a given case, C_* varies at each measuring line; but for a given measuring line, C_* is fairly constant for the three cases. Compared to the laboratory cases with regular waves, there is less cross-shore variation in C_* for a given case, although it is noted that the field measurements do not include the inner surf zone near the still water shoreline. The variation in C_f at a given measuring line for the three cases is also small. The values of C_* and C_f for these field data are smaller than the corresponding values of C_* and C_f listed in Table 2 for the laboratory data of Sultan (1995). (Table 4 compares the average calibration coefficients for all cases listed in Table 1). The mean shear velocity $\overline{u_*}$ given by (7) and (16) depends on $C_* f_b$ and $C_f f_b$, respectively, instead of f_b itself. The calibrated values of C_* and C_f depends on the adopted value of z_0 which affects f_b somewhat, but the values of $C_* f_b$ and $C_f f_b$ remain approximately the same. In other words, the change of z_0 by a factor of 10 will change f_b, C_*, and C_f by roughly a factor of 2.

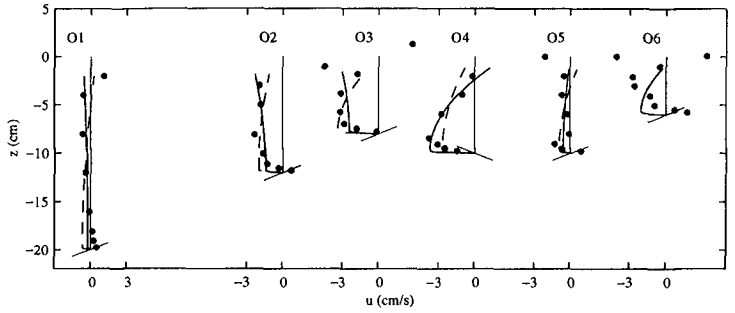

Figure 3: Model predictions for OK92: Measured $\overline{u}$ (•); Predicted, Method 1 (——); and Predicted, Method 2 (– –).

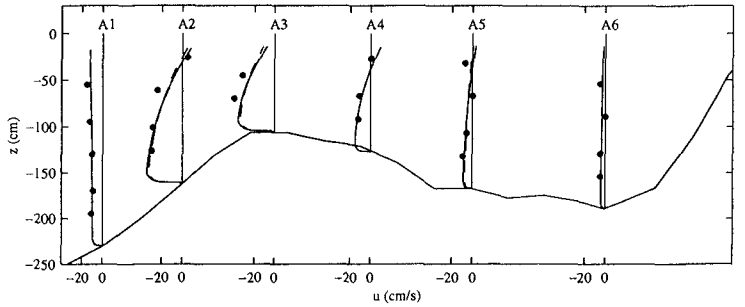

Figure 4: Model predictions for SSP92-A: Measured $\overline{u}$ (•); Predicted, Method 1 with adopted C_* (——); and Predicted, Method 1 with C_{*ave} (– –).

Figure 4 compares the undertow model for Method 1 with the data of SSP92-A using C_* calibrated at each measuring line and the average C_* values for the three cases. The horizontal extent from A1 to A6 is approximately 100 m. Figure 4 indicates that the model predicts the undertow profile over a barred beach for field conditions, provided that the coefficients are adjusted at each measuring line. The values of C_* are larger at A2 and A3 located immediately seaward and on the bar crest, respectively, whereas the values of C_f do not change much across the barred beach. The agreement for Method 2 and for the two other cases SSP92-B and SSP92-C is similar, and the figures are not shown for brevity. For these field data, the boundary layer thickness is estimated to be in the range $4 \leq \delta \leq 11$ cm, and the mean shear velocity is estimated to be in the range $-2.1 \leq \overline{u_*} \leq -0.2$ cm/s. These values are much larger than the laboratory values estimated for S95 and OK92.

Similar to Smith *et al.* (1992), $\overline{\eta}$ and η_{tr} were not given in the paper of Haines and Sallenger (1994), and the assumptions of $\overline{h} \simeq d$ and $\eta_{tr} \simeq 0.3\, H_{rms}$ are made here as well. The roughness height is assumed as $z_0 = 0.05$ cm, and the relative roughness is found to be in the range $88 \leq A_b/k_s \leq 180$. The Reynolds number is found to be in the

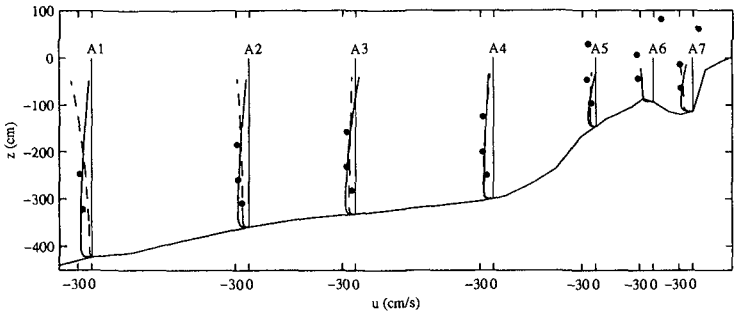

Figure 5: Model predictions for HS94-A: Measured $\overline{u}$ (•); Predicted, Method 1 (——); and Predicted, Method 2 (– –).

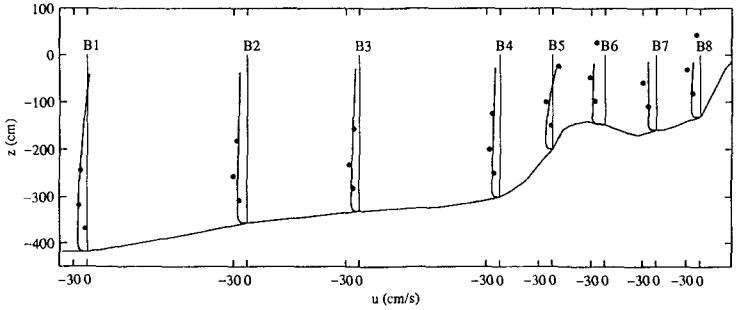

Figure 6: Model predictions for HS94-B: Measured $\overline{u}$ (•); Predicted, Method 1 (——); and Predicted, Method 2 (– –).

range $8 \times 10^5 \leq Re \leq 34 \times 10^5$, indicating rough turbulent flow in the bottom boundary layer (Jonsson, 1966). The cross-shore variations in C_* and C_f are small compared to the laboratory cases.

Figures 5 and 6 show the model agreement for HS94-A and HS94-B. The horizontal extent from A1 to A7 and from B1 to B8 is approximately 300 m. Substantial offshore migration of the bar occurred from October 11 (HS94-A) to October 12 (HS94-B) as explained in Haines and Sallenger (1994). The agreement is good for both methods and for both cases with the calibration coefficients adjusted at each measuring line. For these two cases, the boundary thickness is estimated to be in the range $11 \leq \delta \leq 17$ cm, and the mean shear velocity is estimated to be in the range $-1.5 \leq \overline{u_*} \leq -0.8$ cm/s. These ranges are similar to the field data of SSP92.

VOLUME FLUX BELOW TROUGH LEVEL

As an alternative to specifying the volume flux below trough level using the measurement, the local depth-averaged velocity $\overline{U}$ is estimated using (20) with the measured values of H_{rms} and $\overline{h}$ at the same location. The predictability of the depth-averaged

velocity is discussed in terms of the calibration coefficient C_u which is obtained from (20) using the measured depth-averaged velocity given by $\overline{U} = (Q_t/d_{tr})$ together with the measured values of H_{rms} and $\overline{h}$. If the calibrated values of C_u are fairly constant, (20) may be applied to predict $\overline{U}$. Furthermore, the calibrated values of C_u can be used to assess the roller effect on C_u since $C_u = 1$ assuming no roller effect.

The calibrated values of C_u listed in Table 2 for S95 indicate that C_u is on the order of 1 over most of the shoaling and surf zone. For S9 to S12 in the inner surf zone, C_u is larger than 1, possibly due to the roller effect. The calibrated values of C_u for OK92 are generally less than 1. It is possible that the value of H_{rms} estimated from the significant crest and trough elevations reported by Okayasu and Katayama (1992) may not be very accurate. Noting that $\overline{U}$ is proportional to H_{rms}^2, this estimation error may have resulted in the unexpectedly small values of C_u for OK92. On the other hand, the calibrated values of C_u in for the field data of SSP92 are mostly on the order of unity and tend to be larger over the bar crest region and smaller in the bar trough region in view of the measuring line locations shown in Figure 4. The calibrated values of C_u for HS94 are also on the order of unity for both cases, but C_u tends to be smaller for HS94-A which had a smaller longshore current than HS94-B.

Table 3 summarizes the calibrated values of C_u. The value $\overline{C_u}$ indicated in the table is estimated for each data set by averaging the C_u values over the measuring lines that have qualitatively similar locations in the cross-shore direction, namely outside the surf zone, the breaker zone, the bar-trough zone, and the inner surf zone. In general, Table 3 shows that $\overline{C_u}$ is closer to unity for the laboratory data sets of S95 and OK92 than for the field data sets of SSP92 and HS94. There appears to be no systematic variation of $\overline{C_u}$ in the cross-shore direction as may be expected from the effect of rollers associated with regular breaking waves. For the irregular wave data in the laboratory, the roller effect is not very pronounced; and $C_u = 1$ is a reasonable approximation. For the field data, $\overline{C_u}$ tends to be larger than unity, and the magnitude of the undertow velocities may have been modified by the wave directionality and alongshore variation of wave and current fields.

Table 3: Summary of calibrated values of C_u.

Data	Outside surf zone		Breaker zone		Bar/trough zone		Inner surf zone	
Set	Line	$\overline{C_u}$	Line	$\overline{C_u}$	Line	$\overline{C_u}$	Line	$\overline{C_u}$
S95	S1,S2	1.2	S3-S5	0.7	N/A[1]		S9-S12	2.1
OK92	O1	0.3	O2,O3	0.6	O4-O6	0.7	N/A[2]	
SSP92-A	A1	2.7	A2,A3	3.2	A4-A6	1.3	N/A[2]	
SSP92-B	B1	1.9	B2,B3	2.6	B4-B6	1.1	N/A[2]	
SSP92-C	C1	1.6	C2,C3	3.5	C4-C6	1.6	N/A[2]	
HS94-A	A1-A4	1.5	A5,A6	0.8	A7	2.8	N/A[2]	
HS94-B	B1-B4	2.1	B5	0.5	B6-B8	3.7	N/A[2]	

[1] Trough region not applicable to data of S95

[2] No inner surf zone measurements for these data sets

CONCLUSIONS

Existing undertow models based on a local balance of the horizontal momentum equa-

tion can predict the order of magnitude of the undertow if empirical parameters are calibrated for each data set. Moreover, the literature is divided among regular or irregular waves and laboratory or field conditions with each model typically calibrated for one of these condition only. Rarely is it shown whether the empirical input is universal. For example, Okayasu and Katayama (1992) used empirically adjusted representative wave heights to get reasonable agreement with a model which was calibrated in an earlier paper under similar laboratory conditions. Haines and Sallenger (1994) employed a vertically uniform eddy viscosity which varied at each measuring line, and they attempted to parameterize this variation using their field data only.

Table 4 summarizes the types of data sets considered in this paper and in Cox and Kobayashi (1997), listing the average calibration coefficients with the standard deviation given in parenthesis. These averages are crude in that they do not distinguish between breaking and nonbreaking waves, but they serve to indicate the variability of the coefficients for the different data sets. Table 4 indicates that C_* and C_f are similar for both regular and irregular waves in the laboratories. For all of the data sets, Method 2 using C_f appears to be the most consistent in terms of the small standard deviation relative to the mean value. It was noted earlier in this paper and in Cox and Kobayashi (1997), however, that the predicted undertow is more sensitive to small changes in the calibration coefficient C_f for Method 2 than C_* for Method 1.

Table 4: Summary of calibration coefficients.

Literature Cited	Lab/ Field	Wave Cond.	Bathy.	C_*		C_f		C_u	
Sultan (1995)	Lab	Irreg	P, S	0.09	(.04)	1.0	(.2)	1.3	(.8)
Okayasu and Katayama (1992)	Lab	Irreg	B, S	0.06	(.02)	1.4	(.4)	0.6	(.3)
Smith *et al.* (1992)	Field	Irreg	B, R	0.03	(.02)	0.22	(.01)	2.0	(1.1)
Haines and Sallenger (1994)	Field	Irreg	B, R	0.03	(.01)	0.61	(.02)	2.0	(1.1)
Cox *et al.* (1995)	Lab	Reg	P, R	0.05	(.03)	0.47	(.04)	—	—
Hansen and Svendsen (1984)	Lab	Reg	P, S	0.10	(.04)	1.0	(.3)	—	—
Nadaoka and Kondoh (1982)	Lab	Reg	P, S	0.10	(.05)	0.9	(.2)	—	—

Note: P=Plane, B=Barred; S=Smooth, R=Rough

The consistency of the average values of C_u between the two field data sets suggests that (20) with $C_u \simeq 2$ might yield reasonable approximations of the depth-averaged undertow velocity $\overline{U}$, but the standard deviation is 1.1 and fairly large. The values of C_* and C_f for the field data tend to be smaller than those for the laboratory data, but these values of C_* and C_f are affected somewhat by the adopted value of z_0 as well as by the presence of longshore currents. Furthermore, errors associated with use of the model where the volume flux and calibration coefficients are not known are approximately 100% or roughly a factor of 2.

Finally, the values of C_* for all the data sets in Table 4 are definitely less than $C_* = (2/\pi) = 0.64$ based on (6). Consequently, (6) overpredicts the mean bottom

shear stress. The alternative equation (16) with $\overline{f} = C_f f_b$ has been proposed by Cox and Kobayashi (1997) to mitigate the shortcomings of (6), but (16) is physically unsatisfactory because it neglects wave effects. Therefore, it may be concluded that the mean cross-shore bottom shear stress is poorly understood. The state of the art for the alongshore bottom shear stress in the surf zone is similar (e.g. Garcez Faria *et al.*, 1998).

ACKNOWLEDGMENTS

This work was partially sponsored by the U.S. Army Research Office, University Research Initiative under contract No. DAAL03-92-G-0116, by the National Science Foundation under grant No. CTS-9407827, and by the National Science Foundation CAREER Award CTS-9734109..

REFERENCES

Cox, D.T. and Kobayashi, N., 1996. Undertow profiles in the bottom boundary layer under breaking waves. *Proc. 25th Int. Conf. on Coastal Engrg.*, ASCE, 3, 3194–3206.

Cox, D.T. and Kobayashi, N., 1997. A kinematic undertow model with a logarithmic boundary layer. *J. Waterway, Port, Coastal, and Ocean Engrg.*, 123 (6), 354–360.

Garcez Faria, A.F., Thornton, E.B., Stanton, T.P., Soares, C.V. and Lippmann, T.C.. 1998 Vertical profiles of longshore currents and related bed shear stress and bottom roughness. *J. Geophys. Res.*, 103 (C2), 3217–3232.

Grant, W.D. and Madsen, O.S., 1979. Combined wave and current interaction with a rough bottom. *J. Geophys. Res.*, 84 (C4), 1797–1808.

Haines, J.W. and Sallenger, A.H., 1994. Vertical structure of mean cross-shore currents across a barred surf zone. *J. Geophys. Res.*, 99 (C7), 14223–14242.

Hansen, J.B. and Svendsen, I.A., 1984. A theoretical and experimental study of undertow. *Proc. 19th Int. Conf. on Coastal Engrg.*, ASCE, 2246–2262.

Jonsson, I.G., 1966. Wave boundary layers and friction factors. *Proc. 10th Int. Conf. on Coastal Engrg.*, ASCE, 127–148.

Kamphuis, J.W., 1975. Friction factor under oscillatory waves. *J. Waterway, Harbors and Coastal Engrg.*, 101 (2), 135–144.

Nadaoka, K. and Kondoh, T., 1982. Laboratory measurements of velocity field structure in the surf zone by LDV. *Coastal Engrg. in Japan*, 25, 125–145.

Okayasu, A. and Katayama, H., 1992. Distribution of undertow and long-wave component velocity due to random waves. *Proc. 23rd Int. Conf. on Coastal Engrg.*, ASCE, 883–893.

Smith, J.M., Svendsen, I.A., and Putrevu, U., 1992. Vertical structure of the nearshore current at DELILAH: Measured and modeled. *Proc. 23rd Int. Conf. on Coastal Engrg.*, ASCE, 2825–2838.

Sultan, N., 1995. Irregular wave kinematics in the surf zone. Ph.D. Dissertation, Texas A&M University, College Station, Texas.

Thornton, E.B., Humiston, R.T., and Birkemeier, W., 1996. Bar/trough generation on a natural beach. *J. Geophys. Res.*, 101 (C5), 12097–12110.

WAKE WASH OF HIGH-SPEED CRAFT IN COASTAL AREAS

Jens Kirkegaard[1], Henrik Kofoed-Hansen[1] and Berry Elfrink[1]

Abstract

In recent years fast ferries have been introduced on many ferry routes throughout the world. Particularly when operating in shallow waters and near the coast, the waves generated by these ferries give rise to conflicts with recreational use of beaches and coastal waters. Also the potential coastal erosion caused by a changed wave impact has been a matter of concern. The paper presents the results of studies carried out with the objective of providing an unbiased description of these wave phenomena, which has served as basis for a new legislation for regulation of fast ferry operation. The coastal erosion potential was studied and sediment transport simulations showed that the long-periodic ship-generated waves give rise to beach accretion and steepening of the cross-shore profile.

Introduction

It is known that the waves generated by high-speed craft (HSC) in shallow water are substantially different from the waves generated by conventional ships as a consequence of the higher speed and the size of these modern vessels. This results in different wave impact – also denoted wake wash – in coastal areas. It has been observed that HSC operating in the transcritical and supercritical speed range generate diverging waves in groups of both long-periodic and short-periodic waves. This paper primarily describes the long-periodic wave behaviour. Even though these waves are transient, they are similar to swell and thus may cause changes to beaches in areas not usually exposed to swell or severe local seas. Also the safety of nearshore recreational boaters may be reduced and

[1] *Danish Hydraulic Institute, Agern Allé 5, DK-2970 Hørsholm, Denmark, Fax: +45 45 76 25 67, e-mail: jkj@dhi.dk*

the long waves may increase the risk for people bathing and fishing as the long-periodic waves reach the shore without warning.

Several HSC in the form of catamaran and monohull fast ferries have been introduced on ferry routes in Denmark. Due to the shallow waters conditions in Danish waters the wave effects along the coast were immediately recognized and received much attention. Similar experience has been found in a number of other countries, eg UK, Ireland, USA and New Zealand.

The paper present results and analysis of recent full-scale wake wash measurements from a few of these Danish ferry routes. The measurements have been supplemented by wave propagation modelling in order to develop methods to predict the areas of particular concern. These prediction methods are required in connection with planning of new ferry routes or alteration of present routes to obey new Danish regulation concerning fast ferry operation.

The results of the wake wash studies were included in a report by the Danish Maritime Authority (1997) together with other studies on the effect on the external environment, including noise, emissions, impact on birds and marine life and marine safety.

Wave Generation by High-Speed Craft

When a ship moves through the water, it makes waves and suffers wave resistance. Typically, an advancing ship generates a set of waves at both its bow and stern as a consequence of pressure gradients along the hull. For a ship moving steadily in water of uniform finite depth, the nature of the wash which it creates will closely depend upon two non-dimensionless parameters; the length-based Froude number, $F_{nl}= V_s/\sqrt{gL_w}$, and the depth-based Froude number, $F_{nh}= V_s/\sqrt{gh}$. Here, V_s is the ship speed, g is the acceleration due to gravity, L_w is a characteristic length of the ship and h denotes the water depth.

In the subcritical speed range (ie $F_{nh} < 0.6$-0.7), the wave system consists of diverging and transverse waves in a restricted wedge-shaped Kelvin wake, where the cusp angle is about $\pm 19.5°$ and almost independent of the ship speed, see eg Kostyukov (1959) and Newman (1977). In this speed range, the wave period of the diverging waves is proportional to the ship speed ($T \approx 0.27 V_s$, V_s in knots). For depth-Froude numbers beyond 1 (supercritical speed range), the transverse waves disappear and the wave system is characterised by a Havelock-like wave pattern taken a convex form as illustrated in the aerial photograph shown in Figure 1. This is typically the case for HSC operating in coastal water. The divergent waves are now contained within an angle that depends on the speed of the ship. In the transcritical speed range (F_{nh}~ 0.9-1.1), transverse and divergent waves merge together into wave fronts nearly straight and perpendicular to the ship's course. High-amplitude waves are typically generated for speeds in this speed range. If also $F_{nl} \sim 0.5$, ie in the vicinity of the primary hump, where maximum wave resistance occurs, particularly high waves can be generated.

Figure 1. Aerial photograph of wave pattern generated at supercritical speed. The vessel speed is V_s= 35 knots and the water depth is h= 13-14 m. The Froude numbers are F_{nh} ~ 1.5 and F_{nl} ~ 0.7. The overall length of the catamaran is approximately 78 m.

Even though a considerable amount of theoretical and experimental research effort has been devoted to HSC operating within the transcritical and supercritical speed range, particularly in shallow water channels (eg Johnson, 1958), yet no simple methods exist for ship wave prediction similar to Sorensen and Weggel (1986), see also Weggel and Sorensen (1984). These are only applicable for subcritical ship speeds.

Full-scale Measurements

A number of comprehensive full-scale measurement programmes have recently been carried out at various locations in Denmark and abroad (eg Kalundborg Fjord, Lindholm Dyb, Tunø Harbour and Odden Ferry Terminal, Denmark, and in Derwent River and Norfolk Bay, Tasmania). One of the objectives was to evaluate the consequences of wake wash from high-speed ferries as well as for route planning in order to reduce environmental impacts. The measurement programmes covered various navigation conditions for the involved catamarans, which have a service speed of 35-45 knots. Also wake wash caused by conventional ferries having a service speed of about 17 knots was measured. The ship-generated waves were measured at various water depths (2 m to 25 m) and at various distances to the navigation track. A few results of the comprehensive measurement campaigns carried out in Kalundborg Fjord are presented and discussed in Kofoed-Hansen and Mikkelsen (1997), see also Kofoed-Hansen and Kirkegaard (1996) and Kirkegaard et al (1998).

Wave generation

The measurements show that a catamaran advancing with a supercritical speed generally generates a wave system characterised by groups of both short-periodic and long-periodic waves as illustrated in the time series of surface elevation shown in Figure 2a (F_{nh} ~ 1.39, F_{nl} ~ 0.74). It is seen that the long waves have periods in the range of 7-9 s and the short

waves 2-4 s. Figure 2b shows that in the subcritical speed range (F_{nh} ~ 0.66, F_{nl} ~ 0.34), the wave period is approximately 5 s, which is in reasonable agreement with Kelvin's classical theory. For a ship speed near the critical speed (F_{nh} ~ 0.93, F_{nl} ~ 0.47), the generated long-periodic waves are high as expected. From Figure 2c, it is seen that the maximum wave height is approximately H_{max} ~ 1.3 m.

In Figure 3, the relationship between the measured maximum wave height of the long-periodic wave component (T> 5s) and the depth-Froude number is depicted. A realistic trend line is also indicated. All measured data have been adjusted so they correspond to a distance of approximately 700 m (~ 10 ship-lengths) from the navigation track using the trend line shown in Figure 4. Although the scatter of the data is relatively high, it is seen that the highest waves appear in the transcritical speed range. The critical Froude number is slightly smaller than the theoretical value of one, which is in agreement with experience from model tests and CFD calculations. For supercritical speeds, it is also seen that the wave height is less than in deep water (ie subcritical speed). The reason for this is a lower pressure due to an increased particle velocity between the ship hull and the seabed.

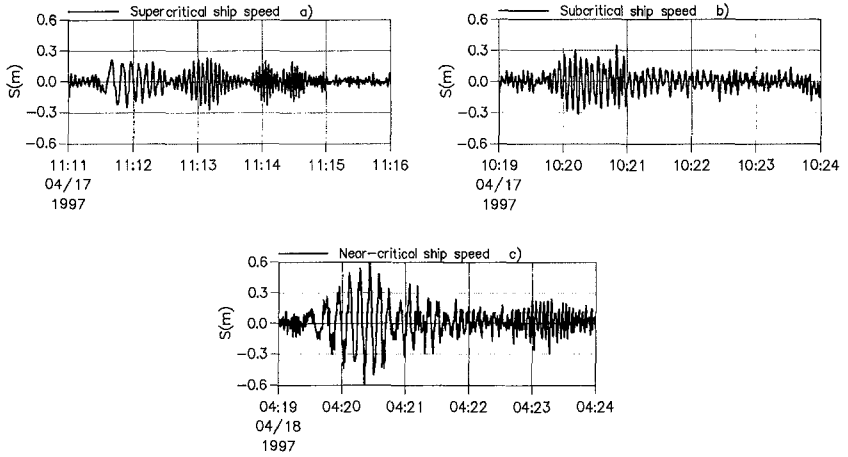

Figure 2. Time series of measured surface elevation generated by a HSC catamaran at Lindholm Dyb, Denmark. a) supercritical speed ($V_s \approx$ 36 knots, $h \approx$ 18 m, $F_{nh} \approx$ 1.39, $F_{nl} \approx$ 0.74), b) subcritical speed ($V_s \approx$ 17 knots, $h \approx$ 18 m, $F_{nh} \approx$ 0.66, $F_{nl} \approx$ 0.34), c) near-critical speed ($V_s \approx$ 24 knots, $h \approx$ 18 m, $F_{nh} \approx$ 0.93, $F_{nl} \approx$ 0.47). The distance between the measurement buoy and the navigation track was approximately 300-400 m.

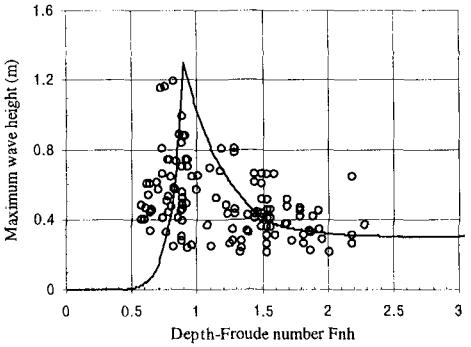

Figure 3. Maximum wave height of the long-periodic waves versus the depth-Froude number. The measured data (ooo) have been corrected to be valid in a distance of 700 m (~ 10 ship lengths) from the ship track. (—) indicates a trend line.

The influence of the distance from the navigation route on the maximum zero-crossing wave height, ie the wave decay due to diffraction, is illustrated in Figure 4. The figure shows the maximum wave height versus the perpendicular distance between the ship track and the Waverider buoy. The data are not affected by shoaling and refraction effects as the water depth is in the range of 10-30 m. It is seen that the wave decay is exponential, which is in agreement with Crapper (1984), page 125.

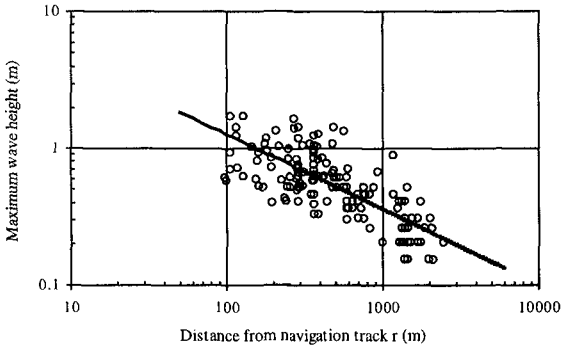

Figure 4. Maximum wave height of the long-periodic waves versus the distance from the ship track. The measured data (ooo) have been based on various field campaigns involving catamarans only. The trend line (—) is given by $H_{max} = 16r^{-0.55}$, where r (in meters) denotes the distance from the track.

Usually ship-generated waves are assumed to be caused by the ship hull alone, and the wave formation from the propulsion system is neglected. Based on a number of recent model tests, however, Taatø et al (1998) concluded that the propulsion system on large HSC (water jets) may cause increased wave heights of 20-40 per cent compared to the bare hull.

Wave propagation and transformation

The wave height, and to some extent, the wave period change during the wave propagation due to diffraction of the short-crested waves as well as to nonlinear wave interactions and wave breaking. When the long-periodic transient waves reach shallow water, the nonlinear shoaling results in rapid growth of the waves which ultimately break, typically as plunging breaker, and may cause transient run-up on the beach.

The photographs shown in Figures 5 and 6 illustrate an example of an HSC-generated wave pattern under propagation towards the coast.

Figure 5. Photograph of wave pattern generated by a mono-hull fast ferry at Hundested, Denmark.

Figure 6. Photograph of a plunging breaker east to Gedser Harbour, Denmark. A monohull fast ferry generated the wash.

Figure 7 shows two time series of wake wash measured at 2-3 m water depth. The wave train shown on the left panel was caused by a passing HSC with its service speed, and the right panel shows the wake wash caused by the same HSC operated in the transcritical speed range. It clearly illustrates that very large transient waves may occur in shallow water without any warning and cause transient currents and run-up. The consequence of this type of wave impact is discussed in the next section.

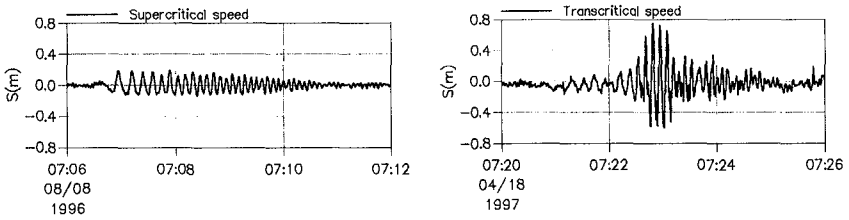

Figure 7. Time series of measured surface elevation in shallow water. Left panel shows the wake wash caused by an HSC operating in the supercritical speed range and the right panel for a transcritical speed. The water depth and distance to the navigation track are 2.4 m and 1500 m (left panel) and 3.2 m and 1100 m (right panel).

Sediment Transport and Coastal Impact

As the waves approach the coastline, changes in wave shape, size and direction occur due to transformation mechanisms such as refraction, shoaling and breaking. Mass transport in the direction of wave propagation occurs due to the wave orbital motion and the surface rollers in the breaker zone. If the bed shear forces generated by the wave orbital motion exceed a critical value, transport of bed sediments is initiated.

Long-shore sediment transport

Oblique incident natural waves give rise to littoral currents in the surf zone driven by the radiation stress gradient. For ship-generated waves, the long-shore current is not established due to the short duration of the wave event. The usual large run-up of the ship waves, however, may give rise to a long-shore sediment transport in the swash zone due to the zigzag motion of the water and sediment particles. Under natural conditions, the bulk of the littoral transport occurs in the surf zone. The long-shore component of the sediment transport in the swash zone is small compared to the transport in the surf zone Elfrink (1997).

Cross–shore sediment transport

In natural waves the mass transport perpendicular to the coast is balanced by means of a return current driven by the sloping water surface, the wave set-up. The vertical

distribution of the shear stress under breaking and non-breaking waves was analysed by Deigaard and Fredsøe (1989) and Deigaard (1993).

In ship-generated waves the balance between onshore directed flow due to the mass transport and offshore directed flow due the sloping water surface is not established due to the relative short duration of the wave event. The mass transport occurs during the passing of breaking waves, the return flow occurs later. The response time depends on the distance from the shoreline. The result is that onshore velocities occur over the entire water column during the wave event. Offshore-directed velocities, to balance the net drift occur later after the passage of the wave train. During the passage of the wave train, the level of turbulence and the suspended sediment concentrations are higher than during the return flow period. Therefore a net onshore transport of sediment occurs.

In order to illustrate the sediment transport mechanisms, a number of simulations were performed with the model presented in Elfrink et al (1996). The model was specially customised in order to account for the non-equilibrium conditions with regard to the turbulence levels, the mean flow, and the suspended sediment concentrations. The time series of water surface elevation shown in Figure 7 (left panel) was used as boundary conditions. The wave transformation on a beach slope of 1:50 was simulated with a wave model based on the Boussinesq type equations presented in Madsen et al (1997). Figure 8 shows the simulated wave orbital velocity (upper panel) at a water depth of 0.65 m. At this water depth the waves are fully breaking. The calculated instantaneous sediment flux is also shown in Figure 8 (lower panel). It is noticed that the highest sediment fluxes occur under the wave crests and that the resulting sediment transport is directed onshore (positive values).

Coastal Impact

The run-up height is higher for the long-periodic ship-generated waves than for natural wind waves with the same height. Thus, the swash zone of the beach will become wider and higher due to the ship waves caused by HSC.

The simulations showed an increasing onshore sediment transport rate towards the shore. This gives rise to a tendency of steepening of the cross-shore beach profile and sediment accumulation in the run-up zone. If the total amount of wave energy originating from the ship-generated waves is of the same order of magnitude as the energy from natural waves, this can lead to permanent changes in the cross-shore profile. The profile-steepening is counteracted by the natural waves. If the wave conditions are dominated by natural waves, the impact of the ship-generated waves on the cross-shore profile is negligible.

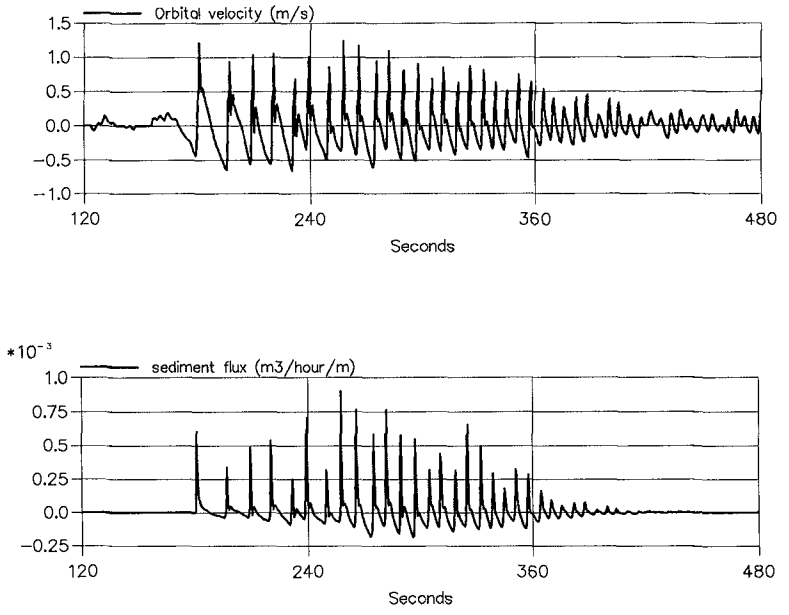

Figure 8. Time series of simulated wave orbital velocity (upper panel) and sediment flux (lower panel) caused by waves generated by a HSC. The water depth is 0.65 m.

Criteria of Acceptable Wake Wash

To ensure safe navigation of small craft in shallow water and leisure activity the Danish Maritime Authority has per May 1997 issued a governmental order that requires the HSC owner/operator to document that the ship-generated waves do not exceed a prescribed criterion along the entire route. The wake wash criterion is presently formulated as

$$H_h \leq 0.5\sqrt{\frac{4.5}{T_h}} \tag{1}$$

where H_h is the maximum wave height (in meters) of the long-periodic waves having a mean wave period of T_h (in seconds). The criterion is applicable at a still water depth of 3 m. Assuming that the mean wave period of the long-periodic waves is approximately 9 s at 3 m of water depth, the criterion gives H_h= 0.35 m. The background for this criterion is briefly described below, see also Kofoed-Hansen and Kirkegaard (1996).

Despite the fact that wash generated by HSC is substantially different from wash caused by conventional ships and ferries, the choice of criterion of acceptability must reflect a connection between these two types of wash, where the latter is generally accepted by the public. Characteristic measures such as wave energy, maximum wave height prior to breaking and wave run-up on the coast have been used tentatively in the formulation of a criterion. A criterion based on the maximum wave height immediately before breaking was originally suggested as the most reasonable choice because it is directly connected to public's experience at sea.

Based on analysis of experimental data, the original criterion was formulated as

$$H_{HSC} \leq \beta_b^{3/2} \sqrt{\frac{T_c}{T_{HSC}}} H_c \qquad (2)$$

which is applicable at about 3 m of water depth and for wave periods longer than 4-5 s. H indicates a maximum wave height at 3 m of water depth and T the related wave period. Index HSC refers to a High-Speed Craft, whereas index c refers to a conventional ferry. The decision parameter, β_b, is indicated in the equation $H_{b,HSC} = \beta_b H_{b,c}$, where H_b is the wave height immediately before breaking. The criterion in Eq. (1) appears immediately by setting $\beta_b = 1$, $H_c = 0.5$ m and $T_c = 4.5$ s, which may be taken as very rough estimate of wash caused by a conventional ferry (in Kalundborg Fjord, Denmark) at a distance of 1-2 km from the track. It should be mentioned that the criterion does not state how the wake wash will break on the coast. Even though the wave height is less than the above-mentioned limit at 3 m of water depth, the wave height can be considerably higher in water depths less than 3 m due to the shoaling.

Legislation, Regulation and Approval

The conflicts between the ferries on the one side and environmental and recreational interests on the other have prompted the Danish authorities to impose certain restrictions on the operation of HSC. With this objective the Environmental, Coastal and Maritime Authorities introduced new legislation in 1997. The legislation relates to environmental protection of the marine environment, coastal protection and safe navigation and take into account waves but also noise, emissions and disturbance of marine life.

It is now required that a shipping company shall obtain approval from the authorities before it establishes a high-speed ferry route operating on a Danish port or puts a new high-speed ferry into service on an existing route. With respect to wave impact, the shipping company shall document that the ferry on the proposed route does not exceed the wave height criterion described above.

Prediction of wake wash in coastal areas

A numerical model capable of calculating ship-generated waves, wave propagation and wave transformation in non-homogeneous media is the ultimate tool when new regulations and approval procedures are introduced for HSC. Today's CFD methods are used to

compute the wave field around ships advancing in deep or shallow water, but the wave propagation and transformation towards a coastline are seldom not considered, see Larsson (1997). Time-domain models based on depth-integrated Boussinesq type equations, eg Madsen and Sørensen (1990), can be justified for practical purposes in shallow water. As for conventional CFD models, the computational effort may be huge for large domain areas why approximate and efficient methods are needed in practice.

Based on the knowledge of the waves generated along the route, the ship-generated wave climate in larger coastal and shallow water regions can be assessed using a phase-averaged model describing the most important physical processes (including wave decay) the waves are undergoing during their propagation and transformation. An example of a model output is illustrated in Figure 9 showing the computed maximum wave height and the wave directions. The HSC is navigating along the edge of the model in direction of the arrow. The figure shows distinctive focusing of wave energy in a number of areas, which is in agreement with field observations on the site. Even though such types of models neglect the transient effect of the wash, they are extremely helpful in eg route planning of new and existing HSC routes.

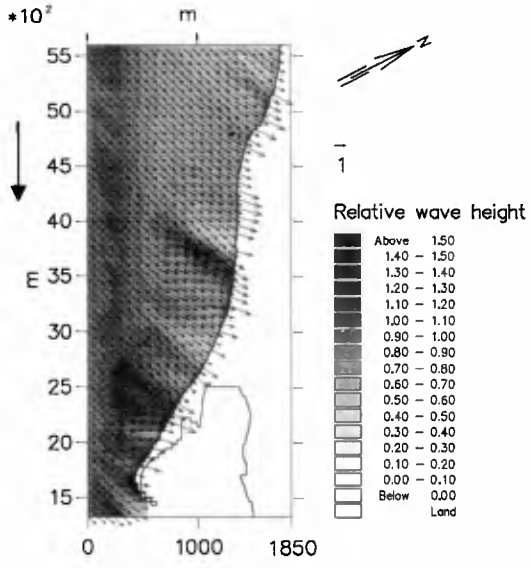

Figure 9. Wave propagation and transformation in Kalundborg Fjord, Denmark. The contour values show the relative wave height defined as the local wave height divided by the wave height at the boundary (the navigation route). The direction of the arrows indicates the wave propagation direction.

Conclusions

Wake wash generated by HSC is markedly different from waves from conventional ships. Wave measuring programs have demonstrated that HSC generates diverging wave patterns consisting of groups of long-period waves and short-periodic waves. The long waves from large car-carrying fast ferries are typically of more than 9 s wave period. These waves have a relatively larger wave height growth during shoaling and wave refraction caused by sea floor irregularities appears in deeper water. The result is that the waves when reaching the shore may cause higher breaking waves and larger run-up than traditional ship waves and the breakers are more often plunging. The waves will arrive faster than ordinary Kelvin waves and particularly during calm whether conditions, people on the beach will not be prepared for a breaking wave appearing without any warning. This is a main reason for the public concern over wake wash from HSC.

The full-scale measurements have also confirmed the significance of the vessel speed versus water depth, expressed in the depth-based Froude number. When operating at near the critical Froude number (~ 1.0), the wave generation is maximum. HSC will operate at critical speed during acceleration and deceleration and due to depth variations several times during transit. It is important that passage of critical speed is carefully planned in order not to coincide with sensitive coastal areas.

Due to the different wave characteristics and the repeated exposure to groups of long waves some variation of coastal characteristics may be experienced near HSC routes. The effect is mainly a steepening of the beach face and grading of sediments. However, the effects of ordinary storm waves will typically dominate the general coastal development.

The inherent conflict between fast ferry operation and recreational use of Danish coastal waters due to wake wash have to be solved by the authorities. New legislation has been made to cope with this issue and today a shipping company has to demonstrate that wake wash does not exceed certain limits along the route and that the environmental impact is limited.

Acknowledgement

The studies described in this paper have primarily been financed by the Danish Maritime Authority, Cat-Link A/S and Scandlines A/S. The co-operation with staff members of DMA, the involved shipping companies and Danish Car Ferry Association is greatly appreciated. Thanks also to Karim A. Rahka, International Research Centre for Computational Hydrodynamics (ICCH), for performing the Boussinesq wave simulations used for the study of cross-shore sediment transport.

References

Crapper, G.D. (1984), "Introduction to water waves", Ellis Horwodd Limited.

Deigaard, R. and J. Fredsøe (1989), "Shear stress distribution in dissipative water waves", *Coastal Engineering*, 13, 357-378.

Deigaard, R. (1993), "A note on the three-dimensional shear stress distribution in the surf zone", *Coastal Engineering*, 20, 47 - 59.

Danish Maritime Authority (1997), "Report on the impact of High-Speed Ferries on the external environment", 22pp.

Elfrink, B. (1997), "Longshore sediment transport in the swash zone", *PhD Thesis*, Series papers No 63, Institute of Hydrodynamics and Hydraulic Engineering (ISVA), Technical University of Denmark.

Elfrink, B., R. Deigaard, I. Brøker, E.A. Hansen and P. Justesen (1996), "Modeling of 3D sediment transport in the surf zone, *Proc. 25nd International Conference on Coastal Engineering*, Orlando, FL, USA, ASCE.

Johnson, J.W. (1958), "Ship waves in navigation channels", *Proc. 6th International Conference on Coastal Engineering*, Berkley, CA, USA, ASCE, 666-690.

Kirkegaard, J., N. Højtved and H.O.H. Kristensen (1998), "Fast ferry operation in Danish Waters", *29th International Navigation Congress*, The Hague, The Netherlands.

Kofoed-Hansen, H. and J. Kirkegaard (1996), "Technical investigation of wake wash from fast ferries", Danish Hydraulic Institute, Report No 5012, 41pp.

Kofoed-Hansen, H. and A.C. Mikkelsen (1997), "Wake wash from fast ferries in Denmark", *Proc. 4th International Conference on Fast Sea Transportation*, Sydney, Australia, 471-478.

Kostyukov, A.A. (1959), "Theory of ship waves and wave resistance", State Union Publishing House for Shipbuilding Industry, Leningrad, Translation by Max Oppenheimer, Jr, Effective Communications Inc, Iowa City, Iowa, 400 pp.

Larsson, L. (1997), "CFD in ship design - prospects and limitations", *Ship Tech. Res.*, 44, 133-154.

Madsen, P.A. and O.R. Sørensen (1990), "Extension of Boussinesq equations to include wave propagation in deeper water and wave-ship interaction in shallow water", *Proc. 22nd International Conference on Coastal Engineering*, Delft, The Netherlands, ASCE, 3112-3126.

Madsen, P.A., H.A. Schäffer and O.R. Sørensen (1997), "Surf zone dynamics simulated by a Boussinesq type model. Part I: Model description and cross-shore motion of regular waves", *Coastal Engineering*, 32, 255-288.

Newman, J.H., (1977), "Marine Hydrodynamics", MIT Press, Cambridge, Mass., 402 pp.

Weggel, J.R. and R.M. Sorensen (1986), "Ship wave prediction for port and channel design", *Proc. Ports '86*, Oakland, CA, 797-814.

Sorensen, R.M. and J.R. Weggel (1984), "Development of ship design information", *Proc. 19th International Conference on Coastal Engineering*, Houston, TX, ASCE, 3227-3243.

Taatø, S.H., C. Aage and M.M. Arnskov (1998), "Waves from propulsion systems of fast ferries", *Proc. 14th International Fast Ferry Conference and Exhibition*, Copenhagen, Denmark.

WAVE PROPAGATION DIRECTIONS UNDER REAL SEA STATE CONDITIONS

Joachim Grüne[1]

Abstract

This paper deals with the analysis of wave propagation directions from wave climate measurements in field. A simple method is presented to analyse wave approach directions from signals of a current meter and a wave gauge in time domain. Results using this method of analyzation are demonstrated exemplarily with data from field monitoring.

Introduction

Wind waves coming in from deeper parts of the shelf in areas with extremely restricted water depths, keep their general three-dimensional characteristic with respect to the water particle movement. Even when the breaking wave crests seem to be transformed into a considerable two-dimensional behavior, the wave-induced velocities keep their three-dimensionality, however often with a distinct strengthening towards a main axis system.

It is well known, that wind direction and wave approach direction don't agree necessarily in areas with restricted water depths like the wadden seas in the German Bight. This is due to the strong influence of the complex three-dimensional underwater topography on wave climate propagation. Thus, forecasting the wave propagation direction sometimes can be very difficult and a more detailed knowledge about wave approach on wadden seas is desirable.

In general, some different methods are used to evaluate wave approach directions. These methods depend on the type of sensors which are used for field measurements of wave climate and may be the following ones:

[1] Dipl.-Ing., Senior researcher, Operation and Research Manager of Joint Central Institution " Coastal Research Centre " (**F Z K**) of University Hannover and Technical University Braunschweig, Merkurstrasse 11, 30419 Hannover, Germany

- One method uses the analysis in time domain from two synchronously recorded signals of the velocity components from a two - component velocity sensor in horizontal plane (method A).

- Another method uses the analysis from three synchronously recorded signals: two signals of the components from a velocity sensor as in method A and additionally one signal of the surface elevation from a wave staff. This analysis is done either in frequency domain (method B) or in time domain (method C).

The evaluation of wave approach direction with analyzation method A only works sufficiently for strongly orientated velocities, which seldom occur in real sea state wave climate.

About the evaluation with analyzation method B it has been reported in a lot of previous papers. Analysing the co- and quad-spectra in frequency domain from data triplets of the two horizontal velocity components and the water surface elevation, the directional distribution and from this the main wave approach may be estimated. This method is very complex and in most papers the essential details of this method never are described.

The evaluation of wave approach from the same data triplets using an analysis in time domain (method C) is much more simple compared with such in frequency domain. In addition to the easy practicability this method has a clear physical sense. Due to these advantages this paper will be focussed on this method.

Field measuring locations and equipment

The data used for the estimation of wave approach direction were measured within a comprehensive field research program on wave climate and wave run-up. This program has been running in cooperation with the Regional State Board for Water Management (ALW Heide, supervision Dipl.-Ing. J. Gärtner) of the State of Schleswig-Holstein for many years at 4 different locations at the landside borders of the wadden sea and in the Elbe river estuary in the German Bight. The data presented in this paper, are recorded at the wadden sea location Heringsand at the coastline of the Dithmarscher Küste, which is shown in Fig. 1. The field locations and the measuring equipments already were described in previous papers in connection with first results on wave run-up (Grüne, 1996) and on wave climate (Grüne, 1997 and Wang & Grüne, 1997).

At each of these locations roughly 1 km in front of the dykeline a support pile with the measuring sensors is installed. The surface elevations are estimated from the records of a pressure cell, using the 1st order theory with empirical transfer function. The velocity components are measured in horizontal plane with an electromagnetic two-component sensor. The sensors are connected by cables with a computer controlled recording system, which is placed in a shelter behind the dyke.

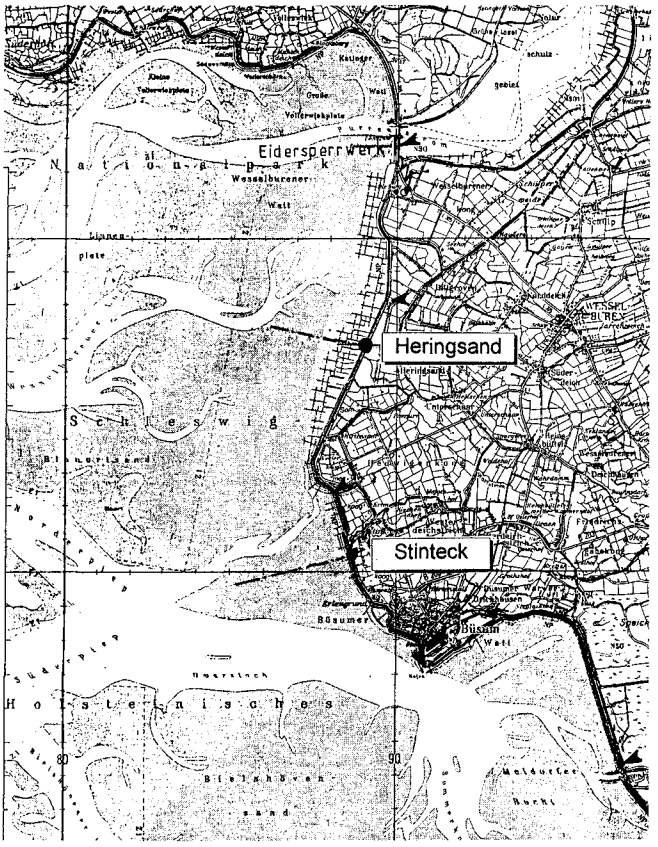

Fig. 1 Measuring locations at the Dithmarscher Küste

Definitions and modalities of analysing wave approach directions

As already mentioned, this paper is focussed on analysing wave approach directions in time domain, using a data triplet of surface elevation η and two rectangular velocity components V_y (normal to dykeline) and V_x (parallel to dykeline) in a horizontal plane as shown in Fig. 2 schematically. An example of such a synchronously recorded data triplet is shown in Fig. 3, where the time histories of the signals of the wave gauge WP1 and the horizontal velocity components S1Y and S1X are plotted for a period of 95 seconds. This example will be used in this paper, to explain the analyzation method.

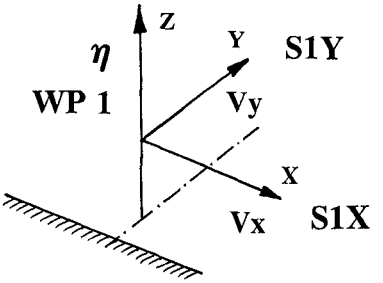

Fig. 2 Scheme of coordinate system of installed sensors

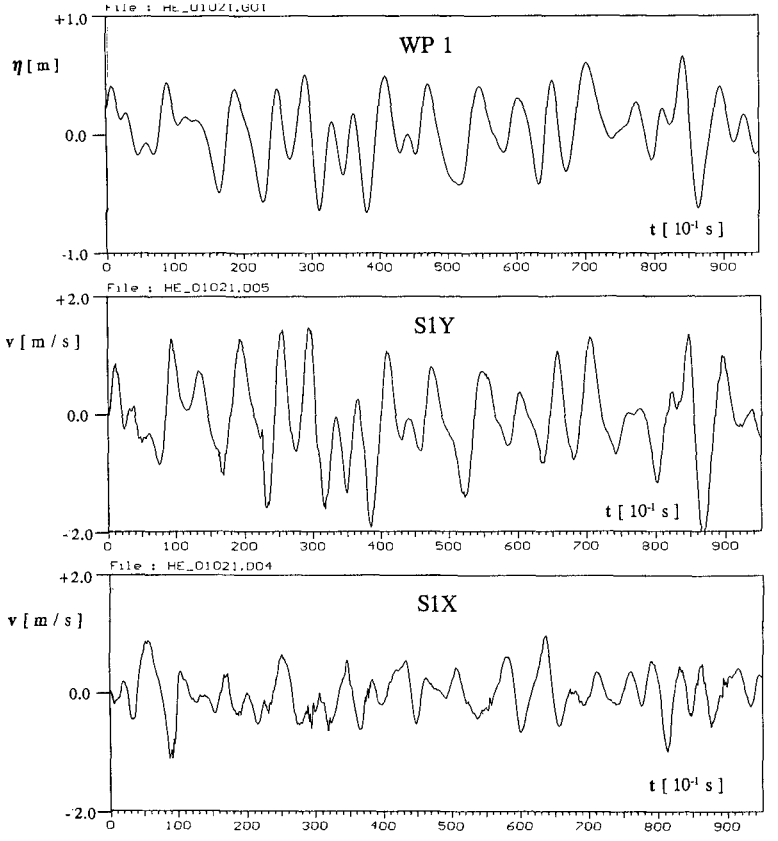

Fig. 3 Example of synchronously recorded wave and velocity data

The data of the two horizontal velocity components V_x and V_y as well as those of the surface elevation η, shown in Fig. 3, are recorded digitally with 10 Hz. With the data from the time period in Fig. 3 the vector course of the two velocity components is plotted in Fig. 4. This course plot seems to have a main direction roughly along the Y-axis. But using the least square correlation method alternating for both independent velocity components V_x and V_y, a mean value from both regressions of - 39.8° will be calculated. This method (one possibility for method A as mentioned before) will create mostly such similar failure results due to the fact, that the mean value from two independent regression lines each with a bad correlation tends always around 45 degrees. A comparison with the result from Fig. 8 (Aw = - 15.6°), which is evaluated with method C as explained later, indicates, that this method don't lead to sufficient results.

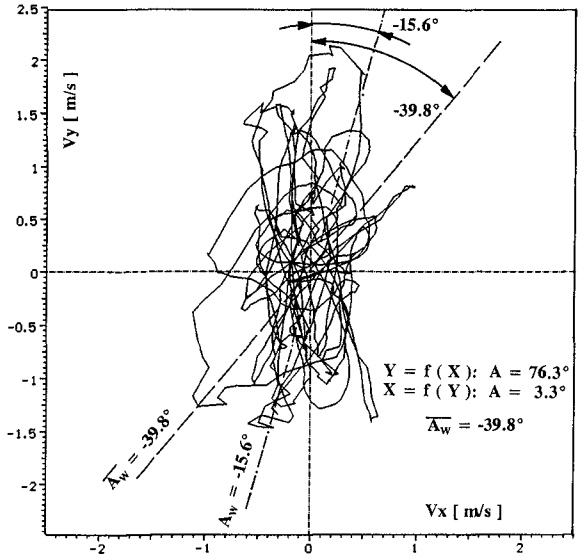

Fig. 4 Velocity vector course of velocity data S1X and S1Y from Fig. 3

But nevertheless, the vector course data itself are very helpful for an evaluation of wave approach directions as demonstrated in Figs. 5 a and 5 b, which give a kind of anatomy of a data triplet in time domain. The time history of surface elevation data η (WP 1) from Fig. 3 has been used to split the wavetrain in 17 consecutive waves, each labelled with continious number 1 to 17. Wave crests and wave troughs of all 17 waves are marked and labelled with time. For this procedure the unscaled pressure data may be used, a transfer to real surface elevations is not necessary. Below the time history of the surface elevation the vector course with the two horizontal velocity components V_x and V_y is plotted separately for each wave event. The vector positions at the dividing troughs between each of the consecutive waves are connected with a dotted line.

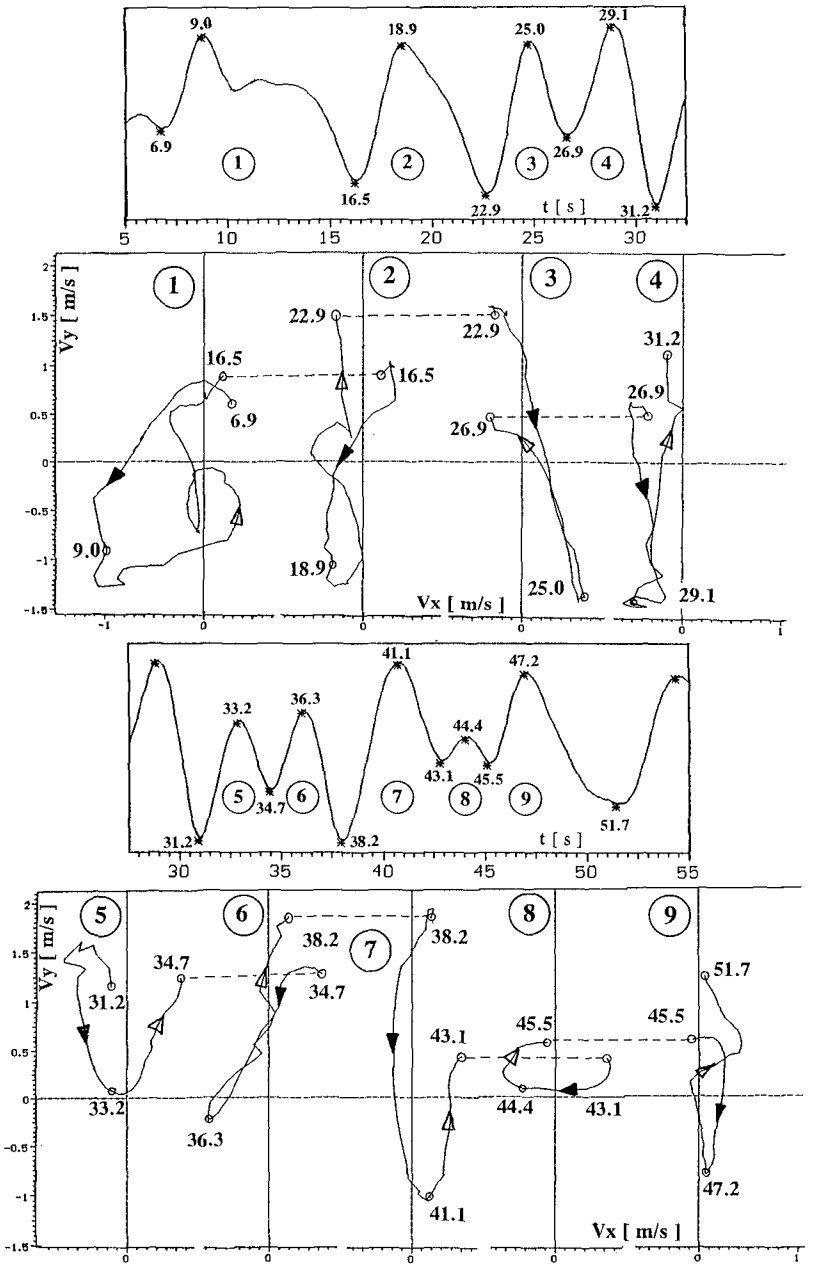

Fig. 5 a Surface elevation and velocity vector course of consecutive waves

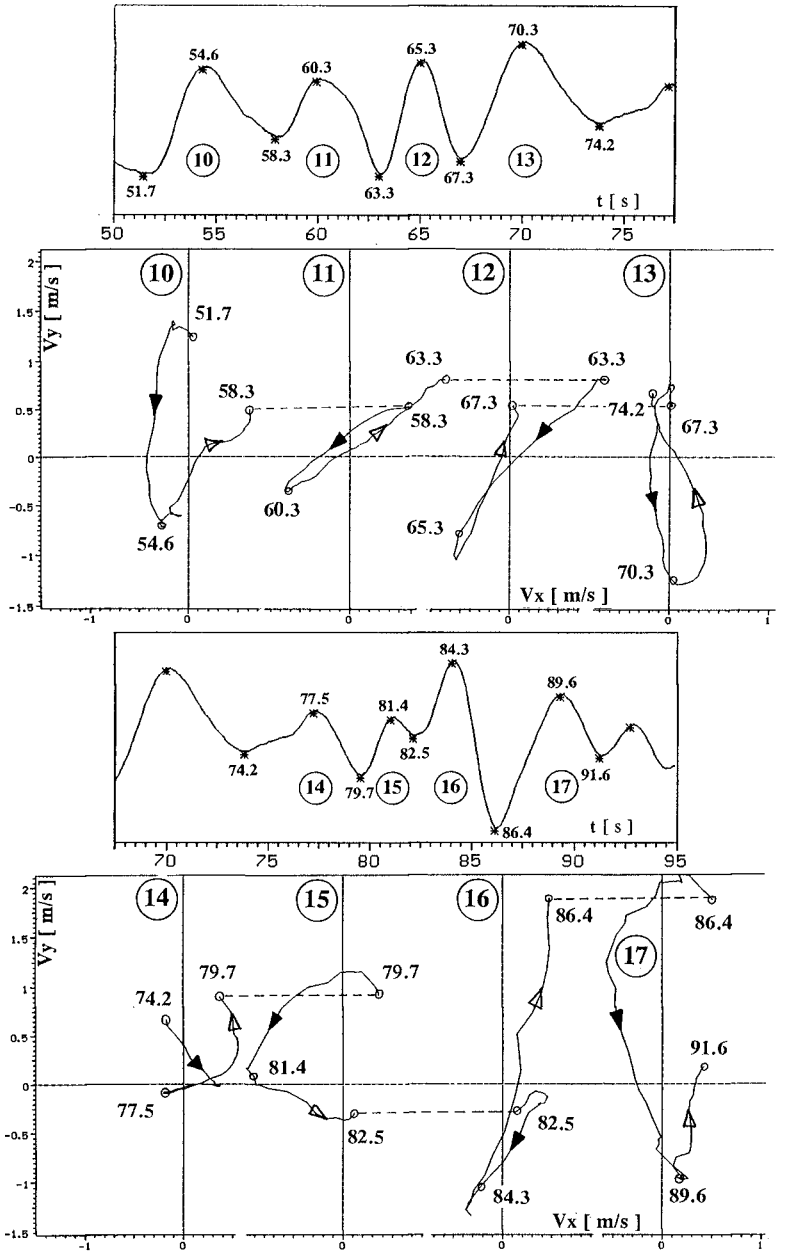

Fig. 5 b Surface elevation and velocity vector course of consecutive waves

Comparing the vector plots of the separated waves in the wavetrain in Figs. 5 a and 5 b, one finds a more or less distinct changing of the approach direction of the water particles at each wave crest and wave trough, which is self-evident for pure two-dimensional waves. This leads to the evaluation of wave approach directions for real sea state conditions from the vector course data between wave crests and troughs. The wave approach directions for such a mode are defined in Fig. 6 schematically.

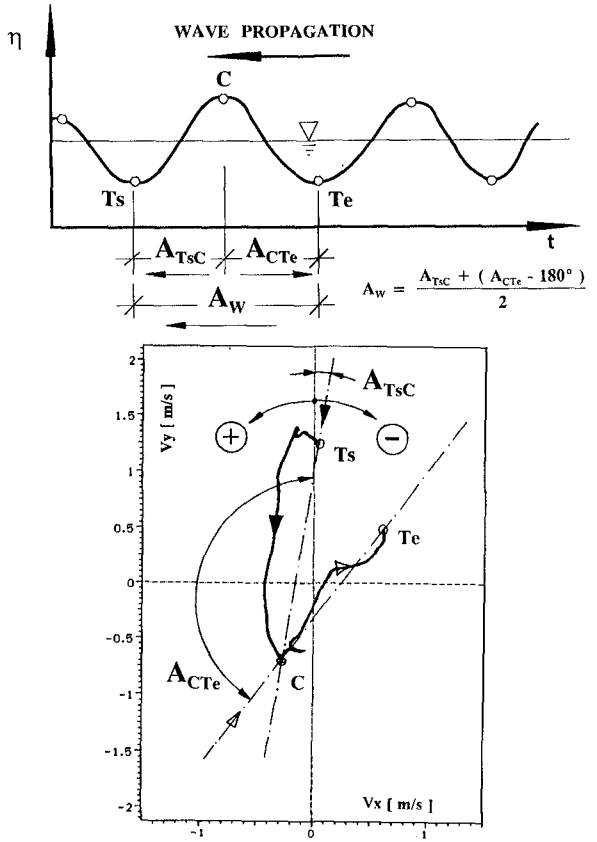

Fig. 6 Definitions for wave approach directions

The definitions in Fig. 6 may be described as follows:

The direction A_{TsC} is defined as mean direction between trough Ts and crest C. Ts is the trough at the start of the wave event according to the time and C is the crest, both are identified from the surface elevation in time history. Troughs and crests are related to time. According to physical sense this means the oncoming rising front of the

wave. A_{TsC} is determined as angle between normal direction (Y - axis of horizontal plane) and linear connection between vector course positions at trough Ts and crest C, as defined in the lower part of Fig. 6, where the rules of sign for the directions A_{TsC} and A_{CTe} are defined as well. The vector course of the oncoming rising front is marked with a black arrow in all figures.

The direction A_{CTe} is defined as mean direction between crest C and trough Te, where Te is the trough at the end of the wave event and this part of the vector course is marked with an open arrow in all figures.

A_W is defined as the total approach direction of each wave event. A_W is calculated as the mean value of A_{TsC} and A_{CTe}. It must be noticed, that A_{TsC} and A_W have approximately the same directions as the main direction of wave propagation has, whereas A_{CTe} has the opposite direction (see also the lower part of Fig. 6, where the rule of sign is defined).

The vector plots in Figs. 5 a and 5 b demonstrate the manifoldness of the vector course anatomy and its complexibility. The vector course of event Nr. 1 in Fig. 7 (right plot) confirms, that nearly each small crest or trough of surface elevation (left plot) creates a significant changing of course direction, even within a defined wave event.

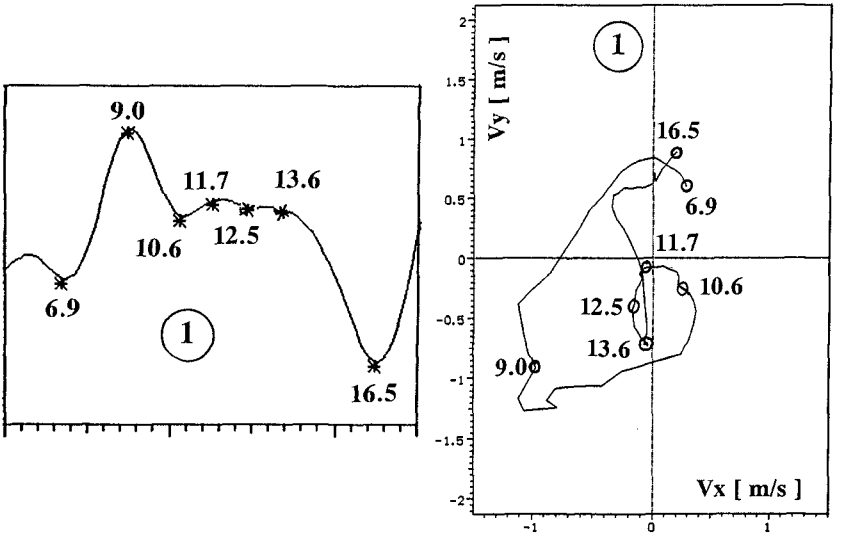

Fig. 7 Example of a wave with complex velocity vector course

Comparing all wave events in Figs. 5 a and 5 b one can find wave events, where the vector courses are as well straightened relatively strong within each wave event and the directions A_{TsC} and A_{CTe} don't differ very much from each other (e.g. wave events

Nr. 2, 3, 4, 6, 11, 12 and 16). Nevertheless, the mean directions A_W differ from those events next to distinctly.

Furthermore there are wave events, where the direction of A_{TsC} differ considerable from that of A_{CTe}, which means a changing of main direction within the wave event (e.g. Nr. 5, 8, 10, 14 and 15). From these events it is obvious, that mostly the chaotic vector courses may be created by the smaller waves between larger ones (e.g. event Nr. 8, 14 and 15).

All estimated approach directions from the test example in Figs. 5 a and 5 b with totally 17 consecutive wave events are plotted in Fig. 8. Significant differences between the different defined directions within one wave event only occur for the smaller waves like e. g. Nr. 8 and 15, as already mentioned before. The result for the mean approach direction (A_W = -15,6°) is compared in Fig. 5 with the results, using method A with the mean value of two independent correlations with the digitally recorded (equidistant with 10 Hz) velocity data. The failure of using the components alone in such a manner is manifest.

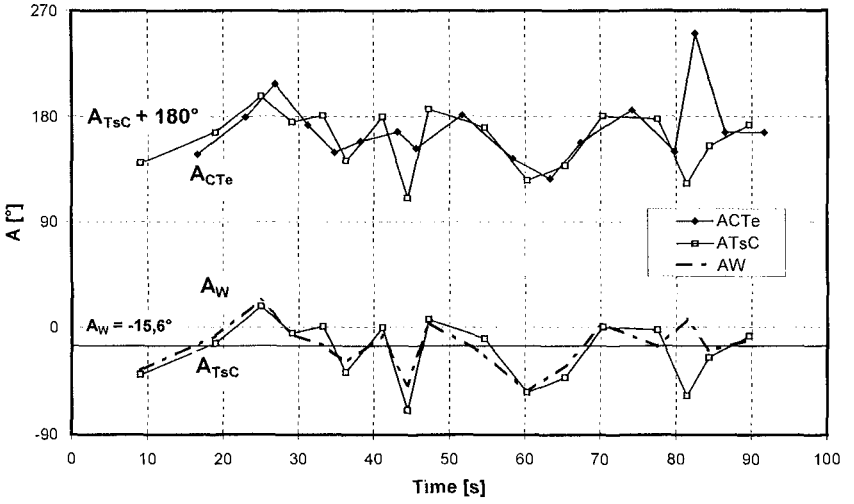

Fig. 8 Wave approach directions evaluated from the waves in Figs. 5a and 5b

First results

As already mentioned, the evaluated approach directions of consecutive waves in a wave train have strong fluctuations. This comes out clearly in Fig. 9, where the evaluated values for A_{TsC} and A_{CTe} are plotted as time history for a period of 15 minutes, measured in field. But beyond a certain time period the mean values are relatively

constant. In Fig. 9 for example the fat line in the upper part stands for the A_{TsC} mean values of 9 consecutive time periods, each 100 seconds long. The differences compared with the mean value of the total period (A_{TsC} = 305,9°) are very small. It must be noticed, that in Fig. 9 and in all following figures the wave approach directions are transferred to the geodetic coordinate system with 0° = North.

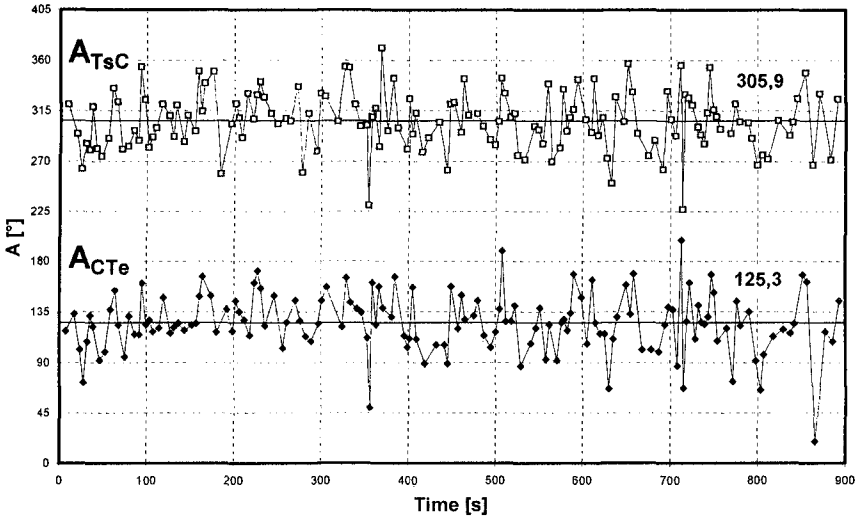

Fig. 9 Fluctuations of A_{TsC} and A_{CTe} during a period of 15 minutes

The values for A_{TsC} and A_{CTe} from the example in Fig. 9 are plotted as frequency distributions in Fig. 10. The mean values of A_{TsC} and (A_{CTe} + 180°) for the total period differ only 0.6 degrees from each other. The agreements with the calculated Normal - distributions are quite good. The total range of fluctuation of the evaluated approach directions is roughly ± 70° and the standarddeviation is roughly 26°. The frequency distribution of the total wave approach directions A_W is plotted in Fig. 11 . Similar wide sectors of fluctuation of wave approach were found for other measurements. With respect to the influence on wave run-up these results indicate, that a possible reduction on wave run-up values due to oblique wave approach should be smaller than expected by excisting formulae, verified with long-crested sea state.

Results of wave approach directions measured during one storm surge event are given in Fig. 12 examplarily. The stillwaterlevel SWL, the local winddirection R_0, the local windvelocity U_0 and the measured wave approach directions A_W are plotted as time history. Each plotted point is the result (mean value) of one of the time periods, which have each a duration of 15 minutes and were recorded consecutively.

During this storm surge event the local wind velocities U_0 as well as the local wind directions R_0 were relatively constant, whereas the wave approach directions A_W

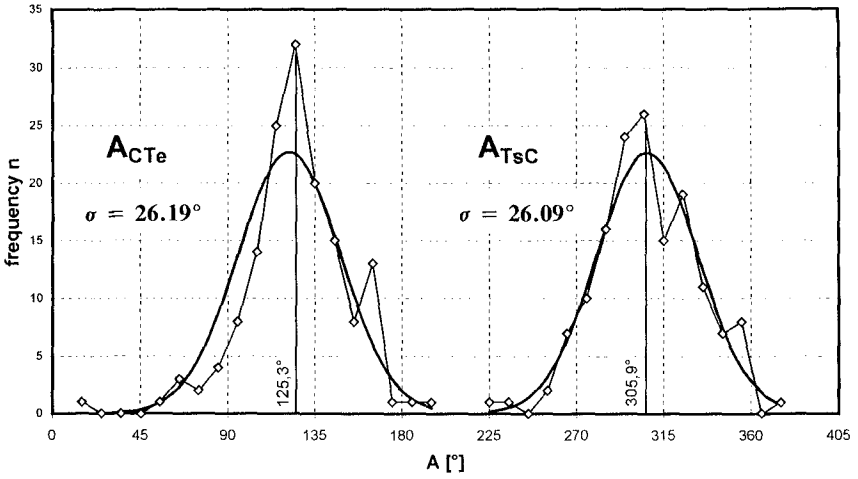

Fig. 10 Frequency distributions of A_{TsC} and A_{CTe} from the data in Fig. 9

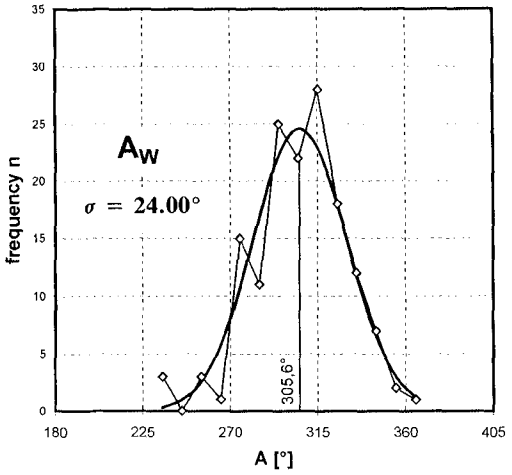

Fig. 11
Frequency distribution of A_W from the data in Fig. 9

partly differ considerable from the wind directions R_0. It is well known, that in such areas the wave propagation direction is strongly influenced by the local morphology and that waves are even propagating against the wind, as far as they run along gullies. Thus, it must be expected, that the differences between winddirection and wave approach direction are mainly caused by the influence of the morphology. Comparing the time histories of the wind- and wave approach direction in Fig. 12 it can be stated, that the differences between both directions decrease with increasing water depth.

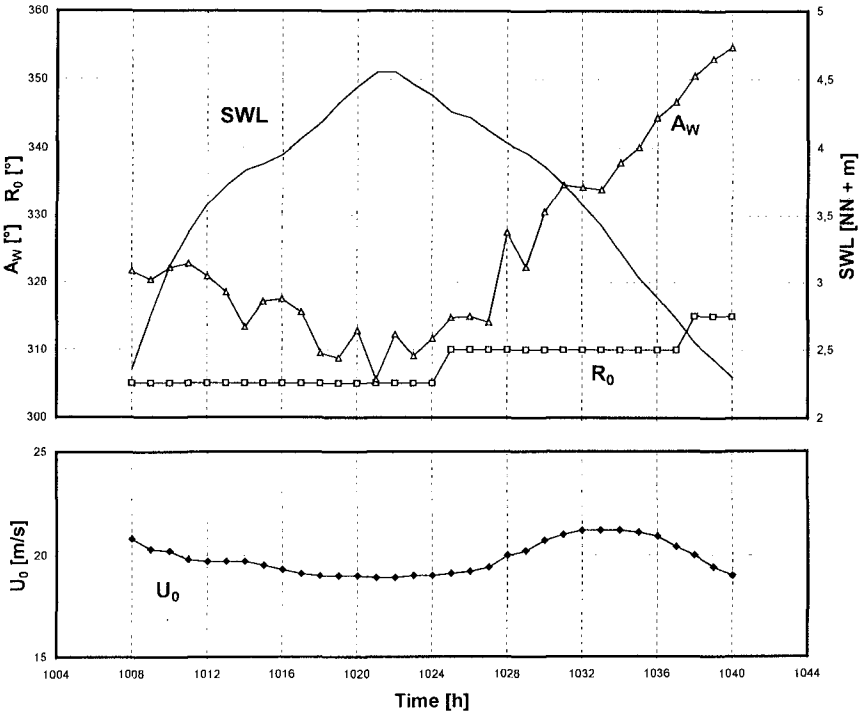

Fig. 12 Time histories of stillwaterlevel SWL, local winddirection R_0, local windvelocity U_0 and wave approach directions A_W during a storm surge

From the morphological conditions around the location Heringsand in Fig. 1 it may be supposed, that the mean wave propagation directions during the rising and falling part of the storm surge stillwaterlevel are adjusted to the end of the main gully.

The influence of water depth comes out clearly in Fig. 13, where the difference between the wave approach direction and the local wind direction A_W - R_0 is plotted versus the stillwaterlevel SWL. The phaseshift A_W - R_0 decrease with increasing water depth, but with different order of magnitude for rising and falling part of the storm surge stillwaterlevel. The phaseshift of the falling part of the storm surge has roughly up to twice the value of that of the rising part, whereas in the summit range it tends to zero. The different phaseshift for rising and falling part may be explained partly by the general trend of tidal motion from South to North in this part of the German Bight. From the ongoing analysis similar results are found for other storm surge events, often

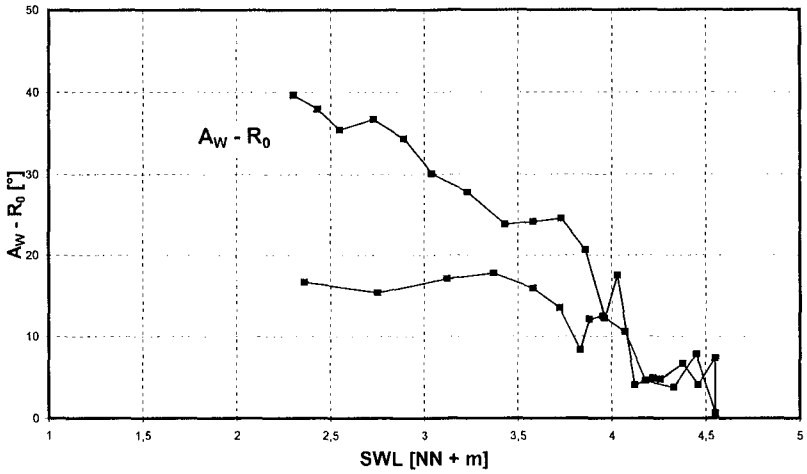

Fig. 13 Phaseshift between wave approach directions A_W and winddirection R_0

in a more complex shape, especially for storm surges with lower summits of stillwaterlevel. Furthermore it was found that the phaseshift also depends on the absolut winddirection and that gullies like the one at Stinteck location have strong influence. All results confirm the strong influence of the local morphology.

Conclusion

For the analysis of wave approach directions from triplet field data of surface elevation and horizontal velocity components a simple method is dicussed with the aid of an example and first results are presented from measurements during a storm surge event. These results indicate the wide range of fluctuations of wave approach directions as well as the strong influence of morphological conditions on approach directions. This topic has to be investigated during the ongoing research work in more detail, especially with the data recorded at the locations in the Elbe river estuary.

References

Grüne J., 1996 Field study on wave run-up on seadykes.
Proc. of 25th. Intern. Conf. on Coastal Eng. (ICCE'96), Orlando, USA

Grüne J., 1997 Field study on wave climate in wadden seas and in estuaries.
Proc. of 3rd. Intern. Symp. on Ocean Wave Meas. and Analysis (WAVES'97), Virginia Beach, USA.

Wang Z. & Grüne J., 1997 The effect of foreland on wave climate changes.
Proc. of 3rd. Intern. Symp. on Ocean Wave Meas. and Analysis (WAVES'97), Virginia Beach, USA.

On the Accuracy of Parabolic Wave Models

Hakeem K. Johnson[1] and Sanne Poulin[2]

Abstract

Errors in parabolic equation models (PEM) for wave refraction and diffraction are investigated by examining the case of waves propagating over a planar bathymetry for which the analytical solution is well known. The models investigated are: i) lowest order parabolic approximation (Simple method), ii) Padé approximation and iii) Minimax approximation models.

Errors in wave heights, wave directions, radiation stresses and resulting longshore currents are investigated analytically and by numerical tests using the parabolic equation model MIKE 21 PMS. The results indicate that, while the predicted wave directions are generally accurate, the wave heights, radiation stresses and longshore currents can contain significant errors depending on the parabolic approximation used.

Introduction

Parabolic equation models (PEM) for wave refraction/diffraction are frequently used in coastal engineering practice for the computation of wave parameters, radiation stresses and associated wave-induced nearshore currents in coastal areas. The PEM approach is attractive since it is computationally more efficient than the complete elliptic mild-slope model, and it provides useful engineering results for refraction/diffraction problems (in the absence of significant reflection) in the coastal area (Berkhoff et. al., 1982, Johnson et. al., 1994).

[1] Dr Nik and Associates, 20-2 Jalan Setiawangsa 10, Taman Setiawangsa, 54200 Kuala Lumpur, Malaysia.

[2] Danish Hydraulic Institute, Agern Allé 5, DK-2970 Hørsholm, Denmark

The parabolic equation model is derived as an approximation to the elliptic mild slope equation (derived by Berkhoff, 1972) governing the refraction, shoaling, diffraction and reflection of linear water waves propagating on mildly sloping bathymetry. The lowest order parabolic approximation is obtained by assuming a principal wave direction (x-direction) and neglecting backscatter. Kirby (1986) extended this approximation to allow waves propagating at large angles to the assumed principal direction. Many numerical models have been developed based on these approximations. One such wave model is the MIKE 21 Parabolic Mild Slope (PMS) model, which is based on the equations derived by Kirby (1986).

As a result of the underlying assumptions, PEM do not exactly reproduce the refraction coefficient for waves approaching the coast at an angle. This introduces errors in the nearshore wave heights and radiation stresses and, consequently, in the wave-driven longshore currents. The magnitude of the errors depends on the type of parabolic approximation.

In this paper, we attempt to quantify the errors and give suggestions for minimizing the influence of the errors in real applications. This is achieved by examining the simple case of wave propagation over straight and parallel depth contours for which an analytical solution exists.

This paper is broadly divided into two parts. In the first part, the PEM is used to derive evolution equations for wave heights and directions over straight and parallel contours. This is compared with the analytical solution, and thus the errors in the PEM are obtained. In the second part, results of numerical tests using MIKE 21 PMS are compared with the analytical solution in order to quantify the errors in the various parabolic approximations. Finally, some conclusions are derived regarding an optimal PEM for practical situations.

Parabolic Equation Model

The starting point for the analysis is the general parabolic equation derived by Kirby (1986) for linear waves in the absence of currents. Kirby removed the rapidly varying term from the mean free surface potential ϕ, to obtain a slowly varying complex function A (see Eq. 1), which is used as the primary variable in the parabolic equation

$$\phi = A(x,y)e^{ik_0 x} \tag{1}$$

In Eq. 1, k_0 is a characteristic wave number, typically chosen as the average wave number along the y-direction, and x is the principal wave direction. Kirby obtained the parabolic equation given in Eq. 2.

$$A_x + i(k_o - \beta_1 k)A + \frac{A}{2c_g}(c_g)_x + \frac{\sigma_1}{\omega c_g}(cc_g A_y)_y + \frac{\sigma_2}{\omega c_g}(cc_g A_y)_{yx} + \frac{W}{2c_g}A = 0 \quad (2)$$

where

$$\sigma_1 = i\left(\beta_2 - \beta_3 \frac{k_o}{k}\right) + \beta_3\left(\frac{k_x}{k^2} + \frac{(c_g)_x}{2kc_g}\right) \quad (3)$$

$$\sigma_2 = -\frac{\beta_3}{k} \quad (4)$$

The subscripts x, y respectively represent differentiation with respect to x and y, i is the imaginary unit, k is the local wave number, c_g is the local group velocity, ω is the circular wave frequency, β_1, β_2 and β_3 are the coefficients of the parabolic approximation, and W is a dissipation term (e.g. bottom dissipation, wave breaking). The β-coefficients are given in Table 1 for various parabolic approximations.

Approximation	β_1	β_2	β_3
Simple	1	-0.5	0
Padé (1,1)	1	-0.75	-0.25
Minimax 10°	0.999999972	-0.752858477	-0.252874920
Minimax 20°	0.999998178	-0.761464683	-0.261734267
Minimax 30°	0.999978391	-0.775898646	-0.277321130
Minimax 40°	0.999871128	-0.796244743	-0.301017258
Minimax 50°	0.999465861	-0.822482968	-0.335107575
Minimax 60°	0.998213736	-0.854229482	-0.383283081
Minimax 70°	0.994733030	-0.890064831	-0.451640568
Minimax 80°	0.985273164	-0.925464479	-0.550974375

Table 1. Coefficients for various parabolic approximations.

The lowest order parabolic approximation is denoted as the Simple approximation in Table 1. The Minimax approximations minimize the error in the wave number over the entire aperture width associated with it. However, this does not preclude that the error for specific directions (within the aperture width) may be large.

Parabolic Equation Model for Straight and Parallel Depth Contours

The evolution equations for wave heights and directions are derived here for the case of straight and parallel depth contours and no dissipation (W = 0). The Cartesian co-ordinate system is chosen such that the y-axis is parallel to the coastline.

The mean free surface potential for plane, progressive waves can be written as:

$$\phi = A^*(x,y)e^{i\Psi} \quad ; \qquad \Psi = \int_x k\cos\theta\, dx + \int_y k\sin\theta\, dy \tag{5}$$

where $A^*(x,y)$ is the amplitude function (equals half of the wave height H) and Ψ is the phase function. Combining Eqs. 1 and 5, the slowly varying mean surface potential can be expressed as:

$$A = A^*(x,y)e^{i(\Psi - k_0 x)} = \frac{H}{2}(x,y)e^{i(\Psi - k_0 x)} \tag{6}$$

Thus, the derivatives in Eq. 2 can be found as a function of $A^*(x,y)$ and Ψ. For example, A_y is obtained as:

$$A_y = \left\{A^*(x,y)\cdot i\Psi_y + A_y^*\right\}e^{i(\Psi - k_0 x)} \tag{7}$$

For straight and parallel depth contours, the wave height H, wave number k, phase speed c, and group velocity c_g, are all constant along the contours (y-direction). Introducing these constraints and rearranging, Eq. 2 gives:

$$A_x = \frac{\left\{i(\beta_1 k - k_0) - \left[\frac{(c_g)_x}{2c_g} - k\sigma_1 \sin^2\theta - \frac{k^2\sin^2\theta}{\omega c_g}\sigma_2 (cc_g)_x\right]\right\}}{1 - k\sigma_2 \sin^2\theta} A \tag{8}$$

Using Eq. 6, an expression for A_x/A in terms of the wave height and phase can be written as:

$$\frac{A_x}{A} = \frac{H_x}{H} + i(\Psi_x - k_0) = \frac{H_x}{H} + i(k\cos\theta - k_0) \tag{9}$$

Equating the real and imaginary parts of Eq. 9 with those of Eq. 8, the following evolution equations for wave height H and direction θ are derived from the PEM

$$\frac{H_x}{H} + \frac{(c_g)_x}{2c_g} - 2\beta_3 \frac{S^2/k^2}{(1+\beta_3 S^2/k^2)}\frac{k_x}{k} = 0 \tag{10}$$

$$\cos\theta = \left(\frac{\beta_1 + \beta_2 S^2/k^2}{1 + \beta_3 S^2/k^2} \right) \tag{11}$$

where $S = k \sin\theta$.

Exact solution for straight and parallel depth contours

The evolution equations for the exact solution are derived from Snell's law and the conservation of energy flux. According to Snell's law, $k \sin\theta$ = constant = S. This can be alternatively written as:

$$\cos\theta = \sqrt{1 - \left(\frac{S}{k} \right)^2} \tag{12}$$

Eq. 12 may be accurately approximated as (see Figure 1):

$$\cos\theta = \left(\frac{\beta_1 + \beta_2 S^2/k^2}{1 + \beta_3 S^2/k^2} \right) \tag{13}$$

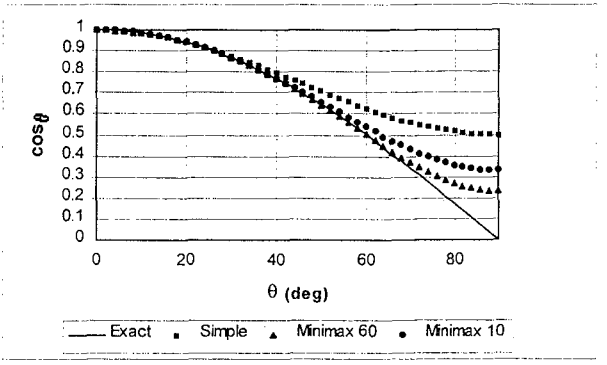

Figure 1. Approximate expressions for $\cos\theta$ using β coefficients for Simple, Minimax 10° and Minimax 60° PEM.

The conservation of energy flux equation is written as:

$$H^2 c_g \cos\theta = \text{constant} \tag{14}$$

Differentiating Eq. 14 with respect to x, the exact evolution equation for the wave height is obtained as:

$$\frac{H_x}{H}+\frac{(c_g)_x}{2c_g}+\frac{(\cos\theta)_x}{2\cos\theta}=0 \tag{15}$$

Inserting Eq. 13 (using Minimax 60° coefficients, indicated by *) into Eq. 15, an almost exact evolution equation (Eq. 16) for wave height is obtained.

$$\frac{H_x}{H}+\frac{(c_g)_x}{2c_g}+\frac{\beta_1^*\beta_3^*-\beta_2^*}{(\beta_1^*+\beta_2^*S^2/k^2)(1+\beta_3^*S^2/k^2)}\frac{S^2/k^2}{}\frac{k_x}{k}=0 \tag{16}$$

Eq. 16 can be readily compared with the corresponding evolution equation from the PEM, Eq. 9.

Errors

Since Eqs. 11 and 13 are identical, it is clear that the errors in wave directions are small in PEM, as long as Eq. 13 is a good approximation to Eq. 12. This covers a wide range of directions (as shown in Fig. 1), even for the lowest order approximation. Thus, calculated wave directions from PEM would be generally accurate.

Comparing Eqs. 10 and 16, it is obvious that the PEM evolution equation for the wave height is different from the analytical solution, resulting in errors.

In order to relate the errors to physically meaningful properties such as the shoaling coefficient K_s, and refraction coefficient K_r, the wave height at an inshore location is written as:

$$H=H_0K_sK_r \tag{17}$$

where H_0 is the wave height at an offshore location. Differentiating Eq. 17 with respect to x and dividing through by $H=H_0K_sK_r$ gives:

$$\frac{H_x}{H}-\frac{K_{s,x}}{K_s}-\frac{K_{r,x}}{K_r}=0 \tag{18}$$

Comparing Eqs. 18 and 15, it is clear that the second term in Eq. 15 (and in Eqs. 10 and 16) is related to the shoaling coefficient, while the third term is related to the refraction coefficient. Thus, while the shoaling coefficient is exactly reproduced in PEM, the refraction coefficient in PEM contains some errors. The refraction terms in Eqs. 10 and 16 are reproduced below:

$$\left[\frac{K_{r,x}}{K_r}\right]_{PEM}=\frac{2\beta_3S^2/k^2}{1+\beta_3S^2/k^2}\frac{k_x}{k} \tag{19}$$

$$\left[\frac{K_{r,x}}{K_r}\right]_{exact} = \frac{\left(\beta_2^* - \beta_1^*\beta_3^*\right)}{\left(\beta_1^* + \beta_2^* S^2/k\right)} \frac{S^2/k^2}{\left(1+\beta_3^* S^2/k^2\right)} \frac{k_x}{k} \tag{20}$$

For waves approaching perpendicular to the coast ($\theta = 0$), $S = 0$, and both refraction terms are zero. Thus, in this special case, the wave heights in the PEM are calculated correctly, since there is no refraction. The same is true for constant water depth where $k_x = 0$.

It is also seen that the refraction term in the parabolic equation model is identically zero for all angles if the Simple approximation is used, since $\beta_3 = 0$. Thus, the Simple approximation does not account for refraction effects at all.

For oblique incidence (and varying depth), we define λ as the ratio of the refraction term in the PEM to that in the exact solution.

$$\lambda = 2\beta_3 \frac{\left(\beta_1^* + \beta_2^* S^2/k^2\right)}{\beta_2^* - \beta_1^*\beta_3^*} \frac{\left(1+\beta_3^* S^2/k^2\right)}{\left(1+\beta_3 S^2/k^2\right)} \tag{21}$$

The ideal situation is $\lambda = 1$. This corresponds to the case where the refraction term is exactly reproduced in PEM. For $\lambda < 1$, the refraction term is underestimated in PEM (i.e. not enough refraction), while for $\lambda > 1$, the refraction term is over-exaggerated (i.e. too much refraction). In the case of the Simple approximation, the refraction term is not reproduced at all, i.e. λ=0. In Figure 2, $(\lambda - 1)$ is shown as a function of wave direction θ for various parabolic approximations given in Table 1 (except Simple).

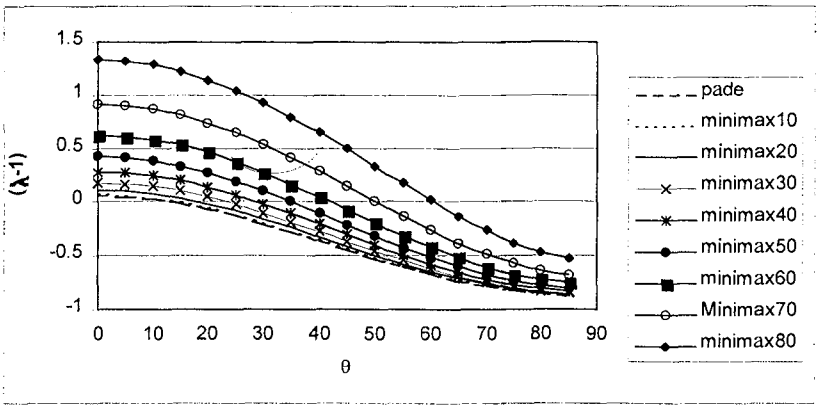

Figure 2. Error in the refraction term as a function of incident wave direction for various parabolic approximations.

It is seen from Figure 2 that the Padé approximation gives the minimum error for small angles of incidence, 0° to 20°. For larger angles, the Minimax 50° or Minimax 60° give the minimum error on average.

Using Eq. 18, we write:

$$\left(\frac{H_x}{H}\right)_{PEM} = \left(\frac{(K_s)_x}{K_r}\right)_{exact} + \lambda\left(\frac{(K_r)_x}{K_r}\right)_{exact} \tag{22}$$

$$\left(\frac{H_x}{H}\right)_{exact} = \left(\frac{(K_s)_x}{K_r}\right)_{exact} + \left(\frac{(K_r)_x}{K_r}\right)_{exact} \tag{23}$$

Using Eqs. 22 and 23, the error in wave height obtained with the PEM at a distance Δx from the offshore location is obtained as:

$$H_{\Delta x,PE} - H_{\Delta x,exact} = (\lambda - 1)H_0 \Delta x \cdot \left(\frac{(K_r)_x}{K_r}\right)_{exact} \tag{24}$$

The refraction coefficient $K_r = \sqrt{\cos\theta_i / \cos\theta_0}$, where θ_i is the inshore wave direction which decreases towards the shore (with increasing x), hence $(K_r)_x/K_r$ is always less than 0. Thus, it follows that if $\lambda > 1$, the inshore wave height will be underestimated (since the refraction effect is over-exaggerated). The converse is true for $\lambda < 1$. For $\lambda = 1$, the error is identically zero. However, there is no PEM that gives $\lambda = 1$ for any range of wave directions. For example, if Padé approximation is used, the parabolic equation model will overestimate the inshore wave heights for most wave directions (> 15°).

Radiation stresses

The next important question is what effect these errors have on wave-driven longshore currents calculated using the parabolic equation model. For straight and parallel depth contours, the important radiation stress gradient term for these currents is

$$\left(\frac{\partial S_{xy}}{\partial x}\right)_{exact} = \frac{\sin\theta}{c}\frac{\partial E c_g \cos\theta}{\partial x} = S_{xy}\left\{2\frac{H_x}{H} + \frac{(c_g \cos\theta)_x}{c_g \cos\theta}\right\}_{exact} \tag{25}$$

Outside the surf zone (disregarding bottom friction), the right-hand side should be zero, since there is no dissipation. Performing the differentiation of the second term in the curly braces and rearranging, we obtain:

$$\frac{1}{S_{xy}}\left(\frac{\partial S_{xy}}{\partial x}\right)_{exact} = 2\left(\frac{H_x}{H}\right)_{exact} + \left(\frac{(\cos\theta)_x}{\cos\theta}\right)_{exact} + \left(\frac{(c_g)_x}{c_g}\right)_{exact} \tag{26}$$

A similar expression is obtained for the parabolic equation model. The last term in Eq. 25 is the shoaling term, which is identical both in the exact and the parabolic case. The second term is the refraction term.

Using Eqs. 22 and 23, and remembering that $(\cos\theta)_x/\cos\theta = (K_r)_x/K_r$, the difference between the exact and the PEM expression for the radiation stress term is obtained as shown below:

$$\begin{aligned}
&\frac{1}{S_{xy}}\left(\frac{\partial S_{xy}}{\partial x}\right)_{PEM} - \frac{1}{S_{xy}}\left(\frac{\partial S_{xy}}{\partial x}\right)_{exact} \\
&= 2\left\{\left(\frac{H_x}{H}\right)_{PEM} - \left(\frac{H_x}{H}\right)_{exact}\right\} + \left(\frac{(\cos\theta)_x}{\cos\theta}\right)_{PEM} - \left(\frac{(\cos\theta)_x}{\cos\theta}\right)_{exact} \\
&= 2(\lambda-1)\left(\frac{K_{r,x}}{K_r}\right)_{exact} + 2(\lambda-1)\left(\frac{K_{r,x}}{K_r}\right)_{exact} = 4(\lambda-1)\left(\frac{K_{r,x}}{K_r}\right)_{exact}
\end{aligned} \tag{27}$$

Outside the surf zone, we therefore see that:

$$\frac{1}{S_{xy}}\left(\frac{\partial S_{xy}}{\partial x}\right)_{PE} = 4(\lambda-1)\left(\frac{K_{r,x}}{K_r}\right)_{exact} \tag{28}$$

which is generally non-zero, meaning that currents are generated which should not be there. Only when $S = 0$ (or the depth is constant) is the right-hand side zero, as it should be, for all wave directions. The type of current generated depends on λ. If $\lambda > 1$, $\partial S_{xy}/\partial x < 0$, and spurious currents are generated which may look realistic. On the other hand, when $\lambda < 1$, $\partial S_{xy}/\partial x > 0$ and clearly unrealistic currents are generated in the "opposite" direction to wave propagation.

In the following second part, numerical examples are presented in order to quantify the errors.

Numerical Examples

The parabolic approximations implemented in MIKE 21 PMS will now be compared with the analytical solution on a beach with straight and parallel depth contours. The slope is 1:50 and the water depth at the toe of the slope is 10m. The shore is parallel to the y-axis and the wave direction is measured from the x-axis. A monochromatic wave is considered, with wave height H=1m at 10m depth and wave period T=8s.

The results in Figures 3 to 5 are shown as functions of the wave direction at the toe of the slope, for a location halfway up the slope, where the depth is 5m. Note that the errors generally increase with decreasing water depth. However, in very shallow water, when wave breaking becomes important, the energy dissipation due to wave breaking is likely to

be more important than the refraction error in the PEM. This aspect was not investigated in this study.

In Figure 3, the relative errors (in %) in the wave directions calculated using the parabolic equation model are shown. It is seen that the errors are less than 1%, even for directions as large as 70°. This confirms that wave directions are calculated accurately using the parabolic equation model.

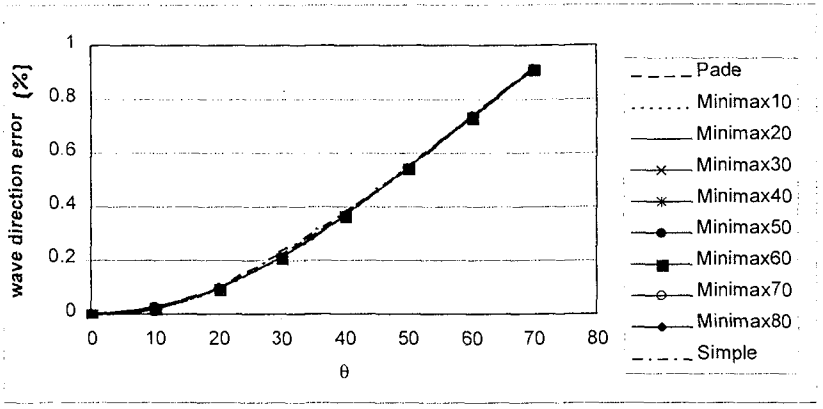

Figure 3. Relative errors in wave directions at 5m depth.

In Figure 4, the corresponding relative errors in wave heights are shown. As expected, these errors are much larger, especially for the Simple approximation. For very large wave directions (directions > 50°), the Minimax 80° performs well, however, it produces much larger errors for smaller directions. Generally, the various approximations are very accurate (less than 5% error) for directions up to 50°.

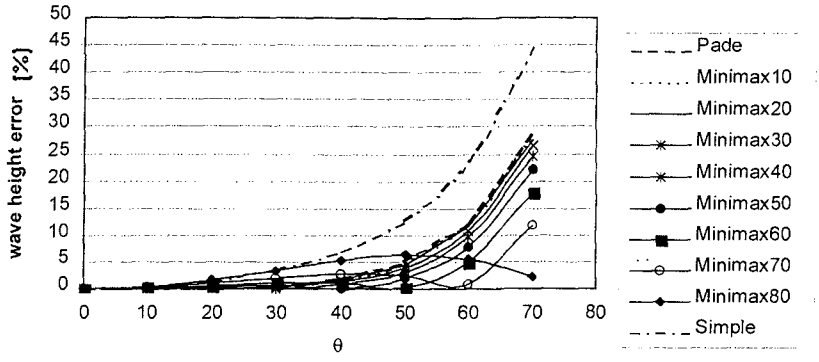

Figure 4. Relative errors in wave heights at 5m depth.

Figure 5 shows the relative errors in the radiation stress term S_{xy}. Notice that it is not the radiation stress *gradient* that is shown. It is again seen, that the Simple approximation only works well for very small directions and that the Padé approximation and the Minimax 10°-30° approximations are almost identical. The errors for larger wave directions decrease with increasing aperture width in the Minimax approximation. However, the Minimax approximation with large aperture width (Minimax 70°, Minimax 80°) gives bigger errors than the other PEM for small wave directions.

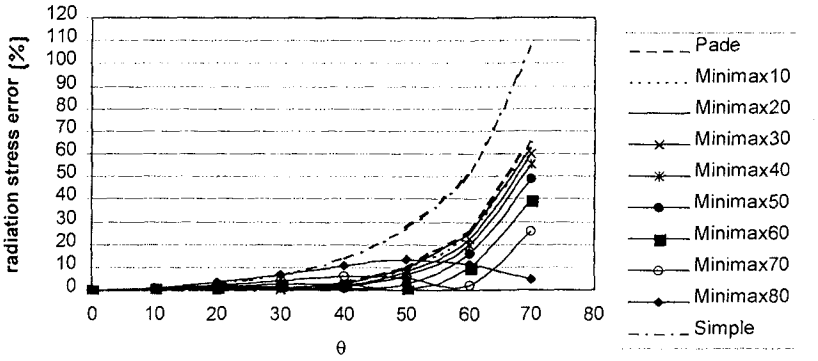

Figure 5. Relative errors in the radiation stress term S_{xy} at 5m depth.

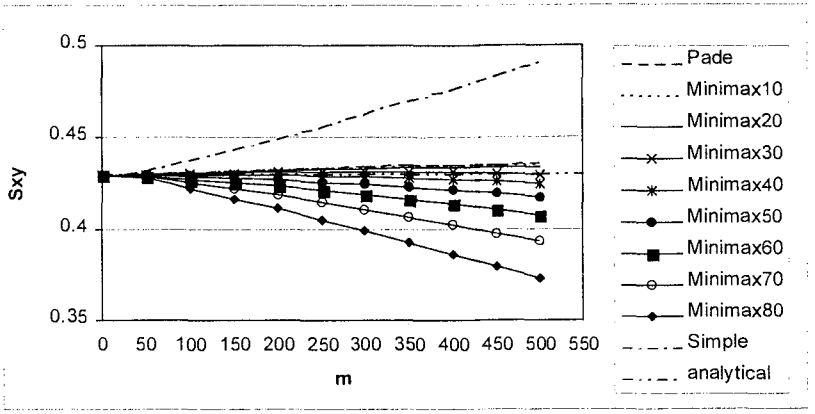

Figure 6. Radiation stresses S_{xy} as a function of distance towards the shore (x). The wave direction at the toe of the slope is 30°.

In Figure 6, S_{xy} is shown as a function of the distance towards the shore (x) for the case where the wave direction at the toe of the slope is 30°. From this figure, we can see the magnitude of the gradient $\partial S_{xy}/\partial x$ that generates the false currents in the parabolic equation model. The Simple approximation has a large positive gradient, which gives clearly unrealistic currents. The Padé and the Minimax 10-30 approximations have very small gradients. These gradients will not generate significant currents. The higher Minimax approximations generate spurious currents in this case because the gradients are negative.

The magnitude of the currents can be seen in Figure 7 where the longshore current profiles are given for four cases. The first three show the performance of the Simple approximation, the Minimax 40° and the Minimax 80° approximation for an angle of incidence of 30°. The Minimax 40° approximation is very good in this case, there is almost zero current outside the surf zone, whereas the two others generate modest currents. The fourth case shows the current profile for the Simple approximation for the case of a large incident wave direction (60°). In this case, the false current offshore of the surf zone is seen to be of a significant magnitude compared with the surf zone current.

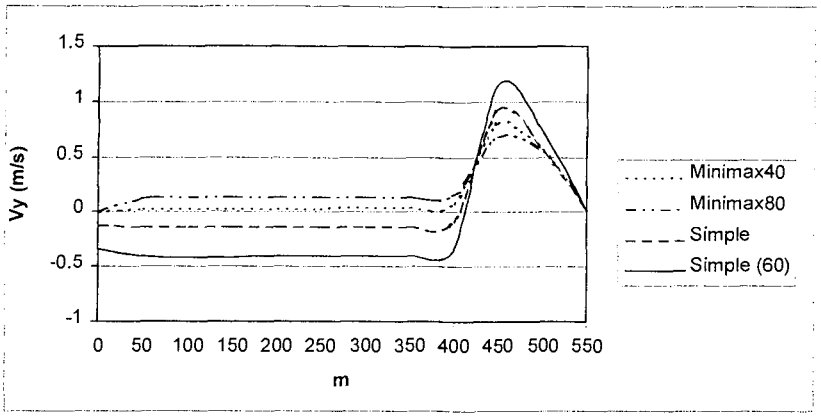

Figure 7. Longshore current profiles.

Conclusions

The investigations in this paper show that the predicted wave directions from PEM models are generally accurate. However, wave heights, radiation stresses and longshore currents predicted from PEM can contain significant errors depending on the parabolic approximation used. The error arises because of the inexact representation of the refraction coefficient in PEM.

In the examples given here, it was easy to quantify the errors and identify the false longshore currents. However, for a complex bathymetry as usually encountered in nature, it will generally not be as easy, and we must emphasize the importance of making a proper choice of parabolic approximation. Also, in real applications the incident wave field will be directional, and thus, what works for one wave direction may not work for another.

Definitely, the Simple approximation should not be used in cases where the waves approach at an angle. In most practical cases, using a Minimax 50° or 60° approximation should work well, since this gives, on the average, a small error in the refraction coefficient over a large range of wave directions (0° to 60°) that will normally be encountered in practice. For cases where the wave directions in the study area are known a-priori to be less than 30°, the Padé approximation is recommended.

References

Berkhoff, J.C.W (1972). 'Computation of combined refraction-diffraction', *Proc. 13th International Conf. on Coastal Engineering,* Vancouver, Canada, 1972, pp. 471-490.

Berkhoff, J.C.W, N. Booij and A.C. Radder (1982). 'Verification of numerical wave propagation models for simple harmonic linear water waves', *Coastal Engineering,* 6, pp. 255-279.

Danish Hydraulic Institute (1996). 'MIKE 21 PMS Users guide and Reference manual, Version 2.6'. Danish Hydraulic Institute, DK-2970 Hørsholm, Denmark.

Johnson, H., I. Brøker and J.A. Zyserman (1994). 'Identification of some relevant processes in coastal morphological modelling', *Proc. 24th International Conf. on Coastal Engineering,* Kobe, Japan, 1994 pp. 2871-2885.

Kirby, J.T. (1986). Rational approximations in the parabolic equation method for water waves, Coastal Engrg. Vol. 10, pp. 355-378.

A Refraction-Diffraction Model for Irregular Waves

Q. Gao[1], A.C. Radder[2]

Abstract

A numerical model for wave refraction and diffraction has been used to compute irregular waves. The model is based on the parabolic approximation, but, by combining with the perfect boundary condition, it is suitable for waves propagating with large incident angles. The irregular waves are modelled through linear superposition of wave components. In order to apply the model to field cases, however, the numerical computations were carried out with one representative frequency while retaining spectral representation of the directionality of waves. This approximation has been examined by the laboratory conditions of Vincent & Briggs; The model's performances in the field cases were also investigated.

Introduction

Recently, two distinct wave models have been used to determine wave properties in two-dimensional near shore zones. One is the so-called parabolic wave model based upon the mild-slope equation, the other is the phase averaged model based on the balance equation for wave energy or wave action. Both models are implemented according to Eulerian approach of wave propagation and wave information is available at the mesh-points of a regular grid. The phase averaged model (for example see Holthuijsen et al. 1989, Holthuijsen et al. 1993), if fully discretized in frequency and direction domain, can trustworthy account for various physical processes such as wave generation, dissipation and nonlinear wave-wave interaction. While this greatly improves representation of the random, short-crested waves, the absence of diffraction in the governing equation can lead to inaccuracy in the case of waves with small directional spreading. The parabolic model (see, for example, Radder,1979, Kirby & Dalrymple, 1983) not only contains the processes of wave transformation such as shoaling, refraction and diffraction, but also can include various other physical influences such as wave growth and dissipation (see Vogel et al. 1988), and the model can be easily implemented on nearshore area. However, the parabolic model has its inherent shortcomings: waves must propagate in one

[1] Researcher, Rijkswaterstaat, Institute for Inland Water Management and W&W Treatment/RIZA, Postbus 17, 8200AA, Lelystad, The Netherlands

[2] Senior Researcher, Rijkswaterstaat, National Institute for Coastal and Marine Management/RIKZ, Postbus 20907, 2500EX, The Hague, The Netherlands

principal direction, say x-direction, since the diffraction effect is restricted to y-direction; and the model deals only with regular waves. A numerical model for irregular waves has been developed which is based on the parabolic approximation and which is suitable for waves with large incident angle (see Gao et al. 1993). In the model a careful treatment of the lateral boundary condition was introduced to prevent the contamination from undesirable side effects (see also Dalrymple & Martin, 1992), it not only makes computation very efficient, but also leads the physical interpretation of the computed results straightforward.

The model has been applied to the laboratory cases with fully spectral form. The results compare well with the experiment of wave transformation over the elliptical shoal carried out by Vincent & Briggs(1989), which usually can not be handled properly by a phase averaged model. When the model is applied to the field cases, the computer effort will be very excessive. We will define a representative frequency, mean frequency of waves, instead of full discretization in frequency domain, while the spectral representation of the directionality of waves is still retained as we consider on the coastal area the directional spreading of waves more important than the spectral representation in the frequency domain. The improvement of the model has been found when it was applied to estuary Haringvliet (a closed branch of the Rhine estuary). The model has also been applied to the tidal area of Friesche Zeegat.

Model Equations

In case of an irregular wave field we consider wave components which make fairly large angle θ with the x-direction. The wide angle equation, that describes the transformation of wave potential $\phi(x, y)$, can be derived

$$\left[1-\frac{\varepsilon^2}{2}+\frac{\varepsilon^2}{2k^2}\frac{\partial^2}{\partial y^2}\right]\frac{\partial \phi}{\partial x}=ik\sqrt{1-\varepsilon^2}\left[1+iP_\varepsilon+\frac{1+\varepsilon^2}{2k^2}\frac{\partial^2}{\partial y^2}\right]\phi \qquad (1.a)$$

$$with \quad P_\varepsilon \equiv \frac{1}{2k^2}\left[\sqrt{1-\varepsilon^2}\frac{\partial k}{\partial x}+\varepsilon\frac{\partial k}{\partial y}+\frac{\omega_r}{c c_g}\left(\gamma_d+\nabla\bullet\vec{U}\right)\right] \qquad (1.b)$$

where $\varepsilon=sin\theta$; γ_d is the dissipation coefficient of waves and $\vec{U}$ is the horizontally varying current; c, c_g and ω_r are respectively wave phase velocity, group velocity and relative frequency; wave number k can be calculated according to the linear dispersion relation. The relative frequency is related to the absolute frequency ω by

$$\omega=\omega_r+\vec{k}\bullet\vec{U}, \qquad \omega_r=\sqrt{gk\tanh kh} \qquad (1.c,d)$$

and the local effective depth

$$h(x,y)=d(x,y)+p_a\bullet H(x,y), \quad 0\le p_a\le 1 \qquad (1.e)$$

with $d(x,y)$ indicating water depth and $H(x,y)$ wave height. The dissipation coefficient γ_d can be easily represented, as formulated by Dingemans(1985) and Vogel et al. (1988). If the incident angle θ=0 and if there are no dissipation and current, eq.(1) is then reduced to the eq.(17) of Radder(1979).

Numerical representation of eq.(1) is the discretization of wave potential ϕ in spatial domain (x,y), with $x>0$ and $0<y<y_b$. The discretization in a computational region forms $M+1$ rows in x-direction, with $x_m=m\bullet\Delta x$ (m=0, 1, ...M), and $N-1$ columns in y-direction, with $y_n=n\bullet\Delta y$ ($n=1,2, ...N-1$). The equations for lateral boundaries have to be applied at $n=0$ and $n=N$, to provide enough equations to solve for unknown $\phi_{m,n}$. The solution of $\phi_{m,n}$ is using the Crank-Nicolson method, which is an implicit scheme with second-order accuracy in both Δx and Δy. The details can be found in Gao et al. (1993).

The model has no difficulty to compute two-dimensional spectral waves, with four independent variables x, y, θ and f. The only one dependent variable is wave potential $\phi(x_m, y_n, \theta_i, f_j)$. The computation is as follows: one starts computation at up-wave boundary where $x=0$ and processes in x-direction, the computation in θ-f domain is that one first solves the linear system of one component on a line in y-direction, then processes to next component. The computation can proceed to the next line only after that all wave components in θ-f domain of a line have been determined.

As mentioned, a parabolic wave model requires lateral boundary conditions. An improper treatment of boundary can cause contamination in the computational domain. Therefore, a parabolic model requires a very large computational domain to avoid the contamination of the interesting area from the lateral boundaries, which leads to inefficiency in computation. A perfect transmitting boundary condition (see also Gao et al. 1993; Dalrymple & Martin, 1992) has been established to allow waves to transmit out or into the computational domain without reflection regardless its direction, crest curvature and the strength of the scattering.

The basis for such a boundary condition is that an exact description of waves in the shadow regions (outside of the computational domain) has to be obtained. To this end we assume in these regions that bottom has straight and parallel contour lines to y-direction and that wave dissipation depends only on x, then eq.(1) can be solved analytically for wave potential ϕ. In practice, we use the differential form of wave potential at the lateral boundaries rather than an analytical one in order that it can be combined with the discretized form of eq. (1). The following equation, which is discretized in x-direction, can be derived

$$\frac{\partial \phi}{\partial y}^{m} + k\sigma\,\phi^{m} = \frac{\partial \phi_{inc}}{\partial y}^{m} + k\sigma\,\phi_{inc}^{m} + k\sum_{\iota=0}^{m-1}\rho_{\iota}\left(\phi^{\iota} - \phi_{inc}^{\iota}\right) e^{i\sum_{\iota}^{m} k\delta(x_{\iota})\Delta x} \qquad (2)$$

which is consistent with the discretized form of eq. (1) at the boundaries. Eq.(2) is the so-called perfect transmitting boundary condition, where ϕ_{inc} is the incident wave which can be obtained numerically, coefficients σ, ρ and δ are given as follows:

$$\delta(x) = \frac{\sqrt{1-\varepsilon^2}}{1-\frac{\varepsilon^2}{2}}\left(1+iP_\varepsilon\right), \qquad \sigma = -i\frac{I}{\sqrt{\beta}}e^{i\mu}\left[J_o(\mu) - iJ_1(\mu)\right] \tag{2.a,b}$$

$$\beta = \frac{\varepsilon^2}{1-\varepsilon^2/2}, \qquad \rho_0 = -i\frac{I}{\mu\sqrt{\beta}}\left[Q(m\mu) - Q((m-1)\mu)\right] \tag{2.c,d}$$

$$\rho_\iota = -i\frac{I}{\mu\sqrt{\beta}}\left[2Q((m-\iota)\mu) - Q((m-\iota+1)\mu) - Q((m-\iota-1)\mu)\right] \tag{2.e}$$

with

$$\mu = \frac{1-\varepsilon^2/2}{\varepsilon^2/2}\frac{\sqrt{1-\varepsilon^2}}{4}\left[\frac{1-\varepsilon^2(1+\varepsilon^2)/2 - i\varepsilon^2 P_\varepsilon}{(1-\varepsilon^2)^2}\right]\Delta x\left(k + \int\frac{\partial k}{\partial x}dx\right) \tag{2.f}$$

$$Q(z) = ze^{iz}\left[J_o(z) - iJ_1(z)\right] \tag{2.g}$$

in which $I=+1$ for left hand side boundary where $y=y_b$ and $I= -1$ for right hand side one where $y=0$, J_0 and J_1 being respectively the zero- and first-order Bessel function. Combining the discretized form of eq.(1) with eq.(2) results a linear system with tridiagonal matrix, which can be solved very efficiently.

To illustrate the performance of the perfect transmitting boundary condition, we compared the numerical results of eq.(2) with a simple absorbing boundary condition, given by

$$\cos\theta\frac{\partial\phi}{\partial x} + \sin\theta\frac{\partial\phi}{\partial y} = ikp_s\phi \tag{3}$$

where θ is the angle at which the plane waves propagate and p_s is taken to be 1. A test was carried out for monochromatic waves in water a basis of $500m \times 500m$, with water depth decreasing from $10m$ at $x=0$ to $5m$ at $x=500m$. The incident waves have height 1 meter, period 8s and an angle 30^o with x axis. The spatial resolution is $\Delta x=5m$, $\Delta y=7.5m$. In figure (1a) the computation was carried out with eq. (2) to be applied at both boundaries. The robustness of eq.(2) can easily be seen in left panel of figure 1, where waves are reasonably calculated across the whole computational line. Whereas in figure (1.b) we apply eq.(3) to $y=0$, the boundary of outgoing waves, the distortion in wave field can be easily found.

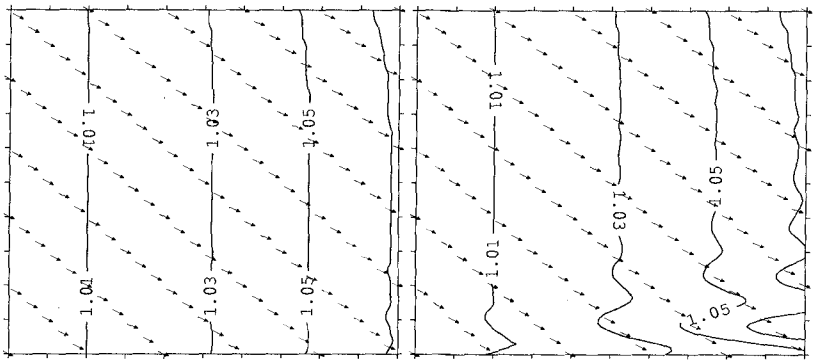

Figure 1. The plane waves propagate at *30°* angle over a shoaling bottom, where arrows indicate the angle at which the waves propagate, and solid line is the iso-line of wave height.

Comparison with The Results of Experiments by Vincent & Briggs

Vincent & Briggs (1989) carried out experiments to simulate regular and irregular random waves in a hydraulic model, which consists of an elliptical shoal and an array of wave sensors. For details of the experiments the reader is referred to Vincent & Briggs. The incident waves which were generated by the spectral wave maker are described by TMA spectrum

$$E(f) = \alpha\, g^2 (2\pi)^{-4} f^{-5} \exp\{-1.25(\frac{f_p}{f})^4 + \ln\gamma \exp[-\frac{(f-f_p)^2}{2\sigma^2 f_p^2}]\}\phi_d$$
$$with\ \ \sigma = \sigma_a = 0.07 \ \ if\ f \le f_p, \quad \sigma = \sigma_b = 0.09 \ \ if\ f \ge f_p; \tag{4.a}$$

where α is the Phillip's constant, f_p the peak frequency, γ the peak enhancement factor, σ the wave shape factor. The shallow water factor ϕ_d is given by

$$\phi_d = 0.5\omega_d^2, \ \ if\ \omega_d < 1; \qquad \phi_d = 1 - 0.5(2-\omega_d)^2, \ \ if\ 1 \le \omega_d \le 2$$
$$\phi_d = 1, \qquad if\ \omega_d > 2; \quad with \quad \omega_d = 2\pi f\sqrt{h/g} \tag{4.b}$$

The directional spreading used in the experiments is the Fourier series representation for the wrapped normal function, which will be approximated in our computations by the following one

$$D(\theta_i) = \frac{1}{2I_s}\cos^s(\theta_i - \theta_o), \quad with \ \ I_s = \int_0^{\pi/2}\cos^s(\theta)d\theta \tag{5}$$

where s is the directional spreading parameter, $\sigma_m = 10$ of the Fourier representation for the directional spreading will be approximated by $s=20$ of eq.(5) and $\sigma_m = 30$ by $s=4$.

A very high resolution in θ-f domain requires excessive computer effort when the model is applied to field cases. To this end, an approximation will be introduced and the accuracy of it will be examined. We are going to define a representative frequency, mean frequency, to approximate the full discretization in frequency domain, while the spectral representation of directionality of waves will be retained. This can not only save the computational cost by one order or more, but also allow us to employ the expressions for wave dissipation and wave growth in the model easily. The representative period is defined as follows

$$f = \frac{1}{E_o} \int f\, E(f)\, df, \quad T = 1/f \ \text{ with } \ E_o = \int E(f)\, df. \tag{6}$$

To examine the performance of this approximation, we compare to the laboratory case N1 and B1 of Vincent & Briggs, where case N1 and B1 have respectively a narrow and broad directional spreading. For each case three computations were carried out with the numerical model. The first computation was carried out with fully spectral form; the frequencies vary from the minimum f_1=0.5Hz to the maximum f_{15}=1.5Hz, with Δf=0.071; the directional sector is 120^o and angular resolution is $\Delta\theta=5^o$ for all cases. The second and third computations were carried out with or without dissipation due to wave breaking; we employ the approximation form of eq.(6), but still keep the directionality of the spectral waves. There are total 15×25=375 wave components per mesh point in the first computation and only 25 in the second and third computation. The input parameters are listed in table 1. The parameters in column 2, 3, 4, 5, 7 and 8 are those used in the first computation and those in column 2, 6 to 8 are used in the second or third computations. The computation consists an area of 20m by 23m and the numerical resolution in spatial domain is $\Delta x=0.1m$, $\Delta y=0.1m$.

case	H(cm)	T_p(s)	α	γ	T(s)	s(eq. 5)	p_a
N1	7.75	1.3	0.0144	2	1.07	20	0.5
B1	7.75	1.3	0.0044	2	1.07	4	0.5

Table 1 The parameters used by the numerical model.

From above computations the following points are to be worthily noted.

1. The model computes the waves in fully spectral form (discretized in both frequency and directional domain) of the laboratory situation with reasonably accuracy and small cpu cost (about 15 minutes on Pentium 90).
2. We find that the differences between the wave heights calculated by the fully spectral form and by the approximation form of eq.(6) are insignificant.
3. Along section 3 discrepancies are found between the computed and measured wave heights in the divergence zones, but the differences decrease for waves with the broad directional spreading.
4. Along section 7-9 of wave propagation direction, the computed and measured wave heights agree reasonably well.
5. It is not conclusive that one can improve the computed results by including wave dissipation in the model.

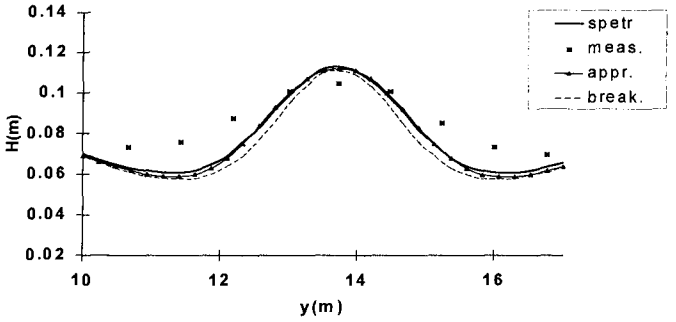

Figure 2a. Comparison between the computed and measured wave heights along the section 3 for case N1. The legends are given as follows: spetr: wave heights computed with fully spectral form; meas: measured heights; appr: computed with the approximation of eq. (6); break: computed with dissipation due to wave breaking.

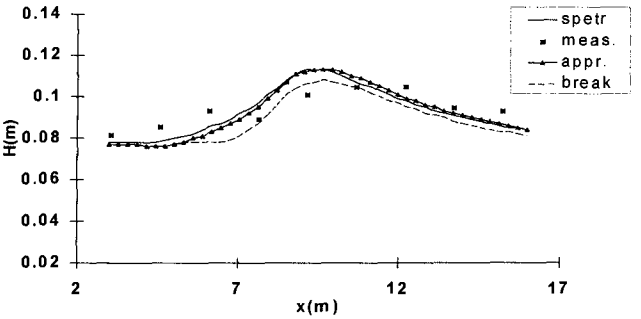

Figure 2b. Along section 7-9 for case N1.

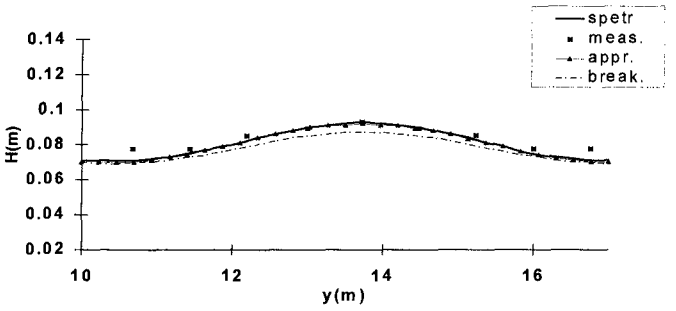

Figure 2c. Along section 3 for case B1.

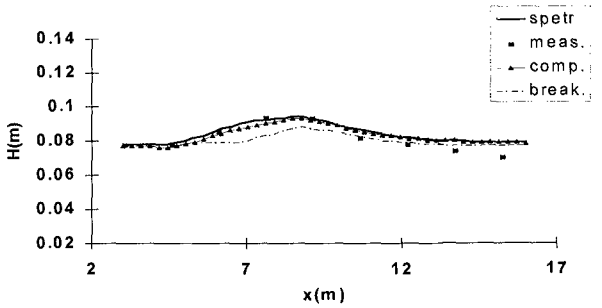

Figure 2d. Along section 7-9 for case B1.

Comparison with Field Measurements

When approaching the shore region, the surface waves will be influenced by a number of factors. Except for wave shoaling and breaking, refraction and diffraction, wind will have a profound effect on waves in a region behind an island or breaker zone. In our model we adopt an empirical expression to account for wave growth due to wind effect(see also Vogel et al., 1988)

$$\gamma_{gr} = -\frac{2c_g}{\tilde{H}_s}\frac{d\tilde{H}_s}{dx}\cos(\theta_w - \theta), \qquad (7)$$

$$with \quad \tilde{H}_s = b\left(1 - \frac{1}{\left(1 - a\sqrt{\tilde{x}_w}\right)^2}\right), \quad and \quad \tilde{H}_s = \frac{gH_s}{U_w^2}, \quad \tilde{x}_w = \frac{gx_w}{U_w^2}$$

where H_s is the significant wave height, U_w, θ_w, θ and x_w are respectively wind speed and direction, wave direction and fetch, coefficient $b=0.30$ and $a=0.009$ were used in the following computations. As mentioned in the previous section we will use a representative period, the mean period, but still keep the directionality of spectral waves in the field cases of the estuary Haringvliet and tidal area Friesche Zeegat.

A. The estuary Haringvliet

The area was chosen to test the model because the wave data in this area is well documented (for details see Andorka Gal, 1995), and because the data set has been extensively used to test the performance of various wave models (see, for example, Vogel et. al, 1988, Holthuijsen et. al,1989). The bathymetry of the estuary and the locations of the measurement are shown in figure 3. The computational area of the present model, which consists of an area of $13600m \times 12400m$, is considerably smaller than those mentioned; the directional sector is 120°. The spatial resolution is $\Delta x=5m$, $\Delta y=10m$ and the angular resolution is $\Delta\theta=15°$, the directional spreading parameter is $s=4$ for all cases. There are total 9 wave components involved in one mesh point. The computations were carried out for the storm situation of 14-15 Oct. 1982. The directional wave buoy WAVEC (see figure 3 at location WA) provides significant wave height, mean wave direction and mean period as up-boundary

conditions; these are listed in Table 2, along with wind and water level. The measured wave heights at other locations were used to check the accuracy of the model. The comparison between the computed and the measured wave heights are given in Table 3. Further the computed wave heights versus the measured ones are shown in figure 4.

	No.1	No.2	No.3	No.4	No.5	No.6
Date/Time	17:00, 14	20:00, 14	22:00, 14	23:00, 14	02:00, 15	04:00, 15
U_w (m/s)	14	14	15	15	13	13
θ_w (degree)	310	310	310	310	310	310
Water level	-0.1m	0.2m	0.85m	1.75m	1.50m	0.45m
H_s(m)	2.58	3.06	3.23	3.54	2.89	2.72
$\overline{T}$(s)	6.0	6.8	6.7	6.7	6.6	6.3

Table 2. The input parameters of the model.

	No.1		No.2		No.3	
	H_{MEAS}	H_{CMP}	H_{MEAS}	H_{CMP}	H_{MEAS}	H_{CMP}
WA	2.58	-	3.06	-	3.23	-
WR1	2.34	2.55	2.65	2.96	2.90	3.13
WR2	2.21	2.17	2.38	2.34	2.53	2.58
WR3	2.21	2.05	2.45	2.28	2.70	2.50
WR4	0.40	0.43	0.48	0.49	0.62	0.56
WR5	0.66	0.79	0.75	0.84	1.05	1.06
WR6	1.16	1.09	1.20	1.28	1.60	1.61
E-75	0.61	0.57	0.74	0.79	0.94	0.95
	No.4		No.5		No.6	
	H_{MEAS}	H_{CMP}	H_{MEAS}	H_{CMP}	H_{MEAS}	H_{CMP}
WA	3.54	-	2.89	-	2.72	-
WR1	3.10	3.40	2.68	2.84	2.49	2.66
WR2	2.63	2.88	2.75	2.67	2.41	2.35
WR3	2.72	2.70	2.68	2.47	2.56	2.24
WR4	0.72	0.80	0.70	0.71	0.44	0.46
WR5	1.45	1.36	1.15	1.26	0.70	0.93
WR6	1.86	1.71	1.95	1.61	1.35	1.32
E-75	1.08	1.08	0.88	0.90	0.63	0.72

Table 3. Comparison of the measured and computed wave heights in Haringvliet.

To measure the performance of the model, we employ the following two statistical expressions, by which the larger waves can not dominate the error quantities; the first one is the relative root-mean-square-error, the second is the performance rate of the model, defined as follows:

$$\varepsilon_{rms} = \sqrt{\frac{1}{N}\sum_{i=1}^{N}\left(\frac{H_{CMP}}{H_{MEAS}} - 1\right)^2}; \quad P_{mdl} = 1 - \frac{\sum_{i=1}^{N}\left(H_{CMP} - H_{MEAS}\right)^2}{\sum_{i=1}^{N}\left(\left|H_{CMP} - \overline{H}_{MEAS}\right| + \left|H_{MEAS} - \overline{H}_{MEAS}\right|\right)^2} \qquad (8.a,b)$$

where H_{CMP} is the computed wave height and H_{MEAS} the measured one, H_{MEAS} is the measured mean wave height. For the data set listed in Table 3 we have ε_{rms}=0.094 and P_{mdl}=76%, these compare favourably to the model CREDIZ(Vogel et al., 1988), which has ε_{rms}=0.17 and P_{mdl}=67%.

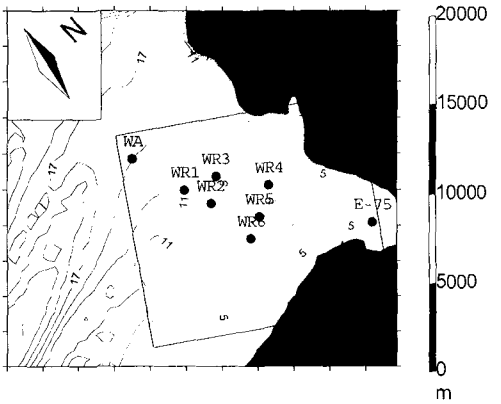

Figure 3 Bathymetry of the estuary Haringvliet and locations of the measurement, where the rectangle indicates the computational area.

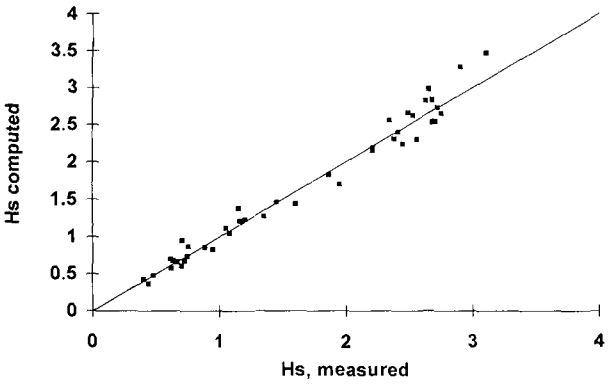

Figure 4 Computed wave heights versus measured ones.

B. The tidal area Friesche Zeegat

The aim is to test the model in a situation of strong tidal current, up which waves propagate. The area was chosen because the wave data from measurements is available (see Dunsbergen, 1995), and tidal currents were calculated with a fair degree of detail. The bathymetry of the area, along with locations of measurement, is shown in figure 5. A shoal, located in the centre of the tidal channel, will shelter most onshore area from the incoming waves. The tidal current, as shown in figure 6a (for

flood case) and figure 7a (for ebb case), will also contribute to deflect the propagation direction of the incoming waves.

The weather situation was that a storm in the North Sea generated waves, which propagated into tidal area. The computations were carried out for the flood case at 06:00 M.E.T., Oct. 9, 1992 and the ebb case at 12:00 M.E.T. Oct. 9 1992 in a rectangular area of 22000m×16000m, the directional sector was taken to be 90°. The waves measured by WAVEC buoy at location **S** is used to provide the model with the up-wave boundary. The input parameters are given in Table 4, where the mean wave direction is the same as wind and is in nautical convention. The wave heights measured at other locations were used to check the performance of the model. The resolution was $\Delta x=5m$, $\Delta y=10m$ and $\Delta\theta=15°$, the directional spreading parameter s=6 is used for flood case and s=10 for ebb case. In these computations only 7 wave components per mesh point are used.

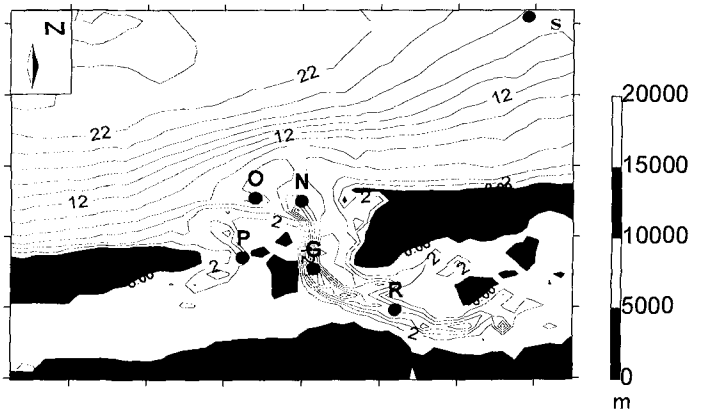

Figure 5 Bathymetry of tidal area Friesche Zeegat with the locations of observation (marked with ●).

	H_s	$\bar{T}$	Water level	U_w	θ_w	s
Flood	2.24	5.6	1.13m	12.0m/s	320°	6
Ebb	3.31	7.4	0.1m	11.5m/s	340°	10

Table 4. The input parameters for the numerical model.

location	N	O	P	G	R
Flood					
H_{MEAS}	1.75	1.90	0.56	0.53	0.31
H_{CMP}	1.72	1.82	0.43	0.40	0.53
Ebb					
H_{MEAS}	1.65	2.62	0.39	0.52	0.43
H_{CMP}	1.94	1.93	0.58	0.59	0.42

Table 5 The measured and computed wave heights for ebb and flood cases.

The comparison between the computed and measured waves is shown in table 5. For the flood case the rms error ε_{rms} is 0.23, the performance rate P_{mdl} is 97% and for the ebb case ε_{rms}=0.27, P_{mdl}=69%. The computed wave fields are shown in figure 6b for the flood case and figure 7b for the ebb case. The following remarks are added here according to the computed results: The varying depth in the area of the tidal inlet deflects the propagation direction of the incoming waves, making them towards the shallow area. In such a situation it is hardly possible for monochromatic waves to penetrate through the channel and to arrive in the onshore region (south of tidal inlet). The eomputations also indicate that in the inlet region the tidal current has profound influence on the computed waves, whereas wind nearly dominates the waves in onshore region.

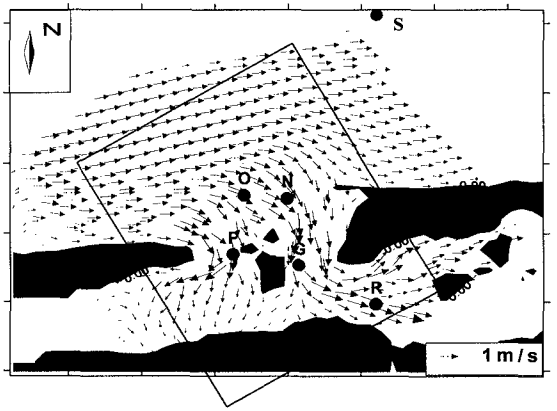

Figure 6a. Tidal current for flood case at 06:00 M.E. T., Oct. 9, 1992 in the area of Friesche Zeegat, where the rectangular line indicates the computational area.

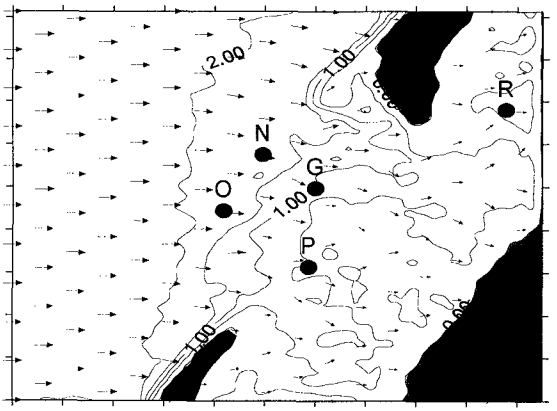

Figure 6b. Computed waves for the flood case, where the iso-lines refer to the wave height and arrows indicate the mean wave direction.

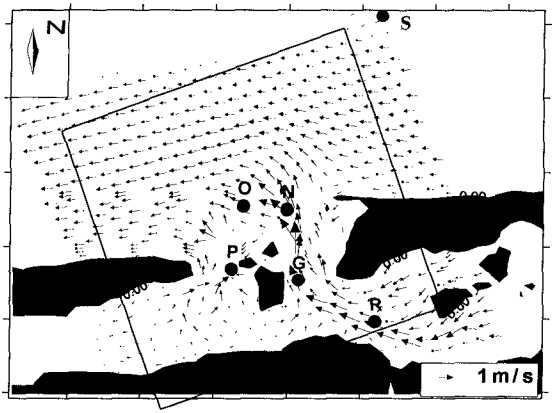

Figure 7a. Tidal current (ebb case) at 12:00 M.E.T. Oct. 9, 1992.

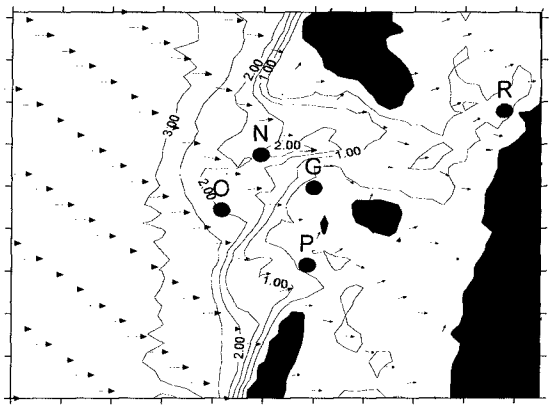

Figure 7b. Computed waves for the ebb case, caption is the same as figure 6b.

Conclusions

The advantage of the parabolic model is that it can be used to compute wave transformation in a large horizontal domain, say, a region of several hundreds of wave length on one side. But when applied to field cases, the model often assumes the incoming waves to be monochromatic. The numerical model presented in this paper can be used to compute irregular waves and regular waves as well. The numerical results have been compared to a number of measurements from hydraulic models as well as field cases on coastal areas. We have the following conclusions: 1, The results show that the model is suitable for waves with large incident angle. 2, Through the linear superposition of regular waves, the model can be used to compute irregular waves; the performance of the model was reasonably good when it was applied to the laboratory cases of Vincent & Briggs. 3, The perfect boundary condition used in the numerical model can allow waves to transmit out or into the computational domain

without causing disturbances in the computational domain, which also makes the computation of waves very efficient. 4, The model can be used to compute waves in field cases and it performs quite well when compared to the observations.

References

Andorka Gal, J.H. 1995. Verification set Haringvliet, Oct. 14, 1982 - Oct. 15, 1982, *Rep. RIKZ-95.112x, Ministry of Transport and Public Works, The Netherlands.*

Dalrymple, R.A. and Martin, P.A. 1992. Perfect boundary conditions for parabolic water-wave models. *Proc. R. Soc. Lond.* A437, pp. 41-54.

Dingemans, M.W., 1985. Surface wave propagation over an uneven bottom. Evaluation of two-dimensional horizontal wave propagation models. *Report W301 part 5, Delft Hydraulics Laboratory* (December 1985).

Dunsbergen, D. W., 1995. Verification set Friesche Zeegat. Oct. 1, 1992 - Nov. 17, 1992, *Rep. RIKZ-95.035, Ministry of Transport and Public Works, The Netherlands.*

Gao, Q., Radder, A.C. and Booij, N. 1993. A numerical wave model for the refraction and diffraction of irregular waves, Description of the wave model CREON. Report 5-93, *Faculty of Civil Engineering, Delft University of Technology, The Netherlands.*

Holthuijsen, L. H., Booij, N., and Herbers, T.H.C., 1989. A prediction model for stationary, short-crested waves in shallow water with ambient current. *Coastal Eng.* 23, pp. 23-54

Holthuijsen, L. H., Booij, N., and Ris, R. C., 1993. A spectral wave model for the coastal zone, *Proc. of 2nd Int. Symposium on Ocean Wave Measurement and Analysis,* New Orleans, 630-641

Kirby, J.T. and Dalrymple, R.A., 1983. A parabolic equation for the combined refraction-diffraction of Stokes waves by mildly varying topography. *J. Fluid Mech.*, 136, pp. 453-466

Radder, A.C., 1979. On the parabolic equation method for water-wave propagation. *J. Fluid Mech.* 95(1), pp. 159-176

Ris, R.C. 1997. Spectral modelling of wind waves in coastal areas. *Ph.D. dissertation, Faculty of Civil Engineering, Delft University of Technology, The Netherlands.*

Vincent, C.L. and Briggs, M.J. 1989. Refraction-diffraction of irregular waves over a mound. *J. Waterway, Port, Coastal and Ocean Engng ASCE* 115(2), pp. 269-284

Vogel, J.A., Radder, A.C. and de Reus, J.H. 1988. Verification of numerical wave propagation models in tidal inlets. *Proc. 21st Coastal Eng. Conf. ASCE, Malaga,* pp. 433-447.

CALCULATION OF VELOCITY FIELD IN 3-D RANDOM WAVES

Yu-xiu Yu* and Ning-chuan Zhang**

ABSTRACT

A method simply treating the governing equation for 3-D wave-motion is proposed in this paper. The Euler's velocity in whole depth can be directly calculated with this method if the wave free surface is given. For the linear waves the wave surface is determined from given directional spectrum (Yu. et al. 1991) or other wave surfaces at near locations with an inversion method proposed in this paper. For the nonlinear waves the wave surface can be determined with the method proposed by Dommermuth and Yue (1987). These methods proposed by authors are tested and verified with numerical simulation, model test or field observation data.

1. INTRODUCTION

The sea wave is a three-dimentional random process. An understanding of the kinematics of waves is critical to the understanding of many processes in the sea from the forcing on structures to nearshore sediment transport. In general the velocity field of sea waves is three dimentional, random, and nonlinear. Due to the complexity of this problem, some scientists only considered its three-dimentionality and random property and the direct linear superposition method was used to calculated the velocity. Others emphasized its nonlinearity and the higher-order unidirectional wave theories were used. Forristall et al (1978) showed that even linear wave theory with directional spereading of wave energy predicts storm wave kinematics of the subsurface flow better than higher-order unidirectional wave theories. But the direct linear method greatly overestimate crest velocities near the surface (Donelan, 1992). Some methods, for example the coordinate stretching method and the extrapolation method were proposed to correct the direct linear method and the results of former are smaller than that of the latter. The measured kinematics in the crests of random waves is bounded by these two modified linear models

* Professor, The State Key Laboratory of Coastal and Offshore Engineering, Dalian University of Technology (DUT), Dalian 116024. China
** Associate Professor, Dept. of Civil Eng. DUT, Dalian 116024, China

(Roderbusch and Forristall, 1982). More recently, Donelan (1992) proposed a new method based on the linear superposition of a sum of freely propagating wave-trains and assume that shorter waves ride on longer ones. But the effect of nonlinearity is not considered yet in this method.

Methods used for the calculation of velocity field in irregular waves fall into two general categories, global and local approximations. The local method attempt to find separate salutions to the governing equations that fit sequential windows in time of the given record, rather than attempting to find a single solution that fits an entire record. The amount of computation work is large.

Prislin and Zhang (1997) presented a newly-developed deterministic methodology for decomposition of nonlinear short-crested irregular waves up to second order in wave steepness into a characteristic set of free-wave components. Based on the decomposed free-wave components, the Directional Hybrid Wave Method (DHWM) allows for prediction of wave properties other then measured and at different locations including wave crests.

Dommermuth and Yue (1987) developed a numerical method for modelling nonlinear gravity waves which is based on the Zakharov equation/mode-coupling idea but is generalized to include interactions up to an arbitrary order M in wave steepness. This method were used to calculate the deformation of a travelling wave (Dommermuth, et al. 1987). In this paper, an inversion method is proposed to determine the wave surface from other wave surfaces at near locations, then it is used as the boundary condition to derive the wave kinematics in 3-D random waves with Dommermuth's idea.

2. NUMERICAL INVERSION OF 3-D RANDOM WAVE SURFACE

The single direction per frequency model (Yu et. al. 1991) is used to describe the 3-D random wave surface at point (x,y):

$$\eta(x,y,t) = \sum_{m=1}^{M} \sum_{i=1}^{I} a_{mi}\cos[\omega_{mi}t + k_{mi}(x\cos\theta_i + y\sin\theta_i) + \epsilon_{mi}] \tag{1}$$

$$a_{mi} = \sqrt{2S(\omega_m,\theta_i)d\omega_m d\theta_i} \tag{2}$$

where M and N are the division numbers of frequency and direction respectively; a_{mi}, ω_{mi}, k_{mi} and ϵ_{mi} are amplitude, frequency, wave number and random initial phase of the component waves; $S(\omega,\theta)$ is the directional spectrum.

Usually, if the directional spectrum is given, the 3-D wave surface can be obtained with Eqs. (1) and (2). It also can be measured. But sometimes we can not measure the wave surface at structure position. In this case, an inversion method is proposed to determined the wave surface from other wave surfaces at near locations. The wave surface can be expanded as a Fourier Series:

$$\eta(x,y,t) = \sum_{j=1}^{J} (A_j\cos\omega_j + B_j\sin\omega_j) \tag{3}$$

where A_j and B_j are the Fourier coefficients. If the length of the wave data is L, then

$$\left.\begin{aligned} A_j &= \frac{2}{L}\sum_{l=1}^{L}\eta(x,y,t_l)\cos\omega_j t_l dt \\ B_j &= \frac{2}{L}\sum_{l=1}^{L}\eta(x,y,t_l)\sin\omega_j t_l dt \end{aligned}\right\} \tag{4}$$

Eq. (3) can be rewrite as

$$\left.\begin{aligned} \eta(x,y,t) &= \sum_{j=1}^{J} a_j\cos(\omega_j t + \beta_j) \\ a_j &= \sqrt{A_j^2 + B_j^2} \\ \beta_j &= \arctan(-B_j/A_j) \end{aligned}\right\} \tag{5}$$

Comparing with Eq. (1) we can get the total phase

$$\beta_j = k_j(x\cos\theta_j + y\sin\theta_j) + \epsilon_j$$

If the wave surfaces, $\eta(x,y,t)$ are measured at I points and $I \geqslant 3$, the total phase for each surfacr can be obtained

$$\left.\begin{aligned} \beta_j^1 &= k_j(x_1\cos\theta_j + y_1\sin\theta_j) + \epsilon_j \\ \beta_j^2 &= k_j(x_2\cos\theta_j + y_2\sin\theta_j) + \epsilon_j \\ &\vdots \quad\quad \vdots \quad\quad \vdots \quad\quad \vdots \\ \beta_j^I &= k_j(x_I\cos\theta_j + y_I\sin\theta_j) + \epsilon_j,\ I \geqslant 3 \end{aligned}\right\} \tag{7}$$

In these equations, only the directions, θ_j and the initial phase ϵ_j of component waves are unknow and they can be obtained from any two equations in principle. For example, from points 1 and 2 (Fig. 1) one can get

$$\theta_{jk} = \alpha_{12} + \cos^{-1}\left(\frac{\beta_j^1 - \beta_j^2}{k_j D_{12}}\right) \tag{8}$$

But in Eqs. (5) and (8), both arctangent and arccosine are multi-value function. Moreover, some component wave's directions are nearly parallel to the line 1-2 and the Eq. (7) for points 1 and 2 is invalid for these component waves. Therefore, at least three measured points are necessary. For each pair of measured point, two equations form a simultaneous equations and the values of θ_j and ϵ_j can be obtained for each component wave except the invalid condition. In general, for n pairs of measured points.

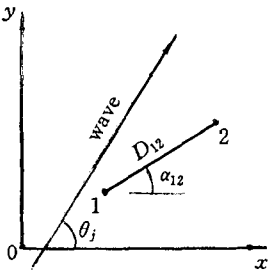

Fig. 1

$$\theta_j = \frac{1}{n}\sum_{k=1}^{n}\theta_{jk} \qquad n \geqslant 3 \tag{9}$$

Then the wave surface at any point can be calculated with Eq. (1) if the wave field is homogenous.

The numerical simulation, the physical simulation and the field wave data are used to examine this method. Five wave gages of vertical line type arranged in T-type array (Fig. 2a) were used in the field observation (Liu and Yu, 1995). The wave data were recorded simultaneously for 1200 seconds every hour and the time interval, Δt is 0.25s. Fig. 2(b) shows an example of the comparison of wave surfaces between field data at point 1 and the numerical inversion result form these at

points 2, 3, 4 and 5. It shows that this method is successful and its precision is dependent on the length of data, $N\Delta t$, the distance, R from measured points to predicted point and the spatial homogeneity of wave field. According to the numerical simulation result, when $R/L_s=1.0$, number of points $N\geqslant 2000$, when $R/L_s=10$, $N\geqslant 3000$ and when $R/L_s=20$, $N\geqslant 4000$, where L_s is the significant wave length. But in nature, the wave field is not exactly homogenous, so the validity of this method is limited to a few wave length from the measurement sites.

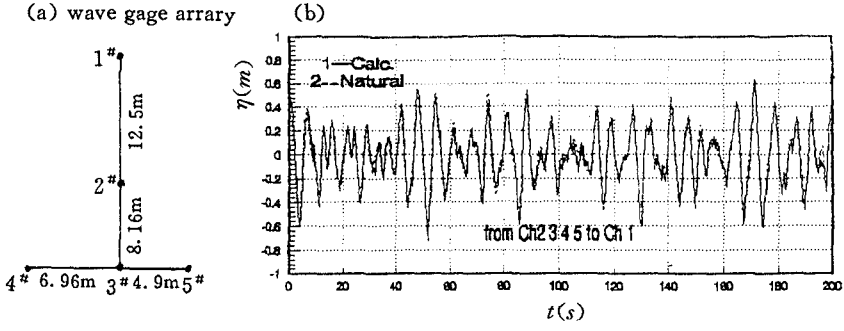

Fig. 2 A comparison of wave surfaces between field data (----) and numerical inversion (——)

3 CALCULATION OF VELOCITY FIELD

3.1 Governing Equations

The irrotational wave motion of a homogeneous, incompressible and inviscid fluid is considered. The origin is located at the mean water level and the vertical axis z is positive upward. The wave flow can be described by a velocity potential $\phi(x,y,z,t)$ such that within the fluid ϕ satisfies Laplace's equation:

$$\Delta\phi=\frac{\partial^2\phi}{\partial x^2}+\frac{\partial^2\phi}{\partial y^2}+\frac{\partial^2\phi}{\partial z^2}=0 \tag{10}$$

$$x_s(y,t)\leqslant x\leqslant\infty;\ -\infty<y<\infty;\ -d(x,y)\leqslant z\leqslant\eta(x,y,t)$$

where $x_s(y,t)$ denote the coordinate x of boundary between water and land at time t. $\eta(x,y,t)$ is the free surface of wave. For determining the velocity potential, the following boundary conditions should be satisfied

Kinematics condition at bottom

$$\left.\frac{\partial\phi}{\partial\eta}\right|_{z=-d}=0 \tag{11}$$

Kinematics condition at free surface

$$\left.\frac{\partial\phi}{\partial z}\right|_{z=\eta}=\frac{\partial\eta}{\partial t}+\left.\frac{\partial\eta}{\partial x}\frac{\partial\phi}{\partial x}\right|_{z=\eta}+\left.\frac{\partial\eta}{\partial y}\frac{\partial\phi}{\partial y}\right|_{z=\eta} \tag{12}$$

Dynamic condition at free surface

$$\left.\frac{\partial\phi}{\partial t}\right|_{z=\eta}+g\eta+\frac{1}{2}(\nabla\phi\cdot\nabla\phi|_{z=\eta})+\frac{p_s(x,y,t)}{\rho}=0 \tag{13}$$

$x\to\infty$ or $y\to\infty$ or $z\leftarrow\infty$; $\phi(x,y,z,t)$ and $\eta(x,y,t)$ are finite.

Initial condition

$$\eta(x,y,t)|_{t=0} = \eta_0(x,y) \tag{14}$$

$$\nabla\phi(x,y,z,t)|_{t=0} = \nabla g(x,y,z) \tag{15}$$

where $\nabla g(x,y,z)$ denote the initial velocity potential and it should satisfy the irrotational condition. It is very difficult to solve Eq. (10) directly to study the wave kinematics and some simplification is necessary.

3.2 Simplified Treatment Method

Dommermuth and Yue (1987) presented an approximate model for wave motion. The velocity potential at wave surface is defined as (Zakharov. 1968):

$$\phi^s(x,y,t) = \phi(x,y,\eta(x,y,t),t) \tag{16}$$

where, $z=\eta(x,y,t)$ denotes the free surface. In terms of ϕ^s, the kinematic and dynamic boundary conditions on the free surface are respectively

$$\left.\begin{aligned} &\eta_t + \nabla_{\bar{r}}\phi^s \cdot \nabla_{\bar{r}}\eta - (1 + \nabla_{\bar{r}}\eta \cdot \nabla_{\bar{r}}\eta)\varphi_z(x,y,\eta,t) = 0 \\ &\phi^s_t + g\eta + \frac{1}{2}\nabla_{\bar{r}}\phi^s \cdot \nabla_{\bar{r}}\phi^s - \frac{1}{2}(1 + \nabla_{\bar{r}}\eta \cdot \nabla_{\bar{r}}\eta)\phi^2_z(x,y,\eta,t) = 0 \end{aligned}\right\} \tag{17}$$

where $\bar{r}=\{x,y\}$ is the position vector, $\nabla_{\bar{r}}=\left\{\frac{\partial}{\partial x},\frac{\partial}{\partial y}\right\}$ denotes the horizntal gradient.

The initial conditions at wave surface are

$$\phi(x,y,0) = q_1(x,y) \tag{18}$$

$$\eta(x,y,0) = q_2(x,y) \tag{19}$$

where $q_1(x,y)$ and $q_2(x,y)$ are given.

If the wave elevation, $\eta(x,y,t)$ and the velocity potential at free surface, $\phi^s(x,y,\eta,t)$ are expressed with the Fourier integral which satisfy the continuous equation and the bottom boundary condition, Eq. (17) is expressed as the equations concerning Fourier amplitude and these equations are solved by a perturbation method, whose key idea is that $\phi_z(x,y,\eta,t)$ is to be expressed as the function of ϕ and η. Dommermuth and Yue (1987) assumed that ϕ and η are $O(\varepsilon)$ quantities, where ε, a small parameter, is a measure of the wave steepness. We consider a consistent approximation up to and including a given order M in ε, and write ϕ in a perturbation series in ε.

The surface vertical velocity

$$\phi_z(x,y,\eta,t) = \sum_{m=1}^{M}\sum_{K=0}^{M-m}\frac{\eta^K}{K!}\sum_{n=1}^{N}\phi_n^{(m)}(t)\frac{\partial^{K+1}\psi_n(x,y,0)}{\partial z^K} \tag{20}$$

Substitute (20) into (17) and yields the final result

$$\left.\begin{aligned} &\eta_t + \nabla_{\bar{r}}\phi^s\nabla_{\bar{r}}\eta - (1 - \nabla_{\bar{r}}\eta \cdot \nabla_{\bar{r}}\eta)\left\{\sum_{m=1}^{M}\sum_{K=0}^{M-m}\frac{\eta^K}{K!}\sum_{n=1}^{N}\phi_n^{(m)}(t)\frac{\partial^{K+1}\psi_n(x,y,0)}{\partial z^{K+1}}\right\} = 0 \\ &\phi^s_t + \eta + \frac{1}{2}\nabla_{\bar{r}}\phi^s \cdot \nabla_{\bar{r}}\phi^s - \frac{1}{2}(1 + \nabla_{\bar{r}}\eta \cdot \nabla_{\bar{r}}\eta) \\ &\qquad\left\{\sum_{m=1}^{M}\sum_{K=1}^{M-m}\frac{\eta^K}{K!}\sum_{n=1}^{N}\phi_n^{(m)}(t)\frac{\partial^{K+1}\psi_n(x,y,0)}{\partial z^{K+1}}\right\}^2 = 0 \end{aligned}\right\} \tag{21}$$

Where $(\ )^m$ denote a quantity of $O(\varepsilon^m)$, $\phi_n^{(m)}$ is called modal amplitude, $\psi_n(x,y,0)$ is given as follows:

$$\psi_n = \frac{\cosh k_n(z+d)e^{ik_n\vec{r}}}{\cosh k_n d} \tag{22}$$

where k_n is the wave number of n*th* characteristic wave. The modal amplitude, $\phi_n^{(m)}(t)$ can be treated as the function of ϕ^s and η and can be obtained by solving successively at increasing order the following equations

$$\left.\begin{aligned} &\sum_{n=1}^{N}\phi_n^{(1)}\psi_n(x,y,0) = \phi^s \\ &\sum_{n=1}^{N}\phi_n^{(m)}\psi_n(x,y,0) = \sum_{K=1}^{m-1}\frac{\eta^K}{K!}\left.\frac{\partial^K\left(\sum_{n=1}^{N}\phi_n^{(m-K)}\psi_n(x,y,z)\right)}{\partial z^K}\right|_{z=0} \\ &\qquad m = 2,3,\cdots,M \end{aligned}\right\} \tag{23}$$

Eq. (21) is the generalization to Mth order in wave steepness, ϵ of penturbation equations. For the finite ϵ, Dommermuth (1987) had proven that $|\psi_n(x,y,\eta_{max})/\psi_n(x,y,\eta_{min})|$ will rapidly increase along with n increasing. It means that the penturbation equation will exactly consistent coverge to the original equation.

For treating the three dimentional problem with both nonlinear and randomness the following model are proposed.

3.3 Wave Motion Equation under Known Wave Surface

When the surface elevations of a random wave are known, among two boundary condition equations at free surface only the potential function ϕ^s is to be determined. so we can choice either the kinematics boundary condition or the dynamic boundary condition as the boundary condition at known free surface. Thus the problem of solving velocity field under known wave surface is transformed into the boundary-value problem of Laplace equation in a given area, $x_1 \leqslant x \leqslant x_2$; $y_1 \leqslant y \leqslant y_2$; $-d \leqslant z \leqslant \eta(x,y)$ as Fig. 3 shown.

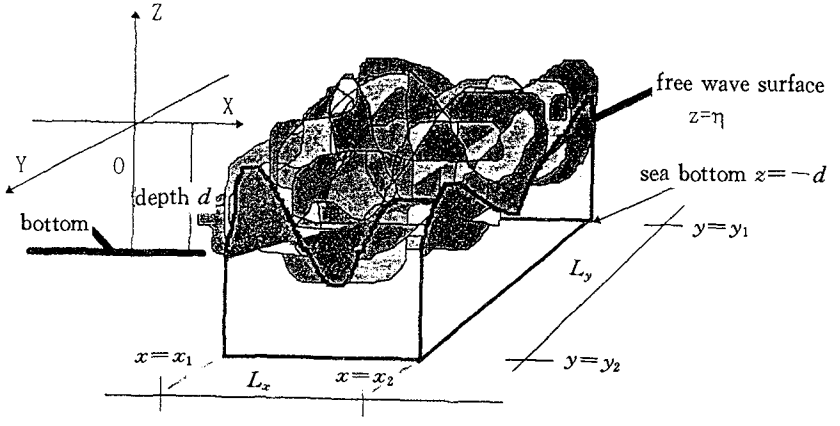

Fig. 3 Sketch of computation area

In given area, this boundary-value problem can be divided into two parts:

Part 1. Solve the surface protential function, $\phi^s(x,y,t)$ at free surface. Using Dommermuth's expression method, substituting (20) into (12), one can get the governing equation:

$$\eta_t = \sum_{m=1}^{M}\sum_{K=0}^{M-m}\frac{\eta^K}{K!}\sum_{n=1}^{N}\phi_n^{(m)}(t)\frac{\partial^{K+1}\psi_n(x,y,z)}{\partial z^{K+1}}\bigg|_{z=0} - \eta_x\phi_x^s - \eta_y\phi_y^s \qquad (24)$$

Part 2. In the given area, solve the Laplace equaton given as Eq. (10). Their boundary conditions are

At bottom $z=-d$, as same as Eq. (11)

At free surface $z=\eta$, use the results in Part 1. The potential function at surface is used as the first kind of boundary condition.

At four profiles of $x=x_1, x=x_2, y=y_1$ and $y=y_2$ it is given directly by the linear potential function:

$$\phi(x,y,z,t) = \sum_{m=1}^{M}\sum_{i=1}^{I}\frac{a_{mi}g}{\omega_m}\frac{\cosh k_m(z+d)}{\cosh(k_m d)} \times \sin[k_m(x\cos\theta_i + y\sin\theta_i) + \omega_m t + \epsilon_{mi}] \qquad (25)$$

As well know the accuracy of linear theory is enough except at where close free surface. If the computation area is large enough, the effect of the linear error on the computed results at the center point of this area can be negligible.

3.4 Numerical Method

The governing equation is solved with a finite diference method. Becaused the simplified governing equation is very simple, any special treatment is not needed for its computation.

3.4.1 Computing potential function at free surface.

At a given time the wave surface elevation, $\eta(x,y,t)$ and the linear potential function $\phi^s(x,y,t)$ are given so that the modal amplitude, $\phi_n^{(m)}(t)$ of velocity potential satisfys the Dirichirt boundary condition. Because the calculation reange is $z\leqslant 0$, so the amplitude $\phi_n^{(m)}(t)$ in the range of computational cuboid can be given with a pseudospectral method (Gottlieb and Orszag. 1977). The basic of the psendospectral method is the Fourier sesies expansion of periodic function and the Chebyshev polynomial expansion of a general function and the expansive coefficients are obtained with FFT. Here the FFT is done for wave number k (for frequency in general). In each order of solving proess, the number of k requested is equal to that of Fourier item.

For calculate $\phi_x^s(x,y,t)$, considering the nonlinear interaction between the component waves of different period, the order of the perturbation, M should be four. In this case, from Eq. (20) one can get:

$$\begin{aligned}\phi_x^s(x,y,t) = \sum_{n=1}^{N} e^{ik_n x}\{&\phi_n^{(1)}[k_n\tanh(k_n d) + \eta k_n^2 + \frac{\eta^2}{2}k_n^3\tanh(k_n d) + \frac{\eta^3}{6}k_n^4] \\ &+ \phi_n^{(2)}[k_n\tanh(k_n d) + \eta k_n^2 + \frac{\eta^2}{2}k_n^3\tanh(k_n d)] \\ &+ \phi_n^{(3)}[k_n\tanh(k_n d) + \eta k_n^2] + \phi_n^{(4)}[k_n\tanh(k_n d)]\}\end{aligned} \qquad (26)$$

Then calculate ϕ' at discrete points with iterative method.

3.4.2 Calculate ϕ in the given area.

3.4.3 Matching the boundary conditions

At the boundary between free surface and four profiles of $x=x_1$, $x=x_2$, $y=y_1$ and $y=y_2$ the boundary conditions are not continuative. Because the potential function at free surface is obtained by Eq. (24) and those at four profiles are given by linear wave theory. The Lagrange's insertion formula is used to matching the boundary conditions. For the deep water take the bottom bonndary at $z=-\frac{d}{2}$ and the potential function is also given by linear theory, it is in harmony with that at four profiles.

3.4.4 Solve difference equation group

The successive overrelaxation (SOR) method is used to solve the difference equation. The relaxation factor is equal to 1.5.

3.5 Reliability Examination of Numerical Method.

3.5.1 Errors due to linear boundary conditions

A regular wave is considered, its $H=15$cm, $T=1.5$s and depth $d=41.3$m. Two boundary conditions are artificially constructed, one is a linear boundary and at the boundary between wave surface and four profiles, the boundary conditions are matching with Lagrange's insertion. Another is taken as $\phi_0(z)\cdot G(z)$ and the definition of $G(z)$ is shown in Fig. 4(a). The computational parameters are perturbation order $M=3$, Fourier trunction number $N=16$. Computation area $x_1=0$, $x_2=2.0$m, node spacing $\Delta x=0.05$m, $\Delta z=0.01$m. Fig. 4(b) shows that the potential functions $\phi(i,j)$ at different depth obtained from linear boundary condition are in agreement with that obtained from another boundary condition beyond the eighth node. So it is concluded that for calculating the potential function at the center of area 2×2m the linear boundary condition is available with enough accuracy.

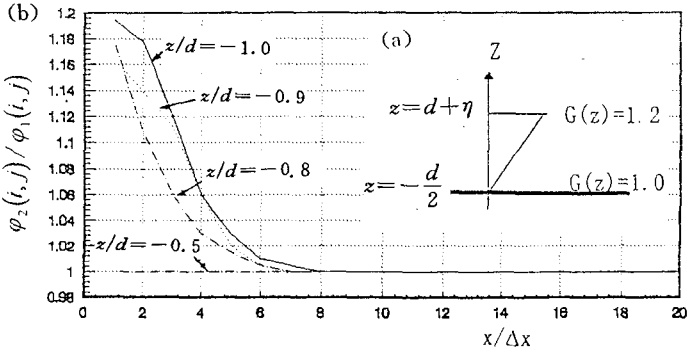

Fig. 4 Errors due to linear boundary condition

3.5.2 The effect of perturbation order number M

Taking $M=1, 2, 3$ and 4 respectively calculate the velocity v_x in a regular

wave as above mentioned at $x=1.0$m, $z/d=-0.25$. As Fig. 5 shows that the velocity for $M=3$ is almost the same as that for $M=4$ and even if $M=2$ its result is acceptable.

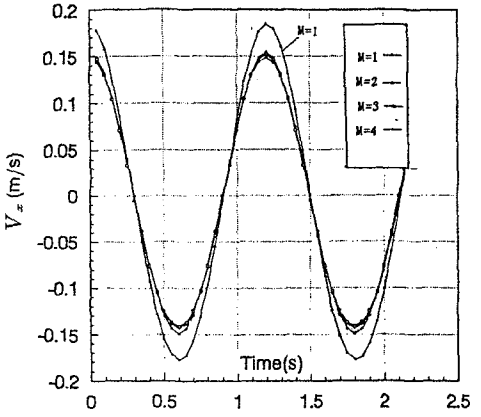

Fig. 5 Comparison of calculation results with different M for velocity V_x

3.5.3 Comparison between numerical calculation and wave theories

The linear theory, 2nd Stokes and 3rd Stokes wave theories and the numerical method are used to calculate the velocity v_x respeitively in a regular wave. The results show that at the crest phase the velocity v_x calculated by numerical method is almost the same as that from 3rd Stokes wave theory.

3.6 Velocity Field in 3-D Random Waves—Model Test

The velocity field in regular wave, unidirectional random wave and 3-D random wave were experimentally studied in the State Key Laboratory of Coastal and Offshore Engineering, Dalian University of Technology, China. The wave basin is 55m long, 34m wide and 1.3m deep. The multi-directional wave-maker consists of 70 independent segments of 0.4m wide. Wave absorbers were placed along the basin walls to prevent wave reflection from the walls. A wave gage array consisted of 8×8 gages was set 6.5m apart from the wave plate. The gage spacings were about 0.25m. An Acoustic Doppler Velocimeter (ADV) was put near the center of the wave gage array to measure three flow velocity components. The data of wave elevations and velocities were acquired simultaneonsly by computer. The sampling interval was 0.05s and the data length is 512—1024 (regular waves)、4096(unidirectional waves) and 8192 points (3-D random waves). The water depth was kept 0.413m. The velocities were measured at $Z=-0.303$m, -0.196m, -0.109m and -0.018m respectively. For the last case, the ADV was out of water at trough phase.

The JONSWAP spectrum, $\gamma=3.3$ and the Mitsuyasu-type spreading function, $G_0\cos^{2s}\frac{\theta}{2}$, was used to simulate the 3-D random waves with the Single Direction Per Frequency Model (Yu et al, 1991). $H_{\frac{1}{3}}=0.047\sim 0.145$m, $T_{H\frac{1}{3}}=1.09\sim$

1.88s. The measured directional spectrum was estimated by the Bayesian Approah (Hashimoto et al, 1987). The numerical inversion method was used to obtain the wave surface at ADV's position from the wave surfaces at 5 near locations. Then it was used to claculated the velocities and compared with the measured ones by ADV.

Fig. 6 shows an example of the comparisom between calculated and measured velocity hostories in an oblique 2-D random wave. Two velocity histories are agreeable each other.

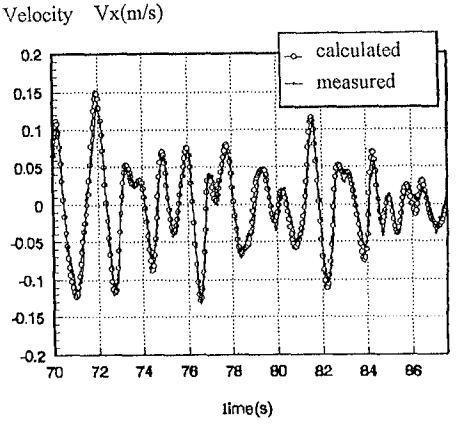

Fig. 6 Comparison between calculated and measured velocity histories in an oblique random wave

The example of the compareson between the calculated and measured velocities v_x, v_z in a 2-D random wave at the position $z=-0.018$m is shown in Fig. 7. Two sets of velocity history are agreeable. But for the trough phase, the ADV is out of the water so the measured velocities are equal to zero.

For the 3-D random waves the example of the comparison between the measured and calculated velocities is shown in Fig. 8. The wave spreading parameter, $s=50$. The velocities are measured at the position 0.304m above bottom. Two sets of velocity history are basically consistent. In this case the accuracy of velocity calculation is also dependent on that of the wave surface inversion.

3.7 Effects of nonlinearity on velocity

For the unidirectional wave, the direct linear method and Donelan's linear method (1992) are used to calculate the velocities at different depth and their results are compared with that by the nonlinear numerical method. Their ratios are shown in Fig. 9. The measured results are also shown in this figure by closed circles. It is found that when $z/d<-0.25$ all of three methods can predict the avaible velocities which is close to the measured ones. But when $z/d\to 0$ two linear

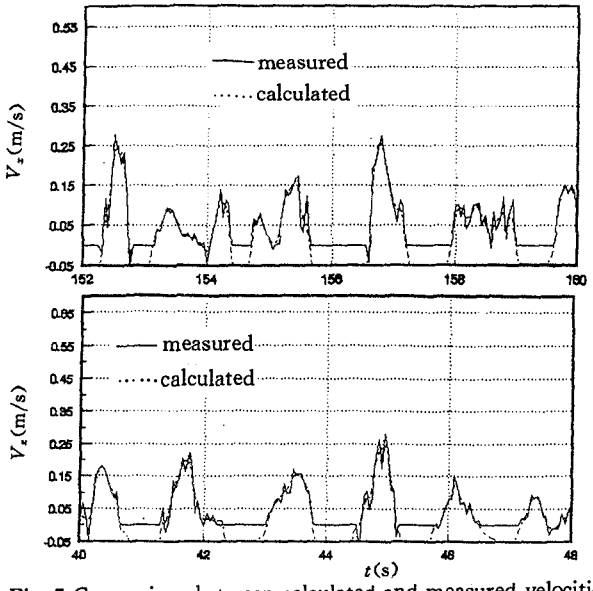

Fig. 7 Comparison between calculated and measured velocities in a 2-D random wave (H_s=4.88cm, T_s=1.39s)

mthods over-predict the velocities. For 3-D waves, the general variation tendency is the same as for 2-D waves.

Fig. 10 shows the comparison between calculated and measured velocities v_x and v_y at wave crest for 3-D random wave. The linear method overestimate the velocities and the nonlinear numerical method predict the velocities closed to measured ones.

4. CONCLUSIONS

A numerical method calculating the 3-D velocity field under a given random wave surface directly by the governing equations is proposed in this paper. It is verified with the exprimental study that this methed can predicte 3-D velocities at different locations including wave crest with high accuracy. The direct linear method usually greatly overestimates the crest velocities near the surface.

The wave surface needed for velocity calculation can be numerically simulated from directional spectrum or determined from other wave surfaces at near locations with an inversion method proposed in this paper. The inversion method is verified with model test and field data.

The effects of nonlinearity of waves on the velocities at positions near still water level are not negligible. The experimental results show that this effect of 2-D waves is more than that of 3-D waves and this effect on vertical component velocity is more than that on horizontal component velocity.

Acknowledgments—This project is supported by the Foundation of State Key

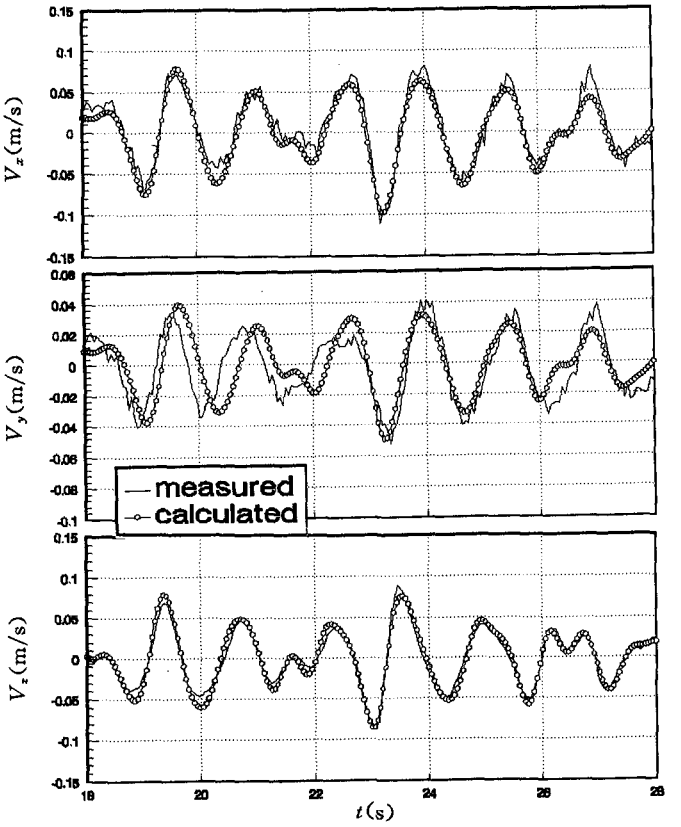

Fig. 8 Comparison between calculated and measured velocity histories in 3-D wave (H_s=5.1cm, T_s=1.38s, s=50, d=41.3cm, z=−10.9cm)

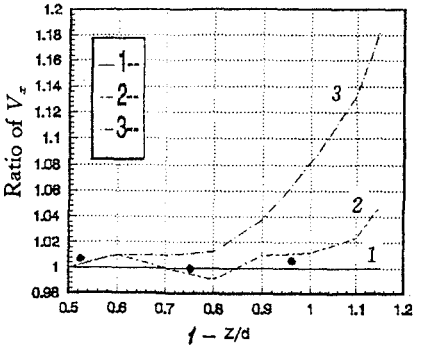

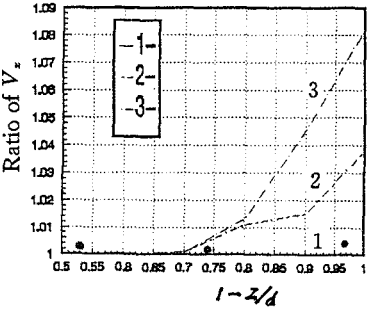

Fig. 9 Effects of nonlinearity on velocities V_x and V_z (H/d=0.36, H/L=0.122, 1-nonlinear method; 2-Donelan; 3-direct linear method)

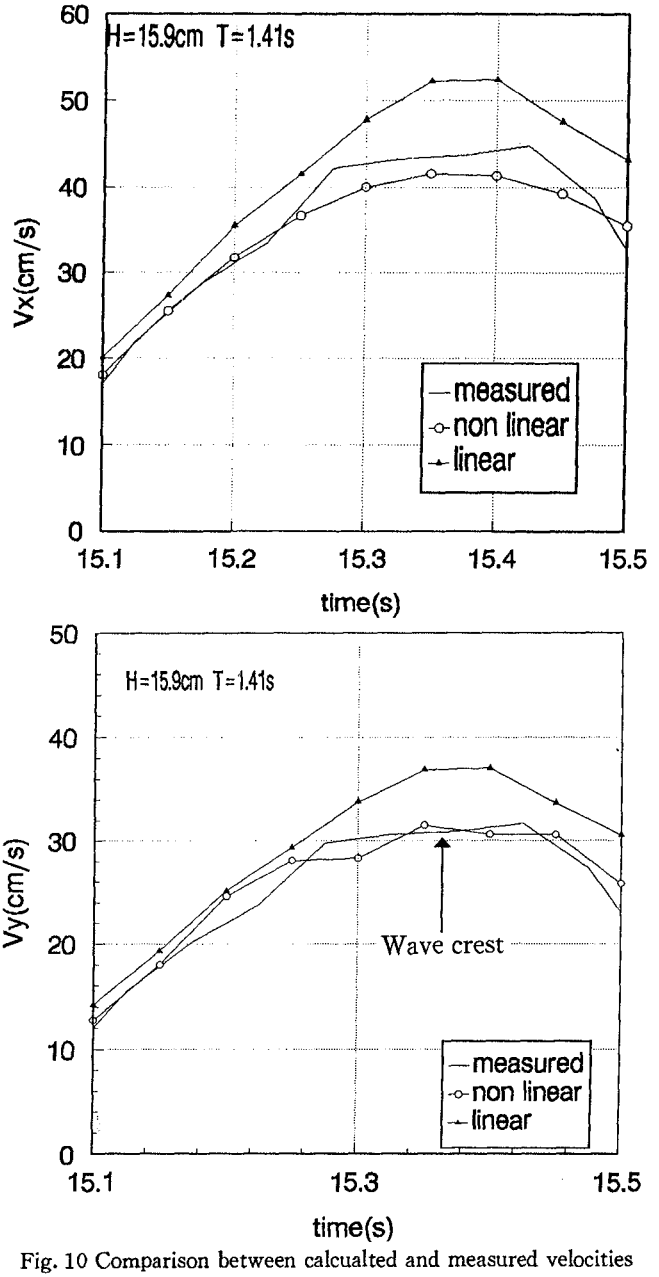

Fig. 10 Comparison between calcualted and measured velocities v_x and v_y at wave crest for 3-D wave.
(d=41.3cm, z=−1.8cm, H_s=12.3cm, T_s=1.39s)

Laboratory of Coastal and Offshore Engineering, China. The anthors sincecely wish to express their appreciation to Mrs. Y. Sun, M. N. Go and Mr. Z. C. Jiang for their great helps to this study.

REFERENCES

Dommermuth D. G. and Yue K. P. ,(1987), A high-order spectral method for the study of nonlinear gravity waves. J. Fluid Mech. Vol. 184, 267-288.

Donelan M. A. , Anctil F. and Doering J. C. (1992). A simply method for calculating the velocity field beneath irregular waves, Coastal Engineering, 16, 199-224.

Forristall G. Z. , Ward E. G. , Cardone, V. J. Borgmann, L. E. (1978), The directional spectra and kinematics of surface gravity waves in tropical storm Delia, J. Phys. Ocean, 8. 888-909.

Gottlieb, D. and Orszag, S. A. (1977), Numerical analysis of spectral methods, SIAM.

Hashimoto N. , Kobune, K. , Kambyama Y. (1987), Estimation of directional spectrum using the Bayesian Approach and its application to field data analysis, Report of the Port and Harbour Research Institute. Vol. 12, 57-100.

Prislin I. and Zhang J. (1997), Pridiction of wave kinematics under the wave crest in short-crested irregular gravity waves, IAHR Seminar, Multidirectional Waves and Their Interaction with Structures, 357-370.

Rodenbuch G. and Forristall, G. E. , (1982). Three crest kinematics models compared to MaTS data and OTS data. MaTS Report VM-1-4B. Netherlands Marine Technological Research Program.

Yu, Y. X. , Lin S. X. and Li L. (1991), Numerical simulation of multidirectional random waves. Proc. 1st Inter. Offshore and Polar Engineering Conf. 26-32.

Zakharov V. E. (1968),Stability of periodic waves of finite amplitude on the surface of a deep fluid. J. Appl. Mech. Tech. Phys. 9, 190-194.

ON THE REFLECTION OF SHORT-CRESTED WAVES IN NUMERICAL MODELS

Michael Brorsen [1] and Jacob Helm-Petersen [1]

Abstract

The paper concerns the reflection performance of so-called 'sponge' layers, which are used to model partially reflecting (porous) structures in a numerical model domain. Various compositions of sponge layers and their performance with respect to wave reflection, main direction of propagation, and directional spreading have been investigated. The numerical model used in this study was a finite difference model based on the time-dependent mild-slope equation. Comparisons are made with reflection measured in physical experiments with short-crested waves. The results obtained so far indicate that in several cases partial reflection of short crested waves can be described satisfactorily in numerical models by use of sponge layers.

Introduction

An accurate modelling of reflection may be of great importance when the wave disturbance in a harbour is estimated by use of a numerical model.

In order to obtain a correct partial reflection from a porous structure under arbitrary wave conditions, it is necessary to set up a 3D numerical model to describe the flow in the porous structure. This would lead to a computational effort that normally cannot be afforded in a practical investigation of wave disturbance in a harbour.

Models based on depth integrated flow equations are nearly always applied in practical investigations of wave fields in order to reduce the computational effort. Typical examples of depth integrated equations are Boussinesq equations or mild-slope equations.

In models based on Boussinesq equations it is rather easy to model the depth integrated flow in a porous structure with vertical front. Terms describing the

[1]Hydraulics & Coastal Engineering Laboratory, Dept. of Civil Engineering
Aalborg University, Sohngaardsholmsvej 57, DK-9000 Aalborg

dissipation are included in the governing equations, and dissipation as well as reflection can be modelled rather accurately in such numerical models, at least in case of head on waves (Madsen and Warren, 1984). A major drawback of these models is the necessary substantial computational effort, and some 'tuning' is normally still necessary to obtain a correct reflection coefficient.

Models based on mild-slope equations may demand much less computational effort, especially if partial reflection could be modelled by implementation of a simple boundary condition for the surface elevation or the velocity potential at the structure. With such a type of boundary condition one has to specify the reflection coefficient beforehand and this demands an estimate of the yet unknown wave steepnees. In principle an iterative approach is therefore necessary.

Furthermore, it is not straightforward to obtain an analytical boundary condition which combines good performance with respect to the angle of incidence of the waves and easiness of implementation into the numerical model see e.g. Behrendt (1986) and Dingemans (1997).

The present paper concerns the reflection performance of so-called 'sponge' layers, which are used to model partially reflecting (porous) structures in the numerical model domain. The applied sponge layer technique was first described by Larsen and Dancy (1983). This technique is very easy to implement into finite difference models and has been used extensively to model open boundaries, i.e. boundaries where the goal is no reflection at all.

Various compositions of sponge layers and their performance with respect to wave reflection, main direction of propagation, and directional spreading have been investigated with models based on the finite difference method.

Attention has also been paid to the effects due to the discretization of an oblique structure with straight front in a finite difference model. Here an oblique structure means a structure, where the front of the structure is not aligned with a grid line in the model domain. For such a structure the straight front will be discretized into shorter pieces in the numerical model which might influence the reflection from the structure. Comparisons are made with reflection measured in physical experiments with short-crested waves (Helm-Petersen, 1994).

Numerical model

The numerical model was based on the time-dependent mild-slope equation, see e.g. Kirby et al. (1992) and Dingemans (1997). In this equation the vertical dependence is extracted from the velocity potential $\phi(x, y, z, t)$ according to

$$\phi(x, y, z, t) = f(z, h) \cdot \varphi(x, y, t) \tag{1}$$

where

$$f(z, h) = \frac{\cosh k(z + h)}{\cosh kh} \tag{2}$$

Here $\varphi(x, y, t)$ is the velocity potential at $z = 0$, h is the local still water depth, k is the local wave number and z a vertical co-ordinate.

Assuming small variations in the seabed topography (mild slopes) and first order wave theory leads to the model equations

$$\eta = -\frac{1}{g}\varphi_t \tag{3}$$

and

$$\eta_t + \frac{\partial}{\partial x}(A\varphi_x) + \frac{\partial}{\partial y}(A\varphi_y) - B\varphi = 0 \tag{4}$$

where

$$A(x,y) = \frac{1}{2k}\left[1 + \frac{2kh}{\sinh(2kh)}\right]\tanh(kh) = \frac{c\,c_g}{g} \tag{5}$$

$$B(x,y) = \frac{k}{2}\left[1 - \frac{2kh}{\sinh(2kh)}\right]\tanh(kh) = \frac{\omega^2 - k^2\,c\,c_g}{g} \tag{6}$$

and ω is the circular frequency, c is the phase velocity and c_g is the group velocity.

If equation (3) is substituted into equation (4) the result is the hyperbolic time-dependent mild-slope equation. This equation is able to handle refraction, shoaling, diffraction and reflection of linear, irregular waves provided that the sea state can be described by a narrow frequency spectrum (Dingemans, 1997) with a dominant carrier frequency $\bar{\omega}$.

In this study the numerical solution was based on an explicit finite difference discretization of equation (3) and equation (4). The computational domain was divided into quadratic boxes, and central differences were used for spatial as well as time derivatives. Both η and φ were calculated at the center of each box (but at different new time levels, $(n+1/2)\,\Delta t$ and $(n+1)\,\Delta t$, respectively) from the discretized equations:

$$\begin{aligned}\frac{\eta_{i,j}^{n+\frac{1}{2}} - \eta_{i,j}^{n-\frac{1}{2}}}{\Delta t} \simeq\ & B_{i,j}\varphi_{i,j}^n \\ & - \frac{A_{i+1,j} - A_{i-1,j}}{2\Delta x} \cdot \frac{\varphi_{i+1,j}^n - \varphi_{i-1,j}^n}{2\Delta x} \\ & - A_{i,j}\frac{\varphi_{i-1,j}^n - 2\varphi_{i,j}^n + \varphi_{i+1,j}^n}{(\Delta x)^2} \\ & - \frac{A_{i,j+1} - A_{i,j-1}}{2\Delta y} \cdot \frac{\varphi_{i,j+1}^n - \varphi_{i,j-1}^n}{2\Delta y} \\ & - A_{i,j}\frac{\varphi_{i,j-1}^n - 2\varphi_{i,j}^n + \varphi_{i,j+1}^n}{(\Delta y)^2}\end{aligned} \tag{7}$$

$$\eta_{i,j}^{n+\frac{1}{2}} = -\frac{1}{g}(\varphi_t)_{i,j}^{n+\frac{1}{2}} \simeq -\frac{1}{g}\frac{\varphi_{i,j}^{n+1} - \varphi_{i,j}^n}{\Delta t} \tag{8}$$

In each time step $\eta_{i,j}^{n+1/2}$ was first calculated by equation (7) and then $\varphi_{i,j}^{n+1}$ was calculated by equation (8).

Fully reflective boundaries were modelled by forcing the flow to be zero between the two boxes on each side of the boundary. This was obtained by setting the values of φ at the two boxes to be equal.

Partially reflective boundaries were modelled by use of sponge layers. A reduction factor $\mu < 1$ is specified for each box in the sponge layer. In each time step the surface elevation, η, was calculated in each box within the entire domain. Hereafter, also at each time step, the η-values in sponge layers are multiplied by the corresponding μ-factors. Thus energy was extracted from the system. The width (no of boxes) of a sponge layer, denoted W_s, and the μ-values corresponding to a desired reflection coefficient were found by trial and error for head on waves in a numerical wave flume.

The factor μ was found from the expression

$$\mu = \frac{1}{(a-1)(\frac{n}{N})^b + 1} \tag{9}$$

where n (the type of the sponge box) is an integer between 1 and N, a and b are constants. Open boundaries were modelled by sponge layers where the type n was varied linearly from the beginning of the sponge layer to the boundary of the computational domain. The reflection coefficient from such a layer was typically only a few percent if the width of the sponge layer was approximately 2 times the wave length corresponding to the peak frequency of a sea state.

A single summation wave generation model (Miles, 1989) was applied to generate the short crested sea state. Hence each wave component had a unique frequency, whereas several wave components were travelling in the same direction. This can be expressed as

$$\eta(x,y,t) = \sum_{l=1}^{L}\sum_{m=1}^{M} A_{lm}\cos(\omega_{lm}t - k_{lm}(x\cos\theta_m + y\sin\theta_m) + \phi_{lm}) \tag{10}$$

where

$$\omega_{lm} = 2\pi f_{lm}$$
$$= 2\pi(M(l-1)+m)\Delta f + 2\pi f_{min} \tag{11}$$
$$A_{lm} = \sqrt{2S(f_{lm})H(f_{lm},\theta_m)M\Delta f\Delta\theta} \tag{12}$$
$$\theta_m = (m-1)\Delta\theta - \theta_{max} \tag{13}$$

ϕ_{lm} is a random phase, $S(\cdot)$ and $H(\cdot)$ are the wave energy spectrum and the directional spreading function, respectively.

The waves were generated in the numerical model by the method described in Larsen and Dancy (1983) by adding or removing volume along a gridline, referred to as the wave generation line. In order to generate a single wave component

$$\eta_I = a\sin(kx' - \omega t + \varphi) \tag{14}$$
$$= a\sin(k\cos\theta x^* + k\sin\theta x^* - \omega t + \varphi) \tag{15}$$

travelling in the direction θ, see Figure 1, the necessary volume to be added at each generation box at each time step was calculated from equation

$$\Delta\eta = \frac{2\,c_e\eta_I \cos\theta\Delta t}{\Delta x} \tag{16}$$

where c_e is the energy velocity defined (Suh et al., 1997) as

$$c_e = \bar{c}_g \frac{\bar{\omega}}{\omega}\sqrt{1+\frac{\bar{c}}{\bar{c}_g}\left((\frac{\omega}{\bar{\omega}})^2-1\right)} \tag{17}$$

Here the overbar is associated with the applied carrier frequency.

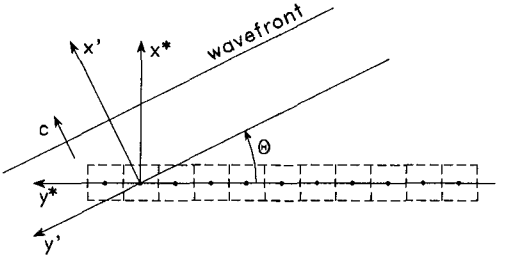

Figure 1: Definition of parameters.

Analysis of data

Directional spectra were estimated by use of the software package PADIWA (1997), which is based on the Bayesian Directional Spectrum Estimation Method - BDM (Hashimoto and Kobune, 1988). This method estimates the spreading function $H(f,\theta)$, and the directional spectrum $S(f,\theta)$ was found from

$$S(f,\theta) = H(f,\theta)\,S(f) \tag{18}$$

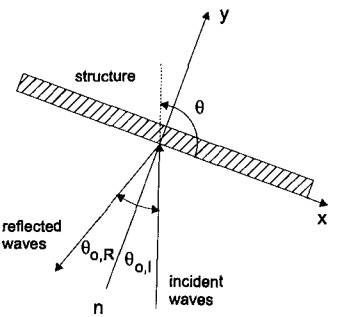

Figure 2: Definition sketch of propagation angles.

From Figure 2 it is seen that waves propagating in directions between 0° and 180° were incident waves, and waves propagating in directions between 180° and 360° were reflected waves. Having estimates of $H(f,\theta)$ in K directions at each frequency, the main propagation directions for incident and reflected waves, see Figure 2, were found from

$$\theta_{o,I}(f) = \sum_{k=1}^{K/2} \theta_k \, H(f,\theta_k) \, \Delta\theta - 90^\circ \tag{19}$$

$$\theta_{o,R}(f) = 270^\circ - \sum_{k=K/2+1}^{K} \theta_k \, H(f,\theta_k) \, \Delta\theta \tag{20}$$

and the variances of the directional spreading functions from

$$\sigma^2_{\theta,I}(f) = \sum_{k=1}^{K/2} (\theta_k - \theta_{o,I}(f))^2 \, H(f,\theta_k) \, \Delta\theta \tag{21}$$

$$\sigma^2_{\theta,R}(f) = \sum_{k=K/2+1}^{K} (\theta_k - \theta_{o,R}(f))^2 \, H(f,\theta_k) \, \Delta\theta \tag{22}$$

The frequency dependent reflection coefficient (defined as the ratio between wave heights) was found from

$$R(f) = \sqrt{\frac{S_R(f)}{S_I(f)}} \tag{23}$$

and the total reflection coefficient from

$$C_R = \sum \frac{S_I(f) + S_R(f)}{\sum [S_I(f) + S_R(f)]} \, R(f) \tag{24}$$

Numerical simulations

In all simulations the following setup was applied:

- computational domain : 120×208 boxes
- box size : $dx = dy = 0.125$ m
- water depth : $h = 0.61$ m
- Jonswap frequency spectrum ($\gamma = 3.3$), significant wave height $H_s = 0.10$ m and peak period $T_p = 1.5$ secs. Energy outside the frequencies $0.66\, f_p$ and $2\, f_p$ was cut off
- Mitsuyasu spreading function i.e.

  $H(f,\theta) = const \cdot \cos^{2s}(\frac{\theta-\theta_o}{2})$ with $s = 15$ ($\Leftrightarrow \sigma_{\theta,I}(f) = 20^\circ$)

- time step : $dt = 0.05$ sec
- short-crested sea: 220 wavelets
  (20 frequency bands ($L = 20$) each with 11 directions ($M = 11$))
- the sponge layer coefficients were calculated by equation (9) with $a = 1.3$, $b = 1.8$ and $N = 50$.

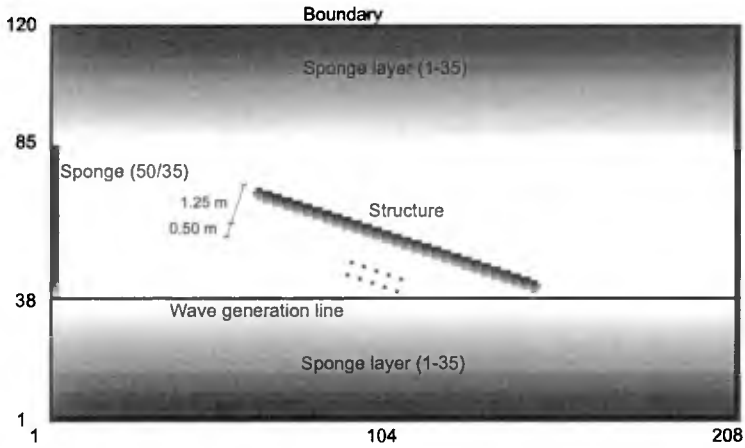

Figure 3: Model setup. Structure with stepped front (1:3), $C_R \approx 55\%$.

Different types and placement of structures were investigated, but the wave generation line and the 2 fully absorbing sponge layers were in all simulations situated as shown in Figure 3. In case of oblique structures an additional sponge layer with $W_s = 2$ and types 50 and 35 was applied at the left boundary of the domain.

In all simulations surface elevation time series were sampled at 10 positions in a 0.5 m×0.5 m grid placed parallel with the front of the actual structure at a distance of 1.25 m, see Figure 3. These time series provided the data for the reflection analysis. The elevation time series were sampled with a frequency of 10 Hz, i.e. every second time step and the duration of each time series was 18 minutes.

The applied setup of measuring positions is not considered optimal, but was chosen in order to get the same setup which was used in similar physical experiments (Helm-Petersen, 1994). In these physical experiments reflection coefficients from a breakwater with a vertical, porous front were determined by use of the same type of analysis applied in the present numerical simulations.

The estimation of the directional spectrum was based on subseries having a duration of 25.6 secs corresponding to a spectral resolution of $\Delta f = 0.039$ Hz. The directional resolution was chosen to 5° corresponding to $K = 72$ directions.

Structures with straight front

In those cases the structure was parallel with the wave generation line. The following reflection conditions were simulated:

- fully reflective front
- partially reflective front, $C_R \approx 85$ %, corresponding to a sponge layer with $W_s = 1$ and $n = 20$ or $\mu = 0.95$
- partially reflective front, $C_R \approx 55$ %, corresponding to a sponge layer with $W_s = 3$ and $n = 20, 25, 35$ corresponding to $\mu = 0.95, 0.92, 0.86$

The results from these simulations are shown in Figures 4 – 7.

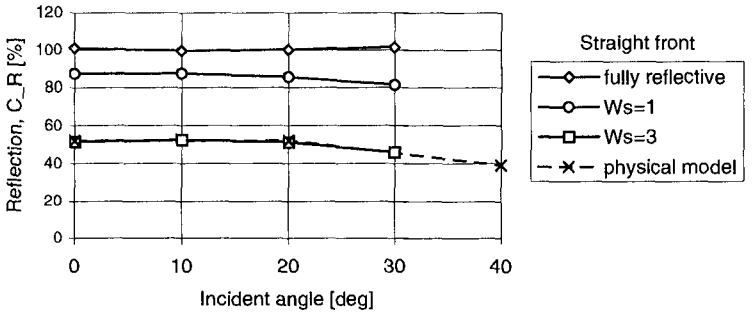

Figure 4: Reflection coefficients. Numerical models with *straight* front and physical model (Helm-Petersen, 1994).

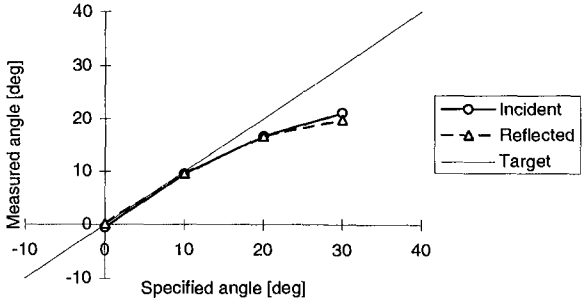

Figure 5: Main propagation angles. Numerical model with *straight* front, $C_R = 100\%$.

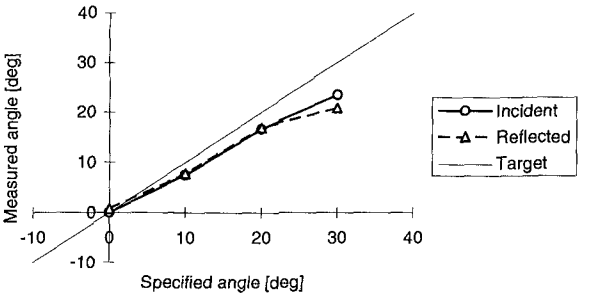

Figure 6: Main propagation angles. Numerical model with *straight* front, $C_R \approx 85$ %, $W_s = 1$.

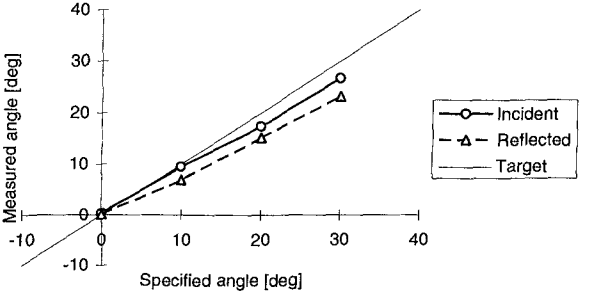

Figure 7: Main propagation angles. Numerical model with *straight* front, $C_R \approx 55$ %, $W_s = 3$.

Structures with stepped front

The oblique structures were forming angles of 9.5° (1:6), 18.4° (1:3) or 26.6° (1:2), respectively, with the computational grid. Hence the discretized front of the models were stepped. The model setup for a structure forming an angle of 18.4° (1:3) with the computational grid is shown in Figure 3. The following conditions were simulated for the three oblique structures:

- fully reflective front.
- partially reflective front, $C_R \approx 55$ %, $W_s = 3$.

The setup of the sponge layers are shown in Figures 8–9, and the results from these simulations are shown in Figures 10 –14.

Discussion of results

For a structure having the front aligned with a grid line in the model domain it was found that sponge layers provide a very reasonable reflection of short-crested

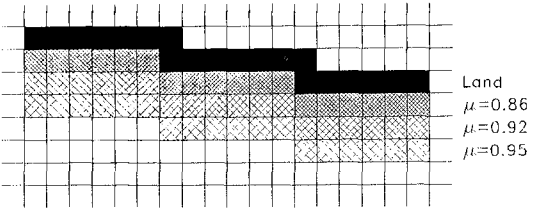

Figure 8: Structure with stepped front (1:6), $C_R \approx 55$ %, $W_s = 3$.

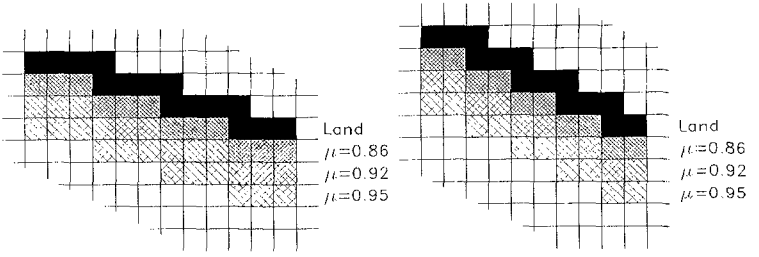

(a) 1:3 (b) 1:2

Figure 9: Structures with stepped front, $C_R \approx 55$ %, $W_s = 3$.

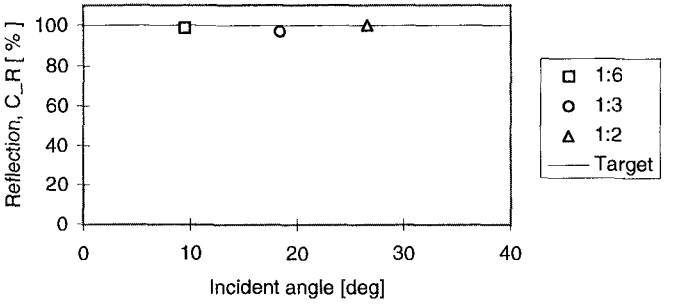

Figure 10: Reflection coefficients. Structures with *stepped* front, fully reflective.

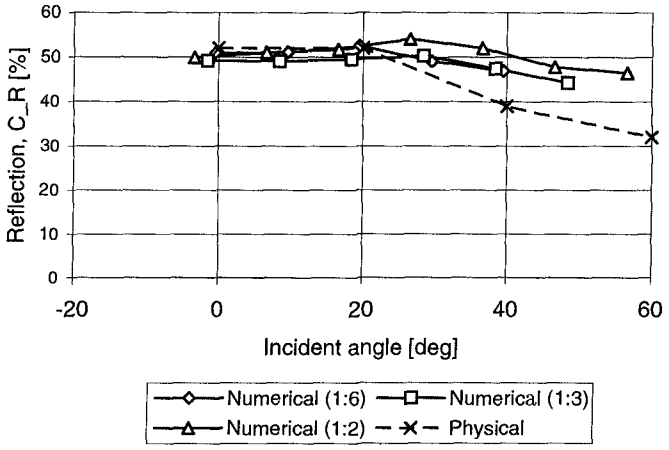

Figure 11: Reflection coefficients. Structures with *stepped* front, $W_s = 3$.

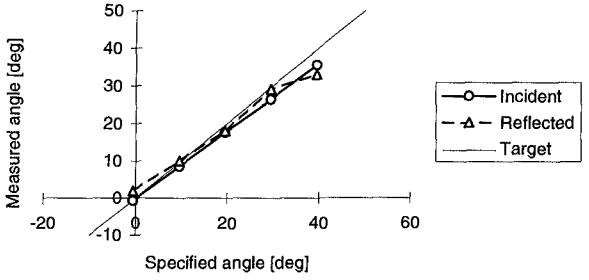

Figure 12: Main propagation angles. Structure with *stepped* front (1:6), $C_R \approx 55$ %, $W_s = 3$.

waves. The variation of the total reflection coefficient C_R with the angle of incidence (main propagation direction) was the same in the numerical and in the physical model in case of a partially reflective front, see Figure 4. Furthermore the main propagation directions of the waves was reflected into directions corresponding to Snell's law, see Figures 5–7. This was also found in the physical experiments. Some deviation between the specified and measured main incident angles are seen for angles larger than 20-30°. In the numerical simulations it was only possible to generate wavelets propagating at angles of approximately 65° from the line of generation and therefore the directional spectrum had to be truncated at angles where considerable energy was present. This might be the main cause to the deviation between the specified and measured main incident angles.

Also in case of oblique structures with a straight front discretized into a stepped front it was found that sponge layers provide a very reasonable reflection of short-crested waves. The total reflection coefficient C_R was modelled correctly op to

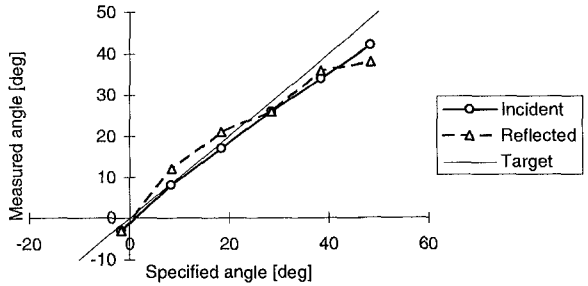

Figure 13: Main propagation angles. Structure with *stepped* front (1:3), $C_R \approx 55$ %, $W_s = 3$.

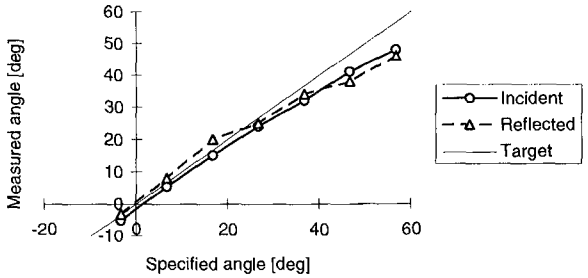

Figure 14: Main propagation angles. Structure with *stepped* front (1:2), $C_R \approx 55$ %, $W_s = 3$.

approximately 20°'s angle of incidence (main propagation direction) in the numerical model. For larger angles the variation of C_R in the numerical simulations had the correct trend, but C_R-values from numerical simulations were somewhat larger than the corresponding C_R-values from the physical experiments, see Figure 11. The main propagation direction of the waves was also in case of stepped fronts reflected into directions corresponding to Snell's law, see Figures 12–14. Due to the oblique structure larger angles of incidence could be obtained, but also in these simulations some deviations between specified and measured main incident angles were seen. Average values of the relative directional spreading, defined as $\sigma_{rel} = \sigma_{\theta,R}/\sigma_{\theta,I}$, are shown in Table 1. It is seen that simulations with partially reflective structures having $C_R \approx 55\%$ typically had a relative spreading $\sigma_{rel} \approx 1.25$. A relative spreading larger than one is to be expected for a partially reflective structure, and in physical experiments with vertical fronts having $C_R \approx 55\%$ (Helm–Petersen, 1994) $\sigma_{rel} \approx 1.20$ was found.

Conclusions

The 3D reflection performance of sponge layers applied in numerical models has been investigated considering short-crested waves. In general the results from the numerical simulations compare well to results from physical experiments carried

Width of layer W_s	type of front	Reflection coeff. C_R [%]	Relative spreading $\sigma_{rel} = \frac{\sigma_{\theta,R}}{\sigma_{\theta,I}}$
0	straight	100	1.00
1	straight	85	1.05
3	straight	55	1.33
3	stepped (1:6)	55	1.18
3	stepped (1:3)	55	1.24
3	stepped (1:2)	55	1.19

Table 1: *Relative directional spreading.*

out with caissons having perforated vertical fronts, and it is found that appropriate 3D reflection can be obtained with respect to the total reflection coefficient, main propagation direction of the reflected waves and the relative directional spreading.

Acknowledgements

Part of this work has been carried out under the frame work programme *Marine Techniques 2* (Marin Teknik 2) of the Danish Technical Research Council.

References

Behrendt, L. (1985), A finite element model for water wave diffraction including boundary absorption and bottom friction, ISVA Series Paper 37, Technical University of Denmark.

Dingemans, M. W. (1997), Water Wave Propagation over Uneven Bottoms, Part 1, Advanced Series on Ocean Engineering–Volume 13, World Scientific.

Hashimoto, N. and K. Kobune (1988). Directional spectrum estimation from a Bayesian approach. In Proc. 21st International Conference on Coastal Engineering, Malaga, Spain, pp. 62-76.

Helm–Petersen, J. (1994). Reflection from caissons in multidirectional seas. In *3rd MCS Project Workshop, MAS2-CT92-0047, Monolithic (vertical) Coastal Structures.*

Kirby, J. T., C. Lee and C. Rasmussen (1992), Time-Dependent Solutions of the Mild–Slope Wave Equation, Proc. 23rd International Conference on Coastal Engineering, Venice, Italy, pp. 391-404.

Larsen, J. and H. Dancy (1983). Open boundaries in short wave simulations - a new approach. Coastal Engineering, Volume 7, pp. 285-297.

Madsen, P. A. and I .R. Warren (1984). Performance of a numerical short wave

model. Coastal Engineering, Volume 8, pp. 73-93.

Miles, M. D. (1989). A note on directional random wave synthesis by the single-summation method, XXIII Congress, IAHR, Ottawa, Canada, vol. C, pp. 243-250.

PADIWA (1997). A Package for Directional Wave Analysis. Hydraulics and Coastal Engineering Laboratory, Aalborg University.

Suh, K. D., C. Lee and W. S. Park (1997). Time dependent equations for wave propagation on rapidly varying topography. Coastal Engineering, Volume 32, pp. 91-117.

Breaking Waves and Induced Currents on Coastal Structures

Entin A. Karjadi[1] and Nobuhisa Kobayashi[2]

Abstract: A horizontally two-dimensional, time dependent numerical model for obliquely incident shallow water waves with arbitrary incident angles is developed to predict the temporal and spatial variations of the free surface elevations and fluid velocities on inclined coastal structures. As a first attempt, use is made of periodic lateral boundary conditions, which limits the computations to regular waves on the slope of alongshore uniformity. The numerical method and the seaward and landward boundary algorithms are fairly general and expected to be applicable to irregular waves as well. The computed results for plunging waves on a rough 1:3.5 slope with the incident angles in the range of $0° - 80°$ are presented.

Introduction

The three-dimensional hydrodynamics processes on and around coastal structures are little known in comparison to the nearshore hydrodynamics on sandy beaches. As a result, no predictive model is available to predict breaking waves and induced currents on and around these inclined structures.

The available data are still limited because the experiments in directional wave basins to examine the effects of incident wave angles and directionality on design variables such as wave runup (De Wall and Van der Meer 1992) and wave reflection (Isaacson *et al.* 1996) were conducted mostly for straight structures on horizontal bottom. In addition, since these experiments include more design parameters and are much more time-consuming than unidirectional wave flume experiments, measurements are normally limited to free surface oscillations at several locations and do not provide detailed understanding of oblique wave dynamics on steep rough slopes.

Existing time-dependent models for waves on inclined coastal structures are limited mostly to normally-incident waves as reviewed by Kobayashi (1995). Liu *et al.* (1995) solved the finite-amplitude, shallow-water equations numerically to predict solitary wave runup around a circular island with a 1:4 side slope. Kobayashi and Karjadi (1996) and Kobayashi *et al.* (1997) developed numerical models for oblique irregular waves with small incident angles but these models can not be used to examine the

[1]Department of Civil Engineering, Bandung Institute of Technology, Jalan Ganesha 10, Bandung 40132, Indonesia. E-mail: entin@coastal.udel.edu

[2]Professor and Associate Director, Center for Applied Coastal Research, University of Delaware, Newark, DE 19716, USA. E-mail: nk@coastal.udel.edu

effects of incident wave angles on the important quantities for the design of coastal structures.

In this paper, a two-dimensional, time-dependent numerical model for finite-amplitude, shallow-water waves with arbitrary incident angles is developed to examine the effects of incident wave angles on oscillatory and time-averaged wave characteristics on a steep rough slope. As a first attempt, use is made of periodic lateral boundary conditions. Consequently, computations are limited to regular waves on the slope of alongshore uniformity. Incident nonlinear waves at the toe of the slope are specified as input to the model. Reflected waves are predicted at the toe of the slope to examine the height, shape, angle and phase shift of reflected waves as a function of the incident wave angle. Computed waterline oscillations are analyzed to obtain wave runup, setup and run-down as a function of the incident wave angle. Furthermore, the computed spatial and temporal variations of the free surface elevation and horizontal velocities are analyzed to elucidate the detailed wave mechanics on the steep rough slope.

Numerical Model

The normalized depth-integrated continuity and horizontal momentum equations in shallow water may be expressed in the conservative vector form as

$$\frac{\partial \mathbf{U}}{\partial t} + \frac{\partial \mathbf{E}}{\partial x} + \frac{\partial \mathbf{F}}{\partial y} + \mathbf{G} = 0 \tag{1}$$

with

$$\mathbf{U} = \begin{bmatrix} h \\ hU \\ hV \end{bmatrix} ; \quad \mathbf{E} = \begin{bmatrix} hU \\ hU^2 + h^2/2 \\ hUV \end{bmatrix} ; \quad \mathbf{F} = \begin{bmatrix} hV \\ hUV \\ hV^2 + h^2/2 \end{bmatrix} ;$$

$$\mathbf{G} = \begin{bmatrix} 0 \\ h\frac{\partial z_b}{\partial x} + f(U^2+V^2)^{1/2}U \\ h\frac{\partial z_b}{\partial y} + f(U^2+V^2)^{1/2}V \end{bmatrix} \tag{2}$$

where the symbol are depicted in Fig. 1 with the prime indicates the physical variables; x' = horizontal coordinate taken to be positive landward with $x' = 0$ at the toe of the slope; y' = horizontal coordinate parallel to the toe alignment and taken to be positive in the downwave direction; h' = water depth; U' = depth- averaged cross-shore velocity; V' = depth-averaged alongshore velocity; g = gravitational acceleration; η' = free surface elevation above the still water level (SWL). The vertical coordinate z' is taken to be positive upward with $z' = 0$ at SWL. The bottom elevation is located at $z' = z'_b$ with $z'_b = (\eta' - h')$ and the spatial variation of z'_b is assumed to be known.

The normalized variables without the primes in (1) and (2) are defined as

$$t = \frac{t'}{T'} \; ; \; x = \frac{x'}{\sigma H'} \; ; \; y = \frac{y'}{\sigma H'} \; ; \; U = \frac{U'}{\sqrt{gH'}} \; ; \; V = \frac{V'}{\sqrt{gH'}} \tag{3}$$

$$h = \frac{h'}{H'} \; ; \; \eta = \frac{\eta'}{H'} \; ; \; z_b = \frac{z'_b}{H'} \; ; \; f = \frac{1}{2}\sigma f'_b \; ; \; \sigma = \frac{T'\sqrt{gH'}}{H'} \tag{4}$$

where T' and H' = incident wave period and height, respectively; f'_b = bottom friction factor which is allowed to vary spatially; and σ = ratio of the horizontal and vertical

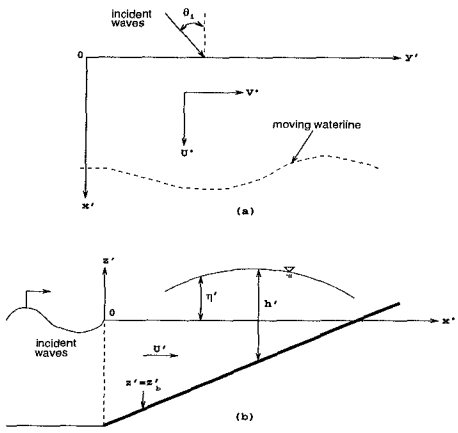

Figure 1: Definition sketch.

length scales which is assumed to satisfy $\sigma^2 \gg 1$ in shallow water (*e.g.*, Kobayashi and Wurjanto 1992).

Equation (1) is solved numerically to compute the temporal and spatial variations of h, U and V where $\mathbf{E}$, $\mathbf{F}$ and $\mathbf{G}$ depend on $\mathbf{U}$ only for given z_b and f. The mean water depth $\overline{h}$ and the mean velocities $\overline{U}$ and $\overline{V}$ are then obtained by time-averaging the computed h, U and V where the overbar indicates time-averaging.

To interpret the computed spatial variations of $\overline{h}$, $\overline{U}$, and $\overline{V}$, the time-averaged continuity and momentum equations are derived from (1)

$$\frac{\partial}{\partial x}(\overline{hU}) + \frac{\partial}{\partial y}(\overline{hV}) = 0 \tag{5}$$

$$\frac{\partial}{\partial x}(S_{xx}) + \frac{\partial}{\partial y}(S_{xy}) + \overline{h}\frac{\partial \overline{\eta}}{\partial x} + \tau_{bx} = 0 \tag{6}$$

$$\frac{\partial}{\partial x}(S_{xy}) + \frac{\partial}{\partial y}(S_{yy}) + \overline{h}\frac{\partial \overline{\eta}}{\partial y} + \tau_{by} = 0 \tag{7}$$

with

$$S_{xx} = \overline{hU^2} + \frac{1}{2}\overline{(\eta - \bar{\eta})^2} \quad ; \quad S_{xy} = \overline{hUV} \quad ; \quad S_{yy} = \overline{hV^2} + \frac{1}{2}\overline{(\eta - \bar{\eta})^2} \tag{8}$$

$$\tau_{bx} = \overline{f(U^2 + V^2)^{1/2}U} \quad ; \quad \tau_{by} = \overline{f(U^2 + V^2)^{1/2}V} \tag{9}$$

where S_{xx}, S_{xy} and S_{yy} = time-averaged momentum fluxes similar to radiation stresses (Longuet-Higgins 1970); and τ_{bx} and τ_{by} = time-averaged bottom shear stress in the x and y-directions. The accuracy of the time-dependent numerical model is checked using (5)-(7) with (8) and (9) because the computed h, U and V must satisfy the corresponding time-averaged equations.

The derivation of the depth-integrated energy equation corresponding to (1) is similar to that of Kobayashi and Wurjanto (1992). The time-averaging normalized

energy equation corresponding to (1) may be expressed as

$$\frac{\partial}{\partial x}(F_x) + \frac{\partial}{\partial y}(F_y) = -D_f - D_B \tag{10}$$

with

$$F_x = \overline{hU[\eta + \frac{1}{2}(U^2 + V^2)]}\ ;\ \ F_y = \overline{hV[\eta + \frac{1}{2}(U^2 + V^2)]}\ ;\ \ D_f = f\overline{(U^2 + V^2)^{1.5}} \tag{11}$$

where F_x and F_y = time-averaged energy flux per unit width in the x and y-directions, respectively; and D_f and D_B = time-averaged rate of energy dissipation per unit horizontal area due to bottom friction and wave breaking, respectively. The dissipation rate D_B is related to the vertical variations of horizontal velocities and shear stresses outside the bottom boundary layer which are not predicted in this two-dimensional model. As a result, D_B is computed using (10) with (11) for the computed h, U and V using (1). The computed D_B must be positive or zero.

The computer program is developed using the MacCormack method (MacCormack 1969) which has been used successfully for the computation of two-dimensional transient open channel flow with bores (Chaudhry 1993). The finite difference grid of constant grid size Δx and Δy is used to solve (1). The values of Δx and Δy must be small enough to resolve the rapid spatial variation of the wave motion on the slope. The initial time $t = 0$ is taken to be the time when the incident wave train arrives at the seaward boundary and there is no wave action in the computation domain. The waterline in the numerical model is defined as the location where the instantaneous water depth h equals a small value δ, which is taken as $\delta = 10^{-3}$ in the subsequent computation. The time step size Δt varies for each time step and determined using an approximate numerical stability criterion proposed by Thompson (1990).

It is very difficult to specify incoming waves through the lateral boundaries into the computation domain and allow outgoing waves to propagate out of the computation domain without any numerical reflection from the lateral boundaries. As a first attempt, the periodic lateral boundary conditions are used here, although these conditions are appropriate only for regular waves on the slope of alongshore uniformity. For the periodic lateral boundaries, the nodes along the lateral boundaries are treated as the interior nodes.

The seaward boundary of the numerical model is located at the toe of the slope along the y-axis as shown in Fig. 1. In the region $x \leq 0$, the bottom is assumed to be horizontal so that a regular wave theory on the horizontal bottom may be used to specify the normalized incident wave train $\eta_i(t, y)$ at $x = 0$ in the following form:

$$\eta_i(t, y) = F_i(p) \qquad \text{at} \quad x = 0 \tag{12}$$

with

$$p = t - \lambda y \quad ; \quad \lambda = \frac{T'\sqrt{gH'}}{L'} \sin\theta_i \tag{13}$$

where F_i = periodic function with respect to the phase p such that $F_i(p + 1) = F_i(p)$; L' = dimensional incident wavelength; θ_i = incident wave angle as shown in Fig. 1; and λ = inverse of the normalized alongshore wavelength. The alongshore wavelength, $L'/\sin\theta_i$, is constant on the slope of alongshore uniformity because of Snell's law (*e.g.*,

Dean and Dalrymple 1984). The function F_i depends on the wave theory used for a specific application. To satisfy the initial conditions of no wave action in the region $x \geq 0$, use is made of $\eta_i = tF_i$ for $0 \leq t < 1$ and $\eta_i = F_i$ for $t \geq 1$. To satisfy the periodic lateral boundary conditions, the computation domain width is taken as $0 \leq y \leq \lambda^{-1}$.

The seaward boundary algorithm for obliquely incident and reflected waves is not well established because no unique direction of propagation for characteristic variables exists for multidimensional hyperbolic equations including (1) (*e.g.*, Thompson 1990). Several algorithms including that of Van Dongeren and Svendsen (1997) were tried to produce the periodic wave motion on the slope which satisfies the time-averaged equations (5)-(7). In addition, the computed reflected wave train must become periodic and propagate along the y-axis in a manner similar to (12). The algorithm satisfying these requirements is developed using the method of cross-shore characteristics.

A smoothing procedure is applied to damp numerical high-frequency oscillations which may appear at the rear of the steep front of a breaking wave. Use is made here of the relatively simple procedure described in Chaudhry (1993). The procedure of the numerical method and boundary conditions is described in detail in Kobayashi and Karjadi (1999).

Computed Wave Motions on Steep Slope

The developed two-dimensional model becomes practically the same as the one-dimensional model of Kobayashi *et al.* (1987) for normally-incident waves which was compared with the large-scale riprap tests reported by Ahrens (1975). Since there are no appropriate data available to verify this two-dimensional model, test 18 of Ahrens (1975) is used as an example in this paper. The computation results for test 12 with surging waves are presented in Kobayashi and Karjadi (1999).

For test 18, the riprap slope was 1:3.5; the still water depth at the toe of the slope, $d' = 4.57$ m; the incident wave period $T' = 4.2$ s; the incident wave height $H' = 1.01$ m; the median mass of the riprap, $M_{50} = 34$ kg; and the density of the riprap, $\rho_a = 2710$ kg/m^3. The nominal diameter of the riprap defined as $D_{n50} = (M_{50}/\rho_a)^{1/3}$ was $D_{n50} = 0.232$ m. The test was limited to normally incident waves with $\theta_i = 0$. Computation is also made for the incident wave angle $\theta_i = 10°$, 20°, 30°, 40°, 50°, 60°, 70° and 80°. The ratio σ of the horizontal and vertical length scales defined in (4) is $\sigma = 13$, which satisfies the shallow water assumption of $\sigma^2 \gg 1$. The surf similarity parameter given by $\xi = \sigma \tan\theta/\sqrt{2\pi}$ is $\xi = 1.5$. The Ursell number $U_r = 5.7$ and the incident wave $\eta_i'(t', y')$ at the seaward boundary is computed using the Stokes second order theory (Kobayashi and Karjadi 1994). The bottom friction factor f_b' is taken as $f_b' = 0.3$ (Kobayashi *et al.* 1987). The damping coefficient κ for smoothing high-frequency numerical oscillations is taken to be very small ($\kappa = 0.01$) so as to minimize the numerical dissipation, although the numerical high-frequency oscillations become more visible as shown in Figs. 2 and 3 later.

The computation domain is taken as $0 \leq x \leq 1.95$ and $0 \leq y \leq \lambda^{-1}$ except for $\theta_i = 0$ because $\lambda = 0$ for $\theta_i = 0$. For $\theta_i = 0$, use is made of the value of λ corresponding to $\theta_i = 10°$. The number of nodes in the x and y-directions are taken as 162 and 161,

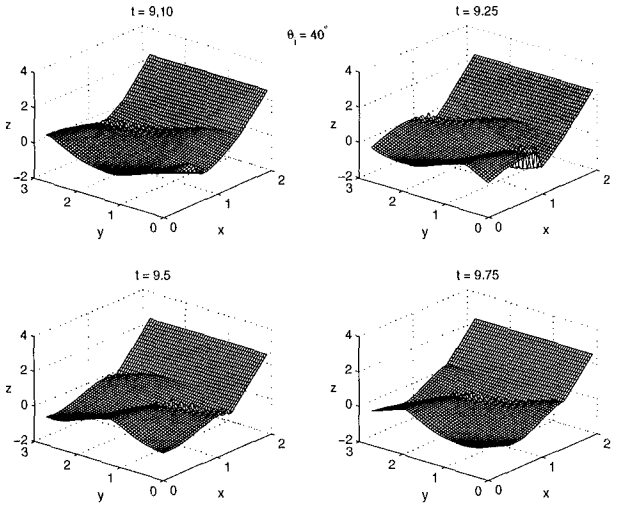

Figure 2: Spatial variations for free surface elevation η at time $t = 9, 9.25, 9.5, 9.75$ and 10.

respectively. The time step size Δt is on the order of 0.0003. The computation is made for $0 \leq t \leq 10$ and the time-averaging is performed for the last wave period $9 < t \leq 10$.

In the following, the computed results for $\theta_i = 40°$ are presented as an example. Fig. 2 shows the spatial variations of the free surface elevation η at time $t = 9$, 9.25, 9.5, 9.75 and 10 for $\theta_i = 40°$. The computed spatial variations at $t = 9$ and 10 are identical because the periodicity is established before $t = 9$. In the region of no water with $h = (\eta - z_b) = 0$, use is made of $\eta = z_b$ to depict the bottom elevation z_b of the slope. Fig. 2 indicates the oblique waves breaking and propagating along the slope.

Fig. 3 shows the temporal variations of η, U and V at $x = 0$, 0.35, 0.71, 1.16 and 1.40 along the cross-shore line at $y = 1.35$ where $\lambda^{-1} = 2.73$ for $\theta_i = 40°$. The waterline at SWL is located at $x = 1.20$. The lower limit of the free surface elevation η at $x = 1.16$ and 1.40 corresponds to the bottom elevation z_b at those locations. The cross-shore velocity U at $x = 1.16$ and 1.40 indicates wave uprush ($U > 0$) of a short duration and wave down-rush ($U < 0$) of a longer duration. The longshore velocity V at $x = 1.16$ and 1.40 becomes more unidirectional ($V > 0$) because the large alongshore velocity occurs only during the short wave uprush. Fig. 3 also shows that the computed wave motion becomes periodic after a few waves unlike the longshore velocity V on a gentle smooth slope (Kobayashi and Karjadi 1994).

Fig. 4 shows the cross-shore variations of the maximum, mean and minimum values of η, U and V during the last wave period $9 < t \leq 10$. The root-mean-square (rms) values of the oscillatory components $(\eta - \overline{\eta})$, $(U - \overline{U})$ and $(V - \overline{V})$ are the standard deviations of η, U and V, which represent the oscillatory wave motion intensity.

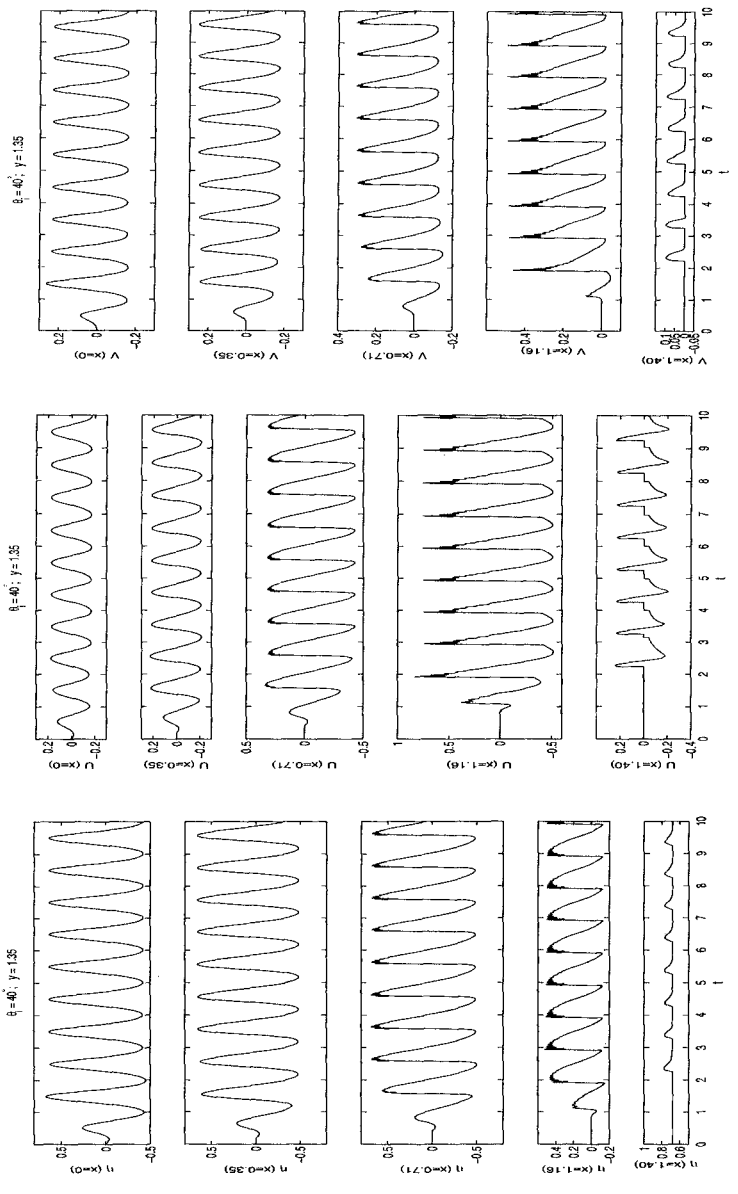

Figure 3: Temporal variations of free surface elevation η, cross-shore velocity U, and longshore velocity V at five cross-shore locations.

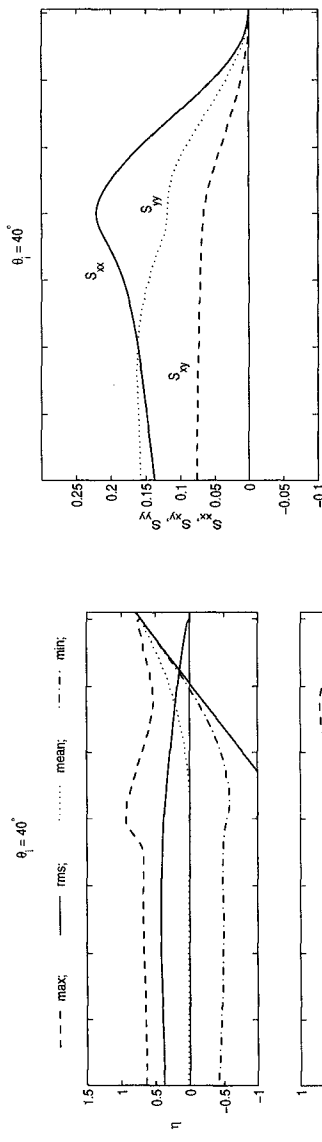

Figure 4: Cross-shore variations of maximum, root-mean-square, mean and minimum values of η, U and V.

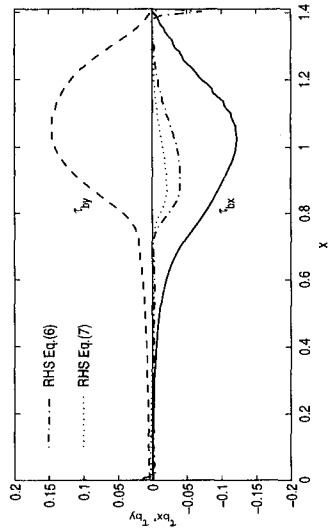

Figure 5: Cross-shore variations of time-averaged momentum quantities.

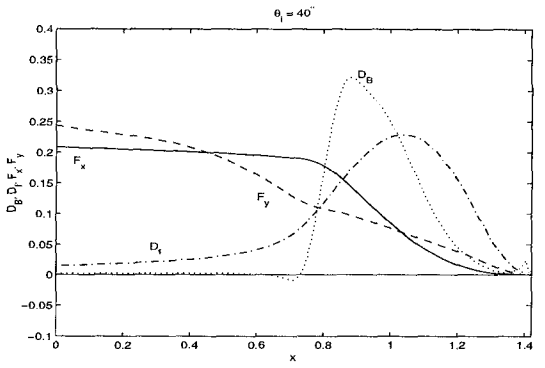

Figure 6: Cross-shore variations of time-averaged energy quantities.

The quantities shown in Fig. 4 are uniform alongshore. The 1:3.5 slope indicated by the solid straight line is added in the top panel to indicate the swash zone of wave uprush and down-rush on the slope. The rms wave intensity decreases landward in the swash zone. The largest U occurs near the still waterline while the largest η and V occur seaward of the still waterline. The mean cross-shore velocity $\overline{U}$ is negative and represents the cross-shore return current. The mean alongshore velocity $\overline{V}$ is the wave-induced longshore current which becomes as large as the standard deviation of V in the swash zone on the steep rough slope. The longshore current can become dominant on a gentle smooth slope (*e.g.*, Kobayashi and Karjadi 1994).

The computed alongshore volume flux $\overline{hV}$ is uniform alongshore. The time-averaged continuity equation (5) requires $\overline{hU} = 0$ to satisfy the no flux condition into the impermeable slope. The computed cross-shore volume flux $\overline{hU}$ satisfies this requirement.

The cross-shore variations of the momentum fluxes S_{xx}, S_{xy} and S_{yy} are depicted in Fig. 5, which also shows the bottom shear stresses τ_{bx}, τ_{by} and the time-averaged momentum equations (6) and (7). S_{xx} increases landward and decreases in the swash zone, whereas S_{yy} and S_{xy} is approximately constant seaward of the swash zone. The bottom shear stresses are important in the swash zone where the zone of $\tau_{bx} < 0$ and $\tau_{by} > 0$ corresponds approximately to the zone of $\overline{U} < 0$ and $\overline{V} > 0$ shown in Fig. 4. The computed time-averaged quantities are uniform alongshore. There is a small residual on the right hand side (RHS) of (6) and (7) due to the numerical dissipation, although the numerical damping coefficient $\kappa = 0.01$ is very small. For surging waves, the residuals for (6) and (7) were practically zero (Kobayashi and Karjadi 1999).

Fig. 6 shows the cross-shore variations of the time-averaged energy fluxes F_x and F_y and the time-averaged energy dissipation rates D_f and D_B due to bottom friction and wave breaking, respectively. The computed values of these quantities are uniform alongshore. Fig. 6 indicates that D_B is maximum at the location where η and V are maximum as shown in Fig. 4. The cross-shore and alongshore energy flux F_x and F_y decreases in the swash zone.

The reflected wave profile $\eta_r(t,y)$ along $x = 0$ is obtained as $\eta_r = (\eta - \eta_i)$ with η being the computed free surface elevation at $x = 0$. All the computed time series η_i and η_r at the 161 nodes along $x = 0$ for $0 \leq t \leq 10$ are plotted as a function of $p = (t - \lambda y)$ in Fig. 7. The 161 time series of η_i do not coincide for $-1 \leq p < 1$ because of the adjustment of η_i to satisfy the initial conditions of no wave action in the computation domain. The reflected wave profile η_r becomes periodic with respect to p after a few waves. This implies that the alongshore wavelengths of the incident and reflected waves are the same where λ for the incident waves is defined in (13). If the incident and reflected wavelengths are the same, $\sin\theta_i = \sin\theta_r$ where θ_r = reflected wave angle. This assumption is generally adopted to separate incident and reflected waves using linear wave theory (*e.g.*, Isaacson *et al.* 1996).

The reflection coefficient r and the phase shift θ_r are estimated to examine their variations with respect to $\theta_i = 0° - 80°$. The estimation of r and θ_r is based on the periodic portions of η_i and η_r shown in Fig. 7. The reflection coefficient r is defined here as the ratio of the standard deviation of η_r to that of η_i. The phase shift ϕ_r is obtained as the shift of the crests of the incident and reflected wave profiles plotted as a function of $(t - \lambda y)$. For $\theta_i = 40°$, the incident and reflected waves are in phase as shown in Fig. 7, where the phase shift remains the same by adding an integer to ϕ_r.

Fig. 8 shows the computed values of r and ϕ_r as a function of θ_i. The computed values of $r = 0.056$ for $\theta_i = 0°$ is compared with available empirical formulas. The formula of Seelig and Ahrens (1995) predicts $r = 0.18$ for the rough impermeable slope assumed in the present computation. On the other hand, the formula of Davidson *et al.* (1996) predicts $r = 0.08$. The computed reflection coefficient r in Fig. 8 increases from $r = 0.056$ for $\theta_i = 0°$ to $r = 0.32$ for $\theta_i = 80°$. Most of the regular wave data by Isaacson *et al.* (1996) indicated the increase of r with $\theta_i = 0° - 60°$. As for the phase shift ϕ_r, Sutherland and O'Donoghue (1998) proposed two empirical formulas for the range $0° \leq \theta_i \leq 60°$. These formulas can be expressed as $\phi_r = 2.5(\cos\theta_i)^{0.71}$ and $\phi_r = 2.2(\cos\theta_i)^{0.625}$ for this specific case and are plotted in Fig. 8. The computed phase shifts are almost within the empirical curves for $0° \leq \theta_i \leq 60°$.

The waterline elevation Z_r' above SWL is defined as the free surface elevation measured by a hypothetical wire placed at a vertical distance of δ_r' above the bottom and parallel to the slope in the cross-shore direction. Since the nominal stone diameter was 23.2 cm, use is made of $\delta_r' = 0.4$, 2 and 4 cm which may represent the possible range of the roughness of the irregular bottom surface. All the computed time series of Z_r along the 161 cross-shore lines for $0 \leq t \leq 10$ are plotted as a function of $p = (t - \lambda y)$ for $\delta_r' = 0.4$, 2 and 4 cm. Fig. 9 shows that the computed waterline oscillations become periodic after a few waves. The normalized alongshore wavelength of the waterline oscillations on the slope is the same as the incident alongshore wavelength λ^{-1} at $x = 0$. This indicates the validity of Snell's law for obliquely incident waves on the slope of alongshore uniformity. Fig. 9 also indicates that wave down-rush with a thin layer of water is sensitive to the wire height δ_r'.

The periodic portions of Z_r are used to obtain the maximum, mean, minimum and standard deviation and values of Z_r. The maximum Z_r is the wave runup R_u, which is shown in Fig. 10, and the minimum Z_r is the wave rundown. The wave runup R_u is not sensitive to $\delta_r' = 0.4$ - 4 cm. The computed value of R_u for $\theta_i = 0°$ is 1.05 in comparison

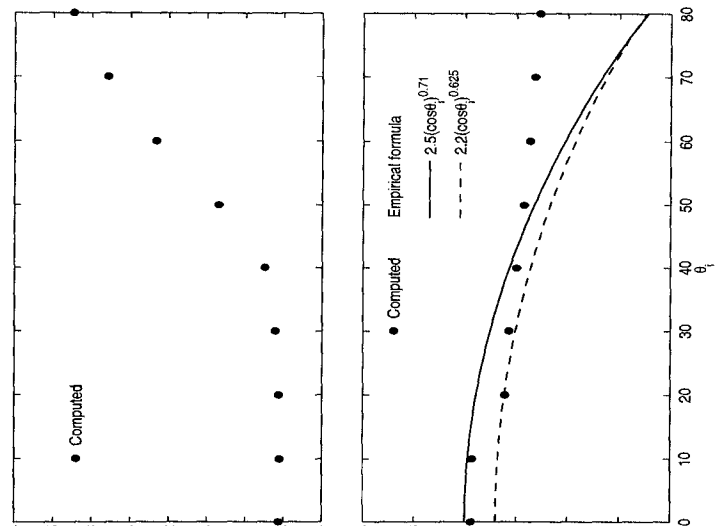

Figure 8: Reflection coefficient r and phase shift ϕ_r as a function of incident wave angles θ_i in degrees.

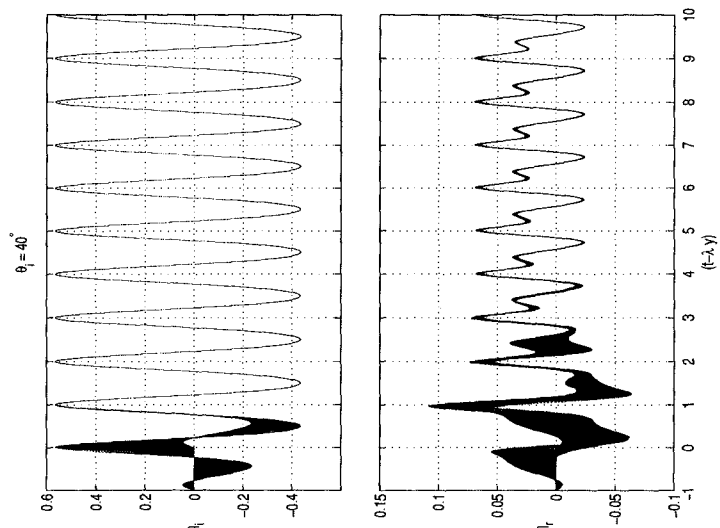

Figure 7: Incident and reflected wave profiles as a function of shifted time $(t - \lambda y)$.

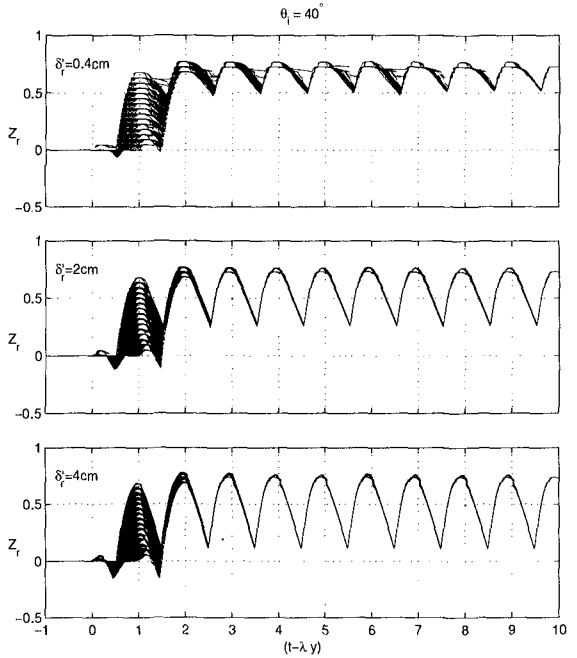

Figure 9: Waterline elevations Z_r for water depth $\delta_r' = 0.4, 2$ and 4 cm as a function of shifted time $(t - \lambda y)$.

to $R_u = 1.06$ observed visually in test 18 by Ahrens (1975). The empirical relationship shown in Fig. 10 is based on the runup reduction factor $\gamma = R_u(\theta_i)/R_u(\theta_i = 0°)$ proposed by De Wall and Van der Meer (1992). For unidirectional irregular waves, $\gamma = 1$ for $0° \leq \theta_i \leq 10°$, $\gamma = \cos(\theta_i - 10°)$ for $10° \leq \theta_i \leq 63°$, and $\gamma = 0.6$ for $63° \leq \theta_i \leq 80°$. The decrease of the computed regular wave runup with the increase of θ_i is consistent for small θ_i but larger for large θ_i. On the other hand, Fig. 11 shows the wave runup R_u, the mean waterline elevation $\overline{Z_r}$, the standard deviation σ_r, and the wave run-down R_d for $\delta_r' = 2$ cm. The computed R_u, $\overline{Z_r}$ and R_d decrease with the increase of θ_i, whereas the standard deviation of Z_r representing the intensity of the waterline oscillation about the mean $\overline{Z_r}$ remains approximately constant. Correspondingly, the value of $(R_u - R_d)$ remains approximately constant.

Conclusions

A two-dimensional, time-dependent numerical model for finite-amplitude, shallow-water waves with arbitrary incident angles is developed to provide an additional tool for the design of coastal structures. The utility of this numerical model is to obtain the detailed wave motions in the vicinity of the still waterline which are difficult to

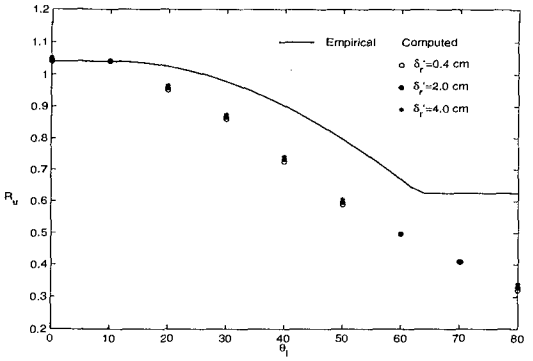

Figure 10: Wave runup R_u for $\delta_r' = 0.4, 2$ and 4 cm as a function of θ_i in degrees.

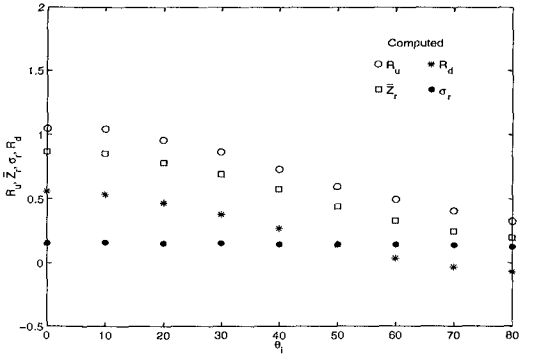

Figure 11: Wave runup R_u, setup $\overline{Z_r}$, standard deviation σ_r, and run-down R_d for δ_r'=2 cm as a function of θ_i in degrees.

measure in experiments. The use of periodic lateral boundary conditions has limited the present computations to regular waves on the slope of alongshore uniformity. The numerical method and the seaward and landward boundary algorithms presented here are general and expected to be applicable to irregular waves as well.

The time-averaged continuity, momentum and energy equations are used to check the accuracy of the numerical model as well as to examine the spatial variations of the time-averaged quantities. For the computed plunging waves, the energy dissipation rate due to wave breaking is significant as shown in Fig. 6. This dissipation appears to have produced the residuals in (6) and (7) as shown in Fig. 5. The computed reflected waves and waterline oscillations are shown to have the same alongshore wavelength as the incident waves.

The numerical model will need to be compared with new experiments that will

include the temporal and spatial variations of the free surface elevation and velocities. It is also essential to generalize the lateral boundary algorithm for irregular waves. An algorithm similar to the seaward boundary algorithm used here might be applied if the incident waves at the lateral boundaries could be specified as input.

Acknowledgement

This work was supported by the National Oceanic and Atmospheric Administration Office of Sea Grant, Department of Commerce, under Grant No. NA56RG0147 (Project SG97 R/OE-23).

References

Ahrens, J.P. (1975). "Large wave tank tests of riprap stability." Tech. Memo No. 51, U.S. Army Coast. Engrg. Res. Ctr., Ft. Belvoir, Va.

Chaudhry, M.N. (1993). *Open-channel flow.* Prentice Hall, Englewood Cliffs, N.J.

Davidson, M.A., Bird, P.A.D., Huntley, D.A., and Bullock, C.N. (1996). "Prediction of wave reflection from rock structures: An integration of field & laboratory data." *Proc., 25th Coast. Engrg. Conf.*, ASCE, New York, N.Y., 2, 2077–2086.

Dean, R.C., and Dalrymple, R.A. (1984). *Water wave mechanics for engineers and scientists.* Prentice Hall, Englewood Cliffs, N.J.

De Wall, J.P., and Van der Meer, J.W. (1992). "Wave runup and overtopping on coastal structures." *Proc., 23rd Coast. Engrg. Conf.*, ASCE, New York, N.Y., 2, 1758–1771.

Isaacson, M., Papps, D., and Mansard, E. (1996). "Oblique reflection characteristics of rubble-mound structures." *J. Wtrwy., Port, Coast., and Oc. Engrg.*, ASCE, 122(1), 1–7.

Kobayashi, N. (1995). "Numerical models for design of inclined coastal structures." *Wave forces on inclined and vertical wall structures*, N. Kobayashi and Z. Demirbilek, eds., ASCE, New York, N.Y., 118–138.

Kobayashi, N., and Karjadi, E.A. (1994). "Swash dynamics under obliquely incident waves." *Proc., 24th Coast. Engrg. Conf.*, ASCE, New York, N.Y., 2, 2155–2168.

Kobayashi, N., and Karjadi, E.A. (1996). "Obliquely incident irregular waves in surf and swash zones." *J. Geophys. Rcs.*, 101(C3), 6527–6542.

Kobayashi, N., Karjadi, E.A.(1999). "Obliquely incident wave reflection and runup on steep rough slope." *J. Wtrwy., Port, Coast., and Oc. Engrg.*, ASCE, (submitted).

Kobayashi, N., Karjadi, E.A., and Johnson, B.D. (1997). "Dispersion effects on longshore currents in surf zones." *J. Wtrwy., Port, Coast., and Oc. Engrg.*, ASCE, 123(5), 240–248.

Kobayashi, N., Otta, A.K., and Roy, I. (1987). "Wave reflection and runup on rough slopes." *J. Wtrwy., Port, Coast., and Oc. Engrg.*, ASCE, 113(3), 282–298.

Kobayashi, N., and Wurjanto, A. (1992). "Irregular wave setup and run-up on beaches." *J. Wtrwy., Port, Coast., and Oc. Engrg.*, ASCE, 118(4), 368–386.

Liu, P.L.-F., Cho, Y.S., Briggs, M.J., Kanoglu, U., and Synolakis, C.E. (1995). "Runup of solitary waves on a circular island." *J. Fluid Mech.*, 302, 259–285.

Longuet-Higgins, M.S. (1970). "Longshore currents generated by obliquely incident sea waves." *J. Geophy. Res.*, 75(33), 6778–6801.

MacCormack, R.W. (1969). "'The effects of viscosity in hypervelocity impact cratering." Pap. 69-354, *Am. Inst. Aeronaut. and Astronaut.*, New York, N.Y.

Seelig, W.N., and Ahrens, J.P. (1995). "Wave reflection and energy dissipation by coastal structures." *Wave forces on inclined and vertical wall structures*, N. Kobayashi and Z. Demirbilek, eds., ASCE, New York, N.Y., 28–51.

Sutherland, J., and O'Donoghue, T. (1998). "Wave phase shift at coastal structures." *J. Wtrwy., Port, Coast. and Oc. Engrg.*, ASCE, 124(2), 90–98.

Thompson, K.W. (1990). "Time-dependent boundary conditions for hyperbolic systems, II." *J. Comp. Phys.*, 89, 439–461.

Van Dongeren, A.R., and Svendsen, I.A. (1997). "Absorbing-generating boundary condition for shallow water models." *J. Wtrwy., Port, Coast., and Oc. Engrg.*, ASCE, 123(6), 303–313.

ALES Shallow-Water Flow Solver with Non-Hydrostatic Pressure: Wave Applications

J. G. Zhou[1] and P. K. Stansby[2]

Abstract

A shallow-water flow solver with non-hydrostatic pressure in σ coordinates has been developed to include effects due to the moving grid, referred to as the ALES approach. The formulation is outlined for 2D vertical plane problems and tested against experimental data for wave flows over plane beds, bars and trenches. Agreement with experiment is generally good and the importance of non-hydrostatic pressure and moving-grid terms is demonstrated.

Introduction

Conventional shallow-water flow models based on hydrostatic pressure can provide accurate results for many engineering problems. However, the model will not be accurate for problems in which there is significant gradient of either bed topography or free surface. A recent study by Stansby and Zhou (1998) has shown that the influence of non-hydrostatic pressure on current flow over a trench with bottom slope greater than 1:5 can be significant. The solver developed for non-hydrostatic pressure applies also to wave flows. Accurate predictions of wave flows including viscous/turbulence effects are of importance in coastal and ocean engineering projects such as harbors, channel dredging, pipeline trenching and storm-surge barriers. In this paper, we present a shallow-water flow solver to predict waves over a plane bed, a trapezoidal trench and a bar and compare with experimental data. The model is based on the unsteady Reynolds-averaged Navier-Stokes equations in ALE (Hirt, 1970) description which is able to account for the moving mesh with non-hydrostatic pressure. The equations are solved in the σ coordinate system and the eddy viscosity is calculated using the standard $k-\epsilon$ model. The method is referred to as ALES. The computations are also compared with the model with hydrostatic pressure alone.

Flow Model

The unsteady Reynolds-averaged Navier-Stokes equations for incom-

[1]Research Associate, Hydrodynamics Research Group, School of Engineering, The University of Manchester, Manchester M13 9PL, UK

[2]Professor, Hydrodynamics Research Group, School of Engineering, The University of Manchester, Manchester M13 9PL, UK

pressible flow in a 2-D vertical plane can be written with the ALE description for incompressible flow, with the Boussinesq assumption for the time-averaged Reynolds stress in σ coordinates as

$$\frac{\partial u}{\partial x} + \frac{\partial w}{\partial z} = 0 \tag{1}$$

$$\frac{\partial (hu)}{\partial t} + \frac{\partial (huu)}{\partial x} + \frac{\partial (\omega u)}{\partial \sigma} - w_g \frac{\partial u}{\partial \sigma} = -gh\frac{\partial \eta}{\partial x} - \frac{h}{\rho}\frac{\partial \tilde{p}}{\partial x} + h\frac{\partial}{\partial x}\left(\nu_e \frac{\partial u}{\partial x}\right) + \frac{\partial}{\partial \sigma}\left(\frac{\nu_e}{h}\frac{\partial u}{\partial \sigma}\right) \tag{2}$$

$$\frac{\partial (hw)}{\partial t} + \frac{\partial (huw)}{\partial x} + \frac{\partial (\omega w)}{\partial \sigma} - w_g \frac{\partial w}{\partial \sigma} = -\frac{1}{\rho}\frac{\partial \tilde{p}}{\partial \sigma} + h\frac{\partial}{\partial x}\left(\nu_e \frac{\partial w}{\partial x}\right) + \frac{\partial}{\partial \sigma}\left(\frac{\nu_e}{h}\frac{\partial w}{\partial \sigma}\right) \tag{3}$$

$$\frac{\partial \eta}{\partial t} + \frac{\partial}{\partial x}\int_{-1}^{0} hu d\sigma = 0 \tag{4}$$

where x is the horizontal coordinate and σ the vertical dimensionless coordinate defined below; η is the water surface elevation above horizontal datum; h is water depth; u and w are the velocity components in the horizontal and vertical directions; $\omega = hd\sigma/dt$ (defined below); w_g is the grid velocity in the vertical direction; g is the gravitational acceleration; $\tilde{p}$ is the non-hydrostatic pressure; ρ is the fluid density; ν_e is the eddy viscosity; where

$$\sigma = \frac{z-\eta}{h}, \qquad \omega = w - u\left(\sigma\frac{\partial h}{\partial x} + \frac{\partial \eta}{\partial x}\right) - \left(\sigma\frac{\partial h}{\partial t} + \frac{\partial \eta}{\partial t}\right)$$

$\omega = 0$ when $\sigma = -1$ or $\sigma = 0$, corresponding to the bed and the free surface. The continuity equation (1) is not transformed into σ coordinates because the non-hydrostatic pressure is calculated in real space.

The eddy viscosity ν_e is defined by the standard $k-\epsilon$ equations (Rodi, 1993), which can be written in σ coordinates as

$$\frac{\partial (hk)}{\partial t} + \frac{\partial (huk)}{\partial x} + \frac{\partial (\omega k)}{\partial \sigma} - w_g \frac{\partial k}{\partial \sigma} = h\frac{\partial}{\partial x}\left(\frac{\nu_e}{\sigma_k}\frac{\partial k}{\partial x}\right) + \frac{\partial}{\partial \sigma}\left(\frac{\nu_e}{h\sigma_k}\frac{\partial k}{\partial \sigma}\right) + hP - h\epsilon \tag{5}$$

$$\frac{\partial(h\epsilon)}{\partial t}+\frac{\partial(hu\epsilon)}{\partial x}+\frac{\partial(\omega\epsilon)}{\partial\sigma}-w_g\frac{\partial\epsilon}{\partial\sigma}=h\frac{\partial}{\partial x}\left(\frac{\nu_e}{\sigma_\epsilon}\frac{\partial\epsilon}{\partial x}\right)$$
$$+\frac{\partial}{\partial\sigma}\left(\frac{\nu_e}{h\sigma_\epsilon}\frac{\partial\epsilon}{\partial\sigma}\right)+hc_{1\epsilon}\frac{\epsilon}{k}P-hc_{2\epsilon}\frac{\epsilon^2}{k} \tag{6}$$

Solution of the Equations

Spatial discretization is in finite-volume form on a staggered mesh following Stansby (1997). For a cell i, k the equations (2)-(4) can be discretized in time from time level n to $n+1$ with time step δt, as

$$\frac{\eta_i^{n+1}-\eta_i^n}{\delta t}+\frac{\partial}{\partial x}\int_{-1}^{0}h_i^n[\theta u_{i,k}^{n+1}+(1-\theta)u_{i,k}^n]d\sigma=0 \tag{7}$$

$$h_i^n\frac{u_{i,k}^{n+1}-u_{i,k}^n}{\delta t}+\frac{\partial(huu)_{i,k}^n}{\partial x}+\frac{\partial(\omega u)_{i,k}^n}{\partial\sigma}-w_{gi,k}\frac{\partial u_{i,k}^n}{\partial\sigma}=$$
$$-gh_i^n\left[\theta\frac{\partial\eta_i^{n+1}}{\partial x}+(1-\theta)\frac{\partial\eta_i^n}{\partial x}\right]-\frac{h_i^n}{\rho}\frac{\partial\tilde{p}_{i,k}^n}{\partial x}+u_{i,k}\frac{\partial h_i}{\partial t}$$
$$+h_i^n\frac{\partial}{\partial x}\left(\nu_e\frac{\partial u_{i,k}^n}{\partial x}\right)+\frac{\partial}{\partial\sigma}\left(\frac{\nu_e}{h_i^n}\frac{\partial u_{i,k}^{n+1}}{\partial\sigma}\right) \tag{8}$$

$$h_i^n\frac{w_{i,k}^{n+1}-w_{i,k}^n}{\delta t}+\frac{\partial(huw)_{i,k}^n}{\partial x}+\frac{\partial(\omega w)_{i,k}^n}{\partial\sigma}-w_{gi,k}\frac{\partial w_{i,k}^n}{\partial\sigma}=$$
$$-\frac{1}{\rho}\frac{\partial\tilde{p}_{i,k}^n}{\partial\sigma}+w_{i,k}^n\frac{h_i^{n+1}-h_i^n}{\delta t}$$
$$+h_i^n\frac{\partial}{\partial x}\left(\nu_e\frac{\partial w_{i,k}^n}{\partial x}\right)+\frac{\partial}{\partial\sigma}\left(\frac{\nu_e}{h_i^n}\frac{\partial w_{i,k}^{n+1}}{\partial\sigma}\right) \tag{9}$$

The equations (7)-(9) are solved for η efficiently by the conjugate gradient method. Similarly, Eqs. (5) and (6) are discretized and solved.

The continuity equation (1) can be used to derive an equation for non-hydrostatic pressure in real space as

$$\begin{aligned}a_P p'_P &= a_E p'_E+a_W p'_W+a_U p'_U+a_D p'_D\\ &+ a_{EU}p'_{EU}+a_{ED}p'_{ED}+a_{WU}p'_{WU}\\ &+ a_{WD}p'_{WD}+a_0\end{aligned} \tag{10}$$

in which p' is the correction of the no-hydrostatic pressure. The coefficients such as a_P and the details are described by Stansby and Zhou (1998).

The σ mesh is refined near the bed and surface as in Stansby (1997).

Results

1. Wave over a plane bed

A wave over a plane bed is simulated. A mesh of 600x20 cells is used with $\delta x = 0.1\ m$, $\delta t = 0.05\ s$, and $h_0 = 1.0\ m$. The period T is 4 s. The amplitude of uniform sinusoidal velocity at inflow is $U_0 = 0.2\ m/s$. Fig. 1 shows velocity vectors at $t = 100\ s$. Clearly, regular waves are propagating along the channel.

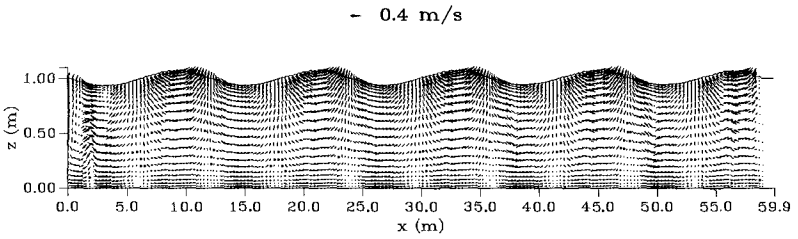

Figure 1: Wave over a plane bed

2. Wave over a bar with small side slope

The progressive wave considered here is the same as that studied experimentally by Beji et al. (1992). The wave flume is sketched in Fig. 2. The wave height is 2.0 cm and the period T is 2.0 s. A mesh of 320x21 cells is

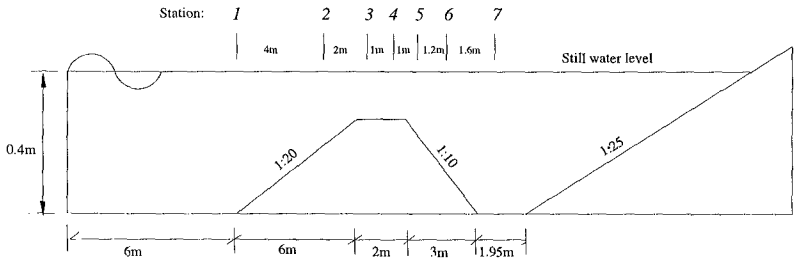

Figure 2: Sketch of the wave flume

used with $\delta x = 0.1\ m$ and $\delta t = 0.005\ s$. For the inflow boundary conditions, $U_0 = 0.09\ m/s$ which generates a wave of 2.01 cm height and $h_0 = 0.4\ m$.

Results after 17.5 s are shown in Figs. 3-5 with experimental data, showing good agreement. Results from the σ model without incorporating the moving grid are also plotted in Fig. 5. It is clear that the ALES model is superior to the σ model.

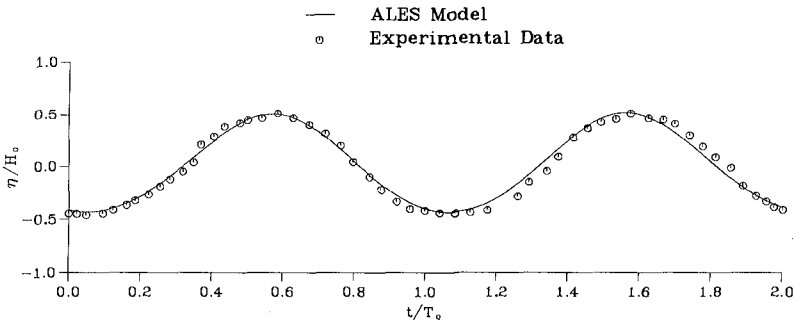

Figure 3: Comparison between model and experiment of the wave profile at station 1

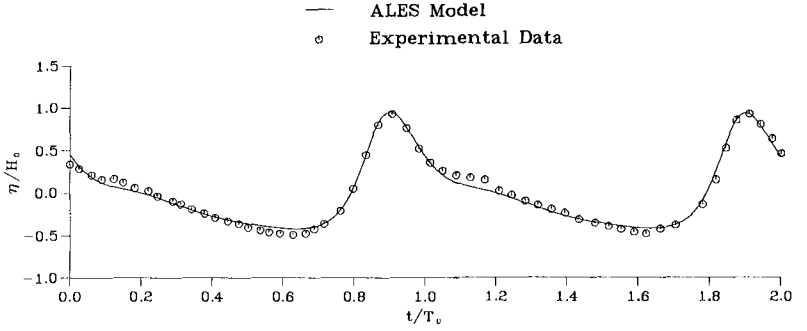

Figure 4: Comparison between model and experiment of the wave profile at station 3

3. Wave over a bar with steep side slope

Here a progressive wave over a bar with steep slope is considered. The flume is the same as that in the experiment by Ohyama et al. (1995) and is sketched in Fig. 6. The wave height is 5.0 cm and the period T is 2.01 s. A mesh of 600x21 cells is used with $\delta x = 0.1$ m and $\delta t = 0.005$ s. $U_0 = 0.2$ m/s generates a wave of 5.006 cm height and $h_0 = 0.5$ m. Results are presented after 33 s.

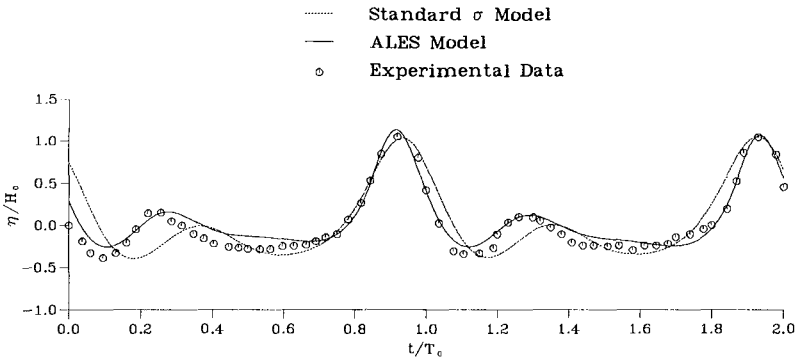

Figure 5: Comparison between model and experiment of the wave profile at station 5

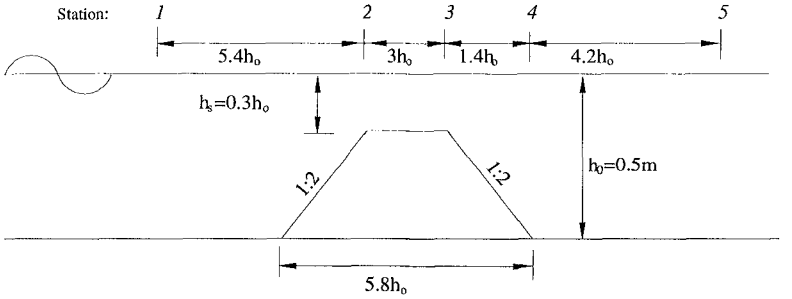

Figure 6: Sketch of experimental arrangement for wave over a bar with steep side slope

A comparison between experimental data and computations for station 3 is depicted in Fig. 7. The figure shows that the agreement is good. The results from the standard σ model are also plotted in the figure for comparison. Again, this shows that the ALES model is superior due to the incorporation of grid velocity

4. Comparison with hydrostatic model

In order to show the difference between the results predicted with and without non-hydrostatic pressure, a wave over a trench with the same geometry as described by Alfrink and van Rijn (1983) is simulated. A mesh of 170x20 cells is used in the numerical computation with $\delta x = 0.1\ m$, $\delta t = 0.01\ s$, $U_0 = 0.2\ m/s$ and $h_0 = 0.2\ m$. The period T is 3 s. Comparison of the surface

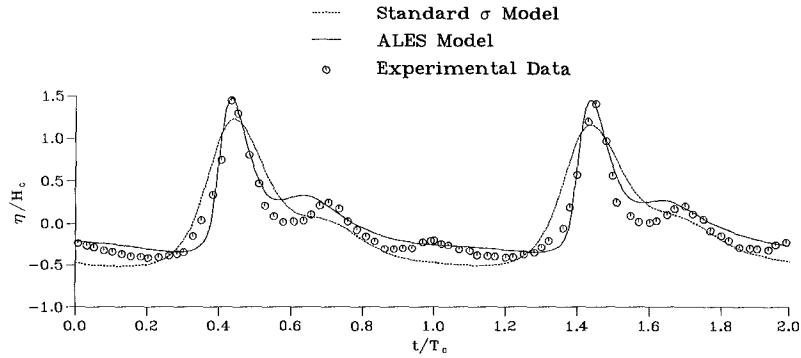

Figure 7: Comparison between model and experiment of the wave profile at station 3

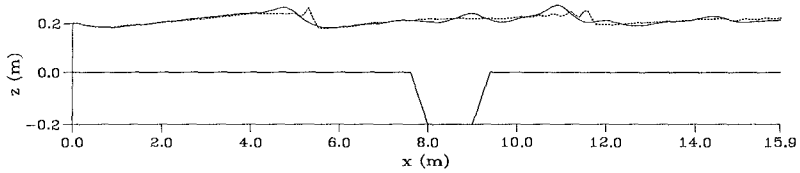

Figure 8: Comparison of surface profiles at $t = 20\ s$ with and without non-hydrostatic pressure: dashed line denotes the surface from hydrostatic pressure model

profiles is shown in Fig. 8.

5. A wave flow over a trench

A current over a trench has been investigated numerically and experimentally (Alfrink and van Rijn, 1983; Basara and Younis, 1995; Stansby and Zhou, 1998). No experimental studies of wave flow over a trench have been reported in the literature to our knowledge. However, this is an important problem in coastal engineering and is investigated numerically here. The trench used is the same as that investigated experimentally for a current (Alfrink and van Rijn, 1983) and is sketched in Fig. 9. A mesh of 170x30 cells is used in the numerical computation with $\delta x = 0.1\ m$, $\delta t = 0.01\ s$, $U_0 = 0.08\ m/s$ and $h_0 = 0.2\ m$. The wave height is $h_w \approx 0.2h_0$ and the period T is 1 s. The streamlines are shown at $t = 20\ s$ in Fig. 10. The reflection coefficient is $K_r \approx 0.38$ and the transmission coefficient is $K_t \approx 0.44$, estimated after 4 wave crests have passed the trench. As comparison, a current over the trench

is shown in Fig. 11 (Stansby and Zhou, 1998).

6. A wave/current flow over a trench

Waves often occur in combination with a current. Here a wave/current flow over the same trench is simulated. To retain the same wave height, $U_0 = 0.2\ m/s$ and inflow boundary condition for velocity u is specified as

$$u_{in} = \frac{u_*}{\kappa} log_e \left(\frac{30.0(z - z_0)}{k_s} \right) + U_0 sin(2\pi t/T) \tag{11}$$

where $u_* = 0.033\ m/s$, $\kappa = 0.4$, $k_s = 0.002\ m$ and $z_0 = 0.00067\ m$. This gives wave height $H = 0.038\ m$ and mean current velocity $\overline{u} \approx 0.387\ m/s$.

Fig. 12 shows the streamlines at $t = 8.4\ s$. At this moment, there is clearly separation in the trench. There is also flow separation in the trench when $t = 8.7\ s$ as shown in Fig. 13. However, separation appears to disappear when $t = 8.9\ s$ as shown in Fig. 14. This highly unsteady separation is in contrast to the stable separation in a steady current (see Fig. 11) and attached flow in a wave alone.

Conclusions

In this paper, we present the application of the ALES model to wave flows. The results have shown that the ALES model is more accurate than the conventional shallow-water flow model in σ coordinate. When there is significant variation in either free surface or bed topography, the effect of the non-hydrostatic pressure on flows should not be ignored.

References

Alfrink, B. J. and van Rijn, L. C. (1983). Two-equation turbulence model for flow in trench, *Journal of Hydraulic Engineering, ASCE* **109**(3): 941–958.

Basara, B. and Younis, B. A. (1995). Predictions of turbulent flows in dredged trenches, *Journal of Hydraulic Research* **33**(6): 813–824.

Beji, S., Ohyama, T., Battjes, J. A. and Nadaoka, K. (1992). Transformation of nonbreaking waves over a bar, *Coastal Engineering 1992, Proc. 23rd Int. Conf.*, Vol. 1, Venice, Italy, pp. 51–61.

Hirt, C. W. (1970). An arbitrary lagrangian-eulerian computing technique, *Proc. 2nd Int. Conf. on Numerical Methods in Fluid Dynamics*, Berkeley, USA.

Ohyama, T., Kioka, W. and Tada, A. (1995). Applicability of numerical models to nonlinear dispersive waves, *Coastal Eng.* **24**: 297–313.

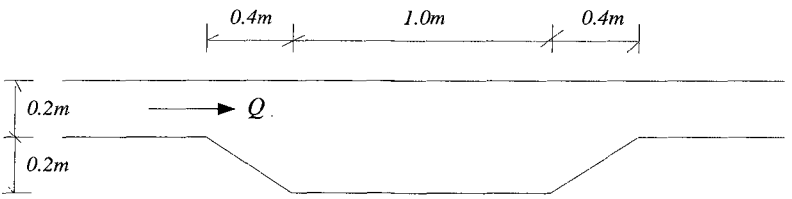

Figure 9: Sketch of the trench used in experiments (Alfrink and van Rijin, 1983)

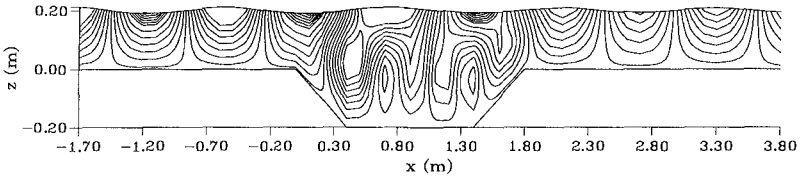

Figure 10: Streamlines for the wave over the trench $t = 20\ s$

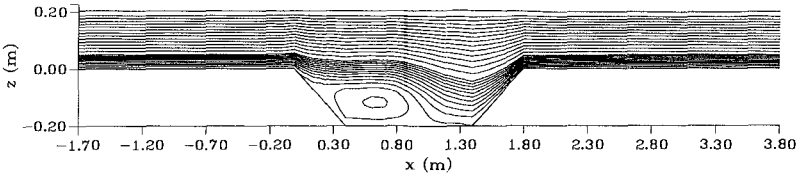

Figure 11: Streamlines for current flow over the trench (from Stansby and Zhou, 1998)

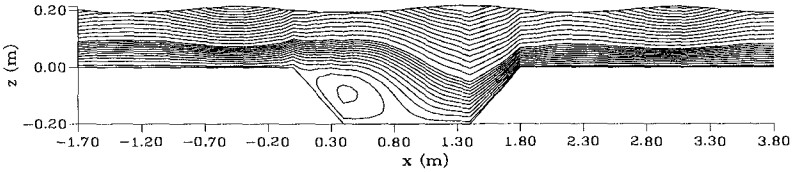

Figure 12: Streamlines for the wave/current flow over the trench: $t = 8.4\ s$

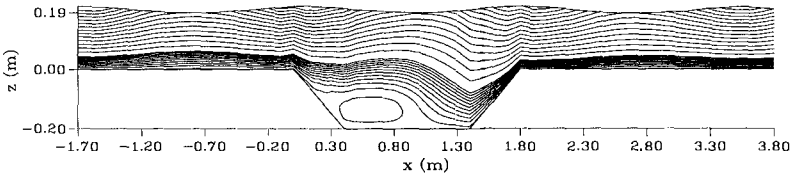

Figure 13: Streamlines for the wave/current flow over the trench: $t = 8.7\ s$

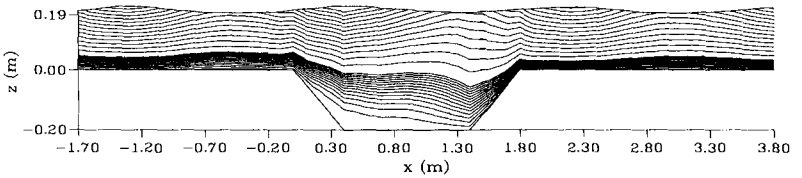

Figure 14: Streamlines for the wave/current flow over the trench: $t = 8.9\ s$

Rodi, W. (1993). *Turbulence models and their applications in hydraulics*, 3rd edn, IAHR.

Stansby, P. K. (1997). Semi-implicit finite volume shallow-water flow and solute transport solver with $k - \epsilon$ turbulence model, *Int. J. Num. Meth. Fluids* **25**: 285–313.

Stansby, P. K. and Zhou, J. G. (1998). Shallow-water flow solver with non-hydrostatic pressure: 2D vertical plane problems, *Int. J. Num. Meth. Fluids* **28**: 541–563.

Linear and Nonlinear Modeling of Long Waves Propagating around Channel Bends

By Aimin Shi[1] and Michelle H. Teng[2], M. ASCE

Abstract

In the present study, the transmission and reflection of long waves traveling through right-angled channel bends of constant depth and width are investigated by using numerical simulation based on the linear and nondispersive long wave equations. The present linear results are compared with the results obtained by Shi, Teng and Wu (1998) based on the weakly nonlinear and dispersive Boussinesq equations. The objective is to examine the difference between linear and nonlinear modeling of long waves propagating through curved channels.

Introduction

It is of practical interest to coastal engineers to understand how tides and other long ocean waves are transmitted and reflected through curved river inlets and harbors. In the past, several excellent studies were carried out on the related subject including the studies by Rostafinski (1976) on long acoustic waves in curved ducts, by Webb and Pond (1986) on Kelvin waves in channel bends, and by Kirby, Dalrymple and Kaku (1994) on short water waves through wide channel bends. Most of the previous studies were based on the linear wave theory and focused on waves propagating through smoothly curved channels, except in Miles' (1947) pioneer study where analytical solutions were obtained for linear acoustic waves traveling through sharp-cornered 90°-bends. Miles' solution is valid for long waves propagating in relatively narrow ducts whose width is less than half the wavelength.

In recent studies by Shi and Teng (1996), Shi, Teng and Wu (1998), the previous analytical studies were extended to investigate the propagation of a solitary wave through both smoothly curved and sharp-cornered 90°-bends by using numerical simulation based

[1] Researcher, Environmental Fluid Dynamics Research, Jamesburg, NJ 08831, USA.
[2] Associate Professor, Department of Civil Engineering, University of Hawaii at Manoa, Honolulu, HI 96822, USA.

on Wu's (1981) weakly nonlinear and dispersive Boussinesq equations. Solitary waves propagating through various narrow and wide channel bends were studied. Two parameters, namely, the bending curvature and the ratio of channel width b to effective wavelength λ_e, were found to be the dominant factors that affect the transmission and reflection of a solitary wave through curved channels. For solitary waves traveling through sharp-cornered 90°-bends, the transmission (reflection) coefficient, i.e., ratio of the leading transmitted (reflected) wave amplitude along the channel centerline to the initial wave amplitude, was found to depend on a single dimensionless parameter, namely, b/λ_e. Quantitatively, the transmission (reflection) coefficient was found to decrease (increase) as b/λ_e increases. Based on the numerical results, empirical power laws for predicting the transmission and reflection coefficients as functions of b/λ_e were obtained. For solitary waves traveling through smooth channel bends, the initial wave was observed to be almost completely transmitted in both narrow and wide bends with little backward reflection.

In the present study, the same cases studied in Shi, Teng and Wu (1998) will be revisited by applying the linear nondispersive long wave equations. The objective is to investigate the difference between linear and nonlinear modeling of long waves propagating through channel bends.

Governing Equations

In the recent study of Shi, Teng and Wu (1998), the numerical simulation of long waves propagating through curved shallow water channels of constant depth was based on the generalized weakly nonlinear and dispersive Boussinesq model (i.e., the gB model)

$$\zeta_t + \nabla \cdot [(h+\zeta)\nabla\phi] = 0 \tag{1}$$

$$\phi_t + \frac{1}{2}(\nabla\phi)^2 + \zeta - \frac{h^2}{3}\nabla^2\phi_t = 0 \tag{2}$$

where ζ is the wave elevation relative to the unperturbed water surface, h (=1) the water depth, ϕ the depth-averaged velocity potential, t time, and $\nabla = (\partial_x, \partial_y)$ with x, y being the spatial coordinates in the longitudinal and lateral directions, respectively. All the variables are in dimensionless form, with length scaled by h, and time by $\sqrt{h/g}$. The boundary conditions were unperturbed water surface at $x = \pm\infty$, and zero normal velocity at the channel walls.

In the present study, the following linear and nondispersive long wave equations

$$\zeta_t + h\nabla^2\phi = 0 \tag{3}$$

$$\phi_t + \zeta = 0 \tag{4}$$

are applied along with the same boundary conditions as described above.

The long waves studied are solitary waves whose initial wave profile and speed are given by (Teng 1997, Teng and Wu 1992, Shi, Teng and Wu 1998):

$$\zeta(x,t) = \frac{\alpha \operatorname{sech}^2 \beta(x - x_0 - ct)}{1 + \alpha \tanh^2 \beta(x - x_0 - ct)} \tag{5}$$

$$c = \left\{ \frac{6(1+\alpha)^2}{\alpha^2(3+2\alpha)} [(1+\alpha)\ln(1+\alpha) - \alpha] \right\}^{1/2} \tag{6}$$

where α is the wave amplitude, $\beta = [3\alpha / 4(1+0.68\alpha)]^{1/2}$, c the wave speed, and x_0 the initial wave position. Here the effective wavelength λ_e of a solitary wave is defined as the wavelength within which the wave elevation ζ is greater than 1% of the amplitude α. Based on (5), λ_e can be calculated by

$$\lambda_e = \frac{2}{\beta} \ln \frac{(1+0.01\alpha)^{1/2} + 0.99^{1/2}}{(0.01+0.01\alpha)^{1/2}} \tag{7}$$

Numerical Results

In Shi, Teng and Wu (1998), the Boussinesq model (1), (2) was solved by using an iterative predictor-corrector finite difference scheme (Wang, Wu and Yates 1992) to simulate the propagation of solitary waves through 90°-channel bends. The numerical results for solitary waves traveling through sharp-cornered 90°-bends revealed an interesting phenomenon that in a narrow channel bend, the initial wave is almost completely transmitted with little reflection, while in a wide channel, the amplitude of the reflected wave becomes much greater than the transmitted wave. It was also found that the transmission and reflection coefficients depend on only one dimensionless parameter, namely, the ratio of channel width b to wavelength λ_e. This implies that, when studying long wave transmission and reflection through channel bends, whether a channel is "wide" or "narrow" is judged by comparing the channel width with the wavelength, rather than with the water depth. Based on the numerical results, empirical power laws for predicting the transmission and reflection coefficients through sharp-cornered 90°-bends were obtained as

$$\frac{\alpha_T}{\alpha} = \begin{cases} 1, & 0 < b/\lambda_e < 0.2 \\ 0.28(b/\lambda_e)^{-0.72}, & 0.2 \le b/\lambda_e < 1.0 \end{cases} \tag{8}$$

$$\frac{\alpha_R}{\alpha} = \begin{cases} 1.19(b/\lambda_e)^{0.9}, & 0 < b/\lambda_e < 0.4 \\ 0.58(b/\lambda_e)^{0.14}, & 0.4 \le b/\lambda_e < 1.0 \end{cases} \tag{9}$$

where α is the initial wave amplitude, and α_T and α_R are amplitudes of the leading transmitted and reflected waves, respectively. For solitary waves traveling through smoothly curved channel bends, it was found that the waves are almost completely transmitted with little backward reflection in both narrow and wide channels.

In the present study, the linear and nondispersive long wave equations (3), (4) are solved by using the 4th-order Runge-Kutta scheme. The scheme is first tested on solitary waves traveling in a straight channel where closed-form solution (5), (6) exists. Our results show that after a solitary wave travels for about 60 water depths, the amplitude changes by only 0.1%. The accuracy of the numerical simulation is also examined by monitoring the mass and energy conservation at each computational step. Both the Runge-Kutta scheme and the scheme by Wang et al. (1992) are found to conserve mass and energy accurately. In all the simulations, including the cases involving waves traveling through sharp-cornered channel bends, the maximum errors in mass and energy conservation are 1.2% and 4.2% with Wang et al.'s scheme in solving the nonlinear Boussinesq model, and 2.2% and 1.9% with the Runge-Kutta scheme in solving the linear wave equations.

Numerical results of a solitary wave of initial amplitude $\alpha = 0.3$ propagating through a sharp-cornered 90°-bend of width $b = 5$ are shown in Fig. 1 (linear results) and Fig. 2 (nonlinear results). Figures 1 (a) and 2 present the two-dimensional wave field at different time instants based on the linear and nonlinear results, while Fig. 1 (b) and (c) show the detailed comparison between the linear (dashed line) and nonlinear (solid line) results for transmitted and reflected wave profiles along the channel centerline. From these results, we observe that, the Boussinesq model can predict more detailed (e.g., Fig.1 (a) and Fig.2, near the sharp corner) and more realistic (e.g., Fig.1 (c), the transmitted wave profile) wave features than the linear wave equations. In addition, there are some quantitative differences between the two models in predicting the transmitted and reflected wave amplitude and speed. The linear wave equations predict a slightly smaller (larger) transmitted (reflected) wave amplitude, and a slower speed which is expected. Despite these small differences, the linear and nonlinear wave models are seen to be fundamentally consistent with each other in predicting the transmission and reflection of solitary waves propagating through sharp-cornered channel bends. This consistency is further shown in Fig. 3 (a) and (b) where numerical results from fifteen simulations involving different initial wave amplitude and different channel width are plotted together. In this figure, the connected solid and dashed lines are based on the least-square fitting of the numerical data points, and the solid line also represents the empirical power laws given by (8) and (9). We can see that, similar to the nonlinear results based on the Boussinesq model, the data points for the transmission (and reflection) coefficient based on the linear and nondispersive model (3) and (4) also fall along one curve when plotted against b/λ_e, hence revealing the same similarity parameter that governs the phenomenon.

The linear results for a solitary wave of initial amplitude $\alpha = 0.3$ traveling through a smooth 90°-bend of width $b = 5$ are presented in Fig. 4 (a) and (b). Comparing with the nonlinear results (Shi, Teng and Wu 1998, Fig.9 (a), p.171), we find that the nonlinear

and dispersive Boussinesq model again provides more detailed wave features, such as the lateral wave variation in the trailing region, than the linear model. In addition, based on the linear equations, the back of the transmitted wave is slightly steeper than the front of the wave, which is less realistic than the wave profile predicted by the Boussinesq model (see comparison in Fig.4 (b)). Nevertheless, both models predict that for long waves traveling through smoothly curved channels, the initial wave is almost completely transmitted with little backward reflection. In addition, the values for the leading transmitted wave amplitude predicted by the two models are quite consistent.

In our numerical simulation, the wave speed based on both models is calculated. Here we define the average wave speed as the total longitudinal distance traveled along the channel centerline divided by the corresponding travel time. Detailed numerical results on the wave speed of an initial solitary wave of $\alpha = 0.3$ traveling in different curved channels are presented in Table 1. These results show that the linear waves travel with critical wave speed, slower than the nonlinear waves, which is consistent with the wave theory.

	Channel Width b	Linear Wave Speed	Nonlinear Wave Speed
Smooth 90°-Bends	1	0.998	1.133
	5	0.980	1.122
	10	0.940	1.093
Sharp-Cornered 90°-Bends	1	0.996	1.154
	5	1.006	1.142
	10	1.092	1.183

Table 1. Comparison between wave speeds based on the linear and nonlinear models

Conclusion

For long waves propagating through smooth and sharp-cornered channel bends, it is found that the weakly nonlinear and dispersive Boussinesq model and the linear nondispersive long wave equations are fundamentally consistent with each other in predicting the amplitude of the leading transmitted and reflected waves. Beyond this fundamental consistency, we also find that the Boussinesq model can predict slightly more detailed wave features and more realistic wave profiles.

Acknowledgement

The numerical computations were performed on Cray c90 at the San Diego Supercomputer Center which is supported by the U.S. National Science Foundation. Helpful suggestions and discussions from Professor Howell D. Peregrine and Professor Robert Dalrymple at the 26th International Conference on Coastal Engineering in Copenhagen are greatly appreciated.

References

Kirby, J.T., Dalrymple, R.A. and Kaku, H. (1994). "Parabolic approximations for water waves in conformal coordinate systems." *Coastal Engrg.*, 23, 185-213.

Miles, J. W. (1947). "The diffraction of sound due to right-angled joints in rectangular tubes." *J. Acoust. Soc. Am.*, 19(4), 572-579.

Rostafinski, W. (1976). "Acoustic systems containing curved duct sections." *J. Acoust. Soc. Am.*, 60, 23-28.

Shi, A. and Teng, M.H. (1996). "Propagation of solitary wave in channels of complex configurations." *Proc. of 2nd Int. Conf. on Hydrodynamics,* Balkema, Rotterdam, The Netherlands, 349-354.

Shi, A., Teng, M.H. and Wu, T.Y. (1998). "Propagation of solitary wave through significantly curved shallow water channels." *J. of Fluid Mech.*, 362, 157-176.

Teng, M.H. and Wu, T.Y. (1992). "Nonlinear water waves in channels of arbitrary shape." *J. of Fluid Mech.*, 242, 211-233.

Teng, M.H. (1997). "Solitary wave solution to Boussinesq equations." technical note, *J. of Waterway, Port, Coastal and Ocean Engrg.*, 123(3), 138-141.

Wang, K.H., Wu, T.Y. and Yates, G.T. (1992). "Three-dimensional scattering of solitary waves by vertical cylinder." *J. of Waterway, Port, Coastal and Ocean Engrg.*, 118(5), 551-556.

Webb, A.J. and Pond, S. (1986). "The propagation of a Kelvin wave around a bend in a channel." *J. of Fluid Mech.*, 169, 257-274.

Wu, T.Y. (1981). "Long waves in ocean and coastal waters." *J. of Engrg. Mech.*, 107(3), 501-522.

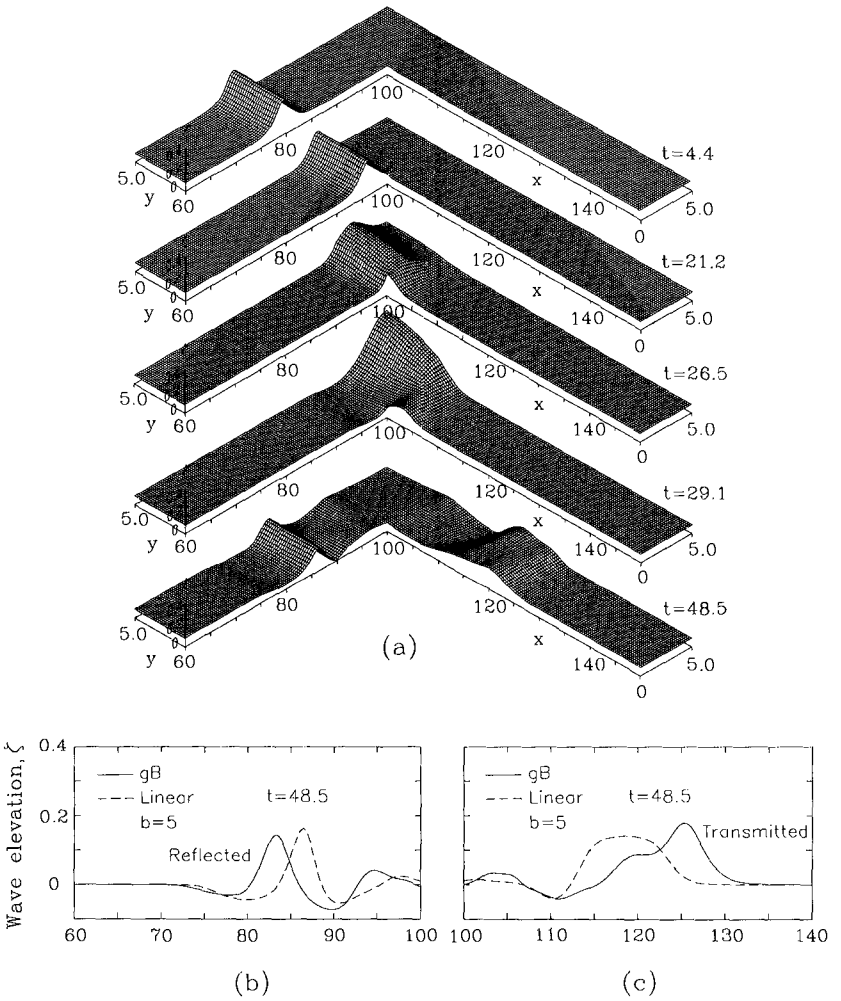

Figure 1. Propagation of a solitary wave of initial amplitude $\alpha = 0.3$ through a sharp-cornered channel bend of width $b = 5$. (a) wave field at different time instants based on the linear nondispersive wave equations; (b) and (c): comparison between the linear (dashed line) and the nonlinear (solid line) results for the reflected and transmitted wave profiles along the channel centerline.

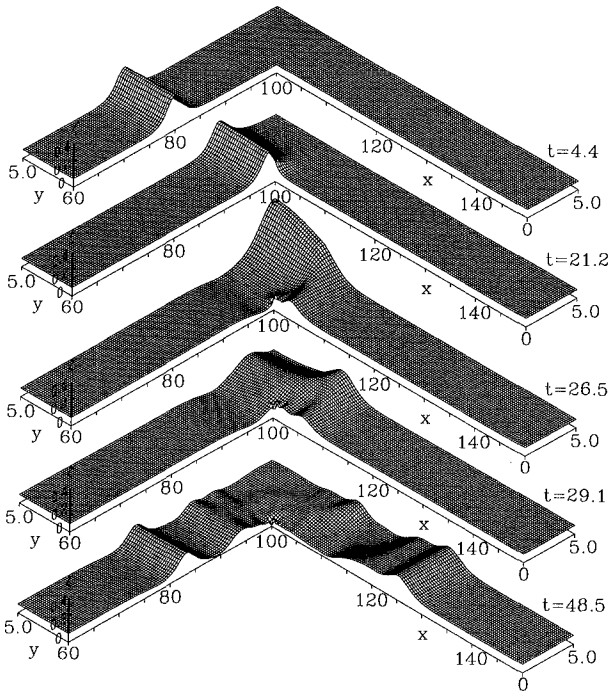

Figure 2. Propagation of a solitary wave of initial amplitude $\alpha = 0.3$ through a sharp-cornered channel bend of width $b = 5$ based on the weakly nonlinear and dispersive Boussinesq model.

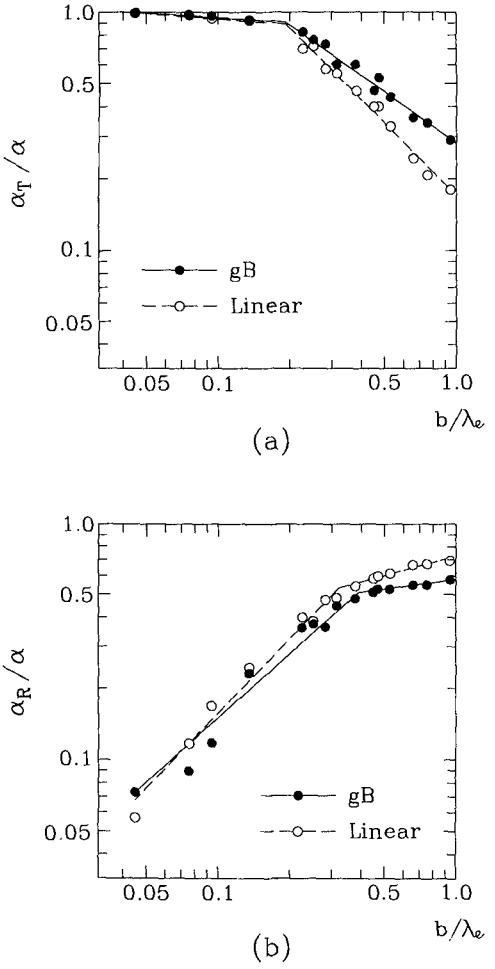

Figure 3. Plots of (a) transmission coefficient and (b) reflection coefficient v.s. the ratio of channel width b to effective wavelength λ_e for solitary waves propagating through sharp-cornered 90°-bends.

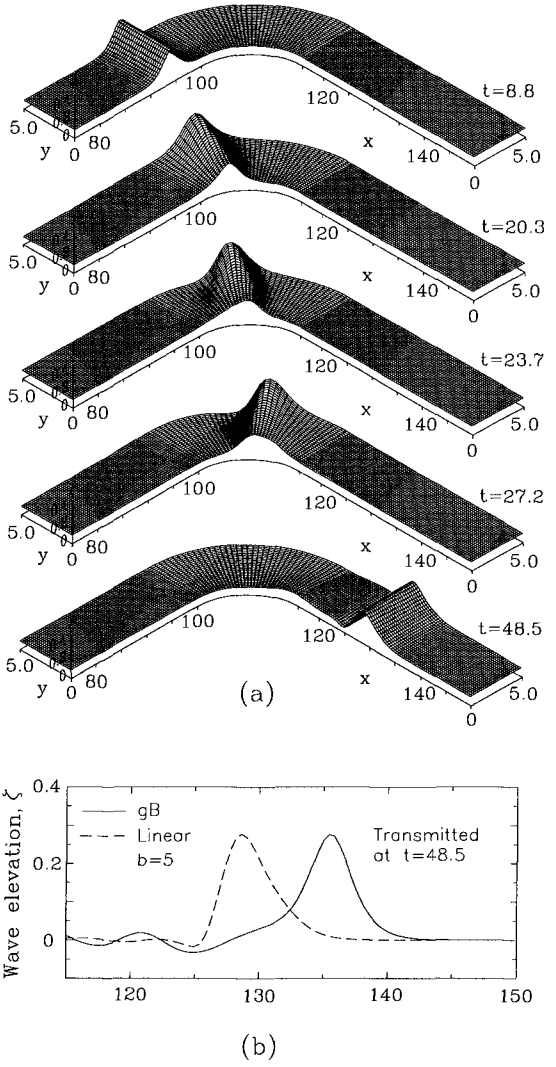

Figure 4. Propagation of a solitary wave of initial amplitude $\alpha = 0.3$ through a smooth channel bend of width $b = 5$. (a) wave field at different time instants based on the linear nondispersive wave equations; (b): comparison between the linear (dashed line) and the nonlinear (solid line) results for the transmitted wave profiles along the channel centerline.

Mass Transport of Progressive Edge Waves : A Comparison between the Full and Shallow-Water Wave Theories

K. M. Mok[1] & Harry Yeh[2]
[2]Member of ASCE

Abstract

The differences between the full and shallow-water wave theories for edge waves are reviewed. Detailed comparisons between the solutions of the second-order mass transport velocities within the laminar boundary layer obtained through the two theories are carried out for the first three edge-wave modes. The results clearly show that the error of the shallow-water approximation is larger as the mode number gets larger, and/or the beach slope gets steeper. It is also found that the magnitude of shallow-water approximation error increases in the offshore direction first, then it decreases as the distance approaches further offshore due to the energy decay in that direction. The affecting area of the shallow water approximation is relatively larger for the longshore transport than for the cross-shore transport in higher-mode edge waves. The significant differences between the full and shallow water-wave solutions in the near shore region identified in the present study issue a warning to the modellers of coastal hydrodynamics and nearshore topography, who utilize the shallow water approximation.

Introduction

Edge waves, the waves trapped near the shoreline on a uniformly sloping beach due to wave refraction, were discovered by Stokes (1846). The crest of Stokes' edge wave on a plane beach is perpendicular to the shoreline, it propagates along the shore with the wave amplitude decaying exponentially offshore. Other edge wave modes, besides the Stokes mode, were found by Eckart (1951) through the shallow water-wave theory and Ursell (1952) through the full water wave theory.

[1] Associate Dean, Assistant Professor, Faculty of Science and Technology, University of Macau, PO Box 3001, Macau.
[2] Professor, Box 352700, Dept. of Civil Engr., University of Washington, Seattle, WA 98195, USA

The assumptions associated with the full water wave theory are inviscid and homogeneous fluid, irrotational fluid motion, constant pressure on the free surface, negligible surface tension effect, and only gravity as the restoring force. For the shallow-water wave theory, the assumptions are the same as the full water theory with further simplification; the vertical fluid acceleration is neglected which means that the pressure variation with depth within the fluid domain is hydrostatic, and the horizontal component of the velocity field is uniform over the whole depth. With these assumptions, the problem formulated with the shallow water approximation is reduced to two-dimensional by the depth-integration. The mathematical descriptions of a mode-n progressive edge wave through the shallow water theory (Eckart, 1951) are

$$\phi_s = \frac{a_n g\beta}{\omega}\exp(-k_n y')L_n(2k_n y')\sin(k_n x-\omega t), \tag{1}$$

$$\eta_s = a_n\beta\exp(-k_n y')L_n(2k_n y')\cos(k_n x-\omega t), \tag{2}$$

with the dispersion relation,

$$\omega^2 = gk_n(2n+1)\beta, \tag{3}$$

where n is a non-negative integer (n = 0, 1, 2, 3, ...) representing the offshore mode number, (x, y', z) are the Cartesian coordinates of the alongshore, horizontally offshore and vertically upward directions (the shoreline is at y' = 0 and z = 0), ϕ is the velocity potential, η is the displacement of the water surface from the equilibrium position, a_n is the wave run-up amplitude on the beach, β is the beach sloping angle from the horizontal, ω (= 2π/wave period) is the angular frequency and k (= 2π/wavelength) is the wavenumber in the longshore direction, and $L_n(\bullet)$ is the Laguerre polynomial of order n, which is defined as

$$L_n(s) = \frac{e^s}{n!}\frac{d^n}{ds^n}\left(e^{-s}s^n\right). \tag{4}$$

The counter parts of (1) to (3) by the full water wave theory (Ursell 1952) are

$$\phi = \frac{\alpha_n g}{\omega}\Big[\exp(-k_n y'\cos\beta + k_n z\sin\beta) + \sum_{m=1}^{n} A_{mn}\Big\{\exp\big[-k_n y'\cos(2m-1)\beta - k_n z\sin(2m-1)\beta\big] + \exp\big[-k_n y'\cos(2m+1)\beta + k_n z\sin(2m+1)\beta\big]\Big\}\Big]\sin(k_n x-\omega t), \tag{5}$$

$$\eta = \alpha_n\Big[\exp(-k_n y'\cos\beta) + \sum_{m=1}^{n} A_{mn}\Big\{\exp\big[-k_n y'\cos(2m-1)\beta\big] + \exp\big[-k_n y'\cos(2m+1)\beta\big]\Big\}\Big]\cos(k_n x-\omega t), \tag{6}$$

where

$$A_{mn} = (-1)^m\prod_{j=1}^{m}\frac{\tan(n-j+1)\beta}{\tan(n+j)\beta}, \tag{7}$$

and α_n is a constant. The corresponding dispersion relation is given by

$$\omega^2 = gk_n \sin(2n+1)\beta \tag{8}$$

Ursell (1952) further showed that the number of possible trapped modes depends upon the beach sloping angle β with the maximum mode number n (a non-negative integer) satisfying

$$(2n+1)\beta \le \frac{\pi}{2}. \tag{9}$$

Stokes mode which is also called the mode 0 corresponds to $n = 0$, and edge waves with $n \ge 1$ are termed higher-mode edge waves. It is noted that Eckart's (1951) solution does not give any limitation to the value of the mode number n for a given beach slope; i.e. one cannot distinguish between the trapped modes and those that radiate energy offshore; as $n \to \infty$, the shallow-water wave solution corresponds to the perfectly reflected cross-shore wave (Whitham, 1976) which is obviously not a (trapped) edge-wave mode. To show the discrepancies between the full water-wave solution and the shallow-water wave approximation, Yeh (1986) plotted the surface profiles obtained by the two theories for the first three modes ($n = 0, 1, 2$) on a beach of 15° ($\beta = \pi/12$) slope as shown in figure 1. He showed that the full water-wave and the shallow-water wave solutions have good agreement for the mode-0 edge wave, but the two solutions deviate from each other as either n or y' increases; these deviations reflect the failure of the shallow-water wave

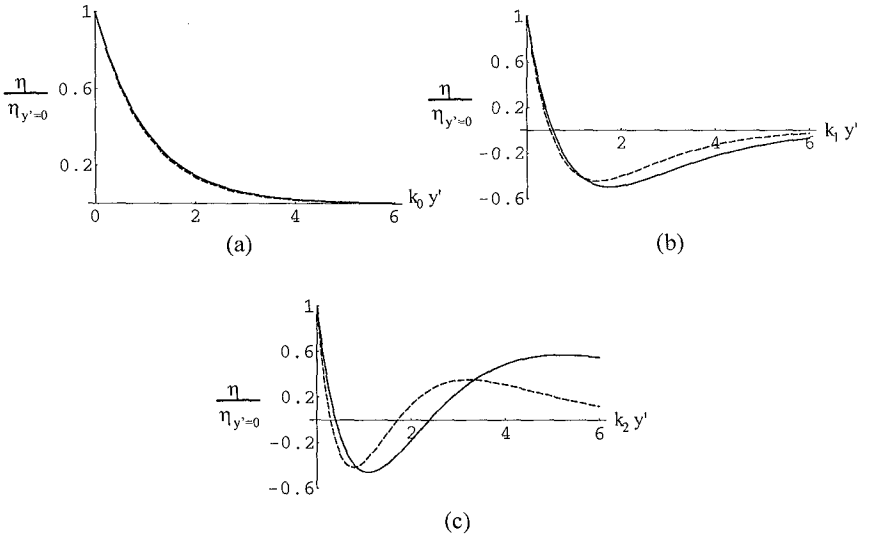

Figure 1. Offshore surface profiles of various edge-wave modes with $\beta = \pi/12$; (a) $n = 0$, (b) $n = 1$, (c) $n = 2$. ——— full theory; ---------- shallow-water approximation.

approximation as $y' \to \infty$ (in deep water). A more general comparison of the water-surface profiles predicted by the full water-wave solution and the shallow water-wave approximation can be demonstrated qualitatively by plotting the normalized difference ε for a range of beach slope and offshore distance;

$$\varepsilon = \frac{\eta_s}{\eta_{s,\, y'=0}} - \frac{\eta}{\eta_{y'=0}}. \tag{10}$$

Figure 2 shows the difference ε for the mode-0, mode-1 and mode-2 edge waves. It is noted that the plot range of the beach slope β is determined by (9). The $\varepsilon = 0$ plane represents the perfect agreement between the two theories. It is clearly shown that the deviation of ε from the zero plane increases both with the beach slope and the mode number. These deviations indicate the failure of the shallow water approximation in deep water. Quantitative comparison of the water surface as shown in figure 2 is given by Mok (1995b) who plotted the contour maps of the difference ε for the mode-0, 1, and 2 edge waves.

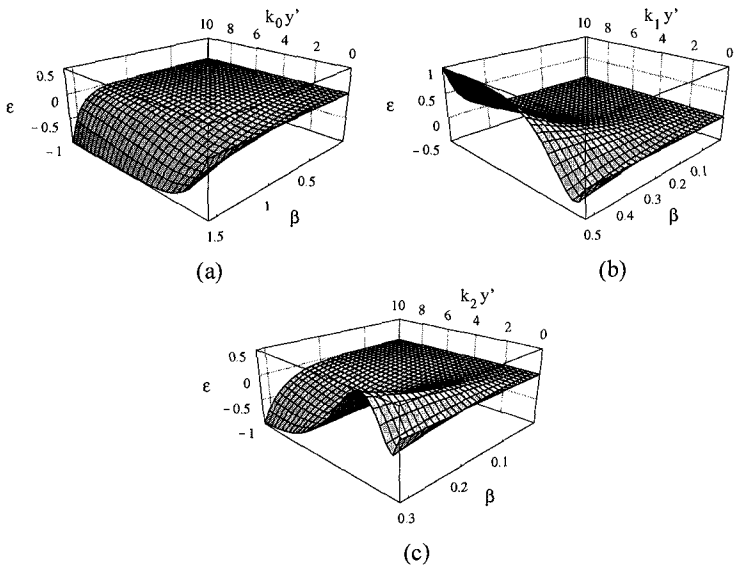

Figure 2. Differences on the water-surface elevation between the full water-wave theory and the shallow-water wave approximation for the (a) mode-0, (b) mode-1, (c) mode-2 edge waves.

In the natural beach environment, various field observations show that edge waves with the mode number less than 5 could be significant nearshore (Munk, Snodgrass & Gilbert, 1964; Huntley & Bowen, 1973; Huntley, 1976; Huntley, Guza & Thornton, 1981; Oltman-Shay & Guza, 1986). Due to the rhythmic characteristics of edge waves in the longshore direction, they can be related to many nearshore morphological features such as the formation of systematically spaced rip currents, nearshore circulation (Bowen & Inman, 1969), crescentic bars, some rhythmic topographical patterns nearshore (Bowen & Inman, 1971; Holman & Bowen, 1982), and beach cusps (Bowen & Inman, 1971; Guza & Inman, 1975; Huntley & Bowen, 1978; Guza & Bowen, 1981). The effects of edge wave on the coastal topography are due to its time-averaged Lagrangian mass-transport velocities (wave induced currents). Even if the magnitude of the induced current might be small, incipience of sediment detachments from the bottom might be caused by the disturbance such as turbulence induced by wave breaking. Then, the fate of the detached sediments might be controlled by the minute-but-persistent time-averaged wave induced currents, and eventually change the sea-bed topography.

Due to simplicity, many of the previous edge-wave mass-transport models (e.g. Bowen & Inman (1971) and Holman & Bowen (1982)) are based on the shallow-water wave theory and the transport velocity is evaluated only at the outer edge of the boundary layer. The question remained is "How much error will the shallow-water approximation introduce to the mass-transport velocity?". In the present study, the second-order mass-transport velocity at the outer edge of the bottom laminar boundary layer derived based on the full water-wave theory is compared with that obtained by the shallow-water-wave theory to identify the differences.

Mass Transport at the Outer Edge of the Bottom Boundary Layer

According to the thin laminar boundary layer theory, the flow field within the bottom viscous layer is driven by the outer irrotational oscillatory flow which is described by the velocity potential. A comparison between (1) and (5) shows that the shallow water solution has the vertical (z-direction) structure of the irrotational flow field removed due to the depth integration operation. This approximation is acceptable when the beach slope or the mode number is small as the vertical structure of the flow field depends on the sine of these two parameters (see (5)). Nevertheless, when the beach slope or the mode number becomes large, the failure of the shallow water approximation is apparent. When the shallow water approximation introduces error into the forcing (the outer irrotational flow field) of the bottom boundary layer, it will pass the error down to the induced second-order mass transport velocity.

Using the full water-wave solution of the velocity potential (5) with the coordinates rotated by the beach slope β,

$$\phi = \frac{\alpha_n g}{\omega}\Big\{\exp(-k_n y) + 2\sum_{m=1}^{n} A_{mn}\exp\left[-k_n y\cos(2m\beta)\right]\cosh\left[k_n z\sin(2m\beta)\right]\Big\}\sin(k_n x - \omega t), \quad (11)$$

Mok & Yeh (1998) and Mok (1992) derived the second-order mass-transport velocity within the thin laminar bottom boundary layer for all modes of progressive edge waves propagating along a uniformly sloping beach. Their solutions are evaluated at the outer edge of the boundary layer here to give the longshore and cross-shore mass-transport velocities ($\overline{u}_L$, $\overline{v}_L$),

$$\overline{u_L} = (\alpha_n g)^2\left(\frac{k_n}{\omega}\right)^3\left\{\frac{3}{2}\left[\exp(-k_n y) + 2\sum_{m=1}^{n} A_{mn}\exp[-k_n y\cos(2m\beta)]\right]\cdot\left[\sum_{m=1}^{n} A_{mn}\sin^2(2m\beta)\exp[-k_n y\cos(2m\beta)]\right] + \frac{1}{2}\left[\left(\exp(-k_n y) + 2\sum_{m=1}^{n} A_{mn}\exp[-k_n y\cos(2m\beta)]\right)^2 + \left(\exp(-k_n y) + 2\sum_{m=1}^{n} A_{mn}\cos(2m\beta)\exp[-k_n y\cos(2m\beta)]\right)^2\right]\right\}, \quad (12)$$

$$\overline{v_L} = -(\alpha_n g)^2\left(\frac{k_n}{\omega}\right)^3\left\{\exp(-k_n y) + 2\sum_{m=1}^{n} A_{mn}\cos(2m\beta)\exp[-k_n y\cos(2m\beta)]\right\}\cdot\left\{-\frac{1}{2}\left[\exp(-k_n y) + \sum_{m=1}^{n} A_{mn}[1+\cos^2(2m\beta)]\exp[-k_n y\cos(2m\beta)]\right] + \left[\sum_{m=1}^{n} A_{mn}\sin^2(2m\beta)\exp[-k_n y\cos(2m\beta)]\right]\right\}, \quad (13)$$

where, the coordinates (x, y, z) are measured longshore, offshore along the bottom and perpendicular to the beach. Based on the mass-transport velocity solutions at the outer edge of the boundary layer given by Hunt & Johns (1963) and the velocity potential given in (1), the second-order mass-transport velocity for progressive edge waves can also be estimated by the shallow-water wave theory. The mass-transport velocities in the longshore and cross-shore directions are, respectively,

$$\overline{u_{L_s}} = (a_n g\beta)^2\left(\frac{k_n}{\omega}\right)^3\frac{1}{4}\Big\{5\exp(-k_n y')[L_n(2k_n y')]^2 - \frac{3}{k_n^2}\exp(-k_n y')L_n(2k_n y')\frac{d^2}{dy'^2}[\exp(-k_n y')L_n(2k_n y')]$$

$$+\frac{2}{k_n^2}\left(\frac{d}{dy'}[\exp(-k_n y')L_n(2k_n y')]\right)^2\Big\}, \tag{14}$$

$$\overline{v_{L_S}} = (a_n g\beta)^2\left(\frac{k_n}{\omega}\right)^3 \frac{1}{4k_n}\frac{d}{dy'}[\exp(-k_n y')L_n(2k_n y')]\cdot$$

$$\Big\{\exp(-k_n y')L_n(2k_n y') - \frac{3}{k_n^2}\frac{d^2}{dy'^2}[\exp(-k_n y')L_n(2k_n y')]\Big\}. \tag{15}$$

Comparison between the Full and Shallow-Water Wave Solutions

Since the coordinate y' for the shallow-water wave solution is measured horizontally offshore and the coordinate y for the full water-wave solution is along the beach bottom, the mass-transport velocities calculated by the shallow-water wave solution are evaluated at position y' but plotted against the corresponding y location ($y = y'/\cos\beta$) in order to be compared with the full water-wave solution. To show the characteristics of the longshore and cross-shore mass transport velocities of progressive edge waves and to be consistent with Yeh's (1986) comparison, the mass-transport velocity profiles obtained by the two theories on a beach of $\pi/12$ slope is plotted to view the differences. The $\beta = \pi/12$ selection restricts the discussions only on the mode-0, mode-1 and mode-2 edge waves according to (9). For both longshore and cross-shore mass-transport velocities of a mode-0 edge wave, the full and shallow-water wave solutions agree with each other (the differences are indistinguishable so that the results are not presented). However, as the mode number becomes larger, the differences appear. Figure 3 shows the longshore and cross-shore mass-transport velocities of a mode-1 edge wave, respectively. It is shown that the differences between the full and shallow-water wave solutions are small. For the longshore transport (figure 3a), the shallow-water wave solution is slightly larger at $k_1 y < 1.68$ and smaller at $k_1 y > 1.68$ than the full water-wave solution. For the cross-shore transport (figure 3b), the two solutions agrees qualitatively. The main differences between them are the locations of the zero mass-transport (zero-crossing) and the offshore locations of the local minimum and maximum. In general, the locations of the zero-transport, local minimum and local maximum predicted by the shallow-water wave theory occur closer to the shore than those predicted by the full water-wave theory. Figure 4 shows the longshore and cross-shore mass-transport velocities of a mode-2 edge wave, respectively. The differences between the full and shallow-water wave solutions are evident. The main differences are the offshore locations of the local minima, local maxima and zero crossings; the shallow-water wave theory still predicts those locations closer to the shore than the full water-wave theory does.

Further general comparisons between the two theories are carried out for the longshore and cross-shore mass transport velocities by plotting the normalized difference

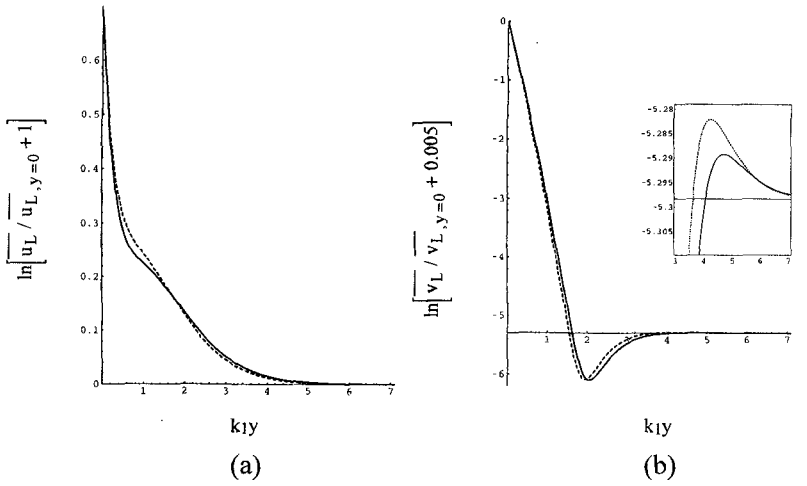

Figure 3. Mass-transport velocity at the outer edge of the boundary layer of a mode-1 progressive edge wave with $\beta = \pi/12$. ——— is the full water-wave solution; ---------- is the shallow-water wave solution. (a) Longshore component, (b) Cross-shore component.

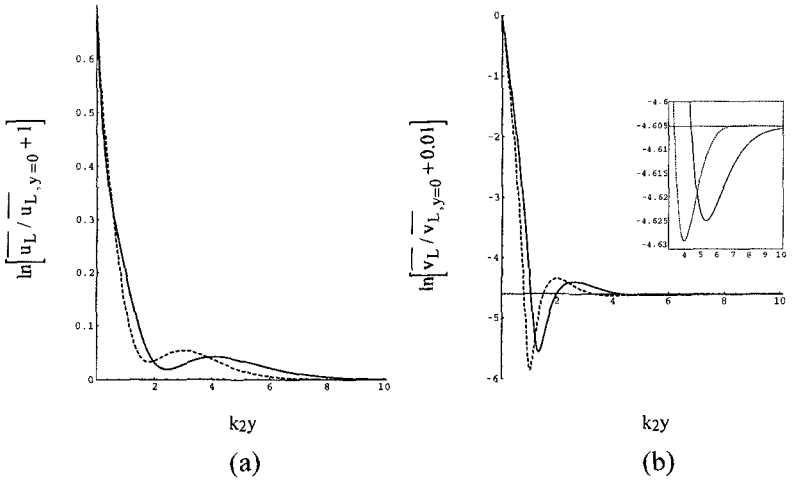

Figure 4. Mass-transport velocity at the outer edge of the boundary layer of a mode-2 progressive edge wave with $\beta = \pi/12$. ——— is the full water-wave solution; ---------- is the shallow-water wave solution. (a) Longshore component, (b) Cross-shore component.

Δu_L and Δv_L for a range of beach slope and offshore distance;

$$\Delta u_L = \frac{\overline{u_{L_s}}}{u_{L_s,y=0}} - \frac{\overline{u_L}}{u_{L,y=0}}, \tag{16}$$

$$\Delta v_L = \frac{\overline{v_{L_s}}}{v_{L_s,y=0}} - \frac{\overline{v_L}}{v_{L,y=0}}. \tag{17}$$

The comparison scheme is to assume that both of the solutions have the same magnitude at the shoreline and see how they deviate from each other as the beach slope and the offshore distance increase. Figure 5 shows the differences Δu_L and Δv_L for a mode-0 edge wave. It is noted that the error chart is valid for both the longshore and cross-shore transports due to the similar offshore structure that they possess. Each line in figure 5 represents the longshore (or cross-shore) transport difference between the two solutions (full and shallow) on beaches of various slope β. For a given beach slope, the magnitude of the error increases offshore from zero to a local maximum then it decreases. The increase of error in the offshore direction at location near the shore reflects the failure of the shallow water approximation due to the increasing water depth. The maximum error of a mode-0 edge wave occurs at $k_0 y < 0.5$ for the entire range of beach slope ($\beta \leq \pi/2$).

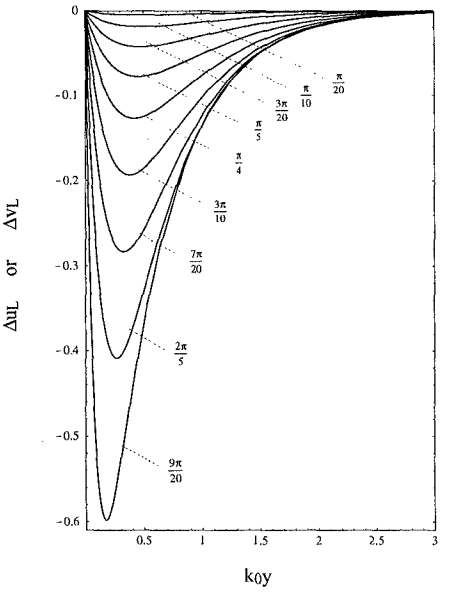

Figure 5. Error chart of the longshore (or cross-shore) transport between the full and shallow-water wave theories for a mode-0 edge wave on various beach slopes.

The decrease of the relative error at further offshore location is due to energy decay in that direction; i.e. the magnitude of the mass-transport velocity is small at location far offshore due to the exponential decay and therefore the relative error between the two solutions becomes small there. On the other hand, the relative error between the two solutions increases with the increasing beach slope for a given offshore location k_0y. This characteristic clearly indicates the effects of the water depth. As the water depth at a fixed offshore location becomes larger with the larger beach slope, the error of the shallow water approximation becomes larger. In fact, this behaviour is expected to be the same for the other edge-wave mode and will not be addressed again in the following discussions for the higher-mode edge waves.

For a mode-1 edge wave, the variation of the error for longshore and cross-shore transports differs. Figure 6 shows the longshore-transport difference Δu_L of a mode-1 edge wave. For the shown beach-slope range, the errors increase offshore from zero to local maxima at $0.5 < k_1y < 0.8$, then it decreases offshore to local minima at $2.0 < k_1y < 2.7$. The magnitudes of the local maxima are larger (about 1.7 times for the case of $\beta = \pi/6$) than the local minima. Nevertheless the magnitude of the error decreases gradually at $k_1y > 2.7$. Again, the increase of error in the offshore direction at location near the shore reflects the failure of the shallow water approximation due to the increasing water

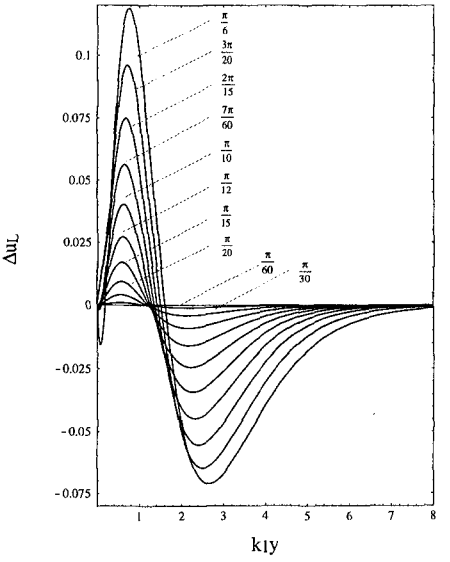

Figure 6. Error chart of the longshore transport between the full and shallow-water wave theories for a mode-1 edge wave on various beach slopes.

depth while the decrease of error at location further offshore ($k_1y > 2.7$) is due to the energy decay as discussed earlier. For the cross-shore mass transport comparison, figure 7 shows the difference Δv_L for a mode-1 wave. Similar to the longshore transport, the magnitudes of the cross-shore transport errors increase in the offshore direction with formation of local minima and maxima at $0.1 < k_1y < 0.2$ and $2.2 < k_1y < 3.0$, respectively. However, the magnitudes of the local minima are much larger (about 7 times for the case of $\beta = \pi/6$) than the local maxima. This significant magnitude difference is caused by the rapid decay of the cross-shore transport velocity in the offshore direction (see figure 3b). Comparing the longshore and cross-shore transport error variation (figures 6, 7), it is clear that the error introduced by the shallow water approximation has a relatively wider offshore coverage for the longshore transport than for the cross-shore transport. Again this is due to the different offshore energy decaying rates of the two transport velocities as shown in figure 3. Note that the complexity of the offshore variation and the existence of local maxima, minima and zero crossings are due to the intersection of the two solutions at various offshore locations (see figure 3).

For the mode-2 edge wave, variation of the error is similar to that of a mode-1 edge wave qualitatively but with more complexity. Detailed description of the comparison is not given for the mode-2 edge wave. Figures 8 and 9 show the longshore-

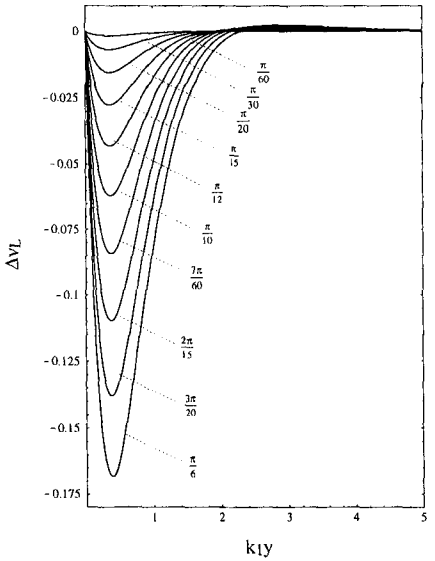

Figure 7. Error chart of the cross-shore transport between the full and shallow-water wave theories for a mode-1 edge wave on various beach slopes.

transport difference Δu_L and the cross-shore transport difference Δv_L for a mode-2 edge wave, respectively. Generally, the error still increases with the beach slope and the offshore distance and forms local maxima and minima. The affecting area of the shallow water approximation is still larger for the longshore transport than for the cross-shore transport.

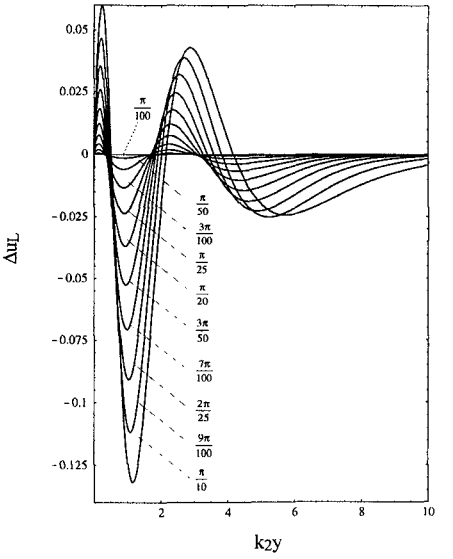

Figure 8. Error chart of the longshore transport between the full and shallow-water wave theories for a mode-2 edge wave on various beach slopes.

Conclusions

Due to its simplicity, many edge-wave mass-transport models are based on the shallow-water approximation. The use of the shallow-water approximation seems reasonable if the beach slope is mild, or only relatively low-mode edge waves are considered. The present study shows that the significant differences between the full and shallow water-wave solutions as the beach slope gets steeper, the distance is farther from the shoreline, or the mode number gets larger issue a warning to the modellers of coastal hydrodynamics and nearshore topography, who utilize the shallow water approximation. Even the present comparison of the two solutions are carried out for mass transport located at the outer part of the boundary layer, it should be noted that there may be major drawbacks on the usage of the mass transport velocity at this location to model the nearshore topography formation. According to Mok's (1995a) experimental verification

and discussions on Dore's (1975) mass transport solution for the Stokes progressive edge wave, the cross-shore transport is bidirectional; the transport is in the inshore direction near the bottom of the boundary layer, while it is in the offshore direction in the upper part of the boundary layer. Evidently, using only the mass-transport velocity at the outer edge of the boundary layer may give an incomplete picture or even misleading prediction of the edge waves' influences on the coastal regions.

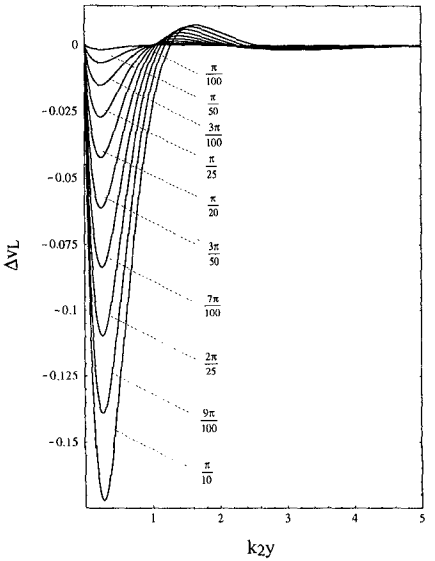

Figure 9. Error chart of the cross-shore transport between the full and shallow-water wave theories for a mode-2 edge wave on various beach slopes.

Acknowledgements

The work for this paper was supported by the US Office of Naval Research (N00014-87-K-0815). The preparation and publication fee of this paper is kindly supported by the University of Macau and the Fundação Oriente.

References

Bowen, A. J. and Inman, D. L. (1969). "Rip-currents: 2. Laboratory and field observations." J. Geophys. Res., 74, 5479-5490.

Bowen, A. J. and Inman, D. L. (1971). "Edge waves and crescentic bars." J. Geophys. Res., 76, 8662-8671.

Dore, B. D. (1975). "Wave-induced vorticity in free-surface boundary layers: application to mass transport in edge waves." J. Fluid Mech., 70, 257-266.

Eckart, C. (1951). "Surface waves on water of variable depth." Wave Report No. 100, Univ. of Calif., Scripps Institution of Oceanography, Calif.

Guza, R. T. and Bowen, A. J. (1981). "On the amplitude of beach cusps." J. Geophys. Res., 86, 4125-4132.

Guza, R. T. and Inman, D. L. (1975). "Edge waves and Beach Cusps." J. Geophys. Res., 80, 2997-3012.

Holman, R. A. and Bowen, A. J. (1982). "Bars, bumps, and holes: models for the generation of complex beach topography." J. Geophys. Res., 87, 457-468.

Hunt, J. N. and Johns, B. (1963). "Currents induced by tides and gravity waves." Tellus, 15, 343-351.

Huntley, D. A. (1976). "Long-period waves on a natural beach." J. Geophys. Res., 36, 6441-6449.

Huntley, D. A. and Bowen, A. J. (1973). "Field observations of edge waves." Nature, 243, 160-162.

Huntley, D. A. and Bowen, A. J. (1978). "Beach cusps and edge waves." Proc., 10th Int. Conf. on Coastal Engrg., 1378-1393.

Huntley, D. A., Guza, R. T. and Thornton, E. B. (1981). "Field observations of surf beat: 1. Progressive edge waves." J. Geophys. Res., 86, 6451-6466.

Mok, K. M. (1992). "Higher-mode edge waves." Ph.D. thesis, Univ. of Wash., Seattle, Wash.

Mok, K. M. (1995a). "An experimental study on mass transport of progressive Stokes edge waves." Proc., XXVI IAHR Congress, London, UK, 3, 186-191.

Mok, K. M., (1995b). "Edge waves - the differences between the full and shallow water-wave theories." Proc., 17th Conf. on Ocean Engrg. and 1995 Cross-Strait Conf. on Port and Coastal Development, Tainan, Taiwan, 1, 393-405.

Mok, K. M., and Yeh, H. (1998). "On mass transport of progressive edge waves." In Preparation.

Munk, W., Snodgrass, F. and Gilbert, F. (1964). "Long waves on the continental shelf: an experiment to separate trapped and leaky modes." J. Fluid Mech., 20, 529-554.

Oltman-Shay, J. and Guza, R. T. (1986). "Infragravity edge wave observations on two California beaches." J. Phys. Oceanogr., 17, 644-663.

Stokes, G. G. (1846). "Report on recent researches in hydrodynamics." Rep. 16th meeting Brit. Assoc. Adv. Sci., 1-20 = Math. Physics Papers, 1, 157-187, Cambridge, 1880.

Ursell, F. (1952). "Edge waves on a sloping beach." Proc., R. Soc. Lond. A, 214, 79-97.

Whitham, G. B. (1976). "Nonlinear effects in edge waves." J. Fluid Mech., 74, 353-368.

Yeh, H. H. (1986). "Experimental study of standing edge waves." J. Fluid Mech., 168, 291-304.

Coherent Motions in the Bottom Boundary Layer under Shoaling and Breaking Waves

Daniel T. Cox[1] and Nobuhisa Kobayashi[2]

ABSTRACT: Laboratory measurements of the instantaneous horizontal and vertical velocities induced by regular waves spilling on a rough, impermeable slope were analyzed to elucidate the nature of turbulence generated in the bottom boundary layer and by wave breaking. In the bottom boundary layer outside the surf zone, both the absolute shear stress $|\tau'|$ and the turbulent kinetic energy k' exhibited intermittent behavior where the instantaneous values were often several times greater than the phase-averaged values. The motions occurred with the passing of each regular wave, however, and the phase-averaged values described the turbulent fluctuations reasonably well. A quadrant analysis showed that the turbulent velocities u' and w' were strongly correlated and oriented in either the first and third quadrants with $u'w' > 0$ during the acceleration phases or in the second and fourth quadrants with $u'w' < 0$ in the deceleration phase. The Reynolds stress contributions for this unsteady flow case depended strongly on the phase. Inside the surf zone, $|\tau'|$ and k' were marked by intense, intermittent events which did not occur with the passing of each wave and which were roughly two orders of magnitude larger than the phase-averaged values. This intermittent motion extended into the wave bottom boundary layer. Near trough level, the intermittent events were phase-dependent, and the intense motion was primarily in the fourth quadrant. Near the bottom, the intermittent events were less phase- dependent. A preliminary analysis of the intensity and duration of the intermittent events indicated that coherent events occurred for about 10% of the record and accounted for approximately 50% of the motion, whereas intense events occurred for about 2% of the record and accounted for approximately 20% of the motion. These statistics clearly indicated that the intense, coherent events were intermittent and infrequent but contributed significantly to the magnitude of the absolute shear stress and turbulent kinetic energy.

INTRODUCTION

Progress in understanding nearshore sediment suspension has been aided by the development of concentration sensors with high temporal resolution based on either optic or acoustic principles. Using these techniques, researchers have shown that nearshore sediment suspension is characterized by intermittent events and that these events, particularly inside the surf zone, can not be explained simply in terms of the free surface

[1]Asst. Prof., Ocean Engrg. Prog., Dept. of Civil Engrg., Texas A&M Univ., College Station, TX 77843-3136, USA; Email: dtc@arlo.tamu.edu; Tel: (409) 862 3627; Fax: (409) 862 8162.

[2]Prof. and Assoc. Dir., Center for Applied Coastal Res., Univ. of Delaware, Newark, DE 19716, USA; Email: nk@coastal.udel.edu; Tel: (302) 831 8044; Fax: (302) 831 1228.

elevation or local wave-induced horizontal velocity. A number of mechanisms have been put forward to explain the intermittent behavior of nearshore sediment suspension [e.g., *Jaffe et al.*, 1984; *Beach and Sternberg*, 1988; *Nadaoka et al.*, 1988; *Hanes*, 1991; *Hay and Bowen*, 1994]. Coherent fluid motions, such as bursting events in the boundary layer and large eddies produced by wave breaking, are plausible mechanisms but have received little attention due to a lack of suitable measurements, particularly estimates of the instantaneous vertical turbulent velocity, momentum flux and kinetic energy in the nearshore. In light of this, this paper identifies intermittent, coherent fluid motions under regular waves in three areas: (1) outside the surf zone and inside the bottom boundary layer where turbulence is generated at the boundary, (2) inside the surf zone in the interior region below trough level and above the bottom boundary layer where turbulence is generated primarily by wave breaking and (3) inside the surf zone and inside the bottom boundary layer where both mechanisms may be important. The term "bottom boundary layer" used in this paper is in reference to the wave bottom boundary layer which was shown to exist inside the surf zone [e.g., *Cox et al.*, 1996].

EXPERIMENT

The nature of nearshore turbulence generated in the bottom boundary layer and by wave breaking is investigated using a laboratory flume since repeatability of the wave condition allows the turbulent signal to be extracted by phase-averaging. The experiment was conducted in a 33 m long, 0.6 m wide, and 1.5 m deep wave flume with a 1:35 impermeable slope, corresponding to a dissipative beach. A physical bottom roughness was added to the slope to increase the boundary layer roughness and boundary layer thickness so that the bottom boundary layer would be fully rough turbulent for non-breaking waves. The roughness was prepared by gluing sand grains with a median grain diameter of $d_{50} = 1.0$ mm to Plexiglas sheets and then taping these sheets over the entire slope. The adopted roughness in this small-scale experiment would correspond to gravel on a natural beach if geometric similitude were applied.

Six measuring lines were established, noted L1 to L6, and their cross-shore position relative to the spilling breakers can be described as follows: L1 was in the shoaling region seaward of breaking, L2 was at the break point defined as the onset of aeration in the tip of the wave crest, L3 was in the transition region where the wave changed from organized motion to a turbulent bore, and L4 to L6 were in the inner surf zone where the saw-toothed wave shape was a well-established turbulent bore. The free surface elevation, η, was measured at each measuring line using capacitance-type wave gages with a sampling rate of 100 Hz. The horizontal, cross-shore velocity, u, and the vertical velocity, w, were measured at a number of elevations at each measuring line by a fiber-optic laser-Doppler velocimeter (LDV). The effective sampling rate was in excess of 1×10^3 data points per second, and the data were reduced by band averaging to a sampling rate of 100 Hz. The flume was filled with fresh water to a depth of 0.4 m in the flat section of the tank, and regular waves were generated with a wave period of $T = 2.2$ s. Fifty regular waves were measured at each elevation, and the turbulent signal was extracted by phase-averaging.

Table 1 summarizes the measuring line locations and elevations. The second column indicates the horizontal coordinate, x, for each measuring line which is defined positive onshore with $x = 0$ at L1, where L1 was 9.8 m from the still water shoreline. The third

column indicates the depth d below the still water level to the top of the Plexiglas sheet. The fourth column indicates the phase-averaged wave height H. The fifth column indicates the range of measuring elevations analyzed near the bottom with the number of elevations given in parenthesis. The vertical coordinate z_m is defined positive upward with $z_m = 0$ on the bottom at each measuring line. The thickness of the wave bottom boundary layer is estimated to be approximately 1 cm based on the maximum shear velocity and angular wave frequency which is consistent with observations for this data set [*Cox et al.*, 1996].

Table 1: Measuring line locations and elevations.

Line	x	d	H	Range of z_m (cm) analyzed				Dropout Rate
No.	(cm)	(cm)	(cm)	BBL		Interior		(%)
L1	0	28.00	13.22	0.20–1.10	(7)	1.60–24.10	(10)	0.6–2.1
L2	240	21.14	17.10	0.20–1.10	(7)	1.60–16.10	(8)	0.4–2.5
L3	360	17.71	12.71	0.20–1.10	(7)	1.60–14.10	(9)	0.3–8.6
L4	480	14.29	8.24	0.20–1.10	(7)	1.60–12.10	(8)	0.4–15.4
L5	600	10.86	7.08	0.20–1.10	(7)	1.60–9.10	(9)	0.6–3.1
L6	720	7.43	5.05	0.20–1.10	(7)	1.60–6.10	(6)	1.0–3.5

The sixth column indicates the range of measuring elevations in the interior region outside the bottom boundary layer to trough level with the number of elevations given in parenthesis. The seventh column indicates the range of the dropout rate for all elevations at each measuring line. The dropout rate is expressed as a percent and is typically low (less than about 2%), except near trough level for L3 and L4 due to aeration by the bores. Statistics presented in this paper were compared extensively using two types of time series, one in which the dropouts were excluded and a second in which the dropouts were replaced by a linear interpolation of the nearest points. For all elevations except those immediately below trough level at L3 and L4, there was no significant difference in the statistics using the two types of time series. In this paper, only the time series in which the dropouts were replaced by a linear interpolation are presented for clarity. As summarized in Table 1, the data set consists of a total of 86 measuring elevations from the bottom to trough level over six measuring lines. The following sections present the instantaneous and phase-averaged turbulence using three representative elevations: L2 at $z_m = 0.30$ cm inside the bottom boundary layer outside the surf zone, L5 at $z_m = 7.10$ cm in the interior region inside the surf zone, and L5 at $z_m = 0.30$ cm inside the bottom boundary layer inside the surf zone.

INSTANTANEOUS AND PHASE-AVERAGED TURBULENCE

The instantaneous free surface elevation, η, and the horizontal and vertical velocities, u and w, were phase-averaged over the fifty waves. The turbulent signals were defined as the difference of the instantaneous signals and phase-averaged signals and are expressed $\eta' = (\eta - \eta_a)$, $u' = (u - u_a)$, and $w' = (w - w_a)$ where the subscript a denotes a phase-averaged quantity and the prime denotes a turbulent quantity. The phase-averaged quantities include both the organized wave-induced motion and the mean motion. The instantaneous turbulent momentum flux may be defined $\tau'/\rho = -u'w'$ where ρ is the

fluid density and τ'_a is the phase-averaged Reynolds shear stress. The absolute value of the phase-averaged Reynolds shear stress, $|\tau'_a|$, is normally related to the concentration of suspended sediments at the bed or to the pick-up of bottom sediments. This approach may be reasonable if $|\tau'_a|$ represents most of the fluctuations in $|\tau'|$. The notation of $\tau' = -u'w'$ without the assumed constant ρ is used in this paper for simplicity. The instantaneous turbulent kinetic energy per unit mass k' is also of interest since it is not clear whether suspended sediments near the bed respond to $|\tau'|$ or k'. Since the cross-tank component of velocity, v, was not measured for this experiment, the turbulent kinetic energy per unit mass in this paper is defined as $k' = (u'^2 + w'^2)/2$ which is less than the actual k' including the contribution of v'^2.

Figure 1 shows the temporal variations of the instantaneous and phase-averaged free surface elevation, horizontal and vertical velocities, absolute shear stress, and turbulent kinetic energy for L2 at $z_m = 0.30$ cm for $20 \leq t/T \leq 25$ where t is time with $t = 0$ at the beginning of the 50 waves. The instantaneous and phase-averaged free surface elevation η and η_a in Figure 1a are difficult to distinguish and indicate the repeatability of the wave form. The wave shows strong asymmetry in both the horizontal and vertical planes. Figures 1b and 1c show the instantaneous and phase-averaged horizontal velocities, u and u_a, and vertical velocities, w and w_a. The phase-averaged horizontal velocity is dominant and much larger than the horizontal turbulent fluctuation. This assumption of a relatively weak turbulent intensity in a locally steady flow has been used in the analysis of surf zone turbulence [*George et al.*, 1994]. The phase-averaged vertical velocity w_a is small at this elevation and throughout most of the water column except near trough level, and the vertical turbulent fluctuation is dominant w' in comparison to w_a. Note that u and w were measured simultaneously and that the LDV and wave gage were synchronized to the wavemaker signal. Since multiple runs were repeated at the same measuring line, however, the velocity and free surface measurements presented in this figure and in Figure 2 are not synoptic.

Figures 1d and 1e show the instantaneous and phase-averaged variations of the absolute shear stress, $|\tau'|$ and $|\tau'|_a$, and turbulent kinetic energy, k' and k'_a. Both $|\tau'|$ and k' exhibit intermittent behavior where the instantaneous values are often several times greater than the phase-averaged values. Nevertheless, this motion occurs with the passing of each wave, and the phase-averaged values describe the turbulent fluctuations reasonably well with the following features: relatively low turbulence in the trough, an increase with the approaching wave crest (acceleration) which continues with the passing of the wave crest (deceleration). Elevations in the range $0.20 \leq z_m \leq 1.10$ cm exhibited similar behavior. Elevations for $z_m > 1.10$ cm above the bottom boundary layer outside the surf zone show very little turbulent motion [e.g., *Cox et al.*, 1994].

Figure 2 is similar to Figure 1 but for L5 inside the surf zone in the interior region at $z_m = 7.10$ cm where turbulence is generated by wave breaking. Comparison of η and η_a in Figure 2a shows the variability of the free surface inside the surf zone, particularly at the roller region on the crest of the wave. Inspection of the entire record $0 \leq t/T \leq 50$ did not reveal any large deviations in the instantaneous time series from the phase-averaged time series in the trough region, however. On the other hand, Figures 2b and 2c show intense, coherent motion in the horizontal and vertical velocities at $t/T \simeq 21$ and $t/T \simeq 24$. Inspection of the entire record $0 \leq t/T \leq 50$ for this elevation and for

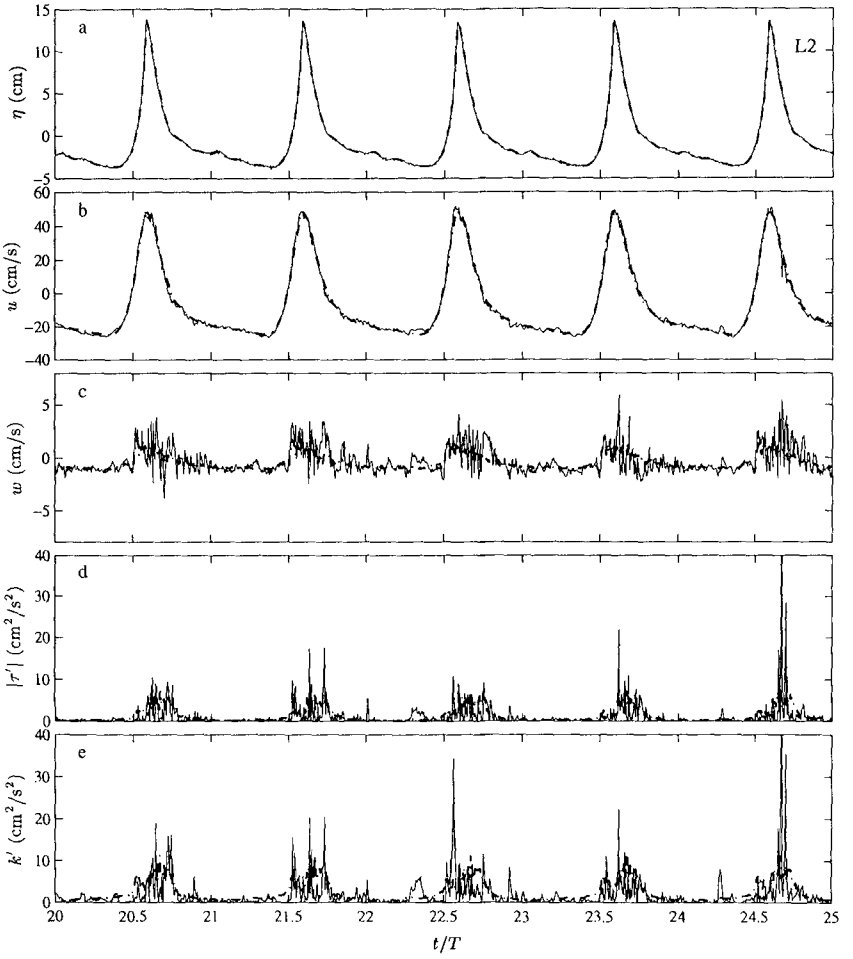

Figure 1: Temporal variation of (a) η, (solid) and η_a (dash-dot); (b) u (solid) and u_a (dash-dot); (c) w (solid) and w_a (dash-dot); (d) $|\tau'|$ (solid) and $|\tau'|_a$ (dash-dot); and (e) k' (solid) and k'_a (dash-dot) in the range $20 < t/T < 25$ for L2 at $z_m = 0.30$ cm.

the other elevations inside the surf zone indicates that these intense turbulent events are intermittent, that they do not occur with the passing of each wave, and that the motions extends into the bottom boundary layer. The intense turbulent velocity fluctuations are of the same magnitude as the phase-averaged horizontal velocity, and the motion generally occurs with the passing of a wave crest and spreads downwards.

Figures 2d and 2e show the instantaneous and phase-averaged absolute shear stress and turbulent kinetic energy. Similar to L2, $|\tau'|$ and k' are well correlated. However, $|\tau'|$ and k' are an order of magnitude larger than in the bottom boundary layer outside the surf zone. Since the intense motion does not occur with each wave, this motion is more intermittent and can not be explained in terms of the phase-averaged quantities. In the bottom boundary layer inside the surf zone, the motion is characterized by intense, intermittent turbulence generated by wave breaking and less intense but more frequent turbulence generated at the boundary (Figure not shown).

Figures 3a–c show smoothed spectra of k' and k'_a at the representative locations. The spectral densities are plotted as a function of the frequency, $f*$, normalized by the wave period $T = 2.2$ s. The spectra of k'_a were computed using phase-averaged time series repeated over 50 waves. All spectra were computed with detrended time series and were smoothed using band-averaging with 20 degrees of freedom. Figure 3a shows that the spectrum of k' can be reasonably well represented by the spectrum k'_a, and that the low frequency components are small outside of the surf zone. Figure 3b shows that the spectrum of k'_a describes a small portion of the k' spectrum at the fundamental harmonic. Figure 3c shows that the spectrum k' is poorly represented by the spectrum k'_a inside the bottom boundary layer inside the surf zone. Figures 3b and 3c also show large low frequency components which are due to the intermittent nature of the eddies generated by wave breaking. The spectra for $|\tau'|$ and $|\tau'|_a$ are similar to those shown in Figure 3. These observations of small low frequency motion outside the surf zone and large low frequency motion inside the surf zone are consistent with observations of sediment suspension in a wave flume under regular waves [*Dally and Barkaszi*, 1994].

QUADRANT ANALYSIS

In this section, a quadrant analysis is used to identify coherent motions in the instantaneous turbulent velocity time series. For unidirectional flow in the marine atmospheric boundary layer, *Boppe and Neu* [1995] used the quadrant technique to identify coherent motions and to quantify the bursting process. Associated with the bursting process are "ejections" where low speed fluid is brought up from the boundary layer and "sweeps" where high speed fluid rushes down from the outer layer. For unidirectional flow, motion in the second quadrant where $u' < 0$ and $w' > 0$ corresponds to ejections and motion in the fourth quadrant where where $u' > 0$ and $w' < 0$ corresponds to sweeps. Both ejections and sweeps contribute positively to the Reynolds stress since $\tau'/\rho = -u'w'$.

Figure 4 shows quadrant plots of u' and w' at 20 phases for the entire 50 waves in the range $0 \leq t/T < 50$ for L2 at $z_m = 0.30$ cm. The time in the first quadrant for each panel indicates the phases for which the data were plotted. For example, $t_a/T = 0.05$ indicates that the data plotted in that panel correspond to all data in the range $0 \leq t_a/T < 0.05$ over the fifty waves where t_a/T is the normalized phase

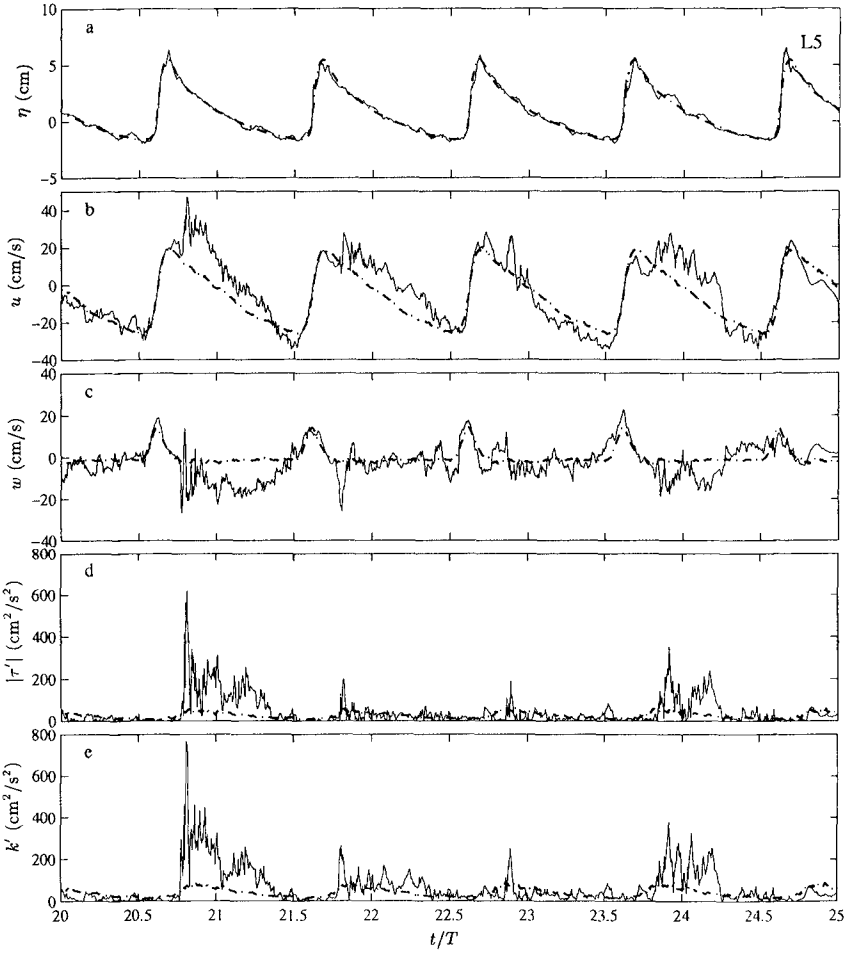

Figure 2: Same as Figure 1 for L5 at $z_m = 7.10$ cm.

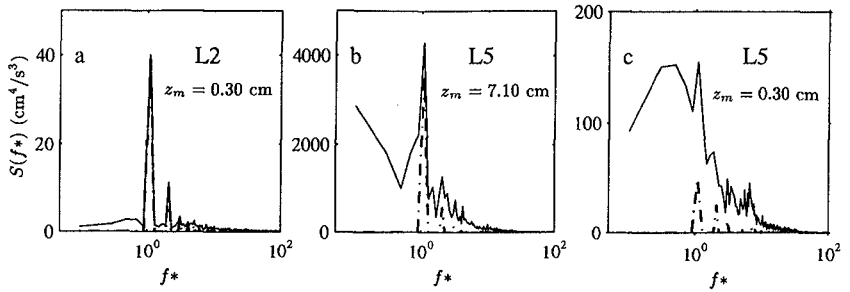

Figure 3: Spectral densities of k' (solid) and k'_a (dash-dot). NDOF = 20.

over one wave period. The four horizontal bars plotted along the vertical axis indicate (from top to bottom) the phase-averaged free surface elevation, η_a; the phase-averaged horizontal velocity, u_a; the local acceleration of the horizontal velocity, $\partial u_a/\partial t$; and the vertical gradient of the horizontal velocity $\partial u_a/\partial z$. The plotted values of η_a, u_a, $\partial u_a/\partial t$, and $\partial u_a/\partial z$ in each panel were averaged over that interval and were scaled by the maximum absolute value of the phase-averaged variable shown in the lower right of the figure. Temporal and spatial derivatives were estimated using a centered finite difference. The scaling is such that the maximum absolute value of the phase-averaged variable is equal to the upper limit of u' on the abscissa of that figure. For example, η_a = 13.5 cm would correspond to u' = 15 cm/s in Figure 4. Although the phase-averaged variables may be difficult to interpret quantitatively in this figure, they give a useful qualitative comparison of the relative phases of these important variables.

In Figure 4, the top horizontal bar indicates that the wave crest occurs at t_a/T = 0.65, and the wave height decreases until reaching a minimum near t_a/T = 0.40. Comparison of the first and second bars indicates that η_a and u_a are generally in phase. The undertow is small compared to the maximum wave-induced velocity, $|\overline{u_a}|/|u_a|_{max} \simeq 0.14$. The third horizontal bar indicates that local deceleration of the flow starts at t_a/T = 0.65, is a minimum at t_a/T = 0.70, and deceleration continues until t_a/T = 0.35. At t_a/T = 0.40, the flow accelerates and reaches a maximum acceleration at t_a/T = 0.55. The bottom horizontal bar indicates that the vertical gradient of the horizontal velocity reaches a minimum at t_a/T = 0.50 and a maximum at t_a/T = 0.70. This gradient is large at this elevation compared to the elevations above the bottom boundary layer, and this gradient is not in phase with either the horizontal velocity or the local acceleration.

Figure 4 shows that the turbulent motion is most intense during periods of large local acceleration (t_a/T = 0.55, 0.60) and large local deceleration (t_a/T = 0.65, 0.70, 0.75). In the trough region, both the turbulent motion and the fluid acceleration is small. The horizontal and vertical velocity fluctuations are of similar magnitude and are generally much smaller than the phase-averaged horizontal velocity. Perhaps the most striking feature of Figure 4 is that the turbulent motion is strongly correlated and oriented in either the first and third quadrants with $u'w' > 0$ during the acceleration phases or in the second and fourth quadrants with $u'w' < 0$ in the deceleration phase.

This indicates that unidirectional flow results such as estimates of the Reynolds stress contributions can not be extended directly for oscillatory flow. The Reynolds stress contributions for this unsteady flow case depend strongly on the phase.

Similar to Figure 4, Figure 5 shows quadrant plots at 20 phases for L5 at $z_m = 7.10$ cm. The wave crest and maximum phase-averaged horizontal velocity occur at $t_a/T = 0.75$. The undertow is large, $|\overline{u_a}|/|u_a|_{max} \simeq 0.25$, and the vertical gradient of the horizontal velocity is small compared to L1 at $z_m = 0.30$ cm. The largest fluctuations of u' and w' occur after the passage of the wave crest and in the trough region ($t_a/T = 0.95, 0.95, 1.0, 0.05, 0.10, 0.15, 0.2$). For the quadrant plots in this range, the large fluctuations occur primarily in the fourth quadrant, corresponding to sweeps where high speed fluid ($u' > 0$) rushes downward ($w' < 0$) due to wave breaking. The phase-averaged horizontal velocity is generally positive in this range $u_a > 0$, but because the undertow is strong, u_a can become negative even when $\eta_a > 0$. The instantaneous values of u' and w' during sweeps can be as large as $|u_a|_{max} = 26.18$ cm/s in Figure 5.

INTENSE COHERENT EVENTS

An analysis on the intensity and duration of the intermittent turbulent events is presented here similar to that by *Jaffe and Sallenger* [1992] for suspended sediments. Coherent events are defined in this paper when the magnitude of $|\tau'|$ or k' exceeds a critical value. Since setting the critical values is somewhat subjective, the following procedure adopted from *Jaffe and Sallenger* [1992] was used. A coherent event was defined as $|\tau'| \geq (m + \sigma)$ where m is the mean of $|\tau'|$ over the entire 50 waves at that elevation and σ is the standard deviation. An intense event was defined as $|\tau'| \geq (m + 3\sigma)$. This analysis was also used to detect events in k' where coherent events are defined as $k' \geq (M + \sigma_k)$ and intense events are defined as $k' \geq (M + 3\sigma_k)$ where M is the mean and σ_k is the standard deviation of k' at that elevation. It is noted that the wave phase is not considered in this simplified analysis. Figure 6 illustrates the procedure with a portion $|\tau'|$ in the range $20 \leq t/T \leq 25$ for L5 at $z_m = 7.10$ cm. The lower dash-dot line shows the threshold $(m + \sigma)$ for the coherent events, and the upper dash-dot line shows the threshold $(m + 3\sigma)$ for the intense events. The corresponding detection of coherent events and intense events are shown by the solid lines above the $|\tau'|$ time series.

Statistics of coherent events and intense events for $|\tau'|$ and k' were computed for all elevations listed in Table 1. Table 2 compares the statistics of $|\tau'|$ and k' at L1 and L2 outside the surf zone. Statistics shown in this table are averages of the first four elevations near the bottom $z_m = 0.20, 0.25, 0.30$, and 0.40 cm since these elevations were fairly similar in terms of m, σ, and n_1/n. In this table, n_1 is the number of coherent events out of a total number of data points, $n = 11000$, for which $|\tau'| \geq (m+\sigma)$; and m_1 is the average value of $|\tau'|$ for the coherent events. The second column essentially indicates the duration of the coherent event as a percent of the total record, $(n_1/n) \times 100$; and the third column indicates the percent of the motion contained in the coherent events in relation to that in the entire time series, $[(n_1 m_1)/(nm)] \times 100$. The subscript "3" indicates statistics computed using the definition of intense events, and the capital letters are used to distinguish coherent events and intense events computed using k'. In general, the statistics for the coherent events and intense events are similar for definitions based on $|\tau'|$ or k'. However, from L1 to L2, $(n_1 m_1)/(nm)$ and $(N_1 M_1)/(nM)$ are similar but $(n_3 m_3)/(nm)$ and $(N_3 M_3)/(nM)$ increase by approximately 15%, indicating

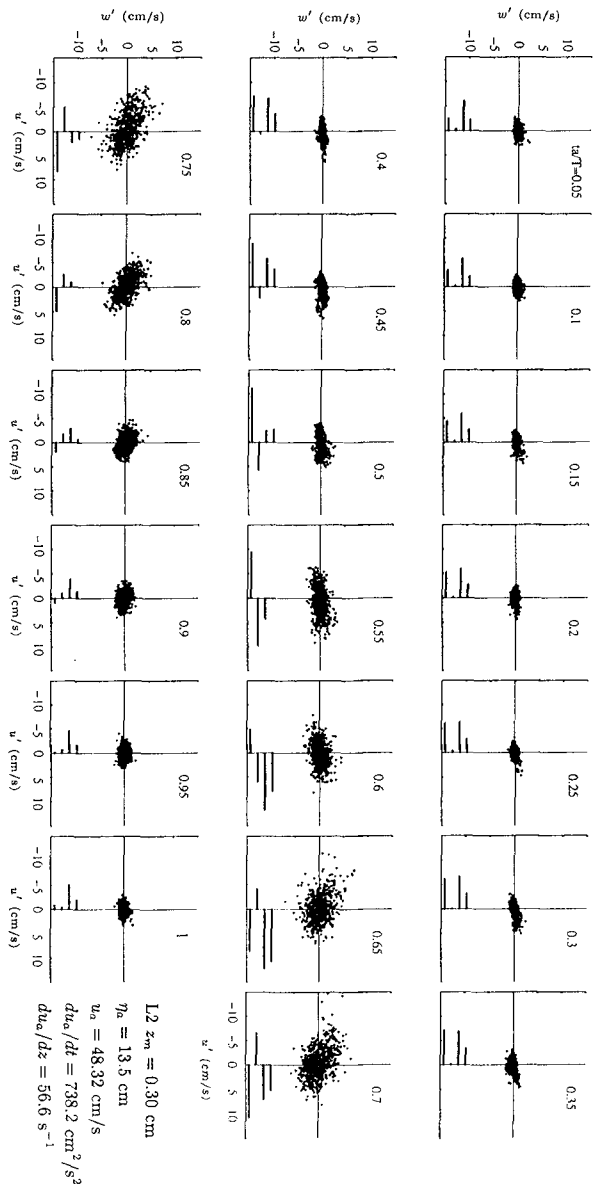

Figure 4: Quadrant plots at 20 phases for L2 at $z_m = 0.30$ cm. Figure explained in text.

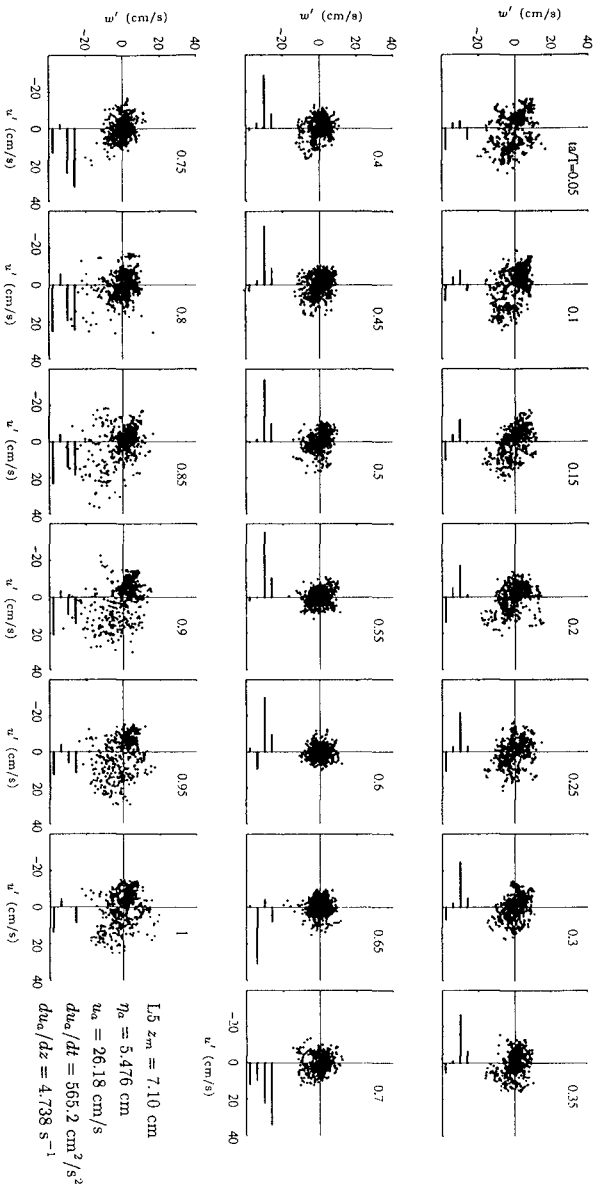

Figure 5: Same as Figure 4 for L5 at $z_m = 7.10$ cm.

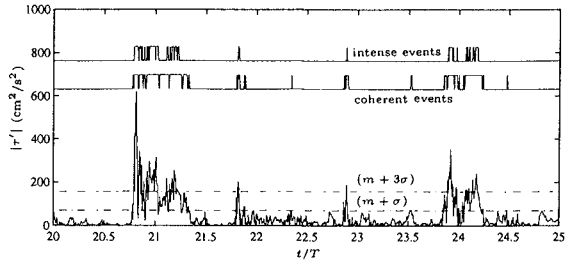

Figure 6: Detection of coherent events and intense events based on $|\tau'|$ for L5 at $z_m = 7.10$ cm.

Table 2: Coherent events and intense events detected using $|\tau'|$ and k' for L1 and L2 averaged at each measuring line. Standard deviation in parenthesis

Line No.	$\lvert\tau'\rvert$				k'			
	Coherent Events		Intense Events		Coherent Events		Intense Events	
	$\frac{n_1}{n}$ %	$\frac{n_1 m_1}{nm}$ %	$\frac{n_3}{n}$ %	$\frac{n_3 m_3}{nm}$ %	$\frac{N_1}{n}$ %	$\frac{N_1 M_1}{nM}$ %	$\frac{N_3}{n}$ %	$\frac{N_3 M_3}{nM}$ %
L1	8.6 (0.9)	49.1 (0.6)	1.9 (0.2)	20.8 (2.3)	10.0 (1.5)	48.0 (0.6)	2.1 (0.1)	18.4 (3.4)
L2	6.9 (0.6)	49.5 (4.6)	1.8 (0.2)	24.2 (2.6)	8.1 (0.6)	47.5 (4.4)	1.9 (0.3)	21.1 (2.1)

that the magnitude of the intense events increases landward before breaking.

Table 3 lists the statistics of coherent events and intense events inside the surf zone. The statistics were averaged from $z_m = 0.20$ cm to trough level for all elevations at L3 to L6, and the standard deviations are given in parenthesis. The average statistics for L4, L5, and L6 in the inner surf zone are remarkably similar and suggest that it should be possible to parameterize the intense, coherent motion inside the surf zone. The average statistics for L3 in the transition region are different from those in the inner surf zone, and this suggests that the statistics could also vary with breaker type. Tables 2 and 3 shows that coherent events and intense events are of short duration, occuring for approximately 10% and 2% of the record, respectively, but contain a large portion of the turbulent motion, approximately 50% and 20%, respectively.

Table 3: Coherent events and intense events detected using $|\tau'|$ and k' for L3 to L6 averaged at each measuring line. Standard deviation in parenthesis

Line No.	$\lvert\tau'\rvert$				k'			
	Coherent Events		Intense Events		Coherent Events		Intense Events	
	$\frac{n_1}{n}$ %	$\frac{n_1 m_1}{nm}$ %	$\frac{n_3}{n}$ %	$\frac{n_3 m_3}{nm}$ %	$\frac{N_1}{n}$ %	$\frac{N_1 M_1}{nM}$ %	$\frac{N_3}{n}$ %	$\frac{N_3 M_3}{nM}$ %
L3	9.6 (1.3)	44.5 (1.5)	2.0 (0.2)	17.4 (2.0)	10.7 (1.4)	42.8 (2.7)	2.0 (0.2)	14.4 (2.3)
L4	7.5 (1.3)	43.7 (2.3)	1.7 (0.3)	19.6 (1.9)	8.5 (1.7)	42.4 (3.0)	1.9 (0.4)	18.1 (2.2)
L5	7.6 (1.1)	43.5 (1.7)	1.7 (0.3)	19.5 (1.9)	8.5 (1.8)	41.1 (3.1)	1.8 (0.4)	17.1 (2.2)
L6	7.9 (0.8)	43.5 (1.9)	1.7 (0.2)	19.1 (1.6)	8.8 (1.3)	41.8 (3.2)	1.9 (0.4)	17.0 (2.3)

CONCLUSIONS

In the bottom boundary layer outside the surf zone, the phase-averaged horizontal velocity is dominant and much larger than the horizontal turbulent fluctuation. The phase-averaged vertical velocity is small, and the vertical turbulent fluctuation is dominant. Both $|\tau'|$ and k' exhibit intermittent behavior where the instantaneous values are often several times greater than the phase-averaged values. The motions occur with the passing of each regular wave, however, and the phase-averaged values described the turbulent fluctuations reasonably well. In the interior region below trough level inside the surf zone, the horizontal and vertical velocity records showed intense, intermittent turbulent events that did not occur with the passing of each wave. The intense turbulent fluctuations were of the same magnitude as the phase-averaged horizontal velocity. The instantaneous quantities of $|\tau'|$ and k' could not be explained in terms of the phase-averaged quantities. The intermittent turbulent events extended into the bottom boundary layer inside the surf zone. The infrequent but intense turbulence generated by wave breaking is an order of magnitude larger than the turbulence generated locally at the boundary.

Spectra of k' showed that the low frequency motion is small outside the surf zone and that the low frequency motion due to the intermittent turbulence from wave breaking increases inside the surf zone. Spectra of k' are reasonably well represented by spectra of k'_a outside the surf zone and poorly represented by spectra of k'_a inside the surf zone. This conclusion was the same for the spectra of $|\tau'|$ and $|\tau'|_a$.

A quadrant analysis was used to show the relative contributions to the Reynolds stress as a function of wave phase. In the bottom boundary layer outside the surf zone, the turbulent motion was strongly correlated and oriented in either the first and third quadrants with $u'w' > 0$ during the acceleration phases or in the second and fourth quadrants with $u'w' < 0$ in the deceleration phases. In the interior region below trough level inside the surf zone, large fluctuations occurred primarily in the fourth quadrant, corresponding to sweeps where high speed fluid rushed downward due to wave breaking. These large motions did not occur with each wave but were phase-dependent near trough level. Near the bottom, the large motions were less dependent on phase and may be related to a more random arrival of eddies in the bottom boundary layer. The horizontal turbulent fluctuations increased relative to those outside the surf zone, whereas the vertical turbulent fluctuations were similar.

To analyze the intensity and duration of the intermittent turbulent events, two thresholds were used to distinguish coherent events and intense events. The analysis showed that coherent events occurred for about 10% of the record and accounted for approximately 50% of the turbulent motion. Intense events occurred for about 2% of the record and accounted for approximately 20% of the turbulent motion. These statistics indicated that coherent and intense events are infrequent but contribute significantly to the magnitude of $|\tau'|$ and k' and possibly the suspension of bottom sediments.

These results are based on one experiment of regular laboratory waves spilling on a fixed, rough bottom. Further work with plunging waves, irregular waves, and movable beds will be necessary to generalize these conclusions. Nevertheless, this is an important step to show that instantaneous turbulence even for regular waves are dominated by

intense, intermittent events. Furthermore, this may explain difficulties in correlating suspended sediment concentrations and transport rates to phase-averaged or ensemble-averaged horizontal velocities. Parameterization and prediction of the intense events is left for further work but would likely be beneficial in developing predictive models for sediment suspension inside the surf zone.

Acknowledgments

This work was sponsored by the National Science Foundation CAREER Award CTS-9734109.

REFERENCES

Beach, R.A., and R.W. Sternberg, Suspended sediment transport in the surf zone: Response to cross-shore infragravity motion, *Mar. Geol.*, 80, 61–79, 1988.

Boppe, R.S., and W.L. Neu, Quasi-coherent structures in the marine atmospheric surface layer, *J. Geophys. Res.*, 100 (C10), 20635–20648, 1995.

Cox, D.T., N. Kobayashi, and A. Okayasu, Vertical variations of fluid velocities and shear stress in surf zones, in *Proceedings of the 24th International Conference on Coastal Engineering*, 98–112, Am. Soc. Civ. Eng., New York, 1994.

Cox, D.T., N. Kobayashi, and A. Okayasu, Bottom shear stress in the surf zone, *J. Geophys. Res.*, 101 (C6), 14337–14348, 1996.

Dally, W.R., and S.F. Barkaszi, High-resolution measurements of sand suspension by plunging breakers in a large wave channel, in *Proceedings of Coastal Dynamics*, 263–277, Am. Soc. Civ. Eng., New York, 1994.

George, R.A., R.E. Flick, and R.T. Guza, Observations of turbulence in the surf zone, *J. Geophys. Res.*, 99 (C1), 801–810, 1994.

Hanes, D.M., Suspension of sand due to wave groups, *J. Geophys. Res.*, 96 (C5), 8911–8915, 1991.

Hay, A.E., and A.J. Bowen, Coherence scales of wave-induced suspended sand concentration fluctuations, *J. Geophys. Res.*, 99 (C6), 12749–12765, 1994.

Jaffe, B.E., and A.H. Sallenger, The contribution of suspension events to sediment transport in the surf zone, in *Proceedings of the 23rd International Conference on Coastal Engineering*, Am. Soc. Civ. Eng., 2680–2693, 1992.

Jaffe, B.E., R.W. Sternberg, and A.H. Sallenger, The role of suspended sediment in shore-normal beach profile changes, in *Proceedings of the 19th International Conference on Coastal Engineering.*, 1983–1996, Am. Soc. Civ. Eng., New York, 1984.

Nadaoka, K., S. Ueno, and T. Igarashi, Sediment suspension due to large scale eddies in the surf zone, in *Proceedings of the 21st International Conference on Coastal Engineering*, 1646–1660, Am. Soc. Civ. Eng., New York, 1988.

EXPERIMENTAL STUDY ON NON-LINEAR WAVE BOUNDARY LAYERS

Hitoshi Tanaka[1], Hiroto Yamaji[2] and Ahmad Sana[3]

Abstract

A mechanical generation method of an asymmetric oscillatory flow has been proposed by the authors (Tanaka et al., 1997, 1998), though, its applicability to an actual experiments has not been thoroughly examined yet. In the present study, laboratory experiments are carried out for an asymmetric oscillatory flow in a U-shaped oscillating tunnel to make comprehensive investigation on the validity of the generation method under both laminar and turbulent condition using air and water respectively as working fluid.

Introduction

In numerous experimental studies on oscillatory boundary layers, a U-shaped oscillating tunnel has been effectively utilized in place of a wave flume (e.g., Jonsson, 1963). Use of this type of facility enables us to generate oscillating motion with the period almost similar to prototype wave motion. Most of the existing experimental facilities are, however, restricted to sinusoidal oscillation, equivalent to fluid motion induced by linear waves. In reality, waves are generally asymmetric more or less due to non-linear effect. In order to generate corresponding asymmetric oscillatory flow in a U-tunnel, it requires a highly expensive sophisticated equipment to control the piston movement, the reason being for scarcity of the experiments in this regard. For example, Nadaoka et al.(1994, 1996) and Ribberink and Al-Salem (1994) performed some experiments by using a computer-controlled piston system to study the characteristics of asymmetric oscillatory boundary layers.

Recently, the authors have proposed a rather simple and inexpensive piston mechanism, by which an asymmetric oscillation simulating fluid motion under non-linear waves is produced mechanically, and preliminary experiments have already been done using this generation method (Tanaka et al., 1997, 1998). However, number of experimental cases performed using this system is too limited to judge whether or not it works in actual experiments under various conditions. In the present study, the applicability of this generation method is examined at low and high Reynolds numbers.

1 Professor, Department of Civil Engineering, Tohoku University, Aoba, Sendai 980-8579, Japan. Phone & Fax:(+81)-22-217-7451, e-mail: tanaka@ tsunami2.civil.tohoku.ac.jp
2 Laboratory Assistant, ditto.
3 Research Associate, ditto.

Mechanical Generation of Asymmetric Oscillatory Flow

The schematic description of the piston mechanism to generate asymmetric oscillatory motion is shown in Fig.1. According to Tanaka et al.(1997,1998), time-variation of the velocity induced by the piston system is

$$\frac{U}{U_c} = \frac{(b_* - 1)(b_* \cos \omega t - 1)}{(b_* - \cos \omega t)^2} \tag{1}$$

where U is the horizontal velocity, U_c: peak velocity of U during wave crest, ω is the angular frequency ($=2\pi/T$, T: wave period), t is the time, $b_*=b/a$ and the definitions of b, and a are found in Fig.1.

Time-variation of the velocity given by Eq.(1) is plotted in Fig.2, where A_s denotes the asymmetry of the velocity variation defined as (Dibajnia and Watanabe 1992, Ribberink and Al-Salem 1994)

$$A_s = \frac{U_c}{U_c + U_t} \tag{2}$$

and U_t is the magnitude of the trough velocity. Since the velocity variation of Eq.(1) is symmetric about the crest, only the first half of the wave cycle is shown in Fig.2. The dotted lines with open circles in Fig.2 denotes the first-order solution of cnoidal wave theory given by

$$\frac{U}{U_c} = \mathrm{cn}^2\left(\frac{2Kt}{T}; k\right) - \overline{\mathrm{cn}^2} \tag{3}$$

where cn is the Jacobian elliptic function with modulus k, K is the complete elliptic integral of the first kind, and the bar denotes time average. In the above equation, the asymmetry of the velocity is more predominant with the increase of k, whereas the asymmetry of Eq.(1) is dependent on b_*. These two parameters governing the asymmetry can be correlated as follows (Tanaka et al., 1997, 1998). According to Eq.(3), A_s defined by Eq.(2) is

$$A_s = \frac{1}{k^2}\left(1 - \frac{E}{K}\right) \tag{4}$$

where E is the complete elliptic integral of the second kind of modulus k. On the other hand, the expression for A_s induced by the present generation system is obtained from Eq.(1).

$$A_s = \frac{b_* + 1}{2b_*} \tag{5}$$

Thus, by equating Eqs.(4) and (5), we obtain

$$\frac{1}{k^2}\left(1 - \frac{E}{K}\right) = \frac{b_* + 1}{2b_*} \tag{6}$$

Figure 3(a) shows how A_s varies with the change of k^2 calculated from Eq.(4), whereas Fig.3(b) denotes the relationship between b_* and k^2 obtained from Eq.(6). Figure 3(c) is drawn to show the relationship between q and k^2.

Figure 2 shows a comparison between Eq.(1) and Eq.(2) thus correlated. In Fig.2, it is seen that Eq.(1) and the exact solution of the cnoidal wave theory, Eq.(3), show surprisingly excellent agreement, especially at smaller values of A_s. Theoretical treatment of Tanaka et al. (1997,1998) revealed that Eq.(1) can be derived from Eq.(3) using an approximate formula for the elliptic function in the form of infinite product in terms of nome, q ($=\exp(-\pi K'/K)$, $K'(k) = K(\sqrt{1-k^2})$).

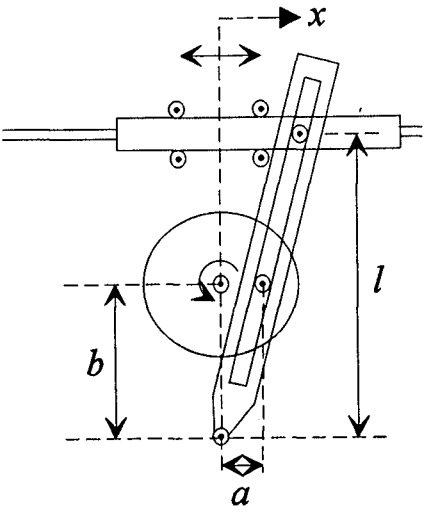

Fig.1 Mechanical generation method of an asymmetric oscillatory movement proposed by Tanaka et al.(1997,1998)

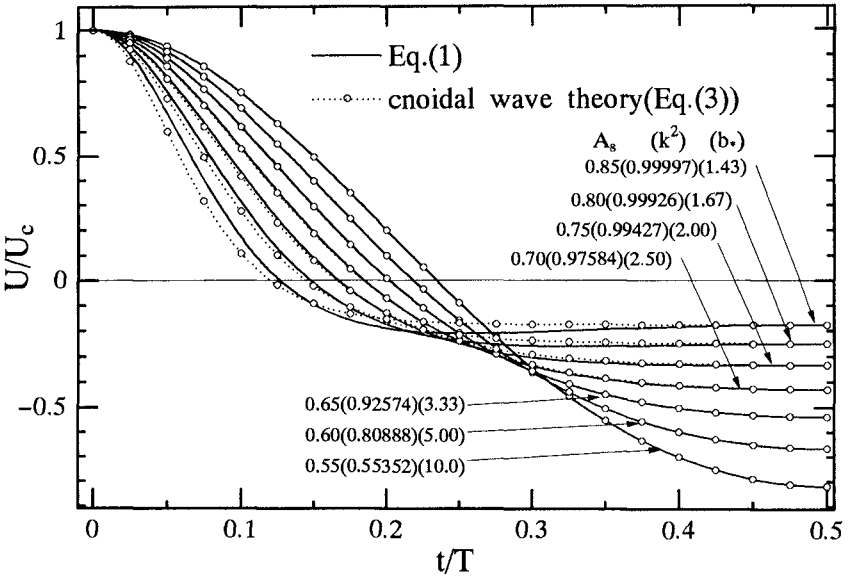

Fig.2 Time-variation of free-stream velocity

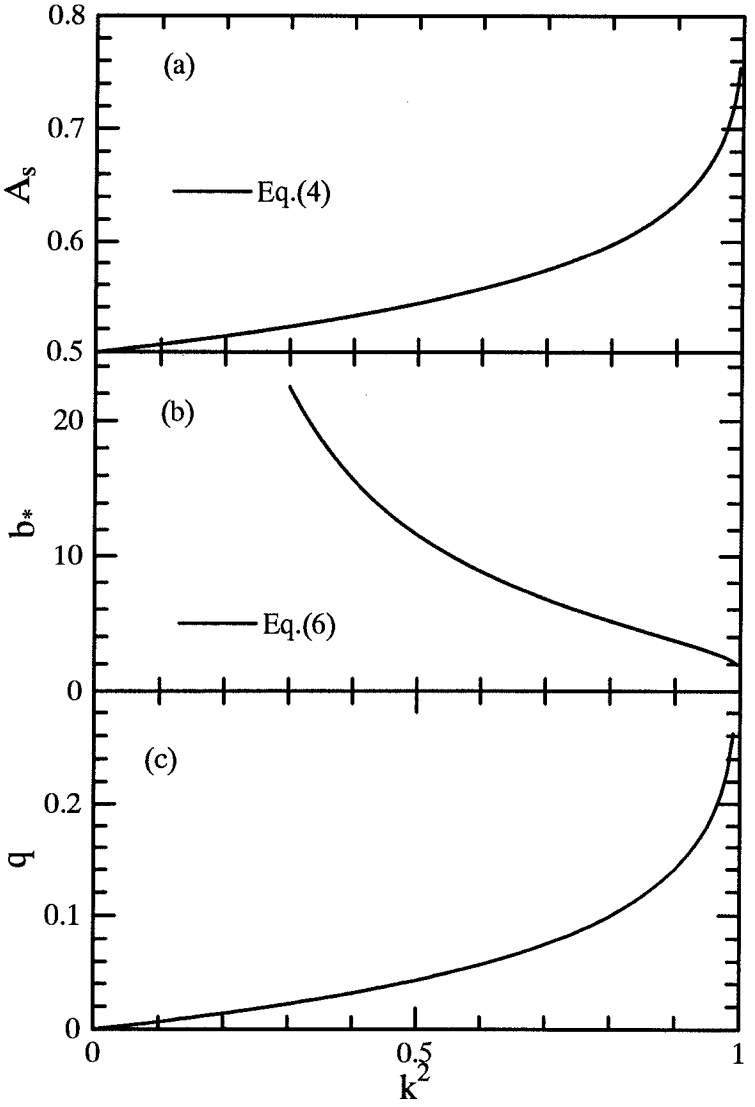

Fig.3 Relationship between A_s, b_*, q and k^2

Furthermore, Tanaka et al. (1997,1998) correlated b_* with Ursell number, U_r, as follows:

$$\text{for } U_r<90: \quad b_* = \frac{32\pi^2}{3U_r} + \tanh^{4/3}\left\{(U_r/70)^{3/4}\right\} \tag{7}$$

$$\text{for } U_r>90: \quad b_* = \frac{1}{1-\frac{8}{\sqrt{3U_r}}} \tag{8}$$

in which the definition of Ursell number is

$$U_r = \frac{HL^2}{h^3} \tag{9}$$

where H, L and h are the wave height, the wave length and the water depth, respectively. Figure 4 shows the accuracy of the approximate formulae, Eqs.(7) and (8), in which the exact relationship is obtained from Eq.(10). (Shuto, 1974)

$$k^2K^2 = \frac{3}{16}U_r \tag{10}$$

For designing an actual oscillating facility, Eqs.(7) and (8) can be used to determine b_* of piston system for a given Ursell number. Meanwhile, if A_s value is given instead of U_r as an experimental condition, corresponding b_* value is easily computed from Eq.(5).

$$b_* = \frac{1}{2A_s - 1} \tag{11}$$

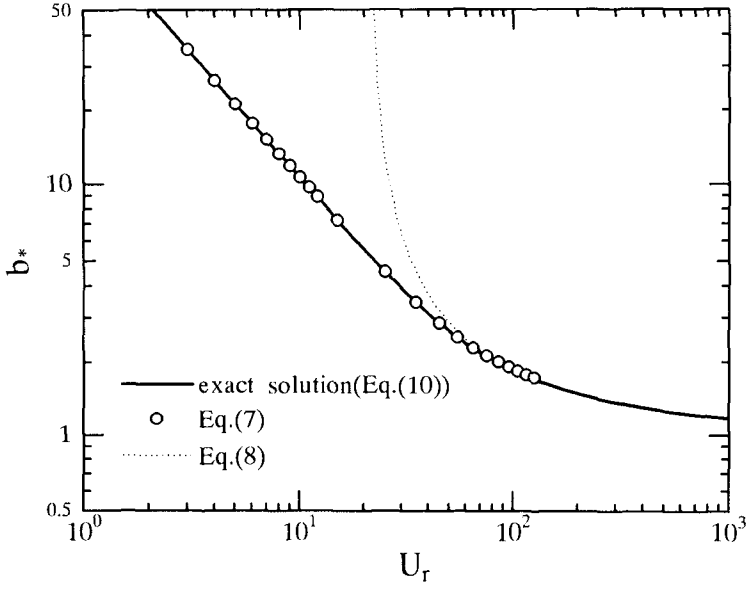

Fig.4 Relationship between b_* and Ursell number

Experimental Set-up and Experimental Condition

The present experiments were performed in a U-shaped oscillating tunnel with smooth walls seen in Fig.5 and Photo 1. The vertical risers of the tunnel were connected to the piston movement system described in the previous section. The velocities were measured with the help of a one-component fiber-optic laser doppler velcimeter (LDV) in forward scatter mode.

Table 1 Experimental condition

	working fluid	$T(s)$	$U_c(cm/s)$	$U_f(cm/s)$	A_s	R_δ
Case 1	air	2.15	161.3	88.0	0.64	345
Case 2	water	2.38	89.3	56.9	0.61	824

Table 1 shows the experimental conditions for the experiments presented herein. In this table, R_δ is the Reynolds number defined in terms of the crest velocity and the Stokes layer thickness.

$$R_\delta = \frac{U_c\sqrt{2\nu/\omega}}{\nu} \tag{12}$$

where ν is the molecular viscosity of the fluid.

As to the present days, the critical Reynolds number in case of asymmetric oscillatory boundary layer has not been studied in detail. As a first approximation, the value for purely sinusoidal oscillatory boundary layers may be considered to be applicable. According to an experimental study of Hino et al. (1976), transition from laminar to turbulence occurs around R_δ=550 in a sinusoidal wave boundary layer. It may be thus anticipated that Case 1 may be in laminar regime, whereas Case 2 may be turbulent, although the representative velocity in the definition is different between sinusoidal and asymmetric oscillatory flow.

Experimental Results and Discussions

Case 1

Figure 6(a) shows the temporal variation of velocity at the axis symmetry in the wind tunnel. It is seen that the measurement and the theory, Eq.(1), shows excellent agreement.

The open and closed circles in Figs.6(b) and 6(c) show the profile of measured mean velocity in horizontal direction. The solid lines denote an analytical solution for laminar asymmetric oscillatory flow expressed in terms of Fourier series (Schäffer and Svendsen, 1986).

$$u = \sum_{n=1}^{m} \left[a_n \left\{\sin n\omega t - \exp(-\beta_n z)\sin(n\omega t - \beta_n z)\right\} + b_n \left\{\cos n\omega t - \exp(-\beta_n z)\cos(n\omega t - \beta_n z)\right\}\right] \tag{13}$$

where a_n, b_n are the coefficients obtained by Fourier analysis of the measured free stream velocity, β_n is the Stokes layer thickness for each harmonics,

$$\beta_n = \sqrt{n\omega/2\nu} \tag{14}$$

and z is the vertical coordinate taken positive upward from the wall surface. In the

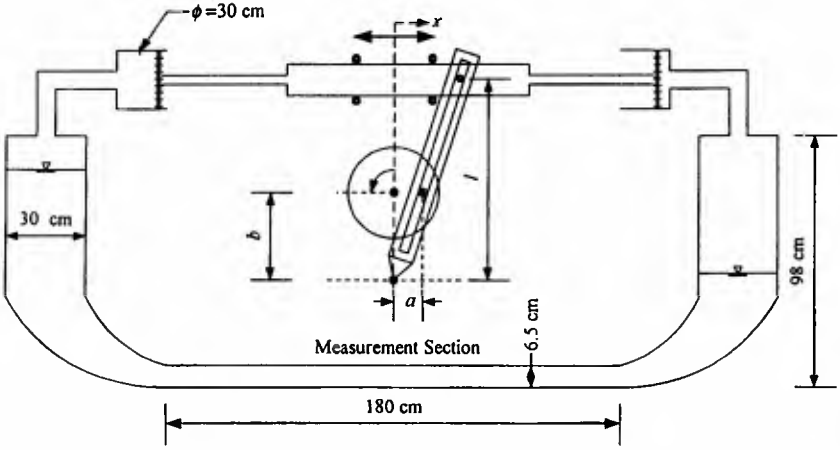

Fig.5 Experimental set-up

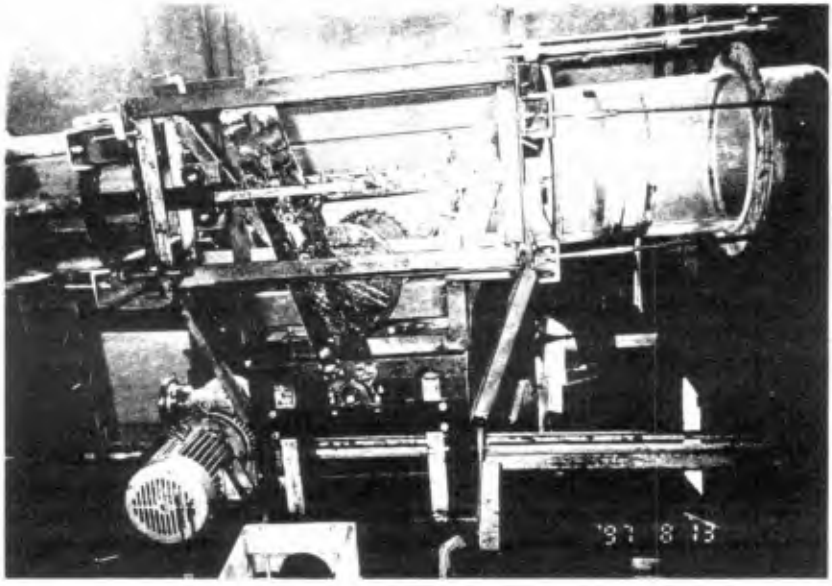

Photo 1 Piston system

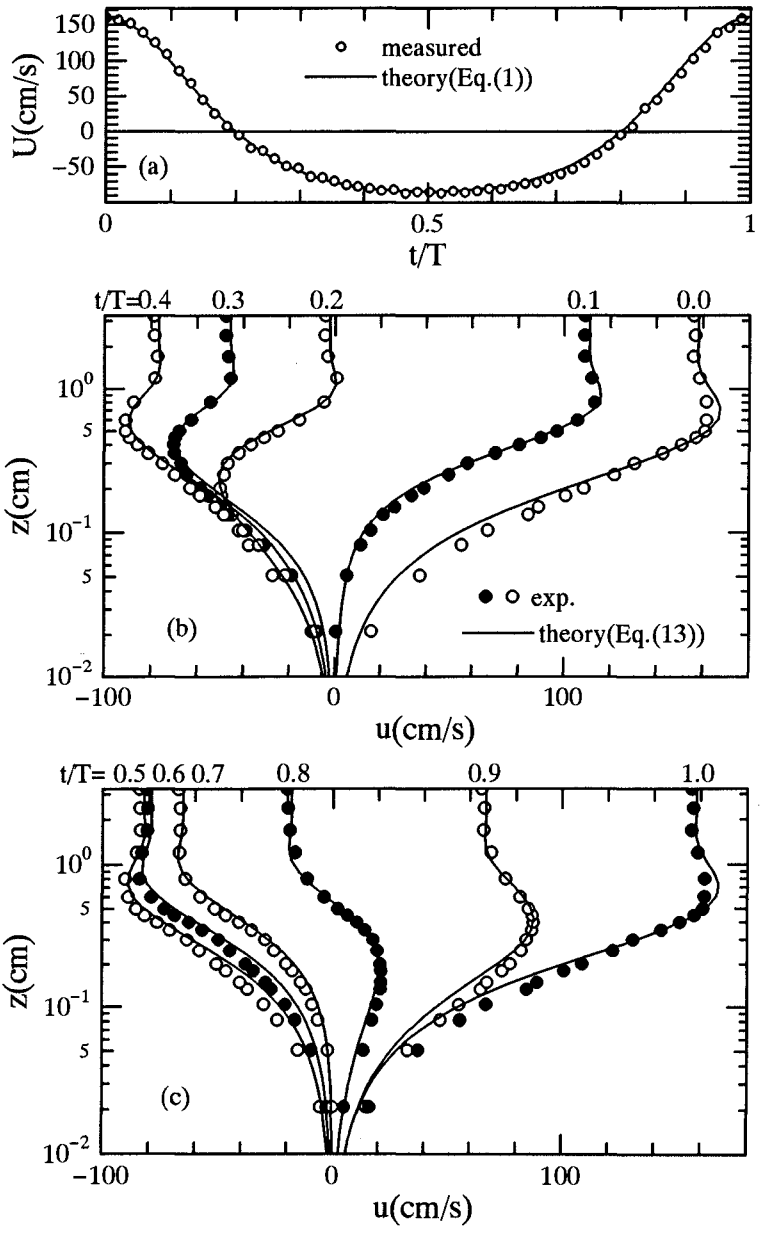

Fig.6 Velocity profile in a wind tunnel

present computation, the total number of terms in Eq.(13), m, is 5 to achieve sufficient accuracy. It is seen that the agreement between the measurement and the theory in Fig.6 is excellent, suggesting the validity of the present generation system.

Figure 7 depicts the time-variation of the wall shear stress from the experiment and the laminar theory,

$$\tau_0(t) = \rho \sum_{n=1}^{m} \sqrt{n\omega\nu}\left\{a_n \sin(n\omega t + \frac{\pi}{4}) + b_n \cos(n\omega t + \frac{\pi}{4})\right\} \tag{15}$$

In the experiment, $\tau_0(t)$ is evaluated by multiplying the measured near-wall velocity gradient to the kinetic viscosity of the fluid. It is seen that the time-variation of the measurement shows reasonable agreement with the theory, although small difference is seen near the peak. As may be recalled, in case of purely sinusoidal wave boundary layer in laminar flow regime, shape of the wall shear stress is also sinusoidal, but there exit a phase difference of $\pi/4$ between free-stream velocity and τ_0. It may be noted that from Eq.(15) that following the same basic principle, every component of the wall stress has a phase lead of $\pi/4$ from the corresponding velocity component. But after the addition of these components with different frequency, the shape of the resultant wall shear stress profile is altogether different from the corresponding free-stream velocity over the wave cycle.

Judging from Figs.6 and 7, it can be concluded that the present generation system works very well for the use of wave boundary layer experiment under non-linear waves.

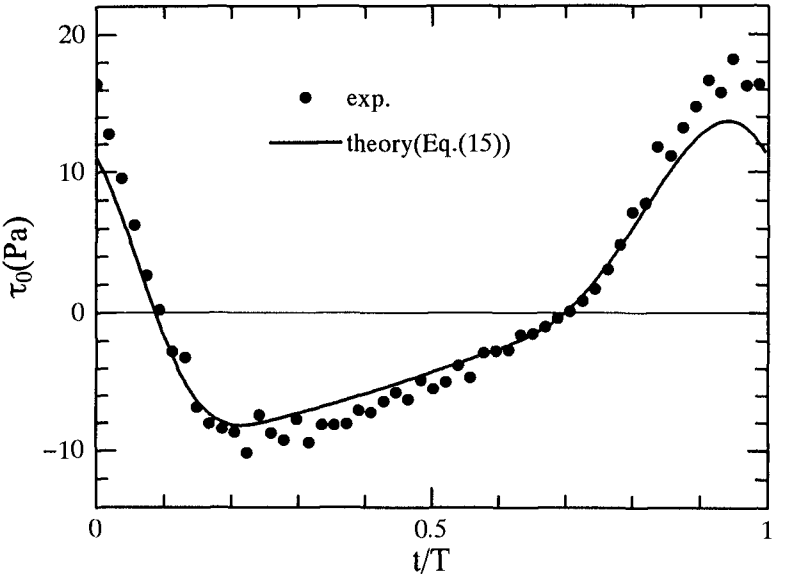

Fig.7 Time-variation of bottom shear stress

Case 2

During the experiment with water as working fluid, it was observed that the temporal free-stream velocity showed slight deviation from Eq.(1). Therefore, it was necessary to open both the valves on top of the risers in order to get the velocity in close agreement with the theory (Fig.8(a)). The velocity profile thus obtained is shown in Fig.8 at selected phases. The laminar solution, Eq.(13), is also plotted in Figs.8(b) and 8(c) along with numerical solution based on k- ε model. Among various versions of k- ε model, Jones and Launder's (1972) low-Reynolds number model is employed in the present study, based on Sana and Tanaka's (1996) comparative study of the existing models. Detailed computation method is already described elsewhere (Tanaka and Sana, 1994, Sana and Tanaka, 1996).

In contrast to Fig.6, the experimental result in Figs.8(b) and 8(c) shows distinct difference from the laminar solution. The velocity profile at the beginning of deceleration phase (t/T=0.0) shows better agreement with k- ε model prediction, especially where the velocity overshooting occurs. But during the course of deceleration, it seems that the model fails to cope with the flow situation. During deceleration, both of the experiment and model show logarithmic behavior, although the boundary layer thickness is different each other. As the flow proceeds to acceleration in the trough phases, the model predictions begin to conform to the data very well. In the next deceleration phase during the trough phase (t/T=0.5-0.7), the model prediction is satisfactory. During the next acceleration phase (t/T=0.8-0.9), an excellent agreement is found between prediction of the model and the experimental data.

Figure 9(a) depicts turbulence intensity measured in an oscillating tunnel. As may be observed around t/T=0.5, turbulence is generated with time near the wall, yet with a lower rate as compared to that in crest period around t/T=0.1. During the trough period, the contours are almost horizontal, suggesting small variation in the turbulence intensity in that region. This is distinct difference from sinusoidal boundary layer and in accordance with what might be anticipated on the basis of the flat free-stream velocity during trough period, where the behavior similar to a steady flow should be observed. The contour plot obtained from the model prediction is shown in Fig.9(b). Since the model provides the total turbulent kinetic energy k, x-direction fluctuating component u' is obtained using Nezu's (1977) expression to correlate k and u' in a steady open channel flow. It is seen that the k- ε turbulence model can very well reproduce the fluctuating velocity near the wall.

Conclusions

The following conclusions can be drawn from this experimental study on non-linear wave boundary layers:

(1) It is confirmed that the generation method of an asymmetric oscillatory flow proposed by Tanaka et al. (1997, 1998) can be effectively utilized in a laboratory experiment for both air and water as working fluid.

(2) The low-Reynolds number k- ε model by Jones and Launder (1972) shows good performance to predict mean velocity profile except decelerating phases under wave crest. As for turbulence intensity in x-direction, the overall agreement is satisfactory between the model prediction and experimental data.

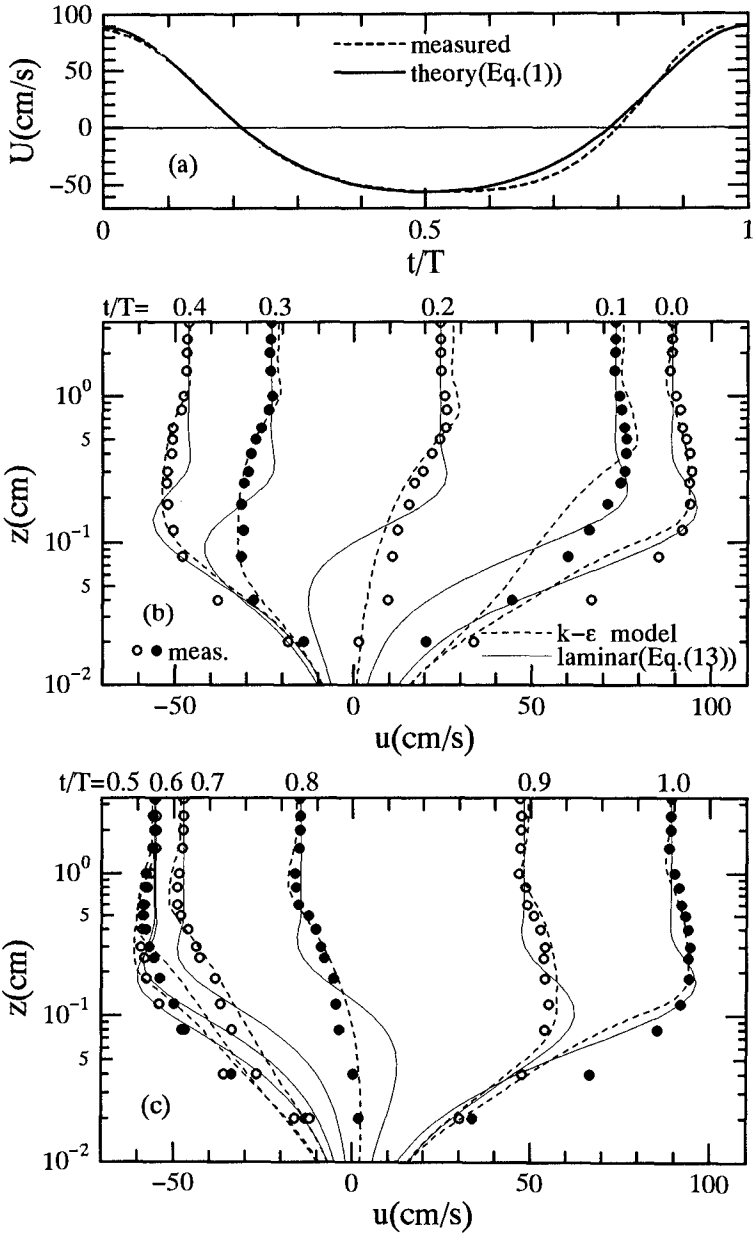

Fig.8 Velocity profile in an oscillating tunnel

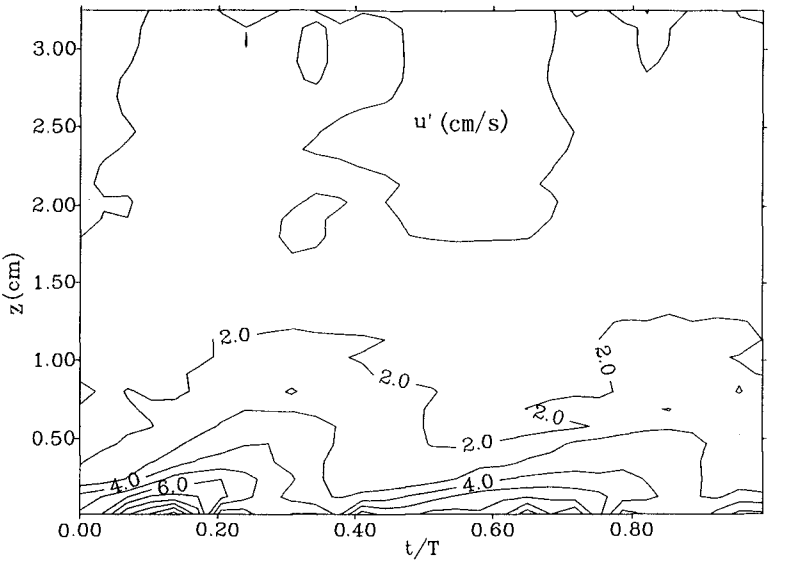

(a) Measurement

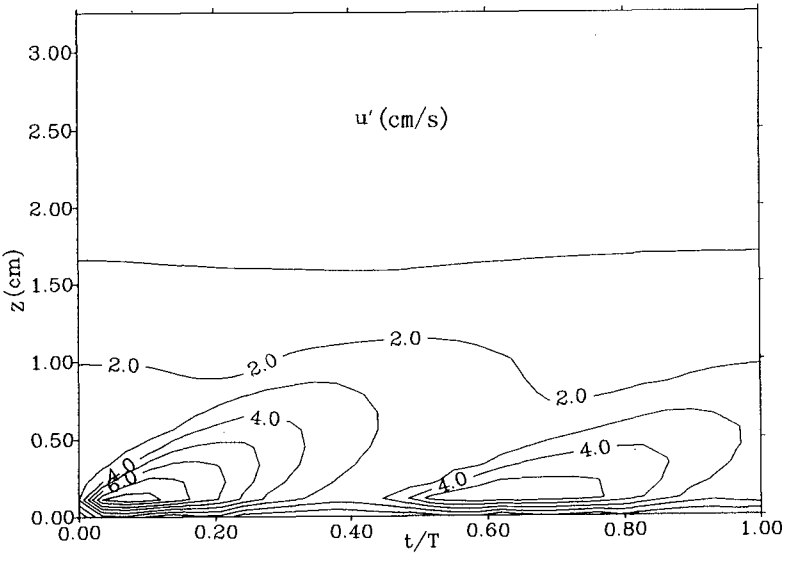

(b) k- ε model computation

Fig.9 Turbulence intensity in an asymmetric wave boundary layer

Acknowledgments

A part of this study was financially supported by Grant-in-Aids of Ministry of Education, Science and Culture, Japan.

References

Dibajnia, M. and Watanabe, A., 1992. Sheet flow under nonlinear waves and currents, *Proceedings of 23rd International Conference on Coastal Engineering*, pp.2015-2028.

Hino, H., Sawamoto, M. and Takasu, S., 1976. Experiments on transition to turbulence in an oscillatory pipe flow, *Journal of Fluid Mechanics*, Vol.75, pp.193-207.

Jones, W.P. and Launder, B.E., 1972. The prediction of laminarization with a two-equation model of turbulence, *International Journal of Heat and Mass Transfer*, Vol.15, pp.301-314.

Jonsson, I.G., 1963. Measurements in the turbulent wave boundary layers, *Proceedings of 10th International Congress IAHR*, pp.85-90.

Nadaoka, K., Yagi, H., Nihei, Y. and Nomoto, K., 1994. Characteristics of turbulent structure in asymmetrical oscillatory flow, *Proceedings of Coastal Engineering*, Vol.41, pp.141-145. (in Japanese)

Nadaoka, K., Nihei, Y., Yagi, H., Y. and Nomoto, K., 1996. Characteristics of turbulent structure in asymmetrical oscillatory flow, *Proceedings of Coastal Engineering*, Vol.43, pp.441-445. (in Japanese)

Nezu, I., 1977. Turbulent structure in open channel flows, Dr. Eng. Dissertation, Kyoto Univ. (in Japanese)

Ribberink, J.S. and Al-Salem, A.A., 1994. Sediment transport in oscillatory boundary layers in case of rippled beds and sheet flow, *Journal of Geophysical Research*, Vol.99, No.C6, pp.12707-12727.

Sana, A. and Tanaka, H., 1996. The testing of low Reynolds number k- ε models by DNS data for an oscillatory boundary layer, *Flow Modeling and Turbulence Measurements VI*, pp.363-370.

Schäffer, H.A. and Svendsen, I.A., 1986. Boundary layer flow under skew waves, *Progress Report, No.64, Inst. Hydrodyn. and Hydraulic Engineering, Tech. Univ. Denmark*, pp.12-23.

Shuto, N., 1974. Nonlinear long waves in a channel of variable section, *Coastal Engineering in Japan*, Vol.17, pp.1-12.

Tanaka, H. and Sana, A., 1994. Numerical study on transition to turbulence in a wave boundary layer, *Sediment Transport Mechanisms in Coastal Environments and Rivers*, pp.14-25.

Tanaka, H., Yamaji, N., Sana, A. and Shuto, N., 1997. A new generation method of asymmetric oscillatory motion simulating cnoidal waves, *Journal of Hydraulic, Coastal and Environmental Engineering JSCE*, Vol.565, No.II-39, pp.111-118. (in Japanese)

Tanaka, H., Yamaji, H., Sana, A. and Shuto, N., 1998. A generation method asymmetric oscillatory motion simulating cnoidal waves, *Coastal Engineering Journal*. (in press)

A 2-DV NUMERICAL SOLUTION FOR THE TURBULENT WAVE BOUNDARY LAYER UNDER BREAKING WAVES

Nguyen The Duy[1], Tomoya Shibayama[2] and Akio Okayasu[3]

Abstract

This paper presents a numerical solution for the bottom boundary layer (BBL) in the surf zone. The upper boundary of the BBL is determined through the solution of a breaking waves model. Different turbulence models have been tested to determine the distribution of turbulent kinetic energy, energy dissipation and eddy viscosity in the BBL. Finally, the vertical profiles of horizontal velocity can be found out through the solution of the governing equations of the BBL.

Introduction

A quantitative study of the hydrodynamics of the bottom boundary layer (BBL) is necessary for determining precisely the near-bottom shear stress, a major driving force in predicting the transport of sediment in coastal areas. Various studies on the mechanics of the wave boundary layers under non-breaking condition have been reported in the literature (e.g. Kajura 1968, Kamphuis 1975, Grant and Madsen 1979, Trowbridge and Madsen 1984, Larson 1995, etc.). Under breaking waves, however, development in the study of the BBL has been limited because of the following unsolved or unsatisfactorily solved problems.

(1) The free stream velocity at the upper edge of the BBL, an important boundary for solving BBL flow, still cannot be determined properly by available 1-D or 2-DH breaking wave models. Outside the BBL, it is necessary to solve a 2-DV breaking wave model in order to determine directly the upper boundary condition of the BBL from computed vertical profile of water particle velocity. For this purpose, the breaking waves model presented by Duy et al. (1996), Duy and Shibayama (1997) has been applied in the present study.

(2) The effect of turbulence induced by waves breaking on the turbulence structure of the BBL is still not understood adequately. In this study, it is assumed that in

[1] Dr. Eng., Dept. of Civil Eng., Ho Chi Minh University of Technology, 268 Ly Thuong Kiet, Q.10, Ho Chi Minh City, Vietnam.

[2] Dr. Eng., Professor, Dept. of Civil Eng., Yokohama National University, Hodogaya-ku, Yokohama 240, Japan.

[3] Dr. Eng., Assoc. Prof., Dept. of Civil Eng., Yokohama National University, Hodogaya-ku, Yokohama 240, Japan.

case of a surf zoue formed by spilling breakers, the transfer of turbulence from the upper layer to the BBL is negligible and therefore the turbulence production resulted from shear is dominant in the BBL.

(3) The lack of reliable measured velocity data that cau be used for verifying a BBL model in the surf zone.

Model formulation

At each time level of computation, a three-step procedure is utilized to solve the 2-DV flow equations for the BBL. This solution procedure is illustrated in the flow diagram below.

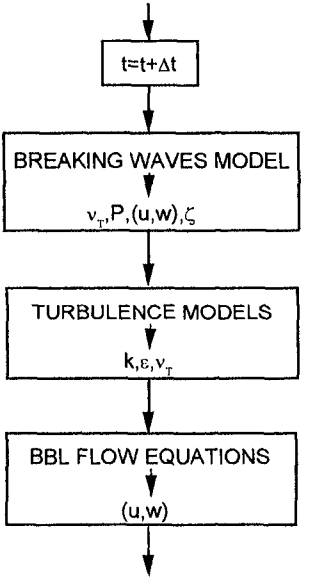

Figure 1. Flow diagram of solution procedure.

- In the first step, the breaking waves model is solved for the water domain outside the BBL (the upper layer) to determine the wave variables in 2-DV plane such as water surface, pressure field and velocity field. The result of this solution provides the values of velocity vectors at the upper boundary of the BBL.
- In the second step, turbulence structure of the BBL is iuvestigated through the solution and comparison of the following turbulence models: eddy viscosity model, k-model and $k\varepsilon$-model. From this solution, it is possible to find out the distribution of eddy viscosity, turbulent kinetic energy and energy dissipation inside the BBL.
- In the final step, the results obtained from the previous two steps are used as input data to solve the governing equations for the BBL. From which, the velocity field in the BBL can be determined.

The governing equations and boundary conditions used in the second and third step of the solution procedure are described briefly as follows.

In a 2-DV plane, the flow in the BBL can be modeled by the following equations

$$\frac{\partial u}{\partial x}+\frac{\partial w}{\partial z}=0 \tag{1}$$

$$\frac{\partial u}{\partial t}+u\frac{\partial u}{\partial x}+w\frac{\partial u}{\partial z}-\frac{1}{\rho}\frac{\partial \tau_{zx}}{\partial z}=\frac{\partial u_e}{\partial t}+u_e\frac{\partial u_e}{\partial x} \tag{2}$$

where (u, w): Reynolds-averaged velocity vector; τ_{zx}: Reynolds shear stress; u_e: free stream velocity. The momentum term due to turbulent motion can be expressed as

$$\frac{1}{\rho}\frac{\partial \tau_{zx}}{\partial z}=\nu_T\frac{\partial}{\partial z}\left(\nu_T\frac{\partial u}{\partial z}\right) \tag{3}$$

In (2), the momentum terms on the right hand side are the forcing function reflecting the process of water motion in the region outside the BBL. Along the edge of the BBL, these momentum terms can be determined by using the 2-DV turbulent flow model for breaking waves developed by Duy et al. (1996).

The boundary conditions for the BBL equations are introduced in the following.

$$u=0,\ w=0 \quad \text{for} \quad z=0 \tag{4}$$

$$u\to u_e,\ w\to w_e \quad \text{for} \quad z\to\infty \tag{5}$$

and at the seaward and shoreward boundary (side boundaries), a logarithmic distribution is assumed for the vertical profile of horizontal velocity in the BBL

$$u=u_e\ln\left(C_1z+C_2\right) \quad \text{for} \quad x=0 \text{ or } x=x_{\max} \tag{6}$$

in which the constants C_1 and C_2 are determined by using the boundary conditions (4) and (5)

$$C_1=\frac{e-1}{\delta} \tag{7}$$

$$C_2=1 \tag{8}$$

where δ is the thickness of the BBL and e the natural logarithmic base.

At the side boundaries, the vertical velocities are determined by substituting Eq. (6) into the mass conservation, Eq. (1), and then solve for w.

In addition to the above boundary conditions, it is necessary to know the distribution of the eddy viscosity in the BBL to solve (1) and (2). Three different solutions of the eddy viscosity are investigated in the present study.

In the first solution, the following equation of the eddy viscosity, or also known as the eddy viscosity model, is applied for the entire boundary layer thickness (e.g., Kajura 1968, Grant and Madsen 1979)

$$\nu_T=\kappa u_* z \tag{9}$$

where κ is the Karman constant (κ=0.4), z the vertical elevation from the bottom and u_* the friction velocity

$$u_*=\sqrt{0.5f_w u_{em}^2} \tag{10}$$

where f_w is the wave friction factor and u_{cm} the maximum horizontal velocity at the upper boundary of the BBL. Eq. (10) expresses a linear distribution of the eddy viscosity inside the BBL. In fact, this time-invariant eddy viscosity has been originally developed to simulate non-breaking wave boundary layers.

The second solution of the eddy viscosity is based on the transport equation for turbulent kinetic energy, or the *k*-equation, which in a 2DV-plane reads

$$\frac{dk}{dt} = \frac{\partial}{\partial x}\left(\frac{\nu_T}{\sigma_k}\frac{\partial k}{\partial x}\right) + \frac{\partial}{\partial z}\left(\frac{\nu_T}{\sigma_k}\frac{\partial k}{\partial z}\right) + \frac{PROD}{\rho} - c_2\frac{k^{3/2}}{l_d} \tag{11}$$

in which

$$\frac{dk}{dt} = \frac{\partial k}{\partial t} + \frac{\partial (uk)}{\partial x} + \frac{\partial (wk)}{\partial z} \tag{12}$$

PROD is the turbulence production, c_2 a constant, and l_d the length scale of turbulence

$$l_d = \kappa \sqrt[4]{c_2}\, z \tag{13}$$

In the *k*-equation, the eddy viscosity is determined by the following expression

$$\nu_T = l_d \sqrt{k} \tag{14}$$

Under breaking waves condition, the turbulence production in the BBL can be assumed to be resulted from two different sources: one is the transfer of breaker-generated turbulence from the upper layer to the BBL, denoted by *TRANS*, and one is caused by shear inside the BBL.

$$PROD = TRANS + \rho \nu_T \left(\frac{\partial u}{\partial z}\right)^2 \tag{15}$$

In case of spilling breakers, as mentioned above, it may be reasonable to assume that

$$TRANS \to 0 \quad \text{for} \quad z \to 0 \tag{16}$$

Therefore, the turbulence production resulted from shear is dominant in the BBL, and Eq. (15) becomes

$$PROD = \rho \nu_T \left(\frac{\partial u}{\partial z}\right)^2 \tag{17}$$

The boundary conditions for the *k*-equation are

$$k = \frac{1}{\sqrt{c_2}} \nu_T \frac{\partial u}{\partial z} \quad \text{for} \quad z = \frac{k_N}{30} \tag{18}$$

and

$$\frac{\partial k}{\partial z} = 0 \quad \text{for} \quad z \to \infty \tag{19}$$

in which k_N is the bed roughness.

Eq. (18) is derived by assuming that there is local equilibrium between production and dissipation close to the bottom. Eq. (19) is based on the assumption (16), i.e. there is no flux of turbulent kinetic energy at the upper boundary.

At the side boundaries, a uniform distribution of turbulent kinetic energy in the x-direction is assumed.

The third solution of the eddy viscosity is based on the transport equations for turbulent kinetic energy and dissipation, or the $k\varepsilon$-equations, which in a 2DV-plane reads

$$\frac{dk}{dt} = \frac{\partial}{\partial x}\left(\frac{\nu_T}{\sigma_k}\frac{\partial k}{\partial x}\right) + \frac{\partial}{\partial z}\left(\frac{\nu_T}{\sigma_k}\frac{\partial k}{\partial z}\right) + \nu_T\left(\frac{\partial u}{\partial z}\right)^2 - \varepsilon \tag{20}$$

$$\frac{d\varepsilon}{dt} = \frac{\partial}{\partial x}\left(\frac{\nu_T}{\sigma_\varepsilon}\frac{\partial \varepsilon}{\partial x}\right) + \frac{\partial}{\partial z}\left(\frac{\nu_T}{\sigma_\varepsilon}\frac{\partial \varepsilon}{\partial z}\right) + c_{1\varepsilon}\varepsilon\frac{\nu_T}{k}\left(\frac{\partial u}{\partial z}\right)^2 - c_{2\varepsilon}\frac{\varepsilon^2}{k} \tag{21}$$

$$\nu_T = c_\mu \frac{k^2}{\varepsilon} \tag{22}$$

where σ_k, σ_ε, $c_{1\varepsilon}$, $c_{2\varepsilon}$ and c_μ are empirical constants.

The boundary conditions for the $k\varepsilon$-equations are

$$k = \frac{1}{\sqrt{c_2}}\nu_T\frac{\partial u}{\partial z} \quad \text{for} \quad z = \frac{k_N}{30} \tag{23}$$

$$\frac{\partial k}{\partial z} = 0 \quad \text{for} \quad z \to \infty \tag{24}$$

$$\varepsilon = (c_2)^{3/4}\frac{k^{3/2}}{\kappa z} \quad \text{for} \quad z = \frac{k_N}{30} \tag{25}$$

$$\frac{\partial \varepsilon}{\partial z} = 0 \quad \text{for} \quad z \to \infty \tag{26}$$

And similar to the k-equation, uniform distributions of k and ε in the x-direction are also assumed at the side boundaries.

In the second and third step of the solution procedure (Figure 1), the governing equations and corresponding boundary conditions are solved by the finite difference method, using a fully implicit scheme. On a sloping bottom, in order to establish a linear numerical mesh in which the grid lines are parallel to the coordinates axes, the (x,z) domain is transformed to the (ξ,η) domain as shown in Figure 2.

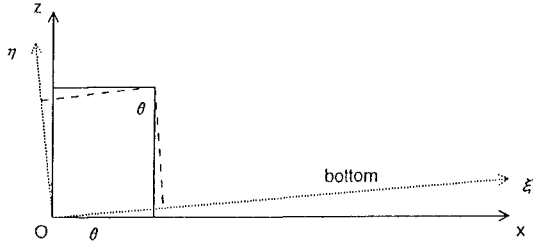

Figure 2. Coordinates transformation for numerical solution.

The functional relationship between the (x,z) and (ξ,η) coordinates systems is expressed by

$$x = \xi \cos\theta - \eta \sin\theta \tag{27}$$

$$z = \xi \sin\theta + \eta \cos\theta \tag{28}$$

From (27) and (28), the Jacobian matrix of the transformation can be determined as follows

$$J = \begin{bmatrix} \frac{\partial \xi}{\partial x} & \frac{\partial \xi}{\partial z} \\ \frac{\partial \eta}{\partial x} & \frac{\partial \eta}{\partial z} \end{bmatrix} = \begin{bmatrix} \cos\theta & \sin\theta \\ -\sin\theta & \cos\theta \end{bmatrix} \tag{29}$$

The first derivatives of the velocity components in the computational domain are then determined by the chain rule, using the Jacobian matrix (29)

$$\begin{bmatrix} \frac{\partial u}{\partial x} & \frac{\partial u}{\partial z} \\ \frac{\partial w}{\partial x} & \frac{\partial w}{\partial z} \end{bmatrix} = \begin{bmatrix} \frac{\partial u}{\partial \xi} & \frac{\partial u}{\partial \eta} \\ \frac{\partial w}{\partial \xi} & \frac{\partial w}{\partial \eta} \end{bmatrix} \begin{bmatrix} \frac{\partial \xi}{\partial x} & \frac{\partial \xi}{\partial z} \\ \frac{\partial \eta}{\partial x} & \frac{\partial \eta}{\partial z} \end{bmatrix} \tag{30}$$

while the time derivative ($\partial/\partial t$) remains unchanged in the transfomed domain.

Numerical results

Some numerical results of the present model are compared with the laboratory data of Cox et al. (1996). In this experiment, an extensively detailed measurement of surf zone hydrodynamics was reported for the case of a spilling breaker. The velocity profiles were measured at different locations in a surf zone by using a laser-Doppler velocimeter. At each location, 30 measuring points were set along the verical line, of which 10 points were located in the near-bottom area. In the experiment, the wave period was 2.2 s, the water depth in the constant depth section was 0.4 m, and the wave height was 17.10 cm at breaking. The 1:35 bottom slope was filled with natural sand of 1.0 mm median grain diameter. The boundary layer thickness was found to be appoximately 1 cm in this experiment.

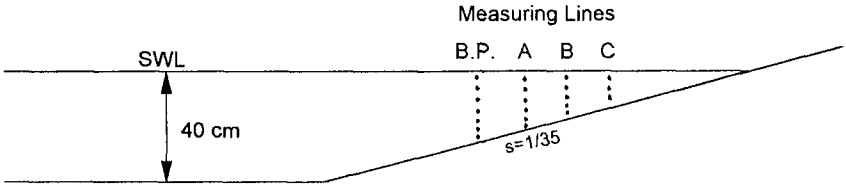

Figure 3. Locations of measuring lines in the surf zone.

In Figure 3, according to the experimental observation, section A is in the transition region where the wave form goes from organized motion to a turbulent bore; and sections B and C are in the inner surf zone where the saw-toothed wave shape is a well-developed turbulent bore.

Figure 4 shows a result obtained in the first step of the solution procedure (Figure 1), that is the time series of horizontal velocity at different positions outside the BBL which are computed by the breaking waves model of Duy et al. (1996). In this figure, the variable X denotes horizontal distance from the shoreline of the still water, subscript "b" denotes the breaking point, and z is the vertical elevation from the

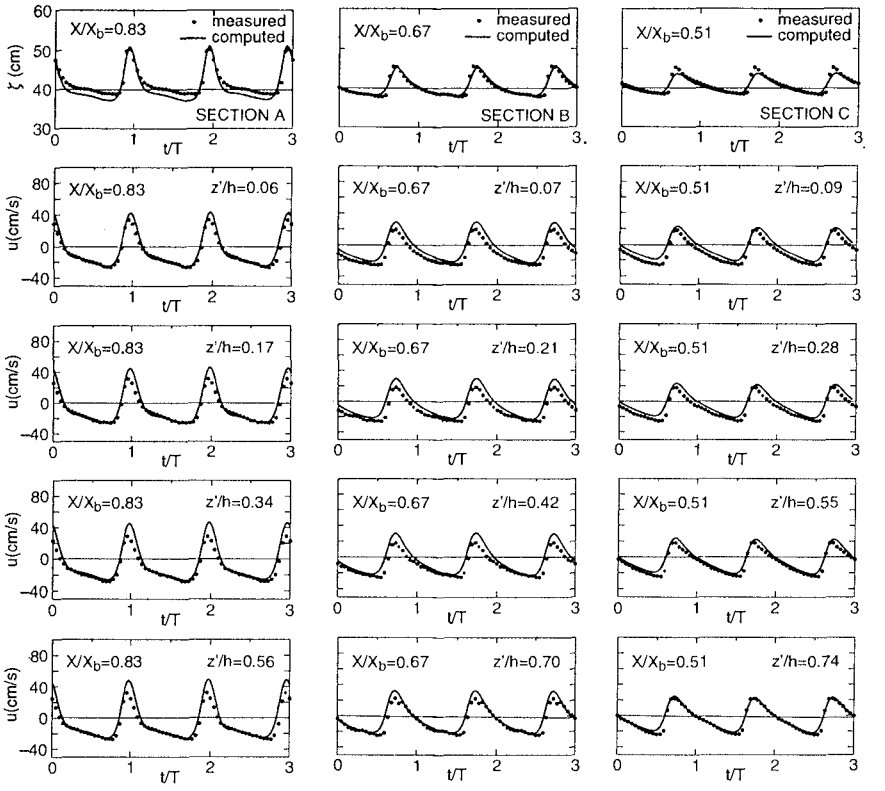

Figure 4. Time series of water surface elevation ζ and horizontal velocity u.

bottom. The comparisons show that the model is capable of simulating the deformation of the velocity profiles as wave propagates shoreward and of producing the high nonlinearity of the velocity profiles in shallow water area. As a general tendency, in the transition region (section A), the model results overestimate the peak values of horizontal velocity at elevations far away from the bottom. At sections in the inner surf zone (sections B and C), reasonable agreements are obtained between the simulated and measured velocities.

In the second step of computational procedure, the turbulence structure of the BBL is examined through the solutions of different turbulence models.

Figure 5 presents the water surface computed by the breaking waves model and the distribution of turbulent kinetic energy in the BBL computed by the k-equation. The wave decay due to energy dissipation in the surf zone can be observed from the surface elevations at different phases. At each phase, it can be seen that the developing cores of k are originated from the bottom and correspond to the locations of wave crests at the water surface. And as wave moves shoreward, the magnitude of k decreases gradually. This distribution pattern of k may be caused by the following: (1) the assumption that turbulence production resulted from shear is dominant in the BBL, and

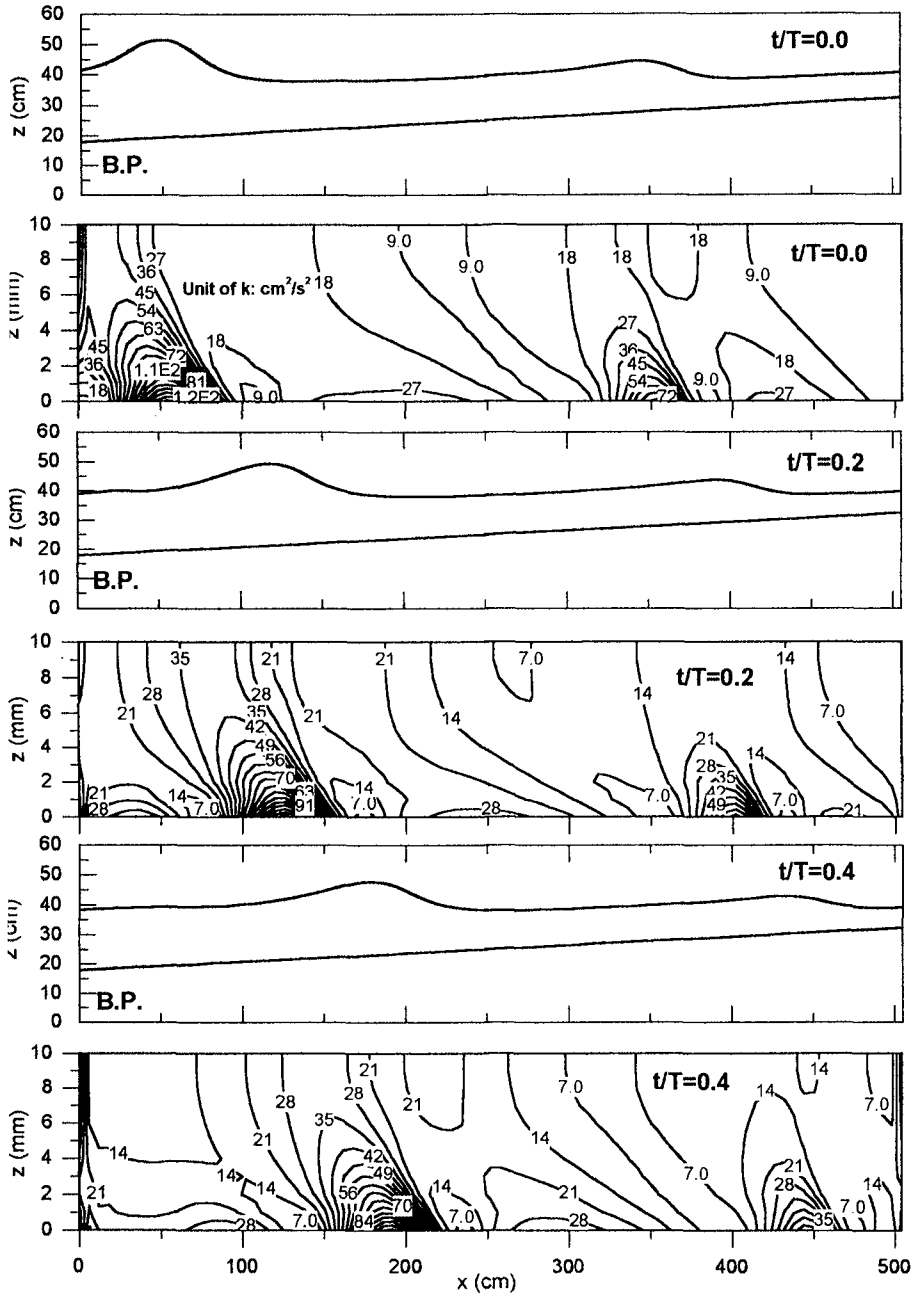

Figure 5. Distribution of turbulent kinetic energy in the bottom boundary layer in a surf zone (solution of the k - equation)

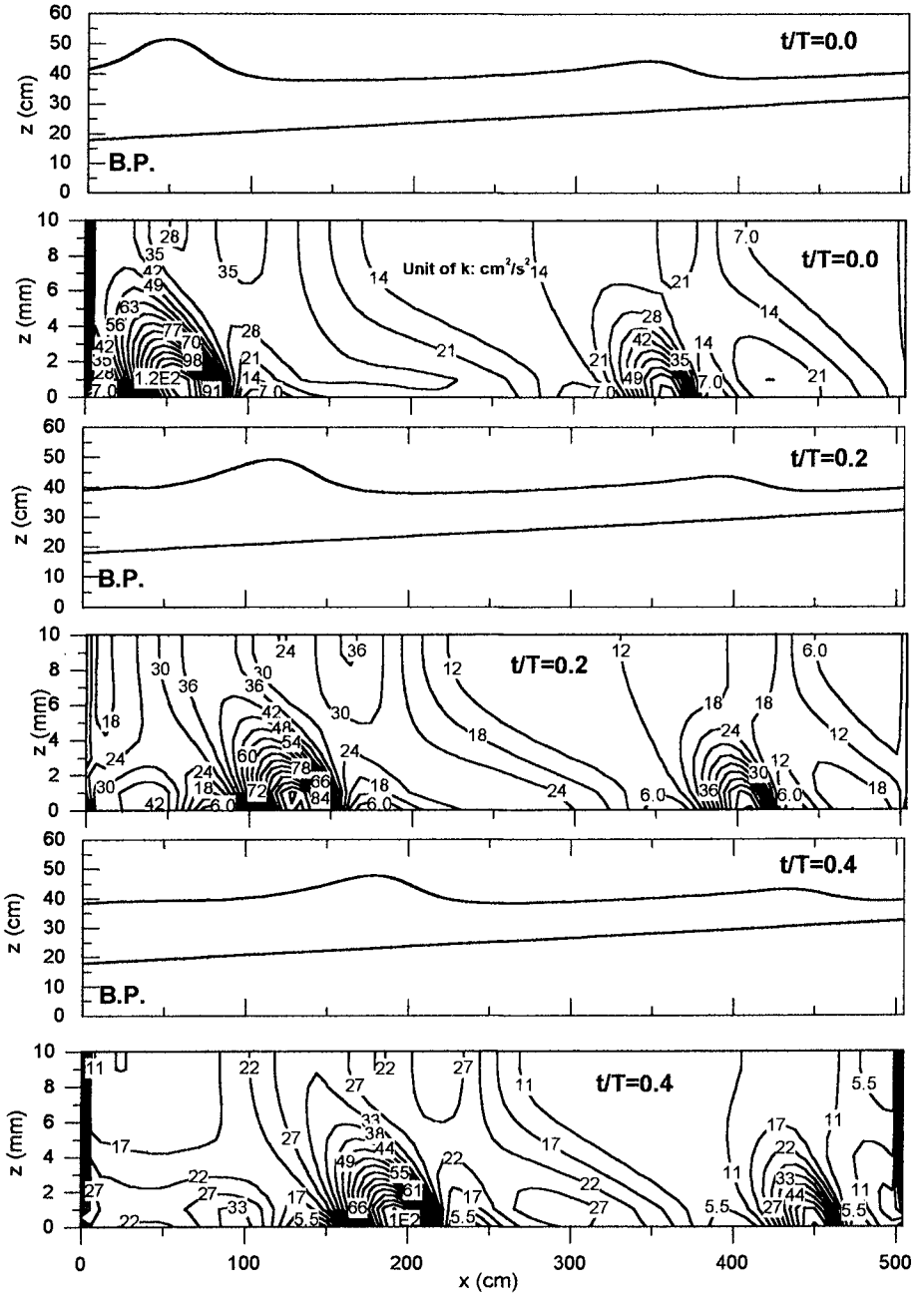

Figure 6. Distribution of turbulent kinetic energy in the bottom boundary layer in a surf zone (solution of the $k\varepsilon$-equations).

(2) the effect of the upper boundary, which is expressed by the forcing function on the right hand side of Equation (2).

Figure 6 also presents the distribution of turbulent kinetic energy in the BBL for different phases, but from the solution of the $k\varepsilon$ - equations. Very similar distributions of k can be seen for the solutions of the k-equation and the $k\varepsilon$ - equations. Quantitatively, the differences in k magnitude between the above two models are less than 5%.

The numerical results of turbulent kinetic energy are compared with laboratory data as shown in Figure 7. The time series of k at different positions in the BBL again indicate that the results of the k-equation and the $k\varepsilon$ - equations are very similar. The comparison with laboratory data shows that the agreement between computed and measured values is not good around the peak of k. At other phases of the wave period, reasonable agreements are obtained.

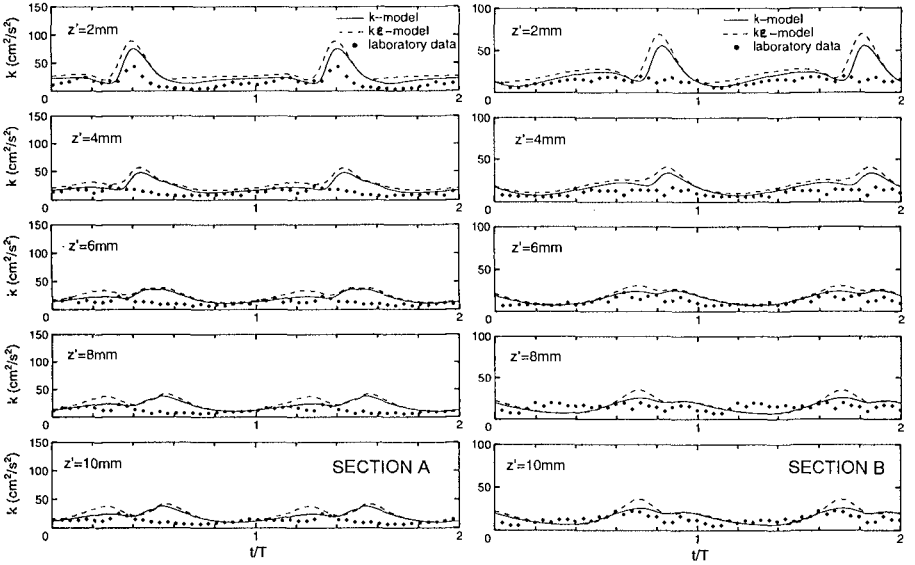

Figure 7. Time series of turbulent kinetic energy in the bottom boundary layer.

Figure 8 also plots a result of the $k\varepsilon$ - equations, that is the distribution of energy dissipation, ε, in the BBL. Similarly to the distribution of k, zones of large energy dissipation are also originated from the bottom and correspond to the locations of wave crests at the water surface. This means that large dissipation occurs where there exists high turbulent kinetic energy. The magnitude of energy dissipation is smaller at locations closer to the shoreline. With known distributions of k and ε, the distribution of eddy viscosity in the BBL can be determined as shown in Figure 9.

With known distribution of the eddy viscosity, Equations (1) and (2) can be solved to determine the velocity field in the BBL. Figure 10 presents the computed vertical profiles of horizontal velocities inside the BBL corresponding to different distributions of the eddy viscosity. There are certain differences between these three velocity profiles. However, they exhibit the similar features as follows: (1) when the flow

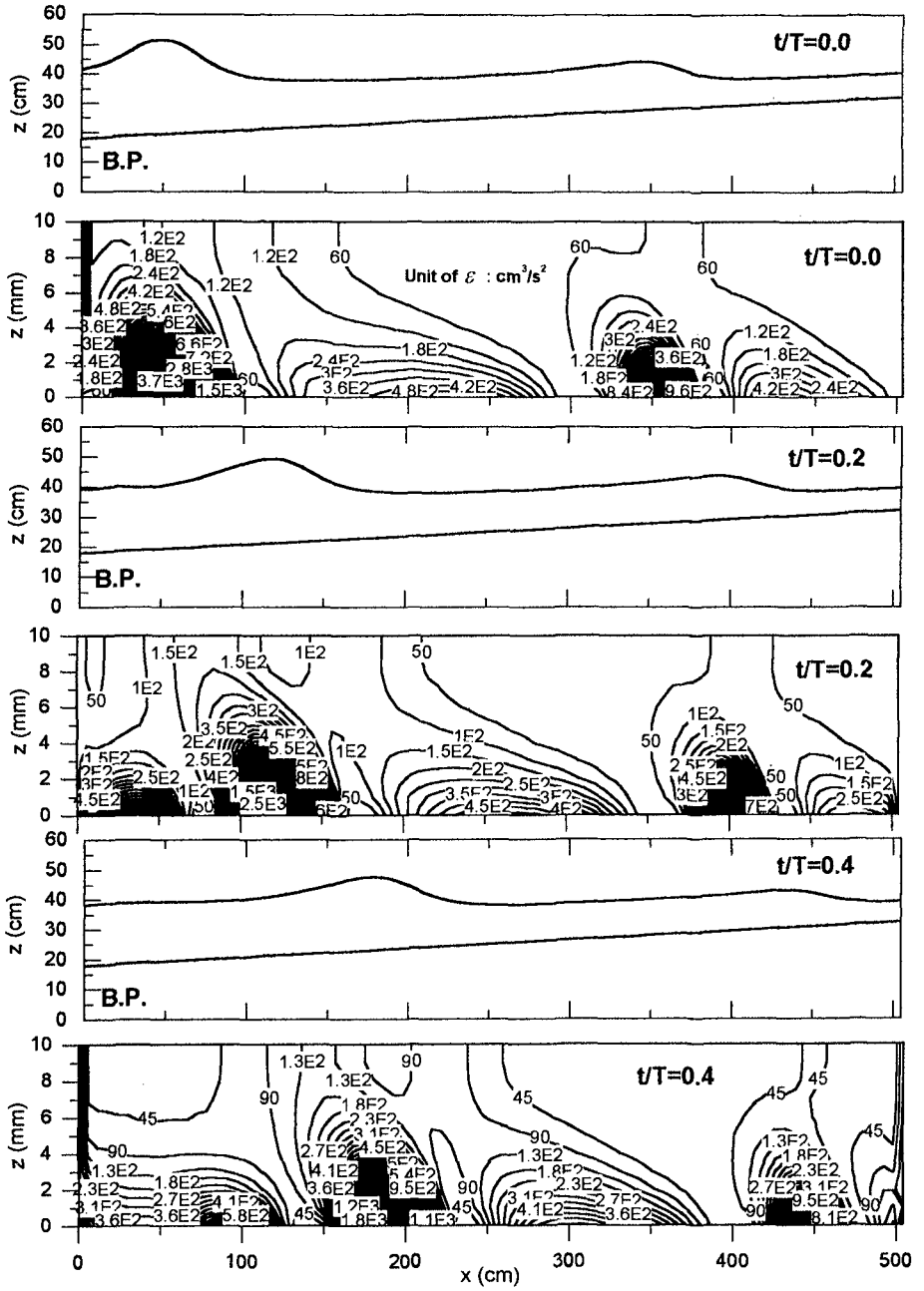

Figure 8. Distribution of energy dissipation in the bottom boundary layer in a surf zone (solution of the $k\varepsilon$-equations).

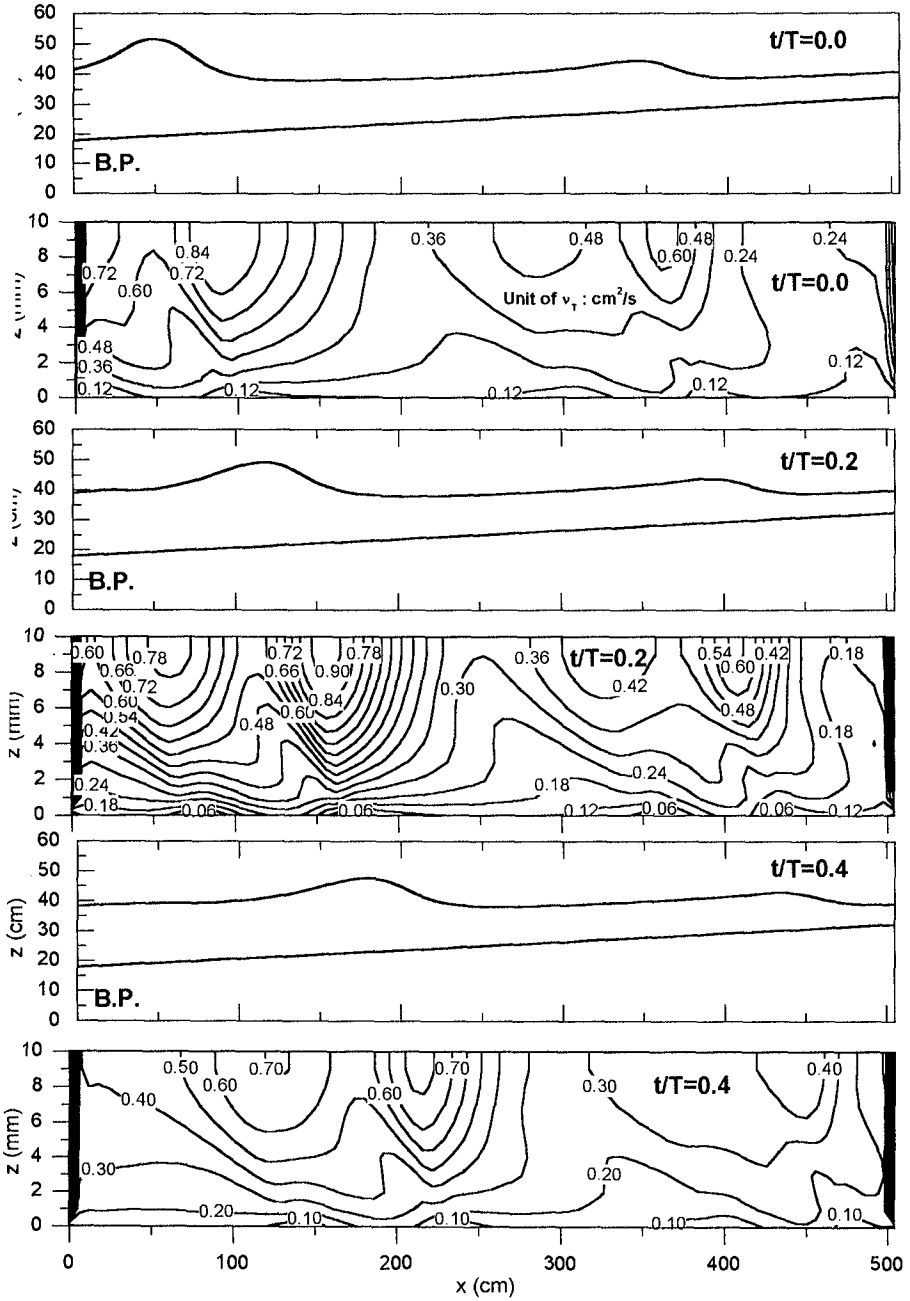

Figure 9. Distribution of eddy viscosity in the bottom boundary layer in a surf zone (solution of the $k\varepsilon$ - equations)

changes direction, the near-bottom velocity always turns before the free stream velocity, both in the increasing and the decreasing stages of the water surface; this indicates a phase difference between the near-bottom velocity and the free stream velocity, a typical feature of oscillatory boundary layers that has been also observed for non-breaking waves, (2) as a result of the nonlinearity and asymmetry of the time variation of the water surface and the free stream velocity in the surf zone, the velocity amplitude of the shoreward flow is larger than that of the seaward flow, and (3) the velocity amplitude is largest at certain elevation inside the BBL, not at the upper edge of the layer. The comparison with laboratory data show that the numerical model is capable of predicting reasonably the velocity profiles inside the boundary layer for most phases of the wave period. However, at the phases when the velocities of the seaward flow reach their maximum values, the slope of the measured velocity profile at the area very close to the bottom tends to decrease and the present model fails to predict such change.

For the specific comparison shown in Figure 10, the calculation of the standard deviations indicates that when solving equations (1) and (2) with the eddy viscosity computed by the k-model, best agreement is obtained between the simulated velocity profiles and laboratory data.

Conclusions

Under breaking waves condition, the flow inside the BBL was modeled by solving numerically the 2-DV governing equations for the bottom boundary layer for the entire surf zone. The comparisons with laboratory data show that the numerical model is capable of predicting reasonably the distribution of turbulent kinetic energy as well as the velocity profiles inside the boundary layer for most phases of the wave period.

References

Duy, N.T., T. Shibayama, and A. Okayasu, A 2-DV numerical solution for the turbulent wave boundary layer under breaking waves, in *Book of Abs. of 26th Coastal Engineering Conference,* 550-551, ASCE, Copenhagen, 1998.

Duy, N.T. and T. Shibayama , A convection-diffusion model for suspended sediment in the surf zone, *J. of Geophys. Res., 102* (C10), 23169-23186, 1997.

Duy, N.T., T. Shibayama, and A. Okayasu, A turbulent flow model for breaking waves, in *Proceedings of 25th Coastal Engineering Conference,* 200-212, ASCE, Orlando, 1996.

Cox, D.T., N. Kobayashi, and A. Okayasu, Experimental and numerical modeling of surf zone hydrodynamics, *Res. Report No. CACR-95-07,* Center for Applied Coastal Res., Univ. of Delaware, 1996.

Grant, W.D. and O.S. Madsen, Combined wave and current interaction with a rough bottom, *J. of Geophys. Res., 84*(C4), 1797-1808, 1979.

Kajura, K., A model of the bottom boundary layer in water waves, *Bull. Earthquake Res. Inst., 46,* 75-123, 1968.

Larson, M., Closed-form solution of turbulent wave boundary layer, *Proc. of Coastal Eng., JSCE, 42*(1), 26-30, 1995.

Trowbridge, J. and O.S. Madsen, Turbulent wave boundary layers, 1, Model formulation and first-order solution, *J. of Geophys. Res., 89*(C5), 7989-7997, 1984.

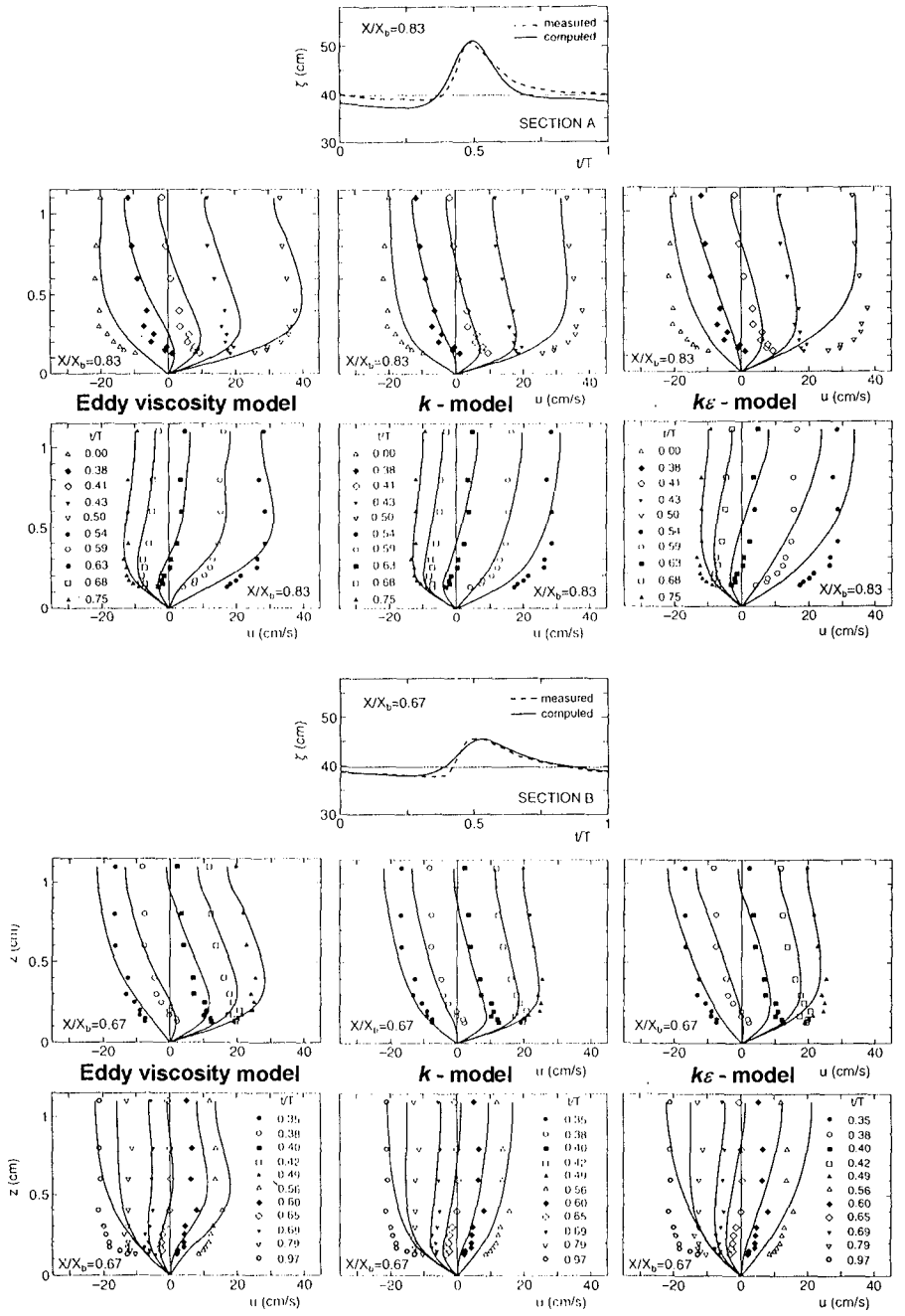

Figure 10. Comparison of vertical profiles of horizontal velocity inside the bottom boundary layer for the use of different distributions of the eddy viscosity.

WAVE MODELLING IN THE WISE GROUP

L. Cavaleri[1] and L.H. Holthuijsen[2]

ABSTRACT

The WISE group is a group of investigators who have agreed to jointly (i) study the physical processes affecting waves in shallow water, (ii) develop numerical codes to explicitly represent these processes in operational models and (iii) verify these wave models in real coastal conditions. The group meets once per year in Europe or North America to discuss progress and coordinate future plans. Since the first meeting in 1993, interesting results have been obtained in all of the three aspects, including operational third-generation spectral wave models for shallow water (one of which has been released in public domain).

INTRODUCTION

When in 1992 the highly successful third-generation wave model WAM for ocean applications (WAMDI group, 1988; Komen et al., 1994) was completed, several members of the WAM group turned their attention to coastal regions where of course they encountered coastal engineers with their large diversity of wave models notably the second-generation HISWA model (Holthuijsen et al., 1988). In the following year, these WAM members and members of the HISWA group and others met and decided to jointly approach the study of Waves In Shallow water Environments (WISE). In this first meeting the WISE group agreed to develop (operational) wave models for coastal regions in which all relevant physical processes would be represented explicitly. Three tasks were correspondingly defined: (i) to study the physical processes affecting waves in shallow water, (ii) to develop numerical codes to represent these processes in operational models and (iii) to verify these wave models in real coastal conditions. We wish to emphasize that the WISE group does not necessarily exhaust all the activities in the field. However, it includes a fairly large and comprehensive part of it.

---

[1] Istituto Studio Dinamica Grandi Masse, 1364 San Polo, 30125 Venice, Italy

[2] Delft University of Technology, Department of Civil Engineering and Geosciences, Stevinweg 1, 2628 CN Delft, the Netherlands

THE WISE GROUP

The WISE group is an informal group of some 50 active members (individuals) from some 15 countries, mostly from Europe and N. America but also from Australia, Japan, S. America and the Middle East. The home institutions of these members are both public and private with a wide range of interests from applied research to daily marine operations (e.g., ministries, harbour authorities, army & navy, universities, research institutions, consultants). The WISE group as a whole is coordinated by the present authors. The group meets once every year, alternating between Europe and N. America. Meetings were held in Thessaloniki (Greece, 1993), Ensenada (Mexico, 1995), Venice (Italy, 1996), San Francisco (USA, 1997) and Leuven (Belgium, 1998). The next meeting shall convene in Annapolis (USA, 1999). The WISE group has three working groups corresponding to the above three tasks. Each group communicates and coordinates common interests (e.g., joint funding, exchange of visiting scientists and students, computer codes and observational data). During the meetings, scientific and operational progress in each group is reported in plenary meetings which are also used to discuss common interests such as large-scale joint efforts, funding opportunities and sharing of data and computer codes. The WISE meetings are organized in a very informal way, without any written report or proceedings, and with an open continuous discussion during and after the individual presentations. The latest findings are regularly shown at the meeting for constructive discussion about future steps. The WISE group as such is not funded by any agency but some (subgroups of) WISE members are funded contingent on their participation in the WISE group and their willingness to share results with other WISE members.

SHALLOW-WATER WAVE MODELS

Two families of numerical wave models can be used effectively in shallow-water. These are (a) phase-resolving models which are based on vertically integrated, time-dependent mass and momentum balance equations and (b) phase-averaged models, which are based on a spectral energy (or action) balance equation. The phase-resolving models require a spatial resolution that is a small fraction of the wave length. They are therefore limited to relatively small areas of the order of a dozen wave lengths (i.e. order of 1 km). The phase-averaged models do not require such fine resolution so that they can be used in much larger areas, the limitation being the size of the ocean basin (with the conventional resolution of 50 - 100 km for ocean applications). The reason for using both models is that some processes cannot be adequately handled in one or the other. For instance, diffraction and triad wave-wave interactions can at present not or only approximately be modeled in phase-averaged models whereas wind-generation cannot be modeled in phase-resolving models with any operational feasibility. Since the first WISE meeting in 1993, the role of these types of models in the group has evolved. The interest of most WISE members is aimed at the region between the deep ocean and the surf zone (it includes islands, shoals, tidal flats and estuaries; e.g., Fig. 1). This has resulted in a support-oriented role of the phase-resolving models (source of basic results) and an operationally-oriented role for the phase-averaged models (source of operational products). It must be emphasized that this evolution in the WISE group does not distract from the operational importance of the phase-resolving models in small-scale areas where they may well perform better than any phase-averaged model (in particular when diffraction is important).

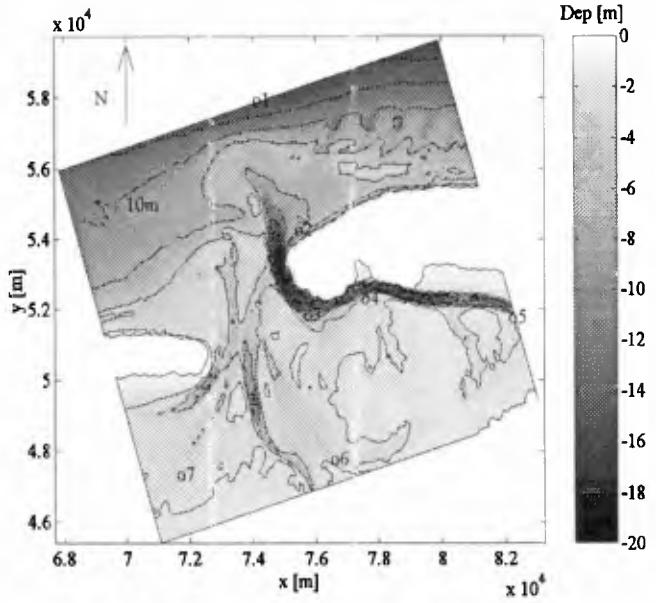

Fig. 1 An example of the type of area of interest to the WISE group: the Norderneyer Seegat (Germany). Depth contour lines with 2 m interval.

Phase-averaged energy balance models are often formulated in terms of the two-dimensional energy density varying in spectral space, geographic space and time, $E(\sigma,\theta;x,y,t)$. The energy balance can then be written as (e.g. Hasselmann et al., 1973):

$$\frac{\partial}{\partial t}E + \frac{\partial}{\partial x}c_x E + \frac{\partial}{\partial y}c_y E + \frac{\partial}{\partial \sigma}c_\sigma E + \frac{\partial}{\partial \theta}c_\theta E = S \qquad (1)$$

The first term in the left-hand side of this equation represents the local rate of change of energy density in time, the second and third term represent propagation of energy in geographical space (with propagation velocities c_x and c_y in x- and y-space, respectively). The fourth term represents shifting of the relative frequency due to (time) variations in depths (with propagation velocity c_σ in σ-space). The fifth term represents depth-induced refraction (with propagation velocity c_θ in θ-space). The expressions for these propagation speeds can be taken from linear wave theory (e.g., Mei, 1983; Dingemans, 1997). Interactions with ambient currents are readily included by extending all of these propagation speeds consistent with linear wave theory and by replacing energy density in the balance equation by action density (defined as the energy density E divided by the relative frequency σ). This formulation is for Cartesian coordinates. It is readily changed into a formulation in spherical coordinates for applications on oceanic scales. The term S ($=S(\sigma,\theta)$) at the right hand side of the action balance equation is the source term in terms

of energy density representing the effects of generation, dissipation and nonlinear wave-wave interactions.

The most important phase-resolving models are Boussinesq models. These are essentially wave propagation models without source terms and they are commonly formulated in terms of the surface elevation and some depth-averaged velocity (the long-wave equations corrected for the vertical velocity distribution), e.g.:

$$\frac{\partial \eta}{\partial t} + \frac{\partial \{(h+\eta)u_x\}}{\partial x} + \frac{\partial \{(h+\eta)u_y\}}{\partial y} = 0$$

$$\frac{\partial u_x}{\partial t} + u_x\frac{\partial u_x}{\partial x} + u_y\frac{\partial u_x}{\partial y} = -g\frac{\partial \eta}{\partial x} + \sum C_x \qquad (2)$$

$$\frac{\partial u_y}{\partial t} + u_x\frac{\partial u_y}{\partial x} + u_y\frac{\partial u_y}{\partial y} = -g\frac{\partial \eta}{\partial y} + \sum C_y$$

in which η is the sea surface elevation, h is mean water depth, u_x and u_y are the depth averaged velocity components in x- and y-direction respectively, g is gravitational acceleration and $\sum C$ is the sum of all correction terms to represent effects of the vertical velocity distribution. Some Boussinesq models include processes of dissipation by adding particular boundary conditions at the surface, notably a roller to represent depth-induced breaking (e.g. Schäffer et al., 1993).

Recent developments which integrate the two approaches of the energy balance and the Boussinesq models are reported below.

ACHIEVEMENTS

Most of the progress in task (i) of WISE has come from the phase-resolving models, providing input for the development of the phase-averaged models. The most fundamental development here has been an explicit formulation for the evolution of wave phases in shallow water which can be used in energy balance models. It involves the introduction of the bispectrum. Representing the random surface elevation in the Boussinesq equations as the sum of a large number of harmonic components with complex amplitudes eventually leads to evolution equations for amplitudes and biphases (or the bispectrum). The bispectrum $B(\sigma_1,\sigma_2)$ is defined as the Fourier transform of the third-order correlation function $R(\tau_1,\tau_2)$, analogous to the definition of the energy density spectrum $E(\sigma)$ which is defined as the Fourier transform of the second-order correlation function $R(\tau)$:

$$E(\sigma) = \int_{-\infty}^{+\infty} R(\tau)\exp(-i\sigma\tau)\,d\tau$$
$$B(\sigma_1,\sigma_2) = \int_{-\infty}^{+\infty} R(\tau_1,\tau_2)\exp[-i(\sigma_1\tau_1+\sigma_2\tau_2)]\,d\tau_1\,d\tau_2 \qquad (3)$$

where τ, τ_1 and τ_2 are time lags. The essence of the bispectrum is that it represents the coupling between triads of wave components with phases φ_l, φ_m and φ_{l+m}. Madsen and Sørensen (1993) thus obtained a discrete spectral version of the (phase-resolving) Boussinesq model which explicitly formulates the triad wave-wave interactions. In deep water these interactions can be ignored but in shallow water they often generate a

secondary, high-frequency peak in the wave spectrum. This spectral Boussinesq model is phase-resolving in the sense that the phases of the wave components are an integral part of the formulation (in contrast to the random-phase assumption in phase-averaged models). Because of its spectral nature, it allows a blending with phase-averaged models in a hybrid approach: the energy balance equation (partially dependent on the biphases) can be supplemented with a phase evolution equation (which in turn depends on the energy spectrum). The first step in implementing this explicit formulation of triad interactions in a phase-averaged model was taken by Eldeberky and Battjes (1995). They used an approach somewhat similar to the discrete interaction approximation (DIA) of the quadruplet wave-wave interactions of Hasselmann et al. (1985) for deep water. Eldeberky and Battjes consider only self-self triad interactions for uni-directional waves in their model (the lumped triad approximation, LTA, Eldeberky, 1996) and they avoided the use of an explicit phase-evolution equation by locally estimating the biphase $\varphi_l + \varphi_m - \varphi_{l+m}$ from the local wave steepness and local relative water depth (Ursell number). The next step, i.e. to fully blend the spectral energy balance model with a bispectral model has been taken by Herbers and Burton (1997). They explicitly compute the biphase and the energy density of short-crested waves on a plane beach in the absence of generation and dissipation. It should be relatively straightforward to expand this propagation model to arbitrary bathymetry. But adding source terms to represent the effect of generation and dissipation of wave energy on the biphase seems difficult.

Another phase-resolving model, the mild-slope equation (Berkhoff, 1972) is the basis for attempts to include diffraction in phase-averaged models. The essence is that diffraction modifies the conventional dispersion relationship from the linear wave theory and consequently the refraction term in the phase-averaged models (the propagation velocity c_θ in θ-space, Booij et al., 1997; Rivero et al., 1997):

$$c_\theta = \frac{c_g}{k}\frac{\partial k}{\partial m} + \frac{c_g}{2(1+\delta)}\frac{\partial \delta}{\partial m} \tag{4}$$

where $\delta = \nabla\cdot(cc_g\nabla a)/k^2cc_g a$ and in which k is the separation constant (e.g. Dingemans, 1997), determined from linear wave theory with $\sigma^2 = gk\tanh kd$ (normally referred to as the wave number $2\pi/L$ where L is the wave length but not in this context where the difference is essential). The phase speed is c, the group velocity is c_g and m is the direction normal to the wave direction. The first term in the right-hand side of Eq. (4) is the conventional refraction representation and the second term is obviously the diffraction addition in terms of the amplitude a of a harmonic wave. A spectral formulation of diffraction (i.e. in terms of energy or action density) is not available. Since the second-order derivatives in the expression for δ are linear in amplitude, an ad-hoc approach would be to replace the amplitude by the square root of energy density $E = E(\sigma,\theta)$ per spectral wave component $\delta \approx \nabla\cdot(cc_g\nabla\sqrt{E})/k^2cc_g\sqrt{E}$. Preliminary attempts to compute diffraction in this way are being made (Booij et al., 1997; Rivero et al., 1997), but an adequate numerical formulation has not yet been developed.

Progress with phase-averaged modelling in this task (i) as been mostly in depth-induced breaking. It has been observed in laboratory conditions (e.g., Battjes and Beji, 1992; Vincent et al., 1994) that depth-induced wave breaking of waves with a unimodal spectrum hardly affects the shape of the spectrum (the changes in spectral shape are mostly due to triad wave-wave interactions). This has led to a simple spectral version

(Eldeberky and Battjes, 1995) of an earlier expression for the overall dissipation of waves breaking in shallow water that is based on a bore model (Battjes and Janssen, 1978; Thornton and Guza, 1983). Outside the WISE group Elgar et al. (1997) have shown with a detailed analysis of observations that the dissipation is often proportional with the square of the frequency. But the effect of this on the spectrum seems often to be masked by the simultaneous effects of triad wave-wave interactions (Chen and Guza, 1997). More observations in the surf zone will further contribute to the understanding of this phenomenon.

In task (ii) the main progress has been achieved with new numerical codes of phase-averaged models and adaptations of the WAM code. A serious problem with the codes of phase-averaged ocean wave models such as the WAM model (but also similar third-generation models such as the WAVEWATCH model, Tolman, 1991) for applications in shallow water is that their numerical schemes are explicit. This implies that they are subject to the Courant criterion of numerical stability: the time step in the computations is limited by the spatial resolution of the model. In open ocean applications this is usually not a problem (the spatial resolution is of the order of 100 km and the propagation time step is of the order of 15 min). For coastal applications however this is a problem because the required spatial resolution is often of the order of 100 m or less and the corresponding time step would be about 10 s or less in water of 10 m depth. This is operationally unacceptable and new ways for integrating the energy balance have to be found. One successful optimization has been to use a larger time step for integrating the physical processes than for wave propagation (the WAVEWATCH model, Tolman, 1991; the WAM model, Luo et al., 1997). This permits reasonably efficient computations down to a spatial resolution of about 1 km (in particular on vector machines, as these models vectorize well). Another attempt is being made with a hybrid scheme: piecewise propagation along rays between grid points (in the TOMAWAC model of Benoit et al., 1996). This numerical scheme is unconditionally stable but time steps larger than corresponding to the spatial resolution (i.e. $\Delta t > \Delta x / c_g$) ignore the variations in the physical processes at that spatial resolution since spatial variations in the processes are not considered within the time step Δt. This approach is therefore still subject to the Courant criterion (for reasons of spatial resolution of the physical processes rather than numerical stability). An implicit scheme that avoids the stability problem has been developed by Booij et al. (1996) in their SWAN model. It sweeps through the computational area in four 90° quadrants with an upwind scheme that is unconditionally stable and does not suffer from the limitation of the hybrid approach. However, the present implementation is based on a first-order, upwind scheme which is rather diffusive. This seems acceptable for small-scale regions (25 km or less) but it needs to be replaced by a higher-order scheme for larger scales. It operates on arbitrarily small spatial resolution (varying from 1 km to 10 m in field conditions to 0.1 m in laboratory conditions). A third-order upwind scheme is presently being developed in SWAN for Cartesian and spherical coordinates (which would allow long-distance propagation over the oceans). The TOMAWAC model and the SWAN model are extensions of the WAM model in the sense that they supplement the processes that are represented in the WAM model (Cycles 3 and 4 of that model) with the LTA of the triad wave-wave interactions, spectral depth-induced wave breaking and several options for bottom friction. Vectorization has not been considered in the design of SWAN as it is aimed at relatively small (nonvectorizing) computers. Like the WAM model, to all

intents and purposes the SWAN model is available in the public domain (home page, http:// swan@ct.tudelft.nl).

To validate numerical wave models that are being developed, a standard test bank is under construction containing academic cases of wave propagation in deep and shallow water with and without ambient currents for which analytical solutions are available. Real field cases with detailed observations are also included. Some are fairly complex (e.g., tidal inlets), others are sufficiently simple that they can be generalized (e.g. idealized fetch-limited wave generation).

The wave models often need coupling to other models, either to be driven by models such as atmospheric and circulation models or to drive other models such as circulation models (with wave induced radiation stresses) and morphodynamic or ecological models. Also, some wave models need to be nested into other wave models to achieve high-resolution results or to shift to other physical processes (e.g. to include diffraction). Work in these aspects is being carried out at several levels in the WISE group. From a scientific point of view the effect of wind variations in coastal regions is being investigated by coupling coastal atmospheric models with coastal wave models (in particular orographic and boundary-layer effects along mountainous coastlines and behind barrier islands). The effects of tidal currents on the coastal wave climate are similarly investigated by coupling coastal wave models with tide-driven coastal circulation models. To numerically accommodate such interactions with circulation models, the TOMAWAC model is formulated on a triangular grid and the SWAN model has recently been adapted to operate on a non-orthogonal curvi-linear grid. To carry out computations from large scale to small scale, the SWAN model can be nested into the WAM model (SWAN accepts output directly from the WAM model; Luo and Flather, 1997). To pre- and post-process the input and output of such sets of models (both numerically and graphically), dedicated tools are being developed based on ARCINFO (Kaiser, 1994), ARCVIEW and MATLAB.

In task (iii) a number of fairly large field campaigns has been carried out with very useful results. A most interesting field campaign was carried out in nearly ideal shallow-water generation conditions in Lake George in Australia (e.g. Young and Verhagen, 1996). The observations of this campaign provide much needed characteristics of the wind-induced growth of waves in limited water depth. It has already served (and will continue to do so) to verify or calibrate models of the WISE group. Several other large field campaigns have been executed off fairly open coasts along the east coasts of the USA and England and along the rather convoluted coast in the north of the Netherlands and Germany. It is expected that the wave models of WISE members will be verified against these observations. Such verification has already been carried out for the SWAN model (Figs. 2 and 3). The rms-error of the significant wave height and mean wave period computed with SWAN in these (and other, similar) conditions was typically about 10% of the incident values (note that locally the relative error can be much larger as the local waves may be much lower).

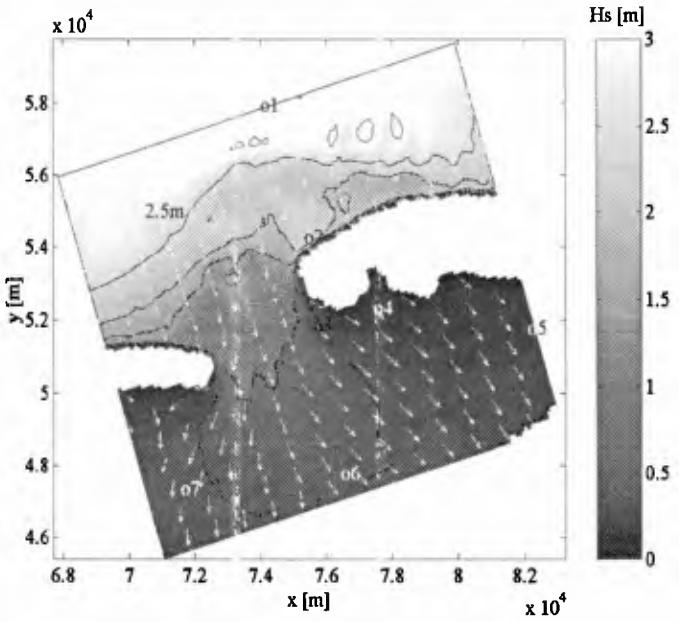

Fig. 2 Significant wave height and mean wave direction (unit vectors) computed with the SWAN model in the Norderneyer Seegat (Germany, see Fig. 1; six buoy locations indicated). Significant wave height contour line interval 0.5 m.

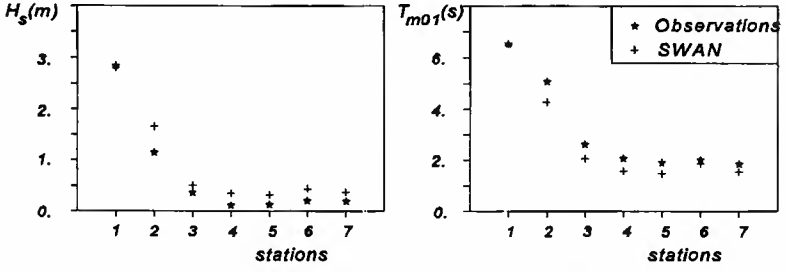

Fig. 3 The significant wave height and mean wave period in the Norderneyer Seegat (Germany, see Fig. 1) observed at the six buoy locations of Fig. 2 and computed with the SWAN model.

OUTLOOK

Although considerable progress has been made in the WISE group over the last few years, several basic aspects are still unresolved and the verification of the existing computer codes has been rather limited. Moreover, the numerical quality of the present codes pose unnecessary constraints on their operational applicability. With the present and future R&D programs of WISE members, these aspects will improve. In addition, relatively new model technology such as real-time data assimilation based on buoy and satellite observations will be introduced in the forecasting of waves in coastal regions. The outlook for these developments is optimistic because both in Europe and in the USA, funding is available to continue research and development at an increased pace. With the release of the SWAN model in the public domain, next to the WAM model, these developments can be concentrated in two widely available, supplementary computer codes.

ACKNOWLEDGEMENTS

The achievements in the WISE group are a credit to individual members who, we hope, have benefited from the discussions and interactions with other members. The group as a whole proceeds with its own momentum which we, as chairmen, hope to maintain with our logistical efforts.

REFERENCES

Battjes, J.A. and J.P.F.M. Janssen, 1978: Energy loss and set-up due to breaking of random waves, *Proc. 16th Int. Conf. Coastal Engineering*, ASCE, 569- 587

Battjes, J.A. and S. Beji, 1992: Breaking waves propagating over a shoal, *Proc. 23rd Int. Conf. Coastal Engineering*, ASCE, 42-50

Benoit, M., F. Marcos and F. Becq, 1996: Development of a third-generation shallow-water wave model with unstructured spatial meshing, *Proc. 25th Int. Conf. Coastal Engineering*, ASCE, Orlando, in press

Berkhoff, J.C.W., 1972: Computation of combined refraction-diffraction, *Proc. 13th Int. Conf. Coastal Engineering*, ASCE, 471-490

Booij, N, L.H. Holthuijsen and R.C. Ris, 1996, The "SWAN" wave model for shallow water, *Proc. 25th Int. Conf. Coastal Engineering*, ASCE, Orlando, in press

Booij, N., L.H. Holthuijsen, N. Doorn and A.T.M.M. Kieftenburg, 1997, Diffraction in a spectral wave model, *Proc. WAVES'97*, ASCE, in press

Chen, Y. and R.T. Guza, 1997: Modelling of breaking surface waves in shallow water, *J. Geophys. Res.*, 102, C11, 25035-25046

Dingemans, M.W., 1997: Water wave propagation over uneven bottoms. Part 1 -linear wave propagation, Advanced Series on Ocean Engineering, 13, World Scientific, 471 p.

Eldeberky, Y. and J.A. Battjes, 1995: Parameterization of triad interactions in wave energy models, *Proc. Coastal Dynamics Conf. '95*, Gdansk, Poland, 140-148

Eldeberky, Y., 1996: Nonlinear transformation of wave spectra in the nearshore zone, Ph.D. thesis, Delft University of Technology, Department of Civil Engineering, The Netherlands

Elgar, S., R.T. Guza, B. Raubenheimer, T.H.C. Herbers and E.L. Gallagher, 1997: Spectral evolution of shoaling and breaking waves on a barred beach, *J. Geophys. Res.*, 102,C7, 15797-15805

Hasselmann, K., T.P. Barnett, E. Bouws, H. Carlson, D.E. Cartwright, K. Enke, J.A. Ewing, H. Gienapp, D.E. Hasselmann, P. Kruseman, A. Meerburg, P. Müller, D.J. Olbers, K. Richter, W. Sell and H. Walden, 1973: Measurements of wind-wave growth and swell decay during the Joint North Sea Wave Project (JONSWAP), *Dtsch. Hydrogr. Z. Suppl.*, **12**, A8

Hasselmann, S., K. Hasselmann, J.H. Allender and T.P. Barnett, 1985: Computations and parameterizations of the linear energy transfer in a gravity wave spectrum. Part II: Parameterizations of the nonlinear transfer for application in wave models, *J. Phys. Oceanogr.*, **15**, 11, 1378-1391

Herbers, T.H.C. and M.C. Burton, 1997, Nonlinear shoaling of directionally spread waves on a beach, *J. Geophys. Res.*, **102**, C9, 21,101-21,114

Holthuijsen, L.H., Booij, N. and T.H.C. Herbers, 1989: A prediction model for stationary, short-crested waves in shallow water with ambient currents, *Coastal Engineering*, **13**, 23-54

Kaiser, R., W. Liebig and H.D. Niemeyer, 1994: Mutual benefits of combined mathematical wave model and geographic information system application, *Proc. Int. Conf. Hydrodyn. '94*, Wuxi (China), China Ocean Press

Komen, G.J., Cavaleri, L., Donelan, M., Hasselmann, K., Hasselmann, S. and P.A.E.M. Janssen, 1994: *Dynamics and Modelling of Ocean Waves*, Cambridge University Press, 532 p.

Luo, W. and R. Flather, 1997: Nesting a nearshore wave model (SWAN) into an ocean wave model (WAM) with application to the southern North Sea, in: *Computer Modelling of Seas and Coastal Regions III*, J.R. Acinas and C.A. Brebbia (eds.), Computational Mechanics Publications, 253-264.

Luo, W., R. Flather and J. Monbaliu, 1997: An efficient computational scheme for the use of the third-generation WAM model in coastal regions, *J. Waterway, Port, Coastal and Ocean Engineering*, in press

Madsen, P.A. and O.R. Sørensen, 1993: Bound waves and triad interactions in shallow water, *Ocean Engineering*, **20**, 4, 359-388

Mei, C.C., 1983: *The applied dynamics of ocean surface waves*, Wiley, New York, 740 p.

Rivero, F.J., A.S. Arcilla and E. Carci, 1997: Implementation of diffraction effects in the spectral wave energy conservation equation, IMA Conference on Wind-over-wave Couplings: Perspectives and Prospects, University of Salford, in press

Schäffer, H.A., R. Deigaard and P.A. Madsen, 1993, A Boussinesq model for wave breaking in shallow water, *Coastal Engineering*, 20, 185-202

SWAMP group, 1985: *Ocean wave modelling*, Plenum Press, New York and London

Thornton, E.B. and R.T. Guza, 1983: Transformation of wave height distribution, *J. Geophys. Res.*, **88**, C10, 5925-5938

Tolman, H.L., 1991: A third-generation model for wind waves on slowly varying, unsteady and inhomogeneous depths and currents, *J. Phys. Oceanogr.*, **21**, 6, 782-797

Vincent, C.L., J.M. Smith and J. Davis, 1994: Parameterization of wave breaking in models, *Proc. of Int. Symp.: Waves - Physical and Numerical Modelling*, Univ. of British Columbia, Vancouver, Canada, M. Isaacson and M. Quick (Eds.), Vol. II, 753-762

WAMDI group, 1988: The WAM model - a third generation ocean wave prediction model, *J. Phys. Oceanogr.*, **18**, 1775-1810

Young, I.R. and L.A. Verhagen, 1996: The growth of fetch limited waves in water of finite depth. Part 1: Total energy and peak frequency, *Coastal Engineering*, **29**, 47-783

A Long Term Wave Hindcast System Using ECMWF Winds

Yoshio Hatada[1] and Masataka Yamaguchi[2]

Abstract

A long-term shallow water hindcast system for the evaluation of wave climate is applied to consecutive computation of nearshore waves over a period of 9 years from 1986 to 1994 at 6 wave measurement stations of the Pacific coast of Japan. The data of the wind fields was acquired from the ECMWF wind data sets. Comparison between hindcasts and measurements is made for wave climate represented by not only significant waves and mean wave direction but also frequency-integrated directional wave energy and directional spectrum in addition to time variation of significant waves and mean wave direction. The conclusion is that the newly-revised system is fairly useful for a reasonable and computationally efficient evaluation of the wave climate at the level of spectral representation.

Introduction

Evaluation of long term wave conditions over several years, the so called wave climate, is of great importance for the mitigation of wave-induced disasters such as beach erosion and so on. The authors (1990, 1991, 1992, 1993, 1995, 1997) developed a long term shallow water wave hindcast system which makes it possible to consecutively follow wave conditions over several years with reasonable accuracy. Applicability of the system was verified by close agreement between computations and measurements for time series and climatic characteristics of significant waves and mean wave direction over 2 to 8 years at several locations around the coasts of Japan.

The system consists of a wind estimation model and a wave estimation model. Wind estimation is due to the application of the Bijvoet model (1957), in which input data are atmospheric pressure data obtained every 3 hours at irregularly-distributed points on the weather charts. Accordingly, tremendous efforts are required to acquire atmospheric pressure data sets, which make it

[1] Research Assistant, Dept. of Civil and Environmental Eng., Faculty of Eng., Ehime Univ., Bunkyocho 3, Matsuyama 790-8577, Ehime Pref., Japan

[2] Professor, Dept. of Civil and Environmental Eng., Faculty of Eng., Ehime Univ., Bunkyocho 3, Matsuyama 790-8577, Ehime Pref., Japan

practically impossible to extend data sets over several years, and the accuracy of the estimates at the Pacific coast of Japan in the cases of complicated wind fields associated with movement of intense typhoons and low systems is not high owing to the use of a simple wind model.

This paper presents a revised system for the estimation of wave climate around the coasts of Japan by using wind data sets provided by ECMWF (European Centre for Medium-range Weather Forecasts) for atmospheric pressure data sets in the former system as input conditions. Wave hindcasting is conducted over 9 years (1986-1994) at 6 wave measurement stations in the Pacific coast of northern Japan. In order to investigate the validity of the system, wave climates represented by not only significant waves and mean wave direction but also frequency-integrated directional wave energy and directional spectrum in addition to time variations of significant waves are compared with those obtained from measured wave data.

Description of the System

(1) Wind Estimation

Wind data at a height of 10 m (U_{10}, θ_w) is gathered from uninitialized analysis surface wind data sets in ECMWF/TOGA Advanced Operational Analysis Surface and Diagnostic Fields Data Sets. This is hereafter called the ECMWF wind data. The ECMWF wind data is provided every 6 hours on a spherical grid system with a space resolution of 1.125 degree for a period of Jan. 1, 1986 to Sept. 16, 1991 and with a space resolution of 0.5625 degree for a period of Sept. 17, 1991 to Dec. 31, 1994. The wind data with a time resolution of 6 hours is bilinearly interpolated onto a Cartesian grid system with a grid size of 80km set on the Northwestern Pacific Ocean area over a period of 9 years from Jan. 1, 1986 to Dec. 31, 1994.

(2) Wave Estimation

A shallow water wave prediction model (Yamaguchi et al., 1987), which traces the change of directional spectrum along a refracted ray of each component focusing on a hindcast point is applied for long-year wave hindcasting in order to save computer processing time. The model belongs to a decoupled propagation model classified into the first generation. The source function consists of linear growth term by the Phillips mechanism, exponential growth term by the Miles mechanism and energy dissipation term by opposing winds, bottom friction and pseudo-viscosity. Energy dissipation due to wave breaking is evaluated by imposing the limitation of a saturated spectrum.

Wave ray is traced on the nesting grid system composed of the Northwestern Pacific Ocean with a medium grid size of 5 km and a small sea area surrounding the hindcast point with a fine grid size of 1 km. At the land boundary, the directional spectrum is set at zero. At the open boundary, the directional spectrum is given, which is obtained from the product of a modified Pierson-Moskowitz spectrum using local wind speed and the $\cos^{l}\theta$ type angular spreading function using local wind direction. In the wave hindcast, 25 frequency components ranging from 0.04 to 0.5 Hz and 19 to 37 directional components,

determined by taking into account angular width of a wave window at each hindcast point, are employed.

Figure 1 shows the grid system used in the wave computation and location of 6 wave hindcasting points. The use of a nested grid system with high topographical resolution yields a reasonable estimate of waves in coastal sea water. Wave hindcast points are 5 coastal stations such as Sendai-shinko (water depth h=20m), Soma (h=16m), Onahama (h=19m), Hitachinaka (h=30m) and Kashima (h=23m), and an offshore station of Iwakioki (h=154m). Wave measurements at 6 stations have been conducted by the Second District Port Construction Bureau of the Ministry of Transport, Japan. These stations constitute some parts of NOWPHAS (Nationwide Ocean Wave information network for Ports and HArbourS) managed by the Port and Harbour Research Institute of the Ministry of Transport. The measured data (Coastal Development Institute of Technology, 1992-1995) and analyzed results for wave climate (Kobune et al., 1988-1991, Nagai et al., 1992, Nagai et al., 1993-1996) have been published as annual reports. Coastal stations where measurement data of significant waves and mean wave direction are acquired are located within a distance of 1 to 2 km from

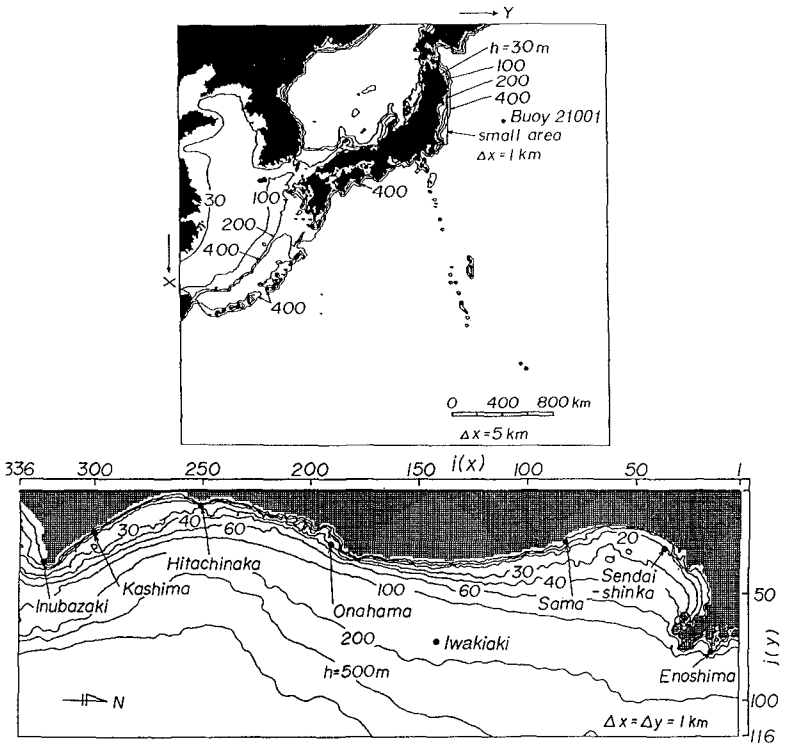

Figure 1. Medium and Fine Grid Systems of the Northwestern Pacific Ocean, Contour Plot of Water Depth and Location of Wave Hindcast Points

the coast. The offshore station Iwakioki, where measurement data of not only significant waves but also directional spectra and frequency-integrated directional energy using a multi-gauge array are acquired, is located 42 km off the Pacific coast in the Tohoku district of northern Japan. In wave hindcasting, the ECMWF wind data over the area with a time resolution of 6 hours is linearly interpolated every 1 hour on time domain and then is bilinearly interpolated onto a wave ray of each component.

Verification of the System

(1) Wind Climate

Figure 2 shows the comparison between ECMWF analysis winds and measured winds for monthly-averaged wind speed and occurrence rate of wind speed over 10 m/s, and directionally-grouped occurrence rate of wind speed over 10 m/s at Buoy 21001 of the Japan Meteorological Agency. A close agreement between analyzed and measured data is obtained, in spite of the discrepancy that analyzed data tends to indicate a slightly stronger concentration to the NW direction than does the measured data. But there is a possibility that the measured data at the buoy may be used in the data assimilation of the ECMWF analysis winds. In this case, a close agreement would be a natural result.

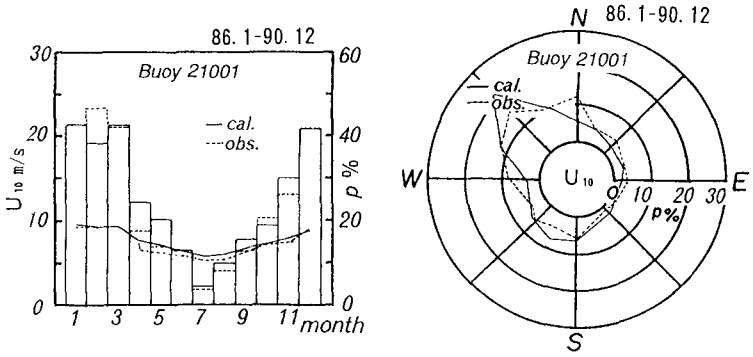

Figure 2. Comparison of Analysis Data and Measurement Data for Monthly-Variations of Mean Wind Speed and Occurrence Rate of Strong Winds, and Yearly-Average of Directionally-Grouped Occurrence Rate of Strong Winds

(2) Time Variations of Significant Waves and Mean Wave Direction

Comparison between computed and measured results was conducted for the time variations of significant wave height $H_{1/3}$, significant wave period $T_{1/3}$ and mean wave direction $\overline{\theta}$ over a period of 9 years from 1986 to 1994 at 6 measurement stations. Two examples of the comparison over 3 months in summer at the offshore station (Iwakioki) and at the coastal station (Onahama) are given in Figure 3. Calm sea states associated with low swell continue in summer except for some less frequent periods of passage of typhoons. The system generally reproduces the measured time variations of waves with reasonable accuracy,

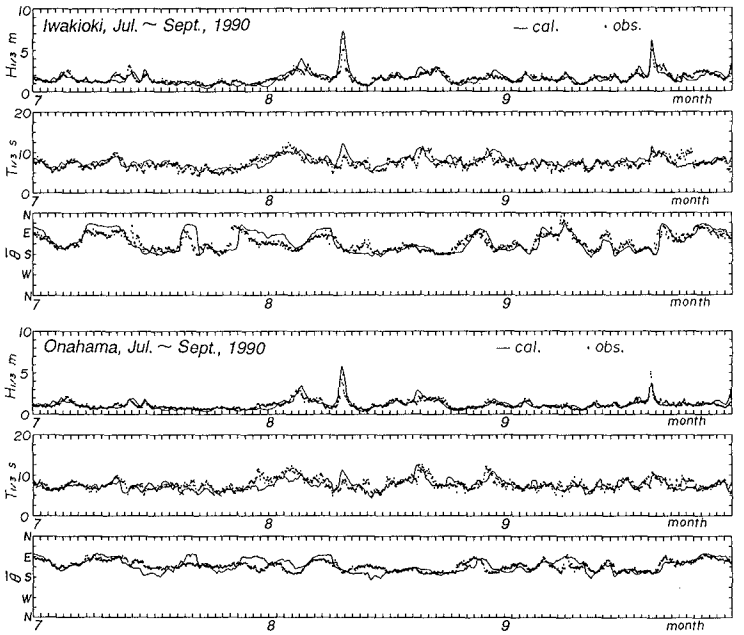

Figure 3. Comparison between Hindcast and Measurement for Time Variations of Significant Waves and Mean Wave Direction over 3 Months.

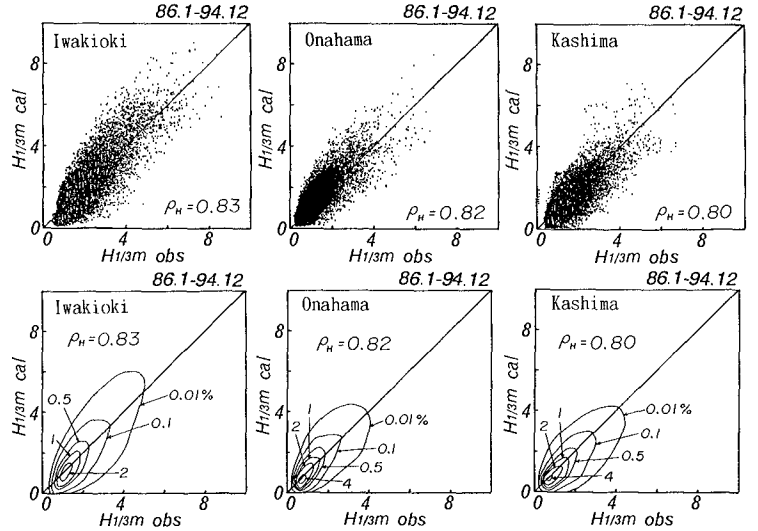

Figure 4. Scatter Diagram between Hindcast and Measurement for Significant Waves and Contour Plot of Relative Occurrence Frequency in a Segment of Wave Height at 3 Stations

although a slight overestimation is observed for the typhoon period.

Figure 4 illustrates some examples of the scatter diagrams between hindcast and measurement for individual significant wave height obtained every 2 hours over 9 years and the contour plot for relative frequency of data contained in a small segment of wave height. Individual data gathers and distributes almost symmetrically around the line indicating a perfect correlation, but the tendency of somewhat excess evaluation to higher waves is found at both Iwakioki and Onahama. It may be said that the hindcasted wave height follows the measured wave height fairly well, taking into account complicated wind and wave fields in an open ocean area, in which case the correlation coefficient ρ_H ranges from 0.80 to 0.83.

(3) Wave Climate for Significant Waves and Mean Wave Direction

Various kinds of mean wave statistics for representing wave climate are obtained from the time series of computed and measured wave data. Figure 5 shows the comparison for monthly averages of significant waves and occurrence rate of high waves greater than 2 m at 6 wave measurement stations. The system evaluates well a general pattern of the seasonal change of the wave climate in the Pacific coastal area of northern Japan, in which high wave conditions associated with frequent passage of intense low pressures occur in spring and autumn, and comparably calm sea states continue in summer. In detail, the system tends to overestimate the occurrence rate of higher waves and to underestimate the wave period in winter particularly at coastal stations. The former results may be caused by the still insufficient grid resolution of 1 km used for the coastal sea area. The latter may be explained as a result of wave computation in a restricted area with artificial open boundary. In winter and in the latter half of autumn, strong landward northwesterly monsoon winds prevail frequently and regularly over the area. Consequently, waves hardly grow by landward winds at coastal sea areas because of the short fetch condition, but low swell-like waves with a longer period propagate from the Pacific Ocean. This means that waves with lower height and longer period reach the coastal area in these seasons. The system may not give a proper estimate for the arrival of low swell-like waves probably due to the above-mentioned reason.

Histograms of wave height grouped every 0.5 m at 6 stations are compared in Figure 6. The system produces well the overall distribution of the histograms for measurement data. But the system tends to underestimate the occurrence rate in the highest rank and the second highest rank, and to overestimate the occurrence rate in the other ranks. Figure 7 indicates the comparison of hindcast and measurement for correlation between wave height and wave period. A higher correlation between wave height and wave period is observed at the offshore station (Iwakioki) where wind waves reach from all directions. This results in the contourlines extending in the right-upward direction. At 5 coastal stations where onshore winds do not give rise to the growth of wind waves and low swell-like waves reach in monsoon seasons, the contourlines show a flatter distribution compared to those at the offshore station. The system yields general features in the correlation diagrams, although each contourline in the hindcast is situated on the shorter period side to the one in the measurement because of underestimation for low swell-like waves.

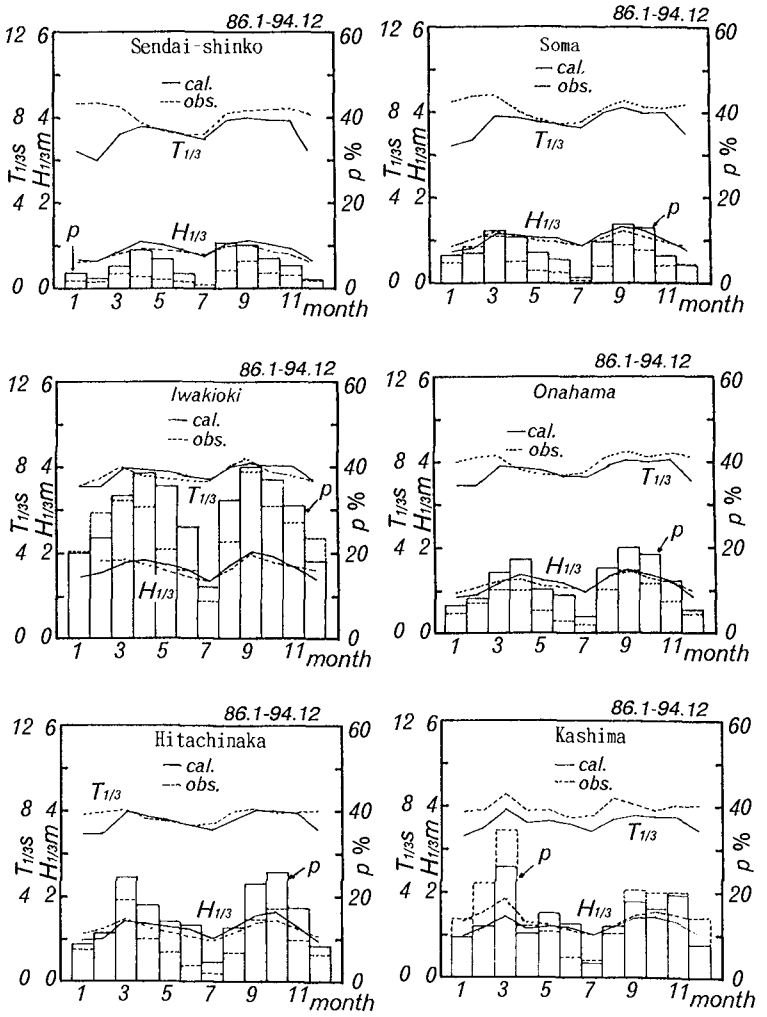

Figure 5. Comparison of Hindcast and Measurement for Monthly Variations of Mean Significant Waves and Occurrence Rate of High Waves

The directionally-grouped occurrence rates of high waves over 2 m at 6 stations are given in Figure 8. Close agreement between hindcast and measurement is found at the offshore station and 3 coastal stations. At 2 coastal stations (Hitachinaka and Kashima), the distribution in the hindcast indicates counterclockwise deviation from the one in the measurement by a directional

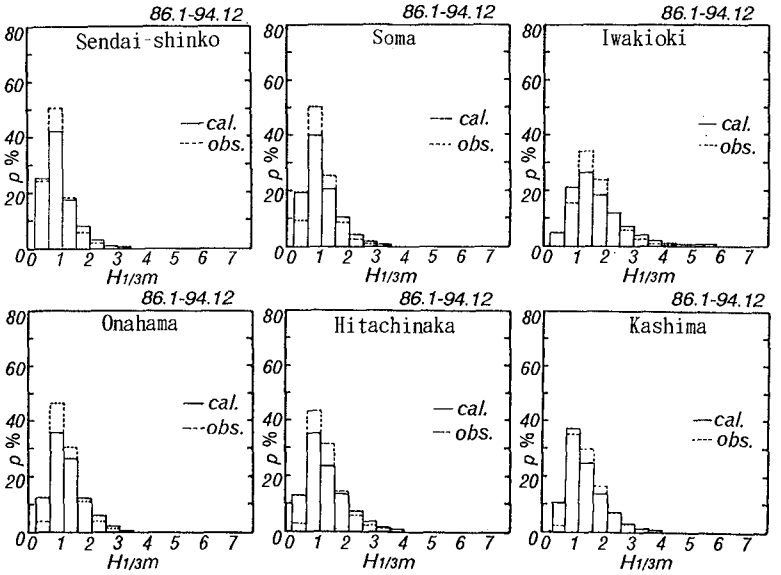

Figure 6. Comparison of Hindcast and Measurement for Histograms of Wave Height

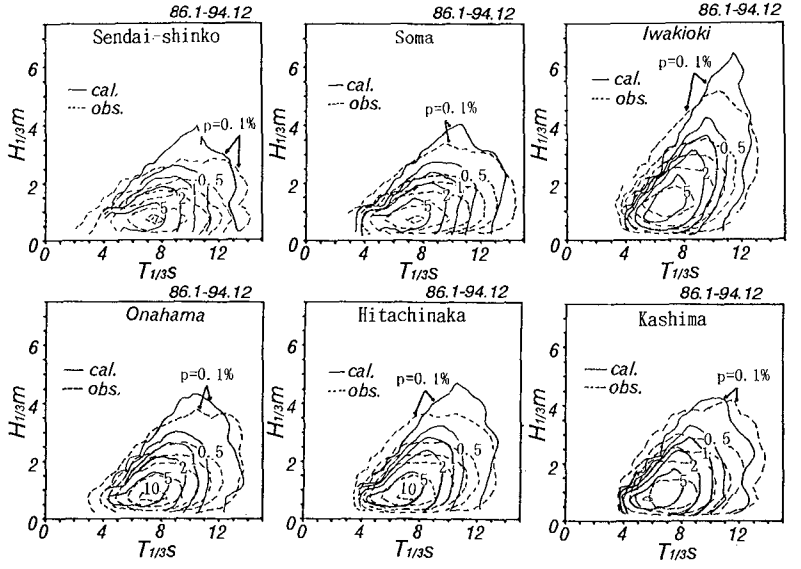

Figure 7. Comparison of Hindcast and Measurement for Correlation between Wave Height and Wave Period

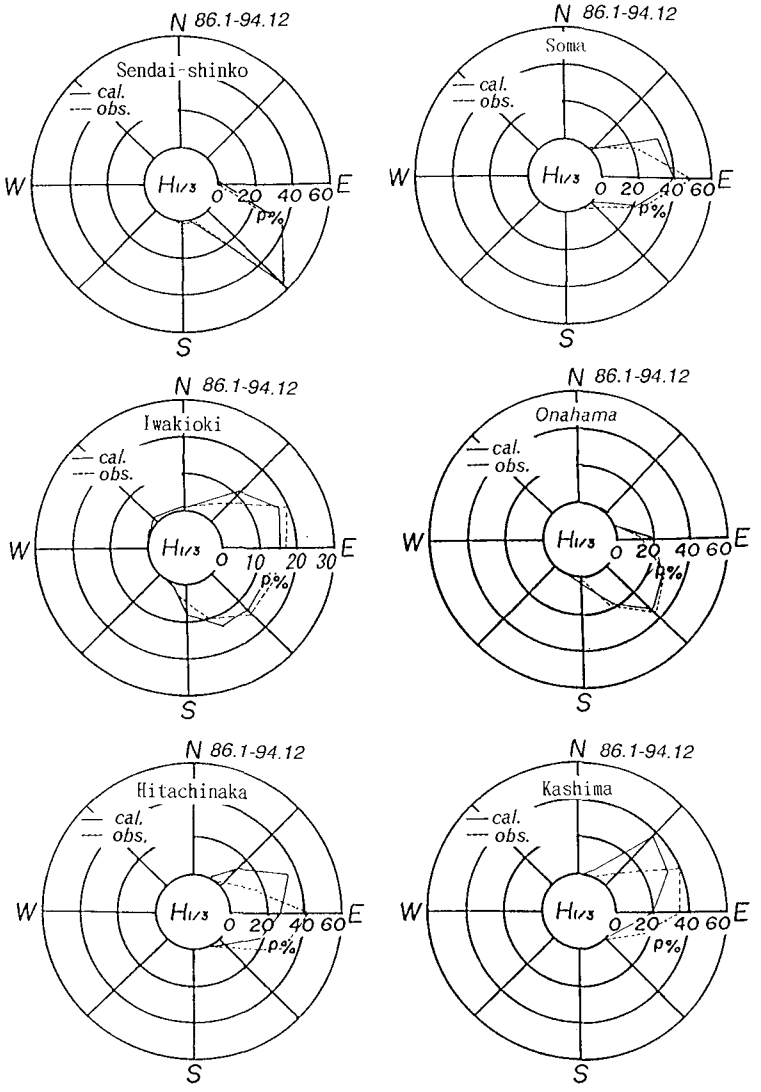

Figure 8. Comparison of Hindcast and Measurement for Directionally-Grouped Occurrence Rate of High Waves Exceeding 2 m

segment (22.5 degree). The reason is not clear, but an insufficient topographical resolution in the nearshore wave computation may contribute to the small discrepancy. While the wave window for high waves at the offshore station has a wider directional range, the wave window at the coastal stations becomes narrower by the presence of the surrounding land topography and the effect of wave refraction during propagation. The system reproduces fairly well the change of the

directional distribution of mean wave direction associated with the propagation from the offshore area to the coastal area.

(4) Wave Climate for Directional Energy and Directional Spectrum

As mentioned above, directional spectra have been analyzed using wave data measured over long years with a multi-gauge array at the offshore station (Iwakioki) by a group of the Port and Harbour Research Institute of the Ministry

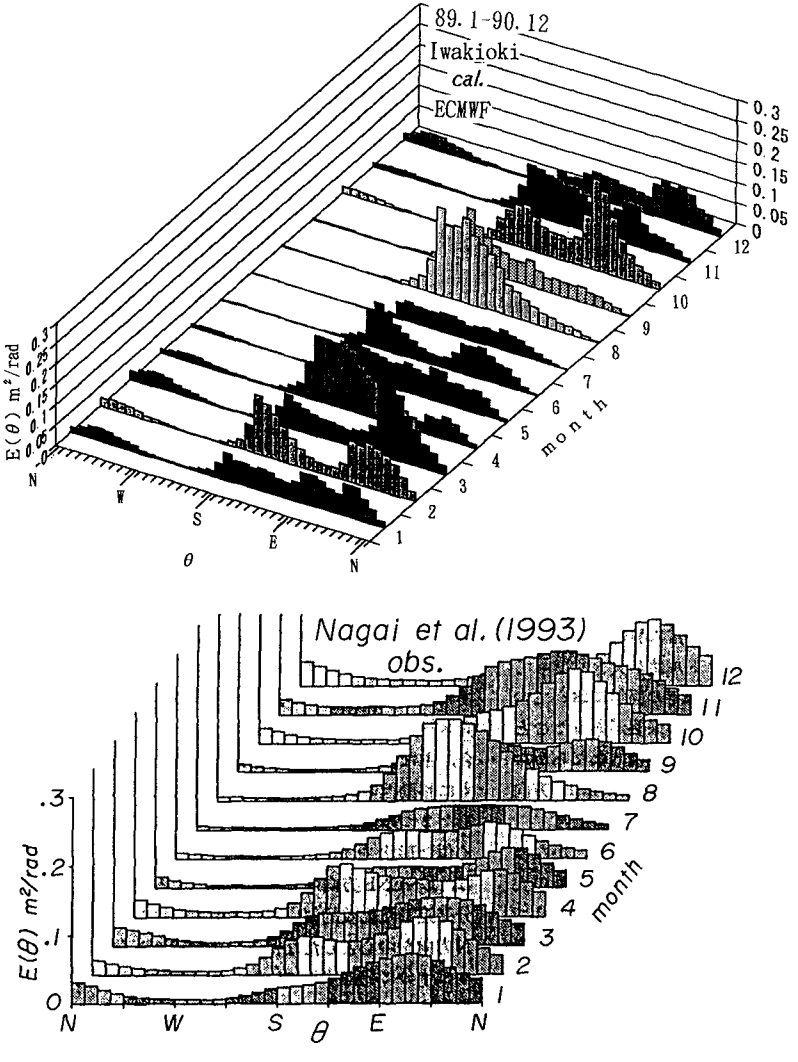

Figure 9. Comparison of Hindcast and Measurement for Monthly-Averaged Directional Energy

of Transport (Nagai et al, 1993, Shimizu et al. 1996). Figure 9 illustrates the comparison of hindcast and measurement for monthly mean of frequency-integrated directional wave energy E(θ) of every 2 hours for the period of 1989 to 1990, in which the measurement data is analyzed by Nagai et al. (1993) using the BDM (Bayesian Directional spectrum estimation Method) proposed by Hashimoto (1987). In winter, directional energy is concentrated in directional ranges of E to NE, and in spring, it has two peaks at the S and NE directions. In summer, directional energy for the S direction is greatly augmented with the passage of intense typhoons, and in autumn, predominant directional energy ranges from E to SE directions. The seasonal change of directional energy is highly correlated with the weather conditions in the concerned sea area. It may be said from the comparison that a gross feature of the seasonal change is reasonably evaluated with use of the present system except for the insignificant difference in directional distribution of each month.

Figure 10 shows the evaluation and measurement (Shimizu et al., 1996) for directional spectrum E(f, θ), normalized frequency-integrated directional energy E(θ) and frequency spectrum E(f) averaged over 7 years, in which the value of the contour line for analyzed directional spectrum was not given in their report. Directional spectrum is analyzed with use of EMEP (Extended Maximum Entropy Principle method) proposed by Hashimoto et al. (1993). General patterns of directional spectrum distribution, directional energy distribution with two peaks and frequency spectrum distribution are rather similar in both results based on the hindcast and measurement.

In order to have a closer look at the applicability of the system, comparison of the spectral informations mentioned above is made at each month. Figure 11 shows examples of monthly-averaged spectral characteristics representing each season. In February, a peak of directional energy is seen in the NE direction, but another peak of directional energy in the S direction is slightly overestimated. In May, the hindcast seems to indicate a clockwise shift of peak direction by a directional segment compared to the analysis. In August, the mutual correspondence seems to be acceptable, but in November, directional range with high energy is

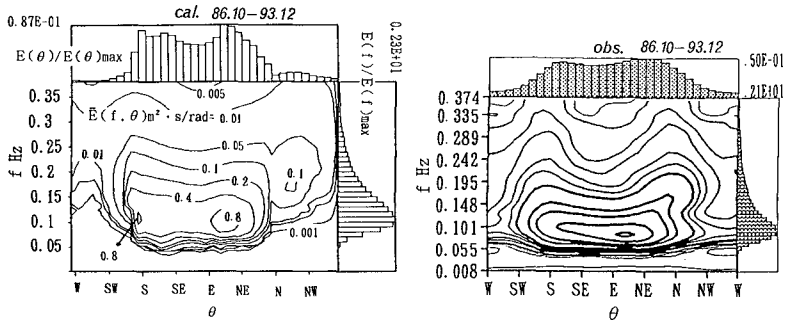

Figure 10. Comparison of Hindcast and Measurement for Directional Spectrum, Directional Energy and Frequency Spectrum Averaged over 7 Years

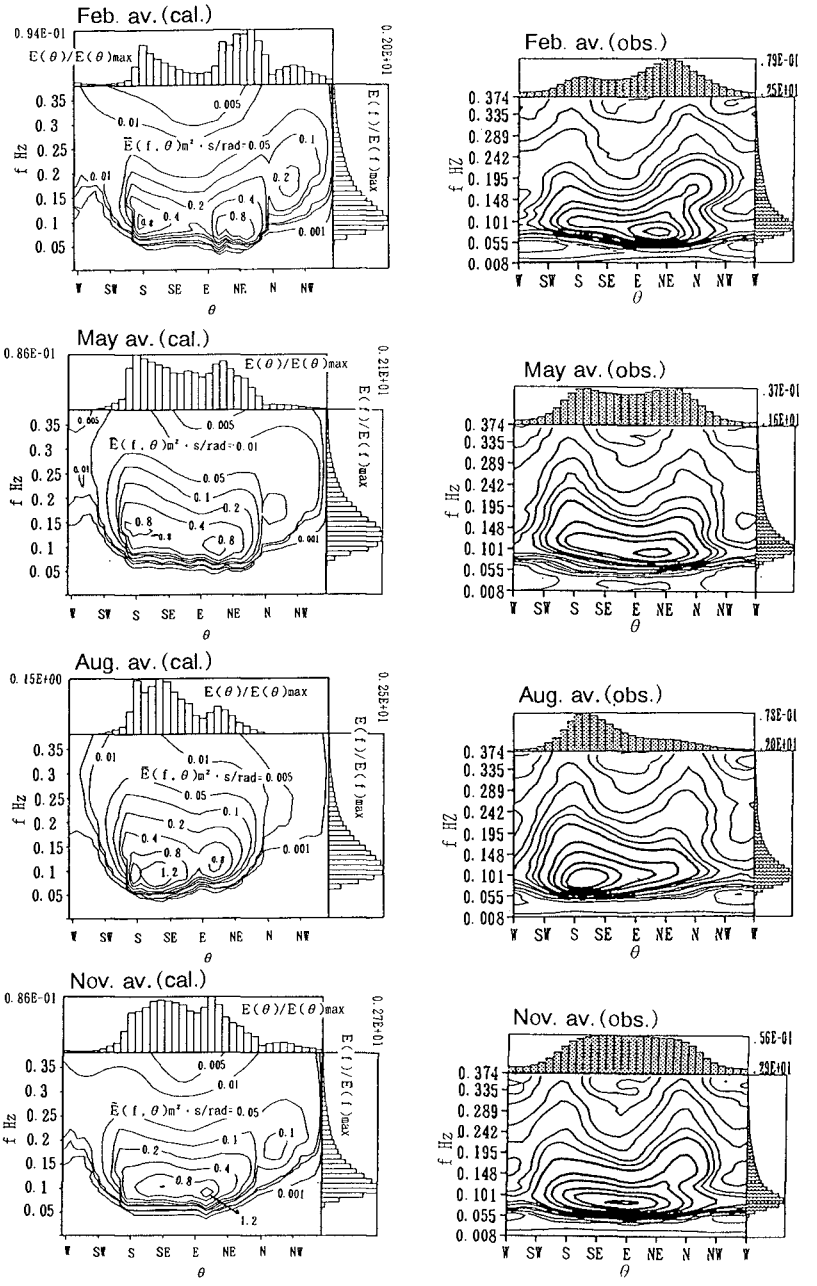

Figure 11. Comparison of Hindcast and Measurement for Monthly-Averaged Directional Spectrum, Directional Energy and Frequency Spectrum

somewhat narrower in the hindcast than in the analysis. In addition, directional energy from W to SW direction is underestimated through all seasons. In spite of such discrepancy observed in detail, the overall pattern of the directional distribution of wave energy in the hindcast is in reasonable agreement with that in the analysis. This may lead to the conclusion that the present system is amply applicable for the estimation of long-term wave climate at the level of spectral representation.

Conclusions

Consecutive wave computations over 9 years were carried out at 6 wave measurement stations near the Pacific coast of northern Japan by using a long term wave hindcasting system. Close correlation between hindcast and measurement emphasizes that a newly-revised system, in which the ECMWF wind data sets are incorporated as input data is fairly useful for reasonable and efficient evaluation of the wave climates represented by not only significant waves and mean wave direction but also directional spectrum and its frequency-integrated directional wave energy.

Acknowledgements

The authors are indebted to Mr. M. Ohfuku, technical officer of our department and Mr. T. Matsugi, graduate course student of Civil and Ocean Engineering, Ehime University for their sincere assistance during the study. The authors express their thanks to the ECMWF which provided " ECMWF 1986-1994 The Description of the ECMWF/WCRP Level III -A Global Atmospheric Data Archive". Thanks are also due to the Second District Port Construction Bureau of the Ministry of Transport, the Japan Meteorological Agency and the Coastal Development Institute of Technology for kindly offering measured wind and wave data including NOWPHAS data.

References

Bijvoet, H.C. (1957) : A new overlay for the determination of the surface wind over sea from surface weather charts, KNMI, Mededelingen en Verhandelingen, Vol.71, pp.1-35.

Coastal Development Institute of Technology (1992-1995) : Annual report of nationwide measurement data of ocean waves for ports and harbours -NOWPHAS-, VOl.1 (1991) -Vol.4 (1994).

Hashimoto, N. (1987) : Estimation of directional spectrum from a Bayesian approach, Rep. Port and Harb. Res. Inst., Vol.26, No.2, pp. 97-125 (in Japanese).

Hashimoto, N. et al. (1993) : Extension of maximum entropy principle method (MEP) for estimating the directional ocean wave spectrum, Rept. Port and Harb. Res. Inst., Vol.32, No.1, pp.3-25 (in Japanese).

Hatada, Y. and M. Yamaguchi (1992): Eight years wave hindcast and analysis of wave climate, Proc. 23th ICCE, Vol.I, pp.267-280.

Hatada, Y. and M. Yamaguchi (1997): Eight years wave hindcast at the coastal area of the East China Sea and estimation of wave climate, WAVES 97, Vol.2, pp.911-924.

Kobune, K. et al. (1988-1991): Annual report on wave properties at the network stations, Tech. Note Port and Harb. Res. Inst., No.612 (1986), No.642 (1987), No.666 (1988), No.712 (1989) (in Japanese).

Nagai, N. et al. (1992): Annual report on wave properties at the network stations, Tech. Note Port and Harb. Res. Inst., No.721 (1990) (in Japanese).

Nagai, N. et al. (1993): On the properties of the directional wave spectra observed in deep seas (1st report: the field observation off Iwaki), Rept. Port and Harb. Res. Inst., Vol.32, No.2, pp.45-112 (in Japanese).

Nagai, et al. (1993-1996): Annual report on nationwide ocean wave information network for ports and harbours (NOWPHAS), Tech. Note Port and Harb. Res. Inst., No.745 (1991), No.770 (1992), No.796 (1993), No.821 (1994) (in Japanese).

Shimizu, K. et al. (1996): On the properties of the directional wave spectra observed in deep seas (2nd report: 7-year statistics of the directional wave spectra off Iwaki), Rept. Port and Harb. Res. Inst., Vol.35, No.1, pp.65-89 (in Japanese).

Yamaguchi, M. et al. (1987): A shallow water wave prediction model at a single location and its applicability, Jour. JSCE, No.381/II-7, pp.151-160 (in Japanese).

Yamaguchi, M. et al. (1990): Estimation of wave climate along the coast of Japan Sea based on wave hindcasting, Jour. Natural Disas. Sci., 9-3, pp.18-42 (in Japanese).

Yamaguchi, M. et al. (1991): Applicability of a long term shallow water wave hindcast system to the estimation of wave climate along the coastal area of the East China Sea, Jour. Natural Disas. Sci., 10-3, pp.187-199 (in Japanese).

Yamaguchi, M. and Y. Hatada (1993): Estimation of wave climate and extreme waves in the coastal area of Nansei Islands based on wave hindcasting, Proc. 3rd Taiwan-Japan Joint Seminar on Natural Hazards Mitigation, pp.234-247.

Yamaguchi, M. et al. (1995): Applicability of a long term shallow water wave hindcast system, Proc. Coastal Eng. in Japan, Vol.42, pp.331-335 (in Japanese).

NUMERICAL SIMULATIONS OF DIRECTIONALLY SPREAD SHOALING SURFACE GRAVITY WAVES

Françoise BECQ[1], Michel BENOIT[1], Philippe FORGET[2]

ABSTRACT

The study aims at investigating the non-linear triad interaction process affecting shoaling surface gravity wave fields in shallow water areas. Attention is specifically paid to analyse the effects of these second-order non-linearities on the directional distribution of incident waves. A stochastic approach was chosen to model the triad interaction process. Three source terms have been implemented in the spectral wave model TOMAWAC developed at the Laboratoire National d'Hydraulique (LNH). The model results are compared to the laboratory data of Nwogu (1994).

1. INTRODUCTION:

This work focusses to the study of the non-linear interactions between triplets of waves which occur in the nearshore zone. These non-linearities, of lower order than the four wave interactions, are usually considered as the main exchange mechanism for wave energy of an irregular wave train towards sub- (long waves) and super-harmonics (bound higher order waves) (e.g. Freilich and Guza, 1984). The strength of these near-resonant interactions is governed by the phase mismatch between the bound and free wavenumbers. As for decreasing water depth the waves tend to become non-dispersive, the phenomenon is enhanced towards the shore. The effect of the transfer of energy associated with near-resonant wave interactions is not only distortions of the frequency spectrum, but also modifications of the directional spreading of energy. Elgar et al. (1993) observed that directionally bi-modal wave spectra can give rise to a new directional peak. This implies that both collinear and non-collinear triad interactions are important.

Boussinesq equations have been extensively used to establish evolution equations for the amplitudes and phases of unidirectional waves propagating over a mildly sloping bottom. The models (e.g. Freilich and Guza (1984), Madsen and Sorensen (1993)) are able to correctly reproduce the generation of harmonics. The quality of the results incited us to extend the deterministic model of Madsen and Sorensen (1993) to bidimensional situations. The model is presented in part 2.

[1]EDF - Laboratoire National d'Hydraulique, 6 quai Watier, 78400 Chatou, FRANCE

[2]L.S.E.E.T Université de Toulon et du Var, BP 132, 83957 La Garde, FRANCE

Alternatively, stochastic (phase-averaged) models are more useful to predict the evolution of directional wave spectra. The shallow water three-waves interaction process is simulated by including a source term in the energy balance equation. From the works of Zakharov et al. (1992), Eldeberky et al. (1996) proposed a directionally coupled source term. Some misbehaviours of this non-linear model were pointed out by the authors. We studied more particularly the problem of energy conservation and the ability to generate new directional peaks (which was not demonstrated in Eldeberky, 1996). For practical applications, Eldeberky et al. (1996) recommended the use of the parametrized LTA (Lumped Triad Approximation) model proposed by Eldeberky and Battjes (1995) and Eldeberky (1996). This model has been applied in the wave propagation model SWAN developed at Delft University of Technology (Ris, 1997). The LTA model is characterised by the restriction to self-self interactions leading to a great computational efficiency. From the 2D spectral deterministic equation presented in §2, we developed a new stochastic model. To solve the classical problem of closure, we used the works of Holloway (1980) who assumes that the sum over fourth-order moments draws some contribution from third-order moments through a coupling coefficient interpreted as a broadening of the resonance condition. The three formulations for phase-averaged models are presented in part 3. They are implemented in the spectral wave model TOMAWAC developed at the LNH (Benoit et al., 1996) and they have been compared to the experimental laboratory results presented by Nwogu (1994) (§4).

2. DETERMINISTIC APPROACH:

Deterministic Boussinesq (SB) model:

Starting from their extended Boussinesq equations, Madsen and Sorensen (1993) derived a set of deterministic evolution equations for the amplitudes and phases of unidirectional waves propagating over a mildly sloping bottom. We extended the model to bidimensional situations by use of the 2D Boussinesq equations of Madsen and Sorensen (1992):

$$\frac{\partial \zeta}{\partial t} + \vec{\nabla}.\vec{P} = 0 \qquad (1)$$

$$\frac{\partial \vec{P}}{\partial t} + \left[\frac{\vec{P}}{h+\zeta}\left(\vec{\nabla}.\vec{P}\right) + \left(\vec{P}.\vec{\nabla}\right)\frac{\vec{P}}{h+\zeta}\right] + g(h+\zeta)\vec{\nabla}\zeta - \left(B+\frac{1}{3}\right)h^2\vec{\nabla}\left(\vec{\nabla}.\frac{\partial \vec{P}}{\partial t}\right)$$
$$-\frac{h}{6}\left(\vec{\nabla}.\frac{\partial \vec{P}}{\partial t}\right)\vec{\nabla}h - \frac{h}{6}\left(\vec{\nabla}h.\vec{\nabla}\right)\left(\frac{\partial \vec{P}}{\partial t}\right) - \frac{h}{6}\vec{\nabla}h \otimes \left(\vec{\nabla} \otimes \frac{\partial \vec{P}}{\partial t}\right) \qquad (2)$$
$$-Bgh^2\left(\vec{\nabla}h.\vec{\nabla}\right)\left(\vec{\nabla}\zeta\right) - Bgh^2\left(\vec{\nabla}.\vec{\nabla}\zeta\right)\vec{\nabla}h - Bgh^3\vec{\nabla}\left(\vec{\nabla}.\vec{\nabla}\zeta\right) = 0$$

where ζ is the free surface elevation, $\vec{P}$ is the depth-integrated velocity and h is the water depth. These equations include a linear parameter B which improves the dispersion properties and the shoaling mechanisms associated with the model. The optimal value $B=1/15$ was obtained by the authors by a fit to the reference linear shoaling coefficient predicted by the Stokes first-order theory. The standard form of the Boussinesq equations can be recovered by setting $B=0$.

The extended Boussinesq equations are combined into one single equation. For this, the partial derivative in time of the continuity equation is substracted to the partial derivative in space of the momentum equation. This leads to:

$$L = M + N \tag{3}$$

where:

$$L = \zeta_{tt} - gh\vec{\nabla}.\vec{\nabla}\zeta + Bgh^3\vec{\nabla}.\left(\vec{\nabla}\left(\vec{\nabla}.\vec{\nabla}\zeta\right)\right) - \left(B+\frac{1}{3}\right)h^2\vec{\nabla}.\left(\vec{\nabla}\zeta_{tt}\right) \tag{4}$$

$$M = g\vec{\nabla}h.\vec{\nabla}\zeta + (2B+1)h\vec{\nabla}h.\vec{\nabla}\zeta_{tt} - 5Bgh^2\vec{\nabla}h.\vec{\nabla}\left(\vec{\nabla}.\vec{\nabla}\zeta\right) + \frac{h}{6}\vec{\nabla}h.\left(\vec{\nabla}\otimes\left(\vec{\nabla}\otimes\vec{P}_t\right)\right) \tag{5}$$

$$N = \vec{\nabla}.\left[\frac{\vec{P}}{h+\zeta}\left(\vec{\nabla}.\vec{P}\right) + \left(\vec{P}.\vec{\nabla}\right)\frac{\vec{P}}{h+\zeta}\right] + g\vec{\nabla}\zeta.\vec{\nabla}\zeta + g\zeta\vec{\nabla}.\vec{\nabla}\zeta \tag{6}$$

L contains the lowest order and dispersive terms, M represents the effects of slowly varying depths on the wave propagation and N models the non-linear effects due to wave coupling. Now, the equation is transformed into the spectral domain. ζ is written as a discrete Fourier series:

$$\zeta(x,y,t) = \sum_{p=-\infty}^{\infty} A_p(x,y)\exp\left[i\left(\omega_p t - \psi_p(x,y)\right)\right] \tag{7}$$

in which p refers to a directional wave component. A_p is the complex Fourier amplitude ($A_{-p} = A_p^*$), ω_p is the angular frequency ($\omega_{-p} = -\omega_p$) and ψ_p is the linear wave phase, linked to the wavenumber by the relation $\vec{\nabla}\psi_p = \vec{k}_p(x,y)$. $\vec{P}$ is linked to ζ through the continuity equation, so:

$$\vec{P}(x,y,t) \approx \sum_{p=-\infty}^{\infty} \vec{c}_p A_p(x,y)\, e^{\left[i\left(\omega_p t - \psi_p(x,y)\right)\right]} \tag{8}$$

where $\vec{c}$ is the wave phase celerity. The Fourier expressions of ζ and $\vec{P}$ are inserted in the equation (3). We follow for this the guideline presented by Madsen and Sorensen (1993) for 1D situations. First derivatives of A_p, k_p and h are assumed to be small, and products of derivatives and higher derivatives of these quantities are neglected. After algebraic manipulations, we get,

- at lowest order, the linear dispersion relation:

$$\frac{\omega_p^2 h}{g} = \frac{\left(k_p h\right)^2 + B\left(k_p h\right)^4}{1 + \left(B + 1/3\right)\left(k_p h\right)^2} \tag{9}$$

- at second order, the coupled differential equations:

$$\frac{\partial A_p}{\partial t} + \vec{C}g_p.\vec{\nabla}A_p + \frac{1}{2}\frac{Cg_p}{k_p}A_p\vec{\nabla}.\vec{k}_p + \frac{S_{3,p} - S_{4,p}}{2S_{1,p}}A_p = \frac{ig}{2S_{1,p}}N_p \tag{10}$$

where $\vec{C}g$ is the group velocity:

$$\vec{C}g_p = \frac{S_{2,p}}{S_{1,p}}\vec{k}_p \tag{11}$$

$$S_{1,p} = \omega_p\left[1 + (B + 1/3)h^2k_p^2\right] \tag{12}$$

$$S_{2,p} = \left[gh + 2Bgh^3 k_p^2 - \left(B + \frac{1}{3} \right) \omega_p^2 h^2 \right] \quad (13)$$

$$S_{3,p} = 4Bgh^3 \frac{-k_p^2 \left[g + 3Bgh^2 k_p^2 - 2(B + 1/3) h \omega_p^2 \right]}{2 \left[gh + 2Bgh^3 k_p^2 - (B + 1/3) h^2 \omega_p^2 \right]} \vec{k}_p . \vec{\nabla} h \quad (14)$$

$$S_{4,p} = -(\vec{k}_p . \vec{\nabla} h) \left[g + 5Bgh^2 k_p^2 - (2B + 1) \omega_p^2 h \right] \quad (15)$$

$$N_p = \sum_{m=1}^{\infty} 2R_{-m,p+m} A_m^* A_{p+m} e^{-i(-\psi_p - \psi_m + \psi_{p+m})} + \sum_{m=1}^{p-1} R_{p-m,m} A_m A_{p-m} e^{-i(-\psi_p + \psi_m + \psi_{p-m})} \quad (16)$$

The left hand side of (10) represents the propagation terms, whereas the right hand side governs the non-linear triads interactions. N models the exchange of energy towards sub and super-harmonics through the coupling coefficient, R, which controls the strength of the interactions. Its expression is given by:

$$R_{p,m} = \left[\frac{1}{2} \left(k_p^2 + k_m^2 + 2 \vec{k}_p . \vec{k}_m \right) + \frac{1}{gh} \left(\frac{\omega_p \omega_m}{\left(k_p k_m \right)^2} \left[\left(k_p^2 + k_m^2 \right) \vec{k}_p . \vec{k}_m + \left(\left(k_p k_m \right)^2 + \left(\vec{k}_p . \vec{k}_m \right)^2 \right) \right] \right) \right] \quad (17)$$

3. STOCHASTIC APPROACHES:

Stochastic Parametrized Zakharov (SPZ) model:

The model proposed by Eldeberky et al. (1996) is based on the so-called Zakharov equation for resonant three-wave interactions (Zakharov, 1968; Zakharov et al., 1992):

$$\frac{\partial a_{\vec{k}_3}}{\partial t} = -i \omega_{\vec{k}_3} a_{\vec{k}_3} - i \iint \left[R_{312} a_{\vec{k}_1} a_{\vec{k}_2} \delta_{3-1-2} + 2R_{132} a_{\vec{k}_1} a_{\vec{k}_2}^* \delta_{1-3-2} \right] d\vec{k}_1 d\vec{k}_2 \quad (18)$$

δ_{3-1-2} is shorthand for $\delta\left(\vec{k}_3 - \vec{k}_1 - \vec{k}_2\right)$ where δ stands for the delta Kronecker symbol. R_{312} is a coupling coefficient depending on the physics of the interacting waves. For surface gravity waves in intermediate water depth, the expression is given by (Stiassnie and Shemer, 1984; Eldeberky et al., 1996):

$$R_{312} = \frac{g^{1/2}}{8\pi\sqrt{2}} \left\{ \left[\vec{k}_3 . \vec{k}_1 - (\omega_3 \omega_1 / g^2) \right] (\omega_2 / \omega_1 \omega_3)^{1/2} + \left[\vec{k}_3 . \vec{k}_2 - (\omega_3 \omega_2 / g^2) \right] (\omega_1 / \omega_2 \omega_3)^{1/2} + \left[\vec{k}_1 . \vec{k}_2 + (\omega_2 \omega_1 / g^2) \right] (\omega_3 / \omega_1 \omega_2)^{1/2} \right\} \quad (19)$$

A statistical formulation of the three-wave interaction process, expressed in term of the correlation functions of the wave field, can be obtained from (18) (Zakharov et al., 1992). Because of non-linearities, the statistical description consists in a series of interconnected equations where each moment evolves according to the next higher-order moment. The problem is closed by assuming that the fourth-order moments can be expressed as a function of the lower order moments. For resonant wave-wave interactions, Zakharov et

al. (1992) used the quasi-gaussian hypothesis. A broadening of the resonance condition is included in the model by the assumption that the fourth-order cumulant depends on the third-order moment through a coupling coefficient Ω which represents a frequency uncertainty among the three interacting waves (Holloway, 1980). A small (but finite) value for Ω is used (Eldeberky et al., 1996). Defining the wave action density $n_{\vec{k}}$ by:

$$\left\langle a_{\vec{k}} a^{*}_{\vec{k}'} \right\rangle = 4\pi^2 n_{\vec{k}} \delta\left(\vec{k} - \vec{k}'\right) \qquad (20)$$

the wave action evolution equation can be expressed as (Zakharov et al., 1992):

$$\frac{dn_{\vec{k}_3}}{dt} = 4 \int\int d\vec{k}_1 d\vec{k}_2 \left[R^2_{312} N_{312}\, \mu_{3-1-2} \delta_{3-1-2} - 2R^2_{132} N_{132}\, \mu_{3-1+2} \delta_{3-1+2} \right] \qquad (21)$$

where N_{312} depends on the spectral action density functions (n_j) of the interacting waves according to:

$$N_{312} = n_1 n_2 - n_3 n_1 - n_3 n_2 \qquad (22)$$

In Holloway's approach, μ_{3-1-2} acts as a spectral filter through the frequency mismatch $(\omega_3 - \omega_1 - \omega_2)$ and through the parameter Ω characterising non-resonant interactions:

$$\mu_{3-1-2} = \frac{\Omega}{\left(\omega_3 - \omega_1 - \omega_2\right)^2 + \Omega^2} \qquad (23)$$

For the resonant conditions: $\vec{k}_3 - \vec{k}_1 - \vec{k}_2 = 0$ and $\omega_3 - \omega_1 - \omega_2 = 0$, the weak wave theory of Zakharov et al. (1992) assumes that $\Omega \to 0$, implying:

$$\mu_{3-1-2} = \pi\, \delta\left(\omega_3 - \omega_1 - \omega_2\right) \qquad (24)$$

Eldeberky et al. (1996) showed by numerical simulations that the spectral source term for triad interactions results in an artificial energy decay/gain. This non-conservative feature was explained by the specification of the filter bandwidth Ω. As done by Hasselmann and Hasselmann (1985) for quadruplets interactions, we exploited the basic symmetry of the triplets interactions to study more accurately the problem of energy conservation. The interaction coefficient R_{312}, as well as N_{312} and μ_{312} are invariant with respect to permutations between waves 1 and 2. So, for the collision:

$$\vec{k}_3 - \vec{k}_1 - \vec{k}_2 = 0 \qquad (25)$$

the changes Δn_i in wave action per unit time for the three wavenumbers can be expressed by:

$$\begin{Bmatrix} \Delta n_{\vec{k}_1} \\ \Delta n_{\vec{k}_2} \\ \Delta n_{\vec{k}_3} \end{Bmatrix} = \begin{Bmatrix} -1 \\ -1 \\ +1 \end{Bmatrix} 4 R^2_{312} N_{312} \mu_{312} \delta\left(\vec{k}_3 - \vec{k}_2 - \vec{k}_1\right) d\vec{k}_1 d\vec{k}_2 d\vec{k}_3 \qquad (26)$$

leading to:

$$\begin{Bmatrix} \Delta F_{\vec{k}_1} \\ \Delta F_{\vec{k}_2} \\ \Delta F_{\vec{k}_3} \end{Bmatrix} = \begin{Bmatrix} -f_1 \\ -f_2 \\ +f_3 \end{Bmatrix} 8\pi R^2_{312} N_{312} \mu_{312} \delta\left(\vec{k}_3 - \vec{k}_2 - \vec{k}_1\right) d\vec{k}_1 d\vec{k}_2 d\vec{k}_3 \qquad (27)$$

(26) and (27) show that, for resonant three wave interactions $f_3 = f_1 + f_2$, only the

conservation of energy applies, as expected (Komen et al., 1994). Non-conservation of energy occurs for near-resonant interactions when the linear dispersion relationship is used to link the wavenumber to the frequency since $f^{lin}(\vec{k}_3) < f^{lin}(\vec{k}_1) + f^{lin}(\vec{k}_2)$. The outcome is a decay of energy during the generation of bound super-harmonics and an increase in energy during the generation of bound sub-harmonics.

For its implementation in a spectral wave model, the SPZ source term is expressed in terms of frequency-directional variance density function $F(f,\theta)$ (Eldeberky et al., 1996):

$$S(\omega_3,\theta_3) = 16\pi^2 g \int_0^{\infty}\int_0^{2\pi} \frac{c_2 Cg_2}{\omega_1 \omega_2^2}\left(T_{312} - 2T_{132}\right) d\omega_1 d\theta_1 \qquad (28)$$

where

$$T_{312} = R_{312}^2\ \mu_{312}\left[\frac{\omega_3}{Cg_3}F_1F_2 - \frac{\omega_1}{Cg_1}F_3F_2 - \frac{\omega_2}{Cg_2}F_1F_3\right] \qquad (29)$$

T_{312} and T_{132} represent the sum ($\vec{k}_3 = \vec{k}_1 + \vec{k}_2$) and difference ($\vec{k}_3 = \vec{k}_1 - \vec{k}_2$) interactions. The formulation is directionally coupled and allows for both collinear and non-collinear interactions.

LTA model:

The parametrized LTA model proposed by Eldeberky and Battjes (1995) and Eldeberky (1996) is based on the evolution equation for complex Fourier amplitudes presented by Madsen and Sorensen (1993). The statistical nature of a wave field allows to transform the equation in term of discrete spectrum of energy. The result is a set of interconnected equations where each moment evolves in terms of the next higher order moment. Assumptions are made on the third-order moment (bispectrum) to close the system. The magnitude of bispectrum (bicoherence) is expressed only in terms of second-order moment (quasi-gaussian hypothesis) whereas a parametrical formulation is given for the phase β (biphase). In order to reduce the computational effort, the triad interactions phenomenon is restricted to self-self interactions. Finally, the net source term is given by (Eldeberky, 1996):

$$\begin{aligned} S_{nl}(f_p) &= S_{nl}^{+}(f_p) + S_{nl}^{-}(f_p) \\ S_{nl}^{+}(f_p) &= \alpha\, c_p\, Cg_p\, R^2_{(p/2,p/2)} \sin\left|\beta_{p/2,p/2}\right| \left[F^2(f_{p/2}) - 2F(f_p)F(f_{p/2})\right] \\ S_{nl}^{-}(f_p) &= -2\, S_{nl}^{+}(f_{2p}) \end{aligned} \qquad (30)$$

$S_{nl}^{\pm}$ represents the positive and negative contributions to the self-interactions; c_p and Cg_p are the phase and group velocities for the p harmonic, R is the sum interaction coefficient derived from the deterministic evolution equation and α is a tuning parameter.

Stochastic Parametrized Boussinesq (SPB) model:

By using the statistical closure hypothesis proposed by Holloway (1980), we built up a stochastic model based on the 2D evolution equation for complex Fourier amplitudes presented in §2. We define the complex wave amplitude C_p as:

$$C_p = A_p\, e^{-i\psi_p} \qquad (31)$$

So, the evolution equation for C_p reads, from (10):

$$\frac{\partial C_p}{\partial t}+\vec{C}g_p.\vec{\nabla}C_p+\frac{1}{2}\frac{Cg_p}{k_p}\vec{\nabla}.\vec{k}_p\,C_p+\frac{S_{3,p}-S_{4,p}}{2S_{1,p}}C_p=-\,i\frac{S_{2,p}}{S_{1,p}}\left(\vec{k}_p.\vec{k}_p\right)C_p + \frac{ig}{2S_{1,p}}\sum_{m=-\infty}^{\infty}R_{m,p-m}C_mC_{p-m} \qquad (32)$$

Since:

$$\frac{\partial\left\langle C_pC_p^*\right\rangle}{\partial t}=\left\langle C_p\frac{\partial C_p^*}{\partial t}\right\rangle+\left\langle C_p^*\frac{\partial C_p}{\partial t}\right\rangle \qquad (33)$$

and,

$$\vec{\nabla}\left\langle C_pC_p^*\right\rangle=\left\langle C_p\vec{\nabla}C_p^*\right\rangle+\left\langle C_p^*\vec{\nabla}C_p\right\rangle \qquad (34)$$

by defining the discrete variance density F_p as:

$$F_p=\left\langle C_pC_p^*\right\rangle \qquad (35)$$

the evolution equation for F_p writes:

$$\frac{\partial F_p}{\partial t}+\vec{C}g_p.\vec{\nabla}F_p+\frac{Cg_p}{k_p}\left(\vec{\nabla}.\vec{k}_p\right)F_p+\frac{S_{3,p}-S_{4,p}}{S_{1,p}}F_p=-\frac{g}{S_{1,p}}\sum_{m=-\infty}^{\infty}R_{m,p-m}\,\mathrm{Im}\left(B_{m,p-m}\right) \qquad (36)$$

where $B_{m,p-m}=\left\langle C_p^*C_mC_{p-m}\right\rangle$ is the bispectrum. When $B=1/15$, Madsen et Sorensen (1992) have shown that the shoaling term corresponding to their extended Boussinesq equations fits quite satisfactorily the shoaling term of the first order Stokes theory (percentage errors less than 6% for $h/\lambda_0<0.3$). So, we write (36) in the following form:

$$\frac{\partial F_p}{\partial t}+\vec{\nabla}.\left(\vec{C}g_pF_p\right)=-\frac{g}{S_{1,p}}\sum_{m=-\infty}^{\infty}R_{m,p-m}\,\mathrm{Im}\left(B_{m,p-m}\right) \qquad (37)$$

where $\vec{C}g$ refers here to the group celerity of the first order Stokes theory.

To derive an expression for the bispectrum, we assume stationary conditions. In the limit $h_x\to 0$, (32) is reduced to:

$$\vec{k}_p.\vec{\nabla}\left(C_p\right)+i\left(\vec{k}_p.\vec{k}_p\right)C_p=\frac{ig}{2S_{2,p}}\sum_{m=-\infty}^{\infty}R_{m,p-m}C_mC_{p-m} \qquad (38)$$

The complex amplitudes, C_p, are expanded in a perturbation series with respect to ε:

$$C_p=\varepsilon C_p^{(1)}+\varepsilon^2C_p^{(2)}+\ldots \qquad (39)$$

and (38) has a simple steady solution:

$$C_p^{(2)}=\frac{ig}{2S_{2,p}}\sum_{m=-\infty}^{\infty}R_{m,p-m}C_m^{(1)}C_{p-m}^{(1)}\,\Delta\left(\vec{k},\vec{x}\right) \qquad (40)$$

with $\Delta\left(\vec{k},\vec{x}\right)=\dfrac{1-e^{-i\int\vec{k}.d\vec{x}}}{i\left(\vec{k}.\vec{k}_p\right)}$ (41)

and $\vec{k}=\vec{k}_p-\vec{k}_{p-m}-\vec{k}_m$ (42)

At lowest order, the bispectrum vanishes (gaussian wave field):

$$\left\langle C_p^{*(1)} C_{p-m}^{(1)} C_m^{(1)} \right\rangle = 0 \tag{43}$$

Here, $\left\langle C_p^* C_{p-m} C_m \right\rangle$ is decomposed as:

$$\left\langle C_p^* C_{p-m} C_m \right\rangle = \left\langle C_p^{*(1)} C_{p-m}^{(1)} C_m^{(2)} \right\rangle + \left\langle C_p^{*(1)} C_{p-m}^{(2)} C_m^{(1)} \right\rangle + \left\langle C_p^{*(2)} C_{p-m}^{(1)} C_m^{(1)} \right\rangle \tag{44}$$

Substitution of the steady contribution of (40) into (44) leads to:

$$\begin{aligned}\left\langle C_p^* C_{p-m} C_m \right\rangle = {} & \frac{ig}{2 S_{2,m} k_m} \sum_{q=-\infty}^{\infty} R_{m-q,q} \left\langle C_q^{(1)} C_{m-q}^{(1)} C_p^{*(1)} C_{p-m}^{(1)} \right\rangle \frac{1}{i\left|\vec{k}_m - \vec{k}_{m-q} - \vec{k}_q\right|} \\ & + \frac{ig}{2 S_{2,p-m} k_{p-m}} \sum_{q=-\infty}^{\infty} R_{p-m-q,q} \left\langle C_q^{(1)} C_{p-m-q}^{(1)} C_p^{*(1)} C_m^{(1)} \right\rangle \frac{1}{i\left|\vec{k}_{p-m} - \vec{k}_{p-m-q} - \vec{k}_q\right|} \\ & + \frac{ig}{2 S_{2,p} k_p} \sum_{q=-\infty}^{\infty} R_{p-q,q} \left\langle C_q^{*(1)} C_{p-q}^{*(1)} C_{p-m}^{(1)} C_m^{(1)} \right\rangle \frac{1}{i\left|\vec{k}_p - \vec{k}_{p-q} - \vec{k}_q\right|}\end{aligned} \tag{45}$$

where $\left\langle C_q^{(1)} C_{m-q}^{(1)} C_p^{*(1)} C_{p-m}^{(1)} \right\rangle$ is the fourth order moment, often referred as the trispectrum. We assume that the sum over the quadruple correlations gives a contribution on the triple correlations (Holloway, 1980). So, (45) transforms to:

$$\begin{aligned}\left(\vec{k}_p - \vec{k}_{p-m} - \vec{k}_m\right)\left\langle C_p^* C_{p-m} C_m \right\rangle = {} & \frac{g R_{m-p,p}}{S_{2,m} k_m} \left\langle C_p^{*(1)} C_p^{(1)} \right\rangle \left\langle C_{p-m}^{*(1)} C_{p-m}^{(1)} \right\rangle \\ & + \frac{g R_{p,-m}}{S_{2,p-m} k_{p-m}} \left\langle C_p^{*(1)} C_p^{(1)} \right\rangle \left\langle C_m^{*(1)} C_m^{(1)} \right\rangle \\ & - \frac{g R_{p-m,m}}{S_{2,p} k_p} \left\langle C_{p-m}^{*(1)} C_{p-m}^{(1)} \right\rangle \left\langle C_m^{*(1)} C_m^{(1)} \right\rangle \\ & + iK \left\langle C_p^* C_{p-m} C_m \right\rangle\end{aligned} \tag{46}$$

where K is the tuning parameter of the model (fixed value). Only the imaginary part of the bispectrum is required to close the evolution equation for the variance density, so:

$$\mathrm{Im}\left(B_{m,p-m}\right) = \frac{g\,K}{K^2 + \Delta k^2} \left[\frac{R_{m-p,p}}{S_{2,m} k_m} F_p F_{p-m} + \frac{R_{-m,p}}{S_{2,p-m} k_{p-m}} F_p F_m - \frac{R_{p-m,m}}{S_{2,p} k_p} F_{p-m} F_m \right] \tag{47}$$

with $\Delta k^2 = \left|\vec{k}_p - \vec{k}_{p-m} - \vec{k}_m\right|^2$

Substitution of equation (47) into (37) leads to:

$$\begin{aligned}& \frac{\partial F_p}{\partial t} + \vec{\nabla}.\left(\vec{C} g_p F_p\right) = \\ & - \frac{g^2}{S_{1,p}} \sum_{m=-\infty}^{\infty} \frac{K}{K^2 + \Delta k^2} R_{m,p-m} \left[\frac{R_{m-p,p}}{S_{2,m} k_m} F_p F_{p-m} + \frac{R_{-m,p}}{S_{2,p-m} k_{p-m}} F_p F_m - \frac{R_{m,p-m}}{S_{2,p} k_p} F_{p-m} F_m \right]\end{aligned} \tag{48}$$

For its implementation in the TOMAWAC spectral wave model, the SPB source term (right hand side of (48)) is expressed in terms of the continuous frequency-directional variance density function $F(f,\theta)$. The source term may be written as:

$$S(f_3,\theta_{\vec{k}_3}) = \int_0^\infty \int_0^{2\pi} \int_0^\infty \int_0^{2\pi} df_1 df_2 d\theta_1 d\theta_2 T_{312}^{SPB} \delta\left(\theta_{\vec{k}_3} - \theta_{\vec{k}_1+\vec{k}_2}\right)\delta(f_3 - f_1 - f_2)$$
$$-2\int_0^\infty \int_0^{2\pi} \int_0^\infty \int_0^{2\pi} df_1 df_2 d\theta_1 d\theta_2 T_{132}^{SPB} \delta\left(\theta_{\vec{k}_3} - \theta_{\vec{k}_1-\vec{k}_2}\right)\delta(f_3 - f_1 + f_2) \quad (49)$$

where T_{312}^{SPB} and T_{132}^{SPB} represent respectively the sum and difference triad interactions. The formulation is directionally coupled and allows for both collinear and non-collinear interactions.

4. NUMERICAL SIMULATIONS:

The three non-linear source terms presented in §3 have been implemented in the spectral wave model TOMAWAC, developed at the Laboratoire National d'Hydraulique (Benoit et al., 1996). Numerical simulations are compared to the experimental laboratory results presented by Nwogu (1994), for the propagation of crossing seas over a constant slope.

Laboratory Basin description (Nwogu, 1994; Nwogu, 1993)

The three-dimensional wave basin (30 m wide, 20 m long and 3 m deep) is located at the Hydraulics Laboratory, National Research Council of Canada. It is equipped with a segmented directional wave generator. Reflections at the basin sidewalls are reduced by wave energy absorbers made of perforated metal sheets. A bathymetric profile was constructed in the basin. It consists in a constant slope beach (1:25) with an impermeable concrete cover. The free surface elevation was measured along the centreline of the basin with a linear array of 23 water level gauges.

Wave conditions imposed at the wave generator

The incident laboratory wave spectrum at the wave generator ($h = 0.56$ m) is bimodal: it is composed of two sea states characterising local sea and swell components (figure 1). The frequency distributions of the sea states are described by a JONSWAP spectrum characterised by the peak period T_p, the significant wave height H_{m0} and the peak enhancement factor γ. The directional distributions are given by the cosine function:

$$D(\theta) = \cos^{2s}(\theta - \theta_0) \quad (50)$$

Table 1 sums up the wave parameters of the target spectrum.

Swell					Local sea				
H_{m0}(m)	T_p(s)	γ	s	θ_0(°)	H_{m0}(m)	T_p(s)	γ	s	θ_0(°)
0.068	2.5	10	22	22.5	0.062	1.5	3.3	6	-22.5

Table 1. Spectral wave parameters characterising the initial spectrum.

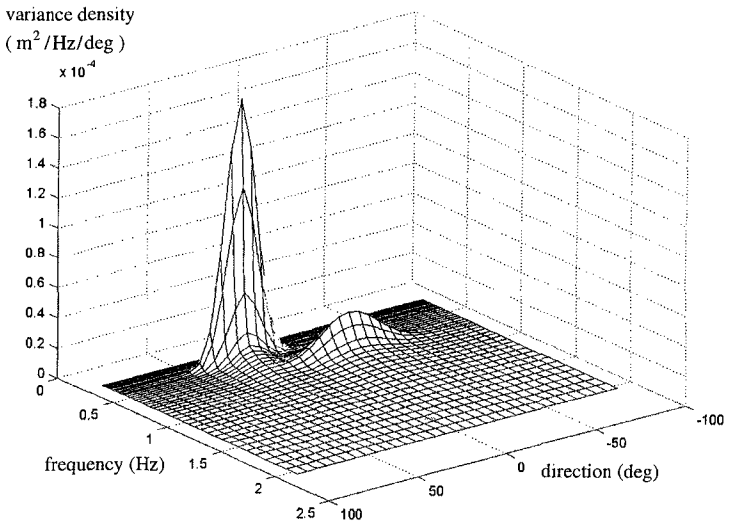

Figure 1 : Directional wave spectrum imposed at the wave generator.

Numerical results

The SPZ source term was activated in the TOMAWAC simulation, with Ω=0.05. The directional wave spectrum obtained in the shallow water area (h = 0.18 m) is presented on figure 2. It shows that the variance density spectrum is affected by refraction, shoaling and non-linear triad interactions. Non-linear wave-wave interactions strongly affect the frequency-directional shape of the spectrum. By collinear wave-wave interactions, energy is transferred from the swell spectral peak towards its two higher harmonics and by non-collinear interactions, energy is transferred from the two primary spectral peaks (swell and local sea) towards the component corresponding to the vector sum of the primary peak wavenumbers. Figure 3 shows a comparison between the non-linear SPZ simulation and measurements for the frequency spectrum. The results obtained with a linear simulation are also presented to point-up the effects of wave-wave interactions on the spectral shape. Figure 3 clearly demonstrates that the non-linear triads interactions cannot be neglected in the shoaling zone. As shown by Eldeberky et al. (1996), the new spectral peaks generated using the SPZ model are shifted towards lower frequencies as compared to measurements. Since the interaction condition between the three interacting waves is imposed through $\delta(\vec{k}_3 - \vec{k}_1 - \vec{k}_2)$, the negative curvature of the linear relationship implies that if $\vec{k}_3 = \vec{k}_1 + \vec{k}_2$, then $f_3 \leq f_1 + f_2$ (Eldeberky et al., 1996).

The simulation using the LTA source term was performed with α=0.5. The numerically simulated shallow water spectrum is presented on figure 4. Since the LTA model is restricted to self-self (collinear) interactions, the simulated shallow water spectrum only shows two new spectral peaks at frequencies $2f_1$ and $2f_2$, where f_1 and f_2 refer here to

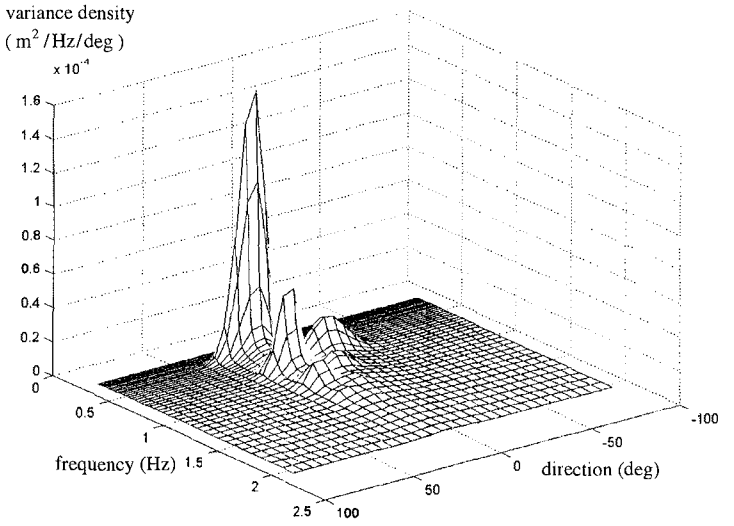

Figure 2: Directional wave spectrum in shallow water (h=0.18m). Non-linear simulation using the SPZ source term.

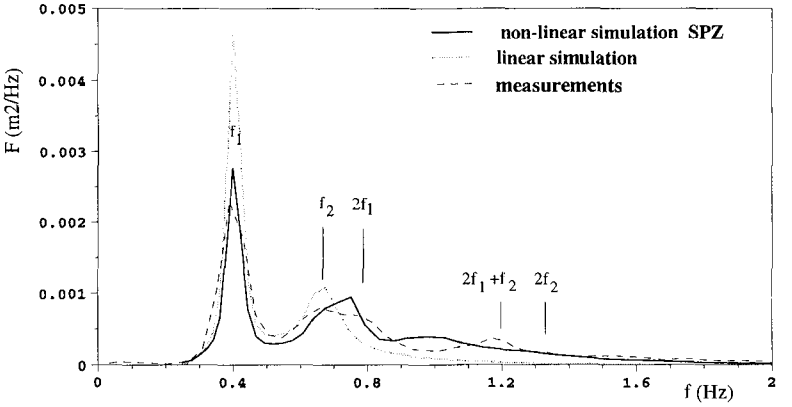

Figure 3: Frequency wave spectrum in shallow water (h=0.18m).

the peak frequencies of the swell and local sea respectively. Figure 5 shows the frequency wave spectrum in shallow water. The energy at $2f_1$ is strongly overestimated by the LTA model, when α=0.5. The transfer of energy towards super-harmonics decreases with α. But, since the LTA model is energy flux conservative and is restricted to self-self interaction, the choice of α requires a balance between an overestimation of the primary peaks or an overestimation of the harmonics.

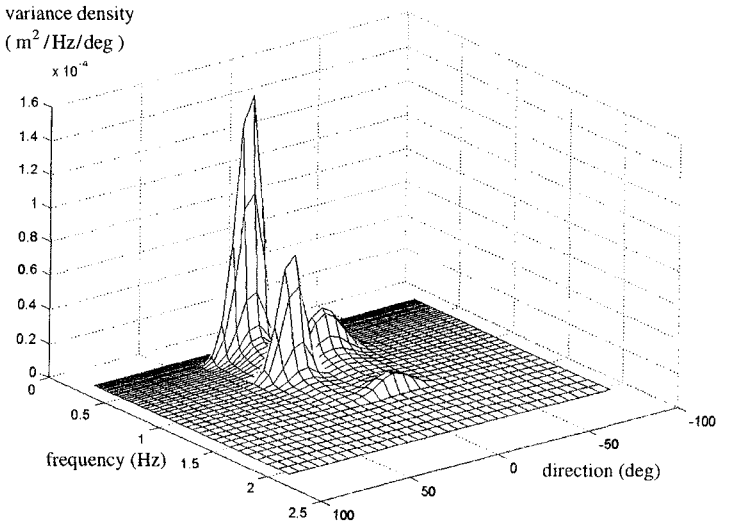

Figure 4: Directional wave spectrum in shallow water (h=0.18m). Non-linear simulation using the LTA source term.

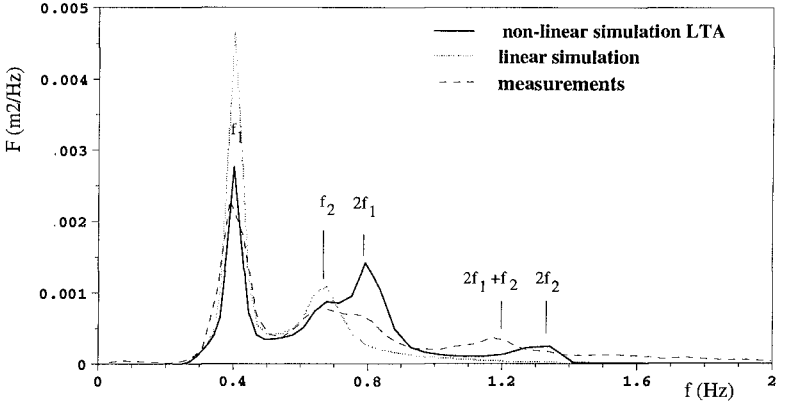

Figure 5: Frequency wave spectrum in shallow water (h=0.18m).

The results obtained with the SPB model are presented on figure 6. Collinear and non-collinear wave-wave interactions are both modelled using the SPB source term. Energy is transferred from the swell spectral peak towards its first and second harmonics. The swell also interacts with the local sea and generates components at the vector sum of the local sea and swell components. A comparison of the model to measurements is presented on figure 7. A relatively good fit to measurements is obtained with the SPB source term.

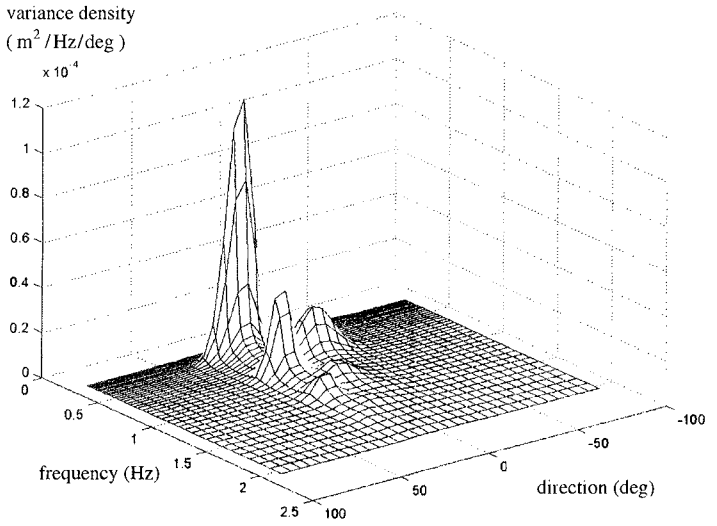

Figure 6: Directional wave spectrum in shallow water (h=0.18m). Non-linear simulation using the SPB source term.

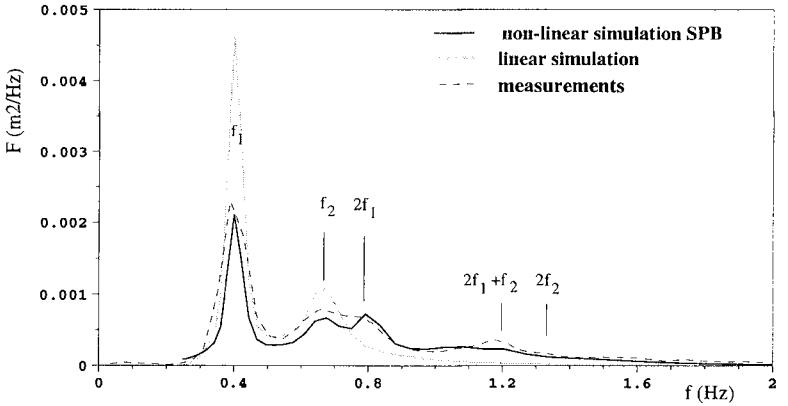

Figure 7: Frequency wave spectrum in shallow water (h=0.18m).

5. CONCLUSIONS:

The spectral deterministic model of Madsen and Sorensen (1993) has been extended to bidimensional situations where combined refraction, shoaling and triads interactions act simultaneously to modify the frequency and directional spreading of the ocean surface energy field. A stochastic source term (SPB) is developed from the deterministic

equations obtained. The model is directionally coupled and implies that the energy transfer among spectral components is governed by collinear and non-collinear near-resonant triad interactions. The consequcnces are not only distortions of the frequency spectrum, but also alterations of the directional spreading of wave energy. This source term has been compared to two other spectral source terms: the LTA and SPZ models. The LTA model is able to catch the main features of energy transfers from the main spectral peaks towards their higher harmonics. It cannot simulate all the new spectral peaks occurring in crossing seas, but it is characterised by a great computational efficiency. The SPZ model and the SPB are directionally coupled and are able to transfer energy to a third component at the sum vector of the primary waves. The SPB model gives the best results since the frequency of the new components corresponds exactly to the sum frequency of the primary waves, whereas with the SPZ model, a shift towards lower frequency is observed (Eldeberky et al., 1996).

6. REFERENCES:

BENOIT M., MARCOS F. and BECQ F. (1996). Development of a third generation shallow-water wave model with unstructured spatial meshing. *Proc. 25th Int. Conf. Coastal Eng.*, pp. 465-478.

ELDEBERKY Y. and BATTJES J.A. (1995). Parametrisation of triads interactions in wave energy models. *Proc. Coastal Dynamics'95*, pp. 140-148.

ELDEBERKY Y. , POLNIKOV V. and BATTJES J.A. (1996). A statistical approach for modeling triad interactions in dispersive waves. *Proc. 25th Int. Conf. Coastal Eng.*, pp. 1088-1101.

ELDEBERKY (1996). Nonlinear transformation of wave spectra in the nearshore zone, Ph.D.-dissertation, Delft University of Technology, Department of Civil Engineering, The Netherlands.

ELGAR S., GUZA R.T. and FREILICH M.H. (1993). Observations of nonlinear interactions in directionally spread shoaling surface gravity waves. *J. Geophys. Res.*, Vol 98, No C11, pp 20299-20305.

FREILICH M.H. and GUZA R.T. (1984). Nonlinear effects on shoaling surface gravity waves. *Phil. Trans. R. Soc. Lond.* A311, pp 1-41.

HASSELMANN S. et HASSELMANN K. (1985). Computations and parameterizations of the nonlinear energy transfer in a gravity-wave spectrum. Part I : A new method for efficient computations of the exact nonlinear transfer integral. *J. Phys. oceanogr.*, Vol. 15, N° 11, pp. 1369-1377.

HOLLOWAY G. (1980). Oceanic internal waves are not weak waves. *J. Phys. Oceanogr.*, 10, pp. 906-914.

KOMEN G.J., CAVALERI L., DONELAN M., HASSELMANN K., HASSELMANN S. et JANSSEN P.A.E.M. (1994). *Dynamics and modelling of ocean waves*, Cambridge University Press, London, 532 pp.

MADSEN P.A. and SORENSEN O.R. (1992). A new form of the Boussinesq equations with improved linear dispersion characteristics. Part 2: a slowly-varying bathymetry. *Coastal Eng.*, 18, pp 183-205.

MADSEN P.A. and SORENSEN O.R. (1993). Bound waves and triads interactions in shallow water. *J. Ocean Eng.* 20 (4), pp 359-388.

NWOGU O. (1993). Alternative form of Boussinesq equations for nearshore wave propagation. *Journal of Waterway, Port, Coastal and Ocean Engineering*, ASCE, 119 (6), pp. 618-638.

NWOGU O. (1994). Nonlinear evolution of directional wave spectra in shallow water. *Proc. 24th Int. Conf. Coastal Eng.*, pp.467-481.

RIS R.C. (1997). Spectral modelling of wind waves in coastal areas. *Communications on Hydraulic and Geotechnical Engineering*. ISSN 0169-6548, report no. 97-4, Delft University of Technology, The Netherlands.

STIASSNIE M. et SHEMER L. (1984). On modifications of the Zakharov equation for surface gravity waves. *J. Fluid Mech.*, Vol. 143, pp. 47-67.

ZAKHAROV V.E (1968). Stability o f periodic waves of finite amplitude on the surface of a deep water, Engl. trans., *J. Appl. Mech. Tech. Phys.*, 4, pp. 86-94.

ZAKHAROV V.E., L'VOV V.S. and FALKOVICH G. (1992). Kolmogorov spectra of turbulence, I. *Wave Turbulence*, Springer verlag.

EFFECTS OF WAVE REFLECTION AND DISSIPATION ON WAVE-INDUCED SECOND ORDER MAGNITUDES

Fernando J. Méndez[1], Iñigo J. Losada[2], Associate Member, ASCE, Robert A. Dalrymple[3], F., ASCE, and M.A. Losada[4], Member, ASCE

Abstract

The influence of reflection and dissipation on wave-induced mean magnitudes is studied. Starting from linear wave theory the second order quantities are derived in terms of transfer functions considering regular as well as irregular waves. It is shown that any reflective and dissipative natural or artificial structure such as a vegetation field, or an emerged or submerged breakwater, induces spatial variations of the mean quantities such as the mean water level, mass flux, energy flux or radiation stress. The evolution of these magnitudes is analogous to their behavior in the surf zone, showing wave damping and modulation. Compared with the experimental results, the models presented are able to reproduce wave height transformation as well as mean water level variations along the dissipative structures with reasonable accuracy.

Introduction

Wave reflection and dissipation are two important wave transformation processes close to structures or at the shoreline. Through the years, research has been carried out in order to understand the role of reflection and dissipation on coastal engineering problems, especially concentrating on wave height evolution. In this paper attention will be paid to how nonlinear quantities obtained from linear wave theory, such as: mass transport, mean water level, momentum flux, energy flux, radiation stress, etc., are affected by wave reflection and

[1] Postdoctoral Researcher. Ocean & Coastal Research Group. Dpto. de Ciencias y Técnicas del Agua y del Medio Ambiente. Universidad de Cantabria. Av. de los Castros s/n. 39005 Santander. Spain.
[2] Associate Professor. Ocean & Coastal Research Group.
[3] Professor and Director, Center for Applied Coastal Research. University of Delaware, Newark, DE 19716.
[4] Professor, Dpto. de Ingeniería Civil. Universidad de Granada. Campus de la Cartuja. 18071 Granada. Spain.

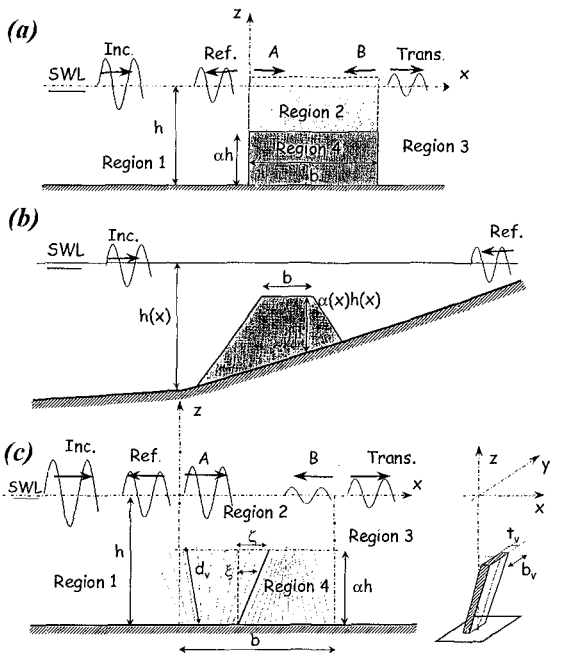

Figure 1. Definition Sketch

dissipation. Reflection and dissipation are considered to be induced by natural (vegetation) or artificial emerged or submerged permeable structures. Dissipation by wave breaking is neglected in most of the cases considered since its effects are well known in the surf zone. The detailed examination of these hydrodynamic mean quantities will be a first step to analyze the influence of the presence of the structure on the morphodynamics of its vicinity.

Theory

Starting from linear wave theory the second order quantities are derived assuming complex reflection and transmission coefficients including magnitude and phase information. The coefficients and wave amplitudes can be calculated solving the first order problem. The models used are able to consider several structure geometries, porous material characteristics and incident wave climates. Therefore, it can be established how each of the second order magnitudes is affected by these parameters.

For an emerged vertical permeable breakwater on a horizontal bottom, Fig. 1*a*, the solution based on an eigenfunction expansion presented in Dalrymple *et al.* (1991) is used to evaluate the first order problem. Regular, oblique incident waves are considered to impinge the structure. As a result the potential inside and outside the structure is known and conse-

quently the free surface evolution, velocity, acceleration and pressure field at any point in the domain considered.
A similar approach is used for a submerged permeable step, Fig. 1*a*, as shown in Losada *et al.* (1996a and b). In these papers the solution also considers irregular incident waves and the model is extended to analyze submerged permeable structures of arbitrary geometry on a sloping bottom, Fig. 1*b*, using a modified mild slope equation. The equation said is suitable to include wave breaking effects via a Dally *et al.* (1985) breaking model or others like the one proposed in Rojakanamthorn *et al.* (1990).
In order to consider a natural reflective, dissipative medium different than a beach a vegetation field is studied, Fig. 1*c*. The wave-induced first order kinematics and dynamics under regular and irregular waves is evaluated extending the work of Kobayashi *et al.* (1993) and Dubi and Torum (1994, 1996) as explained in Méndez (1997).
Once the first order solution is known for any of the structures considered, mean water level, mass flux, energy flux and radiation stresses can be calculated. These magnitudes, time averaged and correct to second order are proportional to the wave height squared. Regular as well as irregular waves are considered.
The expressions of the mean quantities are formulated in a general form in terms of transfer functions which vary depending on the structure considered.

Mass transport

To obtain the total mass flux in the $x-$direction, M_x, the following integration has to be carried out

$$M_x = \overline{\int_{-h}^{\eta} \rho u dz} = \overline{\int_{-h}^{0} \rho u dz} + \overline{\int_{0}^{\eta} \rho u dz} = \overline{\int_{0}^{\eta} \rho u dz} \tag{1}$$

Expressing the horizontal velocity in terms of a Taylor series, to second order and using transfer functions, the mass flux in the $x-$direction for a monochromatic wave train is

$$M_x = \frac{1}{2} a^2 \rho \, \mathrm{Re}[H_\eta H_u^*]\Big|_{z=0} \tag{2}$$

where $(*)$ stands for complex conjugate, ρ is the water density, a the incident wave amplitude and Re[] stands for real part of the magnitude in brackets.
The mass flux can be expressed in terms of the incident directional spectrum of the free surface η, $S_\eta(f)G(f,\theta)$, by applying the results from the linear theory to individual spectral components, Battjes (1974), where $S_\eta(f)$ is a frequency energy spectrum and $G(f,\theta)$ is a directional spreading function. This gives

$$M_x = \rho \int_{-\pi}^{\pi} \int_{0}^{\infty} \mathrm{Re}[H_\eta H_u^*]|_{z=0} \, S_\eta(f) G(f,\theta) df \, d\theta \tag{3}$$

For an incident unidirectional spectrum, $S_\eta(f)$, the mass flux is

$$M_x = \rho \int_{0}^{\infty} \mathrm{Re}[H_\eta H_u^*]|_{z=0} \, S_\eta(f) df \tag{4}$$

Assuming a very narrow incident spectrum (one unique component with amplitude a) we

obtain $\int_0^\infty S_\eta(f)df = \frac{1}{2}a^2$ and, therefore, the mass flux can be expressed as eq. (2).

Mean water level

The second order mean water surface displacement, $\bar{\eta}$, can be evaluated averaging the Bernoulli equation over a wave period. Neglecting third order terms and higher, yields:

$$\bar{\eta} = -\frac{1}{2g}\left(\overline{u^2} + \overline{v^2} - \overline{w^2}\right)\Big|_{z=0} + \frac{\overline{C(t)}}{g} \tag{5}$$

In terms of the transfer functions the mean water level may be expressed as:

$$\bar{\eta} = -\frac{1}{4g}a^2\left(|H_u|^2 + |H_v|^2 - |H_w|^2\right)\Big|_{z=0} + \frac{\overline{C(t)}}{g} \tag{6}$$

where the transfer function expression varies depending on the region where the mean water level has to be evaluated.

Radiation stress

The radiation stress will be affected by the presence of reflected waves and the dissipation induced by the flow through the porous material or breaking. The four components of the radiation tensor in a fluid region are in terms of the transfer functions

$$S_{xx} = \frac{1}{2}a^2\int_{-h}^{0}\rho\left(|H_u|^2 - |H_w|^2\right)dz + \frac{1}{4}\rho g a^2|H_\eta|^2 \tag{7}$$

$$S_{yy} = \frac{1}{2}a^2\int_{-h}^{0}\rho\left(|H_v|^2 - |H_w|^2\right)dz + \frac{1}{4}\rho g a^2|H_\eta|^2 \tag{8}$$

$$S_{xy} = \frac{1}{2}a^2\int_{-h}^{0}\rho\,\mathrm{Re}[H_u H_v^*]dz \tag{9}$$

where h is the water depth.

Above and inside a porous layer the components of the radiation stress due to the wave-induced velocities have to be multiplied by the factor εs

$$\begin{aligned} S_{xx} &= \frac{1}{2}a^2\int_{-h}^{-h+\alpha h}\rho s\varepsilon\left(|H_u|^2 - |H_w|^2\right)dz + \\ &\quad \frac{1}{2}a^2\int_{-h+\alpha h}^{0}\rho\left(|H_u|^2 - |H_w|^2\right)dz + \frac{1}{4}\rho g a^2|H_\eta|^2 \end{aligned} \tag{10}$$

$$\begin{aligned} S_{yy} &= \frac{1}{2}a^2\int_{-h}^{-h+\alpha h}\rho s\varepsilon\left(|H_v|^2 - |H_w|^2\right)dz + \\ &\quad \frac{1}{2}a^2\int_{-h+\alpha h}^{0}\rho\left(|H_v|^2 - |H_w|^2\right)dz + \frac{1}{4}\rho g a^2|H_\eta|^2 \end{aligned} \tag{11}$$

$$S_{xy} = \frac{1}{2}a^2 \int_{-h}^{-h+\alpha h} \rho s\varepsilon \,\mathrm{Re}[H_u H_v^*]dz + \frac{1}{2}a^2 \int_{-h+\alpha h}^{0} \rho \,\mathrm{Re}[H_u H_v^*]dz \quad (12)$$

where ε is the porosity of the porous material and s an inertia coefficient, generally taken to be one and αh is the height of the porous material. Note that $\alpha = 1$ corresponds to an emerged vertical permeable structure.
In the Appendix transfer functions, including evanescent modes, in eqs. (2) to (12) for regular incident waves impinging on a submerged permeable step of height αh are given as an example.

Results

In Fig. 2 the wave height, H_{rms} and the mean water level, $\bar{\eta}$ evolution is presented, under non-breaking conditions, along two different submerged steps of identical geometry and different material (impermeable and permeable with $D_{50} = 2.09$ cm and $\varepsilon = 0.521$). The step geometry is given by $\alpha h = 0.385\, m$ and $b = 0.8$ m. Different incident wave conditions have been also considered in the experiments described in Losada *et al.* (1997). The mean water level variation has been obtained using eq. (6) and (14) to (14).
Fig. 3 shows the experimental results in Rivero *et al.* (1998) versus the numerical results obtained using the mild slope model, Losada *et al.* (1996a) for a submerged breakwater, with 1:1.5 slopes on both sides, a crown width of 0.61 m and constructed with an impermeable core and an armour layer of quarrystones with mean weight of 25 Kg. The water depth at the toe of the structure was 1.50 m. The mean water level variation is solved using the time-averaged and depth-integrated momentum equation

$$\frac{\partial S_{xx}}{\partial x} = -\rho g(h+\bar{\eta})\frac{\partial \bar{\eta}}{\partial x} \quad (13)$$

where S_{xx} is expressed as in eq. (10) and the corresponding transfer functions. Wave breaking takes place along the crest and therefore, it is considered in the modelling using Rojanakamthorn *et al.* (1990), Méndez *et al.* (1998).
In general, there is a good agreement between the experimental and numerical wave height transformation for both the rectangular and the trapezoidal breakwaters under breaking and non-breaking conditions. The modulation of wave height induced by the reflection in front and above the breakwater is very well reproduced by the theory. However, behind the breakwater only the trapezoidal breakwater model does reproduce the modulation well since it considers reflection induced by the slope. This is due to the fact that the eigenfunction model used for the rectangular breakwater assumes the region leewards the structure to be semi-infinite.
Results show that the mean water level presents a set-up induced by the reduction in wave height due to dissipation even without breaking. However, results have shown that the portion of the total set-up induced by wave breaking is more important than the part induced by dissipation inside the pores.
In Fig. 4 the theoretical results for wave height variation and nondimensional mean water

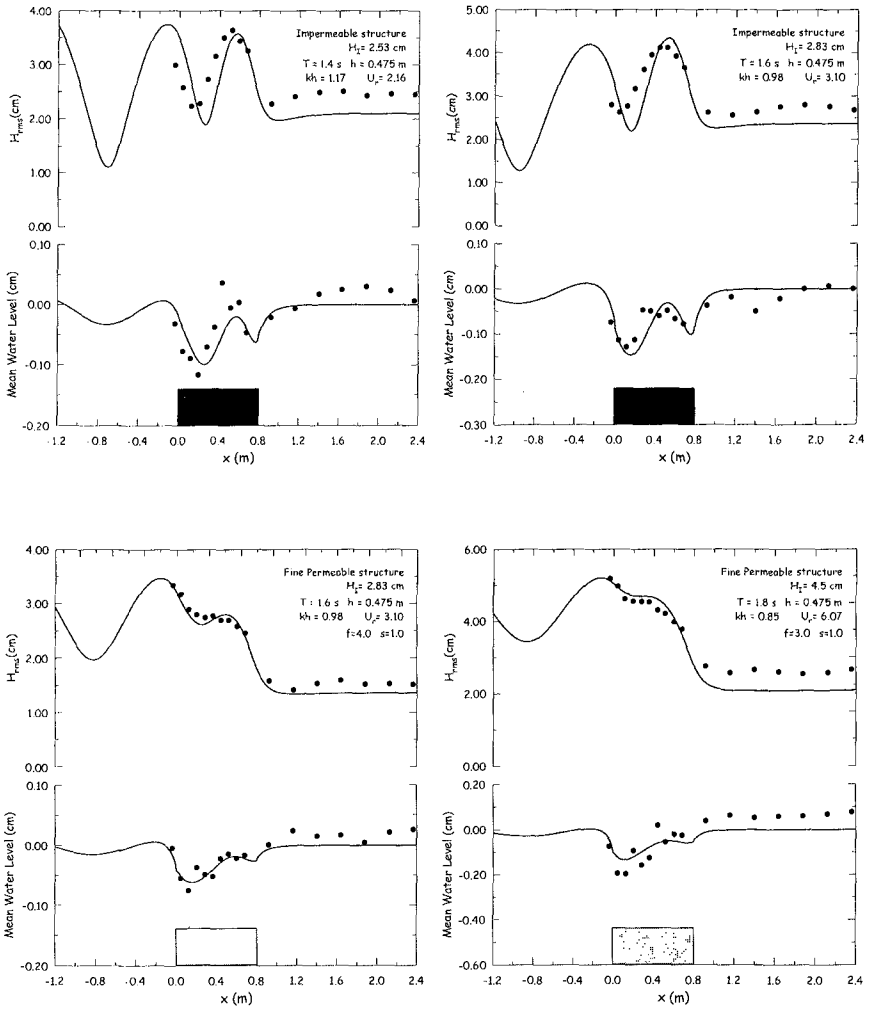

Figure 2. Wave height and mean water level evolution along two different submerged steps (impermeable and permeable)

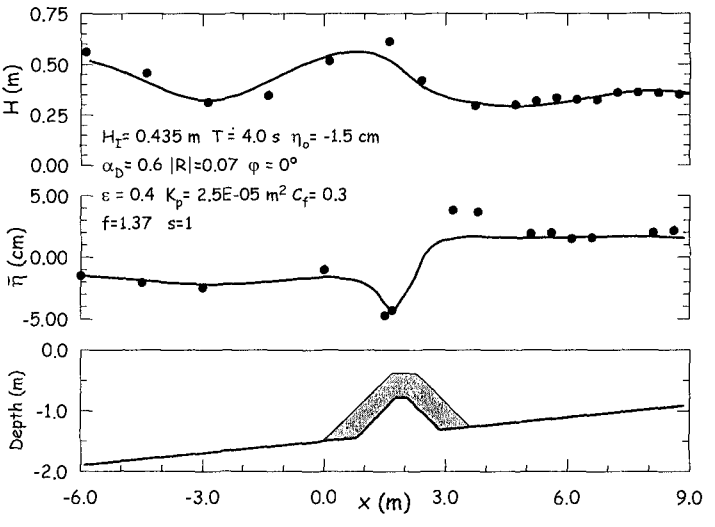

Figure 3. Wave height and mean water level evolution in a submerged breakwater. Comparison between experimental data (Rivero et al., 1998) and numerical model results.

level are compared with the experimental results for artificial seaweed included in Kobayashi *et al.* (1991). Unfortunately, experimental mean water level data are not available. The experiment was carried out in a 27 m long, 0.5 m wide and 0.7 m high wave flume. The artificial seaweed was made of polypropylene strips with a specific gravity $s = \frac{\rho_v}{\rho} = 0.9$. The length, width and thickness of each strip was: $d_v = 0.25\ m$, $b_v = 5.2\ cm$ and $t_v = 0.03\ mm$, respectively. Each of the strips was fixed to a wire net at the bottom of the flume and placed to produce maximum resistance to the incident flow. The vegetation field, located at the center of the flume had a total width of $b = 8\ m$, (Kobayashi *et al.*, 1993, fig. 1). The number of uniformly distributed strips per unit horizontal area was $N = 1110$ and 1490 units/m^2.

The wave height evolution is well reproduced by the model including the modulation in front and above the vegetation field induced by reflection. Associated with the wave height decay along the vegetation field there is a clear wave set-up showing similar modulations as the wave height.

Fig. 5 shows the wave height evolution and mean water level variation on an artificial *laminaria hyperborea* field for regular and irregular wave conditions (*a:* JONSWAP spectrum, $H_{rms,i}$ =1.41 m, $k_p h = 0.65$, $\gamma = 3.3$, $h = 6$ m) and (*b:* JONSWAP spectrum, $H_{rms,i}$ =1.51 m, $k_p h = 0.51$, $\gamma = 3.3$, $h = 6$ m). $H_{rms,i}$, is the incident root-mean-square wave height. The theoretical results are compared with the experimental data in Dubi (1995). C_D is the drag coefficient used for calibration.

The theoretical and experimental results show the modulation induced by the reflection

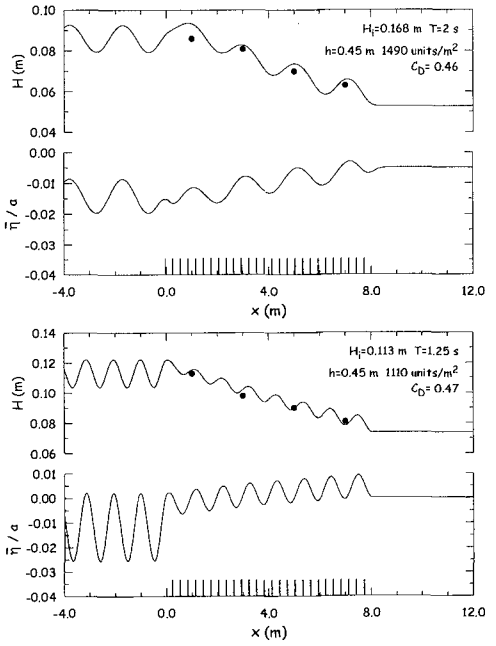

Figure 4. Wave height and mean water level evolution in a submerged vegetation field. Comparison between experimental data (Kobayashi et al., 1991) and numerical model results.

at the front and back face of the vegetation field. This modulation is not present in the theoretical models presented in Dubi and Torum (1994, 1996) since they did not consider the regions offshore and leewards the vegetation field in their first order solution. Comparing with Fig. 4, it can be seen that for irregular waves, the modulation of H_{rms} along the vegetation field is less pronounced than for regular waves. Even if the agreement between theoretical and experimental results is good it has to be pointed out that the artificial seaweed used in Dubi (1995) is characterized by, at least, two degrees of freedom and not only one as assumed by the model presented in this paper. In fact, the kelp plant consists of a stipe, which can be regarded as a slender vertical cylinder with uniformly distributed mass and a frond. Therefore, the obtained C_D represents a depth-averaged value.

The $x-$components of the radiation stress and energy flux are presented in Fig. 6 for a submerged vegetation field. The second order magnitudes are nondimensionalized using the average energy and the energy flux, respectively. For irregular waves and considering a TMA spectrum with the given characteristics, results are shown for two different μ values. The nondimensional friction coefficient μ, is equivalent to the friction coefficient, f, for porous media and can be calculated using Lorentz hypothesis of equivalent work, Méndez

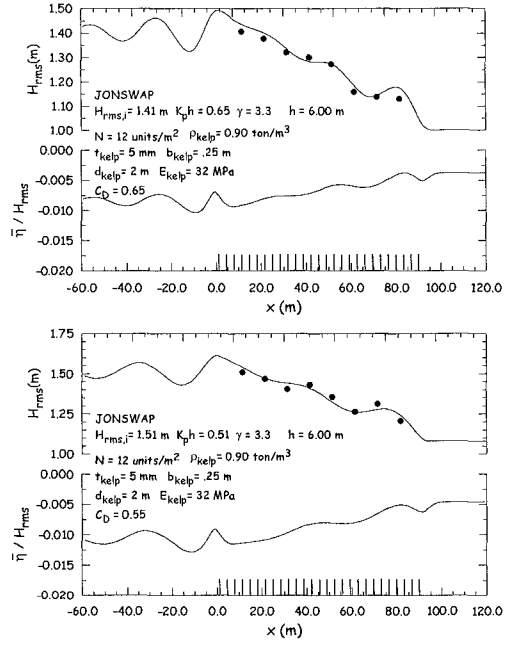

Figure 5. Root-mean-square wave height and mean water level evolution in a submerged vegetation field. Comparison between experimental data (Dubi, 1995) and numerical model results.

(1997). As it can be observed, in front of the vegetation field the energy flux is not very much affected by its presence taking an almost identical value for both μ values considered. However, as the waves propagate along the vegetation field the energy flux strongly decays especially for the higher friction coefficient. In the leeward region the energy flux magnitude is constant since it has been assumed this region to be semiinfinite.

The radiation stress shows a similar pattern only varying in front of the vegetation field, where, for $\mu = 0.5$, the higher reflection induces a modulation of S_{xx}. The strong decay in the radiation stress will result in a set-up along the vegetation field.

For oblique incident regular waves, Fig. 7 presents the evolution of the nondimensional radiation stress component S_{xy} along an emerged permeable vertical structure. Different angles of incidence are considered. From the results it can be concluded that S_{xy} decreases towards the lee face of the vertical structure due to the dissipation induced by the structure. Furthermore, increasing oblique incidence results in higher S_{xy} values until a maximum close to 45^o is reached. For higher angle values S_{xy} decreases due to the fact that S_{xy} is proportional to $\sin 2\theta$.

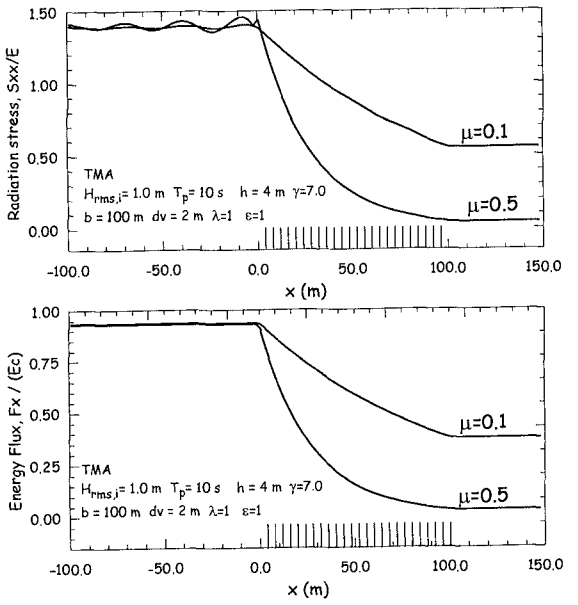

Figure 6. Radiation stress S_{xx} and energy flux evolution in a submerged vegetation field.

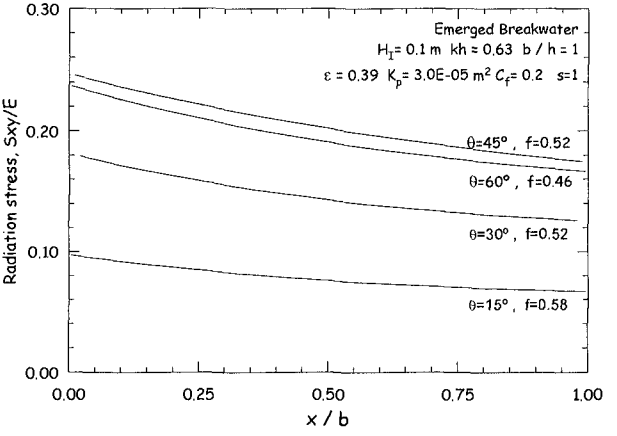

Figure 7. Radiation stress S_{xy} evolution in an emerged permeable breakwater.

Conclusions and further applications

In this paper the influence of reflection and dissipation on wave induced mean quantities is analyzed. The obtained results show that any reflective and dissipative natural, such as vegetation fields, or artificial structure, like emerged or submerged breakwaters induce spatial variations of the mean quantities, water level, mass flux, momentum flux and energy flux, among others, similarly to the surf zone. Computed values are compared to experimental results from different sources. Generally speaking, the agreement between theory and experimentation is very good. From these results the following conclusions may be drawn.

1. The transfer functions are a very convenient and useful tool for computing easy and efficiently the mean quantities in the vicinity of natural or artificial coastal structures.
2. In front of and above the reflective structures considered second order magnitudes are modulated due to the reflection induced by the structure.
3. Over the structure mean momentum flux and mean energy flux are attenuated even if no breaking is present. The dissipation rate is dependent upon wave conditions, breakwater geometry and porous material or vegetation characteristics.
4. The mean water level variations, due to the radiation stress gradients induced by the dissipation associated with both breaking and friction, show a maximum set-down at the beginning of the structure and a progressive increase along the crest reaching its maximum value at the crest or at the leeside of the structure depending on the reflecting conditions. However, it is noticed that the set-up due to breaking is much more important than the one due to dissipation induced by the porous material.
5. The present method can be used to analyze further coastal problems such as: the influence of the mean water level variations on the functionality and stability of breakwaters, the analysis of water table dynamics in shingle beaches, the influence of the presence of dissipative structures on beach profile dynamic models or the evaluation of longshore currents induced by rubble-mound breakwaters, Baquerizo and Losada (1998).

Acknowledgments

This paper is part of the "Surf and Swash Zone Mechanics (SASME)" research project, which is funded by the Comission of the European Communities in the framework of the Marine Science and Technology Programme (MAST) under contract No. MAS3-CT95-0081.

Appendix

In this Appendix the transfer functions, including evanescent modes, in eqs. (2) to (12) for regular incident waves impinging on a submerged permeable step of height αh are given as an example.

$$H_\eta(x) = \begin{cases} \sum_{n=0}^{\infty} \left[e^{-iq_n x} + R_n e^{iq_n x}\right] & x \le 0 \\ \sum_{n=0}^{\infty} \left[A_n e^{-iQ_n x} + B_n e^{iQ_n(x-b)}\right] & 0 \le x \le b \\ \sum_{n=0}^{\infty} T_n e^{-iq_n(x-b)} & x \ge b \end{cases} \tag{A.1}$$

$$H_u(x,z) = \begin{cases} \sum_{n=0}^{\infty} iq_n I_n(z) \left[-e^{-iq_n x} + R_n e^{iq_n x}\right] & \begin{cases} x \le 0 \\ -h \le z \le 0 \end{cases} \\ \sum_{n=0}^{\infty} iQ_n M_n(z) \left[-A_n e^{-iQ_n x} + B_n e^{iQ_n(x-b)}\right] & \begin{cases} 0 \le x \le b \\ -h + \alpha h \le z \le 0 \end{cases} \\ \sum_{n=0}^{\infty} iQ_n P_n(z) \left[-A_n e^{-iQ_n x} + B_n e^{iQ_n(x-b)}\right] & \begin{cases} 0 \le x \le b \\ -h \le z \le -h + \alpha h \end{cases} \\ \sum_{n=0}^{\infty} -iq_n I_n(z) T_n e^{-iq_n(x-b)} & \begin{cases} x \ge b \\ -h \le z \le 0 \end{cases} \end{cases} \tag{A.2}$$

$$H_v(x,z) = \begin{cases} \sum_{n=0}^{\infty} -i\lambda I_n(z) \left[e^{-iq_n x} + R_n e^{iq_n x}\right] & \begin{cases} x \le 0 \\ -h \le z \le 0 \end{cases} \\ \sum_{n=0}^{\infty} -i\lambda M_n(z) \left[A_n e^{-iQ_n x} + B_n e^{iQ_n(x-b)}\right] & \begin{cases} 0 \le x \le b \\ -h + \alpha h \le z \le 0 \end{cases} \\ \sum_{n=0}^{\infty} -i\lambda P_n(z) \left[A_n e^{-iQ_n x} + B_n e^{iQ_n(x-b)}\right] & \begin{cases} 0 \le x \le b \\ -h \le z \le -h + \alpha h \end{cases} \\ \sum_{n=0}^{\infty} -i\lambda I_n(z) T_n e^{-iq_n(x-b)} & \begin{cases} x \ge b \\ -h \le z \le 0 \end{cases} \end{cases} \tag{A.3}$$

$$H_w(x,z) = \begin{cases} \sum_{n=0}^{\infty} \frac{dI_n(z)}{dz} \left[e^{-iq_n x} + R_n e^{iq_n x}\right] & \begin{cases} x \le 0 \\ -h \le z \le 0 \end{cases} \\ \sum_{n=0}^{\infty} \frac{dM_n(z)}{dz} \left[A_n e^{-iQ_n x} + B_n e^{iQ_n(x-b)}\right] & \begin{cases} 0 \le x \le b \\ -h + \alpha h \le z \le 0 \end{cases} \\ \sum_{n=0}^{\infty} \frac{dP_n(z)}{dz} \left[A_n e^{-iQ_n x} + B_n e^{iQ_n(x-b)}\right] & \begin{cases} 0 \le x \le b \\ -h \le z \le -h + \alpha h \end{cases} \\ \sum_{n=0}^{\infty} \frac{dI_n(z)}{dz} T_n e^{-iq_n(x-b)} & \begin{cases} x \ge b \\ -h \le z \le 0 \end{cases} \end{cases} \tag{A.4}$$

where $q_n = \sqrt{k_n^2 - \lambda^2}$, $\lambda = k_o \sin\theta$, θ is the wave incidence angle and k_o the progressive wavenumber in the offshore region. $I_n(z)$, $M_n(z)$ and $P_n(z)$ are depth functions in the different regions defined associated to the nth evanescent mode, Losada *et al.* (1996a). R_o and T_o are the reflection and transmission coefficients, R_n and T_n are the nondimensional coefficients of the evanescent mode n, and k_n is the eigenvalue (wave number) that satisfies the standard dispersion relationship

$$\sigma^2 = g k_n \tanh k_n h \tag{A.5}$$

where σ is the wave frequency.
aA_n and aB_n are the complex amplitudes of the waves propagating above the breakwater and $Q_n = \sqrt{K_n^2 - \lambda^2}$. For normal incidence $Q_n = K_n$.
The complex wavenumber K_n can be determined using the complex dispersion equation derived by Losada *et al.* (1996a) for wave propagation over a porous medium,

$$\sigma^2 - gK_n \tanh K_n h = F_n[\sigma^2 \tanh K_n h - gK_n] \tag{A.6}$$

where

$$F_n = \left(1 - \frac{\varepsilon}{(s - if)}\right) \frac{\tanh K_n \alpha h}{1 - \frac{\varepsilon}{(s-if)} \tanh^2 K_n \alpha h}$$

and f is a linearized friction coefficient that can be obtained using the Lorenz equivalent work hypothesis, Sollitt and Cross (1972). This coefficient depends on the intrinsic characteristics of the permeable material K_p, intrinsic permeability, C_f turbulent friction coefficient and porosity ε. The evaluation of f is flow dependent, therefore the problem has to be solved by iterations, Losada *et al.* (1996a).

References

- Baquerizo, A. and Losada, M.A. (1998). "Longitudinal current induced by oblique waves along coastal structures." Accepted for publication *Coastal Engineering.*
- Battjes, J.A. (1974). *Computation of set-up, longshore currents, run-up and overtopping due to wind-generated waves.* Ph.D. Thesis. Technical University, Delft, 244 pp.
- Dally, W.R., Dean, R.G. and Dalrymple, R. A. (1985). "Wave height variation across beaches of arbitrary profile." *Journal of Geophysical Research,* Vol. 90(C6), pp. 11917-27.
- Dalrymple, R.A., Losada, M.A. and Martin, P. (1991). "Reflection and transmission from porous structures under oblique wave attack". *Journal of Fluid Mechanics.* Vol. 224, pp. 625-644.
- Dubi, A. and Torum, A. (1996). "Wave energy dissipation in kelp vegetation." *Proc. 25th Coastal Engineering Conference,* ASCE, New York, N.Y., pp. 2626-2639.
- Dubi, A. (1995). *Damping of water waves by submerged vegetation. A case study on Laminaria Hyperborea.* Ph. D. Thesis, University of Trondheim, The Norwegian Institute of Technology, Trondheim, Norway, 143 pp.
- Dubi, A. and Torum, A. (1994). "Wave damping by kelp vegetation." *Proc. 24th Coastal Engineering Conference,* ASCE, New York, N.Y., pp. 142-156.
- Kobayashi, N., Raichle, A.W. and Asano, T. (1993). "Wave attenuation by vegetation." *Journal of Waterway, Port, Coastal, and Ocean Engineering,* ASCE, Vol.119, No.1, pp. 30-48.
- Kobayashi, N., Raichle, A.W. and Asano, T. (1991). "Prediction of wave attenuation by vegetation and seaweed." *Research Report No. CACR-91-07,* Center for Applied Coastal Research, University of Delaware, 55 pp.
- Losada, I.J., Silva, R. and Losada, M.A. (1996a). " 3-D non-breaking regular wave

interaction with submerged breakwaters." *Coastal Engineering.* ELSEVIER, Vol. 28, pp. 229-248.

- Losada, I.J., Silva, R. and Losada, M.A. (1996b). " Interaction of non-breaking directional random waves with submerged breakwaters." *Coastal Engineering.* ELSEVIER, Vol. 28, pp. 249-267.
- Losada, I.J., Patterson, M.D. and Losada, M.A. (1997). "Harmonic generation past a submerged porous step." *Coastal Engineering.* ELSEVIER, Vol. 31, pp. 281-304.
- Losada, I.J., Dalrymple, R.A. and Losada, M.A. (1998). "Wave-induced mean flows in vertical rubble mound structures." Submitted to *Coastal Engineering.* ELSEVIER.
- Méndez, F.J. (1997). *Flujos medios inducidos por las ondas de gravedad en medios reflejantes y disipativos naturales o artificiales.* Ph.D. Thesis. University of Cantabria. 344 pp. (In Spanish).
- Méndez, F.J., Losada, I.J. and Losada, M.A. (1998). "Mean magnitudes induced by regular waves in permeable submerged breakwaters". Submitted to *Journal of Waterway, Port, Coastal, and Ocean Engineering,* ASCE.
- Rojanakamthorn, S., Isobe, M. and Watanabe, A. (1990). "Modeling of wave transformation on submerged breakwater." *Proc.* 22nd *Coastal Engineering Conference*, ASCE, New York, N.Y. pp. 1060-1073.
- Rivero, F.J., S.-Arcilla, A., Gironella, X. and Corrons, A. (1998). "Large–scale hydrodynamic experiments in submerged breakwaters". *Proc. Coastal Dynamics '97*, ASCE, Virginia. pp. 754-762.
- Sollitt, C.K. and Cross, R.H. (1972). "Wave transmission through permeable breakwaters". *Proc.* 13th *Coastal Engineering Conference.* ASCE. New York, N.Y. pp. 1827-1846.

Green-Function Analysis of a Wave Field over Arbitrary Bathymetry

Hitoshi Nishimura [1] and Moon-Su Kwak [2]

Abstract

A parabolic approximation of the mild slope equation was derived in terms of polar coordinates to describe waves diverging from a point source. Numerical solutions of the equation were used to extend the application of Green-function method to a wave field over arbitrary bathymetry. Validity of the equation obtained and usefulness of the numerical model were demon-strated through trial computations of wave diffraction, refraction and multiple reflection in model basins and in an actual harbor.

Introduction

Green-function method is the most convenient and rational method for analyzing a wave field including diffraction and multiple reflection. It is, however, difficult to apply the method to a basin with non-uniform depth. Barailler and Gaillard's (1967) approach to cope with this problem was not quite successful, and so far computation of this type has been performed only under the condition of uniform depth.

In the method of this type, distribution of wave sources is assumed on every physical or computational boundary, and a horizontally two-dimensional wave field in question is expressed by superposition of waves emitting from all these sources. Application of the method will be readily extended if we could numerically give such unit solutions for arbitrary bathymetry to replace the Hankel function for a horizontal bed. For this purpose, first a parabolic equation is derived after Radder (1979) in the framework of polar coordinates, and then its numerical solutions are superposed to describe wave fields in model and actual harbors.

[1] Professor, Institute of Engineering Mechanics, University of Tsukuba, Tennodai, Tsukuba, Ibaraki 305-8573, Japan.

[2] Graduate Student, Doctoral Program in Engineering, University of Tsukuba

Parabolic Equation for Unit Solutions

The polar coordinate system will be convenient to describe circular waves emitting from a point source, and it is preferable to provide a rather simple basic equation for them since it has to be numerically solved as many times as the number of wave sources distributed. In this context, a parabolic approxi-mation of the mild slope equation seems to be suitable. Note that a significant part of wave diffraction is automatically taken into account through super-position of unit solutions in the present scheme.

The mild slope equation with respect to the complex wave amplitude is written as

$$\nabla\left(CC_g\nabla\psi\right) + k^2CC_g\psi = 0 \tag{1}$$

where k is the wave number, C is the phase velocity, and C_g is the group velocity of waves, all depending on the local water depth.

As is widely known, a conversion of the dependent variable

$$\phi = \sqrt{CC_g}\cdot\psi \tag{2}$$

reduces the above equation to the form of Helmholtz equation

$$\nabla^2\phi + k^2\phi = 0 \tag{3}$$

or, in terms of the polar coordinates $(r,\ \theta)$,

$$\frac{\partial^2\phi}{\partial r^2} + \frac{1}{r}\frac{\partial\phi}{\partial r} + \frac{1}{r^2}\frac{\partial^2\phi}{\partial\theta^2} + k^2\phi = 0 \tag{4}$$

Now, ϕ is decomposed into two parts ϕ^+ and ϕ^-, each corresponding to waves diverging from and converging to the origin:

$$\phi = \phi^+ + \phi^- \tag{5}$$

and its gradient is also decomposed in the form of

$$\frac{\partial\phi}{\partial r} = A^+\phi^+ + A^-\phi^- \tag{6}$$

Eliminating ϕ^- from these two expressions, we obtain

$$\phi^+ = -\frac{A^-}{A^+ - A^-}\phi + \frac{1}{A^+ - A^-}\frac{\partial\phi}{\partial r} \tag{7}$$

Introduction of asymptotic expressions of Hankel function

$$\phi^{\pm} \approx \sqrt{\frac{2}{\pi kr}} \cdot \exp\left[\pm i\left(kr - \frac{\pi}{4}\right)\right] \tag{8}$$

leads to

$$\frac{\partial \phi^{\pm}}{\partial r} = \left(-\frac{1}{2r} \pm ik\right)\phi^{\pm} \tag{9}$$

or, through comparison with Eq. (6),

$$A^{\pm} = -\frac{1}{2r} \pm ik \tag{10}$$

It is noted that the derivatives of the wave number k were ignored; the validity of such approximation was discussed by Corones (1975).

Equation (7) is then rewritten as

$$\phi^{+} = \alpha\phi + \beta\frac{\partial \phi}{\partial r} \tag{11}$$

where

$$\alpha = \frac{1}{2} - \frac{i}{4kr}, \qquad \beta = -\frac{i}{2k} \tag{12}$$

and, therefore,

$$\frac{\partial \phi^{+}}{\partial r} = \frac{\partial \alpha}{\partial r} + \left(\alpha + \frac{\partial \beta}{\partial r}\right)\frac{\partial \phi}{\partial r} + \beta\frac{\partial^2 \phi}{\partial r^2} \tag{13}$$

Using Eq. (4), the second derivative term can be eliminated as

$$\frac{\partial \phi^{+}}{\partial r} = \left(\frac{\partial \alpha}{\partial r} - \beta k^2 - \frac{\beta}{r^2}\frac{\partial^2}{\partial \theta^2}\right)\phi + \left(\alpha + \frac{\partial \beta}{\partial r} - \frac{\beta}{r}\right)\frac{\partial \phi}{\partial r} \tag{14}$$

Considering Eqs. (5) and (6) and excluding the converging waves, we finally obtain a parabolic equation for diverging waves as follows:

$$\frac{\partial \phi}{\partial r} = \left(-\frac{1}{2r} + ik + \frac{i}{8kr}\right)\phi + \frac{i}{2kr^2}\frac{\partial^2 \phi}{\partial \theta^2} \tag{15}$$

Computation of Unit Solution

To solve Eq. (15) for a wave source, the area of interest is covered by a local r-θ grid with its origin at the source point (Fig. 1). The equation as well as variables is discretized, where the Crank-Nicolson scheme is adopted as in normal Cartesian coordinate analyses. In this case, the origin is a singular point that rejects numerical treatment. A Hankel function solution, therefore, has to be assumed in a very small circular region around the origin, that is, a small area of uniform depth is supposed in the

immediate vicinity of the source point. Starting from the outer edge of the central region, outward marching scheme computation is repeated until reaching the computational boundary.

Validity of the basic equation (15) was examined through trial computation under the simplest condition of uniform depth. Figure 2 shows the numerically calculated amplitude and phase of diverging waves in comparison with the Hankel function. It is seen that the numerical solution is sufficiently accurate except for the close vicinity of the origin. Introduction of asymptotic expression in the derivation of the equation inevitably causes abrupt reduc-tion of accuracy near the origin. Our tentative conclusion is that the equation describes diverging waves with sufficient accuracy for the range of $kr > 0.8$.

Figure 2 illustrates calculated crestlines of diverging waves over varying depth. In this example, straight and parallel depth contours were assumed with linearly varying wave celerity in the on-offshore (x) direction, so that wave refraction can be analytically solved as also shown in the figure. A good agreement is observed between numerical and analytical solutions except for extremely shallow water area, where the relatively coarse computational grid (large grid spacing-wavelength ratio) resulted in reduction of accuracy.

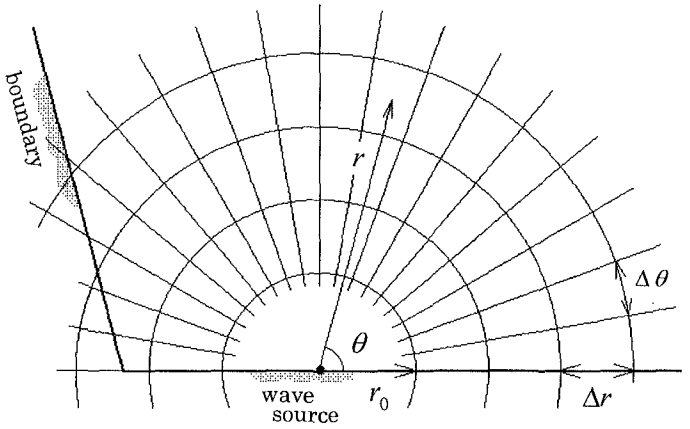

Figure 1. Computational r-θ grid.

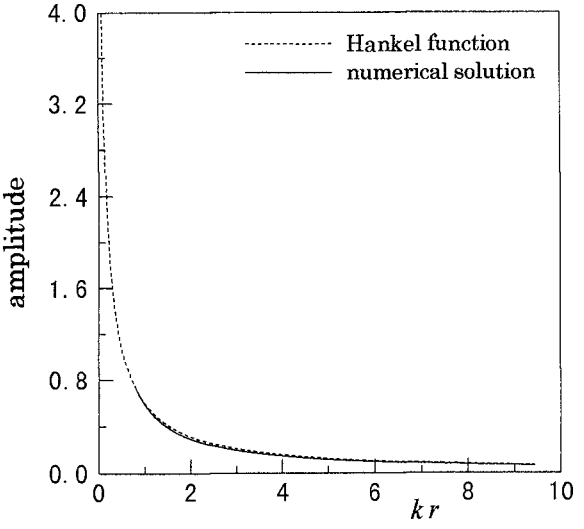

(a) Amplitude

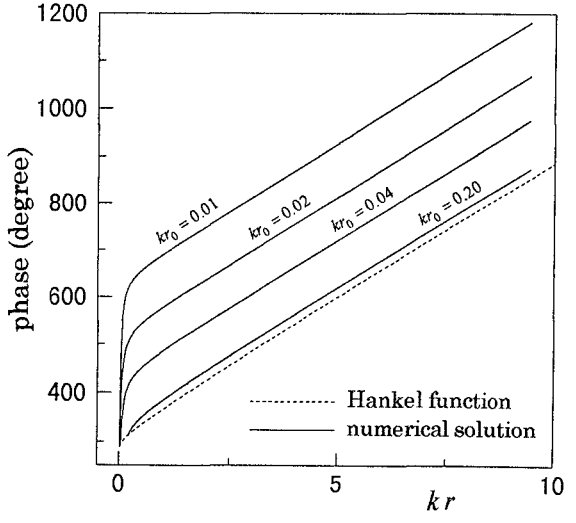

(b) Phase

Figure 2. Comparison of numerical solution with the Hankel function.

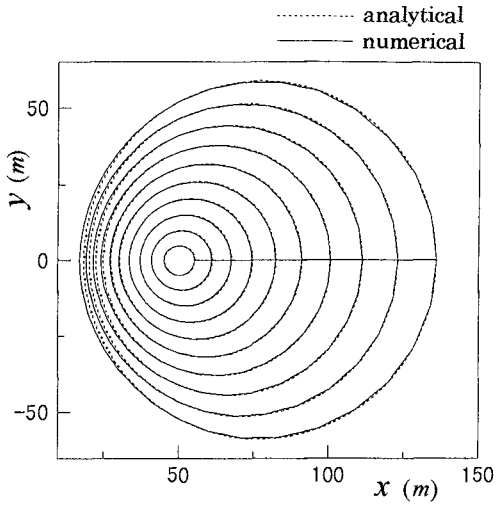

Figure 3. Numerical and analytical solutions for diverging waves from a point source over varying depth.

Application of Generalized Green-Function Method

A water region of interest is first divided into several convex polygonal subregions surrounded by physical and imaginary (artificial) boundaries. Physical boundaries are more or less reflective, and imaginary boundaries are either absorbing or transmissive (merely separating subregions). Continuation conditions of both surface elevation and gradient are imposed along a common boundary connecting two subregions. Wave sources are distributed on every boundary, each producing a field of diverging waves.

One can avoid this procedure of region dividing. If the entire water area is regarded as one region, then all the wave sources have global influence even beyond the physical boundaries. Definition of subregions and local wave sources for it makes the physical implication of each source much more explicit, some representing wave reflection and the other wave transmission. This is important for simple and rational treatment of partial reflection and transmission of waves. In addition to this, computational labor is largely saved by handling multiple subregions of smaller size when unit wave fields are numerically calculated.

An overall wave field in a subregion is given by summation of unit waves from all the sources on its boundaries, automatically satisfying the linear basic equation. Intensities of the wave sources are to be determined

so as to satisfy all the boundary conditions imposed. Rational treatment of boundary conditions of various types was discussed by Nishimura et al. (1994, 1997). Note that the source intensities cannot be correctly determined on the basis of local energy conservation (See also Lee, 1971).

(1) Model harbor with sloping bottom

Figure 3 illustrates a model harbor whose bottom is uniformly sloped. The plan shape of the model was specified by Coastal Engineering Committee, JSCE, for comparison of computational methods. The entire region was divided into four subregions R_1 to R_4 as shown in the figure, and the above described Green-function method was applied to this problem. All the boundaries were divided into small segment of 1/20 wavelength, and the effect of each segment was represented by a wave source located at its middle point. Refraction of unit waves were taken into account by applying the parabolic equation (15) for surface elevation and gradient of unit waves. Reflection coefficient was assumed to be unity for vertical walls and 0.4 for wave absorbing boundaries.

The relative wave height distribution thus obtained is described in Fig. 4 in comparison with the result of hydraulic experiments conducted under similar conditions. It is seen that the computation well reproduces a complicated field of standing waves after multiple diffraction due to breakwaters and multiple reflection due to harbor walls. Diffracted waves

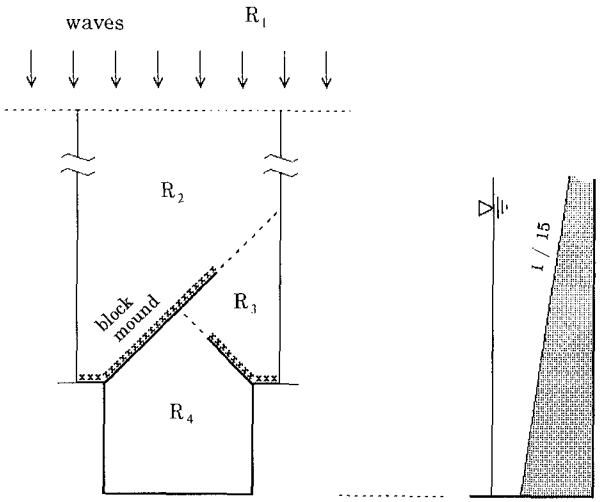

Figure 4. Model basin with sloping bottom.

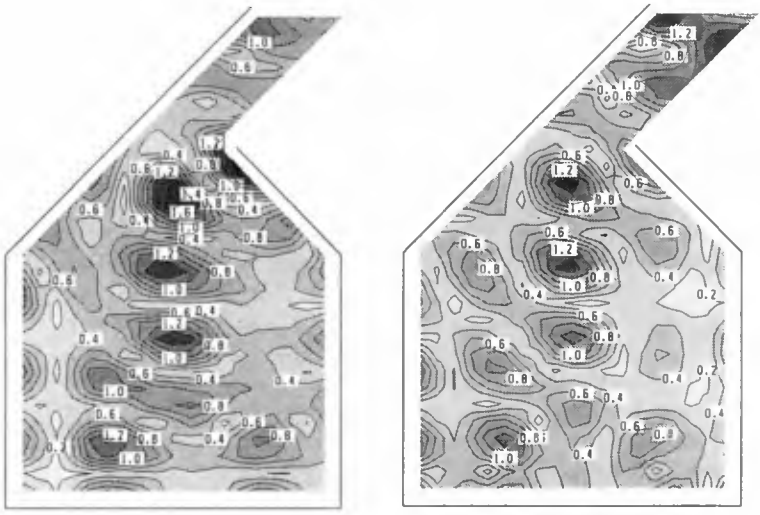

(a) Experiment (b) Calculated

Figure 5. Distribution of relative wave height (period = 0.70s).

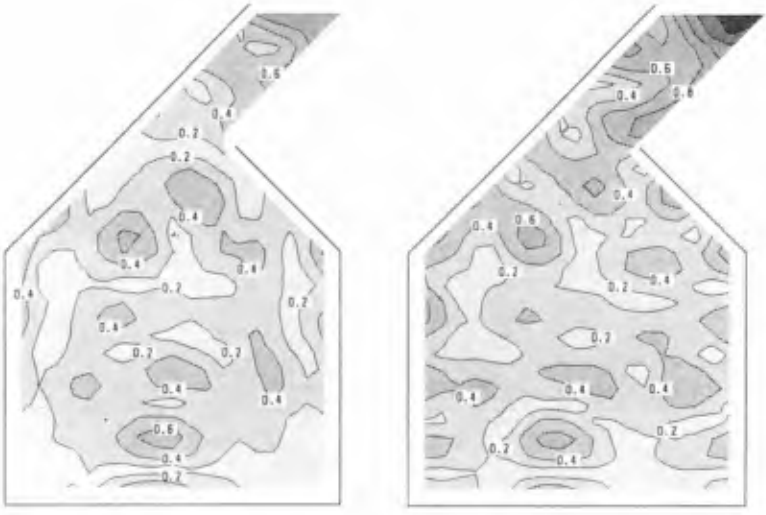

(a) Experiment (b) Calculated

Figure 6. Distribution of relative wave height (period = 0.72s).

are often underestimated in numerical models of direct integration type, but no such tendency is observed here. Sound estimation of wave diffraction is a notable merit of this method.

Under the condition of multiple reflection, a slight difference in the wave period causes significant change in the wave height distribution as demon-strated in Fig. 5. Computation well follows this sensitive response of the basin.

(2) Actual basin with arbitrary bathymetry

For further examination of the present method, it was applied to a wave field in Soma Harbor, Fukushima Pref., Japan. Figure 6 shows location of the harbor as well as depth contours in and around it. The incident wave height and period were assumed at 3.5m and 8.0s. A comparison of calculation and experiment is given in Fig. 7, where the agreement is again reasonable. Slight reduction in accuracy as compared with the previous example may be ascribed to the uncertain evaluation of reflection coefficients (assumed at 0.9 for vertical walls and 0.3 for absorbing walls) and lower resolution (boundary segments of 1/10 wavelength).

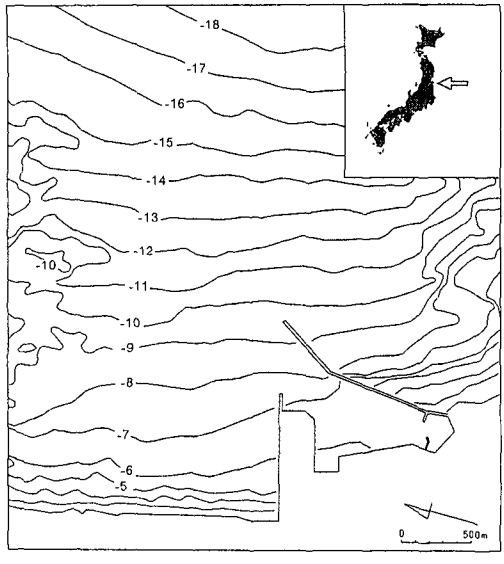

Figure 7. Soma Harbor.

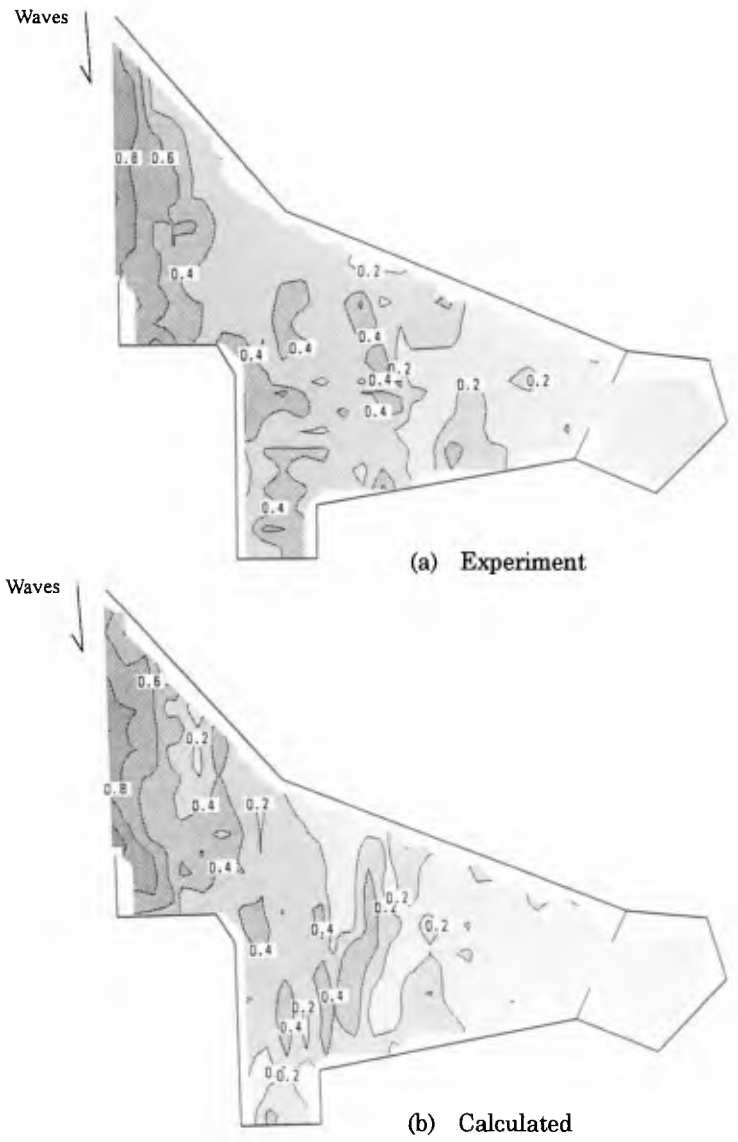

Figure 8. Distribution of relative wave height in Soma Harbor.

Concluding Remarks

A parabolic equation for waves diverging from a point source was derived using asymptotic expression of the Hankel function. It proved that numerical solutions of the equation well works as unit waves in applying the Green-function method to a basin with arbitrary bathymetry. This numerical model quite accurately simulates refraction, diffraction and multiple reflection of waves, providing a useful tool for linear analysis of a horizontally two-dimensional wave field.

Acknowledgment

The authors' gratitude is due to Tetra Co., Ltd., for kindly providing experimental data both for the standard model basin and for Soma Harbor.

References

Barailler, L. and P. Gaillard (1967): Évolution récente des modèles mathématiques d'agitation due á la houl, Calcul de la diffraction en profondeur non uniforme, La Houile Blanche, Vol.22, No.8, pp.861-869.

Corones, J. (1975): Bremmer series that correct parabolic approximations, J. Math. Analy. and Appl., Vol.50, pp.361-372.

Lee, J.-J. (1971): Wave-induced oscillations in harbour of arbitrary geometry, J. Fluid Mech., Vol.45, Part 2, pp.375-394.

Nishimura, H., M. Matsuoka and A. Matsumoto (1994): A generalized Green-function method for wave field analysis, Proc. 24th ICCE, Vol.1, pp.442-454.

Nishimura, H. and M.-S. Kwak (1994): Rigorous formulation of an open boundary condition in Green-function analysis of a wave field, Proc. 7th ICCCBE, Vol.3, pp.2011-2016.

Radder, A. C. (1979): On the parabolic equation method for water-wave propagation, J. Fluid Mech., Vol.95, Part 1, pp.159-176.

Wave Propagation over a Bar and Wave Induced Bed Pressure Gradients.

Dr. ing. Øivind A. Arntsen[1]

Abstract

Wave induced pore pressure and instantaneous liquefaction are known to occur and cause loss of bearing capacity of sand. Wave bottom pressure $\bar{p}$ forms the boundary condition for the wave induced pore pressure. It is believed that not only variation of the pressure itself, but also the variations of its first and second order spatial derivative play an important role in the formation of liquefaction. An experimental and a preliminary numerical study on unidirectional water wave propagation over a bar are presented. Emphasis is placed upon investigation on the wave induced pressure gradient at the seabed. Single sinusoidal, two-component sinusoidal and five-component sinusoidal waves are investigated in a wave flume of constant water density ρ. Only the results for single sinusoidal waves are reported herein. The variation of the dimensionless pressure gradient $C_p = (\partial \bar{p} / \partial x) / (\rho g)$ was within ± 0.4 for all experiments with a tendency of larger values for downslope gradients (negative values) than for upslope. (g is the acceleration gravity). The numerical results, based on the two-dimensional Green-Naghdi theory for fluid sheets - level II, compare well for sea bed pressures and gradients, but the sea surface does not fit the observations so well.

The Numerical Model

Introduction

A new generation water wave model concept has developed during the last two decades. Its fundamental principle is known as the Green-Naghdi theory of fluid sheets,

[1] Associate professor, Department of Structural Engineering, NTNU, N-7034 Trondheim, Norway.
E-mail: oivind.arntsen@bygg.ntnu.no

hereafter referred to simply as GN theory (Green, Laws and Naghdi, 1974). The foundation for its application in water waves is discussed in the original work of Green and Naghdi (1986, 1987).

Webster and Kim (1990) use this theory to investigate the dispersion of large amplitude gravity waves in deep water. A level III GN-theory (a nonlinear 2D fluid sheet model) is used to simulate a train of steep regular waves and a random wave record corresponding to steep seas measured during hurricane Camille. An analysis of the simulated random wave record shows that linear dispersion, Airy theory with Wheeler stretching, often assumed for referring a random wave train from one point in space to another, does not result in conservative estimates of two important quantities used in design: the crest elevation and particle velocity under the crest. In regular waves the model reproduce (and confirmed by laboratory experiments) the tendency that the leading edge of a packet of relatively steep waves always appears to break before very many waves are created.

Demirbilek and Webster (1992a,1992b) derived a version of the GN-theory applicable for shallow water to moderate water depths and where the water depth may vary rapidly. The model named GNWAVE3 is as a nonlinear 2D numerical wave flume that simulates the wave transformation in shallow water in a finite difference scheme. Areas of applications may be wave transformation over submerged obstacles, reflections of waves, time history of bottom-mounted pressure gage measurements for estimation of surface wave conditions in coastal design projects. The theory is particularly suited for the collision of waves with natural and man-made structures, and their impact on preventive and hydraulic structures. The model is intended to be implemented in the Coastal Modeling System (CMS) provided by the Waterways Experiment Station, U.S. Army Corps of Engineers, Vicksburg , USA.

The purpose of using GNWAVE3 in this project is to study the feasibility of its application on the computation of wave motion over a bar. Later, it would be of interest to compare the performance of this model to results obtained with numerical wave flumes based on more conventional wave models (e.g. the Boussinesq formulation) and with more data from field and/or laboratory experiments.

Overview of theory

This overview follows the description of the model development given in Demirbilek and Webster (1992a). The GN approach to water wave theory is fundamentally different from the perturbation methods used in classical wave theory. In contrast to the Stokes and Boussinesq theories, the equations of motion in the GN theory are derived by enforcing exact kinematic and dynamic boundary conditions on the free surface and on the bottom, and by enforcing conservation of mass, but approximating the conservation of momentum. In short, the treatment of the field equation and nonlinear boundary conditions by perturbation methods and GN theory are the antithesis of one another. The essential clue

of GN wave theory is that the vertical dependence of the kinematics of the fluid flow is restricted and prescribed a-priori. That is, a set of shape-functions (like the e^{kz} in deep water Airy theory) that serve as a basis for the vertical dependence is introduced. In this way the method achieves a simplification by reducing the computational domain from three dimensions to two (or from two dimensions to one in the case of 2D flows). The theory also yields governing equations for the flow, which are solved numerically in a more efficient manner than those from a conventional finite-difference, finite-element or similar schemes.

In the following, the theoretical development behind GNWAVE3 is outlined. Although GNWAVE3 is a model for 2D inviscid flow, the development of GN theory in general is not at all limited to such fluids. The governing equations are the GN level II shallow water equations originally constructed by Shields (1986) and reported by Shields and Webster (1988). The coordinate system Oxyz, with the Oz axis oriented vertically up and the Oxy plane horizontal and corresponding to the undisturbed free surface. We assume that the fluid velocity $v(x,y,z;t) = (u, 0, w)$ can be approximated as

$$v(x, z; t) = \sum_{n=0}^{2} W_n(x; t)\, \psi_n(z) \tag{1}$$

where

$$W_n = (u_n, 0, w_n)\,; \quad n = 0,1,2 \tag{2}$$

are vector coefficients associated with the shape-functions $\psi_n(z)$. The vector coefficients are unknown spacial- and time-dependent functions to be determined as a part of the solution. In the general GN-theory the number of shape-functions is not fixed to three. The theory put restrictions on the choice of shape-functions to those that possess the following property:

$$\frac{d\psi_m}{dz} = \sum_{r=0}^{n} a_r^m\ \psi_r\,, \qquad (n \le m) \tag{3}$$

a_r^m are some constants. There are many function sets that satisfy (3). For instance, Webster and Kim (1990) use $\psi_n(z) = z^n\, e^{\alpha z}$, $n = 0,1,2$ as their set of shape-functions for deep-water waves. In GNWAVE3 polynomial functions $\psi_n(z) = z^n$ form the shape-function set. The linear function $\psi_1 = z$ was selected since it coincides with the z dependence found in linear shallow water wave theory.

The kinematic assumption (1) is inserted into the equations for conservation of mass, conservation of momentum (Euler equations), and the kinematic boundary conditions on the free surface $z = \beta(x; t)$ and at the bottom $z = \alpha(x,t)$. These equations are all satisfied identically by this method. When (1) is substituted into the momentum equation and the resulting equation is required to be satisfied everywhere in the fluid domain, many more equations than the required number would be obtained. To overcome this difficulty, the shape-functions ψ_m are used as weighting functions to develop the required number of equations to be solved. Euler's equations are multiplied by each $\psi_n(z)$ and integrated from

the sea bottom to the free surface. The weighted momentum equations express the conservation of momentum in some integral sense and consequently the conservation of momentum is satisfied only approximately. The determination of the evolution equations in terms of derivatives of the primary variables requires a prodigious amount of algebraic manipulation. For theory of level I or of level II it is not too difficult to obtain this by hand, however, for higher level of the theory mathematical symbolic processors should be used.

In GNWAVE3 the velocity profile is modeled as

$$u(x, z; t) = u_0(x;t) + u_1(x;t)z + u_2(x;t)z^2 \tag{4}$$

$$w(x, z; t) = w_0(x;t) + w_1(x;t)z + w_2(x;t)z^2 \tag{5}$$

Fulfillment of the continuity equation implies that $u_2(x;t) \equiv 0$, and consequently the horizontal velocity profile is restricted to linear variation with depth.

It is now possible to eliminate the vertical vector coefficients as well as the integrated pressure coefficients. The final sets of governing equations involving the three unknown functions $\beta(x;t)$, $u_0(x;t)$, $u_1(x;t)$ (free surface elevation and the two remaining coefficients of the horizontal velocity respectively) are rather difficult to derive without the help of mathematical symbolic software.

Although the equations may seem large and complicated they may be integrated with little difficulty. Together they form a system of three coupled, partial differential equations that are of first order in time and of third order in space and the highest order of mixed derivatives are of first order in time and second order in space. Thus the system of equations can be summarized as

$$\boldsymbol{A}\dot{\xi} + \boldsymbol{B}\frac{\partial \dot{\xi}}{\partial x} + \boldsymbol{C}\frac{\partial^2 \dot{\xi}}{\partial x^2} = \boldsymbol{g}\,; \qquad \xi \equiv (\beta, u_0, u_1)^T. \tag{6}$$

The matrices $\boldsymbol{A}$, $\boldsymbol{B}$, $\boldsymbol{C}$ and the vector $\boldsymbol{g}$ are functions of x and β, u_0, u_1 and their derivatives. With prescribed boundary conditions at both ends of the domain the equations can be solved through a numerical technique. The domain of x over which a solution to the equations is desired is assumed to be a finite difference scheme of uniformly spaced grids in the x-direction spaced a distance Δx apart. Time is assumed to be discretised with intervals Δt. The spatial distribution of $\dot{\xi}$ is first found by a central difference technique combined with a forward backward substitution. The updated values for ξ is obtained through a two step forward explicit scheme.

The Pressure Relation

Taking the vector dot product between the vectored equations of motion and the vertical unity vector $\boldsymbol{e}_3$ and integrating from the sea bed to the free surface, we obtain an explicit expression for the bottom pressure ($\boldsymbol{e}_1$ is the x-direction unity vector).

$$\int_\alpha^\beta \left(\frac{\partial(\rho v)}{\partial t} + u\frac{\partial \rho v}{\partial x} + w\frac{\partial \rho v}{\partial z} \right) \cdot \boldsymbol{e}_3 dz = \int_\alpha^\beta \left(-\frac{\partial p}{\partial x}\boldsymbol{e}_1 - \frac{\partial p}{\partial z}\boldsymbol{e}_3 - \rho g \boldsymbol{e}_3 \right) \cdot \boldsymbol{e}_3 dz$$

$$\Downarrow$$

$$\int_\alpha^\beta \left(\frac{\partial(\rho v)}{\partial t} + u\frac{\partial \rho v}{\partial x} + w\frac{\partial \rho v}{\partial z} \cdot \boldsymbol{e}_3 \right) dz = \int_\alpha^\beta \left(-\frac{\partial p}{\partial z} - \rho g \right) dz = -\left(p_\beta - p_\alpha \right) + \rho g(\alpha - \beta) \tag{7}$$

Assuming the surface pressure p_β equal to zero and denoting the bottom pressure $p_\alpha \equiv \bar{p}$ this results in:

$$\bar{p} = -\rho g(\alpha - \beta) + \int_\alpha^\beta \left(\frac{\partial(\rho v)}{\partial t} + u\frac{\partial \rho v}{\partial x} + w\frac{\partial \rho v}{\partial z} \cdot \boldsymbol{e}_3 \right) dz \tag{8}$$

Within the limits of level II theory and uneven bottom this expression can be rewritten in terms of the variables u_0 and u_1 and their derivatives with respect to time and horizontal variation and β in addition to the known bottom variation $\alpha(x)$. The resulting equation is:

$$\bar{p} = \bar{p}_r + \bar{p}_{u_0 t}\frac{\partial u_0}{\partial t} + \bar{p}_{u_0 tx}\frac{\partial^2 u_0}{\partial x \partial t} + \bar{p}_{u_1 t}\frac{\partial u_1}{\partial t} + \bar{p}_{u_1 tx}\frac{\partial u_1}{\partial x \partial t} \tag{9}$$

where

$$\begin{aligned}
\bar{p}_r = &- \{\rho g(\alpha-\beta) - \rho(\alpha-\beta)^2\left(\frac{\partial u_0}{\partial x}\right)^2/2 + \rho\left(\frac{\partial \alpha}{\partial x}\right)^2(\alpha-\beta)u_1(2u_0+(\alpha+\beta)u_1)/2 \\
&+\rho\frac{\partial^2\alpha}{\partial x^2}(\alpha-\beta)(u_0+\alpha u_1)(2u_0+(a_0+\beta)u_1)/2 \quad - \quad \rho\frac{\partial \alpha}{\partial x}(-\alpha+\beta)\frac{\partial u_0}{\partial x}(u_0+\beta u_1) \\
&+\rho(\alpha-\beta)^2\frac{\partial^2 u_0}{\partial x^2}(3u_0+(\alpha+2\beta)u_1)/6 \quad - \quad \rho(\alpha-\beta)^2(\alpha+\beta)\frac{\partial u_0}{\partial x}\frac{\partial u_1}{\partial x}/2 \\
&+\rho\frac{\partial \alpha}{\partial x}(\alpha-\beta)((3\alpha-\beta)u_0+\alpha(\alpha+\beta)u_1)\frac{\partial u_1}{\partial x}/2 \quad - \quad \rho(\alpha-\beta)^2(\alpha+\beta)^2\left(\frac{\partial u_1}{\partial x}\right)^2/8 \\
&+\rho(\alpha-\beta)^2\left(4(2\alpha+\beta)u_0+3(\alpha+\beta)^2u_1\right)\frac{\partial^2 u_1}{\partial x^2}/24\}
\end{aligned}$$

$\bar{p}_{u_0 t} = -\frac{\partial \alpha}{\partial x}(\alpha-\beta)\rho$, $\bar{p}_{u_0 tx} = -(\alpha-\beta)^2\rho/2$, $\bar{p}_{u_1 t} = -\alpha\frac{\partial \alpha}{\partial x}(\alpha-\beta)\rho$ and
$\bar{p}_{u_1 tx} = -(\alpha-\beta)^2(2\alpha+\beta)\rho/6$.

Initial Conditions

For this shallow water study it is assumed that the time history of the waves is known at $x = 0$. The waves are input not only as local wave height history $\beta(0,t)$, but also as a history of the corresponding values of the other variables in this Level II theory ($u_0(0,t)$ and $u_1(0,t)$). These variables are obtained from the solution of steady waves on a flow (linearized for small wave amplitude and flow speed = - celerity of the waves). These linear solutions for waves propagating with a celerity c are:

$$\beta(0,t) = \beta_0 \cos(kx - \omega t) = \beta_0 \cos(k(x - ct)) \tag{10}$$

$$u_0(0,t) = \beta_0 \frac{12g\left(20 + 7(kd_S)^2\right)}{c\left(240 + 104(kd_S)^2 + 3(kd_S)^4\right)} \cos(\omega t) \tag{11}$$

$$u_1(0,t) = \beta_0 \frac{120g(kd_S)^2}{cd_S\left(240 + 104(kd_S)^2 + 3(kd_S)\right)} \cos(\omega t) \tag{12}$$

$$c = \sqrt{\frac{24gd_S\left((kd_S)^2 + 10\right)}{240 + 104(kd_S)^2 + 3(kd_S)^4}} \tag{13}$$

where d_S is the still water depth at the wave generator and g is the acceleration of gravity. Thus, $u(0,z,t) = u_0(0,t) + u_1(0,t)\,z$ is the horizontal particle velocity at the wave paddle. Here z is measured positive upwards from the seabed. Figure 1 compares the distribution to that obtained from Airy wave theory, in the case of a $T = 2.3$ s wave period and a H=0.2 m high wave in water depth of 0.6 m and of a 9.65 s wave of 3.0 m height in 35 m waterdepth.

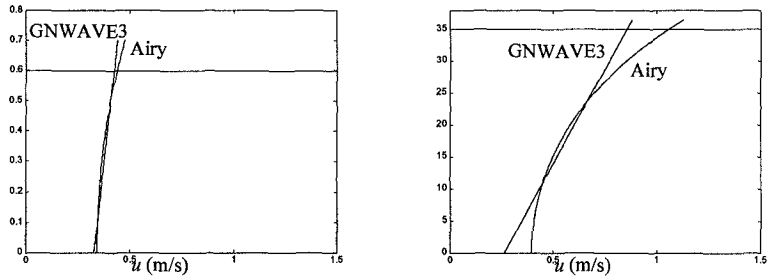

a) $H = 0.2$ m, $T = 2.3$ s, $d_S = 0.6$ m b) $H = 3.0$ m, $T = 9.65$ s, $d_S = 35$ m.

Figure 1. Wavemaker boundary conditions (horizontal particle velocity) in GNWAVE3 compared to Airy linear wave theory.

The boundary condition at the other end of the wave flume is modeled either as fully reflective or fully open.

GNWAVE3 Performance Example

A simple test run of GNWAVE3 shows its capability of time-simulation of waves. This test run is performed with wave-data from one of the experimental runs, but with constant water depth equal to 0.70 m. Other inputs to the model is the same as for the reference experiment *bp136150* described later. A time-series recording at x=5 meters is shown in Figure 2 and a snapshot of the surface elevation after 39.95 seconds is shown in Figure 3. The time function in Figure 2 has been analyzed with respect to zero-upcrossings and also a peak-to-peak analysis to establish two sequences of wave periods. Similarly the function in Figure 3 has been analyzed with respect to zero-upcrossings, and the sequence of identified wave-lengths was found. The results are seen in Figure 4 together with the average values. In Table 1 the derived wave parameters are compared to values obtained by Airy wave theory and by an analytical nonlinear model known as the Fourier-series model, both available in (ACES, 1992). The Fourier-series model requires knowledge of the vertically integrated flow in the flume. It was set equal to zero in this example.

GNWAVE3, which is a numerical model based on the first principles of conservation of momentum and continuity of mass demonstrates stability and accuracy that of sufficient quality for this example test. E.g. the deviations between GNWAVE3 results and Airy theory are less 0.5 % both in wavelength and celerity.

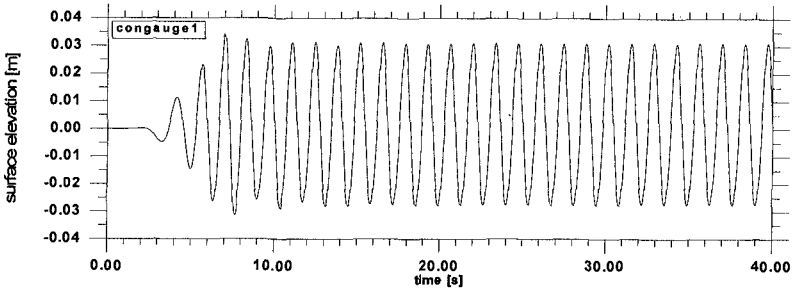

Figure 2. Time-series of the surface elevation at x = 5 meters.

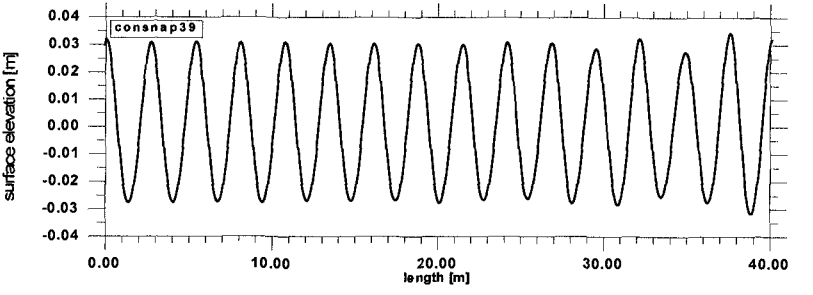

Figure 3. Snapshot of the surface at time 39.95 sec.

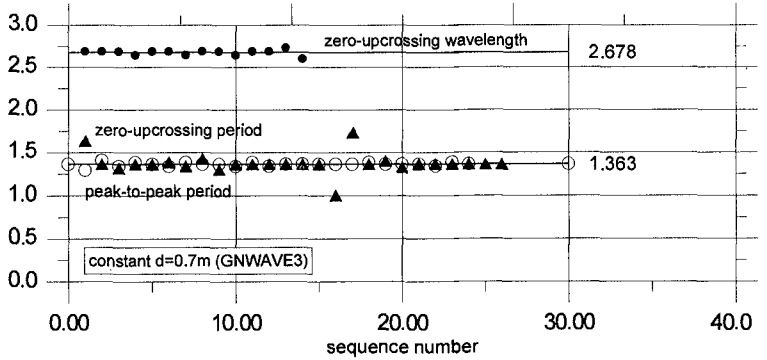

Figure 4. Sequences of wavelengths and wave periods

Table 1. Wave parameters computed from three different wave models

Parameter (input) Froude scaling	GNWAVE3 protype values (M=1:50)	AIRY THEORY protype values (M=1:50)	FOURIER-SERIES protype values (M=1:50)
H (3.00 m)	2.90 m (num. res.)	3.00 m (input)	3.00 m (input)
T (9.645 s)	9.638 s (num. res.)	9.645 s (input)	9.645 s (input)
d (35.0 m)	35.0 m (input)	35.0 m (input)	35.0 m (input)
λ	133.9 m (num. res.)	134.5 m (num. res.)	135.0 m (num. res.)
c	13.89 m/s (num.res.)	13.95 m/s (num. res.)	13.98 m/s (num. res.)

Laboratory Experiments

Setup

The experimental setup is shown in Figure 5. The experiments were carried out in a wave flume with a trapezoidal bar. The flume is 40 m long, 5m wide. Around the bar the water depth was 0.70 m, on the bar plateau the depth was 0.25 m. Free surface waves were measured by parallel-wire resistance gauges at three stations. Two pressure sensors of type Kistler 4043 were installed in the sea bed near the top break of the slope at a location were waves were expected to break. The numerical model was gauged at the same five locations, see Table 2 and Figure 5. Gauge 1 measures surface elevation at the beginning of the slope, Gauge 2 measures the surface elevation near the top break of the slope, Gauge 3 measures the surface elevation on the bar plateau. Gauge 4 and Gauge 5 measures bottom pressures at Gauge 2, from which the bottom pressure gradient can be estimated by computing the differences. All the gauges were leveled to zero before each run, thus only the dynamical part of the processes were recorded. The accuracy of the gauges is indicated in Table 2. However some zero-drift was detected during the analysis of data, thus the mean levels of the processes have been somewhat adjusted before the final presentation.

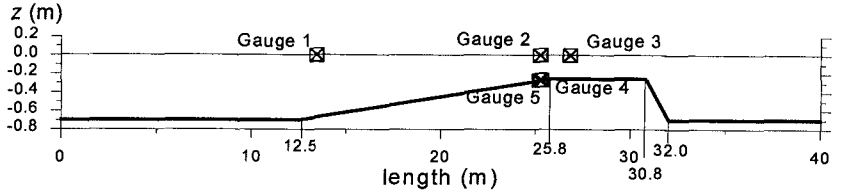

Figure 5. Experimental set up. Measures in meters.

Table 2. Gauge locations and accuracy

Gauge	process	x (m)	z (m)	accuracy
1	water level, η_1	13.42 (x_1)	0.000	$\pm 2mm$
2	water level, η_2	25.25 (x_2)	0.000	$\pm 2mm$
3	water level, η_3	26.82 (x_3)	0.000	$\pm 2mm$
4	pressure , p_4	25.30 (x_4)	-0.265	$\pm 50Pa$
5	pressure, p_5	25.20 (x_5)	-0.268	$\pm 50Pa$

Results

The experiments included one-component, two-component and five-component sinusoidal waves. The results shown below are for one-component waves only. Preliminary inspection of the other runs reveals similar pressure gradients . Results for both breaking and nonbreaking waves are included. Table 3 summarizes the results in which;

- H_1 is an estimate for the wave height at Gauge 1; = $(\eta_{1,max} - \eta_{1,min})$.
- T is an estimate for the wave period = average time between peeks over about a 20 s interval.
- H_2 is an estimate for the wave height at Gauge 2; = $(\eta_{2,max} - \eta_{2,min})$.
- H_0 is the deep water wave height given by the Airy theory shoaling coefficient (computed from H_1, T and d_1; d_1 - the still water depth at Gauge 1).
- λ_0 is the deep water wave length; = $gT^2 / 2\pi$.
- λ_S is the wave length in the constant depth part of the flume in front of the slope determined by the Airy wave theory: $\lambda_S = 2\pi/k_S$ where k_S is given by: $\omega^2 = gk_S \tanh k_S d_S$ and $\omega = 2\pi / T$; d_S - the water depth at start of the slope).
- C_p is the dimensionless dynamic pressure gradient defined as:

$$C_p = \frac{1}{\rho g}\frac{\partial \bar{p}}{\partial x} \approx \frac{1}{\rho g}\frac{p_4 - p_5}{x_4 - x_5} \quad . \tag{14}$$

Column of positive index refers to positive values, column of negative index refers to negative values.

- H_2/d_2 is a breaking wave index (rule of thumb: waves break for approx. 0.78). (d_2 = depth at Gauge 2).

- ξ is a local Irribarren number defined as $\xi = \mathrm{tg}\theta / \sqrt{H_2 / \lambda_0}$.
- Ir is the Irribarren number based on deep water wave height, i.e. $Ir = \mathrm{tg}\theta / \sqrt{H_0 / \lambda_0}$

The three latter parameters are used as dimensionless variables for graphical presentation. They appear to be powerful parameters to determine for which wave conditions large pressure gradients are favorable. Figure 6 shows the variability of C_p with respect to these dimension-less numbers. It is seen that the values of C_p are all within ±0.4 and that the largest values occur for the steepest waves just about breaking. The Irribarren number is often used for breaker type classification (Battjes, 1974), as listed below in Table 3. According to this table all runs should have resulted in spilling breakers. That was not the case. In Table 4 is listed the observed type of breakers. When these observations are held together with the results in Table 3, we see that the plunging breakers are associated with the largest values of C_p. $|C_p|<0.4$ is believed not sufficient to cause liquefaction in a saturated seabed. If the seabed contains a fraction of gases these levels may be sufficient. (Moshagen, 1997).

Table 3 Summary of the wave conditions and the main derivations

reference	H_1 [cm]	T [s]	H_2 [cm]	H_0[cm]	λ_0[cm]	λ_S [cm]	C_{p+} [-]	C_{p-} [-]	H_2/d_2 [-]	ξ [-]	Ir [-]
bp100100	13.8	1.07	13.1	14.2	179	176	0.22	0.23	0.49	0.123	0.118
bp100120	16.6	1.07	17.8	17.1	179	176	0.25	0.27	0.67	0.106	0.108
bp100121	17.1	1.07	18.1	17.6	179	176	0.27	0.26	0.68	0.105	0.106
bp100130	19.2	1.07	19.5	19.8	179	176	0.23	0.27	0.74	0.101	0.100
bp100140	20.0	1.07	19.8	20.6	179	176	0.24	0.29	0.75	0.100	0.098
bp100150	18.2	1.07	19.1	18.8	179	176	0.23	0.29	0.72	0.102	0.103
bp116150	22.3	1.18	16.2	23.7	217	210	0.22	0.20	0.61	0.122	0.101
bp126150	19.1	1.25	22.1	20.3	244	232	0.25	0.35	0.83	0.111	0.116
bp136150	18.1	1.36	22.0	19.5	289	268	0.24	0.36	0.83	0.121	0.128
bp145150	18.1	1.45	22.0	19.7	328	296	0.24	0.36	0.83	0.129	0.136
bp154150	15.8	1.55	22.3	17.3	375	326	0.33	0.37	0.84	0.137	0.155
bp160150	15.9	1.56	21.5	17.4	380	330	0.27	0.31	0.81	0.140	0.156
bp165150	15.2	1.65	23.0	16.6	425	358	0.23	0.37	0.87	0.143	0.169
bp200200	17.2	2.13	22.6	18.3	708	500	0.22	0.33	0.85	0.187	0.207
bp300100	6.7	3.15	8.4	6.4	1548	786	0.13	0.12	0.32	0.452	0.518

Table 4 Breaker type index

Breaker type	Irribarren number
Spilling	$0 < Ir < 0.5$
Plunging	$0.5 < Ir < 3.3$
Surging, collapsing	$3.3 < Ir$

Table 5 Observed breaker type and location of regular waves.

reference	remarks
bp100100	No breaking waves on the slope. The wave broke approx. 3.5 m past Gauge 3.
bp100120	Spilling/Plunging breaker occurred approx. 0.8 m past Gauge 2.
bp100121	Spilling/Plunging breaker occurred approx. 0.8 m past Gauge 2.
bp100130	Spilling breaker occurred approx. 0.8 m in front of Gauge 2.
bp100140	Spilling breaker occurred approx. 1.5 m in front of Gauge 2.
bp100150	Spilling breaker occurred approx. 4.0 m in front of Gauge 2.
bp116150	Spilling/Plunging breaker approx. 2.0 m in front of Gauge 2.
bp126150	Plunging breaker approx. at Gauge 2.
bp136150	Plunging breaker approx. at Gauge 2.
bp145150	Plunging breaker approx. 0.8 m behind Gauge 2.
bp154150	Plunging breaker approx. 1.2 m behind Gauge 2.
bp160150	Plunging breaker approx. midway between Gauge 2 and Gauge 3.
bp165150	Plunging breaker approx. midway between Gauge 2 and Gauge 3.
bp200200	Plunging breaker approx. at Gauge 2.
bp300100	No breaking waves.

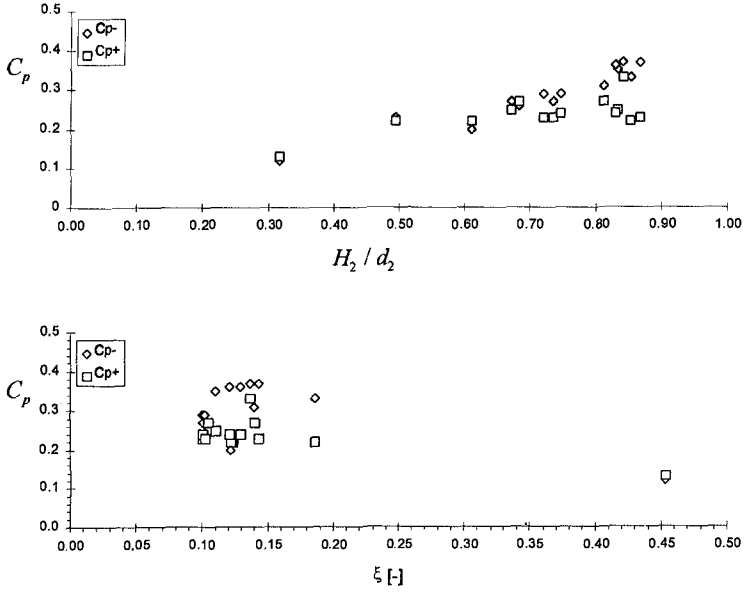

Figure 6 Variation of the dynamic pressure gradient, C_p.

Comparisons - GNWAVE3 and Experimental Results

Raw time-series plots of $\eta_1, \eta_2, \eta_3, p_4, p_5$ and C_p are available for all runs in a separate report (Arntsen, 1996). In this paper only one run will be presented. The output of the model was sampled at flume positions close to those in the physical model. However, since the model operates at discrete time and spacial steps a slight difference in locations are present. The output of the model are "snapshots" at prescribed times, and/or timeseries at prescribed positions. In this run, 5 sets of timeseries were recorded at the gauges 1-5 plus a snapshot at time 30 seconds after switching the model on. The model was set to run for 40 seconds, but collapsed due to "wave breaking" after 30.1 seconds. The spatial discretization was dx = 0.0462 m and the time discretization was dt = 0.0227 s. A snapshot of the surface elevation is shown in Figure 7, while a timeseries of the surface elevation at Gauge 2 is shown in Figure 8. Figure 9 is an intercomparison between observations and results from the numerical model for the run with reference *bp136150.* Although the fit of surface elevations are not so well in shape and phase, the model seem to predict the bed pressure fluctuations excellently. Also the amplitude of the waves before breaking is in good agreement. Breaking is identified by the "noisy" results close to the downslope break-point in Figure 7. It is believed that the model would perform better if that slope has been modeled less steep. Some of the deviations in amplitude are definitively caused by that the model has not run sufficiently long time to establish a stable solution. Cf. the initial disturbances in Figure 8. All considered, the GNWAVE3 seems to be a fairly good tool for the modeling of bed-pressure fluctuations in non-breaking shallow water waves.

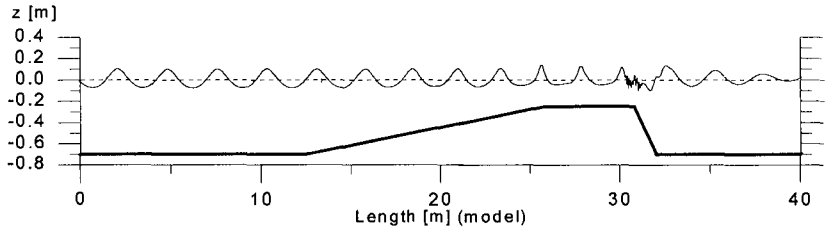

Figure 7 Snapshot of surface elevation (GNWAVE3).

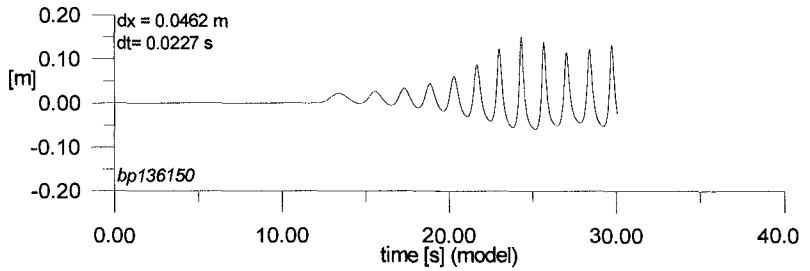

Figure 8 Timeseries of surface elevation at Gauge 2 (GNWAVE3)

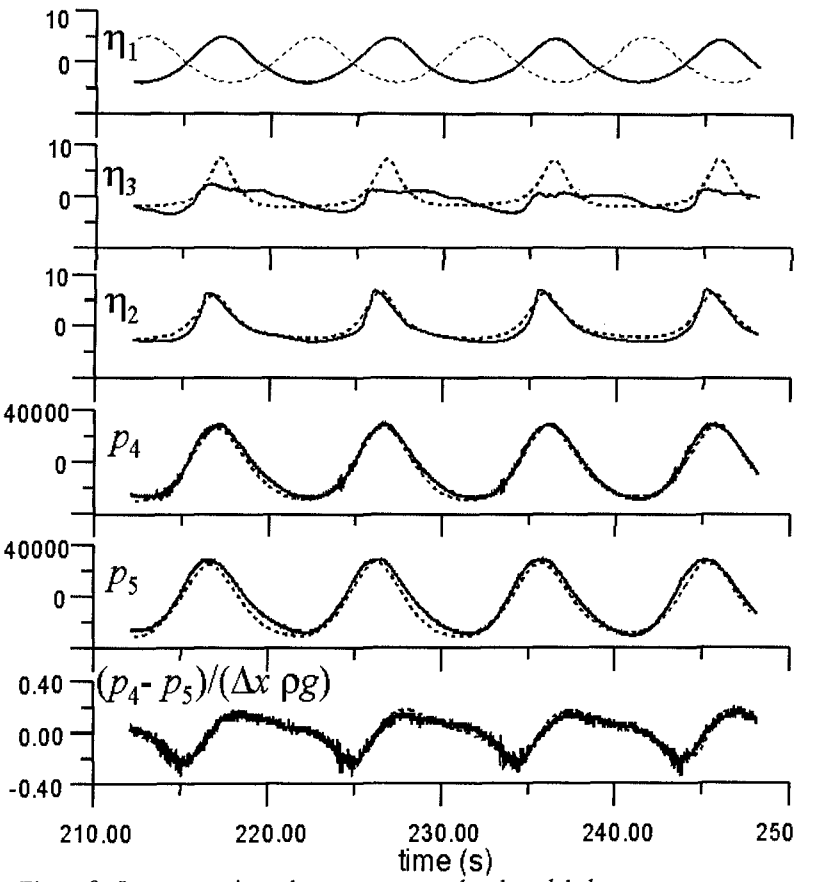

Figure 9 Intercomparisons between measured and modeled (GNWAVE3) wave dynamics over a trapezoidal bar. Prototype scale (M=1:50). H=9.1 m, T=9.6 s, d_S = 35 m. The timeseries are synchronized at Gauge 2 measurements.

Conclusions

GNWAVE3 seems to be a good tool for modeling bottom-pressure fluctuations in non-breaking shallow water waves. The observed levels of pressure gradients are believed not sufficient to cause liquefaction in a saturated seabed. However, if the seabed contains fraction of gases, these levels may be sufficient.

Acknowledgement

This study is partially supported by the Commission of the European Communities, Directorate-General XII for the Science, Research and Development Program Marine Science and Technology (MAST III) Contract No. MAS3-CT97-0097, Scour Around Coastal Structures (SCARCOST).

References.

ACES (1992). "Automated Coastal Engineering System version 1.07. Users-guide & Technical Reference." Coastal Engineering Research Center, Waterways Exp. Station, 3909 Halls Ferry Road, Vicksburg, MS 39180-6199, USA.

Arntsen, Ø.A. (1996). "Wave propagation over a bar and wave induced bed pressure. Plots of recorded time series." Department of structural engineering, NTNU, Trondheim, Norway. Misc. paper.

Battjes, J.A. (1974). "Computation of set-up longshore currents, run-up and overtopping due to wind generated waves." Communications on Hydraulics, Delft University of Technology, report 74-2.

Demirbilek, Z., and Webster, W. (1992a). "Application of the Green-Naghdi Theory of Fluid Sheets to Shallow-Water Wave Problems, Report 1, Model development." Waterways Exp. Station, Vicksburg, MS, USA. Technical Report CERC-92-11.

Demirbilek, Z., and Webster, W. (1992b). "Users Manual and Examples for GNWAVE." Waterways Exp. Station, Vicksburg, MS, USA. Technical Report CERC-92-13.

Green, A.E., Laws, N., and Naghdi, P.M. (1974). "On the Theory of Water Waves." Proc. Roy. Soc. London, A338, 43-55.

Green, A.E., and Naghdi, P.M. (1986). "A Nonlinear Theory of Water Waves for Finite and Infinite Depths." Philos. Trans. Roy. Soc. London, Ser. A320, 37-70.

Green, A.E., and Naghdi, P.M. (1987). "Further developments in a Nonlinear Theory of Water Waves for Finite and Infinite Depths." Philos. Trans. Roy. Soc. London, A324, 47-72.

Moshagen, H. (1996). Personal Communications. STATOIL, Trondheim, Norway.

Shields, J. J. (1986). "A Direct Theory for Waves Approaching a Beach." Ph.D. thesis, University of California, Berkeley, p 137.

Shields, JJ., and Webster, W. C. (1988). "On Direct Methods in Water-Wave Theory." J. Fluid Mech., Vol 197, 171-199.

Webster, W., and Kim, D.-Y. (1990). "The Dispersion of Large-Amplitude Gravity Waves in Deep Water." 10th Naval Hydrodynamic Symp., 1990, 397- 416.

A MULTI-LEVEL MODEL FOR NONLINEAR DISPERSIVE WATER WAVES

Susumu Kanayama[1], Hitoshi Tanaka[2] and Nobuo Shuto[3]

Abstract

To improve the accuracy of depth-integrated models for water waves, it is important to express the vertical characteristic of wave motion properly. In the present study, a multi-level model for nonlinear dispersive water waves is derived, in which vertical profile of horizontal velocity is assumed to be a chain of quadratic portions. The properties of the model in dispersion relation and second order nonlinear interactions turned out to converge to that of the Stokes wave theory, with the increasing number of layers.

Introduction

In many coastal projects, depth-integrated horizontal wave models play very important roll in estimating wave deformation. To improve the accuracy of depth-integrated model, it is important to express the vertical characteristic of wave motion properly. In the long wave model such as widely used Boussinesq equations and modified Boussinesq equations by Nwogu(1993), the vertical distribution of horizontal velocities are assumed to be quadratic. The higher order Boussinesq type equations by Kioka・Kashihara(1995), Madsen et.al(1996), Gobbi・Kirby(1996) and so on, have high accuracy in dispersion and nonlinearlity. In these equations, vertical distribution of horizontal velocities are assumed to be bi-quadratic. Different approaches were used by Nadaoka et.al(1994), Nochino(1994) and Isobe(1994), who expressed the vertical characteristic of wave motion as a combination of some components with properly chosen vertical distribution functions. The components are combined by applying the Galerkin method or variational principle to the Euler equation of motion to yield the coupled vibration equation for water waves, which have high accuracy in dispersion and nonlinearlity. As vertical distribution functions, Nadaoka et.al(1994) employed hyperbolic cosine type function, whereas Nochino(1994) used the Legendre's polynomials, and Isobe(1994) chose even-order polynomial functions.

1 Senior Research Engineer, Inst. Technology , Penta-Ocean construction Co.,Ltd.,1534-1 Yonku-cho, Nishi-nasuno, Nasu, Tochigi, 329-2749, Japan.
2 Professor, Department of Civil Engineering, Tohoku University, Aoba, Sendai 980-8579, Japan.
3 Professor, Faculty of Policy Studies, Iwate Prefectural University, Iwate 020-0173, Japan.

In the present work, with the objective of expressing the vertical characteristics of wave motion properly, a multi-level model for nonlinear dispersive water waves is derived and analyzed, in which vertical profile of horizontal velocity is assumed to be a chain of quadratic portions

Model Equations

The conceptual diagram of the present multi-level model for nonlinear dispersive water waves is shown in Fig.1. Static water depth is divided into several layers, whose number is N and numberd downward. The upper edge of first layer corresponds to still water level, and lower edge of N-th layer to the bottom. d_n is the thickness of n-th layer and $-h_n$ the depth of lower edge, $\mathbf{u}_n$ are level-averaged horizontal velocities, and $\mathbf{u}_b$ the horizontal velocity at the bottom.

Velocities are assumed to be expressed by (1) and (2). Horizontal velocities vary quadratically over a level, and vertical velocities linearly. For individual layer, this is the same as the standard Boussinesq equations.

$$\mathbf{u}(z) = \mathbf{u}_n + \frac{1}{6}(d_n^2 - 3(h_n + z)^2)\nabla(\nabla\cdot\mathbf{u}_n) + \frac{1}{2}(d_n - 2(h_n + z))[\sum_{i=n+1}^{N}\nabla(d_i\nabla\cdot u) + \nabla h_n\nabla\cdot\mathbf{u}_n + \nabla(\mathbf{u}_b\cdot\nabla h)] \quad (1)$$

$$w(z) = -\sum_{i=n+1}^{N} d_i\nabla\cdot\mathbf{u}_i - (h_n + z)\nabla\cdot\mathbf{u}_n - \mathbf{u}_b\cdot\nabla h \quad (2)$$

By substituting (1) into depth-integrated continuity equation (3), the continuity equation of multi-level model is obtained as (4).

$$\frac{\partial\eta}{\partial t} + \nabla\int_{-h}^{\eta}\mathbf{u}dz = 0 \quad (3)$$

$$\frac{\partial\eta}{\partial t} + \sum_{i=1}^{N}\nabla(d_i\mathbf{u}_i) + \nabla(\eta\mathbf{u}_1) - \nabla[\frac{1}{2}\eta(d_1 + \eta)\{\sum_{i=1}^{N}\nabla(d_i\nabla\cdot\mathbf{u}_i) + \nabla(\mathbf{u}_b\cdot\nabla h)\}] \quad (4)$$

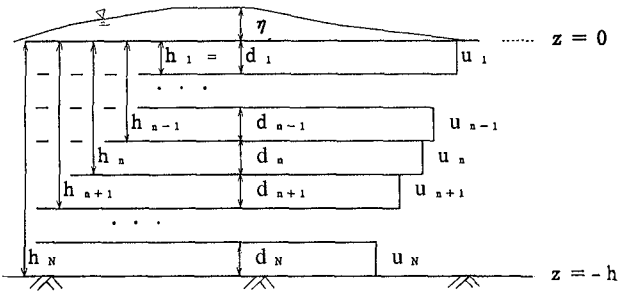

Fig.1 The conceptual diagram of the multi-level model for nonlinear dispersive water waves

Momentum equations are expressed by (6), which are obtained by substituting (1) and (2) to (5), and averaging over individul layer. Equation (5) is the Euler equation of motion modified by using the irrotational condition.

$$\frac{\partial \mathbf{u}}{\partial t} + \frac{1}{2}\nabla(\mathbf{u}_s \cdot \mathbf{u}_s + w_s^2) + g\nabla\eta = -\nabla\int_z^\eta \frac{\partial w}{\partial t}dz' \tag{5}$$

$$\begin{aligned}
&\frac{\partial \mathbf{u}_n}{\partial t} + \frac{1}{2}\nabla(\mathbf{u}_s \cdot \mathbf{u}_s + w_s^2) + g\nabla\eta \\
&= \nabla[\eta\sum_{i=1}^{N} d_i\nabla\cdot\frac{\partial \mathbf{u}_i}{\partial t} + \frac{1}{2}(\eta^2\nabla\cdot\frac{\partial \mathbf{u}_1}{\partial t}) + \eta\frac{\partial \mathbf{u}_b}{\partial t}\cdot\nabla h] \\
&+ \sum_{i=1}^{n-1}\sum_{j=i+1}^{N}\nabla(d_i d_j\nabla\cdot\frac{\partial \mathbf{u}_j}{\partial t}) + \sum_{i=1}^{n-1}\frac{1}{2}\nabla(d_i^2\nabla\cdot\frac{\partial \mathbf{u}_i}{\partial t}) \\
&+ \sum_{i=n+1}^{N}\frac{1}{2}d_n\nabla(d_i\nabla\cdot\frac{\partial \mathbf{u}_i}{\partial t}) - \sum_{i=n+1}^{N}(\nabla h_{n-1})d_i\nabla\cdot\frac{\partial \mathbf{u}_i}{\partial t} \\
&+ \frac{1}{2}\nabla(d_n^2\nabla\cdot\frac{\partial \mathbf{u}_n}{\partial t}) - \frac{1}{6}d_n\nabla(\nabla\cdot\frac{\partial \mathbf{u}_n}{\partial t}) \\
&- \frac{1}{2}d_n(\nabla h_n)\nabla\cdot\frac{\partial \mathbf{u}_n}{\partial t} + \sum_{i=1}^{n-1}\nabla(d_i\frac{\partial \mathbf{u}_b}{\partial t}\cdot\nabla h) \\
&+ \frac{1}{2}d_n\nabla(\frac{\partial \mathbf{u}_b}{\partial t}\cdot\nabla h) - (\nabla h_{n-1})(\frac{\partial \mathbf{u}_b}{\partial t}\cdot\nabla h)
\end{aligned} \tag{6}$$

In the momentum equations(6), $\mathbf{u}_s$ and w_s are the velocities at the free surface, which are expressed by (7) and (8).

$$\begin{aligned}
\mathbf{u}_s &= \mathbf{u}_1 + \frac{1}{6}d_n^2\nabla(\nabla\cdot\mathbf{u}_1) - \frac{1}{2}\eta^2\nabla(\nabla\cdot\mathbf{u}_1) \\
&- (\frac{1}{2}d_1 + \eta)[\sum_{i=n+1}^{N}\nabla(d_i\nabla\cdot\mathbf{u}_i) + \nabla(\mathbf{u}_b\cdot\nabla h)]
\end{aligned} \tag{7}$$

$$w_s = -\sum_{i=1}^{N} d_i\nabla\cdot\mathbf{u}_i - \eta\nabla\cdot\mathbf{u}_n - \mathbf{u}_b\cdot\nabla h \tag{8}$$

$\mathbf{u}_b$ the horizontal velocities at the bottom is determined by the relation(9), combined with $\mathbf{u}_N$ the N-th layer-averaged velocity.

$$\mathbf{u}_b = \mathbf{u}_N + \frac{1}{6}d_N^2\nabla(\nabla\cdot\mathbf{u}_N) + \frac{1}{2}d_N[\nabla(\mathbf{u}_b\cdot\nabla h) + (\nabla h)\nabla\cdot\mathbf{u}_N] \tag{9}$$

Thus, fundamental system of multi-level model is obtained, which is composed of one continuity equation, layers number of momentum equations and bottom condition. For the momentum equations (6), the convenient form is given by (10), in which the contributions of $\mathbf{u}_i$ to $\mathbf{u}_n$ in linear dispersion terms are shown explicitly.

$$\frac{\partial \mathbf{u}_n}{\partial t} + \frac{1}{2}\nabla(\mathbf{u}_s \cdot \mathbf{u}_s + {w_s}^2) + g\nabla\eta$$
$$= \nabla[\eta\sum_{i=1}^{N} d_i \nabla\cdot\frac{\partial \mathbf{u}_i}{\partial t} + \frac{1}{2}(\eta^2\nabla\cdot\frac{\partial \mathbf{u}_1}{\partial t}) + \eta\frac{\partial \mathbf{u}_b}{\partial t}\cdot\nabla h]$$
$$+\sum_{i=1}^{N}\alpha_{n,i}\nabla(\nabla\cdot\frac{\partial \mathbf{u}_i}{\partial t}) + \sum_{i=1}^{N}\beta_{n,i}\nabla\cdot\frac{\partial \mathbf{u}_i}{\partial t} + \gamma_n\nabla\cdot\frac{\partial \mathbf{u}_b}{\partial t} + \delta_n\frac{\partial \mathbf{u}_b}{\partial t} \tag{10}$$

where ,coefficients in linear dispersion terms are given as follows.

$$\alpha_{n,i} = \alpha 1_{n,i} + \alpha 2_{n,i} + \alpha 3_{n,i} + \alpha 4_{n,i} \tag{11}$$

$$\alpha 1_{n,i} = \begin{cases} 0 & (n \le 1) \\ \sum_{m=1}^{n-1} d_m d_i & (n > 1, i > n-1) \\ \sum_{m=1}^{i-1} d_m d_i & (n > 1, i \le n-1) \end{cases} \tag{12}$$

$$\alpha 2_{n,i} = \begin{cases} 0 & (n \le 1) \\ \frac{1}{2}{d_i}^2 & (n > 1, i > n-1) \end{cases} \tag{13}$$

$$\alpha 3_{n,i} = \begin{cases} 0 & (n \ge i) \\ \frac{1}{2} d_n d_i & (n < i) \end{cases} \tag{14}$$

$$\alpha 4_{n,i} = \begin{cases} 0 & (n \ne i) \\ \frac{1}{3}{d_i}^2 & (n = i) \end{cases} \tag{15}$$

$$\beta_{n,i} = \beta 1_{n,i} + \beta 2_{n,i} + \beta 3_{n,i} + \beta 4_{n,i} \tag{16}$$

$$\beta 1_{n,i} = \begin{cases} 0 & (n \le 1) \\ \sum_{m=1}^{n-1} \nabla(d_m d_i) & (n > 1, i > n-1) \\ \sum_{m=1}^{i-1} \nabla(d_m d_i) & (n > 1, i \le n-1) \end{cases} \tag{17}$$

$$\beta 2_{n,i} = \begin{cases} 0 & (n \le 1) \\ d_i \nabla d_i & (n > 1, i > n-1) \end{cases} \tag{18}$$

$$\beta 3_{n,i} = \begin{cases} 0 & (n \ge i) \\ \frac{1}{2} d_n \nabla d_i - d_i \nabla h_{n-1} & (n < i) \end{cases} \tag{19}$$

$$\beta 4_{n,i} = \begin{cases} 0 & (n \neq i) \\ d_i \nabla d_i - \frac{1}{2} d_i \nabla h_i & (n = i) \end{cases} \tag{20}$$

$$\gamma_n = \sum_{m=1}^{n-1} d_m \nabla h + \frac{1}{2} d_n \nabla h \tag{21}$$

$$\delta_n = \sum_{m=1}^{n-1} \nabla (d_m \nabla h) + \frac{1}{2} d_n \nabla (\nabla h) - \nabla h_{n-1} \nabla h \tag{22}$$

A remarkable feature of multi-level model is applicability to quasi-3 dimensional problem with vertical and horizontal closed boundaries. Vertical closed boundaries can be simply treated by setting the corresponding horizontal velocities to be zero. Horizontal closed boundaries can be treated by following manner(Fig.2). Vertical velocities at the horizontal closed boundaries are set to be zero by condition (23), where $-h_B$ is the depth of horizontal closed boundaries which corresponds to the lower edge of nB-th layer. In this case, the number of equations exceed the number of unknowns. To make the system closed ,a new unknown p_B the pressure under the closed boundary should be introduced.

$$w(-h_B) = -\sum_{i=nB}^{N} d_i \nabla \cdot \mathbf{u}_i - \mathbf{u}_b \cdot \nabla h = 0 \tag{23}$$

By expressing the modified Euler equation (5) using p_B, (24) is obtained for the region under the horizontal closed boundary.

$$\frac{\partial \mathbf{u}}{\partial t} + \frac{1}{2} \nabla (\mathbf{u}_B \cdot \mathbf{u}_B) + \nabla (\frac{p_B}{\rho}) = -\nabla \int_z^{-h_B} \frac{\partial w}{\partial t} dz' \tag{24}$$

Equation(24) is expressed with dependent variables of multi-level model as (25). At the side edge of horizontal closed boundary, variable p_B is connected to that of ordinary region.

$$\begin{aligned} &\frac{\partial \mathbf{u}_n}{\partial t} + \frac{1}{2} \nabla (\mathbf{u}_B \cdot \mathbf{u}_B) + \nabla (\frac{p_B}{\rho}) \\ &= \sum_{i=nB+1}^{n-1} \sum_{j=i+1}^{N} \nabla (d_i d_j \nabla \cdot \frac{\partial \mathbf{u}_j}{\partial t}) + \sum_{i=nB+1}^{n-1} \frac{1}{2} \nabla (d_i^2 \nabla \cdot \frac{\partial \mathbf{u}_i}{\partial t}) \\ &+ \sum_{i=n+1}^{N} \frac{1}{2} d_n \nabla (d_i \nabla \cdot \frac{\partial \mathbf{u}_i}{\partial t}) - \sum_{i=n+1}^{N} (\nabla h_{n-1}) d_i \nabla \cdot \frac{\partial \mathbf{u}_i}{\partial t} \\ &+ \frac{1}{2} \nabla (d_n^2 \nabla \cdot \frac{\partial \mathbf{u}_n}{\partial t}) - \frac{1}{6} d_n \nabla (\nabla \cdot \frac{\partial \mathbf{u}_n}{\partial t}) - \frac{1}{2} d_n (\nabla h_n) \nabla \cdot \frac{\partial \mathbf{u}_n}{\partial t} \\ &+ \sum_{i=1}^{n-1} \nabla (d_i \frac{\partial \mathbf{u}_b}{\partial t} \cdot \nabla h) + \frac{1}{2} d_n \nabla (\frac{\partial \mathbf{u}_b}{\partial t} \cdot \nabla h) - (\nabla h_{n-1}) (\frac{\partial \mathbf{u}_b}{\partial t} \cdot \nabla h) \end{aligned} \tag{25}$$

In this manner, the multi-level model proposed in this study can be applied to quasi-3 dimensional problem.

Properties of Model Equations

In this section we will analyze the linear and nonlinear characteristics of the present model. The procedure employed here is fundamentary the same as previous works, for example Madsen et.al(1996).

For simplicity, we treat the one dimensional version of the equations with constant depth, which are expressed by (26), the continuity equation and (27), the momentum equations with the velocities at the free surface expressed by (28) and (29).

$$\frac{\partial \eta}{\partial t}+\sum_{i=1}^{N}\frac{\partial}{\partial x}(d_i u_i)+\frac{\partial}{\partial x}(\eta u_1)-\frac{1}{2}\frac{\partial}{\partial x}[\eta(d_1+\eta)\sum_{i=1}^{N}d_i\frac{\partial^2 u_i}{\partial x^2}] +\frac{1}{6}\frac{\partial}{\partial x}[\eta(d_1{}^2-\eta^2)\frac{\partial^2 u_1}{\partial x^2}] = 0 \tag{26}$$

$$\frac{\partial u_n}{\partial t}+u_s\frac{\partial u_s}{\partial x}+w_s\frac{\partial w_s}{\partial x}+g\frac{\partial \eta}{\partial x} =\frac{\partial}{\partial x}[\eta\sum_{i=1}^{N}d_i\frac{\partial^2 u_i}{\partial t\partial x}+\frac{1}{2}\eta^2\frac{\partial^2 u_1}{\partial t\partial x}]+\sum_{i=1}^{n-1}\sum_{j=i+1}^{N}d_i d_j\frac{\partial^3 u_j}{\partial t\partial x^2} +\frac{1}{2}\sum_{i=1}^{n-1}d_i{}^2\frac{\partial^3 u_i}{\partial t\partial x^2}+\frac{1}{2}\sum_{i=n+1}^{N}d_n d_i\frac{\partial^3 u_i}{\partial t\partial x^2}+\frac{1}{3}d_n\frac{\partial^3 u_n}{\partial t\partial x^2} \tag{27}$$

$$u_s = u_1+(\frac{1}{6}d_1{}^2-\frac{1}{2}\eta^2)\frac{\partial^2 u_1}{\partial x^2}-(\frac{1}{2}d_1+\eta)\sum_{i=1}^{N}d_i\frac{\partial^2 u_i}{\partial x^2} \tag{28}$$

$$w_s = -\sum_{i=1}^{N}d_i\frac{\partial u_i}{\partial x}-\eta\frac{\partial u_n}{\partial x}-u_b\frac{\partial h}{\partial x} \tag{29}$$

We look for solutions of the form expressed by (30) and (31), where ε is a small parameter.

$$\eta = \varepsilon\eta^{(1)}\cos(kx-\omega t)+\varepsilon^2\eta^{(2)}\cos 2(kx-\omega t) \tag{30}$$

$$u_n = \varepsilon u_n{}^{(1)}\cos(kx-\omega t)+\varepsilon^2 u_n{}^{(2)}\cos 2(kx-\omega t)) \tag{31}$$

Substituting them to (26) and (27) ,the equations for first order of ε are given by (32) and (33).

$$\omega\eta^{(1)}+k\sum_{i=1}^{N}d_i u_i{}^{(1)} = 0 \tag{32}$$

$$\omega u_n{}^{(1)}-gk\eta^{(1)}+k\omega[(\sum_{i=1}^{n-1}\sum_{j=i+1}^{N}d_i d_j+\frac{1}{2}\sum_{i=1}^{n-1}d_i{}^2)u_1{}^{(1)}+\frac{1}{3}d_n{}^2 u_n{}^{(1)}] = 0 \tag{33}$$

These are homogenious equations and non-trivial solutions require the determinant of the system to vanish to provide the dispersion relation.

In Fig. 2, the dispersion relation of the present model is compared with that of the linear theory. In this case, thickness of n-th layers are set to be n-times of first layer so that deeper layer has larger thickness. With the increasing number of layers, linear dispersion relation of the multi-level model converges to that of linear theory. Four layers are enough for sufficiently accurate dispersion for kh up to 10.

Distribution of $\{u_n^{(1)}\}$ for various values of kh can also be obtained from (32) and (33), which provide the vertical distribution of linear components of velocities according to (1) and (2). In Fig.3, vertical distribution of horizontal velocity $u(z)$ of the present model is compared with that of the linear theory. Fig. 4 shows plots similar to Fig.3 for vertical velocity $w(z)$. Although larger number of layers is required to reproduce the exact solution as kh increase, plots for N=6 and N=8 show very accurate reproduction so that they are hard to distinguish, for the range of kh smaller than 20.

Similary, the equations for second order of ϵ are given by (34) and (35). From these equations, the second order surface elevation and velocities are obtained, which should be compared with that of Stokes second order wave theory.

$$\omega\eta^{(2)} + k\sum_{i=1}^{N} d_i u_i^{(2)} = \frac{1}{2}k[(1-\frac{1}{6}d_1^2k^2)u_1^{(1)} + \frac{1}{2}d_1k^2\sum_{i=1}^{N} d_i u_n^{(1)}]\eta^{(1)} = 0 \tag{34}$$

$$\begin{aligned}(\omega + \frac{1}{3}kd_n^2)u^{(2)} + k\omega(\sum_{i=1}^{n-1}\sum_{j=i+1}^{N} d_i d_j + \frac{1}{2}\sum_{i=1}^{n-1} d_i^2)u_i^{(2)} - gk\eta^{(2)} \\ = \frac{1}{4}k[(1-\frac{1}{6}d_1^2k^2)u_1^{(1)} + \frac{1}{2}d_1k^2\sum_{i=1}^{N} d_i u_n^{(1)}]^2 \\ -\frac{1}{4}k^3(\sum_{i=1}^{N} d_i u_i^{(1)})^2 - \frac{1}{2}k^2\omega\eta^{(1)}\sum_{i=1}^{N} d_i u_i^{(1)}\end{aligned} \tag{35}$$

The water-surface elevation including second order of ϵ is expressed by equation(36), where H is wave height. On the other hand, according to Stokes second order theory, it also can be expressed by equation(37).

$$\eta = \frac{H}{2}\cos(kx-\omega t) + \frac{H^2\eta^{(2)}}{4(\eta^{(1)})^2}\cos 2(kx-\omega t) \tag{36}$$

$$\eta = \frac{H}{2}\cos(kx-\omega t) + \frac{H^2}{16}k\frac{\cosh kh(\cosh 2kh+2)}{(\sinh kh^3)}\cos 2(kx-\omega t) \tag{37}$$

The amplitude of second term of equation (36) and (37) are compared in Fig.5, both are plotted being divided by wave number. In this case, wave height is 20% of still water depth. It is seen that the results of the present model converge to that of Stokes wave theory, with the increasing number of layers. Thus, it is confirmed that nonlinear interaction characteristic of the present model is accurate up to the second-order.

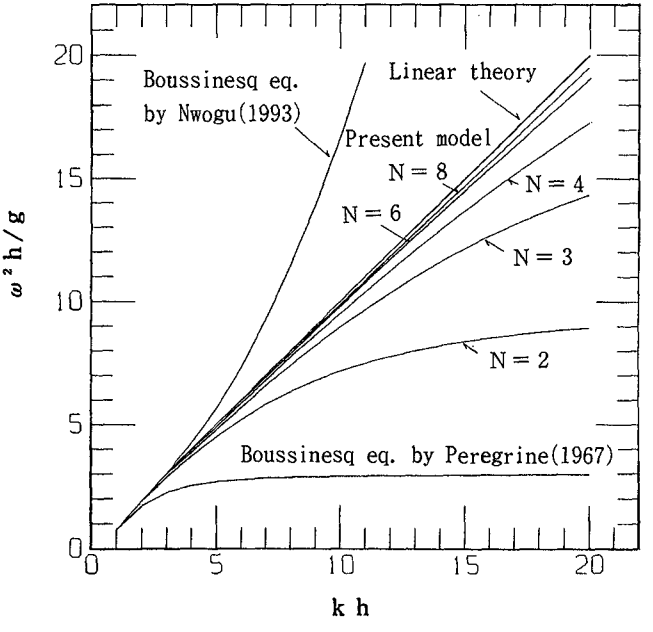

Fig.2 Linear dispersion relation

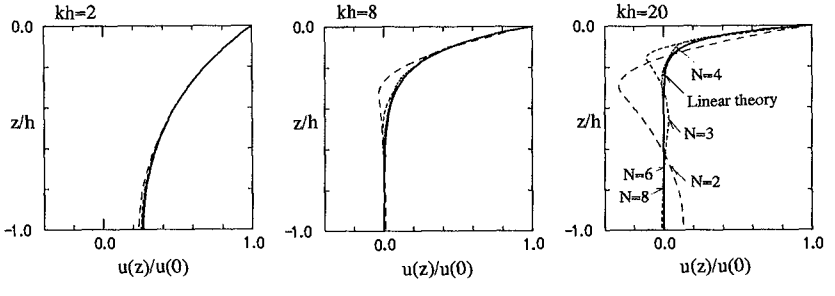

Fig.3 Vertical distribution of linear components of horizontal velocity $u(z)$

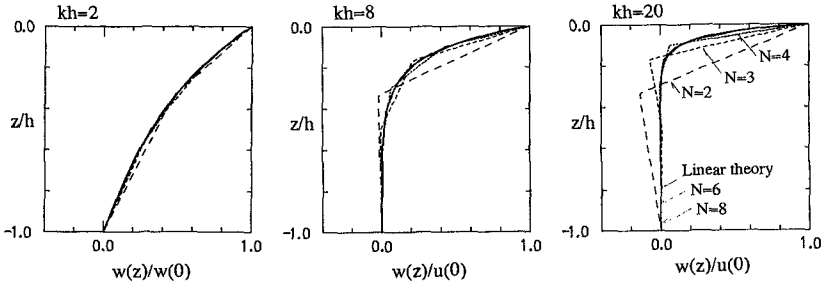

Fig.4 Vertical distribution of linear components of vertical velocity $w(z)$

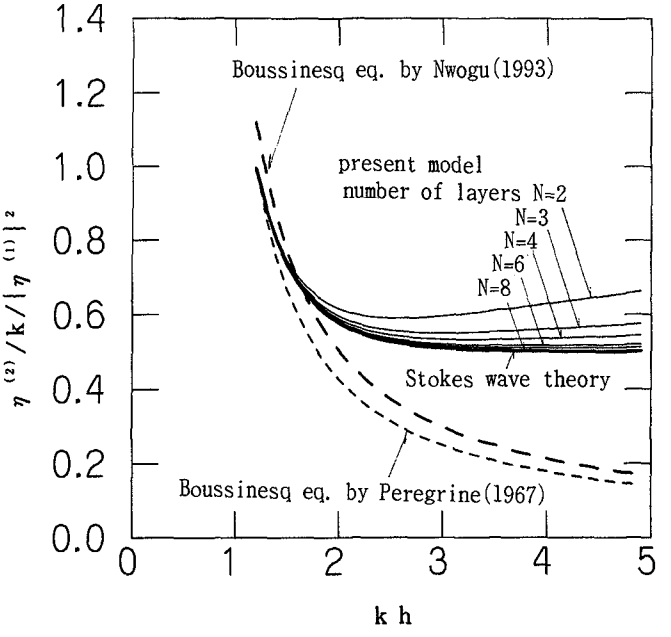

Fig.5 Second-order nonlinear interaction

Numerical Approach

The differential equations are discretized by using a time-centered implicit scheme with variables defined on a space-staggered rectangular grid. The resulting system of difference equations is reduced to a block tridiagonal system, which is solved by generalized Thomas algorithm.

An example of 2-HD simulation with three layers is for oblique wave incidence to sloping beach of 1:20. Regular, unidirectional waves with the period of 10sec and the wave height of 3m are generated at the depth of 24m with the incident angle of 25 deg. In this example, a little simplified version of momentum equation is employed, which are expressed by (38).

$$\frac{\partial \mathbf{u}_n}{\partial t} + (u_n \cdot \nabla)u_n + \frac{1}{d_n}\int_{-h_n}^{-h_{n-1}} w\frac{\partial u}{\partial z}dz + g\nabla\eta$$
$$= \sum_{i=1}^{n-1}\sum_{j=i+1}^{N} d_i d_j \nabla(\nabla \cdot \frac{\partial u_j}{\partial t}) + \sum_{i=1}^{n-1}\frac{1}{2}d_i{}^2\nabla(\nabla \cdot \frac{\partial u_i}{\partial t})$$
$$+ \sum_{i=n+1}^{N}\frac{1}{2}d_n d_i \nabla(\nabla \cdot \frac{\partial u_i}{\partial t}) + \frac{1}{3}d_n{}^2\nabla(\nabla \cdot \frac{\partial u_n}{\partial t}) + \varepsilon_T(\nabla \cdot \nabla)u_n \qquad (38)$$

The third term in left hand side of (38) is expressed by (39) with dependent variables of multi-level model.

$$\frac{1}{d_n}\int_{-h_n}^{-h_{n-1}} w\frac{\partial u}{\partial z}dz = \frac{1}{3}d_n{}^2\nabla u_n\nabla(\nabla \cdot u_n) + \frac{1}{2}\nabla(d_n\nabla u_n\sum_{i=n+1}^{N} d_i\nabla u_i)$$
$$+ (\sum_{i=n+1}^{N} d_i\nabla u_i)(\sum_{i=n+1}^{N} d_i\nabla(\nabla \cdot u_i)) \qquad (39)$$

In this expression, bottom sloping, vertical acceleration over still water surface, and nonlinearity of vertical momentum equation are neglected. In equation(23), ε_T is the eddy viscosity according to breaking wave propagation model by Katayama and Sato(1993).

Fig.6 depicts a perspective views of calculated wave fields. A vector plot of the layer-averaged velocity of first and third layer is shown in Fig.7. Co-existence of longshore current and undertow is well described by the present model.

Next example is wave diffraction simulation by submerged horizontal plate. In this case, linear and 1-dimensional version of multi-level model with five layers is employed. Fig.8 shows the spatial profile of the propagating wave for different relative submerged depth of horizontal plate. The transmission coefficients K_T agree with the result of simulation by boundary element method, which is shown in brackets. Thus, the applicability of present model to quasi-3 dimensional problem is confirmed.

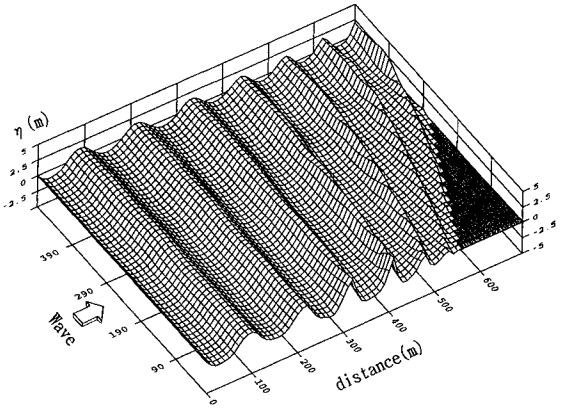

Fig.6 Perspective view of the wave field for oblique wave incidence

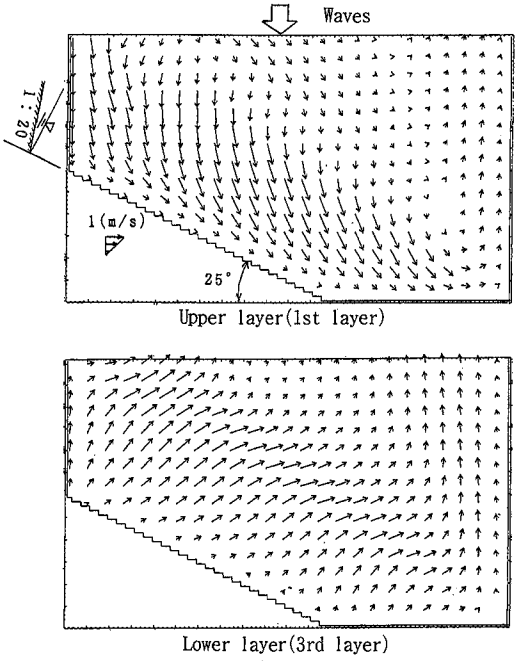

Fig.7 Time-averaged velocity field for oblique wave incidence

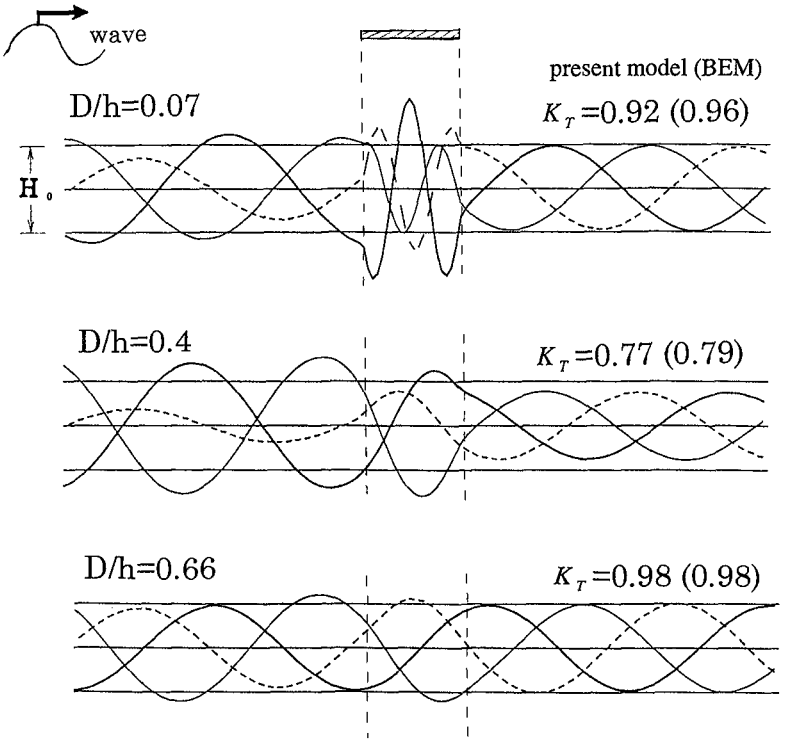

Fig.8 Computation for linear wave diffraction by submerged horizontal plate.

Conclusions

(1)A multi-level model is proposed for computing nonlinear dispersive waves. The accuracy of the model is first examined in terms of the convergence of linear dispersion relation along with quadratic transfer function. It is found that the model gives satisfactory results if the number of layers is properly chosen.
(2)The model is secondly applied to 2-HD wave propagation on sloping beach, and coexisting property of longshore current and undertow can be predicted.
(3)The applicability of the present model to quasi-3 dimensional problem is confirmed by reproducing the diffraction wave field with submerged horizontal plate.

References

Gobbi, M.F. and Kirby, J.T., 1996. A fourth order Boussinesq-type wave model, *Proceedings of 25th International Conference on Coastal Engineering*, pp.1116-1129.

Isobe, M., 1994. Time-dependent mild-slope equations for random waves, *Proceedings of 24th International Conference on Coastal Engineering*, pp.285-299.

Katayama, H. and Sato, S., 1993. A numerical model for simulating random breaking waves based on the Boussinesq equation, *Proceedings of Coastal Engineering*, Vol.40, pp.16-20. (in Japanese)

Kioka, W. and Kashihara, K., 1995. Higher-order Boussinesq equations and their applicability to the wave transformation over a step beach, *Proceedings of Coastal Engineering*, Vol.42, pp.166-170. (in Japanese)

Madsen, P.A., Banijamali, B., Schäffer, H.A. and Sørensen, O.R., 1996. Boussinesq type equations with high accuracy in dispersion and nonlinearity, *Proceedings of 25th International Conference on Coastal Engineering*, pp.95-108.

Nadaoka, K., Beji, S. and Nakagawa, Y., 1994. A fully-dispersive nonlinear wave model and its numerical solutions, *Proceedings of 24th International Conference on Coastal Engineering*, pp.427-441.

Nochino, M., 1994. Coupled vibration equations for irregular water waves, *Proceedings of 24th International Conference on Coastal Engineering*, pp.427-441.

Nwogu, O., 1993. Alternative form of Boussinesq equations for nearshore wave propagation, *Journal of Waterway, Port, Coastal, and Ocean Engineering*, Vol. 119, No.6, pp.618-638.

Recent Extensions to Local Polynomial Approximation Models

Andrew B. Kennedy[1]

Abstract

Local polynomial approximation models for water wave simulation are examined with the aim of improving accuracy and efficiency. Several potential improvements are considered. The first is based on a linearisation of the solution for Laplace's equation and is shown to have good theoretical characteristics. However, it is found to have a fatal instability to high wavenumber bottom disturbances. The second method uses empirical collocation adjustment to provide better agreement with exact solutions for steady waves. This method provides significant improvements in accuracy for a given level of approximation and is recommended for future use.

Introduction

For the computation of water wave evolution over varying topography, there have been two main areas of effort in recent years. One has focused on improvements to Boussinesq-type models, continually increasing the range of validity to encompass deeper and higher waves (Nwogu, 1993., Schäffer and Madsen, 1995, Wei et al., 1995, Gobbi et al., 1998). Despite increasing complexity, solution times remain reasonable enough to consider wave motion in two horizontal dimensions. This remains a very active area of research. At the other extreme from Boussinesq equations are numerical solutions of Laplace's equation using boundary element methods (BEM, e.g. Dold and Peregrine, 1980, Grilli et al., 1994). These offer unparalleled accuracy in any depth and can even compute overturning waves. However, despite significant advances (Wang et al, 1995), they are extremely computationally intensive; enough that large domains for one horizontal dimension can become problematic, and two dimensional computations are extremely limited in scope. Although research continues in this area, boundary element models are considered to be a relatively mature field.

Local polynomial approximation methods (LPA, Kennedy and Fenton, 1996, Kennedy and Fenton, 1997, Kennedy, 1997) were introduced as a way of bridging

[1]Center for Applied Coastal Research, University of Delaware, Newark, DE. 19716 USA.

this gap between highly accurate, computationally intensive models (BEM), and Boussinesq models of moderate accuracy and expense. The basis of these models is a polynomial representation of arbitrary degree in the vertical coordinate combined with a weighted residual solution of the continuity equation for potential flow. For lower levels of approximation, accuracy is comparable to high end Boussinesq equations, while higher levels of approximation can provide accuracy comparable to some implementations of boundary element models. Computational expense lies in between BEM and Boussinesq schemes. A comparison of an advanced Boussinesq and LPA models is given in this volume (Gobbi et al., 1998).

This paper reports recent efforts to improve the accuracy and efficiency of LPA models. Two basic strategies are considered: one which makes further approximations which slightly degrade nonlinear properties, but potentially offers great computational savings, and a second method which improves linear and nonlinear accuracy for a given level of approximation with no increase in computational expense.

Local Polynomial Approximation Model

Local polyonomial approximation models all assume potential flow, and are essentially weighted residual solutions of Laplace's equation combined with potential flow evolution equations. The velocity potential is assumed to vary in the vertical coordinate, z, like a polynomial of some specified degree. This may be represented as

$$\phi(x,y,z) = \sum_{j=0}^{n-1} A_j(x,y) z^j \tag{1}$$

where $A_j(x,y)$ is an initially unspecified function of the horizontal coordinates. The level of approximation, n, controls the degree of polynomial and, hence, the accuracy of the computation. To specify these functions, boundary conditions must be given at the free surface $z = \eta(x,y)$ and bed $z = -h(x,y)$, and continuity must be imposed over the entire flow field. The bottom boundary condition is

$$\phi_z + \phi_x h_x + \phi_y h_y = 0 \quad \text{on } z = -h(x,y) \tag{2}$$

The condition at the free surface specifies the velocity potential

$$\phi(x,y,z = \eta(x,y)) = \phi^{(s)}(x,y) \tag{3}$$

where $\phi^{(s)}(x,y)$ is the known free surface velocity potential. For all methods considered here, these two equations will remain unchanged. In a more general sense, this is not entirely necessary, and Kennedy (1997) presents a method similar to Dommermuth and Yue (1987), which expands (3) about the still water level, with some loss of accuracy. However, in this paper attention instead will be paid to Laplace's equation, which imposes continuity throughout the flow

field. In its most general form, the LPA approximation to the field equation becomes

$$\int_{-h}^{\eta} W_j(x,y)(\phi_{xx}+\phi_{yy}+\phi_{zz})dz = 0, \quad j = 1,\ldots,n-2 \tag{4}$$

where $W_j(x,y)$ are weighting functions, which can take almost any form. Kennedy and Fenton (1996) used polynomial weighting functions, but here, as in Kennedy and Fenton (1997), weighting functions will be taken to be Dirac delta functions. This turns (4) into a set of collocation equations

$$\phi_{xx}+\phi_{yy}+\phi_{zz} = 0 \ \text{ on } z = z_j(x,y), \quad j = 1,\ldots,n-2 \tag{5}$$

The set of collocation points in Kennedy and Fenton (1997) were given as

$$z_j = -h + (\eta + h)\alpha_j \tag{6}$$

where α_j's were chosen so that z_j's were the Gauss-Legendre points for $N = n-2$, using the free surface and the bed as limits. This set was chosen because of continuity considerations, and will be considered as the standard against which the revised methods will be judged.

With the addition of conditions on the lateral boundaries, equations (2-4) form a set of linear equations which may be solved to find the flow field. Once interior velocities are known, the system may be advanced in time using the evolution equations

$$\eta_t = -\left(\int_{-h}^{\eta}\phi_x dz\right)_x + \left(\int_{-h}^{\eta}\phi_y dz\right)_y \tag{7}$$

and

$$\phi_t^{(s)} = -g\eta - \frac{1}{2}\left(\phi_x^2+\phi_y^2+\phi_z^2\right) + \phi_z\eta_t \tag{8}$$

In Kennedy and Fenton (1997), an equation different from (7) was used to update the free surface elevation. This in general did not analytically guarantee conservation of mass for approximate solutions, but because the Gauss-Legendre collocation points were used, overall conservation was guaranteed for levels of approximation $n \geq 4$. However, in this paper different collocation points will be used, and to guarantee overall continuity, (7) is employed.

This system of equations defined by (1-8) may be solved in a variety of ways, for both one and two horizontal dimensions. However, for simplicity, and because of computational constraints, we will limit tests to one horizontal dimension. Here, a good method involves complex polynomials and is detailed in Kennedy and Fenton (1997). This will be the base method used here.

In the previously referenced papers, these models have been shown to provide good accuracy with a reasonable computational cost for a variety of conditions.

However, two possible areas of improvement seem obvious. The first concerns the number of computational variables. According to (1), n variables define the flow field at each computational point. Each of these makes its way into the system of unknowns which must be solved at each time step. If the number of computational unknowns were reduced, computational speed would almost certainly increase. This will form one avenue of exploration. The second concerns the accuracy of any given level of approximation. The weighting functions in (4) were not specified using a strict theoretical basis and indeed none will be used now. Instead, sets of points will be found for different levels of approximation that provide some sort of best fit to a theoretical special case, such as wave celerity over a level bed. For both avenues of improvement, results will then be tested using the experiments of Ohyama et al. (1995), which measured wave transformation over a submerged breakwater.

Improved Speed: Linearised B-Splines

The first effort at improvement will be directed towards increasing computational speed. In the previous section, it was stated that one way to do this would be to reduce the number of computational unknowns that form the system of equations that must be solved at each time step. Unfortunately, despite significant effort, no such technique has been found for the general case of fully nonlinear wave motion in two horizontal dimensions. However, if one small additional approximation is made, a method exists which promises great improvements in computational efficiency. The change that must be made is to the field equation, (6), which becomes

$$z_j = h(-1 + \alpha_j) \tag{9}$$

where α_j's are identical to those previously used. Linearly, computations will be identical but, because collocations are chosen with respect to the still water level and not the instantaneous free surface, nonlinear properties should be slightly worse. However, because collocation points are invariant with time, it is possible to use what we will call the linearised B-spline approximation to speed computatious. This may only be used for one horizontal dimension, as it makes use of the complex polynomial solution method. A detailed discussion of the method (only used there for expansion techniques) is given in Kennedy (1997), but a brief description will be given here. Essentially, because equations (2,5) are homogeneous, it is possible to rewrite the basis functions used in the complex polynomial solution method so that (2,5) are satisfied and the number of equations to be solved is equal to the number of computational points (plus additional boundary conditions). As an additional bonus, the bandwith of the resulting matrix equation is reduced, further increasing speed. The new basis functions are analogous to B-splines, which may also be thought of as methods to eliminate homogeneous equations. It would be possible to rewite these basis functions even when (6) is used, but because the collocation points change with the free surface, they would need to be rederived at each time step, actually

slowing computations. However, with (9), collocation points remain constant with time and the revised basis functions would only need to be computed once, at the beginning of computations.

Before testing the new technique, it is helpful to consider the change to the nonlinear properties caused by the approximation (9). Figure 1 shows the amplitude of the second harmonic of LPA Stokes-type steady waves compared to exact results. Two levels of approximation are shown: $n = 5$, which contains z^4 terms in the velocity potential, and $n = 7$, which contains z^6 terms. The original formulation for the level of approximation $n = 5$ has a second harmonic which remains quite accurate into water of depth $kh = 2\pi$, while the linearised basis functions show greater error at high wavenumbers. Still, error remains small up to a dimensionless wavenumber of $kh = 5$, which is quite good. Using the level of approximation $n = 7$, second harmonics for both the original and linearised versions are extremely accurate to wavenumbers of $kh = 3\pi$.

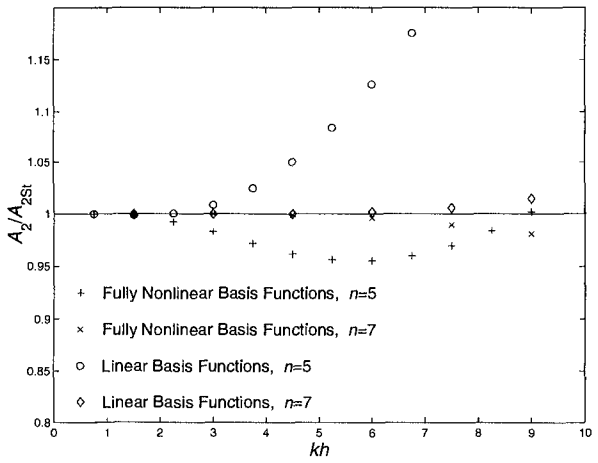

Figure 1: Second harmonics for a second order steady wave compared to Stokes' solution

A special case of subharmonics, second order setdowns under a steady wave were also calculated and provided a major surprise: setdowns using both the fully nonlinear and linearised basis functions were identical. Figure 2 shows setdown magnitudes relative to Stokes' solution plotted on a semi-logarithmic scale. For the level of approximation $n = 5$, results are very good until a dimensionless wavenumber of $kh = 2.5$, when error increases very quickly. For the higher level of approximation $n = 7$, error remains small until around $kh = 4$. For

high wavenumbers, both levels of approximation can show order of magnitude errors in setdown. However, since setdown decays exponentially with increasing wavenumber, for the most part the error is merely a "different flavour of zero", and should make little difference to computations. For very high wavenumbers around $kh = 6$, the lower level of approximation does begin to show errors which may not be negligible in terms of absolute, rather than relative, error.

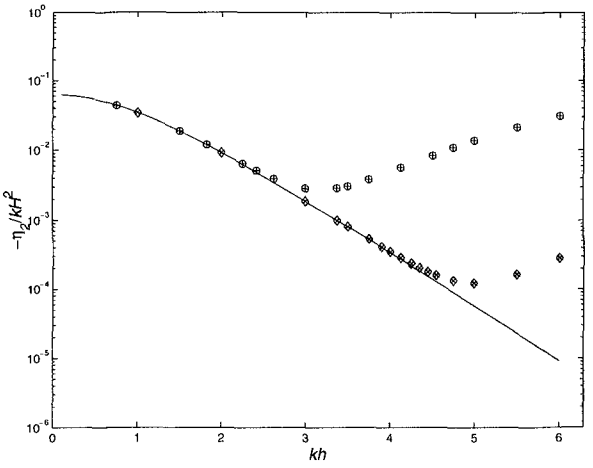

Figure 2: Second order setdown for a second order steady wave compared to Stokes' solution. Symbols identical to previous figure.

These results show a small, but noticeable difference in nonlinear accuracy between the original and linearised basis functions. Computations using the level of approximation $n = 7$ and the linearised basis functions were then tested against the experimental results of Ohyama et al (1995). Figure 3 shows a schematic drawing of the experimental setup, where monochromatic waves propagated over a steep-sided submerged bar. All waves had an initial height $H/h = 0.1$, and cases 2,4, and 6 had periods $T\sqrt{g/h} = 5.94,\ 8.91,\ 11.88$ respectively

It was here that the problems with the linearised B-spline approximation became apparent. For all cases tested, and with all spatial and temporal resolutions used, computations became unstable as waves passed from the crest of the shelf onto the back slope. The reason for this was not readily obvious, but became apparent after some additional analysis. The culprit was a nonlinear instability to short wavelength bottom disturbances. Consider a small amplitude

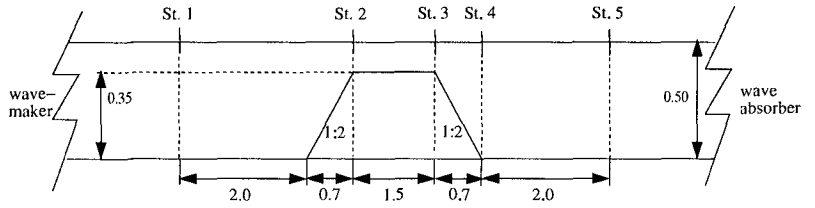

Figure 3: Setup for Experiments of Ohyama et al. (1995). All measurements in m.

sinusoidal bottom disturbance in otherwise quiescent water. The water level is assumed to be at elevation $\eta = 0.5h$, similar to that under the crest of a very large wave. Although this is somewhat different from what happens when the wave crest passes over the sharp corner of the submerged bar, it provides an illuminating demonstration of model response to short wavelength disturbances in topography.

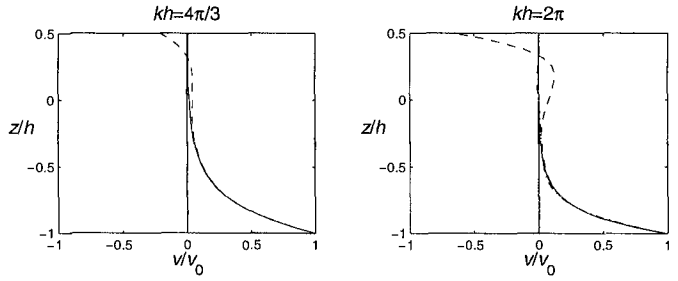

Figure 4: Vertical velocity due to a bottom disturbance, $n = 7$; –, exact; ···, fully nonlinear (obscured) ; - -, linearised basis functions

Figure 4 plots the structure of the resulting vertical velocity field, showing the exact solution using hyperbolic functions, the fully nonlinear LPA solution, and the LPA solution using linearised basis functions, both with the level of approximation $n = 7$. The wavenumbers shown straddle the Nyquist wavenumber used in computations. The fully nonlinear LPA solution closely resembles the exact decaying relation for both short wavenumbers tested, but results using the linearised functions show wild oscillations and large amplitudes above the still water level. This is because the linearised functions have collocation points which extend only from the bed to the still water level. Above this, the linearised basis functions essentially extrapolate the interpolated solution

of Laplace's equation. In contrast, the fully nonlinear solution has collocation points which move with the instantaneous water surface (Eq. (6)). This ensures that solutions of the field equation are interpolations rather than extrapolations, as with the linearised solution. Possible solutions to this dilemma would be to increase the range of collocation points using the linearised functions to above the still water level, but this has its own problems. Both linear and nonlinear performance would deteriorate for any given level of approximation, perhaps enough to cancel out any increase in efficiency. No completely satisfactory solution has yet been found.

This instability to bottom disturbances is also of concern for higher order Boussinesq-type approximations, which extrapolate solutions of Laplace's equation using Taylor series. In fact, the higher order Boussinesq model of Gobbi et al. (1998) has also exhibited instabilities in computational tests with sharp corners (M. Gobbi, pers. commun.). Clearly, the extrapolation of a decaying function with a polynomial remains an area of difficulty.

Improved Accuracy: Revised Collocation

Although the efforts to improve efficiency in the previous section ultimately proved unworkable, results here were much more successful. The question was quite simple: for a given level of approximation, n, find the set of collocation points which best optimises certain analytic properties, and see if this translates to better performance for real computations.

To begin with, the analytic property chosen for comparison was small amplitude phase celerity, as it greatly influences accuracy in comparison with experiments such as Ohyama et al. (1995). The exact celerity was expanded in a Taylor series about the long wavelength limit $kh = 0$, and LPA celerities were made to match as many terms as possible. First of all, we will start with the low level of approximation, $n = 3$, although this level is of little practical use. One free collocation point is available for manipulation, and for any choice of collocation points, the LPA dispersion relationship is accurate to $O(kh^2)$. However, for the choice $\alpha_1 = 1/\sqrt{5}$, dispersion is accurate to $O(kh^4)$. In fact, the resulting dispersion relationship is the [2,2] Padé approximant found in Nwogu (1993) and Wei et al. (1995). For the level of approximation $n = 5$, three collocation points were available, while the base level of accuracy was $O(kh^4)$. With the choice of $\alpha_1 = 0.1255280883$, $\alpha_2 = 0.5008959415$, $\alpha_3 = 0.8419853513$, accuracy is increased to $O(kh^{10})$. For the level of approximation $n = 7$, however, no optimised approximation was found. This was due to the lack of a general solution for dispersion; i.e. dispersion relationships could be found for any particular set of α_j's, but not for the general set. Solutions using the Gauss-Legendre points were close to optimal, but the possibility for improvements remains.

Figure 5 shows the original and improved dispersion relationships compared to the exact small amplitude solution. For the level $n = 3$, the resulting relationship is usable up to the nominal deep water limit of $kh = \pi$, which is a

significant improvement. However, in contrast to the Gauss-Legendre relationship, phase speeds are greatly overpredicted for high wave numbers. For the level $n = 5$ errors in improved phase speed remain less than 1 percent until a dimensionless depth of approximately $kh = 9$. However, this level is still somewhat less accurate than the level of approximation $n = 7$, which has excellent accuracy. Clearly, dispersion relationships can be much improved.

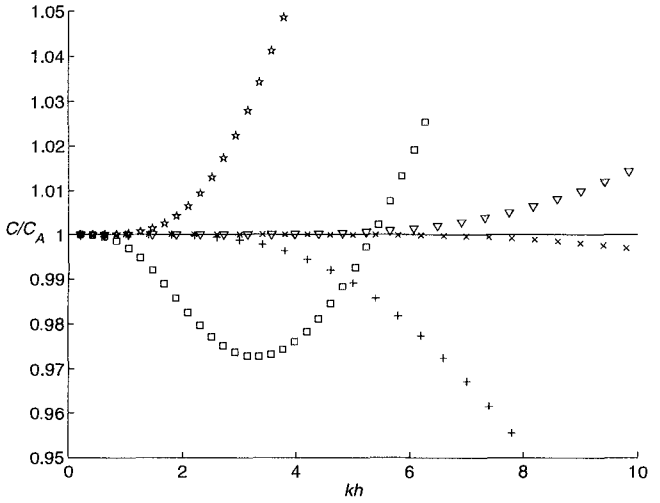

Figure 5: LPA celerities using Gauss-Legendre (GLE) and new collocation points. Squares, GLE $n = 3$; stars, new collocation $n = 3$; +, GLE $n = 5$; triangles new collocation $n = 5$; x GLE $n = 7$

Nonlinear performance is improved as well. Figure 6 shows amplitudes of second harmonics for a steady wave relative to Stokes' solution. For all levels of approximation, results are much asymptotically much improved, although at higher wave numbers, the revised collocation points tend to show greater error. Subharmonics show a similar trend. Figure 7 shows a significant improvement in the accuracy of the steady wave setdown for the levels of approximation $n = 3$ and $n = 5$. Notably, for the level of approximation $n = 5$ using the new collocation points, absolute errors remains small over the entire range considered. Accuracy for the level of approximation $n = 7$, however, remains significantly better.

We will now consider computational results over the topography of Ohyama et al. (1995) which, as mentioned previously, is shown in Figure 3. Fortunately, computations with the revised collocation points showed none of the instabilities

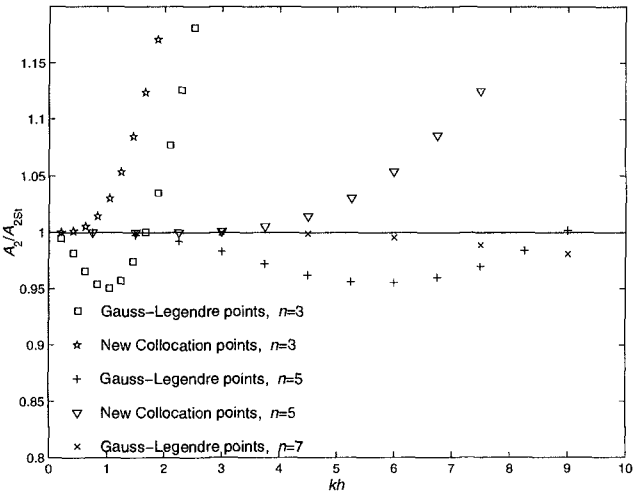

Figure 6: Second harmonics for a second order steady wave compared to Stokes' solution

of the previous section. Full experimental results are available for comparison at both Stations 3 and 5. However, almost any nonlinear model will give good results at Station 3, while good agreement at Station 5 is much more difficult. Therefore, instead of showing results at Station 3, we will merely say that all comparisons were uniformly excellent, no matter what levels of approximation were used. Figure 8 shows results at Station 5 for the level of approximation $n = 5$, for both the original and revised collocation points. For case 2, the shortest wave, computations using the original collocation show some error, while this error is greatly reduced with the revised collocation. For case 4, computations show a similar trend, although the reduction in error is not as large. For case 6, agreement using the improved collocation is quite good, while results using the original formulation show higher harmonics which are visibly too large.

Figure 9 shows results for the level of approximation $n = 7$. For all cases considered, results are excellent, with experimental and computational results nearly identical. Once again, the higher level of approximation gives results somewhat better than the improved lower level.

Discussion and Conclusions

Analytic results and computational tests using the revised collocation points show significant improvements in accuracy for all levels of approximation. Since

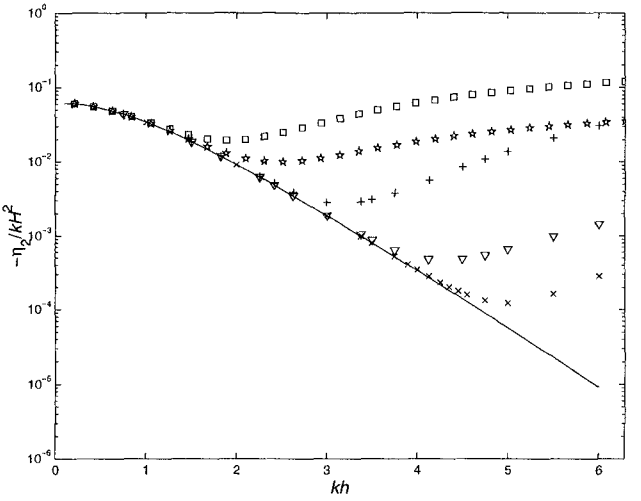

Figure 7: Setdown under a second order wave compared to Stokes' solution. Symbols identical to previous figure.

a change in collocation points provides no increase in computational expense, there seems to be no reason why this new feature should not be adopted as a matter of routine.

It should be possible to increase nonlinear accuracy further by changing the collocation technique itself. If the definition for collocation points (6) is changed to

$$z_j = h(\alpha_j - 1) + \beta_j \eta \tag{10}$$

where α_j's are unchanged, linear dispersion will be the same, but an additional parameter will be available to tune second or third order nonlinear characteristics. Although no comprehensive effort has yet been made to optimise β_k parameters, ad hoc tests show that significant improvement in nonlinear parameters is indeed possible. Figure 10 shows second harmonics computed using (10) using the set $\beta_1 = 0.0319$, $\beta_2 = 1.4018$, $\beta_3 = 1.4297$. Although this set is not fully optimised, significant improvement can be seen. However, manipulation of this sort introduces a dependency on the definition of the still water level which was not present in the previous fully nonlinear LPA solutions. Slight changes in the still water level from what was assumed could lead to significant changes in the model properties if (10) were used, negating any advantage that might be gained. Still, this idea may deserve further consideration.

Another possible area of investigation lies in what quantities should be op-

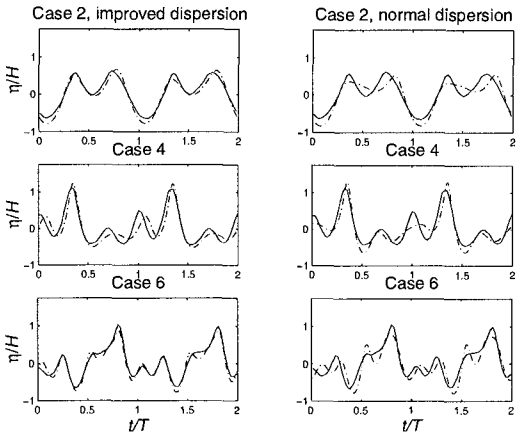

Figure 8: Experimental (—) and computed (-·-) time series at Station 5 for experiment of Ohyama et al., $n = 5$

timised for best results. Previously, linear dispersion was the only analytic quantity used, but the experience with the linearised B-splines suggests that it might be wise to include response to bottom disturbances in the optimisation criteria. Yet another candidate is linear shoaling, although this would involve a significantly more complicated analyis.

Practical performance of the linearised B-spline approximation was quite disappointing, and the solution does not appear to be simple. The basic problem of extrapolating a decaying function is fundamental, and requires careful thought. Several possible solutions were proposed in an earlier section, but all will require testing.

So in conclusion, it can be stated that revised collocation offers significant improvements in accuracy for all levels of approximation considered and should be used on a regular basis. However, the linearised B-spline approximation exhibits a strong nonlinear instability to short wavenumber bottom disturbances, and presently remains unworkable.

References

Dold, J., and Peregrine, D., 1980 "Steep, unsteady water waves: an efficient computational scheme", *Proc. Int. Conf. Coastal Eng.*, Houston, 955-967.

Dommermuth, D.G, and Yue, D.K.P., 1987, "A high-order spectral method for the study of nonlinear gravity waves", *J. Fluid Mech.*, **184**, 267-288.

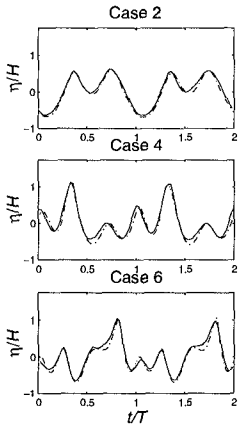

Figure 9: Experimental (—) and computed (---) time series at Station 5 for experiment of Ohyama et al., $n = 7$

Gobbi, M.F., Kennedy, A.B., and Kirby, J.T., 1998, "A comparison of higher order Boussinesq and local polynomial approximation models", *Proc. 26th Int. Conf. Coastal, Eng.*, Copenhagen.

Gobbi, M. F., Kirby, J. T., and Wei, G., 1998 "A fully nonlinear Boussinesq model for surface waves: II. Extension to $O(kh)^4$", *J. Fluid Mech.*, Submitted.

Grilli, S., Subramanya, R., Svendsen, I., and Veeramony, J., 1994, "Shoaling of solitary waves on plane beaches", *J. Waterway, Port, Coastal and Ocean Eng.* **120**(6), 609-628.

Kennedy, A. B., 1997 "The propagation of water waves over varying topography", Ph.D. Thesis, Monash University, Australia, 163pp..

Kennedy, A. B. and Fenton, J. D., 1996 "A fully nonlinear 3D method for the computation of wave propagation", *Proc. 25th Int. Conf. Coastal Eng.*, Orlando, 1102-1115.

Kennedy, A. B. and Fenton, J. D., 1997 "A fully-nonlinear computational method for wave propagation over topography", *Coastal Eng.*, **32**, 137-161.

Nwogu, O., 1993 "An alternative form of Boussinesq equations for nearshore wave propagation", *J. Waterway, Port, Coast., Ocean Engng*, **119**, 618-638.

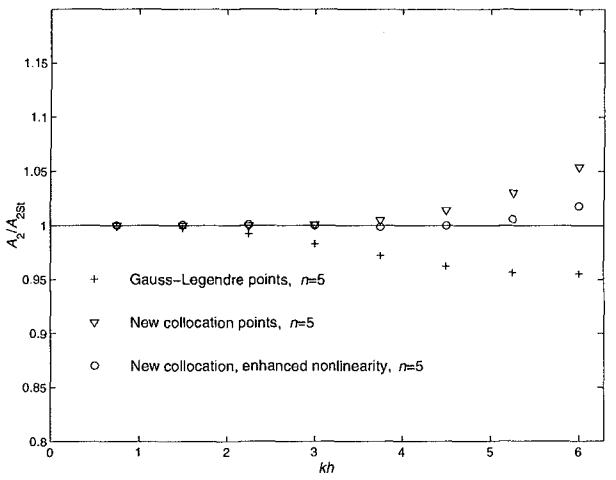

Figure 10: Second harmonics for a second order steady wave compared to Stokes' solution

Ohyama, T., Kiota, W., and Tada, A., 1995 "Applicability of numerical models to nonlinear dispersive waves", *Coastal Eng.*, **24**, 297-213.

Schäffer, H. A. and Madsen, P. A., 1995 "Further enhencements of Boussinesq-type equations", *Coastal Eng.*, **26**, 1-14.

Wang, N.T., Yao, Y., and Tulin, M., 1995, "An efficient numerical tank for nonlinear water waves, based on the multi-subdomain approach with BEM", *Int. J. Numer. Meth. Fluids* **20**, 1315-1336.

Wei, G., Kirby, J. T., Grilli, S. T., and Subramanya, R., 1995 " A fully nonlinear Boussinesq model for surface waves. Part 1. Highly nonlinear unsteady waves. *J. Fluid Mech.*, **294**, 71-92.

Depth inversion for nonlinear waves shoaling over a barred-beach

Stéphan T. Grilli [1], M. ASCE, and Jesper Skourup [2]

ABSTRACT : Characteristics of periodic wave shoaling over a barred-beach are calculated in a fully nonlinear numerical wave tank. Variations of wave elevation, slopes, height, asymmetry, and celerity are discussed. Over and beyond the bar, classical highly nonlinear decomposition phenomena occur in a *modulation region* (MR); in shallower water, shoaling reoccurs. Depth inversion algorithms developed and calibrated for mild slopes are applied to the barred-beach. Expectedly, errors on depth prediction occur in the MR; suggestions for improvements are made.

INTRODUCTION

Depth inversion algorithms

Depth inversion refers to a class of numerical/experimental methods by which the ocean bottom bathymetry in coastal areas is predicted using properties of waves measured on the ocean surface. Such properties are typically obtained by remote sensing or video based technique [see Grilli, 1998, for a brief summary of these] and often consist, in their raw form, in spatial and temporal variations of wave phases. Multiple phase diagrams separated in time can provide estimates of wave celerity and wavelength [hence, wave period] which, in turn, using a dispersion relationship, can provide estimates of the depth variation. Both the quality of the initial data and the accuracy of the dispersion relationship in representing real wave behavior will affect the accuracy of the depth prediction.

Most state-of-the-art methods still use the linear dispersion relationship to carry out depth inversion, according to the methodology outlined above [Dugan,

[1]Distinguished Professor, *Dept. of Ocean Engng., University of Rhode Island, Narragansett, RI 02882, USA*, email: grilli@oce.uri.edu, http://www.oce.uri.edu/~grilli

[2]*Danish Hydraulic Institute, Agern Allé 5, Horsholm DK 2970, Denmark*, email : jes@dhi.dk

1997]. Grilli (1998), however, studied the depth inversion problem for mildly and monotonously sloping beaches and showed, for shallow enough water, nonlinear effects and their influence on wave celerity c cannot be neglected. Such so-called *amplitude dispersion effects* make higher waves travel faster and lead to overestimation of the water depth h, when depth inversion is simply the result of "inverting" the linear dispersion relation. To account for amplitude dispersion effects, wave height data H or, at least, deep water steepness k_oH_o must also be known [k_o and H_o are the deep water wavenumber and wave height, respectively]. For periodic waves, normalized wave steepness kH/k_oH_o was shown by Grilli and Horrillo (1996,1998b) to provide an almost one-to-one relationship with relative depth kh in the shoaling region and, also [surprisingly], to be well predicted by linear wave theory (LWT). Hence, assuming simultaneous observations of surface elevations are available, they suggested that this parameter could be used to model the wave height variation, and thus predict k_oH_o, in the *depth-inversion problem.*

Following this approach, assuming both wave phases and wave height data are available, Grilli (1998) developed a new *Depth Inversion Algorithm* [referred to as DIA1] and validated it for simulated wave data. This algorithm uses a dispersion relation $c(k_oh, k_oH_o)$ which is empirically based on results of computations in a fully nonlinear wave tank [NWT; see next Section]. In all cases, rms-errors on depth inversion with DIA1 were less than a few percent whereas the linear dispersion led to rms-errors 5 to 10 times larger, particularly in the shallower water region. Accurate spatial measurements of wave elevations, for instance using remote sensing techniques such as Synthetic Aperture Radar (SAR), are still quite problematic under the current state of the technology. Hence, to eliminate the need for wave height data, an alternate parameter related to wave skewness, also function of k_oH_o, was identified and shown to be quite sensitive to depth variations (Grilli and Horrillo, 1996,1998b). This parameter is the ratio of forward to backward wave slopes, noted, $s_2/s_1 \simeq L_1/L_2$ [Fig. 1b, assuming $H_1 \simeq H_2$; i.e., a measure of wave left to right spatial asymmetry]. Unlike H, this parameter can also be retrieved from spatial wave phase information. Thus, Grilli (1998) developed a second algorithm [referred to as DIA2], using an empirical relationship $s_2/s_1(k_oh, k_oH_o)$, also fitted to results of computations in the NWT, to predict k_oH_o before the nonlinear dispersion relation is "inverted" to predict depth. Although DIA2 provided slightly larger errors on depth prediction than DIA1, these were still much smaller than when using LWT.

In actual field situations, DIA1 and DIA2 would thus predict the depth variation $h(x)$ in the direction of wave propagation, for waves almost normally incident to the shore [i.e., about cross-shore], based on sets of values of $c(x)$ and $L(x)$ [obtainable from wave phases], and either $H(x)$ (DIA1) or $s_2/s_1(x)$ (DIA2), simultaneously measured at a number of locations x, using remote sensing techniques (Fig. 1). In both algorithms, wave period T is first predicted as the mean of observed L/c values [where $L = (L_c(x) + L_t(x))/2$; Fig. 1b], and k_oH_o is then predicted [with, $k_o = (2\pi)^2/(gT^2)$], either based on wave height data, using the LWT steepness

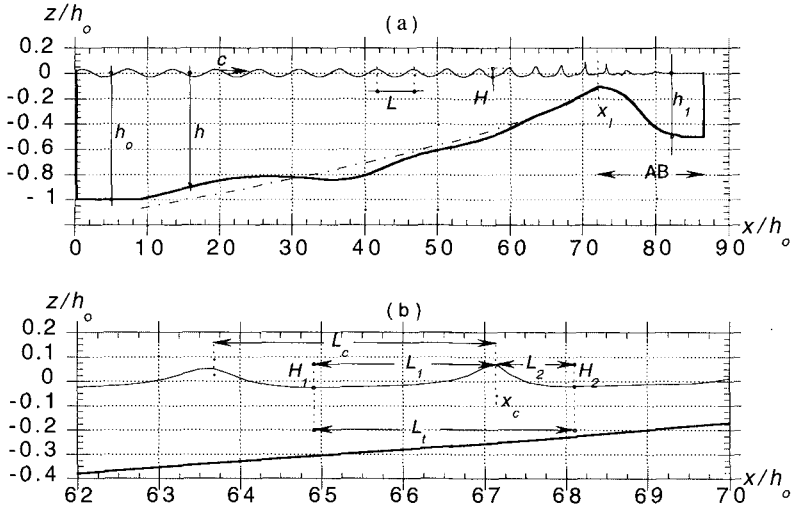

Figure 1: (a) Sketch of periodic wave shoaling computations in the *numerical wave tank*. (——) typical bottom topography and (— - —) least square fit to the topography : $h/h_o = 0.0758\,(74.20 - x/h_o)^{0.64}$ (Dean's profile). (b) Blow-up of part (a) and definition of some of the wave geometric characteristics used in DIA1 and DIA2.

relationship (DIA1), or on wave asymmetry data, using the empirical relationship for $s_2/s_1(k_o h, k_o H_o)$ (DIA2). The celerity relationship $c(k_o h, k_o H_o)$ is finally inverted to predict depth h [see details in Grilli, 1998].

Computation of wave shoaling in a numerical wave tank

Nonlinear properties of periodic waves of height H_o and period T in deep water, shoaling over "cylindrical beaches" with *monotonously decreasing and mildly sloping* depth variation $h(x)$ (Fig. 1), were used by Grilli (1998) to calibrate depth inversion algorithms DIA1 and DIA2.

These properties were obtained by Grilli and Horrillo (1996,1998b), using a two-dimensional (2D) *numerical wave tank* (NWT), which combined [Grilli et al., 1989; Grilli and Subramanya, 1996; Grilli and Horrillo, 1997; Fig. 2a] : (i) a higher-order Boundary Element (BEM) solution of Fully Nonlinear Potential Flow (FNPF) equations in domain Ω; (ii) an exact generation of finite amplitude periodic waves [*Streamfunction Waves*] at the deeper water extremity (Γ_{r1}); and (iii) an *Absorbing Beach* (AB) at the far end of the tank [featuring both free surface absorption on Γ_f

and lateral active absorption (AP) on Γ_{r2}; Clément, 1997]. A feedback procedure was developed to adaptively calibrate the beach absorption coefficient so as to absorb the period-averaged energy of waves entering the AB at $x = x_l$. After absorption of initial transient waves, computations in the NWT reached a *quasi-steady* state for which reflection from the AB was very small. Nonlinear properties of waves were then calculated and validation tests were performed to assess their sensitivity to the AB location and to the resolution of the spatial discretization. Numerical results were compared to laboratory experiments for periodic wave shoaling over a mild slope, and propagation over a bar [Beji and Battjes, 1994]. All the tests were found satisfactory. Details of model equations, numerical methods and validation applications can be found in the above-referenced papers.

Grilli and Horrillo (1996,1998b) calculated shoaling of waves of various heights and periods up to very close to the breaking point, over 1:35, 1:50, and 1:70 slopes, both plane and natural [i.e., with a bathymetry following Dean's (1991) equilibrium beach profile; see, e.g., Fig. 1a]. Local [i.e., variations of shoaling coefficient $K_S = H/H_o$, celerity c, relative wave height H/h, steepness kH, and asymmetry s_2/s_1], and integral properties of shoaling waves were calculated. Due to the low reflection from the slope and the AB, wave properties were found to be very repeatable for successive waves.

For mild slopes, nonlinear properties of waves of different height and period but same deep water steepness k_oH_o were found to be almost identical for the same relative depth kh. This allowed Grilli (1998) to use results for a plane 1:50 slope to calibrate DIAs which were later successfully applied to other slopes. In the shallower water region, linear, weakly nonlinear, and higher-order steady wave theories did not, in general, accurately predict shoaling wave properties, especially for $H/h > 0.15$. Linear wave theory, in particular, was in error by up to 85% for the wave celerity. The weak nonlinearity and/or the lack of wave skewness in these theories were identified as the main sources of errors.

WAVE SHOALING OVER BARRED-BEACHES

General features

Grilli and Horrillo (1998a) used the same NWT as above to calculate periodic wave shoaling over a barred-beach, modeled as a Dean's equilibrium profile with average slope 1:50 (Fig. 2), and a bar located towards the top of the slope, with a 1:20 seaward, a 1:10 shoreward slope, and a crest with nondimensional depth 0.2. [The geometry of this bar is similar to that of Beji and Battjes' (1994) experiments which were used to validate shoaling computations in the NWT.]

Since waves of moderate incident steepness initially behave as predicted by LWT, the computations are initiated in intermediate water depth $h_o^* = 0.6h_o$, in the de-shoaling zone. Corresponding wave characteristics in deep water (depth h_o) are back-calculated using LWT. Three incident waves of nondimensional height $H_o'^* =$

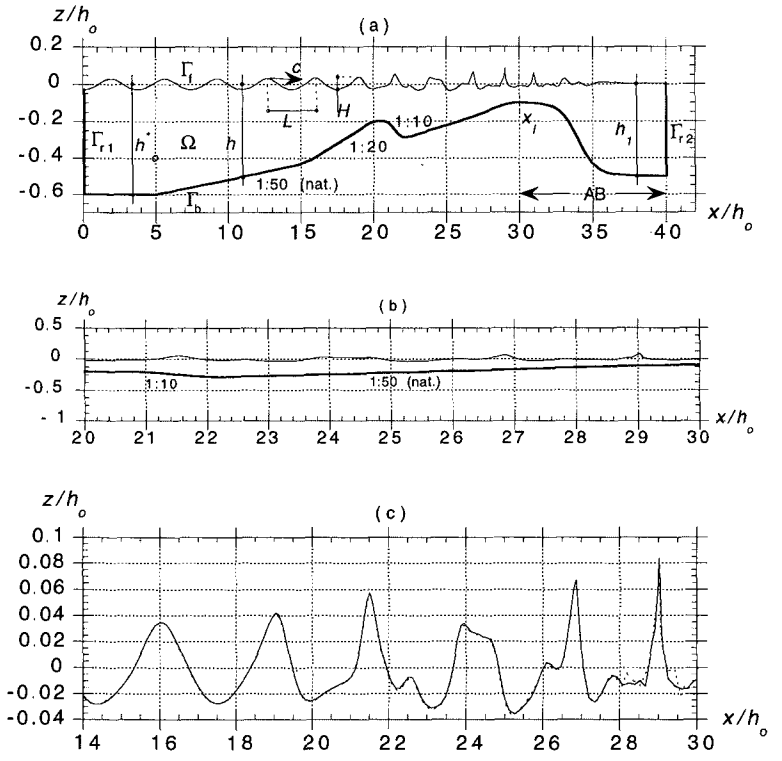

Figure 2: Periodic wave shoaling over a barred-beach. (a) Sketch of NWT. (b) Blow-up of free surface shape in undistorted scale. (c) Free surface shape for case 1 (Table 1) : after $15.75T'$ (——); one period later (- - - - -).

Table 1: Input characteristics of incident waves in the NWT : H'_o deep water wave height; T' wave period; H'^*_o initial wave height in depth $h'^*_o = 0.6$; $k'_o = (2\pi/T')^2$ (linear) deep water wave number; $k_o H_o$ initial wave steepness; $c'_o = T'/(2\pi)$ and$L'_o = c'_o T$, the linear deep water wave celerity and wavelength, respectively. Dashes indicate nondimensional variables (length scale : h_o; time scale : $\sqrt{h_o/g}$, with g, the gravitational acceleration).

No.	H'_o	T'	H'^*_o	k'_o	$k_o h^*_o$	$k_o H_o$
1	0.0635	5.5	0.06	1.305	0.79	0.0852
2	0.0626	6.5	0.06	0.934	0.56	0.0594
3	0.0614	7.5	0.06	0.702	0.42	0.0361

$H^*_o/h_o = 0.06$ and periods $T' = T\sqrt{g/h_o} = 5.5$, 6.5, and 7.5 are successively generated at Γ_{r1}, as exact finite amplitude zero-mass-flux streamfunction waves (Grilli and Horrillo, 1997). General data for these three waves are summarized in Table 1. An AB is specified in the NWT for $x' \geq x'_l = 30$, with a tapered bottom variation aimed at improving energy absorption (Grilli and Horrillo, 1997); the depth at the AB entrance is $h'_l = 0.1$, and $h'_1 = 0.5$ at its extremity. Numerical data in the NWT [i.e., spatial and temporal discretizations] are selected for each case in order to ensure high accuracy of the computations.

A typical result for the calculated free surface shape is shown in Fig. 2, for case 1 (Table 1) at $t' = 86.64 = 15.75T'$ from the (cold) start of the computations. At this stage, the initial transient front has been absorbed in the AB and computations have reached a quasi-steady state. This is confirmed in Fig. 2c which shows two free surface profiles obtained at a one-period time interval : the two profiles are nearly identical, except for small high-frequency oscillations close to the AB entrance ($x' > 28$). Seaward of the bar ($x' \leq 21$), wave shoaling appears qualitatively similar to that obtained for monotonous mild slopes (e.g., Fig. 1) : as waves propagate up the beach, their length reduces, their height increases, and their profile becomes increasingly front/back asymmetric (i.e., skewed), with higher and narrower crests, and longer and shallower troughs. Shoreward of the bar ($x' \geq 21$), however, the free surface profile appears very different from typical shoaling profiles, and decomposes into higher-frequency oscillations. Such decomposition phenomena of waves propagating over obstacles are well known and have been observed, e.g, by Byrne (1969) and Young (1989), and modeled, e.g., by Massel (1983), Rey (1992), Rey et al (1992), Driscoll et al (1992), and Ohyama and Nadaoka (1994). Just before entering the AB, close to the breaking point ($x' \geq 28$), waves somewhat recover the sawtooth/soliton-like shape typical of pre-breaking shoaling waves.

Unlike in Driscoll et al's (1992) and Ohyama and Nadaoka's (1994) work, the present study features a varying beach topography. Hence, when waves reach the bar, due to the initial shoaling over the mildly sloping base-profile of the beach, they are

already significantly nonlinear with a height of about 45% of the local depth, and significant energy transferred to bound second and higher-order harmonics. Upon reaching the deeper water region behind the bar, wave nonlinearity drops and, as over a flat bottom, the higher harmonics are released as free waves. These free waves induce significant spatial modulations of the wave profile, quite apparent in Fig. 2, over some distance but, further onshore, as waves again propagate up the base-profile of the beach and depth decreases, shoaling reoccurs and, for sufficiently shallow depth, the free higher harmonics, again, become bound to the main wave and the wave profile reassumes a typical shoaling shape. Therefore, unlike with underwater obstacles over constant depth, the modulation region shoreward of the bar is limited in extension by the reducing depth, clearly, as a function of incident wavelength, bar berm geometry, and beach slope. In the case of Fig. 2, the modulation region covers a horizontal distance of about 5-6h_o.

Detailed features

Detailed variations of local wave parameters over the barred-beach are now presented and, more specifically, in the modulation region beyond the bar, where wave behavior is irregular. Fig. 3, parts a to d, shows normalized wave harmonics a_i [$i = 1, 2, 3$], height H, slopes s_1 and s_2, and celerity c, respectively, calculated for case 2. [Since results for the three cases are qualitatively similar, only detailed results for case 2 are presented here.] Both the FNPF results for a 1:50 natural slope [i.e., the base-profile of the beach without the bar] and those predicted by LWT for the barred-beach, have been plotted. Fig. 4, parts a and c shows comparisons of normalized wave height and celerity, calculated for cases 1, 2, and 3, as a function of $k_o h$; and part b shows wave front/back asymmetry s_2/s_1 as a function of x/h_o.

In Fig. 3a, as mentioned before, standard wave shoaling occurs in front of the bar ($x' \leq 21$; Fig. 2), where wave energy is continuously transferred from the fundamental to bound higher-order harmonics [the initial slight increase in a_1 is due to reflection by the slope]. As a result, wave shape becomes increasingly skewed and sawtooth-like. Upon passing over the bar berm ($x' > 21$), waves reach the deeper water region beyond the bar and the harmonics are released as free waves. This results in marked oscillations in harmonic amplitudes and in strong spatial modulations of the wave profile. The modulation length for a_2 is approximately 5.6h_o, i.e., about twice the wavelength in the middle part of the modulation region. Waves reassume their sawtooth-like shoaling shape before entering the AB ($x' \geq 30$), and the harmonic amplitudes seem to come back to a prolongation of what they were before reaching the bar.

In Fig. 3b, similarly, the FNPF wave height variation for the barred-beach departs from that corresponding to the base-profile, upon reaching the bar berm. Towards the end of the modulation region beyond the bar, however, the barred-beach results seem to agree better with the latter. As expected from earlier studies, LWT

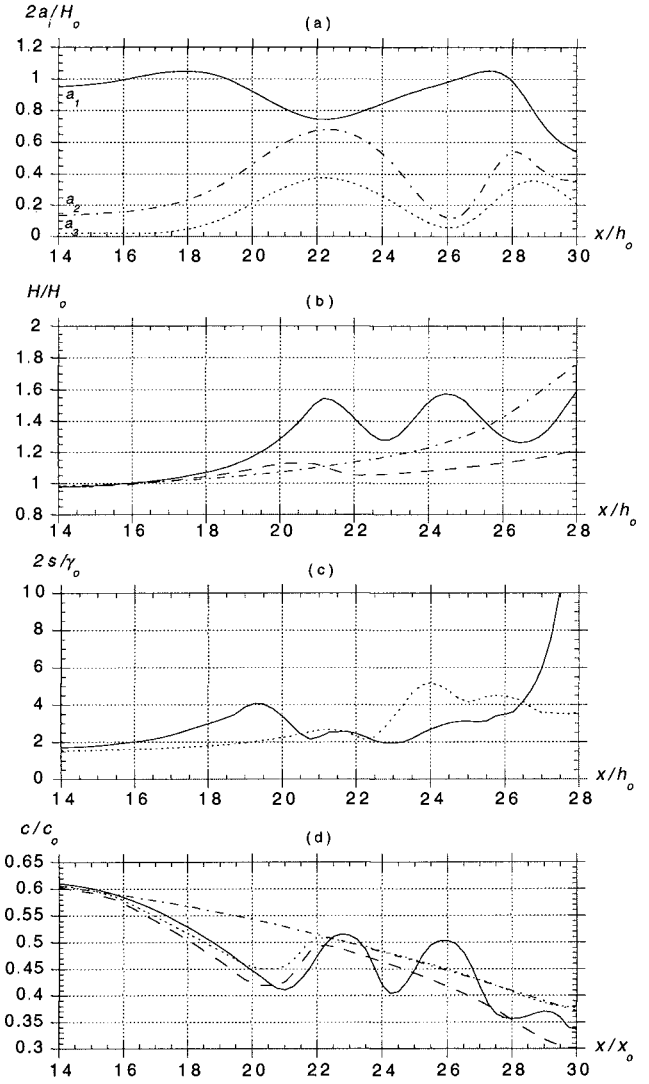

Figure 3: Normalized NWT results for case 2 (Table 1), over barred-beach of Fig. 2, compared with (– – –) LWT results for the same case; (- - -) NWT computations for the natural 1:50 base-profile (without a bar) : (a) First three wave harmonic amplitudes a_i. (b) Wave height (——). (c) Front (——) ($s_2 = H_2/L_2$) and back (- - - -) ($s_1 = H_1/L_1$) wave slopes ($\gamma_o = H_o/L_o$). (d) Wave celerity (——); (- - - -) application of based-profile results to the barred-beach.

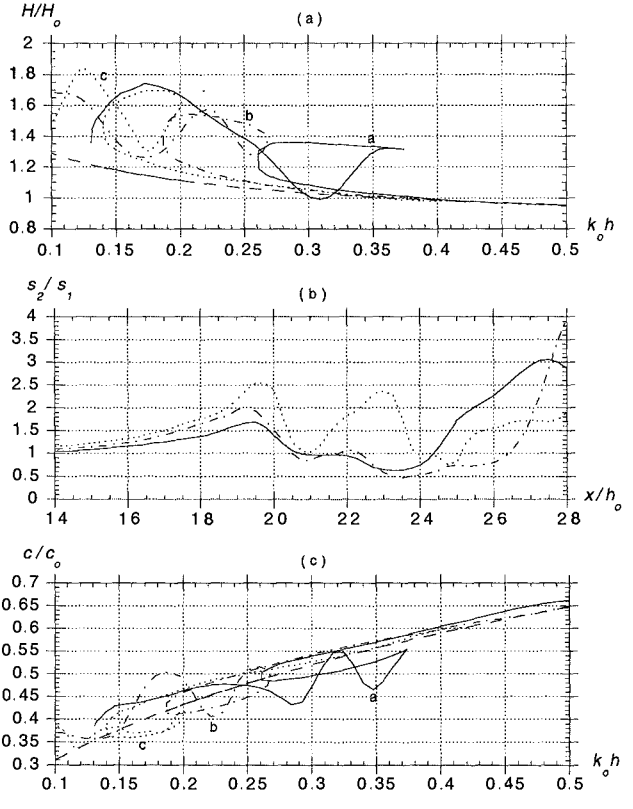

Figure 4: Normalized NWT results as a function of $k_o h$ for cases : (——; a) 1; (– – –; b) 2; and (- - - -; c) 3 in Table 1; and (– – –) indicates LWT results. (a) Wave height. (b) front/back asymmetry. (d) Wave celerity.

significantly underpredicts wave height. In Fig. 4a, due to wave modulations, the FNPF height variations for the barred-beach are multiple-valued functions of relative depth $k_o h$ [whereas LWT gives superimposed single-valued results; this would also be the case for results of the base-profile]. The patterns of wave height variations beyond the bar in the three cases show clear similarities.

In Fig. 3c, prior to reaching the bar, both front and back wave slopes, $s_2 = H_2/L_2$ and $s_1 = H_1/L_1$, continuously increase due to shoaling, with a larger relative increase for the front slope than for the back slope, due to increasing wave skewness. As a result, the front/back asymmetry s_2/s_1 in Fig. 4b, also continuously increases before the bar, from a value of 1 in deep water. For the beach base-profile, Grilli and Horrillo (1996,1998b) showed that this pattern is maintained up to reaching the AB. On the barred-beach, however, the modulations in wave shape beyond the bar induce significant changes in wave slopes. In each case, the wave front slope first reaches a maximum at around $x' = 19$, then drops over the bar berm and stabilizes beyond the bar, to finally increase again. The back slope keeps increasing over and beyond the berm and reaches a maximum at about 4.3 h_o after the front slope reaches its maximum; the back slope then drops until $x' = 25$ [where water depth is about equal to the bar berm depth] and then stabilizes. In Fig. 4b, except for a backward shift in space of $1.5h_o$ or so, equal to the berm width, wave front/back asymmetry seems to correlate well in all cases, with the variations of H/H_o, such as in Fig. 3b for case 2, in the spatial region over and beyond the bar.

In Fig. 3d, the FNPF wave celerity variation for the barred-beach departs from that corresponding to the base-profile upon reaching the bar seaward slope. When corrected for depth, however, the latter results stay accurate until reaching the bar berm at $x' = 20$. This is because the 1:20 seaward slope is mild enough for the FNPF results, calculated for the same depth on the 1:50 natural slope, to apply in the present case. As expected, LWT underpredicts celerity before reaching the bar berm [and increasingly so, the longer the wave]. Celerity increases over and beyond the bar, as a result of the increasing depth, and then strongly oscillates in the modulation region, due to changes in wave height inducing amplitude dispersion effects for the celerity. Finally, just before reaching the AB, wave celerity seems to stabilize and agree better with the FNPF results calculated for the base-profile without the bar. As expected, FNPF results calculated for the base-profile and corrected for depth do not capture the celerity oscillations in the modulation region. They also overpredict celerity over the bar berm. This is also the case for LWT. In Fig. 4c, due to wave modulations, the FNPF celerity variations calculated for the barred-beach, for each case, are multiple-valued functions of relative depth $k_o h$ [whereas LWT gives superimposed single-valued results; this would also be the case for results of the base-profile corrected for depth]. Similarly to wave height, the patterns of wave celerity variations beyond the bar show clear similarities in the three cases.

The results for wave shape and celerity variations over and beyond the bar show that highly nonlinear phenomena of wave decomposition, harmonic generation,

and nonlinear exchanges of energy between harmonics occur and strongly affect the variation of wave parameters, as compared to the case without a bar. A further confirmation of the strong nonlinearity is given by calculating the typical nonlinearity parameters, $\delta = H/h$ and $\varepsilon = kH/2$, as a function of x. Due to shoaling, in all cases, the wave height to depth ratio δ already reaches a large 45 to 50% value over the bar, then drops beyond the bar, due to the increasing depth. For $x' > 25$, as shoaling re-occurs, δ starts increasing again, to eventually reach $\mathcal{O}(1)$ values or more, before waves enter the AB. Similarly, wave steepness, ε, keeps increasing due to shoaling up to reaching a large 0.10 to 0.12 value at the bar; it then oscillates beyond the bar to finally increase again up to 0.12 to 0.17 [for comparison, the deep water steepness of the limiting Stokes wave is $\varepsilon_{ol} = 0.44$].

DEPTH INVERSION OVER BARRED-BEACHES

Results presented in the previous Section for periodic wave shoaling over a barred-beach show how local properties of waves such as H/H_o, s_2/s_1 and c/c_o, differ from the results obtained by Grilli and Horrillo (1996,1998b) for monotonously decreasing mild slopes. Differences mostly occur in the region over and at the lee side of the bar, the so-called *wave modulation region*. As variations of local wave properties with $k_o h$ and $k_o H_o$ are the bases for the depth inversion algorithms DIA1 and DIA2 proposed by Grilli (1998), it is expected that these algorithms will perform poorly to retrieve depth over and directly beyond the bar.

To confirm this prediction, DIA1 was applied to the results of cases 1, 2, and 3 in Table 1. To be fair, the wave height data used to estimate $k_o H_o$ in the algorithm, and the wavelength data used to estimate T, were limited to the monotonously varying region before the bar-berm, over the 1:50 natural base-profile and the 1:20 seaward slope of the berm [for $x' < 20$]. In a real field case, this monotonous part of the data could easily be identified. The corresponding direct prediction of both H [and thus $k_o H_o$] and T gave R^2 values of better than 99.3%. Depth was then retrieved using the celerity computed over the whole barred-beach, by inverting the FNPF celerity predicted on a mild slope for the same incident wave steepness and relative depth [i.e., such as the one plotted in Fig. 3d as curve (- - - -)]. Fig. 5, parts a to c, shows the results of this depth inversion for cases 1 to 3 in Table 1, compared to the actual depth variation and to the prediction of LWT. As expected, before the bar, for $x' < 20$, DIA1 gives quite a good prediction of depth whereas LWT overpredicts depth. Beyond the bar, however, both DIA1 and LWT fail to model the oscillatory behavior of wave celerity (Fig. 3d) and, hence, instead, wrongly predict an oscillatory bottom topography within the wave modulation region. In fact, as wave nonlinearity initially decreases in this region, thus reducing amplitude dispersion effects on the celerity, LWT does a somewhat better job in locating both the berm depth and the shape of the shoreward side of the berm. Beyond the modulation region [$x' \geq 28$], as shoaling more or less re-occurs as would be expected over the base-profile, the depth prediction in DIA1 improves while LWT again overpredicts depth.

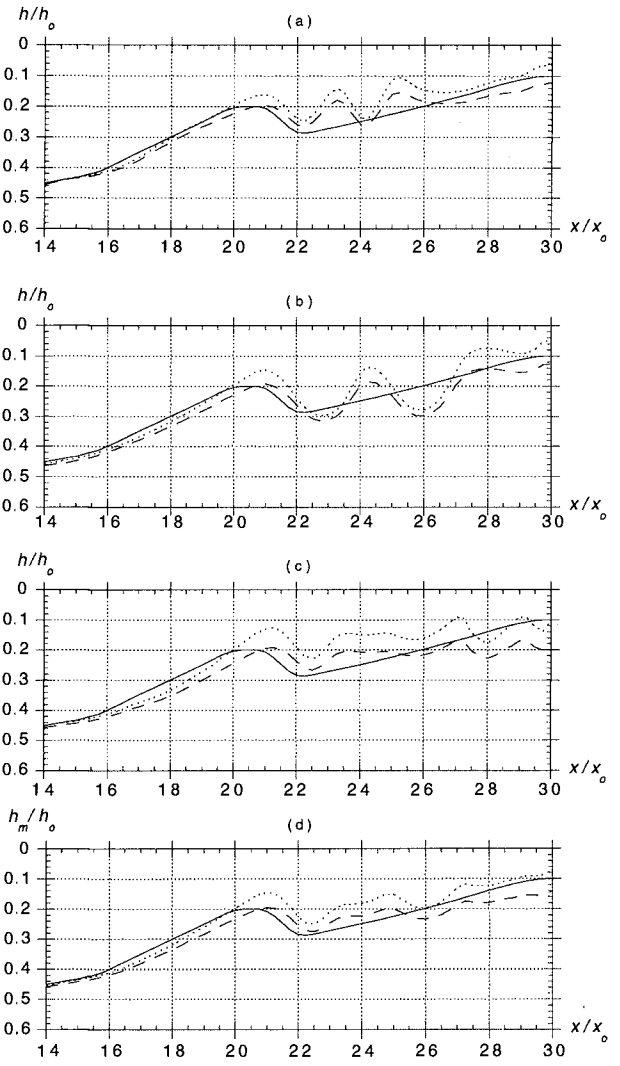

Figure 5: Depth inversion for the barred-beach and cases [Table 1] : (a) 1; (b) 2; and (c) 3. (——) Actual depth variation; (– – –) prediction by inversion of LWT dispersion relation; (- - - -) prediction by application of DIA1.(d) mean of results of the three cases in parts a-c.

In Fig. 5d, the depth predictions for the three cases have been averaged which, due to both different modulation regions and amplitudes of oscillations, somewhat limits the effects of wave decomposition on depth prediction. We thus see that DIA1 provides a good depth prediction for $x' \leq 20$ and $x' > 28$. In between, in the modulation region, depth is underpredicted by DIA1 and, as explained above, LWT does a somewhat better job in predicting depth.

CONCLUSIONS

Shoaling of three periodic waves was calculated over a barred-beach in a two-dimensional fully nonlinear NWT. Results showed that : (i) prior to reaching the bar berm, wave shoaling occurs as over mild slopes; (ii) for waves with large non-linearity over the bar [such as here with $H/h = 0.45 - 0.50$], the increasing depth beyond the bar induces highly-nonlinear *wave decomposition* phenomena, with energy transfer between harmonics and the release of bound higher-harmonics into free waves; (iii) a *modulation region* appears beyond the bar, with a spatial extension function of the incident wave period/length, in which wave parameters such as celerity c, height H, and asymmetry s_2/s_1, become strongly oscillatory; (iv) repetitive patterns of variations of wave *front and back slope* occur in the modulation region; these could be used to locate the berm and predict the extension of the modulation region in DIAs; (v) as *shoaling re-occurs* beyond the modulation region, waves eventually reassume a shape and behavior similar to that observed over mildly sloping beaches; and (vi) since variations of local wave properties over mild slopes are the bases for the earlier depth inversion studies (Grilli, 1998), DIA1, expectedly, performs poorly within the modulation region; its performance is good otherwise.

For DIA1 to perform better in the modulation region, wave parameters would have to be analyzed and parameterized in the algorithm, based on the present and other similar computations of wave characteristics over barred-beaches. This is the object of future extensions to this work.

Acknowledgments

This publication, in part, is based on research sponsored by the US Naval Research Laboratory, Stennis Space Center, grants N-00014-95-1-G607 and N-00014-96-C012, from the Remote Sensing Division (code 7240).

References

Beji, S. and Battjes, J.A., Experimental investigation of wave propagation over a bar. *Coastal Engng.*, **23**, 1-16, 1994.

Byrne, R.J., Field occurrences of induced multiple gravity waves. *J. Geophys. Res.*, **74**, 2590-2596, 1969.

Clément, A., Coupling of two absorbing boundary conditions for 2D time-domain simulations of free surface gravity waves. *J. Comp. Phys.*, **126**, 139-151, 1996.

Dean, R.G., Equilibrium beach profiles : characteristics and applications. *J. Coastal Res.*, **7**(1), 53-84, 1991.

Driscoll, A.M., Dalrymple, R.A. and Grilli, S.T., Harmonic generation and transmission past a submerged rectangular obstacle. In *Proc. 23rd Intl. Conf. on Coastal Engineering* (Venice, Italy), Vol 1, pp 1142-1152. ASCE edition, 1992.

Dugan, J., Bathymetry measurements from long range airborne imaging systems. *Proc. 4th Intl. Conf. on Remote Sensing for Marine and Coastal Environments*, Orlando, Florida, 1997.

Grilli, S.T., Depth inversion in shallow water based on nonlinear properties of shoaling periodic waves. *Coastal Engineering* (in press), 1998.

Grilli, S.T. and Horrillo, J., Fully nonlinear properties of periodic waves shoaling over slopes. In *Proc. 25th Intl. Conf. on Coastal Engineering* (Orlando, Florida), Vol 1, pp 717-730. ASCE edition, 1996.

Grilli, S.T. and Horrillo, J., Numerical generation and absorption of fully nonlinear periodic waves. *J. Engng. Mech.*, **123**(10), 1060-1069, 1997.

Grilli, S.T. and Horrillo, J., Computation of periodic wave shoaling over barred-beaches in a fully nonlinear numerical wave tank. In Proc. ISOPE98 (Montreal, Canada, May 1998) (eds. Chung, J.S., Olagnon, M., Kim, C.H., Koterayama, W.), Vol 3, pp 294-300, 1998a.

Grilli, S.T. and Horrillo, J., Nonlinear properties of periodic waves shoaling over mild slopes. Submitted to *J. Geophys. Res.*, 1998b.

Grilli, S., Skourup, J., and Svendsen, I.A., An efficient boundary element method for nonlinear water waves, *Engng. Analysis with Boundary Elements*, **6**(2), 97-107, 1989.

Grilli, S.T. and Subramanya, R., Numerical modeling of wave breaking induced by fixed or moving boundaries. *Computational Mech.*, **17**, 374-391, 1996.

Massel, S.R., Harmonic generation by waves propagating over a submerged step. *Coastal Engng.*, **7**, 357-380, 1983.

Ohyama, T. and Nadaoka, K., Transformation of a nonlinear wave train passing over a submerged shelf without breaking. *Coastal Engng.*, **24**, 1-22, 1994.

Rey, V., Propagation and local behaviour of normally incident gravity waves over varying topography. *Eur. J. Mech. B: Fluids*, **11**, 213, 1992.

Rey, V., Belzons, M. and Guazzelli, E., Propagation of surface gravity waves over a rectangular submerged bar. *J. Fluid Mech.*, **235**, 453, 1992.

Young, I.R., Wave transformation over coastal reefs. *J. Geophys. Res.*, **94**, 9779-9789, 1989.

NUMERICAL MODEL OF FULLY-NONLINEAR WAVE REFRACTION AND DIFFRACTION

Masahiko Isobe* and Samir Abohadima†

Abstract

Nonlinear mild-slope equations are a set of equations which were derived to analyze fully-nonlinear and fully-dispersive wave transformation. In the present study, it is shown that refraction-diffraction equations including the mild-slope equation, nonlinear shallow water equations and Boussinesq equations are derived as special cases of the nonlinear mild-slope equations. Then, a numerical model is developed for fully-nonlinear wave refraction and diffraction on the basis of the nonlinear mild-slope equations. The model is verified through comparison of numerical results with theoretical and experimental results. Finally, effect of nonlinearity on wave diffraction through a breakwater gap is discussed.

1 Introduction

Mild-slope equation derived by Berkhoff (1972) is used to predict transformation of linear waves due to refraction and diffraction. Boussinesq equations were derived for analyzing transformation of weakly-nonlinear and weakly-dispersive waves, and modified versions have been proposed to apply them in deeper water. However, waves are strongly nonlinear especially in very shallow water.

Nonlinear mild-slope equations are among the equations which were derived recently to analyze fully-nonlinear and fully-dispersive wave transformation. In deriving the equations, the velocity potential is expanded into a series in terms of a given set of vertical distribution functions and then substituted into the Lagrangian defined by Luke (1967). The equations are obtained by applying the variational principle to the Lagrangian. No assumptions are made in the derivation so that they are

*Professor, Department of Civil Engineering, University of Tokyo, 7-3-1 Hongo, Bunkyo-ku, Tokyo 113-8656, Japan. (Email: isobe@coastal.t.u-tokyo.ac.jp)
†Graduate student, ibd. (Email: abohadim@coastal.t.u-tokyo.ac.jp)

applicable even to strongly nonlinear and strongly dispersive waves and more general than any other wave equations derived so far. In the present study, the mild-slope equation, nonlinear shallow water equations, and Boussinesq equations are derived as special cases of the nonlinear mild-slope equations.

Then, a fully nonlinear and fully dispersive numerical model is developed based on the nonlinear mild-slope equations to predict wave refraction and diffraction. Linear dispersion characteristic of the model is first examined by comparing with the small amplitude wave theory. Next, the model is applied to wave transformation due to a circular shoal and diffraction through a breakwater gap. These results show the validity of the present model. Further discussion is made on the effect of nonlinearity on the wave diffraction.

2 Relation Between Nonlinear Mild-Slope Equations and Various Wave Equations

2.1 Nonlinear mild-slope equations

The nonlinear mild-slope equations are derived from the Lagrangian, L, obtained by Luke (1967):

$$\mathrm{L}[\phi,\eta] = \int_{t_1}^{t_2}\iint_A\int_{-h}^{\eta}\left\{\frac{\partial\phi}{\partial t}+\frac{1}{2}(\nabla\phi)^2+\frac{1}{2}\left(\frac{\partial\phi}{\partial z}\right)^2+gz\right\}dz\,dA\,dt \tag{1}$$

where ϕ is the velocity potential, η the water surface elevation, t_1 and t_2 arbitrary times, A arbitrary area on the horizontal plane, h the water depth, g the gravitational acceleration, z the vertical coordinate and t the time. To terminate the above Lagrangian with respect to ϕ and η is equivalent to satisfy the Laplace equation, kinematic bottom boundary condition, and kinematic and dynamic surface boundary conditions.

The vertical distribution of the velocity potential, ϕ, is expressed as a series in terms of a set of vertical distribution functions, Z_α:

$$\phi(\mathbf{x},z,t) = \sum_{\alpha=1}^{N} f_\alpha(\mathbf{x},t)\,Z_\alpha(z;h(\mathbf{x})) \equiv f_\alpha\,Z_\alpha \tag{2}$$

where f_α are the coefficients to Z_α and therefore independent of z, and $\mathbf{x}=(x,y)$ denotes the position vector on the horizontal plane. As is normally the case, the expression of Z_α can include the local water depth $h(\mathbf{x})$ as a parameter. Substitution of the above expression into the definition of the Lagrangian (1) and analytical

integration in the vertical direction yields the following expression:

$$\mathrm{L}[f_\alpha, \eta] = \int_{t_1}^{t_2} \iint_A \chi(f_\alpha, \eta)\, dA\, dt \tag{3}$$

where

$$\begin{aligned} \chi(f_\alpha, \frac{\partial f_\alpha}{\partial t}, \eta, \frac{\partial \eta}{\partial t}) &= \frac{g}{2}(\eta^2 - h^2) + \tilde{Z}_\beta \frac{\partial f_\beta}{\partial t} + \frac{1}{2} A_{\gamma\beta} (\nabla f_\gamma)(\nabla f_\beta) + \frac{1}{2} B_{\gamma\beta} f_\gamma f_\beta \\ &+ C_{\gamma\beta} f_\gamma (\nabla f_\beta)(\nabla h) + \frac{1}{2} D_{\gamma\beta} f_\gamma f_\beta (\nabla h)^2 \end{aligned} \tag{4}$$

and

$$\begin{aligned} &A_{\alpha\beta} = \int_{-h}^{\eta} Z_\alpha Z_\beta \, dz, \qquad B_{\alpha\beta} = \int_{-h}^{\eta} \frac{\partial Z_\alpha}{\partial z} \frac{\partial Z_\beta}{\partial z} \, dz, \; C_{\alpha\beta} = \int_{-h}^{\eta} \frac{\partial Z_\alpha}{\partial h} Z_\beta \, dz, \\ &D_{\alpha\beta} = \int_{-h}^{\eta} \frac{\partial Z_\alpha}{\partial h} \frac{\partial Z_\beta}{\partial h} \, dz, \; \tilde{Z}_\alpha = \int_{-h}^{\eta} Z_\alpha \, dz \end{aligned} \tag{5}$$

To terminate the Lagrangian with respect to f_α and η, the following Euler equations should be satisfied:

$$\frac{\partial \chi}{\partial f_\alpha} = \frac{\partial}{\partial t}\left[\frac{\partial \chi}{\partial (\partial f_\alpha / \partial t)}\right] + \nabla \left[\frac{\partial \chi}{\partial (\nabla f_\alpha)}\right] \tag{6}$$

$$\frac{\partial \chi}{\partial \eta} = \frac{\partial}{\partial t}\left[\frac{\partial \chi}{\partial (\partial \eta / \partial t)}\right] + \nabla \left[\frac{\partial \chi}{\partial (\nabla \eta)}\right] \tag{7}$$

Substituting the definition of χ, Eq. (4), into the above equations and neglecting the second and higher order terms in the bottom slope, we obtain the following equations:

$$Z_\alpha^\eta \frac{\partial \eta}{\partial t} + \nabla(A_{\alpha\beta} \nabla f_\beta) - B_{\alpha\beta} f_\beta + (C_{\beta\alpha} - C_{\alpha\beta})(\nabla f_\beta)(\nabla h) + \frac{\partial Z_\beta^\eta}{\partial h} Z_\alpha^\eta f_\beta (\nabla \eta)(\nabla h) = 0 \tag{8}$$

$$g\eta + Z_\beta^\eta \frac{\partial f_\beta}{\partial t} + \frac{1}{2} Z_\gamma^\eta Z_\beta^\eta (\nabla f_\gamma)(\nabla f_\beta) + \frac{1}{2} \frac{\partial Z_\gamma^\eta}{\partial z} \frac{\partial Z_\beta^\eta}{\partial z} f_\gamma f_\beta + \frac{\partial Z_\gamma^\eta}{\partial h} Z_\beta^\eta f_\gamma (\nabla f_\beta)(\nabla h) = 0 \tag{9}$$

where

$$Z_\alpha^\eta = Z_\alpha|_{z=\eta}, \qquad \frac{\partial Z_\alpha^\eta}{\partial z} = \left.\frac{\partial Z_\alpha}{\partial z}\right|_{z=\eta} \tag{10}$$

Equation (8) is a vector equation with N components and Eq. (9) is a scalar equation, whereas the unknowns are η and f_α ($\alpha = 1$ to N). Thus the above set of partial differential equations evolutional in the horizontal two dimensions are closed if an appropriate set of initial and boundary conditions are given. We call the set as nonlinear mild-slope equations (Isobe, 1994). No assumptions other than the series expression of the velocity potential are made to derive the nonlinear mild-slope equations; therefore the equations include full nonlinearity and full dispersivity as long as sufficient number of terms are used in the series.

Various wave equations such as mild-slope equation, nonlinear shallow water equations and Boussinesq equations are derived theoretically upon ordering nondimensional parameters. Each ordering results in a specific vertical distribution of wave motion. In a sense, ordering and vertical distribution are equivalent, and the validity of a wave equation depends on the accuracy of the vertical distribution instead of the magnitudes of nondimensional parameters used in the assumption. In the following, it is shown that various wave equations are derived from the nonlinear mild-slope equations by giving a proper set of vertical distribution functions.

2.2 Relation with mild-slope equation

The mild-slope equation (Berkhoff, 1972) is a linear refraction-diffraction equation in which vertical distribution is expressed by the hyperbolic cosine function. Hence we first linearize the nonlinear mild-slope equations (8) and (9):

$$Z_\alpha^o \frac{\partial \eta}{\partial t} + \nabla(A_{\alpha\beta}^o \nabla f_\beta) - B_{\alpha\beta}^o f_\beta + (C_{\beta\alpha}^o - C_{\alpha\beta}^o)(\nabla f_\beta)(\nabla h) = 0 \tag{11}$$

$$g\eta + Z_\beta^o \frac{\partial f_\beta}{\partial t} = 0 \tag{12}$$

where the superscript ^{o} denotes the quantity evaluated at the mean water level instead of the water surface. Next we express the velocity potential by only one vertical distribution function of hyperbolic cosine type:

$$\phi(\mathbf{x}, z, t) = f(\mathbf{x}, t)\, Z(z) \tag{13}$$

$$Z(z) = \frac{\cosh k(h+z)}{\cosh kh} \tag{14}$$

where k satisfies the linear dispersion relation. Then, Eqs. (11) and (12) become

$$\frac{\partial \eta}{\partial t} + \nabla\left(\frac{CC_g}{g}\nabla f\right) + \frac{1}{g}\left(k^2 CC_g - \sigma^2\right) f = 0 \tag{15}$$

$$g\eta + \frac{\partial f}{\partial t} = 0 \tag{16}$$

Eliminating η from the above two equations, we obtain the following time-dependent form of the mild-slope equation:

$$\nabla\left(CC_g \nabla f\right) + \left(k^2 CC_g - \sigma^2\right) f - \frac{\partial^2 f}{\partial t^2} = 0 \tag{17}$$

If we assume a sinusoidal oscillation as:

$$f = \hat{f} e^{-i\sigma t} \tag{18}$$

we finally obtain the mild-slope equation:

$$\nabla\left(CC_g\nabla\hat{f}\right)+k^2CC_g\hat{f}=0 \tag{19}$$

Equations for refraction and diffraction of linear random waves are obtained by taking multiple components in Eqs. (11) and (12). The vertical distribution functions are defined as

$$Z_\alpha=\frac{\cosh k_\alpha(h+z)}{\cosh k_\alpha h} \tag{20}$$

$$\sigma_\alpha^2=gk_\alpha\tanh k_\alpha h \tag{21}$$

Then, Eqs. (11) and (12) become

$$\frac{\partial\eta}{\partial t}+A^o_{\alpha\beta}\nabla^2 f_\beta-B^o_{\alpha\beta}f_\beta=0 \tag{22}$$

$$g\eta+\sum_{\beta=1}^{N}\frac{\partial f_\beta}{\partial t}=0 \tag{23}$$

where

$$A^o_{\alpha\beta}=\begin{cases}\dfrac{1}{g}\dfrac{\sigma_\alpha^2-\sigma_\beta^2}{k_\alpha^2-k_\beta^2} & (\alpha\neq\beta)\\ \dfrac{1}{g}c_\alpha^2 n_\alpha & (\alpha=\beta)\end{cases}\qquad B^o_{\alpha\beta}=\begin{cases}\dfrac{1}{g}\dfrac{k_\alpha^2\sigma_\beta^2-k_\beta^2\sigma_\alpha^2}{k_\alpha^2-k_\beta^2} & (\alpha\neq\beta)\\ \dfrac{1}{g}\sigma_\alpha^2(1-n_\alpha) & (\alpha=\beta)\end{cases} \tag{24}$$

From Eqs. (22) and (23), η can be eliminated to yield

$$-\frac{1}{g}\sum_{\beta=1}^{N}\frac{\partial^2 f_\beta}{\partial t^2}+A^o_{\alpha\beta}\nabla^2 f_\beta-B^o_{\alpha\beta}f_\beta=0 \tag{25}$$

By assuming progressive waves with the angular frequency $\hat{\sigma}$ and wave number $\hat{\mathbf{k}}$:

$$f_\alpha=a_\alpha e^{i(\hat{\mathbf{k}}\mathbf{x}-\hat{\sigma}t)} \tag{26}$$

Equation (25) becomes

$$\sum_{\beta=1}^{N}\left(\frac{\hat{\sigma}^2}{g}-B^o_{\alpha\beta}\right)a_\beta=\hat{k}^2\sum_{\beta=1}^{N}A^o_{\alpha\beta}a_\beta \tag{27}$$

To have a nontrivial solution, $\hat{k}^2$ is determined as an eigenvalue for a given $\hat{\sigma}$. It can easily be proved that $\hat{k}=k_\alpha$ for $\hat{\sigma}=\sigma_\alpha$, and therefore the dispersion relation is exactly satisfied at the frequencies σ_α ($\alpha=1$ to N). This suggests that the dispersion relation is accurately satisfied even if the frequency is not equal to either of the selected frequencies. Therefore, transformation of random waves with a wide spectrum can accurately be calculated by Eqs. (22) and (23).

2.3 Relation with nolinear shallow water equations

In the nonlinear shallow water equations (Stoker, 1957), vertical distribution of the pressure is hydrostatic and that of the horizontal water particle velocity is uniform. Therefore we take one component of the vertical distribution function which is uniform:

$$Z = 1 \tag{28}$$

Then, the matrices $A_{\alpha\beta}$, $B_{\alpha\beta}$ and $C_{\alpha\beta}$ defined by Eq. (5) have one component, respectively, as

$$A = h + \eta, \quad B = 0, \quad C = 0 \tag{29}$$

and the nonlinear mild-slope equations (8) and (9) become

$$\frac{\partial \eta}{\partial t} + \nabla \left[(h + \eta) \nabla f \right] = 0 \tag{30}$$

$$g\eta + \frac{\partial f}{\partial t} + \frac{1}{2} (\nabla f)^2 = 0 \tag{31}$$

By rewriting the above equations in terms of $\mathbf{u}$:

$$\mathbf{u} = \nabla \phi = \nabla f \tag{32}$$

the nonlinear shallow-water equations are obtained:

$$\frac{\partial \eta}{\partial t} + \nabla \left[(h + \eta) \mathbf{u} \right] = 0 \tag{33}$$

$$\frac{\partial \mathbf{u}}{\partial t} + (\mathbf{u} \nabla) \mathbf{u} + g \nabla \eta = 0 \tag{34}$$

2.4 Relation with Boussinesq equations

Since the vertical distribution of the horizontal water particle velocity in the Boussinesq equations is expressed by the linear combination of uniform and parabolic components, the following two vertical distribution functions are employed:

$$Z_1 = 1, \quad Z_2 = \frac{(h + z)^2}{h^2} \tag{35}$$

Then, the nonlinear mild-slope equations (8) and (9) become

$$\begin{aligned} \frac{\partial \eta}{\partial t} + \nabla \left[(h + \eta) \nabla f_1 + \frac{(h + \eta)^3}{3h^2} \nabla f_2 \right] + \frac{(h + \eta)^2 (h - 2\eta)}{3h^3} (\nabla f_2)(\nabla h) \\ - \frac{2(h + \eta)\eta}{h^3} f_2 (\nabla \eta)(\nabla h) = 0 \end{aligned} \tag{36}$$

$$\frac{(h+\eta)^2}{h^2}\frac{\partial \eta}{\partial t}+\nabla\left[\frac{(h+\eta)^3}{3h^2}\nabla f_1+\frac{(h+\eta)^5}{5h^4}\nabla f_2\right]-\frac{4(h+\eta)^3}{3h^4}f_2 - \frac{(h+\eta)^2(h-2\eta)}{3h^3}(\nabla f_1)(\nabla h)-\frac{2(h+\eta)^3\eta}{h^5}f_2(\nabla\eta)(\nabla h)=0 \quad (37)$$

$$g\eta+\frac{\partial f_1}{\partial t}+\frac{(h+\eta)^2}{h^2}\frac{\partial f_2}{\partial t}+\frac{1}{2}\left\{\nabla f_1+\frac{(h+\eta)^2}{h^2}\nabla f_2\right\}^2+\frac{1}{2}\left\{\frac{2(h+\eta)}{h^2}f_2\right\}^2 - \frac{2(h+\eta)\eta}{h^3}f_2\left\{\nabla f_1+\frac{(h+\eta)^2}{h^2}\nabla f_2\right\}(\nabla h)=0 \quad (38)$$

The assumption of $\mathrm{O}[H/h] \sim \mathrm{O}[(h/L)^2]$ (H: wave height, h: water depth, L: wavelength) leads to the following ordering:

$$\nabla h \sim \mathrm{O}\left[\sqrt{\varepsilon}\right], \quad \eta \sim f_1 \sim \mathrm{O}[\varepsilon], \quad f_2 \sim \mathrm{O}\left[\varepsilon^2\right] \quad (39)$$

By considering the above ordering, Eqs. (36) to (38) are simplified as

$$\frac{\partial \eta}{\partial t}+\nabla\left[(h+\eta)\nabla f_1+\frac{h}{3}\nabla f_2\right]+\frac{1}{3}(\nabla f_2)(\nabla h)=0 \quad (40)$$

$$\frac{\partial \eta}{\partial t}+\nabla\left[\frac{h}{3}\nabla f_1\right]-\frac{4}{3h}f_2-\frac{1}{3}(\nabla f_1)(\nabla h)=0 \quad (41)$$

$$g\eta+\frac{\partial f_1}{\partial t}+\frac{\partial f_2}{\partial t}+\frac{1}{2}(\nabla f_1)^2=0 \quad (42)$$

Then, because

$$\mathbf{u}=\nabla\phi=\nabla f_1+\frac{(h+z)^2}{h^2}\nabla f_2-\frac{2z(h+z)}{h^3}f_2\nabla h \quad (43)$$

$$\bar{\mathbf{u}} \approx \nabla f_1+\frac{1}{3}\nabla f_2+\frac{1}{3h}f_2\nabla h \quad (44)$$

Equations (40) to (42) are combined to yield the Boussinesq equations (Peregrine, 1967):

$$\frac{\partial \eta}{\partial t}+\nabla\left[(h+\eta)\bar{\mathbf{u}}\right]=0 \quad (45)$$

$$\frac{\partial \bar{\mathbf{u}}}{\partial t}+(\bar{\mathbf{u}}\nabla)\bar{\mathbf{u}}+g\nabla\eta=-\frac{h^2}{6}\frac{\partial}{\partial t}\nabla(\nabla\bar{\mathbf{u}})+\frac{h}{2}\frac{\partial}{\partial t}\nabla\left[\nabla(h\bar{\mathbf{u}})\right] \quad (46)$$

3 Verification of Numerical Model

3.1 Outline of numerical model

A finite difference numerical model is developed based on the nonlinear mild-slope equations, in which the nonlinear equations are solved by simple successive substitution or Newton-Raphson scheme.

Non-reflective boundary conditions are installed along the boundaries by introducing sponge layers in which an energy dissipation term, D, is added to the left side of Eq. (9) (Cruz et al., 1994):

$$D = \epsilon(x) \sum_{\alpha=1}^{N} f_\alpha \tag{47}$$

where

$$\epsilon(x) = \frac{r\epsilon_m}{2(\sinh r - r)} \left[\cosh\left(\frac{rx}{F}\right) - 1\right] \tag{48}$$

$$\epsilon_m = \theta\sqrt{g/h} \tag{49}$$

and F is the width of the sponge layer, $\theta = 1.0$ to 2.0 and $r = 3$. Incident waves are given as a discontinuity at the interface between the actual calculation domain and sponge layer (Ishii et al., 1996). Still water is the initial condition for all calculations.

3.2 Effect of vertical distribution functions

A typical example of sets of vertical distribution functions is a set of polynomial functions:

$$Z_\alpha = \left(1 + \frac{z}{h}\right)^{2(\alpha-1)} \tag{50}$$

The coefficients are easily calculated as

$$Z_\alpha^\eta = \zeta^{2(\alpha-1)} \tag{51}$$

$$A_{\alpha\beta} = \frac{h\,\zeta^{2(\alpha+\beta)-3}}{2(\alpha+\beta)-3} \tag{52}$$

$$B_{\alpha\beta} = \frac{4(\alpha-1)(\beta-1)}{2(\alpha+\beta)-5} \frac{\zeta^{2(\alpha+\beta)-5}}{h} \tag{53}$$

$$C_{\alpha\beta} = 2(\alpha-1)\,\zeta^{2(\alpha+\beta)-4} \left[-\frac{\zeta}{2(\alpha+\beta)-3} + \frac{1}{2(\alpha+\beta)-4}\right] \tag{54}$$

$$D_{\alpha\beta} = \frac{4(\alpha-1)(\beta-1)\,\zeta^{2(\alpha+\beta)-5}}{h} \left[\frac{\zeta^2}{2(\alpha+\beta)-3} - \frac{\zeta}{\alpha+\beta-2} + \frac{1}{2(\alpha+\beta)-5}\right] \tag{55}$$

where

$$\zeta = \frac{h+\eta}{h} \tag{56}$$

The above set of polynomial functions gives an accurate linear dispersion relation even in deep waters (Isobe, 1994); however hyperbolic cosine functions are expected to be more effective in deep water. In the present study, two sets are examined for propagation of permanent waves with various water depths and wave heights. In the

first set (CASE A), the following two functions are taken as the vertical distribution functions:

$$Z_1(z) = 1, \quad Z_2(z) = \left(1 + \frac{z}{h}\right)^2 \tag{57}$$

The second set (CASE B) is

$$Z_1(z) = \left(1 + \frac{z}{h}\right)^2, \quad Z_2(z) = \frac{\cosh k(h+z)}{\cosh kh} \tag{58}$$

in which Z_1 and Z_2 are expected to become effective in shallow and deep waters, respectively.

Figures 1 to **3** show sample results of 1-D propagation of permanent waves. Permanent waves are incident at $x/L = 1$ and a sponge layer is installed from $x/L = 3$ to 9, and thus the actual region is from $x/L = 1$ to 3. The distributions of η/H_1 and H/H_I (H: wave height and H_I: incident wave height), are shown in the

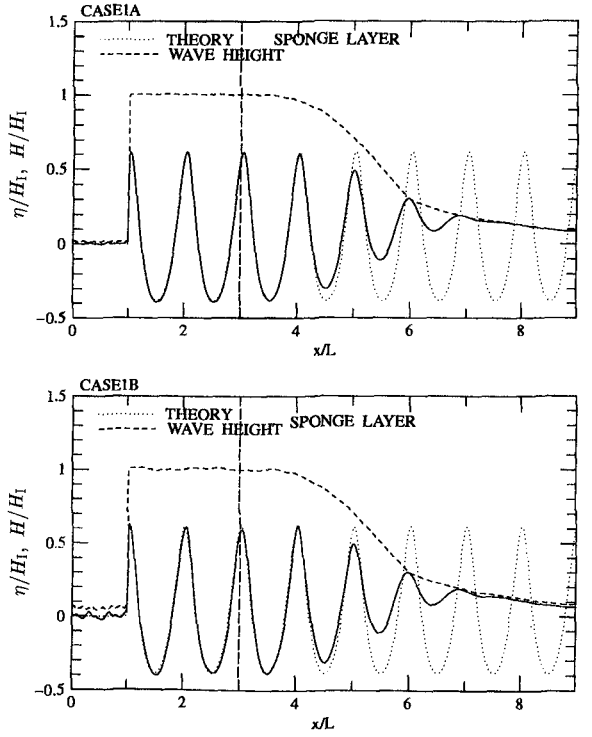

Fig. 1 Comparison between exact and numerical solutions of water surface profile of permanent waves ($h/L_0 = 0.1$, $H_I/h = 0.3$, $H_I/L_0 = 0.03$, $U_r = 16$).

figure. Since **Fig. 1** is for weakly nonlinear waves on an intermediate water depth in which $h/L_o = 0.1$ (h: water depth and L_o: deep water wavelength of linear waves), the agreement with theory is good for the two sets of vertical distribution functions. **Figure 2** is for highly nonlinear waves on a shallow water. Nonlinear effect is well reproduced by the two sets. However, for deep water as shown in **Fig. 3**, difference in wavelength is signigicant in CASE A, indicating that the dispersion effect is not enough. In general, the vertical distribution functions of CASE B are appropriate in deep water, whereas those of CASE A give numerical solution even for near-breaking waves in shallow water.

The numerical model of CASE B is applied to wave diffraction due to a circular shoal for which an experiment is conducted by Ito and Tanimoto (1972). **Figure 4** shows the bottom configuration in the prototype scale and wave height distributions along cross-shore and alongshore directions. The water depth in the uniform region

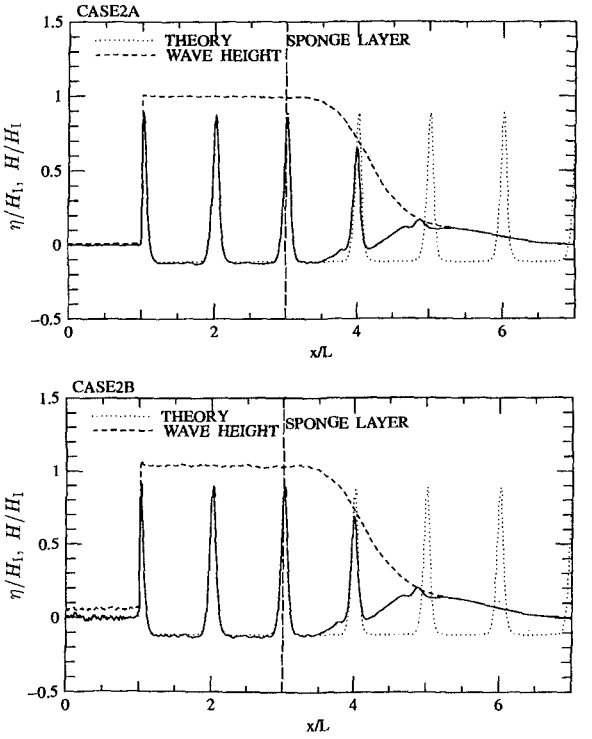

Fig. 2 Comparison between exact and numerical solutions of water surface profile of permanent waves ($h/L_0 = 0.005$, $H_I/h = 0.3$, $H_I/L_0 = 0.0015$, $U_r = 450$).

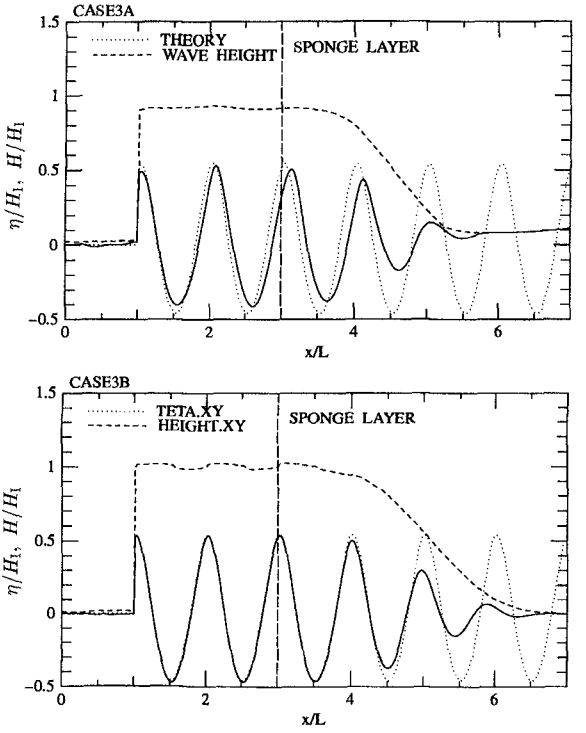

Fig. 3 Comparison between exact and numerical solutions of water surface profile of permanent waves ($h/L_0 = 0.1$, $H_I/h = 0.5$, $H_I/L_0 = 0.05$, $U_r = 0.41$).

is 15m, the wave period 5.1s and the incident wave height 1m, resulting in fairy strong nonlinearity. Comparison of wave height distribution between calculation and measurement indicates the validity of the present model.

3.3 Effect of nonlinearity on wave diffraction

Diffraction of waves through a breakwater gap is calculated to elucidate the effect of nonlinearity on diffraction. **Figure 5** shows an example in which $h/L_0 = 0.05$, $B/L = 2$ (B: gap width and L: wavelength of linear waves), and $H_I/L_0 = 0.0002$, 0.024, and 0.032. As can be seen from comparison among the three figures, nonlinearity accelerates diffraction, causing smaller wave height in direct wave incidence region along $y = 0$ and larger wave height in the shadow region. This implies that the function of breakwater to make a calm region behind it is less effective in

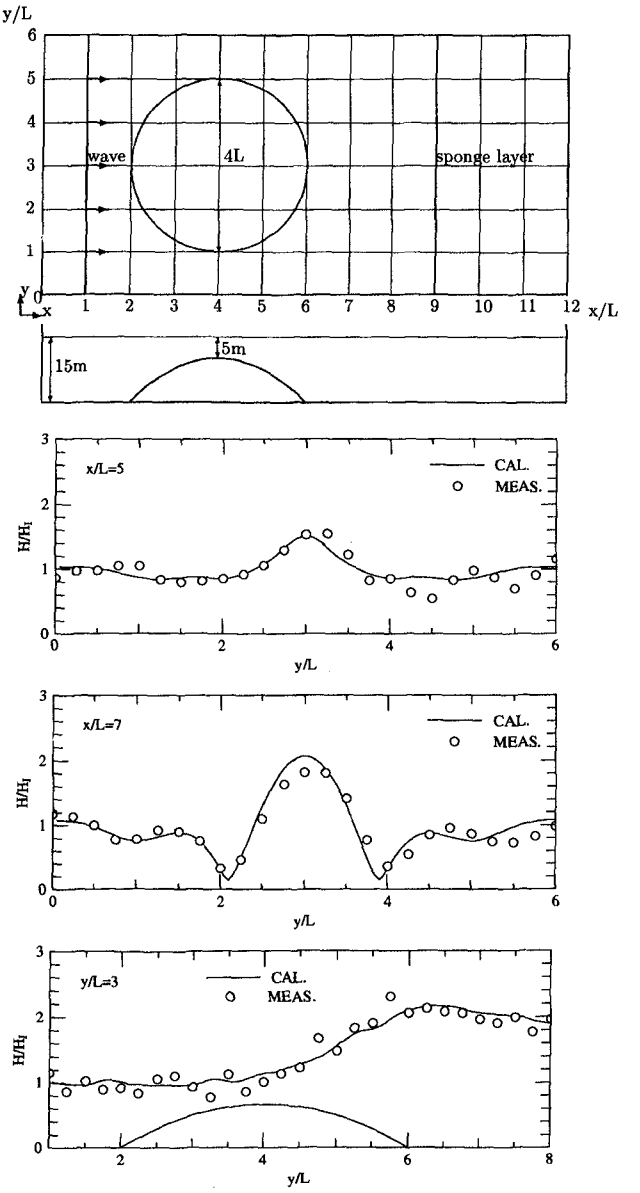

Fig. 4 Comparison of calculated wave height distribution around a circular shoal with measurement by Ito and Tanimoto (1972).

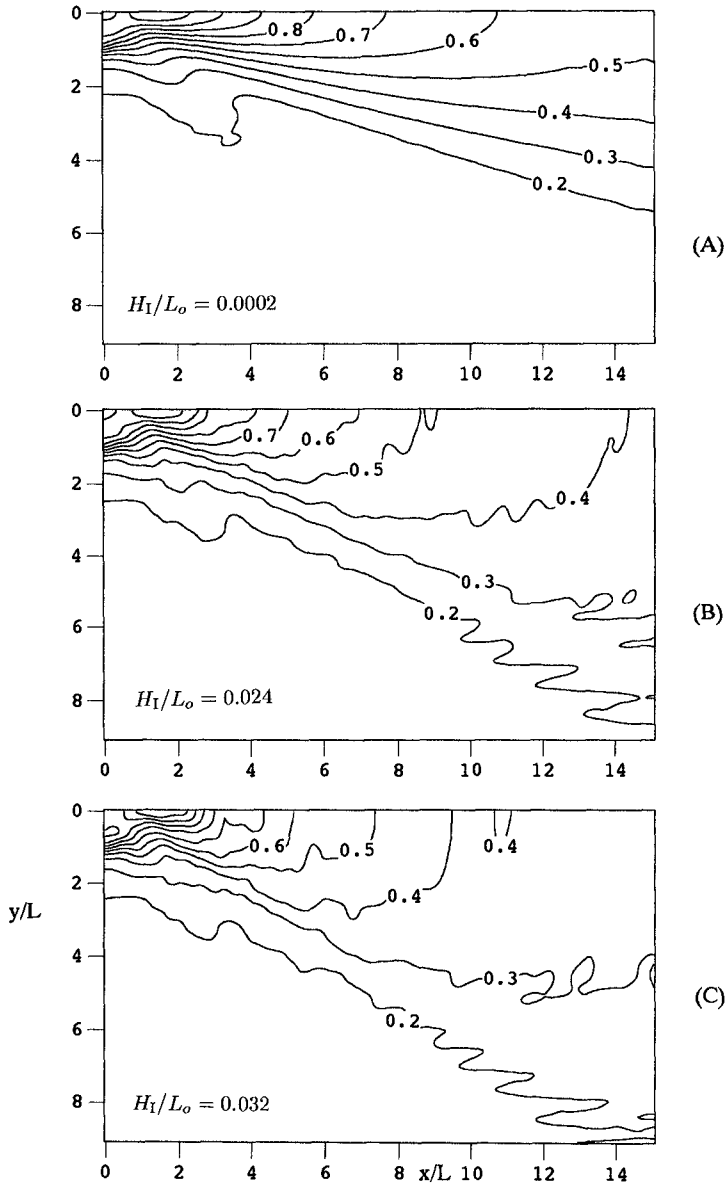

Fig. 5 Effect of wave nonlinearity on diffraction behind a breakwater gap ($B/L = 2$, $h/L_o = 0.05$).

rough wave condition.

4 Conclusion

Nonlinear mild-slope equations are derived only by expanding the velocity potential into a series in terms of a given set of vertical distribution functions and hence include full nonlinearity and full dispersivity. In the former part of the present paper, it was shown that the mild-slope equation, nonlinear shallow water equations and Boussinesq equations can be derived as special cases of the nonlinear mild-slope equations. It was also shown that the dispersion relation is accurately expressed by linearized forms of the nonlinear mild-slope equations.

A numerical model is developed based on the nonlinear mild-slope equations. The validity of the model is verified through calculations of waves of permanent type and wave transformation around a circular shoal. The result for diffraction of waves through a breakwater gap showed the larger diffraction effect for the more nonlinear waves. This suggests the importance to consider nonlinear effect in the diffraction diagrams since they are used to predict tranquility in the shadow region for rough incident waves. Systematic calculations will be made in the future.

References

1) Berkhoff, J. C. W. (1972): Computation of combined refraction-diffraction, *Proc. 13th Int. Conf. on Coastal Engrg.*, ASCE, pp. 471–490.

2) Cruz, E. C. and Isobe, M. (1994): Numerical wave absorbers for short and long wave modelling, Proc. Int. Symp. on Waves — Phys. and Num. Modelling, Univ. British Columbia, Vol. 2, pp. 992–1001.

3) Ishii, T., Isobe, M. and Watanabe, A. (1996): Two-dimensional analysis of wave transformation by rational-approximation-based, time-dependent mild-slope equation for random waves, *Proc. 25th Int. Conf. on Coastal Engrg.*, ASCE, pp. 754–766.

4) Isobe, M. (1994): Time-dependent mild-slope equations for random waves, *Proc. 24th Int. Conf. on Coastal Engrg.*, ASCE, pp. 285–299.

5) Ito, Y. and Tanimoto, K. (1972): A method of numerical analysis of wave propagation, — Application to wave diffraction and refraction —, *Proc. 13th Int. Conf. on Coastal Engrg.*, ASCE, pp. 503–522.

6) Luke, J. C. (1967): A variational principle for a fluid with a free surface, *J. Fluid Mech.*, Vol. 27, pp. 395–397.

7) Peregrine, D. H. (1967): Long waves on a beach, *J. Fluid Mech.*, Vol. 27, pp. 815–827.

8) Pos, J. D. (1985): Asymmetrical breakwater gap wave diffraction using finite and infinite elements, *Coastal Engrg.*, Vol. 9, pp. 101–123.

9) Stoker, J. J. (1957): *Water Waves*, Interscience, New York, 567p.

A Comparison of Higher Order Boussinesq and Local Polynomial Approximation Models

Maurício F. Gobbi[1], Andrew B. Kennedy[2] and James T. Kirby[2]

Abstract

Two recent approaches for computing wave evolution over varying topography are presented: the high order Boussinesq model of Gobbi and Kirby (1998) and the local polynomial approximation (LPA) method of Kennedy and Fenton (1997). Both analytical results and numerical solutions of Gobbi and Kirby (1998) model and two variants of the LPA method are presented and compared with exact solutions and laboratory measurements of waves propagating over submerged features.

Introduction

The increasing availability of high-speed computers has encouraged several researchers to work towards implementing deterministic nonlinear models and their numerical solutions for more accurate predictions of wave transformation in coastal areas. A great deal of effort has been made to extend the validity of $O(\mu^2)$ ($\mu \sim$ depth to length ratio) Boussinesq-type models to both deeper water (eg. Nwogu, 1993; Schäffer *et al.*, 1995) and highly nonlinear conditions (Wei *et al.*, 1995). Recently, noticing that existing Boussinesq models, which assume a second degree polynomial approximation for the velocity potential's vertical (z) dependency, have poor kinematics prediction in deep water, Gobbi *et al.* (1998) have derived a new Boussinesq-type model for a flat bed, which assumes that the velocity potential has a fourth degree polynomial dependency in z. The model's dependent variables are defined to give a (4,4) Padé linear dispersion relationship, and is fully nonlinear. Comparisons of several linear and nonlinear properties with exact solutions show great improvement of Gobbi *et al.* (1998) over Wei *et al.* (1995). A variable depth version of the model has been derived by Gobbi and Kirby (1998), and comparisons with laboratory experimental data show, again, very significant improvement over the model by Wei *et al.* (1995). We shall refer to these fourth order models as GKW98.

[1]Simepar, Caixa Postal 360, Curitiba, PR 80001-970, Brazil.

[2]Center for Applied Coastal Research, University of Delaware, Newark, DE. 19716 USA.

Recently, several local polynomial approximation methods have been developed (Kennedy and Fenton, 1997) which seek to provide local solutions to Laplace's equation in a weighted residual sense by assuming a local polynomial for the velocity potential at each local subdomain, where a subdomain is bounded by the bottom, the free surface, and vertical interfaces. The solution is subject to bottom and free surface constraints and continuity of the velocity and velocity potential at the subdomains' interfaces. With the problem completely specified for a given time, the coefficients of the polynomial are calculated. The kinematic and dynamic free surface boundary conditions are then used to advance the solution in time, and provide new free surface constraints for the next time step. Of the several variants of LPA methods, in this paper we shall look at two cases: both with only one horizontal dimension and fully nonlinear, one with fourth degree (somewhat comparable to GKW98) and one with sixth degree polynomial vertical representation of the velocity potential.

We briefly present both the GKW98 and LPA models, and then look at analytical properties of the linearized models and Stokes second harmonic amplitudes. Finally, the models are compared with experimental data.

Fully Nonlinear, $O(\mu^4)$ Boussinesq Model

This model, which was derived by Gobbi and Kirby (1998), consists of a set of coupled evolution equations which approximate the mass flux and momentum conservation in an arbitrary depth located at elevation $z = -h(x,y)$, where (x,y) are the horizontal spatial coordinates. The dependent variables are the free surface displacement η and the weighted average of the eulerian velocity between two arbitrary elevations, z_a and z_b in the water column, $\tilde{\mathbf{u}}$, with weight parameter β. The choice of of these elevations and the weight parameter are related to the accuracy of the linear dispersion properties of the model. The nondimensionalized mass conservation equation is given by

$$\eta_t + \nabla \cdot \mathbf{M} = 0; \quad \mathbf{M} = \int_{-h}^{\delta\eta} \nabla\phi dz, \tag{1}$$

with

$$\begin{aligned}
\mathbf{M} &= H\left\{\tilde{\mathbf{u}} + \mu^2\left[\left(Ah - \frac{H}{2}\right)(2\nabla hF_{22} + \nabla F_{21}) + \left(Bh^2 - \frac{H^2}{3}\right)\nabla F_{22}\right]\right. \\
&+ \mu^4\left[\left(Ah - \frac{H}{2}\right)(2\nabla hF_{42} + \nabla F_{41} + 2\nabla hF_{44} + \nabla F_{43})\right. \\
&+ \left(Bh^2 - \frac{H^2}{3}\right)(\nabla F_{42} + 3\nabla hF_{45} + \nabla F_{44}) \\
&+ \left.\left.\left(Ch^3 - \frac{H^3}{4}\right)(4\nabla hF_{46} + \nabla F_{45}) + \left(Dh^4 - \frac{H^4}{5}\right)\nabla F_{46}\right]\right\},
\end{aligned} \tag{2}$$

and $H = h + \delta\eta$. The pair of momentum conservation equations is given by

$$\mathbf{U}_t = -\nabla\eta - \frac{\delta}{2}\nabla\left(|\tilde{\mathbf{u}}|^2\right) + \Gamma_1\left(\eta, \tilde{\mathbf{u}}_t\right) + \Gamma_2\left(\eta, \tilde{\mathbf{u}}\right), \tag{3}$$

where

$$
\begin{aligned}
\mathbf{U} \equiv\ & \tilde{\mathbf{u}} + \mu^2 \left[(A-1)\, h\, (2\nabla h F_{22} + \nabla F_{21}) + (B-1)\, h^2 \nabla F_{22} \right] \\
+\ & \mu^4 \left[(A-1)\, h\, (2\nabla h F_{42} + \nabla F_{41} + 2\nabla h F_{44} + \nabla F_{43}) \right. \\
+\ & (B-1)\, h^2\, (\nabla F_{42} + 3\nabla h F_{45} + \nabla F_{44}) \\
+\ & \left. (C-1)\, h^3\, (4\nabla h F_{46} + \nabla F_{45}) + (D-1)\, h^4 \nabla F_{46} \right] \qquad (4) \\
\Gamma_1 \equiv\ & \mu^2 \nabla \left[\delta\eta F_{21t} + \left(2h\delta\eta + \delta^2\eta^2 \right) F_{22t} \right] \\
+\ & \mu^4 \nabla \left[\delta\eta\, (F_{41t} + F_{43t}) + \left(2h\delta\eta + \delta^2\eta^2 \right) (F_{42t} + F_{44t}) \right. \\
+\ & \left(3h^2\delta\eta + 3h\delta^2\eta^2 + \delta^3\eta^3 \right) F_{45t} \\
+\ & \left. \left(4h^3\delta\eta + 6h^2\delta^2\eta^2 + 4h\delta^3\eta^3 + \delta^4\eta^4 \right) F_{45t} \right] \qquad (5) \\
\Gamma_2 \equiv -\ & \mu^2 \delta \nabla \left\{ \tilde{\mathbf{u}} \cdot \left[(Ah - H)\, (\nabla F_{21} + 2\nabla h F_{22}) + \left(Bh^2 - H^2 \right) \nabla F_{22} \right] \right. \\
+\ & \left. \frac{1}{2} \left(F_{21} + 2H F_{22} \right)^2 \right\} \\
-\ & \mu^4 \delta \nabla \left\{ \tilde{\mathbf{u}} \cdot \left[(Ah - H)\, (\nabla F_{41} + 2\nabla h F_{42} + \nabla F_{43} + 2\nabla h F_{44}) \right. \right. \\
+\ & \left(Bh^2 - H^2 \right) (\nabla F_{42} + \nabla F_{44} + 3\nabla h F_{45}) \\
+\ & \left. \left(Ch^3 - H^3 \right) (\nabla F_{45} + 4\nabla h F_{46}) + \left(Dh^4 - H^4 \right) \nabla F_{46} \right] \\
+\ & \frac{1}{2} \left| (Ah - H)\, (\nabla F_{21} + 2\nabla h F_{22}) + \left(Bh^2 - H^2 \right) \nabla F_{42} \right|^2 \\
+\ & \frac{1}{2} \left[\left(F_{21} + 2H F_{22} \right) \left(F_{41} + 2H F_{42} \right. \right. \\
+\ & \left. \left. F_{43} + 2H F_{44} + 3H^2 F_{45} + 4H^3 F_{46} \right) \right] \Big\} \qquad (6) \\
F_{21}(\tilde{\mathbf{u}}) \equiv\ & G \nabla h \cdot \tilde{\mathbf{u}} \qquad (7) \\
F_{22}(\tilde{\mathbf{u}}) \equiv\ & \frac{1}{2} G \nabla \cdot \tilde{\mathbf{u}} \qquad (8) \\
F_{41}(\tilde{\mathbf{u}}) \equiv\ & -|\nabla h|^2 \left[(A-1)\, \nabla h \cdot \tilde{\mathbf{u}} + (B-A)\, h \nabla \cdot \tilde{\mathbf{u}} \right] \qquad (9) \\
F_{42}(\tilde{\mathbf{u}}) \equiv\ & -\frac{1}{2} \nabla^2 h \left[(A-1)\, \nabla h \cdot \tilde{\mathbf{u}} + (B-A)\, h \nabla \cdot \tilde{\mathbf{u}} \right] \qquad (10) \\
F_{43}(\tilde{\mathbf{u}}) \equiv\ & \nabla h \cdot \nabla \left(Ah \nabla h \cdot \tilde{\mathbf{u}} \right) + \frac{1}{2} \nabla h \cdot \nabla \left(Bh^2 \nabla \cdot \tilde{\mathbf{u}} \right) \qquad (11) \\
F_{44}(\tilde{\mathbf{u}}) \equiv\ & \frac{1}{2} \nabla^2 \left(Ah \nabla h \cdot \tilde{\mathbf{u}} \right) + \frac{1}{4} \nabla^2 \left(Bh^2 \nabla \cdot \tilde{\mathbf{u}} \right) \\
-\ & \frac{1}{2} \nabla^2 h \nabla h \cdot \tilde{\mathbf{u}} - \nabla h \cdot \nabla \left(\nabla h \cdot \tilde{\mathbf{u}} \right) \qquad (12) \\
F_{45}(\tilde{\mathbf{u}}) \equiv\ & -\frac{1}{6} \nabla^2 h \nabla \cdot \tilde{\mathbf{u}} - \frac{1}{3} \nabla h \cdot \nabla \left(\nabla \cdot \tilde{\mathbf{u}} \right) - \frac{1}{6} \nabla^2 \left(\nabla h \cdot \tilde{\mathbf{u}} \right) \qquad (13) \\
F_{46}(\tilde{\mathbf{u}}) \equiv\ & -\frac{1}{24} \nabla^2 \left(\nabla \cdot \tilde{\mathbf{u}} \right). \qquad (14)
\end{aligned}
$$

where $G \equiv (1 + \mu^2 |\nabla h|^2)^{-1}$. The nondimensional parameters appearing are δ and μ, characterizing the importance of nonlinearity and dispersion, respectively.

For details on the derivation of the equations above, the values of A, B, C, D (functions of constants β, z_a/h, and z_b/h), and the numerical implementation, the reader is referred to Gobbi *et al.* (1998) and Gobbi and Kirby (1998).

Local Polynomial Approximation Method

The local polynomial approximation method is a finite depth, potential flow technique for computing wave evolution over varying topography. It was designed to provide high accuracy with a reasonable computational cost, and remains general enough that the order of approximation may be easily changed.

The local polynomial approximation method used here is identical to that presented in Kennedy and Fenton (1997). In contrast to the presentation there, where the numerical solution method was highlighted, it is presented here in as a dimensionless set of differential equations for the approximate solution of Laplace's equation coupled with potential flow evolution equations. The velocity potential ϕ is assumed to be represented in the vertical coordinate z, by a polynomial of arbitrary degree

$$\phi(x,z) = \sum_{j=0}^{n-1} A_j(x) z^j \tag{15}$$

where the A_j's are functions only of the horizontal coordinate. The level of approximation n controls the degree of polynomial used and hence the accuracy. Here, the levels of approximation $n = 5$ and $n = 7$ will be used which have, respectively, fourth and sixth degree polynomial approximations in the vertical direction z. The initially unknown functions A_j must be chosen to satisfy the bottom boundary condition at the bed location $z = -h(x)$

$$\phi_z + \phi_x h_x = 0 \quad \text{on } z = -h \tag{16}$$

and also the free surface boundary condition

$$\phi(x, z = \eta(x)) = \phi^{(s)}(x) \tag{17}$$

This leaves $n-2$ constraints needed to completely specify the distribution of the A_j functions. These are found by imposing an approximation to the full field equation at collocation points in the vertical plane

$$\nabla^2 \phi = 0 \quad \text{on } z_j = -h + (\eta + h)\alpha_j, \; j = 1, 2, \ldots, n-2 \tag{18}$$

For all results presented here, collocation points, z_j, are taken to be the Gauss-Legendre points for $N = n - 2$, using the free surface and the bed as limits.

With the addition of global boundary conditions on the lateral boundaries, a set of block-banded linear equations results which completely specifies the problem. Once the system of equations has been solved, the flow field may be

determined and the free surface elevation and velocity potential may be advanced to the next time step using the free surface evolution equations

$$\eta_t = -\left(\int_{-h}^{\eta} \phi_x dz\right)_x \tag{19}$$

$$\phi_t^{(s)} = -\eta - \frac{1}{2}\left(\phi_x^2 + \phi_z^2\right) + \phi_z \eta_t \tag{20}$$

It is very simple to extend the system of equations to three dimensions, but because of computational considerations, this is not advisable. For one horizontal dimension, a good solution technique uses complex polynomials to represent the flow field as detailed in Kennedy and Fenton (1997), but this particular technique cannot be extended into an extra dimension.

Analytical Properties

For very small amplitude waves propagating over a level bottom, a progressive sinusoidal wave solution can be substituted into the linearized constant depth versions of both GKW98 and LPA to give an approximation to the exact linear dispersion relationship. Details can be found in Gobbi *et al.* (1998) for GKW98 dispersion, which results in a (4,4) Padé approximant to the exact relationship, and in Kennedy (1997) for the LPA formulations. Figure 1 shows the ratio to the exact solution of the linear phase speed calculated for GKW98, LPA $n = 5$, and LPA $n = 7$. It is clear that the GKW98 phase speed sits in between the two LPA results in terms of accuracy. Figures 2 and 3 show the vertical profile of the horizontal and vertical velocity amplitudes, respectively, normalized by their value at the free surface, for GKW98 and both LPA results. Notice the effect of the more powerful representation of the vertical dependence in LPA $n = 7$ over both GKW98 and LPA $n = 5$, which are quite comparable. Turning to a second order nonlinear property, figure 4 shows the ratio to the full theory solution of the amplitude of the second harmonic of a Stokes expansion of GKW98 and both LPA's. For this case, both LPA solutions give better result than the GKW98 model. This is probably because the GKW98 model was derived for optimized performance in a linear sense, whereas the LPA method uses the full water column in the specification of the problem.

Comparisons with Laboratory Measurements

In this section we compare the computations from GKW98 and both LPA implementations presented earlier with experimental data of waves propagating over submerged sills. First we use data from Beji and Battjes (1993) and Luth *et al.* (1994) consisting of regular waves propagating over a structure resembling a sand bar. Then we use the data from Ohyama *et al.* (1994) where the submerged structure has much steeper slopes, resembling a submerged breakwater. These two experiments have become quite popular for tests of wave propagation models, and the reader is referred to the original papers for additional information.

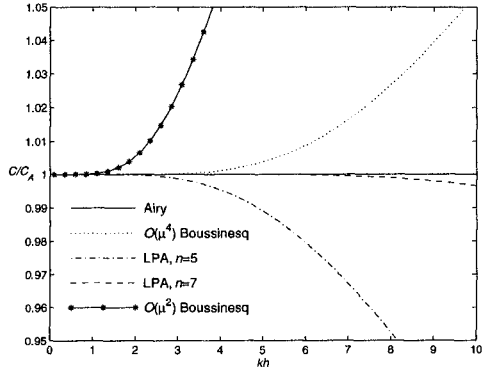

Figure 1: Ratio to exact solution of phase speed.

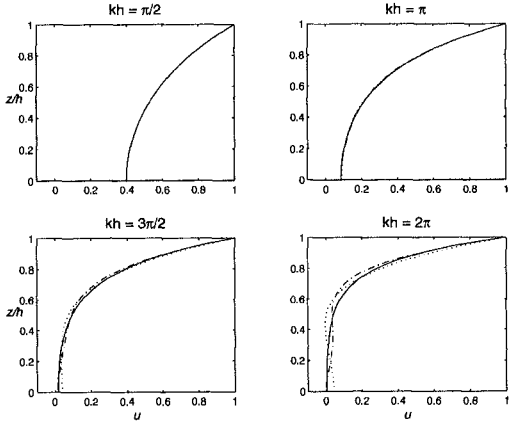

Figure 2: Horizontal velocity profile. Exact (solid), GKW98 (dot), LPA n=5 (dash-dot), LPA n=7 (dash).

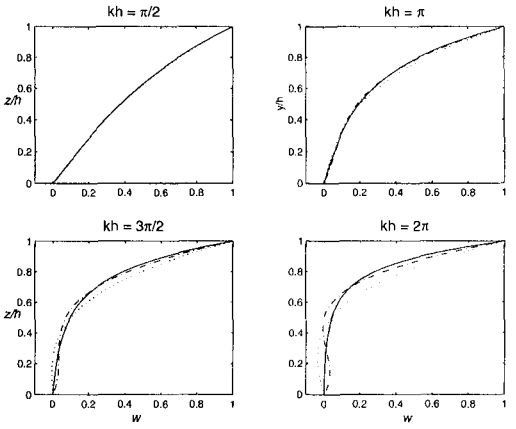

Figure 3: Vertical velocity profile. Exact (solid), GKW98 (dot), LPA n=5 (dash-dot), LPA n=7 (dash).

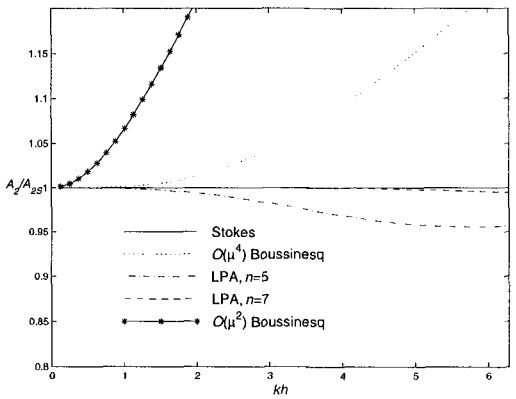

Figure 4: Ratio to full problem solution of Stokes second harmonic amplitude.

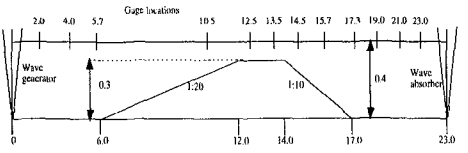

Figure 5: Sketch of wave flume of Delft experiments. All dimensions in (m)

The experiments performed by Beji and Battjes (1993) and Luth *et al.* (1994) have the same geometric characteristics, except for the length scale in Luth *et al.* (1994), which is twice as large as in Beji and Battjes (1993). In Luth *et al.* (1994) all gauge locations used in Beji and Battjes (1993) were repeated, and another run of measurements was performed with the gauges at different locations. Here, we re-scale all measurements to the scales used in Beji and Battjes (1993). The layout of the experimental set-up with the locations of the measurement stations and the geometry of the flume are illustrated in Figure 5.

Three sets of data were collected using different incident wave conditions. We refer to these data sets as cases (a), (b), and (c). In case (b), wave breaking occurred and this case was disregarded. The incident wave amplitude and period were $0.01m$, $2.02s$, and $0.0205m$, $1.01s$, for cases (a) and (c) respectively.

In all cases, the data from gauges at $2.0m$ or $4.0m$ were used to synchronize the data with the models. Figures 6, 7, and 8 show, respectively, comparisons of GKW98, LPA $n = 7$, and LPA $n = 5$, with the case (a) of the Delft experimental data at several gauge locations. For this case, all three models' performance are quite satisfactory, with GKW98 and LPA $n = 7$ showing excellent agreement, while LPA $n = 5$ shows larger discrepancies, due to its less accurate linear phase speed. Similarly, figures 9, 10, and 11 show comparisons with case (c). Notice that because the incident waves in this case are shorter, it is a more demanding case than case (a), especially behind the bar, where nonlinear superharmonics are released as free waves, and are much shorter than the incident wave. For this case, LPA $n = 7$ performs best, followed by the also very good agreement of GKW98, but LPA $n = 5$ has poor agreement behind the structure. This result is in agreement with the linear phase speed results shown in figure 1.

We now compare the numerical results to the Ohyama experimental data. Summarizing the experimental setup, the wave flume is $65m$ long and $1.0m$ wide. The total depth of the flume is $1.6m$. The location of the center of the bar was $28.3m$ from the wavemaker. Figure 12 shows a sketch of the flume. Three tests with incident wave periods $1.34s$, $2.01s$, and $2.68s$, (cases 2, 4, 6, respectively) and fixed amplitude equal to $0.025m$ will be used in the comparisons. No wave breaking occurred in any of the tests. The time series were synchronized with the computations at station 3. Figures 12, 13, and 14 show the comparisons

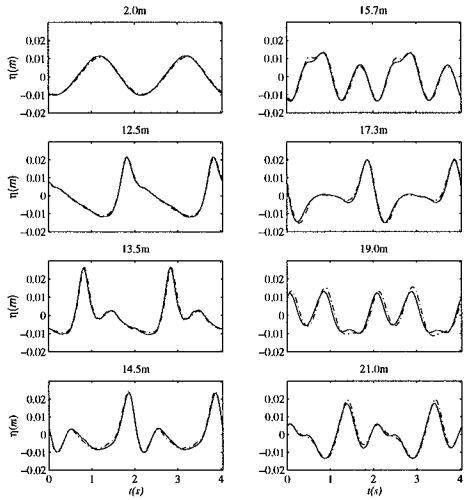

Figure 6: Comparisons of free surface displacement with case (a) of Delft experimental data at several gauge locations. GKW98 (dash-dot), data (solid).

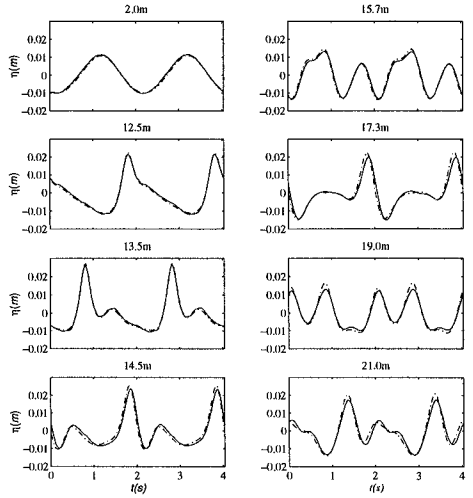

Figure 7: Comparisons of free surface displacement with case (a) of Delft experimental data at several gauge locations. LPA n=7 (dash-dot), data (solid).

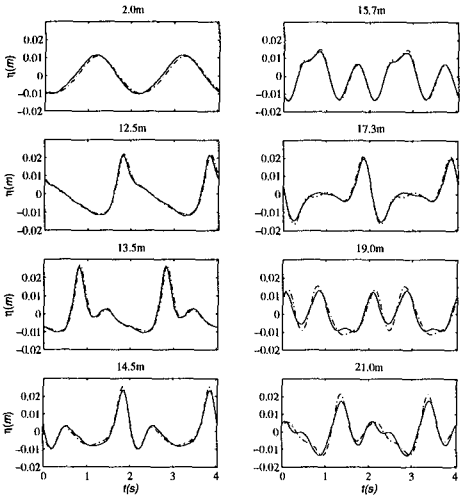

Figure 8: Comparisons of free surface displacement with case (a) of Delft experimental data at several gauge locations. LPA n=5 (dash-dot), data (solid).

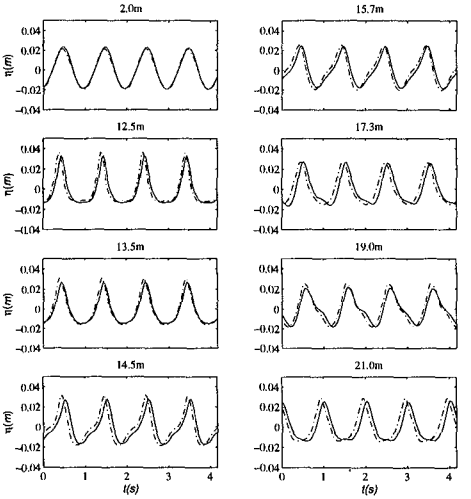

Figure 9: Comparisons of free surface displacement with case (c) of Delft experimental data at several gauge locations. GKW98 (dash-dot), data (solid).

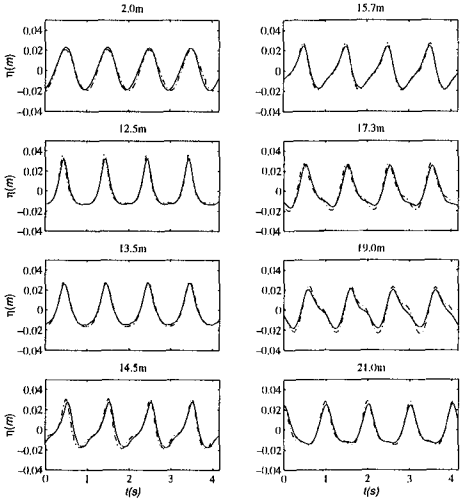

Figure 10: Comparisons of free surface displacement with case (c) of Delft experimental data at several gauge locations. LPA n=7 (dash-dot), data (solid).

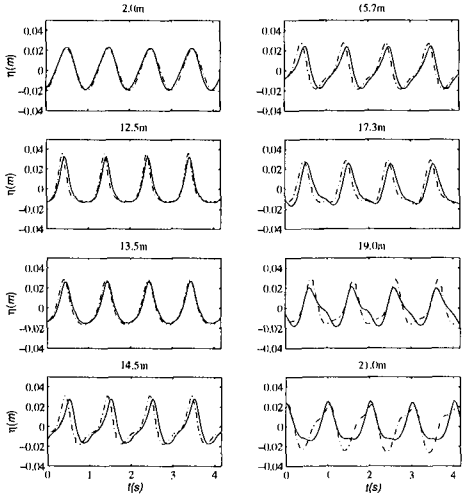

Figure 11: Comparisons of free surface displacement with case (c) of Delft experimental data at several gauge locations. LPA n=5 (dash-dot), data (solid).

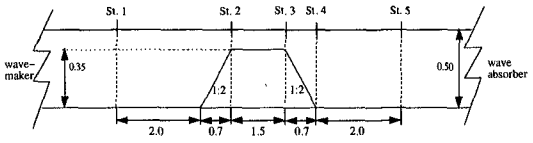

Figure 12: Sketch of wave flume of the Ohyama experiment.

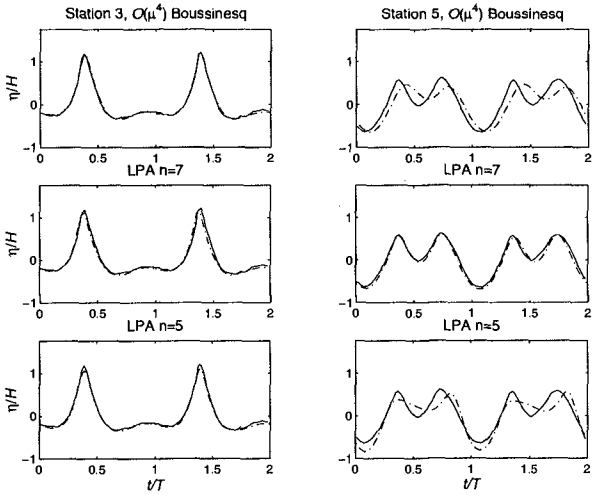

Figure 13: Comparisons of free surface displacement with case 2 of Ohyama experimental data. Computations (dash-dot), data (solid).

for the three cases, and it is possible to see that GKW98 and LPA $n = 5$ are comparable for cases 2 and 4, while LPA $n = 7$ outperforms them for these cases. In case 6, GKW98 and LPA $n = 7$ are comparable, while LPA $n = 5$ shows poorer performance. It might seem surprising that GKW98 does not perform in Ohyama cases 2 and 4 as well as in the Delft cases (a) and (c), since the incident wave conditions are not that different. This is due to the steep bottom slopes in Ohyama's cases which violates the intrinsic mild-slope assumption of GKW98 ($w \ll u$), which the fourth order polynomial for the potential's vertical dependence is not powerful enough to handle, for large enough μ.

Conclusions

Fully nonlinear local polynomial approximations and a $O(\mu^4)$ Boussinesq model were compared both in terms of analytical properties and of agreement

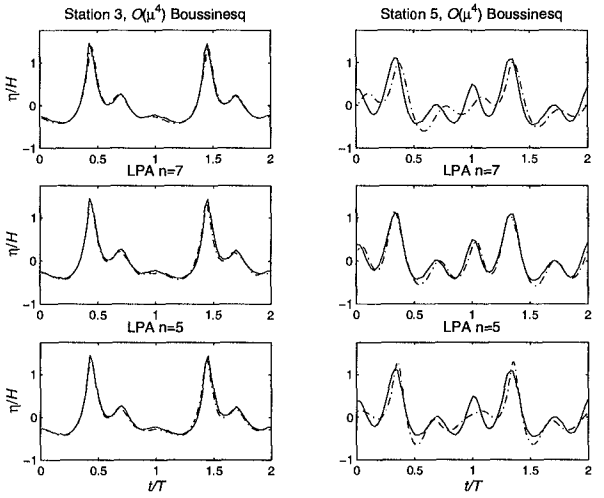

Figure 14: Comparisons of free surface displacement with case 4 of Ohyama experimental data. Computations (dash-dot), data (solid).

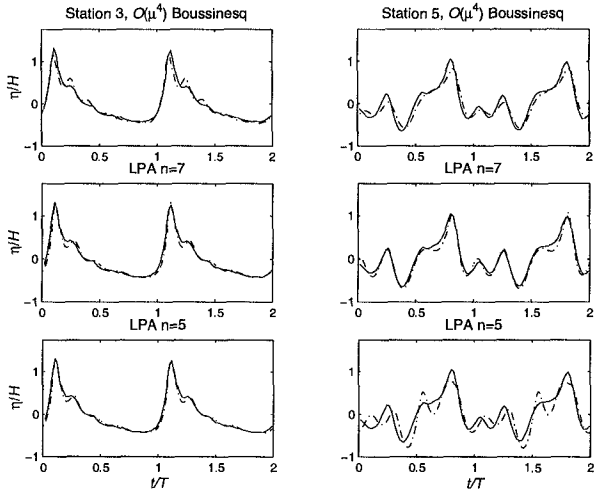

Figure 15: Comparisons of free surface displacement with case 6 of Ohyama experimental data. Computations (dash-dot), data (solid).

with experimental data. In general, because of its more accurate dispersion, the Boussinesq model performed better than the LPA with the same level of polynomial accuracy ($n = 5$), while the sixth degree polynomial LPA ($n = 7$) proved to be more accurate than both. The Boussinesq model has the advantage of being potentially faster in terms of computational time, and its 3-D implementation is more natural than the LPA methods shown here, which uses complex formulation to solve Laplace's equation and therefore cannot be extended to 3-D in an efficient manner. However, it is much simpler to extend the LPA model to any level of accuracy desired. The authors are now working on improvements in nonlinear behavior of Boussinesq models, improvements on dispersion properties of LPA methods, and 3-D implementation of the models.

Appendix: References

Beji, S. and Battjes, J. A., 1993 "Experimental investigations of wave propagation over a bar", *Coastal Eng.*, **19(1,2)**, 151-162.

Gobbi, M. F. and Kirby, J. T., 1998 "Wave evolution over submerged sills: tests of a high-order Boussinesq model", *Coastal Eng.*, Submitted.

Gobbi, M. F., Kirby, J. T., and Wei, G., 1998 "A fully nonlinear Boussinesq model for surface waves: II. Extension to $O(kh)^4$", *J. Fluid Mech.*, Submitted.

Kennedy, A. B., 1997, "The propagation of water waves over varying topography", Ph.D. Thesis, Monash University, Australia, 163pp..

Kennedy, A. B. and Fenton, J. D., 1997, "A fully-nonlinear computational method for wave propagation over topography", *Coastal Eng.*, **32**, 137-161.

Luth, H. R., Klopman, G., and Kitou, N., 1994 "Kinematics of a wave breaking partially on an offshore bar; LDV measurements with and without a net onshore current", Report H-1573. Delft Hydraulics, 40pp..

Nwogu, O., 1993 "An alternative form of Boussinesq equations for nearshore wave propagation", *J. Waterway, Port, Coast., Ocean Engng*, **119**, 618-638.

Ohyama, T., Kiota, W., and Tada, A., 1994 "Applicability of numerical models to nonlinear dispersive waves", *Coastal Eng.*, **24**, 297-213.

Schäffer, H. A. and Madsen, P. A., 1995 "Further enhencements of Boussinesq-type equations", *Coastal Eng.*, **26**, 1-14.

Wei, G., Kirby, J. T., Grilli, S. T., and Subramanya, R., 1995 " A fully nonlinear Boussinesq model for surface waves. Part 1. Highly nonlinear unsteady waves. *J. Fluid Mech.*, **294**, 71-92.

Experiments on nonlinear wave groups shoaling in a tank

L. Shemer[1], Haiying Jiao[2] & E. Kit[3]

Abstract

Evolution of periodically generated wave groups of different shapes that propagate over a sloping beach is studied experimentally and theoretically, by solving numerically the cubic Schrödinger equation. The agreements and disagreements between the experimental and the numerical results are discussed.

Introduction

Real sea waves can be described quite faithfully by JONSWAP spectrum (Hasselmann et al., 1973). One of the important features of this spectrum is its quite narrow frequency band, which results in notable wave groupiness even in the open seas. It has been observed in many field experiments that the distribution of waves in a group approaching the shore becomes more uniform, so that the maximum wave height in the group decreases. Such a transformation of wave groups has important practical consequences, since it affects directly the value of the maximum wave height in the group. The importance of the significant wave height as a design parameter is generally recognized in coastal engineering. This demodulation effect may result from the dissipation in the bottom boundary layer, as well as from the nonlinear and dispersive effects, as shown in numerical simulations based on the Korteweg-de Vries equation by Kit et al. (1995). The reduction in the maximum wave height with decrease of the water depth was also obtained numerically by Barnes and Peregrine (1995). In the present study, the transformation of a deterministic wave group over a sloping beach is investigated experimentally, in a laboratory wave tank, and theoretically, by a numerical solution of

[1] Prof., Dept. of Fluid Mechanics and Heat Transfer, Faculty of Engng., Tel Aviv Univ., Tel Aviv 69978, Israel.
[2] Ph. D. Student, Dept. of Fluid Mechanics and Heat Transfer, Faculty of Engng., Tel Aviv Univ., Tel Aviv 69978, Israel.
[3] Prof., Dept. of Fluid Mechanics and Heat Transfer, Faculty of Engng., Tel Aviv Univ., Tel Aviv 69978, Israel.

model equations. The simplest nonlinear theoretical model which is capable of describing the evolution of propagating wave packet with a narrow spectrum in the range of water depths from deep to intermediate is the so-called cubic Schrödinger equation (CSE) (see, e.g., Mei 1989). This equation was derived first by Zakharov (1968) and Hasimoto & Ono (1972) and has been extensively applied for description of wave group evolution in deep water.

Experimental Facility and Procedure

Experiments are performed in a wave tank that is 18m long, 1.2m wide and filled to a mean water depth of 0.6m. A computer-operated wavemaker is located at one end of the tank. A false bottom made of thick marine plywood is installed in the tank. The effective water depth is 0.3m in the vicinity of the wavemaker. The bottom slope is 1:30 for the length of 7.5m along the tank. The last 5m of the false bottom represent a horizontal flat surface with the effective depth of 0.05m. At the far end of the false bottom is located a wave energy-absorbing beach. Two sets of four wave gauges, each on its own bar, are used in this study. The first set of the gauges is of resistance type, while the second one is of the capacitance type. The distance between the two consecutive probes is 0.4m for the resistance wave gauges and about 0.3m for the capacitance probes. Each probe-supporting bar is mounted on a separate carriage that can be moved along the tank. More sensitive capacitance probes are used for measurements in the shallow water area, while resistance probes are used in the rest of the tank. Detailed measurements of instantaneous surface elevation are carried out at eight fixed measuring stations, thus covering 32 locations along the tank.

Wave groups with three different shapes are selected in this study. The equations describing the driving signal applied to the wavemaker are as following:

$$s(t) = A_0 \sin(\Omega t)\sin(\omega t), \quad \Omega = \omega / 20 \tag{1}$$

$$s(t) = A_0 \left|\sin(\Omega t)\right| \sin(\omega t), \quad \Omega = \omega / 20 \tag{2}$$

$$s(t) = A_0 \exp - (t / 5T)^2 \sin(\omega t), \quad -16T < t < 16T \tag{3}$$

where the carrier wave period $T = 2\pi/\omega$. These signals are repeated periodically. The first two driving signals produce identical wave groups envelopes, but their spectra differ essentially. The forcing signal (1) has a simple bimodal spectrum. The spectrum of (2) consists of a set of discrete frequencies, where 3 dominant modes can be identified. The third signal produces wave groups that are widely separated and have a discrete spectrum, which requires a considerable number of modes for its accurate description. Experiments are carried out for T=0.7 s and for three values of the driving amplitude A_0, corresponding to a nearly linear, nonlinear, and strongly nonlinear wave steepnesses. In the vicinity of the wavemaker, the maximum values of the wave steepness a_0k_0 in the group are approximately 0.07, 0.14 and 0.21. Variation of the wave group velocity along the tank and modification of the wave power spectra are measured.

Theoretical Model

The cubic Schrödinger equation (CSE) for a mild slope is selected as the theoretical model. The CSE is written in a form given by Mei (1989):

$$-i\mu A - iA_X + \alpha A_{\tau\tau} + \beta |A|^2 A = 0 \tag{4}$$

where $A(X,\tau)$ is the complex wave group envelope, and the slow variables are related to the coordinate along the tank x and the time t as

$$X = \varepsilon^2 x; \qquad \tau = \frac{1}{\varepsilon}\int_0^X \frac{dX}{c_g(X)} - \varepsilon t \tag{5}$$

In (5), $c_g = \partial\omega/\partial k$ is the group velocity, k being the local wave number, and $A(X=0, \tau = 0) = a_o/\varepsilon$. The local values of the X-dependent coefficients in the CSE are defined in the dimensionless form by

$$\frac{\mu}{k_o} = \frac{dq}{dX}\frac{(1-\tanh^2 q)(1-q\tanh q)}{k_o[\tanh q + q(\tanh^2 q)]}, \tag{6}$$

$$\frac{\alpha\omega^2}{k_o} = \frac{\omega^2}{k_o c_g^3}\frac{\partial^2\omega}{\partial k^2}, \tag{7}$$

$$\frac{\beta}{k_o^3} = \frac{1}{n}\left[\frac{\cosh 4q + 8 - 2\tanh^2 q}{16\sinh^4 q} - \frac{1}{2\sinh^2 2q}\frac{(2\cosh^2 q + n)^2}{\frac{q}{\tanh q} - n^2}\right], \tag{8}$$

where $q = kh$, $k_0 = k(X=0)$ and the parameter $n = c_g k/\omega$ represents the local value of the ratio of group and phase velocities and is given by

$$n = \frac{1}{2}\left(1 + \frac{2q}{\sinh 2q}\right). \tag{9}$$

It is well know that the coefficient β of the nonlinear term given by (8) and (9) changes its sign at q=1.36. For q>1.36, β>0, corresponding to the focusing condition, while for q<1.36, β<0 and wave energy defocusing occurs. The radian frequency of the carrier wave ω is related to its wave number k by the dispersion relation

$$\omega^2 = kg\tanh q, \tag{10}$$

where g is the acceleration due to gravity. Equation (4) is solved numerically using an implicit finite difference scheme with periodic in τ boundary conditions. Initial conditions at $X = 0$ are in accordance with the shapes defined by (1) to (3). The variation of the surface elevation η is obtained using the complex amplitude $A(X, \tau)$ from the solution of (4) and the relations (5) between the scaled (X, τ) and the physical (x, t) variables as

$$\eta(x,t)=\varepsilon[A(X,\tau)e^{i(kx-\omega t)}+c.c.], \tag{11}$$

where *c.c.* denotes complex conjugate.

Results and Discussion

The results for the wave groups excited by the driving signal given by the equations (1) – (3) are presented in Figures 1 – 3, respectively, for the two extreme values of the forcing amplitude, $a_0k_0 = 0.07$ and $a_0k_0 = 0.21$.

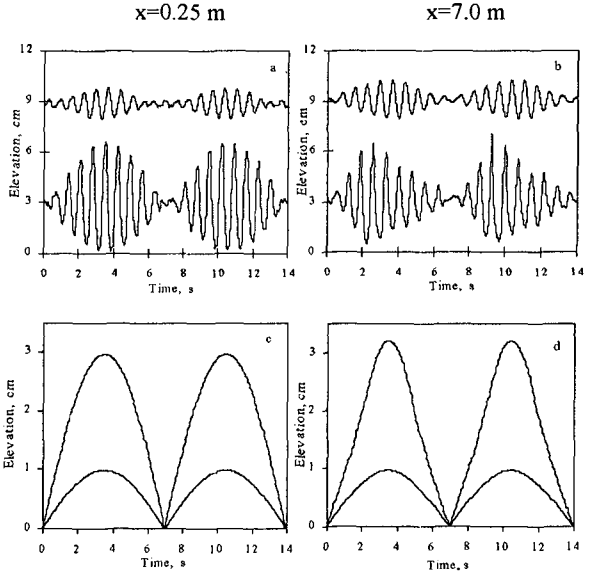

Figure 1. The measured surface elevation (*a* and *b*) and the computed group envelopes (*c* and *d*) for the driving signal (1).

In each Figure, the results are given at two locations along the tank, $x = 0.25$ m, $h = 0.3$ m (Figures *a* and *c*), and $x = 7.0$ m, $h = 0.075$ m (Figures *b* and *d*). The measured variation in time of the instantaneous surface elevation is given in Figures *a* and *b*, where the curves representing the low and the high amplitudes are shifted in the vertical

direction. The corresponding variation in time of group envelopes obtained numerically is given in Figures *c* and *d*.

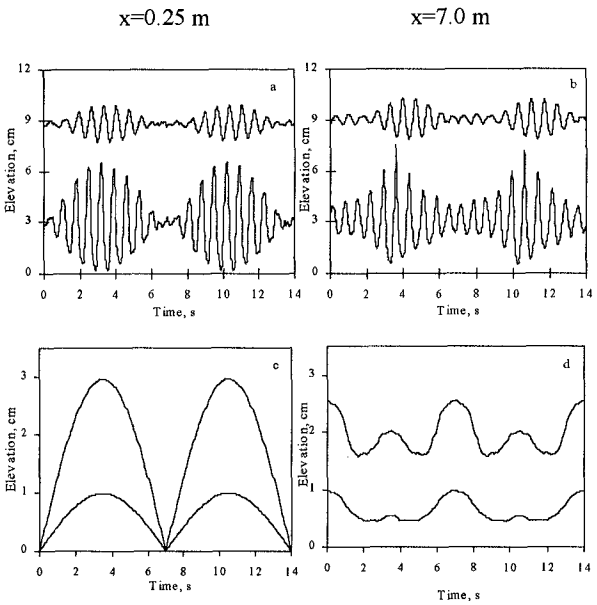

Figure 2. The measured surface elevation (*a* and *b*) and the computed group envelopes (*c* and *d*) for the driving signal (2).

The most striking effect observed in this study is the difference in the evolution of wave groups excited by the driving signals (1) and (2). In the vicinity of the wavemaker, both types of wave groups look practically identical, see Figures 1*a* and 2*a*. At a larger distance, the wave groups generated by (1), Figure 1*b*, tend to retain their identity, although nonlinear effects are clearly visible, while the wave groups excited by (2), Figure 2*b*, are spread significantly. This spreading can be interpreted as the demodulation effect. Certain spreading can also be observed in the detached wave groups excited using (3), Figure 3*b*. For all shapes of the forcing signals, the initially symmetric wave groups at higher amplitude loose their symmetry. The trough-crest asymmetry is clearly visible at high amplitude of forcing at both locations. This asymmetry is a clear indication of the appearance of the higher harmonics in the surface elevation spectrum. In addition to the trough-crest asymmetry, left-right asymmetry is observed at the remote measuring station at high amplitude of forcing. This effect is most prominent for the driving signal (3), Figure 3*b*, although it also can be observed in Figure 1*b*. Note that similar group shapes were observed in experiments and obtained numerically in deep water by solving the modified nonlinear Schrödinger equation (Lo & Mei 1985).

The demodulation effect observed in the experiments away from the wavemaker is clearly seen in the numerical simulation as well, Figure 2*d*. Contrary to that, wave group shapes for the forcing signals (1) and (3) do not change notably, although certain focusing effects can be observed at high amplitude of forcing in Figures 1*d* and 3*d*. It should be mentioned here that the left-right asymmetry observed in the experiments could not be obtained in the framework of the adopted theoretical model, since the CSE conserves the symmetry of the initial conditions. In Figures *c* and *d*, the envelope corresponding to the temporal variation of wave groups at the carrier frequency only is presented, and the contribution of the bound waves at higher harmonics, which leads to the trough – crest asymmetry observed in the experiments, is not accounted for.

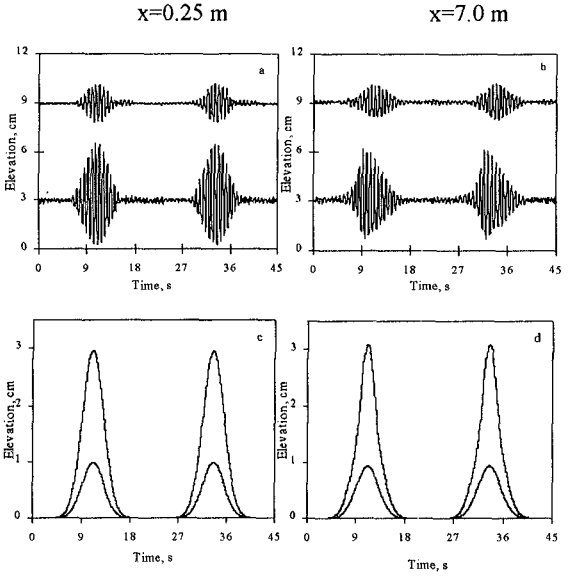

Figure 3. The measured surface elevation (*a* and *b*) and the computed group envelopes (*c* and *d*) for the driving signal (3).

Both the experimental and the numerical results indicate that for the driving signals (1) and (3) no considerable variation in the maximum wave amplitude can be observed for the conditions employed in this study. For the driving signal given by (2), both the experiments and the computations give considerable spreading of the wave energy in the group. The results presented in Figures 1 – 3 thus suggest that the adopted theoretical model is capable of providing a reasonable pattern of wave group evolution over a sloping beach. The CSE can therefore be used to investigate the wave group evolution over larger distances, which could not be verified experimentally due to the limitations of the experimental facility.

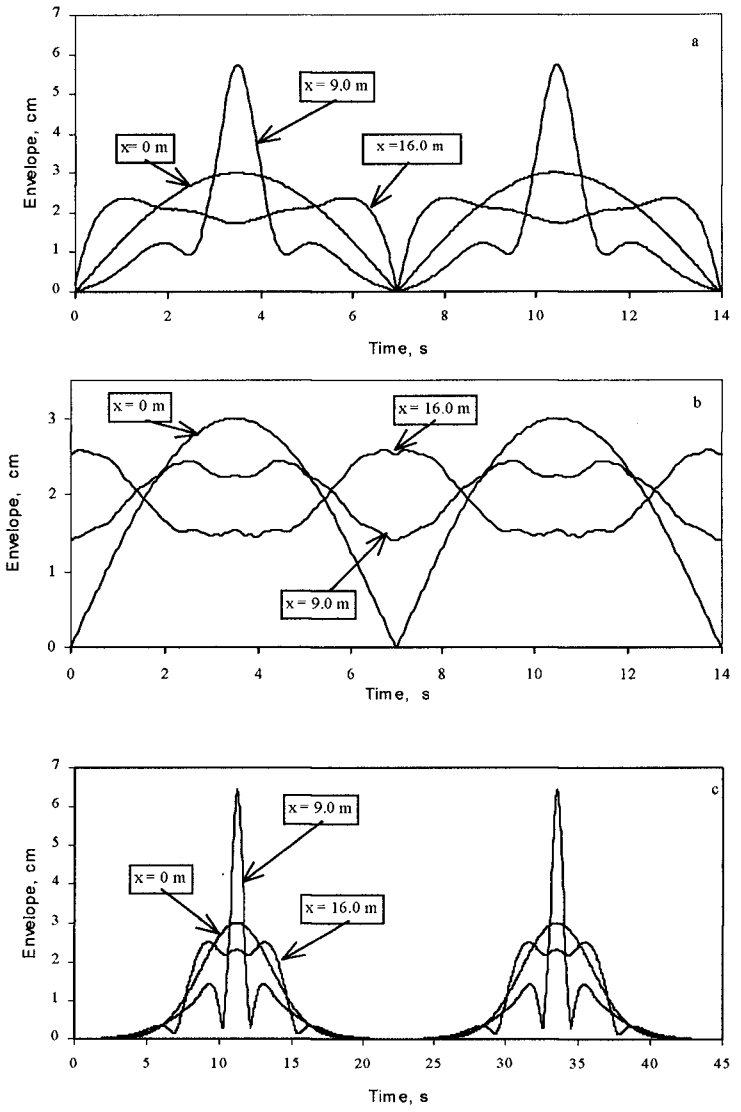

Figure 4. The computed variation of the wave group envelopes with the distance from the wavemaker for the bottom slope 1:30; initial depth h=0.6m. *a*) driving signal (1), *b)* driving signal (2), *c*) driving signal (3).

Computations were therefore performed wave groups of high wave steepness (a_0k_0 = 0.21) for the driving signals given by (1) to (3) for the same slope of 1:30 as in the experiments, but with the initial depth of h=0.6 m. The results at three locations along the tank for the duration corresponding to two wave groups are presented in Figure 4. The locations selected for the presentation correspond to the initial wave group at the wavemaker, x=0 m, h=0.6 m, intermediate depth at x=9.0 m, h=0.3 m, and shallow water at x=16.0 m, h=0.067 m.

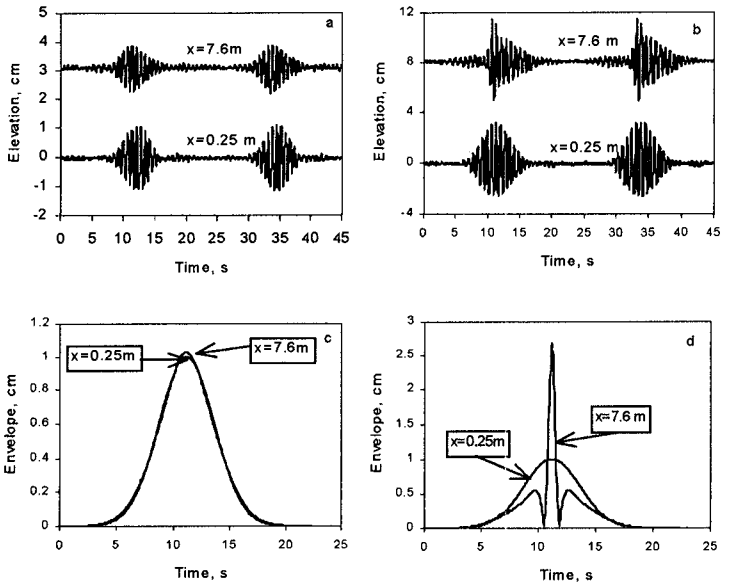

Figure 5. The measured surface elevation (*a* and *b*) and the computed group envelopes (*c* and *d*) for the constant water depth h=0.6m and the driving signal (3).

The qualitative difference in the evolution pattern of wave groups excited by signal (1), Figure 4*a*, and (2), Figure 4*b*, is quite evident. The wave groups excited by the driving signal (1) initially exhibit strong focusing, and the maximum amplitude is nearly doubled at x=9.0 m. As the waves propagate over more shallow water, strong defocusing occurs, and the wave energy is spread nearly uniformly in the group. It should be stressed here that due to the symmetry properties of the driving signal (1) and the CSE (4), the node points in the envelope distribution in time are conserved in the course of the evolution process. This particular feature does not apply to the driving signals (2) and (3). The qualitative difference between the driving signals (1) and (2) is responsible for the different evolution patterns on Figures 4*a* and 4*b*. Contrary to Figure 4*a*, no strong

focusing is observed at the initial stages of evolution for the driving signal (2), and at both locations in Figure 4*b*, x=9.0 m, h=0.3 m, and x=16.0 m, h=0.067 m, the waves are distributed essentially uniformly along the group.

Evolution pattern for the detached groups in Figure 4*c* is similar qualitatively to that observed in Figure 4*a*. Here too, the wave energy is initially focused at x=9.0 m, h=0.3 m. At larger distances from the wavemaker and in more shallow water demodulation is obtained. Although the driving signal (3) does not require conservation of the node points as it is the case for the signal (1), the groups are initially sufficiently separated, so that no substantial interference between the neighboring groups can occur for the time and length scales employed in the present computations.

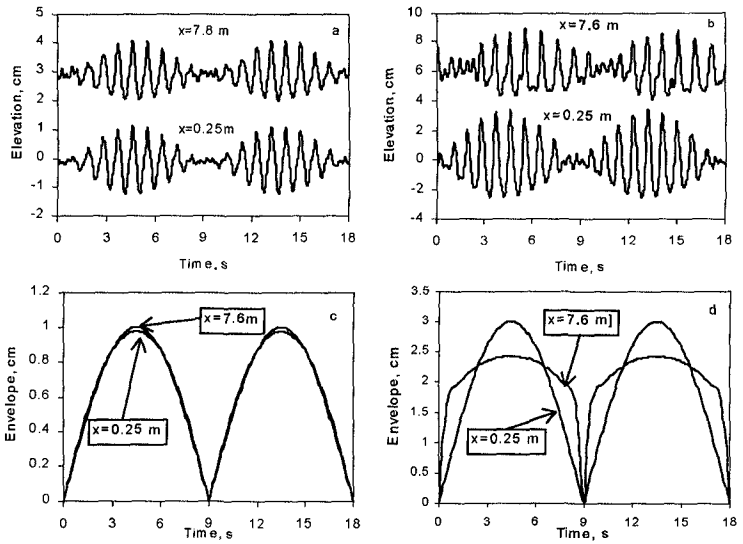

Figure 6. The measured surface elevation (*a* and *b*) and the computed group envelopes (*c* and *d*) for the constant water depth h=0.6m, T=0.9s and the driving signal (3).

These computational results suggest that it may be instructive to study wave group evolution in water of constant depth. The representative experimental and numerical results for the two extreme forcing amplitudes (a_0k_0 = 0.07 and a_0k_0 = 0.21) for the deep (h=0.6 m) and shallow (h=0.012 m) water cases are given in Figures 5 and 6, respectively. The driving signal (3) is used in the results of Figure 5, while the signal (1) is employed in Figure 6.

For the conditions of Figure 5, focusing (increase in the maximum wave amplitude within the group) is obtained for the high forcing amplitude both in the experiments

(Figure 5*b*) and in computations (Figure 5*d*). For the low amplitude of forcing, no significant variation of the maximum wave amplitude along the tank is obtained in Figures 5*a* and 5*c*.

In shallow water the spreading of the wave energy is obtained experimentally for the high amplitude of forcing in Figure 6*b*. The corresponding demodulation effect is observed in the numerical simulations presented in Figure 6*d*. At low amplitude of forcing, no significant effects are observed neither in experiments (Figure 6*a*), nor in computations (Figure 6*c*).

A more detailed analysis of the evolution of nonlinear wave groups in water of a constant intermediate depth is presented in Shemer et al. (1998). The experimental results are compared in this study with the numerical solutions of the CSE. In an additional study, Kit et al. (1998), nonlinear wave group evolution in shallow water is investigated. The measurements of the temporal and spatial variation of the instantaneous surface elevation are supported by the numerical solutions of the Korteweg-de Vries equation.

Concluding remarks

The present study indeed confirms that wave groups propagating over a sloping beach undergo modulation and subsequent demodulation and their wave energy tends eventually to spread more uniformly over the group. In the case of the constant water depth, defocusing is obtained in shallow water, while in deeper water, the trend is opposite and wave energy focusing leading to increase of the maximum wave height above its initial value is observed.

The current investigation reveals that shoaling wave groups having identical initial envelope shapes but different spectral contents may undergo completely different evolution processes. Specifically, groups having a bimodal spectrum, driving signal (1), retain their clear identity in the process of propagation, and their envelope periodically attains zero. For wave groups with the same shape and more complicated spectra, driving signal (2), the wave energy tends to become more uniformly distributed along the group, so that the clear distinction between the groups vanishes.

The simplest possible nonlinear model, the cubic Schrödinger equation, which contains an additional term accounting for mild water depth variation and is thus capable of describing wave group shoaling, is selected here. The coefficient of the nonlinear term in this equation changes its sign in the course of wave group propagation toward the beach.

The total body of experimental and numerical results accumulated in this study indicates that the cubic Schrödinger equation (4) constitutes a reasonable model for studies of shoaling of nonlinear gravity wave groups over a sloping beach. CSE appears to be able to capture successfully the global features of nonlinear wave group transformation for the whole range of the water depth variation employed here. It also reflects correctly

in general the effect of the initial maximum wave steepness $k_o a_o$ on the group evolution pattern. The CSE thus can be considered as a robust, albeit crude model for description of the nonlinear wave group evolution and transformation in water of slowly varying depth.

Acknowledgement

This work was supported in part by a grant from the Israel Science Foundation.

References

Barnes, T., and Peregrine, D.H. 1995 Wave groups approaching a beach: full irrotional flow computations. Int. Conf. on Coastal Research in Terms of Large Scale Experiments, Abstracts, Poland, 7 - 8.

Hasimoto, H. and Ono, J. 1972. "Nonlinear modulation of gravity waves." *J. Phys. Soc. Japan* 33, 805-811.

Hasselmann, K., Barnett, T.P, Bouws, E., Carlson, H., Cartwright, D.E., Enke, K., Ewing, J.A., Gienapp, H., Hasselmann, D.E., Krusemann, P., Meerburg, A., Müller, P., Olbers, D.J., Richter, K., Sell, W., and Walden, H. 1973 "Measurements of wind-wave growth and swell decay during the Joint North Sea Wave Project (JONSWAP)." *Deut. Hydrogr. Z.*, 8, (*suppl. A*).

Kit, E., Pelinovsky, E. and Talipova, T. 1995 Transformation of probability distribution of wind waves in coastal zone. Proceedings of the COPEDEC IV, Brazil, v. 3, 2344-2353.

Kit, E., Shemer, L., Pelinovsky, E., Talipova, T., Eitan, O., and Jiao, H. 1998 Nonlinear wave group evolution in shallow water. Submitted for publication.

Lo, E. and Mei, C.C. 1985 A numerical study of water-wave modulation based on a higher-order nonlinear Schrödinger equation. *JFM* 150, 395-416.

Mei, C.C. 1989 "The Applied Dynamics of Ocean Surface Waves." World Scientific, Singapore.

Shemer, L., Kit, E., Haiying Jiao, and Eitan, O. 1998 Experiments on nonlinear wave groups in intermediate water depth. J. Waterway, Port, Coastal and Ocean Engng., v. 124. Zakharov, V.E. (1968). "Stability of periodic waves of finite amplitude on the surface of deep fluid." *J. Appl. Mech. Tech. Phys.* 2, 190-194.

Zakharov, V.E. 1968 "Stability of periodic waves of finite amplitude on the surface of deep fluid." *J. Appl. Mech. Tech. Phys.* 2, 190-194.

MODULATION OF BICHROMATIC WAVE TRAIN IN A WAVE TANK

Motohiko Umeyama[1]

Abstract

The instability of bichromatic wave train in water of intermediate depth is investigated by means of a perturbation method. The analytical solution, treated as the result of an initial value problem, yields the modulation and disintegration of the wave train, caused by the interaction of two incident waves of finite amplitude. A laboratory study was also conducted to measure the surface elevations of bichromatic waves generated by several types of compound sinusoidal signals. The calculation using the third-order finite-amplitude wave equation is carried out, and its prediction is compared with the measured data obtained under several experimental conditions.

Introduction

For surface waves in water of arbitrary depth, small disturbances cause the instability as the waves propagate after a certain distance. Eventually the instability leads to loss of coherence, while the wave energy distributes over a broad spectrum. Benjamin and Feir(1967), using a perturbation approach, studied the instability of nonlinear deep-water waves, and showed that weakly nonlinear free-surface waves are inherently unstable to modulated periodic disturbances. In the following paper, Benjamin(1967) qualitatively explained the experimental evidence, known as side-band instability, using a second-order perturbation solution, and predicted that the side-band frequency components grow exponentially in time. Their results, however, are limited to the initial instability. Since then, much theoretical effort has been expended to search for an uniformly valid equation describing the behavior of the Stokes' wave train; for example, Lighthill(1967) examined the early stage of the nonlinear modulation of a wave packet using Whitham's theory(1965) based on an averaged Lagrangian, and Chu and Mei(1970) extended the Whitham's theory to derive the modulation equation for slowly varying Stokes' waves. On the

[1]Associate Professor, Department of Civil Engineering, Tokyo Metropolitan University, 1-1 Minamiohsawa, Hachiohji, Tokyo 192-0397, Japan

other hand, Zakharov(1968) derived the cubic Schrödinger equation which predicts the spatial evolution of the wave packet, and later, Zakharov and Shabat(1972) obtained an exact solution of the nonlinear Schrödinger equation. Their solutions predict the disintegration of initially uniform wave train into a definite number of wave groups. Yuen and Lake(1975) proved that Whitham's theory yields the same nonlinear Schrödinger equation when applied consistently to the order considered. All these solutions can be only applied to the case of the monochromatic wave train. The instability of the bichromatic wave train, having a set of discrete frequencies, has been regarded as the similar phenomenon which can be described by the evolution equation of the monochromatic wave. The instability by the bichromatic wave motion develops slowly as waves propagate from the wavemaker, and the growth rate of the instability becomes greater as the wave steepness increases. An example is found in a recent literature by Stansberg(1994), who observed a strong variation of wave pattern downstream the wave tank.

Despite the interest in the subject, few theoretically justifiable equation is available, to date, for predicting modulated surface displacements responsible for bichromatic waves. The purpose of this study is to investigate the modulation and disintegration of the bichromatic wave train in water of intermediate depth. A perturbation method is applied to the velocity potential and the vertical displacement of the water surface. The present equation predicts the surface displacements during the period of transition from a stationary state to a steady state in a finite distance from the wavemaker. The solution explains the instability of the periodic wave train mathematically as a result of the interaction of two incident waves propagating in the same direction.

Theory

Now we consider a two-dimensional irrotational wave motion bounded above by a free surface and below by a rigid horizontal bed, and assume the fluid to be inviscid and incompressible. The Eulerian velocity components of the water particles can be expressed in terms of a velocity potential $\Phi(x,y,t)$ such as

$$u(x,y,t) = \frac{\partial \Phi}{\partial x} \tag{1}$$

$$v(x,y,t) = \frac{\partial \Phi}{\partial y} \tag{2}$$

where $u(x,y,t)$ = horizontal velocity; $v(x,y,t)$ = vertical velocity; x = horizontal coordinate; and y = vertical coordinate measured from the still water level, respectively. For incompressible flow, the velocity potential must satisfy Laplace equation such as

$$\frac{\partial^2 \Phi}{\partial x^2} + \frac{\partial^2 \Phi}{\partial y^2} = 0. \tag{3}$$

The kinematical and dynamical boundary conditions at the free surface are

$$g\eta + \frac{\partial \Phi}{\partial t} + \frac{1}{2}\{(\frac{\partial \Phi}{\partial x})^2 + (\frac{\partial \Phi}{\partial y})^2\} = 0 \quad on\ y = \eta, \tag{4}$$

$$\frac{\partial \eta}{\partial t} + \frac{\partial \Phi}{\partial x}\frac{\partial \eta}{\partial x} - \frac{\partial \Phi}{\partial y} = 0 \qquad on\ y = \eta, \tag{5}$$

where $\eta(x,t)$ = vertical displacement of the water surface measured from $y=0$; g = acceleration due to gravity; and t = time. No fluid can pass perpendicular to the plane horizontal bottom, and therefore the bottom boundary condition is

$$\frac{\partial \Phi}{\partial y} = 0 \qquad \text{on } y=-h, \tag{6}$$

where h = water depth from the still water level.

In the finite-amplitude wave theory, the perturbation method is used to solve eqs.(3), (4), (5) and (6). The dependent variables are defined in terms of a power series, with successively smaller terms defined by a small perturbation parameter raised to a higher power in each succeeding term. Therefore, the velocity potential, vertical displacement and angular frequency for a third-order wave of finite amplitude can be expressed as

$$\Phi = \epsilon\Phi^{(1)} + \epsilon^2\Phi^{(2)} + \frac{1}{2}\epsilon^3\Phi^{(3)} + O(\epsilon^4), \tag{7}$$

$$\eta = \epsilon\eta^{(1)} + \epsilon^2\eta^{(2)} + \frac{1}{2}\epsilon^3\eta^{(3)} + O(\epsilon^4), \tag{8}$$

$$\sigma = \sigma^{(0)} + \epsilon\sigma^{(1)} + \frac{1}{2}\epsilon^2\sigma^{(2)} + O(\epsilon^3), \tag{9}$$

where ϵ = perturbation parameter; σ = angular frequency; and O()= order symbol. The superscripts $^{(1)}$, $^{(2)}$, and $^{(3)}$ denote quantities corresponding to the first-order, second-order and third-order perturbation solutions.

Goda and Abe(1968) developed a progressive wave theory for finite amplitude waves using a power series expansion. The results for a third-order progressive wave are as follows.

The perturbation functions of velocity potential are

$$\Phi^{(1)} = \frac{\sigma^{(0)}\coth k(y+h)}{k^2\sinh kh}\sin(kx-\sigma t), \tag{10}$$

$$\Phi^{(2)} = \frac{1}{k^2}\sigma^{(0)}\alpha_2^{(2)}\cosh 2k(y+h)\sin 2(kx-\sigma t), \tag{11}$$

$$\Phi^{(3)} = \frac{1}{k^2}\sigma^{(0)}\alpha_1^{(3)}\cosh 3k(y+h)\sin 3(kx-\sigma t), \tag{12}$$

in which

$$\alpha_2^{(2)} = \frac{3}{8}\frac{(c^4-1)}{\cosh 2kh},$$

$$\alpha_1^{(3)} = \frac{(c^2+3)(9c^5-22c^3+13c)}{32\cosh 3kh}.$$

The perturbation functions of vertical displacement are

$$\eta^{(1)} = \frac{1}{k}\cos(kx-\sigma t), \tag{13}$$

$$\eta^{(2)} = \frac{1}{k}\beta_1^{(2)}\cos 2(kx-\sigma t), \tag{14}$$

$$\eta^{(3)} = \frac{1}{k}\{\beta_1^{(3)}\cos(kx-\sigma t) + \beta_2^{(3)}\cos 3(kx-\sigma t)\}. \tag{15}$$

in which

$$\beta_1^{(2)} = \frac{3c^3 - c}{4},$$

$$\beta_1^{(3)} = \frac{3c^4 + 8c^2 - 9}{8},$$

$$\beta_2^{(3)} = \frac{3(9c^6 - 3c^4 + 3c^2 - 1)}{32}.$$

The perturbation functions of angular frequency are

$$\sigma^{(0)} = \sqrt{gk \tanh kh}, \tag{16}$$

$$\sigma^{(1)} = 0, \tag{17}$$

$$\sigma^{(2)} = k^2\sigma^{(0)}\frac{9c^4 - 10c^2 + 9}{8}, \tag{18}$$

in which k = wave number; and $c = \coth kh$.

When two incident waves of finite amplitude interact, the free surface conditions in eqs.(4) and (5) cannot be satisfied by a simple superposition of two waves. The two original waves propagating in the same direction deform as a result of the interaction, and the difference due to the deformation results in the formation of nonlinear bichromatic waves. The combination of two (the first and second) incident wave trains with different wave amplitudes, a_I and a_{II}, and a pair of discrete wave periods, T_I and T_{II} is considered here. The solution of bichromatic waves, therefore, must be composed of the first third-order incident wave, second third-order incident wave, and resonance effect. The velocity potential and the surface displacement of bichromatic waves are expressed as

$$\Phi = \epsilon\Phi_I^{(1)} + \epsilon^2\Phi_I^{(2)} + \frac{1}{2}\epsilon^3\Phi_I^{(3)} + \lambda\epsilon\Phi_{II}^{(1)} + (\lambda\epsilon)^2\Phi_{II}^{(2)} + \frac{1}{2}(\lambda\epsilon)^3\Phi_{II}^{(3)}$$
$$+\epsilon^2\Phi_F^{(2)} + \frac{1}{2}\epsilon^3\Phi_F^{(3)}, \tag{19}$$

$$\eta = \epsilon\eta_I^{(1)} + \epsilon^2\eta_I^{(2)} + \frac{1}{2}\epsilon^3\eta_I^{(3)} + \lambda\epsilon\eta_{II}^{(1)} + (\lambda\epsilon)^2\eta_{II}^{(2)} + \frac{1}{2}(\lambda\epsilon)^3\eta_{II}^{(3)}$$
$$+\epsilon^2\eta_F^{(2)} + \frac{1}{2}\epsilon^3\eta_F^{(3)}, \tag{20}$$

in which

$$\epsilon = a_I k_I, \quad and \quad \lambda = \frac{a_{II}k_{II}}{a_I k_I}.$$

In these equations, the subscripts I, II, and F denote the first incident wave, second incident wave, and resonance effect, respectively.

The angular frequency of the third-order incident wave increases with increasing wave amplitude if the wave number is given. For bichromatic waves, therefore, the angular frequency of each incident wave is disturbed in order to obtain the correction terms. Taking into account the secondary effect, the perturbations of angular frequencies are expressed as

$$\sigma_I = \sigma_I^{(0)} + \frac{1}{2}\epsilon^2(\sigma_I^{(2)} + \sigma_{IF}), \tag{21}$$

$$\sigma_{II} = \sigma_{II}^{(0)} + \frac{1}{2}\epsilon^2(\lambda\sigma_{II}^{(2)} + \sigma_{IIF}), \tag{22}$$

where σ_{IF} and σ_{IIF} denote the third-order angular frequencies induced by the interaction of the first and second incident waves, respectively. In the above equations, the first and third order perturbation frequencies are already given in eqs.(16) and (18).

Now, a generalized theory for a bichromatic wave system is formulated to the third order. The dynamical and kinematical free-surface boundary conditions are used to obtain linear partial differential equations for each order of the approximation. In formulating the expressions, it is convenient to replace the nonlinear free-surface boundary conditions in eqs.(4) and (5) by conditions to be satisfied about $y = 0$ instead of $y = \eta$. Expanding eqs.(4) and (5) into a Taylor series in y, and substituting eqs.(19), (20), (21) and (22) into these equations, the boundary conditions for the second and third powers are as follows.

The second-order equations are :

$$g\eta_F^{(2)} + \frac{\partial \Phi_F^{(2)}}{\partial t} = -\lambda\left(\frac{\sigma_I^{(0)}}{\sigma_I}\eta_{II}^{(1)}\frac{\partial^2 \Phi_I^{(1)}}{\partial t \partial y} + \frac{\sigma_{II}^{(0)}}{\sigma_{II}}\eta_I^{(1)}\frac{\partial^2 \Phi_{II}^{(1)}}{\partial t \partial y} + \frac{\partial \Phi_I^{(1)}}{\partial x}\frac{\partial \Phi_{II}^{(1)}}{\partial x} + \frac{\partial \Phi_I^{(1)}}{\partial y}\frac{\partial \Phi_{II}^{(1)}}{\partial y}\right), \quad (23)$$

$$\frac{\partial \Phi_F^{(2)}}{\partial y} - \frac{\partial \eta_F^{(2)}}{\partial t} = \lambda\left(\frac{\partial \eta_{II}^{(1)}}{\partial x}\frac{\partial \Phi_I^{(1)}}{\partial x} + \frac{\partial \eta_I^{(1)}}{\partial x}\frac{\partial \Phi_{II}^{(1)}}{\partial x} - \eta_{II}^{(1)}\frac{\partial^2 \Phi_I^{(1)}}{\partial y^2} - \eta_I^{(1)}\frac{\partial^2 \Phi_{II}^{(1)}}{\partial y^2}\right). \quad (24)$$

The third-order equations for $[\lambda]$ are :

$$\begin{aligned}
\frac{1}{2}\Big(g\eta_F^{(3)} &+ \frac{\partial \Phi_F^{(3)}}{\partial t} + \lambda\frac{\sigma_{IIF}}{\sigma_{II}}\frac{\partial \Phi_{II}^{(1)}}{\partial t}\Big) \\
= &- \lambda\frac{\sigma_{II}^{(0)}}{\sigma_{II}}\eta_I^{(2)}\frac{\partial^2 \Phi_{II}^{(1)}}{\partial t \partial y} - \lambda\frac{\sigma_I^{(0)}}{\sigma_I}\eta_{II}^{(1)}\frac{\partial^2 \Phi_I^{(2)}}{\partial t \partial y} - \frac{\sigma_I^{(0)}}{\sigma_I}\eta_F^{(2)}\frac{\partial^2 \Phi_I^{(1)}}{\partial t \partial y} - \eta_I^{(1)}\frac{\partial^2 \Phi_F^{(2)}}{\partial t \partial y} \\
&- \lambda\frac{\sigma_I^{(0)}}{\sigma_I}\eta_I^{(1)}\eta_{II}^{(1)}\frac{\partial^3 \Phi_I^{(1)}}{\partial t \partial y^2} - \frac{\lambda}{2}\frac{\sigma_{II}^{(0)}}{\sigma_{II}}\eta_I^{(1)^2}\frac{\partial^3 \Phi_{II}^{(1)}}{\partial t \partial y^2} - \lambda\eta_I^{(1)}\frac{\partial \Phi_I^{(1)}}{\partial x}\frac{\partial^2 \Phi_{II}^{(1)}}{\partial x \partial y} - \lambda\eta_{II}^{(1)}\frac{\partial \Phi_I^{(1)}}{\partial x}\frac{\partial^2 \Phi_I^{(1)}}{\partial x \partial y} \\
&- \lambda\eta_I^{(1)}\frac{\partial \Phi_{II}^{(1)}}{\partial x}\frac{\partial^2 \Phi_I^{(1)}}{\partial x \partial y} - \lambda\eta_I^{(1)}\frac{\partial \Phi_I^{(1)}}{\partial y}\frac{\partial^2 \Phi_{II}^{(1)}}{\partial y^2} - \lambda\eta_{II}^{(1)}\frac{\partial \Phi_I^{(1)}}{\partial y}\frac{\partial^2 \Phi_I^{(1)}}{\partial y^2} - \lambda\eta_I^{(1)}\frac{\partial \Phi_{II}^{(1)}}{\partial y}\frac{\partial^2 \Phi_I^{(1)}}{\partial y^2} \\
&- \lambda\frac{\partial \Phi_{II}^{(1)}}{\partial x}\frac{\partial \Phi_I^{(2)}}{\partial x} - \lambda\frac{\partial \Phi_{II}^{(1)}}{\partial y}\frac{\partial \Phi_I^{(2)}}{\partial y} - \frac{\partial \Phi_I^{(1)}}{\partial x}\frac{\partial \Phi_F^{(2)}}{\partial x} - \frac{\partial \Phi_I^{(1)}}{\partial y}\frac{\partial \Phi_F^{(2)}}{\partial y}, \qquad (25)
\end{aligned}$$

$$\begin{aligned}
\frac{1}{2}\Big(\frac{\partial \Phi_F^{(3)}}{\partial y} &- \frac{\partial \eta_F^{(3)}}{\partial t} - \lambda\frac{\sigma_{IIF}}{\sigma_{II}}\frac{\partial \eta_{II}^{(1)}}{\partial t}\Big) \\
= &- \lambda\eta_I^{(2)}\frac{\partial^2 \Phi_{II}^{(1)}}{\partial y^2} - \lambda\eta_{II}^{(1)}\frac{\partial^2 \Phi_I^{(2)}}{\partial y^2} - \eta_F^{(2)}\frac{\partial^2 \Phi_I^{(1)}}{\partial y^2} - \eta_I^{(1)}\frac{\partial^2 \Phi_F^{(2)}}{\partial y^2} \\
&- \lambda\eta_I^{(1)}\eta_{II}^{(1)}\frac{\partial^3 \Phi_{II}^{(1)}}{\partial y^3} - \frac{\lambda}{2}\eta_I^{(1)^2}\frac{\partial^3 \Phi_{II}^{(1)}}{\partial y^3} + \lambda\frac{\partial \eta_I^{(2)}}{\partial x}\frac{\partial \Phi_{II}^{(1)}}{\partial x} + \lambda\frac{\partial \eta_{II}^{(1)}}{\partial x}\frac{\partial \Phi_I^{(2)}}{\partial x} \\
&+ \lambda\frac{\partial \eta_F^{(2)}}{\partial x}\frac{\partial \Phi_I^{(1)}}{\partial x} + \lambda\frac{\partial \eta_I^{(1)}}{\partial x}\frac{\partial \Phi_F^{(2)}}{\partial x} + \lambda\eta_I^{(1)}\frac{\partial \eta_I^{(1)}}{\partial x}\frac{\partial^2 \Phi_{II}^{(1)}}{\partial x \partial y} + \lambda\eta_{II}^{(1)}\frac{\partial \eta_I^{(1)}}{\partial x}\frac{\partial^2 \Phi_I^{(1)}}{\partial x \partial y} \\
&+ \lambda\eta_I^{(1)}\frac{\partial \eta_{II}^{(1)}}{\partial x}\frac{\partial^2 \Phi_I^{(1)}}{\partial x \partial y}. \qquad (26)
\end{aligned}$$

The third-order equations for $[\lambda^2]$ are :

$$\frac{1}{2\lambda}(g\eta_F^{(3)} + \frac{\partial \Phi_F^{(3)}}{\partial t} + \frac{\sigma_{IF}}{\sigma_I}\frac{\partial \Phi_I^{(1)}}{\partial t}) = \cdots, \tag{27}$$

$$\frac{1}{2\lambda}(\frac{\partial \Phi_F^{(3)}}{\partial y} - \frac{\partial \eta_F^{(3)}}{\partial t} - \frac{\sigma_{IF}}{\sigma_I}\frac{\partial \eta_I^{(1)}}{\partial t}) = \cdots. \tag{28}$$

The right hand sides of eqs.(27) and (28) are same as those of eqs.(25) and (26) except for the subscripts I and II which are switched.

By differentiating eq.(23) with respect to t, eliminating η_{F1} from eqs.(23) and (24), and substituting the expressions for $\Phi_I^{(1)}$, $\Phi_{II}^{(1)}$, $\eta_I^{(1)}$, and $\eta_{II}^{(1)}$ into the combined equation, the free-surface boundary condition on $y = 0$ is given by

$$g\frac{\partial \Phi_F^{(2)}}{\partial y} + \frac{\partial^2 \Phi_F^{(2)}}{\partial t^2} = \frac{\lambda}{2k_I k_{II}}\{(\gamma_{11} + \gamma_{12})\sin(\chi_I - \chi_{II}) + (\gamma_{21} - \gamma_{22})\sin(\chi_I + \chi_{II})\}, \tag{29}$$

in which

$$\begin{aligned}
\gamma_{11} &= (\sigma_I - \sigma_{II})\{{\sigma_I^{(0)}}^2 + {\sigma_{II}^{(0)}}^2 - \sigma_I^{(0)}\sigma_{II}^{(0)}(1 + c_I c_{II})\}, \\
\gamma_{12} &= (\frac{k_{II}}{k_I}\sigma_I^{(0)}\sigma_I^2 + \sigma_{II}^{(0)}\sigma_{II}^2 - \frac{k_I}{k_{II}}\sigma_{II}^{(0)}\sigma_{II}^2 - \sigma_I^{(0)}\sigma_I^2), \\
\gamma_{21} &= (\sigma_I + \sigma_{II})\{{\sigma_I^{(0)}}^2 + {\sigma_{II}^{(0)}}^2 + \sigma_I^{(0)}\sigma_{II}^{(0)}(1 - c_I c_{II})\}, \\
\gamma_{22} &= (\frac{k_{II}}{k_I}\sigma_I^{(0)}\sigma_I^2 + \sigma_{II}^{(0)}\sigma_{II}^2 + \frac{k_I}{k_{II}}\sigma_{II}^{(0)}\sigma_{II}^2 + \sigma_I^{(0)}\sigma_I^2),
\end{aligned}$$

where $\chi_I = k_I x - \sigma_I t$; and $\chi_{II} = k_{II} x - \sigma_{II} t$. Eqs.(3), (6) and (29) are satisfied by

$$\Phi_F^{(2)} = \frac{\lambda}{k_I k_{II}}\{\alpha_{F1}^{(2)}\sin(\chi_I - \chi_{II}) + \alpha_{F2}^{(2)}\sin(\chi_I + \chi_{II})\}, \tag{30}$$

in which

$$\begin{aligned}
\alpha_{F1}^{(2)} &= \frac{\gamma_{11} + \gamma_{12}}{2\cosh(k_I - k_{II})h}\frac{\cosh(k_I - k_{II})(y + h)}{\omega'_{I-II} - (\sigma_I - \sigma_{II})^2}, \\
\alpha_{F2}^{(2)} &= \frac{\gamma_{21} + \gamma_{22}}{2\cosh(k_I - k_{II})h}\frac{\cosh(k_I + k_{II})(y + h)}{\omega'_{I+II} - (\sigma_I + \sigma_{II})^2}.
\end{aligned}$$

The corresponding surface displacement is obtained by substituting eq.(30) into eq.(23). Finally the second-order surface displacement by the resonance effect are obtained as

$$\eta_F^{(2)} = \frac{\lambda}{2gk_I k_{II}}\{\beta_{F1}^{(2)}\cos(\chi_I - \chi_{II}) + \beta_{F2}^{(2)}\cos(\chi_I + \chi_{II})\}, \tag{31}$$

in which

$$\begin{aligned}
\beta_{F1}^{(2)} &= \frac{\omega'_{I-II}\gamma_{11} - (\sigma_I - \sigma_{II})^2\gamma_{12}}{(\sigma_I - \sigma_{II})\{\omega'_{I-II} - (\sigma_I - \sigma_{II})^2\}}, \\
\beta_{F2}^{(1)} &= \frac{\omega'_{I+II}\gamma_{21} + (\sigma_I + \sigma_{II})^2\gamma_{12}}{(\sigma_I + \sigma_{II})\{\omega'_{I+II} - (\sigma_I + \sigma_{II})^2\}}, \\
\omega'_{I-II} &= g(k_I - k_{II})\tanh(k_I - k_{II})h, \\
\omega'_{I+II} &= g(k_I + k_{II})\tanh(k_I + k_{II})h.
\end{aligned}$$

The second-order surface displacement by the resonance effect have two components with wave numbers and frequencies consisting of the sums and differences of those of the first and second incident waves. These amplitudes are bounded in time and their magnitude is dependent on the water depth.

To find the third-order velocity potential $\Phi_F^{(3)}$ and surface displacement $\eta_F^{(3)}$, the same procedure is followed in the second-order approximation. Eliminating $\eta_F^{(3)}$ from eqs.(25) and (26), the combined free-surface boundary condition on $y = 0$ is obtained for $[\lambda]$ as

$$\begin{aligned} g\frac{\partial \Phi_F^{(3)}}{\partial y} &+ \frac{\partial \Phi_F^{(3)}}{\partial t^2} - \frac{2\lambda\sigma_{IIF}}{k_{II}}\left(\frac{\sigma_{II}\sigma_{II}^{(0)}c_{II}}{k_{II}} + \frac{g}{2}\right)\sin\chi_{II} \\ &= \frac{2\lambda}{k_I k_{II}}[\{(2\sigma_I - \sigma_{II})b_1 + gb_4\}\sin(2\chi_I - \chi_{II}) \\ &+ \{(2\sigma_I + \sigma_{II})b_2 + gb_5\}\sin(2\chi_I + \chi_{II}) + (\sigma_{II}b_3 + gb_6)\sin\chi_{II}], \end{aligned} \tag{32}$$

in which

$$\begin{aligned} b_1 &= \frac{\sigma_{II}^{(0)^2}\beta_{I1}^{(2)}}{2} + 2\sigma_I^{(0)^2}\alpha_{I2}^{(2)}\sinh 2k_I h - \sigma_I^{(0)}\sigma_{II}^{(0)}\alpha_{I2}^{(2)}(c_{II}\cosh 2k_I h + \sinh 2k_I h) \\ &+ \frac{\sigma_{II}^{(0)^2}k_{II}c_{II}}{8k_I} - \frac{\sigma_I^{(0)}\sigma_{II}^{(0)}k_{II}(c_I + c_{II})}{4k_I} - \frac{\sigma_I^{(0)}\sigma_{II}^{(0)}c_{II}}{2} + \frac{\sigma_I^{(0)^2}c_I}{4} \\ &+ \frac{\sigma_I^{(0)^2}\{\omega'_{I-II}\gamma_{11} + (\sigma_I - \sigma_{II})^2\gamma_{12}\}}{4gk_I(\sigma_I - \sigma_{II})\{\omega'_{I-II} - (\sigma_I - \sigma_{II})^2\}} + \frac{(\gamma_{11} + \gamma_{12})(\sigma_I - \sigma_{II})\omega'_{I-II}}{4gk_I\{\omega'_{I-II} - (\sigma_I - \sigma_{II})^2\}} \\ &- \frac{\sigma_I^{(0)}c_I(\gamma_{11} + \gamma_{12})(k_I - k_{II})}{4\{\omega'_{I-II} - (\sigma_I - \sigma_{II})^2\}} + \frac{\sigma_I^{(0)}(\gamma_{21} - \gamma_{22})\omega'_{I+II}}{4gk_I\{\omega'_{I+II} - (\sigma_I + \sigma_{II})^2\}} \end{aligned}$$

$$\begin{aligned} b_2 &= \frac{\sigma_{II}^{(0)^2}\beta_{I1}^{(2)}}{2} + 2\sigma_I^{(0)^2}\alpha_{I2}^{(2)}\sinh 2k_I h - \sigma_I^{(0)}\sigma_{II}^{(0)}\alpha_{I2}^{(2)}(c_{II}\cosh 2k_I h - \sinh 2k_I h) \\ &+ \frac{\sigma_{II}^{(0)^2}k_{II}c_{II}}{8k_I} - \frac{\sigma_I^{(0)}\sigma_{II}^{(0)}k_{II}(c_I - c_{II})}{4k_I} + \frac{\sigma_I^{(0)^2}c_I}{4} \\ &+ \frac{\sigma_I^{(0)^2}\{\omega'_{I+II}\gamma_{21} + (\sigma_I + \sigma_{II})^2\gamma_{22}\}}{4gk_I(\sigma_I + \sigma_{II})\{\omega'_{I+II} - (\sigma_I + \sigma_{II})^2\}} + \frac{(\gamma_{21} - \gamma_{22})(\sigma_I + \sigma_{II})\omega'_{I+II}}{4gk_I\{\omega'_{I+II} - (\sigma_I + \sigma_{II})^2\}} \\ &- \frac{\sigma_I^{(0)}c_I(\gamma_{21} - \gamma_{22})(k_I + k_{II})}{4\{\omega'_{I+II} - (\sigma_I + \sigma_{II})^2\}} + \frac{\sigma_I^{(0)}(\gamma_{11} + \gamma_{12})\omega'_{I-II}}{4gk_I\{\omega'_{I-II} - (\sigma_I - \sigma_{II})^2\}} \end{aligned}$$

$$\begin{aligned} b_3 &= \frac{\sigma_{II}^{(0)^2}k_{II}c_{II}}{4k_I} - \frac{\sigma_I^{(0)}\sigma_{II}^{(0)}k_{II}c_I}{2k_I} - \frac{\sigma_I^{(0)}\sigma_{II}^{(0)}c_{II}}{2} - \frac{\sigma_{II}^{(0)^2}c_I}{2} \\ &+ \frac{\sigma_I^{(0)^2}\{\omega'_{I-II}\gamma_{11} + (\sigma_I - \sigma_{II})^2\gamma_{12}\}}{4gk_I(\sigma_I - \sigma_{II})\{\omega'_{I-II} - (\sigma_I - \sigma_{II})^2\}} + \frac{(\gamma_{11} + \gamma_{12})(\sigma_I - \sigma_{II})\omega'_{I-II}}{4gk_I\{\omega'_{I-II} - (\sigma_I - \sigma_{II})^2\}} \\ &- \frac{\sigma_I^{(0)}c_I(\gamma_{11} + \gamma_{12})(k_I - k_{II})}{4\{\omega'_{I-II} - (\sigma_I - \sigma_{II})^2\}} - \frac{\sigma_I^{(0)}(\gamma_{11} + \gamma_{12})\omega'_{I-II}}{4gk_I\{\omega'_{I-II} - (\sigma_I - \sigma_{II})^2\}} \end{aligned}$$

$$+ \frac{\sigma_I^{(0)^2}\{\omega'_{I+II}\gamma_{21} - (\sigma_I+\sigma_{II})^2\gamma_{22}\}}{4gk_I(\sigma_I+\sigma_{II})\{\omega'_{I+II} - (\sigma_I+\sigma_{II})^2\}} + \frac{(\gamma_{21}-\gamma_{22})(\sigma_I+\sigma_{II})\omega'_{I+II}}{4gk_I\{\omega'_{I+II} - (\sigma_I+\sigma_{II})^2\}}$$

$$- \frac{\sigma_I^{(0)}c_I(\gamma_{21}-\gamma_{22})(k_I+k_{II})}{4\{\omega'_{I+II} - (\sigma_I+\sigma_{II})^2\}} - \frac{\sigma_I^{(0)}(\gamma_{21}-\gamma_{22})\omega'_{I+II}}{4gk_I\{\omega'_{I+II} - (\sigma_I+\sigma_{II})^2\}}$$

$$b_4 = -\frac{\beta_{I1}^{(2)}\sigma_{II}^{(0)}k_{II}c_{II}}{2} - \alpha_{I2}^{(2)}k_{II}\cosh 2k_Ih - 2\alpha_{I2}^{(2)}\sigma_I^{(2)}k_I\cosh 2k_Ih - \beta_{I1}^{(2)}\sigma_I^{(0)}k_Ic_I$$

$$- \frac{\sigma_{II}^{(0)}k_{II}}{8k_I} - \frac{\sigma_I^{(0)}k_{II}}{4} - \frac{\sigma_I^{(0)}k_I}{2} - \frac{\sigma_{II}^{(0)}k_{II}}{4}$$

$$- \frac{\sigma_I^{(0)^2}c_I\{\omega'_{I+II}\gamma_{21} - (\sigma_I+\sigma_{II})^2\gamma_{22}\}}{4g(\sigma_I+\sigma_{II})\{\omega'_{I+II} - (\sigma_I+\sigma_{II})^2\}} - \frac{\sigma_I^{(0)}c_I(k_I+k_{II})\{\omega'_{I+II}\gamma_{21} - (\sigma_I+\sigma_{II})^2\gamma_{22}\}}{4gk_I(\sigma_I+\sigma_{II})\{\omega'_{I+II} - (\sigma_I+\sigma_{II})^2\}}$$

$$- \frac{(\gamma_{21}-\gamma_{22})(k_I+k_{II})}{4\{\omega'_{I+II} - (\sigma_I+\sigma_{II})^2\}} - \frac{(\gamma_{11}+\gamma_{12})(k_I-k_{II})^2}{4k_I\{\omega'_{I+II} - (\sigma_I-\sigma_{II})^2\}}$$

$$b_5 = \frac{\beta_{I1}^{(2)}\sigma_{II}^{(1)}k_{II}c_{II}}{2} + \alpha_{I2}^{(2)}k_{II}\cosh 2k_Ih - 2\alpha_{I2}^{(2)}\sigma_I^{(0)}k_I\cosh 2k_Ih - \beta_{I1}^{(2)}\sigma_I^{(0)}k_Ic_{II}$$

$$+ \frac{\sigma_{II}^{(0)}k_{II}^2}{8k_I} + \frac{\sigma_I^{(0)}k_{II}}{4} - \frac{\sigma_I^{(0)}k_I}{2} - \frac{\sigma_{II}^{(0)}k_{II}}{4}$$

$$- \frac{\sigma_I^{(0)}c_I\{\omega'_{I-II}\gamma_{11} + (\sigma_I-\sigma_{II})^2\gamma_{12}\}}{4g(\sigma_I-\sigma_{II})\{\omega'_{I-II} - (\sigma_I-\sigma_{II})^2\}} - \frac{\sigma_I^{(0)}c_I(k_I-k_{II})\{\omega'_{I-II}\gamma_{11} + (\sigma_I-\sigma_{II})^2\gamma_{12}\}}{4gk_I(\sigma_I-\sigma_{II})\{\omega'_{I-II} - (\sigma_I-\sigma_{II})^2\}}$$

$$- \frac{(\gamma_{11}+\gamma_{12})(k_I-k_{II})}{4\{\omega'_{I-II} - (\sigma_I-\sigma_{II})^2\}} - \frac{(\gamma_{21}-\gamma_{22})(k_I+k_{II})^2}{4k_I\{\omega'_{I+II} - (\sigma_I+\sigma_{II})^2\}}$$

$$b_6 = -\frac{\sigma_{II}^{(0)}k_{II}^2}{4k_I} - \frac{\sigma_I^{(0)}k_{II}}{2}$$

$$- \frac{\sigma_I^{(0)}c_I\{\omega'_{I-II}\gamma_{11} + (\sigma_I-\sigma_{II})^2\gamma_{12}\}}{4g(\sigma_I-\sigma_{II})\{\omega'_{I-II} - (\sigma_I-\sigma_{II})^2\}} - \frac{(\gamma_{11}+\gamma_{12})(k_I-k_{II})^2}{4k_I\{\omega'_{I-II} - (\sigma_I-\sigma_{II})^2\}}$$

$$+ \frac{\sigma_I^{(0)}c_I(k_I-k_{II})\{\omega'_{I-II}\gamma_{11} + (\sigma_I-\sigma_{II})^2\gamma_{12}\}}{4gk_I(\sigma_I-\sigma_{II})\{\omega'_{I-II} - (\sigma_I-\sigma_{II})^2\}} - \frac{(\gamma_{11}+\gamma_{12})(k_I-k_{II})}{4\{\omega'_{I-II} - (\sigma_I-\sigma_{II})^2\}}$$

$$+ \frac{\sigma_I^{(0)}c_I\{\omega'_{I+II}\gamma_{21} - (\sigma_I+\sigma_{II})^2\gamma_{22}\}}{4g(\sigma_I+\sigma_{II})\{\omega'_{I+II} - (\sigma_I+\sigma_{II})^2\}} + \frac{(\gamma_{21}-\gamma_{22})(k_I+k_{II})^2}{4k_I\{\omega'_{I+II} - (\sigma_I+\sigma_{II})^2\}}$$

$$- \frac{\sigma_I^{(0)}c_I(k_I+k_{II})\{\omega'_{I+II}\gamma_{21} - (\sigma_I+\sigma_{II})^2\gamma_{22}\}}{4gk_I(\sigma_I+\sigma_{II})\{\omega'_{I+II} - (\sigma_I+\sigma_{II})^2\}} + \frac{(\gamma_{21}-\gamma_{22})(k_I+k_{II})}{4\{\omega'_{I+II} - (\sigma_I+\sigma_{II})^2\}}.$$

The final results of $\Phi_F^{(3)}$, $\eta_F^{(3)}$, σ_{IF}, and σ_{IIF} become

$$\Phi_F^{(3)} = \lambda[\frac{\psi_1}{k_Ik_{II}\cosh(2k_I-k_{II})h}\{2\sin\frac{2\sigma_I-\sigma_{II}+\sigma_{F1}}{2}t\sin\frac{2\sigma_I-\sigma_{II}-\sigma_{F1}}{2}t\sin(2k_I-k_{II})x$$

$$+ \sin(2\sigma_I-\sigma_{II})t\cos(2k_I-k_{II})x\}\cosh(2k_I-k_{II})(y+h)$$

$$+ \frac{\psi_2}{k_I k_{II}\cosh(2k_I+k_{II})h}\{2\sin\frac{2\sigma_I+\sigma_{II}+\sigma_{F2}}{2}t\sin\frac{2\sigma_I+\sigma_{II}-\sigma_{F2}}{2}t\sin(2k_I+k_{II})x$$

$$+ \sin(2\sigma_I+\sigma_{II})t\cos(2k_I+k_{II})x\}\cosh(2k_I+k_{II})(y+h)]$$

$$+ \lambda[\textit{same as the above except for the subscripts I and II being switched}], \quad (33)$$

$$\eta_F^{(3)} = \frac{\lambda}{gk_Ik_{II}}[-\psi_1\{(2\sigma_I-\sigma_{II}+\sigma_{F1})\cos\frac{2\sigma_I-\sigma_{II}+\sigma_{F1}}{2}t\sin\frac{2\sigma_I-\sigma_{II}-\sigma_{F1}}{2}t$$

$$+ (2\sigma_I-\sigma_{II}+\sigma_{F1})\sin\frac{2\sigma_I-\sigma_{II}+\sigma_{F1}}{2}t\cos\frac{2\sigma_I-\sigma_{II}-\sigma_{F1}}{2}t\}\sin(2k_I-k_{II}x)$$

$$- \psi_2\{(2\sigma_I+\sigma_{II}+\sigma_{F2})\cos\frac{2\sigma_I+\sigma_{II}+\sigma_{F2}}{2}t\sin\frac{2\sigma_I+\sigma_{II}-\sigma_{F2}}{2}t$$

$$+ (2\sigma_I+\sigma_{II}-\sigma_{F2})\sin\frac{2\sigma_I+\sigma_{II}+\sigma_{F2}}{2}t\cos\frac{2\sigma_I+\sigma_{II}-\sigma_{F2}}{2}t\}\sin(2k_I+k_{II}x)$$

$$+ (2b_1-\psi_1\frac{2\sigma_I-\sigma_{II}}{2})\cos(2\chi_I-\chi_{II})-\psi_1\frac{2\sigma_I-\sigma_{II}}{2}\cos\{(2k_I-k_{II})x+(2\sigma_I-\sigma_{II})t\}$$

$$+ (2b_2-\psi_2\frac{2\sigma_I+\sigma_{II}}{2})\cos(2\chi_I+\chi_{II})-\psi_2\frac{2\sigma_I+\sigma_{II}}{2}\cos\{(2k_I+k_{II})x+(2\sigma_I+\sigma_{II})t\}$$

$$+ \frac{2g(b_3k_{II}-2b_6\sigma_{II}^{(0)}c_{II}}{2\sigma_{II}\sigma_{II}^{(0)}c_{II}+gk_{II}}\cos\chi_{II}]$$

$$+ \frac{\lambda^2}{gk_Ik_{II}}[\textit{same as the above except for the subscripts I and II being switched}], \quad (34)$$

$$\sigma_{IF} = -\frac{2\lambda^2k_I(\sigma_Ib_3+gb_6)}{k_{II}(2\sigma_I\sigma_I^{(0)}c_I+gk_I)}, \quad (35)$$

$$\sigma_{IIF} = -\frac{2k_{II}(\sigma_Ib_3+gb_6)}{k_I(2\sigma_{II}\sigma_{II}^{(0)}c_{II}+gk_{II})}, \quad (36)$$

in which

$$\psi_1 = \frac{2\{(2\sigma_I-\sigma_{II})b_1+gb_4\}}{(2\sigma_I-\sigma_{II})^2-\sigma_{F1}^2},$$

$$\psi_2 = \frac{2\{(2\sigma_I+\sigma_{II})b_2+gb_5\}}{(2\sigma_I+\sigma_{II})^2-\sigma_{F2}^2},$$

$$\sigma_{F1}^2 = g(2k_I-k_{II})\tanh(2k_I-k_{II})h,$$

$$\sigma_{F2}^2 = g(2k_I+k_{II})\tanh(2k_I+k_{II})h.$$

Since $2\sigma_I-\sigma_{II}$ is nearly equal to σ_{F1} in eq.(34), the trigonometric functions $\sin\frac{2\sigma_I-\sigma_{II}-\sigma_{F1}}{2}t$ and $\cos\frac{2\sigma_I-\sigma_{II}-\sigma_{F1}}{2}t$ are slowly varying in comparison with the functions $\sin\frac{2\sigma_I+\sigma_{II}-\sigma_{F1}}{2}t$ and $\cos\frac{2\sigma_I+\sigma_{II}-\sigma_{F1}}{2}t$. The low-frequency factor on $\frac{2\sigma_I-\sigma_{II}-\sigma_{F1}}{2}t$ induces an amplitude modulation on the high-frequency factor on $\frac{2\sigma_I+\sigma_{II}-\sigma_{F1}}{2}t$. The resulting modulated oscillation causes the phenomenon of beats, which are limited to the initial stage.

Experiments

For the purpose of verifying the present wave theory, experiments were conducted in the 26-m-long, 0.5-m-wide, and 0.8-m-deep wave tank at Tokyo Metropolitan University. A piston-type wave generator is placed at one end of the tank, and a wave-absorber is installed at the opposite end to reduce the wave reflection. A series of electronic signals were produced by an arbitrary wave-form synthesizer, which controlled the motion of wave paddle. The surface elevations were measured using resistance wave gauges at four horizontal locations, 10.0, 12.5, 15.0, and 17.5m from the wave paddle. The water depth was varied from 20 to 40cm. In each water depth, several strokes of paddle motion were prescribed. The bichromatic waves composed of a pair of cosine waves have two incident wave amplitudes a_I and a_{II}, and two incident wave periods T_I and T_{II}. The wave conditions used in the present experiment were $T_I = 0.5sec$ and $T_{II} = 0.55sec$, or $T_I = 0.5sec$ and $T_{II} = 0.6sec$ for a pair of bichromatic wave periods and $a_I : a_{II} = 1 : 1, 1 : 2$, or $2 : 1$ for the corresponding ratio of two incident wave amplitudes. In each experimental condition, wave data were collected from four wave gauges continuously at a frequency of 47Hz for about three minutes in order to provide data samples sufficiently long for FFT analyses.

Results

A series of wave records observed at four fixed points and these amplitude spectra are shown in Fig.1. The abscissa and ordinate in figure(a) show the time in seconds, and the surface displacement above the still water level in cm, respectively, while those in figure(b) show the frequency in Hz, and the amplitude in cm, respectively. The periods of the first and second incident waves are $T_I = 0.5sec$ and $T_{II} = 0.55sec$, and the ratio of the first incident wave amplitude to the second incident wave amplitude is $a_I : a_{II} = 1 : 1$. In this case, the water depth is $h = 40cm$. The measured wave profiles are different from the input bichromatic-wave signal, by which the wave paddle motion is prescribed. The wave train at each location exhibits an appreciable modulation, even though the wave form itself is nearly uniform at each point. The modulation becomes smaller as the waves propagate from the wave paddle to the opposite end of the wave tank. Each spectrum contains four major frequency components within relatively narrow range of frequencies. The third-order frequency components by the wave interaction at x=10m are the largest; they decrease their amplitudes rapidly toward the end of the wave tank. Fig.2 shows similar plots of the bichromatic waves for $T_I = 0.5sec$, $T_{II} = 0.6sec$, $a_I : a_{II} = 1 : 1$, and $h = 40cm$. The modulation is not so large in this case. The basic profile of wave train remains the same throughout the entire process. The carrier-frequency and second-harmonic components of incident waves are quite evident but the third-order frequency components by the wave interaction are not seen clearly in the spectrum. The energy transfer within the spectrum is not appreciable, while the dissipation of the total energy is small.

Several free-surface elevations obtained from four different experiments are compared to theoretical results computed by the third-order perturbation equation[(20)]. To describe the natural profile of bichromatic wave train, each calculated

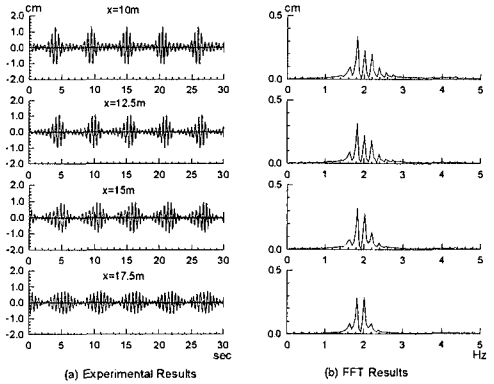

Fig.1 Surface displacements of bichromatic wave train and FFT analyses for $T_I = 0.5sec, T_{II} = 0.55sec, a_I : a_{II} = 1 : 1$, and $h = 40cm$.

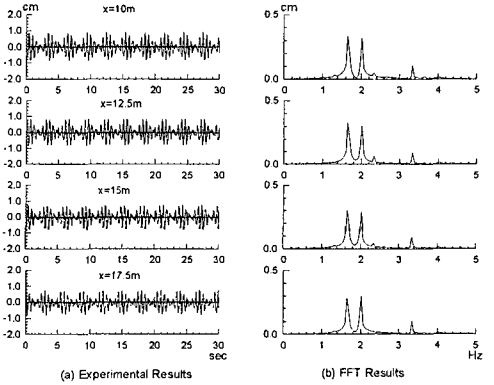

Fig.2 Surface displacements of bichromatic wave train and FFT analyses for $T_I = 0.5sec, T_{II} = 0.6sec, a_I : a_{II} = 1 : 1$, and $h = 40cm$.

value is plotted for thirty seconds at intervals of 0.02 sec. Comparisons of the measured free-surface displacements with the theoretical ones are presented in Figs.3-6. In these figures, (a) shows the experimental data plot, and (b) shows the theoretical profile. A set of time series for $T_I = 0.5sec$, $T_{II} = 0.55sec$, $a_I : a_{II} = 1 : 1$, and $h = 40cm$ are presented in Fig.3(a). The modulation caused by the interaction of two incident waves occurs in all locations, and the resonant nonlinear interaction leads to the disintegration of the wave envelope. The original periods of incident waves, however, remain constant throughout the process of the modulation. Fig.3(b) shows an example of calculated wave profiles for a pair of initial amplitudes, $a_I = a_{II} = 0.37cm$. These initial amplitudes were determined from actual free-surface measurements by the wave gauge at $x = 10m$. Fig.4 shows a comparison of the measured data for $T_I = 0.5sec$, $T_{II} = 0.55sec$, $a_I : a_{II} = 1 : 1$ and $h = 20cm$, and the theoretical calculation for $a_I = a_{II} = 0.34cm$. Although the pe-

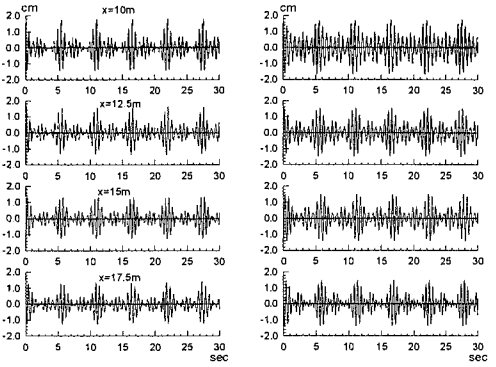

Fig.3 Measured and calculated surface displacements ($T_I = 0.5sec, T_{II} = 0.55sec, a_I : a_{II} = 1 : 1$, and $h = 40cm$).

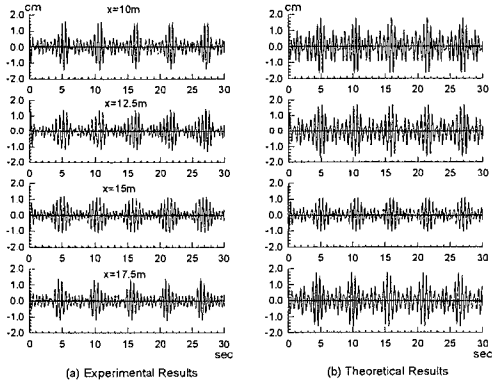

Fig.4 Measured and calculated surface displacements ($T_I = 0.5sec, T_{II} = 0.55sec, a_I : a_{II} = 1 : 1$, and $h = 20cm$).

riods of the first and second incident waves and the ratio of amplitudes of them are the same as those in the previous case, the water depth is shallower. In this case, the modulation is also found at all locations. A basic difference to the previous experiment for $h = 40cm$ is observed under the nodes of the envelope. Fig.5 presents a set of time series for $T_I = 0.5sec$, $T_{II} = 0.55sec$ and $a_I : a_{II} = 1 : 2$, in the water depth of $h = 20cm$, and the calculated surface displacements for $a_I = 0.22cm$ and $a_{II} = 0.44cm$. The agreement between the measured data and the theoretical result is reasonable on the tendency of a change of wave train. Fig.6 shows a set of temporal records of surface displacements for $T_I = 0.5sec$, $T_{II} = 0.6sec$, $a_I : a_{II} = 1 : 2$ and $h = 20cm$. The theoretical results were calculated by the present third-order bichromatic wave equation for $a_I = 0.38cm$ and $a_{II} = 0.76cm$. The measured data are well described by the theoretical curves in spite of such difference in the two wave periods and amplitudes.

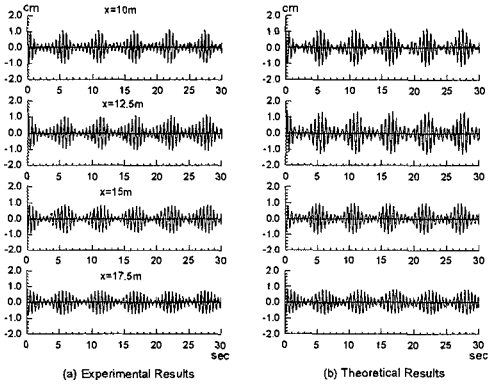

Fig.5 Measured and calculated surface displacements ($T_I = 0.5ecs, T_{II} = 0.55sec, a_I : a_{II} = 1 : 2$, and $h = 20cm$).

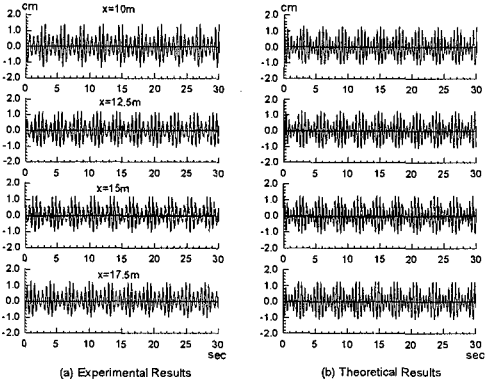

Fig.6 Measured and calculated surface displacements ($T_I = 0.5sec, T_{II} = 0.6sec, a_I : a_{II} = 1 : 2$, and $h = 20cm$).

Conclusions

The equation based on a finite-amplitude approximation was derived to calculate the surface displacements of bichromatic waves in water of intermediate depth. Experiments were also performed to investigate the modulation of bichromatic wave train in our wave tank. From the results of this study, the following conclusions are drawn.

When a wave train is generated by a pure bichromatic-wave paddle motion, the wave train usually modulates in the wave tank. This tendency is more prominent when the difference of the first and second incident wave periods become small; accordingly, measurable modulation did not develop in our tank length, when the bichromatic waves with the periods $T_I = 0.5sec$ and $T_{II} = 0.6sec$ were generated. The water depth affects to the disintegration of wave train; indeed, the modulation

tends to disintegrate into smaller wave envelopes when the water depth increases. The third-order amplitudes by the wave interaction are larger than the first-order amplitudes when the difference between the first and second incident wave periods is smaller. The results obtained in this study are physically valid over the range of our interest.

References

Benjamin, T.B. (1967) : Instability of periodic wave trains in nonlinear dispersive systems, Proc. Roy. Soc. A 299, 59-75.

Benjamin, T.B. and Feir, J.E. (1967) : The disintegration of wave trains in deep water. Part 1. Theory, J. Fluid Mech. 27, 417-430.

Chu, V.C. and Mei, C.C. (1970) : On slowly varying Stokes waves, J. Fluid Mech. 41, 873-887.

Goda, Y. and Abe, Y. (1968) : Apparent coefficient of partial reflection of finite amplitude waves, Rep. Port and Harb. Res. Inst. 7(3), 3-58.

Lighthill, M.J. (1967) : Some special cases treated by the Whitham theory, Proc. Roy. Soc. A 299, 28-53.

Stansberg, C.T. (1994) : Effects from directionality and spectral bandwidth on non-linear spatial modulations of deep-water surface gravity wave trains, Proc. Int. Conf. Coastal Eng. 24, 579-593.

Whitham, G.B. (1965) : A general approach to linear and non-linear dispersive waves using a Lagrangian, J. Fluid Mech. 22, 273-283.

Yuen, H.C. and Lake, B.M. (1975) : Nonlinear deep water waves, Theory and experiment, Phys. Fluids, 18(8), 956-960.

Zakharov, V.E. (1968) : Stability of periodic waves of finite amplitude on the surface of a deep fluid, J. Appl. Mech. Tech. Phys. 2, 190-194.

Zakharov, V.E. and Shabat, A.B. (1972) : Exact theory of two-dimensional self-focusing and one-dimensional self-modulating waves in nonlinear media, Sov. Phys. J. Exp. Theor. Phys. 34, 62-69.

SIMULATION OF NONLINEAR WAVE DEFORMATION BY A SHOAL IN 3D

Paul de Haas [1] and Maarten Dingemans [1]

Abstract

Three-dimensional propagating nonlinear waves can be simulated with a time-domain numerical model based on a boundary integral equation method. For the simulation of nonlinear wave deformation by a shoal, a domain decomposition method is used to increase the efficiency of the model. Features and efficiency of the domain decomposition method are described and its application to the shoal problem is discussed.

1 Introduction

In the modelling of refraction and shoaling of waves, it is important to describe the nonlinear free-surface boundary conditions properly. It is known, for example, that non-linearity opposes convergence and divergence of wave ray paths. In order to assure the correctness of modelling non-linearity, physical experiments are often used.

We present a three-dimensional time-domain numerical model, based on a boundary integral equation method, which computes the propagation of waves with the exact nonlinear boundary conditions over an arbitrary bottom geometry. This method is therefore able to provide additional material suitable for verification. The results of a computation of the model are compared with the shoal experiment (Berkhoff et al. (1982)) in order to determine the accuracy of the model. Because the study of such problems requires large computational effort, the use of efficient numerical techniques is imperative. Here we present a domain decomposition method which reduces the computational costs of the boundary integral equation method considerably.

This paper is organized as follows. First the numerical model is described in Section 2. In Section 3 the domain decomposition method is described and its

[1]Delft Hydraulics, P.O. Box 177, 2600 MH Delft, The Netherlands

efficiency is discussed. In Section 4 the application of the domain decomposition technique to the shoal problem is discussed. Finally some conclusions will be stated in Section 5.

2 Numerical model

2.1 Description

In the mathematical model for nonlinear water waves considered here, the motion of the water is described by the usual potential-flow equations for inviscid irrotational fluid motion with a free surface on water of varying depth. It is described by the field equation for the velocity potential ϕ (Laplace's equation)

$$\Delta\phi = 0, \tag{1}$$

and the boundary conditions on the free surface $\partial\Omega_{FS}$

$$\left.\begin{aligned} \frac{D\phi}{Dt} &= \frac{1}{2}(\nabla\phi)^2 - gz - \frac{p}{\rho} \\ \frac{D\boldsymbol{x}}{Dt}\cdot\boldsymbol{n} &= \frac{\partial\phi}{\partial n} \end{aligned}\right\} \quad \boldsymbol{x} \in \partial\Omega_{FS} \tag{2}$$

and on the bottom $\partial\Omega_B$

$$\frac{\partial\phi}{\partial n} = 0, \ \boldsymbol{x} \in \partial\Omega_B. \tag{3}$$

Appropriate in- and outflow boundary conditions are formulated on the lateral boundaries.

The numerical model consists of a time marching scheme for the evolution of the free surface and its boundary conditions. At every time-step, Laplace's equation for the velocity potential is solved by using a boundary integral equation method (BIEM). In the BIEM, only the boundary of the fluid domain is discretized into quadrangular panels represented by a collocation point in the centre of the panel. For each collocation point a Fredholm integral equation of the second kind equivalent with Laplace's equation is formulated (see e.g. Broeze (1993)). These integral equations are discretized and by using the boundary conditions a system of linear equations is built and subsequently solved. Insertion into equations (2) of the solution obtained in this way, provides the time derivatives which are needed for the time marching scheme.

For the time integration of the collocation points, a Lagrangian description is used in combination with (small) tangential correction velocities to control the grid motion. In the present implementation the Lagrangian description is required to obtain stability near the inflow boundaries, see Broeze (1993). The lateral boundaries move along with the free-surface grid with uniform velocities over each vertical. Due to the Lagrangian motion the grid distorts during the time-domain simulation. For this reason a mixed Eulerian-Lagrangian description is preferred which controls the grid in the inside of the domain and retains the

stability. This is however not implemented in the model yet but seems to be of importance to be used in combination with domain decomposition, as will be pointed out in Section 4. See furthermore Broeze (1993) for a more detailed description of the method employed here.

Boundary integral equation methods are very suitable for solving Laplace's equation on such domains because they only require a discretization of the boundary of the domain. Compared with field discretization methods, the advantages of a BIEM are a much smaller amount of grid points and a natural description of the evolution of the free surface. On the other hand, the computational requirements for some specific parts of the solution algorithm depend superlinearly on the number of collocation points and often form the bottleneck for the computation of large-scale wave problems. These parts are the discretization of the boundary integral equations and the solution of the resulting system of linear equations. The domain decomposition technique is used to tackle these problems.

2.2 Applications

There are a number of applications for which the model can be used. For verification the model can be used to check higher-order wavemaker theory for both translating and rotating wavemakers in two dimensions. In this application the boundary condition related to the moving wavemaker is imposed on the exact position of the wavemaker in time. Because the full nonlinear free surface boundary conditions are solved, the accuracy of the wavemaker theory can be investigated with respect to its order.

The model can also be used for verification of the modelling of the nonlinear free-surface conditions in other wave models, like Boussinesq models. This is especially useful when experimental verification material is hard to get, for example in large scale problems. This also applies to the modelling of wave interaction with bottom topography.

As a simulation model, the numerical model can be useful when interaction with objects is involved, for example with ships. Wave forces and run-up can be determined in order to simulate its motion. A development which has progressed considerably recently, is the simulation of ship and water motion through a simultaneous solution of the equations of motion of the ship and the governing potential flow equations. These are coupled through the boundary conditions on the hull of the ship, which are taken on the exact wet part of the (moving) ship. Development on these kind of computations is still ongoing, see Berkvens (1998).

For most interesting applications however, limited computer capacity often still prohibits the use of the model, especially in three dimensions. Therefore the development of numerical techniques, such as domain decomposition, is needed.

3 Domain decomposition

3.1 *Description*

The domain decomposition method described here consists of a division of the computational domain into subdomains (see Figure 1) and an iterative procedure which generates a sequence of solutions in the subdomains that converges towards the solution in the original domain.

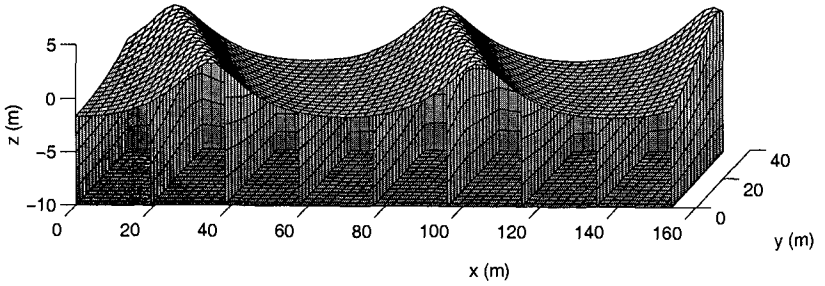

Figure 1: Domain subdivided into 8 subdomains (Panels on the front lateral boundaries are not shown)

Every step of the iterative procedure consists of first solving Laplace's equation for the potential ϕ on the separate subdomains simultaneously and secondly formulating new boundary conditions on the subdomain interfaces. In the latter part the subdomain problems are coupled.

There are many possibilities in the way information can be exchanged between the subdomains. We have chosen here to use the so-called DD/NN-scheme. Every odd step of the iterative procedure Dirichlet conditions are imposed on all interfaces. Neumann conditions are imposed at all even steps. These steps are illustrated in Figure 2 for the first two steps of a two-subdomain problem.

This scheme is also known as a Neumann-Neumann preconditioner in the context of domain decomposition methods for field discretization techniques, see e.g. Le Tallec (1994). In the field of time-domain BIEM's for nonlinear water waves a similar technique was used by Wang et al. (1994) in 2D. In their work interfaces are used to formulate a block-structured matrix which is then solved iteratively. In the present approach the subdivision and the coupling is formulated on the continous level. It is implemented numerically through separate discretizations for all subdomains leading to matrices to be solved per subdomain and a separate coupling algorithm. The present method has been presented in De Haas et al. (1996) where it was applied to the simulation of propagating nonlinear wave groups in 2D. For a general impression of work being done in the field of domain decomposition the reader can consult for instance Quarteroni (1994).

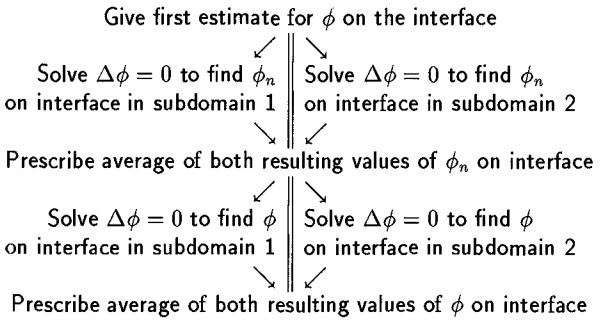

Figure 2: Schematic representation of the DD/NN-scheme

3.2 Implementation and application

In the application of the domain decomposition technique to the time-domain numerical model described here, the domain is divided in one direction only. It is possible to change the subdivision of the domain during the computation which may for example be useful when initially having large subdomains in parts where hardly no waves are present and required CPU time per node is small, and small subdomains in parts where a lot of wave action takes place. We have chosen to use a fixed initial subdivision of the computational domain with subdomains of equal size so that no reorganization of data over the subdomains is necessary and the number of nodes in all subdomains is (approximately) the same.

In the present implementation, each subdomain is treated numerically as a one-domain problem with respect to both the solution of Laplace's equation and the time integration. This implies that for each subdomain the interfaces move as if they were in- and outflow boundaries of this subdomain, moving along with the free-surface grid in a Lagrangian fashion. The subdomain problems are coupled to ensure a unique description of the interface position (the motion of each interface is determined from solutions of the neighbouring subdomains) and they are coupled through the averaging of the interface boundary conditions as required in the iterative process.

3.3 Convergence characteristics

The performance of the domain decomposition method is determined by the convergence of the iterative process. It can be monitored on each interface by considering the jump across the interface between the solutions on both sides. The convergence on the interfaces depends on the geometrical form of the subdomains and on the coupling scheme used. Convergence characteristics for 2D-problems have been outlined in De Haas e.a. (1996) and are repeated here with inclusion

of typical three-dimensional aspects.

- The convergence of the iterative procedure deteriorates if there is more asymmetry near the interfaces due to a disturbed free surface or an uneven bottom. In numerical experiments it was shown that it is mainly determined by the slope in the direction perpendicular to the interface, see De Haas and Zandbergen (1996).
- If either the length-to-height ratios or the length-to-width ratios are not too small (typically larger than 1) then convergence on each interface is not influenced by iterative processes on other interfaces.

Implications of these features with resepect to the division of a computational domain in more than two subdomains can be considered in two ways.

- For a fixed length-to-height ratio L/h of the computational domain, the convergence of the iterative procedure deteriorates as the number of subdomains N increases. For problems with an even bottom a specific number $\tilde{N}$ (and corresponding length $\tilde{l} = L/\tilde{N}$) exists for which the iterative process on one interface is influenced by the iterative processes on neighbouring interfaces.
- For a fixed length-to-height ratio l/h of the subdomains, the convergence rate does not change as the number of subdomains increases, in the case of rectangular subdomains of equal size $l > \tilde{l}$. In applications with a disturbed free surface over an even bottom it is seen that convergence is determined by the interface with the worst convergence. The number of iterations has an upper bound which is independent of N.

Examples of the first type of computation are shown in Section 3.4. The shoal problem treated in Section 4 represents a problem with an uneven bottom.

3.4 Efficiency

The efficiency of the domain decomposition technique is of course related to the convergence of the iterative method. It is considered for the case of a computational domain with a fixed length-to-height ratio and illustrated with an example.

- If for a computational domain with a fixed length the number of subdomains is increased, on the one hand the number of required iterations will increase. On the other hand, the CPU-time to solve Laplace's equation per subdomain decreases, since the subdomains become smaller. In general a certain optimal number of subdomains exists with respect to required computer capacity to solve a given water-wave problem.
- If the computational domain is built from subdomains with a fixed length-to-height ratio and the number of subdomains is increased, the number of iterations increases but remains below a upper bound independent of

the number of subdomains used. Therefore the computational costs per subdomain have an upper bound independent of the number of subdomains and the maximum total computational cost per time step can be given by a function linearly dependent on the size of the computational domain.

Results are shown for the fully nonlinear water wave problem illustrated in Figure 1. This problem involves a Fourier series solution which propagates undisturbed in water of constant depth. It is computed using the method by Rienecker and Fenton for waterdepth $h = 10.0$ m and wavelength $\lambda = 60.0$ m. The computations are started from an initial state prescribed by the solution with the wave direction under an angle of 30° with the positive x-direction, see Figure 1.

In the first example a computational domain of length $L = 153.8$ m is considered with subdivisions into 2, 4 and 8 subdomains. Time domain computations are done over the time interval $[0, 10]$ s. Required CPU times are measured for computations using Gaussian elimination and for computations using a conjugate gradient type of solver for the system of linear equations. To reduce CPU times these computations are performed for a wave height $H = 2.5$ m instead of the wave height $H = 5.0$ m shown in Figure 1. For the investigation of the number of iterations the waveheight $H = 5.0$ m is only used for the 8-subdomain problem. The number of required iterations is shown in Figure 3. The number of required

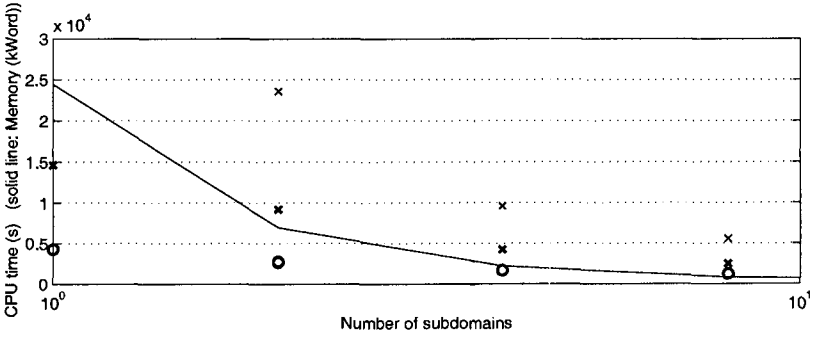

Figure 3: Number of iterations k required per timestep during the computation over the time interval $[0, 10]$ using 2, 4 and 8 subdomains indicated by the thick, medium thick and thin line respectively, for $H = 2.5$ m. The dashed line corresponds to the 8-subdomain computation with $H = 5.0$ m.

iterations for the 2- and 4-subdomain problem is approximately equal. For the 8-subdomain problem the number of required iterations is significantly larger. The variation during the considered time interval is clearly visible for the 8-subdomain problem with $H = 5.0$ m. This variation is related to the varying distortion of the free-surface grid and the connected interfaces. After approximately one wave period the number of required iterations is on the initial level again because all

the free surface collocation points have made the same excursion through space. The initial domain is recovered apart from a Lagrangian drift in the wave propagation direction. See Figure 4 in which the domain at $t = 10.0$ s $\approx 1.53T$ is shown.

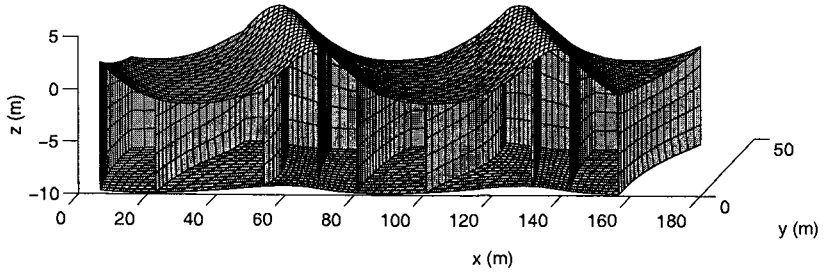

Figure 4: Domain at time level $t = 10$ s using 8 subdomains. Again the networks of the front lateral boundary are not shown.

With respect to the computational requirements results are shown in Figure 5. The following observations are made:

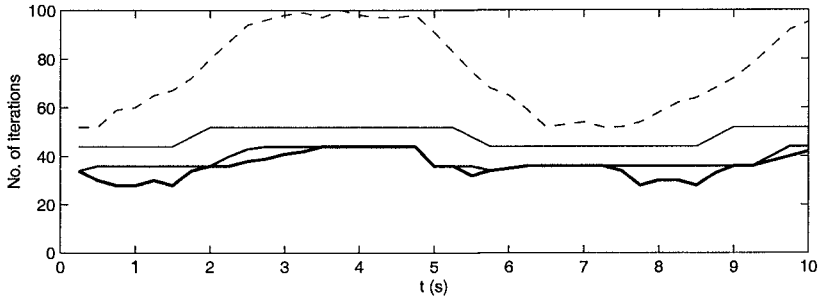

Figure 5: Measured CPU-times using 1, 2, 4 and 8 subdomains with $H = 2.5$ m. Crosses indicate computations using Gaussian elimination and circles indicate computations using CGS. Symbols printed thin indicate CPU-times that are corrected for the performance of the computing system by normalizing with the performance of the 1-domain computation. The solid line indicates the required memory. In cases in which the thin symbols can not be observed, the thin and the thick symbols coincide.

- The CPU-time for the one-domain problem is much smaller using CGS compared with using Gaussian elimination. This is due to the small efficiency of the latter method for large numbers of panels.

- For the computations using Gaussian elimination, the CPU-times for the subdivisions are smaller than the CPU-time for the original one-domain problem. If the results are corrected for the performance of the system still less CPU-time is required except for the two-subdomain problem.
- For the computations using CGS, reductions in CPU-time are obtained in all cases up to a factor 3 when using 8 subdomains. The performance is hardly affected so that it can be concluded that the number of floating point operations is decreased.
- The memory required for these computations is largely decreased when using domain decomposition.

4 Shoal problem

For the intercomparison of some wave propagation models a laboratory experiment was set up at Delft Hydraulics in which a coastal area was schematized, see Berkhoff et al. (1982). The bottom geometry consists of a sloping bottom with slope 1/50 and a shoal. A number of tests were done with different wave conditions. Wave heights were measured along a number of sections. See also Dingemans (1997), sections 4.6 and 5.6.6. Figure 6 shows the geometry of the shoal experiment.

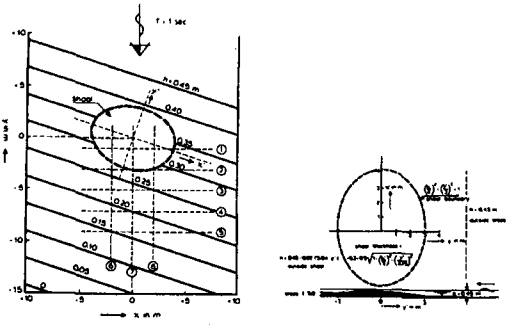

Figure 6: The geometry of the shoal experiment.

The experiment has been used by Broeze (1993) to test the accuracy of the present numerical model. Due to the relatively large domain and the limited number of panels given the available memory at the time, computations were restricted to only a part of the domain and using coarse resolutions. Nevertheless

the results agreed fairly well with the measured data. Figure 7 shows computed and measured wave heights along four sections.

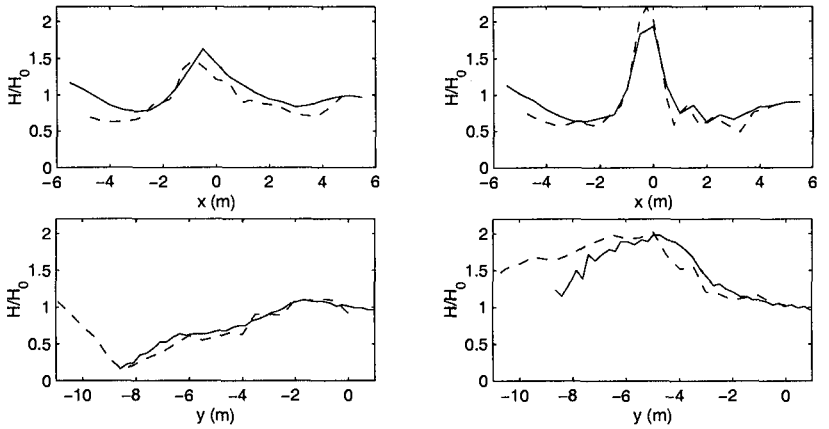

Figure 7: Wave heights relative to height of incoming wave. Computed (solid line) and measured (dashed line) wave heights along sections 2 and 3 (upper two plots) and 6 and 7 (lower two plots).

The domain decomposition technique has the potential to decrease the restrictions mentioned above with respect to the limited available memory. Using domain decomposition more panels can be used taking up the same amount of memory. The computational domain can be increased or a finer resolution can be used.

In application to the shoal problem, however, we found that stability problems occured due to the Lagrangian motion of the grid and a subsequent deterioration of the convergence of the iterative process. These problems were not solved in the limited time available. A representative computation for these problems is shown in Figure 8.

At the time level shown in this figure, the iterative process diverges on the interfaces located near $y = 13.1$ m and $y = 16.5$ m. Most probably it is related to the distortion of the grid on the interfaces, especially on the interface near $y = 13.1$ m. Due to the large variation of wave height in the region behind the shoal, the variation in horizontal velocities of the free-surface grid is large which causes the grid to distort. As a consequence the interface located behind the shoal distorts as well.

Also subdivisions in the direction perpendicular to the incoming wave direction were applied and showed to be much more stable. But still simulation over the time interval $[0, 18]$ s (required to obtain periodic wave height measurements) did not succeed. As pointed out in Section 2, the use of a mixed

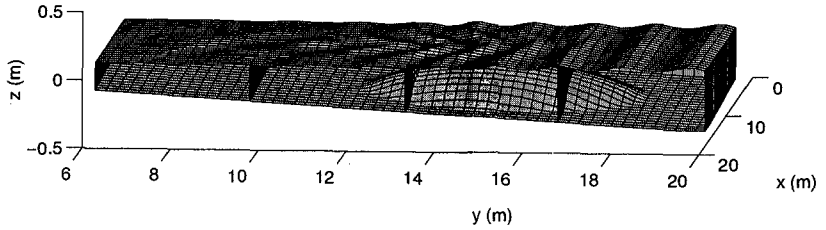

Figure 8: Domain of the shoal-problem at $t = 9.26$ s in the computation using 4 subdomains. The networks in the front lateral boundary are not shown. Waves enter the domain from the right.

Eulerian-Lagrangian method seems to be required to successfully apply the domain decomposition technique.

5 Conclusion

Domain decomposition is a suitable technique to improve the efficiency of boundary integral equation methods, especially in domains originating from water wave problems. In the application to time domain simulations of propagating nonlinear water waves over even bottoms, it leads to large reductions of required computer capacity. In the application to simulations of waves propagating over uneven bottoms, the method still fails. This is probably related to the Lagrangian motion of the free-surface grid and the consequent deterioration of the convergence process.

Acknowledgements

The use of supercomputer facilities was provided by NCF.

References

[1] Berkhoff, J.W.C., (1982). Refraction and diffraction of water waves, wave deformation by a shoal; comparison between computations and measurements, Delft Hydraulics, report W154-VIII, The Netherlands.

[2] Berkvens, P.J.F., (1998). *Floating bodies interacting with water waves; Developments of a time-domain panel method*, Ph.D. thesis, University of Twente, Enschede, The Netherlands.

[3] Broeze, J., (1993). *Numerical modelling of nonlinear free surface waves with a 3D panel method*, Ph.D. thesis, University of Twente, Enschede, The Netherlands.

[4] De Haas, P.C.A., M.W. Dingemans, and G. Klopman, (1996). Simulation of free long-wave generation due to uneven bottoms, in: *Proc. 25th Int. Conf. on Coastal Engng.*, Orlando, **1**, pp. 165-174.

[5] De Haas, P.C.A., and P.J. Zandbergen, (1996). The application of domain decomposition to time-domain computations of nonlinear water waves with a panel method, *J. Comp. Phys.*, **129 (2)**, pp. 332-344.

[6] Le Tallec, P., (1994). Domain decomposition methods in computational mechanics, *Comp. Mech. Adv.*, **1**, pp. 121-220.

[7] Quarteroni, A., Ed., (1994). *Proc. Sixth Int. Symp. on Domain Decomposition Methods for Partial Differential Equations*, Como, June 1992 (AMS, Providence).

[8] Rienecker, M.M. and J.D. Fenton, (1981). A Fourier approximation method for steady water waves. *J. Fluid Mech.* **104**, pp. 119-137.

[9] Wang, P., Y. Yao and M.P. Tulin, (1994). *Int. Journ. of Offshore and Polar Eng.*, 4, pp. 200-205.

Variations in Nonlinearly Evolved Nearshore Spectra and Their Significance in the Estimation of Wave Forces

Serdar Beji[1] and Kazuo Nadaoka[2]

Abstract

Variability of spectral estimates is examined with respect to the nonlinearity of the wave field considered. Both measured field data and numerical simulations are used for checking the extent of variations, which are quantified as histograms that closely follow the chi-square distribution. An absolute assessment of the variations over the entire frequency band of a spectrum is also made and found to approach to a mean of 70% regardless of the frequency concerned. Finally, it is observed that a nonlinearly evolving wave field of initially constant spectral shape gradually assumes a spectral variability, which is characterized by the chi-square distribution. The last finding provides a clue for a possible cause of the variations observed in the estimates of spectra.

Introduction

Despite the important implications concerning uncertainties in the estimation of wave loads, deviations of individual spectral samples from the final spectral estimate, as computed through ensemble averaging and frequency smoothing, appear to have received little attention. Borgman (1972) questioned the validity of the use of the chi-square confidence interval for high sea conditions and tested the accuracy of the method using wave data from a hurricane. His comparison with the theory yielded some discrepancies but the overall conclusion was that the chi-square approximation was acceptable even for hurricane waves. Donelan and Pierson (1983) presented an extensive examination of wind-generated laboratory and field wave data with special emphasis on the sampling variability of the spectral peak. They showed that while the scaling according to the spectral peak would bias the spectral estimates, the sampling variability of the spectra was in good accord with the chi-square distribution. The latter finding is in line with Borgman's (1972) conclusion.

[1] Assoc. Prof., Department of Naval Architecture and Ocean Engineering, Istanbul Technical University, Maslak 80626, Istanbul, Turkey.
[2] Professor, Graduate School of Information Science and Engineering, Tokyo Institute of Technology, 2-12-1 O-okayama, Meguro-ku, Tokyo 152-8552, Japan.

It is well known that nonlinear evolutions of surface gravity waves are highly dependent on the phase values of the interacting wave components. Thus, unlike linear waves, depending solely on the initial phase values, a nonlinear random wave field of a certain spectral shape may evolve quite differently from a wave field of the same spectral shape but different initial phases. Variations in such nonlinearly evolved spectra are not negligible and therefore a closer examination may lead to interesting results. In particular, some hints as to the source of the variability observed in spectral estimates may be gained.

This work first examines the sampling variability of the spectra of field measurements in the nearshore zone (Nakamura and Katoh, 1992) and confirms that the chi-square distribution is a good approximation to these variations. The agreement with the theory is remarkable because for these highly nonlinear waves the surface displacements do not exactly satisfy the Gaussian distribution. Absolute deviations of the individual spectra from the ensembled mean are also computed for the entire frequency band and found to resemble a white-noise with a mean level of approximately 70%. The effect of nonlinearity on the spectral variability is investigated by performing a numerical test, which simulates the nonlinear evolution of an initially constant spectral shape over a gently decreasing depth. The numerical results show that the initially constant spectral shape gradually assumes a variability, which is in accord with the chi-square distribution. This finding indicates that nonlinearity may be a responsible mechanism for the observed spectral variability.

For practical applications, the crucial aspect of the spectral variability lies in the uncertainties it implies in the estimation of wave loads, which is essential for a safe design. Possible further investigations on the subject are mentioned in closing.

Analysis of Field Measurements

The spectral variations are first examined by using field data. Two particular data sets from the field measurements of Nakamura and Katoh (1992) were selected; namely, the data of 25 February 1989 and 28 February 1989. The measurements were performed at the Hazaki Oceanographical Research Facility (HORF) near Kashima, Japan. The site of the field observations was a natural sandy beach facing the Pacific Ocean. Ten ultrasonic wave gauges were used; of which seven were installed on the 427 m-long observatory pier while the remaining three were deployed at water depths of 9 m (Station 8), 14 m (Station 9), and 24 m (Station 10), located respectively at the distances 1.3, 2.1, and 3.2 km from the shoreline.

The data of 25 February 1989 was recorded prior to a storm and displayed a typical sea state with significant wave height H_s=1.5 m and period T_s=4.8 s at the offshore station (Station 10) where the waves were essentially linear. On the other hand, the data of 28 February 1989 was recorded in the aftermath of the storm and the spectrum at Station 10 represented a swell with H_s=2.2 m and T_s=12.4 s; the waves were nonlinear. While the water depths at Stations 10 to 8 were too deep to cause depth-induced breaking, most of the waves at the remaining stations were either breaking or broken.

For computations the data at each station was first segmented into M=12 groups of N=1024 data points and Fourier transformed. Out of the 512 unique Fourier pairs the first 256 components, which covered the frequency range of 0.0-0.5 Hz, were considered sufficient to capture almost all the wave energy present and therefore the subsequent computations were performed by using the first 256 transformed pairs.

For each separate set, comprising the Fourier components a_{nm} and b_{nm} for $n = 1,...,256$ and $m = 1,...,12$ the Fourier amplitudes $C_{nm}^2 = a_{nm}^2 + b_{nm}^2$ were frequency smoothed by a five-point running average

$$\overline{C}_{nm}^2 = \frac{1}{5}\sum_{i=n-2}^{n+2} C_{im}^2 . \tag{1}$$

Using the above frequency smoothed values; a segment averaging was performed

$$\hat{C}_n^2 = \frac{1}{12}\sum_{m=1}^{12} \overline{C}_{nm}^2 , \tag{2}$$

which in turn could be used to obtain the spectral estimates $\hat{S}_n = \hat{C}_n^2 / \Delta f$ with $2 \times 5 \times 12 = 120$ degrees of freedom. Here, $\Delta f = 1/N\Delta t = 1.953 \times 10^{-3}$ Hz, and $\Delta t = 0.5$ s is the sampling interval.

Since it has implicity been assumed that the process is approximately Gaussian, the 90% confidence level for the estimated spectral variance with 120 degrees of freedom may be computed as (see Bendat and Piersol, 1971, p.114)

$$P\left(\frac{120\hat{S}_n}{\chi^2_{120;0.05}} < S_n < \frac{120\hat{S}_n}{\chi^2_{120;0.95}} \right) = 0.90 , \tag{3}$$

where S_n is the true but unknown spectral variance corresponding to the frequency $n\Delta f$. Substituting $\chi^2_{120;0.05} = 146.57$ and $\chi^2_{120;0.95} = 95.70$ gives

$$P(0.82\hat{S}_n < S_n < 1.25\hat{S}_n) = 0.90 , \tag{4}$$

which indicates that the true spectrum is known to within ± 25% or a range of 43% at the 90% confidence level. Figure 1 shows the estimated spectrum with 120 DOF and a single realization with 2 DOF for the data of 28 February 1989 at Station 10.

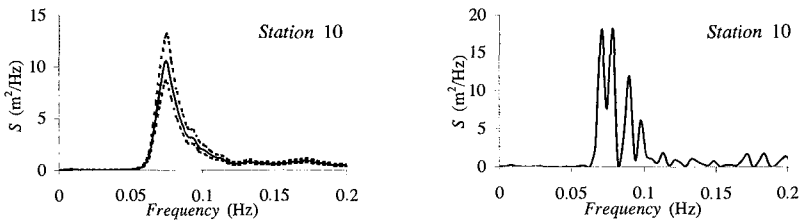

Figure 1. The spectral estimate on the left has 120 degrees of freedom and is within –18 to +25% of the true spectrum at the 90% confidence level. The 90% confidence limits are shown by dashed lines. The spectral estimate on the right is a single realization with 2 degrees of freedom.

Hypothetically, the random variable $r = C_n^2 / S_n \Delta f$ is distributed according to $\exp(-r)$ for r greater than zero. Since S_n is not known, the estimate $\hat{S}_n$ can be used for testing the hypothesis that the computed r values will follow the exponential law.

The computations were done for the data of both 25 and 28 February 1989 using all 12 segments with 256 components covering the frequency range 0.0-0.5 Hz. Consequently, 3072 values of r were obtained. Strictly speaking, vanishingly small values of $\hat{S}_n$ should have been avoided to prevent possible errors, however no problems were encountered and therefore the entire range of $\hat{S}_n$ values was used.

In Figure 2 the histograms for the 3072 values of r for a class interval 0.05 wide is shown over the range $0 < r < 5$ for three selected stations. Each histogram has been normalized by its value in the first interval (0.00-0.05).

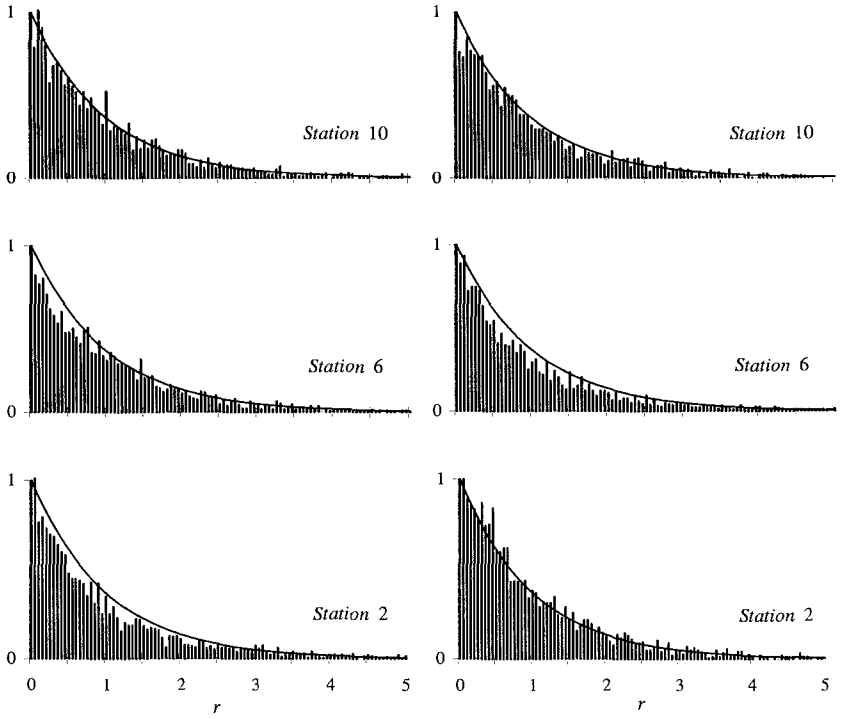

Figure 2. Normalized histograms of the ratio, r, of raw spectral estimates to the smoothed average spectral estimates for Stations 10, 6, and 2. Left column: 25 February 1989, right column: 28 February 1989. The solid line is the theoretical curve exp (-r).

In order to obtain quantitative estimates of the spectral variations, the field data is analyzed in a different manner. Instead of treating the spectral variations regardless of frequency, the mean absolute percentage of deviations from the estimate for each frequency component are computed according to the formula

$$\varepsilon_n = \frac{1}{12}\sum_{m=1}^{12}\frac{\left|\hat{S}_n - C_{nm}^2/\Delta f\right|}{\hat{S}_n}, \tag{5}$$

and then plotted over frequency. Figure 3 shows the results corresponding to the stations shown in Figure 2.

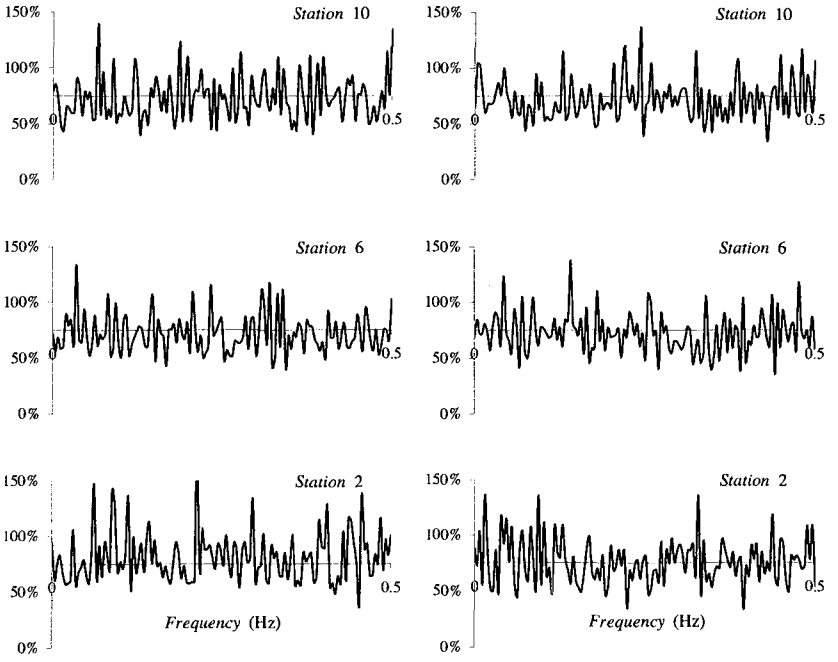

Figure 3. Mean absolute percentage of spectral variations over frequency as computed from equation (5) for the stations of Figure 2.

As it is seen from the above graphs, the mean absolute percentages of individual deviations from the estimated spectral values exhibit a random distribution over frequency with a mean of approximately 75%. Further computations have shown that the number of frequency averaging determines the exact value of the mean percentage with the trend that the higher the number of frequency merging the higher the resulting mean percentage. This is to be expected because the frequency averaging essentially pulls down the estimated spectral shape, resulting in smaller and smaller spectral values. Therefore, if a meaningful mean deviation percentage were to be obtained, it would be best not to introduce any frequency smoothing at all.

As an alternative, instead of C_{nm}^2, one could use $\overline{C}_{nm}^2$ in equation (5) to eliminate the quantitative effect of frequency smoothing. Computations without any frequency smoothing but with different number of FFT points and of ensemble averaging have yielded that the mean absolute deviations center around 70% with no sensitivity to the number of FFT points and to the number of ensemble averaging. Likewise, use of $\overline{C}_{nm}^2$ in equation (5) has yielded nearly the same numerical value for different frequency averaging operations. Thus, it has been concluded that the mean absolute deviations center around 70% with a random-noise type appearance over frequency regardless of the characteristics of the wave field considered.

A possible cause for the noise-like distribution of spectral variations over entire frequency band may be attributed to a nonlinear mechanism allowing continuous energy flow among spectral components. For testing the validity of such a notion, a numerical experiment was carried out with supportive results. The computations and results are described in detail in the following section.

A Numerical Experiment

Using a nonlinear wave model, nonlinear evolution of an initially constant spectral shape over decreasing water depth is now investigated. The wave model may be considered as a generalized KdV equation (Korteweg and de Vries, 1895), which is valid for arbitrary ratios of depth to wavelength (Nadaoka *et.al.*, 1994; Beji and Nadaoka, 1997a)

$$C_g\eta_t + \tfrac{1}{2}C_p(C_p + C_g)\eta_x - \frac{(C_p - C_g)}{k^2}\eta_{xxt} - \frac{C_p(C_p - C_g)}{2k^2}\eta_{xxx} + \tfrac{1}{2}[C_p(C_g)_x + (C_p - C_g)(C_p)_x]\eta + \tfrac{3}{4}g\left(3 - 2\frac{C_g}{C_p} - \frac{k^2C_p^4}{g^2}\right)(\eta^2)_x = 0, \tag{6}$$

where C_p, C_g, and k are respectively the phase and group velocities and the wave-number computed according to the linear theory dispersion relation for a dominant wave frequency ω and a given local depth h, the subscripts x and t indicate partial differentiation with respect to space and time, respectively.

Based on the above unidirectional wave equation a spectral model was developed (Beji and Nadaoka, 1997b; 1998) resulting in a set of evolution equations describing the spatial changes of the component wave amplitudes of a prescribed incident wave field. No detail is given here; the complete derivation can be found in Beji and Nadaoka (1998). It must be indicated that the wave model itself is not crucial so long as it contains a nonlinear mechanism to generate harmonics thus allowing continuous redistribution of energy.

For numerical investigations a uniformly decreasing depth of 1:50 slope followed by a horizontal section is selected. Waves first steepen due to decreasing depth and then the energy exchange takes places as they travel over the shallow constant depth region. The water depth at the incident boundary is 25 m, which reduces to 5 m after a distance of 1000 m. For the next 1000 m, the water depth remains constant at 5 m.

The wave field at the incident boundary is assumed linear with a Bretshneider type spectral shape and a typical mean period $T_m \approx 12$ s. For ensuring the linearity of the incident wave field as well as preventing any possible breaking in the shallow region, the incident mean wave height is taken $H_m = 1.0$ m, a moderate value. Twelve realizations with *constant spectral shape* but *different initial phase* assignments are performed. As in the field measurements, the computations were done using 256 Fourier pairs with $\Delta f = 1.953 \times 10^{-3}$ Hz, and a five-point running average was applied for frequency smoothing. Thus, all the statistical values given in the previous section apply to the numerical simulations as well.

In Figure 4, the left column shows the histograms for three selected stations while the right column gives the mean absolute percentage of spectral variations for the same stations.

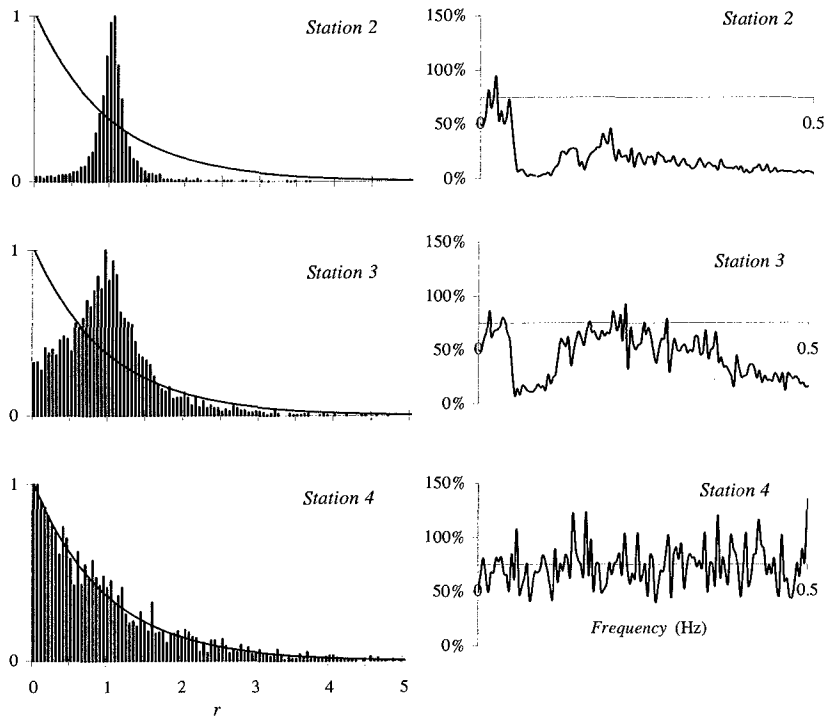

Figure 4. Histograms of spectral variability (left) and mean absolute percentage of variations (right) for an initially constant spectral form at three different locations. Station 1 (not shown) is the incident boundary at x=0 m and h=25 m; Station 2, x=250 m and h=20 m; Station 3, x=750 m and h=10 m; Station 4, x=2000 m and h=5 m. Histograms for Station 2 and 3 are normalized by their largest values whereas histogram for Station 4 is normalized by its value in the first interval, as in Figure 2.

From the graphs for Station 2 it is seen that the histogram is quite unlike the theoretical chi-square distribution (due to the initially imposed unvarying spectral heights for all realizations) but increasing nonlinearity begins manifesting itself in the lower frequency portion of the wave spectrum by introducing an appreciable variability in that particular region. At Station 3, the histogram is broader but still not quite like its theoretical shape. The effect of nonlinearity has now spread to the higher frequency part of the spectrum; however, the main frequency band (0.05-0.12 Hz), which contains the primary energy of the spectrum remains almost unaffected as can be observed by remarkably low percentages of mean absolute variations. The main frequency band is the last to be modified because the sub- and super-harmonics must reach to appreciable levels before they could interact with it. After travelling the shallow constant depth region of 1000 m, the wave field at Station 4 is completely modified by the wide-spread nonlinear interactions and it has attained a spectral variability which is in excellent agreement with the chi-square distribution. Also, the mean absolute percentages of deviations show a white-noise type random distribution over frequency with a mean of 75%, as for the field measurements given in Figure 3. The results of overall computations imply the existence of a nonlinear mechanism behind the observed spectral variability. This nonlinear mechanism needs not be in the form of a second-order nonlinearity as in here, it may be a cubic nonlinearity, *e.g.* the nonlinear Schrödinger equation, or a higher order nonlinearity that would permit energy exchange among spectral components.

While the chi-square distribution is linked to the properties of stationary Gaussian processes, the examination of the field data used here shows that this may not be strictly the case. For instance, computing the histograms for the surface elevation distributions at Stations 10 and 6 of 28 February 1989 data results in the graphs shown in Figure 5. While the distribution of Station 10 may be accepted as Gaussion, the distribution of Station 6 clearly diverges from the theoretical curve. However, the histograms of spectral variabilities for both Station 10 and Station 6 satisfy the theoretical chi-square distribution very closely, as is seen in Figure 2. This particular point was Borgman's (1972) principal motivation for investigating the validity of the chi-square confidence intervals for high sea conditions.

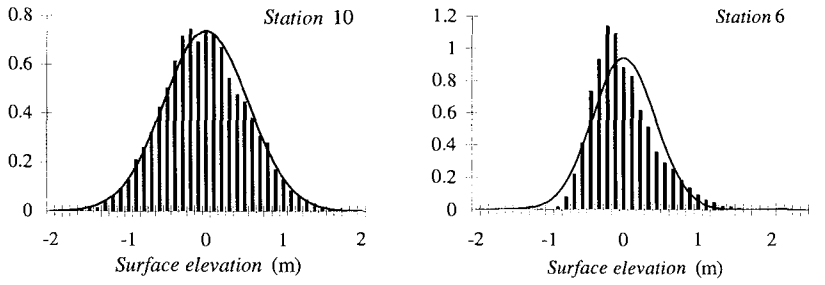

Figure 5. Histograms for distributions of surface displacements for the data of 28 February 1989 at Station 10 and Station 6.

The point that the wave field needs not be truly Gaussian in order that the corresponding spectral variations be chi-square distributed is especially mentioned here because except for a few stations of the data of 25 February 1989, almost all the other data (measured or computed) were actually representing nonlinear waves.

Concluding Remarks

Analysis of the field data comprising linear and highly nonlinear wave fields has confirmed the validity of the standard assumption that the spectral variabilities follow the chi-square distribution. It is also observed that the wave field does not necessarily need to be truly Gaussian for its spectral variability to follow the chi-square distribution. The numerical simulation of a nonlinearly evolving spectrum has shown that an initially constant spectral shape gradually assumes a variability, which is in perfect agreement with the chi-square distribution. Therefore, nonlinear interactions may be at least partially responsible for the variability observed in spectral computations. Once the spectral variability is attained, it remains preserved even if the wave field becomes linear as, for instance, by breaking or moving into deeper regions.

The quantitative assessments of the variability show that on the average 70% deviation of a spectral component from the smoothed and segment averaged value is possible. In estimating the extreme wave loads this percentage may be interpreted as an indicator of the additional transient loads. For making reliable assessments, it is necessary to investigate the actual wave load variations by performing computations with wave fields having such variable spectra.

Acknowledgments

This work was carried out while the first author was at Tokyo Institute of Technology as a visiting faculty member. The authors would like to thank Dr. K. Katoh and Mr. S. Nakamura for providing the field data.

References

Beji, S. and K. Nadaoka, 1997a. A time-dependent nonlinear mild-slope equation for water waves. *Proc. Roy. Soc. Lond. A*, **453**, 319-332.

Beji, S. and Nadaoka, K., 1997b. Spectral modelling of nonlinear shoaling and breaking over arbitrary depths. *Proc. Coastal Dynamics '97*, 285-294.

Beji, S. and K. Nadaoka, 1998. A spectral model for unidirectional nonlinear wave propagation over arbitrary depths. *Coastal Engng.*, Submitted.

Bendat, J.S. and A.G. Piersol, 1971. *Random Data: Analysis and Measurement Procedures*, John Wiley & Sons, pp. 407.

Borgman, L.E., 1972. Confidence intervals for ocean wave spectra. *Proc. 13th Int. Conf. Coast. Engng.*, **1**, 237-250.

Donelan, M. and W.J. Pierson, 1983. The sampling variability of estimates of spectra of wind-generated gravity waves. *J. Geophys. Res.*, **88**, 4381-4392.

Korteweg, D.J. and G. de Vries, 1895. On the change of form of long waves advancing in a rectangular canal and on a new type of long stationary waves. *Phil. Mag.*, **5**, 422-443.

Nadaoka, K., Beji, S. and Nakagawa, Y. 1994. A fully dispersive nonlinear wave model and its numerical solutions. *Proc. 24th Int. Conf. Coast. Engng.*, **1**, 427-441.

Nakamura, S. and Katoh, K., 1992. Generation of infragravity waves in breaking process of wave groups. *Proc. 23 th Int. Conf. Coast. Engng.*, 990-1003.

Wave Refraction across a Current with Strong Horizontal Shearing

Richard R. Simons[1] and Ruairi D. Maciver[2]

Abstract

Experiments have been performed with regular deep-water waves propagating obliquely across a relatively narrow jet-type current. Measurements have been made of wave refraction using an 8-element wave array and 3d acoustic Doppler flowmeters. Results show that wave height and celerity follow the trends predicted by gradually-varied flow theory, but with wave height modulated by weak reflections as the waves pass across the jet. Direction of wave propagation is found to be sensitive to the presence of internal reflections from the shear layers.

Introduction

It is now widely accepted that non-linear wave-current interaction plays an important role in the evolution of coastal flow. Currents are generated by wind stresses, tides and river estuary discharges, and when waves move across such spatially varying mean flows, they experience significant changes in amplitude, celerity, direction, kinematics, and bed friction, all of which affect both their local characteristics and their potential impact on the wider coastal environment.

Many theoretical models of coastal flows are based on the assumption that waves are moving through a gradually varying medium, for instance, where there is a gently sloping seabed or a current contains only weak horizontal shearing. Conventionally, when regular long-crested waves cross a horizontally sheared current, the angle of refraction and Doppler-shifted celerity are determined by application of Snell's Law to the wave orthogonals, while the change in wave height

[1] Senior Lecturer, Department of Civil & Environmental Engineering
UCL, Gower Street, LONDON WC1E 6BT. E-mail: r.r.simons@ucl.ac.uk

[2] Research Assistant, Department of Civil & Environmental Engineering
UCL, Gower Street, LONDON WC1E 6BT. E-mail: ucesf25@ucl.ac.uk

is determined from the conservation of wave action through wave ray tubes (Jonsson, 1990). This form of analysis is appropriate when the width of the shear layer is many times the length of the incident wave, such as where waves propagate across the Gulf Stream. In that particular case, the width of the jet current is approximately 300 times the incident wave length.

However, it is often the case that waves propagate through waters where bathymetry and currents vary rapidly, for instance, where rivers or tidal inlets discharge into the ocean. Under such circumstances the width of the jet may be less than 5 times the incident wave length. An important consequence of such rapidly varying conditions is that significant wave reflection may take place at both shear layers, a phenomenon not normally included in wave refraction models.

There have been a number of attempts to model wave refraction across a rapidly varying current, extending the slowly-varying WKB solution to allow reflections (McKee, 1977; McKee, 1996), or including a vortex sheet to simulate the reflecting shear layer (Smith, 1983; Kirby, 1986). The availability of data against which these theories can be validated has been restricted by the practical difficulties involved in performing equivalent experiments. At a laboratory scale the flow conditions typically achievable can produce refraction of only a few degrees, and the accurate measurement of such small changes presents a significant difficulty. However, motivated by a parallel project at University College Cork to develop a new model, the present paper describes tests carried out under controlled conditions in the UK Coastal Research Facility (UKCRF) at Wallingford aimed at providing both a better understanding of the processes controlling current refraction and data for model validation.

The experiments were designed to investigate the behaviour of waves in water of constant depth as they pass obliquely across a narrow jet-like current with strong horizontal shear. The refraction has been established at several locations across the shore-parallel current from oscillatory velocity vectors and from a directional wave array. The project addresses one of the areas highlighted in a recent review (Thomas and Klopman, 1997) as requiring attention, and offers a unique data set against which models can be tested.

Experiments

The UKCRF has been designed to provide a controlled environment in which various coastal processes can be simulated and investigated at relatively large scale. While the main aim is to provide data for validation of models describing a range of coastal phenomena, it also offers the opportunity to improve fundamental understanding of the physics. The design and capabilities of the basin are described in an earlier paper (Simons *et al.*, 1995).

For the present tests, water depth was fixed at 0.5m above a bed roughened with 10mm diameter granite chippings. A jet-like current was generated in the offshore flat-bed region of the basin. This jet had a Gaussian horizontal distribution of velocity across its nominal width of 7 metres and a streamwise centreline near-surface velocity of 0.25m/s. Long-crested waves, generated in still water offshore from the jet current, were propagated through the jet current before being spent on a 1-in-20 plane beach. Preliminary tests used regular wave periods of both 0.8s and 0.9s, wave heights of 40mm, and angles of incidence between wave orthogonal and shore-normal of 0^0 and $\pm 30^0$. Parameters for the main test programme described here are set out in **Table 1** below.

UK Coastal Research Facility	
Basin dimensions:	36m by 20m (internal)
Test region:	10m alongshore by 9m shore-normal
Water depth:	0.5m
Bed geometry:	horizontal
Bed roughness:	10mm diameter (nominal) stone chippings
Spending beach:	1 in 20 slope (outside test region)
Jet Current	
Centreline velocity:	0.25 m/s at test section
Width:	7.0m (4.0m for $\bar{u}_{50}$) at test section
Horizontal profile:	Gaussian
Flow direction:	shore-parallel
Waves	
Regular wave period:	0.8s
Height:	0.04m (nominal)
Propagation direction:	-30^0, 0^0, 30^0,
h / L	0.50
Prototype scale:	
Depth:	25m
Centreline velocity:	1.75 m/s
Wave period:	6s
Width of jet:	200m

Table 1: Test conditions

Vertical profiles of mean and wave-induced velocities were measured at regular positions across and at three sections along the horizontally varying current using three 3d Nortek acoustic Doppler velocimeters (ADVs) mounted one above the other. Surface elevation was measured using the "Octoprobe", an array of eight wave probes mounted in a fixed geometry, 0.85m long by 0.6m wide, as described by

Teisson and Benoit (1994). The array was traversed across the jet current with one wave probe located exactly above the three ADV velocimeters, and provided wave heights, reflection coefficients and wave propagation direction. Four additional wave probes were also deployed on tripods, at fixed locations in the basin to provide a common reference for phase analysis of all data channels.

The objectives of the test programme were: with no waves present, to establish a stable jet current parallel to the wave generators, and to measure the velocity field across the jet and through the depth at three cross-sections; then, with no jet current flowing, to measure the velocity field for regular long-crested waves propagating obliquely or normal to the shoreline; and finally, with those waves propagating across the jet current, to measure the wave refraction and wave height at regular positions across the jet current, and to determine the Doppler-shifted wave celerity at the same locations.

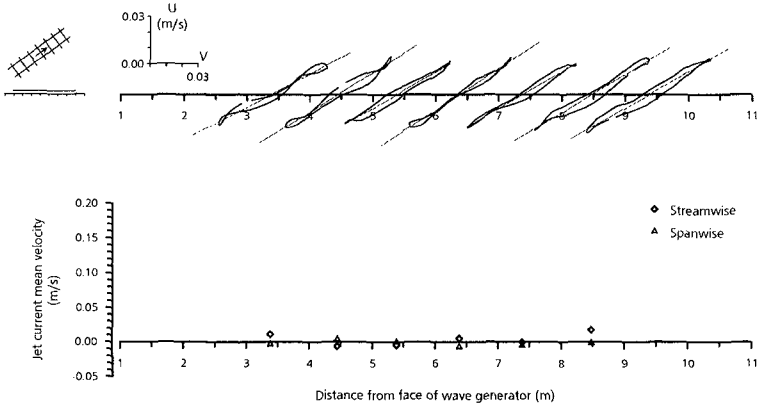

Figure 1: *Horizontal velocity vectors for 30° waves: no current flowing [straight lines indicate mean direction of wave propagation].*

Methods of analysis

To determine the local direction of wave propagation as the waves refract across the jet current, five different methods of analysis were considered.

The first of these ("Method 1") used only data from the ADV velocity probes to generate the ensemble average horizontal velocity vector at phases through the wave cycle. A least-squares method was then adopted to identify the mean direction

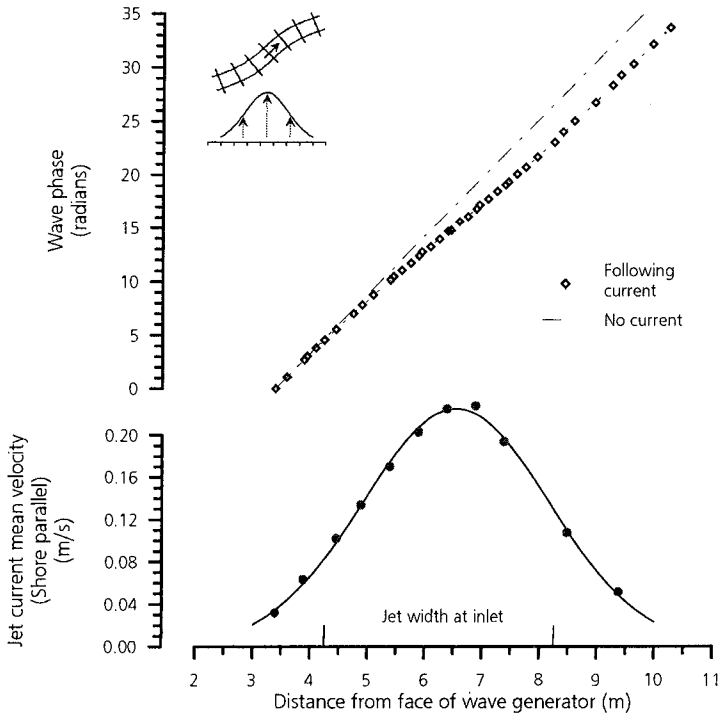

Figure 2: Variation in wave phase on an orthogonal section across the jet current.

of the velocity vector. An alternative method, calculating the direction using only the 1st harmonic of the horizontal velocity vector, yielded almost identical results. It should be noted that the vectors were never the ideal straight lines that a clean, long-crested wave should produce, but were always mildly contorted closed curves, as shown in **fig.1** for a case with no current. This suggests that waves of different frequency or direction of propagation were present in the basin.

"Method 2" used data from the 8 wave probes deployed in the Octoprobe, and related the 1st harmonic phase difference between pairs of probes a known distance apart to the two unknowns, namely, local direction of wave propagation and absolute wave celerity. If the flow field was homogeneous, it would then be possible to produce 7 independent estimates of phase difference and, adopting an appropriate numerical technique, solve for celerity and direction. However, the present tests specifically included rapidly varying currents, and estimates predicted a possible 15% variation in celerity along the length of the Octoprobe. In order to improve the spatial

resolution, it was decided to analyse the data as two separate cross-shaped groups - with 5 probes in each group. Adopting a least-squares optimisation, it was then possible to deduce two independent sets of results for each deployment position. While this method was restricted to identifying the dominant propagation direction at a single incident wave frequency, it was found to be robust, made no assumptions concerning the local wave celerity, and produced reliable results for all test conditions investigated.

"Method 3" looked at the variation in phase of the 1st harmonic along a shore-normal transept as measured by the four co-linear wave probes on the spine of the Octoprobe as it was traversed across the jet current (**fig.2**). At any particular location the rate of change of phase is related directly to the component of celerity in the shore-normal direction. Then, making the (initially unsupported) assumption that the local absolute celerity can be calculated from the incident wave celerity and the local mean velocity (as measured by the ADV probes) using simple Doppler shift, it is possible to calculate the angle of incidence between the jet current and the local direction of wave propagation, in other words, the wave refraction. While this method worked well for the case with waves following the current, it failed to yield solutions for the opposing current case and has not been applied further.

The next ("Method 4") used data from the Octoprobe to produce full directional spectra, providing both the directional distribution of wave energy at the incident wave frequency and the distribution between different frequencies at positions across the jet current. At each deployment location, analysis was performed on two groups of wave probes (with 4 probes in each) to improve spatial resolution. Spectra were calculated using the Iterative Maximum Likelihood Method (Pawka, 1983), adapted to include a dispersion relation varying with direction and local jet current strength. Implicit in this modification is the assumption, used in "Method 3", that the local wave celerity can be calculated from a simple Doppler-shift of celerity from linear wave theory using the local mean current velocity.

Finally, from the data recorded, it would be possible to calculate the wave parameters using collocated measurements of water surface elevation and wave-induced velocities. However, time has so far precluded such analysis.

Results

Preliminary observations with no waves present confirmed that the jet current took on the desired Gaussian horizontal profile, but a gradual increase in width of the jet was noted as it propagated along the basin. However, this change was sufficiently weak to be deemed negligible along the 10m length of basin in which detailed velocity measurements were made. Some meandering of the jet was also detected in the time-series of u and v velocity components, and spectral analysis confirmed

oscillations between 40s and 100s, suggesting streamwise length scales of between 10m and 25m.

With the current turned off, waves of 0.8s period were then propagated shore-normal and at +/- 30^0 to shore-normal to assess both the quality of the waves and the reliability of the measuring and analysis techniques. Time-series of water surface elevations showed that the waves remained regular, with wave heights constant to 5% and no modulation. Spatial variation of wave height suggested reflection coefficients from the beach of less than 5%. The angle of wave propagation was found to be determined to within +/- 1.5^0 of the direction requested at the wave maker using data from the Octoprobe, with slightly poorer estimates from the velocity vector method.

When the waves were propagated across the jet current, the first notable observation was that the jet current had itself been moved laterally - inshore and away from the wave generators by 0.3m when the waves followed the current, offshore and towards the wave generators by 1.4m when the waves opposed the current. This change can be seen in the reference current plotted at the bottom of most subsequent diagrams, and changes in wave properties should be viewed relative to that location.

Fig.3 shows the local wave celerity and angle of propagation measured by the Octoprobe using "Method 2" when waves at 30^0 incidence propagate across the following jet current. The 20% increase in celerity observed at the centre of the jet agrees well with simple 1st order Doppler-shifted theory as used for gradually varied flows (Jonsson, 1990). However, the direction of propagation varies sinusoidally across the jet (oscillating about the predicted refraction pattern), with almost no refraction measurable at the centre and with 6^0 shifts in the two shear layers on either side. IMLM analysis ("Method 4") produced very similar results. In contrast, the propagation angle deduced from the velocity vectors (**fig.4**) shows rather higher angles of refraction - again varying sinusoidally across the jet but phased differently from the results reported above - with a 15^0 shift in the offshore shear layer. Despite the spatial variation in refractive angle, the scale is close to the 6^0 predicted from Snell's Law for slowly varying flow.

Figs.5 & **6** show the corresponding refraction patterns when the waves propagate into the opposing jet current. In this case the 20% decrease in celerity predicted by theory is again well matched to data from the Octoprobe, as is the refracted angle of propagation at the centre of the jet. However, inshore of the jet, the angle of refraction is erratic. The shift in propagation direction towards shore-normal calculated at the centre of the jet from the velocity vectors (particularly using ADV2) is significantly greater than found using the other methods or predicted by gradually-varied theory.

With the waves propagating orthogonally across the jet current, no significant

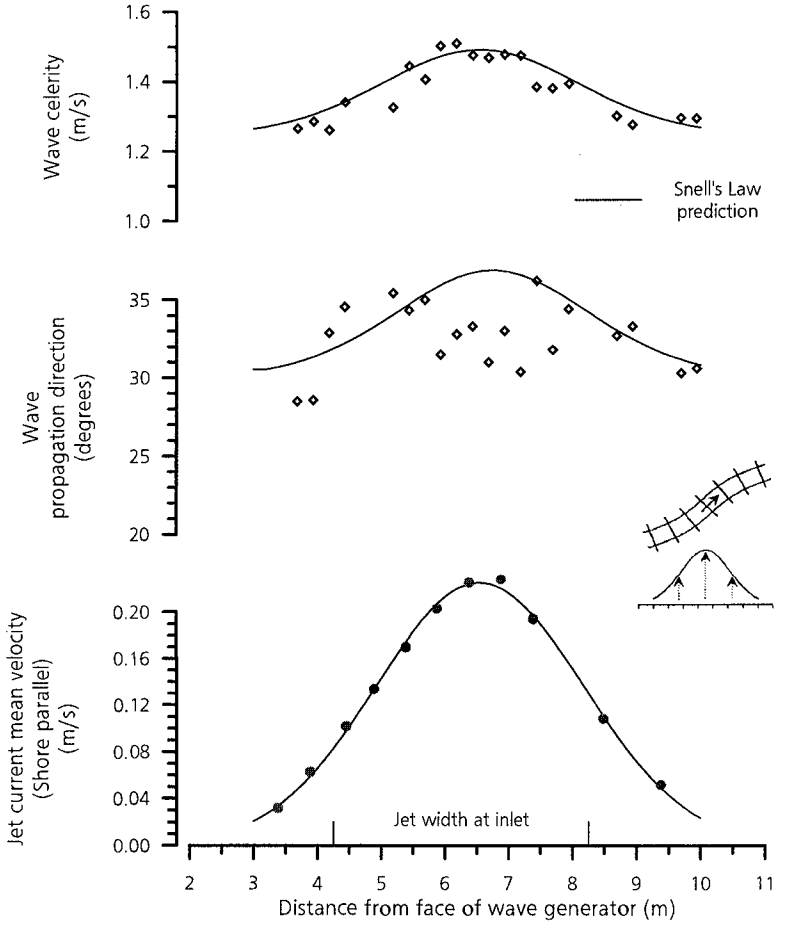

***Figure 3**: Variation of wave celerity and direction (from Octoprobe) across the jet current: following current case.*

changes in celerity or angle of propagation were observed, although the scatter in all data sets was greater than observed in the absence of the current.

Figs.4 & **6** also show the variation in wave height measured across the jet current for the following and opposing current cases respectively. It can be seen that, within the bounds of experimental scatter, the significant wave height indicates a

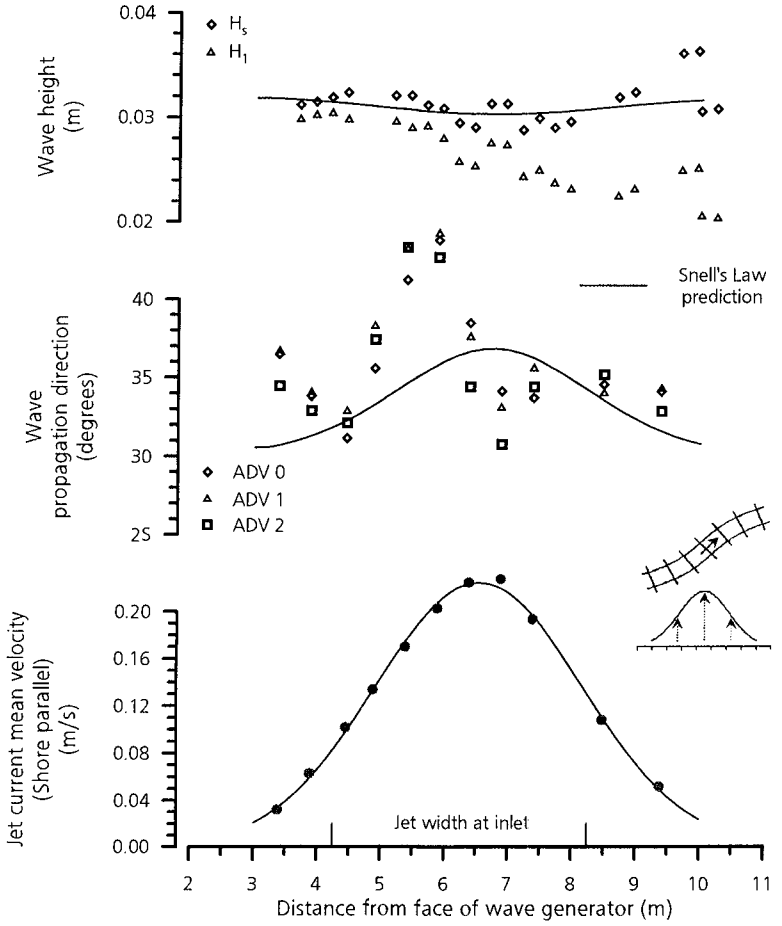

Figure 4: *Variation of wave height and direction (from velocity vectors) across the jet current: following current case.*

partial standing wave pattern (<10%) superimposed on the weak variation in *Hs* predicted by theory as the waves propagate across the jet. In contrast, the graph of 1st harmonic wave height H_1 confirms the reflection pattern but suggests that H_1 decays rapidly across the jet. This apparent anomaly is caused by different methods

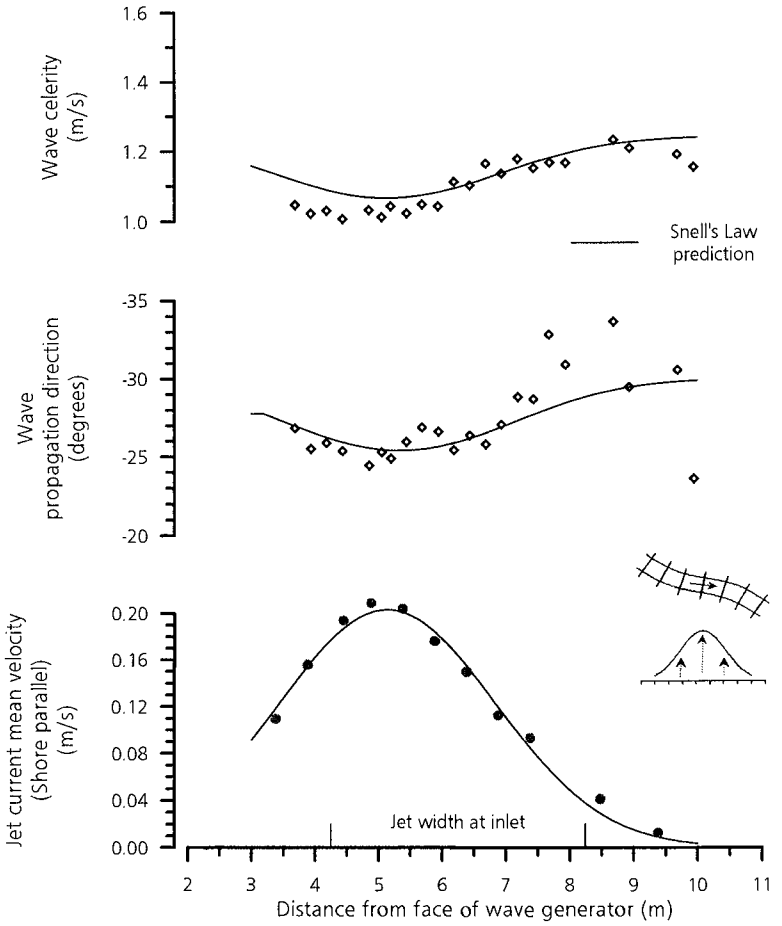

***Figure 5**: Variation of wave celerity and direction (from Octoprobe) across the jet current: opposing current case.*

of analysis: *Hs* has been calculated from the standard deviation of the wave surface time-series, whereas H_1 comes from Fourier analysis of the ensemble-averaged surface profile (phase-locked to one of the offshore fixed wave probes). The problem arises because wave time-series records on the inshore side of the jet current exhibit

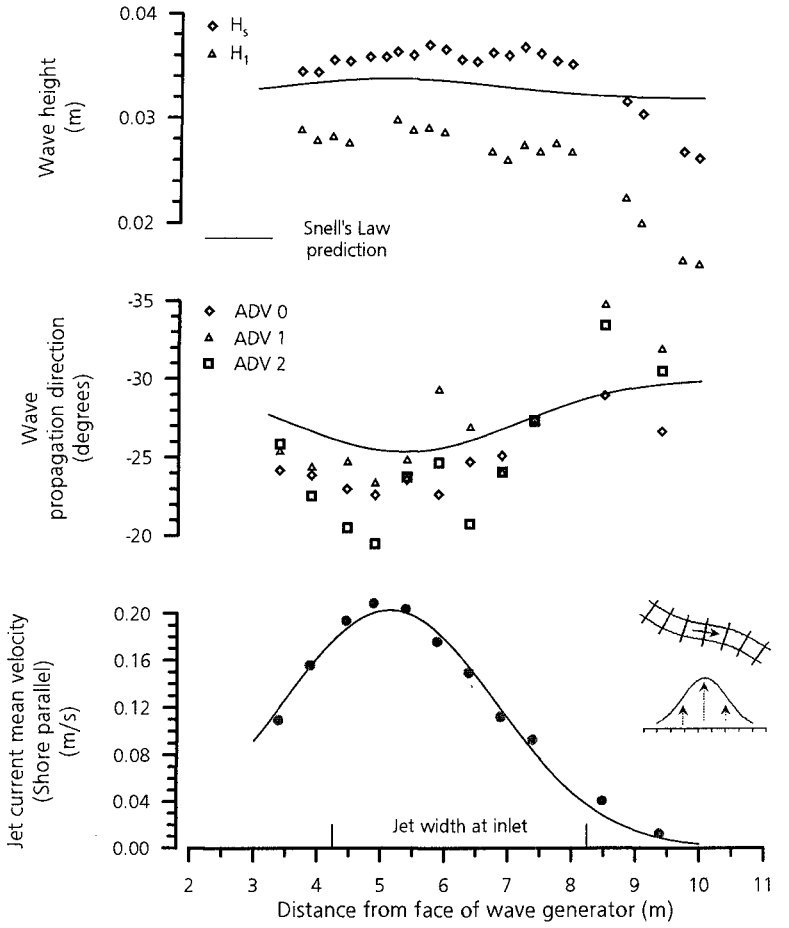

Figure 6: *Variation of wave height and direction (from velocity vectors) across the jet current: opposing current case.*

modulation patterns; these cause the ensemble-averaging process to move in and out of phase, thus reducing the amplitude of the resulting ensemble average and of the wave harmonics calculated from it. Clearly, in this situation, the significant wave height *Hs* is giving the true picture as far as wave height change across the jet is

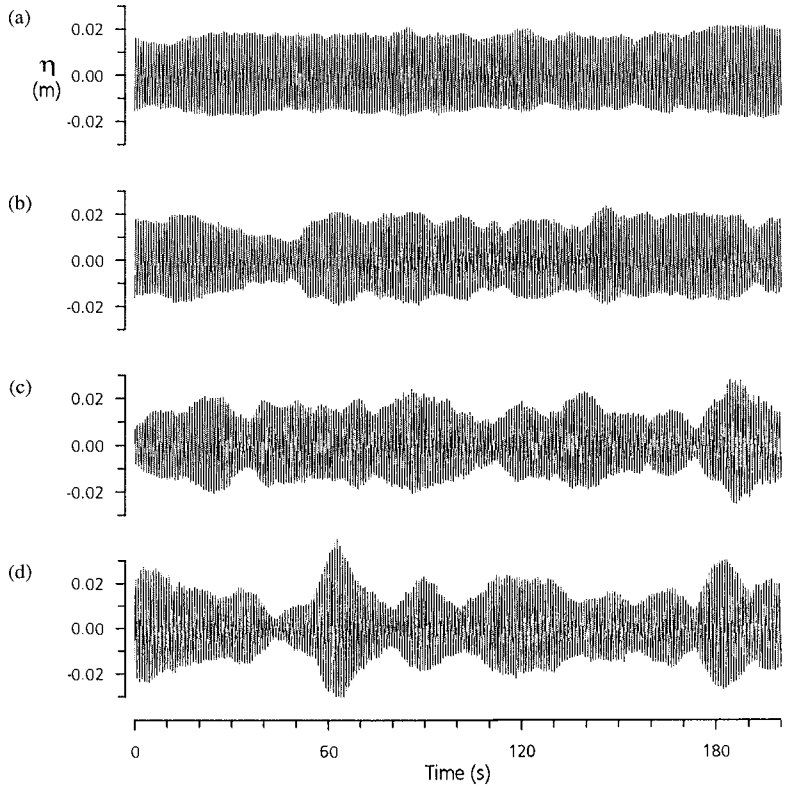

***Figure 7**: Surface elevation time series at locations across the jet current for the wave following current case. (a) 3.4m, (b) 5.4m, (c) 7.4m, (d) 9.4m.*

concerned, and the harmonics should be ignored.

The modulation in wave amplitude referred to above is an interesting phenomenon which needs to be considered when interpreting the results from this study. Time-series of wave surface elevation recorded at various locations across the jet current (**fig.7**) show that while there is some modulation at the offshore edge, the effect is worse inshore, where the waves have already propagated across the jet for some distance. These features generally exhibit time-scales of approximately 30s, which is rather lower than those noted above in relation to the meandering of the jet current.

While it has not yet been possible to model the observations in detail, it is

clear from the descriptions above that the angles of propagation (**figs.3-6**) observed on the jet can be explained as the effect of reflections (<10%) from the jet-current shear layers superimposed on the refraction angle predicted by gradually-varied flow theory. The phase of these reflected waves will vary depending on the exact location of the jet current at the point of reflection; similarly, the phase of the incident waves will depend on the location of the jet at the point where they first enter the shear layer. Hence the wave modulation will be related to the meandering of the jet but will not necessarily correlate with the time variation at any one point along the basin. The resultant wave pattern on the jet will thus be a function of incident wave characteristics, reflection coefficient from the shoreward shear layer, possible secondary internal reflection from the offshore shear layer, the mean horizontal jet current profile, and the temporal and spatial scales of the current meandering.

Conclusions

A significant data set has been acquired, providing information on the transformation of regular waves propagating across a narrow jet-like current with strong horizontal shear. Four methods have been used to measure the refraction of waves on the spatially varying current. One of these methods has been able to provide an independent measure of the local wave celerity on the jet current, and this confirms the predictions from a simple Doppler shift of linear wave theory.

The apparent angle of propagation of the incident waves does not follow a simple variation across the jet, but has been shown to be sensitive to the effect of small waves reflected from the shear layers.

In the absence of the jet current, wave amplitude is constant with time. When the current is added, the wave amplitude becomes modulated by the interaction of the incident waves with reflections from the gradually-meandering shear layer.

When waves are propagated across the jet-like current in a large wave basin such as the UKCRF, the jet is moved laterally. For following waves it translates towards the shoreline; for opposing waves it translates away from the shore.

Acknowledgements

This work was funded by the Commission of the European Communities Directorate General for Science, Research and Development under Contract MAS3-CT95-0011 as part of the KADWCI project: *Kinematics and Dynamics of Wave-Current Interactions*. The authors also wish to express their gratitude to HR Wallingford for allowing use of the UK Coastal Research Facility, and in particular to Adrian Channell for his support in ensuring that the tests were completed on time.

References

Jonsson, I.G. 1990. Wave-current interactions. In "The Sea", editors B. Le Mehaute and D.M. Hanes, Wiley-Interscience, pp.65-120.

Kirby, J.T. 1986. Comments on "The effects of a jetlike current on gravity waves in shallow water". J. Physical Oceanography, 16, pp.395-397

McKee, W.D. 1977. The reflection of water waves by shear currents. Pure Applied Geophys., 115, pp.937-949

McKee, W.D. 1996. A model for surface wave propagation across a shearing current. J. Physical Oceanography, 26, pp.276-278

Pawka, S.S. 1983. Island shadows in wave directional spectra. J. Geophysical Research, 88, C4, pp.2579-2591.

Simons R.R., Whitehouse R.J.S., MacIver R.D., Pearson J., Sayers P., Zhao Y. and Channell A. 1995. Evaluation of the UK Coastal Research Facility. Proc. Coastal Dynamics '95, Gdansk, Poland, pp.161-172.

Smith, J. 1983. On surface gravity waves crossing weak current jets. J. Fluid Mech., 134, pp.277-299.

Teisson C. and Benoit M. 1994. Laboratory measurements of oblique irregular wave reflection on rubble-mound breakwaters. Proc. 24th Int. Conf. on Coastal Engng., Kobe, Japan, Ch.116, pp.1611-1624.

Thomas G.P. and Klopman G. 1997. Wave-current interactions in the nearshore region. In "Gravity waves in water of finite depth", editor J.N. Hunt, Advances in Fluid Mechanics, Computational Mechanics Publications, pp.255-319.

Random Waves on a Vertically-sheared Current

C. Swan[1] and R. L. James[2]

Abstract

This paper considers the interaction between two-dimensional random waves and a co-linear, depth-varying, current. Two rotational wave-current models, capable of incorporating the effects of a depth dependent vorticity distribution, are combined with a conservation equation describing the total energy flux. This provides new solutions capable of predicting the change in a wave spectrum due to the interaction with a current. Comparisons between these solutions and a new data set confirms that a successful wave-current model must incorporate both the Döppler shift associated with the surface current and the near-surface vorticity distribution. Typical design calculations, based on a uniform current approximation, commonly satisfy neither of these constraints. Accordingly, they are shown to provide a poor description of the laboratory data. Furthermore, the nature of the wave-current interaction, which is shown to be significantly larger than the nonlinear wave-wave interactions, involves both a current-induced change in the wave motion and a wave-induced change in the current. While the former is reasonably well understood, the latter remains difficult to predict. Indeed, both parts of this overall interaction are shown to be strongly vorticity dependent.

1. Introduction

The nonlinear interaction between waves and a co-existing current is an important feature of many coastal and offshore environments. Accordingly, several authors have considered the case of regular waves on a variety of current profiles (see, for example, the recent review article by Thomas and Klopman, 1997). In its simplest form the current profile, $U(z)$, is assumed to be uniform with depth. In this case no vorticity is present and it has been conclusively shown that both the dispersion equation and the associated water particle kinematics are well described by a Döppler shifted solution (Fenton, 1985). Likewise, the change in the wave height, ΔH, which arises when the waves first propagate onto the current, can be modelled via the conservation of wave action

[1] Reader and [2] Research Assistant, Department of Civil and Environmental Engineering, Imperial College, London SW7 2BU.

(Thomas, 1990). Alternatively, if it is assumed that the current profile is represented by a linear shear, then a uniform vorticity distribution (ω=dU/dz) is introduced. In this case the wave motion again remains irrotational, but additional vorticity dependent terms arise within the dispersion equation so that the Döppler shifted solution is no longer applicable. In this case the water particle kinematics have been considered by Tsao (1959) and Kishida and Sobey (1988); while a linear formulation of a conservation equation for wave action has been provided by Jonsson *et al.* (1988).

More recently, solutions have been presented which address the case of waves on a current profile that varies arbitrarily with depth. In particular, considerable attention has been paid to cases in which the current profile is strongly sheared close to the water surface. Such cases are practically important since they are representative of a wind-driven current, and may also correspond to a typical estuarine outfall in the near-shore coastal region. In these cases the vorticity distribution is strongly non-uniform and, consequently, the wave motion becomes rotational. In terms of kinematic predictions an analytical model describing this type of interaction has been proposed by Swan (1992) and recently modified by Swan and James (1998); while numerical formulations are provided by Dalrymple (1974), Chaplin (1990), Thomas (1990) and Cummins and Swan (1993). In contrast, the initial wave height change, ΔH, caused by the interaction with a strongly sheared current is more difficult. In the absence of an appropriate (nonlinear) conservation of wave action equation, the conservation of total energy flux, R_x, must be applied.

Although the advances noted above have greatly enhanced our understanding of nonlinear wave-current interactions, they are restricted in the sense that they have principally considered the case of regular waves on currents. In practice the waves observed in most offshore and coastal locations are random, or irregular, with a significant frequency spread. In these cases the design engineer may be primarily concerned with the changes in a wave spectrum due to the interaction with a sheared current. It is this task which the present paper will address. Section 2 commences with a description of the experimental facility in which two-dimensional random waves were super-imposed on a depth-varying current. The essential characteristics of both an analytical wave-current model (Swan and James, 1998) and a multi-layered numerical model (Cummins and Swan, 1993) are briefly outlined in section 3. Using these results, a conservation of total energy flux equation is outlined, and verified with comparisons to a fifth-order conservation of wave action equation (Thomas, 1990) for the simplified case of regular waves on a uniform current. Comparisons between the laboratory data and both the analytical and numerical models are presented in section 4; while section 5 provides some concluding remarks concerning the extent of the wave-current interaction, the importance of the vorticity distribution, and those areas which require further consideration.

2. Experimental Apparatus and Measuring Procedure

The experimental work undertaken within this study was conducted in a purpose built wave-current flume. This facility is located in the Hydraulics Laboratory within the

Department of Civil and Environmental Engineering at Imperial College, London. The flume has an overall length of 25m, a width of 0.3m, and a working depth of 0.7m. The waves are generated by a bottom-hinged, numerically controlled, wave paddle located at one end of the wave flume. At the opposite end the wave energy is absorbed by a large block of poly-ether foam, the front face of which is cut to form a vertical wedge with an included angle of 30°. With this passive absorber in place, the reflection coefficient across a broad range of regular wave conditions was less than 2%. Further details of the wave flume are provided by Baldock *et al.* (1996).

Within the present tests the current was introduced via three loops of pipework. These allow a re-circulating and reversible current with a maximum volume discharge of $0.05m^3/s$. A sketch indicating the layout of the experimental facility is given on figure 1. Measurements undertaken within the wave-current flume include both time-histories of the water surface elevation, $\eta(t)$, recorded at a number of fixed spatial locations, and point measurements of the water particle kinematics to define both the shape of the current profile (acting in the absence of the waves) and the extent of the wave-current interaction. The surface elevation data was recorded via an array of surface-piercing resistance gauges. Individually, these consist of two vertical wires, each with an external diameter of 1mm, placed 10mm apart. Previous experience has shown that these gauges cause almost no disturbance of the flow field, and allow the water surface elevation to be recorded with an accuracy of ±1mm. The velocity data was recorded using a three beam Laser Döppler anemometer based on a 30mW helium-neon laser. This system was established in a forward scatter mode for optimal signal to noise ratio, and allows two components of the water particle velocity to be recorded simultaneously with an accuracy of ±2%. In each of the cases presented the measuring section was located 2.8m downstream of the wave paddle.

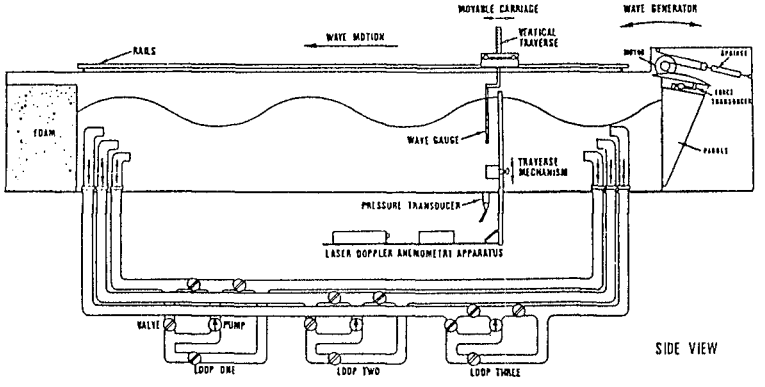

Figure 1. Layout of experimental facility

To create a vertically-sheared current at the measuring section, the mean flow was introduced in the form of an upwelling immediately downstream of the wave paddle (figure 1). With careful modifications of the inlet conditions a steady, two-dimensional,

current was achieved in which the surface velocities were of the order of $U_{z=\eta}\approx 0.6$m/s and the surfaee vorticity was as large as $(dU/dz)_{z=\eta}\approx 2.0$m/s/m. Figure 2a describes the time-variation of the current profile over a period of 3 hours; while figure 2b describes the cross-tank variation. These results clearly suggest that the eurrent profile is both steady and two-dimensional. In contrast, figure 2c describes the downstream variation in the current profile. Although there clearly remains some downstream variation, i.e. $dU/dx\neq 0$, this is at least one order of magnitude smaller than the gradient in the z direction. Hence, we are able to conclude that the nature of the wave-current interaction is dominated by the vertical shear in the current profile.

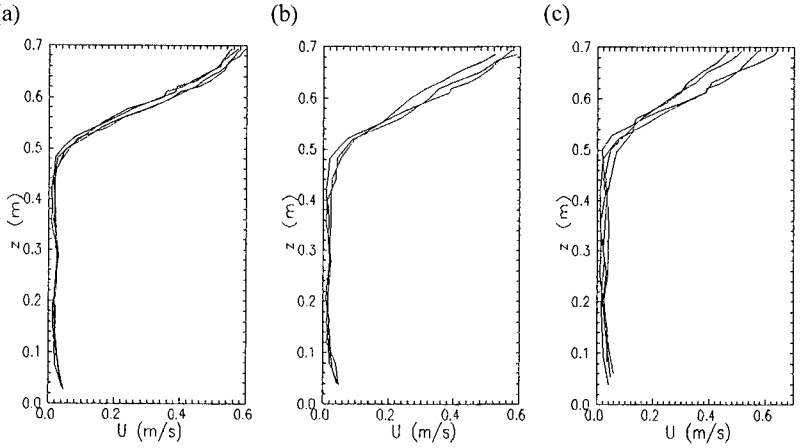

Figures 2a-2c. Characteristics of the current profile.
(a) Variation with time: t=0, 1hr, 2hrs and 3hrs; (b) Cross-tank variation: y=0.25b, 0.5b and 0.75b; (c) Downstream variation: x=0, 1.4m, 2.1m and 2.8m.

3. Modelling Work

In this section we will briefly mention two methods which have previously been applied to the modelling of regular waves on depth-varying currents. The first is the multi-layered numerical model outlined by Cummins and Swan (1993); while the second corresponds to the weakly nonlinear analytical solution described by Swan and James (1998). Although the results of these models are shown to be in good mutual agreement, the latter model is much easier to apply in the context of random waves. Indeed, the agreement between these models is an important finding in itself since it implies that the analytical formulation, which is only accurate to a second-order of wave steepness, has a wider range of applicability than one might expect.

3.1 Numerical Modelling

The scheme proposed by Cummins and Swan (1993) is essentially a five-layered equivalent of the two-layered or bi-linear shear model originally proposed by Dalrymple

(1974). If the computational domain is defined according to figure 3a, the stream function, ψ, in the i^{th} fluid layer, where i=1, ..., 5, is given by:

$$\psi = (c - U_{(i-1)})z - \frac{(U_i - U_{i-1})}{d_{i-1} - d_i}\left(\frac{z^2}{2} + d_{i-1}z\right) + \sum_{n=1}^{N}\left[X_i(n)\sinh\left(\frac{2\pi nz}{\lambda}\right) + Y_i(n)\cosh\left(\frac{2\pi nz}{\lambda}\right)\right]\cos(nkx) \quad (1)$$

where the Cartesian co-ordinates (x,z) have their origin at the mean water surface, z is measured vertically upwards and x in the direction of wave propagation, c is the phase velocity, d_i is the depth of the i^{th} fluid layer, U_i defines the current profile, and λ is the wave length. Within (1) the first term on the right hand side ensures that the solution is steady; the second term defines the current profile, approximated by a series of linear shear currents; while the third term defines the oscillating flow field and includes the unknown coefficients (X_i, Y_i). A solution of this type is appropriate to the description of the equilibrium conditions arising in a combined wave-current flow.

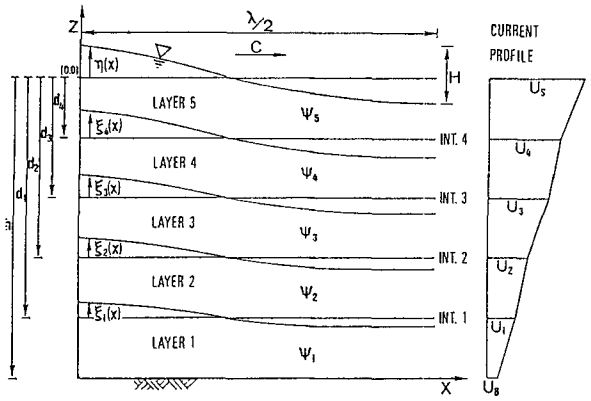

Figure 3a. Co-ordinate arrangement and solution domain

Assuming that the wave height, H, the wave period, T, the water depth, d, and the current profile, $U(z)$ (occurring in the presence of the waves) are defined, the usual boundary conditions coupled with a number of compatibility constraints applied at the interfacial sections ($z=\xi_i$, where i=1, ..., 5) allow the flow field to be solved. Solutions for the wave length, λ, the surface profile, η, the oscillatory velocity components (u,v) and the pressure, p, are thus achieved. Using this approach the order of the approximation was typically set at N=8 for nonlinear waves on a strongly sheared current, and the calculations undertaken on a standard 200MHz personal computer. Detailed comparisons between this model and a data set concerning regular waves on a variety of strongly sheared currents are provided by Swan *et al.* (1998).

3.2 Analytical Modelling

In contrast to the numerical scheme noted above, the analytical model is restricted to a second-order of wave steepness and is based on the orthogonal transformation indicated on figure 3b.

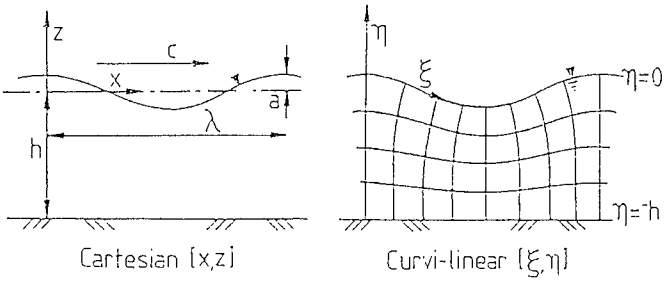

Figure 3b. Co-ordinate arrangement and solution domain

Within the (ξ,η) frame, η=0 defines the free-surface, η=-d, the bottom boundary, and the current profile (again specified in the presence of the waves) is defined by a third-order polynomial such that in a stationary frame of reference:

$$U(\eta) = (P + 2Q\eta + 3R\eta^2 + 4S\eta^3).\delta_s(\eta + md) \tag{2}$$

where P, Q, R and S are constants, η=-md defines the vertical extent of the current, i.e. $0 \le m \le 1$, and δ_s is a step function such that $\delta_s(y)$ is 0 if $y<0$ or 1 if $y \ge 0$. After solving the two-dimensional vorticity equation in general orthogonal co-ordinates for an inviscid fluid, subject to the usual boundary conditions, the stream function, ψ, is given by:

$$\begin{aligned}\psi = &-c\eta + \left(Q\eta^2 + R\eta^3 + S\eta^4\right)\delta_s(\eta + md) - P\eta.\delta_s(-\eta - md)\\ &+ a\left(2Q\eta + 3R\eta^2 + 4S\eta^3 + \frac{6S\eta}{k^2} + f_a\right)\frac{\sinh k(d+\eta)}{\sinh(kd)}\cos(k\xi).\delta_s(\eta + md)\\ &+ a\left(-\frac{3R\eta}{k} - \frac{6S\eta^2}{k} + f_b\right)\frac{\cosh k(d+\eta)}{\sinh(kd)}\cos(k\xi).\ \delta_s(\eta + md)\\ &+ af_c \sinh k(\eta + md)\cos(k\xi).\delta_s(-\eta - md)\end{aligned} \tag{3}$$

where the constant coefficients f_a, f_b and f_c are dependent on the wave characteristics and the current profile. Applying this solution, the velocity components in the (ξ,η) directions are given by:

$$u_\xi = J^{1/2}\frac{\partial\psi}{\partial\eta} \quad \text{and} \quad u_\eta = -J^{1/2}\frac{\partial\psi}{\partial\xi} \tag{4}$$

where the Jacobian, J, is defined by $J=\partial(\xi,\eta)/\partial(x,z)$. Within this solution the first term on

the right side of (3) reflects the translation of the co-ordinate axis; the second and third terms define the current profile; while the remaining terms provide a first approximation to the nonlinear wave-current interaction. Comparisons between this solution, the numerical model discussed in section 3.1, and a number of regular wave cases on strongly sheared currents, are provided in Swan and James (1998). This paper also gives explicit solutions for the Jacobian and the dispersion equation.

3.3 Energy Flux

We have already noted that in the case of nonlinear waves interacting with a strongly sheared current (with non-uniform vorticity) a conservation equation for wave action has not, as yet, been derived. Accordingly, a simpler approach, orginally proposed by Longuet-Higgins and Stewart (1960) in their derivation of the radiation stress tensor, is adopted. This ensures that the total energy flux associated with both the wave and the current is conserved. In effect, the total energy flux comprises three distinct contributions. The first arises due to the rate at which work is done by the pressure, p. If we consider the combined wave-current flow, this contribution is defined by:

$$R_x^1 = \iint p\,u_x\,dz\,dx \tag{5}$$

where u_x is the total horizontal velocity including both the wave and the current components, i.e. $u_x=u+U$. The second contribution arises from the additional transport of kinetic energy and is given by:

$$R_x^2 = \int\int \left(\tfrac{1}{2}\rho\,\underline{u}^2\right) u_x\,dz\,dx \tag{6}$$

where ρ is the density of the fluid and $\underline{u}=u_x+u_z$. Similarly, the third contribution represents an additional transport of potential energy and is given by:

$$R_x^3 = \int\int (\rho\,g\,z)\,u_x\,dz\,dx \tag{7}$$

where g is the gravitational acceleration and d the total water depth. Combining these results gives a total energy flux of $R_x = R_x^1 + R_x^2 + R_x^3$. Assuming that this total flux is constant, one can add the energy flux associated with the current (acting alone) with the energy flux associated with the waves (again acting alone), and equate this to the total energy flux in the combined wave-current environment:

$$R_{x(\text{current})} + R_{x(\text{waves})} = R_{x(\text{waves+current})} \tag{8}$$

If this equation is combined with the results of either the numerical model (section 3.1) or the analytical solution (section 3.2) the wave height change, ΔH, which arises when the wave and the current first interact, can be determined.

To verify this energy flux formulation we first considered a simple waves only situation (no current) and compared the sum of (5), (6) and (7) with the energy flux

calculated according to Ec_g, where E is the energy in one wave length and c_g is the group velocity. Figure 4a presents the results of this comparison for regular waves (T=10s, d=50m) in which Ec_g was calculated using a high-order stream function solution. The observed agreement is clearly very good, with minor deviations only arising in the very steepest waves. In a second test, we considered the case of regular waves (H=7.5m, T=10s, and d=50m) propagating on a uniform current. In this case the wave height change predicted using the present formulation, i.e. (8), coupled with a high-order stream function solution was compared to the linear solution proposed by Bretherton and Garrett (1968) and the fifth-order solution proposed by Thomas (1990). The latter solutions being based upon the conservation of wave action. Figure 4b contrasts these results and shows good agreement between the present energy flux approach and the nonlinear conservation of wave action. Indeed, this figure also highlights the importance of the nonlinear terms when seeking to define the change in wave height.

4. Discussion of Results: Random Waves

The solutions outlined in sections 3.1 and 3.2 were formulated to solve the interaction of regular waves with depth-varying currents. Nonetheless, they can be applied in a 'linear' sense to the individual components of a random or irregular sea in an attempt to determine a first approximation to the changes in the wave spectra. If this approach is adopted, the nonlinear interaction between the individual wave components and the co-existing current are correctly modelled, but the nonlinear wave-wave interactions (together with any subsequent interactions that these components have with the current) are neglected. However, it will be shown that for a typical Pierson-Moskowitz (P-M) spectrum interacting with a strongly sheared current, the nonlinear wave-wave interactions are negligible in comparison to the wave-current interactions. As a result, the present approach should provide a good first approximation to any changes in the wave spectrum.

The first P-M spectrum investigated in the laboratory study had an average zero up-crossing period of T_z=0.94s and a significant wave height (measured in the absence of a current) of H_s=0.062m. This case therefore corresponds to a relatively linear sea state. The characteristics of this spectrum measured on quiescent water (or in the absence of a current) are indicated by the uppermost curve on figure 5a. This spectrum was generated by the summation of 99 individual wave components with random phasing; it was calculated from two time-histories of the water surface elevation, each recorded at 25Hz for a duration of 600s. Preliminary tests confirmed that this spectrum was highly repeatable, being both stationary and ergodic. In subsequent tests the current profile indicated on figure 2a was generated within the wave flume. Having allowed sufficient time for the profile to become stable, an identical signal to that described above was sent to the wave paddle. The resulting water surface elevations, involving the waves on the current, were again recorded and the corresponding spectra calculated in an identical manner. The results of this process are indicated by the second solid line on figure 5a. The effect of the wave-current interaction, in terms of spectral changes, is clearly apparent.

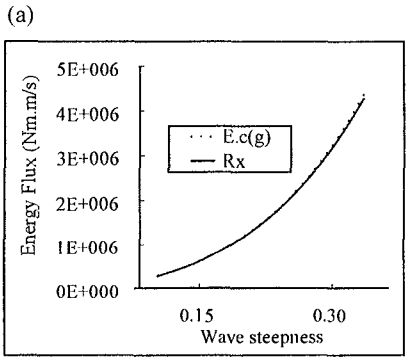

Figure 4a. Energy flux for waves only case

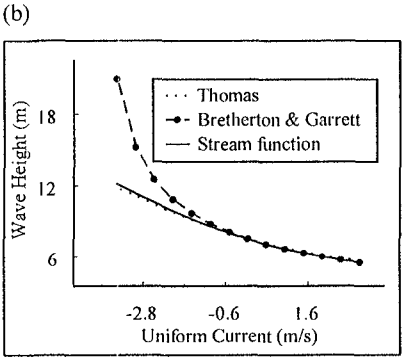

Figure 4b. Wave height change on a uniform current

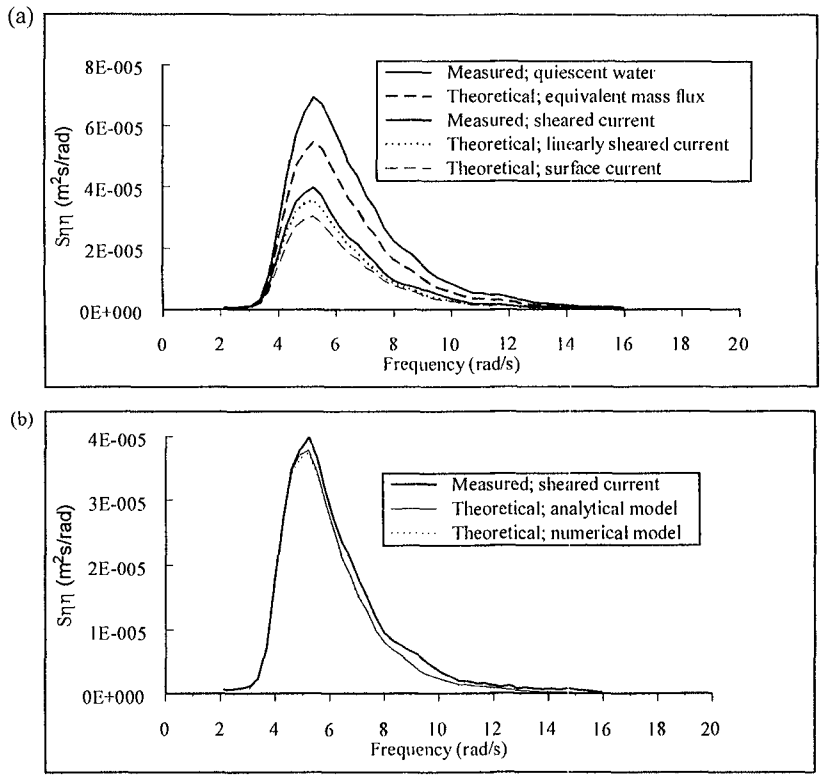

Figure 5a-5b. Changes in a linear spectrum

The remaining curves indicated on figure 5a correspond to the predicted wave spectrum assuming that: (a) the current is uniform with depth and has a value equal to the surface current; (b) the current is uniform with depth and has a value such that the total (depth-integrated) mass flux is conserved; and (c) the current varies linearly with depth. These comparisons suggest that while solution (a) correctly models the Döppler shift, it entirely neglects the vorticity and therefore over-predicts the change in the wave spectrum. Alternatively solution (b), which is commonly applied in a design context, fails to model either the Döppler shift or the vorticity profile, and consequently provides the worst prediction of the wave-spectra on the current. In contrast, the solution which uses a linearly-sheared current correctly describes the Döppler shift, and makes some attempt to model the effects of the vorticity. As a result, this latter model provides an improved description of the measured spectra. Nevertheless, even in this case, there remain significant differences between the measured and predicted data.

In contrast figure 5b compares the wave spectra measured on the current with the results of both the numerical model and the analytical solution described in sections 3.1 and 3.2. In each of these solutions iterative calculations were undertaken to determine the individual wave heights which satisfy the total energy flux constraint (8). In applying this approach it is assumed that there is no transfer of energy between components within the spectrum. This point is further discussed below. Furthermore, it is important to note that although the iterative calculations are relatively straightforward, those based on the numerical model can be somewhat time-consuming. Whereas those based on the analytical model are rapid and easy to apply. In essence, this latter solution is no more difficult to apply than a second-order Stokes' model.

The comparisons provided on figure 5b confirm that both these solutions provide a much improved description of the wave spectra measured in the presence of the current. Indeed, this is to be expected since these models (and only these models) allow the affects of both the Döppler shift and the vorticity distribution to be correctly incorporated. Furthermore, comparisons between figures 5a and 5b suggest that the vorticity can be of equal importance to the Doppler shift when attempting to predict the changes in the wave spectra due to the interaction with a sheared current.

Figures 6a and 6b present a similar sequence of results in which the P-M spectrum measured in quiescent water has an average zero up-crossing period of T_z=0.98s and a significant wave height of H_s=0.090m. In this case the sea-state is more nonlinear, with some evidence of occasional wave breaking. However, the frequency of the breaking events was such that they had no significant influence on the characteristics of the wave spectrum. In figure 6a the measured and predicted spectra show similar trends to those identified on figure 5a, although the differences are inevitably somewhat larger. This is particularly true of the linearly-sheared current (Jonsson *et al.*, 1978) since this neglects the nonlinear terms in the wave-current interaction. Figure 6a also includes an additional curve, which indicates the magnitude of the second-order nonlinear wave-wave interactions (the scale appropriate to this curve is given on the right hand axis). Comparisons between this curve and the change in the wave spectrum due to the interaction with the current confirm that the wave-current interaction is indeed dominant.

(a)

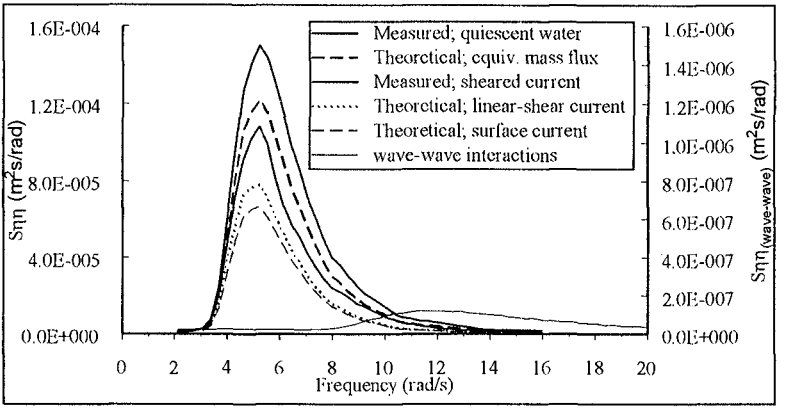

(b)

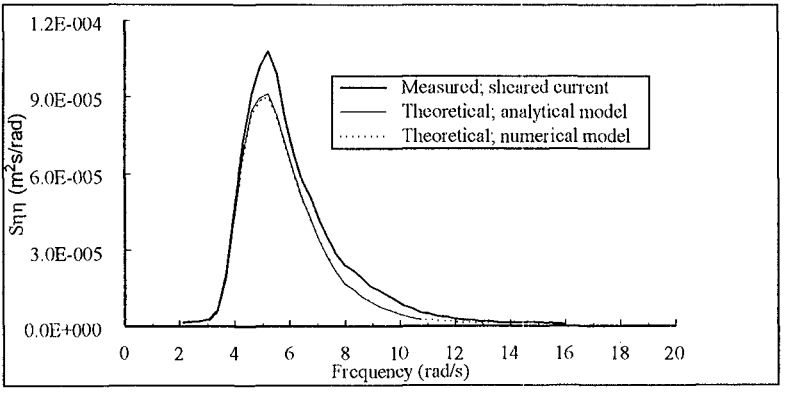

Figure 6a-6b. Changes in a nonlinear spectrum

In Figure 6b the results are (unfortunately) somewhat different from those given on figure 5b. In this case, the comparisons suggest that neither of the present methods provide a good description of the spectral changes, although they do represent a significant improvement over the solutions indicated on figure 6a. However, it is interesting to note that the apparent shortcomings are equally applicable to both the numerical calculations and the second-order analytical model. This suggests that the 'errors' do not arise as a result of higher-order nonlinear terms within the wave-current interaction. Indeed, the present results confirm that the weakly nonlinear analytical model is more widely applicable than one might expect.

The most probable explanation for the 'errors' in figure 6b lie in our treatment of the current profile. In previous studies, concerning regular waves on a vertically-sheared current, considerable effort was made to determine the current profile in the presence of the waves. Indeed, good agreement between the measured and predicted oscillatory velocities was only achieved when this profile was applied within either the analytical solution or the numerical model. In the present case this approach has not been adopted. Indeed, the results presented in figures 5 and 6 were calculated using the current profile measured in the absence of waves. The reason for this difference is clear. In a regular wave case the magnitude of the current was calculated along an empirically determined streamline. This approach allows the characteristics of the current, in particular its gradient, to be determined close to the water surface. In random waves it is simply not possible to undertake such an approach.

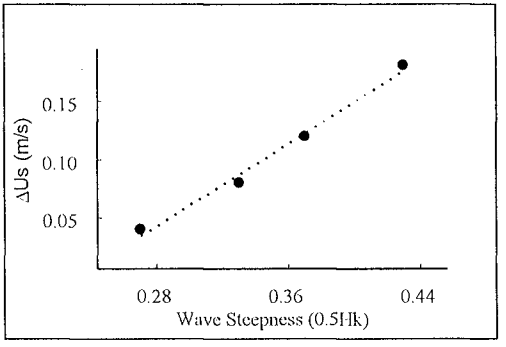

Figure 7. Changes in the surface current (regular waves)

Nevertheless, if we return to our previous regular wave data, it is clear that the extent of the current change is dependent upon the wave height, or more probably the wave steepness. For example, figure 7 considers four regular wave cases and describes the change in the magnitude of the surface current as a function of the wave steepness. Taking into account this change, it is clear that as the steepness of a random sea-state increases, the present methods will provide less reliable results. Furthermore, it is clear that if the change in a wave spectrum due to the interaction with a current is to be adequately predicted, the change in the current due to the presence of the waves must be defined. Recent work by Groeneweg and Klopman (1998) provide a possible method for investigating this effect. However, if the results of recent regular wave studies are to be believed, it would appear that in random waves the current profile will be continuously changing as it attempts to adjust to the local (or instantaneous) wave conditions. In such circumstances it may be very difficult to separate those parts of the fluid motion that relate individually to the wave and the current.

In an attempt to account for the extent of the current change, Δu, particularly that arising close to the water surface, the present study has reconsidered the current change arising in several regular wave cases, and has applied a similar change to the present

study. Having identified a 'modified' current profile, the iterative calculations were repeated and a new wave spectrum determined. The results of this procedure are presented on figure 8. This is identical to the case considered in figures 6a and 6b, and contrasts the spectrum measured in the presence of the waves with two predictions based on the analytical formulation. The first assumes the current remains unchanged; while the second is based upon our best estimate of the changed current profile. The improvement in the solution is clearly significant, and highlights the importance of the wave-induced current change. However, it should be noted that although the peak of the spectrum is in good agreement, its overall shape is no longer self-similar. This clearly raises the possibility of significant energy transfers within the spectrum due to subtle changes in the current profile.

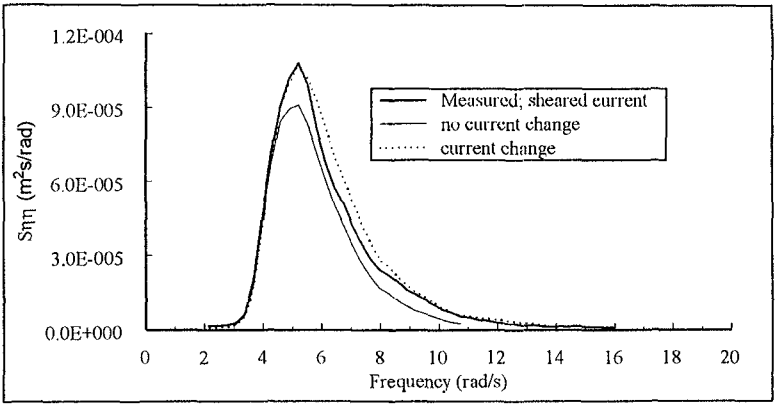

Figure 8. Spectral predictions based on a changed current

5. Concluding Remarks

The present paper has considered the modification of a random wave spectrum due to the interaction with a depth-varying current. New experimental data has been presented, and the results shown to be in reasonable agreement with a new calculation procedure based upon the conservation of total energy flux. Although this solution represents a significant improvement over existing design methods (traditionally based upon a uniform current approximation), difficulties remain concerning the description of a current profile in the presence of waves. Indeed, the present study has clearly demonstrated that in the case of a depth-varying current, the nature of the wave-current interaction involves both a current-induced change in the wave motion, and a wave-induced change in the current. Finally, the present study has also shown that a relatively simple, weakly nonlinear, analytical solution can be surprisingly effective, and provides clear guidance as to the importance of the vorticity distribution.

Acknowledgement

This work was undertaken as part of the MAST project 'The Kinematics and Dynamics of Wave-Current Interactions'. It was funded by the Commission of the European Union Directorate General for Science, Research and Development under contract No. MAST3-CT95-0011.

References

Baldock, T. E., Swan, C. and Taylor, P. H. (1996) A laboratory study of nonlinear surface waves on water. *Phil. Trans. R. Soc., Lond.* A **354**, 649-676.

Bretherton, F. P. and Garrett, G. J. R. (1968) Wavetrains in inhomogeneous moving media. *Proc. Roy. Soc.*, A **302**, 529-554.

Chaplin, J. R. (1990) The computation of nonlinear waves on a current of arbitrary non-uniform profile. OTH 90327, HMSO.

Cummins, I. and Swan, C. (1993) Nonlinear wave-current interactions. *Wave Kinematics and Environmental Forces. Society for Underwater Tech.*, Vol. **29**, pp. 35-51.

Dalrymple, R. A. (1974) Water waves on a bilinear shear current. *Proc. 14th Conf. Coastal Eng., Hamburg*, pp. 626-641.

Fenton, J. D. (1985) A fifth-order Stokes theory for steady waves. *J. waterway, Port, Coastal and Ocean Eng., ASCE*, Vol. **111**, pp. 216-234.

Groeneweg, J. and Klopman, G. (1998) Changes of the mean velocity profiles in the combined wave-current motion described in GLM formulation. Accepted for publication in *J. Fluid Mech.*

Jonsson, I. G., Brink-Kjær, O. and Thomas, G. P. (1978) Wave action and set-down for waves on a shear current. *J. Fluid Mech.*, Vol. **87**, 401-416.

Kishida, N. and Sobey, R. J. (1988) Stokes theory for waves on a linear shear current. *J. Eng. Mech., ASCE*, Vol. **114**, pp. 1317-1334.

Longuet-Higgins, M. S. and Stewart, R. W. (1960) Changes in the form of short gravity waves on long waves and tidal currents. *J. Fluid Mech.*, Vol. **8**, pp. 565-583.

Swan, C. (1992) A stream function solution for waves on a strongly sheared current. *Proc. 23rd. Int. Conf. Coastal Eng., Venice,* Vol. **1**, pp. 684-697.

Swan, C. and James, R. L. (1998) A simple analytical model for surface water waves on a depth-varying current. Submitted to *J. Geophys. Res.*

Swan, C., Cummins, I. P. and James, R. L. (1998) An experimental study of 2-D surface water waves propagating on depth-varying currents. Part 1: Regular waves. Submitted to *J. Fluid Mech.*

Thomas, G. P. (1990) Wave-current interactions: an experimental and numerical study. Part 2. Nonlinear waves. *J. Fluid Mech.* Vol. **216**, pp. 505-536.

Thomas, G. P. and Klopman, G. (1997) Wave-current interactions in the near-shore region. *In 'Gravity waves in water of finite depth', Ed. J. N. Hunt, Advances in Fluid Mechanics, Computational Mechanics Publications*, pp. 255-319.

Tsao, S. (1959) Behaviour of surface waves on a linearly varying flow. *Tr. Mosk. Fiz.-Tekh. Inst. Issled. Mekh. Prikl. Mat.*, Vol. **3**, pp. 66-84.

Wave Setup and Other Tidal Anomalies in Coastal Rivers

Eko Santoso[1], David Hanslow[2], Peter Nielsen[1] & Kevin Hibbert[2]

Abstract

The tailwater level is together with rainfall the most important input to flood modeling in coastal rivers. Thus, the need for an ocean-river interface which can provide tailwater levels for numerical models is obvious. The state of the art is however not very advanced. Detailed waterlevel profiles through the Brunswick River entrance from 500m inside the breakwaters to 150m outside during a wide range of weather conditions revealed that the wave setup through the zone of wave breaking is much smaller than what is being used by practicing modelers in Australia. Barometric effects of the order 1cm per hPa is only a minor part of the tidal anomalies, which range up to 0.8m 500m inside the breakwaters, and wind effects, although not modeled in detail, are estimated to be small on the fairly narrow continental shelf of South East Australia. Tidal anomalies of the order 0.5 to 0.7 metres have been observed in the absence of rainfall and strong local winds during Cyclone Roger in 1993. An offshore record indicated that a substantial fraction of this tidal anomaly (of the order 0.25m) also occurred in 25m of water offshore from the Tweed River on the border between New South Wales and Queensland. This indicates the presence of weather related oceanic forcing of a nature which is not understood in detail.

1. Introduction

The state of the art of flood modeling in coastal rivers at present is not very advanced in general. In particular, the tailwater level, which is an important input to the flood model, is not accurately predicted.

[1]Department of Civil Engineering, The University of Queensland, St. Lucia, Australia 4072. Fax:+61 7 3365 4599

[2] New South Wales Department of Land and Water Conservation, Coastal Branch, 10 Valentine Avenue, Parramatta, NSW 2150.

Precise prediction of tailwater the level is important during both normal and emergency situations. People may benefit from the coastal environment and should be protected from natural disasters. Several past records show that extreme water levels cost millions of dollars to the people and the government. The February 1993 low water level event cost the New South Wales Oyster Industry millions of dollars when the oyster cages became exposed to the air. At the same time, flooding along the coastal rivers costs the NSW Government tens of millions of dollars per annum (Hanslow and Nielsen, 1992). The storm surge event on 17 February 1996 caused heavy inundation in Gold Coast canal jetties and roads (Nielsen, Voisey and Santoso, 1997). Hence, Australia needs better flood models in general and better models of river entrance water levels in particular.

Several weather-related forcing mechanisms have been identified, however, there is still lack of precise quantification for better prediction. A quantitative model of Coriolis effects on longshore currents, as one of the most probable driving forces during cyclone events, is developed.

2. Historical Data

The difference between the measured water levels and the astronomically predicted levels are called tidal anomalies. Extreme water levels, which include large anomalies, have been studied for decades, but still the forcing mechanisms are not quite clear.

2.1. The inverse barometer effect

Extreme water levels usually show significant, negative correlation with the local barometric pressure. Investigations at several tidal stations on the East Coast of Australia found the sea level depressed about half the theoretical amount of 1 cm per hectopascal. Conversely, greater than theoretical values were typical for some locations on the West Coast. On Lord Howe Island the inverse barometer law gives accurate predictions. This is an indication that the continental shelf is influential (Hamon, 1962, 1963, 1966, Robinson 1964). In the Bay of plenty, New Zealand, the inverse barometer law applies accurately over a limited range of periods (Goring and Bell, 1993). Investigation of the Manly Hydraulics Laboratory database shows that the low barometric pressures alone is not appropriate to predict the tidal anomalies. For instance, theoretical barometric set-up during Cyclone Justin (March 1997) accounts for only 25% of the observed tidal anomaly (see Figure 1).

2.2. Wave set-up

Wave set-up, which has been long believed to be an important contributor to extreme water levels, has negligible influence to the overheight water level in most river entrances. Thus, historical data from the Brunswick River (1987 to 1996) show that offshore wave heights are not correlated with the tidal anomalies. In fact, some very high waves coincided with negative tidal anomalies (see Figure 2).

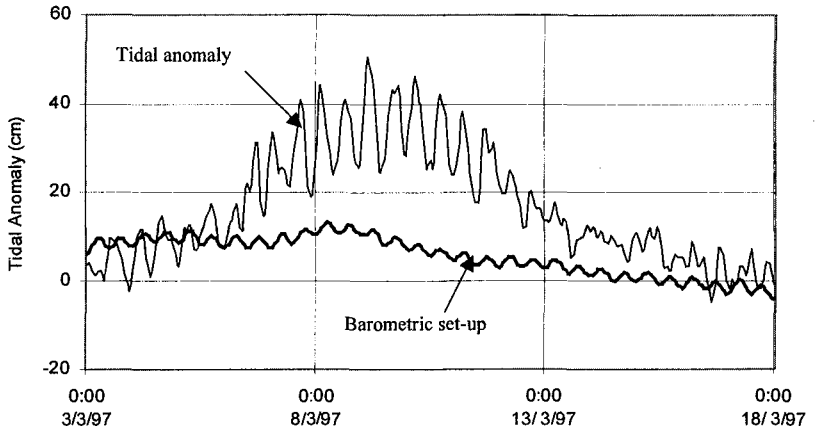

Figure 1. Tidal anomaly and barometric set-up at Rosslyn Bay during Cyclone Justin, March 1997. The theoretical barometric set-up (1 cm/hPa) contributes a minor fraction to the observed tidal anomaly. Data courtesy of National Tidal Facility, Adelaide.

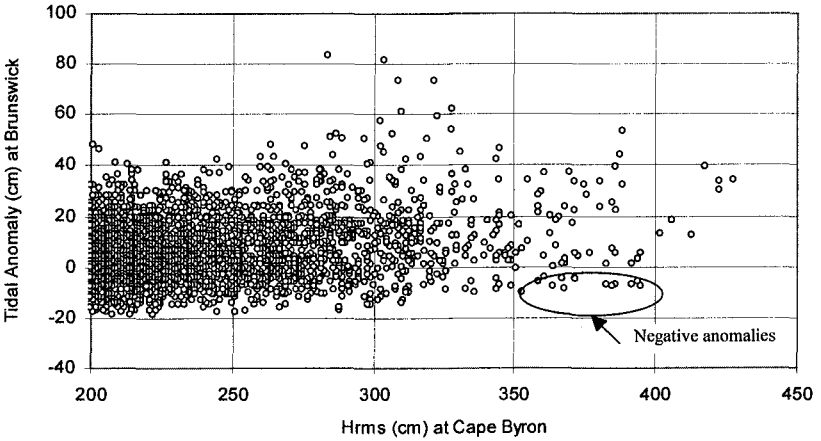

Figure 2. Tidal anomaly versus offshore root mean square wave heights at Brunswick Heads. Even for the very shallow (just navigable by fishing vessels) Brunswick River there is very little correlation between offshore wave height and tidal anomaly just inside the wave breaking in the river. Data courtesy of the MHL, Sydney.

The New South Wales Government has sponsored field investigations at the Brunswick River entrance (Brunswick Heads) over the last decade, headed by Dr. Peter Nielsen. The primary achievement of this work has been detailed water level profiles through the river entrance from 300m inside the breakwaters to 150m outside during a wide range of weather conditions. It was found that different water levels between inner and outer river entrance were caused by hydraulic gradient in the entrance during flood and ebb tides (see page 250, Hanslow and Nielsen, 1992).

2.3. Rainfall

Previous investigations found that rainfall contributes significantly to the tidal anomaly for gauges in rivers with small cross section of river entrance compared with the large river catchment area.

Table 1. The ratio between cross section of river entrance and catchment area. (Data from The Department of Land and Water Conservation NSW, 1997).

Name	Catchment area (km^2)	River entrance cross section (m^2)	Ratio
Gold Coast Seaway	150	3300	2.2×10^{-5}
Tweed River	1100	400	3.6×10^{-7}
Brunswick River	160	160	10.0×10^{-7}
Richmond River	6850	1340	2.0×10^{-7}

Data from the Brunswick River show the correlation between rainfall intensity in the river catchment and tidal anomalies in the river entrance (Figure 3). The plots show vertical clusters, which consist of 6 one-hourly tidal anomalies versus cumulative rainfall for the six hours period. The lower part of each cluster indicates the fresh water flow has not reached the tide gauge yet. The appropriate cumulative time applied in the plot is site specific, dependent on the characteristics of river catchment.

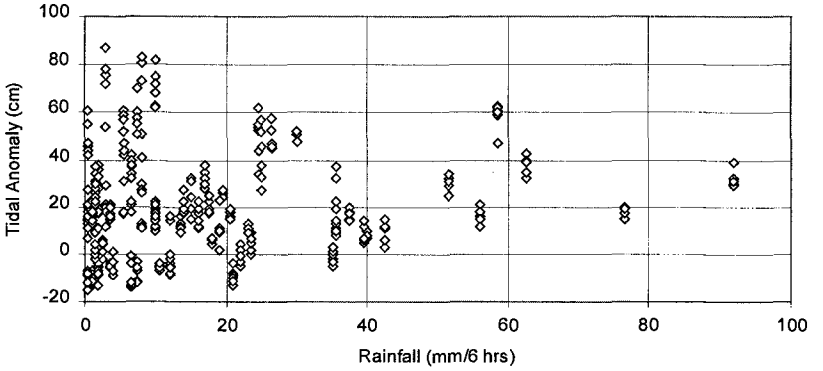

Figure 3. Hourly tidal anomalies versus 6 hourly cumulative rainfall at the Brunswick River. Data courtesy of the MHL, Sydney.

Tide gauges installed in rivers with small entrance to the large catchment ratios such as the Brunswick and the Tweed Rivers are quite sensitive to rainfall. Hence, rainfall over these two catchment areas in the period of 15 to 17 February 1995 contributes significantly to the high tidal anomalies (see Figure 4).

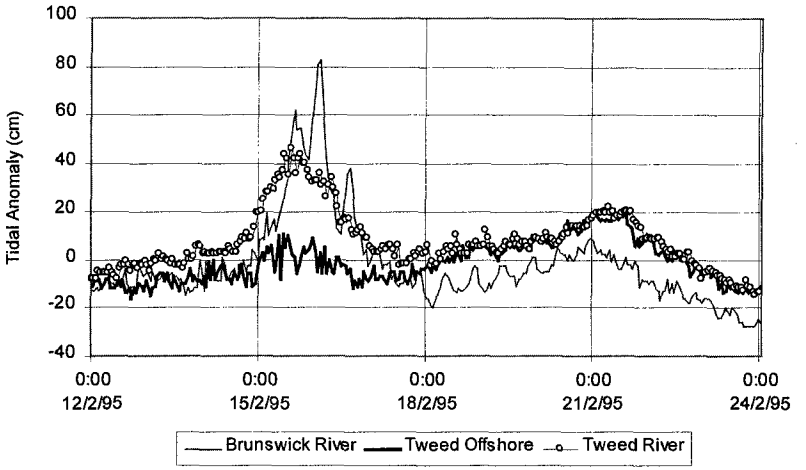

Figure 4. Tidal anomalies generated by heavy rainfall on 16 February 1995 event. Tidal anomalies at the Brunswick and Tweed Rivers are high compared with that of Tweed Offshore, which was not influenced by fresh water flow. Data courtesy of the MHL, Sydney.

2.4. Negative anomalies

Negative anomalies, which cannot be generated by rainfall or wave setup are of interest for evaluating the variation of other driving mechanisms along the coast. Thus, the negative tidal anomalies at the Gold Coast Seaway and at Ballina (at the Richmond River entrance), which are only 80 km apart show quite different trends for the more significant events (see Figure 5). These data imply that along the coast of NSW and Queensland the strength of the oceanic driving mechanisms vary significantly.

3. Long Periodic Waves

Travelling cyclones are some times able to generate long periodic waves. Low barometric pressure at the center of cyclone causes the sea water level to rise in a mound shape. As the cyclone moves into the shallow water, the combination of high wind stresses on the surface and friction on the ocean bed generate long wave (Stark, 1977; Lighthill, 1998).

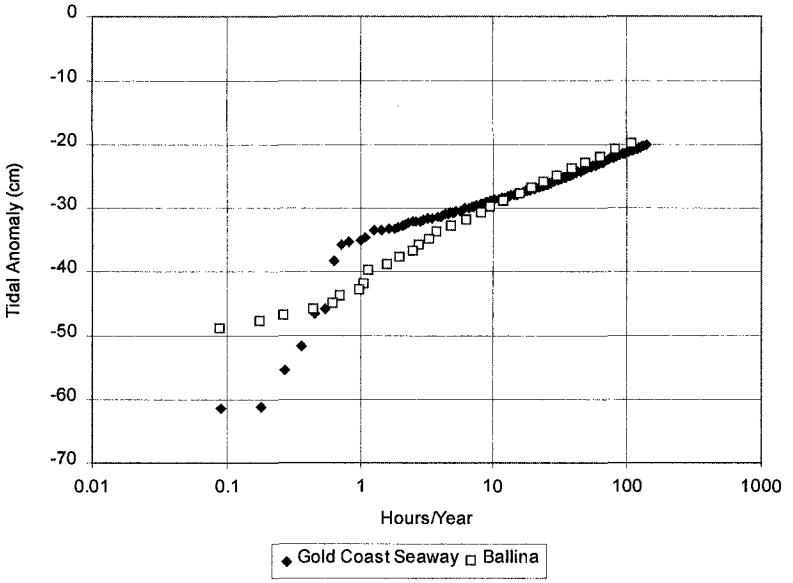

Figure 5. Exceedance plot of negative tidal anomalies at the Gold Coast Seaway and Ballina (at the Richmond River entrance). Data courtesy of MHL, Sydney.

The motion of long waves parallel to a coastline can generate a number of edge wave modes, and only the fundamental mode is stimulated by the large-scale pressure disturbances (Greenspan, 1956). However, Reid (1958) stated that if wind stress is considered, cyclones could generate higher order of edge waves.

The amplitude of the long waves is dependent on the local topography. Shoaling, diffraction and reflection are of primary importance for the extreme water levels along the coast.

The presence of long periodic waves was observed at tidal stations along the East Coast of Australia (Figure 6). The event ten days before Cyclone Violet showed the movement of a long wave. The phase shift of the tidal anomaly peaks of Ballina, Brunswick River and Tweed Offshore around 21 February 1995 were less than a day. This is because the distance between Ballina to Brunswick and Brunswick to Tweed Head are about 30 km and 65 km respectively. The tidal anomaly peaks at Rosslyn Bay and Cape Fergusson, where separated about 700km and 1250km from Brunswick, occurred 3 and 4 days later. Another travelling long wave can be seen in Figure 7, during Cyclone Justin.

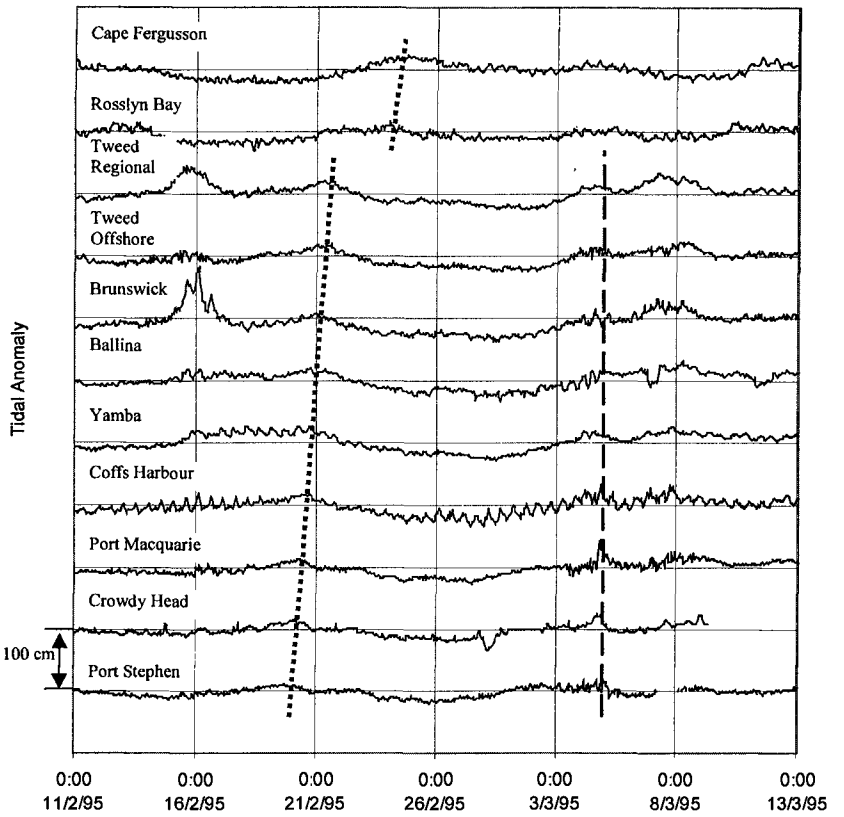

Figure 6. The travelling long wave was marked by north going tidal anomaly peaks during 18-26 February event (dotted line). Cyclone Violet (3-8 March), which came very close to Brunswick generated tiny tidal anomalies along the NSW coast without long wave character (dashed line). Data courtesy of MHL and NTF.

4. Cyclone Justin

As discussed above, travelling cyclones can generate continental shelf waves. Stationary cyclones however, do not have this ability. They generate different types of tidal anomalies. Our best example is Cyclone Justin (March 1997), which was stationary in the Coral Sea, in the North East of Townsville, for about two weeks. Tidal anomalies in the order of 0.5 to 0.8 m were generated along the North Coast of Queensland, but no significant were found south of Mooloolaba (see Figure 7).

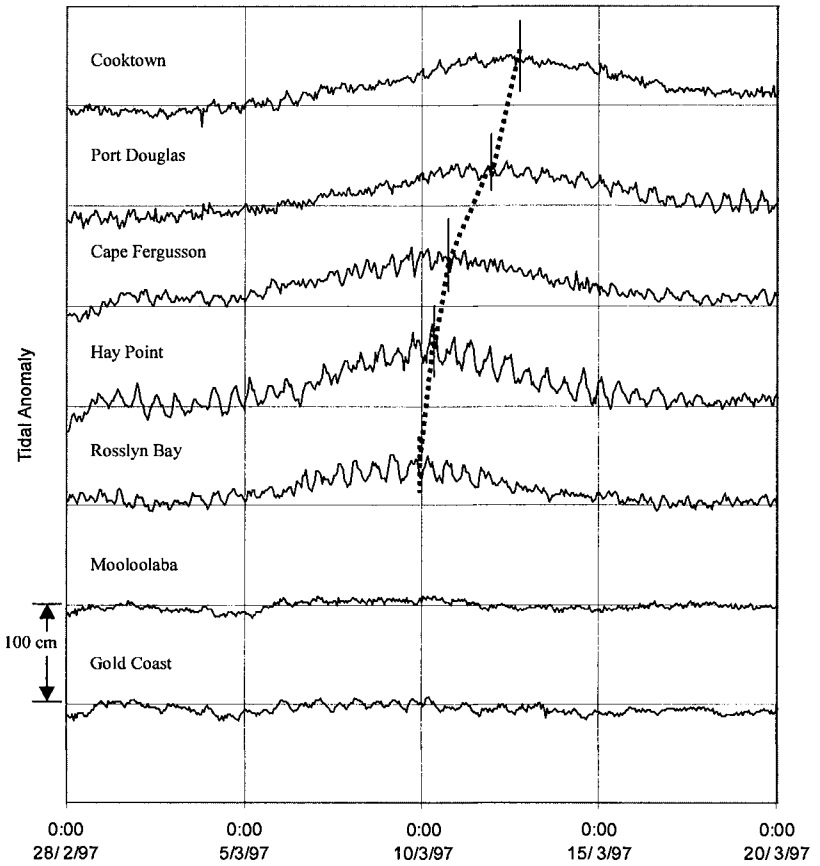

Figure 7: Tidal anomalies generated by Cyclone Justin. The peaks of tidal anomaly move northward from Rosslyn Bay to Cooktown as shown by the dotted line. Data courtesy of MHL, NTF and Queensland Transport.

4.1. Wind set-up

The cyclonic wind component perpendicular to the shoreline may generate set-up in the shallow waters, particularly where the shelf is wide and shallow. The strength and duration of the winds, and the width of continental shelf are important components generating the wind set-up. However, the estimated wind set-up at Rosslyn Bay, about *700 km* southward the center of cyclone, was very small even though it is located on the widest continental shelf in East Australia.

Onshore wind speeds at Rosslyn Bay during the cyclone were quite weak. Taking into account the depth of shelf edge h_o=*200 m*, the width of the continental shelf is W_{shelf}, with the constant shelf gradient $dh/dx=200/W_{shelf}$, wind set-up generated by wind blowing perpendicular to the coast can be estimated as follows (see Nielsen and Hanslow, 1995).

$$\overline{\eta}(h)=\frac{\rho_{air}}{\rho_{sw}gh_o}C_f U_{10}^2 W_{shelf}\ln\left(\frac{h_o}{h}\right) \quad (1)$$

where ρ_{air} and ρ_{sw} are the density of air and sea water respectively, U_{10} is wind speed at *10 m* above sea level, C_f is the sea-air friction coefficient, h is the water depth. By taking ρ_{air} = *1.3 kg/m*^{3}, ρ_{sw} = *1025 kg/m*^{3}, W_{shelf} = *260 km*, U_{10} =*2.5 m/s* (see Figure 8), C_f =*0.002* (Toba et al, 1990), wind set-up at Rosslyn Bay; where the tide gauge is located at *1.8 m* water depth, is estimated to be at most *0.01 m*.

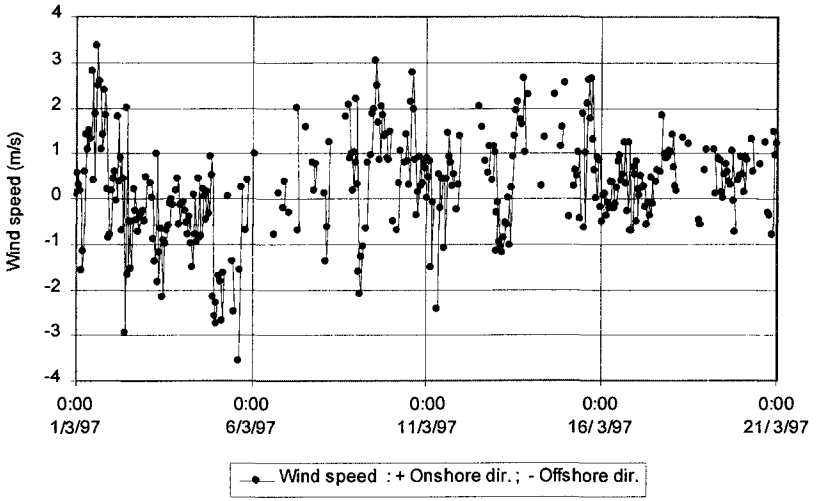

Figure 8. Onshore/Offshore winds at Rosslyn Bay during Cyclone Justin. Taking into account onshore wind of 2.5 *m/s* estimates *0.01 m* wind set-up on the coast.

4.2. Coriolis Effects on Longshore Currents

Cyclone Justin was stationary in the Coral Sea for more than 2 weeks (see Figure 9). Therefore, it is reasonable that clockwise cyclical currents may be generated during the event. Due to the Earth's rotation, north going longshore current will be pushed against the land and that causes a coastal sea level to rise.

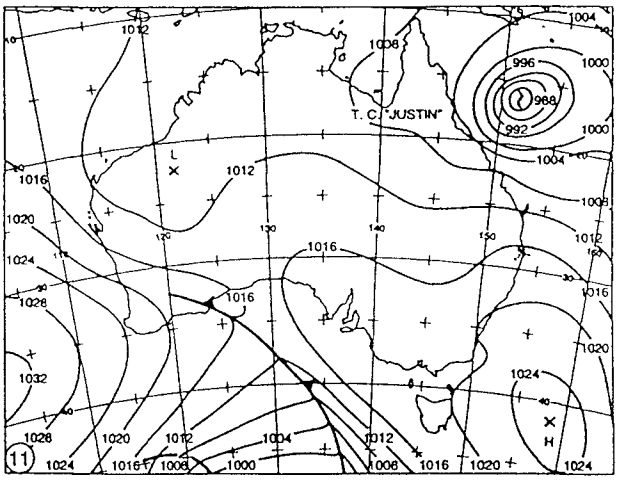

Figure 9. Weather map during Cyclone Justin, March 1997 (Bureau of Meteorology Annual Reports 1997).

The Coriolis effect on longshore current component can quantitatively be modeled as follows (see Figure 10). The Coriolis acceleration is:

$$f = 2\Omega \sin\phi \tag{2}$$

where, Ω is the angular speed of earth's rotation on its axis, ϕ is the latitude of point on earth. The Coriolis acceleration on longsore current U is then Uf. Combine acceleration of gravity and Coriolis forms tilting water level with gradient of:

$$i = \frac{Uf}{g} \tag{3}$$

Taking Cape Fergusson as an example, which is situated at latitude 19^oS and average longshore current at Myrmidon Reef (18^o 16'S, 147^o22'E) of *0.6 m/s*. The Coriolis acceleration is $f = 2 \times 7.2\times10^{-5} \times sin19^o = 4.7\times10^{-5}\ s^{-1}$. The gradient of tilting water level will be $i = Uf/g = 0.6 \times 4.7\times10^{-5}/9.8 = 2.9\times10^{-6}$.

This magnitude indicates that water level to rise 2.9×10^{-3} *m* per kilometer. Assuming uniform flow across the continental shelf near Cape Fergusson, which is approximately *100km* wide, the extra water level height near the shoreline would be $100 \times 2.9\times10^{-3} = 0.29$ *m*.

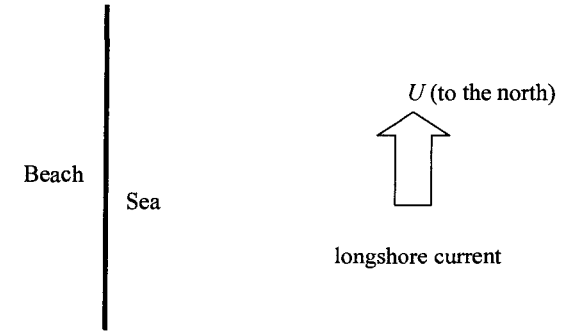

a. Planview

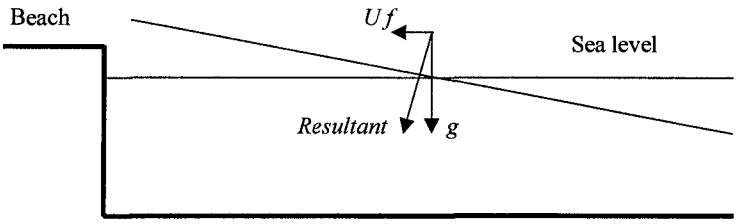

b. Cross section

Figure 10. Hypothetical model of Coriolis effect on longshore current at continental shelf. Northwards longshore current is pushed to the left against the land to cause water level rising along shoreline.

5. Conclusion

Detailed water level profiles through the Brunswick River entrance show that offshore wave height has no correlation to the tidal anomaly. Barometric effects of the order 1cm per hPa and wind set-up are minor parts of the tidal anomalies.

The exceedance plot of negative tidal anomalies is of interest for evaluating the variation of other forcing mechanisms than wind waves and rainfall.

Effects of the Coriolis force on longshore currents are another driving mechanism of tidal anomalies along the East Coast of Australia. During Cyclone Justin, tidal anomalies of the order *0.4* to *0.8* meters were generated along the northern Queensland coast. Up to *50%* of these can be accounted for by the Coriolis effect on wind driven longshore currents.

6. References

Greenspan, H.P. (1956) : The Generation of Edge Waves by Moving Pressure Distributions, *Journal of Fluid Mechanics*, Vol. 1, 574-592

Goring, D. G. & Bell, R. G. (1993) : Effect of Barometric Pressure on Sea Level in the Bay of Plenty, New Zealand, Proc. *11th Australasian Conference on Coastal Engineering*, Townsville, pp 415-419.

Hamon, B. V. (1962) : The Spectrum of Mean Sea Level at Sydney, Coffs Harbour, and Lord Howe Island, *Journal of Geophysical Research*, Vol 67, No 13, pp5147-5155.

Hamon, B. V. (1963) : Correction to The Spectrum of Mean Sea Level at Sydney, Coffs Harbour, and Lord Howe Island, *Journal of Geophysical Research*, Vol 68, No 15, pp 4635.

Hamon, B. V. (1966) : Continental Shelf Waves and The Effects of Atmospheric Pressure and Wind Stress on Sea Level, *Journal of Geophysical Research*, Vol 71, No 12, pp2883-2893.

Hanslow, D. J. & Nielsen, P (1992) : Wave Set-up on Beaches and in River Entrances, *Proc. 23th Int. Conf. Coastal Engineering.*, Venice, pp240-252.

Lighthill, Sir J. (1998) : Fluid Mechanics of Tropical Cyclones, *Theoretical and Computational Dynamics*, 10, pp 3-21

Nielsen, P. and Hanslow, D.J. (1995) : Wave Setup at River Entrances, *Proc 12th Australasian Conf. On Coastal and Ocean Engineering*, pp109-112

Nielsen, P., Voisey, C.J. and Santoso, E.B. (1997) : *Tidal Anomalies in the Southport Broadwater*, Department of Civil Engineering, University of Queensland.

Reid, R.O. (1958) : Effect of Coriolis Force on Edge Waves, (I) Investigation of the Normal Modes, *Journal of Marine Research*, 16(2), 109-144.

Robinson, A.R. (1964) : Continental Shelf Waves and the Response of Sea Level to Water Systems, *Journal of Geophysical Research*, Vol 69, pp367-368.

Stark, K.P. (1977) : Cyclonic surges and their effects, *31st Conference of the Queensland Harbor Boards Association*, Magnetic Island, 31 August

Toba, Y., Iida, N., Kawamura, H., Ebuchi, N. and Jones I.S.F. (1990) : Wave Dependence of Sea-Surface Wind Stress, *Journal of Physical Oceanography*, Vol. 20, No. 5, pp 705-721.

3D Wave-Current Interactions in Wave-Current Channels

Jacco Groeneweg[1] and Jurjen A. Battjes[1]

Abstract

Measurements of mean velocity profiles in a wave-current flume have shown some features for which the mechanism is far from trivial. A 2DV model based on the so-called Generalized Lagrangian Mean formulation is developed to study the influence of waves on the mean motion, the mean horizontal velocity in particular. This influence can be split in two parts, viz. a direct effect of the waves via wave-induced driving forces and an indirect effect of waves via secondary circulations. To include both effects an existing 1DV model is extended by introducing lateral variations including side-wall boundary layers. Resulting formulations have been implemented in an existing 2DV non-hydrostatic numerical flow model. Computations for regular waves following and opposing a turbulent current have been carried out and compared with both experimental results and results from an existing numerical model.

Introduction

Understanding the mechanism of wave-current interaction is of great importance for a good prediction of vertical profiles of horizontal velocities. The study of these profiles is relevant from both a hydrodynamic point of view (bed friction), and a morphodynamic point of view. Observations in laboratory experiments by e.g. Kemp & Simons (1982; 1983) and Klopman (1994) of the effect non-breaking waves on a steady turbulent current over a rigid rough bed show significant and unexpected changes in the profiles of the mean horizontal velocity (see figure 1).

To the authors' knowledge only Nielsen & You (1996) and Dingemans *et al.* (1996) presented theoretical models to explain the wave-induced changes in the Eulerian-mean horizontal velocity profiles. The model of Nielsen & You (1996) is based on a local force balance. In a steady two-dimensional flow the

[1]Delft University of Technology, Department of Civil Engineering and Geosciences, Stevinweg 1, 2628 CN Delft, The Netherlands.

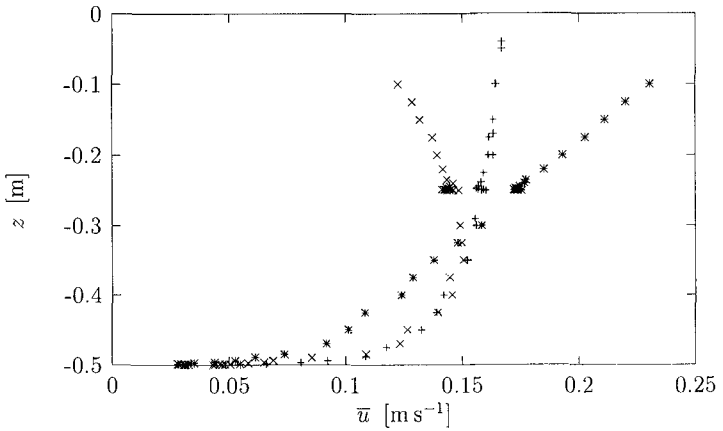

Figure 1: Eulerian-mean velocity profiles for the situation of no waves (+), following waves (×) and opposing waves (∗) of the same size (depth 0.5 m, wave period 1.44 s, wave amplitude 0.06 m). After Klopman (1994).

vertical variation of the total shearing force per unit area of a cross-section was balanced by the horizontal variation of the total normal stress. Assuming linear wave theory, expressions were derived for the mean wave contribution $\langle \tilde{u}\tilde{w} \rangle$ and for the local radiation stress. Although their model gives a qualitative explanation of the physical mechanisms involved, quantitative agreement with Klopman's results was obtained only after a significant ad hoc enhancement of $\langle \tilde{u}\tilde{w} \rangle$ by a linearly depth-dependent empirical factor. The empirical adjustment is based on the fact that the interaction with a current induces extra vorticity of the wave motion.

Dingemans *et al.* (1996) developed a 2DV model, the results of which were compared with the wave flume experiments of Klopman (1994). A detailed description of this model is given in the report of Van Kester *et al.* (1996). The effect of waves has been incorporated by adding the so-called Craik-Leibovich (CL) vortex force, consisting of $\overline{\boldsymbol{u}}^S \times \overline{\omega}$ with $\overline{\boldsymbol{u}}^S$ the Stokes drift and $\overline{\omega} = \nabla \times \overline{\boldsymbol{u}}$ the mean vorticity. Among others Leibovich (1983) showed that under certain assumptions the vortex force is the main term in the ensemble-averaged momentum equations in a so-called GLM formulation. Dingemans *et al.* (1996) observed in their simulations that secondary lateral circulations induced by the CL vortex force caused changes in the vertical structure of the mean horizontal flow. However, due to poor estimates of the Stokes drift and the CL vortex force in the boundary layers, quantitative agreement with Klopman's experimental results was not obtained for situations of waves following or opposing

a current.

Groeneweg & Klopman (1998) developed a 1DV model, based on the Generalized Lagrangian Mean (GLM) formulation. This approach, in which the Lagrangian motion is described in a fixed Eulerian framework, has been introduced by Andrews & McIntyre (1978) in order to obtain a clear separation of the mean and fluctuating motion. In the model lateral variations have been neglected. Comparison with Klopman's results shows both qualitative and quantitative agreement.

An intriguing point is that two models of Nielsen & You (1996) and Groeneweg & Klopman (1998) confirm the theory that changes of the mean horizontal velocity profile are purely caused by phenomena in longitudinal direction, whereas Dingemans *et al.* (1996) suppose the secondary lateral circulations to be the reason for changes in the mean horizontal velocity profile in streamwise direction. Their prediction of the existence of lateral circulations is supported by laboratory measurements of Klopman (1997).

The purpose of this work is to develop a 2DV model, which describes the mean flow under the influence of the wave motion, in a Generalized Lagrangian Mean (GLM) formulation in order to provide more insight in the effect of the secondary circulations on the mean horizontal velocity profile. The work is presently in a preliminary state and the results of the developed 2DV model are not yet completely satisfactory. Therefore, the presentation of the model will not be given in detail and frequent reference is made to Groeneweg & Klopman (1998) (to be denoted as GK hereafter). General formulations of the flow equations in a GLM setting as well as a 1DV application of a combined wave-current problem have been given in detail in that paper.

GLM approach

As already mentioned in the introduction a hybrid Eulerian-Lagrangian approach, the so-called GLM approach, will be adopted to simulate the combined motion of waves and currents in a flume. For the definition of the GLM theory we refer to Andrews & McIntyre (1978), or for an introductory outline to McIntyre (1980) and Dingemans (1997, note 2.10.6). The notation in this paper is exactly the same as applied by GK. Here, only the essential idea of the GLM theory is outlined. A Cartesian coordinate system (x, y, z) is used, where z is the vertical direction, x and y the horizontal coordinates in longitudinal and lateral direction respectively. Central in the GLM description is the mapping $\boldsymbol{x} \rightarrow \boldsymbol{x} + \boldsymbol{\xi}(\boldsymbol{x}, t)$, where $\boldsymbol{\xi}(\boldsymbol{x}, t)$ is a field denoting the displacement about the position $\boldsymbol{x}$. By introducing $\varphi^{\xi}(\boldsymbol{x}, t) = \varphi(\boldsymbol{x} + \boldsymbol{\xi}(\boldsymbol{x}, t), t)$ for an arbitrary particle-related function φ, Andrews & McIntyre (1978) define a Lagrangian

mean operator $\overline{(\,)}^L$ by

$$\overline{\varphi(\boldsymbol{x},t)}^L = \left\langle \varphi^\xi(\boldsymbol{x},t) \right\rangle \,, \tag{1}$$

where in our case $\langle(\,)\rangle$ will be a time-average operator. This implies that the average assigned to the fixed point $\boldsymbol{x}$ is taken over disturbed positions $\boldsymbol{x}+\boldsymbol{\xi}(\boldsymbol{x},t)$. In order that $\boldsymbol{\xi}$ is a true disturbance, it is required that $\overline{\boldsymbol{\xi}(\boldsymbol{x},t)} = 0$. The fluctuation φ^ℓ is defined in a natural way as $\varphi^\ell = \varphi^\xi - \overline{\varphi}^L$, and thus $\overline{\varphi^\ell} = 0$. Finally, the difference between the GLM velocity and Eulerian mean velocity is given by the so-called Stokes drift, $\overline{\boldsymbol{u}}^S = \overline{\boldsymbol{u}}^L - \overline{\boldsymbol{u}}$. A Stokes correction $\overline{\varphi}^S$ can be expressed in terms of fluctuating quantities.

In GK the three-dimensional GLM flow equations have been derived in a general way. Therefore, the lateral 2DV model, providing a local solution in a cross-sectional plane, can be obtained just by neglecting variations in longitudinal direction of GLM quantities, except for the hydrostatic part of the GLM pressure which is related to the GLM surface elevation $\overline{\zeta}^L$. The total pressure $\overline{p}^L$ is decomposed in a hydrostatic and non-hydrostatic part, $\overline{p}^L = \rho g\left(\overline{\zeta}^L - z\right) + \overline{q}^L$. The horizontal gradient of the hydrostatic pressure, $\partial\overline{\zeta}^L/\partial x$, is assumed constant over the entire cross-section and chosen such that the discharge of the combined flow equals the discharge Q of the flow without waves. A cross-section at a distance x from the wave maker is defined as $\Omega(x) = \left\{(y,z) \,:\, -L \le y \le L,\ -h \le z \le \overline{\zeta}^L(x,y,t)\right\}$. Here we restrict ourselves to vertical side walls and a horizontal bottom profile.

The flow equations in GLM coordinates are of the same form as those in Eulerian formulation. Only the wave-induced driving forces in the momentum equations are different, and a wave-related correction in the continuity equation causes the mean velocity to be no longer divergence free.

The wave-induced driving forces are expressed in terms of fluctuating quantities in GK. The 1DV model presented in that paper provides the vertical profiles of the fluctuating quantities as well. In order to take side wall effects into account we adopt a procedure that was also used by Mei *et al.* (1972), who analyzed mass transport caused by progressive waves for a situation of constant viscosity and no initial current. A cross-section $\Omega(x)$ of the flume is subdivided into five regions, viz. the inviscid core region and the boundary layers at the bottom, the free surface and the two side walls. This is sketched in figure 2.

Analogous to the analysis of Mei *et al.* (1972) viscous effects are neglected outside the side wall boundary layers. Consequently, the lateral variations of the amplitude functions of the fluctuating quantities can be neglected. The flow equations for the fluctuating motion are then reduced to those derived for the 1DV problem in GK. The solution of the latter problem will be denoted by $\varphi = \varphi_1$. Following e.g. Mei *et al.* (1972) one can easily show that the first order first harmonic velocity including the no-slip condition at the side walls

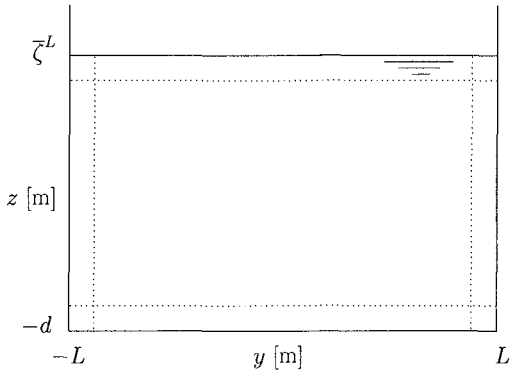

Figure 2: Division of a cross-section $\Omega(x)$ into five regions.

satisfies Stokes' shear wave solution given by

$$\tilde{u} = [1 - \exp(\beta Y)]\,\tilde{u}_1 \,, \tag{2a}$$

$$\tilde{v} = \tilde{v}_1 = 0 \,, \tag{2b}$$

$$\tilde{w} = [1 - \exp(\beta Y)]\,\tilde{w}_1 \,. \tag{2c}$$

with the factor $\beta = (-\mathrm{i}\,\omega_0/\nu)^{1/2}$ and Y the distance to the nearest side wall. The influence of the mean current and variations of the eddy viscosity ν have been neglected in the side-wall boundary layers. To sum up: the 1DV model is used to determine the vertical distribution of the fluctuating quantities. The 2DV profiles are obtained by multiplying the 1DV profile (subscript 1) by a y-dependent factor, which only affects the fluctuating motion in the side-wall boundary layers.

The distribution of the wave-induced driving forces in the entire cross-section can now easily be found by substituting the laterally varying oscillating quantities in the general expressions for the driving forces.

Implementation of GLM equations in existing numerical model

Although the flow equations are given in a GLM formulation, their form is similar to their Eulerian counterpart. For this reason an Eulerian flow solver can be used to integrate the GLM flow equations. We have chosen for the 2DV non-hydrostatic flow solver developed by Van Kester *et al.* (1996). For the numerics in this model one is referred to *loc. cit.* After the wave-induced driving forces $\overline{\boldsymbol{S}}^L$ and the GLM-correction term in the continuity equation have been evaluated, implementation of these terms is straightforward.

The implementation of the boundary conditions at the bottom and sidewalls needs special care. In Van Kester *et al.* (1996) partial-slip conditions are imposed at those boundaries, using a logarithmic law-of-the-wall formulation. This type of boundary condition differs from the no-slip condition used in the 1DV model. Therefore, correct expressions had to be determined for these boundary conditions in a GLM setting. For the time being the simplest possible approach has been adopted. The formulation applied by Van Kester *et al.* (1996) is based on a formulation of Grant & Madsen (1979) and takes the presence of the wave motion into account. Given a shear velocity at a certain distance from the wall, the friction velocity and related shear stress are determined. This formulation is given in an Eulerian framework. In order to obtain the GLM shear stress at a closed boundary, the following algorithm has been applied:

1. The GLM velocity at a certain height or distance from the side wall is transformed to its Eulerian equivalent at the same height.

2. The formulation of Grant & Madsen (1979) which has been applied by Van Kester *et al.* (1996), is used to determine the Eulerian shear stress at the boundary.

3. The Eulerian shear stresses are transformed to GLM shear stresses by adding the Stokes correction of the shear stress under consideration.

Finally, for simulating turbulent flow a turbulence model has to be implemented. In a first approach a classical turbulence model has been used. Any of the turbulence models implemented by Van Kester *et al.* (1996) can be used. For this study a $k - \varepsilon$ model was chosen. In order to take the wave influence into account, boundary conditions for the turbulent kinetic energy and dissipation are related to the shear velocity near the boundary. As mentioned above the shear velocities are determined using a logarithmic law of the wall. For closure of the turbulence model the production term is computed with Eulerian velocities, which are determined by transforming the GLM velocities.

Model results

Mean velocities have been computed for situations of following and opposing waves. In order to compare the model results with experimental data, the initial conditions of one of Klopman's (1994; 1997) measurements have been applied. In the present model a turbulent current with a constant discharge of $Q = 0.08\,\mathrm{m^3\,s^{-1}}$ was generated in a 1.0 m wide flume ($L = 0.50\,\mathrm{m}$) with a still-water depth $h = 0.50\,\mathrm{m}$. A monochromatic wave field following or opposing the current with a wave period $T = 1.44\,\mathrm{s}$ (relative to the flume) and wave

amplitude $a = 0.060\,\mathrm{m}$ is superposed on the current. All presented results refer to the situation at $t = 1600\,\mathrm{s}$ and have been obtained on an equidistant grid with horizontal and vertical resolution $\Delta x = 0.01\,\mathrm{m}$, resp. $\Delta y = 0.0125\,\mathrm{m}$ and a time step $\Delta t = 0.02\,\mathrm{s}$.

In the present 2DV model the wave-induced driving forces depend via the orbital quantities on the factor $\beta = (-\mathrm{i}\omega/\nu)^{1/2}$. In our analysis the quantity ν was assumed independent of the lateral direction. We have taken $\nu = 10^{-4}\,\mathrm{m^2\,s^{-1}}$ in all experiments, representing a turbulent oscillatory motion. This choice for ν leads to a factor β for which $\mathrm{Re}(\beta) = -(\omega/2\nu)^{1/2} \approx -148\,\mathrm{m^{-1}}$.

Since velocity measurements have been carried out at fixed locations and are thus Eulerian, the GLM velocities $\overline{\boldsymbol{u}}^L$ have to be transformed to Eulerian velocities. In this section these are denoted as $\boldsymbol{U}$. As already mentioned $\boldsymbol{U} = \overline{\boldsymbol{u}}^L - \overline{\boldsymbol{u}}^S$.

In figure 3 and 4 the results for the mean velocity distribution in a cross-section at $x = 22.5\,\mathrm{m}$ from the wave maker and the mean horizontal velocity profile in streamwise direction in the center of the flume are shown for the situation of waves propagating in the current direction. The agreement with measurements of Klopman (1997) is only qualitative. The direction of the computed secondary circulation is correct, but the velocity magnitude is a factor 2, and at the side walls even a factor 3 larger than measured. Near the side wall the maximum velocity magnitude is $2.0\,\mathrm{cm\,s^{-1}}$ and in the center $1.6\,\mathrm{cm\,s^{-1}}$. The computed secondary circulations are comparable to those obtained by Dingemans *et al.* (1996). The mean horizontal velocity in the center of the flume is fairly well predicted by the 2DV model. Compared with the measurements of Klopman (1994) and the 1DV results of GK there is a slight overprediction in the lower region of the flume and an underprediction in the higher region.

In figure 5 and 6 the results have been plotted for the situation that waves are propagating in the opposite direction. Once again, the maximum velocity magnitude near the side wall is $2.5\,\mathrm{cm\,s^{-1}}$ and in the center of the flume $1.8\,\mathrm{cm\,s^{-1}}$, which is even an overprediction of Klopman's (1997) experimental data with a factor 4 to 5. The prediction of the mean horizontal velocity profile in streamwise direction is even worse. Whereas for the situation of waves following the current at least the trend was predicted correctly, this is not true in the opposite case. In the upper 40% of the flume the velocity gradient seems to vanish whereas the experiments of Klopman (1994) and the 1DV computations of GK show an increasing velocity gradient.

The side walls should have less effect on the mean velocity profile in the center of the flume when a wider flume is considered. The secondary lateral circulations should then decrease in magnitude. Moreover, the 2DV solution should converge to the 1DV solution as $L \to \infty$. However, we remark that

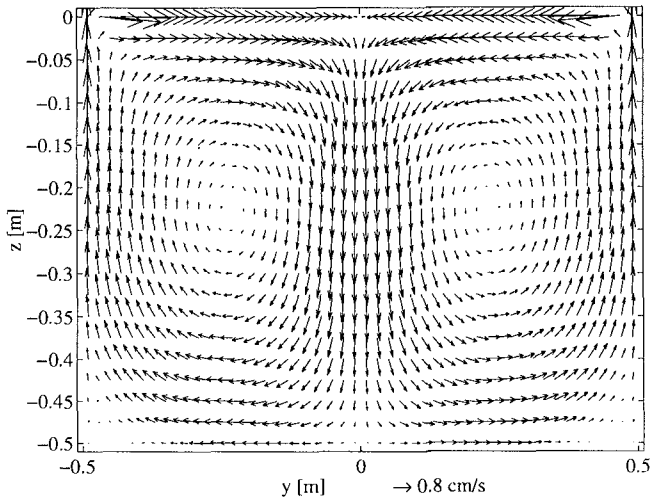

Figure 3: Mean velocity distribution in cross-section for waves following the current. Note difference between horizontal and vertical scale.

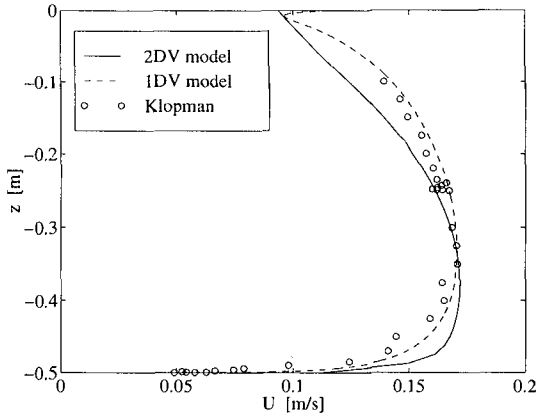

Figure 4: Mean streamwise horizontal velocity profile in center of the flume for waves following the current.

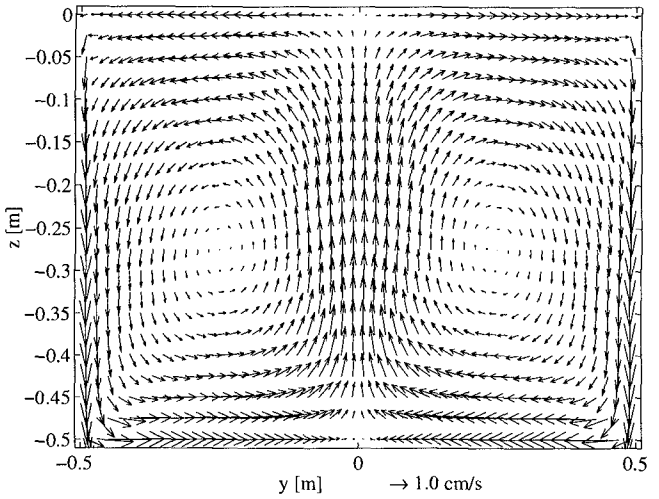

Figure 5: Mean velocity distribution in cross-section for waves opposing the current.

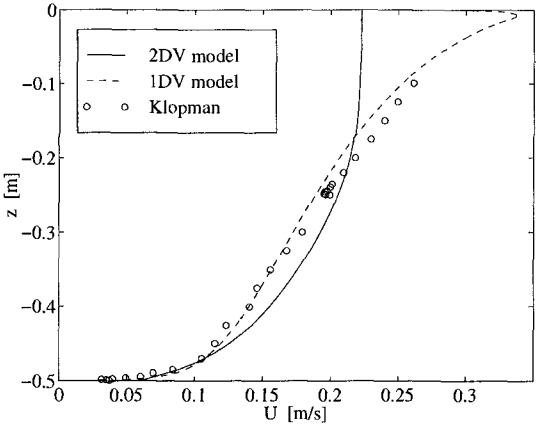

Figure 6: Mean streamwise horizontal velocity profile in center of the flume for waves opposing the current.

some principal differences in the formulation of both models, such as the turbulence model and boundary layer treatment, will induce some differences in the results.

To study the effect mentioned above, the same situation with a following current is considered as before, but now in a 5 m wide flume. The discharge is increased proportionally, $Q = 0.40\,\mathrm{m^3\,s^{-1}}$. In figure 7 the velocity distribution is shown only in the region 50 cm from the left side wall. The velocity magnitude is obviously smaller, at most $0.8\,\mathrm{mm\,s^{-1}}$. A circulation cell can still be observed. Our main interest concerns the mean horizontal velocity profile in the center of the flume as given in figure 8. Comparing this with the distribution obtained in a 1 m wide flume only shows a slight difference.

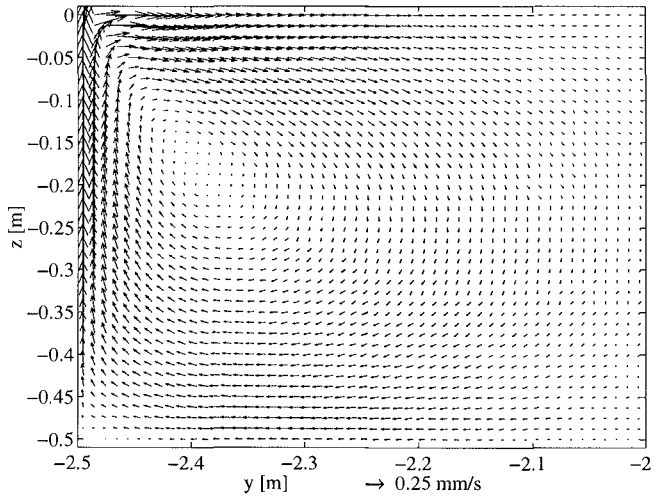

Figure 7: Mean velocity distribution in a part of the cross-section for waves following the current in a 5 m wide flume.

Discussion

Two important philosophies explaining the wave-induced changes in the mean horizontal velocity profiles are known so far. One is based on a 1DV local force balance neglecting lateral variations, and in the other secondary circulations in the cross-section are essential. In order to find out which phenomenon is dominant a 2DV numerical flow model based on the GLM formulation has

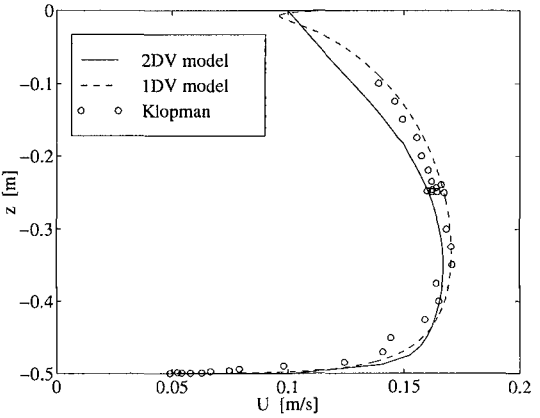

Figure 8: Mean streamwise horizontal velocity profile in center of a 5 m wide flume for waves following the current.

been developed. It is still in a preliminary state and the numerical results obtained so far are not always satisfactory.

Numerical experiments with the 2DV model for a 1 m and a 5 m wide flume give almost similar predictions of the mean horizontal velocity in streamwise direction in the center of the flume and a significant difference for the order of magnitude of the circulations. One might therefore conclude that phenomena in streamwise direction are dominant over those in lateral direction. However, the 2DV model overpredicts the velocity components in vertical and lateral direction measured by Klopman (1997). Two possible reasons are given here. Firstly, the computations have been carried out on a regular grid with a grid size of 1 cm, which was too coarse to represent the side-wall boundary layers well. These are only a few millimeters thick (order β^{-1}). An irregular grid which is finer towards the boundaries has already been implemented. Results of these numerical experiments will be reported in the future.

Secondly, in the formulation of wave effects in the partial slip conditions and the $k-\varepsilon$ turbulence model, the simplest approaches have been applied. GLM quantities are computed by Eulerian based models. Transformations from GLM to Eulerian and vice versa have been carried out only at the beginning and at the end of those processes. Improvement of this approach might lead to better results for the circulations.

Furthermore, extra attention has to be paid to the mean horizontal velocity profile for the situation of opposing waves. Towards the free surface a completely deviant behavior was observed compared to the measurements and

predictions with the 1DV model. The cause of this is unknown for now and will be considered carefully in the near future.

Acknowledgements

This research is supported by the Technology Foundation (STW), The Netherlands. Furthermore, we would like to thank G. Klopman and M.W. Dingemans for their valuable suggestions, and Delft Hydraulics for putting their numerical solver at our disposal.

References

Andrews, D.G. & McIntyre, M.E. 1978. An exact theory of nonlinear waves on a Lagrangian-mean flow. *J. Fluid Mech.*, **89**, 609–646.

Dingemans, M.W. 1997. *Water wave propagation over uneven bottoms.* World Scientific, Singapore.

Dingemans, M.W., van Kester, J.A.Th.M., Radder, A.C. & Uittenbogaard, R.E. 1996. The effect of the CL-vortex force in 3D wave-current interaction. *Pages 4821–4832 of: Proc. 25th Int. Conf. on Coastal Engng, Orlando.* ASCE, New York.

Grant, W.D. & Madsen, O.S. 1979. Combined wave-current interaction with a rough bottom. *J. Geophys. Res.*, **84**(C4), 1797–1808.

Groeneweg, J. & Klopman, G. 1998. Changes of the mean velocity profiles in the combined wave-current motion described in a GLM formulation. *J. Fluid Mech.*, **370**, 271–296.

Kemp, P.H. & Simons, R.R. 1982. The interaction of waves and a turbulent current; waves propagating with the current. *J. Fluid Mech.*, **116**, 227–250.

Kemp, P.H. & Simons, R.R. 1983. The interaction of waves and a turbulent current; waves propagating against the current. *J. Fluid Mech.*, **130**, 73–89.

Klopman, G. 1994. *Vertical structure of the flow due to waves and currents.* Tech. rept. H840.32, Part 2. Delft Hydraulics.

Klopman, G. 1997. *Secondary circulation of the flow due to waves and current.* Tech. rept. Z2249. Delft Hydraulics.

Leibovich, S. 1983. The form and dynamics of Langmuir circulations. *Ann. Rev. Fluid Mech.*, **15**, 391–427.

McIntyre, M.E. 1980. Towards a Lagrangian-mean description of stratospheric circulation and chemical transports. *Phil. Trans. R. Soc. Lond.*, **A296**, 129–148.

Mei, C.C., Liu, P.L-.F. & Carter, T.G. 1972. *Mass transport in water waves.* Tech. rept. 146. M.I.T. Rep. Ralph M. Parsons Lab. Water Resources Hydrodynamics.

Nielsen, P. & You, Z-J. 1996. Eulerian mean velocities under non-breaking waves on horizontal bottoms. *Pages 4066–4078 of: Proc. 25th Int. Conf. on Coastal Engng, Orlando.*

Van Kester, J.A.Th.M., Uittenbogaard, R.E. & Dingemans, M.W. 1996. *The effect of the CL-vortex force in 3D wave-current interaction.* Tech. rept. Z751. Delft Hydraulics.

Vorticity and surf zone currents

D. H. Peregrine[1] and O. Bokhove[2]

Abstract

Water wave breaking is of considerable importance in the transfer of momentum from the waves to currents. Near shore lines most of the water motions are dominated by breaking waves. Recent work on the generation of vorticity by breaking waves and bores in the surf zone on beaches within the shallow water approximation has shown that non-uniformity in the strength of bores is an important source of potential vorticity. This is illustrated by discussing the generation of longshore currents and illustrated with a numerical example of vorticity generation due to a non-uniform bed. These demonstrate that the horizontal excursion of vorticity transported by the incident waves may be a significant factor in interpreting velocity measurements at a fixed site.

Introduction

The role of horizontal eddies in surf zone currents, and the generation of their vorticity are discussed in Peregrine (1995, 1998). The latter paper gives a quantitative measure of vorticity generation by bores, which is briefly recounted below. The aim of this paper is to look at some of the implications of this vorticity generation.

Note: the vorticity that is being discussed here is not the vorticity caused directly by the breaking of the wave and the subsequent organised and turbulent motions on the scale of

[1] Professor of Applied Mathematics, d.h.peregrine@bristol.ac.uk
[2] Research Associate, o.bokhove@bristol.ac.uk
School of Mathematics, Bristol University, University Walk, Bristol BS8 1TW, England

the wave crest. Rather, we are concerned with vorticity on a larger scale, at the scale of the crest length or wave length of the wave, such as is important in describing mean currents generated by breakers.

The usual way to model the transfer of momentum from waves to currents is to average over the wave motion, assuming the waves to be sufficiently regular for this to be appropriate. The resulting equations have a momentum transfer term, that is known as radiation stress following its development by Longuet-Higgins & Stewart (1964). These averaged equations include mean currents and mean pressures: a standard way of studying fluid motion. However, an alternative way of analysing any flow is to consider its vorticity. Peregrine (1995) points out that surf zone flows on beaches of gentle slope are almost two-dimensional flows in the horizontal, and that little attention had been given to the properties of such flows such as are used in the geophysical fluid dynamics for atmospheres and oceans. This has been followed up by numerical modellers including vorticity plots in their results which have clearly shown discrete eddies even when radiation stress is used to drive the currents (Allen, Newberger & Holman,1996; Özkan-Haller & Kirby, 1998; Sancho & Svendsen, 1998).

After summarising the main result on vorticity generation from Peregrine (1998) and noting the importance of potential vorticity in these flows, we present a comparison between the usual radiation stress description of the generation of longshore currents and the view that is obtained by considering potential vorticity generation. Then data from a numerical computation of a normally incident wave meeting a non-uniform bar is shown to generate eddies. The accuracy of this inviscid computation is verified by the maintenance of their potential vorticity as they are convected by the wave motion.

Vorticity generation by bores in shallow water

The simplest dynamic model for waves breaking on a beach of gentle slope is for shallow water. The equations for finite amplitude shallow water waves, e.g. see Stoker (1957), permit waves to steepen until the necessary approximation of gentle surface slopes is no longer valid. In practice, if the variation of surface elevation is large enough compared with the depth, waves break shortly after they steepen significantly. Thus, if details of the breaking and the associated turbulent motions are on shorter length and time scales than are of immediate interest, the breaking event can be modelled as the development of a surface and current discontinuity in the shallow water equations. Such discontinuities are bores and are dynamically consistent if mass and momentum are conserved.

For the development of wave generated currents it is these longer scales that are most relevant. Modelling of waves on a beach with the shallow water equations plus bores has developed from early numerical models (Keller, Levine & Whitham, 1960; Hibberd & Peregrine; 1979) to more effective examples (e.g. Kobayashi & Wurjanto, 1992; Watson, Peregrine & Toro, 1992). These examples are of one-dimensional models, and only now

are models with two horizontal dimensions which include bores being used in this area. However, comparisons with one-dimensional experiments described in Barnes, Peregrine & Watson (1994) show that although fine details of wave breaking are poorly modelled the overall generation of currents is well described.

Kelvin's circulation theorem can be derived for the shallow water equations, as can the conservation of potential vorticity following material particles. Potential vorticity is defined by (vorticity)/(total waterdepth). Note that conservation of potential vorticity implies a change in vorticity for any water that changes its depth. This is a dynamically important feature and generates or absorbs vorticity, but the major point for discussion here is the generation of potential vorticity.

Derivation of Kelvin's circulation theorem and of the material conservation of potential vorticity from the shallow water equations requires that the flows be represented by continuous and differentiable functions. The development of bores introduces a complicating feature: the discontinuity of velocity and depth that represents a bore gives a rate of change of circulation in any material circuit that cuts through the bore unless it has another section through the bore in the opposite direction at a point where the bore has the same properties. It is clear that velocity, and hence circulation along a material line, is changing most rapidly at bores. By considering the effect of a bore on a material circuit over a small time interval Peregrine (1998) derives the rate of change of circulation due to one intersection with the bore. It turns out to have a magnitude equal to the rate of energy dissipation in the bore at that point, divided by the water density. This neat result has the nice feature that to a large extent the rate of dissipation is related to the visible strength of a bore in terms of the intensity of splashing and air entrainment.

However, we need to discuss the large-scale generation of potential vorticity. Peregrine (1998) derives a formula for the generation of vorticity by considering the change in vertical vorticity, Ω, that occurs in an infinitesimal material circuit as it passes through a bore. The result, at a bore that has an increase in water depth from h_1 to h_2, is $\Delta\Omega_A + \Delta\Omega_D$. Here $\Delta\Omega_A$ is the change in vorticity due to the vertical stretching of fluid elements:

$$\Delta\Omega_A = \left(\frac{h_2}{h_1} - 1\right)\Omega,$$

where Ω is the original vorticity of the fluid element. This part represents no change in the pre-existing potential vorticity. On the other hand, the motion of the bore over running water in front of it gives the change of vorticity

$$\Delta\Omega_D = \left[\frac{2h_2}{gh_1(h_1+h_2)}\right]^{\frac{1}{2}} \frac{dE_D}{dy}, \quad \text{where} \quad E_D = \frac{g(h_2-h_1)^3}{4h_1h_2}$$

is the dissipation rate at the bore divided by fluid density. This does represent generation of potential vorticity:

$$\left[\frac{2}{gh_1h_2(h_1+h_2)^3}\right]^{\frac{1}{2}}\frac{dE_D}{dy}.$$

Pratt (1983) also derived this result from manipulation of the shallow water equations and bore relations.

As may be seen, a bore with uniform properties, such that E_D is constant, conserves potential vorticity. On the other hand if the bore varies due to non-uniformities in E_D, then new potential vorticity is generated. Non-uniformities in E_D come from variations in the water depths h_1 and h_2, either because of non-uniformities in the bed, or because of variations along the wave crest. The effect of bed non-uniformities is discussed here. Peregrine (1999) discusses the effect of crest variations for finite length breaking wave crests.

Longshore currents

Figure 1 is a sketch of regular waves incident at an angle on a gently sloping beach which is uniform in the longshore direction; the slightly irregular lines indicate the bores and runup. The x-direction is on shore, and the y-direction along shore. The standard approach to considering the generation of longshore currents, from Longuet-Higgins (1970), is to average over the waves and consider the momentum flux or radiation stress. A short straight line is drawn to illustrate this. Through such a shore-parallel surface the flux of x momentum carried shorewards by the waves, S_{xx}, is reducing towards the shore as the bores dissipate wave energy. The resulting gradient of momentum flux is balanced, in the simplest case by a correponding gradient of the mean surface giving a set up towards the shoreline.

On the other hand, the flux of y momentum carried shorewards by the waves, S_{yx}, is also reducing, but with no pressure gradient to balance it. Since the momentum must be conserved it thus contributes to a longshore current. In fact a balance is reached, either by direct bed friction, or, more likely, by the horizontal eddy viscosity which is enhanced by the long life of almost two-dimensional eddies which are generated by instabilities in the flow, bed irregularities, and/or irregularities in the incident waves.

The vorticity view of the longshore current generation depends on vorticity generation. Again this results from the shoreward diminution of the waves, but now we focus on the bores. Each bore starts abruptly as a wave breaks so that it is at its strongest when created and decays to zero where it meets the shoreline. Thus E_D is continually diminishing shorewards and its gradient leads to vorticity generation as described above. This vorticity is the gradient of the longshore current profile.

The most interesting aspect of this viewpoint comes when we look at the offshore end of the bore where it is created by the initial breaking of a wave crest. Here the bore

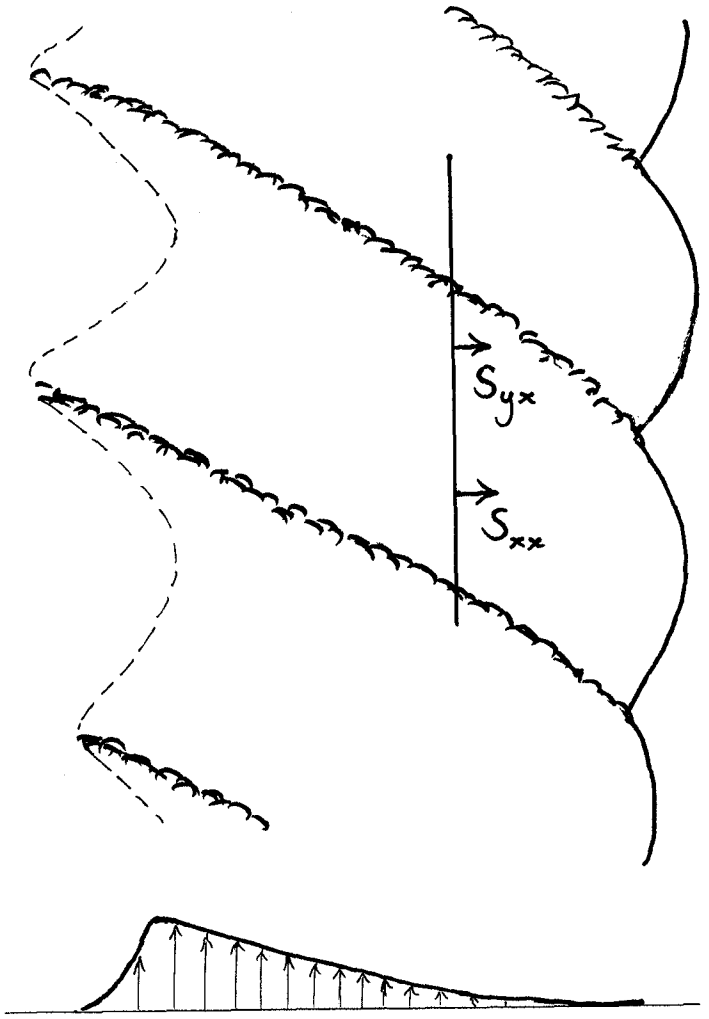

Figure 1. Thc irregular heavy lines sketch the positions of bores due to regular obliquely incident waves approaching a shoreline on the right. The flux of both x- and y-momentum past a shore-parallel line is indicated by arrows. The dashed line is an estimate of the edge of the region of vorticity as it is displaced by the wave motion. The lower profile is a sketch of a longshore current profile in the absence of horizontal mixing.

dissipation has its greatest value and also its greatest gradient, that is from zero offshore from breaking up to its maximum at breaking. This results in generation of vorticity of the opposite sense to that of the rest of the surf zone, as is needed for the longshore current to diminish to zero offshore. This draws attention to the localised generation of vorticity, and hence to a feature that appears to have been overlooked in discussions about the offshore profile of longshore currents. As may be seen in the computational example described in the next section, any vorticity that is generated is convected with the water motions. In particular the horizontal displacements of the incident wave motion are not generally negligible.

As an example consider linear long wave theory on water of constant depth h. For a sinusoidal wave of height H, the total horizontal displacement of the water is $HL/2\pi h$, where L is the wavelength. Note L/h is large for long waves, and H is not small when a wave breaks. The trajectory of the vorticity due to this displacement is sketched with a dashed line in figure 1. Thus any velocity sensor at a fixed position near the breaking point is affected by the vorticity for only part of the wave period. This means that even for perfectly regular waves with no horizontal eddy viscosity, the measured velocity profile could not show the very steep reduction to zero current offshore that the wave averaged approach predicts. This feature of the problem has yet to be studied quantitatively, but a sketch of the velocity profile that would be measured is included in figure 1.

Eddies generated by a non-uniform bar

Vorticity can be generated at a bore because the dissipation, E_D , varies due to variation in the level of the bed. As an illustration we present results from computation of a uniform wave incident normally on a plane beach with a bar. Bed non-uniformity is introduced by having a dip in the elevation of the bar. The contours of the bed and the numerical domain of integration are shown in figure 2. The domain is taken to be periodic in the long-shore direction. A single large wave of elevation propagating towards the shore constitutes the initial condition.

The wave and current motions are modelled by the finite-amplitude shallow-water equations in the dimensionless form:

$$u_t + uu_x + vu_y + h_x = d_x,$$
$$v_t + uv_x + vv_y + h_y = d_y,$$
$$h_t + (hu)_x + (hv)_y = 0.$$

where the coordinates (x, y, t), depth to bed, $d(x,y)$, total water depth, $h(x,y,t)$ and horizontal velocity components, (u,v) are related to the corresponding dimensional variables, starred, by

$$x = x^*/D,\ y = y^*/D,\ t = t^*(\alpha g/D)^{1/2},\ d = d^*/\alpha D,\ h = h^*/D,\ u = u^*/(\alpha g D)^{1/2},\ v = v^*/(\alpha g D)^{1/2}.$$

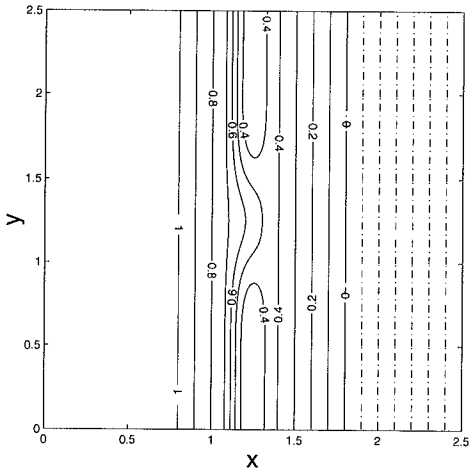

Figure 2: Contour plot of the bed, $d(x, y)$. Those above the initial still water level are shown with dashed lines. Contour interval: 0.1.

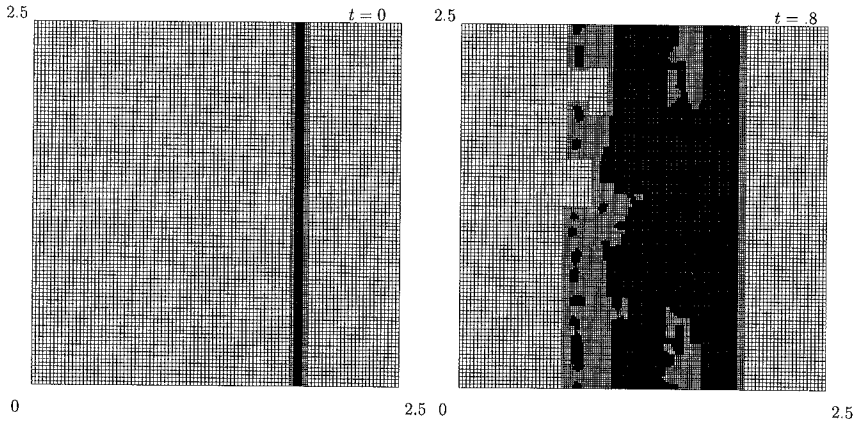

Figure 3: Examples of grid refinement at $t = 0$ and $t = 0.8$.

Here D and α are a reference depth and beach slope respectively: e.g. for a beach of constant slope rising from a horizontal bed, D could be chosen equal to the depth of undisturbed water over the horizontal bed, and α equal to the bed slope. This distortion of variables is used to scale out the beach slope, as is possible when no friction terms are included, see Brocchini & Peregrine (1996) or Hibberd & Peregrine (1979) where a slightly different scaling has the same effect.

The computational domain has a bed that is horizontal and constant unit depth for $x < 0.8$, at which point the bed rises with x with a slope 1. The bar is between $x = 1.05$ and 1.383, formed by adding a the positive sinusoid of amplitude 0.125. The dip is formed by multiplying the bar height by a suitable factor varying in the alongshore direction. Thus the bed is given by:

$$d = 1-(x-0.8)-0.125f(y)\{1+\sin[6\pi(x-1.05)-\pi/2]\}$$

where $$f(y) = 1+\cos(2\pi y/L)\left[\exp\{-(y-L/2)^2/a^2\}+\exp\{-(y-3L/2)^2/a^2\}\right].$$

The width of the domain is $L = 2.5$, and $a = 0.3$. A plot of bed contours is given in figure 2.

The initial conditions are to have water at rest except over the horizontal bed, $0 < x < 0.8$ where

$$u(x,0) = 0.3\,[1+\sin(2\pi x/0.8-\pi/2)]$$
$$h(x,0) = \tfrac{1}{4}u(x,0)^2 + u(x,0).$$

The relationship between u and h is chosen from the properties of simple unidirectional waves to give only onshore propagation initially.

The numerical scheme used is one due to Quirk, "AMRITA", which has adaptive mesh refinement, with a Roe type solver, conserving mass and momentum, and a total variation diminishing scheme that can accurately represent the initiation and propagation of the discontinuities in the solutions that represent bores. It is very similar to the gas dynamic code incorporated in the same program package that is described in Quirk & Karni (1996). The computation reported here includes no dissipation other than that which occurs at bores. The mesh refinement criterion are specified by the user. Refinement is clearly needed at bores, but our preliminary studies of accuracy showed that it is also needed at the shoreline and in regions with vorticity. An important feature for checking is that potential vorticity is conserved following a fluid particle. Figure 3 shows the numerical mesh at the initial time, where only the shore line has refinement since we start with a smooth wave, and as the wave meets the shoreline where much refinement is needed for the more complex flow.

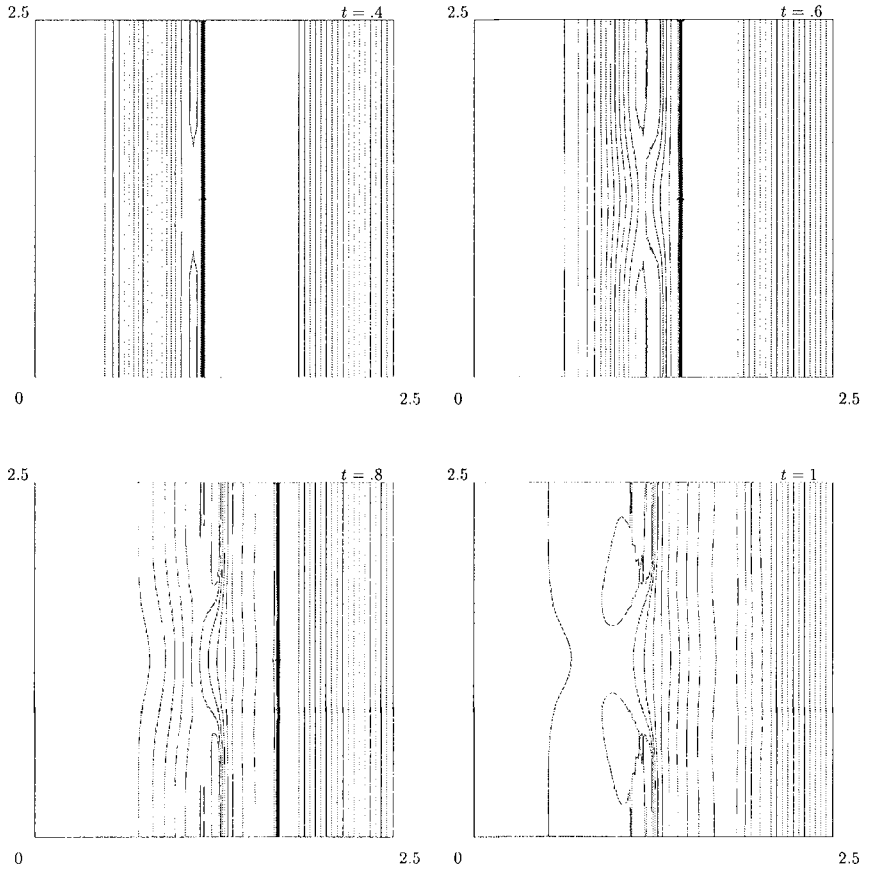

Figure 4: Contours of water surface height, $h - d$, with 25 contours in each of the intervals $[-1.0, -0.04]$ and $[0.04, 1.0]$. Contours of the exposed beach are also included.

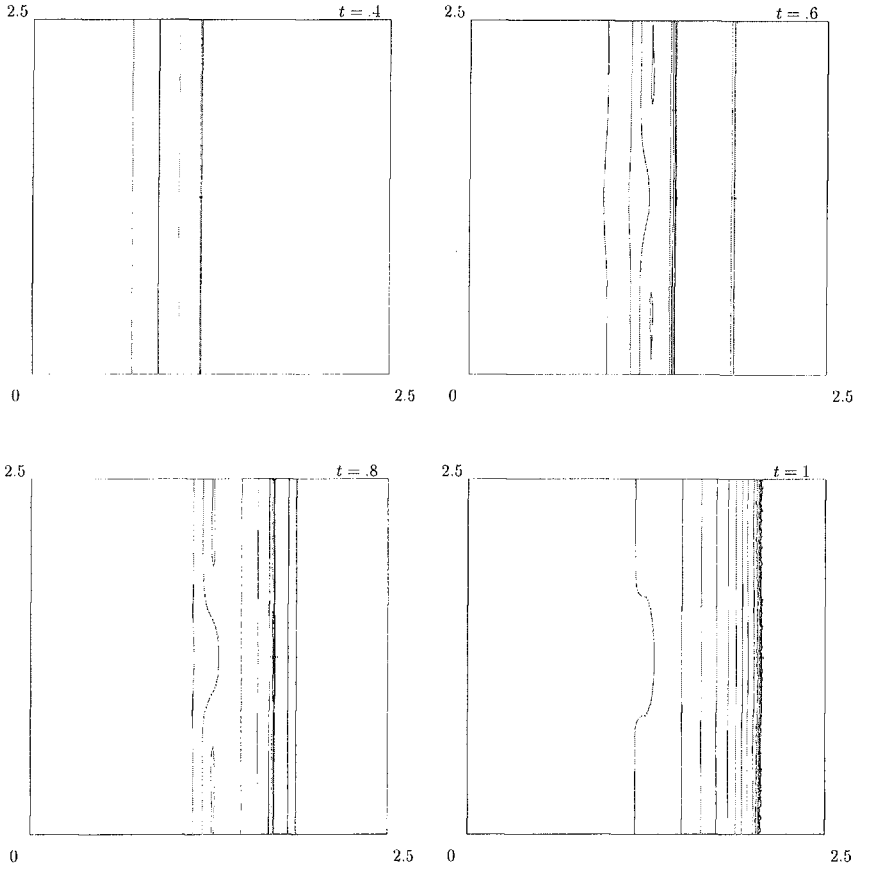

Figure 5: Onshore velocity component, u, with 12 contours in $[-2.5, -0.2]$ and $[0.2, 2.5]$.

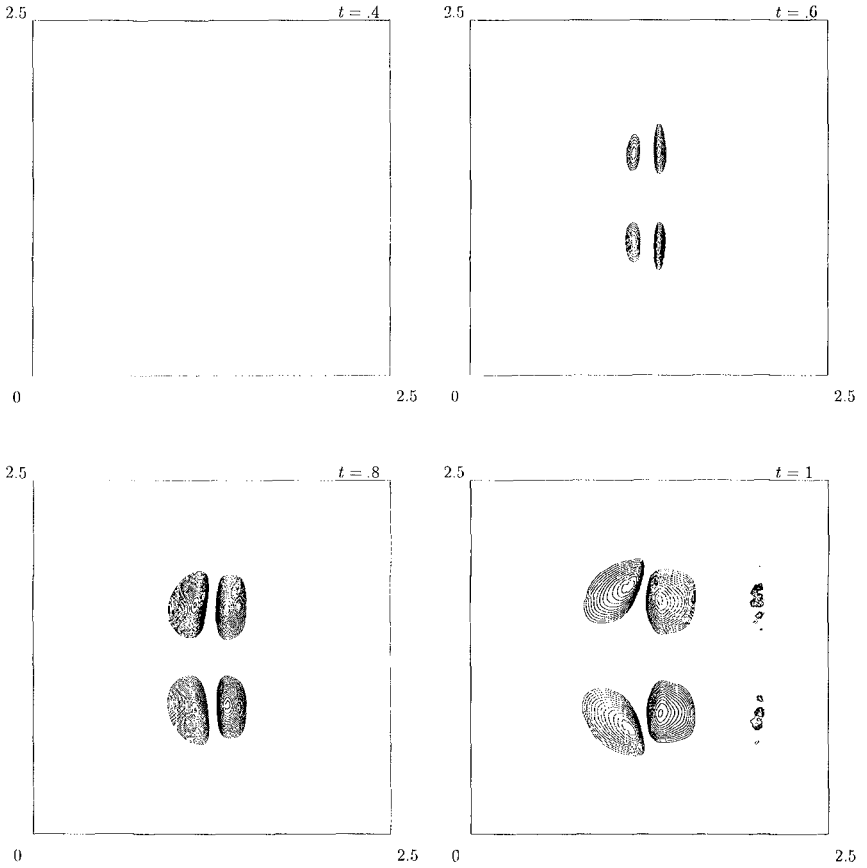

Figure 6: Alongshore velocity component, v, with 20 contours in $[-0.03, -0.015]$ and $[0.015, 0.03]$.

The primary results are shown as contour plots of the surface elevation, and the onshore and alongshore velocity components in figures 4, 5 and 6. As may be seen the bore, the following wave's elevation and the onshore water velocity all become lower over the dip in the bar than they are elsewhere. The alongshore velocity component would be zero if the bar were uniform, so its values give a clear view of the disturbance caused by the dip in the bar.

Potential vorticity at four different times is displayed in figure 7. Since vorticity is obtained from the primary variables by differentiation an increase in numerical noise is likely, and occurs. We have not smoothed the results, some of the noise is closely related to the steep front of the bore and although it mainly translates with the bore some small mesh-scale disturbances appear to be left behind. However, the generated vorticity shows up clearly. In the first frame, at $t = 0.4$, the bore is in the process of passing over the bar and the effect of the dip in generating vorticity at its sides where E_D has a significant gradient is clear. Only part of the vorticity generation has occurred at this time. Note figure 4 shows little discernible deviation in the line of the bore front at any time despite the gradient of its strength induced by the dip in the bar.

By time $t = 0.6$ the bore has passed over the bar and two narrow regions of vorticity have been generated. The bore's position can be seen by the thin spurious contour line just in front of these new eddies. The subsequent frames at later times show how the vorticity is convected shorewards by the forward motion of the water in the wave. The area over which the vorticity is spread increases substantially. This is because the vorticity moves with the water into a shallower region where the water has to spread out. As can be seen the values of the potential vorticity appear to be well conserved, e.g. the peak value hardly changes.

Conclusion

The interpretation of surf zone currents and their generation by considerations of vorticity and potential vorticity are illustrated and discussed here. They give a picture of the currents which is more directly related to the dissipative structure in surf zone waves where almost all the dissipation occurs in breaking and bores. We demonstrate the generation of discrete eddies by relatively small non-uniformities in the bed profile. Also evident in the numerical solutions is a large horizontal convection of the eddies by the wave motion following the bore. This horizontal motion is also relevant to the interpretation of the generation of longshore current profiles by regular waves, and appears to be a matter that should be borne in mind when interpreting velocity measurements from fixed velocity sensors.

Financial support is acknowledged from the Commission of the European Communities, Directorate General XII: Science, Research and Development under MAST contract

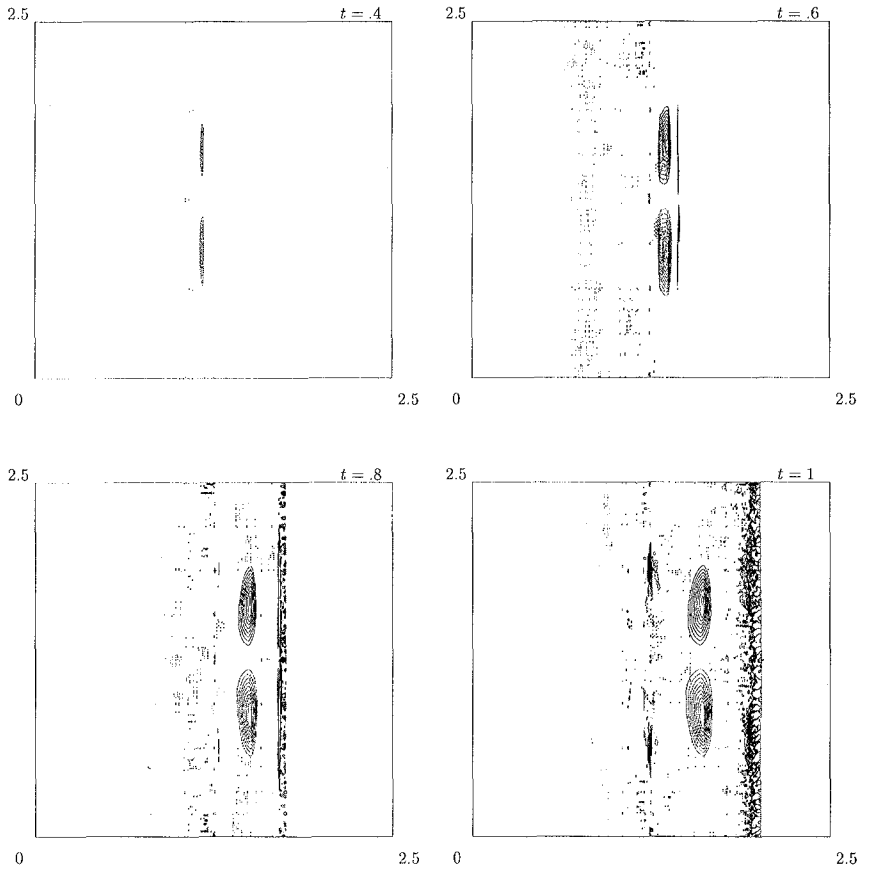

Figure 7: Contours of potential vorticity with 9 contours in $[-0.3, -0.06]$ and $[0.06, 0.3]$.

MAS3-CT97-0081, Surf and Swash Zone Mechanics (SASME), and from the U.S. Office of Naval Research with the NICOP grant N00014-97-1-0791.

References

Allen, J., Newberger, P.A. & Holman, R.A. (1996) Nonlinear shear instabilities of alongshore currents on plane beaches. *J. Fluid. Mech.*, **310**, 181-213.

Barnes, T., Peregrine, D.H. & Watson, G. (1994) Low frequency wave generation by a single wave group, *Proc. Internat. Sympos.* Waves - Physical and Numerical Modelling, Eds. Isaacson, M. & Quick, M., pp.280-286.

Brocchini, M. & Peregrine, D.H. (1996) Integral flow properties of the swash zone and averaging, *J. Fluid Mech.* **317**, pp.241-273.

Hibberd, S. & D.H.Peregrine, D.H. (1979) Surf and run-up on a beach, *Jour.Fluid Mech.*, **95,** pp.323-345.

Keller, H.B., Levine, D.A. & Whitham, G.B. (1960) Motion of a bore over a sloping beach. *J.Fluid Mech.,* **7**, 302-316.

Kobayashi, N. & Wurjanto, A. (1992) Irregular wave setup and run-up on beaches. *J. Waterways, Port Coastal & Ocean Engng.* ASCE, **118**, 368-386.

Longuet-Higgins, M.S., (1970) Longshore currents generated by obliquely incident sea waves. *J. Geophys. Res.*, **75**, 6778-6789.

Longuet-Higgins, M.S. & Stewart, R.N., (1964) Radiation stresses in water waves; a physical discussion, with applications. *Deep-Sea Res.*, **11**, 529-562.

Özkan-Haller, H.T., and Kirby, J.T., (1998) Nonlinear evolution of shear instabilities of the longshore current: a comparison of observations and computations. Submitted to *J. Geophys. Res.*

Peregrine, D.H. (1995) Vorticity and eddies in the surf zone, *Proc. Coastal Dynamics* '95, ASCE. Gydnia, 460-464.

Peregrine, D.H. (1998) Surf zone currents. *Theor. & Computational Fluid Dynamics,* **10**, 295-309.

Peregrine, D.H. & Svendsen, L.A. (1978) Spilling breakers, bores and hydraulic jumps, *Proc. 16th Inter. Conf. Coastal Engng.*, **1,** pp.540-550.

Pratt, L.J., (1983), On inertial flow over topography. Part 1. Semigeostrophic adjustment to an obstacle. *J. Fluid Mech.*, **131**, 195-218.

Quirk, J.J., and Karni, S. (1996) On the dynamics of shock-bubble interaction. *J. Fluid Mech.*, **318**, 129-163.

Sancho, F.E.P. and Svendsen, I.A., (1998) Shear waves over longshore nonuniform barred beaches. *Proc. 26th Inter. Conf. Coastal Engng.*

Stoker, J.J., (1957) *Water waves.* New York, Interscience. xxviii + 567pp.

Watson, G. & Peregrine, D.H. (1992) Low frequency waves in the surf zone, *Proc. 23rd Internat. Conf. Coastal Engng.* ASCE, Venice, **1**, pp.818-831.

Watson, G., Peregrine, D.H. & Toro, E.F. (1992) Numerical solution of the shallow-water equations on a beach using the weighted average flux method, *Computational Fluid Dynamics '92*, **1**, pp.495-502.

Experimental Study of Wave Breaking and Blocking on Opposing Currents

Arun Chawla and James T. Kirby [1]

Abstract

A series of experiments on monochromatic waves being blocked by opposing currents are presented in this paper. A heirarchial pattern in the wave field characteristics was observed with increasing wave amplitude. A shoaling model using a bore dissipation formulation to simulate current limited breaking is compared with the data. It is observed that amplitude dispersion plays an important role in wave blocking and cannot be ignored. For the large amplitude waves side band instabilities radically affect the wave field and prevent wave blocking.

Introduction

Wave blocking occurs in regions (e.g. mouths of river inlets) where the currents are opposing the waves. The opposing current slows down the waves leading to an increase in the wave steepness, which sometimes leads to wave breaking. The waves get blocked when the current is strong enough to prevent the wave energy from traveling upstream. That is when the group velocity C_g goes to zero. The steep waves in front of the blocking point cause considerable navigational hazards and can also effect sediment transport. Since the wave field is dramatically altered through the blocking region, it becomes important for the coastal engineer to be able to quantify under which conditions wave blocking will occur. There is also a limited understanding of energy dissipation due to current limited wave breaking. Thus, from an engineering view point a study of wave blocking and the evolution of the wave field through these blocking points is very important.

Before progressing into the dynamics of wave blocking, it is important to know the conditions under which wave blocking occurs. Consider a two dimensional wave moving on a depth-uniform current U. Then in a frame of reference moving with the current, the equations and solutions for water wave motion are identical to the case of no current. If ω is the wave frequency in a stationary reference frame, and σ is the wave frequency in a reference frame moving with the current, then the phase speed of the wave in the moving reference frame can be related to the phase speed in a

[1]Center for Applied Coastal Research, Dept. of Civil and Environmental Engrng., University of Delaware, Newark, DE 19716, USA. Correspondence e-mail: cwla@coastal.udel.edu

stationary reference frame by

$$\frac{\omega}{k} = \frac{\sigma}{k} + U \tag{1}$$

or

$$\omega - kU = \sigma \tag{2}$$

where k is the wave number and remains unchanged in the two reference frames. The expression for σ depends upon the theory used to obtain the dispersion relation from the equations. Differentiating (2), and setting $C_g = \frac{\partial \omega}{\partial k}$ to zero we then get the condition for wave blocking as

$$\frac{\partial \sigma}{\partial k} = -U \tag{3}$$

From (3) it is obvious that wave blocking can only occur if the wave and current are moving in opposite directions.

A linear uniform asymptotic solution for the waves close to the blocking point was first obtained by Smith (1975), who showed that, for small wave amplitudes, the waves are reflected from the blocking point. These reflected waves get shorter and shorter as they move away from the blocking point. Stiassnie and Dagan (1979) showed that when the required blocking current is close to the maximum current then partial wave reflection occurs. Their solution provided the transition region from no reflection to total reflection of wave energy. Some nonlinear aspects of the waves at the blocking points were also studied by Peregrine and Smith (1979). Both Shyu and Phillips (1990) and Trulsen and Mei (1993) further enhanced the theory of wave blocking by including the effects of surface tension. They showed the existence of a second blocking point which occurs when the reflected waves get so small that surface tension effects become predominant in the dispersion relation.

All the references cited above have concentrated on the study of wave reflection from the blocking point. But wave reflection occurs only if the initial wave amplitude is fairly small. For most practical problems the waves become steep enough to break as they approach the blocking point with very little to no wave reflection. The process is complex and requires an extensive experimental study. Unfortunately there are very few references in the literature to experimental studies of wave blocking. Lai *et al.* (1989) have conducted laboratory studies of the kinematics of the wave-current interaction under blocking conditions but do not discuss any of the dynamics. Sakai and Saeki (1984) have also conducted experiments of waves on opposing currents, but their experimental setup also includes a sloping sea bed. The focus of their study was the combined effect of opposing currents and sloping sea bed on wave transformation and breaking. In their experiments wave breaking occurs in shallow water, and it thus becomes difficult to isolate current limited wave breaking from depth limited wave breaking. There are still a number of unanswered questions, including1, what are the factors affecting wave blocking, how do waves break and dissipate energy under strong opposing current, and how do the wave field characteristics change with increasing nonlinearity. Therefore, we need further experimental studies to get a better understanding of the evolution of the wave field through the blocking region and

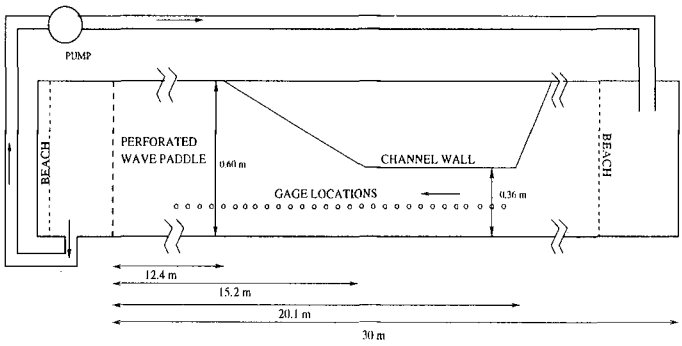

Figure 1: Schematic Plan view of the experimental setup

the dynamics of the wave-current interaction. Keeping this aim in mind the present study was carried out. A series of experiments have been conducted with monochromatic waves to provide some useful insights into the characteristics of the wave field in blocking currents, and the conditions under which the waves get blocked. The experiments have been conducted in relatively deep water so as to minimize the interaction between the bottom bathymetry and the waves. A simple shoaling model for waves on currents combined with a bore dissipation model to simulate wave breaking has also been compared with the data. This has been done with an attempt to quantify current limited wave breaking.

Experimental Setup

The experiments were conducted in the recirculating flume at the Center for Applied Coastal Research. A schematic plan view of the setup is shown in Figure 1. The flume is 30 m long and 0.60 m wide. All the tests were conducted in a water depth of $h = 0.50$ m. Currents are generated with the help of a pump which removes the water from behind the wavemaker and puts it back at the far end. A narrow channel has been created with the help of a false wall so as to be able to generate faster currents in the middle of the flume. A perforated wave paddle is used to generate waves so that the current can be allowed to go through the paddle. Porous beaches have been placed at the two ends of the flume to absorb the waves. All measurements in the $x-$ direction are made from the still position of the wave paddle.

Data was recorded in the form of a time series of the water surface at 29 different locations extending through the channel. Capacitance-type wave gages were used for this purpose. The gage locations are shown by open circles in Figure 1. At each location data was collected for 600 wave periods and wave height estimates obtained using a zero-up crossing method. The current field was measured using an acoustic doppler velocimeter. Figure 2 shows the vertical profile of the mean current (averaged over 330 seconds) at 5 different locations in the flume. Due to the development of

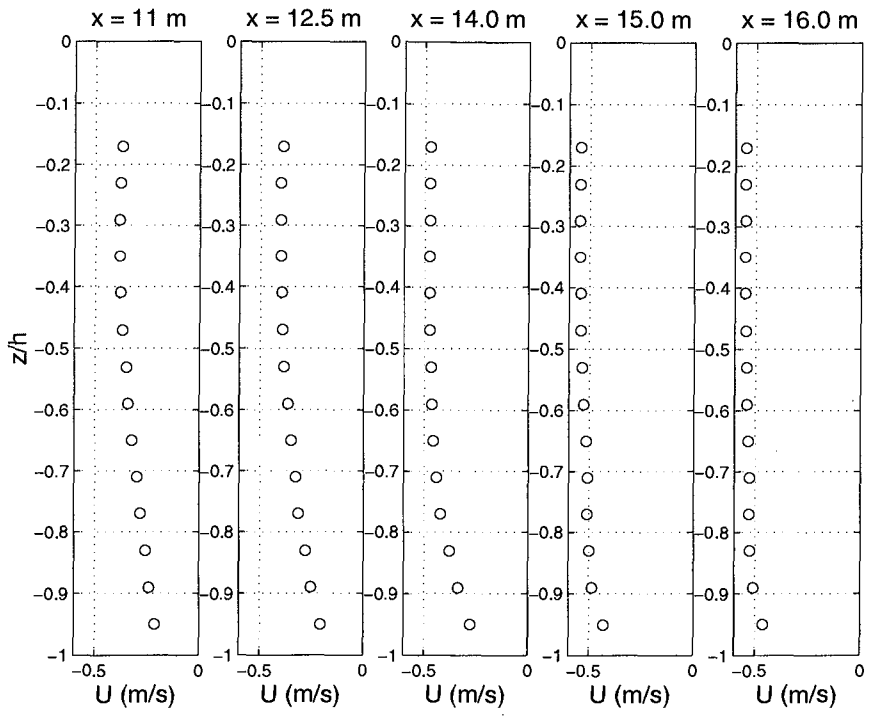

Figure 2: Vertical distribution of the current away from the channel and inside the narrow channel

a bottom boundary layer there is a slight shear in the current profile, specially in the region closer to the wavemaker. But inside the channel the current is more or less depth uniform. Thus, for the remainder of the paper we shall consider a depth averaged value of the current only. As a result of the constriction caused by the narrowing of the channel, the depth averaged current varies from 0.32 m/s at $x = 12.4$ m to its maximum value of 0.53 m/s at $x = 15.2$ m.

Various tests were conducted of which 6 cases will be shown here. The particulars about the tests are given in Table 1. In these cases the blocking point (according to linear dispersion) for the given wave period occurs close to the narrow part of the channel ($x = 14.6$ m). The incident wave amplitude was increased from test 1 to 6 and the characteristics of the wave field observed.

Theoretical Model

Table 1: Test Particulars

Test	T (sec)	H_o (cms)
1	1.2	1.223
2	1.2	1.8
3	1.2	3.344
4	1.2	6.607
5	1.2	9.512
6	1.2	12.61

Bretherton and Garrett (1969) showed that in the presence of currents it is the wave action that is conserved and not the wave energy. Their conservation principle is given by

$$\frac{\partial}{\partial t}\left(\frac{E}{\sigma}\right) + \nabla.\left(\frac{E}{\sigma}C_g\frac{\vec{k}}{k}\right) = 0 \tag{4}$$

where $\frac{E}{\sigma}$ is the wave action and E is defined by linear theory as

$$E = \frac{1}{8}\rho g H^2$$

H being the wave height.

Since we are considering only steady wave conditions, we can neglect the first term in (4). Allowing for the variation of the channel width, integrating across the channel and providing a dissipation function for wave breaking, we get

$$\frac{1}{b}\frac{\partial}{\partial x}\left(\frac{bEC_g}{\sigma}\right) = \frac{D'}{\sigma} \tag{5}$$

where b is the channel width. D' is defined according to the bore dissipation model of Battjes and Janssen (1978), and is given by

$$D' = \frac{-\beta}{\pi}\left(\sqrt{\frac{8}{\rho h}}\right) kE^{3/2} \tag{6}$$

where β is a parameter. To match this dissipation rate with our data we take $\beta = 0.20$. It should be kept in mind that this is ten times lower in magnitude than the value used for modeling waves breaking on a sloping beach (Battjes and Janssen, 1978). This is due to the fact that current limited wave breaking is very different from depth limited wave breaking even though we are using the same formulation to model the two processes. Figure 3 shows a picture of waves breaking on the current. From the picture we can see that the breaking is weak and unsaturated as opposed to the saturated breakers observed in depth limited breaking.

The onset of wave breaking is predicted by Miche's criterion given by

$$H_m = \frac{\alpha}{k}\tanh kh \tag{7}$$

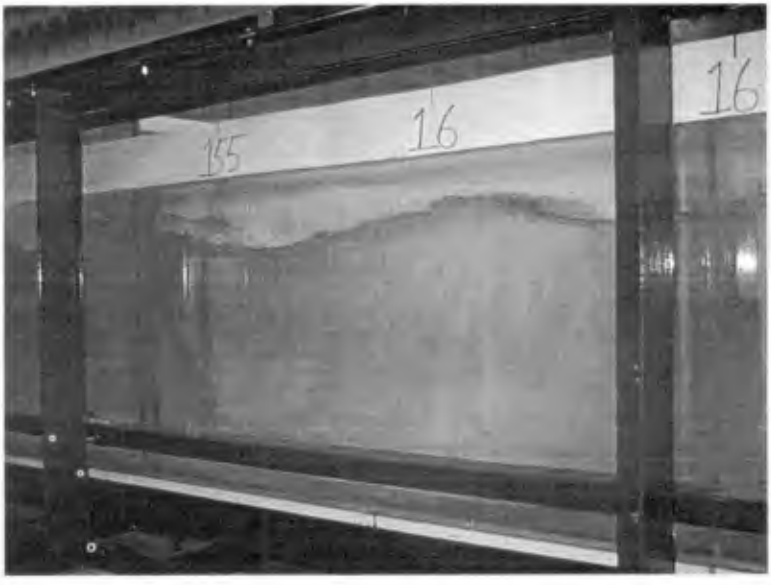

Figure 3: Waves breaking on the current (Test 6)

where α is a parameter. By taking the Stokes wave solution and assuming that at the onset of breaking the fluid velocity at the crest of the wave is equal to the phase velocity, Miche got $\alpha = 0.88$. This value of α has been used in the literature to predict the onset of depth limited breaking (Battjes and Janssen, 1978). However, based on our observations α has a lower value ($\alpha = 0.60$) for current limited wave breaking. Sakai and Saeki (1984) have shown through their experimental results that $\alpha = 0.88$ works reasonably well when there are no opposing currents, but it decreases with increase in the opposing current. The smallest value of α that they got was approximately 0.7. It should be kept in mind that their experiments were carried out in shallow water ($kh \approx 0.63$) where both depth and current play a part in wave breaking, while our experiments were carried out in much deeper water ($kh \geq 2.4$) where the wave breaking is caused only by the opposing current.

Eq. (5) together with (6) gives a model for a wave shoaling and breaking on a current . The model does not account for wave reflection, and thus cannot be used in cases where the waves are reflected from the blocking point. Also, it can be seen from (4) that at the blocking point ($C_g = 0$) the model becomes singular. Thus the model can only be used until the blocking point.

The dispersion relation is given by (2) together with an expression for σ which

depends upon the wave theory used. According to linear wave theory we have

$$\sigma = \pm\sqrt{gk\tanh kh} \tag{8}$$

and according to a third order Stokes wave theory (Bowden, 1948) we have

$$\sigma = \pm\sqrt{gk\tanh kh\left[1+(ka)^2\left(\frac{8+\cosh 4kh-2\tanh^2 kh}{8\sinh^4 kh}\right)\right]} \tag{9}$$

To determine the importance of amplitude dispersion in wave blocking, the model shall be compared with data using both the dispersion relations. From (3) and (9) we can already see that amplitude dispersion tends to increase the required blocking current, by increasing the relative wave frequency σ at a fixed k.

Observations

Out of the 6 test cases, only in test 1 was the incident wave height small enough for the waves to be reflected from the blocking point. Since the gages were too far apart to obtain the envelope of the partial standing waves, the experiments were repeated for this case with the gages densely spaced between $x = 13.7$ m and $x = 16$ m.

Smith (1975) and all subsequent references in the literature on wave reflection from a blocking point have shown that the envelope of the waves through the blocking point is represented by an Airy function, within the context of the linearized theory. From Trulsen and Mei (1993), the wave amplitude near the reflection point is given by

$$a = b_0 Ai(-\alpha^{2/3}(x - x_{st})) \tag{10}$$

where, x_{st} is the location of the blocking point (for our test case $x_{st} = 14.6$ m), b_0 is a constant related to the incident wave amplitude, and α is given by

$$\alpha = \sqrt{\left(\frac{-2\frac{\partial U}{\partial x}k\sigma}{3U^2}\right)\Bigg|_{x=x_{st}}} \tag{11}$$

Matching the data to (10) at $x = 13.7m$ and then comparing the amplitude envelope to the Airy function (Figure 4) we find that (10), which is based on linear theory, gives a good estimate of the actual shape of the amplitude envelope but underestimates the first peak. The accentuation in the wave envelope occurs because the larger wave amplitude close to the blocking point makes nonlinear effects important. The nonlinear term in a cubic Schrodinger equation for a modulating wave-train changes sign at $kh = 1.36$, leading to a self-focusing modulation for $kh > 1.36$, and a defocusing modulation for $kh < 1.36$. The result of the self-focusing mechanism, expected to be dominant here, is to accentuate the height of envelope modulations. A similar effect occurs in the case of an evolving sinusoidal wave front, where in deep water, linear theory again underestimates the first peak of the amplitude envelope in the front (Mei, 1992, page 57, Figure 4.2). It should be noted that these are just

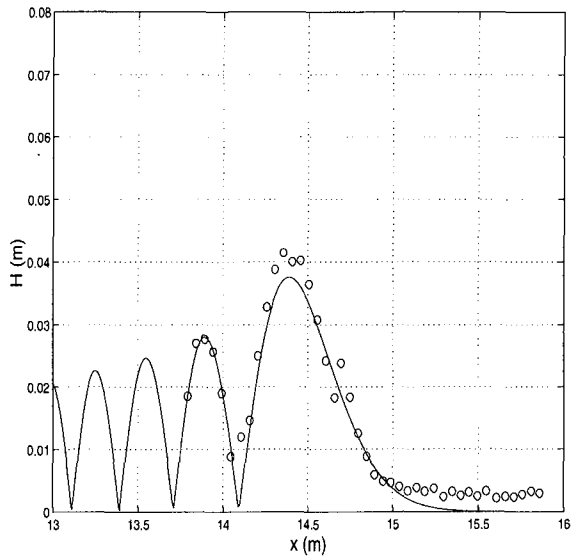

Figure 4: Amplitude envelope of partial standing waves due to reflection from the blocking point. 'Solid line' Airy function. 'Circles' Data

the preliminary findings and a thorough analysis of wave reflection from the blocking point is currently being carried out.

Tests 2 to 6 all have wave breaking with no apparent wave reflection. We can thus compare the data with the numerical model. The comparison is shown in Figure 5. In each of the test cases the wave heights have been normalized by their corresponding incident wave height. The depth averaged velocity distribution is also shown as a function of x. In the case of test 2 the wave shoals as the opposing current is increased and gets blocked before it can reach the maximum limit of the current. Test 3 shows a similar trend but now the blocking point is shifted back further from the wave paddle due to amplitude dispersion caused by the larger wave height. Wave blocking now occurs at the maximum current. In test 4, due to an even larger wave height, the wave reaches the maximum current without getting blocked. At this point, if the wave height does not reduce, the wave will travel right through the channel. But the wave is breaking and thus continues losing energy until the magnitude of the current in the narrow channel is enough to block it. In these three cases we find that the model works very well in predicting the blocking point when using Stokes third order dispersion as opposed to linear dispersion. The model also performs better in estimating the shoaling of the waves before blocking when taking amplitude dispersion into account.

Tests 2 to 4 are similar in the sense that the waves break and get blocked. But

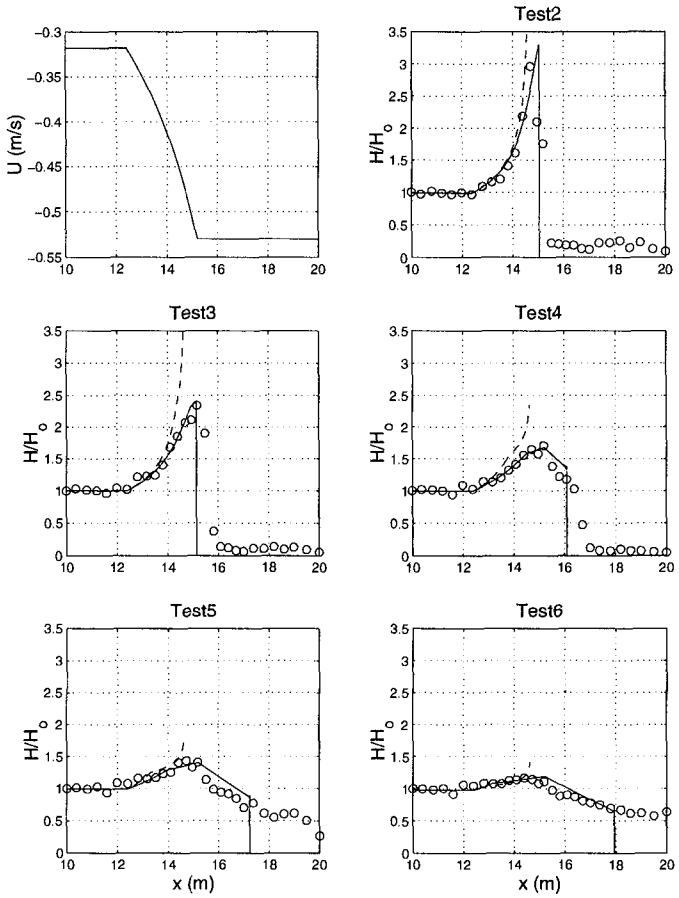

Figure 5: Model to data comparisons of the wave height distribution. 'Solid line' Bore model with Stokes third order dispersion, 'dashed line' Bore model with linear dispersion, 'circles' Data

tests 5 and 6 show a different pattern. From Figure 5 it can be seen that in both cases the waves reach the maximum current, and just as in test 4, propagate into the channel and continue dissipating energy due to wave breaking. However, the waves do not get blocked even when the blocking condition is satisfied for the model. Why? To get a better idea let us consider the wave period distribution as a function of x for the different test cases. From Figure 6 it can be seen that for tests 5 and 6 the wave energy shifts to a lower frequency as it propagates through the channel. For these

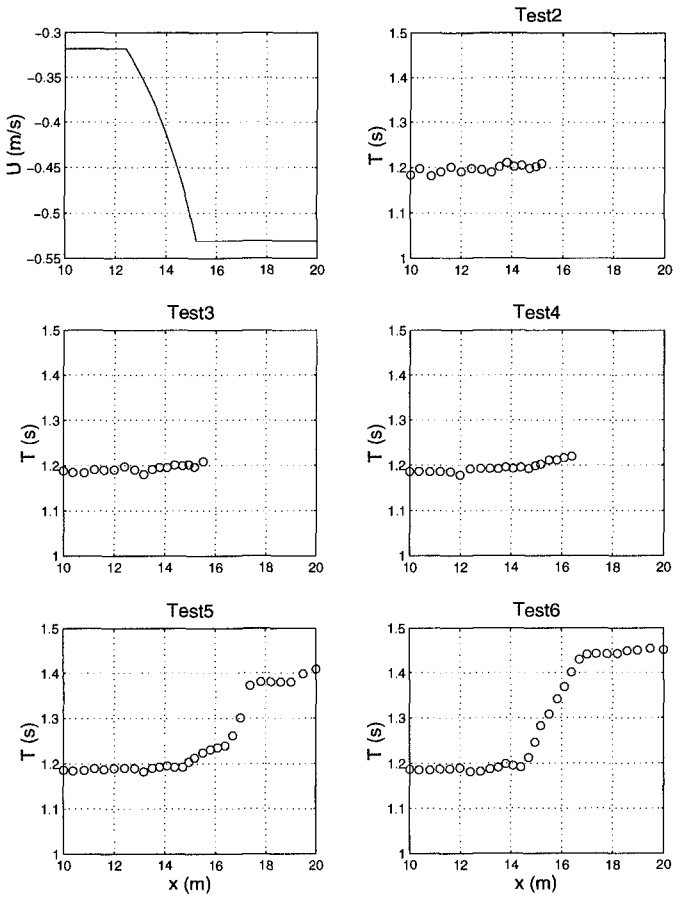

Figure 6: Significant wave period at the different data points obtained by the Zero-upcrossing method. Clear shift in the energy to a lower frequency for Tests 5 and 6

lower frequencies the required blocking current (even in the linear limit) is greater than the maximum current and the waves do not get blocked. The model, on the other hand, is unable to reproduce the shift to lower frequencies and thus predicts that waves are blocked.

The shift in the wave energy to a different frequency is explained by the growth of lower side bands. Benjamin and Feir (1967) showed that in deep water, steep waves

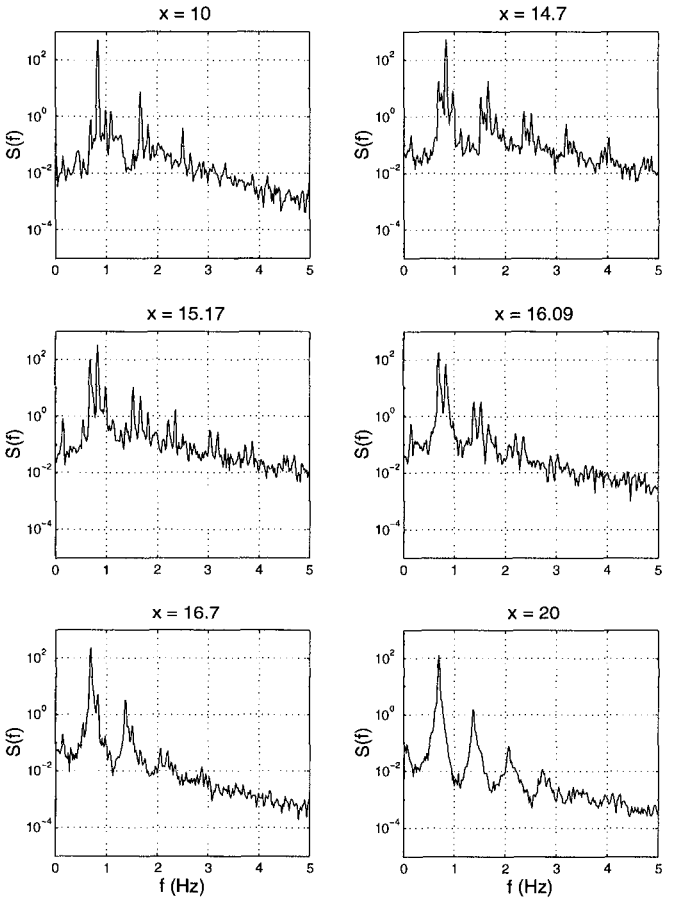

Figure 7: Frequency Spectra for Test 6 at various locations in the channel. Energy is transferred to the lower side band while the primary wave is blocked.

are unstable to disturbances at some frequencies δf away from their fundamental frequency (where δf is a small number). This leads to the growth of bands of energy on either side of the fundamental frequency in the frequency spectra, which are referred to as side bands. The growth of these side band instabilities depends upon the wave steepness and water depth. They become highly pronounced when the waves are riding on opposing currents and have been observed in the laboratory (Lai *et al.*, 1989). As the waves approach the blocking point the group velocity C_g tends to zero and the wave energy travels very slowly. Thus, a significant amount of energy

could be transferred from the fundamental frequency to the side bands even through small spatial distances, as the time of passage of a given wave energy packet through the transition region is relatively long. Since the lower side band requires a stronger blocking current than the primary wave or the upper side band, it could then continue to propagate forward while the other two are blocked.

This is clearly evident in test 6. The frequency spectra at six different gage locations are shown in Figure 7. At $x = 10$ m the wave is away from the channel but the side bands are clearly visible. The fundamental frequency is $f = 0.833Hz$ while the most prominent lower and upper side bands occur at $f = 0.688Hz$ and $f = 0.978Hz$ respectively. As the waves propagate into the channel the growth of these side bands is clearly evident. Going from $x = 14.7$ m to $x = 15.17$ m the energy in the lower side band increases by almost 10 times in less than 0.5 m. In the narrow part of the channel, first the upper side band and a little later the primary wave get blocked. But the wave energy continues to propagate through via the lower side band. A plot of the corresponding time series (Figure 8) shows the shift to a longer wave period. During the transfer of energy to the longer wave period the waves become very groupy. This increases the complexity of the breaking process as the waves tend to break at the crests of the wave groups. A similar pattern was also seen in test 5. Tests 2 to 4 showed no side band instabilities due to the smaller wave steepness.

Conclusions

In this work we have studied a series of monochromatic waves on an opposing blocking current. The wave amplitudes considered varied from small to large. For the smallest wave amplitudes, wave reflection from the blocking point was observed. Preliminary results show that though the amplitude envelope confirms well with the theoretical predictions, discrepancies between the data and theory show up close to the blocking point due to nonlinear effects.

A simple wave action conservation model together with a bore dissipation breaking model is used to simulate the data. Comparisons show that amplitude dispersion plays an important role in wave blocking. A third order Stokes dispersion relation works much better than a linear dispersion relation in predicting the blocking point. Also the predictions of energy decay from the bore model are reasonably accurate upto the blocking point.

For the largest wave amplitudes the wave energy shifts to a lower frequency due to side band instabilities and the waves do not get blocked, while the model predicts wave blocking. The growth of side bands also makes the waves very groupy, and thus in turn increases the complexity of wave breaking. It is clear that side bands in a carrier wave play an important role in determining whether waves are blocked or not, and ignoring them could lead to significant errors in wave modeling. This phenomenon requires further study and efforts are underway to try and predict the growth of these instabilities using a Schrodinger's equation.

A hierarchy in the wave field characteristics has been observed as the wave amplitude is increased. Depending upon the initial wave amplitude and frequency a monochromatic wave on an opposing current could

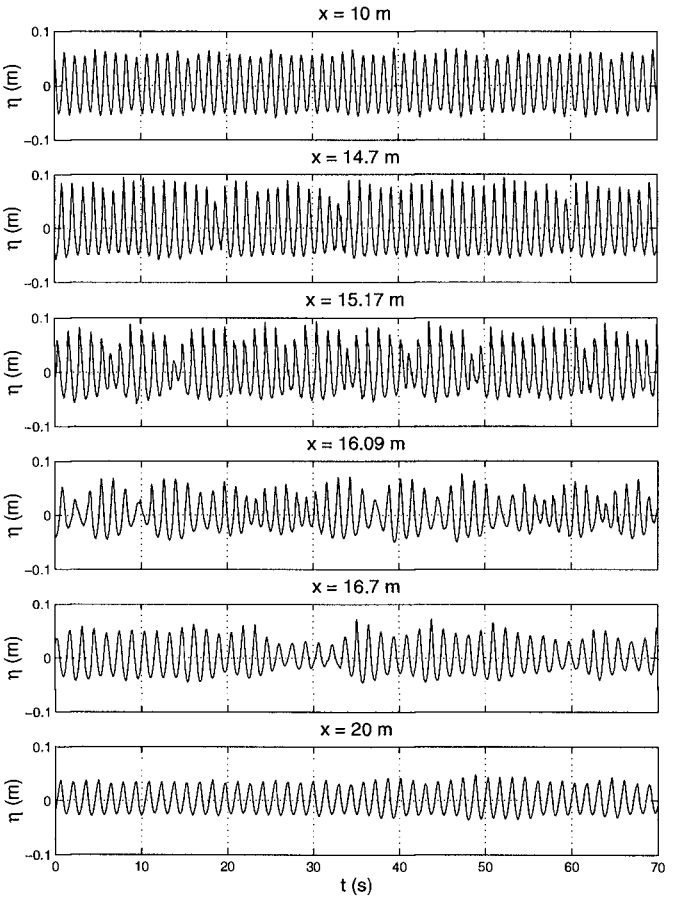

Figure 8: Time series for Test 6 at various locations in the channel.

1. be blocked and reflected,
2. be blocked and break at the blocking point,
3. pass through the maximum current due to amplitude dispersion but break and still get blocked, or
4. transfer significant energy to a lower side band which does not get blocked while the primary wave and the upper side band do.

In a random sea all these different phenomena could be occurring at the same time

making dissipation modeling all the more difficult. Thus the next step is to study wave breaking in groupy and random waves.

Acknowledgments

This research has been sponsored by NOAA Office of Sea Grant, Department of Commerce, under Grant No. NA56RG0162-01 (Project No. R/OE-13) and Grant No. NA56RG0147 (Project No. R/OE-21). The U.S. Government is authorized to produce and distribute reprints for governmental purposes, not withstanding any copyright notation that may appear heron.

References

Battjes, J. A. and Janssen, J. P. F. M. (1978). Energy loss and set-up due to breaking of random waves. In *16th Coastal Engineering Conference Proceedings*, pages 569–587. ASCE.

Benjamin, T. B. and Feir, J. E. (1967). The disintegration of water waves on deep water part 1. theory. *J. Fluid Mech.*, **27**(3), 417–430.

Bowden, K. F. (1948). Some observations of waves and other fluctuations in a tidal current. *Proc. Roy. Soc. London*, **192**, 403–425.

Bretherton, F. P. and Garrett, C. J. R. (1969). Wavetrains in inhomogenous moving media. *Proc. Roy. Soc. London A.*, **302**, 529–554.

Lai, R. J., Long, S. R., and Huang, N. E. (1989). Laboratory studies of wave-current interaction:kinematics of the strong interaction. *J. Geophys. Res.*, **94**(C11), 16201–16214.

Mei, C. C. (1992). *The Applied Dynamics of Ocean Surface Waves*. World Scientific, second edition.

Peregrine, D. H. and Smith, R. (1979). Nonlinear effects upon waves near caustics. *Phil. Trans. Roy. Soc. London*, **292(A)**, 341–370.

Sakai, S. and Saeki, H. (1984). Effects of opposing current on wave transformation. In *19th Coastal Engineering Conference Proceedings*, pages 1132–1148, Houston, Texas. ASCE.

Shyu, J. H. and Phillips, O. M. (1990). The blockage of gravity and capillary waves by longer waves and currents. *J. Fluid Mech.*, **217**, 115–141.

Smith, R. (1975). Reflection of short gravity waves on a non-uniform current. *Math. Proc. Camb. Phil. Soc.*, **78**, 517–525.

Stiassnie, M. and Dagan, G. (1979). Partial reflexion of water waves by non-uniform adverse currents. *J. Fluid Mech.*, **92**(1), 119–129.

Trulsen, K. and Mei, C. C. (1993). Double reflection of capillary/gravity waves by a non-uniform current: a boundary-layer theory. *J. Fluid Mech.*, **251**, 239–271.

Tidal ellipses in the near-shore zone (-3 to -10 m); modelling and observations

Klaas T. Houwman[1] and Piet Hoekstra[1]

Abstract

Based on theoretical considerations it is demonstrated that in the near-shore zone the tidal water level fluctuations are mainly caused by cross-shore volume fluxes. Phase differences between the tidal wave propagating on the shelf and in the shallow near-shore zone create cross-shore surface gradients which result in an onshore directed flow during rising water and an offshore directed flow during falling water. Observations of near bed velocities in the near-shore zone confirm the presence of these currents. It results in an anti clockwise rotating current vector at a water depth of about 10m . Comparisons of these observations with results obtained from a 1-DV flow model show that the tidal ellipses are not the result of Coriolis forces but are generated by the alternating cross-shore water fluxes due to the tide.

Introduction

Generally, in the near-shore zone several mechanism are present which are capable of driving a mean flow, e.g. waves, wind and tides. In literature many studies are focussing on wave driven currents, but hardly any study can be found describing the tidal phenomena in the near-shore zone. In this study we will focus on tidal flow phenomena which can be found in the near-shore zone of the barrier island of Terschelling, the Netherlands. Houwman and Uittenbogaard (1998) investigated the longshore tidal flow at this location by combining modelling and observations. Here emphasis will be given to the tide induced cross-shore flow. Measurements as well as model results will be used to investigate the origin of these currents.

Description of the field site and measurements

[1] Institute for Marine and Atmospheric Research, Utrecht University, Department of Physical Geography, P.O.Box 80.115, 3508 TC Utrecht, The Netherlands.

For the analysis presented in this paper, data will be used obtained from measurements made in the multiple bar system of the barrier island of Terschelling, the Netherlands. These measurements were carried out in the framework of the NOURTEC project (Hoekstra et al., 1994). The field site is fully exposed to the North Sea, with an average annual offshore significant wave height of 1.1m. Tides are semi diurnal with a neap tidal range of about 1.5 m and a spring tidal range of ca. 2.5 m. The tidal wave propagates along the coast from the west to the east with an almost constant speed and shape within several tens of km's at either side of the measurement site. In a cross-shore direction, the inner near shore zone is characterized by several breaker bars parallel to the shoreline (see figure 1).

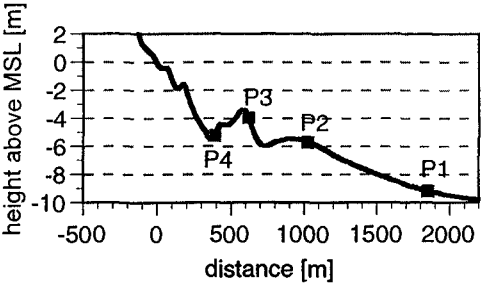

Figure 1: Cross-shore profile with instrumented positions.

The bars are more or less uniform in longshore direction in the area of interest. Several instrumented tripods were placed in a cross-shore transect at position P1, P2, P3 and P4 (see Figure 1) and data was collected over a time period of 2 years during three successive campaigns. All tripods were equipped with two Electro Magnetic Flow meters (EMF) at (nominal) heights of 0.3 m and 1.2 m above the bed and a pressure sensor at 2.2 m above the bed. Each tripod collected data with a sampling frequency of 2 Hz with a burst length of 2048 s and starting at every full hour. These bursts were split up in four subseries of 512 s each and averaged values of these subseries were used for the analyses presented here. Furthermore, from this data set two calm weather events, with a length of about 140 hours each, were selected. The wave height during these periods was in the range of 0.3-0.8 m and wave breaking occurred only landwards of P4. The wind speed during both periods was about 6 m/s.

Flow model

In this study, a one dimensional vertical flow model (1-DV) will be used to support the analysis of measurements. Here the outline of this model will be described briefly. More details, and an evaluation of this model are presented in Houwman and Uittenbogaard (1998). This 1-DV flow model, describes the distribution of the horizontal velocity vector over depth at a single location in the horizontal plane. The equations of motion in cross-shore x and longshore y direction at a particular height z above the bottom are respectively given by:

$$\frac{\partial U}{\partial t} = -g\frac{\partial \zeta}{\partial x} + fV + \frac{\partial}{\partial z}\left(\upsilon_T \frac{\partial U}{\partial z}\right) \quad (1)$$

$$\frac{\partial V}{\partial t} = -g\frac{\partial \zeta}{\partial y} - fU + \frac{\partial}{\partial z}\left(\upsilon_T \frac{\partial V}{\partial z}\right) \quad (2)$$

In this U and V are the orthogonal velocity components in x and y direction respectively. The first left-hand terms describe the rate of change of the velocities. The horizontal pressure gradient is represented by the first right-hand term, with ζ being the water level fluctuation around mean sea level. The Coriolis force is given by the second right-hand term, with the Coriolis parameter $f=2\Omega\sin\Phi$ representing the influence of the earth's rotation. The last right-hand term describes the vertical exchange of horizontal momentum due to the turbulent forces. The eddy viscosity υ_T is calculated from the Kolmogorov-Prandtl expression, using a standard k-ϵ turbulence model. The equations of this turbulence model, with their constant settings, are adopted from Launder and Spalding (1974). Assuming a logarithmic velocity profile in the near-bed region and in the region near the air-water interface leads to the boundary conditions for this k-ϵ turbulence model.
The boundary conditions for the flow equations (1) and (2) can be deduced making the same assumption. The bottom boundary condition for eq.(1) reads:

$$\upsilon_T \frac{\partial U}{\partial z}\bigg|_{z=z_0} = S^2 U\sqrt{U^2+V^2} \quad (3)$$

The parameter S is given by $S = \kappa / \ln(z/z_0)$, with the Von Kármán' constant κ and roughness length z_0. Similar conditions are used at the upper boundary and for eq. (2). The cross-shore water surface gradient $\partial\zeta/\partial x$ is obtained from a method given by Uittenbogaard and Van Kester (1996). They used the depth-integrated version of the equation of motion to calculate the surface gradient. Here this method is applied to calculate the cross-shore surface gradient $\partial\zeta/\partial x$:

$$g\frac{\partial \zeta}{\partial x}\bigg|_t = \frac{\tau_{sx} - \tau_{bx}}{\rho h} + \frac{\overline{U}(t-T_{rlx}) - \overline{U_0}}{T_{rlx}} + f\overline{V} \quad (4)$$

with :
- τ_{sx} = surface shear stress in cross-shore direction
- τ_{bx} = bottom shear stress in cross-shore direction
- h = water depth
- T_{rlx} = some relaxation time span
- $\overline{U}(t\text{-}T_{rlx})$ = depth averaged cross-shore velocity solution at time t - Δt

$\overline{U_0}$ = given depth averaged cross-shore velocity at time t

$\overline{V}$ = depth averaged longshore velocity solved

The cross-shore surface gradient can be calculated from eq. (4) using information about the shear stresses at the boundaries and the depth averaged currents. The shear stress τ_{bx} and the depth averaged currents $\overline{U}(t\text{-}T_{rlx})$ and $\overline{V}$ are obtained from the solution of eq. (1) and (2) while the surface stress component τ_{sx} is an input term of the model (wind stress). The depth averaged velocity $\overline{U_0}$ must be specified and is an input parameter for the model. Using alternatingly eq.(1), (2) and (4), the depth averaged velocity $\overline{U}$ at time t - T_{rlx} approaches the velocity $\overline{U_0}$. The surface gradient then balances the shear stresses at the surface τ_{sx} and the bottom τ_{bx} and the (small) contribution of the Coriolis force. The time step T_{rlx} is taken equal to two times the numerical time step which results in a stable and accurate solution.
The prescribed depth averaged (cross-shore) velocity $\overline{U_0}$ is set to zero for the entire tidal cycle. Note that this does not mean that the cross-shore velocity at each position in the vertical is zero. Finally, specification of the longshore surface gradient $\partial\zeta/\partial y$ and the roughness length z_0 is needed, to apply the model. Here the longshore surface gradient, obtained from measured water levels at two locations along the coast, is used to drive the model. A fixed roughness length z_0 of 0.0033 m was used for all computations, based on the findings of Houwman and Van Rijn (1998) for the same site. All computations were carried out, using 100 grid points equally distributed over the vertical, and 16 time steps in an hour. The model is capable to reproduce the observed longshore velocities accurately as shown by Houwman and Uittenbogaard (1998).

Results

The model was run for the first selected period of 140 hours at position P1 and the calculated flow pattern at 1.2 m above the bed is shown in figure 2. The calculated current ellipse is almost flat and is orientated parallel to the coast. Note that the horizontal and vertical axises are different in this diagram. In principle the combination of the Coriolis force and the cross-shore pressure gradient should produce a clockwise rotating current vector at the surface and an anticlockwise sense of rotation for the current ellipse at the bottom. But at this water depth of about 10 m, the vertical gradient of the Coriolis forcing term is rather small. The depth averaged contribution of the Coriolis force in cross-shore direction $f\overline{V}$ is balanced by the cross-shore water surface gradient. So, the difference between the Coriolis force fV and the depth averaged Coriolis force $f\overline{V}$ is the only net driving force left for the cross-shore flow. The combination of this small driving force and a strong friction in the vertical results in an almost rectilinear flow pattern. Figure 2 also presents the measured flow pattern for the same period and location. In contrast to the predicted flow pattern, the observations show a clear developed ellipse. This ellipse is apparently not caused by Coriolis forces because these were taken into account in the model. The difference between predicted and observed cross-shore velocities can be explained in the following way: In the model the depth averaged cross-shore flow is taken equal to zero. Using this condition one assumes

implicitly that at each location the volume of water involved in the rising or falling of the water level is fully delivered by the longshore tidal flow. This can easily be seen from the continuity equation (5). Taking $\overline{U} = 0$ implies that the first term is balanced by the third term .

$$\frac{\partial \zeta}{\partial t} + \frac{\partial h\overline{U}}{\partial x} + \frac{\partial h\overline{V}}{\partial y} = 0 \qquad (5)$$

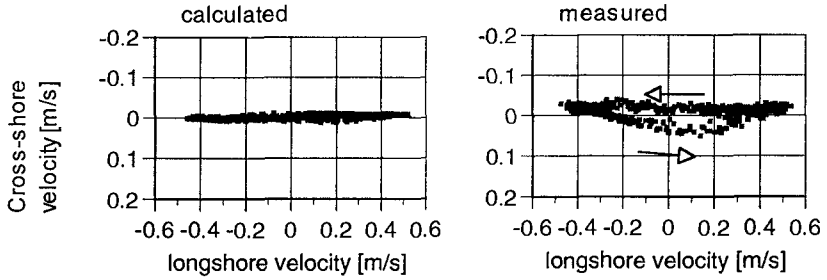

Figure 2: Calculated and measured flow pattern at P1, 1.2 m above the bed.

A scale analysis however, shows that this is not the case in thc near-shore zone. Assuming a tidal wave with amplitude ζ_1 , period T ,wavelength L and depth averaged longshore velocity $\overline{V}_1$, the first and last term in the continuity equation have the following order of magnitude:

$$\frac{\partial \zeta}{\partial t} \approx O\left(\frac{\zeta_1}{T}\right)$$
$$\frac{\partial \overline{V}h}{\partial y} = h\frac{\partial \overline{V}}{\partial y} + \overline{V}\frac{\partial h}{\partial y} \approx O\left(d\frac{\overline{V}_1}{L} + \overline{V}_1\frac{\zeta_1}{L}\right) \qquad (6)$$

The magnitude of these terms becomes comparable at a mean water depth d ≈24m, when typical values for the tidal regime at Terschelling are used. At smaller water depths $\partial\zeta/\partial t$ is significant larger than the $\partial\overline{V}h/\partial y$ term. So, at these water depths a cross-shore flux must be present. The actual magnitude of the $\partial\zeta/\partial t$ and $\partial\overline{V}h/\partial y$ terms can more accurately be deduced using the flow model. The magnitude of the $\partial\overline{V}h/\partial y$ term can be calculated assuming a longshore uniform topography and using the propagation speed of the tidal wave. These computations demonstrate that the term $\partial\overline{V}h/\partial y$ is significant smaller than the $\partial\zeta/\partial t$ term at a mean water depth of 10 m. Averaged over a half tidal cycle, about 22% of the volume of water is delivered by this longshore term at this water depth. At smaller water depths the importance of the $\partial\overline{V}h/\partial y$ term decreases rapidly. For example, at a water depth of 5 m approximately 6% of the volume flux is delivered by the longshore term and at 2 m water depth only 1% can be explained from this. This implies that in the near shore zone the second term in the continuity equation $\partial\overline{U}h/\partial x$, is non-

zero and is mainly responsible for delivering the volume of water associated with the tidal water level fluctuations in the coastal zone. The relative importance of this cross-shore term grows for a decreasing water depth. The underlying reason for this cross-shore flux is the difference in water depth on the shelf and in the near-shore zone. The tidal wave propagates along the coast with a speed determined by the (average) water depth at the shelf. In the shallow near-shore zone the propagation speed would have been less as a result of the smaller water depth, which is of course not possible. The tide in the near-shore zone lags the propagation of the tidal wave at the shelf only slightly. But, this results in co-tidal lines which are not entirely perpendicular to the coast. This is schematically illustrated in figure 3.

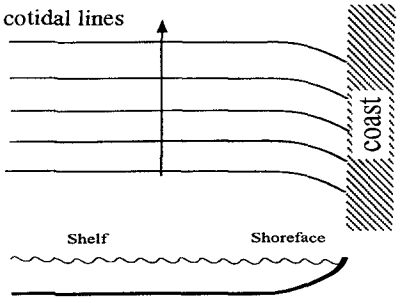

Figure 3: Cotidal lines on the shelf and shoreface.

During rising water the water level in deep water rises faster than in the shallow near shore zone. This results in a cross-shore water surface gradient which drives an onshore directed, cross-shore flow (see figure 4). This flow is (mainly) responsible for increasing the water level in the shallow near-shore zone. During falling water the reversed process will take place and an offshore directed flow will be present, as indicated in figure 4.

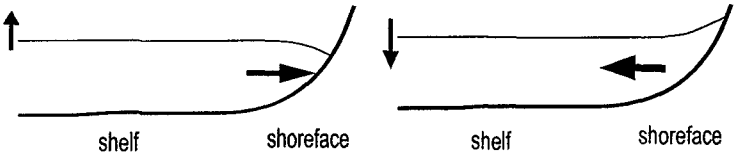

Figure 4: Cross-shore flow due to tide induced surface gradients.

So, in colour full terms spoken, the tidal wave in the near-shore zone is drawn along the coast by the tidal wave travelling on the shelf. The principle of this tide induced cross-shore flow is also described by Pugh (1987). Unfortunately, the magnitude of this cross-shore flow can not be deduced from a 1-DV model, at least a 2-DH model is required. But in the near-shore zone the third term in the continuity equation is relatively small as shown above. Therefore a reasonable approximation of the magnitude of the cross-shore flow can be found after neglecting this longshore term in the continuity equation. After integration in cross-shore direction from a position x_0 to the waterline, see figure 5, the

following expression is found:

$$\overline{U_0} = \frac{x_0}{h}\frac{\partial \zeta}{\partial t} \tag{7}$$

So, the depth averaged flow at a particular position in the near shore-zone depends on the distance to the waterline x_0, the local water depth h and the rate of fluctuation of the water level. The flow $\overline{U_0}$ delivers a water volume to the landwards located zone, equal to the dotted area presented in figure 5.

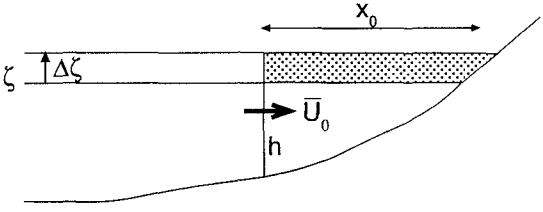

Figure 5: The tide induced cross-shore flow in the near-shore zone.

The distance to the water line x_0 depends on the actual water level and is thus a function of time. It can be calculated from: $x_0 = x_1 + \zeta/\tan\beta$. In this x_1 is the distance to the waterline when $z = 0$ (mean sea level) and $\tan\beta$ is the slope of the beach, which is 0.014 m/m in the Terschelling case. Figure 6 shows the computed cross-shore distribution of the depth averaged cross-shore flow during one tidal cycle. During falling water (time 0 to 5) an offshore (negative) flow is present at all positions and during rising water (time 6 to 11) an onshore (positive) flow exists at each position. Due to the asymmetry of the water elevation curve, the onshore directed currents are larger than the offshore directed ones, but the duration of this latter period is longer. The largest velocities are found just after low tide. At that time the most rapid variation of the water level takes place. The cross-shore distribution of the tidal flow clearly shows a relationship with the morphology. The largest velocities can be found on top of the bars and local minima in the spatial flow distribution coincide with the troughs. Further offshore also rather strong velocities are predicted. But, one has to keep in mind that at water depths larger then ~8 m the contribution of the longshore term in the continuity equation becomes significant resulting in a reduction of $\overline{U_0}$. The magnitude of the cross-shore flow depends on the speed in which the water level is changing. The largest flow velocities coincide with the steepest parts of the tidal elevation curve. For these periods the longshore surface slope is also maximal. Without inertia, this would result in maximum cross-shore and longshore flow at the same time, creating a rectilinear flow pattern oblique to the coast. The influence of the inertia is however significant for the longshore flow, which results in a phase lag between cross-shore and longshore flow. Therefore an anticlockwise rotating current vector can be expected at locations where inertia plays a significant role, see figure 2. In contrast to velocity profiles affected by Coriolis forces this mechanism creates a current vector which rotates in the same direction at every position in the vertical. The direction of rotation has of course nothing to do with Coriolis forces, it is determined by

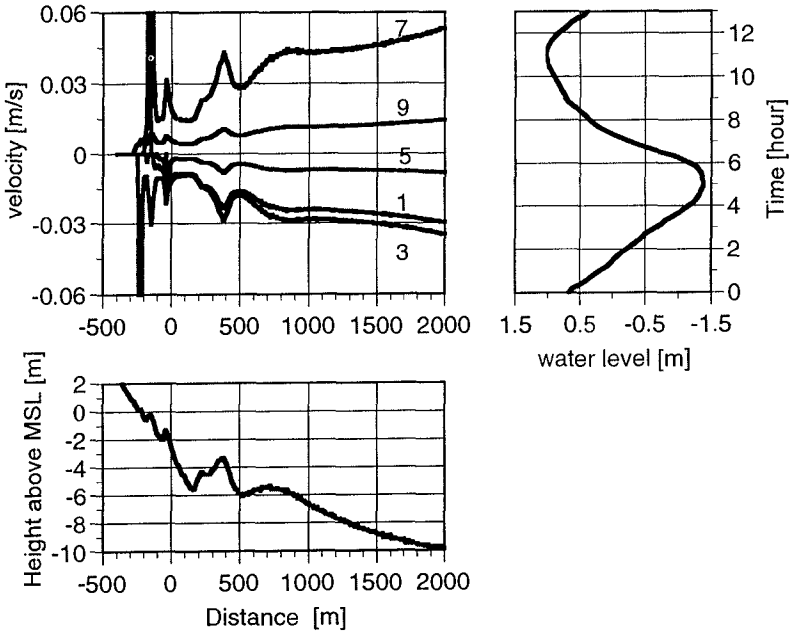

Figure 6: Cross-shore distribution of the tide induced depth averaged cross-shore flow.

the position of the coast, left or right relative to the progressive tidal wave.

This mechanism, generation of a tide induced cross-shore flow, can easily be implemented into the flow model simply using eq. (7) to calculate the model input parameter $\overline{U_0}$ for every time step.

Computations were carried out, using this condition, for the two selected periods of 140 hours each. Figure 7 shows the observed and calculated tidal ellipses during the first period at P1 at 1.2 m and 0.3 m above the bed. The computed as well as the observed flow patterns show ellipses created by an anticlockwise rotating current vector. The predictions agree well with the observations. The tide induced cross-shore velocities at these levels are rather small, with a typical maximum value of about 0.05 m/s at 1.2 m above the bed. Figure 8 shows the flow pattern at P1 during the second period of 140 hours. The computed velocities during this period form an anticlockwise rotating current vector similar to the previous period. The measured velocities however do not show a clear ellipsoidal form. Unfortunately, the orientation of the measured flow pattern is not accurately known due to inaccuracies in the determination of the direction of the flow meter in the frame. So, it is not clear if the phase lag between long and cross-shore flow has become less or that the cross-shore flow is diminished during this period. It is also

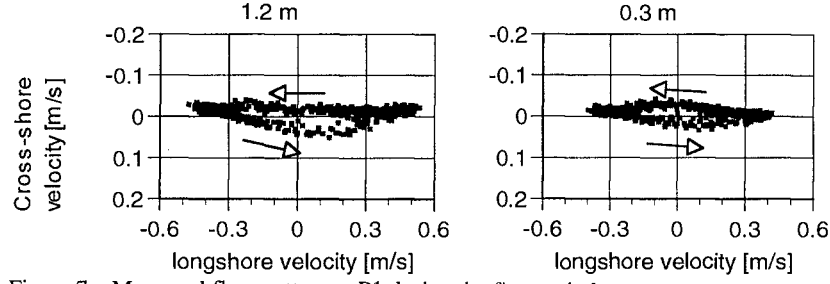

Figure 7a: Measured flow pattern at P1 during the first period

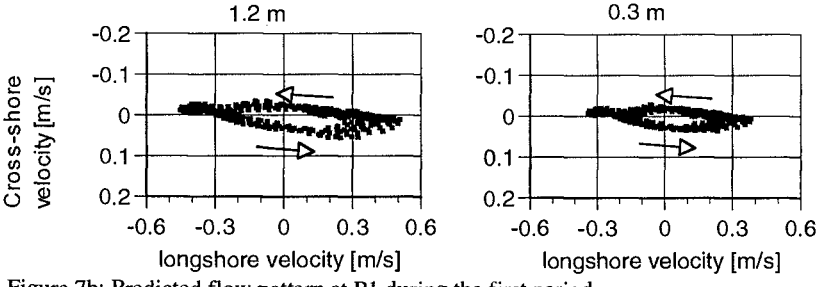

Figure 7b: Predicted flow pattern at P1 during the first period.

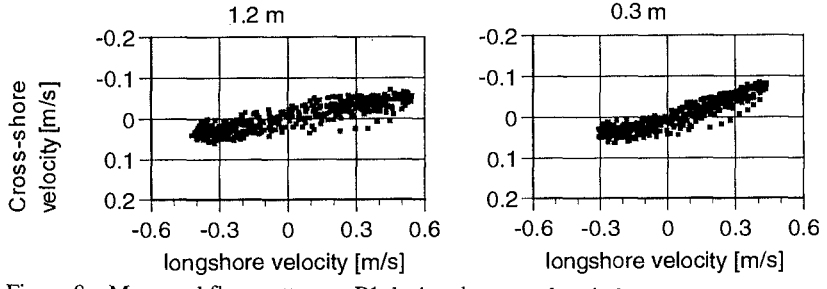

Figure 8a: Measured flow pattern at P1 during the second period.

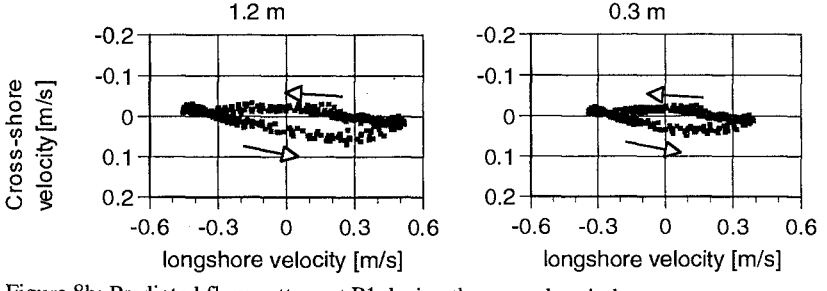

Figure 8b: Predicted flow pattern at P1 during the second period.

unclear why in the second period the observed ellipses are flat, contrary to the ones in the first period, but at station P2 the same phenomena occurred. During the second period the observed velocities at P2 do not form an ellipse in contrast to the predicted ones .The ellipses observed during the first period are shown in figure 9 together with the calculated ones.

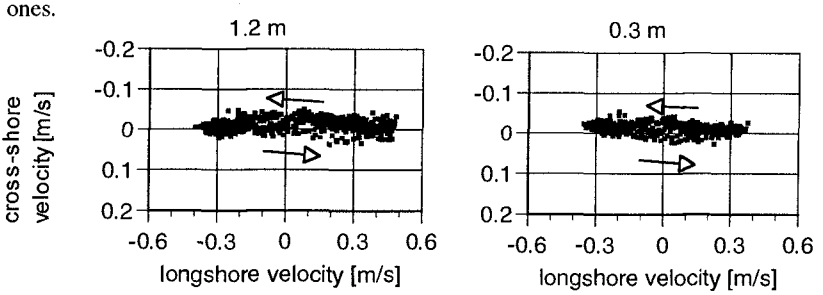

Figure 9a: Measured flow pattern at P2 during the first period.

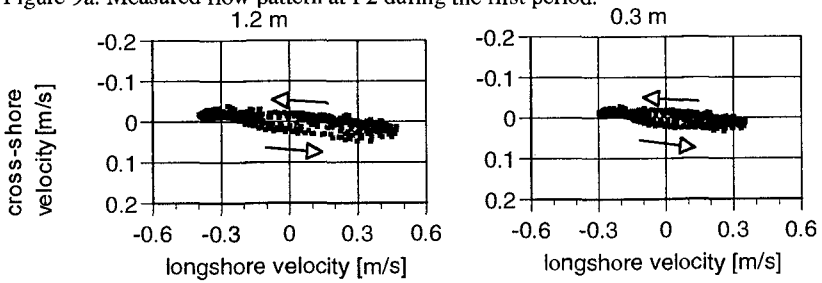

Figure 9b: Predicted flow pattern at P2 during the first period.

Although the observed ellipses are less "open" as the computed ones, they both display similar trends. The onshore velocities are larger than the offshore directed velocities, which is also visible in figure 7 and 8. The shape of the predicted tidal ellipses at P1 and P2 is different, which is the result of a decrease of the phase lag between the longshore and cross-shore flow. The influence of the inertia on the flow at P2 is smaller than at P1 resulting in a reduction of this phase lag. The measured and predicted tidal ellipses during the second period at this position P2 are shown in figure 10. At position P3 and P4 only data from the second period is available. The measured and computed ellipses at station P3 for this period are shown in figure 11. Also here the current vectors predicted by the model rotate in an anticlockwise sense. And again, onshore directed current velocities are larger than the offshore directed ones. At this position with a mean water depth of about 4 m the influence of the inertia on the flow is small, which results in an almost flat ellipse. The main axis of this ellipse makes an angle with the coast line. The predictions and observations do not deviate significantly from each other, taking into account the error band in the orientation of the flow meter.

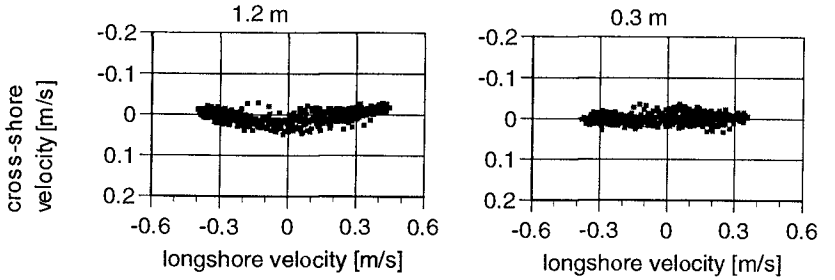

Figure 10a: Measured flow pattern at P2 during the second period.

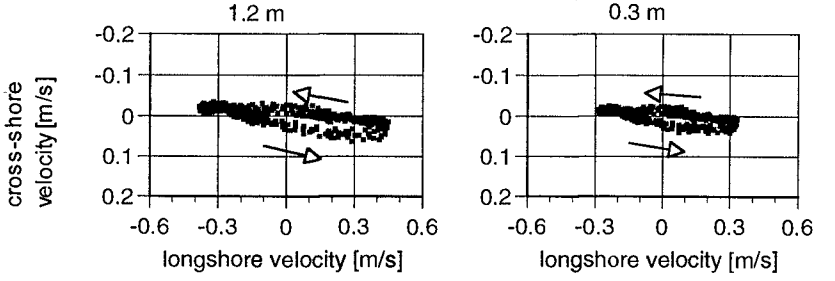

Figure 10b: Predicted flow pattern at P2 during the second period.

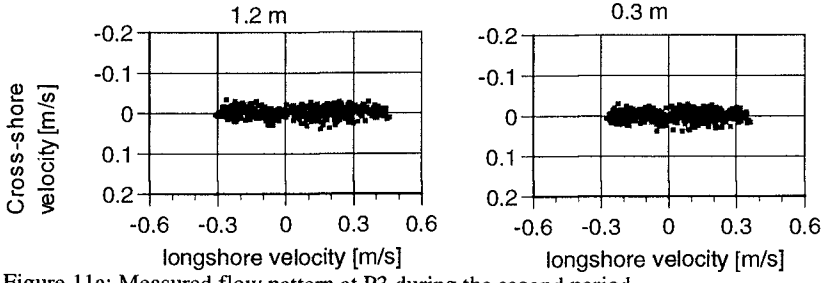

Figure 11a: Measured flow pattern at P3 during the second period.

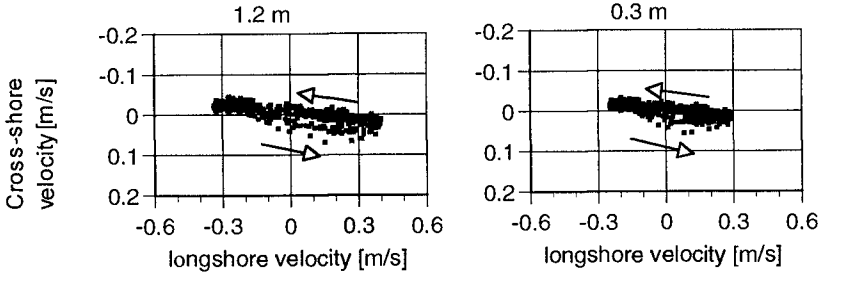

Figure 11b: Predicted flow pattern at P3 during the second period.

Figure 12 shows the measured and predicted current ellipses in the trough at station P4. The observations and the model results indicate that no clear ellipses are developed at this position. This can be explained by the combination of a relative large water depth at this position and the rather small distance to the shore. The measured velocities are somewhat scattered and the flood current at 0.3 m above the bed seems to be deflected. The reason for this is not clear.

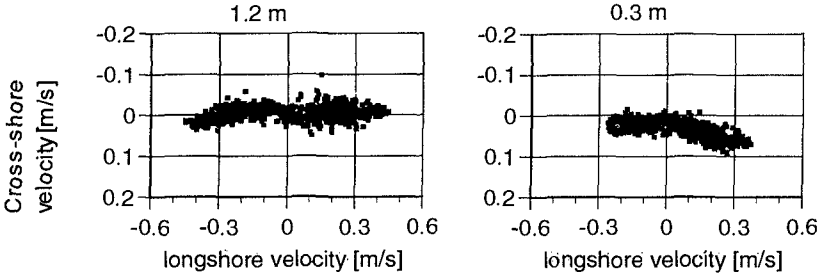

Figure 12a: Measured flow pattern at P4 during the second period.

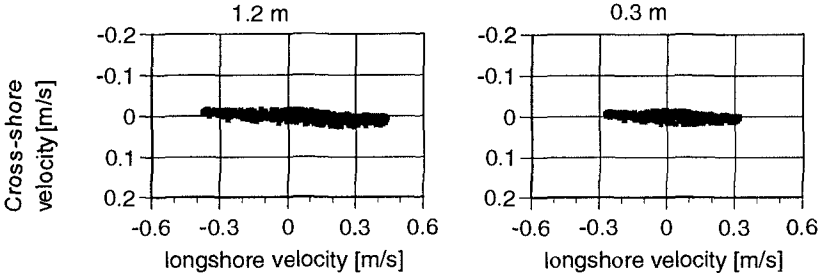

Figure 12b: Predicted flow pattern at P4 during the second period.

Discussion and conclusions

Based on theoretical considerations it is demonstrated that small but persistent cross-shore flows are generated in the near-shore zone due to tidal water level fluctuations. This is confirmed by the comparison between model computations and flow observations. A phase difference between the tidal wave in the near-shore zone and on the shelf creates cross-shore surface gradients which drives a cross-shore flow. At this site the volume flux involved in the tidal fluctuation of the water level in the near-shore zone, at water depths less than 10 m, is mainly delivered by the cross-shore flow. Neglecting the contribution of the longshore flow to this volume flux makes it possible to determine this cross-shore flow. The magnitude of the tide induced cross-shore flow depends on the tidal range, the shape of the tidal curve, the local water depth, the distance to the water line and the slope of the beach. Furthermore, the propagation speed of the tidal wave is important, if one takes the longshore term, the third term in eq. (5), into account.
Based on this, it can be expected that this mechanism is important only for coastal areas

dealing with a meso or macro tide and a gentle sloping beach-shoreface system such as the coast of Terschelling.

The comparison of observed and predicted tidal ellipses demonstrates that the tide induced cross-shore currents can be detected in the field. Predictions of the near bed flow at a water depth of about 10m (location P1) indicate that ellipses can be expected, which were also observed in the field during the first period. But, in contrast to the predictions, no clear ellipse was observed during the second period. A similar result was found at P2. Apparently, the flow pattern can easily be disturbed by other mechanisms. Non-uniformity of the morphology in longshore direction could be an explanation for the difference between measured and predicted ellipses during the second period. But, particular at position P1, the large scale morphology is uniform over several kilometres in longshore direction and is almost identical for both periods. So, it is unlikely that this is the reason for the observed differences. Perhaps wind effects play a role in this, although no significant differences were present during the first and second period. A decrease of the phase differences between longshore and cross-shore velocities, which are small, could explain the diminishing of the open ellipses. A time shift, for any reason whatsoever, in the order of 20 minutes would already give a flat ellipse which makes an angle to the coastline. These flat ellipses have been observed, but the magnitude of the cross-shore flow in those cases can not be determined due to the inaccuracies in the direction of the measured flow vector. At this stage, it remains unclear what the reason is for the disturbance of the ellipse. It is clear though persistent, tide induced cross-shore currents exist. Going from P1 further inshore, the phase difference between longshore and cross-shore near bed flow decreases, resulting in a change of the shape of the tidal ellipse. At P3, the major axis of predicted ellipses is oblique orientated to the coast and the minor axis is only small compared to the one at P1 .

Finally, at P4 a rectilinear flow pattern is predicted, orientated shore parallel, which is the result of the rather large water depth and the short distance to the shore line.

Acknowledgments

This work was carried out in the framework of the NOURTEC project: Innovative Nourishment Techniques Evaluation. It was jointly funded by the Ministry of Transport, Public Works and Water Management in the Netherlands and by the Commission of the European Communities, Directorate General for Science, Research and Development under the Marine Science and Technology programme: MAS2-CT93-0049.

References

Hoekstra, P., Houwman, K.T., Kroon, A., Vessem, P. Van and Ruessink, B.G., 1994:The NOURTEC experiment of Terschelling: process-oriented monitoring of a shoreface nourishment (1993-1996). Proc. Coastal Dynamics'94, ASCE, 402-416.

Houwman, K.T. and Uittenbogaard, R.E., 1998:The vertical distribution of the flow field

in the near-shore zone: a comparison between model results and measured tidal velocities. Submitted to Journal of Physical Oceanography, AMS.

Houwman, K.T. and Van Rijn, L.C., 1998: Modelling the apparent bed roughness under varying wave and current conditions in the field. Submitted to Coastal Engineering, Elsevier.

Launder, B.E. and Spalding, D.B., 1974: The numerical computation of turbulent flows. Computer methods in applied mechanics and engineering, 3, 269-289.

Pugh, D.T., 1987: Tides, surges and mean sea-level. John Wiley & Sons, 472 pp.

Uittenbogaard, R.E. and Van Kester, J.A.Th.M., 1996: Modelling seasonal temperature stratification with TRIWAQ. A preparatory study based on one-dimensional computations, Report Z978, Delft Hydraulics, The Netherlands, 89 pp.

ADCP Observation of Nearshore Current Structure in the Surf Zone

Takao Yamashita*, Hiroshi Yoshioka*, Shigeru Kato*, Lu Ming*
and Chikara Shimoda**

Abstract

Coastal current in the nearshore zone is generated by both breaking waves inside the surf zone and by the wind over the extended area of the coastal and offshore zones. Wind-induced currents as well as wave-induced currents are characterized by strong shear flows and complicated turbulence flow fields. In order to develop mathematical models for these currents, it is essential to formulate wind and wave stresses acting on the sea surface. Unfortunately, there has been no reliable observation of current profile in the surf zone under the condition of strong wind. No extensive information on wind stresses inside the nearshore zone has been made available, primarily because of the challenge of recording these data without facilities such as observation pier or towers.

In this paper we conducted a continuous recording of nearshore current profile and wind stresses in/out the surf zone by using high frequency ADCP (Acoustic Doppler Current Profiler, 1200kHz) installed on the sea bottom under the observation pier of Ogata Wave Observatory, together with 3-component ultrasonic anemometer. This two and half months observation revealed part of the structure of nearshore currents and some characteristics of the wind drag coefficient in the nearshore zone.

1. Introduction

Causes of beach erosion may be natural, as for example entrainment by storm waves or nearshore currents, or they may result from human activity, as for example from coastal structures, which affect waves and currents patterns, from hinterland development which reduced sediment yield, or from the global warming of the atmosphere which produces a rise of sea level. As a consequence, beaches become smaller and smaller. Management and use of the seashore may also affect water quality and the entire ecological system with its natural resources. Beaches play an important role in the global environment, yet beaches are so fragile.

* Disaster Prevention Research Institute, Kyoto University, Gokasho, Uji, Kyoto 611-0011, Japan
** Science Engineering Associates Corporation (SEA Corp.), Ichikawa, Chiba, Japan

Maybe, all over the world, intensively both in the United States and in European countries, the role of beaches as a regulator of the coastal environment, as well as their function as wave absorbers (disaster prevention function) have been recognized for several decades. Soft beach construction by sand nourishment and simple structures seems to be the best choice of beach preservation. A new field, so called "Beach Engineering", emerged, in which beach protection, maintenance, and environmental and economic evaluation have been extensively examined. An interdisciplinary research on coastal environment keeps developing.

Part of this research consists of predicting the evolution of both natural and artificial beaches, and numerical simulations can be used for this purpose. Beach changes result from sediment transport which is controlled by several factors; sediments are moved away by ocean currents and nearshore currents, originated by external forces such as waves and winds. Therefore, numerical models need to combine a model for wind, a model for wave propagation and a model for sediment entrainment. Most nearshore current models have been written as horizontally two dimensional models, assuming the driving shear forces to be originated by the gradient of radiation stresses. However, these models are incomplete because it is assumed that the current profile is uniform in the vertical direction. Although the three-dimensional nature of nearshore currents has been recently studied by numerical simulations, their dynamics is not yet fully understood and their modeling remains a difficult task; to avoid the complexity of three-dimensional models which require long calculations, quasi three-dimensional models have been proposed instead. Whereas models can be run to simulate changes of sea bottom topographies induced by natural factors as well as by nearshore constructions, because of the variety of beaches, of wave and current conditions, and because of the complexity of the processes involved, the results of these simulations lack accuracy. Field observations can then be used as a complementary source of information to understand current mechanisms, long-term beach evolution, and to calibrate the models in each particular case. This requires a substantial amount of data simultaneously for winds, waves and currents in order to calibrate each part of the code - wind module, wave module and current module - as well as the whole coherence of the model. For example, test runs can be performed and model parameters adjusted until numerical results fit field data.

Such a long term observation was carried out by Yamashita et al. (1997) to investigate the structure of nearshore currents in the surf zone along the Ogata coast facing the Japan Sea. Since most erosion occurs in presence of large waves and strong winds, data were recorded during winter time, under such conditions. After an observation of two months, the following characteristics were revealed : (1) nearshore currents have almost uniform vertical distribution in the surf zone, (2) nearshore currents are strongly influenced by the wind, and wind-induced currents are of the same order as wave-induced currents. It was also observed that features of waves, currents and turbulence differ significantly from shallow waters to deep waters. Therefore, mechanisms of momentum transfer between atmosphere and sea deserve further investigations. Effects of both waves and winds need to be taken into account in any nearshore current simulation along this coast.

It is the goal of this study to discuss some aspects of winds, waves and currents

recorded in the surf zone and to get a better understanding of their mutual interaction; the observation was made possible by the presence of the T-shaped observation pier (TOP) of Ogata Wave Observatory, a research facility of the Disaster Prevention Institute (DPRI), Kyoto University. This pier extends from the shoreline into the surf zone and permits continuous and methodic recordings of nearshore data in an area inaccessible by boat under severe winter conditions. The pier also enables constant check out and maintenance of all instruments. Nearshore currents were recorded by two ADCPs. Winds were recorded by a three-components anemometer at a 10m elevation above mean sea level. The influence of wind and waves on current intensity and direction were investigated. A drag coefficient was derived to characterize wind stresses over the surf zone. The drag coefficient was deduced from wind data using the Turbulence Dissipation Method (TDM).

2. Observation of Currents, Waves and Winds in the Nearshore Zone

During winter time, severe erosion is caused by offshore sediment transport along the Japan's coast facing the Japan Sea. It is believed that the strong winds and waves take a significant role in this process, but the mechanisms involved are not yet understood. In this study, the interdependence between winds, waves and currents is examined, based on a set of data recorded in/out the surf zone in order to get a preliminary idea on nearshore-currents structure and dynamics. The observation was carried out using the pier (TOP) with the following instruments: 3-component ultrasonic anemometer for wind shear stresses, seven ultrasonic wave gauges for water surface elevation and wave characteristics and two 1200KHz ADCP set on 1.3m above the sea bottom underneath the pier for current profiles. Dimension and location of instruments are shown in Fig.1.

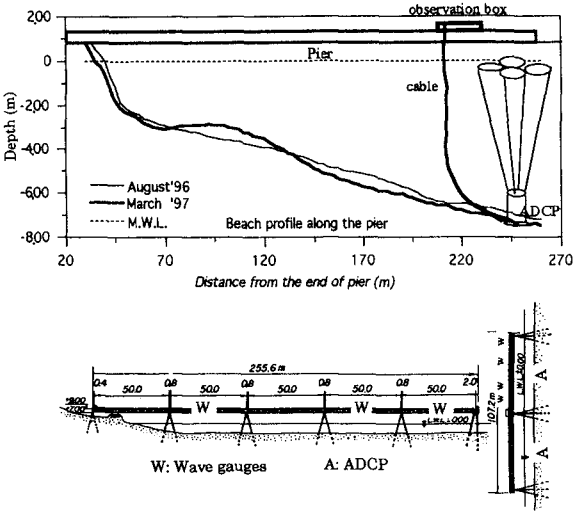

Figure 1 T-shaped observation pier, beach profile and location of instruments

Figure 2 shows (a) the significant wave height of the wave gauge ch.4 and 5, (b) offshore and (c) longshore velocities (4-6m depth average of west ADCP) during the entire observation period. As been shown in Fig.2(b), seven winter storms which generated strong offshore-going currents were recorded. Five cases of them, Case A (Jan. 4-5), Case B (Jan. 6-7), Case C (Jan.18-20), Case D (Jan.31-Feb.1) and Case E (Feb.9-10), are selected to investigate the interdependence between nearshore currents and wind-wave climate. It is observed that strong offshore currents arise only during short periods of less than 24hrs and longshore currents going eastwards are dominant.

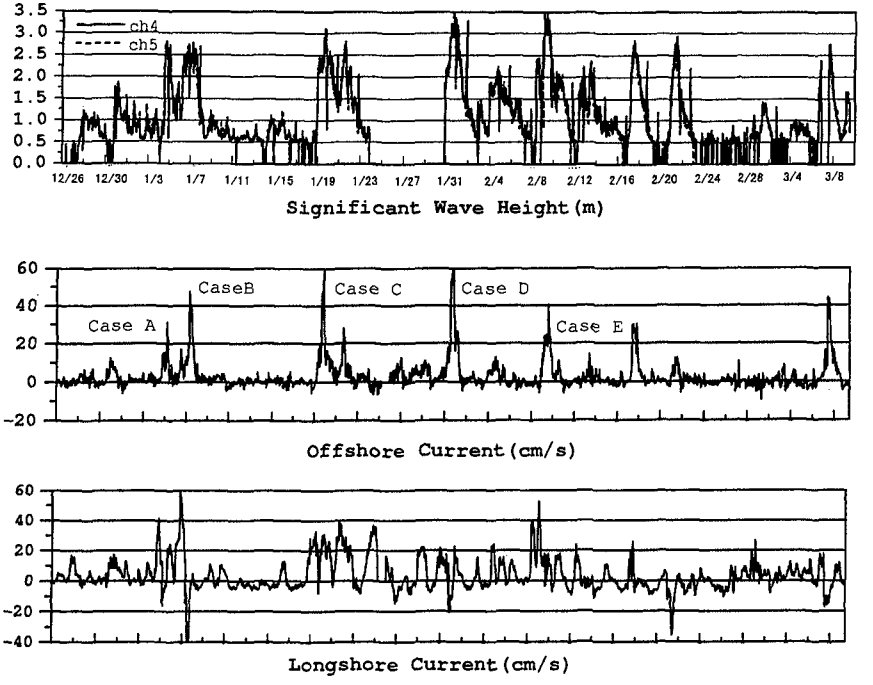

Figure 2 Significant wave height (ch.4 and 5), and 4-6m depth averaged currents of the west ADCP recorded during the entire observation period. Cases A-E indicate the selected ivents in which strong offshore going currents observed.

Top: significant wave height of the wave gauge ch.4 and 5,
Middle: offshore velocity (going offshore is positive),
Bottom: longshore velocity (going eastwards is positive)

3. Interdependence between Nearshore Currents and Wind-Wave Climate

Figures 3 - 7 show interdependence between nearshore currents and wind/wave climate of five selected winter storms (Case A-E in Fig.2(b)). Sub figures refer respectively to time (a) wave climate, (b) wind climate, (c) longshore current profiles, (d) offshore current profiles and (e) nearshore current profiles by vector. As TOP is oriented north-west (48deg from the north, shore-normal), winds blowing from a direction westwards relative to TOP will be referred to as westerly winds. During winter storm winds typically blow from the west, i.e. they are westerly relative to the pier. From these figures, it can be recognized that there are two types of wind/wave climates which cause strong offshore-going currents. One is the type called "end-storm undertow" which is defined that sudden bursts of current occur with changes in wind directions from westerly to easterly with reduction of wind velocity at the end of the winter storms (Cases A, B, E). The other is the type called "mid-storm undertow" which is defined that continuous strong shore-normal(NW) winds generate strong undertow in the midst of storm (Cases C, D). It has been recognized at TOP that when the significant wave height at the gauge ch.4 exceeds 2.5m, TOP is completely inside the surf zone, and when being the range of 2.0-2.5m, breaker point exists in the area of gauge ch.4 to ch.6. If the obvious reduction in the significant wave height between ch.5 and ch.6 is observed, we judge that wave breaking occurred between ch.5 to ch.6. Following are significant nearshore-current characteristics revealed by the 1998 observation:

(a) Velocity profile : Sub figures (c) and (d) in Figs. 3-7 indicate that both longshore and offshore current profiles in the vertical direction are almost uniform in the region under the wave trough level and above the boundary layer when wave and wind climates are stable. Figure 8 shows the hourly changes in vertical profiles of on-offshore (left) and longshore (right) in Case B. Phases A, B and C in the figure are indicated in Fig.4, which are corresponding to before, middle and after the sudden bursts of offshore-going currents.

(b) Longshore currents : Direction of longshore currents is much more sensitive to the wind direction than waves. Its intensity is much stronger than that of on-offshore component except the phase of the sudden bursts of offshore-going currents. These observation facts may indicate that strong longshore current is mainly induced by winds in the wide area of nearshore zone and its direction is shore-parallel. Wave-induced longshore current is much smaller than wind-induced one. This fact suggest us that wind-induced current near the surf zone is the dominant factor of sediment transport under the storm conditions such as typhoon, hurricane and winter monsoon. This effect should be taken into consideration when beach changes and depth of closure are discussed.

(c) On-offshore currents : As mentioned before there are two types of wind climate which cause a strong offshore-going current, those are called here "end-storm undertow" and "mid-storm undertow". These cross shore currents may be generated by unbalance of mean water surface gradient and shear stresses due to both winds and

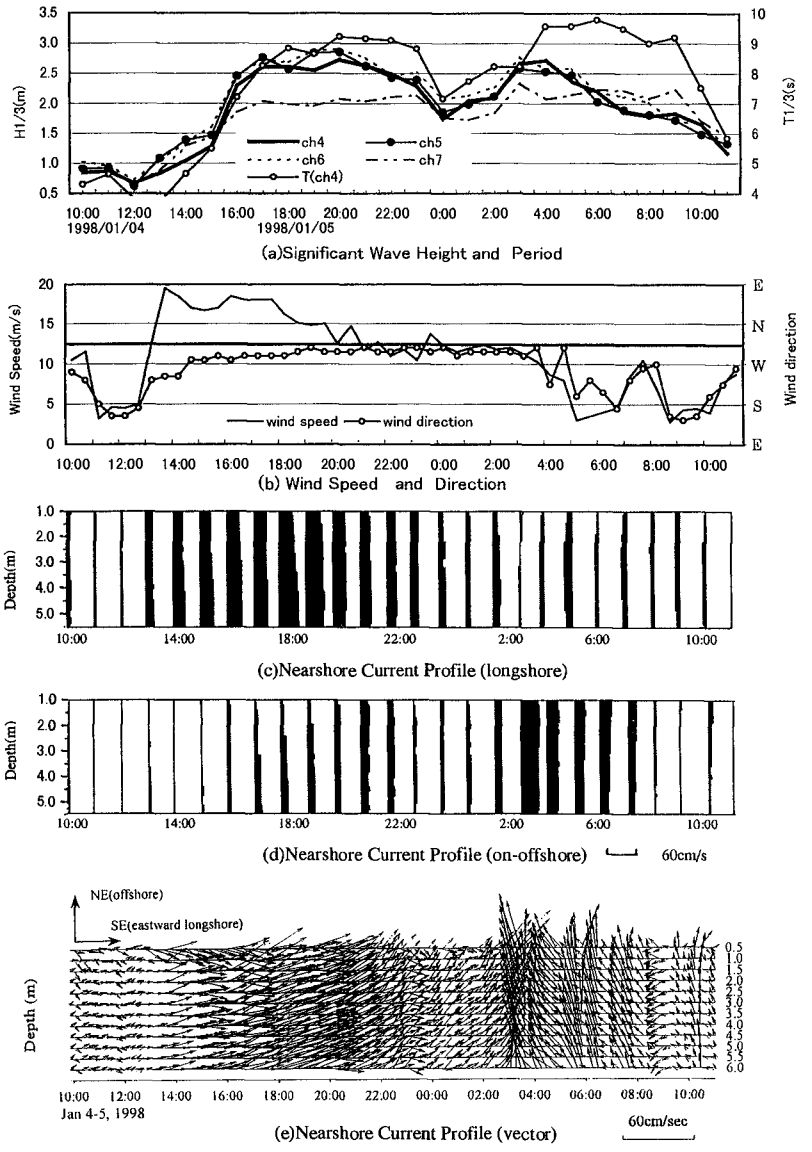

Figure 3 Interdependence between nearshore currents and wind/wave climate of winter storms (Case A).

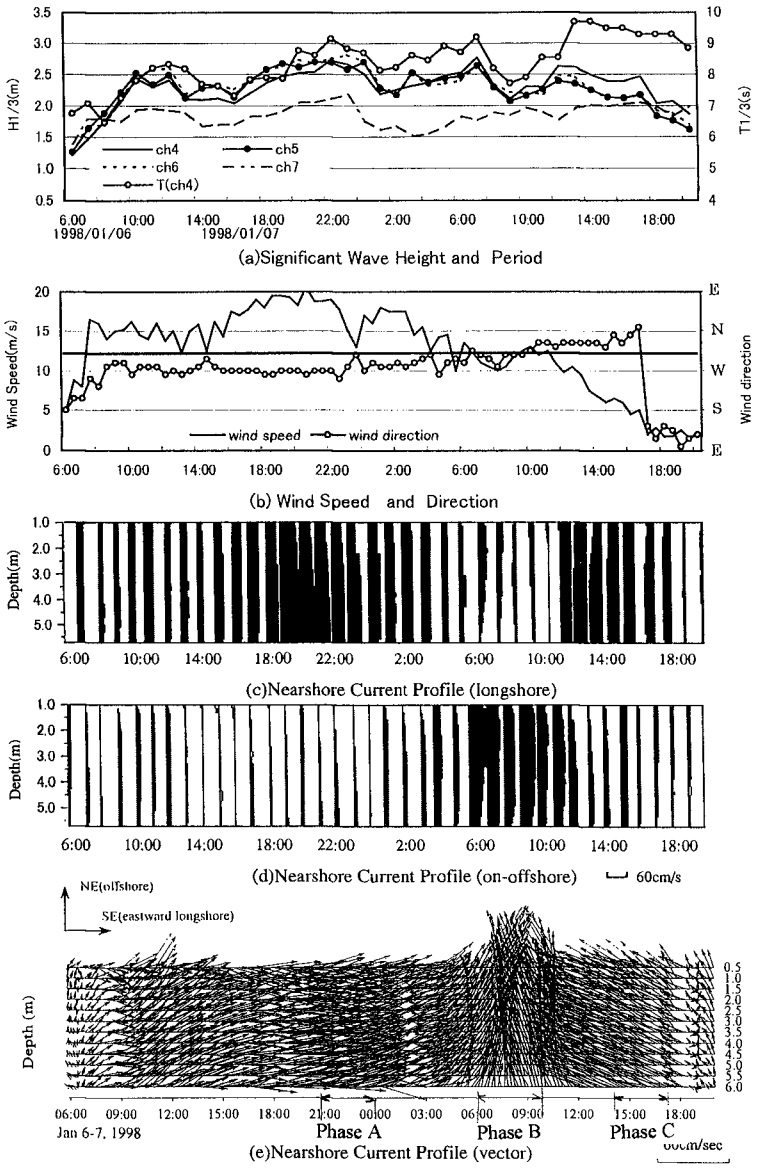

Figure 4 Interdependence between nearshore currents and wind/wave climate of winter storms (Case B).

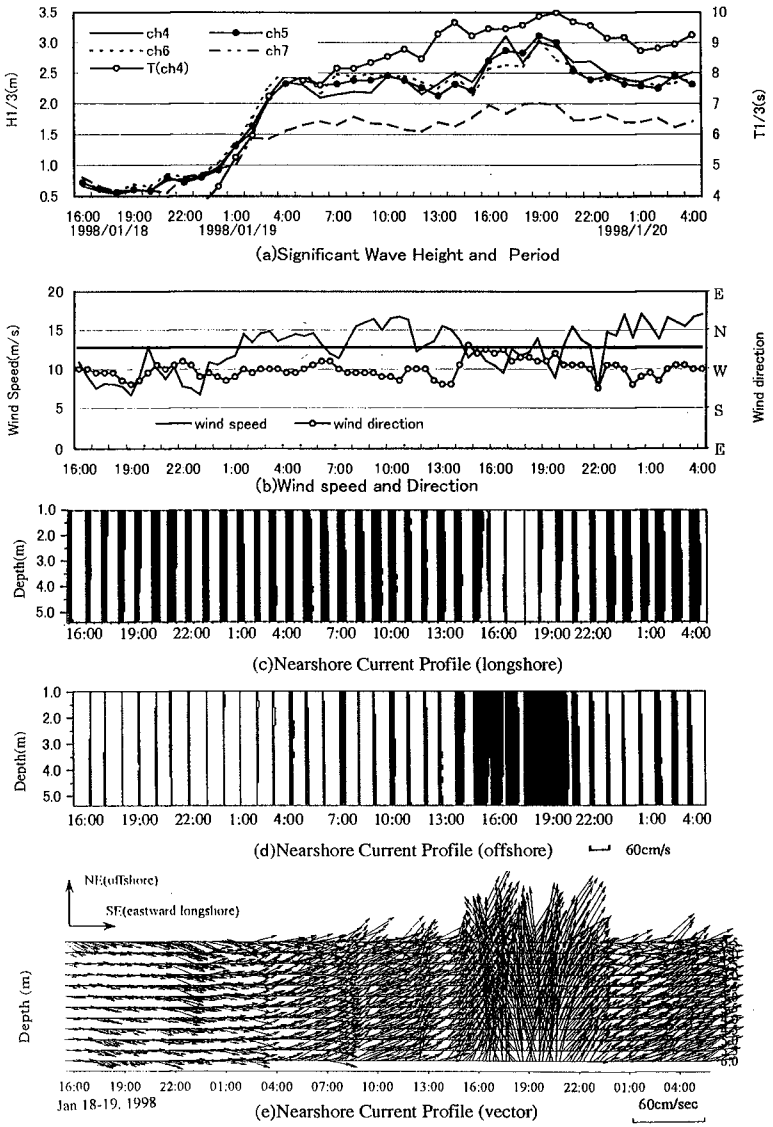

Figure 5 Interdependence between nearshore currents and wind/wave climate of winter storms (Case C).

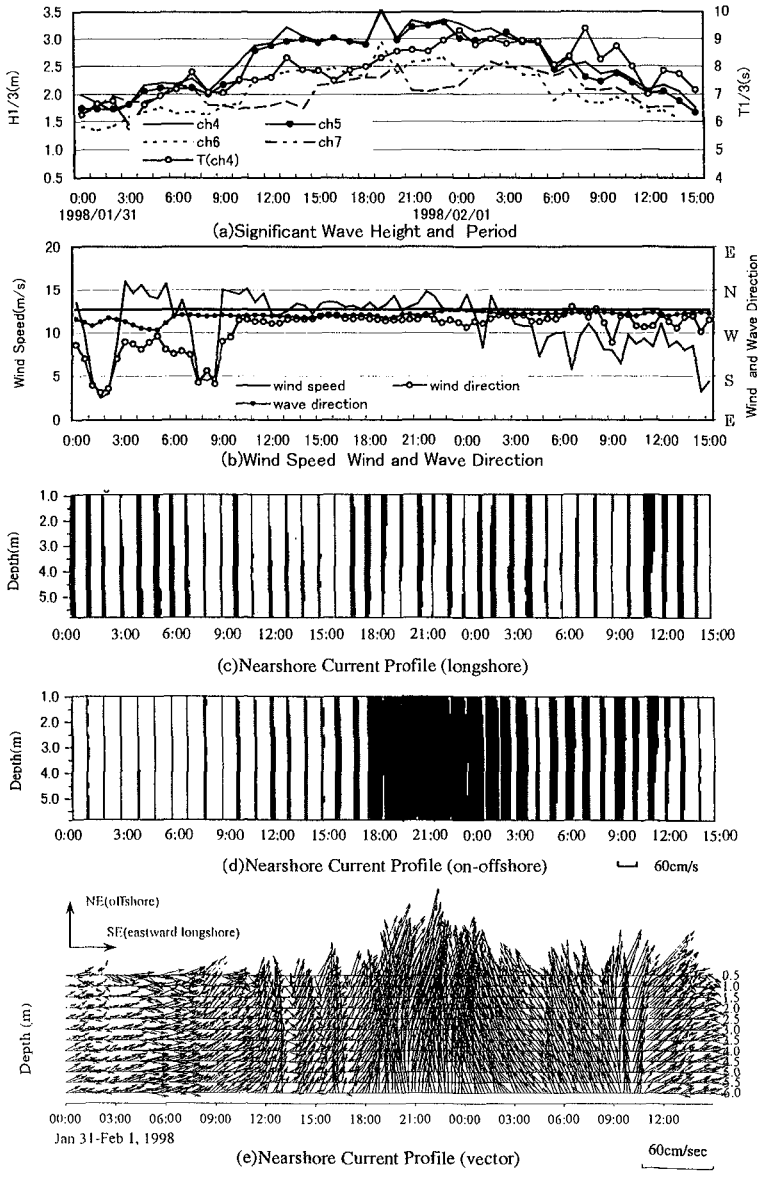

Figure 6 Interdependence between nearshore currents and wind/wave climate of winter storms (Case D).

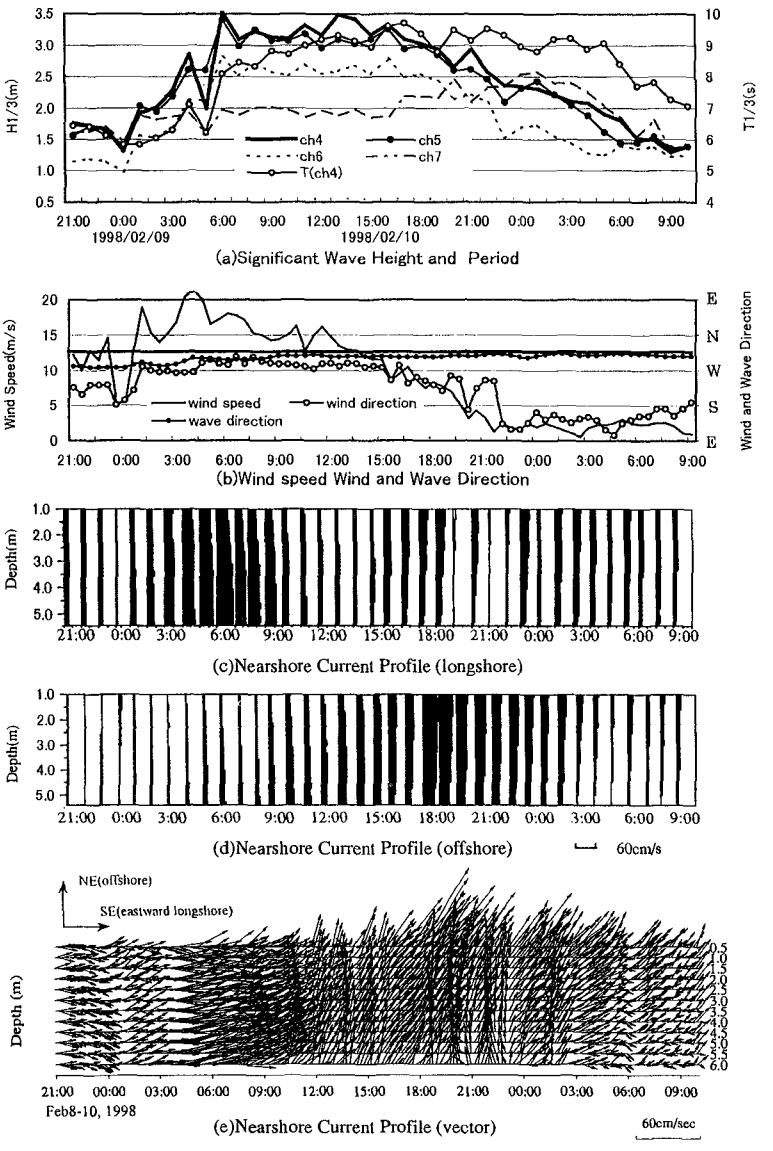

Figure 7 Interdependence between nearshore currents and wind/wave climate of winter storms (Case E).

breaking waves. When wind direction changes and/or wind velocity decreases at the end of winter storm, the type of "end-storm undertow" occurs. When the water surface gradient which is generated by wind and wave-induced cross shore currents loses its balance in the midst of the storm, the type of "mid-storm undertow" occurs. Wave-induced cross shore currents is mainly generated in the surf zone by wave breaking, which may form the velocity profile of the so-called undertow together with wind-induced cross shore currents. Note that the mechanism of this undertow is different from two types of strong offshore-going currents. The intensity of offshore-going sediment transport by "end-storm undertow" and "mid-storm undertow" may have to be made clear to evaluate the total volume of losing sand by storms.

4. Wind Stresses in the Nearshore Zone

As wind-induced current is the main factor of sediment transport, especially longshore transport, evaluation of wind stresses in the nearshore zone is one of the most important tasks of beach change prediction under the storm condition. Stress factors represent the exchange of momentum between atmosphere and ocean, and between ocean and sea bed. Air-sea momentum exchange is controlled by the waves; it is a complex process involving turbulent boundary-layer flow over a moving rough surface, wave generation, non-linear energy transfer between wave components, and wave breaking. Besides, waves also affect the bottom stress by increasing turbulence in the bottom boundary layer and eddy viscosity, hence facilitating momentum transfer. These processes are not very well understood theoretically, especially under strong winds and high waves, and therefore they are not incorporated into the models. If they could be better explained, then, in principle, the accuracy of the corresponding forcing terms in the equations of motion for nearshore currents could be improved.

Following is an analysis of wind data over the surf zone aimed to formulate wind stresses in terms of a drag coefficient. Wind turbulence was measured by a three-components ultrasonic anemometer, located on top of the observation pier, 10m above the mean sea level. Wind data were continuously recorded at a 10Hz sampling frequency, and analyzed by means of the Turbulence Dissipation Method (Yelland et al. ,1996). Wind data observed have been classified into four types according to the wind direction relative to the pier (TOP), as defined in Fig. 9. Almost all winds stronger than 10m/s are from the direction of south-west to north-west (Type I), in which the drag coefficient, C_D, estimated by TDM (10min in every hour) and the average wind speed at 10m, U, obey a linear relationship in a semi-log plot as shown in Fig. 10. The following fitting formula has been obtained:

$$C_D = 0.0223\left(\frac{10}{3}\right)^{-\frac{U}{15}} \tag{1}$$

The drag coefficient usually increases with the wind speed in the ocean, but observed drag coefficient indicates the opposite tendency in the nearshore zone. The effect of long-crestedness and steepness of waves in the shallow water may cause larger drag coefficient and wave breaking may cause such an inverse trend vs wind speeds.

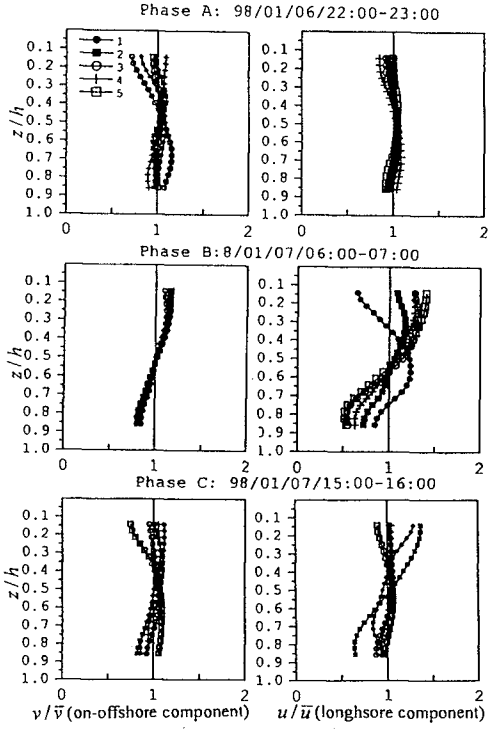

Figure 8 The hourly changes in vertical profiles of on-offshore (left) and longshore (right) in Case B.

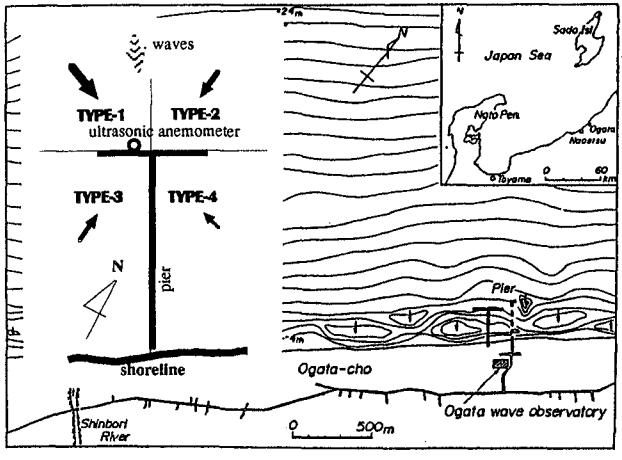

Figure 9 Wind data classification (four types) according to the wind direction relative to the pier (TOP).

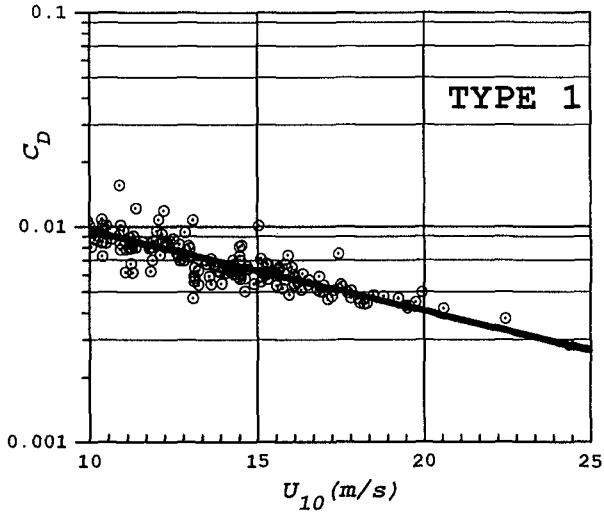

Figure 10 The drag coefficient estimated by TDM and the averaged wind speed.

5. Conclusions

This study is a screening of a set of wind and current data recorded in the surf zone during a two and half months period from an observation pier. Winds and waves were observed simultaneously and continuously in the nearshore zone, at a location alternately inside the surf zone and outside, depending on the state of the sea. This long-term observation revealed the structure of currents and the characteristics of the wind drag in the nearshore zone; main results are summarized below :

(1) There are two types of wind/wave climates which cause strong offshore-going currents. One is the type called "end-storm undertow" which is defined that sudden bursts of current occur with changes in wind directions from westerly to easterly with reduction of wind velocity at the end of the winter storms. The other is the type called "mid-storm undertow" which is defined that continuous strong shore-normal(NW) winds generate strong undertow in the midst of storm.

(2) Both offshore and longshore current profiles are vertically uniform underneath the wave trough level.

(3) Direction of longshore currents is much more sensitive to the wind direction than waves. Strong longshore current is mainly induced by winds in the wide area of nearshore zone and its direction is shore-parallel. Wave-induced longshore current is much smaller than wind-induced one.

(4) Wave-induced cross shore currents is mainly generated in the surf zone by wave breaking, which may form the velocity profile of the so-called undertow together with wind-induced cross shore currents.

(5) Drag coefficient in the near shore zone was empirically formulated with relation to the wind speed in the range of over 10m/s, which shows the opposite tendency to that in deep waters.

Acknowledgements

The authors would like to express our thanks to Mr. Kiyoshi Uchiyama, technician in Ogata Wave Observatory, for his kind help in observations. This study was funded by the Ministry of Education, Science, Sports and Culture of Japan as the Research Project, Grant-in-aid for Scientific Research (1997-1998), contract No.09555157, (the chief researcher, Takao Yamashita, Kyoto University). Support for a part of observation was also received from the NEWJEC Consultants Inc, Osaka, Japan.

References

Yelland, M. J. et al. (1994): The use of the inertial dissipation technique for shipboard wind stress determination, J. Atmos. Oceanic Technology, Vol. 11, pp. 1093-1108.

Yamashita, T., H. Yoshioka, Lu Ming and S. Kato (1997): ADCP observation of Nearshore Current Structure in the Surf Zone, Proc. Coastal Eng., JSCE, Vol.44, pp. 361-365 (in Japanese).

Numerical Modeling of Nearshore Circulation on a Barred Beach with Rip Channels

K.A. Haas, I.A. Svendsen and M.C. Haller[1]

Abstract

A nearshore circulation modeling system has been applied to a closed wave basin with a longshore bar and two rip channels. The major characteristics of the flow pattern have been established by the model including the recirculation cells, the feeder currents and the bias of the rip current toward the center of the basin. Wave current interaction is established as one of the significant mechanisms in the flow. The parameters for the eddy viscosity and the bottom friction have been shown to influence the stability of the flow. The flow is generally fluctuating and large vortex systems are formed. The model results are compared with the experimental data matching magnitudes of mean velocities as well as trends of oscillations.

Introduction

The concept of rip currents was first introduced by Shepard (1936). Since then there have been many attempts to observe rip currents in the field, such as the observations by Shepard *et al.* (1941), Shepard and Inman (1951), McKenzie (1958), and Sonu (1972) to name a few. All of these studies noted that the rip currents were not steady but were transient in nature which contributed to the difficulty in obtaining accurate measurements in the field. Shepard and Inman (1951) noted that the rip current seemed to be pulsating and that eddies were being generated. Rip currents usually are described to be fed by feeder currents, although flow entrainment can be important or even dominate as described by Shepard *et al.* (1941) and McKenzie (1958).

There have also been several theoretical studies of rip currents, such as Arthur (1962) who showed that the conservation of potential vorticity requires the rip currents to become more narrow as they flow offshore. The flow across and behind

[1]Center for Applied Coastal Research, Ocean Engineering Lab, University of Delaware, Newark, DE 19716, USA. Correspondence e-mail: haas@coastal.udel.edu

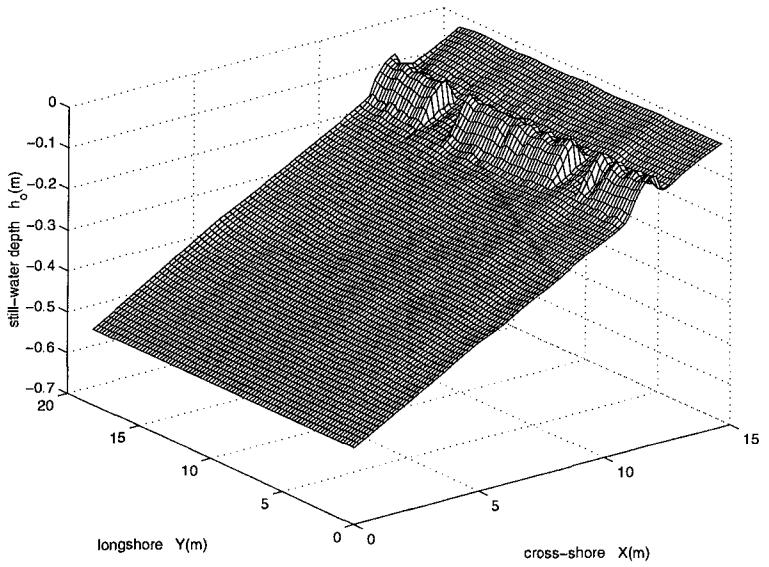

Figure 1: Bathymetry used in model simulations.

longshore bars was analyzed by Dalrymple (1978) using a simple linear model. The cross-shore flow was analyzed by the theoretical and experimental work of Svendsen and Hansen (1986) and Hansen and Svendsen (1986). These works addressed the issue of interaction between the breaking waves and circulation currents and the driving mechanisms for those currents. Computational results of a simplified version of the present model for flow over a rip channel and barred beach showed that on barred beaches with rip channels the longshore variations are important (Sancho *et al.*, 1995). Particularly, the longshore pressure gradients strongly contribute to the longshore momentum balance.

Present Problem

Dalrymple (1978) provided two classifications of the generating mechanisms for rip currents, wave interaction and structural interaction. In this study we look at rip currents in the stuctural interaction class. Specifically, we are modeling the experiment of normal incident waves in a closed wave basin with a longshore bar and two rip channels as outlined by Haller *et al.* (1997a,b). The bathymetry used in the model was taken from a detailed survey of the wave basin and is shown in figure (1). The two rip channels were intended to be symmetric to each other although they clearly have some differences. The bars also exhibit longshore non-uniformities which will have an impact on the circulation.

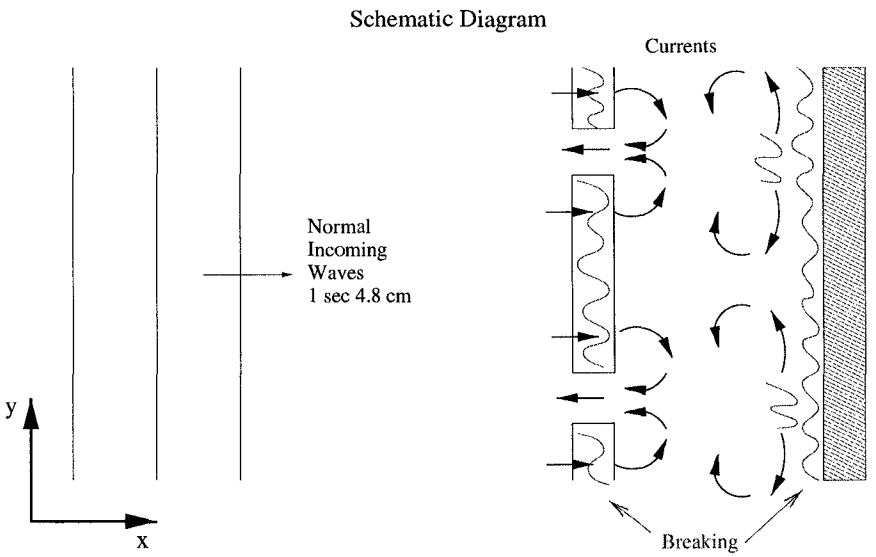

Figure 2: Schematic diagram of wave-averaged flow on a barred beach with rip channels.

Figure (2) shows a schematic diagram outlining the general flow patterns for the nearshore region of the basin. The short waves are normally incident with a period of 1 s and an off-shore wave height of 4.8 cm. These waves propagate toward the shore and start breaking over the bars, as indicated in the drawing, creating a setup in the mean water level. The waves are not breaking as much in the channels, therefore the mean water level is lower in the channels, which creates a longshore pressure gradient from the bars directed toward the channels. This pressure gradient is driving the currents towards the channels, creating the feeder currents for the rips.

Because the waves have not broken as much in the channels, these waves will be larger and therefore break earlier than the waves behind the bar as they approach the shoreline. This will create a larger setup, or a bump in the mean water level, close to the shoreline behind the channel. Therefore, a longshore pressure gradient will drive flow away from the channels creating secondary or recirculation cells close to the shoreline. Note that the circulation is highly dependent on the breaking pattern; if the waves did not break on the bar then there would be no recirculation cells and the feeder currents for the rips would be much smaller.

Model Equations

The model system is the SHORECIRC which consists of a short wave transformation component ("wave driver") and a short wave-averaged component, working

simultaneously to simulate the short and long wave motions, and their interactions, in the nearshore regions. The short wave model REF/DIF (Kirby and Dalrymple, 1994) is used as the wave driver accounting for the effects of bottom induced refraction-diffraction, current induced refraction and wave breaking dissipation by solving the parabolic equation initially developed by Kirby and Dalrymple (1983).

The nearshore circulation model used is SHORECIRC, as described in Van Dongeren *et al.* (1994) and Van Dongeren and Svendsen (1997), which determines the flow pattern by solving the quasi-3D short wave-averaged hydrodynamic equations given below.

$$\frac{\partial \overline{\zeta}}{\partial t} + \frac{\partial \overline{Q}_x}{\partial x} + \frac{\partial \overline{Q}_y}{\partial y} = 0 \tag{1}$$

$$\begin{aligned}
&\frac{\partial \overline{Q}_x}{\partial t} + \rho \frac{\partial}{\partial x}\left(\frac{\overline{Q}_x^2}{h_o + \overline{\zeta}}\right) + \rho \frac{\partial}{\partial y}\left(\frac{\overline{Q}_x \overline{Q}_y}{h_o + \overline{\zeta}}\right) + \rho g \left(h_o + \overline{\zeta}\right) \frac{\partial \overline{\zeta}}{\partial x} \\
&\quad + \frac{\partial}{\partial x}\left(S_{xx} - \overline{\int_{-h_o}^{\zeta} \tau_{xx} dz}\right) + \frac{\partial}{\partial y}\left(S_{yx} - \overline{\int_{-h_o}^{\zeta} \tau_{yx} dz}\right) - \overline{\tau_x^S} - \overline{\tau_x^B} \\
&\quad + \rho \frac{\partial}{\partial x} \overline{\int_{-h_o}^{\zeta} V_{1x} V_{1x} dz} + \rho \frac{\partial}{\partial y} \overline{\int_{-h_o}^{\zeta} V_{1y} V_{1x} dz} \\
&\quad + \rho \frac{\partial}{\partial x} \overline{\int_{\zeta_t}^{\zeta} u_{wx} V_{1x} + u_{wx} V_{1x} dz} + \rho \frac{\partial}{\partial y} \overline{\int_{\zeta_t}^{\zeta} u_{wy} V_{1x} + u_{wx} V_{1y} dz} = 0
\end{aligned} \tag{2}$$

$$\begin{aligned}
&\frac{\partial \overline{Q}_y}{\partial t} + \rho \frac{\partial}{\partial y}\left(\frac{\overline{Q}_y^2}{h_o + \overline{\zeta}}\right) + \rho \frac{\partial}{\partial x}\left(\frac{\overline{Q}_x \overline{Q}_y}{h_o + \overline{\zeta}}\right) + \rho g \left(h_o + \overline{\zeta}\right) \frac{\partial \overline{\zeta}}{\partial y} \\
&\quad + \frac{\partial}{\partial x}\left(S_{xy} - \overline{\int_{-h_o}^{\zeta} \tau_{xy} dz}\right) + \frac{\partial}{\partial y}\left(S_{yy} - \overline{\int_{-h_o}^{\zeta} \tau_{yy} dz}\right) - \overline{\tau_y^S} - \overline{\tau_y^B} \\
&\quad + \rho \frac{\partial}{\partial x} \overline{\int_{-h_o}^{\zeta} V_{1x} V_{1y} dz} + \rho \frac{\partial}{\partial y} \overline{\int_{-h_o}^{\zeta} V_{1y} V_{1y} dz} \\
&\quad + \rho \frac{\partial}{\partial x} \overline{\int_{\zeta_t}^{\zeta} u_{wx} V_{1y} + u_{wy} V_{1x} dz} + \rho \frac{\partial}{\partial y} \overline{\int_{\zeta_t}^{\zeta} u_{wy} V_{1y} + u_{wy} V_{1y} dz} = 0
\end{aligned} \tag{3}$$

where x and y are the cross-shore and longshore directions, the overbar represents wave-averaging, $\overline{\zeta}$ is the mean water level, $\overline{Q_\alpha}$ is the wave-averaged volume flux in the α direction, ρ is the water density, h_o is the still water depth, $S_{\alpha\beta}$ is the radiation stress, $\tau_{\alpha\beta}$ is the turbulent stress, τ_α^S and τ_α^B are the surface and bottom shear stresses in the α direction, $V_{1\alpha}$ is the depth varying portion of the currents and $u_{w\alpha}$ is the short wave velocity. Equation (1) is the conservation of mass, equation (2) the cross-shore or x-momentum balance and equation (3) the longshore or y-momentum balance.

The first three terms in the momentum balances (equations (2) and (3)) are the local accelerations and the convective accelerations. The next term is the pressure

gradient followed by the gradient of the radiation and turbulent stresses. In this study the turbulent normal stresses are neglected (i.e. the terms τ_{xx} and τ_{yy}) because they are usually considered small compared to the turbulent shear stresses. The surface shear stresses are also neglected since we are modeling a closed basin inside a laboratory. The last four terms on the left-hand side are the quasi-3D terms which act as a dispersive mixing mechanism. Traditional nearshore circulation models assume depth uniform currents which would mostly elimimate those four terms. Because this is the beginning of the study, we will also assume depth uniform currents, although, in future studies the importance of depth varying currents will be analyzed in greater detail.

The turbulent shear stresses are modeled by utilizing an eddy viscosity approach given by the following expressions, (Sancho, 1997),

$$\tau_{xy} = \rho\nu_t\left(\frac{\partial V_y}{\partial x} + \frac{\partial V_x}{\partial y}\right) \tag{4}$$

where ν_t is the eddy viscosity given by

$$\nu_t = C_1 u_o h + Mh\left(\frac{D}{\rho}\right)^{\frac{1}{3}}. \tag{5}$$

Here C_1 is a constant coefficient, u_o the bottom orbital velocity, h the total water depth, D the energy dissipation rate per unit area of the short waves, and M a constant taken to be 0.1. This eddy viscosity formulation accounts for both bottom induced and wave breaking turbulence. The first term in equation (5) represents the bottom induced turbulence which is always present and the second term represents the wave breaking turbulence which is only present in the surf zone.

The bottom shear stress is modeled using the generalized friction factor approach for waves and currents as outlined by Svendsen and Putrevu (1993),

$$\tau_\alpha^B = \frac{1}{2}\rho f_{cw} u_o(\beta_1 V_{b\alpha} + \beta_2 u_{o\alpha}) \tag{6}$$

where β_1 and β_2 are given by

$$\beta_1 = \left[\left(\frac{V_b}{u_o}\right)^2 + 2\frac{V_b}{u_o}\cos\theta\cos\mu + \cos^2\theta\right]^{\frac{1}{2}} \tag{7}$$

$$\beta_2 = \cos\theta\left[\left(\frac{V_b}{u_o}\right)^2 + 2\frac{V_b}{u_o}\cos\theta\cos\mu + \cos^2\theta\right]^{\frac{1}{2}}. \tag{8}$$

β_1 and β_2 are weight factors for the current and wave motion respectively and f_{cw} is the bottom friction factor.

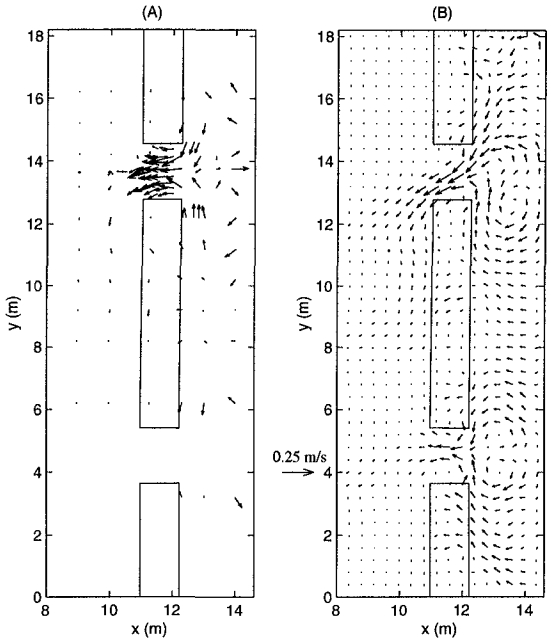

Figure 3: Time-averaged below-trough velocity vectors from (A) experimental data (described by Haller *et al.* (1997b)) and (B) SHORECIRC.

Qualitative Results

Figure (3) shows the below-trough velocity vectors for the experimental data on the left-hand side and the model results on the right-hand side. The experimental data was time-averaged for 819 seconds over the last half of the experiment. Only three velocity gauges were used at a time, however, there was a high rate of repeatability allowing all the time-averaged properties to be examined simultaneously. The model results were time-averaged over 750 seconds after beginning from a cold start for 200 seconds. The model data results from a single model run in which the velocities were the qualitative best fit with the experimental data.

The majority of the experimental data is gathered around the upper rip channel so we will primarily focus on the flow around that rip channel. The rip currents are easily identifiable in the channels for both the experiment and model. In both diagrams of figure (3), the rip currents vanish just seaward of the channel. The rips are also biased toward the center of the basin in both the experiment and the model. The flow leaving the rip channel in the model turns toward the center of the basin and flows back onto the bar and then runs shore parallel, similar to the experimental

results. The magnitude of the rip currents in the channel also are similar. The rip in the model has flow entrainment which causes the rip to widen offshore. The model from Arthur (1962) predicts that the rips should become narrower but that model does not allow for flow entrainment.

The recirculation cells discussed earlier are clearly evident in both the experimental and the model results. However, the experiment shows a stronger shoreward flow behind the channel close to the shoreline, which is not present in the model results. This will be discussed in greater detail later. The two recirculation cells for the upper rip in the model are unequal due to the irregularities in the bathymetry previously mentioned. The flow around the two rip channels also exhibit many differences which is a result of the seemingly minor differences in the bathymetry of the channels. We also noticed that the feeder currents are similar between the two figures with the upper feeder currents being at a slight angle toward the channel and the lower feeder currents being shore parallel. The magnitude of the currents behind the bar are similar between the two cases.

Wave Current Interaction

The wave current interaction is accounted for in the model system and proves to be an important mechanism, particularly around the strong rip currents. The governing equation in REF/DIF accounts for the effect of large currents including the doppler shift due to currents.

The wave current interaction is modeled interactively by initially determining the short waves without currents and then calculating the resulting currents with SHORECIRC. The currents and mean water level are fed back into REF/DIF to determine the new wave field. This process is constantly repeated to provide for the wave current interaction. In the present study the short waves are calculated approximately once every short wave period. The wave field, and therefore the forcing, only has small changes over this short time scale, providing smooth transitions between the different forcings.

The effect of including the wave current interaction is shown in figures (4), (5) and (6). Figure (4) shows the cross-shore sections of the short wave height across the center bar and through the channel for cases with and without wave current interaction. In general, the waves over the bar shoal and break on the bar (as indicated by the steep decline in wave height), then reform, shoal and break at the shoreline. On the other hand, the waves in the channel only have a single break point and, therefore, tend to start breaking earlier as they approach the shoreline. We see that inclusion of the currents causes the wave heights in the channel to increase slightly and the onset of breaking occurs farther offshore in the channel. The comparisons with experimental data shows that these trends, if not the exact magnitudes, are matched. It is more important to match the gradient of the wave heights because the forcing is due to the gradient of the radiation stresses which is proportional to the gradient of the wave height.

Figure (5) shows the mean water level for the same two cross-shore sections with

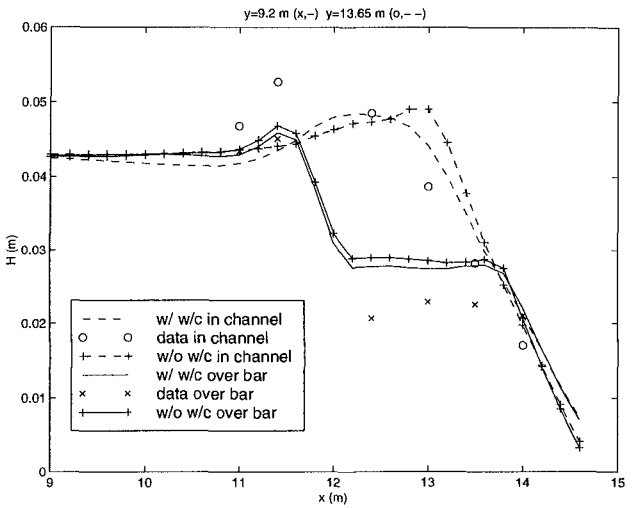

Figure 4: Comparison of time-averaged modeled short-wave height with and without wave current (w/c) interaction to experimental data (described by Haller *et al.* (1997b)).

and without wave current interaction again. The longshore pressure gradient between the channel and the bar is evident between $x = 12 - 13.5$ m. This longshore pressure gradient is reversed, although much smaller, closer to the shoreline. The effect of the wave current interaction on the mean water level is most evident in the channel around $x = 12 - 13.5$ m where the water level is significantly reduced. Everywhere else the differences appear to be insignificant. In particular, the changes along the center of the channel due to the currents turn out to be important, even though they may appear small. However, it is emphasized that although the sine wave theory of REF/DIF has been modified, it does not model the forcing of breaking waves accurately.

Finally, figure (6) shows the vorticity and below trough velocity vectors demonstrating the most significant impact of the wave current interaction on the circulation pattern. The most significant change is that with the wave current interaction included, the rip current does not extend very far offshore of the channel and is biased toward the center of the basin. The recirculation cells are smaller and do not extend over the bar as they do for the case without wave current interaction. The experimental data in figure (3) also shows that the rip vanishes and is biased toward the center of the basin. We have found that this effect is only achieved in the model if we include the wave current interaction.

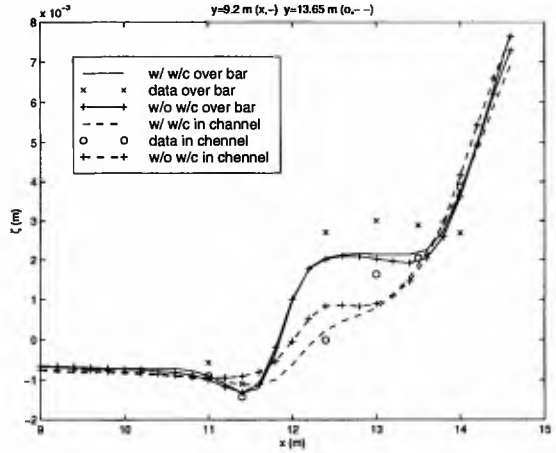

Figure 5: Comparison of time-averaged modeled mean water level with and without wave current (w/c) interaction to experimental data (described by Haller *et al.* (1997b)).

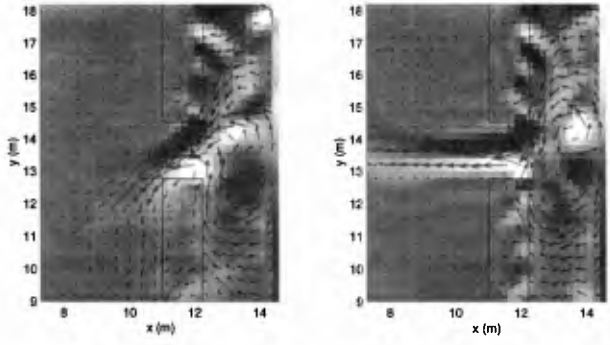

Figure 6: Below trough time-averaged velocity vectors with vorticity contours. The left side is with wave current interaction and right side is without wave current interaction. White contours are positive vorticity and black contours are negative vorticity.

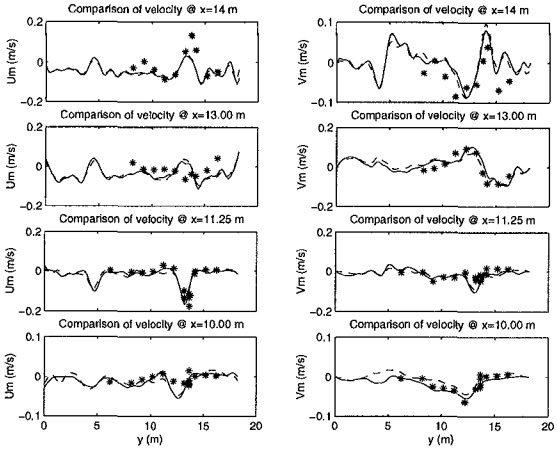

Figure 7: Comparison of time-averaged below-trough velocity for cross-shore (Um) and longshore (Vm) flow with experimental data (described by Haller *et al.* (1997b)). Solid line (-) is for $C_1 = 0.001$, dashed line (- -) is for $C_1 = 0.01$ and asterix (*) is the experimental data.

Selection of Parameters

The important flow parameters which have been adjusted to fit the experimental data are the eddy viscosity coefficient (C_1) and the bottom friction factor (f_w). The parameter C_1 is varied between 0.001 and 0.01. This parameter will change the eddy viscosity due to the bottom induced turbulence. Therefore, changing the parameter will primarily affect the flow outside the surfzone because the term representing breaking wave conditions will dominate inside the surfzone. The friction factor is estimated from Jonsson (1966) and has a range from 0.01 to 0.035 accounting for the uncertainty in bottom roughness and the variable flow conditions.

Figure (7) shows velocity profiles for longshore sections at four cross-shore locations; moving down, at the shoreline ($x = 14$ m), in the trough ($x = 13$ m), over the bar ($x = 11.25$ m) and seaward of the bar ($x = 10$ m). This figure shows two cases with an eddy viscosity coefficient, C_1, of 0.001 and 0.01 and the friction factor being held constant at $f_w = 0.03$. The most significant change occurs in the longshore velocity offshore of the bar, where the velocity for the higher eddy viscosity is slightly reduced. The increased eddy viscosity tends to help stabilize the flow, therefore significantly reducing the meandering of the rip current. Less meandering of the rip current will produce less time-averaged longshore velocity in the rip.

Figure (8) shows velocity profiles of the same longshore sections for $f_w = 0.015$ and $f_w = 0.03$ and C_1 being held constant at 0.001. The variation between the two

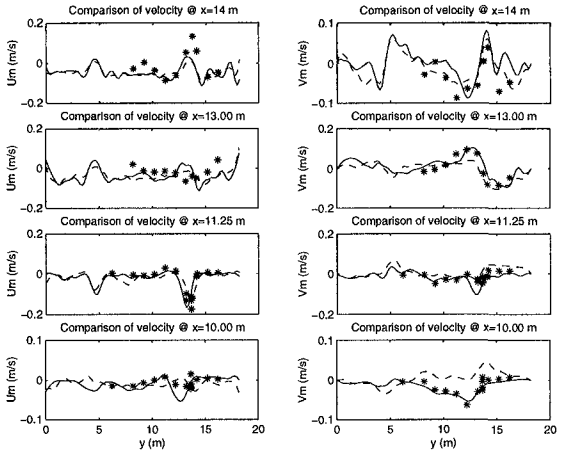

Figure 8: Comparison of time-averaged below-trough velocity for cross-shore (Um) and longshore (Vm) flow with experimental data (described by Haller *et al.* (1997b)). Solid line (-) is for $f_w = 0.03$, dashed line (- -) is for $f_w = 0.015$ and asterix (*) is the experimental data.

cases is much more significant. As with the eddy viscosity, increasing the bottom friction tends to stabilize the flow. The time-averaged cross-shore velocity in the rip current tends to be larger for higher friction factors because less meandering of the current produces less mixing. The longshore velocity for the lower friction case for the farthest offshore sections tends to be antisymmetric (i.e. the current is positive on one side of the rip channel and negative on the other), whereas the higher friction tends to have the longshore current in one direction. The lower friction factor allows the rip to meander fairly equally in both directions whereas the higher friction factor, and experimental data, shows a bias toward the inside of the basin. Even though the higher friction case has smaller instantaneous velocities, the time-averaged velocities in the rip are higher because the flow is more stable with less mixing.

Multiple cases for the range of the eddy viscosity coefficient, C_1 between 0.001 and 0.01, and the bottom friction factor, between $f_w = 0.015$ and 0.03 were run to obtain the best fit with the experiments. From these different cases the best visual match of the currents with the experimental data was selected. The parameters that best fit the data turned out to be $C_1 = 0.001$ and $f_w = 0.03$. These are the same parameters used for the model results in figure (3). The relatively high f_w is in conjuction with the small scale experiment where the boundary layer is in the laminar-turbulent transition region. Figure (9) shows the currents for the final selection of parameters for cases with and without wave current interaction in the same longshore sections as figures (7) and (8). This figure demonstrates that the inclusion of the wave current

interaction improved match with the measured data, particularly the flow around the rips.

Close to the shoreline, the top panels in figure (9), the cross-shore velocity is too small and the longshore velocity is too large. This is probably a result of the recirculation cells in the model being shifted seaward relative to the experiments because the shoreline boundary condition is a wall with an average still water depth around 6 mm. Presumably, utilizing a moving shoreline condition could improve the match with data close to the shoreline. The recirculation cells being shifted seaward could also explain why the cross-shore velocity in the trough (second panel on the left) is less accurately predicted.

Some of the inaccuracies around the rip channels and in the trough region between the bar and the shoreline could be a result of incorrect breaking patterns. The short wave driver uses a bottom induced breaking criteria which causes the waves in the channel to break closer to the shoreline. Visual observation of the experiments showed that the waves in the channels were breaking somewhat earlier due to the increased short wave steepness from the oppossing current. Correctly predicting the breaking pattern and the forcing due to the breaking waves would also improve the comparison with the data, although, in general, the magnitudes of the currents from the model match fairly well with the experimental data.

Finally it may be noticed that only the time-averaged properties of the flow field are presented here because they provide the best means of comparison with the experiments. The time varying properties of the currents and mean water level show many similarities with the experiments. The flow for both cases is unstable. The rip has instabilities on several time scales, typically a faster scale $\sim$ 20 seconds, which appears to be related to the instability of a jet and slower motions with scales $\sim 100 - 300$ seconds. The experiments (Haller *et al.*, 1997b) have shown similar trends. The model also shows eddies being created and shed from the rips as well as from the flow behind the bar. The time series from the experiments show some evidence of eddies passing through the sensors in a similar fashion.

Conclusions

A study on rip currents has been performed by applying a numerical nearshore circulation model system to an experiment in a closed wave basin with a barred beach containing two rip channels. The breaking pattern resulting from this bathymetry has been identified to be an important driving mechanism of the nearshore currents. Significant changes occur when the wave current interaction is included in the model system such as the rip current vanishing quickly offshore and being biased toward one side as is also found in the experiments. In general, the model and experiments are in agreement.

The effect of several flow parameters has been analyzed including the eddy viscosity and the bottom stress. Both parameters are a factor in controlling the stability of the flow. Decreasing either parameter causes the flow to become more unstable. These parameters can be varied to give a qualitative best fit of the modeled cur-

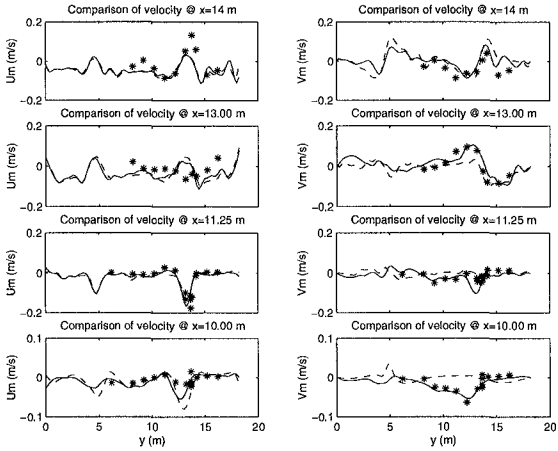

Figure 9: Comparison of time-averaged below-trough velocity for cross-shore (Um) and longshore (Vm) flow with experimental data (described by Haller *et al.* (1997b)). Solid line (-) is with wave current interaction, dashed line (- -) is without wave current interaction and asterix (*) is the experimental data.

rents to the experimental data. Changes in the eddy viscosity does not produce large changes in the flow pattern. Variations in the bottom stress are more important. The values of the two coefficients selected for matching the experimental data are physically realistic. Currents have been assumed depth uniform in this preliminary study.

Acknowledgements

This work was sponsored by Sea Grant, under Award No NA56 NG 0147 and by ONR (contract no N00014-95-C-0075). The US government is authorized to produce and distribute reprints for government purposes non withstanding any copyright notation that may appear herein.

References

Arthur, R. S. (1962). A note on the dynamics of rip currents. *Journal of Geophysical Research*, **67**, 2777–2779.

Dalrymple, R. A. (1978). Rip currents and their causes. In *Proceedings of the 14th Coastal Engineering Conference*, pages 1414–1427.

Haller, M., Dalrymple, R., and Svendsen, I. (1997a). Rip channels and nearshore circulation: Experiments. In *Proceedings Coastal Dynamics*.

Haller, M., Dalrymple, R., and Svendsen, I. (1997b). Experimental modeling of a rip current system. In *Proceedings of the Third International Symposium on Ocean Wave Measurement and Analysis*.

Hansen, J. and Svendsen, I. A. (1986). Experimental investigation of the wave and current motion over a longshore bar. In *Proceedings of the 20th Coastal Engineering Conference*, pages 1166–1179.

Jonsson, I. G. (1966). Wave boundary layers and friction factors. In *Proceedings of the 10th Coastal Engineering Conference*, volume 1, pages 127–148, Tokyo. ASCE.

Kirby, J. and Dalrymple, R. (1994). Combined refraction/diffraction model ref/dif 1, version 2.5. Technical Report CACR-94-22, Center for Applied Coastal Research, University of Delaware.

Kirby, J. T. and Dalrymple, R. A. (1983). A parabolic equation for the combined refraction-diffraction of stokes waves by mildly varying topography. *Journal of Fluid Mechanics*, **136**, 453–466.

McKenzie, P. (1958). Rip current systems. *Journal of Geology*, **66**, 103–113.

Sancho, F. (1997). *Unsteady Nearshore Currents on Longshore Varying Topographies*. Ph.D. thesis, University of Delaware.

Sancho, F., Svendsen, I., Van Dongeren, A., and Putrevu, U. (1995). Longshore nonuniformities of nearshore currents. In *Proceedings Coastal Dynamics*, pages 425–436.

Shepard, F. P. (1936). Undertow, rip tide or rip current. *Science*, **84**, 181–182.

Shepard, F. P. and Inman, D. L. (1951). Nearshore circulation. In *Proceedings of the 1st Coastal Engineering Conference*, pages 50–59.

Shepard, F. P., Emery, K. O., and La Fond, E. (1941). Rip currents: a process of geological importance. *Journal of Geology*, **49**, 337–369.

Sonu, C. J. (1972). Field observations of nearshore circulation and meandering currents. *Journal of Geophysical Research*, **77**, 3232–3247.

Svendsen, I. A. and Hansen, J. B. (1986). The interaction of waves and currents over a longshore bar. In *Proceedings of the 20th Coastal Engineering Conference*, pages 1580–1594.

Svendsen, I. A. and Putrevu, U. (1993). Surf zone wave parameters from experimental data. *Coastal Engineering*, **19**, 283–310.

Van Dongeren, A., Sancho, F., Svendsen, I., and Putrevu, U. (1994). Shorecirc: A quasi-3d nearshore model. In *Proceedings of the 24th Coastal Engineering Conference*, pages 2741–2754.

Van Dongeren, A. R. and Svendsen, I. A. (1997). Quasi-3D modeling of nearshore hydrodynamics. (Ph. D. Dissertation), Res. Report CACR-97-04, Center for Applied Coastal Research, Univ. of Delaware.

APPLICABILITY OF A QUASI-THREE DIMENSIONAL NUMERICAL MODEL TO NEARSHORE CURRENTS

Masamitsu Kuroiwa[1], Hideaki Noda[2] and Yuhei Matsubara[3]

ABSTRACT

This paper presents a quasi-three dimensional numerical model of wave-induced current due to wave breaking so as to make it applicable to the coastal region with the coastal structures. First, applicability of the present model to undertow velocity and longshore current field was investigated. Secondly, laboratory tests were carried out to examine the characteristics of nearshore currents around the detached breakwater. Thirdly, nearshore currents around the breakwater were computed using the present numerical model. Finally, the results of computation were compared with those of laboratory tests and the applicability of the numerical model was discussed.

INTRODUCTION

The objective of this study is to develop a simple quasi-three dimensional model (Q-3D model) of nearshore currents so as to make it applicable to the coastal region with the coastal structures.

The nearshore currents have been previously predicted by using two-dimensional model in the horizontal plane (2DH model). However, in the surf zone the direction of current vectors near water surface is different from that at sea bottom because of effect of undertow velocities. The currents have spiral profiles in the vertical direction. In order to predict the change of beach profile and dispersion of pollutants exactly, it is very important to determine the three dimensional distribution of nearshore currents.

Recently, some models for determining the three dimensional currents have been proposed. Svendsen et al. (1989) presented an analytical model composed of cross-shore and alongshore current velocities. Sanchez et al. (1992) proposed a Q-3D numerical model by combining 2-DH model and one-dimensional model in the vertical direction (1-DV model). Okayasu et al. (1994) proposed a Q-3D numerical model with the effect of the momentum flux due to the large vortexes formed on

1.Reseach associate, Dep. of Civil Eng. Tottori Univ., 4-101,Koyama-minami,Tottori,680,Japan
2.Professor, Dep. of Civil Eng. Tottori Univ., 4-101,Koyama-minami,Tottori,680,Japan
3.Associate professor, Dep. of Civil Eng. Tottori Univ., 4-101,Koyama-minami,Tottori,680,Japan

the front face of breaking waves. These models have been only applied to straight coast without coastal structures. On the other hand, Pechon et al.(1994) have proposed a quasi-three dimensional numerical model and tried to calculate the nearshore current around the coastal structures. However, comparison with measured data has not been done. The applicability of these models should be confirmed by comparing with the measured data and a predicted model on nearshore currents must be completed by above mentioned procedure

In this study, a Q-3D numerical model based on the solution method by developed Koutitas et al. (1980) is proposed. The applicability of the Q-3D model to undertow, longshore currents and nearshore currents around the coastal structures is investigated by comparing with the experimental results.

NUMERICAL MODEL

The present model consists of two modules. Wave and steady current velocity field are determined separately without wave-current interaction.

Wave field module

Wave field can be obtained from the time-dependent mild slope equations proposed by Watanabe et al. (1984). The governing equations are as follows:

$$\frac{\partial Q_x}{\partial t} + \frac{1}{n} C^2 \frac{\partial n\eta}{\partial x} + f_D Q_x = 0 \quad \text{----------(1)}$$

$$\frac{\partial Q_y}{\partial t} + \frac{1}{n} C^2 \frac{\partial n\eta}{\partial y} + f_D Q_y = 0 \quad \text{----------(2)}$$

$$\frac{\partial \eta}{\partial t} + \frac{\partial Q_x}{\partial x} + \frac{\partial Q_y}{\partial y} = 0 \quad \text{----------(3)}$$

where Q_x and Q_y are the depth-integrated flow rates per unit width by waves in the cross-shore (x) and alongshore direction (y) respectively, t the time, C the wave celerity, η the surface elevation, n the ratio of group velocity to C, f_D the attenuation factor by wave breaking. The attenuation factor f_D is estimated as follows:

$$f_D = \alpha_D \tan\beta \sqrt{\frac{g}{h}\left(\frac{\hat{Q}}{Q_r} - 1\right)} \quad \text{----------(4)}$$

$$\hat{Q} = \sqrt{\hat{Q}_x^{\,2} + \hat{Q}_y^{\,2}} \quad \text{----------(5)}$$

$$Q_r = 0.25\sqrt{gh^3} \quad \text{----------(6)}$$

where α_D is the non-dimensional coefficient, which is 2.5. $\tan\beta$ is the bottom slope, $\hat{Q}$ is the amplitude of flow rate, Q_r is the amplitude of the flow rate of recovered waves.

The governing equations for wave field are solved by using the explicit finite difference method on a staggered rectangular grid region.

Nearshore current module

Governing equations

The governing equations are derived from the 3-D Navier-Stokes equations. The equations of motion for Q-3D nearshore currents proposed by Svendsen et al. (1989) may be expressed as

$$\frac{\partial U}{\partial t}+U\frac{\partial U}{\partial x}+V\frac{\partial U}{\partial y}+W\frac{\partial U}{\partial z}=-g\frac{\partial \bar{\zeta}}{\partial x}-\frac{\partial Sxx}{\partial x}-\frac{\partial Sxy}{\partial y}$$
$$+\frac{\partial}{\partial x}\left(\nu_h\frac{\partial U}{\partial x}\right)+\frac{\partial}{\partial y}\left(\nu_h\frac{\partial U}{\partial y}\right)+\frac{\partial}{\partial z}\left(\nu_v\frac{\partial U}{\partial z}\right) \quad \text{---------- (7)}$$

$$\frac{\partial V}{\partial t}+U\frac{\partial V}{\partial x}+V\frac{\partial V}{\partial y}+W\frac{\partial V}{\partial z}=-g\frac{\partial \bar{\zeta}}{\partial y}-\frac{\partial Syy}{\partial y}-\frac{\partial Syx}{\partial x}$$
$$+\frac{\partial}{\partial x}\left(\nu_h\frac{\partial V}{\partial x}\right)+\frac{\partial}{\partial y}\left(\nu_h\frac{\partial V}{\partial y}\right)+\frac{\partial}{\partial z}\left(\nu_v\frac{\partial V}{\partial z}\right) \quad \text{---------- (8)}$$

where U, V and W are steady current velocities in the x, y and z directions, respectively as shown in Figure 1. $\bar{\zeta}$ is the mean water level, Sxx, Sxy, Syx and Syy represent the excess momentum fluxes (radiation stresses) due to waves. These values are estimated by solving the time-dependent mild slope equations (1)-(6), which include the effect of reflection and diffraction around the coastal structures such as detached breakwaters. ν_v and ν_h represent the turbulent eddy viscosity coefficients in the vertical and horizontal direction, respectively. ν_h is estimated by using the method presented by Longuet-Higgins (1970). The eddy viscosity coefficient ν_v plays a very important roll in the determination of the vertical distribution of nearshore currents. The effects of the eddy viscosity coefficients must be examined. Two types of the coefficients are proposed. One is assumed that the value is constant in the vertical distribution. A simple method proposed by Tsuchiya et al. (1986) is used, according to the following relationship:

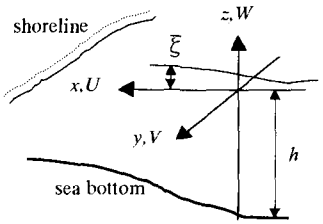

Figure 1 Coordinate system

$$\nu_v = ACH \quad \text{----------(9)}$$

where C is the wave celerity, H is the wave height and A is the non-dimensional constant. A is set to be 0.01. The other is assumed that the coefficient is quadratic function as follows;

$$\nu_v = A_T CH\left(\frac{z+h}{h}\right)^2 + B_T CH \quad \text{----------(10)}$$

where A_T=0.01, B_T=0.001.

The continuity equation is as follow:

$$\frac{\partial U}{\partial x}+\frac{\partial V}{\partial y}+\frac{\partial W}{\partial z}=0 \qquad \text{----------} \quad (11)$$

and the depth-integrated continuity equation is:

$$\frac{\partial \bar{\zeta}}{\partial t}+\frac{\partial \tilde{U}(h+\bar{\zeta})}{\partial x}+\frac{\partial \tilde{V}(h+\bar{\zeta})}{\partial y}=0 \qquad \text{----------} \quad (12)$$

where $\tilde{U}$ and $\tilde{V}$ are the depth-averaged steady currents. The steady current velocity W in the vertical direction is determined from Eq. (11) and the mean water level $\bar{\zeta}$ is determined from Eq. (12).

Boundary conditions and solving method

In this study, shoreline, offshore and side wall in the small basin are assumed fixed boundaries, namely, the velocity components normal to those boundaries can be taken as zero.

The boundary conditions in the mean water surface and bottom are needed to determine the vertical distribution of the currents. In general, the boundary condition at the free surface is the no-flux condition. However, in the case that mass transport due to wave breaking is dominant in the surf zone, shear stress due to water surface rollers must be considered. The stress is given by taking account of the effect of surface roller based on Svendsen's model (1989) as follows

$$\tau_s = A_S \rho g h \tan\beta \left(\frac{H}{h}\right)^2 \left(2.7\frac{h}{L}\right) \qquad \text{----------} \quad (13)$$

where H is the wave height, h the water depth and L the wave length. $\tan\beta$ is bottom slope. A_s is constant value, which is determined empirically by comparing computed nearshore currents with experimental data, that is, A_s =0.5～1.0. The boundary conditions at mean water level are given by

$$\nu_v \left.\frac{\partial U}{\partial z}\right|_{z=\bar{\zeta}} = \tau_s \cos\alpha / \rho \ , \quad \nu_v \left.\frac{\partial V}{\partial z}\right|_{z=\bar{\zeta}} = \tau_s \sin\alpha / \rho \qquad \text{----------} \quad (14)$$

where α is the wave direction.

The boundary conditions at bottom level are given as

$$\nu_v \left.\frac{\partial U}{\partial z}\right|_{z=-h} = \tau_{bx} / \rho \ , \qquad \nu_v \left.\frac{\partial V}{\partial z}\right|_{z=-h} = \tau_{by} / \rho \qquad \text{----------} \quad (15)$$

in which τ_{bx} and τ_{by} are the shear stresses due to bottom friction, which include the effect of interaction between the steady current and wave oscillatory motion.

The equations (7) to (12) are solved by using the hybrid method proposed by Koutitas et al. (1980), which combines the fractional step finite difference method in the horizontal plane with the Galerkin finite element method in the vertical direction.

RESULTS AND DISCUSSIONS

Undertow under spilling breaker

Experimental Apparatus

The laboratory tests under the spilling breaker were carried out in two-dimensional wave tank with beach slope of 1:15. The incident wave height in horizontal bottom where is 40 cm deep was 13.1cm and the wave period was 1.01 sec. The water particle velocities in the surf zone were measured by using the two components Laser Doppler Anemometer (LDA). Measurement points were set at the interval of 1-2 cm distance from 2mm above the bottom to trough level in the vertical direction and 3cm distance in the cross-shore direction.

Computed results and comparisons with measured data

Figure 2 shows an example of the computed results of velocity field in the vertical plane. The present model can predict the wave set-up and circulation flow in the surf zone. It is confirmed that undertow velocities can be reproduced in lower layer. If As=0 in Eq.(13), which shows $\tau s=0$ at mean water surface level in the surf zone, circulation flow may not be generated. Therefore, the shear stress due to surface roller plays an important roll in the production of the undertow velocities.

Figure 3 shows the comparison of vertical distribution of undertow velocities between the calculated results and measured data. The effect of eddy viscosity coefficient to the vertical distribution of nearshore currents was examined. In this figure, solid line and dotted line are the computed results by using the eddy viscosity coefficient of quadratic (refereed Eq. (10)) and constant types (refereed Eq. (9)), respectively, and symbol circle shows experimental results. From these figures, both computed curves which describe the vertical distribution of undertow velocity are coincident, although the eddy viscosity coefficients used are different in both curves, and then, the constant type of eddy viscosity coefficient is used because constant type is simpler than quadratic one. Finally, it is clear that computed curves show good agreement with measured data.

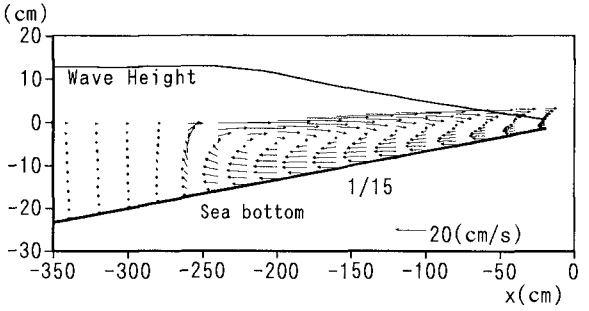

Figure 2 Example of flow pattern in the surf zone obtained from the present model

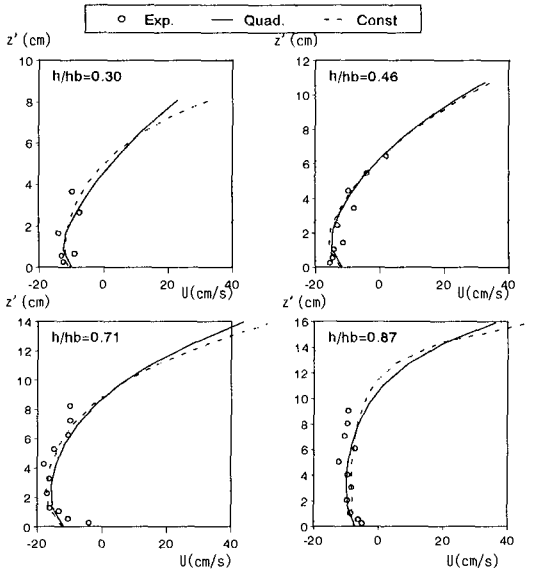

Figure 3 Comparison of vertical distributions of undertow velocities between computed and measured results

Longshore Currents

The present model is applied to determine the vertical profile of longshore currents. The results of calculation are compared with those of laboratory tests conducted by Visser (1991). The wave condition is shown in Table 1. Figure 4 shows the comparison of the depth-integrated longshore current between the computed results and measured data. In this figure, solid line and symbol circles are the computed results and the measured data, respectively. It is found that the computed results agree with the measured data. Figure 5 shows the comparisons of vertical distribution of longshore currents between the computed results and measured data. Figures 5 (a), (b) and (c) correspond to the points as shown in Figure 4. In these figures, solid lines and dotted lines are the computed alongshore components V and cross-shore components U, respectively. Combining the cross-shore and alongshore components, it is clear that the longshore currents have spiral profile in the vertical direction. The computed velocities V agree with the measured longshore velocities.

Table 1 Wave condition of experiments conducted by Visser (1991)

Beach slope	H(cm)	T(s)	θ	Ho/Lo	Breaker type
1:20	7.80	1.02	17	0.052	Plunging

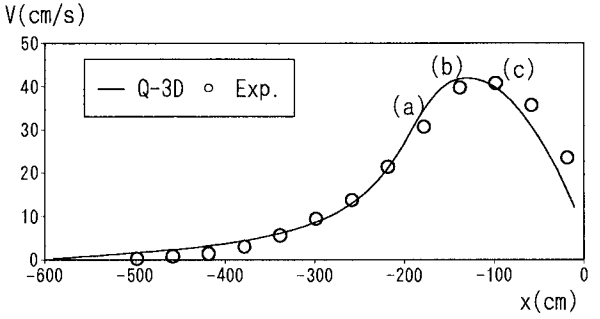

Figure 4 Comparison of the depth-integrated longshure currents between the computed results by suing Q-3D numerical model and the measured data conducted by Visser(1991)

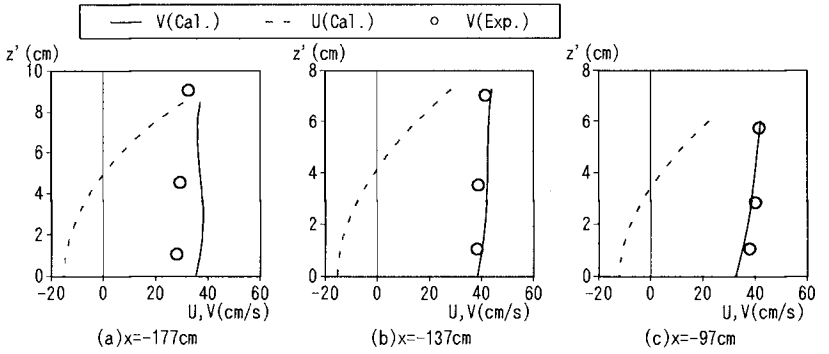

Figure 5 the comparison of vertical distribution of longshore currents between the computed results and measured data.

Nearshore Currents around Detached Breakwater

Experimental Apparatus

The laboratory tests under two regular wave conditions were carried out in the small wave basin(12m×5.0m×0.6m)with the beach slope of 1:10 as shown in Figure 6. The water depth adopted in this experiment was 0.3m at the toe of beach slope. Steal wave-guides along direction of the wave propagation were placed in the basin. The half-detached breakwater model in a width of 1m normal to the incident wave was installed at 0.15m deep on the beach slope.

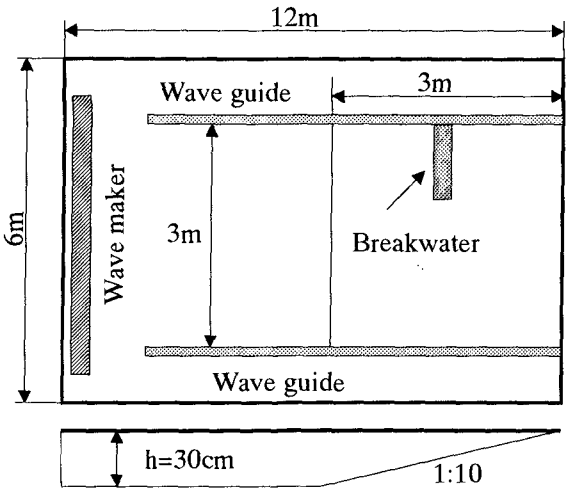

Figure 6 Wave basin and experimental apparatus

The wave condition is shown in Table 2. The surface elevations behind the breakwater model were measured using capacitance type wave gages. Cross-shore and longshore components of water particle velocities below the trough level behind the breakwater model were measured by using bi-axial electro-magnetic velocity meters. The measuring points were arranged with every 20 cm long in the horizontal direction and 2cm high in the vertical one. The velocity data were sampled at interval of 0.02 second. Steady current velocities were determined by time-averaged water particle velocity components.

Table 2 Experimental conditions

Case	H (cm)	T (sec)	Ho	Ho/Lo	Breaker type
1	6.9	1.0	7.53	0.048	Plunging
2	11.25	1.0	12.25	0.079	Spilling

Computed results and comparison with measured data

Figure 7 shows the domain of calculation and an example of distribution of wave height around the detached breakwater calculated from the mild-slope equations. In this figure, dotted line represents breaking line, which is determined as the ratio of water particle velocity to wave celerity, $u_w/C > 0.45$.

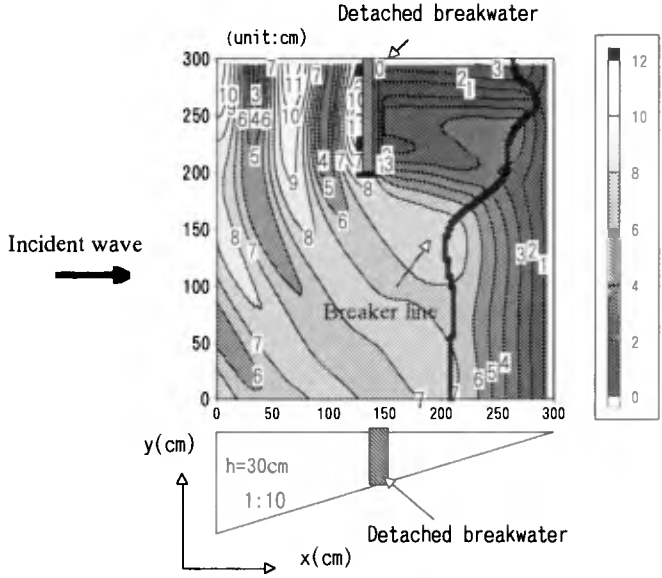

Figure 7 Domain of calculation and an example of wave field calculated from the mild-slope equations(Case 1; Ho=7.53cm, T=1.0s)

Figure 8 shows the comparison of the distribution of wave heights in the cross-shore direction between computed results and measured data for Case1. The computed results show good agreement with the experimental data.

Figures 9(a) and (b) show examples of the computed current vectors at mean water surface level and those at bottom level, respectively. In both figures, it is found that the magnitudes and directions of current vectors at mean water surface level are obviously different from those at bottom. Undertow velocities in the surf zone can be reproduced in the opening of the detached breakwater, and the spiral profiles can be reproduced in the surf zone.

Figures 10(a) and (b) show the vectors of steady current velocity behind the detached breakwater at 2cm above bottom for the experiments of Case1 and 2, respectively. In these figures, solid line and dotted line are breaker line obtained from the experiments and dotted one obtained from the computations. From the result for Case1 it is found that a circulation flow is generated behind the breakwater. On the other hand, the flow pattern for Case2 is non-closed circulation. The distribution of the steady current velocities for Case2 is different from that for Case1, and the magnitude of current velocity for Case2 is larger than that for Case1. It is clarified that the flow pattern depends on the wave condition.

Figures 11(a) and (b) show the computed vectors of steady current velocity at 2cm above bottom for Case1 and 2, respectively. It is found that the results of computations show qualitative agreement with those of experiments in Figures 9(a) and (b).

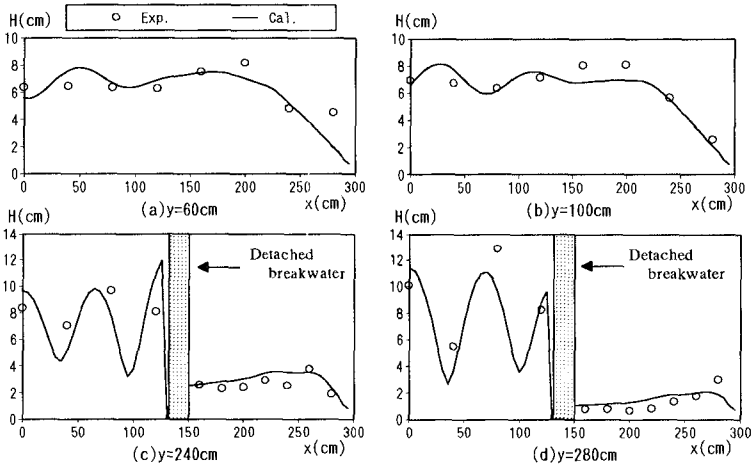

Figure 8 Comparison of wave height distribution between computation and experiment for Case1 (Ho=7.53cm, T=1.0sec)

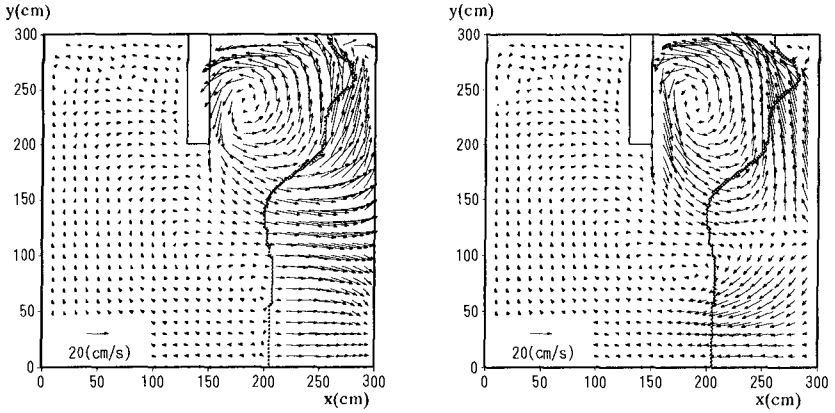

(a)Mean water surface level (b)Bottom level

Figure 9 Distribution of steady current vectors obtained from the present Q-3D model (Case1; Ho=7.53cm,T=1.0sec)

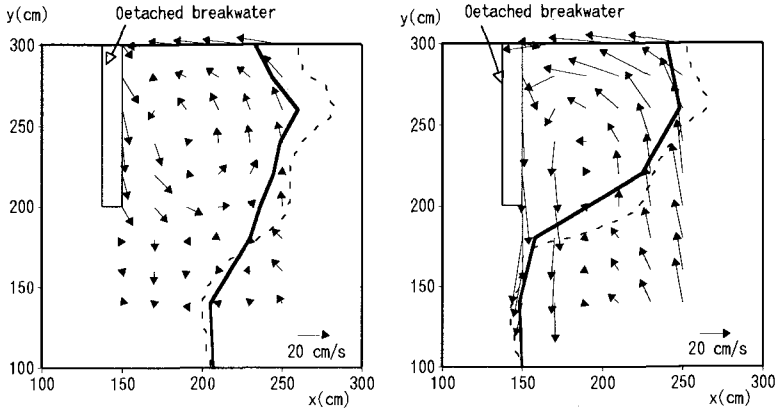

Figure 10 Distribution of current vectors at 2cm above bottom obtained from the laboratory tests

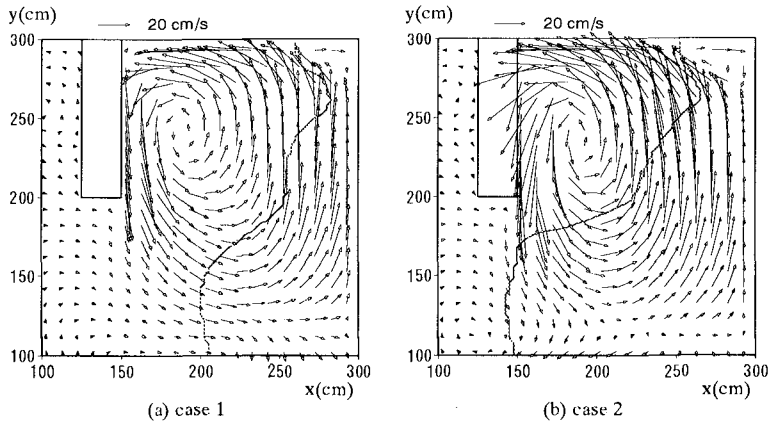

Figure 11 Distribution of current vectors at 2cm above bottom obtained from the present Q-3D model

Figures 12 and 13 show the comparisons between the vertical profiles of the computed results and those of the measured data for Case1 and Case2, respectively. Notations (a),(b),(c) and (d) in these figures correspond to results at the stations A,B,C and D behind the detached breakwater. In these figures, U and V represent cross-shore and alongshore components of steady current, respectively. From the results of measurement for Case1, cross-shore and alongshore current velocities at St.A,C and

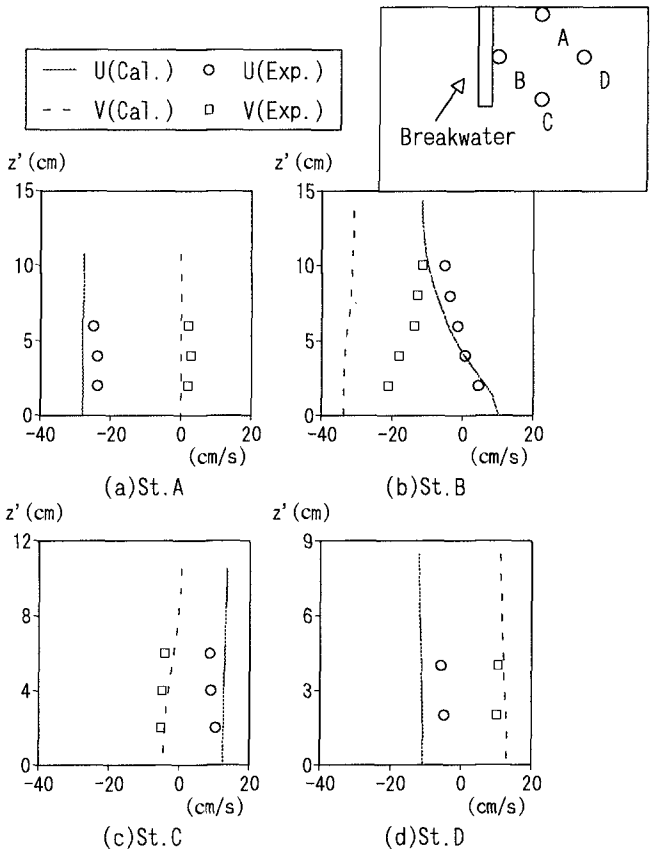

Figure 12 Comparisons of vertical distribution of neashore currents behind the detached breakwater for CASE1(Ho=7.53cm, T=1.0s)

D are almost constant over the depth. It is found that the computed results coincide with the measured data. From the results of experiments at St. B, the magnitude and direction of the cross-shore current U near water surface is different from that near bottom. It is found that nearshore currents in the vicinity of the detached breakwater have spiral distribution in the vertical direction. The computed results for the cross-shore steady current U show good agreement with the measured data. On the other hand, the computed V are overestimated.

From the comparison for Case2 in Figure 13, it is found that the computed current velocities U and V at St.A ,B and D show qualitative agreement with the measured data, and the computed velocity U at St.C in the opening of the breakwater is different from the measured data.

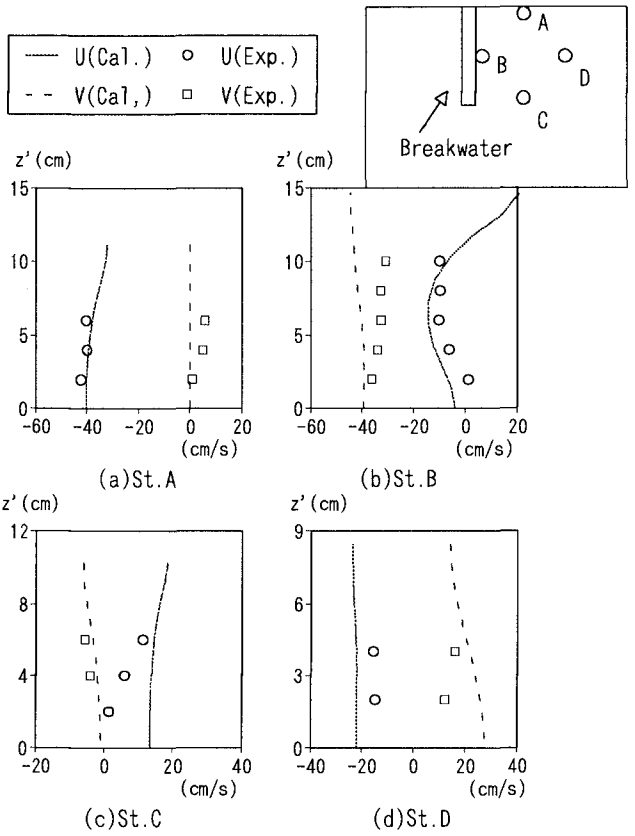

Figure 13 Comparisons of vertical distribution of neashore currents behind the detached breakwater for CASE2(Ho=12.25cm, T=1.0s)

Most computed results show qualitative agreement with the laboratory tests. It was confirmed that the present Q-3D numerical model could apply to the prediction of neasrhore currents around the coastal structures such as the detached breakwater.

CONCLUSIONS

This paper presented a numerical model for estimating the vertical profile of nearshore currents. The computed results were compared with the measured data. The applicability of the Q-3D model to neashore currents was investigated. The main conclusions of this study are summarized as follows:

1) A quasi-three dimensional numerical model of nearshore currents was developed.
2) Undertow velocity and spiral profile in the surf zone can be reproduced by taking account of the shear stress due to breaking wave.
3) The vertical distribution of longshore currents was computed. The results were compared with the results of the laboratory tests conducted by Visser(1991). The computed results agreed with the measured data.
4) From the laboratory tests of the detached breakwater, it was found that the flow patterns behind the breakwater depend on the wave conditions.
5) From the experimental results in the vicinity of the detached breakwater, it was found that the magnitude and direction of nearshore currents near water surface is different from those near bottom from the experiments and it shows spiral distribution in the vertical direction.
6) The results of computation of nearshore currents around the breakwater using present Q-3D model show good agreement with those of experiments. The spiral profiles in the vicinity of the breakwater was computed.
It was confirmed that the numerical model could be applied to the determination of the distribution of currents around coastal structures.

REFERENCES

Koutitas, C. and B. O'Connor (1980): Modeling three-dimensional wind-induced flows, Journal of The Hydraulics Division, HY11, pp.1843-1865.

Longuet-Higgins,M.S.(1970):Longshore currents generated by obliquely incident wave,
J.Geophys. Res., Vol.75, No.33, pp.6778-6789.

Okayasu, A., K.Hara and T. Shibayama (1994): Laboratory experiments on 3-D nearshore currents and a model with momentum flux by breaking wave, Proc. 24th Int. Conf. Coastal Eng., pp.2461-2475.

Pechon P. and C. Teisson(1994): Numerical modelling of three-dimensional wave-driven currents in the surf zone,, Proc. 24th Int. Conf. Coastal Eng.,pp.2503-2512.

Sanchez-Arcilla, A., F.Collado and A.Rodriguez(1992):Vertical varying velocity field in Q-3D nearshore circulation, Proc. 23th Int. Conf. Coastal Eng., pp.2811-2824.

Svendsen, I.A. and R.S. Lorenz, (1989): Velocities in combined undertow and longshore currents, Coastal Engineering, Vol.13, pp.57-79.

Tsuchiya,Y., T.Yamashita and M.Uemoto (1986): A model of undertow in the surf zone, Proc. of 33rd Conf. of Coastal Eng., JSCE, pp.31-35.(in Japanese)

Visser,P.J.(1991):Laboratory measurements of uniform longshore currents, Coastal Eng., Vol.15,pp.563-593.

Watanabe, A. and K. Maruyama (1986): Numerical modeling of nearshore wave field under combined refraction, diffraction and breaking, Coastal Eng. in Japan, Vol.29, pp.19-39.

Three-Dimensional Nearshore Currents Model Based on Vertical Distribution of Radiation Stress

Hisamichi Nobuoka[1], Nobuo Mimura[2] and Hajime Kato[3]

Abstract

Wave-induced currents in a surf zone must be explained by the change of wave motion. The driving force for nearshore currents is the radiation stresses which are defined as the excess momentum flux due to wave motion. However, there is no model which can describe the three-dimensional structure of the nearshore currents. This study aims to develop a model of this kind, in which only wave motion is taken as the driving force to the currents. Governing equations are derived from the Navier-Stokes equations. This model is proved to reproduce the currents measured in the experiments.

1. Introduction

Nearshore currents in a surf zone have a three-dimensional structure (e.g., Svendsen et al., 1989). They have been dealt with by the combination of horizontal and vertical circulations. The generation of the horizontal circulation has been expressed with radiation stresses averaged over a water depth. On the other hand, it is suggested that the vertical circulation including undertow is caused by the imbalance between the momentum flux of wave motion and pressure force in a vertical plane (Dyhr-Nielsen et al., 1970).

Some models for the vertical circulation including undertow take into account the role of rollers associated with wave breaking. These models are classified into two types. One is an undertow model proposed by Svendsen (1984). The undertow model needs to empirically assume the volume rate of the undertow compensating the onshore

[1] Research Associate and [3] Professor, Dept. of Urban & Civil Eng. Faculty of Eng., Ibaraki Univ., Nakanarusawa, Hitachi, Ibaraki, 316, Japan (e-mail hnob@hit.ipc.ibaraki.ac.jp)

[2] Professor, Center for Water Environmental Studies, Ibaraki Univ., Nakanarusawa, Hitachi, Ibaraki, 316, Japan

flux above the wave trough. In a three-dimensional beach, however, the estimation of compensating flow is very difficult, for onshore and offshore flow rates are not necessary balanced in a vertical section. The other type is a model which considers the momentum flux of surface roller as driving force for the vertical circulation. It is not clear, however, how the momentum of surface roller occur.

This study aims to propose a new type of three-dimensional nearshore currents model on the basis of two concepts; i.e., the flux of onshore flow above the trough level and offshore flow under the trough level themselves are variable to be obtain, and a driving force for currents is only wave motion. At first, governing equations are derived from the Navier-Stokes equation. Then, the mechanism to generate time-mean currents are discussed. The predictive capacity in this model is also examined by comparing the computational results with measurements of cross- and long-shore currents in different settings.

2. Governing Equations and Numerical Solution

Basic equations to derive the time-mean equations are the Navier-Stokes equations of continuity (Eq. (1)) and momentum conservation (Eq. (2) and (3)).

$$\frac{\partial u}{\partial x} + \frac{\partial w}{\partial z} = 0 \tag{1}$$

$$\frac{\partial u}{\partial t} + \frac{\partial u^2}{\partial x} + \frac{\partial uw}{\partial z} = -\frac{1}{\rho}\frac{\partial p}{\partial x} \tag{2}$$

$$\frac{\partial w}{\partial t} + \frac{\partial uw}{\partial x} + \frac{\partial w^2}{\partial z} = -g - \frac{1}{\rho}\frac{\partial p}{\partial z} \tag{3}$$

where u, w are the total instantaneous fluid particle velocity in the x and z directions, p is pressure, ρ is the mass density and g is gravity. The terms in y direction are similar to the x terms, but are not presented here for the sake of brevity. Furthermore viscous terms are not expressed now as they will be small except in the bottom boundary.

Equations (1), (2) and (3) are transformed into the Reynolds equations by dividing the velocity components and pressure into three components (Eq. (4)).

$$u = \overline{u} + u_w + u'$$

$$w = \overline{w} + w_w + w'$$

$$p = \overline{p} + p_w + p' \tag{4}$$

where $\overline{u}, \overline{w}, \overline{p}$ are time-mean components, u_w, w_w, p_w are periodic components associated with wave motion, u', w', p' are turbulent fluctuating components. The time-mean quantities in Eq. (4) satisfy the following relation:

$$\overline{u'}, \overline{w'} = 0$$
$$\overline{u}_w, \overline{w}_w = 0 \text{ (except above trough level)} \quad (5)$$

We obtain Eq. (6), (7) and (8) substituting Eq. (4) to Eq. (1), (2) and (3).

$$\frac{\partial(\overline{u} + u_w + u')}{\partial x} + \frac{\partial(\overline{w} + w_w + w')}{\partial z} = 0 \quad (6)$$

$$\frac{\partial(\overline{u} + u_w + u')}{\partial t} + \frac{\partial(\overline{u} + u_w + u')^2}{\partial x} + \frac{\partial(\overline{u} + u_w + u')(\overline{w} + w_w + w')}{\partial z} = -\frac{1}{\rho}\frac{\partial(\overline{p} + p_w + p')}{\partial x} \quad (7)$$

$$\frac{\partial(\overline{w} + w_w + w')}{\partial t} + \frac{\partial(\overline{u} + u_w + u')(\overline{w} + w_w + w')}{\partial x} + \frac{\partial(\overline{w} + w_w + w')^2}{\partial z} = -g - \frac{1}{\rho}\frac{\partial(\overline{p} + p_w + p')}{\partial z} \quad (8)$$

The pressure p at arbitrary height z can be calculated after integrating vertical momentum equation (Eq. (8)) between water surface η and z. The following equation is obtained assuming that interaction between the components is not exist (Assumption-1) and that pressure at the water surface is zero.

$$\begin{aligned}\frac{1}{\rho}(\overline{p} + p_w + p') = {} & g(\overline{\eta} + \eta_w + \eta' - z) \\ & + \frac{\partial}{\partial t}\int_z^{\eta}(\overline{w} + w_w + w')dz \\ & + \frac{\partial}{\partial x}\int_z^{\eta}(\overline{u}\overline{w} + u_w w_w + u'w')dz \\ & - (\overline{w}^2 + w_w^2 + w'^2)\end{aligned} \quad (9)$$

When Eq. (9) is substituted to Eq. (7) with Assumption -1, we can obtain Eq. (10).

$$\frac{\partial \overline{u}}{\partial t} + \frac{\partial \overline{u}^2}{\partial x} + \frac{\partial \overline{u}\overline{w}}{\partial z} = -\frac{\partial}{\partial x}\left\{g(\overline{\eta} - z) + \left[\frac{\partial}{\partial t}\int_z^{\eta}\overline{w}dz + \frac{\partial}{\partial x}\int_z^{\eta}\overline{u}\overline{w}dz - \overline{w}^2\right]\right\}$$
$$-\frac{\partial}{\partial x}\left\{g\eta_w + \left[\frac{\partial}{\partial t}\int_z^{\eta}w_w dz + \frac{\partial}{\partial x}\int_z^{\eta}u_w w_w dz - w_w^{\,2}\right]\right\} - \left\{\frac{\partial u_w}{\partial t} + \frac{\partial u_w^{\,2}}{\partial x} + \frac{\partial u_w w_w}{\partial z}\right\}$$
$$-\frac{\partial}{\partial x}\left\{g\eta' + \left[\frac{\partial}{\partial t}\int_z^{\eta}w'dz + \frac{\partial}{\partial x}\int_z^{\eta}u'w'dz - w'^2\right]\right\} - \left\{\frac{\partial u'}{\partial t} + \frac{\partial u'^2}{\partial x} + \frac{\partial u'w'}{\partial z}\right\} \tag{10}$$

After averaging the Eq. (10) over a wave period, Eq. (11) is finally obtained.

$$\left(\frac{\partial \overline{u}}{\partial t} + \right)\frac{\partial \overline{u}^2}{\partial x} + \frac{\partial \overline{u}\overline{w}}{\partial z} = -\frac{\partial}{\partial x}\left\{g(\overline{\eta} - z) + \frac{1}{T}\int_0^T\left[\frac{\partial}{\partial x}\int_z^{\eta}\overline{u}\overline{w}dz - \overline{w}^2\right]dt\right\}$$
$$-\frac{1}{T}\int_0^T\left[\frac{\partial}{\partial x}\left\{g\eta_w + (u_w^{\,2} - w_w^{\,2}) + \frac{\partial}{\partial x}\int_z^{\eta}u_w w_w dz\right\} - \left\{\frac{\partial u_w w_w}{\partial z}\right\}\right]dt \tag{11}$$
$$-\frac{1}{T}\int_0^T\left[\frac{\partial}{\partial x}\left\{g\eta' + (u'^2 - w'^2) + \frac{\partial}{\partial x}\int_z^{\eta}u'w'dz\right\} - \left\{\frac{\partial u'w'}{\partial z}\right\}\right]dt$$

Here some assumptions are added; the wave components are expressed by small amplitude wave theory (Assumption-2), third-order terms of wave height are sufficiently small and can be neglected (Assumption-3), the gradient of the Reynolds stress in the horizontal direction is much smaller than that of radiation stress based on the Stive et al. (1982) (Assumption-4) and the vertical acceleration of time-mean component is small (Assumption-5). Adding these assumptions, the Eq. (11) for the momentum conservation of the time-mean components becomes the following equation.
From the still water level to the bottom $(-h \le z \le 0)$,

$$\left(\frac{\partial \overline{u}}{\partial t} + \right)\frac{\partial \overline{u}^2}{\partial x} + \frac{\partial \overline{u}\overline{w}}{\partial z} = -\frac{\partial}{\partial x}g(\overline{\eta} - z) - \frac{\partial}{\partial x}(\overline{u}_w^{\,2} - \overline{w}_w^{\,2}) - \frac{\partial \overline{u'w'}}{\partial z} \tag{12}$$

and, for above the still water level $(0 \le z \le \eta)$,

$$\left(\frac{\partial \overline{u}}{\partial t} + \right)\frac{\partial \overline{u}^2}{\partial x} + \frac{\partial \overline{u}\overline{w}}{\partial z} = -\frac{\partial}{\partial x}g(\overline{\eta} - z) - \frac{1}{T}\int_0^T\frac{\partial}{\partial x}g\eta_w\,dt - \frac{\partial \overline{u'w'}}{\partial z} \tag{13}$$

Equation (12) and (13) consist of four terms; acceleration, hydrostatic pressure, radiation stress and the Reynolds stress terms.

The continuity equation (1) becomes Eq.(14) by following the similar process.

$$\frac{\partial \overline{u}}{\partial x} + \frac{\partial \overline{w}}{\partial z} = 0 \tag{14}$$

The water depth is divided into an appropriate number of the horizontal layers. The sketch of layer is shown in Fig. 1. The layer are numbered from top to bottom. The h_i indicates the depth at the lower boundary of the number i th layer. The surface of the first layer is the mean water level $\overline{\eta}$ and the lowest boundary is the bottom surface.

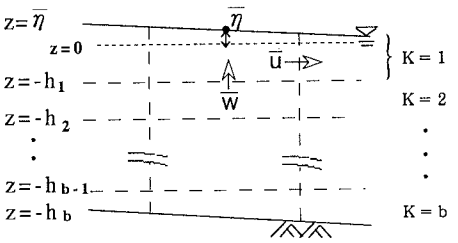

Figure-1 Lay-out of Multi-Layer

In order to obtained the governing equations for each layer, Eq. (12), (13) and (14) are integrated between the upper and lower boundary of each layer with an assumption that the time-mean horizontal velocity $\overline{u}$ is constant in each layer (Assumption-6).

<Momentum Equation>
The Top Layer (k=1)

$$\frac{\partial \overline{P}_1}{\partial t} + \frac{\partial \overline{P}_1 \overline{u}_1}{\partial x} - \overline{u}_1 \overline{w}_1\Big|_{z=-h1} = -g(\overline{\eta} - (-h_1))\frac{\partial \overline{\eta}}{\partial x} - \frac{\partial}{\partial x}\left(\frac{1}{2}\overline{\eta^2} + \int_{h1}^{0}\left(\overline{u_w^2} - \overline{w_w^2}\right)dz\right) - u'w'\Big|_{z=-h1} \tag{15}$$

The Middle Layer (k= i)

$$\frac{\partial \overline{P}_i}{\partial t} + \frac{\partial \overline{P}_i \overline{u}_i}{\partial x} + \overline{u}_i \overline{w}_i\Big|_{z=-hi-1} - \overline{u}_i \overline{w}_i\Big|_{z=-hi} = -g((-h_{i-1}) - (-h_i))\frac{\partial \overline{\eta}}{\partial x} - \frac{\partial}{\partial x}\left(\int_{-hi}^{-hi-1}\left(\overline{u_w^2} - \overline{w_w^2}\right)dz\right) + u'w'\Big|_{z=hi-1} - u'w'\Big|_{z=-hi} \tag{16}$$

The Bottom Layer (k= b)

$$\frac{\partial \overline{P}_b}{\partial t} + \frac{\partial \overline{P}_b \overline{u}_b}{\partial x} + \overline{u}_b \overline{w}_b\Big|_{z=-hb-1} = -g\left((-h_{b-1}) - (-h_b)\right)\frac{\partial \overline{\eta}}{\partial x} - \frac{\partial}{\partial x}\left(\int_{hb}^{-hb-1}\left(\overline{u_w^2} - \overline{w_w^2}\right)dz\right) + u'w'\Big|_{z=-hb} \tag{17}$$

<Continuity Equation>

The Top Layer (k=1)

$$\left(\frac{\partial \overline{\eta}}{\partial t}\right) + \frac{\partial \overline{P}_1}{\partial x} - \overline{w}_1 = 0 \tag{18}$$

The Middle Layer (k= i)

$$\frac{\partial \overline{P}_1}{\partial x} + \overline{w}_{i-1} - \overline{w}_i = 0 \tag{19}$$

The Bottom Layer (k= b)

$$\frac{\partial \overline{P}_b}{\partial x} + \overline{w}_b = 0 \tag{20}$$

where,

$$\overline{P}_i \equiv \int_{-h_i}^{-h_{i-1}} u_i dz \tag{21}$$

The governing equations in the present model are from Eq. (15) to (20). A bottom friction term is added to Eq. (17).

These governing equations are solved numerically with a modified ADI method (Maa, 1990; Sato et al., 1992). The variables to be obtained are time-mean velocity $\overline{u}$, $\overline{w}$ in each layer and time-mean water level $\overline{\eta}$ at the top layer. The radiation stress in each layer is calculated using water particle velocities and water surface elevation calculated by the small amplitude wave theory. The total amount of this stress over the water depth is the same as the conventional radiation stress introduced by Lounguet-Higgins et al.(1964). The Reynolds stresses are represented by the eddy viscosity model. The eddy viscosity coefficients are estimated by the empirical formula introduced by Okayasu et al. (1988), for the onshore area between plunging point and shoreline. For the area off the breaking point, this coefficient is set to be zero. In the area between plunging and breaking points, the coefficient is calculated by linear interpolation. The bottom friction is expressed with a term proportional to the square of time-mean velocity.

3. Theoretical Consideration on the Present Model

As waves approach to the shore, a part of the momentum of wave motion is transferred to a flow. Since the total momentum of water motion in the surf zone is conserved, changes in wave momentum in the horizontal direction should balance with the momentum of time-mean currents. This phenomenon is expressed in the Navie-Stokes momentum equations. Equation (22) is the Navier-Stokes equation expressed by the time-mean and wave components, and is same as Eq. (10) excluding the turbulent term.

$$\frac{\partial \overline{u}}{\partial t} + \frac{\partial \overline{u}^2}{\partial x} + \frac{\partial \overline{uw}}{\partial z} + \frac{1}{\rho}\frac{\partial \overline{p}}{\partial x} = -\left(\frac{\partial u_w}{\partial t} + \frac{\partial u_w^2}{\partial x} + \frac{\partial u_w w_w}{\partial z} + \frac{1}{\rho}\frac{\partial p_w}{\partial x} \right) \qquad (22)$$

The left side shows the balance of the time-mean component while the right side is for the wave component. If the wave momentum decreases, the momentum of flow must increase for conserving the total momentum. The transferred momentum in an averaged wave period is expressed as the difference in the radiation stresses.

When a wave breaks and jet and large vortexes occur, the momentum of jet and vortexes must be supplied from the wave motion. The source of the time-mean momentum of the vortex is also the difference in the radiation stress. In the models for the vertical circulation, the vortex is often dealt as outer source of force to the time-mean flow (e.g. Péchon et al., 1994). However, from the above-mentioned consideration, it is sufficient to take only change in the radiation stress as driving force of the time-mean flow. This is the basic concept of this model.

As the radiation stress is dealt with as an integrated form over a water depth until now, we can not take into consideration its vertical distribution. However, it is needed to express the strong transfer by wave breaking around the water surface. Figure-2(a) shows an example of calculated result for the gradient of radiation stress after wave breaking. The gradient around the surface is the steepest throughout the depth. This result expresses that the momentum is transferred from wave to large vortexes in a wave period. Figure-2(b) shows hydrostatic time-mean pressure at the same point. Comparing the pressure force and radiation stresses, onshore force induced

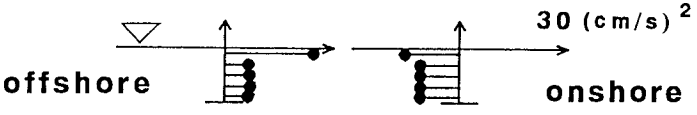

(a) Radiation stresses (b) Pressure

Figure-2 Imbalance of radiation stresses and hydrostatic pressure

by the radiation stress is stronger than offshore pressure force at the top layer. On the other hand, they are opposite in other layers i.e.; offshore force induced by pressure is stronger. This means that the present model can represent the vertical distribution of driving forces and their local imbalance.

These local imbalances of radiation stress and time-mean hydrostatic pressure force indicate how the vertical circulation is generated. The distribution of time-mean water level which causes the gradient of hydrostatic pressure force can be explained by the radiation stress. Then, we can explain the generation of the vertical circulation with radiation stresses as a source of driving force.

4. Comparisons of Results between Simulations and Experiments.

The present model was applied to predict time-mean water level and vertical distribution of on- and off-shore time-mean currents. The following three experiments were chosen for the comparison.

(Case-a) Vertical Circulation and Wave Set-up/Set-down in Wave Flume (2-DV)

In this case, the experiments were divided two sorts. First one was designed to compare the distribution of mean water level and pattern of vertical circulation in a surf zone. The wave flume was 20 m long and 0.6 m wide with a beach of 1/20 slope. The water depth in the uniform area was 35 cm. Two different wave conditions were used; spilling breaker (Case-a-1) and plunging breaker (Case-a-2). Surface elevations and velocity were measured by capacitance-type wave gauge and electromagnetic current meter respectively.

The other experiment was performed by Okayasu et al.(1988), in which vertical distribution of cross-shore current was measured in detail by laser-Doppler velocimeter. The wave flume was 23 m long and 0.4m wide with a 1/20 slope. Water depth in the uniform area is 40 cm. Six lines were chosen to measure the currents. Line-1 is at the breaking point and Line-6 is on the still water shore line. Two conditions of incident wave were chosen; plunging breaker (Case-a-3) and spilling breaker (Case-a-4).

(Case-b) Weak Three-Dimensional Nearshore Currents in Wave Basin

This case was chosen to check the capacity of this model to predict the vertical distribution of long- and cross-shore currents. This experiment was performed by Okayasu et al.(1994), and the currents observed in the experiments was not strong. The condition of the experiment and simulation are shown in Fig.-3. The wave basin has a 1/20 uniform slope which is uniform in the long-shore direction. Wave enters at an angle of 10 degree to cross-shore line.

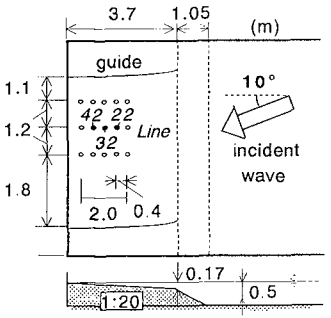

Figure-3 Top and Side View of Wave basin (Case-b)

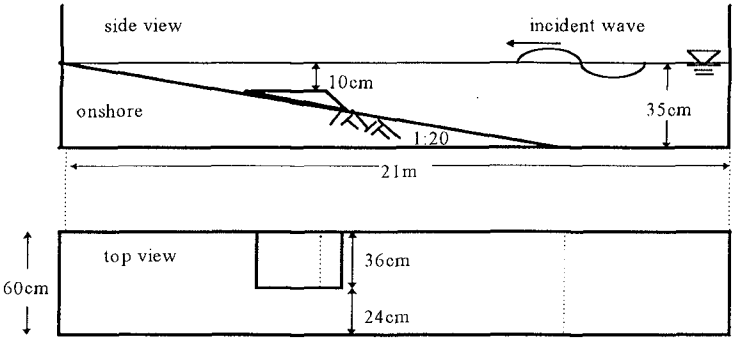

Figure-4 Wave flume with a step (Case-c)

(Case-c) Strong Three-Dimensional Nearshore Currents Around a Step

This case was selected to examine the capacity to predict the three-dimensional nearshore fast currents. Figure-4 shows a schematic diagram of the wave fume. The width of the step were three fifth of the flume width in order to cause three-dimensional currents.

Table-1 shows the conditions of these cases, where Hi and T are height and period of incident waves, and h is the water depth in the offshore.

Table-1 Experimental Condition

	Incident Wave			Breaking Type	Experiment
	Hi (cm)	*T* (s)	*h* (cm)		
Case-a-1	10.0	1.0	35	spilling	Present study
Case-a-2	12.0	2.0	35	plunging	Present study
Case-a-3	8.5	2.0	40	plunging	Okayasu (1988)
Case-a-4	9.87	1.17	40	spilling	Okayasu (1988)
Case-b	5.5	1.33	49.7		Okayasu (1994)
Case-c	7.5	1.75	35	plunging	Present study

(1) Results of Vertical Circulation and Wave Set-up/Set-down (Case-a)

Figure-5(a) and 5(b) show the results of Case-a-1 and Case-a-2 respectively. The line and marks in each figure indicate the mean-water level obtained by the simulation and experiment respectively. Both results of the simulation show good agreement with the experimental results, though wave set-down are slightly overestimated around the wave breaking point. Simulated and measured cross-shore currents are shown by arrows with solid line and broken line respectively. The direction of vertical circulation of both simulated results is onshore at the uppermost level and offshore below the second level which is nearly equal to wave trough level. These patterns correspond to the experimental results.

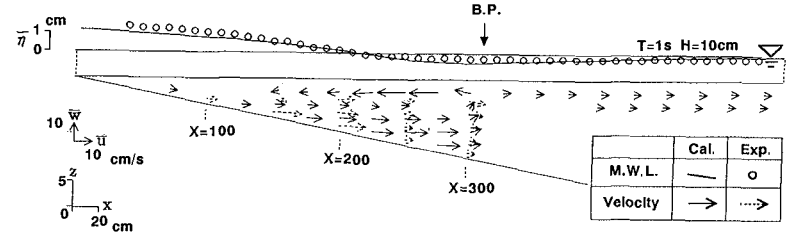

(a) Case-a-1 (Spilling breaking type)

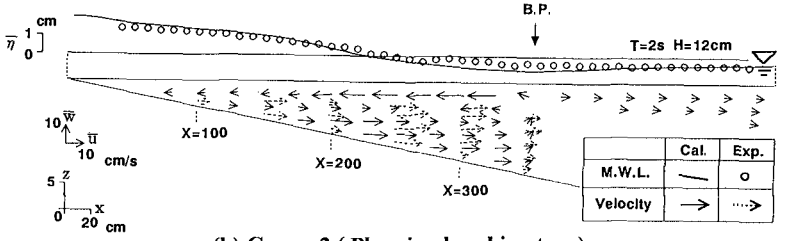

(b) Case-a-2 (Plunging breaking type)

Figure-5 Vertical Circulation and Wave Set-up/Set-down (Case-a)

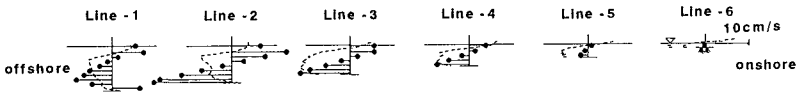

(a) Case-a-3 (Plunging breaking type)

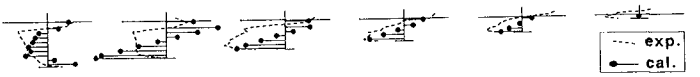

(b) Case-a-4 (Spilling breaking type)

Figure-6 Vertical Distribution of cross-shore current(Case-a)

The calculated results and experimental data measured by laser-Doppler velocimeter are compared in Figure-6(a) and 6(b) in order to examine the vertical distribution of cross-shore current in detail. Simulation results are indicated by filled circles with line and experimental results are by broken lines. From Line-3 to Line-5, where large vortexes progress, simulated vertical distribution show good agreement with experiments. On the other hand, the agreement is not so good at Line-2 and 6, which are near the breaking point and the shore line, respectively.

(2) Results of Weak 3-D Currents (Case-b)

It is important to properly predict time-mean water level, since the gradient of the water level is one of the driving force of currents. Figure-7 shows the comparison for the water level. The results by the present multi-layer model and single layer model which have been used conventionally are indicated by a circle and a triangle respectively. The results of both simulations are in close agreement with that of experiments.

Figure-8(a) shows the vertical distribution of currents simulated simultaneously with the water level. The vertical axis shows the water depth. The horizontal axes show the cross- and long-shore directions. The solid lines show the calculated cross- and long-

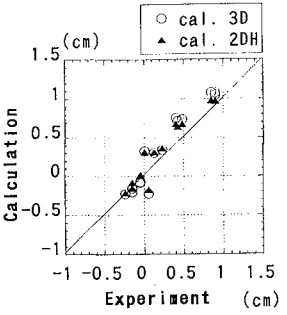

Figure-7 Wave Set-up/Set-down

shore current velocities, and the solid lines with filled circle show the sum of these velocities. On the other hand, the broken lines show the measured currents.

In both results of simulation and experiment, cross-shore currents are onshore above the wave trough level and offshore under the trough level. In the long-shore direction, there is a vertical distribution of the current velocity i.e.; it is slow near the surface, fast in the middle, and slow again near the bottom. The simulated currents velocities agree approximately with experiments in the area where the water depth is a comparatively large as Line-22. On the other hand, in the area where the depth is small as Line-42, the simulated velocities are far slower than experiment. This reason may be that the present model can not yet express the distribution of radiation stress well in the shallow region.

Next, the present multi-layer model is compared with a single layer model which have been used conventionally. For the result of single layer model (Fig.-8(b)), cross-shore current dose not appear and long shore currents are of course uniform over the depth. Such comparison shows the effectiveness of the multi-layer model for the simulation of the three-dimensional structure of the nearshore currents.

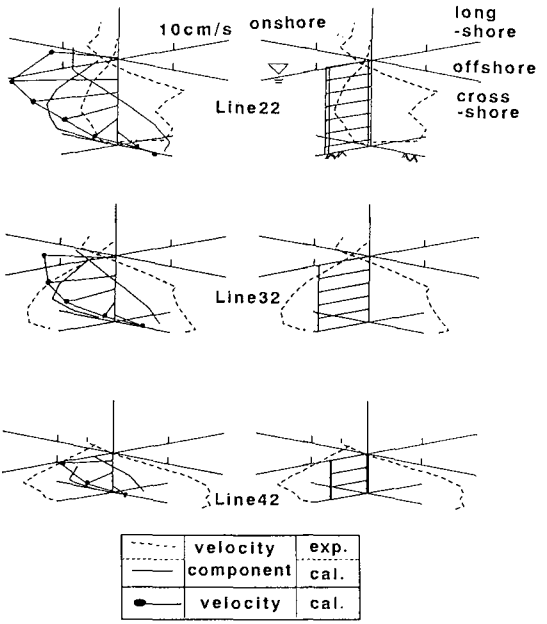

(a)Multi-Layer Model (b) Single-Layer model

Figure-8 Vertical Distribution of Cross- and Long-Shore Currents (Case-b)

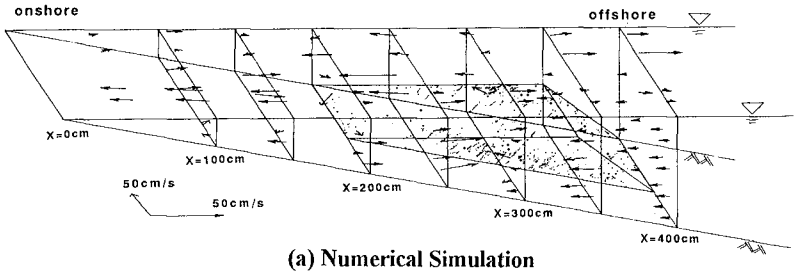

(a) Numerical Simulation

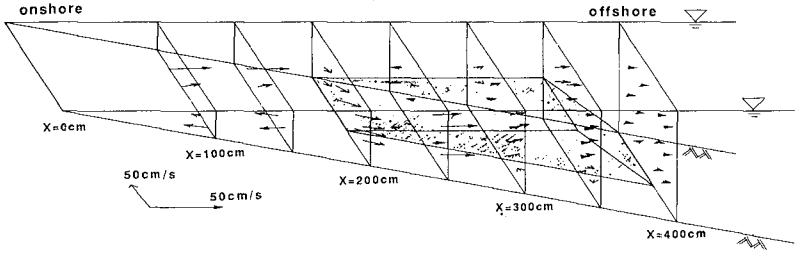

(b) Experiment

Figure-9 Three-dimensional currents around the step (Case-c)

(3) Results of Strong 3-D Currents (Case-c)

Figure-9(a) and (b) show the simulated and measured results of the near-shore currents around the step. The currents were measured only under wave trough by a electromagnetic current meter. In the results of simulation, there are circulations around the step and near the shore line respectively. The circulation around the step is anti-clockwise; i.e., it directs onshore above the step and offshore at the gap of structure. The other circulation show the reverse rotation. Detailed examination of simulated results shows that flow moves from one to another circulation and vice versa. Part of streamlines forms a "8" shape with a two-level crossing. The measured and observed result showed a similar pattern of circulation.

Another remarkable three-dimensional structure is that offshore currents near the bottom of the gap turn to a rising current a long the step in the vicinity of $x=300$ line. This pattern of current is also reproduced in the simulation.

5. Conclusion

In this study, a three-dimensional nearshore current model based on the vertical distribution of the radiation stresses was developed. As the driving force of this model is only radiation stresses, it is comparatively easy to calculate the time mean flow for the

three-dimensional beach. Simulated results for wave set-up/set-down and vertical distribution of cross- and long-shore currents show good agreement with measured data. The above results confirm that this model is effective to estimate three-dimensional nearshore current in the surf zone.

Acknowledgments

The authors are grateful to Dr. A. Okayasu of Yokohama National University for providing valuable experimental data.

Reference

Dyhr-Nielsen M. and T. Sørensen.(1970): Some sand transport phenomena on coast with bars, Proc. 12th. ICCE, pp.855-865.

Longuet-Higgins M. S. and R. W. Stewart (1964): Radiation stresses in water waves ; a physical discussion, with applications, Deep-sea Res.11, pp.529-562.

Maa J. P.-Y.(1990): An efficient horizontal two-dimensional hydrodynamic model, Coastal Engineering, vol.14, pp.1-18.

Okayasu A., T. Shibayama and K. Horikawa (1988) Vertical variation of undertow in the surf zone, Proc. 21st. ICCE, pp.478-491.

Okayasu A., K. Hara and T. Shibayama (1994): Laboratory experiments on 3-D nearshore current and a model with momentum flux by breaking waves, Proc. 24th. ICCE, pp.2461-2475.

Péchon P. and C. Tesson (1994) : Numerical modeling of three-dimensional wave-induced currents in the surf zone, Proc.24th. ICCE, pp.2503-2512.

Sato S. and K. Ueda (1992): Numerical simulation of tide and wind induced currents in Tokyo Bay, JSCE, Vol. 39(1), pp.251-255, (in Japanese).

Stive M. J. F. and H. G. Wind (1982): A study of radiation stress and set-up in the nearshore region, Coastal Engineering, vol.6, pp.1-25.

Svendsen I. A.(1984): Mass flux and undertow in a surf zone, Coastal Engineering, Vol.8, pp.347-365.

Svendsen I. A. and R. Lorenz (1988): Velocities in combined undertow and longshore currents, Coastal Engineering, Vol.13, pp.55-79.

Numerical Simulation of Wave Fields around The Submerged Breakwater with SOLA-SURF Method

Norio Hayakawa,Member*, Tokuzo Hosoyamada* Shigeru Yoshida**
and Gozo Tsujimoto#

Abstract

Bothe two and three dimensional numerical simulation of wave fields around the submerged breakwater is carried out using the SOLA-SURF method. The results of the calculation are compared with the laboratory experiment. It is shown that the side wall boundary condition for the three dimensional calculation of the laboratory tank should be nonviscous(slip-type) to reproduce the experimental data. The calculation method is easily extendible to a field scale case.

Introduction

Numerical simulation of wave fields based on the Navier Stokes(NS) equation has been known to be time-consuming. It has been customarily carried out with some kind of simplifications such as irrotationality for the Boundary Element Method 1, mild slope hypothesis for the long wave approximation, etc. The advancement of the computer technology in recent years, however, has made numerical simulation method based on the NS equation remarkably amenable. It is now possible to integrate the NS equation directly for the simulation of wave fields within a reasonable CPU time.

Also, there is a need for such a study in designing coastal engineering structures of the advanced type. A good example is found in the design of a submerged breakwater around which the flow is quite complicated and the mechanism and extent of scour is not fully understood. In this respect, the need to develop the simulation method of the three dimensional flow structure is quite apparent.

* Nagaoka University of Technology, 1603-1 Kamitomioka-machi, Nagaoka Niigata Japan 940-21

** Nagaoka Technical College, 888 Nishi-Katagai Nagaoka Niigata Japan 940

Kobe City Technical College, 8-3 Higashimachi, Nishiku, Kobe, Japan 651-21

The objective of this study is to develop a three dimensional simulation method of the wave and flow field around a submerged breakwater. The result will be tested with the experimental study in a laboratory wave tank. The numerical simulation method adopted in this study is the SOLA-SURF method (Hirtet al. 1975, Bulgarelli et al. 1984])

SOLA-SURF Method

Numerical schemes to integrate the NS equations can be characterized in the way to treat time development of the water surface. In the SOLA-SURF method, the kinematic condition of water surface is integrated for prediction of the position of water surface for the successive time step. Then the pressure and velocity are adjusted at the same time to satisfy the set of the governing equations, rendering this method quite effective and versatile. With this method, unfortunately, it is impossible to simulate the breaking wave. Aside for the breaking wave, SOLA-SURF method appears to be quite versatile as it directly deals with the NS equations and can be easily extended to the three dimensional wave field.

The formulation of the SOLA-SURF algorithm is given in the reference and will not be repeated here. The basic equations to be solved are three dimensional equation of continuity and Navier-Stokes equations for the incompressible, viscous fluid and these are not listed herein. In this study, the flow inside the permeable breakwater is also analyzed and the basic equations of motion in this case are linear equations of the Darcy flow given as

$$\frac{\partial \vec{v}}{\partial t} = -\varepsilon \nabla (p + gz) - \frac{\varepsilon \nu}{k} \vec{v} \tag{1}$$

$$\nabla \cdot \vec{v} = 0 \tag{2}$$

where $\vec{v}$ is the three dimensional velocity vector, t is time, ε is the porosity, k is the permeability, p is pressure, g is the gravitational acceleration, z is the elevation, and ν is the kinenamic viscosity. Incorporation of Eqs. (1) and (2) into the SOLA-SURF method is easy since these equations are simplified form of the NS equations. At the boundary of the submerged breakwater with water, continuity conditions of velocity and stress components are applied.

Experimental Condition

Laboratory experiments are carried out with a wave tank, 15m long and 0.6m wide. In this tank a model submerged breakwater is placed piling up model blocks of hexa-pod shape for the case of the permeable breakwater. Fig. 1 shows the wave tank set up of this study. The numerical calculation of this study is carried out under the same conditions as the laboratory experiment.

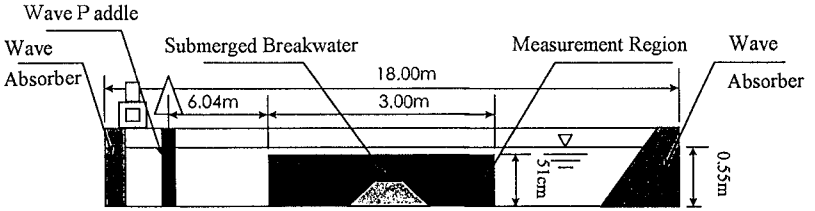

Fig. 1 Wave tank

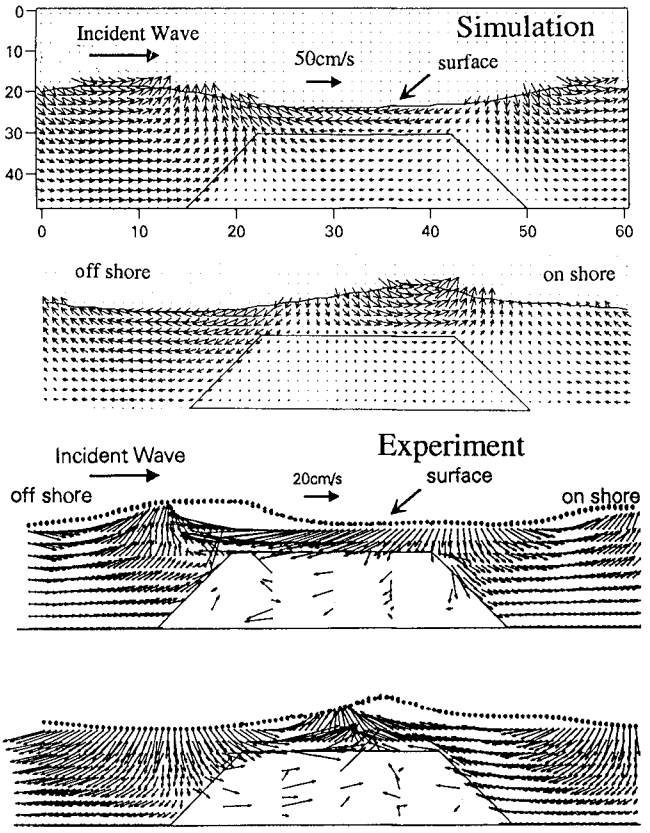

Fig. 2 Comparison of velocity vectors for 2D calculation and lab experiment

The results of the lab study is then compared with the numerical calculation usinf the SO LA-SURF method. For two dimensional study submerged breakwater is placed uniformly over the width, while for three dimensional study the breakwater is placed over the half width of the tank.

The experimental conditions are as follows: incident wave height H of 0.135m, wave period T of 0.15s and water depth h of 0.6m. In the lab experiment, detailed measurement of the velocity vectors is carried out using an electromagnetic current meter to obtain the data that can be compared with the numerical simulation.

Calculation with 2D Breakwater

In this chapter is presented the result with the two dimensional (2D) breakwater, which means that the breakwater is placed to fill the whole width of the wave tank. The objective is to investigate the flow structure around the breakwater in detail and to test the validity of the three dimensional calculation.

Flow structure around 2D breakwater: Figure 2 shows the velocity vector around the submerged breakwater. In this figure, the top two charts indicate the results of simulation with SOLA-SURF method, while the bottom two charts those for the laboratory experiments. The development of wave vector is simulated reasonably well. In the laboratory experiments, the return flow to the offshore direction is observed. This is probably related to the phase difference of wave and horizontal velocity. In the SOLA-SURF method, on the other hand, the return flow is not observed probably because the Sommerfeld's radiation condition for the onshore boundary is effective.

Side wall boundary condition for 3D calculation : Next the three dimensional SOLA-SURF calculation is performed on this 2D breakwater. Fig. 3 gives the resulting water surface elevation. In this calculation, the boundary condition at the side wall of the water tank is set at first as non-slip type, i.e. viscous, condition. It is then observed that there is a considerable gradient in the water surface along the wave ridge, a situation which is not found in the laboratory experiment. This is probably because this calculation is essentially the laminar flow calculation, whereas the flow in the wave tank is at least to some degree turbulent. Therefore, the slip (inviscid) condition for the side wall is adopted for the further calculation. The top and bottom charts of Figure 3 give the calculation result with, respectively, no-slip and slip boundary conditions.

Calculation with 3D Breakwater

To test the validity of the three dimensional SOLA-SURF calculation, it is applied to the three dimensional(3D) breakwater. The 3D breakwater occupies half width of the wave tank with the other half free of breakwater. Fig. 4a and 4b give the water surface profile and Fig. 5 and 6 give velocity vectors for both permeable and impermeable submerged

breakwaters. In these figures the submerged breakwater is placed to the left half of the wave tank looking in the direction of the wave propagation, occupying from 6.6 to 7.4m in the across-shore distance and 0.0 to 0.3m in the long-shore distance.

Figure 4 shows that the wave profile is deformed over the submerged breakwater section, with somewhat less deformation above the half width over which the breakwater is not present, showing the effect of the 3D calculation. The wave deformation around the impervious breakwater(Fig. 4a) is more remarkable than that for the permeable breakwater(Fig. 4b).

Fig. 5 and 6 give the comparison of velocity vectors at the plane 2.5cm over and 17.5cm under the top surface of the submerged breakwater, respectively. Fig. 5 indicates that the water over the breakwater flows out to the part free of breakwater, which corresponds to the phase of the water surface elevation between these two areas observed in Fig. 4. The impervious breakwater, compared to the permeable breakwater, tends to give more pronounced difference in velocity vectors. Fig. 6 shows that the flow tends to turn around the corner of the breakwater. It is also remarkable that there exists significant amount of flow inside of the permeable breakwater.

Conclusion

Itt is shown that numerical simulation of three dimensional wave field over a submerged breakwater is possible with the SOLA-SURF method. The breakwater in this case can be impervious or permeable. Simulation results are, on comparison with the laboratory experiments, qualitatively satisfactory.

Appendix-Reference

Bulgarelli, U., Casulli, V., and Greenspan, D.(1984): Pressure Methods for the Numerical Solution of Free Surface Fluid Flows, Pinerige Press Swansea U.K., pp.323.

Hirt, C.W., Nichols, B.D. and Romero,N (1975): SOLA-A Numerical Solution Algorithm for Transient Fluid Flows, Los Alamos Scientific Laboratory LA-5852, pp.1-50.

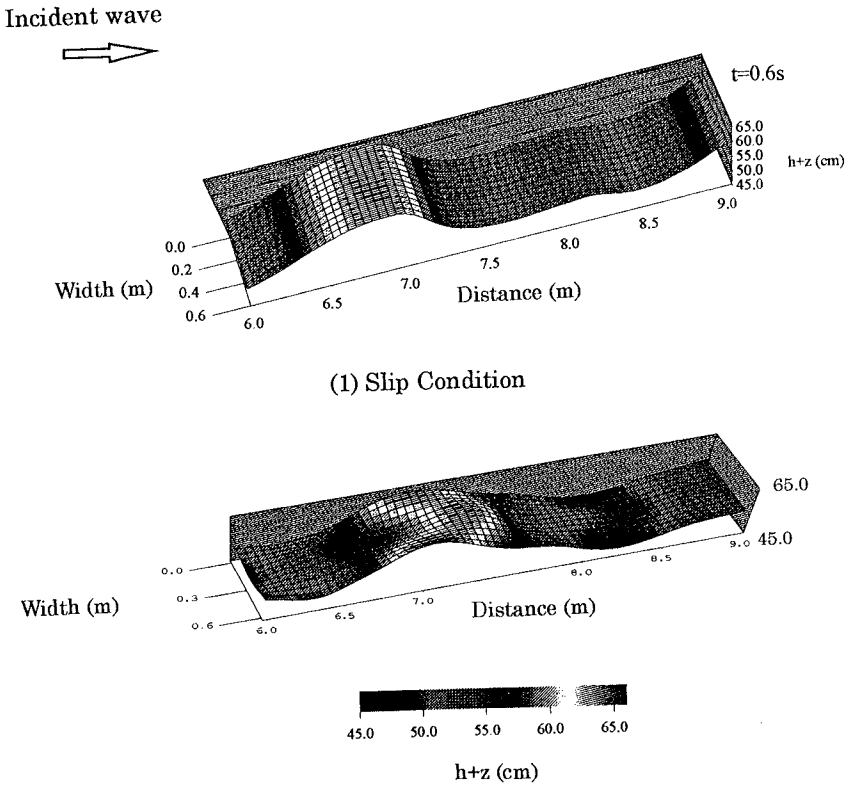

Fig. 3 Side wall Condition of the three dimensional calculation

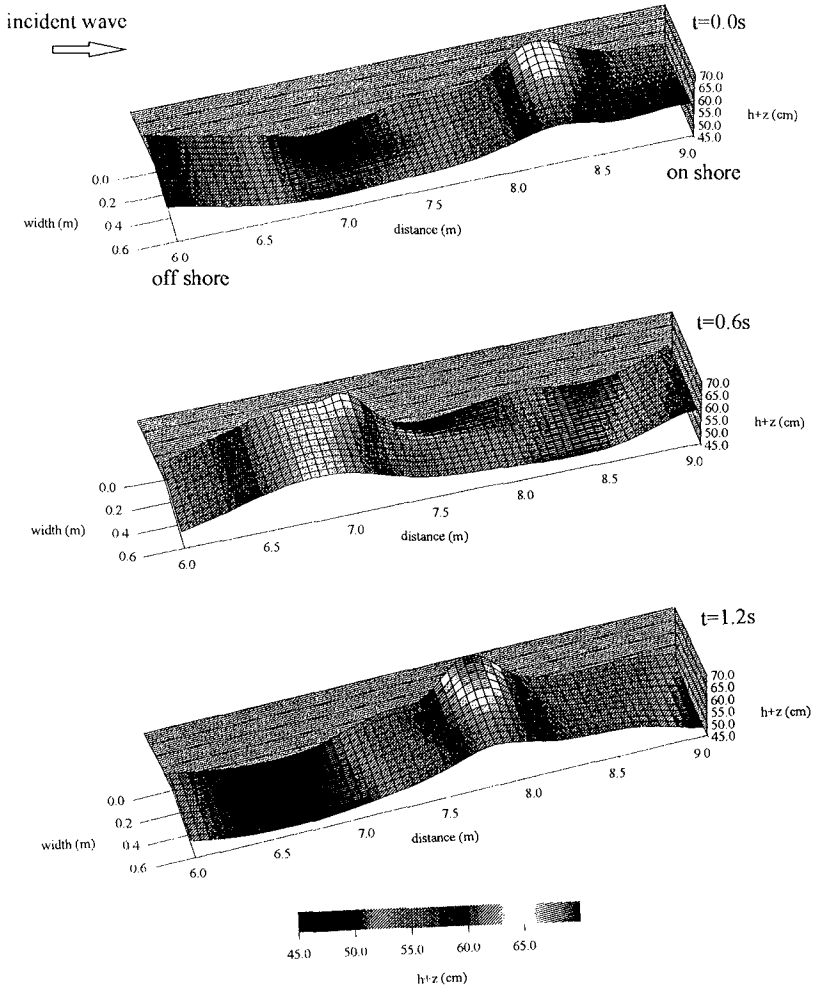

Fig. 4a Water Surface profile for 3D calculation over impervious breakwater

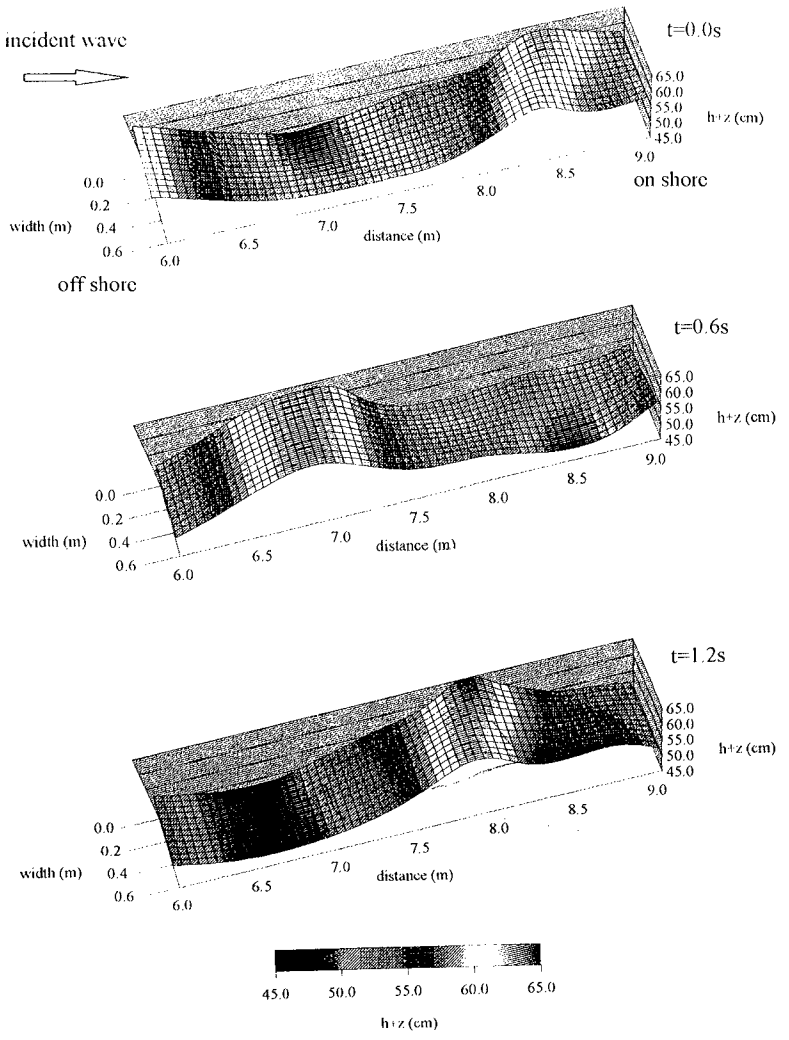

Fig. 4b Water Surface profile for 3D calculation over permeable breakwater

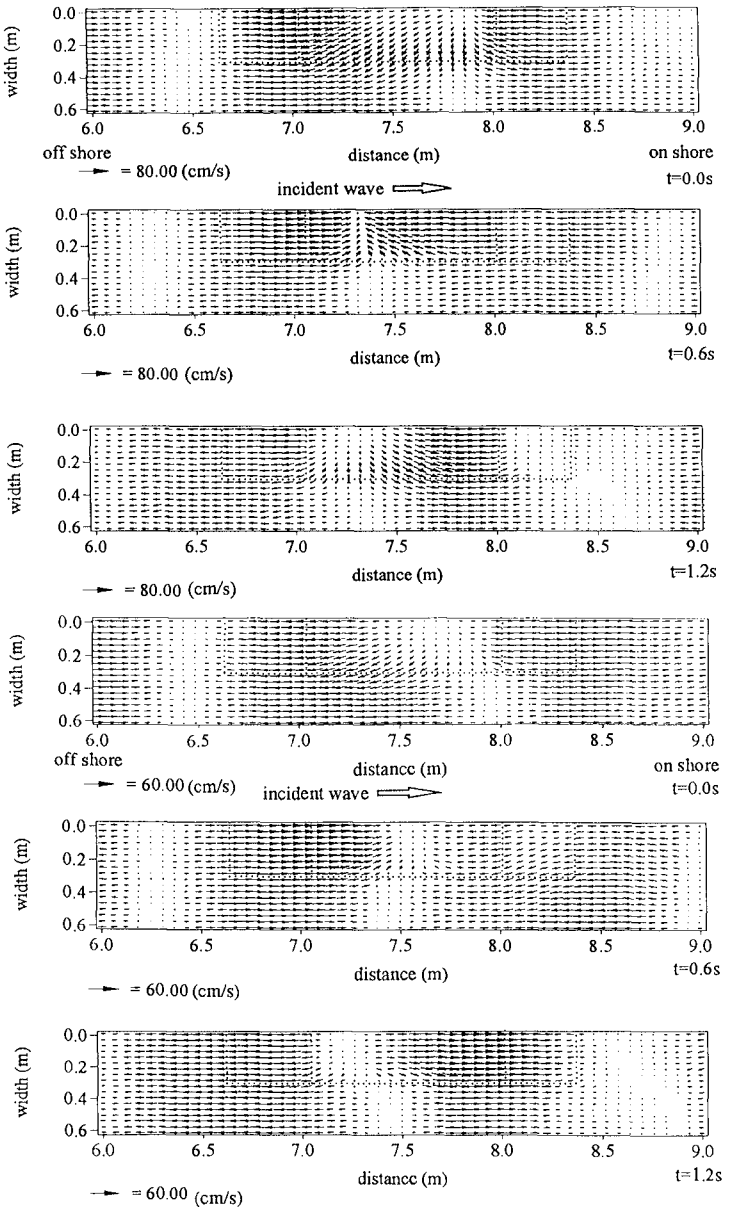

Fig. 5 Horizontal velocity vectors of 3D calculation

(Top three figures for impervious breakwater and bottom three for permeable one.)

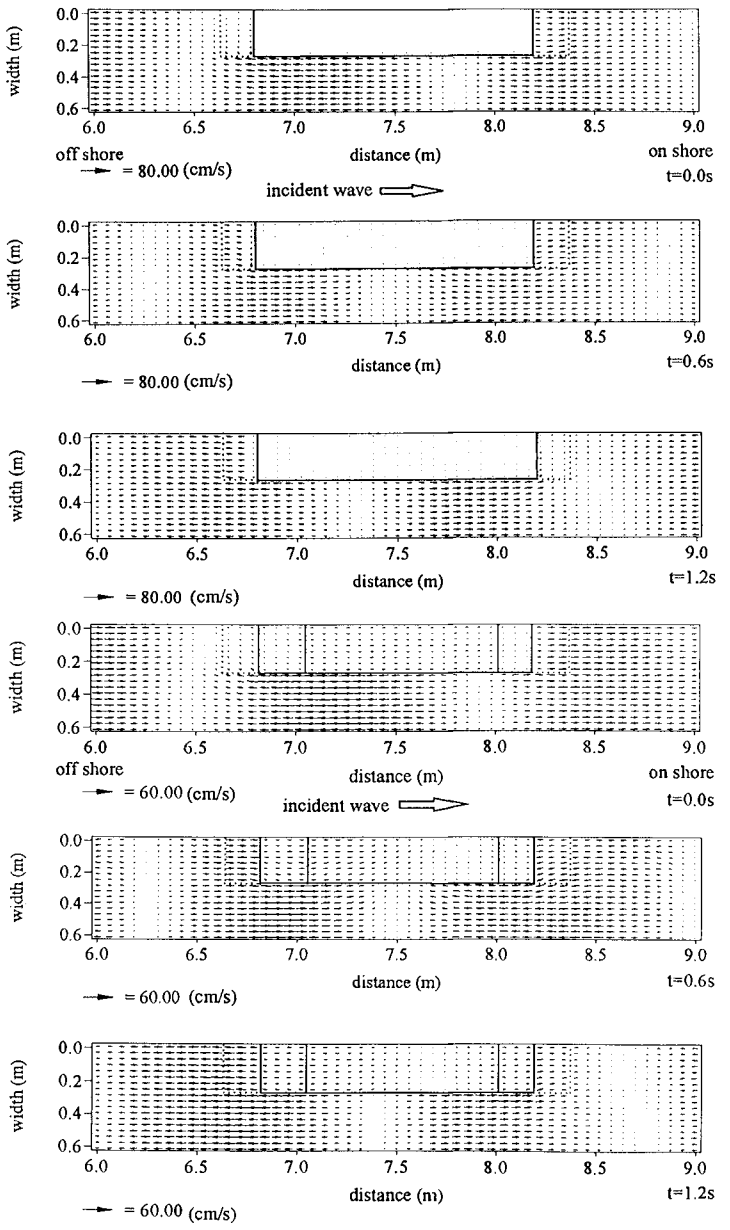

Fig. 6 Horizontal velocity vectors of 3D calculation
(Top three figures for impervious breakwater and bottom three for permeable one.)

NUMERICAL ANALYSIS OF WAVE BREAKING DUE TO SUBMERGED BREAKEWATER IN THREE-DIMENSIONAL WAVE FIELD

Koji KAWASAKI[1] and Koichiro IWATA[2]

ABSTRACT

The wave breaking and post-breaking wave deformation due to a submerged breakwater in a three-dimensional wave field have been investigated numerically and experimentally in this study. The calculated and measured results have revealed that the breaking limit and the breaker types are almost independent of the relative structure length W/L_i ($0.5 \leq W/L_i \leq 2.5$), and that the horizontal and vertical circulation flows are formed around the submerged breakwater. It is also found that the wave breaking in three-dimensional wave field is affected strongly by the wave refraction, different from the two-dimensional case. The numerical calculation method based on a SOLA-VOF method has been developed and has reproduced well laboratory experiments in case of a weak breaker such as the Spilling breaker.

INTRODUCTION

Accurate prediction and evaluation of wave breaking process due to a submerged breakwater are important in view of multi-purpose utilization of coastal sea area as well as the wave dynamics. Researches have ever been conducted to evaluate numerically and experimentally the wave breaking and its deformation due to the submerged breakwater. Most of these researches are, however, limited to a two-dimensional wave field (for examples, Petit et al., 1994 ; van Gent et al., 1994 ; Sabeur et al., 1996 ; Iwata et al., 1996).

The main purpose of this study is to discuss numerically and experimentally the wave breaking process due to a submerged breakwater in a three-

1) Research Associate, Dept. of Civil Eng., Osaka Univ., Osaka 565-0871, JAPAN
2) Professor, Dept. of Civil Eng., Nagoya Univ., Nagoya 464-8603, JAPAN

dimensional wave field. First, elaborate three-dimensional laboratory experiment was conducted to study the breaking limit, the breaker type, the breaking position and the wave deformation after breaking in the regular wave field, in relation to the relative dimensions of submerged breakwater to the waves. Next, the numerical calculation method based on the SOLA-VOF method (Hirt and Nichols, 1981) is developed to investigate the wave breaking process due to the submerged breakwater. The validity of the present method is verified by comparing with the experimental results.

LABORATORY EXPERIMENTS

Three kinds of laboratory experiments, such as Series I on the breaking limit, breaker type and breaking position, and Series II and III regarding the wave deformation and the water particle velocity field after breaking, were carried out in a three-dimensional wave basin (28m in length, 8m in width and 0.8m in depth) at Nagoya University. In the experiments, the relative width B/L_i, the relative submerged depth R/h and the relative height D/h of the submerged breakwater were fixed as B/L_i=0.3, R/h=0.4 and D/h=0.6, where B is the structure width, R the submerged depth, D the structure height, and L_i the wavelength at the still water depth h. The still water depth was kept constant at 40cm. The relative submerged breakwater length W/L_i was as-

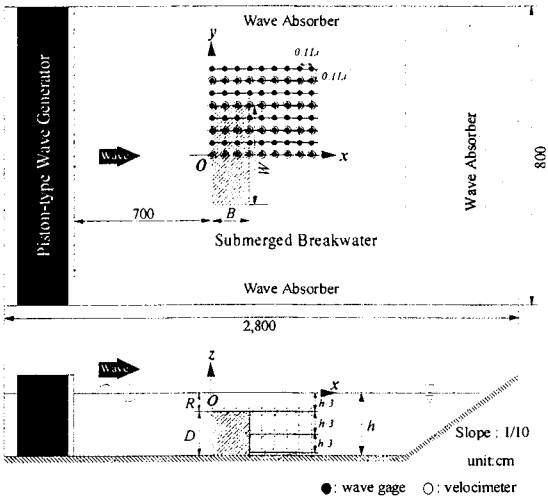

Fig. 1 Definition sketch of wave basin

signed as W/L_i=0.5, 1.0, 1.5, 2.0 and 2.5. The regular waves with different wave periods T_i=0.8, 1.2 and 1.68s were generated so as to propagate perpendicularly to the submerged breakwater. The incident wave height H_i was, in Series I, carefully changed to find out the breaking limit and the breaker types. On the other hand, H_i in Series II and III were chosen so that the following non-linearity parameter Π (Goda, 1983) was 0.08 and 0.09 for three different wave periods.

$$\Pi = \frac{H_i}{L_i} \coth^3\left(\frac{2\pi h}{L_i}\right) \tag{1}$$

Note that the above-stated conditions were selected so that the breaker type became the Spilling breaker.

For each experimental condition, the water surface profile η was measured with capacitance-type wave gages at $0.1L_i$ interval mesh points within the square region of $2.0L_i$ in x-axis and $1.5L_i$ in y-axis, as shown in Fig. 1. The horizontal water particle velocities u and v at three different depths on each mesh point were also measured with electromagnetic type velocimeters. Moreover, the wave breaking process was recorded using a video tape recorder.

NUMERICAL CALCULATION METHOD

A numerical model has been developed to study the wave breaking process due to the submerged breakwater in the three-dimensional wave field (Kawasaki, 1998). The model utilizes a SOLA-VOF method (Hirt and Nichols, 1981) as well as a non-reflective wave generator (Brorsen and Larsen, 1987). Further, an added dissipation zone is adopted to treat the open boundaries (Hinatsu, 1992).

The wave field is governed by the continuity equation (Eq.(2)) and Navier-Stokes equations (Eq.(3) $\sim$ (5)) for incompressible fluid. The free surface is treated by introducing a function F that represents the fractional volume of the cell occupied by the fluid, as in Eq.(6).

$$\frac{\partial u}{\partial x} + \frac{\partial v}{\partial y} + \frac{\partial w}{\partial z} = q = \begin{cases} q^*/\Delta x_S & \text{at } x = x_S \\ 0 & \text{at } x \neq x_S \end{cases} \tag{2}$$

$$\frac{\partial u}{\partial t} + u\frac{\partial u}{\partial x} + v\frac{\partial u}{\partial y} + w\frac{\partial u}{\partial z} = -\frac{1}{\rho}\frac{\partial p}{\partial x} + \nu\nabla^2 u \tag{3}$$

$$\frac{\partial v}{\partial t} + u\frac{\partial v}{\partial x} + v\frac{\partial v}{\partial y} + w\frac{\partial v}{\partial z} = -\frac{1}{\rho}\frac{\partial p}{\partial y} + \nu\nabla^2 v + \frac{\nu}{3}\frac{\partial q}{\partial y} \tag{4}$$

$$\frac{\partial w}{\partial t} + u\frac{\partial w}{\partial x} + v\frac{\partial w}{\partial y} + w\frac{\partial w}{\partial z} = -g - \frac{1}{\rho}\frac{\partial p}{\partial z} + \nu\nabla^2 w + \frac{\nu}{3}\frac{\partial q}{\partial z} - \gamma w \tag{5}$$

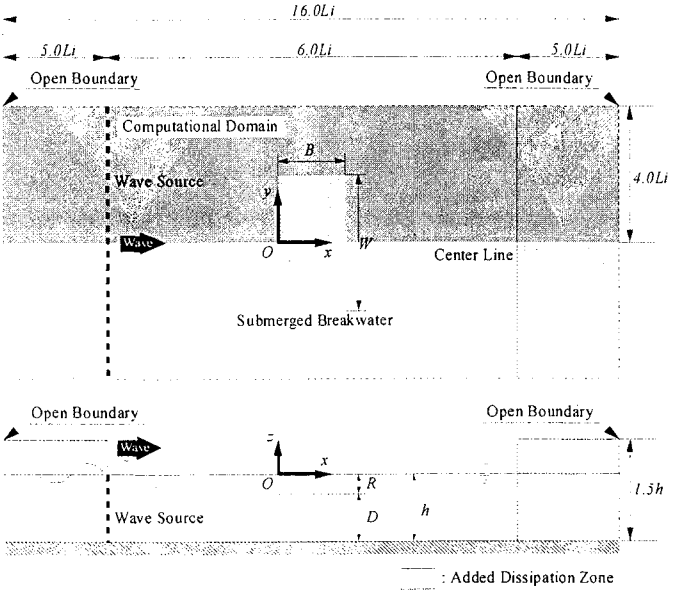

Fig. 2 Definition sketch of computational domain

$$\frac{\partial F}{\partial t}+\frac{\partial(Fu)}{\partial x}+\frac{\partial(Fv)}{\partial y}+\frac{\partial(Fw)}{\partial z}=Fq \tag{6}$$

where the Cartesian coordinate system (x,y,z) is used. u, v and w are the velocity components in respective direction of x, y and z. q is the wave generation source with its strength $q^*/\Delta x_S$ only assigned at source line $(x=x_S)$, in which q^* is twice horizontal velocity component of the generated wave (the third-order Stokes wave in this study), and Δx_S is the mesh size in x-direction at $x=x_S$. t is the time, p the pressure, ρ the fluid density, ν the kinematic viscosity, g the gravitational acceleration, and $\nabla=(\partial/\partial x,\partial/\partial y,\partial/\partial z)$. γ is the positive wave dissipation factor and equals 0 except for the added dissipation zone.

As shown in Fig. 2, the computational domain (shaded portion) is the half side of total region because it was confirmed from laboratory experiments that the wave breaking phenomenon was almost symmetrical for the center line of the submerged breakwater. The computational domain is $16.0L_i\times4.0L_i\times1.5h$ in the respective directions of x, y and z. The positive x-direction is onshoreward. The vertical z-axis is taken positive upward with its origin being on the still water level. The mesh sizes Δx, Δy and Δz are

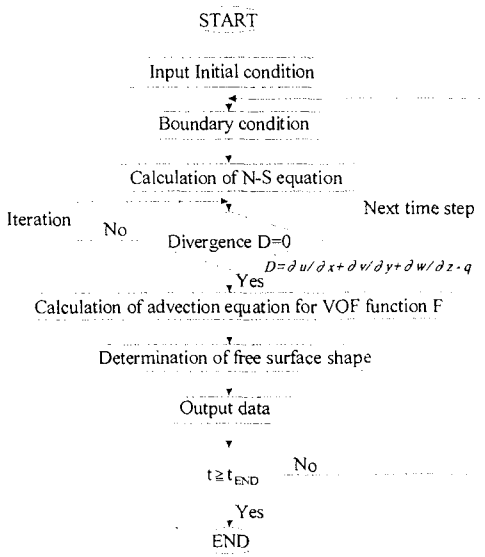

Fig. 3 Flow chart of numerical calculation

$1/50L_i$, $1/50L_i$ and $1/40h$ in respective directions of x, y and z. The time interval Δt is kept constant at 0.001s so as to satisfy the Courant condition at every time step.

The flow chart of the present numerical scheme is shown in Fig. 3. The Navier-Stokes equations (Eqs.(3) $\sim$ (5)) are used to calculate the first approximation of the velocities at the next time step. However, the calculated velocities do not satisfy, in general, the continuity equation Eq.(2). Therefore, to satisfy the continuity equation completely, the velocities and the pressure are repeatedly adjusted. Next, using the thus obtained velocities, the behavior of the free-surface is evaluated by calculating the advection equation Eq.(6).

Stable numerical computation is carried out by repeating the above-mentioned procedures under suitable boundary conditions at each time step.

RESULTS AND DISCUSSIONS

(a) Breaking Limit, Breaker Types and Breaking Position

Figure 4(a) and (b) illustrate the critical relative wave height for the wave breaking $(H_i/L_i)_c$ or $(H_i/R)_c$ in relation to the relative structure length W/L_i, in which W/L_i=∞ means the two-dimensional experimental results

(Iwata et al., 1996). The breaking limit Eq.(7) at the constant depth derived by Miche (1944) is also shown for comparison. In this study, the wave breaking is defined as the instance when the wave front became vertical.

$$\left(\frac{H_i}{L_i}\right)_c = 0.142 \tanh\left(\frac{2\pi h}{L_i}\right) \tag{7}$$

The wave breaking first occurs, in general, at both side edges of the submerged breakwater and then spreads, with wave propagation, to the onshore center line of the structure. As shown in Fig. 4(a) and (b), W/L_i little effects the breaking limit under $1.0 \leq W/L_i \leq 2.5$. According to Fig. 4(b), the critical relative wave height $(H_i/R)_c$ is 0.35 for h/L_i=0.2 and 0.41 for h/L_i=0.4, which are smaller than their respective two-dimensional values (W/L_i=∞) ; $(H_i/R)_c \cong 0.39$ for h/L_i=0.2 and $(H_i/R)_c \cong 0.49$ for h/L_i=0.4. In other words, the wave in three-dimensional wave field is likely to break under smaller incident wave height than the case of two-dimensional field. This is thought to be largely attributed to the wave refraction by the abrupt change of water

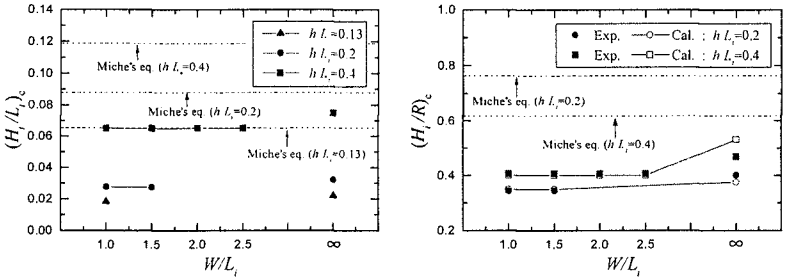

(a) Relation of $(H_i/L_i)_c$ and W/L_i (b) Relation of $(H_i/R)_c$ and W/L_i

Fig. 4 Breaking limit

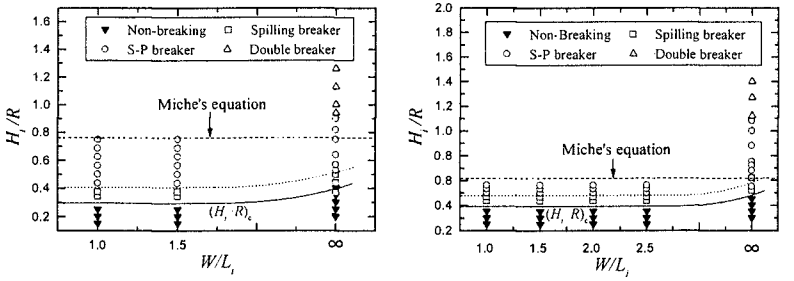

(a) h/L_i=0.2 (b) h/L_i=0.4

Fig. 5 Breaker types

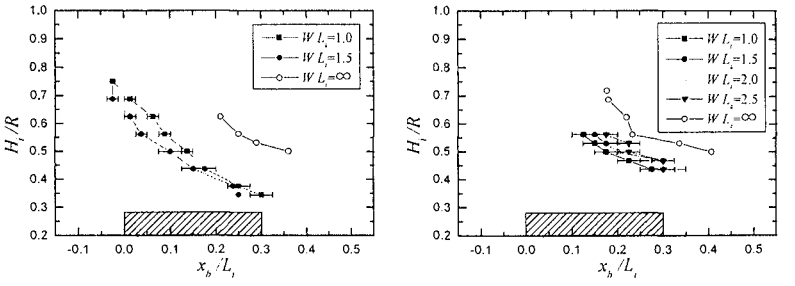

(a) h/L_i=0.2 (b) h/L_i=0.4

Fig. 6 Breaking Position

depth. Figure 4(b) also indicates that the breaking limit calculated with the present numerical calculation method coincides with experimental values.

Laboratory experiments reveal, as shown in Fig. 5, that the breaker types are classified into Spilling breaker (□), S-P breaker which means an intermediate type between Spilling and Plunging breakers (○), and Double breaker (△). The Double breaker is defined as twice breaking in front of and above the structure due to the wave-induced return flow (Katano et al., 1992). It is also found out from Fig. 5 that regardless of W/L_i, the breaker type changes from Spilling to S-P breaker with an increment of H_i/R under $0.5 \leq W/L_i \leq 2.5$. The occurrence range of each breaker type can be graphically given in Fig. 5(a) and (b). This would show that the magnitude of the wave-submerged breakwater interaction becomes smaller with an increment of h/L_i.

Figure 6 shows the relationship between x_b/L_i and H_i/R with parameter of W/L_i in case of h/L_i=0.2 and 0.4, where x_b is the distance from the front face of the submerged breakwater to the breaking point. Regardless of W/L_i, the breaking point shifts to the offshore side with an increase of H_i/R. In Fig. 6(a), x_b/L_i=-0.05 is attained for $H_i/R \geq 0.7$ because of forming the partial standing wave. Moreover, the breaking point in the three-dimensional case shifts to the offshore side as compared with the two-dimensional case.

(b) Wave Deformation

Figure 7 indicates one example of the wave height distribution, in which the breaker type is a weak Spilling breaker. The wave height above the submerged breakwater becomes larger than the incident wave height ($H/H_i \geq 1.0$), especially the wave height at the side edge of the submerged breakwater (y/L_i=0.3) is much larger.

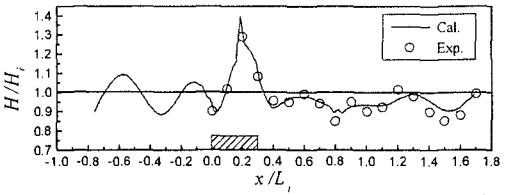

(a) Along the breakwater side edge (y/L_i=0.3)

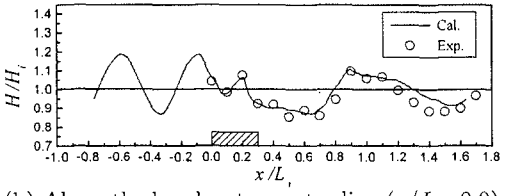

(b) Along the breakwater center line (y/L_i=0.0)

Fig. 7 Comparison of wave height variation between computation and laboratory experiment (H_i/L_i=0.05, h/L_i=0.2, W/L_i=1.0)

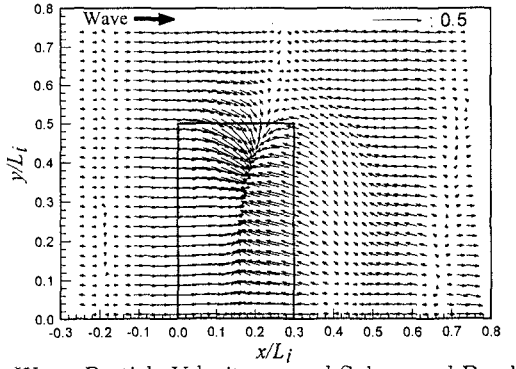

Fig. 8 Water Particle Velocity around Submerged Breakwater (h/L_i=0.2, H_i/L_i=0.05, W/L_i=1.0 ; z/h=-0.15, t/T_i=7.0)

The reason of this can be explained from Fig. 8, which shows the water particle velocity at z/h=-0.15 when the free-surface at the side edge of the structure becomes extremely large. According to this figure, the direction of the velocity is converged near the side edge of the structure due to the wave refraction by an abrupt change of the water depth. Therefore, as already mentioned, it can be thought that the wave height at the side edge of the submerged breakwater becomes extremely large mainly by the effect of the

wave refraction.

As shown in Figs. 7 and 9, the water surface profiles as well as the wave height before and after wave breaking, computed with the present numerical calculation method, are in good agreement with those of the laboratory experiments. In addition, as shown in Fig. 10 (the case of a weak Spilling breaker), the computed water particle velocities agree well with the experimental values. Therefore, the present numerical calculation method can evaluate well the breaking wave deformation in case of the Spilling breaker.

The calculation results, as demonstrated in Fig. 11, reveals that the diffracted wave is generated around the structure and that the partial standing wave is formed in front of the structure. It is also found that the relative structure length W/L_i affects the wave height above the structure.

(c) Wave Spectra

Figure 12 shows the spatial distribution of the non-dimensional wave height spectrum $2A(f)/H_i$, where $A(f)$ is the amplitude spectrum and f is the wave frequency. It is obvious that the decreasing region of the fundamental harmonic component coincides with the increasing region of the second harmonic component. This would indicate the shift of the wave energy of the fundamental harmonic component to that of the second harmonic component. The fundamental harmonic component increases again in the range of the non-breaking reformed wave (roughly $x/L_i \geq 1.0$), while the second harmonic component is decaying with wave propagation. The amplitude variation of the second harmonic component is seen to be periodic at the onshore side of the structure. Therefore, similar to Massel's results (1983) for non-breaking waves in two-dimensional wave field, it can be judged that the free second harmonic component wave is generated even under the condition of wave breaking.

(d) Mean Velocity Field

Figure 13 shows the numerical and experimental results for the mean velocity field around the submerged breakwater. It is recognized from Fig. 13(i) and (ii) that there is the strong mean onshore velocity near the free-surface at onshore side of the submerged breakwater. This is due to the wave breaking above the submerged breakwater. The mean offshore velocity, i.e. the return flow is also found to be caused near both the side of the structure ($0.5 \leq y/L_i \leq 1.0$) and the bottom. Thus, it is clear that the return flow takes place to compensate the onshore mass transport around the still water level caused by wave breaking. Judging from the above-stated, it can be said that

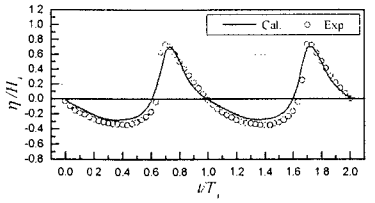

(a) On the crown
(x/L_i=0.2, y/L_i=0.0)

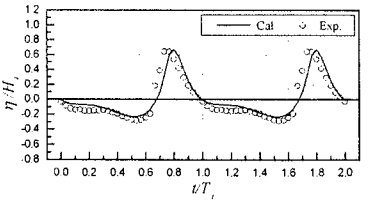

(b) On the crown
(x/L_i=0.3, y/L_i=0.0)

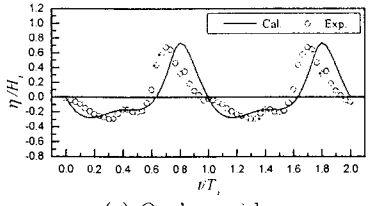

(c) Onshore side
(x/L_i=0.6, y/L_i=0.1)

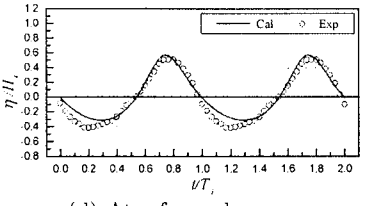

(d) At reformed range
(x/L_i=1.1, y/L_i=0.3)

Fig. 9 Time history of the water surface profile
(H_i/L_i=0.05, h/L_i=0.2, W/L_i=1.0)

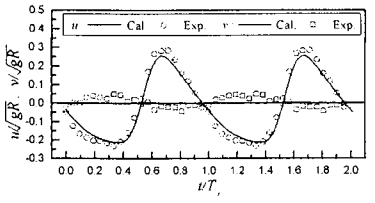

(a) On the crown
(x/L_i=0.1, y/L_i=0.0)

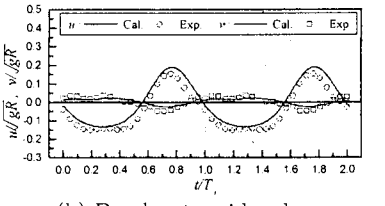

(b) Breakwater side edge
(x/L_i=0.3, y/L_i=0.6)

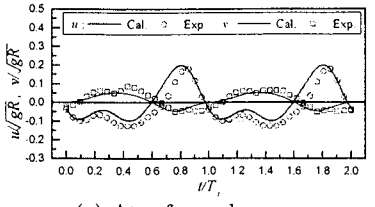

(c) At reformed range
(x/L_i=0.5, y/L_i=0.4)

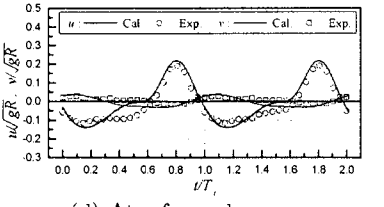

(d) At reformed range
(x/L_i=0.8, y/L_i=0.02)

Fig. 10 Time histories of the water particle velocities
(H_i/L_i=0.029, h/L_i=0.13, W/L_i=1.0 ; z/h=-0.3)

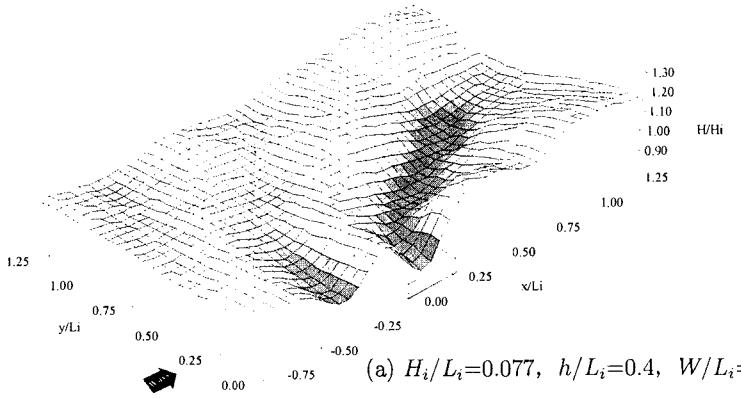

(a) H_i/L_i=0.077, h/L_i=0.4, W/L_i=0.5

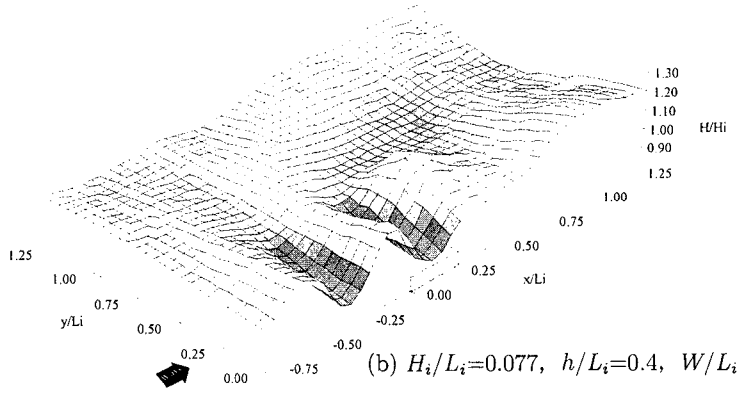

(b) H_i/L_i=0.077, h/L_i=0.4, W/L_i=1.0

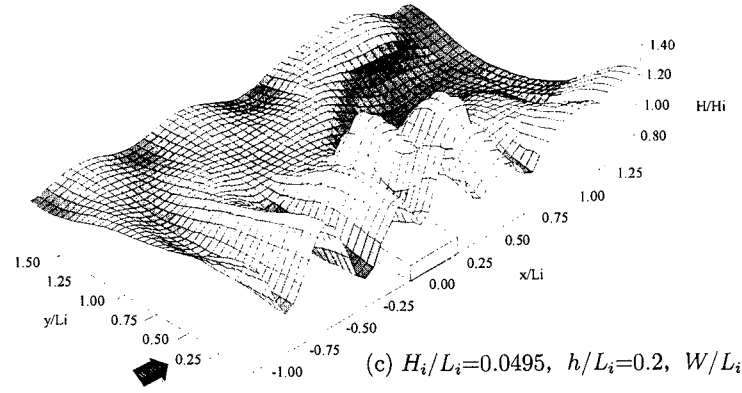

(c) H_i/L_i=0.0495, h/L_i=0.2, W/L_i=1.5

Fig. 11 Spatial distribution of computed wave height around structure

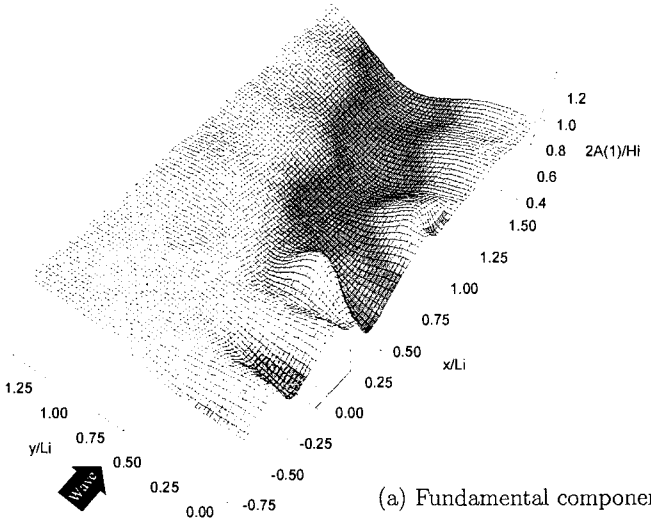

(a) Fundamental component

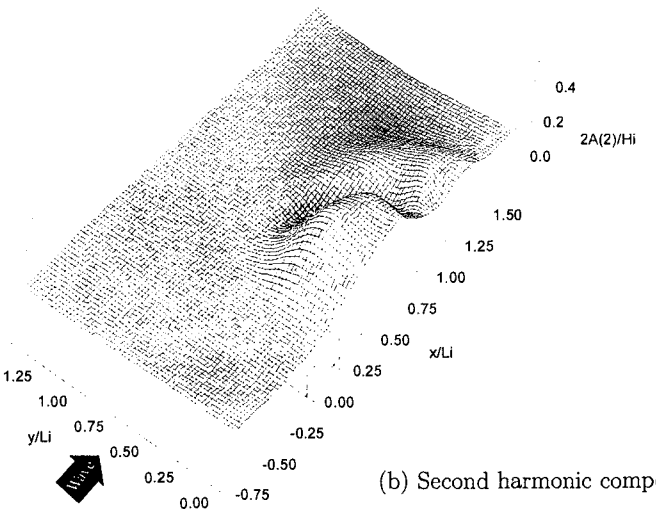

(b) Second harmonic component

Fig. 12 Computed spatial distribution of Fourier component wave amplitude (h/L_i=0.2, H_i/L_i=0.05, W/L_i=1.0)

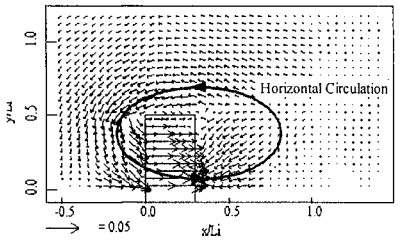

(a) z/h=-0.3

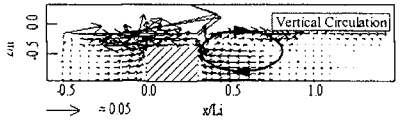

(b) y/L_i=0.0

(i) Numerical Results

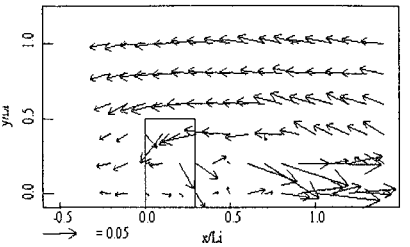

(a) z/h=-0.3

(ii) Experimantal Results

Fig. 13 Mean Velocity Field around Submerged Breakwater (h/L_i=0.2, H_i/L_i=0.055, W/L_i=1.0)

two circulation flows, that is, the horizontal and vertical circulation flows are formed around the submerged breakwater.

CONCLUSIONS

Main conclusions in this study are summarized as follows:

1) The breaking limit and the breaker types are almost independent of the relative structure length W/L_i in the range of $0.5 \leq W/L_i \leq 2.5$.
2) The breaker type changes from Spilling to an intermediate breaker between Spilling and Plunging breakers (S-P breaker) with an increment of the relative incident wave height H_i/R.
3) The breaking position shifts to the offshore side as H_i/R becomes larger.
4) The free second harmonic component wave is possibly generated from the edge side of the submerged breakwater.
5) The horizontal and vertical circulation flows are formed around the submerged breakwater.
6) The present numerical calculation model with the SOLA-VOF method has been found to evaluate well the wave deformation before and after breaking in case of weak breakers like the Spilling breaker.

REFERENCES

Brorsen, M. and Larsen, J.(1987). "Source generation of nonlinear gravity waves with boundary integral equation method", *Coastal Eng.*, Vol. 11, pp. 93–113.

Goda, Y.(1983). "Description of wave nonlinearity with a unified parameter", *Proc. 30th Japanese Conf. on Coastal Eng.*, pp.39–43 (in Japanese).

Hinatsu, M.(1992). "Numerical simulation of unsteady viscous nonlinear waves using moving grid system fitted on a free surface", *J. Kansai Soc. Naval Architects Japan*, No.217, pp.1–11.

Hirt, C.W. and Nichols, B.D.(1981). "Volume of Fluid (VOF) method for the dynamics of free boundaries", *J. Comp. Phys.*, Vol. 39, pp.201–225.

Iwata, K., K. Kawasaki and D.-S. Kim(1996). "Breaking limit, breaking and post-breaking wave deformation due to submerged structures", *Proc. of 25th ICCE, ASCE*, Vol.2, pp.2338-2351.

Katano, A., S. Murakami and M. Hattori(1992). "Relevant parameters representing energy dissipation due to submerged breakwaters", *Proc. Coastal Eng., JSCE*, Vol. 39, pp. 646–650 (in Japanese).

Kawasaki, K.(1998). "Fundamental study on wave breaking and post-breaking deformation due to submerged structure", *Dissertation, Nagoya University*, 186p (in Japanese).

Massel, S.R.(1983). "Harmonic generation by waves propagating over a submerged step", *Coastal Eng.*, Vol. 7, pp.357–380.

Miche, A.(1944). "Mouvements ondulatories de la mer en profendeur constante ou decroissante, forme limit de la houle lors de som déferlement", *Application aux digues maritimes, Ann. Ponts et Chausees*, Tome 114 (in French).

Petit, H.A.H., P. Tönjes, M.R.A. van Gent and P. van den Bosch(1994). "Numerical simulation and validation of plunging breakers using a 2D Navier-Stokes model", *Proc. 24th ICCE, ASCE*, Vol.1, pp.511–524.

Sabeur, Z.A., N.W.H. Allsop, R.G. Beale and J.M. Dennis(1996). "Wave dynamics at coastal structures : Development of a numerical model for free surface flow", *Proc. 25th ICCE, ASCE*, Vol.1, pp.389–402.

van Gent, M.R.A., Tönjes, H.A.H. and van den Bosch, P.(1994). "Wave action on and in permeable structure", *Proc. 24th ICCE, ASCE*, Vol. 2, pp.1739–1753.

CLASSIFICATION OF WAVE LOADING ON MONOLITHIC COASTAL STRUCTURES

Andreas Kortenhaus[1], Hocine Oumeraci[2]

Abstract

The paper uses the 'parameter map' which has been developed under PROVERBS (Probabilistic Design Tools for Vertical Breakwaters) in the frame of the ongoing MAST III programme of the European Union (EU contract no. MAS3-CT95-0041) to classify the wave loading on monolithic coastal structures and to identify the conditions leading to wave impacts. Data from four different hydraulic model tests have been used to verify and extend the parameter map. As a result an updated version is proposed for further design purposes.

1. Introduction

Waves approaching the shoreline from the open sea are transformed by various processes like shoaling, diffraction and refraction before they eventually break on the sloped foreshore. In conjunction with any coastal structure at the shoreline wave breaking is more complex to estimate and various methods have been developed to account for this phenomenon.

One of the most recent studies on this topic is conducted by a multinational European research group under the MAST III programme of the European Union within the PROVERBS project ('Probabilistic Design Tools for Vertical Breakwaters'). Within PROVERBS a parametric decision map has been developed to provide an easy-to-use guidance for the breaker type to be expected in front of vertical structures as a function of various geometric and wave parameters (*Allsop et al., 1996*; *Oumeraci, 1997*).

[1] Dipl.-Ing., Research Assistant, Leichtweiß-Institut, TU Braunschweig, Beethovenstr. 51a, 38106 Braunschweig, Germany, e-mail: a.kortenhaus@tu-bs.de

[2] Prof. Dr.-Ing., University Professor, Managing Director of Leichtweiß-Institut, TU Braunschweig

This parameter map (Fig. 1) has been cross-checked against various structures and parameter variations but is still under further development. More work is needed to fill the gaps and add possible modifications of parameters. A contributions into this direction was made by *Kortenhaus and Oumeraci (1997)* who summarized small- and large-scale model tests and gave some advice on the use of slightly varied parameters and parameter ranges.

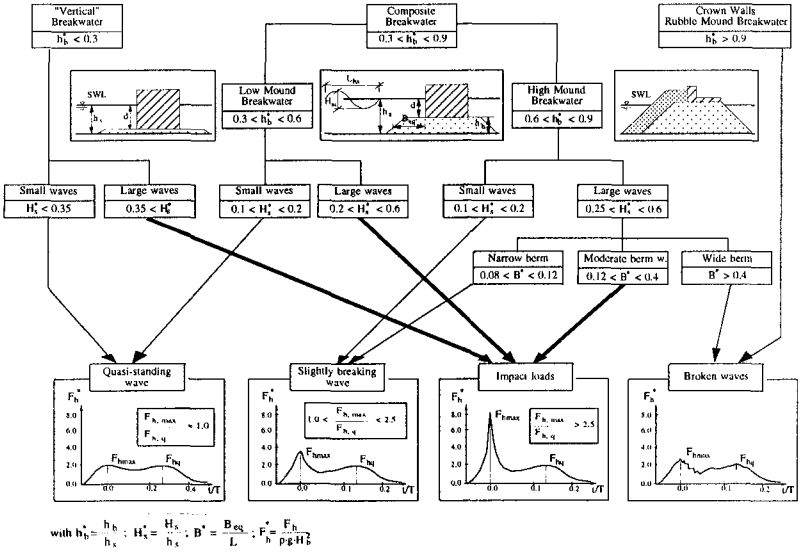

Figure 1. Parameter Map of PROVERBS (*Oumeraci, 1997*)

Very little information within the parameter map is yet available for composite type breakwaters with a very high mound. The aim of this paper is to feed and extend the aforementioned map with more detailed information obtained from large-scale model tests on innovative high mound composite breakwaters (HMCB) performed in the Large Wave Flume (GWK) of Hannover, Germany.

2. The Parameter Map Concept

The parameter map is a simple, easy-to-use map to identify wave loading on monolithic coastal structures. In the following some parameters and notations are defined. Furthermore, the input of the map (structure types) and the output (breaker types) are described in more detail.

(a) Governing Parameter

All parameters related to the various structure types are defined in Fig. 2. Three dimensionless parameters are needed to use the map and identify the breaker type at the structure. The occurrence or non-occurrence of impact breakers at the wall can be predicted by these parameters at the following three decision levels:

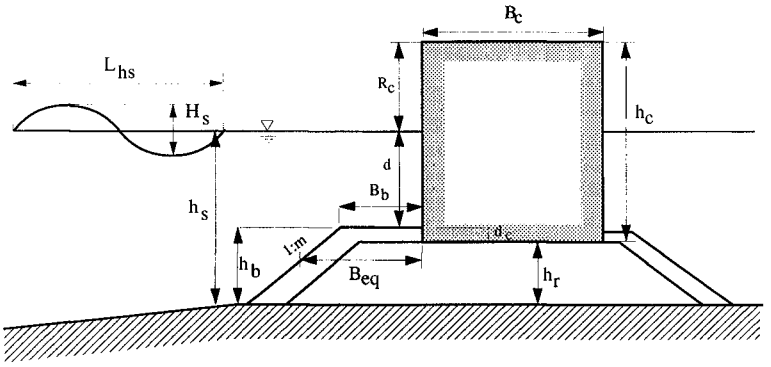

Figure 2. Definitions of Parameters

1. *Relative berm height* $h_b^* = h_b/h_s$: h_b is the height of the berm and h_s is the water depth at the toe of the rubble foundation; h_b^* represents the most important input parameter for the depth limited wave breaking in front of the breakwater, but also defines the type of structure (vertical breakwater, low or high mound breakwater, crown wall).
2. *Relative wave height* $H_s^* = H_s/h_s$: H_s is the significant wave height at the toe of the rubble foundation. H_s^* was found to be decisive for wave breaking where waves with small H_s^* do not break whereas higher waves could break at the structure thus inducing extreme impact pressures and forces. If H_s^* exceeds a certain maximum value (for details see *Muttray et al., 1998*) the wave breaks on the berm and only broken waves will reach the structure.
3. *Relative berm width* $B_{eq}^* = B_{eq}/L_{hs}$: B_{eq} is the equivalent berm width in front of the structure which is defined as $B_{eq} = B_b + (0.5 \cdot h_b \cdot m)$. The wave length L_{hs} is the local wave length in the water depth h_s determined by the peak period of the waves. B_{eq}^* describes the effect of the berm width on the occurrence of the impact loading.

(b) Main Structure Types

Principally, four types of breakwaters can be distinguished. These types can be characterised by h_b^*, together with the most typical type of waves in front of these walls.

Vertical Wall Breakwater (VWB): this type is characterised by a very low bedding layer without any mound. The relative berm height h_b^* varies from 0.0 to 0.3. There is almost no wave breaking in front of these vertical breakwaters but mostly standing or slightly breaking waves occur. Under extreme wave height conditions wave may break at the wall (wave - wave interaction).

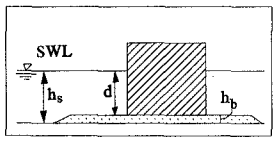

Low and High Mound Breakwaters (LMB and HMB): they consist of a rubble mound layer of various thickness and a caisson structure sitting on top of this mound. The relative berm height h_b^* varies from 0.3 to 0.9. Low mound breakwater (LMB, $h_b^* = 0.3 \div 0.6$) and high mound breakwater (HMB, $h_b^* = 0.6 \div 0.9$) can be distinguished. This type of breakwater can cause severe breaking at the wall and high loads at the structure.

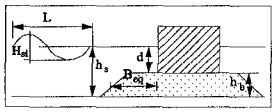

High Mound Composite Breakwater (HMCB): a new type of composite type breakwater developed at PHRI, Japan with a very high rubble foundation and a smaller superstructure than standard vertical breakwaters is characterized by $h_b^* \approx 0.9 \div 1.0$. Depending on the water level at the structure only breaking waves or already broken waves can be observed at the structure, i.e. it represents a transition between a caisson breakwater and a crown wall of a rubble mound breakwater.

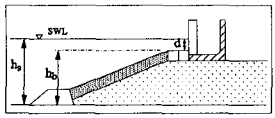

Crown walls (CW): crown walls are located on top of a rubble mound layer and usually the water level is below the berm so that generally $h_b^* > 1$. Most crown walls are designed for broken waves only.

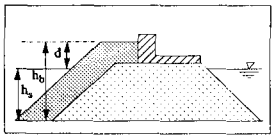

(c) Main Breaker Types

From the parameter map four different breaker types may be distinguished. These types are classified by typical force time series showing their characteristics (*Oumeraci and Kortenhaus, 1997*).

Quasi-standing waves in front of vertical structures can be observed for smaller wave heights so that the incident waves are more or less fully reflected by the wall and do not break. The typical force history does not show significant peaks but alters slowly over time (quasi-static force).

Slightly breaking waves occur when the wave height is slightly increased and the waves start to break in front of a breakwater. Sometimes this breaking occurs at the wall, thus inducing a first peak in the force time series which is higher than the second (quasi-static) peak.

Wave impacts generally occur when the berm in front of the structure induces a breaker with the breaking point just in front of the wall. Many different types of impact breakers were already described (*Oumeraci and Kortenhaus, 1997*)

but they are very difficult to be classified only by means of wave and geometric parameters. Therefore, the parameter map does not give any detail on the type of breaker or on the frequency of its occurrence. In all cases the force history shows a clear and high first peak which is significantly higher than the second 'quasi-static' peak.

If the breaking point is far enough in front of the wall (e.g. in case of a wide berm or extremely shallow water in front of the structure) only a *broken wave* will reach the structure. In this case a force history is obtained which is generally superimposed by high frequency oscillations due to a large air content in the water. The order of magnitude of the forces is the same as for slightly breaking waves.

3. Experimental Setup

In a joint research project between Port and Harbour Research Institute (PHRI), Japan and Leichtweiß-Institut (LWI), Germany the wave load and hydraulic performance and the loading of an innovative high mound composite type breakwater have been investigated.

Figure 3. Front View of Model Breakwater With Vertical Wall in the GWK

The most important dimensions, locations of measurement devices, information about the test setup and results of these tests can be found in *Muttray et al. (1998)*. A slit-type breakwater and a solid wall breakwater on a very high mound have been tested. Within this study results of the solid wall breakwater have been used only (acronym: CERI) to assure comparison with other data sets on vertical breakwaters.

Fig. 3 shows the front view of the model breakwater in the Large Wave Flume (GWK) where the foreshore, the rubble foundation and the caisson structure can easily be identified. The rubble foundation consists of rock of 0.5 to 5.0 kgs with an armour layer of 40 kg Accropodes. The caisson structure is made of reinforced concrete with a solid wall and a slit-type wall (pillars).

Three more data sets on composite type breakwaters have been used in this paper. These additional data sets were taken from the following large-scale and small-scale investigations performed at various institutes in the U.K. and Germany:

Random waves have been used on a composite type breakwater in a small-scale 2D flume at HR Wallingford. Various modifications of rubble mound geometry have been tested representing the most comprehensive data set (more than 200 tests) to support the parameter map (acronym: HR). These tests have been described in more detail in *Allsop et al. (1996)*.

Regular and random waves have been tested in large-scale model tests performed in 1993 and 1994 in the Large Wave Flume of the 'Coastal Research Center', a joint institution of the University of Hannover and the Technical University of Braunschweig, Germany. Due to the large scale only one geometry has been tested but water level and wave parameters were varied extensively thus resulting in about 80 tests with random waves and 60 tests with regular waves (acronym: GWK). For more details on test setup see *Kortenhaus and Oumeraci (1997)*.

Regular and random waves have also been used for small-scale model tests performed at the Franzius-Institute of University of Hannover, Germany in 1993 (*Oumeraci et al., 1995*). About 80 tests with regular waves and 120 tests with wave spectra have been conducted which were all used for feeding the parameter map (acronym: WKS).

The type of waves and the range of relative parameters for all tests are summarized in Tab. 1.

Tab. 1: Overview of Data Sets Used for Analysis

Acronym	Waves	$h_b^* = h_b/h_s$	$H_s^* = H_s/h_s$	$B_{eq}^* = B_{eq}/L_{hs}$
CERI	R, S	0.75 - 1.00	0.17 - 0.49	0.03 - 0.07
HR	S	0.43 - 1.00	0.21 - 0.53	0.09 - 0.33
GWK	R, S	0.46 - 0.63	0.12 - 0.56	0.11 - 0.30
WKS	R, S	0.57 - 0.79	0.11 - 0.46	0.18 - 0.54

R = Regular waves, S = Spectra (random waves)

4. Classification of Breaker Types

The breaker types classified in section 2 are sometimes very difficult to distinguish from the force or pressure time series they induce at the wall. Therefore, a procedure had to be found to identify these breakers by means of both video observation and analysis of force histories.

In Fig. 4 a slightly breaking wave is shown when it breaks at the wall. Fig. 5 shows a wave breaking in a reasonable distance before reaching the wall so that this may be classified as 'broken wave' whereas Fig. 6 shows a wave breaking directly at the structure thus inducing high pressure and force peaks. From photos like this and video frames of all of the tests an identification of the respective breaker type was performed. However, it has been found from the analysis that the procedure to classify the breaker types is different for regular and random waves. This will be described in more detail in the following sections.

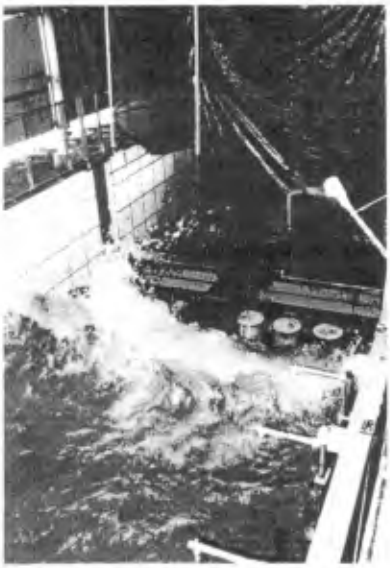

Figure 4. Slightly Breaking Wave

Figure 5. Already Broken Wave

Figure 6. Impact Breaker

(a) Regular Waves

Regular waves are generally easier to handle than random waves as they generate regular signals at wave gauges and pressure transducers given that a wave absorber is available behind the structure and the wave reflection control at the wave paddle works properly. In this case, these waves can easily be characterised by mean values of pressures and forces and only one breaker type exists.

As already mentioned the distinction of breaker types could be very difficult from force histories only, particularly, if complex berm geometries are involved as this is the case for high mound breakwaters. It is therefore strongly recommended (i) to use video analysis of the tests for distinction of breaker types and (ii) to use available time series of pressures (preferably in the vicinity of the still water level) or horizontal forces to check the breaker type identification. The latter step is required because very often it cannot be observed from the video whether a wave breaks as a slightly breaking wave or as an impact breaker. This, however, can easily be identified by the force or pressure signal showing a clear sharp peak in the case of an impact breaker.

(b) Random Waves

(i) Flow Chart Procedure

For random waves it is not practicable to identify each single wave in a wave test by means of video analysis. Furthermore, each breaker type may occur in a single test. The main goal, however, is to identify a characteristic breaker type for each of the tests performed. Therefore, a different approach is needed which may be summarized as follows:

In Fig. 7 the analysis starts with a time series analysis of the random wave test. From this the occurrence probability of impact breakers P_{Fh} can be obtained which is described in more detail within the next section. If P_{Fh} is higher than 5% of all waves in the test, it is assumed to be sufficiently large to design the breakwater for impact breakers. If this is not the case, videos from the test are needed to identify the prevailing characteristics of the waves in the individual test. This allows for a fast video analysis so that a minimum of time is needed.

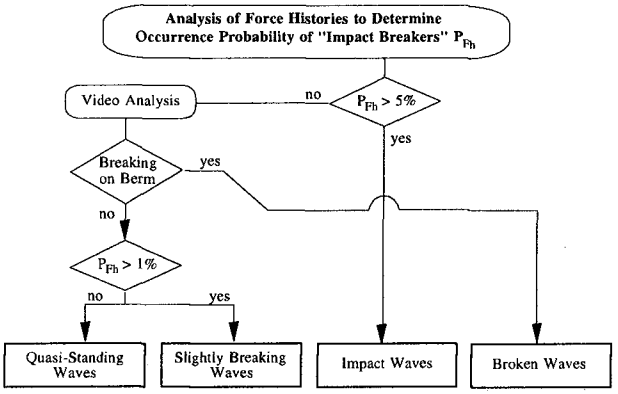

Figure 7. Flow Chart for Identification of Breaker Types for Random Wave Tests

If the video analysis shows some breaking waves at the structure the time series analysis (P_{Fh}) is needed again to distinguish between 'quasi-standing' waves ($P_{Fh} < 1\%$) and 'slightly breaking' waves ($P_{Fh} \geq 1\%$). Thus, the principal breaker type of the test has been found and will be assigned to the related test.

(ii) Time Series Analysis of Impact Breakers

Impact breakers can be identified from horizontal force histories integrated at the front wall of the breakwater. Therefore, an automatic procedure has been set up to identify these impacts.

In Fig. 8 a typical force time series of random waves is shown where the left vertical axis represents the horizontal force in model units and the right axis the relative horizontal force (non dimensionalised by $\rho \cdot g \cdot H_{si}^2$); the horizontal

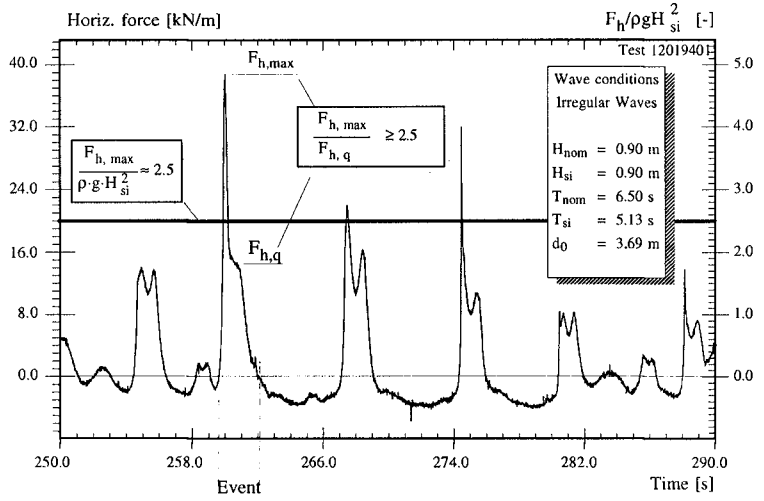

Figure 8. Definition of Impact Breakers from Force Time Series

axis is the time in model units. Two criteria were adopted to identify impact breakers:

1. the relative horizontal force $F_h/\rho \cdot g \cdot H_{si}^2$ should be larger than 2.5; and
2. the ratio of the maximum horizontal force $F_{h,max}/F_{h,q}$ (first peak over second peak for each single event) must be larger than 2.5 as well.

If these criteria are applied to force time series the number of impact breakers can be found by simply counting the number of impacts and dividing by the number of all events (waves) in one test.

5. Results

All data from the various data sets have been analysed as described above and breaker types have been assigned to each of the tests. Therefore, the next step is to identify the areas of the parameter map where these data fit. For this purpose the first two relative parameters h_b^* and H_s^* described in section (b) are plotted against each other (Fig. 9).

The boxes in Fig. 9 indicate the branches of the parameter map as given in Fig. 1. Each box is labelled by the type of breaker which has to be expected for these relative parameter. All observed breaker types for each data point are indicated by different symbols and a second symbol for each point gives the type of tests in which it has been observed.

Following the parameter map for most data points the breaker type seems to be dependent on the relative berm width B_{eq}^*. Within this box all breaker types were observed thus indicating that the relative berm height and the relative wave height are not sufficient to classify the breaker type. However, outside this box some data points can be found with $h_b^* = 1.0$ (i.e. water level in height of the

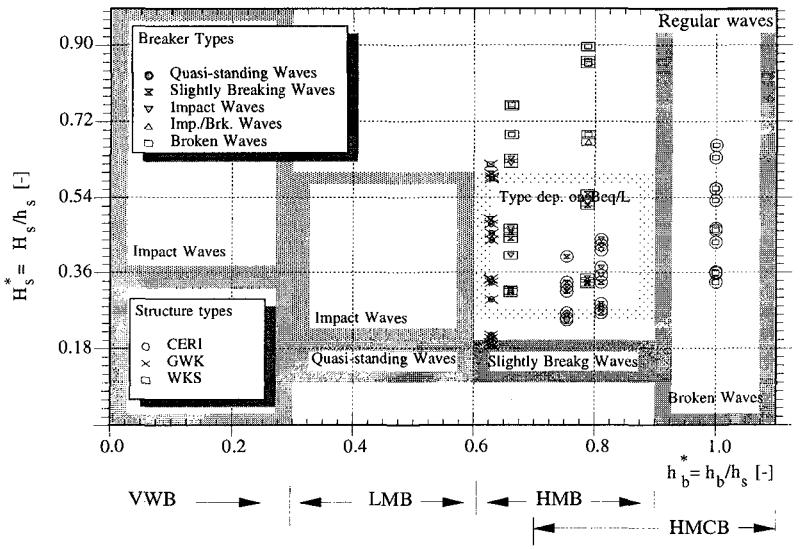

Figure 9. H_s^* vs h_b^* for Regular Wave Tests (All Data Sets)

berm level) which fall in the box of 'broken waves'. The observed breaker types match the parameter map prediction very well so that the map is verified in this region.

For $H_s^* > 0.6$ the data points indicate that the waves will break before reaching the structure. For most of the data points beyond this margin 'broken waves' were observed only. Therefore, the parameter map can be extended in this region.

In Fig. 10 the same plot is shown for random waves. Again, most data points fall in the region of the parameter map in Fig. 1 where a further distinction by the relative berm width B_{eq}^* is required. All other data seem to support the branches of the parameter map in the same way than for regular waves. Additionally, the gap in between 'small waves' and 'large waves' is filled by some data points showing mainly 'quasi-standing' waves but some 'slightly breaking' as well. Therefore, an extension of the parameter map for this region is proposed where a further distinction by the relative berm width will be required.

In a second analysis step all data have been plotted for the region where the predicted breaker type is dependent on the relative berm width. In Fig. 11 the relative wave height is plotted versus the relative berm width B_{eq}^*. Again, all boxes indicate the region of the parameter map which are labelled according to the respective breaker type the parameter map predicts. It should be noted that only data are plotted which fall in the region of the map with a relative berm height of $h_b^* = 0.6 \div 0.9$. All other data were removed from the plot.

From Fig. 11 it can be seen that there are almost no data to support the regions of narrow and wide berms so that most of the data points are within the

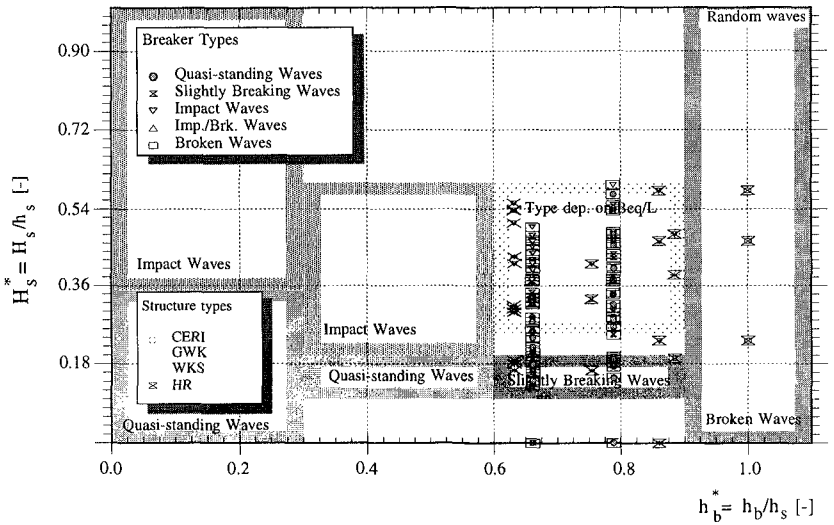

Figure 10. H_s^* vs h_b^* for Random Wave Tests (All Data Sets)

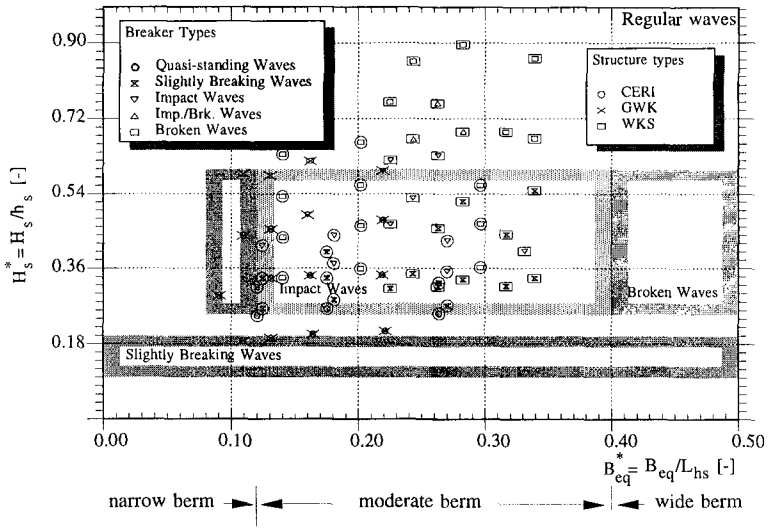

Figure 11. H_s^* vs B_{eq}^* for Regular Wave Tests ($h_b^* = 0.6 \div 0.9$, All Data Sets)

box of 'impact breakers' and above. Within this box no further distinction between breaker types can be made, i.e. that all breaker types are more or less spread all over this area. Therefore, more data would be useful testing the influence of narrow and wide berms, and further analysis is needed to find a criterion for further

discrimination of the breaker types. For practical use, however, all data falling in the aforementioned region of 'large waves' and 'moderate berm widths' should be handled as 'impact breakers' and designers have to realise that impacts could occur at the wall.

Together with the amendments of the map already discussed in this paper the following revised parameter map is proposed for the prediction of the most probable loading cases in front of vertical structures (Fig. 12).

The updated map comprises the following modifications and extensions:

- verification of 'broken waves' for 'crown wall' type breakwaters with a relative berm height $h_b^* > 0.9$;
- extension of the map for high mound composite type breakwaters (HMCB) for $h_b^* = 0.9$ to 1.0;
- extension of the parameter map for regions of relative wave heights $H_s^* > 0.6$ ('very large waves');
- modification of range of relative wave heights $H_s^* = 0.20$ to 0.60 for 'large waves'.

6. Concluding Remarks and Future Work

A 'parameter map' has been developed under PROVERBS (Probabilistic Design Tools for Vertical Breakwaters) in the frame of an ongoing MAST III programme of the European Union (under contract no. MAS3-CT95-0041) to classify the wave loading on monolithic coastal structures and to identify which breaker type leads to impact loading.

Data from four different model tests have been used to verify and extend the parameter map so that an updated version (Fig. 12) is proposed for further design purposes.

However, due to some limitation in the data sets the following future work remains to be done:

- All data sets were based on a foreshore slope of 1:50. It is therefore questionable whether the behaviour of waves approaching the structure over steeper slopes is predictable by the present parameter map. More data are therefore needed to extend the parameter map in this respect.
- Almost no data are yet available for very narrow and very wide berms so that the respective regions of the map are based on very few data only. Further model tests or prototype experience are also needed to verify the map in those regions.
- The boundary between high mound breakwater (HMB) and high mound composite breakwater (HMCB) was set to $h_b^* = 0.9$. More data analysis is needed to specify this boundary.

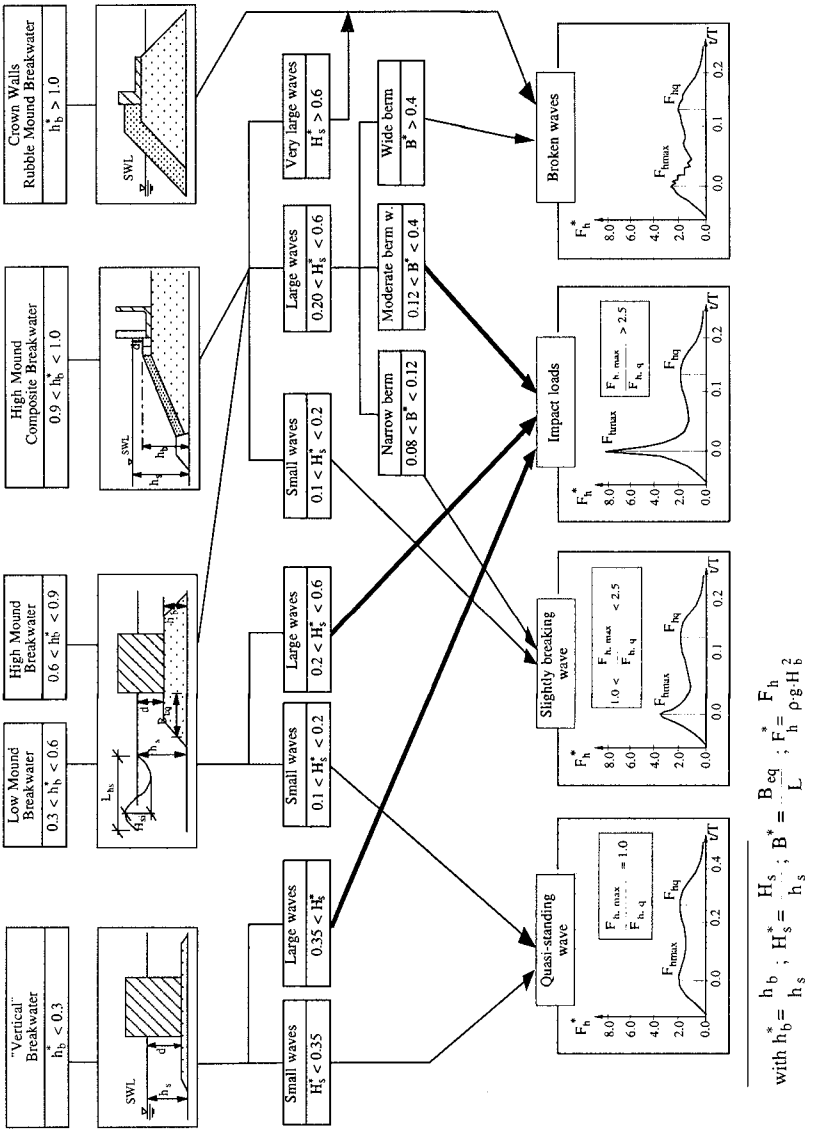

Figure 12. Updated Parameter Map to Identify Loading Cases

Acknowledgements

The hydraulic model tests in the GWK on the high mound composite type breakwater were funded by Port and Harbour Research Institute, Japan (PHRI) and Coastal Engineering Research Institute, Japan (CERI). Further analysis of these data with respect to breaking wave aspects were funded by the European Union under contract MAS3-CT95-0041 (PROVERBS). Additional support was given by the German Research Council (DFG) within the basic research project 'Design Wave Parameters in Front of Structures With Different Reflection Properties' (OU 1/3-1). Those supports are gratefully acknowledged.

The use of various data sets for the parameter map was only possible due to the kind support by researchers from HR Wallingford (Prof. William Allsop and Kirsty McConnell), PHRI and CERI, Japan. In particular, special thanks are due to the kind support by Dr. S. Takahashi (PHRI) and Dr. K. Kimura (CERI) who collaborated with LWI in two joint research projects in 1996 and 1998, respectively.

References

ALLSOP, N.W.H.; VICINANZA, D.; MCKENNA; J.E. (1996): Wave forces on vertical and composite breakwaters. *Strategic Research Report. Hydraulic Research Wallingford*, SR 443, Wallingford, U.K., 94 pp.

KORTENHAUS, A.; OUMERACI, H. (1997): Supplementary data for response map. *Proceedings 1st Overall Project Workshop, MAST III, PROVERBS-Project: Probabilistic Design Tools for Vertical Breakwaters*, Las Palmas, Gran Canaria, Annex 1B, 15 pp.; 4 Annexes.

MUTTRAY, M.; OUMERACI, H.; SHIMOSAKO, K.; TAKAHASHI, S. (1998): Hydraulic performance at a high mound composite type breakwater. *Proceedings International Conference Coastal Engineering (ICCE)*, ASCE, Copenhagen, Denmark, no. 26, 14 pp.

OUMERACI, H.; KORTENHAUS, A.; KLAMMER, P. (1995): Displacement of caisson breakwaters induced by breaking wave impacts. *Proceedings of the International Conference of the Institution of Civil Engineers - Advances in coastal structures and breakwaters*, Clifford, J.E., London, U K.: Thomas Telford Ltd., Paper 3, pp. 50-63.

OUMERACI, H. (1997): Wave impact loading and dynamic response of vertically faced breakwaters - European research project MAST III/PROVERBS. *1st German-Chinese Joint Seminar on Recent Developments in Coastal Engineering*, Wismar, Germany, no. 1, 22 pp.; 1 Annex.

OUMERACI, H.; KORTENHAUS, A. (1997): Wave impact loading - tentative formulae and suggestions for the development of final formulae. *Proceedings 2nd Task 1 Workshop, MAST III, PROVERBS-Project: Probabilistic Design Tools for Vertical Breakwaters*, Edinburgh, U.K., Annex 1.0.2, 13 pp; 3 Annexes.

LAGRANGIAN MEASUREMENTS OF ACCELERATIONS IN THE CRESTS OF BREAKING AND BROKEN WAVES.

Søren Peter Kjeldsen [1], Pierre Bonmarin [2], Michael. G. Skafel [3], William. M. Drennan [4].

Abstract.

The present investigation reports synoptic measurements and analysis of particle accelerations and kinematics of plunging crests in deep water wave groups. The unexpected occurrence of unusully large waves has been documented on numerous occasions. While little is known about the statistics of these waves, even less is known of the dynamical conditions under which they occur. Nonlinear interactions among individual waves travelling within a group on an opposing current have been identified as an important mechanism in the formation of giant waves in deep waters in the ocean. In this study, the non-linear packet-focusing technique is used to generate steep, deep water plunging waves in two laboratory flumes. In one of these flumes the plunging breakers were generated on opposing currents. The kinematics of these waves are measured just up-wave of the onset of plunging, and these results are compared to those of a superposition model, a modified stretching model, and a model based on Stokes 3rd order theory combined with a linear wave spectrum for an irregular sea on an opposing current, developed for the present study. The present model represents the velocity beneath the plunging breakers significantly better than the two other models.

1. Introduction.

Breaking waves play an essential role in air-sea interactions, and in assesment of impact loads on both fixed and floating coastal structures, platforms and ships see (Kjeldsen, 1997). Further breaking waves are very important for mixing and spreading of oil pollution in the upper surface layers of the sea. The dynamic action of the crest of a plunging breaker thus becomes particularly important. Even now when theoretical and numerical treatments of the breaking problem have progressed, controlled experimental measurements for development and calibration of numerical ocean basins are needed. The present investigation reports synoptic measurements and analysis of particle accelerations and kinematics of plunging crests. Furthermore a third order simulation technique is developed in order to predict wave kinematics in extreme waves occurring in irregular seas containing coalescing wave groups.

[1] The Norwegian Maritime Academy, Ladehammerveien 6. 7004 Trondheim, Norway.
[2] IRPHE Institute. IOA Laboratory. Avenue de Luminy. Case 903. 13288 Marseilles.France.
[3] National Water Research Institute. P.O. Box 5050, Burlington. ON. L7R 4A6, Canada.
[4] Rosentiel Schoool of Marine and Atmospheric Sciences. University of Miami. FL 33176 U.S.A.

2. Experiments.

One series of experiments were performed in the large (40 m long) Air-Sea Interaction Simulation Facility of the I.O.A. laboratory of the I.R.P.H.E. Institute, located in Marseille. The wave generation technique developed by (Kjeldsen 1982) was used for production of plunging breaking crests in deep water wave groups. A visualization technique (Bonmarin 1989) makes the wave profile visible and an associated image analysis process allows measurements of both the water surface geometry, crest front steepness and asymmetry (Kjeldsen & Myrhaug 1978), (IAHR/PIANC 1986), as well as detailed measurements of accelerations of tracer particles dragged away by breaking and broken waves. Ten experiments designated by the reference of A11 to A21 were performed.

Another series of experiments were performed in the large wave tank at the Canada Centr for Inland Waters. The tank dimensions are 100 m in length, 4.5 m in width and the water depth for all runs were 1 m.The water surface elevations were measured using four capacitanc type water surface piercing wave staffs; two were fixed in the tank and two were on a movabl carriage. The velocity was measured with an acoustic Doppler current meter (Sontek ADV-1) mounted on the carriage. The surface elevation data and the velocity data for each run were logged on the current meter computer at 25 Hz. A mean flow in the tank, in the opposite direction to the wave travel, was generated with a pump. The flow entered the tank through a diffuser in the floor about 36 m downwave from the measuring station, and left the tank immediatly in front of the wave board, also through a floor diffuser. Mean flows (U_M) of 0.04 and 0.095 m/sec were used for the experiments.

3. Results.

A Lagrangian measurement technique is needed in order to measure particle accelerations accurately in non-linear waves, see (Longuet-Higgins 1986.) In order to develop such a technique the wave-following properties of the tracer particles were mapped. A calibration experiment was performed with a symmetric regular wave with steepness ak = 0.31. Fig 1 shows the measured trajectory, and a theoretical trajectory predicted by second order wave theory. A significant Stokes drift in agreement with the theory was obtained. This relative goo agreement between experiment and theory validates the choice of the floating particles.
In the breaking waves the different steps of the measurements were i) the reconstruction of th trajectory of the floating particles, ii) measurements of their celerity, and iii) the measurement of their acceleration, these two last measurements being deduced from the trajectory. Fig. 2 shows an example of surface elevation and location of tracer particles in a plunging breaker developing in deep water. Fig. 3 shows the reconstruction of the trajectories of floating particles, one of them colliding with a breaking crest. Fig 4 shows an example of measured horizontal velocities of two particles P2 and P3, shown in the experiment A15,as it develops in Fig. 2. The horizontal velocities are normalized with the wave phase velocity c. Particle P3 reaches a horizontal velocity equal to the wave phase velocity, as can be seen.

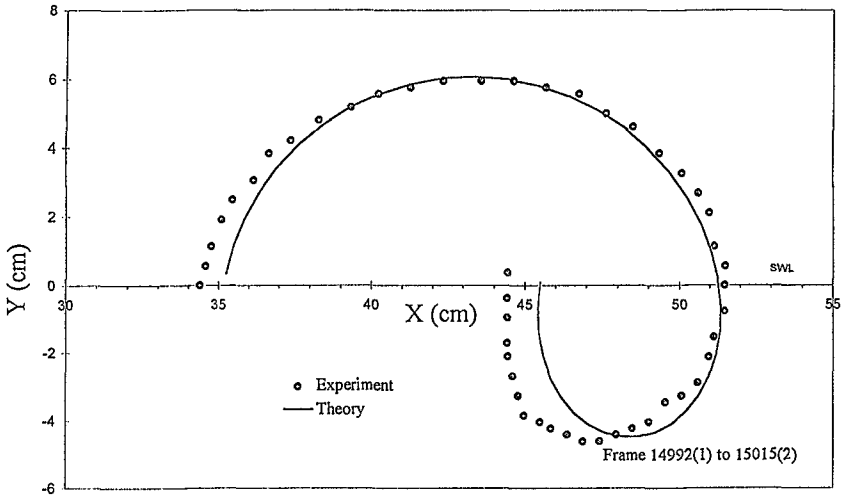

Fig. 1. Comparison of trajectories of a floating particle moving on a quasi symmetrical crest (ak=0.31), and second order Stokes wave theory.

Fig 5 then shows measured horizontal accelerations of the particles P2 and P3, normalized with the gravity acceleration. The horizontal acceleration of particle P3 reaches a value of 1.35 times the gravity acceleration

Particle P3 reaches a vertical acceleration 0.78 times the gravity acceleration. Fig 6 shows the total acceleration of this particle. The acceleration of the floating particles increases rapidly in the non-breaking region and reaches a maximum value at the time when the overturning part of the crest collides with them. Total acceleration vectors up to 1.55 g were measured at the free surface. Maximum acceleration and maximum velocity are nearly in phase in these breaking waves, leading to large wave forces, and a significant capsizing potential if encounter happens with small floating objects (small boats, rescue floats or wave buoys).

If wave forces are computed on structural elements of a steel jacket or a tension leg platform then both the particle velocity and the acceleration must be known, and data from the established data bank are used for calibration of the 3-order kinematic model developed in this study for extreme waves in irregular seas with or without currents.

Wave particle accelerations in non-linear waves can not easily be deduced from Eulerian measurements. The wave crests show an asymmetrical shape at the breaking onset (Kjeldsen 1997), and work is in progress to establish a correlation between surface particle accelerations and wave asymmetry, see (Kjeldsen, Bonmarin & Duchemin 1998).

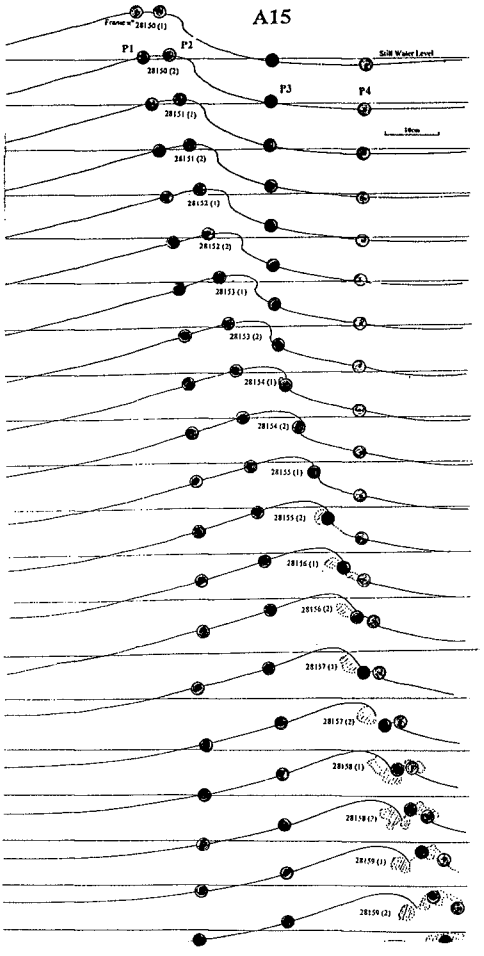

Fig. 2. Surface elevation and location of tracer particles in a plunging breaker developing in deep water. Experiment A15, frame period 0.02 sec.

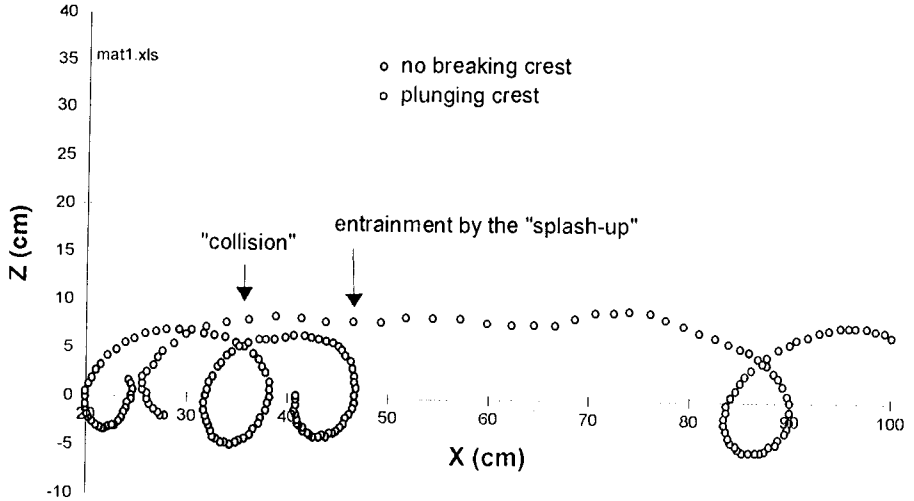

Fig. 3. Trajectory of a floating paticles.

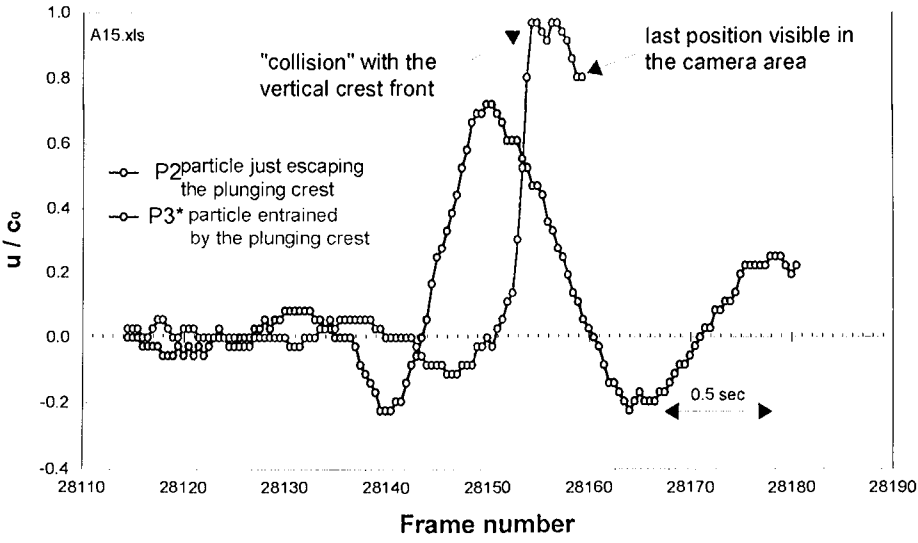

Fig. 4. Horizontal velocity of floating particles. Experiment A15.

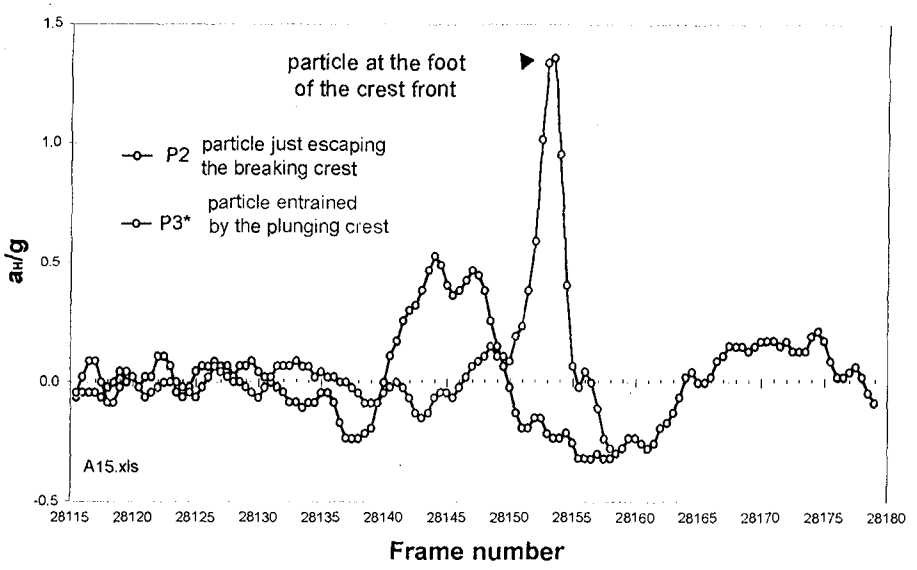

Fig. 5. Horizontal acceleration of floating particles. Experiment A15.

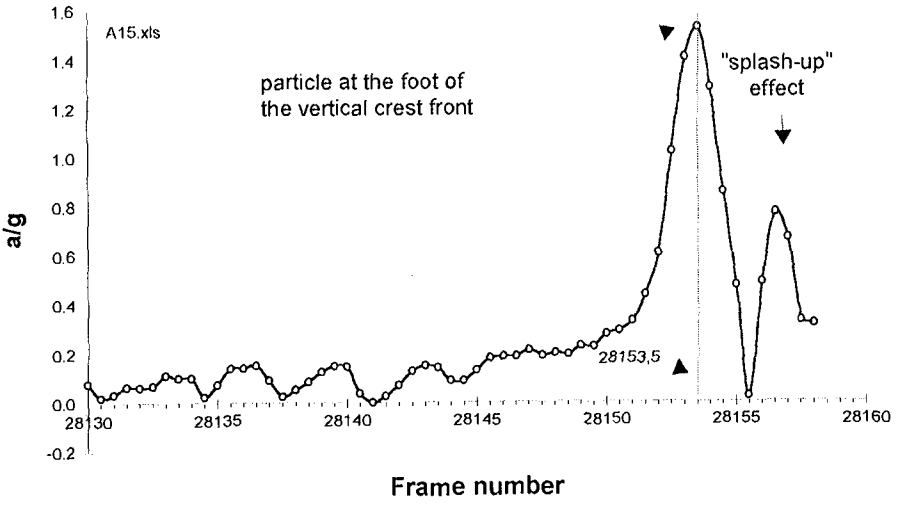

Fig. 6. Total acceleration of floating particle. Experiment A15.

4. Kinematic Models.

In the offshore industry a stretching theory developed by (Wheeler 1970) has traditionally been used for prediction of kinematics of irregular sea states. In this study, we use a modified stretching model (Lo and Dean 1986) as representative of this class of model. (Donelan et al. 1992) report that it produces velocities very similar to the Wheeler method). We also used the superposition method proposed by (Donelan et al. 1992), based on the linear superposition of a sum of freely propagating wave trains. Even when adapted to account for a possible mean flow, these linear models do not adequately represent the velocity beneath the coalescing wave group.

In the present study we therefore developed a third order simulation of the kinematics in steep wave crests, see (Skafel, Drennan and Kjeldsen 1997). This third order simulation technique is based on a combination of two earlier models. The first of these was developed by (Kishida and Sobey 1988) and simulates a Stokes third order wave train on a current with a linear profile.

This model is then used both for cases where non-linear waves propagate on opposing currents, and for cases without currents. However this model does not give a complete description of the wave spectrum developed by the command signal in the wave flume. Therefore the superposition model developed by (Donelan et al. 1992) is also used. The procedure for computation then becomes:

- 1. A third order wave train interacting with a current with a constant vorticity is computed.
- 2. The third order wave train is subtracted from the experimentally obtained surface elevation.
- 3. The kinematics of the remaining wave signal is analysed using the superposition model of (Donelan et al. 1992).
- 4. Finally the solutions obtained in steps 1) and 3) above are added, using the surface of the non-linear wave as mean water level for the additional wave components, in agreement with the concept behind the development of (Donelan et al. 1992).

5. Model Comparison.

Fig 7 shows an example from CCIW experimentsof internal maximum horizontal velocities measured below extreme wave crests. The mean predicted velocity profiles beneath the crests using the modified stretching model, the superposition model, and the present third order model are shown in Fig. 8 along with the experimental laboratory profiles. All the kinematic models were run for the surface elevation time series of all the laboratory runs (26 experiments with the same condition). The resulting mean profiles, along with twice the standard deviations about the means are plotted. The narrowness of the spread of the standard deviations presented in Fig. 8 serves as an indication of the excellent reproducability of the wave trains. Fourier analysis of each surface profile was used to find the peak frequency, and hence the peak wave number k_0. The mean peak wave number for all 26 runs, in this case k_0=1.38 m^{-1} was used for normalisation. It can be seen here that the modified stretching model underpredicts the velocity significantly throughout the profile. The superposition model more nearly represents the data. The new third order model developed here best reproduces the data. It slightly underestimates the velocity, lying just outside the two standard deviation range. A further development of the new model is in progress. (Kjeldsen, Skafel, Drennan 1998).

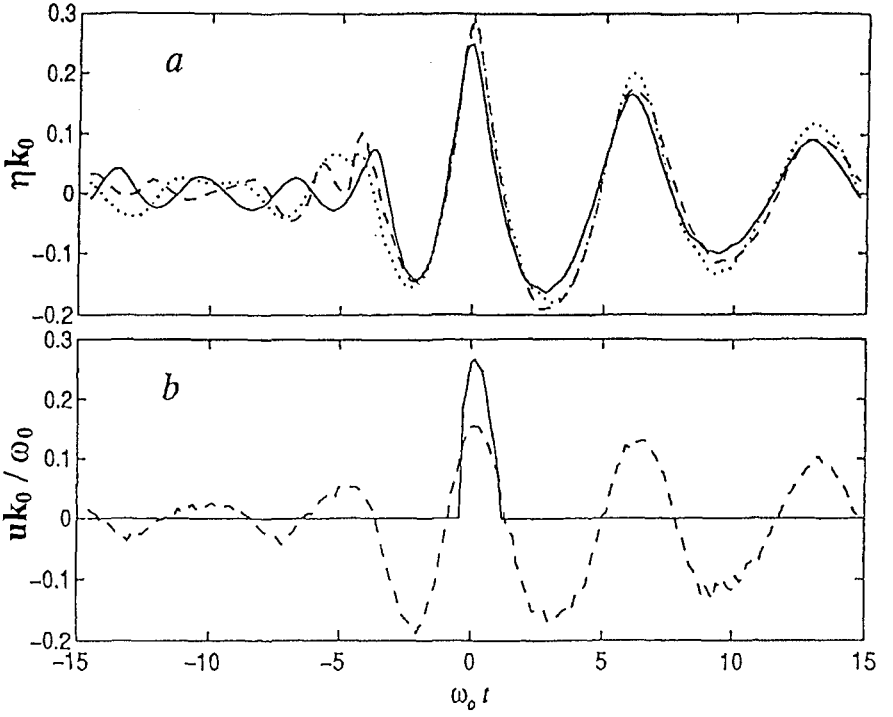

Fig. 7. Panel a shows the time series of the water surface elevation, just upwave of breaking, normalized by the peak wave number ($k_0 = 1.38$), and frequency ω_0. U_M is the mean current velocity of opposing current.

——— : $U_M = 0$ cm/sec. — — — : $U_M = 4$ cm/sec. - - - - - - : $U_M = 9.5$ cm/sec.

Panel b shows the corresponding normalized horizontal orbital velocity u for $U_M = 9.5$ cm/sec.

——— : 4 cm above the still water level. — —: 20 cm below the still water level.

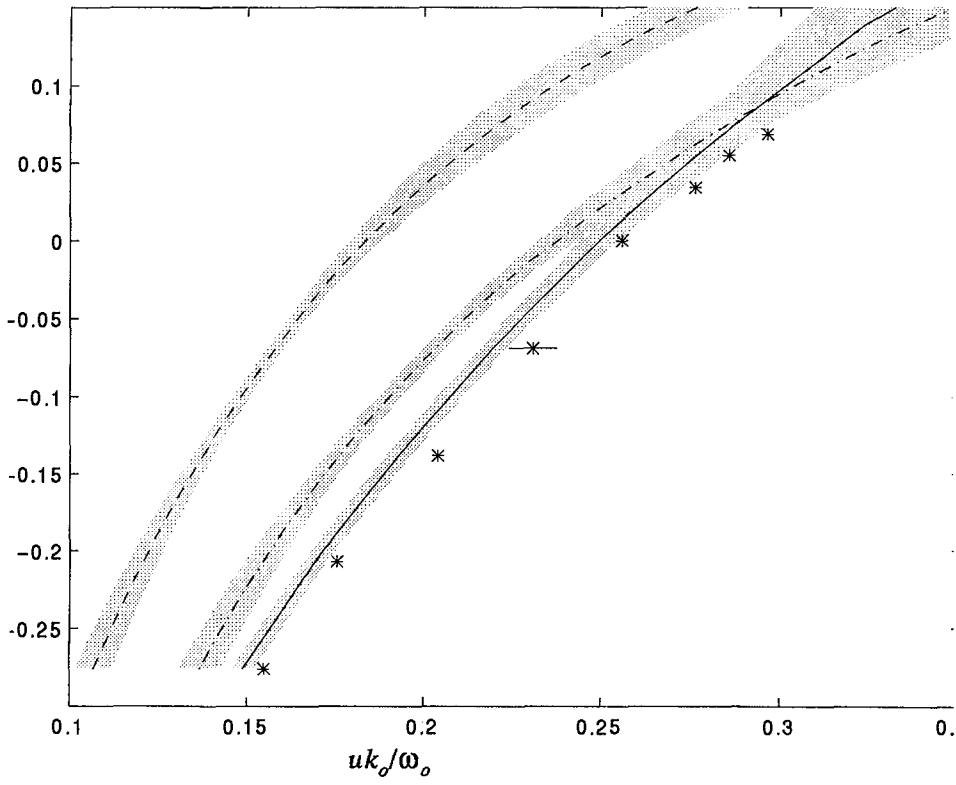

Fig. 8. Maximum horizontal orbital velocities (u) beneath the crest just upwave of breaking, normalized by k_0 and ω_0, versus elevation (z) normalized by k_0.
*** : measured values. — — — : mean of linear superposition model.**
—·—: mean of modified stretching model. _____ : present model.
The horizontal bar on the data point at the elevation of 0.05 represents two standard deviations about the mean. The shaded areas around the model lines enclose twice the standard deviations.

6. Conclusions.

1. A new third order kinematic model simulating the velocity beneath extreme waves has beer developed.; it represents the velocity beneath extreme waves occuring in irregular seas with o without current better than the modified Wheeler stretching model and the linear superpositior model.
2. The new third order kinematic model can easily be adopted to take into account the directional spreading in a non-linear directional sea state interacting with a current.
3. A Lagrangian measurement technique is needed in order to measure particle accelerations in non-linear waves. By means of a visualisation technique it was possible to measure both the Lagrangian particle accelerations in breaking wave crests, and Stokes drift in steep waves as well as particle drift caused by breaking wave crests.
4. Both horizontal and vertical accelerations were measured not so far from the ones predicted by the numerical model developed by (Vinje & Brevig 1980.) Total particle accelerations up to 1.55 g were measured in plunging breakers occurring in deep water.
5. The behaviour of the tracer particles is similar to the one of free floating oceanographic buoys (operated at sea without moorings as in parts of the LEWEX experiment, see (Beal 1989)). If buoys are moored it is well known that they follow a more linear mode. Moored buoys will therefore not measure particle accelerations in non-linear breaking waves correctly.
6. The behaviour of the tracer particles is also similar to the one of rescue floats deployed after a ship accident in a swell. Drift of rescue floats at sea is also depending on wind, and drag coefficients related to float design. Accurate modelling of surface drift of smaller objects is very important for management of search and rescue operations at sea.
7. The wave generation technique of (Kjeldsen 1982), modified for opposing currents, was able to generate unusually large plunging breakers with crest front steepnesses in the range 0.25 - 0.41, similar to observations on the Norwegian Continental Shelf.

7. Further Work.

1. Results are also obtained for spilling and plunging breakers on beaches. These will be dealt with in a seperate report.
2. A further development of experimental technique using smaller particles and a high speed camera is considered.
3. A further development of the new kinematic model incorporating an overturning jet on the steep irregular wave is considered, in order to simulate capsizing of smaller objects in a numerical ocean basin.

8. Acknowledgement.

This work was supported in part by NATO, Scientific Affairs Division within the research programme on «Giant Waves caused by wave-wave and wave-current interactions.» under contract no. 930137. Canada, France and Norway participated in this international research programme.

9. References.

Beal R.C. (editor) (1989) « Measuring, Modelling, Predicting and Applying Directional Ocean Wave Spectra. - A record of the Labrador Sea Extreme Waves Experiment.« The Johns Hopkins University Press, Baltimore and London.

Bonmarin P. (1989).»Geometric properties of deep-water breaking waves». J Fluid Mech. Vol 209, pp 405-433.

Donelan M.A., Anctil F., and Doering J.C. (1992).»A simple method for calculating the velocity field bemneath irregular waves.» Coastal Engineering. Vol 16. pp 399-424.

I.A.H.R./P.I.A.N.C. (1986).»List of Sea State Parameters.» Supplement to bulletin No. 52.

Kishida N. and Sobey R.J.(1988).»Stokes theory for waves on linear shear current»J.Engineering Mech. Vol 114. pp 1317-1334.

Kjeldsen S.P., Myrhaug D. (1978) « Kinematics and Dynamics of Breaking Waves.» Report STF60 A78100 Norwegian Hydrodynamic Laboratories. Trondheim. Norway.

Kjeldsen S.P. (1982).»2- and 3-dimensional deterministic freak waves.». Proc. 18th Internat. Conf. on Coastal Engineering. ASCE, Cape Town, pp 677-694..

Kjeldsen S.P.(1997).»Examples of Heavy Weather Damages caused by Giant Waves.» SNAJ Bulletin of The Society of Naval Architechts of Japan. Vol 828 1997/10 pp 744-748.

Kjeldsen S.P., Skafel M.G.,Drennan W.M. (1998) « Modelling of Velocities in Giant Waves.» (in press.)

Kjeldsen S.P., Bonmarin P. & Duchemin L. (1998).»Lagrangian measurements of accelerations in the crests of breaking and broken waves.» Applied Ocean Research 1998. (in press)

Lo J.M. and Dean R.G.(1986).»Evaluation of modified stretched linear wave theory.» Proc. 20th Intern. Conf. on Coastal Eng. ASCE, Taipei, pp 522-536.

Longuet-Higgins M.S.(1986).»Eulerian and Lagrangian wave measurements.» J. Fluid Mech. Vol. 173, pp 683-707.

Skafel M.G., Drennan W.M. & Kjeldsen S.P. (1997).» Modelling of Velocities in Unusually Large Waves.» Canadian Coastal Science and Engineering Association. Proc. of the 1997 Canadian Coastal Conference. 21-24 may 1997. Guelph, Ontario. Canada..

Vinje T., Brevig P. (1980) « Breaking Waves on Finite Water Depths. A numerical study.» Report The Norwegian Institute of Technology and Norwegian Hydrodynamic Laboratories. Trondheim. Norway.

Wheeler J.D. (1979).»Method for calculating forces produced by irregular waves.» J. Petroleum Tech. March, pp. 359-367.

Numerical Simulation of Breaking Waves by Large Eddy Simulation and VOF Method

Qun Zhao[1] and Katsutoshi Tanimoto[2]

Abstract

In this paper, the VOF method for free surface flow is applied to simulate breaking waves incident on a submerged reef. An efficient numerical wave channel with two absorbing boundaries is developed. Corresponding boundary conditions are prescribed. Smagorinsky's sub-grid scale model is incorporated to account for the sub-grid scale turbulence. Numerical results are compared with laboratory measurements.

Introduction

Owing to the extremely complicated wave manner caused by the wave nonlinearity and breaking, a complete satisfactory theory for wave deformation on uneven topographies seems to be not attainable so far. Small-scale model tests and field observations are still dominant in the traditional study. Nevertheless, small-scale model tests suffer from the scale effects, while large-scale model tests are too expensive.

The booming progress in computer technology in the past decade witnesses the continuous improvements in computational fluid dynamics. With today's personal computer, it is possible to solve the Naiver-Stokes equations for coastal engineering problems.

The VOF method developed by Hirt and Nichols(1981) is among the best candidates for solving free surface flow problems due to its clearness and simplicity of

[1]Post doctoral fellow, Dept. of Civil Eng., Saitama Univ., Shimo-Okubo 255, Urawa, Saitama 338-8570, Japan. E-mail:zhao@envi.env.civil.saitama-u.ac.jp

[2]Professor, ditto. Tel/Fax:+81-48-858-3561, E-mail:tanimoto@envi.env.civil.saitama-u.ac.jp

tracing free surface. Besides, this method is especially useful for calculating breaking waves, since the free surface is not necessarily required to be single. Several studies based on the VOF method to simulate breaking waves have been reported recently(van der Meer *et al.*, 1992; Lemos, 1992; Petit *et al.*, 1994; van Gent *et al.*, 1994; Sabeur *et al.*, 1996; Kawasaki and Iwata, 1997; Lin and Liu,1998; etc.).

However, most of these studies either ignore the sub-grid scale turbulence totally, which implies that the sub-grid scale energy dissipation purely relies on the numerical viscosity appeared in the finite difference schemes; or use a constant eddy viscosity of the same order as that of Reynolds Averaged Navier-Stokes(RANS) equations.

Lemos(1992), Lin and Liu(1998) demonstrate two-dimensional breaking wave models based on the Reynolds Averaged Navier-Stokes equations separately. Both of them used the $k-\varepsilon$ model with standard coefficients. Lemos used a linear closure for the Reynolds stress terms, while Lin and Liu used a nonlinear closure to account for the anisotropic turbulence. Nevertheless, Lemos' results were not compared with experimental measurements directly. Lin and Liu's results showed that their model could give generally good agreement at the inner surf zone. Near the breaking point, however, the $k-\varepsilon$ model always overestimates the eddy viscosity, and thus leads to an underestimation of surface elevation. If we consider the breaking point is the transition point from laminar flow to turbulent flow, this in one way suggests the limitation of the $k-\varepsilon$ model in predicting the flow transition. Besides, there are too many coefficients in the $k-\varepsilon$ model, and this makes it difficult for calibration.

In the present paper, therefore, we are trying to use a space filter to account for the sub-grid scale turbulence. It is expected that the sub-grid scale turbulence is more isotropic and less flow dependent, therefore, the closure model can be simpler and less sensitive to the parameterization. However, due to the very high Reynolds number and limited computer resources, we restrict the present study to two-dimensional problem.

Numerical Formulation

The governing equations are the mass conservation equation for incompressible flows:

$$\frac{\partial u_j}{\partial x_j} = 0 \tag{1}$$

and the Navier-Stokes equations:

$$\frac{\partial u_i}{\partial t} + u_j \frac{\partial u_i}{\partial x_j} = -\frac{1}{\varrho}\frac{\partial p}{\partial x_i} + \nu \frac{\partial}{\partial x_j}[(\frac{\partial u_i}{\partial x_j} + \frac{\partial u_j}{\partial x_i})] + g_i \tag{2}$$

in which ϱ and ν are the fluid density and kinematic viscosity, respectively. g_i is the gravitational acceleration at the ith direction, u_i is the velocity component, and p is the pressure. Here $i = 1, 2$ correspond to horizontal (x) and vertical (z) directions, respectively, j is dummy.

Assuming that the sub-grid scale turbulence is isotropic, the filtered Navier-Stokes equations and the continuity equation read:

$$\frac{\partial \overline{u}_j}{\partial x_j} = 0 \tag{3}$$

$$\frac{\partial \overline{u}_i}{\partial t} + \overline{u}_j \frac{\partial \overline{u}_i}{\partial x_j} = -\frac{1}{\rho}\frac{\partial \overline{p}}{\partial x_i} + \nu \frac{\partial}{\partial x_j}[(\frac{\partial \overline{u}_i}{\partial x_j} + \frac{\partial \overline{u}_j}{\partial x_i})] - \frac{\partial}{\partial x_j}(\overline{u_i u_j} - \bar{u}_i \bar{u}_j) + g_i \tag{4}$$

The top-hat filter(cell volume) is applied in the above equations, and the over-bars denote the resolvable scale quantities (for example $\overline{u}_i$):

$$\overline{u}_i(x,z,t) = \frac{1}{\Delta x \Delta z}\int_{x-\frac{1}{2}\Delta x}^{x+\frac{1}{2}\Delta x}\int_{z-\frac{1}{2}\Delta z}^{z+\frac{1}{2}\Delta z} u_i(\zeta,\eta,t)d\zeta d\eta \tag{5}$$

Where Δx and Δz are the mesh sizes of the finite- difference equations in x and z directions, respectively. The $\overline{u}_i$ is the filtered velocity component; $\overline{p}$ is the filtered pressure. The new terms appeared in the filtered equations are:

$$(\overline{u_i u_j} - \bar{u}_i \bar{u}_j) = L_{ij} + C_{ij} + R_{ij} \tag{6}$$

with L_{ij}, C_{ij}, R_{ij} referred as the Leonard term, the cross term and the sub-grid scale(SGS) Reynolds term, respectively:

$$L_{ij} = \overline{\bar{u}_i \bar{u}_j} - \bar{u}_i \bar{u}_j \tag{7}$$

$$C_{ij} = \overline{\bar{u}_i u'_j} + \overline{u'_i \bar{u}_j} \tag{8}$$

$$R_{ij} = \overline{u'_i u'_j} \tag{9}$$

The prime denotes a SGS quantity. Notice that the sum of the Leonard term and the cross term ($L_{ij} + C_{ij}$) is small comparing with the SGS Reynolds stress (Deardorff, 1970), and thus can be neglected. Therefore, we finally obtain the filtered Navier-Stokes equations in which the SGS Reynolds stress need to be modeled.

Applying Boussinesq's eddy-viscosity hypothesis, the SGS Reynolds stress is given by:

$$R_{ij} = -2\nu_T S_{ij} \tag{10}$$

where

$$S_{ij} = \frac{1}{2}(\frac{\partial \overline{u}_i}{\partial x_j} + \frac{\partial \overline{u}_j}{\partial x_i}) \tag{11}$$

is the strain rate tensor of the resolved scales. Smagorinsky's model gives:

$$\nu_T = (C_S \Delta)^2 |S| \tag{12}$$

$$\Delta = (\Delta x \Delta z)^{\frac{1}{2}} \tag{13}$$

in which ν_T is SGS eddy viscosity, Δ is SGS length scale for two-dimensional problems, and $C_s = 0.10$.

Equation (12) is used otherwise of the fluid except at the solid boundary, where the van Driest damping function is applied to the SGS length scale. At free surface, the closure for the SGS Reynolds stress is less certain, we apply Smagorinsky's model at the present stage.

Besides the above equations, a volume of fluid function (F) is used to define the fluid region in the VOF method. A unit value of F corresponds to a cell full of fluid, while a zero value indicates that cell contains no fluid. Cells with F values between zero and one represent the water-air interface. The governing equation of F function is given by:

$$\frac{\partial F}{\partial t} + \bar{u_j}\frac{\partial F}{\partial x_j} = 0 \tag{14}$$

Numerical Methods

The governing equations are discretized using a staggered grid where the velocities are located at the cell faces, the pressures and the F functions are settled at each cell center. The time increment is achieved by the Euler scheme and the convective terms are approximated by the third-order difference scheme due to stability consideration.

In order to obtain accurate result, boundary conditions must be treated very carefully. In the present study, the boundary conditions for resolved field have been summarized into three kinds, namely, the lateral boundary conditions, the free surface boundary conditions and the solid boundary conditions.

The lateral boundary conditions include the inflow boundary and the out flow boundary(open boundary). At the inflow boundary, we choose to generate the incident wave by simulating a piston-type wave-maker. The wave paddle is driven by the second order Stokes wave theory (Hughes, 1993), and an absorbing wave-maker system(Zhao, 1998) which is essentially same as that in the physical experiment. This method is particularly effective for our case, where waves are generated at deeper water region and encounter a reflective structure(submerged reef with a steep reef face). The secondary wave for this case is very small according to our study. The example of second order Stokes waves incident on a vertical wall is shown in Fig. 1, where T is the wave period, h is the still water depth, H_{in} denotes the incident wave height, L is the incident wavelength calculated by linear wave theory, and η is the water surface relative to the still water level.

At the open boundary, an artificial boundary condition has to be given to truncate the computational domain from the infinite physical domain, but without rendering disturbances to the inside area. For wave problems, this is normally fulfilled by the well-known Sommerfeld radiation boundary condition. However, the wave dispersion induced by wave nonlinearity and breaking makes it difficult to use one wave celerity to represent the whole wave field. Hence, a damping zone(Arai, 1993) and the Sommerfeld radiation condition are combined at the open boundary.

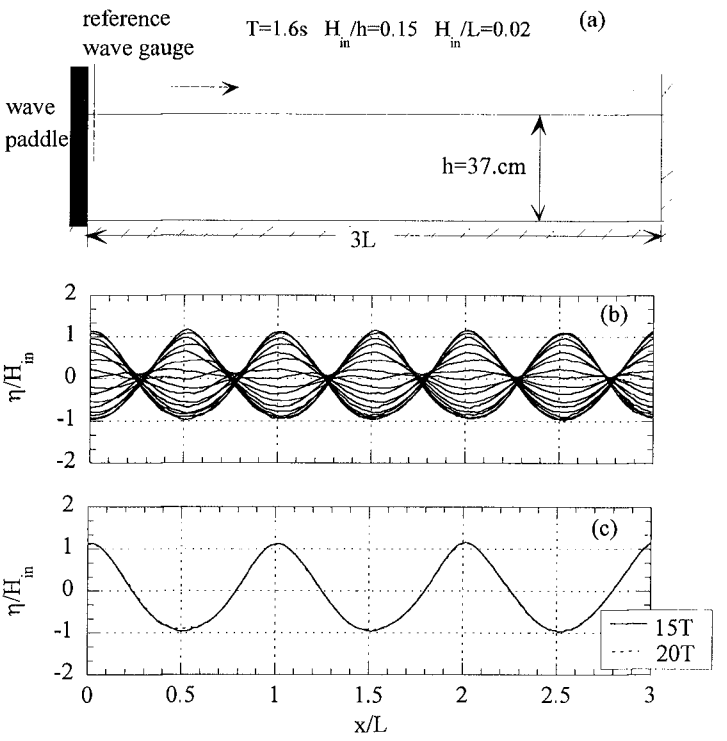

Fig.1 Nonlinear wave incident on a vertical wall
(a) calculation condition; (b) wave profile in one wave period;
(c) wave profile at time 15 wave period and 20 wave period

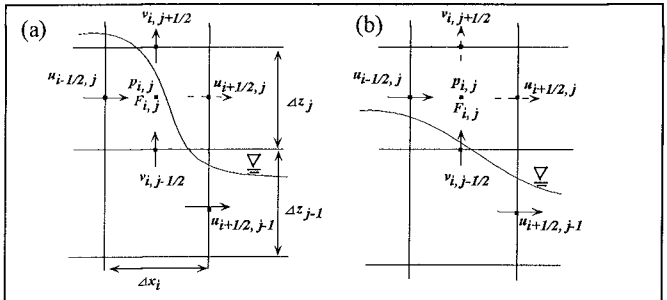

Fig.2 Examples of surface cells partially open to the air
The solid arrows denote the velocities normally calculated;
the dash arrows denote the velocities obtained by extrapolation

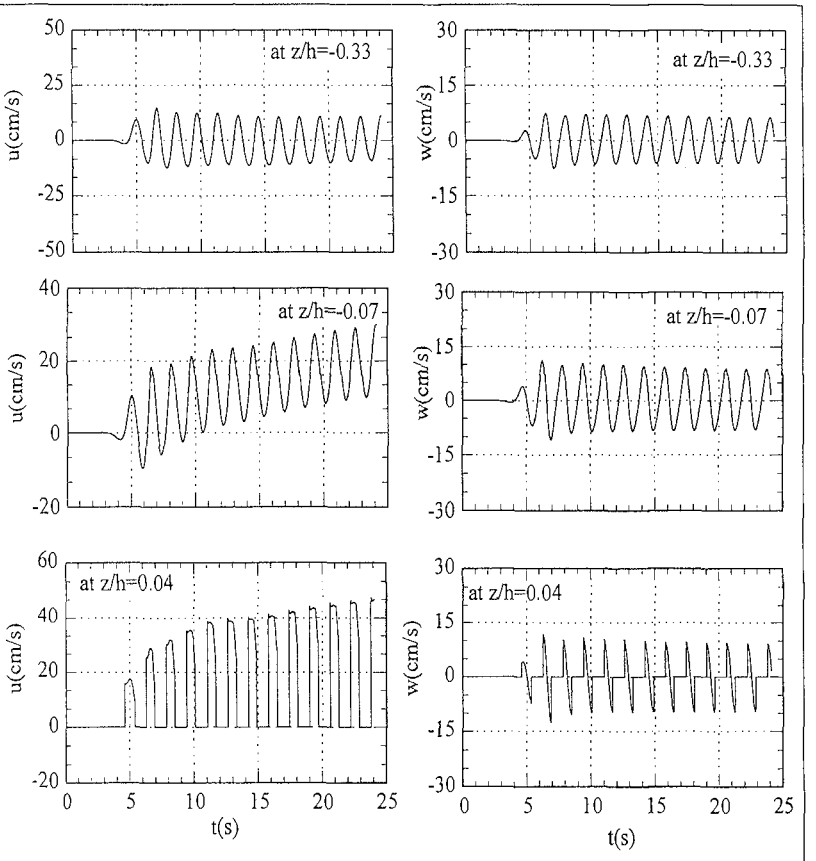

Fig. 3 Orbital velocities calculated by original VOF method
at different vertical locations: inside the water(z/h=-0.33),
at the trough level(z/h=-0.07) and above the still water level(z/h=0.040)

The free surface boundary conditions include the dynamic and the kinematic boundary conditions. The dynamic boundary condition is satisfied by $\tilde{p} = 0$ at the free surface. The pressures at the surface cells are calculated by linear extrapolation from the cells inside the fluid domain. The kinematic boundary condition is automatically satisfied by Eq.(14). However, special care must be paid to the treatment of velocities at surface cells . The examples are shown in Fig. 2 , where parts of the cell faces are exposed to the air. For these cases, the momentum equations for water can not be used. The determination of these values is quite arbitrary. In the original VOF method(Hirt and Nichols, 1981) and some other methods related to the VOF method(ex. Ashgrizon and Poo, 1991), these velocities are obtained by the continuity equation. In the calculation of solitary

wave, Chan and Street(1970) used vertical extrapolation to obtain these velocities, therefore, the continuity equation is not forced at the surface cells. Actually, the approximation of the former method is acceptable provide the flow in nonperiodic. But it brings considerably errors for periodic problem. Figure 3 shows the calculated results by the original VOF method at different vertical positions.

It is seen that the influence of the free surface boundary increases considerably as the vertical position approaches to the surface. And this effect is more pronounced for the horizontal velocities than the vertical velocities. Accordingly, in our calculation, we used the extrapolation to obtain the horizontal velocities. For example, $u(i+\frac{1}{2},j)$ in Fig. 2 can be approximated as:

$$u_{i+\frac{1}{2},j} = [u_{i-\frac{1}{2},j}*0.5*(\Delta z_j+\Delta z_{j-1})+u_{i+\frac{1}{2},j-1}*\Delta x_i]/[\Delta x_i+0.5*(\Delta z_j+\Delta z_{j-1})] \quad (15)$$

In case the vertical velocity is also exposed to the air (Fig. 2(b)), the vertical velocity can be obtained by the continuity equation. As for the case shown in Fig. 2(a), there is no way to satisfy the continuity equation in the surface cells. The results of the modified calculation are shown in Fig. 4.

In the numerical simulation, still water level is given at time $t = 0$. No initial superimposed condition has been introduced to the sub-grid scale variables.

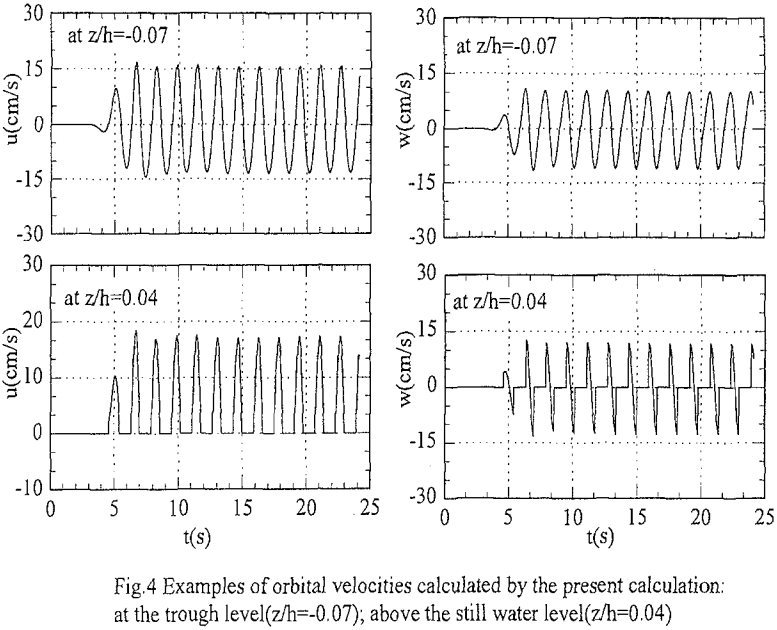

Fig.4 Examples of orbital velocities calculated by the present calculation: at the trough level(z/h=-0.07); above the still water level(z/h=0.04)

Verification with Experimental Measurements

1.Experimental Setup

Finally, breaking waves propagating on a submerged reef are numerically calculated and verified with previous experimental data(Nakamura 1995).

Figure 5 shows the experimental setup and coordinates layout. The wave channel is 17.0 meters long. The model reef is fully impervious and 32.5cm high with a seaward reef face of 1 : 2. Regular waves were generated by a computer controlled piston type wave-maker. Water surface elevations were measured by capacitance-type wave gauges. In the experiment, only six wave gauges were available. The first two gauges(from the wave paddle) were served as reference gauges for incident waves. The other 15 locations of water surfaces were obtained by moving the remained four wave gauges prior to each run. In each run, data were recorded simultaneously from 6 channels at sampling time interval of 50ms. Velocities and pressures were measured at three locations(I, II and III) on the slope of the reef for case A. The $L_1/4$ in the figure denotes a quarter of incident wavelength calculated by linear wave theory. The incident wave characters are given in Table 1 in which x_b is the measured position nearest to the breaking point.

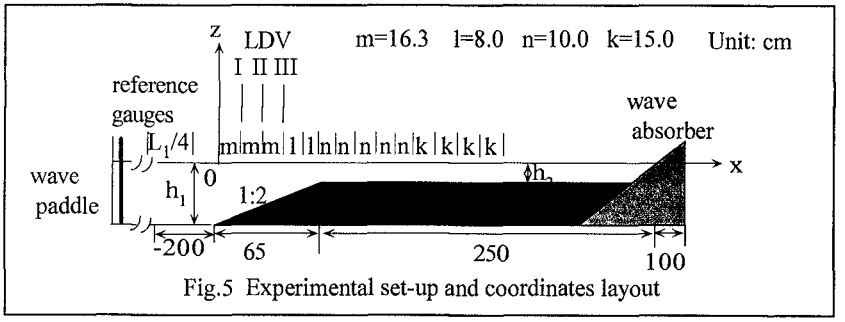

Fig.5 Experimental set-up and coordinates layout

Case	h_1	h_2	T	H_{in}	L_1	x_b
A	45.0cm	12.5cm	1.6s	6.60cm	296.2cm	105.0cm
B	37.5cm	5.0cm	1.6s	5.64cm	276.4cm	57.0cm

Table 1. Simulated cases

In the calculation, incident waves are generated at the left boundary. In order to avoid the pressure divergence at the initial stage, incident wave heights were slowly increased to H_{in}, where H_{in} is the incident wave height obtained by comparing the surface elevations at reference gauge with the physical experiments. The calculated surface elevations were obtained by integration of the F function from the bottom of the channel to the water surface. In the position where air entrainment appears inside the fluid domain, the F function was set to 1 to keep consistency in the experimental measurements. In order to limit effects of wave reflection from the end of the wave channel, the analysis of the experimental data was restricted to the first fully grown-up four or five waves in a record.

2.Calculation Results

Figure 6 shows the normalized vertical distribution of velocities, phase difference and dynamic pressures of case A in which H is the local wave height. To be succinct, only the results of position III are presented here. Besides the experimental results and the numerical simulation, the first order Biesel theory with slight modification(Zhao *et al.*, 1996) is also presented. The general agreements among the analytical solution, the numerical simulation and the experimental results are good. The numerical simulation and the experimental measurement show the same trend of skewness in the vertical velocity and phase difference.

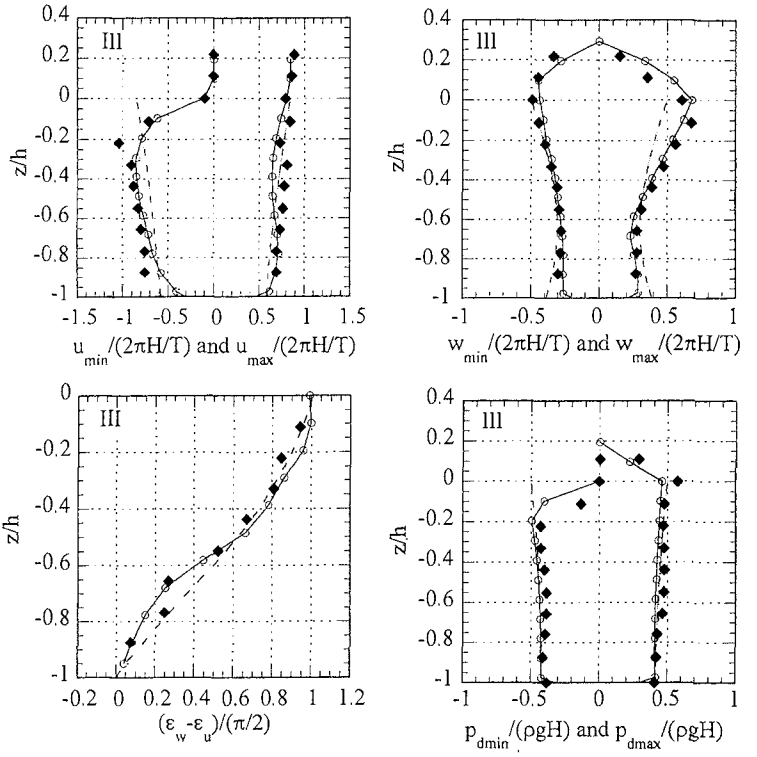

Fig.6 Vertical distribution of maximum and minum orbital velocities, phase differences and dynamic pressures

Figure 7 shows the simulated time series of surface elevations together with experimental measurements. Both the measured and calculated surface elevations include the reflective waves from the submerged reef.

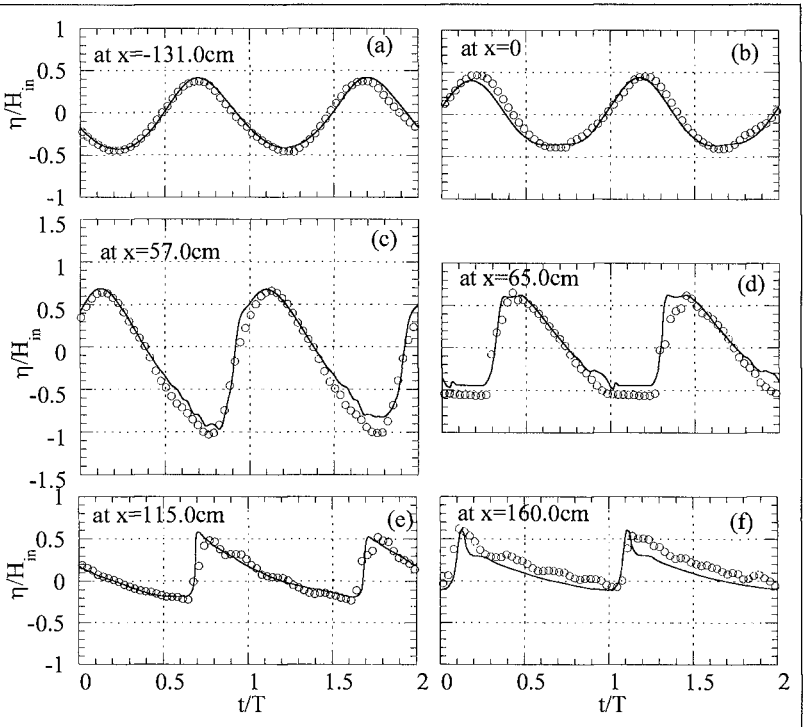

Fig.7 Comparison of surface elevations(Case B) at positions: before wave breaking (a,b); near the breaking point(c) ; after wave breaking(d,e,f)

○ Measured ——— Calculated

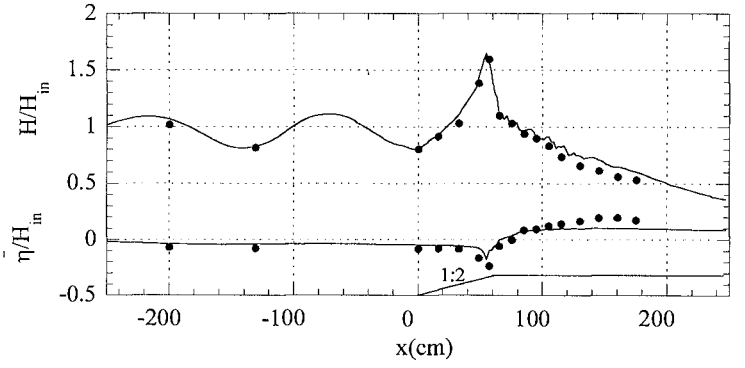

Fig.8 Comparison of wave height and mean water level distribution

The wave height distribution and mean water level changes are presented in Fig. 8. It is seen that the numerical simulation can give very good results of breaking waves incident on a submerged reef at the reflection side, near the breaking point, and at the transmission region. However, the calculation intends to underestimate the mean water level changes.

Figure 9 shows the filtered vorticity distribution of case B where BP denotes the position of measured breaking point. According to the calculation, the vortices in the figures are generated by two mechanisms, one is by the breaker, and the other one is by the presence of the submerged reef.

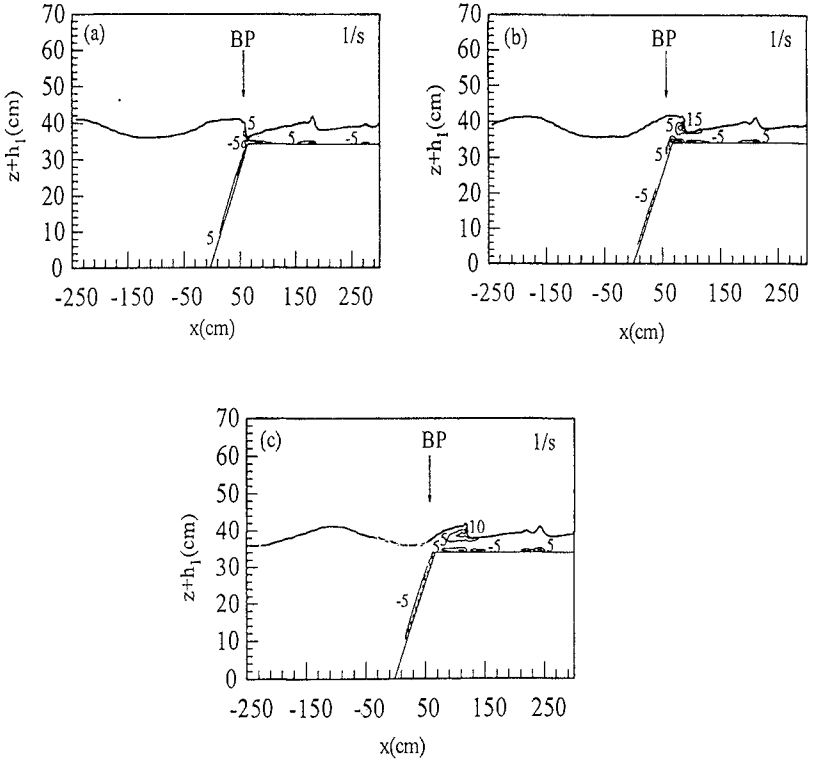

Fig. 9 Vorticity distribution at different phases:
approaching the breaking point(a); after wave breaking(b,c)

The figure indicates that the vortex generated by the breaker is initiated at the toe of the wave front. This vortex is further convected and diffused to almost the whole wave crest.

The other kind of vortices is due to the appearance of the submerged reef. Clockwise and counter-clockwise vortices are generated alternatively depending on the phase of the wave motion. These vortices are not as strong as the one generated by the breaker. They are also convected by the wave.

The figure also shows that for the present condition, the vortex generated by the breaker is confined above the trough level.

It should be noticed that the present model, as well as other two-dimensional models, lacks the three-dimensional vortex stretching mechanism. However, two-dimensional vortex stretching is enabled due to the numerical viscosity.

In Fig.10 we show the spatial distribution of the sub-grid scale eddy viscosity normalized by kinematic viscosity. The calculation shows that the highest eddy viscosity, about 120 times of the kinmeatic viscosity, is appeared slightly after the measured breaking point. The SGS eddy viscosity is smaller than those calculated from Reynolds-averaged equations. This is because that in the present method, only parts of the turbulence whose length scales are smaller than the mesh sizes are modeled. In the RANS models, all fluctuations are modeled. However, it seems premature to say at this stage that the fluctuations appeared in our calculation are turbulence. The fact that F is a step function and the air bubbles which occasionally appeared in the fluid may also contribute to these fluctuations. Further study is necessary. At the present stage, our model can only capture the major flow.

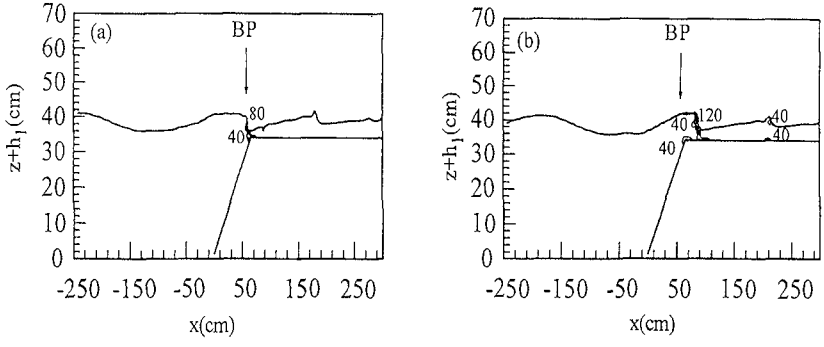

Fig.10 Normalized SGS eddy viscosity at:
approaching the breaking point(a); after wave breaking(b)

Conclusions and Further Improvements

In this paper, the VOF method is applied to simulate breaking waves incident on a submerged reef. In the calculation, an absorbing wave-maker is adopted to handle the wave reflection from the structure. In order to account for the sub-grid scale turbulence, a space filter is applied. The closure is given by Smagorinsky's model. The comparison between the simulation and experimental measurements showed satisfactory agreements. Future work would use a modified SGS model instead of Smagorinsky's SGS model, or develop 3D models to scrutinize the turbulent flow more carefully. The studies of air-water mixing and non-negligible density variations are also necessary.

Acknowledgements

The work presented here is part of the Ph.D. study of the first author. She is grateful to the Japanese Government and the Japan Society of Promotion of Science for granting her the Monbusho Scholarship and the JSPS fellowship to make this study and the presentation possible. The invaluable suggestions from Prof. Kiyoshi Horikawa, Emeritus of the University of Tokyo, and Dr.Vu Thanh Ca, Saitama University, are gratefully acknowldged.

References

Arai, M., Paul, U.K.,Cheng, L.Y. and Inoue,Y.(1993): A technique for open boundary treatment in numerical wave tanks. *Journal of the Society of Naval Architects of Japan,* **173**, 45-50.

Ashgriz, N. and Poo, J.Y.(1991): FLAIR: Flux line-segment model for advection and interface reconstruction. *J.Comput. Phys.,* **93**, 449-468.

Chan, R.C. and Street, R.L.(1970): A computer study of finite amplitude water waves. *J.Comput. Phys.,* **6** , 68-94.

Deardorff, J.W. (1970): A numerical study of three- dimensional turbulent channel flow at large Reynolds numbers. *J.Fluid Mech.,* **41, part 2** , 453-480.

Hirt, C.W. and Nichols, B. D.(1981): Volume of fluid (VOF) method for the dynamics of free boundaries. *J.Comput. Phys.,* **39** , 201-225.

Hughes, S.A.(1993): Physical models and laboratory techniques in coastal engineering. World Scientific. 333-379.

Kawasaki, K. and Iwata, K.(19978): Numerical analysis of two-dimensional plane wave deformation due to submerged structure(in Japanese). *Proc.of Coastal Engineering, JSCE* , **44(1)** , 81-85

Lemos, C.M.(1992): A simple numerical technique for turbulent flows with free surfaces. *Int. J. Numer. Methods. Fluids.* **15** , 127-146.

Lin, Pengzhi and Liu, Philip L.-F.(1998): A numerical study of breaking waves in the surf zone. *J. Fluid Mech.* **359** , 239-264.

Nakamura, S.(1995): Experimental study on wave velocities on a steep slope bottom(in Japanese). Bachelor thesis. Saitama University.

Petit, H.A.H., van Gent, M.R.A. and van den Bosch, P.(1994) : Numerical simulation and validation of plunging breakers using a 2D Navier-Stokes model. *Proc. 24th Int. Conf. on Coastal Eng., ASCE* , 511-524.

Sabeur, Z.A., Allsop, N.W., Beale, R.G. and Dennis, J.M.(1996): Wave dynamics at coastal structures: development of a numerical model for free surface flow.

Proc. 25th Int. Conf. on Coastal Eng., ASCE, 339-402.

van der Meer, J. W., Petit, H.A.H., van den Bosch, P., Klopman, G. and Broekens, R.D. (1992): Numerical simulation of wave motion on and in coastal structures. *Proc. 23rd Int. Conf. on Coastal Eng., ASCE*, 1772-1784.

van Gent, M.R.A., Tonjes, P., Petit, H.A.H., van den Bosch, P.(1994): Wave action on and in permeble structures. *Proc. 24th Int. Conf. on Coastal Eng., ASCE*, 1739-1753.

Zhao, Q., Nakamura, S. and Tanimoto, K.(1996):Distribution of particle velocities due to waves on very steep slope bottom. IAHR-APD, Langkawi, Maylaysia.

Zhao, Q.(1998):Wave kinematics on a submerged reef with a steep seaward face. Ph.D. thesis, Saitama University.

INFLUENCE OF STEEP SEABED SLOPES ON BREAKING WAVES FOR STRUCTURE DESIGN

N.W.H. Allsop[1], N. Durand[2] & D.P. Hurdle[3] ‡

ABSTRACT

Prediction of limiting wave heights in conditions of depth-induced breaking is subject to considerable uncertainties, yet the (local) wave height is probably the most important input variable in design of coastal, harbour or shoreline structures subject to wave action.

This paper presents selected results from laboratory experiments to measure depth-limited wave breaking over steep bed slopes (1:50, 30, 20, and 1:10) in fully random wave conditions. Experimental measurements are compared with predictions for H_{rms}, H_s and H_{max} under shoaling and breaking. The effects of shoaling and breaking on the wave height distributions are explored. An alternative empirical method to predict $H_{1/3}$ and H_{max} is suggested.

1. INTRODUCTION

1.1 Is there a problem?

Many coastal structures and some harbour breakwaters are constructed in relatively shallow water depths where the larger wave heights that constitute the primary input parameters in structure design are significantly influenced by depth-limited breaking. Prediction methods to calculate hydraulic or stability responses of these structures generally use the incident significant wave height (H_s) as primary input variable, often defined in the water depth at the seaward toe of the structure, h_s. Where wave breaking has significant influence on design wave heights, this approach therefore requires that prediction methods for depth-limiting must be robust and reliable.

‡ [1] Professor (associate) University of Sheffield, c/o HR Wallingford, Howbery Park, Wallingford, Oxon OX10 8BA, U.K. e-mail: w.allsop@sheffield.ac.uk

[2] Visiting Researcher at HR Wallingford, Howbery Park, Wallingford, OX10 8BA UK

[3] Senior Engineer, Alkyon Hydraulic Consultancy, PO Box 248, 8300 AE Emmeloord, Netherlands

Design methods for wave overtopping, armour movement and related responses require values of the incident significant wave height, $H_{1/3}$. In contrast, calculations of wave forces using Goda's method often use an upper limit estimate of H_{max} such as $H_{1/250}$. Neither of these values are reliably derived from wave breaking prediction methods which use spectral measures.

A few design methods use offshore wave heights in deeper water, say H_{so}, and use empirical methods to predict the response directly, calibrated for a range of simple bed slopes. The best-known examples are methods developed by Goda (1975, 1985) to predict overtopping or forces on vertical walls which use a single equivalent sea bed slope. Such methods assume that each approach bathymetry may be represented by a simple bed slope, and that the empirical prediction methods fully represent the effects of different wave transformations on the response of interest.

Most experimental studies on wave breaking have been on bed slopes shallower than 1:30, typically 1:50 or 1:100. On these slopes, wave shoaling is relatively mild, and wave breaking reasonably well understood, but there is growing evidence that steep bed slopes transform waves differently and give more severe hydraulic and structure responses. Jones & Allsop (1994), Southgate & Stripling (1996), Hamm & Peronnard (1997), Nelson (1997) and McConnell & Allsop (1998) demonstrate not only that many methods to predict wave conditions under breaking suffer from significant limitations, but that some responses seem to be particularly influenced by local sea bed slopes, in some instances to an extent not covered by using local wave heights in the calculations. These seem to be especially noticeable for slopes steeper than 1:50.

1.2 Research studies

New or improved methods to predict wave behaviour and breaker heights are needed to improve safety of structures constructed in the surf zone. In the first instance, a series of hydraulic model studies were completed by HR Wallingford for the Flood & Coast Defence division of the Ministry of Agriculture, Fisheries and Food (MAFF) to provide more information on wave breaking behaviour. Co-operation with Alkyon Consultancy & Research and TUDelft in the Netherlands to share laboratory and field data on wave breaking is intended to ensure as large and reliable a dataset as possible. It should however be noted that the results presented in this particular paper represent only part of the data, and relatively simple levels of analysis.

Other studies on wave breaking at vertical or composite breakwaters have been conducted as part of the EU PROVERBS project, see particularly Calabrese & Allsop (1998). Those studies have concentrated on whether wave conditions, depth and geometry will cause wave impacts on the wall, and are not intended to predict breaking / broken wave heights, so will not be addressed further here.

2. PREDICTION METHODS FOR WAVE BREAKING

This paper does not attempt to give an overall review of prediction methods for wave breaking, but draws on the review by Southgate (1995). Additional papers or reports are cited where they amplify or up-date that review. It may be noted that many of the methods cited by Southgate give information only at a single point, but in design of realistic structures, it is important that predictions be valid over a wide range of

relative depths / breaking regions. Predictions of wave breaking are tested here against measurements from the onset of breaking onwards.

The primary cause for wave breaking in deep water is that the wave steepness exceeds the fundamental limit given for individual waves by:

$$(H / L)_{max} = 0.142 \quad (1)$$

In shallow water, the main processes of interest in wave breaking may be divided into two. The first processes are those of wave transformations up to, but not beyond, the point of breaking. These include refraction and diffraction (neither discussed further here), and shoaling (here of considerable interest). These processes involve no significant loss of energy and are essentially reversible. The second set of processes are those which occur from breaking onwards. These processes involve significant loss of energy and are not reversible. It is noted that in some analysis, effects of shoaling and then breaking have been somewhat confused. Confusions may also have arisen from differences between regular waves (where all waves behave the same) and random waves (in which breaking positions and other features vary with period and height of each wave). These differences are particularly evident where methods to predict wave breaking have been developed using regular waves only, but are then applied to "real sea" cases where waves are random.

A final source of confusion is the use of significant wave height H_s in design methods, and numerical models to predict wave conditions, without more careful definition of its derivation, be it spectral ($H_s = H_{m0}$) or statistical ($H_s = H_{1/3}$). Differences between $H_{1/3}$ and H_{m0} were first highlighted by Thompson & Vincent (1984) and described more recently by Hamm & Peronnard (1997). The main problem arises where one method has been used to define wave conditions in model testing used to derive empirical design methods, and then a different method is used to derive design wave conditions. Comparisons in this study have shown that differences between $H_{1/3}$ and H_{m0} are greatest for low wave steepnesses when non-linear shoaling is pronounced.

2.1 Flat bed slopes

For very shallow bed slopes, usually taken as flatter than 1:100, it is often assumed that a simple limit to the individual wave height relative to local water depth may be given by:

$$H_{max} / h = 0.78 \quad (2a)$$

Later researchers showed that this limit, suggested by McCowan based on solitary wave theory (see Southgate, 1995), might be increased to $H_{max} / h = 0.83$. Perversely, Le Mehaute appears to give a much lower limit of individual wave height relative to local water depth:

$$H_{max} / h = 0.55 \quad (2b)$$

2.2 Sloping seabeds

The methods most frequently used in practical design calculations for structures are those by Weggel (1972), Goda (1975) and Owen (1980). Weggel used regular wave test data to derive simple empirical expressions to predict maximum wave heights in depth h_s:

$$H_{max} / h_s = b / (1 + a\, h_s /(gT^2)) \quad (3a)$$

wnere coefficients a and b are defined in terms of the seabed slope m:

$$a = 43.75\,(1 - \exp(-19m)) \quad (3b)$$

$$b = 1.56\,/(1 + \exp(-19.5m)) \quad (3c)$$

Goda (1975) developed a prediction method for irregular wave breaking, even suggesting a method to transform the wave height distribution under breaking conditions. For shoaling, Goda used Shuto's method instead of simple linear wave methods to give the shoaling coefficient K_s.

For wave breaking where $h/L_{po} \geq 0.2$:

$$H_{1/250} = 1.8\,K_s\,H_{so} \quad (4a)$$

For $h/L_{po} < 0.2$:

$$H_{1/250} = \min\{\,(\beta_0^* H_{so} + \beta_1^* h),\ \beta_{max}^* H_{so},\ 1.8\,K_s\,H_{so}\,\} \quad (4b)$$

where:

$$\beta_0^* = 0.052\,(H_{so}/L_{po})^{-0.38} \exp(20m^{1.5}) \quad (4c)$$

$$\beta_1^* = 0.63 \exp(3.8m) \quad (4d)$$

$$\beta_{max}^* = \max\{\,1.65,\ 0.53(H_{so}/L_{po})^{-0.29} \exp(2.4m)\,\} \quad (4e)$$

Where $H_{1/3}$ is needed in design, Goda suggested a similar method for $H_{1/3}$.

For $h/L_{po} \geq 0.2$:

$$H_{1/3} = K_s\,H_{so} \quad (4f)$$

For $h/L_{po} < 0.2$:

$$H_{1/3} = \min\{\,(\beta_0 H_{so} + \beta_1 h),\ \beta_{max} H_{so},\ K_s H_{so}\,\} \quad (4g)$$

where:

$$\beta_0 = 0.028\,(H_{so}/L_{po})^{-0.38} \exp(20m^{1.5}) \quad (4h)$$

$$\beta_1 = 0.52 \exp(4.2m) \quad (4i)$$

$$\beta_{max} = \max\{\,0.92,\ 0.32(H_{so}/L_{po})^{-0.29} \exp(2.4m)\,\} \quad (4j)$$

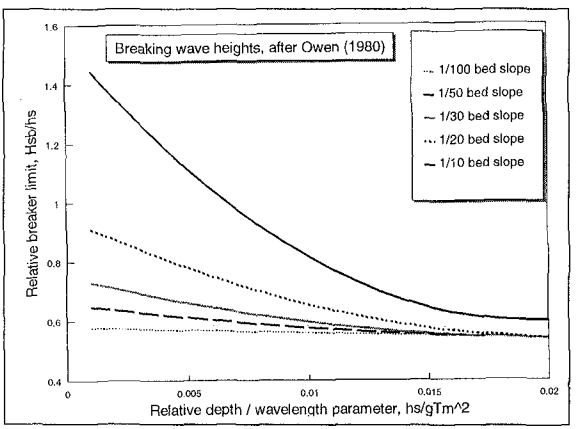

Figure 1 Simple breaking curves, after Owen

Noting that for steep bed slopes, waves may shoal substantially before breaking starts, Owen (1980) developed a simple method to provide first-estimates of the upper limit to the (significant) wave height H_{sb} in any water depth h_s for each of five bed slope. The method was derived as a part-way point in predicting wave overtopping of seawalls, and was not itself validated against any data on breaking wave heights. Owen's simple curves were derived graphically, see Figure 1, but were later described by empirical equations relating breaker index H_{sb}/h_s to relative depth $h_s/\,gT_m^2$:

Slope	Breaking limit, H_{sb}/h_s	
1/100	$H_{sb}/h_s = 0.58 - 2\,(h_s/ gT_m^2)$	(5a)
1/50	$H_{sb}/h_s = 0.66 - 10.583\,(h_s/ gT_m^2). + 229.17\,(h_s/ gT_m^2)^2$	(5b)
1/30	$H_{sb}/h_s = 0.75 - 20.083\,(h_s/ gT_m^2) + 479.17\,(h_s/ gT_m^2)^2$	(5c)
1/20	$H_{sb}/h_s = 0.95 - 38.417\,(h_s/ gT_m^2) + 895.83\,(h_s/ gT_m^2)^2$	(5d)
1/10	$H_{sb}/h_s = 1.54 - 97.83\,(h_s/ gT_m^2) + 2541.67\,(h_s/ gT_m^2)^2$	(5e)

In analysing laboratory and field data for slopes up to 1:20, Battjes & Stive (1984) did not detect any systematic dependence of wave conditions on slope, but did find an influence of wave steepness. They developed an expression for a breaking coefficient, taken by Southgate (1995) to give the limiting r.m.s. wave height:

$$H_{rms} / h = 0.5 + 0.4 \tanh (33\, H_{rms,o} / L_{po}) \quad (6)$$

The literature gives relatively little advice on changes to wave height distributions with breaking, but Simm (1991) cites equations for extreme wave heights $H_{0.1\%}$ and $H_{1\%}$ probably originating from Klopman & Stive (1989):

$$H_{1\%} = 1.517\, H_s / (1+(H_s/h_s))^{1/3} \quad (7a)$$

$$H_{0.1\%} = 1.859\, H_s / (1+(H_s/h_s))^{1/2} \quad (7b)$$

2.3 Numerical models

During this study, many of the wave measurements were also compared with two numerical models: WENDIS and COSMOS2D. **WENDIS** is a Wave ENergy DISsipation model, designed to estimate near-shore wave conditions at coastal structures where *shoaling* (linear shoaling theory), *bed friction* (Hunt and Bretschneider & Reid), and *wave breaking* (Weggel) may be significant. **COSMOS2D** is a numerical model of near-shore hydrodynamics, sediment transport and morphological changes which includes wave transformation by *refraction*, *shoaling* (linear wave theory), *bed friction* and *wave breaking* (Battjes & Stive and Weggel). Some of these comparisons were discussed by Durand & Allsop (1997).

3. EXPERIMENTAL STUDY

Wave conditions were measured using statistical (and later spectral) methods for 2 or 3 water levels over five different bed slopes:

1:50, indicative of shallow sand beach slopes;
1:30 and 20, indicative of steeper sand beaches;
1:10 and 1:7, indicative of rock coasts and shingle beaches.

The results discussed in this paper were mostly derived from supplementary tests conducted by the visiting researcher on a 1:30 slope, with some comparisons with data from the main series of tests on bed slopes of 1:50, 1:20 and 1:10. Additional data for a 1:10 slope by Allsop (1990) and on a 1:20 slope by Southgate & Stripling (1996) has not yet been included in these analyses.

3.1 Outline of experiments

The main tests used uni-modal or bi-modal seas, 30 wave conditions divided into six sequences of five tests, described by Hawkes et al (1998)and Coates et al (1998):

a) Wind-sea only

b) More wind-sea (80%) than swell (20%)
c) Equal wind-sea and swell
d. More swell (80%) than wind-sea (20%)
e. Swell only

Swell and wind sea conditions used standard JONSWAP spectra (γ=3.3) defined by H_s and T_p. Bi-modal conditions combined two JONSWAP spectra, each defined by H_s and T_p. Supplementary tests of wave breaking included a few regular wave conditions; some modified spectra of different spectral peakedness (γ=1 to 7), and a few rectangular spectra. Other measurements in tests reported by Hawkes et al (1998) and McConnell & Allsop (1998) included wave overtopping discharges, rock armour stability, and wave pressures / forces on vertical walls.

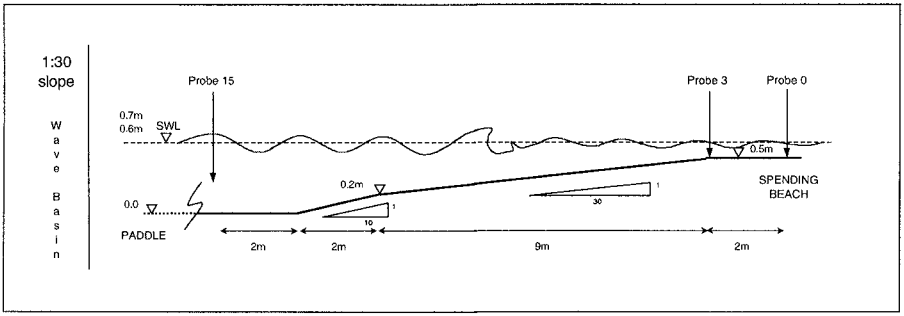

Figure 2 Configuration for supplementary tests on 1:30 bed slope

Most of the tests on wave breaking used the Absorbing Flume at Wallingford with a working length of 36m, and equipped with a random wave generator with computer-controlled absorption system. In each instance, the sea bed slope was terminated in a horizontal section below water, behind which was a gravel beach to absorb remaining wave energy. The supplementary tests on 1:30 slope used a 6m wide flume within a wave basin with two mobile piston paddles, and the 1:30 slope itself was slightly unusual as it featured a short steep (1:10) approach ramp at the toe, Figure 2.

Up to 16 wave probes were placed along the test sections, usually 1 or 2 probes in deep water near the wave paddle, 3 or 4 being placed along the horizontal section at the top of the slope, and the remaining probes up the slope. Each test was run for 500 waves or longer, sampled at 20 Hz (model) giving an average of 20-60 points per wave. In general, wave measurements were analysed statistically using a zero down-crossing definition for each wave. Selected data files were later also analysed spectrally, and some of the results of this analysis are discussed by Hurdle et al (1998) in an accompaning paper.

4. RESULTS

4.1 Parameters derived

Most wave measurements discussed here are presented as significant wave heights, $H_{1/3}$. Both spectral and statistical methods have been used to derive wave heights during these studies, but most weight in this paper will be given to statistical measures of wave height, particularly $H_s = H_{1/3}$. This should avoid problems of confusion

between H_{m0} and $H_{1/3}$ highlighted originally by Thompson & Vincent (1984), and most recently by Hamm & Peronnard (1997).

Two other measures of wave heights may be used. The maximum wave height H_{max} will depend on sample size, and is itself relatively unstable. In this study, H_{max} is generally given by $H_{99.8\%}$ or $H_{99.9\%}$. A more stable measure of wave height favoured by morpho-dynamic researchers is root mean square wave height, H_{rms}, defined spectrally as $H_{rms} = H_{m0}/\sqrt{2}$.

The main measures of wave period used here are the spectral peak period, T_p or mean period T_m. The peak period is more stable than the mean period measured either spectrally or statistically, and is less susceptible to distortion by measurement or calculation errors. Sea states have been categorised by the (fictional) steepness, $s_{po} = H_{so}/L_{po}$, where $L_{po} = gT_p^2/2\pi$, or the equivalent using the mean period, $s_{mo} = H_{so}/L_{mo}$.

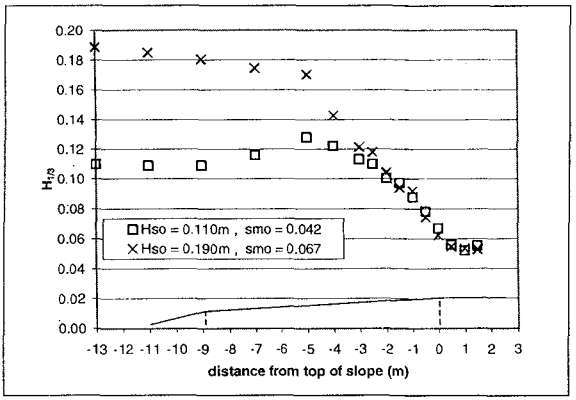

Figure 3 Effect of wave height on breaking for constant wave period, 1:30 slope

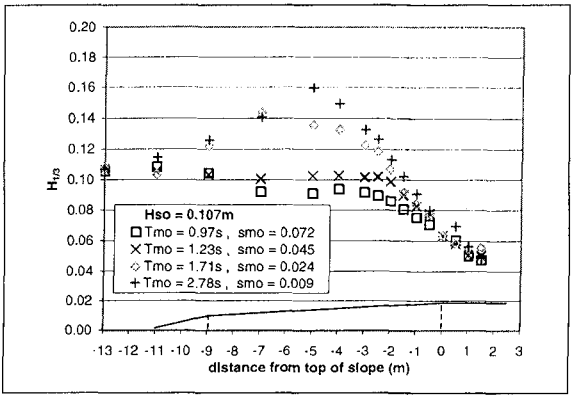

Figure 4 Effect of wave period on breaking for constant offshore wave height, 1:30 slope

4.2 General shoaling and breaking

The complex nature of breaking under random waves precludes any presentation of all features in a single graph. The initial form of presentation by Durand & Allsop (1997) is used here for the first few examples with measurements of local significant wave height against distance along the test flume, see Figure 3.

This presentation allows the effect of shoaling to be identified as waves react to the rising seabed. The onset of breaking occurs at the peak of the wave height, although in some tests this onset was quite difficult to assess. Breaking continues as the waves move into shallower water or, for some tests, over the

horizontal bed at the top of the slope, even if at a slower rate. For most of these tests, rates of breaking appear to be relatively constant for a particular bed slope, but breaking starts at different points along the slope and at different depths, depending upon offshore conditions.

The lowest steepness waves in Figure 4, $s_{mo} = 0.009$, shoal more than low steepness waves, $s_{mo} = 0.024$, or than the moderate steepness waves, $s_{mo} = 0.045$. The conditions shown in Figure 4 show little increase in wave height due to shoaling for wave steepnesses of $s_{mo} \geq 0.045$, but breaking starts quite far up the approach slope. Lower wave steepnesses show more shoaling, reach a greater wave height and breaking starts earlier.

Durand & Allsop (1997) compared transformations of the same (offshore) wave condition for bed slopes of 1:10, 1:20, and 1:30. Wave breaking on the 1:10 and 1:20 slopes was delayed compared with the 1:30 slope, as might be expected, but the breaking appeared to occur in similar water depths. Over the steeper slopes, the process of breaking and energy dissipation was compressed into rather shorter distances.

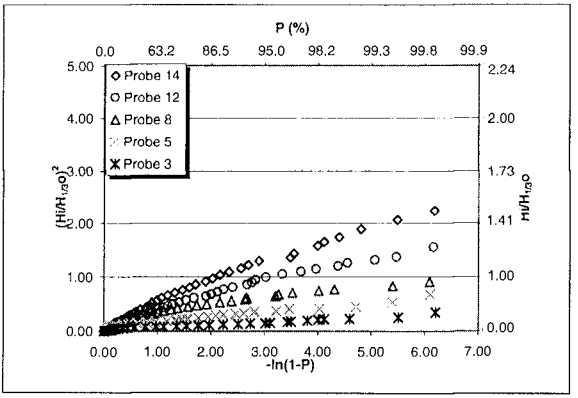

Figure 5 Individual wave heights, $s_{po} = 0.054$, 1:30 slope

4.3 Wave height distributions

Distributions of individual wave heights are not neccessarily of great interest to sediment and wave transformation modellers, but for designers of coastal / harbour or shoreline structures, changes to the distribution of wave heights, particularly to the probabilities of larger individual heights, are of considerable interest.

In deep water, individual wave heights, H_i, generally conform to a Rayleigh distribution. Such distributions plot as straight lines in the format used in Figures 5-8, where individual wave heights are presented as $(H_i/H_{s0})^2$, and non-exceedance probabilities as -ln(1-P). On these scales, -ln(1-P) = 2.0 corresponds to $H_{1/3}$ for a true Rayleigh distribution, $H_{98\%}$ is given by -ln(1-P) = 3.91, $H_{99\%}$ is given by -ln(1-P) = 4.61, and $H_{99.6\%}$ by -ln(1-P) = 5.52.

In Figures 5-8, wave probe 14 is in deepest water, probe 12 is about 2m (model) up the 1:30 slope, probes 8 and 5 are over the slope, and probe 3 is at the top of the slope.

Under breaking, the largest waves in the distribution break first, reducing towards the breaking limit. After some breaking, it is likely that a proportion of the energy will be re-distributed, perhaps combining with waves that have shoaled further. In still

shallower depths, further breaking will then apply over a greater part of the wave height distribution.

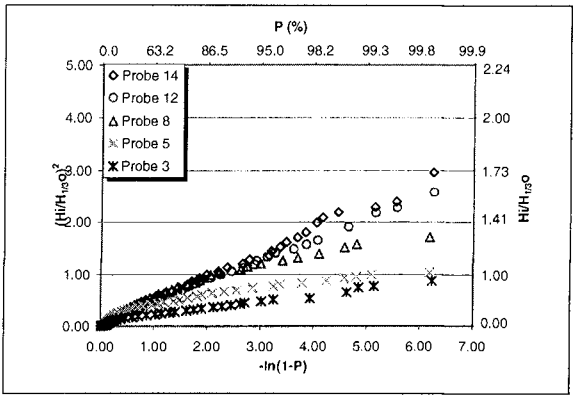

Figure 6 Individual wave heights, s_{po} = 0.034, 1:30 slope

Some of these processes are illustrated for a typically steep storm sea state (s_{po} = 0.054) in Figure 5. These results do not support the suggestion that individual waves above the breaking limit ($H_i > H_b$) will fall to that limit whilst waves smaller than the breaking limit are unaffected.

Even in the relatively shallow water in these test facilities, wave heights at the gauge in deepest water (probe 14) give only a slight curve away from the theoretical Rayleigh distribution. The effect of breaking for this sea state is relatively uniform, shown by the steady decrease of wave heights at each successive probe from that in deepest water (probe 14) to the shallowest (probe 3).

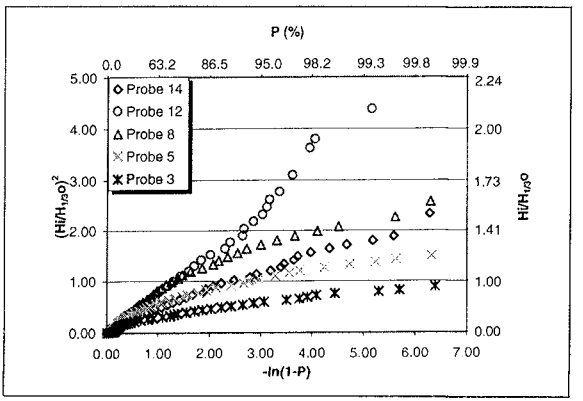

Figure 7 Individual wave heights, s_{po} = 0.018, 1:30 slope

Results for a smaller wave height and lower wave steepness (s_{po} = 0.034) shown in Figure 6 more closely match normal expectations. Individual heights up to H_s (given here by $H_{1/3}$ at -ln(1-P)=2.0) are hardly affected by wave breaking up to probe 8. There are however noticeable reductions in wave heights above 98%, reducing $H_{99.4\%}$ by perhaps 20%. This behaviour will be important for any response that is more strongly influenced by the largest waves in the distribution. Further inshore at probes 5 and 3, the effect of wave breaking again gives more uniform reductions of wave height across the full range of exceedance values.

Retaining the same offshore significant wave height, but further reducing the wave steepness to s_{po} = 0.018 in Figure 7, and s_{po} = 0.007 in Figure 8 gives more surprising

results, although some of these effects might have been anticipated from the shoaling behaviour shown by some of the results examined by Durand & Allsop (1997).

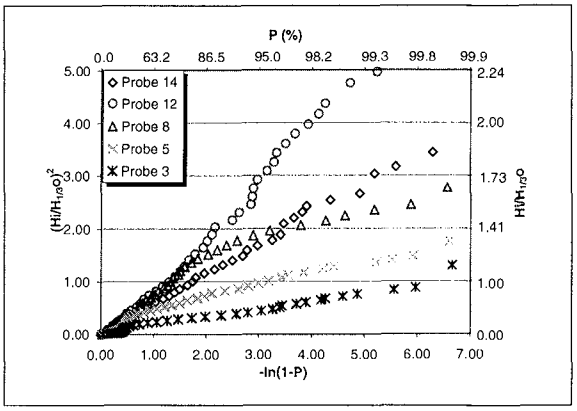

Figure 8 Individual wave heights, s_{p0} = 0.007, 1:30 slope

In Figure 7, the largest waves occur over the start of the approach slope (probes 12 and 8), particularly noticeable for wave heights above $H_{1/3}$. For very low steepnesses in Figure 8, wave heights at $H_{1/3}$ and higher non-exceedance levels increase markedly from the seaward point (probe 14) up the early part of the approach slope (probes 12 and 8). At this last position (probe 8), breaking only reduces individual wave heights below their offshore value above about 98% non-exceedance. Breaking only starts to reduce $H_{1/3}$ by probe 5, well up the approach slope.

4.4 Comparison with prediction methods

As discussed above, random waves do not give a single breaking point, so the identification of onset of breaking under random waves is difficult and may give inaccurate results. For simple prediction methods, more useful comparisons are with wave heights measured after the onset of breaking. These comparisons are however complicated by different definitions of wave height given by the different prediction methods. Weggel's and Goda's methods give estimates of wave heights close to the maximum, H_{max} and $H_{1/250}$, Owen's simple method gives estimates of H_{sb}.

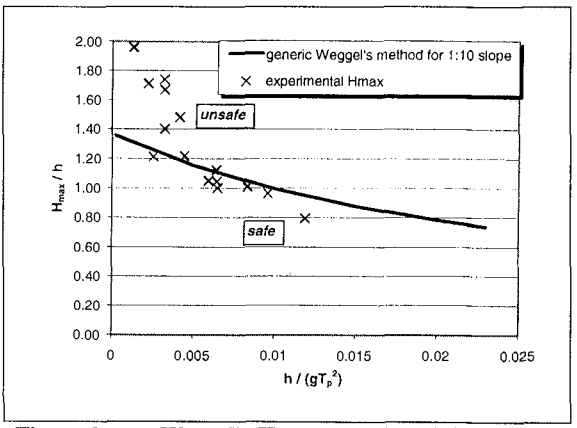

Figure 9 Weggel's H_{max} prediction, 1:10 slope

Considering first maximum wave heights, measurements of H_{max} shown relative to the local water depth as H_{max}/h_s are compared with predictions using Weggel's method for a bed slope of 1:10 in Figure 9, for a slope of 1:30 in Figure 10, and for a slope of 1:50 in Figure 11. The results have been taken from the point of breaking (indicated by the first

reduction of H_s , see for example Figures 3 & 4). Weggel's method does not predict shoaling, so no comparison is made for positions seaward of the breaking point.

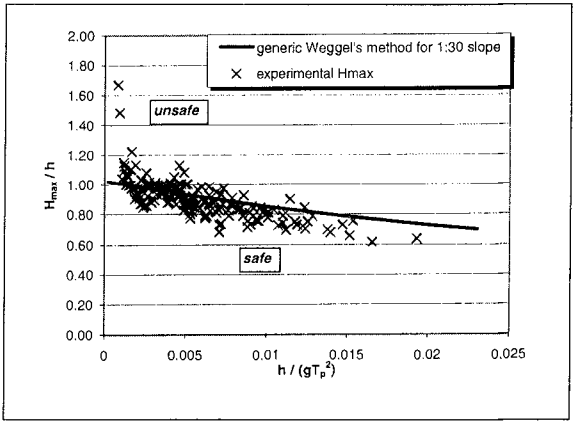

Figure 10 Weggel's H_{max} prediction, 1:30 slope

For the 1:10 slope in Figure 9, Weggel's prediction gives relative breaking heights H_{max}/h_s up to 1.4 at the lowest values of relative depth. Measured maximum wave heights significantly exceed the predicted values for $h/gT_p^2 < 0.005$, suggesting that the prediction method may give unsafe results in this region. Safer predictions for the 1:10 slope are given for $0.005 < h/gT_p^2 < 0.015$.

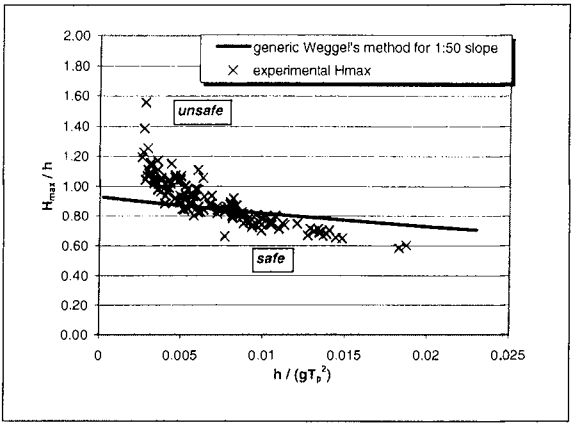

Figure 11 Weggel's H_{max} prediction, 1:50 slope

For the 1:30 slope in Figure 10, Weggel's prediction gives relative hreaking heights H_{max}/h_s up to about 1.0 at the lowest values of relative depth. Measured maximum wave heights significantly exceed predicted values for $h/gT_p^2 < 0.002$, suggesting that the prediction method may give unsafe results in this region. Safer predictions for the 1:30 slope are given for $0.002 < h/gT_p^2 < 0.02$.

For the 1:50 slope in Figure 11, Weggel's prediction gives relative breaking heights H_{max}/h_s up to about 0.9 at the lowest values of relative depth measured here. Maximum wave heights however significantly exceed predicted values for $h/gT_p^2 < 0.007$, suggesting that Weggel's method may give unsafe results in this region. Safer predictions for the 1:50 slope are given for $0.007 < h/gT_p^2 < 0.02$, but the prediction method does still not seem to reproduce well the general effect of increasing breaker index with decreasing relative depth h/gT_p^2.

Measurements of H_{max} from tests on the 1:30 slope were compared with predictions by Weggel's and Goda's methods by Durand & Allsop (1997). It was noted that only

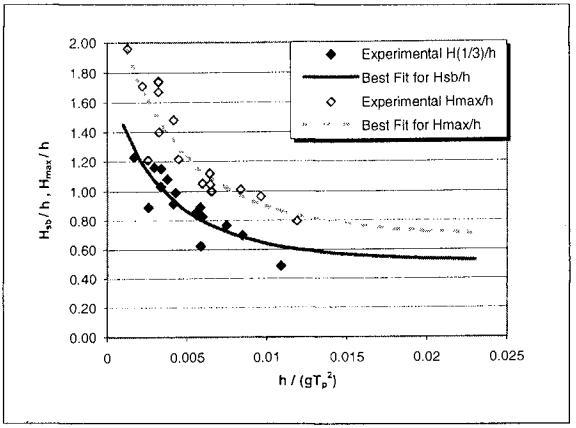

Figure 12 New prediction, 1:10 slope

a few design methods for coastal structures / breakwaters use the maximum wave height, or $H_{1/250}$ as used by Goda for wave forces on caissons. Most such methods require predictions of $H_{1/3}$. Goda's predictions for $H_{1/3}$ would therefore be potentially more useful, but these predictions agreed less well with measurements of $H_{1/3}$ than the agreement with H_{max}.

An alternative approach was therefore sought in which a revised empirical method was fitted to results for bed slopes of 1:10, 1:30 and 1:50, see figures 12-14. In deriving the new empirical method, it was important that the new method will:

a) reproduce the general form of breaking with respect to h/gT_p^2;
b) reproduce reliably the asymptote at high relative depths;
c) give better description of the breaking limits at low values of h/gT_p^2;
d) describe limits for H_s and H_{max} using equations of the same form.

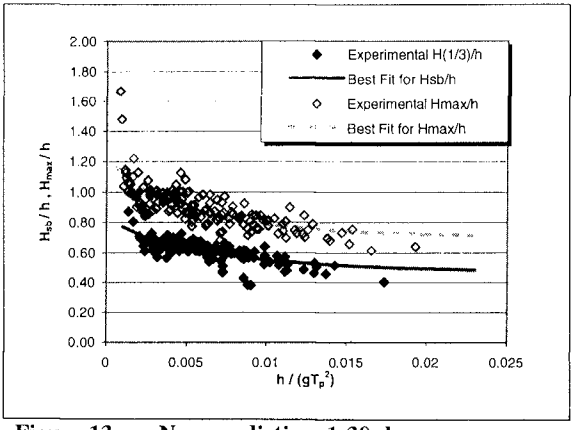

Figure 13 New prediction, 1:30 slope

It was also intended that the new method would be simple to apply in desk study calculations.

A form of equation relating both H_s / h_s and H_{max} / h_s to relative depth h/gT_p^2.was sought. Each potential method was tested against data from these studies for H_s and H_{max}, and for bed slopes of 1:10, 1:30 and 1:50. The equation was:

$$y = y_\infty + (y_0 - y_\infty)\, e^c \qquad (8)$$

where $y = H_{max} / h_s$ or $H_{1/3} / h_s$ $\qquad x = h_s / gT_p^2$

and $c = -bx^{0.78}$

Values of the coefficients were derived by minimising total errors in the fit to measured wave heights from these studies, and are summarised in Table 1:

Table 1: Coefficients for eqn 8

	Bed slope		
Coefficients for $H_{1/3}$	**1:50**	**1:30**	**1:10**
$(y_0 - y_\infty)$	0.831	0.394	1.394
b	69.33	44.78	69.88
y_∞	0.419	0.464	0.513
Coefficients for H_{max}			
$(y_0 - y_\infty)$	1.22	0.587	1.937
b	79.72	69.83	79.94
y_∞	0.621	0.700	0.679

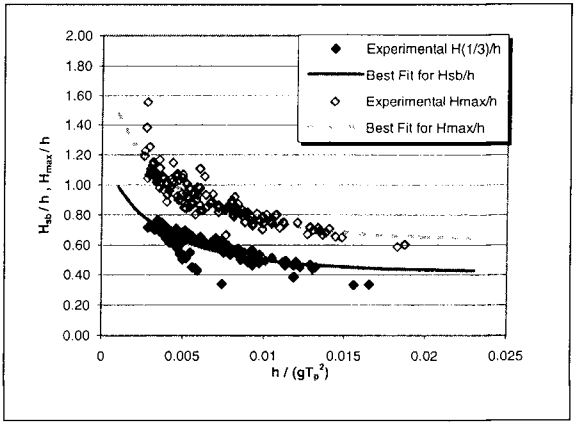

Figure 14 New prediction, 1:50 slope

5. CONCLUSIONS

These studies have demonstrated that present methods to predict inshore wave conditions on steep bed slopes for structure design suffer some important limitations.

Wave shoaling is particularly important in increasing wave heights on steep bed slopes, but requires the use of non-linear methods such as Shuto's to give the full increase of wave height over steep bed slopes.

Weggel's method is widely used to represent wave breaking in many numerical methods, but under-predicts breaking for low relative depths. A new set of equations / coefficients have been developed and are suggested here. Whilst still requiring further checking, the new methods seem relatively robust.

ACKNOWLEDGEMENTS

This paper is based on studies by the Coastal Group of HR Wallingford supported by the UK Ministry of Agriculture, Fisheries, and Food under Research Commissions FD02 and FD07, and by the EU's MAST project PROVERBS under MAS3-CT95-0041. Additional support was given by the University of Sheffield and HR Wallingford. The authors of this paper gratefully acknowledge assistance in processing data by Kirsty McConnell and Rob Jones. Particular thanks for help in deriving the new empirical method are due to Ivano Melito and Sebastien Bourban

REFERENCES

Allsop N.W.H (1990) "Rock armouring for coastal and shoreline structures: hydraulic model studies on the effects of armour grading" Report EX 1989, HR Wallingford.
Battjes J.A. & Stive M.J.F. (1984) "Calibration and verification of dissipation model for random breaking waves" Proc. 19th ICCE, Houston, publn. ASCE, New York.
Calabrese M. & Allsop N.W.H. (1998) "Prediction of wave breaking and impacts: summary of simplified method" Proc. 2nd Overall Workshop of PROVERBS Project, February 1998, Naples, publn. University of Braunschweig.
Coates T.T., Jones R.J. & Bona P.F.D. (1998) "Wind / swell seas and steep approach slopes: technical report on wave flume studies" Technical Report TR 24, HR Wallingford, Wallingford.
Durand N. & Allsop N.W.H. (1997) "Effects of steep bed slopes on depth-limited wave breaking" Proc. Conf. Waves '97, Virginia Beach, publn ASCE, New York.
Goda Y. (1975) "Irregular wave deformation in the surf zone " Coastal Engineering in Japan, Vol 18, pp13-26, JSCE, Tokyo.
Goda Y. (1985) "Random seas and maritime structures" University of Tokyo Press, Tokyo.
Hamm L. & Peronnard C. (1997) "Wave parameters in the nearshore: a clarification" Coastal Engineering Vol. 32, pp 119-135, Elsevier Scientific, Amsterdam.
Hawkes P.J., Coates T.T. & Jones R.J. (1998) "Impact of bi-modal seas on beaches and control structures" Research Report SR 507, HR Wallingford, Wallingford.
Hurdle D.P., van Vledder G.P. de Ronde J.G. & Allsop N.W.H. (1998) "Prediction of coastal design conditions in shallow water" Proc 26th ICCE, Copenhagen, ASCE.
Jones R.J. & Allsop N.W.H. (1994) "Rock armoured beach control structures on steep beaches" Proceedings 24th ICCE, Kobe, Japan, publn. ASCE, New York.
Klopman G. & Stive J.F. (1989) "Extreme waves and wave loading in shallow water" Paper to E & P Forum Workshop, 25-26 October 1989, Rueil Malmaisson, Paris
McConnell K.J. & Allsop N.W.H. (1998) "Wave forces on vertical walls: the influence of wind / swell seas and steep approach slopes" Strategic Research Report SR 509, HR Wallingford, Wallingford.
Nelson R. (1997) "Height limits in top down and bottom up wave environments" Coastal Engineering Vol. 32, pp 247-254, Elsevier Scientific, Amsterdam.
Owen M. W. (1980) "Design of sea walls allowing for wave overtopping" Report EX 924, Hydraulics Research, Wallingford.
Simm J.D. (Editor) (1991) "Manual on the use of rock in coastal and shoreline engineering" Special Publication 83, CIRIA (with CUR, the Netherlands), London.
Southgate H.N. (1995) "Prediction of wave breaking processes at the coastline" In Potential Flow of Fluids, Vol. 6 of Advances in Fluid Mechanics, Rahman E. (Editor), Computation Mechanics Publications, (available as HR published paper No 99)
Southgate H.N. & Stripling S. (1996) "Measurements of wave breaking in the UK Coastal Research Facility" Proc. 25th ICCE, Orlando, USA, publn. ASCE, New York.
Thompson E.F. & Vincent C.L. (1984) "Shallow water wave height parameters" Jo. Waterway, Port, Coastal and Ocean Engineering, Vol. 110, No 2, May 1984, Proceedings ASCE, New York.
Weggel J.R. (1972) "Maximum breaker height" Jo. Waterway, Harbour and Coastal Eng. Div., Proc. ASCE, Vol. 98, No WW4, pp 529-548, publn. ASCE, New York.

INFLUENCE OF FALSE WAVES ON WAVE RECORDS STATISTICS

Marcos H. Giménez[1], Carlos R. Sánchez-Carratalá[2], and Josep R. Medina[3], Member ASCE

ABSTRACT

Wave discretization is a usual procedure in ocean engineering for the statistical analysis of wave records. Different criteria can be used for performing that discretization. The orbital criterion presents important advantages with respect to the zero-up-crossing criterion, more commonly used. These criteria provide significantly different statistical results, as shown when applied to wave records from the scalar Waverider buoy of Valencia, off the Mediterranean Spanish coast.

INTRODUCTION

Statistical parameters, as the significant wave height and the mean wave period, are commonly used in coastal and maritime engineering applications. However, wave statistics depend on the criterion used for discretizing waves in a wave record. The zero-up-crossing (ZUC) criterion is the most widely used up to now. Recently, Giménez *et al.* (1994a) have proposed a new criterion for discretizing waves that is based in the analysis of the combined vertical and horizontal movement of a particle in the sea surface, and not only of its vertical movement as done by the other available criteria. The so-called *orbital criterion* has been shown to be more consistent and robust, and to have less variability than the ZUC criterion.

This paper presents the different results obtained when applying the ZUC and orbital criteria for the statistical analysis of wave records from a waverider buoy installed in front of the Valencia harbour in the Spanish coast. The accomplished comparison of both criteria in the time domain clearly shows the superiority of the

[1] Professor, Dept. of Applied Physics, Universidad Politécnica de Valencia, EUITI, Camino de Vera s/n, 46022-Valencia, Spain.

[2] Professor, Dept. of Applied Physics, Universidad Politécnica de Valencia, ETSICCP, Camino de Vera s/n, 46022-Valencia, Spain.

[3] Professor, Dept. of Transportation, Universidad Politécnica de Valencia, ETSICCP, Camino de Vera s/n, 46022-Valencia, Spain.

orbital criterion for the statistical analysis of wave records, giving results in better accordance with theoretical values.

ORBITAL CRITERION AND FALSE WAVES

In the ZUC criterion, a discrete wave is defined by two consecutive up-crossings of the mean level, that is, a complete cycle of vertical movement. As a consequence, results are very sensitive to the presence of small ripples in the sea surface as well as to the unavoidable noise in the measuring and transmission systems. In the orbital criterion, a discrete wave corresponds to a complete rotation of a surface point around its mean position. This rotation involves a complete cycle of both vertical and horizontal movement. For this reason, there could be ZUC waves that are not orbital waves: they are called false waves, since they lack some important properties that one would like to be fulfilled by progressive waves.

Fig. 1(a) shows a piece of a real wave record with three zero-up-crossings, denoted as A, B, C, and therefore two waves AB and BC according to the ZUC criterion. Fig. 1(b) shows the corresponding orbital representation in the complex plane, making it clear that there is only one complete rotation from A to C. Therefore, there is only one wave according to the orbital criterion, as indicated in Fig. 1(c). The aforementioned can also be applied to the piece of wave record shown in Fig. 2.

ADVANTAGES OF THE ORBITAL CRITERION

The presence of noise in a wave record results in the appearance of small waves that do not actually exist. Giménez *et al.* (1994a) have shown that most of them are false waves. Since the orbital criterion eliminates false waves, it is less sensitive to noise than the ZUC criterion. For instance, a 5% of noise results in an underestimation of the actual mean wave period of about a 5% -same level as noise- when using the orbital criterion. On the contrary, the error tends to be as high as a 20-25% when using the ZUC criterion. Furthermore, the orbital criterion is physically more consistent and, as proved by Giménez *et al.* (1994b), the mean period of orbital waves presents less sampling variability than the mean period of ZUC waves. Using ARMA random wave numerical simulations, Sánchez-Carratalá (1995) has pointed out the very good fitting of the sampling variability of many sea state parameters achieved when the orbital criterion for discretizing waves is used.

Advantages of the orbital criterion can be extended to the analysis of directional seas. As proposed by the IAHR Working Group on Wave Generation and Analysis (1989), the mean wave direction is commonly used as the representative direction of a directional sea state. The mean direction was defined by Longuet-Higgins (1957), and corresponds to the direction in which the energy is propagated. Therefore, its determination is essential in the study of many engineering problems, such as evaluation of longshore sediment transport or pollutant propagation and dispersion. Giménez and Sánchez-Carratalá (1997) have shown that the mean direction is the direction that presents the maximum number of orbital waves. Therefore, energy propagation is associated with orbital waves rather than with ZUC waves.

INFLUENCE OF THE DISCRETIZATION CRITERION ON WAVE STATISTICS

As mentioned above, Figs. 1 and 2 show two examples of the presence of false waves in real wave records. However, there is a significant difference between both of them. On the one hand, the false wave in Fig. 1 has its crest before its trough, and henceforth will be named crest-trough or CT-type false wave. On the other hand, the false wave in Fig. 2 has its trough before its crest, and consequently will be named trough-crest or TC-type false wave. It can be noted that the presence of false waves of any type results in one orbital wave whose wave period is the sum of the two corresponding ZUC wave periods. Therefore, the mean orbital wave period $\overline{T}_r$ will always be greater or equal than the mean ZUC wave period $\overline{T}_z$.

As shown by Longuet-Higgins (1958), following Rice (1954), the mean ZUC wave period for Gaussian waves is T_{02}. On the other hand, Giménez *et al.* (1994a) have proved, both mathematically and numerically, that the mean orbital wave period is T_{01}. The value of these spectral parameters is given by the following expression:

$$T_{ij} = \sqrt[j-i]{\frac{m_i}{m_j}} \tag{1}$$

where m_n is the *n*th order moment of the variance spectrum $S_\eta(f)$:

$$m_n = \int_0^\infty f^n S_\eta(f)\,df \tag{2}$$

and f is the frequency. It can be mathematically proved that $T_{01} \geq T_{02}$, in accordance with the fact that $\overline{T}_r \geq \overline{T}_z$.

The way in which a false wave affects the wave heights of a wave record depends on its type. On the one hand, a CT-type false wave, as the one shown in Fig. 1, results in a small ZUC wave followed by a higher one; the height of the corresponding orbital wave is the same as the higher ZUC wave. On the other hand, a TC-type false wave, as the one shown in Fig. 2, results in two medium-sized ZUC waves; the height of the corresponding orbital wave is higher than both ZUC waves. As a consequence, the value of any statistical wave height parameter (mean wave height, root mean square wave height, significant wave height) is greater for orbital waves than for ZUC waves. Furthermore, the distribution of orbital wave heights presents less small waves (because of CT-type false waves), less medium-sized waves (because of TC-type false waves) and more high waves (because of TC-type false waves).

The elimination of small ripples observed in real wave records is a usual procedure in ocean engineering. For instance, Rye (1974) and Thompson and Seelig (1984) propose to remove the waves whose height or period do not reach certain threshold values, because these waves are considered of secondary interest for

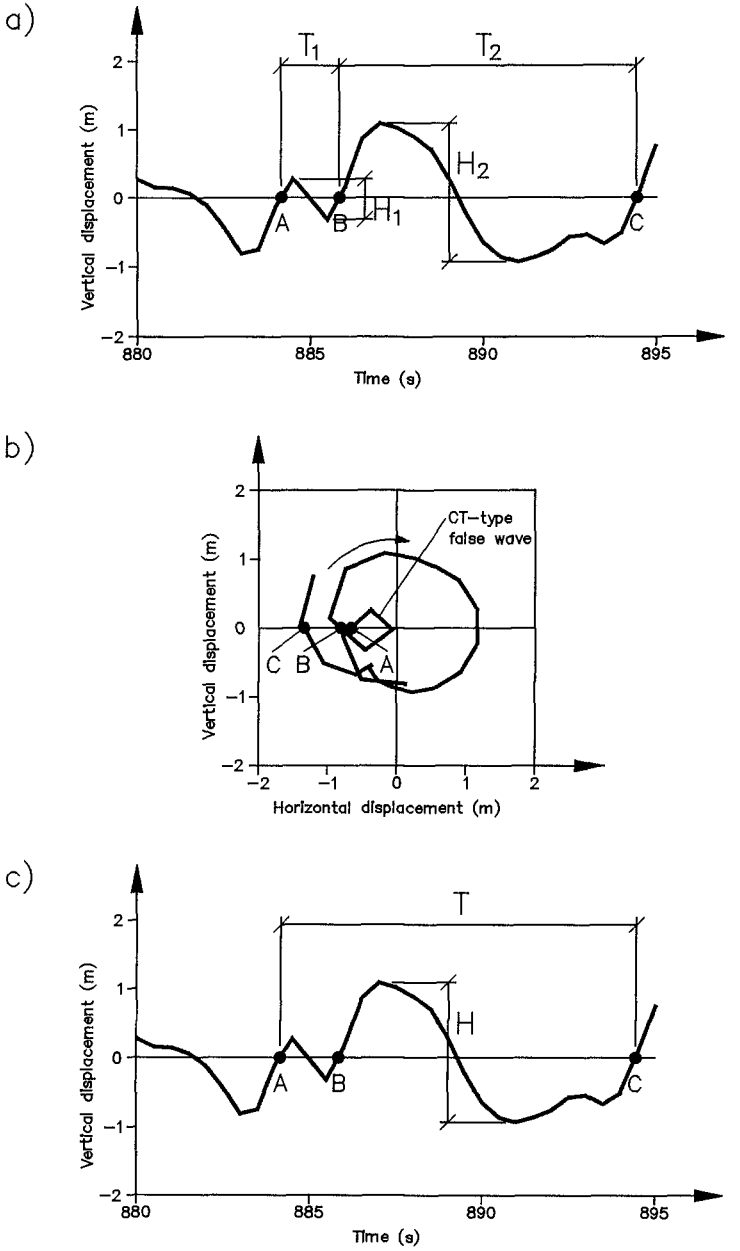

Figure 1. Example of CT-type false wave in wave record 0900010395V: a) ZUC waves; b) orbital analysis; c) orbital wave.

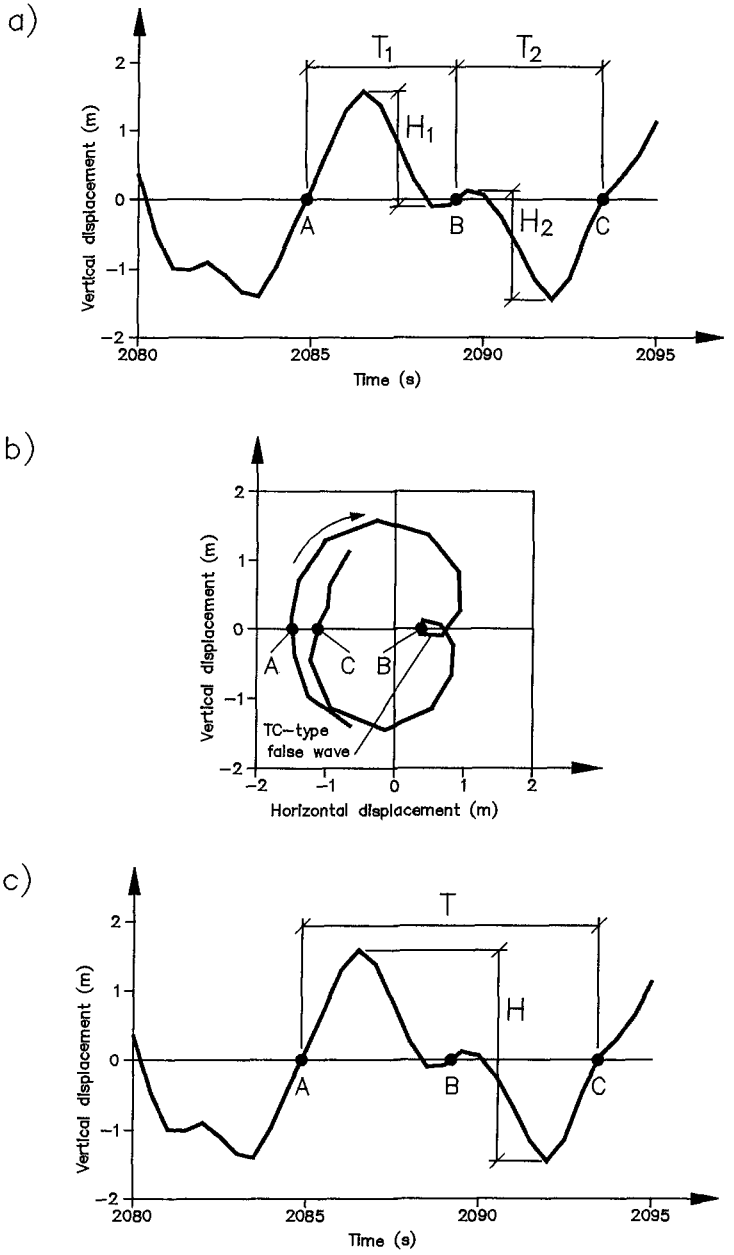

Figure 2. Example of TC-type false wave in wave record 0100010395V: a) ZUC waves; b) orbital analysis; c) orbital wave.

RECORD No.	1	2	3	4
Denomination	0100010395V	0500010395V	0900010395V	1300010395V
Date	3-1-95	3-1-95	3-1-95	3-1-95
Hour	1:00	5:00	9:00	13:00

Table 1. Description of the analyzed wave records.

engineering applications. These threshold values are obviously arbitrary, and they generally only remove the ripples that are ZUC waves, that is, the CT-type false waves. In this sense, the orbital criterion is more consistent and not arbitrary, and can be effectively used to avoid the effect of noise in wave records as suggested by Kitano and Mase (1998).

Using numerical simulations, Giménez *et al.* (1994b) have proved that wave statistics are altered by the selection of the wave discretization criterion. Pires-Silva and Medina (1994) have obtained significant differences in the mean periods of wave records from a waverider buoy located off the west coast of Portugal. In the next section, the results of applying the orbital and ZUC criteria to wave records from the scalar buoy of Valencia are analyzed.

WAVE RECORDS STATISTICS

The scalar buoy of Valencia is a Waverider buoy located in front of the Valencia harbour, off the Mediterranean Spanish coast, at 20 m water depth. Table 1

RECORD No.	1	2	3	4
m_0 (m^2)	0.579	0.469	0.486	0.404
T_{01} (s)	6.73	6.78	7.18	6.44
T_{02} (s)	6.14	6.10	6.51	5.85
$(8m_0)^{1/2}$ (m)	2.15	1.94	1.97	1.80
H_{m0} (m)	3.04	2.74	2.79	2.54
π_f (%)	8.9	10.0	9.2	9.3
Q_e	2.23	2.68	3.86	2.57
γ_{Qe}	0.80	1.63	3.75	1.44

Table 2. Spectral parameters of the analyzed wave records.

indicates the analyzed wave records, that have been taken from a storm with a return period of about 2 years, happened on March 1, 1995. Record length is 5120 points, and sampling interval 0.5 s. Fig. 3 shows the smoothed variance spectra of the analyzed records, with 32 degrees of freedom in each spectral component.

Spectral parameters

Table 2 shows some spectral parameters of the wave records. The parameters m_0, T_{01} and T_{02} have been defined in Eqs. (1) and (2), while $(8m_0)^{1/2}$ and $H_{m0}=4m_0^{1/2}$ are, respectively, the spectral estimations of the root mean square wave height and the significant wave height. The parameter $\pi_f=1-T_{02}/T_{01}$, that appears in Table 2 as a percentage, is the spectral estimation of the rate of false waves (see Giménez *et al.*, 1994a). Q_e is the spectral peakedness parameter introduced by Medina and Hudspeth (1987), divided by two for correcting its sampling bias, as indicated by van Vledder (1992) following Elgar *et al.* (1984). Finally, γ_{Q_e} is the peak enhancement factor of the JONSWAP-Goda spectrum (see Goda, 1979) that has the same value of Q_e.

Statistical parameters

Table 3 shows the number of orbital waves, N_r, and ZUC waves, N_z, that result of applying both criteria to the analyzed wave records. The parameter $p_f=1-N_r/N_z$, expressed in Table 3 as a percentage, is the rate of ZUC waves that are false waves. As it can be observed, its value is about a 10% for the storm under consideration.

Table 4 presents a set of wave height and period statistical parameters. The parameters $\overline{T}$, H_{rms} and $H_{1/3}$ are, respectively, the mean wave period, root mean square wave height and significant wave height. The subscripts *r* or *z* are used to indicate whether the orbital or the ZUC criterion has been applied. The relations between the values corresponding to both criteria are also given. As predicted by the theory, the mean orbital wave period is greater than the corresponding ZUC value, about a 10% for the analyzed wave records. The same can be stated for the characteristic orbital wave heights, that are greater, about a 5-7% in the case of H_{rms} and a 2-4% in the case of $H_{1/3}$, than the corresponding characteristic ZUC wave heights.

Figs. 4 and 5 show, respectively, the distributions of normalized wave heights and wave periods of the analyzed wave records. According to the theory, the use of

RECORD No.	1	2	3	4
N_r	376	368	351	383
N_z	411	408	390	431
p_f (%)	8.5	9.8	10.0	11.1

Table 3. Number of waves and percentage of false waves in the analyzed wave records.

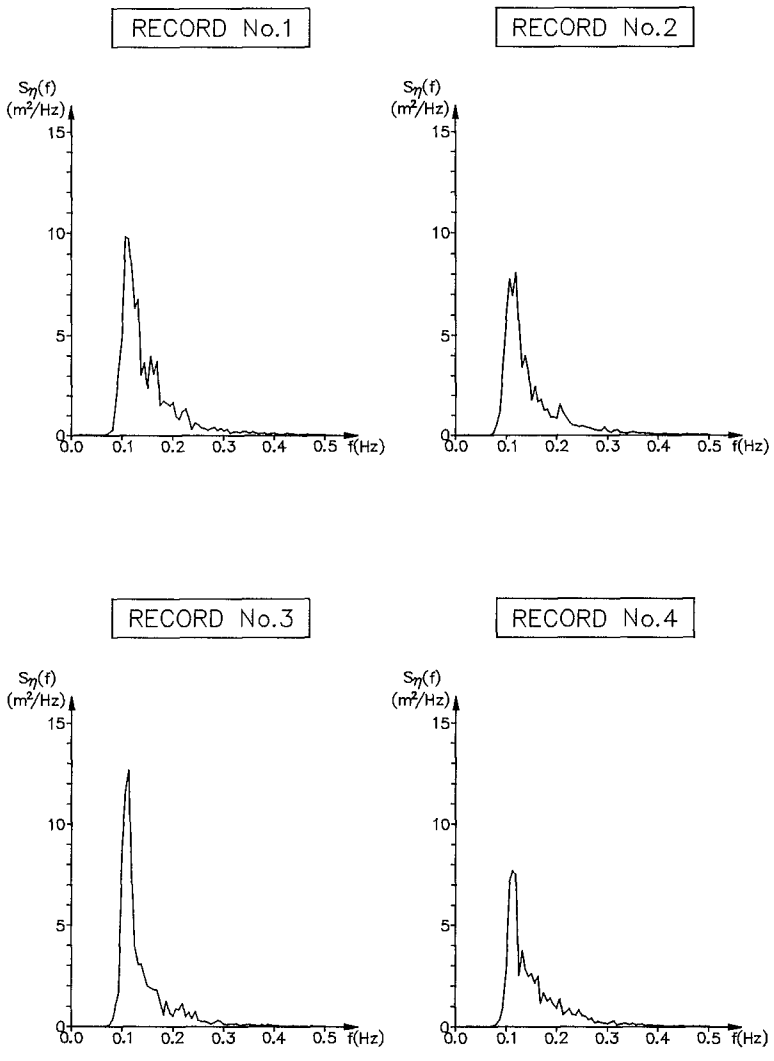

Figure 3. Smoothed variance spectra of the analyzed wave records.

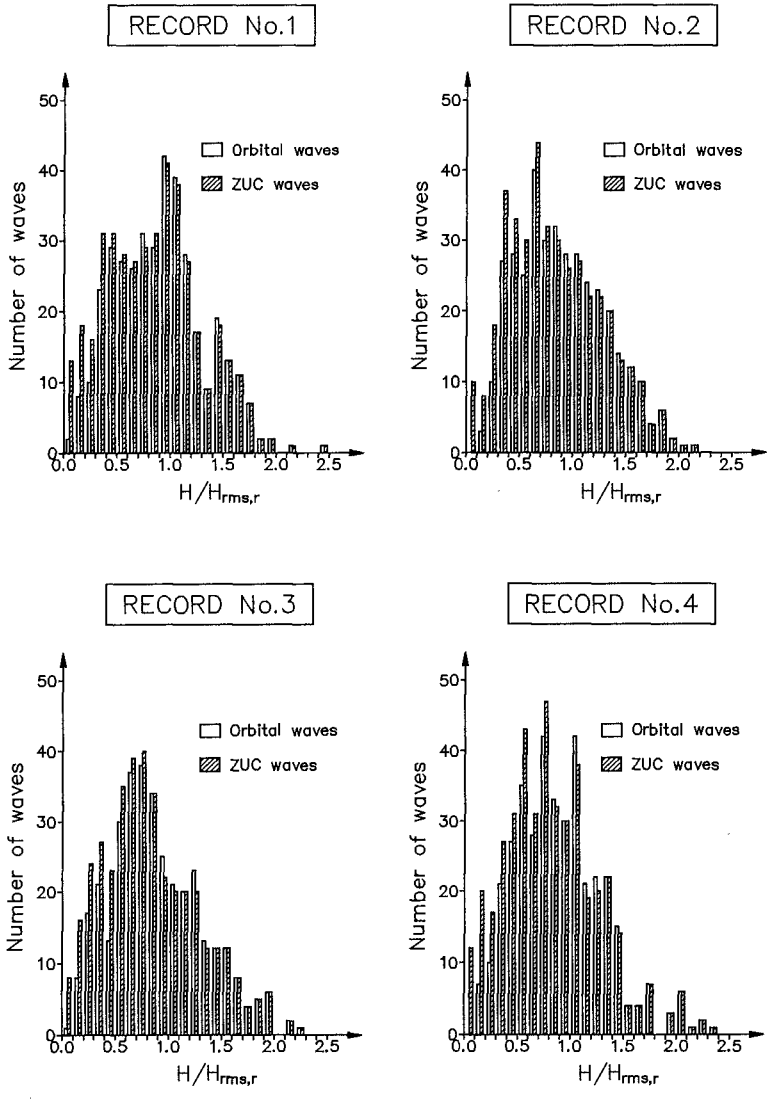

Figure 4. Distributions of normalized wave heights of the analyzed wave records.

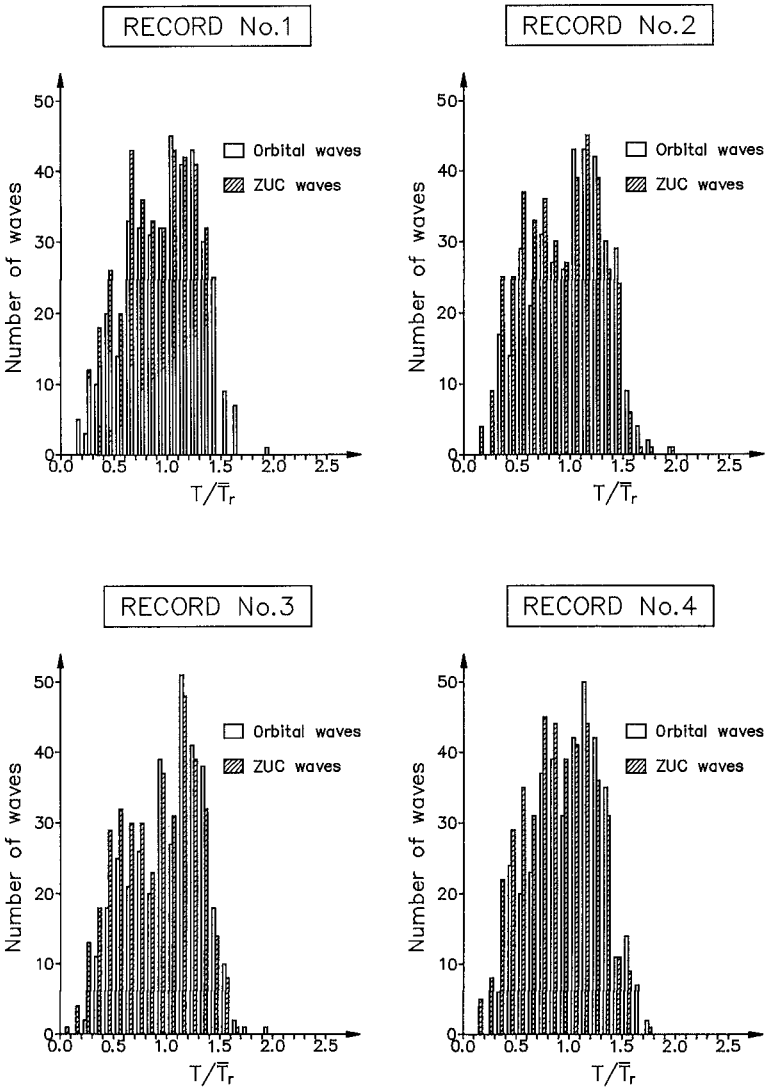

Figure 5. Distributions of normalized wave periods of the analyzed wave records.

RECORD No.	1	2	3	4
$\bar{T}_r$ (s)	6 78	6 93	7 25	6 65
$\bar{T}_z$ (s)	6 20	6 25	6 53	5 91
$\bar{T}_r / \bar{T}_z$	1 093	1 109	1 111	1 125
$H_{rms,r}$ (m)	2 15	1 93	1 98	1 81
$H_{rms,z}$ (m)	2 05	1 83	1 87	1 70
$H_{rms,r} / H_{rms,z}$	1 049	1 059	1 059	1 067
$H_{1/3,r}$ (m)	2 96	2 69	2 79	2 49
$H_{1/3,z}$ (m)	2 89	2 61	2 69	2 40
$H_{1/3,r} / H_{1/3,z}$	1 024	1 029	1 036	1 037

Table 4. Statistical parameters of the analyzed wave records

the orbital criterion results in less small and medium-sized waves, and more high waves Furthermore, the number of short period waves decreases, while the number of large period waves increases

Table 5 indicates, both for the orbital and the ZUC criteria, the values of the covariance coefficient between successive wave heights

$$c_{HH}(1) = \frac{\frac{1}{N-1}\sum_{i=1}^{N-1}\left(H_i - \bar{H}\right)\left(H_{i+1} - \bar{H}\right)}{\sigma_H^2} \qquad (3)$$

RECORD No.	1	2	3	4
$c_{HH,r}$ (1)	0 337	0 351	0 426	0 226
$c_{HH,z}$ (1)	0 298	0 332	0 366	0 199
$c_{HH,r}$ (1) / $c_{HH,z}$ (1)	1 131	1 057	1 164	1 133
$c_{HT,r}$ (0)	0 612	0 609	0 608	0 551
$c_{HT,z}$ (0)	0 720	0 723	0 701	0 690
$c_{HT,r}$ (0) / $c_{HT,z}$ (0)	0 850	0 843	0 866	0 799

Table 5. Covariance coefficients of the analyzed wave records

where $\overline{H}$ and σ_H are, respectively, the mean and standard deviation of wave heights Table 5 also includes the values of the covariance coefficient between wave height and wave period

$$c_{HT}(0) = \frac{\frac{1}{N}\sum_{i=1}^{N}(H_i-\overline{H})(T_i-\overline{T})}{\sigma_H \sigma_T} \quad (4)$$

where $\overline{T}$ and σ_T are, respectively, the mean and standard deviation of wave periods

As shown in Table 5, $c_{HH}(1)$ for orbital waves is up to a 16% greater than the corresponding value for ZUC waves This difference is a consequence of the elimination of small ripples in the sea surface that can significantly distort the length of run of wave groups (see Giménez *et al* , 1999) On the contrary, $c_{HT}(0)$ has a smaller value, about a 15-20%, when applying the orbital criterion In fact, most of the false waves that can be found in a wave record have both small height and small period, and therefore they contribute to a greater value of $c_{HT}(0)$ when the ZUC criterion -that does not eliminate those false waves- is used

Relations between statistical and spectral parameters

Table 6 presents the relations between statistical parameters and their corresponding spectral estimations observed in the analyzed wave records The following results can be remarked both the mean orbital wave period $\overline{T}_r$ and mean ZUC wave period $\overline{T}_z$ are close to their respective theoretical values, T_{01} and T_{02}, the root mean square orbital wave height is almost equal to its spectral estimation, while the corresponding results with ZUC waves differ about a 5%, the significant orbital wave height differs about a 2% with respect to its spectral estimation, while this

RECORD No.	1	2	3	4
$\overline{T}_r / T_{01}$	1 006	1 023	1 011	1 032
$\overline{T}_z / T_{02}$	1 010	1 025	1 002	1 010
$H_{rms,r} / (8m_0)^{1/2}$	0 998	0 998	1 004	1 007
$H_{rms,z} / (8m_0)^{1/2}$	0 952	0 943	0 948	0 943
$H_{1/3,r} / H_{m0}$	0 972	0 982	0 999	0 980
$H_{1/3,z} / H_{m0}$	0 949	0 954	0 965	0 946
p_f / π_f	0 961	0 977	1 082	1 205

Table 6. Relations between statistical and spectral parameters of the analyzed wave records

difference increases to about a 5% in the case of ZUC waves; the false waves rate can oscillate over an interval of $\pm 20\%$ around its spectral estimation.

CONCLUSIONS

The results obtained with the application of the zero-up-crossing criterion for the analysis of real wave records are very sensitive to the presence of small ripples of secondary interest in ocean engineering, as well as to the unavoidable noise in the measuring and transmission systems. On the contrary, the orbital criterion is more consistent and robust, and avoids the arbitrary selection of threshold levels for removing small ripples in the statistical analysis.

The accomplished analysis of wave records from the scalar buoy of Valencia makes clear the influence of the selected discretization criterion on wave records statistics. The orbital wave heights and periods are, on the average, greater than the corresponding ZUC values, and show a better accordance with their corresponding spectral estimations.

ACKNOWLEDGEMENTS

The authors gratefully acknowledge the collaboration of the Departamento Técnico de Clima Marítimo (Puertos del Estado), that provided the wave records used in the development of the present work.

REFERENCES

Elgar, S., Guza, R.T., and Seymour, R.J. (1984). "Groups of waves in shallow water." *J. Geophysical Research*, 89(C3), 3623-3634.

Giménez, M.H., and Sánchez-Carratalá, C.R. (1997). "Influence of false waves in the determination of wave energy propagation near the coast." *Proc. 3rd International Conference on Computer Modelling of Seas and Coastal Regions. COASTAL 97*, J.R. Acinas and C.A. Brebbia, eds., La Coruña, Spain, 283-291.

Giménez, M.H., Sánchez-Carratalá, C.R., and Medina, J.R. (1994a). "Analysis of false waves in numerical sea simulations." *Ocean Engineering*, 21(8), 751-764.

Giménez, M.H., Sánchez-Carratalá, C.R., and Medina, J.R. (1994b). "False waves in wave records and numerical simulations." *Proc. 24th International Conference on Coastal Engineering*, ASCE, Kobe, Japan, 192-206.

Giménez, M.H., Sánchez-Carratalá, C.R., and Salinas, I. (1999). "Influence of wave discretization criterion on wave grouping characteristics." *Proc. 1st International MEDCOAST Conference on Wind and Wave Climate of the Mediterranean and the Black Sea*, Antalya, Turkey (submitted).

Goda, Y. (1979). "A review on statistical interpretation of wave data." *Rep. Port and Harbour Research Institute*, Yokosuka Japan, 18(1), 5-32.

IAHR Working Group on Wave Generation and Analysis (1989). "List of sea-state parameters." *J. Waterway, Port, Coastal, and Ocean Engineering*, ASCE, 115(6), 793-808.

Kitano, T., and Mase, H. (1998). "New theoretical aspects of statistical properties of narrow-banded random waves." *Ocean Engineering*, 25(2-3), 183-193.

Longuet-Higgins, M.S. (1957). "The statistical analysis of a random, moving surface." *Phil. Trans. Roy. Soc. London*, Ser. A, 249, 321-387.

Longuet-Higgins, M.S. (1958). "On the intervals between successive zeros of a random function." *Phil. Trans. Roy. Soc. London*, Ser. A, 246, 99-118.

Medina, J.R., and Hudspeth, R.T. (1987). "Sea states defined by wave height and period functions." *Proc. IAHR Seminar on Wave Analysis and Generation in Laboratory Basins*, 2nd IAHR Congress, Lausanne, Switzerland, 249-259.

Pires-Silva, A.A., and Medina, J.R. (1994). "False waves in wave records." *Ocean Engineering*, 21(8), 765-770.

Rice, S.O. (1954). "The mathematical analysis of random noise." *Selected Papers on Noise and Stochastic Processes*, Nelson Wax, ed., Dover Publications, New York.

Rye, H. (1974). "Wave group formation among storm waves." *Proc. 14th International Conference on Coastal Engineering*, ASCE, Copenhagen, Denmark, 164-183.

Sánchez-Carratalá, C.R. (1995). *Statistical and spectral evaluation of numerical random wave simulation techniques*. Ph.D. Thesis, S.P. Universidad Politécnica de Valencia, SPUPV-95.2088, Valencia, Spain (in Spanish).

Thompson, E.F., and Seelig, W.N. (1984). "High wave grouping in shallow water." *J. Waterway, Port, Coastal, and Ocean Engineering*, ASCE, 110(2), 139-157.

van Vledder, G.Ph. (1992). "Statistics of wave group parameters." *Proc. 23rd International Conference on Coastal Engineering*, ASCE, Venice, Italy, 946-959.

Changing of local wave climate due to ebb delta migration

Ralf Kaiser[1] & Hanz D. Niemeyer[1]

Abstract:

Field measurements highlighted enormous changes in the attenuation of waves propagating from offshore across the ebb delta on the shore face of the East Frisian island of Norderney. The application of mathematical wave model SWAN made evident that the migration of the ebb delta is the cause of these changes. The results are very important for coastal protection measures.

Introduction

The fate of a combined shore face and beach nourishment on the East Frisian island of Norderney (fig. 1) was evaluated. This study was part of the NOURTEC project (Innovative Nourishment Technologies) [Niemeyer et al. 1995] in the framework of the MAST II - Program of the Commission of the European Communities and commissioned to Danish, Dutch and German institutions. Necessarily investigations on local wave climate were incorporated basing as well on field measurements as on mathematical wave models [Niemeyer et al. 1997].

Fig. 1: Location map with stations of directional wave buoy measurements ⊙

[1] Coastal Research Station of the Lower Saxonian Central State Board for Ecology, P.O. Box 1221, 26534 Norderney/East Frisa, Germany

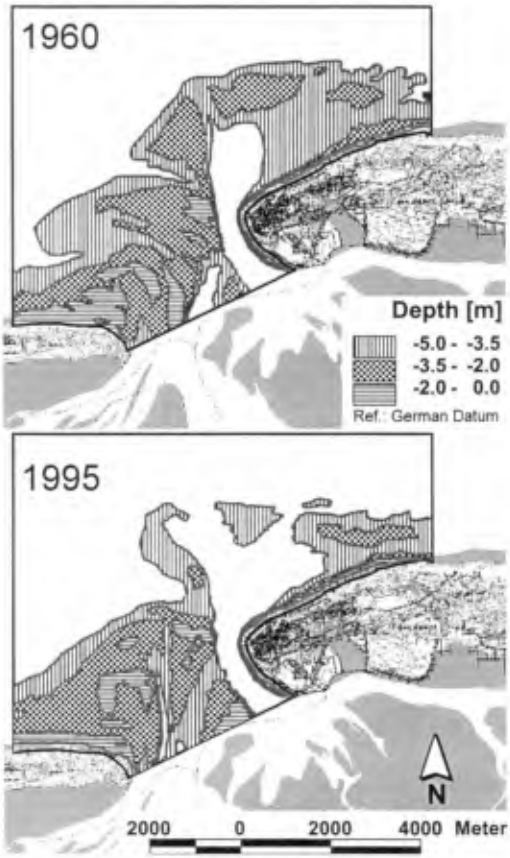

Fig. 2: Change of the higher ebb delta shoals of the Norderneyer Seegat between 1960 and 1995

Field measurements were carried out by directional wave riders (fig. 1); both the well-established second generation model HISWA [Holthuijsen & Booij 1987; Booij & Holthuijsen 1992] and the newly developed third generation model SWAN [Ris 1997; Holthuijsen et. al 1997] have been applied, where the latter is referred to in this paper. The joint application of field measurements and mathematical modeling is regarded as an effective approach for gaining as well reliable data as spatial information on local wave climate.

Field measurements in the offshore area and on the shore face of the island of Norderney highlighted enormous changes in wave damping on the ebb delta of the tidal inlet. In comparison to results from earlier investigations [Niemeyer 1987] waves propagating across the ebb delta are significantly lesser attenuated than before. Even for conditions with no remarkable set-up above mean high tide the shelter effect of the ebb delta for the northwestern shoreface of the island was remarkably reduced.

This change in the shoreface wave climate is a result of the changes of the ebb delta morphology of the Norderneyer Seegat in the last 35 years (fig. 2). Whereas the southwestern part of the system has not changed decisively, the central section has suffered substantial erosion particulary in the upper part. Even the -5m line (with respect to German Datum, which is about mean sea level) which is regarded as the base line of the ebb delta system has two openings, allowing the penetration of higher waves on the shoreface.

In order to get a deeper and more systematic insight into background of these processes runs with the mathematical wave model SWAN [RIS et al. 1995] have been carried out for four distinct morphological situations of the area seaward of the tidal inlet and the northwestern shore of the island of Norderney: the bathymetries of 1960, 1975, 1990 and 1995 were used as a basis for model topography.

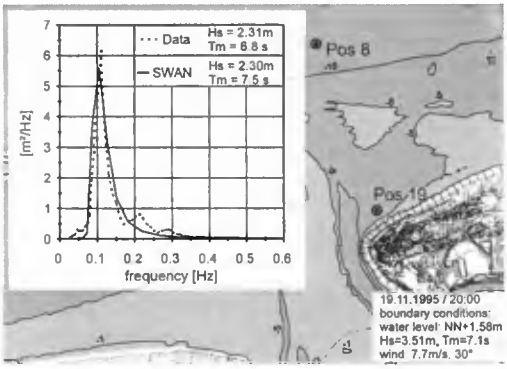

Fig. 3: Comparison of the measured and calculated energy spectrum at Pos. 19

Verification and Sensitivity study

The verification was carried out for several distinct water levels and offshore wave boundary conditions. The results for Pos. 19 are generally good und sometimes excellent (fig. 3). It became apparent that the fitting of model results and measurements or the northwestern shoreface of Norderney improves, if the TRIAD option in SWAN is switched off. With this setting SWAN generally gives a good representation of the spectrum with a slight underprediction of the significant wave height and slight overprediction of the mean wave period at Pos. 19. For other positions in the inner part of the inlet the incorparation of the TRIAD interaction gives the better results. Since the major interest of this study is focussed in wave climate on the shoreface of the north western beach, in all runs discussed for this case the TRIAD interaction have been switched off.

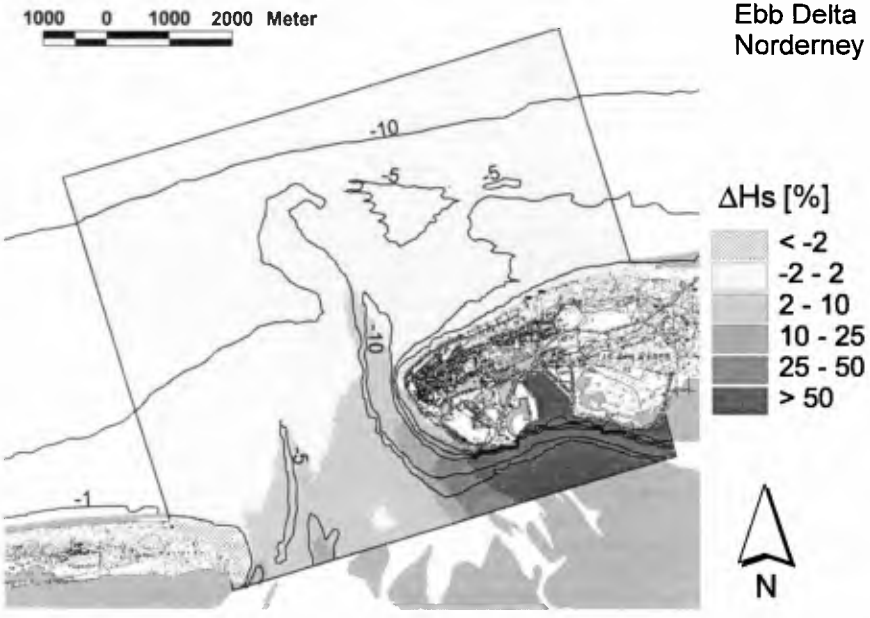

Fig. 4: Increase of significant wave heights due to uniform local wind; boundary conditions: Water level: MSL+1.58m; Hs=3.51m, Tm=7.1s; Wind: 7.7 m/s, 30°

Checking the neccessity of a local varying wind field a crude estimation can be done in comparing model results with a uniform wind field to a run with out any wind (fig. 4). The difference between wave heights for situations with no wind and uniform wind are smaller than 2% on the shoreface. Therefore it is not necessary to imply here a local varying wind field. Further inwards in the inlet and especially behind the island the influence of the local wind becomes substantial, so that there might be the demand for a local varying wind field.

It became also significantly evident that the application of the third generation model SWAN delivers results matching much better the prototype data than with the second generation model HISWA achivable (Niemeyer & Kaiser 1998). Furthermore SWAN delivers full spectral information.

Morphological changes of the ebb delta

The comparison of the topography for the distinct four situations makes significant morphological changes evident (fig. 5): Whereas the ebb delta is becoming even more pronounced after 1960 with a climax in 1975 the later surveys in 1990 and 1995 highlight a reduction of the shallows with heights above German datum NN - 5 m accompanied by a migration and seaward directed deepening of the main inlet channel between 1990 and 1995: Both morphological changes enhance onshore wave penetration in direction of the island's northwestern shores.

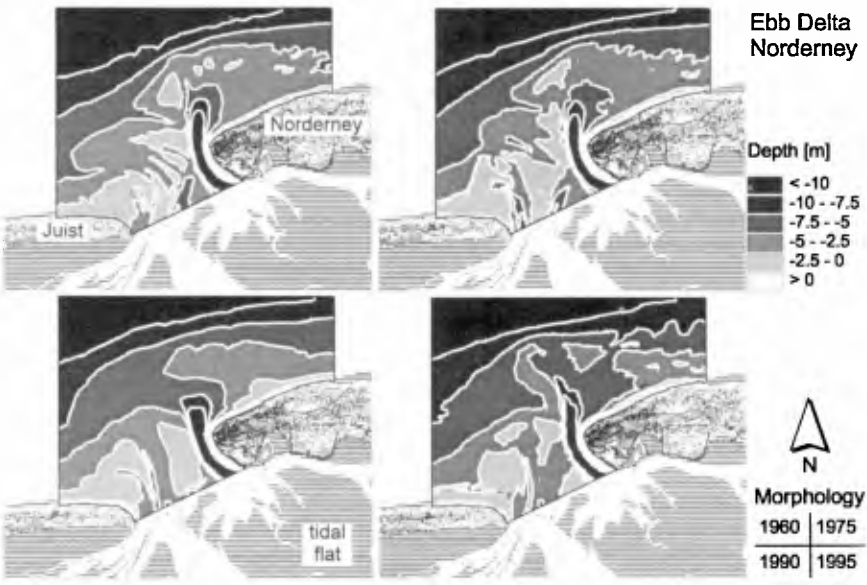

Fig. 5: Bathymetry of the seaward area of the western part of the island of Norderney with the ebb delta in 1960, 1975, 1990 and 1995 (depths related to German datum NN= MSL)

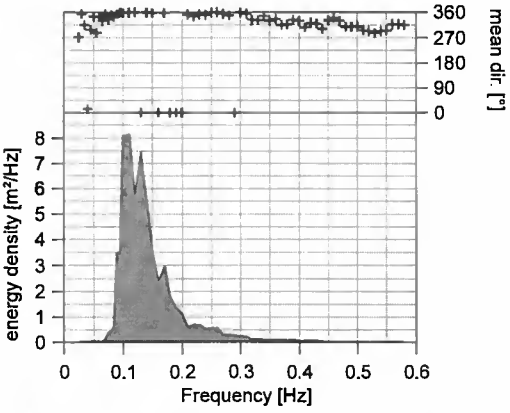

Fig. 6: Measured spectrum at the seeaward boundary at 17.11.95, 04:58

Model results

ordinary tide

The models have been run for distinct water levels and offshore wave parameters as seaward boundary conditions. Exemplary for an ordinary tide the results of a run with the following boundary conditions are highlighted here which have been gained from field measurements: Set-up of about 0,3m above MHWL (in sum equivalent to a water level of NN + 1,42 m) and an offshore wave field (fig. 6) with a significant wave height Hs = 2,98 m and a peak period Tp = 6,4 s. Wind comes from 344° with a velocity of 8.2 m/s. The model runs with SWAN confirm the impression already gained from field measurements with respect to the penetration of

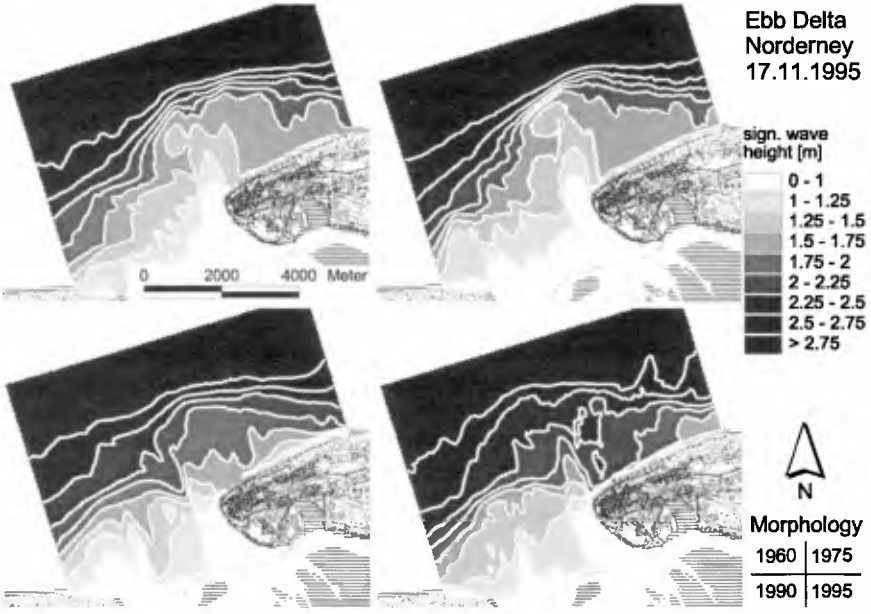

Fig. 7: Significant wave heights in the offshore area, in the tidal inlet Norderneyer Seegat and on the northwestern shoreface of the island of Norderney in 1960, 1975, 1990 and 1995. Boundary conditions: Water level: MSL+1.42m; Wind: 8.2m/s, 344°

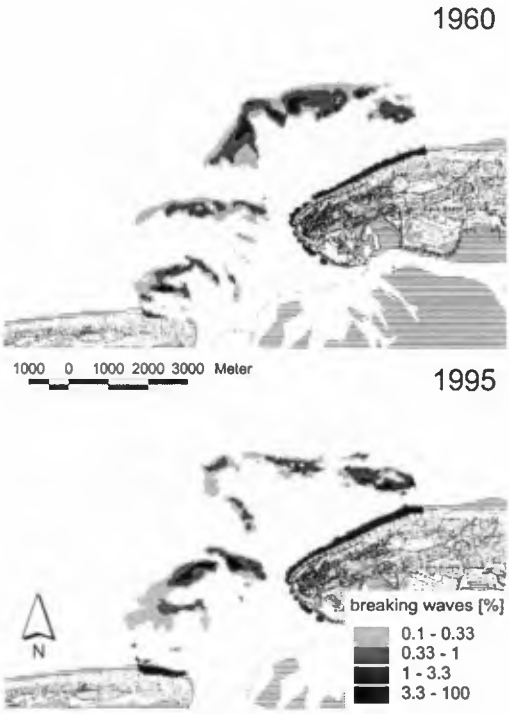

Fig. 8: Percentage of breaking waves in the 'normal' situation of 10.01.95 calculated with the morphology of 1960 and 1995

higher waves onto the northwestern shoreface of the island of Norderney (fig. 7): For the situations of 1960 and 1975 no significant changes occur. But already for the topography of 1990 higher waves with 1,75 m < Hs < 2,00 m propagate across the ebb delta though not appearing nearshore. For the topography of 1995 waves with heights with this order of magnitude occur on a large part of the shoreface. This increase in nearshore wave energy has the same trend as prototype data; the measured wave heights on the shoreface are even slightly higher than those being computed with the model for the same offshore conditions.

The comparison between the portion of breaking waves for the topography of 1960 and 1995 highlights the change in wave transformation over the bars of the ebb delta (fig. 8). In 1960 there is a broad breaker zone at the offshore edge of the eastern ebb delta and two successive breaker systems in the western part. In 1995 there is much lesser wave breaking on the shoals of the ebb delta in its central and eastern part. Also the formerly existing two breaker zones in the western part have changed into a more pronounced single one due to the higher shoals of 1995 in that area.

In order to make the effect of this change in local wave climate more evident for the dynamics on the northwestern shore face and beaches of the island of Norderney the computed significant wave heights for all four morphological situations are compared at 17 selected points at the edge of shore face and beach parallel to the island's northwestern shore (fig. 9). For the situations of 1960 and 1975 there are no remarkable changes in wave climate. The significant wave heights are of the same order of magnitude on the whole stretch of the northwestern shore face. In 1990 there is an increase of wave heights up to 40%, particularly in the stretch between the reference points 3 and 5 but they decrease further downdrift and become even smaller in the eastern part of the study area. In 1995 wave height have additionally increased in all places downdrift of point 4 (fig. 9).

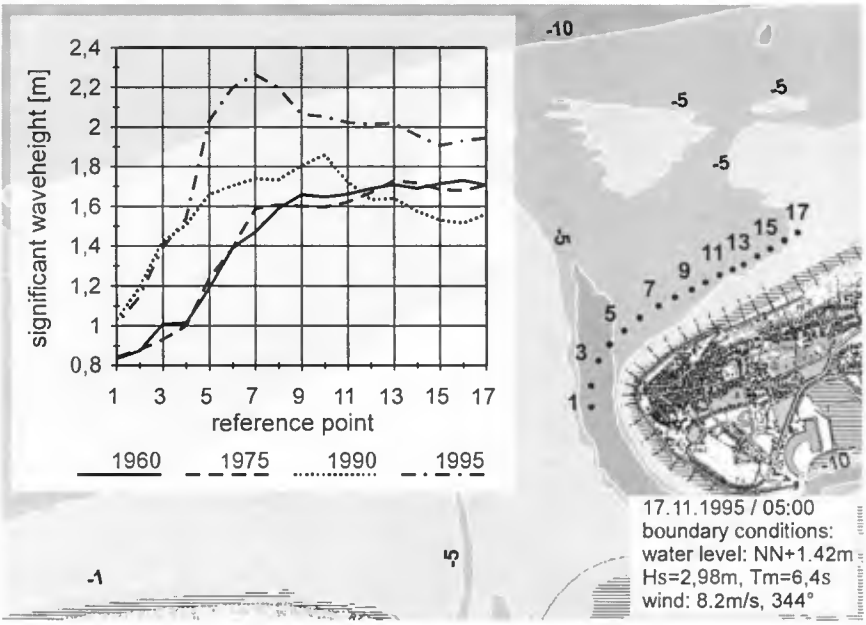

Fig.9: Significant wave heights at the edge of shoreface and beach parallel to the northwestern shore of the island of Norderney according to the bathymetry in 1960, 1975, 1990 and 1995 (computed with SWAN)

The difference between the four morphological situations absolutely has to be considered in comparing the effectiveness of different beach nourishments in the last 35 years. The unfavorable boundary conditions of 1995 compared to the previous situations are another indication for the superior effectiveness of the combined nourishment executed in the framework of NOURTEC project.

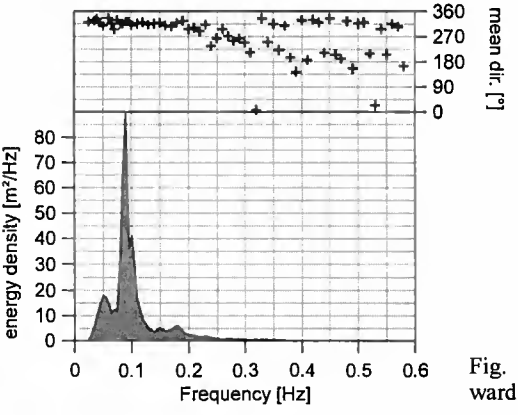

Fig. 10: Measured spectrum at the seaward boundary at 10.011.95, 04:56

storm condition

Explanatory for wave conditions during a storm are the results of a run with the following boundary conditions which have been gained from field measurements in January 1995: Set-up of about 2,3m above MHWL (in sum equivalent to a water level of NN + 3.46 m) and an offshore wave field (fig. 10) with a

significant wave height Hs = 6.41 m and a peak period Tp = 11.1 s. Wind direction is 295° with a velocity of 22 m/s. As well as for the results for the ordinary tidal conditions here occur also only small differences between the local wave heights calculated for the morphologies of 1960 and 1975 (fig. 11). Nevertheless, in 1990 higher waves in the order of 2.5 - 2.75 m arrive at the north western shoreface of the island. Also, a penetration of higher waves into the inlet is evident. In 1995 the erosion in the central part of the ebb delta has reduced the effectiveness of the ebb delta remarkably to act like a breakwater. Wave attenuation is there less pronounced leading to higher energy dissipation on the shoreface with a more pronounced breaker zone.

Also fro the storm conditions a quantitative comparison has been carried out for the the significant wave heights at 17 selected points at the edge of shoreface and beach parallel to the island's northwestern shore (fig. 12) on the basis of the results of the mathematical model. As well as for the ordinary tide condition the situations of 1960 and 1975 show no remarkable changes in wave climate for storm conditions. The significant wave heights are of the same order of magnitude on the whole stretch of the northwestern shore face. In 1990 there is an increase of wave heights starting at reference point 2 reaching its maximum at point 9 with about 15%, decreasing further down drift and become even smaller in the eastern part of the study area. In 1995 the wave heights are nearly in the same order of

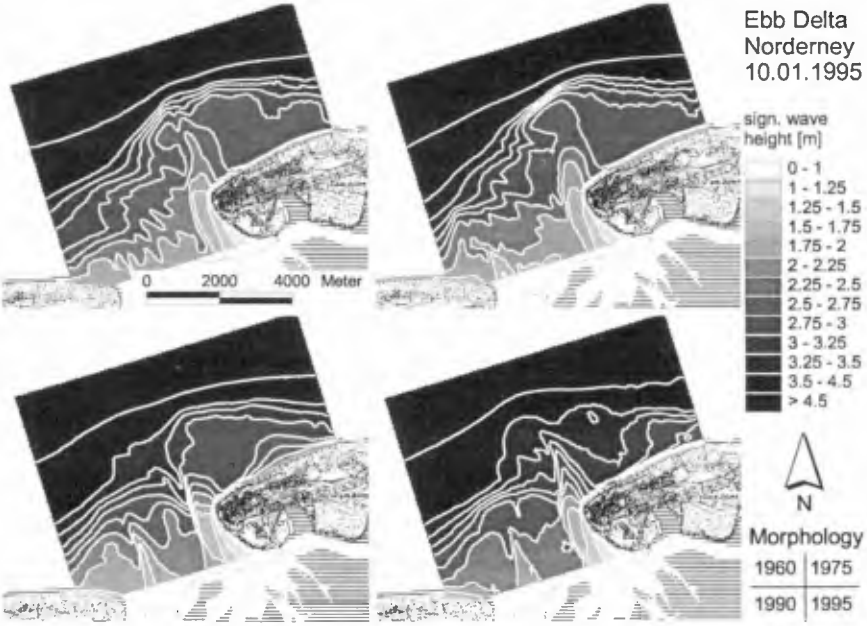

Fig. 11: Significant wave heights in the offshore area, in the tidal inlet Norderneyer Seegat and on the northwestern shoreface of the island of Norderney in 1960, 1975, 1990 and 1995. Boundary conditions: Water level: MSL+3.46m; Wind: 22m/s, 295°

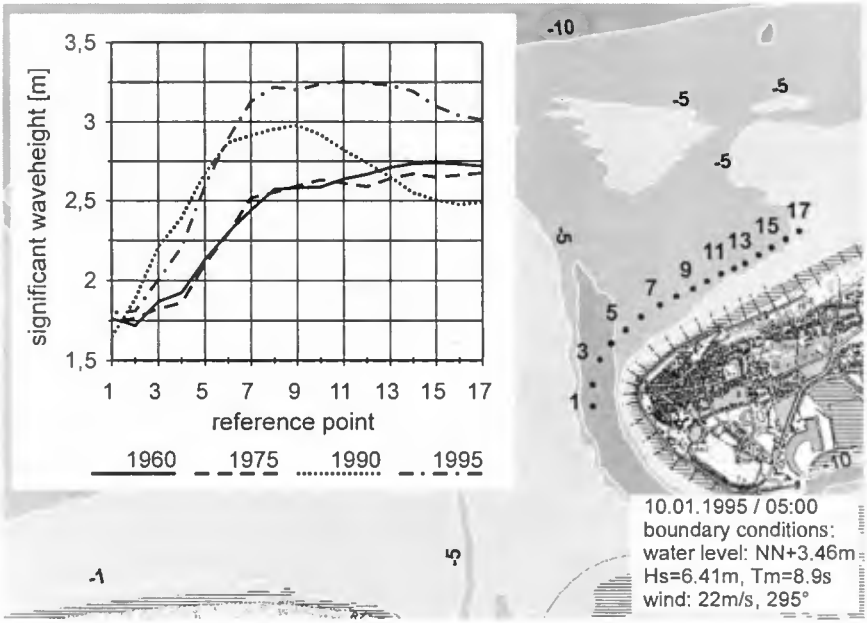

Fig. 12: Significant wave heights at the edge of shoreface and beach parallel to the northwestern shore of the island of Norderney according to the bathymetry in 1960, 1975, 1990 and 1995 (storm condition, computed with SWAN)

magnitude as in 1990 up to reference point 6 but then further increasing down drift and remaining on a high level up to the end of the investigation area. The maximum increase in wave height is about 20% between the reference points 8 and 10 comparing the 1960 and 1995-situation.

Conclusivly the relation of wave heights on the shoreface and the offshore wave boundary condition has been calculated both for the ordinary tide and the storm situation (fig. 13). On the one hand the results hightlight the presently decreased capability of the ebb delta to reduce the offshore wave energy. For ordinary tidal high water levels even waves with a significant height of about 3 m reach the shoreface only reduced by 25 % (reference point 7). In the other case the wave heights (Hs = 6.4m at the offshore boundary) during a storm event with a set-up above MHWL of about 2.3m were reduced at least by 50%. These figures are remarakably smaller than for the modified situations of earlier states

Comparing the morphological states of 1960 and 1995 the consequences of the ebb delta migration can be differentiated for different boundary conditions: For the storm condition there is an increase at the shoreface in the maximum from 40% to 50% of the offshore wave height. This increase starts slowly at the western edge and is then nearly the same downdrift of point 6. For the ordinary tide and the morphology of 1960 the relation of foreshore to offshore wave height starts at nearly the same value as for the storm condition,

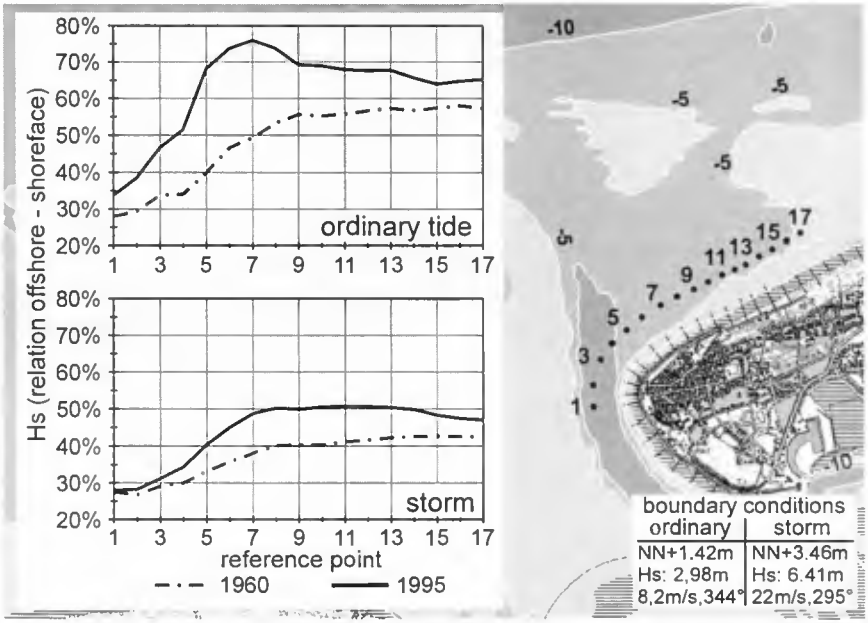

Fig: 13: Relation of the significant waveheight offshore of the ebb delta and on the shoreface for ordinary tide conditions and during a storm event calculated with the bathymetries of 1960 and 1995

increasing further down drift and reaching it maximum im point 9 with about 58%. The situation of 1995 is in contrast to that much faster increasing with a distinctive maximum between the points 4 and 9. As a consequence the foreshore wave height in 1995 is at point 7 about 75% of the offshore wave height compared to only 50% in 1960. This is also reflected in the higher erosion rates in that stretch (Niemeyer et al. 1997).

Conclusion

Wave climate studies have been carried out for distinct bathymetries of ebb delta, shoreface and tidal inlet by application of the mathematical wave model SWAN. It has proved to be a suitable tool for the reproduction of the wave climate in an environment with heterogenous morphological pattern. The results of the verification runs show a good agreement for the wave parameters in the whole study area and the same for the spectrum on the shoreface. It is important to have sufficient areal wave data for the verification in different stages of the transformation of the wave field. The application of the third generation model SWAN leads to an improved fitting of model results and field data in comparison to the earlier used second generation model HISWA.

The changes of the ebb delta morphology of the Norderneyer Seegat within the last 35 years caused a higher impact of waves on the north western shoreface. Consequently both beach erosion and losses of nourished material increase remarkably.

For ordinary tides changes of wave climate on the shoreface are relatively higher than for storm conditions.

Acknowledgement

This investigations have been carried out in the framework of the NOURTEC project of the COMMISSION OF THE EUROPEAN COMMUNITIES (Contract MAS-CT93-0049) and additionally benefitted from national funds of the GERMAN FEDERAL MINISTRY FOR EDUCATION AND RESEARCH (BMBF) and the LOWER SAXONIAN MINISTRY FOR THE ENVIRONMENT. The authors have substantially benefitted from the joint cooperation in this European project with their Danish and Dutch partners. They are also very grateful for the assistance and support by Messrs Günther Brandt, Detlef Glaser, Thomas Hartkens, Peter Heddinga, Holger Karow, Heiko Knaack and Georg Münkewarf.

References

Booij, N. & L.H. Holthuijsen (1992): "HISWA user manual. Prediction of stationary, short-crested waves with ambient currents", TU Delft, Faculteit d. Civ. Techn.

Holthuijsen, L.H. & N. Booij (1992): "A grid model for shallow water waves", Proc. 20th Intern. Conf. o. Coast. Eng. Taipei, ASCE, New York

Holthuijsen, L.H., R.C. Ris, N. Booij (1997): "A third generation model for near-shore waves with ambient currents", Proc. 25th Intern. Conf. o. Coast. Eng. , ASCE, New York, 668-676

Niemeyer, H. D. (1987): " Changing of wave climate due to breaking on a tidal inlet bar ", Proc. 20th Intern. Conf. Coast. Eng. Taipei/ROC-Taiwan , ASCE, New York

Niemeyer, H. D.; E. Biegel, R. Kaiser; H. Knaack, C. Laustrup, J.P.M. Mulder, R. Spanhoff & H. Toxvig (1995): "general aims of the NOURTEC project - effectiveness and execution of artificial beach and shoreface nourishments", Proc.4th Conf. o. Coast & Port. Eng. i. Develop. Countr., Rio de Janairo/Brazil.

Niemeyer, H. D.; Kaiser, R.;Knaack, H. (1997): "Effectiviness of a combined beach and shoreface Nourishment on the island of Norderney/East Frisia , Germany". Proc. 25th Intern. Conf. Coast. Eng. Orlando/USA, ASCE, New York

Niemeyer, H. D. & R. Kaiser (1998): "Effects of ebb delta migration on local wave climate". Proc. 3rd Intern. Conf. Hydrodyn., Seoul

Ris, R.C. (1997): "Spectral modelling of wind waves in coastal areas". Communications on Hydraulic and Geotechnical Engineering, Delft University of Techn., Ph.D. thesis, 160p.

Sensitivity of wind wave simulation to coupling with a tide/surge model with application to the Southern North Sea

J. Monbaliu*, C.S. Yu† and P. Osuna*

Abstract

The wave-current interaction process in a one way coupled system for the Southern North Sea region was studied. To this end, a modified version of the third-generation spectral wave model WAM was run in a three level nested grid system, taking into account the hydrodynamic fields (coupled version) computed by a tide/surge model. The resolution in these three grids corresponds roughly to 35 km (coarse), 5 km (local) and 1 km (fine). Hydrodynamic information was only available at the resolution of the local grid. Results are compared with those of the same version without considering the interaction with tide and surges (uncoupled version). The emphasis is on the results from the local grid calculations. The sensitivity to the source of boundary conditions (coupled vs. uncoupled) and to the frequency of information exchange is investigated. Also the spectral evolution is studied.

Numerical results in the local grid are in good agreement with buoy data. The phase and amplitude of the modulations of wave period observed from the buoy data are quite well reproduced by the coupled version. The model results in the local grid did not show much sensitivity to the source of boundary condition information, nor were they very sensitive to the information update frequency of the hydrodynamic fields. The directional spectra computed in the coupled mode show a broader energy distribution and a more rapid growth. The fine grid results only differ marginally from the local grid results due to the limited resolution of the hydrodynamic fields used.

*Laboratory of Hydraulics, K.U.Leuven, de Croylaan 2, B-3001 Heverlee, Belgium.
†Dept. of Marine Env. and Eng., NSYSU, Lien-Hai Road 70, Kaoshiung 804, Taiwan.

1 Introduction

Wind generated waves can be affected considerably when they interact with currents. When waves propagate on an inhomogeneous and unsteady current field, some particular characteristics of the wave signal are modified, e.g. wavelength, amplitude, frequency, direction, etc. A review of the theoretical aspects concerning the wave–current interaction can be found in Jonsson (1990).

In coastal regions with appreciable tide, the varying water depth as well as the varying currents influence the wave pattern. Besides of the current interaction processes, interaction with the bottom introduce a series of linear and non-linear mechanisms in the spectral transformation (Shemdin et al., 1980). According to Graber and Madsen (1988), in finite–depth waters the shape of the spectrum is to a great extent influenced by the bottom friction term.

By coupling a third generation wave model with a two-dimensional or three-dimensional current model, improved estimates of wave parameters or improved estimates of surge levels can be obtained. Improved parameter estimates for wave conditions are, next to a help for safer navigation and design of coastal structures, of considerable interest for the estimation of sediment movement since wave action can determine to a large extent the resuspension, deposition rate, and transport of sediments (Mei et al., 1997). Coupling can be done at different levels of complexity. Complex coupled systems can have dynamic interactions, where changes in one model also affect the processes in the other model(s) and an iterative numerical procedure might become necessary. The simplest configuration is a loose one way coupling where information from one model is transferred to another model. Considerable work has already been done. Two literature examples are given to illustrate the concept. Mastenbroek et al., (1993) studied the effect of waves on the calculation of storm surges in the North Sea. They reported that taking the dependence of the drag coefficient on the sea state into account, it is possible to improve the storm surge predictions. Tolman (1990) studied the effect of currents on the wave field in applications with a relatively coarse space resolution.

In this work, we explore the dependence of the wave evolution on an inhomogeneous, unsteady current field in finite–depth waters and this at intermediate spatial resolution (O(5 km)). To this end the third-generation WAM model (Günther et al., 1994) was modified (Luo and Sclavo, 1997; Monbaliu et al, 1998) and it was implemented for applications in the North Sea. The hydrodynamic fields were computed by a tide/surge model and transfered off-line to the wave model. The main goal here is to investigate the sensitivity of the results at the local scale to the frequency of information exchange and to the source of boundary conditions in a loose one way coupled system.

2 The numerical models

2.1 The wave model

The wave model used is the third generation WAM *Cycle_4* model (Günther et al., 1994). The model solves an energy balance equation for the spectrum $\mathrm{F}(f,\theta)$ as a function of the wave frequency, f, wave direction, θ, and the geographical position, $\mathbf{x}$, and time, t. The standard version of WAM propagates the energy over a calculational grid in Cartesian coordinates $\mathbf{x}(x,y)$ for small area applications or in spherical coordinates $\mathbf{x}(\phi,\lambda,r)$ for model applications over large areas as to take into account the swell propagation over great circles. For this work the last option is used. The WAM model permits the inclusion of a stationary current background and uses the relative frequency, σ, as a coordinate. Under these conditions, the energy transport equations solved in the WAM *Cycle_4* model code is equivalent to the action density transport equation. The transport equation for the evolution of the wave spectrum $F(t,\phi,\lambda,\sigma,\theta)$ then reads

$$\frac{\partial F}{\partial t} + (\cos\phi)^{-1}\frac{\partial}{\partial\phi}(\dot{\phi}\cos\phi F) + \frac{\partial}{\partial\lambda}(\dot{\lambda}F) + \sigma\frac{\partial}{\partial\sigma}\left(\dot{\sigma}\frac{F}{\sigma}\right) + \frac{\partial}{\partial\theta}(\dot{\theta}F) = S_{tot}, \qquad (1)$$

where the expressions $\dot{\phi}$, $\dot{\lambda}$, $\dot{\sigma}$, and $\dot{\theta}$ represent the rate of change of energy in the space $(\phi,\lambda,\sigma,\theta)$. At the right hand side of (1), S_{tot} is the function representing the source and sink functions, and the conservative non-linear transfer of energy between wave components. In the present application, it includes wind input S_{in}, non-linear quadruplet wave-wave interactions S_{nl}, whitecapping dissipation S_{ds} and bottom friction dissipation S_{bf}. Standard values were used for the empirical coefficients in the source terms. The model has been used in a quasi-steady approach, assuming that the current and the water depth vary only slowly. A detailed description of the physics incorporated in WAM *Cycle_4* model and its numerical implementation can be found in Komen et al., (1994). Details on the improvements, alterations and additions for application in nearshore regions can be found in Luo and Sclavo (1997) and Monbaliu et al. (1998).

2.2 The tide/surge model

The hydrodynamic (u,v,η) fields are computed with a model based on the shallow water equations. The spherical coordinate expressions for this set of equation are (Washington and Parkinson, 1986)

$$\begin{aligned}\frac{\partial u}{\partial t} &+ \frac{u}{R\cos\phi}\frac{\partial u}{\partial\lambda} + \frac{v}{R}\frac{\partial u}{\partial\phi} - \frac{uv\tan\phi}{R} - 2\varpi\sin\phi v \\ &= -\frac{g}{R\cos\phi}\frac{\partial\eta}{\partial\lambda} - \frac{1}{\rho R\cos\phi}\frac{\partial P_a}{\partial\lambda} - \frac{\tau_{b\lambda}}{\rho(h+\eta)} + \frac{\tau_{s\lambda}}{\rho(h+\eta)} \\ &+ A_h\left[\nabla^2 u + \frac{u}{R^2}(1-\tan^2\phi) - 2\frac{\tan\phi}{\cos\phi}\frac{\partial v}{\partial\lambda}\right], \qquad (2)\end{aligned}$$

$$\frac{\partial v}{\partial t} + \frac{u}{R\cos\phi}\frac{\partial v}{\partial \lambda} + \frac{v}{R}\frac{\partial v}{\partial \phi} - \frac{u^2\tan\phi}{R} + 2\varpi\sin\phi u$$
$$= -\frac{g}{R}\frac{\partial \eta}{\partial \phi} - \frac{1}{\rho R}\frac{\partial P_a}{\partial \phi} - \frac{\tau_{b\phi}}{\rho(h+\eta)} + \frac{\tau_{s\phi}}{\rho(h+\eta)}$$
$$+ A_h\left[\nabla^2 v + \frac{v}{R^2}(1-\tan^2\phi) + 2\frac{\tan\phi}{\cos\phi}\frac{\partial u}{\partial \lambda}\right], \quad (3)$$

$$\frac{\partial \eta}{\partial t} + \frac{1}{R\cos\phi}\left[\frac{\partial}{\partial \lambda}((h+\eta)u) + \frac{\partial}{\partial \phi}((h+\eta)v\cos\phi)\right] = 0, \quad (4)$$

where (u, v) are the horizontal (λ, ϕ) components of the velocity, ρ the sea water density, g the acceleration due to the gravity, ϖ the angular speed of the earth's rotation, η the water elevation (with respect to mean sea level), h is the mean depth, P_a the atmospheric pressure, $(\tau_{b\lambda}, \tau_{b\phi})$ the bottom stress components due to friction, $(\tau_{s\lambda}, \tau_{s\phi})$ the surface stress components due to wind, A_h the depth averaged kinematic eddy viscosity, and ∇^2 denotes the horizontal Laplacian operator in spherical coordinates. Equations (2) and (3) are the vertically integrated momentum equations and equation (4) states the conservation of mass. The information concerning the numerics can be found in Yu (1993).

3 Model implementations

3.1 WAM model implementations

Three nested grid were used: one coarse grid of which the domain extends up to 70N (Figure 1) as to capture the swell generated outside but traveling into the region of interest; a local grid covering part of the Southern North Sea basin (Figure 2); and a high resolution grid which takes into account the most important details of the bathymetry near the Flemish coast (not shown). The emphasis in this study is on the results obtained for the local grid.

The spectrum $\mathrm{F}(f, \theta)$ was discretized using 12 directions and 25 frequencies with the standard logarithmic distribution. Both the coupled and uncoupled versions of the WAM model were run over the same grid and the option for energy propagation in spherical coordinates was used for all runs.

From the time series of wave parameters calculated from buoy data we used the *significant wave height*,

$$\mathrm{Hs} = 4\sqrt{m_0}, \quad (5)$$

and the *zero upcrossing period*,

$$\mathrm{Tm}_{02} = \sqrt{m_0/m_2}, \quad (6)$$

where

$$m_i = \int\int \mathrm{F}(f,\theta) f^i df d\theta. \quad (7)$$

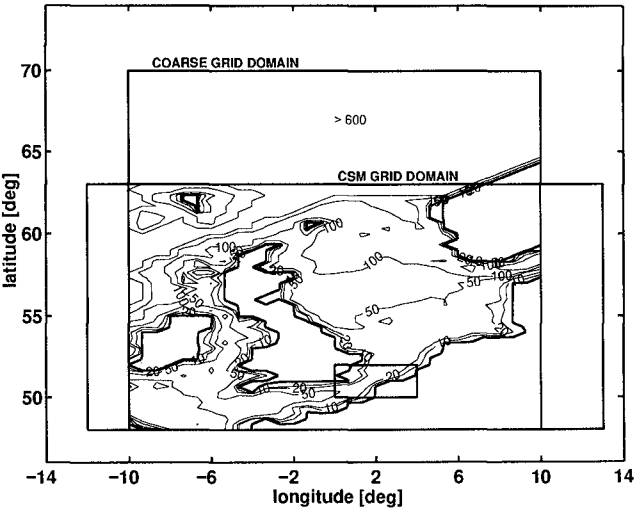

Figure 1: Coarse and CSM grid domain. The coarse grid bathymetry is included. Boundary condition for a nested local grid (region indicated by the square) are generated. Depth values are in meters.

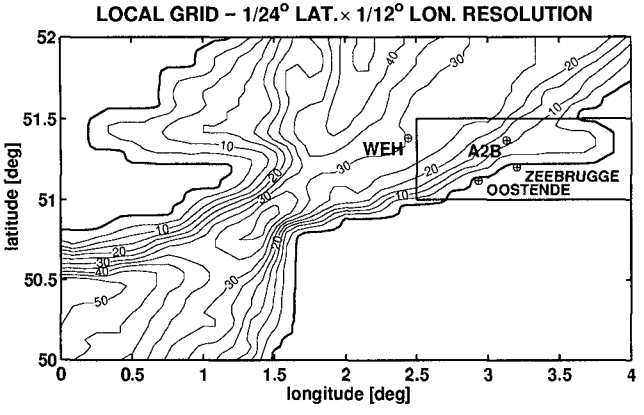

Figure 2: Local grid bathymetry with location indication of the WEH and A2B buoys. Boundary condition for a fine grid (region indicated by the square) are generated. Depth values are in meters.

Wind data are six-hourly winds for the North Sea region produced by UKMO (United Kingdom Meteorological Office). The wind data were interpolated onto the coarse grid points. This wind data set was then also used for the two nested grids, where they were interpolated internally in the WAM-model. Time interpolation was not used. Details concerning the different grids and integration time steps used are given in Table 1.

Table 1: Types, geographical coverage, resolution, and time step (advection and source terms) for each grid used.

GRID	AREA	RESOLUTION (LAT × LON)	TIME STEP	
			Advection	Source
WAM MODEL (Type–A Grid)				
Coarse	48.0N - 70.0N 10.0W - 10.0E	$(1/3)^o \times (2/3)^o$	20 min	20 min
Local	50.0N - 52.0N 0.0E - 4.0E	$(1/24)^o \times (1/12)^o$	4 min	20 min
Fine	51.0N - 51.5N 2.5E - 4.0E	$(1/96)^o \times (1/96)^o$	30 sec	10 min
CSM Model (Type–C Grid)				
CSM	48.0N - 63.0N 12.0W - 13.0E	$(1/24)^o \times (1/12)^o$	10 min	–

3.2 Surge model implementation

The hydrodynamic fields were obtained from a Continental Shelf Model (CSM) which solved the set of equations (2)–(4) with a spatial coverage and resolution indicated in Table 1. The model was forced at the boundary with eight tidal constituent. No surge effect was taken into account. Current (u, v) and elevation (η) fields were generated on a Type–C grid. These fields were linearly interpolated to the local and fine WAM type–A grids. Note that η points from the CSM grid correspond to the local grid WAM points. For the coarse grid, the closest values of (u, v) were assigned to each wet point of the WAM grid. For the hydrodynamic data from 63°N to 70°N needed in the WAM coarse grid coupled run, the values at the 63°N points were taken.

4 Results

4.1 Introduction

The performance of coupled and uncoupled versions of the WAM was tested on a one-month period (February 1993) for the coarse and local grid. The fine grid version was run only for a 15-day period due to the high computational effort required.

In what follows, time series at the locations WEH (Westhinder) and A2B from both coupled and uncoupled WAM results are compared with the available buoy data. The sensitivity to 'coupled' information in the boundary conditions, and to the frequency of information exchange is addressed for the local grid application. The evolution of 1D–spectra and 2D–spectra in 'coupled' and 'uncoupled' mode are discussed.

4.2 Time series

Time series calculated by WAM at station WEH (30m depth) show a good agreement with buoy data, especially for significant wave height (Hs) values during high-wave events (see Figure 3). The small modulations visible in the buoy data at WEH seem well reproduced by the coupled version of WAM. However, the presence of some modulations in the uncoupled run results suggests that part of the modulations in the signal must come from wind variability. The bias for Hs in the coupled and uncoupled results is -0.072m and -0.143m, respectively. The intercomparison between results from coupled and uncoupled models show differences (coupled - uncoupled) in Hs smaller than 0.25m, with a mean difference of 0.02m. Modulations of Tm_{02} , corresponding to the dominant semidiurnal tide period, are quite clear in the buoy data (Figure 3). The importance of including the hydrodynamic fields is highlighted qualitatively by the good agreement between buoy data and WAM-coupled results for Tm_{02}. This is not directly reflected in the value for the bias for Tm_{02}, which were 0.032s for the coupled and 0.034s for the uncoupled run, respectively. The model results themselves showed differences up to 1.0s, with a mean difference of -0.15s.

In the more shallow A2B station (11m depth), overestimation of model results with respect to buoy data is observed, both in Hs and in Tm_{02} (Figure 4). Although it is possible to reduce the observed differences by tuning of the empirical coefficient in the bottom friction term (see Luo and Monbaliu, 1994, Luo et al., 1996), this was not done since it was not considered important for the scope of this work. At this station, the bias was -0.128m and -0.116m for Hs and -0.846s and -0.965s for Tm_{02} in the coupled and uncoupled mode, respectively. The importance of tidal modulations is again observed at this location and it is qualitatively well reproduced in the coupled run. Differences between coupled and uncoupled model results do not exceed 0.25m in Hs and 1.0s in Tm_{02}, whereas the mean difference in the Hs and Tm_{02} value was 0.014m and -0.217s, respectively.

4.3 Sensitivity to boundary conditions

In order to explore the necessity to run in coupled mode on a coarse grid in order to supply good boundary conditions for a subsequent nested run, the application on the local grid was run once using boundary conditions from the coupled and once from the uncoupled coarse grid run. In both cases, results showed clearly the tidal modulation effect on Tm_{02} (Figure 5a). The observed differences are small and most of the time do not exceed 5%, which seem to suggest that running the coarse grid

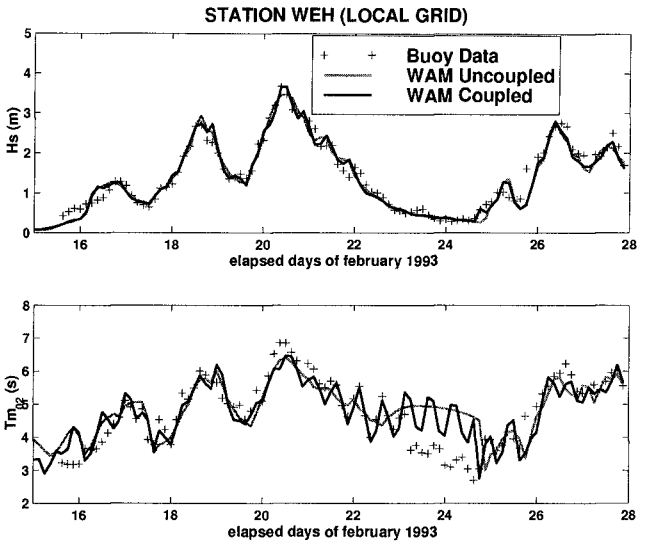

Figure 3: Time series of significant wave height (Hs) and zero upcrossing period (Tm_{02}) at station WEH of the local grid.

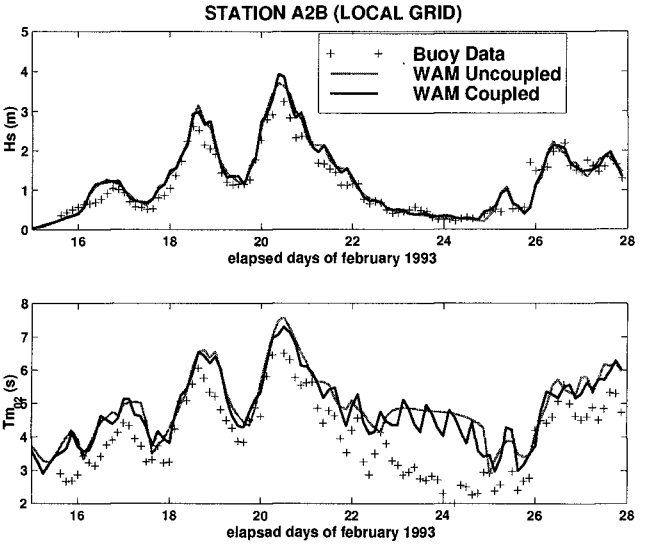

Figure 4: Time series of significant wave height (Hs) and zero upcrossing period (Tm_{02}) at station A2B of the local grid.

application in coupled mode, does not have a dramatic influence on the local grid runs. Tide–induced modulations, at least on the space scales used here, are mainly a local effect.

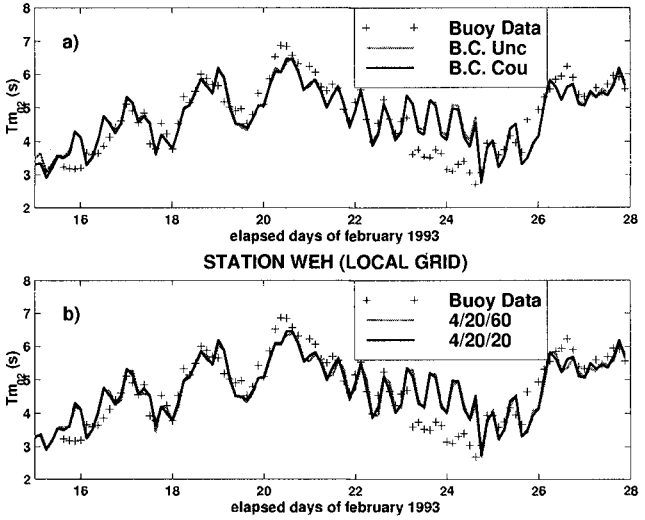

Figure 5: Time series showing the sensitivity to: (a) boundary conditions, and (b) information exchange of Tm_{02} at station WEH.

4.4 Sensitivity to frequency of information exchange

In a coupled system, an important factor to define is the frequency of information transfer between model components. In this work, hydrodynamic fields were updated every 20 minutes (standard coupled mode), which seems suitable for the temporal scale of tide variability. In order to investigate the sensitivity of the model results to the frequency of information exchange, the coupled model on the local grid was also run with an update of the hydrodynamic fields every 60min. The results were compared with those of the standard run. The time series of Tm_{02} presented in Figure 5b, show differences smaller than 5%. Some details in the modulation are missed. For this spatial scale and with current and depth fields which vary only slowly in time and space, the main variation in the spectral periods are well reproduced by the Doppler shift. As one can observe from the time series, the tidal modulations respond mainly to the semidiurnal tidal constituent M2. Further decrease of the frequency of information exchange will lead to increased loss of information.

4.5 Spectral evolution

In order to clarify the observed differences in the time series, it is appropriate to analyze how the spectral shape evolves in the presence of a current field. In Figure 6 we can observe the history of the 1D–spectra at station WEH as calculated by the coupled and uncoupled version of WAM. The frequency shifting effect is clearly observed as modulation with a period corresponding to the semidiurnal tidal constituent. These modulations are mainly observed at intermediate and low frequencies, where the effect is not masked by the wind variability.

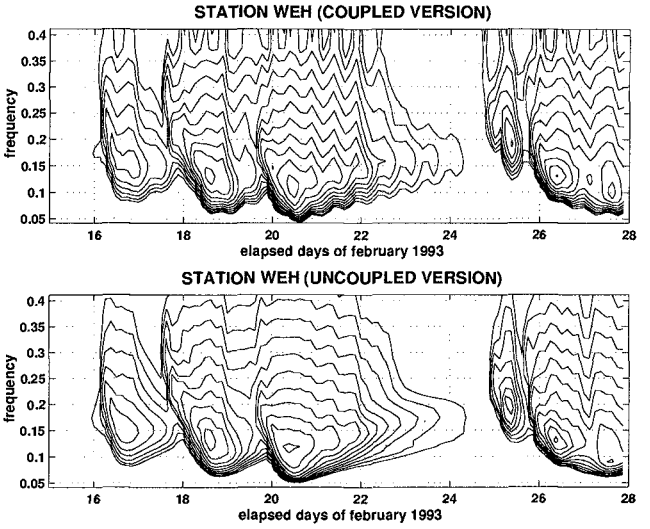

Figure 6: Evolution of the 1D spectra calculated by WAM coupled and uncoupled at location WEH. A logaritmic distribution of contour labels is used in both cases.

A definitive insight to clarify the differences in time series is the intercomparison of directional spectra. Hubbert and Wolf (1991) and Holthuijsen and Tolman (1991) studied the propagation of a wave spectrum across a current eddy. They found that the interaction with the current produce changes in the shape of the spectra (broadening and bimodality at some parts of the whirl) associated to the current induced refraction. The coupled runs produced slightly broader spectra than the uncoupled version, mainly at small angles between wave and current direction. An illustration of is given in Figure 7. Starting from almost the same spectrum (date: 93022515), it is possible to observe six hours later a fast growth of energy in the spectrum calculated by the coupled version. The fast growth is due to the wind, which remained relatively constant in magnitude and direction during that period. This produced a shifting of the mean wave direction toward the wind direction, almost 90 degrees from the original direction. Note that the WAM-model does not

have a linear 'Phillips' term in its wind input source function. It was not investigated in how far this is responsible for the lack of growth in the uncoupled version.

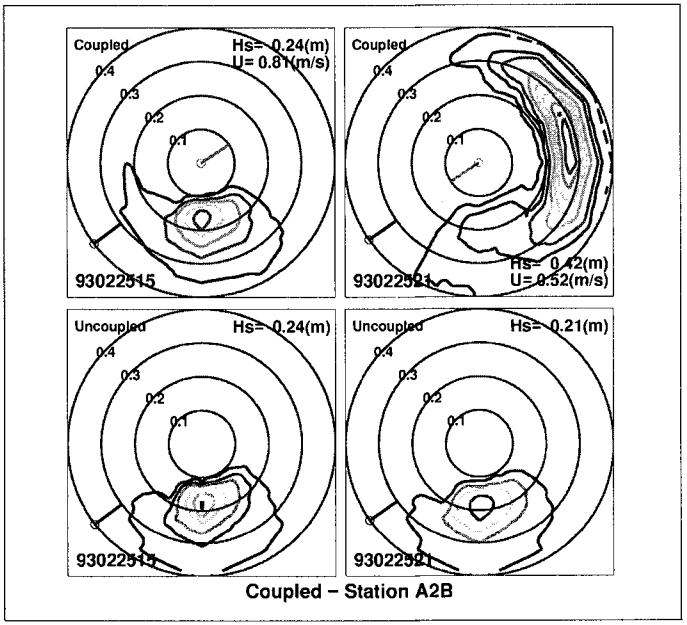

Figure 7: 2D spectra at station A2B calculated by WAM coupled and uncoupled. Significant wave height (Hs), wind direction (dark line) and date are always indicated. For coupled results, current magnitude (U) and current direction (light line) are indicated. The same contour labels were used in all figures (1, 5, and from 10 to 100% every 10% of $0.1 m^2/Hz/deg$).

4.6 Further work

The fine grid bathymetry for the Flemish Coast is much more complicated than can be anticipated from Figure 2. Many sand banks more or less parallel with the coast are present. Their spatial scale is small such that they dissapear from the local grid resolution. A fine grid wave model was nested in the local grid (see section 3.1). For the hydrodynamic fields linear interpolation from the CSM-grid (equal to the local wave model grid) to the fine grid was used. Comparison of time series at A2B from the local and fine grids showed only negligible differences. This is not unexpected since all the variability in the current field induced by the local bathymetry is not represented in the interpolated current field. If the details of the bathymetry are not taken into account in the calculation of the hydrodynamical variables, the directions of the waves and the currents become more and more perpendicular as

one approaches the coast. This produces a neglegible effect of the currents on the characteristics of the wave field. The next logical step is therefore to use the same resolution for the hydrodynamic and the wave field calculations.

5 Conclusions

A modified version of the third generation spectral wave model WAM was used in a three level nested grid application to study the interaction of waves with currents. Numerical results from the local grid showed a very good agreement with buoy data. At the shallower station A2B some slight modulations (approximately ± 0.1m) of the significant wave height were observed. Tidal effects were better visible as modulations on the wave period. These last effects were larger at the station WEH than at the station A2B.

Local grid results using boundary conditions from a coarse uncoupled run were qualitatively and quantitatively as good as the results considering boundary information from a coupled coarse run. This indicates that the results in the local grid are not sensitive to 'coupled' or 'uncoupled' boundary information. The results also do not seem very sensitive to the update frequency (from 20 to 60min) of the hydrodynamic information. This means that at least for this local grid application, currents and water depths vary slowly and that the doppler shift reproduces to a large extent the hydrodynamic interactions.

Tidal modulations with a period corresponding to the semidiurnal tidal constituent were observed in all the frequency components of the spectra. The directional spectra computed by the coupled version of WAM had a broader energy distribution and a more rapid energy growth was observed in changing wind conditions.

The neglegible differences between local and fine grid results were attributed to a lack of spatial resolution in the hydrodynamic field. The next logical step is therefore to use the same spatial resolution for the wave and for the hydrodynamic calculations.

Acknowledgments

The buoy data were provided by AWK of the Ministry of the Flemish Community. This study is carried out with financial support from the PROMISE project under the EC-MAST III PROGRAMME, contract MAS3 CT 9500025.

References

Günther, H., S. Hasselmann, and P.A.E.M. Janssen, 1994: User manual of the WAM Cycle 4. Report nr. 4, Hamburg.

Graber, H.C., and O.S. Madsen, 1988: A finite-depth wind-wave model. Part I. Model description. *J. Phys. Oceanogr.* **18**, 1465-1483.

Hubbert, K.P., and J. Wolf, 1991: Numerical investigation of depth and current refraction of waves. *J. Geophys. Res.*, **96**, 2737–2748.

Holthuijsen, L., and H.L. Tolman, 1991: Effects of the Gulf Stream on ocean waves. *J. Geophys. Res.*, **96**, 12755–12771.

Jonsson, I.G, 1990: Wave–current interactions. In B. Le Mehaute and D.M. Hanes (Eds.), *The Sea*, Ocean Engineering Science, Vol 9(A), p65–120. Wiley, New York.

Komen, G.J., L. Cavaleri, M. Donelan, K. Hasselmann, S. Hasselmann, and P.A.E.M. Janssen, 1994: *Dynamics and modelling of ocean waves.* Cambridge University Press.

Luo, W., and J. Monbaliu, 1994: Effects of the bottom friction formulation on the energy balance for gravity waves in shallow water. *J. Geophys. Res.*, **99**, 18501–18511.

Luo, W., J. Monbaliu, and J. Berlamont, 1996: Bottom friction dissipation in the Belgian coastal region. *Proc. 25th Int. Conf. Coastal Eng.*, Florida, 836–849.

Luo, W., and M. Sclavo, 1997: Improvement of the third generation WAM model (Cycle 4) for applications in nearshore regions. Internal report no. 116, Proudman Oceanographic Laboratory.

Monbaliu, J., R. Padilla, P. Osuna, R. Flather, J. Hargreaves, J.C. Carretero, S. Espinar, and H. Günther, 1998: A shallow water version of the WAM spectral wave model. Report nr. 52, Proudman Oceanographic Laboratory. *To be published.*

Mastenbroek, C., G. Burgers, and P.A.E.M. Janssen, 1993: The dynamical coupling of a wave model and a storm surge model through the atmospheric boundary layer. *J. Phys. Oceanogr.*, **23**, 1856–1866.

Mei, C.C., S. Fan, and K. Jin, 1997: Resuspension and transport of fine sediments by waves. *J. Geophys. Res.*, **102**, 15807–15821.

Shemdin, O.H., S.V. Hsiao, H.E. Carlson, K. Hasselmann, and K. Schulze, 1980: Mechanisms of wave transformation in finite-depth water. *J. Geophys. Res.* **85**, 5012-5018.

Tolman, H.L., 1990: Wind wave propagation in tidal seas. *Communications on hydraulic and geotechnical engineering*, Delft University of Technology. Report nr. 90–1.

Washington, W.M., and C.L. Parkinson, 1986: *An introduntion to three-dimensional climate modelling.* Oxford University Press.

Yu, C.S., 1993: Modelling Shelf Sea Dynamics, Ph.D. thesis, Department of Civil Engineering, K.U.Leuven, Belgium.

PROBABILITY DISTRIBUTION OF WAVE HEIGHT IN FINITE WATER DEPTH

Michel K. Ochi[1]

Abstract

This paper presents probability density functions applicable to peaks, troughs and peak-to-trough excursions of coastal waves with finite water depth in closed form. It is found that for a non-Gaussian waves for which the skewness of the distribution is less than 1.2, the probability density function of peaks (and troughs) can be approximately represented by the Rayleigh distribution with a parameter which is a function of three parameters representing the non-Gaussian waves. The agreement between the probability density functions and the histograms constructed from data obtained by the Coastal Engineering Research Center is satisfactory.

Introduction

It has been known that waves in finite water depth (hereafter defined as coastal waves) are, in general, considered to be a nonlinear, non-Gaussian random process. The profile of wave peaks (positive side) is sharp as contrasted to the round profile of the troughs (negative side) as shown in Figure 1. The degree of difference in the positive and negative sides of the wave profile can be presented mathematically in terms of skewness. It is highly desirable that the statistical properties of peaks and trough amplitudes be presented separately, and then the properties of wave height (peak to trough excursion) may be obtained through the distribution function applicable to the sum of two independent

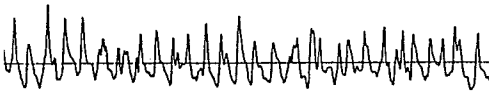

Figure 1: A portion of the time history of shallow water wave record obtained by CERC during ARSLOE Project

[1] Professor, Department of Coastal & Oceanographic Engineering, University of Florida, Gainesville, Florida 32611, U.S.A.

random variables (peaks and troughs). Furthermore, it is requisite that the probability distributions of peaks and troughs be developed from the distribution representing a non-Gaussian wave profile; the same approach as considered for derivation of the Rayleigh probability distribution for Gaussian waves in deep water.

Only a limited number of studies has been carried out on the probability distribution of coastal wave height. It is often assumed in these studies that the wave profile is amplitude modulated and follows the Stokes expansion to the second or third components; Tayfun (1980), Arhan and Plaistad (1981), among others. There is some reservations, however, in applying Stokes theory for shallow water waves unless the expansion includes higher order terms. Furthermore, it is advisable not to assume any preliminary form of the wave profile for derivation of its probability distribution.

Another approach for derivation of the probability distribution of wave amplitudes is to apply the Gram-Charlier series distribution representing coastal wave profiles; Ochi and Wang (1984) for example. The results, however, are not promising since the Gram-Charlier series distribution is not given in closed form and the density function at times becomes negative for large negative displacements.

On the other hand, several empirical probability distributions applicable for coastal wave heights have been developed from analysis of observed data. These include Kuo and Kuo (1975), Goda (1975), Ochi, Malakar and Wang (1982) and Hughs and Borgman (1987), among others.

In the present paper, the probability function applicable to amplitudes of response of a nonlinear mechanical system (Ochi 1998) is applied to coastal waves. That is, the probability density function applicable to peaks and troughs of wave data are presented separately in closed form as a function of three parameters representing non-Gaussian waves. Since these three parameters have been presented as a function of water depth and sea severity (Robillard and Ochi, 1996), the probability density function of wave amplitudes of coastal waves can be evaluated for a specified water depth and sea severity.

Probability Distribution of Wave Peaks

For derivation of the probability distribution representing statistical properties of wave peaks, a peak envelope process, denoted by $\xi(t)$, shown in Figure 2 is considered.

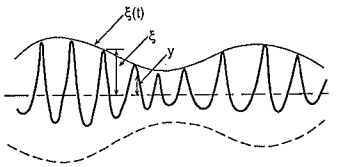

Figure 2
Definition of the envelope process of peaks of non-Gaussian wave

The non-Gaussian random waves y(t) are expressed as a function of normal random process and its square. That is,

$$y(t) = U(t) + a\{U(t)\}^2 \tag{1}$$

where "a" is a constant and U(t) is a Gaussian wave with mean μ_* and variance σ_*^2; all of these parameters can be evaluated from data. The parameter "a" represents the intensity of non-Gaussian wave characteristics; the larger the a-value the stronger the nonlinearity. We may consider Y and U to be random variables for a given time of y(t) and u(t), respectively, and the functional relationship given in Eq.(1) is inversely expressed as follows (Ochi and Ahn 1994):

$$U = \frac{1}{\gamma a}\left(1 - e^{-\gamma a Y}\right) \tag{2}$$

where $\gamma = 1.28$ for $y > 0$, 3.00 for $y < 0$.

It is noted that the random variable U defined in Eq.(2) is normally distributed with sample space $(-\infty, 1/\gamma a)$ instead of $(-\infty, \infty)$ as originally defined. However, this restriction does not affect the distribution of U, in practice, since the value of $(\mu_* + 3\sigma_*)$ where the density function of the normal variate U becomes almost zero, is much smaller than $1/\gamma a$. Hence, the sample space $(-\infty, 1/\gamma a)$ is essentially equivalent to $(-\infty, \infty)$.

For the random variable U associated with the peak envelope process, the mean value is μ_* but the variance is that affiliated with the positive (peak) side only which can be evaluated by

$$\sigma_1^2 = 2\int_0^\infty y^2 f(y)\,dy$$

$$= \frac{2}{\lambda_1^2}\left\{\frac{1}{2}\left(\lambda_1\sigma_*\right)^2 + \sqrt{2/\pi}\left(\lambda_1/\sigma_*\right) + \frac{3}{2}\left(\lambda_1/\sigma_*\right)^4\right\} \tag{3}$$

where $\lambda_1 = a\gamma$, $\gamma = 1.28$ for the positive y.

The probability density function f(y) in Eq.(3) represents a non-Gaussian random wave profile and is given by

$$f(y) = \frac{1}{\sqrt{2\pi}\sigma_*}\exp\left\{-\frac{1}{2(\gamma a\sigma_*)^2}\left(1 - \gamma a\mu_* - e^{-\gamma a y}\right)^2 - \gamma a y\right\} \tag{4}$$

Next, we may define the random variable V by subtracting the mean value μ_* from the random variable U. That is,

$$V = U - \mu_* = \frac{1}{\lambda_1}\left(1 - e^{-\lambda_1 Y}\right) - \mu_* \tag{5}$$

We may write the cosine and sine components of V as V_c and V_s, respectively, and the joint probability density function of V_c and V_s is given by a statistically independent bi-variate normal distribution with zero mean and a common variance σ_1^2. That is,

$$f(v_c, v_s) = \frac{1}{2\pi\sigma_1^2}\exp\left\{-\frac{1}{2\sigma_1^2}\left(v_c^2 + v_s^2\right)\right\} \tag{6}$$

By applying the change of random variable technique and by using the relationship given in Eq.(5), the joint probability density function $f(V_c, V_s)$ is transformed to the joint probability density function $f(y_c, y_s)$. Furthermore, we may write Y_c and Y_s as a function of amplitude and phase. That is,

$$\begin{aligned} Y_c &= \xi \cos\tau \\ Y_s &= \xi \sin\tau \end{aligned} \tag{7}$$

where ξ = amplitude (peak), τ = phase.

Then, we can derive the joint probability density function of ξ and τ as follows:

$$\begin{aligned} f(\xi,\tau) = \frac{\xi}{2\pi\sigma_1^2}\exp\Bigg\{ & -\left(\frac{1-\lambda_1\mu_*}{\lambda_1\sigma_1}\right)^2 - \lambda_1\xi(\cos\tau + \sin\tau) \\ & + \frac{1-\lambda_1\mu_*}{\lambda_1^2\sigma_1^2}\left(e^{-\lambda_1\xi\cos\tau} + e^{-\lambda_1\xi\sin\tau}\right) \\ & - \frac{1}{2\lambda_1^2\sigma_1^2}\left(e^{-2\lambda_1\xi\cos\tau} + e^{-2\lambda_1\xi\sin\tau}\right)\Bigg\}, \\ & 0 \le \xi < \infty, \quad 0 \le \tau \le 2\pi. \end{aligned} \tag{8}$$

In order to obtain the marginal density function of ξ by integrating Eq.(8) with respect to τ, the exponential parts of the 3rd and 4th term of Eq.(8) are expanded to a series of $\lambda_1\xi$ and we may take terms up to $(\lambda_1\xi)^2$. We can then derive the following probability density function of peaks $f(\xi)$.

$$f(\xi) = \frac{(1+\lambda_1\mu_*)\xi}{\sigma_1^2}\, e^{-\left\{\frac{(\lambda_1\sigma_1^2-\mu_*)^2}{(1+\lambda_1\mu_*)\sigma_1^2} + \frac{1+\lambda_1\mu_*}{2\sigma_1^2}\xi^2\right\}} I_0\left\{\sqrt{2}\left(\lambda_1 - \frac{\mu_*}{\sigma_1^2}\right)\xi\right\}$$

$$0 \le \xi < \infty. \qquad (9)$$

The detailed description of the derivation of Eq.(9) is given in the reference Ochi (1998).

In the case of Gaussian waves, μ_* as well as λ_1 are both zero, and the variance σ_1^2 reduces to σ^2. Hence, Eq.(9) becomes

$$f(\xi) = \frac{\xi}{\sigma^2}\, e^{-\frac{\xi^2}{2\sigma^2}} \qquad (10)$$

which is the Rayleigh probability density function applicable for amplitudes of narrow-band Gaussian waves.

In Eq.(9), let us write

$$\frac{\sigma_1^2}{1+\lambda_1\mu_*} = s_1^2$$

$$\frac{\sqrt{2}\left(\lambda_1\sigma_1^2 - \mu_*\right)}{1+\lambda_1\mu_*} = c_1 \qquad (11)$$

then, we have the probability density function of the positive amplitude as

$$f(\xi) = \frac{\xi}{s_1^2}\exp\left\{-\frac{1}{2s_1^2}\left(c_1^2 + \xi_1^2\right)\right\}\cdot I_0\left(c_1\xi / s_1^2\right) \qquad (12)$$

The above equation is the probability density function applicable for the sum of two statistically independent random processes; one being a narrow-band Gaussian random process with zero mean and variance s_1^2, the other a sine wave with amplitude c_1, both having the same frequency (Rice 1945). This implies that the probability density function of the envelope of the positive side of the non-Gaussian waves given in Eq.(9) is equivalent to the probability density function of the envelope of a random process consisting of the sum of a narrow-band Gaussian wave with zero-mean and variance $\sigma_1^2/(1+\lambda_1\mu_*)$ and a sine wave with amplitude $\sqrt{2}\,(\lambda_1\sigma_1^2-\mu_*)/(1+\lambda_1\mu_*)$. This result provides insight as to the structure of the probability distribution function of wave height in finite water depth.

It is further possible to simplify Eq.(12) for non-Gaussian waves for which the skewness of the distribution is less than approximately 1.2. That is, we may approximate the modified Bessel Function in Eq.(12) as

$$I_o(z) \sim \exp\left\{z^2 / 5\right\}, \qquad \text{where } z < 3.0 \tag{13}$$

A comparison of the approximate formula and $I_o(z)$ is shown in Figure 3. By applying the approximation given in Eq.(13), the probability density function given Eq.(12) can be expressed in the following form:

$$f(\xi) = K \cdot \left(\frac{1}{s_1^2} \exp\left\{c_1^2 / 2s_1^2\right\}\right) \cdot \xi \exp\left\{-\frac{1}{2s_1^2}\left(1 - \frac{2c_1^2}{5s_1^2}\right)\xi^2\right\} \tag{14}$$

$$0 < \xi < \infty$$

where K is a normalization factor determined from the condition that the integration of Eq.(14) in the sample space be unity. Then we have

$$f(\xi) = \frac{1}{s_1^2}\left(1 - \frac{2c_1^2}{5s_1^2}\right)\xi \cdot \exp\left\{-\frac{1}{2s_1^2}\left(1 - \frac{2c_1^2}{5s_1^2}\right)\xi^2\right\} \tag{15}$$

$$0 < \xi < \infty$$

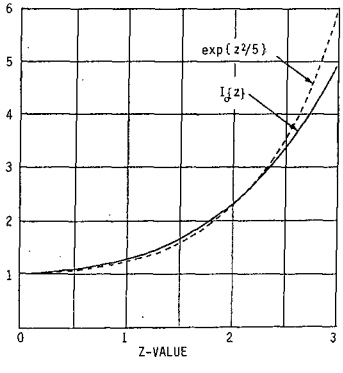

Figure 3
Comparison between the modified Bessel function $I_o(z)$ and its approximate formula

This is the Rayleigh probability density function. Thus, it is found that amplitudes of the positive part of non-Gaussian waves may be approximately distributed following the Rayleigh probability distribution with the parameter $(2s_1^2)/\{1-(2c_1^2/5s_1^2)\}$.

Figure 4 shows a comparison of the exact (Eq.9) and the approximate (Eq.15) probability density functions with the histogram constructed from data shown in Figure 1. The data shown in the

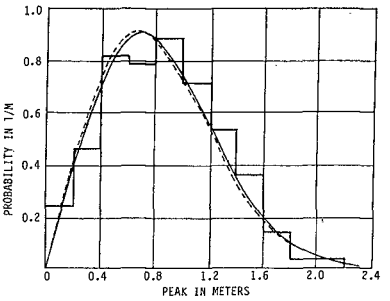

Figure 4
Comparison of exact (solid line) and approximate (dashed line) probability density functions applicable for peaks of a non-Gaussian wave with the histogram constructed from data

figure are obtained at Duck, North Carolina, by the Coastal Engineering Research Center during the ARSLOE Project. As seen, the difference between the exact and approximate density functions is very small and they represent well the histogram of peaks.

Derivation of Probability Distribution of Wave Troughs

The probability density function applicable to troughs of non-Gaussian waves, denoted by $f(\eta)$, has essentially the same form as Eq.(9). The parameter λ_1 and variance σ_1^2 in Eq.(9), however, should be replaced by λ_2 and σ_2^2, respectively, which are appropriate for troughs. The variance σ_2^2 for the trough envelope process can be evaluated by subtracting σ_1^2 from twice the data variance σ^2 computed including both positive and negative displacements from the mean value. That is, the probability density function is given by

$$f(\xi) = \frac{(1+\lambda_2\mu_*)\eta}{\sigma_2^2} \; e^{-\left\{\frac{\left(\lambda_2\sigma_2^2-\mu_*\right)^2}{\left(1+\lambda_2\mu_*\right)\sigma_2^2}+\frac{1+\lambda_2\mu_*}{2\sigma_2^2}\eta^2\right\}} \; I_o\left\{\sqrt{2}\left(\lambda_2-\frac{\mu_*}{\sigma_2^2}\right)\eta\right\}$$

$$0 \le \eta < \infty \qquad (16)$$

where $\sigma_2^2 = 2E\left[y^2\right] - \sigma_1^2$

$\lambda_2 = a\gamma$ with $\gamma = 3.00$

As in the case for the probability distribution of peaks, the probability distribution of envelope of troughs is equivalent to that of a random process consisting of the sum of a narrow-band Gaussian wave with zero-mean and variance $\sigma_2^2/(1+\lambda_2\mu_*)$ and a sine wave with amplitude $\sqrt{2}\,(\lambda_2\sigma_2^2-\mu_*)/(1+\lambda_2\mu_*)$. These may be denoted by s_2^2 and c_2, respectively. Furthermore, the probability density function may be expressed approximately by the following Rayleigh probability distribution:

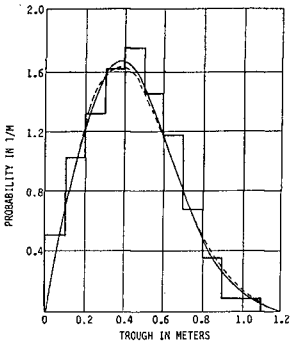

Figure 5
Comparison of exact (solid line) and approximate (dashed line) probability density functions applicable for troughs of a non-Gaussian wave with the histogram constructed from data

$$f(\eta) = \frac{1}{s_2^2}\left(1 - \frac{2c_2^2}{5s_2^2}\right)\eta \cdot \exp\left\{-\frac{1}{2s_2^2}\left(1 - \frac{2c_2^2}{5s_2^2}\right)\eta^2\right\}$$

$$0 < \eta < \infty \qquad (17)$$

Figure 5 shows a comparison between the exact (Eq.16) and approximate (Eq.17) probability density functions applicable for the troughs of non-Gaussian waves and the histogram constructed from data. As seen, the difference between the exact and approximate density functions is extremely small and the overall agreement between the histogram and density functions is satisfactory.

Probability Distribution of Wave Height

Wave height is defined as a peak-to-trough excursion. As stated earlier, peak and trough envelope processes are independently considered for probability distribution of peaks and troughs of non-Gaussian waves. The results of analysis have shown that large peak envelopes and large trough envelopes do not occur simultaneously, in general. Correlation between the two envelopes is rather small; hence, it is assumed that peaks and troughs are statistically independent and thereby the probability density function of peak-to-trough excursions may be obtained as a convolution integral of the two probability density functions, $f(\xi)$ and $f(\eta)$. That is

$$f(\zeta) = \int_0^\infty f_\xi(\xi)\, f_\eta(\zeta - \xi)\, d\xi \qquad (18)$$

where $f_\xi(\ )$ and $f_\eta(\ )$ represent the probability density functions given in Eqs.(9) and (16), respectively, for the exact density functions, and Eqs.(15) and (17), respectively, for the approximate density functions.

The integration given in Eq.(18) cannot be analytically carried out for the exact density functions because of the product

of two modified Bessel functions involved. The probability density function of ζ, therefore, is numerically evaluated. The convolution integral for the two approximate probability density functions given in Eqs.(15) and (17), however, can be analytically carried out. It is the sum of two independent Rayleigh distributions. That is, by writing the parameters of the Rayleigh distributions applicable for the peaks and troughs as

$$R_1 = \left(2s_1^2\right)\Big/\left\{1 - \left(2c_1^2 / 5s_1^2\right)\right\}$$
$$R_2 = \left(2s_2^2\right)\Big/\left\{1 - \left(2c_2^2 / 5s_2^2\right)\right\} \qquad (19)$$

the probability density function of the sum of the Rayleigh distribution, denoted by $f(\zeta)$, becomes

$$f(\zeta) = \frac{2\xi}{R_1} e^{-\frac{\xi^2}{R_1}} \cdot \frac{2(\zeta - \xi)}{R_2} e^{-\frac{(\zeta - \xi)^2}{R_2}} d\xi$$

$$= \frac{2\zeta}{(R_1 + R_2)^2}\left(R_1 e^{-\frac{\zeta^2}{R_1}} + R_2 e^{-\frac{\zeta^2}{R_2}}\right)$$

$$+ \frac{2\sqrt{\pi}}{R_1 + R_2} e^{-\frac{\zeta^2}{R_1 + R_2}} \sqrt{\frac{R_1 R_2}{R_1 + R_2}} \left(\frac{2}{R_1 + R_2}\zeta^2 - 1\right)$$

$$\times\left\{\Phi\left(\sqrt{\frac{2R_2}{R_1(R_1 + R_2)}}\,\zeta\right) - \Phi\left(-\sqrt{\frac{2R_1}{R_2(R_1 + R_2)}}\,\zeta\right)\right\}$$

$$0 < \zeta < \infty \qquad (20)$$

where Φ = cumulative distribution function of the standardized normal distribution.

Figure 6 shows a comparison between the exact (Eq.18) and approximate (Eq.20) probability density functions for the peak-to-trough excursions and the histogram constructed from the same wave data as used for the histograms of peaks and troughs. The difference between the exact and approximate density functions is negligibly small, and the theoretical density functions agree reasonably well with the histogram. Included also in the figure is the Rayleigh probability density function applicable for Gaussian waves commonly considered for analysis of deep water waves. The probability density function for the Gaussian wave assumption substantially deviates from the histogram.

The cumulative distribution function of the wave height can be evaluated by integrating Eq.(20) with respect to ζ. The derivation of the distribution function, however, may be much easier using the

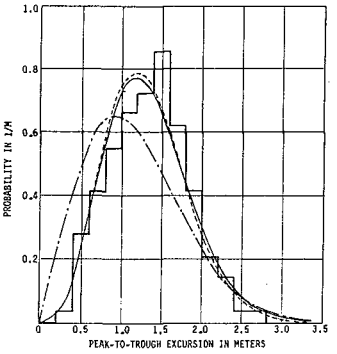

Figure 6
Comparison between exact (solid line) and approximate (dashed line) probability density functions developed based on non-Gaussian concept, Gaussian concept (chain line) and histogram constructed from data

following approach since the distributions of the peaks and troughs are assumed to be statistically independent. That is

$$F(\zeta) = \iint_{\xi+\eta\le\zeta} f(\xi,\eta)d\xi\, d\eta = \int_0^{\zeta}\left(\int_0^{\zeta-\xi} f(\eta)\, d\eta\right) f(\xi)\, d\xi \tag{21}$$

By applying Eqs.(15) and (17), and with the parameters given in Eq.(19), we have

$$F(\zeta) = 1 - \frac{1}{R_1+R_2}\left[R_1 e^{-\frac{\zeta^2}{R_1}} + R_2 e^{-\frac{\zeta^2}{R_2}}\right.$$

$$\left. + 2\zeta\sqrt{\frac{\pi R_1 R_2}{R_1+R_2}}\, e^{-\frac{\zeta^2}{R_1+R_2}}\left\{\Phi\left(\sqrt{\frac{2R_2}{R_1(R_1+R_2)}}\,\zeta\right) - \Phi\left(-\sqrt{\frac{2R_1}{R_2(R_1+R_2)}}\,\zeta\right)\right\}\right]$$

$$0 < \zeta < \infty \tag{22}$$

It may be of interest to see how the shape of the probability distribution of amplitudes of coastal waves changes when wave energy propagates from deep to shallow water. Figure 7 shows an example of the probability density functions of peaks and troughs along with wave records simultaneously measured at four locations (60 m, 151 m, 456 m and 12 km offshore) during the ARSLOE Project. The waves obtained at the 12 km offshore are considered to be Gaussian at the time of measurement. As seen, the mode of the Rayleigh distribution applicable to non-Gaussian waves shifts to the smaller values as waves approach the shoreline. In particular, the rate of change of the probability density function of troughs is much faster than that

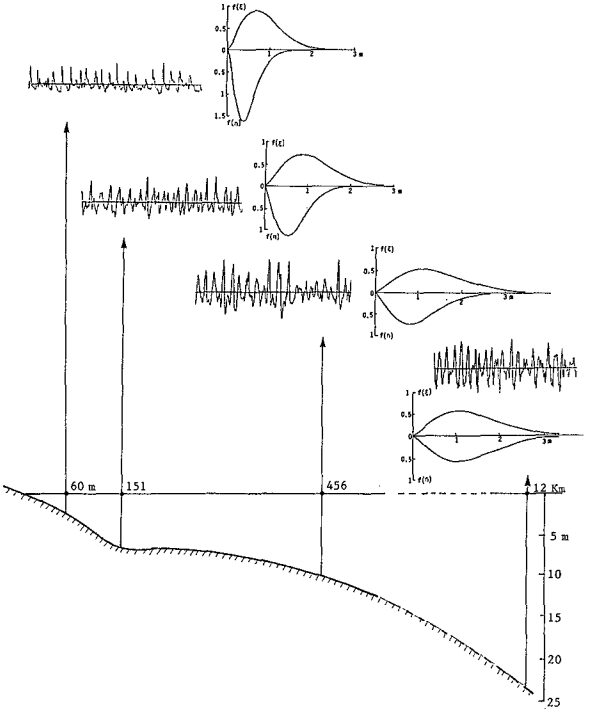

Figure 7 Probability density functions of wave peaks and troughs obtained from data at various locations in the nearshore zone

of peaks. This is understandable since wave troughs are much more susceptible to bottom effect.

Significant Wave Height

Significant wave height defined as the average of the highest one-third wave heights, denoted by H_s, is most commonly used for representing the severity of random waves. It can be evaluated by

$$H_s = 3\int_{\zeta_*}^{\infty} \zeta f(\zeta)\, d\zeta \tag{23}$$

where ζ_* = the value of wave height ζ for which $F(\zeta) = 2/3$,
$f(\zeta)$ = probability density of wave height.

Table 1
Comparison between computed and measured significant wave heights

Water Depth (M)	Significant Wave Height in meters		
	Non-Gaussian Concept	Gaussian Concept	Measured
2.32	1.97	1.86	1.92
6.53	2.56	2.48	2.52
10.07	3.72	3.69	3.70

Equation (23) yields a very simple result for deep water : $4\sqrt{m_o}$ where m_o is the area under the spectral density function. For non-Gaussian waves, however, the computation of Eq.(23) is rather complicated. After some mathematical manipulations, we can derive

$$H_s = 3\left[\left(\frac{R_1}{R_1+R_2}\right)^2\left[\zeta_* e^{-\frac{\zeta_*^2}{R_1}} + \sqrt{\pi R_1}\left\{1-\Phi\left(\sqrt{2/R_1}\zeta_*\right)\right\}\right] + \sqrt{\pi}\sqrt{\frac{R_1R_2}{R_1+R_2}}e^{-\frac{\zeta_*^2}{R_1+R_2}}\left(\frac{2}{R_1+R_2}\zeta_*^2+1.1\right)\right] \quad (24)$$

Comparisons of significant wave heights computed by Eq.(24) and those evaluated from data obtained at three water depths is shown in Table 1. Included also in the table are those computed by using the formula applicable for deep water. As seen in the table, significant wave heights computed based on non-Gaussian and Gaussian concepts do not differ more than 6 per cent, and the significant wave height obtained from measured data is between the two computed values for a given water depth. As shown in Figure 6, the probability density function of wave height for non-Gaussian waves intersects that of Gaussian waves at a large wave height. This results in the centers of gravity of the highest one-third of these two probability density functions (significant wave heights) may not be too far apart.

In order to supplement the above-mentioned statement, Figure 8 is prepared. The figure shows the cumulative distribution function of wave heights computed at two water depths based on Gaussian and non-Gaussian concepts. As seen, the two cumulative distribution functions slowly approach each other with increase in wave height and intersect at a certain high wave height. The value of the significant wave height is slightly greater than the wave height at

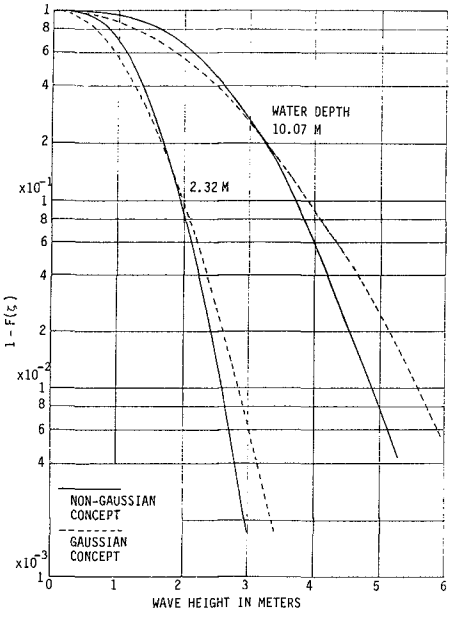

Figure 8
Comparison of cumulative distribution functions of wave heights computed based on Gaussian and non-Gaussian concepts

the point of crossing, but much less than the height where the two distribution functions start separating widely. Since the computation of significant wave height based on the Gaussian concept is quite simple, and since computed significant wave height is close to that computed using the formula for non-Gaussian waves, it may be concluded that the formula to evaluate significant wave height in deep water may also be applied approximately to non-Gaussian waves as far as the evaluation of significant wave height is concerned.

Conclusions

Probability density functions applicable to peaks, troughs and peak-to-trough excursions of coastal waves with finite water depth are presented separately in closed form. It is found that the probability density function applicable to peaks (and troughs) consists of the sum of narrow-band Gaussian waves and sine waves having the same frequency. It is also found that for non-Gaussian waves for which the skewness of the distribution is less than 1.2, the probability density function of peaks (and troughs) can be represented approximately by the Rayleigh distribution with a parameter which is a function of three parameters representing the non-Gaussian waves. Since these three parameters have been presented as a function of water depth and sea severity, the probability density function of amplitudes of coastal waves can be evaluated for a specified water depth and sea severity. The

agreement between the probability density functions and the histograms constructed from data obtained by the Coastal Engineering Research Center during the ARSLOE Project is satisfactory.

The significant wave height of non-Gaussian coastal waves is analytically derived. The results of the computations show that computed significant wave height is close to that evaluated by applying the formula for waves in deep water (Gaussian waves). Therefore, since the computations based on the Gaussian concept are quite simple, it may be used for non-Caussian waves as far as the evaluation of significant wave height is concerned.

Acknowledgments

The author is grateful to Ms. Laura Dickinson for typing the manuscript.

References

Arhan, M.K. and Plaisted, R.O. (1981), Nonlinear deformation of sea-wave profiles in intermediate and shallow water, *Oceanol.* Acta, 2, 107-115.

Goda, Y. (1975), Irregular wave deformation in the surf zone. Coastal Eng. Japan, **18**, 13-26.

Hughs, S.A. and Borgman, L.E. (1987), Beta-Rayleigh distribution for shallow water wave heights. Proc. Conf. Coastal Hydrodynamics, 17-31.

Kuo, C.T. and Kuo, S.J. (1975), Effect of wave breaking on statistical distribution of wave heights. Proc. Civil Eng. in the ocean, Ame. Soc. Civil Eng., 1211-1231.

Ochi, M.K., Malakar, S.B. and Wang, W.C. (1982), Statistical analysis of coastal waves observed during the ARSLOE Project, Report COEL/TR-045, University of Florida.

Ochi, M.K. and Wang, W.C. (1984), Non-Gaussian characteristics of coastal waves. Proc. 19th Coastal Eng. Conf., **1**, 516-531.

Ochi, M.K. and Ahn, K. (1994), Probability distribution applicable to non-Caussian random process, *J. Prob. Eng. Mechanics*, **9**, 4, 255-264.

Ochi, M.K. (1998), Probability distribution of peaks and troughs of non-Caussian random processes, *Journal, Prob. Eng. Mech.*, 13, 4, 291-298.

Rice, S.O. (1945), Mathematical analysis of random noise, *Bell System Tech. Jour.*, 24, 46-157.

Robillard, D.J. and Ochi, M.K. (1996), Transition of stochastic characteristics of waves in the nearshore zone, *Proc. 25th Coastal Eng. Conf.*, 1, 878-888.

Tayfun, M.A., (1980), Narrow-band nonlinear sea waves, *Journal Geophy. Res.*, **85**, C3, 1548-1552.

Increase of wave height in the North Pacific Ocean

Kozo Okada[1], Yasushi Suzuki[2], Yoshihiro Utsunomiya[3]
and Yoshihiro Watanabe[4]

Abstract

We analyze annual variations and the long-term tendency of wave heights along the coast of Japan, based on observed data for more than 10 years. And we analyze the trend of wave heights over the last 10 years in the North Pacific with hindcast data. As a result of the analysis, the wave height has shown an increase trend at most stations along the Pacific coast of Japan. The average increase rate is 0.6cm/year. The estimated wave height by a wave model also shows an increased trend in the North Pacific Ocean. Since there is a correlation relation between 500hPa height anomaly at specific areas and the wave height anomaly at each station, an increase trend of wave height in the Northern Hemisphere is supposed to be related to the change in an atmospheric planetary wave pattern.

Introduction

In recent years, there has been a growing interest in the climate change represented by the global warming and the influence of the climate change to the world. It is shown by numerical calculations of climate models that if carbon dioxide keeps on being exhausted at the current levels, a surface atmospheric temperature will rise more than 2 ℃ 100 years later. It is imagined that the global warming makes not only the sea level rise but also causes changes of meteorological and ecological system in the oceans.

Ocean waves are important natural conditions for the design of ships and harbors and for the prevention of coastal disasters. It is important for these purposes to understand the current state of a long-term change in ocean waves, which is believed to be related closely to the climate change.

In this paper we analyze the long-term change of ocean waves along the coast of Japan and in the North Pacific Ocean. We use observational data obtained for more

[1]Executive engineer, Japan Weather Association, Sunshine60, 3-1-1, Higashi-Ikebukuro, Toshimaku, Tokyo 170-6055, Japan

[2]Vice senior researcher, Remote Sensing Technology Center of Japan, 1-9-9, Minatoku, Tokyo 106-0032, Japan

[3]Engineer, Japan Weather Association Kansai hdqrs., 3-16-11, Higashi-Imazato, Higashinariku, Osaka 537-0011, Japan

[4]Director, Japan Weather Association, Sunshine60, 3-1-1, Higashi-Ikebukuro, Toshimaku, Tokyo 170-6055, Japan

than 10 years at most stations along the coast of Japan, and 10-year global hindcast data by a wave model. As a result of the analysis, it is shown that the wave height has had the increasing trend over the past 10 to 20 years at most stations along the Pacific coast of Japan and in the North Pacific Ocean.

It is shown that annual variations of ocean wave height at stations are related to the strength of anomaly from the normal monthly mean of 500hPa height of the atmosphere and the strength of Asian monsoon, according to the correlation analysis with a wave height and 500hPa height. It is suggested from these that there is a possibility of the increasing tendency of wave height in the North Pacific to originate in the change of the weather related to an atmospheric circulation in the middle layer.

Data analysis

Figure 1 shows major wave observation stations in Japan. Open circle is the Meteorological Agency's station, and closed circle is the Harbor Bureau's. Japan Meteorological Agency has been executing the wave observation at 11 stations along the coast of Japan for about 22 years from 1976 to present, for the purpose of wave watch and wave forecast for the fishery, the safe navigation and marine leisure in coastal areas. Harbors Bureau in Ministry of Transport has been observing coastal waves at about 44 stations for about 26 years from 1972 to present for the harbor design and the maintenance.

Fig.1 Location of coastal wave observation stations.

Almost all locations of these observation stations are in 1 or 2 kilometers offing from the shore. The depth is about 50m at these stations. Ultrasonic type wave meters are placed at the bottom of the ocean to measure the sea surface level. The observation interval is two hours at the Harbors Bureau's station. It is three hours in the routine observation at Meteorological Agency, but is one hour in the urgent observation like the case of a typhoon. Significant wave height and other parameters are calculated from the record of sea level for 20 minutes. The sampling time is 0.25sec or 0.5sec.

We chose the data from the stations where observations have been continued for a long period without a displacement of the position or an interruption of the observation. Table 1 shows the stations and the period of data chosen for analysis along the Pacific coast. Table 2 is those along the Sea of Japan coast. We use a monthly mean significant wave height, as an index to represent a long-term tendency of ocean waves. Hereafter we use the word the monthly mean wave height to mean the monthly mean significant wave height. A monthly mean wave height is not calculated if the data are not available for more than 80 percents of the time in a month.

Table 1 The period of data analysis (the Pacific coast).

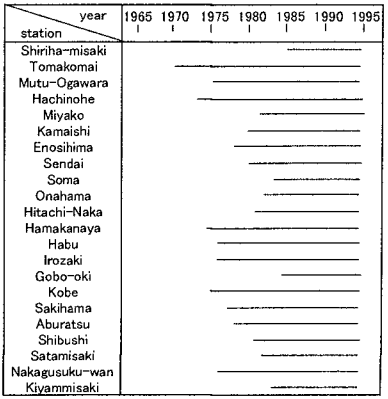

Table 2 The period of data analysis (the Japan Sea coast).

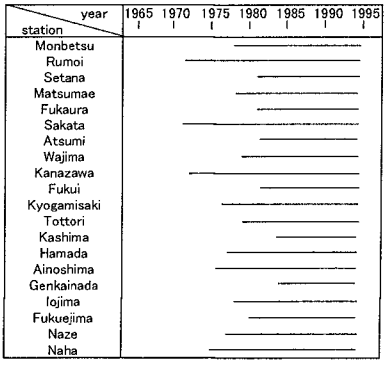

Figure 2 shows a seasonal change of the monthly mean wave height and the 12 months running mean at the coast of Japan Sea (the top figure) and the coast of Pacific Ocean (the bottom figure). As can be seen, the monthly mean wave height at the coast of Japan Sea exhibits seasonal variations, low in summer and high in winter. High waves are caused by a strong wind in the northwest of the Asian monsoon in the Sea of Japan in winter.

On the other hand, the monthly mean wave height at the Pacific coast generally fluctuates over a period of about six months. The wave height is larger in both spring and autumn and is lower in both winter and summer at the Pacific coast. For this weather factor, it is thought that although monsoonal wind blows in the northwest in winter, waves don't greatly develop at the Pacific coast, because the Fetch is short in this direction. Waves develop in spring and autumn at the Pacific coast, because depressions occur with the period of a few days in the Sea of Japan or the East China Sea and move from the southwest toward northeast through Japan while developing in these seasons. Moreover, swells and wind waves develop under the influence of typhoons in autumn.

The thick solid line shows the variation with a several years period both at the Sea of Japan and the Pacific coast. When we pay attention to the coast of Japan Sea, we can see the annual variation of wave height has an increasing wave height in 1981, 1984, 1986, and 1988. In these years, the wave height develops in winter (figure 3). Therefore, the annual mean wave height is chiefly controlled by the mean wave height in winter at the coast of Japan Sea.

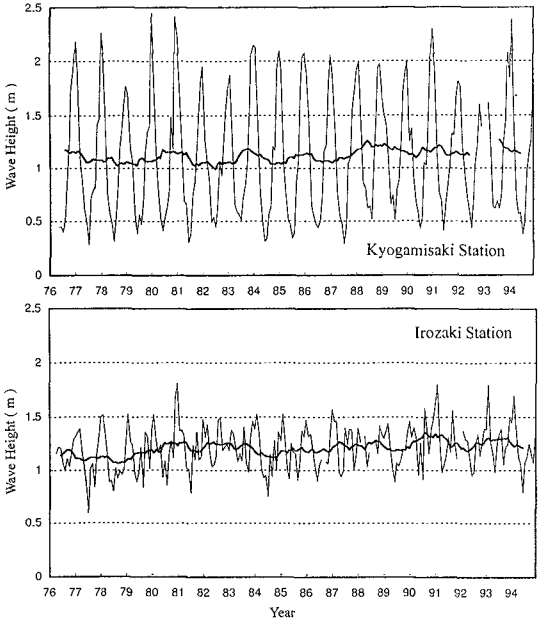

Fig.2 Annual variation of monthly mean wave height (thin line) and 12 months running mean (thick line). (top figure; the Japan Sea coast, bottom figure; the Pacific coast)

On the other hand, it is shown that the seasonal mean wave height at the Sea of Japan coast in winter has a correlation with the seasonal mean temperature at 500hPa height over the Sea of Japan (Figure 3). The solid line with open circles is the seasonal mean temperature in winter at 500hPa height over the Sea of Japan. The dashed line with closed triangles is a seasonal mean wave height in winter at the coast of Japan Sea. These time series show peaks at the same years. For example, in 1981, 84 and 86. It is known that the temperature at 500hPa over the Sea of Japan is related to the intensity of cold air mass on the Asian continent in winter. When the temperature is lower, the intensity of cold air mass is strong and the northwest monsoon wind is strong. It is thought that such a weather condition develops wave heights more than a usual year in the Sea of Japan. After all, it is suggested that the variation of wave heights with a several years period in the Sea of Japan depend on a change in the intensity of Asian monsoon in winter.

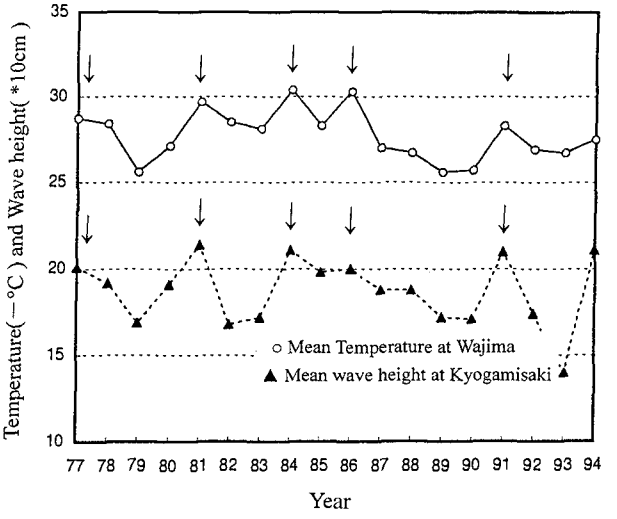

Fig.3 Time series of mean wave height in winter at Kyogamisaki and mean temperature in winter at 500hpa height over the Japan Sea.

We determined the long-term tendency of the monthly mean wave height by a least square method at observation stations, where data has existed for more than 10 years from a year before 1985 to 1994 (Table 1, 2). Figure 4 gives the examples of the time series of the monthly mean wave height and the linear trend at the Pacific coast (the top figure) and the Japan Sea coast (the bottom figure). The wave heights show the increasing trend at these stations.

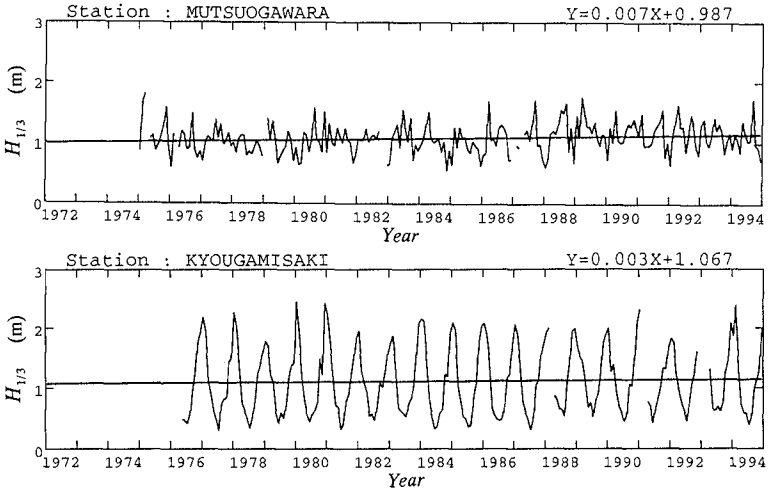

Fig.4 Time series of monthly mean wave height and the liner trend.
(top figure; the Pacific coast, bottom figure; the Japan Sea coast)

The trend of wave heights was gotten in a nationwide coast. Figure 5 shows the rate of change of wave heights per year at each station along the coast of Japan. According to this result, the long-term tendency of wave height at the coast of the Sea of Japan differs from one station to another (the bottom figure). The tendency is not uniform along the coast of the Sea of Japan. On the other hand, the monthly mean wave height at the Pacific Ocean coast shows the increasing tendency in most observation stations. The average rate of the increasing tendency is about 0.6cm/year along the coast of the Pacific Ocean (the top figure).

Figure 6 shows the long-term tendency in each season. In spring from March to May (the top of left side figure), the decreasing tendency is shown at many stations along the Pacific Ocean coast, and the increasing tendency is shown at many stations along the Sea of Japan coast. In summer from June to August, the increasing tendency is shown at most stations along the Sea of Japan coast, but the tendencies are not uniform along the Pacific Ocean coast. In autumn and winter a remarkable wave height increasing is shown at most observation stations along the Pacific Ocean coast. It is found from these that the increase of wave height at the Pacific Ocean coast has occurred in autumn and winter.

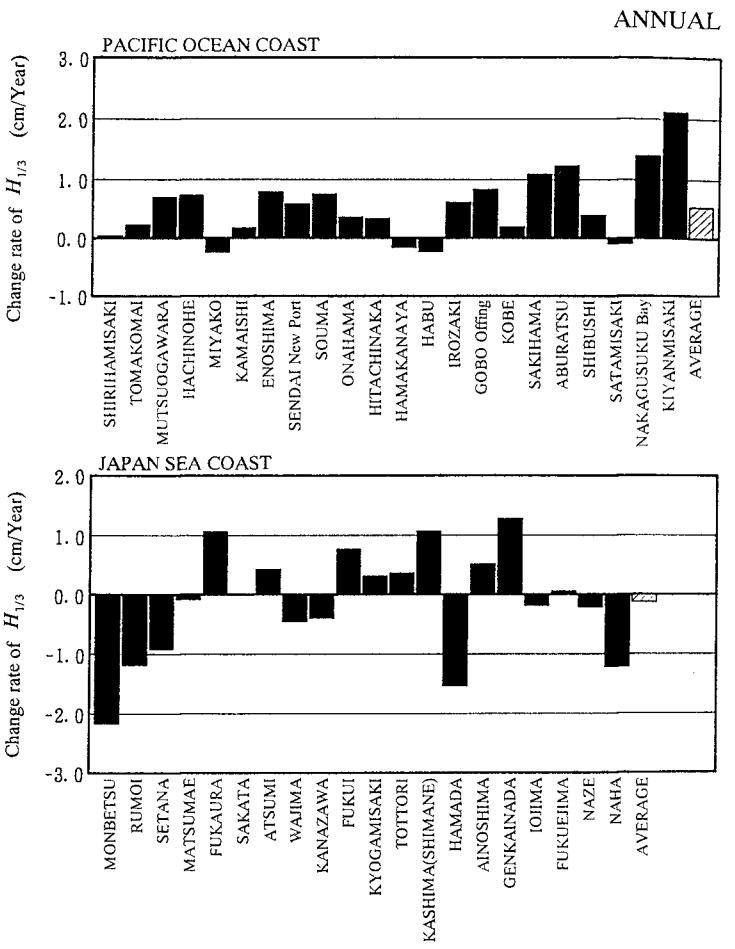

Fig.5 Long-term change rate (cm/year) of the significant wave height. (top figure; the Pacific coast, bottom figure; the Japan Sea coast)

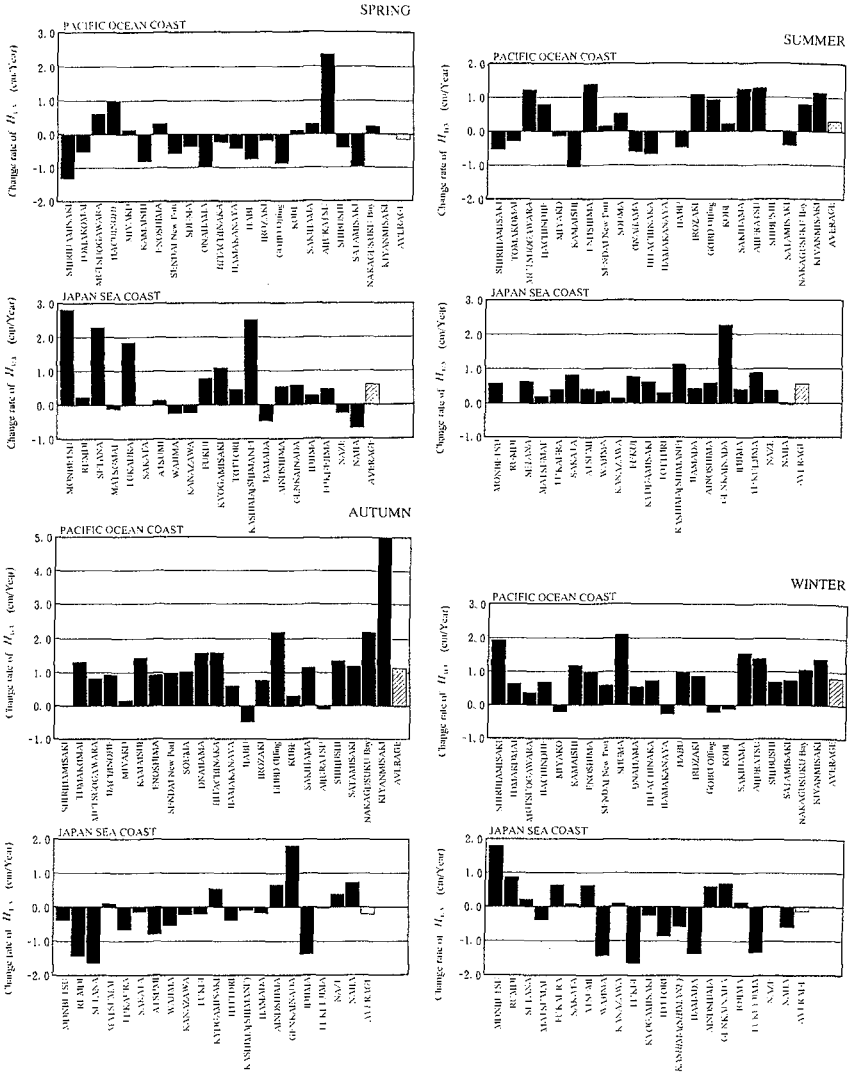

Fig.6 Long-term change rate (cm/year) of SWH in seasons.

Result of wave model

We analyzed the long-term variation of wave heights in the North Pacific Ocean by the wave model, that was developed by Suzuki and Isozaki(1994). This model is classified as the third generation model, which is based on the energy balance equation and considers a non-linear effect among wave components. The source functions of this model consist of the empirical formula of Mitsuyasu-Honda(1982) connected to Hsiao and Shemdin(1983) for the input energy by wind, the empirical formula obtained by dimension analysis for dissipation by whitecapping, and the effective calculation of wave components for nonlinear interaction between waves, respectively. This model uses the hybrid upstream difference scheme for the advection calculation of energy. As for the calculation accuracy of this wave model, the root mean square error of wave height is less than 1m, and the accuracy is very high for practical wave forecasts (Figure 7).

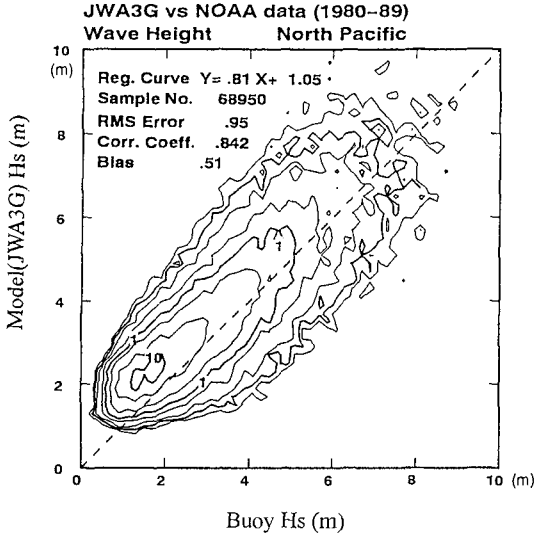

Fig.7 Scatter plot of modeled and measured significant wave height for NOAA buoys in the North Pacific.

The global wave variation in the last ten years has been analyzed by using this model and the wind data of the European Centre for Medium-range Weather Forecasts. An analyzed wind of ECMWF was converted to 10m-wind above a sea surface by using an observed wind at NOAA and JMA buoys and used. The analysis period is 10 years from 1985 to 1994. During this period, the ECMWF model was modified and the accuracy was improved.

Figure 8 shows a global distribution of the trend in wave height for 10 years from 1985 to 1994. The contour interval is 20cm. According to this, one of the largest increasing trends of wave height is shown in the center of the North Pacific Ocean. The maximum value is about 60cm in the last ten years. The increase of wave height is about 20cm at the Pacific coast of Japan over ten years. This magnitude is nearly the same as that of the rate of the increase obtained from the observation data along the coast. It is interesting that both the calculated wave height and the observed one show the increasing tendency with the same magnitude along the Pacific cost of Japan.

The wave height in the middle latitude area of the North Atlantic Ocean shows an increasing tendency, as it does in the North Pacific Ocean. On the other hand, the decreasing tendency of wave height is shown in the high latitude area of the Southern Hemisphere. This reason is not clear yet.

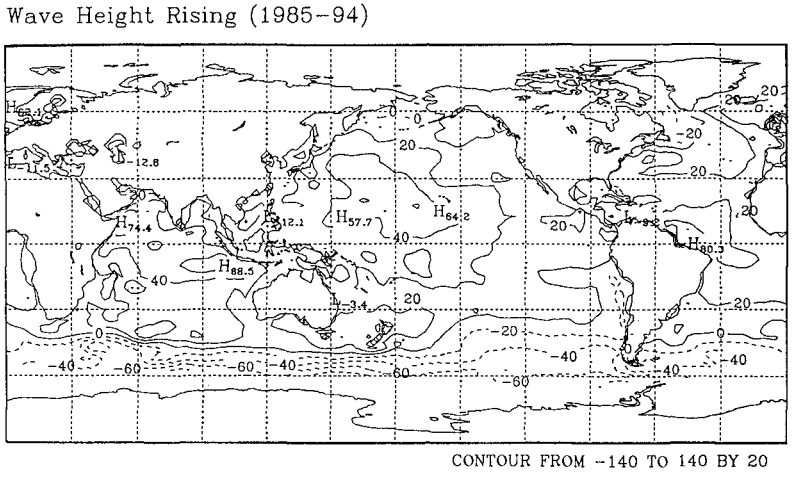

Fig.8 Increase of wave height during 10 years from 1985 to 1994. Contour lines show the total increase of wave height. Solid lines indicate positive values (increase) and dashed lines indicate negative values (decrease). The increase was obtained by fitting a linear regression curve to the monthly mean wave height.

Discussion

As shown above, the wave height shows the tendency of increase at most of the observation stations along the Pacific coast of Japan. The increasing tendency is shown in all seasons except spring (Figure 6). It is also shown that the increasing tendency is especially dominant in autumn and winter. As the primary weather factor causing the wave height increase, it is thought that the number of typhoon approaching to and hitting Japan has been increasing recently, and that atmospheric depressions develop more frequently in winter around Japan, since Asian Monsoon

tends to be weak in recent winters.

According to the numerical simulation by a wave model, the trend of wave height over the recent 10 years shows a tendency of increase in the North Pacific Ocean with a maximum of 6cm/year (Figure 8). A long-term tendency in the mid latitude area of the North Atlantic Ocean is also an increase, with the rate of approximately 2cm/year according to the hindcast data. The order of magnitude of this rate is equal to the result of the analysis of E.Bouws et al (1996) from the wave chart for 27 years from 1961 to 1987, though both these analysis periods are different. It is also interesting that the wave height shows an increasing tendency in both the North Pacific and the North Atlantic Oceans.

As one of the primary factors of a long-term change of ocean waves, there is a possibility that the change of atmospheric circulation in the upper layers is related to this. Figure 9 shows a correlation relation between an anomaly of monthly mean wave height at Sendai and 500hPa height at latitude 45°N longitude 155°E in winter.

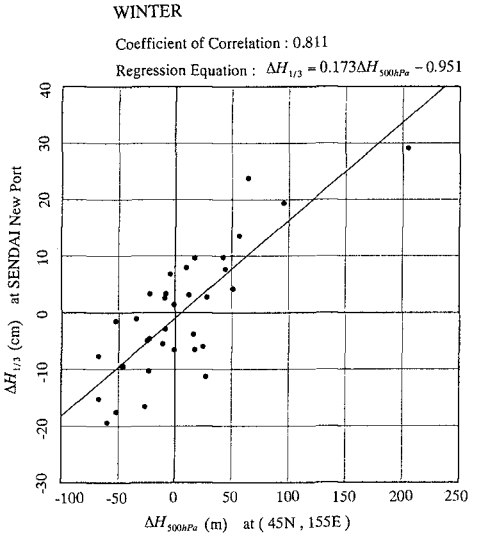

Fig.9 Scatter plot of anomaly of monthly mean wave height at Sendai and anomaly of monthly mean 500hPa height at 45° N, 155° E.

Figure 10 shows the distribution of correlation coefficient between an anomaly of monthly mean wave height from a climatic value at Sendai and an anomaly of monthly mean 500hPa height in the Northern Hemisphere. It is shown that there are three places with evident correlation relation between anomaly of ocean wave height and 500hPa height in this figure. The correlation relation between the anomaly of 500hPa height and wave height is shown to exist also at other wave observation stations. This means that when atmospheric circulation fields in the upper layer

change compared with ordinary states, a weather system at the ground surface tied to these circulation changes too, and as a result, wave statistics values change. Therefore, wave height showing the increase tendency in the North Pacific Ocean suggests the possibility that the weather system at the ground surface is changing.

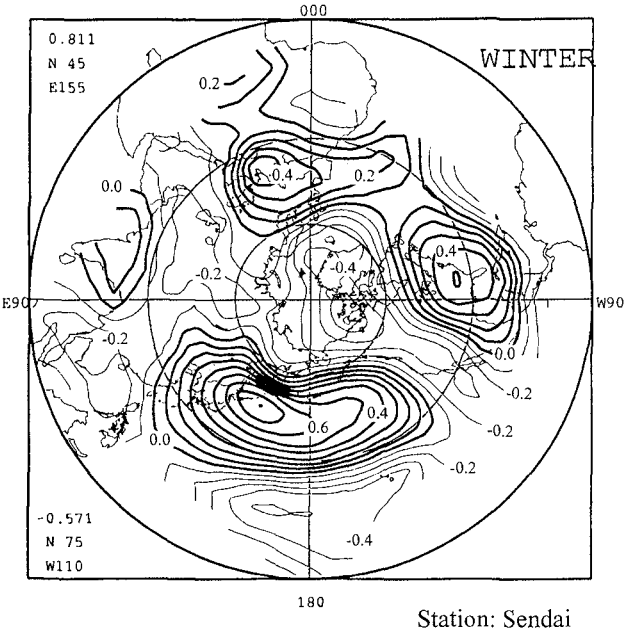

Fig.10 Correlation coefficients between anomaly of monthly mean wave height at Sendai and anomaly of monthly mean 500hPa height in the northern Hemisphere in winter. Thick contour lines indicate plus correlation and thin lines indicate minus correlation.

Conclusion

A long-term tendency of monthly mean wave height has shown the tendency of increase at most observation stations along the Pacific coast of Japan. The increasing tendency of wave height based on the observation data does not contradict with the numerical calculation result. Therefore, there is a possibility that wave height has increased over the recent ten years in the North Pacific Ocean.

The following is thought as this factor. It has been shown that the anomaly of monthly mean wave height at each wave observation station has a high correlation with the anomaly of 500hPa height in a specific area. This suggests that the change in the planetary wave pattern in the upper layer of atmosphere generate the changes of wave climate. For instance, in the winter when the planetary wave moves to the north and locates in a higher latitude area than a usual year, it tends to cause a warm winter in Japan. At that time the monthly mean wave height tends to be larger than usual

along the Pacific coast of Japan, since synoptic-scale weather disturbances are frequently generated in such a warm winter.

The long-term change in weather systems related to a planetary wave is thought to be one of the factors controlling the wave height increase tendency in the North Pacific. However, the evidence or the mechanism of the change in the weather disturbance has not been clarified yet. It is indeed necessary to investigate the change in the weather disturbance activity.

References

Bouws, E., D. Jannik, and G. J. Komen (1996): The Increasing Wave Height in the North Atlantic Ocean, Bull. of Amr. Meteor. Soc., 77, 2275-2277.

Mitsuyasu, H. and T. Honda (1982): Wind-induced growth of water waves, J. Fluid Mech., 123, 425-442.

Hsiao, S. V. and O. H. Shemdin (1983): Measurements of wind velocity and pressure with a wave follower during MARSEN, J. Geophys. Res., 88(C14), 9841-9849.

Nagai, T., K. Sugahara, N. Hashimoto, T. Asai, S. Higashiyama, and K. Toda (1994): Introduction of Japanese NOWPHAS System and its Recent Topics, Proc. Int. Conf. on Hydro-Technical Engg. for Port and Harbor Construction in Yokosuka, 67-82.

Okada, K., Y. Utsunomiya, and Y. Watanabe (1997): The long-term prediction method for ocean waves by using a parameter of middle stratum atmosphere, Proc. 44th Japanese Conf. Coastal Engg., JSCE, 44, 461-465 (in Japanese).

Suzuki, Y. and I. Isozaki (1994): On the development of a global ocean wave model JWA3G, Proc. Pacific Ocean Remote Sensing Conf. in Melbourne, Australia, 195-201.

Acknowledgment

The present study was carried out as part of the Improvement of Precision of Wave Information Program, which has been supported by the Nippon Foundation. The authors gratefully acknowledge Japan Meteorological Agency and Harbors Bureau in Ministry of Transport for providing wave observation data. The authors are also grateful to Prof. Y. Ogura for his fruitful advice.

ANALYSIS OF WAVE DATA AT SINES

Carlos Pita [1] and Fernando Abecasis [2]

Abstract

The aim of this paper is to summarise the main results obtained from wave data collected in the Portuguese west coast near Sines Harbour. In spite of special attention given to wave characteristics during storm occurrences, some considerations about mean wave regimen will be done.

Introduction

Sines Harbour is located in the South part of Portuguese west coast (fig. 1).

Fig. 1

Acquisition of wave data is made in a regular basis at Sines since 1973, with some interruptions for maintenance of recorder devices or caused by buoys mooring problems. Unfortunately only after 1981 data processing is carried out systematically. So, at this moment, available data cover a period of 18 years, period of time still insufficient for a good definition of extreme values, but interesting to provide information about the tendencies of these extreme values, specially when compared with design conditions.

Two Datawell directional wave buoys are installed at depths of -100 m CD and -50 m CD. In spite of some small variations in the positions of these buoys, after their removal for maintenance needs, it may be assumed (taking into account mathematical model results) that, for wave regimen characterisation, data from each depth may be considered as recorded at the same point.

(1) - Civil Engineer, Consultant, WW - Consultores de Hidráulica e Obras Marítimas, Lda., Avenida Ventura Terra, 11 - R/C, 1600 LISBOA, PORTUGAL

(2) - Civil Engineer, Consultant, HIDROTÉCNICA PORTUGUESA, Apartado 5058, 1702 LISBOA Codex, PORTUGAL

Wave Data

Wave data is nowadays obtained in a continuous form. Records are segmented in parts with a duration of about 20 minutes, which are subjected to an on-line computation at Administração do Porto de Sines (APS) facilities. This analysis allows the computation, for each record, of maximum individual wave height, Hmax, significant wave height, Hs, mean period, Tz and main direction.

These 20 minutes records are also digitally registered. In a subsequent treatment, done by the portuguese hydrographic service, Instituto Hidrográfico (IH), parameters like peak period or wave height and wave period distributions are also computed.

In present paper most of used results where obtained from APS on-line computations, complemented in some cases by the evaluation of wave parameters done at IH. The results of some studies performed by Laboratório Nacional de Engenharia Civil (LNEC) and by IH are also used.

Storm Waves

It was assumed by the Portuguese coastal engineers, taking into account their experience about wave conditions in the Portuguese west coast, that a "storm" occurs when there is one exceedance of a significant wave height of 5.0 meters. In the case of Sines there is a "storm" if the significant wave height of 5.0 meters is exceeded at least in one of the two wave buoys.

Considering this definition, a total of 57 storms happened since the beginning of 1981 until February 1998.

In table I the main characteristics of these storms, namely maximum values of Hs, Hmax and associated main direction are presented for the two wave buoys. The total time of exceedance of Hs = 5.0 meters is also presented, with a maximum error in each storm of +1 hour.

According to this table, since 1981 storm total duration is around 1.000 hours (aprox. 42 days) with maximum yearly duration in 1989 (about 200 hours) and 1996 (222 hours) - fig. 2.

Wave conditions are in general more severe at the depth of -100 m CD than at -50 m CD (as it was expected) - figures 3 and 4, with maximum values of:

- Depth -100 m CD: Hs = 9.6 m
- Depth -50 m CD: Hs = 9.0 m

Anyway, largest Hmax had occurred at buoy at -50 m CD, with a value of 16.1 m, against a value of Hmax = 14.7 m at -100 m CD.

TABLE I
SINES WAVE STORMS (1981-98)

Nr.	Year	Month	Day	Buoy at -100 m CD			Buoy at -50 m CD			Storm Duration (hrs.)
				Maximum Values		Main	Maximum Values		Main	
				Hmax	Hs	Direction	Hmax	Hs	Direction	
1	1981	March	28-31	8.3	5.5	-	6.7	4.5	-	< 12
2		December	28-30	13.6	8.7	-	16.1	9.0	-	< 67
3	1982	January	11-12	8.9	5.6	-	8.0	4.9	-	< 12
4			19	8.3	6.0	-	9.0	4.9	-	< 6
5		February	15-16	8.6	5.4	-	9.1	5.0	-	< 6
6		October	16-17				-	4.5 (1)	-	-
7		November	7-8		No		15.8	7.9	-	< 31
8			14		Data		7.7	5.0	-	< 6
9	1983	April	22				7.6	4.1 (1)	-	-
10		December	15-23	12.3	6.0	-				< 19
11	1984	January	26-27	9.6	5.5	-				< 3
12		October	5	8.2	5.1	-		No		< 3
13	1985	February	8-9	8.5	5.2	-				< 6
14		December	23-26	9.1	5.9	-		Data		< 18
15	1986	January	2-3	8.8	5.4	-				< 21
16		February	17 (2)	14.7	9.6	-				< 27
17		November	14	8.2	5.0	-	7.7	5.0	-	< 6
18	1987	January	13	11.0	7.4	-	10.8	7.2	-	< 15
19		February	2-3	8.0	5.2	-	8.3	5.3	-	< 12
20			11	10.0	7.2	-	11.4	5.8	-	< 15
21		October	15-16	10.7	5.9	-	7.4	4.4	-	< 6
22	1988	January	6	9.0	5.3	-				< 1
23		February	6-7	10.3	5.9	-				< 9.5
24	1989	February	26	11.0	5.4	311		No		< 25
25		April	9	10.2	5.4	280		Data		< 9
26		November	19-20	12.3	7.3	288				< 33
27			22	9.7	6.3	277				< 9
28		December	16-19	11.7	7.4	286	10.3	6.6	281	< 73
29			21-22	9.4	6.0	284	10.3	5.7	283	<17
30			25-27	11.7	6.8	300	10.3	6.2	290	< 32
31	1990	Jan./Feb.	30-1	12.7	7.7	302	10.0	6.6	281	<42.5
32		October	22	10.6	6.3	309	9.3	5.7	291	<8.5
33	1991	Feb./March	28-1	11.1	6.7	311	8.6	5.2	295	<10
34		March	6-7	10.6	5.7	298	8.8	5.1	288	<15
35	1992	February	13	8.8	5.6	306	5.8	3.5	286	<9
36		March	30-31	10.3	5.6	308	7.3	3.9	294	<20
37		May	25-26	7.8	5.0	315	6.0	3.4	286	<6
38		December	8	8.0	5.1	304		No		<6
39			16	12.5	6.0	304		Data		<6
40	1993	October	16	11.3	6.7	289	10.2	5.8	286	<7
41		November	6	7.5	5.0	314	7.4	3.9	294	<3
42	1994	February	3 - 5	10.7	5.8	313				<32
43	1995/6	Dec./Jan.	31-1	-	6.8	293				<20

(Cont.)

TABLE I - Cont.

Nr.	Year	Month	Day	Buoy at -100 m CD			Buoy at -50 m CD			Storm
				Maximum Values		Main	Maximum Values		Main	Duration
				Hmax	Hs	Direction	Hmax	Hs	Direction	(hrs.)
44	1996	January	6-15	-	8.8	293				<188
45			19	-	5.0	293				<2
46			23	-	5.6	225				<4
47		April	1 - 2	-	6.8	325				<17
48		November	11-12	-	6,8	315		No		< 8
49		December	11-13	-	5,2	225				< 3
50	1997	February	16-19	-	6,6	315				< 6
51			19-20	-	6,6	315		Data		< 11
52		November	24-26	-	7,8	290				< 56
53	1998	January	1	-	5,4	315				< 2
54			5	-	6,1	315				< 3
55			7-8	-	6,1	315				< 4
56			12-13	-	5,6	225				< 4
57		February	2-3	-	6,6	270				< 11

Notes:

(1) - Identified as a "storm" due to the occurrence of Hs > 5.0 meters in other points of portuguese coast. As there is no data from the buoy positioned at -100 m CD, it was impossible to confirm deep water conditions.

(2) - Due to a problem with the measurement devices, records do not cover all the storm. Storm duration could not be properly evaluated.

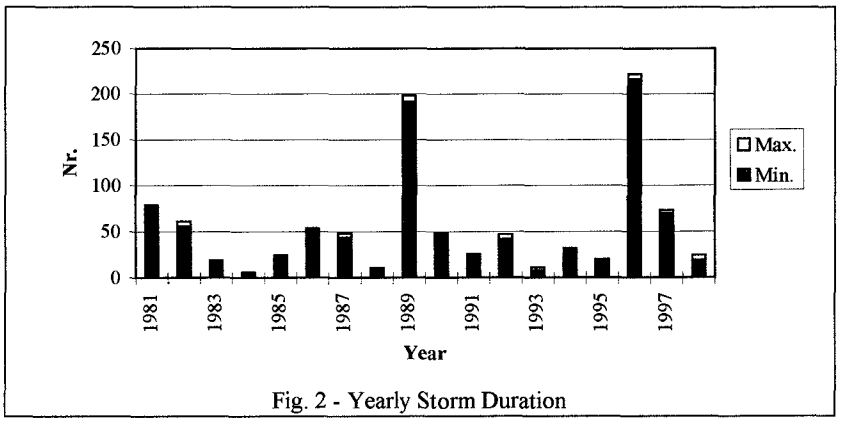

Fig. 2 - Yearly Storm Duration

More frequent values of Hmax and Hs are:

- Depth -100 m CD: Hmax between 10.3 and 10.7 m
  Hs between 5.3 and 5.7 m
- Depth -50 m CD: Hmax between 7.3 and 7.7 m
  Hs between 4.8 and 5.2 m

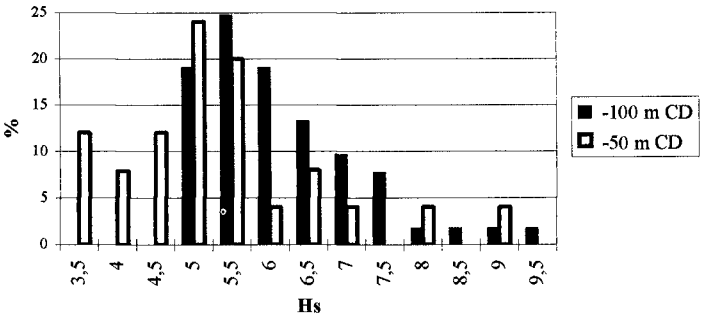

Fig. 3 - Percentages of Occurrence of Hs

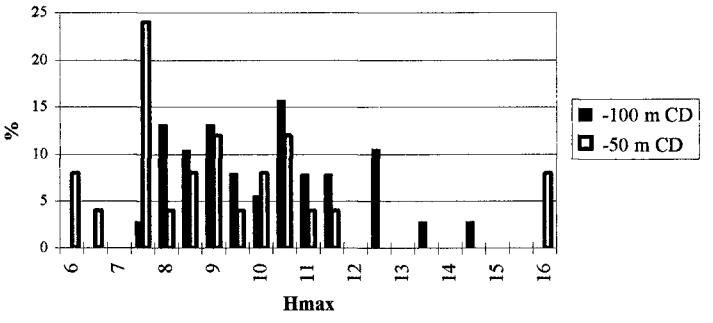

Fig. 4 - Percentages of Occurrence of Hmax

Wave directions during storms at a depth of -100 m CD are dominant in the sector 270° - 320°, with a few occurrences from 225° (SW). At -50 m CD existing data are not enough to get good conclusions, but a concentration between 280° and 300° seems to occur, as it was expected, if refraction effects are taken into account (Fig. 5).

Wave Parameters

Wave Heights Distribution

Theoretically, assuming a Rayleigh distribution for individual wave heights during any record of each storm, the parameters H_{max} (maximum individual wave height of each record), H1 (average of 1% higher wave heights of the record), H10 (average of the

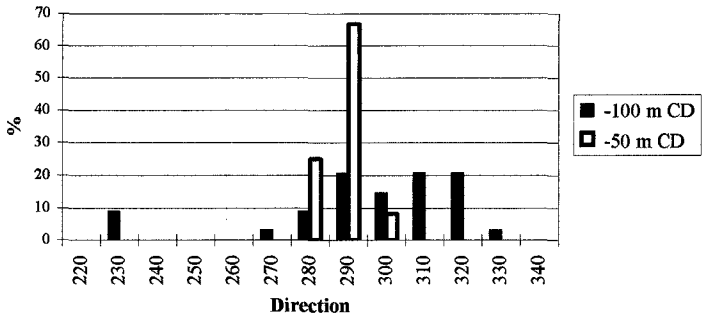

Fig. 5 - Percentage of Occurrence of Storm Directions

10% higher wave heights of the record) are related with Hs (average of 33,3% highest wave heights of the record) by the following relationships:

$$H^{NA}_{max} = \sqrt{\frac{\ln NA}{2}}\ Hs \qquad (1)$$

in which NA is the number of waves of the record and H^{NA}_{max} is the average maximum wave height expected in a record with a number of waves Na and a significant wave height, Hs,

$$H1 = 1.668\ Hs \qquad (2)$$

$$H10 = 1.273\ Hs \qquad (3)$$

To evaluate the validity of these relations, individual records from the buoy positioned at a depth of -100 m CD obtained during storm conditions were analysed. Results are presented at figures 6 to 8.

These results suggest the following comments and conclusions:

a) As each record contains less than 150 waves, the parameter H1 has no statistical meaning. The group of the 1% higher waves is composed by one single wave, and, in consequence, H1 = Hmax. No conclusion can be obtained about the correctness of the relation H1 = 1.668 Hs. Anyway, the tendency of the results is that values evaluated by theoretical relationship are higher than observed values - Fig. 6.

Fig. 6 - Relations between H1 and Hs

b) Average values of the relation H10/Hs are around 1.23 and 1.27, in the range of 0 to -2% around theoretical value. At the peak of the storm, these oscillations are larger, varying between +0,5% and -7.3%. Maximum and minimum values of this relation oscillate around +5% and -9% of theoretical value.

These oscillations are small enough to conclude that theoretical values are very close to the real ones and can be used to evaluate H10 in the absence of computed values - Fig. 7.

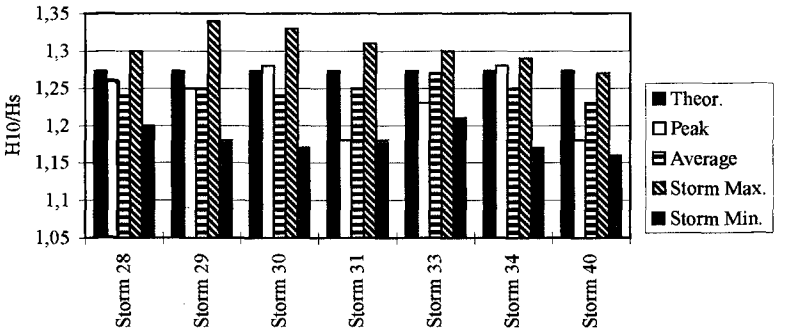

Fig. 7 - Relations between H10 and Hs

c) Relations between Hmax and Hs have average values of 1.5 to 1.6, as expected from theoretical results. Anyway, the results show a large scatter and, at the peak of the storm, these relations can oscillate ±20% around theoretical value - Fig. 8.

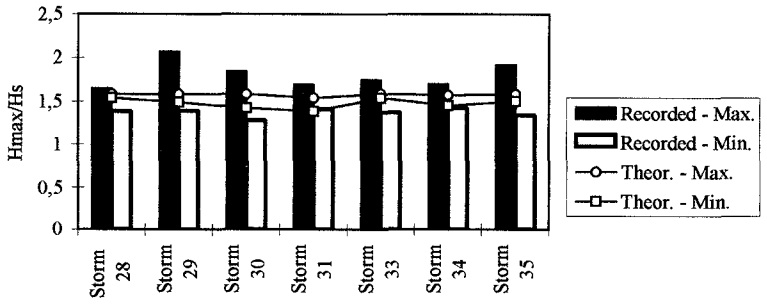

Fig. 8 - Relations between Hmax and Hs

Relationships between Wave Heights, Directions and Peak Periods

In figure 9 is done a presentation of the value of Tp associated to the maximum Hs in each storm. This presentation illustrates that parameter Tp has a large scatter in recorded wave storms at Sines. The same conclusion can be obtained considering maximum Tp at each storm and associated values of wave directions (fig. 10) and Hs at the same record (fig. 11).

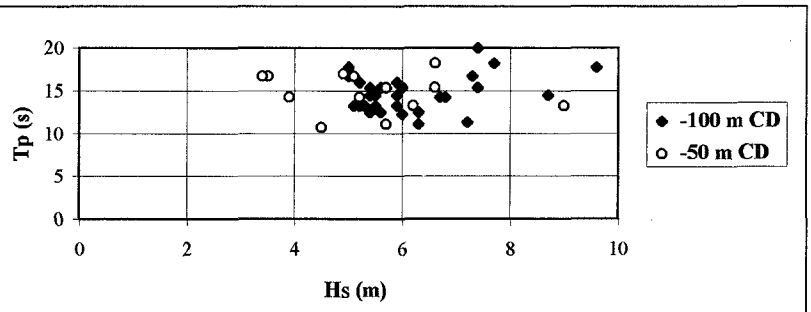

Fig. 9 - Relations between (Hs)max at each storm and associated peak periods

Anyway, it must be noticed that large values of Tp can occur at Sines, as, during more than 50% of the storms, Tp values higher than 15 seconds were computed at both wave buoys (Table VI). It is also interesting to recognise that records done at the same hour in both wave buoys do not show the same value of Tp, with differences that can reach 2 seconds (Table VII). Anyway, in both positions most frequent values occur for Hs between 4 and 6 meters and Tp from 15 to 18 seconds (Table VI).

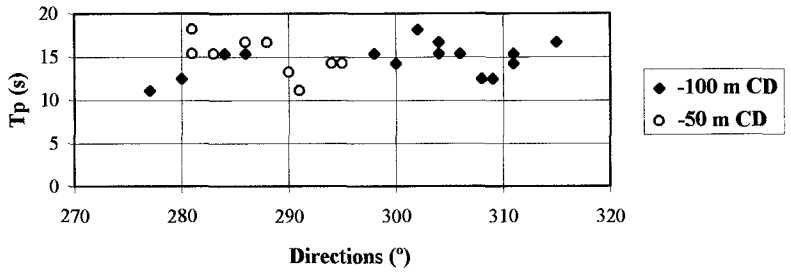

Fig. 10 - Relations between Directions and associated peak periods at the peak of the storms

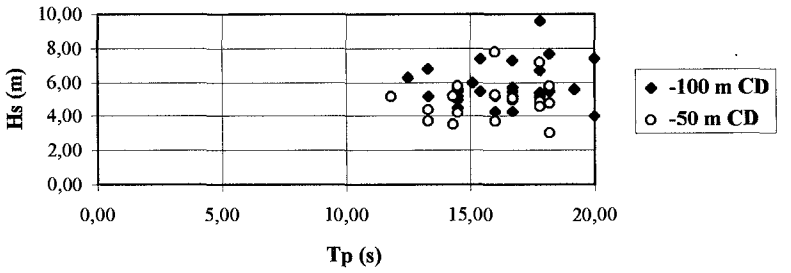

Fig. 11 - Relations between (Tp)max at each storm and associated Hs

TABLE VI
Distributions of (Tp)max and associated Hs
Wave Buoy at -100 m Cd (Sample of 35 values)

		Hs (m)				
		2 - 4	4 - 6	6 - 8	8 - 10	TOTAL
Tp (s)	9 - 12	-	2.9%	-	-	2.9%
	12 - 15	-	22.9%	5.7%	-	28.6%
	15 - 18	-	**39.9%**	11.4%	2.9%	54.2%
	18 - 21	-	8.6%	5.7%	-	14.3%
	TOTAL	-	74.9%	22.8%	2.9%	

Wave Buoy at -50 m CD (Sample of 22 values)

		Hs (m)				
		2 - 4	4 - 6	6 - 8	8 - 10	TOTAL
Tp (s)	9 - 12	-	4.5%	-	-	4.5%
	12 - 15	9.1%	22.7%	-	-	31.8%
	15 - 18	4.6%	**31.8%**	9.1%	-	45.5%
	18 - 21	4.6%	13.6%	-	-	18.2%
	TOTAL	18.3%	72.6%	9.1%	-	

TABLE VII
Examples of Values of Tp at the same hour in both depths (at the peak of the storms)

-100 m CD	-50 m CD	-100 m CD	-50 m CD
12,5 s	12.0	16.5	14.5
13,5 s	14.5	16.5	16.5
13,55 s	14.5	16.6	16.6
14,5 s	13.5	16.5	18.0
15,0 s	18.0	17.5	16.0
15,2 s	17.0	18.0	18.0
15,2 s	16.0	18.1	18.1
16,0 s	16.0	19.0	18.5
16,0 s	14.5	20.0	18.0

These conclusions were checked in a study conducted by IH and LNEC (ref. [1]), where it was stated that:

a) Significant Wave Heights:

A strong correlation between siginificant wave heights was found (91%). According to linear model and from a general way significant wave heights at -50 m CD are about 80 - 90% of significant wave heights at -100 m CD.

b) Peak Periods

Correlation coefficient between records obtained at the two points is about 76 to 77%.

Wave Propagation

The importance of previous results is due to a large discussion, which took place after west breakwater accident in 1978, about the possibility of occurrence of energy concentrations on the breakwater.

In fact, a lot of refraction studies were carried out at different institutions after 1978 accident at Sines west breakwater, with very different conclusions, some of them pointing out the possibility of occurrence of wave concentrations on the breakwater.

Mathematical studies or physical model tests with regular waves carried out either at LNEC (Portugal) and LCHF (France) concluded by the possibility of occurrence of refraction coefficients up to 1.5 or even higher.

On the other hand, tests in a physical model with irregular waves performed at DHL (Netherlands) lead to the conclusion that do not occur refraction coefficients higher than 1.1. Besides, the reaches of the breakwater in which the occurrence of energy concentrations could be expected were not the same in the different studies.

The differences in the conclusions of different studies can be explained by the use of different techniques (traditional refraction diagrams with different bottom digitalisation, model studies with regular waves or with random waves).

At figure 12 relations between existing wave data collected with directional wave buoys at depths of -100 m CD and -50 m CD are presented. In spite of an important dispersion, these results seem to show that:

- For wave directions at depth -100 m CD below 300 degrees, a relation between significant wave heights of 0.9 to 1.0 may be expected, with a variation of directions lower than 10° towards the perpendicular to the breakwater (the direction of which is 270°);
- For wave directions at deep water between 300 and 310°, relations between wave heights at depths of -50 m CD and -100 m CD of 0.6 to 0.9 can occur, with variations on the direction of 14 to 22°;
- For wave directions higher than 310°, relations lower than 0.8 between significant wave heights can be expected;
- No influence of peak period was found in these relations.
- Anyway in the referred study conducted by IH and LNEC, it was found for the Mean Direction of Peak Period a small correlation coefficient (0,88). The direction in the deeper water location shows a rotation of about 12° North with reference to lower water depths.

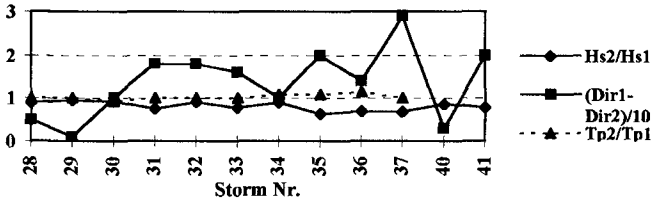

Simbology:
1 - Buoy at -100 m CD
2 - Buoy at -50 m CD

Fig. 12 - Relations between Significant Wave Heights, Wave Directions and Peak Periods at -100 m CD and -50 m CD

It must be stated that these results are preliminary, additional analysis and a physical explanation for them being required (for instance, to evaluate how much they were affected by local winds or by reflections in the breakwater).

Wave regimen - Extreme Values

During initial studies of Sines West Breakwater a wave climate was defined, conducting to the extreme values presented in Table VIII.

After 1978 accident, during the studies about the rehabilitation of the breakwater, PRC Harris defined, mainly based in hindcast studies performed by WES, a new deep water wave climate, supported in a Gumbel distribution. This climate was

used, taking into account refraction and difraction effects, in the design of all the breakwaters existing at Sines harbour. Extreme values of this climate are also presented in Table VIII.

Return Period	Extreme Values of Hs	
	Initial Design (Bertlin, 1973)	Repair Works (Harris, 1981)
10 years	8.5 m	10.0 m
20 years	9.3 m	11.8 m
50 years	10.3 m	13.0 m
100 years	11.0 m	14.0 m

Since 1981 a lot of additional storm data were collected, as indicated at Table I. In general, maximum waves occur during the winter, which in Portugal is, in what sea conditions is concerned, between October and March. It is the author's opinion that a "maritime year" is extended from October until October of next year (like the hydrologic year).

Yearly maximum individual and significant wave data according to the previous definition are the following in the period from 1980/1 until 1997/8:

TABLE IX
Yearly Maximum Values of Hmax and Hs

Year	Buoy at -100 m CD		Buoy at -50 m CD		Year	Buoy at -100 m CD		Buoy at -50 m CD	
	Hmax	Hs	Hmax	Hs		Hmax	Hs	Hmax	Hs
1980/1	13,6	8,7	16,1	9,0	1989/90	12,7	7,7	10,3	6,6
1981/2	8,9	5,6	9,1	5,0	1990/1	11,1	6,7	9,3	5,7
1982/3	-	-	15,8	7,9	1991/2	10,3	5,6	8,8	5,1
1983/4	12,6	6,0	-	-	1992/3	12,5	6,0	-	-
1984/5	8,5	5,2	-	-	1993/4	12,5	6,5	10,2	5,8
1985/6	14,7	9,6	-	-	1994/5	10,7	5,8	-	-
1986/7	11,0	7,4	11,4	7,2	1995/6	-	8,8	-	-
1987/8	10,7	7,2	7,4	4,4	1996/7	-	6,8	-	-
1988/9	11,0	5,4	-	-	1997/8	-	7,8	-	-

Using Gumbel and Log-Normal Distributions the Extreme Values of Hs and Hmax associated to different Return Periods were computed. They are presented at Table X.

Presented values for -50 m CD depth were computed using a very small time series (10 values) and should be considered with additional caution, specially because a sample of 17 values was available for the depth of -100 m CD.

Obtained values are between adopted design values after west breakwater accident and those established initially. In spite of, once again, the importance of being very careful about these conclusions, it is important to the owner of the harbour and to its users to be confident that wave action influence on the structures have a high probability of being from safe side.

TABLE IX
EVALUATION OF EXTREME VALUES
A.- Maximum Wave Heights

	-100 m CD (Deep Water)		-50 m CD (Deep Water)	
Return Period	**Gumbel Distribution**	**Log-normal Distribution**	**Gumbel Distribution**	**Log-normal Distribution**
5 years	13,0	13,7	14,1	14,3
10 years	14,1	15,0	16,4	16,9
20 years	15,1	16,1	18,6	19,1
25 years	15,5	16,6	19,5	19,9
50 years	16,6	17,2	21,8	22,4
100 years	17,8	19,1	24,0	24,8

B.- Significant Wave Heights

Return Period	**Gumbel Distribution**	**Log-normal Distribution**	**Gumbel Distribution**	**Log-normal Distribution**
5 years	8,0	8,2	7,9	7,8
10 years	8,9	9,0	9,1	8,1
20 years	9,8	9,7	10,2	9,8
25 years	10,1	10,0	10,6	10,0
50 years	11,0	10,7	11,8	11,0
100 years	11,9	11,4	13,0	11,9

Wave regimen - Mean Values

Measured mean wave conditions are clearly in accordance with values defined by Frederick R. Harris in their studies. Main results are summarised in figure 13.

These results show that, as expected, predominant wave directions are in the reach WNW to W and that only in 10% of the time (38 days per year) Hs exceeds 3.0 meters.

Conclusions

- A total of 57 wave storms occurred at Sines since 1981, with a total duration of about 1.000 hours with Hs ≥ 5.0 meters.

- Maximum recorded values of wave heights were:
  - at a depth of -100 m CD: Hs = 9.6 m
    Hmax = 14.7 m
  - at a depth of -50 m CD: Hs = 9.0 m
    Hmax = 16.1 m

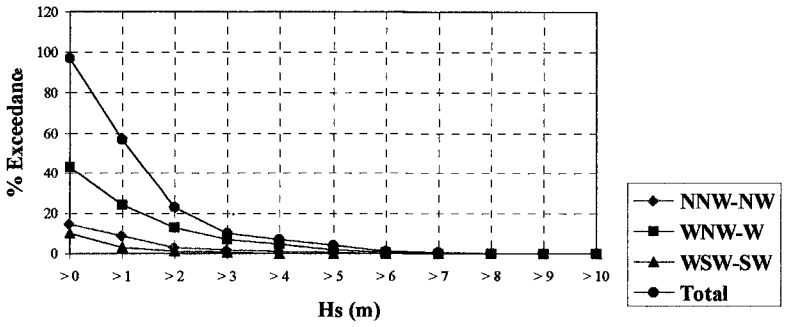

Fig. 13

- Using existing data and assuming that statistical distributions of yearly maximum values of Hs and Hmax are Gumbel or Log-normal, the following extreme values of Hs and Hmax were obtained for a depth of -100 m CD:
  - •With a return period of 10 years:
    Hs from 8.9 to 9.0 meters
    Hmax from 14.1 to 15.0 meters
  - •With a return period of 50 years:
    Hs from 10.7 to 11.0 meters
    Hmax from 16.6 to 17.2 meters
  - •With a return period of 100 years:
    Hs from 11.4 to 11.9 meters
    Hmax from 17.8 to 19.1 meters

BIBLIOGRAPHY:

[1] - LNEC/INSTITUTO HIDROGRÁFICO, 1993 - "Correlação entre Parâmetros Espectrais nas Estações SINESDW1 e SINESDW6", NATO PO-WAVES, Report 10/93-A, November 1993

[2] - FREDERICK R. HARRIS/CONSULMAR, 1981 - "PORT OF SINES. EXTENSION OF MULTIPURPOSE BERTH. Part 1 - Wave Penetration Study", August 1981.

[3] - PRET/ENVIMODE, 1997 - "Terminal Definitivo de Carga Geral do Porto de Sines. EP3 - Execução de Modelação Matemática da Agitação", March 1997.

ON THE STATISTICAL VARIABILITY OF WAVE HEIGHT AND PERIOD PARAMETERS

Carlos R. Sánchez-Carratalá[1], and Marcos H. Giménez[2]

ABSTRACT

A new method for the determination of short-term variability of some commonly used wave height and period parameters is presented. The new TFD method combines some previously available time and frequency domain approaches, optimizing their application and giving greater accuracy with easy implementation. Short-term variability predicted by the new TFD method is consistently higher than the one obtained with theoretical frequency domain expressions, and proves to be in very good agreement with sampling variability observed in Gaussian, non-periodic and non-deterministic random wave records generated with stable ARMA numerical simulators.

INTRODUCTION

Random nature of ocean waves and their modelling as a stochastic process are basic assumptions commonly used in engineering problems. Although a great deal of effort has been dedicated to describe the statistical behaviour of some important sea state parameters, many problems related to their short-term variability still remain unsolved. Short-term variability can be defined as the statistical sampling variability of any time or frequency domain parameter when it is calculated from a finite length wave record that is supossed to be taken from a theoretically infinite length realization of the underlying stochastic process. Knowledge of short-term variability is important in many practical applications, such as: assessment of wave climate uncertainty; risk-based design and economic analysis of offshore and coastal structures; estimation of maintenance and insurance costs of maritime works; and design of physical or numerical experiments.

[1] Professor, Dept. of Applied Physics, ETSICCP, Universidad Politécnica de Valencia, Camino de Vera s/n, 46022-Valencia, Spain.

[2] Professor, Dept. of Applied Physics, EUITI, Universidad Politécnica de Valencia, Camino de Vera s/n, 46022-Valencia, Spain.

Although continuous measurement of the sea surface movement is no problem with most modern wave recorders -like scalar and directional bouys or coastal and satellite radars-, wave climate non-stationarity makes necessary to divide long wave records into finite length time (space) intervals, if the commonly assumed stationarity (homogeneity) hypothesis is to be fulfilled, at least in a wide sense. Furthermore, many ongoing measurements are being made over short intervals and much existing data are in this form. Sampling variability can be reduced at the expense of a lost of resolution in the time or frequency domain by averaging over time intervals or frequency bands, but it can still be important for some purposes. This means that, even assuming ergodicity, we are forced to face up to sampling variability in practical applications.

One of the main difficulties found in theoretical developments for estimating short-term variability has its origin in the use of a specific wave discretization criterion for the analysis of wave records in the time domain (zero-up-crossing, zero-down-crossing, orbital, etc.). Two basic approaches have been proposed in the last decades to overcome this problem: (1) a numerical approach in the time domain (TD approach) that is based in the numerical simulation of random wave records (e.g., Goda, 1977, 1987); and (2) an analytical approach in the frequency domain (FD approach) that takes advantage of some relations between time domain and frequency domain parameters (e.g., Tucker, 1957; Cavanié, 1979; Giménez et *al.*, 1994b). Some interesting contributions to the theoretical and experimental study of sampling variability of spectral estimates and spectral integrals are discussed in Donelan and Pierson (1983), Young (1986), Elgar (1987) and Forristall *et al.* (1996), among others.

This paper presents a new method for the determination of short-term variability of some widely used wave height and period parameters. The new combined *time and frequency domains method* (TFD method) integrates the two aforementioned approaches, optimizing their application and giving greater accuracy with easy implementation.

VARIABILITY OF WAVE HEIGHT PARAMETERS

Henceforth, we will use the subscript R -in connexion with a time or frequency domain parameter- to point out that it has been calculated from a wave record of duration T_R. Additionally, we will use the subscript r -in connexion with a time domain parameter- to indicate that the orbital criterion for discretizing waves has been applied for the statistical analysis of a wave record. In the orbital criterion a discrete wave is defined by a complete rotation of a sea surface particle around its mean position. The orbital criterion has proved to be more consistent and robust (see Giménez *et al.*, 1994a) and to present less sampling variability (see Giménez *et al.*, 1994b) than the commonly used zero-up-crossing criterion. Furthermore, as shown by Giménez and Sánchez-Carratalá (1997), energy propagation in directional seas is closely related with orbital waves.

Making use of the approximate expression (A.13) obtained in Appendix A for the coefficient of variation of the product of two random variables x and y, we have that when:

$$x=\sqrt{m_{0,R}}\ ;\ y=\frac{H_{1/p,r,R}}{\sqrt{m_{0,R}}} \tag{1}$$

the coefficient of variation of $H_{1/p,r,R}$ is approximately given by:

$$\nu\left[H_{1/p,r,R}\right]\simeq\sqrt{\nu^2\left[\sqrt{m_{0,R}}\right]+\nu^2\left[H_{1/p,r,R}/\sqrt{m_{0,R}}\right]} \tag{2}$$

where $\nu[\cdot]$ is an operator denoting the population coefficient of variation of the random variable considered as argument; $H_{1/p,r,R}$ is the mean orbital wave height of the $1/p$ highest waves in a wave record of duration T_R (specifically, when $p=1$ we obtain the mean wave height, $H_{1/1,r,R}=\bar{H}_{r,R}$; and when $p=3$ we obtain the significant wave height, $H_{1/3,r,R}$); and $m_{n,R}$ is the nth order spectral moment of a wave record of duration T_R.

On the one hand, the value of $\nu\left[\sqrt{m_{0,R}}\right]$ in Eq. (2) can be calculated analytically in the *frequency domain* using the following approximate expression derived by Cavanié (1979):

$$\nu\left[\sqrt{m_{0,R}}\right]\simeq\sqrt{\frac{1}{4T_R m_0^2}\int_0^{+\infty}S_\eta^2(f)\,df} \tag{3}$$

where f is the cyclic frequency; $S_\eta(f)$ is the variance spectrum of the process; and m_n is the nth order spectral moment of the process. Eq. (3) can be reformulated using the well-known spectral peakedness parameter Q_e proposed by Medina and Hudspeth (1987), so that:

$$\nu\left[\sqrt{m_{0,R}}\right]\simeq\sqrt{\frac{Q_e}{8N_{w,r,R}}} \tag{4}$$

where $N_{w,r,R}=T_R/T_{01}$ is the spectral estimation of the number of orbital waves in a wave record of duration T_R; and $T_{01}=m_0/m_1$ is the spectral estimation of the mean orbital wave period of the process, as shown by Giménez *et al.* (1994a).

On the other hand, the value of $\nu\left[H_{1/p,r,R}/\sqrt{m_{0,R}}\right]$ in Eq. (2) should be calculated numerically in the *time domain* using a harmonic DSA random wave numerical simulator (see Tuah and Hudspeth, 1982), as suggested by Sánchez-Carratalá (1995). This kind of simulator has no variability in the frequency domain for a record duration equal to its recycling period, and thus:

$$\nu\left[H_{1/p,r,R}/\sqrt{m_{0,R}}\right]=\nu_{H\text{-}DSA}\left[H_{1/p,r,R}\right]\propto n_{H\text{-}DSA}\left[H_{1/p,r,R}\right] \tag{5}$$

where $n[\cdot]$ is an operator denoting the sample coefficient of variation of the random variable considered as argument

The value of $n_{H\text{-}DSA}[H_{1/p,r,R}]$ has been calculated for different wave height parameters ($p=1,3,10$), different record durations ($T_R=2^k\Delta t$, $k=6,7,\ ,13$, $\Delta t=1$ s), and different peak enhancement factors of a JONSWAP-type spectrum ($\gamma=1,3\ 3,7$), using samples of 200 wave records generated with an H-DSA(2^{k-1})-FFT numerical simulator, that is, a harmonic wave superposition simulator with 2^{k-1} one-sided DSA frequency components, implemented with an FFT algorithm According to theoretical and numerical evidence (see, e g , Goda, 1987), the results obtained have been fitted with a least squares technique to a function of the following type

$$n_{H\text{-}DSA}\left[H_{1/p,r,R}\right]\propto kT_R^{-n} \tag{6}$$

Table 1 gives the coefficients $k=k(p,\gamma)$ and $n=n(p,\gamma)$ in Eq (6), obtained for each wave height parameter ($p=1,3,10$) and each peak enhancement factor ($\gamma=1,3\ 3,7$), with T_R in seconds

SEA STATE PARAMETER	$\gamma=1$		$\gamma=3.3$		$\gamma=7$	
	k	n	k	n	k	n
$\bar{H}_{r,R}$	0 8656	0 5279	0 8583	0 5136	0 8191	0 4965
$H_{1/3,r,R}$	1 2644	0 6190	1 2334	0 6152	1 2674	0 6114
$H_{1/10,r,R}$	2 0142	0 5751	2 0054	0 5592	1 6094	0 5125
$\bar{T}_{r,R}$	0 8501	0 5062	0 8078	0 5026	0 7184	0 4940

TABLE 1 Coefficients k and n in Eqs (6) and (11) for different sea state parameters (T_R in seconds)

VARIABILITY OF WAVE PERIOD PARAMETERS

Making use of the approximate expression (A 13) obtained in Appendix A for the coefficient of variation of the product of two random variables x and y, we have that when

$$x=T_{01,R}\ ;\ y=\frac{\bar{T}_{r,R}}{T_{01,R}} \tag{7}$$

the coefficient of variation of $\bar{T}_{r,R}$ is approximately given by:

$$\nu\left[\bar{T}_{r,R}\right]\simeq\sqrt{\nu^2\left[T_{01,R}\right]+\nu^2\left[\bar{T}_{r,R}/T_{01,R}\right]} \tag{8}$$

where $\bar{T}_{r,R}$ is the mean orbital wave period of a wave record of duration T_R; and $T_{01,R}=m_{0,R}/m_{1,R}$ is the spectral estimation of the mean orbital wave period of a wave record of duration T_R.

On the one hand, the value of $\nu\left[T_{01,R}\right]$ in Eq. (8) can be calculated analytically in the *frequency domain* using the following approximate expression derived by Giménez et *al.* (1994b):

$$\nu\left[T_{01,R}\right]\simeq\sqrt{\frac{1}{T_R m_0^2}\int_0^{+\infty}\left(T_{01}f-1\right)^2 S_\eta^2(f)\,df} \tag{9}$$

On the other hand, the value of $\nu\left[\bar{T}_{r,R}/T_{01,R}\right]$ in Eq. (8) should be calculated numerically in the *time domain* using a harmonic DSA random wave numerical simulator, as suggested by Sánchez-Carratalá (1995). This kind of simulator has no variability in the frequency domain for a record duration equal to its recycling period, and thus:

$$\nu\left[\bar{T}_{r,R}/T_{01,R}\right]=\nu_{H\text{-}DSA}\left[\bar{T}_{r,R}\right]\simeq n_{H\text{-}DSA}\left[\bar{T}_{r,R}\right] \tag{10}$$

The value of $n_{H\text{-}DSA}\left[\bar{T}_{r,R}\right]$ has been calculated for different record durations ($T_R=2^k\Delta t$, $k=6,7,\ldots,13$; $\Delta t=1$ s), and different peak enhancement factors of a JONSWAP-type spectrum ($\gamma=1,3.3,7$), using samples of 200 wave records generated with an H-DSA(2^{k-1})-FFT numerical simulator. According to theoretical and numerical evidence (see, e.g., Goda, 1987), the results obtained have been fitted with a least squares technique to a function of the following type:

$$n_{H\text{-}DSA}\left[\bar{T}_{r,R}\right]\simeq k\,T_R^{-n} \tag{11}$$

Table 1 gives the coefficients $k=k(\gamma)$ and $n=n(\gamma)$ in Eq. (11), obtained for each peak enhancement factor ($\gamma=1,3.3,7$), with T_R in seconds.

Table 2 gives a comparison between short-term variability predicted by the FD approach and the new TFD method, for each peak enhancement factor ($\gamma=1,3.3,7$), and for a record duration of about 100 waves. According to these results, sampling

variability of wave height and period parameters included in this study, is systematically underestimated by the presently available frequency domain expressions

SEA STATE PARAMETER	$\frac{\nu_{TFD}[x_R]}{\nu_{FD}[x_R]}-1$ (%)		
	$\gamma=1$	$\gamma=3.3$	$\gamma=7$
$\bar{H}_{r,R}$	10 7	7 6	5 9
$H_{1/3,r,R}$	7 0	4 1	3 0
$H_{1/10,r,R}$	28 7	21 5	17 4
$\bar{T}_{r,R}$	56 6	54 3	56 7

TABLE 2 Comparison between short-term variability predicted by the FD approach and the new TFD method for different sea state parameters (T_R in seconds) ($N_{w,r,R}=100$)

CONTRAST WITH NUMERICAL SIMULATIONS

The new TFD method herein presented has been compared with sampling variability estimates obtained by numerical simulation, in order to test its performance Samples of 100 wave records with about 1000 waves each one (N=8192, $\Delta t=1$ s), corresponding to different sea states characterized by a JONSWAP-type spectrum ($\gamma=1,3$ 3,7), have been generated using an AR(100)-RT(0 05) numerical simulator, that is, a digital linear filter with 100 autoregressive parameters, fitted with the robust technique proposed by Medina and Sánchez-Carratalá (1991), with only a 0 05% of white noise in the target spectrum Digital filters obtained with the robust technique are always stable, and present extremely low fitting errors according to the hierarchic criteria introduced by Medina and Sánchez-Carratalá (1988) for qualifying ARMA representations of ocean wave spectra

Figs 1, 2, 3 and 4 show the evolution of the coefficient of variation of $\bar{H}_{r,R}$, $H_{1/3,r,R}$, $H_{1/10,r,R}$, and $\bar{T}_{r,R}$, respectively, as a function of the number of waves $N_{w,r,R}$, for different peak enhancement factors ($\gamma=1,3$ 3,7). The continuous thin line represents the sampling variability predicted by the new TFD method according to Eqs (2) or (8), while the dashed thin lines are an estimation of the corresponding 95% confidence intervals The thick line represents the sampling variability obtained from a sample of numerically simulated wave records, showing the overall good performance of the new TFD method for predicting sampling variability of wave height and period parameters in random Gaussian seas.

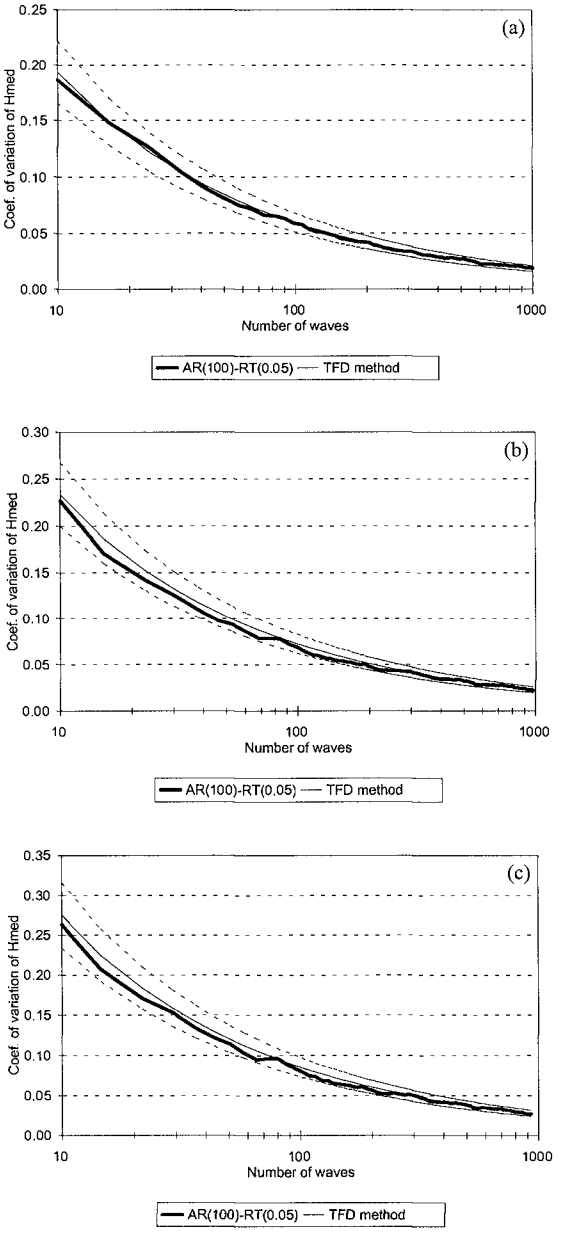

FIGURE 1. Evolution of $\nu\left[\bar{H}_{r,R}\right]$ as a function of $N_{w,r,R}$; Δt=1 s; JONSWAP target spectrum (H_{m_0}=4.0 m; f_p=0.1 Hz; σ_a=0.07; σ_b=0.09; f_{min}=0.5f_p, f_{max}=6.0f_p).
(a) γ=1; **(b)** γ=3.3; **(c)** γ=7.

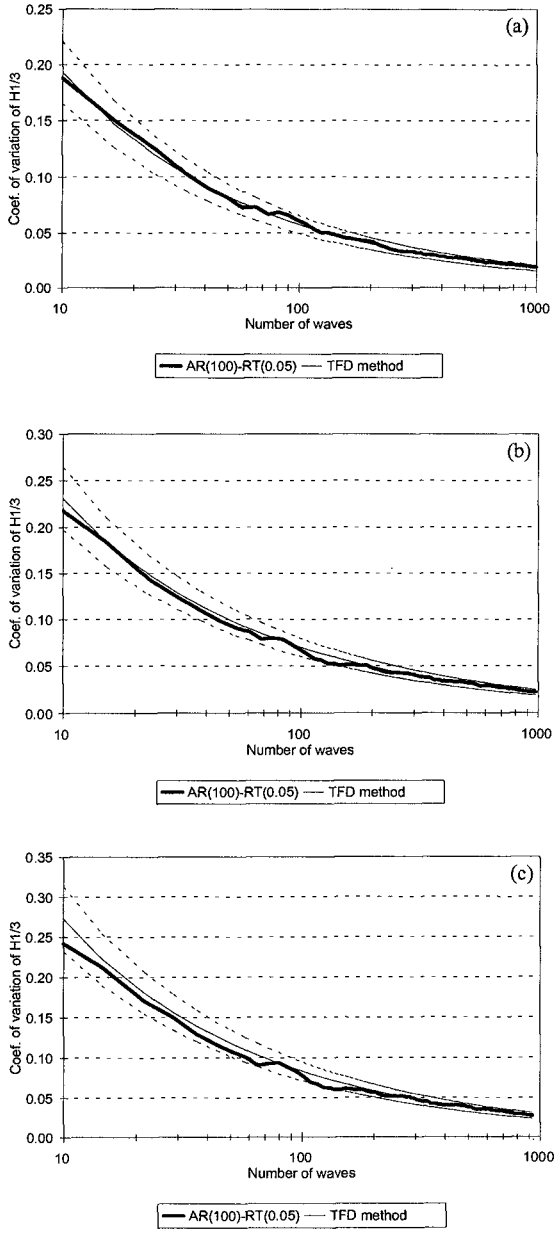

FIGURE 2. Evolution of $\nu\left[H_{1/3,r,R}\right]$ as a function of $N_{w,r,R}$; $\Delta t=1$ s; JONSWAP target spectrum ($H_{m_0}=4.0$ m; $f_p=0.1$ Hz; $\sigma_a=0.07$; $\sigma_b=0.09$; $f_{min}=0.5f_p$, $f_{max}=6.0f_p$).
(a) $\gamma=1$; **(b)** $\gamma=3.3$; **(c)** $\gamma=7$.

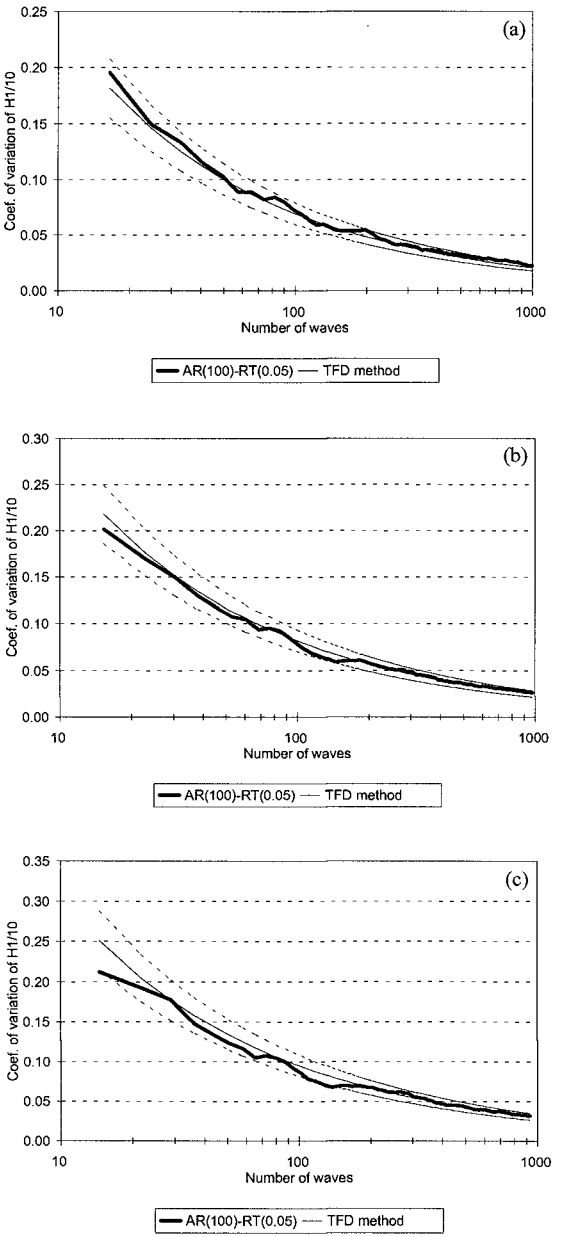

FIGURE 3. Evolution of $v\left[H_{1/10,r,R}\right]$ as a function of $N_{w,r,R}$; Δt=1 s; JONSWAP target spectrum (H_{m_0}=4.0 m; f_p=0.1 Hz; σ_a=0.07; σ_b=0.09; f_{min}=0.5f_p, f_{max}=6.0f_p).
(a) γ=1; **(b)** γ=3.3; **(c)** γ=7.

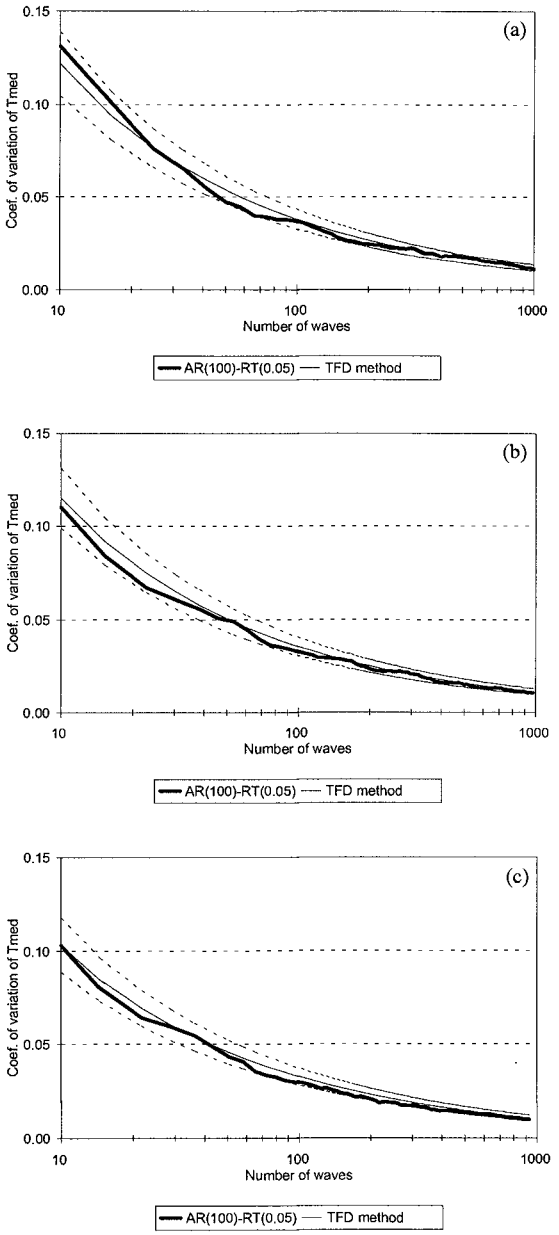

FIGURE 4. Evolution of $\nu\left[\overline{T}_{r,R}\right]$ as a function of $N_{w,r,R}$; $\Delta t=1$ s; JONSWAP target spectrum ($H_{m_0}=4.0$ m; $f_p=0.1$ Hz; $\sigma_a=0.07$; $\sigma_b=0.09$; $f_{min}=0.5f_p$, $f_{max}=6.0f_p$).
(a) $\gamma=1$; **(b)** $\gamma=3.3$; **(c)** $\gamma=7$.

CONCLUSIONS

A new method for the determination of short-term variability of some commonly used wave height and period parameters has been developed as a combination of some previous time and frequency domain approaches. Short-term variability predicted by the new *time and frequency domains method* (TFD method) is consistently higher than the one obtained with theoretical frequency domain expressions. The difference is specially notorious for $H_{1/10,r,R}$ (17~29%) and $\overline{T}_{r,R}$ (54~57%).

Results obtained with the new TFD method have proved to be in very good agreement with sampling variability observed in Gaussian, non-periodic and non-deterministic random wave records generated with stable ARMA numerical simulators, thus constituting a straightforward and reliable alternative for the prediction of short-term variability of many time domain parameters.

APPENDIX A. Coefficient of variation of the product of two random variables

Let x and y be two random variables distributed in the interval $[0,+\infty[$ with a joint probability density function $p(x,y)$. The aim of this Appendix is to obtain an approximate expression for the coefficient of variation of the product xy.

Let a be a random variable defined as the following function of x and y:

$$a = a(x,y) = xy \tag{A.1}$$

The first and second order partial derivatives of a with respect to x and y are:

$$\begin{cases} \dfrac{\partial a}{\partial x} = y \;\; ; \;\; \dfrac{\partial a}{\partial y} = x \\ \dfrac{\partial^2 a}{\partial x^2} = 0 \;\; ; \;\; \dfrac{\partial^2 a}{\partial y^2} = 0 \;\; ; \;\; \dfrac{\partial^2 a}{\partial x \partial y} = 1 \end{cases} \tag{A.2}$$

A Taylor series expansion of a around the point (x_0,y_0) gives:

$$\begin{aligned} a = (a)_0 &+ \frac{1}{1!}\left(\frac{\partial a}{\partial x}\right)_0 (x-x_0) + \frac{1}{1!}\left(\frac{\partial a}{\partial y}\right)_0 (y-y_0) + \\ &+ \frac{1}{2!}\left(\frac{\partial^2 a}{\partial x^2}\right)_0 (x-x_0)^2 + \frac{1}{2!}\left(\frac{\partial^2 a}{\partial y^2}\right)_0 (y-y_0)^2 + \frac{1}{1!1!}\left(\frac{\partial^2 a}{\partial x \partial y}\right)_0 (x-x_0)(y-y_0) + \ldots \end{aligned} \tag{A.3}$$

On substituting (A.2) in (A.3) for $x_0 = E[x]$ and $y_0 = E[y]$, we obtain the following exact expression for a:

$$a = E[x]E[y] + E[y](x - E[x]) + E[x](y - E[y]) + (x - E[x])(y - E[y]) =$$
$$= E[x]E[y]\left[1 + \frac{(x - E[x])}{E[x]} + \frac{(y - E[y])}{E[y]} + \frac{(x - E[x])(y - E[y])}{E[x]E[y]}\right] \quad (A.4)$$

where $E[x]$ is the expected value of the random variable x.

Hence, the mean value of a is:

$$E[a] = \int_0^{+\infty}\int_0^{+\infty} a\,p(x,y)\,dx\,dy =$$
$$= E[x]E[y]\left(1 + \frac{C[x,y]}{E[x]E[y]}\right) = E[x]E[y](1 + c[x,y]\,v[x]\,v[y]) \quad (A.5)$$

where $C[x,y]$ and $c[x,y]$ are, respectively, the covariance and the normalized covariance of the random variables x and y; and $v[x]$ is the coefficient of variation of the random variable x, given by:

$$v[x] = \frac{\sigma[x]}{E[x]} \quad (A.6)$$

where $\sigma[x]$ is the standard deviation of the random variable x.

Let b be a random variable defined as the following function of x and y:

$$b = b(x,y) = x^2y^2 \quad (A.7)$$

that is, $b = a^2$.

The first and second order partial derivatives of b with respect to x and y are:

$$\begin{cases} \dfrac{\partial b}{\partial x} = 2xy^2 \;\; ; \;\; \dfrac{\partial b}{\partial y} = 2x^2y \\ \dfrac{\partial^2 b}{\partial x^2} = 2y^2 \;\; ; \;\; \dfrac{\partial^2 b}{\partial y^2} = 2x^2 \;\; ; \;\; \dfrac{\partial^2 b}{\partial x \partial y} = 4xy \end{cases} \quad (A.8)$$

A Taylor series expansion of b around the point (x_0,y_0) gives:

$$b=(b)_0+\frac{1}{1!}\left(\frac{\partial b}{\partial x}\right)_0(x-x_0)+\frac{1}{1!}\left(\frac{\partial b}{\partial y}\right)_0(y-y_0)+ \\ +\frac{1}{2!}\left(\frac{\partial^2 b}{\partial x^2}\right)_0(x-x_0)^2+\frac{1}{2!}\left(\frac{\partial^2 b}{\partial y^2}\right)_0(y-y_0)^2+\frac{1}{1!1!}\left(\frac{\partial^2 b}{\partial x\partial y}\right)_0(x-x_0)(y-y_0)+\ldots \tag{A.9}$$

On substituting (A.8) in (A.9) for $x_0=E[x]$ and $y_0=E[y]$, we obtain the following approximate expression:

$$b\simeq E^2[x]E^2[y]+2E[x]E^2[y](x-E[x])+2E^2[x]E[y](y-E[y])+ \\ +E^2[y](x-E[x])^2+E^2[x](y-E[y])^2+4E[x]E[x](x-E[x])(y-E[y])= \\ =E^2[x]E^2[y]\left[1+2\frac{(x-E[x])}{E[x]}+2\frac{(y-E[y])}{E[y]}+\right. \\ \left.+\frac{(x-E[x])^2}{E^2[x]}+\frac{(y-E[y])^2}{E^2[y]}+4\frac{(x-E[x])(y-E[y])}{E[x]E[y]}\right] \tag{A.10}$$

Hence, the mean value of b is:

$$E[b]=\int_0^{+\infty}\int_0^{+\infty}bp(x,y)\,dx\,dy\simeq \\ \simeq E^2[x]E^2[y]\left(1+\frac{\sigma^2[x]}{E^2[x]}+\frac{\sigma^2[y]}{E^2[y]}+4\frac{C[x,y]}{E[x]E[y]}\right)= \\ =E^2[x]E^2[y](1+\nu^2[x]+\nu^2[y]+4c[x,y]\nu[x]\nu[y]) \tag{A.11}$$

Now from (A.5) and (A.11) we find that the square of the coefficient of variation of a is given by:

$$\nu^2[a]=\frac{\sigma^2[a]}{E^2[a]}=\frac{E[b]-E^2[a]}{E^2[a]}\simeq \\ \simeq\frac{E^2[x]E^2[y](\nu^2[x]+\nu^2[y]+2c[x,y]\nu[x]\nu[y]-c^2[x,y]\nu^2[x]\nu^2[y])}{E^2[x]E^2[y](1+2c[x,y]\nu[x]\nu[y]+c^2[x,y]\nu^2[x]\nu^2[y])} \tag{A.12}$$

Assuming that $\nu[x]\ll 1$, $\nu[y]\ll 1$ and $c[x,y]\ll 1$, we obtain the following approximate expression for the coefficient of variation of the product xy:

$$\nu[xy]\simeq\sqrt{\nu^2[x]+\nu^2[y]} \tag{A.13}$$

REFERENCES

Cavanié, A.G. (1979). "Evaluation of the standard error in the estimation of mean and significant wave heights as well as mean period from records of finite length." *Proc. International Conference on Sea Climatology*, 73-88.

Donelan, M., and Pierson, W.J. (1983). "The sampling variability of estimates of spectra of wind-generated gravity waves." *J. Geophysical Research*, 88(C7), 4381-4392.

Elgar, S. (1987). "Bias of effective degrees of freedom of spectrum." *J. Waterway, Port, Coastal, and Ocean Engineering*, ASCE, 113(1), 77-82.

Forristall, G.Z., Heideman, J.C., Leggett, I.M., Roskam, B., and Vanderschuren, L. (1996). "Effect of sampling variability on hindcast and measured wave heights." *J. Waterway, Port, Coastal, and Ocean Engineering*, 122(5), 216-225.

Giménez, M.H., and Sánchez-Carratalá, C.R. (1997). "Influence of false waves in the determination of wave energy propagation near the coast." *Proc. 3rd International Conference on Computer Modelling of Seas and Coastal Regions*, J.R. Acinas and C.A. Brebbia, eds., La Coruña, Spain, 283-291.

Giménez, M.H., Sánchez-Carratalá, C.R., and Medina, J.R. (1994a). "Analysis of false waves in numerical sea simulations." *Ocean Engineering*, 21(8), 751-764.

Giménez, M.H., Sánchez-Carratalá, C.R., and Medina, J.R. (1994b). "False waves in wave records and numerical simulations." *Proc. 24th International Conference on Coastal Engineering*, ASCE, Kobe, Japan, 192-206.

Goda, Y. (1977). "Numerical experiments on statistical variability of ocean waves." *Rep. Port and Harbour Research Institute*, Yokosuka, Japan, 16(2), 3-26.

Goda, Y. (1987). "Statistical variability of sea state parameters as a function of wave spectrum." *Proc. IAHR Seminar on Wave Analysis and Generation in Laboratory Basins*, 22nd IAHR Congress, Laussanne, Switzerland, 237-248.

Medina, J.R., and Hudspeth, R.T. (1987). "Sea states defined by wave height and period functions." *Proc. IAHR Seminar on Wave Analysis and Generation in Laboratory Basins*, 22nd IAHR Congress, Laussanne, Switzerland, 249-259.

Medina, J.R., and Sánchez-Carratalá, C.R. (1988). "Comparisons of numerical random wave simulators." *Proc. 21st International Conference on Coastal Engineering*, ASCE, Torremolinos, Spain, 941-955.

Medina, J.R., and Sánchez-Carratalá, C.R. (1991). "Robust AR representations of ocean spectra." *J. Engineering Mechanics*, ASCE, 117(12), 2926-2930.

Sánchez-Carratalá, C.R. (1995). *Statistical and spectral evaluation of numerical random wave simulation techniques*. Ph.D. Thesis, S.P. Universidad Politécnica de Valencia, SPUPV-95.2088, Valencia, Spain (in Spanish).

Tuah, H., and Hudspeth, R.T. (1982). "Comparisons of numerical random sea simulations." *J. Waterway, Port, Coastal, and Ocean Division*, ASCE, 108(WW4), 569-584.

Tucker, M.J. (1957). "The analysis of finite-length records of fluctuating signals." *British J. Applied Physics*, 8, 3-41.

Young, I.R. (1986). "Probability distribution of spectral integrals." *J. Waterway, Port, Coastal, and Ocean Engineering*, ASCE, 112(2), 338-341.

Duration in Wave Climate Analysis

Rodney J. Sobey*and Leah S. Orloff†

Abstract

The relationship between sea state intensity, sea state duration and frequency is pursued in the context of wave data from five sites in U.S. waters. A rational methodology is presented for the interpolation and extrapolation of measured trends, based on extreme value series for intensity, given duration. The inevitable short duration data base problem is addressed by routine application of the triple annual maximum methodology. A format is suggested for IDF data preparation and presentation. Examples are given for wave climate data on the Pacific and Atlantic coasts of the United States.

Introduction

The long term history of wave conditions at a particular site exhibits similar variability to other climate variables such as atmospheric pressure, precipitation, stream flow, temperature and wind speed. Wave measurement programs have only recently become commonplace. Apart from the relatively short duration of available data sets, analysis techniques in wave climate have followed, where appropriate, the established practices for other climate variables.

Though by no means universal, a common trend in wave measurement practice is a twenty minute burst sample every hour. This is the practice, for example, of the National Data Buoy Center (NDBC), for the numerous surface buoys in its network throughout U.S. waters. Each burst sample provides a single wave climate intensity estimate, typically the significant wave height H_s.

Wave climate attention has often focused on frequency analyses of the intensity alone. Extreme value analyses, leading to intensity-frequency summaries, are relatively routine, except for extrapolation uncertainties that are a direct consequence of the short duration of existing wave data series.

*Professor, Department of Civil and Environmental Engineering, University of California, Berkeley, CA 94720, U.S.A.

†Graduate Student, Department of Civil and Environmental Engineering, University of California, Berkeley, CA 94720, U.S.A.

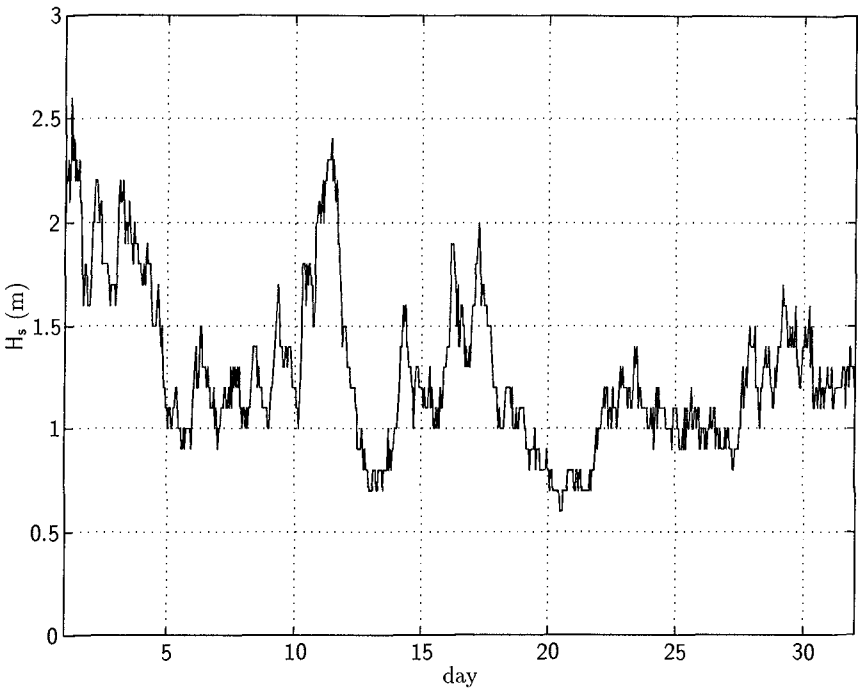

Figure 1: Historical wave climate record at NDBC Buoy 46026 off San Francisco, California for July, 1988.

But there is also a time scale to an historical record of a local wave climate; Figure 1, for example, shows a month of data from the NDBC buoy 46026 off San Francisco, California. The intensity is the significant wave height estimate from hourly burst samples. There is considerable interest in the duration or persistence of the sea state intensity, in applications ranging from the planning of engineering operations at sea to the closure of tidal inlets into coastal wetlands.

In a wave climate, both the intensity or wave height H and the duration D of sea state exceedance of this intensity are random variables. In most wave monitoring programs, burst-sample-averaged intensity is routinely characterized by the significant wave height; H throughout is identified as the significant wave height. Intensity-duration-frequency curves are an interpreted presentation of the joint distribution

of intensity and duration, with CDF $F_{H,D}(h,d)$ and PDF $f_{H,D}(h,d)$. h and d are realizations of the random variables H and D respectively.

In surface water hydrology, it is a common practice to summarize precipitation records as IDF (intensity-duration-frequency) curves, and not just as intensity-frequency curves. An IDF-style presentation can be equally useful in wave climate characterization. In this paper, the relationship between sea state intensity, sea state duration and frequency will be pursued. Initial attention will be directed to the trends suggested by measured data. This leads to a rational methodology for the interpolation and extrapolation of measured trends and a suggested format for IDF data preparation and presentation.

Observational Data

Field data suitable for the extraction of coupled intensity-duration information must be able to resolve sea state durations. At a minimum, hourly observations of H seem necessary. Some historical data sets with 3 or 6 hours between burst samples cannot adequately resolve the expected range of sea state duration.

Given that the historical record has adequate time resolution, intensity and duration data may be extracted from the record in three different ways, as

(a). joint intensity-duration observations,

(b). duration, given intensity, observations, and

(c). intensity, given duration, observations.

Each of these approaches has intrinsic value. There is potentially useful information in a focus on both population and extreme value events. In particular, an extreme value analysis of data sets (b) or (c) is a basis of the IDF-style presentations.

The measured wave climate records used in the present study have been taken from the NOAA Marine Environmental Buoy Database (National Oceanic and Atmospheric Administration (1992) and supplements), available on CDROM. Details of the two sites on which attention has been focussed are listed in Table 1. Data gaps of one or two hours in these records were filled by linear interpolation. Exceedance intervals interrupted by longer gaps have been ignored.

Annual maximum series for duration given intensity that are extracted from this data often have no entries in some years for the higher intensities. Unfortunately, this identifies a major weakness of efforts to extrapolate the duration given intensity data to extreme events, like the 100 year event, that are well beyond the overall duration of the data record. Fortunately, the alternative extreme value presentation of this same data, as intensity given duration, largely circumvents this difficulty.

Site	Location	Water depth (m)	Record duration	Climate years	Maximum H_s (m)	Mean H_s (m)
San Francisco, CA NDBC 46026	37.75N, 122.82W	54.3	July 1982 -December 1994	12	7.6	1.7
Portland, ME NDBC 44007	43.53N, 70.14W	18.9	February 1981 -December 1994	13	7.3	0.9

Table 1: Wave Data Base

Intensity, given Duration, Observations

Extreme value analyses is based on direct extraction of sea state intensity at a given duration. A moving window search has been adopted to identify the largest intensity h that is continuously exceeded over the target duration. The search may be applied over any period that is sufficiently long to include several storm hydrographs; a week would generally be sufficient, a month would certainly be. The width of the moving window is the target duration d; values of 1, 2, 3, ... 12, 15, 18, ... 36, 42, 48, ... 72, 84, 90, ... 144 hours have routinely been adopted.

In the expectation of using either annual maximum series (AMS) and triple annual maximum series (TAMS), the moving window search has been applied over all periods of one calendar month in the historical record. For each target duration, this provides a data series of monthly maximum intensities that are maintained in the record for the target duration. These monthly maximum series are then organized into climate years and ranked in descending order of magnitude to define the TAMS series, which includes H_1, the series of annual maximum intensity, H_2, the series of the annual second largest monthly maximum intensity, and H_3, the series of the annual third largest monthly maximum intensity. Extreme value analyses may be based on these data series.

An immediately apparent feature of these observations is the sparsity of the data. The longer records in the entire NOAA data base have twelve to sixteen climate years. Reliable information is concentrated at average recurrence intervals of less than 5 years. Yet extrapolation to 100 year events is routinely expected.

The present study adopts a generic and very direct approach. There is no insistence on a single probability distribution and there is a direct focus on the inevitable interest in the longer recurrence intervals, extending to 100 years. Attention is directed to extreme value series and extreme value distributions.

Intensity, given Duration - Interpolation and Extrapolation of Extreme Value Series

While the existing wave climate literature has mostly focussed on the conditional distribution for duration given intensity, an equally appropriate representation of intensity-duration-frequency curves is available from the conditional distribution for intensity given duration, with CDF $F_H(h \mid d)$ and PDF $f_H(h \mid d)$. The NOAA observational data appears to be more sympathetic to this approach. It also retains the familiarity of intensity-frequency analyses.

Following the adoption of a specific distribution to aide interpolation and extrapolation, the distribution CDF and PDF become $F_H(h \mid d; p_1, p_2, \dots)$ and $f_H(h \mid d; p_1, p_2, \dots)$ respectively. The distribution parameters $p_1(d), p_2(d), \dots$ are dependent on the given intensity d. Once the distribution is established, intensity (h), duration (d) and frequency (the return period or average recurrence interval T_R) are related as

$$1 - \frac{\Delta t}{T_R} = F_H(h \mid d; p_1, p_2, \dots) \tag{1}$$

in which Δt is the time interval of the observational data series to which $F_H(h \mid d; p_1, p_2, \dots)$ or $f_H(h \mid d; p_1, p_2, \dots)$ has been fitted. For AMS data, Δt is 1 year. An IDF-style presentation might have duration as the abscissa, intensity as the ordinate and frequency as the parameter of a family of curves. The PDF, CDF, mean and variance for a range of candidate two-parameter distributions have been listed in Table 2.

The classical approach would separately address the intensity data at each duration. Given an AMS series for intensity at that duration and the choice of the extreme value distribution (say from Table 2) to aide interpolation and extrapolation, the probability model would be fitted to the AMS data by probability plotting, by the method of moments, by the least squares method or by the method of maximum likelihood. Knowing the parameters of the distribution, the CDF is completely defined together with the preferred interpolation within the range of the data. The preferred extrapolation beyond the range of the data is also defined. Confidence bands on the extrapolation would finally be estimated, often following the Central Limit theorem or the Kite (1975) method of moments.

This classical approach however does not take full advantage of the data. The data sets are very short and AMS series can be supplemented through controlled recognition of marginally less extreme events. Partial duration series (the peak-over-threshold method) or triple annual maximum (TAMS) series have both been used to advantage in this context. The classical approach also does not acknowledge that data at different durations remain samples from the same wave climate. Using all the

Distribution	CDF PDF μ σ^2	Parameters
Extreme Value 1 (Gumbel)	$F_Y(y) = \exp[-\exp(-\frac{y-v}{u})]$ $f_Y(y) = \frac{1}{u}\exp[-\frac{y-v}{u} - \exp(-\frac{y-v}{u})]$ $\mu = \gamma u + v, \quad \gamma = 0.5772\ldots$ $\sigma^2 = \pi^2 u^2/6$	u, v
Extreme Value II	$F_Y(y) = \exp[-(\frac{u}{y})^\alpha]$ $f_Y(y) = \frac{\alpha}{u}(\frac{u}{y})^{\alpha+1}\exp[-(\frac{u}{y})^\alpha]$ $\mu = u\Gamma(1-1/\alpha)$ $\sigma^2 = u^2\Gamma(1-2/\alpha) - \mu^2$	α, u
Extreme Value III (Weibull)	$F_Y(y) = 1 - \exp[-(\frac{y}{u})^\alpha]$ $f_Y(y) = \frac{\alpha}{u}(\frac{y}{u})^{\alpha-1}\exp[-(\frac{y}{u})^\alpha]$ $\mu = u\Gamma(1+1/\alpha)$ $\sigma^2 = u^2\Gamma(1+2/\alpha) - \mu^2$	α, u
Log Normal	$F_Y(y) = \frac{1}{2}[1 + \mathrm{erf}(\frac{\ln y - \alpha}{2^{1/2}\beta})]$ $f_Y(y) = \frac{1}{y(2\pi)^{1/2}\beta}\exp[-\frac{(\ln y - \alpha)^2}{2\beta^2}]$ $\mu = \exp(\alpha + \beta^2/2)$ $\sigma^2 = (\exp(\beta^2) - 1)\exp(2\alpha + \beta^2)$	α, β

Table 2: Candidate Extreme Value Distributions for random variable Y

extreme value data together has the potential to provide a superior prediction of the IDF curves. The TAMS approach has been extended to this purpose.

A TAMS Methodology for Wave Climate IDF

Typical record durations from the NOAA data base identify a very familiar problem in wave climate analysis. The record duration, a decade or so, must be significantly extrapolated to provide estimates of the 50 and 100 year events that are expected from frequency analyses. For the NOAA data in Table 1, the AMS series have twelve or thirteen data points, sufficient for a reliable estimate of perhaps a 25 year event. And these are the long established stations in the data base.

The extrapolation uncertainty can be mitigated by using additional data from the complete duration series, using either a partial duration series or a triple annual maximum series (Sobey and Orloff 1995). The latter approach has been adopted as the basis for the present analysis.

The results of an initial exploratory analysis, using the Sobey and Orloff algorithm on the TAMS data for each duration for the data at Portland, Maine, is shown as the markers in Figure 2. Each of the four Table 2 extreme value distributions has been TAMS-fitted to the data. The TAMS series extracted from the data at the different durations are not unrelated, being extracted from the same historical record. It is not surprising that some of the distribution parameters, such as u and v for Extreme Value I, follow a very consistent trend. Some data scatter is expected, and is an endemic problem of geophysical field data, especially from a relatively short duration record. Nevertheless, the declining probability levels of the longer duration events anticipates smoothly-evolving trends in the distribution parameters. For example, smoothed estimates of both u and v are monotonically decreasing with D in Figure 2a.

Figures 2a through d provide some visual measure of the relative acceptability of each of the four extreme value distributions. The Extreme Value I results (Figures a) look very plausible, the trends being monotonic and the data scatter relatively minor. The Extreme Value II results (Figures b) do not appear acceptable; the u trends is plausible but the jumps in the α response would seem to preclude this distribution as a candidate for data interpolation and extrapolation. The results for Extreme Value III (Figures c) are relatively smooth, except for the α response at large D, where also the response seems no longer monotonic. There is a suggestion that this distribution is also unacceptable. The Log Normal (Figures d) results are relatively encouraging. Both α and β are monotonically evolving, though the data scatter for β is moderately coarse. This result is perhaps acceptable, but seemingly less so than Extreme Value I for this data set.

The trends exhibited by both Table 1 data sets were roughly similar. On a visual basis, the Extreme Value II and III distributions were rejected as suitable candidates for interpolation and extrapolation. The Extreme Value I trends were relatively smooth and monotonic. The Log Normal β parameter trends were less smooth and not always monotonic. On this visual measure, the Extreme Value I distribution is preferred fir these data sets. But selecting the appropriate distribution for data interpolation and extrapolation is a subjective process. It must be guided by the trends of the particular data set and also by measures of analysis acceptability in addition to a purely heuristic interpretation. Data sets from other geographical sites may be very different.

Similar analyses for all Table 1 data sites were completed. Collectively, such figures and tables provide the information upon which a selection of an extreme value

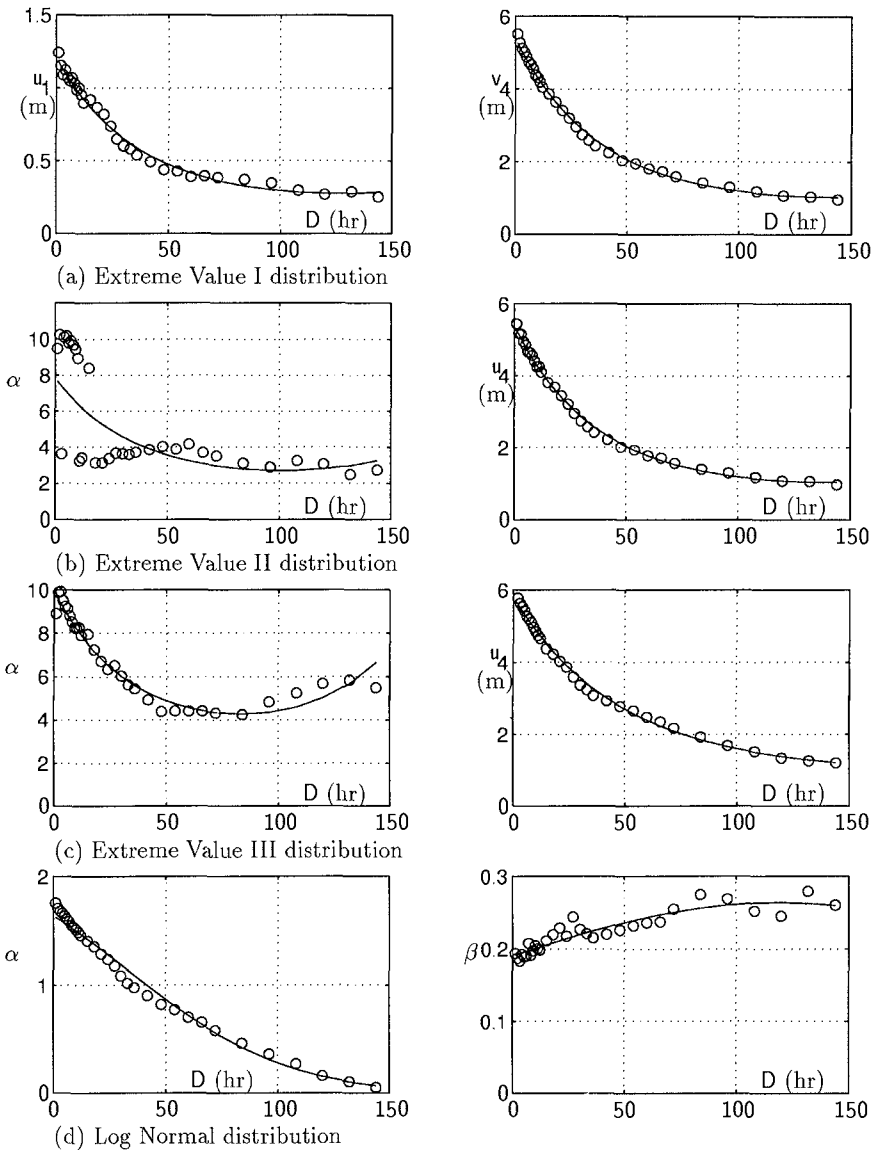

(a) Extreme Value I distribution

(b) Extreme Value II distribution

(c) Extreme Value III distribution

(d) Log Normal distribution

Figure 2: TAMS-predicted distribution parameters for Table 2 Extreme Value distribution from NDBC Buoy 44007 off Portland, Maine. Markers are TAMS predictions at individual durations; solid line is the Equation 2 curve fit to these individual duration predictions.

Site	Distribution	p_i	a_i	b_i	c_i
San Francisco, CA	Extreme Value I	u	-0.0193	-0.0103	3.89e-05
NDBC 46006		v	1.52	-0.0111	3.85e-05
	Log Normal	α	0.459	-0.00855	2.12e-05
		β	-1.66	-0.00143	1.37e-05
Portland, MN	Extreme Value 1	u	0.191	-0.0234	9.29e-05
NDBC 44007		v	1.68	-0.0233	8.15e-05
	Log Normal	α	0.495	-0.00767	-0.000101
		β	-1.66	0.00547	-2.30e-05

Units of a_i, b_i and c_i assume D in hours; u and v in m; α and β are dimensionless.

Table 3: Parameters of Equation 2 curve fits to Extreme Value I and Log Normal distribution parameters.

distribution must be based. As with most extreme value analyses in the natural environment, this choice remains somewhat subjective.

IDF Summaries for US Waters

Given a choice of extreme value distribution, intensity-duration-frequency curves can be constructed.

Interpolation and extrapolation of results such as Figure 2 may be facilitated by smoothing the trends to the empirical curve

$$p_i(d) = \exp\left[a_i + b_i d + c_i d^2\right] \tag{2}$$

where p_i (i = 1,2) are the distribution parameters. There is no fundamental basis for such a relationship, except that it does reasonably follows the $p_i(d)$ trends. Least squares curve fits of Equation 2 to the data in Figure 2 and similar for other sites define the parameters a_i, b_i and c_i. These curve fits for all four of the Table 2 distributions are included as the solid lines on Figure 2 for the Portland, Maine site. Parameters for Extreme Value I and Log Normal at all the Table 1 sites are listed on Table 3. These distributions seem to be the most plausible for these sites, though this may not be the case for other sites.

Given an extreme value distribution and the p_i parameters as a smooth function of duration D, an IDF curve can be constructed for a given average recurrence interval T_R from solutions to Equation 1.

$$1 - \frac{\Delta t}{T_R} = F_H\left(h|d; p_1(d), p_2(d)\right) \tag{3}$$

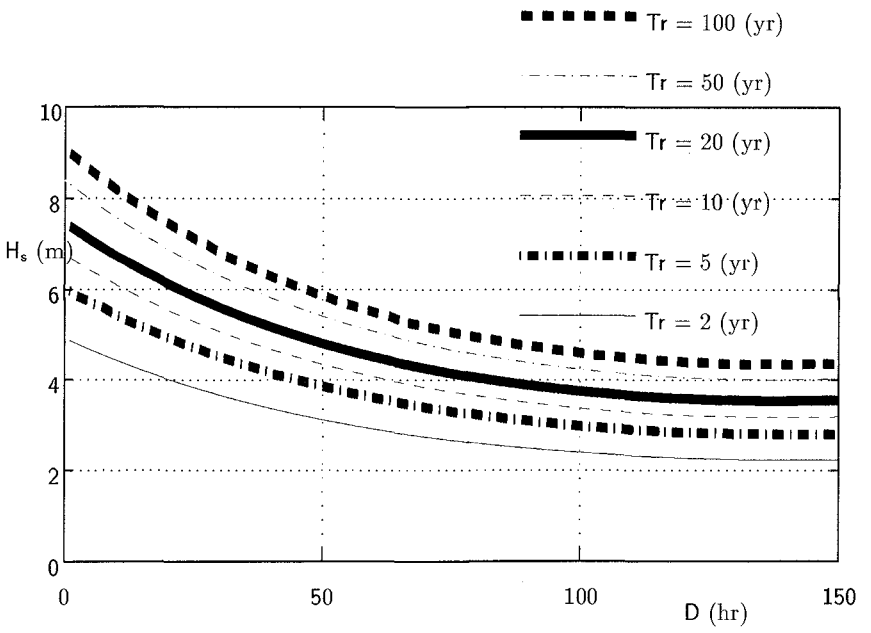

Figure 3: Extreme Value I Prediction for IDF curves at NDBC Buoy 46026 off San Francisco, California.

This is an implicit algebraic equation in $h(d; T_R)$, which can be solved for each duration by standard numerical algorithms such as Newton-Raphson, regula falsi or the secant method. As a result of the smoothing implicit in the Equation 2 curve fits, these solutions will also be smoothly varying. Completing these solutions for a range of appropriate average recurrence intervals, typically 2, 5, 10, 20, 50 and 100 years provides the classical IDF presentation.

IDF predictions from the Extreme Value I and Log Normal distributions for the San Francisco, California and Portland, Maine sites are shown as Figures 3 through 6. These predictions show excellent trend agreement but only moderate magnitude agreement. More can not be expected, these figures once again demonstrating the fragility of extreme value analyses from short duration data.

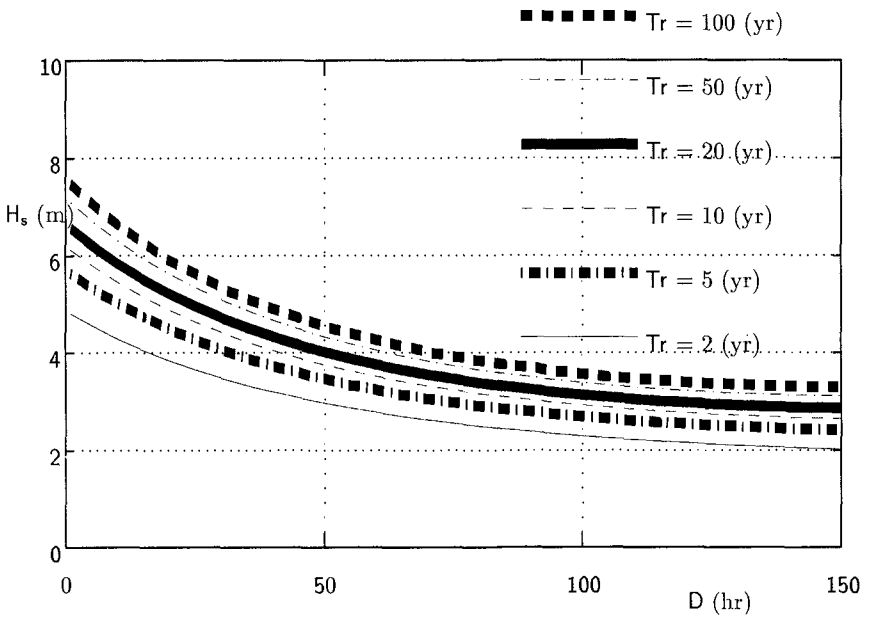

Figure 4: Log Normal Prediction for IDF curves at NDBC Buoy 46026 off San Francisco, California.

Conclusions

The relationship between sea state intensity, sea state duration and frequency is pursued in the context of wave data from the NOAA Marine Environmental Buoy Database at two sites in U.S. waters.

Detailed attention has been given to extreme events, where the popular approach has been a focus on duration, given intensity. Existing studies have mostly utilized wave data from the European and Japanese waters. Analyses have mostly been based on an assumption that the conditional distribution of the population of duration, given intensity, follows the Weibull distribution. This distribution does not seem especially appropriate in U.S. waters.

The present approach is a direct focus on extreme events, through extreme value data extracted from observational records. IDF (intensity-duration-frequency) summaries may originate from the conditional extreme value distribution for duration,

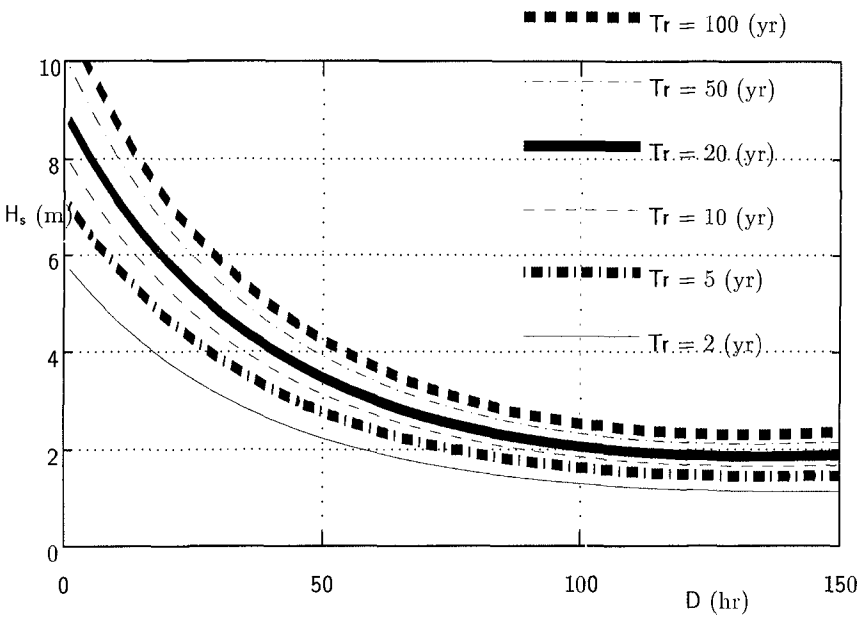

Figure 5: Extreme Value I Prediction for IDF curves at NDBC Buoy 44007 off Portland, Maine.

given intensity, or from the conditional extreme value distribution for intensity, given duration. Extracting the data as duration, given intensity, results in significant data gaps for the more extreme intensities. Intensity, given duration, data appears to be much less problematic.

A rational methodology is presented for the interpolation and extrapolation of measured trends, based on extreme value series for intensity, given duration. The inevitable short duration data base problem is addressed by routine application of the triple annual maximum methodology.

A format is suggested for IDF data preparation and presentation. Examples are given for wave climate data on the Pacific and Atlantic coasts of the United States.

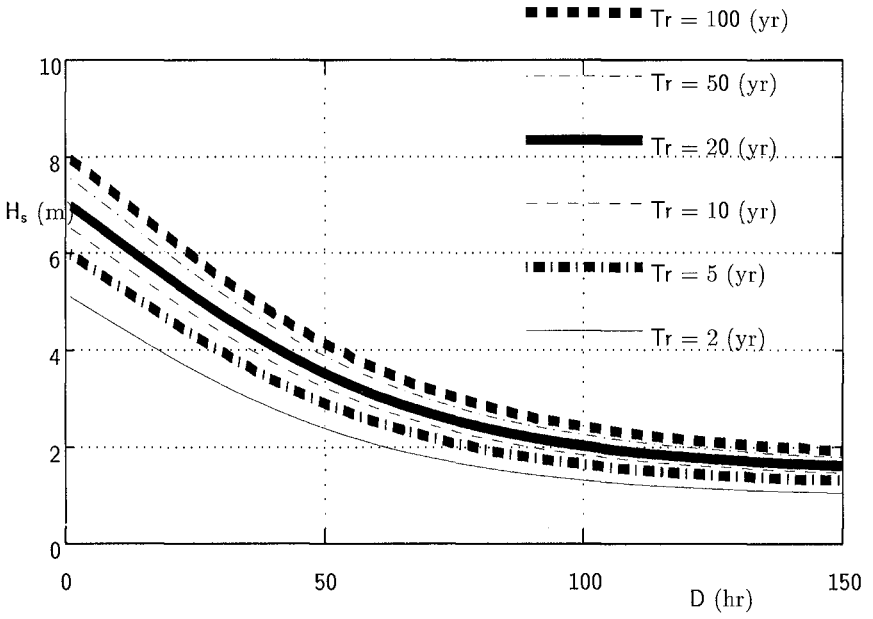

Figure 6: Log Normal Prediction for IDF curves at NDBC Buoy 44007 off Portland, Maine.

Acknowledgements

This paper is funded in part by a grant from the National Sea Grant College Program, National Oceanic and Atmospheric Administration, U.S. Department of Commerce, under grant number NOAA NA66RG0477, project number R/OE-36 through the California Sea Grant College System, and in part by the California State Resources Agency. The views expressed herein are those of the authors and do not necessarily reflect the views of NOAA or any of its sub-agencies. The U.S. Government is authorized to reproduce and distribute for governmental purposes.

Support through a U.S. Environmental Protection Agency STAR Fellowship to Leah S. Orloff is also acknowledged.

References

Kite, G. W. (1975). Confidence limits for design events. *Water Resources Research 11*, 48–53.

National Oceanic and Atmospheric Administration (1992). NOAA marine environmental database. CD-ROM NODC-32. Updates NODC-38, -39, ...

Sobey, R. J. and L. S. Orloff (1995). Triple annual maximum series in wave climate analysis. *Coastal Engineering 26*, 135–151.

Encounter Probability of Individual Wave Height

Zhou Liu[1] and Hans F. Burcharth [2]

Abstract

Some coastal and offshore structures, e.g. offshore platforms and vertical wall breakwaters in deep water, are often designed according to a design individual wave height.

The conventional method for the determination of the design individual wave height is first to obtain the design significant wave height corresponding to a certain exceedence probability within a structure lifetime (encounter probability), based on the statistical analysis of long-term extreme significant wave height. Then the design individual wave height is calculated as the expected maximum individual wave height associated with the design significant wave height, with the assumption that the individual wave heights follow the Rayleigh distribution.

However, the exceedence probability of such a design individual wave height within the structure lifetime is unknown.

The paper presents a method for the determination of the design individual wave height corresponding to an exceedence probability within the structure lifetime, given the long-term extreme significant wave height. The method can also be applied for estimation of the number of relatively large waves for fatigue analysis of constructions.

1. Introduction

Some coastal and offshore structures, e.g. offshore platforms and vertical wall breakwaters in deep water, are often designed according to a design individual wave height.

The determination of the design individual wave height is based on a long-term wave measurement or hindcast. Most often the data set consist of maximum

[1]Assistant Professor, Ph.D.

[2]Professor, dr.techn., Department of Civil Engineering, Aalborg University, Denmark

significant wave heights for the most severe storms within a number of years. An extreme significant wave height is the peak value of the significant wave height in a storm which exceeds a predefined threshold.

The conventional method for the determination of the design individual wave height is first to obtain the design significant wave height corresponding to a certain exceedence probability within a structure lifetime (encounter probability), based on the statistical analysis of the extreme data set. Then the design individual wave height is calculated as the expected maximum individual wave height associated with the design significant wave height (sea state), with the assumption that the individual wave heights follow the Rayleigh distribution.

For example, if the design level for the design significant wave height is a return period of 100 years (T=100 years), then by extreme analysis we find out that $H_s^{100\ years} = 10.2\ m$. With the assumption that the individual wave heights follow the Rayleigh distribution, the expected maximum individual wave height associated with the design significant wave height is

$$(H_{max})_{mean} \approx \left(\sqrt{\frac{\ln N}{2}} + \frac{0.577}{\sqrt{8\ \ln N}} \right) H_s^{100\ years} \tag{1}$$

where N is the number of individual waves related to $H_s^{100\ years}$. In engineering practice it is normally assumed that N is in the order of 1000 for the stationary peak of the storm, which corresponds to $(H_{max})_{mean} = 19.7\ m$.

However, the return period of such design individual wave height remains unknown.

The paper presents a method for determination of the return period of a design individual wave height. The encounter probability of the design individual wave height, i.e. exceedence probability within structure lifetime L, is

$$p = 1 - \exp\left(-\frac{L}{T}\right) \tag{2}$$

The only input of the method is an extreme data set (minimum input). The accuracy of the result can be improved if more information are available, e.g. the duration of the storms, joint distribution of wave height and period etc.

The method can also be applied for estimation of the number of relatively large waves for fatigue analysis of constructions.

2. Distribution of individual wave height in a storm: $F_L(H)$

Because the structures are located in deep water, it is assumed that, with a given significant wave height H_s, the individual wave height H follows the Rayleigh distribution:

$$F_R(H) = 1 - \exp\left(-2\left(\frac{H}{H_s}\right)^2\right) \tag{3}$$

However, the significant wave height is varying throughout a storm. Based on some prototype records it is assumed that H_s grows and decays linearly between the threshold of significant wave height, $H_{s,t}$, and the peak significant wave height $H_{s,p}$. For the convenience, an equivalent storm history is used, cf. Fig. 1.

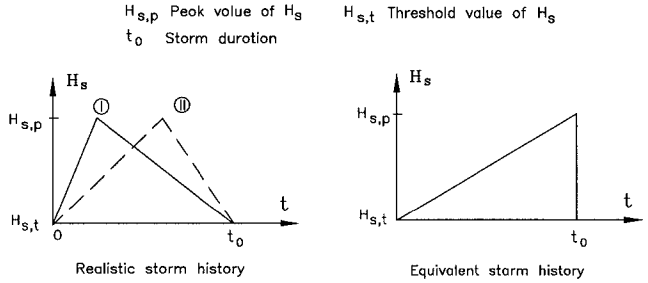

Fig. 1. Realistic storm history and the equivalent storm history (Burcharth et al. 1992).

If it is further assumed that the average wave period within a storm is constant and independent of H_s, then the distribution of individual wave height in a storm is

$$F_S(H) = \int_{H_{s,t}}^{H_{s,p}} F_R(H) \frac{1}{H_{s,p} - H_{s,t}} \, \mathrm{dH}_s$$

$$= 1 - \frac{1}{H_{s,p} - H_{s,t}} \int_{H_{s,t}}^{H_{s,p}} \exp\left(-2\left(\frac{H}{H_s}\right)^2\right) \mathrm{dH}_s \tag{4}$$

Note that $F_S(H)$ is independent of storm duration.

Fig. 2. shows an example of the difference between the individual wave height distribution in a storm and the Rayleigh distributions corresponding to $H_{s,t}$ and $H_{s,p}$, respectively.

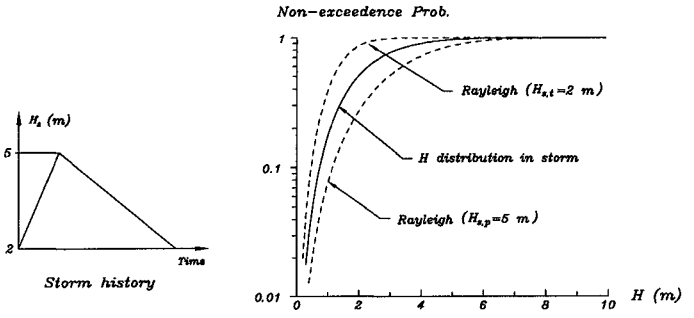

Fig. 2. Example of individual wave height distribution in a storm.

3. Long-term distribution of significant wave height: $F(H_s)$

The long-term distribution of significant wave height is obtained by the statistical analysis of the extreme data set. The general procedure is:

1) Choice of the extreme data set based on long-term wave height measurement/hindcast
2) Choice of several theoretical distributions as the candidates for the extreme wave height distribution
3) Fitting of the extreme wave heights to the candidates by a fitting method.
4) Choice of the distribution based on the comparison of the fitting goodness among the candidates

For more details please refer to Burcharth et al. (1994). The obtained long-term distribution of H_s gives information on the occurrence probability of storms over the threshold $H_{s,t}$ (which can be converted to the number of the storms in the structure lifetime), and the corresponding peak value $H_{s,p}$ in the storms.

4. Long-term distribution of individual wave height: $F_L(H)$

If we keep the assumption that the average wave period is constant and independent of the significant wave height, the long-term distribution of individual wave height can be expressed as (cf. Fig. 3)

$$F_L(H) = \int_{H_{s,t}}^{\infty} F_S(H)\, f(H_s)\, \mathrm{dH}_s \tag{5}$$

where $f(H_s)$ is the density function of the long-term significant wave height distribution, obtained by the extreme analysis, and $F_S(H)$ is the distribution of individual wave height in a storm.

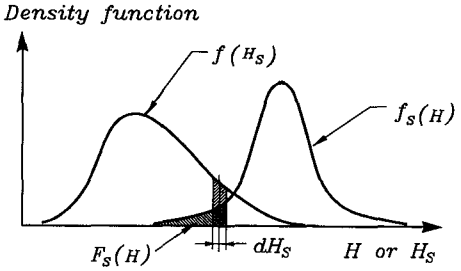

Fig. 3 Illustration of the integral in eq (5).

5. Return period and encounter probability of design individual wave height

According to the definition of return period, the return period of the individual wave height H is

$$T = \frac{1}{\lambda' (1 - F_L(H))} \tag{6}$$

where λ' is the number of individual waves related to extreme storm, i.e. all H_s in the storm $\geq H_{s,t}$, and $F_L(H)$ is the long-term distribution of individual wave height.

The only unknown in eq (6) is λ'. Obviously the value of λ' depends on the threshold level $H_{s,t}$. The lower $H_{s,t}$, the larger λ'.

Smith (1988) investigated by field measure the relation between $H_{s,t}$ and P, occurrence probability of the event $H_s \geq H_{s,t}$. The threshold $H_{s,t}$ is represented by the number of extreme storms per year, λ. The definition of λ and P is illustrated by Fig. 4.

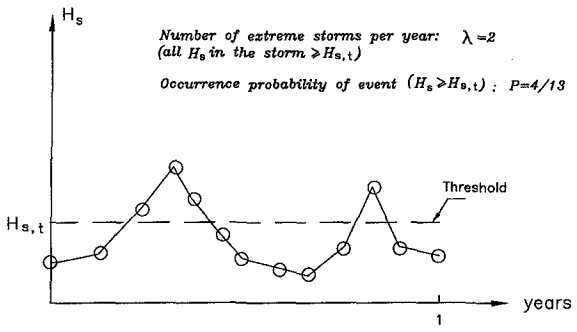

Fig. 4. Illustration of definition of λ and P.

The locations of the field measurement are given in Table 1. They represent a wide geographical spread and variety of wave conditions. Each location includes 58,440 significant wave heights by hindcast study three hours apart from January 1, 1956 to December 31, 1975 (20 years).

Table 1. Locations investigated by Smith (1988)

Site	mean wave height in 20 years (m)
Atlantic City, New Jersey	0.65
Nagshead, North Carolina	0.65
Daytona Beach, Florida	0.67
Newport, Oregon	2.76
Half-Moon Bay, California	2.14

A linear regression analysis for all locations gives

$$P = 0.003\ \lambda \tag{7}$$

with a correlation coefficient of 0.97. λ' can be calculated based on eq (7), as will be shown in the next example. Then the return period and encounter probability of the individual wave height can be calculated by eqs (6) and (2), respectively.

6. Example

Extreme data set

An extreme wave data set for the 15 most severe storms in a period of 20 years for a deep water location in Mediterranean Sea is given in Table 2. The data set is obtained by hindcast study. The threshold level for identifying the extreme storms is $H_{s,t} = 3\ m$.

Table 2. Extreme wave data set.

Rank i	Peak $H_{s,p}$ metres	Peak period T_P seconds	Wave direction degrees
1	9.32	14.0	143
2	8.11	14.1	139
3	7.19	13.4	123
4	7.06	10.8	123
5	6.37	11.9	143
6	6.15	11.1	185
7	6.03	12.3	135
8	5.72	10.5	176
9	4.92	10.7	150
10	4.90	10.6	129
11	4.78	11.8	161
12	4.67	9.9	120
13	4.64	9.2	122
14	4.19	10.5	137
15	3.06	11.1	154

Long-term distribution of significant wave height

The number of extreme storm per year is $\lambda = 15/20$. By fitting the peak significant wave height to the Weibull distribution

$$F(H_s) = 1 - \exp\left[-\left(\frac{H_s - H_{s,t}}{A}\right)^k\right] \tag{8}$$

where $H_{s,t} = 3\ m$, we obtain the Weibull distribution parameters $A = 3.24$ and $k = 1.83$.

By inserting the definition of return period T

$$T = \frac{1}{\lambda\,(\,1 - F(H_s)\,)} \tag{9}$$

into eq (8), we obtain

$$H_s = A\left(-ln(\frac{1}{\lambda T})\right)^{\frac{1}{k}} + H_{s,t} \tag{10}$$

The fitting is depicted in Fig. 5.

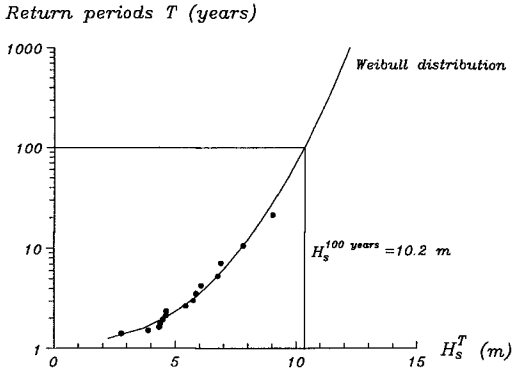

Fig. 5. Fitting of extreme data set to Weibull distribution.

If the design level for the design significant wave height is a return period of 100 years (T=100 years), we get $H_s^{100\ years} = 10.2\ m$.

By eq (1) with $N = 1000$, the expected maximum individual wave height associated with the design significant wave height is $(H_{max})_{mean} = 19.7\ m$. In the following we will try to obtain the return period and encounter probability of $(H_{max})_{mean}$.

Long-term distribution of individual wave height: $F_L(H)$

The long-term distribution of individual wave height is calculated by eq (5) and shown in Fig. 6.

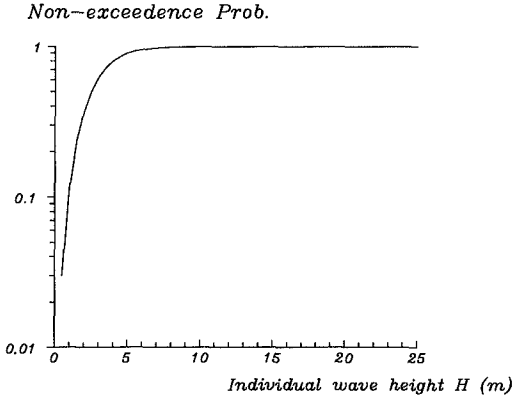

Fig. 6. Long-term distribution of individual wave height.

Return period and encounter probability of individual wave height

By eq (7) we get the occurrence probability of the event $(H_s \geq H_{s,t})$

$$P = 0.003\lambda = 0.0025$$

If we assume that the average wave period is $\overline{T} = 12\ s$ (average wave period in Table 2), the number of individual waves per year is

$$365 \times 24 \times 60 \times 60/\overline{T} = 2,628,000$$

and the number of individual waves related to the extreme storm is

$$\lambda' = 2,628,000 \times P = 6750$$

The return period of individual wave height is calculated by eq (6) and shown in Fig. 7.

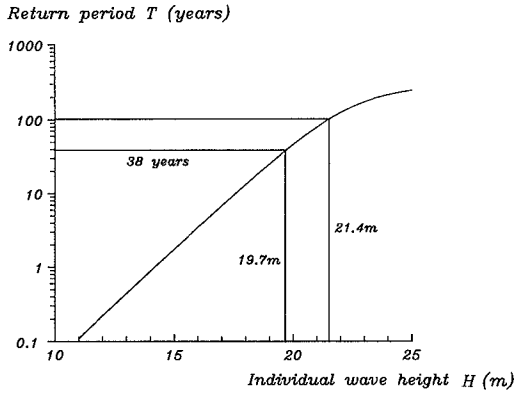

Fig. 7. Return period of individual wave height.

It can be seen from Fig. 8 that the return period of $(H_{max})_{mean} = 19.7\ m$ is 38 years. By Fig. 8 we can also choose a design individual wave height corresponding to a certain return period, e.g. $H^{100\ years} = 21.4\ m$.

Fig. 8 gives the encounter probability of individual wave height within a structure lifetime of 25 years.

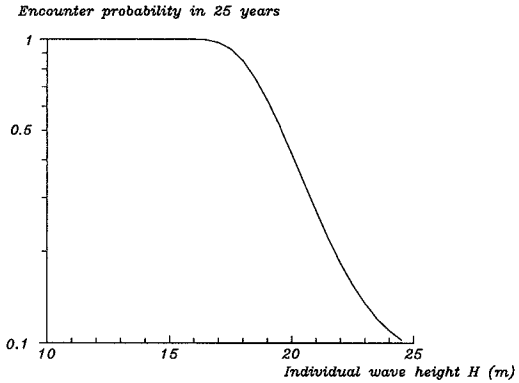

Fig. 8. Encounter probability of individual wave height.

7. Conclusions

- A method for estimation of return period and encounter probability of individual wave height has been developed. The method is based on extremely limited wave information (extreme data set). Improvement of the estimate can be expected if more information, e.g. the storm duration, is available.

- The method can also be applied for estimation of the number of relatively large waves for fatigue analysis of constructions.

8. Acknowledgement

Our colleague Peter Frigaard is gratefully acknowledged for fruitful discussions on the paper.

9. References

Burcharth, H.F. and Frigaard, P. (1992) *Ciervana Breakwater, Puerto Autonome de Bilbao: Model test results.* Department of Civil Engineering, Aalborg University, Denmark, 1992

Burcharth, H.F. and Zhou Liu (1994) *On the extreme wave height analysis.* Proceedings of HYDRO-PORT'94, Yokosuka, Japan, 19-21 October, 1994

Liu, Z. and Burcharth, H.F (1996) *Design wave height related to structure lifetime.* Proceedings of the 25th International Conference on Coastal Engineering, Orlando, USA, 1996.

Smith, O.P. (1988) *Duration of extreme wave conditions.* Journal of Waterway, Port, Coastal and Ocean Engineering, Vol. 114, No. 1, January 1988.

Sobey, R.J., Chandler, B.D. and Harper, B.A. (1990) *Extreme waves and wave counts in a hurricane.* Proceedings of the International Conference on Coastal Engineering, ASCE, 1990.

WAVE RUN-UP AND OVERTOPPING: PROTOTYPE VERSUS SCALE MODELS

Julien DE ROUCK[1], Raf VERDONCK[1], Peter TROCH[1], Luc VAN DAMME[2], Flemming SCHLÜTTER[3], John DE RONDE[4]

ABSTRACT

The determination of the crest level is one of the most important points in the design of sloping coastal structures. The crest level of sloping coastal structures is governed by wave run-up and overtopping. Recent measurement results of run-up on prototype have indicated that wave run-up may be underpredicted by scale model tests. So full scale measurements of wave run-up is necessary. At the same time the overtopping discharge on a prototype breakwater will be measured. Within the MAST III - OPTICREST project, these measurements will be carried out at coastal structures at two locations: Zeebrugge (Belgium) and Petten (The Netherlands). The results obtained from these prototype measurements will be compared with those from scale model tests and will be used to calibrate numerical models. This paper also presents the contents of the OPTICREST project.

1 INTRODUCTION

In the past few decades, the dimensions of seagoing vessels have increased strongly. As a result, many harbours have been constructed in open sea. Harbours need to facilitate smooth and unhindered transfer of passengers and cargo between vessels and land. In order to prevent storms from impeding these harbour activities, the harbour area has to be sheltered.

Sloping structures, such as rubble mound breakwaters are often used for such harbour sheltering purposes. Yet some aspects of their design still remain unsolved. One of these aspects is the crest level. The level to which breakwaters should be built is governed by the phenomena of wave run-up and overtopping. A wave run-up level is

[1] University of Ghent, Dept. of Civil Eng., Technologiepark 9, B-9052 Ghent, Belgium
[2] Ministry of the Flemish Community, Coastal Division, Vrijhavenstraat 3, B-8400 Oostende, Belgium
[3] Aalborg University, Hydraulics and Coastal Eng. Lab., Sohngaardsholmvej 57, DK-9000 Aalborg, Denmark
[4] Rijkswaterstaat, Kortenaarkade 1, PO Box 20907, NL-2500 ex The Hague, The Netherlands

defined as the vertical distance between the Still Water Level (SWL) and the highest point reached by the wave up-rush on the slope.

Recent research (De Rouck et al., 1996; Troch et al., 1996b) showed that wave run-up may be underpredicted by model tests. Since the design of the crest level of sloping coastal structures is based on such tests, or on formulae derived from such tests, this has serious implications.
In order to establish better design rules for the crest level of sloping coastal structures, prototype measurements of wave run-up and overtopping are essential.
Section 2 describes the discrepancies that have been observed between prototype and scale model measurements of wave run-up.
Section 3 provides a theoretical background on the subjects of run-up and overtopping.
Section 4 describes prototype wave run-up and overtopping measurements on a rubble mound breakwater and prototype measurements of run-up on a sea dike.
Finally section 5 presents a project description of OPTICREST.

2 DISCREPANCIES BETWEEN PROTOTYPE AND SCALE MODEL WAVE RUN-UP

During the MAST II project 'Full scale dynamic load monitoring of rubble mound breakwaters' (MAS2-CT92-0023), wave run-up was measured on the NW breakwater of the Zeebrugge harbour (Belgium). The prototype measurements were compared with run-up levels obtained from scale model tests. The breakwater was modelled in three different laboratories: Aalborg University, Denmark; Flanders Hydraulics, Belgium; University College Cork, Ireland. The run-up levels observed in the scale model tests fit well with experimental design curves. However, as shown in figure 1 the prototype measurements, were approximately 50% higher (De Rouck et al., 1996). This difference confirms the experience in many harbours that wave overtopping is much higher during exploitation, than was expected during design.

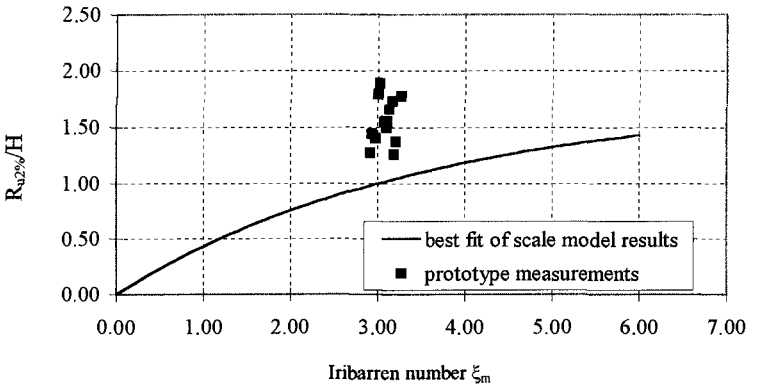

Figure 1. Wave run-up levels with 2% exceedance probability, obtained from prototype and scale model measurements.

All prototype results were obtained during one storm event. Due to the observed wave characteristics and the breakwater geometry, all data are concentrated in an area of Iribarren numbers around 3. Future measurements in a wider range of Iribarren numbers are necessary to confirm this trend for higher full scale run-up levels.

Nowadays, the design of the crest level of sloping coastal structures is based on scale model tests, or on design rules based on such tests. So the aforementioned discrepancy between prototype and scale model run-up levels has very serious consequences: 'the discharge outside will be higher than expected for a given crest level' or 'to limit the discharge to a given value, the crest has to be built higher'.
Therefore, further research is necessary.

3 THEORETICAL BACKGROUND

To get a better insight in the problem first a short theoretical background both on wave run-up and wave overtopping is given. So the reader easily can find out which parameters are important with regard to run-up and overtopping.

3.1 Wave run-up

Extensive laboratory testing on wave run-up has been performed by Losada, Van der Meer and others, leading to design rules used today.

Losada and Giminez - Curto (1981) present a formula to calculate run-up on rough slopes:

$$\frac{R_u}{H} = A \cdot (1 - \exp(-B \cdot \xi)) \tag{1}$$

where R_u = run-up level (m), H = wave height (m), ξ = Iribarren number (-), A and B = experimental coefficients (-) (A = 1.322; B = -0.966).

This formula is based on tests using **regular** waves. The slopes that were tested, were rip-rap slopes.

The formula for wave run-up on rough slopes, proposed by Van der Meer and Stam (1992), takes the form:

$$\frac{R_{ux\%}}{H_s} = a \cdot \xi_m \quad \text{for} \quad \xi_m \leq 1.5 \tag{2}$$

$$\frac{R_{ux\%}}{H_s} = b \cdot \xi_m^c \quad \text{for} \quad \xi_m \leq 1.5 \tag{3}$$

$$\frac{R_{ux\%}}{H_s} \leq d \quad \text{for permeable structures} \tag{4}$$

where: $R_{ux\%}$ = the run-up level (m) with an exceedance probability of x%, H_s = the significant wave height (m), ξ_m = the surf similarity parameter or Iribarren number (-), based on the mean period, a, b, c and d = experimental coefficients (-) depending on the exceedance probability x.

The coefficients for different probabilities of exceedance are given in table 1.

Probability of exceedance (%)	coefficient a (-)	coefficient b (-)	coefficient c (-)	coefficient d (-)
0.13	1.12	1.34	0.55	2.58
1	1.01	1.24	0.48	2.15
2	0.96	1.17	0.46	1.97
5	0.86	1.05	0.44	1.68
10	0.77	0.94	0.42	1.45
significant	0.72	0.88	0.41	1.35
mean	0.47	0.60	0.34	0.82

Table 1. Coefficients to be used in the formulae (2)-(4) by Van der Meer & Stam (1992) to calculate run-up on rough slopes.

The formula by Van der Meer is based on tests using **irregular** waves. The slopes that were tested, were rip-rap slopes, ranging from 1:2 to 1:6. Wave steepness ranged from 0.004 to 0.06.

Recently a general expression of wave run-up for **irregular** waves has been published (Burcharth, 1998; Van der Meer et al., 1998).

$$\frac{R_{ux\%}}{H_s} = (A\xi + C)\gamma_r \gamma_b \gamma_h \gamma_\beta \qquad (5)$$

where

$R_{ux\%}$ run-up level exceeded by x% of the incident waves

ξ surf similarity parameter, e.g. ξ_{op}

A, C coefficients dependent on ξ and x but related to the reference case of a smooth, straight impermeable slope, long-crested head-on waves and Rayleigh distributed wave heights

γ_r reduction factor for influence of surface roughness; $\gamma_r = 1$ for smooth slopes

γ_b reduction factor for influence of a berm; $\gamma_b = 1$ for non-bermed profiles

γ_h reduction factor for influence of shallow water conditions where the wave height distribution deviates from the Rayleigh distrbution; $\gamma_h = 1$ for Rayleigh distributed waves

γ_β factor for influence of angle of incidence β of the waves; $\gamma_\beta = 1$ for head on long-crested waves, i.e. $\beta = 0°$. The influence of directional spreading in short-crested waves is included in γ_β as well

The coefficients A and C, together with estimates of the coefficient of variations for R_u, are given in Table 2. The symbol R_{us} means the significant R_u.

ξ	R_u	ξ-limits	A	C	$\frac{\sigma_{Ru}}{R_u}$
ξ_{op}	$R_{u2\%}$	$\xi_p \leq 2.5$	1.6	0	app. 0.15
		$2.5 < \xi_p < 9$	-0.2	4.5	
	R_{us}	$\xi_p \leq 2.0$	1.35	0	app. 0.1
		$2.0 < \xi_p < 9$	-0.25	3.0	

Table 2. Coefficients in eq (5) for run-up of long-crested irregular waves on smooth impermeable slopes (Burcharth, 1998).

Within the MASTIII-project MAS3-CT97-0116 'The optimisation of crest level design of sloping coastal structures through prototype monitoring and modelling' (OPTICREST) measurements on site will be carried out on the NW rubble mound breakwater in Zeebrugge (rough permeable) and the sea dike in Petten (smooth impermeable). The main difference is the roughness and the void ratio of the armour layer. So only γ_r will be discussed in more detail here. For variations of γ_b, γ_h and γ_β reference is made to De Waal and Van der Meer (1992) and Van der Meer et al. (1998).

The original factor γ_r given in TAW (1974) and in the SPM (1984) has been updated based on experiments including large scale tests with random waves. The new γ_r values taken from de Waal and Van der Meer (1992) are valid for $1 < \xi_{op} <$ 3-4. For larger ξ_{op} values the γ_r factor will slowly increase to 1.

Type of slope surface	γ_r
Smooth, concrete, asfalt	1.0
Smooth block revetment	1.0
Grass (3 cm length)	0.90 – 1.0
1 layer of rock, diameter D_n ($H_s/D = 1.5 - 3.0$)	0.55 – 0.6
2 or more layers of rock, ($H_s/D = 1.5 - 6.0$)	0.50 – 0.55

Table 3. Surface roughness reduction factor γ_r in eq. (5), valid for $1 < \xi_{op} <$ 3-4. (de Waal and van der Meer, 1992)

3.2 Overtopping

The experimental study of overtopping also has led to a number of empirical formulae. Several formulae which relate a dimensionless average discharge to a dimensionless freeboard have been published. The freeboard of a structure is defined as the vertical distance between the Still Water Level (SWL) and the crest of the structure. This type of formulae are called 'simple regression models'.

Another approach to calculate overtopping discharges is the use of 'weir models'. These models are based on a theoretical derivation which considers the crest of a structure to be a weir.

It has to be emphasised that the formulae give average overtopping discharges. These values should be used very carefully when thinking about admissible overtopping discharges. The intensity of water hitting a specific location is very much dependent on

the geometry of the structure and the distance from the front of the structure. The maximum intensities might locally be up to two orders of magnitude larger than the average discharge.
Moreover, what is regarded as acceptable conditions is to a large extend a matter of local traditions and individual opinions.
Some background on both models for calculating the average discharge are presented.

3.2.1 Simple regression models

The advantage of simple regression models over weir models is that they are very easy to use. The disadvantage is that they do not fulfil the boundary conditions:

- When the crest becomes very high, the overtopping discharge should be zero.
- When the freeboard is zero, the overtopping discharge should remain finite.

Owen (1980) relates a dimensionless freeboard to a dimensionless discharge by an exponential relationship:

$$Q_* = A \cdot \exp\left(\frac{-B \cdot R_*}{r}\right) \tag{6}$$

The dimensionless variables are defined as:

$$Q_* = \frac{Q}{T_m g H_s} = \frac{Q}{\sqrt{g H_s^3}} \cdot \sqrt{\frac{s}{2\pi}} \tag{7}$$

and

$$R_* = \frac{R_c}{T_m \cdot \sqrt{g H_s}} = \frac{R_c}{H_s} \cdot \sqrt{\frac{s}{2\pi}} \tag{8}$$

where: A and B = experimental coefficients (-), r = coefficient (-) ranging from 0 to 1 to account for the roughness of the slope, Q = mean overtopping discharge per meter crest length ($m^3/s.m$), T_m = mean wave period (s), g = gravitational acceleration (m/s^2), s = wave steepness (-), R_c = freeboard (m).

The parameter ranges tested by Owen were: R_* ranging from 0.05 to 0.30, Q_* ranging from 10^{-6} to 10^{-2}, slope ranging from 1:1 to 1:4, d/H_s (where d = water depth (m)) ranging from 1.5 to 5.5 and $H_s/L_{0,mean}$ (where $L_{0,mean}$ = mean deepwater wave length) ranging from 0.035 to 0.055.

Allsop & Bradbury (1988) propose a different relationship between a dimensionless freeboard and a dimensionless discharge:

$$Q_* = A \cdot F_*^{-B} \tag{9}$$

The dimensionless variables are defined as:

$$Q_* = \frac{Q}{T_m g H_s} = \frac{Q}{\sqrt{g H_s^3}} \cdot \sqrt{\frac{s}{2\pi}} \tag{10}$$

and

$$F_* = \frac{R_c}{H_s}\frac{R_c}{T_m\sqrt{gH_s}} = \frac{R_c^2}{H_s^2}\cdot\sqrt{\frac{s}{2\pi}} \tag{11}$$

where A and B = experimental coefficients (-).

Other formulae are discussed by Burcharth (1998).

A more recent regression model is given by Van der Meer et al. (1998):

$$\frac{q}{\sqrt{gH_s^3}} = \frac{0.06}{\tan\alpha}\cdot\gamma_b\cdot\xi_{op}\cdot\exp\left(-4.7\cdot\frac{R_c}{H_s}\cdot\frac{1}{\xi_{op}\cdot\gamma_b\gamma_f\gamma_\beta\gamma_v}\right) \tag{12}$$

With as a maximum:

$$\frac{q}{\sqrt{gH_s^3}} \le 0.2\cdot\exp\left(-2.3\cdot\frac{R_c}{H_s}\cdot\frac{1}{\gamma_f\gamma_\beta}\right) \tag{13}$$

where: q = mean overtopping discharge per meter crest length (m^3/s.m), α = slope angle (rad), ξ_{op} = the Iribarren number (-) calculated with the peak period and the deepwater wave length, γ_b = a reduction factor (-) to account for the effect of a berm, γ_f = a reduction factor (-) to account for the roughness of the slope, γ_β = a reduction factor (-) to account for the effect of oblique wave attack, γ_v = a reduction factor (-) to account for the effect of a vertical wall.
Full discussion of the influence of a berm, roughness, oblique wave attack, etc... can be found in van der Meer et al. (1998).

3.2.2 Weir models

As an exemple the first weir model, developed by Kikkawa et al. (1968) is presented. Based on theoretical considerations, the following formula is derived:

$$\frac{Q}{\sqrt{2g}\cdot H_0^{3/2}} = \frac{2}{15}\cdot M\cdot(1-K_0)^{5/2} \tag{14}$$

Where: H_0 = deep water wave height (m), K_0 = a dimensionless freeboard (-), M = experimental coefficient (-).
The left hand side of equation (14) can be considered as a dimensionless discharge. Thus this equation gives a relationship between a dimensionless discharge and a dimensionless freeboard. It holds the advantage over a simple regression model that it contains more physics and satisfies both boundary conditions:

- When the freeboard equals the highest run-up level, K_0 becomes 1 and the discharge becomes 0.
- When the freeboard is zero, K_0 becomes zero and the discharge remains finite.

4 PROTOTYPE MEASUREMENTS OF RUN-UP AND OVERTOPPING

In order to investigate whether there are systematic differences between run-up levels and overtopping discharges measured in (small) scale models and on full scale, in-situ measurements in Zeebrugge will proceed within OPTICREST. Also in-situ measurements of run-up will be carried out on a smooth sea dike in Petten (The Netherlands). At both locations tide and wind data are available through a nationally funded project.

The main objectives of OPTICREST are:
- Provide designer with improved design rules for the crest level design of sloping coastal structures
- Verify and calibrate scale models for run-up with full scale data
- Calibrate numerical models with full sale data and model test data

The partners of the OPTICREST project are
- University of Gent (Coordinator)
- Flemish Community (Coastal Division; Flanders Hydraulics)
- Aalborg University
- Leichtweiss Institut für Wasserbau
- University College Cork
- Delft Hydraulics
- Rijksinstituut voor Kust en Zeeën
- Universidad Politechnica de Valencia
- Instituto Hidrografico

The project runs from 1 March 1998 till 28 February 2001.

4.1 Zeebrugge (Belgium)

The port of Zeebrugge is situated on the eastern part of the Belgian coastline and is protected by two main breakwaters (Fig. 2). The Zeebrugge breakwater constitutes a conventional rubble mound breakwater with an armour layer of 25 ton grooved cubes.

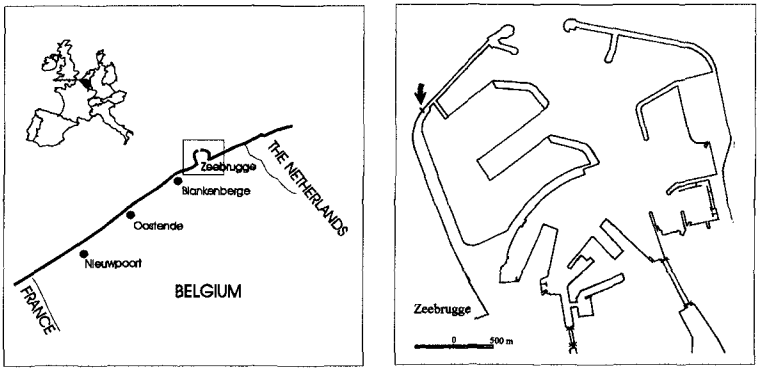

Figure 2. Location of the prototype run-up measurement system on the NW breakwater at the Zeebrugge harbour (Belgium).

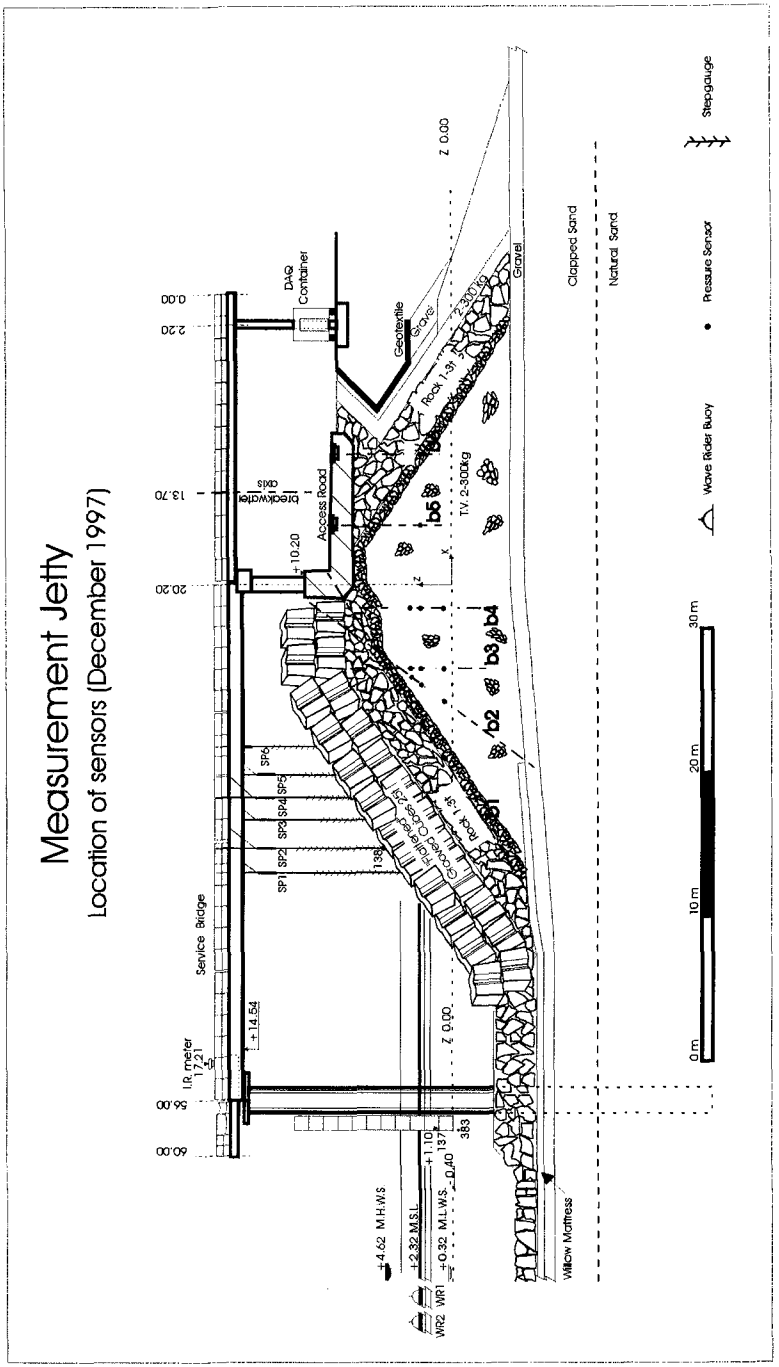

Figure 3. Crosssection of the Zeebrugge rubble mound breakwater with the instrumentation.

A measurement jetty of 60 m length is constructed on the NW breakwater (Fig. 3). It is supported by a steel tube pile at the breakwater toe and by two concrete columns on top of the breakwater.

Run-up is measured using six vertical stepgauges, placed along the breakwater slope. At the bottom, the stepgauges are attached to an armour unit. At the top they are supported by the jetty. Each stepgauge has a number of electrodes, spaced vertically at 20 cm intervals. Each submerged electrode produces an output voltage. The summation of these voltages leads to an output signal that contains the information about the water level with a 20 cm resolution. Using the six stepgauges, this information is available at six positions along the breakwater slope. Specially developed software computes the water surface profile on the slope as the polygon connecting the water surface levels measured by the six stepgauges. The instantaneous run-up level is taken as the intersection of the slope with an extrapolated line through the highest two water surface levels measured at that instant. (Figure 4)

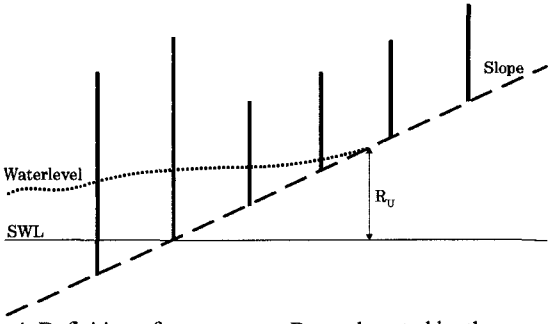

Figure 4. Definition of wave run-up Ru as detected by the stepgauges.

A device to measure overtopping will be installed on the breakwater in autumn 1998. Overtopping will be measured by a screen, catching the overtopping water which will then be collected in a container (Fig. 5). The container will be continuously emptied by a weir. The volume of water in the container, as well as the discharge over the weir will be calculated from the water surface level in the container.

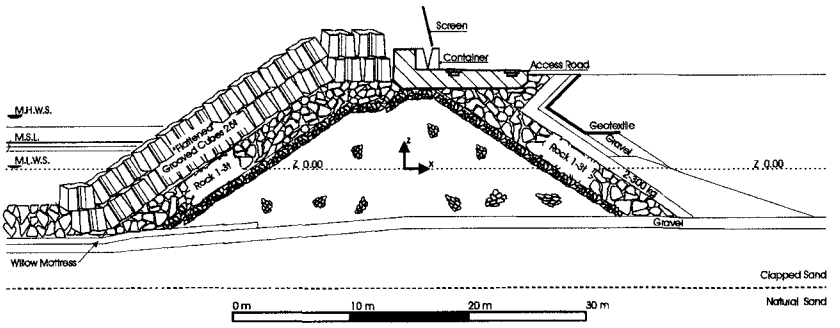

Figure 5. Prototype measurement of overtopping.

Wave data are obtained from two wave rider buoys close to the breakwater, at 165 m and 215 m in front of the breakwater, and from three wave rider buoys located at 5 km, 30 km and 45 km from the structure.

4.2 Petten (The Netherlands)

The Petten sea dike is situated in the northern part of The Netherlands (Fig. 6). The Petten coastal region is very suitable for a measurement campaign as the iso-baths are approximately parallel to the coastline. The bathymetry is characterised by a bar and a dike onshore.

The Petten sea dike consists of a lower slope, made of basalt stones on approx imately. a 1:3.5 slope. Above the lower slope an asphalt berm (1:13.5) and an asphalt slope (1:2.75) form the higher protection. Figure 7 shows the crosssection of the dike.

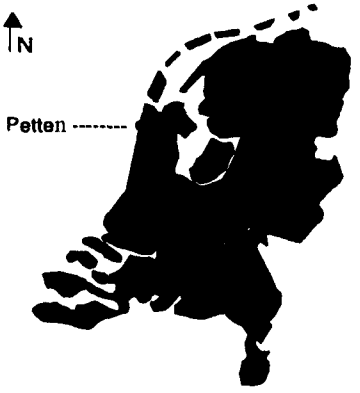

Figure 6. Location of the prototype run-up measurement system on the Petten sea dike (The Netherlands).

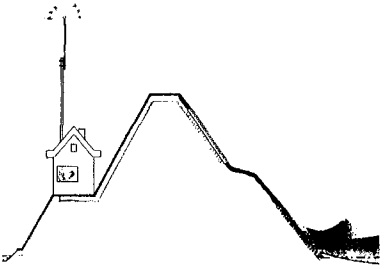

Figure 7. Cross section of the Petten sea dike (distorted scale).

Figures 8 and 9 show the bathymetry and the instrumentation.

Data concerning the wave climate are collected by wave rider buoys (Mp2 and Mp4) and by directional wave riders (Mp1 and Mp5). Just in front of the bar, a wave staff and a water level meter (Mp3) measure the incoming waves. In front of the dike the waves are measured by a wave staff and a pressure sensor (Mp6 and Mb6).
The wave run-up is measured, using a staff gauge placed along the slope of the sea dike (Mp7). The staff gauge consists of a number of electrodes spaced at 10 cm intervals. The vertical distance between the electrodes is approximately 3.5 cm

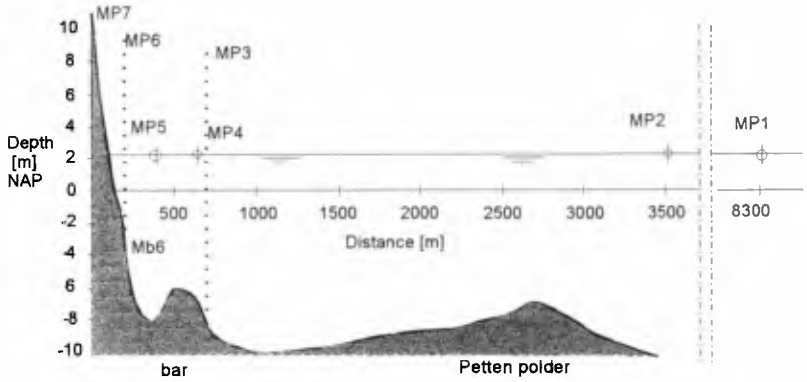

Figure 8. Bathymetry and instrumentation at the Petten sea dike.

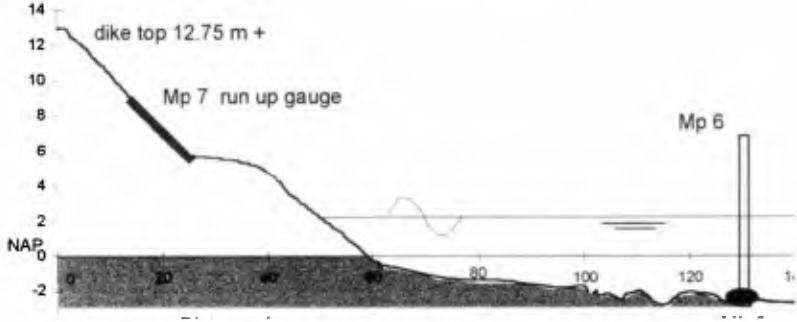

Figure 9. Bathymetry and instrumentation in front of the Petten sea dike

5 FURTHER PROJECT DESCRIPTION

5.1 Laboratory investigations

Both the Zeebrugge and the Petten site will be modelled in scale model tests. Run-up levels and overtopping discharges will be measured. In the scale model tests, both in-situ measured spectra and standard spectra will be used. Special attention will be paid to the influence of the foreshore bathymetry.
Two dimensional and three dimensional tests will be carried out.

5.1.1 Two dimensional testing

Deviations between the scale model results and the prototype measurements will be determined and the influence of different scale effects will be investigated. This may lead to changes in building models for the two sites. The models will then be re-built and the basic tests re-run.

5.1.2 Three dimensional tests

Three dimensional tests will be carried out for models of the Zeebrugge and the Petten site. The scaling will be as close as possible to the scales used in the two dimensional tests.
These tests will attempt to validate the prototype results and continue to investigate the influence of such parameters as wave height, period, water depth, angle of wave attack, directional spreading, currents, foreshore bathymetry and structure geometry.

5.1.3 Link between prototype and laboratory results

One of the conclusions of the MAST II project 'Full scale dynamic load monitoring of rubble mound breakwaters', was that wave run-up is underpredicted by model tests. This may be due to several factors, such as: measuring systems, wind, roughness, randomness of sea conditions, etc... The purpose of the comparison between prototype and laboratory results is to quantify these effects in order to allow better predictions of run-up levels and overtopping quantities from laboratory tests.

5.2 Numerical modelling

It has to be expected that numerical models will play a very important role in future research and design of coastal structures. Therefore it is of paramount importance that these models are as reliable as can be achieved. Up to now, these models have been calibrated against scale model test results only. In the OPTICREST project, they will also be calibrated against full scale data.

5.3 Outlook

Existing design techniques for sloping coastal structures, which include the use of mathematical and physical models have not prevented severe failures. Such failures have disastrous consequences, such as loss of life, loss of business, damage to property, economic ruin, ... Reliable design methodologies are essential.
Full scale measurements of run-up and overtopping will provide better insights in the phenomena and will lead to better mathematical and physical models. This will lead to a better design method of the crest of sloping coastal structures. With our coast being used more than ever before, these results will be very valuable.

6 ACKNOWLEDGEMENTS

This research originated during the EC MAST II project MAS2-CT92-0023 'Full scale dynamic load monitoring of rubble mound breakwaters'. The run-up and overtopping research will go on in the EC MAST III project MAS3-CT97-0116 'The optimisation of crest level design of sloping coastal structures through prototype monitoring and modelling', coordinated by J. De Rouck. The financial support by the EC is greatly acknowledged.
Also the financial support of the government of both Belgium (Flanders) and the Netherlands is acknowledged.

7 REFERENCES

Allsop N.W.H., Bradbury A.P, 1988, *Hydraulic performance of breakwater crown walls,* HR Wallingford, Rep. SR 146.

Andorka Gal J.H., 1996, *Verification set Petten,* Ministry of transport, public works and water management, Directorate-General for public works and water management, National Institute for coastal and Marine Management, RIKZ.

Burcharth H.F., 1998 , *Hydraulic responses – wave run-up, rundown and overtopping,* OPTICREST, start-up workshop, Ghent, March 1998.

De Rouck J. and Troch P., editor, 1996, *Full scale dynamic load monitoring of rubble mound breakwaters,* (MAS2-CT92-0023) Detailed Scientific report, vol 1 and vol 3, March 1996.

De Waal J.A., Van der Meer J.W., 1992, *Wave run-up and overtopping on coastal structures,* Proc. 23th ICCE, 1992, Venice.

Holterman S.R., 1998, *Golfoploop bij dijken met ondiep voorland,* Final year thesis, Technische Universiteit Delft.

Kikkawa H., Shi-igai H., Kono T., 1968, *Fundamental study of wave overtopping on levees,* Coastal Engineering in Japan, Vol. 11, p. 107-115.

Losada M.A., Gimenez Curto L.A., 1981, *Flow characteristics on rough, permeable slopes under wave action,* Journal of Coastal Eng., 4, p. 187-206.

Owen M.W., 1980, *Design of sea walls allowing for wave overtopping,* Rep. EX 924, HR Wallingford.

SPM, 1984, *Shore Protection Manual.,* Coastal Engineering Research Center, Waterways Experiment Station, U.S. Army Corps of Engineers.

TAW, 1974, *Wave run-up and overtopping,* Technical Advisory Committee on Water Defence. Govern. Publishing Office, The Hague .

Troch P, De Somer M., De Rouck J., 1995, *Full scale dynamic load monitoring of rubble mound breakwaters,* Proc. 2nd MAST days and EUROMAR market, 7-10 Nov. 1995, Sorrento.

Troch P., De Somer M., De Rouck J., Van Damme L., Vermeir D., Martens J.P., Van Hove C., 1996, *In-situ load monitoring of rubble mound breakwaters,* Proc. 11th Int. Harbour Congress, Antwerp, pp. 331-334.

Troch P., De Somer M., De Rouck J., Van Damme L., Vermeir D., 1996, *Full scale dynamic load monitoring of rubble mound breakwater,* 25th ICCE, 1996, Orlando, pp. 1916-1929.

Troch, P., De Rouck J., Van Damme L., 1998, *Instrumentation and prototype measurements at the Zeebrugge rubble mound breakwater,* Accepted for publication in Coastal Engineering, Special issue on instrumentation.

Van der Meer J.W., Stam C.J., 1992, *Wave run-up on smooth and rock slopes of coastal structures,* Journal of Waterway, Port, Coastal and Ocean Eng., Vol. 118, No. 5, p. 534-550.

Van der Meer J.W., Tönjes P., de Waal J.P., 1998, *A code for dike height design and examination,* International Conference on Coastlines, Structures and Breakwaters '98, 19-20 March 1998, Institution of Civil Engineering – London U.K.

WAVE RUNUP AND REFLECTION ON COASTAL STRUCTURES IN DEPTH-LIMITED CONDITIONS

Joel R. Rathbun, Daniel T. Cox, and Billy L. Edge[1]

Abstract

An experimental study was performed to measure the effects of depth-limited conditions on wave runup and reflection from coastal structures. The measurements are compared with existing empirical formulas. An existing model to predict wave runup is shown to overpredict the runup and a clear trend of increased wave runup in depth-limited conditions is shown. A new empirical model is presented that includes the effects of depth-limited conditions on wave runup. Existing models to predict wave reflection based on the surf similarity parameter are shown to fail to collapse the measured data onto a single line. A recently developed model based on a number of parameters is shown to accurately predict wave runup in cases where no wave breaking occurred before the structure. However, at the shallower water depths where wave breaking occurred seaward of the structure, the model underpredicted the reflection coefficient. This model was modified to increase its accuracy in depth-limited conditions based upon the laboratory results presented in this study.

Introduction

Wave runup and wave reflection are two important variables that have to be taken into account by engineers in designing safe and effective coastal structures. A number of researchers have proposed empirical formulas to quantify these variables; however, there have been relatively few studies undertaken with depth limited conditions. These conditions are of practical interest due to the large number of coastal structures present throughout the world that are located in areas where these types of conditions occur during storms.

From the few studies that have included shallow water cases, some researchers have found that wave runup and reflection tend to decrease in depth-

[1]Dept. of Civil Engineering, Texas A&M University, College Station, TX 77843 USA; Tel: (409) 842-3627 Fax: (409) 862-3627 Email: dtc@arlo.tamu.edu.

limited conditions (e.g., Seelig and Ahrens, 1995; Van der Meer and Janssen, 1995). Interestingly, Kobayashi and Raichle (1994) found that the overtopping rate for a coastal revetment located inside the surf zone was underestimated by prediction methods developed for deep water cases. Similarly in an extensive investigation on overtopping rates of vertical walls in shallow water conditions, Besley et al. (1998) found that in cases where wave breaking occurred due to depth-limited conditions, previously developed methods significantly underestimated overtopping discharge. This leads to an apparent contradiction as it has been generally thought that higher levels of wave runup cause increased overtopping.

This study seeks to shed some light on the discrepancy between models that predict decreasing runup with decreasing depth and models that predict increasing overtopping with decreasing depth. A laboratory investigation of wave runup and reflection on a coastal structure in shallow water with both breaking and non-breaking waves was undertaken. Empirical models for both wave runup and wave reflection on riprap revetments were evaluated. A brief description of the experiment and the essential findings of this research are presented in this paper. A full description of the experiment and a detailed analysis and discussion of the findings is presented in Rathbun (1998).

Experimental Setup

The experiments were conducted in the long wave flume at Texas A&M University. The dimensions of the flume were 32 m long by 0.9 m wide by 1.2 m deep. The flume was equipped with a flap type wavemaker capable of generating irregular waves. A mild slope, 1:35, was installed over most of the length of the flume, consisting of sections of marine plywood coated with an epoxy paint mounted on an aluminum frame. The edge of the mild slope was caulked to the side of the flume to ensure that no wave energy was transmitted to the water below the mild slope. The toe of the mild slope was located 10.73 m from the wavemaker. A capacitance type wave gage consisting of two wires strung between a steel backbone was installed along the slope of the revetment to measure the water line oscillation along the slope of the revetment. The wires were placed as close to the rocks on the revetment as possible, without actually touching any rocks. The average distance between the wires and the stones on the revetment was approximately 0.75 cm.

The model coastal structure that was used for the tests was an impermeable revetment consisting of a plywood board supported by a steel frame, on which a filter layer and armor layer were placed. This type of impermeable revetment was chosen as it is a common type of coastal structure found throughout the world. The revetment was located on the mild slope, 27.28 m from the wavemaker. Test runs were made on revetments with two different slopes, 1:1.5 and 1:3, during the course of the investigation. A thin layer of silicone was spread over the plywood board to hold the bottom layer of filter stone from sliding down the slope for the steeper 1:1.5 case. During construction

of the revetment, the armor stones were individually placed on the revetment to ensure a high degree of interlocking between adjacent stones. Both the filter and armor layers were two stone dimensions in thickness. The filter stone was river stone gravel and the armor stone was crushed granite. The specific gravity of the armor and filter stone was 2.65 and 2.50 respectively with the median rock size of 278.2 g for the armor stone and 23.8 g for the filter stone. These rock sizes produced an armor layer thickness of 9.4 cm and a filter layer thickness of 4.2 cm.

The control signal for the wavemaker was derived from the TMA spectral form using a random-phase scheme. The value of the peak enhancement factor, γ, used to generate the TMA spectrum was $\gamma = 3.3$. Additional tests were performed using a narrower spectrum, $\gamma = 20$, but these test runs are not discussed in this paper. The interested reader is referred to Rathbun (1998). The free surface elevation at nine wave locations and the runup along the slope of the revetment was recorded at a rate of 25 Hz for the duration of each test. The majority of the tests were 615.36 seconds in duration. This resulted in approximately 400 to 600 runup events per test run depending on the wave period. A small number of shorter tests were performed to gage the effects of the test length on the results. These tests were 327.68 seconds in length, resulting in approximately 250 runup events per test run.

The incident and reflected wave conditions were resolved at three locations in the flume using the method of Goda and Suzuki (1976) modified for three gage pairs. The first set of three wave gages, array A, was located at the toe of the mild slope 15.75 m from the toe of the structure and 10.32 m from the wave maker. Array B was located 2 m seaward of the toe of the structure and array C was located at the toe of the structure. The location of each array corresponds to the location of the gage closest to the structure at which the incident and reflected waves were resolved. The separation between the gage closest to the structure and the middle gage at each gage array was 30 cm and the separation between the middle gage and the gage farthest from the structure was 50 cm.

A measure of the percentage of broken waves at the toe of the structure, *Br*, was obtained by visual observation. The observer stood immediately adjacent to the tank and counted the number of waves that were broken at the toe of the structure out of a series of 100 waves. For the majority of the tests, *Br* was recorded for two successive counts of 100 waves and the results were averaged. For the small number of tests that were shorter in duration *Br* was recorded for only one series of 100 waves. After some initial observation and discussion, two observers could obtain *Br* to within a difference of 3% or less of each other. Only waves that reached the structure as white water bores were recorded as broken. If a wave broke over the sloping foreshore and reformed before reaching the structure, it was not counted as broken. For the surf conditions encountered in this investigation, this phenomenon occurred infrequently.

Test runs were made at three water depths, $d_s = 0.400$, 0.200 and 0.105 m, at the toe of the structure with the 1:1.5 revetment in place and at two water depths, $d_s = 0.200$ and 0.105 m, with the 1:3 revetment in place. Table 1 outlines the range of variables that were tested during the investigation. θ is the slope of

the structure, d_s is the depth at the toe of the structure, H_{mo} is the incident significant wave height at the toe of the structure defined as $4.004\sqrt{m_o}$ where m_o is the zeroth moment of the wave spectrum, ξ_{Lo} is the surf similarity parameter given as $\xi_{Lo} = \tan\theta/(H_{mo}/L_o)^{1/2}$ where L_o is the deepwater wavelength given as $L_o = gT_p^2/2\pi$ where T_p is the peak wave period, and g is the acceleration due to gravity. The measured reflection coefficient, K_{rm}, is defined as $K_{rm} = (E_i/E_r)^{0.5}$ where E_i is the incident wave energy and E_r is the reflected wave energy at the toe of the structure.

Table 1. Range of Parameters Tested

Cot θ	d_s (cm)	H_{mo} (cm)	T_p (s)	ξ_{Lp}	K_{rm}	H_{mo}/d_s
1.5, 3	10.5, 20.0, 40.0	5.2 –14.5	1.1 – 2.3	1.5 – 7.5	0.15 – 0.66	0.14 – 0.77

Wave Runup

The most common approach taken for wave runup prediction has been to relate the relative runup to the surf similarity parameter. Typically the deep water wavelength, L_o is used to define the surf similarity parameter, ξ_{Lo}. However, Ahrens and Heimbaugh (1988) found that a more accurate model could be developed with a surf parameter using the local wavelength. This new surf parameter is defined as $\xi_{Lp} = \tan\theta/(H_{mo}/L_p)^{1/2}$ where L_p is the local wavelength found using linear wave theory. In Fig. 1 the relative runup, $R_{2\%}/H_{mo}$, is plotted against ξ_{Lp}. The two percent runup elevation, $R_{2\%}$, is defined as the runup elevation above SWL that is exceeded by two percent of the individual runup elevations in the time series. Also shown is the prediction model proposed by Ahrens and Heimbaugh (1988) given as

$$\frac{R_{2\%}}{H_{mo}} = \frac{a\xi_{Lp}}{1 + b\xi_{Lp}} \tag{1}$$

where a and b are empirical coefficients given by Ahrens and Heimbaugh as a = 1.154 and b = 0.202. Note that in (1), $R_{2\%}$ has replaced R_{max} where R_{max} is the maximum runup elevation above SWL in the time series. The R_{max} values that Ahrens and Heimbaugh's model used were derived from test runs with a length of 256 s, that is from 100-200 waves. For tests of short duration such as this, R_{max} will probably be close to $R_{2\%}$ of the present tests (Van der Meer and Stam 1993). As can be seen from this figure, the model overpredicts the relative runup observed in the test runs for $\xi_{Lp} > 2.5$.

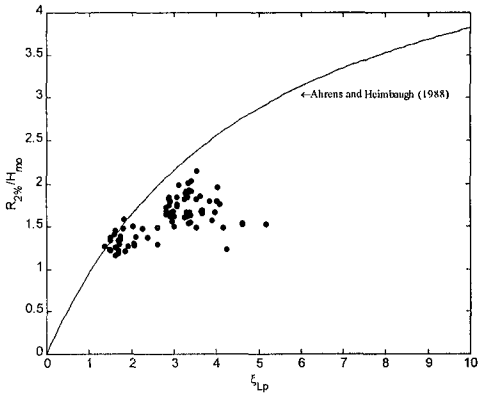

FIG. 1 $R_{2\%}/H_{mo}$ as a Function of ξ_{Lp}, and Compared with Ahrens and Heimbaugh (1988)

One of the principal concerns of this research was the effect of depth limited conditions on wave runup. The figure shows that, in general, as the water depth is decreased the relative runup increases for a given value of the surf similarity parameter. This is in contrast to the work of Van der Meer and Janssen who suggest using a reduction factor for conditions with a shallow foreshore.

The effect of depth-limited conditions on wave runup may be better illustrated by considering the percentage of broken waves at the toe, in other words, the percentage of waves that break on the sloping foreshore before reaching the structure and reach the structure as white water bores. Fig. 2 shows the relative runup, $R_{2\%}/H_{mo}$, as a function of the surf similarity parameter, ξ_{Lp}, with the data grouped according to the percentage of broken waves at the toe of the structure, Br. The data are divided into three groups: $Br = 0$, $0 < Br < 40$ and $Br > 40$. It can be seen in Fig. 2 that as Br increases the relative runup increases for a given value of the surf parameter.

A parameter that describes the wave conditions at the toe of the structure that can be used in a formula to predict wave runup other than Br is required because methods to predict Br are not readily available. A common parameter that is often used to define if breaking condition exist is the ratio of the wave height to the water depth -- in this case H_{mo}/d_s. For the tests performed in this investigation the onset of broken waves at the toe of the structure occurred at approximately $H_{mo}/d_s = 0.4$ and the percentage of broken waves increased sharply with increasing H_{mo}/d_s after that point.

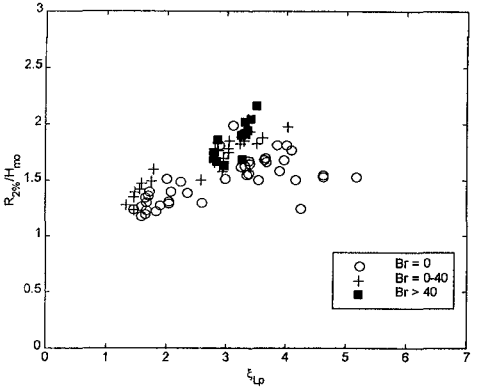

FIG. 2. $R_{2\%}/H_{mo}$ as a Function of ξ_{Lp} with *Br* Indicated

The relative runup, $R_{2\%}/H_{mo}$ as a function of ξ_{Lp} is shown in Fig. 3 with the data divided into groups of $H_{mo}/d_s \leq 0.4$ (non-breaking waves) and $H_{mo}/d_s > 0.4$ (breaking waves). It can be seen in Fig. 3 that for cases where $H_{mo}/d_s > 0.4$ the relative runup is higher for a given value of ξ_{Lp}. Curves of a form similar to Equation (1) were fit to all of the data points and as well, to only the points where $H_{mo}/d_s < 0.4$ (non-breaking cases). The coefficients a and b are $a = 2.108$ and $b = 0.939$ when the curve is fit to all of the data and $a = 2.181$ and $b = 1.062$ for the curve fit to the data where $H_{mo}/d_s \leq 0.4$. This curve is also shown in Fig. 3 with $a = 2.181$ and $b = 1.062$. The R^2 statistic (the square of the correlation coefficient) when Equation (1) is used to predict the relative runup for all of the test cases is $R^2 = 0.373$. If only the cases where $H_{mo}/d_s < 0.4$ are considered, the R^2 value using Equation (1) to predict the relative runup is $R^2 = 0.384$.

The underprediction of Equation (1) for cases with depth-limited conditions (breaking conditions) when the empirical coefficients a and b are determined from cases without depth-limited conditions (non-breaking cases) can be accounted for through the use of an enhancement factor based on H_{mo}/d_s. The resulting model takes the form of the existing equation developed from the test runs where $H_{mo}/d_s < 0.4$ (non-breaking cases) divided by an enhancement factor in cases where $H_{mo}/d_s > 0.4$. This new model is given as

$$\frac{R_{2\%}}{H_{mo}} = \frac{a\xi_{1,p}}{1 + b\xi_{1,p}} \frac{1}{\gamma_{ds}} \tag{2}$$

where γ_{ds} is the enhancement factor based on H_{mo}/d_s. γ_{ds} is given by

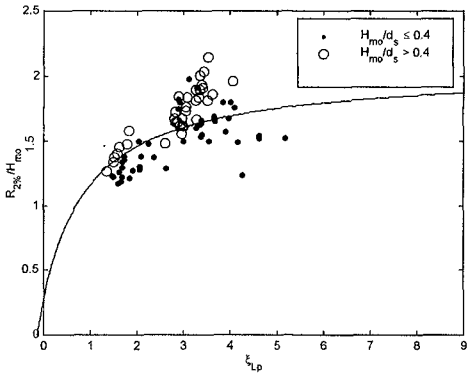

FIG. 3. Influence of H_{mo}/d_s on $R_{2\%}/H_{mo}$

$$\gamma_{ds} = 1 - c\left(\frac{H_{mo}}{d_s} - 0.4\right)^d \qquad \text{for} \quad \gamma_{ds} > 0.4 \tag{3}$$

$$\gamma_{ds} = 1 \qquad \text{for} \quad \gamma_b \leq 0.4 \tag{4}$$

The empirical coefficients a and b remain $a = 2.181$ and $b = 1.062$. The values for the coefficients associated with the enhancement factor were found to be $c = 0.220$ and $d = 0.389$. The R^2 value for this model fit to the laboratory data was $R^2 = 0.567$, an improvement of 52% over the R^2 value found using Equation (1) with no enhancement factor.

The effectiveness of the new model can be seen in Fig. 4 where $R_{2\%}/H_{mo}$ multiplied by the enhancement factor γ_{ds} as a function of ξ_{Lp} along with the new model, Equation (2), is shown.

Other wave breaking parameters may be used to describe the wave conditions at the toe of the structure. Allsop et al. (1995) found that wave overtopping of vertical walls may be underestimated in cases where equations describing non-breaking waves are used in cases where breaking waves predominate due to a shallow sloping foreshore. For simple vertical walls on a shallow sloping foreshore, a wave breaking parameter, h_m*, was defined which dictates whether waves at the structure are dominated by what the authors termed impact waves (breaking) or by deflecting/pulsating waves (non-breaking). h_m* includes the deepwater wave steepness along with the ratio of the water depth to the wave height and is given by

$$h_m^* = \left(\frac{d_s}{H_s}\right)\left(\frac{2\pi H_s}{g T_m^2}\right) \tag{5}$$

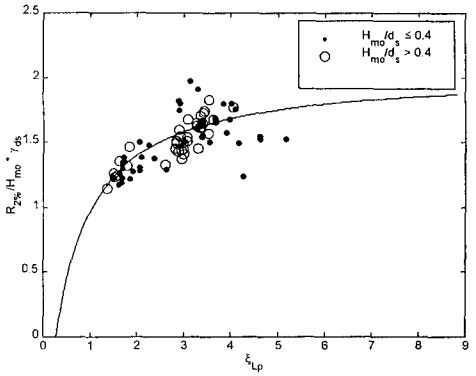

FIG. 4. $R_{2\%}/H_{mo} * \gamma_{ds}$ as a Function of ξ_{Lp} with Equation (2)

The formulation of h_m* reflects the fact that waves are more likely to break if the wavelength or the wave height is large compared to the water depth. The authors found that deflecting (non-breaking) waves dominate when h_m* > 0.3 and impacting (breaking) waves dominate when h_m* < 3.

The wave breaking parameter h_m* can be modified using T_p in place of T_m, and H_{mo} in place of H_s. This new parameter, h_p*, defined as

$$h_p * = \left(\frac{d_s}{H_{mo}}\right)\left(\frac{2\pi H_{mo}}{gT_p^2}\right) \tag{6}$$

may be more advantageous for use in a practical design formulation for two reasons. First, T_p is more stable than T_m measured either spectrally or statistically and is less susceptible to distortion by measurement/calculation errors (Durand and Allsop 1997). Second, most modern wave forecast models predict H_{mo} rather than H_s and many field measurements are reported as H_{mo}.

A similar methodology that was followed when developing a prediction model with an enhancement factor based on H_{mo}/d_s can be used to formulate a model with an enhancement factor based on h_p*. This new model is given by

$$\frac{R_{2\%}}{H_{mo}} = \frac{a\xi_{Lp}}{1 + b\xi_{Lp}} \frac{1}{\gamma_b} \tag{7}$$

where γ_b is the enhancement factor based on h_p*. γ_b is given by

$$\gamma_b = \left(1 - (0.25 - h_p *)^c\right) \qquad \text{for } \gamma_b < 0.25 \tag{8}$$

$$\gamma_b = 1 \qquad \text{for } \gamma_b \ge 0.25 \tag{9}$$

With no enhancement factor, the coefficients of the model if only the tests runs where h_p* ≥ 0.25 (the non-breaking cases) are considered are a= 2.075 and b=0.990 with an R^2 value of 0.500. A value for the enhancement factor coefficient of c = 1.380 was found. The R^2 value found using Equation (7) to predict the

relative runup was $R^2 = 0.652$. This represents a 74% improvement over $R^2 = 0.373$ that was found for using Equation (1) with coefficients based on all of the test runs (non-breaking and breaking cases). $R_{2\%}/H_{mo}$ multiplied by the enhancement factor γ_b as a function of ξ_{Lp} along with Equation (7) is shown in Fig. 5.

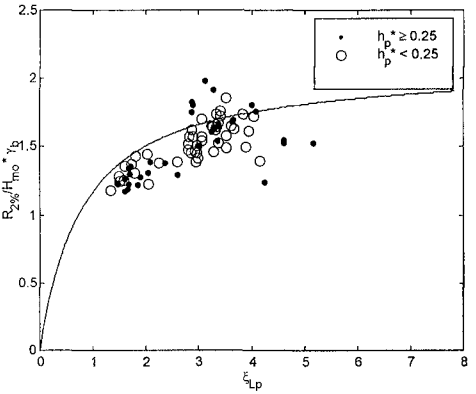

FIG. 5. $R_{2\%}/H_{mo}$ * γ_b as a Function of ξ_{Lp} with Equation (7)

The addition of a wave steepness term ($2\pi H_{mo}/gT_p^2$) to a depth term (d_s/H_{mo}) in the enhancement factor resulted in a slightly improved model for wave runup. The R^2 value of the model with an enhancement factor based on h_p* was $R^2 = 0.652$ compared with $R^2 = 0.567$ for the model with an enhancement factor based on H_{mo}/d_s. This represents an additional improvement of 15%.

Table 2 is a summary table showing the formulas that have been developed to predict the runup along with the values of the empirical coefficients. Also shown in the table are the R^2 values for each model.

Wave Reflection

The measured reflection coefficient at the toe of the structure, K_{rm} is a function of ξ_{Lp}, the surf similarity parameter found using the local wavelength at the toe of the structure. In Fig. 6 the data are grouped according to d_s. In this figure, a trend of higher reflection coefficients for a given value of the surf similarity parameter with decreasing depth can be seen. The measured reflection coefficients for the test runs where $d_s = 0.105$ m are generally higher than the test runs where $d_s = 0.20$ m which are in turn generally higher than the test runs where $d_s = 0.40$ m. Interestingly, this trend can also be seen in Fig. 7 where K_{rm} is plotted as a function of ξ_{Lo} although the effect of d_s is not as pronounced. When $R_{2\%}/H_{mo}$ is plotted as a function of ξ_{Lo} with d_s indicated, the effect of d_s on $R_{2\%}/H_{mo}$ is not as evident.

TABLE 2. Summary of Runup Formulas

Formula	a	b	c	d	R^2
$\frac{R_{2\%}}{H_{mo}} = \frac{a\xi_{Lp}}{1+b\xi_{Lp}}$	2.108	0.939	-	-	0.373
$\frac{R_{2\%}}{H_{mo}} = \frac{a\xi_{Lp}}{1+b\xi_{Lp}} \frac{1}{\gamma_{ds}}$ $\gamma_{ds} = 1 - c\left(\frac{H_{mo}}{d_s} - 0.4\right)^d$ for $\gamma_{ds} > 0.4$ $\gamma_\beta = 1$ for $\gamma_b \le 0.4$	2.181	1.059	0.220	0.389	0.567
$\frac{R_{2\%}}{H_{mo}} = \frac{a\xi_{Lp}}{1+b\xi_{Lp}} \frac{1}{\gamma_b}$ $\gamma_b = \left(1 - (0.25 - h_p^*)^c\right)$ for $\gamma_b < 0.25$ $\gamma_b = 1$ for $\gamma_b \ge 0.25$	2.070	0.846	1.380	-	0.652

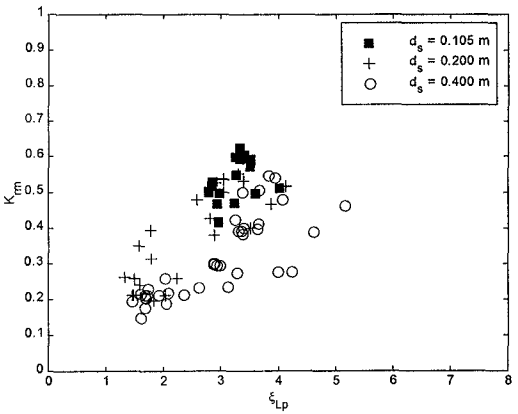

FIG. 6. K_{rm} as a function of ξ_{Lp} with d_s Indicated

A different approach to describe the effects of depth-limited conditions on wave reflection was employed than was used to describe wave runup in depth-limited conditions. There are several limitations to using the surf similarity parameter to parameterize wave reflection. For example, with all variables fixed, the observed reflection coefficient increases with an increasing wave height, while most models based on the surf similarity alone predict the opposite (Seelig and Ahrens 1995). Additionally, the reflection, which has been shown here and

by others (e.g., Davidson et al., 1996; Ward and Ahrens, 1992) to be influenced by the water depth at the toe of the structure, has been typically ignored in prediction models. For these reasons, the method of Seelig and Ahrens (1995) was analyzed in detail to see whether it could be used to describe wave reflection in depth-limited conditions without modification, and if the model failed in depth-limited conditions, what modifications would be required to extend the model to include cases where depth-limited conditions exist.

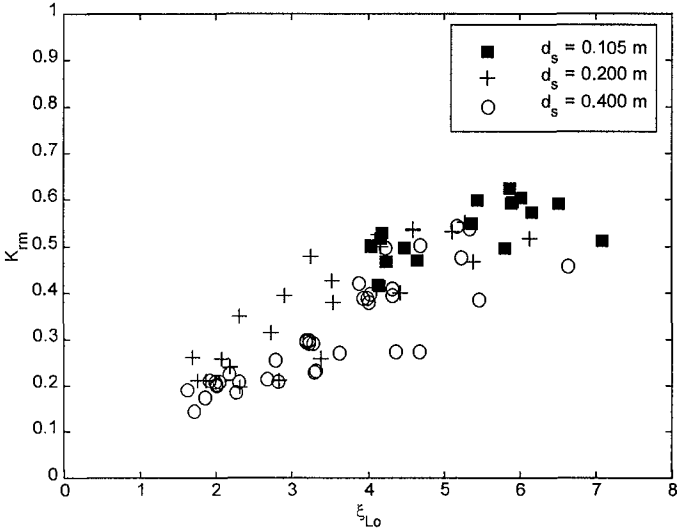

FIG. 7 K_{rm} as a Function of ξ_{Lo} with d_s Indicated

Seelig and Ahrens (1995) make use of H_{mo}/d_s as a water depth parameter in their formulas. As was discussed earlier and shown in Fig. 2 , H_{mo}/d_s can be used to describe the wave conditions at the toe of the structure and correlates well with *Br*. *Br* increases sharply from zero for values of $H_{mo}/d_s > 0.4$. The measured and predicted reflection coefficients found using the model of Seelig and Ahrens is shown in Fig. 8. Here the data points are separated into groups of less or greater than $H_{mo}/d_s = 0.4$. It is clear from the figure that the model underpredicts the reflection coefficient for values of $H_{mo}/d_s > 0.4$. Seelig and Ahrens' formulation for breaking conditions contains H_{mo}/d_s as a depth term with an empirical coefficient. This formula may be adjusted as

$$Kr = 1 - \exp\left[-0.06(\xi_{Lo})^{2.4} - a\left(\frac{H_{mo}}{d_s}\right) * fr\right] \tag{10}$$

where a is the empirical coefficient associated with the depth term. The correction factor fr is given by

$$fr = 0.16 + \left(-0.4 + 0.5(P) * \ln\left(\frac{D_{50}}{H_{mo}}\right)\right) \tag{11}$$

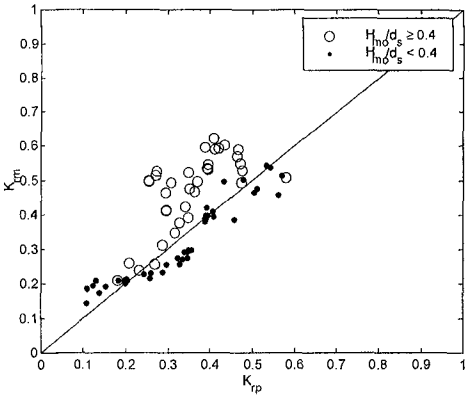

FIG. 8 Measured and Predicted Reflection Coefficient with H_{mo}/d_s Indicated Using Seelig and Ahrens (1995)

Seelig and Ahrens (1995) suggested a value for a of 0.5 for cases where $H_{mo}/d_s < 0.4$ and 0.6 for cases where $H_{mo}/d_s > 0.4$. This coefficient was reevaluated using the present data for the cases where $\xi_{Lp} < 2.5$ and $H_{mo}/d_s > 0.4$. Based on the analysis of this subset of tests it is recommended that the empirical coefficient, a, be raised from 0.6 to 0.76. The R^2 value for the measured data where $H_{mo}/d_s > 0.4$ and $\xi_{Lp} < 2.5$ with the predicted values using Equation (10) with $a = 0.76$ is $R^2 = 0.823$. This compares with $R^2 = 0.720$ for the measured data where $H_{mo}/d_s > 0.4$ and $\xi_{Lp} < 2.5$ with the predicted values using Equation (10) with $a = 0.5$, a difference of 13%.

Seelig and Ahrens' formula for non-breaking also contains a depth term. This equation may be adjusted as

$$K_r = \frac{1}{1 + \lambda^{1.57} \exp(\theta)} \tag{12}$$

where

$$\lambda = \frac{d_x \cot\theta}{L_p} \tag{13}$$

and

$$\alpha = 2.29\left[(\cot\theta)^{0.3}\left(\frac{D_{50}}{L_p}\right)^{0.15}\left(1+\frac{H_{mo}}{d_s}\right)^{b}+\frac{P^{0.4}}{(\cot\theta)^{0.7}}\right] \tag{14}$$

where P is the Van der Meer permeability factor, and the empirical coefficient for the depth term, b, is given in Equation (14). Based on an analysis of the tests where $\xi_{Lp} > 4$ and $H_{mo}/d_s > 0.4$, it is recommended that the coefficient b be lowered from 1.5 to 1.2. The R^2 value for the non-breaking cases using to predict the reflection is $R^2 = 0.239$. Using Equation (12) and the new value for b of 1.2, $R^2 = 0.481$, an improvement of 64%.

The method for predicting reflection coefficients for transition cases where $2.5 < \xi_{Lp} < 4.0$ remains unchanged from Seelig and Ahrens (1995) except that the new formulation for shallow water cases where $H_{mo}/d_s < 0.4$ is to be used. The transitional reflection coefficient K_{rt} is given by

$$K_{rt} = \left(\frac{4-\xi_{1,o}}{1.5}\right)K_{rb} + \left(\frac{\xi_{1,o}-2.5}{1.5}\right)K_{rnb} \tag{15}$$

where K_{rnb} is the predicted reflection coefficient for non-breaking waves given by Equation (10) and K_{rb} is the predicted reflection coefficient for breaking waves given by Equation (12).

The reflection coefficients for the transitional cases where $2.5 < \xi_{Lp} < 4.0$ are predicted using Equation (15) with the modified formulas. The R^2 value for the transition cases using Equation (15) and the original formulas of Seelig and Ahrens is $R^2 = 0.748$, and $R^2 = 0.794$ for the transitional cases using the new formulations.

The measured and predicted reflection coefficients for all of the test runs are shown in Fig. 9. The data are separated according to H_{mo}/d_s. The data points indicated by a solid dot are the cases where $H_{mo}/d_s < 0.4$ (no wave breaking before structure). The predicted reflection coefficients for these points were determining using the original methods of Seelig and Ahrens (1995). The data points indicated by a circle are the cases for which $H_{mo}/d_s > 0.4$ (wave breaking before structure). For these points the modifications to the methods of Seelig and Ahrens (1995) for depth-limited conditions was used.

Conclusions

Accurate methods to predict wave runup and wave reflection from coastal structures that are both robust and relatively simple to use are required by engineers to design safe and cost effective protection systems. Many studies have been undertaken to quantify these parameters; however, there have been relatively few investigations performed with depth-limited conditions.

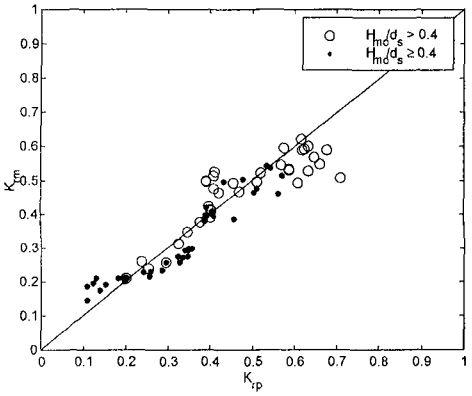

FIG. 9 Measured and Predicted Reflection Coefficients Using Modified Seelig and Ahrens (1995)

Previously developed models to predict 2% wave runup level, which are almost exclusively based on some form of the surf similarity parameter, accurately predict the general trend of increasing wave runup with increasing surf similarity parameter. However, some of the models overpredict $R_{2\%}$ (Ahrens and Heimbaugh 1988) while others underpredict $R_{2\%}$ (Van der Meer and Janssen 1995).

A clear trend of increasing wave runup with decreasing depth for a given value of ξ_{Lp} was observed. This could have serious implications for design engineers since empirical models that are based solely on model tests undertaken in relatively deep water may be non-conservative for design cases where the revetment is located in the surf zone.

A new empirical model to predict the 2% runup level on coastal revetments was presented that incorporates the effects of depth-limited conditions. The model takes the form of existing models (Ahrens and Heimbaugh 1988) that had been tested and employed often in the coastal field, and makes use of a new enhancement factor to account for the effects of depth-limited conditions.

The empirical formulas of Seelig and Ahrens (1995) for wave reflection from coastal structures accurately predicted the reflection coefficients for the cases where the water depth at the toe of the structure was relatively deep and no wave breaking occurred before the structure. However, at the shallower water depths where wave breaking occurred over the sloping foreshore in front of the structure, the model underpredicted the reflection coefficients. A modification to empirical coefficients of the depth terms, H_{mo}/d_s, in the formulas was made for cases where $H_{mo}/d_s > 0.4$ to extend the model to accurately predict the reflection coefficient in depth-limited conditions.

References

Ahrens, J. P., and Heimbaugh, M. S. (1988). "Irregular wave runup on riprap revetments." *J. Wtrwy., Ports, Coast., and Oc. Engrg.*, 114 (4), 524-530.

Allsop, N. W. H., Besley, P., and Madurini, L. (1995). "Overtopping performance of vertical and composite breakwaters, seawalls and low reflection alternatives." *Proc. MCS Project*, Paper 4.6, University of Hanover.

Besley P., Stewart T. and Allsop N. W. H. (1998). "Overtopping of vertical structures: new prediction methods to account for shallow water conditions." *Proc. Coast. Struc. and Break. Conf. '98,* ICEL.

Davidson, M. A., Bird, P. A. D., Bullock, G. N. and Huntley, D. A. (1996). "A new non-dimensional number for the analysis of wave reflection from rubble mound breakwaters." *Coastal Engrg.*, 28, 93-120.

Durand, N., and Allsop, N. W. H., (1997). "Effects of steep bed slopes on depth-limited wave breaking." *Proc. Waves '97*, ASCE, New York, NY, 1400-1413.

Goda, Y. G., and Suzuki, Y. (1976). "Estimation of incident and reflected waves in random wave experiments." *Proc., 15th Coast. Engrg. Conf.*, ASCE, New York, NY, 828-845.

Kobayashi N., and Raichle A. W. (1994). "Irregular wave overtopping of revetments in surf zones." *J. Wtrwy, Ports, Coast., and Oc. Engrg.*, ASCE, 120(1), 56-73.

Rathbun, J. R. (1998). "Wave runup and reflection from coastal structures in depth-limited conditions." M.S. Thesis, Texas A&M University, College Station, TX.

Seelig. P. E., and Ahrens, J. P. (1995). "Wave reflection and energy dissipation by coastal structures." *Wave Forces on Inclined and Vertical Wall Structures* (Kobayashi and Demirbiliek, eds.) ASCE, 28-51.

Van der Meer, J. W., and Stam, C. J. M. (1992). "Wave runup on smooth and rock slopes of coastal structures." *J. Wtrwy, Ports, Coast., and Oc. Engrg.*, 118(5), 534-550.

Van der Meer, J. W., and Janssen, J. P. F. M. (1995). "Wave runup on smooth and rock slopes of coastal structures." *Wave Forces on Inclined and Vertical Wall Structures* (Kobayashi and Demirbiliek, eds.) ASCE, 1-27.

Ward, D. L., and Ahrens, J. P. (1992). "Laboratory study of a dynamic berm revetment." *TR-CERC-92-1*, USACE, Vicksburg, MS.

WIND EFFECTS ON RUNUP AND BREAKWATER CREST DESIGN

Josep R. Medina[1]

Abstract

Estimation of the run-up and overtopping rates corresponding to breakwaters is a critical aspect for designing. Although it is widely assumed that onshore winds significantly increase runup and overtopping, very few design rules and experimental data have been published to estimate the effects of wind on runup and overtopping. A conventional and several *cuenco amortiguador* breakwater cross sections were tested at the UPV wind and wave test facility using wind velocities up to 10 m/s. A neural network modeling using simulated annealing was developed to analyze the experimental results. A preliminary analysis of the results found that wave overtopping was sensitive to wind speed (U>0), while runup seems sensitive only to high wind speed (U> 8 m/s). The runup measurements using capacitance wave gauges placed along the slope are dependent on the distance from the theoretical profile; therefore, a pair of wave gauges placed at $D_{n50}/3$ and 2 $D_{n50}/3$ were used to calculate the measured runup on the conventional breakwater. A significant discrepancy was found between the visual observations of runup on the conventional breakwater and the measured runup using the capacitance wave gauges; it seems that capacitance wave gauges underestimate the runup because of the alteration of the capacity of the water due to air intrusion during the breaking process.

Introduction

Runup and overtopping are two very important issues in planning and designing mound breakwaters. Both the overestimation and the underestimation of runup and overtopping rates of sloping structures during a lifetime have a major impact on the long-term economic efficiency, they unnecessarily increase construction costs or damage to ships, equipment and property protected by the structure. Runup

1) Professor, *Departamento de Transportes, Univ. Politécnica de Valencia, Camino de Vera s/n*, 46022 Valencia, SPAIN. // E-mail: jrmedina@tra.upv.es

and overtopping depend on a variety of structural and environmental variables; armor roughness, structural shape, water depth, bottom slope and core permeability must be taken into consideration for an adequate estimation of the runup during its lifetime. Furthermore, wind waves (heights, periods and directions), long waves (tides, storm surges, shelf waves, seiches, etc.), and onshore winds must be properly characterized in order to define the environmental conditions at the construction site.

Although it is widely assumed that onshore winds significantly increase runup and overtopping, very few design rules and experimental data have been published to estimate the effects of wind on runup and overtopping. SPM(1984) provided the following empirical correction factor for overtopping rates to take into account the winds

$$k = 1.0 + W_f\left(\frac{h - d_s}{R} + 0.1\right)\sin\alpha \qquad (1)$$

in which α is the structure slope, h is the height of the structure crest from the bottom, d_s is the depth at the structure toe, R is the runup on the structure that would occur if the structure were high enough to prevent overtopping corrected for scale effects, and W_f is an empirical coefficient depending on wind speed (W_f = 0.0, 0.5 and 2.0 for wind speed = 0, 30 and 60 miles per hour). However, the wind correction factor given by Eq. 1 can only be used as a general guide with little reliability because no reference to experimental observations is given by SPM(1984).

Ward et al.(1994 and 1996) used the wind and wave test facility at Texas A&M University (32.0 m-long, 0.6 m-wide and 0.9 m-deep). The effects of strong onshore winds on runup and overtopping of both smooth and rough coastal revetments were studied. Wind speeds of 6.5 m/s (50% of blower capacity) showed little effect on runup and overtopping, but wind speeds of 12 m/s (75% of blower capacity) or higher greatly increased both runup and overtopping. The maximum wind speed used in the experiments by Ward et al.(1994 and 1996) was 16 m/s. One of the most relevant final comments of Ward et al.(1994) was that scaling relationships need to be explored to allow runup and overtopping to be considered and applied to prototype coastal structures.

Troch et al.(1996) compared runup and rundown measurements obtained from the prototype monitoring system of the Zeebrugge breakwater, using vertically placed step gauges, with measurements on scaled models from a number of laboratories. Compared to the laboratory runup measurements, it appears that runup on prototype is about 50% higher than runup estimated in laboratories. On the contrary, wave rundown on the prototype was in accordance with laboratory data. An obvious difference between the prototype and laboratory experiments compared by Troch et al.(1996) is the onshore wind, which is present in the prototype but not in the laboratories; therefore, there is a point to support the idea that onshore wind may be the main factor used to explain the

difference in dimensionless runup obtained in the prototype and laboratories.

The spray of salt-water particles transported by strong winds over breaking waves, usually related to high runup and overtopping events, may also cause significant losses in coastal areas (see Matsunaga et al., 1994); experiments in wind tunnels seem to be of critical importance to provide adequate design guidelines to face these phenomena. Matsunaga et al.(1994) and Hashida et al.(1996) used a wind and wave test facility of 32.0 m-long, 0.6 m-wide and 1.30 m-deep. The wind speeds used ranged from 9 m/s to 19 m/s.

Because of the importance of accurate estimates of runup and overtopping rates for adequate breakwater crest designing, within the project OPTICREST (see Rouck et al., 1998) prototype measurements of runup, overtopping and spray will be taken at Zeebrugge (Belgium) and laboratory tests will be conducted in the wind and wave facility at the *Universidad Politécnica de Valencia* (UPV). This paper shows some preliminary results from tests on deep water models of breakwaters: (1) *cuenco amortiguador* type and (2) Zeebrugge type. The dimensions of the UPV wind and wave facility are 30.0 m-long, 1.2 m-wide and 1.2 m-deep, and the maximum wind speed used in the experiments was 10 m/s.

Wave and Wind Tunnel Testing

Most of the work published on wind tunneling is refers to experimental information useful for solving aerodynamic problems for the aeronautical industry. Compared to supersonic and hypersonic wind tunnels, low-speed wind tunnels are facilities using U<150 m/s; however, our problem belongs to a very special case of the relatively small nonaeronautical group classified as boundary-layer wind tunnels (BLWT) which typically use air at atmospheric pressure and operating speeds in the range of 10 m/s to 50 m/s (see WTMBS, 1987). Aeroelastic simulations in BLWT for buildings and structures and experiments in meteorological and environmental wind tunnels are under relatively similar constrains to those necessary for modeling waves, run-up, overtopping and spray; however, maritime applications have additional problems like the variations of MWL induced by wind and the resonant infragravity waves in wave flumes and basins. As a first approximation, Froude and Reynolds numbers appear to be more important than Cauchy, Rossby and Mach numbers for modeling run-up and overtopping.

Fig. 1 shows a longitudinal cross section of the UPV wind and wave test facility (dimensions in cm). The wavemaker is a piston type hydraulic controlled able to generate regular and irregular waves without active absorption. The power of the blower is controlled manually to fix a specific wind speed for each test; the wind speed is measured between the air intake and the model. Only regular waves were used in the experiments described in this paper; the maximum wind speed was 10 m/s and the number of waves was selected to prevent multirreflected waves from attacking the

model. The time series for controlling the wavemaker movement were calculated using the classical frequency domain transfer function for piston movement (see Goda, 1985) with an additional linear transition function in the time domain to prevent unrealistic accelerations of the wave paddle at the beginning and the end of each test. The maximum estimated incident wave heights attacking the model was compared to the maximum measured and visual runup.

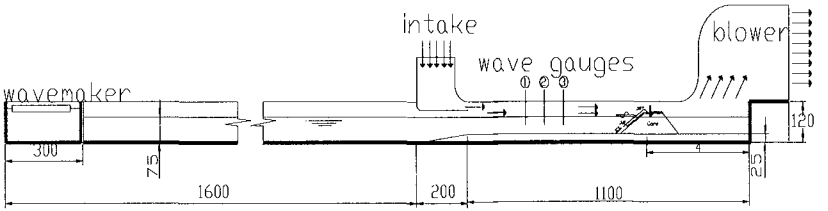

Figure 1. Longitudinal Cross Section of the UPV Wind and Wave Test Facility

The appropriate scaling relationships between wind speed, wave celerity and wave group velocity are not known for a proper modelization of the runup and overtopping phenomena (see Ward et al., 1994). Therefore, Froude similarity was chosen and a variety of wind speeds in the range of 0 to 10 m/s were used to study runup in the UPV wave and wind test facility. A neural network modeling was used to analyze the results given the lack of knowledge about the proper dimensionless variables to be considered and the number of significant structural variables to be taken into account.

Neural Network Modeling Using Simulated Annealing

The Neural Network (NN) systems belong to a group of relatively new optimization techniques commonly used in artificial intelligence (see Ansari and Hou, 1997). Neural networks (NN), simulated annealing (SA), genetic algorithms (GA) and fuzzy systems (FS) are some of the new optimization techniques which have proven to be very effective in solving difficult optimization problems. In particular, the NN are a computing device inspired by the function of the neurological system of the brain; they are composed of many parallel and interconnected computing units named artificial neurons. There are a variety of NN models which may be classified (see Kosko, 1992) depending on whether they learn with supervision and whether they contain feedbacks. On the one hand, the human brain belongs to the group of highly complex unsupervised NN with feedbacks; on the other hand, the relatively simple supervised feedforward NN is the most common structure used for NN modeling.

Usually, a supervised feedforward multilayer NN with only one hidden layer and a backpropagation learning algorithm is used for NN modeling of laboratory

experiments. Mase et al.(1995) used a NN model with backpropagation to re-analyze laboratory measurements first examined by Van der Meer(1988) in assessing the stability of rubble-mound breakwaters. Van Gent and Van den Boogaard(1998) used a NN model with backpropagation to analyze horizontal forces on vertical breakwaters measured by a group of laboratories. The number of artificial neurons in the first layer is fitted to the number of input variables (structural and environmental variables), the number of neurons in the third layer is fitted to the number of output variables (structural response variables), and the number of neurons in the hidden layer has to be subjectively chosen to avoid both over-simplicity and overlearning. If the number of neurons in the hidden layer is too small, the NN may be too simple to properly describe the relationship between input and output variables. If the number of neurons in the hidden layer is too large, the NN model fits the data used for learning but it does not fit the test data which are not used in the learning process. Therefore, the NN has not captured the characteristics of the underlying process and it is said that the NN has overlearned. The overlearning problem in this kind of NN modeling is related to the ratio between number of parameters in the NN model and the number of data sets used in the learning process; if this ratio is higher than 10%, the overlearning problem is likely to occur. Because the number of NN parameters roughly grows linearly with the product of the number of neurons in the input layer by the number of neurons in the hidden layer, the complexity of the model is greatly limited by the amount of data available. Furthermore, because the backpropagation algorithm used in the NN teaching is a gradient descent method, the model may probably find a local optimum NN instead a global optimum NN.

In order to reduce the shortcomings in the use of the gradient descent backpropagation algorithm, a simulated annealing (SA) algorithm has been implemented to define the appropriate NN for modeling the results of the runup experiments described in this paper. The SA is a common tool in artificial intelligence (see Ansari and Hou, 1997); SA simulates the process in which liquids crystalize: at high temperatures the energetic particles are free to rearrange, while at low temperatures the particles lose mobility, finally reaching a state of equilibrium, having minimum energy. The entropy of a substance decreases monotonically during annealing, leading the substance to an ordered crystalline structure if the temperature is slowly lowered to relax to thermal equilibrium at each temperature. Alternative implementations of the SA concept are described by Laarhoven and Aarts(1992) who also provide a review of SA methods and their applications. In the tests presented in this paper, incident and reflected waves were separated using the new LASA method (see Medina, 1998) which is a time-domain method able to deal with nonstationary and nonlinear wave trains using local approximations and simulated annealing.

In this paper, a NN structure similar to that used by Mase et al.(1995) was considered, but instead of using a backpropagation algorithm, a SA algorithm was used in the NN learning process. Two-parameter artificial neurons similar to those used by Mase et al.(1995) were considered; the sigmoidal curve was defined by one threshold parameter and one amplification parameter for the logistic function. Each connection

between neurons of consecutive layers has its corresponding weighting parameter. In addition to the common multilayer feedforward NN structure (named principal NN), a parallel structure of boolean parameters was considered to either activate or disactivate the parameters of the NN (named activation structure). Each parameter of the principal NN has its corresponding boolean activation parameter in the activation structure. If a boolean parameter is set to "1" the corresponding parameter in the principal NN works normally; on the contrary, if a boolean parameter is set to "0" the corresponding parameter in the principal NN works with the corresponding defect value. The defect values are zero for the weighting parameters in connections among neurons, zero for threshold parameters in neurons, and one for amplification parameters of the logistic function in neurons. The use of a feedforward NN associated with a parallel activation boolean structure allows for an optimization of the NN topology. The SA algorithm will not only optimize the parameters of the NN, but also the topology, disconnecting parameters, neurons, and inputs if they are not relevant to improve the NN model. Fig. 2 shows a typical NN model using SA for optimization; in addition to the disconnected input and hidden neurons, some of the remaining active neurons have one or no active parameters.

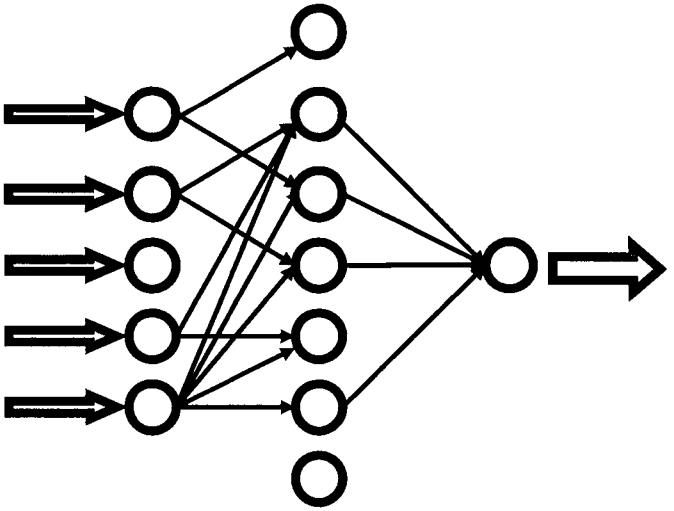

Figure 2. Typical NN Model Using Simulated Annealing

The NN model after the SA optimization is a parsimonious NN. The ratio between the number of NN active parameters and the number of data sets used for the learning process ranged from 3% to 5%; therefore, it is easy to understand why no overlearning problem was detected in any of the applications made in this paper. The use of a SA algorithm to optimize the NN model provided more than just good models to relate input variables (H, Ir, ...) with output variables (runup); it gave a clear

indication of what input variables were irrelevant for modeling the process under study. This characteristic is quite convenient when NN modeling is used to analyze phenomena and processes which are little known, as is the case of the influence of wind on runup and overtopping considered in this paper.

In order to obtain the parsimonious NN mentioned above, certain details of the most critical aspects of the SA algorithm used in this paper must be described. Medina(1998) defines a SA algorithm in seven steps: (1)cost function, (2)generation mechanism, (3)initial solution, (4)initial control parameter, (5)reduction of control parameter, (6)length of Markov chains, and (7)stop criterion. In this paper, the most critical points are the cost function and the generation mechanism; the initial solution was a principal NN of parameters with random values in a given interval and the activation structure with all activation parameters set to "1". Steps 4 to 7 may be critical given time constrains, but in this case a reasonably good NN model can be obtained in a few minutes with a personal computer.

The cost function used in this paper for the SA algorithm has two components: the relative mean squared error and the ratio between the number of active parameters and the number of data sets used for the NN learning process. If only the relative mean squared error is used as a cost function, the resulting NN model using SA would be a least squares model similar to that obtained with the backpropagation algorithm. It may pose as an additional advantage for the SA algorithm because it prevents becoming trapped in a local minimum. However, the main advantage of the SA algorithm is obtained when a factor measuring parsimony is added to the cost function; in this case, the SA not only find good estimates of the NN parameters, but SA also eliminates those which are not significant to explain the relationship between input and output variables. The relative weight between the two factors in the cost function is decided by the operator; in this paper, the weight of relative mean squares error factor was three times the weight of the parsimony factor. Indeed, although the relative weight of the parsimony factor was very low, the impact on the NN topology is significant.

The generation mechanism defines the new NN in the neighborhood of the old NN. In this paper, a random change of parameters and magnitude of parameters, as well as a random change of the boolean parameters in the activation structure is made to create the new NN in the neighborhood of the old NN. However, the probability of changes in the activation structure must be controlled for an adequate exploration of the search space. During the first Markov chains, when the temperature is high and the NN parameters are far from the optimum, the activation structure must be set to "1" to prevent its anticipated convergence to a sub-optimal solution. Once the SA has found a reasonably good NN model, a solution similar to what would be obtained using a backpropagation algorithm, then a small probability of change from "1" to "0" and from "0" to "1" is fixed for the parameters in the activation structure. With this small probability of activation and disactivation of parameters and connections between neurons, the SA also explores alternative NN topologies by pruning the useless NN connections.

Experiments with *Cuenco Amortiguador* Breakwater Models

Fig. 3 shows the two *cuenco amortiguador* type breakwater cross sections tested in the UPV wave and wind tunnel shown in Fig. 1. The *cuenco amortiguador* concept is a special breakwater crest design introduced two decades ago in Spain by Aguado-Gallego and Sánchez-Naverac(1978). The idea was to reduce the breakwater crest elevation in cases where the aesthetic conditions were very restrictive, as is the case in many touristic areas. During the last two decades, several *cuenco amortiguador* type of breakwaters have been built in Spain (Fuengirola, Marbella, Torre del Mar, Denia, etc.). The design rules currently used in Spain for this type of breakwaters are based on a series of scale model tests provided by Aguado-Gallego and Sánchez-Naverac(1978) with regular waves without wind. These authors identified twelve structural and environmental variables, not the wind, but the experiments only covered a limited number of cases. The main conclusion was that breakwater crest elevation could be reduced by about 30% with respect to the currently used Iribarren rule*: crest elevation is approximately equal to 1.5 the design wave height.* However, it is obvious that the crest width and cap elevation depends critically on runup and overtopping which are related to onshore winds. Therefore, a series of experiments were conducted to check the influence of onshore winds on the runup as measured on the crown wall of the *cuenco amortiguador* breakwater cross section shown in Fig. 3, which is related to the overtopping rate of the conventional armor.

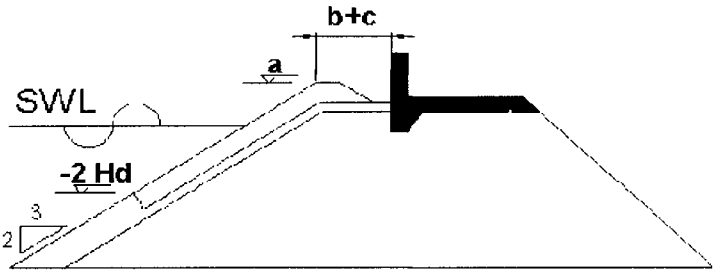

Figure 3. *Cuenco Amortiguador* Breakwater Cross Section.

The armor was built of angular quarrystones for deep water conditions; the median weight was W_{50}= 130g, the slope was 3/2 and the armor, filter and core stones were the same as those used in the tests described by Medina(1992). In the experiments described in this paper, a conventional and a D-armor cross section were also tested but no significant difference in runup was observed; therefore, in this paper the test results refer only to the conventional armor section shown in Fig. 3. Based on the preliminary results found by Aguado-Gallego and Sánchez-Naverac(1978), the structural variables selected to be analyzed in this paper were the armor crest elevation and the total width of the *cuenco*. The higher the armor crest elevation on the SWL (a) and the wider the *cuenco amortiguador* (b+c), the lower the runup measured on the crown wall. The

selected environmental variables were: wave height, Iribarren's number and wind speed. The armor crest elevation refers to the SWL and was fixed to {a}= 4.0 D_{n50} for the first series of experiments; however, the tests were repeated increasing and decreasing the water level by 1.35 D_{n50} in order to analyze the influence of a change in the armor crest elevation. Three *cuenco amortiguador* widths were considered in the experiment: {b+c}= 5.0 D_{n50}, 6.5 D_{n50} and 10.0 D_{n50}.

Because of the special profile of the *cuenco amortiguador* breakwater, the runup measured on the crown wall is directly related to the overtopping rate on the crest of the armor layer. Therefore, the effects of onshore wind on runup measured on the crown wall of the *cuenco amortiguador* breakwaters may be considered similar to the effects of wind on the overtopping of conventional breakwaters. If the volume of water overtopping the armor layer is small, the overtopped water is drained through the *cuenco amortiguador* without reaching the crown wall and the measured runup is null. On the contrary, if the overtopped volume is large, the runup on the crown wall increases with increasing overtopping rates. The runup was visually measured on a scale fixed on the crown wall and was defined as the distance between the maximum water elevation on the crown wall and the SWL; if the water did not reach the crown wall, the runup was considered zero.

375 tests with regular waves were completed using wind speeds between 3 and 10 m/s; in addition, 875 tests were completed without wind. In only 25% of the tests the observed overtopping rate was large enough to reach the crown wall; in the other 75% of the tests, the measurement of runup was Ru=0. NN modeling is usually appropriate to analyze multivariable nonlinear relationships between input and output variables when there is a large amount of data and the knowledge about the underlying process is low (see Kosko, 1992). However, a first direct application of the NN methodology using SA described above gave only a poor result with a correlation coefficient lower than 60% between measured Ru and estimated Ru. The main reason for this poor result was attributed to the extremely high nonlinear relationship between the measured Ru (the output variable) and the structural and environmental variables (input variables), with 75% null Ru in the data.

The analysis of the poor results obtained with the first direct application of the NN methodology shown above led to a second NN modeling considering a chain of two different NN for two different purposes. The first NN were used as classifiers of data in two groups: input associated with Ru=0 and input associated with Ru>0. The second NN were used to estimate the Ru when the first NN identified conditions for reaching the crown wall (Ru>0). This NN modeling using a chain of two different neural networks gave satisfactory results with a correlation coefficient between measured Ru and estimated Ru higher than 90%. About 80% of the data were randomly chosen for the NN learning process while the rest of the data was used for testing the NN model. The ratio between the number of parameters in the NN using SA ranged from 3% to 5% and no overlearning problem was detected. Fig. 4 compares the observed Ru on the crown wall and the estimated Ru using the described NN modeling.

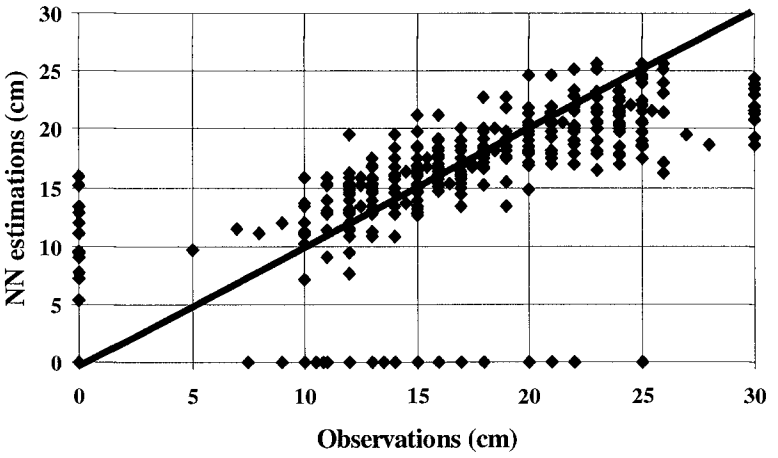

Figure 4. Measured vs Estimated Ru of the *Cuenco Amortiguador*

Five input variables were used in both NN: wave height (H), Iribarren's number (Ir), wind speed (U), crest elevation (a) and *cuenco amortiguador* width (b+c). It is interesting to point out that the SA process eliminated only the input wind speed (U) from the NN used as classifier; this fact suggests that the wind speed is not relevant for predicting if the water will reach the crown wall or not. However, the wind speeds were not eliminated from the NN which predicted the Ru once the conditions were classified as Ru>0 by the first NN. This asymmetric behavior suggests that onshore wind has an irrelevant effect on runup of conventional breakwaters but a significant effect on large overtopping discharges of conventional breakwaters.

Experiments with the Zeebrugge Type Breakwater Model

Troch et al.(1996) described the prototype monitoring system of the Zeebrugge breakwater, equipped with high precision vertical step resistance wave gauges to measure runup and rundown. Fig. 5 shows the deep water Zeebrugge type breakwater cross section tested in the UPV wind and wave facility (dimensions in cm); the armor layer was made of regular cubes instead of the antifer cubes placed in the Zeebrugge breakwater. The nominal diameters of the armor layer, secondary layer and core were D_{n50}=6.00 cm, 1.71 cm, and 1.26 cm respectively. The runup was measured visually placing cubes with different colors at different levels, using two capacitance wave gauges placed along the slope at distances of 2 cm and 4 cm from the theoretical profile, and using two wave gauges placed vertically through the armor layer. The maximum elevation of water on the armor was directly measured by the two inclined wave gauges and by visual observation; the vertical wave gauges provided additional measurements at fixed points, but this additional information is not analyzed in this paper.

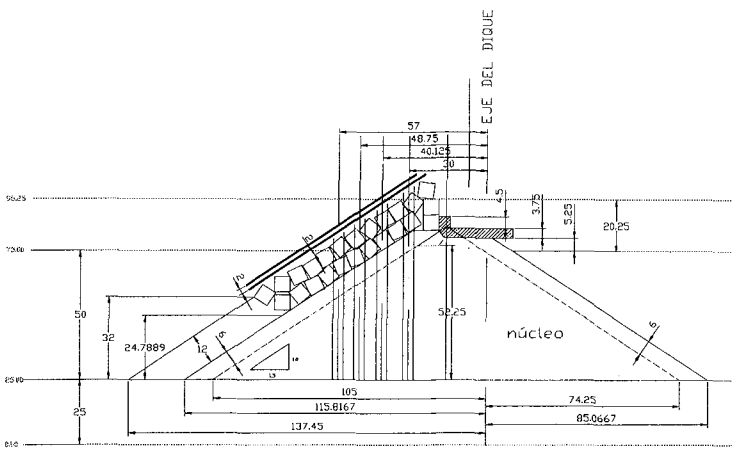

Figure 5. Cross Section of Deep Water Zeebrugge Type Breakwater Model

A series of tests with regular waves, changing wave height (H), Iribarren's number (Ir), and wind speed were carried out in the UPV wind and wave facility. 385 data sets relating the input conditions (H, Ir and U) and the output (Ru) were used to apply the NN methodology using SA described above. However, before starting the NN modeling of runup corresponding to this conventional breakwater, it was first necessary to clarify what should be considered the runup of a wave breaking on a sloping structure. Visual observation of runup may be biased in comparison to measurements of runup taken with wave gauges. On one hand, the human eye is subjective in estimating the maximum elevation of the water level on the slope. On the other hand, it is impossible to place the wave gauge exactly in the external profile of the armor where the runup should be measured, and wave gauges are not calibrated to take into consideration the air intrusion generated during the breaking process.

The Ru measured by the two inclined wave gauges were highly correlated but biased; usually, the runup measured by the wave gauge nearest to the theoretical profile were higher. Therefore, a linear estimation of the runup on the theoretical profile was calculated from the runup measurements taken by the two wave gauges parallel to the slope at distances 1/3 D_{n50} and 2/3 D_{n50} respectively. Fig. 6 compares this linearly estimated runup versus visual observations of runup and measured runup by the wave gauge closest to the theoretical profile (sensor 4). Because measured runup decreases depending on the distance of the inclined wave gauge from the theoretical profile, and it is impossible to place the wave gauge exactly in the theoretical profile, the two wave gauges linearly estimated runup were considered in Fig. 7 as the actual measured runup of the sloping structure. Fig. 6 clearly shows a significant bias between measured and visual observations of runup on a conventional sloping structure. In this case, the wave gauges measured the capacity of the instrument in the water and were unable to take

into consideration the air intrusion always present during the breaking process. Therefore, runup measured on a prototype scale should be expected to be higher than runup measured in the laboratory with wave gauges, although the measured runup in the laboratory was corrected to take into consideration the distance of the wave gauge from the theoretical profile. Additionally, a precise description of the experimental setup and the variables is necessary to compare results from different laboratories.

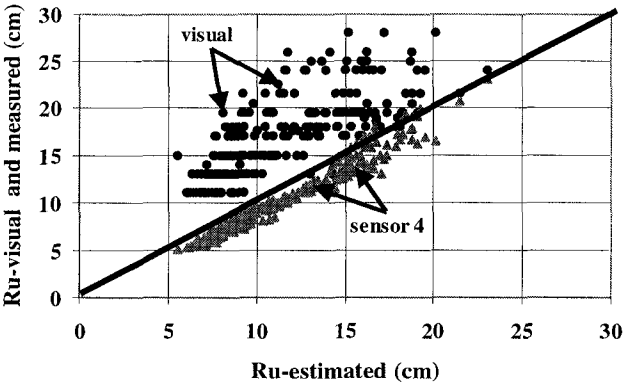

Figure 6. Comparison of Visually Observed vs Measured Runup

The visually observed runup was significantly higher than the linearly calculated runup based on the measurements taken by the two wave gauges placed parallel to the slope, but the dispersions of the visual observations shown in Fig. 6 were also much higher. The NN modeling methodology described previously was applied to the input-output data sets using the linearly calculated runup as the output Ru on the sloping structure. Wind speed was not eliminated as a significant input variable by the SA process, but the NN produced Ru very sensitive only to inputs H and Ir. According to the result of the NN modeling, Ru was insensitive to low wind speed and increased slightly only to high wind speed (U>8m/s).

Fig. 7 compares the output of the NN model and the runup measured using the two wave gauges parallel to the slope; the overlearning problem was not detected, the correlation coefficient was higher than 90% and the ratio number of parameters to number of data sets was lower than 5%.

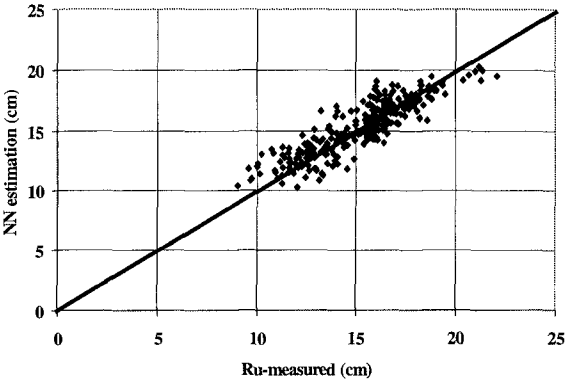

Figure 7. Neural Network Estimation of Ru

Conclusions

Deep water model tests on breakwaters models of the *cuenco amortiguador* type and a Zeebrugge type were conducted in the UPV wind and wave facility using regular waves and windspeeds up to 10 m/s. The parsimonious neural network models obtained by simulated annealing were found to be very effective in modeling both the runup and the overtopping of conventional breakwaters. The preliminary results from the tests described in this paper are qualitatively in agreement with those obtained by Ward et al.(1996) referring to runup, in the sense that runup is affected only by high onshore wind speeds (U> 8 m/s). Contrary to the results obtained by Ward et al.(1996), a significant influence of onshore winds on overtopping was also found for low wind speeds. The NN modeling using SA not only provided adequate models but also guided the research indicating the most significant variables to be considered in describing the processes under study. Therefore, the NN methodology presented in this paper may be useful not only to analyze runup and overtopping, but also to analyze other little known phenomena.

Acknowledgements

This research was funded by *the Dirección General de Investigación Científica y Técnica* (Spanish Ministry of Education) and the E. C. through grant PB94-0534 and MAS3-CT97-0116 OPTICREST Project . The author wishes to acknowledge the assistance of José Andreu, Jesús Ceniceros and José A. González in collecting the laboratory data. Additionally, it should be mentioned that Vicent Esteban designed the new UPV wind facility, José Aguilar and Juan J. Navarro renewed the UPV wavemaker software, and Adolfo Conesa and Juan J. Conesa developed the NN software.

References

Aguado-Gallego, A. and Sánchez-Naverac, V.(1978). Nuevo Tipo de Sección para Diques en Talud con Espaldón, (in Spanish). *Revista de Obras Públicas*, May 1978, 353-359.

Ansari, N., and Hou, E.(1997). *Computational Intelligence for Optimization.* Kluwer Academic Publishers, Boston, USA.

Goda, Y.(1985). *Random Seas and Design of Maritime Structures.* University of Tokyo Press, Tokyo, Japan.

Hashida, M., Matsunaga, N., and Irie, I. (1996). Landward Transport of Spray Generated from a Wave Absorbing Sea Wall. *Proc. ICCE'94,* ASCE, 219-231.

Kosko, B.(1992). *Neural Networks and Fuzzy Systems: A Dynamic Systems Approach to Machine Intelligence.* Prentice Hall, Englewood Cliffs, New Jersey, USA.

Laarhoven, P.J.M. van, and Aarts, E.H.L.(1987). *Simulated Annealing: Theory and Applications.* Kluwer Academic Publishers, Dordrecht, The Netherlands.

Mase, H., Sakamoto, M., and Sakai, T.(1995). Neural Network for Stability Analysis of Rubble-Mound Breakwaters. *J. of Waterway, Port, Coastal and Ocean Engineering*, 121(6), 294-299.

Matsunaga, N., Hashida, M., Mizui, H., and Sugihara, Y. (1994). Quantity of Spray Transported by Strong Winds over Breaking Waves. *Proc. ICCE'94,* ASCE, 219-231.

Medina, J.R.(1992). A Robust Armor Design to Face Uncertainties. *Proc. ICCE'92,* ASCE, 1371-1384.

Medina, J.R.(1998). Estimation of Incident and Reflected Waves Using Simulated Annealing . *J. of Waterway, Port, Coastal and Ocean Engineering* (in review).

Rouck, J. de, Troch, P., Damme, L. van, Eelen, B., and Schlütter, F.(1998). Wave Run-up: Prototype versus Scale Models. *Book of Abstracts of the ICCE'98*, LOC of ICCE'98, 632-633.

***Shore Protection Manual*(1984).** Coastal Eng. Res. Center, Dept. of the Army, Waterways Exp. Stat., Vicksburg, Miss.

Troch, P., De Somer, M., De Rouck, J., Van Damme, L., Vermeir, D., Martens, J.P., and Van Hove, C.(1996). Full Scale Measurements of Wave Attenuation Inside a Rubble Mound Breakwater. *Proc. ICCE'96,* ASCE, 1916-1929.

Van der Meer, J.W. (1988). Deterministic and Probabilistic Design of Breakwater Armor Layer. *J. of Waterway, Port, Coastal and Ocean Engineering*, 114(1), 66-80.

Van Gent, M.R.A., and Van den Boogaard, H.F.P.(1998). Neural Network and Numerical Modelling of Forces on Vertical Structures. *Book of Abstracts of the ICCE'98*, LOC of ICCE'98, 384-385.

Ward, D. L., Wibner, C. G., Zhang, J., and Edge, B.(1994). Wind Effects on Runup and Overtopping. *Proc. ICCE'94,* ASCE, 1687-1699.

Ward, D. L., Zhang, J.,Wibner, C. G. and Cinotto, C.M. (1996). Wind Effects on Runup and Overtopping of Coastal Structures. *Proc. ICCE'96,* ASCE, 2206-2215.

***Wind Tunnel Model Studies of Buildings and Structures* (1987).** Task Committee on Manual Practice for Wind Tunnel Testing of Buildings and Structures of the Committee on Aerodynamics of the Aerospace Division. ASCE Manuals and Reports on Engineering Practice No. 67.

Some Design Aspects of an Absorbing 3D Wavemaker

Hemming A. Schäffer[1]

ABSTRACT

A new absorbing multidirectional wavemaker is under development at the Danish Hydraulic Institute. In this process numerous aspects of the design and control of multielement wavemakers as well as the theory for wave generation and active absorption have been considered. This paper focuses on two specific and specialized points. First, the influence of finite segment width on the wave field generated is analysed for different types of paddle front. In this connection a new criterion for the truncation of directional spectra to be generated is suggested. Second, the appearance and reduction of aliasing problems for 3D active absorption is discussed. Aliasing appears due to the spatial sampling typically used for obtaining a hydrodynamic feedback in the absorption procedure.

INTRODUCTION

A traditional wavemaker is controlled independently of the waves present in its vicinity. Thus, if the waves generated by the wavemaker are reflected from some boundary or construction in the flume or basin, then full re-reflection takes place when these waves return to the wavemaker. The result is an undesirable distortion of the incident wave field.

An absorbing wavemaker attempts to eliminate this problem by including some hydrodynamic feedback signal in the paddle control. Simultaneously with the usual wave generation, reflected waves are absorbed by moving the paddle appropriately.

Absorbing wavemakers for wave flumes are now routinely used in a number of laboratories. For multidirectional wavemakers the simplest option is to use independent absorption control systems for each wavemaker segment. This gives a quasi-3D system, which does not account for wave obliqueness in the absorption procedure. Nevertheless, a quasi-3D system provides a significant improvement over a traditional segmented wavemaker. In very recent years, fully 3D systems have been pursued. Wave obliqueness
is accounted for through a coupling between the control of neighbouring paddle segments. For a review of active absorption methods with emphasis on 3D systems, see Schäffer and Klopman (1997).

[1] Danish Hydraulic Institute, Agern Allé 5, DK-2970 Hørsholm, Denmark, e-mail: has@dhi.dk

At the last ICCE, we presented a fully 3D theory for active absorption of multidirectional waves (Schäffer and Skourup, 1996). Within the framework of linear waves, this theory was developed in the wavenumber-frequency domain (k_y,ω), using the wavenumber component along the wavemaker. The result was a 2D transfer function $F(k_y,\omega)$, relating the amplitude of the wavemaker position $X_a(k_y,\omega)$ to the amplitude of the surface elevation measured along the wavemaker $A(k_y,\omega)$. The same transfer function appeared in the combined generation/absorption problem. Phase relations were accounted for, since F, X_a and A were complex. In order to obtain a physically realisable representation, a 2D digital recursive filter was developed. This filter was designed to have a transfer function approximating $F(k_y,\omega)$, thus giving the wavemaker paddle position $X(m\Delta y,n\Delta t)$ as output when provided with the surface elevation $\eta_0(m\Delta y,n\Delta t)$ measured along the wavemaker as input. Here, y is the coordinate along the wavemaker and t is time. The space-time domain was sampled at $(y,t)=(m\Delta y,n\Delta t)$ where Δy equals the individual paddle width of the segmented wavemaker. A wave elevation gauge was assumed to be mounted on each segment. Schäffer and Skourup tested the absorption algorithm in a numerical wave tank based on the Boundary Integral Equation Method and concluded that the system gave a significant improvement over a quasi-3D system.

One of the shallow water facilities at Danish Hydraulic Institute is now being upgraded with a multidirectional wavemaker and the active absorption system is an important part of this development. The new wavemaker is scheduled to be ready in 1999 and thus the practical performance of the system will be published at a later occasion. The present paper reports a number of investigations made in connection with the design of the multidirectional wavemaker front.

SELECTED DESIGN CONSIDERATIONS

The active absorption depends on the elevation measured directly on the paddle front of the wavemaker. This makes the local wave field very important and it gives a renewed interest in phenomena like evanescent modes and spurious wave generation due to finite paddle width. Since the surface elevation is measured at discrete points in space, aliasing problems must also be considered.

Spurious Waves and Evanescent Modes for Different types of paddle front

The finite spatial resolution Δy of a segmented wavemaker results in spurious waves (see eg Sand, 1979). Let the wavelength along the wavemaker be $L_y=2\pi/|k_y|$ and let the wave direction be θ then if $L_y/\Delta y > \sin|\theta|/(1+\sin|\theta|)$, these appear only as evanescent modes confined to the vicinity of the wavemaker. For high frequencies and large obliqueness, the resolution becomes very coarse, and spurious progressive waves are generated. Since spurious waves in general influence the local wave field and since spurious progressive waves contaminate the whole wave basin, it is interesting to know how large they get. This depends on the variation of the paddle front, and thus we have studied three different types of paddles with a) a constant, b) a linear and c) a cubic spline variation between the discrete points at which the position is controlled. Type a) is often called 'the staircase approximation', while b) is known as a vertically hinged paddle. Type c) requires a flexible paddle and it has probably never been used in practice.

One problem with the flexible paddle is that it needs to be sufficiently rigid to sustain the wave forces. We have estimated that the power required to bend the paddle is consequently in the same order of magnitude as the power required to generate the waves. However, we have

included the flexible paddle in the analysis anyway as it represents the best interpolation one could possibly obtain for this type of problem.

In this paper, we shall refer to the three types of paddle fronts by the shape of their segments, namely as constant, linear and spline elements, respectively. For $L_y/\Delta y=5$, Fig. 1 shows a sketch for each of the three types of elements in comparison with the sinusoid to be approximated.

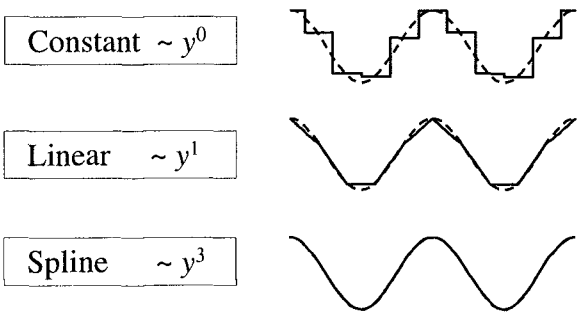

Figure 1. Different types of paddle fronts considered: constant, linear and cubic spline elements. Resolution: $L_y/\Delta y=5$.

Part of this investigation has been made before (Sand, 1979, types a) and b)), with the emphasis on progressive spurious waves. The purpose of the present analysis is twofold. First, we establish a more elaborate condition than just cutting at $L_y/\Delta y = \sin|\theta|/(1+\sin|\theta|)$ when truncating a directional spectrum to be generated. The condition suggested limits the amplitude of progressive spurious waves and it depends on the type of wave paddle. This further supports the decision on which paddle type to chose in multidirectional wavemaker design. Second, we calculate the local wave field in detail for use in connection with active absorption.

Let the paddle position, $X(y_m,t)$ be given as a sinusoid with amplitude X_a sampled at equidistant points,

$$X(y_m,t) = X_a \exp[i(\omega t - k_y y_m)], \quad y_m = m\Delta y \tag{1}$$

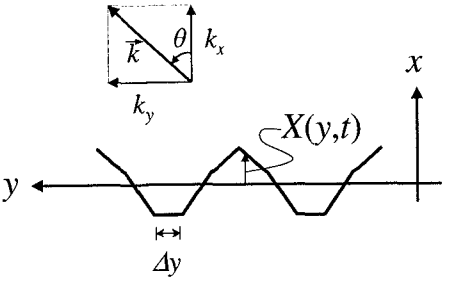

Figure 2. Definition sketch.

see Fig. 2 for a definition sketch. The continuous position, $X(y,t)$ is then determined by the type of paddle front, i.e. the type of interpolation. Generally, we may write

$$X(y,t) = \xi(y) X_a \exp[\omega t], \quad \xi(y_m) = \exp[-ik_y y_m] \tag{2}$$

For constant elements, we have

$$\xi(y) = \xi(y_m), \quad y_{m-1/2} \le y \le y_{m+1/2} \tag{3}$$

For linear and spline elements the interpolation can be written as

$$\begin{aligned} \xi(y) = {} & A(y)\xi(y_m) + B(y)\xi(y_{m+1}) + \\ & + C(y)\xi''(y_m) + D(y)\xi''(y_{m+1}), \quad y_m \le y \le y_{m+1} \end{aligned} \tag{4}$$

where

$$A(y) = (y_{m+1} - y)/\Delta y, \quad B(y) = (y - y_m)/\Delta y \tag{5}$$

For spline elements, we get

$$C(y) = \frac{\Delta y^2}{6} A(A^2 - 1), \quad D(y) = \frac{\Delta y^2}{6} B(B^2 - 1) \tag{6}$$

while these cubic terms vanish for linear elements, i.e. $C(y)=D(y)=0$. For the spline case, it may be verified that (3) and (4) ensure continuity in both $\xi(y)$ and $\xi''(y)$ at $y=y_m$. Further requiring that also $\xi'(y)$ is continuous at $y=y_m$ gives a linear system of $N=L_y/\Delta y$ equations relating $\xi''(y_n)$ to $\xi(y_n)$, assuming an integer number of elements per wavelength along the wavemaker. Due to periodicity of the problem, the coefficient matrix involved is circulant, i.e. each row is identical to the previous one except for being rotated one place to the right. Using the Discrete Fourier Transform, this linear system can be solved for any value of N to give

$$\xi''(y_m) = \xi(y_m)\, 6 \frac{\cos(k_y \Delta y) - 1}{\cos(k_y \Delta y) + 2} \tag{7}$$

It may be shown, that both this and the following results can also be obtained under the assumption that N is a rational number. For continuity reasons we further conjecture that also irrational values of N are allowed. For simplicity, however, we shall maintain the assumption of integer N in the following derivations. Expanding $\xi(y)$ in a Fourier series

$$\xi(y) = \sum_{n=-\infty}^{\infty} a_n \exp[ink_y y], \quad a_n = \frac{1}{L_y} \int_0^{L_y} \xi(y) \exp[-ink_y y]\, dy \tag{8}$$

it turns out that all but every N'th coefficient vanish, and the remaining ones appear for $n=pN-1$, where p is an integer. The result may generally be expressed as

$$\xi(y) = \sum_{p=-\infty}^{\infty} a_p \exp[-ik_{yp} y], \quad k_{yp} = k_y - pk_{\Delta y}, \quad k_{\Delta y} = \frac{2\pi}{\Delta y} \tag{9}$$

irrespective of the type of paddle front. After quite some algebra, we get

$$a_p = \begin{cases} \beta_p, & \text{constant elements,} \\ \beta_p^2, & \text{linear elements,} \\ \dfrac{3}{2+\cos(k_y \Delta y)} \beta_p^4, & \text{spline elements,} \end{cases} \qquad \beta_p = \frac{\sin\left(\frac{k_{yp}\Delta y}{2}\right)}{\frac{k_{yp}\Delta y}{2}} \tag{10}$$

where the first two results were given by Sand (1979). It appears that in all three cases the power of β_p equals the order of the interpolating polynomial plus one. The primary component given by p=0 represents the desired motion, while all other components are spurious modes due to finite resolution. The perfect sinusoid recovers for $N \to \infty$ (or $k_y \Delta y \to 0$) for which $a_0 \to 1$ and $a_p \to 0$, $p \neq 0$. Figure 3a shows $|a_p|$ for $p \in [-2;2]$ versus $1/N = k_y / k_{\Delta y}$ for constant elements. Similar curves are shown in Fig. 3b for linear elements and in Fig. 3c for spline elements, where c_{-1}, c_{-2} and c_2 are hardly visible. While increasing the order of interpolation clearly improves the results when $1/N$ is small, the main spurious component dominates over the primary component for any type of interpolation when the resolution is more coarse than corresponding to the Nyquist limit, i.e. when $1/N$>1/2. This illustrates the importance of resolution and the limited possibility for improvements by high order interpolation. Irrespective of the type of interpolation all paddles move in phase if $1/N$=1 and the wavemaker reduces to a long-crested wavemaker. This is in line with (9), since for $N \to 1$, we have $k_{y1} \to 0$, $a_1 \to 1$ and $a_p \to 0$, $p \neq 1$.

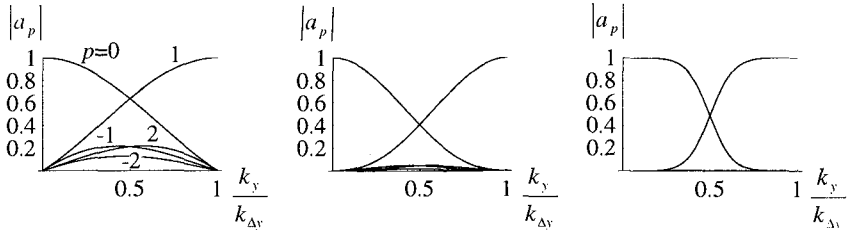

Figure 3. Fourier coefficients $|a_p|$ versus $1/N = k_y / k_{\Delta y}$ for $p \in [-2;2]$. Left plot: constant elements; middle plot: linear elements; right plot: spline elements.

While the above results give an indication on how well the ideal sinusoid is reproduced by a given type of segmentation, it does not show which waves will be generated. Summing up the solution (see e.g. Dean and Dalrymple, 1984) for each sinusoidal paddle mode, the surface elevation of the waves generated by the paddle movement from (9) can be written as

$$\eta(x,y,t) = X_a \sum_{p=-\infty}^{\infty} a_p \sum_{j=0}^{\infty} e_{jp} \exp\left[i(\omega t - k_{xjp} x - k_{yp} y)\right] \tag{11}$$

where

$$e_{jp} = \frac{k_j}{k_{xjp}} c_j, \quad k_{xjp} = \sqrt{k_j^2 - k_{yp}^2}, \quad \omega^2 = g k_j \tanh k_j h \tag{12}$$

Here k_j and c_j are the wavenumber and the Biésel transfer function, respectively. These are real for $j=0$ and imaginary for $j>0$ representing evanescent modes. For a piston-type wavemaker, we have

$$c_j = \frac{2\sinh^2 k_j h}{k_j h + \sinh k_j h \cosh k_j h} \tag{13}$$

see e.g. Schäffer (1996) for other types of wavemakers. While $j>0$ gives evanescent modes for any value of p, progressive modes require that $j=0$ and that p is sufficiently small as to get $|k_{yp}|<k$. Singularities appear in the transition from progressive to evanescent modes, since the square root in (12) vanishes when

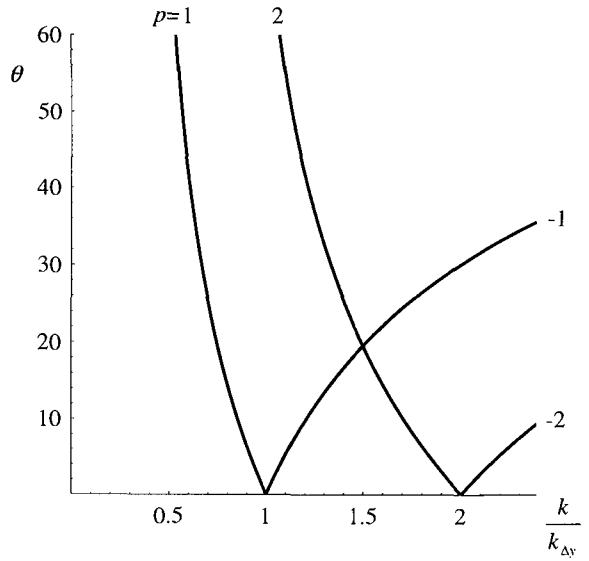

Figure 4. Singularities for spurious wave amplitudes, see (14).

$$\left| p\frac{k_{\Delta y}}{k} - \sin\theta \right| = 1 \tag{14}$$

where θ is the angle between the wavenumber vector and the wavemaker orthogonal. These singularities are shown in Fig. 4 for $p = \pm 1, \pm 2$. Swapping signs for p and θ gives the same image but mirrored in the abcissa. The singularity for p=0 is outside the range of the figure, since it appears for $\theta = \pm 90^\circ$. Obviously, it is desirable to stay away from the singularities, since at these points the mode in question can be expected to grow until nonlinearity or dissipation put an end to it. A criterion often used in multidirectional wave generation is that no progressive spurious modes should be allowed. This criterion is met (and only met) by staying to the left of the singularity curve for p=1 (and for p=-1 for negative θ) in Fig.4, i.e. requiring $k/k_{\Delta y} < 1/(1+\sin|\theta|)$. However, theoretically this may still give arbitrarily high evanescent mode amplitudes and this is one possible source of cross modes sometimes seen to build up near the wavemaker eventually ruining the physical experiment.

For comparison with Fig. 4 and the figures shown later, contours of resolution, $k_y/k_{\Delta y}$=1/2, 1/5 and 1/10 versus $k/k_{\Delta y}$ and θ are shown in Fig. 5.

Usually, the desired wave is progressive, and omitting the zero's for the subscripts j and p on the wavenumber components, we have

$$\eta_{00}(x,y,t) = A_{00}\exp[i(\omega t - k_x x - k_y y)],$$
$$A_{00} = \frac{X_a a_0 c_0}{\cos\theta}, \quad (k_x, k_y) = k(\cos\theta, \sin\theta) \tag{15}$$

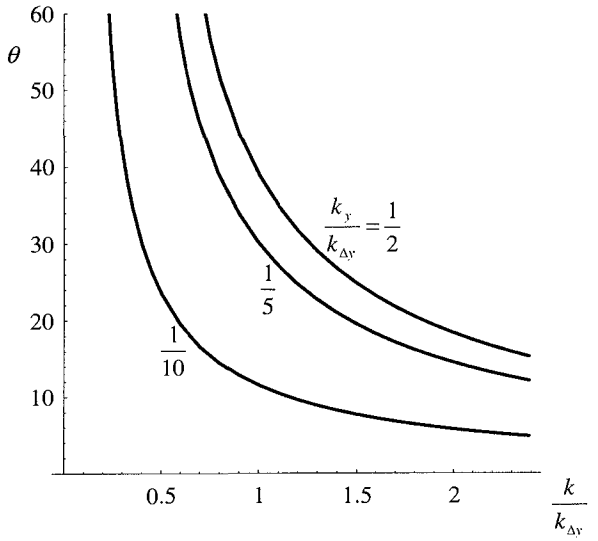

Figure 5. Hyperbolas showing constant resolution.

Sand (1979) concentrated on the number of evanescent modes as well as on the Fourier coefficients for the paddle motion, a_p. However, as pointed out by Christensen (1995), it is rather the magnitude of the resulting waves which is interesting from a wave generation point of view. Generating spurious waves is not a problem as long as their magnitude is sufficiently small. Thus, we look at the amplitude, A_{0p} of the dominant mode (j=0) for the p'th spurious wave relative to the desired wave amplitude, A_{00}. From (11), we get

$$\frac{A_{0p}}{A_{00}} = \frac{a_p}{a_0} \frac{\cos\theta}{\sqrt{k^2 - k_{yp}^2}} \tag{16}$$

which is again singular when (14) is satisfied. As a rational criterion for whether or not we should include a given desired wave component in the generation of a multidirectional sea state, we suggest to require

$$\left| A_{0p} / A_{00} \right| \leq \varepsilon \tag{17}$$

This requirement should be met for all values of p given some small value of the parameter ε. For each p (17) produces two limiting curves, one on the progressive-wave side of the singularity and one on the evanescent-mode side. Including also the singularities, Fig. 6 shows the results using $\varepsilon = 0.2$ for a constant element wavemaker and $p = \pm 1, \pm 2$. The shading indicates the allowable combination of direction, θ and scaled wavenumber, $k / k_{\Delta y}$. The grouping of curves

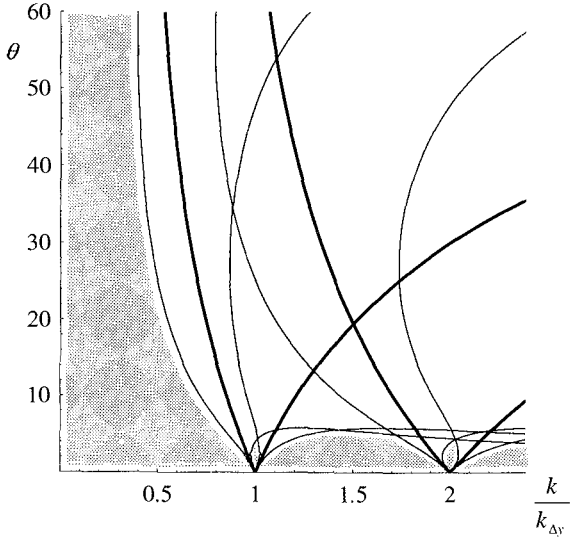

Figure 6. Limiting curves for wave generation defined by (17) with $\varepsilon = 0.2$. Paddle type: constant elements. Thick curves repeat the singularities from Fig. 4.

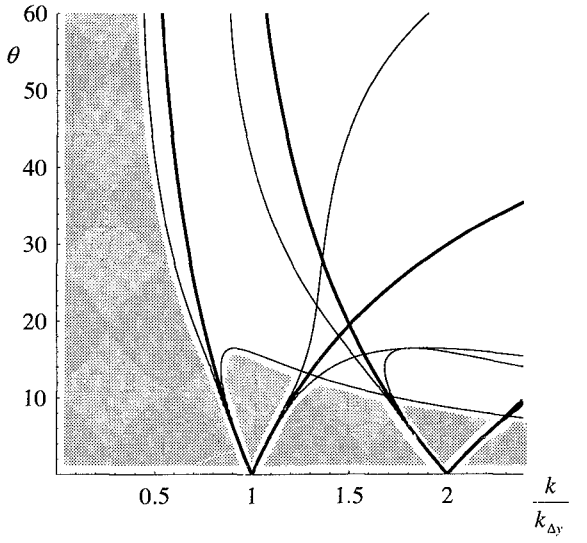

Figure 7. As Fig. 6, but for linear elements.

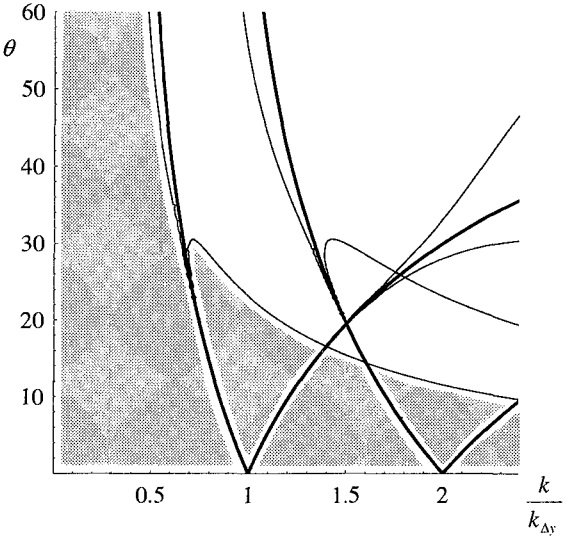

Figure 8. As Fig. 6, but for cubic spline elements.

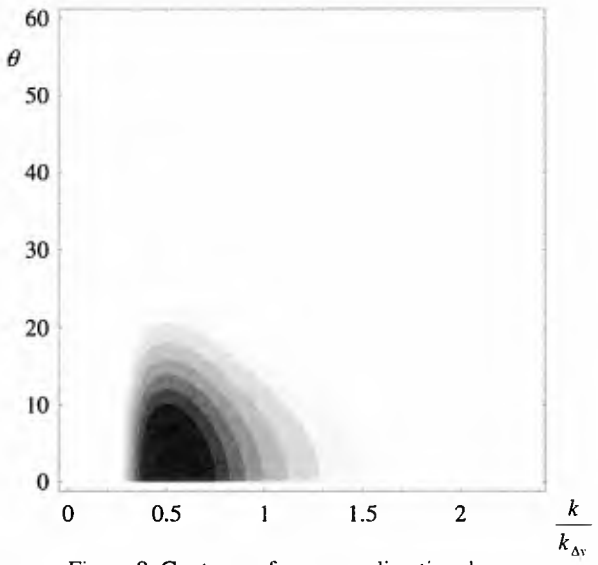

Figure 9. Contours of a narrow directional spectrum.

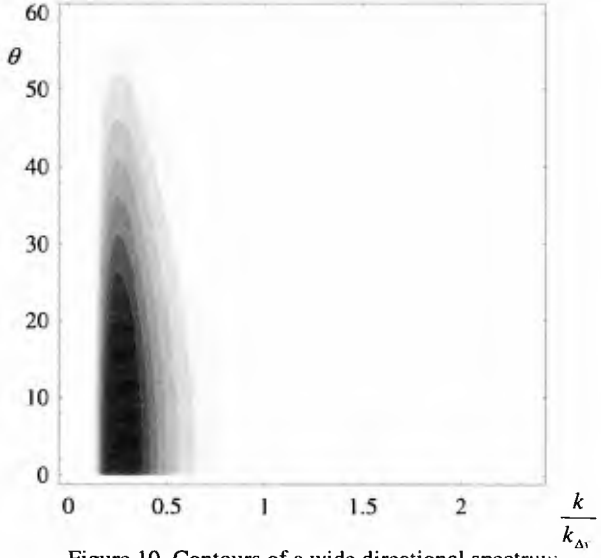

Figure 10. Contours of a wide directional spectrum

in sets of three for each value of p is more evident in Fig. 7 which shows similar results but for linear elements. The range of applicability is somewhat increased, but mainly for small. The limit of what a flexible paddle front could provide is seen in Fig. 8 showing the results for cubic spline elements. Although the improvement is evident, we note that again the advantage is quite small for waves with oblique mean direction.

For comparison with the allowable regions in Figs. 6-8, Figs. 9 and 10 show two examples of directional spectra. For both spectra the frequency variation is a Pierson-Moskowitz spectrum and the directional distribution is proportional to $\cos^{2s}(\theta/2)$. Ten equidistant contours are shown between the directional spectral peak value and zero. In Fig. 9 the directional distribution is quite narrow with s=40 corresponding to a directional spread of σ_θ=13°. The spectral peak is at $k/k_{\Delta y}$=1/2 e.g. corresponding to a peak frequency f_p at 1.25Hz for a segment width of Δy=0.5m (using the deep water dispersion relation). In comparison with the allowable regions in Figs. 6-8 it appears that the linear segments show a significant improvement over the constant ones (the staircase approximation) and the cubic splines give yet an improvement. However, shifting the mean direction in Fig. 9 to for example 30°, this advantage disappears as only one side of the directional distribution can be generated. In Fig. 10 the directional distribution is quite wide with s=6 (σ_θ=32°), while the peak is now at $k/k_{\Delta y}$=1/4 corresponding to f_p=0.88Hz assuming Δy=0.5m and deep water theory. For this case the difference between the three types of paddle front is rather small even for zero mean direction.

Spatial Aliasing

Collecting for example surface elevation time series usually involves a discrete sampling of a continuous measurement. In order to avoid aliasing, a suitable lowpass filter is applied to the analogue signal before the digital sampling takes place. The situation is quite different when measuring the surface elevation at equidistant points along the wavemaker. In this case, the surface elevation is sampled directly in discrete space. Thus, no underlying continuous measurement is available for eliminating aliasing in the sampling process. Assuming that the sampling interval equals the segment width, aliasing takes place for $L_y/\Delta y$ <2, (equivalent to the Nyquist frequency). Aliasing wraps wavenumbers k_y to

$$\tilde{k}_y = k_y + nk_{\Delta y} \tag{18}$$

where n is determined so that

$$-\frac{k_{\Delta y}}{2} < \tilde{k}_y < \frac{k_{\Delta y}}{2} \tag{19}$$

Assuming that k_y is inside the Nyquist range, the spurious wavenumbers $k_{yp} = k_y - pk_{\Delta y}$ given in (9) are all outside this range and aliasing wraps them back to get $\tilde{k}_{yp} = k_y$. Naturally, sampling the Fourier series for the paddle position (9), the original expression in (2) recovers as can be confirmed by checking that for all types of elements we have

$$\sum_{p=-\infty}^{\infty} a_p = 1 \tag{20}$$

For the surface elevation in (11), however, the transfer function e_{jp} modifies the terms in the summation so that the sampled elevation varies with type of element. This modification, however, is not a problem as it can be easily computed.

Other sources of short waves contaminating the system through aliasing must be anticipated. Nonlinearity is bound to give higher harmonics, both directly in the wave generation itself and indirectly through reflections from possible fixed or floating structures. Since the waves from these sources are unknown, we are not able to compensate for their influence. Consequently, a 3D active absorption system based on a discretely spatially sampled surface elevation will misinterpret very short waves as longer waves and thus try to absorb these longer waves, which do not exist. In this attempt, the system will generate unwanted waves.

Since the surface elevation is sampled both in space and time, the dispersion relation in principle makes it possible to overcome the spatial aliasing by lowpass filtering in the time domain. The frequency domain transfer function of such a lowpass filter transforms into the wavenumber domain, k. However, the desired effect is to restrict energy to small values of the wave number projection, k_y. Since for progressive waves $k \geq k_y$ the aliasing problem can be solved by eliminating frequencies for which $L/\Delta y<2$ (or $k/k_{\Delta y}>1/2$), where $L=2\pi/k$ is the wave length. Unfortunately, this requires a quite severe filtering, which we have found to impose unacceptable limits to the range of application for the active absorption system. Note, however, that wave generation and active absorption can be separated so that the filtering only affects the active absorption range and not the generation range.

In search for other means of reducing the potential problem of aliasing, we examine the effect of spatial averaging between consecutive surface elevation gauges. Let the gauge distance equal the segment width and let each gauge be centred between two control points, i.e. at $y=(m+1/2)\Delta y$. (This arrangement is not feasible for constant elements, as the paddle position is discontinuous at these points.) Spatial averaging between two gauge signals is equivalent to a multiplication in the k_y domain by the transfer function

$$H_1(k_y\Delta y)=\cos\left(\frac{k_y\Delta y}{2}\right) \tag{21}$$

as depicted in Fig. 6a. This is a notch filter, which has the desirable property that it removes all energy at the Nyquist wavenumber $k_y/k_{\Delta y}=1/2$ (and uneven multiples of 1/2), and the undesirable property of no reduction of energy for integer values of $k_y/k_{\Delta y}$. In combination with this spatial averaging, the time domain lowpass filtering as mentioned above can be less restrictive with a slightly higher cut-off frequency. However, as we still do not find this combination satisfactory, we shall investigate the consequences of doubling the number of surface elevation gauges placing these at $y=(m+1/2)\Delta y/2$. Aliasing now follows (18) and (19) with $\Delta y/2$ in place of Δy and spatial average among two neighbouring gauges corresponds to the transfer function

$$H_2(k_y\Delta y)=\cos\left(\frac{k_y\Delta y}{4}\right) \tag{22}$$

as shown in Fig. 6b. Combining (21) and (22), we get

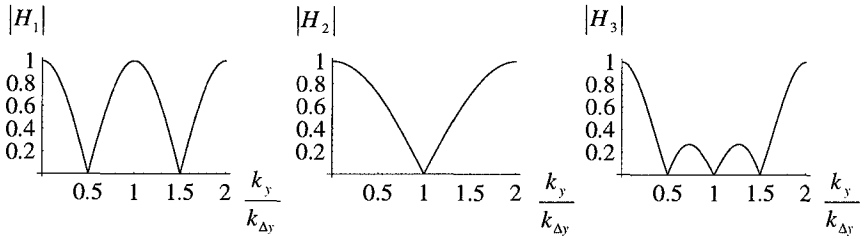

Figure 11. Transfer functions (21)-(23) for spatial averaging reducing aliasing problems.

$$H_3(k_y\Delta y) = \cos\left(\frac{k_y\Delta y}{2}\right)\cos\left(\frac{k_y\Delta y}{4}\right) = \frac{1}{2}\cos\left(\frac{k_y\Delta y}{3}\right) + \frac{1}{2}\cos\left(\frac{k_y\Delta y}{4}\right) \qquad (23)$$

Here the first version is given by $H_3=H_1H_2$ as obtained by two consecutive spatial averages between two neighbouring values, while the second formulation is found by considering the process as one spatial average between four neighbouring gauges. By this combination, we have obtained a stop band as seen in Fig. 6c. Consequently the supporting time domain filter can use a much higher and less restrictive cut-off frequency and still significantly reduce the contamination of the active absorption system due to short-wave aliasing. This solution has been chosen for the new multidirectional wavemaker under construction at DHI. A more elaborate analysis involving variable coefficients in the spatial averages did not show an overall improvement.

CONCLUSIONS

With regard to the type of wavemaker paddle front (Fig. 1) no differences appear in the limitations for multidirectional wave generation if the traditional cut-off in frequency and direction is used i.e. requiring no *progressive* spurious waves. A more elaborate criterion has been proposed, which reduces the application range slightly for very oblique waves in order to avoid large evanescent spurious waves. These could be the source of destructive cross modes and would in particular be unwanted when using surface elevation signals at the paddle front for hydrodynamic feedback to and active absorption system. On the other hand the new criterion permits a wider frequency range for very small obliqueness and increasingly much so for the more sophisticated segment type.

Both progressive and evanescent spurious waves should be recognized in surface elevation measurements at the paddle front for active absorption. In this connection aliasing of short-wave energy due to finite segment width and in particular due to other sources should be recognized. Means of reducing the aliasing problem have been discussed. A combination of better spatial resolution of elevation measurements and time-domain low-pass filtering in the active absorption system is suggested.

Acknowledgement. Part of this study was financed by the Danish National Research Foundation.

REFERENCES

Christensen, M. (1995). *Generation and active absorption of 2- and 3-dimensional linear water waves in physical models.* PhD Thesis. Series paper **11**, Hydraulics & Coastal Engng. Lab, Aalborg University, 90 pp.

Dean, R.G. and R.A. Dalrymple (1984). Water wave mechanics for engineers and scientists. Prentice Hall.

Sand, S.E. (1979). Three-dimensional deterministic structure of ocean waves. PhD Thesis. Series paper 24, Inst. Hydrodyn. and Hydr. Engng. (ISVA), Tech. Univ. of Denmark, 177 pp.

Schäffer, H.A. and J. Skourup (1996). Active absorption of multidirectional waves. Proc. 25th Int. Conf. on Coastal Engng., Orlando, FL, USA, pp 55-66.

Schäffer, H.A. and G. Klopman (1997). Review of multidirectional active wave absorption methods. Proc. IAHR-Siminar: Multidirectional Waves and their Interaction with Structures, San Francisco, CA, USA, pp 131-158. Also submitted to J. Waterway, Port, Coastal and Ocean Engng.

Generation of Double Peak Directional Wave by Dual Mode Snake-Type Wave Maker

Tetsuya Hiraishi and Katsuya Hirayama [1]

Abstract

The dual-mode snake-type directional random wave maker has been developed in order to reproduce double peak directional waves, long period waves and directional waves with oblique principal wave direction. Results from a series of wave generation tests demonstrate that the dual-mode generator system is suitable to reproduce the the target wave conditions with good accuracy.

Introduction

Various types of directional random wave generators have been developed to reproduce experimentally the wave condition similar to real sea waves. Especially, the recent development of active absorption theories of multi-directional waves (Ito,K.,et al.,1996) has made it possible to install a directional wave generator with three generator faces (multi-face directional wave generator)(Ito et al.,1996, Hiraishi et al.,1995). A wide area in the basin is possible to be employed as the effective test area(Funke et al.,1987) by the establishment of multi-face wave generators.

Meanwhile, recent systematic and large-scale field observation(Nagai et al.,1993) demonstrates that the directional spectrum observed offshore often has two peaks at different directions as shown in **Figure 1.** Each peak direction is usually apart more than 90° each other. Such double-peak directional waves are considered to be composed of 'wind wave' component with relatively short periods and 'swell' with long periods. Reproduction of double-peak directional waves is of great importance to carry out experimental study on the stability of offshore structures and navigating ships. A new type directional wave maker has been developed for the generation of double peak directional waves as well as the multi-face wave generation with active absorption (Hirakuchi et al.,1992).

Moreover, long period waves with period longer than swell become important for estimation of the stability and safety of floating structures and large cargo vessels moored to berths. Because long waves' periods are near to natural periods of the system composed of a ship and mooring ropes, their

[1] Wave Laboratory, Port and Harbour Research Institute, Nagase 3-1-1, Yokosuka, Japan 239-0826

penetration into harbors may cause large surge motion and breakage of the ropes by resonance (Hiraishi,1997a). Periods of long waves range usually from 50 to 100 s in prototype (Hiraishi,1997b). The main energy of long period waves propagate as free waves from the offshore area. A standard spectrum of long period waves has been proposed to estimate influences of long period waves in harbor planning (Hiraishi,1998).

The proposed profile of a standard spectrum includes the short period components(wind wave and swell) and long period wave components. The spectral density of long period wave components is constant and its level is determined by results in field observation. In order to reproduce the long period components evaluated in the standard spectrum, relatively large stroke are necessary. The newly developed directional wave maker should be also applicable to the generation of combination of short and long period waves.

The following section describes the applicability of the newly developed wave generator with segmented piston-type paddles.

Frame of Dual-Mode Snake-type Wave Generator

Figure 2 shows a conceptional design of the directional wave generator with double faces and with double operation modes. The generator consists of 50 and 30 drive shafts respectively on each side. **Figure 3** shows cross section of the wave maker. The generator is named "Dual-mode snake-type wave generator" because of two generator faces. A paddle 130cm heigh is attached

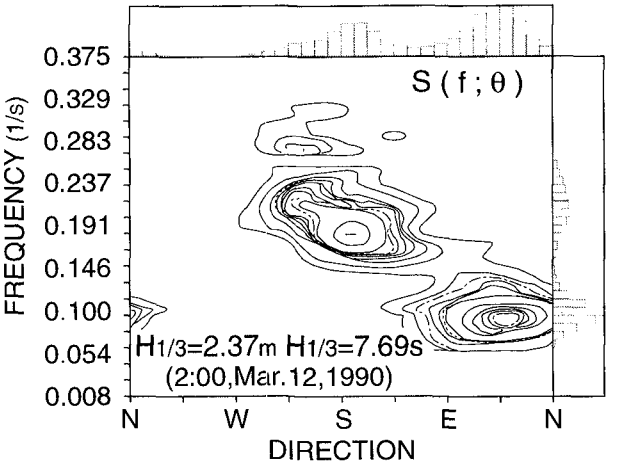

Figure 1 Observed directional spectrum with double peaks

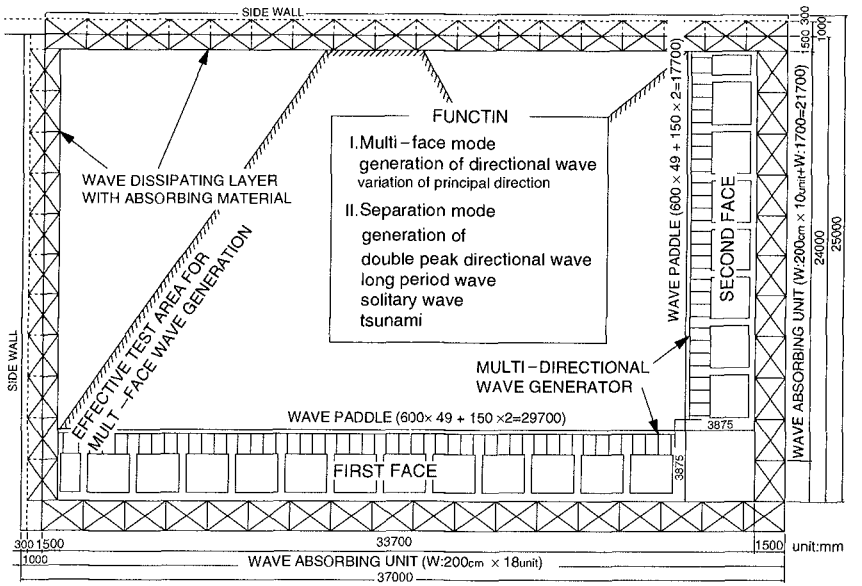

Figure 2 Arrangement of Dual-mode serpent type wave generator

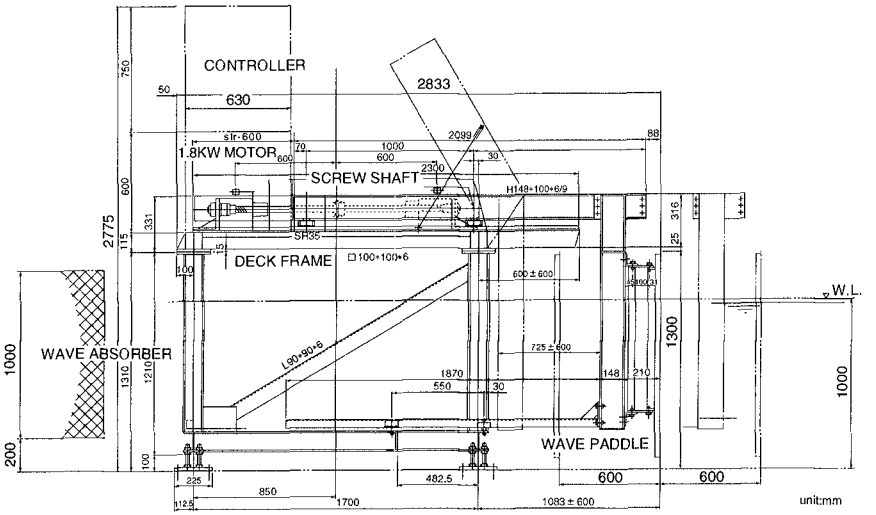

Figure 3 Cross section of wave generator unit

between adjoining two drive shafts. Wave paddles are displaced by the mechanical screw shaft system. The maximum water depth and wave height for generation is 100 and 30cm respectively. Each wave paddle is equipped with two wave sensors on its surface to measure the variation of water surface elevation at the front to carry out the active wave absorption for obliquely propagating waves (Ito et al.,1996). The side walls of the basin are covered with the wave dissipating layer composed of the wave energy absorbing material (Takayama et al.,1991). The wave energy absorbing layer is available to prevent waves reflected at the side walls without the generator faces and generated backward paddles. The generation face indicated below in Fig.3 is named "First face", and the right face "Second face" **Photograph 1** shows the overview of the dual-face serpent type wave generator.

The operation modes consist of the following two methods:

(a) Multi-face Mode :

The both of First and Second faces are operated as a single generator system to make single-peak multi-directional waves. The same target directional wave condition is given to the both faces with different phases. The paddle displacements in the both faces are synthesized according to the single summation model (Takayama and Hiraishi,1989) for directional wave generation. During operation, the re-reflected oblique wave components from wave paddle are prevented by the active wave absorption motion. The effective test area is much larger than a single face directional wave maker. The image of effective test area in the dual-mode generator is shown in Fig.3 as an area surrounded with broken lines.

A connecting removable pannel is attached at the corner between First and Second faces. The width of the pannel is variable corresponding to the positions of the adjoining paddles in the both faces. The position-shifted

Photograph 1 Overview of Dual-mode wave generator

pannel is proposed to prevent the wave height reduction on the straight line stretching obliquely from the corner(Hiraishi et al.,1995).

(b) Separation Mode :

Each of First and Second face is operated in the different target wave condition in the separation mode. Therefore, First face wave maker is available to the generation of directional wind waves with short periods when Second face generates 'swell' with longer periods. For the generation, both faces are controlled with the active absorption function. The double peak directional waves are reproduced in the separation mode.

Long period waves with the periods longer than those in swell are generated in the separation mode. A rigid pier was installed at the corner connecting First and Second face. Therefore, no wave is induced due to motion of the corner part. The pier becomes a guide walls to the both faces. In the separation mode, both faces are applicable to reproduce the directional waves with long period wave components by employing the long driving shafts of 100cm.

Experimental Evaluation of Applicability of Wave Generator

(a) Absorption of Oblique Wave

One of the important functions of the generator is the active absorption function to oblique waves. Ito et.al.(1996) has already investigated the applicability of three-point measurement array system for active absorption. We investigated applicability of the active absorption system of the dual-mode serpent type wave generator operated in the separation mode. **Figure 4** shows location of wave gages to measure incident and reflected wave heights. In the test, the oblique regular waves were generated from Second face. The wave angle in the basin is defined as the normal propagation angle from First generator face becomes 0°. The wave angle normal to Second face is defined to be 90°.

In the oblique wave absorption test, the angle of waves generated from Second face became 135°. **Figure 5** shows the wave profiles measured in the wave gages W.1 and W.2 in case of the operation in the active absorption. The target wave height and period in the generation signal is 5.0cm and 2.0sec respectively. The water depth is 60cm. The generated wave train may be reflected on First surface if the active absorption function does not work. In Fig.5 for the active absorption methods, the wave heights measured at W.2 were small. Their heights were about 0.5cm in the maximum, which corresponds to 10% of the height of waves measured at W. 1. Therefore, the active absorption function for oblique waves is suitable in the basin.

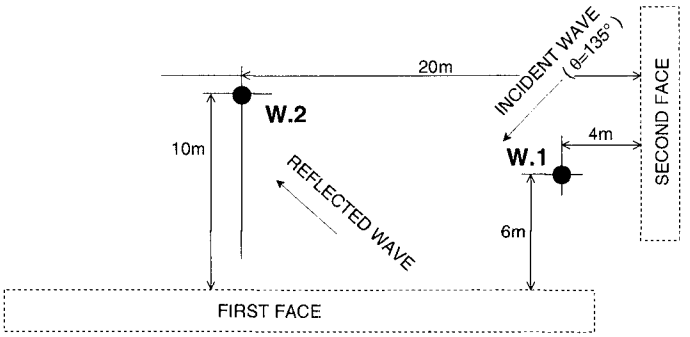

Figure 4 Measurement point of oblique wave profile

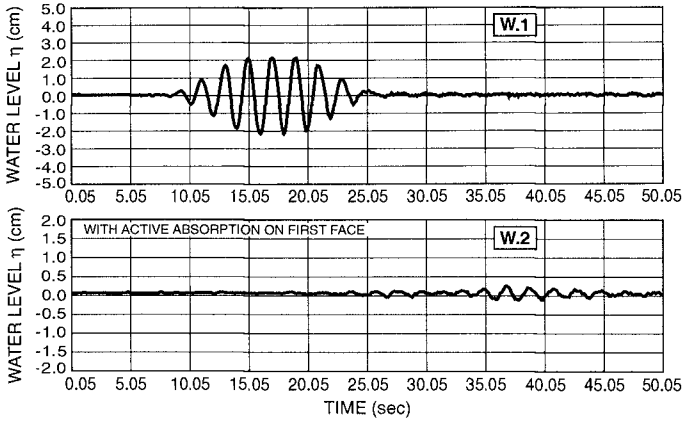

Figure 5 Wave profile measured at W. 1 and W. 2

(b) Directional Waves Generated in the Multi-face Mode

Figure 6 shows the arrangement of wave gage array to analyze the directional spectrum. The extended maximum entropy principle (EMEP, Hashimoto et al., 1994) was mainly employed to obtain the directional spectrum from simultaneously measured wave profiles. The Bretschneider -Mitsuyasu type frequency spectrum and the Mitsuyasu-type directional function (Goda, 1985) is applied to form the directional spectrum. Directional spectrum is given generally by,

$$S(f;\theta) = S(f)\,G(\theta;f) \qquad (1)$$

The Bretschneider–Mitsuyasu spectrum $S(f)$ is expreesed as,

$$S(f) = 0.257 H_{1/3} T_{1/3} (T_{1/3} f)^{-5} \exp[-1.03 (T_{1/3} f)^{-4}] \quad (2)$$

where f, $T_{1/3}$ and $H_{1/3}$ represents the frequency, significant wave height and period. The Mitsuyasu directional function is expressed as,

$$G(\theta ; f) = G_0 \cos^{2s} (\theta / 2) \quad (3)$$

where θ is the azimuth measured from counterclockwise from the principal wave direction. G_0 is a constant to normalize the directional function.

$$G_0 = \left(\int_{\theta min}^{\theta max} \cos^{2s} \left(\frac{\theta}{2} \right) d\theta \right)^{-1} \quad (4)$$

The parameter S_{max} represents the angular spreading parameter (Goda and Suzuki,1975) which may give the energy concentration to the principal wave direction. The smaller S_{max} corresponds to the wider spreading of wave energy. Goda and Suzuki(1975) has suggested the parameter S_{max} becomes about 10 for the normal wind waves. The location of wave gage array is included in the effective test area for First face generator.

Figure 7 shows comparison of the target and experimentally obtained contour map of directional spectrum at the center of basin for waves generated in condition of $S_{max}=5$. In the figures, the vertical and horizontal axis represents the frequency and wave direction respectively. During generation, Second face is working as the wave dissipating layer with active absorption. If the obliquely propagating components may be reflected at Second face, the obtained directional function may be distorted by the effect of obliquely reflected waves in energy contour map for wave with oblique principal direction because of the wide spreading of wave energy with $S_{max}=5$. The obtained directional spectrum contour in Fig.7 becomes symmetric, which means the effects by reflection waves are negligible. The obtained wave spectral contour in the left figure becomes similar to the target ones in the right. Therefore, the dual mode snake–type wave generator is applicable to reproduce directional waves with wider spreading of wave energy.

One of the large advantages to employ the dual–mode snake type wave generator is the possibility to make directional waves with oblique principal wave direction θ_p. We tested the applicability of generation of directional waves with the principal direction of $\theta_p = 45^\circ$. In order to generate the directional waves of $\theta_p = 45^\circ$, the appropriate motion of connecting board is inevitable.

Figure 8 shows comparison of the target and obtained directional spectrum in contour expression. The right and left figure represents the target and obtained wave energy contour map respectively. The obtained contor becomes similar to the target one. The peak of spectrum density appears at $\theta = 45^\circ$ at the both cases of target and obtained contours. We compared the directional function at the peak frequency to have a detail check of the principal wave direction. The input parameter S_{max} for synthesizing wave signals is 25.

Figure 9 shows the directional function at the peak frequency f_p of the target and obtained directional waves. In the figure, the profiles analyzed in

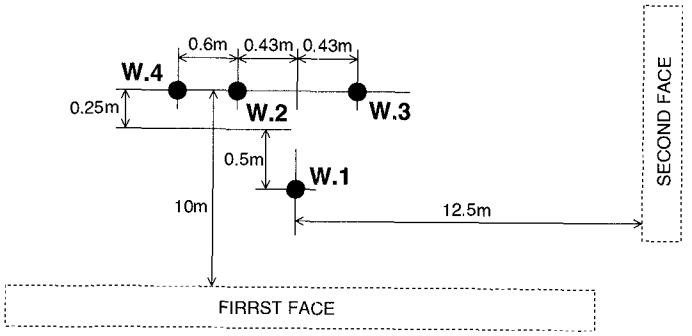

Figure 6 Measurement point of directional wave spectrum generated in multi-face mode

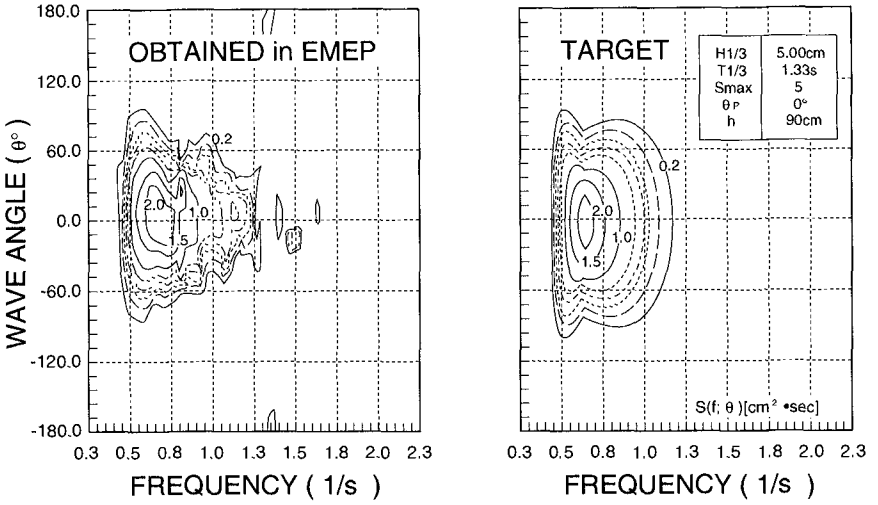

Figure 7 Comparison of measured and target directional spectrum in energy contour map

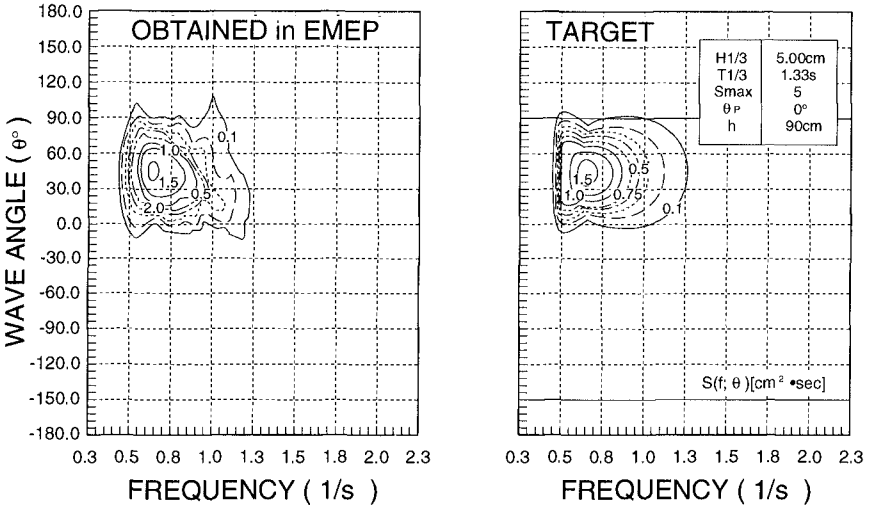

Figure 8 Measured and target directional spectrum for case of oblique principal wave direction

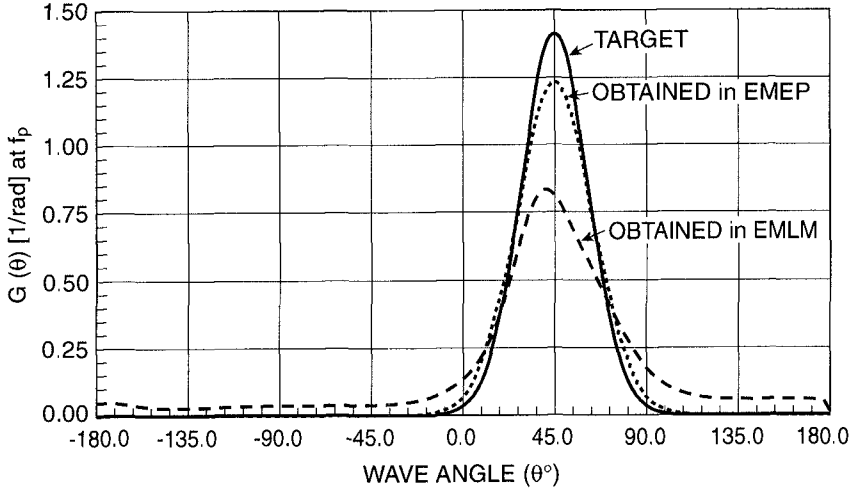

Figure 9 Comparison of directional function at peak frequency f_p of measured and target waves with oblique principal direction

EMEP and in the Extended Maximum Likelyfood Method (EMLM) (Isobe, 1988) are indicated in the dot and broken line respectively. The directional function profile analyzed in EMEP agrees with the target one indicated in the solid line. Meanwhile, the profile analyzed in EMLM shows the peak lower than the target. The mehod of EMEP is more appropriate to obtain the directional spectrum from the wave data simultaneously measured in a wave gage array than the method of EMLM. The peak angle of obtained directional function agrees well to the target of 45°. The multi-face mode operation of the serpent type wave generator is applicable to generate the directional waves with the oblique principal wave direction expressed as $\theta_p = 30°, 45°$ and so on.

(c) Long Period Wave

In order to investigate the efficiency and stability of floating structures in oceans, the reproduction of long period waves is important. **Figure 10** shows comparison of the obtained and target frequency spectrum of uni-directional random waves including the long period wave components. The uni-directional waves were generated from Second face and First surface was employed as a fixed guide wall. In the figure, the solid line represents the target frequency spectrum. The target spectrum has a constant level in the long period wave range. The broken line represents the experimentally obtained spectrum. The

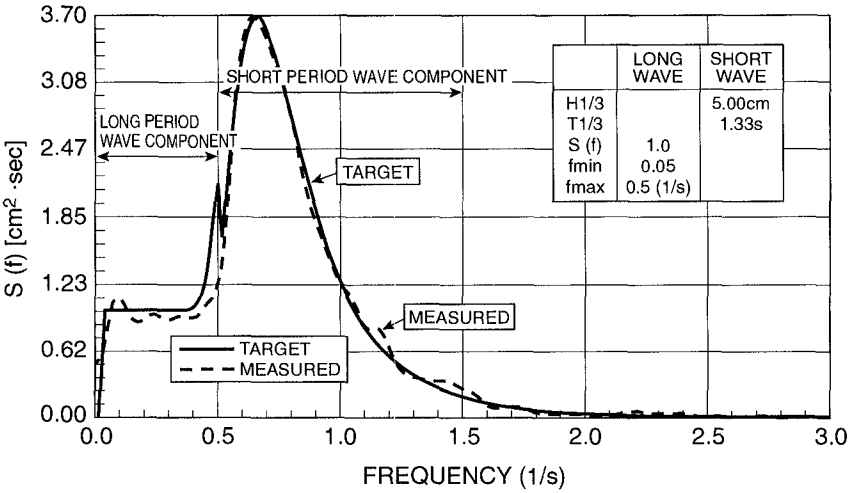

Figure 10 Measured and target wave frequency spectrum including short and long period wave component

obtained spectrum agrees well with the target even in the range of long period waves. Therefore, the generator with long stroke is expected to be applied to generate the uni-directional wave condition with free long period wave components in the experimental basin.

(d) Double-peak Directional Wave

In the evaluation tests, wind waves are generated by First-face and swell by Second face. The propagating angle of wind waves and swell is 0° and 90° respectively. The target period of generated wind waves and swells is 1.33 and 2.0sec respectively. **Figure 11** shows the measured directional spectrum at the basin center. The target conditions of wind wave and swell component is indicated as 'WAVE-1' and 'WAVE-2' respectively in the upper-left side table. In the figure, the two-dimensional directional spectrum is represented. The two dimensional directional spectrum is given by,

$$G_2(\theta)=\int_0^\infty S(\theta;f)df \qquad (5)$$

The profile analyzed in EMEP has peaks at the same to the target angles. The energy level of swell component at θ =90° is slightly smaller than the target. In the wind wave components generated by First surface, the obtained peak angle and energy level agrees well with those of target spectrum. Therefore, the double-peak directional waves can be reproduced with good accuracy in dual-face directional wave generator.

Figure 12 shows comparison of the directional function at the peak frequency of swell components. The directional function's peak angle and energy level agree with those of target respectively. For the wind wave components, the peak angle slightly differs from the target, however, the differences are less than 20°. Considering the directional function at peak frequency, the dual-mode snake type wave generator is expected to be applicable to genarate double-peak directional random waves.

Figure 13 shows the frequency spectrum measured at the gage W.1. In the case for Fig.13, the target significant wave period for wind waves and swell is 1.0 and 2.2sec respectively. In the figure, the target frequency spectrum is represented in the solid line and the obtained by the broken line. The frequency spectrum of generated waves agrees well with the target spectrum and they have spectral profiles with two peaks typically observed in the double-peak directional wave condition in the field (Nagai et al.,1993). The good agreements in the directional function and frequency spectrum profile between the measured and target double-peak directional waves demonstrate the possibility of the generator to reproduce the complicated sea conditions composed of wind waves, swell and long period waves.

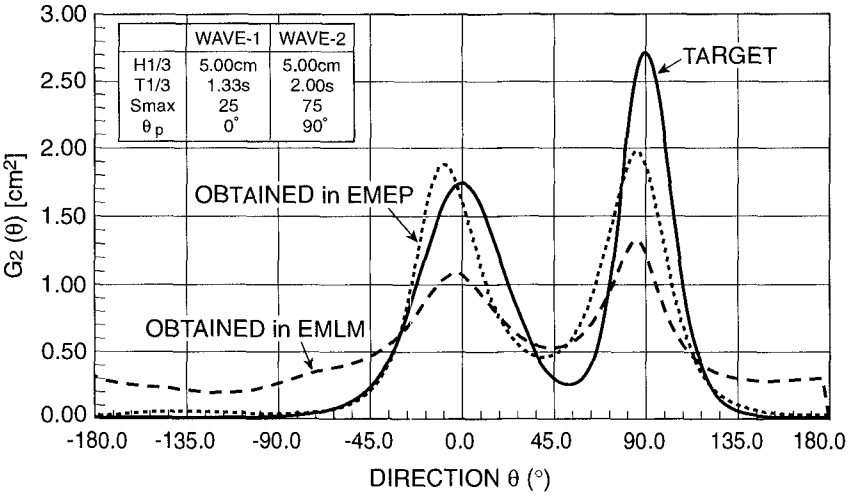

Figure 11 Comparison of two dimensional directional spectrum of measured and target double–peak directional wave

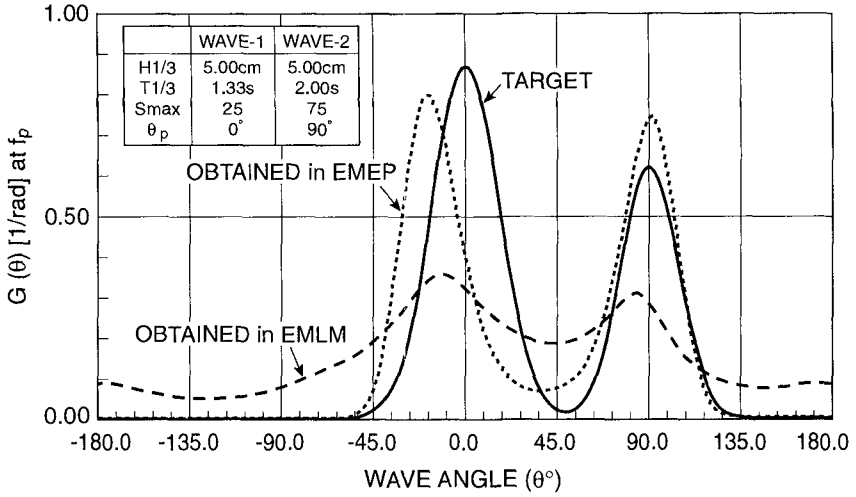

Figure 12 Comparison of directional function at f_p of measured and target double–peak directional wave

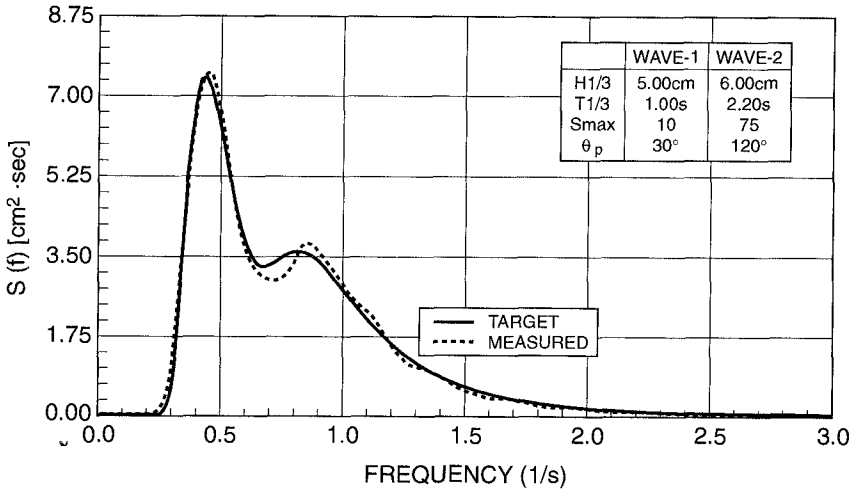

Figure 13 Comparison of frequency spectrum of measured and target double–peak directional wave

CONCLUSIONS

A Dual–mode snake type wave generator has been newly developed. The generator is composed of First and Second faces and is operated in the multi–face and the separation mode. The generator is available to reproduce;

i) directional waves with oblique principal direction,
ii) long period waves,
iii) double–peak directional waves,

REFERENCES

Funke E.R. and M.D.Miles (1987). "Multi –directional wave generation with corner reflectors," *Technical Rep. of National Res. Council Canada,* TR–HY–021,17p.

Goda Y.(1985). "Random seas and design of maritime structures," *University of Tokyo Press*, pp.27–33.

Goda Y.and Y.Suzuki (1975). "Computation of refraction and diffraction of sea waves with Mitsuyasu's directional spectrum," *Technical Note of Port and Harbour Res. Inst.*, No.230, 45p.

Hashimoto N.,T.Nagai and T.Asai (1994). "Extension of maximum entropy principle method(MEP) for estimating directional wave spectrum," *24th Inter. Conf. Coastal Engineering*, Vol.1, pp.232–246.

Hiraishi T., T.Kanazawa and H.Fujisaku (1995). "Development of multi–face directional random wave maker, " *Proc. 5th Inter. Offshore and Polar Engi. Conf.*,Vol.3, pp.26–33.

Hiraishi T., Y.Atsumi, S.Sekiguchi and T.Kawaguchi (1997a). "Observation of long period wave and ship motion in Tomakomai–port, " *Proc. 7th Inter. Offshore and Polar Engi. Conf.*, Vol.3, pp.546–551.

Hiraishi T.(1997b). "Characteristics of long–period waves observed in a port," *Proc. 7th Inter. Offshore and Polar Engi. Conf.*, Vol.3, pp.254–258.

Hiraishi T.(1998). "Observed frequency spectrum of long period waves," *Proc. 8th Inter. Offshore and Polar Engi. Conf.*, Vol.3.

Hirakuchi ,H.,R.Kajima,T.Shimizu and M.Ikeno (1992). "Characteristics of absorbing directional wavemaker, " *25th Inter. Conf. Coastal Engineering*, Vol.1, pp.281–294.

Isobe M.(1988) . "Measurement of wave direction," Chapter 3, *Nearshore Dynamics and Coastal Processes*, edited by K.Horikawa, University of Tokyo Press, pp.407–422.

Ito K.,H.Katsui,M.Mochizuki and M.Isobe (1996). "Non–reflected multi directional wave maker theory and experiments of verification," *Proc. 25th Inter. Conf. Coastal Engineering*, Vol.4, pp.443–456.

Nagai T.,N.Hashimoto and T.Asai (1993). "On the properties of the directional wave spectra observed in deep seas –1st report : The field observation off Iwaki–," *Report of the Port and Harbour Research Institute*, Vol.32, No.2, pp.45–114.

Takayama T.and T.Hiraishi (1989). "Reproducibility of directional random waves in laboratory wave simulation," *Rept. of Port and Harbour Res. Inst.*,Vol.28,No.4,pp.3–24.

Takayama T., N.Ikeda and Y.Kosugi (1991) . "Hydraulic model tests on directional random wave transformation in Kamaishi bay, " *Report of the Port and Harbour Research Institute*, Vol.30, No.1, pp.69–136.

Extreme Multi-Directional Waves

T.B. Johannessen[1] & C. Swan[2]

Abstract

The present paper concerns the nonlinear description of large waves in which the wave energy is spread in both the frequency and the directional domains. A new series of experimental observations are briefly described in which a large number of deep-water focused wave groups were generated in a large wave basin. For each combination of frequency bandwidth and directional spread the intensity of the wave, measured in terms of a linear amplitude sum, was varied from a near-linear condition to the limit of incipient wave breaking. Comparisons between this laboratory data and a new fully nonlinear, multi-directional, numerical model are used to validate the modelling procedure and highlight the importance of the directionality. In particular, the results show that for a given linear amplitude sum an increase in the directional spread leads to a reduction in the magnitude of the nonlinear wave-wave interactions. Conversely, the maximum nonlinear crest elevation, observed just prior to the onset of wave breaking, increases with the directional spread assuming the frequency bandwidth remains constant. From a practical perspective, the paper demonstrates that an accurate representation of an extreme ocean wave requires a model that incorporates nonlinearity, unsteadiness and directionality. The present model satisfies these requirements.

1. Introduction

It is well known that the largest ocean waves, which are by definition highly nonlinear, do not arise as part of a regular wave train, but occur as individual events within a random or irregular sea. Indeed, field data confirms that the most severe storms are typically characterised by a relatively broad-banded frequency spectrum implying a

[1] Senior Engineer, Kvaerner Oil and Gas, Oslo, Norway

[2] Reader, Department of Civil and Environmental Engineering, Imperial College, London, SW7 2BU.

wide distribution of energy within the frequency domain. As a result, the largest waves, arising due to the constructive interference or focusing of the frequency components (see Tromans et al., 1991), only arise at one point in space and time and are thus commonly referred to as transient waves. More recently, it has also been shown that such waves will have a significant distribution of energy in the directional domain. For example, Jonathan et al. (1994) have considered several severe storms arising in the northern North Sea, and show that the wind waves have a typical directional spread corresponding to a normal distribution with a standard deviation of 30°.

Having established that large wave events are nonlinear, transient and directional, it is perhaps surprising to note that the commonly applied design solutions either include the nonlinearity or the unsteadiness, but seldom both, and typically neglect the underlying directionality. For example, a linear random wave theory provides a first approximation to the dispersive properties of a sea state, and hence models the transient nature of individual waves, but entirely neglects the nonlinearity. In contrast, a nonlinear regular (or steady) wave theory, either based upon a Stokes' expansion (Fenton, 1985) or a stream function formulation (Dean, 1965), includes the nonlinearity but neglects the unsteadiness. More recently, an alternative design solution proposed by Baldock and Swan (1994) includes both the nonlinearity and the unsteadiness, and has been shown to be effective in a wide range of water depths (Smith and Swan, 1996). However, even in this latter model the omission of directionality represents a serious restriction.

Evidence as to the importance of directionality in the evolution of large waves has recently come to light in comparisons between two-dimensional laboratory data and field measurements. For example, Baldock et al. (1996) provides observations of extreme two-dimensional wave groups, produced by the focusing of energy due to frequency dispersion. These results show that the nonlinear wave-wave interactions may increase the maximum crest elevation by as much as 30% above that predicted by the linear sum of the underlying wave components. In contrast, the analysis of field data (Rozario et al., 1993) suggests that while nonlinearity is undoubtedly important, the corresponding increase in the maximum crest elevation is substantially less than 30%. An obvious explanation for this difference lies in the directionality of the field data.

The present paper will address this point and will provide comparisons between a fully nonlinear, multi-directional, wave model and a new series of laboratory observations undertaken in a large wave basin. Section 2 commences with a brief description of the numerical model; while section 3 outlines the nature of the experimental study. Comparisons between these results are provided in section 4, with particular attention given to both the maximum crest elevations and the underlying water particle kinematics. In section 5 some additional numerical calculations are provided to examine the nature of the nonlinear wave-wave interactions arising in the vicinity of the largest wave crests, and in particular their dependence upon the directionality of the wave field. The paper concludes in section 6 by highlighting the practical implications of the present study.

2. Numerical Modelling

The numerical model outlined within this section is an extension of the two-dimensional time-stepping formulation originally proposed by Fenton and Rienecker (1980). In its original form this scheme represents one of several potential flow solutions, each capable of accurately modelling the evolution of a two-dimensional nonlinear wave train (e.g. Longuet-Higgins and Cokelet, 1976, Dold and Peregrine, 1984, and Dommermuth et al., 1988). In the context of the present study the scheme outlined by Fenton and Rienecker (1980) was adopted because, although it is less efficient (computationally) than many of the other schemes, it is expandable to three-dimensions. Assuming that a fluid flow is both inviscid and irrotational a velocity potential, ϕ, defined by $\underline{u}=\nabla\phi$, where $\underline{u}$ is the velocity vector, can be expressed as:

$$\Phi(x,y,z;t) = \sum_{m=0}^{\infty} Cos(mk_y y) \sum_{n=0}^{\infty} \left(\left(A_{nm} Cos(nk_x x) + B_{nm} Sin(nk_x x) \right) \frac{\cosh\left(k_{nm}[z+d]\right)}{\sinh\left(k_{nm} d\right)} \right) \tag{1}$$

where (x,y,z) are the usual Cartesian co-ordinates with z defined vertically upwards from the mean water level, z=-d defines the bottom boundary, and (x,y) are the horizontal co-ordinates which are orientated such that the x-axis defines the mean wave direction (see section 3 below). Furthermore, $k_{nm} = \sqrt{(nk_x^2 + mk_y^2)}$ where (k_x,k_y) define the large fundamental length scales, $\lambda_x=2\pi/k_x$ and $\lambda_y=2\pi/k_y$, over which the solution is assumed periodic in the x and y directions respectively. Likewise, the free surface elevation, which must be similarly periodic in space, is given by:

$$\eta(x,y;t) = \sum_{m=0}^{\infty} Cos(mk_y y) \sum_{n=0}^{\infty} \left(\left(a_{nm} Cos(nk_x x) + b_{nm} Sin(nk_x x) \right) \right) \tag{2}$$

Both equations (1) and (2) utilise the fact that the experimental wave fields are symmetric in y (see section 3 below), although this is not a formal necessity. Furthermore, the series coefficients A_{nm}, B_{nm}, a_{nm}, b_{nm} are assumed to be functions of time only. In this form the velocity potential satisfies the governing field equation ($\nabla^2\phi=0$) representing mass continuity and the bottom boundary condition corresponding to a flat impermeable bed ($\phi_z=0$ on z=-d). The remaining constraints represent the nonlinear free surface boundary conditions (both kinematic and dynamic) evaluated on the water surface ($z=\eta$). After some re-arrangement these can be written as:

$$\Phi_t = -\left(g\eta + \tfrac{1}{2}(\Phi_x^2 + \Phi_y^2 + \Phi_z^2) \right) \tag{3}$$

$$\eta_t = \Phi_z - \left(\Phi_x \eta_x + \Phi_y \eta_y \right) \tag{4}$$

where g is the acceleration due to gravity.

Longuet-Higgins and Cokelet (1976) were the first to note that in this form the right hand side of equations (3) and (4) involve no time derivatives. As a result, if an initial spatial description of the water surface elevation, $\eta(x,y,z)$, and its associated velocity potential, $\phi(x,y,z)$, are known, it is possible to time-march the solution such that η and ϕ can be defined at all subsequent times. In the present cases the initial conditions, at some early time prior to the occurrence of a large wave event, can be calculated from linear or second-order theory on the basis that the wave group is fully dispersed. To apply this procedure it must be assumed that no significant wave energy lies above the truncation wave numbers Nk_x and Mk_y. Provided this is indeed the case, equations (3) and (4) can be solved at $2N(M+1)$ spatial locations in order to define the time derivatives of the coefficients $\left(A_{nm_t}, B_{nm_t}, a_{nm_t}, b_{nm_t}\right)$. This corresponds to a grid spacing equal to half the wavelength of the shortest wave component. Once the time derivatives of the coefficients have been determined, the solution can be time-stepped using the Adams, Bashford, Moulton formulation (Gear, 1971) and the solution procedure repeated.

Within the present scheme the time derivatives of the free surface coefficients may be evaluated using a Fast Fourier Transform (FFT). Unfortunately, the time derivatives of the velocity potential are functions of η, and must be evaluated by solving a set of linear simultaneous equations using a lower-upper (LU) matrix decomposition. As a result, the numerical formulation is time consuming, and requires parallel computing power for the steepest directional wave cases. The present numerical formulation was implemented on a Fujitsu AP1000 parallel computer. On this machine the most computationally demanding wave groups may be evaluated accurately with run times of up to 16 hours. Full details of this numerical procedure are given in Johannessen and Swan (1998a).

3. Experimental Investigation

The purpose of the experimental study was to investigate a large number of focused wave groups in which the underlying wave components were spread in both the frequency and the directional domains. The experimental work was undertaken in the wide wave basin at the University of Edinburgh. This facility has a plan area of 25m x 11m, a uniform water depth of 1.2m, and is equipped with 75 numerically controlled wave paddles each 0.3m wide. To limit the occurrence of reflected waves, large passive absorbers were located at the downstream end of the wave basin and along one of the side-walls. A sketch showing the layout of this facility is given on figure 1.

Preliminary tests confirmed that within this facility waves could be generated within a directional range of $\theta=\pm 45°$and a frequency range of $0.6\text{Hz} \le f \le 1.7\text{Hz}$. Within the present tests, three separate frequency spectra were investigated. The first corresponds to a broad-banded spectrum (denoted by case B), and includes waves within the period range $0.6\text{s} \le T \le 1.4\text{s}$; while the second corresponds to a narrow-banded spectrum (denoted by case D), and includes waves within the period range $0.8\text{s} \le T \le 1.2\text{s}$. The third spectrum (denoted by case C) is intermediate to cases B and D and corresponds to a period range of $0.7\text{s} \le T \le 1.3\text{s}$. Within each of these cases a large number of wave

components, of equal amplitude, were uniformly spaced within the respective period range. This gives a corresponding amplitude spectrum, a(f), which, in each case, decays according to f^{-2} (figure 2a).

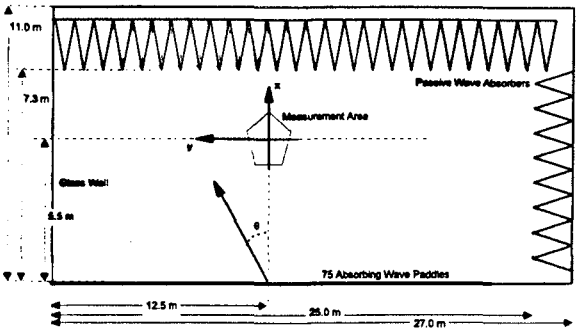

Figure 1: Experimental apparatus.

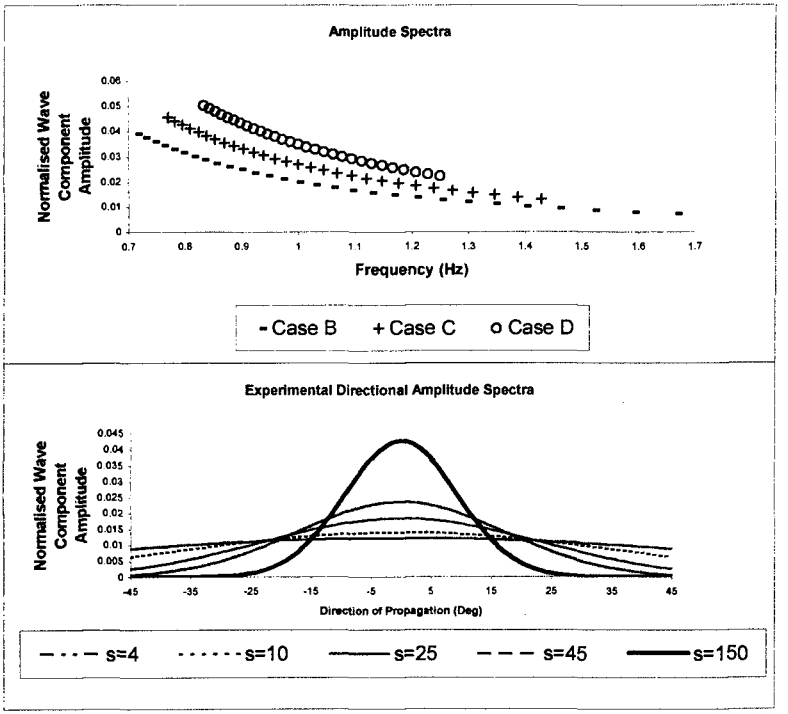

Figure 2a-b: Experimental amplitude spectra.
(a) In the frequency domain; (b) In the directional domain.

To quantify the directional spread of the wave components, the Mitsuyasu spreading parameter, s, was employed, where the directional amplitude spectrum, $a(\theta)$, is defined by:

$$a(\theta) = \lambda \cos^{s}(\theta/2) \tag{5}$$

where θ denotes the wave direction measured relative to the x-axis and λ is a normalising coefficient. For each of the three frequency spectra, 6 directional spreads were adopted (s=∞, 150, 45, 25, 10, 4); where s=∞ corresponds to a unidirectional wave field, s=150 a very long-crested wave field, and s=4 a short-crested wave field. Graphical representations of these directional spreads are given on figure 2b. For each combination of frequency and directional spread a minimum of 4 input amplitude sums (A) were employed, where A corresponds to the linear sum of the component wave amplitudes. To address the widest range of wave conditions, the input amplitudes for each case were increased from A=20mm (corresponding to a linear wave group) to $A=A_{max}$, where the latter values correspond to the onset of incipient wave breaking. In total some 88 individual wave groups were considered. A full discussion of this data is outside the scope of the present paper and is given in Johannessen and Swan 1998b.

For each of the wave fields described above, the surface elevation was sampled at 45 spatial locations in the vicinity of the linearly predicted focus position (x=0, y=0). These measurements were made using standard surface-piercing wave gauges that are estimated to have an accuracy of ±1mm. In addition, for a number of selected wave cases (15 in total) the x-component of the horizontal wave-induced velocity was recorded at closely spaced vertical elevations underneath the measured position of the maximum crest elevation. This velocity data was obtained using a one component laser Doppler anemometer that was estimated to have an accuracy of ± 2%.

As part of our preliminary measurements, considerable time was spent calibrating and validating the wave basin. The usual problems associated with wave reflections, which are notoriously strong in many wave basins, did not pose a significant problem in the present study. This is because the nature of a focused wave group is such that the waves are almost completely dispersed when they reach the downstream absorbers. Consequently, any energy reflected or scattered from the wave absorbers is negligible when compared with the energy density in the vicinity of the extreme event. The success of the calibration process is clearly demonstrated in figures 3a-3c. These results concern the narrow-banded wave spectrum (case D), with the largest possible directional spread (s=4, corresponding to a very short-crested sea state), and an input amplitude of A=20mm. This represents the smallest input amplitude and should, therefore, be in good agreement with a linear model. Figure 3a concerns the time-history of the water surface at the focus position, $\eta(t)$; figure 3b describes a spatial description of the surface elevation along the centreline $\eta(x)$; and figure 3c describes the horizontal velocity profile, u(z), beneath the maximum crest elevation. In all cases the measured data is in very good agreement with the linearly predicted behaviour. Agreements of this type are essential if one is to interpret the nature of the nonlinear wave-wave interactions arising with larger input amplitudes.

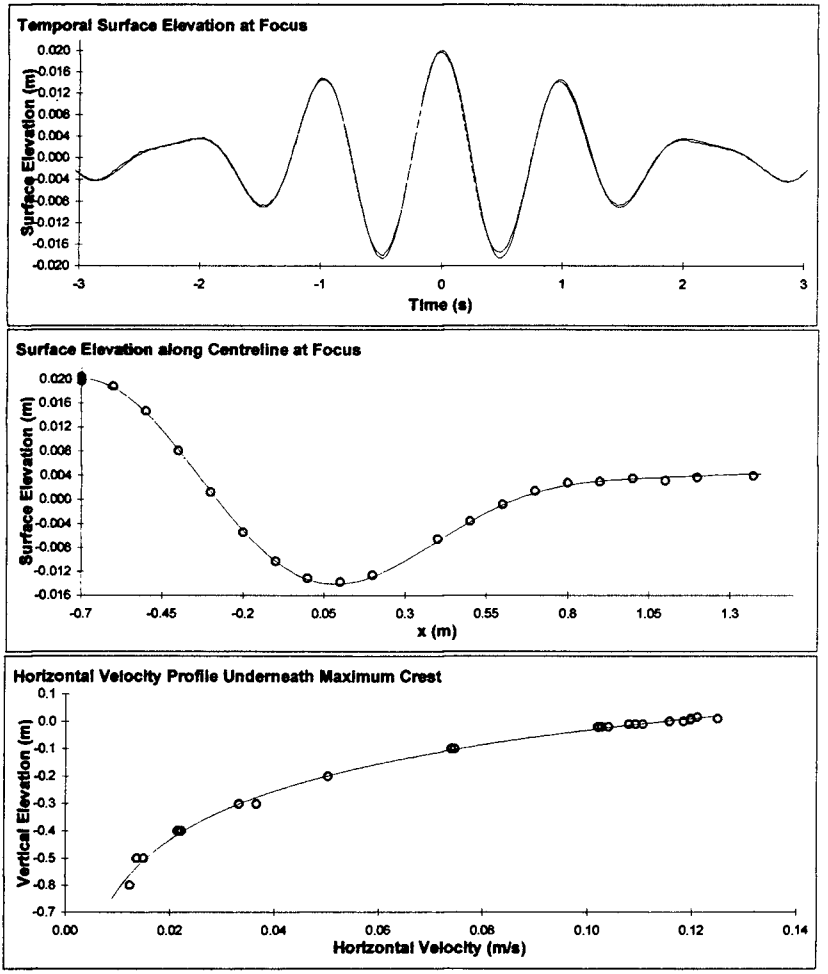

Figures 3a-3c: Comparisons with a linear wave group.
——— linear theory; ..... , o experimental data.

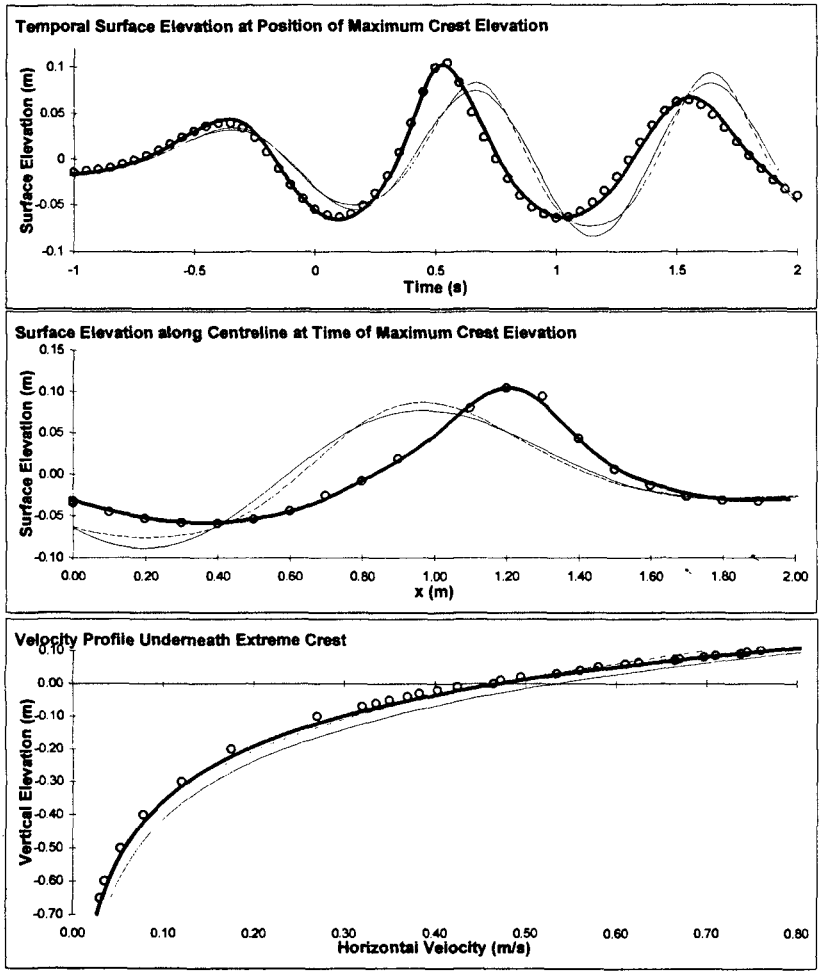

Figures 4a-4c: Comparisons with a nonlinear wave group.
o experimental data; ▬▬ numerical model; ——— linear theory;
..... second-order theory .

4. Discussion of Results

Figures 4a-4c again concern the narrow-banded spectrum (case D) with a large directional spread (s=4), but now corresponds to a highly nonlinear wave group with an input amplitude of A=93mm. In this case the measured data is compared to the results of the numerical model (section 2), a linear solution, and a second-order solution based upon the wave-wave interactions identified by Longuet-Higgins and Stewart (1960) and further considered by Sharma and Dean (1981). In each of these figures the results of the numerical model are in very good agreement with the measured data. Furthermore, figure 4a, which concerns the time-history of the water-surface elevation measured at the position of the maximum crest elevation, suggests that the largest wave crest occurs after the linearly predicted focus event (t=0). Similarly, figure 4b, which presents a spatial description of the water surface elevation at the time of the maximum crest elevation, suggests that the largest wave crest also occurs downstream of the linearly predicted focus (x=0). These shifts in the focus time and position are consistent with those observed in unidirectional wave groups (Baldock et al., 1996). Furthermore, comparisons between the measured data and both the linear and the second-order solutions, suggest that significant energy shifts occur in the vicinity of the largest wave event.

In figure 4c comparisons with the horizontal velocity data, recorded beneath the largest wave crest, again confirm that the numerical model provides the best description of the measured data. However, the data also appears to be in reasonable agreement with the second-order solution, with the exception of a 15% under-prediction that arises very close to the water surface. This latter result is in marked contrast to the unidirectional data presented by Baldock et al. (1996).

To further examine the success of the numerical model, figure 5 again concerns frequency spectrum D, with s=4 and A=93mm. In this figure, time-histories of the water surface elevation are presented at four spatial locations: x=0, or the linearly predicted focus position; x=0.6m; x=1.2m, which is the observed position of the maximum crest elevation; and x=1.8m. At each of these locations the numerical model is in good agreement with the measured data, and is shown to be very different from either the linear or the second-order solutions.

To isolate the effect of the directional spread, two further comparisons were undertaken. Firstly, the linear sum of the component wave amplitudes generated at the wave paddles were held constant (A=55mm), and the global maximum crest elevations measured for a range of directional spreads for each frequency spectrum. This data is presented on figure 6a. Comparisons between these results clearly suggest that the effect of introducing a directional spread is to dramatically reduce the maximum crest elevation. Furthermore, the bulk of this reduction occurs between a unidirectional wave group (1/s=0, where s is again the Mitsuyasu spreading parameter) and a long-crested wave group with small directional spread. Since the local increase in the crest elevation (above that predicted by linear theory) arises due to the nonlinear wave-wave interactions, and almost certainly involves a shift of energy into the higher frequencies, the data presented

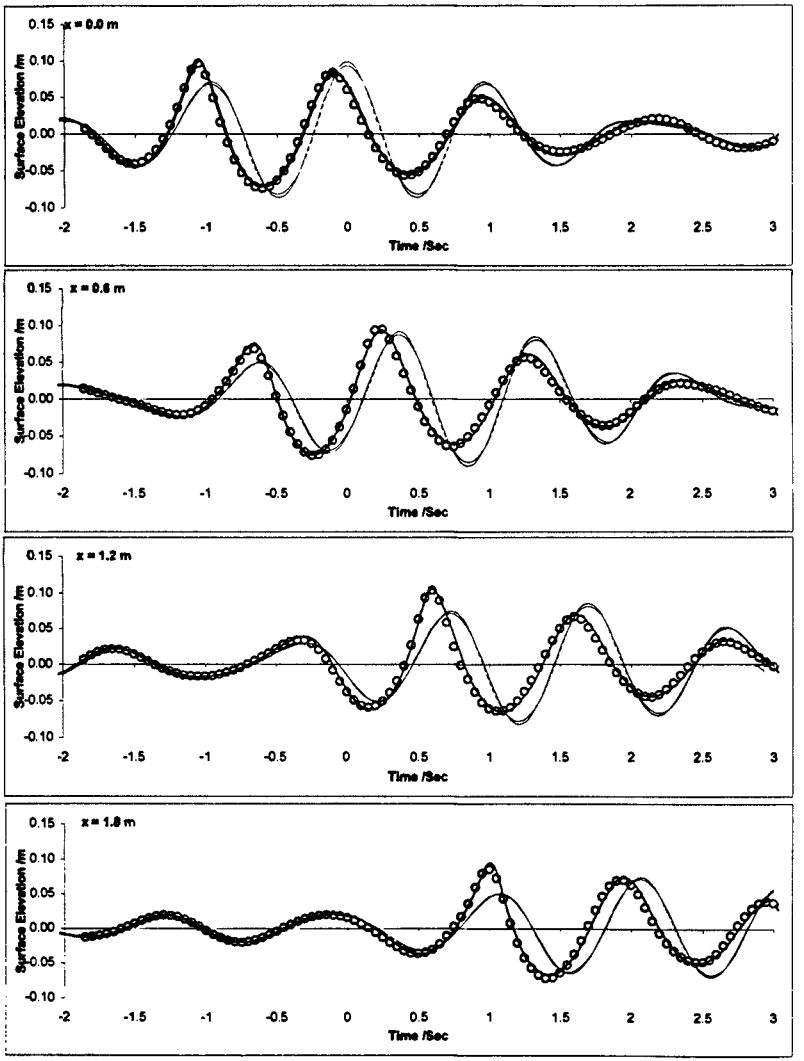

Figure 5: Evolution of a nonlinear wave group.
▬▬ experimental data; **o** numerical model; ——— linear theory;
····· second-order theory .

on figure 6a represents a weakening of the nonlinear wave-wave interactions due to the underlying directionality. Although further analysis of this data is required, it is believed that this effect is caused by a reduction in the absolute wave front steepness and curvature. This is due to the fact that in a directional wave this steepness can be distributed around the perimeter of the wave, and is not constrained in one plane. If this is indeed the case, it clearly explains why extreme unidirectional waves (generated in the laboratory) appear more nonlinear than those observed in the open ocean.

The data presented on figure 6a also has implications for the limiting wave height. If increasing directionality reduces the nonlinearity, this perhaps implies that a larger linear amplitude sum (A) is required to induce incipient wave breaking. To examine this point, a second set of comparisons were undertaken in which the amplitude of the wave components generated at the wave paddles was progressively increased until there was evidence of incipient wave breaking in the vicinity of the focus position. This allowed the variation in the maximum possible crest elevation, for a given underlying frequency bandwidth, to be recorded as a function of the directional spread. This data is presented on figure 6b and clearly suggests that the limiting crest elevation increases with the directional spread. Indeed, figure 6b suggests that the difference between a unidirectional wave group (1/s=0) and a short-crested wave group (with 1/s=0.25) can lead to an increase in the limiting crest elevation by as much as 25%.

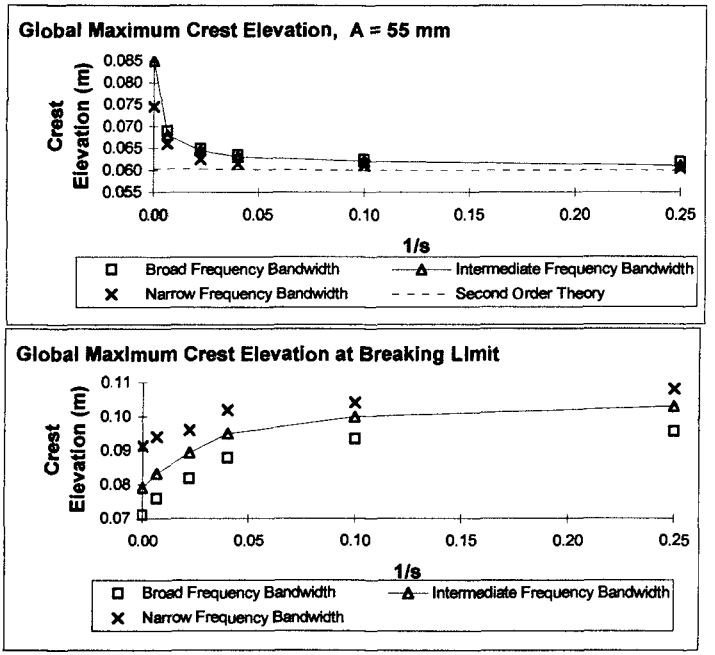

Figures 6a-6b: Maximum crest elevation. (a) A=55mm, (b)A=A_{max}.

5. Nonlinear Interactions and Energy Shifts

To examine the nature of the nonlinear wave-wave interactions and the associated energy shifts, the numerical model was used to simulate the narrow-banded spectrum (case D) with four different directional spreads. In each of these cases the input amplitude sum (A) was such that the largest waves were on the limit of wave breaking. Details of the directional spreads and the input amplitudes are given in table 1.

Wave case.	Directional spread, s.	Input amplitude, A
1	∞ (Unidirectional)	61mm
2	150	71mm
3	45	78mm
4	4	93mm

Table 1: Numerical simulations

Applying a Fast Fourier Transform to the numerically predicted time-history of the water surface elevation, $\eta(t)$ at the position of the largest wave crest allowed the frequency content to be accurately defined. The results of this analysis, applied to each of the wave cases given on table 1, are present on figure 7. In addition, the solid line indicated above the power spectra defines the linear input of the wave components generated at the paddles (for s=4, A=93mm), while the dashed lines indicated on the right hand side of the figure define the range of the second-order frequency sum terms.

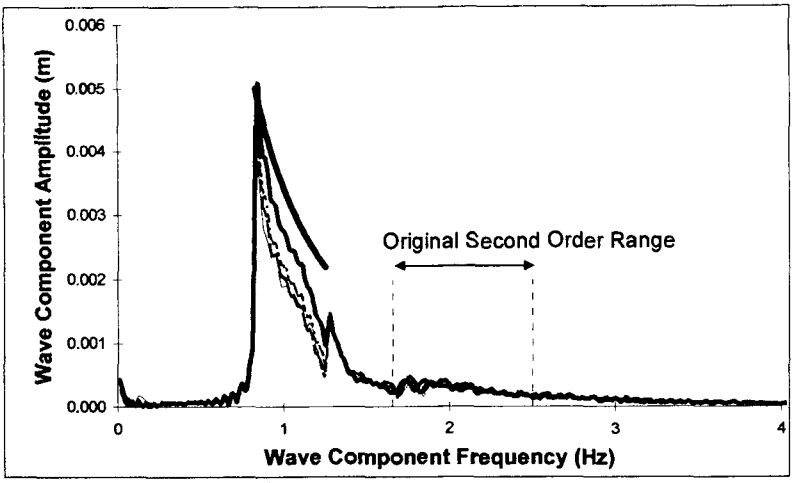

Figure 7: Frequency spectra.

These results clearly suggest that there is a 'loss' of energy from within the linear input range. However, this energy is not primarily transferred to the second-order frequency-sum terms, as one might expect, but appears as significant energy at frequencies just larger than the upper limit of the linear input range (ie. $f \approx 1.3$Hz). Furthermore, although the energy distribution within the linear input range varies between the four cases, due to the different linear amplitude sums; the energy immediately outside the linear range appears to be virtually identical. Given that each of these waves is on the limit of incipient wave breaking, it would seem plausible that the growth of energy within these high frequencies plays a major role in defining the characteristics of extreme wave groups. Furthermore, the energy level indicated on figure 7 appears to represent a threshold value beyond which wave breaking will occur. Detailed analysis of these observed energy transfers is provided by Johannessen and Swan (1998b).

6. Concluding Remarks

The nonlinear evolution of a large number of directional wave groups has been investigated experimentally, and a new numerical model shown to be in good agreement with the laboratory data. The principle advantage of this numerical model is that it represents the only solution that rigorously includes nonlinearity, unsteadiness and directionality. Furthermore, it does not require a detailed description of the nonlinear water surface profile (something which is seldom available in practice) since it is based upon a linear description of the underlying wave spectrum. From a practical point of view the results presented in this paper confirm that for a given linear crest height (or input amplitude sum, A) and frequency bandwidth, the effect of increasing directionality is to significantly reduce the nonlinearity of a wave group. This explains the significant differences between two-dimensional wave flume experiments and field data. However, as a consequence of this reduced nonlinearity, the maximum nonlinear crest elevation that may be obtained, before further growth is limited by wave breaking, increases with the directionality of the wave field provided the frequency bandwidth is held constant. This has important implications for the specification of a 'design' wave, and highlights the need to fully include the nonlinearity, unsteadiness and directionality in both model testing and numerical calculations.

Acknowledgements

The present study has formed part of the research programme 'Uncertainties in Loads on Offshore Structures' sponsored by EPSRC through MTD Ltd and jointly funded with: Amoco (UK) Exploration Company, BP Exploration Operating Co Ltd, Brown & Root Ltd, Exxon Production Research Company, Health and Safety Executive, Norwegian Contractors a.s., Shell UK Exploration and Production, Den norske Stats Oljeselskap a.s. and Texaco Britain Ltd. EPSRC Grant Reference GR/J23976. The authors are also grateful for further funding from the Norwegian Research Council (norges Forskningsråd).

References

Baldock,T.E. & Swan,C. ,(1994) ,'Numerical calculations of large transient water waves' , Appl. Ocean Res., **16**, pp 101- 112.

Baldock,T.E., Swan,C. & Taylor,P.H., (1996), 'A laboratory study of non-linear surface waves on water', Phil. Trans. Roy. Soc. London, Ser. A, **354**, pp 649-676.

Dean, R.G., (1965), 'Stream function representation of non-linear ocean waves', J. Geophys. Res., **70**, pp 4561-4572.

Dold,J.W. & Peregrine, D.H., (1984), 'Steep unsteady waves: an efficient computational scheme', Proc. 19th Int. Conf. Coastal Engineering, ASCE, **1**, pp 955 -67.

Dommermuth, D.G., Yue, K.P., Lin, W.M. & Rapp, R.J. (1988). 'Deep-water plunging breakers: a comparison between potential theory and experiment.' J. Fluid Mech., **189**, pp 423-442.

Fenton,J.D. ,(1985),'A fifth order Stokes' theory for steady waves', J. Waterways, Port, Coastal and Ocean Engng. ,**111**, pp 216-234.

Fenton,J.D. & Rienecker,M.M., (1980), 'Accurate numerical solutions for nonlinear waves', 7th Int. Conf. on Coastal Engng., Sydney, **1**, pp 50-69.

Gear,S.W., (1971), 'Numerical initial value problems in ordinary differential equations', Englewood Cliffs Inc., Prentice Hall.

Johannessen,T.B. & Swan,C. (1998a), 'A Fourier solution for three-dimensional surface water waves. Submitted to J. Fluid Mech.

Johannessen,T.B. & Swan,C. (1998b), 'A laboratory study of directionally spread surface waves on water'. Submitted to Phil. Trans. Roy. Soc. Ser. A.

Jonathan, P.,Taylor,P.H. & Tromans,P.S., (1994), 'Storm Waves in the Northern North Sea', Proc. 7th Int. Conf. on the Behaviour of Offsh. Str., Mass., **2**, pp 481-494.

Longuet-Higgins,M.S. & Stewart,R.W.,(1960) 'Changes in the form of short gravity waves on long waves and tidal currents', J. Fluid Mech., **8**, pp 565-583.

Longuet-Higgins,M.S. & Cokelet,E.D.,(1976), 'The deformation of steep surface waves on water. A numerical method of computation', Proc. Roy. Soc., Ser. A, **350**, pp 1-26.

Rozario, J.B., Tromans, P.S., Taylor, P.H. & Efthymiou, M., (1993), 'Comparisons of loads predicted using 'New Wave' and other wave models with measurements on the Tern structure', In: 'Wave Kinematics and Environmental Forces', Soc. Underwater Tech., Kluwer, **29**, pp 143-158.

Sharma,J.N. & Dean,R.G., (1981), 'Second-Order Directional Seas and Associated Wave Forces', Society of Petroleum Engineers J., 4, pp 129-140.

Smith, S., & Swan, C., (1996), 'Kinematic predictions in large shallow water waves', Proc. 25th Int. Conf.. Coastal Engng., Orlando, Florida. **1**, pp 502-515.

Tromans,P.S.,Anaturk,A. & Hagemeijer,P.,(1991), 'A new model for the kinematics of large ocean waves - application as a design wave', Proc. 1st Int. Offshore and Polar Engng. Conf., **3**, Edinburgh, pp 64-71.

Low Frequency Surf Zone Response to Wave Groups

Merrick C. Haller [1], Uday Putrevu [2], Joan Oltman-Shay [2], and Robert A. Dalrymple [1]

Abstract

The nearshore potential vorticity balance of Bowen and Holman (1989) is expanded to include the forcing from wave group-induced radiation stresses. Model results suggest that the forcing from radiation stresses can drive oscillations in the longshore current that have a spatial structure similar to linear shear instabilities of the longshore current. In addition, the forced response is nearly resonant when the forcing has scales (k, σ) similar to the linearly most unstable mode. Thus, we suggest that the wave groups may provide an initial perturbation necessary for the generation of shear instabilities of longshore currents and enough forcing to overcome frictional damping.

Analysis of data from the SUPERDUCK (1986) field experiment reveals that wave groups were present on days when strong low frequency surf zone motion (shear waves) existed. In addition, some of these groups are shown to have periods and longshore spatial structures comparable to the observed shear wave motions suggesting that incident wave groups are present on this open coast with the required spatial and temporal structure to initiate the low frequency oscillations in the longshore current.

1 Introduction

Shear waves are low-frequency (10^{-3} to $10^{-2}Hz$) vortical motions of surf zone currents. The kinematics of these waves are closely linked to the mean longshore current (Oltman-Shay et al., 1989). Bowen and Holman (1989) suggested that shear waves are generated due to a shear instability of the mean longshore current. Subsequent

[1]Center for Applied Coastal Research, Ocean Engineering Lab, University of Delaware, Newark, DE 19716, USA. Correspondence e-mail: merrick@coastal.udel.edu

[2]NorthWest Research Associates, Inc., P.O. Box 3027, Bellevue, WA 98009, USA.

work (see Shrira et al., 1997 for a complete set of references) has shown that the shear instability model is capable of explaining many of the observed characteristics. However, the instability theory fails to predict the following two features – both related to the effects of bottom friction. First, the instability theory predicts a low-frequency cutoff below which no shear waves are generated (Dodd, 1994; Shrira et al., 1997). Second, instability theory predicts that shear waves should be damped by friction on planar beaches. Both of these predictions are at odds with observations at Duck, NC and Santa Barbara (Leadbetter), CA beaches (Dodd et al., 1992).

Recently, the work of Shrira et al. (1997) showed that both shortcomings of the instability theory could potentially be explained by an explosive instability mechanism. In particular, they showed that shear waves that would otherwise be damped out by friction could grow due to resonant triad interactions provided their initial amplitudes exceed a critical value. However, how such initial (small amplitude) shear waves are generated remains unexplained. In this paper, we show that the direct forcing from wave groups could provide the initial amplitudes required by the resonant interaction model of Shrira et al. (1997). This mechanism follows earlier work by Hamilton and Dalrymple (1994).

The outline of this paper is as follows. Section 2 discusses the theoretical formulation. An example calculation in section 3 shows that direct forcing from wave groups leads to a larger response at shear wave scales, which may provide the initial amplitudes required by the resonant interaction model. In section 4 we analyze data from the SUPERDUCK experiment and find that there is evidence that the forcing required to set up these initial oscillations existed. Data from the experiment at Leadbetter Beach (a planar beach) could not be used in the wave group analysis because the offshore wave array was too short to resolve wave group scales. The final section is devoted to a few concluding remarks.

2 Theoretical formulation

The depth-integrated, short-wave-averaged equations of horizontal momentum read

$$\frac{\partial u}{\partial t} + u\frac{\partial u}{\partial x} + v\frac{\partial u}{\partial y} = -g\frac{\partial \eta}{\partial x} + \tau_x - \frac{\tau^b_{xz}}{\rho h}, \tag{1}$$

$$\frac{\partial v}{\partial t} + u\frac{\partial v}{\partial x} + v\frac{\partial v}{\partial y} = -g\frac{\partial \eta}{\partial y} + \tau_y - \frac{\tau^b_{yz}}{\rho h}, \tag{2}$$

where u and v are depth-averaged horizontal velocities in the cross-shore (x) and longshore (y) directions, respectively; η is the free surface displacement; g is the acceleration due to gravity; $\tau^b_{\alpha z}$ ($\alpha = x, y$) are the bottom shear stresses; and h is the total depth (it includes wave-induced set-down and set-up). Finally, τ_x and τ_y represent the forcing due to the radiation stresses.

We consider the case of a long straight coast. We separate all quantities into steady and time varying parts and assume that steady terms are independent of the longshore coordinate, e.g.,

$$\eta(x,y,t) = \eta_0(x) + \eta_1(x,y,t), \tag{3}$$

where η_1 represents the small ($|\eta_1| \ll |\eta_0|$) modulation effect of the wave groups. All other quantities are defined in an analogous fashion. We assume that the steady current has only a longshore component. That is, we assume

$$u = u_1(x,y,t) \tag{4}$$

$$v = V(x) + v_1(x,y,t). \tag{5}$$

Following Dodd et al. (1992), we parameterize the bottom friction using a linear law. In particular, we assume that $\tau^b_{xz} = \rho\mu u$, and $\tau^b_{yz} = \rho\mu v$, where $\mu = \frac{2}{\pi} c_f U_o$ is the friction coefficient, and U_o is the amplitude of the orbital velocity of the incident short waves and is assumed constant.

These definitions for velocity and bottom shear stress are now substituted into equations (1) and (2). The resulting equations are separated into steady and unsteady parts. We find that the steady problem reduces to the familiar cross-shore momentum balance determining wave set-up and set-down, and the longshore momentum balance governing the generation of the mean longshore current. The unsteady problem is of particular interest here since it governs the dynamics of the low frequency motion in the nearshore.

Following Bowen and Holman (1989), we make the rigid lid assumption, thus, the nondivergence of the continuity equation allows us to introduce a transport stream function, Ψ, such that $\Psi_y = -u_1 h$ and $\Psi_x = v_1 h$ (subscripts (x,y) denote partial differentiation). This leads to the following equation for the stream function:

$$\left(\frac{\partial}{\partial t} + V\frac{\partial}{\partial y} + \frac{\mu}{h}\right)\left(\frac{\Psi_x h_x}{h^2} - \frac{\Psi_{yy}}{h} - \frac{\Psi_{xx}}{h}\right) + \Psi_y\left(\frac{V_x}{h}\right)_x + \frac{\mu h_x \Psi_x}{h^3} = \frac{\partial \tau_{x,1}}{\partial y} - \frac{\partial \tau_{y,1}}{\partial x}, \tag{6}$$

where subscripts denote partial differentiation (except for the definition of $\tau_{\alpha,1}$, $\alpha = x,y$). For simplicity, we concentrate on periodic solutions. Hence, we assume that the stream function may be expressed as

$$\Psi = \Re e\left\{\psi(x)\, e^{i(ky-\sigma t)}\right\}, \tag{7}$$

where $\sigma = 2\pi/T$ (T = wave period) represents the wave frequency and $k = 2\pi/L$ (L = longshore wavelength) is the wavenumber. The amplitude of the stream

function, $\psi(x)$, is in general complex. In addition, the forcing due to radiation stresses will also be assumed proportional to $e^{i(ky-\sigma t)}$, and expressed as

$$\frac{\partial \tau_{x,1}}{\partial y} - \frac{\partial \tau_{y,1}}{\partial x} = \Re e \left\{ F(x,k)\, e^{i(ky-\sigma t)} \right\}. \tag{8}$$

Note that the homogenous version of (6) ($F = 0$) is an eigenvalue problem. Nontrivial solutions for ψ exist only for certain values of the eigenvalues, σ. These frequencies represent the natural frequencies of the system. If the system is forced at (or near) these frequencies, then there is the potential for a large response.

In general, the natural frequencies of (6) are all complex, whereas the forcing frequency has to be real. Therefore, the possibility of exact resonance is somewhat limited for this system. However, there is still a potential for a large response if the frequency mismatch is small.

3 An example calculation

In this section we present an example calculation that illustrates the nature of the forced response. First, we need to specify the longshore current, the wavenumber and frequency of the forcing, and the friction factor. Wherever possible, we choose these parameters such that they are representative of those measured at Santa Barbara's Leadbetter beach. We make this choice because, as mentioned in the introduction, Dodd et al. (1992) found that the shear instability theory predicts that shear waves should be damped out by friction on this planar beach.

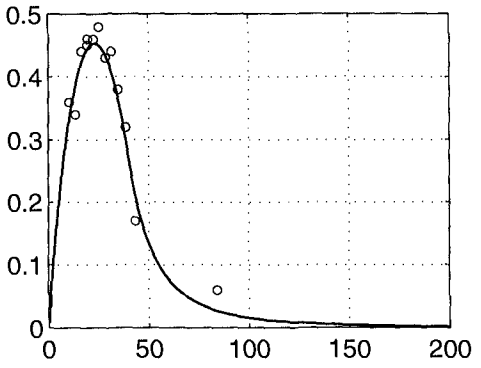

Figure 1: Cross-shore variation of the modeled longshore current (solid line) using the model of Longuet-Higgins (1970), circles represent measured data from Leadbetter Beach, Santa Barbara, February 4, 1980. Note: $x = 0$ is the position of the mean shoreline.

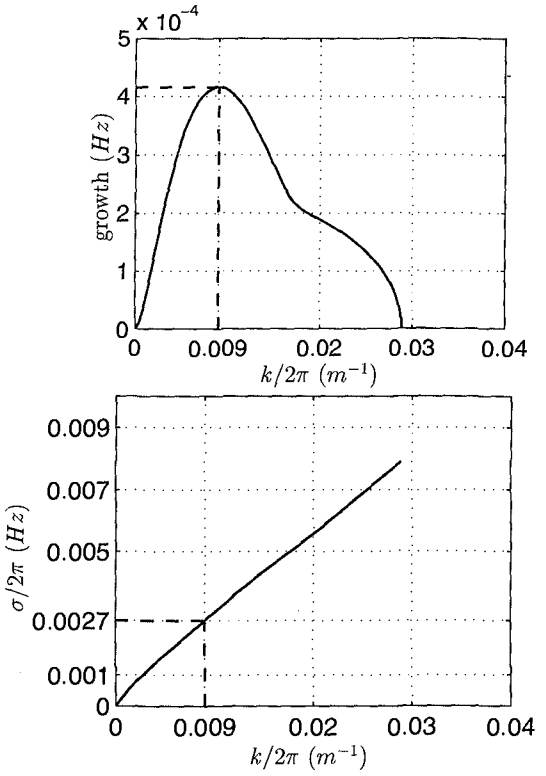

Figure 2: a) Linear growth rate and the b) dispersion relation for the most unstable modes of the homogeneous system for the longshore current profile shown in Figure 1.

The longshore current profile used in our calculations (along with the measured current values) is shown in Figure 1. To first get an estimate of the natural frequencies of the system, we solve the inviscid, homogeneous version of (6) (i.e. $\mu = 0$, $F = 0$). The results are shown in Figure 2. Figure 2a shows the growth rates of the most unstable mode for each wavenumber and Figure 2b shows the real part of the frequency. Dodd et al. (1992) obtained a similar dispersion curve and stated that it compares reasonably well with observations, however, they also found that the inclusion of realistic bottom friction will damp out the instability. Thus, the observations are unlikely to have resulted due to an instability of the longshore current profile. Here we investigate whether radiation stress forcing could have provided the small amplitude shear waves required of the explosive instability mechanism

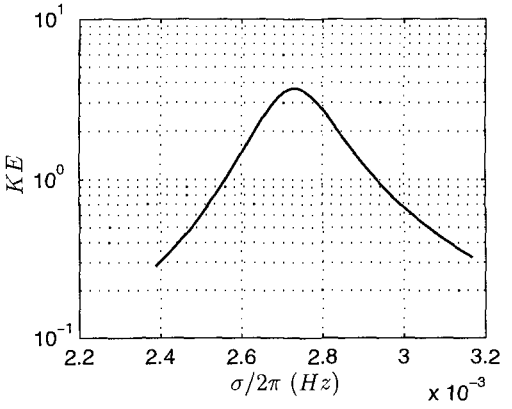

Figure 3: The variation of kinetic energy (KE) as a function of the forcing frequency for a forcing spatial scale of $k = 0.0566\,rad/m$. Shown is the forced system response (equation 6, $F = 0.05 h_x e^{-(x-x_b)^2}$) for the frictional dissipation coefficient: $\mu = 0.00372$.

Shira et al., 1997. To do that we have to first specify the forcing function. In our example calculation (6), we use

$$F = -.0025\, i\, g\, k\, h_x\, e^{-(x-x_b)^2}, \tag{9}$$

where x_b is the distance from the mean shoreline to the breaker location. We obtained this form of the radiation stress forcing term based on the stationary forcing used by Bowen (1969, see Eq. 32). In its present form, we have assumed the forcing to be longshore propagating and have limited the forcing amplitude to a region very close to the zone of initial breaking. This was done in order to include in a simple way the tendency for the breaker line to oscillate in the cross-shore direction with the modulations of the incident waves which destroys most wave grouping shoreward of the initial breaking region. However, the results are not sensitive to the form of the forcing decay away from the breaker line.

As a measure of the forced response, we use the total kinetic energy averaged over a wavelength and period and integrated over x:

$$\overline{KE} = \int_0^\infty \frac{1}{TL} \int_0^T \int_0^L \frac{(u_1^2 + v_1^2)h}{2} dy\, dt\, dx. \tag{10}$$

The variation of shear wave kinetic energy, as a function of forcing frequency, is shown in Figure 3 for a forcing spatial scale of $k = 0.0566\,rad/m$. This k value has the largest growth rate in the unforced, homogeneous system (Figure 2a) and the value of $\mu = 0.0269\,m/s$ is suggested by the model-data comparisons of Dodd

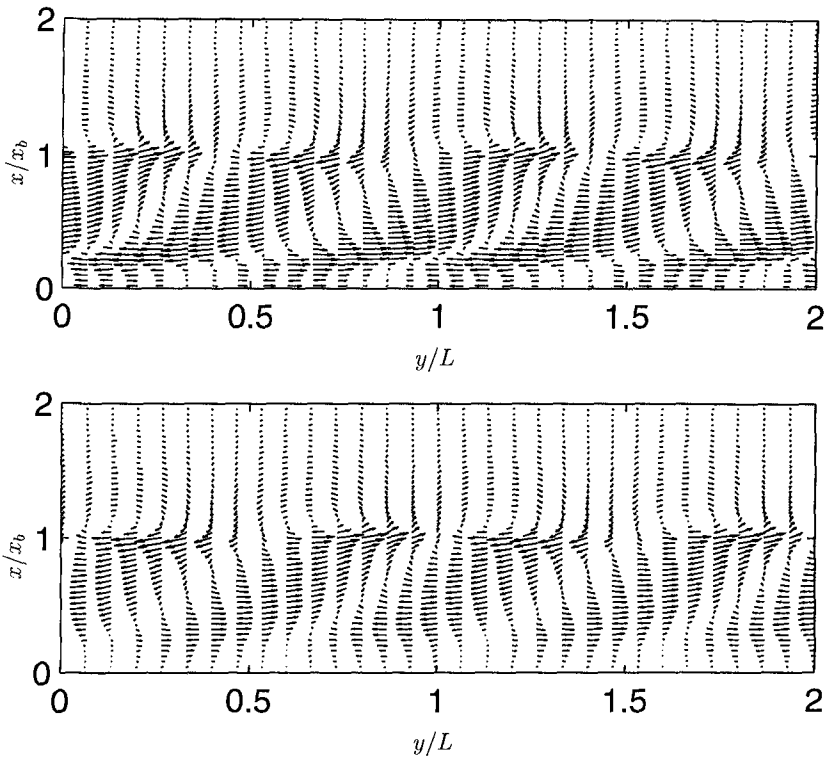

Figure 4: a) Velocity distribution from solution of homogeneous system, $k = 0.0566\,rad \cdot m^{-1}$. b) Velocity distribution from solution of forced system including dissipation, $k = 0.0566\,rad \cdot m^{-1}$, $\mu = 0.00372$.

et al. 1992. It is important to note that, though not shown here, the μ value does not alter the frequency of the maximum kinetic energy ($0.0027\,Hz$); the peak frequency consistently falls near the resonant frequency of the unforced system ($\sigma/2\pi = 0.0027\,Hz$ in Figure 2b).

A comparison of the forced and free shear wave velocity fields is presented in Figure 4 a and b. Figure 4a shows the velocity field of the free, undamped, shear instability ($\mu = 0, F = 0$). The magnitude and pattern of this field is remarkably similar to the forced, damped shear wave field (Figure 4b, $\mu = 0.00372$, F as defined in eq. 9). Note that the longshore phase difference between the two figures is arbitrary.

Figures 3 and 4 suggest an alternative shear wave generation mechanism for a

beach such as Leadbetter where shear waves cannot be generated from an instability of the longshore current (assuming realistic frictional damping). These figures show that given forcing with spatial and temporal scales near those of the shear waves, the system can preferentially excite frequency-wavenumber scales that satisfy the free system and generate wave patterns with similar magnitude and form to the free, undamped shear waves. It is then plausible that these forced motions could resonantly grow via the explosive instability mechanism suggested by Shrira et al. (1997).

4 Field Data Analysis

The results from the calculations in Section 3 suggest that if wave group energy is present near the most unstable shear wave mode (from linear theory) in frequency-wavenumber space, the possibility of a near-resonant surf zone response to this forcing exists and an explosive instability generation can occur. In the following, field data from the SUPERDUCK experiment are analyzed for the presence of radiation stress forcing at the scales of shear waves.

The SUPERDUCK experiment was conducted by the U.S. Army Corps of Engineers in October of 1986 at Duck, North Carolina. The beach at this site trends NW-SE and is centrally located within a 100-km barrier spit (Crowson et al., 1988). The beach slope is typically 1:20 in the surf zone and decreases to 1:200 offshore. In addition, the bathymetry is characterized by a three-dimensional bar system which often becomes linear during storms (Lippmann, 1989).

Surf zone velocity records were obtained from a longshore array of ten Marsh-McBirney bidirectional electromagnetic current meters located approximately 55 m offshore from the mean shoreline in the trough of the bar (Oltman-Shay et al., 1989). The array had a minimum sensor separation of 10 m and total longshore extent of 510 m.

The incident wave climate was obtained by a linear array of 10 bottom-mounted pressure sensors located approximately 800 m offshore in 8 m water depth and spanning 255 m in the longshore direction. The array elements had a minimum sensor separation of 5 m. The wave fields measured during the experiment were highly variable but often consisted of longer period swell from the south along with shorter period wind-generated waves from the north and the surf zone usually extended approximately 100 m from the shoreline. Data for all sensors were sampled at 2 Hz during 4-hour measuring periods centered about high and low tides and the 4-hour tidal range was $\sim$ 20 cm with a shoreline excursion of 2 m.

The work of Oltman-Shay et al. (1989) showed that the vortical motions, due to shear instabilities of the longshore current (or shear waves), reside in the lower end of the infragravity band ($0.001 < f < 0.01$ Hz) with longshore wavelengths $100 < L < 1000$ m. Typical two-dimensional (f, k) spectra of measured surf zone velocities (u,v) from the SUPERDUCK data set contain a ridge of energy spanning this range of frequencies and wavelengths.

Offshore Wave Groupiness

To look for radiation stress forcing with similar scales to shear waves, we examine the incident wave envelopes associated with wave groups using the pressure records from the offshore (8 m depth) array. Each of the pressure records were divided into sections 2048 s in length, demeaned and then detrended (using a least squares quadratic fit). The pressure records were converted to records of water surface elevation using the pressure response factor according to linear theory. The wave records were then bandpass filtered (0.06 – 0.30 Hz) to remove low (infragravity) frequency and high (wave harmonics, turbulence) frequency energy outside of the wind wave band. Time series of wave envelopes were computed from the filtered wave records using the Hilbert transform method (Melville, 1983). The specific data runs used in the present analysis represent a subset of the entire SUPERDUCK data set. Data selection was based on whether energetic shear wave motions were present in the nearshore current records during the data run and by data quality and availability considerations. The incident wave conditions during the data runs used herein are considered typical for the field site. If a groupiness factor for each record is defined by $\sqrt{2} \cdot \sigma_A/\overline{A}$, where σ_A is the standard deviation of the wave envelope, $\overline{A}$ is the mean, and GF varies from $0 \rightarrow O(1)$ then the average GF for these records is ~ 0.75; suggesting significant wave grouping was present offshore of the surf zone on the days analyzed herein. In addition, previous work using data from this field site has indicated that wave grouping can persist into the surf zone (List, 1991; Haller and Dalrymple, 1995).

Offshore Wave Groups and Surf Zone Shear Waves

Phase and coherence between the wave group time series of the offshore pressure sensors were calculated and plotted, as a function of sensor alongshore separation, to estimate the longshore scale and propagation direction of the incident wave groups. The offshore wave group phase and coherence plots were then compared with the (surf zone) shear wave phase and coherence plots computed from the longshore current records. All cross-spectra were computed using the standard Fast Fourier Transform method after first dividing each time series into 13 ensembles 2048 s in length with 50% overlap and tapering with a Hamming window. The number of spectral components was then reduced by half using a 2-point average resulting in a resolution of $\Delta f = .001$ Hz and 44 degrees of freedom (d.o.f.).

Using the longshore current records, the range of frequencies which contained spatially coherent shear waves was determined for each data run (usually 0.001 – 0.006 Hz). Typically, the shear waves demonstrated strong coherence for longshore distances of $\sim$ 200 m. Oltman-Shay et al. (1989) showed that cross-shore current records also indicated coherent shear waves of similar scale. However, offshore wave group spatial coherence was found to typically be less than 100 m. The tendency for wave groups to have low spatial coherence is not unexpected since wave grouping is likely a random process and is therefore broad banded in wavenumber at a given frequency. This is in contrast to shear waves, which are the result of

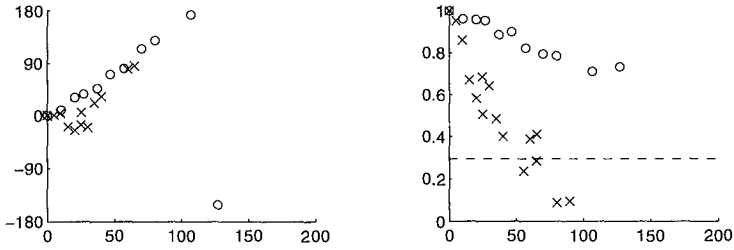

Figure 5: Comparison of (a) relative phase vs. lag, (b) coherence vs. lag for shear waves (**o**) and offshore wave groups (**x**) at frequency 0.003 Hz. Dashed line represents 85% confidence interval, 44 d.o.f.. Data is from October 15 at 0945 EST sensors LA 1-6, LX 1-5.

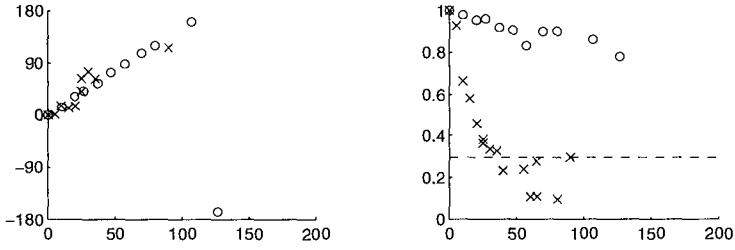

Figure 6: Comparison of (a) relative phase vs. lag, (b) coherence vs. lag for shear waves (**o**) and offshore wave groups (**x**) at frequency 0.003 Hz. Dashed line represents 85% confidence interval, 44 d.o.f.. Data is from October 16 at 1020 EST sensors LA 1-6, LX 1-5.

a resonant process and tend to be narrow banded in wavenumber. In addition, wave group spectra tend to exhibit more statistical uncertainty then the original wave/current records and very long wave records are needed in order to obtain truly stationary estimates of wave grouping (Nelson et al., 1988). To limit the processing of incoherent data, the offshore array was limited to six closely spaced sensors with a maximum lag of 90 m. The nearshore array was similarly limited to five sensors with a maximum lag of 130 m.

Using the wave group cross-spectra, the range of existing shear wave frequencies were searched for the presence of spatially coherent wave groups. Relatively few

cases were found in which the offshore wave groups were clearly shown to have scales similar to shear waves. In many cases the wave groups did not exhibit significant coherence. In addition, there were cases where coherent wave groups existed but with scales different from shear waves and those will not be discussed here. The cases which best demonstrate that wave groups can exist offshore at similar spatial scales as shear waves are shown in Figures 5-6.

For comparison, the relative phase and coherence vs. longshore lag of the shear waves is plotted together with those of the offshore wave groups. The slope (+/-) of phase vs. lag indicates the direction of propagation (upcoast/downcoast) for the given motion and the figures show that the offshore wave groups at these frequencies were propagating in the same direction as the shear waves. The comparisons of coherence indicate that wave groups lose coherence at much shorter distances than shear waves ($\sim$ 50 m). The 85% confidence interval is also shown for reference (dashed line). The relative phase for lags which did not demonstrate coherence above the 85% confidence level are not plotted.

Surf Zone Wave Groups and Shear Waves

The computations in Section 3 assumed that incident wave heights had a longshore progressive 2-D structure near the breaker line that swiftly decayed shoreward due to wave breaking. It is expected that any wave grouping present at the offshore array would persist and possibly increase in amplitude towards the breaker line due to shoaling. However, since the offshore array was about eight surf zone widths (x_b) from the shoreline, the cross-shore current records measured at the nearshore array (located $\sim x_b/2$) were also examined for any evidence of wave grouping persisting shoreward of the breaker line. To do this, it was necessary to assume that, in the range of incident wave frequencies ($0.06 < f < 0.3$ Hz), the auto-spectra of the u velocities have the same shape as sea surface elevation spectra at the same location, since there were no pressure sensors in the nearshore (longshore) array. Figure 7 indicates this assumption is reasonable. The choice of cross-shore velocities for the wave group analysis was made because the u auto-spectra were more energetic at incident wave frequencies due to the near normal incidence of the waves at this nearshore location. The u velocity records were converted to surf zone wave (current) envelopes in the same manner as the offshore wave records (neglecting the pressure to water surface conversion).

A result from the phase and coherence analysis of the surf zone wave envelopes is shown in Figure 8. The linear phase progression in the longshore direction demonstrates that a certain amount of wave grouping was present in the surf zone during the data run taken the morning of October 18. It should be noted that the bandpass filtering operation was tested with different windows (Hamming, Hanning) to rule out the possibility of leakage of the energetic shear wave motions into the incident wave band during filtering. The offshore wave envelopes did not show strong spatial coherence at this frequency suggesting that wave grouping was locally induced during this data run.

The results of the cross-spectral analysis for this subset of SUPERDUCK data

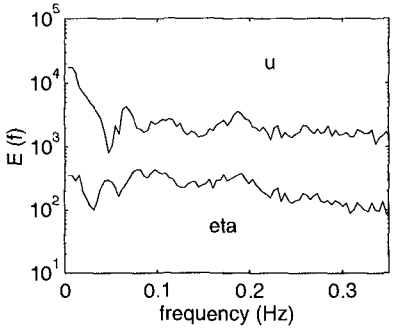

Figure 7: Comparison of auto-spectra of cross-shore velocity and water surface elevation from nearly co-located surf zone sensors. Data is from October 18 at 1140 EST.

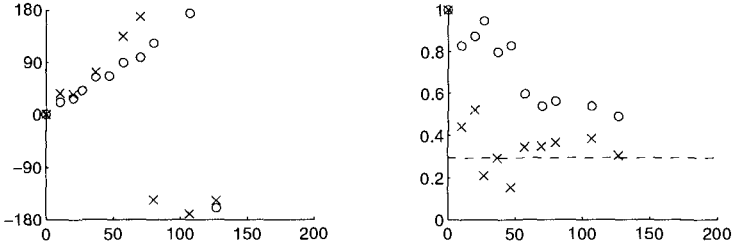

Figure 8: Comparison of (a) relative phase vs. lag, (b) coherence vs. lag for shear waves (**o**) and surf zone wave groups determined from cross-shore velocity records (**x**) at frequency 0.003 Hz. Dashed line represents 85% confidence interval, 44 d.o.f.. Data is from October 18 at 1140 EST sensors LX 1-5.

demonstrate that wave grouping at shear wave and other scales can exist in the field. The calculations presented in Section 3 indicate that the response to such forcing will occur primarily at shear wave scales and that the velocity field will closely resemble the velocity field under free shear waves. Thus, it is likely that direct forcing from wave groups might provide the initial perturbations required for shear wave growth.

5 Conclusions

The inclusion of a forcing term due to wave group induced radiation stresses in the nearshore potential vorticity balance of Bowen and Holman (1989) shows that incident wave groups can force a surf zone response similar to shear waves. If the forced response has similar scales (k, σ) to the linear most unstable mode, the response is nearly resonant.

Field data were examined for the presence of wave group forcing with scales similar to the observed shear waves. Analysis of phase and coherence shows that wave grouping of shear wave scales was sometimes present during the SUPERDUCK experiment. The results suggest that wave grouping can exist to perturb the nearshore velocity field at temporal and spatial scales of the shear instabilities.

In addition, it is interesting to view the results presented here in light of the recent work of Shira et al. (1997). Their work indicates that the range of unstable scales for shear waves excited by the explosive instability mechanism is much larger than that determined by the linear instability mechanism. This suggests that the presence of any of a wide range of coherent wave group spatial scales can force any of a wide range of initial instabilities to feed the explosive instability mechanism. Also, they show that the explosive instability occurs, even when all linear instabilities are damped by bottom friction, as long as the initial perturbations exceed a certain amplitude.

The wave group forcing mechanism presented here and the results of Shrira et al. (1997) provide a possible explanation for the observation of shear wave instabilities at Leadbetter Beach, CA. Dodd et al. (1992) found that linear instability theory did not predict instabilities for that beach unless the frictional damping was decreased by decreasing the friction coefficient, c_f, to unrealistic values. In light of the above, it can be hypothesized that the shear waves observed at Leadbetter Beach may have been generated via the explosive instability mechanism with wave groups providing the initial instabilites.

Acknowledgments

Funding for U. Putrevu and J. Oltman-Shay was provided by ONR Coastal Dynamics under contract number N00014-96-C-0075. Funding for M. Haller and R. Dalrymple was provided by the Army Research Office through University Research Initiative Grant DAAL 03-92-G-0116. The authors wish to thank Bob Hamilton for providing some of the software used in the data analysis and Bill Birkemeier, Peter Howd, Ed Thornton, and the staff at the Army Corps Field Research Facility (FRF) at Duck, NC, for their contributions to the field data acquisition and distribution (the 8 m array is still maintained as part of the FRF infrastructure).

References

Bowen, A. J., and R. A. Holman, Shear instabilities of the mean longshore current, 1. Theory, *J. Geophys. Res.,94,* 18023-18030, 1989.

Crowson, R. A., W. A. Birkemeier, H. M. Klein, and H. C. Miller, SUPERDUCK nearshore processes experiment: Summary of studies. CERC Field Research Facility, *Tech. Rep. CERC-88-12,* 81 pp., Coastal Eng. Res. Cent., Vicksburg, MS, 1988.

Dodd, N., J. Oltman-Shay, and E. B. Thornton, Shear instabilities in the longshore current: A comparison of observation and theory, *J. Phys. Oceanogr., 22,* 1, 62-82, 1992.

Haller, M. C., and R. A. Dalrymple, Looking for wave groups in the surf zone, Proceedings of Coastal Dynamics '95, 81-92, 1995.

Hamilton, R. P., and R. A. Dalrymple, Wave group forcing in low frequency surf zone motion, Center for Applied Coastal Research, *Res. Rpt. CACR-94-23,* 1994.

Lippmann, T., The stability and spatial variability of sand bar morphology, M.S. Thesis, 132 pp., Oreg. St. Univ., Corvallis, 1989.

List, J. H., Wave groupiness variations in the nearshore, *Coastal Eng.,* 15, 475-496, 1991.

Longuet-Higgins, M. S., Longshore currents generated by obliquely incident sea waves, 2, *J. Geophys. Res., 97,* (33), 6790-6801, 1970.

Melville, W. K. Wave modulation and breakdown, *J. Fluid Mech., 128,* 489-506, 1983.

Nelson, R. C., P. D. Treloar, and N. V. Lawson, The dependency of inshore long waves on the characteristics of offshore short waves, *Coast. Eng.,* 12, 213-231, 1988.

Oltman-Shay, J., P. A. Howd, and W. A. Birkemeier, Shear instabilities of the mean longshore current, 2. Field observations, *J. Geophys. Res., 94,* 18,031-18,042, 1989.

Shrira, V. I., V. V. Voronovich, and N. G. Kozhelupova, Explosive instability of vorticity waves, *J. Phys. Oceanogr., 27,* 542-554, 1997.

Wave Dynamics and Revetment Design on a Natural Reef

Thomas Jensen[1], Peter Sloth[1] and Vagner Jacobsen[1]

Abstract

In connection with hydraulic studies of a new coastal resort development on the south-east coast of Bali in Indonesia, a three-dimensional (3D) physical model study was carried out. The study was aimed at the determination of the wave transformation over a shallow natural reef in front of the resort and for the design of the rubble mound revetments to be built for coastal protection. Due to the heavy wave breaking on the reef, physical model tests were the only viable avenue for obtaining a reliable design of the revetment structures located behind the shallow reef area. The stability of the armour layer as well as the overtopping of the revetments were equally important aspects of this part of the study, since not only should the resort be protected against storm waves, but visitors should also be able to comfortably visit the coastal areas during more normal wave conditions.

This paper mainly concerns the wave dynamics on the reef. Due to the limited water depth the wave conditions were dominated by heavy wave breaking and the associated release of the bound long-period wave components in the wave groups of the incident wave train. These long-period wave components caused a dynamic water level set-up with long-period variations in front of the revetments (surf beats). The depth-limited wave conditions on the reef and the dynamic water level set-up had major influence on the evolution of damage and overtopping of the revetments and made the design of the revetments particularly complex.

[1] Danish Hydraulic Institute, Agern Allé 5, DK-2970 Hørsholm, Denmark. Fax: +45 4517 9186
e-mail: thj@dhi.dk, prs@dhi.dk and vj@dhi.dk

Introduction

Bali Turtle Island Development Project is a major tourism-related coastal development project located on the south-east coast of Bali, Indonesia. The site location is shown in Figure 1. The project involves around 3.7 km^2 of land reclamation constructed on an existing reef facing the Lombok Strait, which connects to the Indian Ocean. The completed reclamation will include three artificial lagoons, four artificial pocket beaches, six artificial headlands and a causeway/bridge connection to the Balinese mainland. Figure 2 shows the existing and the reclaimed Turtle Island and Figure 3 shows an aerial photo of the land reclamation in progress.

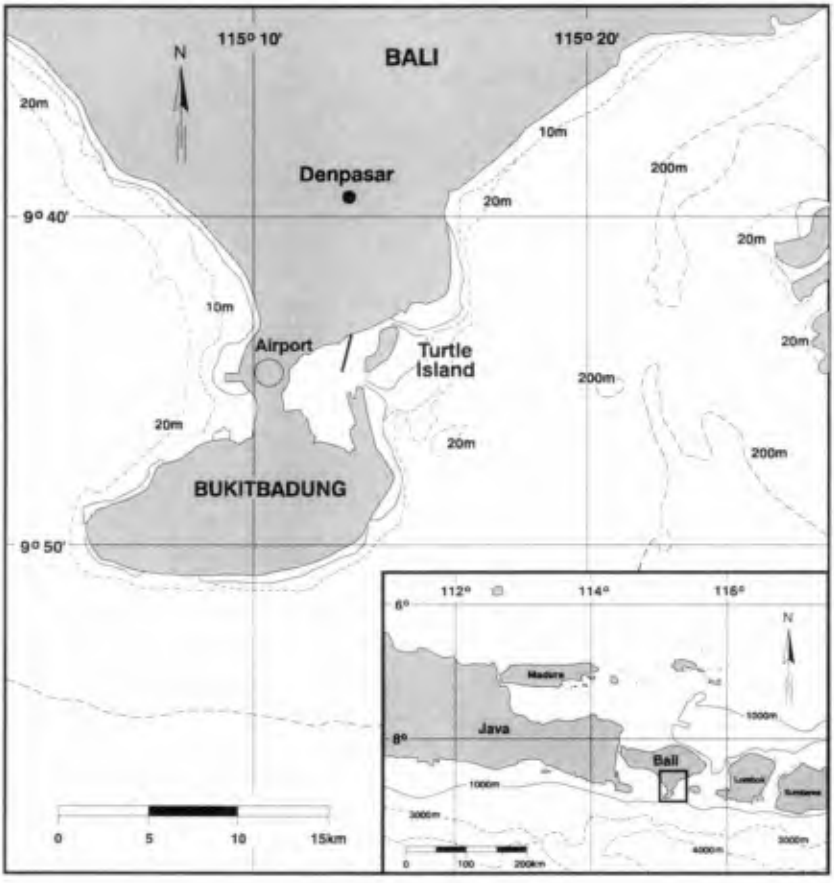

Figure 1. Site location.

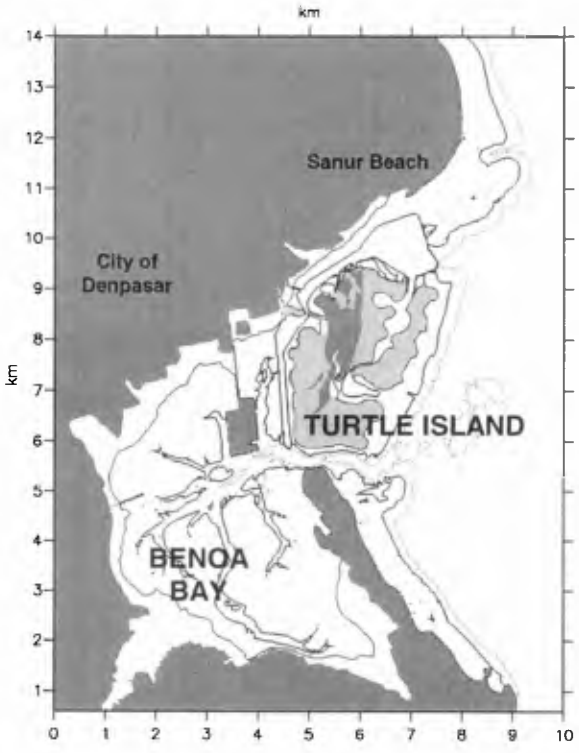

Figure 2. The existing and the reclaimed (light shaded) Turtle Island.

Figure 3. Aerial photo of the reclamation works in progress.

To aid the contractor, Penta Ocean Construction Company, in the detailed design works for Bali Turtle Island Development, hydraulic investigations were carried out by Danish Hydraulic Institute (DHI). Thc overall project involved the following aspects:

- Determination of environmental design conditions (waves, water levels, etc)
- Hydraulic design of the primary revetment protection using physical modelling
- Assessment of impact upon navigation
- Spreading of dredged material
- Water quality impact assessment
- Coastal impact assessment (beach stability and sediment morphology)
- Environmental monitoring during dredging.

This paper concerns the physical modelling used for design and optimisation of the revetments and for studying the wave transformation over the reef in front of the extended Turtle Island. An overview of the development project as a whole and detailed information on the other aspects of the project are given in the accompanying ICCE '98 paper by Driscoll et al (1998) as well as in Driscoll et al (1997) and Sloth et al (1997).

Physical Modelling

Onc of the challenges faced in the project was the design of the revetments used as coastal protection of the headlands. Due to the heavy wave breaking and complex wave dynamics on the reef in front of the revetments, the design procedure was far from trivial. Physical model tests were the only viable avenue for obtaining a reliable design of the revetment structures located behind the shallow reef area. The physical model tests comprised the following two tasks:

- Wave transformation tests
- Revetment stability and overtopping tests

In addition to predicting the necessary information on the wave conditions on the reef for revetment design, the results of the wave transformation tests were used to calibrate numerical models used for the prediction of eg beach stability (see Driscoll et al, 1998).

The purpose of the revetment stability and overtopping tests was to optimise the design of the revetments to be built as coastal protection of the headlands on the extended Turtle Island. This optimisation involved the determination of the required size of stones for the revetment armour as well as the determination of the optimum crest height of the revetments to obtain both an aesthetic design and acceptable levels of overtopping discharge. Not only should the resort be protected against storm waves, but visitors should also be able to admire the scenery at sea and comfortably visit the area during more normal wave conditions. Therefore, both stability and overtopping were equally important aspects of the investigations in the physical model.

The model was constructed in scale 1:40 in one of DHI's wave basins, and covered a prototype area of approximately 1200 m by 1200 m. The extent of the physical model is shown in Figure 4. Based on detailed local surveys, the reef was modelled to detail out to a water depth of 13 m relative to Port Datum (PD–LAT) corresponding to 14.3 m relative to mean sea level (MSL). Figure 5 shows a sketched cross-section of the reef, and Figure 6 shows the overall layout of the physical model.

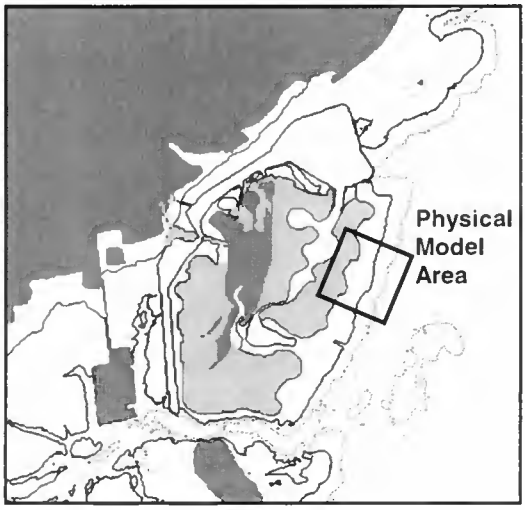

Figure 4. Extent of physical model area.

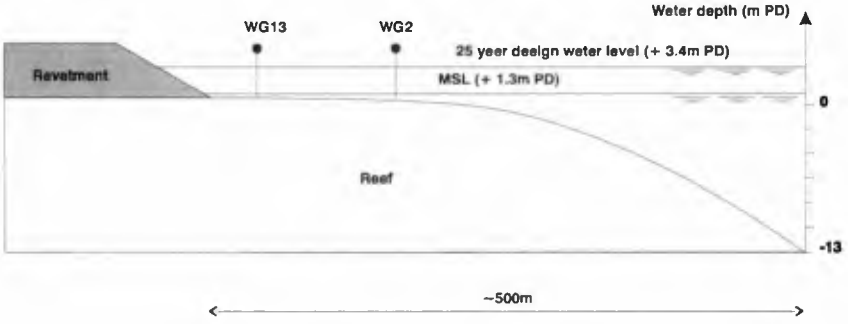

Figure 5. Sketch of a typical cross-section of the reef (distorted length scale).

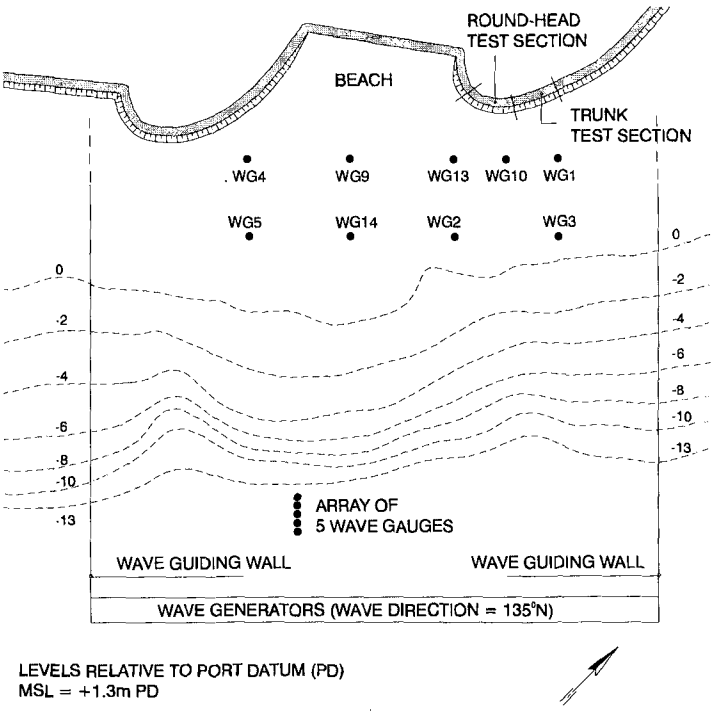

Figure 6. Layout of physical model.

All model tests were carried out with long-crested, irregular waves (Pierson-Moskowitz spectra) with significant wave heights (H_{m0}) ranging from $H_{m0} \approx 1$ m to $H_{m0} \approx 5$ m and peak periods (T_p) of between $T_p \approx 8$ s and $T_p \approx 17$ s. Two different water levels were used in the tests, one corresponding to mean high water spring (+1.1 m MSL or approximately 1.5 m of water depth on the reef), and one corresponding to the 25-year design water level (+2.1 m MSL or approximately 2.5 m of water depth on the reef). Two different angles of wave incidence were investigated in the tests, 135°N (head-on waves) and 155°N (oblique waves). Only the results obtained with the 25-year design water level (+2.1 m MSL) and head-on waves (135°N) are addressed in this paper. The applied wave conditions at the boundary of the physical model were based on an extensive numerical model study of the nearshore wave climate, in which offshore wave conditions from the Indian Ocean were transformed into the area of interest. This aspect of the study is described further in Sloth et al (1997). The following extreme wave conditions were identified:

- 1-year condition: $H_{m0} = 3.0$ m, $T_p = 12.7$ s
- 10-year condition: $H_{m0} = 4.0$ m, $T_p = 12.7$ s
- 100-year condition: $H_{m0} = 4.5$ m, $T_p = 12.7$ s

During the tests, waves were measured at nine locations on the reef (see Figure 6). The incident waves were determined by reflection analysis using an array of five wave gauges in front of the reef. In the revetment stability and overtopping tests, the overtopping discharge and the stability of the revetment armour were monitored for a number of different revetment configurations (size of armour stone, crest height and crest width). A sketch of the general layout of the revetments test section is shown in Figure 7. Figure 8 shows a photo of the revetment test section.

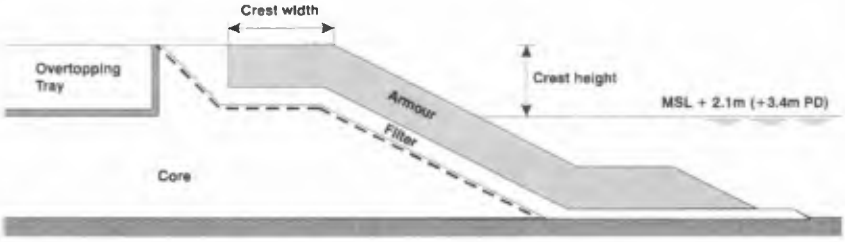

Figure 7. Cross-section of revetment test section.

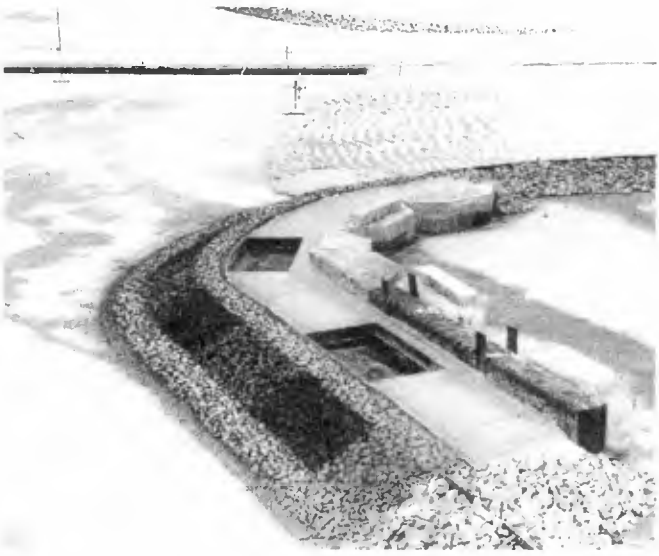

Figure 8. Photo of revetment test section.

Wave Dynamics on the reef

During severe wave conditions, a relatively large rise in the mean water level on the reef was observed. This stationary water level set-up increased with the incident significant wave height ($H_{m0,i}$) reaching approximately 0.4 m for the 25-year wave conditions.

In addition to this stationary water level set-up, a dynamic set-up was also observed on the reef. When the individual waves in a wave group break, the bound long waves associated with the wave groups are released on the reef as free long waves. These long waves cause a dynamic water level set-up or surf beat. Figure 8 shows wave spectra of surface elevations measured outside the reef (WG12) and on the reef (WG2) for four different incident wave conditions. The long-period waves on the reef are seen clearly in the spectra obtained at WG2 as substantial energy at frequencies below 0.05 Hz (periods (T) longer than 20 s).

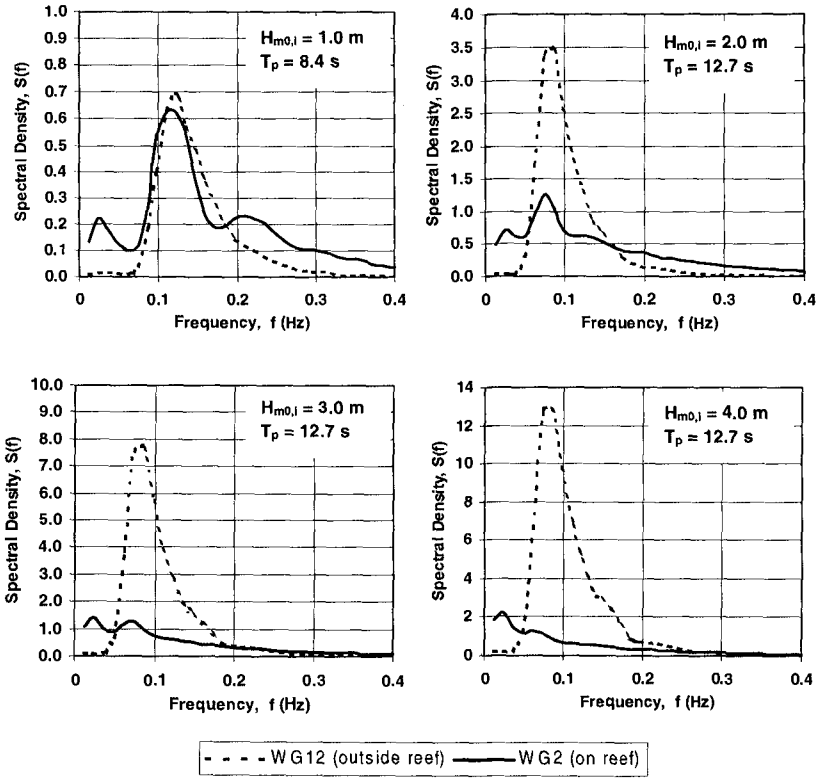

Figure 8. Measured wave spectra on the reef and outside the reef.

The dynamic water level set-up caused by the long-period waves on the reef is also seen in the time series in Figure 9, which shows the measured surface elevations at WG12 (outside the reef) and at WG2 (on the reef). For WG2 low-pass filtered and high-pass filtered signals (for T < 25 s and T > 25 s) are also shown. It is seen from Figure 9 that for this incident wave condition, the amplitude of the dynamic set-up is occasionally in the order of 1 m.

It should be noted that even though the model (as any other physical model) cannot be deemed totally free of model effects, the observed dynamic set-up was proven not to be significantly influenced by eg seiching of the laboratory basin or re-reflections from the wave paddle.

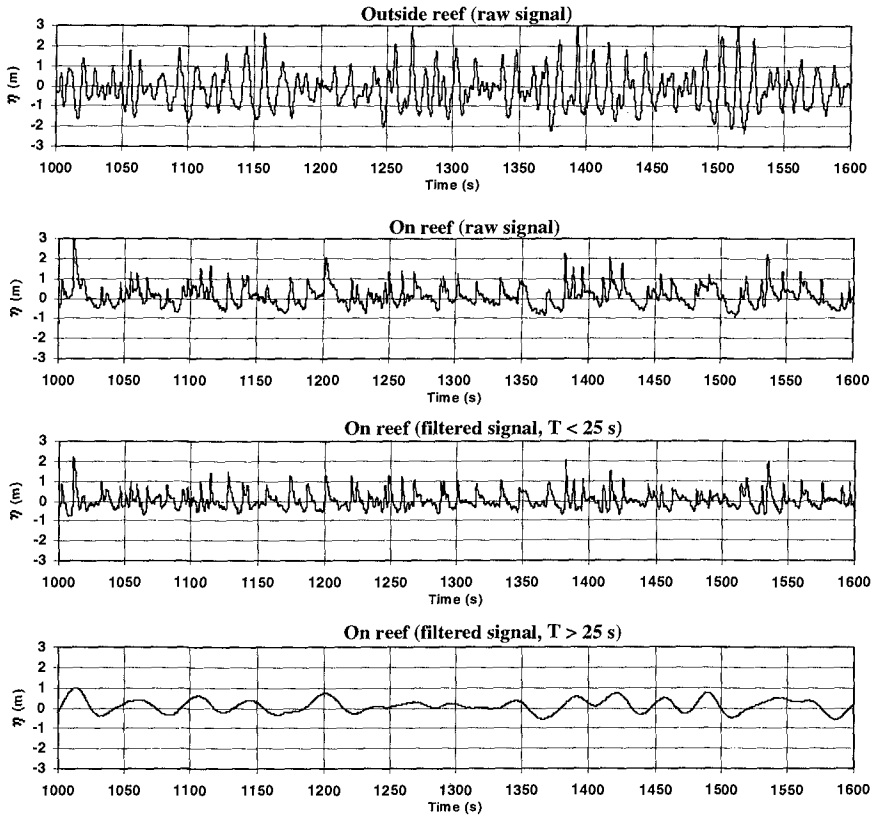

Figure 9. Time series of surface elevations on the reef ($H_{m0,i}$ = 4.0 m, T_p = 12.7 s).

Prototype wave measurements presented by Sulaiman et al (1994) for the reef off Sanur Beach just north of Turtle Island on the Balinese mainland (see Figure 2) also showed the presence of long-period wave components on the reef.

Since the long-period waves on the reef were generated by the wave breaking, the amount of long-period energy on the reef increased with the incident significant wave height ($H_{m0,i}$). This can be seen in Figure 10, which shows the standard deviation of the long-period wave components (T > 25 s) at WG13 on the reef as a function of $H_{m0,i}$. The standard deviation has been derived from time series low-pass filtered at 0.04 Hz.

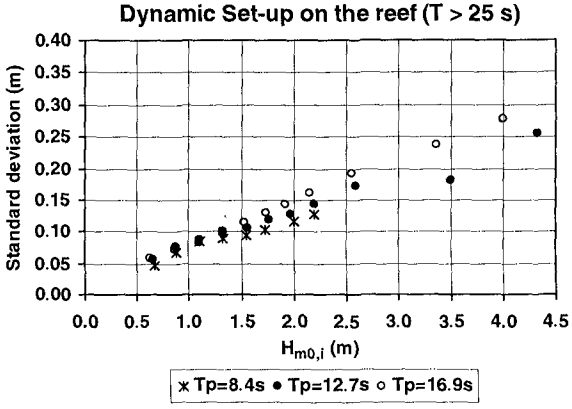

Figure 10. Standard deviation of the dynamic set-up on the reef versus $H_{m0,i}$.

So far only the long-period wave components (T > 25 s) have been addressed, but also the short-period wave components (T < 25 s) were analysed. The wave parameters presented in the following have been derived from time series where all energy with periods longer than 25 s has been removed by high-pass filtering. For the three different wave periods investigated in the wave transformation tests, Figure 11 shows wave parameters (H_{m0}, H_{max}, H_{mean} and T_z) at WG13 on the reef as a function of the incident significant wave height, $H_{m0,i}$.

H_{m0} is the spectral estimate of the significant wave height on the reef (calculated as four times the standard deviation of the surface elevation). The three parameters H_{max} (the maximum wave height), H_{mean} (the mean wave height) and T_z (the mean zero-crossing period) have been estimated from zero-crossing analysis of the high-pass filtered time series.

It should be noted that due to the altered wave height distribution on the reef, the presentcd H_{m0}-values on the reef do not necessarily correspond to $H_{1/3}$, which is often used to define the significant wave height as the average of the highest one-third of the waves in a sea state.

From Figure 11, it is seen that irrespective of the incident wave period, the mean zero-crossing period on the reef approaches a constant value of approximately 6 s. This general reduction in wave period is a consequence of the heavy wave breaking occurring over the reef. The changes in wave period and reduction of wave energy on the reef can also be seen from the recorded surface elevations and the wave spectra on the reef (Figures 9 and 8, respectively). The wave spectra on the reef cover a wider range of frequencies than the incident spectrum. The field measurements at Sanur Beach by Sulaiman et al (1994) also showed broader wave spectra and reduction in wave period on the reef.

Figure 11 also shows that the incident wave periods have minor influence on the wave heights on the reef. The effect of depth-limited waves is clearly illustrated, since the maximum wave height on the reef is reached for an incident significant wave height of approximately $H_{m0,i}$ =2 m, corresponding to less than the 1-year wave condition outside the reef.

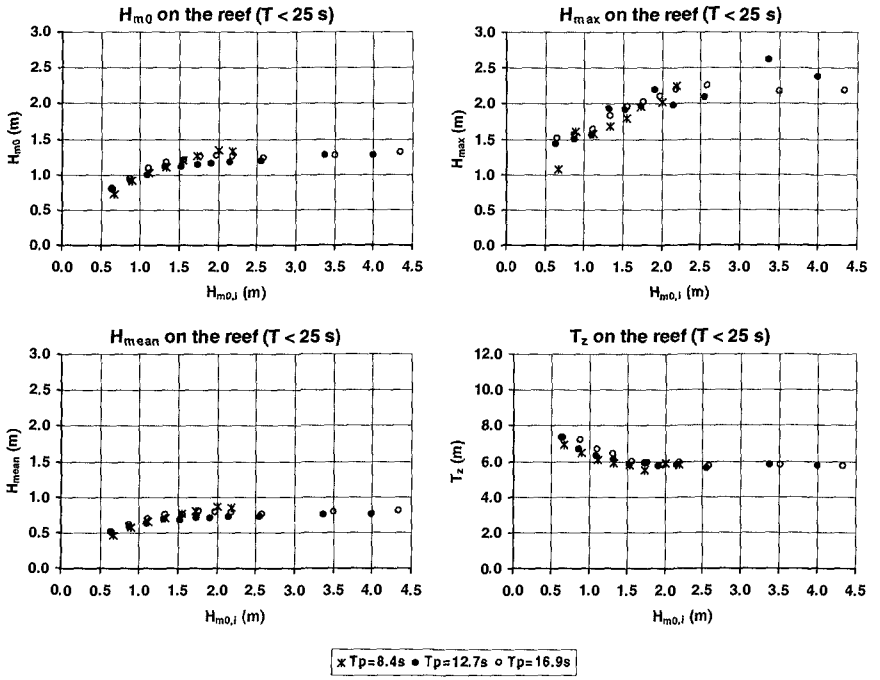

Figure 11. Wave conditions at WG13 on the reef (short-period wave components).

Consequences of Wave Dynamics on Revetment Design

The following two phenomena induced by the shallow reef were particularly crucial with respect to design and optimisation of the revetment structures:

- The depth-limited wave condition
- The dynamic water level set-up

Depth Limited Waves – Size of Revetment Armour Stones:

The maximum wave condition on the reef was reached for a significant wave height outside the reef of approximately $H_{m0} = 2$ m, which is substantially lower than the 1-year wave condition outside the reef.

As a consequence of this depth-limited wave condition on the reef, the more frequent wave conditions will impose almost the same wave impacts on the structure as rare events such as the 25-year design condition. This means that the damage induced by the 25-year condition outside the reef will also be induced by a 'normal' wave condition with a return period of less than one year. Since the damage to the revetment armour is cumulative, it was of paramount importance to weigh the consequences of the depth-limited waves into the considerations of an appropriate design criterion for the damage to the revetment armour. Furthermore, the depth-limited wave conditions eliminated any use of empirical formulae for predicting the necessary size of the armour stones to be used on the revetments.

Basically, the depth-limited wave conditions cause the design waves for the structure to occur more often, and as a consequence of this, the probability of failure of the structure within a given lifetime increases. Therefore, a 'no damage' criterion was adopted for the design of the revetment armour. This means that no progressive damage to the revetment armour should occur for the maximum wave condition on the reef. This 'no damage' design criterion led to the recommendation of revetment armour stones somewhat larger than expected.

Dynamic Set-up – Revetment Crest Dimensions:

With the highest amplitudes of the dynamic set-up (surf beat) exceeding 1 m for the most severe wave conditions, it is evident that the long wave energy on the reef was a crucial parameter as regards the overtopping on the revetments. Any use of existing empirical formulae for predicting the consequences of a given revetment profile with respect to overtopping was eliminated due to these special conditions.

Basically, the dynamic set-up on the reef results in increased water level in front of the structure, and thereby a lower revetment free board. Hence, the overtopping is increased dramatically. The results of the model tests led to the recommendation of a revised crest height and crest width of the revetments to meet the requirements of acceptable overtopping.

The effect of long waves on the design of coastal structures has previously been addressed by eg Kamphuis (1996) and Kamphuis (1998), the latter also presented at ICCE '98. Kamphuis argues that the presence of long waves and the resulting increase of water level in front of a structure cause an increase of the design wave height for a structure in shallow water. Essentially, this means that in areas with more typical slopes towards the coastline the design wave height in shallow water is not only a function of the water depth at the toe of the structure but also a function of the long wave activity. However, this is not seen from the results of the present model study (see Figures 10 and 11) because of the relatively wide and shallow reef.

Conclusions

In connection with hydraulic studies of the Bali Turtle Island Development Project, 3D physical modelling was carried out for determination of the wave transformation over the shallow reef in front of the new resort and for the design of the rubble mound revetments to be built for coastal protection.

In the design of the revetments, stability of the armour layer as well as overtopping of the revetments were equally important aspects, since not only should the resort be protected against storm waves, but the aesthetic value of the design should also be taken into account.

The physical model study showed that the maximum wave height on the reef was limited by the water depth on the reef and that this wave height corresponded to less than a 1-year wave condition outside the reef. This depth-limitation eliminated the use of any empirical formulae for predicting the necessary size of the stones for the revetment armour, and made the implementation of a 'no damage' design criterion essential.

The presence of significant amounts of long wave activity (dynamic set-up) was identified on the reef as a consequence of the heavy wave breaking and the associated release of bound long waves into free waves. This dynamic set-up caused a significant increase of the overtopping on the revetments and prevented the use of existing empirical formulae for overtopping prediction.

The present case study is a perfect example of a study in which the use of physical modelling as a design tool was essential in order to develop a sound and viable solution to a problem which offhand may seem rather simple to the design engineer.

The study also illustrates how important non-linear wave phenomena such as bound long waves released by wave breaking can be for the design of a coastal structure. For many years the importance of these non-linear wave phenomena on for example movements of floating bodies and seiching in harbours has been recognised, but their effect on the design of coastal structures such as rubble mound revetments and breakwaters in shallow water has to some extent been neglected. The present study clearly shows that when designing coastal structures in shallow water, the effect of long waves should be taken into account.

Acknowledgement

This paper is based on work carried out under contract from Penta Ocean Construction Co Ltd on behalf of Pt Bali Turtle Island Development (BTID).

References

Driscoll, A.M., Foster, T., Pedersen, C. and Tateishi, Y. (1998). *Integrated Design Optimization for a Tropical Land Reclamation: Bali Turtle Island Development*, Proc. of 26th ICCE, Copenhagen, Denmark, 1998.

Driscoll, A.M., Foster, T., Rand, P. and Tateishi, Y. (1997). *Environmental Modelling and Management of Marine Construction Works in a Tropical Environment*, Proc. of the 2nd Asian and Australasian Ports and Harbours Conference, Ho Chi Minh City, Vietnam, 1997.

Kamphuis, J.W. (1996). *Experiments on Design Wave Height in Shallow Water*, Proc. of 25th ICCE, Orlando, USA, 1996.

Kamphuis, J.W. (1998). *The Effect of Long Waves on Flume Experiments*, Proc. of 26th ICCE, Copenhagen, Denmark, 1998.

Sloth, P., Jensen, T., Jacobsen, V. and Tateishi, T. (1997). *The Combined Use of Mathematical and Physical Modelling for Coastal Resort Development*, Proc. of 2nd Asian and Australasian Ports and Harbours Conference, Ho Chi Minh City, Vietnam, 1997.

Sulaiman, D.M., S. Tsutsui, H. Yoshioka, T. Yamashita, S. Oshhiro and Y. Tsuchiya (1994). *Prediction of the Maximum Wave on the Coral Flat.* Proc. of the 24th ICCE, Kobe, Japan, 1994.

COASTAL ENGINEERING 1998

Volume 2

CONFERENCE PROCEEDINGS

June 22-26, 1998
Falconer Hotel
Copenhagen, Denmark

EDITED BY
Billy L. Edge

ASCE American Society of Civil Engineers
1801 ALEXANDER BELL DRIVE
RESTON, VIRGINIA 20191–4400

Abstract: This proceedings, *Coastal Engineering 1998*, contains over 270 papers presented at the 26th International Conference on Coastal Engineering which was held in Copenhagen, Denmark, June 22-26, 1998. The proceedings is divided into five parts: 1) characteristics of coastal waves and currents; 2) long waves and storm surges; 3) coastal structures; 4) coastal processes and sediment transport; and 5) coastal, estuarine, and environmental problems. The individual papers include such topics as the effects of wind, waves, storms, and currents as well as the study of sedimentation, erosion, and beach nourishment. Special emphasis is given to case studies of completed engineering projects. With the inclusion of both theoretical and practical information, these papers provide the civil engineer and professionals in related fields with a broad range of information on coastal engineering and coastal processes affecting design and operations in the coastal zone.

Cover photo and all photos on section breaker pages 71, 1153, 1393, 2263, and 3373 provided by Danish Hydraulic Institute.

Library of Congress Cataloging-in-Publication Data

Coastal engineering 1998: proceedings of the twenty-sixth international conference: 22-26 June 1998, Falconer Hotel, Copenhagen, Denmark / edited by Billy L. Edge.
p. cm.
"Held under the auspices of the Coastal Engineering Research Council of the American Society of Civil Engineers."
Includes bibliographical references and index.
ISBN 0-7844-0411-9
1. Coastal engineering–Congresses. 2. Ocean waves–Congresses. 3. Shore protection –Congresses. I. Edge, Billy L. II. Coastal Engineering Research Council (U.S.)
III. International Conference on Coastal Engineering (26th: 1998: Copenhagen, Denmark)
TC203.5.C6184 1999 98-55126
627'.58–dc21 CIP

Any statements expressed in these materials are those of the individual authors and do not necessarily represent the views of ASCE, which takes no responsibility for any statement made herein. No reference made in this publication to any specific method, product, process or service constitutes or implies an endorsement, recommendation, or warranty thereof by ASCE. The materials are for general information only and do not represent a standard of ASCE, nor are they intended as a reference in purchase specifications, contracts, regulations, statutes, or any other legal document.
ASCE makes no representation or warranty of any kind, whether express or implied, concerning the accuracy, completeness, suitability, or utility of any information, apparatus, product, or process discussed in this publication, and assumes no liability therefore. This information should not be used without first securing competent advice with respect to its suitability for any general or specific application. Anyone utilizing this information assumes all liability arising from such use, including but not limited to infringement of any patent or patents.
Photocopies. Authorization to photocopy material for internal or personal use under circumstances not falling within the fair use provisions of the Copyright Act is granted by ASCE to libraries and other users registered with the Copyright Clearance Center (CCC) Transactional Reporting Service, provided that the base fee of $8.00 per chapter plus $.50 per page is paid directly to CCC, 222 Rosewood Drive, Danvers, MA 01923. The identification for ASCE Books is 0-7844-0411-9/99/ $8.00 + $.50 per page. Requests for special permission or bulk copying should be addressed to Permissions & Copyright Dept., ASCE.

Copyright © 1999 by the American Society of Civil Engineers, All Rights Reserved.
Library of Congress Catalog Card No: 98-55126 ISBN 0-7844-0411-9
Manufactured in the United States of America.

Contents

VOLUME 1

Keynote Presentations

The Art of Coastal Engineering 1
Torben Sorensen

The European Research Programmes in Coastal Engineering 15
Hans-Werner Partenscky

Beach Nourishment: A Limited Review and Some Recent Results 45
Robert G. Dean

Part I: Characteristics of Coastal Waves and Currents

The Modelling of a Spilling Breaker: Strong Turbulence at a Free Surface 72
M. Brocchini and D.H. Peregrine

Time-Dependent Depth-Integrated Turbulence Modeling of Breaking Waves 86
Kazuo Nadaoka and Osafumi Ono

Wave Crest Interaction in Water of Intermediate Depth 98
C.C. Bird and D.H. Peregrine

Energy Dissipation Model for Irregular Breaking Waves 112
Winyu Rattanapitikon and Tomoya Shibayama

Stochastic Modelling of Nonlinear Waves in Shallow Water 126
Henrik Kofoed-Hansen and Jørgen H. Rasmussen

Comparing First, Second, and Third Generation Coastal Wave Modelling 140
L.H. Holthuijsen, N. Booij, and I.J.G. Haagsma

Wave Transformation near a Quasi-1D Coast 150
J.H. Andorka Gal, L.H. Holthuijsen, J.C.M. de Jong, and
A.T.M.M. Kieftenburg

A New Formulation of Deterministic and Stochastic Evolution Equations for Three-Wave Interactions Involving Fully Dispersive Waves 161
Per A. Madsen and Yasser Eldeberky

The Horizontal Eddies in the Offshore Zone 175
Li Li and Robert A. Dalrymple

Nonlinear Distribution of Nearshore Free Surface and Velocity 189
Nobuhito Mori and Nobuhisa Kobayashi

Evolution Equations for Edge Waves and Shear Waves on Longshore Uniform Beaches 203
James T. Kirby, Uday Putrevu, and H. Tuba Özkan-Haller

On the Viscous Destabilization of Longshore Currents 217
Uday Putrevu, James T. Kirby, Joan Oltman-Shay, and H. Tuba Özkan-Haller

Shear Waves over Longshore Nonuniform Barred Beaches 230
F.E. Sancho and I.A. Svendsen

Trapped and Free-Wave Propagation in Channels and Harbours 244
João A. Santos and D.H. Peregrine

A Boussinesq Model for Breaking Waves: Comparisons with Experiments 258
Jayaram Veeramony and Ib A. Svendsen

Nearshore Wave Dynamics Simulated by Boussinesq Type Models 272
Ole R. Sørensen, Per A. Madsen, and Hemming A. Schäffer

A 2D Model of Waves and Undertow in the Surf Zone 286
Brian A. O'Connor, Shunqi Pan, John Nicholson, Neil MacDonald, and David A. Huntley

Field Measurements of Undertow on Longshore Bars 297
Yoshiaki Kuriyama

Application of an Undertow Model to Irregular Waves on Barred Beaches 311
Douglas L. Kennedy, Daniel T. Cox, and Nobuhisa Kobayashi

Wake Wash of High-Speed Craft in Coastal Areas 325
Jens Kirkegaard, Henrik Kofoed-Hansen, and Berry Elfrink

Wave Propagation Directions under Real Sea State Conditions 338
Joachim Grüne

On the Accuracy of Parabolic Wave Models 352
Hakeem K. Johnson and Sanne Poulin

A Refraction-Diffraction Model for Irregular Waves 366
Q. Gao and A.C. Radder

Calculation of Velocity Field in 3-D Random Waves 380
Yu-xiu Yu and Ning-chuan Zhang

On the Reflection of Short-Crested Waves in Numerical Models 394
Michael Brorsen and Jacob Helm-Petersen

Breaking Waves and Induced Currents on Coastal Structures 408
Entin A. Karjadi and Nobuhisa Kobayashi

ALES Shallow-Water Flow Solver with Non-Hydrostatic Pressure: Wave Applications 422
J.G. Zhou and P.K. Stansby

Linear and Nonlinear Modeling of Long Waves Propagating around Channel Bends 433
Aimin Shi and Michelle H. Teng

Mass Transport of Progressive Edge Waves: A Comparison between the Full and Shallow-Water Wave Theories 443
K.M. Mok and Harry Yeh

Coherent Motions in the Bottom Boundary Layer under Shoaling and Breaking Waves 457
Daniel T. Cox and Nobuhisa Kobayashi

Experimental Study on Non-Linear Wave Boundary Layers 471
Hitoshi Tanaka, Hiroto Yamaji, and Ahmad Sana

A 2-DV Numerical Solution for the Turbulent Wave Boundary Layer under Breaking Waves 484
Nguyen The Duy, Tomoya Shibayama, and Akio Okayasu

Wave Modelling in the WISE Group 498
L. Cavaleri and L.H. Holthuijsen

A Long Term Wave Hindcast System Using ECMWF Winds 509
Yoshio Hatada and Masataka Yamaguchi

Numerical Simulations of Directionally Spread Shoaling Surface Gravity Waves 523
Françoise Becq, Michel Benoit, and Philippe Forget

Effects of Wave Reflection and Dissipation on Wave-Induced Second Order Magnitudes 537
Fernando J. Méndez, Iñigo J. Losada, Robert A. Dalrymple, and M.A. Losada

Green-Function Analysis of a Wave Field over Arbitrary Bathymetry 551
Hitoshi Nishimura and Moon-Su Kwak

Wave Propagation over a Bar and Wave Induced Bed Pressure Gradients 562
Øivind A. Arntsen

A Multi-Level Model for Nonlinear Dispersive Water Waves 576
Susumu Kanayama, Hitoshi Tanaka, and Nobuo Shuto

Recent Extensions to Local Polynomial Approximation Models 589
Andrew B. Kennedy

Depth Inversion for Nonlinear Waves Shoaling over a Barred-Beach 603
Stéphan T. Grilli and Jesper Skourup

Numerical Model of Fully-Nonlinear Wave Refraction and Diffraction 617
Masahiko Isobe and Samir Abohadima

A Comparison of Higher-Order Boussinesq and Local Polynomial Approximation Models 631
Maurício F. Gobbi, Andrew B. Kennedy, and James T. Kirby

Experiments on Nonlinear Wave Groups Shoaling in a Tank 645
L. Shemer, Haiying Jiao, and E. Kit

Modulation of Bichromatic Wave Train in a Wave Tank 656
Motohiko Umeyama

Simulation of Nonlinear Wave Deformation by a Shoal in 3D 670
Paul de Haas and Maarten Dingemans

Variations in Nonlinearly Evolved Nearshore Spectra and Their Significance in the Estimation of Wave Forces 682
Serdar Beji and Kazuo Nadaoka

Wave Refraction across a Current with Strong Horizontal Shearing 692
Richard R. Simons and Ruairi D. Maciver

Random Waves on a Vertically-Sheared Current 706
C. Swan and R.L. James

Wave Setup and Other Tidal Anomalies in Coastal Rivers 720
Eko Santoso, David Hanslow, Peter Nielsen, and Kevin Hibbert

3D Wave-Current Interactions in Wave-Current Channels 732
Jacco Groeneweg and Jurjen A. Battjes

Vorticity and Surf Zone Currents 745
D.H. Peregrine and O. Bokhove

Experimental Study of Wave Breaking and Blocking on Opposing Currents 759
Arun Chawla and James T. Kirby

Tidal Ellipses in the Nearshore Zone (-3 to -10m): Modelling and Observations 773
Klaas T. Houwman and Piet Hoekstra

ADCP Observation of Nearshore Current Structure in the Surf Zone 787
Takao Yamashita, Hiroshi Yoshioka, Shigeru Kato, Lu Ming, and Chikara Shimoda

Numerical Modeling of Nearshore Circulation on a Barred Beach with Rip Channels 801
K.A. Haas, I. A. Svendsen, and M.C. Haller

Applicability of a Quasi-Three Dimensional Numcrical Model to Nearshore Currents 815
Masamitsu Kuroiwa, Hideaki Noda, and Yuhei Matsubara

Three-Dimensional Nearshore Currents Model Based on Vertical Distribution of Radiation Stress 829
Hisamachi Nobuoka, Nobuo Mimura, and Hajime Kato

Numerical Simulation of Wave Fields around the Submerged Breakwater with SOLA-SURF Method 843
Norio Hayakawa, Tokuzo Hosoyamada, Shigeru Yoshida, Gozo Tsujimoto

Numerical Analysis of Wave Breaking Due to Submerged Breakwater in a Three-Dimensional Wave Field 853
Koji Kawasaki and Koichiro Iwata

Classification of Wave Loading on Monolithic Coastal Structures 867
Andreas Kortenhaus and Hocine Oumeraci

Lagrangian Measurements of Accelerations in the Crests of Breaking and Broken Waves 881
Søren Peter Kjeldsen, Pierre Bonmarin, Michael G. Skafel, and William M. Drennan

Numerical Simulation of Breaking Waves by Large Eddy Simulation and VOF Method 892
Qun Zhao and Katsutoshi Tanimoto

Influence of Steep Seabed Slopes on Breaking Waves for Structure Design 906
N.W.H. Allsop, N. Durand, and D.P. Hurdle

Influence of False Waves on Wave Records Statistics 920
Marcos H. Giménez, Carlos R. Sánchez-Carratalá, and Josep R. Medina

Changing of Local Wave Climate Due to Ebb Delta Migration 934
Ralf Kaiser and Hanz D. Niemeyer

Sensitivity of Wind Wave Simulation to Coupling with a Tide/Surge Model with Application to the Southern North Sea 945
J. Monbaliu, C.S. Yu, and P. Osuna

Probability Distribution of Wave Height in Finite Water Depth 958
Michel K. Ochi

Increase of Wave Height in the North Pacific Ocean 972
Kozo Okada, Yasushi Suzuki, Yoshihiro Utsunomiya, and Yoshihiro Watanabe

Analysis of Wave Data at Sines 985
Carlos Pita and Fernando Abecasis

On the Statistical Variability of Wave Height and Period Parameters 999
Carlos R. Sánchez-Carratalá and Marcos H. Giménez

Duration in Wave Climate Analysis 1013
Rodney J. Sobey and Leah S. Orloff

Encounter Probability of Individual Wave Height 1027
Zhou Liu and Hans F. Burcharth

Wave Run-up and Overtopping: Prototype Versus Scale Models 1039
Julien De Rouck, Raf Verdonck, Peter Troch, Luc Van Damme, Flemming Schlütter, and John De Ronde

Wave Run-up and Reflection on Coastal Structures in Depth-Limited Conditions 1053
Joel R. Rathbun, Daniel T. Cox, and Billy L. Edge

Wind Effects on Run-up and Breakwater Crest Design 1068
Josep R. Medina

Some Design Aspects of an Absorbing 3D Wavemaker 1082
Hemming A. Schäffer

Generation of Double Peak Directional Wave by Dual Mode Snake-Type Wave Maker 1096
Tetsuya Hiraishi and Katsuya Hirayama

Extreme Multi-Directional Waves 1110
T.B. Johannessen and C. Swan

Low Frequency Surf Zone Response to Wave Groups 1124
Merrick C. Haller, Uday Putrevu, Joan Oltman-Shay, and Robert A. Dalrymple

Wave Dynamics and Revetment Design on a Natural Reef 1138
Thomas Jensen, Peter Sloth, and Vagner Jacobsen

VOLUME 2

Part II: Long Period Waves, Storm Surges, and Wave Groups

Long Waves in Flume Experiments 1154
J. William Kamphuis

Probabilistic Model for Tsunami-Wave Elevation along the Alborán Seacoast 1168
M. González and R. Medina

Long-Period Wave Responses in a Harbor with a Narrow Mouth 1182
Weon Mu Jeong, Kil Seong Lee, and Woo Sun Park

Application of Computer Modeling for Harbor Resonance Studies of Long Beach and Los Angeles Harbor Basins 1196
Jiin-Jen Lee, Ching-Piau Lai, and Yigong Li

Attenuation of Very Long Waves by a Large Resonator as an Outer Harbor 1210
Takayuki Nakamura and Satoshi Morita

Application of Physical Model in Long Wave Studies for the Port of Long Beach 1222
Ying-Keung Poon, Frederic Raichlen, and James (Kimo) Walker

Nautical Design Studies: Haifa Port Extensions 1236
J.A. Zwamborn, F. Di Castro, M. Radomir, and J.T.M. van Doorn

Wave Propagation Modeling for Pusan New Harbor 1250
Jang-Won Chae and Weon Mu Jeong

The Studies for the Resonance of Hwa-Lian Harbour Agitated by Typhoon Waves 1263
Chien-Kee Chang, Chung-Ching Chien, and Hsiang-Maw Tzeng

Application of Mathematical Modeling in Optimizing Layout of a Large Industrial Fishery Harbour 1276
P.P. Gunaratna, P. Justesen, D.S. Abeysirigunawardena, and H.-J. Scheffer

Characteristics of Long-Period Flow Velocity Fluctuations around Tomakomai Harbor 1290
Hiroya Kinoshita, Hideki Hoshi, Youichi Atsumi, Shin-ichiro Sekiguchi, and Toshihiko Yamashita

Transformation of Wave Groups and Accompanying Long Waves in Shallow Water 1299
M. Mizuguchi and H. Matsutate

Observation and Simulation of Low-Frequency Waves on Two Natural Beaches 1313
Satoshi Nakamura and Nicholas Dodd

Quasi 3-D Effects in Infragravity Waves 1323
A.R. Van Dongeren, I.A. Svendsen, and U. Putrevu

Numerical Modelling of Long Wave Ship Motions 1337
John R. Headland and Ying-Keung Poon

Response of Moored Vessels in Buffington Harbour 1350
E.P.D. Mansard, T. Faure, and K. MacIntosh

Statistical Wave Forecasting through Kalman Filtering Combined with Principal Component Analysis 1364
Noriaki Hashimoto, Toshihiko Nagai, and Masanobu Kudaka

Data Assimilation and Nested Hydrodynamic Modelling in Storm Surge Forecasting 1378
Rafael Cañizares and Henrik Madsen

Part III: Coastal Structures

Berm Breakwaters: Influence of Stone Gradation, Permeability, and Armouring 1394
Jørgen Juhl and Peter Sloth

Berm Breakwaters: Fifteen Years Experience 1407
Sigurdur Sigurdarson, Gisli Viggosson, Sigtryggur Benediktssson, Sigurdur Einarsson, and Omar Bjarki Smarason

The First Berm Breakwater in Hong Kong 1421
K.C. Ander Chow, Charles P. Fournier, P.F. Ma, and W.Y. Shiu

On the Stability of Berm Breakwaters in Shallow and Deep Water 1435
Alf Tørum

The Economic Analysis of "Soft" Versus "Hard" Solutions for Shore Protection: An Example 1449
David R. Basco

Uncertainty Analysis of Coastal Projects 1461
Jim W. Hall, John P. Davis, and David I. Blockley

Preventing Natural Breaching of the Major Sand Spit Protecting the Port of Walvis Bay 1475
J.S. Schoonees, L. Lenhoff, and A.J. Raw

Phenomena in Standing Wave Impact on a Horizontal Plate 1489
Piotr Wilde, Kazimierz Szmidt, and Eugeniusz Sobierajski

Two and Three-Dimensional Pressure-Impulse Models of Wave Impact on Structures 1502
Deborah J. Wood and D. Howell Peregrine

Thyborøn Barriers: A Master Case of Coastal Engineering 1516
Per Roed Jakobsen, Ida Brøker, Jesper Holt Jensen, Ann Skou, and Sanne Poulin

Application of Shore Protection Schemes in Hornbæk 1530
Mads Peder Jørgensen, Peer Skaarup, Karsten Mangor, and Jørgen Juhl

Design and Construction of Seawater Exchange Breakwaters 1539
Sadamitsu Akeda, Yasushi Yamamoto, Katsutoshi Kimura, and Kenji Yano

Application of Overtopping Models to Vertical Walls against Storm Surges 1553
Holger Schüttrumpf, Andreas Kortenhaus, and Hocine Oumeraci

Advanced Assessing of the Stability of Existing Placed Block Revetments 1567
Adam Bezuijen and Gerard A.M. Kruse

Design of Revetments in the Öresund Link: Reclaimed Artificial Island and Peninsula 1576
Jeppe Blak-Nielsen, Helge Gravesen, and Niels Lykkeberg

Design of Alternative Revetments 1587
M. Klein Breteler, K.W. Pilarczyk, and T. Stoutjesdijk

Inventory of the Stability of Existing Placed Block Revetments in the Netherlands 1601
Theo Stoutjesdijk, Mark Klein Breteler, and Hans Johanson

Second Order Wave Interaction with a Large Structure 1613
Bjarne Büchmann, Jesper Skourup, and David L. Kriebel

On the Effect of Two-Layer Thickness by High-Specific Gravity Armor Blocks on Wave Reflection 1625
Masahiro Ito, Yuitch Iwagaki, Hiroshi Murakami, Kenji Nemoto, Masato Yamamoto, and Minoru Hanzawa

Development of Two-Dimensional Numerical Wave Flume for Wave Interaction with Rubble Mound Breakwaters 1638
Peter Troch and Julien De Rouck

Nonlinear Wave Forces on a Rubble Covered Pipeline 1650
William G. McDougal, Norimi Mizutani, and Ayman M. Mostafa

Sea Level Set-up Behind Detached Breakwaters 1665
J.H. Loveless, D. Debski, and A.B. MacLeod

Coastal Erosion Caused by Construction of an Artificial Island and Performance of Beach Nourishment 1679
Ryuichiro Nishi, Takaaki Uda, Michio Sato, Masakazu Wakita, Yasuro Ohtani, and Takahiro Horiguchi

On the Design of Shore-Parallel Breakwaters 1693
J.A. Zyserman, I. Brøker, H.K. Johnson, K. Mangor, and K. Jørgensen

Shore Parallel Breakwaters and Beach Nourishments 1706
Jan van de Graaff, Henk Steetzel, Bram Bliek, and Hans de Vroeg

Sediment Transport around a Mound Breakwater: The Toe Erosion Problem 1720
Asunción Baquerizo and Miguel A. Losada

Stability of Near-Bed Rubble-Mound Structures 1730
César Vidal, Íñigo J. Losada, and Francisco L. Martín

Coastal Defense Structures in NSW, Australia 1744
S.J. Wyllie, D.B. Lord, I.F.W. Jayewardene, and T. Young

Alderney Breakwater: Scheme Evolution 1758
Paul B. Sayers, N. William H. Allsop, and Alan A. Hill

Breakwater Repair: Monitoring, Modelling, and Construction 1775
S. Pillay, D. Phelp, and A. Bartels

Digital Imaging Processing Techniques for the Aerial Field Monitoring of Harbour Breakwaters 1789
Gavin Hough and David Phelp

Design of Rock Armoured Single Layer Rubble Mound Breakwaters 1800
T. Hald, A. Tørum , and T. Holm-Karlsen

The Form of the Mound of Rubble Dumped by a Barge 1814
J.K. Vrijling and G. van Oord

Hydraulic Model Test of Stability of Amenity-Oriented Breakwater 1824
Shoji Kunitomi, Hajime Mase, and Tomotsuka Takayama

Stability of Mound Breakwaters: Dependence on Wave Reflection 1833
Cristina López, Miguel A. Losada, and Nobuhisa Kobayashi

Impact Structural Response of Core-Loc 1846
George F. Turk and Jeffrey A. Melby

Results of Field Monitoring of the New Core-Loc Breakwater at Port St. Frances, South Africa 1857
D. Phelp, A. Holtzhausen, and J. Melby

The First Core-Loc Breakwater 1871
Anton H. Holtzhausen

Damage Progression on Breakwaters 1884
J. A. Melby and N. Kobayashi

The Influence of Pressure Fluctuations on the Flow between Armour Elements 1898
Robert Booij, Wim S.J. Uijttewaal, Patrick van Os, Harry L. Fontijn, and Jurjen A. Battjes

Wave Kinematics on Breakwater Heads and Stability of Armour Layers under Multidirectional Waves 1906
Yoshiharu Matsumi, Akira Kimura, and Kenichi Ohno

A Statistical Tool for Breakwater Design 1920
Rodolfo Silva, Georges Govaere, and Francisco Martin

Cost Comparison of Breakwater Types 1934
W.H. Tutuarima and K. d'Angremond

Wave Forces on Solid and Perforated Caisson Breakwaters: Comparison of Field and Laboratory Measurements 1945
L. Franco, M. de Gerloni, G. Passoni, and D. Zacconi

Wave Impacts on Caisson Breakwaters Situated in Multidirectionally Breaking Seas 1959
P. Frigaard, H.F. Burcharth, and J.P. Kofoed

Prototype Measurements of the Dynamic Response of Caisson Breakwaters 1972
Alberto Lamberti and Luca Martinelli

Experimental and FEM Simulation of the Dynamic Response of a Caisson Wall against Breaking Wave Impulsive Pressures 1986
Shigeo Takahashi, Muneo Tsuda, Kojiro Suzuki, and Ken-ichiro Shimosako

Wave Transmission at Submerged Rubblemound Breakwaters 2000
Stuart R. Seabrook and Kevin R. Hall

Vertical Circulation Induced by a Submerged Breakwater 2014
A. Sánchez-Arcilla, F. Rivero, X. Gironella, D. Vergés, and M. Tomé

2DH Morphological Modelling of Submerged Breakwaters 2028
S.C. van der Biezen, J.A. Roelvink, J. van de Graaff, J. Schaap, and L. Torrini

Wave Pressure Distribution on Permeable Vertical Walls 2042
Hendrik Bergmann and Hocine Oumeraci

Impact Loadings on Vertical Walls in Directional Seas 2056
N.W.H. Allsop and M. Calabrese

Wave Forces on a Vertical Wave Barrier 2069
David Kriebel, Charles Sollitt, and William Gerken

Statistical Distribution of Horizontal Wave Forces on Vertical Breakwaters 2082
Janice McKenna and William Allsop

Neural Network Modelling of Forces on Vertical Structures 2096
Marcel R. A. van Gent, and Henk F. P. van den Boogaard

Pore Pressures in Vertical Breakwater Foundations 2110
C. Zwanenburg, M.B. de Groot, T. J. Kvalstad, and A. van Hoven

Economic Optimal Design of Vertical Breakwaters 2124
H. G. Voortman, H.K.T. Kuijper, and J.K. Vrijling

Design of Vertical Wall Caisson Breakwaters Using Partial Safety Factors 2138
Hans F. Burcharth and John Dalsgaard Sørensen

Lateral Versus Longitudinal Artificial Reef Systems 2152
Yoshimi Goda and Hiroshi Takagi

Development of a New Type of Reef Breakwater: Theoretical and Experimental Study 2166
Shohachi Kakuno, Masao Endoh, Yiming Zhong, Takaaki Shigematsu, and Kazuki Oda

Performance of Submerged Active Breakwaters in a Hydraulic Model 2179
K.R. Hall and M.P. Fischer

Wave Force and Stability of Armor Units for Composite Breakwaters 2193
Katsutoshi Kimura, Yuzo Mizuno, and Michifumi Hayashi

Hydraulic Performance of a High Mound Composite Breakwater 2207
M. Muttray, H. Oumeraci, K. Shimosako, and S. Takahashi

Double Walled, Low Reflection Wave Barriers 2221
R.J. Cox, P.R. Horton, and S.H. Bettington

Wave Overtopping of Rubble Mound Breakwaters 2235
Mogens Hebsgaard, Peter Sloth, and Jørgen Juhl

Directional Wave Overtopping Estimation Model and Experimental Verification 2249
Tetsuya Hiraishi and Haruhiro Maruyama

Part IV: Coastal Processes and Sediment Transport

The Morphological Changes along the Northern Coast of the Nile Delta 2264
John B. Herbich, Abdel-Fattah Elfiky, and Gamal H. Elsaeed

Modelling the Morphological Sensitivity of Large Nontidal Coastal Areas to Climatological Changes 2269
H. Weilbeer and W. Zielke

North-Coast of Texel: A Comparison between Reality and Prediction 2281
Rob Steijn, Dano Roelvink, Dick Rakhorst, Jan Ribberink, and Jan van Overeem

Littoral Processes in a Prograding Coast: The Case Study of the Atlantic Ocean Coast of Uruguay 2294
Luis Teixeira, Juan Montaña, and Miguel Losada

Turbidimetric Measuring of Suspended Sediment Concentration in the Coastal Zone 2303
Ruben D. Kos'yan, Igor S. Podymov, and Sergey Yu. Kuznetsov

Characteristics of Suspended Sediment Transport in the Surf Zone of Irregular Waves and Their Reproduction by a Cross-Shore Beach Deformation Model 2317
M. Ikeno and T. Shimizu

Cross-Shore Sediment Transport: A Field Test of the Bailard Energetics Model 2331
Troels Aagaard, Brian Greenwood, and Jørgen Nielsen

Field Observations of Small Scale Sedimentation Processes 2344
Daniel M. Hanes, Eric D. Thosteson, Yeon-Sihk Chang, Craig Conner, and Chris E. Vincent

Littoral Transport under Complex Wave Fields: Pecém, Northeast Brazil 2353
Berry Elfrink, Domenico Accetta, Berenice Motta Vargas, and Wagner Santos Scisinio Dias

Morphological Modelling Using a Modified Multi-Layer Approach 2368
Henk J. Steetzel, Hans de Vroeg, Leo C. van Rijn, and Jean-Marie Stam

Parameterizing Beach Erosion/Accretion Conditions 2382
John P. Ahrens and Edward B. Hands

Determining Depth from Remotely-Sensed Images 2395
Robert A. Dalrymple, Andrew B. Kennedy, James T. Kirby, and Qin Chen

VOLUME 3

On the Predictability of Nearshore Bar Behaviour 2409
Stefan Aarninkhof, Claire Hinton, and Kathelijne Wijnberg

Laboratory Evaluation of Instrumentation Used in Field Studies of Wave-Sediment Interactions 2423
J.J. Williams, P. Bell, L.E. Coates, A.E. Davies, P.J. Hardcastle, J.D. Humphery, S.P. Moores, L.C. van Rijn, P.D. Thorne, and K. Trouw

Size Gradation Effects in Sediment Transport 2435
Y. Chatelus, I. Katopodi, M. Dohmen-Janssen, J.S. Ribberink, P. Samothrakis, B. Cloin, J.C. Savioli, J. Bosboom, B.A. O'Connor, R. Hein, and L. Hamm

Phase-Lag Effects in Oscillatory Sheet Flow 2449
C. Marjolein Dohmen-Janssen, Gizella van der Hout, and Jan S. Ribberink

Cross-Shore Graded Sediment Transport: Grain Size and Density Effects 2463
R.L. Koomans, R.J. de Meijer, and L.B. Venema

Cross-Shore Sediment Transports on a Cut Profile for Large Scale Land Reclamations 2475
Martijn Onderwater, Dano Roelvink, and Jan van de Graaff

Optimum Size of Distorted Ripple Train for the Control of Cross-Shore Sediment Transport 2489
Satoshi Takewaka, Isao Irie, Masahiro Uchida, Hirokazu Sakamoto, and Nobuyuki Ono

The Effect of Sediment Composition on Cross-Shore Bed Profiles 2495
Leo C. van Rijn

The Breaching of Sand Investigated in Large-Scale Model Tests 2509
Cees van Rhee and Adam Bezuijen

A Dimensionless Parameter Describing Sea Cliff Erosion 2520
Akira Mano and Shigenori Suzuki

The Sand Trapping Trench as a Countermeasure To Control Wind-Blown Sand on Beaches 2534
Shintaro Hotta, Katsumori Hatanaka, Hiroyoshi Tanaka, and Kiyoshi Horikawa

Coastal Sediment Transport: The COAST3D Project 2548
R.L. Soulsby

Modelling of a Three-Layer Sediment Transport System in Oscillatory Flow 2559
Leszek M. Kaczmarek and Rafal Ostrowski

Analytical Model for Wave-Related Transport 2573
Judith Bosboom, Gert Klopman, Ad Reniers, and Marcel J.F. Stive

Vertical Length Scales of Nearshore Suspension Events 2587
D.L. Foster, A.J. Bowen, and A.E. Hay

Sediment Resuspension under Non-Breaking Waves: Predicting Sediment "Pulses" as a Function of Groupiness 2595
José A. Jiménez, Agustín Sánchez-Arcilla, and German Rodríguez

Coherent Doppler Sonar: Sediment Flux and Turbulent Velocitics in a Wave Flume 2607
Len Zedel and Alex Hay

Eddy Viscosity Models for Wave Boundary Layers 2615
Ole Secher Madsen and Paulo Salles

Measurement of Shear Stress on a Moveable Bed 2628
Kelly L. Rankin, Michael S. Bruno, and Richard I. Hires

Evaluation of Longshore Sediment Transport Models on Coarse Grained Bcaches Using Field Data: A Preliminary Investigation 2640
Erik van Wellen, Andrew J. Chadwick, Mark Lee, Brian Baily, and John Morfett

Motions of Pebbles on Pebble Beach 2654
Ichiro Deguchi, Masanobu Ono, Susumu Araki, and Toru Sawaragi

ONELINE: A Numerical Model for Shoreline Change 2668
Mohamed Dabees and J. William Kamphuis

Seasonal Shoreline Variations by Cross-Shore Transport in a One-Line Model under Random Waves 2682
Hans Hanson and Magnus Larson

Coastline Evolution in Response to a Major Mine Sediment Discharge on the Namibian Coastline 2696
G.G. Smith and G.P. Mocke

Longshore Patterns of the Sea Bottom Morphology 2710
Giovanna Vittori, Huib de Swart, and Paolo Blondeaux

Simple Models for Equilibrium Profiles under Breaking and Non-Breaking Waves 2722
Magnus Larson and Randall A. Wise

Equilibrium Terraced and Barred Beaches 2736
Mark D. Orzech and Nobuhisa Kobayashi

Breaker Bar Formation and Migration 2750
Bart T. Grasmeijer and Leo C. van Rijn

Beach Evolution on the Southern North Sea Coast 2759
Daniel J. Leggett, Jeremy P. Lowe, and Nicholas J. Cooper

Extracting Morphologic Information from Field Data 2773
Nathaniel G. Plant and Rob A. Holman

Nonlinear Time-Averaged Model in Surf and Swash Zones 2785
Bradley D. Johnson and Nobuhisa Kobayashi

Swash Zone Morphodynamics and Sediment Transport Processes 2799
K. Todd Holland, Asbury H. Sallenger, Britt Raubenheimer, and Steve Elgar

Field Measurements of Swash Induced Pressures within a Sandy Beach **2812**
D.P. Horn, T.E. Baldock, A.J. Baird, and T.E. Mason

Flow Structures in Swash Zone **2826**
H.H. Hwung, K.S. Hwang, W.S. Chiang, and C.F. Lai

Modelling Large-Scale Dynamics of Hel Peninsula, Poland **2837**
Marek Szmytkiewicz, Ryszard B. Zeidler, Grzegorz Różyński, and Marek Skaja

Morphodynamics of Shoreface-Connected Ridges **2851**
A. Falques, D. Calvete, H.E. de Swart, and N. Dodd

The Spatial Variability of Large Scale Sand Bars **2865**
C.R. Worley, T.C. Lippmann, J.W. Haines, and A.H. Sallenger

Modeling the Dynamics of a Bar System at Duck, North Carolina, USA **2877**
B. Boczar-Karakiewicz, W. Romańczyk, J.L. Bona, and E.B. Thornton

Depth of Closure: Improving Understanding and Prediction **2888**
Robert J. Nicholls, Magnus Larson, Michele Capobianco, and William A. Birkemeier

Short-Term Relatively Deep Sedimentation on the Ebro Delta Coast: Opening the Closure Depth **2902**
Vicente Gracia, José A. Jiménez, Agustín Sánchez-Arcilla, Jorge Guillén, and Albert Palanques

Spatial and Temporal Behavior of Depth of Closure along the Holland Coast **2913**
Claire Hinton and Robert J. Nicholls

Depth of Closure and Seabed Variability Patterns **2926**
Grzegorz Różyński, Zbigniew Pruszak, Tomasz Okrój, and Ryszard Zeidler

2DH Non-Linear Dispersive Wave Modelling and Sediment Transport in the Nearshore Zone **2940**
Theofanis V. Karambas

Comparison of Storm Longshore Transport Rates to Predictions **2954**
Herman C. Miller

Depth of Erosion under Storm Conditions **2968**
John F.A. Sleath

Numerical Investigation of Sediment Transport for Combined Waves and Currents **2980**
Juan Savioli

A Morphodynamic Model for River and Estuary Management **2992**
Volker Barthel and Ulrich Zanke

Random Wave Modelling Approach Included in a Beach Deformation Model **3008**
Ioan Nistor and Tomoya Shibayama

Geomorphological Modelling in Coastal Waters **3022**
Morteza Kolahdoozan, Roger A. Falconer, and Yiping Chen

Beach Recharge Design and Bi-Modal Wave Spectra 3036
T.T. Coates and P.J. Hawkes

Management of Beach Nourishment in an Open Sand System 3046
Hans H. Dette

Beach Fills in Europe: Projects, Practices, and Objectives 3060
L. Hamm, H. Hanson, M. Capobianco, H.H. Dette, A. Lechuga, and R. Spanhoff

Evaluation of the Effect of 20 Years of Nourishment 3074
Christian Laustrup and Holger Toxvig Madsen

Zurriola Beach Evolution Two Years after Nourishment 3086
José C. Santas, José M. Medina, Alejandro Caballero, Adolfo Uriarte, and Vicente Esteban

Model Tests for Evaluating Beach Nourishment Performance 3096
Massimo Tondello, Piero Ruol, Mauro Sclavo, and Michele Capobianco

Assessment of Depth of Closure on a Nourished Beach: Terschelling, The Netherlands 3110
S.W. Marsh, R.J. Nicholls, A. Kroon, and P. Hoekstra

Post-Stabilization Morphology of Oregon Inlet, North Carolina 3124
Brian P. Joyner, Margery F. Overton, and John S.Fisher

Predictive Model of Three-Dimensional Development and Deformation of a River Mouth Delta by Applying Contour Line Change Model 3138
Takaaki Uda, Hiroshi Yamagata, Ken-ichi Katoh, and Naohiro Akamatsu

Field Investigation on Sediment Transport into the Submarine Canyon in the Fuji Coast with the New Type Tracers 3151
Shigenobu Tanaka, Koji Yamamoto, Hitoshi Ito, Toshiharu Arisawa, and Toshimitsu Takagi

Sea Breeze Climatology and Nearshore Processes along the Perth Metropolitan Coastline, Western Australia 3165
G. Masselink and C.B. Pattiaratchi

Field Observation of Erosion and Accretion Waves on Shizuoka and Shimizu Coasts in Suruga Bay in Japan 3178
Naoki Itabashi and Takaaki Uda

Coastal Erosion at Keta Lagoon, Ghana: Large Scale Solution to a Large Scale Problem 3192
R.B. Nairn, K.J. MacIntosh, M.O. Hayes, G. Nai, S.L. Anthonio, and W.S. Valley

Morphological Vulnerability Index: A Simple Way of Determining Beach Behavior 3206
Óscar Ferreira, Rui Taborda, and J. Alveirinho Dias

Homogeneity Aspects in Statistical Analysis of Coastal Engineering Data 3215
P.H.A.J.M. van Gelder and J.K. Vrijling

A Simple Method To Predict Long-Term Morphological Changes 3224
Dano Roelvink, Alain Boutmy, and Jean-Marie Stam

Coastal Morphologic Variability of High Energy Dissipative Beaches 3238
Peter Ruggiero, George Kaminsky, and Nathaniel Plant

Effect Resonance on Morphology of Tidal Channels 3252
Willem T. Bakker

Inlet Cross-Sectional Area Calculated by Process-Based Model 3265
Nicholas C. Kraus

Stabilisation of the Tidal Entrance at Hornafjordur, Iceland 3279
Gisli Viggosson, Sigurdur Sigurdarson, and Bjorn Kristjansson

Application of a Long-Term Evolution Model of Tidal Inlets to the Design of a Navigation Channel, The Navia Inlet Case 3293
R. Medina, M.A. Losada, P. Lomónaco, and A. Baquerizo

Change of Mean Tidal Peaks and Range Due to Estuarine Waterway Deepening 3307
Hanz D. Niemeyer

Inlet Dynamics from Semi-Annual Surveys 3318
Owen W. Callard, William R. Dally, and Kathy FitzPatrick

Nearshore Coastal Processes Adjacent to a Tidal Inlet 3331
Thomas O. Herrington, Michael S. Bruno, Majid Yavary, and Kelly L. Rankin

Inlet Impacts on Local Coastal Processes 3345
Rajesh Srinivas and R. Bruce Taylor

Long-Term Morphological Development of the Accumer Ee Tidal Inlet and Its Impact on Island Beaches and Engineering Responses 3359
U. Abels, H. Kunz, G. Ragutzki, and H.-J. Stephan

Part V: Coastal, Estuarine, and Environmental Problems

Integrated Design Optimization for a Tropical Land Reclamation: Bali Turtle Island Development 3374
Andrew M. Driscoll, Tom Foster, Claus Pedersen, Palle Mikkelsen, and Yukimitsu Tateishi

The Influence of Marina Construction in Beach Stability: El Milagro Case Study 3388
J. Galofré, F.J. Montoya, and R. Medina

Man Made Beaches Balancing Nature and Recreation 3401
Ulf Anderskouv, Hanne Bach, Dan B Hasløv, and Karsten Mangor

Environmentally Friendly Coastal Protection: The ECOPRO Project 3412
Brendan Dollard

Coastal Restoration Considerations 3425
Karsten Mangor

Integrated Approach on the Safety of Dikes along the Great Dutch Lakes 3439
Jentsje van der Meer, Harry de Looff, and Peter C.G. Glas

Maintenance Dredging Required after Port Extensions at Walvis Bay 3453
R.C. Coppoolse and J.S. Schoonees

Accuracy in Spill Monitoring: Turbidity Distribution and Conversion Factors 3466
Klavs Høgh, Iris Buxbom, and Trine Borum Bojsen

Defining an Unusual Littoral Regime To Optimize Dredging at East London 3479
A.K. Theron and J.S. Schoonees

The Development of Sand Waves and the Maintenance of Navigation Channels in the Bisanseto Sea 3490
Kazumasa Katoh, Hidetoshi Kume, Keiji Kuroki, and Junzo Hasegawa

Coastal Disaster Prevention Works in Japan 3503
Ichio Motono and Susumu Naruse

Breach Erosion in Sand-Dikes 3516
Paul J. Visser

Bayesian Estimation of Quantiles for the Purpose of Flood Prevention 3529
J.M. van Noortwijk, and P.H.A.J.M. van Gelder

Flood Protection in the Danish Wadden Sea Area 3542
Jens Otto Andersen

Dispersion of Wave Action 3553
James M. Buick and Tariq S. Durrani

Predicting and Evaluating Turbidity Caused by Dredging in the Environmentally Sensitive Saldanha Bay 3561
S.A. Luger, J.S. Schoonees, G.P. Mocke, and F. Smit

Simulation of the Behavior of Oxygen-Deficit Water in Tokyo Bay by Three-Dimensional Water Quality Model 3575
Nobuo Mimura, Mitsuhiro Tsukada, and Masaharu Suzuki

Watertable Fluctuations in a Sandy Ocean Beach 3588
B. Raubenheimer, R.T. Guza, and Steve Elgar

Seepage Effects on Sediment Transport by Waves and Currents 3601
T.E. Baldock and P. Holmes

The Settlement, Hardness and Liquefaction of Sand Beds Due to Fluctuating Water Pressure 3615
Takaaki Minamimura, Masaki Niiyama, Takao Akutu, Kenji Yano, and Toshihiko Yamashita

A Method for Estimating the Bed Velocities Produced by a Ship's Propeller Wash Influenced by a Rudder 3624
G.A. Hamill, J.A. McGarvey, and P.A. Mackinnon

Design of Scour Protection for the Bridge Piers of the Øresund Link 3634
Lars Kirkegaard, Mogens Hebsgaard, and Ole Juul Jensen

Experimental Analysis of Wave-Induced Liquefaction in a Fine Sandbed 3643
Kojiro Suzuki, Shigeo Takahashi, and Yoon-Koo Kang

Long-Period Oscillations in a Harbor with a Fluid Mud Bottom **3655**
Wataru Kioka, M. Akter Hossain, and Kenji Kashihara

Non-Uniformity in the Wind Generated Gravity Waves Phase Distribution **3668**
Germán Rodríguez, C. Guedes Soares, E. Pérez Martell, and J.C. Nieto

Subject Index **3681**

Author Index **3691**

Part II: Long Period Waves, Storm Surges, and Wave Groups

Waves from Fast Ferry Breaking on the Coast of Zealand

Waves Generated by Fast Ferry at Hundested, Zealand

LONG WAVES IN FLUME EXPERIMENTS

J. William Kamphuis, M.ASCE[1]

Abstract

This paper addresses the influence of long waves on the design wave height of structures in shallow water. Wave heights, wave periods, depths of water at the structure, time of wave measurement, length of the wave-guides were all varied in 29 series of two-dimensional hydraulic model tests. The results indicated that long wave activity is an important design parameter for breakwaters in shallow water. The wave height at breaking and long wave reflection from the structure are the primary parameters influencing long wave activity.

Introduction

This paper is based on two-dimensional hydraulic model tests to determine the design wave for structures in shallow water. An earlier paper - Kamphuis (1996) reported that *design wave height* was not simply related to the depth of water at the structure toe, as is normally assumed. *Design depth* was found to be the sum of the water depth and a fraction of the breaking wave height. A preliminary expression for design depth was given as:

$$d_{des} = d_T + 0.1H_b \qquad (1)$$

[1] Faculty of Civil Engineering, Delft Technical University, Netherlands; Department of Civil Engineering, Queen's University, Kingston, Ontario, Canada, K7L 2R4. Tel: 613-545-2148, E-Mail: kamphuis@civil.queensu.ca

where d_T is the depth of water at the toe of the structure. The wave height, H is determined from the wave spectrum (H_{mo}) and H_b is the breaking H_{mo} wave height. This is a significant increase in design depth for structures in shallow water, considering that H_b can be much greater than d_T. Further research is now underway to determine the actual physical causes that modify design depth. Part of that research is the analysis of long wave activity near the structure and that is the basis of the present paper.

The Tests

An initial set of tests was performed in 1995. The experimental setup is shown in Fig. 1. Water level fluctuations were recorded for 16 sets of conditions (Table 1). Each test consisted of water level records at 64 locations (one stationary probe and a rack of 9 moving probes placed at 7 locations). Six to 11 different incident wave spectra with offshore wave heights (H_{mo}) varying from 0.04 to 0.18 m were tested. Subsequent to these tests, other data sets were obtained in 1997 to provide better estimates of wave setup, to determine the increase of long wave activity with time, to isolate the influence of length wave guides and to test the actual breakwater stability. Each of the 1997 tests used 16 wave gauges at fixed locations. The test parameters for all tests are summarized in Table 1.

Table 1
Test Conditions

	Depth at Structure (cm)			
T(sec)	**0.04**	**0.05**	**0.064**	**0.08**
0.8	6	2	9	10
1.0	4	3 *	1	11 * t
1.2	5	7	8 *	12 * t G
1.5	13	14 *	15 * G	16 * t G

The numbers refer to the 1995 tests (each with 6 to 11 incident wave heights).
(*) denotes 1997 tests (each with 3 incident wave heights).
(t) denotes tests for time dependence (at 2, 5, 10 and 20 minutes).
(G) denotes tests with different lengths of wave guides (27, 18 and 9 m).

The basic 1997 tests were a repetition of selected 1995 tests, except that a more realistic model breakwater was used. In 1995 a large, high rubble mound structure was used that could not be damaged and was overtopped only by the highest waves. The 1997 the rubble mound addressed stability and was therefore more realistic, sustained damage and was not so high. Three offshore wave heights were run for each 1997 test. To determine time dependence of the long wave, the waves were measured beginning at 2, 5, 10 and 20 minutes after the start of the test for Tests 11, 12 and 16. The standard measurement time used in all other tests was to begin recording of the waves 5 minutes after the start of the test. Finally, the effect of the lengths of the wave guides were tested for Tests 12,

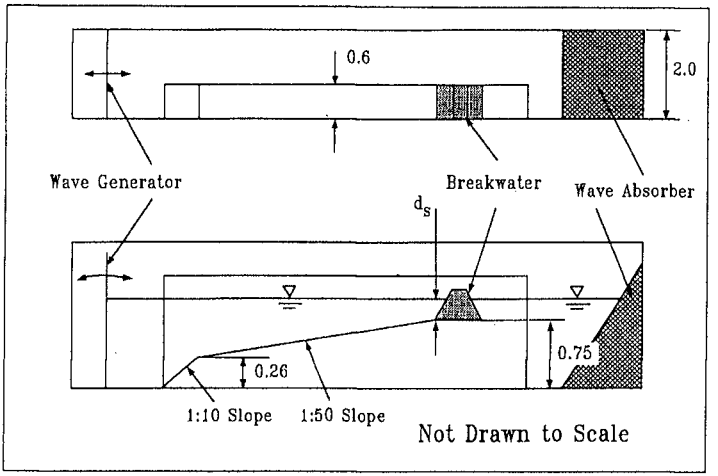

Figure 1 - Experimental Setup

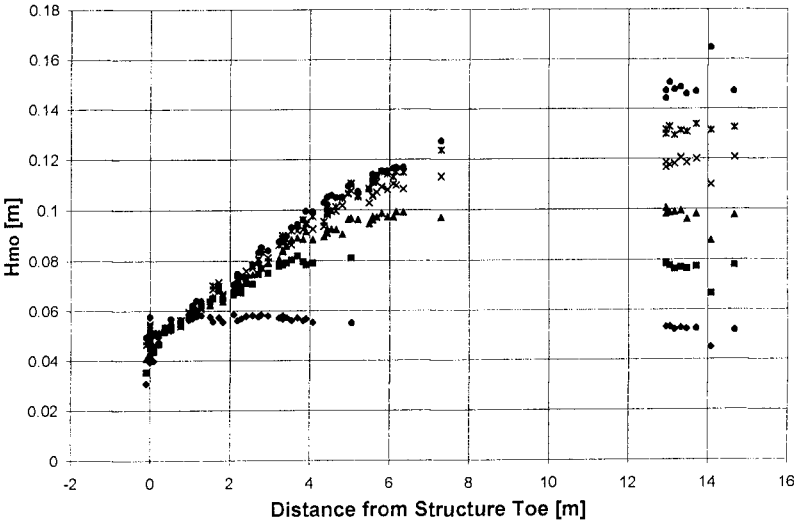

Figure 2 - Wave Height Profile

15 and 16, using the original guide length of 27.1 m and shorter lengths of 18.3 and 9.5 m (thus roughly 27, 18 and 9 m).

Primary analysis

Preliminary analysis of each data set consisted of frequency analysis. For the 1997 tests wave setup was determined. Zero-crossing analysis was performed for some of the 1995 records. Figure 2 presents the frequency analysis of Test 7. Test results for six offshore incident wave heights are shown, varying from 5.4 to 14.4 cm. It is seen that H_{mo} decreases after breaking and then increases close to the structure. This increase in H_{mo} is due to long wave activity. To investigate this further, the long- and short wave components of the signal needed to be separated. Wave spectrum analysis showed that a minimum in the wave spectrum occurred at about $f_p/2$ as shown in Fig. 3. This was used to filter the water level signal to produce separate short wave and long wave signals (Figs. 4 and 5).

Wave Setup and Seiche

The first physical process that could modify the design depth in Eq. 1 would be *wave setup*. The measured wave setup at the structure, however, was much less than 0.1 H_b as shown in Fig. 6 and thus the depth modification in Eq. 1 cannot be explained by wave setup alone. The details of the wave setup analysis will be presented in another paper.

During the tests, it was noticed that the highest short waves at the structure always coincided with the *crest* of the long wave and therefore it can be expected that the long wave has an influence on the design depth. Particularly because the wave generator did not have capability to absorb long wave energy, it is first necessary to see if any of the long wave activity is due to resonance of certain frequencies with the wave flume *(seiche)*. The natural frequencies of the wave flume in Fig. 1 were therefore determined by eigenvalue analysis. These natural periods were found to be as in Table 2. The peak periods of the long waves were found to be unrelated to these natural periods. There were no peaks in the measured long wave spectra at either the fundamental frequency or its harmonics. Clearly seiche was not a consideration in these tests.

Table 2
Natural Periods of the Experimental Setup

	Depth at Structure (d_s) m			
Period (sec)	**0.04**	**0.05**	**0.064**	**0.08**
First Harmonic	35.2	34.9	33.3	32.5
Second Harmonic	18.4	17.9	17.3	16.8
Third Harmonic	12.4	12.1	11.6	11.3
Fourth Harmonic	9.4	9.1	8.8	8.5

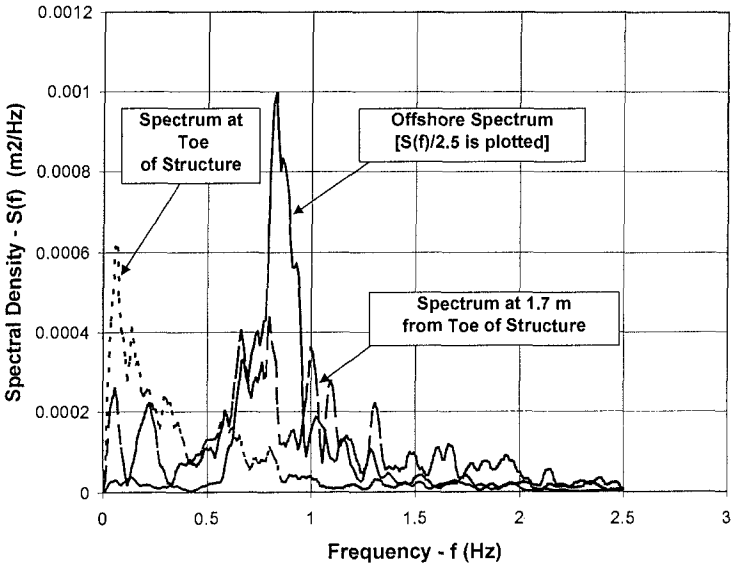

Figure 3 - Separation of Long- and Short Wave Spectra at $f_p/2$

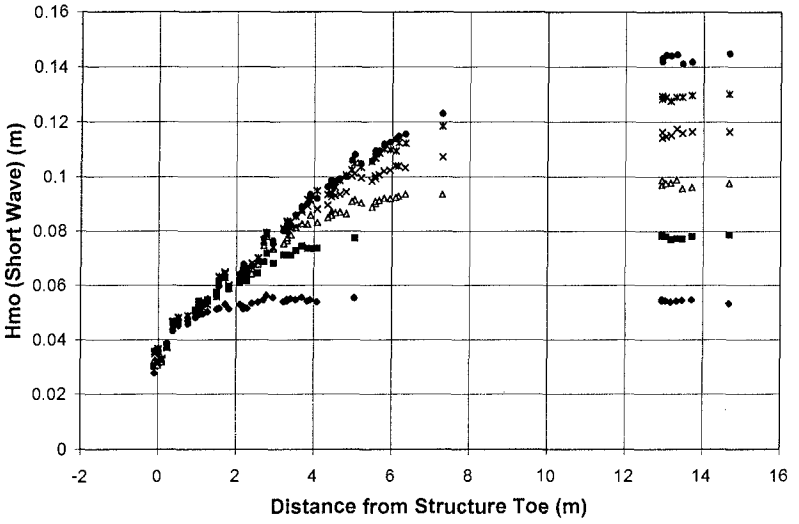

Figure 4 - Short Wave Height Profile

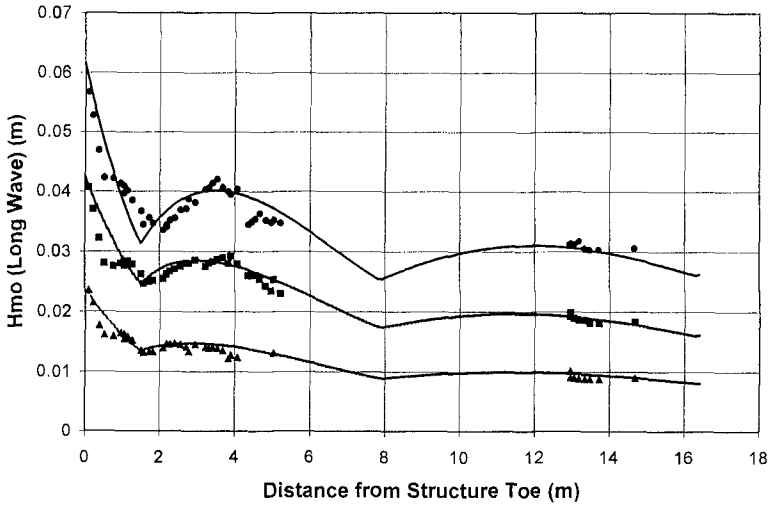

Figure 5 - Long Wave Height Profile

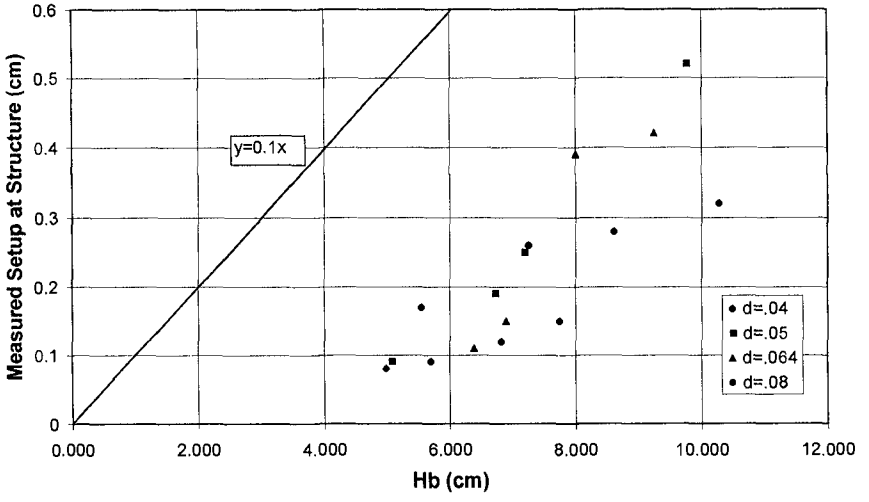

Figure 6 – Measured Wave Setup at Structure Toe

Long Wave Profiles

The long wave profiles (Fig. 5) can be adequately described by combining an absorbed and a standing long wave. At the structure:

$$H_{LW} = H_{LW,I} + H_{LW,R} = H_{LW,A} + H_{LW,S} = H_{LW,A} + 2H_{LW,R} \quad (2)$$

where H_{LW} is H_{mo} of the long wave, I denotes incident, R is reflected, A is absorbed and S is standing.

To keep it simple, we used the approach of Lamb (1932) who solved the linearized long wave equations to show that the standing long wave envelope over a sloping bottom may be approximated by a Bessel function. This approach is also illustrated by Shah and Kamphuis (1996). For the present tests, the expression needed some adjustment because d_T was not zero. The absorbed long wave portion is assumed to consist of a bound long wave up to the breaking point and a free long wave up to the structure. The shoaling expression for the bound long wave of Longuet-Higgins and Stewart (1964) was found to overestimate the shoaling, because the 1:50 foreshore slope does not allow the shoaling long wave to reach equilibrium. The free long wave was found to obey Green's Law. Offshore, the trough of the bound long wave accompanies the highest waves in the group, but close to the structure, the crest of the long wave accompanies the highest waves. This represents a 180° shift from outside the breaker to the shore, noted also by other authors. The detailed work on the long wave profiles will be presented in another paper.

Long Waves at the Structure

To determine the influence of long waves on structural stability and design conditions, we investigated the long wave action *at the toe of the structure*. The long wave height there may be expressed as:

$$H_{LW} = f(H_b, d_s, T, g, \mu, \rho, m, t, L_g) \quad (3)$$

where H refers to H_{mo}, H_{LW} is the long wave height at the structure, H_b is the breaking wave height, T the peak period of the short wave, g the gravitational acceleration, μ and ρ are the dynamic viscosity and density of the water, m is the slope of the foreshore, t is time and L_g is the length of the wave guide. Note that d_b was not used in this function, since it is closely related to (not independent of) H_b as shown in Fig. 7.

Dimensional analysis of Eq. 3 yields:

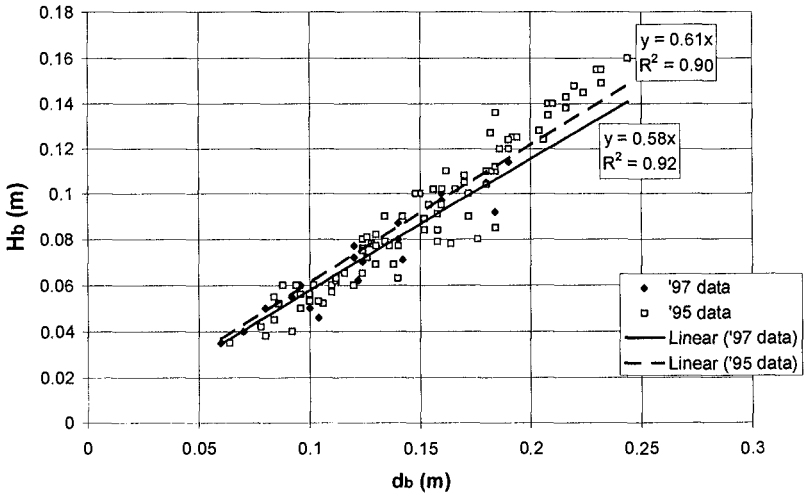

Figure 7 - Breaking Wave Height and Breaker Depth

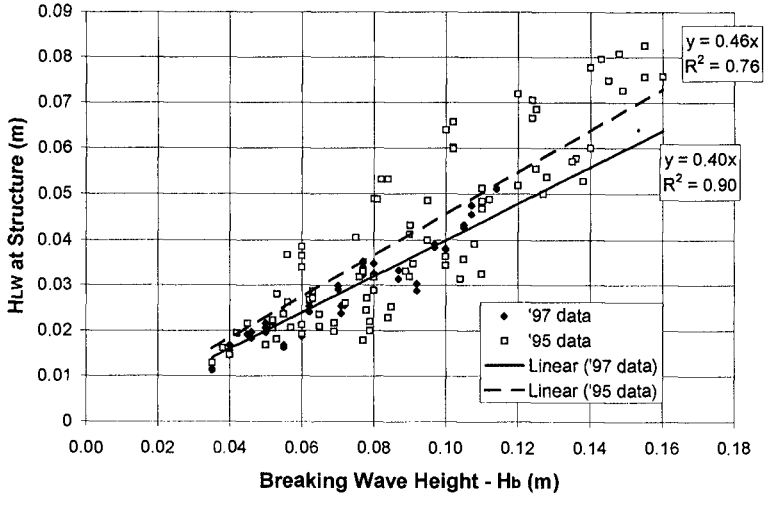

Figure 8 - Long Wave Height at the Structure and Breaking Wave Height

$$\frac{H_{LW}}{H_b} = \phi\left(\frac{H_b}{gT^2}, \frac{d_s}{H_b}, \frac{\sqrt{gH_b}H_b}{\mu/\rho}, m, \frac{t}{T}, \frac{L_g}{gT^2}\right) \quad (4)$$

where the ratios represent relative long wave height, steepness of the short waves, relative depth at the structure, wave height Reynolds number, foreshore slope, the number of waves and the relative length of the wave guides. In these tests, typical model Reynolds numbers are of the order of 10^6 and viscous scale effects are expected to be small. The foreshore slope was kept constant at 1:50. That is quite similar to prototype slopes, but its effect was not specifically tested.

The long wave height at the structure was closely related to the breaking wave height, as shown in Fig. 8. Thus the ratio H_{LW}/H_b is valid as a basic dependent variable. Both the 1995 and the basic 1997 data sets are plotted in Fig. 7. It is seen that there is a difference between the two sets of results. The 1995 set results in $H_{LW}=0.46H_b$ and the 1997 results give $H_{LW}=0.40H_b$.

Effect of Depth at the Structure and Wave Period

Figure 9 shows that the depth of water at the structure does not seem to affect the results, but the influence of wave period is substantial as shown in Fig. 10. When H_{LW}/H_b is plotted against the wave period related steepness parameter H_b/gT^2, as in Fig. 11, it is seen that there are again two different populations for the 1995 and 1997 data.

A reflection coefficient was defined (at the structure) as:

$$K_R = \frac{H_{LW,R}}{H_{LW,I}} = \frac{\frac{1}{2}H_{LW,S}}{(H_{LW,A} + H_{LW,S} - \frac{1}{2}H_{LW,S})} = \frac{H_{LW,S}}{(2H_{LW,A} + H_{LW,S})} \quad (5)$$

Fig. 12 shows that the effect of H_b/gT^2 on K_R is very similar to its effect on H_{LW}/H_b. Thus most of the dependence of H_{LW}/H_b on H_b/gT^2 must be explained by long wave reflection. From detailed analysis of the long waves, it was shown (to be published) that, on average $H_{LW,A}\cong 0.26H_b$ for both the 1995 and 1997 tests. For the 1997 tests, $H_{LW,R}\cong 0.07H_b$, on average. Thus, using Eq. 2, $H_{LW}=\{0.26+2(0.07)\}H_b=0.40H_b$, which is the same as in Fig. 8. For the 1995 tests $H_{LW,R}$ was found to be $0.12H_b$, which would result in $H_{LW}=0.50H_b$. However, the scatter in these results was much greater – the standard deviation of the coefficient is 0.06. Therefore $H_{LW}=0.46H_b$ in Fig. 8 corresponds well and the difference between the two sets of results can be completely ascribed to the difference in long wave reflection between the high 1995 breakwater and the

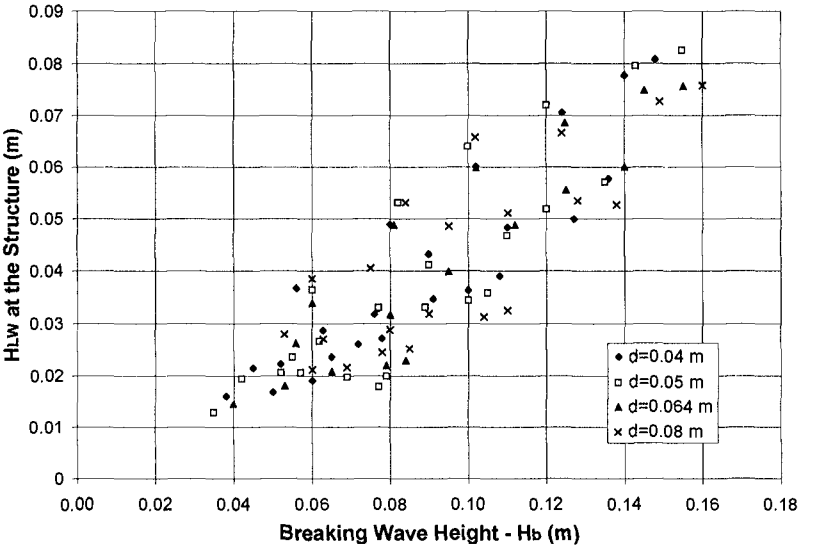

Figure 9 - Effect of Depth of Water at the Structure on H_{LW}/H_b (1995 data)

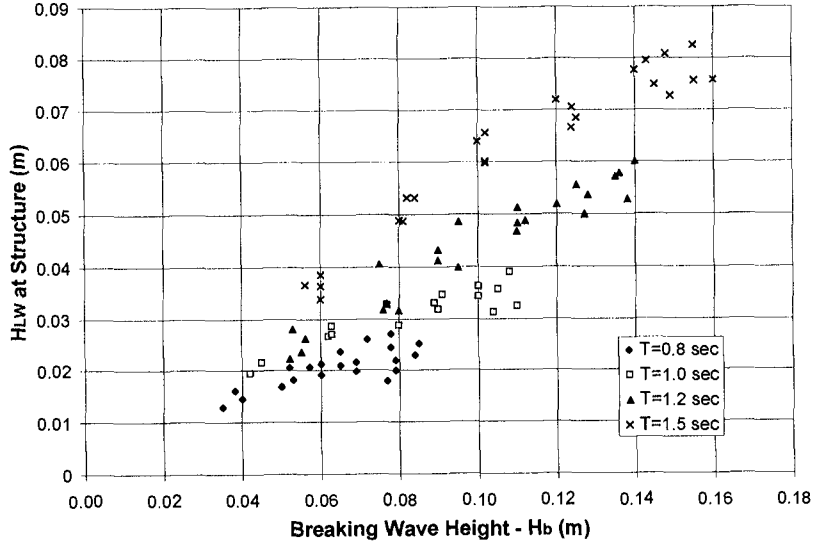

Figure 10 - Effect of Wave Period on H_{LW}/H_b (1995 data)

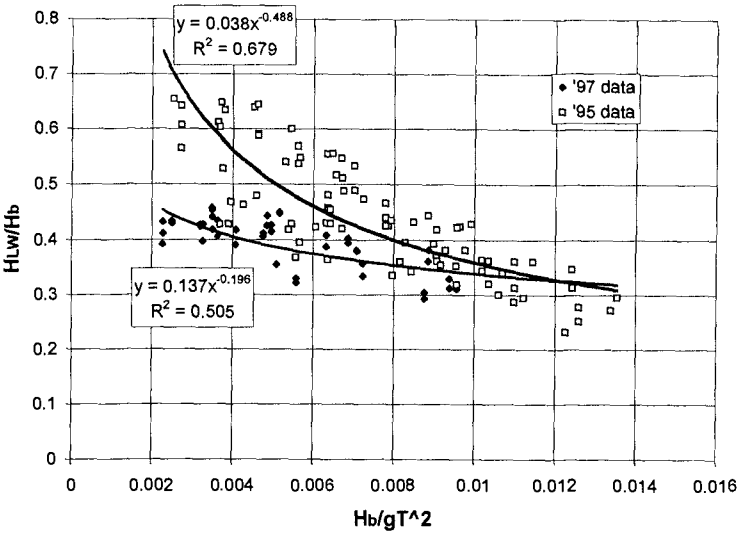

Figure 11 - Effect of H_b/gT^2 on H_{LW}/H_b

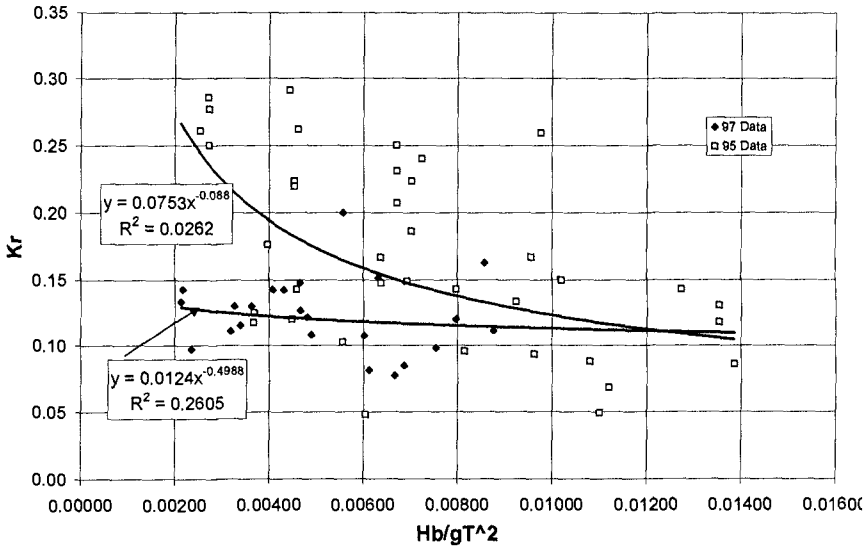

Figure 12 – Long Wave Reflection Coefficient

lower 1997 breakwater that was damaged in the later stages of the tests. If we assume the 1997 tests to be typical of a functioning breakwater, it would appear that long wave height at a structure in shallow water may be approximated by

$$H_{LW} \cong 0.4H_b \quad (6)$$

This is substantial. For structures in very shallow water, the resulting long wave height can easily exceed d_T, which would mean exposure of the toe of the structure and extensive overtopping.

Effect of Time of Measurement and Length of Wave Guides

Figure 13 shows the effect of time of measurement on the long wave activity for Test 12B. It is seen that the results of 2, 10 and 20 minutes compare quite closely with the standard time of 5 minutes used in all the other tests. When the coefficients of all such analyses are summarized as in Fig. 14, it is seen that there is no discernible effect of time of measurement. Analysis of the lowest and highest values shown in Table 3 indicates that if there is any increase in long wave activity with time, it is only marginal.

To test the effect of the length of the wave-guides, the incident waves varied a little from test to test and therefore it was necessary to analyze H_{LW}/H_b. Figure 15 shows no great effect. Analysis of the highest and lowest values in Table 4 shows that the 27 m wave guides resulted most often in the highest long waves, but does not show a consistent decrease in long wave height with wave guide length.

Table 3
Occurrences of Lowest and Highest Values for Measurement Times

	2 Min.	10 Min.	20 Min.
Lowest	4	3	1
Highest	2	3	3

Table 4
Occurrences of Lowest and Highest Values for Wave Guide Lengths

	27 m.	18 m.	9 m.
Lowest	0	5	4
Highest	6	2	1

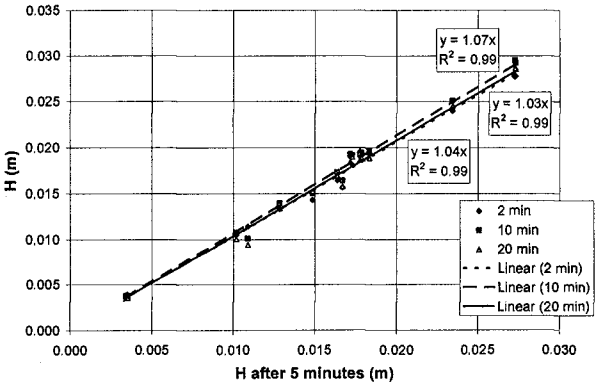

Figure 13 – Effect of Time of Measurement (Test 12B)

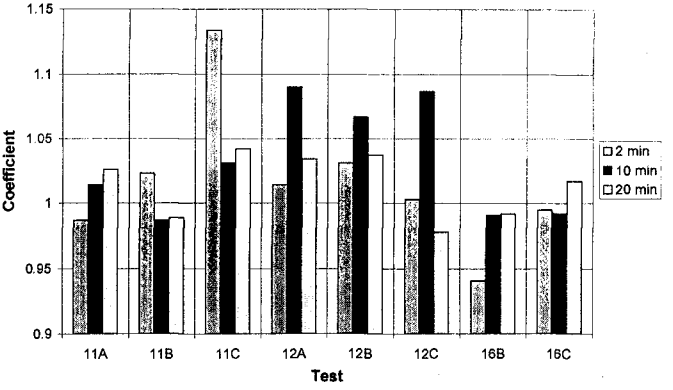

Figure 14 –Time of Measurement

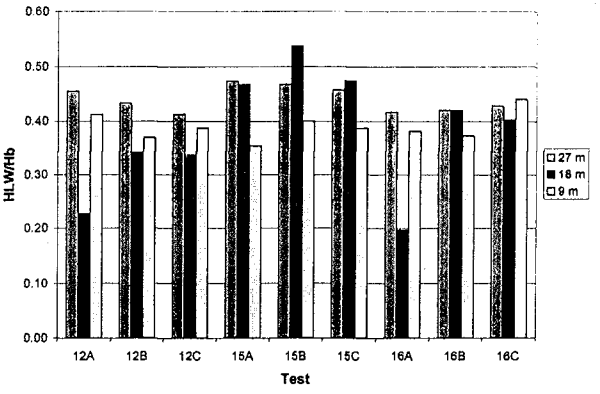

Figure 15 –Length of Wave Guides

Conclusions

The following conclusions with respect to long waves may be drawn from the work presented here. The experiments were performed with a rubble mound breakwater structure placed in shallow water, fronted by a constant 1:50 slope.

a) The wave height decreased from the breaker to the structure, but increased very close to the structure.
b) The increase in wave height was due to long wave activity.
c) Long wave height at the structure was related to:
   - breaking (short) wave height.
   - wave period, most likely through the variation in long wave reflection coefficient with wave steepness.
d) Long wave height was not related to:
   - depth of water at the structure.
   - resonant wave action (seiche) in the wave flume.
   - the time when the long wave activity is measured.
   - to the length of the wave guides.

With respect to design wave height for the structure in shallow water:

e) Kamphuis (1996) has shown that the design wave height is not simply related to depth of water at the structure, but to a design depth.
f) Design depth at the structure in shallow water was shown to be substantially increased by a function of breaking wave height.
g) The design depth increase postulated in Kamphuis (1996) cannot be due to wave setup alone.
h) The long wave activity near the structure is more than sufficient to be the cause the increase in design depth.

References:

Kamphuis, J.W. (1996), "Experiments on Design Wave Height in Shallow Water", *Proc. 25th Int. Conf. on Coastal Eng.*, ASCE, Orlando, pp 221-232.

Lamb, H. (1932), *"Hydrodynamics"*, 6th Ed. Cambridge U. Press, pp 273-280.

Shah, A.M. and J.W. Kamphuis (1996), "The Swash Zone - a Focus on Low Frequency Motion", *Proc. 25th Int. Conf. on Coastal Eng.*, ASCE, Orlando, pp 1431-1442.

PROBABILISTIC MODEL FOR TSUNAMI-WAVE ELEVATION ALONG THE ALBORÁN SEACOAST

M. González[1,2] and R. Medina[1]

Abstract

In this study the tsunami-wave run-up along the Alborán Seacoast (Spain) have been evaluated. An indirect statistical method has been used to estimate the tsunami risk along the southeastern Spanish coast. This method can be summarized as: (1) analysis of the global neotectonic setting, the geodynamic processes as well as seismicity of the region; (2) tsunami source model; (3) generation, propagation and run-up numerical models; and (4) the risk model. The purpose of this study is to establish tsunami-wave elevation at the shoreline versus the return period curves for different locations along the Alborán seacoast. It is concluded that, the tsunamis generated in the Alborán basin have a medium-to-low intensity, with the most important elevations in the Málaga, Adra and Melilla areas.

Introduction

The Alborán seacoast is located along the southwestern Mediterranean Sea and occasionally, this area is affected by tsunami water waves (see figure 1 where some of the tsunamigenic epicenters are shown).

During the last few decades, the southeastern coast of Spain (Almería, Málaga and Marbella) has suffered an enormous transformation due to the tourism "boom" and the demand for coastal use. For this reason, a great number of infrastructures have been built (marinas, beaches, highways, boardwalks, hotels, etc.), which could be affected by tsunamis. The objective of this study is to establish the tsunami-wave elevation risk along the Alborán Sea. Since the frequency of occurrence, location, and magnitude of tsunamigenic earthquakes are random, the risk analyses must be based on probabilistic considerations.

1 Ocean & Coastal Research Group. Departamento de Ciencias y Técnicas del Agua y del Medio Ambiente. Universidad de Cantabria. 39005 Santander, Spain. E-mail: mao@puer.unican.es
2 Facultad de Ingeniería. Dpto. de Mecánica de Fluidos y Ciencias Térmicas. Universidad del Valle. A.A. 25360. Cali (Colombia)

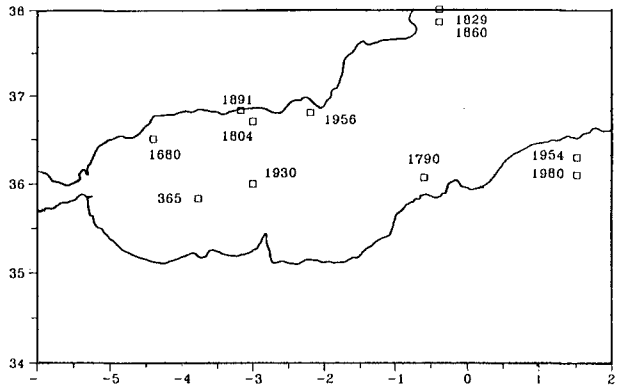

Figure 1. Historical tsunamigenic events

Tsunami hazard has been investigated using various approaches. Where historical information and measurements regarding tsunami inundation are available, a direct statistical analysis has been used (Houston, 1977; Wiegel, 1970); where such data are scarce the concept of indirect analysis has been applied. The indirect approach, as carried out by Houston et al. (1974) and García et al. (1975), consists essentially of utilizing: (1) the historical information available in order to estimate the frequency of tsunamis of various intensities at the sources, and (2) the knowledge of tsunami wave propagation based on hydrodynamic considerations to compute the risk of a tsunami at the site.

The catalog of tsunamis that have occurred along the Alborán seacoast includes only a few events, since tsunamis are rather infrequent and since, in the past, positive scientific attention to these natural phenomena was scarce or even absent in the Alborán seacoast as in many other countries. Given this, no data concerning the source parameters (bed sea dislocations, source area, etc.) are available. In this study, a tsunami risk analysis following the idea of Houston et al. (1974) and García et al. (1975) is performed. However, seismological and probabilistic models similar to Lin et al. (1986) are used in order to determine the seabed dislocations in the source area.

The indirect method applied in this study can be summarized as:

- Selection of the tsunamigenic sources and seismic parameters.
- Tsunami source model (seismological model).
- Hydrodynamic numerical models (generation, propagation and run-up).
- Risk model.

Tsunamigenic Sources

Taking into account the global neotectonic setting, the geodynamic processes as well as the seismicity of the considered region, it is possible to determine potential tsunamigenic

sources, whether or not they are historically active. It is likely that the major cause of catastrophic tsunamis is underwater shallow focus earthquakes of Richter magnitud 5.0 or greater (Iida, 1970, 1963). However, not all such earthquakes produce tsunamis since the generation mechanism is usually associated with vertical dislocations of the sea floor in dip-slip faults normal or reverse faults.

Neotectonic features

The Alborán Sea in the southwestern Mediterranean is a very active region of the wide area of continental collision generated by the northward movement of the African plate relative to the European plate (Dewey et al., 1989). The unusual tectonic situation of a small sea caught between two major plates is characterized by a complex sea floor physiography, with several basins separated by structural highs and ridges (Maldonado et al., 1992a, c; Woodside et al., 1992). Furthermore, some authors (Udías et al., 1976; Buforn, 1988b, c; Udías et al., 1992 and Mezcua et al., 1997) have proposed different geodynamic models based on source mechanisms of earthquakes, that permit the determining of the fault system in the Alborán Sea. The tectonic features are characterized by a fault system composed of short strike-slip faults and short dip-slip faults, as shown in figure 2. This short fault system is due to the crustal shocks of the African and European plates, where a beniof or subduction zone is not evidenced.

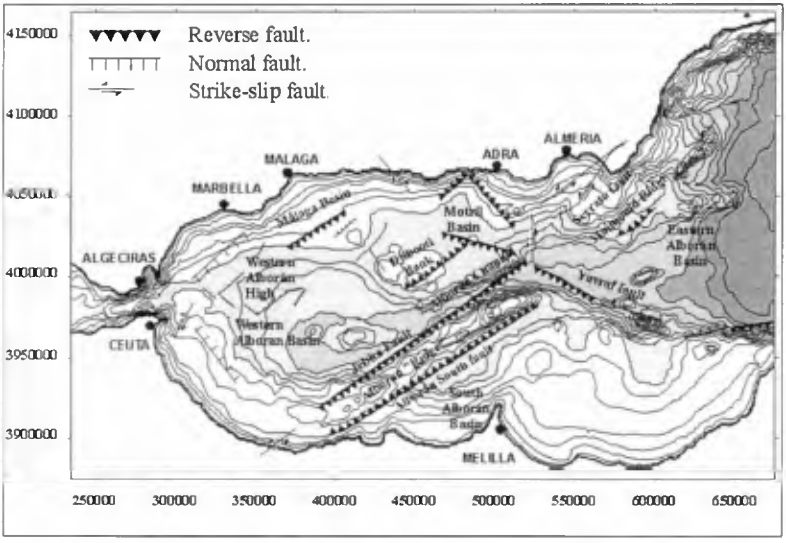

Figure 2. Schematic summary of principal neotectonic and geomorphologic elements in the Alborán Sea

Seismic pattern

The spatial distribution of seismicity could be considered a manifestation of the lithospheric weakness zone where the stresses applied are released, that, joined with some seimic parameters, permit the choice of potential tsunamicgenic sources. The Alborán Sea presents high seismic activity, with moderate earthquake magnitudes and shallow epicenters. The earthquakes are associated with the local fault system.

The data for the earthquakes were taken from: (1) the Spanish National Seismic Catalog from the period 1916-1996: (2) the Spanish seismic risk maps from the National Geographic Institute (NGI) from the period 1320-1920. In figure 3, different Richter magnitudes of the earthquakes from the 1916-1996 period are shown for ($M_s \geq 5.0$).

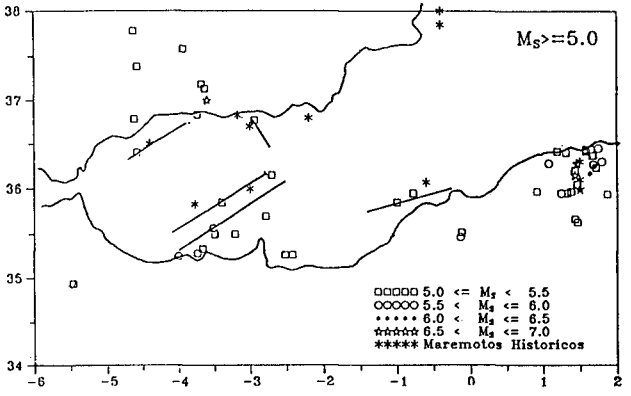

Figure 3. Relocated seismicity ($M_s \geq 5$), for the period 1916 - 1996 and potential tsunamigenic sources

Potential faults

Five potential tsunamigenic sources have been selected for the Alborán Sea, taking into account: (1) the historical tsunami data (figure 1); (2) the analysis of the dip-slip faults (normal and reverse); and (3) analysis of seismicity. This kind of analysis is used as an important tool to estimate the potential for tsunamigenic earthquakes (Alami and Tinti, 1991). Only the seismic data with magnitude greater than 5.0 on the Richter scale with focal depths less than 50 km and greater than 20 km, are included in the analysis (Iida, 1963, 1970).

Tsunamis of distant origin (Italian and Greek sources) are not considered a threat to the study area. Furthermore, although the Atlantic Ocean sources (Azores - Gibraltar fault system) can generate great tsunamis, they do not cause any perceivable perturbations in the Alborán Sea. Historical events and numerical simulations confirm that the Strait of Gibraltar acts as an important tsunami filter. In figures 3 and 5, the five potential tsunamigenic sources

selected for the Alborán Sea area are shown.

Tsunami Source Model

In this study, the offset is assumed to be a vertical ascendant movement generated by submarine earthquakes of tectonic origin, which are associated with the five selected potential sources. It is also assumed that the sources are simple straight faults with a focus located in the middle point (see figure 5). The bed displacement is defined by: (1) the source location; (2) the plane area of the ground displacement, S; (3) the average offset or vertical dislocation, D; and (4) the velocity of the displacement, $\xi(t)$. Figure 4 shows a diagram of the bed movement.

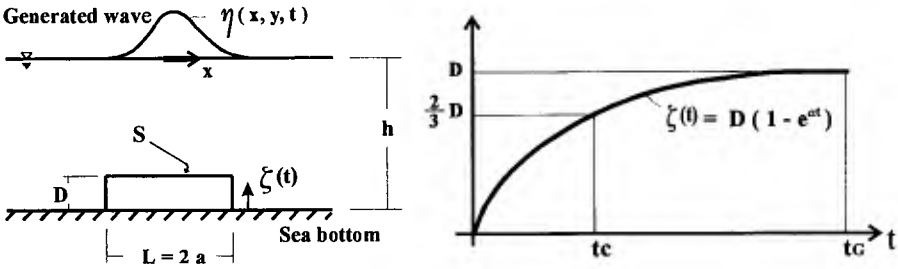

Figure 4. Schematic sea bottom displacement

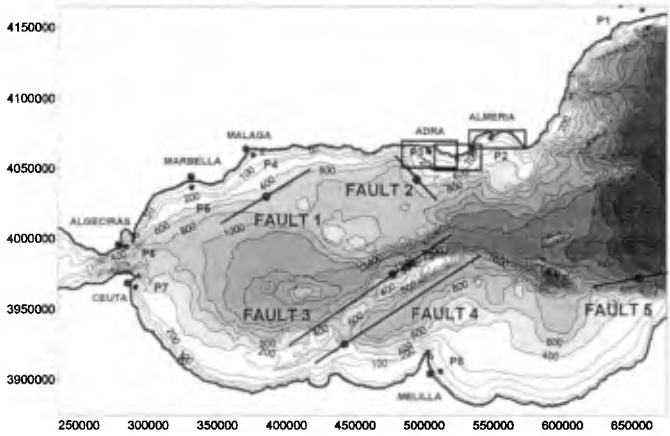

Figure 5. Location map showing global and detailed grids and potential tsunamigenic sources

The most widely used quantitative measure of the strength of an earthquake has been its magnitude (M_s). However, it is well-known that there is difficulty in relating magnitude with other important source characteristics such as strain-energy release, fault offset, stress drop and source dimensions, etc. (Kanamori and Anderson, 1975). For large earthquakes, the seismic moment denoted M_o, is defined as:

$$M_o = \mu S D \tag{1}$$

In which μ= rigidity of the medium (μ= 2 - 3 · 10^{11} dyne - cm^2).

Tsunamigenic earthquakes of tectonic origin are those submarine earthquakes on shallow faults and of large magnitude. As such, tsunamigenic earthquakes are most conveniently measured by seismic moment. In fact, tsunami records in the Pacific have been correlated with and used to calibrate seismic moments (Kanamori, 1977).

The number of occurrences of earthquakes with seismic moment, M_0, greater than or equal to m_0 has been shown to be given as:

$$N(m_0) = \alpha\, m_0^{-\beta} \tag{2}$$

where α and β are numerical constants determined from earthquake records. Discussion of values of these quantities is given by Molnar (1979) as well as by Kanamori and Anderson (1975) and the Fundación Leonardo Torres Quevedo (1997). Equation (2) will be used to determine the probability distribution function of seismic moment in the section "Risk model for tsunamis".

Important physical dimensions of an earthquake are the offset: vertical dislocations and, length and width of ground dislocation. Based on earthquake data, Kanamori and Anderson (1975) obtained the empirical relation between the seismic moment M_o and the source, S, given as:

$$M_o = C_1 S^{\frac{3}{2}} \tag{3}$$

In which $C_1 = 1.23 \cdot 10^7$ dyne - cm^2 width S measured in km^2.

In order to relate seismic moment, M_o, with Richter magnitude, M_s, different authors have proposed empirical relations. Mezcua et al. (1991) obtained for the Azores-Gibraltar-Alborán Sea, the following empirical relationship:

$$\text{Log } M_o = 1.16\, M_s + 17.93 \tag{4}$$

An expression that can be used to relate M_s with source parameters.

In this study an elliptical ground displacement in plan view is assumed, with an exponential time-displacement function which Hammack (1972) defined as:

$$\xi(t) = D\,(1 - e^{-\alpha t}) \quad 0 < t < t_G \tag{5}$$

with $\alpha = 1.1/t_c$, where t_c is the time to rise 2/3 D (t_c ~1 - 20 g.) and t_G is the total generation time (1 - 2 min.).

In accordance with the tsunami source model, the most important parameters that have to be determinated are the source location and the seismic moment, M_o.

Hydrodynamic Numerical Models

In order to simulate tsunami generation and propagation a coupled numerical model was applied. The run-up in some cross-shore locations was estimated matching the coupled model with a one-dimensional, time-dependent numerical model.

Tsunami Generation numerical model

Many authors have applied an elliptical water surface shape similar to the ground displacement for the waves near the source (Houston et al., 1980; Lin et al., 1986; Camfield, 1992). This kind of surface water displacement has also been applied in this study, defined as:

$$\eta(x, y, t) = \xi(t)\left[1 - \left(\frac{x}{a}\right)^2 - \left(\frac{y}{b}\right)^2\right]^{\frac{1}{2}} \tag{6}$$

where $\xi(t)$ is the equation (5), and the coordinate system origin for the x and y axes is located in the middle of the ellipsoid (or source area).

Tsunami Propagation numerical model

Nonlinear, nondispersive, shallow water equations were used to model the propagation of tsunamis in the Alborán Sea.

For a distant tsunami, traveling distance could be much greater than the characteristic wave length of the tsunami. In these cases, both the frequency dispersion and coriolis terms

could play an important role (Liu et al., 1994). However, due to morphological characteristics of the Alborán Sea (see figure 5) which is a small basin (approximately 400 km length, 200 km width and water depth less than 2 km) these two terms can be neglected.

As tsunamis propagate into the shallow water region, wave amplitude increases and wave length decreases due to shoaling. The nonlinear convective inertia force becomes increasingly important while the importance of frequency dispersion diminishes (Liu et al., 1994).

The model equations are solved by an implicit finite difference method. The finite difference scheme is similar to that presented by Leendertse (1970). The model used, as a temporal initial condition, the elliptical deformation of the water surface presented by the relations (5) and (6). An absorbing boundary condition is employed for the seaward boundary and a reflecting condition in the coastline.

A global propagation grid 440 x 290 km^2 was adopted (see figure 5). The numerical computational mesh size and time-step size were fixed, $\Delta x = \Delta y = 1000$ m, $\Delta t = 5$ s. for propagation and $\Delta t = 0.5$ s. for the wave generation. In order to reduce numerical errors, the spatial grid size should be such that one local wave length includes more than 20 grid points. Therefore, a finer spatial grid size was adopted, $\Delta x = \Delta y = 200$ m for water depth less than 50 m. Three finer grids between Adra and Almería are shown in figure 5.

A propagation tsunami example generated in fault 5 ($M_s = 7.5$), is shown in figure 6, where the computed water surface appears at t = 18 min. and t = 33 min.

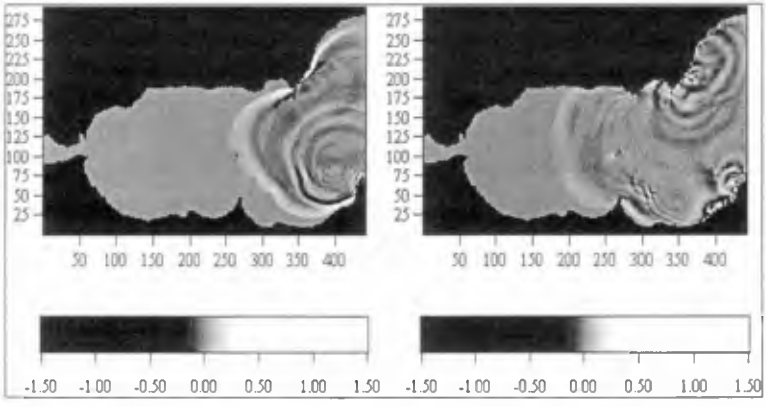

Figure 6. Propagation example tsunami wave elevation (t = 18 and 33 min.), epicenter at fault 5, with $M_s = 7.5$

Tsunami Run-up Numerical Model

A one-dimensional, time-dependent numerical model (Kobayashi et al, 1994 a), is used to simulate the tsunamis flow over some cross-shore profiles along the coast between Adra and Almería. The finite amplitude shallow-water equations (mass, momentum and energy) including the effects of bottom friction over rough impermeable cross-shore slopes, are solved numerically in the time domain using an explicit dissipative lax-wendroff finite-difference method (Kobayashi and Otta, 1987). The run-up model used, as seaward boundary, the tsunami-wave elevation recorded at a numerical gauge in the finer grid. Several cross-shore profiles were selected, starting seaward in 10 m water depth and including the topography of high and low coastal areas.

The bottom friction factor (f) was not considered constant along a cross-shore profile. In profile areas with smooth slopes, as is the case in sandy beaches a $f = 0.005$ was used. On the other hand, a $f = 0.01$ was used in rough slopes, for example in urban areas and step structure slopes.

Risk Model

The tsunamigenic earthquake is not a deterministic phenomenon; both source location and seismic moment, M_o, have to be defined as random variables. Since the occurrence of future tsunamis is difficult to predict, risk analyses must be based on probabilistic considerations. One of the elements involved is the probability of tsunami inundation of various levels at a given place in a given return period. This probability is generally referred to as hazard or risk.

Eight points (see figure 5) of the Alborán seacoast and some cross-shore profiles between Adra and Almeria were selected to perform the risk analysis. The risk analysis consists of: (1) A Monte Carlo simulation, which is based on a probabilistic model in order to obtain the synthesized record of tectonic deformations of the seabed; (2) The tsunami source model, which permits us to relate the physical dimensions (S, D) of the displaced bottom source [eq. (1) and (3)]; and (3) the hydrodynamic numerical models which are used to simulate propagation and run-up of the tsunami caused by each of the synthetic seabed deformations.

Probabilistic model for tsunamigenic earthquakes

In order to obtain the synthesized record of seabed deformations, it is necessary to define the three basic random variables involved in risk analysis: (1) the occurrence of tsunamigenic earthquakes events; (2) the earthquake source; and (3) the seismic moment, M_o.

The tsunamic mean frequency of occurrence was obtained based on the eight events which occurred in the last 200 years, due to the fact that there is no historical catalog of tsunamis before 1800. Therefore, it is assumed that one tsunami event occurs once every 25 years on average.

As stated previously, five potential individual faults, were selected. However, the probability of occurrence of tsunamigenic earthquakes in each one of these is different. In order to obtain these probabilities, the following hypothesis are assumed: (1) the faults are independent and once every 25 years one event occurs in one of the five faults; (2) a tsunamigenic earthquake originates from a single, well-defined, straight fault; (3) earthquakes can occur anywhere along a fault with equal likelihood but the focal point is located in the middle of a straight fault (see figure 5); and (4) the probability of occurrence of tsunamigenic earthquakes of a specific fault increases, with the number of events with Richter magnitudes ($M_s > 5$) and focal depths ($D_f < 50$ km). Figure 7 shows the probability function obtained for each one of the potential faults.

The probability distribution function, $F_{M_o}(m_o)$ of M_o was determined, using equation (2) by Lin and Tang (1982), as:

$$F_{M_o}(m_o) = \left[1 - \left[\frac{m_{ol}}{m_o}\right]^{\beta}\right] \cdot \left[1 - \left[\frac{m_{ol}}{m_{ou}}\right]^{\beta}\right]^{-1} \quad m_{ol} \le m_o \le m_{ou} \tag{7}$$

where m_{ol} is the lower magnitud of seismic moment, in accordance with (Iida, 1970, 1963), $m_{ol} = 10^{23.73}$dyne-cm ($M_s = 5.0$ on Richter scale). The maximal energy released by a earthquake in a fault, is limited depending on the neotectonic and the geodynamic of the potential fault. Due to the characteristics of the Alborán Sea, m_{ou} was defined as $m_{ou} = 10^{26.65}$ dyne-cm ($M_s = 7.5$). Equation (7) was applied for the five potential faults (see figure 8), taking into account the seismological data to obtain β, and the empirical relation between M_s and M_o (equation 4).

Results

The risk analysis due to tsunamis is represented by curves which permit us to obtain the maximal tsunami-wave elevation in given sites along the Alborán seacoast for two confidence levels (50% and 99.99%) and return period (years).

As an example of these curves, figures 9 and 10 show the risk analysis in the city of Adra. Figure 9 shows the run-up in a cross-shore city profile and the figure 10 represents the horizontal flooded landward distance, measured from local mean water level. In figure 11, for a return period of 2,500 years, the risk analysis for different places along the Alborán Sea in water depths of 6 m is shown. This figure shows a higher risk in areas near Adra, Málaga and Melilla. The complete results and propagation details can be found in Fundación Leonardo Torres Quevedo (1997).

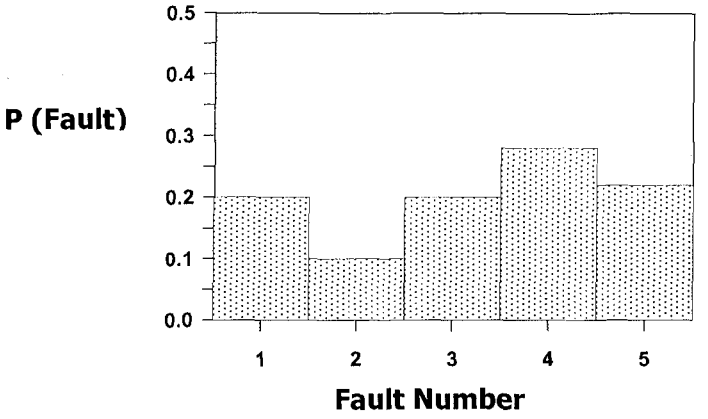

Figure 7. Probability function of tsunami occurrence in potential faults

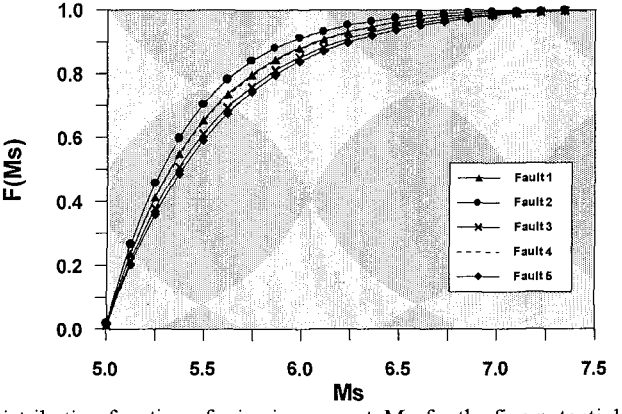

Figure 8. Distribution function of seismic moment, M_0, for the five potential faults.

Conclusions

- Given the global neotectonic setting, the geodynamic processes as well as the seismicity of the Alborán Sea, the tsunamis generated in the area present a medium-to-low intensity.
- Five potential tsunamigenic faults have been determined in the area (figure 5).
- Using simple tsunami source, hydrodynamic and risk models, tsunami risk in different sites along the Alborán Sea has been computed.
- Due to morphological characteristics and the setting of potential faults, zones close to Málaga, Adra and Melilla have a greater tsunami wave elevation than the rest of the Alborán Sea locations.

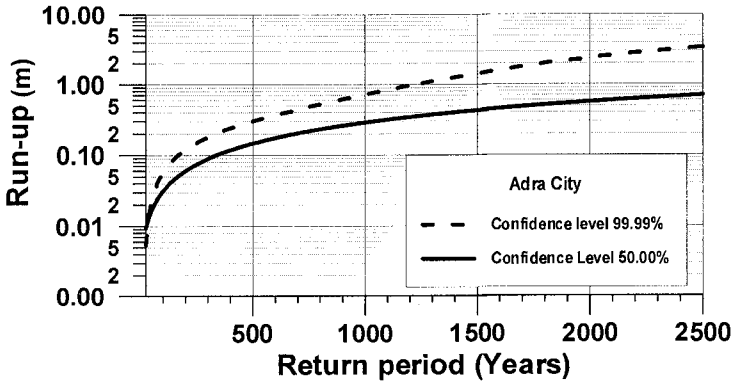

Figure 9. Tsunami risk example. Run-up in the city of Adra

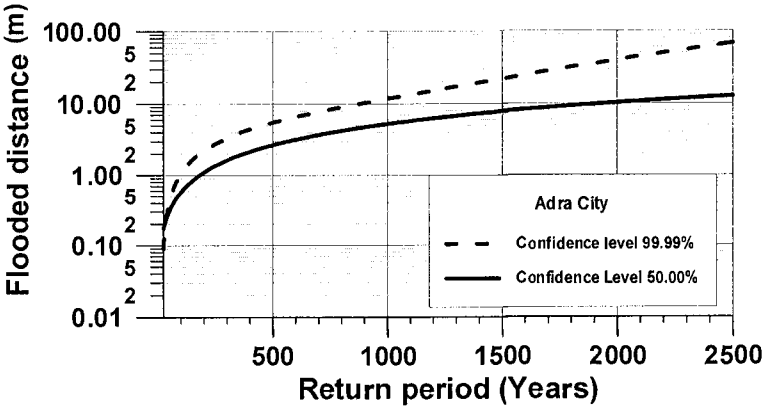

Figure 10. Flooded landward distance in the city of Adra (distance measured from the mean water level)

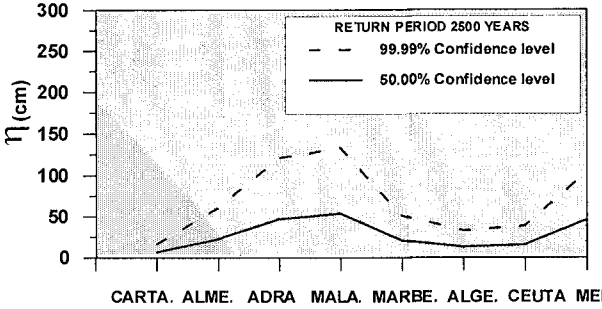

Figure 11. Tsunami risk example. The 2,500 year return period curve in different points along the Alborán Sea (h = 6 m)

Acknowledgements

This research has been partially supported by the "Dirección General de Costas del Ministerio del Medio Ambiente", and the "Comisión Interministerial de Ciencia y Tecnología" under the project MAR96-1135.

References

Alami, S.O. and S. Tinti (1991). *A preliminary evaluation of the tsunami hazards in the Moroccan coasts*, The International Journal of the Tsunami Society, Vol. 9, N. 1.

Camfield, F.E. (1992). *Tsunami effects on coastal structures*, Journ. of Coastal Research Special Issue, N. 12: Coastal Hazards, pp. 177-187.

Dewey, J.F., W.C. Pitman, W.B.F. Ryan and J. Bonnin (1974). *Plate tectonics and the evolution of the Alpine system*, Bull. Geol. Soc. America, 84, 3137-3180.

Fundación Leonardo Torres Quevedo (1997). *Estudio de riesgo de inundación y evaluación de daños por acción de maremotos en el litoral del sureste español (Mar de Alborán)*. Ocean & Coastal Research Group, Universidad de Cantabria.

García, A.W. and J.R. Houston (1975). *Type 16 flood insurance study: Tsunami predictions for Monterey and San Francisco Bays and Puget Sound*, Technical Report H-75-17, Hydraulic Laboratory U.S. Army Engineer, Waterways Experiment Station, Vicksburg, Mississippi.

Hammack, J.L. (1972). *Tsunamis. A Model of their generation and propagation*, California Institute of Technology. Report N. KH-R-38, 337 pages.

Houston, J.R., R.D. Carver and D.G. Marckle (1977). *Tsunami-wave elevation frequency of occurrence for the Hawaiian Islands*, Technical Report H-77-16, Hydraulics Laboratory, U.S. Army Engineer Waterways Experiment Station, Vicksburg, Miss.

Houston, J.R. and A.W García (1974). *Type 16 flood insurance study: Tsunami predictions for Pacific coastal communities*, Technical report H-74-3, US Army Engineer, Waterways Experiment Station, Vicksburg, Miss.

Houston, J.R. (1980). *Type 19 flood insurance study: Tsunami predictions for southern California*. Technical report HL-80-18, US Army Engineer, Waterways Experiment Station, Vicksburg, Miss.

Iida, K. (1963). *Magnitude, energy and generation and mechanisms of tsunamis and a catalog of earthquakes associated with tsunamis*, Proc. of the 10th Pacific Science Congress Symposium. International Union of Geodesy and Geophysics U.G.G.I., Monograph 24, pp. 7-18.

Iida, K. (1970). *The generation of tsunamis and the focal mechanisms of earthquakes*, ADAMS, W.M, ed. tsunamis in the Pacific Ocean, Honolulu, Hawaii, East-West Center Press, pp. 3-18.

Kanamori, H. and D.L. Anderson (1975). *Theoretical basis of some empirical relations in seismology*, Bull. of the Seismological Society of America. Vol. 65, N. 5, pp. 1073-1095.

Kanamori, H. (1977). *The energy release in great earthquakes,* Journal of Geophysical Research. Vol. 82, N. 2, pp. 2981-2987.

Kobayashi, N. and A.K. Otta (1987). *Wave reflection and run-up on rough slopes*, Journal Waterway, Port, Coastal and Ocean Engineering, ASCE, 113 (2), 171 – 186.

Kobayashi, N. and M. Poff (1994 a). *Numerical model RBREAK2 for random waves on impermeable coastal structures and beaches*, Research Report N° CACR-94-12, Center for Applied Coastal Research. University of Delaware, Newark, Delaware.

Kobayashi, N. and A.W. Raichle (1994 b). *Irregular wave overtopping of revetments in surf zones,* Journal Waterway, Port, Coastal and Ocean Engineering, ASCE, 120 (1), 56-73.

Leendertse, J.J. (1970). *A water-quality simulation model for well-mixed estuaries and coastal seas: Vol 1. Principles of computation*, RM-6230-RC. Rand Corp., Santa. Monica, California.

Lin, I. -C. (1982). *A preliminary investigation of tsunami*, ltazard, Bulletin of the seismological Society of America. Vol. 72., N. 6, pp. 2323-2337.

Lin, I.-C and C.C. Tong (1986). *Tsunami hazard*, Jour. of Engineering Mechanics. Vol. 122, N. 9, pp. 874-887.

Liu, P.L. and Y. Cho (1994). *Numerical simulation of tsunami propagation and inundation with application to Hilo, Hawaii*, School of Civil and Environmental Engineering, Cornell University, Ithaca.

Maldonado, A., A.C. Campillo, A. Mauffret, A. Alonso, J. Woodside and J. Campos (1992a). *Alborán Sea late Cenozoic tectonic and stratigraphic evolution*, Geo-Marine Letters 12: pp. 179-186.

Maldonado, A. and M.C. Comas (1992c). *Geology and geophysics of the Alborán Sea: an introduction*, Geo-Marine Letters 12: pp. 61-65.

Mezcua, J., J. Rueda and E. Buforn (1991). *Seismic deformation in the Azores-Alborán Sea region*, Instituto Geográfico Nacional de España. Monografía n° 8, pp. 205-211.

Mezcua, J. and J. Rueda (1997). *Seismological evidences for a delamination process in the lithosphere under the Alborán Sca*, Instituto Geográfico Nacional, Madrid. In Press.

Ministerio de Obras Públicas y Urbanismo (1990). R.O.M. 02-90. *Acciones en el proyecto de obras marítimas y portuarias*, Madrid, Spain.

Molnar, P. (1979). *Earthquake reoccurrence intervals on plate tectonics*, Bull. Seism. Soc. Am. 69, pp. 115-133.

Udías, A., A. López Arroyo and J. Mezcua (1976). *Seismotectonic of the Azores-Alborán region*, Tectonophysics 31: pp. 259-289.

Udías A. y E. Burforn (1992). *Sismicidad y sismotectónica de las béticas*, Física de la tierra, N. 4, 109-123. Editorial Complutense de Madrid.

Wiegel, R.L. (1970). (Ed.), Earthquake Engineering, Chapter 11, Prentice-Hall, Englewood Cliffs, N.J., pp. 253-306.

Woodside, J.M., A. Maldonado A. (1992b). *Styles of compressional neotectonics in the eastern Alborán Sea*, Geo-Marine Letters 12: pp. 111-116.

Long-Period Wave Responses in a Harbor with Narrow Mouth

Weon Mu Jeong[1], Kil Seong Lee[2] and Woo Sun Park[1]

Abstract

Field measurements of long-period wave have been preformed for the Gamcheon Harbor in Korea. A Galerkin finite element model based on the extended mild-slope equation has been developed for simulating harbor oscillation more accurately. Infinite and joint elements are introduced to accomodate radiation condition at infinity and matching conditions at harbor mouth for the consideration of the energy loss due to flow separation, respectively. Comparisons with the results obtained by hydraulic experiments by Lepelletier (1980) show that the present model gives fairly good results. Model results reveal that the influence of entrance loss at the harbor mouth is considerably significant. From the application to the Gamcheon Harbor it is seen that the computed resonant periods and amplification ratios well agree with the measured results. The entrance loss effects were found to be insignificant unless the incident wave height is large.

Introduction

Long-period harbor oscillations could create unacceptable vessel movements leading to the downtime of moored ships. It is practically very difficult to prevent long-period harbor oscillations, but extension of breakwaters at the harbor mouth could be a countermeasure in part. Narrowing a harbor mouth might give rise to increase in the energy loss due to flow separation near the mouth, which in turn makes resonant periods of the harbor become longer, especially for the Helmholtz resonant mode. Referring to Lepelletier (1980), the reduction of a harbor mouth can reduce the amplification ratios of Helmholtz mode considerably.

[1]Senior Research Scientist, Coastal and Harbor Engineering Research Center, Korea Ocean Research and Development Institute, 1270 Sa-dong, Ansan, Kyeonggi-do, 425-170, Korea
[2]Professor, School of Civil, Urban and Geo-Systems Engineering, Seoul National University, San56-1, Sinrim-dong, Kwanak-ku, Seoul, 151-742, Korea

This study includes field measurements for short- and long-period waves around the Gamcheon Harbor in Korea, and the development of a finite element model based on the extended mild-slope equation, which incorporates the bottom frictional dissipation and the entrance loss due to flow separation. The present model can also handle the harbor resonance problems in a harbor with non-straight coastlines. The model is verified through the comparisons with Lepelletier (1980)'s experimental results. Finally, the model is applied to the Gamcheon Harbor with narrow mouth and compared with field measurements.

Field Measurement

Field measurements for short- and long-period waves have been performed around Gamcheon Harbor which is located at the east-southern coast of Korea. The harbor is 4,000 m long, 1,150 m wide and has entrance of 240 m wide. In spite of narrow mouth, this commercial harbor is suffering from severe downtime problems in summer season. The measurement period was from November 27 to December 13 in 1997. Four pressure-type wave gauges (PWG), and one Aanderaa RCM-9 current meter were deployed at locations shown in Figure 1. Sampling intervals for the pressures at Sts. P1 and P4 were set to 5 seconds, while pressure data at Sts. P2 and P3 were gathered in the interval of 1 second. Current velocities from RCM-9 were averaged over 1 minute.

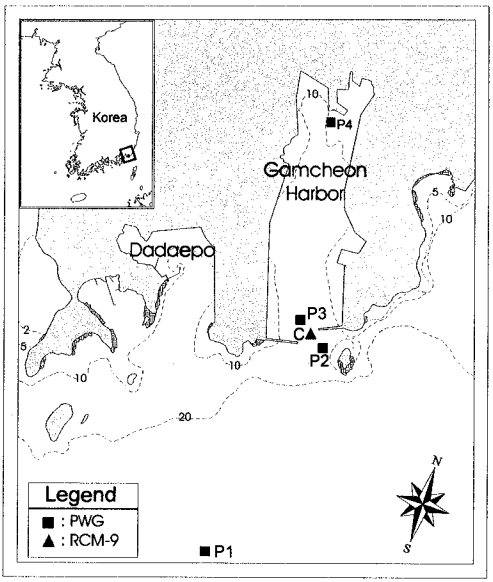

Figure 1. Location Map of Field Measurements.

After filtering tidal components from pressure signals using a Butterworth high-pass filter in MATLAB, spectral analyses of the 16 sets of filtered pressure data were performed. Figure 3 shows the power spectral densities of long-period wave data set no. 6 obtained at the four stations. We can find the first and second resonant modes appear near 2,000 seconds and 600~700 seconds, respectively. It is noted that the period of Helmholtz resonant mode of Gamcheon Harbor is 27.0~33.3 minutes, and the second and third resonant periods appear at 9.4~12.1 and 5.2~6.2 minutes, respectively. Figure 3 shows the power spectral densities of current velocity normal to the harbor mouth. It is noted that the maximum value appears around 28.2~31.9 minutes corresponding to the Helmholz mode.

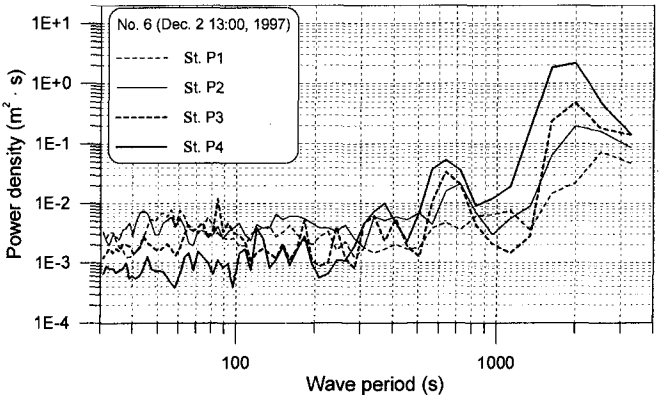

Figure 2. Power Spectral Densities Obtained at Sts. P1~P4.

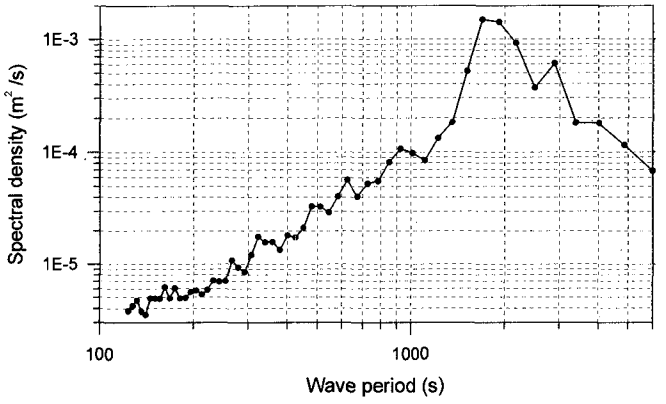

Figure 3. Power Spetral Densities for Observed Velocity at St. C.

Galerkin Finite Element Model

Theoretical Formulation

A Cartesian coordinate system (x, y) and a cylindrical coordinate system (r, θ) are employed for mathematical formulation. The domain in the model is divided into two regions as shown in Figure 4. One is a near field region (Ω_1) that is modeled as conventional finite elements and the other is a far field region (Ω_2) that is represented as infinite elements of which shape functions satisfy the radiation condition at infinity. In the far field region, the water depth is assumed to be constant in the radial direction, but the depth in the circumferential direction varies with the value of the interface between the far and near field regions, Γ_I. To take into account the entrance loss at the narrow harbor mouth, the near field region is again divided into two sub-regions, that is inner (Ω_{1i}) and outer regions (Ω_{1o}) of the harbor (see Figure 4).

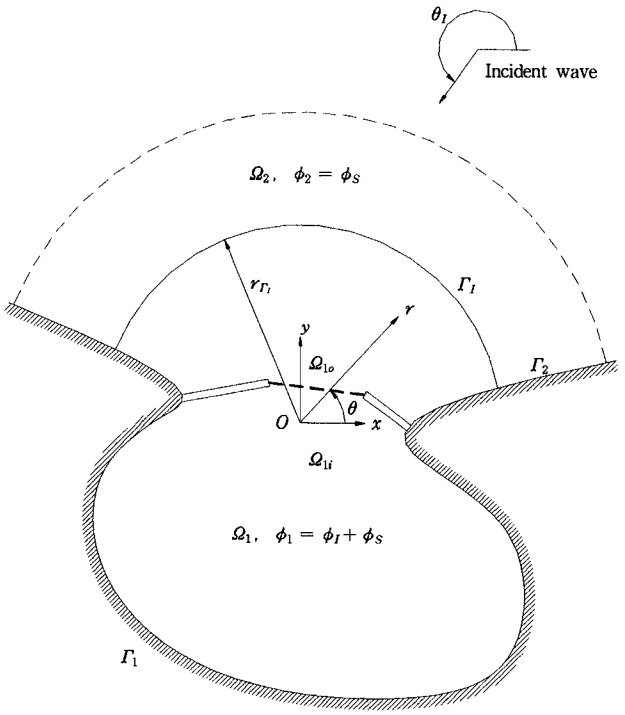

Figure 4. Definition Sketch for Boundary Value Problem.

The monochromatic and simple time harmonic waves propagating over a steeply sloped sea bed with variable depths in both regions may be described as follows (Massel, 1993; Suh et al., 1997).

$$\nabla \cdot (CC_g \nabla \phi_i) + \frac{C_g}{C} \omega^2 \phi_i - \omega^2 \{R_1 (\nabla h)^2 + R_2 \nabla^2 h\} \phi_i = 0 \tag{1}$$

in which $\nabla = (\partial/\partial x)\hat{i} + (\partial/\partial y)\hat{j}$, $\hat{i}$ and $\hat{j}$ are unit vectors in the directions of x and y, respectively, ϕ_i is the two-dimensional spatial complex valued velocity potential, the subscript i denotes the near field region for $i = 1$ and the far field region for $i = 2$, ω is the angular frequency, $h(x, y)$ is the water depth, R_1 and R_2 are coefficients for second-order bottom effects corresponding to the squared bottom slope $(\nabla h)^2$ and the bottom curvature $\nabla^2 h$ (see Suh et al., 1997). Wave celerity, C and group velocity, C_g are given as

$$C = \sqrt{\frac{g}{k} \tanh kh} \tag{2}$$

$$C_g = \frac{C}{2}\left(1 + \frac{2kh}{\sinh 2kh}\right) \tag{3}$$

in which k is the wave number.

To consider the effects of wave absorbing, the partial reflection boundary condition is introduced along the solid boundaries, which was proposed by Mei and Chen(1975) as a function of an empirical reflection coefficient, K_r normal to the solid boundaries. This boundary condition is represented as

$$\frac{\partial \phi_1}{\partial n} = \alpha \phi_1 \qquad \text{on } \Gamma_1 \tag{4a}$$

$$\frac{\partial (\phi_2 + \phi_I)}{\partial n} = \alpha (\phi_2 + \phi_I) \qquad \text{on } \Gamma_2 \tag{4b}$$

in which ϕ_1 is the total velocity potential in the near field region, ϕ_2 is the scattered wave potential in the far field region, ϕ_I is the incident wave potential, n is outward normal to the solid boundary, and α is expressed as

$$\alpha = ik \cos\theta_I \frac{1 - K_r}{1 + K_r} \tag{5}$$

in which θ_I is the angle of the incident wave normal to the solid boundary.

The matching boundary condition on Γ_I can be expressed as

$$\phi_1 = \phi_2 + \phi_I \tag{6a}$$

$$\frac{\partial \phi_1}{\partial n} = -\frac{\partial(\phi_2 + \phi_I)}{\partial n} \tag{6b}$$

The scattered wave potential, ϕ_2 in the far field region must satisfy the Sommerfeld radiation condition at infinity.

$$\lim_{r\to\infty} \sqrt{r}\left(\frac{\partial \phi_2}{\partial r} - ik\phi_2\right) = 0 \tag{7}$$

The incident wave potential is given as

$$\phi_I = -\frac{igA_0}{\omega} e^{ikr\cos(\theta-\theta_I)} \tag{8}$$

in which A_0 is the amplitude of incident wave and θ_I is the attack angle of incident wave.

Two matching conditions were introduced on the interface boundary of two sub-regions, i.e., velocity and pressure continuity conditions at the harbor mouth (Unluata and Mei, 1975). For the entrance loss effects, the following matching conditions are introduced.

$$u_i = u_o \tag{9}$$

$$\frac{p_i}{\rho} = \frac{p_o}{\rho} + \frac{1}{2}\frac{f_e}{g} u_o|u_o| + \frac{l_j}{g}\frac{\partial u_o}{\partial t} \tag{10}$$

where, u is the flow velocity, p is the pressure, the subscript i denotes the inner region and o denotes the outer region, ρ is the fluid density, f_e is the loss coefficient and l_j is the jet length. The quadratic non-linear energy loss term was linearized by using Lorentz transformation and equating depth averaged power, that is,

$$\frac{1}{2}\frac{f_e}{g} u_o|u_o| = \frac{1}{2}\alpha u_o \tag{11}$$

where, the linearized loss coefficient α is given by

$$\alpha = \frac{8}{9\pi}\frac{f_e}{g}\overline{u_o}\tanh kh \frac{5+\cosh 2kh}{2kh+\sinh 2kh} \tag{12}$$

where, $\overline{u_o}$ indicates the wave mean velocity.

In the above equations, f_e and l_j are determined by hydraulic experiments for various cross-sections. We used f_e based on the inverse Strouhal number, $u_e/a\omega$ suggested by Lepelletier (1980). Then the linearized matching condition can be given by

$$\frac{\partial \phi_{1i}}{\partial n} = -\frac{\partial \phi_{1o}}{\partial n} \tag{13}$$

$$\frac{\partial \phi_{1i}}{\partial n} = \frac{1}{\frac{ia}{\omega} + \frac{l_j}{g}}(\phi_{1o} - \phi_{1i}) \tag{14}$$

in which ϕ_{1i} and ϕ_{1o} are complex velocity potentials of the inner and outer regions, respectively. For the jet length, a simple formula suggested by Morse and Ingard (1968) is used.

Finite Element Formulation

- Discretization of Fluid Domain

To discretize the fluid domain in the standard finite element manner, it is necessary to describe the unknown potential, ϕ_i, in terms of the nodal potential vector, $\{\phi_i^e\}$, for an element (e), and the prescribed shape function vector, $\{N\}$, as follows:

$$\phi_i = \{N\}^T\{\phi_i^e\} \tag{15}$$

Using Galerkin's technique, the boundary value problem can be re-formulated as integral equations. Using following definition of the residual for each element

$$\{R^e\} = -\int_{\Omega_i^e}\{N\}\left[\nabla\cdot(CC_g\phi_i) + \frac{C_g}{C}\omega^2\phi_i - \omega^2\{R_1(\nabla h)^2 + R_2\nabla^2 h\}\phi_i\right]d\Omega_i^e \tag{16}$$

and Green's second identity, and introducing the above boundary conditions, the system equation can be obtained for each element. Taking the residual as zero gives following simultaneous equations:

$$\sum_e^n\left\{\left([K^e_{\Omega_i}] + [K^e_{\Gamma_i}] + [K^e_{\Gamma_{mi}}]\right)\{\phi_i^e\} + \{F^e_{\Gamma_i}\} + \{F^e_{\Gamma_{Ii}}\} + \{F^e_{\Omega_i}\}\right\} = \{0\} \tag{17}$$

in which $[K^e_{\Omega_1}]$, $[K^e_{\Gamma_1}]$, $[K^e_{\Gamma_{m1}}]$, $\{F^e_{\Gamma_1}\}$, $\{F^e_{\Gamma_{I1}}\}$, and $\{F^e_{\Omega_1}\}$ are the element system matrices given by for the near field region:

$$[K^e_{\Omega_1}] = \int_{\Omega^e_1} \left[CC_g \left(\left\{ \frac{\partial N}{\partial x} \right\} \left\{ \frac{\partial N}{\partial x} \right\}^T + \left\{ \frac{\partial N}{\partial y} \right\} \left\{ \frac{\partial N}{\partial y} \right\}^T \right) - \omega^2 \left(\frac{C_g}{C} - \{R_1(\nabla h)^2 + R_2 \nabla^2 h\} \right) \{N\}\{N\}^T \right] d\Omega^e_1 \tag{18a}$$

$$[K^e_{\Gamma_1}] = \int_{\Gamma^e_1} CC_g \alpha \{N\}\{N\}^T d\Gamma^e_1 \tag{18b}$$

$$[K^e_{\Gamma_{m1}}] = \int_{\Gamma^e_{m1i}} CC_g \frac{\partial \phi_{1i}}{\partial n} \{N\} d\Gamma^e_{m1i} + \int_{\Gamma^e_{m1o}} CC_g \frac{\partial \phi_{1o}}{\partial n} \{N\} d\Gamma^e_{m1o} \tag{18c}$$

$$\{F^e_{\Gamma_1}\} = \{0\} \tag{18d}$$

$$\{F^e_{\Gamma_{I1}}\} = - \int_{\Gamma^e_I} CC_g \frac{\partial(\phi_2 + \phi_I)}{\partial n} \{N\} d\Gamma^e_I \tag{18e}$$

and for the far field region:

$$[K^e_{\Omega_2}] = \int_{\Omega^e_2} \left[CC_g \left(\left\{ \frac{\partial N}{\partial r} \right\} \left\{ \frac{\partial N}{\partial r} \right\}^T + \frac{1}{r^2} \left\{ \frac{\partial N}{\partial \theta} \right\} \left\{ \frac{\partial N}{\partial \theta} \right\}^T \right) - \omega^2 \left(\frac{C_g}{C} - \{R_1(\nabla h)^2 + R_2 \nabla^2 h\} \right) \{N\}\{N\}^T \right] d\Omega^e_2 \tag{19a}$$

$$[K^e_{\Gamma_2}] = \int_{\Gamma^e_2} CC_g \alpha \{N\}\{N\}^T d\Gamma^e_1 \tag{19b}$$

$$[K^e_{\Gamma_{m2}}] = 0 \tag{19c}$$

$$\{F^e_{\Gamma_2}\} = \int_{\Gamma^e_2} CC_g \left(\alpha \phi_I - \frac{\partial \phi_I}{\partial n} \right) \{N\} d\Gamma^e_2 \tag{19d}$$

$$\{F^e_{\Gamma_{I2}}\} = - \int_{\Gamma^e_I} CC_g \frac{\partial(\phi_1 - \phi_I)}{\partial n} \{N\} d\Gamma^e_I \tag{19e}$$

- Finite, Infinite and Joint Elements

The inner region is modeled by using three-noded triangular elements, in which the water depth h, the square of bottom slope $(\nabla h)^2$, and the curvature $\nabla^2 h$ are assumed to be constant for the convenience of numerical calculation. In order to model efficiently the radiation condition at infinity, a two-noded infinite element is developed. The shape function of the element is given by

$$\{N\} = N_r(\xi)\{N_\theta(\eta)\} \quad \text{for } 0 \le \xi \le \infty, \ -1 \le \eta \le 1 \tag{20a}$$

$$\{N\} = N_r(\xi) \quad \text{for } 0 \le \xi \le \infty \tag{20b}$$

in which $\{N_\theta(\eta)\}$ is the Lagrange shape function, and $N_r(\xi)$ is the shape function in the radial direction given by

$$N_r(\xi) = \frac{\sqrt{r_{\Gamma_I}}}{\sqrt{\xi + r_{\Gamma_I}}} e^{(ik-\varepsilon)\xi} \tag{21}$$

in which ε is the artificial damping parameter($\varepsilon < k$), and r_{Γ_I} is the distance to the infinite elements from the origin as shown in Figure 4. The artificial damping parameter has been introduced to make the integration in Eq. (19e) in the radial direction bounded. After the integration is completed analytically, the value of ε is taken to be zero. The shape function, $N_r(\xi)$, in the radial direction, except for the artificial damping parameter, have been derived from the asymptotic expression for the first kind of Hankel's function in the analytical boundary series solutions such as

$$\phi_S \propto \frac{1}{\sqrt{r}} e^{ikr} \tag{22}$$

The above shape functions satisfy the radiation condition at infinity.

- Matching the Inner and Outer Regions

Using the matching boundary conditions in Eq. (6), the total system matrices can be assembled as

$$\sum_e^n \left\{ ([K^e_\Omega] + [K^e_\Gamma])\{\phi^e_i\} + \{F^e_\Gamma\} + \{F_{\Gamma_I}\} \right\} = \{0\} \tag{23}$$

in which

$$[K^e_\Omega] = [\ K^e{}_{\Omega_1}], \quad [\ K^e{}_{\Omega_2}] \tag{24}$$

$$[K^e_\Gamma] = [\ K^e{}_{\Gamma_1}], \quad [\ K^e{}_{\Gamma_2}], \quad [\ K^e{}_{\Gamma_m}] \tag{25}$$

$$\{F^e_\Gamma\} = \{\ F^e{}_{\Gamma_2}\} \tag{26}$$

$$\{\ F^e{}_{\Gamma_I}\} = -\int_{\Gamma^e_I} CC_g \frac{\partial \phi_I}{\partial n}\{N\} d\Gamma^e_I - ([\ K^e{}_{\Omega_2}] + [\ K^e{}_{\Omega_2}])\{\phi^e_I\} \tag{27}$$

and $\{\phi_I^e\}$ is the vector of the incident wave potential corresponding to the nodal points.

Numerical Analyses and Discussions

Verification of the present model

To prove the validity of present model, numerical analyses have been performed for a rectangular harbor used by Lepelletier (1980) in hydraulic experiments. Two types of rectangular harbor have been tested. One is a fully open harbor (a/b = 1.0, a is width of a harbor entrance, b is width of harbor) and the other is a partially open one (a/b = 0.2). In Figures 6 and 7, numerical results without and with entrance losses are presented with the experimental results by Lepelletier (1980), respectively. As shown in figures, the calculated amplification ratios considering energy loss effects due to flow separation coincide very well with the experimental results. Neglecting energy loss effects obviously over-estimates the ratio.

In general, the length of jet-flow, l_j has been taken to be zero. As the l_j increases, the resonant periods move toward longer periods and amplification ratios at the resonant conditions increase. These phenomena have been confirmed in this verification. As shown in Figure 7, amplification ratios for the case with l_j = 0.0284 m are smaller than those for the case with $l_j = 0$. This is due to shifting of the first resonant condition. The results considering the effects of the jet-flow are better fitted to the measured results. As mentioned before, the length of the jet-flow is estimated from the theoretical formula proposed by Morse and Ingard (1968) which was derived for the narrow channel with a thin gate. It may be required to develop a new formula for estimating the length of jet-flow at the harbor mouth more accurately.

Application of the present model

To prove the applicability of the present model to the real case and to investigate the characteristics of long-period oscillations in a harbor with narrow mouth, numerical analysis was performed for the Gamcheon Harbor shown in Figure 1. As previously mentioned, field measurements were carried out using four PWGs and one RCM-9. For the direct comparison of the field measurements and calculated results, the informations for the incident waves such as wave heights and directions are estimated. However, it is nearly impossible to obtain the accurate informations from the limited set of field measurements, especially for long- period waves. Therefore, the incident wave angles were assumed to be equal to the main direction of short-period waves previously measured. A wave height for each wave frequency was determined from comparisons of the estimated and measured results at two stations, P1 and P2 at the outside of the

harbor. The estimated incident long-period wave heights were in the range of 0.03~0.07 m.

The amplification ratios at the innermost station, P4 are plotted in Figure 8. In this figure, hollow black circles indicate 13 measured data and black squares indicate the estimated results. The resonant periods and amplification ratios simulated by the present model are well agree with the measured results. To investigate the effects of the entrance losses in the real situation, the numerical analysis without considering the entrance losses was performed. The effects of the entrance losses were however almost insignificant in the whole tested range, except for the slight difference near the first resonant condition. This may be due to the fact that the incident wave heights are small in the present case. The entrance losses might be effective when the incident wave height is large as the case of attacking of tsunami.

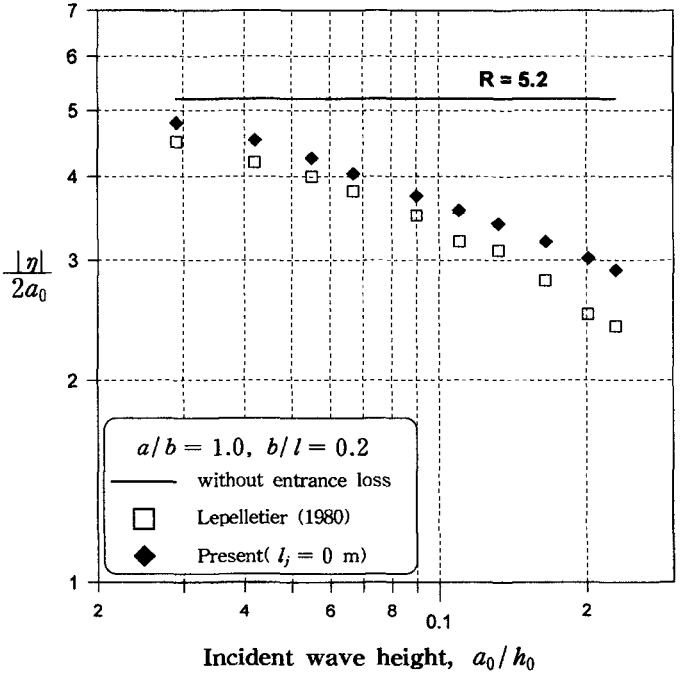

Figure 6. Variation in Amplification Ratios with respect to Incident Wave Heights for a Fully Open Rectangular Harbor (a/b = 1.0).

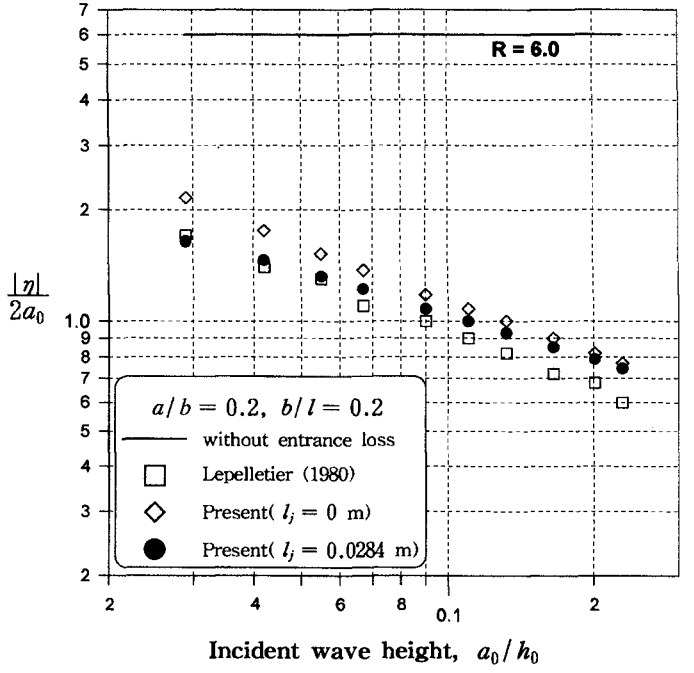

Figure 7. Variation in Amplification Ratios with respect to Incident Wave Heights for a Partially Open Rectangular Harbor (a/b = 0.2).

Conclusions

In this paper, the long-period wave oscillations in a harbor with narrow mouth has been studied. Field measurements were performed for a harbor with narrow mouth, Gamcheon Harbor in Korea. A Galerkin finite element model based on the extended mild-slope equation was developed which can handle the entrance losses due to flow separation. Verification of the present model was proved through the comparison of the estimated and experimental results. Comparisons of estimated and measured data in field shows that the present model gives quite reasonable results.

The effects of the entrance losses are insignificant unless the incident wave height is large. This may be true for tsunami. It was also found that strong jet-flow can affect the resonant condition, i.e., the resonant periods are moving toward longer period and amplification ratios are amplifying especially for the resonant conditions, as the jet-flow is being strong.

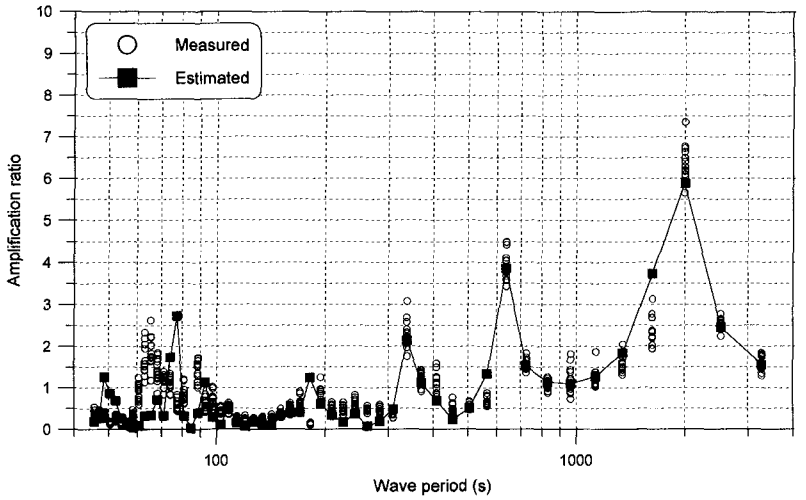

Figure 8. Comparison of Measured and Calculated Results for Gamcheon Harbor.

Acknowledgements

Partial support for this research was provided by Korea Ocean Research and Development Institute through Project Nos. BSPE 97625-00-1055-2 and BSPE 97608-00-1052-2. The authors would like to thank to their colleagues for providing field data.

References

Chen, H. S. (1986). "Effects of bottom friction and boundary absorption on wave scattering." *Applied Ocean Research*, Vol. 8, No. 2, pp. 99-104.

Jeong, W. M., Chae, J. W., Jun, K. C., Lee, J. C., and Cho, H. Y. (1997). *A study on the propagation of bound waves.* Korea Ocean Research and Development Institute, BSPE 97625-00-1055-2, 174 p. (in Korean).

Jeong, W. M., and Park, W. S. (1996). "Sensitivity analysis on hybrid element model for harbor oscillation." *J. Korean Society of Coastal and Ocean Engineers*, Vol. 8, No. 2, pp. 174-184. (in Korean).

Lepelletier, T. G. (1980). "Tsunamis - harbor oscillations induced by nonlinear transient long waves." *Report No. KH-R-41*, W. M. Keck Lab. of Hydrodynamics and Water Resources, CIT, Pasadena, C.A.

Liu, P. L.-F. (1986). "Effects of depth discontinuity on harbor oscillations." *Coastal Engrg.*, Vol. 10, pp. 395-404.

Massel, S. R. (1992). "Extended refraction-diffraction equation for surface waves." *Coastal Engrg.*, Vol. 19, pp. 97-126.

Morse, P. M., and Ingard, K. U. (1968). *Theoretical acoustics*. McGraw-Hill Inc., New York.

Suh, K. D., Lee, C., and Park, W. S. (1997). "Time-dependent equations for wave propagation on rapidly varying topography." *Coastal Engrg.*, Vol. 32, pp. 91-117.

Unluata, U., and Mei, C. C. (1975). "Effects of entrance loss on harbor oscillations." *J. of Waterways, Harbours and Coastal Engrg. Div.*, ASCE, Vol. 101, No. WW2, pp. 161-180.

APPLICATION OF COMPUTER MODELING FOR HARBOR RESONANCE STUDIES OF LONG BEACH & LOS ANGELES HARBOR BASINS

Jiin-Jen Lee[1], Member, Ching-Piau Lai[2], Member, and Yigong Li[3], Member

ABSTRACT

One of the major engineering problems for large harbors with container ship operation is the motion of moored ships due to long wave activity. In order that the wave-induced ship-motions may be effectively controlled, the response characteristics of the harbor basin due to incident waves must be accurately determined. This study focuses on the application of a computer model in the harbor resonance study in connection with modification of harbor basins. The computer model used is a finite element model with the mild-slope equations as the governing equations. Various boundary conditions are incorporated in the model: fully and partially reflecting boundaries, permeable boundary. Energy losses across the harbor entrance due to flow separation and frictional loss at the bottom are also incorporated in the model. Good comparison between the computer model results and the physical model data of the Los Angeles-Long Beach harbor basin has been obtained.

The computer model has been applied to the large scale harbor basin of Los Angeles & Long Beach Harbors. Effects on response characteristics due to incident wave system with and without breakwater at Pier J in Long Beach Harbor have been determined. The construction of the proposed breakwater outside Pier J in Long Beach Harbor appears to be effective in reducing the wave amplification for wave period less than 140 sec. The wave period associated with resonant peak has been shifted to 170 sec. or higher. With the advancement of computing power, it is found that computer model offers a very powerful alternative to physical model in the study of wave response characteristics. All the computation reported herein are done by Pentium 2-300 MHz personal computer.

1. Professor of Civil Engineering, University of Southern California, Los Angeles, CA 90089-2531
2. Principal Engineer, Environmental and Ocean Technology, Inc., Arcadia, CA 91006
3. Project Engineer, Moffatt & Nichol Engineers, Long Beach, CA 90807

1. INTRODUCTION

One of the most important engineering tasks in the planning and design of a new harbor or modification of an existing harbor is the determination of the response characteristics of the harbor basin to the incident wave system. The long wave induced harbor resonance may cause unwanted motion of berthed ships, delaying the loading or unloading of cargo. It may even damage the ship or dock facilities and cause breaking of mooring lines and fenders. The response characteristics could be determined by either physical modeling or by computer modeling. Advancement in the computer modeling technique has progressed to the point that a convenient computer model can be applied to model a complicated harbor basins using personal computer including incident wave system of relatively short wave period range.

This study focuses on the effect of the proposed breakwater at Pier J on the reponse characteristics of the harbor basin.

2. THEORY OF THE COMPUTER MODEL

The computer model used for the present study is a finite element model. The governing equation is the well known mild-slope equation with appropriate boundary conditions as specified in the following:

Mild-slope wave equation:

$$\nabla\cdot(CC_g\nabla\Phi)+\frac{C_g\omega^2}{C}\Phi=0 \tag{1}$$

Boundary conditions:

$$\frac{\partial\Phi}{\partial n}=0 \qquad \textit{(for fully reflecting boundary)} \tag{2}$$

$$\frac{\partial\Phi}{\partial n}=-i\alpha k\Phi-\frac{i\alpha}{2k}\frac{\partial^2\Phi}{\partial S^2} \qquad \textit{(for partially absorbing boundary)} \tag{3}$$

$$\frac{\partial\Phi_T}{\partial n}=i\kappa\kappa_t\Phi_I \qquad \textit{(for permeable boundary)} \tag{4}$$

$$\Phi_1=\Phi_2+\Delta\Phi=\Phi_2+\frac{g}{i\omega}f_e|U|\frac{U}{2g} \qquad \textit{(for entrance boundary)} \tag{5}$$

$$\lim_{r\to+\infty}\sqrt{r}\left(\frac{\partial}{\partial r}-ik\right)\Phi_S=0 \quad where \quad \Phi_S=\Phi-\Phi_I \ (at\ infinity) \tag{6}$$

The energy dissipation due to bottom friction is described as an instantaneous complex energy flux, E_f, out through the bed under the water,

$$E_f=\tau_b U_b \tag{7}$$

where τ_b is the instantaneous complex shear stress at the bed.

τ_b can be expressed in terms of the water particle velocity near the bed as follows:

$$\tau_b=\frac{1}{2}\rho K_b|U_b|U_b \tag{8}$$

Here K_b is a dimensionless frictional coefficient, U_b is the near-bottom water particle velocity and can be expressed in term of the velocity potential Φ as follows:

$$U_b=\left(\frac{\partial\Phi}{\partial s}\right)_b=\nabla\Phi e^{-i\omega t}\left(\frac{1}{\cosh kh}\right) \tag{9}$$

Insert (9) into (7), we obtain

$$E_f=\frac{\rho}{g}e^{-2i\omega t}f_\omega\left(\frac{1}{\cosh kh}\right)^2(\nabla\Phi)^2 \tag{10}$$

Upon integrating (10), we introduce a new bottom friction coefficient, $f_w=\frac{1}{2}gK_b|U_b|$. Thus the resulting equation can be written as:

$$\int_A\left[\int E_f dt\right]dA=\frac{\rho}{g}e^{-2i\omega t}\int_A\frac{i}{2\omega}f_\omega\left(\frac{1}{\cosh^2 kh}\right)(\nabla\Phi)^2 dA \tag{11}$$

We introduce a quadratic headloss law at the harbor entrance. It is convenient to define $K_e=\frac{f_e}{2g}|U_0|$, where $|U_0|$ is taken as the average velocity at the harbor entrance computed based on the case of no entrance loss, and express the entrance loss, ΔH, as follows:

$$\Delta H=f_e\frac{U^2}{2g}=f_e|U_0|\frac{U}{2g}=K_e U. \tag{12}$$

where U is the new entrance velocity to be computed in the model, and f_e is the entrance loss coefficient similar to the one defined by Lapelletier (1980).

The Galerkin's method and shape function are used to transform the governing's equation and boundary conditions into a matrix form by discretizing the domain of interest into a finite number of elements. The Gaussian quadrature method is used for numerical integration terms.

By using $\Phi = N_i\Phi_i$, $\nabla\Phi = \nabla N_i\Phi_i = B_i\Phi_i$ and $\Phi_s = N_s c$, $\frac{\partial\Phi_s}{\partial r} = P_s c$, the finite element weak formulation can be obtained as follows:

$$[K][\Psi] + [Q] = [0] \tag{13}$$

where ψ are all unknown matrices, and

$$K = \begin{bmatrix} [[M]] & [[M_2]] \\ [[M_2]'] & [[M_1]] \end{bmatrix}$$

$$[M] = \int_A (CC_g B^T B - \frac{C_g\omega^2}{C} N^T N)\,dxdy - \int_{\partial B} i\omega C_g \alpha N^T N ds + \int_{\partial T} i\omega C_g K_t^2 N^T N ds$$
$$- \int_A \frac{i}{\omega} f_\omega (\frac{1}{\cosh^2 \kappa h}) B^T B dxdy - \int_{\partial E} i\omega CC_g [(1-K_j)N^T B - K_e B^T B] ds$$

$$[M_1] = \int_{\partial A} CC_g P_s^T N_s ds$$

$$[M_2] = \int_{\partial A} CC_g N^T P_s\, ds$$

$$[Q_1] = \int_{\partial A} CC_g N^T \frac{\partial\Phi_I}{\partial n_A} ds$$

$$[Q_2] = \int_{\partial A} CC_g P_s^T \Phi_I ds$$

$$K_e = \frac{f_e |U_0|}{2g}$$

This computer model takes into account the diffraction, refraction, reflection, boundary absorption, bottom friction, and separation losses at harbor entrance or other entrance to inner basins. Especially noteworthing is the ability of this computer model to obtain responses in the relatively short wave period range which was considered prohibitive heretofore. This was accomplished by the use of "substructuring technique" and "automatic mesh generation" system. The substructuring technique has been developed by dividing the entire modeling basin into several irregular shaped basin with solutions

matched at each of the imaginary common boundaries. The automatic mesh generation program is incorporated so that this computer model could be used as an effective iteration design tool to arrive at the desirable harbor geometry for a given permissible wave response within the harbor.

3. RESULTS AND DISCUSSIONS

One of the major objectives of this study is to use the computer model to investigate the basin response characteristics to incident waves which are related to any proposed modification of the harbor layout with the ultimate objective of reducing the dependence on physical model in reaching engineering decisions. At the very least, the computer model could be used to guide the use of physical model so that the physical models could be more efficiently conducted.

The layout of the Long Beach / Los Angeles harbor model basin is presented in Figure 1. This physical model basin was constructed by the Coastal Engineering Research Center of the Waterways Experiment Station of the U.S. Army Corps of Engineers. Also included in the figure are the location of all the wave height measuring gages used in the model basin.

Two computer model grid systems have been used and are shown in Figure 2 and Figure 3. Figure 2 is a smaller model which covers the harbor basin mostly in Long Beach Harbor region. This model grid has 14,895 nodal points with 6,325 elements. Also indicated in the grid layout are three of the incident waves directions.

Figure 3 shows the grid layout of a larger model it contains the entire model basin used in the physical model (as shown in Figure 1). It consists of 31,538 nodal points and 13,263 elements. One of the motivations of using this huge model is to utilize of the results of the physical model for verification of the computer model.

It should be noted that because of the nature of the long period wave, the wave length is long compared with characteristic length of the harbor basin, a true incident wave system for an open sea condition can not be achieved in the physical model. Instead, it is a wave generator system at one end of the harbor model basin surrounded by reflecting walls at the model boundaries.

Thus, in order to compare the computer model results with the physical model data, it is necessary to construct the computer model so that it will be identical to the physical model (that is a wave generator is placed at one end of the model basin, with reflecting boundaries comprising the three walls of the model basin).

An attempt has been made to compare the results of a computer model with a wave

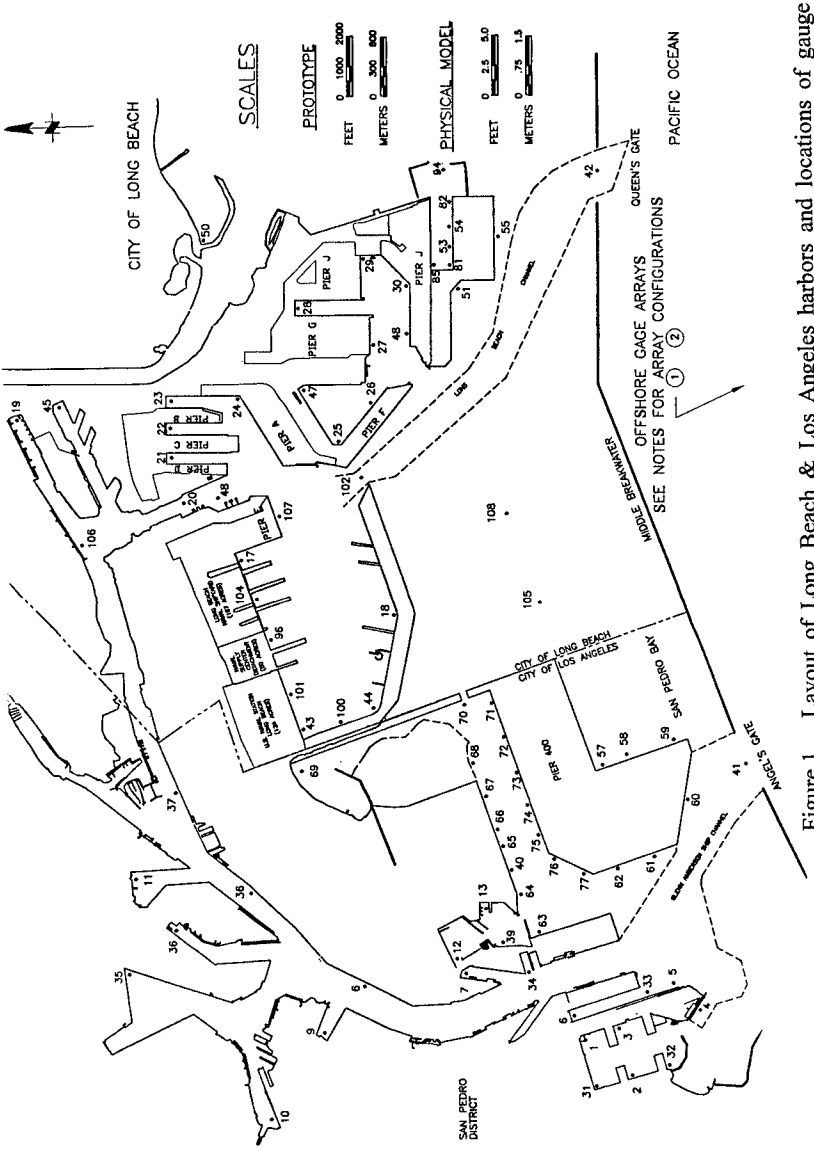

Figure 1 Layout of Long Beach & Los Angeles harbors and locations of gauge stations

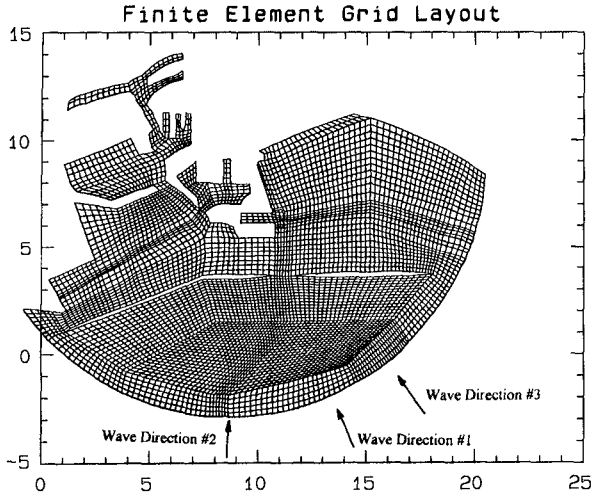

Figure 2 The finite element grid layout of small scale model (6325 elements, 14895 nodal points)

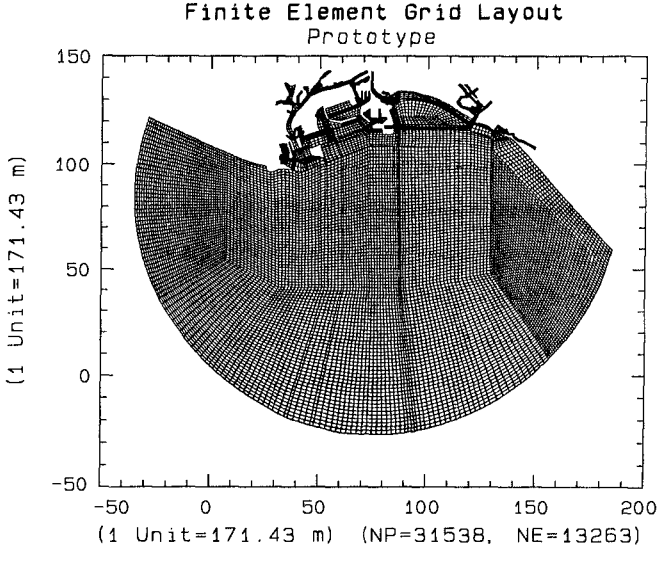

Figure 3 The finite element grid layout of large scale model (13263 elements, 31538 nodal points)

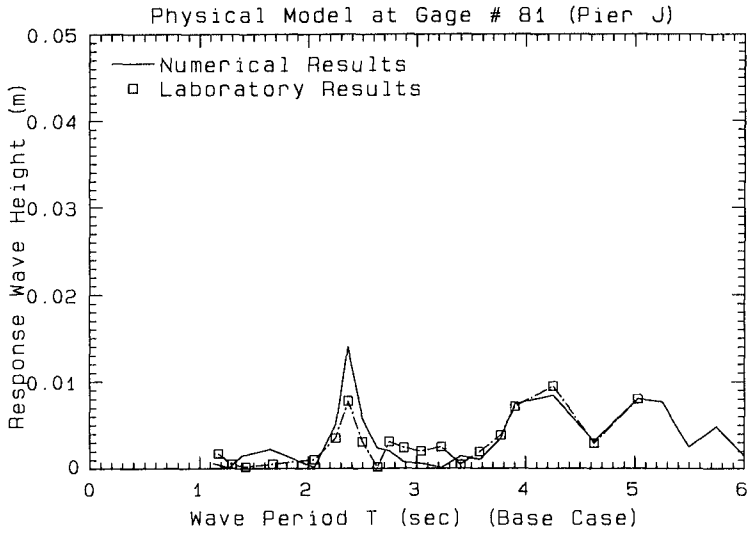

Figure 4 Comparison of response curves between the present numerical results and WES experimental results at gage #81 (Pier J)

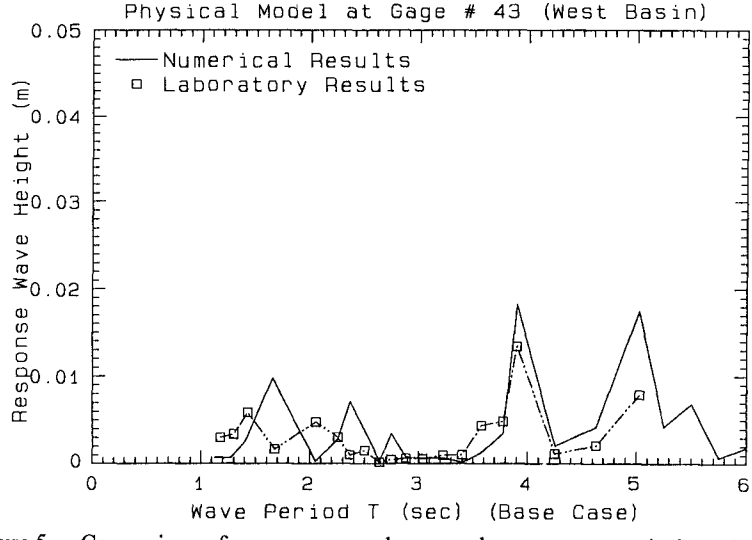

Figure 5 Comparison of response curve between the present numerical results and WES experimental results at gage #43 (West Basin)

generator system with the physical model data using the exact wave generator strokes registered by the physical models. This comparison is presented in Figures 4 and 5 for two gaging stations. These two figures show the comparison of the computed and measured wave heights at the specified stations as a function of the model wave periods. Gage #81 is located at the inner corner of the Pier J basin in Long Beach Harbor. Gage #43 is located at the left corner of the Long Beach West Basin. It can be seen that the comparisons are good in general further verifying the usefulness of the computer models.

The computer model with large grid layout covering a wide area of the harbor basin as shown in Figure 3 has been applied to study the effect of basin modification on long period wave response characteristics.

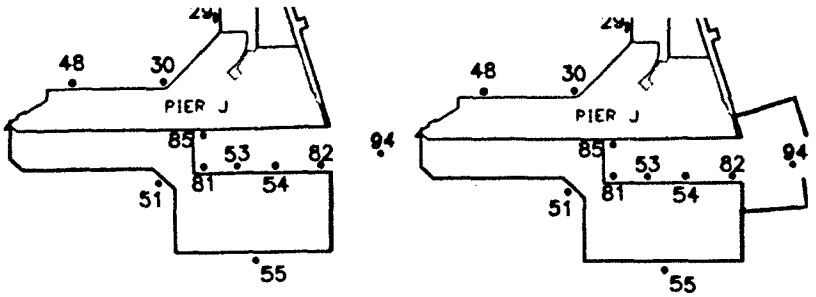

Figure 6 Detail layout of Pier J basin of Long Beach harbor without breakwater and with breakwater

Figure 6 shows the plan view of the harbor modification at Pier J. The sketch on the left shows the Pier J basin without the breakwater (the basin layout prior to the construction of the breakwater). The sketch on the right of Figure 6 shows the layout for the breakwater. It is clear that the introduction of the breakwater modifies the characteristic length of the harbor basin. The longitudinal length of the Pier J basin is increased by approximately 44%.

The response curves for four different gaging stations are presented in Figures 7 through 10 for Gage #81, #85, #82 and #94. Gage #81 and #85 are located at the back end of Pier J basin. Since the variations of water surface elevation for the wave period range under study is mainly in the longitudinal direction; thus, response curves for Figure 7 & 8 are almost identical. Comparing the two curves in both Figure 7 & 8 two major effects of the breakwater can be clearly shown: (1) The amplification factors for wave periods less than 140 sec. has been greatly reduced due to the introduction of the breakwater. (2) The major resonant mode at T=130 sec. has been shifted to T=170 sec.

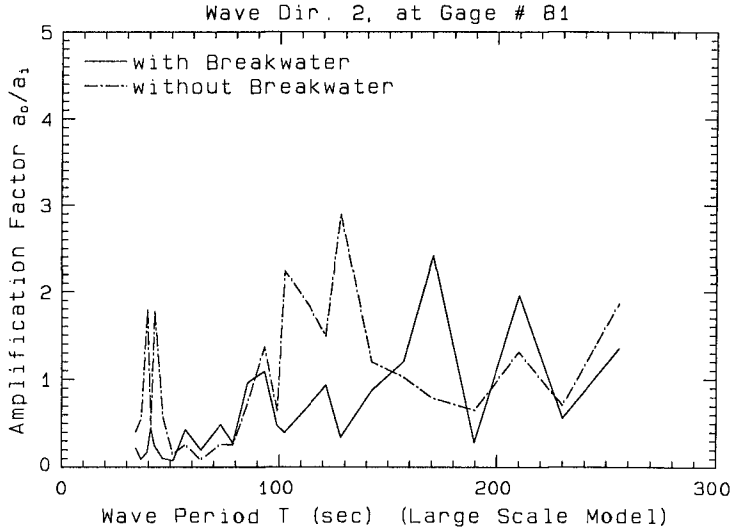

Figure 7 Comparison of computed response curves with and without breakwater at gage #81

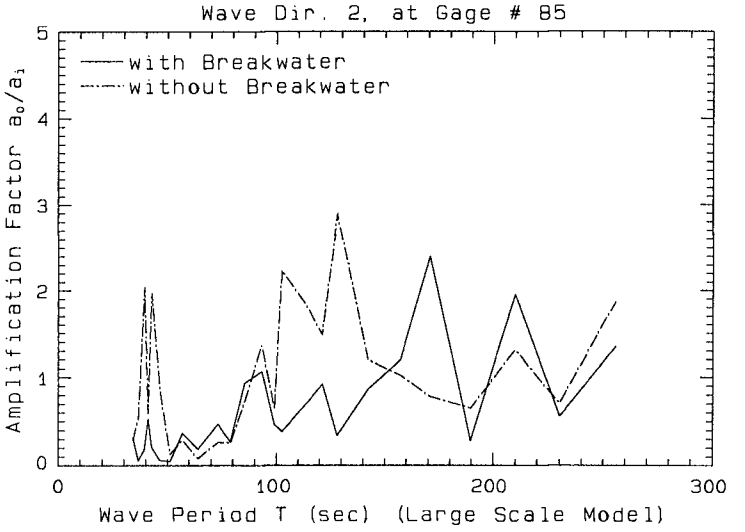

Figure 8 Comparison of computed response curves with and without breakwater at gage #85

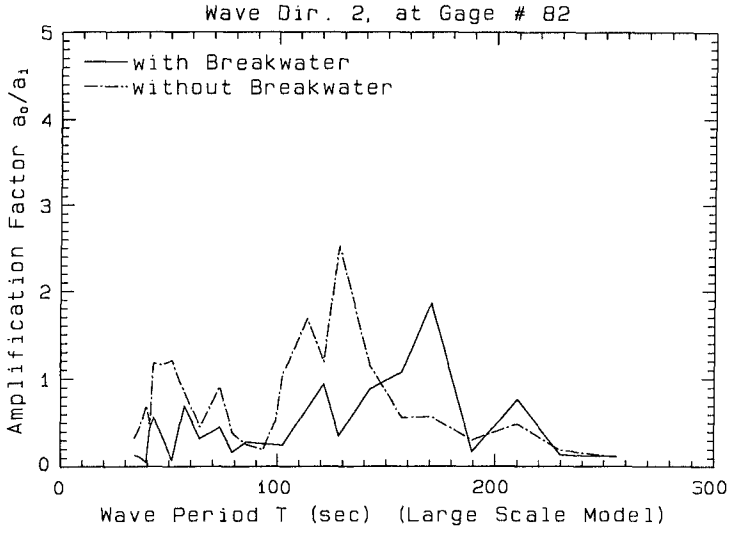

Figure 9 Comparison of computed response curves with and without breakwater at gage #82

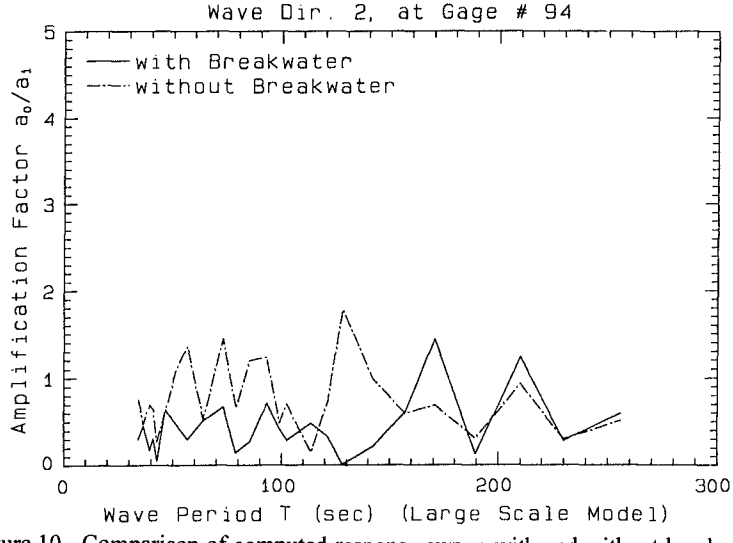

Figure 10 Comparison of computed response curves with and without breakwater at gage #94

By comparing the response curves shown in Figures 9 & 10 for the conditions with and without breakwater, it is also found that the two key features just mentioned also hold true here. Therefore, the introduction of the breakwater clearly shift the resonant wave period to higher values hopefully into the region not relevant to periods associated with possible ship motions.

Comparison of the computer model results with available field data at a location corresponding to that for gage #81 is presented in Figure 11.

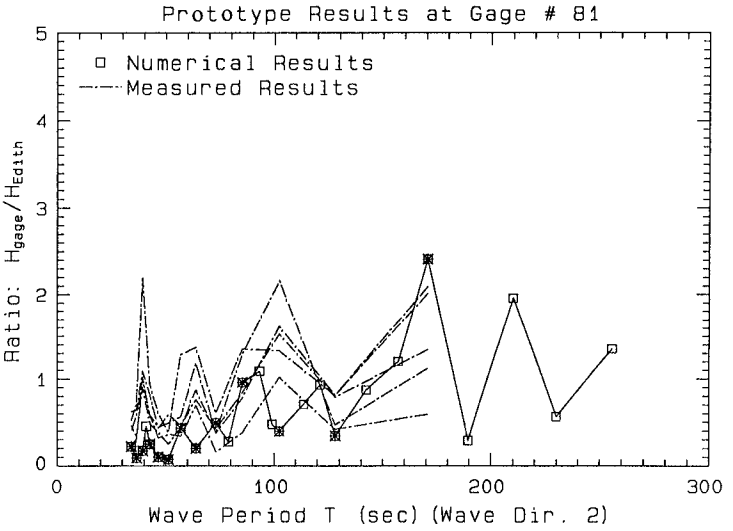

Figure 11 Comparison of response curves between the present numerical results and field measured data at gage #81

Field data were obtained during a three months period, December 1997, January and February 1998. Five sets of field data are included in Figure 11. Obviously without knowing the actual incident wave direction it is not certain what definitive conclusion can be drawn from them. However, it appears that some of the resonant modes are captured in the computer model even though the field data show considerable scatter. It should be noted that the computer results shown are for incident wave direction #2, with breakwater at Pier J Basin and with large scale grid layout (as that shown in Figure 3).

4. CONCLUDING REMARKS

Computer models by nature are an approximate solution to the more complicated prototype conditions. For important engineering projects one should use both the computer models and physical models. However, at the present time the computer model has been advanced to a degree that it can largely reduce (although not eliminate) the need for physical models. At the very least, the computer model can be used effectively for preliminary planning work and to serve as a guide to the use of physical model if the latter is still needed for important projects.

The results presented herein show that the computer model nicely reproduces the data obtained from the physical model. The introduction of the breakwater at Pier J at Long Beach Harbor effectively reduces the wave amplitude response for wave period less than 140 sec. It also shifted the resonant wave period to period larger than 170 sec., hopeful this will be in the wave period range not very significant for ship motion problem.

5. ACKNOWLEDGEMENT

The authors are appreciative of the funding support of the Port of Long Beach and Port of Los Angeles. The helpful comments of Professors Robert Dean, C.C. Mei and Fredric Raichlen during the course of this study are greatly appreciated. The authors also acknowledge the help and encouragement of Dr. Ying Poon and the late Dr. James Walker of Moffatt & Nichol Engineers, during the course of this study.

6. REFERENCES

1. Behrendt, L., Johnson, I. G. and Skovgaard, O. (1985), "A finite Element Model for Water Wave Diffraction Including Boundary Absorption and Bottom friction," Series Paper No. 37, Institue of Hydrodynamics and Hydraulic Engineering, Technical University of Denmark.
2. Berkhoff, J. C. W. (1972), "Computation of Combined Refraction-Diffraction," Proc. 13th Coastal Eng. Conf., Vancouver 1972, ASCE, Vol. 1, Chap. 24, pp 471-490.
3. Chen, H.S. and Mei, C.C. (1974), "Oscillations and Wave Forces in An Offshore Harbor" (Application of Hybrid Finite Element Method to Water Wave Scattering), Report No. 190, Ralph M. Parsons Laboratory, Water resources and Hydrodynamics, M.I.T.
4. Lai, C.P., Lee, J.J., Wu, F. (1993), "Computer Aided Design of Harbors for Diffraction Refraction and Dissipations of Incident Waves," Proc. 15th Conf. On Ocean Engineering in Republic of China, Nov. 1993, pp 405-418.
5. Lee, J.J. (1969), "Wave Induced Oscillations in Harbors of Arbitrary Shape," Report KH-R-20, W.M. Keck Laboratory of Hydraulics and Water Resources, California

Institute of Technology.
6. Lee, J.J. (1971), "Wave Induced Oscillations in Harbors of Arbitrary Geometry," Journal of Fluid Mechanics, Vol. 45, pp 375-394.
7. Lee, J.J. and Raichlen, F. (1971), "Wave Induced Oseillations in Harbors with Connected Basins," Report KH-R-26, California Institute of Technology.
8. Lepelletier Thierry Georges (1980), "Tsunamis-Harbor Oscillations Induced by Nonlinear Transient Long Waves," Report KH-R-41, California Institute of Technology.
9. Raichlen, F., Lee, J.J. and Walker, James R. (1997), "Physical Modeling of Harbor Resonance," Proceedings Wave '97, Virginia Beach, VA, Nov. 1997.

ATTENUATION OF VERY LONG WAVES BY A LARGE RESONATOR AS AN OUTER HARBOR

Takayuki Nakamura[1], M. ASCE and Satoshi Morita[2]

Abstract

A large resonator which has a similar size of the outer basin of a double-basin type harbor is designed by the Wave Filter Theory. This resonator aims to protect an inner basin from incoming very long waves which may cause long-period motions of moored ships at piers. Performance of the designed resonator is examined by the physical and numerical experiments. It was confirmed that the large resonator designed by the Wave Filter Theory is effective for protecting the inner basin from very long waves with a period of 30s or longer. However, the aspect ratio of the resonant basin should be nearly equal to 2:1 for the effective reduction as pointed out by Valembois(1953).

Introduction

It has become known that infragravity waves having a period of about one minute or longer may cause long-period ship motions in a harbor. Especially, a moored ship at piers sometimes experiences large amplitude motions by these long-period waves. In this study, a large resonator that is presumed as the outer basin of a double-basin type harbor is proposed as one of countermeasures to reduce such long-period ship motions.

Valembois(1953) has already presented an idea of resonators to reduce incoming waves to harbors and canals by installing resonators at the entrance. Recently, Nakamura et al(1996) have shown a rational method to design a resonator, which is called the Wave Filter Theory. They also reported that the theory is useful for designing a resonator that is effective for the specified wave conditions. However, the designed resonator is mainly for wind waves having a wave period of 10s or so.

In this study, by using the Wave Filter Theory, a resonator that is effective for very long waves is first obtained. The resonator as the outer harbor of a double-basin type is assumed. Laboratory and numerical experiments were carried out to examine the effectiveness of the resonator.

[1] Associate professor, Department of Civil and Environmental Eng., Ehime University, 3 Bunkyo-cho, Matsuyama City, Ehime 790, Japan. (Email: nakamura@coe.ehime-u.ac.jp)

[2] Research Engineer, Technical Research and Development Institute, Kumagai-gumi Co. Ltd., Onigakubo, Tsukuba City, Ibaragi, Japan.

Large Resonators Designed by the Wave Filter Theory

In the Wave Filter Theory, a rectangular resonator as shown in Fig.1 is assumed. Based on the theory (Nakamura et al 1996), we can estimate the necessary dimensions of l_2, l_1 and b_3 for given b_0 and the required effective frequency band as follows.

$$\left.\begin{aligned} b_3 &= \frac{m b_0}{\sqrt{2(1-m^2)}} \\ l_2 &= \frac{1}{\pi f_c}\sqrt{\frac{gh(1-m^2)}{2}} \\ l_1 &= \frac{m\sqrt{gh}}{2\pi f_c} \end{aligned}\right\} \qquad (1)$$

where g is the gravitational acceleration, h is a water depth, and m is a function of the critical frequency f_c and the pole frequency f_∞ of an effective frequency band ($f_c<f<f_\infty$)of a wave resonator and is given by

$$m = \sqrt{1-\left(\frac{f_c}{f_\infty}\right)^2} \qquad (2)$$

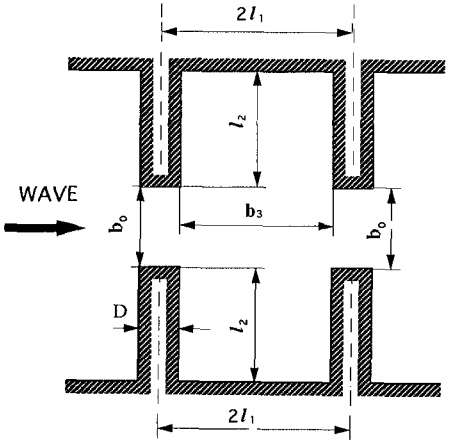

Fig.1 Definition sketch of a resonator.

Table 1 Design conditions and results of a resonator.

TYPE	b_0	$T_\infty(=1/f_\infty)$	$Tc(=1/f_c)$	b_3	l_2	D	b_3/l_2	h
(A)	310m	43s	80s	344m	166m	26m	2.07	30m
(B)	600m	81s	135s	566m	312m	30m	1.82	30m
(C)	300m	65s	180s	550m	159m	30m	3.50	12m

The pole frequency f_∞ corresponds to a frequency at which wave transmission through a resonator becomes the lowest.

Table 1 shows typical results on the horizontal dimensions of resonators for various design conditions. Resonators with a wide entrance are presumed for passing ships. The aspect ratio of a resonant basin of these resonators, b_3/l_2, ranges from 1.8 to 3.5. Valembois (1953) pointed out that the aspect ratio of the resonant basin should be about 2 for the effective protection.

Effects of the Aspect Ratio of a Resonant Basin on the Wave Transmission

To examine the effectiveness of the designed resonators specified in Table 1, we calculated wave transmission characteristics through a linear array of the resonators by the vertical line source Green's function method (Nakamura 1994). This numerical method takes into account the effect of an infinite array of bodies by considering an infinite number of mirror image sources. In the computation, the reflection coefficient of the wall of resonators is assumed to be 0.8 for modeling the practical situations.

Figs.2～4 show the computation results on the wave transmission through an infinite array of the resonators, Type(A), (B) and (C) in Table 1, respectively. The wave transmission characteristic is specified by the wave height ratio K_T, which is defined by

$$K_T = (H_T)_{rms} / H \tag{3}$$

where $(H_T)_{rms}$ is a root-mean-square value of transmitted wave height along the array direction, and H is an incident wave height. The rms value of transmitted wave height is necessary to account for the short-crested wave pattern about an array of resonators, especially under the condition $\lambda/L>1$ (λ: center-to-center distance between the adjacent resonators, L: wave length). It has become known that wave patterns about an infinite array of identical bodies under the condition $\lambda/L>1$ are short-crested even though in the region far from the array (Dalymple & Martin 1990 and Nakamura 1994). In other condition $\lambda/L<1$, the wave pattern is long-crested and the definition of K_T coincides with that of a well known transmission coefficient.

From these figures, it is seen that the value of K_T for each array of resonators, Type (A), (B) and (C), is comparatively small for the presumed effective range of wave period as shown in Table 1. The spike-like variation of K_T is due to the wave resonance in the transverse direction. Under the transverse resonant condition, a center-to-center length of the adjacent resonators λ is equal to a wave length L. In the numerical computation, this resonant condition corresponds to the singular point at where one of eigenfunctions of the Green's function becomes indefinite.

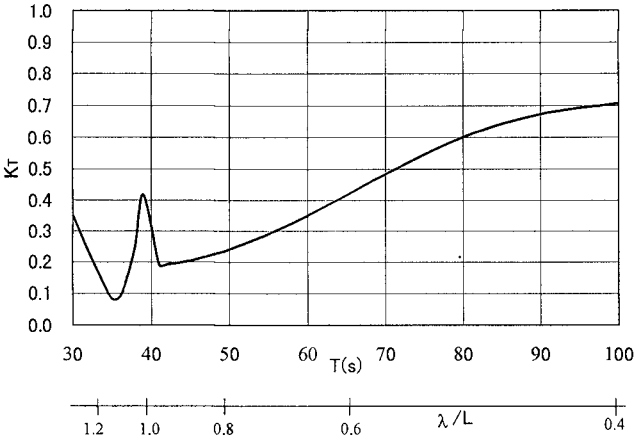

Fig.2 Dimensionless transmitted wave height through the arrayed resonators of Type (A) ; water depth h=30m.

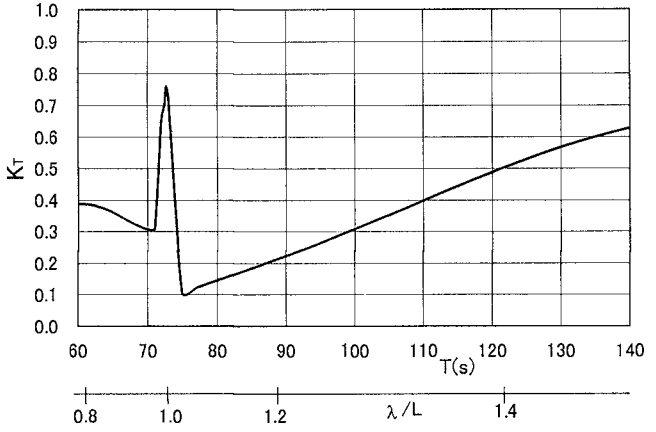

Fig.3 Dimensionless transmitted wave height through the arrayed resonators of Type (B) ; water depth h=30m.

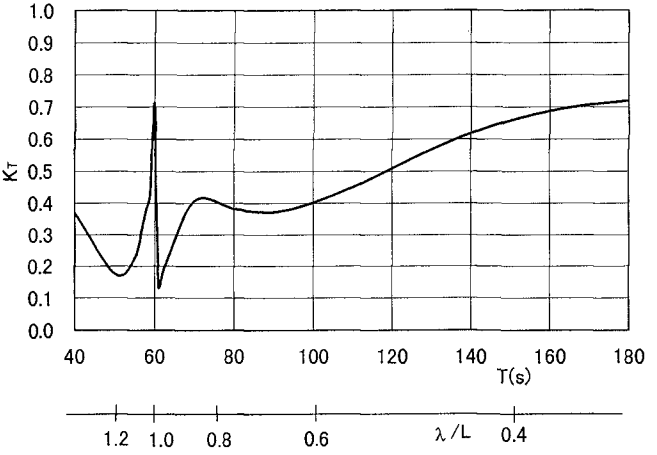

Fig.4 Dimensionless transmitted wave height through the arrayed resonators of Type (C) ; water depth h=12m.

From inter-comparison among these figures, we can see some difference with the performance of the resonators. For instance, Type (A) and (B) resonators show the much lower K_T value than Type (C) resonator in the presumed effective wave period range. It may be caused by the difference of aspect ratios of a resonant basin b_3/l_2. The aspect ratio is about 2 for Type(A) and (B) resonators, which is equal to the aspect ratio recommended by Valembois (1953). On the other hand, the aspect·ratio of Type (C) resonator is 3.5. Therefore, it is better to design a resonator in such a way that the aspect ratio of a resonant basin is about 2. However, it is noted that the entrance width b_0 of a resonator is also an important factor to determine the performance.

As a result, we can use the Wave Filter Theory to get a rough estimate of geometrical dimensions of a wave resonator that is effective for the given frequency range. However, it is hard to know the degree of effectiveness of the resonator by the theory. In this case, we have to rely on the numerical computation method.

Experimental Results in a Channel for Regular and Irregular Waves

In order to check the validity of the design results by the Wave Filter Theory, we carried out model tests in a long channel. The channel is 1.2m heigh, 1m wide and 26m long. The distorted model was applied to avoid the difficulties arising from the wave nonlinearities. The model scale is 1/324 in the horizontal dimensions and 1/167 in the vertical dimension. Type (A) resonator in Table 1 was basically used. The setup of a model resonator is shown in Fig.5. Considering the mirror image effect of both side walls, only a half of the resonator was placed in a long channel. The wave field in this channel is equivalent to the one around an infinite array of identical resonators when the wave reflection from side walls is perfect. In the experiment, the allocation pitch length λ of the arrayed resonators is equal to double of a channel width, i.e. 2m.

We used two different types of model resonators with the same dimensions, but having different reflection characteristics. One model is made of plywood and has a high reflective

nature. The other model consists of low-reflective walls covered with porous materials on the surface. It was confirmed by the other experiment that the reflection coefficient of the low-reflective wall is approximately 0.8.

In order to be able to analyze the short-crested wave pattern around a resonator in the channel, we set a linear array of five wave gauges in the transverse direction to measure transmitted waves through a resonator. Wave conditions used in the experiment are largely classified into two categories, i.e. regular and irregular waves.

In the case of regular waves, wave period T_m ranges from 1.2 s to 3.5s (in prototype scale T=22~64s) and wave height H_m is fixed at about 3cm (in prototype scale H=5m).

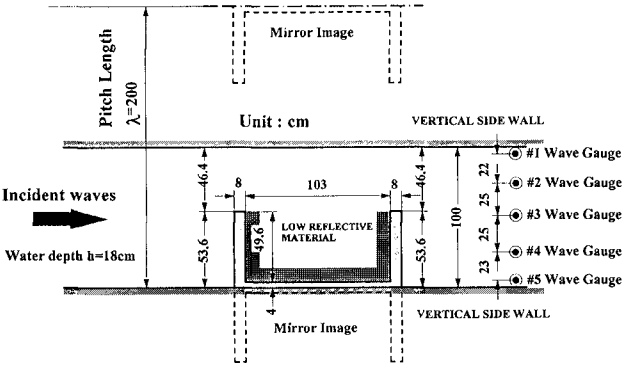

Fig.5 Experimental setup; Type (A) resonator.
(In case of low reflective walls)

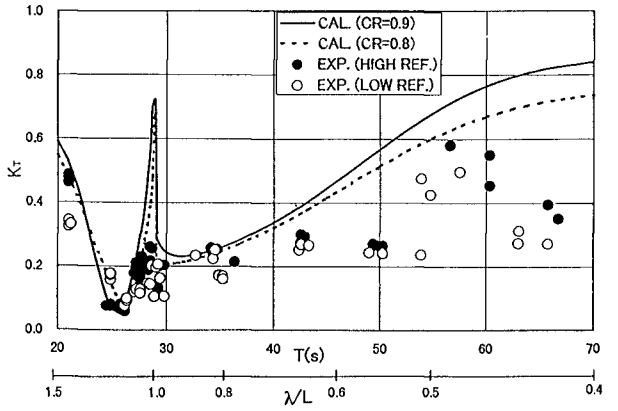

Fig.6 Dimensionless transmitted wave height through the arrayed resonator for regular waves.

For the case of irregular waves, the Bretschneider spectrum was used as a target frequency spectrum. At present, the frequency characteristic of infragravity waves has not been clarified. Therefore, we just account for the irregular nature of wave trains in the field.

Fig.6 shows typical results for regular waves, where the rms transmitted wave height ratio K_T is plotted as a function of wave period T in the prototype scale. The parameter λ/L is also plotted as a second horizontal axis.

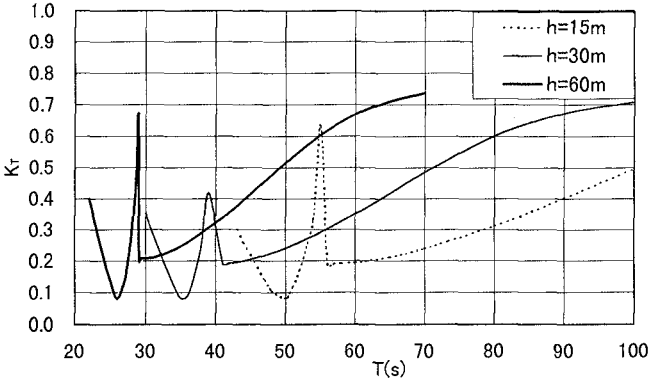

Fig.7 Variations of K_T of Type(A) resonator with water depth.

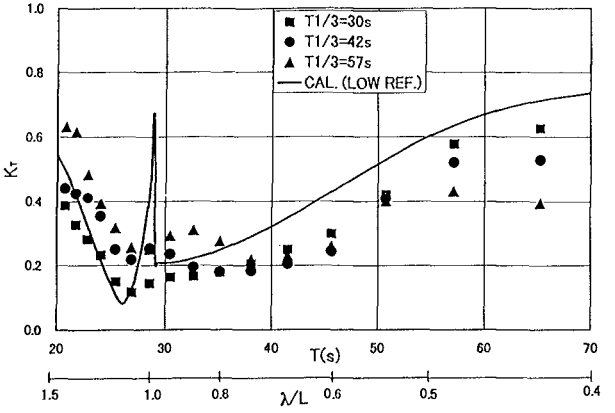

Fig.8 Dimensionless transmitted wave height through the arrayed resonator for irregular waves.

In the figure, two different results are shown. One is for the resonator consisting of high reflective walls and the other consists of dissipative walls covered with porous materials. Further, in the figure, the computed result by the Green's function method is also plotted. In the computations, the distorted model was used as a real structure. Hence the water depth is assumed to be 60m in the prototype scale.

Except the condition near the transverse resonance at $\lambda/L=1$, we can see the reasonable agreement between the computed and experimental results. However, for longer wave period conditions, the measured value of K_T is smaller than the computed one. It may be partly caused by the frictional damping on the sea bed.

From the comparison between the two experimental results for the low- and high-reflective wall cases, it is seen that there is little influence of the different wall types on the wave transmission.

Fig.7 shows the effect of water depth on the performance of resonators. In the figure, the computed results of K_T for the arrayed resonators with the same horizontal dimensions (Type (A)), but for three different water depths, are shown. It is apparent that the effective range of wave period shifts to the side of longer waves with deceasing water depth h. This is eaused by the decrease of wave length with water depth. This tendency can also predicted by Eq.(1).

Fig.8 shows the result of K_T for irregular waves with different significant wave periods $T_{1/3}$, where K_T is defined as a transfer function in the frequency domain. We can see the similar tendency to the result of regular waves. From the examinations described above, we can say that the large resonator is effective for reducing very long waves of both regular and irregular wave trains.

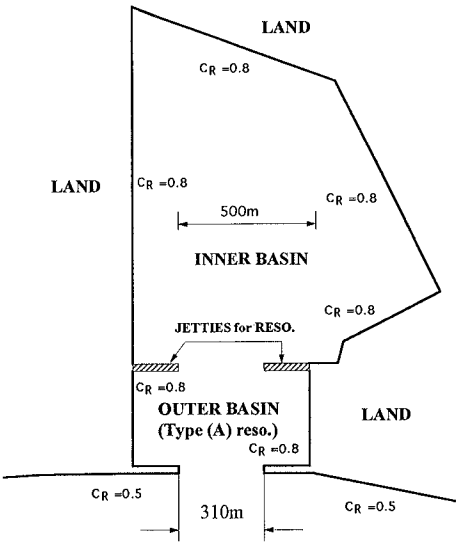

Fig.9 Layout of a model harbor and reflection coefficients on the boundary.

Numerical Experiment on the Harbor Tranquility

In order to confirm the effectiveness of the resonator as an outer harbor of a double-basin type, we carried out numerical experiments based on the vertical line source Green's function method (Isaacson 1978 and Nakamura et al 1985).

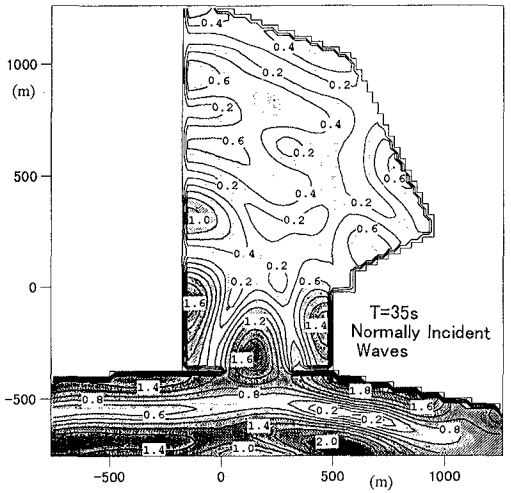

Fig.10 Wave height distributions around the original harbor (T=35s, normal incidence).

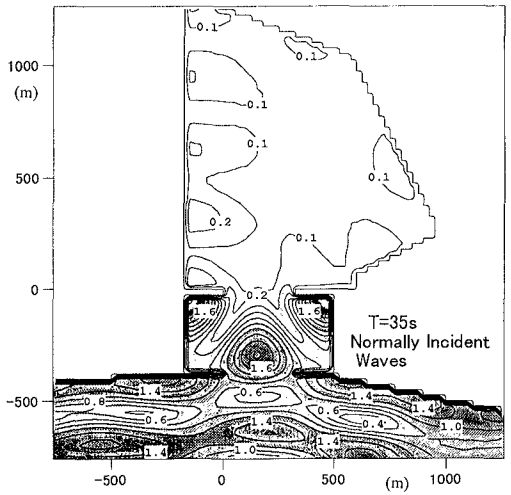

Fig.11 Wave height distributions around the harbor with a resonator (T=35s, normal incidence).

Fig.9 shows a layout of an original harbor adopted in the numerical experiment. It is assumed that the water depth h is constant around the harbor and is equal to 30m. Reflection characteristics of harbor boundaries are specified in the figure by the reflection coefficients C_R. When we add two jetties in a harbor as shown in dashed lines in the figure, the harbor becomes a double-basin type with the resonator of Type (A) as an outer basin.

Fig. 10 and 11 show the comparisons of wave height distributions between two different models, i.e., the original harbor and the one with the type (A) resonator as an outer harbor as seen in Fig.9, respectively. In these figures, the dimensionless wave height ratio to an incident wave height is plotted. The normal incidence of waves to the harbor entrance is presumed.

We can see that the resonator designed by the Wave Filter Theory is very effective to reduce long-period waves incoming to the inner basin. However, we can also see a subsidiary effect of the resonator, i.e., higher waves in the resonator including at the harbor entrance. It may be thought that there is little or no influence on passing ships because of a small amplitude of very long waves. Fig.12 shows another example, where the wave period T is longer than the case of Fig.11. It is again confirmed that the resonator plays an effective protector for incoming waves to the inner basin.

Finally, Fig.13 shows the result of wave height distributions in case of obliquely incident waves to the harbor entrance. The inclination angle is 30-degree from the normal incident direction. It can be seen that the performance of a resonator is not affected by the incident angle of waves.

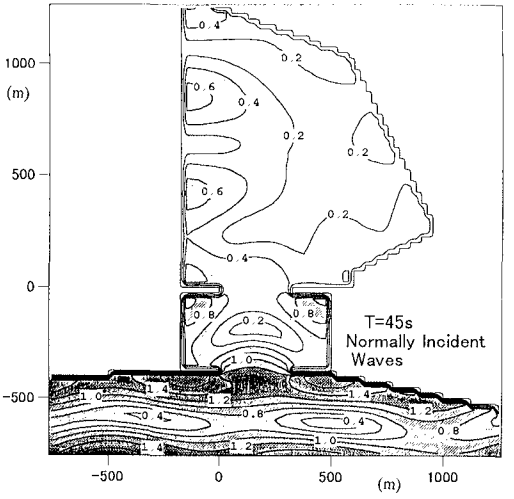

Fig.12 Wave height distributions around the harbor with a resonator (T=45s, normal incidence).

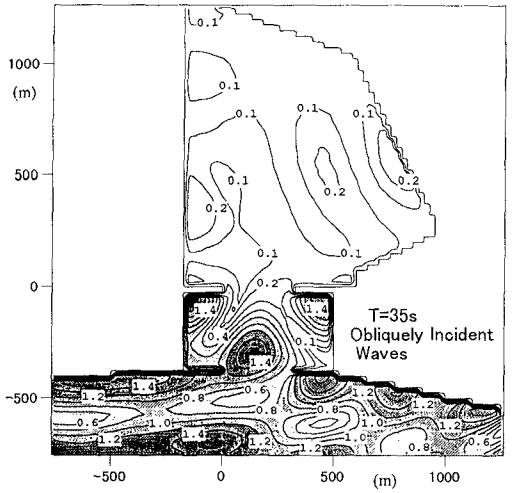

Fig.13 Wave height distributions around the harbor with a resonator (T=35s, oblique incidence).

Conclusion

The Wave Filter Theory is very useful to design a large resonator as the outer basin of a double-basin type harbor for protecting the inner basin from very long waves, which may cause long period motions of a moored ship at the piers. It was confirmed experimentally that the large resonator as the outer basin is effective for reducing both regular and irregular waves in the inner basin.

It is suggested that the aspect ratio of a resonant basin should be the order of 2:1 for the effective protection of the inner basin from incoming waves. However, it is noted that the entrance width of a resonator is also an important factor to determine the performance.

References

Dalrymple, R.A. and Martin, P.A. (1990) : Wave diffraction through offshore breakwaters. Journal of the Waterway, Port, Coastal and Ocean Engineering Division, ASCE, Vol.116, No.6, pp.727-741.

Isaacson, M.Q. (1978): Vertical cylinders of arbitrary section in waves. Journal of the Waterway, Port, Coastal and Ocean Engineering Division, ASCE, Vol.104, No.WW4, pp.309-324.

Nakamura, T. and Oku, Y. (1985): A method of numerical analysis on wave diffractions about a vertical structure of arbitrary section, Proc. of 32nd Japanese Conf. on Coastal Eng., pp.594-598.

Nakamura, T, Mochizuki, H and Morita, S. (1996): Performance of a resonator designed by the Wave Filter Theory - Applicability to a harbor, Proc. 25th Coastal Eng. Conf., ASCE, pp.1208-1292.

Nakamura, T. (1994): Wave directional change by an array of breakwaters, Proc. of Inter. Symp. Waves - Physical and Numerical Modeling, pp.1069-1078.

Valembois, J. (1953): Investigation of the effect of resonant structures on wave propagation, Proc. of Minnesota International Hydraulics Convention, pp 193-199.

Application of Physical Model in Long Wave Studies for The Port of Long Beach

Ying-Keung Poon[1], Frederic Raichlen[2], and James (Kimo) Walker[3]

INTRODUCTION

The increase in container shipping demand has lead to rapid expansion of container terminal facilities. The Port of Long Beach have expanded their operations by landfills in areas more exposed to waves in less protected areas of the harbors. At the same time, container ships have been increasing in size and more rapid cycle time of cargo transfers by container cranes have demanded tranquil berths to minimize vessel motions. The availability of tranquil water and the need for faster crane cycle times have been in conflict.

The Port of Long Beach constructed a container terminal near the entrance to the harbor in 1992 for Maersk shipping lines. The 2,300 ft wharf is backed by over 100 acre of terminal and gate area and has four post panamax size container cranes. The terminal operates with a trucking and rail facility. Immediately after construction of the terminal in 1992, the first ships of over 900-ft size experienced excessive ship motions. These motions produced a surge measured up to 10 ft with periods on the order of one minute. Sway motions were about 20 to 40 seconds, and when coupled with the surge caused damage to fenders, represented a safety issue by mooring line breakage, and substantially reduced container crane productivity.

This paper summarizes the use of physical model studies in the design of a breakwater to attenuate vessel surge motions at Pier J berths to acceptable levels. In assessing the performance of a breakwater configuration, two different criteria were considered. The

[1] Senior Coastal Engineer, Moffatt & Nichol Engineers, 250 W. Wardlow Road, P.O. Box 7707, Long Beach, CA 90807, USA
[2] Professor, Civil & Mechanical Engineering Dept., California Institute of Technology, Pasadena, CA 91125, USA
[3] Senior Vice President, Moffatt & Nichol Engineers

first criterion was based on comparing the long wave energy in Pier J with a proposed breakwater arrangement in place to the wave energy at existing conditions. This criterion was used to quantify the improvement in wave conditions in Pier J and hence to compare the performance of different alternatives. The second criterion was based on comparing the long waves at Pier J with those at the South East Basin at the Port of Long Beach, at where container ship operations had not experienced major ship motion. The long wave attenuation criterion selected for the Pier J Breakwater design was therefore set to match or be below the existing wave conditions within South East Basin.

EXPERIMENTAL PROGRAM

Model Description

The effectiveness of the Pier J Breakwater in reducing the long wave in Pier J was tested at the US Army Engineer Waterways Experiment Station (WES) Los Angeles and Long Beach Harbors (LA/LB) model. The LA/LB model was originally constructed to conditions in the early 1970's and has been periodically updated to account for changes in the LA/LB Harbors. The model has a vertical scale of 1:100 and a horizontal scale of 1:400. The model shoreline extends from 2 miles northwest of Point Fermin to Huntington Beach, and reproduces the Pacific Ocean bathymetry seaward of the harbor out to the -300 ft MLLW contour. The total model area covers about 44,000 ft^2, which represents 253 sq. miles in prototype.

A wave generator composed of 13 individual segments, each independently controlled by a computer, was located at the far end of the wave basin. Details of the generator design and modes of operation can be found in Outlaw et al. (1997). A sketch of the physical model basin, wave generators and offshore wave gages is shown in Figure 1.

Breakwater Configurations

Seventeen different breakwater configurations were tested. These configurations are shown in Figure 2, and represent modifications from the original "J6" configuration identified in a prior study by Sargent and Thomas (1995) as effective in reducing the long wave energy at Pier J.

A total of twenty-three sets of tests were conducted. These include the seventeen different configurations, two tests for the existing (base) conditions, and four additional tests for construction phasing (J20, J21, J22 and J23).

Detailed descriptions of each breakwater configuration are not provided herein. However, the rationale in selecting these different test configurations is summarized as follows:

1. Compare the performance of the breakwaters with a rectangular layout (J6 and J8) with those breakwaters with a triangular layout (J9 and J11);

2. Optimize the performance of the rectangular layout by varying the length of the breakwaters (J6, J8, and J12 through J19);

3. Test the importance of the permeability of the breakwaters (J6, J15 and J19) in reducing the long wave energy in Pier J; and

4. Identify the importance of different long wave attenuation mechanisms such as blocking the incident wave (O1), enhancing the separation losses (P1, O1 and J18), and reducing the trapped long wave energy (J11).

Test Conditions

Both monochromatic waves and random wave spectra were tested. Eleven wave periods were selected for most of the monochromatic wave tests which included 151.5, 128.3, 110.3, 99.0, 80.2, 72.3, 60.2, 47.8, 41.9, 37.2 and 32.7 seconds. These wave periods were chosen based on the response of the basin during an initial test with a uniform random wave. Some of the test configurations shown in Figure 2 (BS2, J10, J11, N1, O1 and P1) were tested with only four wave periods (151.5, 128.3, 110.3 and 37.2 seconds). The final configuration J19 was tested with five additional wave periods (160.0, 141.1, 120.0, 106.0 and 91.0 seconds), which results in a total of sixteen periods tested.

Ten wave gages were used for data collection. These included five in Pier J, two in the South East Basin, one at the Queen's Gate entrance, and two offshore gages (one near Platform Edith). The gage locations and their designated numbers are shown in Figure 3. For the final test for J19, an additional gage was placed near the entrance to the Pier J. Wave gages were also deployed in other locations in the Port of Long Beach and Port of Los Angeles to investigate whether proposed modifications would exacerbate any existing surge conditions outside the Pier J project site.

Data Analysis

The monochromatic wave test results revealed that the incident wave conditions measured at a gage near Platform Edith location are subject to multiple wave reflections within the model basin. Reflected waves from the breakwaters, reflected waves from other model boundaries, and re-reflected waves from the wave machine contaminated the wave record at Platform Edith after a short time.

An example time series of recorded waves at four different gage locations is shown in Figure 4. In the figure, Gage 16 is at Platform Edith; Gage 42 is at the Queen's Gate entrance; Gage 81 is near the end of Pier J; and Gage 29 is in the South East Basin. This

example record shows that it takes about 5 seconds for the waves to reach Platform Edith and about another 25 seconds for the waves to travel from Edith to Queen's Gate. This means that it takes about 50 seconds for the reflected waves from the Federal Breakwaters to reach Edith. In another 10 seconds, the reflected waves will travel to the wave generator and be re-reflected to Edith. The effect of these reflected and re-reflected waves to the wave record at Edith is clearly shown in the figure.

In calculating the wave amplification factor – the ratio of the measured wave height at a specified location to that at Edith, only the uncontaminated (before wave reflection affects the Edith reading) wave record was used in the calculation.

The test with the uniform spectrum, which requires a long wave record for spectral analysis, is inherently contaminated and therefore not suitable in defining wave amplifications. In this study, the optimized breakwater configuration was therefore chosen based on the results of the monochromatic wave tests. The spectral wave results were used only for studying the general response of the basin over a range of wave periods.

MODEL RESULTS

In general, the monochromatic wave tests showed that for similar total breakwater lengths, the rectangular layout is more efficient in attenuating the long waves than the triangular layout. For the rectangular layout, the longer the breakwater segments the better the performance. In addition, the permeability of the breakwater was found to be an important factor in determining the performance of the breakwaters. The less permeable breakwater cross section performs better than the more permeable sections.

Due to the large number of tests and large amount of analyzed data, only the most relevant and important test results are presented here. These results were chosen to illustrate and elaborate the general conclusions stated above. In addition, only measurements at Gages 81 (located near the end of Pier J, which usually shows the greatest long wave amplification within Pier J, are shown. However, wave measurements at all gages were analyzed and their results were evaluated in determining the best breakwater configurations.

Effect of Permeability

The amplification factors measured at Gage 8I for configurations J6 and MI are shown in Figures 5. The two test configurations used identical breakwater layouts. While J6 has permeable breakwater cross-sections, MI has impermeable breakwater sections. The results showed that in general, the impermeable breakwater performs better in attenuating the long waves. Data taken at other gage locations showed the same general trend.

Since the breakwater permeability was found to be an important factor in the performance of the breakwaters, proper modeling of long wave transmission through a breakwater in a distorted scale model was further evaluated in a two-dimensional flume. The model stone size providing the best match of permeability of the prototype design (determined from a 1:30 undistorted scale flume model test) was specified for use in the final test with Configuration J19.

Effect of Breakwater Length

The length of the breakwater segments for the rectangular layout was found to be important. In general, wave amplifications in Pier J were found to be less for the breakwater configurations with longer segments. However, this improvement in performance is less sensitive to the length of the breakwater segments running in the north-south direction (i.e., parallel to the Pier J entrance) compared to the lengths of the breakwater segments extending eastward from the Pier J Berth (i.e. parallel to the berthing slips). In the following discussions, the average length of the two north-south breakwater segments is designated as L_1, while the average length for the two east-west sections is designated as L_2. A definition sketch of L_1 and L_2 is shown on the last configuration in Figure 2.

Effect of L_1

The amplification factors measured at Gage 81 for configurations J08 and J15 are shown in Figure 6. These two configurations have roughly the same L_2 of about 600 feet but L_1 differs by about 200 feet. The results show that J08 with longer L_1 of 1,000 feet has slightly less amplification factors compared to those for J15 with L_1 of about 800 feet. However, the differences in the amplification factors are in general very small.

Effect of L_2

Amplification factors at Gages 81 configurations J12, J14, J15 and J17 are shown in Figure 7. For these four tests, the shortest L_2 is about 370 feet (J12) and the longest L_2 is about 965 feet (J17). Note that these four test configurations do not have the same L_1, the latter ranges between 600 to 800 feet. As discussed above, the length L_1 does have some effect on long wave attenuation in Pier J, but not to a great extent.

In Figure 7, the dot-dash line connects the amplification factors for J12, which has the shortest L_2 of 370 feet. The solid line represents results for J17, which has the longest L_2 of 965 feet. The results show that there is a great difference in the amplification factors between these two configurations. In most of the tested wave periods, J17 has amplification factors of only about half or less of those amplification factors for J12.

The effects of L_2 on long wave attenuation at Pier J were further examined by comparing their performance relative to the existing condition (base case) for five critical wave periods. These include three longer periods of 151.5, 128.3 and 110.3 seconds which are important for ship surge motions; and two shorter periods of 41.9 and 37.2 seconds which are important for ship sway motions.

Figure 8 plots the amplification factors relative to the base case versus the length of the east-west breakwater segment L_2 at Gage 81. The amplification factors are taken from test results for breakwater configurations J12, J15, J14 and J17; which have different L_2 of 370, 600, 810 and 965 feet, respectively. Except for the longest period of 151.5 seconds, all the four configurations resulted in substantial reduction in wave amplification factors compare to the existing conditions. There is also a general trend of reduced amplifications with the increase in L_2. The reductions in the amplification factors are substantial when the breakwater length L_2 extends from 360 to 600 feet. When the breakwater extends beyond 600 feet, the amplification factors reduce less rapidly and seem to level off when the L_2 approaches about 1,000 feet.

Separation Loss

Exploratory tests were conducted by visual observations for a few selected wave periods for configurations P1 and O1. These tests were designed to determine whether enhancement of the separation losses would have measurable impact on surge. The results of these very basic tests, however, did not support the importance of the separation losses in attenuating the long waves in Pier J. After J17 was chosen for the final test, a full test with all the eleven wave periods was conducted to further examine the importance of separation losses. The test was conducted with configuration J18, which has similar layout as J17. The only difference between J17 and J18 is that while J17 has the traditional sloping breakwater head sections, J18 has vertical sheet piles installed at the breakwater head sections leading to the Pier J basin. These vertical sheet piles for J18 were intended to increase the flow separation at the basin entrance and hence should have induced greater separation loss compare to J17.

Figure 9 compares the amplification factors at Gage 81 for J17 and J18. The methodology and results did not indicate that it would be warranted to investigate alternatives based on increasing separation losses.

FINAL TEST WITH J19

After reviewing all the results, it was determined that J17 had the best performance among all the configurations tested. A final test was therefore conducted with Configuration J19, which was a modification of J17. This final configuration J19 differs from J17 in two major aspects. First, the lengths of the breakwater segments were

extended to the maximum allowable for the site as limited by dredging and ship maneuvering room. Second, a less permeable breakwater cross-section was specified.

The performance of J19 was compared to J17 in Figure 10. This figure shows the wave amplification factors measured at Gages 81 for J17 and J19. The results show that the less permeable J19 breakwater did result in smaller wave amplifications at Gage 81. Similar results were found for other gage locations.

As mentioned earlier, the criterion for long wave attenuation at Pier J is set to be the same or less long wave energy compared to those long wave energy at the South East Basin. The wave amplification factors measured at Pier J with the final test configuration J19 in place are therefore compared with those amplification factors measured at the South East Basin. These comparisons are shown in Figure 11. In the figure, solid symbols denote wave amplification factors measured in Pier J (Gages 81, 82, 85, 53 and 54), while open symbols are used to show measured results in the South East Basin (Gages 29 and 30). The wave amplification factors at Gage 81 for existing condition (base case) are also shown in the figure for comparison.

In general, with the J19 breakwater configuration in place, wave amplification factors at Pier J are comparable to those at the South East Basin. For the shorter wave periods between 30 to 70 seconds, the amplification factors at Pier J are close to those at the South East Basin. For the longer wave periods of between 90 to 130 seconds, waves at Pier J are slightly higher than those at the South East Basin. However, these wave amplifications at Pier J already represent reduction by a factor 1/2 to 1/3 compared with existing conditions. Even longer wave periods, of between 140 and 160 seconds, waves amplifications at Pier J are in general smaller than those at the South East Basin.

SUMMARY

In summary, although configuration J19 does not completely meet the criterion of reducing the long waves in Pier J to be the same as or lesser than the wave conditions at the South East Basin, it is the most effective among all the tested configurations and also represents substantial improvement over existing conditions. Hence, the J19 Breakwater configuration was selected. The Pier J layout with the J19 Breakwater (hatched) is shown in Figure 12.

REFERENCES

Outlaw D.G., Durham, D.L., Chatham, C.E., and Whalin, R. W. (1977), "Los Angeles and Long Beach Harbors' Model Study: Report 4, Model Design," Technical Report H-75-4, US Army Engineer Waterways Experiment Station, Vicksburg, MS.

Sargent F.E., and Thomas, L.J. (1995), "Port of Long Beach Pier J Slip Study – Draft Report," US Army Corps of Engineers Waterways Experiment Station Tech. Report CERC-95-X.

ACKNOWLEDGMENTS

Work described in this paper was conducted by Moffatt & Nichol Engineers (M&N) for the Port of Long Beach (POLB), Long Beach, California. Dan Allen was the Chief Harbor Engineer; Doug Sethness was the Deputy Chief Harbor Engineer. Mr. Richard Weeks and Mr. Maxwell Sweeney were Project Managers for POLB at different time. A Technical Review Committee (TRC) reviewed the methodology and results, and provided guidance. Members of the TRC included Professors Frederic Raichlen, Robert Dean, Chaing C Mei and Captain Braendekilde. Physical model tests were conducted at the US Army Engineer Waterways Experiment Station Coastal Engineering Research Center (CERC). Personnel at CERC working on the project included Mr. Dennis Markle, Mr. Bill Seaberg and Mr. Frank Sargent.

APPENDIX – CONVESION FACTORS

Multiply	By	To Obtain
feet	0.3048	Meters
mile	1.6093	Kilometers
acre	0.4047	Hectares

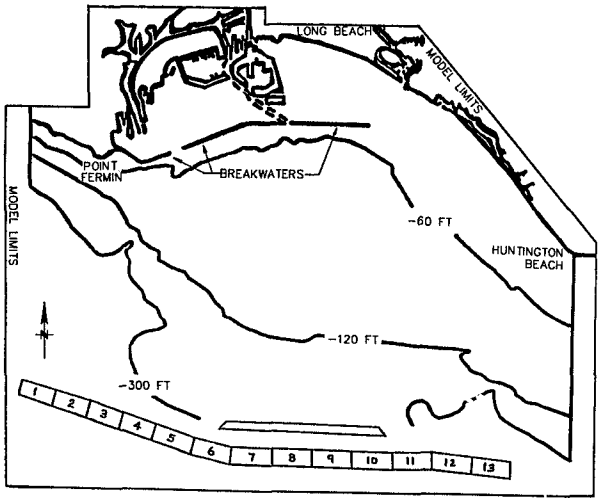

Figure 1: Physical Model Layout

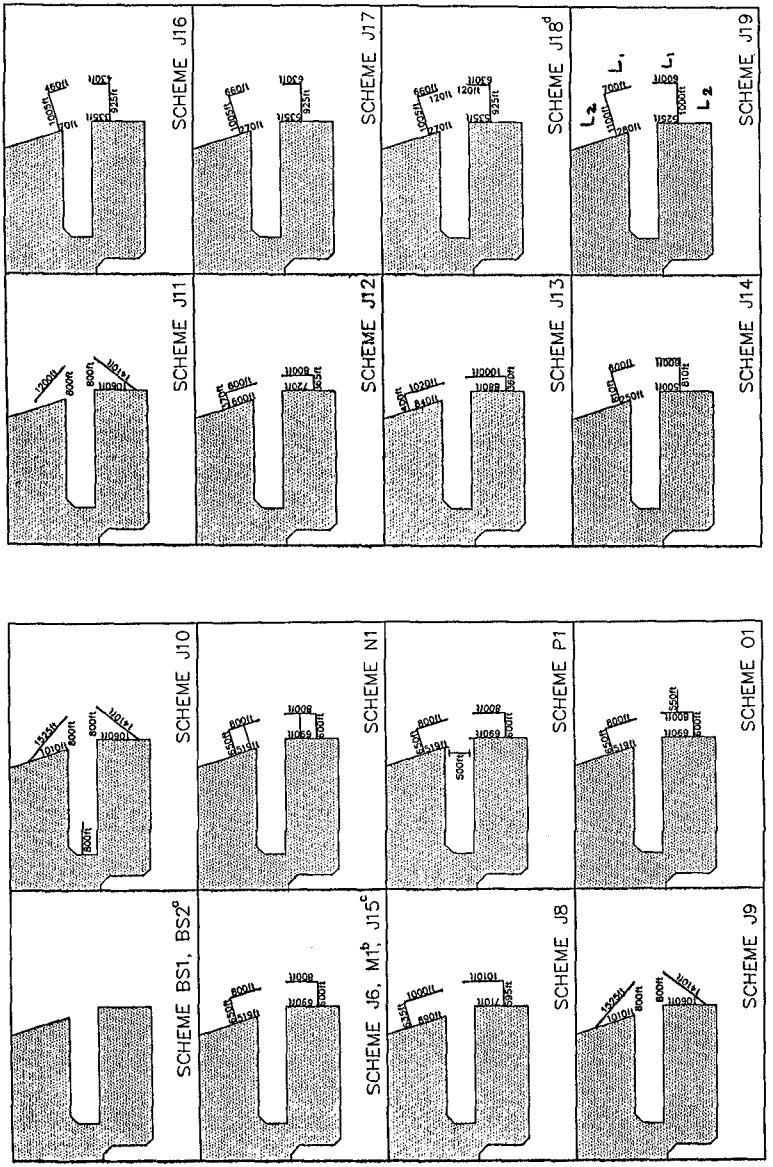

Figure 2: Schematics of Different Breakwater Configurations

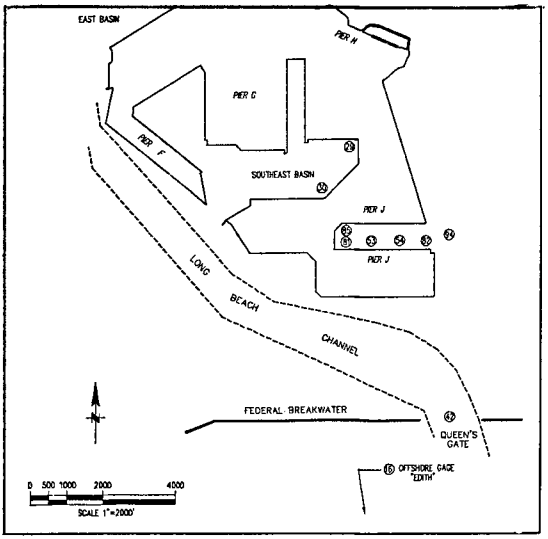

Figure 3: Gage Locations

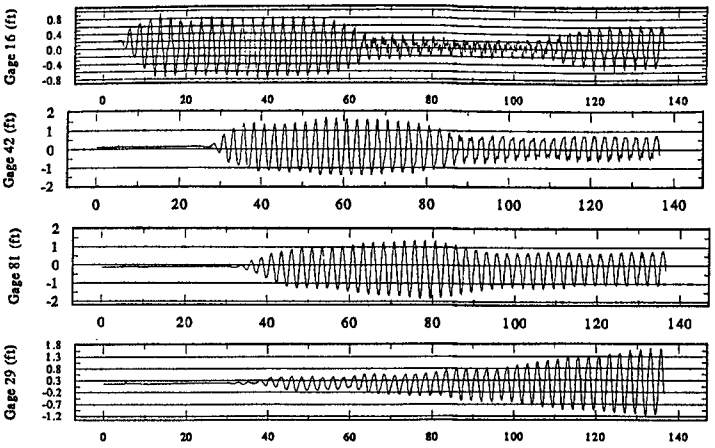

Figure 4: Example Water Surface Elevation Time History

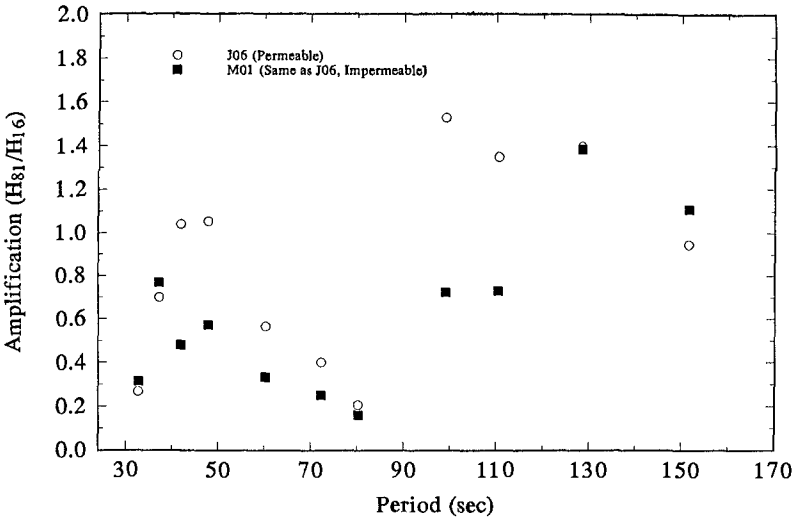

Figure 5: Effect of Breakwater Permeability on Long Wave Attenuation

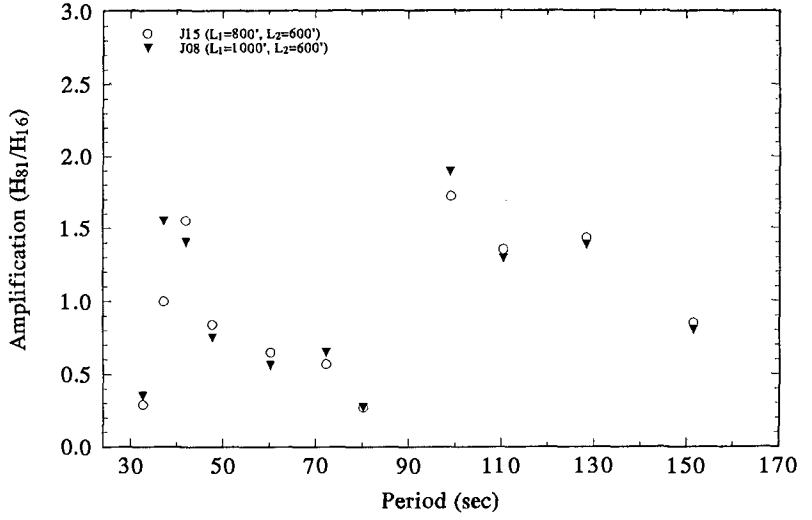

Figure 6: Effect of Length L_1 on Long Wave Attenuation

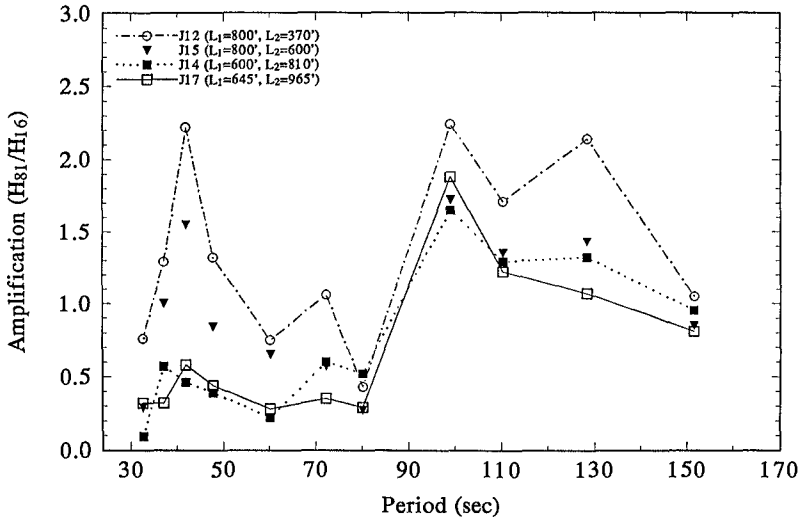

Figure 7: Effect of Length L_2 on Long Wave Attenuation

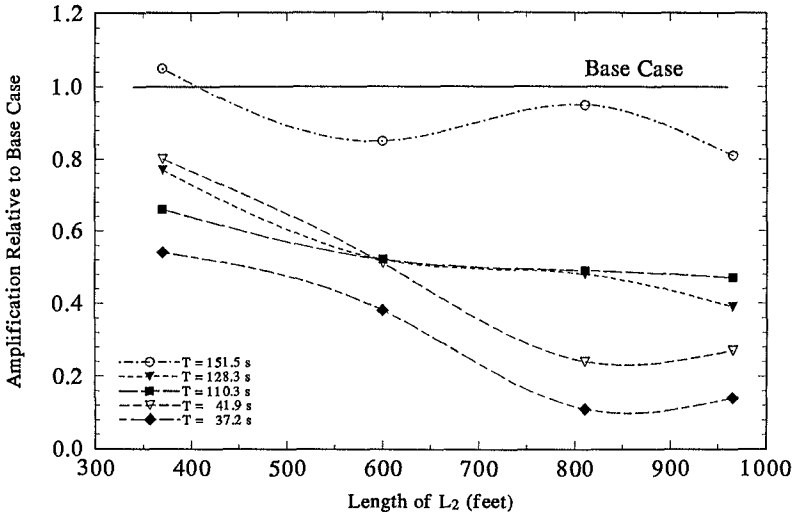

Figure 8: Effect of Length L_2 on Long Wave Attenuation for Five Critical Periods

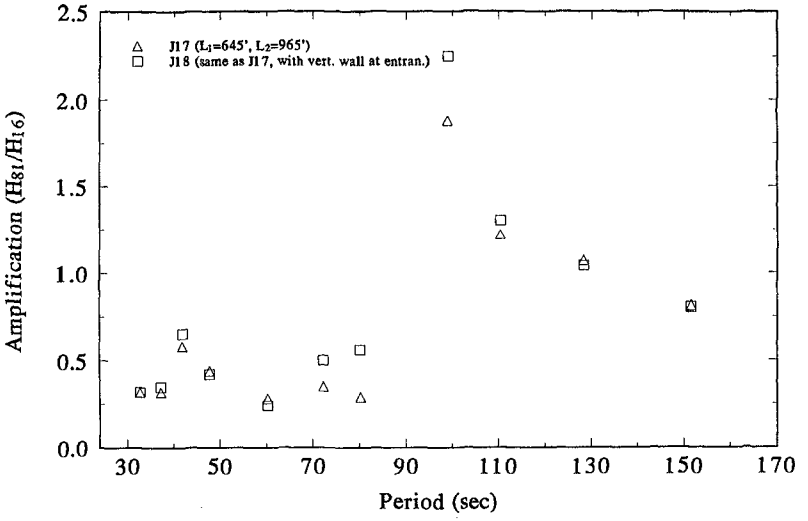

Figure 9: Effect of Enhanced Separation on Long Wave Attenuation

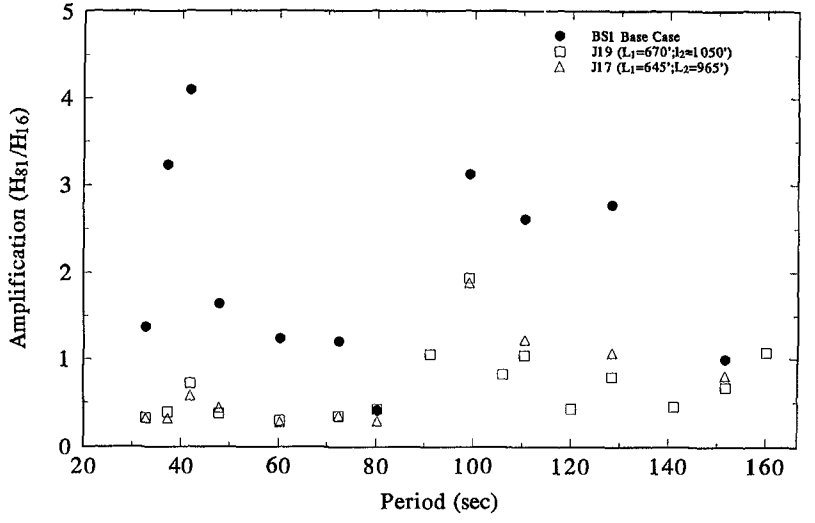

Figure 10: Comparison between J19 and J17 with the Base Case

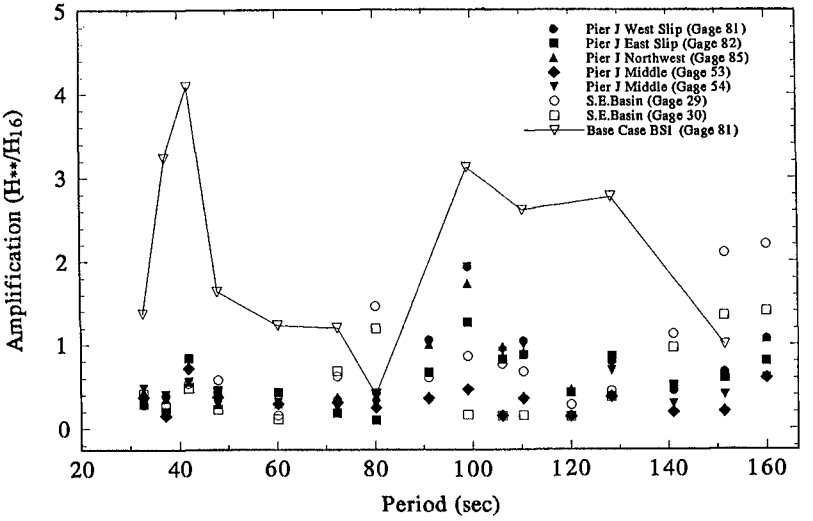

Figure 11: Comparison between J19 and the South East Basin

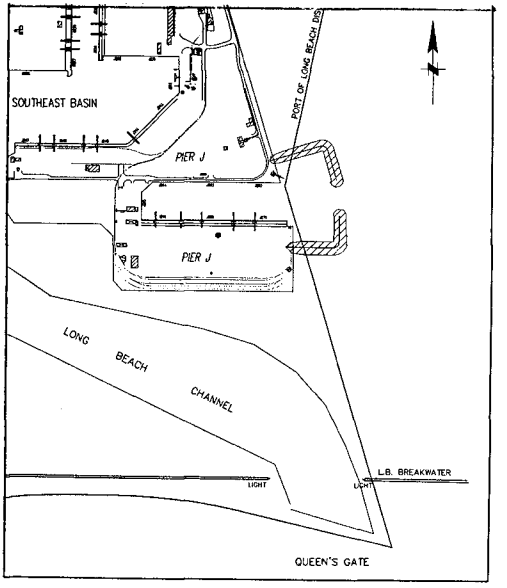

Figure 12: Selected J19 Breakwater (Hatched) to Reduce Surge Motion

NAUTICAL DESIGN STUDIES
HAIFA PORT EXTENSIONS

JA Zwamborn[1], F Di Castro[2], M Radomir[2] and JTM van Doorn[3]

ABSTRACT

Detailed studies have been undertaken to assist in the design of major extensions to the port of Haifa. Both numerical and physical model studies were done to optimise the mooring conditions vis á vis the harbour approach and entrance layout. The adopted layout deviates from the normal straight approach to the harbour entrance. This layout, together with suitable aids to navigation, was found to be **nautically acceptable**, and generally better with regard to mooring conditions, on the basis of **extensive nautical design studies**.

INTRODUCTION

The **Port of Haifa** is situated at the southern end of Haifa Bay, which is about 12 km long by 6 km wide, with Mount Carmel at the south and Akko at its north end (see Figure 1). The original main breakwater with a length of 2,25 km was built in 1931. It was extended by 600 m during 1978/79 to protect the newly constructed container or eastern quay. At the same time, the harbour entrance area was dredged to a nominal depth of - 14 m LSD (Land Survey Datum). In recent years, the eastern quay has been extended by 300 m and a piled passenger jetty has just been completed at the western end of the harbour.

The Kishon harbour is situated east of the main port area close to Haifa's main industrial area. The harbour entrance is dredged to a depth of - 12 m LSD and it is protected by a 400 m long rubble mound breakwater. It is the home of the Israeli shipyard and repair industry.

As part of the **Master Plan** for the development of the Port of Haifa a 500 m main breakwater extension and several new container, general cargo and bulk quays are planned together with a new approach and entrance channel. Initial numerical wave agitation studies showed unacceptably high downtimes for the original layout, particularly for Quay no. 4 (re. Figure 2). Further studies were therefore undertaken to increase the operability of all the new

1 Coastal and Harbour Engineering Advisor, IPRA, 5 Province Ave, Stellenbosch, 7600, South Africa

2 Design Engineer, Israel Ports and Railways Authority, 74 Petach Tikva Road, Tel Aviv, 61201, Israel

3 Past Project Manager, Maritime Simulation Centre the Netherlands, Van Uvenweg 9, Wageningen, the Netherlands

berths to acceptable levels but, at the same time, to ensure good navigational conditions in the approach and entrance to the port.

These **studies** included :

- studies of the main breakwater layout giving the best protection against wave penetration
- a desk study of the nautical design of the entrance
- preliminary full-mission manoeuvring simulations
- a full simulation programme for the accepted layout.

The results of these studies are briefly described in the following sections.

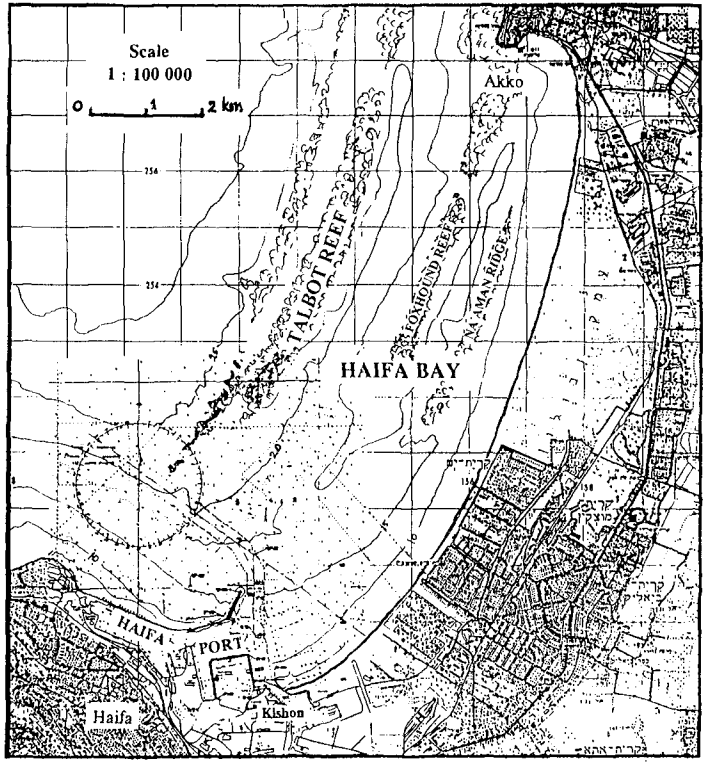

Fig. 1 Haifa Port in Haifa Bay

HAIFA PORT EXTENSION

The **Haifa Port Area Development Plan** was prepared by the Israeli Ports and Railways Authority (IPRA), with the assistance of Israeli and international experts in various fields. The primary goals of the development are to prepare Haifa Port to meet operational demands which require a high level of service efficiency. This is intended to be accomplished by staged development through the year 2020, as required by demand. The primary goals are as follows :

- furnish a high level of service which means an average waiting time for berths of not more than one hour per vessel
- develop the western part of the Haifa Port as a passenger port
- assure port accessibility by various transport modes (roads and railway)
- optimize integration of the port complex into the metropolitan area by coordinated development planning with surrounding systems
- develop the port hinterland for industrial, commercial and port services
- ensure environmental protection, quality of life and maximum safety.

The three primary components of the development plan are **breakwaters**, **layout** & designated usage of quays and port operational areas. The development of **Haifa East** will be implemented in the following phases (refer Figure 2):

Phase I - Haifa East "A" and Haifa East "B" by the year 2003.

Phase II - Haifa East "C" and "D" future developments based on demand.

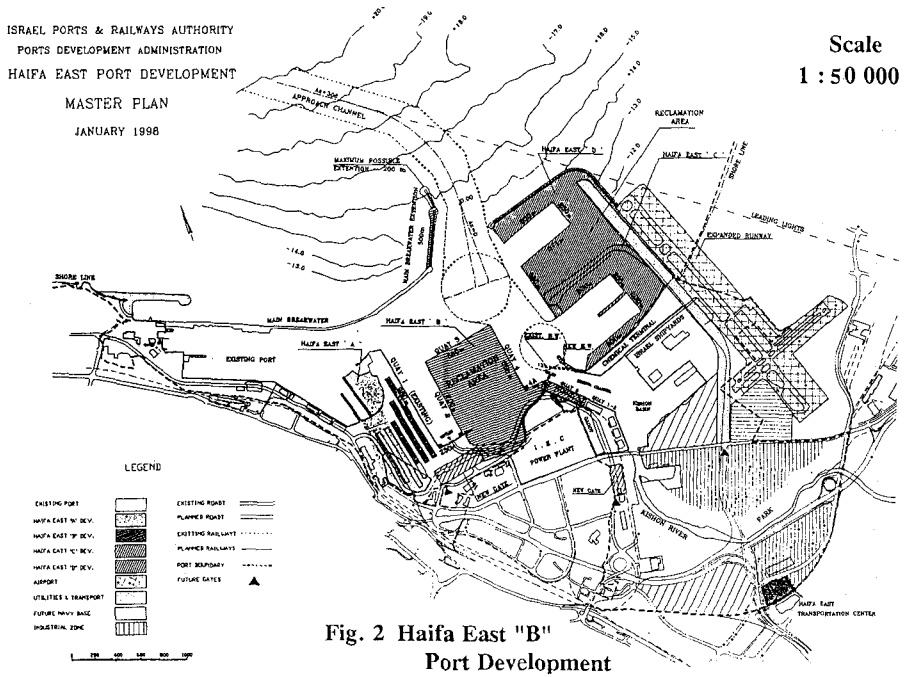

Fig. 2 Haifa East "B" Port Development

With the completion of works envisioned under the development plan, the port would have a total of 6 500 m of operational quays (plus another 900 m of service quays) and 245 ha of operational area.

Phase I calls for the construction of 700 meter of container quay and 1 900 meter of general and dry bulk cargo quays in Haifa East "B". Container operational areas will be expanded by 50 ha, general and dry bulk cargo areas by 15 ha. The quays in the western sector of the port (1 600 m) are to be used by passenger ships and ships serving the Dagon grain silos. The western end of the port will then be designated as a passenger ship port and will be integrated into the city's urban fabric. This transformation will have a sweeping impact on the development of the City of Haifa.

The main breakwater must be extended by 500 m to allow Phase I development. The existing Kishon north breakwater must be removed and replaced along a new alignment, with a 200 m long breakwater, refer Figure 2.

Upon the completion of Phase I, the container terminal will be centralized in the area including Haifa East "A" and the western side of Haifa East "B". The western end of the Port will no longer be used for container handling operations. General cargo will be handled in the Kishon Port (as it is currently) and on the northern and eastern quays of Haifa East "B". A transport corridor physically connecting the Kishon Port with the main Haifa Port is planned. The water inlet of the Electric Power Station's cooling basin will be maintained as a bridge in the transport corridor. The warm water from the Electric Power Station will be canalized in a closed conduit and its outlet will be located between Quays nos 1 and 2.

Phase II is intended for expansion of the existing chemical terminal as an alternative to the fuel jetty and tankfarm and for handling general cargo and bulks by grabs (Haifa East "C" and "D"). Expansion of the existing airport is planned, as shown in Figure 2.

The mix of ships using the Port, has impact on two primary aspects of the port development plans :

- the physical layout of the port including quay length, water depth, basin size, operational areas, breakwaters and entrance channel dimensions
- the design of the operational concept, including personnel and handling equipment plans and work procedures.

The following **design vessels** (LoaxBxT) were used by the planners for the Haifa Port extensions :

a) Post Panamax Container Vessels up to 84 000 dwt (318x42,8x14).
b) Bulk Ships 60 000 dwt (225x32x12,5),Bulk Ships 100 000 dwt (280x40x15) and Coal Ships 150 000 dwt (295x44x17).

c) General Cargo Ships 25 000 dwt (190x25x10,6).
d) Chemical Tankers 12 000 dwt (160x18,4x8,3).
e) LPG Tankers 22,000 dwt (170x23x9,7).

The following development plan characteristics were set based on the above design vessel assumptions :

- entrance channel water depths (max. 20 m);
- quayside water depths, 14 and 16,5 m for Bulk and General Cargo Ships, 15,5 m for Post Panamax Container Ships, 19 m for Coal Carriers, 12 and 10 m in the Kishon Port to be used by smaller Bulk Carriers and General Cargo Ships;
- basin width between quays 250 m;
- turning circle diameter 600 m.

WAVE PENETRATION AND MOORING STUDIES

Both numerical and physical model studies were done to optimise the harbour layout with respect to limiting wave agitation. Due to the semi-protected position of the Port of Haifa (see Figure 1), storm waves from the dominant W'ly and WNW'ly directions become mainly NW'ly but also NNW'ly. Because ships must approach from the same NW'ly direction, due to the presence of the Talbot Reef, protection against wave penetration becomes rather problematic and several layouts have been studied in the numerical model before physical model tests were done.

The **numerical model** studies employed three separate modules, a non-linear shoaling module, the linear DHI agitation model MIKE 21 EMS and a linear wave-ship interaction module developed by the Coastal and Marine Engineering Research Institute (CAMERI) in Haifa. For more details on this approach, refer to Di Castro *etal* (1997). The **physical model** was built to a scale of 1 in 150 at the CAMERI laboratory in Haifa. As a first step, the numerical model results were compared with those of the physical model for the **existing** harbour conditions. Acceptable agreement was found, both in the short and long wave heights and in the downtimes for the 60 000 dwt bulk carrier and the 30 000 dwt container ship moored at the existing eastern quay (refer Di Castro *etal*). Operabilities were found to be **97,0 %** and **96,1 %** for the numerical model and **97,9 %** and **96,7 %** for the **physical** model (limited prototype data suggests 2 % to 4 % downtime which is in close **agreement**).

After calibration, three basic layouts were modelled in the numerical model, namely the '**original**' design (Figure 3) with four different alignments of Quay no. 4 from maximum skew (kinked extension of Quay no. 5) to 90° square (parallel to Quay no. 2), the '**alternative**' design which provides maximum protection against wave penetration (Figure 4) and the '**final**' design (Figures 4, insert, and Figure 2).

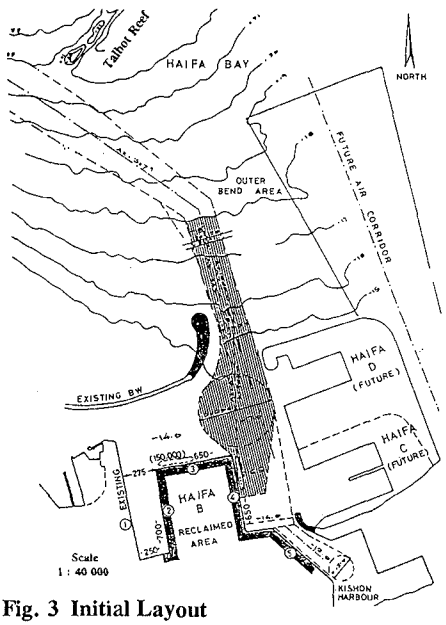

Fig. 3 Initial Layout Haifa Port Extensions

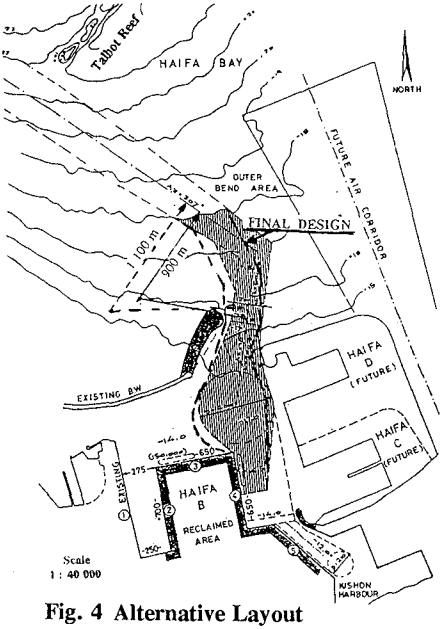

Fig. 4 Alternative Layout Haifa Port Extensions

The test results for the original layout showed that the 'parallel' Quay no. 4 has the lowest downtimes and this quay-wall layout was therefor used for all further modelling. The 'alternative' design, with the head of the breakwater extension moved about 150 m east, was found to be significantly **better** in the eastern part of the port extension, including the Kishon Port, although conditions at Quays nos 1 and 2 became slightly worse. Mainly based on navigational considerations the entrance channel of the 'alternative' layout was revised, without changing the position of the breakwater head, which resulted in the 'final' design. The 'final' layout was studied, both with the numerical models and the physical model and the results showed generally **acceptable downtimes** for all the berths of Haifa East "B", namely operabilities for the various design ships moored at the relevant Quays nos 1 to 5 from **95,2 % to 98,8 %** for the **numerical** model and from **96,6 % to 99,6** for the **physical** model. Considering that these operabilities assume 100 % occupancy of design ships (sensitivity studies showed that downtimes for smaller ships are generally significantly less), these results were considered **acceptable**, based on present experience in the port.

NAUTICAL HARBOUR ENTRANCE DESIGN

The nautical design efforts were concentrated on the Post Panamax **container** vessel of 84 000 dwt (maximum draught 14,0) loaded to **12,5 m** draught (**71 900 dwt**) to berth at Quay no. 2, a **150 000 dwt** coal carrier to be berthed at Quay no. 3, the **100 000 dwt** bulk carrier to berth at Quay no. 4 (north) and the **25 000 dwt** general cargo ship entering the Kishon Port.

Wave conditions in the approach and entrance area are rather mild and the swell direction is mainly NW. The following refracted design data (in %) apply to the entrance area in 16 m depth (the 'long term' data are largely visually recorded data) :

Wave Direction	$H_{mo} > 1,5$ m	
	'Long term' wave data '58 -'96	Directional Waverider '93 -
NW	3,43	0,77
NNW	0,53	0,10
All directions	3,96	0,87

Thus, since the available 30 t bollard pull Voith-Schneider tractor tugs can be made fast in waves up to H_{mo} = 1,5 to 1,8 m (refer Halber *etal*, 1985), these tugs could **assist outside** the protection of the breakwaters for **at least 96 % of the time**.

The dominant **wind** directions are W, NW and SE while the strongest winds come mainly from W'ly, E'ly and SE'ly directions. Wind speeds in excess of 10 m/s (20 knots) occur only 2,9 % of the time (all directions) while speeds in excess of **15 m/s** (30 knots), which limits ship handling and crane operation, occur less than **3 days** per year.

The 'original' channel alignment shown in Figure 3 was 345° with an approach route of 307°. This design was based on the accepted criterion of a **straight** harbour entrance channel (refer PIANC, 1997 and also Halber *etal*, 1985). However, a more easterly position of the breakwater extension would provide better protection against the NW'ly waves and the 'Alternative' entrance design shown in Figure 4 was developed with the breakwater head moved about 150 m east, an entry channel at 10° with the same approach route of 307° and a nominal 63°-radius bend of 900 m or about 3 ship lengths. PIANC (1997) quotes a minimum of 2,8 lengths for unassisted entry but in the case of Haifa, **tug assistance** in the bend area would anyhow be **possible** up to at least 96 % of the time.

This layout proved to be **superior** from a wave protection point of view but further improvements were made as follows (see insert Figure 4) :

- the head of the breakwater extension remained unchanged but the 500 m extension was made straight
- the turning circle and the head of the future Haifa D breakwater were moved 50 m west
- the entrance channel was revised to have a single-radius (1 100 m) bend of 53°
- the channel design allows a further lengthening of the breakwater due north of 200 m, if found necessary (see Figure 2).

This provided a single-radius entry route into the main port area (container basin) of ample

radius. No change was sofar made to the original approach route of 307° into Haifa Bay because it is virtually fixed by the presence of the Talbot Reef and the future air corridor (refer Figures 1 and 3). However, when considering the aids to navigation, it was found that by making a minor change in the approach route from 307° to 306°, the back leading light could be fixed to a very prominent grain elevator building (refer Figure 2).

This 'final' layout was used for the preliminary and detailed ship manoeuvring studies described below.

FULL-MISSION MANOEUVRING SIMULATOR

The MSCN **real-time simulator** with the full mission bridge and a 360° visual image was used for the Haifa Port extension manoeuvring simulation studies. This facility consists of a real **ship bridge** located in the centre of a cylindrical projection wall on which the graphics image is projected. A separate wing console is available for manoeuvring close to berth. Among the standard equipment of the bridge is a software controlled radar with full ARPA functionality.

Behind the bridge is the **simulation manager's** position. He can follow the manoeuvres directly as he has a view on the bridge, but he also controls all aspects of the simulations using a dual-headed workstation. On the left hand screen a **birds-eye view** of the simulation is presented. All environmental conditions can be called up on this screen. The track following target vessels are also controlled from this screen with respect to track and velocity. The right hand screen is used for the **control** of the simulation. It is used for the selection of conditions, control of tugs, control of environmental settings (visibility, wave heights and wind speed/direction) and it gives information about the status of the own ship (velocity, rate of turn and relative wind speed). At any time the simulation manager can halt the simulation and, if required, reposition the vessel. It is even possible to play-back a manoeuvre. During the simulations the simulation manager can follow the conversation on the bridge using the intercom. Tug orders are normally transmitted by VHF.

During the simulation studies the following **instruments** were available on the 'bridge' :

RPM indicators of engine and bow thrusters;	dopplerlog;
rate of turn indicator(s);	sallog;
rudder indicator(s);	wind indicator (speed and direction);
compass and course indicator;	VHF and intercom.

The data base includes information regarding the new **lay-out** of the port according to existing data of surveys, sea charts, local maps and the design drawings of the new situation. Both the 'original' and 'final' designs were included with access channel depths of 16, 18.5 and 20 m, depending on the design ship. All data regarding the critical **environmental conditions** were made available by the Israel Ports and Railways Authority and these data were digitized and imported into the database. For the environment (waves, wind and currents) it

is possible to include a so called grid in order to take into account the spatial variation of the environment. Furthermore effects of variations in time are also included in the simulations, for instance, wind gusting and slowly varying drift forces. These variations in time are, like in nature, stochastic which makes every simulation unique.

The **visual image** was prepared using photographs, maps, charts and drawings. For each situation two outside views were prepared, a day and a night version. In the night version special emphasis was laid on the so-called cultural lights. Lights on the quays and in town, producing backlight but also giving additional position information to the pilot. Of course also the **aids to navigation**, buoys and leading lights, were implemented. A so called 'minimum scheme' was applied in order to find out which aids had to be added in order to secure safe manoeuvring. For a number of destinations, moored ships were included at various quays thus reducing the available space and making the manoeuvres more complicated.

The **mathematical models** applied are waterdepth/draft sensitive, consequently the manoeuvring characteristics are depending on the waterdepth, an important aspect of manoeuvring in shallow water. Special emphasis was paid to the wave drift forces calculated for the various ship types. When the vessel runs aground in the simulator the simulation halts sothat the reason for this can be evaluated. A realistic collision behaviour with spring action, damping and longitudinal friction, depending on the properties of the fendering, was included along the quay walls. Bank suction was only included in the Kishon area, as this is a relatively narrow passage with restricted width and depth.

Most realistic is a simulation with **tugs** as own ships sailed from other available bridges. However the own-ship tugs are not always practical and in the Haifa simulation tugs operated by the simulator manager were used. All tug forces are modelled realistically and the transitions between the pulling/pushing directions conform with reality. The forces are dependent of speed, pulling/pushing direction, velocity of own ship and current. The tugs can be positioned in a realistic position awaiting the approach of the vessel. They are also visible in the visual image. When the pilot requests assistance, the tugs will approach and upon command they will make fast. All this is performed with **realistic time delays** including stochastic variation. Pulling/pushing will be effected on order. In the Haifa simulations four 30t bollard pull Voith-Schneider tugs were available for assisting the vessel.

For a new port development, the **selection of the pilots** who should execute the simulations is an important issue. It is beyond doubt that experienced pilots must be used. Local pilots have the advantage that they are familiar with the port and the procedures normally applied. However in case of an increase in maximum ship size they lack the experience with the specific vessels. To overcome this problem in the Haifa port study we have worked with one local pilot and one Dutch pilot who has experience with the specific ship size. This was a successful approach also with regard to knowledge/experience transfer.

PRELIMINARY MANOEUVRING SIMULATIONS

Although tug assistance in the channel bend is considered feasible most of the time, it was decided by the IPRA to carry out a preliminary programme of manoeuvring simulations to check on the **nautical feasibility** of the curved entrance channel which goes against normal harbour entrance design rules.

These preliminary simulations were done on the full-mission simulator at MSCN/MARIN, Wageningen over a period of three days by a Dutch and an Israeli pilot. Only the **largest ships** were used, namely the Post Panamax container vessel (84 000 dwt) loaded to 71 900 dwt and the 150 000 dwt bulk carrier. Also, rather **extreme conditions** were used, namely : Condition 1 with 10 m/s (**20 knots**) W wind, 1 m/7 s NW waves and 0,2 m/s E'ly current, and Condition 2 with 20 m/s (**40 knots**) W wind, 2 m/9 s NW waves and 0,4 m/s E'ly current.

Leading lights were used to define the approach route, the back light being 4,7 km from the start of the bend at a height of 30 m above sea level and the front one 2,9 km away at a height of 15 m (see Figure 2). Four navigation buoys were used, **no. 1** at the Talbot Reef, **nos 2** and **4** at the start of the bend and no. **3** at the entrance, opposite the new breakwater head.

The preliminary simulations included 15 entry manoeuvres (both during daylight and at night) and 4 departures with the container vessel (T = 12,5 m) and 8 entries and 1 departure with the 150 000 dwt bulk carrier (T = 17,0 m). Thus, a total of 28 actual test runs, excluding 5 familiarisation runs. The runs started about ½ mile (900 m) seaward of buoy no. **1** and it was assumed that the **pilot** had boarded before buoy no. 1. The container vessel was berthed at Quay no. 2 (north) and the bulk carrier at Quay no. 3 (centre). Two 30 t tugs joined the ship in the bend area. For condition 1 (H_{mo} = 1 m) the tugs could start to make fast outside, for Condition 2 (H_{mo} = 2 m), they could only make fast when the wave height had reduced to H_{mo} =1,5 m. It was assumed to take 5 minutes to fasten one tug. Two more tugs were waiting inside and could be used, if required.

Although it was intended to also check the 'original' layout, the early results with the 'final' layout were very positive and all the preliminary runs were done for this layout. On the basis of this limited simulation programme it was found that the 'final' layout was indeed **feasible**. Rudder and propeller use were moderate and three tugs should be sufficient, except for the 40 knot (20 m/s) wind condition when the tug capacity was considered marginal for the container vessel. It was therefore decided to reduce this test condition for the further simulations to a more realistic wind speed of 30 knots (15, 0 m/s). Even when the container ship's power was reduced by 25 per cent for some runs, no particular problems were encountered.

Based on the preliminary three-day simulation study it was **concluded** that the 'final' layout was, not only nautically **acceptable**, but probably preferable to the original layout with the straight entrance channel section. This is because the single bend design is such that the entry manoeuvre becomes quite 'natural'. It was also found that the aids to navigation (leading lights and 4 buoys) appeared sufficient but necessary for safe navigation.

On the basis of these results it was decided to continue with the main simulation study using the 'final' entrance design.

COMPREHENSIVE MANOEUVRING SIMULATION STUDY

The main simulation study consisted of two weeks of simulations at MSCN/MARIN by two Israeli and two Dutch pilots. The **purpose** of these studies was to check on the nautical design of the extended port, according to the 'final' design, with particular emphasis on :

- the approach, entrance and turning area layouts and the channel widths
- the location and extent of the manoeuvring areas and mooring basins
- the need for and adequacy of the aids to navigation
- the minimum required tug use and the overall manoeuvring safety vis á vis weather conditions.

The simulations were done with the following ships :

- Post Panamax Container Vessel (T = 12,5 m) to be berthed at Quay no. 2;
- 150 000 dwt Bulk Carrier (T = 17 m and 11,8 m) to be berthed at Quay no. 3;
- 100 000 dwt Bulk Carrier (T = 15 m and 10 m) to be berthed at Quay no. 4;
- 25 000 dwt General Cargo Ship (T = 10,6 m) to be berthed at Quay no. 5 (Kishon).

The following **environmental conditions** were used in the simulations :

Swell	Direction	-		-		NW		NNW	
	H (m)	0		0		1	2	1	2
	T (s)	0		0		7	9	7	9
Wind	Direction	E		SE		W		NW	
	Speed (m/s)	10	20/15	10	20/15	10	20/15	10	20/15
Current	Direction	-		-	W	E		-	W
	Speed (m/s)	0		0	0,20	0,20	0,4	0	0,20
Starting Speed (knots)		5	6	5	6	6	7	6	7
Condition		**1**	**2**	**4**	**5**	**7**	**8**	**9**	**10**

In total, 102 manoeuvring runs were performed as follows (outbound in ballast) :

Runs	Inbound	Outbound	Night	75 % Power	Total
Post Panamax Container Vessel	47	10	9	4	57
General Cargo Ship	13	-	3	-	13
100 000 dwt Bulk Carrier	12	4	2	-	16
150 000 dwt Bulk Carrier	22	4	1	-	26
Totals	94	18	15	4	102

The results of the simulations are shown in Figure 5 where the results are **combined** for the different wind directions W, E, SE and NW and for the three main design ships (excluding the 100 000 dwt bulk carrier). Some minor channel boundery transgressions are noted on the inside of the bend and near the head of the future Haifa D breakwater. MSCN/MARIN recommended straightening of the western channel boundery but since this would come in the way of a possible further main breakwater extension, it was decided to anchor an **additional buoy, no. 6**, here. Also, an additional buoy, **no. 5**, is anticipated to avoid possible transgression of the eastern channel boundery (refer Figure 6).

Apart from these minor changes, the harbour **entrance design** was found to be **effective** and **nautically safe.**

FINAL LAYOUT AND AIDS TO NAVIGATION

Based on the design studies and the preliminary and detailed ship manoeuvring simulations it was found that :

- the approach, entrance, turning and mooring areas are **satisfactory** for safe operation for waves up to H_{mo} = 2 m and 20 to 30 knots (10 to 15 m/s) wind for the container vessel and up to 40 knots (20 m/s) for the bulk carriers
- the **limiting** conditions for operation will be bringing aboard of pilots and the use of service craft, not the channel design
- the revised Kishon entrance was found to be **satisfactory** although, due to the change from the present entry conditions, pilot **training** on a simulator will be advisable
- under adverse conditions, only the **bow-out** manoeuvre of the container vessel is sufficiently **safe** but for the bulk carriers both the bow-out and bow-in manoeuvres can be made safely
- normally **two tugs**, used inside the port, are sufficient although for some conditions three and even four tugs are advisable (also depending on the type of ship and for speed of operation)
- the **aids** to navigation as used in the simulations are generally sufficient but **necessary** for safe navigation and manoeuvring although two additional buoys are envisaged based on the minor transgressions
- the pilot boarding and manoeuvre starting points used are satisfactory

- pilot training is envisaged for the new conditions, particularly for manoeuvring into the container basin and the new Kishon entrance and to confirm the need and effectiveness of the additional buoys nos 5 and 6.

The 'final' design, including all the envisaged aids to navigation are shown in Figure 6. This layout was also used for the detailed numerical and physical model tests described above for the **mooring conditions**. Preliminary numerical model studies did indicate that a longer breakwater extension (600m) would indeed **further reduce** wave heights inside the port sothat this remains a future option, if needed.

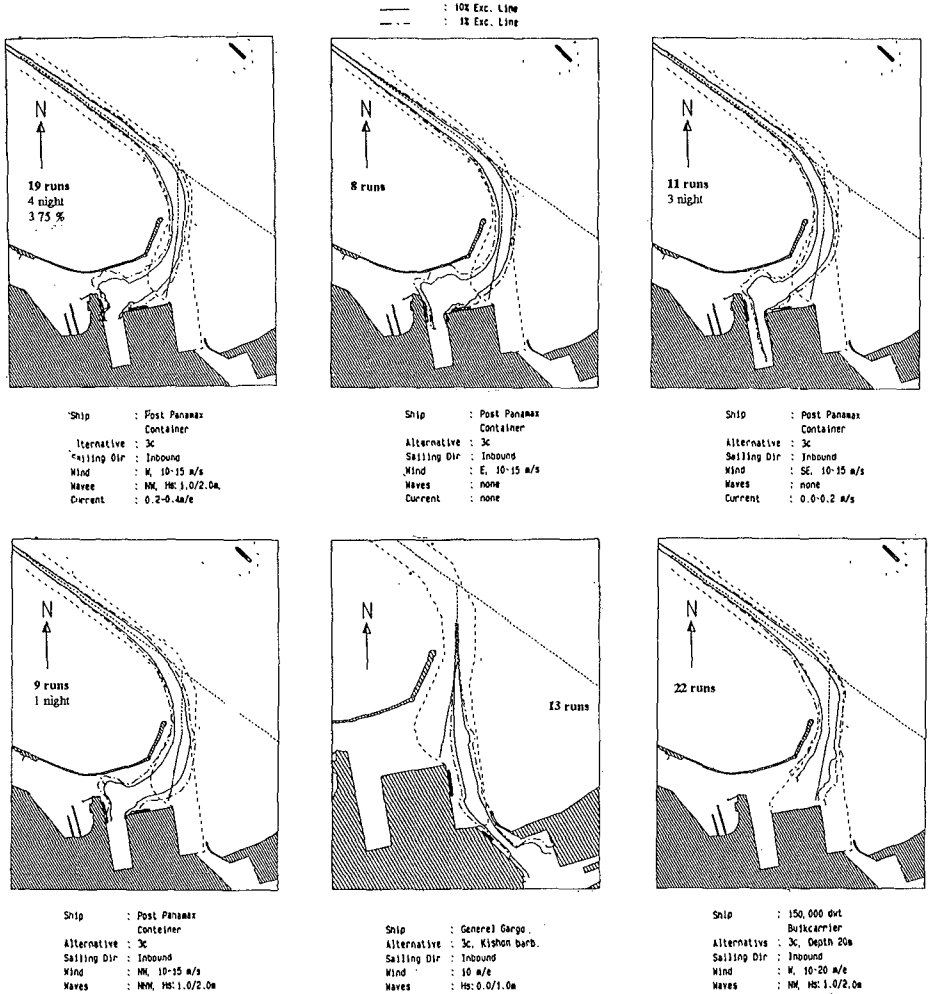

Fig. 5 Combined Simulation Tracks per Wind Direction

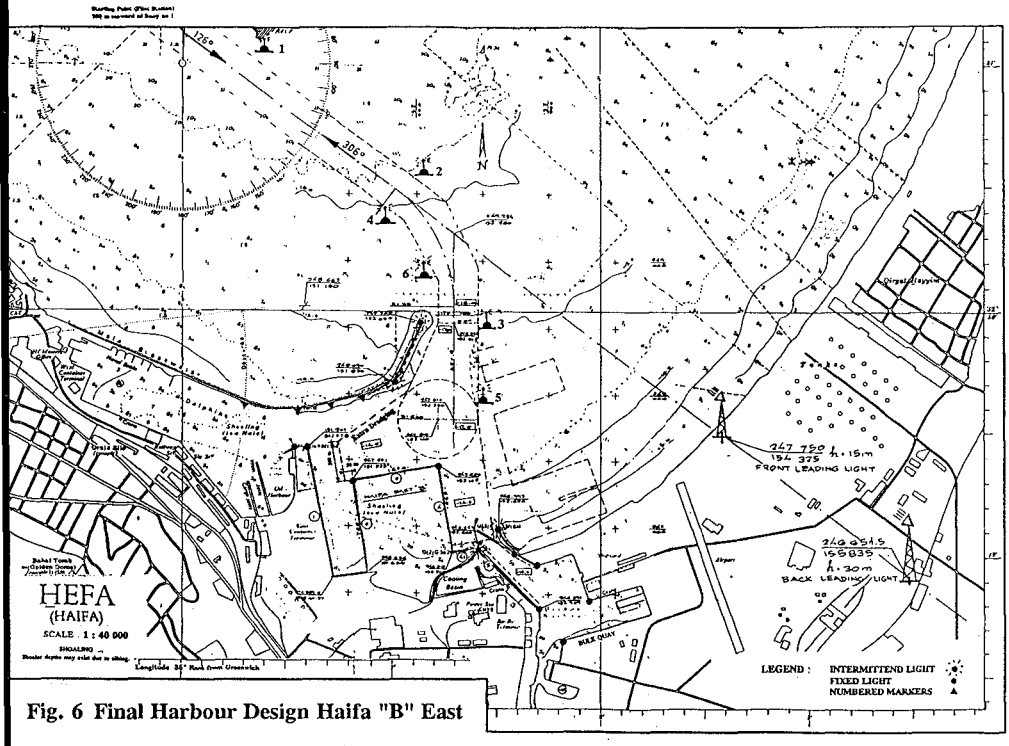

Fig. 6 Final Harbour Design Haifa "B" East

CONCLUSIONS

Forced by circumstances, a **curved approach** to the entrance of the planned extensions to the Port of Haifa, was designed in the 'final' layout. Detailed nautical studies not only proved the adequacy of this layout but they showed the distinct **advantages** of this particular design. At the same time, **maximum protection** against wave penetration was achieved.

These satisfactory results were reached by an **integrated design** process which included a nautical desk study design supported by an extensive programme of full mission manoeuvring simulations and detailed numerical and physical model studies.

REFERENCES

Di Castro, F *etal.* A numerical Model for Studying the Motion of Berthed Ships in Harbours. Proc. Coastal Engineering 97, La Corũna, Spain, June 1997.

Halber, D *etal.* Design of Ashdod Port Extension, Coal Unloading Terminal for 150 000 dwt Bulk Carriers. Proc. 26th PIANC Congress, Brussels, June 1985.

PIANC (1997) Approach Channels, a Guide for Design. Supplement to Bulletin no. 95, Brussels, June 1997.

Wave Propagation Modeling for Pusan New Harbor

Jang-Won Chae[1] and Weon Mu Jeong[2]

Abstract

For the basic design of Pusan New Harbor that will be the third largest container hub-port in the world, extensive wave measurements and wave propagation modeling were made. They are mainly for estimating shallow-water design wave height and determining breakwater alignment to acquire harbor tranquility. The directionality of short crested waves is proved to be very important when they propagate through the waterway. Bounded long-period waves with a small amplification were observed in the shallow water area, which might cause horizontal motions of the container ship moored at a berth aligned to the south. Modified and extended numerical wave models are found to be reasonably good at simulating the measured wave propagation phenomena. Hybrid modeling was made to evaluate harbor tranquility combining numerical and physical modeling results.

Introduction

With the rapid economic growth in the region of North-East Asia, Pusan New Harbor, which is located at the south-east end of the Korean Peninsula, is to be developed in order to cope with massive annual increase of trading goods (51 million tons in 1995). Then it will be the third largest container hub-port in the world and handle nine million TEUs per year (Ministry of Maritime and Fisheries, 1996). The proposed harbor site is located at the area of very shallow water of depth less than 5 m in which tidal flat is well developed due to the sediments from the Nakdong river as shown in Figure 1. The harbor basin and approaching channel are to be dredged up to 15 m below the chart datum.

[1]Director, Coastal and Harbor Engineering Research Center, Korea Ocean Research and Development Institute, 1270 Sa-dong, Ansan, Kyeonggi-do, 425-170, Korea
[2]Senior Research Scientist, Coastal and Harbor Engineering Research Center, KORDI, Korea

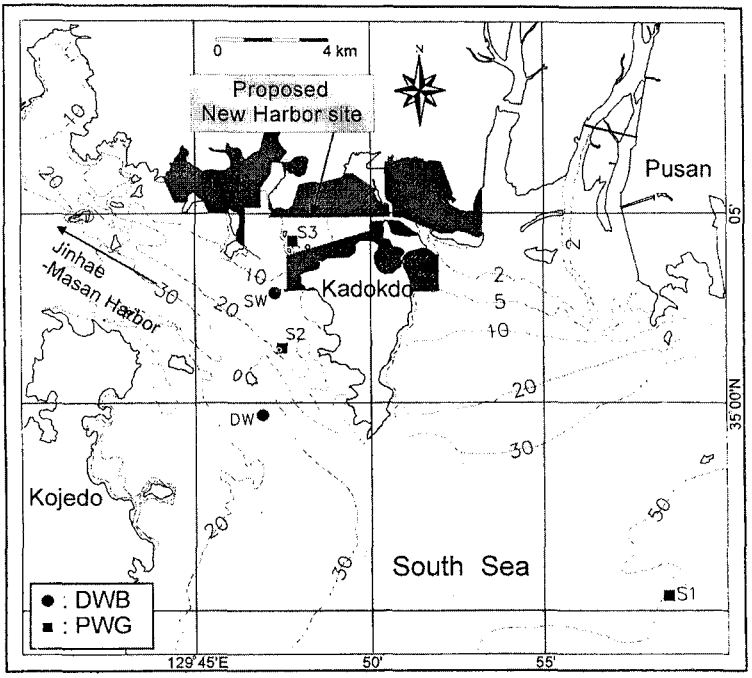

Figure 1. Measuring Stations around Pusan New Harbor.

Even though the site is sheltered from typhoon attacks in summer, both the waves coming from the south and long-period waves bounded in swell waves can penetrate into the harbor. The short-period waves might be strongly influenced by the complex bottom topography, reflections by the irregular coastal line and small islands, and tidal currents. Numerical modeling of the waves propagating through the waterway and penetrating into the harbor is essential for the determination of breakwater alignment which guarantees a harbor tranquility.

The concerned area is so large that it was divided into three regions for the numerical analysis. Short-period wave models were chosen to calculate effectively the irregular wave propagation because of their computational accuracy and efficiency. Hybrid modeling was done for the harbor tranquility analysis in combination with numerical and physical modeling results. The modified Chen's model (Jeong et al., 1996) was used for the long-period harbor oscillation. Extensive field measurements of short- and long-period waves were made in order to analyze wave propagation and statistical characteristics.

Field Measurement and Data Analysis

In order to analyze irregular wave propagations, the relationship between short- and long-period waves and harbor oscillations, extensive field measurements were carried out at five reference stations for three months as shown in Figure 1. Using two Datawell directional waverider buoys, short-period waves were measured at Sts. DW and SW for about 27 min. at every hour. Long-period waves were also measured simultaneously at Sts. S1～S3 for three months at the interval of 5 s.

Directional frequency spectra of the short-period waves were obtained using the maximum entropy method (Kobune and Hashimoto, 1986). After filtering low frequeney waves using the Butterworth high-pass filter, spectral analyses were made for each record of 16,384 data points (about 22.8 hours) using the standard FFT method. The spectrum was obtained by averaging over 64 raw harmonics.

Significant wave heights at St. SW were 40～60% of those at St. DW as shown in Figure 2. But the wave periods are almost the same each other at the two stations. Waves are narrow-banded at St. DW while waves are broad-banded and have non-negligible reflection components at St. SW. More details of the spectral changes can be seen in Figures 3～5. The frequency spectra have a very narrow-banded and single sharp peak, which is a typical shape of swell waves (see Figure 3). Even though swell waves, which have a narrow-banded spectrum, propagated through the waterway of about 8 km in the main direction (SSE), its significant wave height reduced half in average.

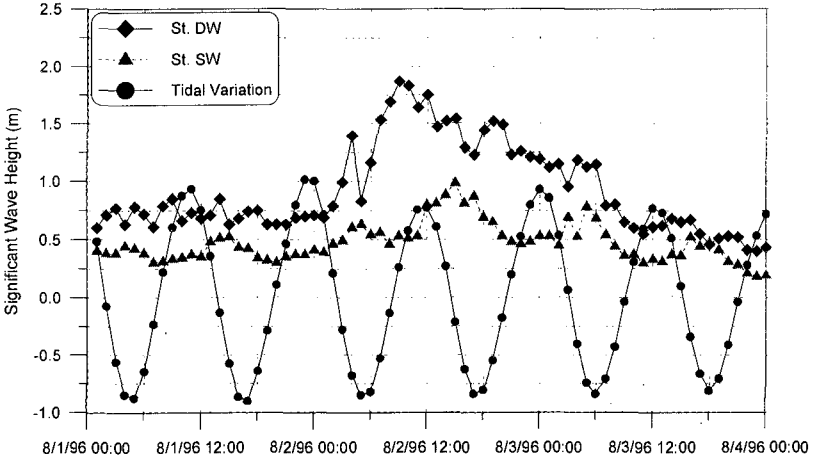

Figure 2. Variation of Significant Wave Height (H_s) at Stations DW and SW.

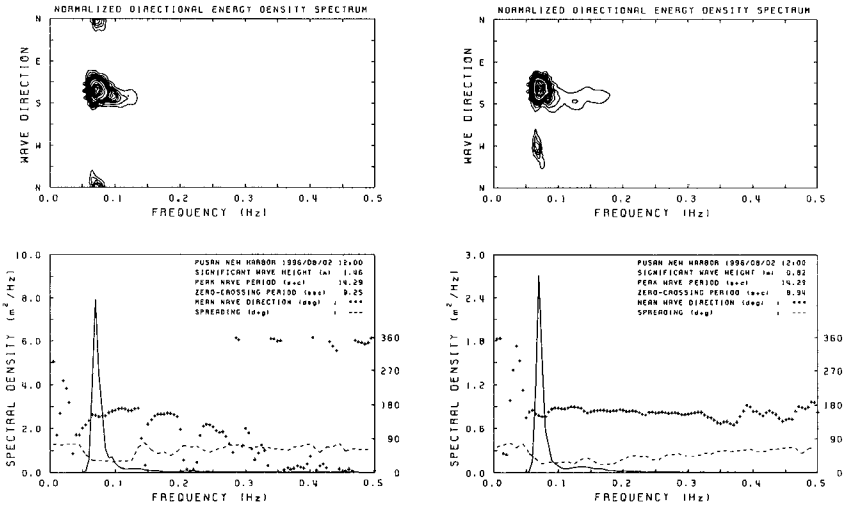

Figure 3. Frequency and Directional Wave Spectra Measured at Stations DW (Left) and SW (Right) (12:00~12:27, Aug. 2, 1996).

When the waves propagated from St. DW to St. SW, they were also affected by the tidal currents. The maximum current speed was about 60 cm/s. At high water (no current) spectral shape change was very small but energy level was decreased by half mainly due to refraction (Figure 3). However, in the following current condition, spectrum became wide in both direction and frequency bands, and wave height decreased by 60%. In the opposing current condition (Figure 4), the spectrum were less broad-banded than one in the following current (Figure 5). Significant wave height at St. DW decreased at St. SW by 40%. Reflected wave components were appeared, which might be due to currents or mooring line

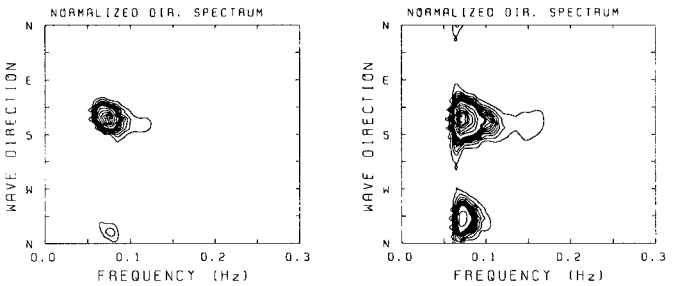

Figure 4. Directional Wave Spectra Measured at Stations DW (Left) and SW (Right) (14:00~14:27, Aug. 2, 1996).

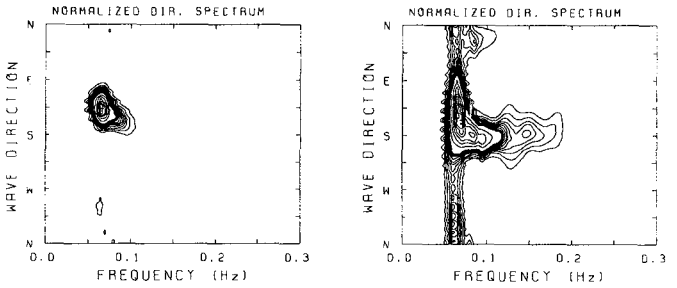

Figure 5. Directional Wave Spectra Measured at Stations DW (Left) and SW (Right) (08:00~08:27, Aug. 2, 1996).

system of the buoy. The mooring line was slightly modified by substituting a part of the polypropylene rope with thin steel wire of 10 m long in order to prevent the rope from cutting by fishing activities.

From this analysis it can be said that the wave height increased about 10% by the opposing current effects. The major factor on the wave transformation through the channel is the refraction of waves due to its bathymetry. To some extent current is responsible. Therefore consideration of directional distribution of the waves is most important for the refraction in the calculation of the wave propagation through the channel.

It is shown that long-period waves were observed at St. S1 and slightly amplified at St. S3. As shown in Figure 6 the spectrum has major peak in the short-period band and bounded waves are in the periods of 60 s to 150 s. The long-period waves were slightly amplified at St. S3 in shallow water area. Those waves might induce the ship moored at the berth to surge and sway because the periods are close to those of resonant modes of the ship and mooring system.

Short-Period Wave Propagation Modeling

As the modeling area of 49 km × 31 km shown in Figure 7 is so large that it was divided into three regions depending on the phenomena of wave transformation and the limitation of wave propagation models. With given deep-water wave height H_s and frequency-directional spectrum $S(f, \theta)$ the irregular waves at the input boundary can be generated (Goda, 1985). Additional wave growth was ignored during their propagation in the modeling area. The wave model was used to calculate 286 discrete spectral components. The total wave height can be obtained by adding each components.

For the calculation of wave propagation in the large offshore region in Figure 7, the RCPWAVE model (Ebersole et al., 1986) was used because of its

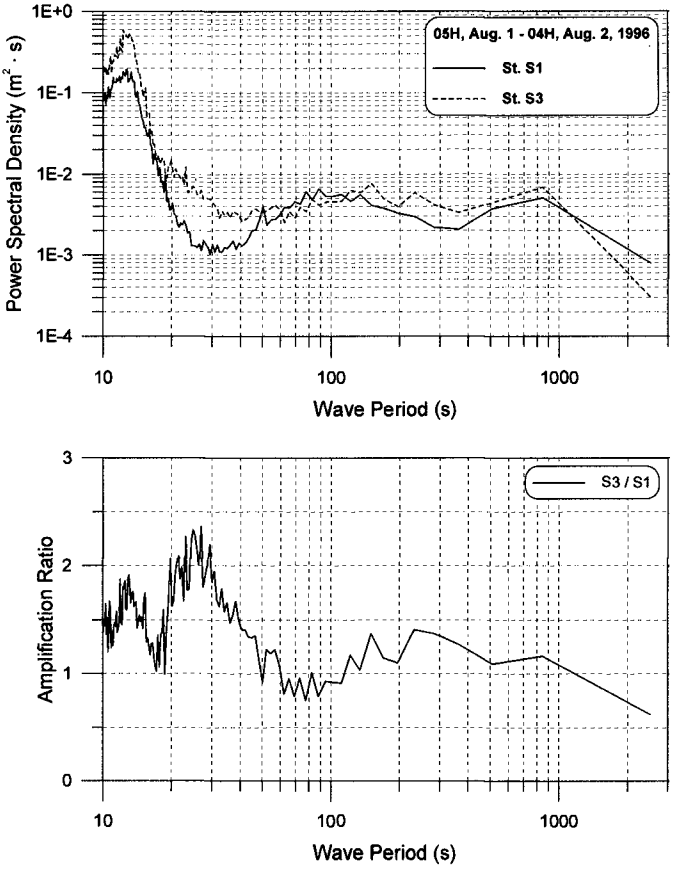

Figure 6. Spectra Obtained from Pressure Data at Sts. S1 and S3 and their Amplification Ratios.

computational efficiency and sufficient accuracy. The area was divided into 195 × 124 rectangular cells and the grid size was 250 m.

Estimation of Shallow-Water Design Wave Height for Breakwater

For the calculation of short-crested wave propagating in the complex coastal waterway (subregion A) and penetrating into the harbor (subregion B), a hyperbolic-type wave model HCORD (eg. Copeland, 1985) based on the mild-slope equation was used.

The HCORD is modified in order to simulate partial wave reflection by

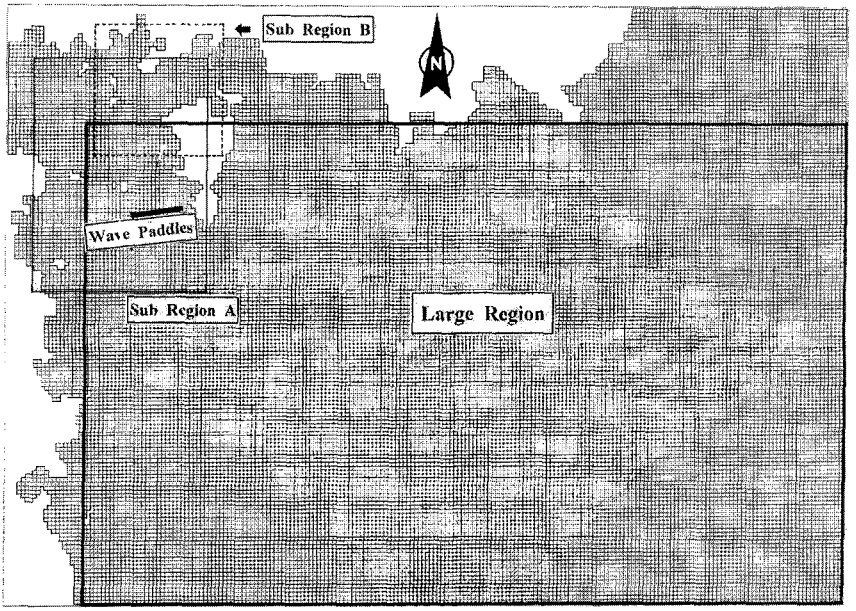

Figure 7. Map Showing Computational Domains for Short-Period Wave Propagation Modeling, and Location of Wave Paddles in the Physical Modelling.

absorbing wave energy normal to the solid boundary. The method is not correct in theory but gives numerical results within 10% error compared with the field data (Jeong et al., 1997).

Input wave conditions were provided at the boundary of the subregion B by the RCPWAVE results. The HCORD was applied to 5 discrete directional components ($\Delta\theta = 22.5^\circ$) with a representative frequency of the waves (Goda, 1985). It is mainly because of the grid size limitation (herein 1/10 wavelength) and computational capacity of engineering workstation. The subregion A was divided into 1,650,000 grids and the size is 10 m$\times$10 m. It took about 6 hours for computing one irregular wave propagation by engineering workstation.

The computation results agree well with the measured data in terms of wave height and direction. They were also compared with the data obtained from three-dimensional hydraulic model tests which used a JONSWAP (multi-frequency) spectrum with one direction. The physical model produced larger waves than the field data and it was tuned with the data. One of the calculation results is shown in Figure 8, where shallow water design wave heights were obtained for various breakwater alignments.

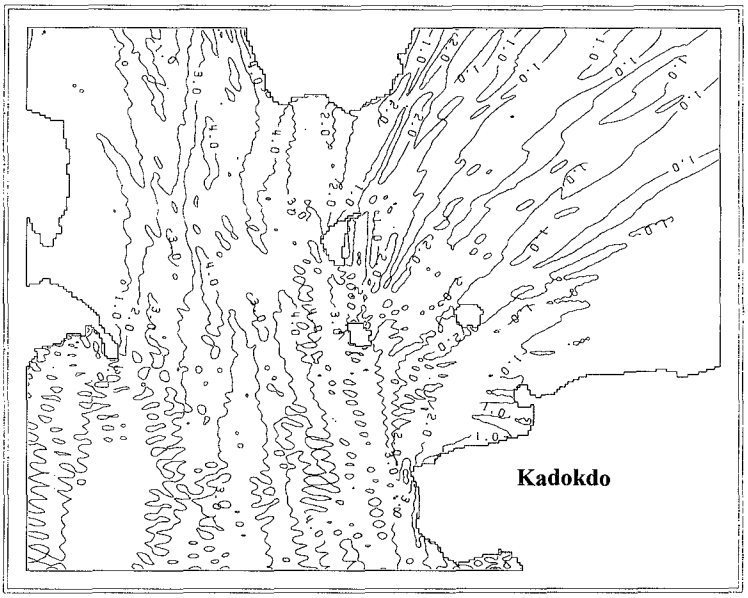

Figure 8. Calculated Significant Wave Heights around Pusan New Harbor (Incident Deep-Water Wave Height = 10 m, Period = 15 s, Direction = S10 ° W, Present State).

Harbor Tranquility Analysis

Harbor tranquility is essentially to reduce motions of ships moored at anchorage or along a wharf. Even though physical factors are involved for the analysis of harbor tranquility (Goda, 1985), a practical approach of wave height evaluation was used for simplicity in the designing stage. Harbor tranquility should be maintained above a certain level of harbor operation rate (95～97.5% in Korea) in order to have feasibility with respect to safety of loading/unloading and operational efficiency. Combined numerical and physical modeling results were used in order to estimate wave height distribution in the harbor. The limiting wave height criteria for loading/unloading were chosen as 0.3 m for small vessel, 0.5 m for general cargo, and 0.3 m for north and south container ship terminals.

Four-year data of six hourly hindcasted waves at deepwater were used, which are in the form of the joint distribution of significant wave height, period and direction. They were further reanalyzed to know the days of exceedance of the significant wave height above certain levels during a year at the container and cargo terminals in the harbor. Among the data set 12 cases of waves were chosen

for the calculation because only limited number of directional wave components can propagate into the harbor. Those waves are in the direction of SSW, S and SSE with periods of 7 s, 9 s, 12 s, and 15 s.

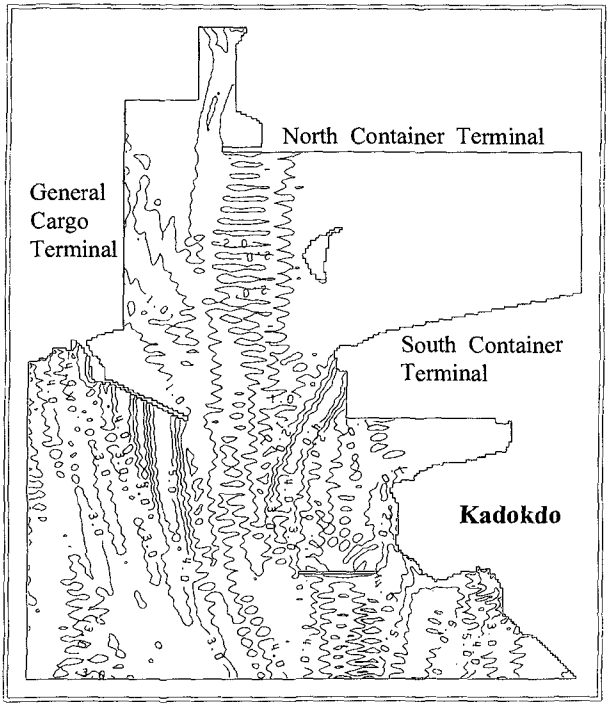

Figure 9. Calculated Wave Heights around Pusan New Harbor (Incident Deep-Water Wave Height = 10.1 m, Period = 14 s, Direction = S, Final Layout).

Two wave models of RCPWAVE and HCORD were used to calculate the wave propagation from deep water (large region) to shallow water (subregions A, B) shown in Figure 7. One of the computational results is shown in Figure 9, which is the wave heights in meter at the final harbor layout for the design wave condition. Hydraulic modeling results were adopted to estimate the wave heights inside the harbor depending on the wave condition at the entrance of the harbor given by HCORD. In order to reduce the strong wave reflection from the vertical wall with right angle to the north end of the general cargo terminal a beach with 1/3 slope was applied. As shown in Table 1 harbor operation rates were

evaluated for small vessel, general cargo, and container terminals. Mean annual rate of the harbor operation is estimated at 98.7 %.

Table 1. Numbers of Waves Exceeding a Criteria and Harbor Operation Rate.

Terminal \ Wave		SSW				S				SSE				Total	Harbor Operation Rate (%)
		7s	9s	12s	15s	7s	9s	12s	15s	7s	9s	12s	15s		
General Cargo		0	32	9	6	5	6	13	11	17	5	2	2	108	98.2
Small Vessel		0	65	13	12	32	16	21	22	30	8	6	9	234	96.0
North Container	W*	0	49	9	9	12	10	17	16	24	7	3	4	160	97.3
	C*	0	8	3	2	0	3	4	1	4	1	0	0	26	99.6
	E*	0	3	1	0	0	0	2	0	1	0	0	0	7	99.9
South Container	W*	0	20	7	3	2	4	8	5	5	3	0	1	58	99.0
	C*	0	6	3	2	1	3	4	1	4	1	0	0	25	99.6
	E*	0	3	1	1	0	1	2	0	2	1	0	0	11	99.8

* W : West, C : Center, E : East part of the Terminal.

Long-Period Wave Modeling

Long-period wave oscillations in a harbor may cause unacceptable vessel motions, excessive mooring forces and fender reactions leading to the breaking of mooring lines and fender system. The typical natural periods of a reasonable harbor or moored vessel are of the order of magnitude of minutes (Nagai et al., 1994). One of the sources that generate the offshore long-period waves of 2~3 minutes is the wave set-down traveling with the wave group velocity.

For the analysis of harbor oscillations a long-period wave model HOMETA was developed, which is similar to Chen (1986)'s HARBD but improved with the extended mild-slope equation (Massel, 1992). Some details of the model equations and calculation method are given in Jeong et al. (1996). The model application to new harbor oscillation is focused herein.

The modified model was applied to calculate the wave amplification due to group bounded and free long waves, which were generated during the storm wave condition and resonated in the new harbor. The calculation area was taken large enough to cover offshore measurement station S1 as shown in Figure 1. The water depth of the far-field area (analytic solution region in HARBD model) is assumed to be constant. Reflection coefficients vary from 0.95 (natural beach) to 0.99 (vertical sea wall) and also vary depending on the magnitude of frequency (i.e., from 0.4 for 15 s to 0.98 for 180 s waves at energy absorbing boundary). The numbers of triangular elements are 22,222 and its size is small enough to

resolve 30 s period wave in the water of 15 m depth. Numerical computation has been made for the 54 component waves of period ranging from 60 s to 1,400 s and comparisons were made with experimental data. The amplification ratio is $\sqrt{S_i(f)/S(f)}$, where $S_i(f)$ is the spectral density at the i-th point in the domain and $S(f)$ at offshore station.

The model was validated with the measured data, and then it was applied to predict harbor amplification by dominant frequency wave components observed at St. S1. Figures 10 and 11 show the amplification ratios at Sts. C12 (south), C13 (center), and C14 (north) of general cargo terminal, and Sts. C26 (west), C28 (center), and C30 (east) of north container terminal. First and second modes of the harbor oscillations are expected to be amplified but their energy levels are so low that they can not generate large water level variation and strong current. However the bounded waves of period from 100 s to 200 s will be amplified at St. C12 in the general cargo terminal. As the waves might be critical for the surging motion of ship sized several 10,000 DWG, this should be considered for the mooring line and fender system in the detail design stage.

Conclusion

From the field measured directional wave spectra and numerical modeling, the directionality of short crested waves is proved to be very important when they

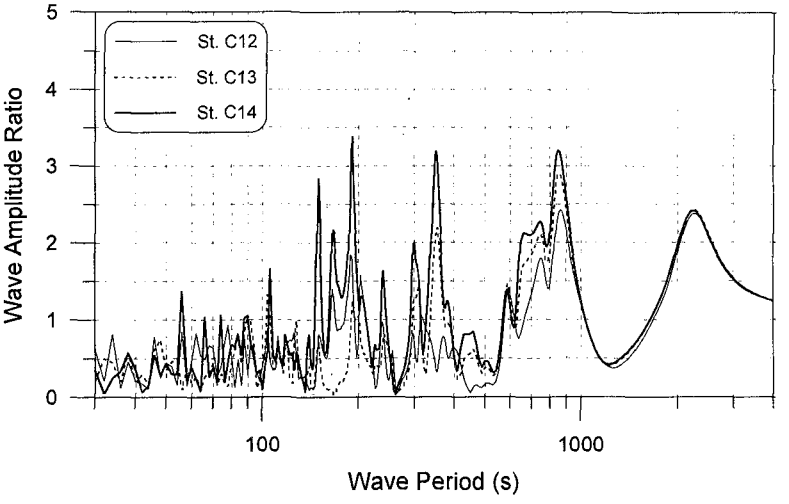

Figure 10. Computed Amplification Ratios for Wave Periods of 30 to 4,000 seconds at Stations C12, C13 and C14 of General Cargo Terminal.

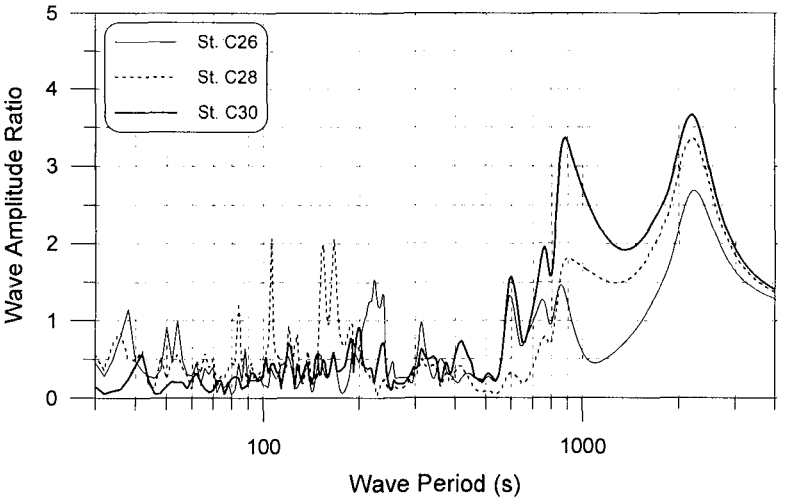

Figure 11. Computed Amplification Ratios for Wave Periods of 30 to 4,000 seconds at Stations C26, C28 and C30 of North Container Terminal.

propagate through the complex coastal waters. Bounded long-period waves were observed in the shallow water area with a small amplification. These might cause horizontal motions of a container ship moored at a berth aligned to the south. Both the modified and extended numerical wave models are accurate enough to simulate the measured wave propagation phenomena. Based on the computational results of short/long-period waves, proper counter-measures were recommended.

Acknowledgements

This work has been financially supported by the Ministry of Maritime and Fisheries, Korea under the Project No. BSPE 97608-00-1052-2. The authors are grateful to their colleagues for collecting the field data, and Mr. S. B. Oh for his collaboration in Hanah Engineering Consultant. We thank prof. Goda for his advices on the harbor tranquility analysis.

References

Chen, H. S. (1986). "Effects of bottom friction and boundary absorption on water wave scattering." *Applied Ocean Research*, 8(2), 99-104.

Copeland, G. J. M. (1985). "A practical alternative to the mild-slope wave equation." *Coastal Engrg.*, 9, 125-149.

Ebersole, B. A., Cialone, A., and Prater, M. D. (1986). "Regional coastal processes numerical modeling system; Report 1, RCPWAVE - A linear wave propagation model for engineering use." *Technical Report CERC-86-4*, WES, US Army Corps of Engineers, Vicksburg, Miss., USA.

Goda, Y. (1985). "Random seas and design of maritime structures." University of Tokyo Press, 323p.

Jeong, W. M., Chae, J. W., Park, W. S., and Jung, K. T. (1996). "Field measurements and numerical modeling of harbor oscillations during storm waves." *Proc. 25th Int. Conf. Coastal Engrg.*, ASCE, 1268-1279.

Jeong, W. M., Lee C., and Chae, J. W. (1997). "Analysis of harbor tranquility in Pohang New Harbor using a hyperbolic model with multi-directional incoming waves." *J. of Korean Society of Coastal and Ocean Engineers*, 9(2), 97-104. (in Korean)

Kobune, K., and Hashimoto, N. (1986). "Estimation of directional spectra from the maximum entropy principle." *Proc. 5th Int. Offshore Mech. and Arctic Engrg. Symp.*, ASME, 1, 80-85.

Massel, S. R. (1992). "Extended refraction-diffraction equation for surfaces waves." *Coastal Engrg.*, 19, 97-126.

Ministry of Maritime and Fisheries. (1996). "Basic planning of Pusan New Harbor Development - Summary." 176p. (in Korean)

Nagai, T., Hashimoto, N., Asai, T., Tobiki, I., Ito, T., Toue, T., Kobayashi, A., and Shibata, T. (1994). "Investigation of the harbor tranquility based on wave group characteristics." *HYDRO-PORT'94*, 203-215.

The Studies for the Resonance of Hwa-Lian Harbour Agitated by Typhoon Waves

Chien-Kee Chang
Chung-Ching Chien
Hsiang-Maw Tzeng

Abstract

Hwa-Lian Harbour is located at the north-eastern coast of Taiwan, where is relatively exposed to the threat of typhoon waves from the Pacific Ocean. In the summer season, harbour resonance caused by typhoon waves which generated at the eastern ocean of the Philippine. In order to obtain a better understanding of the existing problem and find out a feasible solution to improve harbour instability. Typhoon waves measurement, wave characteristics analysis, down-time evaluation for harbour operation, hydraulic model tests are carried out in this program.

Under the action of typhoon waves, the wave spectra show that inside the harbors short period energy component has been damped by breakwater, but the long period energy increased by resonance hundred times. The hydraulic model test can reproduce the prototype phenomena successfully. The result of model tests indicate that by constructing a jetty at the harbour entrance or building a short groin at the corner of terminal #25, the long period wave height amplification agitated by typhoon waves can be eliminated about 50%. The width of harbour basin 800m is about one half of wave length in the basin for period 140sec which occurs the maximum wave amplification.

I . Introduction

Hwa-Lian Harbour is an artificial harbour built on a steep and narrow east coast of Taiwan. More than 4000m long breakwater was constructed to protect the harbour basin against incident waves from the Pacific Ocean. Figure 1 shows the location and layout of the harbour, which has 25 wharves after the fourth stage expansion. In the summer season, harbour resonance may be agitated by typhoon waves which generated at the east of the Philippine. Harbour resonance, may cause down time for harbour operation, or even break the ship mooring lines.

Institute of Harbour Marine Technology(IHMT)
No. 83, Lin-Hai Rd., Wuchi, Taichung District, Taiwan,
Fax. No: 886 04 6571329 , E-mail ckcihmt@ms6.hinet.net

Field investigation has been carried out since 1989, a waverider has been deployed at the outside of the harbour. In 21 June 1990, Typhoon Ofelia formed at the eastern ocean of the Philippine, and moved toward Taiwan in NNW direction. Finally made landfall with the eye of typhoon striking at 17km south of Hwa-Lian Harbour. One hour before landfall, the maximum wave height 20.5m, period 16.0sec was recorded; The corresponding significant wave height and period were 13.9m and 14.1 sec respectively. Time series of wave height and period are plotted as shown in figure 2. Four commercial vessels were berthed at the terminal, two of them escaped for survival when significant wave hight was greater than 4m; the mooring lines of two other ships were broken and the harbour facilities were damaged while wave height increased rapidly.

In November 1992, there were three typhoons Elise, Hunt and Gay. The center of those typhoons were located at SE direction and more than thousand kilometers away from Hwa-Lian. But, the harbour basin was agitated by swells generated by typhoon and berthed ships were forced to leave the harbour for survival.

In order to get a better understanding of the harbour hydraulic environment during the threat of typhoon, an intensive research program had been carried out by the Institute of Harbour and Marine Technology (IHMT) since March 1993. Field investigation, hydraulic model test and numerical computation are included in this research project. This paper present field investigation wave characteristics, down time of harbour operation, model test for different amendment layouts.

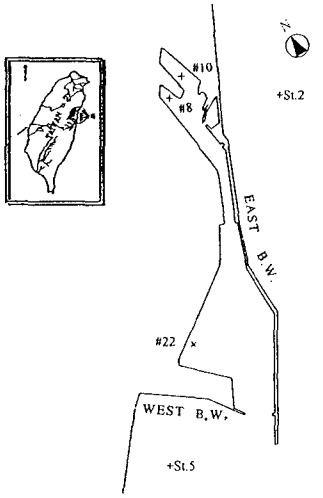

Figure1 Layout of Hwa-Lian Harbour and Location of Instruments

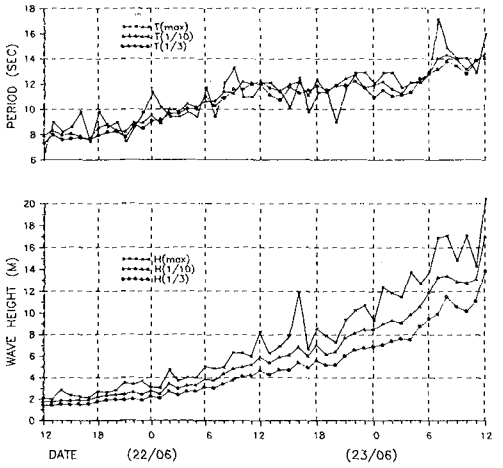

Figure 2 Time Series of Wave Height and Period for Ofelia Typhoon

II. Field Investigation

Figure 1 shows the location of wave stations. The permanent station, St.2 locates at outside of the harbour, a directional wave-rider and current meter have been installed since 1989. At the harbour entrance, St.5 and terminal stations located at water front of terminal #8, #10, #22, four pressure type wave gauges were installed prior to typhoon wave attacked Hwa-Lian Harbour. At the offshore station, St.2 offshore incident waves were recorded 20 min every two hours with sampling rate 1.28Hz. At the harbour basin and entrance stations waves were recorded 34min every hour with 1 Hz sampling rate.

III. Wave Characteristics

The paths of six typhoons which occurred in the summer of 1994 are plotted as shown in figure 3. IHMT had succeeded to obtain wave data inside and outside of the harbour synchronously during Typhoon Tim, Fred and Gladys moved toward Hwa-Lian Harbour. Figure 4 shows time series of wave height variation for the offshore station St.2, the harbour entrance station St.5 and terminal stations #22,#8 ,#10. The sheltering coefficient is defined as the ratio of wave height between the terminal station or the harbour entrance station and the offshore station. The sheltering coefficient and corresponding incident wave direction recorded at St.2 are plotted as shown in the upper and middle diagrams of figure 4. For a specific time, the location of typhoon center, the incident wave height, wave direction and sheltering coefficients at the harbour entrance station St.5, terminal stations #22, #8, #10 are tabulated in table 1.

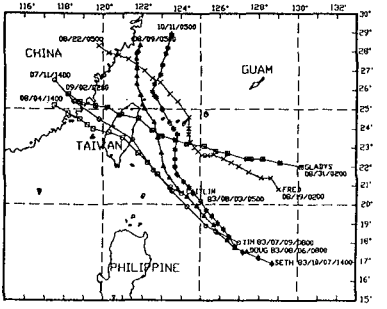

Figure3 Paths of 6 Typhoons Occurred in 1994

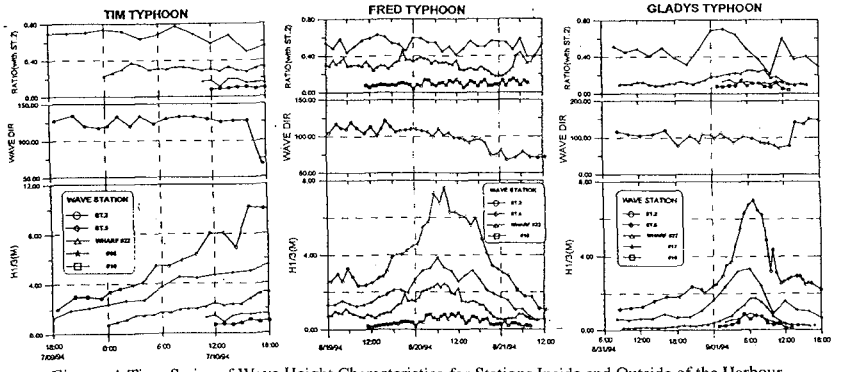

Figure 4 Time Series of Wave Height Characteristics for Stations Inside and Outside of the Harbour

Table 1 indicates that the sheltering coefficients of harbour entrance and terminal stations depend on the incident wave direction and sheltering environment. The incident wave direction have good relationship with the location of the typhoon center. For example, the center of Typhoon Tim was 600km in SE of Hwa-Lian, incident wave came from 125^0, wave height coefficient reduced from 0.6 at the harbour entrance to 0.1 at the inner basin terminal #10; the center of Typhoon Fred located at 100km in ESE and moved toward Hwa-Lian in WNW direction, wave height increased from 2.6m to 4.9m, incident wave direction decreased from 115^0 to 95^0, the sheltering coefficient decreased accordingly. But, when the center of typhoon approached Hwa-Lain, the incident wave direction and sheltering coefficients were changed rapidly by local wind field.

TABLE 1 SUMMARY OF INCIDENT WAVES AND WAVE HITH COEFFICIENT

TYPHOON NAME	TIME (M/D/H)	CENTER LOCATION (KM)	WAVE DIRECTION (O)	INCIDENT WAVE Hs (m)	SHELTERING OEFFICIENT St.5	#22	#8	#10	(TYPHOON CENTER) NOTE
TIM	07/09/ 18:00	SE (600)	125	2.0	0.65	0.33	0.17	0.1	MOVED NW
	07/10/ 14:00	SE (200)	130	7.0	0.55	0.32	0.15	0.1	BEFORE LANDFALL
	07/10/ 16:00	SE (140)	130	10.2	0.49	0.27	0.15	0.1	BEFORE LANDFALL
FRED	08/19/ 00:00	ESE (1000)	115	2.6	0.52	0.30	-	0.1	MOVED WNW
	08/20/ 18:40	E (200)	95	4.9	-	0.19	-	0.1	MOVED NNE
	08/21/ 02:00	ENE (250)	75	2.9	0.45	0.38	-	0.11	MOVED NNE
GLADYS	08/31/ 08:00	ESE (700)	115	1.2	0.45	0.1	-	-	MOVED WNW
	09/01/ 00:00	ESE (300)	100	2.4	0.67	0.2	-	0.09	BEFORE MOVED TOWARD H.L
	09/01/10:0 0	E (60)	80	4.4	0.36	0.18	-	0.13	BEFORE LANDFALL
	09/01/ 14:00	WNW (100)	145	2.9	0.35	0.1	-	-	AFTER LANDFALL, CHANGE WIND DIR

Energy spectra for waves recorded at the permanent station St.2 and terminal stations #22, #8 and #10 are plotted as shown in figure 5. After the sheltering of the breakwater, the short period wave energy measured at terminal stations were reduced tremendously. The degree of energy density reduction depends on the sheltering condition. At the outer basin the energy density ratio between terminal #22 and incident wave is about 1/10; at the inner basin the ratio between #8 or #10 and incident wave decreases further to 1/100. On the other hand, long period waves from 140sec to 160sec recorded in the harbour basin, the energy density were amplified hundred folds. The detail time series water surface for various wave stations are plotted in figure 6, which shows water surface recorded at harbour stations have rather long periodic motion in comparison with that of incoming wave recorded at St.2.

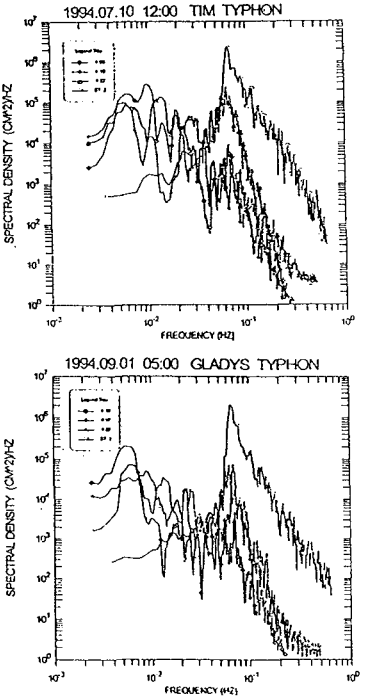

Figure5 Energy Spectra for Stations Inside and Outside of the Harbour

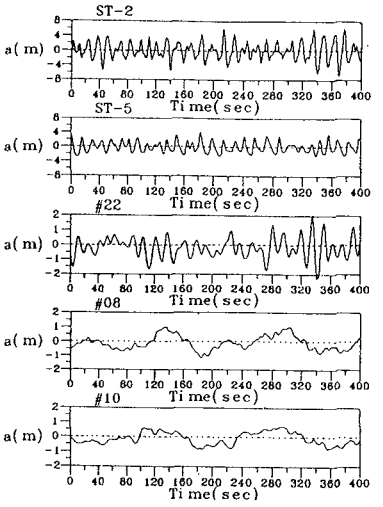

Figure6 Detail Time Serces of Water Surface Motion for Stations Inside and Outside of the Harbour

IV Down-time Evaluation

According to the berthing records of Hwa-Lian Harbour indicate that in the summer season, down time for harbour operation due to the action of typhoon wave has occurred at least once every year since 1985. Based on the status of berthing conditions provided by Hwa-Lian Harbour Bureau from 1990 and the corresponding paths of the typhoon, as shown in figure 7, issued by the Central Weather Bureau, table 2 shows the summary of typhoon generated swells that made harbour instability and caused down time for harbour operation.

Based on the advance typhoon path, the leaving location which listed in column 4 of table 2, is defined as the location of typhoon, while berthing ship commences to leave the harbour due to agitation of swells. By assuming the propagation velocity of swill is 50 km/hr, the initial time and location were estimated as shown in column 5 of table 2. The initial time and location are defined as the time and location that typhoon generated swells which might arrive the harbour and force ships to leave the harbour for safety. The analysis results of initial and leaving locations are plotted as shown in figure 8. The swell generated at the initial location arrives the harbour and causes ships to leave the harbour for survival, while the center of typhoon moves from initial location to leaving location.

Table2 Summary Of Down Time For Berthing Conditions Corresponding Typhoon Status

(1) DATE (YYMMDD)	(2) TYPHOON NAME	(3) DOWNTIME OF BERTHING CONDITION: TIME (DHR)	WHARF NUM	SHIP TONNAGE (DWT)	(4) LEAVING LOCATION (°,°N/E)	(5) INITIAL CONDITION: TIME	LOCATION	DISTANCE (KM)
9005	OPELIA	29/13:30 13:30	#19 #10	9,000 7,000	19°N 125°E	24/20:00	17.6° 134°E	700
9008	BECKY	30/11:30 14:00	#19 #6	12,000 9,000	18.5 19.5	30/00:00	19.5° 125.5	650
9008	YANCY	1706:30 17:30	#14 #17	9,000 8,000	20° 17.5	17/18:00	19.6° 126.6	900
9009	DOT	09/03:01	#4	3,000	21.5 12.4	09/06:00	18.6° 119.6	1050
9010	RUTH	29*** 30***	#18 #15 #14	19,900 9,000 9,000	18.5 12.5	30/06:00	17.6° 117.6	950
9009	TED	21*** 22***	#16 #19 #11	19,900 9,000 9,900	19.5 12.5	20/12:00	18.6° 120.6	850
9011	ELSIE	09/13:30 18:30 20:30	#17 #6 #20 #19	- - 35,000 77,000	20.5 13.5	09/12:00	16.5° 119.6	1100
9011	HUNT	20/15:00 19:00	#19 #25	- -	20.5 13.5	19/06:00	15.5 119.6	1450
9011	GAY	26/04:00 10:00	#11 #10 #20	- 7,000	18.5 13.5	26/06:00	17.6 119.5	2000
9106	KORYN	20***	#6 #4 #14 #10 #18 #8 #11	7,000 19,900 9,000 8,000 7,000 9,000	EAST 12°	25/06:00	15.1 126.1	1050
9108	TASHA	15***	#19	31,200	19.0 17.0	19/14:00	17.8 134.3	920
9108	YANCY	01***	#19 #15 #20 #5 #10 #11	30,000 11,000 30,000 9,000 19,000 9,900	20.5 12.0 0.0	31/12:00	20.7 126.5	840
9109	ABE	11/23:01	#19	30,000	21.0 12.3 0.0	11/14:00	20.5 122.8	920
9407	TIM	06/23:30 07:01 08:30	#25 #23 #17	9,000 25,000 14,000	19.0 13.3 0.0	06/19:01	18.0 117.0	850
9408	CAITLIN	17/06:30 17:20	#24 #10	9,000 7,600	22.5 12.0 0.0	18/06:00	20.6 118.0	700
9408	DOUG	09/15:30 16:01 17:01	#23 #22 #24	13,000 13,000 39,000	18.5 13.0 0.0	16/23:00	17.2 120.1	950
9408	FRED	19/17:00 17:30 17:40 18:30	#6 #19 #20 #24	3,970 12,000 9,900 39,000	22.5 12.0 0.0	19/22:00	20.8 120.1	650
9408	GLADYS	30/18:01 19:40 21:31	#10 #25 #3	19,900 36,000 3,970	22.5 17.5 0.0	30/21:00	23.7 119.5	1000
9410	SETH	06/03:01 08:00	#6 #22	3,970 9,900	19.5 12.9 0.0	07/00:00	16.5 120.5	1150

NOTE: /** TIME UNKNOW

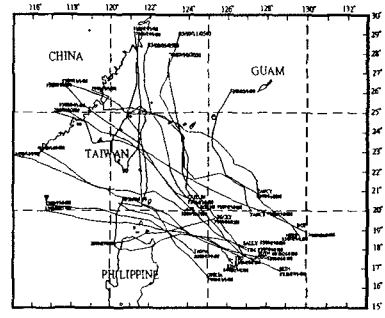

Figure7 The Paths of Typhoon that Have Caused Down Time for Harbour Operation Since 1990

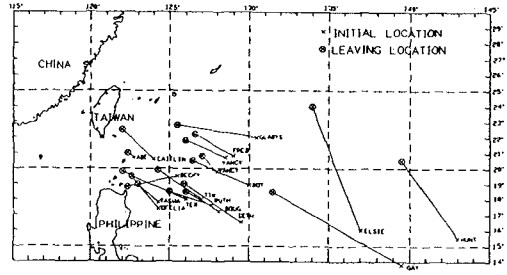

Figure8 The Initial and Leaving Locations of Typhoon that Caused Down-Time For Harbour Operation

IV Down-time Evaluation

According to the berthing records of Hwa-Lian Harbour indicate that in the summer season, down time for harbour operation due to the action of typhoon wave has occurred at least once every year since 1985. Based on the status of berthing conditions provided by Hwa-Lian Harbour Bureau from 1990 and the corresponding paths of the typhoon, as shown in figure 7, issued by the Central Weather Bureau, table 2 shows the summary of typhoon generated swells that made harbour instability and caused down time for harbour operation.

Based on the advance typhoon path, the leaving location which listed in column 4 of table 2, is defined as the location of typhoon, while berthing ship commences to leave the harbour due to agitation of swells. By assuming the propagation velocity of swill is 50 km/hr, the initial time and location were estimated as shown in column 5 of table 2. The initial time and location are defined as the time and location that typhoon generated swells which might arrive the harbour and force ships to leave the harbour for safety. The analysis results of initial and leaving locations are plotted as shown in figure 8. The swell generated at the initial location arrives the harbour and causes ships to leave the harbour for survival, while the center of typhoon moves from initial location to leaving location.

V. Model Tests

The main purpose of model test is to find out a feasible amendment layout to eliminate long period wave energy inside the basin amplified by harbour resonance. The optimum layout will be proposed for the improvement of Hwa-Lian Harbour in the future project.

Model tests were conducted in a 62m long and 57m wide wave basin. Regular and irregular wave generator, wave gauges and data acquisition system have been equipped in the laboratory. Hwa-Lian Harbour was built in the basin by using model scale 1:150. Both regular and irregular waves were simulated in the model tests. In the primary stage, 14 layouts were tested by regular wave for qualitative analysis. Prototype incident wave height 0.75m, and wave period ranges from 10sec to 180sec were reproduced in the model tests. The existing and three amended layouts as shown in figure 9 were selected for further tests by irregular waves. The spectra of Tim typhoon waves recorded at offshore of Hwa-Lian Harbour and JONSWAP spectra were simulated in irregular wave tests.

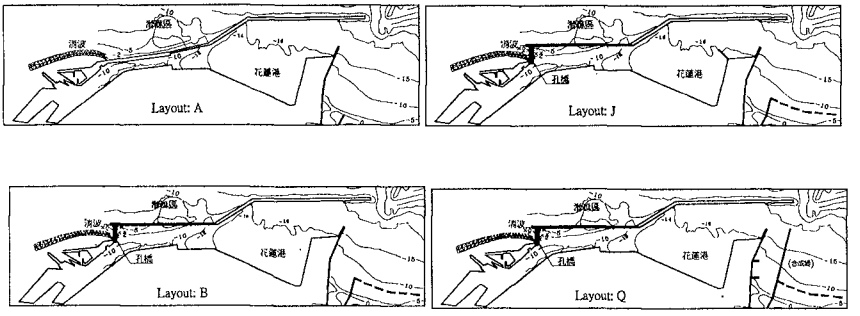

Figure 9 Layout of the Model Tests

Wave data in front of the wave paddle (incident wave) , harbour entrance and inside the basin were recorded at 30 locations in the model tests to evaluate wave disturbance of the harbour protected by breakwater. Figure 10 and 11 show wave height ratio versus incident wave period at terminal #22 of the outer basin and terminal #8 of the inner basin for primary 12 layouts. The wave height ratio is defined as the ratio of wave height between a specific location at the basin and offshore incident station. Figure12 and 13 show the detail wave height ratio of terminal #22 and #8 for the existing and three amendment layouts. The results of the existing layout indicate that the short period wave is sheltered by breakwater, the wave height ratio at #22 of the outer basin is about 0.4 and the ratio at #8 of the inner basin in less than 0.15. But for the 140sec long period wave height ratio, the amplification factor is more than 3.4 at #22 and about 2.0 at #8. The short period wave height ratios of outer and inner basins obtained in model tests and measured in field investigation are quite consistence in case of the same direction of incident wave.

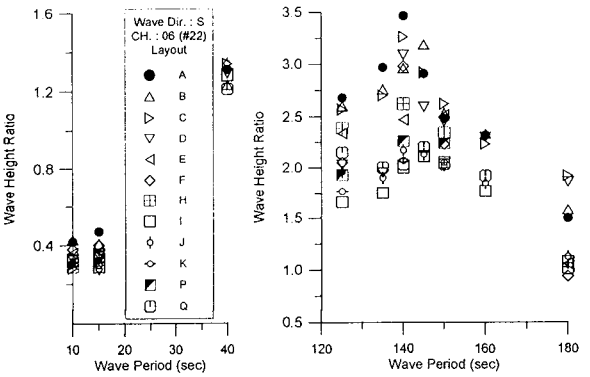

Figure 10 Wave Height Ratio of the Terminal #22 for 12 Layouts

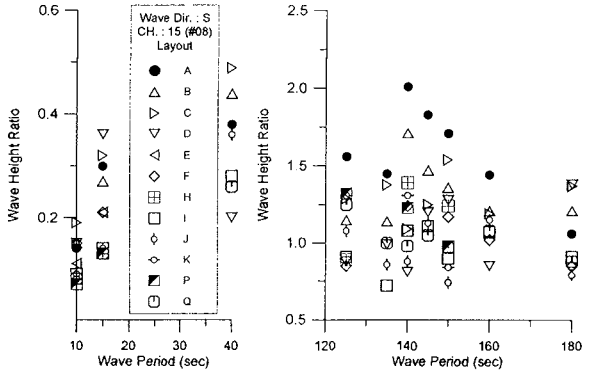

Figure 11 Wave Height Ratio of the Terminal #8 for 12 Layouts

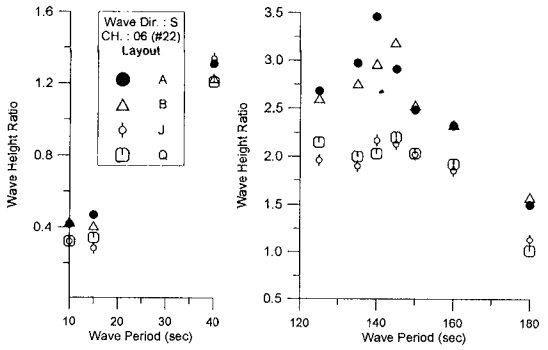

Figure 12 The Detail Wave Height Ratio of the Terminal #22 for 4 Layouts

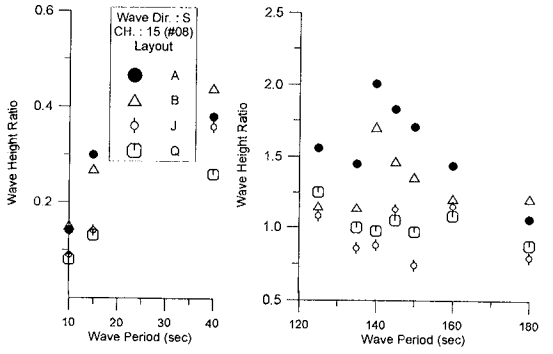

Figure 13 The Detail Wave Height Ratio of the Terminal #8 for 4 Layouts

The amendment layout B, rebuilds the old portion of the eastern breakwater, installs perforated rubble breakwater at the north end. This layout doesn't improve the short period wave height ratio of the outer basin. But, the ratio of the inner basin decreased, because some portion of incident wave energy of inner basin transmits through perforated breakwater. Layout B does not change the geometry of the outer basin, the resonance mechanism of the long period wave is existing. The long period wave height amplification remains the same scale as the existing layout. Layout J, a short groin is constructed at the turning corner of the terminal #25 which located beside the navigation channel. The mode of wave resonance is broken by the interaction of groin and long period wave height in the basin is eliminated by the disturbance of refraction waves. Layout Q, builds a jetty at the harbour entrance and eastern breakwater remains the same as layout B. It is obvious that the jetty and the west breakwater forms as a resonant basin at the harbour entrance, the incident long period wave energy is damped by the transverse waves in the basin. The test results show that the long period wave height amplification due to resonance decreases more than 40%. The short period wave height ratio of terminals #22 and #8 for layout J and Q are smaller in comparison with those of layout A and B.

Based on 4096 sampling data recorded at each run of model test (about 205 seconds), wave spectra were analyzed by using FFT method. The wave spectra of four layouts are plotted as shown in figure 14. In order to find out the difference of three wave spectra, which measured at incident location, terminal #22 and terminal #8, were plotted in a figure for the same layout. By simulating waves recorded in Tim typhoon, the spectrum has peak period 1.25sec in model or 15.3sec in prototype and no extraordinary long period wave energy component. The test results indicate that the short period wave energy density at terminal #22 and at terminal #8 is reduced by the sheltering of breakwater. There are not much difference for various layouts in the short period wave.

The spectra show that long period 11.8sec and 5.6sec in model or 144sec and 67sec respectively in prototype, the energy density at the inner and outer basins are enlarged by harbour resonance. Long wave period 144sec is quite consistency with regular wave period 140sec that caused the maximum wave amplification. Low frequency energy density at terminal #22 and #8 amplifies about 30 times for layout A and B. The shape of spectra for layout J and Q are quite similar as those of layout A and B, but low frequency energy density becomes smaller. In order to get a better quantitative understanding, the frequency is divided into two intervals, low frequency band between 0.06Hz and 0.3Hz, and main frequency band between 0.8Hz and 1.2Hz. There are corresponding to prototype wave period 204.1 sec to 40.8 sec for long period wave band and 15.3sec to 10.2sec for main period wave band. The sum of wave energy for low frequency and main frequency bands are tabulated in Table 3 and plotted as shown in figure15 and figure16. In all layouts, long period wave energy component contained in the incident wave measured at offshore (ch:09) is very limited. But, the terminal #22 and #8 in the harbour basin of layout A , long period wave energy component enlarged by harbour resonance. The reduction of long period wave energy component is not significant for layout B , that is similar as regular wave tests. Layout J and Q, long period wave energy component inside the basin gets much better, especially layout Q. On the other hand, figure16 shows the main period wave energy component. The incident wave obtained at offshore station is much higher than those measured at terminal #22 and #8 in the basin.

Table 3 shows the wave height ratio computed by the view point that wave height is the square root of wave energy. Because the long period wave energy for irregular wave is the sum of energy in the range of 40 sec and 204sec. Hence, the wave height ratio listed in table 3 can be considered as the average of the wave height ratio for the same period of regular wave tests. The result of irregular wave tests are quite consistency with those of regular wave tests as show in figure 12 and 13.

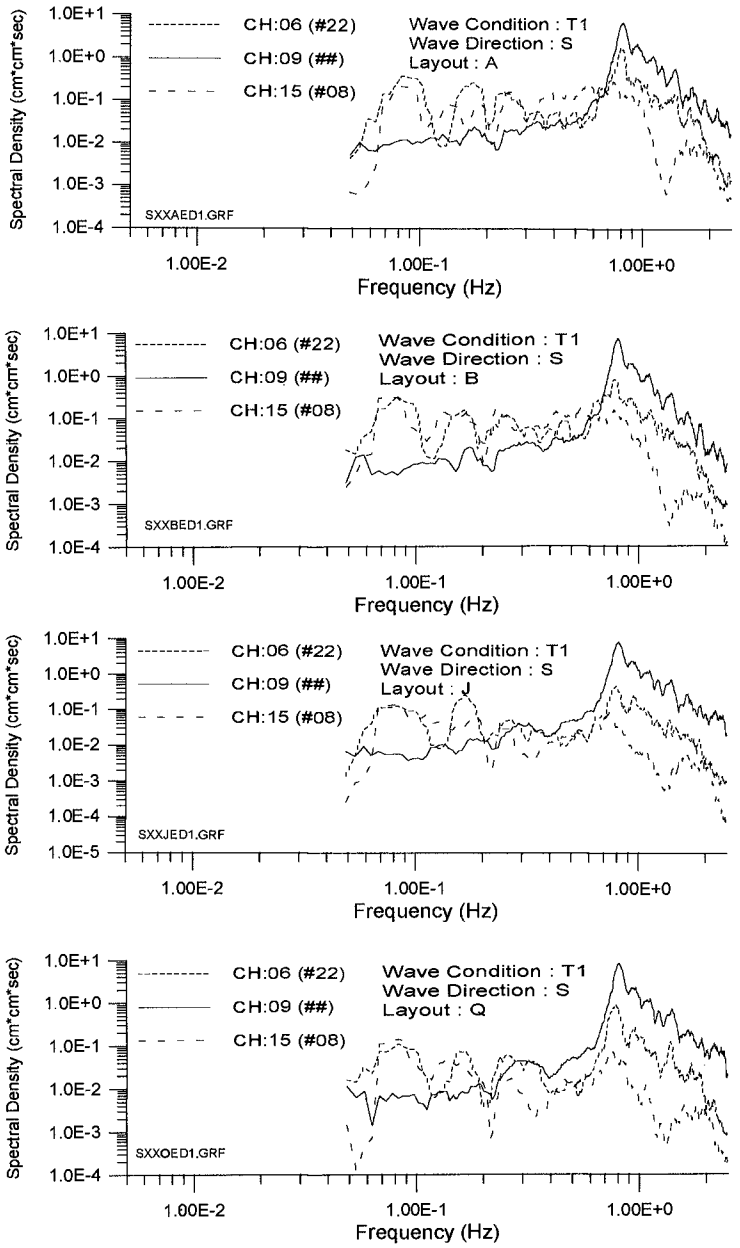

Figure 14 Wave Spectra Measured at Incident Location (# #), Terminal #22 and #8 for Different Layout in Model Tests

Table3 Wave Energy and Wave Height Ratio of Long Period and Main Period Wave Bands for Different Layouts

	Energy of Long Period Wave Band (cm×cm)				Energy of Main Period Wave Band (cm×cm)			
Layout	A	B	J	Q	A	B	J	Q
Offshore Incident	0.71	0.60	0.68	0.70	152.5	143.1	181.0	170.0
Terminal #22	6.50 (3.0)	4.53 (2.8)	3.38 (2.2)	2.00 (1.7)	28.1 (0.43)	15.3 (0.33)	11.0 (0.25)	13.6 (0.28)
Terminal #8	3.91 (2.3)	4.83 (2.8)	2.05 (1.7)	1.51 (1.5)	5.5 (0.19)	3.5 (0.16)	0.9 (0.07)	1.1 (0.08)

Note: ( ) the wave height ratio is defined as the square root of (terminal wave energy /incident wave energy).

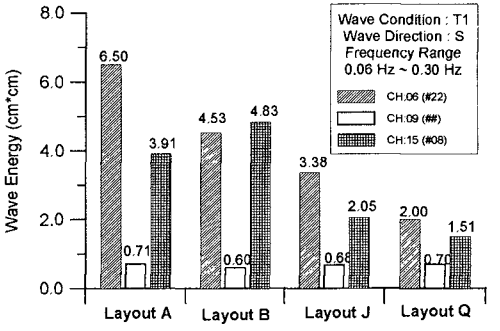

Figure 15 Wave Energy of Low Frequency Band Inside and Outside the Harbour for Different Layouts

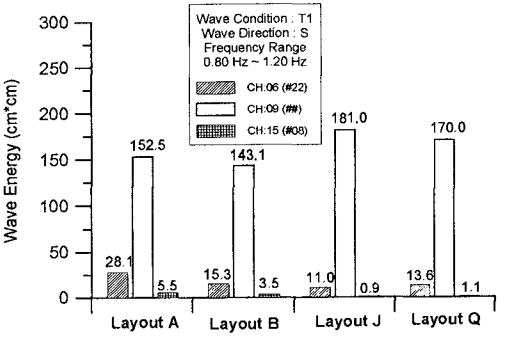

Figure 16 Wave Energy of Main Frequency Band Inside and Outside the Harbour for Different Layouts

VI. Discussion

1. The spectra of the offshore permanent station shows no extraordinary long period wave energy component. Because the accelerator of wave rider can not detect low frequency motion. A pressure type wave gauge had been installed at the offshore station at typhoon season in 1996. The spectrum of waves measured by pressure type wave gauge indicates that typhoon wave has long period energy component at the offshore station.

2. Long period wave energy amplified by harbour resonance can be reproduced in hydraulic model by using either regular wave or irregular wave. The amplification ratio in prototype is larger than that in model, because the friction loss at small scale physical model is larger than in the field.

3. The shape of the outer basin is like a triangle, the maximum width is about 800m which equals a half wave length of period 140sec approximately. Hence the harbour basin is resonated in transverse direction which is consistent with the video records of ship motion under the action of typhoon wave and the visual aspect in the model test. Layout B doesn't change the harbour geometry, the resonance amplitude remains the same order of magnitude. Layout J constructs a short groin at the basin or layout builds a jetty at the harbour entrance, the long period wave energy can be eliminated by breaking the resonance mode or disturbing the incident waves.

4. Down-time harbour operation due to the berthing ship motion enlarged by the agitation of long period harbour resonance. Although, layout J and Q can reduce the long period wave energy, but it still exist in the basin. It is necessary to perform ship motion test to evaluate down-time harbour operation for various feasible layouts.

5. By taking ship maneuvering and sediment at the entrance into consideration, at this stage layout Q is proposed for the harbour improvement in the future.

Reference

1. Chang, Chien-Kee, Tzeng, Hsiang-Maw Preliminary Investigation for Instability of Hwa-Lian Harbour Basin, Proc. 15th Conf. On Ocean Engineering, Tainan, Taiwan, Nov. 1993.(Chinese)

2. Chang, Chien-Kee Investigation on the Disaster of Typhoons in 1995, IHMT Special Report No. 99, Dec.1994. (Chinese)

3. Chang Chien-Kee, Tzeng Hsiang-Maw Long-Period Wave and Associated Agitation in Harbour Caused by Typhoon Waves. Proc. Fourth International Conference on Coastal and Port Engineering in Developing Countries, Rio de Janeiro, Brazil, 1995.

4. Chang, Chien-Kee Final Report for the Studies of Hwa-Lian Harbour Improvement, IHMT Special Report No.131, Dec. 1996.(Chinese)

5. Chien, Chung-Ching Tzeng, Hsiang-Maw Oceanographic Investigation Around Taiwan, IHMT Yearly Report, June, 1993.(Chinese)

6. Chien Chung-Ching etal Wave Sheltering Test for the Amendment Layout of Breakwater of Hwa-Lian Harbour, IHMT Special Report No.152 Nov. 1997.

APPLICATION OF MATHEMATICAL MODELING IN OPTIMIZING LAYOUT OF A LARGE INDUSTRIAL FISHERY HARBOUR

P.P. Gunaratna,[1] Member, ASCE, P. Justesen[2], D.S. Abeysirigunawardena[3], and H-J, Scheffer[4]

Abstract

Mathematical modelling of nearshore oceanographic conditions was carried out, in connection with a large industrial fishery harbour planned to be implemented in a coastal stretch protected by two reefal systems, on the western coast of Sri Lanka. MIKE 21, a two dimensional mathematical modelling system with a wide range of coastal engineering applications, and LITPACK, a one dimensional coastal processes modelling system, were extensively used in this study. The major features of modelling were the successful simulation of wave transmission over reefs and wave overtopping mass flux induced currents behind the innermost reef.

The validated model under existing conditions was used to optimise the harbour layout with safe navigational access, acceptable wave agitation within the basin and adequate sediment by-pass capacity at the entrance. The wave and other hydrodynamic parameters for the economical design of harbour breakwaters were also obtained. A well calibrated hydrodynamic model covering most of the western coast of Sri Lanka also evolved as a by-product of this study.

Introduction

Dikkowita is a small coastal town located on the western coast of Sri Lanka, 6 km north of the capital city, Colombo (Figure 1.). The coastal environment around Dikkowita is characterised by the presence of two distinct sandstone reefal systems (Figure 1.). The outer reef, known as the "Offshore Reef", is located at an average distance of 1 km from the

[1]Senior Research Engineer, Lanka Hydraulic Institute Ltd., John Rodrigo Mawatha, Katubedda, Moratuwa, Sri Lanka.
[2] Head, Hydro Informatics Technologies, Danish Hydraulic Institute, Agern Alle 5, DK-2970 Hørsholm, Denmark.
[3] Research Engineer, Lanka Hydraulic Institute Ltd., John Rodrigo Mawatha, Katubedda, Moratuwa, Sri Lanka.
[4]Coastal Processes Expert, ADB-Sri Lanka Fisheries Sector Development Project, 22 Tickel Road, Colombo 8, Sri Lanka.

coastline, about 2.5 m to 3 m below mean sea level (MSL). This reef has a significant gap in it fronting Dikkowita. The inner reef, commonly known as the "Secondary Reef", is generally located under or in front of the beach. This reef has got disconnected from the coastline south of Dikkowita and again merges with the coastline further northwards, forming a kind of a narrow basin. The maximum distance between the coastline and the secondary reef within this basin is about 200 m. The level of the secondary reef is quite variable consisting of exposed segments above sea level, and certain submerged segments as much as 4 m below MSL. The dual protection provided by these two reefal systems has made Dikkowita an attractive site for locating a coastal fishery harbour.

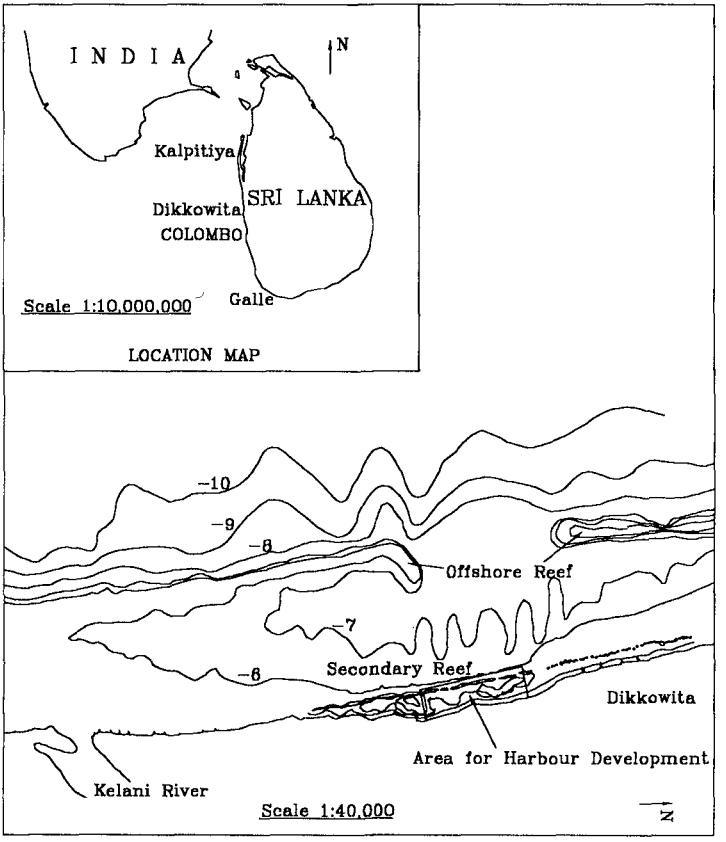

Figure 1. Coastal Environment Around Dikkowita, Sri Lanka

About 2 km south of Dikkowita lies the outfall of the Kelani River, which is the major source of sediment supply to a long coastal stretch northward of it. However, due to intensive sand mining taking place in the lower reaches, the sand supply from the river to the downdrift coasts has declined. Based on the findings of a National Sand Study (Delft Hydraulics and Netherlands Economic Institute, 1992) the present rate of sand supply may be estimated to be around 100,000 m^3/year compared to 400,000 m^3/year in 1961. This has led to severe erosion of down drift beaches and has required the implementation of coast protection measures.

Under the Asian Development Bank (ADB) assisted Sri Lanka Fisheries Sector Development Project, the site at Dikkowita was identified as having the potential to develop an industrial fishery harbour, which will cater to large deep sea fishing vessels. The technical feasibility study in this connection was carried out by Lanka Hydraulic Institute Ltd. (LHI), Sri Lanka in association with the Danish Hydraulic Institute (DHI) and PortConsult Consulting Engineers, Denmark. Coastal Engineering Investigations formed a major component of this feasibility study.

Mathematical Modelling

Most of the coastal engineering aspects were addressed through the application of MIKE 21 and LITPACK mathematical models developed at the Danish Hydraulic Institute (DHI), Denmark. In addition, certain numerical desk calculations were carried out to supplement the model computations. A substantial volume of data acquired through a dedicated field investigation campaign (LHI et al., 1996) and from previous studies (Behnsen, 1994 and LHI, 1994), was used in the setting up and validation of the mathematical models.

MIKE 21 is a two dimensional modelling system with a wide range of coastal engineering applications. A variety of computational modules are available within MIKE 21 for simulating hydrodynamics, wave dynamics, sediment transport, advection-dispersion processes, etc. LITPACK is a one dimensional coastal processes modelling system mainly used for computation of sediment transport and associated beach profile and coastline changes.

Offshore Wave Climate and Extreme Waves

The offshore wave climate within the study area is characterised by the presence of year round swell waves, approaching from the narrow directional band 210° - 230° north and locally generated sea waves strongly influenced by the south west monsoonal winds. Based on findings of a wave study for the south west coast of Sri Lanka (Scheffer et. al., 1994) and on-site measurements (LHI, 1994), the wave climate representative around 15m water depth could be established. The average significant wave height of swell waves was found to be 0.9 m during the south west monsoon season (May to September) and 0.5m outside this period. The sea waves were seen to dominate during the south west monsoon season with an average significant wave height of 1.5 m. Apart from this, certain extreme occurrences of sea waves due to local depressional storms, with average significant wave height exceeding 3.5 m have been recorded during the intermonsoon period October to November.

The extreme occurrences of wave heights around 15m water depth were established through extrapolation of recorded significant wave heights. Several probability distributions (Fischer and Tippet, Weibull etc.) were fitted and monthly maximum wave heights as well as the actual distribution of wave heights were considered in arriving at the final estimates of extreme waves. The significant wave height (H_{m0}) and the mean wave period (T_{02}) of 100 year return period wave were determined as 5.47 m and 7.8 sec, respectively. The corresponding values established for 1 year return period wave were 2.82 m and 6.3 sec, respectively.

Nearshore Wave Propagation Modelling

Nearshore wave propagation modelling was carried out to establish spatial variation of wave climate within the reefal system for wave driven littoral current computations as well as for establishing wave parameters for the design of breakwater structures. For this purpose, two wave modules within MIKE 21 (NSW - Nearshore Spectral Wave and PMS - Parabolic Mild Slope) were used. Both these wave modules are based on an irregular and directional description of wave field and considers shoaling, refraction and energy dissipation due to wave breaking and bottom friction. The PMS module has the added capability to account for diffraction effects caused by coastal structures and bathymetric features.

A nested set up of NSW and PMS modules was employed with the NSW model extending offshore up to an average water depth of 15m, and the PMS model contained within it, with its offshore boundary positioned some distance outside the offshore reef. Both models were oriented with offshore boundary parallel to the general direction of shoreline in the study area (255° north). In the NSW model, the grid spacings used were 50 m in the direction parallel to offshore boundary and 10 m in the perpendicular direction. In the PMS model a 5m grid resolution was used in both directions.

The model computations with respect to wave transmission over the offshore and secondary reefs were verified using simultaneous wave recordings within and outside the reefal system. The model simulations were seen to over predict wave heights inshore of the offshore reef when compared with actual wave recordings, for moderate offshore wave heights. This discrepancy was seen to get reduced with increasing offshore wave height. The model parameters which were used to control wave transmission over the offshore reef were those which govern wave breaking.

In MIKE 21, wave breaking is governed by a maximum allowable wave height (H_m) given by:

$$H_m = \gamma_1 k^{-1} \tanh \frac{\gamma_2 kd}{\gamma_1} \quad (1)$$

where, k is the wave number, d is the water depth and γ_1 and γ_2 are wave breaking parameters. The parameter γ_1 which control breaking due to wave steepness was set to 1.0 (Battjes and Jensen, 1978) and γ_2 which controls water depth limited wave breaking was set to 0.8 (Holutuijsen et al., 1989). The wave attenuation over a steeply sloping submerged reef

cannot be simply described by conventional breaker parameters. The main reason for simulated wave heights being somewhat higher compared to actual wave recordings can be attributed to this reason. However, since simulations provided a conservative estimate of wave heights behind the offshore reef, allowing for this discrepancy as a margin of safety, further refinement of wave transmission computations was not effected.

The wave heights behind he secondary reef was found to depend on wave heights outside of it as well as the tidal elevation. Empirical relationships were obtained for this wave height dependency through the analysis of simultaneous wave measurements on either side of the secondary reef for different water level ranges. The model simulated wave heights were seen to closely follow these wave height dependencies (Figure 2.). In order reproduce this wave transmission over the secondary reef, it was necessary to artificially lower exposed segments of the reef, as model computation ceases once an exposed "land" grid point is encountered.

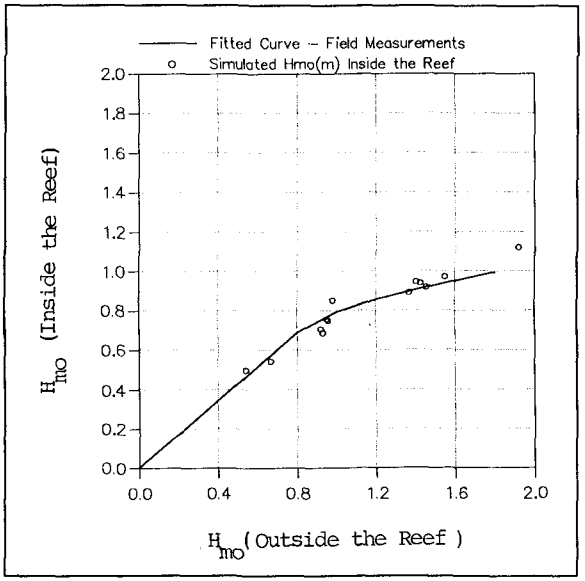

Figure 2. Verification of Wave Transmission Over the Secondary Reef H_{m0} (Outside the Reef) vs H_{m0} (Inside the Reef)

The calibrated wave model setup was used to simulate wave incidences which characterise year round wave climate as well as extreme wave occurrences. The simulation of 100 year extreme wave event is illustrated in Figure 3. The proposed harbour layout is also included in this illustration. The attenuation of waves over the offshore reef and penetration of waves through the gap in this reef is clearly seen from the significant wave height contour pattern.

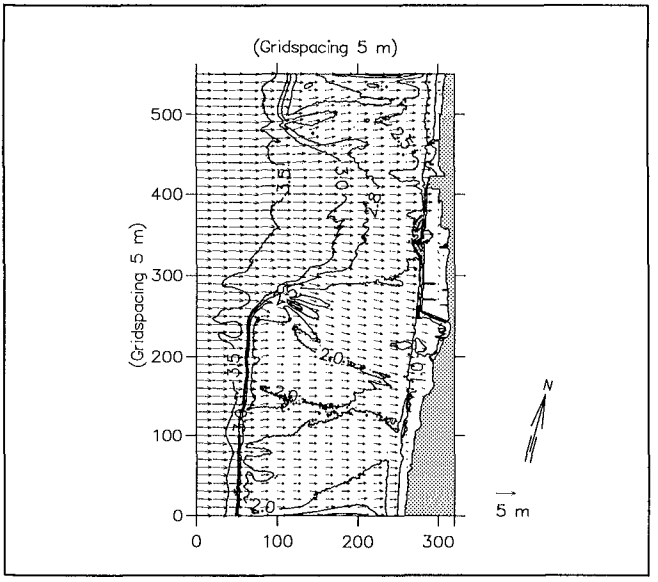

Figure 3. Simulation of 100 Year Return Period Wave at 0.0 m MSL

Hydrodynamic Modelling

MIKE 21's hydrodynamic module (MIKE 21 HD), based on the finite difference solution of full non-linear equations of conservation of mass and momentum integrated over the vertical was used to establish hydrodynamic conditions within the study area, under pre and post harbour construction stages. The hydrodynamics off the western coast of Sri Lanka is characterised by weak tidal velocities combined with intermittent wind influences. The average tide and wind combined flow velocities are in the range 0.15 to 0.25 m/s. The variation of tidal range along the coast is also found to be marginal with about 0.7 m during spring tide and 0.15 m during neap tide. In order to establish compatible boundary conditions for hydrodynamic modelling in such an environment, it was necessary to originate hydrodynamic modelling from a "Regional Model" covering a large sea area (Gunaratna et al., 1997).

The bathymetry and location of the Regional Model, which spans across most of the western coast of Sri Lanka is illustrated in Figure 4. This model was 230 km x 71 km in extent and was set up on a 1000 m x 1000 m grid. The model boundary conditions for the simulation of tidal flows was obtained through a detailed analysis of tidal wave propagation pattern of principal tidal constituents in the Indian Ocean (Gunaratna et al., 1997). The model computations were validated by comparison with tidal data available from a number of stations alongshore. Having validated the model for tidal flows, certain wind driven flow events were simulated by adjusting the wind friction coefficient.

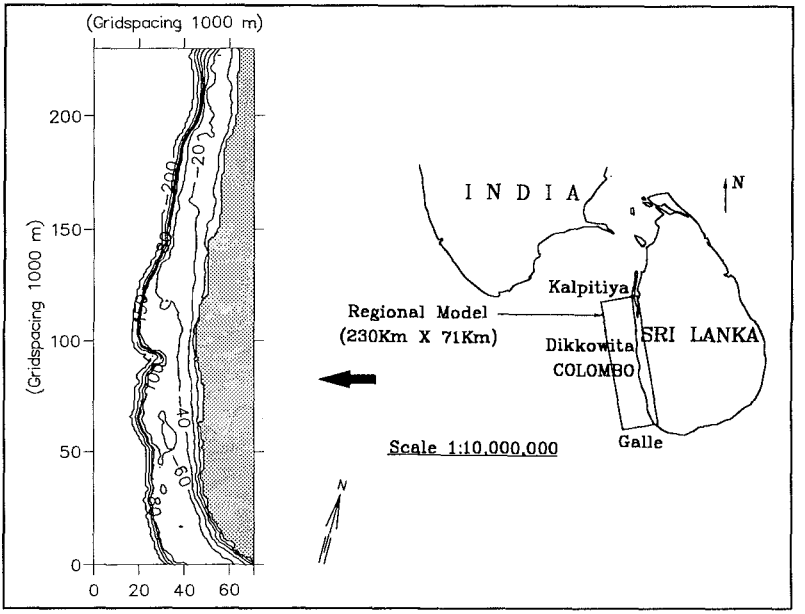

Figure 4. Regional Hydrodynamic Model

The hydrodynamics within the study area were simulated by stepping down from the Regional Model through a set of nested sub-models. The basic details of this model setup is given in Table 1. The "transfer boundary conditions" for carrying out simulations within a sub-model were extracted by simulations within the next highest level model. The simulation of wave overtopping currents and littoral currents were carried out in the lowest level HD2 and HD3 sub-models, respectively.

Hydrodynamic Model	Size	Grid Resolution	Time Step
Regional (HDR)	71 km x 230 km	1000 m x 1000 m	360 sec
HD0	25 km x 13.75 km	125 m x 125 m	90 sec
HD1	4.35 km x 2.75 km	50 m x 50 m	60 sec
HD2	2250 m x 600m	10 m x 10 m	30 sec
HD3	900 m x 500 m	5 m x 5 m	2 sec

Table 1. MIKE 21 Hydrodynamic Model Set Up

In the modelling of wave overtopping induced currents, the wave overtopping mass flux over reef segments was assumed to be described by the following expression for a discharge in the wave direction in the roller of a spilling breaker (Fredsøe, et al., 1992)

$$q = \frac{k_1 H_{m0}^2 \cos\beta}{T_{02}} \quad (2)$$

where, q=wave overtopping mass flux per unit length; and H_{m0} , T_{02} are the significant wave height and mean wave period, respectively, outside the secondary reef; β is the angle of wave incidence; and k_1 is a non-dimensional calibration coefficient.

The simulations were carried out at HD2 model level by employing a strategically synthesised combination of point sources behind the secondary reef that represent wave overtopping mass fluxes over reef segments. An identical number of point sinks were introduced on the other side of the reef segments for conserving the mass. An instantaneous picture of the simulated current pattern is illustrated in Figure 5. Simultaneous instrument recordings of two dimensional currents inside the reef and directional waves outside the reef were used as the basis for validation of model computations (Figure 6.).

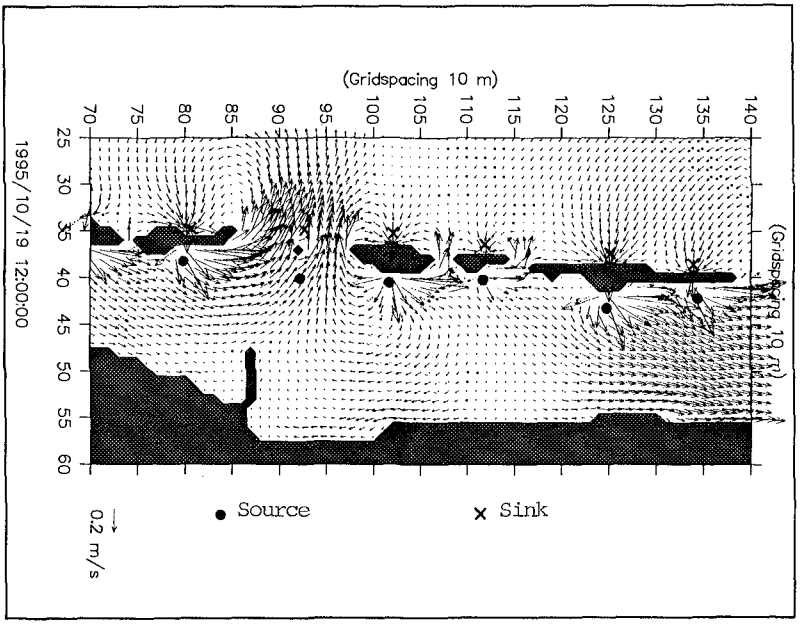

Figure 5. Simulation of Wave Overtopping Currents Behind the Secondary Reef

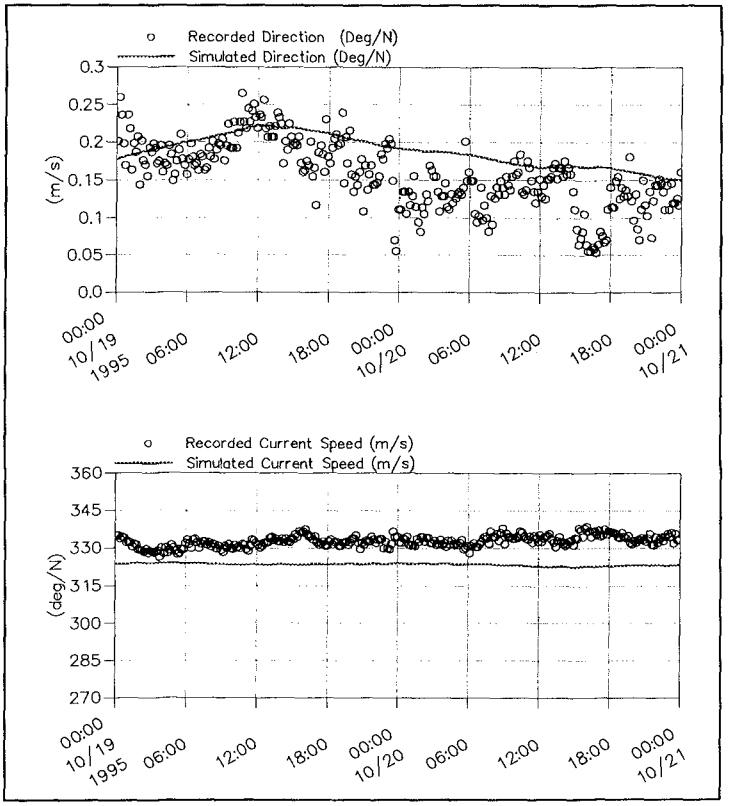

Figure 6. Simulated and Recorded Currents Behind the Secondary Reef

Optimization of Harbour Layout

A preliminary harbour layout was conceptualised by incorporating an optimal basin area of 11.7 hectares (117,000 m^2) behind the secondary reef into the harbour basin. The secondary reef itself was to function as the outer toe of the main breakwaters connected by return breakwaters to land. The harbour was planned to accommodate 400 fishing craft ranging in size from 40 feet (12.2 m) to 100 feet (30.5 m).

The calibrated hydrodynamic and wave propagation models under existing conditions were used as the primary basis, to simulate post-harbour construction scenarios through additional model computations. The remaining sections of this paper outline the wave disturbance, sediment transport and sedimentation computations carried out for layout optimization.

Wave Disturbance Modeling

The wave conditions within the harbour basin and harbour entrance was modelled using MIKE 21's Boussinesq Wave Module (MIKE 21 BW). MIKE 21 BW is primarily used for modelling of wave disturbance within harbours due to penetration of regular and irregular wave trains, taking into account shoaling, refraction, diffraction, and partial reflection and absorption of wave energy by harbour structures. The input wave conditions for wave disturbance modelling were obtained by NSW/PMS model simulations.

The simulations for selected swell and sea wave incidences which characterise the year-round wave climate were carried out within the BW model set up incorporating the entire harbour basin and the approach channel. The overall wave heights were derived by combing sea and swell wave heights:

$$H^2_{m0,overall} = H^2_{m0,swell} + H^2_{m0,sea} \quad (3)$$

where, $H_{m0,overall}$, $H_{m0,swell}$ and $H_{m0,sea}$ are the overall, swell and sea significant wave heights, respectively.

Having established the annual wave height exceedances from model simulations, the internal layout of the harbour and the entrance configuration was suitably modified to maintain wave disturbance within acceptable limits. The allowable significant wave height limits (not to exceed 1 week per year) used were 0.4 m to 0.6 m for loading/unloading operations at a quay and 0.6 m to 0.8 m for safe mooring in the basin.

In Figure 7, the significant wave heights for a wave incidence with an estimated exceedance of 1 week per year is illustrated for the optimised harbour layout. It was necessary to effect several modifications in the basic layout to limit wave disturbance within acceptable limits. The modifications carried out included, the provision of a forebay area at the entrance and a sandy beach fronting the entrance for energy dissipation and sloping rubble mound faces as much practically possible as the internal faces of harbour structures for effective wave energy absorption.

In addition to wave disturbance due to short period waves, the possibility of harbour resonance due to long period oscillations was also examined by using a combination of MIKE 21 BW and HD models. Several simulations carried out with different wave periods indicated that undesirable wave heights due to long period oscillations will not result within the harbour basin.

At the entrance, curved breakwater arms extends up to a water depth of 5.4 m below MSL. The main operational area of the harbour is to be dredged up to 4.5m below MSL while in the southern part of the basin a depth of 3 m below MSL is to be provided. The model simulations confirmed that under the wave conditions that may be expected throughout the year, these water depths are sufficient to ensure safe navigation into and out of the harbour and safe operation within the harbour for the range of anticipated craft sizes.

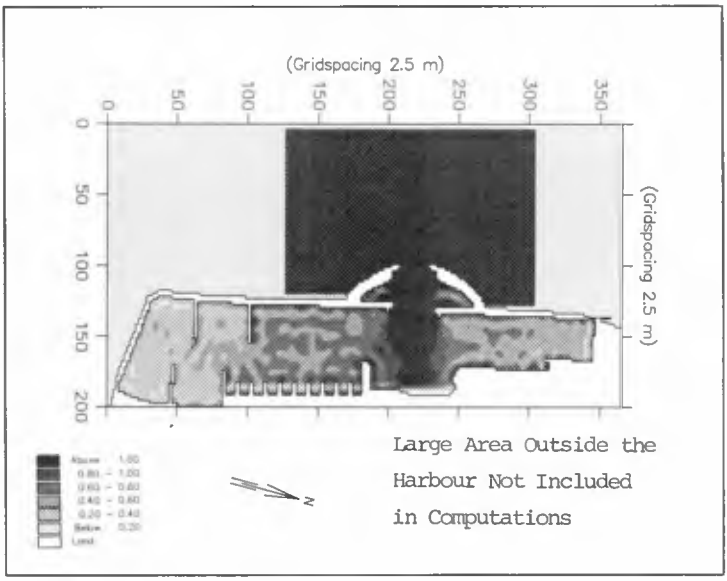

Figure 7. Simulated Significant Wave Heights Exceeded 1 Week per Year

Sediment Budget Computations

A sediment budget for the study area was obtained in the initial phase by quantifying different components as accurately as possible. The establishment of the sediment budget was based on LITPACK model computed sediment transport capacities across selected transects, volumetric bed level change computations based on repetitive surveys and available information on sediment supply from the Kelani River.

The analysis of all available sediment data from the study area and sediment transport mechanisms led to an identification of four distinct transport zones. These were the inner trough area behind the secondary reef, outer trough between the two reefs, the wave breaking zone on the outer slope of the secondary reef and the area around the Kelani River mouth. This analysis also identified that the average characteristics of sediments in motion due to longshore currents can be represented by that of a graded sediment mixture with a mean grain size (d_{50}) of 0.6 mm.

LITPACK model computations carried out using this information revealed that sediment transport capacities northwards and southwards of the proposed harbour site, where the secondary reef has merged with the coastline, are around 200,000 m^3/year. This is in excess of the present estimated sediment supply rate from Kelani River of 100,000 m^3/year. Therefore, progressive erosion of fine material can be expected to take place until bed armouring result in an equilibrium situation.

LITPACK computations indicated variable sediment transport capacities along the stretch where secondary reef has got disconnected with the coastline, but in general being in excess of the sediment supply rate. Diver inspections of the secondary reef carried out in this area revealed that it consists of fragmented sandstone with hardly any sediment accumulations within the crevices. This observation itself is an indication of the sediment transport potential being higher than the sediment supply rate.

The volumetric bed level change computations showed that on an average about 3,500 m3/year of sediment is lost from the basin area planned to be occupied by the harbour. This figure represents the net difference of sediment eroded by the wave overtopping currents and the sediment spilling over the secondary reef into the basin. The construction of the harbour will result in a loss of these erosion products from the basin area to down drift coasts. However, such a moderate deficiency in sediment discharge will be unlikely to create significant erosional problems.

Assessment of Sedimentation Impacts of the Harbour

Two dimensional sediment transport computations were carried out for the post-harbour construction stage to ascertain whether a sufficient sediment transport capacity exist in front of the harbour entrance to by-pass the incoming sediment supply. For this purpose, MIKE 21's sediment Transport Module, MIKE 21 ST was used.

MIKE 21 ST computes sand transport capacity at each node of a rectangular grid computational domain for which hydrodynamic and wave characteristics have been established. The model could account for effects of both breaking and non-breaking waves on transport of non uniform spatially varying sediment sizes. The currents could be tidal, wind-driven, wave-driven or a combination of the three. The grain size and the gradation of sediments may vary throughout the model area.

The hydrodynamic scenarios for computing sediment transport considering selected wave incidences combined with tide and wind driven flows were established within MIKE 21 HD3 model (Figure 8.). The computed sediment transport potentials for the selected wave incidence scenarios were extrapolated considering their seasonal occurrence percentages and the fractional contribution to the transport potential as indicated by LITPACK computations. These calculations revealed that the entrance configuration of the proposed harbour with curved double breakwater arms will be able to by pass the present estimated sand supply of 100,000 m3/year. This also implies that there would be no additional lee-side erosion due to the construction of the fishery harbour, apart from the first few years, which is required for the adjustment of bathymetry adjacent to the entrance.

The sedimentation within the harbour basin was assessed through desk calculations, considering three basic mechanisms of sedimentation, viz., tidal exchange, eddy exchange and long period oscillations. The calculations made under conservative assumptions estimated the annual siltation within the harbour basin to be about 5 cm. The long period oscillations was found to be the most important mechanism contributing to about 80 percent of the estimated siltation.

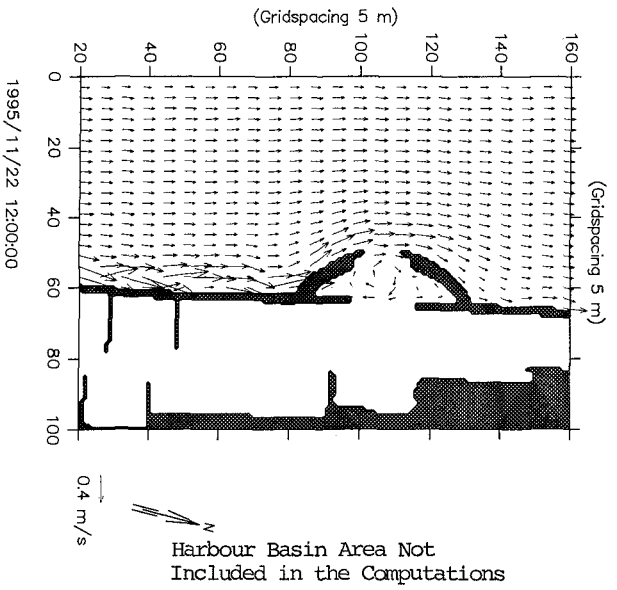

Tide and Wind Driven Flow Combined with the Wave Incidence:
H_{m0} = 1.25m, T_{02} = 11.2 sec and Mean Wave Direction = 202.5° from north at -15m MSL

Figure 8. A Simulated Hydrodynamic Scenario for Sediment Transport Computations

Concluding Remarks

The hydrodynamic, wave and sediment transport phenomena in a complex reef protected coastal stretch could be successfully simulated through the application of MIKE 21 and LITPACK mathematical models. The study also resulted in the evolution of a hydrodynamic model for the western coast of Sri Lanka. This model which has undergone further refinement and validation since its initial development, has been subsequently used as the primary basis in a number of costal engineering applications at other locations.

Acknowledgments

The work described in this paper was conducted as a part of the technical feasibility study for the proposed fishery harbour at Dikkowita, Sri Lanka. The authors of this paper wish to thank Ministry of Fisheries and Aquatic Resources Development, Sri Lanka, for providing the opportunity to be involved in this study, conducted under the ADB Sri Lanka Fisheries Sector Development Project.

Appendix - References

1. Battjes, J.A., and Jansen, J.P.F.M. (1978). "Energy Loss and Setup due to breaking of Random Waves", Proceedings of the 16th International Conference on Coastal Engineering, Hamburg, Germany, pp 569-587.

2. Behnsen, H., "Project Report - Colombo North" (1994). Prepared for the Coast Conservation Department of Sri Lanka.

3. Delft Hydraulics and Netherlands Economic Institute (1992), "National Sand Study for Sri Lanka - Phase One", A Report Prepared for Ministry of Foreign Affairs, The Netherlands and Central Environment Authority of Sri Lanka.

4. Fredsøe, J. and Deigaard, R. (1992). "Mechanics of Coastal Sediment Transport", World Scientific, Singapore.

5. Gunaratna, P.P., Justesen, P., Abeysirigunawardena, D.S. (1997). " Modelling of Hydrodynamics off the Western Coast of Sri Lanka", Proceedings of the Second Indian National Conference on Harbour and Ocean Engineering, Thiruvanathapuram, India, pp. 241-250.

6. Holthuijsen, L.H., Booij, N., and Herbers, T.H.C. (1989) "A Prediction Model for Stationary, Short Crested Waves in Shallow Water with Ambient Current", Coastal Engineering, Vol. 13, pp 23-54.

7. Lanka Hydraulic Institute Ltd. (LHI), Sri Lanka (1994). "Final Report on Colombo Wave Measurements", Prepared for Sri Lanka Ports Authority.

8. Lanka Hydraulic Institute Ltd. (LHI) Sri Lanka, Danish Hydraulic Institute (DHI), Denmark, PortConsult Consulting Engineers, Denmark, and Associated Management Services Ltd., Sri Lanka (1996). "Dikkowita Fishery Harbour - Feasibility Report", Prepared for the Ministry of Fisheries and Aquatic Resources, Sri Lanka.

9. Scheffer, H-J, Fernando, K.R.M.D.,and Fittschen, T. (1994). "Directional Wave Climate study - South West Coast of Sri Lanka", A Report Prepared by CCD-GTZ Coast Conservation Project, Sri Lanka.

Characteristics of long-period flow velocity fluctuations around Tomakomai Harbor

Hiroya Kinoshita[1], Hideki Hoshi [2], Youichi Atsumi [3],
Shin-ichiro Sekiguchi [3], Toshihiko Yamashita [2]

1. Abstract

Studies of flows near the coast from the viewpoint of coastal engineering have focused on tidal currents and nearshore currents that are generated by waves in breaker zones. However, on-site observations have shown that there also exist strong flows with long periods of several days. As these long-period flows have a high velocity even at deep water levels outside breaker zones, they are thought to play an important role in the offshore drift-sand phenomenon and in the convection and diffusion of floating larvae of marine organisms. Through analysis of observation date on wind velocity and flow velocity recorded around Tomakomai Harbor, the temporal and spatial characteristics of long-period velocity fluctuations of these flows were clarified. We confirmed the existence of and clarified the characteristics of long-period flow velocity fluctuations around Tomakomai Harbor that have a period of 3～4 days and propagate in a westerly direction at a phase velocity of approximately 2.0km/h. These long-period flow velocity fluctuations can be estimated by the storm surge formula that assumes wind stress to be the extemal force and Coriolis force to be the restoring force.

2. Introduction

Studies of flows near the coast from the viewpoint of coastal engineering have focused on tidal currents and nearshore currents that are generated by waves in breaker zones. However, on-site observations have shown that there also exist strong flows with long periods of several days. Adams and Buchwald (1969) pointed out that wind stress parallel to the coastline is

[1] Sumitomo Metal Industries, LTD. 1-3, Otemachi 1-chome, Chiyoda-ku, Tokyo 100-8113, Japan
[2] Laboratory of Coastal and Offshore Engineering, Division of Environment and Resources Engineering, Hokkaido University, N-13 W-8, Kita-ku, Sapporo 060-8628, Japan
(Fax:+81-11-726-2296, E-mail: y-toshi@eng.hokudai.ac.jp)
[3] Hokkaido Development Bureau, N-8 W2, Kita-ku, Sapporo 060-8511, Japan

important for the occurrence of shelf waves. Nakamura (1990) showed from the results of on-site observations carried out over a period of many years on the coast of Fukushima that there exist southward-propagating flow velocity fluctuations with a period of 3 or 4 days, propagating the direction with the shoreline on the right,and he reported that these flows correspond to the second mode of shelf waves. He also pointed out that these flows affect the drifting and diffusion of floating bivalve larvae. Sato (1995) reported the existence of a strong flow at a depth of 15m off the Hokuriku coast that reaches a speed of up to 1m/s along the coastline and reported that this flow is mainly caused by wind stress and Coriolis force. Yasuda et al. (1995) pointed out that not only wind stress but also the effect of momentum transportation due to offshore breakers is important in the generation of strong flows outside the breaker zone.As these flows with long periods of several days have a high velocity even at deep water levels outside breaker zones, they are thought to play an important role in the offshore drift-sand phenomenon and in the convection and diffusion of floating larvae of marine organisms. However, there have been very few field studies conducted on these flows. Moreover, these strong flows are caused not only by a large variety of factors such as wind stress, offshore breakers, differences in density and shelf waves but also by combinations of these factors, making it difficult to clarify the physical mechanisms of flow occurrence.

Therefore, in this study, through analysis of observation data on flow velocity and wind velocity recorded around Tomakomai Harbor, we attempted to clarify the temporal and spatial characteristics of long-period velocity fluctuations of these flows, and the correlation between flow velocity and wind velocity. Next, we performed numerical calculation of these flows using a storm surge formula, and by a comparison with the observation results, we were able to investigate the mechanisms that generate these flows.

3. On-site observation data

The observation data used for the analysis were flow and wind velocities measured at the sites around Tomakomai Harbor shown in Fig. 1. Flow velocity data included long-term continuous observation data collected at one site and short-term observation data collected at multiple sites. The long-term continuous observation data of flow velocity were measured by an NC-2 current meter set at 23.5 m under the sea surface and at 1m above the sea bottom at site A, which is located 2.5km offshore from the west harbor (see Fig. 1). Velocity data (90-sec mean velocity) collected every hour from January 1990 to August 1995 were used for the analysis. The short-term data were measured by a RCM-4 current meter set at 5m below sea surface at

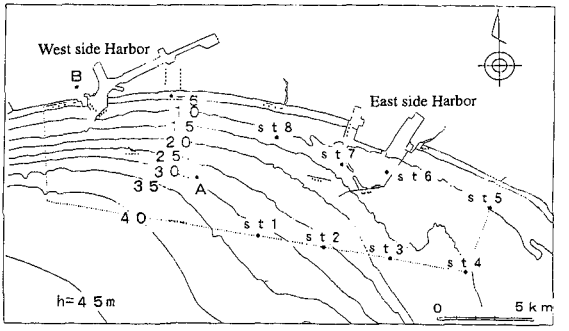

Fig.1 Observation sites around Tomakomai Harbor

eight observation sites (St. 1～St. 8) around the east harbor (see Fig. 1). The offshore sites, St. 1～St. 4, run almost parallel to the shoreline, and the water is shallower on the east side. At St. 1～St. 8, 20-min mean flow velocities were measured at 20-min intervals over a period of 30 days four times a year (in June, July, October and February). Wind velocity was measured at 10m above the ground at site B (see Fig. 1). Wind velocity data obtained every hour during the same period as the recording of long-term continuous flow velocity were used for the analysis.

4. Characteristics of long - period flow velocity fluctuations

4.1 Temporal characteristics of flow velocity fluctuations

Fig. 2 shows flow velocity data obtained over a one-month period in October 1993. As can be seen in the figure, there were flow velocity fluctuations with periods of 12.5 hours and 25 hours attributed to the tides. There were also flow velocity fluctuations with shorter periods and flow velocity fluctuations with long periods of 4～6 days. The flows with long-period flow velocity fluctuations were mainly in an east-west direction, parallel to the shoreline. In the present study, we focused on these flow velocity fluctuations with a long period of several days. In order to show the components of these long-period fluctuations, we calculated the 25-hour moving averages of the flow velocity raw data used in Fig. 2 and extracted the flow velocity fluctuations with periods shorter than tidal periods. The results are shown in Fig. 3. As can be seen in the figure, the periods of the flow velocity fluctuations are 4～7 days.

Next, we divided the raw data of flow velocities for October 1993 shown in Fig. 2 into two components: the component of flows in a direction parallel to the shoreline and the component of flows in a direction perpendicular to the shoreline. Fig. 4 shows the power spectrums for these

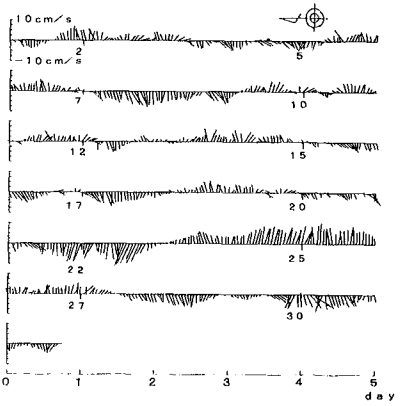

1 ～ 31 Oct. 1993

Fig.2 Temporal characteristics of flow velocity

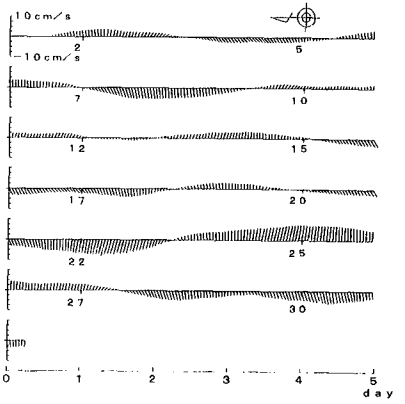

1 ～ 31 Oct. 1993

Fig.3 25-hour moving average of flow velocity

two components. The spectrums were calculated by MEM using 700 data values obtained every hour over a period of 30 days. For the flow velocity component in a parallel direction to the shoreline, the spectrum density is greatest at a period of about 150 hours (about 6 days).These long-period fluctuations correspond to the velocity fluctuations with periods of 4～7 days in Figs. 2 and 3 and were dominant flow fluctuations in October 1993. A comparison of the parallel and perpendicular components of flow velocity shows that the parallel components of these long - period flow velocity are dominant. A spectrum of flow velocity fluctuations observed every month over a period of 6 years showed that strong flow velocity fluctuations with a long period of several days were dominant throughout the year except in the early summer and mid-summer months from May to July. Nakamura (1990) reported that flow velocity fluctuations with long periods of several days could be observed off the coast of Fukushima throughout the year except for summer, when there is a great difference between daily maximum and minimum water temperatures caused by thermocline. These observation results are similar to the results of our observations of flow velocity fluctuations off the coast of Tomakomai.

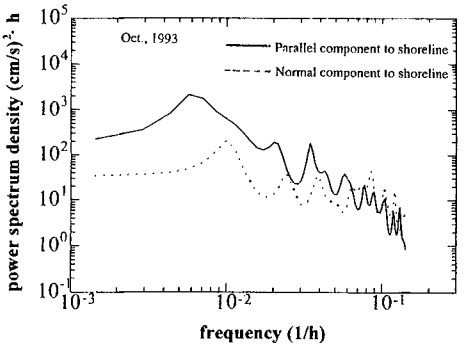

Fig.4 Power spectrum of flow velocity

4.2 Spatial characteristics of flow velocity fluctuations

Fig. 5 shows the measurements of flow velocity from September 28 to October 7, 1993 at St. 1 ～ St. 8 around the east harbor. This observation period is almost the same as the first ten days in Fig. 2. As can also been seen in this figure, the dominant flow velocity fluctuations were those with a period of several days, and most of these flows were in an east-west direction. As can be seen in Fig. 5, flow velocity fluctuations have the following spatial characteristics. St. 1 ～ St. 4 (offshore sites) showed almost the same tendencies in flow velocity fluctuations. The intensities of flow velocity fluctuations were almost the same at St. 1 and St. 4, while St. 2 and St. 3 showed larger flow velocity fluctuations. For example, on September 28, when there was a dominant eastward flow, the maximum flow velocity fluctuation at St. 1 and St. 4 was about 15cm/s, while the flow velocity fluctuation at St. 3 reached a maximum of 30cm/s. This difference is thought to be due to the acceleratory effect caused by the breakwater in the harbor; this effect should be considered when dealing with the issue of drift sand around a breakwater, especially in deep water around the end of the breakwater. As can be seen in the figure, St. 5 also showed similar flow velocity fluctuations to those at St. 1 ～ St. 4.

On the other hand, St. 8 showed similar flow velocity fluctuations to those at St. 1 ～ St. 4 when an eastward flow was dominant at the offshore sites, but the flow direction at St. 8 was opposite to that at St. 1 ～ St. 4 on September 29, October 4 and October 7, when an westward flow was dominant at St. 1. It is thought that a westward flow with a velocity

fluctuation period of several days changes direction at St. 8 after circling around the back of the breakwater. This type of circulatory flow around a large harbor could be effective for preventing the drifting and diffusion of floating larvae of bivalves such as surf clams. A flow in the opposite direction to that at St. 1 was rarely seen at St. 5. This is thought to be due to the shape of the breakwater, although many points still remain unclear. However, this phenomenon is thought to be an important factor in assessing the effects on the coastal environment, and especially the hydraulic environment, of large harbors, and further investigation of this phenomenon is needed. The flow velocity fluctuations at St. 6 and St. 7 (nearshore sites) are much smaller than those at other sites; most of the flow velocity fluctuations at these two sites have short periods that accord with the tides.

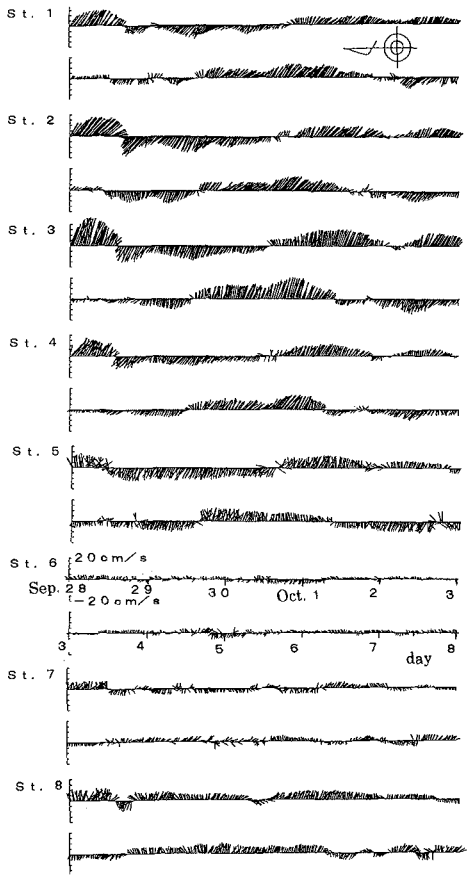

Fig.5 Spatial characteristics of flow velocity fluctuations around the east side of Tomakomai Harbor

A comparison of the flow velocity fluctuation data from October 1 to October 7 in Figs. 2 and 5 for site A and St. 1, which are located relatively close together (see Fig. 1), shows that although these two sites have similar flow velocity fluctuations, the flow velocity at site A, where measurements were conducted near the sea bottom, is only about half that at St. 1. The vertical distribution of flow velocity fluctuations with long periods is also important for transport problems of matter such as drift sand.

Since St. 1 ~ St. 4, sites that are not affected greatly by the harbor (see Fig 5), showed very similar flow velocity fluctuations, we calculated the correlations of east-west and north-south flows between these sites using 25-hour moving averages of the observation data obtained

at each site. Fig. 6(a) and (b) show the correlation coefficients C(τ) between flow velocities at St. 4 and those at St. 1 ~ St. 3 for a 30-day period in October 1993. The distances between St. 3 and St. 4, St. 2 and St. 4, and St. 1 and St. 4 are 4.0km, 7.5km, and 10.9km, respectively. As can be seen in the figures, the correlation coefficients between all of the sites are high (over 0.9) for both the east-west and north-south components. Also, the time lag (τ) increases as the westward distance from St. 4 increases, and the correlation coefficient decreases slightly as the distance between sites increases. These results indicate that flow velocity fluctuations with long periods propagate about 10km to the south with little change in form. This property is the same as that of shelf waves along coasts in the northern hemisphere, the direction of propagation being with the shoreline on the right.

Table 1 shows the time lags between sites in various observation periods and the phase velocities of flow velocity fluctuations in these observation periods. The table shows that flow velocity fluctuations were always in an east-to-west direction and that the phase velocity ranged from 1.5~3.0 km/h.

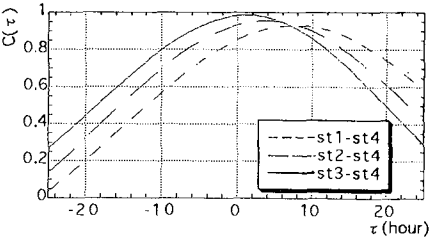

(a) East - West velocity component

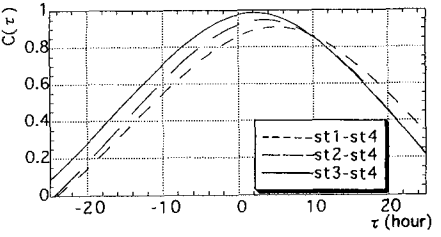

(b) North - South velocity component

Fig.6 Cross correlation of long - period flow velocities between these sites

Table 1 Correlation coefficient and phase velocity

Month	Year	Sites	Correlation coefficient	Time lag (min)	Phase velocity (km/h)
May	1993	st2-st4	0.88	300	1.5
May	1993	st3-st4	0.97	90	2.7
Oct.	1993	st1-st4	0.93	460	1.4
Oct.	1993	st2-st4	0.95	240	1.9
Oct.	1993	st3-st4	0.98	80	3.0
Jan.	1994	st1-st4	0.91	300	2.2

4.3 Correlation between flow and wind velocities

Fig. 7 shows the raw data of wind velocities recorded during the same period in October 1993 as that in Fig. 2. As can be seen in the figure, wind velocity data also have fluctuations with periods of several days. A comparison with the data in Fig. 2 shows that there is a clear correlation between flow velocity and wind velocity fluctuations and that wind velocity fluctuations

is slightly faster for change in phase than flow velocity fluctuations.

Fig. 8 shows the same power spectrums for wind velocity as those calculated for flow velocity in Fig. 4. The majority of winds blowing in a direction parallel to the shoreline had a velocity fluctuation period of about 150 hours. This is similar to that of the flow velocity fluctuations shown in Fig. 4.

We calculated the correlation coefficients between flow velocities at site A and wind velocities at site B. Table 2 shows the correlation coefficients that were greater than 0.8. The correlation coefficients between flow and wind velocities in the months not shown in the table were also relatively high; for example, the correlation coefficients were 0.7~0.8. for other months in 1993. The time lags of flow velocity are also shown in the table. In the case of a high correlation coefficient between flow and wind velocities, there was a time difference of 6 to 11 hours between sea flow and wind. The above results show that a sea flow is generated approximately 6 to 11 hours after a strong wind starts to blow, suggesting that tangential stress acting on the sea surface due to wind is important for the external forces that cause flow velocity fluctuations with long-term periods.

Velocity fluctuations in flows off the coast of Tomakomai with periods of 4~7 days showed a strong correlation with wind. As possible factors affecting wind, we investigated the positional relationship between low and high atmospheric pressures and the relationship between wind and flow velocities. The following results were obtained. When low and high atmospheric pressures pass over

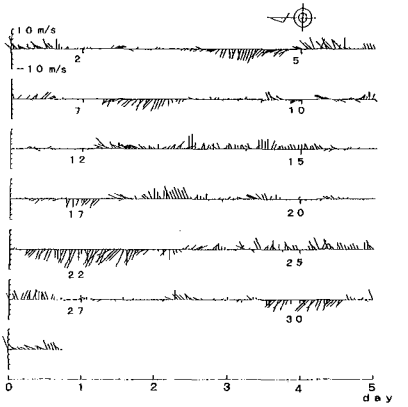

1 ~31 Oct. 1993

Fig.7 Temporal characteristics of wind velocity

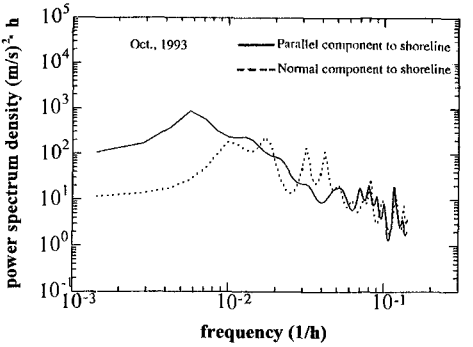

Fig.8 Power spectrum of wind velocity

Table 2 Correlation coefficient and time lag

Month	Year	Correlation coefficient	Time lag (hour)
Nov.	1990	0.89	11
Oct.	1991	0.83	9
Apr.	1992	0.83	10
May	1992	0.89	6
Aug.	1993	0.85	6
Mar.	1994	0.84	8
Aug.	1995	0.81	10

Tomakomai together, flow velocity fluctuations with long periods occur. When there is low pressure to the west and high pressure to the east of Tomakomai, westward wind and sea flows occur, and when there is low pressure to the east and high pressure to the west of Tomakomai, eastward wind and sea flows occur. These results suggest that wind velocity, which is largely determined by the atmospheric pressure pattern, and fluctuations in the sea surface due to changes in atmospheric pressure affect flows.

5.Numerical calculation of long-period flow velocity fluctuations

A flow velocity fluctuation with a long period of several days is thought to be generated by wind stress and atmospheric pressure fluctuations accompanying the passing of a low atmospheric pressure, and Coriolis force as restoring force.At a first step, numerical calculation was performed by similar method with Sato (1995) using a basic formula for storm surge.An outline the numerical calculation is as follows:

$$\frac{\partial M}{\partial t}+\frac{\partial}{\partial x}\left(\frac{M^2}{d}\right)+\frac{\partial}{\partial y}\left(\frac{MN}{d}\right)-fN+gd\frac{\partial \eta}{\partial x}+\frac{d}{\rho_w}\frac{\partial p_0}{\partial x}-\frac{\partial \tau_{sx}}{\rho_w}-\frac{\partial \tau_{bx}}{\rho_w}-\varepsilon\left(\frac{\partial^2 M}{\partial x^2}+\frac{\partial^2 M}{\partial y^2}\right)=0$$

$$\frac{\partial N}{\partial t}+\frac{\partial}{\partial x}\left(\frac{MN}{d}\right)+\frac{\partial}{\partial y}\left(\frac{N^2}{d}\right)-fM+gd\frac{\partial \eta}{\partial y}+\frac{d}{\rho_w}\frac{\partial p_0}{\partial y}-\frac{\partial \tau_{sy}}{\rho_w}-\frac{\partial \tau_{by}}{\rho_w}-\varepsilon\left(\frac{\partial^2 N}{\partial x^2}+\frac{\partial^2 N}{\partial y^2}\right)=0$$

$$\frac{\partial \eta}{\partial t}+\frac{\partial}{\partial x}M+\frac{\partial}{\partial y}N=0$$

Where, x , y : the parallel and the vertical co-ordinates to shoreline, d : water depth, f : coefficient of Coriolis force, g : acceleration of gravity, ρ_w : density of sea water, τ_s :shear stress on the sea surface, τ_b : shear stress on the seabed, and ε : horizontal coefficient of eddy viscosity.Subscripts x and y represent the components of flow that are parallel to the shoreline and perpendicular to the shoreline, respectively.

The topographical conditions were simplified to a shoreline running parallel to the x direction with a 1/100 uniform slope and no harbor. Coriolis factors within the area of calculation were assumed to be constant, and we used f-plane approximation and values at 42° North Latitude. An square area of 600km × 600km was used for the calculation. At the shoreline boundary, M and N = 0, and all other boundaries were closed. The grid width was 10km, and time steps were 30 sec. As the results of past calculation showed that fluctuation in atmospheric pressure has little effect on flows, atmospheric pressure was not included in the present calculation.Observed date of wind velocity were used as extemal force in this calculations.

Fig. 9 shows observed flow velocity, 25-hour moving average flow velocity, observed wind velocity, 25-hour moving average wind velocity (all at site A in Fig. 1), and calculated flow velocity 10km offshore for the period from Oct. 1 to Oct. 15, 1993. Although a direct comparison between observed and calculated flow velocities is not possible, since observation data of flow velocity were obtained at a site approximately 2.5km offshore and calculations of

flow velocity were made at a point 10km offshore, the qualitative agreement between observed and calculated flow velocities is good. Moreover, the phase velocity of the calculated flow velocity fluctuations at a point 10km offshore is 2.5 km/h, which agrees well with the results of on-site observations (see Table 1, Oct. 1993). However, there are time differences of a half day to one day between the calculated and observed flow velocities. Further study is required to resolve this discrepancy.

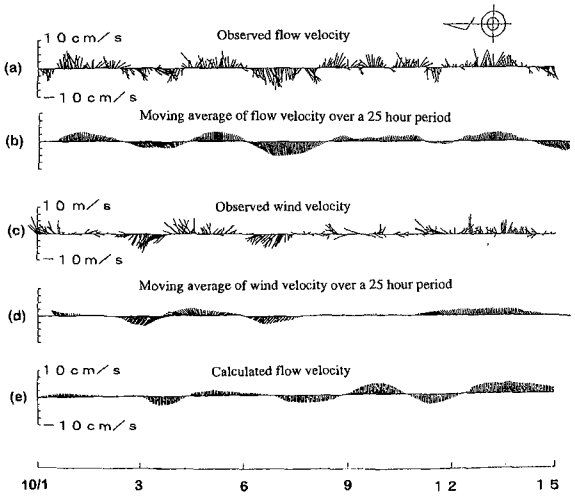

Fig.9 Relationship among observed flow velocity,observed wind velocity and calaculated flow velocity

6.Conclusions

We confirmed the existence of and clarified the characteristics of long-period flow velocity fluctuations around Tomakomai Harbor that have a period of 3～4 days and propagate in a westerly direction at a phase velocity of approximately 2.0km/h. These long-period flow velocity fluctuations can be estimated by the storm surge formula that assumes wind stress to be the external force and Coriolis force to be the restoring force.

7. References

Adams,J.K.and V.T.Buchwald(1969) : The generation of continental shelf waves, J.F.M.,35, pp.815-826.

Sato,S.(1995) : Characteristics of waves and currents induced by low pressures in Japan Sea,Journal of Hydraulic,Coastal and Environmental Engineering , JSCE , No.521/II -32 , pp.113-122(in Japanese).

Nakamura,Y.(1990) : Studies of the fishing fround formation of Skhalin surf clam and Hydraulic environments in coastal region , Dr. thesis , Tokyo Univ.of Fisheries(in Japanese).

Transformation of wave groups and accompanying long waves in shallow water

Mizuguchi, M. and H. Matsutate

Abstract

Interaction of short waves modulation and long waves evolution is studied. Existence of free long waves is taken into account. Laboratory experiment and numerical simulation with coupled equations are performed. Mechanism of the modulation is discussed. The distance, below which the modulation may be neglected, is evaluated.

Introduction

Figure 1 shows an example of wave record obtained in Hasaki pier, PHRI, MOT in Japan. Strong grouping of short waves is present. Long period component is filtered out numerically with cut-off frequency 0.04 Hz. Magnitude of the long waves is 1/10 of wind waves. Bounded long waves to grouping waves may be evaluated by applying the following Longuet-Higgins and Stewart (1962) solution.

$$\eta_b = -Sxx(x-c_g t)/\rho(gd-c_g^2) \qquad (1)$$

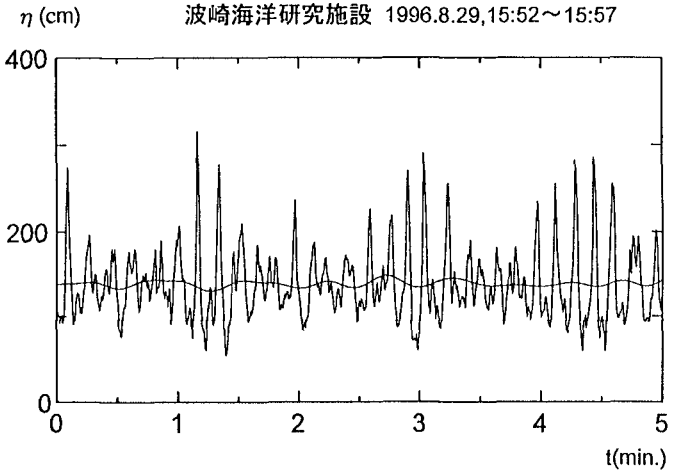

Fig. 1 Long waves in the field (where water is shallow and about 5m deep)

Dept. Civil Eng., Chuo Univ., Bunkyo-ku, Tokyo JAPAN 113

where η_b is the surface profile of the bound long waves, Sxx is the radiation stress of short waves, c_g is the group velocity of short waves, d is the water depth. Rough calculation of Eq.(1) gives 1.0 m in terms of wave height for η_b, with d=5 m, wave period T=10 s, maximum amplitude of short waves a_{max}=1.1 m, minimum amplitude a_{min}=0.3 m. Observed long waves are much smaller than that of bound long waves as is widely pointed out.

Why is the observed long waves much smaller than that of bound long waves. A very plausible explanation may be found in Nagase and Mizuguchi(1996) that free long waves, being generated simultaneously while the bound waves developes in the process of shoaling, nearly cancels out the bound one. Then long waves observed is much smaller than the bound one unless those two are separated well as shown in Fig. 2.

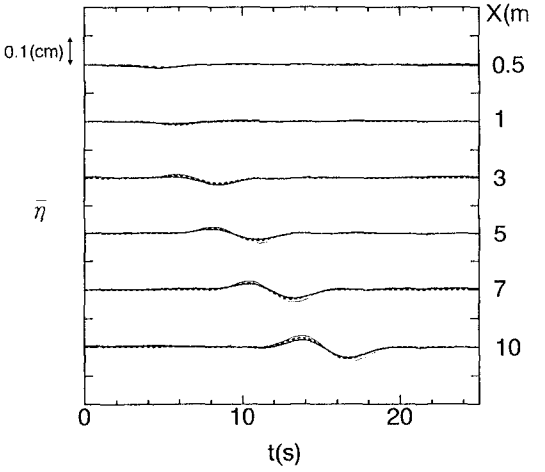

Fig. 2 Long waves accompanying a group of waves (Mizuguchi and Toita, 1996) X is the distance from the wave maker. Thick solid line: experiment, broken line; first-order theory. For information on short waves, see the reference.

In Fig. 2, no significant long waves is observed near the wave maker. Free long waves, which is needed to satisfy the boundary condition at the wave maker, is c_g/c times the bound waves, where c is the phase speed of the long waces. As they travel, long waves appear to be growing both in experiment and in theory. Free long waves, generated at the wave maker, propagate faster than the bound waves (or set-down waves) and start to separate each other. The separation can be observed only for this kind of single group of waves.

In this figure, one can also notice small difference between the experimental results and the theoretical one growing with the distance from the wave maker. The purpose of present study is to examine this difference. This difference is of second-order and very small in Fig. 2, but may be significant in some situation and worth to be investigated. The first-order theory assumes that short waves propagates with no change of group form. Previous nonlinear theory of wave modulation does not take into account of the free long waves. No systematic experimental investigation has not yet published, either.

Laboratory experiment

First we conducted a series of laboratory experiments to see how significant the change of wave group (or wave modulation) is. Figure 3 shows our experimental setup. Wave flume is 40m long and 30 cm wide and equipped with a piston-type wave maker.

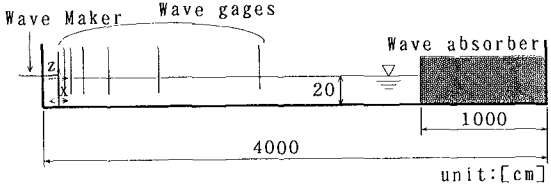

Fig. 3 Wave flume and experimental setup

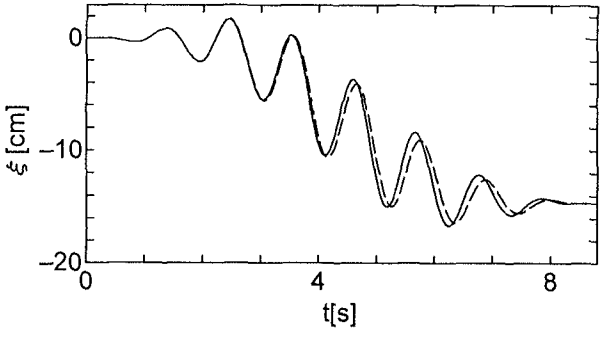

Fig. 4 An example of signal for wave maker (Case 2)
Solid line is calculated by Eq.(2) and broken line after Mizuguchi and Toita(1996).

We use single group of short waves for its simplicity as in Mizuguchi and Toita(1996). An example of wave maker signal is shown in Fig. 4. Displacement of wave maker ξ is obtained by numerically integrating the following equation.

$$d\xi/dt=u_w(0,t)+u_l(0,t)+\xi_l\partial u_w/\partial x \quad (2)$$

where u_w and u_l denote horizontal velocities of short waves and long waves respectively. u_w is given by linear wave theory and u_l is by

$$u_l=r(c_g/d)\eta_b(x,t) \quad (3)$$

where r is the quantity to control the generation of long waves. ξ_l is the displacement of the wave maker for long wave componenet and is given by

$$\xi_l=\int_0^t u_l(0,t)dt \quad (4)$$

The last term in Eq.(2) is newly added to compensate rather large value of ξ_l.

Ten cases are chosen as shown in Table 1. Standard case is Case 1, where generation of free long waves is suppressed by putting r=1. Finite amplitude effects may be seen in Cases 2 and 3. Effects of dispersion may be studied both in Cases 4 and 5 with different number of waves in a group and in Cases 6 and 7 with different wave period of short waves. Effects of free long waves may be observed in Cases 8, 9 and 10. Water depth is 20 cm throught the experiment.

Table 1 Experimental cases

case	a_{max} [cm]	T[s]	N_g	r	$(\eta'_0)_{min}$ [cm]	kd	ka_{max}	Us_{max}	Uss_{max}
1	2	1.1	8	1	-0.223	0.92	0.092	9.36	11.86
2	4	1.1	8	1	-0.891	0.92	0.184	18.73	23.72
3	1	1.1	8	1	-0.056	0.92	0.046	4.68	5.93
4	2	1.1	6	1	-0.223	0.92	0.092	9.36	11.86
5	2	1.1	12	1	-0.223	0.92	0.092	9.36	11.86
6	2	0.8	8	1	-0.116	1.42	0.142	3.94	6.27
7	2	1.6	8	1	-0.475	0.59	0.059	22.52	25.09
8	2	1.1	8	0	-0.223	0.92	0.092	9.36	11.86
9	2	1.1	8	-1	-0.223	0.92	0.092	9.36	11.86
10	2	1.1	8	2	-0.223	0.92	0.092	9.36	11.86

$$Us_{max} = 2a_{max}L^2/d^3 \ , \ Uss_{max} = 2ga_{max}T^2/d^2$$

Analytical description

In order to discuss the experimental results, knowledge on the theoretical background is very helpful. It is known that for long waves under grouping short waves, mass continuity equation is given as

$$\partial\eta_l/\partial t+d\partial u_l/\partial x=0 \tag{5}$$

and momentum equation is as

$$\partial u_l/\partial t+g\partial\eta_l/\partial x=-(n'-1/4)g\partial|A|^2/\partial x \tag{6}$$

where A is the complex amplitude of short waves. For short waves, the complex amplitude A follows

$$\partial A/\partial t+c_g\partial A/\partial x+i[\alpha\partial^2 A/\partial x^2+\beta'|A|^2A$$
$$+\{(k/d)(c_g-c/2)\eta_l+ku_l\}A]+\text{dissipation}=0 \tag{7}$$

where

$$\alpha=-(\partial^2\omega/\partial k^2)/2$$

$$\beta'=(\omega k^2/16\sinh^4 kd)\{2\sinh^2 2kd(1-\tanh kd/kd)+9\}$$

Equation (7) is written explicitly for η_l and u_l. Conventional form may be found in Mei(1989). Dissipation term is modeled after Masc(1987), where dissipation due to viscosity at side walls is included in addition to that at bottom. The traditional Schrodinger-type equation for wave modulation is obtained by substituting only the forced solution of Eqs.(5) and (6), while assuming the functional form of $A(x-c_gt)$, into Eq.(7) and neglecting the dissipation term.

Equations (5) to (7) may describe the second-order phenomena of long wave evolution and modulation of short waves for any initial and/or boundary condition. Standard finite difference technique is employed to solve Eqs.(5) to (7) numerically. Care is needed to give the boundary condition at the wave maker to be smooth enough.

Experimental results and comparison with theories

In the analysis of the laboratory data, long waves is simply filtered out numerically. Envelope of short waves is calculated by applying numerical filter to the absolute value of short wave surface fluctuation(List, 1992). Bound long

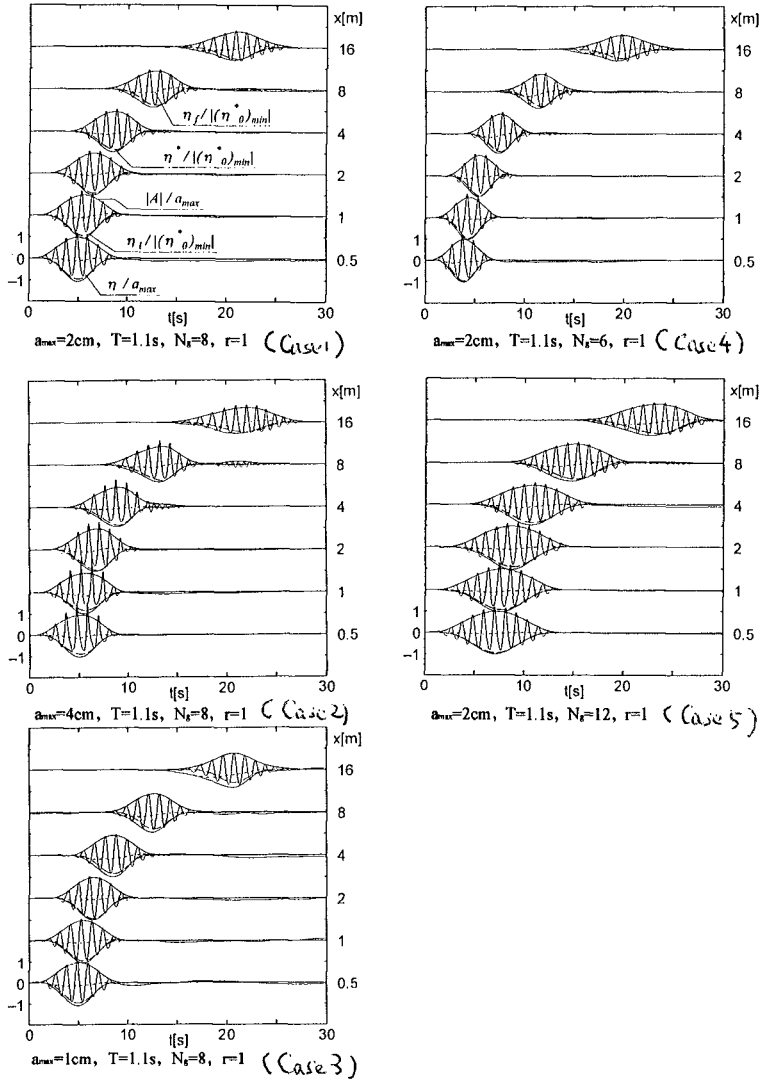

Fig. 5a Experimental results (Case 1 to 5)

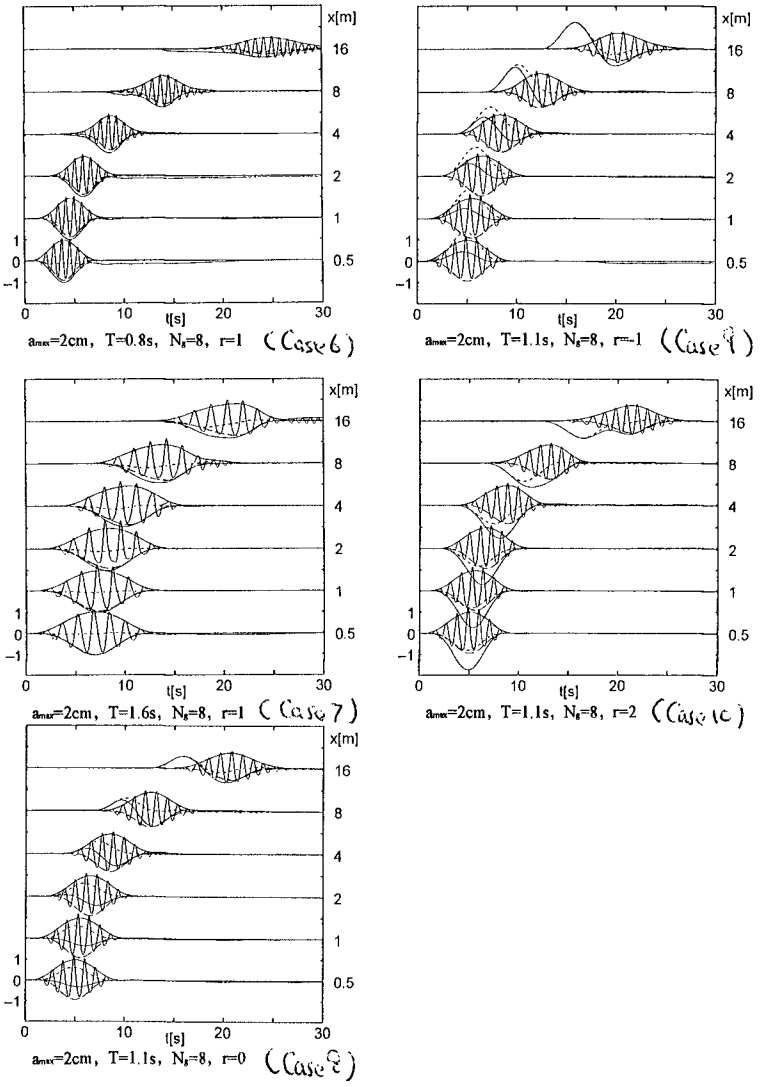

Fig. 5b Experimental results (Case 6 to 10)

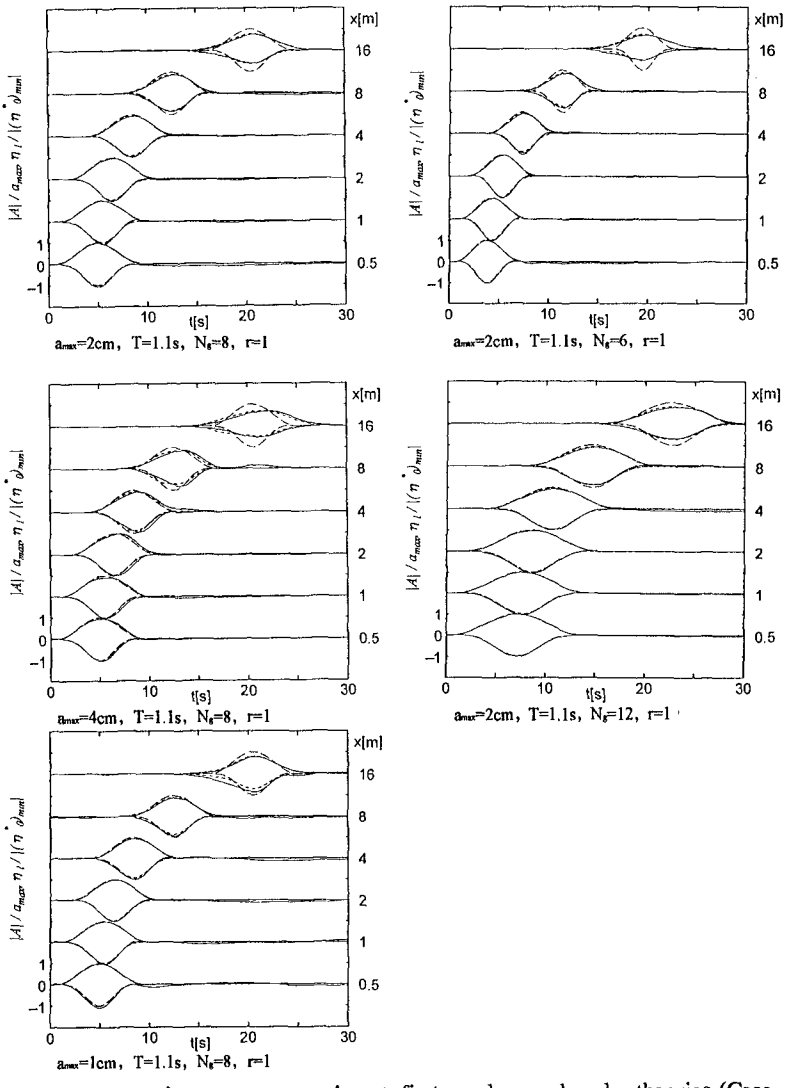

Fig. 6a Comparison among experiment, first- and second-order theories (Case 1 to 5). Lines in upper half of each figure show envelope profiles and theose in lower half long wave profiles.

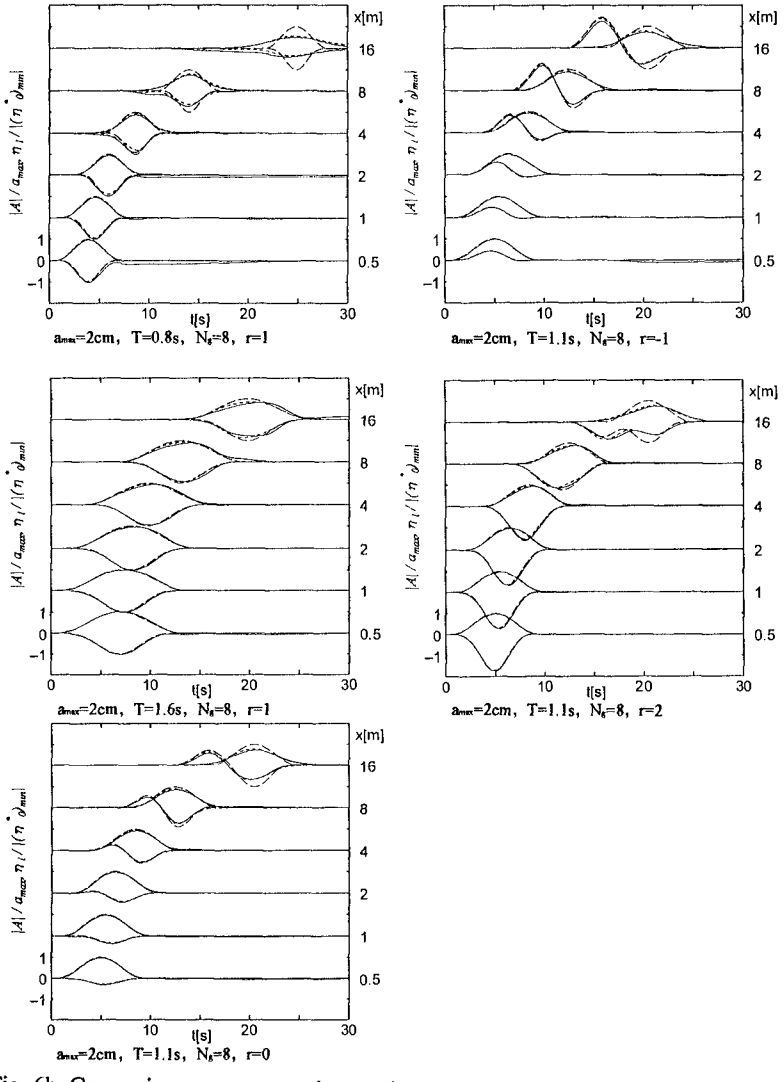

Fig. 6b Comparison among experiment, first- and second-order theories (Case 6 to 10)

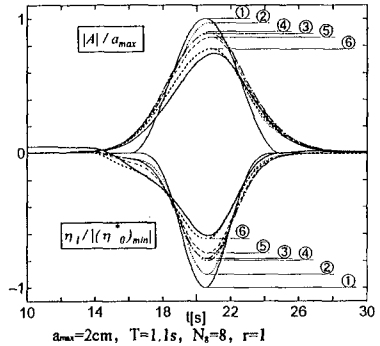

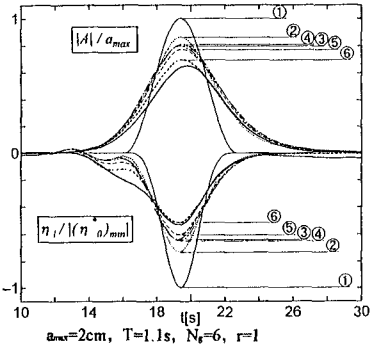

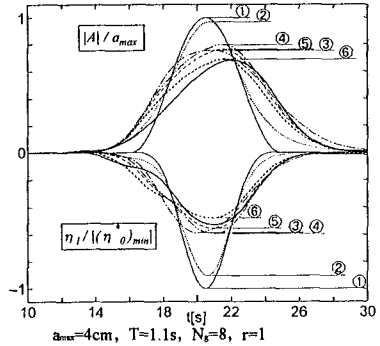

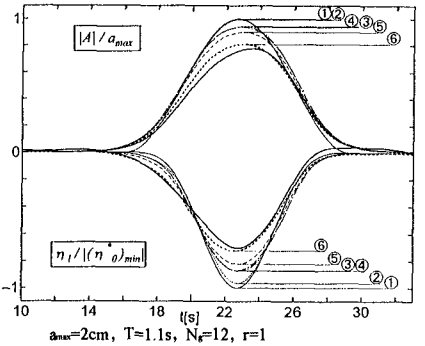

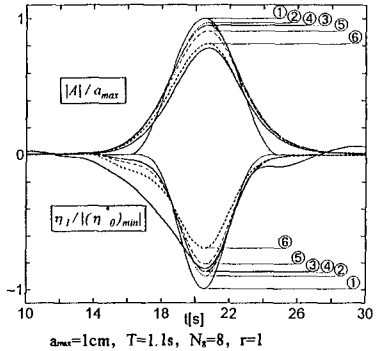

Fig. 7a Contribution of each term in Eq.(5) (case 1 to 5)

Lines in upper half of each figure show envelope profiles and theose in lower half long wave profiles.

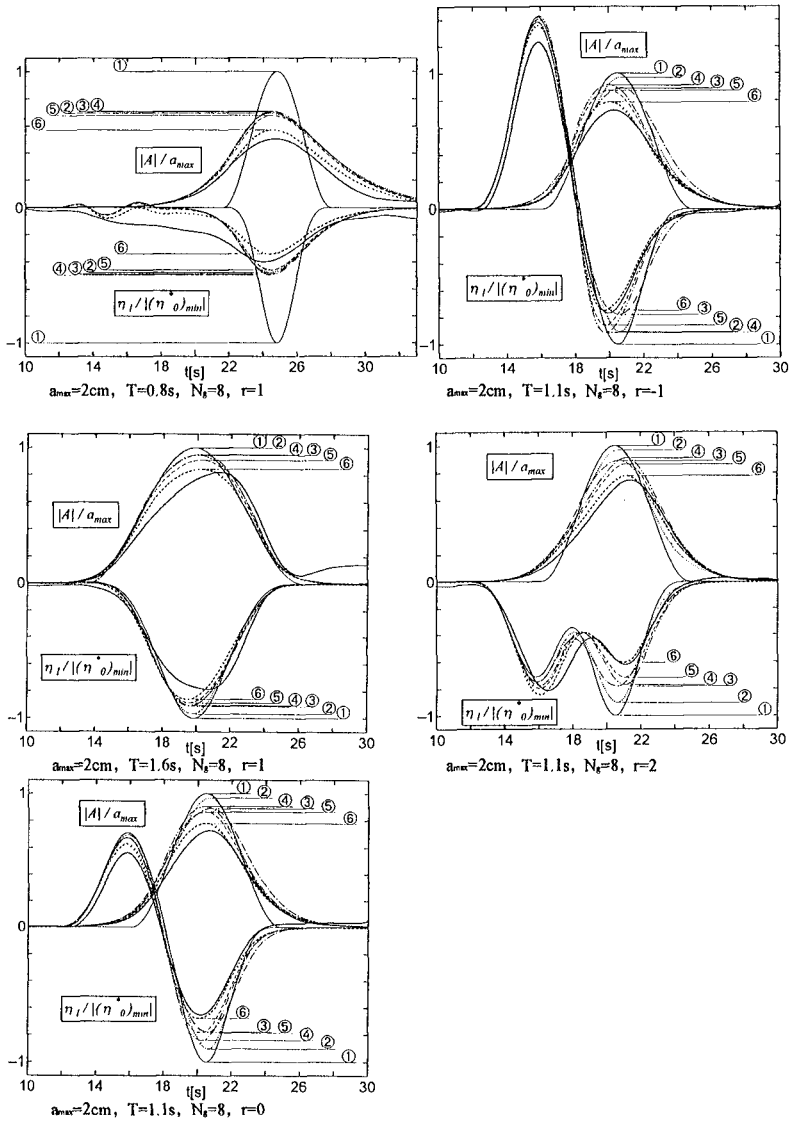

Fig. 7b Contribution of each term in Eq.(5) (case 6 to 10)

waves is calculated as LHS solution, that is by Eq.(1), with the evaluated short wave envelope. Free long waves is defined as the difference between the observed long waves and the calculated bound one.

In all cases both envelope of short waves and long wave (or set-down wave) flatten more or less as they propagate away. In Case 2, phase modulation (change of wave period of short waves) as well as amplitude modulation is clearly seen. Large velocity of bound long waves is responsible. Free second (higher) harmonics are also present, being left behind. In more linear case Case 3, change of wave group is naturally slower. In this case experimental error in long waves could be significant as its magnitude is very small. In Cases 4 and 5, effect of dispersion due to the curavature of $|A|$ is showing. In Cases 6 and 7, effect of the coefficient $\alpha(=\omega''(k))$ for linear dispersion is evident. Cases 8, 9 and 10 show that effect of free long waves may appear in another group of waves travelling ahead.

Comparisons with first- and second-order theories are made in Figs. 6(a) and (b). They may be summarized as in the following. Near the wave maker three of them, experiment, the analytical solution of the first-order theory (Mizuguchi and Toita, 1996) and numerical simulation of Eqs.(5) to (7), agree well for all cases. First-order theory starts to fail to agree with other two at some point. Even after the first-order theory fails, the coupled Eqs. (3) to (5) well describe experimental results.

Discussions on wave modulation

We evaluate degree of contribution of each term by truncating the modulation equation at different position shown below.

$$\partial A/\partial t + c_g \partial A/\partial x + i[\alpha \partial^2 A/\partial x^2 + \beta' |A|^2 A$$
$$\text{--(1)} \qquad \text{--(2)}$$

$$+\{(k/d)(c_g - c/2)\eta_l + ku_l\}A] + \text{dissipation} = 0 \qquad (7')$$
$$\text{--(3)/} \quad \text{--(4)} \quad \text{--(5),(6)}$$

where, in Stage (3) the bound long wave solution is used in this interaction term, in practice Schrodinger-type equation is used. In Stage (5), dissipation only at bottom is included. Stage (1) corresponds to the analytical solution of first-order. Numerical results in Stage (1) to (6) are plotted together with experimental results in Figs 7(a) and (b). Comparison are made for data at x=16m, farthest measuring point from the wave maker. Overall comparison tells that the first-order theory is rather good. For second-order effects, dissipation (in particular at side wall) is always non-negligible in this scale of experimnts. Other second-order effects plays their each role as is expected. In particular following points may be marked. In Case 2, the flattening effect of bound long waves on wave modulation is most

significant, as the difference between Stage (2) to (3) is largest. The cubic nonlinear term is not important as it contributes to sharpening the grouping profile. In Cases 4 and 6, especially in the latter, effect of linear dispersion term (from Stage (1) to (2)) is dominant. Small difference between the experiment and the full thory is noticable in these magnified figures. They may come from either errors in the experiment or higher order effects in theory.

Then the distance X^*, below which rms difference in envelope profile between first-order theory and full second-order theory is less than 5% is calculated by using numerically simulated results with the coupled euations and plotted in Fig. 8. Free waves at the wave maker are suppressed and dissipation neglected. When ka_{max} is large, flattening due to interaction with bound waves is significant and the distance is at most one-quarter of group length. When ka_{max} is small, linear dispersion term $\alpha x\{\text{curavature}\}$ determines the distance, which is of order one wave group length. Significant shoaling of field waves occurs in rather short distance (a few km?), which is of order of one wave group length. The first-order treatment may be sufficiently accurate.

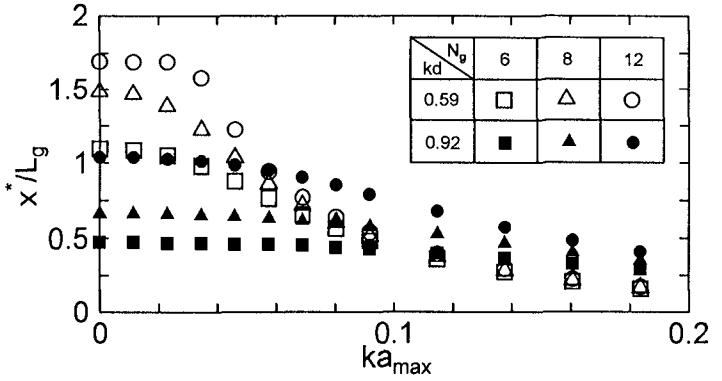

Fig. 9 Traveling distance of negligible change in envelope
L_g is the length of the wave group

Conclusions

1)Coupled equations (5) and (7) can describe well the modulation of short wave group and evolution of long waves in a wide range of experimental results.

2) The second-order effects may be insignificant for shoaling field waves,

although the effect of free long waves could not be fully assesed as the long waves travels ahead of grouping waves.

References

List, J.H.(1992), A model for the generation of two-dimensional surf beat, J.G.R., Vol. 97, C4, 5623-5635.

Longuet-Higgins, M.S. and R.W. Stewart(1962), Radiation stress and mass transport in gravity waves, with application to "surf beat", J.F.M., Vol. 13, 481-504.

Mase, H., K. Matumoto and Y. Iwagaki(1987), Effect of viscous damping on wave group modulation, Proc. of Coastal Engineering, JSCE, Vol. 34, 189-193. (in Japanese)

Mei, C.C.(1989), The applied Dybamics of Ocean Surface Waves, World Scientific, 740 p.

Mizuguchi, M. and H. Toita(1996), Generation of second-order long waves by a wave group in a flume and its control, Proc. 25th ICCE, Orlando, USA, 493-501.

Nagase, S. and M. Mizuguchi(1996), Laboratory experiment on long wave generation by time-varying breakpoint, Proc. 25th ICCE, Orlando, USA, 1307-1320.

Observation and Simulation of Low-frequency Waves on Two Natural Beaches

Satoshi NAKAMURA [1] and Nicholas DODD [2]

Abstract

Field observations of low-frequency wave on natural beaches are carried out. The ratio of the wave height of low-frequency wave near the shoreline to the wind wave height at the offshore has positive correlation with the surf similarity parameter. Using the field data, a validation of a numerical model was made. The model includes basic mechanisms of low-frequency wave generation that low-frequency wave increases with shoaling of wind waves groups, they are released from wave groups due to wave breaking and wind wave period becomes longer due to run-up to the beach. The model results tend to be excessively computed against field data.

Introduction

Low-frequency waves, with wave periods in the order of minutes, appear in the surf zone most noticeably when pronounced wind wave groups exist offshore. Generation of bound or free low-frequency waves can be conclusively explained that the structure of wave group changes. Therefore the low-frequency waves are made everywhere when the wind wave groups change its shape. At the offshore, obtained wave data contain low-frequency waves of all direction from different origin such as bound low-frequency waves grown beneath wind wave group, free low-frequency waves generated near the wave breaking points and from the breakwaters and the shoreline, and low-frequency waves caused by wind wave refraction. In the surf zone, the low-frequency waves, which are mainly generated by wave breaking and become standing waves, occasionally cause rapid nearshore bar migration and berm shape changes by running-up beyond the berm crest.

In this paper, field observations are presented. The simultaneous data of offshore and nearshore low-frequency waves are obtained. A numerical model which includes mechanisms of low-frequency wave generation is used to simulate the observed dynamics.

[1]Marine Environment Division, Port and Harbour Research Institute, 3-1-1 Nagase, Yokosuka 239-0826, Japan

[2]Coastal Group, HR wallingford, Howbery Park, Wallingford, OX10 8BA, UK.

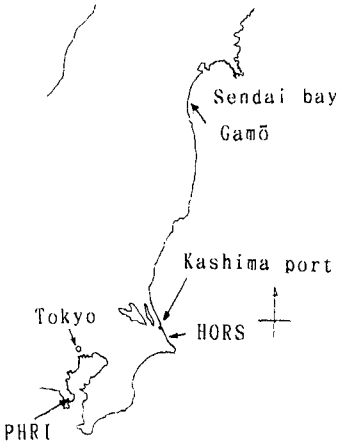

Figure 1: Map of observation sites

Field observation

Study sites

Field studies of low-frequency waves and wave groups have been carried out at two sites of the east coast of Japan (see fig.1).

One field observation has been carried out at a seashore site near Gamō tidal lagoon in the Sendai bay on the Pacific coast since 1997 for the study of wave run-up with the low-frequency waves on a berm and of offshore wave groups. In this observation, wave data were collected continuously with sampling 0.5s intervals using only 2 wave gages at the offshore and near the shoreline. Figure 2 shows the beach profile at Gamō and location of the wave gages. The offshore wave gage, which is set on the sea bottom at 4km offshore from the shoreline and 20m depth, measures the sea surface elevation using ultrasonic wave. The nearshore ultra-sonic wave gage is attached in the air on a scaffold at the shoreline. A highly-sensitive CCD camera and video recorder, which is set on the berm, is used to record the wave run-up and over-topping events beyond the berm crest. During observation period, an over-topping event does not record unfortunately. We do not use video data in this paper.

Another field observation was carried out at Hazaki Oceanographical Research Station (HORS) in 1989 (see Nakamura and Katoh, 1992) for the study of the propagation of incident wave groups and the low-frequency nearshore

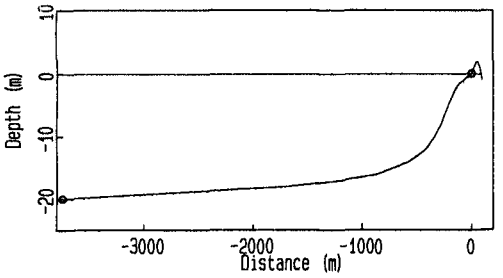

Figure 2: Beach topography of Gamō beach

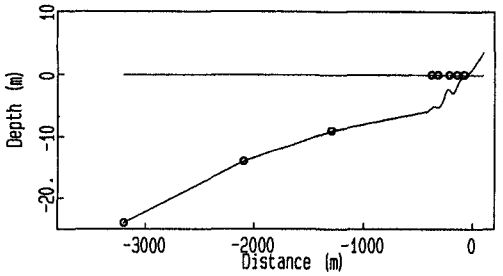

Figure 3: Beach topography of HORS

wave motion in the storm condition. Figure 3 shows the beach profile at HORS and location of the wave gages. This data set contains simultaneous recordings of 10 wave gages from the shoreline to 3.2km offshore during a storm.

Data analysis

A set of wave record, which length is approximately 2 hours, separated in the frequency band upper 0.04Hz and the low-frequency band using FFT method. Significant wind wave heights, H_S, and periods, T_S, are calculated from the higher band wave record using zero-up-cross method. Significant low-frequency wave heights, H_L, and periods, T_L, are calculated same way. For the numerical model input, the wave energy time series is calculated from the wave envelope

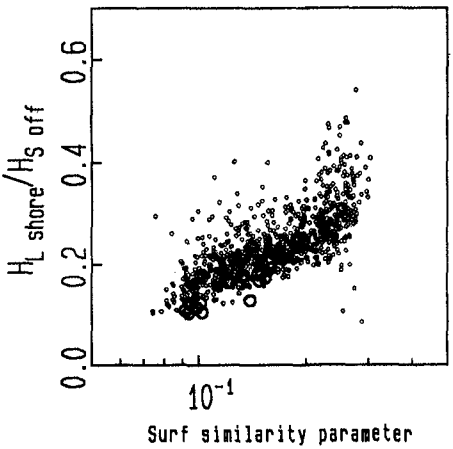

Figure 4: Ratio of the low-frequency wave height in the surf zone to the significant wave height in the offshore vs. surf similarity parameter

using Hilbert transform (see Hudspeth and Medina, 1988) of the wind wave record is used.

Figure 4 shows the ratio of low-frequency wave height near the shoreline, H_{Lshore}, to offshore wind wave height, H_{Soff}, against the surf similarity parameter, $\tan\beta_b/\sqrt{H_{Soff}/L_{Soff}}$, where $L_{Soff} = 1.56 * T_{Soff}^2$ is offshore wave length and $\tan\beta_b$ is the slope of the surf zone in case of Gamō $\tan\beta_b = 1/70$ and in case of HORS $\tan\beta_b = 1/60$. In figure 4, small circles indicate the data obtained at Gamō and large circles at HORS. The ratio of H_{Lshore}/H_{Soff} has positive correlation with the surf similarity parameter. In both cases, the plots seem to be scattered on a line. This fact suggests that height of low-frequency waves in the surf zone becomes large not only as height of offshore wave becomes large but on condition that beach profile and waves fill some requirements.

Figure 5 shows the ratio of low-frequency wave height at the offshore, H_{Loff}, to offshore wave height, H_{Soff}, against the surf similarity parameter. There are two groups of plots in figure 5. One is the ratio of H_{Loff}/H_{Soff} has positive correlation with the surf similarity parameter. Another group is the ratio has no correlation with the surf similarity parameter. The feature of this group is that it appear in Gamō data at the calm condition several days after the storm and it does not appear in HORS data. According to the NOWPHAS

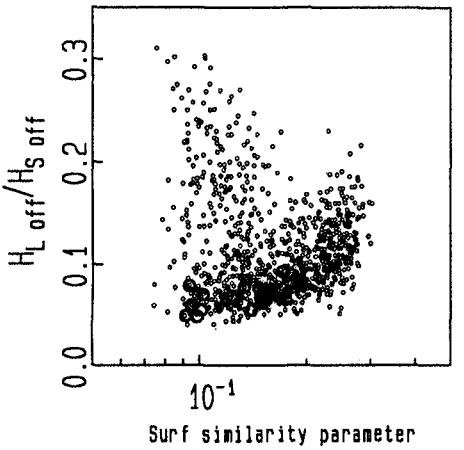

Figure 5: Ratio of the low-frequency wave height to the significant wave height in the offshore vs. surf similarity parameter

data PHRI (1996), at Sendai New Port where is nearest observation point of Gamō, the relative frequency of calm condition ($H_s \leq 0.5m$) is 24.5% and the distribution of incident wave direction is narrow (main direction is SE) and at Kashima Port where is nearest point of HORS, the relative frequency of calm condition is 2.5% and the distribution of incident wave direction is wide (main direction is E). Comparing Gamō with HORS, as Gamō beach is located at the inner part of the bay, heights of significant wind wave quickly decrease after storm due to an effect of interception of Sendai bay. I suppose that trapped small amplitude low-frequency waves in Sendai bay are observed at offshore Gamō beach.

Numerical model

Low-frequency wave model

The numerical model of low-frequency waves uses an upwind, Godunov-type finite volume method to solve the equations. This method alleviates the problem of tracking multiple shorelines, which can occur over barred beaches (see Dodd, 1998; Nakamura and Dodd, 1997). The numerical equations used in the model are the one-dimensional depth-integrated and time-averaged non-linear shallow water equations of mass (eq.1) and momentum (eq.2), in which the

radiation stress gradient is included as a forcing term, and the energy balance of fluctuating motion equation (eq.3) (see e.g. Roelvink, 1993; Zou and Dodd, 1994) includes the interaction of wind wave energy and low-frequency waves.

$$\frac{\partial D}{\partial t} + \frac{\partial (DU)}{\partial x} = 0, \tag{1}$$

$$\frac{\partial (DU)}{\partial t} + \frac{\partial}{\partial x}\left(DU^2 + \frac{1}{2}gD^2\right) = gD\frac{\partial h}{\partial x} - \frac{\partial}{\partial x}\left(\frac{S_{11}}{\rho}\right) - \tau_b, \tag{2}$$

$$\frac{\partial E}{\partial t} + \frac{\partial}{\partial x}[(c_g + U)E] + \frac{\partial}{\partial x}(US_{11}) = -\mathcal{D}, \tag{3}$$

where D is the total mean water depth, U is the mean velocity, h is the still water depth, τ_b is a bottom friction term, $\mathcal{D}$ is a dissipation term,

$$E = \frac{\rho g}{8}H^2, \tag{4}$$

$$c_g = \frac{1}{2}\frac{\omega}{k}\left(1 + \frac{2kD}{\sinh 2kD}\right), \tag{5}$$

and

$$S_{11} = E\left(2\frac{c_g}{c} - \frac{1}{2}\right). \tag{6}$$

The interaction terms appear effective close to the shoreline where wave speed and water velocity are nearly equal. To calculate low-frequency waves generation nearshore zone, we use here the 1D model as that the wind wave was being incident on the coastline at the normal angle is supposed for reason that both of near HORS and Gamō beach topography have little change into alongshore direction. To simulate trapped low-frequency wave by alongshore topography such as edge waves, of course, the 2D model has to be used.

Simulations

In this model, the radiation stress gradient works as a forcing term. So, the distribution of the radiation stress seriously affects on the model results. As this model calculate radiation stress using a simple function of wave height (eqs.4-6), we compare the wave height distribution between the field data and the model result. Figure 6 is a comparison of the distribution of mean wind wave height in storm condition ($H_s = 2.4m$, $T_s = 11.8s$) at HORS. Solid line is a model result that is calculated from each steps of the distribution of wave energy simulated by giving a time series of wind wave energy at the offshore boundary. Roelvink's wave dissipation model($\gamma = 0.65$ and as following Roelvink $\alpha = 1.0, n = 10$) is used in this model results. Circles indicate the field data. The model results of nearshore mean wave height has a good

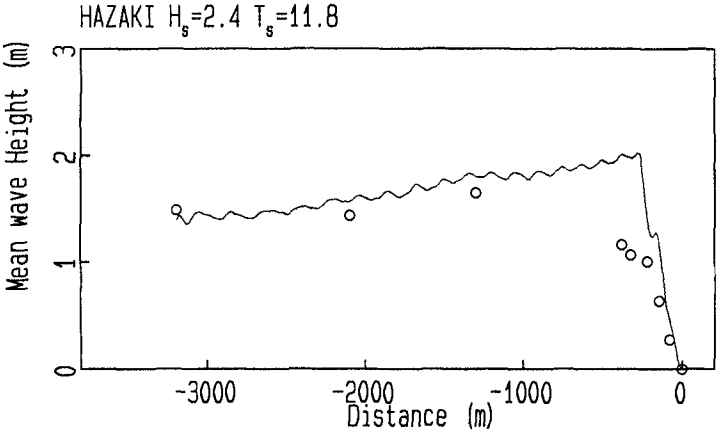

Figure 6: Comparison of mean wave height distribution between field data and model results

agreement with field data but the results of mean wave height near the wave breaking point is over estimated.

Figure 7 shows a comparison of the distribution of low-frequency wave height in same wave condition of fig.6. Bold solid line is a model results. Thin solid line is a model result of mean water level (no comparison with field data). Circles are field data. In model result, low-frequency wave height is calculated excessively. The distance between the field data of low-frequency wave height near the shoreline and the model result of that can be reduced using a large bottom friction coefficient at this region. We do not use such adjustment because it is not essential. At the shoreline (0m), low-frequency wave height in field is not calculated because run-up waves come rarely at this point.

Comparisons

Comparisons of low-frequency wave height between the field data and the model results are done with chose 13 data sets, which are embraced in the group that the ratio of H_{Loff}/H_{Soff} has positive correlation with the surf similarity parameter, in Gamō data sets and 15 data sets in HORS data sets.

Figure 8 shows a comparison of low-frequency wave heights near the shore-

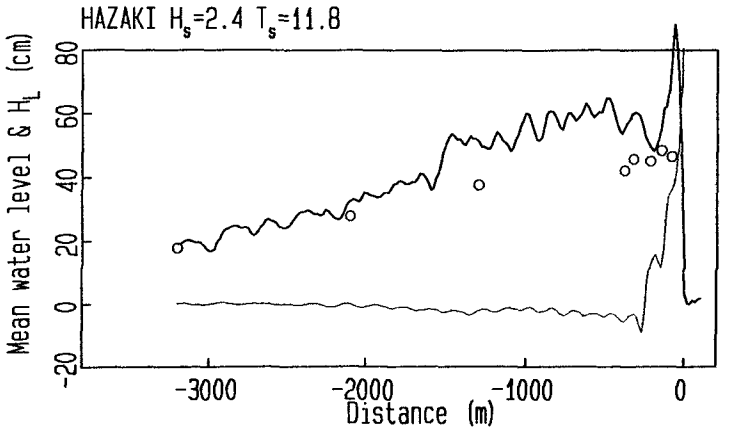

Figure 7: Comparison of low-frequency wave height distribution between field data and model results

line between field data and model results. Small boxes indicate the Gamō data and large boxes the HORS data. The model results become excessive estimation of wave height in proportion that low-frequency wave height in field becomes large. This tendency is explained as the model feature at fig.7.

Figure 9 shows a comparison of low-frequency wave heights in the offshore between field data and model results. Small boxes indicate the Gamō data and large boxes the HORS data. There are three under-estimated results. Except three data, the model results are well computed.

Conclusions

During the observation period at Gamō, a few simultaneous observation records using offshore and nearshore wave gages were gotten. Conspicuous run-up events at Gamō as water invade a lagoon beyond the crest of sand dune aren't observed by video records.

At offshore Gamō beach, the small amplitude of low-frequency waves are observed in calm condition until several days after storms. Comparing Gamō with HORS, as Gamō beach is located at the inner part of the bay, heights of significant wind wave quickly decrease after storm due to an effect of interception of Sendai bay. There seems to be trapped small amplitude low-frequency

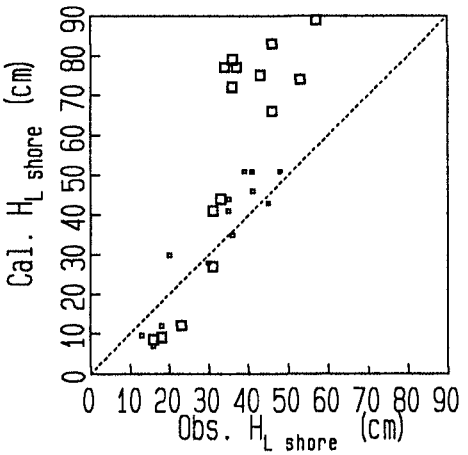

Figure 8: Comparison of low-frequency wave heights near the shoreline between field data and model results

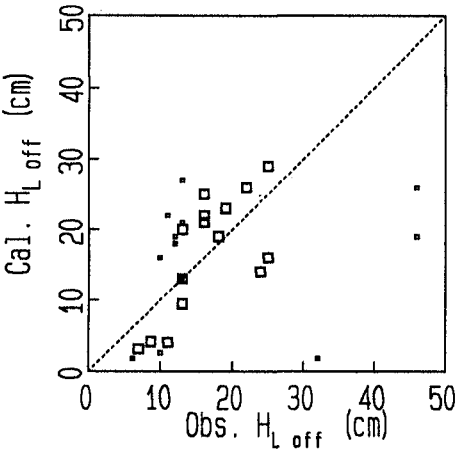

Figure 9: Comparison of low-frequency wave heights in the offshore between field data and model results

waves in Sendai bay.

The computation result of the low-frequency wave tends to be excessively computed. This cause is to compute the energy of the wind wave excessively. To do the better simulation, the wind wave energy dissipation and the bottom friction of the low-frequency wave must be well computed. The way to the better simulation seems to be essential difference that wind wave breaking on the surface low-frequency motion, the radiation stress in breaking waves and sediment moving by low-frequency current.

References

N. Dodd. A numerical model of wave run-up, overtopping and regeneration. *J. Water. Port Coast. Ocean Eng.*, 1998. To appear.

R. T. Hudspeth and J. R. Medina. Wave group analysis by the Hilbert transform. In *Proc. 21st Int. Conf. Coastal Eng.*, pages 884–898, Malaga, 1988. A.S.C.E.

S. Nakamura and N. Dodd. A numerical model of low-frequency wave motion on a beach and over reefs. In *Proc. of Waves'97*, 3rd Int. Symp. On Ocean Wave Measurement and Analysis, 1997. A.S.C.E.

S. Nakamura and K. Katoh. Generation of infragravity waves in breaking process of wave groups. In *Proc. 23rd Int. Conf. Coastal Eng.*, pages 990–1003, Venice, 1992. A.S.C.E.

PHRI. Nowphas 1997-1994. Technical report, Port and Harbour Research Institute, MOT, 1996.

J. A. Roelvink. *Surf beat and its effect on cross-shore profiles.* PhD thesis, Delft University of Technology, 1993.

Z. Zou and N. Dodd. A nonlinear surf beat model. In *Proc. 24th Int. Conf. Coastal Eng.*, pages 1961–1974, Kobe, 1994. A.S.C.E.

QUASI 3-D EFFECTS IN INFRAGRAVITY WAVES

A.R. Van Dongeren[1], I.A. Svendsen[2], and U. Putrevu[3]

ABSTRACT: *The present paper describes a numerical study of infragravity waves forced by obliquely-incident wave groups. In this study, the depth-integrated, shortwave-averaged nearshore circulation model SHORECIRC (Van Dongeren et al., 1994), which includes the quasi three-dimensional effects, is used. The governing equations that form the basis of the model, as well as the numerical model and the boundary conditions are described. The model is applied to the case of leaky infragravity waves. The magnitude of the quasi 3-D terms and their effect on the infragravity wave envelope is analyzed, and the velocity profiles of the infragravity waves are shown.*

INTRODUCTION

The depth-integrated, shortwave-averaged nearshore circulation model SHORECIRC (Van Dongeren *et al.*, 1994) belongs to the class of quasi-3D (Q3D) models, which combine the effect of the vertical structure with the simplicity of two-dimensional horizontal (2DH) models.

Several approaches to the development of Q3D models can be found in the literature. De Vriend & Stive (1987) split the current into primary and secondary flow profiles based on the assumption that the primary velocity profiles are the same in the cross-shore and longshore direction. In a different approach, Svendsen & Lorenz (1989) determined the vertically-varying longshore and cross-shore currents separately under the assumption of weak dependence. Svendsen & Putrevu (1990) formulated a steady state version of the nearshore circulation model using analytical solutions for the 3D current profiles in combination with a numerical solution of the depth-integrated 2D horizontal equations for a long straight coast. They split the current velocity into a depth-invariant component and a component with a vertical variation with zero mean flow integrated over the central layer. Sánchez-Arcilla *et al.* (1990, 1992) presented a similar concept.

Putrevu & Svendsen (1992) and Svendsen & Putrevu (1994) recognized that the current-current and current-wave interactions neglected in previous investigations induce a non-linear dispersion mechanism, analogous to the dispersion of solutes (Taylor, 1954). This mechanism significantly augments the lateral turbulent mixing

[1]Associate Researcher, Netherlands Centre for Coastal Research, Delft University of Technology, P.O. Box 5048, 2600 GA, Delft, The Netherlands. email: A.vanDongeren@ct.tudelft.nl

[2]Distinguished Professor, Center for Applied Coastal Research, University of Delaware, Newark, DE 19716, USA. email: ias@coastal.udel.edu

[3]Research Scientist, NorthWest Research Associates, Inc., 14508 NE 20th Street, Bellevue, WA 98007, USA. e-mail: putrevu@nwra.com.

and accounts for the difference in magnitude between the vertical and horizontal mixing in the case of a longshore current on a long, straight coast.

The time-dependent version of this model, called SHORECIRC, was presented in Van Dongeren *et al.* (1994) for the special case of longshore uniformity in both the bathymetric and hydrodynamical conditions. The generalized quasi 3-D governing equations were derived in Putrevu & Svendsen (1997a,b) and Van Dongeren & Svendsen (1997a).

Recently, SHORECIRC has been used to study a number of nearshore phenomena, such as shear instabilities over longshore-varying bathymetries (Sancho *et al.*, 1997, 1998) and rip currents over a bar (Haas *et al.*, 1998).

In the present paper SHORECIRC will be used to study infragravity waves forced by obliquely-incident wave groups and the associated quasi 3-D effects on a cylindrical coast.

GOVERNING EQUATIONS

The depth-integrated, time-averaged mass and momentum equations incorporated in SHORECIRC are derived from the Reynolds' equations which are integrated over depth and averaged over the shortwave period largely following the procedure outlined in Phillips (1977) and Mei (1983). In the present approach, which is given in more detail in Putrevu & Svendsen (1997a,b) and Van Dongeren & Svendsen (1997a), the total horizontal velocity of the long and short waves is further split into a depth-uniform long wave part $\tilde{V}_\alpha$, a depth-varying long wave part $V_{1\alpha}$ and a short-wave contribution $u_{w\alpha}$, so that

$$u_\alpha(x,y,z,t) = \tilde{V}_\alpha(x,y,t) + V_{1\alpha}(x,y,z,t) + u_{w\alpha}(x,y,z,t) \tag{1}$$

We define $\overline{u_{w\alpha}} \equiv 0$ below trough and define the shortwave-induced volume flux above the trough level as

$$Q_{w\alpha} \equiv \overline{\int_{\zeta_t}^{\zeta} u_{w\alpha}\, dz} \tag{2}$$

where ζ_t denotes the trough level of the short-wave motion. The total flux $\tilde{Q}_\alpha$ can then be written as

$$\tilde{Q}_\alpha \equiv \overline{\int_{-h_o}^{\bar{\zeta}} u_\alpha\, dz} = \tilde{V}_\alpha\, h + \int_{-h_o}^{\bar{\zeta}} V_{1\alpha}\, dz + Q_{w\alpha} \tag{3}$$

where h_o is the still water depth, $\bar{\zeta}$ is the surface elevation of the long (or IG) wave motion, and $h = h_o + \bar{\zeta}$ is the total depth. With this result, the depth-integrated shortwave-averaged conservation of mass can be written as

$$\frac{\partial \bar{\zeta}}{\partial t} + \frac{\partial \tilde{Q}_\alpha}{\partial x_\alpha} = 0 \tag{4}$$

where the index α represents the horizontal x, y directions, and z is the vertical coordinate, defined from the still water level (SWL) up.

Using the same splitting procedure, the horizontal conservation of momentum can be expressed as

$$\frac{\partial \bar{Q}_\beta}{\partial t} + \frac{\partial}{\partial x_\alpha}\left(\frac{\bar{Q}_\alpha \bar{Q}_\beta}{h}\right) + \frac{\partial}{\partial x_\alpha}\overline{\int_{\zeta_t}^{\zeta} (u_{w\alpha} V_{1\beta} + u_{w\beta} V_{1\alpha})\, dz} +$$

$$\frac{\partial}{\partial x_\alpha}\int_{-h_o}^{\bar{\zeta}} V_{1\alpha} V_{1\beta}\, dz = -g h \frac{\partial \bar{\zeta}}{\partial x_\beta} - \frac{1}{\rho}\frac{\partial}{\partial x_\alpha}\left[S_{\alpha\beta} - \overline{\int_{-h_o}^{\zeta} \tau_{\alpha\beta}\, dz}\right] + \frac{\tau_\beta^S - \tau_\beta^B}{\rho} \quad (5)$$

where β is index notation for the horizontal x and y directions, $\tau_{\alpha\beta}$ represents the turbulent shear stresses, τ_β^S is the surface stress and τ_β^B is the bottom stress. The radiation stress is defined as[1]

$$S_{\alpha\beta} \equiv \overline{\int_{-h_o}^{\zeta} (p\,\delta_{\alpha\beta} + \rho u_{w\alpha} u_{w\beta})\, dz} - \delta_{\alpha\beta}\frac{1}{2}\rho g h^2 \quad (6)$$

The governing equations (4) and (5) would be readily solvable numerically if the depth variation of the long wave velocity $V_{1\alpha}$ were known. However, this would require a three-dimensional grid and therefore a large computional time. In order to reduce the computational time, the depth-dependent terms can be replaced by semi-analytical solutions, which are functions of the depth-integrated terms. In this so-called quasi 3-D approach only a two-dimensional numerical model is needed. This substitution can be achieved by using the local (i.e., *not* depth-integrated), time-averaged momentum equations (see e.g., Svendsen & Lorenz, 1989), which after some manipulations can be written as (Putrevu & Svendsen, 1997a,b; Van Dongeren & Svendsen, 1997a)

$$\frac{\partial V_{1\beta}}{\partial t} - \frac{\partial}{\partial z}\left(\nu_t \frac{\partial V_{1\beta}}{\partial z}\right) = -\beta_\beta + \frac{1}{\rho h}\frac{\partial}{\partial x_\alpha}\left(S_{\alpha\beta} - \overline{\int_{-h_o}^{\zeta} \tau_{\alpha\beta}\, dz}\right) - \frac{\tau_\beta^S - \tau_\beta^B}{\rho h}$$

$$- V_{1\alpha}\frac{\partial \tilde{V}_\beta}{\partial x_\alpha} - \tilde{V}_\alpha \frac{\partial V_{1\beta}}{\partial x_\alpha} - W\frac{\partial V_{1\beta}}{\partial z} \quad (7)$$

where

$$\beta_\beta = \frac{\partial}{\partial x_\alpha}\left(\overline{u_{w\alpha}u_{w\beta}} - \overline{w_w^2}\right) + \frac{\partial \overline{u_{w\beta}w_w}}{\partial z} - \frac{\partial}{\partial x_\alpha}\left(\nu_t\left(\frac{\partial \tilde{V}_\alpha}{\partial x_\beta} + \frac{\partial \tilde{V}_\beta}{\partial x_\alpha}\right)\right) \quad (8)$$

In this expression w_w denotes the vertical short-wave velocity and ν_t is the turbulent eddy viscosity.

Eq. (7) can be solved more easily if we split the depth-varying velocity into two parts

$$V_{1\beta} = V_{1\beta}^{(0)} + V_{1\beta}^{(1)} \quad (9)$$

[1]This definition is symbolically similar to Mei (1983), who uses a different definition of $u_{w\alpha}$, however. He requires $\overline{\int_{-h_o}^{\zeta} u_{w\alpha}\, dz} = 0$.

where the first part is primarily the (slowly time-varying) component generated by the local external forcing, which are the first five terms on the RHS of (7), while the second, smaller contribution is generated by the advective terms (the last three terms on the RHS) in (7). Hence, we can solve for $V_{1\beta}^{(0)}$, which represents the first approximation to the depth-varying part of the infragravity velocity profiles.

In the present paper we further assume a quasi steady-state. This means that we can solve the first part of (7) by integration twice over depth with two boundary conditions: a slip boundary condition at the bottom and a conservation of mass condition over the vertical. If we define

$$f_\beta \equiv \beta_\beta - \frac{1}{\rho h}\frac{\partial}{\partial x_\alpha}\left(S_{\alpha\beta} - \overline{\int_{-h_o}^{\zeta} \tau_{\alpha\beta}\, dz}\right) + \frac{\tau_\beta^S - \tau_\beta^B}{\rho h} \tag{10}$$

the solution of (7) becomes

$$V_{1\beta}^{(0)} = \frac{f_\beta}{2\,\nu_t}\,\xi^2 + \frac{\tau_\beta^B}{\rho\,\nu_t}\,\xi - \left(\frac{f_\beta}{6\,\nu_t}\,h^2 + \frac{\tau_\beta^B}{\rho\,\nu_t}\,\frac{h}{2} + \frac{Q_{w\beta}}{h}\right) \tag{11}$$

where the vertical coordinate z has been transformed to a new coordinate ξ, under the transformation $\xi = z + h_o$, which means that $\xi = 0$ at the local bottom and $\xi = h = h_o + \bar{\zeta}$ at the mean surface elevation.

Putrevu & Svendsen (1997a,b) show that this expression is the first approximation to the time-dependent solution of (7). Hence, in the quasi-steady approximation the velocity profiles are quadratic and known so that the quasi 3-D coefficients (12) - (15) can be expressed in terms of the coefficients of the velocity profiles.

Following the derivation of Putrevu & Svendsen (1997) and Van Dongeren & Svendsen (1997a), which is omitted here for brevity, we can define the coefficients

$$D_{\alpha\gamma} \equiv \frac{1}{h}\int_{-h_o}^{\bar{\zeta}} V_{1\alpha}^{(0)} \int_z^{\bar{\zeta}} \frac{1}{\nu_t} \int_{-h_o}^{z} V_{1\gamma}^{(0)}\,(dz)^3 \tag{12}$$

$$M_{\alpha\beta} \equiv \int_{-h_o}^{\bar{\zeta}} V_{1\alpha}^{(0)}\, V_{1\beta}^{(0)}\, dz + V_{1\alpha}^{(0)}(\bar{\zeta})\, Q_{w\beta} + V_{1\beta}^{(0)}(\bar{\zeta})\, Q_{w\alpha} \tag{13}$$

$$\begin{aligned} A_{\alpha\beta\gamma} \equiv & -\int_{-h_o}^{\bar{\zeta}} V_{1\alpha}^{(0)} \int_z^{\bar{\zeta}} \frac{1}{\nu_t}\left(\frac{\partial}{\partial x_\gamma}\int_{-h_o}^{z} V_{1\beta}^{(0)}\, dz - V_{1\beta}^{(0)}\frac{\partial h_o}{\partial x_\gamma}\right)(dz)^2 \\ & -\int_{-h_o}^{\bar{\zeta}} V_{1\beta}^{(0)} \int_z^{\bar{\zeta}} \frac{1}{\nu_t}\left(\frac{\partial}{\partial x_\gamma}\int_{-h_o}^{z} V_{1\alpha}^{(0)}\, dz - V_{1\alpha}^{(0)}\frac{\partial h_o}{\partial x_\gamma}\right)(dz)^2 \end{aligned} \tag{14}$$

and

$$\begin{aligned} B_{\alpha\beta} \equiv & \frac{1}{h}\int_{-h_o}^{\bar{\zeta}} V_{1\alpha}^{(0)} \int_z^{\bar{\zeta}} \frac{1}{\nu_t} \int_{-h_o}^{z} V_{1\beta}^{(0)}\,(dz)^3 - \frac{1}{h}\int_{-h_o}^{\bar{\zeta}} V_{1\alpha}^{(0)} \int_z^{\bar{\zeta}} \frac{1}{\nu_t} V_{1\beta}^{(0)}\,(h_o + z)\,(dz)^2 \\ & -\frac{1}{h}\int_{-h_o}^{\bar{\zeta}} V_{1\beta}^{(0)} \int_z^{\bar{\zeta}} \frac{1}{\nu_t} V_{1\alpha}^{(0)}\,(h_o + z)\,(dz)^2 \end{aligned} \tag{15}$$

These expressions appear when the solution for $V_{1\alpha}^{(0)}$ is substituted into the depth-dependent integrals in the conservation of momentum equation (5), which - after some algebra - becomes

$$\frac{\partial \bar{Q}_\beta}{\partial t} + \frac{\partial}{\partial x_\alpha}\left(\frac{\bar{Q}_\alpha \bar{Q}_\beta}{h} + M_{\alpha\beta}\right) - \frac{\partial}{\partial x_\alpha}\left[h\left(D_{\beta\gamma}\frac{\partial \tilde{V}_\alpha}{\partial x_\gamma} + D_{\alpha\gamma}\frac{\partial \tilde{V}_\beta}{\partial x_\gamma} + B_{\alpha\beta}\frac{\partial \tilde{V}_\gamma}{\partial x_\gamma}\right)\right]$$
$$+ \frac{\partial}{\partial x_\alpha}\left[A_{\alpha\beta\gamma}\tilde{V}_\gamma\right] = -g\,h\frac{\partial \bar{\zeta}}{\partial x_\beta} - \frac{1}{\rho}\frac{\partial}{\partial x_\alpha}\left(S_{\alpha\beta} - \overline{\int_{-h_o}^{\zeta} \tau_{\alpha\beta}\,dz}\right) + \frac{\tau_\beta^S - \tau_\beta^B}{\rho} \quad (16)$$

where an eddy viscosity closure for the turbulent shear stresses (e.g., Rodi, 1980) is used.

NUMERICAL MODEL

In the version of SHORECIRC used in this paper, eqs. (4) and (16) are solved using a central finite difference scheme on a fixed spatial grid with an explicit second-order Adams-Bashforth predictor and a third-order Adams-Moulton corrector time-stepping scheme. Additionally, the program evaluates (11) in order to calculate the quasi 3-D coefficients (12) - (15).

At the seaward boundary an absorbing-generating boundary condition which is capable of simultaneously generating and absorbing obliquely-incident long waves with a minimum of reflection is implemented, see Van Dongeren & Svendsen (1997b) for details.

At the shoreline, an inundation-drainage procedure, as described in Van Dongeren & Svendsen (1997a), is used which allows for time-varying run-up and run-down of the shortwave-averaged shoreline. At the lateral (shore-normal) boundaries a periodicity condition is used.

QUASI 3-D EFFECTS IN LEAKY INFRAGRAVITY WAVES

In this analysis the model is applied to the case of leaky infragravity waves forced by obliquely-incident wave groups. We will focus on the effect of the quasi 3-D coefficients defined in (12) - (15) and the corresponding quasi 3-D terms in the momentum equation (16).

In our investigation we will choose a very simple bathymetry consisting of a plane beach rising from an offshore shelf, see Fig. 1a for a definition sketch. On the offshore shelf we assume that the depth varies so gently that the waves stay in local equilibrium and that at the toe of the coastal slope the set-down wave corresponds to the equilibrium bound wave found by Longuet-Higgins & Stewart (1962, 1964). This avoids the difficulty encountered by e.g. Lippmann *et al.* (1997) in justifying the use of long wave theory in the deep water part of their plane slope. It also enables us to specify the conditions at the toe as a simple boundary condition for the inflow to the coastal slope. In the present study we limit the analysis to a plane coastal slope to facilitate a comparison to analytical results, but it should be emphasized that the model can be run on an arbitrary bottom topography.

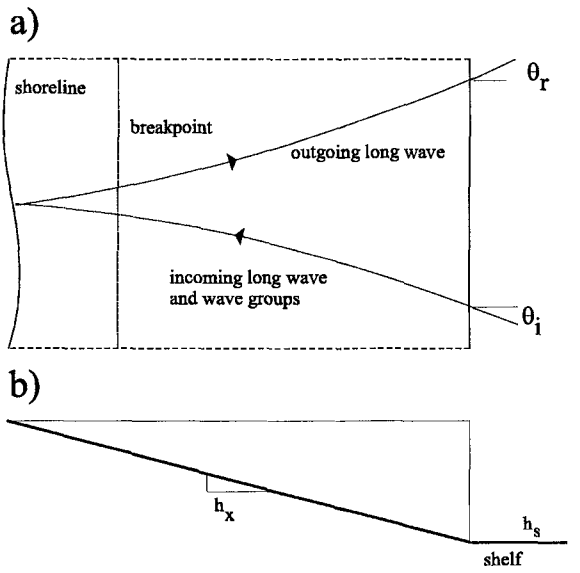

Figure 1: Definition sketch of obliquely-incident and obliquely-reflected infragravity waves. a) plan view; b) cross-section.

The incident wave groups consist of two sinusoidal short wave components that have a slightly different frequency but have the same direction of propagation as a given depth.

Given this short-wave forcing, the radiation stress $S_{\alpha\beta}$ can be written as (generalizing from Schäffer (1994))

$$S_{\alpha\beta} = \rho g P_{\alpha\beta} \begin{cases} H_1^2 \, (1 + 2\delta \cos(2\vartheta)) \,, & h \geq h_b \\ \gamma^2 h_o^2 \, (1 + 2\delta \, (1 - \kappa) \cos(2\vartheta)) \,, & h \leq h_b \end{cases} \tag{17}$$

where H_1 is the height of the carrier wave and the wave height modulation $\delta = H_2/H_1$ is the ratio of the wave heights of the secondary wave to the primary wave in the group. In this formulation it is assumed that δ is small. κ is the breaking parameter, as defined by Schäffer (1994). The breaking criterion is $H_1 = \gamma h_o$, $P_{\alpha\beta}$ is the nondimensional shape parameter for the short waves, and ϑ is the phase function defined following Schäffer (1994).

As these wave groups propagate towards shore at the group speed c_g, they refract towards the shore-normal direction whereby it is assumed that both short wave components refract in the same way and that they do not diverge. The incoming bound infragravity wave that propagates with the groups in the same direction will

also refract in. As the wave groups shoal onto the beach and the short waves are dissipated, this incoming IG wave is modified by the wave group transformation and is released. It will then reflect off the shore and propagate and refract seawards as a free long wave, see Fig. 1 for a definition sketch.

In the following case the input parameters are: shelf depth $h_s = 3\,m$ and mean short-wave frequency $\omega = 1.8\,s^{-1}$, so that the wavenumber $k_s = 0.397\,m^{-1}$. The wave height of the primary short wave on the shelf $H_{1,s} = 2\,a_{1,s} = 0.6\,m$ and the wave height modulation $\delta = 0.1$. The frequency modulation is chosen as $\epsilon = 0.1$. The breaking index is $\gamma = 0.75$, and we choose first to consider a fixed breakpoint $\kappa = 0$. The beach slope is chosen as $h_x = 1/20$. Finally, the angle of incidence on the shelf is chosen as $\theta_{i,s} = 22.37^o$ with the normal, which corresponds to an alongshore wave length of the infragravity wave of 150 meters. The angle of incidence is less than the limiting angle of incidence $\theta_{i,s}^{max} = 37.07^o$, so that the infragravity wave motion is "leaky," i.e., the outgoing long waves reach the shelf and are not trapped.

On the shelf we will assume an incoming equilibrium bound long wave (Longuet-Higgins & Stewart, 1962, 1964) which propagates in the direction of the wave groups. The longshore domain length is chosen equal to the longshore projection of the infragravity wave length.

Fig. 2 shows the normalized envelope of the IG wave as a function of the cross-shore coordinate h_o/h_s, where the origin is at the still water shoreline and unity is at the toe of the slope. The dash-dotted lines indicate linear solution by Schäffer & Svendsen (1988). The dashed lines indicate the envelope computed by the present model *without* the quasi 3-D terms. It can be seen that the nonlinear terms in the equations shift the (quasi) nodes shoreward and have some effect on the amplitude of the anti-nodes. The solid lines indicate the solution computed by the full quasi 3-D model. The quasi 3-D terms change the horizontal distribution of the IG wave amplitudes, especially around the breakpoint and in the surf zone. This will be analyzed in more detail below.

In order to calculate the quasi 3-D terms in the momentum equations, we have to determine the vertical variation of the infragravity wave particle velocities from (11). It is illustrative to use this numerical output and plot the IG particle velocity profiles at various locations and at various time-instances.

Fig. 3 shows the IG particle velocity profiles for three different locations (h_o/h_s = 0.42, 0.17 and 0.07) and at five time intervals of the infragravity wave period. The motion is a result of the forcing by the obliquely-incident wave groups, and of the incoming IG wave and the obliquely-reflected IG wave. It is important to notice that the steady part of the short-wave forcing drives a steady longshore current and a steady undertow, which are both included in the figure, and that the time-varying part of the forcing cause a variation of the velocity profiles over an IG period, so in essence the infragravity wave motion is riding on top of a relatively strong current.

Since the breakpoint is located at $h_o/h_s = 0.3$, the location $h_o/h_s = 0.42$ is outside the surf zone. The IG wave velocity profiles at that location show a little

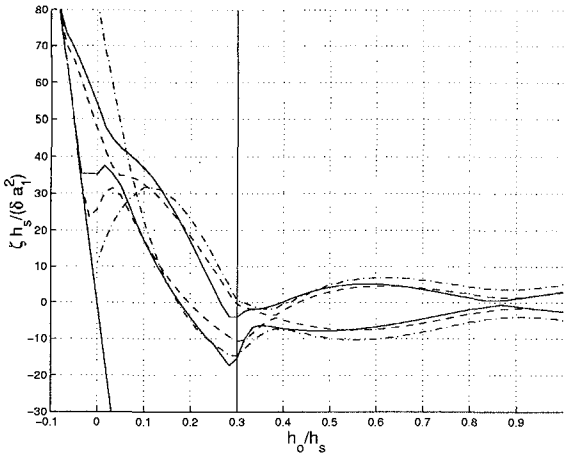

Figure 2: Envelope of the surface elevation of an IG wave vs. cross-shore distance: linear analytical solution by Schäffer & Svendsen (1988) (dash-dot line), SHORECIRC without Q-3D terms (dashed line), and SHORECIRC with Q-3D terms (solid line). The breakpoint is located at $h_o/h_s = 0.3$.

bit of curvature in the cross-shore direction and essentially vary linearly with depth in the longshore direction. The two locations inside the surf zone show much more variation. In particular the cross-shore velocity profiles vary significantly over one infragravity wave period, especially at $h_o/h_s = 0.07$.

The details of the variation of the velocity profiles can better be seen in Fig. 4, which shows the projections of the profiles in the longshore and cross-shore direction. Fig. 4 (a) shows the cross-shore velocity (commonly called the "undertow") normalized by the local long-wave celerity $c_o = \sqrt{g\,h_o}$ versus normalized depth at $h_o/h_s = 0.42$, which is located well outside the surf zone, for ten intervals per infragravity wave period. It can be seen that the profiles are slightly curved and also that the vertical gradient varies substantially with time. This is due to the (time-varying) forcing f_x in (11), which is a function of the radiation stress gradients, the pressure gradient and the gradients in the short-wave velocities.

Fig. 4 (b) shows the longshore velocity V at the same location. Due to the relatively small angle of incidence of the short-wave groups, the forcing induced by the short waves in the y direction is also small. This leads to the profiles with only a slight curvature. The profiles exhibit a non-zero mean over depth due to the momentum that has advected out of the surf zone mostly due to the dispersive mixing (Svendsen & Putrevu, 1994).

The cross-shore profiles in Figs. 4 (c) and (e) exhibit the typical characteristic time-

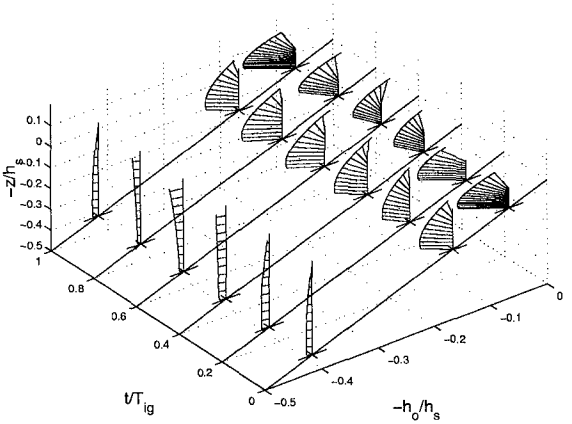

Figure 3: Infragravity wave profiles for three locations ($h_o/h_s = 0.42$, 0.17 and 0.07) and for five time instances of the infragravity wave period. The breakpoint is located at $h_o/h_s = 0.3$.

varying undertow profile in the surf zone that was previously shown by Putrevu & Svendsen (1995). The longshore profiles in Figs. 4 (d) and (f) are slightly more tilted than the longshore current profile in Fig. 4 (b) because inside the surf zone a strong mean forcing is present due to the difference between the radiation stress gradient and the pressure gradient. The time variation of the longshore profiles is not very large because the short-wave groups have refracted to near normal incidence inside the surf zone.

The relative magnitude of the quasi 3-D coefficients can be calculated directly from the model results using the definitions (12) - (15). For brevity we will only present the results for the coefficients $B_{\alpha\beta}$ and $D_{\alpha\beta}$.

Fig. 5 shows the variation of the $B_{\alpha\beta}$ and $D_{\alpha\beta}$ coefficients versus the cross-shore coordinate for five time intervals of the infragravity wave period. In the figures $h_o/h_s = 0$ corresponds to the still water shoreline and $h_o/h_s = 1$ to the toe of the beach.

We see that the B and D coefficients exhibit a quite large variation over an IG wave period, which indicates that the local time-varying forcing is very important. It can also be seen that the magnitude of all coefficients is significantly larger than the magnitudes which would have been found for the case of no groupiness ($\delta = 0$), which is indicated by the thick solid line. The values increase significantly across the breakpoint, since the "undertow" profiles become much more curved inside the surf zone due to the increased forcing. Because of the simple short-wave modeling, this transition in curvature occurs very rapidly, which increases the cross-shore gradients of the quasi 3-D coefficients.

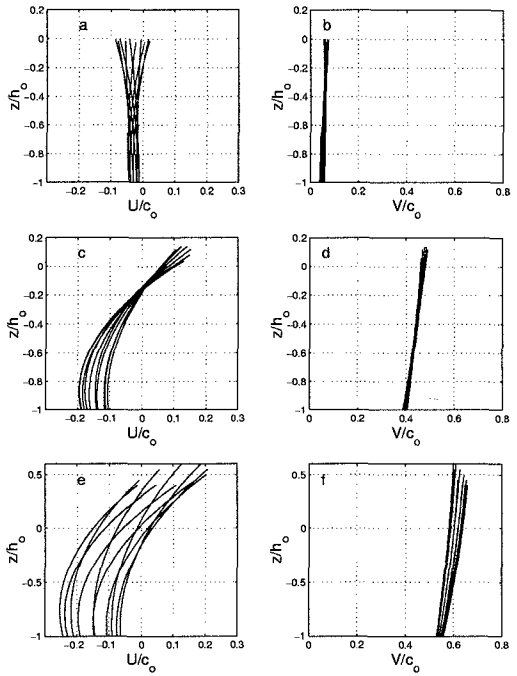

Figure 4: IG wave particle velocities in the cross-shore and longshore direction normalized by the longwave celerity c_o vs. normalized depth for ten intervals per IG wave period: (a) Cross-shore velocity U at $h_o/h_s = 0.42$. (b) Longshore velocity V at $h_o/h_s = 0.42$. (c) U at $h_o/h_s = 0.17$. (d) V at $h_o/h_s = 0.17$. (e) U at $h_o/h_s = 0.07$. (f) V at $h_o/h_s = 0.07$.

We see that the D_{xx} and B_{xx} coefficients are larger than the D_{xy} and B_{xy} coefficients, which are in turn larger than the D_{yy} and B_{yy} coefficients. This is because the short-wave groups refract towards the shorenormal, which means the forcing f_x in (11) becomes dominant over the forcing in the longshore direction. Eq. (11) also implies that the cross-shore velocities are more curved than the longshore velocities which could already be seen in Fig. 4. This curvature of the velocity profiles directly influences the magnitude of the dispersive coefficients.

An assessment of the quasi-3D effects is obtained by looking at the magnitude of the terms in the momentum equations in which these quasi 3-D coefficients appear. The analysis is performed at an arbitrary time after the periodic state of the IG waves has been reached and is strictly speaking only valid for this particular time. However, the magnitude of the terms in the equations at this time instance are

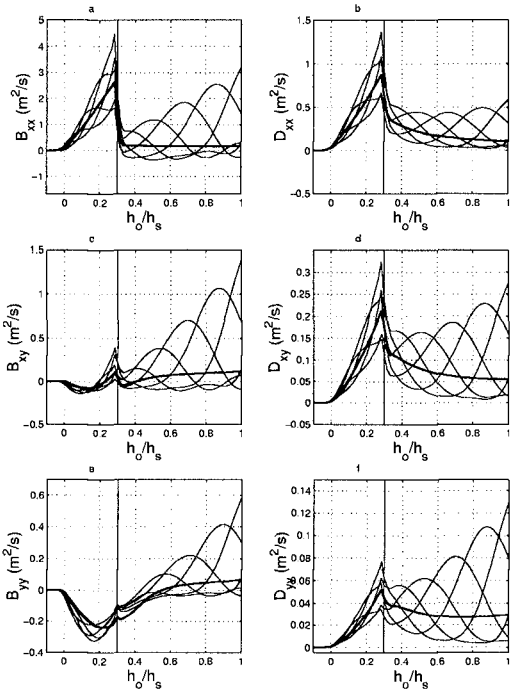

Figure 5: Magnitude of B and D coefficients vs. cross-shore distance h_o/h_s for five intervals per IG wave period: (a) B_{xx}. (b) D_{xx}. (c) B_{xy}. (d) D_{xy}. (e) B_{yy}. (f) D_{yy}. The stillwater shoreline is located at $h_o/h_s = 0$ and the breakpoint at $h_o/h_s = 0.3$. Also shown as the thick solid line is the magitude of the terms for the case of no groupiness $\delta = 0$.

characteristic for their magnitudes at any time in the periodic state. The conclusions that are drawn from this analysis are therefore considered representative for the case in question.

For reasons of clarity Fig. 6 only shows the most important terms in the equations. We first analyze the terms in the x momentum equation (16) versus h_o/h_s, see Fig. 6 (a). The terms shown are the pressure gradient, the radiation stress gradient $\frac{\partial S_{xx}}{\partial x}$ and the local acceleration. Of the quasi 3-D terms, the $\frac{\partial M_{xx}}{\partial x}$ term is large only locally at the breakpoint. This is due to the choice of $\kappa = 0$, which causes the cross-shore velocity profiles to undergo a rapid change over a short distance around the break point. (Notice that M_{xx} is equivalent to the momentum correction factor in hydraulics.) The term is positive, which leads to a negative pressure gradient in

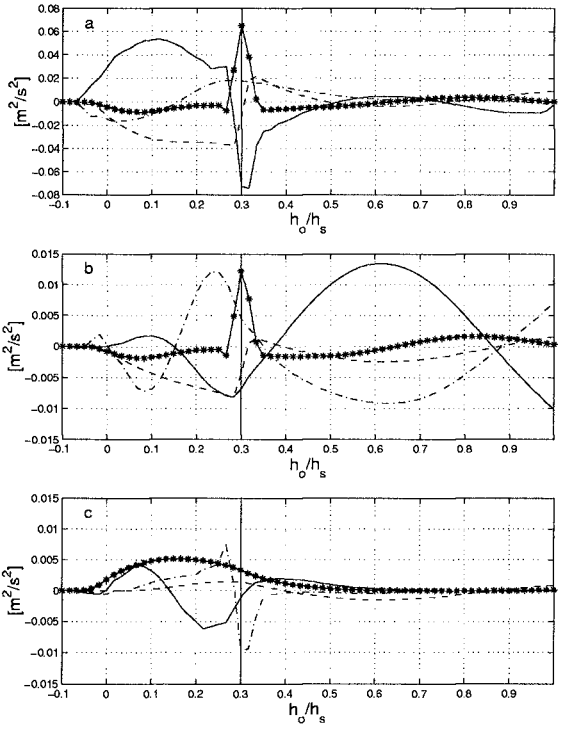

Figure 6: Magnitude of significant terms in the momentum equations vs. cross-shore distance h_o/h_s: (a) x-momentum equation: pressure gradient (solid), radiation stress gradient $\partial S_{xx}/\partial x$ (dashed), local acceleration (dash-dotted) and $\partial M_{xx}/\partial x$ (stars). (b) y-momentum equation: pressure gradient (solid), radiation stress gradient $\partial S_{xy}/\partial x$ (dashed), local acceleration (dash-dotted) and $\partial M_{xy}/\partial x$ (stars). (c) y-momentum equation: advective acceleration $\frac{\partial}{\partial x}\left(\frac{\bar{Q}_x \bar{Q}_y}{h}\right)$ (solid), $\partial S_{yy}/\partial y$ (dashed), $-\frac{\partial}{\partial x}\left(h\, D_{xx} \frac{\partial \bar{V}}{\partial x}\right)$ (dash-dotted) and bottom friction(stars). The stillwater shoreline is located at $h_o/h_s = 0$ and the breakpoint at $h_o/h_s = 0.3$.

the balance. In the inner surf zone, this term is found comparable to other terms, and is negative, which causes an increase in the pressure gradient and explains the difference between the envelopes of Fig. 2. In general, however, the dispersive mixing terms are of minor importance in the cross-shore momentum balance.

The dominating terms in the y-component of (16) are shown in Fig. 6 (b) and (c). Those terms are the local acceleration, the pressure gradient, the radiation shear stresses $\frac{\partial S_{xy}}{\partial x}$ and $\frac{\partial S_{yy}}{\partial y}$, the advection term $\frac{\partial}{\partial x}\left(\frac{\bar{Q}_x \bar{Q}_y}{h}\right)$, and the bottom friction. However, we also see that two Q3D terms, $\frac{\partial M_{xy}}{\partial x}$ and $\frac{\partial}{\partial x}\left(h\, D_{xx} \frac{\partial \bar{V}}{\partial x}\right)$ are important. The first term is significant around the breakpoint for the same reason that the $\frac{\partial M_{xx}}{\partial x}$ was in the x momentum equation. The second term is of the same order of magnitude as the 2-DH terms inside the surf zone and is the same that was found to be in the dispersion of momentum in the case of a steady longshore current (Svendsen & Putrevu, 1994). In this case where the shear in the longshore current is also large, this term is again important.

CONCLUSIONS

A numerical study of the forcing of leaky infragravity waves by obliquely-incident wave groups is performed using the SHORECIRC model which incorporates all quasi 3-D terms. It is shown that some of these terms have a significant effect on the envelope of the infragravity waves. The magnitude of the quasi 3-D terms is analyzed and compared to the size of the terms which are retained in conventional nonlinear shallow water models. This shows that the quasi 3-D terms have a significant size around the break point and in the surf zone. The velocity profiles of the infragravity waves inside the surf zone exhibit a large curvature and time variation in the cross-shore direction, and a small - but essential - depth variation in the longshore direction. Outside the surfzone the velocities in the longshore direction are small, while in the cross-shore direction only the upper part of the profile is curved.

ACKNOWLEDGMENTS

This work is a result of research sponsored by NOAA Office of Sea Grant, Department of Commerce, under Award No. NA 56 RG 0147 (Project No. R/OE-17) and by the U.S. Army Research Office, University Research Initiative under Contract No. DAAL03-92-G-0116. Additional funding has been provided by the Netherlands Centre for Coastal Research, Delft University of Technology, and WL|Delft Hydraulics. The U.S. Government is authorized to produce and distribute reprints for government purposes notwithstanding any copyright notation that may appear herein.

REFERENCES

De Vriend, H.J. and M.J.F. Stive (1987). "Quasi-3D modelling of nearshore currents." *Coastal Engineering, 11*, pp. 565-601.

Haas, K.A., I.A. Svendsen and R.A. Dalrymple (1998). "Numerical modeling of nearshore circulation on a barred beach with rip channels." *Proc. of the 26th International Conference on Coastal Engineering*, this volume.

Lippmann, T.C., R.A. Holman and A.J. Bowen (1997). "Generation of edge waves in shallow water." *J. of Ceophys. Res., 112, C4*, pp. 8863-8879.

Longuet-Higgins, M.S. and R.W. Stewart (1962). Radiation stress and mass transport in gravity waves with application to 'surf-beats'. *Journal of Fluid Mechanics, 8*, pp. 565-583.

Longuet-Higgins, M.S. and R.W. Stewart (1964). Radiation stress in water waves, a physical discussion with applications. *Deep Sea Research, 11*, pp. 529-563.

Mei, C.C. (1983). *The applied dynamics of ocean surface waves.* John Wiley and Sons, New York, 740 pp.

Phillips, O.M. (1977). *The dynamics of the upper ocean.* Cambridge University Press, 336 pp.

Putrevu, U. and I.A. Svendsen (1992). "A mixing mechanism in the nearshore region." *Proc. of the 23rd International Conference on Coastal Engineering*, pp. 2758-2771.

Putrevu, U. and I.A. Svendsen (1995). "Infragravity velocity profiles in the surf-zone." *Journal of Geophysical Research, 100, C8*, pp. 16,131-16,142.

Putrevu, U. and I.A. Svendsen (1997a). "Dispersive mixing in the nearshore." *Proc Coastal Dynamics '97*, pp. 207-216.

Putrevu, U. and I.A. Svendsen (1997b). "Shear dispersion of momentum in the nearshore." Submitted.

Rodi, W. (1980). *Turbulence models and their application in hydraulics.* Int'l Assoc. for Hydraulic Res., Delft, The Netherlands, 104 p.

Sánchez-Arcilla, A., F. Collado, C. Lemos and F. Rivero (1990). "Another quasi-3D model for surf-zone flows." *Proc. of the 22nd International Conference on Coastal Engineering*, pp. 316-329.

Sánchez-Arcilla, A., F. Collado and A. Rodriguez (1992). "Vertically varying velocity field in Q-3D nearshore circulation." *Proc. of the 23rd International Conference on Coastal Engineering* , pp. 2811-2824.

Sancho, F.E.P., I.A. Svendsen and U. Putrevu (1997). "Modeling of longshore currents over alongshore nonuniform topographies: Effects of second order terms." Submitted to *J. of Geophys. Res.*

Sancho, F.E.P. and I.A. Svendsen (1998). "Shear waves over longshore nonuniform barred beaches." *Proc. of the 26th International Conference on Coastal Engineering*, this volume.

Schäffer, H.A. and I.A. Svendsen (1988). Surf heat generation on a mild slope beach. *Proc. of the 21st International Conference on Coastal Engineering*, pp. 1058-1072.

Schäffer, H.A. (1994). "Edge waves forced by short-wave groups." *J. Fluid Mech., 259*, pp. 125-148.

Svendsen, I.A. and R.S. Lorenz (1989). "Velocities in combined undertow and longshore currents." *Coastal Engineering, 13*, pp. 55-79.

Svendsen, I.A. and U. Putrevu (1990). "Nearshore circulation with 3-D profiles." *Proc. of the 22nd International Conference on Coastal Engineering*, pp. 241-254.

Svendsen, I.A. and U. Putrevu (1994). "Nearshore mixing and dispersion." *Proc. Roy. Soc. Lond. A., 445*, pp. 1-16.

Taylor, G.I. (1954). "The dispersion of matter in a turbulent flow through a pipe." *Proc. of the Royal Society of London. Series A*, 219, pp. 446-468.

Van Dongeren, A.R., F.E. Sancho, I.A. Svendsen and U. Putrevu (1994). "SHORECIRC: A quasi 3-D nearshore model." *Proc. of the 24th International Conference on Coastal Engineering*, pp. 2741-2754.

Van Dongeren, A.R. and I.A. Svendsen (1997a). "Numerical modeling of quasi 3-D nearshore hydrodynamics." Ph.D. Dissertation. Research report No. CACR-97-04, Center for Applied Coastal Research, University of Delaware, Newark, 243 p.

Van Dongeren, A.R. and I.A. Svendsen (1997b). "An absorbing-generating boundary condition for shallow water models." *Journal of Waterway, Port, Coastal and Ocean Engineering, 123*, no. 6, pp. 303-313.

Numerical Modeling of Long Wave Ship Motions

John R. Headland, P.E.[1], Ying-Keung Poon, P.E.[2]

Abstract

This paper presents a state-of-the-art numerical model for ship motion analyses along with an application of the model to a seiche problem in the Port of Long Beach, California. The practical uses of the model are emphasized along with a discussion of the efficacy of the modeling approach as a tool for decision-making.

Introduction

The tolerance for delays or inefficient cargo transfer at modern marine terminals due to environmental conditions (i.e., wind, waves or currents) is very low. Competition among shipping lines (and competition among the ports who desire to have the same shipping lines as tenants) demands marine terminals with uninterrupted service. Accordingly, the problem of excessive ship motions has been of particular concern in the development of new marine terminals. Additionally, recent trends in container ship design and terminal development has sparked renewed interest in ship motion problems. Specific developments include: (1) terminals located in areas exposed to harsher environmental conditions; (2) container ships that are larger but do not use commensurately stronger mooring/fender arrangements; and (3) a desire for higher loading/unloading rates which require little or no vessel movement.

The following paragraphs describe a methodology that can be used to simulate the motions of a moored vessel exposed to long waves. The hybrid approach combines the best features of physical and numerical modeling technology. This paper is one in a series on Los Angeles and Long Beach Harbor. The companion papers focus on other aspects of long wave behavior in the Ports (Lee et al, 1998, Poon et al, 1998, Raichlen et al 1998 and Walker et al 1998). Figure 1 shows the overall port complex. The specific application concerns ship motion experienced at the Pier J

[1] Vice President, Moffatt & Nichol Engineers, 342 Madison Ave. Suite 902, NY,NY 10173, Phone: 212-983-0441;Fax: 212-983-0243.

[2] Senior Coastal Engineer, Moffatt & Nichol Engineers, 250 W. Wardlow Road, P.O. Box 7707, Long Beach, CA 90807, Phone: 562/426-9551; Fax: 562/424-7489.

terminal located in the Port of Long Beach. This terminal is presented in Figure 2 and shows protective breakwaters that were constructed to reduce ship motions.

Modeling Approach

Overall, the problem to be addressed is that of a moored vessel located in a geometrically complicated harbor exposed to long waves or seiche. From a practical point of view, the modeling approach is normally used to evaluate various design elements (for a new facility) or corrective actions (for an existing facility) that will reduce ship motions to an acceptable minimum.

Physical models have historically served as the most reliable means for assessing wave-induced ship motion problems. In recent years, however, numerical modeling technology has advanced to the point where reliable estimates can be made for relatively short waves (i.e. waves less than 25 seconds) in open water using time domain ship motion models. The predictive fidelity of these numerical models has generally been confirmed through comparisons with physical model tests. In most cases, these comparisons have been made for open water conditions or for conditions with a solid quaywall, i.e., the vessel is exposed directly to waves from the open sea.

In most harbor applications, vessels are moored within protected basins where they are exposed to waves, which have been diffracted through a harbor basin entrance or reflected from the walls of the basin, or both. The complications associated with diffracted/reflected waves make it difficult to apply typical mooring dynamics models without considerable approximation and this is why physical models are often used to confirm the results of mooring models for final design.

Physical models have been used successfully to examine both harbor disturbance and ship motion problems. Distorted physical models are generally required for large harbors and can be used to examine harbor resonance. Unfortunately, distorted physical models cannot be used to examine ship motion problems due to difficulties associated with achieving similitude.

Numerical models can be used to examine both harbor disturbance and ship motion problems. In practice, application of numerical models for short waves is problematic due to requirements for relatively small element sizes which can result in an unwieldy computational effort. Inasmuch as moored ships tend to respond at both short periods (< 25 seconds) and relatively long periods (> 1 minute) any modeling approach must be capable of simulating the full range of wave periods.

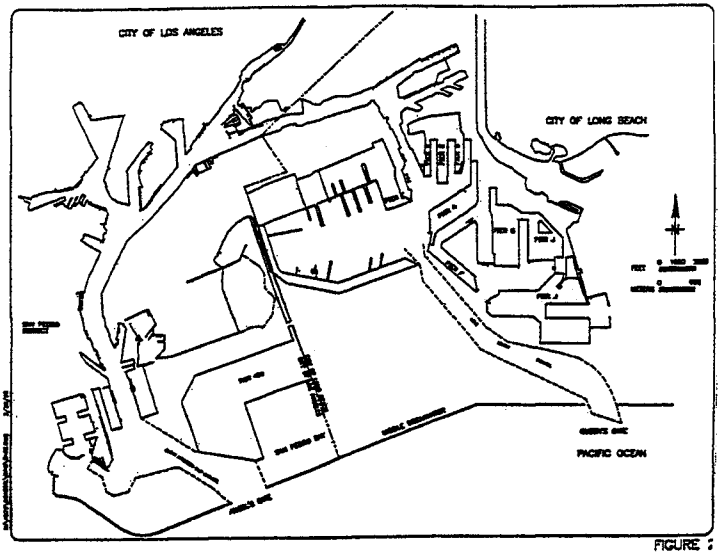

Figure 1. Ports of Los Angeles and Long Beach, California

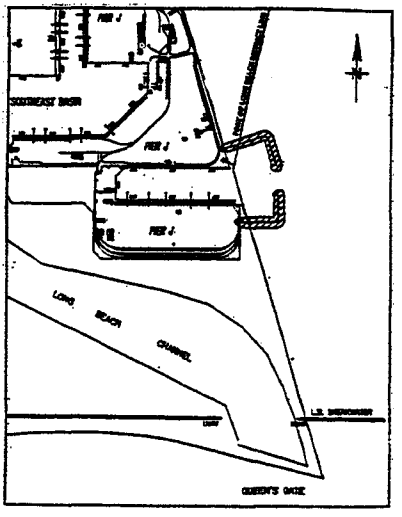

Figure 2. Pier J in the Port of Long Beach

The hybrid approach presented in the present paper involves the combined use of physical and numerical models. A complete description of the physical model used to evaluate long wave problems in the Port of Los Angeles and Long Beach is described in Poon, et al (1998). It suffices to say here that the physical model encompasses the entire harbor complex and was used to evaluate wave amplification factors at various locations throughout the harbor including Pier J. Wave amplification factors derived from the physical model results were used to establish boundary conditions for a local numerical model in the vicinity of Pier J. Additionally, results from the physical model were also used to calibrate amplification factors at interior points in the numerical model mesh. While the physical model results were useful in calibrating the numerical model as regards harbor oscillations, the physical model was of no use in calibrating the mooring model. Reference to Poon, et al (1998) will show that the physical model was used to identify the preferred solution for the Pier J situation. Specifically, the preferred solution was to construct new breakwaters at the entrance to the Pier J basin, see Figure 3. The remainder of this paper focuses on the numerical model and model results regarding the ability of the proposed breakwaters to reduce ship motions.

Ship Motion Simulation Models

A moored ship responds to wave excitation in six degrees of freedom: three translational motions - surge, sway and heave; and three rotational motions - roll, pitch and yaw. An illustration of these motions is shown in Figure 3. The motion response of a container ship at berth is normally dominated by surge motion.

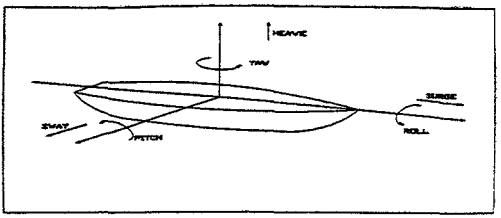

Figure 3 Definition Sketch of Ship Motion in Six Degrees of Freedom

Ship motion analyses were calculated with two numerical models - HYDRO and TDBERTH. HYDRO applies the finite element method (FEM) to solve the wave-ship-berth interaction, treating the oscillating system of a berthed ship in a harbor as a fully three-dimensional system. Overall, the analysis consists of two successive steps. The HYDRO model calculates harbor basin response, the ship hydrodynamic coefficients (i.e. added mass and damping coefficients) and the first and second order wave forces in the time domain. HYDRO models the hydrodynamics of the ship and the harbor basin simultaneously. This feature of the HYDRO model is critical for long wave problems where interactions occur between the incident long waves, the harbor basin and the moored vessel. TDBERTH computes ship motions in the time domain using results from

the HYDRO model. Specifically, TDBERTH solves for ship motions, mooring line forces, and fender reactions.

HYDRO Model

The HYDRO model solves the wave/harbor/ship interaction problem in terms of potential flow theory. The six modes of ship motion are expressed as:

$$x_j = x_{aj}\, e^{-i\omega t}, \quad j=1,2,....6$$

where x_j is a displacement for j = 1,2,3 and a rotation for j=4,5,6 and x_{aj} is the corresponding complex amplitude, t is the time, and ω is the radian wave frequency.

The total velocity potential describing the flow field is written as :

$$\Phi = \phi_0 e^{-i\omega t} + \sum_{j=1}^{6} \phi_j x_{aj} e^{-i\omega t} + \phi_7 e^{-i\omega t}$$

$$= \Phi_w + \Phi_f + \Phi_s$$

where Φ_w = potential of the incident wave

Φ_f = potential of the waves generated by the ship motion

Φ_s = potential of the scattered waves

Each of these velocity potentials also has to satisfy the Laplace Equation, i.e.

$$\nabla^2 \phi_j = 0, \quad j = 0,1,...,7$$

The HYDRO model employs the finite element method to solve the above equations together with the appropriate boundary conditions.

After the velocity potential has been determined, the wave loading on the ship and the hydrodynamic coefficients can be calculated by using the pressure equation. The fluid pressure at any point in the fluid domain can be obtained from the linearized Bernoulli equation:

$$p = -p\frac{\partial}{\partial t}\Phi - \rho g z$$

where ρ is the fluid density, g the acceleration due to gravity and z the depth below water surface.

The total force, F_i, acting on the ship can then be obtained by integrating the pressure over the surface of the ship. Applying Newton's second law of motion, the pressure

equation and the solution of the velocity potentials, the equations of motion of the ship in matrix form can be written as:

$$m_{ij}\ddot{x}_j + K_{ij}x_j = \zeta_a f_{ei} e^{-i\omega t} + f_{ij}\dot{x}_{aj} e^{-i\omega t}$$

where m_{ij} = six-by-six mass matrix of the ship

K_{ij} = hydrostatic restoring force (moment) matrix

x_j = motion vector

f_{ej} = wave exciting forces and moments per unit wave

f_{ij} = forces and moments per unit ship motion

ζ_a = wave amplitude

The added mass and damping coefficients can be found upon separation of the Real and Imaginary parts of the above equation.

In addition to the first order wave forces, a ship is also subjected to second-order mean and low frequency wave drift forces. These forces are partially attributable to the velocity-square terms in the Bernoulli's equation, partially attributable to the elevation variation of the water surface and partially attributable to first-order ship motions. HYDRO computes these forces based on the perturbation method developed by Pinkster and Van Oortmerssen (1977).

TDBERTH Model

Vessel motions and mooring line/fender forces were computed using a six-degree of freedom numerical model TDBERTH. TDBERTH integrates the equations of motion in the time domain by standard numerical methods. The model formulation is similar to that developed by Van Oortmerssen (1975).

The governing equations of motion, which account for motion in six degrees of freedom, are as follows:

$$\sum_{j=1}^{6}\left[(M_{kj}+m_{kj})\ddot{x}_j + \int_{-\infty}^{t} K_{kj}(t-\tau)\dot{x}_j(\tau)d\tau + b_{kj}\dot{x}_j + C_{kj}x_j\right] = F_{kw}(t) + \sum_{i=1}^{n_l} L_{ik}(t) + \sum_{i=1}^{n_f} N_{ik}(t)$$

$$k=1,2,\ldots 6$$

Where:

x_j, $\dot{x}_j$, $\ddot{x}_j$ = displacement, velocity, and acceleration in the j-th mode

M_{kj} = inertia matrix

C_{kj} = hydrostatic restoring force matrix

K_{kj} = impulse response function matrix

m_{kj} = constant added mass matrix

$F_{kw}(t)$ = wave exciting force in kth mode

$L_{ik}(t)$ = mooring line force in kth mode from line i

$N_{ik}(t)$ = fender force in kth mode from fender i

k = denotes mode of motion, (i.e. 1 (surge),
2 (sway), 3 (heave), 4 (roll), 5 (pitch), 6 (yaw))

n_l = number of mooring lines

n_f = number of fenders

The inertia matrix, M_{kj}, and hydrostatic restoring force matrix, C_{kj}, are computed using standard methods of naval architecture. The impulse-response function matrix, K_{kj}, and the constant added mass coefficient, m_{kj}, are computed as follows:

$$K_{kj} = \frac{2}{\pi}\int_0^\infty b_{kj}(\omega)\cos\omega t d\omega$$

$$m_{kj} = a_{kj}(\omega^*) + \frac{1}{\omega^*}\int_0^\infty K_{kj}(t)\sin\omega^*\tau d\tau$$

Where:

a_{kj} = frequency-dependent added mass

b_{kj} = frequency-dependent damping coefficient

The above frequency dependent hydrodynamic coefficients were computed using the HYDRO model.

The wave exciting force, $F_{kw}(t)$, is computed as follows:

$$F_{kw}(t) = \sum_0^n f_k^{(1)}(\omega_n)a_n\cos(\omega_n t + \varepsilon_n + \varepsilon_k)$$
$$+ \sum_0^n \sum_0^m f_k^{(2)}(\omega_n)a_n a_m \cos((\omega_n t + \varepsilon_n) - (\omega_m t + \varepsilon_m))$$

Where:

$f_k^{(1)}(\omega_n)$ = first order wave transfer function in k-th mode for n-th wave component

$f_k^{(2)}(\omega_n)$ = second order wave transfer function in k-th mode for n-th wave component

ε_k = phase of first order wave transfer function in k-th mode for n-th wave component

a_n = wave amplitude of n-th wave component

ε_n = phase of n-th wave component

ω_n = frequency of n-th wave component

The first and second order wave transfer functions were computed using the HYDRO code. The above formula was used to simulate first and second order wave force time-histories resulting from an incident wave spectrum composed of n-waves having amplitudes a_n and frequencies ω_n.

Simulation Conditions

Several container ships were examined and the characteristics of each are shown in Table 1. The mooring configuration used for each simulation is shown in Figure 4 and consists of 10 lines and 17 fenders. Two mooring configurations were examined, namely: (1) conventional nylon lines and (2) mixture of nylon and steel lines. The lines were assumed to be 20 cm (8 inch) in circumference with a breaking strength of 832 kN (187 kips). The fender spacing was assumed to be 15.2 m (50 ft). Both the lines and fenders had non-linear load-deflection curves.

Table 1: Characteristics of Container Ships

	LBP* (ft)	Beam Width (ft)	Draft (ft)	Dead Wt. (ton)
M-Class	294	32.2	12.2	60,350
A-Class	201	30.5	10.0	30,950
F-Class	317	42.8	12.5	85,350

* Length-Between-Perpendiculars

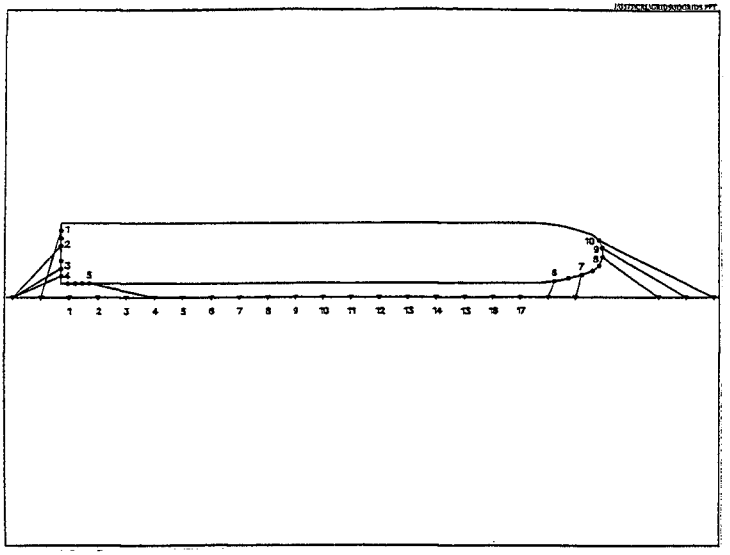

Figure 4. Mooring Geometry

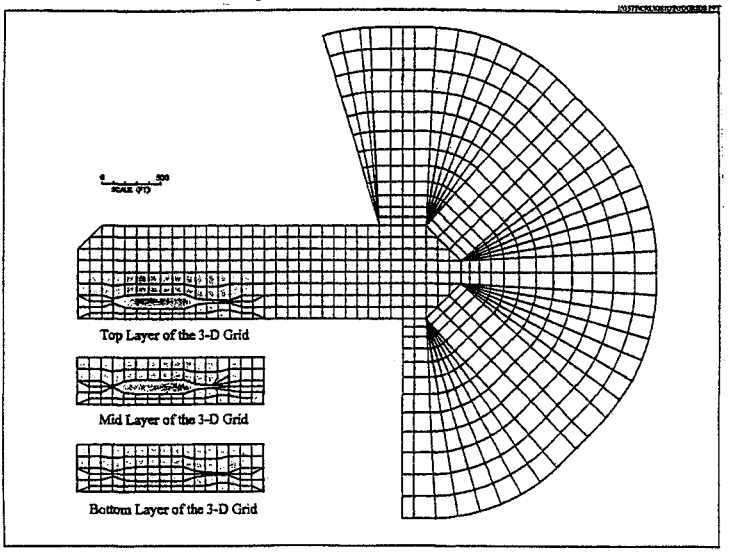

Figure 5. Finite Element Mesh

The container ship was moored at either the eastern or western berth of the nearly rectangular harbor (366 m by 975 m) with uniform water depth of 15.2 m (50 ft). The finite element grid used for numerical modeling is shown in Figure 5. The grid consisted mainly of a two-dimensional (2D) region with an embedded three-dimensional (3D) region (hatched area) to properly schematize the modeled ship. The 3D grid consisted of five layers, with the top three layers constructed to fit the ship, and two bottom layers representing the water between the ship and the basin floor.

The wave condition at the harbor basin entrance was chosen such that there were substantial surge motions under base conditions. The wave spectrum at the harbor entrance has the same spectral shape as the average spectrum measured by the US Army Corp of Engineers (1993) at Platform Edith, the latter is located about eight miles south of the Ports of Los Angeles and Long Beach.

Simulation Results

Ship motion response for each mooring/fender configuration was computed in the time domain with the TDBERTH model for a two-hour simulation period. Example time series of motions, line forces and fender forces are shown in Figures 6, 7 and 8.

The above figures show the moored container ship response to be a mixture of 1st order and 2nd order wave responses at low frequency. Overall, the vessel response in surge is dominated by motions having periods near the natural period of the moored ship system (i.e., about 1.5-2 minutes). Results of the simulations are presented in Table 3 in terms of normalized peak-to-peak surge motions for a representative wave condition.

Table 3 Normalized Peak-to-Peak Surge Motions for an M-Class Vessel

	Western Berth		Eastern Berth	
	Synthetic Lines	Steel/Synthetic Lines	Synthetic Lines	Steel/Synthetic Lines
Existing	100%	100%	100%	100%
Breakwater	51%	96%	55%	21%

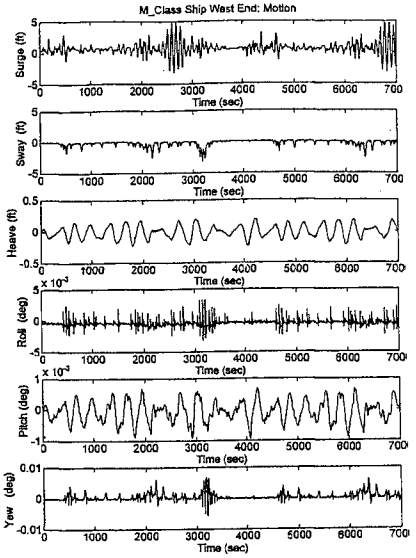

Figure 6. Motion Time Histories

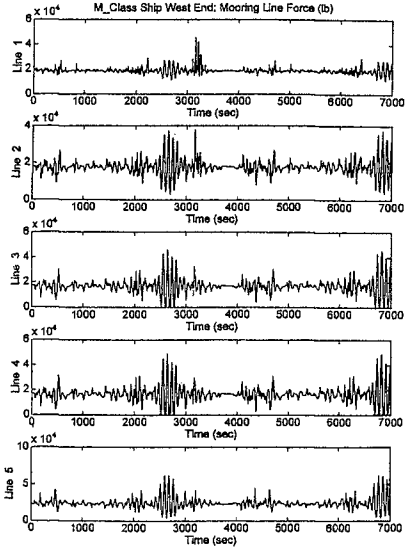

Figure 7. Mooring Line Time Histories

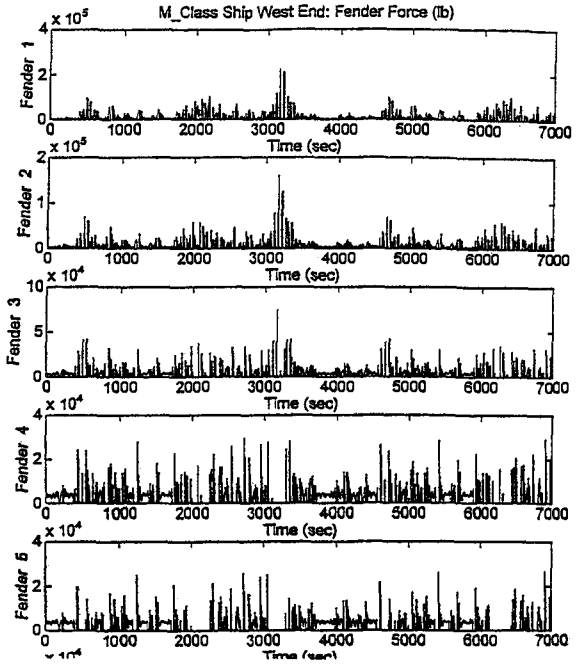

Figure 8. Fender Force Time Histories

Table 3 shows that the breakwater will substantially reduce surge motions for most of the simulations. For example, the existing surge motions are reduced to 51% of existing conditions with the breakwater for a vessel moored at the western end of the basin using all synthetic lines. Interestingly, the motions are not significantly reduced for a vessel moored by a combination of synthetic and steel lines at the western berth. The above results show that the proposed breakwaters would significantly reduce problematic vessel motions for conventional moorings at either berth. The results also show that it is important to consider both the mooring configuration and the location of the vessel within the harbor.

Summary

A methodology for examining ship motions excited by long waves has been presented. The hydrid approach combines the strengths of physical and numerical modeling. Physical model results are used to define boundary conditions for, and calibration of, the numerical model. The numerical model described in this paper provides a powerful and flexible means for examining complicated mooring problems. The model was recently used to examine the efficacy of constructing breakwaters to reduce ship motions at a berth in Long Beach Harbor, California. The model showed the proposed breakwaters would significantly reduce vessel

motions under most conditions. The breakwaters were constructed and preliminary experience indicates that the breakwaters have been successful.

The state-of-the-art in modeling of ship motions is mathematically advanced, however, additional model testing and field data collection efforts are necessary to gain as much confidence in ship/basin models as there presently exists in open sea models. A systematic series of physical model tests involving a vessel moored in simple basin geometries is recommended to advance the currently available modeling technologies.

References

Lee, J.J., Lai, C. and Li, Y., "Application of Computer Modeling for Harbor Resonance Studies of Long Beach Harbor Basins," ICCE'98 Copenhagen, Denmark, 1998.

Pinkster, J.A. and G. van Oortmerssen, "Computation of the First and Second Order Wave Forces on Oscillating Bodies in Regular Waves," Proc. Second International Conf. on Numerical Ship Hydrodynamics, University of California, Berkeley, Sept. 1977.

Poon, Y.K., Raichlen, F. and Walker, J, "Application of Physical Models in Long Wave Studies for the Port of Long Beach," ICCE'98 Copenhagen, Denmark, 1998.

Raichlen, F.R., Dean, R. and Mei, C.C., "Application of Computer Modeling for Harbor Resonance Studies of Long Beach Harbor Basins," ICCE'98 Copenhagen, Denmark, 1998.

U.S. Army Corps of Engineers, Waterways Experiment Station," Los Angeles and Long Beach Harbors Model Enhancement Program, Improved Physical Model Harbor Resonance Methodology," Technical Report CERC-93-17, September 1993.

Van Oortmerssen, I.G., "The Motions of a Moored Ship in Waves," Publication No. 510, Netherlands Ship Model Basin, Wageningen, The Netherlands, 1976.

Walker, J.R., Sethness, D.,Boudreau, R.H.,Poon, Y.K.,"Solutions To Long Wave Induced Ship Motions At the Port of Long Beach," ICCE'98 Copenhagen, Denmark, 1998.

RESPONSE OF MOORED VESSELS IN BUFFINGTON HARBOUR

E.P.D. Mansard[1], T. Faure[1] and K. MacIntosh[2]

ABSTRACT

In a temporary facility built within Buffington Harbour, it was proposed to operate two floating vessels as casinos. An extensive program of physical and numerical model investigations was undertaken to design a harbour and mooring layout that would ensure effective operation with minimal downtime for casino operations. Through a sophisticated model testing program, the motions of the floating vessels were established for different sea states. These motions were then used as inputs to a ship simulator where client representatives participated in the full scale simulations in order to select the sea states that would cause discomfort to clients.

INTRODUCTION

Lehigh Portland Cement Company is the owner of Buffington Harbour facilities in East Chicago. Barden Developments and Trump Indiana proposed to operate two floating casino vessels in a recently constructed temporary harbour facility built within the existing Buffington Harbour. The facility is now complete and the two vessels are in place. Figure 1 shows an overall view of the harbour and the casino ships.

The two vessels are moored on either side of a floating barge/passenger loading dock, which services both vessels. The vessels leave the harbour and enter Lake Michigan whenever weather conditions permit, otherwise operations continue while moored. Being a temporary facility intended for several years' use only, it was important to keep costs down, while providing protection from waves to enable operation under most environmental conditions. This includes entry/exit to the harbour.

Baird & Associates was retained by Lehigh Portland Cement Company to develop preliminary and final designs for marine structures required to protect the vessels, and also to carry out tasks such as permitting, preparation of contract documentation,

[1] Canadian Hydraulics Centre, National Research Council of Canada, Ottawa, ON K1A 0R6 Canada
[2] W.F. Baird & Associates Ltd., 1145 Hunt Club Rd., Suite 1, Ottawa, ON K1V 0Y3 Canada

contractor negotiations and construction supervision. Analysis of environmental parameters (wave climate and water levels), physical and numerical model investigations of harbour wave agitation and response of the vessels, were parts of this study (Baird & Associates, 1996).

The Canadian Hydraulics Centre of the National Research Council of Canada was contracted by Baird & Associates to undertake physical model investigations to determine vessel motions and related mooring line loads for a variety of lake and harbour wave conditions. This information was required to establish downtime during which casino operations should be suspended due to excessive vessel motions.

PHYSICAL MODEL INVESTIGATIONS

Figure 2 shows a photograph of the two model casino vessels and the loading barge under study, while Figure 3 presents the layout of the harbour basin that was tested in the physical model. The model scale used for this study is 1:45.

This harbour layout, considered optimal, was established through a wave agitation study carried out earlier by Baird & Associates. Six different harbour concepts were studied under different combinations of wave heights and directions. This final harbour concept, with the proposed structures for casino operations, was tested as part of the ship mooring study, by measuring directly the response of the vessels induced by wave heights prevailing inside the test basin.

It should also be pointed out that physical model tests were carried out to assess the stability of the breakwater materials (armour, filter and core stone) on the north rubble mound structure. The potential impact of a storm during construction was also determined in a separate series of tests where the breakwater was constructed to varying degrees of completion and then subjected to a storm event. As a result of this work it was recommended that a 100 ft long revetment section, which extends along the west breakwall to the north of the north rubble-mound structure, be constructed (see Figure 3).

VESSEL CHARACTERISTICS

All three vessels, Trump Princess, Barden I and the barge were built at a 1:45 scale. Care was taken to reproduce as accurately as possible the salient characteristics of the vessels, including their hydrostatic conditions. Given below are some of the main characteristics of the vessels:

Characteristics	Trump Princess	Barden I	Barge
Length (LWL)(ft)	226	291	295
Beam (ft)	74	72	54
Draft (ft)	10.5	12	3.5
Displacement (tonne)	3570	2934	1584

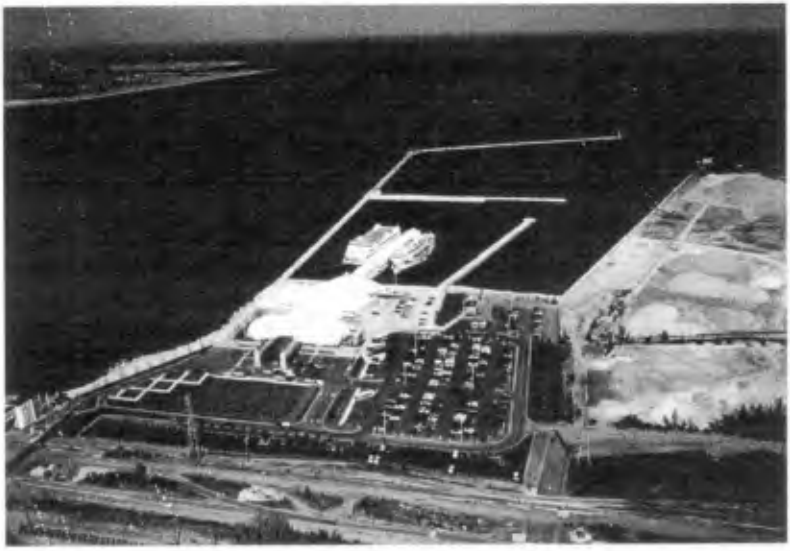

Figure 1: Overall View of Buffington Harbour and the Casino Facilities

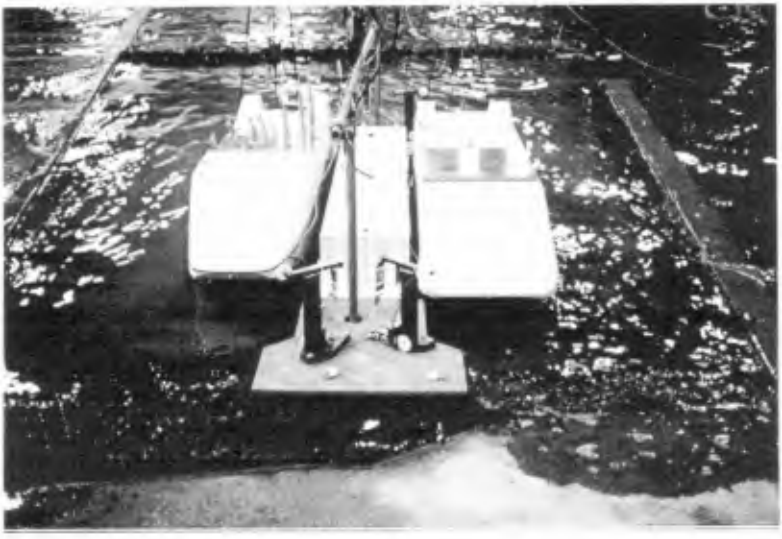

Figure 2: Photograph of Model Vessels in the Test Basin

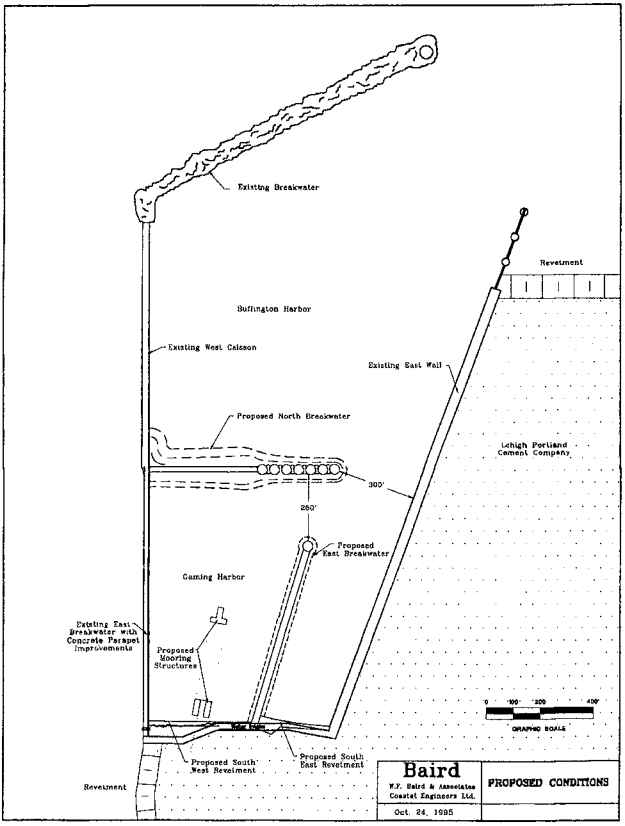

Figure 3: Proposed Layouts of the Harbour and the Breakwater

WAVE CLIMATE

A wave machine located outside the model harbour generated the waves in the harbour. The drive signals to this wave generator, were already available from the initial phase of this study when the optimization of the harbour was investigated. To create these driving signals, irregular wave time series, having a record length of 20 minutes prototype, were synthesized from a spectrum using the random phase spectrum method.

An array of three gauges was deployed near the offshore region to monitor the water surface elevations and to resolve the incident and reflected wave fields from them. The range of wave heights (H_{m0}) and peak period (T_p) used during the testing program is shown in Table 1.

MEASURED VALUES	
H_{m0} (ft)	T_p (s)
4.7	7.2
5.6	7.2
6.4	5.9
6.7	7.8
7.1	10.1
9.2	9.0
11.4	9.0

Table 1: Incident Wave Characteristics during the Ship Mooring Tests

The waves were run from two different directions: 41 degrees East of North and 56 degrees East of North. The water level was varied from 4.7 ft to 6.4 ft (with reference to low water datum) in order to reflect the range in design water levels expected for this temporary harbour. Some additional tests were also carried out using sea states H_{m0} = 8 and 10 ft, with T_p= 8s.

MOORING

Mooring Line Simulation

Figures 4 and 5 show the layout of the mooring lines, with the locations of the bollards on the barge, the end piers and both ships. From these locations, a line length was derived for each mooring, to which 4 to 6 feet was added in order to include the distance between the fairlead and the bollards onboard the ship.

All lines were made of 2 5/8 inch diameter double braid polyester assumed to have a constant unit stiffness EA = 2.353 x 10^3 kips per foot of elongation per unit length, over the expected range of tensions. The bow and stern moorings were made of three lines in parallel, whereas the spring lines were only single lines. The net stiffness of each mooring was (n EA)/L, where n is the number of lines per mooring.

A thin steel cable attached to a set of springs simulated the elasticity of each mooring line. The springs were pre-calibrated to the desired load/elongation characteristics of the lines. Each line was also connected to a load cell to monitor the instantaneous loads. The hardware was designed in such a way that variable levels of pre-tension can easily be set in the mooring system (see Figure 6).

Static Verification of the Mooring Line Simulation

In order to verify that the mooring line simulation and the load cells gave the appropriate results, a simple static experiment was performed. A known force was applied horizontally at mid ship of the Trump Princess, pulling the ship away from the barge. At

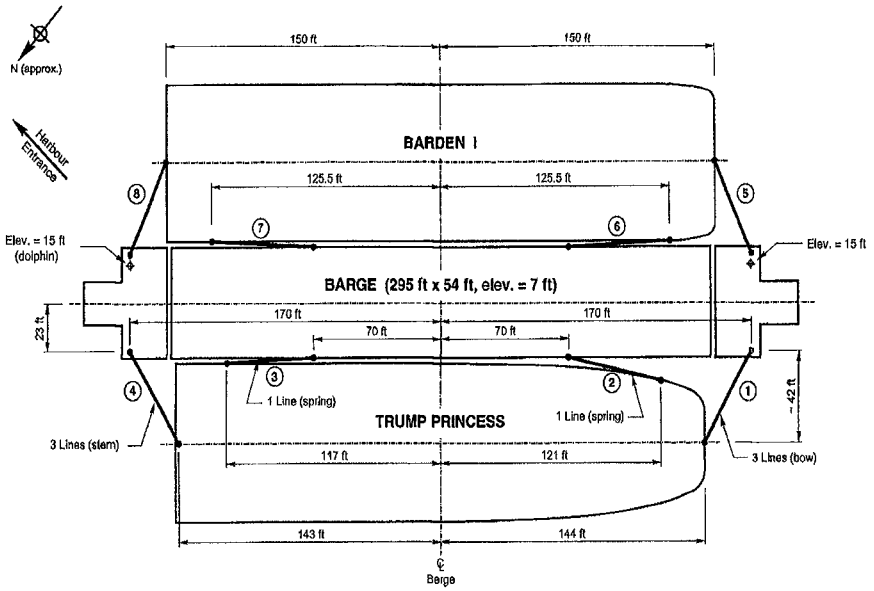

Figure 4: Buffington Harbour Moorings – Plan View

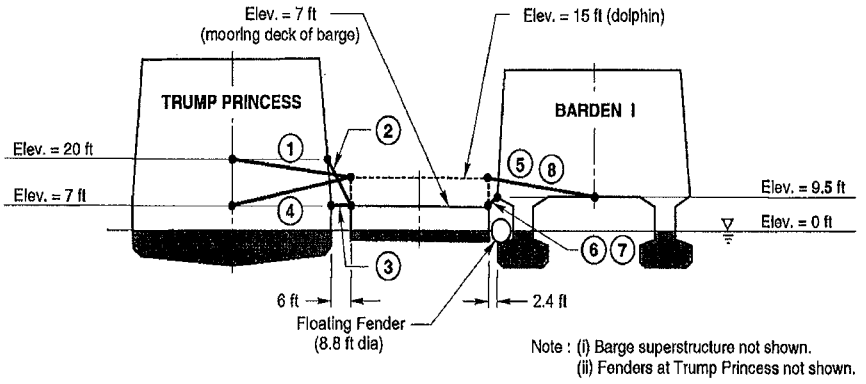

Figure 5: Buffington Harbour Moorings – End View

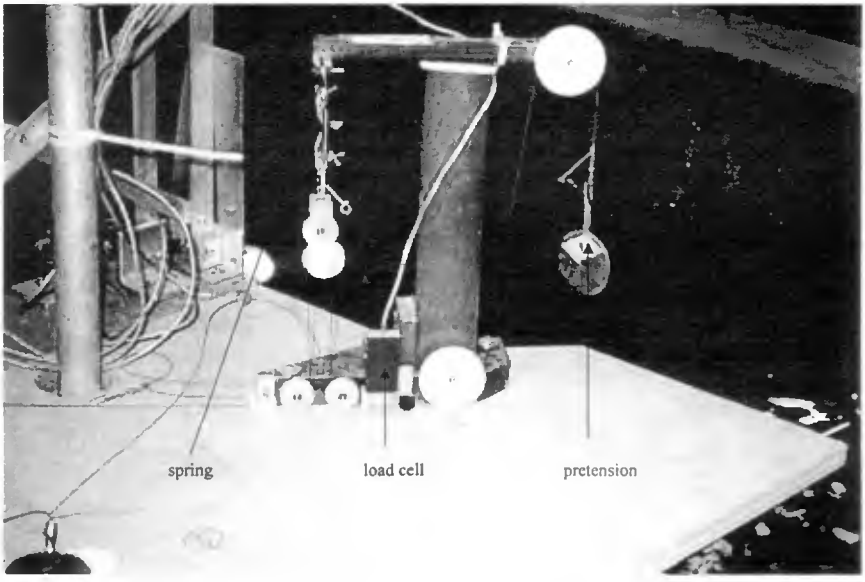

Figure 6: Mooring Line Simulator

the same time the two spring lines were disconnected to ensure that only the two port bow and stern lines were under tension. These line tensions were sampled and analyzed by the same software used during the project. Table 2 shows the theoretical tensions required to balance the system based on the geometry of the moorings, and the measured values.

Weight	Bow Port Line Tensions (kips)			Stern Port Line Tensions (kips)		
(kg)	Theory	Measured	Diff (%)	Theory	Measured	Diff (%)
1.003	105.84	110.29	4.0	106.13	108.68	2.3
2.004	211.45	217.17	2.6	212.04	212.11	0.0

Table 4. Mooring Tensions During Static Tests

The difference between the theoretical and the measured values shows the effect of the line friction when it goes around the fairleads. This test was a static test. It is expected that during dynamic simulations, these differences would be smaller since a dynamic friction coefficient is usually smaller than a static one.

Fenders

For the Trump Princess, three fenders were installed on the barge at the 7-ft elevation (above Low Water Datum). They consisted of a piston and a linear spring inside a cylinder bolted to the barge deck. The spring stiffness corresponded approximately to 130

kips/ft. The contact surface between the ship and the fender (the plastic head of the piston) was very small.

For the Barden 1, two fenders were installed to simulate Yokohama fenders as proposed by naval architects. They consisted of a circular pipe simulating round fenders 8.8 ft in diameter and 11.8 ft long, floating on the water surface and free to move, but within limits. These pipes could be considered as having no elasticity in compression.

INSTRUMENTATION

Two different types of instrumentation were used to measure the six degrees of freedom of motion on the vessels: Qualisys and accelerometers.

Qualisys

During the harbour tests, one of the ship models was instrumented with the Qualisys position system. This optical tracking system was used to measure the vessel position in six degrees of freedom. Its principle of operation is as follows: A light beam is sent from two fixed cameras which reflect from an array of eight reflective markers mountcd on the vessel. The reflected light is captured by the cameras and processed by a computer/video system, which calculates the exact position of each reflected light beam every millisecond. Software is then used to convert the light positions into x, y, and z positions for the vessel. This results in a very accurate measurement of surge, heave and sway of the vessel within ±0.5 mm (±1 inch prototype) and roll, pitch and yaw angles within ±0.1 degrees. Note that the low frequency motions of the vessels can be measured accurately by this system.

The marker array is surveyed to locate the relative position of each marker and the array position relative to the vessel. To provide synchronization with the mooring forces data, a vertical heave accelerometer was installed on each vessel. It also provides a cross-check with the heave motion measured by the Qualisys system. To obtain the motions of the second ship, each test was repeated with the Qualisys system installed on the other ship. Care was taken to ensure that the repeated tests provided similar estimates of mooring line loads.

Accelerometers

The six degrees of freedom motions of the vessels can also be measured by an array of seven accelerometers. These units are precision linear servo accelerometers that are specifically designed for high accuracy applications at frequencies from 0 to 100 Hz. The QA-900 servo electronics generates a current that maintains a seismic element in a position-captured mode. The current required to keep the sensor mass stationary is thus proportional to the applied acceleration. These sensors have a measurement range of ±1 g, a resolution of 5 μg and a maximum linearity error of 30μg.

To obtain the displacements from the accelerations, an iterative analysis procedure was used to solve the full nonlinear differential equations that relate the various rigid body

displacement motions to the local accelerations measured at the seven discrete points. This iterative procedure employs a technique based on the Fast Fourier Transform (FFT).

The analysis method has been validated by comparing tests undertaken with a precision optical tracking system as described in Miles (1986). Within its valid frequency range, it can measure ship model motions with a typical accuracy of ± 1mm in surge, sway and heave and ±0.1 degree in roll, pitch and yaw. This instrumentation was used to measure the pitch and roll motions of the barge. Small plastic screws inside fixed aluminum brackets at the bow and stern restrained the barge. This provided freedom in heave, pitch and roll but prevented any significant surge, sway or yaw motion.

The barge was also equipped with a light vertical line running over a pulley to a small weight so that heave displacement at the midship point on the centerline could be measured directly. This was done by using a calibrated potentiometer that measured the angle of rotation of the pulley, which was linearly proportional to the heave displacement of the barge at the centre point.

TEST REPEATABILITY

Since the Qualisys system can measure the motions of only one vessel at a time, the tests were repeated in order to measure the motions of both the vessels (Trump Princess and Barden I) under each wave condition. Therefore it was essential that similar results were obtained when the tests were repeated. There were also two other issues: potential resonance build-up inside the harbour basin, and inadequacy of sampling rate. Additional sensitivity tests were therefore undertaken in order to address these two issues as well. These tests are described below.

Same Test

All tests were repeated at least once to be able to measure the motion of both ships with the same Qualisys system. In both instances, the mooring line tensions were measured, allowing a direct comparison. The cumulative distribution of the peak tensions calculated from these results indicated good repeatability. The small differences that were found could be attributed to the friction forces from the fenders against the ships and from the lines passing through the fairlead.

Wave Build-up in the Model

In order to ensure that there is no wave build-up in the model due to possible basin resonance, some tests were run for 40 minutes full scale instead of 20 minutes. The first 20 minutes and the next 20 minutes were analyzed separately. No differences in peak tension were found, implying that there is no wave build-up in the basin.

Effect of Data Sampling Rate

All channels were sampled by the data acquisition system at a rate of 20Hz. Additional tests were also undertaken at a higher sampling rate of 100 Hz to determine whether or not all peaks in the mooring tensions were measured properly or if there were other high

frequency phenomena. Once again the cumulative distribution of the peaks were examined. They were similar, implying that the 20 Hz sampling rate was sufficient.

TEST RESULTS

Mooring Line and Fender Loads

The mooring lines and fenders were modelled for all three vessels with each one requiring a unique setup to match the proposed prototype configuration. These tests included pretensioning the lines, modelling line elasticity, and fender stiffness. Mooring tensions were measured for each mooring line of both the Trump and Barden vessels (see an example of a graphical output of these measured tensions in Figure 7).

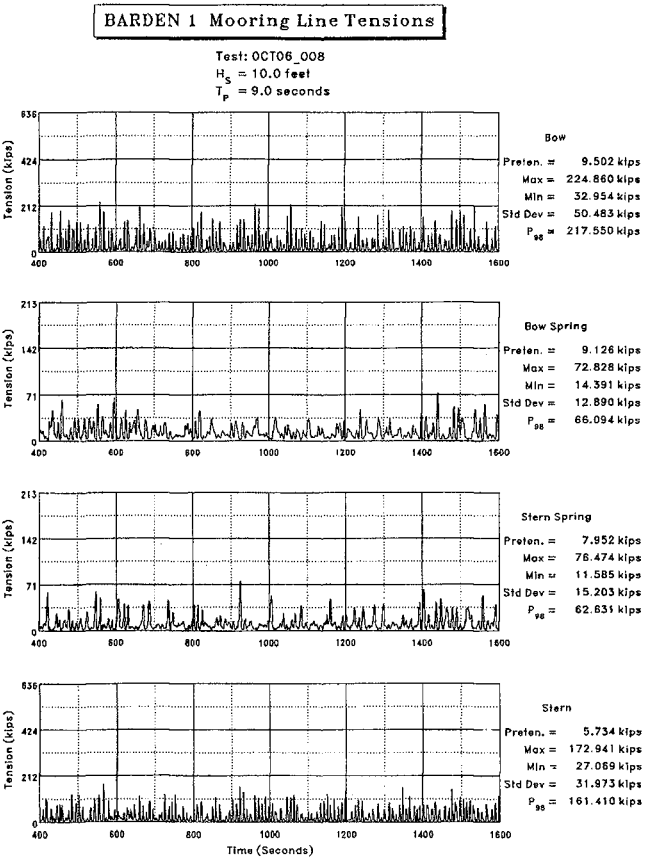

Figure 7: Example Output of Barden I Mooring Line Tensions

From the time series of the mooring line tensions, the peaks (defined as the maximum occurring between two average values) were identified and statistically analyzed. These time series and also some basic statistics of the line tensions associated with each mooring line (pretension, maximum, minimum, standard deviation, and 98 percentile loading level) were summarized for each test conducted as shown in Figure 7. Note that the maximum scale in the Y-axis corresponds to the estimated breaking strength of the lines.

Motions

The six degrees of freedom motions of the two vessels derived from the Qualisys system corresponded to the motions at the centre of gravity of each vessel. By additional calculations, the motions and accelerations corresponding to the gaming room locations could easily be estimated. The summary results were then presented in terms of the significant amplitude for each degree of freedom. It is equal to twice the standard deviation of the motion, and is analogous to the concept of significant wave height (which is equal to four times the standard deviation). Figure 8 shows the increase in significant amplitudes of the various motions with the wave height, for Barden I.

The passengers will board the vessels from gangways located on the barge. To obtain the motions of the gangways, the relative motions between the vessels and the barge were also calculated.

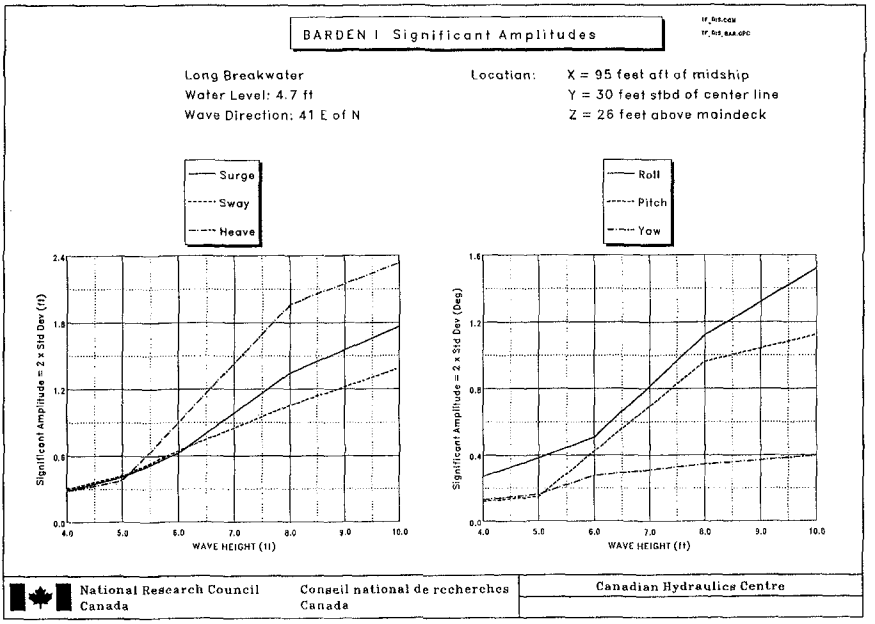

Figure 8: Six Degrees of Freedom Motions of Barden I

PASSENGER COMFORT

Determining the frequency of occurrence of ship motions, which exceed acceptable motions for client comfort, was a very important task in the design of the entire harbour facility. For this purpose, the motions and accelerations at various positions on both the gaming and loading barge vessels were computed in order to provide inputs to a full-scale ship simulator. The full scale simulator was utilized by representatives of both the Trump Princess and Barden as well as the naval architects, coastal engineers, and a human resources consultant, at the Marine Institute in St. John's, Newfoundland. During these tests, a series of gradually increasing motion and acceleration data sets were used to drive the simulator. The participants were inside the simulator room, but were not provided with external visuals (equivalent to casino without windows). The majority of the simulations were conducted for the most aft outside gaming position on the third level of the Trump vessel as this represents the most active part of the vessel during a storm condition. Other areas tested included more central gaming areas such as the first deck towards the centre of the vessel. These areas were tested to determine whether or not it would be feasible to continue gaming in some areas of the vessel should motions become excessive in the most active areas.

These tests, in combination with the motion and mooring line tension data sets and naval architects' input, resulted in a decision by the Trump and Barden representatives to limit gaming operations after wave exceed a significant wave height of 6 feet, and a peak wave period of 8 s or higher, offshore of Buffington harbour. Wave height levels of 6 feet (with peak periods less than 8s) or lower were considered acceptable for gaming at any position on the vessel. The surge motion was the most critical to passenger comfort.

FINAL RESULTS

The participation of the entire project team including naval architects, ship captains and representatives of Barden and Trump Princess during the test program facilitated the selection of the best possible design of the harbour facility. For example, the ship captains were able to maneuver the scaled ships through the model harbour entrance and the model harbour basin. They were able to observe vessel behaviour under a variety of wave conditions both while moored inside the basin and while offshore. Their comments were critical in choosing the optimal harbour layout. Similarly, the naval architects were able to observe the complex interactions that occur between the three floating vessels and to review the forces on each mooring line, which impacted the design of the mooring structures and the mooring arrangement. It also influenced the design of mooring points on the vessels themselves and the access points(gangways).

As a result of the mooring tension tests, the ship simulator tests, and design team meetings to discuss the related issues, three specific operating and related mooring conditions resulted. They are defined as follows:

Condition 1: Open Lake Cruising
Condition 1 mooring covers routine operations when the boat will be departing the harbour at regularly scheduled two-hour intervals, and then returning to the dock to exchange passengers. During this operation, one bowline, one stern line and one each forward and aft spring line will be deployed to moor the boats. This mooring arrangement will be adequate to permit safe loading and unloading of passengers, and will allow rapid deployment and release of mooring lines. The maximum permissible conditions of the wave and wind environment is expected to be limited by vessel maneuverability inside the gaming basin. At present this limiting environment is undefined and will be determined with experience. Environmental loading on the vessel is expected to be low.

Condition 2: Operating Alongside the Dock
When waves on the lake will produce vessel motions that are uncomfortable or unsafe to passengers, or winds are too high to permit safe maneuvering in or out of the harbour, gaming operations may be permitted with the vessels moored alongside the dock. In this case a heavy duty mooring system will be deployed which will secure the vessel to the dock, and will help limit vessel motions in surge and sway.

Condition 3: Survival
When wave conditions inside the harbour result in vessel motions that exceed limits determined for passenger comfort or safety, gaming operations will be shut down, and the passengers and unnecessary personnel will disembark. Additional storm mooring lines will be deployed to the breakwater dolphins, if they have not been rigged. The stern anchor line should also be connected. The gangways will then be pulled back from the vessels and the vessels will be moved off to the storm mooring position, approximately 40 feet off the dock. These conditions are expected to occur for 70 hours per year, on average. Five different storm-mooring configurations were tested in the physical model in order to find an optimal one.

CONCLUSIONS

The physical model provided results that were crucial for effective operation of the harbour with minimal downtime, and for determining an optimal design of the mooring layout and harbour structures.

By combining the frequency of occurrence of storms and the clients determination of acceptable level of motion, it was possible to make timely cost benefit decisions relating to harbour design and permissible wave agitation levels, while meeting the clients operational requirements and schedule objectives.

REFERENCES

Miles, M.D., 1986. Measurement of six degree of freedom motion model motions using strap down accelerometers, Proceedings of 21st American Towing Tank Conference, Washington, D.C. August, pp. 369-375

Faure, T., Miles, M., Pelletier, D. and Mansard, E., 1996. Model study of moored vessels in Buffington Harbour, NRC Controlled technical report, HYD-CTR-006

Baird & Associates Ltd., 1996. Physical environment and model investigations of Buffington Harbour, Report prepared for Lehigh Portland Cement Co.

Statistical Wave Forecasting through Kalman Filtering Combined with Principal Component Analysis

Noriaki Hashimoto[1], Toshihiko Nagai[2] and Masanobu Kudaka[3]

Abstract

Statistical wave forecasting methods have been applied because of their convenience. Most of them, however, include some drawbacks from the statistical or numerical viewpoints. In this paper, these drawbacks are discussed and a new statistical wave forecasting method utilizing the Kalman filter technique combined with Principal Component Analysis (PCA) is proposed in order to mitigate the drawbacks. The applicability and reliability of the proposed method is examined for five wave observation stations around Japan through simulations based on 5-years of wave data and weather charts.

Introduction

Adequate wave forecasting is indispensable for the safe operations of cargo handling, optimum management of port construction projects, and navigating and/or mooring vessels. There are two kinds of wave forecasting methods. One is a numerical model describing the physical process between winds and waves. The other is an empirical model based on a statistical relationship between the weather and the wave data obtained in the past.

The former method has been widely used for wave hindcasting for estimating design wave conditions. The reliability of the method has been discussed in several papers so far. Practical computation with this method, however, requires special knowledge of both the atmospheric and wave systems. Also, a large investment in computations is sometimes required.

On the other hand, the latter method commonly utilizes simple statistical relationships among criterion variables and predictor variables using obtained data.

---

[1] Chief, Hydrodynamics Laboratory, Marine Environment Division, Port and Harbour Research Institute, Ministry of Transport, 1-1 Nagase 3-chome, Yokosuka 239-0826, Japan

[2] Chief, Marine Observation Laboratory, Hydraulic Engineering Division, ditto.

[3] Chief, Wave Information Laboratory, ECOH Co., Ltd., 2-6-4 Kitaueno, Taito-ku, Tokyo 110-0014, Japan.

The statistical method has advantages in that it is easy to handle and does not require special knowledge in practical computations. Because of these advantages, several statistical models have been proposed so far. The most commonly used model is the multiple regression model in which the wave characteristics, such as significant wave height and period at a specific point, and the atmospheric pressure data and/or wind data at several points are interrelated. However, from numerical viewpoints, most of the existing models contain several drawbacks such as multicollinearity among predictor variables, over-fitting of the criterion variable to the data, and over adoption of predictor variables in the model.

For these reasons, it necessitates the development of a reasonable statistical model in which the dynamical behavior of each variable and the statistical relation among variables are properly taken into consideration to eliminate the above drawbacks. Before applying the model, it is necessary to examine the model in detail for the real data obtained in various sea conditions for practical applications.

In this paper, we propose a new statistical wave forecasting model utilizing the Kalman filter technique combined with Principal Component Analysis (PCA) in order to mitigate the above-mentioned drawbacks of the conventional statistical wave forecasting models.

Drawbacks of the conventional statistical wave forecasting methods

In the normal procedure of wave forecasting by using a numerical model, first, the wind field is calculated from the weather charts. Once the wind field is calculated, the generation, development and attenuation of the wave field can be calculated from the wind data. Usually, in numerical computations, a proper grid size is adopted to obtain accurate and reliable results. However, if the same grid size is applied to the statistical wave model, and the data for the predictor variables are given on the same grid points, such fine grid size sometimes cause inferior prediction. This is because of the high correlation among predictor variables themselves, which causes the multicollinearity in the correlation matrix of the predictor variables. In such situations, the data on such fine grids are no longer proper predictor variables. However, if a rough grid size is adopted for predictor variables to eliminate the above multicollinearity problem, important small scale atmospheric pressure patterns will be overlooked and the accuracy of the wave forecasting will be reduced. This is one of the problems for the conventional statistical wave forecasting method.

When analyzing the time series of atmospheric pressure data, the spectrum of the atmospheric pressure includes energies in a considerably wide range of frequencies including seasonal and yearly changes. If the atmospheric pressure data are directly applied for establishing the equations for short-term wave forecasting, unnecessary long-term components of the energy included in the data may cause biases in the relation between the criterion variable and the predictor variables. This leads to the deterioration of the prediction accuracy.

Over-fitting of the criterion variable to the data and over-adoption of predictor variables in the model are also common matters to be attended in the statistical model, which sometimes cause the prominent delay of the predicted values to the real values, and the predicted values tend to be more unstable.

In order to mitigate the above-mentioned drawbacks of the conventional statistical wave forecasting models, this new statistical wave forecasting model is developed which properly considers the dynamical behavior of each variable and the statistical relation among.

Definition of the "wave forecast" used in this study

First, to eliminate any possible confusion, the meaning of the word "forecast" used in this study should to be clarified. The word "forecast" is generally used to estimate an unknown situation based on the information obtained at present or in the past. However, in this study, we assume that the accurate weather information at the time for wave forecasting has already been known, which is assumed to be predicted by some other methods. That is, when we try to forecast waves 24 hours ahead, the accurate weather chart 24 hours ahead has already been obtained and wave data observed at the time are also available. Though the accuracy of the wave forecast strongly depends on the accuracy of the weather information, we examine only the accuracy of waves forecasted by the proposed method under the condition that the accurate weather information is given. Though the forecasted weather chart may include some errors, it is beyond our research to examine the accuracy of the weather chart.

Wave data and atmospheric pressure data used in this study

The computation for wave forecasting is carried out using the atmospheric pressure data read every 12 hours at the grid points of 500km×500km shown in **Figure 1**. Five years of atmospheric pressure data, from 1980 to 1984, are used in this study. The locations of the wave forecasting points are denoted by the upper case letters in **Figure 1**. At each location, wave observations have been obtained every 2 hours for many years. Though the grid size is very rough compared to the numerical model, the forecasted wave heights using this grid size is acceptable for practical applications as shown later.

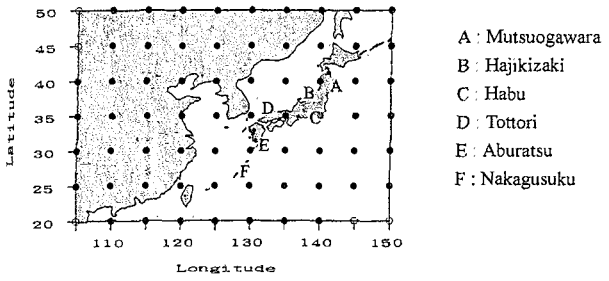

Figure 1 Wave observation stations and grid points of atmospheric pressure data

Statistical wave forecasting model utilizing Kalman filter combined with Principal Component Analysis (PCA)

Figure 2 shows the flow chart of the procedure of wave forecasting by using the Kalman filter combined with Principal Component Analysis (PCA). The model employed here consists of three parts. The first is the real-time filtering by using the Kalman filter. The second step is the PCA. The final step is the wave forecasting by the time-dependent regression model utilizing the Kalman filter. By obtaining new wave information and atmospheric pressure data, these three steps are repeated to update the wave forecasting equation and improve the accuracy of the wave forecasting. The procedure of each step is introduced in detail in the following.

1) Real-time filtering of the atmospheric pressure data by the Kalman filter

The first step in **Figure 2** is the real-time filtering by the Kalman filter. Using their technique, the time series of atmospheric pressure data on the grid points are separated into two components, i.e., a long-term component (longer than one-week period) and the remaining short-term component. The outline of the Kalman filter is as follows.

The equations of the state space representation are expressed by:

$$\mathbf{x}_n = \mathbf{F}_n \mathbf{x}_{n-1} + \mathbf{G}_n \mathbf{v}_n \quad \text{(System Equation)} \tag{1}$$

$$\mathbf{y}_n = \mathbf{H}_n \mathbf{x}_n + \mathbf{w}_n \quad \text{(Observation Equation)} \tag{2}$$

where $\mathbf{x}_n$: state vector ($k \times 1$), $\mathbf{v}_n$: system noise (Gaussian white noise with mean vector O and covariance matrix $\mathbf{Q}_n$) ($m \times 1$), $\mathbf{y}_n$: observation vector ($l \times 1$), $\mathbf{w}_n$: observation noise (Gaussian white noise with mean vector O and covariance matrix $\mathbf{R}_n$) ($l \times 1$) and $\mathbf{F}_n$, $\mathbf{G}_n$, $\mathbf{H}_n$: respectively ($k \times k$), ($k \times m$) and ($l \times k$) matrix.

To estimate the state vector $\mathbf{x}_n$ in Equation (1) on the basis of the observation vector $\mathbf{y}_n$ in Equation (2), the following one-step prediction and filtering are recursively applied through Equations (3) - (7).

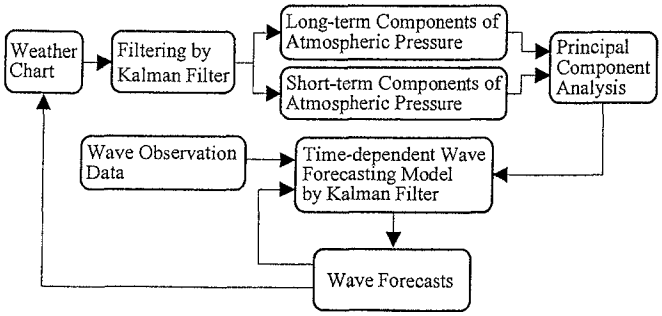

Figure 2 Flow chart of the proposed wave forecasting procedure

[One-step prediction]

$$\mathbf{x}_{n|n-1} = \mathbf{F}_n \mathbf{x}_{n-1|n-1} \tag{3}$$

$$\mathbf{V}_{n|n-1} = \mathbf{F}_n \mathbf{V}_{n-1|n-1} \mathbf{F}_n^t + \mathbf{G}_n \mathbf{Q}_n \mathbf{G}_n^t \tag{4}$$

[Filtering]

$$\mathbf{K}_n = \mathbf{V}_{n|n-1} \mathbf{H}_n^t (\mathbf{H}_n \mathbf{V}_{n|n-1} \mathbf{H}_n^t + \mathbf{R}_n)^{-1} \quad : \text{Kalman gain} \tag{5}$$

$$\mathbf{x}_{n|n} = \mathbf{x}_{n|n-1} + \mathbf{K}_n (\mathbf{y}_n - \mathbf{H}_n \mathbf{x}_{n|n-1}) \tag{6}$$

$$\mathbf{V}_{n|n} = (\mathbf{I} - \mathbf{K}_n \mathbf{H}_n) \mathbf{V}_{n|n-1} \tag{7}$$

where $\mathbf{x}_{n|j} = E(\mathbf{x}_n \mid \mathbf{Y}_j)$ and $\mathbf{V}_{n|j} = E(\mathbf{x}_n - \mathbf{x}_{n|j})(\mathbf{x}_n - \mathbf{x}_{n|j})^t$

For separating long-term and short-term components of the atmospheric pressure, equation (8) is assumed as the observation equation of equation (2).

$$y_n = t_n + w_n \quad \text{(Observation equation)} \tag{8}$$

where y_n : the observed value, t_n : the long-term component and w_n : the short-term component.

Since the long-term component is a slowly varying value, Equation (9) is assumed as the system equation of equation (1).

$$\Delta^k t_n = v_n \quad \text{(System equation)} \tag{9}$$

where Δ^k : k-th order difference operator, and the second order difference operator is applied in this study as $t_n - 2t_{n-1} + t_{n-2} = v_n$.

Figure 3 shows the example of the spectra of the logarithm of the significant wave height measured at Mutsuogawara port and the atmospheric pressure data at a point. The spectra of the separated time series data of long-term component and short-term component are shown in the figure. As seen in the figure, appropriate separation

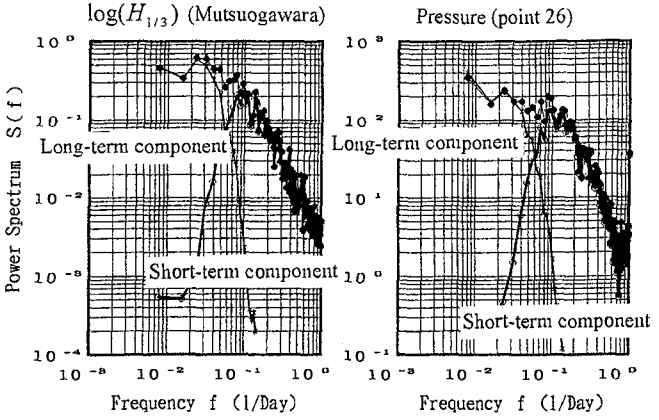

Figure 3 Spectra of the logarithm of the significant wave height at Mutsuogawara port and atmospheric pressure with the separated components

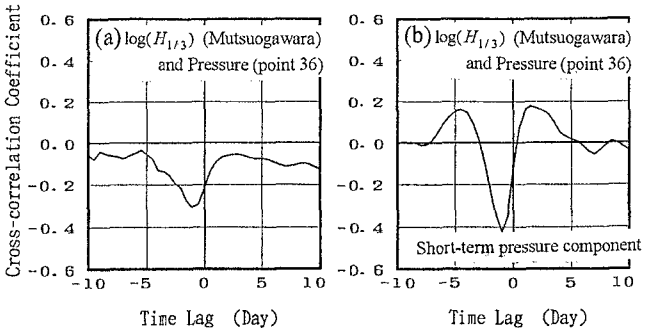

Figure 4 Cross-correlation coefficients between the logarithm of the significant wave height at Mutsuogawara port and the atmospheric pressure data

can be done by the Kalman filter by choosing a proper value of the trade-off parameter σ_v^2/σ_w^2, where σ_v^2 and σ_w^2 are the variances of v_n and w_n in equations (9) and (8), respectively. The trade-off parameter of the Kalman filter is used to control the magnitude of the change of the model in each time step of the computations. That is, by changing the value of σ_v^2/σ_w^2, the ratio of the energy of the separated long-term component and the short-term component can be controlled.

Figure 4 shows the cross-correlation coefficients between the logarithm of the significant wave height measured at Mutsuogawara port and the atmospheric pressure data at a point. The cross-correlation coefficient in figure (a) was estimated from the original atmospheric pressure data. The cross-correlation coefficient in figure (b) was estimated from the short-term atmospheric pressure component separated from the original data. The cross-correlation coefficient in figure (a) shows distinct positive and negative peaks with clear time lag between the two time series, though figure (b) shows vague negative peaks and time lag.

The purpose of separating the atmospheric pressure data into two components is to reduce negative effects from the long-term component to the short-term forecasting. This is necessary since we focus on the short-term wave forecasting and the long-term component may cause a bias in the relation between the criterion variable and the predictor variables.

2) Principal Component Analysis of atmospheric pressure data

The second step is the PCA by which the separated time series data on the grid points are projected onto the empirical eigen-vectors obtained from each component of the atmospheric pressure data on the grid points. Here, the empirical eigen-vectors are preliminarily computed by using the past three-years' atmospheric pressure data. The outline of the PCA is as follows.

Atmospheric pressure field $P_{z,t}$ can be approximately expressed by the

superposition of the eigen-vectors $e_{n,z}$ with weighting coefficients $c_{n,t}$:

$$P_{z,t} = \sum c_{n,t} e_{n,z} \tag{10}$$

where atmospheric pressure field $P_{z,t}$ is normalized by the mean value and standard deviation of $P(x,y,t)$, and each eigen-vector $e_{n,z}$ is assumed to be orthogonal to each other as

$$\sum e_{n,z} e_{m,z} = \delta_{n,m} \tag{11}$$

Then the eigen-vector $e_{n,z}$ can be estimated by solving the following equation.

$$\mathbf{A} = \lambda_{\mathbf{n}} \mathbf{e}_{\mathbf{n}} \tag{12}$$

where λ_n: eigen-value, $a_{i,j}$ is the (i,j) component of matrix $\mathbf{A}$ and is expressed by

$$a_{i,j} = \frac{1}{n_z n_t} \sum_{t=1}^{n_t} P_{i,t} P_{j,t} \tag{13}$$

Using the orthogonal condition of the eigen-vector, the weighting coefficient $c_{n,t}$ can be obtained by

$$c_{n,t} = \sum P_{z,t} e_{n,z} \tag{14}$$

Figure 5 shows examples of the eigen-vectors of the long-term component of the atmospheric pressure system. From the left to the right in **Figure 5**, each figure shows the 1-st, the 2-nd, the 3-rd, and the 4-th principal component, respectively.

As seen in the figure, the 1-st component is invariable with respect to time t. This component seems to be the average of the atmospheric pressure system. The 2-nd component seems to show the phenomenon in which the atmospheric pressure

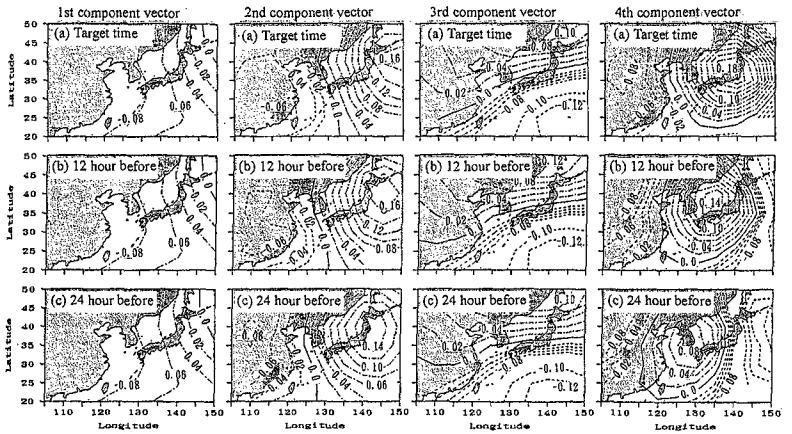

Figure 5 Components of PCA for target time and 12, 24 hours before target time

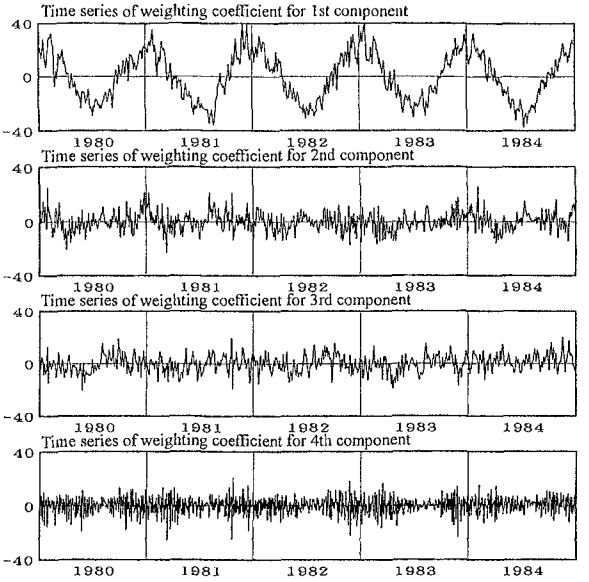

Figure 6 Time series of the weighting coefficients of the PCA

system moves from the west to the east. The 3-rd component shows from the south to the north. The 4-th component from the south-west to the north-east with the developing pressure system. The behavior of the atmospheric pressure system is assumed to be approximated by the superposition of these orthogonal empirical eigen patterns in this study.

The weighting coefficient of each eigen-vector is stored to be used in the following 3-rd step computation. Through this procedure, the atmospheric pressure data on the grid points are transformed and condensed into fewer, yet more efficient and independent predictor variables. The purpose of introducing the PCA is to avoid the unfavorable effect of multicollinearity of the atmospheric pressure data on the space-time grid points, by which new predictor variables are generated through the PCA. **Figure 6** is an example of the time series of the weighting coefficient $c_{n,t}$, which is used as the predictor variable in the next step.

3) Time dependent regression model for wave forecasting by Kalman Filter

The final step is the wave forecasting where the weighting coefficients previously obtained are used as the input data for the time-dependent regression model utilizing the Kalman filter.

The equation for the time-dependent regression model is assumed by

$$\log_{10} H_{1/3} = a_0 + \sum_{i=1}^{N} a_i z_i + \varepsilon \tag{15}$$

This equation can be reduced to

$$y_n = H_n x_n + w_n \quad \text{(Observation equation)} \tag{16}$$

where $y_n = \log_{10} H_{1/3}$, $x_n = (a_0, a_1, \cdots, a_N)^t$, $H_n = (1, z_1, z_2, \cdots, z_N)$, $w_n = \varepsilon$ and the weighting coefficient $c_{n,t}$ is expressed as z_i for convenience.

If the coefficient a_n is slowly varying value, then

$$\Delta^k x_n = v_n \quad \text{(System equation)} \tag{17}$$

where Δ^k is the k-th order difference operator, and the first order difference operator is applied in this study as $a_n - a_{n-1} = v_n$.

The trade-off parameter defined by σ_v^2/σ_w^2 is used to control the magnitude of the change of the model in each time step of the computations, where σ_v^2 and σ_w^2 are the variances of v_n and w_n in equations (17) and (16), respectively. **Figure 7** shows examples of the variations of the time series of the state variables a_i $(i = 0, \cdots, N)$. Figure (a) shows the results calculated with $\sigma_v^2/\sigma_w^2 = 10^{-3}$, while figure (b) shows the results calculated with $\sigma_v^2/\sigma_w^2 = 10^{-10}$. When choosing a small trade-off parameter, the time variations of the state variables a_i $(i = 0, \cdots, N)$ can be suppressed so as to fluctuate around the mean values as seen in figure (b). The rapid change of the state variables a_i $(i = 0, \cdots, N)$ in figure (a) seems to reflect the over-fitting of the model to the data. In other words, the problem of the over-fitting can be reduced by choosing a proper value of the trade-off parameter σ_v^2/σ_w^2 in the model.

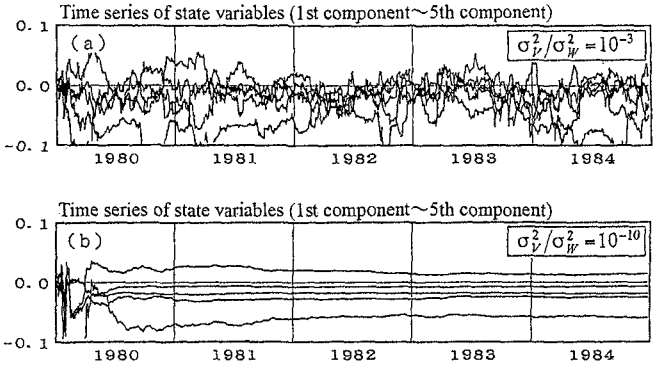

Figure 7 Time series of the state variables a_i $(i = 0, \cdots, N)$ of the time-dependent regression model

The purpose of adopting a time-dependent regression model utilizing Kalman filtering is to detect a gradual change such as a seasonal variation in the atmospheric and wave systems, and to reflect it in the forecasting model to improve the accuracy of the wave forecasting.

These three steps are repeated for each time step. That is, by obtaining new wave data or atmospheric pressure data, the wave forecasting equation is updated to improve the accuracy of the wave forecasting.

Numerical simulations of wave forecasting based on 5-years of data

The applicability and reliability of the proposed method is examined for six wave observation stations around Japan, shown in **Figure 1,** through simulations based on 5-years of wave data and weather charts.

Figure 8 shows the accuracy of the proposed method applied for Mutsuogawara port. The horizontal axis is the lead time for wave forecasting. The vertical axis is the standard deviation of the prediction errors. It is seen that the predicted wave height by the proposed method shows different characteristics depending on the magnitude of the trade-off parameter, σ_v^2/σ_w^2, of the Kalman filter used in the 3-rd step. The trade-off parameter controls the magnitude of the change of the coefficients in each time step of the computations. If an appropriate trade-off parameter is chosen, the wave height errors, predicted several-steps-ahead, can be controlled within an allowable range, although the prediction error of one-step-ahead may not be the minimum. In other words, the problem of the over-fitting of the criterion variable to the data can be resolved by choosing an appropriate value of the trade-off parameter in the model.

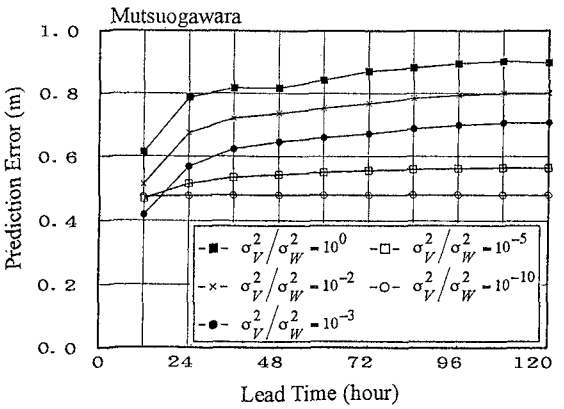

Figure 8 Accuracy of the proposed method (Error vs. lead time)

	Consideration of the separation of long-term component and short-term component	Trade-off parameter σ_v^2 / σ_w^2
(a)	×	10^{-3}
(b)	×	10^{-10}
(c)	○	10^{-3}
(d)	○	10^{-10}

Table 1 Simulation conditions for wave forecasting

To examine the validity of the proposed method, we applied the proposed method for 4 different computation conditions. **Table 1** shows the 4 cases. **Figure 9** shows the scatter diagram between the observed wave height and the forecasted wave height for a lead time of 120 hours under the 4 different conditions for Mutsuogawara port.

The low correlation coefficient between the forecasted value and the observed value can be seen in the case (a) where the separation of the long-term component is not considered, and the trade-off parameter is also inappropriate. In the case (b), the trade-off parameter is properly chosen though the separation of the long-term component is not considered. In this case, the correlation coefficient is improved compared to the case (a). However, prominent bias between the forecasted value and observed value can be seen. In the case (c) where the separation of the long-term

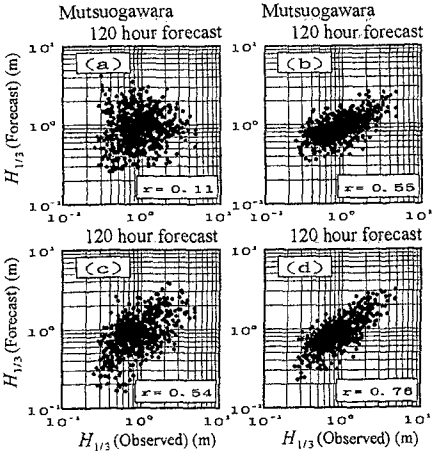

Figure 9 Scatter diagram between the observed wave height and the forecasted wave height for a lead time of 120 hours under the 4 different conditions

component is considered while the trade-off parameter is not appropriate, the correlation coefficient is not improved when compared to the case (b) although it does not show the prominent bias. In the case (d) where the separation of the long-term component is considered and the trade-off parameter is appropriate, this case shows the highest correlation coefficient in the 4 cases and does not show the prominent bias between forecasted and observed values.

From these comparative results obtained under the different conditions using the same data, it is demonstrated that each technique introduced in each step of the proposed method is effective. It is also demonstrated that the accuracy of the proposed method for short-term wave forecasting is better than the other methods (Kobune, et.al., 1988, 1990 and Suda and Yuzawa, 1983) when an appropriate trade-off parameter is properly chosen.

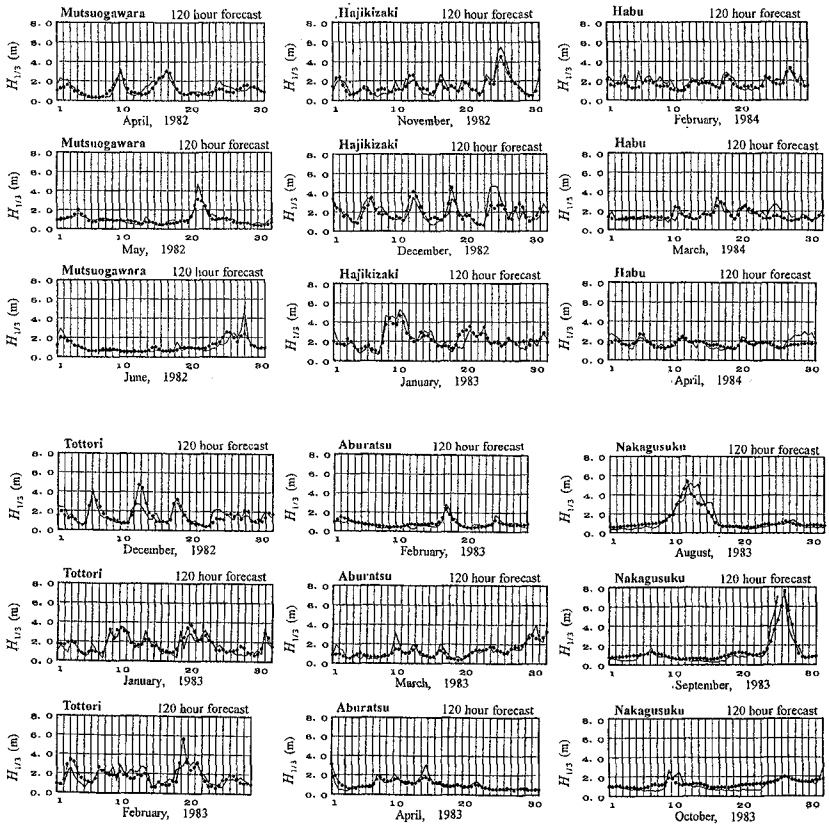

Figure 10 Comparison of the time series of the forecasted wave heights (●) for a lead time of 120 hours and the observed wave height (solid line)

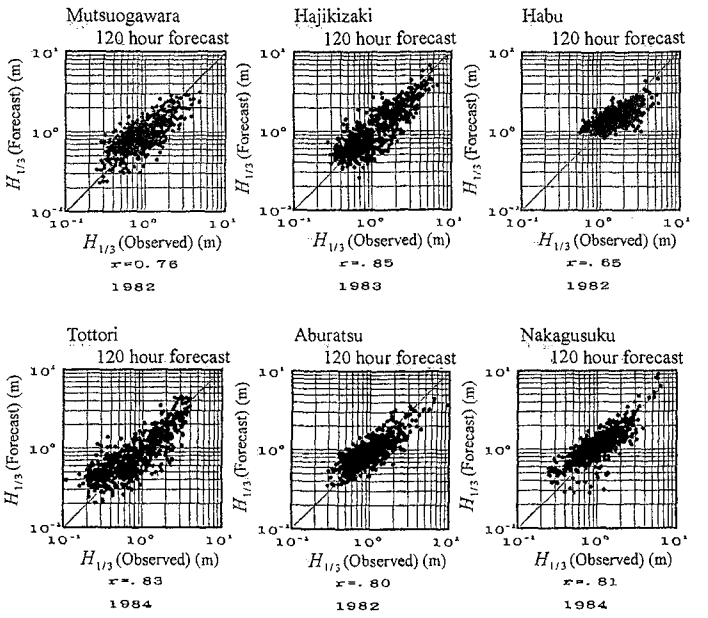

Figure 11 Scatter diagram between the observed wave heights and the forecasted wave heights for a lead time of 120 hours.

The examinations of the wave forecasting for other observation stations were carried out using the atmospheric pressure data at 500km × 500km grid points around the wave observation stations shown in **Figure 1**. **Figure 10** shows an example of the comparison of the time series of the forecasted wave heights for a lead time of 120 hours and the observed wave height, where ● is the forecasted wave height and solid line is the observed wave height. As seen in the figure, the tendency of the time delay of the forecasted wave height to the real wave height is not recognized although most of the conventional statistical wave forecasting methods show such a drawback (Kobune, et.al., 1988, 1990 and Suda and Yuzawa, 1983).

Figure 11 shows the scatter diagram between the observed wave heights and the forecasted wave heights for a lead time of 120 hours. The examples for 6 wave observation stations around Japan are shown in the figure. All the data in one year are plotted in the figure. These examples demonstrate that the reliability of the proposed method for short-term wave forecasting can be acceptable for practical use if errors are allowed to a certain extent.

Conclusions

The overall conclusions of this study are summarized below.

1) The proposed method utilizing the Kalman filter combined with Principal Component Analysis can be a useful tool for a short-term wave forecast if errors are allowed to a certain extent.
2) If an appropriate trade-off parameter is chosen in the model, the wave height errors predicted several-steps-ahead can be controlled within an allowable range, although the prediction error one-step-ahead may not be the minimum.
3) The proposed method is easy to handle, which enables us to use the proposed method with a small personal computer.

Acknowledgement

We wish to express our sincere gratitude to Mr. Sidney Walter thurston III for critical review and valuable comments on this paper.

References

Kobune, K. and N. Hashimoto (1988): On the reliability of the wave forecasting by the multiple regression model, Coastal Engineering in Japan, Vol. 31, No.2, pp.199-205.

Kobune, K., N. Hashimoto and Y. Kameyama (1990): On the reliability of wave forecasting by Emprical wave forecasting models, Technical Note of P.H.R.I., No.673, 42p (in Japanese).

Suda, H. and A. Yuzawa (1983): A fundamental study on the queuing theory of the open sea berth based on the wave forecasting, Proc. Of JSCE, Vol.339, pp.177-185.

Data Assimilation and Nested Hydrodynamic Modelling in Storm Surge Forecasting

Rafael Cañizares[1] and Henrik Madsen[1]

Abstract

A data assimilation method for state updating in a hydrodynamic model is presented. The method is based on the extended Kalman filter in which the error covariance matrix is approximated by a matrix of lower rank using a square-root factorisation (reduced rank square-root filter). Results from a test of the Kalman filter in a regional model of the North Sea and Baltic Sea are presented. In this respect, the influence of using nested hydrodynamic models together with data assimilation techniques is illustrated and discussed. The test reveals that assimilation of water level measurements from coastal stations significantly improves the model results.

Introduction

During the last decades, the interest of predicting water level rising as a consequence of storm surges has grown considerably. In countries that are affected by this phenomenon substantial efforts are made to predict storm surges so far ahead in time that appropriate actions can be taken.

The combination of numerical weather prediction models and hydrodynamic models forms the main frame of an operational storm surge forecast system (Bode and Hardy, 1997). The hydrodynamic model uses the predicted meteorological wind and pressure data to provide a prediction of the water level field. The storm surge prediction, however, is not always as accurate as desired which can mainly be ascribed to

1. Simplifications of the description of the physical processes in the numerical hydrodynamic model.
2. Bias in the meteorological forcing prediction.

[1] International Research Centre for Computational Hydrodynamics and Danish Hydraulic Institute, Agern Allé 5, DK-2970 Hørsholm, Denmark. rct@dhi.dk; hem@dhi.dk

3. Inaccurate open boundary conditions.

The main errors in the hydrodynamic model are, respectively, simplifications of the physical processes in the numerical model equations and application of a too coarse spatial resolution to adequately resolve the dynamics of the system. To reduce the errors caused by the former problem more complex models should be considered, whereas for the latter problem the model has to be applied in a finer grid which can be defined locally by using nested hydrodynamic models (Vested et al, 1995). Nested models allow to have a finer resolution in areas where required while a coarser resolution can be maintained in the rest of the model domain.

The uncertainties of the meteorological forcing and the open boundary conditions as well as uncertainties of the physical model parameters can be accounted for by using data assimilation. In data assimilation, model and measurements of the system are combined in order to obtain a better estimate of the state of the system. Data assimilation algorithms, however, can become prohibitive when applied in large scale models due to the huge computational cost associated with this kind of applications. New algorithms, such as the reduced rank square-root (RRSQRT) Kalman filter (Verlaan and Heemink, 1995) have solved this problem. The RRSQRT filter is a suboptimal scheme of the extended Kalman filter that uses a square-root algorithm as well as a lower rank approximation of the error covariance matrix.

The RRSQRT filter has been integrated into an existing hydrodynamic modelling system that solves the vertically integrated equations of continuity and momentum in two horizontal directions (Cañizares et al, 1998). When measurements are available, the Kalman filter is adopted for updating the state of the system. In storm surge forecasting, the updated state is then used as initial conditions for the forecast simulation.

The paper is organised as follows. In the first section the applied numerical hydrodynamic model is described. In sections two and three the general Kalman filter updating scheme and the RRSQRT filter are presented and the implementation in the hydrodynamic model is described. Sections four and five outline the specific features of the nested version of the hydrodynamic model and the implementation of the filter in this type of model. Finally, a test case is presented where the Kalman filter is applied in a regional model of the North Sea and Baltic Sea.

The deterministic numerical model

In the present study, the data assimilation method has been implemented in the hydrodynamic module of the MIKE 21 modelling system which solves the vertically integrated equations of continuity and conservation of momentum (shallow water equations) in two horizontal directions (DHI, 1995). The equations that are solved are those of:

Continuity:

$$\frac{\partial \xi}{\partial t} + \frac{\partial p}{\partial x} + \frac{\partial q}{\partial y} = S_0 - e \tag{1}$$

x-momentum:

$$\frac{\partial p}{\partial t} + \frac{\partial}{\partial x}\left(\frac{p^2}{h}\right) + \frac{\partial}{\partial y}\left(\frac{pq}{h}\right) + gh\frac{\partial \xi}{\partial x} + \frac{g\frac{p}{h}\sqrt{\frac{p^2}{h^2}+\frac{q^2}{h^2}}}{C^2} - fVV_x - \frac{h}{\rho_w}\frac{\partial}{\partial x}(P_a) - \Omega q - E\left(\frac{\partial^2 p}{\partial x^2} + \frac{\partial^2 p}{\partial y^2}\right) = S_{ix} \tag{2}$$

and y-momentum:

$$\frac{\partial q}{\partial t} + \frac{\partial}{\partial y}\left(\frac{q^2}{h}\right) + \frac{\partial}{\partial x}\left(\frac{pq}{h}\right) + gh\frac{\partial \xi}{\partial y} + \frac{g\frac{q}{h}\sqrt{\frac{p^2}{h^2}+\frac{q^2}{h^2}}}{C^2} - fVV_y - \frac{h}{\rho_w}\frac{\partial}{\partial y}(P_a) - \Omega p - E\left(\frac{\partial^2 q}{\partial x^2} + \frac{\partial^2 q}{\partial y^2}\right) = S_{iy} \tag{3}$$

where:

x,y	Horizontal coordinates [m].
t	Time [s].
h	Water depth [m].
ξ	Surface elevation [m].
p,q	Flux densities in x and y directions [$m^3/s/m$]. $(p,q) = (v_x h, v_y h)$ where v_x and v_y are the depth averaged x and y velocities [m/s].
S_0	Source magnitude per unit horizontal area [m/s].
S_{ix}, S_{iy}	Source impulse in x and y directions [m^2/s^2].
e	Evaporation rate [m/s].
E	Eddy viscosity coefficient [m^2/s]
g	Acceleration due to gravity [m/s^2].
C	Chezy bed resistance coefficient [$m^{1/2}/s$].
Ω	Coriolis parameter [s^{-1}].
f	Wind friction factor [-].
V, V_x, V_y	Wind speed and wind speed components in x and y directions [m/s].
p_a	Atmospheric pressure [$kg/m/s^2$].
ρ_w	Density of water [kg/m^3].

At closed boundaries the flow perpendicular to the boundary is set to zero. At open boundaries the surface elevation is prescribed. With these boundary conditions and with prescribed initial values of surface elevations and flux densities, (1)-(3) form a well-posed boundary value problem.

MIKE 21 uses a finite difference approximation to solve the partial differential equations where the variables are defined on a space-staggered rectangular grid with surface elevations at grid points and fluxes midway between grid points (Leendertse, 1964). A time-centered alternating direction implicit (ADI) scheme is adopted. The equations are solved in one-dimensional sweeps, alternating between x and y directions. In the x-sweep, the continuity equation and the momentum equation in the x direction are solved with respect to ξ at time step k+1/2 and p at time step k+1 using the known variables ξ_k, p_k, $q_{k-1/2}$, and $q_{k+1/2}$. In the y-sweep, the continuity equation and the momentum equation in the y direction are solved with respect to ξ_{k+1} and $q_{k+3/2}$ using $\xi_{k+1/2}$, $q_{k+1/2}$, p_k, and p_{k+1}.

Implementation of the Kalman filter in MIKE 21

For implementation of the Kalman filter in MIKE 21, the numerical model has to be formulated in a state-space form. The state variables to be considered are surface elevations and depth averaged x and y velocities in every point of the horizontal grid. The Kalman filter algorithm is based on a recursive two-time step formulation. The numerical scheme in MIKE 21, however, involves the y velocity at three time steps. To express this scheme using only two time steps, the y velocity at time steps k+1/2 and k-1/2 are included in the state vector. The numerical scheme based on (1)-(3) can then be written

$$x_k = \Phi(x_{k-1}, u_k) \tag{4}$$

where $x_k = (\xi_k, v_{x,k}, v_{y,k+1/2}, v_{y,k-1/2})$ is the state vector, and u_k is the forcing of the system in terms of the surface elevations at open boundaries and the meteorological forcing components in the momentum equations (wind stress and pressure gradient).

For modelling the uncertainty of the system, it is assumed that model errors are mainly related to errors in the forcing components. The error processes are assumed to be less spatially variable than the water flow process (Heemink, 1990), and the discrete error processes can thus be defined on a grid G2 that is coarser than the model grid G1. A stochastic representation of the system equation (4) can then be written

$$x_k = \Phi(x_{k-1}, u_k + \Lambda\varepsilon_k) \tag{5}$$

where ε_k contains the model error in every grid point of G2, and Λ is a matrix that represents the sequence of linear interpolations between G2 and G1.

For the system, measurements z_k of the state are assumed to be available at certain points in the model grid G1. The stochastic representation of the measurement equation reads

$$z_k = C_k x_k + \eta_k \tag{6}$$

where C_k is a matrix that describes the relation between measurements and state variables, and η_k is a random measurement error with zero mean and known covariance matrix R_k.

When measurements are available, cf. (6), the model forecast and the measurements can be combined to obtain an updated estimate of the state of the system. The Kalman filter update of the state vector and the error covariance matrix P_k is given by

$$x_k^a = x_k^f + K_k(z_k - C_k x_k^f) \tag{7}$$

$$P_k^a = P_k^f - K_k C_k P_k^f \tag{8}$$

where K_k is the Kalman gain matrix

$$K_k = P_k^f C_k^T \left[C_k P_k^f C_k^T - R_k\right]^{-1} \tag{9}$$

which serves as a weighting function of model forecast and measurements and depends on the associated errors P_k^f and R_k. In (7)-(9) superscripts f and a refer to, respectively, forecast and analysis (or update).

For large systems, the propagation of the error covariance matrix (determination of P_k^f) is the main bottleneck. This step requires $2n$ as much computing effort as is required to advance the deterministic model itself (n being the dimension of the state vector). Applications to large systems are prohibitive under such conditions, and hence approximations of the Kalman filter, reducing the computational effort, have to be used. The technique described below, the reduced rank square-root filter, introduced in (Verlaan and Heemink, 1995) and (Verlaan, 1998), is based on an approximation of the error covariance matrix.

The Reduced Rank SQuare RooT (RRSQRT) filter

For non-linear model dynamics an extended Kalman filter can be formulated in which the propagation of the error covariance matrix is based on a statistical linearisation of the model equation. Considering a white noise process for the model errors, the forecast step is given by

$$x_k^f = \Phi(x_{k-1}^a, u_k) \tag{10}$$

$$P_k^f = F_k P_{k-1}^a F_k^T + G_k(\Lambda Q_k \Lambda^T) G_k^T$$
$$F_k = \left.\frac{\partial \Phi}{\partial x}\right|_{x=x_k^f}, \; G_k = \left.\frac{\partial \Phi}{\partial u}\right|_{x=x_k^f} \tag{11}$$

where Q_k is the covariance matrix of the system noise, defined on grid G2.

The RRSQRT approximation of the extended Kalman filter uses a square-root algorithm as well as a lower rank approximation of the error covariance matrix (Verlaan and Heemink, 1995). Denote by S the approximation of rank M of the square root of the error covariance matrix. The propagation of the error covariance matrix is then given by

$$S_k^f = \left[F_k S_{k-1}^a \middle| G_k \Lambda Q_k^{1/2} \right] \tag{12}$$

where $Q_k^{1/2}$ is the square-root of Q_k. The matrix S_{k-1}^a has M columns where M is chosen much smaller than the dimension n of the state vector. To calculate the derivatives in F_k and G_k a finite difference approximation of $\Phi(\bullet)$ is adopted. Thus, the propagation of the error covariance matrix requires M plus p (the total number of noise points) model integrations, which is much smaller than the $2n$ integrations required in (11).

The propagation step in (12) increases the number of columns in the error covariance matrix from M to $M + p$. To reduce the number of columns, and hence keep the rank of the matrix constant throughout the simulation, a lower rank approximation of S_k^f in (12) is applied by keeping only the M leading eigenvectors of the error covariance matrix. The reduction can be achieved either by a singular value decomposition of S_k^f or by an eigenvalue decomposition of the matrix $(S_k^f)^T S_k^f$ (Cañizares et al., 1998).

For uncorrelated measurement errors, a sequential updating scheme can be applied (Maybeck, 1979). This algorithm avoids the expensive calculation and storage of P_k^f as well as the matrix inversion in (9) for the calculation of the Kalman gain. The procedure used in the present study follows (Potter, 1967), i.e.

$$a_{k,i} = \left[S_k^f\right]^T C_i^T \tag{13}$$

$$\gamma_{k,i} = \frac{1}{\left[a_{k,i}\right]^T a_{k,i} + \sigma_{k,i}^2} \tag{14}$$

$$K_{k,i} = S_{k,i-1}^a a_{k,i} \gamma_{k,i} \tag{15}$$

$$S^a_{k,i} = S^a_{k,i-1} - K_{k,i} a^T_{k,i} \frac{1}{1+\sqrt{\gamma_{k,i}\sigma^2_{k,i}}}, \quad S^a_{k,0} = S^f_k \tag{16}$$

$$x^a_{k,i} = x^a_{k,i-1} + K_{k,i}\left[z_{k,i} - C_i x^a_{k,i-1}\right], \quad x^a_{k,0} = x^f_k \tag{17}$$

where C_i is the i^{th} column of matrix C, $z_{k,i}$ is the i^{th} measurement, and σ_i is the standard deviation of the measurement noise.

The filter can use time-coloured noise. In this case the state vector is augmented with variables that represent the estimated value of the noise. For the propagation of the state vector and the error covariance matrix new equations have to be defined for the RRSQRT filter (see Madsen and Cañizares, 1998). Moreover, the error covariance matrix has to be normalised prior to the eigenvalue decomposition. For further details on the RRSQRT algorithm see (Cañizares, 1998).

Special features of the MIKE 21 nested model

The nested version of the MIKE 21 model solves the hydrodynamic equations simultaneously in a number of dynamically nested grids. An important difference between nesting and boundary transfer from a coarse model to a finer one is that in nesting the information between grids travel in two directions, i.e. from the coarse to the fine grid and vice versa. On the other hand, in a boundary transfer model information travel only from the coarse to the fine grid. The two techniques are also denoted two-way and one-way nesting, respectively.

In order to ensure model stability and smooth transition between areas, certain constraints are imposed. The most important are:

- Open boundaries can only be defined in the coarsest grid.
- The spatial resolution from one level to another is reduced by a fixed factor (grid reduction factor), which is equal to 3.
- The water depths in common grid points along the internal boundaries must be equal in both the coarse and the fine grid. Between the common points along the internal boundary, the water depths in the fine grid are linearly interpolated using the values at the common points.
- The water depth in the coarse grid has to be identical in three points orthogonal to the internal boundary (at the border and one point at each side). Therefore the first four points orthogonal to the internal boundary in the fine grid have the same water depth. The intention of these corrections is to avoid instabilities in the internal boundaries.

Further details about the nested model can be found in (DHI, 1995).

Implementation of the RRSQRT filter in the nested model

The main features of the implementation of the RRSQRT filter in the nested model are:

- The model is propagated using the complete nested model.
- The error covariance matrix is represented in the coarsest grid (the main area). Hence, the number of variables considered in this matrix is the same as if only the coarsest grid is considered.
- The error covariance matrix is propagated using the complete nested model. The model error is interpolated from the main grid to the internal grids.
- If the measurement position is located in a grid point of an internal area, the value is extrapolated to the main area. Thus, vector C_i represents the relation between the position of the measurement in the fine grid and the surrounding positions in the coarsest grid.
- The Kalman gains K_i correspond to variables in the main area. The gains are interpolated from the main grid to the internal grids.

Under these assumptions, the associated cost of the data assimilation scheme in the nested model is comparable to application in the model defined in the coarse area. The main difference is that the time associated with a run of the nested model is larger than for the model defined in the coarse area. For further details on the application of the RRSQRT in the nested hydrodynamic model see (Cañizares, 1998).

Application: a regional model of the North Sea and Baltic Sea

The Kalman filter has been applied to a regional model covering the North Sea and the Baltic Sea. Two open boundaries are defined in the North Sea between, respectively, Stavanger and Orkney Island (northern boundary) and Dover and Calais (southern boundary). A coarse model is defined with a grid size of 9 nautical miles (16670 m) in both directions. A nested area of the inner Danish waters has been defined in order to obtain a better and more detailed description of the water level and current fields in this area. The local model is defined in a grid with origin in (48,18) of the coarse grid and a grid size of 3 nautical miles (5667 m), i.e. one third of the grid size of the coarse model. The model setup and bathymetry are shown in Figure 1.

At the two open boundaries, the water level is specified. For the simulation period, wind velocity fields and pressure fields are available every three hours and they are linearly interpolated at every model time step (set equal to 10 min.). The flow resistance is defined with a Manning number equal to 32 $m^{1/3}/s$ in the entire model domain. The model is initialised on 01/10/97 at 00:00 with water level and velocity fields obtained from a spin-up simulation of 48 hours.

The performance of the RRSQRT filter in both the standard hydrodynamic model (HD) and the nested hydrodynamic model (NHD) is tested. In the simulations, water level data from 14 coastal stations are assimilated and the results are validated

against data from another 7 available coastal stations. The positions of the, in total, 21 stations are shown in Figure 1.

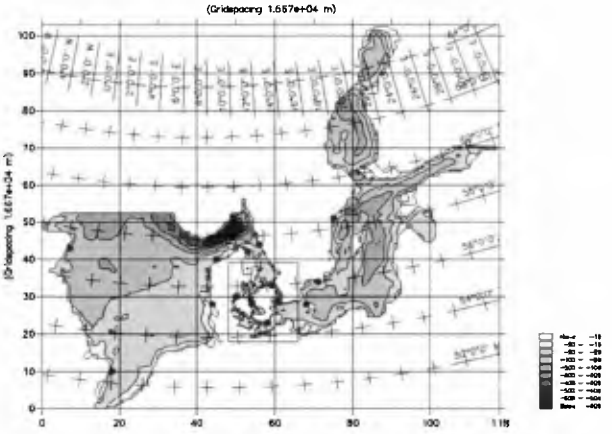

Figure 1. North Sea and Baltic Sea model model setup and bathymetry (depth in meters). A nested area is defined for the inner Danish waters. Water level stations are represented with circles (measurement stations) and squares (validation stations).

A simulation period of three days from 01/10/97 00:00 to 03/10/97 00:00 was applied where continuos measurement of water levels were available at the 21 stations. Based on an initial sensitivity test the following parameters for the Kalman were used:

- The rank of the error covariance matrix is set equal to 100.
- The grid reduction factor between the noise grid and the coarse model grid is set equal to 8.
- Time-coloured noise is defined using a first order autoregressive model with a lag-one autocorrelation coefficient of 0.97.
- The noise in the meteorological forcing components of the momentum equation is defined using an exponential spatial correlation model with a correlation coefficient of 0.9 and a standard deviation that varies in space. The magnitude of the standard deviation varies from 0.0005 m^2/s^2 in the North Sea to 0.0001 m^2/s^2 in the Baltic Sea.
- At the northern boundary noise is defined using a spatial correlation coefficient of 0.95, standard deviation of 0.1 m, and a grid reduction factor of 3. At the southern boundary the same parameters are used except for the grid reduction factor, which is set to 1, i.e. it coincides with the model grid.
- The standard deviation of the measurement noise is set equal to 0.05 m.

Measurements were available every 20 minutes, and hence the updating step of the RRSQRT filter takes place every second time step.

In order to evaluate the performance of the filter the root mean square error (RMSE) between the observed and updated water levels are calculated and compared with the RMSE of the deterministic model simulation for both models. The RMSE has been calculated using the last 36 hours of simulation in order to reduce the influence from the initialisation of the filter. Figures 2 and 3 present the RMSE for the measurement and the validation stations, respectively, obtained from the deterministic and the updated HD and NHD models. Table 1 shows the global (spatial average) values of the RMSE for the different models.

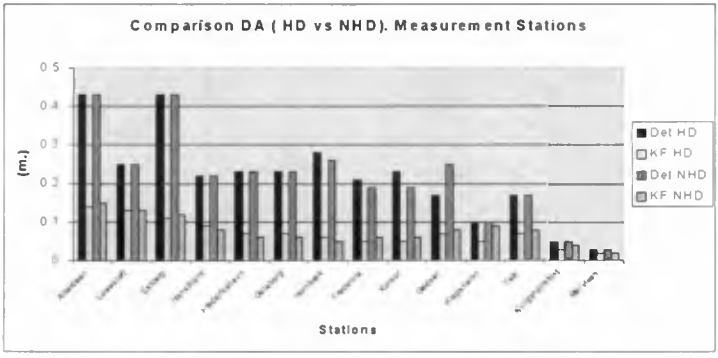

Figure 2. RMSE for the deterministic (Det) and the updated (KF) hydrodynamic (HD) and nested hydrodynamic (NHD) models at measurement stations.

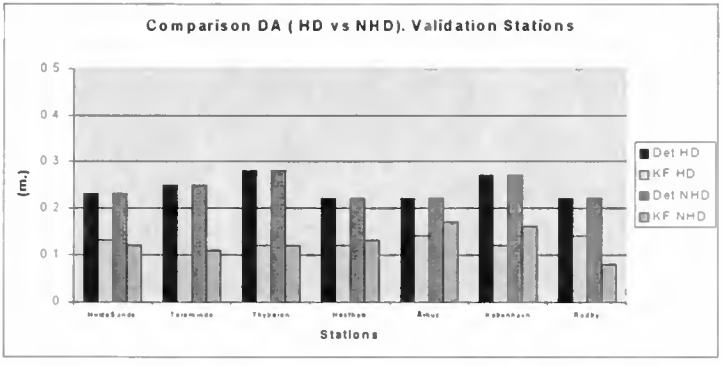

Figure 3. RMSE for the deterministic (Det) and the updated (KF) hydrodynamic (HD) and nested hydrodynamic (NHD) models at validation stations.

Table 1. Global (spatial average) RMSE values for the deterministic and the updated hydrodynamic (HD) and nested hydrodynamic (NHD) models.

	Deterministic RMSE (m) HD	Kalman filter RMSE (m) HD	Deterministic RMSE (m) NHD	Kalman filter RMSE (m) NHD
Measurement stations	0.218	0.072	0.216	0.077
Validation stations	0.240	0.126	0.240	0.127

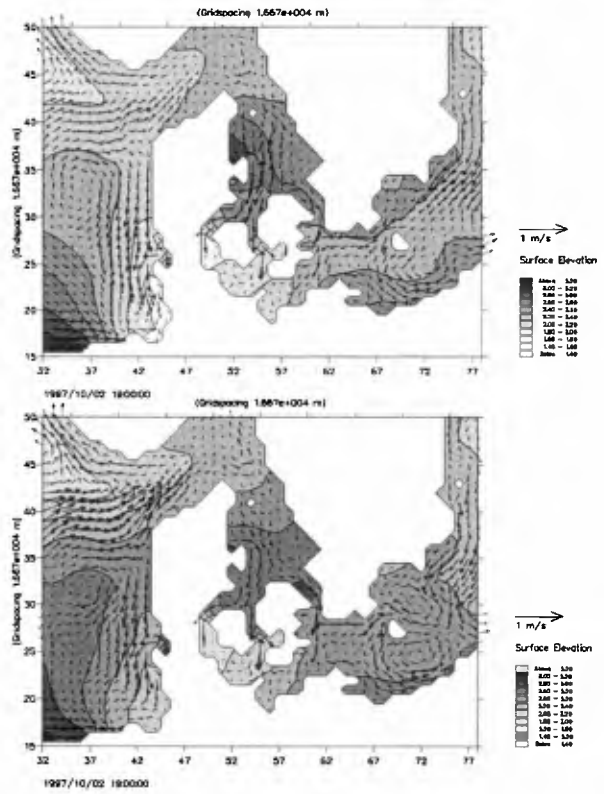

Figure 4. Water level and velocity field for the inner Danish waters at 02/10/97 19:00 calculated from the deterministic model (top) and the Kalman filter (bottom) using the hydrodynamic model (HD).

The HD and NHD deterministic models yield basically the same results. The use of a detailed description in the inner Danish waters improves the simulation only in some of the stations while providing worse results in others. This is a direct consequence of a poor schematisation of the area between Denmark and Sweden in the finer grid, resulting in worse results at the stations located at the southern part of the fine grid (Gedser and Klagshamn). The simulation at the other stations located in the nested area is improved using the finer resolution. No further efforts for calibrating the models have been done.

The Kalman filter for the HD as well as for the NHD model efficiently corrects the water levels in all parts of the regional model. At measurement points a global value of the RMSE equal to 0.072 m for the HD and 0.077 for the NHD have been obtained which is only slightly higher than the assumed standard deviation of the measurement noise (0.05 m). At validation points the corrections are not that significant but they still present a marked improvement (about 50% reduction of the RMSE) in all regions when compared with the deterministic models. In general, the results obtained in this case, in terms of reducing errors in water levels, are not improved by using a finer grid. Since the state vector is defined in the coarse grid, corrections in the fine area are obtained by interpolating the error estimated by the filter in the coarse area. The introduction of this new approximation causes a slightly worse performance of the filter in the finer grid. The use of a finer resolution is more important for corrections of the velocity field as illustrated below.

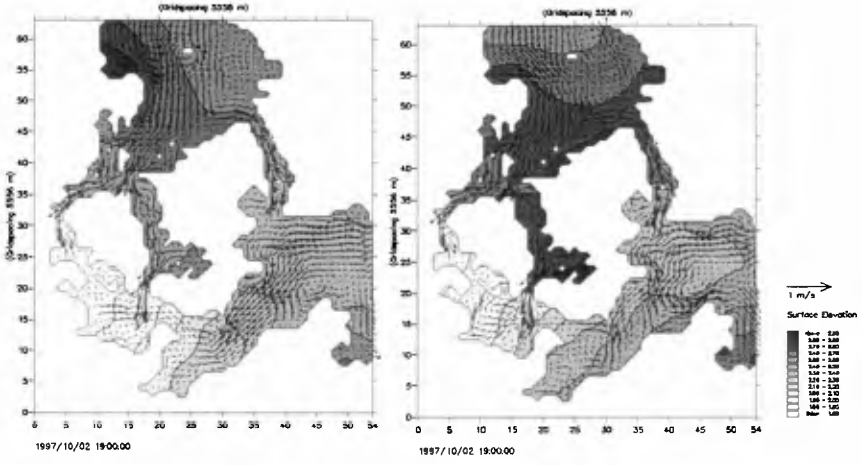

Figure 5. Water level and velocity field for the detailed area of the inner Danish waters at 02/10/97 19:00 calculated from the deterministic model (left) and the Kalman filter (right) using the nested hydrodynamic model (NHD).

Water level and velocity fields for the deterministic and updated models at 02/10/1997 19:00 are presented in Figures 4-5. Important differences in the velocity field can be observed in these figures. The flux entering the Danish waters from the North Sea is not well represented in the deterministic solution. The updated model provides higher water levels in the entrance to the Baltic Sea than in the deterministic model. In general, the updated model is able to reproduce the high water level elevation in the inner Danish waters and the northern coasts of Germany and Poland. When using a finer resolution, the velocity field is better represented. In this case, larger currents are obtained in the updated model, especially in areas with strong water level gradients. The type of global improvements presented in Figures 4-5 is maintained during the entire simulation.

Conclusions

A data assimilation method based on the RRSQRT filter has been implemented in a hydrodynamic model that solves the shallow water equations simultaneously in a number of dynamically nested areas with different resolutions. The use of a finer resolution grid in some areas of the model rapidly increases the number of computational points in the model. The state vector has been defined on the main (coarsest) grid in order to reduce the computational cost and the storage requirements of the Kalman filter. This implementation, however, did not improve the corrections of water levels in the detailed area as compared with the corrections obtained using only one area with a coarse resolution. Although this result may be partly caused by a poor schematisation of the nested model, more accurate results are expected if variables in all points of the nested grids are defined in the state vector, and hence avoiding the interpolation of the Kalman gain from the coarse to the fine grid.

The application example reveals that the use of data assimilation significantly improves the global model results. In storm surge forecasting, the improved estimate of the state of the system is then used as initial conditions for the forecast simulation. In the cases where the main interest is on water level predictions, as in the case in storm surge forecasting, the implementation using only one area of the regional model with a coarse resolution can provide sufficient accuracy. On the other hand, for prediction of currents more detailed information is required, and in this case nested modelling combined with data assimilation should be applied.

Acknowledgement

This study was funded by the Danish National Research Foundation through the International Research Centre for Computational Hydrodynamics (ICCH). Their support is greatly appreciated.

Appendix. References

Bode, L. and Hardy, T.A. (1997) Progress and recent developments in storm surge modelling. J. Hydraul. Eng., ASCE, 123(4), 315-331.

Cañizares, R., Heemink, A.W. and Vested, H.J. (1998) Application of advanced data assimilation methods for the initialisation of storm surge models, J. Hydraul. Res., 36(4), 655-674.

Cañizares, R. (1998) On the application of data assimilation in regional coastal models, Ph.D. thesis, IHE Delft and Delft University of Technology, The Netherlands.

DHI (1995) MIKE 21 HD (Hydrodynamic module), Release 2.5, User guide and reference manual, Danish Hydraulic Institute.

Heemink, A.W. (1990) Identification of wind stress on shallow water surfaces by optimal smoothing, Stochastic Hydrol. Hydraul., 4, 105-119.

Madsen, H and Cañizares, R. (1998) Comparison of extended and ensemble Kalman filter for data assimilation in coastal area modelling, Submitted to International Journal for Numerical Methods in Fluids.

Maybeck, P.S. (1979) Stochastic Models, Estimation and Control, Mathematics in Science and Engineering, Vol. 141-1, Academic Press, New York.

Leendertse, J.J. (1964) Aspects of a Computational Model for Water Wave Propagation, M.I.T. Instrumentation Laboratory, Memo SGA 5-64, Cambridge, Massachusetts.

Potter, J.E. (1967) Matrix Augmentation, Rand Memorandum, RH-5299-PR, Santa Monica, California.

Verlaan, M. and Heemink. A. W. (1995) Reduced rank square root filters for large scale data assimilation problems, In Second International Symposium on Assimilation of Observations in Meteorology and Oceanography, 247-252. World Meteorological Organization.

Verlaan, M. (1998) Efficient Kalman filtering algorithms for hydrodynamic models, Ph.D. Thesis, Delft University of Technology, The Netherlands.

Vested, H.J., Nielsen, H.R., Jensen, H.R. and Kristensen K.B. (1995) Skill assessment of an operational hydrodynamic forecast system for the North Sea and Danish Belts, Quantitative Skill Assessment for Coastal Ocean Models, Coastal and Estuarine Studies, 47, 373-396, American Geophysical Union, Washington DC.

Part III: Coastal Structures

Groin at Fjaltring, Danish North Sea Coast

Coast Protection at Lønstrup, Danish North Sea Coast

Berm Breakwaters – Influence of Stone Gradation, Permeability and Armouring

Jørgen Juhl[1] *and Peter Sloth*[2]

Abstract

The difference in reshaping of a traditional berm breakwater constructed of two stone classes and a more stable armoured type of berm breakwater with the largest berm stones used as an armour layer has been studied through physical model tests at the Danish Hydraulic Institute. A total of eight series of model tests were carried out in a wave flume with the aim of studying the effect of different armouring of the berm. The test results are described in the form of profile development, recession of the berm, waves generated by overtopping and wave reflection.

Further, four series of flume tests were carried out for studying the influence of the width of the stone gradation for the berm material and the permeability of the berm material. Two stone gradations and three permeabilities of the berm material were tested.

Finally, four test series were carried out for studying the influence of scour protection on the scouring in front of the berm breakwater and the behaviour of the berm breakwater.

Introduction

The permeability of rubble mound breakwaters is known to have an effect on the armour layer stability. An armour layer placed on an impermeable core is less stable than an armour layer placed on a core of permeable stone material. This aspect is included in the stability formulae for rubble mound breakwaters established by van der Meer (1988).

1 *COWI, Parallelvej 15, DK-2800 Lyngby, Denmark, e-mail: jju@cowi.dk, Fax: +45 45 97 21 14*

2 *Danish Hydraulic Institute, Agern Allé 5, DK-2970 Hørsholm, Denmark, e-mail: prs@dhi.dk, Fax: +45 45 179 186*

In some cases, the stability of rubble mound breakwaters has been increased by going from two layers of stones in the armour layer to three or four layers. One of the features of berm breakwaters is the energy dissipation in the permeable berm, but this can be reduced if the permeability is reduced due to a high content of fines.

Research presented by Hall and Kao (1991) has shown that the reshaping of berm breakwaters is influenced by the stone gradation. They found, for $D_{n,85}/D_{n,15}<3$, that reducing the gradation width of the armour stones reduced the reshaping.

Experience from Iceland has shown that it is in most cases advantageous to construct berm breakwaters of more than two stone classes. The idea being that the largest stones are used where they will be most effective, ie as an armour layer protecting the berm. Armoured berm breakwaters made of several stone classes like a traditional breakwater require more sorting of stones, but at the same time the increased stability means that the overall dimensions can be reduced. Examples of the Icelandic experience with berm breakwaters are given by Sigurdarsson et al (1995) and Juhl and Jensen (1995).

Local scour can occur at a breakwater constructed on a sandy seabed and may endanger the overall stability due to sliding of the main armour layer if the toe and scour protection is failing. The scouring pattern is a function of the water depth, wave conditions, sediment characteristics, breakwater configuration, and reflection characteristics as described by Arneborg et al (1996). Further, a simultaneous current at the breakwater will influence the scouring.

Scouring in front of a berm breakwater constructed without a sufficient scour protection may result in berm stones sliding into the scour hole, which will lead to further reshaping of the protecting berm.

Model Set-up and Test Programme

Model Set-up

Physical model tests were carried out in a 23 m long and 0.60 m wide wave flume with the aim of studying profile reshaping and wave overtopping of berm breakwater profiles. A fixed bed foreshore with a slope of 1:80 was constructed in the flume.

The profiles used in the first 12 test series are shown in Figure 1. The water depth in front of the berm was 0.25 m for all tests. Profiles 1 to 8 were tested to compare the reshaping of a berm breakwater constructed of two stone classes with the reshaping of a more stable type of berm breakwater with the largest stones armouring the berm.

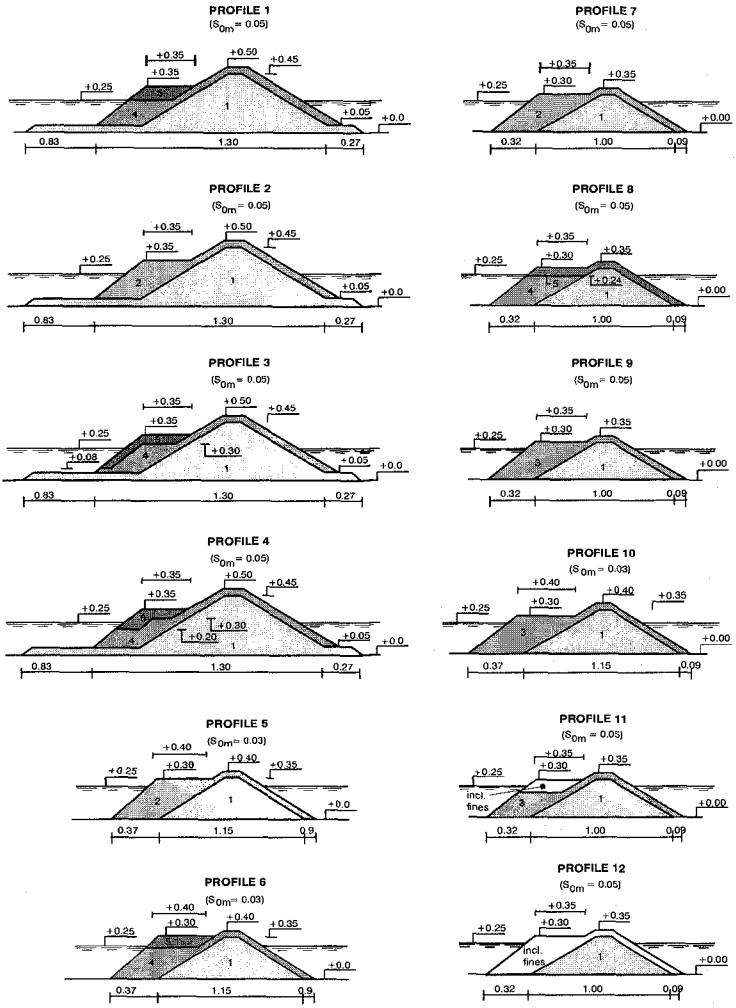

Figure 1 *Tested berm breakwater profiles. Stone class characteristics are presented in*

Profiles 1 to 4 were relatively high-crested breakwaters not allowing wave overtopping. Three alternative berm breakwaters of the armoured type (Profiles 1, 3 and 4) were tested and compared to tests with a traditional berm breakwater consisting of two stone classes (Profile 2). The subsequently tested four profiles were more low-crested breakwaters with the crest elevation and berm width adjusted to take into account different wave steepness (S_{om}=0.03 and 0.05).

The berm breakwaters were constructed of two or three stone classes, ie one for the core and scour protection and one or two for the berm, crest and rear side protection. The traditional berm breakwaters (Profiles 2, 5 and 7) were constructed of two stone classes, a relative wide stone gradation for the berm, $D_{n,85}/D_{n,15}$=1.80, having a nominal diameter, D_{n50}, of 0.022 m (stone class 2) and a core with a nominal stone diameter of 0.011 m (stone class 1). A summary of the stone classes used is presented in Table 1.

Table 1 *Summary of stone classes. The density of the stone material was measured to* ρ_S=2.68 t/m^3.

Stone class	Description	W_{50} (g)	$D_{n,50}$ (m)	$D_{n,85}/D_{n,15}$	Profiles
1	Core material	3.5	0.011	2.30	All
2	Berm material	30.2	0.022	1.80	2, 5, 7
3	Berm material	35.4	0.024	1.40	9, 10, 11, 12
4	Berm material	20.5	0.020	1.65	1, 3, 4, 6, 8
5	Armour layer	78.0	0.031	1.20	1, 3, 4, 6, 8

In testing of the armoured type of berm breakwaters, the berm stones (class 2) were separated into two classes, the lower fraction to be used for the berm (stone class 4) and the higher fraction to be used as an armour layer (stone class 5). This means that the same stones were used for all tested profiles.

Profiles 9 and 10 were tested using berm material with a more narrow stone gradation, $D_{n,85}/D_{n,15}$=1.40, having a nominal diameter, D_{n50}, of 0.024 m (stone class 3). Profiles 11 and 12 were tested for studying the influence of the permeability of the berm material. The permeability was reduced by adding fine material (average weight of 0.24 g) to the narrow stone gradation, either to the surface zone of the berm or to the entire berm.

Four series of model tests were carried out for studying the scouring in front of a traditional berm breakwater having a high crest and a wide berm. In order to assess the scouring, the seabed below and 1.5 m in front of the breakwater was made of fine sand with d_{50}=0.17 mm.

Test Programme

Each test series consisted of five to nine test runs each with a duration corresponding to 2,000 waves. Test runs were carried out with the following deepwater conditions: $H_o = H_{mo}/\Delta D_{n,50} =$ 2.0, 2.5, 3.0, 3.5 and 4.0, where $H_{mo}(=4\cdot\sqrt{m_o}$, where m_o is the zero'th moment of the recorded surface elevations) is the wave height, Δ is the relative density and $D_{n,50}$ is the nominal stone diameter. H_o is also called the stability number and is for the armoured berm breakwaters calculated using $D_{n,50}$ for the entire berm material (0.022 m). Further, the long-term development was studied with H_o=4.0 for Profiles 1 to 3.

The deepwater wave steepness is given by the ratio between the wave height, H_{mo}, and the deepwater wave length, L_{om}, calculated on basis of the mean wave period, T_{om}:

$$S_{om} = H_{mo}/L_{om} = 2\pi/g*H_{mo}/T_{om}^2$$

The tests were carried out in test series with fixed wave steepness in deep water, S_{om}=0.03 respectively 0.05, ie the wave steepness in front of the berm breakwater varied due to differences in wave shoaling and wave breaking on the foreshore.

Two test series were carried out to study scouring in front of a berm constructed directly on a sandy seabed. The first test series consisted of nine test runs with a wave steepness of S_{om}=0.05 and the second test series of six test runs with a wave steepness of S_{om}=0.03 and two additional test runs with S_{om}=0.02 (the last with the water depth reduced to 0.20 m).

A 0.05 m thick scour protection layer below the berm and extending 0.50 m in front of the berm was introduced in the third test series. In the fourth test series, the scour protection material was placed as a 0.10 m layer covering the front slope of the berm. The idea being that the first waves hitting the breakwater will reshape the scour protection material into a combined toe and scour protection. For both test series, four test runs were carried out with S_{om}=0.03 and two additional test runs with S_{om}=0.02 (the last with the water depth reduced to 0.20 m).

Measurements and Analysis

The waves were measured by a total of nine resistance type wave gauges, ie three in deep water, five in shallow water in front of the breakwater, and one behind the breakwater for measuring the overtopping generated waves (only Profiles 4 to 12).

A multigauge technique was used for separating the incoming and reflected waves, and subsequently determining the incoming significant wave height and the reflection coefficient both in deep water and in front of the breakwater. The waves reflected from the breakwater were absorbed by the wave generator applying DHI's AWACS system (Active Wave Absorption Control System).

The breakwater profiles were measured after each test for every 0.10 m across the flume (five profiles) before initiation of the tests and after each test run. The profiling was made by two lasers, one laser running on a beam placed across the breakwater for measuring the vertical distance to the breakwater and another laser for measuring the horizontal position of the other laser.

Analysis of the five profiles measured after each test run (for each 0.10 m across the flume) showed that the differences were very small, and thus the five profiles were averaged for the subsequent analysis. Analysis of the recorded profiles was made for determining the recession of the berm, ie erosion of the crest of the berm as shown in Figure 2. The waves behind the breakwater caused by wave overtopping were analysed with respect to the maximum wave height, H_{max}, and the spectral wave height, H_{m0}.

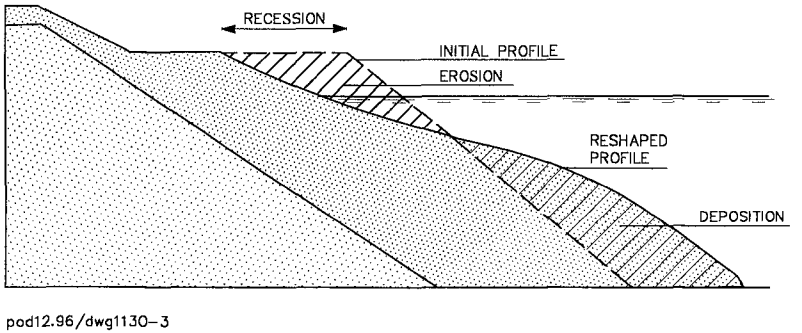

Figure 2 *Definition of berm recession.*

Presentation of Results

Profile developments, berm recessions, overtopping generated waves and reflection coefficients were analysed for the twelve tested profiles with the aim of studying the influence of berm armouring, berm free board, wave steepness, width of stone gradation of the berm material and permeability of the berm material. Finally, the results of the four series of tests carried out for studying the scouring were analysed.

Influence of Armouring

Three alternative berm breakwaters of the armoured type (Profiles 1, 3 and 4) were tested and compared to tests with a traditional berm breakwater consisting of two stone classes (Profile 2). Figure 3 shows the berm recession as function of the stability number calculated on basis of the wave height in front of the breakwater and $D_{n,50}$=0.022 m.

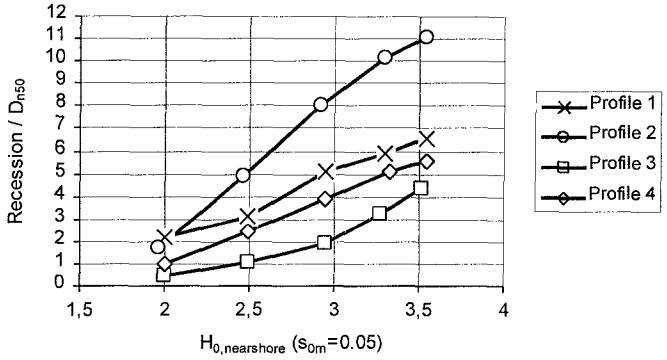

Figure 3 *Dimensionless recession (recession/$D_{n,50}$) as function of the nearshore stability number. Note: $D_{n,50}$ is for the entire berm.*

All three armoured type breakwaters showed significantly less erosion volume and berm recession compared to the traditional berm breakwater. The profile resulting in the smallest erosion volume and berm recession was Profile 3 (an armour layer at the top and at the front of the berm) followed by Profile 4 (armour layer placed as a hammer head), whereas Profile 1 (armour at the top of the berm) showed a little less effect, but has an advantage in construction.

Figure 4 shows the berm recession for the three armoured type berm breakwaters relative to the recession of the traditional berm breakwater as function of the near shore stability number. The increased stability of the armoured berm breakwaters implies that the overall dimensions can be reduced compared to a traditional berm breakwater, which will reduce the construction costs.

Comparisons of the test results for Profiles 7 and 8 (lower crest and berm elevation) also showed a significant reduction in the erosion volume and berm recession using the largest stones for armouring of the berm. The effect of the armouring was somewhat less pronounced for Profiles 5 and 6, run with a wave steepness of S_{om}=0.03.

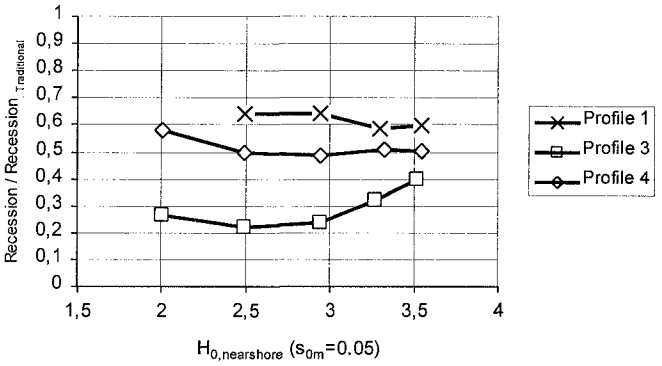

Figure 4 *Relative berm recession (recession of armoured berm breakwater/recession of traditional berm breakwater) as function of the nearshore stability number.*

Testing of Profiles 1 to 3 included long duration tests consisting of 10,000 waves with a stability number H_o=4.0. The results showed that an equilibrium profile was reached after about 8,000 waves, assuming no deterioration of the stones.

For the test series with a high crest elevation (Profiles 1 to 4), the overtopping generated waves were very small, whereas for the test series with a lower crest elevation (Profiles 5 to 8), the overtopping generated waves measured 1 m behind the centreline of the breakwater were analysed. For wave heights up to a stability number corresponding to about 3, the waves behind the breakwater were mainly due to transmission through the breakwater, whereas for larger incoming waves, overtopping became dominant.

Figure 5 shows the transmission coefficients (including overtopping generated waves) calculated on basis of the spectral wave height behind the breakwater as function of the nearshore stability number. The overtopping wave heights were found to be smaller for the armoured type of berm breakwater (Profiles 6 and 8) than for the traditional berm breakwater constructed of two stone classes (Profile 5 and 7). The effect on the wave overtopping is mainly due to the reduced berm reshaping for the armoured berm breakwater. The maximum wave height varied only a little for the different profiles.

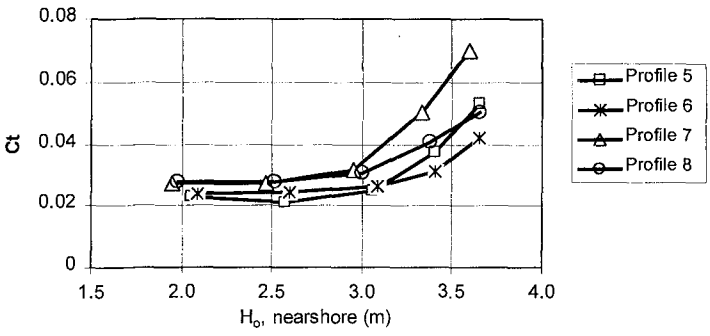

Figure 5 *Wave transmission coefficients based on the spectral wave height of the overtopping generated waves as function of the nearshore stability number.*

The reflection coefficients for the tested berm breakwaters are a function of both wave conditions and breakwater profiles. This means that the reflection conditions are changing with the berm reshaping during the test runs, and thus the results are average values over the period of each test run. The reflection coefficients were found to be higher for the armoured type of berm breakwater compared to the traditional berm breakwater constructed of two stone classes due to the reduced profile reshaping.

Influence of Stone Gradation

Tests were carried out with two stone gradations, a wide stone gradation having $D_{n,85}/D_{n,15}$=1.80 (Profiles 5 and 7) and a more narrow having $D_{n,85}/D_{n,15}$=1.40 (Profiles 9 and 10).

It was found that the wider stone gradation resulted in larger erosion volume and berm recession. Therefore, also the rear side stability was reduced for the wider stone gradation. In a wide stone gradation, the smaller stones will partly fill the voids between the larger stones resulting in a reduced permeability, which for the considered stone gradations are expected to cause increased erosion volume and berm recession due to decreased energy dissipation in the berm.

Larger overtopping generated waves were found for the tests with the wide stone gradation (Profiles 5 and 7) than for the tests with the more narrow stone gradation (Profiles 9 and 10).

A significant increase in the reflection coefficients was found for the tests with the narrow stone gradation due to the reduced berm reshaping.

Influence of Permeability

Wave run-up and overtopping conditions are significantly influenced by the presence of fine material in the berm material reducing the permeability and thus the energy dissipation, which is one of the main features of berm breakwaters. The permeability of a berm breakwater may be reduced by the presence of finer materials, which could be either in the surface of the berm or in the entire berm. The first case could occur if eg a temporary construction road on the berm is not removed after completion of construction and the latter case as an outcome of deficient design or construction.

The influence of the permeability was studied by testing of two profiles with finer material added either to the top of the berm or to the entire berm constructed from stones with the narrow gradation, $D_{n,85}/D_{n,15}$=1.40. An increase in the erosion volume and berm recession was observed by adding finer material to the top of the berm (Profile 11). Adding finer material to the entire berm (Profile 12) led to a further increase in the erosion volume and berm recession. Further, a significant increase in overtopping was found, resulting in severe damage to both crest and rear side. Figure 6 shows the influence on the berm recession by reducing the permeability of the berm.

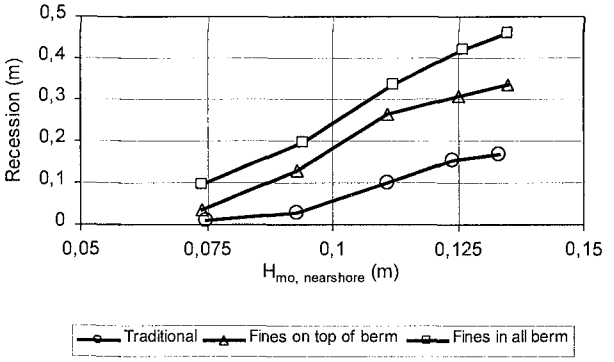

Figure 6 *Influence of permeability on berm recession.*

Scouring

A total of four test series were carried out for a qualitative study of the influence on the scour development in front of a berm breakwater and on the berm reshaping for two types of scour protection. The tests also included a study of the influence of the wave steepness.

The two profiles without a scour protection layer showed subsidence of berm stones into the sandy seabed, which resulted in larger berm recession. The tests showed the development of a larger scour hole in front of the breakwater for the tests with the smallest wave steepness.

Introduction of a scour protection layer moved the scour hole out in front of this. Further, no subsidence of berm stones into the sandy seabed was found and thus the reshaping of the berm was reduced.

Finally, a test series was carried out with the scour protection material placed as a 0.10 m layer covering the front slope of the berm, the idea being that the material under the exposure of the first waves will reshape into a toe and scour protection. During the reshaping process, some of this scour protection material was mixed into the berm material. The resulting reduced permeability led to increasing wave run-up and overtopping reducing the stability of the structure.

Conclusions

Model tests were carried out in a wave flume with the aim of studying the difference in reshaping of a traditional berm breakwater constructed of two stone classes and an armoured type berm breakwater with the largest berm stones used as an armour layer covering a part of or the berm. Further, the influence of the width of the stone gradation for the berm material and the permeability of the berm material was studied.

Finally, tests were carried out for studying the scouring in front of a breakwater without any scour protection followed by testing of two types of scour protection.

Wave conditions in front of and behind the breakwater were measured together with the profile development. All test series consisted of five test runs (H_o=2.0, 2.5, 3.0, 3.5 and 4.0, in deep water), each with a duration corresponding to 2,000 waves. However, for Profiles 1, 2 and 3, another 8,000 waves with H_o=4.0 were run for studying the long-term stability.

The main conclusions of this study can be summarised as follows:

- Comparisons between traditional berm breakwaters and berm breakwaters of the armoured type showed a reduction in the erosion volume and recession of the berm for the latter. An armour layer protecting both the top and the front of the berm (Profile 3) was found to be more effective than both the hammerhead solution (Profile 4) and a thicker layer at the top of the berm (Profile 1).
- A reduction in the berm width can be obtained by using the largest stones as an armour layer. However, the effects vary with a range of parameters, eg wave steepness, stone gradation, permeability, and breakwater geometry.
- A reduction in the wave overtopping was found for the armoured type of breakwater mainly due to the reduced berm reshaping.
- The reflection from a berm breakwater is dominated by the slope of the reshaping profile, and thus the wave reflection from the armoured type of breakwater was larger than for the traditional berm breakwater.
- An increase in the berm freeboard is associated with an increased berm volume and was found to reduce the reshaping of the berm.
- The berm reshaping was found to increase for decreasing wave steepness, ie increasing wave period.
- Tests made with two stone gradations showed larger erosion volume and berm recession for the wider stone gradation.
- Tests with fine material added to either the top of the berm or the entire berm (reducing the permeability) showed a significant increase in the berm recession and wave overtopping.
- Subsidence of berm stones into the sandy seabed was found for the profiles without a scour protection layer
- Introduction of a scour protection layer extending 0.50 m (model) in front of the berm moved the scour hole out in front of this, and no subsidence of berm stones into the sandy seabed was found and thus the reshaping of the berm was reduced
- During reshaping of the scour protection material placed as a 0.10 m layer covering the front slope of the berm, some of this finer material was mixed into the berm material. This reduced the permeability and led to increased wave run-up and overtopping.

Acknowledgements

The present study was carried out as a part of the research project on Berm Breakwater Structures co-sponsored by the European Commission under contract MAS2-CT94-0087 (1994-97).

The model tests were carried out at the Danish Hydraulic Institute, and the authors wish to thank Mr Per Vedel Brøndsted, Mr Erik Mathiesen, Ms Renata Archetti and Mr Nikolay Lissev for their assistance in carrying out the model tests and doing the initial analysis of the measurements.

References

Arneborg, L; Asp Hansen, E; Juhl, J (1996): *Modelling of local scour in front of vertical breakwaters*. Submitted to Coastal Engineering.

Hall, KR; and Kao, JS (1991): *The influence of armour stone gradation on dynamically stable breakwaters*. Coastal Engineering, 15.

Van der Meer, JW (1988): *Rock slopes and gravel beaches under wave attack*. PhD Thesis, publication No 396, Delft Hydraulics, The Netherlands.

Sigurdarson, S; Viggosson, G; Benediktsson, S; and Smarason, OB (1995): *Berm breakwaters and quarry investigations in Iceland*. International Conference on Coastal and Port Engineering in Developing Countries, Rio de Janeiro, Brazil.

Juhl, J; and Jensen, OJ (1995): *Features of berm breakwaters and practical experiences*. International Conference on Coastal and Port Engineering in Developing Countries, Rio de Janeiro, Brazil.

Berm Breakwaters, Fifteen Years Experience

Sigurdur Sigurdarson[1], Gisli Viggosson[1], Sigtryggur Benediktsson[1], Sigurdur Einarsson[1] and Omar Bjarki Smarason[2]

Abstract

Berm breakwaters have been designed and constructed in Iceland since 1983. Over twenty rubble mound structures of the berm type have been constructed so far, fourteen were new structures, whereas the remaining six were improvements or repairs of existing breakwaters. During 1998 two berm breakwaters are being extended. Further two structures will be built every year for the next 2-3 years.

Although some of the berm structures in Iceland have already experienced the design or near to design wave conditions, only minor profile changes have been observed. Valuable experience has, however, been learned from the inspection of the reshaped profile of one structure.

The initial idea of berm breakwaters was that they should be wide voluminous structures, built of two stone classes with a wide size gradation. The Icelandic type of berm breakwaters has however been developed into a less voluminous, more stable structure, where large emphasis is put on maximising the outcome of the armour stone quarry and utilising this to the benefit to the design.

Introduction

At the Icelandic Maritime Administration (IMA) a variant of the original berm breakwater constructed of one or two stone classes has been developed. This variant can be described as "a tailor-made size graded berm" (Sigurdarson et al, 1996). The berm structure is build up of several size-graded layers. The largest stones are placed on top of the berm and some times also at its front, where they will be most effective in order to reinforce the structure, Figure 1. Smaller stones are used in the inner layers of the berm, even smaller than in the original berm breakwater, increasing the utilisation of the quarried material. The reinforcement of the berm has made it possible to reduce the berm width, which reduces the volume of the structure. The use of larger stones more narrowly graded on top and at the front of the berm has been

[1] Icelandic Maritime Administration, Vesturvor 2, 200 Kopavogur, Iceland
[2] Stapi Ltd. – Consulting Geologists, Armuli 19, 108 Reykjavik, Iceland

proved in model tests to decrease reshaping of the berm (Sigurdarson et al, 1998). This is due to a combination of larger permeability and the ability of the structure to swallow the wave more rapidly.

Development of design process

The design process for berm breakwaters in Iceland has been developed through the years in close co-operation with all partners involved, designers, geologists, supervisors, contractors and local governments. At the same time, the designers have been directly involved in the hydraulic model studies and supervision of the construction of the breakwaters. Instead of looking at the berm as a mass of stones, the design focuses more on each unit. It has become clear that "no construction unit is as far from being standardised as the armour rock in the primary cover layer with regard to form, strength and durability" as stated by Viggosson (1990).

Wave load and possible quarry yield

The design philosophy of berm breakwaters aims at optimising the structure with respect to wave load and possible yield from an armourstone quarry. The estimated yield from an armourstone quarry is used as an integrated part of the design process in an attempt to optimise the utilisation of the quarry.

Collaboration between designer and geologist

Close collaboration between the designer and geologist in the preparation of berm breakwater projects has been proven very effective over the years (Smarason et al, 1998). This has resulted in better designs and better use of the quarried material. This collaboration gives the designer the chance to fully utilise all rock classes from the quarry and has often resulted in 100% utilisation of the quarries. Close co-operation between the geologist, the project supervisor and the contractor is often

Figure 1. The Bolungarvik breakwater in 1995 two years after construction.

necessary to achieve maximum results in the quarry. Blasting and sorting of armourstone is by no means an easy task and slight alteration of spacing and tilt of drillholes may at times help to improve blasting results. It has to be realised that the contractor and the buyer should work as a team aiming for the same goal. Experienced contractors rely on the predicted quarry yield curves in their bidding.

The origin of the Icelandic Berm Breakwater

In the late seventies and early eighties many researchers and engineers were occupied with the idea of equilibrium slope and the importance of permeability (Bruun and Johannesson, 1976). Lessons were learned from 19th century breakwaters, like the breakwaters in Plymouth, England, and Cherbourg, France. These breakwaters were built by dumping all quarried material at the breakwater site. It was stated that when "maturing" the breakwaters might develop an S-shape.

In the early eighties the berm breakwater was introduced. For the protection of a runway extension in Unalaska, Alaska, Hall et al (1983) proposed a wide berm of one rock class, where the armour system was designed so that essentially 100% of the quarry was utilised. The stability of the armour layer was to develop during early stages of wave attack. Model tests showed that with greater thickness of the armour layer, the smaller the stones needed to be.

Gradually the ideas of berm breakwaters developed more and more to a dynamic or reshaping breakwaters. Van der Meer and Pilarczyk (1986) grouped berm breakwaters or S-shape profiles as having a stability parameter, $Hs/\Delta D_{n50}$, between 3 and 6. It became the general idea that berm breakwaters were only applicable where large stones were of limited supply. These structures were built up of a homogeneous berm of relatively small stones with wide size gradation.

The natural dynamic structure

What can we learn from nature about dynamic movements of stones? First we will look at gravel or shingle beaches and then move to larger units in rock slopes or boulder beaches.

Gravel or shingle beaches are in some places built up of stones, which are all of similar size as a result of sorting by the sea. The fines have been sorted from the shingle and are found in less exposed areas of the beach. These beaches can have a stability parameter, $Hs/\Delta D_{n50}$, in the range of 50 to 200. As a result of a uniform particle size the gravel beaches have a high permeability. They form a dynamic profile often with a rather steep slope. What happens when we try to scale up the experience from these gravel beaches?

In some places around Iceland rock slopes or boulder beaches exist. The boulder reef at Rif, Figure 2, is an example of this. The height of the reef, which is in an area of 4 m tidal difference at spring tide, is about 5 to 6 m above low water level, with front slope of about 1:4.5 to 1:8. Seen from distance this reef looks like the ideal dynamic berm breakwater. Rounded boulders of several hundreds of kilos up to 1 or 2 tonnes form the surface of the reef. The stability parameter, $Hs/\Delta D_{n50}$, is in the range 3 to 6. This natural dynamic structure looks quite permeable. But looking in-between

the boulders on the surface, smaller stones appear, some tens of kilos in weight. When they are picked up it can be seen that voids are plugged by gravel and sand. Less than 1 m from the surface of the reef all voids are filled up with small particles. The reef is a wide structure with a flat slope over low water level. The natural armouring, which can be looked at as two layers of stones, is in a dynamic action during storms. The waves are breaking on the slope causing high uprush and overtopping. But the reef is by no means a porous structure that swallows up the wave energy.

Figure 2. The boulder reef at Rif is a natural dynamic structure.

The dynamic berm breakwaters

Similar trends can be seen in the reshaped berm breakwater at Bakkafjordur in north-east Iceland (Sigurdarson et al, 1998). The berm breakwater at Bakkafjordur was built in 1983 and 1984 from stones of rather poor quality quarried at the breakwater site. Deterioration of the stones has accelerated a dynamic development of the profile. In the winter 1992/93 the breakwater is believed to have experienced waves close to the design load. The berm was eroded up to the crest and an unstable S-profile had developed. Repair took place in 1993 and in spite of the poor quality of the rock it was decided to use the local quarry again. In the autumn of 1995, the structure was exposed to the design storm. Video recordings from the storm show breaking waves in front of and on the structure, resulting in heavy overtopping. Inspection of the reshaped profile showed that deterioration of the stones had caused filling and plugging of voids and the structure did not function as a berm breakwater any longer, Figure 3. The main conclusion that can be drawn from the Bakkafjordur breakwater is that in a dynamic structure stones will break and the voids will gradually be filled up with smaller stones. This will decrease the ability of the structure to dissipate wave energy. Inspection at the site led to the conclusion that the poor quality (highly altered tholeiite basalt) of the stones in the Bakkafjordur breakwater only accelerated a development that would occur over a longer time period if it was built of better quality stones.

Figure 3. The slope of the reshaped Bakkafjordur breakwater.

The rolling stones

The first concerns regarding rock quality came up at the same time as the berm breakwater was introduced in the early eighties (Poole et al, 1983). Those concerns were from the start a part of the development of the Icelandic berm breakwater. As stated before, no construction unit is as far from being standardised as the armour rock. Usually a large portion of natural stones used in breakwater construction has some fractures or other defects. When the stones start to move or roll up and down the slope and hit each other, high abrasion and splitting of stones will occur.

The presence of fines on the reshaped slope of a berm breakwater will result in plugging and filling up of voids, and an increase in the forces acting on each rock unit on the slope. This in turn will accelerate the dynamic movements of the stones and increase their breaking and splitting.

Rocking of stones in a berm breakwater can be accepted, but not rolling. The only rolling stones that last the rock 'n' roll are The Rolling Stones them selves.

Design Procedures

When designing the Icelandic type of berm breakwater the goal is that it shall be statically stable. Some deformation of the berm is allowed under design conditions, but reshaping into an S-shape is not allowed. It is recognised that the reshaping will increase during the lifetime of the structure, because of insufficient stone quality and repeated wave action. The design approach is not to fulfil certain prescribed stability parameters, $Hs/\Delta D_{n50}$, but to look at the correlation between the armour stone quarry, size distribution and quality; the design wave, height, period and direction; water depth; function of the breakwater, for what purpose is it built, is wave overtopping a

problem or not. In many cases we have been able to design berms with a high stability of the armouring layer without any extra cost.

Design parameters

Various parameters have been proposed to describe the berm profile, like the horizontal width of the berm or the cross-sectional area of the berm from surfacc to bottom. These parameters are not good to compare different design. Differences in upper and lower slope can change the width parameter significantly although the structure is almost the same. Deep water / shallow water or if the berm does not extend to the sea bottom influences the area parameter very much, although the structure may function the same. The width parameter has on the other hand no information on the location of the core relative to the inner edge of the berm, which is important, as the berm can extend under the upper slope and still function to swallow up the wave energy.

In order to be able to compare different berm structures with regard to stability and overtopping two parameters have been defined that describe the thickness and the volume of thc berm, Figure 4. The first parameter is the horizontal thickness of the berm from surface into the core, B, measured at design water level. In the case that the core height is lower than the berm height, the parameter is measured to the extended core slope. The other parameter, A, is the cross-sectional area of rock under and over the aforementioned line from surface into core, one wave height down and one up (1.5 wave height down could also be considered). The area is measured into the centreline of the crest structure. Both parameters are made dimensionless with wave height, B/Hs and A/Hs^2. Design guidelines for these parameters, dependent on the stability parameter, $Hs/\Delta D_{n50}$, are under development.

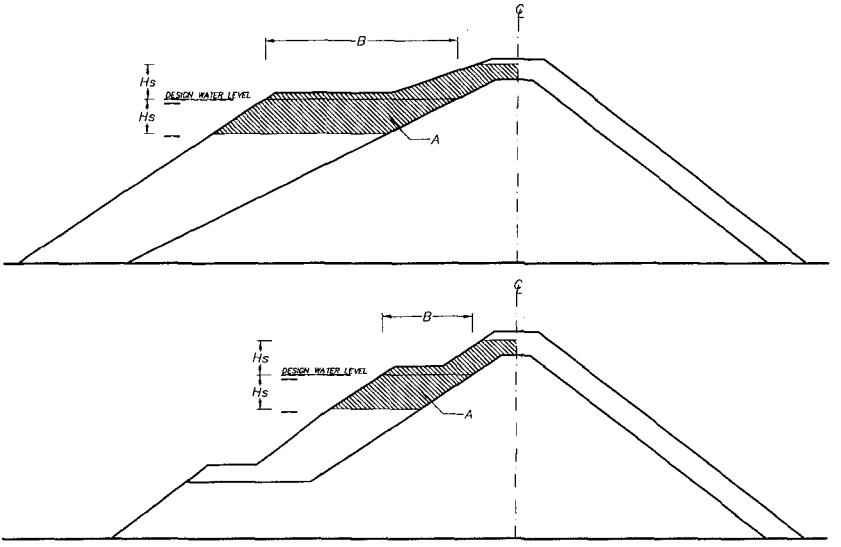

Figure 4. The parameters proposed for description of berm thickness.

Construction

A berm breakwater can be constructed using readily available land based methods and less specialised construction equipment compared to the construction of a conventional breakwater. Usual equipment comprises of a drilling rig, two or three backhoe excavators, sometimes a front loader, and some trucks, Figure 5. When the first berm breakwaters were built, bulldozers were used to push stones to the berm. That resulted in breakage of stones and too many fines that plugged the voids. Backhoe excavators with open buckets or prong, up to 75 tonnes, are used to place stones. The number of trucks depends largely on the transport distance. Tolerance for the placement of stones is greater than for the conventional breakwater design. Usually no underwater placement is necessary, as the front slope is steep. Placement of stones in a slope of 1:1.3 has been achieved down to 8 -10 m water depth.

Figure 5. From the construction of the Dalvik breakwater during the winter 1994-95.

Experience from Iceland shows that small local contractors can quickly adopt the necessary technique to construct berm breakwaters successfully (Sigurdarson et al 1997). The risk during construction is much lower and repairs are also much easier than for the conventional breakwaters. Each breakwater project is tendered out and there is competitive bidding for the works from up to 10 contractors. The lowest bid is usually accepted.

Good interlocking of carefully placed stones is advantageous at the front and the edge of the berm. Experience from many breakwater projects has shown that working with several stone classes and placement of stones only increases the construction cost insignificantly. The construction period of larger projects often extends over two years and experience has shown that partially completed berm breakwaters function well through winter storms. Repairs are much easier than for the conventional breakwaters.

Construction cost has been cut considerably in some recent projects by using dredged material, usually coarse sand and gravel, as a part of the inner core of the structure. Although the berm breakwater is constructed of several layers the advantage of using simple construction methods are still achieved. The advantage of sorting the stone mass into several stone classes to strengthen the structure is far greater than the relatively low additional cost.

Recent developments in berm breakwater design have aimed at using extra large stones (16-25 tonnes) in the more exposed parts of the structures with high wave load. The reason is twofold. Firstly, many of the better quarries are found to produce 10 to 20% of armourstones exceeding 10 tonnes in size. And secondly, heavier machines with greater capacity, like large backhoe excavators, have recently become more readily available from contractors. A relatively low percentage (1-3%) of the largest stone class can be an advantage for most breakwaters. This is not only true for these extra large stone classes but also applies to lower wave load conditions and where quarries with lower size distribution are used.

The Berm Breakwater Structure MAST Project

The design philosophy of the tailor-made size graded structure has proven to reduce deformation of the berm and at the same time lead to a less expensive structure. IMA has recently participated in a European MAST project Berm Breakwater Structure (Sigurdarson et al, 1998) and (Juhl et al, 1998). A series of model tests were carried out in a wave flume at the Danish Hydraulic Institute. The difference in reshaping of a berm breakwater constructed of two stone classes was compared with armoured Icelandic type structure. One of the conclusions of the MAST project was that the Icelandic type structures showed a reduction in erosion volume and recession of the berm compared to the original berm breakwaters. The Icelandic design with armouring on top of and at the front of the berm, allows a significant reduction in the berm width, which varies with a range of parameters as for example wave steepness, stone gradation and breakwater geometry.

Comparative Cost Analysis

Conventional rubble mound versus dynamic berm breakwater

Several studies have been published comparing conventional rubble mound breakwater to dynamic stable berm breakwater. Ligteringen et al (1992) has published a comparative evaluation of various breakwater structures for a site between the islands of Lamma and Cheung Chau in Hong Kong. The water depth ranges between 10 and 18 m. The seabed consists of 15 to 25 m thick, soft marine deposits overlying alluvium. The site is exposed to typhoon generated waves with significant wave height of about 6.0 m. A comprehensive range of breakwater and geotechnical solution has been taken into consideration. In the second stage evaluation construction cost is given for a dynamic berm and a conventional rubble mound breakwater for three breakwater layouts. The cost for the berm type ranges between 67% and 86% of the cost for the conventional rubble mound.

Hauer et al (1995) has made a detailed comparison between a conventional statically stable breakwater and a dynamically stable berm breakwater. Two types of

quarry yield curves are used, a wide curve and a steep curve. According to this study the differences depend strongly on the way the quarry yield is subdivided into different stone classes for both types of breakwaters. Overproduction of the lighter stone classes is necessary to satisfy the demand for the heaviest armour stone classes. And it is stated that the extent of this overproduction has decisive influence in the comparison of the total cost. This is in very good agreement with experience from Iceland.

They conclude that for the specific harbour layout and the specific wave conditions considered in this study the construction of the berm breakwater instead of a conventional rubble mound breakwater resulted in considerable savings. Up to 64% savings of the total cost could be achieved for transport distances from quarry to construction site of 0 to 25 km. For extremely long transport distances, 250 km, 30% savings could still be achieved

Icelandic type berm breakwater versus conventional rubble mound breakwater

First a comparative cost analysis will be presented between the Icelandic berm breakwater and the conventional rubble mound breakwater. Then the difference between the Icelandic and the dynamic approach will be discussed.

The following cost comparison is influenced by a breakwater being designed in a moderate wave climate in Iceland. The structure stands on an 11 m water depth, where the mean spring tidal difference is about 4 m. The design wave height is Hs 3.0 m with mean period of Tz 9.2 s, the mean high water spring tide is +4.0 m and the design water level is +4.7 m. A conventional cross section is designed with a front

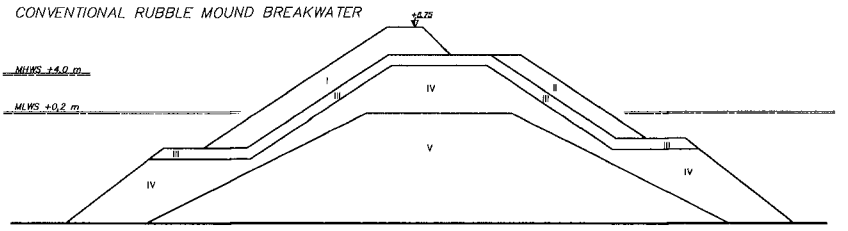

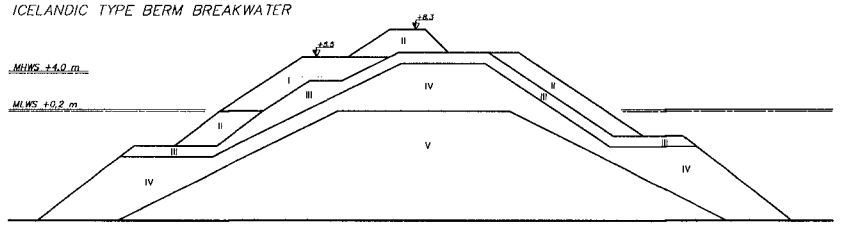

STONE CLASSES FOR BOTH CROSS SECTIONS

CLASS	WEIGHT	MEAN WEIGHT	STABILITY PARAMETER	QUARRY YIELD
I	3.0 t < W ≤ 8.0 t	$W_{50} \geq$ 4.7 t	1.4	10%
II	1.0 t < W ≤ 3.0 t	$W_{50} \geq$ 1.7 t	2.0	13%
III	0.2 t < W ≤ 1.0 t	$W_{50} \geq$ 0.5 t	3.0	17%
IV	QUARRY RUN			
V	DREDGED SAND			

Figure 6. Cross-sections for the comparison between the conventional rubble mound breakwater and the Icelandic type berm breakwater.

slope of 1:1.5, a crest elevation of +8.75 and a toe structure at the front at –3.5 m, Figure 6. The required average mass of stone is determined according to the methods of van der Meer (1988 and 1993). Designing for damage factor S = 2.1, practically start of damage, storm duration of 3 hours, the mass density of the basaltic rock 2.85 tonne/m^3, the required average mass of stone, M_{50}, is 4.7 tonne. Armour stone classes are class I, 3 to 8 tonne. The harbour side is protected be class II, 1 to 3 tonne stones and class III, 0.3 to 1, tonne stones are used as filter layer on both sides. The available armour stone quarry is expected to give about 10% in class I, 13% in class II and 17% in class III.

To make the comparison not to favourable for the berm design, the same stone size is used on top of and at front of the berm as for the armour layer on the conventional breakwater, meaning an unusually high stability for a berm breakwater, Figure 6. The harbour side of the two cross-sections is completely the same, as is the toe structure on the front side, the only difference being the front of the structures from crest down to toe.

The cost estimate is very dependent upon the distance to the quarry. In general, quarries for production of armour stones and core material are within a distance of 10 to 15 km from the construction site. If the distance to a suitable armour stone quarry is more than that, another quarry closer to the structure is usually used for production of the core material. In the calculated example, the distance from the quarry to the breakwater site is about 10 km.

It is also common to use dredged material in the inner part of the core for economical reasons. The price difference of using dredged material instead of trucking the available quarried material in the case of the conventional breakwater is about 20% per m^3 in this case. Table 1 sums up key parameters in the cost comparison.

	Conventional rubble mound breakwater	Icelandic type berm breakwater
Total volume of breakwater	801 m^3/m	846 m^3/m
Total volume of materials from quarry	398 m^3/m	414 m^3/m
Total volume of dredged sand	403 m^3/m	432 m^3/m
Total volume of rocks larger than 3 t	61 m^3/m	33 m^3/m
Total quarried material needed for production of rock	610 m^3/m	420 m^3/m
Excess quarried material	200 m^3/m	
Extra cost due to excess production	25%	
Extra cost due to larger total volume		10%
Machine needed for placing large stones	Crane 60 t	Excavator 45 t
Armour stone placing rate	30 stones/hour	60 stones/hour
Relative cost of machine per hour	2	1
Relative cost of placing armour stone	4	1
Extra cost due to placing of armour stones	10%	
Number of capable contractors	2	10
Extra cost due to limited competition	5 – 20%	
Relative total cost	**130% - 150%**	**100%**

Table 1. Comparative cost analysis between the Icelandic type berm breakwater and the conventional rubble mound breakwater.

In total there is a 15% difference in cost in producing and transporting stones and core material, 10% difference in placing the material and 5 to 20% difference in limited competition. This adds up to 30 to 50% higher cost for the conventional breakwater. Even in a moderate wave climate, the difference is this high and with higher design wave height the difference will increase. Also, a poorer quarry yield will increase this difference. Although a better quarry yield lowers the difference, the difference in placing and limited competition will still remain. This should answer the question, why we retain the berm concept, even though the structure aims at static stability with a number of different rock gradings.

Icelandic type berm breakwater versus dynamic berm breakwater

In the example above, a dynamic structure would need to be of the order of 10% more voluminous than the Icelandic berm breakwater and the dynamic berm would need at least 25% more volume of stones than the Icelandic type berm. The cost of this far exceeds the cost for sorting and placing several stone classes. The largest waste in the two-stone class berm breakwaters is twofold. Firstly, large stones are used or are lost into places where they are not nceded, at large water depth or inside the structure close to the core. And secondly, the contractor is not asked to produce close to the maximum yield from the quarry.

The cost comparisons with the Icelandic type berm breakwater are not comparable with the aforementioned studies, Ligteringen et al (1992) and Hauer et al (1995), since they may rely on different assumptions.

Recent examples

The Dalvik breakwater

The Dalvik breakwater, which was constructed in 1994 and 1995, is 320 m long and has a volume of 104,000 m^3. The available quarry was of good quality with predicted quarry yield of 46 to 54% over 0.3 tonne. As the wave load was moderate, the design anticipated the use of dredged material in the inner part of the core, coarse sand or gravel, up to 30% of the total volume of the structure. The dredged mound experienced a winter storm before protected with material from land, but only minor

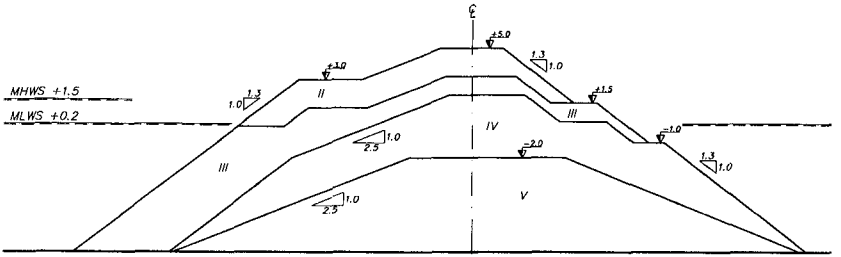

STONE CLASSES

CLASS	WEIGHT	MEANWEIGHT	STABILITY PARAMETER
I	4.0 t < W ≤ 8.0 t	W_{50} ≥ 5.3 t	1.2
II	1.5 t < W ≤ 4.0 t	W_{50} ≥ 2.3 t	1.6
III	0.3 t < W ≤ 1.5 t	W_{50} ≥ 0.7 t	2.3
IV	QUARRY RUN		
V	DREDGED SAND/GRAVEL		

Figure 7. Cross-section of the Dalvik breakwater

deformation of the mound was measured. Figure 7 shows a cross-section of a trunk section. Class II rock, 1.5 to 4.0 tonne rock with stability parameter 1.6, covers the berm in two layers from low water level up to the crest and in one layer on the rear side. Class III rock is used between class II and the core material. The reason for class III extending down to sea bottom was that the design anticipated that all quarried material was placed with land based equipment. In order to increase the thickness of the berm around design water level a flat slope, 1:2.5, of the core is chosen. Class I rock, $\geq$ 4 tonne, is used on top of the berm at the breakwater head. The design fully utilises all stones over 0.3 tonne with an overproduction in both classes I and II. A 100% utilisation of all quarried material was achieved in spite of the use of dredged material.

The Husavik breakwater

The Husavik harbour located on the north east coast of Iceland is exposed to waves and swells from north-west to north-east. The outer breakwater, a concrete pier, was widened and protected from overtopping in 1989 to 1990 by a berm structure (Sigurdarson et al, 1995). Still the pier did not shelter the harbour sufficiently well and in the summer of 1997 a contractor was hired to construct a 100 m long breakwater, as an extension to the pier. Figure 8 shows a cross-section of an outer trunk section. One of the features of this design is that the front slope of the berm is more flat than usual, 1:1.5 over elevation –1.0. This is done to increase the stability of the berm. Another feature is the location of the core in relation to the crest or the inner edge of the berm. This location aims at minimising the total volume of the structure. On the breakwater head and outer most 20 m class I rock covers the front and top of the berm, but class II rock on the rest of the structure. The upper slope, crest and back slope are on the other hand covered by class III rock, as is the front slope under –1.0 m in elevation. The inner part of the structure is built up of class IV rock. The design aims at fully utilising all rocks from the quarry over 0.5 tonne, given that the contractor produces close to the maximum quarry yield, which is 35%.

In the autumn of 1997 sudden changes in the use of the harbour became evident. This development made an alteration in the location of the breakwater

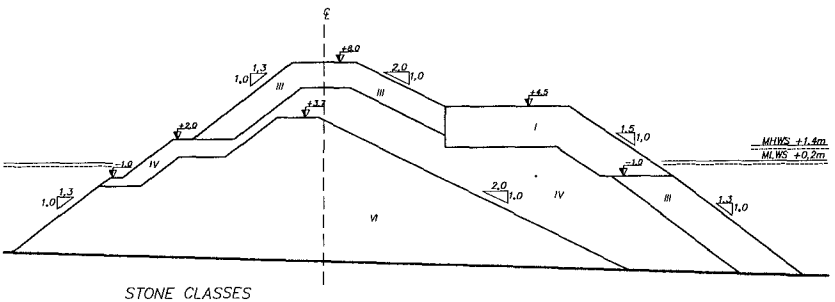

STONE CLASSES

CLASS	WEIGHT	MEAN WEIGHT	STABILITY PARAMETER
I	10,0 t < W ≤ 16,0 t	$W_{50} \geq$ 12,0 t	1.7
II	5,0 t < W ≤ 10,0 t	$W_{50} \geq$ 6,7 t	2.1
III	2,0 t < W ≤ 5,0 t	$W_{50} \geq$ 3,0 t	2.5
IV	0,5 t < W ≤ 2,0 t	$W_{50} \geq$ 1,0 t	3.3
VI	QUARRY RUN		

Figure 8. Cross-section of the Husavik breakwater

necessary. The new location is in a more exposed area. Since funds were not available for a full construction the contract was renegotiated so that rocks were produced and stored near the new location.

Conclusion

Instead of a dynamic approach to berm breakwater the Icelandic type aims at a more stable structure. The use of larger stones more narrowly graded on top and at the front of the berm increases the permeability and the ability of the structure to swallow the wave more rapidly.

Although the Icelandic berm requires larger stones than the dynamic type it aims at maximising the utilisation of all quarried material. And often only a small fragment of the quarried material is used to reinforce the structure. It has been proven in many projects that the Icelandic berm lowers the construction cost significantly. Large, voluminous, dynamic structures may be attractive in some special cases. It is, however, believed that the narrower, stable Icelandic berm has a much wider usage. In the dynamic approach an uncontrolled movements of stones will occur which can not be accepted, especially in the breakwater head.

Cost comparison between the Icelandic type berm breakwater versus conventional rubble mound breakwater show significant reduction in the construction cost. The Icelandic berm breakwaters have proved to withstand design or near to design wave condition with only minor profile changes, Figure 9.

Figure 9. The Bolungarvik breakwater in 1996 after having experienced the design storm lasting for at least two days in January 1995.

References

Bruun, P. and Johannesson, P. (1976). "Parameters Affecting the Stability of Rubble Mounds." J. Waterways, Port, Coastal and Ocean Eng, ASCE, 102(2), 141-164

Hall, K.R., Baird, W.F. and Rauw, C.I. (1983). "Development of a wave protection scheme for a proposed offshore runway extension." Coastal Structures 83, ASCE, Washington DC.

Hauer, M, Op den Velde, W., Vrijling, J.K. and d'Angremond, K. (1995). "Comparison construction costs conventional rubblemound breakwaters/ berm breakwater." Proc. 3rd Seminar on Ports and Inland Waterways, Goa, Publ. by PIANC/PCDC, Brussels.

Juhl, J. and Sloth, P. (1998). "Berm Breakwaters - Influence of Stone Gradation, Permeability and Armouring." Proc. 26th ICCE, Copenhagen.

Ligteringen H., Rowe H. J. D., Hight D., Zwetsloot P.A.J., Hayman Joyce, J. and Chan, K.K., (1992). "The preferred concept for the Lamma breakwater, Western Harbour, Hong Kong," Proc. Ports 2000, International Conference on Port Development for the Next Millennium, A Hong Kong Inst. of Eng. Public.

Poole, A.B., Fookes, P.G., Dibb, T.E. and Hughes, D.W. (1983). "Durability of rock in breakwaters." Breakwaters, Design and Construction. Thomas Telford, London, 31-42.

Sigurdarson, S; Viggosson, G; Benediktsson, S; and Smarason, O.B. (1995). "Berm breakwaters and quarry investigations in Iceland." Proc. COPEDEC IV, Rio de Janeiro, Brazil. 1204-1218.

Sigurdarson, S., Viggosson, G., Benediktsson, S. and Smarason, O.B. (1996). "Berm Breakwaters, Tailor-Made Size Graded Structures." Proceed. of 11th Int. Harbour Congress.

Sigurdarson, S., Einarsson, S., Smarason, O.B. and Viggosson, G. (1997). "Berm Breakwater in the tidal inlet of Hornafjördur, Iceland." MEDCOAST, Malta.

Sigurdarson, S., Juhl, J., Sloth, P, Smarason, O.B. and Viggosson, G. (1998). "Advances in Berm Breakwaters." Coastlines, Structures and Breakwaters Conference, London.

Smarason, O.B., Sigurdarson, S., Benediktsson, S. and Viggosson, G. (1998). "Applications of Armourstone Size Prediction from Discontinuity Measurements in Rock bodies." Fifth Annual One Day Meeting, UK Armourstone Users Group, HR Wallingford.

van der Meer, J.W. and Pilarczyk, K.W. (1986). "Dynamic stability of rock slopes and gravel beaches." Proc. 20th ICCE, Taipei.

van der Meer, J.W. (1988). "Rock slopes & gravel beaches under wave-attack." Ph.D. thesis, Delft University of Technology.

van der Meer, J.W. (1993). "Conceptual design of rubble mound breakwaters." Delft Hydraulics.

Viggosson G. (1990). "Rubble Mound Breakwaters in Iceland." Journal of Coastal Research, SI 7, pp. 41-61, Fort Lauderdale, Florida, Spring 1990.

The First Berm Breakwater in Hong Kong

K C Ander Chow[1], Charles P Fournier[2], P F Ma[3] and W Y Shiu[4]

Abstract

An alternative berm type breakwater was proposed at the South Breakwater of the Typhoon Shelter at Hei Ling Chau, Hong Kong. The required berm width and the stone sizes were initially determined using a numerical model. The proposed berm breakwater was then tested using physical modelling approach. The testing programme made use of both two dimensional and three dimensional hydraulic model studies to assess the stability of the trunk and head sections respectively. Both tests confirmed that the proposed berm type breakwater would perform satisfactorily and the reshaped profiles would not encroach on the core material.

Introduction

To meet the forecast demand for typhoon shelter space in Hong Kong, it is recommended that a typhoon shelter at Hei Ling Chau be constructed to provide about 50 hectares of effective anchorage area. As the typhoon shelter would be located at the southwest of Hei Ling Chau, three breakwaters (see Figure 1) with a total length of about 2.6 km would be required in order to provide a safe and calm anchorage area. Among these three breakwaters, the South Breakwater will be exposed to the severe waves approaching from the southeast direction. Various types of breakwater have been considered for the design of the South Breakwater. However, if the South Breakwater was to be designed as a conventional rock armoured breakwater, it was estimated that an armour rock size of 17t was required. This is generally not commercially available in large quantity in Hong Kong. Precast concrete units could be used instead of amour rocks, but in this case 4t to 9t of cubes,

[1] Director, Scott Wilson (Hong Kong) Ltd., 38/F Metroplaza Tower 1, 223 Hing Fong Road, Kwai Fong, New Territories, Hong Kong, People's Republic of China.
[2] Associate, Baird & Associates, 1145 Hunt Club Road, Suite 1, Ottawa, Ontario, Canada K1V 0Y3.
[3] Senior Engineer, Civil Engineering Department, the Government of the Hong Kong Special Administrative Region, 101 Princess Margaret Road, Homantin, Kowloon, Hong Kong, People's Republic of China.
[4] Government Civil Engineer, Civil Engineering Department, the Government of the Hong Kong Special Administrative Region, 101 Princess Margaret Road, Homantin, Kowloon, Hong Kong, People's Republic of China.

tetrapods or accropods would be required, which will require large works area for construction and thus increase the construction cost.

As an alternative option, the dynamically stable berm type breakwater was considered. With this type of breakwater, the size of armour rocks required would be smaller than that for a conventional breakwater. The construction cost would be lowered. The profile of the breakwater will, however, adjust to severe storm events. The dynamically stable berm type breakwater is thus considered as the preferred form of construction for the South Breakwater. In this paper, development of the berm type breakwater from the outline design to the verification using a physical model is presented.

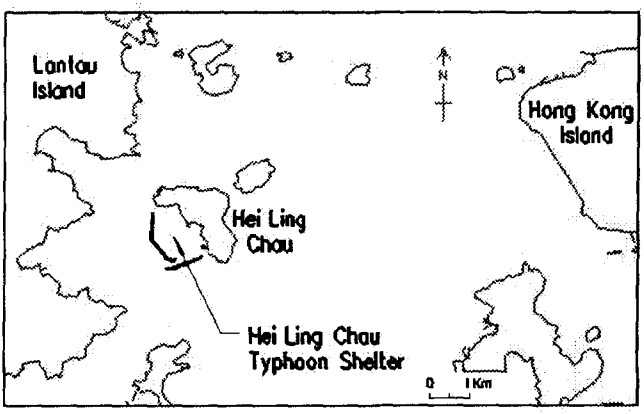

Figure 1 Typhoon Shelter at Hei Ling Chau, Hong Kong

Berm Breakwater Concept

The berm breakwater design consists of a porous berm of armour stones which dissipates wave energy. The stones are expected to move under wave action leading to a stabilised and consolidated equilibrium profile. As a result, the shear strength of the stone mass and the resulting overall stability of the structure increases as the stones settle, nest and interlock. The geometry of the breakwater is a function of the prototype stone gradation and the design wave conditions.

The initial width of the berm determines the extent to which the profile reshapes. Berm breakwaters may be designed so that:

(i) full reshaping of the berm occurs (dynamic)
(ii) only a slight rounding of the outer edge of the berm occurs (static)

The dynamic design is a more common form of the berm breakwater and is the concept which has undergone the most extensive investigation. This type of structure is very cost effective and allows for maximum utilization of the quarry material. By knowing the quarry yield and the relative volumes of core to armour, the quarry yield can simply be split such that a production balance between core and armour is maintained for full utilization of the quarry. The dynamic berm concept has been implemented at a number of prototype locations in Australia, Canada, Iceland, the South Pacific and the USA with great success.

The static design approach requires approximately 70 - 80 % more material and is therefore more costly. However the factor of safety is increased. Static berms have been utilized in Australia, Iceland and the South Pacific.

Implementation of the berm concept at Hei Ling Chau also presents several advantages to the contractor involved with construction of the breakwater. The berm design is simple and thus an easier structure to build. With the berm alternative, it is only important to ensure that the full berm width is placed according to the design. Minimum underwater inspection is required due to the fact that the seaslope will change with time and thus may be built at the angle of repose of the stones. Furthermore, the armour layer is built up out from the core until the required berm width is achieved. Feasibility of the berm breakwater applications in Hong Kong can be found in Chow and Sayao (1991).

Wave Climate and Design Storm

The extreme waves attack at the south of Hei Ling Chau are mainly generated by typhoons. There were no measured wave data available at the study site, the design wave conditions were derived using wave hindcasting techniques. The extreme offshore wave climate was hindcast using a parametric wind wave generation model developed by the Hong Kong Polytechnic University (Li et al 1992). For waves approaching from the south and southeast of Hei Ling Chau, various numerical models considering the effects of refraction, shoaling, bottom friction and wave breaking were applied to derive the nearshore wave climates. The derived design wave conditions can be found in Table 1. The Storm No. roughly represents the return period of the design storm.

Table 1. Design Wave Condition

Storm No.	Water Level (mCD)	Significant Wave Height H_s (m)	Significant Wave Period T_m (s)
2	2.8	2.4	8.5
10	3.2	3.6	11.6
100	3.7	4.0	13.9
250	3.8	4.2	14.7

Conceptual Design

Based on the above design storm, a quarry stone size of 17t was computed to be required for the conventional breakwater. However, this stone size is generally not locally available in large quantity commercially. Using the software BREAKWAT acquired from Delft Hydraulics, a conceptual design of the berm breakwater was carried out. The software showed that a width of berm of 12 m and a median rock size of 2 t and 4.5 t were found to be appropriate for the trunk and head sections respectively under the design storm conditions. Typical cross-section of the proposed berm breakwater profile can be found in Figure 2.

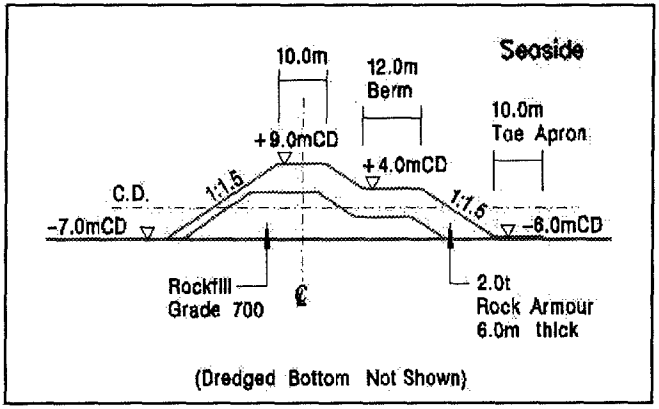

Figure 2. Typical Trunk Section of the Berm Breakwater

Physical Model Tests

To confirm the conceptual design, Scott Wilson was engaged by the Port Works Division of the Civil Engineering Department to undertake physical hydraulic model tests at the Hydraulics Laboratory of the National Research Council (NRC) in Canada. The testing programme made use of both two dimensional (2D) and three dimensional (3D) hydraulic model studies to assess the stability of the trunk and head sections respectively.

Testing Facilities and Model Set-up

The 2D berm breakwater stability tests and the 3D physical hydraulic model tests were carried out in the 14 m coastal wave flume and the multi-directional wave basin at NRC respectively.

Figure 3 illustrates the layout of the 2D model test structures in the 14 m flume (dimensions in model units), the irregular wave-generator and the location of the wave probes used to measure both the wave climate and reflection coefficients. Two model berm breakwater cross sections were tested (side by side) in the 2D model; one with a 12 m berm width and a second with a 18 m berm. As a consequence of this arrangement, both model structures were subjected to the identical wave climate.

Figure 4 illustrates the layout of the 3D model test structure in the Multidirectional Wave Basin, the location of the wave probes used to measure the wave climate and the location of the profile lines selected to record profile reshaping. The 3D model berm breakwater structure consisted of a 90 m trunk section, the full 75 m transition and the complete head. The wave basin is an indoor wave tank which is approximately 30 m by 20 m. The maximum depth of water is approximately 2.5 m. The segmented wave machine (60 individual paddle segments, total paddle length of 30 m) utilized in this basin is capable of producing model significant wave heights of 1 m, and can reproduce the interaction of irregular waves from different directions, i.e. truly three dimensional sea states. The basin is sufficiently large such that a 90° change in wave direction can occur at any point during the design storm without moving either the model structure or the wave machine. This means that many directions of wave attack may be modelled in this facility.

Because the bathymetry of the site at Hei Ling Chau is characterized by a very flat slope, the seabed topography for both 2D and 3D models was not modelled. That is, all tests were conducted with a fixed horizontal bottom located at elevation -7.0 mCD. The wave flume had a series of capacitance-type wave gauges located at strategic locations to measure the wave characteristics. The measured wave records were analyzed using zero crossing analysis and variance spectral density analysis to produce wave parameters and spectral plots respectively.

Both 2D and 3D physical model tests followed the Froude model law (U.S. Army, 1979). It consisted of an undistorted, two-dimensional, fixed bed model, with a geometric scale of 1:30. The model was sufficiently large to avoid Reynold's effects (U.S. Army, 1984).

Required Stone Sizes

Armouring requirements for the trunk section of the model structure was specified in the Project Brief as Type 13 with the following parameters:

Parameter	Specified	Acceptable Range
M_{15}	1000 Kg	1000 - 1500 Kg
M_{50}	2000 Kg	1900 - 2100 Kg
M_{85}	3000 Kg	2600 - 3800 Kg
M_{85}/M_{15}	3.0	2.5 - 3.3

Armouring requirements for the transition and head of the model structure was specified in the Project Brief as Type 14 with the following parameters:

Parameter	Specified	Acceptable Range
M_{15}	3200 Kg	3200 - 4000 Kg
M_{50}	4500 Kg	4300 - 4600 Kg
M_{85}	6400 Kg	5000 - 6500 Kg
M_{85}/M_{15}	2.0	1.8 - 2.1

The Type 13 stone used in the 2D tests was also used for the trunk section in the 3D tests. Model armour stone was sorted in the laboratory to yield a gradation which closely represents the above specified values for the Type 13 and Type 14 materials.

Waves, Water Levels and Wave Measurements

Irregular waves were synthesized by specifying a JONSWAP wave energy density spectrum with γ of 3.3 for both models. Wave measurement probes were positioned at various locations to measure water level fluctuations. These probes are representative of wave conditions generated by the wave machine, and the wave condition in front of the test structures. The specified wave climates and water levels for the 2D and 3D tests can be found in Tables 2 and 3 respectively.

Table 2 Specified Wave Climate and Water Level Conditions for 2D Tests

Run Segment	Significant Wave Height Hs (m)	Peak Wave Period Tp (s)	Water Level (mCD)	Number of Waves
Run 1	2.4	11	2.8	1000
Run 2	3.6	15	3.2	1500
Run 3	4.0	18	3.7	2000
Run 4	4.0	20	3.7	2000
Run 5	4.2	19	3.8	2000

Table 3 Specified Wave Climate and Water Level Conditions for 3D Tests

Run Segment	Significant Wave Height Hs (m)	Peak Wave Period Tp (s)	Direction of Wave Attack	Water Level (mCD)	No. of Waves
Run 1	2.4	11	30°	2.8	1000
Run 2	3.6	15	30°	3.2	1500
Run 3	4.0	18	30°	3.7	2000
Run 4	2.4	11	60°	2.8	1000
Run 5	3.6	15	60°	3.2	1500
Run 6	4.0	18	60°	3.7	2000
Run 7	4.0	20	60°	3.7	2000
Run 8	4.2	19	60°	3.8	2000

Prior to testing the stability of the model structures, the waves were calibrated to the specified conditions. That is, for each Run, the (initially) synthesized wave train was generated in the model basin for a limited period of time. Data samples were recorded and analyzed. As a consequence, adjustments of the synthesized wave trains were required to "tweak" the waves to match those specified wave climate (see Tables 2 and 3). However, when the generated wave heights (at the wave machine) were increased for both 2D and 3D tests, more waves broke offshore of the berm structure resulting in a reduced wave climate and a significantly transformed spectral shape. By studying the spectral plots collected at the laboratory, it is believed that the longer period waves underwent transformation to another spectral form due to finite depth conditions.

Berm Breakwater Profiling Device

An automated berm breakwater profiling device was installed and used in the basin to record profile development. The device is an extremely simple mechanism used to measure any 2D (X,Z) surface profile be it a berm breakwater profile or a beach profile. The device operates on the concept of rolling a wheel over a surface and tracking the X,Z location of that wheel with a real time recording system. To accomplish this, a post and beam assembly was installed over the berm breakwater as shown in Figure 5. On the top surface of the beam, a mouse is moved from one end of the beam to the other by means of a hand crank, which pulls the mouse by a cable in tension. The horizontal location of the mouse is measured by a linear potentiometer at a frequency of 20 Hz. This measurement is the mouse location X_1 (see Figure 5) relative to some fixed reference point.

Two Dimensional Wave Flume Tests

A series of 2D berm breakwater stability tests were carried out in the 14 m coastal wave flume. Under the synthesized wave climate, both the 12 m and 18 m model berm breakwaters performed well. The reshaped profiles did not encroach on the core material, and the crest and backslope model armour material were stable under all wave conditions specified. The toe protection armour stone was also determined to be statically stable under the tested conditions.

Van der Meer (1987) has developed the parameter "S" which relates to the "damage" measure of a conventional breakwater structure. In the context of berm breakwater, the parameter "S" does not relate to damage, but rather to the degree of reshaping of the profile. Van der Meer defines "S" as

$$S = \frac{A}{(D_{n50})^2}$$

where A is the eroded area and D_{n50} is the nominal diameter of the armour stone associated with the 50% value of the mass distribution curve.

The actual value of S is not important, but rather the rate of change of S with respect to the number of waves. Since S really represents the degree of reshaping (in the context of berm breakwaters), one is interested in determining at what locations in the storm profile the rate of change of S is large, i.e. the profile is reshaping significantly, and subsequently, when the rate of change of S becomes small, i.e. reshaping has stabilized.

Figure 6 shows the values of S as a function of cumulative waves for each berm structure. It is apparent from these curves, that the rate of change of S is greatest in Run 3, which indicates that the greatest reshaping of the berm profiles occurred during this storm segment.

On a previous project, it was shown that a 9 m berm in 2D tests reshaped in a dynamically similar manner as an 11 m berm in 3D (all other parameters held constant) (Fournier et al, 1990). Therefore, the 3D tests will be more conservative estimates of breakwater stability than the 2D counterparts. To confirm the stability of the test section, 3D model tests were conducted for the 12 m berm breakwater design.

Three Dimensional Wave Basin Tests

Under the synthesized wave climate, the model berm breakwater performed well. The reshaped profiles did not encroach on the core material, and the crest and backslope model armour material were stable under all wave conditions specified. The toe protection armour stone was also determined to be statically stable under the tested conditions.

During Runs 4 to 8, longshore transport of the armour material occurred due to the 60° oblique angle of wave attack. The material was transported along the trunk towards the transition. Because of this longshore transport, the trunk profiles in close proximity to the transition actually built up due to deposition of Type 13 stone. The source of the transported material was the trunk section closest to the wave machine. As a result, a scour hole was developed in Run 5. To maintain integrity of the test and to simulate the supply of armour stone from a structure much longer than that which was modelled, "artificial feeding" of Type 13 armour stone was performed at the scour hole location. The rate of stone feeding was roughly in accordance with the rate of scouring.

Conclusions

With the aid of the software BREAKWAT, a berm breakwater with 12 m berm width was adopted for the South Breakwater of the Hei Ling Chau Typhoon Shelter. The proposed berm breakwater was tested in a 2D wave flume and a 3D wave basin. In the 2D and 3D physical modelling tests, the proposed structure would reshape, but without excessive damage, under the design storm conditions. Both 2D and 3D tests confirmed that the proposed 12 m berm breakwater performed satisfactorily and the reshaped profiles did not encroach on the core material..

Acknowledgements

This paper is published with the permission of the Director of Civil Engineering, the Government of the Hong Kong Special Administrative Region, People's Republic of China.

References

Chow, K. C. A., and Sayao, O.J. (1991). *Berm breakwater alternative for harbour and shore protection.* Proceedings of International Workshop on Technology for Hong Kong's Infrastructure Development, The Hong Kong University of Science & Technology, 437-452.

Li, C. W., Li, Y. S. and Chau, K. W. (1992). *Estimation of extreme incoming wave conditions of Hong Kong using a "third-generation" discrete-spectral wave model.* Hong Kong Polytechnic.

Fournier, C., Sayao, O. J., and Caldas, P. (1990). *Berm breakwater contamination study, Sergipe Marine Terminal, Brazil.* International Conference on Coastal Engineering, ASCE. Delft, The Netherlands. July. 3194-3206.

U.S. Army Corp of Engineers, (1979). *Coastal Hydraulic Models.* Coastal Engineering Research Center.

U.S. Army Corp of Engineers. (1984). *Shore Protection Manual.* 4th Edition, Coastal Engineering Research Center.

Van der Meer, J. W. (1987). *Stability of breakwater armour layers - design formulae.* Coastal Engineering, Elsevier, Vol. 11, 219-239.

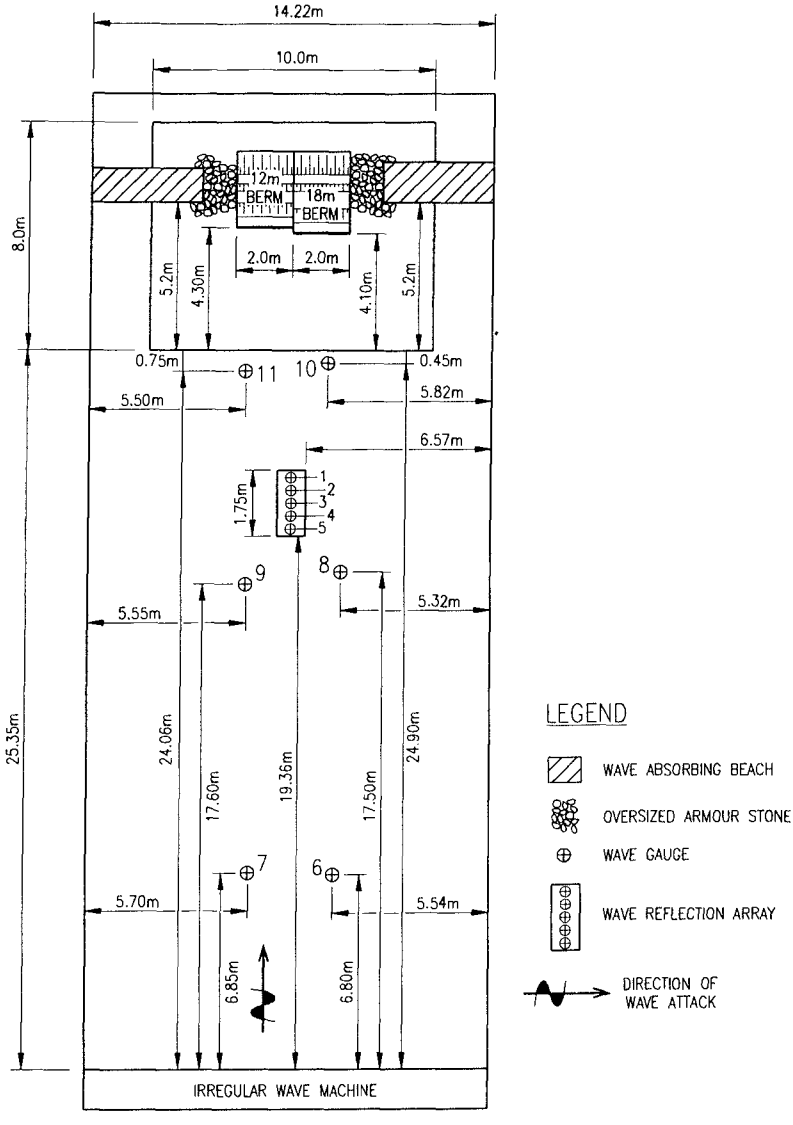

Figure 3 Layout of Model in 14m Wave Flume

Scale 1:200

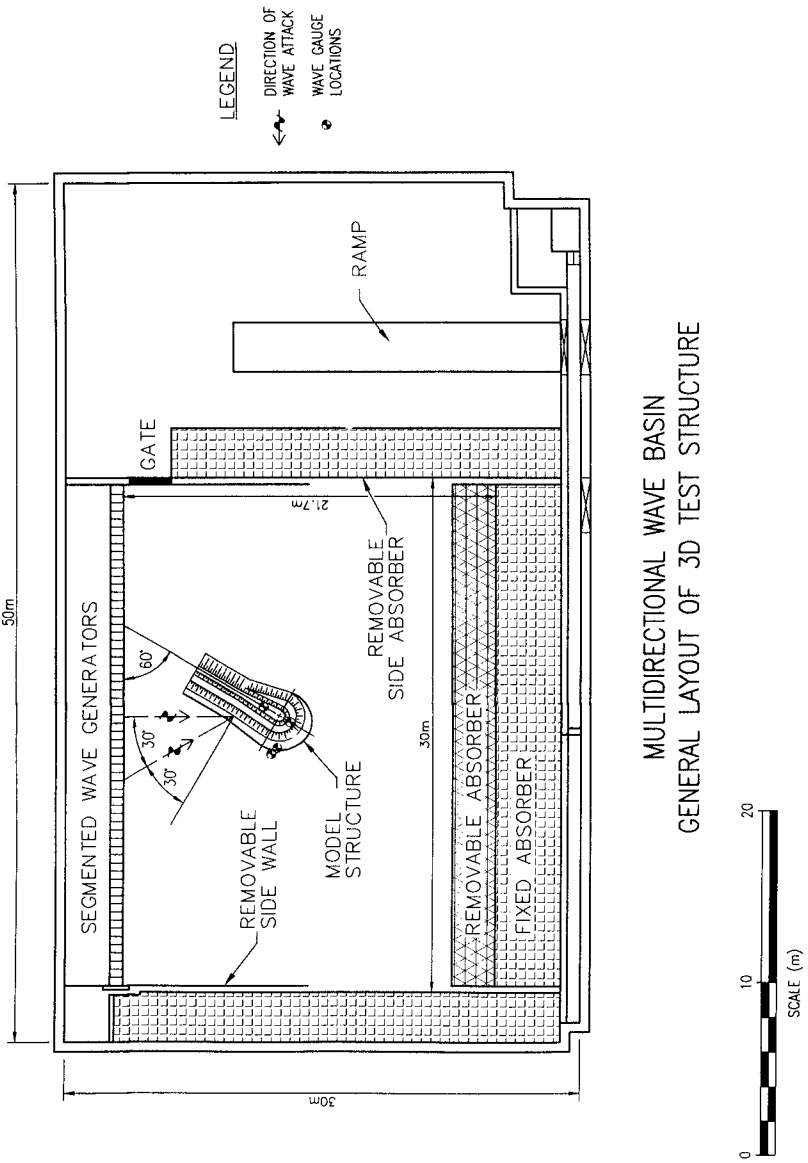

Figure 4a General Layout of 3D Test Structure

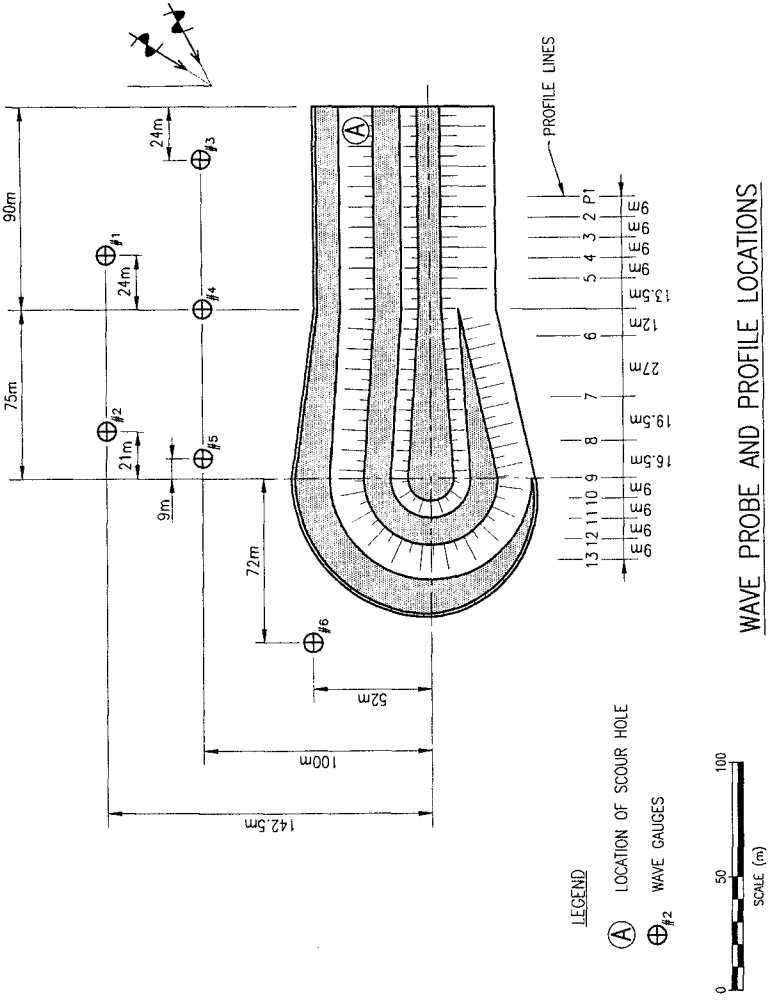

Figure 4b Wave Probe and Profile Locations

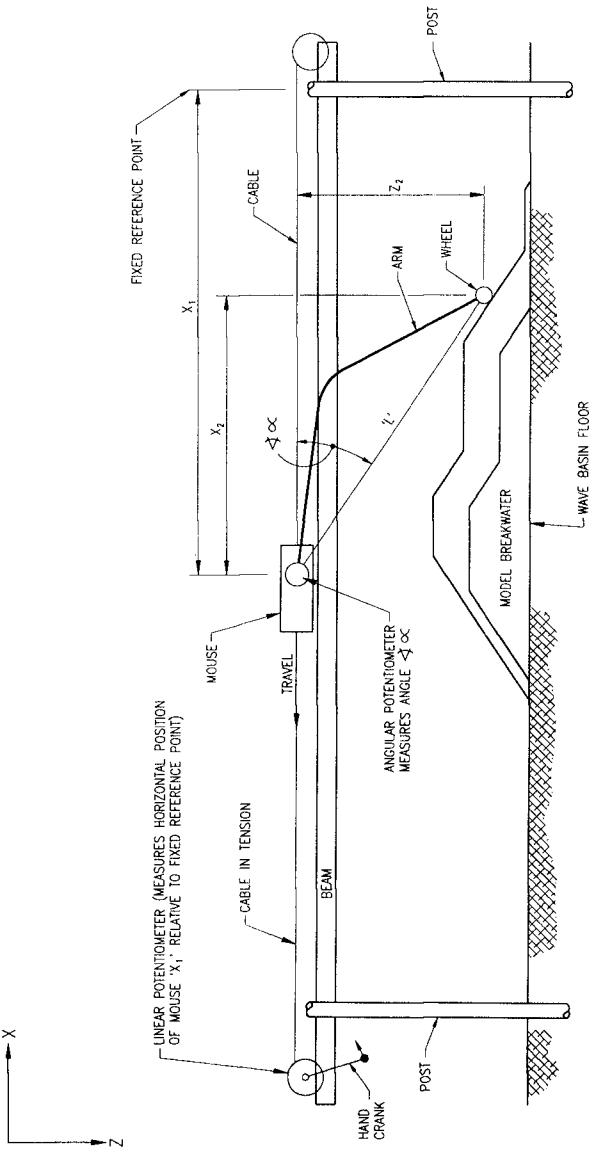

Figure 5 Schematic of Automated Berm Breakwater Profiling Device

Not to Scale
Concept Diagram Only

Physical Modelling for the South Breakwater of the
Hei Ling Chau Typhoon Shelter

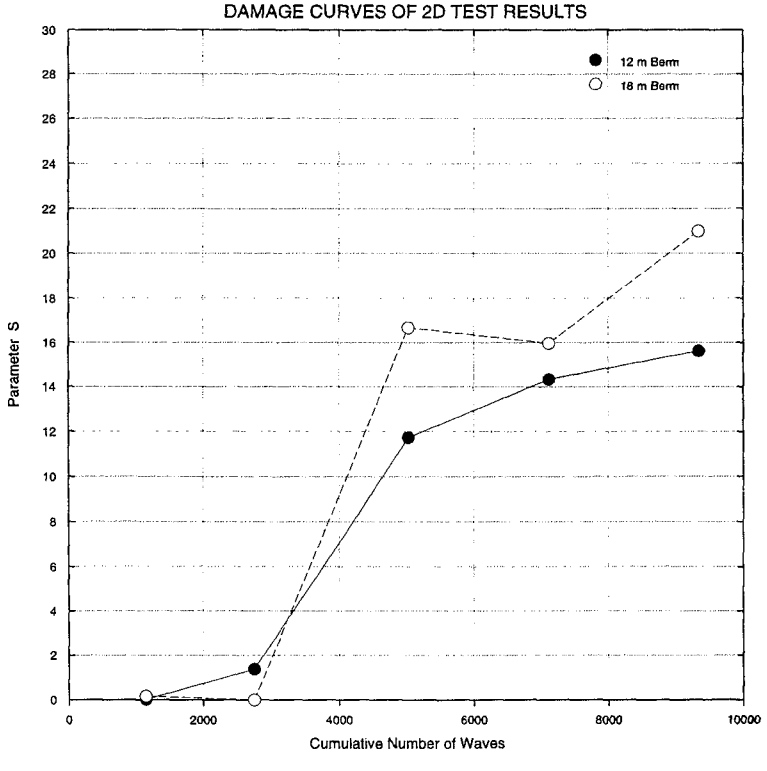

Figure 6 Damage "S" Value Curves

On the stability of berm breakwaters in shallow and deep water.

Alf Tørum[1]

Abstract.

The paper describes laboratory tests on berm breakwaters in shallow water, e.g. in water depths where waves might break before they break on the breakwater. Analysis have been made of test results for breakwaters in shallow and deep waters and a unified design equation is presented for the berm recession of berm breakwaters in shallow and deep water.

Introduction.

Rubble mound berm breakwaters are increasingly used throughout the world. The main advantage of the berm breakwater is that lower stone weights are required on a berm breakwater than on a conventional rubble mound breakwater of quarried rock.

During the EU MAST II Berm Breakwater Structures project model tests were carried out for a berm breakwater, including a breakwater head, in deep water at the Danish Hydraulic Institute, DHI (1995), Juhl et al (1996), while tests in shallow water on a trunk section and including a head were carried out at SINTEF, Tørum (1997), as supplementary tests to the more extensive tests at DHI. In addition 2D tests were carried out at DHI, DHI (1996), Juhl and Sloth (1998). "Deep water" means in this context that the waves will not break until they break on the breakwater, while "shallow water" means that some of the larger waves will break before they arrive at the breakwater due to depth limitation. In the present paper we describe the shallow water tests carried out at SINTEF and give some brief results from them. We further include results from other tests series, notably from Andersen and Fleming (1991), DHI(1995), Lissev (1993), Tørum (1988) and Tørum (1997, 1997A) to arrive at an equation for the recession of the berm as a function of the stone diameter, the wave height and wave period. This equation can be considered as a design equation for the berm recession.

[1]Professor dr.ing. SINTEF Civil and Environmental Engineering
Department of Coastal and Ocean Engineering
7034 Trondheim, Norway.

Model Test Set-up.

The SINTEF "shallow" water model test set-up is shown in Figure 1. The waves were generated in 0.70 m water depth. After travelling for approximately 15 m, the waves climbed a slope of 1:30 to a horizontal plateau where the water depth was 0.25 m and where the breakwater model was placed.

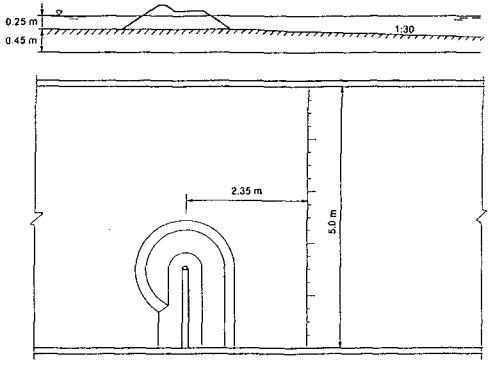

Figure 1. Test set-up.

Three different cross-sections were tested, A, B and C, Figure 2. Section A is almost a copy of the section tested at DHI, except that the water is shallower and except that the initial slope of the outer slope of the berm was 1:1.5 while this slope was 1:1.1 for the DHI tests. The gradation of the berm stones was such that $D_{15} \approx 0.018$ m, $D_{50} \approx 0.022$ m and $D_{85} \approx 0.030$ m.

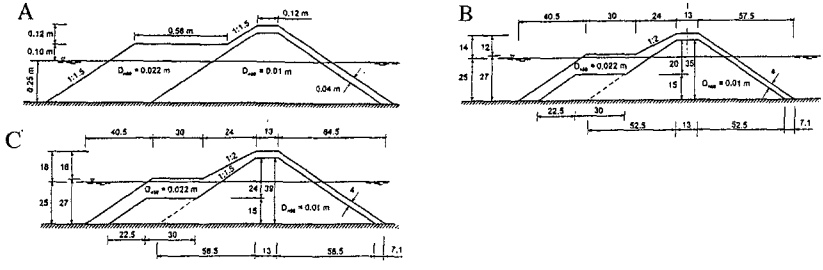

Figure 2. Tested cross-sections, A, B and C.

Wave measurements.

Wave measurements were carried out without the breakwater model being present in the flume. The wave measurements were carried out at the location of the centreline of the breakwater head with water depth 0.25 m, and in the deepest part of the flume, where the water depth was 0.70 m. The target spectra in "deep" water were JONSWAP spectra with an enhancement factor $\gamma = 3.0$.

Figures 3 and 4 show the relation between the measured significant wave heights, $H_s = H_{mo}$, and the measured zero-upcrossing periods, T_z, at water depths 0.70 m and 0.25 m respectively. The measured peak period, T_p, is also shown. However, the peak periods are not as "robust" as the zero-upcrossing periods as it may be somewhat arbitrary for which frequency the peak in the calculated spectrum will occur.

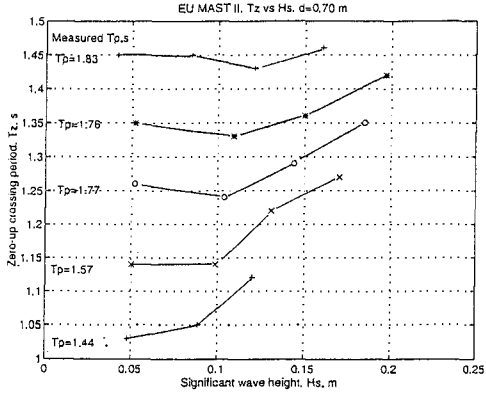

Figure 3. Measured zero-upcrossing periods T_z, peak periods, T_p, and significant waveheights, $H_s = H_{mo}$. Water depth d = 0.70 m.

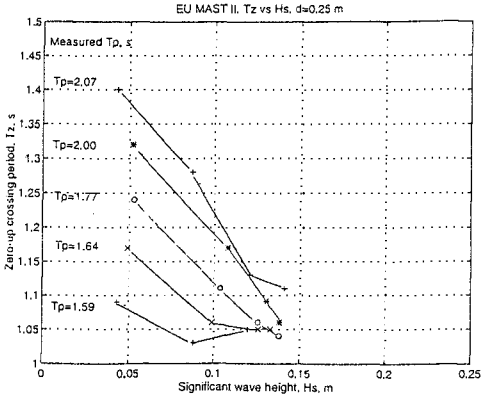

Figure 4. Measured zero-upcrossing periods, T_z, peak periods, T_p, and significant wave heights, $H_s = H_{mo}$. Water depth d = 0.25 m.

In shallow water the highest waves will break. Thus the ratio between the maximum wave height, H_{max}, and the significant wave height, H_{mo}, is expected to be lower in shallow water than in deep water. $H_{mo} = 4\ (m_o)^{0.5}$, where m_o = area under the spectrum. Figure 5 shows this ratio for different significant wave heights for T_p=1.77s

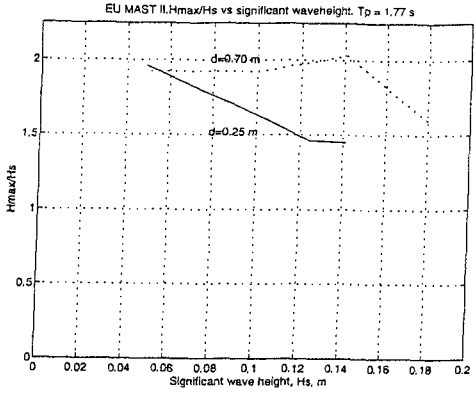

Figure 5 Ratio H_{max}/H_s ($H_s = H_{mo}$) for wave period $T_p = 1.77$ s and for water depth d = 0.70 and 0.25 m.

Test program.

The test program we used was approximately the same as for the DHI tests, DHI (1995), Juhl et al (1996) with respect to the number of waves for each wave step, except that we included a very long test run at the end of each test series. All tests were carried out with a target steepness of the waves of $s = 2\pi H_s/gT_z^2 = 0.05$, where g= acceleration of gravity.This is the same steepness as used for most of the DHI tests.After discussions with other partners in the EU MAST II Berm Breakwater Structures project we decided to use, as has been common practise, the zero up-crossing period in deep water (d = 0.70 m) and H_{mo} from shallow water (local wave height at d = 0.25 m) when calculating the steepness s. The test program is shown i Table 1. Here $D_{n50} = (W_{50}/\rho_s)^{0.333}$ and $\Delta=(\rho_s/\rho_w)-1$, W_{50} = fifty percent of the stones are larger (and smaller) than W_{50}, ρ_s= specific mass of the stones and ρ_w = specific mass of the water.

Table 1. Test program for the shallow water tests at SINTEF.

$H_s/\Delta D_{n50}$	Number of waves.
2.05	2000
2.40	2000
2.85	2000
3.40	2000
≈3.85	2000
2.05	1000
2.40	1000
2.85	1000
3.40	1000
≈3.85	1000
≈3.85	10.000

The wave conditions during the shallow water testing at SINTEF are shown in Table 2.

Table 2. Wave conditions during the 3D tests in shallow water at SINTEF.

"Deep " water.	"Shallow" water				
T_p s	H_s m	$Ho=H_s/\Delta D_{n50}$	T_p s	s_{op}	s_s
1.05	0.086	2.05	1.05	0.049	0.049
1.14	0.101	2.40	1.06	0.049	0.058
1.24	0.120	2.85	1.09	0.049	0.064
1.35	0.138	3.40	1.09	0.048	0.074
1.45	0.160	3.85	1.10	0.048	0.084

As mentioned it was the wave steepness based on the "deep" water wave periods that was the governing factor for establishing the test program waves. However, it is the steepness based on the shallow water wave period that the breakwater "feels". Hence this steepness should have been used rather than the steepness based on the "deep" water wave period. In the unified analysis (see later) we have used the wave periods for shallow water.

The tests were run in the following way:

After building the breakwater model the wave/breakwater parameter Ho, the stability number, was increased in steps according to Table 1. 2000 waves were run for each step. Profiles were taken with a laser distance measurement system, generally after each step. The distance between each profile was 0.10 m and the distance between each measurement point in a profile was 0.02 m.

After this reshaping process with five Ho steps, Ho up to 3.85, the steps were repeated again, but now with 1000 waves in each step. Since no "damaging" effects occurred on Breakwaters A and C at the end of this sequence of runs, we continued to run 10.000 waves with Ho = 3.85.

For Breakwater B the planned test program was the same as for Breakwaters A and C. However, when running the tests a slight damage on the rear side due to wave overtopping occurred for Ho = 3.40 in the first wave step sequence (the sequence with 2000 waves for each step). For Ho = 3.85 the damage on the rear side was so large that we decided to terminate this step after approximately 1600 waves.

Test results for the 3D tests in shallow water at SINTEF.

We will present only some few of the results from this particular study and later include the results in an analysis of the reshaping of berm breakwaters were we also include results from other test series.

Figures 6 and 7 show an oblique "view" of Breakwater A before and after the testing, while Figure 8 shows one of the profiles before the test started and after completion of the test program for Breakwater A.

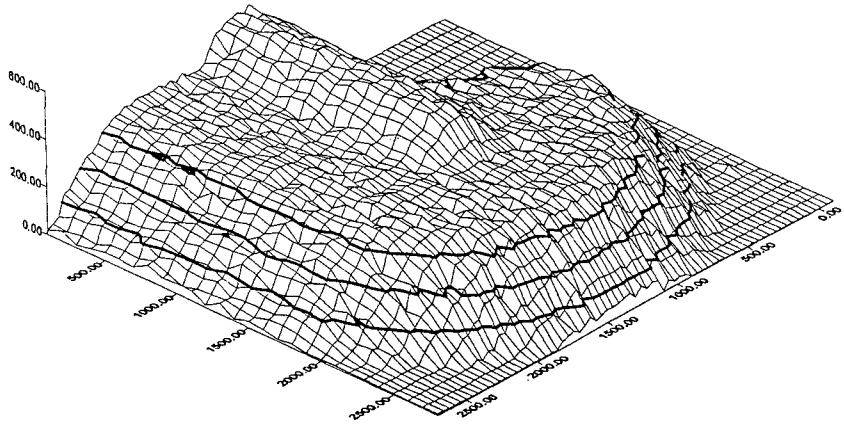

Figure 6. Oblique view of Breakwater A before testing.

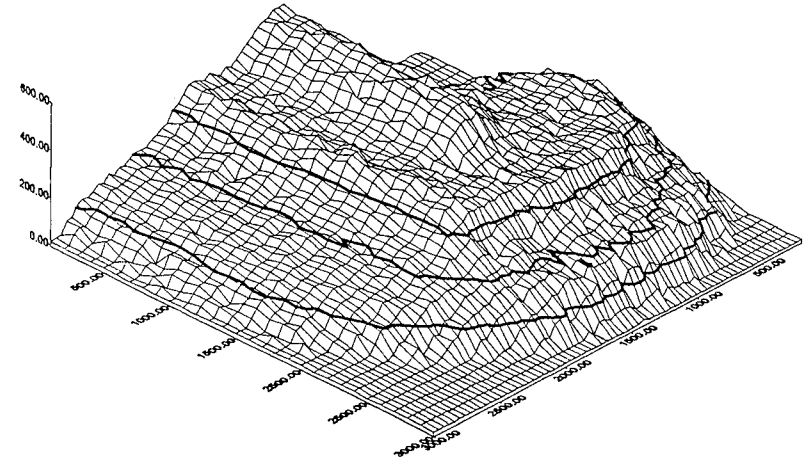

Figure 7. Oblique view of Breakwater A after testing.

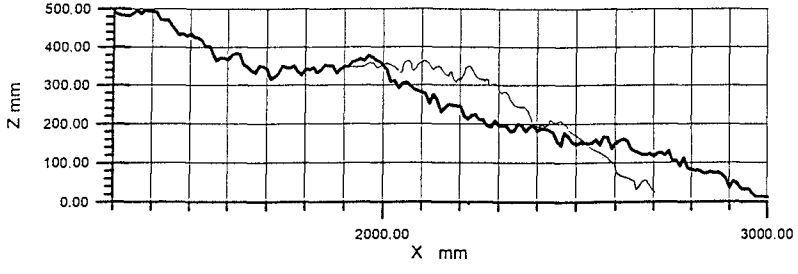

Figure 8. Breakwater A. Cross-sections at 1200 mm before and after testing.

Both Breakwater A and C were considered to be dynamically stable in the sense that no core material was visible after the testing had been completed and no dammage had occurred on the rear side. Also it was noted that not much of the berm stones on the breakwater head had been thrown into the area behind the breakwater.

We took stone samples of the surface stone material at the still water line and at the toe of the berm after completing the test program for Breakwater C. It was interesting to note that the stones at the toe are significantly larger, (D_{n50}), than at the still water line. At first instance this observation may seem unexpected because the smaller stones are easiest to move. Westeren and Tørum (1997) measured the wave forces on a single armour unit placed at different positions along the slope of a reshaped berm breakwater. They found that the highest forces occurred above the still water line, and than to some extent as "impact" forces. This fact together with the observation of the smallest stones at the still water line support the concept that the stones are "knocked" loose above and around the still water and roll down the slope. The larger stones have a larger momentum and rolls more easy than the smaller stones. Hence the larger stones tend to move a longer distance than the smaller stones. The effect is probably the same as we see in a rock slide, where the largest stones are located at the toe of the slide.

Figure 8 reveals that only a part of the berm of Breakwater A was reshaped during the SINTEF "shallow" water tests. The DHI "deep" water test results, DHI (1995), Juhl et al (1996), show that for the same test program that almost the whole width of the berm was reshaped. When analysing the results with respect to an understanding of the differences, we saw that tests carried out under apparently similar conditions in different laboratories have given what we at first instance will consider as significant result differences. We will therefore review some of these test and include the results in a unified analysis.

Analysis of berm breakwater test results from different tests series.

The following analysis is mainly considering the two-dimensional case with waves normal to the breakwater axis.

The geometry of a berm breakwater is defined by notations as shown in Figure 9, while Figure 10 show notations for the reshaped berm breakwater. f_h = berm width, f_v = berm height, w = crest width, R_c = crest height, d = water depth, m and n defines the "inner" and "outer" slopes, Rec = recession of the reshaped berm, l_s = step length, h_s = step height, A_1 = eroded area and A_2 = deposited area.

Occasionally we will also see from berm breakwater test results that some of the berm stones will move above the original berm elevation. This phenomenon could be very pronounced for finer material than normally found in berm breakwater berms, e.g. van der Meer (1988), but is not very pronounced for berm breakwaters.

The most relevant non-dimensional parameters used for the analysis of berm breakwater test results are the following:

$$Ho = \frac{H_s}{\Delta D_{n50}} \qquad (1)$$

$$HoTo = \frac{H_s}{\Delta D_{n50}} \sqrt{\frac{g}{D_{n50}}} T_z \qquad (2)$$

Ho was introduced by Hudson (1958) (as the stability number N_s) and HoTo was introduced by van der Meer (1988) as a dimensionless wave period parameter. Typical values for berm breakwaters are Ho < 3 and HoTo < 100.

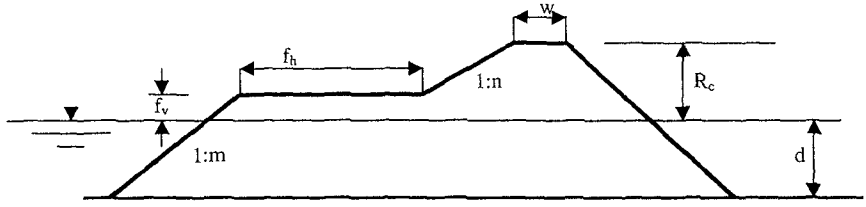

Figure 9. Geometry definitions of a berm breakwater.

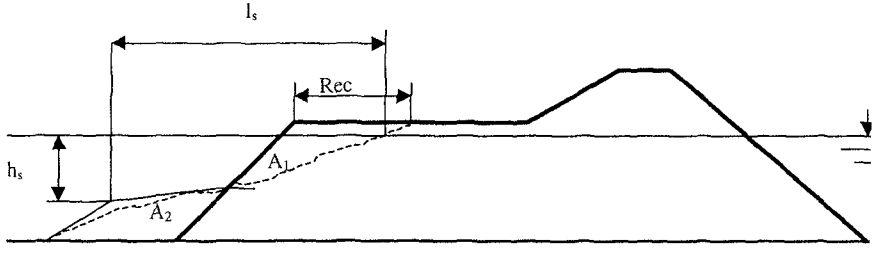

Figur 10. Reshaping parameters of a berm breakwater.

Figure 10 shows that from a continuity point of view the areas A_1 and A_2 must be equal for the two-dimensional case. van der Meer emphasised on the step length l_s and step height h_s (among other geometrical parameters) as a kind of "universal" parameters as they were found to be to a large extent independent of the original profile slope etc observed in his tests, at least for large values of HoTo (HoTo > 1000). van der Meer (1988) obtained values for h_s and l_s as well as the shape of the profile from tests on straight slopes with HoTo = 100 - 50.0000. Based on some limited number of tests van der Meer gave also an indication of how h_s and l_s was dependent on the waterdepth. When the values of h_s and l_s and the profile shape are known it is a matter of trial and error procedure to find the recession such that $A_1 = A_2$. However, van der Meer (1988) did not cover so well the lower range of HoTo (HoTo < 100) as found for berm breakwaters.

We have tried to measure values of h_s and l_s from different profiles from different berm breakwater test series. Our conclusion is that it not so easy to obtain values of h_s and l_s with any good accuracy. Hence it is not so easy to predict the

recession, Rec, with any accuracy either. We will therefore consider the direct measurement of the recession, Rec. This is a length parameter that can be measured with a reasonable good precision and it is a vital parameter for berm breakwater design.

Based on test results from different berm breakwater test series in "deep" water we have in the diagram of Figure 11 plotted the dimensionless parameter Rec/D_{n50} vs. HoTo. The results are from Andersen and Fleming (1991), DHI (1995) (DHI 3D tests), Lissev (1993), Tørum (1988), Tørum (1997, 1997A).

The main characteristics of the test series are the following:

Andersen and Fleming (1991):
Water depth d = 0.67 - 0.90 m, berm height f_v = 0.10 and 0.20 m, berm width f_h = 0.65 m, outer slope 1 : 1.1 , stone diameter D_{n50} = 0.034 m, wave steepnes s = 0.05

DHI (1995)
Water depth d = 0.55 m, berm height f_v = 0.10 m, berm width f_h = 0.65 m, outer slope 1 : 1.1, stone diameter D_{n50} = 0.022 m, wave steepnes s = 0.03 and 0.05

Lissev (1993)
Water depth d = 0.79 m, berm height f_v = 0.08 m, berm width f_h = 0.65 m, outer slope 1 : 1.25, stone diameter D_{n50} = 0.034 m, wave steepnes s = 0.045

Tørum (1988)
Water depth d = 0.50 m, berm height f_v = 0.10 m, berm width f_h = 0.45 m, outer slope 1 : 1.5, stone diameter D_{n50} = 0.029 m, wave steepnes s = varying 0.018 - 0.075

Tørum (1997A)
Water depth d = 0.40 m, berm height f_v = 0 m, berm width f_h = 0.59 and 1.09 m outer slope 1 : 1.3, stone diameter D = 4 - 60 mm, D_{50} = 15 mm (gradation curve values), wave steepnes s = 0.05

To some of the data points in Figure 11 a second degree polynomial fit has been provided, based on the "least square" principle. There are some minor differences in these test series with respect to test set-up and test programs. But they are not that different and we will consider the test series to be reasonable homogenous.

Based of van der Meer's concept we see that the recession, Rec, of a homogenous berm for a given wave condition could be dependent of the berm height, f_h, and the water depth h. We see however from Figure 11 that there is not much of a difference in results of the tests with f_v = 0.10 m and f_v = 0.20 m.

For "shallow" water there are fewer results than for "deep" water. We have in Figure 12 plotted data from tests at DHI (1996) and SINTEF, Tørum (1997A). We have for HoTo used the wave height and wave periods as measured at the shallow water location. For the SINTEF tests the T_z values were measured, while for the DHI tests the wave spectrum was measured and T_z has been taken as $T_z = T_{02}$.

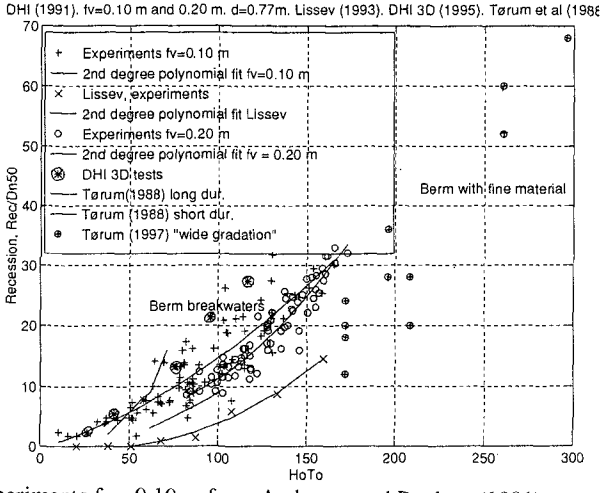

+ Experiments f_v = 0.10 m from Andersen and Poulsen (1991).
o Experiments f_v = 0.20 m from Andersen and Poulsen (1991).

Figure 11. Recession of the berm of berm breakwaters from different test series. "Deep" water.

If we compare the results of Figures 11 and 12 we see that the results are comparable when the local wave parameters are used to calculate HoTo.

There is a considerable scatter in the test results shown in Figure 11. The scatter is between different tests in the same series of tests at a specific laboratory and between test series in different laboratories. But the scatter is probably not more than we normally find for breakwater testing

We have not been able to resolve why there are differences and scatter in the results. We will thus presently consider the scatter of the data as "natural" scatter and consider all results of equal value. Based on this consideration we have in Figure 13 plotted the results from Figure 11 and Figure 12 in the same diagram. We have in Figure 13 ommitted the data from Tørum (1997A) since those data were from tests on aberm of quarry run material not typical for berm breakwaters.

We have provided a second degree polynomial fit to the data. We also tested out a third and a fourth degree polynomial fit, but these fits did not appear to be more accurate than the second degree polynomial fit.

The equation for the second degree polynomial fit is given by:

$$\frac{Rec}{D_{n50}} = 0.00073908(HoTo)^2 + 0.0498855(HoTo) + 0.604 \qquad (3)$$

This equation may be considered as a design equation for the recession of the berm.

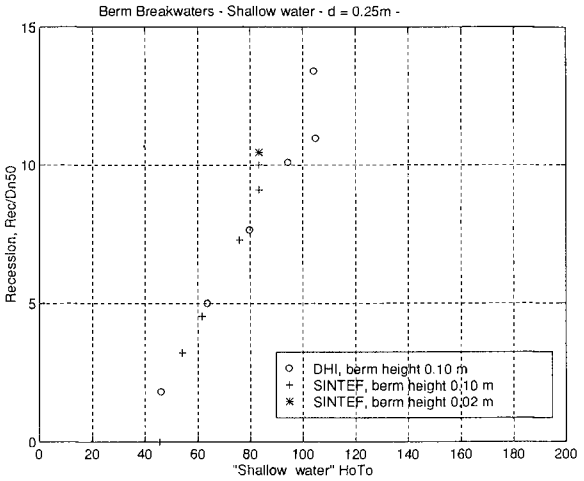

Figure 12. Recession of the berm of berm breakwaters from different test series. "Shallow" water. Note that HoTo is based wave parameters measured at the "shallow" water location of the breakwater.

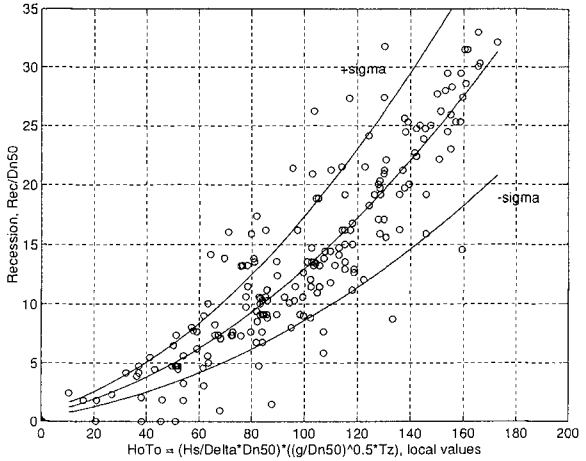

Figure 13. Recession of the berm of a berm breakwater in "shallow" and "deep" water as function of "local" HoTo-values. 2nd degree polynomial fit $\pm\sigma$

The scatter of the data has been analysed in the following way:

$$\frac{f - f_k}{f_k} = f(HoTo) \tag{4}$$

where f = datapoint for a given HoTo-value
f_k= value after 2nd degree polynomial fit
f(HoTo) = function of HoTo

The result of this analysis is shown in Figure 14 where we have also indicated the standard deviation $\sigma = 0.337$. We have also included the "2nd degree polynomial fit" $\pm \sigma$ in Figure 13.

We have further in Figure 15 shown the data compared to a normal distribution function. The design equation, Eq. (3) and the scatter information may be used in a probabilistic analysis of berm breakwaters.

DHI (1996), Juhl and Sloth (1998), carried out tests on "islandic" type berm brakwaters. The idea is to place the largests blocks from the quarry on top of the berm as a composite breakwater. We have analysed the results of these tests in a similar way as we analysed the results from the tests with homogenous berms. For D_{n50} we used the D_{n50} for the largest stones on top of the berm. The results are shown in Figure 16 where we also have plotted the design equation, Eq. (3). The design equation works also reasonably well for the composite berm breakwater.

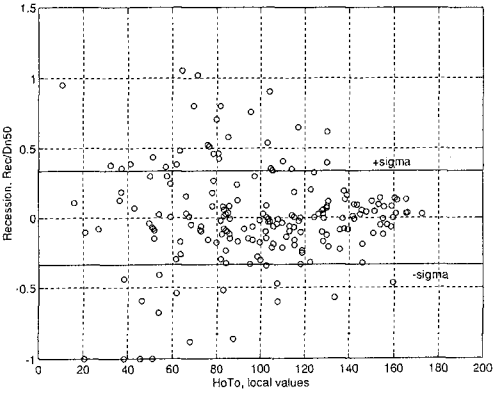

Figure 14. $(f-f_k)/f_k$ as function of HoTo (local values). The standard deviation sigma = $\sigma = 0.337$.

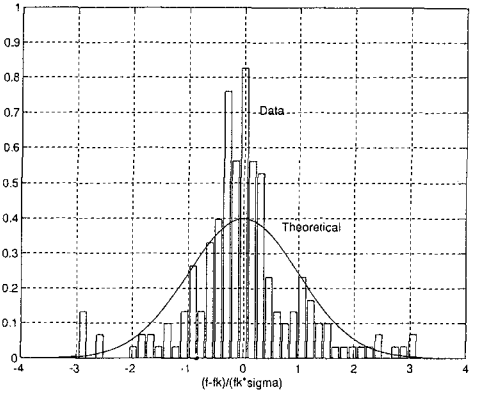

Figure 15 Standardised distribution of $(f - f_k)/f_k$ compared to a theoretical normal distribution.

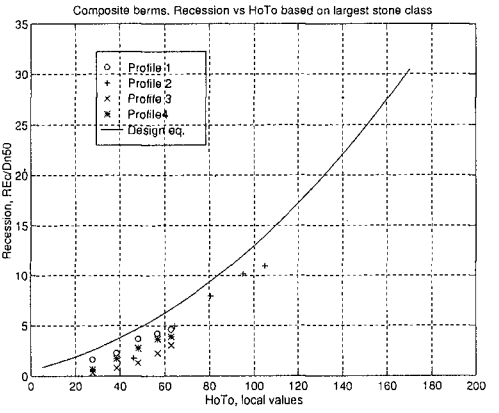

Figure 16. Recession vs. HoTo for composite berm breakwaters. "Local" wave parameters. D_{n50} of largest stone class. Profile 2 is a homogenous profile. Design eq. is Eq (3).

Discussion and conclusion.

We have analysed two-dimensional test results and arrived at a simple design equation for the recession of the berm of a berm breakwater without major overtopping. This equation may be used, at least in the conceptual design phase, for berm breakwaters in water depths and for storm duration that are normally encountered for berm breakwaters.

If the waves are oblique to the breakwater, the lateral transport of the stones have to be considered, e.g. Alikhani et al (1996).

There is no well establish criteria for which stability number Ho or wave period parameter HoTo the design should be accepted. Such criteria should apparently be linked to the mechanical strength of the stones.

Acknowledgement.

This study was funded by the European Communities Research Program MAST II under contract MAST-Contract MAS2-CT94-0087 Berm Breakwater Structures and by the Norwegian Coast Directorate. We appreciate very much this financial support. We also appreciate the many discussions with the other partners of the project.

References.

Andersen, John Fleming and Poulsen, C. (1991) MAST Berm breakwaters. Thesis (carried out at DHI) Danmarks Ingeniør Akademi - Bygningsretning. (in Danish).

DHI (Danish Hydraulic Institute) (1995): EU MAST II Berm Breakwater Structures. Draft report.

DHI (Danish Hydraulic Institute) (1996): EU MAST II Berm Breakwater Structures. Influence of the permeability and stone gradation. Draft report, October 1996.

Hudson, R. (1958): Design of Quarry stone cover layers for rubble mound breakwaters. Waterways Experiment Station, Research Report No. 2-2, 1958.

Juhl, J., Alikhani, A., Sloth, P. and Archetti, R. (1996): Roundhead stability of berm breakwaters. Proc. 25th International Conference on Coastal Engineering, Orlando, Florida, USA, 2 - 6 September 1996.

Juhl, J. and Sloth, P. (1998): Berm Breakwaters - influence of stone gradation, permeability and armouring. Proc. 26th International Conference on Coastal Engineering, Copenhagen, Denmark, 21 - 26 June 1998.

Lissev, N. (1993): Influence of the core configuration on the stability of berm breakwaters. Report R-6-93. Department of Structural Engineering, University of Trondheim, Norwegian Institute of Technology.

Tørum, A., Næss, S., Instanes, A. and Voll, S. (1988): On berm breakwaters. Proc. 23rd International Conference on Coastal Engineering, Spain, June 1988.

Tørum, A. (1997): Berm breakwaters. EC MAST II Berm Breakwater Structures. SINTEF Report STF22 F97250.

Tørum, A. (1997A): Stabilitet av røysfylling mot bølger. (Stability of a quarry run berm against water waves). SINTEF Report STF22 F97250 (in Norwegian).

Westeren, K. and Tørum, A. (1997): Irregular wave induced forces on armour unit on berm breakwaters. EU research project Berm Breakwater Structures MAST II. Final Report, May 1997.

van der Meer, J. (1988): Rock slope and gravel beaches under wave attack. Delft Hydraulics. Publication No. 396. Doctoral thesis approved by Delft University of Technology.

The Economic Analysis of "Soft" Versus "Hard" Solutions for Shore Protection: An Example

David R. Basco, Ph.D., P.E.[1] Mem. ASCE

Abstract

This paper presents the design and economic analysis for two alternatives (soft-versus-hard) for shore protection of facilities at the US Navy's Fleet Combat Training Center, Dam Neck, Virginia, USA. Three key factors are discussed that resulted in the selection of the soft alternative (dune construction and beach nourishment) which also included a buried seawall/revetment structure beneath the dune to provide a unique solution for shore protection. Construction was completed in the fall of 1996 and the results of the first year's monitoring effort are presented. The advantages of the soft alternative are many (environmental, recreational, etc.) and may even include the economic advantage as demonstrated in this paper for one site on the Atlantic Ocean.

Introduction

The perception exists that renourished beaches (i.e., the "soft" alternative) for shore protection costs more than seawalls and revetments ("hard" alternative) over the design life of the project (Smyth, 1996). Beach nourishment is perceived as an endless expense whereas massive concrete seawalls and stone revetments require little maintenance. Economic analysis of the total, life-cycle costs of "soft" versus "hard" shore protection alternatives are needed to provide some real evidence in this debate.

The design and economic analysis for two alternatives (soft-vs-hard) for shore protection of facilities at the US Navy's Fleet Combat Training Center, Dam Neck, Virginia on the Atlantic Ocean below Virginia Beach, Virginia USA (Fig. 1) are described below. Approximately $95 million of structures including the gunnery range were threatened by historic erosion averaging 0.7 m/yr and recent years of severe storm activity that damaged the existing dune-beach system. Fig. 2 shows the Bachelor Officers

[1] Professor of Civil Engineering and Director, the Coastal Engineering Centre, Old Dominion University, Norfolk, VA 23529, USA

Quarters (BOQ) protected by the dune-beach system (top, aerial photo[2]) and by an artificial, stone armour layer revetment (bottom, graphic artist schematic[3])

The soft alternative (Fig. 2, top) also included a rebuilt dune system with buried seawall/revetment structure that together provided a unique solution for shore protection in the US. The retreat alternative was far too expensive and unacceptable because the gunnery range must be located adjacent to the coastline for effectiveness and safety reasons.

Design Criteria

The design criteria was for storm damage mitigation against the one percent chance, annual storm surge event (2.65m, NGVD, 1972 adj.) and related wave conditions (H_{mo} = 4.82 m, T_p = 13.7 s) in a nearshore water depth of about 9 m. Design life selected was 25 years with an interest rate of 9.5 percent that was two points above the prime lending rate (1994) for the economic study of life cycle costs. The beach was to be restored whenever conditions returned to 1995 beach widths which were less than 12 m (MHW) at some locations.

Composite average, median grain size was 0.29mm for the native beach.

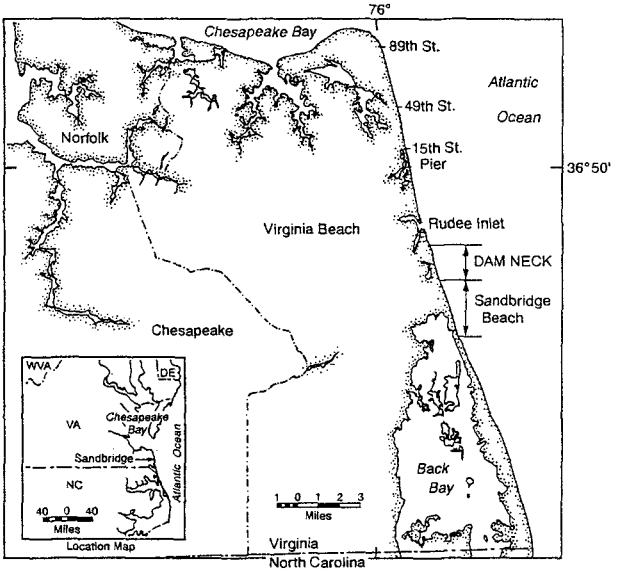

Figure 1 Location Map, Dam Neck, Virginia

[2] Steve MacGregor, MacGregor Enterprises, Norfolk, VA, USA
[3] Mariusz Mijal, Glenn and Sadler Consultants, Norfolk, VA, USA

Figure 2 Protection alternatives for Bachelor Officer's quarters showing dune/beach/ buried seawall as constructed (top) and concrete armour units as artists conception (bottom)

Key Factors in Design Alternatives

Hard Revetment

Fig. 3 displays a plan view of the BOQ, the Enlisted Man's (EM) Club and the gunnery range to be protected by over 1100 meters of revetment including tapered ends. Offshore contours are relatively straight and parallel to the shoreline to permit the use of one nearshore profile (August, 1994 at the EM Club) as representative for all sections.

The design wave height for the stability analysis of the stone armour layer was obtained by considering all the factors that influenced the design water depth at the structure toe. The (1) beach profile is at its lowest expected position at the *end* of the 25 year design life; (2) the flattened, winter condition profile is employed and ; (3) toe scour during storms must also be included. These conditions produced a below sea level elevation (-1.8m) for the hard structure that greatly increased the initial costs for the revetment.

Two numerical models were employed to calculate the design wave height at the structure toe for varying berm elevations with results shown in Fig. 4. The SBEACH model (Larsen and Kraus, 1989) and the SZED model (Baumer, 1991 based on Thornton and Guza, 1983) both produced similar results and a design wave height of 2.5m. A 4.3 ton (US) natural stone or a 2.3 ton (US) artificial armour block unit (CORE-LOC) was required for stability. In short, the design was based on beach conditions expected during a major storm at the end of the design life (with no beach remaining, Fig. 2) and not on today's condition of the beach.

Fig. 5 is a cross-section of the armoured revetment design with crest elevation at +6.71m (+22.0) to minimize overtopping.

Soft System

The soft system alternative consisted of three components:

(1) a buried rock seawall/revetment with crest elevation at +5.49m and toe elevation of +2.7m;

(2) a rebuilt dune with crest elevation at +6.71m and crest width of 15.2m, and;

(3) a renourishment beach with design width of 23m at +2.13m berm elevation,

as depicted in Fig. 6. The buried structure was placed well back in the dune and 1.2m beneath the dune crest so that dune volume during storms was still available to feed the beach. This combination "soft" system is believed to be unique for shore protection in the US. The buried rock structure was first proposed by Headland, (1991) for Dam Neck. The buried seawall design concept has been constructed at other locations around the world (e.g. van der Graff, 1998, personal communication).

A key factor in the cost analysis for the dune design was the development of "damage" curves as shown in Fig. 7 (Basco and Shin, 1997). Again, the beach profile numerical model SBEACH (Larsen and Kraus, 1989) was utilized over a wide range of storm surge elevations, S relative to the design storm surge level, S_D = 2.77m (MSL) to estimate the volume change in dune cross-section, i.e. damage to the dune. Classical, probabilistic methods for estimating future dune damage and subsequent costs analogous to maintenance costs for rubble mound structures were then employed (Basco and Shin,

Figure 3 Plan view of armoured structure to protect Bachelor Officer's quarters (left), Enlisted Man's club (center) and gunnery range (right)

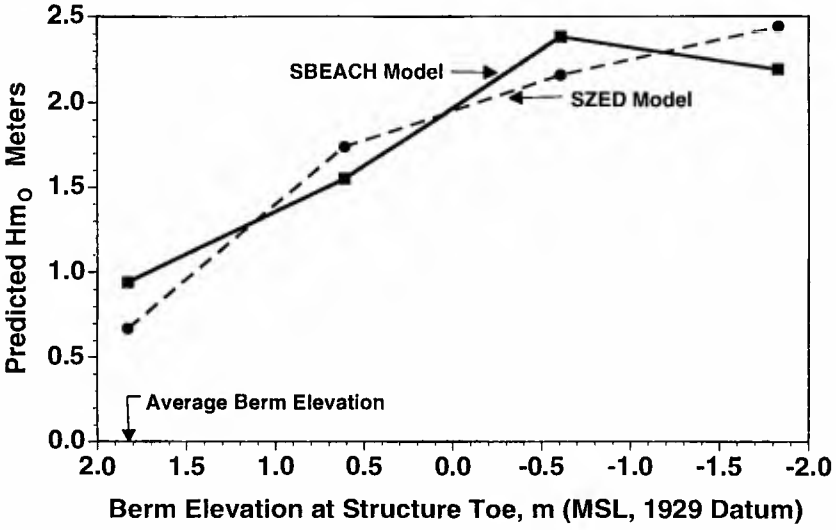

Figure 4 Spectral significant wave height -vs- elevation of beach profile at toe of structure - modeled results

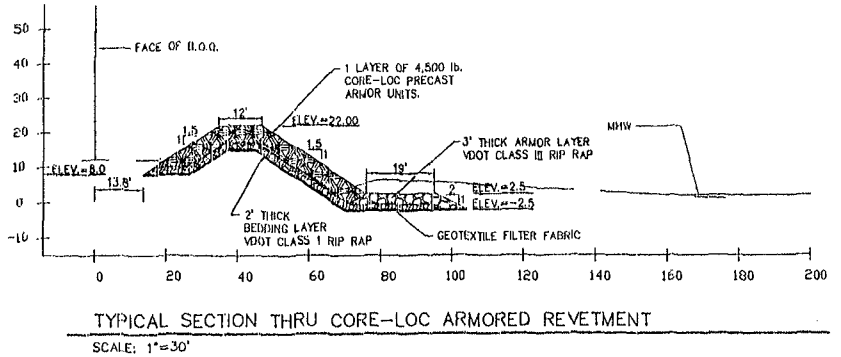

Figure 5 Cross-section of armoured revetment design (hard alternative)

1997). Dune damage curves were estimated at the end of a beach renourishment cycle (8 - 9 yrs) when the beach profile approximates before nourishment conditions. As a safety margin, the secondary, buried structures traps some sand (Fig. 7, with seawall) but serves as shore protection in case two severe storms should be encountered in one hurricane season.

Another key factor in the economics of the soft alternative was identification (Kimball and Dame, 1989) and utilization of a suitable, long term borrow site for sand required for periodic beach nourishment. The offshore borrow area is in Federal government water (beyond the 3 mile limit) about 5 km from Dam Neck. Over 30 million cubic meters of excellent beach material (d_{50} = 0.34 mm) is available for the design life so that the unit costs estimated at $\$6.67/m^3$ ($5/cy) will be reasonable.

Finally, the relatively low annual erosion rate at the site (0.7 m/yr) also contributed to an 8 - 9 year estimate for the renourishment cycle and the relatively lower costs for the soft alternative.

Comparison of Alternatives

Costs

Table 1 summarizes the cost comparison for the hard and soft alternative designs. The new CORE-LOC, artificial, armour unit (Melby and Turk, 1997) was slightly less expensive than natural stone and resulted in a unit cost of slightly over $7200/m for a 1103m revetment.

Table 1 Cost of Alternatives, millions $

Type	Initial Cost, $	Maint. Costs, $	Total Unit Costs, $
Hard	7.746 M	0.204 M	7200
Soft	3.657 M	2.979 M	6016

The soft alternative costs per unit meter were also based upon this length for shore protection (Fig. 3) but the design beach was longer (1600 m) to increase its life. As shown in Table 1, the life-cycle costs favor the soft alternative, in this example. The life-cycle unit costs were $6016 per meter and included almost $3 million in maintenance costs for two nourishment events. These are "present worth" maintenance expenses.

Decision Criteria

Costs are only one criteria in the decision matrix for choosing the soft or hard alternative. Table 2 summarizes all the criteria used to evaluate the alternatives. The sole advantage of the armoured revetment is lower annual maintenance costs. All others favored the dune-beach buried seawall system.

The soft alternative provides a recreational and environmentally useful (turtle nesting habitat) beach at the end of the design life. The permitting agencies, public perceptions, and public relations (image) of the US Navy also favored the soft alternative. Both alternatives provide the same level of shore protection.

The dune/beach/buried seawall, i.e. "soft" alternative was selected for final design and construction.

Table 2 Decision Criteria - Advantages

Criteria	Alternatives	
	Soft	Hard
Shore Protection	✓	✓
Economics		
- Initial Costs	✓	
- Maintenance Costs		✓
- Total Costs	✓	
Environment	✓	
Recreation	✓	
Permits	✓	
Public Perceptions	✓	
Navy Image	✓	
Combined	✓	

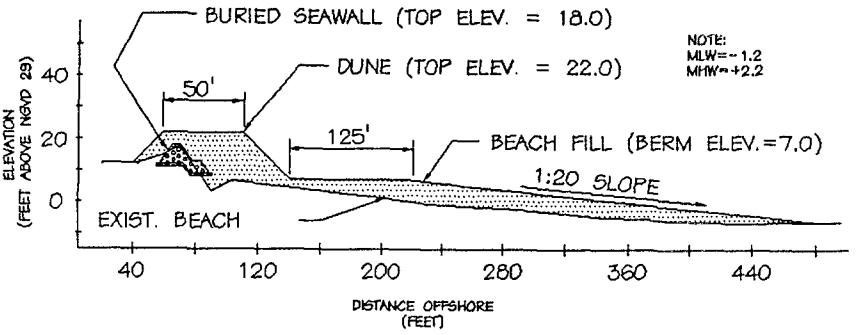

Figure 6 Cross-section of dune/beach/buried seawall design (soft alternative)

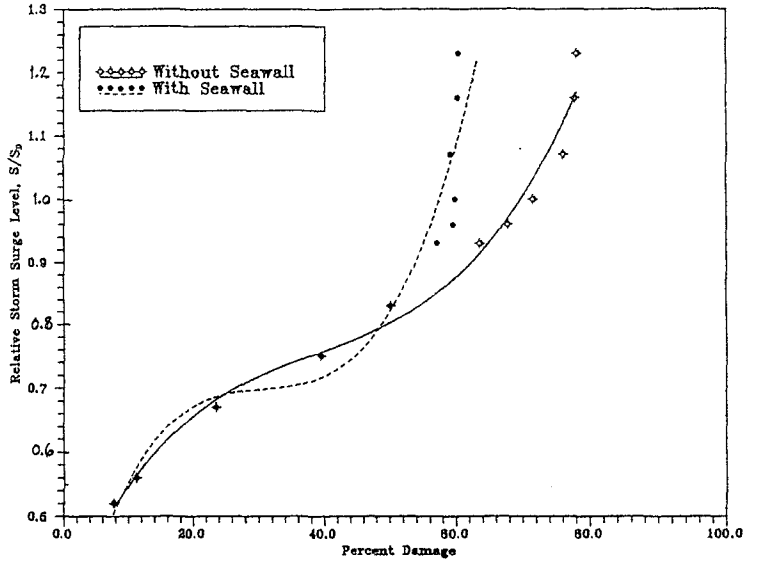

Figure 7 Dune damage curves (from Basco and Shin, 1997)

Final Design, Construction, Monitoring

Final Design

At the Navy's request, the final design was to extend the useful life of the initial beach fill to 12-13 years so that only one renourishment event was expected over the 25 year design life. This required an increase in the beach length (2804 m) including 150 m tapers at both ends for an average length of 2679 m. The design width was also increased to about 38 m to give an average section design fill of 34.4 m^3/m (85.9 cy/ft). The Corps of Engineers' Technical Note, CETNII-32 (CETN, 1994 revised) was employed to estimate the dry beach design width for intersecting profiles since the borrow material was coarser than the native beach material.

End losses for a finite beach fill were estimated using the analytical solution for a one line model of beach fill following Dean, (1992) as discussed further below.

Construction

The major portion of the dune with buried seawall/revetment was constructed in the fall of 1995. Fig. 8 is a photo showing dune/seawall construction and Fig. 9 pictures the final dune before beach nourishment which began in the summer of 1996. The initial placement volume as measured by nearshore sled survey in November, 1996 was about 520,000 m^3 or about 9.4 percent less than the design placement volume. The difference was due to (1) the lack of a true, pre-placement survey (June 1995 survey employed); (2) early erosion occurring between the end of beach fill construction and the initial survey in November 1996; and (3) the dredging contractor not filling the design template. All three factors combined probably contributed to the difference.

Monitoring

A three year monitoring effort is underway to determine volume change of the dune and renourished beach. Sled surveys of beach profiles at 17 locations out to closure depth are being made over a 4875 m reach that extends beyond the beach nourishment project on both ends. The initial year of monitoring (completed October 1997) accounted for all the initial fill volume. The percentage of beach fill volume remaining after year one of the monitoring effort was 84.8 percent over the project length of 2679 m.

Fig. 10 displays the percent volume remaining (crosses) of the nourished beach including intermediate surveys (Mar 1997, June 1997) over the initial year. The dashed line with sediment diffusion coefficient G equal to 0.065 $miles^2$/year was employed for design. End losses are estimated from the diffusion equation

$$\frac{\partial y}{\partial t} = G \frac{\partial^2 y}{\partial x^2} \tag{1}$$

where y (x, t) is the shoreline position in the one-line model for shoreline change (Dean, 1992). The G coefficient depends upon many factors, but mainly the annual wave energy climate striking the beach. A nearshore wave gauge (VA001) is available nearby to measure the waves and is being employed in the monitoring effort. Wave year 1997 (October 96 - September 97) had higher than normal wave energy, yet the sand loss measured followed the theoretical design curves for lower wave energy. Monitored results after three full wave years will (hopefully) be presented at the ICCE `2000

Figure 8 Photograph of dune with buried seawall/revetment under construction

Figure 9 Photograph of completed dune structure before beach renourishment

conference. The actual life of the beach is a key factor in the economics of the "soft" alternative.

Conclusions

On eroding shorelines, hard structures pin the shoreline location, flatten and deepen the profile. Design of hard structures must be for conditions at the end of the design life, when no beach may exist, not for today's beach conditions. The economics of the soft alternative depend upon many factors including (1) historic erosion rate; (2) relative grain size of borrow material, location and long-term volume in borrow area; (3) cross-sectional volume and length of beach fill. The soft alternative maintains a flexible shoreline location and natural beach conditions even at the end of the design life. The advantages of the soft alternative are many (environmental, recreational, etc.) and may even include an economic advantage as demonstrated in this paper for one site on the Atlantic Ocean at Dam Neck, Virginia, USA.

Acknowledgements

The project engineer was R.B. Cummings II, P.E. for Glenn and Sadler, Inc., Norfolk, VA, the consulting engineering firm for the Navy Facilities Engineering Command (NAVFAC) responsible for military base construction projects. Mr. Rick Kahler and Mr. Jim Wood were the responsible engineers for NAVFAC. Mr. Steve Perrot presently directs the monitoring effort for Glenn & Sadler, Inc. The author is a special consultant to Glenn & Sadler on this project.

References

Basco, D.R. and C.-S. Shin (1997) "Dune Damage Curves and Their Use to Estimate Dune Maintenance costs", Proceedings, 25th ICCE (Orlando) ASCE, NY, 2969-2981.

Baumer, J.C. (1991) "Bar Effects on Energy Losses in Surf Zones", Master of Engineering project report, Department of Civil Engineering, Old Dominion University, Norfolk, VA, May.

CETN (1995) "Beach Fill Volume Required to Produce Specified Dry Beach Width", CETN II-32, CERC, WES, Vicksburg, September.

Dean, R.G. (1992) "Beach Management: Design Principles" in Design and Reliability of Coastal Structures, Short Course lecture notes, Venice Italy (part of 23rd ICCE)October.

Headland, J.R. (1991) "Erosion Study of Fleet Combat Training Center, Dam Neck", Final Report, NAVFAC, Alexandria, VA, September.

Kimball, S.M. and Dame, J.K. (1989) "Geotechnical Evaluation of Sand Resources on the Inner Shelf of Southern Virginia", (2 volumes), Final Report, VIMS, Gloucester Pt, VA, August.

Larsen, M. and Kraus, N.C. (1989) "SBEACH: Numerical Model for Simulating Storm Induced Beach Change", Rept 1, Tech. Rept., CERC, WES, Vicksburg, MS.

Melby, J.A. and Turk, G.F. (1995) "CORE-LOC: Optimized Concrete Armour Units", PIANC Bull. No. 87-5, p.5-21.

Smyth, J. (1997) "Ban on Seawalls May Fail Because of Federal Budget Cuts, Lawsuits", quoted in Virginian Pilot, newspaper article, April 9.

Thornton, E.G. and Guza, R.T. (1983) "Transformation of Wave Height Distributions in Surf Zone", Jour. Geoph. Res., vol. 88, c 10, p.5925-5938.

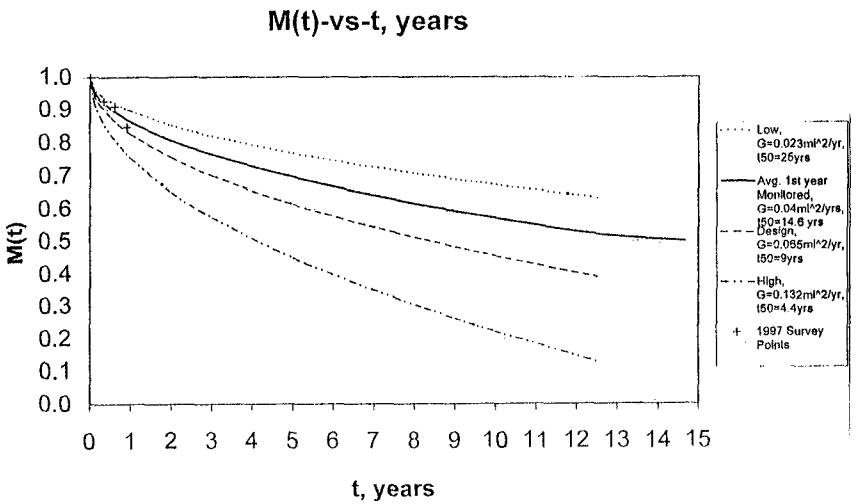

Figure 10 Percent of beach fill remaining versus time (years) for theory (Dean, 1992) and measured results of year one monitoring.

UNCERTAINTY ANALYSIS OF COASTAL PROJECTS

Jim W. Hall[1], John P. Davis[2] and David I. Blockley[3]

Abstract

The nature of uncertainty in coastal engineering is discussed with reference to an empirical study of practising coastal engineers in the UK. This study provided evidence which indicates that a complex multi-disciplinary set of issues are taken into account in decision making only some of which are explicitly articulated. It is argued that current approaches to handling uncertainty based on reliability theory provide an important but incomplete perspective on a rich and complex topic. An approach to uncertainty modelling based on Interval Probability Theory is proposed. Process modelling is used to track the sources of uncertainty in analysis, design and decision making and to integrate different types of evidence. This approach to uncertainty analysis, which involves exploring and accounting for the sources and nature of uncertainty in decision making, is illustrated with reference to sea defence projects on the East Coast of the UK.

Introduction

The coastal engineer is confronted with uncertainty in the random nature of hydraulic loads, in the complexity of structural, morphological and environmental responses, in the diversity of decision objectives and in the fallibility of the human systems which implement coastal defences. The engineer is, nonetheless, expected to make dependable, timely and transparent decisions. To do so requires an understanding of the nature of uncertainty and appropriate techniques for managing it.

The research described in this paper is a merger of three streams of enquiry:

1. a programme of interviews with UK experts and practitioners in coastal engineering to elicit contemporary knowledge on the sources and management of uncertainty;

[1] Jim.Hall@bristol.ac.uk, Lecturer, Department of Civil Engineering, University of Bristol, Queens Building, University Walk, Bristol, BS8 1TR, UK
[2] John.Davis@bristol.ac.uk, Reader, Department of Civil Engineering, University of Bristol
[3] D.Blockley@bristol.ac.uk, Dean, Faculty of Engineering, University of Bristol

2. investigation of theoretical approaches to representing uncertainty in hydraulic engineering including probability theory (both frequentist and Bayesian), fuzzy sets, the Dempster-Shafer theory of evidence and interval probability theory;
3. contemporary developments in generic modelling of human and physical processes.

The research is based on a systems approach which takes account of the richness of sensitivities and interactions which characterise both the natural and human aspects of the coastal zone. This research, which lies on the socio-technical interface, is intended to provide a link between the scientific and largely reductionist theoretical approach to engineering practice and the difficulties of actual practice itself. The research has resulted in development of new methods for assessment and management of uncertainty in coastal engineering projects.

This paper begins with a description of an empirical study of the nature and sources of uncertainty in coastal engineering. Some of the limitations of a purely probabilistic approach to representing uncertainty are discussed before introducing an new approach based on process modelling and interval probabilities. An implementation of this approach for decision support is discussed with reference to example projects.

Descriptive study of practising coastal engineers

Worthwhile decision support tools must be founded on an understanding of the problem domain to which they are to be applied. Decision support systems have failed in the past because they are culturally incompatible with the organisation in which they are applied (Platt, 1994). These problems can be minimised by careful descriptive analysis of the problem domain before proceeding towards decision support.

Descriptive analysis of complex processes on the socio-technical interface is not straightforward. Many of the issues taken into account in decision-making are unquantifiable and may not even be made explicit. To make sense of these issues an investigative technique called Grounded Theory developed by Glaser and Strauss (1967) for field work in the social sciences was used to analyse the problems which coastal engineers encounter in practice. Grounded Theory is a general methodology that aims to develop theory from qualitative data. Theory is in the form of conceptual models of the phenomenon under consideration. The word 'grounded' derives from the concept that the theory generated is 'grounded' in data. Grounded Theory is therefore believed to provide more reliable and more complete understanding than is achievable by conducting an informal consultation exercise or questionnaire surveys. Details of the Grounded Theory study and analysis are reported in Hall et al. (1998a). A series of semi-structured interviews were held with eight practising flood and coastal defence engineers from a variety of backgrounds in the UK. The interview data was analysed in detail with a view to identifying

- characteristics of the decision making process in coastal engineering;
- sources of uncertainty in decision making;
- current approaches to coping with uncertainty.

The interview data demonstrated that

- A complex set of socio-technical issues are taken into account during decision-making only some of which are explicitly stated. Technical issues play an important part but interact with other issues and are not necessarily paramount.

- Individual decisions are integrated in an ongoing infrastructure management process.
- In the UK intuitive and implicit methods of taking uncertainty into account in decision-making are currently much more prevalent than explicit methods. This is despite increasing emphasis on risk-based methods from government and researchers.
- Sources of uncertainty in decision-making are diverse but can be categorised as being 'modelling issues', 'values issues', 'communication', and 'environmental constraints'. The term 'modelling' is being used in the most general sense. The term 'environmental' is used here to refer to surrounding institutional, political and cultural issues outside the immediate control of the decision-maker.

The findings of the empirical study have guided the subsequent research which aims to satisfy identified needs

- to provide a systematic overview of the coastal management process;
- to address the issue of model uncertainly;
- to support the *process* of obtaining and manipulating data and then making decisions;
- to provide a measure of the *dependability* of the processes which lead up to a decision;
- to keep track of the sources and sensitivities to uncertainty in a decision.

Methods of representing uncertainty

Uncertainty is a rich and diverse topic which has been addressed in quantitative, linguistic and symbolic terms. Of all the methods for handling uncertainty, probability theory has by far the longest tradition and it is the best understood. That of course does not imply that it should be beyond criticism as a method of handling uncertainty. It does, however, mean that it is relatively well tested and well developed and can act as a standard against which other more recent approaches may be measured (Krause and Clark, 1993).

Blockley et al. (1983) argued that the additivity axiom or law of excluded middle in probability theory is an assumption which can be difficult to justify under circumstances involving sparse data and incomplete and possibly inconsistent knowledge. This and other re-evaluations of the axioms of probability theory since the 1970s have lead to the development of various alternative and generalised calculi for quantitative handling of uncertainty, including fuzzy set theory, the Dempster-Shafer theory of evidence, mass assignment theory and interval probability theory which is discussed later in this paper. Hall et al. (1998b) proposed a pragmatic approach to uncertainty where the axioms of the probability calculus are matched to the characteristics of the situation in hand. The fundamental problem with quantitative uncertainty methods is one of mapping messy real world situations onto precise mathematical syntax. Several different approaches can provide useful evidence on which to base a decision.

In coastal engineering, as in other fields, probability theory has been developed into a sophisticated and useful tool. Reliability theory and probabilistic risk assessment are now well established methods for coping with the uncertainty inherent in many of the parameters which coastal engineers input into their models. However it is inevitable

that some of the response functions used in probabilistic models will be more dependable than others. For example quantitative models of breaching the low clay embankments which act as flood defences in many areas of the UK are still of limited dependability. Doubtless quantitative understanding of more challenging failure mechanisms will increase in future. More effective and less intrusive methods of obtaining information about the strength of coastal defence structures will be developed, though for the time being methods of obtaining detailed information about the internal constitution of flood defence embankments are very costly. Nonetheless, there will always be a limit to the level of risk analysis that it is practical and economic to undertake. Some failure mechanisms will always be better understood than others. Decision processes need to reflect that fundamental disequilibrium of information. Without some understanding of the dependability of input distributions and of response functions, the data generated by probabilistic methods can be difficult to interpret and in the wrong hands quite misleading.

It is important to recognise that the numbers generated by reliability calculations are hardly scientific (in the Popperian sense) as they cannot normally be falsified. They are better viewed as deductions from a set of premises. Some of those premises will be better supported by evidence than others. Yet unless a procedure is adopted for recording and auditing the premises used in a reliability calculation the ultimate deduction will be of limited value.

Some attempt has been made to address the issue of modelling or systems uncertainties in the theoretical representations of the physical behaviour of structures by use of one or more extra basic variables in the constitutive reliability equation. The value assigned to this variable may for example depend on whether physical model studies have been conducted or not. The empirical evidence supporting this approach is questionable and, as Blockley (1998) argues, its use is inadequate because the level of sophistication of handling such a difficult and important part of the total uncertainty is very much less than for the relatively straightforward issue of parameter uncertainty.

Structural reliability calculations are therefore now widely recognised as only one part of the assessment of structural safety. The results of such calculations are not 'true' probabilities of failure, rather they are 'notional' probabilities of failure. Even in the relatively constrained context of the process industries, calculations of failure probabilities conducted by independent expert teams around Europe have been shown to typically differ by up to three orders of magnitude and in some cases differences were as large a five orders of magnitude (Lemkowitz et al., 1995). It is not unreasonable therefore to have misgivings about the numbers which are generated in reliability calculations in coastal engineering. These calculations do not generally include the behaviour of individuals and almost never include organisational factors such as organisational culture.

It is clear from the analysis conducted in the UK that engineers have difficulty in communicating even quite basic probabilistic concepts of flood risk, not to mention the distinction between notional and statistical probabilities, to the populations at risk. Reliability calculations are seldom transparent to stakeholders who have an interest in the outcome of those calculations. The consequence of adopting authoritarian technocratic approaches which are not transparent is that the co-operation from politicians and the public, which is necessary to implement flood defence works, will not be forthcoming (Beck, 1992). If therefore engineers are not to undermine their own best endeavours on society's behalf for safety, efficiency and sustainability they need to recognise the social construction of risk and acknowledge that their reliability calculations provide but one rather incomplete perspective on a complex phenomenon.

The normative theory of decision making under risk and uncertainty provides a rational theoretical framework for decision making in coastal engineering. By linking risks with costs it, in theory, provides a mechanism for optimising investment in coastal engineering. However, besides the problems associated with computing probabilities described above, there are profound difficulties in eliciting the value (or utility) functions required to compare the attributes of different options. It may be extremely difficult to project some fuzzy values onto a numerical scales. For example it may be hard to state precisely whether a particular coastal defence is sustainable or not. In order to make a decision experts will usually resort to linguistic descriptions of the sustainability, which cannot be manipulated within normative decision theory.

Moreover, all of the possible outcomes of a decision must be predetermined in precise terms for a probabilistic decision analysis. This limits the applicability of probability theory for coping with fuzzy events or incomplete situations. These problems are becoming more apparent when we address more complex multi-disciplinary problems. For example, there is currently much interest in making the coast more resilient. To do so involves restoring natural systems and enhancing flexibility and diversity. Much of the value of a resilient coastline is its capacity to cope with the unforeseen and unpredictable, in particular climate change. These benefits cannot be fully evaluated in probabilistic terms. Moreover, a resilient coastline will be highly dependent on human systems of monitoring and management. Predicting the reliability of these systems represents a particular challenge in complex, dynamic situations because some behaviour is truly unforeseen and so by definition is not included in the reliability model. Unfortunately many engineering failures are the unforeseen consequences of human actions (Blockley, 1980). Collingridge (1980) suggests that unforeseen outcomes in socio-technical systems can be controlled by:

- monitoring,
- reducing the cost of error,
- reducing the corrective response time,
- reducing the cost of remedy,
- keeping one's options open (adopting flexible solutions, enhancing variety).

The intention of these strategies is to improve the robustness of a plan or design in the face of events which are not predictable by the models available to the planner or designer at the moment of decision making. It may be necessary to weigh the apparent loss of expected value involved in adopting a robust decision, against the apparent loss of flexibility in adopting the "optimal" decision. The balance will tend to favour robustness in conditions of high uncertainty (Rosenhead et al., 1972).

The foregoing arguments should not lead to the rejection of reliability calculations and probabilistic decision theory. Thesc approaches provide important evidence on which to base decisions. However, engineers should recognise the need to broaden their perspective and explore ways of enriching current methods in order to merge qualitative and quantitative perspectives. A systems approach recognises that an infrastructure can be described at a number of different levels of resolution and from a number of different perspectives. Reliability theory can be fitted within this more general framework.

Process Modelling

The issues raised in the proceeding discussion have been addressed by broadening attention from specific data (which are the focus of probability theory) to include the *process* of obtaining and manipulating data and then making decisions. The quality of a design will inevitably reflect the process by which it was produced (Platt and Blockley, 1994). Modelling both human and physical processes in generic terms is now an important research theme at the University of Bristol. One of the main theoretical and practical challenges is establishing an appropriate model structure. The structure represents the flow of information and control during a project, and in particular the flow of information towards important design and management decisions. Both hierarchical and cyclic models have been explored. In hierarchical terms, process can be modelled using a series of sub-processes. Figure 1 illustrates some of the processes in one of the case studies examined in this research. The hierarchy represents and integrates processes which manipulate evidence of different pedigree, from numerical model studies to more qualitative geomorphological analysis. Note that the process model is a descriptive commentary of how the processes *were conducted*, not a normative model of how the process *should have been conducted.*

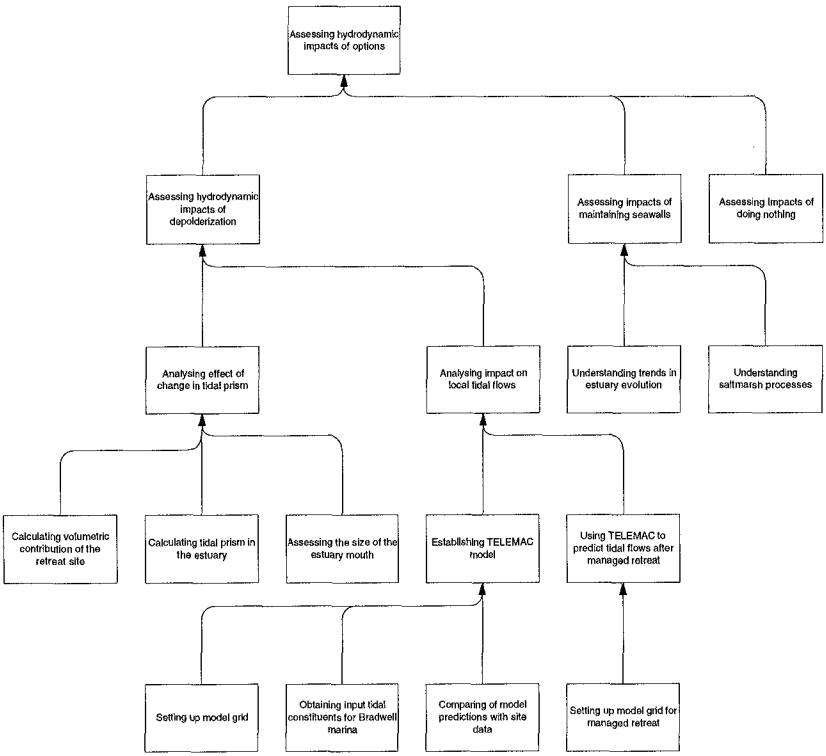

Figure 1 A section of the process hierarchy relating to the Orplands project

Engineers should be concerned with the *dependability* of a process to deliver an appropriate level of function - its quality, or fitness for purpose. An understanding of the dependability of a process can be gained by scrutinising the activities which are

involved in that process and considering evidence of their dependability and the interactions between them. Evidence will range from the size of data sets to testimony of the experts involved.

Looking upwards through the process hierarchy, processes become increasingly general in definition. Thus statements of national policy which represent the top level in a hierarchy of concepts are necessarily expressed in fuzzy linguistic terms such as "sound" and "sustainable". In the UK, Shoreline Management Plans are the next stage below national policy in the hierarchy of concepts, defining policy for a given stretch of coastline. Precise statements, often expressed in numerical rather than linguistic terms, are necessary at project and operational levels. Process modelling enables coherent integration of the hierarchical decision making which characterises modern coastal management. The interface between human and organisational processes and physical processes is handled using the same language which should enable clearer and smoother flow of information.

Interval Probability Theory

Having established a logical hierarchy of processes the next stage is to find a means of expressing uncertainty in each process. The approach adopted here has been to express the dependability of each sub-process using an interval number and calculate how the various uncertainties affect the processes above them using Interval Probability Theory (Cui and Blockley, 1990). An interval number, on the range [0,1], is used to represent the belief in the dependability of a concept.

$$P(E) = [S_n(E), S_p(E)]$$

where

$P(E)$ is the measure of belief in the dependability of a concept E,

$S_n(E)$ represents the extent to which it is certainly believed that E is dependable,

$1 - S_p(E) = S_n(\overline{E})$ represents the extent to which it is certainly believed that E is not dependable, and

$S_p(E) - S_n(E)$ represents the extent of uncertainty of belief in the dependability of E.

Evidence or belief is mapped onto interval numbers using membership functions similar to those used in fuzzy set theory. Three extreme cases illustrate the meaning of this interval measure of belief:

$P(E) = [0,0]$ represents a belief that E is certainly not dependable,

$P(E) = [1,1]$ represents a belief that E is certainly dependable, and

$P(E) = [0,1]$ represents a belief that E is unknown.

The interval $S_n(E) = S_p(E)$ implies that there is no uncertainty in the evidence and corresponds to the theory of classical probability. Thus, whilst Interval Probability Theory is founded on the axioms of probability theory, it allows support for a conjecture to be separated from the support for the negation of the conjecture. It can therefore handle situations where incompleteness is an important issue, because the problem domain need not be completely specified in order to obtain meaningful inferences.

The idea of interval representation has attracted numerous researchers (Dempster, 1969, Shafer, 1976 and Baldwin, 1986). Cui and Blockley (1990) developed previous

work by introducing the parameter ρ which represents the degree of dependence between evidence. Inference rules based on the assumptions of dependence (notably fuzzy set theory (Bier, 1992)) or independence are therefore special cases of IPT.

If ρ is expressed as an interval number $[\rho_l, \rho_u]$ the intersection is

$$S_n(E_1 \cap E_2) = \rho_l(S_n(E_1) \wedge S_n(E_2))$$

$$S_p(E_1 \cap E_2) = \rho_u(S_p(E_1) \wedge S_p(E_2)).$$

The inference mechanism is the total probability theorem

$$P(H) = P(H|E)P(E) + P(H|\overline{E})P(\overline{E})$$

which can be rewritten as

$$P(H) = P(H|E)P(E) + P(H|\overline{E})(1 - P(E)).$$

Dubois and Prade (1990) showed that when all the terms are expressed as interval numbers the bounds on $P(H)$ are

$$\left.\begin{array}{ll} S_n(H) = S_n(H|E)S_n(E) + S_n(H|\overline{E})(1 - S_n(E)); & S_n(H|E) \geq S_n(H|\overline{E}) \\ S_n(H) = S_n(H|E)S_p(E) + S_n(H|\overline{E})(1 - S_p(E)); & otherwise \end{array}\right\}$$

and

$$\left.\begin{array}{ll} S_p(H) = S_p(H|E)S_p(E) + S_p(H|\overline{E})(1 - S_p(E)); & S_p(H|E) \geq S_p(H|\overline{E}) \\ S_p(H) = S_p(H|E)S_n(E) + S_p(H|\overline{E})(1 - S_n(E)); & otherwise \end{array}\right\}.$$

Dubois and Prade only dealt with one item of evidence E. Recently Hall et al. (1998c) have developed a generalised approach to finding the least conservative bounds on the inference for any number of items of evidence. In multi-dimensional problems the simplex algorithm is used to find the least conservative bounds.

An interval approach is attractive because of the much increased flexibility it provides for representing uncertainty knowledge when compared with conventional probability theory. On the other hand it significantly increases the dimensionality of the inference problem. Analysis of any inference problem is therefore a compromise between, on the one hand, having degrees of freedom constrained in a way which does not do justice to the complexities of the situation and, on the other, having to input large amounts of instance-specific information or generating large amounts of uncertainty. The method used will depend on the nature of the problem under consideration. Interval Probability Theory is suitable in situations involving sparse or conflicting data, whilst more precisely defined situations can be effectively tackled with more conventional quantitative approaches.

Implementation of IPT for process modelling

A software tool has been developed which combines visual representation of hierarchical processes with uncertainty propagation using Interval Probability Theory. By combining Interval Probability Theory with process modelling an overall measure of the dependability of the process leading up to a decision can be obtained.

Figure 2 shows a typical working screen. The processes are arranged in a logical

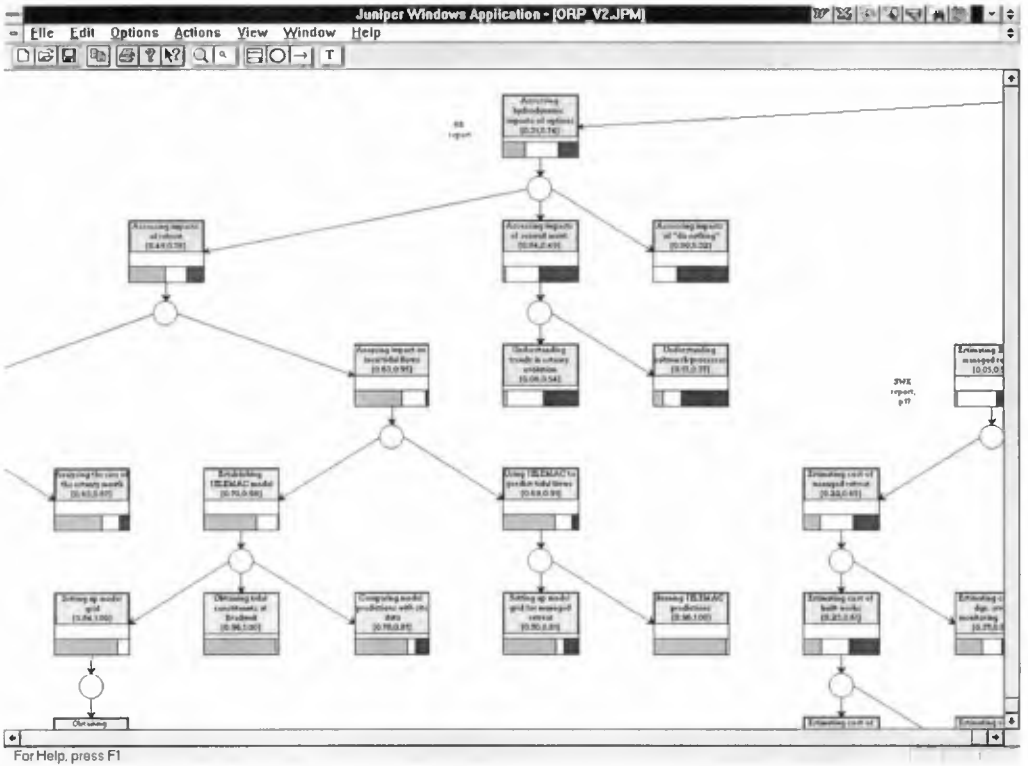

Figure 2 A process model showing the evidence relating to the decision to implement depolderization at Orplands

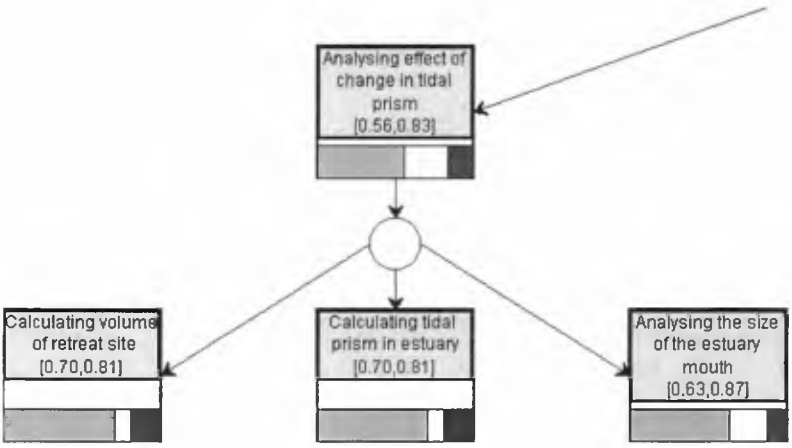

Figure 3 Detail from the process hierarchy

hierarchy. Each process is analysed to identify sub-processes which contribute to the success of the process. The process is decomposed in this way down to a level of resolution appropriate for the problem in hand.

Figure 3 is a detail from the screen shown in Figure 2. The processes are titled and the probability intervals shown as pairs of numbers under the title and graphically as coloured bars at the bottom of each process box. The left bar is coloured green and the right bar red, representing the evidence for or against the success of the process respectively. Between the two bars is a white area representing the uncertainty.

Interval values are input by the user for all of the 'leaf' processes in the hierarchy. At every node in the hierarchy values of the dependency parameter ρ and of the conditional probabilities which express the structure of the inference problem are input by the user. Using this information the software calculates the interval probability which represents the evidence for success of the top process in the hierarchy, which is a logical consequence of all of the interval probabilities input elsewhere in the hierarchy. It is therefore possible to explore the influence of low level processes on the uncertainty in the overall design, modelling or decision making process. Knowledge of the overall dependability, which is provided by the top level interval number can be used to inform and enhance decision making. In this way the process model and interval numbers provide commentary on the process of obtaining and manipulating evidence. The decision maker thereby obtains a means of comparing different predictions (which may be expressed in probabilistic or deterministic terms) which have been obtained from different models. Hall et al. (1998c) also proposed an approach whereby the interval probabilities generated from modelling the dependability of an analysis process can be combined with the probabilistic information generated by that process, for example in the form of a probability of failure, to generate bounds on probability of failure.

Case Studies

Uncertainty analysis which combines process modelling with interval probability theory has been applied to two contrasting flood defence projects on the East Coast of England.

Orplands seawall managed retreat project

One of the projects is a depolderization (managed retreat) project on an estuary in Essex. The dykes which protected a few square kilometres of low grade agricultural land were in need of major repair. To avoid the high cost of repair it was decided to abandon the dykes and retreat the defence line inland. This has had the added benefit of reinstating an area of saltmarsh habitat and reducing stress on the eroding estuary. The scheme was planned based on the experience of the experts involved, supported with some quantitative analysis which was carried out by consultants. The uncertainty analysis was carried out to assess the dependability of the process of choosing to implement the depolderization rather than any of the other options.

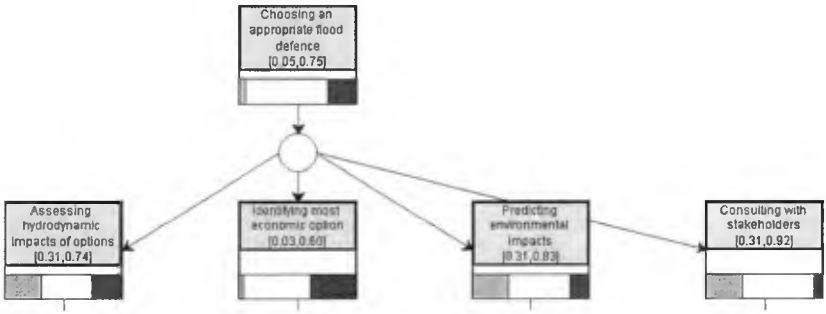

Figure 4 High level processes in the Orplands model

Figure 4 shows the high level process in the process model. The hierarchy shown in Figure 1, 2 and 3 are lower level parts of the same process model. The model was constructed using documented evidence in the form of reports and correspondence relating to the project, together with testimony of the engineers involved. On the basis of this evidence the support for the top process of "choosing an appropriate flood defence" was calculated to be [0.05, 0.75] which represents rather low dependability with low confidence in that assessment. The uncertainty model therefore demonstrated that there was substantial uncertainty in the overall process of choosing an appropriate defence option when this was not necessarily made clear in the documentation relating to the project.

The interval probabilities relating to the sub-processes shown in Figure 4 are listed in Table 1. The main reason why the dependability of the top process was calculated to be low was because of the low support for the economic appraisal process which in the UK has a great influence on the overall dependability of the decision making process. The economic appraisal was found to have dependability [0.03, 0.60]. The lower bound on this interval is a dominant influence on the lower bound of the top process. The economic appraisal was found to be of low dependability because of the complexity of the failure mechanisms at the site, upon which the economic assessment of flood risk depended. Failure probabilities (which are necessary aspects of the economic benefit assessment) were assigned using expert judgement and were not

particularly dependable. To reduce uncertainty in the decision making process would require investment in an improved assessment of flood risk.

Table 1 Support for top level sub-processes after revisions

	Sub-process	Support interval	Verbal mapping
A	Assessing hydrodynamic impacts of options	[0.31, 0.74]	Moderate dependability with moderate confidence
B	Identifying the most economic option	[0.03, 0.60]	Low dependability with low confidence
C	Predicting environmental impacts	[0.31, 0.83]	Moderate to high dependability with low confidence
D	Consulting with stakeholders	[0.31, 0.92]	Moderate dependability with low to very low confidence

The findings of the uncertainty model should not be used in isolation but should complement the information relating to the options which was generated during the economic appraisal, hydraulic and environmental assessment and consultation exercise. These indicated that depolderization was a favourable option which was robust to changes in key parameters in the decision making process. Testing of the uncertainty model suggested that for a project of this size (the estimated cost of the project was only £87k) it would on balance be appropriate to proceed cautiously without further analysis, especially in view of the high cost associated with reducing the uncertainty of key processes.

Construction and use of the uncertainty model forced reflection on how the different activities and studies which had been undertaken contributed to the strategic decision to implement the depolderization project. The final model structure was confirmed by the Environment Agency's project manager to be a good representation of the processes leading up to the strategic decision.

The Lincshore beach nourishment project

The second project used as a case study was a £71 million beach nourishment scheme which is being implemented over a number of years. The scheme has been the subject of detailed numerical model studies and is being intensively monitored. There was therefore much more evidence on which to base the design of the scheme than at the Orplands site.

The first phase of the uncertainty analysis for this project proceeded in the same way as the Orplands project described above, examining the strategic decision to implement beach nourishment rather than any of the other options evaluated during the feasibility study. This demonstrated once again that the risk assessment and economic appraisal process were the main sources of uncertainty in the overall decision. The analysis then proceeded to model the current decision making process relating to the renourishment strategy for the coming five years. This demonstrated how probabilistic modelling to optimise the beach nourishment programme could be combined with hierarchical modelling of the decision making process using Interval Probability Theory.

Conclusions

A descriptive study, using methods developed in the social sciences, has identified principal sources of uncertainty in decision making. Descriptive studies of this type are an important precursor to the design and development of decision support systems.

It has been argued that reliability theory provides an important but incomplete picture of uncertainty in coastal engineering. It cannot be assumed that traditional methods of dealing with uncertainty are as efficient as they could be or that they will continue to be effective in increasingly complex coastal management systems in which more interactions and sensitivities are taken into account. Engineers need to be prepared to explore new methods to give efficiency, safety and sustainability in the defences for which they are responsible. A range of techniques are available for managing uncertainty so engineers should be prepared to draw upon appropriate techniques, remembering that all measures of uncertainty are not absolute measures but are aids in the process of managing uncertainty (Blockley, 1985).

Interval Probability Theory has been found to be a useful approach which accounts for the incompleteness and dependency between items of evidence in an evidential reasoning framework. Interval Probability Theory is an appropriate way of modelling uncertainty in complex situations involving sparse of conflicting information.

Process models of coastal engineering projects have been constructed with Interval Probability Theory. These supplement and enhance existing approaches to uncertainty including reliability methods. These models have been used to support the management of coastal engineering projects on the East Coast of the UK. Two case studies have demonstrated the extent of uncertainty in key decisions during project planning and design. They have highlighted that the a key source of uncertainty and indicated where investment would have to be directed to reduce uncertainty. Moreover, the analysis forced reflection on how the different activities and studies contributed to strategic decisions.

Uncertainty analysis involves giving a overview of where uncertainty lies in a decision. By identifying the most significant sensitivities and sources of uncertainty and by making the most of available information it helps to enable better decision making for coastal engineering projects.

Acknowledgements

The research described in this paper was partly funded by HR Wallingford and the Environment Agency. The co-operation of members of staff at the Ministry of Agriculture Fisheries and Food, the Environment Agency, North Norfolk District Council, HR Wallingford, ABP Research and Consultancy, Sir William Halcrow and Partners, and Posford Duvivier is gratefully acknowledged.

References

BALDWIN, J.F. Support logic programming. *Int. J. Intelligent Systems*, Vol. 1 (1986), pp.73-204.

BECK, U. *Risk Society: Towards a New Modernity*. London: Sage, 1992.

BIER, V.M. Fuzzy set theory, probability theory and truth functionality. in *Analysis and Management of Uncertainty: Theory and Applications* edited by B.M. Ayyub, M.M. Gupta and L.N. Kanal. Amsterdam: Elsevier, 1992, pp.65-78.

BLOCKLEY, D.I. *The Nature of Structural Design and Safety*. Chichester: Ellis Horwood, 1980.

BLOCKLEY, D.I. Reliability of responsibility? *Structural Safety*, Vol. 2 (1985) pp.273-280.

BLOCKLEY, D.I. Risk based structural safety methods in context. *Structural Safety*, in print, 1998.

COLLINGRIDGE, D. *The Social Control of Technology*. Milton Keynes: The Open University Press, 1980.

CUI, W. and BLOCKLEY, D.I. Interval probability theory for evidential support. *Int. J. Intelligent Systems,* Vol. 5 (1990) pp.183-192.

DEMPSTER, A.P. Upper and lower probability inferences for families of hypotheses with monotone density ratios. *Annals of Math. Statist.*, Vol. 40, No. 3 (1969) pp.953-969.

DUBOIS, D. and PRADE, H. A discussion of uncertainty handling in support logic programming. *Int. J. Intelligent Systems*, Vol. 5 (1990) pp.15-42.

GLASER, B.G. and STRAUSS, A.L. *The Discovery of Grounded Theory: Strategies for Qualitative Research*. New York: Aldins, 1967.

HALL, J.W. and DAVIS, J.P. Process modelling and decision support for flood and coastal defence systems, in *Hydroinformatics '98: Proceedings of the 3rd International Conference on Hydroinformatics*, Copenhagen, Denmark, August 24-26, 1998, edited by V.M. Babovic and L.C. Larsen. Rotterdam: Balkema, 1998a, Vol.1, pp.285-292.

HALL, J.W., BLOCKLEY, D.I., and DAVIS, J.P. Non-additive probabilities for representing uncertain knowledge, in *Hydroinformatics '98: Proceedings of the 3rd International Conference on Hydroinformatics*, Copenhagen, Denmark, August 24-26, 1998, edited by V.M. Babovic and L.C. Larsen. Rotterdam: Balkema, 1998b, Vol.2, pp.1101-1108.

HALL, J.W., BLOCKLEY, D.I., and DAVIS, J.P. Uncertain inference using interval probability theory. *Int. J. Approximate Reasoning*, in print, 1998c.

KRAUSE, P.J. and CLARK, D.A. *Representing Uncertain Knowledge: An Artificial Intelligence Approach*. Oxford: Intellect Books, 1993.

PLATT, D.G. and BLOCKLEY, D.I. Process modelling in civil engineering design. *Design Studies*, Vol. 15, No. 3 (1994) pp.317-331.

PLATT, D.G. *Process Modelling and Process Support Environments for Design Management*. Ph.D. thesis, University of Bristol, 1994.

ROSENHEAD, J., ELTON, M. and GUPTA, S.K. Robustness and optimality as criteria for strategic decisions. *Operation Research Quarterly*, Vol. 23 (1972) pp.413-431.

SHAFER, G., *A Mathematical Theory of Evidence,* Princetown: Princetown University Press, 1976.

SMETS, P., The transferable belief model and other interpretations of Dempster-Shafer's model, in *Uncertainty in Artificial Intelligence 6* edited by P.P. Bonissone, M. Henrion, L.N. Kanal and J.F. Lemmer, Amsterdam: North-Holland, 1991.

PREVENTING NATURAL BREACHING OF THE MAJOR SAND SPIT PROTECTING THE PORT OF WALVIS BAY

J S Schoonees [1], L Lenhoff [2] and A J Raw [3]

Abstract

During seasonal storms, waves wash over the major peninsular sand spit protecting the Port of Walvis Bay. The possibility of breaching of the spit was assessed and conceptual measures were proposed to prevent breaching. Aeolian, longshore and cross-shore sand transport rates were computed. Modelling was done of beach profile changes during storms. It was found that the spit would probably not be breached during a single storm. Sand nourishment, methods to prevent erosion, and methods to induce accretion in vulnerable areas were considered to prevent breaching. A contingency plan was recommended involving the use of low-cost shore protection.

1. Introduction

Major coastal sand spits are common features along the Namibian and Angolan coasts of Africa. Examples of these can be found at Walvis Bay (central Namibia; Figure 1), Sandwich harbour (50 km south of Walvis Bay), Baia dos Tigres (southern Angola, about 70 km north of the mouth of the Kunene River) and Lobito (central Angola).

Walvis Bay, which is the biggest deep-water port in Namibia (Figure 1), is protected against wave action by the Walvis Peninsula. This long (about 10 km) but low-lying (about +1 m to mean sea level, MSL) sand spit is growing northwards because of the net northbound longshore transport. However, during storms at high tide, the waves wash over a section of the sand spit (at Donkie Bay; Figure 1), causing concern that natural breaching may occur. This can be a real threat. At

[1] Research engineer and

[2] Marine geologist, CSIR, P O Box 320, Stellenbosch, 7599, South Africa

[3] Port engineer, Namibian Ports Authority, P O Box 361, Walvis Bay, Namibia

Baia dos Tigres natural breaching of the 41 km long spit occurred, leaving an 11 km wide gap in the spit and destroying safe anchorage. At Sandwich harbour extremely dynamic sand banks and channels occur. If breaching does occur at Walvis Bay, the port would have to contend with significant wave action hindering navigation and quay operations. Furthermore, shifting sand banks which are hazardous to shipping, may form in the shipping channel and result in increased maintenance dredging. Because of the seriousness of the consequences and the cost of closing a gap in the spit, a study was undertaken to assess the possibility of breaching of the Walvis Peninsula and propose conceptual measures to prevent it (CSIR, 1996).

The aims of the study were: an initial assessment of the possibility of breaching, the gathering of essential data required for this task, and the proposal of conceptual measures (e.g. shore protection) to prevent breaching. For the study, beach and hydrographic surveys were conducted of the low-lying area (Donkie Bay) and of Pelican Point (the tip of the Walvis Peninsula). It was essential to obtain accurate information on sand spit levels in order to determine the extent of the problem and the most suitable solution. A survey of the Pelican Point area was conducted to assist in estimating the longshore sand transport rate along the Walvis Peninsula.

2. Environmental data

2.1 Historical data

Although charts of the study area date back to 1796, the first reliable map was compiled in 1885 by the British Navy. Subsequently a number of charts and aerial photographs became available which illustrate the development of the spit over the past 100 years. From these data an average annual growth rate could be determined, which has a direct bearing on the longshore sediment transport rate in the area - an aspect which will be discussed in more detail in Section 3.2 below.

2.2 Bathymetry and topography

To assess the present configuration of the Walvis Peninsula, detailed bathymetric and topographical surveys of Pelican Point and its surrounds as well as the area around Donkie Bay were conducted. Echo-sounding and conventional land surveying techniques were used to obtain detailed elevation contours at 1 m intervals. The data show that the Walvis Peninsula is a low-lying spit with an average height of about +1.0 m to MSL, sloping steeply towards deeper water, especially at Pelican Point.

A cross-section at Donkie Bay (Profile 2) is shown in Figure 2. The profiles at Donkie Bay are very similar; however, the crest of the dune is the lowest in Profile 2.

2.3 Waves

The dominant deep-sea waves, obtained from voluntary observing ships

(VOS), originate from the southerly, south-south-westerly and south-westerly sector. Due to the orientation of the peninsula, the Port of Walvis Bay is protected from these dominant waves. The median significant wave height is 1.1 m and the median peak wave period is 11.6 s as obtained from accurate Waverider data measured in 50 m water depth (Figure 1).

2.4 Sediment grain size

Sand samples taken from the wetted beach and the sea bottom at Donkie Bay and Pelican Point show that the average median grain size (D_{50}) is about 0.35 mm, that is, medium sand.

3. Sediment transport analysis

3.1 Aeolian transport

About 6 years of wind data collected near the Walvis Lagoon (Figure 1) were used to compute seasonal and annual wind-blown sand transport rates on the Walvis Peninsula, using the method proposed by Swart (1986). The average of the median grain sizes (0.33 mm) of the samples taken on land across the Walvis Peninsula was applied.

It was found that the dominant transport is towards the north-eastern and north-western sectors with distinct seasonal variations. The net northward movement of sand is equal to the difference between the northbound and southbound transports, which is about 38 m^3/year per m. By using the average width of the Walvis Peninsula (605 m), it was calculated that the potential net northbound aeolian transport is approximately 23 000 m^3/year.

3.2 Longshore transport

Longshore sediment transport usually takes place from south to north along the western shore of the Walvis Peninsula. The tip of the Walvis Peninsula acts as a total trap for sand moving alongshore with the result that the spit is growing over time. By determining the volume of sand deposited over a period of time, the net longshore transport rate can be calculated. An analysis of the historic data (old maps and aerial photographs) showed that Pelican Point grew at an average rate of about 17.4 m/year between 1885 and 1980. Between 1980 and 1996 Pelican Point has prograded over a total distance of 340 m (determined accurately from the surveys), that is 22.6 m/year on average. In contrast to growth at the tip the eastern coastline configuration of the spit did not change between 1980 and 1996. Along the western flank, however, a significant shift took place around Donkie Bay, resulting in a decreased width in this area, which gave rise to the present concerns regarding breaching.

Based on all the available statistical information, a prediction was made with respect to the expected location of Pelican Point in the year 2006, that is, in 10 years' time. Using geographical information system (GIS) techniques, it was found that a total of 8.83 million m^3 of sediment will be required to enable the growth of

Pelican Point to achieve its predicted shape in 2006. This implies an average annual addition of 883 000 m^3 of sediment. If the Walvis Peninsula is considered a total sediment trap, the figure of 883 000 m^3/year represents the net northward sediment transport rate along this coastline.

One should subtract the net northbound aeolian transport (23 000 m^3/year) from the calculated volumetric rate of 883 000 m^3/year. Thus the net northbound longshore transport rate along the western shore of the Walvis Peninsula is considered to be 860 000 m^3/year.

3.3 Cross-shore transport

Erosion by offshore sand transport (during storms) can potentially cause breaching of the Walvis Peninsula. Modelling of cross-shore transport and the associated beach profile changes was therefore carried out.

The Sbeach cross-shore transport/morphological model (Larson and Kraus, 1989) was chosen for predicting beach profile variations due to storms. In a comprehensive review, Schoonees and Theron (1995) found that this is one of the best models currently available. The theoretical basis is acceptable and the model has been extensively verified (Schoonees and Theron, 1995). In addition, it can simulate dune overwash which can be important in the Donkie Bay case. No calibration data are available for the Donkie Bay case and the results should therefore be regarded as first estimates only. However, since Sbeach is a well-verified model against prototype data, the results are considered to be realistic.

Profile 2 was selected because the crest of the dune is the lowest in this profile (Figure 2), thus representing the most critical scenario. A median grain size of 0.35 mm was used for the profile. Two storms were modelled, namely, storms having significant wave heights (H_s) of 3 m and 4 m respectively. These wave heights correspond roughly to the 1-in-1 year (3.6 m) and the 1-in-10 year (4.4 m) conditions. More extreme wave heights were not chosen because it has previously been found that medium-sized waves occurring over longer periods cause more erosion than short-lived, high-wave events. The peak wave periods (T_p) associated with these wave heights are 11.7 s and 12.5 s respectively. The durations of these two storms were 68 h and 41 h respectively. The water-level variation was obtained from the most extreme tides predicted for 1996: from -0.94 m to +0.89 m to MSL (the latter value approaches the highest astronomical tide of +1.02 m to MSL).

Figure 2 shows the progressive erosion of the beach profile for the 3 m storm. An offshore bar formed at a depth of about -5 m to MSL. The predicted maximum horizontal erosion of 23.5 m (and 18.8 m for the 4 m storm) occurred at 0 m to MSL. Because of its longer duration, the 3 m storm caused slightly more erosion than the 4 m storm. Based on experience, these values appear realistic. As indicated by Figure 2, it is unlikely that the dune crest will be flattened, although the model does predict overwash as has been observed on site. Smaller waves will therefore not be able to erode the beach continually. However, it should be borne in mind that the model could not be calibrated for Walvis Bay due to a lack of data.

The results are therefore preliminary only. In addition, only two storms were modelled.

4. Possible breaching of the Walvis Peninsula

The possible breaching of the Walvis Peninsula was approached in two ways: firstly, by analysing measured beach profile variations (in a horizontal plane) from other sites and secondly, by modelling storm erosion as explained above.

Beach profile variations have been recorded on exposed beaches along the Southern African coastline. Typically the maximum, natural, horizontal storm erosion for exposed beaches is between 30 m and 95 m over the long term.

The predicted maximum horizontal erosion of 23.5 m compares well with the range of measured erosion. The beach profile modelling showed that overwash will most probably not flatten the dune (Figure 2). However, caution is necessary because it was not possible to calibrate the model (Sbeach) for Walvis Bay.

When considering the width of the Walvis Peninsula, which is at least 500 m wide, it is clear that it is highly unlikely that the peninsula could be breached by a single storm. Erosion of no more than 50 m can be expected during one storm. However, a potential danger exists for wave action to flatten the frontal dune (although this was not predicted in the beach profile modelling). This could possibly cause smaller, more commonly occurring waves to flatten the peninsula with breaching occurring eventually.

It is therefore recommended that the Donkie Bay area be inspected weekly and also immediately after heavy seas to ensure that flattening of the dune is noticed timeously. In the event of flattening, emergency protection can be installed (see Chapter 5) to prevent breaching. It is further recommended that bi-monthly beach surveys be conducted of the Donkie Bay area.

5. Conceptual measures to prevent breaching

5.1 General

A number of generic measures can be employed to prevent breaching of the Walvis Peninsula. These measures are: sand nourishment, methods to prevent erosion, and methods that induced accretion in the vulnerable areas.

A number of factors should be considered when evaluating the suitability of these measures. These factors include availability of construction materials and equipment, cost of construction, accessibility of the construction site and whether a temporary or permanent solution is required.

5.2 Sand nourishment

Sand can be brought in artificially to widen the vulnerable section of the peninsula (Donkie Bay). Possible methods for bringing in sand from nearby areas where there is abundant sand are: by means of trucks, pumping, or bulldozing sand into the sea just south of the Donkie Bay area. Especially in the case of bulldozing, the sea can be used to transport the sand towards the Donkie Bay area.

The extra sand can serve as an emergency measure by filling up or feeding an eroded section, or by acting as a buffer against future erosion. It is most likely that sand nourishment will be only a temporary solution. If applied correctly, it can, however, be an effective and low-cost solution.

5.3 Methods to prevent erosion

There are a number of different methods for preventing erosion. These include low-cost shore protection, a rock berm (armour), a gabion structure, and a sheetpile wall.

The CSIR has done extensive research into *low-cost shore protection.* Initially, a literature survey was done and new concepts were developed which were tested in the laboratory. Thereafter, a one-day field exercise was conducted. This was followed by a full-scale test at Hermanus (an exposed site) in November 1992. A 3 m high dune (sand wall) of 110 m length was constructed, which was protected by four different configurations of low-cost protection structures. The detailed results of this test are discussed in Theron *et al.* (1994). Based on these results, the three most promising protection methods were found to be sandbags, sand sausages (Figure 3) or a combination of both. In two subsequent cases sandbag groynes were also used successfully in False Bay near Cape Town.

Low-cost protection and breakwaters are in use around the world. In Mexico several major coastal structures have been built (Porraz, 1976, 1987) which have withstood a number of hurricanes. Dette and Raudkivi (1994) devised a shore protection system (Figure 4) very similar to the CSIR design shown in Figure 3. They tested it in the Large Wave Flume in Hannover, Germany before a successful prototype application on the island of Sylt in the North Sea. The defence has withstood storms from 1991 up to at least the date of the publication (1994). Dette and Raudkivi (1994) also mentioned a similar successful deployment in Fidji for hurricane protection.

The main advantages of low-cost shore protection are that it is relatively easy and fast to build and remove and that the building material (usually sand) is locally available. The disadvantages are that the protection is mostly temporary (that is, withstanding a 2 to 6 month period of wave attack) and that degradation of the geotextile material will eventually occur due to ultra-violet radiation from the sun.

Profile 2 (Figure 2) is the most vulnerable section of the Walvis Peninsula. If the top of the dune is flattened during a storm, it is possible to protect the peninsula with a double row of tightly stacked (1 m^3) sandbags placed as shown in Figures 5 and 6 around the eroded area. These emergency measures are, however, only essential if significant erosion has already occurred.

For protecting the Walvis Peninsula permanently, a dynamically stable *rock berm,* consisting of smaller rock, will most probably be cheaper (also in the long term) than a statically stable rock protection. Allowance will have to be made for scour in front of the structure. By placing enough rock, a sacrificial toe can be

constructed which will partially fall into the expected scour hole in front of the rock protection. Figure 7 shows a conceptual rock berm (median rock mass (w_{50}) = 1 150 kg) for protecting the vulnerable Donkie Bay area. This type of design has proved its adequacy in prototype in a similar situation at Saldanha near Cape Town (CSIR, 1994). Such a rock berm can be placed in the same position as the low-cost shore protection (Figure 5). Three-dimensional effects need to be considered. For example, wave overtopping can cause the formation of pools of water behind the rock berm which will rush back to sea at the lowest point of the berm, causing a dangerous and erosive return current.

Other possible methods of preventing erosion at the Walvis Peninsula are *gabions* and a *sheetpile wall*. Gabions are susceptible to failure if they are continually exposed to wave action. This is mainly due to abrasion and corrosion of the wire of the gabions. A sheetpile wall will probably be very expensive. Allowance also has to be made for the extra scour in front of such a wall because of wave reflection. Therefore, these two methods do not appear to be appropriate for the Walvis Peninsula.

5.4 Methods that induce accretion

There are different methods that can be employed to induce accretion of sand in the Donkie Bay area. These include: one or more groynes to trap the longshore transport of sediment, the construction of a headland to trigger the formation of a half-heart bay, and the trapping of wind-blown sand.

One-line theory (Larson *et al.*, 1987) was chosen to predict the shoreline evolution caused by the construction of different *groynes*. The theory predicts the position of a single contour line over time (taken to be the shoreline or 0 m to MSL contour). Despite simplifying assumptions such as the theory being only applicable for small wave approach angles and that no net cross-shore sediment transport takes place, one-line theory has been proved to give good results in Japan (Hanson and Kraus, 1986), the United Kingdom (Brampton and Goldberg, 1991), the USA (Hanson *et al.*, 1989) and Southern Africa (Coppoolse *et al.*, 1994).

Three different groynes extending to -1.5 m, -3 m and -5 m to MSL were simulated in the model. These groynes are 61 m, 86 m and 116 m long if measured from the +2 m to MSL contour. The simulation runs were for a groyne just north of the vulnerable Donkie Bay section at alongshore distance (or Chainage) 4 000 m (Figure 5). At Chainage 3 800 m (the corner of Donkie Bay), the shoreline turns sharply westwards forming Donkie Bay. In addition, two groynes of 61 m length each, one at the above-mentioned position at Chainage 4 000 m and one at 350 m further northward along the Walvis Peninsula at Chainage 4 350 m, were also simulated. This was done because it is considerably cheaper to build two 61 m groynes than one long groyne. In addition, the 61 m groynes will only extend to -1.5 m to MSL, which means that they can be constructed from land using sandbags (Theron, *et al.*, 1994).

As input parameters, the net longshore transport obtained in Section 3.2, a

representative wave incidence angle at the breaker line (4°), a total height (above and below the water) over which nearshore profile changes take place (12 m), and beach slopes and water depths at the groynes obtained from the surveys were used.

Figure 8 represents the shoreline evolution caused by the 116 m groyne. Note that the original coastline is at a cross-shore distance of 200 m. Accretion of about 69 m takes place reasonably rapidly next to the groyne. Equilibrium is reached after about two years with little significant accretion occurring after a year. This means that significant bypassing will take place almost immediately after the groyne has been constructed, thus limiting downdrift erosion. At 200 m south of the groyne (in the corner of Donkie Bay) eventual accretion of approximately 63 m (12 m after 1 month) can be expected. The sand will form an appreciable extra buffer against storm erosion.

Two 61 m groynes were also modelled to evaluate the effects on the beach (Figure 9). It can be seen from this figure that, initially, some erosion is evident north (to the right) of the first groyne (at Chainage 4 000 m), after which significant bypassing takes place and accretion occurs (in the order of 19 m). Because of the relatively high longshore transport rate and the short groynes, the coast will be close to equilibrium after about 6 months.

Downdrift erosion of about the same magnitude as the accretion can be expected to the north of the groyne (or the northernmost groyne in the case of two groynes). However, if erosion occurs when the peninsula is wide (more than 500 m) and not vulnerable, it is considered acceptable.

Half-heart bays can be used to stabilise a coast. However, in the case of the Walvis Peninsula, this will mean that at least one major headland will have to be constructed because the peninsula is an exposed coastline with high longshore transport. Because of the high cost, this option is not considered viable.

Aeolian sand can be *trapped* by erecting geotextile fences across the Walvis Peninsula. Because of the low aeolian transport rate of about 23 000 m^3/year, it will take a long time to achieve appreciable accretion at Donkie Bay. To be conservative, only the width of dry sand on the peninsula should be considered and not the total width of the peninsula at Donkie Bay because moisture limits sand transport by wind. If this is done, the net northbound aeolian transport is only about 3 040 m^3/year. The accretion against the fences will therefore be small and it will take a long time to achieve significant results. The additional protection offered against storm erosion will therefore be small in the short to medium term, which is the required time span.

Although the solution is initially cheap, considerable maintenance is envisaged. Access to Pelican Point for lighthouse personnel, anglers, etc. will be hindered because of the fences. The fences are also prone to damage by vandalism. Trapping wind-blown sand is therefore not regarded as a suitable option.

6. Conclusions and recommendations

It is highly unlikely that the Walvis Peninsula would be breached during a

single storm. There is, however, the potential danger that wave action could flatten the frontal dune (although this is not predicted in the beach profile modelling). Flattening of the frontal dune could possibly cause smaller more commonly occurring waves to flatten the peninsula with breaching occurring eventually. It is therefore recommended that the Donkie Bay area be inspected weekly and also immediately after heavy seas to ensure that flattening of the dune is noticed timeously. In the event of flattening, emergency protection can be installed to prevent breaching. Bi-annual beach surveys of the area are recommended.

Because it is unlikely that the peninsula would be breached during a single storm, it is not deemed necessary to opt for the best permanent solution, namely a rock berm. Such a permanent solution will obviously be more expensive than a temporary solution. However, it is strongly recommended that a contingency plan be drawn up in order to facilitate a timeous response in case of an emergency. It is recommended that 1 m^3 bulk bags be bought and kept in storage at Walvis Bay for such an emergency. These can be used either as low-cost shore protection (Figures 5 and 6) or to construct one or two short groynes (Figure 9). Arrangements should also be made for obtaining a large excavator (on metal tracks; 20 tonnes) at short notice to fill and transport the bulk bags. The low-cost shore protection and groyne(s) should be designed in detail because experience has shown that the method of construction and deployment can have a profound effect on the overall success of the protection (Theron *et al.*, 1994).

It is also advisable to a have a bulldozer available at short notice. Bulldozing sand into the surf zone upstream of the damaged (eroded) area can help to delay erosion, thus buying time for placing the bulk sandbags. It is also advisable, though not essential, to build one short (61 m) groyne. The advantages are that an additional buffer of sand will be formed thereby reducing the possibility of a breach and that the construction will serve as a training exercise for deployment of low-cost protection during an emergency. In addition, by monitoring the beach accretion, calibration data for modelling shoreline evolution resulting from the groyne will be obtained to confirm the predictions presented above. The disadvantage of the construction of the groyne is that unnecessary cost will be incurred. On the other hand, such a groyne will most probably cost less than the more extensive remedial protection required in an emergency.

Acknowledgement

The permission granted by the Namibian Ports Authority to publish this paper is gratefully acknowledged.

References

Brampton, A H and Goldberg, D G (1991). Mathematical model of groyned shingle beaches. *Coastal Sediments* '91, ASCE, Vol. 2: 1842-1855, Seattle.

Coppoolse, R C, Schoonees, J S and Botes, W A M (1994). Physical impacts of the disposal of dredger spoil at Richards Bay, South Africa. *28 PIANC*, Seville, Section II-1, pp 73-85.

CSIR (1994). Photographic, hydrographic and topographic monitoring of the Saldanha Bay spending beach breakwater, May 1993. *CSIR Report* EMAS-C 94110, Stellenbosch.

CSIR (1996). Preventing natural breaching of the peninsula at Walvis Bay. *CSIR Report* ENV/S 96072, Stellenbosch.

Dette, H H and Raudkivi, A J (1994). Beach nourishment and dune protection. *24 Intern. Conf. on Coastal Eng.*, Vol. 2: 1934-1945.

Hanson, H and Kraus, N C (1986). Forecast of shoreline change behind multiple coastal structures. *Coastal Eng. in Japan*, Vol. 29: 195-213.

Hanson, H, Kraus, N C and Nakashima, L D (1989). Shoreline change behind transmissive detached breakwaters. *Coastal Zone* '89, ASCE: 568-582.

Larson, M, Hanson, H and Kraus, N C (1987). Analytical solutions of the one-line model for shoreline change. WES, CERC, *Technical Report* CERC-87-15, Vicksburg.

Larson, M and Kraus, N C (1989). SBEACH: numerical model for simulating storm-induced beach change. Report 1: Empircal foundation and model development, *Tech. Rep.* CERC-89-9, WES, CERC, Vicksburg.

Porraz, M (1976). Textile forms slash cost of coastal zone structures. *Ocean Industry*, Vol. 11(10): 61-64 and 116.

Porraz, M (1987). High tensile geotextiles for low cost harbour facilities. *2 COPEDEC*, Beijing, China, pp 1263-1271.

Schoonees, J S and Theron, A K (1995). Evaluation of 10 cross-shore sediment transport/morphological models. *Coastal Engineering* 25: 1-41.

Swart, D H (1986). Prediction of wind-driven sediment transport rates. *20 Intern. Conf. on Coastal Eng.*, ASCE, Taipei, Vol. 2: 1595-1611.

Theron, A K, Coppoolse, R C and Schoonees, J S (1994). Low-cost coastal protection measures using textiles. *29 PIANC*, Seville, Spain. Section II, Subject 4, pp 109-118.

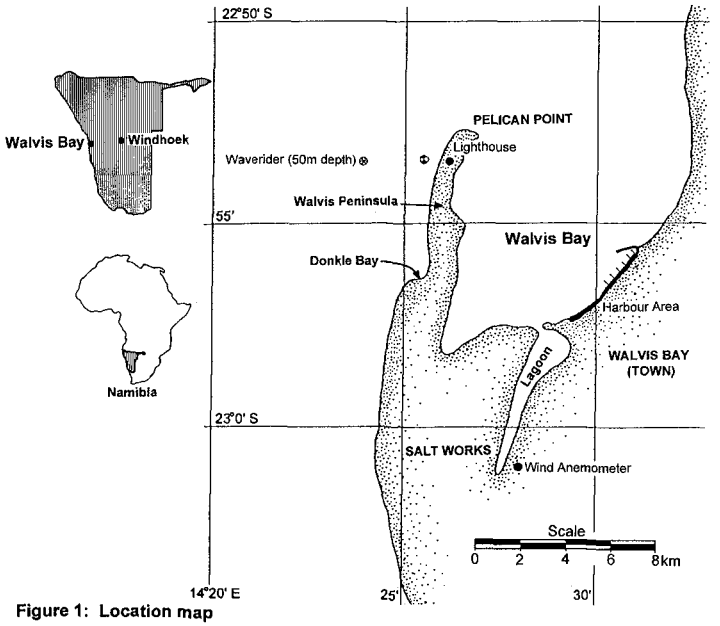

Figure 1: Location map

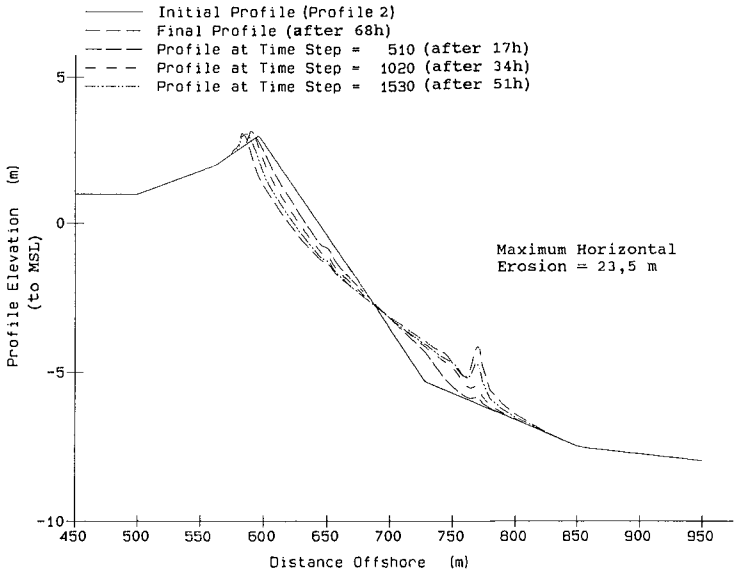

Figure 2: Profile evolution during the 3 m storm

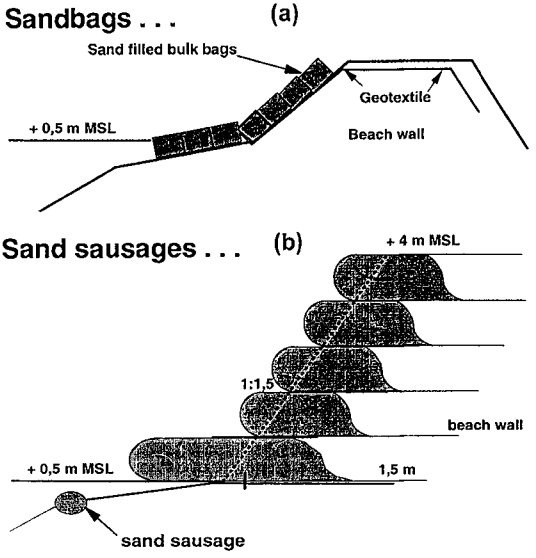

Figure 3: Low-cost shore protection using sandbags and sand sausages

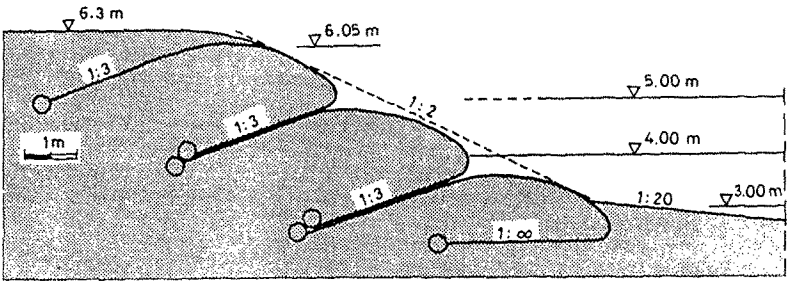

(FROM DETTE AND RAUDKIVI, 1994)

Figure 4: Geotextile membrane tested in the large wave flume

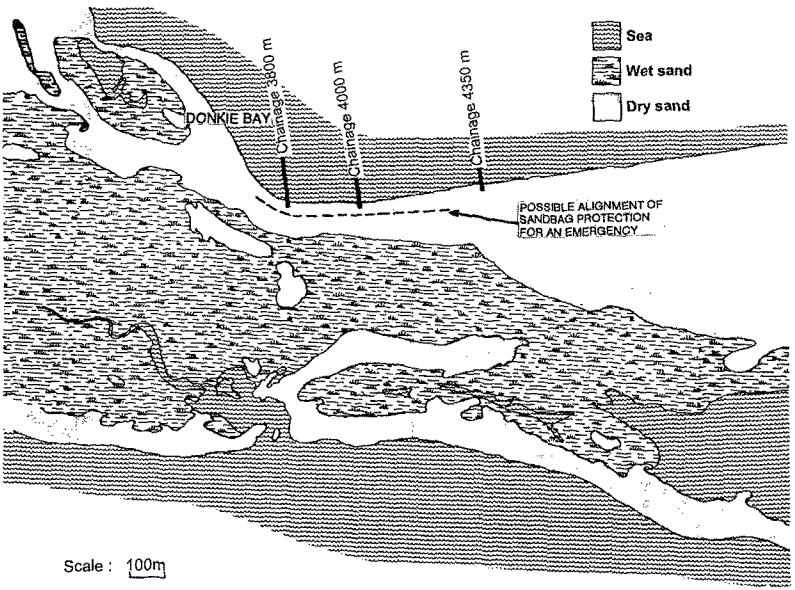

Figure 5: Possible position of the sandbag protection

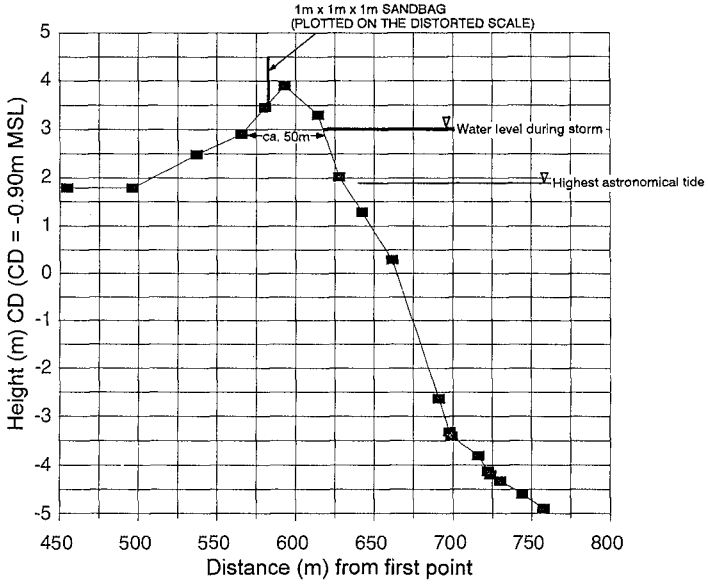

Figure 6: Position of the sandbag protection on the profile

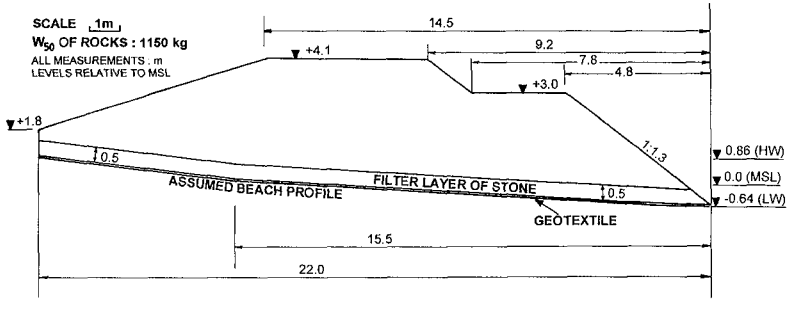

Figure 7: Cross-section of rock berm

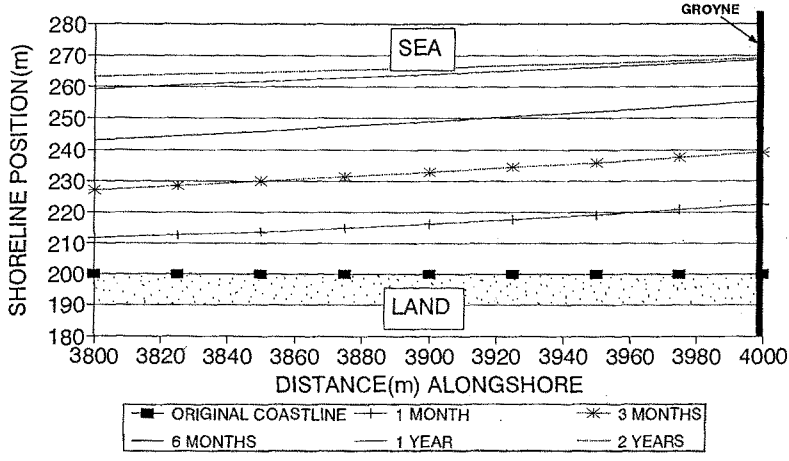

Figure 8: Shoreline evolution caused by the 116 m long groyne

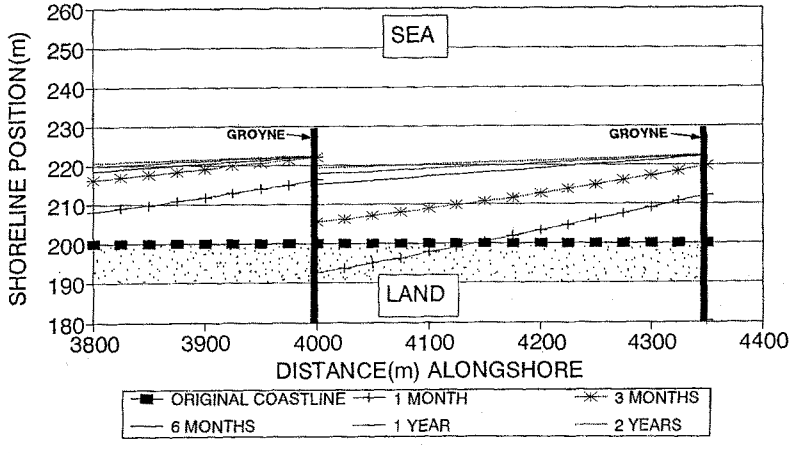

Figure 9: Shoreline evolution caused by two 61 m long groynes

PHENOMENA IN STANDING WAVE IMPACT ON A HORIZONTAL PLATE

Piotr Wilde, Kazimierz Szmidt and Eugeniusz Sobierajski [1]

Abstract

The paper deals with experimental and theoretical investigations of dynamics of a plate–fluid system. In experiments, a horizontal plate was suspended elastically in a wave flume and loaded with impact pressure forces resulting from growing water waves. The data obtained in experiments has revealed the essential role of the elasticity of the plate and its supports as well as the fluid compressibility in estimating the structure-fluid interactions. Therefore, in order to get a better insight into the problem considered, harmonic vibrations of an elastic band plate submerged in an infinite domain of compressible fluid have also been examined. The solution obtained and formulae derived enable to calculate the fluid pressure induced by the plate vibrations.

1. Introduction.

In offshore engineering we have a wide variety of problems associated with water wave forces acting on offshore structures. Among them, there are also cases of horizontal plates (or plate like elements of a structure) loaded with abrupt pressure forces resulting from growing sea waves. Examples are sea piers and suspended breakwaters under the action of water forces of short duration. A theoretical description of the mentioned problem is very difficult because of a complicated structure of the equations of the fluid motion together with the relevant boundary conditions, especially at moving boundaries of the fluid domain. Therefore, in describing the structure – fluid interaction, we are forced to resort to approximate methods, which, in principle, should be verified by experimental investigations. For this purpose and, to learn more about the phenomena, experimental investigations of dynamics of a horizontal plate in contact with water have been performed in the wave flume of the Institute of Hydro -Engineering of PAS in Gdańsk. The performed experiments allowed for collecting information important in creating approximate computational models which describe the structure-fluid interaction with an acceptable accuracy.

[1] Institute of Hydro-Engineering, Polish Academy of Sciences, ul. Kościerska 7, 80-953 Gdańsk, Poland

2. Laboratory experiments.

The experimental set-up is shown schematically in Fig.1. It consists of the following main components: the model of a horizontal plate constructed in the form of a box with frame skeleton and casing made of aluminium alloy, the system of springs and strings, the piston type wavemaker and the system of pressure, wave and acceleration gauges together with a recording unit. The horizontal plate was suspended elastically in the wave flume over the still water level by means of a system of prestressed elastic springs at a chosen distance from the wavemaker. In order to obtain reliable results, we looked for a wave problem that could be controlled. Therefore, at a first step, we have chosen the case of standing water waves growing with time. In order to obtain these waves, additional rigid vertical plate was installed in the flume, just in the neighbourhood of the horizontal plate. In this way, the wavemaker together with the vertical plate formed a rectangular basin of water with its own set of eigenfrequencies.

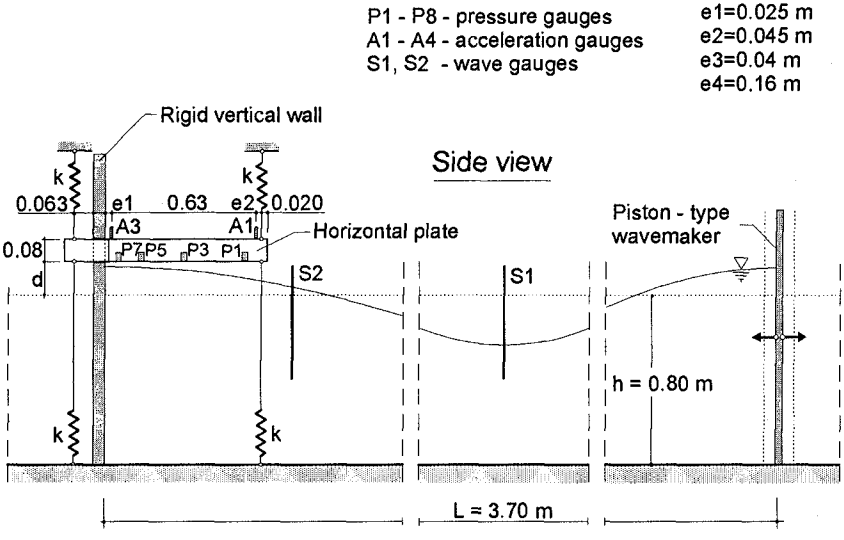

Fig. 1. The horizontal plate in the wave flume.

During experiments the wavemaker frequency was chosen to be equal to the first and the second lowest natural frequencies of the water test section and thus, the lengths of the generated waves were equal to the distance between the wavemaker and the vertical plate and, twice the distance, respectively. Due to the resonance, the harmonic motion of the wavemaker, starting from rest and moving with a relatively small amplitude, led to the standing surface wave with amplitude growing in time. The growing wave crest could reach the horizontal plate level at a certain moment of time and thus, the impact pressure phenomenon occurred. The generated waves were measured by means of two or three wave gauges, the vibrations of the plate - by four acceleration gauges and, the distribution of the impact pressure – by eight pressure gauges, respectively. The latter gauges were installed in two rows on the lower surface of the plate.

The data recorded in experiments has the form of a sequence of numbers corresponding to the assumed sampling frequency. The electronic devices used in

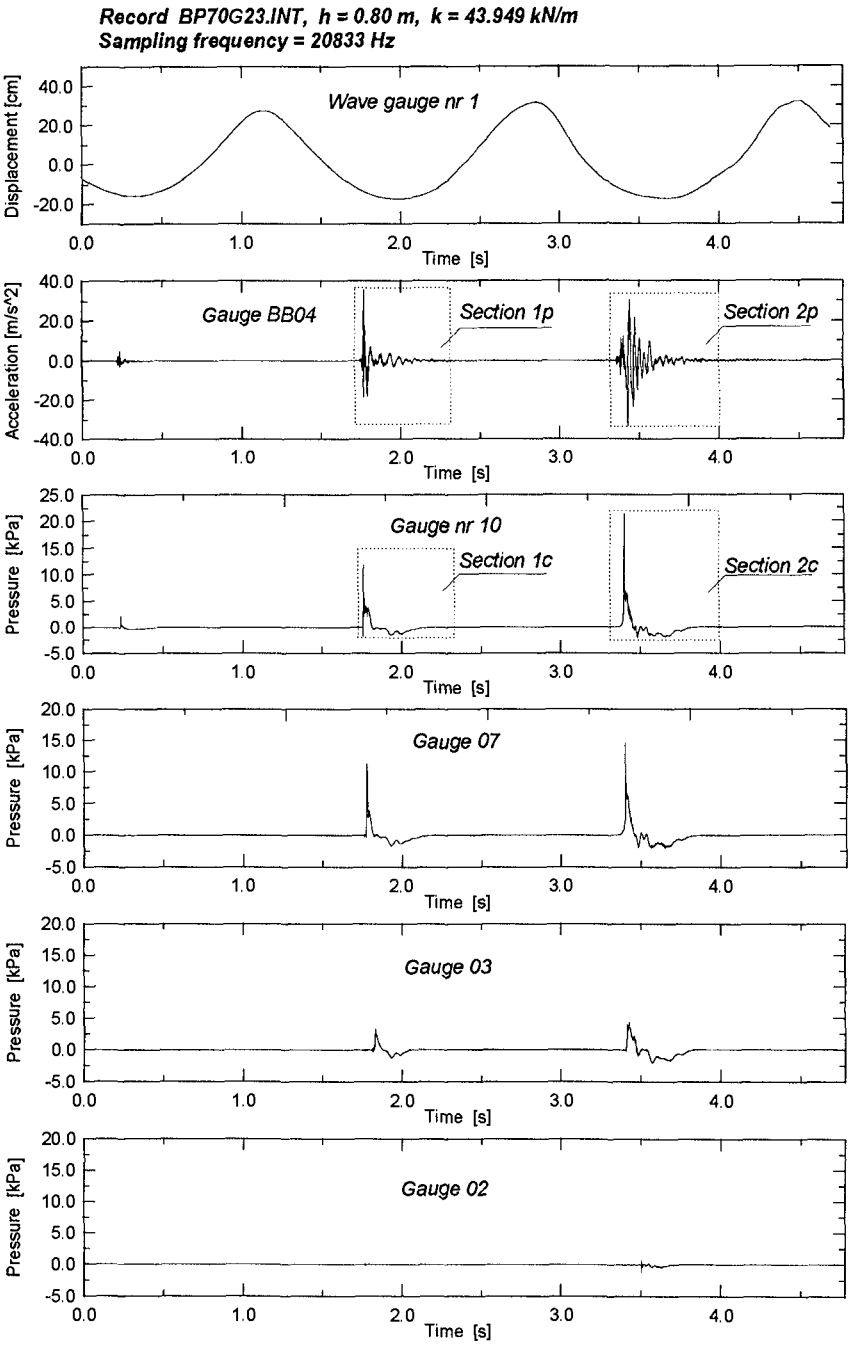

Fig. 2. The measured acceleration and pressures for standing waves.

experiments allowed to register the data numbers with the maximum sampling frequency equal to 20,833 Hz. These records were then processed with the help of the Kalman filter which enabled us to decompose the vibrations into components corresponding to dominant frequencies of the system mentioned.

The experiments started with the identification of the considered dynamical system in air. By applying an initial displacement of the plate, which was then released, the free vibrations of the plate were obtained. The spectral density of the acceleration record of the vibrations showed three eigenfrequencies: 24 Hz, 38Hz and 416 Hz corresponding to the vertical, rotational and flexural displacements of the plate,

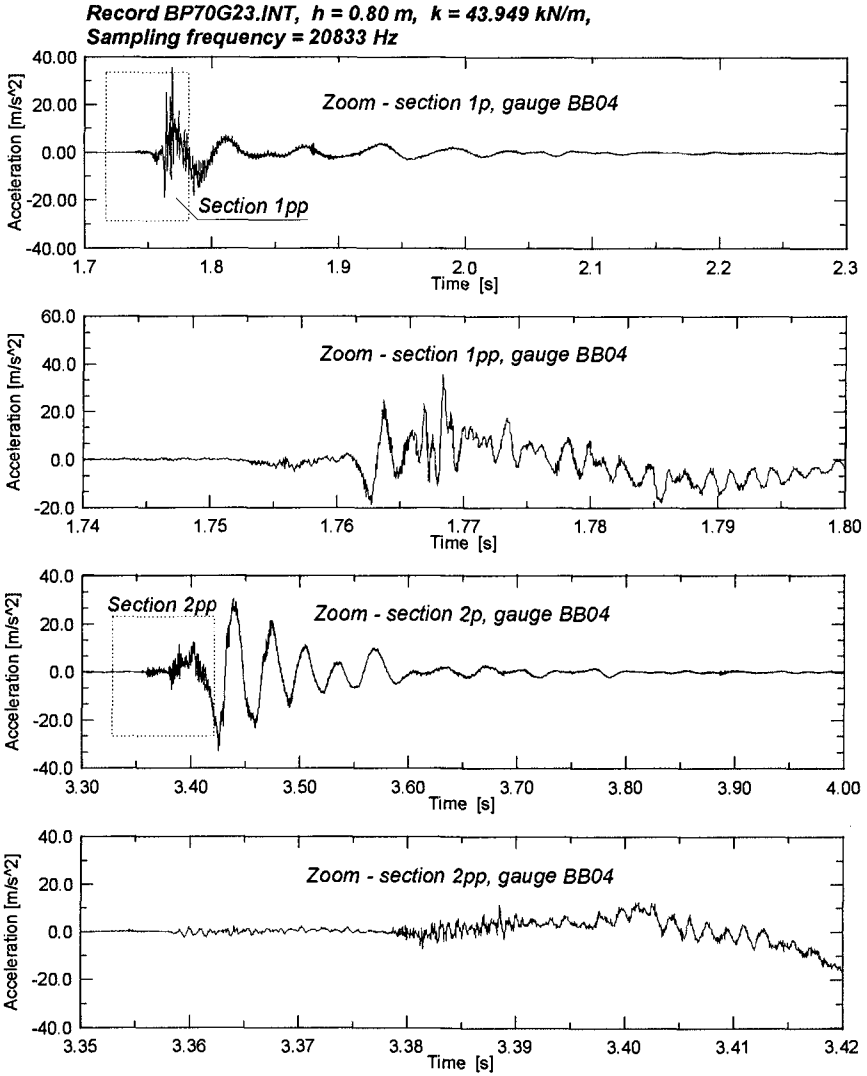

Fig. 3. The analysis of measured acceleration.

respectively. The two lowest frequencies detected correspond to the plane rigid body motion of the plate, while the third one is associated with a deformation of it. The plate as a box structure has many eigenfrequencies and the highest frequency detected is the lowest one of the plate.

The basic experiments of the plate loaded with water wave forces were performed for a relatively large number of particular cases corresponding to the chosen rigidity of the springs, the chosen gap width between the lower surface of the plate and the still water surface and, the assumed amplitude and length of the generated wave (the distance between the vertical plate and the wavemaker was a parameter in the experiments mentioned). With respect to the amount of data obtained, we attached here only few illustrative examples. Typical results of an experiment performed are shown in Fig.2 and in Fig.3, where the plots of the water wave, acceleration of the plate and the pressure acting on the plate surface are depicted. This experiment can be divided into a number of stages. The first one lasts from the outset of the generator motion to the moment of the maximum height of the surface wave, just before water

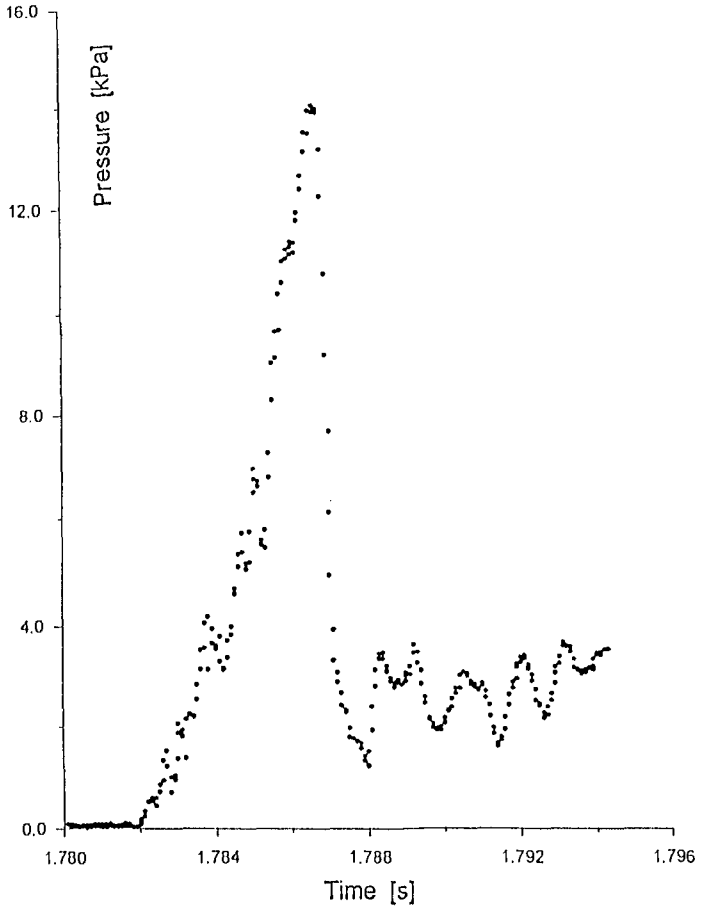

Fig. 4. The impact pressure of a standing wave.

strike at the plate. Then, we have a very short second stage during which the plate receives a finite impulse of the pressure forces. The registered measurements pointed the existence of acoustic waves propagating with sound velocity. With the end of this short stage the third – transitive stage begins during which the free damped vibrations of the plate take place. This third stage may be assumed to last till the next water strike at the plate. Since the water flow is not fully periodic in time, we cannot speak about periodic behaviour of the system at hand and thus, the second wave impact on the plate is assumed to be the beginning of the fourth stage and so on. From the plots in Fig.2. it may be seen that in addition to the range of frequency mentioned above we have now also the frequency of order 1 Hz relevant to the gravitational wave. Besides, the zoom sections shown in Fig.3. reveal the important feature of the impact pressure phenomenon, namely, a wide range of frequencies associated with the system as a whole. The frequencies vary from 1 Hz of the generation of water waves, through 10-30 Hz relevant to rigid body motion of the plate and approx. 200-400 Hz of the lowest eigenfrequency of the box structure. In addition to these frequencies, we have also higher frequencies corresponding to higher modes of vibrations of the box structure and dilatational waves propagating within the fluid. The higher frequencies of the system considered and thus, the influence of the dilatational waves on the system behaviour are of primary importance, especially in proper estimation of the impact pressure forces. This can also be seen in Fig.4. where the distribution of pressure recorded by pressure gauges installed on the plate is given. From the plot it follows, that the time range of the impulse pressure is very narrow and thus, in describing the impact pressure phenomenon, the small compressibility of the fluid as well as the elasticity of a structure must be taken into account. At the same time, because of the small interval of the impulse action on the plate, the higher modes of the system motion can be investigated independently from the lowest modes associated with the surface gravitational waves.

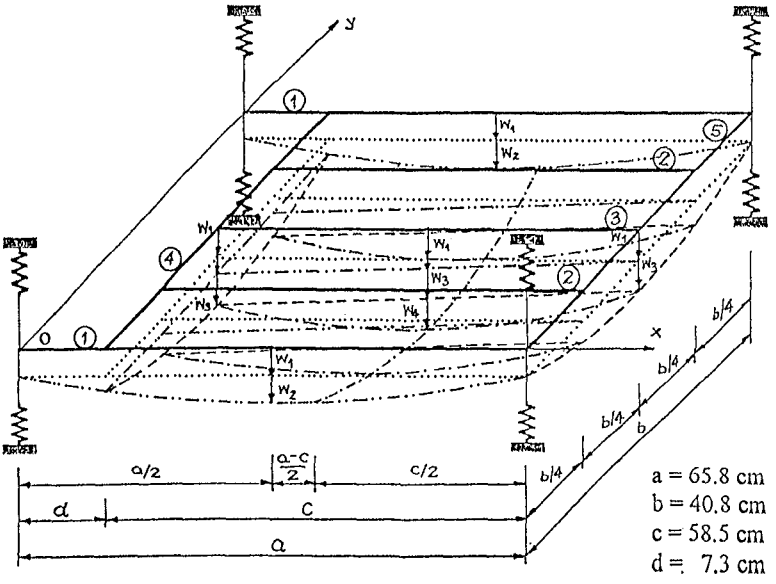

Fig. 5. The theoretical model of the plate.

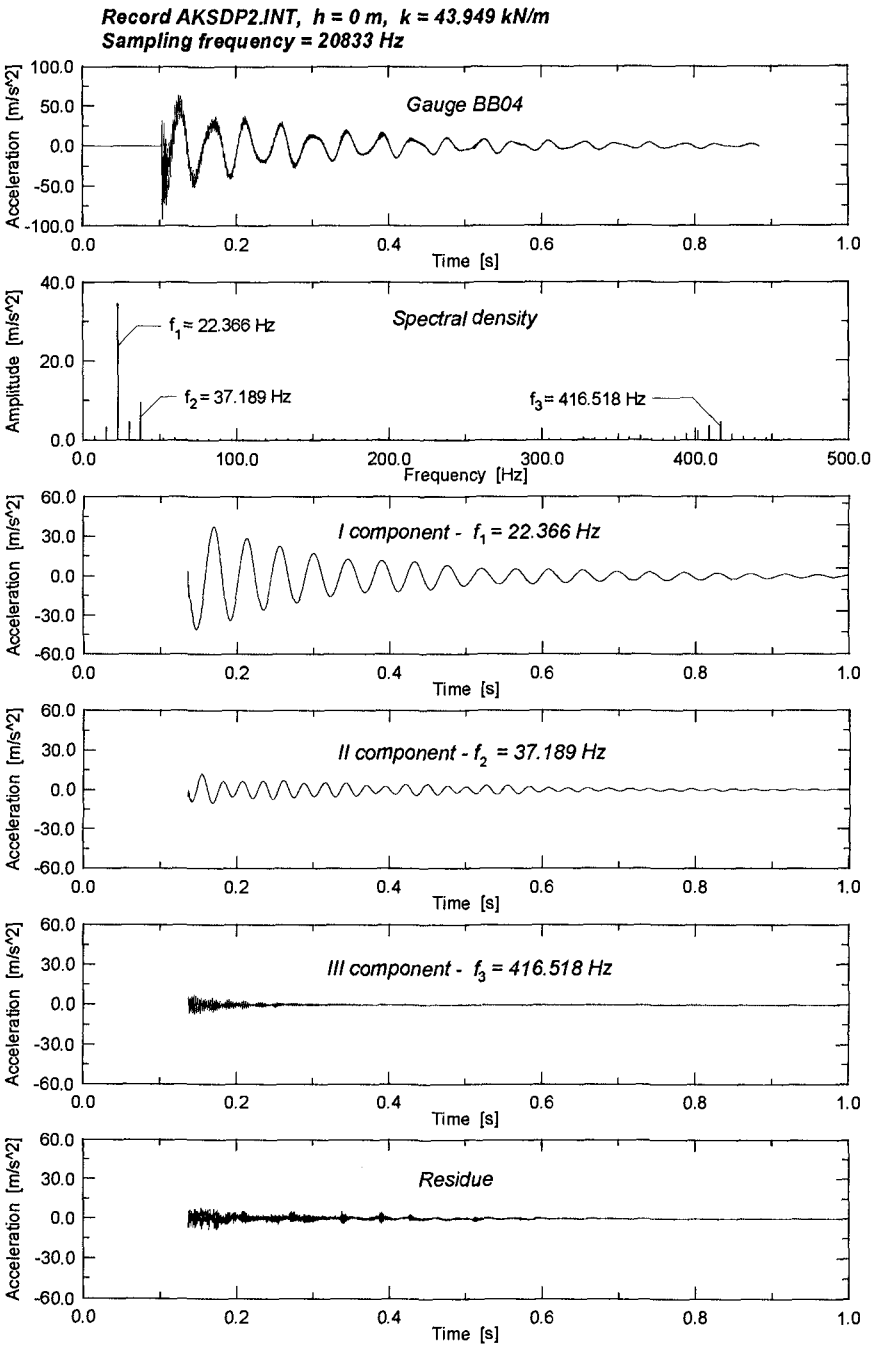

Fig. 6. The decomposition of acceleration in free vibration in air (initial displacement).

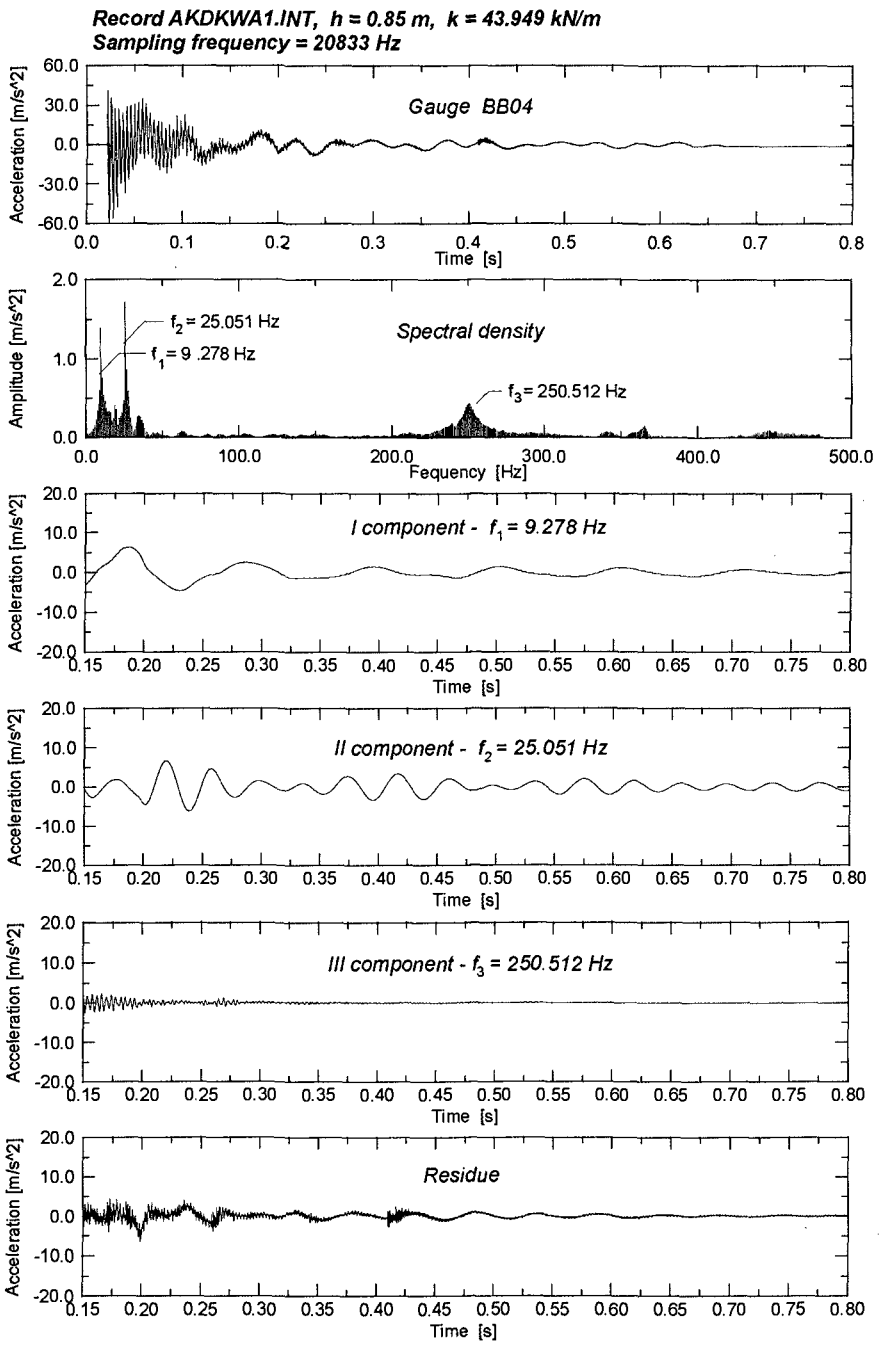

Fig. 7. The decomposition of vibrations in contact with water (initial displacement).

Therefore, the basic experiments mentioned so far were supplemented with experiments concerning vibrations of the plate initially resting on the surface of calm water (floating plate). The vibrations were induced by initial displacements of the plate or, by a hammer strike on it. In order to identify the lowest eigenmodes of the plate vibrations, the theoretical model of the plate shown in Fig.5. was constructed. The experiments started with vibrations of the plate in air. Some of the results obtained are illustrated in Fig.6, where the acceleration record is presented. The experimental results were confirmed in theoretical calculations based on a simplified

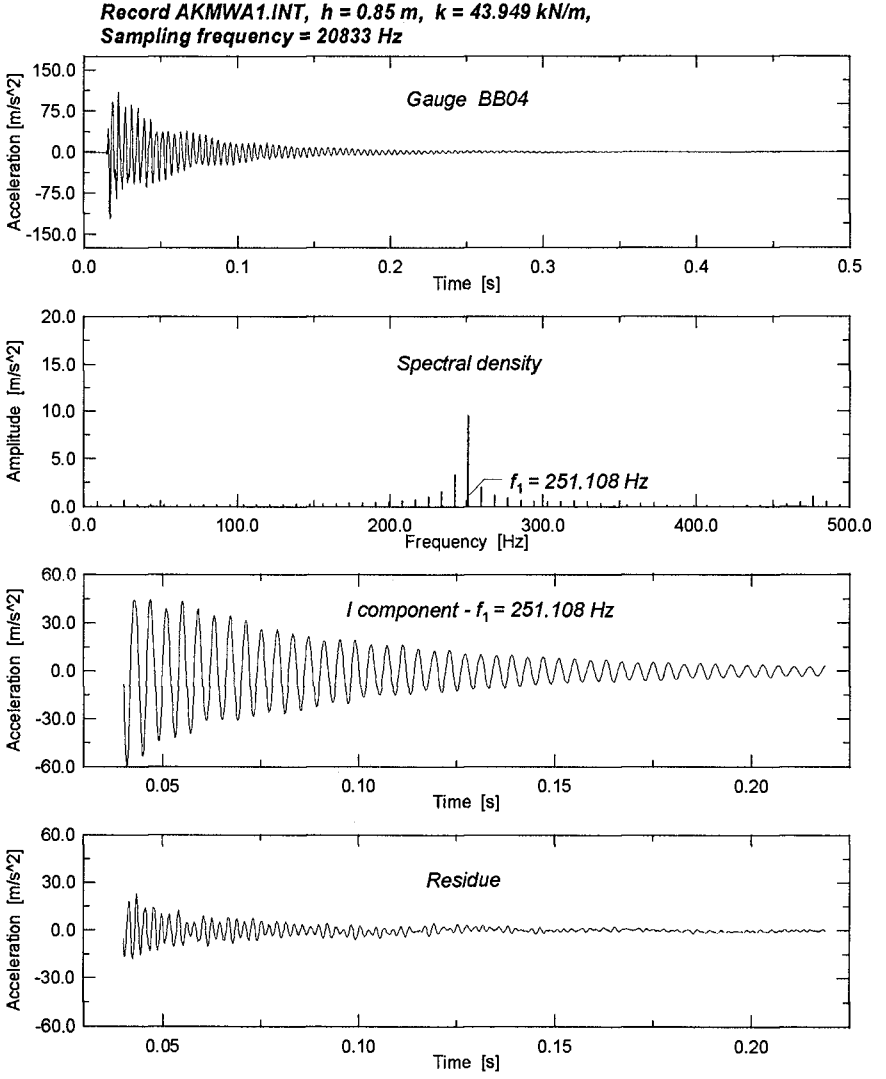

Fig. 8. The vibrations in contact with water induced by an impulse (hammer test).

model of the dynamical system shown in Fig.5. A similar test was performed for the plate having a contact with water. Like in the previous case, the vibrations of the plate were induced by an initial displacement of it. The results obtained in the experiments are shown in Fig.7. The spectral density of the plate vibrations in contact with water is shifted to the left (in the direction of lower values) as compared to the case of vibrations in air. The changes of eigenfrequencies are due to covibrating masses of fluid. The vibrations of the plate induced by a hammer strike are illustrated in Fig.8. where an acceleration record is shown. When compared to the afore-going cases we have here almost exclusively one component corresponding to flexural vibrations of the plate. This is a result of the method used to induce the vibrations of the system mentioned From the acceleration plots it is seen, that the vibrations of the system are damped. In the case of vibrations in air we have the so called structural damping resulting from energy dissipation within the material (the mechanical energy is transformed into heat and dissipated in cyclic deformations). In the case of vibrations of the plate – fluid system, the damping is a result of the dissipation of energy mentioned above and the transmission of energy outside the structure by dilatational waves. It is worth to add, that during reflections of the propagating waves from the flume boundaries, some energy is transmitted outside the fluid.

3. Fluid compressibility and a structure-fluid interaction.

From the experiments performed it follows, that in analysis of a structure loaded with impact pressure forces of fluid and, or vibrating in contact with fluid, the elastic deformation of the structure and the small compressibility of the fluid must be taken into account. Accordingly, for higher frequencies of the vibrations, the dilatational waves generated play an important role in proper estimation of the structure – fluid dynamical interactions. In order to get a better insight into the phenomena considered, the problem of harmonic vibrations of a structure submerged in an infinite domain of compressible fluid has been investigated. In particular, we have confined our attention to the plane problem of harmonic vibrations of an infinite elliptical cylinder immersed in the compressible fluid domain. The solution derived corresponds to the vibrations of the cylinder in the direction of the smaller axis of the ellipse. In the limit, the smaller axis of the ellipse was assumed to decrease to zero and, the solution for the ellipse approached the solution for an elastic infinite plate vibrating in the fluid. In this way, the solution for the ellipse was converted into the solution for the plate. For comparison, a similar problem for an infinite circular cylinder was also considered. The solutions obtained enable us to calculate the resultant force R of the fluid pressure acting on the cylinder or thin plates vibrating in fluid:

$$R = \ddot{w}(t)\cdot\rho\cdot\pi\cdot b_x^2\cdot F_M(h) + \dot{w}(t)\cdot\omega\cdot\rho\cdot\pi\cdot b_x^2\cdot F_T(h), \quad h = \frac{\omega\cdot a}{c}, \tag{1}$$

where: ρ is the fluid density, ω is the angular frequency of vibrations , a is the radius of the cylinder, c is the velocity of sound in fluid, $\dot{w}$ and $\ddot{w}$ are the velocity and the acceleration of the cylinder (or the plate). In the case of the cylinder $b_x = a$ and, in the case of the plate $2b_x = 2a$ is the plate width. The resultant force has two components: the first one corresponding to the covibrating mass of fluid, and the second – describing the damping of vibrations. The plots of the resultant components for the rigid body vertical motion of the circular cylinder and a band plate are shown in Fig.9. Similar plots of the resultant components for the flexural and rotational vibrations of the plate are presented in Fig.10. From the plots it is seen, that with

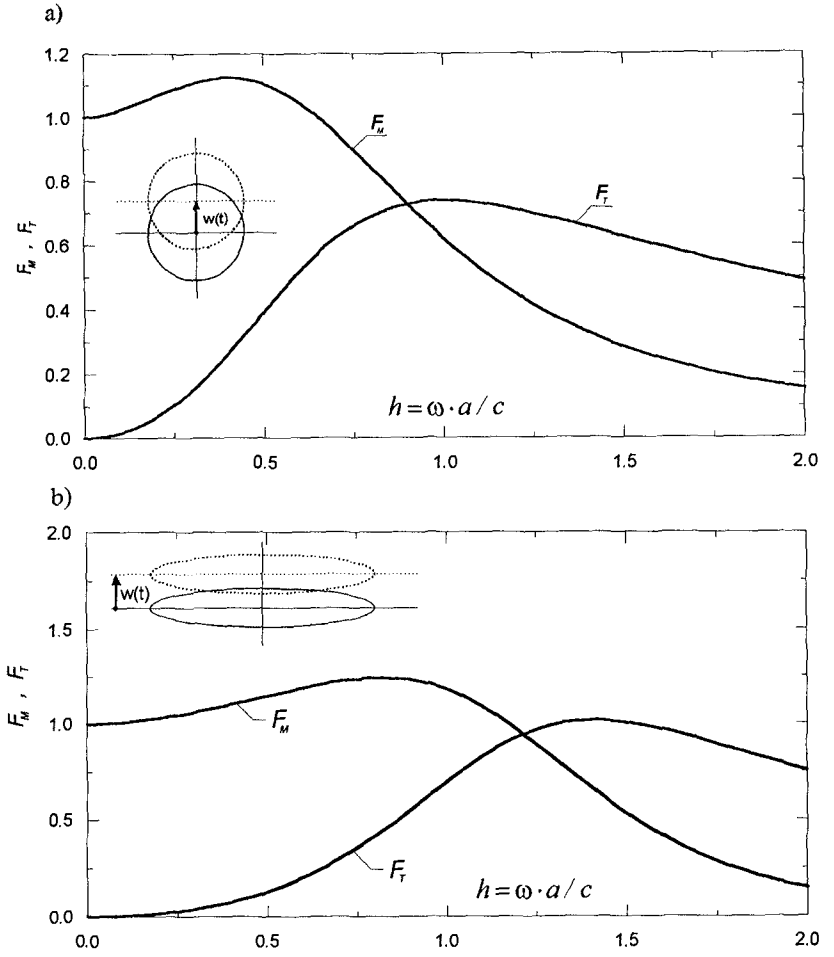

Fig. 9. The influence of compressibility. The coefficients $F_M(h)$ and $F_T(h)$ for vertical vibrations of a circular cylinder (a) and, a band plate (b).

neglecting the fluid compressibility in description of the problem considered , no information about damping of structure vibrations can be obtained. In other words, the fluid compressibility is important in proper estimation of the covibrating mass of fluid and is essential in calculating damping of vibrations.

4. Conclusions.

The phenomenon of impact pressure forces induced by water waves has been examined experimentally by means of a horizontal plate supported elastically in a hydraulic flume. The pressure, wave and acceleration gauges allowed for recording the relevant parameters in the time domain. With respect to the results of the experiments, a theoretical solution to the problem of harmonic vibrations of an elastic band plate submerged in an infinite domain of compressible fluid has also been

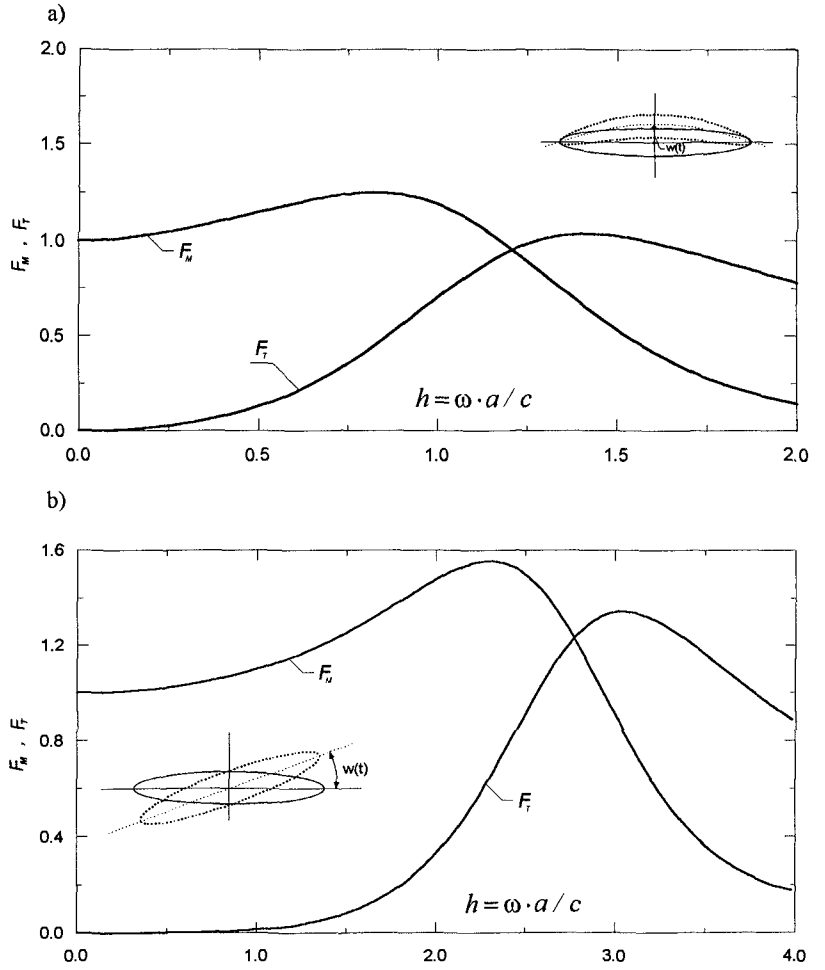

Fig. 10. The influence of compressibility. The coefficients $F_M(h)$ and $F_T(h)$ for flexular (a) and, rotational (b) vibrations of a band plate.

derived. From the results of experimental and theoretical investigations performed, the following conclusions may be withdrawn:

a) The value of the impulse strongly depends upon the elasticity of the supports of the plate. Thus, the problem has to be studied as a problem in hydro-elasticity.
b) In the first stage, due to the impact, progressive dilatational waves appear in water and a lot of eigenfrequencies of the structure are initiated. This stage is difficult to be described by a theoretical model.
c) In the next stage damped vibrations appear. In our experiments we observed not only damped rigid body motions, but also damped vibrations due to bending of the plate

d) For higher eigenfrequencies, the compressibility of the fluid and the propagation of dilatational waves have to be taken into account. To get reliable results we had to measure and register the data with 20,000 Hz frequency for each gauge.
e) The experiments with vibrations of the structure placed on the surface of the water due to initial displacement or impulse show that the calculated covibrating mass is in good agreement with experimental values and, the theoretical dissipation of energy due to the propagation of dilatational waves is a reasonable estimate for damping for high frequencies.
f) In our experiments the impact was repeated, but the consecutive presure impulses were random.

Acknowledgement.

A part of this research was supported by the State Committee for Scientific Research, Poland, within grant Nr 7 T07E 067 10.

References.

1. Blevins R.D., 1986, – *Flow – Induced Vibrations*, R.E.Krieger Publishing Company, Malabar, Florida.
2. Lamb H. , 1975, – *Hydrodynamics*, Cambridge University Press.
3. Moon P., Spencer D.E., 1966 – *Field theory for engineers* (in Polish), PWN, Warszawa.
4. Morse P.M., Feshbach H. – *Methods of Theoretical Physics* (in Russian), Izdatielstwo Inostrannoj Litieratury, Moskwa, vol.I – 1958, vol.II – 1960.

Two and three-dimensional pressure-impulse models of wave impact on structures.

Deborah J. Wood [†] and D. Howell Peregrine [‡]

Abstract

For violent wave impacts against sea walls and breakwaters Cooker and Peregrine (1990,1992) suggest the use of a pressure-impulse model. Here the model is used for three-dimensional examples.

1. Introduction

When a wave is breaking or near breaking when it hits a wall then very high, short lived, pressures can occur. Though this peak in pressure occurs for only a short period of time the magnitude is often many times larger than any other pressures associated with the impact, and maybe enough to cause damage to a structure such as a sea wall or breakwater. This peak in pressure is quite difficult to predict because, as Bagnold noted (Bagnold, 1939), pressures for similar waves vary considerably, whereas pressure impulse (the integral of pressure with respect to time, over the duration of the impact) has less variation.

Pressure impulse, as given in Lamb (1932) and Batchelor (1967), has been used to provide a theoretical model for wave impact by Cooker and Peregrine (1990, 1992, 1995). Chan (1994) and Losada, Martin and Medina (1995) have shown that this theory compares well with experiment. Pressure impulse theory has been further used for impacts in containers (Topliss, 1994) and impacts under a deck (Wood and Peregrine, 1996). A useful property of pressure-impulse theory is the relative insensitivity to the geometry of the problem.

[†]Research assistant, School of Mathematics, University of Bristol, University Walk, Bristol, BS8 1TW, UK, (*Deb.Wood@bristol.ac.uk*)

[‡]Professor of Applied Mathematics, School of Mathematics, University of Bristol, (*D.H.Peregrine@bristol.ac.uk*)

Many theoretical and experimental studies of wave impact on a vertical wall are two-dimensional. However, it is clear that for a wave impacting on a structure, such as a breakwater, the impact is rarely two-dimensional. Nevertheless, if the wave crest is sufficiently wide at impact then the impact can be considered to be two-dimensional towards the centre of the wave. This is where the highest pressures are expected to occur. Here we present three-dimensional examples which can be used directly, or to judge when the two-dimensional result is adequate.

2. Pressure impulse

Let p be the excess pressure over atmospheric. The pressure impulse P is defined by

$$P = \int_{t_1}^{t_2} p dt, \tag{1}$$

where t_1 and t_2 are the times just before and after impact respectively.

Choosing units made dimensionless with the water density, ρ, a typical impact velocity, U, and length scale, H, the total depth of water at impact, we follow Cooker and Peregrine (1990, 1992, 1995) and simplify the equation of motion to

$$\frac{\partial \mathbf{u}}{\partial t} = -\nabla p, \tag{2}$$

for the short time interval, Δt, of the impulse, when for almost all the velocity field the rate of change of velocity, $\mathbf{u}$, is the dominant term. Integration with respect to time over the duration of the impact gives:

$$\mathbf{u}_2 - \mathbf{u}_1 = -\nabla P, \tag{3}$$

where $\mathbf{u}_2$ and $\mathbf{u}_1$ are the velocities after and before impact respectively. Now we assume the water is incompressible before and after impact, and so we have $\nabla.\mathbf{u}_2 = \nabla.\mathbf{u}_1 = 0$. Therefore we need to solve

$$\nabla^2 P = 0 \tag{4}$$

in the fluid domain, subject to appropriate boundary conditions.

The boundary conditions can be grouped into three different types:

1)At the free surface the $p = 0$, so

$$P = 0. \tag{5}$$

2)At points on a rigid boundary where impact occurs the velocity component perpendicular to the boundary is taken to be zero after impact, and some function of position, V, before impact. Using the normal component of equation (3) we find:

$$\partial P/\partial n = V, \tag{6}$$

where n is in the normal direction to the surface pointing into the fluid. We often choose V to be uniform in space, for want of better information, as a reasonable

simplifying assumption. Then, choosing V to be the velocity scale U, and to be in the direction towards the wall, equation (6) simplifies to give:

$$\partial P/\partial n = -1. \tag{7}$$

3)At points on a fixed rigid boundary where no impact occurs the velocity normal to the boundary is zero both before and after impact, and thus

$$\partial P/\partial n = 0. \tag{8}$$

The far-field condition is that $P \to 0$.

Hence, to find a pressure-impulse model for an impact problem we must solve Laplace's equation subject to these boundary conditions. In this paper P is non-dimensional, to get back to dimensional quantities simply multiply P by ρUH. Note that since accelerations are assumed much greater than gravity, see equation (2), this approach only applies to violent impacts.

3. Impact on a wall.

Chan (1994), figure 19, examines the model from Cooker and Peregrine (1990, 1992) and looks at plots of pressure impulse down the wall, varying the depth of water but keeping the impact region size constant. As the water depth becomes the large, there is a 'tail' to the pressure impulse distribution down the wall. Cooker and Peregrine (1995) gives the infinite depth solution, which when integrated gives logarithmic divergence giving a total impulse that is infinite. This shows that for deep water cases this model is inadequate. This emphasises the importance of examining three-dimensional effects.

3.1. Three-dimensional impact on a wall.

Consider the impact of a body of water on a patch of a wall. Cooker and Peregrine (1995) noted that unless the width of the impacting water is quite small the actual shape of the wave away from the impact region is relatively unimportant. So we simplify the free surface to be horizontal and let A denote the area of the patch. We use the boundary conditions described in section 2. On the free surface the usual condition of $P = 0$ is required. The patch is where impact takes place so we need $\partial P/\partial y = V(x, z)$, with y in the direction normal to the patch and into the water, with x and z as shown in figure 1. On the rest of the wall no impact occurs so we require $\partial P/\partial y = 0$. Along the bottom of the region of the fluid, on $z = -1$, we have a solid boundary so $\partial P/\partial z = 0$. We also need $P \to 0$ as we move far away from the impact patch. So a solution to Laplace's equation subject to the boundary conditions shown in figure 1 is required.

We can solve this problem in terms of a Fourier series expansion and a Fourier integral. The boundary conditions on the planes $z = 0$ and $z = -1$ enable the separation of the z dependence giving an expression for P:

$$P(x, y, z) = \sum_n P_n(x, y) \sin(\lambda_n z), \tag{9}$$

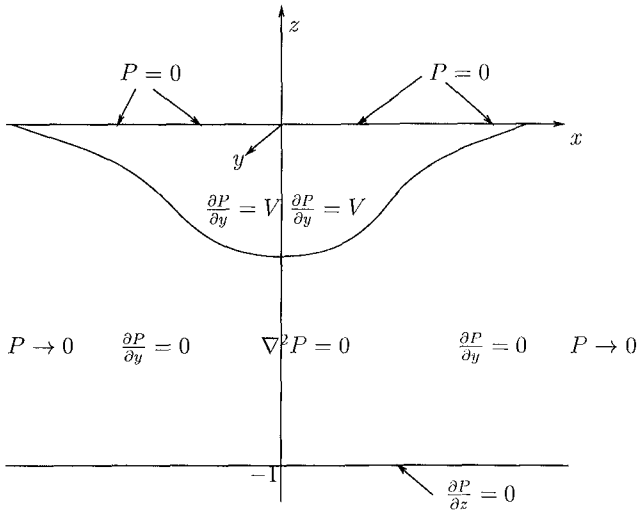

Figure 1: Impact on a patch of a wall. View facing wall.

where $\lambda_n = (n + 1/2)\pi$. A Fourier transform of the problem is taken in the x direction. We assume that the patch is symmetric about $x = 0$ for simplicity. Hence the Fourier cosine transform is defined as:

$$\overline{P_n}(k, y) = \int_{-\infty}^{\infty} P_n(x, y) \cos(kx) dx. \tag{10}$$

The boundary condition on the impact patch becomes:

$$\sum_n \frac{\partial P_n(x, 0)}{\partial y} \sin(\lambda_n z) = V(x, z). \tag{11}$$

Multiply by $\sin(\lambda_r z)$ and integrate with respect to z:

$$\frac{\partial P_r(x, 0)}{\partial y} = 2 \int V(x, z) \sin(\lambda_r z) dz, \tag{12}$$

where the integration in z is, for a given x, over values of z on the patch. Finally we transform this equation in x to give:

$$\frac{\partial \overline{P_n}(k, 0)}{\partial y} = 2 \int \int_A V(x, z) \sin(\lambda_n z) \cos(kx) dz dx, \tag{13}$$

where the integration is over the patch area A.

The transform in x of Laplace's equation leads to:

$$\frac{\partial^2 \overline{P_n}}{\partial y^2} - (k^2 + \lambda_n^2)\overline{P_n} = 0. \tag{14}$$

To simplify the notation we use $m^2 = (k^2 + \lambda_n^2)$. In future expressions it must be remembered that m is dependent on k and n. We require $P(x, y, z) \to 0$ as $y \to \infty$, which means that solving equation (14) gives:

$$\overline{P_n}(k, y) = A_n(k)\mathrm{e}^{-my}, \tag{15}$$

where $A_n(k)$ are functions of k, to be found using the boundary condition at the wall. Then equations (13) and (15) give:

$$A_n(k) = -\frac{2}{m}\int\int_A V(x, z)\sin(\lambda_n z)\cos(kx)dxdz. \tag{16}$$

The final step is to take the inverse transform of equation (15) and substitute into equation (9) to obtain the Fourier sum for P:

$$P(x, y, z) = \sum_n \frac{1}{\pi}\int_0^\infty A_n(k)\mathrm{e}^{-my}\sin(\lambda_n z)\cos(kx)dk, \tag{17}$$

with $A_n(k)$ given by equation (16).

Next consider the specific case of a rectangular patch of depth d and width $2a$ (symmetric about $x = 0$). $V(x, z) = -1$ on the patch. Now we can carry out the integration in equation (16) directly to obtain

$$A_n(k) = -\frac{4}{k\lambda_n m}\sin(ka)\left[1 - \cos(\lambda_n d)\right]. \tag{18}$$

Using (17), for this specific case, we obtain the Fourier sum for P:

$$P(x, y, z) = -\sum_n \frac{4}{\pi\lambda_n}\left[1 - \cos(\lambda_n d)\right] I(n, x, y)\sin(\lambda_n z), \tag{19}$$

where

$$I(n, x, y) = \int_0^\infty \frac{\sin(ka)\cos(kx)\mathrm{e}^{-(k^2+\lambda_n^2)^{1/2}y}dk}{k(k^2 + \lambda_n^2)^{1/2}}. \tag{20}$$

To evaluate pressure impulse for this problem the Fourier series must be truncated. For a patch of height 0.1 the difference between taking 20 and 50 terms is only 4% and for a patch of height 1, the difference is substantially less. The integration is carried out using NAG routine D01ASF, which treats the integral as a Fourier cosine transform. This enables us to evaluate pressure impulse for this problem. Of particular interest are the contours of pressure impulse on the wall itself, as shown in figure 2 for a patch of height 0.2 and width 2.

The total impulse is 1.085 and 0.085 for patches of width 2 and depths 1 and 0.2 respectively. If integration is only taken over the central width $2a$ then

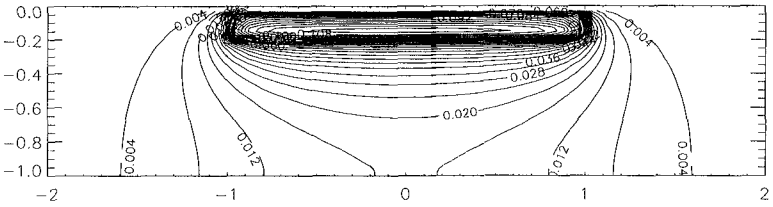

Figure 2: Pressure-impulse contours for impact on a patch of a wall where the patch covers the top 20% of the wall below the water level and is width 2.

the corresponding values are 0.878 and 0.074. As expected the larger the area of impact the larger the total impulse. Figure 3 shows a plot of total impulse against depth of water (the total impulse has been temporarily been scaled to have depth of impact 1 as our length scale H, to compare with Chan (1994)), where the integration is over the central width of $2a$, and the impact region is the top distance 1. We note that the total impulse seems to tend to a finite value instead of increasing with depth of water below the impact region, as predicted by the two-dimensional solution. It is more realistic that as the depth of water at the wall becomes very deep that the total impulse tends to a finite value.

Figure 4 shows a comparison of the pressure impulse on the wall for the two-dimensional impact model and down the centre line of the three-dimensional 'patch' model. For the comparison impact on the top 20% of the depth of water is used. Even when the patch width is twice the water depth at the wall the 'patch' model shows a lower pressure impulse down the centre line than is found using the two-dimensional model. For narrower patches the difference is more significant. The difference between the pressure impulse down the centre line for the three-dimensional 'patch' and two-dimensional models is much larger if we move away from the centre line.

Figure 5 is a plot of pressure impulse at the base of the wall under the centre of the patch for varying values of d (the depth of the impact patch). As expected increasing the depth of impact increases the pressure impulse at the base of the wall. Figure 6 shows a plot of P/P_m offshore on the bed along the line of symmetry for a comparison of the Cooker and Peregrine two-dimensional model, and the 'patch' model with a patch of length 0.5, 1 and 2 all for $d = 0.5$ and depth of water 1. P_m is the value of P at the middle bottom of the wall. This shows that once the pressure impulse has been scaled by the value at the wall all the curves are similar in nature. However, as expected once the patch length is 1 or smaller there is a significant difference between the values predicted by the two-dimensional model and the 'patch' model.

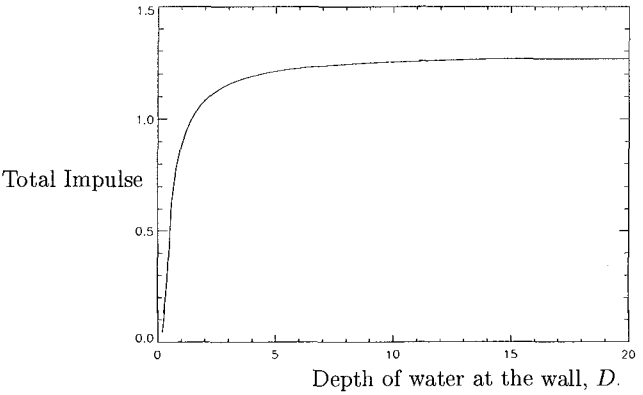

Figure 3: Total impulse against depth of water at the wall, for three-dimensional impact on a patch of a wall, where the integration is over the central width of $2a$ ($a = 1$), and the impact region is the top portion of depth 1. The total impulse has been temporarily rescaled (for this diagram only) to have the unit length scale as the depth of impact, and D as the depth of water at the wall.

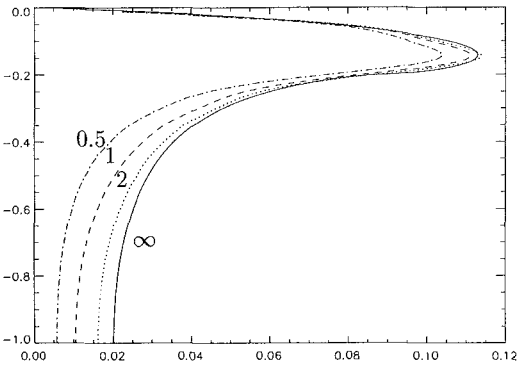

Figure 4: Pressure impulse along the centre line for the for patches of width 0.5, 1, 2, and two dimensional model (∞) of impact on a wall, with impact on the top 20%.

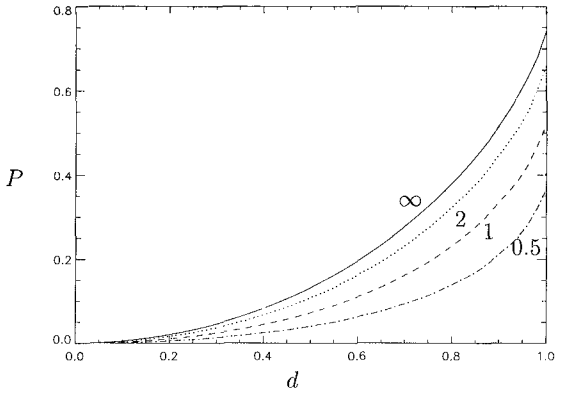

Figure 5: Pressure impulse at the base of the wall in line with the centre of the patch for patches of width 0.5, 1, 2, and two-dimensional model (∞), varying the depth of the impact region.

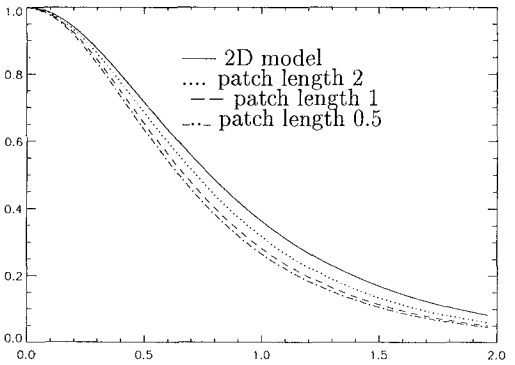

Figure 6: Plot of P/P_m offshore on the bed along the centre of the line of symmetry for a comparison of the Cooker and Peregrine two-dimensional model, and the 'patch' model with a patch of length 0.5, 1 and 2. $d = 0.5$, depth of water 1. P_m is the value of P at the middle bottom of the wall.

4. Semi-infinite patch of impact.

We need to have a clearer way of comparing the 'patch' model and the two-dimensional case. If the patch is sufficiently long, at or towards the centre of the patch the solution is the same as for the two-dimensional case. Hence, for a given length of patch, we need to estimate how far into the patch it is reasonable to assume that the solution has become two-dimensional. For a finite patch, this is difficult to assess as both ends of the patch have an effect on the solution. So we next consider a semi-infinite patch.

Figure 7 shows the problem we need to solve for impact on a semi-infinite region of the wall. We again take our length scale H as the depth of water at the wall, and work in dimensionless quantities. As we need to impose the

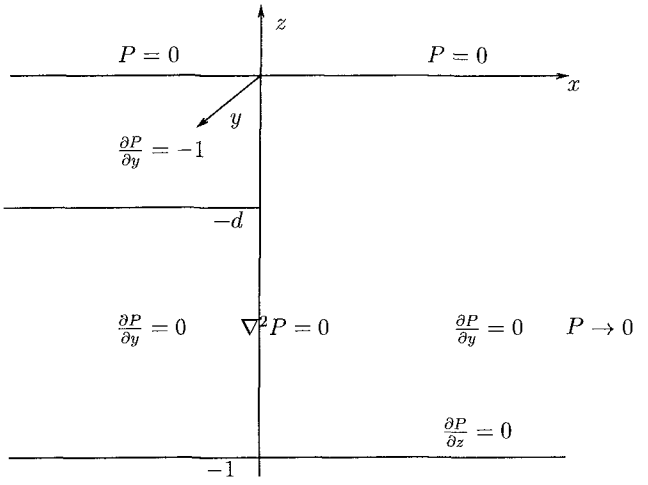

Figure 7: Impact on a semi-infinite patch of a wall. View facing wall.

forcing condition on the patch over a semi-infinite region we solve using a slightly different method to that used for the finite patch. We split the problem up into the two regions $x < 0$ and $x > 0$, the solutions to which we will denote as P_l and P_r respectively. We then use continuity of P and $\partial P/\partial x$ along the line $x = y = 0$, to find the solution. We consider first the solution in the left hand region. As $x \to -\infty$ the solution will tend to the two-dimensional solution for impact on a wall (denoted now by P_{2D}). If we subtract the solution, P_{2D}, for the two-dimensional problem off P_l then the remaining problem whose solution is P_{re} is the same as in left hand region of figure 7 except that the condition over the patch is now $\partial P/\partial y = 0$. So $P_{re} = P_l - P_{2D}$, we solve this problem for P_{re} and then $P_l = P_{re} + P_{2D}$. In a similar manner to the solution of the finite

patch model we take a Fourier transform of the problem, for P_{re}, but this time the Fourier transform is a Fourier-cosine transform in the y direction (since we'll need to match with the right hand side along $x = 0$).

$$\overline{P_{re}}(x, k, z) = 2\int_0^\infty P_{re}(x, y, z)\cos(ky)dy. \tag{21}$$

The solution is given by:

$$P_{re} = 2\int_0^\infty \sum_n A_n(k)\mathrm{e}^{mx}\sin(\lambda_n z)\cos(ky)dk, \tag{22}$$

where $\lambda_n = (n + \frac{1}{2})\pi$, $m^2 = k^2 + \lambda_n^2$, and the A_n are obtained by the continuity conditions given at $x = 0$.

The solution to the two-dimensional problem (Cooker and Peregrine 1990,1992, rescaled to have the length scale as the depth of water at the wall) is given by

$$P_{2D} = -\sum_n \frac{2}{\lambda_n^2}[1 - \cos(\lambda_n d)]\sin(\lambda_n z)\mathrm{e}^{-\lambda_n y}, \tag{23}$$

hence

$$\begin{aligned} P_l = {} & 2\int_0^\infty \sum_n A_n(k)\mathrm{e}^{mx}\sin(\lambda_n z)\cos(ky)dk \\ & - \sum_n \frac{2}{\lambda_n^2}[1 - \cos(\lambda_n d)]\sin(\lambda_n z)\mathrm{e}^{-\lambda_n y}. \end{aligned} \tag{24}$$

Solution in the right hand region is similar to P_{re}. The conditions at $z = 0$, $z = -1$ and on the wall are the same. However we require P_r to be positive, and to decrease to zero as $x \to \infty$ instead of being negative and increasing to zero as $x \to -\infty$ (as P_{re}). The change in sign in front of the x is to satisfy the conditions at $x = \pm\infty$, and the negative in front of the whole expression is to ensure continuity of pressure-impulse gradient at $x = 0$. Hence P_r is given by $-P_{re}(-x, y, z)$:

$$P_r = -2\int_0^\infty \sum_n A_n(k)\mathrm{e}^{-mx}\sin(\lambda_n z)\cos(ky)dk, \tag{25}$$

From continuity of P at $x = 0$ we find that:

$$\begin{aligned} A_n(k) &= \frac{1}{\pi\lambda_n^2}[1 - \cos(\lambda_n d)]\frac{\lambda_n}{k^2 + \lambda_n^2} \qquad k \neq 0 \\ A_n(0) &= \frac{1}{2\pi\lambda_n^3}[1 - \cos(\lambda_n d)] \qquad k = 0. \end{aligned} \tag{26}$$

Integration is carried out in a similar manner to that used in the evaluation of the pressure impulse for the finite patch impact. Hence P is given by equation (24) for $x < 0$ and equation (25) for $x > 0$, with A_n given in equation (26).

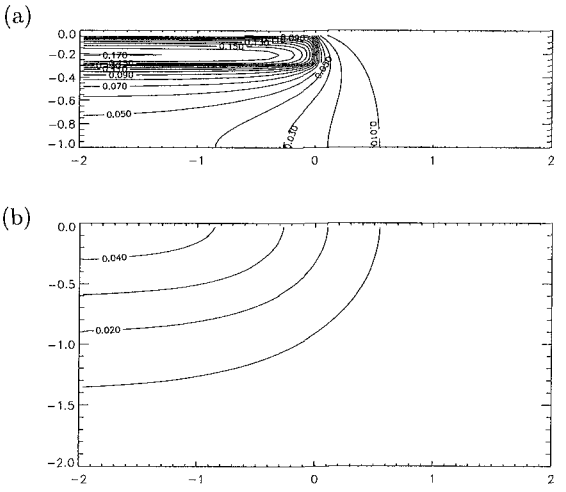

Figure 8: (a) Pressure-impulse contours, for the semi-infinite patch, on the wall for a patch of depth 0.3. (b) Pressure-impulse contours, for the semi-infinite patch, on the bed in front of the wall for a patch of depth 0.3.

Figures 8 (a) and (b) show pressure impulse contours, for the semi-infinite patch, on the wall and base respectively for a patch of depth 0.3.

When the patch is of depth 0.3 the values calculated by the two-dimensional model only approximate the three-dimensional values well at a distance into the patch of two times the depth of the water i.e. the width of influence of the boundary conditions outside of the patch is twice the depth of the water. Figure 9 is a plot of P along the bottom of the wall for different depths of patch (scaled by the two-dimensional model value). If we examine this then we can see that the depth of impact has little effect on the influence distance of the three-dimensional boundary into the patch. If we look at a distance of 0.5 into the patch (along the bottom of the wall), we can see that the pressure impulse is only approximately 0.775 and 0.850 of the two-dimensional value for patches of depth 0.2 and 1.0 respectively.

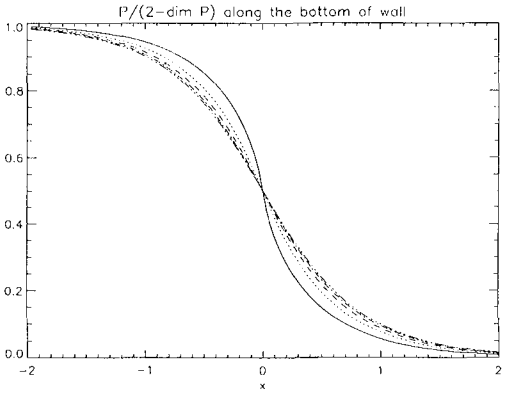

Figure 9: P/(2D value) for the semi-infinite patch as a function of position along the base of the wall, for $d = 0.2, 0.4, 0.6, 0.8, 1.0$ (from left to right in the top half of the graph).

This semi-infinite solution can be used to give an alternative derivation of the rectangular patch case, namely:

$$x > \frac{a}{2}, \quad P_r(x - \frac{a}{2}, y, z) - P_r(x + \frac{a}{2}, y, z) \tag{27}$$

$$-\frac{a}{2} < x < \frac{a}{2}, \quad P_l(x - \frac{a}{2}, y, z) - P_r(x + \frac{a}{2}, y, z) \tag{28}$$

$$x < -\frac{a}{2}, \quad P_l(x - \frac{a}{2}, y, z) - P_l(x + \frac{a}{2}, y, z) \tag{29}$$

$$\tag{30}$$

5. Conclusions

The Cooker and Peregrine (1990,1992) pressure-impulse model for impact on a plane vertical wall has been used for three-dimensional examples. The extension of this work to the impact on a semi-infinite patch of wall allowed conclusions to be drawn as to what distance into the patch we could assume two-dimensionality. The length of influence was found to be about twice that of the height of the wall. Interestingly, this distance of influence is little affected by the percentage of the water depth involved in impact. We conclude that if the wave impact width is greater than four times the height of the wall, then a two-dimensional model can be used to predict peak pressure impulse. However for waves with crest width less than twice the water depth three-dimensional effects play a significant role and should be included.

It is thought that comparison with experiment would lead to greater understanding of three-dimensional effects. However, the difficulties associated with estimating the width of the wave crest at impact from experiment means that as yet this has not been possible.

Acknowledgements

Support of the U.K. EPSRC and the European Commission, Directorate General XII, Science, Research and Development, contract number MAS3-CT95-0041, is gratefully acknowledged.

References

BAGNOLD, R.A. (1939). Interim report on wave pressure research. *J. Inst. Civil Engrs* **12**, 201-226.

BATCHELOR, G.K. (1967). *An Introduction to Fluid Dynamics* Cambridge University Press.

CHAN, E.S. (1994). Mechanics of deep water plunging-wave impacts on vertical structures. *Coastal Engng* **22**, 115-133.

COOKER, M.J. & PEREGRINE, D.H. (1990). A model for breaking wave impact pressures. *Proc. 22nd Internat. Conf. Coast. Engng., ASCE* 1473-1486.

COOKER, M.J. & PEREGRINE, D.H. (1992). Wave impact pressure and its effect upon bodies lying on the sea bed. *Coastal Engng.* **18** 205-229.

COOKER, M.J. & PEREGRINE, D.H. (1995). Pressure-impulse theory for liquid impact problems. *J. Fluid Mech.* **297** 193-214.

LAMB, H. (1932). *Hydrodynamics.* 6th Edn. Cambridge University Press.

LOSADA, M.A., MARTIN, F.L. & MEDINA, R. (1995). Wave kinematics and dynamics in front of reflective structures. *Wave forces on inclined and vertical wall structures. ASCE* editors N. Kobayashi & Z. Demirbilek 282-310

TOPLISS, M.E. (1994). Water wave impact on structures. Ph.D. dissertation, University of Bristol.

WOOD, D.J. & PEREGRINE, D.H. (1996) Wave impact beneath a horizontal surface. *Proc. 25th Internat. Conf. on Coastal Engineering Orlando, ASCE* vol 3, 2573-2583

Thyborøn Barriers – A Mastercase of Coastal Engineering

Per Roed Jakobsen[1], Ida Brøker[2], Jesper Holt Jensen[3], Ann Skou[4], Sanne Poulin[4]

Abstract

Thyborøn, Denmark is placed at the entrance to a fjord system, which connects the North Sea with Kattegat. The inlet acts as a trap for the littoral transport from both sides. The adjacent barrier beaches suffer from severe erosion, which is alleviated by large structures and nourishment. The entrance was formed only 135 years ago and is still undergoing morphological changes. During its lifetime engineers have investigated various schemes for stabilising the shoreline – the most radical suggestion has been to close the entrance to avoid the ongoing loss of beach material. The present paper presents the major findings of a comprehensive study of the hydrographic and geological conditions, the coastal processes and the morphological evolution.

Background

In 1862 the North Sea breached a since then permanent gap in the 22 km long Thyborøn Barriers and created a coastal scenario which over the years has occupied and challenged Danish coastal engineers. Shortly after the breach the construction of a large groyne system was initiated. Today the barrier beaches are managed by maintenance of the structures, controlled withdrawal, and major nourishment with about 750,000 m^3/year of coarse sand.

There are three major reasons for taking a conclusive review of the behaviour of the system:

1. A law of 1970 was prepared on the final assumption, that it was acceptable to leave the Channel open. Danish Coastal Authority is conditioned to monitor the development. Does the assumption hold at the 25-year anniversary?
2. Despite 135 years of dynamic evolution, the system has not yet achieved a full equilibrium since profile steepening is ongoing as well as long-term changes in channel configuration.
3. Modern model tools enable a more detailed and integrated description of processes allowing for improved verification of project assumption such as littoral transport in original and now steep profiles.

1 Director, Danish Coastal Authority (DCA), Højbovej 1, DK 7620 Lemvig, E-mail ki@kyst.dk
2 Head of Department, Danish Hydraulic Institute (DHI), Agern Allé 5, DK 2970 Hørsholm, E-mail ibh@dhi.dk
3 Project engineer, Danish Coastal Authority (DCA), Højbovej 1, DK 7620 Lemvig
4 Coastal engineer, Danish Hydraulic Institute (DHI), Agern Allé 5, DK 2970 Hørsholm

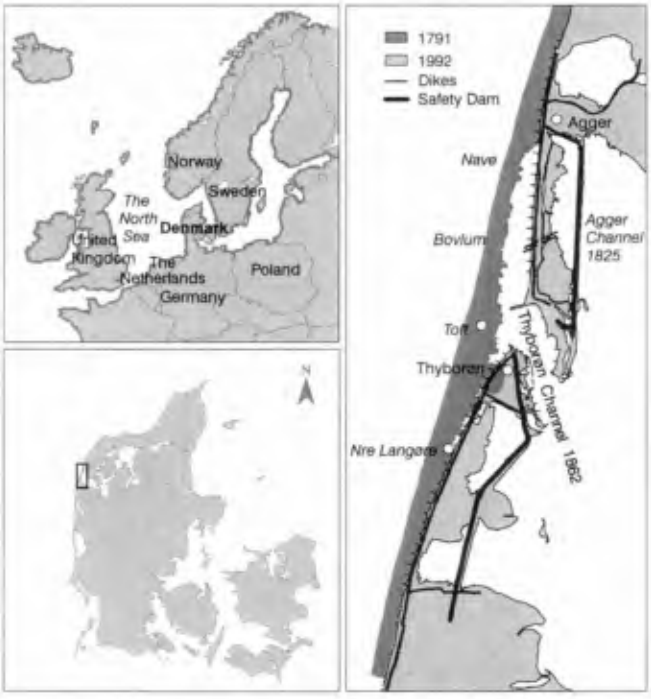

Figure 1. Location map, including overall system description and 205 years of development.

Historical Review

The generation of the present barriers started around year zero as a part of smoothening of the coastline. From the Icelandic sagas is known that there has been a connection between the fjord and the North Sea since there are narratives of the vikings' passing on to the North Sea through the Limfjord in the 11'th century. The barrier system at the earliest closed about year 1100.

There have been multiple breaches in the barriers during the period from 1600 until 1800, but none serious until 1825 where the Agger channel was formed and it lasted until 1868. The most severe breach came in 1862 and formed the Thyborøn Channel. Immediately after this the retreat of the coastline started.

Since the construction of the groyne system, the initial flattening of the coast profiles, caused by the excessive recession of the shoreline, was replaced by a gradual steepening of the sea-bed seaward of the groynes, which is ongoing but declining. In the 1930s, this steepening gave rise to deep concern among the responsible engineers who felt that disaster was looming ahead. They feared that the coast profiles were becoming so steep that even a short serie of severe storms could generate such effects that control of the development would be lost. This was called "The Theory of Disaster".

On this basis an act was passed by Parliament in 1946 whereby the Thyborøn Channel would be closed such that the loss of sand from the seacoasts to the Limfjord would be stopped and the seacoasts thereby stabilised. The project included the construction of 16 km of "safety" embankments placed approximately 2 km behind the coastline as well as the building of two major breakwaters and two sluices for vessels and salt water inflow, respectively.

Before the works to close the Channel were commenced, Per Bruun (1954) in his doctoral thesis, Coast Stability, raised serious doubts as to the "disaster theory" which was the basis for the project and proposed new investigations of the problems. Along similar lines, Helge Lundgren in 1954 and 1956 made specific proposals for new investigations, including scale model tests with movable bed to be carried out in Holland, particularly with a view to keeping the channel open and to saving a major part of the project costs.

The government followed these recommendations and a range of studies of various aspects of the problem were initiated, the most important ones of which were carried out at the Technical University of Denmark headed by Helge Lundgren and Torben Sørensen, Lundgren (1968).

The crucial question of whether the steepening of the coast profiles indicated a risk of disastrous development was resolved by an analysis demonstrating that the steepening was simply a question of the coast profiles adjusting to the reduced shoreline recession achieved by the construction of the groyne system, Sørensen (1961). This realisation in fact eliminated the basis for the very expensive and in many ways controversial project. The soundings of coast profiles over 125 years have confirmed the validity of this analysis.

However, the project had a number of other aspects, which also required analysis and considerations. Among those were the statistics of storm flood levels in the North Sea at Thyborøn.

In consequence of these investigations, the 1946-law was repealed in 1970 under the condition that the Danish Coastal Authority should follow the situation for at least 50 years. This was done the first time in 1975. The major conclusion in this work was that the steepening almost had stopped and that the system to some extent was stable.

Today the system configuration is the following. The length of the barrier islands is 22 km and the number of groynes, about 400 m long, in the system is 78. The maximum retreat of coastline since 1862 is 1.5 km, see figure 1. Coastline retreat rate was previously 1-2 m/year but is now mitigated by yearly nourishment. Net erosion in the system is 1.1 Mio m^3/year, channel shoals deposition is about 500 – 700,000 m^3/year and longshore transport from each side is 2 – 500,000 m^3/year. Coastal protection scheme today consists of maintenance of hard structures and yearly nourishment at about 775,000 m^3/year. (485,000 at beach and dike and 290,000 on shore face).

Total value today of the whole system has been estimated to about 1000 Mio DKK (170 Mio US$). Costs of nourishment and withdrawal of groynes and buffer dikes in line with coastline retreat on 1 – 2 m/year are equal, which leaves full flexibility for the detailed policy for coastal maintenance.

Hydrographic conditions

The astronomical tide on this coast is very small, max. 0.3 m, whereas extreme high water levels caused by wind set-up with westerly winds may reach 3.

To give an impression on the weather conditions at the West Coast of Jutland, wind, wave and extreme water level conditions for Thyborøn are shown in figure 2.

Directional wave measurements have been undertaken since 1991. These detailed measurements supplement 15 years of wave height recordings and have formed the basis for the statistical analysis of the wave conditions.

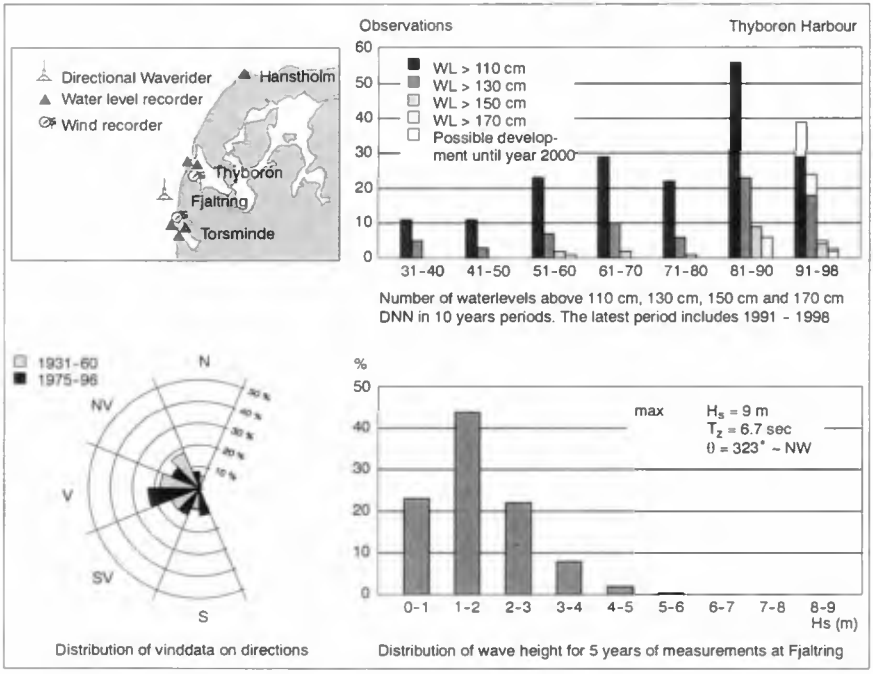

Figure 2. Wave climate and positions of the measurement stations

Geology

The upper layers of the barriers consist of sand and gravel while below –6 m, marine clay can be found to a great extent, eg. about 30 m at Thyborøn. Underneath this are glacial deposits.

The clay layer has been found until 75 km further to the west of the present coastline out on 'Jutland Reef', which consists mainly of deposits of eroded glacial material. This indicates that the glacial formations in the early Holocene period extended further to the west protecting a calm basin where the clay layer could be deposited.

The start of the barriers buildup as a part of the formation of the present glacial coastline is dating back to the start of our era, and the barriers properly closed early in the 12th century, as explained in the historical review.

Sediment transport processes

The sediment transport processes around the inlet have been studied and quantified through a comprehensive set-up of numerical models, see Brøker et al (1996) for details. The various modules comprise a depth-integrated hydrodynamic model MIKE 21HD, a spectral wind wave model MIKE 21 NSW, which is used to transfer waves from the measurement station to the entrance, a mild slope wave model MIKE 21 PMS for the more detailed calculation of wave fields in the entrance area, and a deterministic intra-wave period model for transport of non-cohesive sediment, MIKE 21 ST, see Deigaard et al (1986). The areas covered by the numerical models and the measurement stations, required to drive the modelling complex, are shown in figure 3.

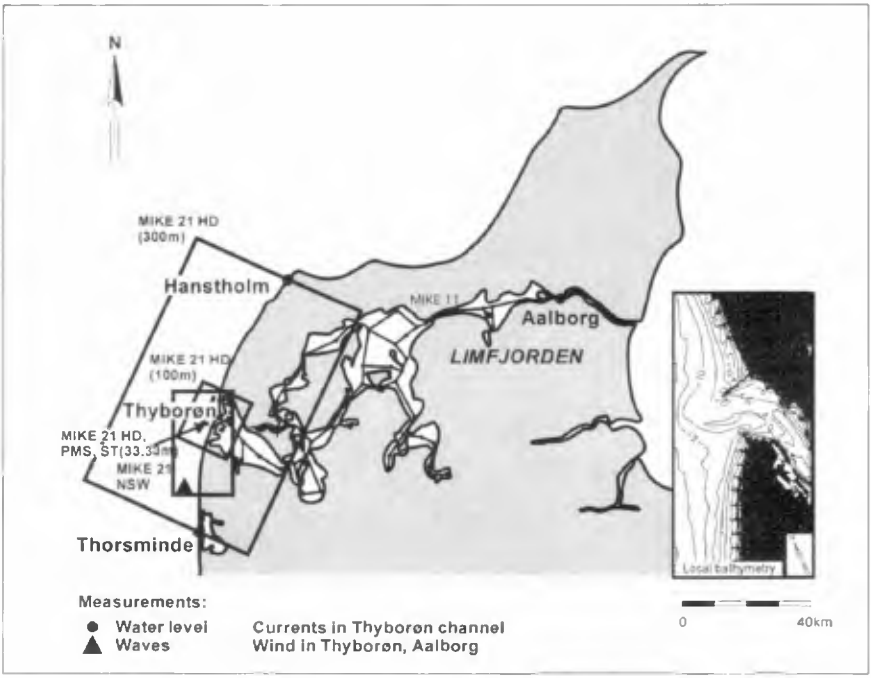

Figure 3. Areas covered by hydrodynamic, wave and sediment transport models, and location of measurement stations.

The meteorology is dominated by low-pressure systems travelling from West towards East. The westerly winds and waves are responsible for the morphological development of the coast. Typically, in the beginning of a westerly storm, the water level rise off Thyborøn, and, due to the connection across the peninsula of Jutland, strong in-going currents may last for the entire storm period, 3 – 5 days. Strong outgoing currents seldom occur in combination with severe wave action. Waves from southwesterly directions cause northward littoral drift along the barrier beaches.

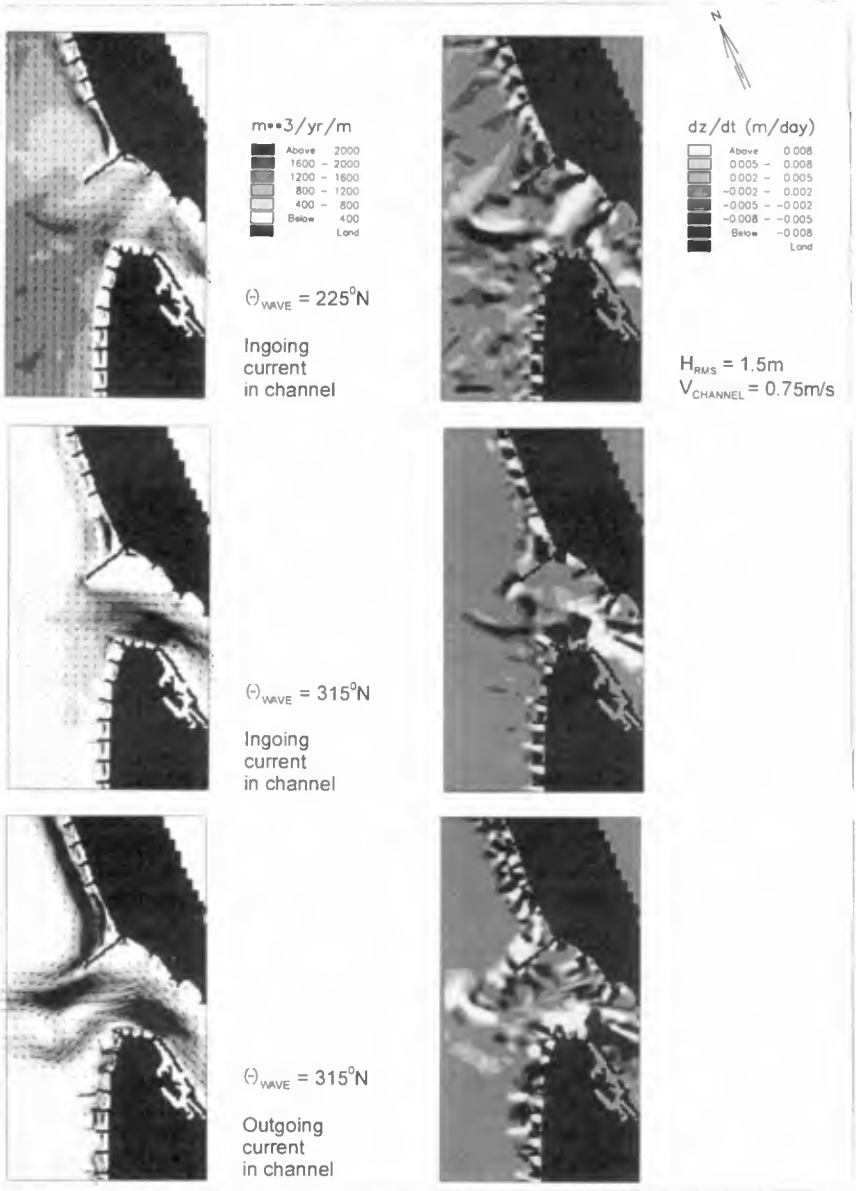

Figure 4. Sediment transport and corresponding initial morphological change, top: south-westerly storm, middle: northwesterly storm, bottom: northwesterly storm. H_{rms} lies in the interval 1-2 m in all 3 cases.

The entrance is too wide to allow for any significant natural bypass and most material is deposited in the entrance area. During northwesterly storms, the littoral drift is southgoing, and for these wave directions the layout of the entrance allows for significant wave penetration into the channel. Therefore, during north-westerly storms, the sediment is kept in suspension further into the channel, and it may be transported all the way through the channel before it deposits on the shoals on the inside of the channel. The net effect of these proceses are that littoral drifts for both barriers are directed towards the central channel.

Transport patterns and the corresponding initial morphological changes for cases with south-westerly and northwesterly waves combined with in-going current and northwesterly waves combined with out-going current are depicted in figure 4. It is seen how the channel tends to migrate to the East during in-going flow and towards west during out-going flow. These calculations correspond to a distribution of sediment properties described from about 240 bed samples in the area.

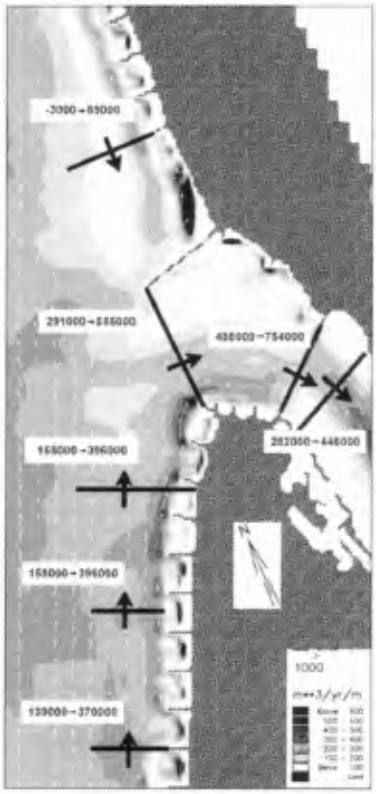

Figure 5. Average sediment transport pattern for the years 1991-1997, net transport across 7 cross-sections for the mildest and the roughest year during the period.

The yearly transport and morphological development are functions of the yearly climate, and at the present location even small variations in the dominant wave conditions change the sediment balances significantly. The modelling complex has been used to quantify this variability. Both the water level and the currents in the channel are strongly correlated to the instantaneous wave conditions. The frequency of occurrence of combinations of wave height and direction, water levels and currents in the channel have been analysed based upon 6 years of simultaneous measurements of water levels and waves, and 1 year of simulations of the currents through the 'fjord' which crosses the peninsula of Jutland, see figure 3 and Brøker et al. (1996).

The waves, currents and sediment transport have been modelled in detail for a number of historical events in total 25 days. 448 different combinations of waves, water level off the channel and current through the channel have been picked from the simulations. These sediment transport patterns are subsequently weighted to reflect the yearly transport pattern for different periods of time. Figure 5 shows the weighted sediment transport pattern for the years 1991-1997 and the integrated transport capacity through certain sections for the mildest and the roughest years of the period.

It appears that the transport capacity off the southern barrier-island increases slightly towards the entrance giving rise to the erosion which today is compensated by nourishment. Inside the channel the calculations indicate ongoing redistribution of material and a loss of material to the internal shoals. The sediment transport capacities inside the channel area have been adjusted to account for the presence of the non-erodible clay surface.

Profile Steepening

Foresighted engineers started profile surveys only 12 years after the final breach in 1862. With few interruptions, such as during the Second World War, the profiles have been surveyed every second year ever since and the database now forms a unique basis for evaluating the long-term trends of profile development, notably steepening of the profiles. The volume of eroded sand along the coast and profile development have been calculated based on these surveys.

From the geological study, the position of the clay surface is known, which means that it has been possible to calculate erosion along the coast for the sand layers only. The sediment balance has been calculated for 4 periods, 1874-1900, 1900-1936, and 1936-1978 and at last 1978-1992. For the first two periods the calculations are carried seaward to a depth of –8 meter DNN. In 1930s, DCA started measuring seaward to a depth of –16 m DNN. The calculations for the last two periods are therefore carried out to this depth. The results are shown in figure 6.

The results clearly show the large erosions immediately after the breach in the barriers. This continued in the following years also after the construction of the groynes. As the steepening began the erosion decreased.

On the basis of the long series of profile sounding the retreat of the coastline, the cliff and the 7, 8, 10 an 16 meter depth contours have been calculated. The results just off the town of Thyborøn are shown in figure 7.

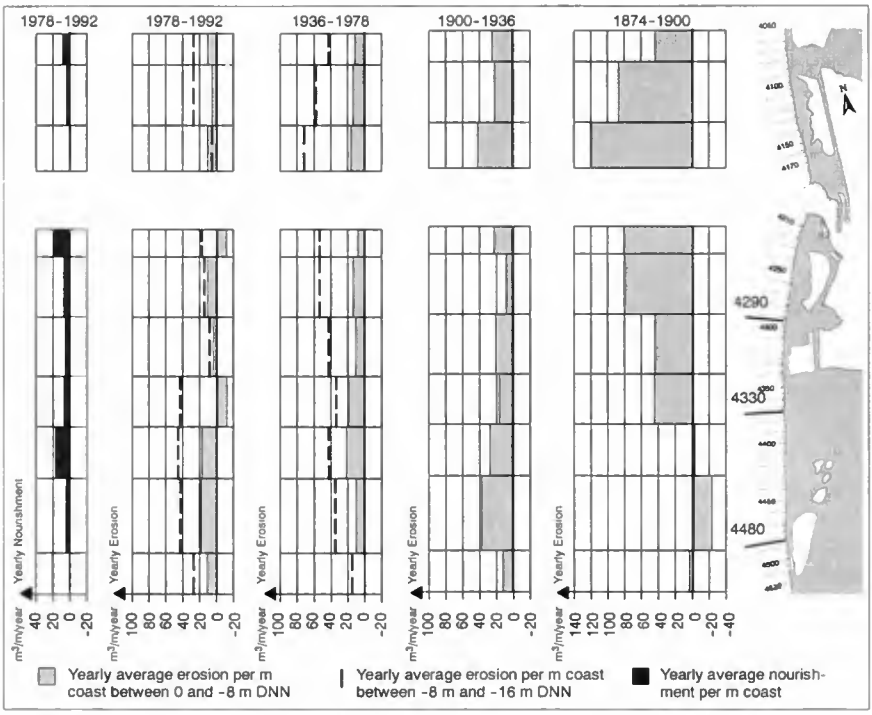

Figure 6. Calculated eroded and nourished volumes for four periods

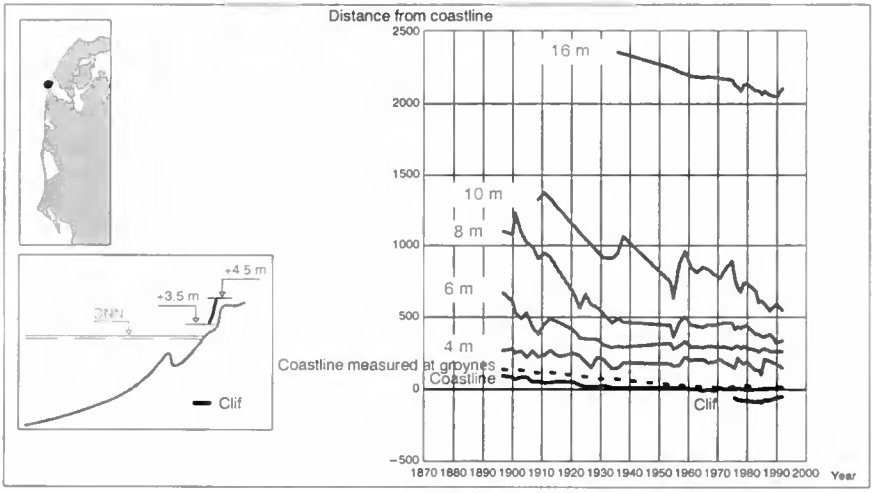

Figure 7. Profile development off Thyborøn town

Figure 7 clearly shows the importance of long-term surveying, the yearly and in periods large fluctuations are so large that say even 25 years of monitoring could have been misleading.

Now with 125 years of data at hand it is possible to extract reliable long-term trends from the otherwise confusing data. From figure 7 it is seen that the retreat of all elements was larger in the beginning of the period compared with the retreat today. For the coastline, the four, and 6-meter depth contours, the retreat has stopped. The depth contours off the groynes are still retreating. This leads to the conclusion that the steepening of the profiles has not yet stopped along all sections of the coast as earlier concluded in the 1975. This is especially true close to the inlet. It should however be noted that the wind and wave conditions were extremely severe for allmost 20 years after 1975. Examples of historical and more recent profiles are shown in figure 8.

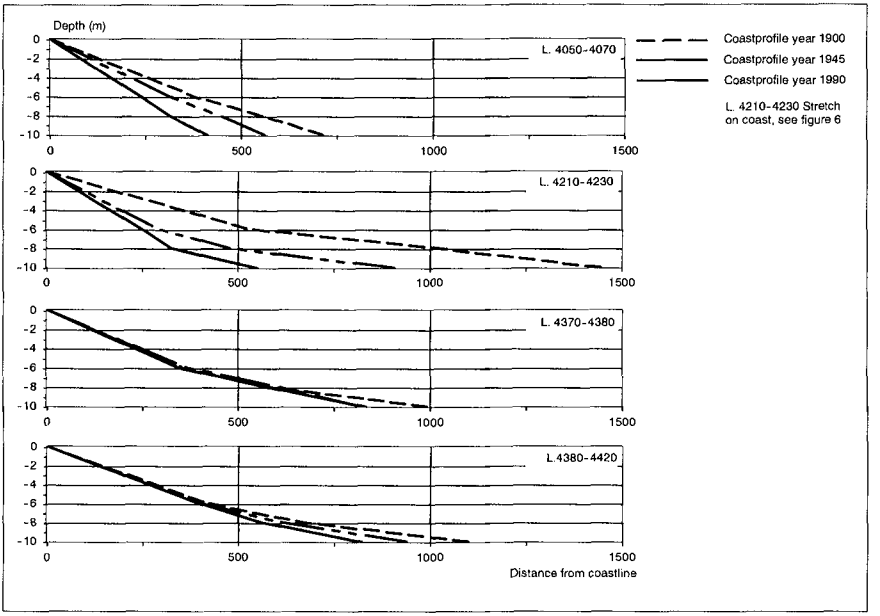

Figure 8. Profile steepening for selected stretches along the barriers.

The effects of the profile steepening on the sediment transport capacity have been quantified by modelling of waves, currents and sediment transport for a historical storm using a recent bathymetry and a bathymetry constructed from the old profile measurements. Figure 9 shows the comparison of simulated sediment transport fields and integrated transport along the barrier islands at one time step during the simulation at which the waves come from southwest, H_{rms} = 1.5 m. It is clearly seen that the transport zone has become very narrow in 1994 and the total littoral drift as well as the gradient of the littoral drift have declined. The groynes have been moved backward in pace with the ongoing erosion, however leaving submerged parts still active on the seabed. The erosion rates are significantly reduced compared to a hundred years ago due to the steepening of the coastal profiles. These simulations

illustrate the sediment transport processes which are reflected in the measurements of the morphological evolution of the area.

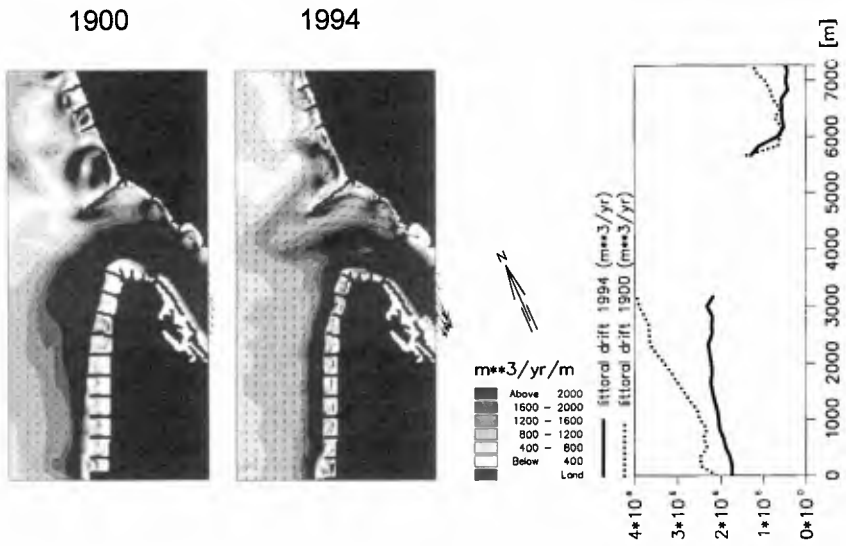

Figure 9. Examples of sediment transport rates, historical and recent bathymetries, H_{rms}= 1.5 m, dir. 255°, mean current in the channel 1.25 m/s. Comparison of integrated littoral drift.

Sediment budget

Both south and north of the barriers there exists a nodal point for the littoral transport from which the net transport is directed towards the central channel. Based on the data which lead to figure 6, the total volume of eroded sand between the northern and southern nodal point has been calculated. Depending on the distance from the coastline taken into account, which is from the top of dunes until 12 op to 16 meters depth, the volume range is 450.000-600.000 m^3/year for the stretch from the southern nodal point up to the channel and 150.000-200.000 m^3/year from the northern point down to the channel. This gives of total of 600.000-800,000 m^3/year between the two nodal points.

Calculations of shoal deposit behind the barriers has been carried out based on soundings of the shoals in 1972 and in 1991. The calculations leads to the conclusion that 500.000-700.000 m^3 is deposited on the shoals every year.

The numerical model gives some ranges for the transport capacity through 7 sections along the sea shore and through the channel, see figure 5. The transport capacity through the central part of the channel is 5-750,000 m^3/year for the mildest and roughest year, respectively, du-

ring the period 1991-1997. The transport capacity along the coastline varies between 0-100,000 m^3/year for the northern barrier and 150,000-400,000 m^3/year for the southern barrier.

Combining these information's ranges for the overall longshore sediment budget can be obtained.The northgoing transport is in the range 3-500,000 m^3/year and the south-going is op to 200,000 m^3/year. The transport rate through the channel is 500,000-700,000 m^3/year. This is illustrated in figure 10.

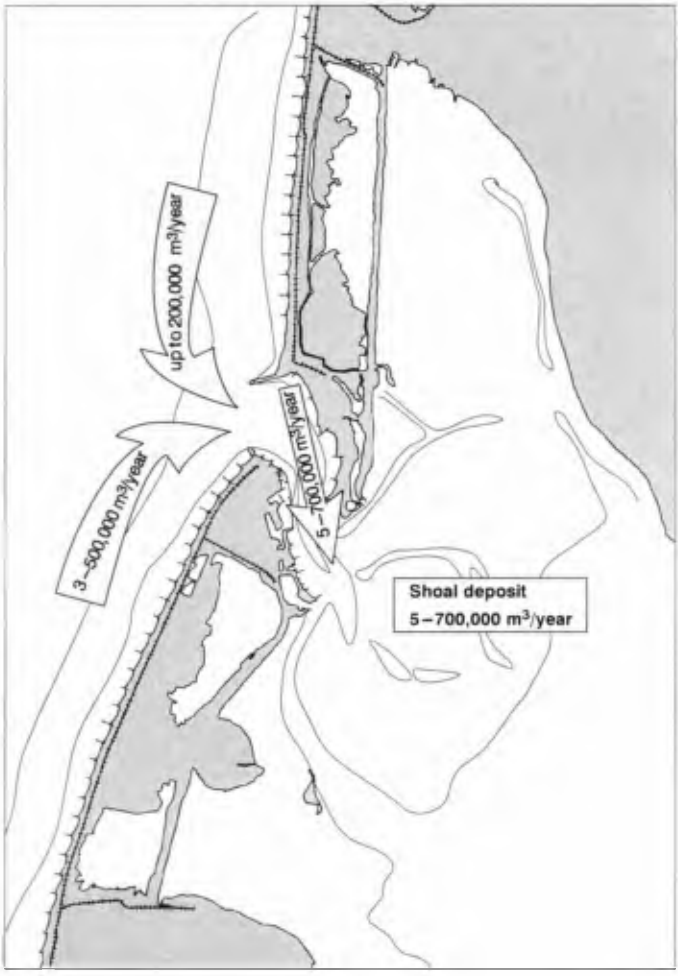

Figure 10. Overall sediment budget for the barriers

The safety level for Thyborøn

The extreme water levels at Thyborøn have been reassessed based on data from the passed 20 years. Figure 11 shows a comparison of extreme analysis results based on the data for the periods 1931 to 1975, from 1975 to 1995 and the full data set. The period just after 1975 covers a number of very extreme events, and therefore the analysis, based on the latest period only, shows a somewhat higher level than the analysis from the first period and the full serie. The dikes have been reinforced, the beach better maintained and the total system will therefor be able to provide flood protection in a 1000 event even accounting for the new analysis of extreme water levels.

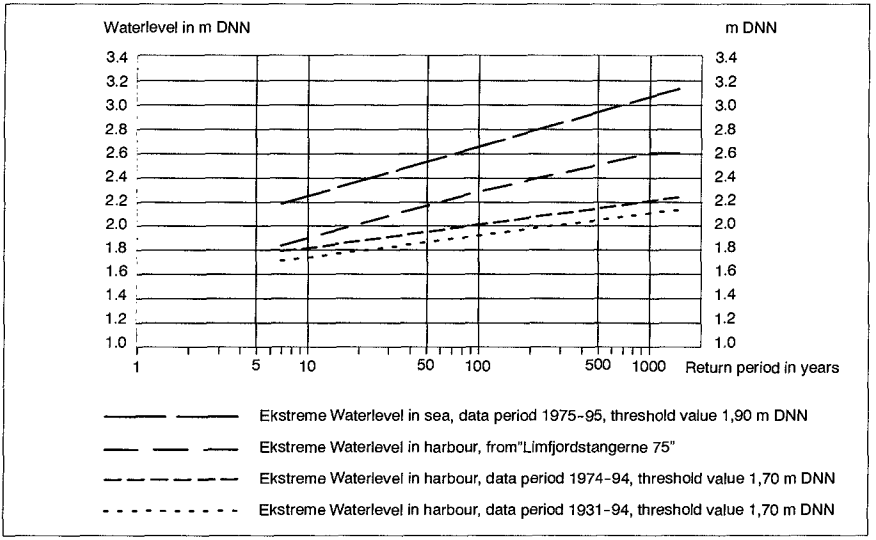

Figure 11. Old and new statistics for the extreme water levels at Thyborøn.

Further, it has been investigated if there should be a certain limit to extreme water levels at Thyborøn due to the nearness of more open and deeper waters to the north. Simulations in a numerical model of the North Sea were performed for a recorded storm scaled to predicted extreme conditions. The simulations showed that the extreme water levels are functions of the barometric conditions mainly, and that a limit could not be identified.

Overall Conclusion

- Although the outer part of the profiles close to the inlet is still getting steeper, the rates of steepening are significantly decreased and the nearshore zone can be kept stable by comprehensive nourishment.
- The safety level at Thyborøn is still 500-1000 years.
- Numerical modelling has greatly supported the understanding of the coastal processes around and in the Thyborøn Channel. Comparison between modelled sediment transport

for a historical and a recent bathymetry has illustrated that relevant processes are sufficiently well represented in the models to reflect the major morphological changes. Inside the channel the modelling has illustrated how different hydrographic conditions lead to different morphological developments such as migration of the channel and very varying depositions in the entrance area.

- Calculations of erosion on the coast, calculations of deposit material on inlet shoals and numerical calculations of the littoral transport capacity have helped gaining a more narrow range for the littoral sediment budget along the barriers.

REFERENCES

Bruun, P. (1954): Coast Stability. Doctor thesis. Copenhagen 1954

Brøker, I., Zyserman, J.Z., Jakobsen P.R. (1996): Thyborøn coastal investigations 1995: New lessons from an old coastal problem, Proceedings of the 25th International conference on Coastal Engineering, Orlando, USA pp.4703-4716.

Deigaard R., Fredsøe J., Brøker Hedegaard I. (1986): Suspended Sediment in the surf zone. Journal of Waterway, Port; Coastal and Ocean Eng. ASCE, Vol 112, No 1 pp 115 -128

Lundgren H., et. al. (1968): Report to government no. 472 concerning Thyborøn Channel (in Danish)

Mikkelsen, S.C.(1977): The effects of groins on beach erosion and channel stability at the Limfjord barriers, Denmark. Proceedings of Coastal Sediment 77, Charleston, USA, 1977

Sørensen, T. (1961): The Development of Coastal Profiles on a Receding Coast Protected by groins. Proceedings 7th International Conference on coastal Engineering. Netherlands pp 846-846.

Sørensen, T., Fredsøe, J., Jakobsen, P.R., (1996) History of Coastal Engineering in Denmark, History and Heritage of Coastal Engineering, ASCE 1996.

APPLICATION OF SHORE PROTECTION SCHEMES IN HORNBÆK

Mads Peder Jørgensen [1]
Peer Skaarup [2]
Karsten Mangor [3]
Jørgen Juhl [4]

ABSTRACT

Hornbæk Harbour was built more than a hundred years ago on a sandy coast with predominant eastward longshore sediment transport. After construction of the harbour the littoral transport was disrupted leading to a large accretion of sand upstream of the harbour whereas lee-side erosion occurred downstream of the harbour. Soon problems were experienced due to sedimentation in the harbour entrance and in the beginning of the century a breakwater was constructed for blocking the sand transport. This breakwater was later extended and finally a lee-side breakwater was constructed.

Hornbæk harbour represents a classical case of the problems encountered when constructing a harbour on a coast with littoral drift. Only in recent years focus has been put on environmental issues and the present project shows a good example of remedial measures by involving a number of shore protection schemes.

The applied shore protection schemes consist of beach nourishment, beach de-watering and maintenance of shingle beaches along with extension and repair of existing slope protection. On completion of the project a monitoring programme has been started in order to track the development of the coastline in response to the beach nourishment scheme.

1. HORNBÆK HARBOUR - HISTORICAL ASPECTS

Hornbæk is situated in Denmark in the northern part of Zealand as seen in Figure 1. The harbour is largely sheltered from waves from all directions except from the northwest.

Hornbæk harbour represents the classical case of harbour construction on a uniform coast with pronounced longshore sediment transport. Before construction of any transverse structures the coastline was near-stable even though there is a significant eastward longshore transport of sediment.

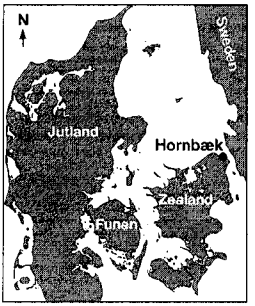

Figure 1 - Denmark.

[1] Coastal Engineer. COWI, Consulting Engineers and Planners A/S. Dept. of Ports, Waterways and Coastal Engineering. Parallelvej 15, DK-2800 Lyngby, Denmark. Mail: mpj@cowi.dk
[2] Engineer, Project Manager. Frederiksborg Amt. Teknik & Miljø. Amtsgården, Kongens Vænge 2, DK-3400 Hillerød, Denmark. Mail: ps@fa.dk
[3] Chief Engineer, Coastal Engineering and Environment. Danish Hydraulic Institute, Agern Allé 5, DK-2970 Hørsholm, Denmark, Mail: KM@DHI.dk
[4] Senior Coastal Engineer. COWI, Consulting Engineers and Planners A/S. Dept. of Ports, Waterways and Coastal Engineering. Parallelvej 15, DK-2800 Lyngby, Denmark. Mail: jju@cowi.dk

Subsequent construction of the harbour has had the effect of blocking this longshore transport resulting in accretion upstream of the harbour (west) and lee-side erosion downstream of the harbour (east).

The harbour originated as a shore-connected single breakwater creating a sheltered area for mooring fishing vessels.

As shown in Figure 2 the breakwater west of the original basin has been extended gradually from 1878 to 1924 in response to continuous upstream accretion and sedimentation in the protected area east of the breakwater.

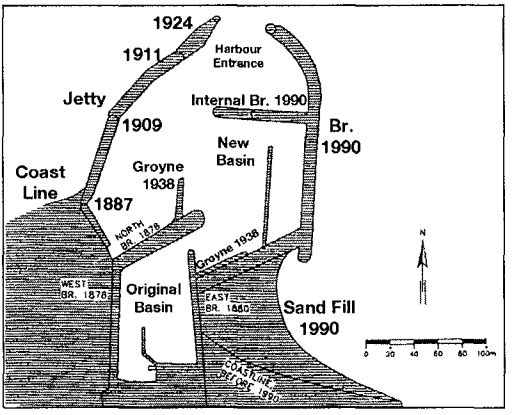

Figure 2 - Development of Hornbæk Harbour 1878-1990.

Due to the continuous sedimentation and increased cost of dredging, a new secondary breakwater was constructed in 1990. Sand dredged from the harbour basin was placed as sand fill east of the harbour forming a small beach area. The construction of the eastem breakwater reduced the sedimentation in the fore harbour from several thousand cubic metres to a few thousand cubic metres a year. In recent years the western breakwater has been renovated, which also involved a more smooth plan shape mirroring the eastern breakwater and this has even further reduced sedimentation of the fore harbour. There is, however, still a requirement for annual maintenance dredging of the access channel.

The continuous extension of the breakwater has had a dramatic effect on the town of Hornbæk. Due to the pronounced accumulation of sand upstream of the harbour the main activities of the town has moved from fishing operations towards recreation and tourism. The beach west of the harbour is today one of the most popular beaches on Zealand and through the fifties and sixties the town hosted a reputed health resort which emerged into a beach hotel and has in later years become a hospital.

2. COASTAL PROCESSES

The construction of the harbour has significantly influenced the morphology in the area. The coastline west of the harbour has accreted continuously necessitating the extension of the western breakwater. The retreat of the coastline east of the harbour has occurred more slowly due to self-armouring of the seabed with gravel and stones originating from erosion in moraine tills. This implies that the erosion in the considered area is mainly caused by storms in conjunction with high water.

The development of lee-side erosion east of the harbour and accretion west of the harbour is seen in Figure 3. From 1880 to 1997 the lee-side erosion has been of the order-of-magnitude of 50 m whereas the advance of the coastline to the west has been in the order of 100 m.

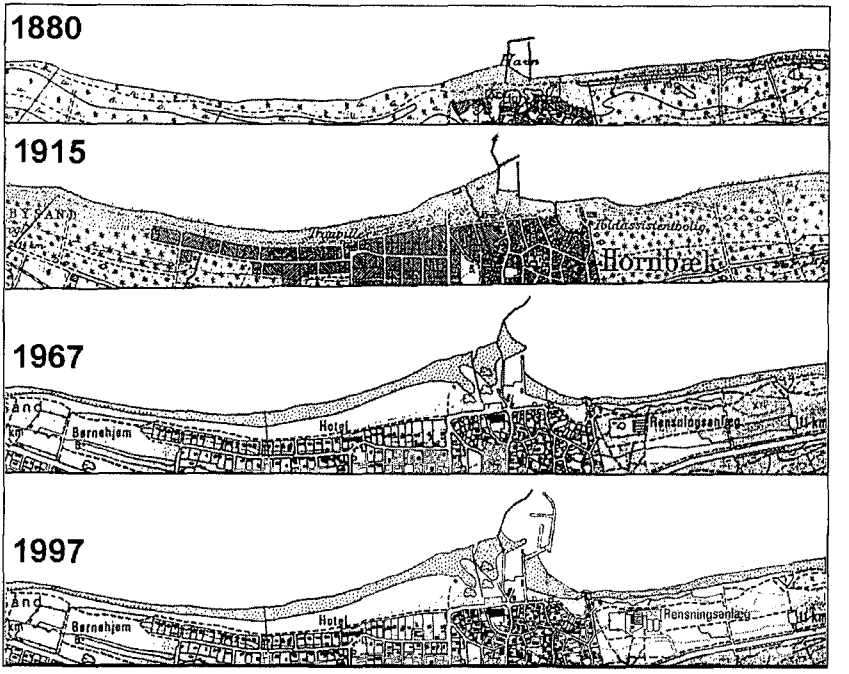

Figure 3 - Development of the coastline adjacent to Hornbæk Harbour, 1880-1997.

Throughout the years approximately 7,000 m^3 of sand has been mined from the accretion area each year in order to minimise sedimentation problems in the harbour entrance. The sand was used by local contractors and has thus been missing in the sediment budget east of the harbour.

Before the construction of the eastern breakwater the yearly maintenance dredging was approximately 15,000 m^3, most of which was dumped in deep waters. After construction of the eastern breakwater, approximately 4,000 m^3 of sand has been dredged yearly in the harbour entrance and in the access channel and deposited in the shallow water area east of the harbour.

The coastal areas adjacent to Hornbæk Harbour are dominated by waves coming from the northwest originating from the large fetch areas in Kattegat. Waves coming from west and from the direction range north to east are limited due to sheltering effects from Zealand and Sweden (Figure 1).

Based on a study of the wave climate and storm surges a numerical study of the littoral drift budget was carried out using the LITPACK modelling system. Findings from this study was used for assessing the amount of sand needed for beach nourishment east of the harbour. Figure 4 shows a detail of the sediment budget for the harbour area in 1995. The cumulated transports show a net accumulation of sediment in the region just east of the harbour of around 2,000 m^3/yr.

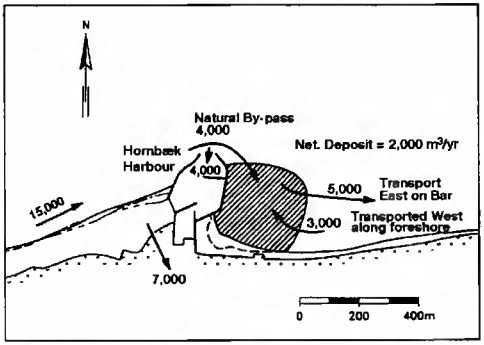

Figure 4 - Sediment at Hornbæk Harbour, before nourishment and artificial bypassing.

Sediment trapped in the harbour mouth (4,000 m^3/yr) is dumped near-shore along the beach east of the harbour resulting in a total transport of 6,000 m^3/yr further east along the coast.

The sediment is clearly deposited in the formation of a large shoal (Figure 5) which is expected to connect with the beach area further east of the harbour closing off a shallow water area. At this point in time there will probably be a decision about whether to fill in the shallow water area creating a wide beach or about relocating the sediment in the shoal to the coastline proper.

Figure 5 - Aerial view of Hornbæk Harbour.

3. SURVEYS AND DETAILED DESIGN

Consulting services covered the following main topics:

- Assessment and modelling of the coastal processes
- Preparation of alternative schemes for shore protection
- Surveys
- Detailed design and preparation of tender documents
- Construction supervision
- Monitoring of the beach development

A series of surveys was made including bathymetric and topographic measurements and borings at sea for determining the soil conditions. A detailed design was produced for the selected protection schemes and was followed by preparation of tender documents divided into beach nourishment and slope protection, respectively. The design detailed:

- Beach Nourishment, 7-14.000 m^3/yr for five years in succession.
- Maintenance of shingle beaches
- Repair of existing slope protection
- Extension of the slope protection at the most exposed location (100 m berm and an additional 10 m protection of the slope)

Upon receipt of the tenders for the beach nourishment, it was decided to have the sand by-passed by dredging and pumping instead of using trucks as the pumping solution was preferable from an environmental point of view.

4. SHORE PROTECTION SCHEMES

The present project is part of a larger plan for the area financed by the County of Frederiksborg (lead partner) together with the Municipality of Helsingør and the State Forest District of Kronborg. Other parts include the following:

- About 1.5 km west of the harbour another project including the beach face dewatering concept has been completed. The purpose is to stabilise and widen the beach in this area which is considered one of the best bathing resorts in the northern part of Zealand.
- The outer breakwaters of the harbour have been modified within the last 10 years with the purpose: to increase the capacity of the harbour, to minimise the sedimentation and to increase the natural bypass of sand.

The final project focused on rehabilitation of a 2.5 km stretch of coastline east of the harbour where protection was needed against further erosion. The project included general repair of existing slope protection and extension of the slope protection in the form of a berm at the most exposed location. Furthermore the shingle beaches were replenished in order to slow down erosion and finally, beach nourishment was carried out along 300 m of the coastline just east of the harbour. The beach nourishment was

carried out through bypassing of sand from the accretion area west of the harbour, which has also reduced sedimentation in the harbour entrance. Figure 6 shows the repair works and extension of the existing slope protection. A 100 m long berm is placed along the toe of the slope protection. In front of the berm a 1 m thick layer of shingle is placed acting as a kind of nourishment.

Figure 6 - Placing of geotextile and armour.

Figure 7 shows the berm shortly after completion. The waves have washed some of the shingle ashore which conceals the larger part of the berm structure and allows for safe passage along the beach.

Figure 7 - Berm Structure on completion

Beach nourishment was carried out east of the harbour in order to improve the quality of the beach in this partly self-armoured area. A total of about 12,000 m^3 of sand was bypassed by dredging in the accretion area west of the harbour and pumping in a pipeline to the nourishment zone east of the harbour. This was performed in April 1997 and April 1998. It is planned to repeat the beach nourishment each year for the next three years and probably more years after. Figure 8 shows the nourishment zone just after nourishment has taken place. The size of the nourishment area is approximately 300 m by 40 m.

Figure 8 - Aerial View of Beach Nourishment upon Completion of Works

Figure 9 shows the estimated sediment budget for the harbour area while nourishment is taking place (compare with Figure 4). For the given example 12,000 m^3/yr of sediment is mined west of the harbour and used as nourishment east of the harbour. The western breakwater has been rounded and sedimentation in the access channel has decreased to 2,000 m^3/yr. The corresponding maintenance dredging of 2000 m^3/yr is dumped nearshore east of the harbour.

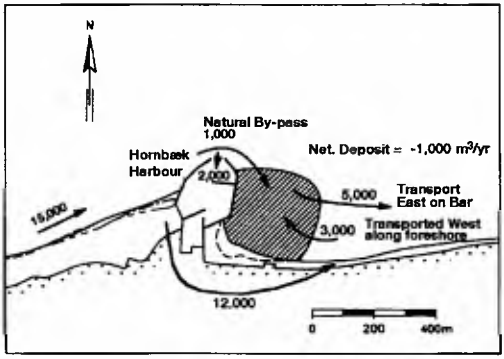

Figure 9 Sediment budget including artificial nourishment

The littoral transport west of the harbour remains the same, resulting in a natural bypass of 1,000 m^3/yr to the shoal. The shoal is also receiving 3,000 m^3/yr from the east coast and looses 5,000 m^3/yr towards east, resulting in an annual loss of sand from the shoal of 1,000 m^3/yr. The shore east of the harbour now receives 2,000 m^3/yr from the shoal and 14,000 by artificial nourishment resulting in a supply to the downdrift shore of 16,000 m^3/yr.

In total the beach nourishment scheme has the effect of maintaining the stable beach west of the harbour, reducing sedimentation in the access channel, improved beach quality east of the harbour (compared to sedimentation on the shoal) and increased littoral transport further east along the coast for the benefit of the downdrift shore.

5. MONITORING

The beach east of the harbour was surveyed prior to initiation of the beach nourishment and again after finalization. Monitoring will take place twice a year throughout the next four years in order to assess erosion and changes in beach profiles. Thereby the quantity of future requirements for beach nourishment will be assessed.

At this point in time measurements of the location of the shoreline and bathymetric surveys of the nourishment zone have been conducted in March 1997, November 1997 and March 1998. The bathymetric surveys of the nourishment zone show relocation of submerged shoals and other sand formations as well as the presence of dunes on the shore. Apart from this the preliminary monitoring results show the coastline being practically stable during the last year. This is mainly because the surveys of March 1997 and March 1998 were conducted just prior to nourishing. The survey from October 1997 shows no evidence of the nourished sand, which indicates that the majority of the material has been transported eastward along the beach as planned. This is in agreement with the philosophy of the nourishment project, which is a gradual rehabilitation of the beach east of the harbour by nourishing locally along a 300 m long section in close vicinity of the harbour. Surveys conducted in coming years are expected to reveal trends in the interaction between the native and the nourished material as well as the effectiveness of the nourishment programme.

6. CONCLUSIONS

Accretion has been taking place west of Hornbæk Harbour over decades, however, the accretion area has stabilised many years ago. The extension of the western breakwater has caused a large offset of the littoral transport in comparison with the original coastline. Historically, most of the normally bypassed sand was trapped in lee of the single western breakwater from where is was dredged and dumped in deep waters, which means that it was lost for the downdrift coastline.

Since 1990 where the eastern breakwater was constructed, sedimentation and maintenance dredging has decreased from 15,000 m^3 to 2,000 m^3 per year. The remaining bypassed sand has accumulated in the shallow area east of the harbour but separated from the coastline. The conclusion with respect to the impact of the harbour on the downdrift coast is that the harbour has caused lee-side erosion in the entire period of its existence.

The selected shore protection scheme for 2.5 km of coastline east of the harbour consisted of beach nourishment with 12,000 m^3 of sand mined west of the harbour and 2,000 m^3 dredged in the harbour entrance, maintenance work on shingle beaches along with extension and strengthening of exposed parts of the slope protection.

The new wide and sandy beach east of the harbour attracted many guests during the first summer but as expected a significant part of the sand was transported eastwards during the winter season. Additional beach nourishment will be carried out the next four years during spring time. Twice a year the development of the new beach will be monitored. The monitoring results will form the basis for assessing the amount of sand to be pumped from the accretion area to the new beach in the coming years.

This project is carried out respecting the natural processes of the sand transport along the coast and thus represents an example of the Consultant's planning with nature instead of against it, so-called shore protection in lieu of coastal protection.

7. ACKNOWLEDGEMENTS

The authors wish to thank Architect Dan Hasløv from Hasløv and Kjærsgaard for assisting with aestethic view points in the studies of the various protection schemes and O. Juul Jensen, COWI for advice on the coastal structures.

Design and Construction of Seawater Exchange Breakwaters

Sadamitsu AKEDA[1], Yasushi YAMAMOTO[2], Katsutoshi KIMURA[3] and Kenji YANO[4]

Abstract

The establishment of breakwaters in Japanese ports has progressed in recent years and has greatly improved the calmness in the ports. However, the seawater exchange within and outside of the port has greatly decreased. In ports near urban areas, in particular, the inflow of domestic and industrial wastewater, and the accumulation of sludge are causing a variety of environmental problems. Therefore, it is necessary to solve two contradictory technical problems: improving seawater exchange while at the same time improving calmness in the port.

An armored caisson breakwater with intake holes has been developed to conduct external seawater into the port using wave energy. In this paper, the hydraulic characteristics and the practical design of this structure will be presented.

Introduction

In ports near urban areas located in inner bay, the various water environmental problems have occurred due to the inflow of domestic and industrial wastewater, and the accumulation of sludge. It is necessary to urgently improve the water environment in these ports. Therefore, it is required that port structures promote the seawater exchange, which is contradictory to original functions such as structural resistiveness against wave action and the maintenance of the calmness in the port.

An armored caisson breakwater is one of the most popular breakwater structure in Japan. It excels in decreasing reflected and transmitted waves, and in being stable in stormy wave conditions. By 2-D & 3-D hydraulic model tests and field tests, the Civil

1) National Research Institute of Fisheries Engineering; Ebidai, Hasaki, Ibaraki, 314-0421 JAPAN
2) Hokkaido Development Bureau; Nishi-2, Kita-8, Kita, Sapporo, 060-8511 JAPAN
3) Civil Engineering Research Institute; Hiragishi 1-3, Toyohira, Sapporo, 062-0931 JAPAN
4) Hokkaido Tohkai University; Minamisawa 5-1-1, Minami, Sapporo, 005-0825 JAPAN

Engineering Research Institute has researched and developed an armored caisson breakwater with intake holes, which enabled the seawater exchange within and outside of the port, while making the most of its excellent hydraulic characteristics (C.E.R.I. et al., 1991-1995, 1997). Fig.1 shows the conceptual drawing of the armored caisson breakwater with intake holes.

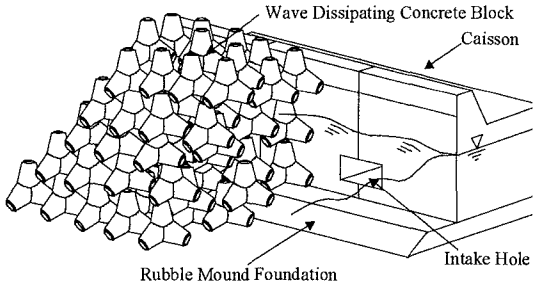

Fig.1 Conceptual Drawing of an Armored Caisson Breakwater with Intake Holes

Experimental Set-up

In the armored caisson breakwater, wave-dissipating blocks installed in front of the breakwater bodies dissipate incident wave energy, and raise the mean water level by wave-setup. The principle of seawater exchange of the armored caisson breakwater with intake holes is the generation of one-way flow into the port through intake holes, using the increase in the mean water level within wave-dissipating blocks (Sarukawa et al., 1993).

Although the seawater exchange is promoted by the increase in the size of intake holes, the wave transmission into the port through intake holes is also increased, and the calmness in the port is decreased. There are also unsolved problems regarding the procedure of design calculation on wave force. Therefore, to confirm the hydraulic functions of the armored caisson breakwater with small or large intake holes, and to establish the structurally resistive design against wave action, 2-D hydraulic model tests were conducted on the following research items.

1) the wave transmission through intake hole
2) the increase in the mean water level within wave-dissipating blocks
3) the intake flow
4) the wave pressure distribution for the structurally resistive design against wave action
5) the influence of the opening ratio ε of intake holes on the wave transmission and the intake flow

Fig.2 shows the experimental models for 2-D hydraulic model tests. The definition of opening ratio ε of intake hole was as follows. The opening ratio ε of intake hole was changed to 16.8, 10.5 and 5.0%.

$$\varepsilon = \frac{\text{an area of cross section of intake holes}}{\text{an area of underwater cross section of breakwater including rubble mound foundation}} \times 100\ (\%)$$

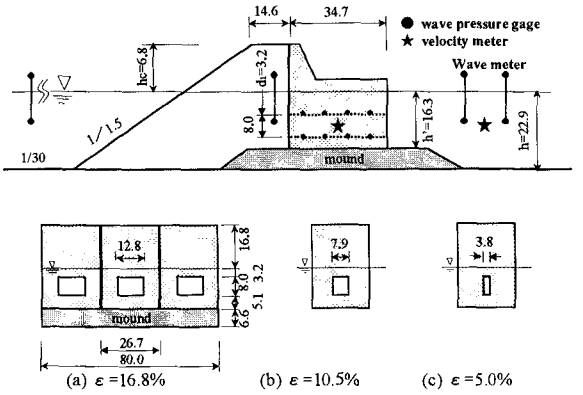

Fig.2 Experimental Models for 2-D Hydraulic Model Tests

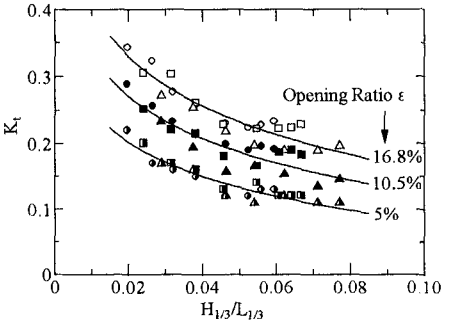

Fig.3 Wave Transmission Coefficient

Hydraulic Characteristics

(1) Wave transmission

An understanding of the wave transmission through intake hole is very important, when considering the size and the arrangement of intake holes, and their influence on the utilization of the port in stormy wave conditions. Fig.3 shows the relationship between the wave steepness $H_{1/3}/L_{1/3}$ and the wave transmission coefficient Kt with the opening ratio ε as a parameter. As the wave steepness $H_{1/3}/L_{1/3}$ decreased, and as the opening ratio ε increased, the wave transmission coefficient Kt of the armored caisson breakwater with intake holes increased, on condition that 2-D hydraulic model tests were conducted under condition without the wave transmission by wave overtopping.

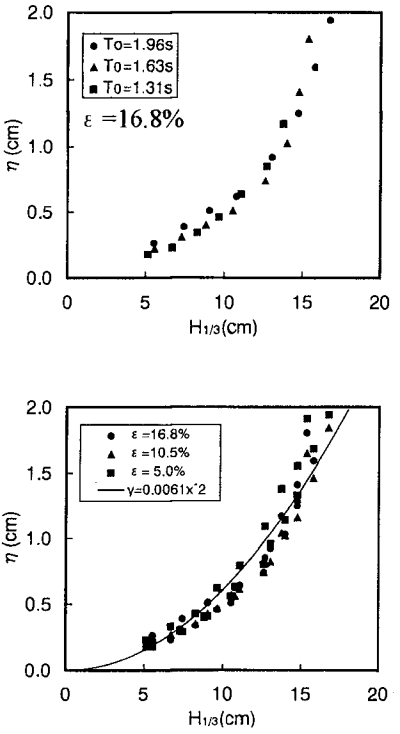

Fig. 4 Increase in the Mean Water Level within Wave-dissipating Blocks

(2) The increase in the mean water level within wave-dissipating blocks

Fig.4 shows the relationship between the wave height $H_{1/3}$ and the increase in the mean water level η_{mean} within wave dissipating blocks, with the opening ratio ε and the wave period $T_{1/3}$ as parameters. The increase in the mean water level η_{mean} within wave-dissipating blocks was not related to the opening ratio ε and the wave period $T_{1/3}$, but was in proportion to the square of the wave height $H_{1/3}$, which was equivalent to the wave energy-loss dissipated within wave-dissipating blocks.

(3) Intake flow

Fig.5 shows the relationship between the increase in the mean water level η_{mean} within wave-dissipating blocks and the mean velocity U_{mean} through intake hole. The mean velocity U_{mean} was in proportion to the dimensionless velocity $(2g\,\eta_{mean})^{0.5}$. "g" is the acceleration of gravity. If the increase in the mean water level η_{mean} within wave dissipating blocks exceeding a certain level does not occur, the portward one-way flow through intake hole does not occur. Similar results were obtained through field tests in

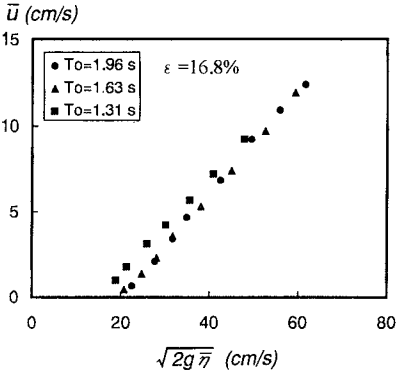

Fig.5 Increase in the Mean Water Level within Wave-dissipating Blocks and Mean Velocity through Intake Hole

Urakawa port (Akeda et al.,1996). As shown in Fig.5, it means that the seawater exchange can not be expected from the armored caisson breakwater with intake holes, unless there is the increase in the mean water level exceeding a certain level, in other words, the wave height exceeding a certain level.

(4) Outflow into inner port from intake hole

When using the inside of the armored caisson breakwater with intake holes as a quaywall, it is necessary to understand the influence of the outflow into the inner port from intake hole. Fig.6 shows the damping characteristics of the outflow from intake hole. The damping factor U/U_0 was defined as shown in Fig.6. The outflow from intake hole decreased as the distance from intake hole increased, and almost leveled off when x/h=1.5-2.5. When the opening ratio ε was 16.8%, the damping factor U/U_0 was 0.3-0.4 when x/h=1.5-2.0.

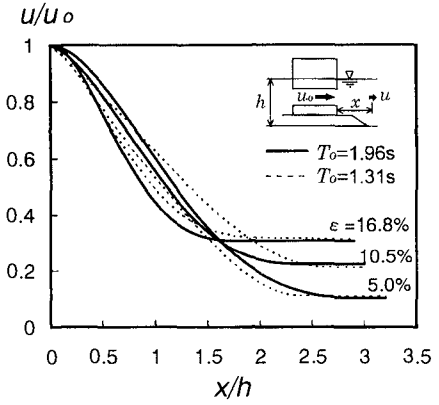

Fig.6 Damping Characteristics of the Outflow

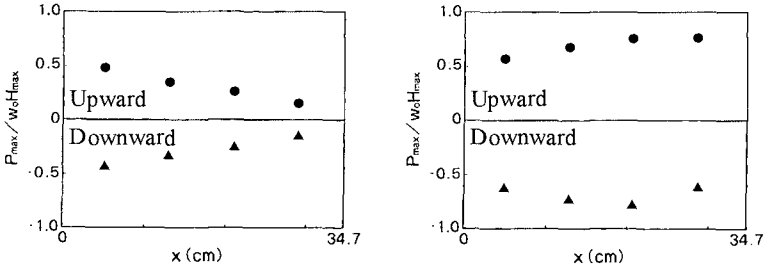

Fig.7 Wave Pressure Distribution (T_0=1.96s, H_0'=21.3cm)

Design wave pressure

(1) Wave pressure distribution

When the intake hole is put on relatively shallow position, the impact wave pressure

acts on the inside of intake hole. Fig.7 shows an example of the wave pressure distribution on the top and the bottom of intake hole. The horizontal axis is the distance from the front-end of intake hole. The vertical axis is the dimensionless wave pressure P_{max}/w_0H_{max}. The left figure is the case when the intake hole is put on relatively deep position. The wave pressure distribution was largest at the front-end of intake hole, then decreased linearly toward the rear-end of intake hole. The upward and downward wave pressure distribution in intake hole were almost symmetrical. The right figure is the case when the intake hole is put on relatively shallow position. The wave pressure distribution was not attenuated toward the rear-end of intake hole.

Fig.8 shows the influence of the crown depth of intake hole on the dimensionless wave pressure P_{max}/w_0H_{max}. The horizontal axis is the dimensionless crown depth of intake hole $d_1/H_{1/3}$. The vertical axis is P_{max}/w_0H_{max}. d_1 was the crown depth of intake hole. When the wave-dissipating blocks were installed in front of the breakwater bodies, P_{max}/w_0H_{max} was almost constant at 0.2-0.4 when $d_1/H_{1/3}$ was larger than 0.2. When $d_1/H_{1/3}$ was smaller than 0.2, the impact wave pressure did not occur even though P_{max}/w_0H_{max} increased. When the wave-dissipating blocks were not installed in front of the breakwater bodies, P_{max}/w_0H_{max} was almost constant at 0.3-0.4 when $d_1/H_{1/3}$ was larger than 0.4. It was observed that P_{max}/w_0H_{max} increased with the decrease in $d_1/H_{1/3}$, and the impact wave pressure occurred when $d_1/H_{1/3}$ was smaller than 0.3.

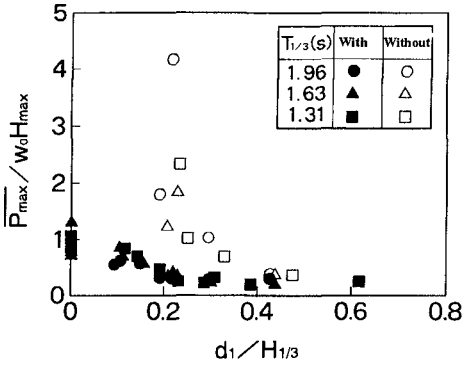

Fig.8 Influence of the Crown Depth of Intake Hole on the Dimensionless Wave Pressure in Intake Hole

(2) Wave pressure formula

Fig.9 shows the wave pressure distribution used for the structurally resistive design against wave action. The horizontal wave pressure and the uplift pressure acting on the front and the bottom of the breakwater body can be determined on the basis of the modified Goda's formula (Yamamoto et al., 1997). In consideration of the influence of intake hole, the horizontal wave pressure is not acted on the vertical surface of "opening part". The uplift pressure is acted on the top of intake hole, and triangularly

distributed toward the rear-end of intake hole, with an intensity of wave pressure at the front-end of intake hole of p_{u2}. The difference between the horizontal intensity of wave pressure acting on the top and the bottom of intake hole is defined as p_{u2}.

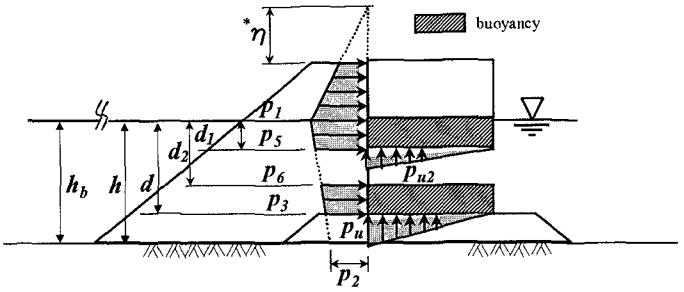

Fig.9 Design Wave Pressure Distribution

The details of the wave pressure formula are as follows:

$$\eta^* = 1.5\lambda H_D$$

$$p_1 = \lambda \alpha_1 w_0 H_D$$

$$p_2 = \frac{p_1}{\cosh(2\pi h / L)}$$

$$p_3 = \alpha_3 p_1$$

$$p_u = \lambda \alpha_1 \alpha_3 w_0 H_D$$

$$p_{u2} = p_5 - p_6 = \frac{d_2 - d_1}{h'}(p_1 - p_3)$$

$$\alpha_1 = 0.6 + \frac{1}{2}\left[\frac{4\pi h / L}{\sinh(4\pi h / L)}\right]^2$$

$$\alpha_2 = \min\left[\frac{h_b - d}{3h_b}\left(\frac{H_D}{d}\right)^2, \frac{2d}{H_D}\right]$$

$$\alpha_3 = 1 - \frac{h'}{h}\left[1 - \frac{1}{\cosh(2\pi h / L)}\right]$$

Where,

η^*: the wave height where the intensity of wave pressure becomes 0 (m)

p_1: the intensity of wave pressure on the still water level (tf/m^2)

p_2: the intensity of wave pressure on the sea bottom (tf/m^2)

p_3: the intensity of wave pressure at the bottom of the upright wall (tf/m^2)

p_5: the intensity of wave pressure on the top of the intake hole (tf/m^2)

p_6: the intensity of wave pressure on the bottom of the intake hole (tf/m^2)

p_u: the intensity of uplift pressure at the front leg of the bottom of the upright wall (tf/m^2)

p_{u2}: the intensity of uplift pressure at the front of the intake hole, $p_{u2}=p_5-p_6$(tf/m^2)

h: the water depth at the front of the upright wall (m)

h_b: the water depth at a distance 5 times longer than the significant wave height from the front of the upright wall to the offshore side (m)

d_1: the water depth at the top of the intake hole (m)

d_2: the water depth at the bottom of the intake hole (m)

w_0: the unit volume weight of sea water (tf/m^3)

H_D: the wave height used for design calculation (m)

L: the wave length used for design calculation at the water depth of h (m)

λ: the wave pressure reduction rate by covering with wave-dissipating blocks (λ=0.8)

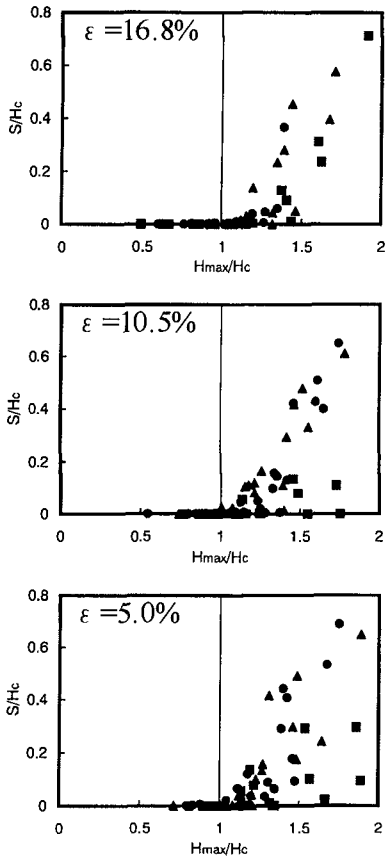

Fig.10 Sliding Distance

Fig.10 shows the relationship between the sliding distance and the critical sliding wave height. The horizontal axis is H_{max}/H_c. H_{max} is the maximum wave height. H_c is the critical sliding wave height calculated by the wave pressure formula. The vertical axis is the dimensionless sliding distance S/H_c. S is the sliding distance. Because S/H_c increased dramatically over $H_{max}/H_c=1$ regardless of the opening ratio ε, the above-mentioned wave pressure formula was thought to be reasonable.

Field Test in Urakawa Port

(1) Measuring conditions

In Urakawa port on the Pacific coast of Hokkaido, the armored caisson breakwater with a intake hole with the opening ratio of 5.0% was constructed to conserve the water quality and promote the seawater exchange. A field test on the hydraulic functions of this structure was conducted from October 26 to November 16, in 1995. The following items were observed:

1) the wave condition (wave height, wave period) in front of the breakwater (at 150m offshore, the depth of 8m)

2) the water pressure (at the front-end and the rear-end of intake hole)

3) the intake flow

Fig.11 shows the layout of measuring instruments. Fig.12 shows the time histories of the wave conditions in front of the breakwater of $H_{1/3}$, $T_{1/3}$, the difference in the mean water level in front-end and rear-end of intake hole of $\Delta\eta$, and the mean velocity through intake hole of U_{mean}. The difference in the mean water level were calculated on the basis of the difference in the water pressure in front-end and rear-end of intake

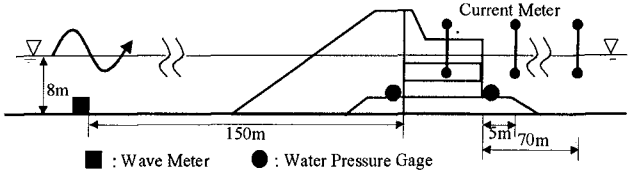

Fig.11 Layout of Measuring Instruments in Field Test

hole. At 8 a.m. on November 8, when the maximum wave ($H_{1/3}$=4.40m, $T_{1/3}$=8.6s) occurred, the difference in the mean water level in front-end and rear-end of intake hole was $\Delta \eta$=6.9cm, and the mean velocity through intake hole was U_{mean}=46.1cm/s. The observed value was equivalent to the inflow of seawater of about 10,000 tons per hour.

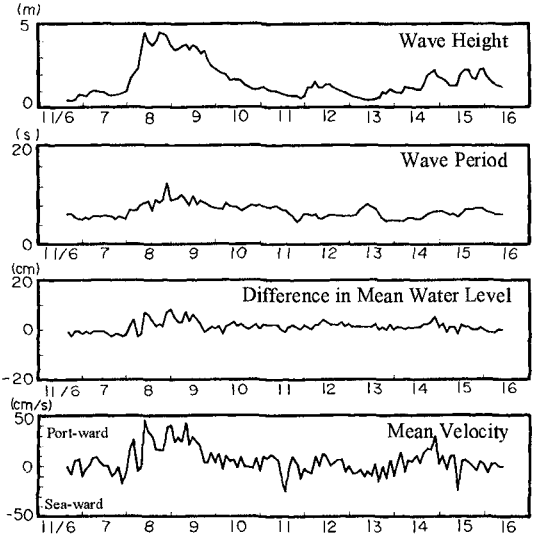

Fig.12 Time Histories of Observation Data

(2) Flow velocity through intake hole

Fig.13 shows the relationship between the wave height in front of the breakwater $H_{1/3}$ and the difference in the mean water level in front-end and rear-end of intake hole $\Delta \eta$. It was found from 2-D hydraulic model tests that the increase in the mean water level within wave-dissipating blocks was not related to the opening ratio ε or the wave period, but was in proportion to the square of the wave height. In field test, the difference in the mean water level in front-end and rear-end of intake hole $\Delta \eta$ was in proportion to the square of the wave height in front of the breakwater $H_{1/3}$, in case of the long-period waves with the wave period $T_{1/3}$ of 8 sec or longer. In case of the short-period waves with the wave period $T_{1/3}$ of shorter than 8 sec, there was hardly any difference in the mean water level in front-end and rear-end of intake hole due to the small incident wave height.

Fig.14 shows the relationship between the difference in the mean water level in front-end and rear-end of intake hole $\Delta \eta$ and the mean velocity in intake hole U_{mean}.

In the same way as in 2-D hydraulic model tests, the mean velocity in intake hole U_{mean} was in proportion to the a half power of the difference in the mean water level in front-end and rear-end of intake hole $\Delta\eta$. From the relationship shown in Figs.13 and Fig.14, it was found that the mean velocity in intake hole was in proportion to the wave height in front of the breakwater.

(3) Effect of the long-period oscillation

Fig.15 shows an example of the fluctuation of the mean water level in the port $\Delta\eta$ and the mean velocity in intake hole U_{mean} observed at 8 a.m. of Nov.13. The wave condition were the wave height of $H_{1/3}$=0.44m, and the wave period of $T_{1/3}$=8.4sec. Under relatively calm wave conditions, when the wave period $T_{1/3}$ is 6 to 7 seconds or shorter and the wave height $H_{1/3}$ is 1.5m or smaller, the external force which causes the seawater exchange is thought to be the long-period oscillation in the port with a period

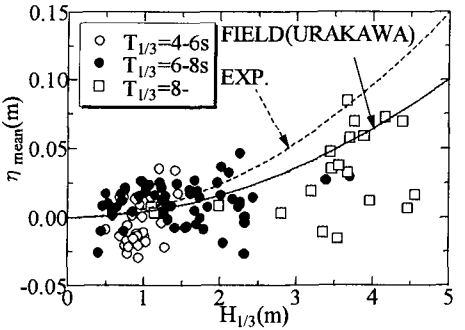

Fig.13 Wave Height in Front of Breakwater and Difference in the Mean Water Level in Front-end and Rear-end of Intake Hole

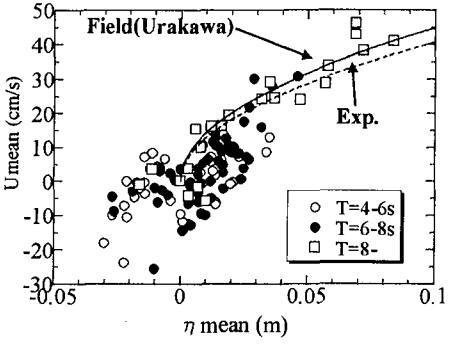

Fig.14 Difference in the Mean Water Level in Fron-tend and Rear-end of Intake Hole and Mean Velocity in Intake Hole

of over 10 minutes and an amplitude of several centimeters. As shown in Fig.15, an oscillatory flow with a flow velocity amplitude of 20 to 40cm/s was observed, and it was equivalent to a seawater exchange of several hundred tons per hour. From the above results, it was found that long-period oscillation in the port would contribute to seawater exchange within and outside the port under relatively calm wave conditions.

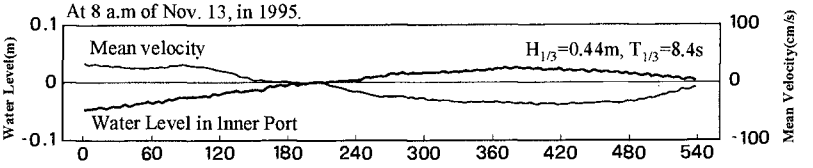

Fig.15 Long-period Oscillation in the Port and Mean Velocity through Intake Hole

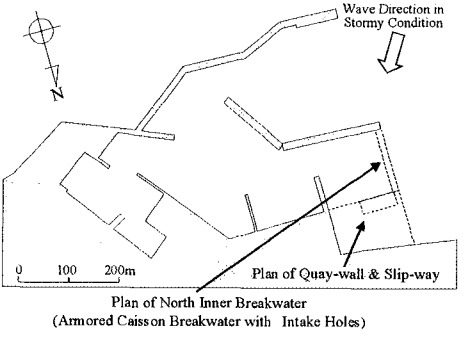

Fig.16 Plan View of Kudoh Fishing Port

Case study on Kudoh Fishing Port

In Kudoh Fishing Port on the Sea of Japan coast of Hokkaido, the construction of an armored caisson breakwater with intake holes with a large opening ratio was planned to improve the calmness in the port. 2-D&3-D hydraulic model tests and numerical analysis were conducted to determine the inflow condition of external seawater and the calmness in the port, to examine the effectiveness of the construction of the armored caisson breakwater with intake holes in Kudoh Fishing Port (Akeda et al.,1998). Fig.16 shows a plan view of the Kudoh Fishing Port. The opening ratio ε was about 16 to 22%, based on the installation depth of the north inner breakwater.

(1) Seawater exchange by tides

If the north inner breakwater is an impermeable structure, the seawater exchange by tides can not be expected, the seawater exchange rate will be decreased to 1/100 to 1/50 of the present (without the north inner breakwater). Although the seawater exchange rate will be decreased to 1/6 to 1/5 of the present if the north inner

breakwater is the armored caisson breakwater with intake holes, there will be no problem concerning water quality in the port.

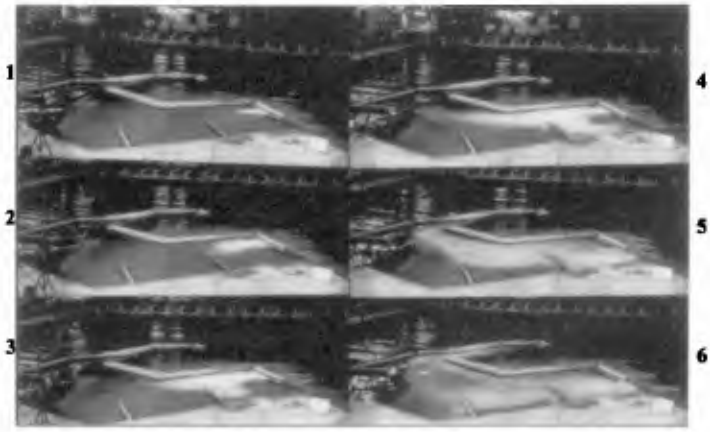

Fig.17 Results of Visualization Experiment on the Inflow ($T_{1/3}$=12.0s, $H_{1/3}$=5.3m)
NO.1 is after 8 min. NO.2 is after 26 min. NO.3 is after 38 min.
NO.4 is after 77 min. NO.5 is after 100 min. NO.6 is after 124 min.

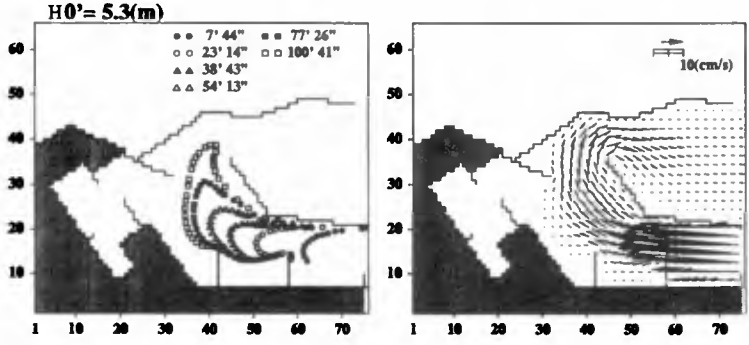

Fig.18 Results of Numerical Analysis on the Inflow ($T_{1/3}$=12.0s, $H_{1/3}$=5.3m)

(2) Seawater exchanges by waves

Fig.17 shows an example of the results of a visualization experiment of the inflow by waves, when the north inner breakwater is the armored caisson breakwater with intake holes. Numbers in the Fig.17 are the field-converted hours after external seawater flowed into the port. Under all experiment conditions, the dye tracer injected into the intake hole flowed into the port without spreading outside the port at all. It was found that the armored caisson breakwater with intake holes were effective in

inducing seawater even with oblique incident waves. The numerical analysis of seawater exchange using a 3-D multi-stratified flow model (Fujihara et al.,1997) was conducted under the same condition as that of the visualization experiment of the inflow of external seawater. Fig.18 shows the numerical analysis result with the same condition as Fig.17. As shown in Fig.18, the tracer distribution and the velocity vector of the inflow external seawater obtained by the numerical analysis almost corresponded with the results of the 2-D hydraulic model tests.

If the north inner breakwater was the armored caisson breakwater with intake holes, it is expected that, in addition to the seawater exchange of 0.5 times/day by tides, the seawater exchange of 3.4 times/day would occur when $T_{1/3}$=12.0s and $H_{1/3}$=5.3m, which were equivalent to wave heights generated several times a year. The seawater exchange of 0.6 times/day would occur when $T_{1/3}$=8.0s and $H_{1/3}$=1.9m, which is equivalent to wave heights generated once or twice a month.

(3) Calmness in the port

Present wave heights (without a north inner breakwater) and future wave heights (with an armored caisson breakwater with intake holes as the north inner breakwater) in the basin for small fishing boat inside of the north inner breakwater were compared. Here, the wave height ratio was defined as the ratio of mean wave height in the basin for small fishing boat to transiting wave height at the position of the north inner breakwater. The wave height ratio was large (0.3 to 0.4) in the basin for small fishing boat inside of the north inner breakwater, due to the direct invasion of waves from the base of the north inner breakwater in the west side of the port. The wave height ratio was particularly high (0.50 to 0.65) in front of the slipway. It was found that, in the future, the wave height ratio would decrease to 0.1 to 0.2 in the basin for small fishing boat and the effect of construction of the north inner breakwater on the calmness in the port would be significant. The rate of effective working days of the quaywall and slipway would also be improved to the required level.

Conclusions

The main results of this research were as follows.

(1)As the wave steepness $H_{1/3}/L_{1/3}$ decreased, and as the opening ratio ε increased, the wave transmission coefficient Kt of the armored caisson breakwater with intake holes increased.

(2)The increase in the mean water level η_{mean} within wave-dissipating blocks was not related to the opening ratio ε and the wave period $T_{1/3}$, but was in proportion to the square of the wave height $H_{1/3}$. The mean velocity U_{mean} through intake hole was in proportion to the dimensionless velocity $(2g\,\eta_{mean})^{0.5}$. The results of field test in Urakawa port were similar to one of 2-D hydraulic model tests.

(3)The horizontal wave pressure and the uplift pressure acting on the front and the bottom of the breakwater body can be determined on the basis of the modified Goda's formula, in consideration of the influence of intake hole.

(4)The amount of seawater exchange could be determined by numerical analysis using

a 3-D multi-stratified flow model.
(5)The validity of the design procedure and the effectiveness of improvement of the seawater exchange could be confirmed through the construction of breakwaters in Setana port (1991-), Urakawa port (1994), Fukushima fishing port (1996-) and Kudoh fishing port (1996-1997).

The armored caisson breakwater with intake holes is excellent in high stability against waves, and can be designed in the same way as a conventional method. Also, it does not require special construction methods and large machinery. The dissemination and the popularization of this technology is expected in the future.

References

S.Akeda, Y.Yamamoto, K.Yano, K.Kimura and T.Onodera(1996): Field Survey on Seawater Exchange Breakwater in Urakawa Port, *Proceedings of Coastal Engineering*, VOL.43, JSCE, pp.1221-1225, (in Japanese)

S.Akeda, Y.Yamamoto, K.Kimura and S.Mifune(1998): Seawater Exchange on an Armored Breakwater with Intake Holes, *Proceedings of Civil Engineering in the Ocean*, VOL.14, JSCE, pp.531-534, (in Japanese).

Civil Engineering Research Institute et al.(1991-1995): Development of Seawater Exchange Breakwater, *Proceedings of the 34th-38th Annual Conference of Hokkaido Development Bureau*, (in Japanese).

Civil Engineering Research Institute et al.(1997): Development of Environment-Friendly Port Structures, *Proceedings of the 40th Annual Conference of Hokkaido Development Bureau*, pp.143-157, (in Japanese).

M.Fujihara, S.Akeda and T.Takeuchi(1997): A Numerical Experiment on Structure-induced Upwelling in Stratified Flow Field, *Transactions of the Japanese Society of Irrigation, Drainage and Reclamation Engineering*, NO.191, pp.117-126, (in English).

Y.Sarukawa, Y.Mizuno, T.Sasajima, K.Kimura and T.Takahashi(1993): A Seawater Exchange Characteristics of Breakwater with Intake Holes Covered with Wave-dissipating Blocks, *Proceedings of Coastal Engineering*, VOL.40, JSCE, pp. 971-975, (in Japanese).

Y.Yamamoto, K.Kimura, K.Yano, S.Akeda, Y.Takeda and K.Sekiguchi(1997): Design Wave Force on Perforated Caisson Breakwater with Wave Dissipating Blocks, *Proceedings of Civil Engineering in the Ocean*, VOL.13, JSCE, pp.549-554, (in Japanese).

Application of Overtopping Models to Vertical Walls against Storm Surges

Holger Schüttrumpf[1], Andreas Kortenhaus[2], Hocine Oumeraci[3]

Abstract

The use of different wave overtopping models has been analysed. These overtopping models were applied to vertical walls with different geometries built for the protection against storm surges in the harbour of Hamburg (Germany). A comparison of existing overtopping test data and results from specific hydraulic model tests for existing geometries in Hamburg was also performed. A simple design diagram to predict both the overtopping rate q and the required freeboard R_C is presented. Furthermore, a simple engineering approach is proposed for the reduction of the horizontal wave load of the harbour walls due to wave overtopping. Finally, conclusions are drawn to come up with a "general overtopping formula" and further research work is outlined.

1. Introduction

The harbour of Hamburg is located on both sides of the river Elbe about 100 km upstream of the river mound (German Bight). The harbour area is divided in many harbour basins with bordering stock areas (Fig. 1). The river Elbe at this location is influenced by the tide resulting in a tidal range of about 2 m in Hamburg. During storm surges the water is pushed upstream the river Elbe from the German Bight and during high floods parts of the harbour are submerged. The cargo areas ("polders") are protected against storm surges by harbour walls with a total length of about 100 km. In Hamburg different geometries are used. Fig. 2 shows a classification of the typical harbour walls.

The local wave conditions during storm surges are as follows: the freeboard is higher than 0.2 m, the significant wave heights vary between 0.1 m and 0.7 m, the

1) Dipl.-Ing., Research Engineer. Leichtweiß-Institut for Hydraulics. Department of Hydraulic and Coastal Engineering. Technical University of Braunschweig. Beethovenstr. 51a. 38106 Braunschweig. Germany. E-Mail: H.Schuettrumpf@tu-bs.de

2) Dipl.-Ing., Research Engineer. Leichtweiß-Institut for Hydraulics. E-Mail: A.Kortenhaus@tu-bs.de

3) Prof. Dr.-Ing., University Professor. Head of Department. Managing Director. Leichtweiß-Institut for Hydraulics. E-Mail: H.Oumeraci@tu-bs.de

mean wave periods between 1.0 s and 4.0 s and the wave directions between 0° and 90°. The water depth h_S is about 15.0 m for design conditions and the average design wind velocity is about 20 m/s. Short crested wave conditions can be expected during high floods.

From above it can be seen that the design conditions in Hamburg for wave overtopping are very complex and an easy-to-use guideline is wanted to calculate wave overtopping. Within a case study the available reports, published and unpublished data have been collected and adapted for the Hamburg harbours walls. The main objectives of this study were:

Figure 1. Port of Hamburg

(1) to identify the most reliable model to predict wave overtopping of vertical walls,

(2) to present an easy-to-use design diagram for the selected model and several applications to different geometries and wave conditions incl. comparisons to other models,

(3) to develop an engineering approach for the reduction of horizontal forces due to overtopping and

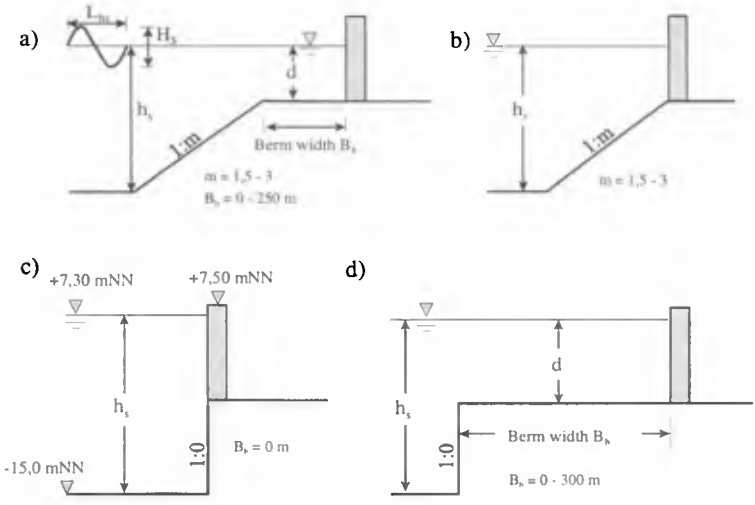

Figure 2. Typical harbour wall geometries

(4) to outline the problems which have to be solved in order to come up with a "general overtopping formula".

2. Influencing Parameters

Wave overtopping is influenced by several parameters which can be identified and classified in the following way (Fig. 2 and 3):

- Structural Parameters:

  Structure Type, crest height and width, berm width, height and slope (Fig. 2)

- Wave parameters and water depth:

  wave height, period and direction, spectral quantities, water depth in front of the structure

- Wind parameters: Wind velocity and direction

- Scale and model effects

- Measured quantities: average overtopping rate, individual overtopping rate, number of overtopping waves

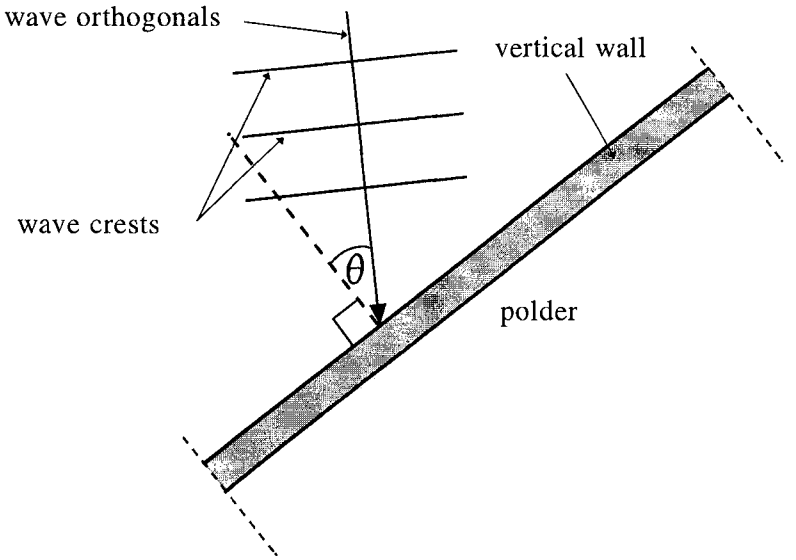

Figure 3. Definition of angle of wave attack

3. Available Overtopping Models

Various overtopping models have been established over the last decades considering more or less of the aforementioned parameters. The most relevant investigations will be summarized in the following with respect to the geometric conditions in Hamburg.

GODA (1985) presents nondimensional diagrams for vertical harbour walls (Type b in Fig. 2) with different foreshore slopes based on small-scale model tests (wave flume) with irregular waves with and without rubble foundation.

DOUGLASS (1984) compares the GODA method with the SPM method (WEGGEL, 1976) and concludes that the two methods show reasonable good agreement for relative water depths h_S/H_S = 0.4 and h_S/H_S = 0.75. For higher ratios of h_S/H_S the SPM overpredicts GODA. AHRENS and HEIMBAUGH (1989) performed model tests with wave spectra for seven test setups, considering a large variety of structure types. DAEMRICH (1991) performed model tests with wave spectra including wave direction (longcrested waves) for the Hamburg harbour wall type a in Fig. 2 (Fig. 4). MÜHLESTEIN (1992a,b) tested the Hamburg harbour wall type without berm and foreshore (Type c in Fig. 2) in a wave flume and a wave basin using wave spectra and wind (Fig. 5).

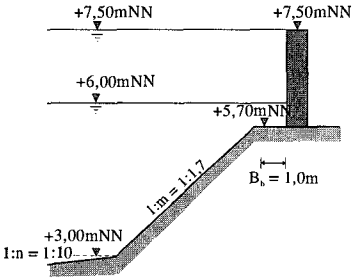

Figure 4. Model Tests by DAEMRICH (1991)

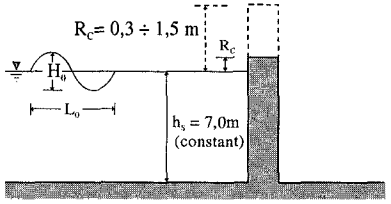

Figure 5. Model Tests by MÜHLESTEIN (1992 a,b)

FRANCO et al. (1995) compiled model data (2D and 3D) from several European laboratories within the MAST II MCS-project (MAS2-CT 92-0047) and added own data (Type c in Fig. 2) from multidirectional wave tests. He proposed the following exponential relationship to calculate the average overtopping rate (in the following referred to as MCS-formula):

$$\frac{q}{\sqrt{g\,H_S^3}} = a\,\exp\left(-b\,\frac{R_C}{H_S}\,\frac{1}{\gamma_i}\right) \qquad (1)$$

with: q = average overtopping rate [$m^3/(s\cdot m)$]

H_S = significant wave height [m]

R_C = freeboard [m] (measured with respect to SWL)

γ_i = non dimensional reduction coefficient [-]

a, b = nondimensional coefficients (recommended: a=0.082; b=3.0 for normal wave attack and no directional spreading)

For oblique wave attack FRANCO recommends $\gamma_\theta=\cos\theta$ (for $\theta<37°$) and $\gamma_\theta=0{,}79$ (for $\theta>37°$) for longcrested waves and $\gamma_\theta=0{,}83$ (for $\theta\leq 20°$) and

$\gamma_\theta=\cos(\theta-20°)$ (for $\theta>20°$) for shortcrested waves.

The influence of wind on wave overtopping is considered by HAYAMI et al. (1966), IWAGAKI et al. (1966) and DE WAAL (1996) for vertical walls. They found that firstly wind has an influence on wave overtopping by affecting the wave profile which again influences the breaker type (breaking occurs earlier, breaker number becomes smaller) and the breaking point moves seaward. Secondly basic spray is transported landward from the sea and thirdly the so called "green water" overtopping increases. Model tests are available for "green water" overtopping resulting in the following findings:

- For most experimental conditions wave overtopping increases due to wind except for very small relative water depths ($h_S/L_0 \leq 0$).
- A quantitative description of the wind influence is still not available due to the scaling problems of wind (drops, drop transport capacity, shear stress between wind and water).

Therefore, further investigations are necessary to check the influence of wind on wave overtopping by large-scale model tests and field measurements.

None of the investigations has yet considered the width of the berm (Type a and Type d in Fig. 2). It is questionable whether the approach by VAN DER MEER et al. (1998) for smooth slopes can be used in the same way or has to be adapted for vertical walls. VAN DER MEER et al. (1998) considered the influence of a berm by introducing a reduction factor γ_b which is defined as:

$$\gamma_b = 1 - \frac{B_b}{L_{berm}} \left(1 - 0.5 \left(\frac{d}{H_S} \right)^2 \right) \qquad (2)$$

with: d = distance between the middle of the berm and still water level (SWL)

B_b = width of berm [m]

L_{berm} = horizontal distance between the two points which are $1.0 \cdot H_S$ below and above the middle of the berm on the structure [m]

H_S = significant wave height [m]

Table 1 shows a comparison of the geometric wall configurations in Hamburg with the model setups of the main investigations used in this paper.

4. Comparison of Model Data to Overtopping Models

Chapter 3 has shown that only the approach by FRANCO considers short- and longcrested waves. Therefore, this approach is compared to the model test results from MÜHLESTEIN (1992a, b) and DAEMRICH (1991) with longcrested waves. These studies were performed to test the geometrical conditions in Hamburg so that comparisons between model data and MCS-formula will show the applicability of the formula for different conditions. Subsequently, the model tests by DE WAAL (1996) for shallow water are introduced in the analysis (s. Table 1).

Table 1. Parameter Used by the Different Investigations (Notations s. Figs. 2-4)

Parameter	Hamburg	MÜHLE-STEIN	DAEMRICH	GODA	DE WAAL	FRANCO
Berm	yes	no	yes (1:1.7)	no	no	yes (1:3)
H_S/L_0 [-]	0.01÷0.1	0.007÷0.017	0.043÷0.057	0.012÷0.036	0.01÷0.04	0.02÷0.04
R_C/H_S [-]	>0.43	0.32÷5.56	0÷1.5	0.45÷1.73	1.0÷2.5	1.18; 1.5; 1.63
θ [°]	0÷90	0, 20, 45	0, 20, 40	0	0	0÷60
v_{Wind} [m/s]	20	0 and 20	0	0	0	0
h_S/H_S [-]	21÷150	7.45÷25.92	7.0÷16.7	0.45÷1.73	1.0÷3.0	4.7÷4.8
tan [-]	1:∞	1:∞	1:10	1:10; 1:30	1:50	1:∞
spectra	short crested	long crested	long crested	wave flume	wave flume	short- and longcrested
model scale	1:1	1:10	1:20	no info.	no info.	1:30
Type (Fig. 2)	a-d	c	b	c	c	a, b, c

A comparison to the MCS-formula is shown in Fig. 6 for tests by MÜHLESTEIN (1992a,b). From Fig. 6 a very good agreement between MCS-formula and model tests can be obscrved for overtopping rates higher than $q \approx 0.1$ l/(s·m). For lower overtopping rates there is a considerable scatter in the results which is common in many model tests. A similar scatter can be found in model tests by OWEN (1980) and VAN DER MEER et al. (1998).

The same conclusions can be drawn when the MCS-formula is plotted against data from DAEMRICH (1991) (Fig. 7). The difference between calculated and measured overtopping rates increases with a decrease in the overtopping rate (below 5 l/(s·m)). It can be concluded that the MCS-formula results in fairly smaller overtopping rates for small overtopping rates especially for oblique wave attack ($\theta = 40°$). For high overtopping rates (q>100 l/(s·m)) the MCS-formula overestimates the overtopping rate. This fact probably results from missing overtopping tests for R_C=0 by FRANCO. Using the model results by DAEMRICH the range of applicability of the MCS-formula is extended for low relative freeboards, higher wave steepnesses and a small steep berm. In Fig. 8 a comparison between the MCS-formula and the overtopping tests by DE WAAL (1993) is shown. In this case the range of applicability of the MCS-formula is extended for high freeboards (small overtopping rates). The scatter of the data is considerable.

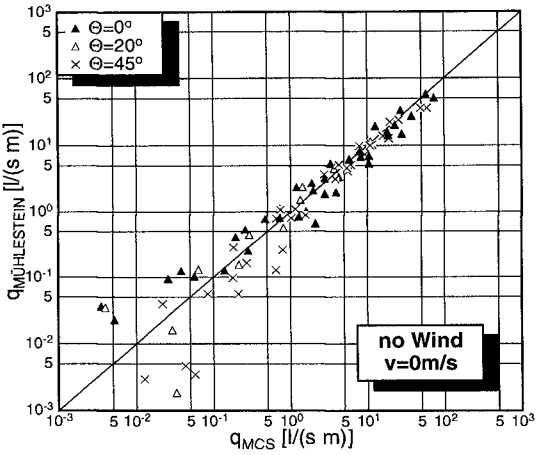

Figure 6. MÜHLESTEIN data versus MCS-formula

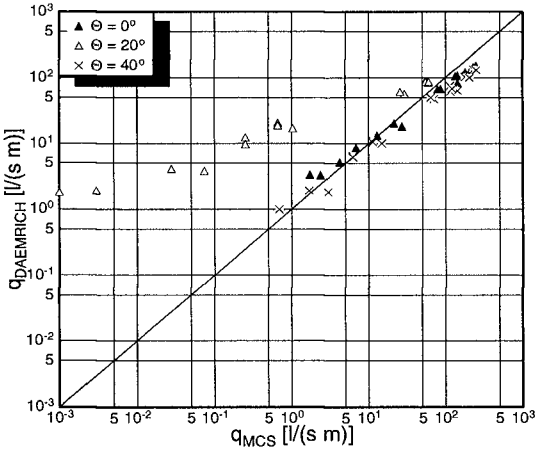

Figure 7. DAEMRICH data versus MCS-formula

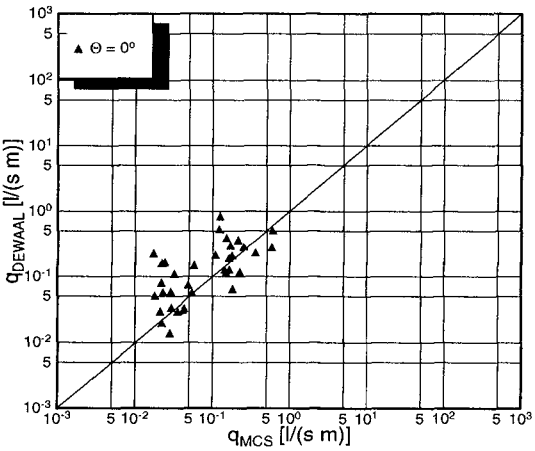

Figure 8. DE WAAL data versus MCS-formula

5. Design Diagram for Wave Overtopping

The comparison between different model data sets and the MCS-formula shows that FRANCOs formula is a reasonable good approach to predict wave overtopping for many different vertical wall geometries. Therefore, this equation has been plotted in a diagram which has been first presented by MÜHLESTEIN (1992) and which is represented in a modified version in Fig. 9 by using Eq. (1).

The overtopping rate can be calculated by entering the diagram with the significant wave height H_S and the freeboard R_C. On the other hand, the requested freeboard can be calculated by using the significant wave height H_S and a critical average overtopping rate q.

The diagram is valid for longcrested waves. For shortcrested waves the freeboard R_C must be divided by γ_θ=0.83 (for $\theta \leq 20°$) or γ_θ=cos(θ-20°) (for $\theta > 20°$) and only the line for θ=0° in the left diagram can be used.

From Table 1 and chapter 4 the range of validity of this diagram is obvious. It can be used for relative freeboard heights R_C/H_S=0÷5, wave steepnesses H_S/L_0=0.007÷0.057 and relative water depths between h_S/H_S=4.7÷deepwater. Furthermore reasonable scatter has to be expected for overtopping ratios lower than 5.0 l/(s·m). Oblique wave attack has to be treated very carefully, because of higher possible overtopping rates.

6. Influence of Wave Overtopping on Wave Forces

The influence of the wave overtopping rate on the wave loading of the wall has not yet been investigated. Many investigations have been performed concerning

wave pressures at the front of vertical walls due to waves (e.g. GODA, 1985; KORTENHAUS et al., 1996) but to the authors knowledge the reduction of pressures due to wave overtopping still remains an unsolved problem. Two main aspects can be distinguished which are dependent on the quantity of wave overtopping:

- indirect reduction of wave forces due to reduction in wave reflection,
- direct reduction of wave forces due to wave overtopping

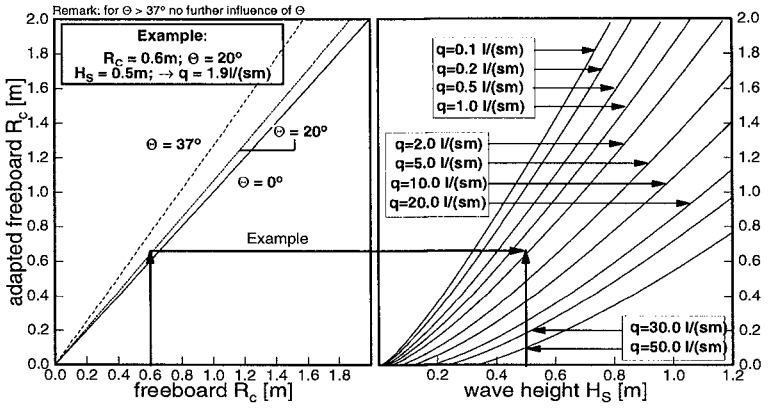

Figure 9. Easy-to-use design diagram for long-crested waves

6.1. Indirect Reduction of Wave Forces due to Reduction of Wave Reflection

DAEMRICH (1991) published data on the reflection coefficient influenced by wave overtopping. The reflection coefficient is defined as:

$$C_r = \frac{H_{S,r}}{H_{S,i}} \tag{3}$$

A reanalysis of DAEMRICH's data (1991) shows a decreasing trend of the reflection coefficient with increasing overtopping rate. This trend is obvious but the scatter of the data is considerable. Unfortunately, model tests on the influence of wave overtopping on wave reflection are still lacking, so that further comparison is not possible.

6.2. Direct Reduction of Wave Forces by Wave Overtopping

Overtopping will lead to a reduction of the horizontal load on the wall. To date this phenomenon has given very little attention in literature and to the authors

knowledge only very few hydraulic model tests have been conducted with a relatively low crest height where considerable amount of overtopping occurred.

The present working assumption for design is to cut the pressure figure at the top of the wall if any overtopping occurs. A typical example for a comparison of cases with and without overtopping is given in Fig. 10. Fig. 10b shows how the pressure distribution is cut at the top of the wall. The pressure ordinate at the top of the wall can be calculated from an interpolation between the ordinate at the height of the design water level (DWL) and the point above the water level where the pressure would be zero if the wall was high enough.

However, this method does not result in a significant decrease of the load. Therefore, an additional approach is proposed. Two boundary conditions are defined: in Fig. 10a the calculated pressure distribution just reach the top of the wall (Case I) whereas in Fig. 10c the design water level (DWL) has reached the top of the wall (Case II). In the latter case wave induced hydro-dynamic pressures cannot exist any more. So this case can be designed by using simple hydrostatic approach. Between cases I and II further reduction of wave pressures and forces should be considered (Fig. 10b).

In Case II the wave-induced loading has to be zero at the top of the wall. Especially for impact breakers this is not the case when the pressure figure is simply cut off at the top of the wall (a pressure head of p_1 in the height of the DWL is still calculated by any design formulae). Therefore, this procedure will result in a too high pressure at the top of the wall.

A factor k_{Fh} is introduced that significantly reduces the loading. This factor accounts for the fact that the pressure distribution and the force in Fig. 10c (Case II) has to be zero and has its maximum at an infinite high wall (Fig. 10a). A reduction of horizontal forces F_h can then be obtained by:

$$F_{h,ov} = k_{F,h} \cdot F_h \tag{4}$$

and for the moment M_h the reduction is given by:

$$M_{ov} = k_{F,h} \cdot M_h \tag{5}$$

In Eq.(4) $F_{h,ov}$ is the reduced force, F_h is the horizontal force according to the design method used and $k_{F,h}$ is the reduction factor for overtopping as given by Eq.(6).

$$\begin{aligned} k_{F,h} &= 1 && \text{für } \eta_* \le R_c \\ k_{F,h} &= \sqrt[3]{\frac{R_c}{\eta_*}} && \text{für } \eta_* > R_c \end{aligned} \tag{6}$$

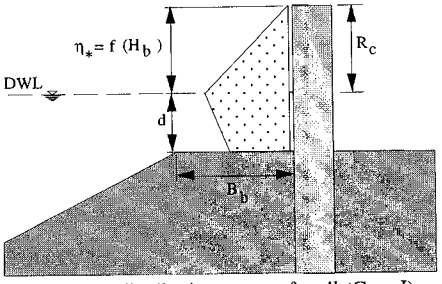

a) Pressure distribution at top of wall (Case I)

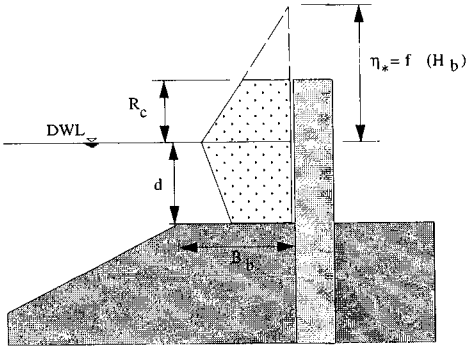

b) Consideration of overtopping

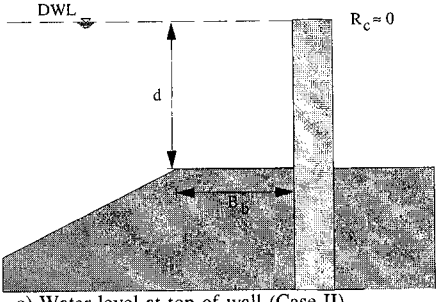

c) Water level at top of wall (Case II)

Figure 10. Comparison of Pressure Distributions With and Without Overtopping

In Eq.(6) η_* is the distance of the highest point of the pressure distribution to the design water level and R_c is the freeboard of the wall (see Fig. 10). Cutting the pressure distribution at the top of the wall is independent from this approach and will be taken into account in all cases. The k_{Fh} factor results in the lower curves shown in Fig. 11 for three different loading cases (1:standing waves; 2:impact waves; 3:broken waves).

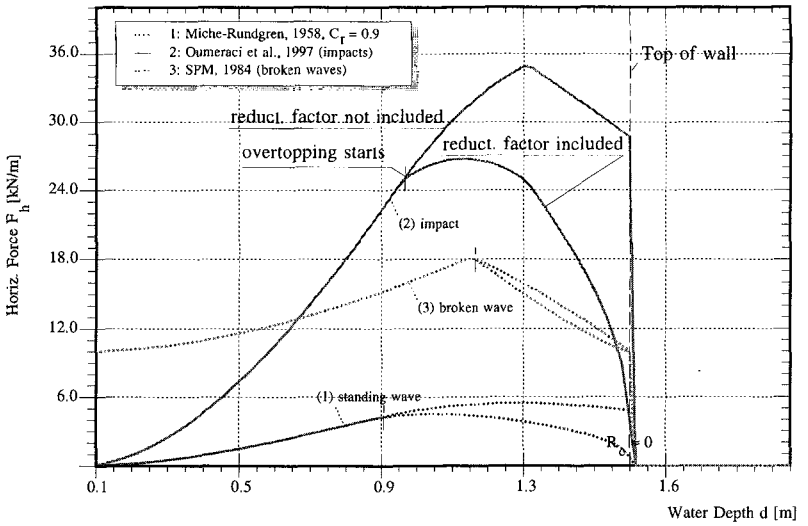

Figure 11. Reduction of horizontal force by reduction factor k_{Fh}

These curves are assumed to be closer to reality than the common method of cutting the pressure distribution. However, for more accurate methods hydraulic model tests should be performed where the reduction of horizontal forces due to overtopping can be measured.

7. Summary and Recommendations for Future Research Work

Many research work has been performed for wave overtopping on vertical walls during the last years. Available papers and data have been reviewed with respect to the various geometric conditions in Hamburg. The most universal overtopping model has been selected and presented in a diagram for practical engineering use. Problems and restrictions of this model have been outlined. Finally an engineering approach for the reduction of wave forces by wave overtopping was shown. The results presented in this paper are in use for the design of about 100km vertical wall length in Hamburg.

From this study the following problems using available model tests and overtopping data have been encountered:

- A variety of overtopping models are available. It is however important to consider both reliability and simplicity when recommend any overtopping model for design.
- The influence of the different berm widths on wave overtopping is insecure. Therefore, more research work conducting model tests is necessary, especially for long berms.
- The influence of wave overtopping on the structure load has not yet been investigated. Consequently, new research work has to concentrate on the direct and indirect influence of wave overtopping. As a first working assumption it is proposed to use the approach presented in this paper.
- The influence of wind on wave overtopping is still under discussion and further research work is needed here.

Acknowledgements

This study has been initiated and supported by the Hamburg harbour authority "Strom- und Hafenbau", Germany. This collaboration is gratefully acknowledged. However, without the basic research project OU 1/2-1 on "Hydrodynamic loading of the inner slope of sea dikes by wave overtopping" supported by the German Research Council (DFG), the practical results presented in this paper would not have been achieved. The very useful comments by Dr. Daemrich (Franzius-Institut, Hannover, Germany) in the preparation of this paper are also gratefully acknowledged.

References

AHRENS, J.P.; HEIMBAUGH, M.S. (1988) Seawall Overtopping Model. Proceedings of the 21st Conference on Coastal Engineering. Malaga, Spain

CERC (1984) Shore Protection Manual. Coastal Engineering Research Center

DAEMRICH, K.F. (1991) Modellversuche zum Wellenüberlauf an Polderwänden. Mitteilungen H. 72. Franzius-Institut für Wasserbau und Küsteningenieurwesen. pp. 353-367; (in German)

DE WAAL, J.P. (1995) Wave Overtopping of Vertical Coastal Structures - Influence of Wave Breaking and Wind. Delft Hydraulics Report No. H 1635.

DE WAAL, J.P.; TÖNJES, P. and VAN DER MEER, J.W. (1996) Wave Overtopping of Vertical Structures including Wind Effect. Proceedings of the 25th Int. Conference on Coastal Engineering. Orlando. USA. pp. 2216-2229.

DOUGLASS, S.L. (1984) Irregular Wave Overtopping Rates. Proceedings of the 19th Int. Conference on Coastal Engineering. Houston. USA. pp. 316-327.

FRANCO, C.; FRANCO, L.; RESTANO, C. and VAN DER MEER, J.W. (1995) The effect of Wave obliquity and Short-Crestedness on the Overtopping Rate and Volume Distribution on Caisson Breakwaters. Final Project Proceedings. MAST II-MCS.

GODA, Y. (1985) Random Seas and Design of Maritime Structures. University of Tokyo Press.

HAYAMI, S.; ISHIHARA, T. and IWAGAKI, Y. (1966) Some Contributions to Hydraulic Model Experiments in Coastal Engineering. Proc. 10th Int. Conf. on Coastal Engineering.

IWAGAKI, Y; TSUCHIYA, Y u. INOUE, M. (1966) On the Effect of Wind on Wave Overtopping on Vertical Seawalls. Bull. Disas. Prev. Inst.. Kyoto University. Vol. 16. Part 1. No. 105. S. 11-30

KORTENHAUS, A.; MILLER, C. and OUMERACI, H. (1996) Design of Vertical Walls against Storm Surge. Proceedings of the 25th Int. Conf. on Coastal Eng.. pp. 1403-1416

MÜHLESTEIN, D. (1992a) Hydraulische Untersuchungen von Wellenüberlauf an HWS-Wänden und Wellenauflauf an Deichen. Final Report. Danish Hydraulic Institute. Project No. 6734. (in German)

MÜHLESTEIN, D. (1992b) Hydraulische Untersuchungen von Wellenüberlauf an HWS-Wänden. Final Report. Danish Hydaulic Institute. Project No. 6930. (in German)

OUMERACI, H. and KORTENHAUS, A. (1996) Bemessung von Hochwasserschutzwänden im Hamburger Hafen. (Design of vertical walls in the harbour of Hamburg) Report No. 799. Leichtweiss-Institut for Hydraulics. (unpublished) (in German)

OUMERACI, H. u. KORTENHAUS, A. (1997) Wave Impact Loading, tentative formula and suggestions for the development of final formulae - Discussion note. Proceedings 2nd Task 1 Workshop. MAST III. PROVERBS-Project: Probabilistic Design Tools for Vertical Breakwaters. Edinburgh

OWEN, M.W. (1980) Design of seawalls allowing for wave overtopping. Hydraulics Research Wallingford, Report No. EX 924

RUNDGREN, L. (1958) Water Wave Forces - A theoretical and Laboratory Study. Kungliga Tekniska Hoegskolans Landlingar. No. 122. Stockholm

SIEFERT, W. (1991) Zum Wellenüberlauf an Hochwasserschutzwänden. HANSA Schiffahrt - Schiffbau - Hafen. No. 12 (in German)

WEGGEL, J.R. (1976) Wave Overtopping Equation. Proceedings of the 15th Int. Conf. on Coastal Eng.. Honolulu. pp. 2737-2755

VAN DER MEER, TÖNJES, P. u. DE WAAL, J.P. (1998) A code for dike height design and examination. Coastal Structures. London.

Advanced assessing of the stability of existing placed block revetments

Adam Bezuijen and Gerard A.M. Kruse[1]

Abstract

Quality assessment of dikes is being set up in the Netherlands. The existing placed block revetments are a part of this assessment. In cases where a routine assessment is insufficient to come to a definitive conclusion, legislation prescribes a more advanced assessment. In this paper, the possibilities of such an advanced assessment are investigated. Three locations were selected for this assessment. The paper describes the experiments, field tests and calculations performed and concludes with the results of the assessment. Permeability of filter layer and cover layer appears much lower than expected, which influences the possible failure mechanism. The residual strength of a clay layer of 0.8 m underneath the blocks appears to be limited.

Introduction

In the Netherlands, where 60% of the land is below sea level, the quality of the water retaining structures is of extreme importance. Now legislation is in progress to come to a regular assessment of the strength of all the water retaining structures.

Figure 1: Type of revetment dealt with. On the lower left side of the picture the filter layer filled with fines can be seen.

The first placed block revetments were evaluated in 1996 according to a provisional version of the legislation to come. In principle this is a routine assessment, with three possible results: 1. the structure is safe, 2. it needs further testing, 3. it is unsafe. This routine assessment used general rules on stability, based on model tests and experience, but always on the safe side. This routine assessment will be described in a paper of Stoutjesdijk et al. (1998). The first results of this routine assessment showed that there are quite a number of revetments with scored 2 or 3, further testing or unsafe.

[1] Consultants, Strategic Research Departement, Delft Geotechnics, P.O. Box 69, 2600 AB Delft, The Netherlands.

Advanced assessment

To check the results of the routine assessment a more detailed assessment is performed for the revetments at selected locations. This, what is called, advanced assessment, has also been performed to investigate the possibilities of such a specific assessment and if it is worthwhile to make this a standard procedure for revetments, that did not pass the routine assessment.

The test results of the selected locations were 2 or 3 after the routine assessment mentioned before. In the assessment, described in this paper, samples were taken from the filter layer, the material between the blocks of the revetment and the subsoil. The permeability of the various layers has been determined in situ and is used to calculate the loading on the revetment, using wave conditions specially determined for the location in study. In cases where blocks had been placed directly on a clay substratum, the quality of the substratum has been evaluated. Furthermore, the clamping forces between the blocks were measured.

After selection of the locations (based on the routine assessment), it appeared that the revetments of these locations were to be improved in 1997. This offers the opportunity to see much more of the filter layers and clay layers than would have been possible without this improvement.

Locations

Three locations were selected. All these locations were along the Western Scheldt. One is on the northern side of the estuary, near the village Borssele. Two are located close together at the southern side near the hamlet Griete.

The location at the northern side would not experience extreme loading during highest storm surges. The highest water levels in the Western Scheldt are expected during spring tide and violent storm from the Northwest, during these conditions this revetment is on the high shore.

The two other locations are at the lee shore during extreme storm conditions. These two locations had the same revetment. At one of the locations, the revetment is placed on a dike of sand covered with a clay layer of approximately 0.8 m thickness. At the other location, the new dike is an enlargement of an old dike of clay material. The old clay dike can present a residual strength to the dike if the revetment is damaged.

The type of revetment is shown in Fig. 1. Concrete blocks are placed on a filter layer below the high water level. Above the high water level the blocks are placed directly on a clay layer. The photo is taken near Borssele, where the entire cover layer is constructed with square concrete blocks. Near Griete the lower part of the revetment was constructed with basalt blocks as a cover layer. Cross-sections of the dike and revetment near Borssele and near Griete at the location where the old clay dike is incorporated in the dike, are shown in Fig. 2 and Fig. 3. The cross-section of the dike near Griete without the old dike is the same except that the old clay dike is missing.

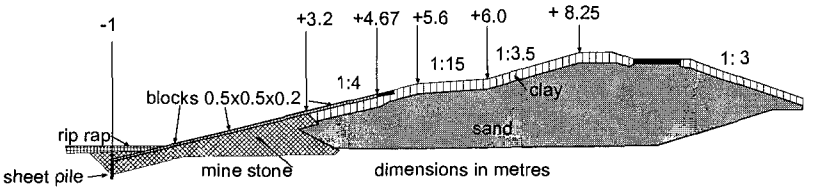

Figure 2: Cross-section of dike near Borssele. Heights are indicated in metres with respect to NAP. The mine stone can be described as coarse mudstone gravel.

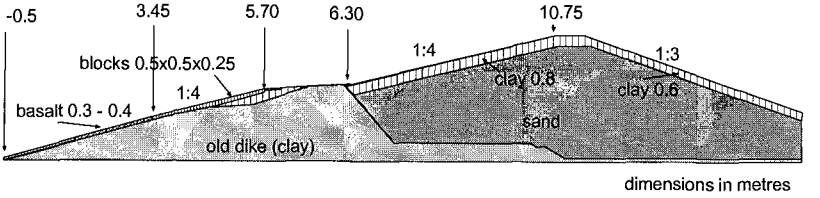

Figure 3: Cross section of dike near Griete. Heights are indicated in metres with respect to NAP. Section where the old (clay) dike is incorporated in the new one.

Results field tests

General

No damage was found where the revetment was placed on a filter layer. Some settlement was found where blocks were placed directly on clay at both locations.

Clamping forces

Pull out tests showed that most of the blocks are well clamped between their neighbours and that a loose block is an exception. There was not much difference between the concrete and basalt blocks. This result confirms earlier measurements (Stoutjesdijk et al. 1992).

The results of the tests on these locations are summarised in Table 1. In this table, the column 'height' is the height with respect of NAP, approximately equal to the mean sea level. At each height, 10 blocks were tested. These blocks were selected blocks. Blocks were chosen from which it was assumed that they could be pulled out of the revetment more easily than the average block. This assumption was based on wider joints between the blocks or some settlement of the block. The maximum possible pull out force was 9 kN. When non-of the 10 blocks in a row were removed with this force, the maximum deformation at this force is given in Table 1. It appears that only in the lower rows at the location Griete some basalt blocks could be removed (in each row 2 of the 10 blocks were removed). Removing was only possible at relatively

Table 1 : Minimum force needed to pull out a block from the revetment or maximum displacement at 9 kN pull out force for 10 blocks in a row.

locati-on	height m +NAP	result
Bors-sele	2.51	3.6 mm
	2.05	2.7mm
	5.59	6.1mm
Griete	3.58	1.5mm
	3.26	6.01 kN
	2.61	6.18 kN

high forces of more than 10 times the block weight. The concrete blocks could not be removed with the maximum 9 kN pull out force. The maximum movement that was measured when pulled with 9 kN was less than 0.01 m in all cases.

Permeability of cover layer and filter

It appeared from the samples taken that all layers have a very low permeability. Values less than 10^{-6} m/s were found in the laboratory, less than the permeability of sand. Field tests, as described by Stoutjesdijk et al (1992), performed by the Dutch Public Work Department resulted also in low permeability values although on average higher values than found in the laboratory. Values ranged between 10^{-6} up to 10^{-4} m/s. Sieve analysis showed that the joints between the blocks are filled with sand and fines as well as the filter layer underneath the blocks. The difference in grain size and premeability was small between the 3 locations.

Most likely, the migration of fines, and the presence of organic slimes have led to the low permeabilities measured. When a block revetment is placed on a filter layer, the normal way of construction is to place the blocks on a thin layer of gravel. Underneath the gravel is a layer of mine stone (coarse mudstone gravel) that is placed on the subsoil of the dike (sand or clay). Just after construction, the permeability of the gravel is higher than that of the mine stone. However, it appears from the field tests that fines that are transported by water in the estuary can migrate in the gravel, but not in the mine stone (due to the smaller grains in the mine stone). This resulted in a gravel layer with a lower permeability than the mine stone layer underneath.

During the research, it was questioned whether the fines will be washed out from the joints and the gravel during extreme storm events, but no evidences what will happen could be obtained. On what is found in the field tests, it is assumed that fines can be washed out from the joints of the cover layer. However, it is unlikely that fines are washed out of the filter layer because of the small joints between the blocks and the limited duration of an extreme storm event.

Clay

To investigate the subsoil below the revetment, a trench was made at all locations. The various layers in the subsoil could be distinguished from the sidewalls from this trench. An example is shown in Fig. 4.

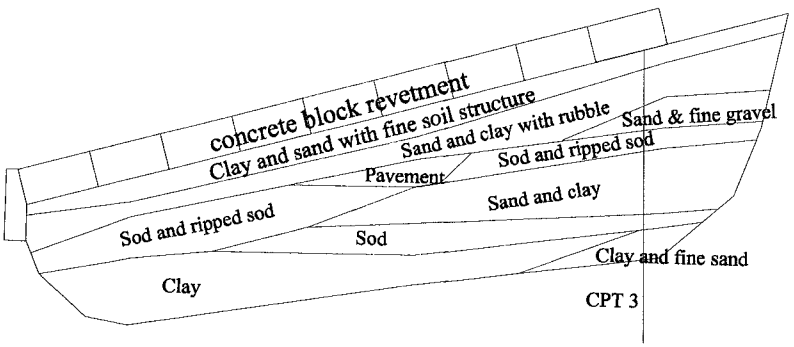

Figure 4: Cross-section through retvetment under layers and subsoil.

At 2 locations a clay liner of 0.8 m thickness on a sand core was encountered. The other the substratum of the block revetment consisted of material supplemented to an existing dike body of clay material (as shown in Fig. 3).

As is common for the upper 1 m of clay in the unsaturated zone of dikes, it has experienced soil formation, and has a soil structure. This structure disrupts the integrity of the clay liners on sand completely. Based on pedological characteristics, it was found that the clay had not been properly densified during construction at the 2 locations with clay liners on sand, and appeared to exist of lumps of clayey material with sand partings. At one location wide, 2 – 5 mm, vertical cracks ran through a thinner section of the clay, and were connected to mine stone below the liner (see Fig. 2). These cracks lead to further erosion of the clay as can be seen from Fig. 5.

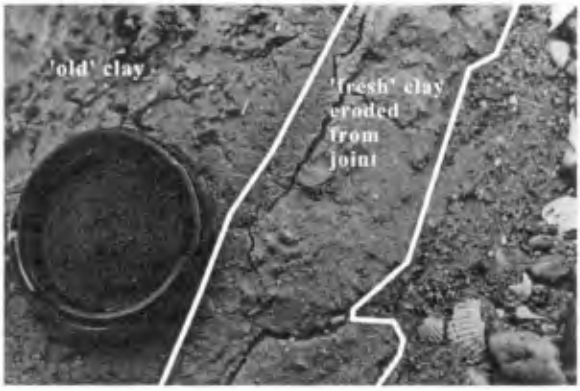

Figure 5: Clay underneath blocks in a revetment. Flow through cracks leads to erosion of the clay.

At the third location the substrate of the block revetment consisted of clay and rubble applied to an already existing dike. The outline of the former dike could be traced by indications of the former grass sods and dike pavement (see Fig. 4). The old dike body had a soil structure entirely comparable to present day soil structure under grassland, but at much denser packing, making it more stiff and less permeable.

The residual strength, expressed in the time it would take to remove the clay substratum of the dike, is very little for clay liners with soil structure on sand, and contributes less than 0.5 to 1 hour for extreme storm and wave conditions. The much denser and stiffer clay body of the older dike at the third location, and its sheer thickness, will make it withstand design loads during a storm surge period.

CPT's were used to assist in determining the overall build up of the dike, and to determine characteristics of clay liners. For the latter purpose the features discerned in the CPT graphs have to be correlated to information derived from sampling pits, however.

Failure mechanism

The failure mechanisms for placed block revetments on a filter layer are described by Burger et al. (1990) and Bezuijen et al. (1987). However, these failure mechanisms were derived from model tests. In these model tests no fines were present between the blocks and in the filter layer, resulting in a much higher permeability for both of these layers in the model, compared with these field locations. Lifting of the

blocks appears to be caused by the pressures on the slope and wave induced flow in the filter layer. During wave rundown, there is a water flow from the filter layer through the cover layer. This water flow can push a block out of the revetment (Bezuijen et al. 1990). Calculation methods have been derived to calculate the stability of the blocks. In these calculation methods, the flow in the filter layer is calculated as a function of the measured or schemed wave pressure distribution on the slope (Bezuijen and Klein Breteler, 1996).

For the revetments studied here, it is unlikely that flow in the filter layer can really contribute to lifting of the blocks. Due to the low permeability the discharge will only be limited leading to minor block movements. From what is seen in the field, it is more likely that flow underneath the blocks results from a small joint between the blocks and the filter layer. Whether this flow can lead to failure of the blocks in the revetment will be described in the next section.

Numerical calculations

The numerical calculations were focussed on the influence of joints between the blocks and the filter layer on the stability. The flow through such a joint can be described with the same equations as the flow through a permeable filter layer. However, in this case the 'filter layer' in the numerical model, represents the joint and has a finite length. In such a situation, largest uplift pressures over the blocks can occur when the waves causes steep pressure gradients on the slope.

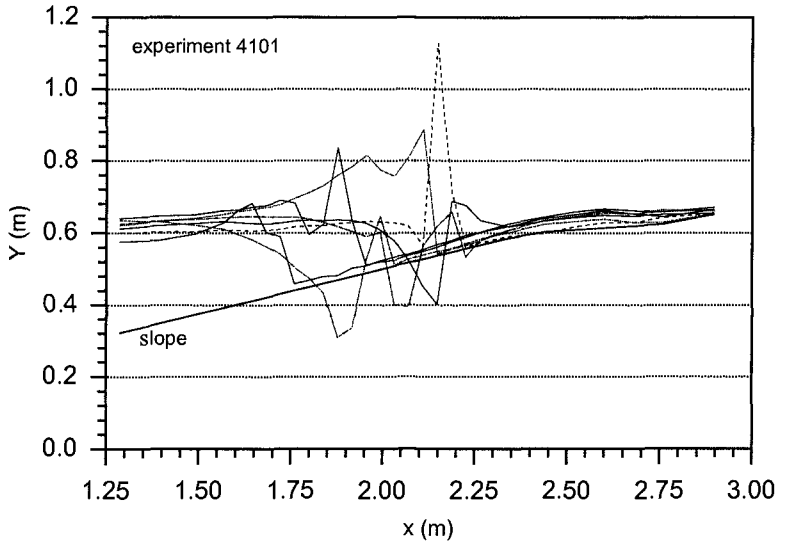

Figure 6: Measured wave pressures on slope at various moments with high pressure gradients. Data from small-scale model tests.
Irregular wave: $H_s = 0.103$ m, $T_p = 2.48$ s.

Wave pressures were available from a series of small-scale model tests. In these tests, the pressure was measured with 25 pressure gauges. Tests were run with

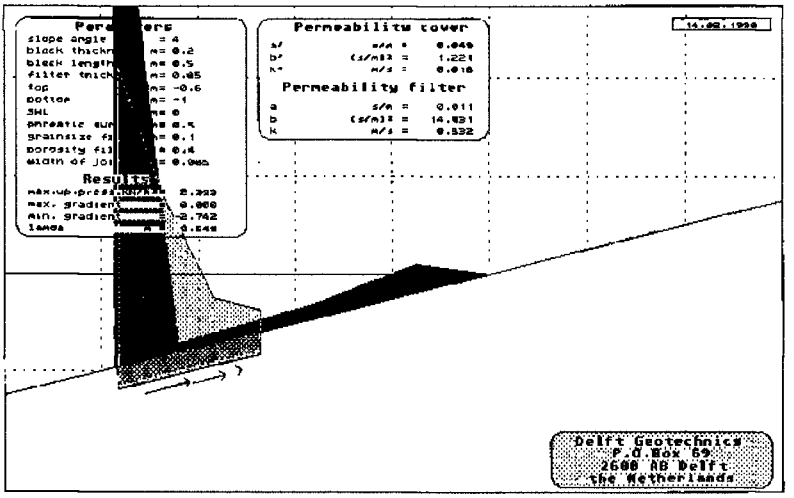

Figure 7: Result STEENZET calculation. Pressures during wave impact. See also text. The distance between the dotted lines is 1 m.

irregular waves on a slope with a berm, as was present at these locations. From the tests the moments with steepest wave pressure gradients between two adjacent pressure gauges were selected. An example of such a selection is shown in Fig. 6. From this figure it appears that high wave pressure are present during wave impact, when there is a peak in the wave pressure, but also at some moments of low wave pressure. These moments occur just after the wave impact and then wave pressures lower than the atmospheric pressure can be measured. After this selection was made calculations where run with the STEENZET program to find what moments are most critical for the stability. These are the moments with the largest uplift pressure. These calculations were run for a joint of 3 or 4 block lengths. The waves were scaled up to the expected wave height at the various locations. For the wave pressures shown in Fig. 6 a scaling factor of 12.72 is used, which means that the actual wave height that is simulated in the calculations is 1.31 m with a wave period of 6.6 s. This is the maximum wave height to be expected at the toe of the revetment near Borssele. The extreme wave height for the revetment near Griete can be up to 2.5 m for a water level of 6 m + NAP.

Some results are shown in Figures 7 and 8. In these figures the blocks on the slope where the assumed joint below the blocks is present, are indicated. The black area is the measured wave pressure distribution (in m water). The part from the still water line until the lowest block is shown. Only the wave pressure distribution above the blocks has a consequence for the calculated pressure in the joint. The STEENZET program was designed for this extreme wave impact events and therefore the wave pressure is drawn through the results.

The calculated pressure in the joint below the blocks is indicated with the grey area (again in m water). The maximum uplift pressure is indicated, if this pressure is higher than the under water weight of the blocks, the revetment is potentially unstable because a block can be lifted. At the two locations described in this paper, the under

water weight of the concrete blocks was 2.7 kN/m^2. For the basalt, this was 3.4 kN/m^2. The figures show that the low wave pressure that can occur directly below the wave impact can result in the largest uplift pressures. In this situation, the uplift pressure of 5 kN/m^2 is well above the pressure corresponding to the underwater weight of the blocks.

Further calculations with the STEENZET program have shown that for this situation the loading during impact is far more severe than the loading during maximum wave run down. The maximum loading depends largely on the length of the joint underneath the blocks. A larger joint leads to a much larger loading.

These results show that a block can become unstable when there is as small joint underneath the blocks. However, it is still difficult to determine an objective failure criterion based on these results. Since the wave pressures used, were measured during wave impact, the large gradients in the wave pressure measured will exist only for a short period. In such a short period, it is not possible that a block is lifted completely out of the revetment. If however some movement of the blocks occurs during this period, then the following waves can cause damage. Comparing the maximum uplift pressures with the pull out forces that were found, no damage has to be expected, but the pull out tests were performed on one single block. During wave attack, an uplift pressure can be present over a row of blocks and wave impacts can result in minor adjustments of the blocks leading to different clamping forces. It is therefore assumed that an uplift pressure of nearly two times the weight of the concrete blocks can result in instability. To get quantitative information it is necessary to perform large-scale model tests on revetments with comparable low permeable cover layers and filter layers and to analyse the measured pressures.

The situation for the basalt is less critical than for the concrete blocks, because of the larger joints between the basalt. In cases where there is a joint between the ba-

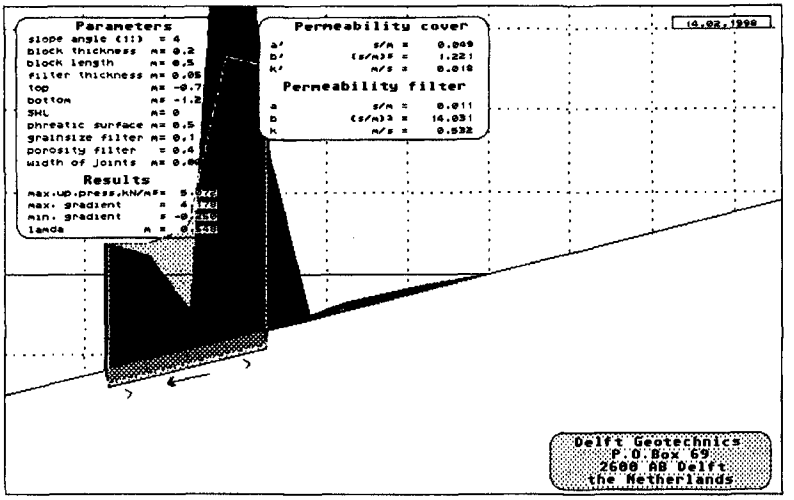

Figure 8: Result STEENZET calculation. Pressures below area of wave impact. See also text. The distance between the dotted lines is 1 m.

salt blocks and the filter layer there is also the possibility for pressure relief through the joints between the blocks. Furthermore the basalt is only placed at the lower parts of the revetment, up to a water level of 3.45 m + NAP, while the design wave attack is expected at a higher water level of approximately 5.5 m +NAP.

Conclusions

- The permeability of cover layer and filter layer in an existing revetment with sand and fines between the blocks and in the filter layer is much lower than of a newly build revetment. This will lead to other failure mechanisms than normally tested on in model tests or calculation models. Quality of workmanship preventing space between blocks and filter layer (due to settlement or erosion) will become more important to evaluate stability. The clamping forces between the blocks increase stability, but also can conceal open space underneath the blocks.
- Due to the low permeability the failure mechanism differ from the failure mechanism that are normally seen in model tests, with more permeable cover layer and filter layers. This means that model tests for existing revetments should be performed modelling the actual situation and not the as built situation.
- Since it not to be expected that about 0.8 m of clay in the unsaturated zone of dikes can withstand erosion for a significant amount of time, it is relevant to find out where such conditions occur. The erosion resistance of clay cores of dikes requires further research.
- Assessment of the quality of revetments still needs 'engineering judgement'. Further research is needed to come to an objective assessment.

References:

Bezuijen, A., Klein Breteler, M., and Bakker, K.J. (1987). "Design criteria for placed block revetments and granular filters." *Proc., 2nd COPEDEC,* China Ocean Press, 2, 1852-1866.

Bezuijen, A., Wouters, J., and den Adel, H. (1990). "Numerical simulation of the motion of a loose revetment block." *Proc. 22nd ICCE*, ASCE, New York, N.Y., 1606-1619.

Bezuijen, A., Klein Breteler, M. (1996). "Design formulas for block revetments." *J. wtrwy, Port, Coastal and Oc. Engrg.,* ASCE, 122(6), 281-287.

Burger, A.M., Klein Breteler, M., Banach, L., Bezuijen, A., and Pilarczyk. K.W. (1990), "Analytical design method for relatively closed block revetments." *J. wtrwy, Port, Coastal and Oc. Engrg.,* ASCE, 116(5), 525-544.

Stoutjesdijk, T., Klein Breteler, M., Johanson, H., (1998), "Inventory of stability of existing placed block revetments in the Netherlands", *To pres. ICCE Copenhagen.*

Stoutjesdijk, T., Rigter, B., Bezuijen, A., 1992, "Field measurements on placed block revetments." *Proc. 23rd ICCE 1992*, ASCE, New York, N.Y.

Design of Revetments in the Öresund Link. Reclaimed Artificial Island and Peninsula

Jeppe Blak-Nielsen[1] (M.Sc.), Helge Gravesen[2] (M.Sc.) and Niels Lykkeberg[3] (M.Sc.)

Abstract

The basic and detailed design of revetments and breakwaters in the Öresund Link were carried out by the Consultant, Carl Bro a/s[4] for the Contractor, Öresund Marine Joint Venture, ÖMJV[5], based on design requirements and additional background information given by the Owner, Öresundskonsortiet, ÖSK. Final design was to be approved by the Owner, but with the liability of the Consultant/Contractor and with due consideration to the contractors method of construction. As part of the design process and in order to fulfil given geometrical restrictions the design requirements where further elaborated based on results of physical model tests and desk studies of critical assumptions. Some of the aspects and considerations in that process are discussed below.

Introduction

The Öresund Link creates a fixed link from Denmark to Sweden. As part of the Link, a 4 km long artificial island, named Peberholm, south of the island Saltholm and a Peninsula east of Amager have been constructed, see the overall layout in Fig. 1. The Link carries both rail and road traffic, from the Peninsula to the new island in a 3.5 km immersed tunnel, and from the island to Sweden on a 7.8 km double deck bridge with cable-stayed central spans. The Peninsula includes approx. 3.5 km permanent revetments. The artificial island includes approx. 8.5 km of permanent revetments and 1 km of semi-submerged breakwaters at the eastern and western ends. Further, approximately 2 km of temporary revetments and breakwaters were designed and constructed along with 3 temporary, sheltered and 3 unprotected work harbours.

[1] Engineer at Ports and Marine Engineering, Carl Bro a/s (E-mail : jnnanl@carlbro.dk)
[2] Specialist at Ports and Marine Engineering, Carl Bro a/s (E-mail : hlganl@carlbro.dk)
[3] Head of department for Ports and Marine Engineering, Carl Bro a/s (E-mail : nkdanl@carlbro.dk)
[4] Carl Bro a/s, Granskoven 8, 2600 Glostrup, Denmark.
[5] ÖMJV consists of : Per Aarsleff A/S, Denmark
Great Lakes Dredge & Dock Company, USA
Ballast Needam Dredging, the Netherlands

A total of approximately 8.000.000 m^3 of dredged material has been placed in the reclaimed areas behind permanent revetments and breakwaters consisting of approximately 650.000 m^3 coarse pebbles, 130.000 m^3 filter stones and 250.000 m^3 armour stones.

A brief description of the design requirements and calculations for design of typical cross sections of the revetments in the 14 km coastal structures is given below. The discussion is mainly on wave heights and the correlation with high water level used in the design of armour layer and in calculations of overtopping. Also the formal proof of the stability of the toe and scour protection is discussed in further detail.

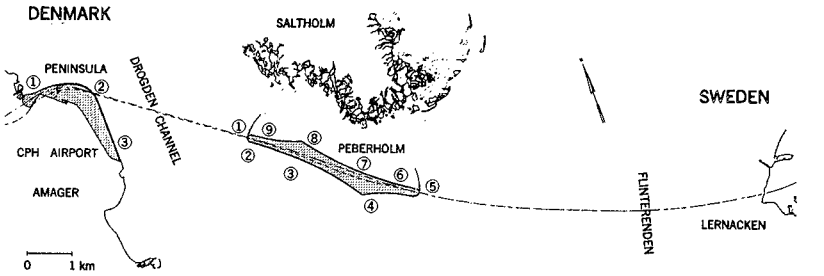

Figure 1. Layout of the Öresund Link - Reclamation Works

As Consultant for design Carl Bro a/s carried out the tender, basic and detailed design of revetments and breakwaters for the Contractor Öresund Marine Joint Venture, (ÖMJV) based on design requirements given by the Owner, Öresundskonsortiet, (ÖSK). Desk studies and physical model tests revealed that the design requirements had to be re-evaluated to make the final structure fulfil geometrical requirements also given by the Owner.

Design Requirements

Significant wave heights and water levels with a 10, 100 and 10,000 year return period where given for specific locations in the Öresund area as design requirements. The wave data were given for two positions on the alignment of the Link (one in the Drogden Channel and one in Flinterenden). Also a set of data for Drogden lighthouse situated approx. 8 km south of the link was given. The requirements were based on field data and numerical wave and water level modelling (MIKE 21 NSW and MIKE 21 HD) performed by Danish Hydraulic Institute, DHI. The numerical modelling was carried out with no island or peninsula present.

Further results from the study done by DHI were available as Background Information, and wave climate data reduced due to friction and wave breaking over the shallow areas was given along the entire length of the Link alignment as well as for 6 points south of the future artificial island. From this a wave climate depending on water depth was developed and used in the Tender Design, see Table 1 below.

The above described approach for determining the design wave heights was not accepted by the Owner and for the basic and detailed design of the armour layer more conservative wave heights were specified in order to reduce the risk of damages. Data from "deep" water were to be applied unreduced on the revetments and breakwaters according to the criteria given below. The results from the numerical modelling were only accepted by the Owner for design of the northern perimeter of the reclaimed island. Also the criteria $H_s < 0.6h$, where H_s is the significant wave height and h is the local water depth at design water level, was given by the Owner, but due to large water depth not applied.

The basis for design requirements for wave heights applied in the final design can be summarised by the following :

Peninsula (P1-P3) : Wave data from Drogden Channel
Western part of the Island (I1) : Wave data from Drogden Channel
Southern perimeter (I2-I4) : Interpolation between Drogden and Flinterenden
Eastern part of the Island (I5) : Wave data from Flinterenden
Northern perimeter (I6-I9) : Results from numerical model increased by 1.15

The positions at the island, I1-I9 and peninsula, P1-P3 are indicated in Figure 1 and the wave heights used for designing armour stones etc. are listed in Table 1.

Location		Tender Design		Final Design (Armour layer)		Final Design (Overtopping)	
		H_s (m)	HWL (m)	H_s (m)	HWL (m)	H_s (m)	HWL (m)
Peninsula	1	1.5	+1.00	1.6	+1.50	1.4	+1.35
	2	1.5	+1.50	1.6	+1.50	1.4	+1.35
	3	1.5	+0.50	1.6	+1.50	1.3	+1.15
Island	1	2.0	+1.50	1.7	+1.50	1.5	+1.35
	2	2.0	+0.50	1.8	+1.50	1.5	+1.10
	3	2.0	+0.50	2.0	+1.50	2.0	+1.00
	4	2.0	+0.50	2.5	+1.50	2.2	+0.90
	5	2.0	+1.50	2.5	+1.50	2.2	+1.30
	6	1.2	+1.00	1.1	+1.50	1.1	+1.35
	7	1.2	+1.00	1.3	+1.50	1.2	+1.35
	8	1.2	+1.00	1.1	+1.50	1.0	+1.35
	9	1.5	+1.00	1.1	+1.50	1.0	+1.35

Table 1. Wave heights and High Water Levels (100 year return period). Water levels include expected level increase of 0.15 m over 100 years.

The water level in the Öresund region is governed by wind and barometric pressure, and tide is only limited. The Öresund link is constructed on a sill, that creates a dividing line between the salty waters in Kattegat to the north and the brackish water of the Baltic Sea to the south and east. A large difference in water level can occur across the sill, and the exact water level at the Link is difficult to determine.

The design requirements stated that if no other studies were performed the conservative wave heights should be used fully correlated with maximum high water level in the design and especially for calculations of overtopping. The correlated high water levels used in the Tender Design were based on data as presented in Background Information. Figure 2 below indicates a correlation between high water levels and waves from northerly directions, while this does not seem to be the case for waves from southerly directions. Due consideration was also given to the high risk sections around the tunnel portals and the abutment area (point P2, I1 and I5 in Figure 1) by using full correlation between maximum wave heights and water levels.

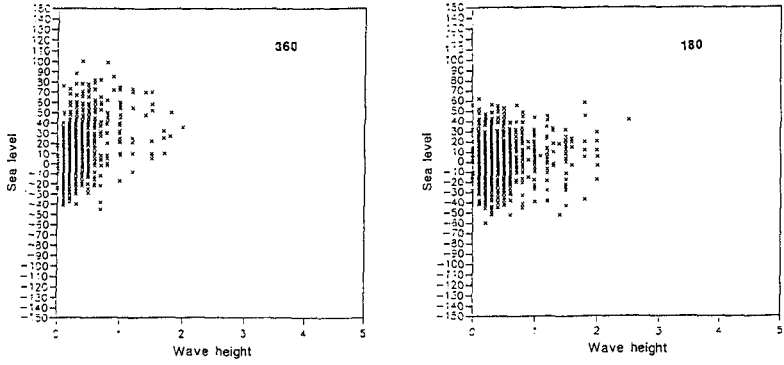

Figure 2. Wave heights and correlated water levels. Data from 1962-1984 (Waves from Northerly (360) and southerly (180) directions)

This however resulted in an unacceptable large volume of predicted overtopping that theoretically would endanger the overall stability of the structure. Hence a detailed statistical investigation was carried out for data on observed water levels and wave heights at Drogden Lighthouse 1962-1984 in order to establish a more accurate description of the correlation. The data was sorted according to wave height and high water level and curves of correlation could be determined, cf. Figure 3 and 4 which include selected results. The limited period of observation meant that a full set of design curves could not be evaluated, and an engineering approach in determining the curves for large wave heights was accepted by the Owner. The less conservative wave heights found in the numerical modelling were specified by the Owner to be used for the calculation of the overtopping, and with a given wave height the correlated high water level was determined. This resulted in the design wave heights and water levels also listed in Table 1. It must be noted that the high water levels listed in Table 1 includes a general increase of 0.15 m of the water levels in the Öresund region over 100 years.

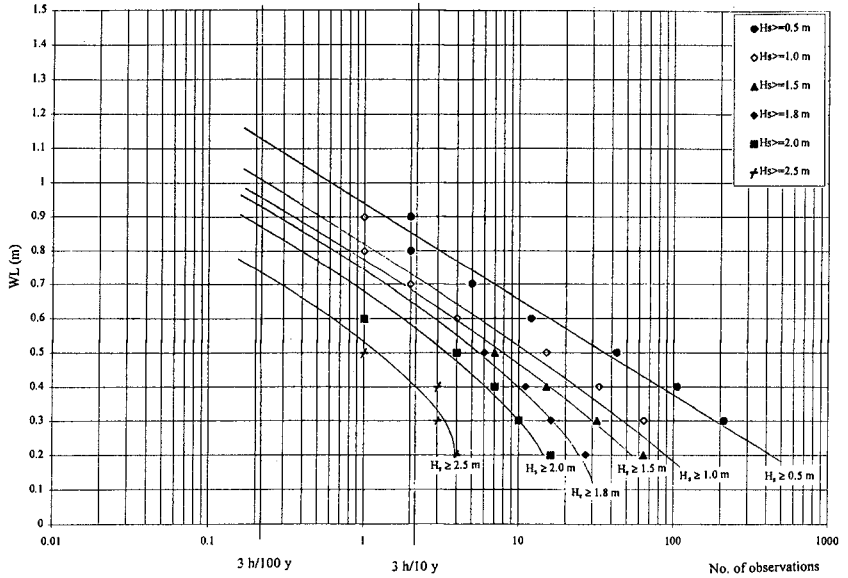

Figure 3. Correlation between water level and wave height
(Waves from southerly directions, based on data from 1962-1984)

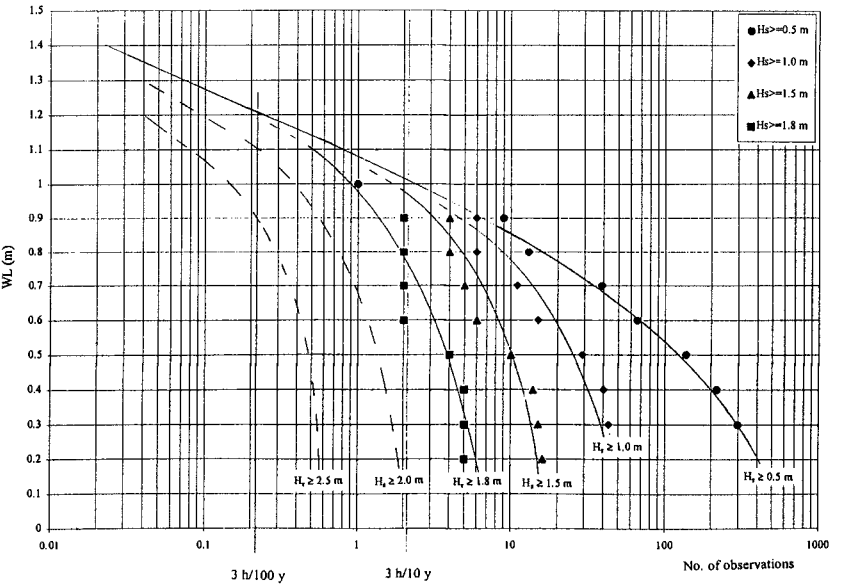

Figure 4. Correlation between water level and wave height
(Waves from northerly directions)

Typical cross sections

In Figure 5 and Figure 6 two typical cross sections of revetments in the Öresund Link are given. Figure 5 shows a normal cross section with the filter stone layer extended behind the crest as a protection against overtopping. Figure 6 illustrates the design adopted at the tunnel portal and abutment area. The vertical wall was part of the geometrical requirements given by the Owner as part of the design basis.

The core of the revetment consists of coarse pebbles ($W_{50\%}$ = 1.0-3.5 kg) which were specified in the design requirements. The filter stones ($W_{50\%}$ = 16-80 kg) follow the filter criteria towards core and armour layer. As already noted above the Owner had specified the interface between backfill and core to be multiple layers of sand, which are difficult and costly to place. In order to greatly simplify and reduce the number of operations the Owner agreed to substitute the layers of sand with a geotextile, which could be proven to have the same effect.

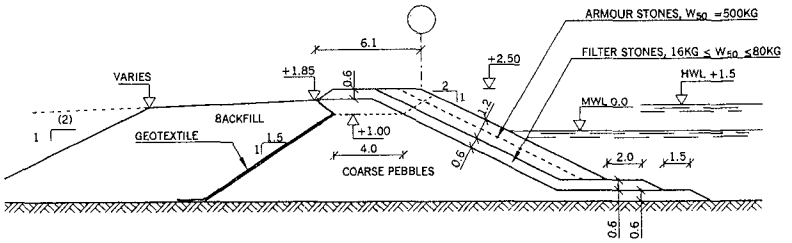

Figure 5. Typical cross section. Low crest

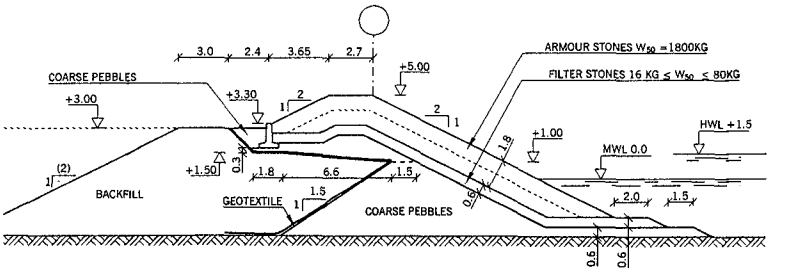

Figure 6. Typical cross section. High crest.

As an important part of the design basis for armour layer, crest, toe and scour protection a series of physical model test were performed for the revetments and breakwaters. From the results simple design criteria could be found.

Armour stones

The formulae given in (Meer, 1987) were approved by the Owner in the design requirements for calculating the armour stone size. Further the damage level was defined as the damaged cross sectional area relative to the total cross sectional area of armour stones. This gives a non-logical dependency between armour stone size and water depth / crest level. Theoretically a higher crest or deeper water required smaller armour stones for identical wave climates. In stead the results of the physical model tests were used to establish design criteria for the stability number, N. Δ is the relative density and $D_{n,50\%}$ is the nominal diameter of the armour stone.

$$N = H_s/\Delta D_{n,50\%} = 1.45 \text{ for damage level of 2 \%} \quad (1)$$
$$N = H_s/\Delta D_{n,50\%} = 1.85 \text{ for damage level of 5 \%} \quad (2)$$

The design requirements specified that the armour stone size for the sections at the tunnel portal and at the abutment were designed for 2% damage in a wave climate with 100 year return period and for 5% damage in a 10,000 year return period. The remaining permanent revetments and breakwaters are designed for 5% damage for a 100 year return period.

The armour stones were grouped in a limited number of stone classes in agreement with the Contractor, but due to repeated changes in design requirements throughout the construction phase this number had to be increased. A list of the armour stones used is given in Table 2, where the locations refer to Figure 1.

Location		H_s (m)	$W_{50\%}$ (kg)
Peninsula	1	1.6	500
	2	1.6	1,000
	3	1.6	500
Island	1	1.7	1,800
	2	1.8	1,000
	3	2.0	1,000
	4	2.5	1,800
	5	2.5	3,700
	6	1.1	1,000
	7	1.3	500
	8	1.1	300 / 200
	9	1.1	1,000

Table 2. Armour stone size with corresponding 100 year wave height.

The armour stones on the northern perimeter have been designed to withstand a temporary situation (5% damage for a 10 year return period) without the low crested breakwaters, the Whiskers, at the eastern and western tip of the island. Further it can be noted that the temporary revetments and breakwaters protecting the compounds used as a construction site have been constructed from materials that can be reused in the construction of the whiskers ($W_{50\%}$ = 1,800 kg armour stones).

Toe and scour protection

Initially the toe and scour protection was designed based on experience and a large redundancy was built into the structure. The toe structure was questioned by the Owner, and a detailed investigation was carried out based on the results of the physical model tests. Design curves are shown in Figure 7, where H_s is the significant wave height, N is the stability number and h_t is the water depth over the toe or scour protection.

The physical model tests showed a general smoothing of the edge of the coarse pebbles and minor damage (less than 5%) to the layer of filter stones. Both layers were at least dynamically stable and the overall stability was not endangered in any of the tests. It was accepted by the Owner, that the curve obtained for the filter stones could be used as a design curve for both toe and scour protection. Based on results presented in (CIRIA/CUR, 1991) and other previous studies the design curve was then extended to be valid for $h_t/H_s > 0.6$. Also H_s could be limited by $H_s = 0.5h$ in stead of the criteria $H_s = 0.6h$ used for the design of the armour layer.

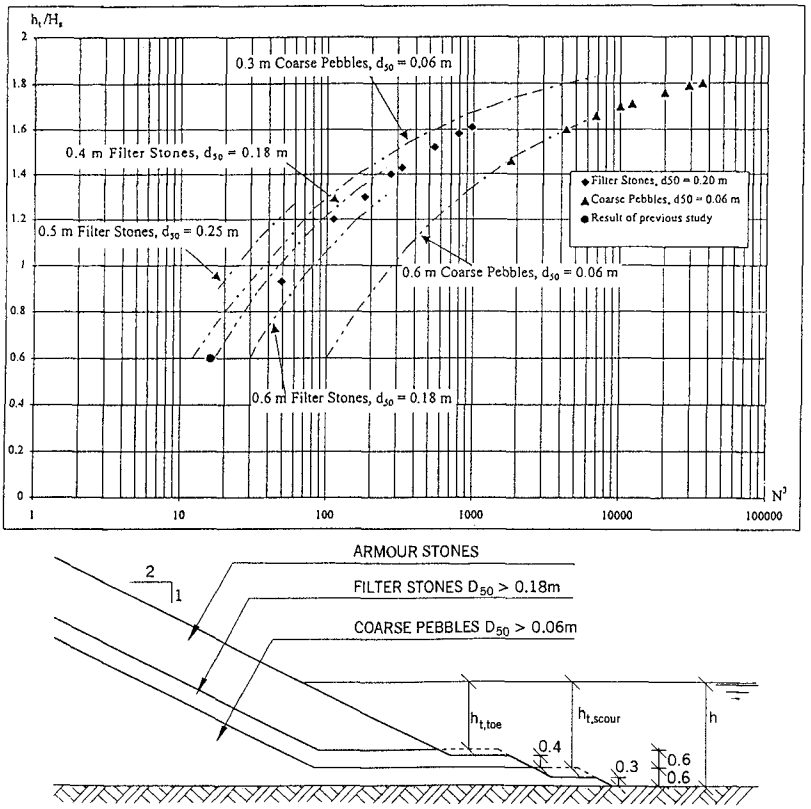

Figure 7. Design curves for toe and scour protection

As can be seen from Figure 7 a toe with 0.6 m layers of filter stones on coarse pebbles including a large redundancy could not be proven theoretically stable due to the shallow water over the toe. By including a smoothing, where the layer thickness was allowed reduced (0.6 m to 0.4 m for filter stones in the toe and 0.6 m to 0.3 m for the coarse pebbles in the scour protection), the structure could be proven theoretically stable for the following water depths, h :

0.4 m Filter stones in toe stable for	$h > 1.45$ m
0.3 m Coarse pebbles in scour protection stable for	$h > 0.45$ m

The Owner then accepted a smoothing of the toe in general to a slope of 1:6, and by using (Meer, 1987) the toe and scour protection could be proven theoretically static stable for the following water depths, h :

Filter stones in toe stable with slope 1:6 for	$h < 1.20$ m
Coarse pebbles in scour protection stable with slope 1:6 for	$h < 0.35$ m

No formal proof of the static stability of the toe and scour protection could be obtained for the intermediate water depths, but the Owner agreed that there is no reason why the structure should be especially unstable for these water depths.

A study of the sediments in the seabed in the area showed mainly coarse materials with limited chances of extensive scour in spite the increase in current speed due to concentration around the island and peninsula. On sections with a large ratio of sand in the seabed the toe and scour protection was extended by 1 m to a total of 3.0 m width of the toe.

Hence the initial design of the toe and scour protection was finally accepted with only minor increase of the toe width on exposed sections, but as a part of the accept, the Owner specified a monitoring programme commencing after handover.

Overtopping

The initial theoretical calculations of overtopping in the Tender Design showed an unacceptable amount that would endanger the overall stability of most sections of the revetments. Based on the physical model tests a formula for calculating the mean volume rate of overtopping, Q_m without correction for the influence of wind was derived by using the structure of a formula by Bradbury et. al. as given in (CIRIA/CUR, 1991).

$$Q_m = gH_sT_z \cdot 2.8 \cdot 10^{-5} \cdot (\Delta h/H_s)^{-7} \qquad (3)$$

Using this formula the overtopping volumes were recalculated using maximum wave heights correlated with maximum water levels. This also showed an unacceptable amount of overtopping, and a the crest levels were recommended raised. The physical model tests indicated a recommended freeboard of not less than $\Delta h = 1.35H_s$ for an overall stable structure. The crest levels were fixed by the Owner, and hence the Owner initiated discussions on the correlation between waves and high water levels. Finally agreement was reached on design criteria with less conservative wave heights

and correlated water levels as given in Table 1. This reduced the overtopping significantly but additional protection of the crest was still necessary. Especially on the southern perimeter of the island, where the crest is down to +3.0 m, a layer of filter stones behind the crest of armour stones is placed.

The Owner further granted that the Contractor would not be responsible for overtopping causing flooding of building sites or erosion of the unbound service road / backslope of clay till bunds.

As an indication of the theoretically calculated amounts of overtopping for different sections of the revetments a list is given in Table 3 for a wave climate and high water level situation with a 100 return period. The volume is measured behind the crest of armour stones.

Location		H_s (m)	HWL (m)	Crest level (m)	Q_m (m^3/h/m)
Peninsula	1	1.4	+1.35	+2.50	54.0
	2	1.4	+1.35	+3.25	2.0
	3	1.3	+1.15	+2.50	19.0
Island	1	1.5	+1.35	+5.00	0.06
	2	1.5	+1.10	+5.00	0.04
	3	2.0	+1.00	+3.00	23.0
	4	2.2	+0.90	+3.00	35.0
	5	2.2	+1.30	+5.00	0.9
	6	1.1	+1.35	+3.00	0.9
	7	1.2	+1.35	+3.00	1.6
	8	1.0	+1.35	+3.00	0.4
	9	1.0	+1.35	+3.00	0.4

Figure 3. Calculated overtopping for situation with 100 year return period

The permanent structures should also withstand a situation with a 10,000 year return period, where the volumes of overtopping are 10-50 times as large. Again the overall stability could be endangered if the backfill is eroded, but the Owner accepted liability for this failure mode and for erosion of the service road behind the revetment.

Conclusion

The revetments and breakwaters in the Öresund Link were described in design requirements given by the Owner, ÖSK, including certain requirements for loads, layout, geometrical dimensions and levels as well as specifications for materials used. The method of construction used by the Contractor, ÖMJV also gave rise to certain requirements for the detailed design carried out by the Consultant, Carl Bro a/s.

Mainly the design is based on general design criteria for armour stone size, design of toe and scour protection as well as a critical crest level, all evaluated from a series of physical model tests. The design of some elements in the revetments and breakwaters were more or less given through requirements in the contract, but it is

noted that multiple layers of sand as a filter towards the back fill were substituted by a geotextile.

The input data as regards wave characteristics and water levels were specified by the Owner based on a conservative evaluation of the numerical modelling of the Öresund region for design of armour stones. Hence an additional factor of safety was included in the design of the armour layer.

Full correlation between waves and high water levels combined with requirements to geometry, lay out etc. given by the Owner, theoretically resulted in an unacceptable large volume of predicted overtopping endangering the overall stability of the structure. Correlation curves were derived based on a detailed statistical investigation of observed wave heights and correlated water levels. The Owner then specified less conservative wave heights for the evaluation of overtopping, but still additional protection of the crest was found necessary. The Owner then agreed that the Contractor would not be responsible for damages to areas behind the revetments due to overtopping.

The initial design of the toe and scour protection was questioned by the Owner, but formal proof of static stability based on physical model tests, could be made for most water depths by including a smoothing of the large redundancy built into the structure. Interestingly the large redundancy theoretically made the toe and scour protection less stable due to a reduced distance to the surface. An engineering approach was accepted for intermediate water depths but a monitoring programme was required by the Owner.

References

CIRIA/CUR, 1991 : Manual on the use of rock in Coastal and Shoreline engineering, CIRIA special publication 83 cue report 154.

Meer, J.W. van der 1987 : Stability of Breakwater Armour Layers - Design Formulae

DESIGN OF ALTERNATIVE REVETMENTS

M. Klein Breteler[1], K. W. Pilarczyk[2], T. Stoutjesdijk[3]

Abstract

Within the scope of the research on the stability of open slope revetments, much knowledge has been developed about the stability of placed (pitched) stone revetments under wave load (CUR/TAW 1995) and stability of rock under wave and current load (CUR/CIRIA 1991).
Until recently, no or unsatisfactory design tools were available for a number of other (open) types of revetment and for other stability aspects. This is why the design methodology for placed block revetments has recently been extended in applicability by means of a number of desk-studies for other (open) revetments:

- interlock systems and block mats;
- gabions;
- concrete mattresses;
- geosystems, such as sandbags and sand sausages;

and other stability aspects, such as: flow-load stability, soil-mechanical stability and residual strength.
This paper aims at giving a summary of the increased knowledge, especially that concerning the design tools that have been made available. The details behind it can be found in (Pilarczyk et al 1998).

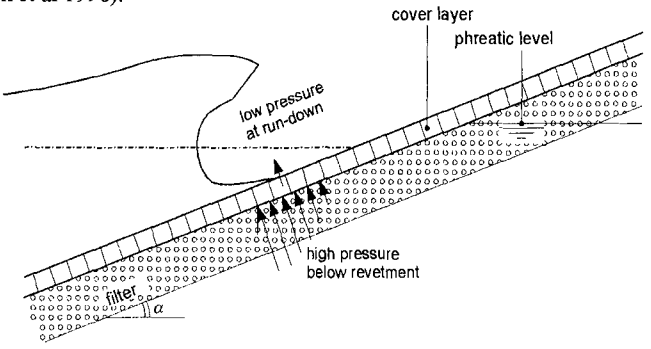

Figure 1, Pressure development in a revetment structure

[1]Delft Hydraulics, P.O.Box 177, 2600 MH Delft, The Netherlands, Fax +31-15-2858582
[2]RWS, Hydraulic Engineering Division, P.O. Box 5044, 2600 GA Delft, The Netherlands
[3]Delft Geotechnics, P.O. Box 69, 2600 AB Delft, The Netherlands

1 THEORETICAL BACKGROUND OF WAVE LOADING

Wave attack on revetments will lead to a complex flow over and through the revetment structure (filter and cover layer). During wave run-up the resulting forces by the waves will be directed opposite to the gravity forces. Therefore the run-up is less hazardous then the wave run-down. Wave run-down will lead to two important mechanisms:

- The downward flowing water will exert a drag force on the cover layer and the decreasing freatic level will coincide with a downward flow gradient in the filter (or in a gabion). The first mechanism can be schematised by a free flow in the filter or gabion with a typical gradient equalling the slope angle. It may result in sliding.
- During maximum wave run-down there will be an incoming wave that a moment later will cause a wave impact. Just before impact there is a 'wall' of water giving a high pressure under the point of maximum run-down. Above the run-down point the surface of the revetment is almost dry and therefore there is a low pressure on the structure. The high pressure front will lead to an upward flow in the filter or a gabion. This flow will meet the downward flow in the run-down region. The result is an outward flow and uplift pressure near the point of maximum wave run-down (Figure 1).

The schematised situation can be quantified on the basis of the Laplace equation for linear flow:

$$\frac{\partial^2 \phi}{\partial y^2} + \frac{\partial^2 \phi}{\partial z^2} = 0 \qquad (1)$$

with: $\phi = \phi_b =$ potential head in the filter or a gabion (m)
$y =$ coordinate along the slope (m)
$z =$ coordinate perpendicular to the slope (m)

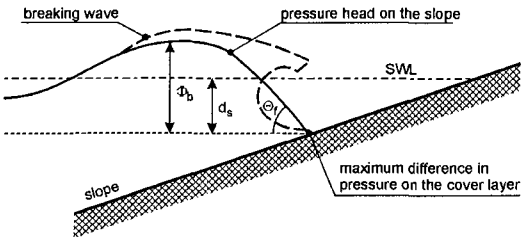

Figure 2 Schematization of pressure head on a slope

After complicated calculations the uplift pressure in the filter or a gabions can be derived. The uplift pressure is dependent on the steepness and height of the pressure front on the cover layer (which is dependent on the wave height, period and slope angle, see Figure 2), the thickness of the cover layer and the level of the freatic line in the filter or a gabion. In case of gabions, it is not dependent on the permeability of the gabions, if the permeability is larger then the subsoil. The equilibrium of uplift forces and gravity forces leads to the following (approximate) design formula (Pilarczyk et al 1998):

$$\frac{H_{scr}}{\Delta D} = f\left(\frac{D}{\Lambda \xi_{op}}\right)^{0.67} \quad \text{with} \quad \Lambda = \sqrt{\frac{bDk}{k'}} \qquad (2a)$$

or

$$\frac{H_{scr}}{\Delta D} = f\left(\frac{D}{b}\frac{k'}{k}\right)^{0.33} \xi_{op}^{-0.67} \qquad (2b)$$

or $$\frac{H_{scr}}{\Delta D} = F\,\xi_{op}^{-0.67} \qquad (2c)$$

where H_{scr} = significant wave height at which blocks will be lifted out [m]; ξ_{op} = $\tan\alpha/\sqrt{(H_s/(1.56T_p^2))}$ = breaker parameter [-]; T_p = wave period at the peak of the spectrum [s]; Λ = leakage length [m], $\Delta = (\rho_s - \rho)/\rho$ = relative volumetric mass of cover layer [-]; b = thickness of a sublayer [m], D = thickness of a top layer [m], k = permeability of a sublayer [m/s], k' = permeability of a top layer [m/s], f = stability coefficient, mainly dependent on structure type, $\tan\alpha$ and friction [-]; F = total (black-box) stability factor [-].
The leakage length (Λ) and stability coefficient are explained in detail in the next section.

2 STRUCTURAL RESPONSE

2.1 Wave-load approach

There are two practical design methods available: the black-box model and the analytical model. In both cases, the final form of the design method can be presented as a critical relation of the load compared to strength, depending on the type of wave attack:

$$\left(\frac{H_s}{\Delta D}\right)_{cr} = \text{function of } \xi_{op} \qquad (3a)$$

For revetments, the basic form of this relation is:

$$\left(\frac{H_s}{\Delta D}\right)_{cr} = \frac{F}{\xi_{op}^{2/3}} \text{ with maximum } \left(\frac{H_s}{\Delta D}\right)_{cr} = 8.0 \qquad (3b)$$

In which: F = revetment (stability) constant (-), H_s = (local) significant wave height (m), Δ = relative density (-), D = thickness of the top layer (m), and ξ_{op} = breaker parameter (-).
The relative density is defined as follows:

$$\Delta = \frac{\rho_s - \rho_w}{\rho_w} \qquad (4a)$$

with: ρ_s = density of the protection material and ρ_w = density of water (kg/m^3). For porous top layers, such as sand mattresses and gabions, the relative density of the top layer must be determined, including the water-filled pores:

$$\Delta_t = (1 - n)\cdot\Delta \qquad (4b)$$

In which: Δ_t = relative density including pores (-) and n = porosity of the top layer material (-).
The breaker parameter is defined as follows:

$$\xi_{op} = \frac{\tan\alpha}{\sqrt{H_s / L_{op}}} \qquad (5)$$

The wave steepness S_{op} is defined as:

$$S_{op} = \frac{H_s}{L_o} = \frac{2\pi H_s}{g T^2} \qquad (6)$$

In which: $$L_{op} = \frac{g}{2\pi} T_p^2 \qquad (7)$$

with: α = slope angle (°), L_{op} = deep-water wavelength at the peak period (m), and T_p = wave period at the peak of the spectrum (s).

The advantage of this black-box design formula is its simplicity. The disadvantage, however, is that the value of F is known only very roughly for many types of structures.
The analytical model is based on the theory for placed stone revetments on a granular filter (pitched blocks). In this calculation model, a large number of physical aspects are taken into account. In short, in the analytical model nearly all physical parameters that are relevant to the stability have been incorporated in the "leakage length": $\Lambda = \sqrt{(bDk/k')}$. The final result of the analytical model may, for that matter, again be presented as a relation such as Eq. 3 where $\mathbf{F} = f(\Lambda)$.
With a system without a filter layer (directly on sand or clay, without gullies being formed under the top layer) not the permeability of the filter layer, but the permeability of the subsoil (eventually with gullies/surface channels) is filled in.

To be able to apply the design method for placed stone revetments under wave load to other systems, the following items may be adapted:

- the revetment parameter **F**;
- the (representative) strength parameters Δ and D;
- the design wave height H_s;
- the (representative) leakage length Λ;
- the increase factor Γ on the strength.

Only suchlike adaptations are presented in this summarising review. The basic formulas of the analytical model are not repeated here. For these, reader is referred to (CUR/TAW 1995).

2.2 Flow-load stability

There are two possible approaches for determining the stability of revetment material under flow attack. The most suitable approach depends on the type of load:

- flow velocity: 'horizontal' flow, flow parallel to dike;
- discharge: downward flow at slopes steeper than 1:10, overflow without waves; stable inner slope.

When the flow velocity is known, or can be calculated reasonably accurately, Pilarczyk's relation (Pilarczyk et al 1998) is applicable:

$$\Delta D = 0.035 \frac{\Phi}{\Psi} \frac{K_T K_h}{K_s} \frac{u_{cr}^2}{2g} \qquad (8)$$

in which: Δ = relative density (-), D = characteristic thickness (m), g = acceleration of gravity (g=9.81 m/s^2), u_{cr} = critical vertically-averaged flow velocity (m/s), Φ = stability parameter (-), Ψ = critical Shields parameter (-), K_T = turbulence factor (-), K_h = depth parameter (-), and K_s = slope parameter (-).
These parameters are explained below.

Stability parameter Φ:
The stability parameter Φ depends on the application. Some guide values are:

Revetment type	Continuous toplayer	Edges and transitions
Riprap and placed blocks	1.0	1.5
Blockmats, gabions, washed-in blocks, geobags, and geomattresses	0.5	0.75

Shields parameter Ψ :
With the critical Shields parameter Ψ the type of material can be taken into account:

- riprap, small bags $\Psi \approx 0.035$
- placed blocks, geobags $\Psi \approx 0.05$
- blockmats $\Psi \approx 0.07$
- gabions $\Psi \approx 0.07$ (to 0.10)
- geomattresses $\Psi \approx 0.07$

Turbulence factor K_T:
The degree of turbulence can be taken into account with the turbulence factor K_T. Some guide values for K_T are:

- Normal turbulence:
  abutment walls of rivers $K_T \approx 1.0$
- Increased turbulence:
  river bends
  downstream of stilling basins $K_T \approx 1.5$
- Heavy turbulence:
  hydraulic jumps
  sharp bends
  strong local disturbances $K_T \approx 2.0$
- Load due to water (screw) jet: $K_T \approx 3.0$ (to 4.0)

Depth parameter K_h:
With the depth parameter K_h, the water depth is taken into account, which is necessary to translate the depth-averaged flow velocity into the flow velocity just above the revetment. The depth parameter also depends on the development of the flow profile and the roughness of the revetment.
The following formulas are recommended:

fully developed velocity profile: $$K_h = \frac{2}{\left(\log\left(\frac{12h}{k_s}\right)\right)^2} \quad (9a)$$

non-developed profile: $$K_h = \left(\frac{h}{k_s}\right)^{-0.2} \quad (9b)$$

very rough flow ($h/k_s < 5$): $$K_h = 1.0 \quad (9c)$$

In which: h = water depth (m) and k_s = equivalent roughness according to Nikuradse (m).
In the case of dimensioning the revetment on a slope, the water level at the toe of the slope must be used for h.
The equivalent roughness according to Nikuradse depends on the type of revetment/ geosystem. For riprap, k_s is equal usually to twice the nominal diameter of the stones, for bags it is approximately equal to the thickness (d), for mattresses it depends of the type of mattress: k_s of about 0.05 m for smooth types and about the height of the rib for articulating mats.

Slope parameter K_s:
The stability of revetment elements also depends on the slope gradient under which the revetment is applied, in relation to the angle of internal friction of the revetment. This effect on the stability is taken into account with the slope parameter K_s, which is defined as follows:

$$K_s = \sqrt{1-\left(\frac{\sin\alpha}{\sin\theta}\right)^2} = \cos\alpha \sqrt{1-\left(\frac{\tan\alpha}{\tan\theta}\right)^2} \quad (10a)$$

or

$$K_s = \cos\alpha_b \quad (10b)$$

with: θ = angle of internal friction of the revetment material, α = transversal slope of the bank (°), and α_b = slope angle of river bottom (parallel along flow direction) (°).
The following values of θ can be assumed as a first approximation: 40° for riprap, 30° to 40° for sand-filled systems, and 90° for stiff and anchored mortar-filled mattresses and (cabled) blockmats ($K_s = \cos\alpha$). However, for flexible non-anchored mattresses and blockmats (units without contact with the neighbouring units) this value is much lower, usually about 3/4 of the friction angle of the sublayer. In case of geotextile mattress and blockmats connected to geotextile lying on a geotextile filter, θ is about 15° to 20°.

The advantage of this general design formula of Pilarczyk is that it can be applied in numerous situations. The disadvantage is that the scatter in results, as a result of the large margin in parameters, can be rather wide.
With a downward flow along a steep slope it is difficult to determine or predict the flow velocity, because the flow is very irregular. In such case formulas based on the discharge are developed (Pilarczyk et al 1998).

2.3 Soil-mechanical stability

The water motion on a revetment structure can also affect the subsoil, especially when this consists of sand.
Geotechnical stability is dependent on the permeability and stiffness of the grain skeleton and the compressibility of the pore water (the mixture of water and air in the pores of the grain skeleton). Wave pressures on the top layer are passed on delayed and damped to the subsoil under the revetment structure and to deeper layers (as seen perpendicular to the slope) of the subsoil. This phenomenon takes place over a larger distance or depth as the grain skeleton and the pore water are stiffer. If the subsoil is soft or the pore water more compressible (because of the presence of small air bubbles) the compressibility of the system increases and large damping of the water pressures over a short distance may occur. Because of this, alternately water undertension and overtension may develop in the subsoil and corresponding to this an increasing and decreasing grain pressure. It can lead to sliding or slip circle failure, see Figure 3.

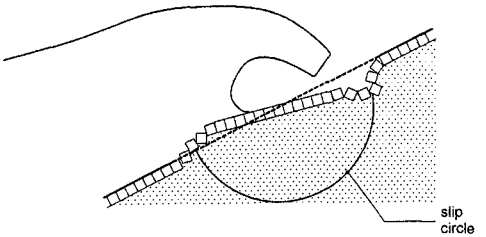

Figure 3 Schematised development of S-profile and possible local sliding in the base (sand)

The design method with regard to geotechnical instability is presented in the form of design diagrams. An example is given in Figure 4 (more diagrams and details: see Pilarczyk et al, 1998). The maximum wave height is a function of the sum of the cover layer weight (ΔD) and filter thickness (b_f).

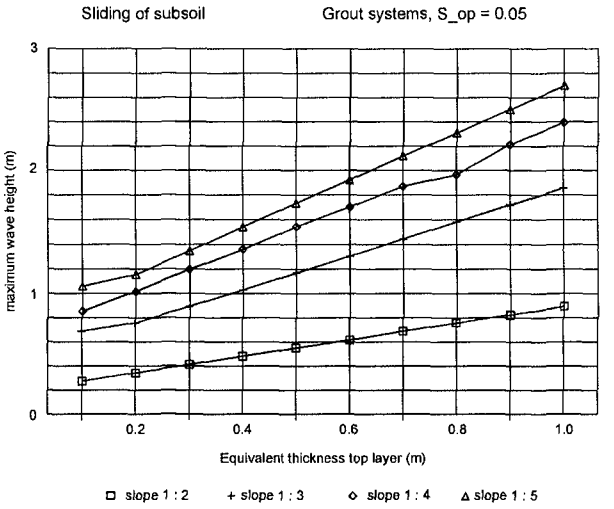

Figure 4, Geotechnical stability, design diagram for grouted systems and $H_s/L_{op} = 0,05$

3 STABILITY CRITERIA FOR BLOCKMATS

3.1 System description

A (concrete) blockmat is a slope revetment made of (concrete) blocks that are joined together to form a "mat", see Figure 5. The interconnection may consist of cables from block to block, of hooks connecting the blocks, or of a geotextile on which the blocks are attached with pins, glue or other means. The spaces between the blocks are usually filled with rubble, gravel or slag.

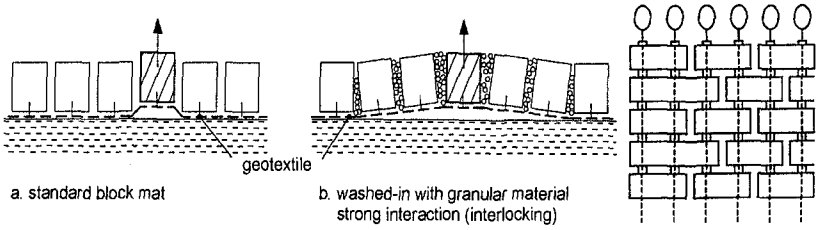

Figure 5 Examples of blockmats

The major advantage of blockmats is that they can to be laid quickly and efficiently and partly under water. Blockmats are more stable than a setting of loose blocks, because a single stone cannot be moved in the direction perpendicular to the slope without moving other nearby stones. It is essential to demand that already with a small movement of an individual stone a significant interactive force with the surrounding stones is mobilised. Large movements of individual blocks are not acceptable, because transport of filter material may occur. After some time, this leads to a serious deformation of the surface of the slope.

The blockmats are vulnerable at edges and corners. If two adjacent mats are not joined

together, then the stability is hardly larger than that of pitched loose stones.

3.2 Design rules with regard to wave load

Table 1 gives an overview of useable values for the revetment constant **F** in the black-box model for linked blocks (blockmats).

Type of revetment		**F (-)**
Linked blocks on sand		5 to 6
Linked blocks on clay	good clay	5 to 6
	mediocre clay	4.5 to 5
Linked blocks on a granular filter	favourable construction	5 to 6
	normal construction	4 to 5
	unfavourable construction	3 to 4

Table 1 Recommended values for the revetment parameter F for blockmats (the lower values refer to blocks connected to geotextile while the higher ones refer to cabled blocks).

The terms "favourable", "normal" and "unfavourable" refer to the composition of the granular filter and the permeability-ratio of the top layer and the filter layer (see CUR/CIRIA, 1991). In a case of fine granular filter and relatively permeable top layer the total composition can be defined as "favourable'. In a case of very coarse granular layer and less permeable top layer the composition can be defined as "unfavourable". In a case of blocks connected to a geotextile and concrete-filled mattresses on a filter layer the construction can be usually defined as between "unfavourable" and "normal", and the stability factor F = 3.0 to 3.5 (max. 4.0) can be applied. For blockmats and permeable mattresses on sand F = 5 (max. 6.0) can be applied. The higher values can also be used in cases that the extreme design loading is not very frequent or when the system is (repeatedly) washed in by coarse material providing additional interlocking.
This wide range of recommended values for **F** only gives a first indication of a suitable choice.

Furthermore it is essential to check the geotechnical stability with the design diagrams (see for example Figure 4 and for a full set of diagrams see Pilarczyk et al 1998).

4 STABILITY CRITERIA FOR CONCRETE-FILLED MATTRESSES

4.1 Concrete Mattresses

Characteristic of concrete mattresses are the two geotextiles with concrete or cement between them. The geotextiles can be connected to each other in many patterns, which results in a variety of mattress systems, each having its own appearance and properties. Some examples are given in Figure 6.

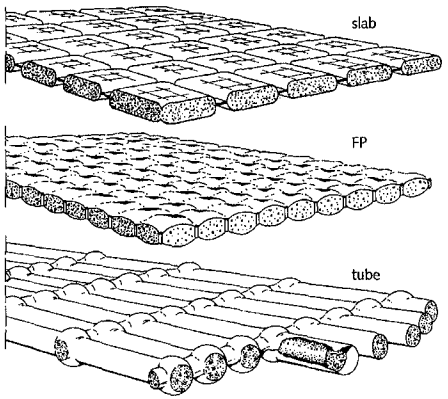

Figure 6 Examples of concrete-filled mattresses

The permeability of the mattress is one of the factors that determine the stability. It is found that the permeability given by the suppliers is often the permeability of the geotextile, or of the so-called Filter Points. In both cases, the permeability of the whole mattress is much smaller. A high permeability of the mattress ensures that any possible pressure build-up under the mattress can flow away, as a result of which the uplift pressures across the mattress remain smaller.
In general, with a subsoil of clay and silty sand the permeability of the mattress will be higher than the permeability of the subsoil. Therefore the water under the mattress can usually be discharged without excessive lifting pressures on the mattress.
The permeability of the mattress will be lower than the permeability of the subsoil or sub layers if a granular filter is applied, or with a sand or clay subsoil having an irregular surface (gullies/cavities between the soil and the mattress). This will result in excessive lifting pressures on the mattress during wave attack.

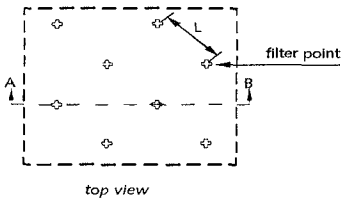

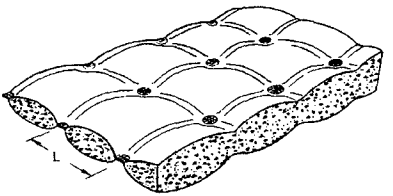

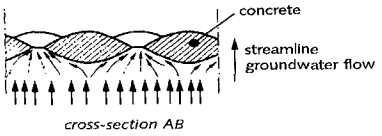

Figure 7, Principles of permeability of Filter Point Mattress

4.2 Design rules with regard to wave load

The failure mechanism of the concrete mattress is probably as follows:

- First, cavities under the mattress will form as a result of uneven subsidence of the subsoil. The mattress is rigid and spans the cavities.
- With large spans, wave impacts may cause the concrete to crack and the spans to collapse. This results in a mattress consisting of concrete slabs which are coupled by means of the geotextile.
- With sufficiently high waves, an upward pressure difference over the mattress will occur during wave run-down, which lifts the mattress (Figure 1).
- The pumping action of these movements will cause the subsoil to migrate, as a result of which an S-profile will form and the revetment will collapse completely.

It is assumed that local settlement of the subsoil will lead to free spans of the concrete mattress. Then, the wave impact can cause the breaking of these spans, if the ratio of H_s/D is too large for a certain span length. A calculation method is derived on the basis of an empirical formula for the maximum wave impact pressure and the theory of simply supported beams. The collapsing of small spans (less then 1 or 2 m) is not acceptable, since these will lead to too many cracks.
The empirical formula for the wave impact is (Klein Breteler et al 1998):

$$\frac{F_{impact}}{\rho g} = 7.2\, H_s^2 \tan\alpha \qquad (11)$$

With: F_{impact} = impact force per m revetment (N).

Calculation has resulted in an average distance between cracks of only 10 to 20 cm for a 10 cm thick mattress and wave height of 2 m. This means that at such a ratio of H_s/D the wave impacts will chop the mattress to pieces. For a mattress of 15 cm thick and a wave height of 1,5 m the crack distance will be in the order of 1 m.
Apart from the cracks due to wave impacts, the mattress should also withstand the uplift pressures due to wave attack. These uplift pressures are calculated in the same way as for block revetments. For this damage mechanism the leakage length is important.
In most cases the damage mechanism by uplift pressures is more important then the damage mechanism by impact.

The representative/characteristic values of the leakage length for various mattresses can be assumed as follow:

	Leakage length Λ (m)		
Mattress	on sand*)	on sand**)	on filter
Standard - FP	1.5	3.9	2.3
FPM	1.0	3.9	2.0
Slab	3.0	9.0	4.7
Articulated (Crib)	0.5	1.0	0.5

*) good contact of mattress with sublayer (no gullies/cavities underneath)
**) pessimistic assumption: poor compaction of subsoil and presence of cavities under the mattress

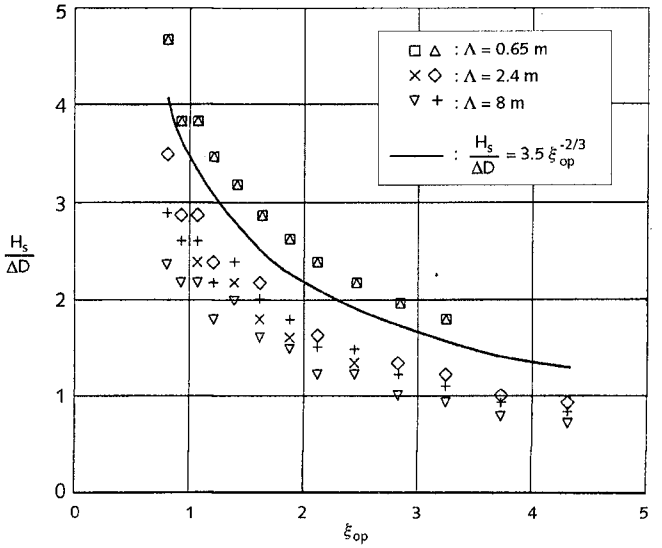

Figure 8 Calculation results for concrete mattresses ($H_s/\Delta D < 4$ because of acceptable crack distance due to impacts on spans).

Taking into consideration the above failure mechanisms, the following design (stability) formula has been derived for the mattresses (Eq. 3b):

$$\frac{H_s}{\Delta D} = \frac{F}{\xi_{op}^{2/3}} \quad with: \left[\frac{H_s}{\Delta D}\right]_{max} = 4 \tag{12}$$

with:

$$D = \frac{\text{mass per } m^2}{\rho_s} \quad \text{(which can be called } D_{effective} \text{ or } D_{average})$$

Δ = relative volumetric mass of the mattress (-) = $(\rho_s - \rho)/\rho$
ρ_s = volumetric mass of concrete (kg/m^3)
F = stability factor, see table (-)

For an exact determination of the leakage length, one is referred to the analytical model (Klein Breteler et al 1998). However, besides the mattresses of a type as, for example, the tube mat (Crib) with relative large permeable areas, the other types are not very sensitive to the exact value of the leakage length. It can be recommended to use the following values of F in design calculations:

- F = 2.5 or ($\leq$ 3) - for low-permeable mattresses on (fine) granular filter,
- F = 3.5 or ($\leq$ 4) - for low-permeable mattress on compacted sand,
- F = 4.0 or ($\leq$ 5) - for permeable mattress on sand or fine filter ($D_{f15} < 2$ mm).

The higher values can be applied for temporary applications or when the soil is more resistant to erosion (i.e. clay), and the mattresses are properly anchored.

5 STABILITY OF GABIONS

5.1 Introduction

Gabions are made of rectangular baskets of wire mesh, which are filled with stones. The idea of the protection system is to hold the rather small stones together with the wire mesh. Waves and currents would have easily washed away the small stones, but the wire mesh prevents this. A typical length of gabions is 3 to 4 m, a width of 1 to 3 m and a thickness of 0.3 to 1 m. The gabions with small thickness (less then 0.5 m) and large length and width are usually called Reno-mattresses.
An important problem of this protection system is the durability. Frequent wave or current attack can lead to a failure of the wire mesh because of the continuously moving grains along the wires, finally cutting through. Another problem is the corrosion of the mesh. Therefore meshes with plastic coating or corrosion resistant steel are used. On the other hand the system is less suitable where waves and currents frequently lead to grain motion.

5.2 Hydraulic loading and damage mechanisms

Wave attack on gabions will lead to a complex flow over the gabions and through the gabions. During wave run-up the resulting forces by the waves will be directed opposite to the gravity forces. Therefore the run-up is less hazardous then the wave run-down.
Wave run-down, as it was already mentioned in Section 2, will lead to two important mechanisms:

- The downward flowing water will exert a drag force on top of the gabions and the decreasing freatic level will coincide with a downward flow gradient in the gabions.
- During maximum wave run-down there will be an incoming wave that a moment later will cause a wave impact. Just before impact there is a 'wall' of water giving a high pressure under the point of maximum run-down. Above the run-down point the surface of the gabions is almost dry and therefore there is a low pressure on the gabions. The interaction of high pressure and low pressure is shown in Figure 1.

A simple equilibrium of forces leads to the conclusion that the section from the run-down point to the freatic line in the filter will slide down if:

- if there is insufficient support from gabions below this section
- if the downward forces exceed the friction forces: (roughly) $f < 2 \cdot \tan\alpha$

with: f = friction of gabion on subsoil; α = slope angle.
From this criterion we see that a steep slope will easily lead to the exceeding of the friction forces, and furthermore a steep slope is shorter then a gentle slope and will give less support to the section that tends to slide down.

Hydrodynamic forces, such as wave attack and current, can lead to various damage mechanisms. The damage mechanisms fall into three categories:

1. Instability of the gabions
   a) The gabions can slide downwards, compressing the down slope mattresses
   b) The gabions can slide downwards, leading to upward buckling of the down slope mattresses
   c) All gabions can slide downwards
   d) Individual gabions can be lifted out due to uplift pressures
2. Instability of the subsoil
   a) A local slip circle can occur, resulting in a S-profile
   b) The subsoil can wash away through the gabions
3. Durability problems
   a) Moving stones can cut through the mesh
   b) Corrosion of the mesh
   c) Rupture of the mesh by mechanical forces (vandalism, stranding of ship, etc.).

5.3 Stability of gabions under wave attack

An analytical approach of the development of the uplift pressure in the gabions can be obtained by applying the formulas for the uplift pressure under an ordinary pitched block revetment, with as leakage length: $\Lambda = 0.77\ D$.
With this relation the stability relations according to the analytical model are also applicable to gabions. Substitution of values, which are reasonable for gabions, in the stability relations according to (CUR/CIRIA 1991) provides stability relations which indeed match the a line through the measured points.
After complicated calculations the uplift pressure in the gabions can be derived (Klein Breteler et al, 1998). The uplift pressure is dependent on the steepness and height of the pressure front on the gabions (which is dependent on the wave height, period and slope angle), the thickness of the gabions and the level of the freatic line in the gabions. It is not dependent on the permeability of the gabions, if the permeability is larger then the subsoil. The equilibrium of uplift forces and gravity forces leads to the following (approximate) design formula (Eq. 3b):

$$\frac{H_s}{\Delta D} = F \cdot \xi_{op}^{2/3} \quad \text{with } 6 < F < 9 \text{ and slope of 1:3 } (\tan\alpha = 0.33) \tag{13}$$

with: H_s = significant wave height of incoming waves at the toe of the structure (m)
Δ = relative density of the gabions (usually: $\Delta \approx 1$)
D = thickness of the gabion (m)
F = stability factor (-)
ξ_{op} = breaker parameter (-) = $\tan\alpha/\sqrt{(H_s/(1.56T_p^2))}$
T_p = wave period at the peak of the spectrum (s)

It is not expected that instability will occur at once if the uplift pressure exceeds the gravity forces. On the other hand, the above result turns out to be in good agreement with the experimental results.

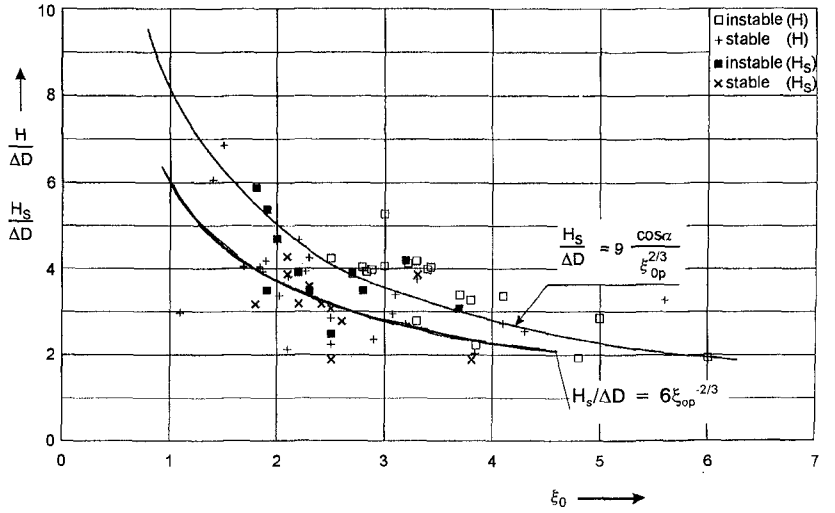

Figure 9: Summary of test results ((Ashe 1975) and (Brown 1979)) and design curves

The experimental verification of stability of gabions is rather limited. Small scale model tests have been performed by Brown (1979) and Ashe (1975), see Figure 9.

5.4 Motion of filling material

It is important to know if the filling material will start to move during frequent environmental conditions, because it can lead to rupture of the wire mesh. Furthermore the integrity of the system will be effected if large quantities of filling material is moved.
During wave attack the motion of the filling material usually only occurs if $\xi_{op} < 3$ (plunging waves). Based on the Van der Meer's formula for the stability of loose rock (CUR/CIRIA, 1991) and the assumption that the filling of the gabion will be more stable then loose rock, the following criterion is derived (Van der Meer formula with permeability factor: $0.1 < P < 0.2$; number of waves: $2000 < N < 5000$; and damage level: $3 < S < 6$):

$$\frac{H_s}{\Delta_f D_f} = \frac{F}{\sqrt{\xi_{op}}} \qquad \text{with } 2 < F < 3 \qquad (14)$$

with: H_s = significant wave height of incoming waves at the toe of the structure (m)
Δ_f = relative density of the grains in the gabions (usually: $\Delta \approx 1.65$)
D_f = diameter of grains in the gabion (m)
F = stability factor (-)
ξ_{op} = breaker parameter (-) = $\tan\alpha/\sqrt{(H_s/(1.56T_p^2))}$
T_p = wave period at the peak of the spectrum (s)

6 CONCLUSIONS

Altemative systems can be a good and mostly cheaper altemative for more traditional materials/systems. These new systems deserve to be applied on a larger scale.
The newly derived design methods and stability criteria will be of help in preparing the preliminary alternative designs with these systems. However, there are still many uncertainties in these design methods. Therefore, experimental verification and further improvement of design methods is necessary. Also more practical experience at various loading conditions is still needed.

REFERENCES

CUR/TAW 1995, Design Manual for Pitched Slope Protection, CUR report 155, A.A. Balkema (Publ.), Rotterdam.

CUR/CIRIA, 1991, Manual on use of rock in coastal engineering, CUR/CIRIA report 154 Gouda, Netherlands.

Pilarczyk, K.W. (editor), 1998, Dikes and revetments, Published by A. Balkema, Rotterdam, ISBN 90 5410 455 4.

Ashe, G.W.T., 1975, Beach erosion study, gabion shore protection, *Hydraulics Laboratory*, Ottawa, Canada

Brown, C., 1979, Some factors affecting the use of maccaferi gabions, *Water Research Lab.*, Australia, report 156.

Klein Breteler, M. et al, 1998, Alternatieve open taludbekledingen (Alternative open slope revetments, in Dutch), Delft Hydraulics, H1930.

Inventory of the stability of existing placed block revetments in the Netherlands

Theo Stoutjesdijk[1]
Mark Klein Breteler[2]
Hans Johanson[3]

Abstract

This paper describes the results of a nationwide inventory of the stability of existing placed block revetments in the Netherlands. The inventory is now complete at a basic level: the revetments have been tested using simple stability criteria. These criteria are described in this paper and the main results of the inventory are presented and discussed.

Introduction

In coastal engineering much emphasis is placed on designing coastal structures and description of the physical behaviour of these structures. It is less common to evaluate the actual performance of existing coastal structures in view of todays safety standards and todays knowledge.

In the Netherlands a nationwide inventory of the stability of the existing 8 million square metres of placed block revetments has been performed. This paper is about the reasons why, the methods used and the results.

The paper will start with a short historic overview. This historic overview will eventually lead to the current legal framework, which prescribes a periodical testing of the safety of water-retaining structures. The testing of placed block revetments is only a small part of this procedure.
Four failure mechanisms have been tested: migration of sublayers, geotechnical stability, stability of the top layer and residual strength of the sub-layers. A short description of the failure mechanims and the testing method for each failure mechanism is included.

After that the results of the inventory are presented and discussed. As it will appear, remedial actions are necessary. The actions which are currently being undertaken will be described.

---

[1]Senior Project Manager, Delft Geotechnics, P.O.Box 69, 2600 AB Delft, The Netherlands
[2]Delft Hydraulics, P.O. Box 177, 2600 MH, Delft, the Netherlands
[3]Rijkswaterstaat, Dept. of Road and Hydraulic Engineering, P.O.Box 5044, 2600 GA, Delft, the Netherlands

Historic overview

Since approximately the 13th century the Dutch have been building dikes to protect the hinterland from flooding. With increasing water levels and subsidence of the land nowadays huge bodies of sand and clay are necessary to provide protection against storm surges and high water levels.

The outer slope of the dikes along the coast, the estuaries, inner lakes and tidal rivers is subject to wave attack. In history several methods, including wooden piles and rip-rap, have been used to stop erosion of the outer slope of the dike. Due to a limited availability of sufficient quantities of rip-rap within transportation distance, a system in which the stones were placed by hand in a closed pattern came into use. In recent years, natural stone is more and more replaced by concrete elements, which can be placed by machines, but the principle remains the same. This type of slope protection is called a placed block revetment. Among other types of slope protection, placed block revetments are now commonly found in the Netherlands.

In 1953 a major storm (a once per 200 years storm) occurred, and large areas in the South Western part of the Netherlands were flooded. Although many dikes were breached or suffered severe damage, almost all stone revetments in the tidal zone survived this event.
After 1953 it was understood that one of the main reasons of the storm disaster was the fact that the dikes were not high enough to withstand extreme storm surges. A new philosophy, based on statistic evaluation of water levels, prescribed that the dikes should be high enough and strong enough to withstand water levels and storm conditions with a recurrence period of 1.250, 2.000, 4.000 or even 10.000 years, depending on the economical value of the protected area.
As a result of this new safety standard most dikes had to be improved, which meant that the crest height had to be raised considerably and that the dike slopes had to be flattened. Most of these reinforcement works have taken place in the sixties and seventies. An example of a cross-section of a dike before and after reinforcement is given in Figure 1.

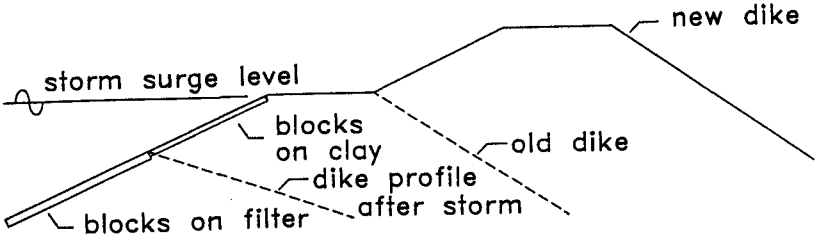

Figure 1 Cross-section of a dike before and after reinforcement

In Figure 1 it is shown that in 1953 in the tidal zone natural stones placed on a filter layer were present. In many cases this part of the revetment survived the storm and can still be present. During the reinforcement works new slope protection, often consisting of blocks on placed directly on clay, was used to protect the higher part of the slope up to the storm surge level. In the example given in Figure 1, the old dike has been damaged severely by overflow of water and subsequent erosion. However, there are also large stretches in which the original clay dike is still present today. The meaning of this fact will become apparent later in this paper.

It is fair to say that most placed block revetments have been constructed based mainly on experience, without the present day knowledge. Without design rules, only the local experience could be taken into account. If a certain location proved to be damaged frequently during seasonal storms, this revetment would be replaced by another type of revetment or by thicker stones of the same type. However, experience normally does not exceed a period of for instance 30 to 50 years.

Since approximately 1980 fundamental research into the stability of placed block revetments is being perfomed. New design methods are based on the results of this fundamental research. The new design criteria are such that a once per for instance 2000 years or 4000 years storm has to be withstood. That there is a gap between experience (i.e. a period of 30 to 50 years) and the scientific approach (thousands of years) seems obvious. In the following the consequences will become clear.

Legal framework

In 1993 and 1995 the Netherlands experienced high and sometimes critical river water levels. It appeared that there was sometimes a lack in maintenance, especially regarding dike height. This has lead to a speed up of new legislation that has two purposes:

1. existing structures have to be tested for their ability to perform their task of retaining water during extreme conditions. If necessary, the structures have to be improved to meet todays safety standards.
2. the required level of safety has to be maintained by a periodical testing of these structures.

The testing procedure is such that all known failure mechanisms have to be taken into account. Examples are overflow and overtopping due to insufficient dike height, dike failure due to a large scale slip circle failure of the soil body and so on. The failure mechanism of inundation due to failure of the slope protection is another example.

Among technicians, the general feeling was that extrapolation from experience (i.e. conditions that occur in a period of maximum 100 years) to conditions that occur only once every 4000 years would lead to the conclusion that in many cases the stability of existing placed block revetments would be insufficient. Some case studies confirmed this expectation. That was the reason why the Dutch Ministry of Transport and Public Works commissioned Delft Geotechnics to carry out an inventory of the stability of existing placed block revetments in the Netherlands.

General testing procedure

There are several levels at which the stability of revetments can be tested (see also Figure 2):

- the basic level, using for instance results of large scale model tests or rules of thumb as a reference to recognize evidently safe and evidently insufficiently safe revetments and exclude them from further testing. Note that in this black box approach there is a large range of uncertainty.
- for the 'doubtfull' revetments the possibility of detailed testing is open. Detailed testing consists in large lines of two components: one has to know more about the construction and an analytical method instead of the black box model is used to test the stability.
- if there remains doubt an advanced testing procedure is started: the most sophisticated means and expertise can be used and a numerical model can be used to evaluate the stability. Bezuijen (Bezuijen, 1998) describes the results of the experience with case studies.

The inventory of existing revetments has at this moment only been completed at the basic level.

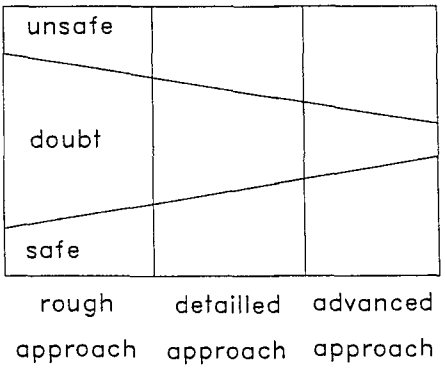

Figure 2 Different levels of testing

Elements of the testing procedure for placed block revetments

The placed block revetments are tested on four different failure mechanisms. These mechanisms are described in the following four paragraphs. In Figure 3 a scheme showing the procedure is given.
In the first step experience plays an important role in the procedure. A 'safe' result of the testing procedure can only be obtained if all criteria regarding the geotechnical stability, the migration of sublayers and the stability of the top layer are met. If the stability of the top layer is insufficient, but there is sufficient residual strength, the result is 'sufficiently safe'. This is not an ideal situation, because during extreme conditions the top layer will be damaged, and will have to be replaced.

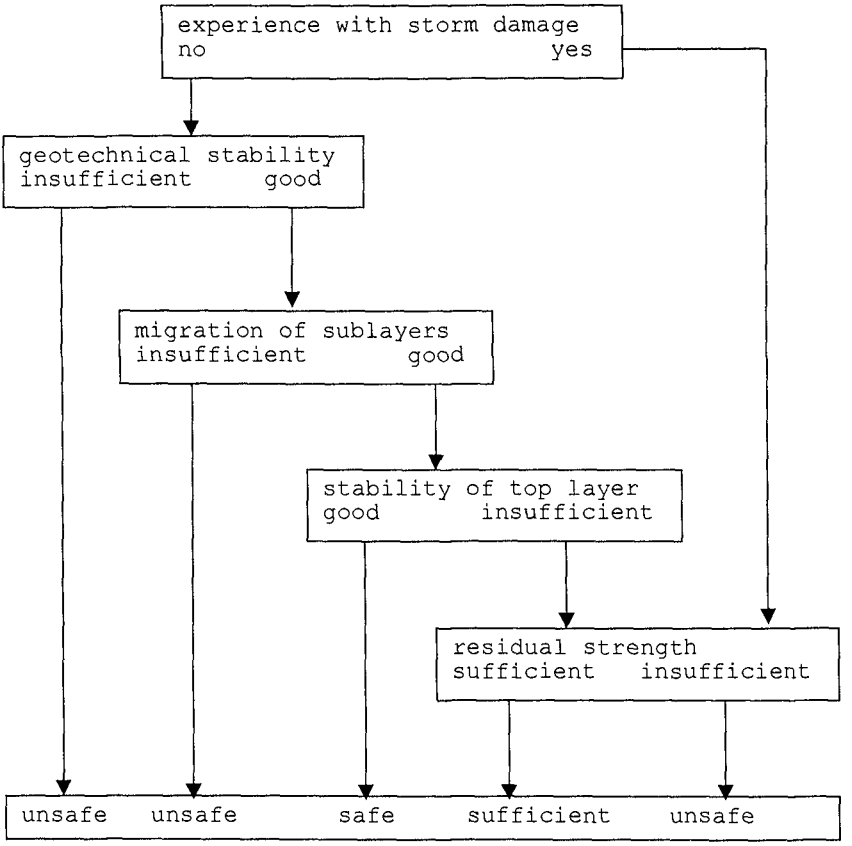

Figure 3 Scheme of testing placed block revetments

Geotechnical stability

One failure mechanism is geotechnical instability. As shown in Figure 4 water pressures on the outside of the construction differ from the internal water pressures inside the core of sand. Close beneath the surface these differences can be so extreme that locally the soil stability is lost and a shallow slide failure takes place. Figure 5 shows a schematic presentation of a slide failure of the subsoil.

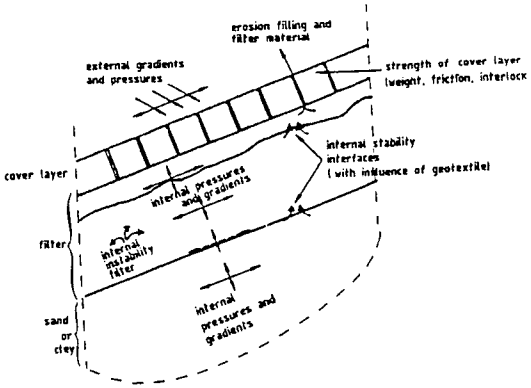

Figure 4 Components of loads and structure

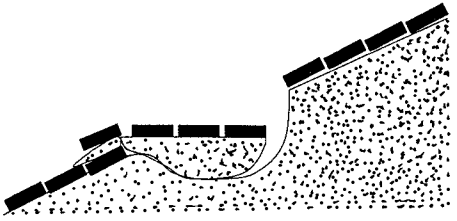

Figure 5 Slide failure of the subsoil

This type of failure is less likely to occur if the slope angle is less steep or the weight of the top layers, including filter layer and clay layer, increases. Therefore, if one the two following conditions is true, there is no risk of a slide failure due to pressure differences:

- if the slope is less steep than 1 : 4 and there are no indications from practice that indicate possible problems, or:
- if the slope is less steep than 1 : 3 and the thickness of the top layers (blocks, filter and/or clay) is larger than 1.2 m.

If these conditions are not met, the simple testing method provides graphs in which the pressure differences in the subsoil are compared to the weight of the top layers which is required to prevent the subsoil from sliding. The outcome is dependant on wave height, wave steepness, slope angle and sand grain size. If there still remains doubt, a more sophisticated analysis is required, see for instance (Bezuijen, 1991).

Migration of sublayers

The second failure mechanism is migration of sublayers. Sub-layers can be either the filter material, sand from the core or clay beneath the blocks. Migration of sublayers can be described as the washing out of filter material, sand or clay from beneath the blocks, thus causing scttlement of the blocks and a decrease in stability. The basic level of testing is therefore to see whether or not settlement of blocks has taken place. If this is not the case, and the revetment has been placed more than 5 years ago, apparently migration of sublayers is not a big problem. When in doubt, the normal rules regarding filter layer stability or sand and clay tightness of geotextiles can be applied for blocks placed on a filter layer and sand.

Experience shows that for blocks placed on clay, migration of the clay from beneath the blocks is always a problem. In a period of five to ten years holes and channels with dimensions of centimetres or even decimetres have been discovered beneath the blocks. As these holes and channels increase, the stability of the top layer decreases. This is one of the reasons why blocks placed directly on clay, which has been used frequently in the Netherlands in the sixties and seventies, nowadays proves to be an unfavourable construction. If this construction is to be used at all, a geotextile should be applied to prevent erosion of the clay.

Stability of the top layer

The stability of the top layer is governed by the wave conditions on one side, and the weight of the blocks and the permeabilities of top layer and sublayers on the other hand. There are several publications describing these relationships, for instance (Bezuijen, 1996) and (Pilarczyk, 1998). These relationships have been extensively investigated and are well understood. Large scale model tests have been

used to verify the modelling and the design criteria.
At the basic level of testing only the results of these large scale model tests are used to evaluate the stability of existing revetments. Figure 6 shows an example of a testing graph, that can be used to determine which revetments are evidently safe and revetments which are evidently not safe. On the x-axis the wave breaking parameter ξ is given. On the y-axis the ratio between wave height and weight of the top layer is set out. This is a simple black box approach. Between safe and not safe there is a large range of doubtfull stability. Revetments which end up in this doubtfull range require further investigation to reach a final score.

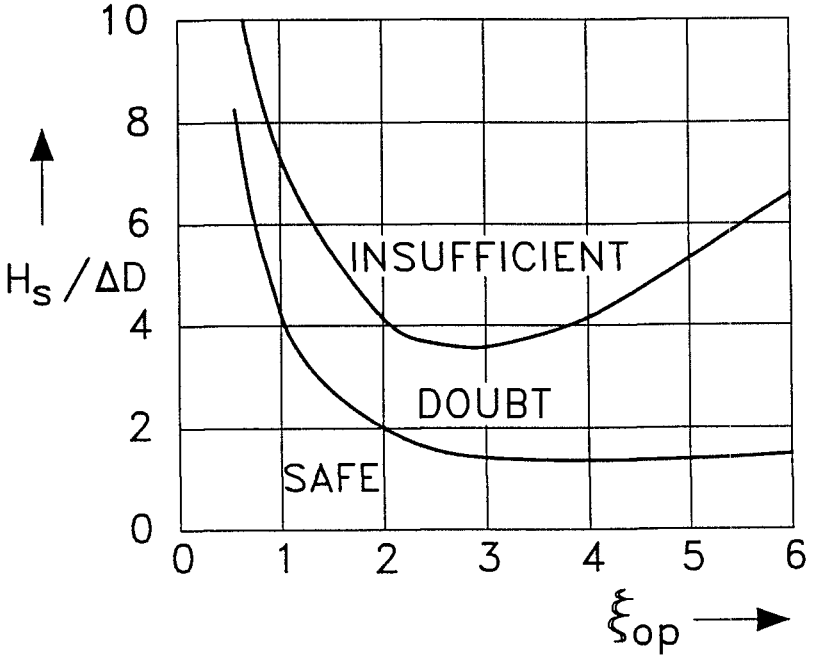

Figure 6 Example of testing graph for top layer stability

In (Stoutjesdijk, 1992) and (Stoutjesdijk, 1996) it is stated that physical properties of constructions 'in the field' can differ quite dramatically from those of newly build constructions of large scale model tests, due to aging effects. Such an aging effect is for instance the fact that in the tidal zone both the filter layer and the top layer have been washed in with sand, silt, shells and other material. As also discussed in (Bezuijen, 1998) it is difficult to test these aged constructions. The

testing graphs are based on model tests and can not be used for aged revetments. However, in 1998 large scale model tests have been performed on constructions which have been deliberately filled with a clayey material to simulate aged constructions in the tidal zone. These tests indicate that the stability of these revetments is not less than that of a new revetment. On the other hand it is at this moment not possible to prove that aged revetments are more stable than new revetments. However, as long as the stability of revetments does not decrease with age, it is possible to test aged constructions the same way as new constructions.

Residual strength and safety

Once the top layer has failed there may be a residual strength, because clay may be able to some extent to resist wave attack. As far as we know right now, clay layers of small thickness (less than 0.8 m) dry out and crack. This is a proces that progresses in time. Therefore the resistance to wave attack of clay on existing revetments is small. If however a large body of clay, for instance the remains of an old clay dike form part of the existing dike, the residual strength may be sufficient to resist the design storm.
The best reference for the erosion resistance of clay are large scale model tests, performed in the Delta Flume of Delft Hydraulics in 1993. The clay for these tests has been cut out of existing dike slopes. Because of drying out and cracking of the clay, the residual strength proved to be limited: a layer of 0.8 m clay showed progressive damage within a matter of hours with a significant wave height of 1.5 m.

The testing method compares the period that the clay layer is exposed to wave attack, with the residual strength of clay, which is expressed in terms of 'the period during which a clay layer of certain thickness can resist wave attack'. It appears that the thickness of the clay layer is an important quantity. As the thickness increases, the drying out and cracking of the clay is less pronounced and therefore the erosion resistance increases. This thought has already lead to the idea of using very thick clay layers or clay layers under flat slopes as a revetment type instead of a hard defence such as a placed block revetment.
A validated model for the erosion proces of clay under wave attack is not yet available, and therefore detailed testing of this aspect is not possible.

Results of the inventory

A total of 8 million square metres of placed block revetments has been tested at the basic level. Figure 7 gives a bar chart with the main result. Almost a quarter of these revetments proved to be evidently unsafe. About one third was evidently safe. The rest, almost half of the surface will have to be further investigated to come to a final conclusion.

This further investigation will take place in the coming years. If we

speculate on the final outcome of this further investigation it may well be the case that approximately half of all existing revetments proves to be insufficiently safe and will have to be improved.

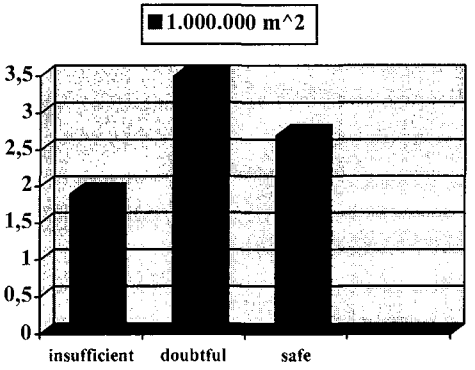

Figure 7 Main result of the inventory

Based on these results an estimation of the expected cost of remedial actions has been made. A total amount of about half a billion US dollars should be spent to improve the existing revetments.

Discussion of results

These results at first sight seem startling. However, on second sight the result is much as should be expected in view of the historic facts. Most existing revetments have been constructed based on experience only, without the design aids available today. Todays safety standards have been raised much higher than in the past, because of new ways of thinking about safety and increasing economical activities behind the dikes. Only about the last two decades the fundamental knowledge regarding the stability of revetments has been developed. If we add up all these factors it seems no more than logical that existing revetments may well be insufficient regarding todays standards.

Another point to consider is that the inventory at this point in time has only taken place at the basic level. Further investigation at a detailed and advanced level may lead to somewhat different views.
Furthermore we have to be conscient of the fact that todays knowledge is not perfect either. For instance, there is a large activity in the area of calculating the correct wave conditions for testing of revetments, we do not know enough about interaction between blocks and we can until today not specify the infuence of aging

on the stability of revetments.

Despite all these considerations it is demonstrated clearly by this inventory that the testing of existing coastal structures against todays safety standards can be a usefull action. In the Netherlands this testing is now prescribed by law, probably as the first country in the world.
It can be stated that this idea represents a rational approach towards safety, and it is necessary to accept the consequences of the transition to this new philosophy. It is fair to say that, after spending a lot of money, the safety against flooding in the Netherlands will have been increased to a significantly higher level. This would never have been reached without this action.

Remedial actions

At the moment several actions are being taken by Rijkswaterstaat, the Dutch Ministry of Public Works:

- clearly insufficient revetments are being improved. The entire operation will take 10 to 15 years to be completed
- detailed and advanced testing of doubtfull revetments will take place in the coming years. This means that the exact parameters in the field will have to be determined to allow a more sophisticated evaluation of the stability of these revetments
- fundamental research is being performed to provide as much of a contribution as possible on sharper testing procedures and ways to facilitate detailed and advanced testing.
- large scale model tests at the Delta flume of Delft Hydraulics are being performed (see Figure 8). Most of these tests concern possible remedial alternative revetment types (Klein Breteler, 1998), but also for instance aged constructions are part of the investigation.

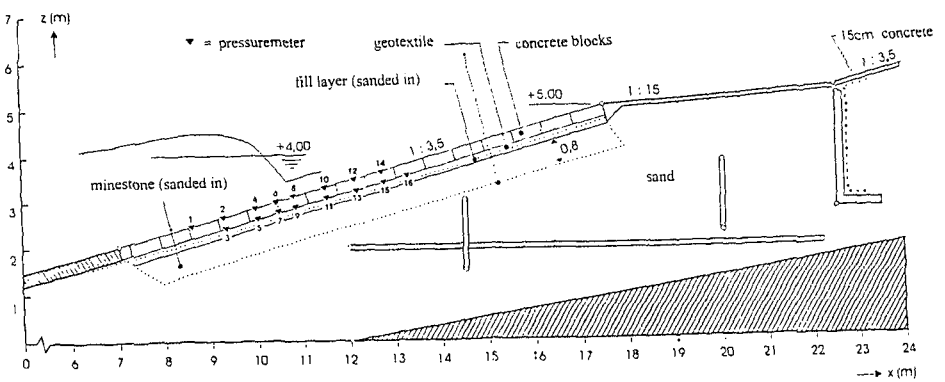

Figure 8 Large scale model test on aged placed block revetment

Conclusion

As it appears today, we are faced with a substantial problem. The challenge is to contribute as much as possible to the solution. The final statement is that, although the inventory of existing structures has brought to light significant problems regarding the stability of placed block revetments, the outcome of this action will be that safety has been brought in accordance with todays demands. It is better to know of a problem and be able to solve it, than not to know there is a problem until it's too late. Therefore the concept of evaluating existing coastal structures with the present day knowledge and testing them against current safety standards should be whole-heartedly supported.

References

(Bezuijen, 1991) *Geotechnical failure of revetments*, A. Bezuijen, Coastal Zone '91, Los Angeles

(Bezuijen, 1996) *Design formulas for block revetments,* Adam Bezuijen and Mark Klein Breteler, Journal of Waterway, Port, Coastal and Ocean Engineering, November/December 1996

(Bezuijen, 1998) *Advanced assessing of the stability of existing placed block revetments*, Adam Bezuijen and Gerard A. M. Kruse, Paper no. 219, 26th International Conference on Coastal Engineering, Copenhagen 1998

(Klein Breteler, 1998) *Design of alternative revetments*, M. Klein Breteler, K. W. Pilarczyk and T. P. Stoutjesdijk, Paper no. 221, 26th International Conference on Coastal Engineering, Copenhagen 1998

(Pilarczyk, 1998) *Seawalls, dikes and revetments,* Chapter 12: Design criteria for placed block revetments, edited by K. W. Pilarczyk, 1998

(Stoutjesdijk, 1992) *Field measurements on placed block revetments,* T. P. Stoutjesdijk, A. Bezuijen and B. P. Rigter, 23rd International Conference on Coastal Engineering, Venice 1992

(Stoutjesdijk, 1996) *Aging and stability of placed block revetments,* Theo Stoutjesdijk, Hans Johanson and Mark Klein Breteler, 25th International Conference on Coastal Engineering, Orlando 1996

SECOND ORDER WAVE INTERACTION WITH A LARGE STRUCTURE

Bjarne Büchmann [1], Jesper Skourup [2] and David L. Kriebel [3]

Abstract

Wave diffraction around a large vertical circular bottom mounted cylinder is considered. Results from a 3D second-order numerical time domain Boundary Element Model, a 3D second-order semi-analytical frequency domain model and experiments are compared and show good agreement over a wide range of wave frequencies and wave steepnesses. In general the agreement between the calculated and experimental results is satisfactory even in some cases where second-order Stokes' wave theory is not *a priori* expected to provide accurate results. The two numerical models have thus been validated against each other and validated against experiments. It is noted that the inclusion of second-order effects is important for the accurate estimation of run-up on a structure.

1 INTRODUCTION

Wave interaction with a large cylindrical structure is considered. The Keulegan-Carpenter number is small and thus inertial effects are dominant. Hence, potential theory can be applied. Conventional methods for estimating the influence on the wave field due to the presence of a large structure are often based on linear wave theory. However, second-order effects may be important and can lead to a significant increase of *e.g.* the run-up on a structure when compared to run-up calculated using linear theory. In the present paper a 3D time domain Boundary Element Model (BEM) correct to second order (see Büchmann *et al.*, 1998) is used for simulating the three dimensional interaction between waves and a structure. Comparisons are made with the run-up envelope results from the second-order semi-analytical frequency domain model by Kriebel (1990) as well as with experimental results by Kriebel (1992) for all the test cases considered by Kriebel (1992). Comparisons are also made to the well known first-order solution by MacCamy and Fuchs (1954) (see Skourup and Bingham, 1996, for further first order comparisons.)

[1] Department of Hydrodynamics and Water Resources (ISVA), DTU, DK-2800 Lyngby, Denmark

[2] International Research Centre for Computational Hydrodynamics (ICCH), Danish Hydraulic Institute, Agern Allé 5, DK-2970 Hørsholm, Denmark

[3] NAOME Department, 590 Holloway Road, Annapolis, MD 21402, USA

2 NUMERICAL MODELS

The BEM is formulated and implemented up to second order with the wave stcepness as perturbation parameter. The kinematic and dynamic free surface conditions are Taylor expanded about the mean free surface position and perturbation expansions are applied to the free surface elevation and to the velocity potential there. Hence, the boundary value problem is formulated at each order in a time-invariant geometry. The velocity potential and the free surface elevation are separated into incoming (known) and scattered components, and the boundary value problem at each order is then solved for the scattered parts alone. The scattered waves are all outgoing (of the domain) and the lateral boundary conditions can thus be formulated as radiation conditions. In the present work the lateral boundaries are modeled as active wave absorbers (as known from physical wave tank facilities). These may be used in combination with a sponge layer on the free surface in order to ensure an efficient absorption over a wide range of wave frequencies. Further details about the model can be found in Skourup (1996) and in Büchmann *et al.* (1998).

A closed-form frequency domain solution correct to second order for the diffraction of Stokes waves around a large vertical circular bottom mounted cylinder is given by Kriebel (1990). At first order the solution corresponds to the usual linear diffraction theory. At second order, however, the solution consists of a combination of forced waves due to the non-linear wave–wave interaction of the first order incident and scattered waves, and free waves due to the interactions of the forced waves with the cylinder. Further details about this semi-analytical frequency domain model can be found in Kriebel (1990, 1992).

3 STUDY PARAMETERS

Since both the numerical time domain model and the semi-analytical frequency domain model employ a Stokes' expansion method on the non-linear free surface conditions, it is expected that both models are limited to waves of small to medium wave steepness. Thus, it is appropriate to compare the wave steepness used in the experiments to the maximal wave steepness for the given frequency and water depth. Fenton (1990) gives a rational-function approximation for this maximum wave height by fitting to numerical results for progressive waves of maximum steepness.

$$\frac{H_{\max}}{h} = \frac{0.141063\frac{L}{h} + 0.0095721\left(\frac{L}{h}\right)^2 + 0.0077829\left(\frac{L}{h}\right)^3}{1 + 0.0788340\frac{L}{h} + 0.0317567\left(\frac{L}{h}\right)^2 + 0.0093407\left(\frac{L}{h}\right)^3} \tag{1}$$

Here H is the wave height, L is the wave length and h is the water depth. As a measure of the non-linearity of the wave the relative wave steepness, S, *i.e.* the wave steepness relative to the maximum steepness, can be introduced as

$$S(k,H) = \frac{kH}{(kH)_{\max}} = \frac{H}{H_{\max}} \tag{2}$$

where $k = 2\pi/L$ is the wave number.

It is well known that a secondary crest appears in the trough of the primary wave when Stokes' second-order theory is used for very steep waves. This is often used as an upper

limit to this theory by imposing a "no secondary crest" condition. For progressive waves of permanent form the condition can be written as

$$\left(\frac{H}{L}\right)_{\max} = \frac{1}{4f_\eta(kh)} \quad , \qquad f_\eta(kh) = \frac{\pi}{4}(3\coth^3 kh - \coth kh) \tag{3}$$

see *e.g.* Svendsen and Jonsson (1980) for details. Equivalently the ratio, a^{21}, between the second-order wave amplitude and the linear wave amplitude can be used to limit the theory. The "no secondary crest" condition then corresponds to $a^{21} < 0.25$. For progressive Stokes waves of permanent form a^{21} is

$$a^{21} = \frac{1}{8}kH(3\coth^3 kh - \coth kh) \tag{4}$$

It should be noted that the second-order Stokes' progressive wave theory may show considerable error when compared to *e.g.* the stream function wave theory even without violating the limit $a^{21} < 0.25$.

For a blunt body in waves a partially standing wave system is located in front of the structure. Thus it may be more appropriate to use the "no secondary crest" condition for Stokes' second-order standing waves as an upper limit. The criterion for plane standing waves is somewhat more restrictive than for progressive waves, especially in deeper waters, and can be expressed as *e.g.*

$$\left(\frac{H^{(s)}}{L}\right)_{\max} = \frac{1}{4f_\eta^{(s)}(kh)} \quad , \qquad f_\eta^{(s)}(kh) = \frac{\pi}{4}(3\coth^3 kh - \coth kh + 2\coth 2kh) \tag{5}$$

where $H^{(s)}$ is the height of the incident wave.

It is evident that numerical models based on Stokes' theory should not be employed to model waves in the cnoidal wave regime. The Ursell parameter $U = HL^2/h^3$ can be used as an indication of the wave regime. Thus, for H/h larger than, say, 10% an Ursell parameter $U = 40$ can be used to divide the Stokes' waves regime from the cnoidal waves regime.

The Keulegan-Carpenter number, KC, is an important parameter for indication of the relative importance of viscous effects. A value of KC less than about two to three indicates that viscous effects are not of importance for wave–structure interaction. Using linear Stokes theory at the mean water level to predict the maximum horizontal velocity, $u_{\max}$, KC can be written on the form

$$KC = \frac{u_{\max}T}{2a} = \frac{\pi}{2}\frac{kH}{ka\tanh kh} \tag{6}$$

where T is the wave period and a is the radius of the cylinder.

4 EXPERIMENTS

Kriebel (1992) conducted a series of experiments to find the run-up around the circumference of a vertical circular bottom mounted cylinder in various regular wave conditions. A

definition sketch showing the geometry and main variables is given in Figure 1. The test conditions ranged from fairly low wave steepness to very steep waves where wave breaking around the cylinder was observed. In some cases super-critical run-up occurred in the form of a vertical jet on the cylinder. Since the potential theory models considered in this work are limited to non-breaking waves, these test cases are not considered in detail here. Also in the cases where breaking was observed in the experiments the agreement between the two second-order numerical models is good, but the results deviate significantly from the results found in the experiments.

In Table 1 the parameters for the test cases considered are given. In addition to parameters mentioned previously, the ratio of the cylinder diameter, D, to the wave length is also given:

$$D/L = ka/\pi \tag{7}$$

It is noted from Table 1 that the Keulegan-Carpenter number KC is small in all the test cases considered. Thus, it is expected that inertial effects are predominant and potential theory can be applied.

To give an overview of the range of wave conditions used, a scatter diagram of the wave height relative to the water depth against the wave length relative to the water depth is

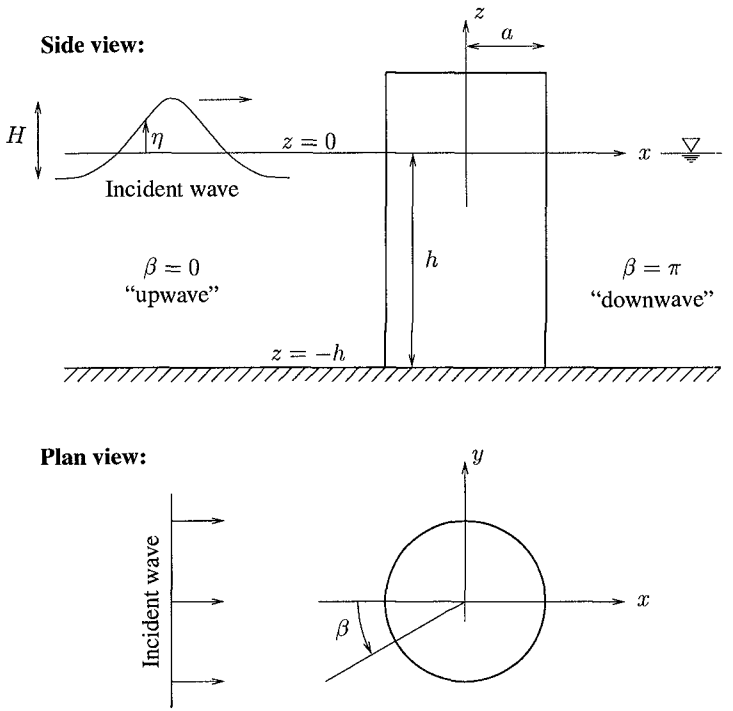

Figure 1: Definition sketch.

depicted in Figure 2. It is noted that the waves are very close to breaking in a few of the cases. In the cases used in this work (shown with squares) the relative wave steepness, S, varies from 15% to 72% (see also Table 1). It is noted that the "no secondary crest" condition for progressive second-order Stokes waves (3) is violated in three of the test cases used, while in many of the cases this limit is exceeded using the standing wave criterion (5). Thus it is clear that in many of the test cases it would be appropriate to use a model based on a Stokes theory of order larger than two, or even a model based on a fully non-linear wave theory. Therefore, the present study also gives indications of the validity range of the two numerical models.

5 RESULTS

Using the time domain BEM the influence on the wave field due to the presence of a fixed structure is computed as mean values over some wave periods. The parts of the time series where initial conditions or reflections from the lateral boundaries can be seen are not used. The run-up on a bottom mounted vertical circular cylinder is calculated in this paper, but this specific shape of the structure is not a restriction to the BEM. The wave run-up is

Figure	ka	kh	kH	S	KC	a^{21}	D/L
3a	0.271	0.750	0.132	0.257	1.20	0.167	0.09
3b	0.271	0.750	0.178	0.346	1.62	0.225	0.09
3c	0.271	0.750	0.215	0.418	1.96	0.272	0.09
4a	0.308	0.853	0.085	0.150	0.63	0.081	0.10
4b	0.308	0.853	0.137	0.242	1.01	0.130	0.10
4c	0.308	0.853	0.182	0.322	1.34	0.173	0.10
4d	0.308	0.853	0.250	0.442	1.84	0.237	0.10
4e	0.308	0.853	0.296	0.523	2.18	0.281	0.10
5a	0.374	1.036	0.122	0.189	0.66	0.078	0.12
5b	0.374	1.036	0.205	0.318	1.11	0.131	0.12
5c	0.374	1.036	0.286	0.444	1.55	0.183	0.12
5d	0.374	1.036	0.385	0.597	2.08	0.247	0.12
5e	0.374	1.036	0.402	0.623	2.17	0.257	0.12
6a	0.481	1.332	0.186	0.252	0.70	0.079	0.15
6b	0.481	1.332	0.317	0.429	1.19	0.135	0.15
6c	0.481	1.332	0.438	0.593	1.64	0.187	0.15
($\star$)	0.481	1.332	0.530	0.718	1.99	0.226	0.15
7a	0.684	1.894	0.391	0.470	0.94	0.117	0.22
7b	0.684	1.894	0.572	0.688	1.37	0.171	0.22
($\star$)	0.631	1.745	0.683	0.838	1.64	0.204	0.22
8	0.917	2.536	0.631	0.724	1.09	0.166	0.29
($\star$)	0.917	2.536	0.806	0.925	1.40	0.212	0.29

Table 1: Parameters for the test cases used in this work, and thus also the experiments conducted by Kriebel (1992). The figure numbers correspond to the figures in this work. An asterisk denotes an experiment where wave breaking or vertical jetting was observed.

computed correct to second order by first solving the linear problem and then using this result as input to the second-order problem. The linear results are compared with the well known linear diffraction theory solution by MacCamy and Fuchs (1954), while the second-order results are compared with the semi-analytical solution and with experimental results – both by Kriebel (1992). All the test cases from Kriebel (1992) have been reproduced in the present work and good agreement is found between the results of the two numerical models for all cases considered here. (see Figures 3 to 8). In the figures the BEM results for the linear run-up are shown with dashed lines and the second-order run-up with solid lines. The analytical linear run-up (*i.e.* the MacCamy and Fuchs solution) is shown with crosses and the second-order semi-analytical solution with diamonds. Experimental results are shown with squares. Due to symmetry only the run-up around half the circumference of the cylinder is depicted.

The agreement between the two linear solutions is excellent for all cases considered. For the maximum run-up on the cylinder the difference between the results of the present linear time domain BEM and the ditto analytical solution is less than 0.5%.

The agreement between the BEM and the semi-analytical second-order run-up by Kriebel (1992) is also good. It can be seen for all cases that the second-order wave run-up is sig-

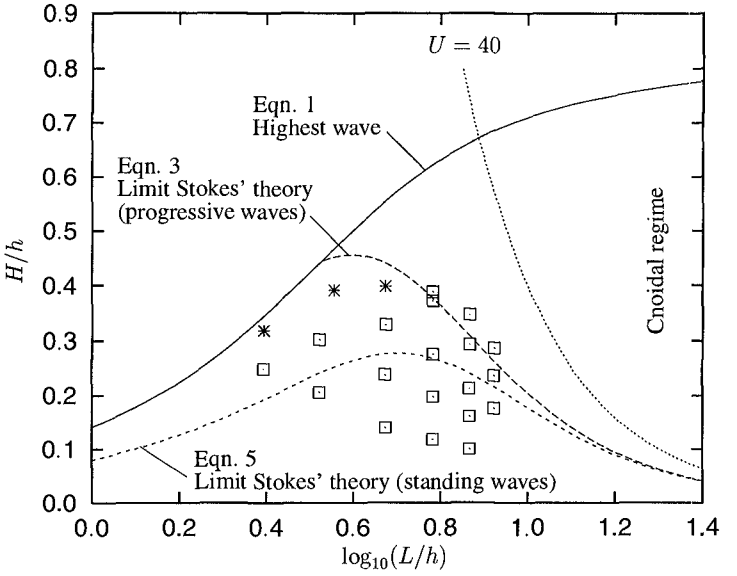

Figure 2: Scatter diagram of the expcriments by Kriebel (1992) used in this work (⊡) and experiments with observed wave breaking or vertical jetting (*). Also shown is the highest wave (Fenton, 1990) (—), the limit for Stokes' second-order progressive waves (----), the limit for Stokes' second-order standing waves (----), and the Ursell number U=40 (----).

nificantly larger than the linear wave run-up. For assessment of wave overtopping or deck slamming on gravity-based bottom mounted structures this is of significant importance.

The experimental results by Kriebel (1992) show larger run-up both on the front and on the lee side of the cylinder than predicted by linear theory. Thus significant non-linear diffraction effects are represented in the experimental data. The second-order results compare reasonably well with the experiments in all but the most severe cases (see Figs. 4d-e, 5d-e and 7b). It should be noted that in all these latter cases the "no secondary crest condition" for second-order standing waves (5) has been violated.

A vertical cross-section of a wave envelope in the direction of the main wave propagation direction is shown in Figure 9 as an example of the good agreement between the 3D BEM and the semi-analytical second-order solution in the fluid domain away from the cylinder. The cross-section is taken along the x-axis, *i.e.* with $y = 0$ (see Fig. 1.) It is noted from the figure that the agreement is good even though a fairly small computational domain has been used for the time domain BEM.

6 CONCLUSIONS

A comparison has been made between the 3D second-order time domain Boundary Element Model by Büchmann *et al.* (1998) and the second-order semi-analytical frequency domain solution by Kriebel (1990) for calculation of run-up on a large vertical circular bottom mounted cylinder. Good agreement has been found between results from the two models.

Comparison between the second-order results and the experimental results by Kriebel (1992) show reasonably good agreement except in cases with strongly non-linear waves. By comparing with solutions of the linear wave diffraction problem, it is demonstrated that second-order effects are important for assesment of *e.g.* wave overtopping or deck slamming on gravity based bottom mounted structures.

7 ACKNOWLEDGEMENTS

This work was funded in part by the Danish National Research Foundation.

REFERENCES

Büchmann, B., Skourup, J. and Cheung, K. F., (1998). Run-up on a structure due to second-order waves and a current in a numerical wave tank. To appear in *Applied Ocean Research.*

Fenton, J. D., (1990). Nonlinear wave theories. *The Sea*, edited by B. Le Mehaute and D. M. Hanes, vol. 9, chap. 1, 5–25. John Wiley & Sons, New York.

Kriebel, D. L., (1990). Nonlinear wave interaction with a vertical circular cylinder. Part I: Diffraction theory. *Ocean Engineering*, **17**(4), 345–377.

Kriebel, D. L., (1992). Nonlinear wave interaction with a vertical circular cylinder. Part II: Wave run-up. *Ocean Engineering*, **19**(1), 75–99.

MacCamy, R. C. and Fuchs, R. A., (1954). Wave forces on piles: A diffraction theory. Tech. Memo. 69, U.S. Army Corps of Engineers, Beach Erosion Board, Washington D.C.

Skourup, J., (1996). Active absorption in a numerical wave tank. *Proceedings of the 6th International Offshore and Polar Engineering Conference*, vol. 3, 31–38, Los Angeles, USA.

Skourup, J. and Bingham, H. B., (1996). Active absorption of radiated waves in a 3D boundary element model. *Proceedings of the 11th International Workshop on Water Waves and Floating Bodies*, Hamburg, Germany.

Svendsen, I. A. and Jonsson, I. G., (1980). Hydrodynamics of Coastal Regions. Den Private Ingeniørfond, Technical University of Denmark, 2nd edn.

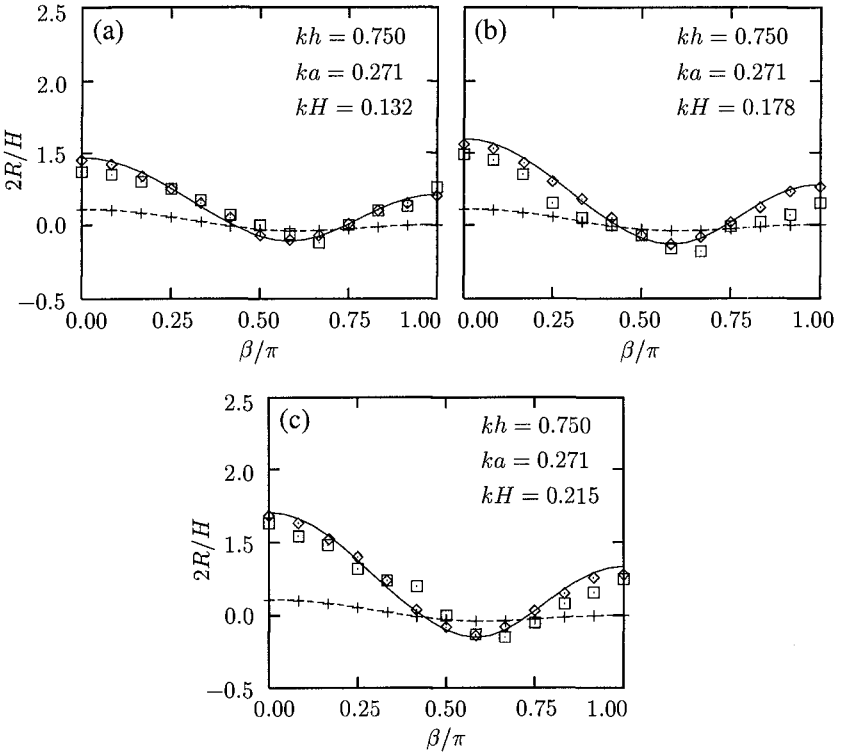

Figure 3: Run-up, R, as function of the angle, β, around a cylinder for $kh = 0.750$ and $ka = 0.271$. Numerical results to first order (----) and to second order (—). Analytical results by MacCamy and Fuchs (1954) (+). Semi-analytical results (◇) and experimental results (□) by Kriebel (1992).

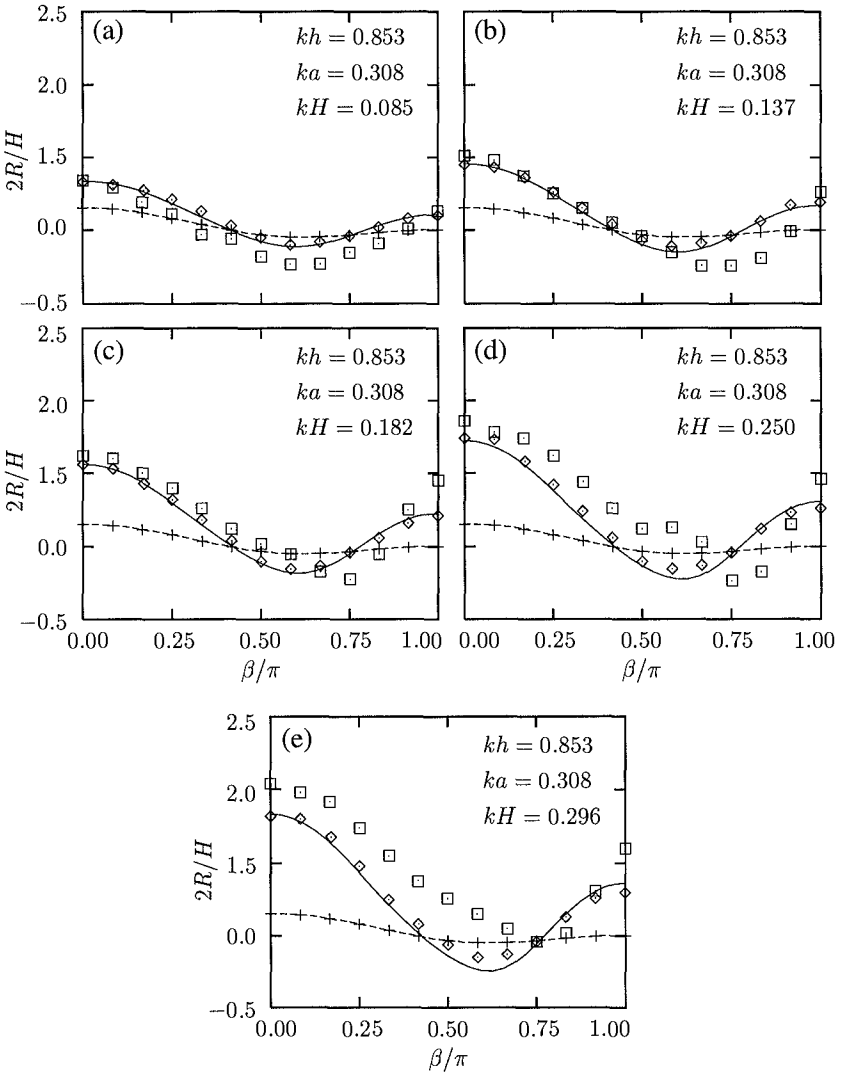

Figure 4: Run-up, R, as function of the angle, β, around a cylinder for $kh = 0.853$ and $ka = 0.308$. Numerical results to first order (---) and to second order (—). Analytical results by MacCamy and Fuchs (1954) (+). Semi-analytical results (◇) and experimental results (□) by Kriebel (1992).

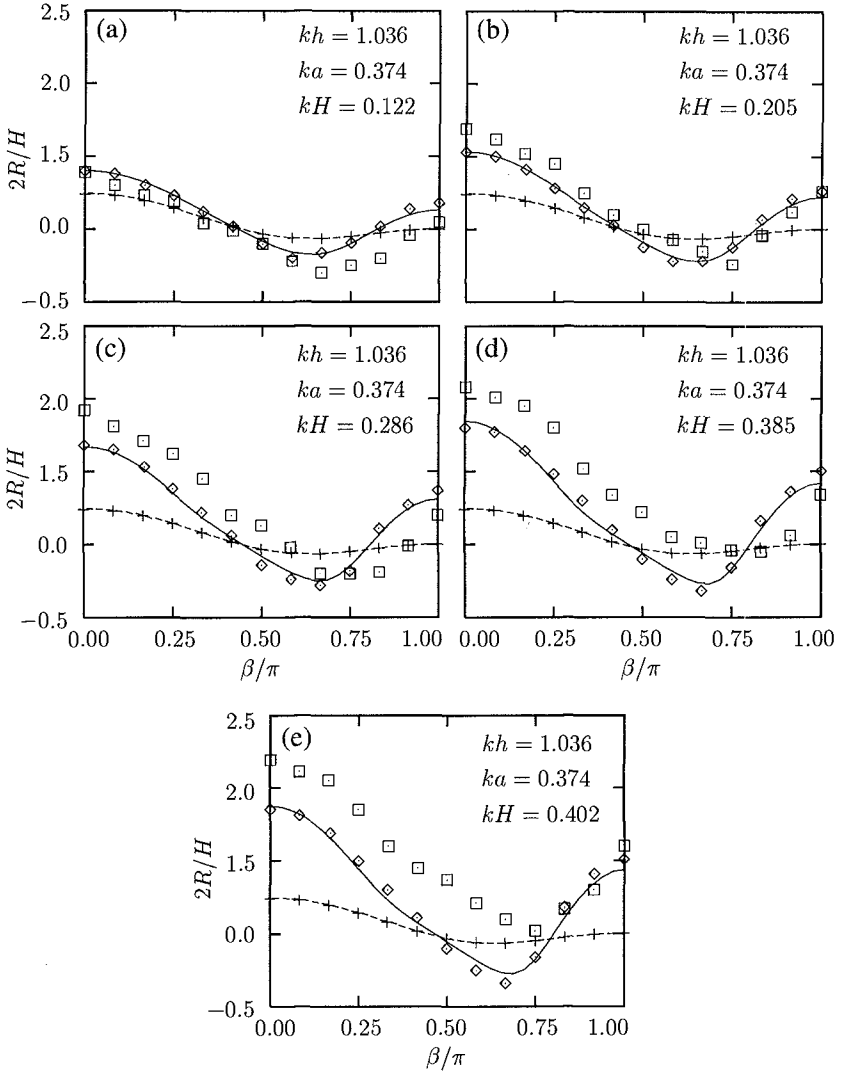

Figure 5: Run-up, R, as function of the angle, β, around a cylinder for $kh = 1.036$ and $ka = 0.374$. Numerical results to first order (---) and to second order (—). Analytical results by MacCamy and Fuchs (1954) (+). Semi-analytical results (◇) and experimental results (□) by Kriebel (1992).

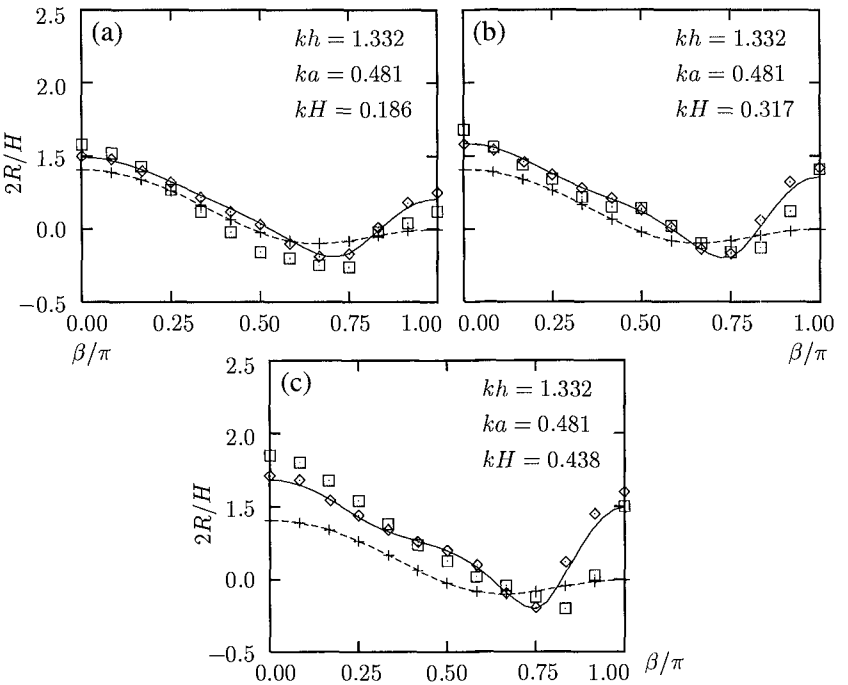

Figure 6: Run-up, R, as function of the angle, β, around a cylinder for $kh = 1.332$ and $ka = 0.481$. Numerical results to first order (---) and to second order (—). Analytical results by MacCamy and Fuchs (1954) (+). Semi-analytical results (◦) and experimental results (□) by Kriebel (1992).

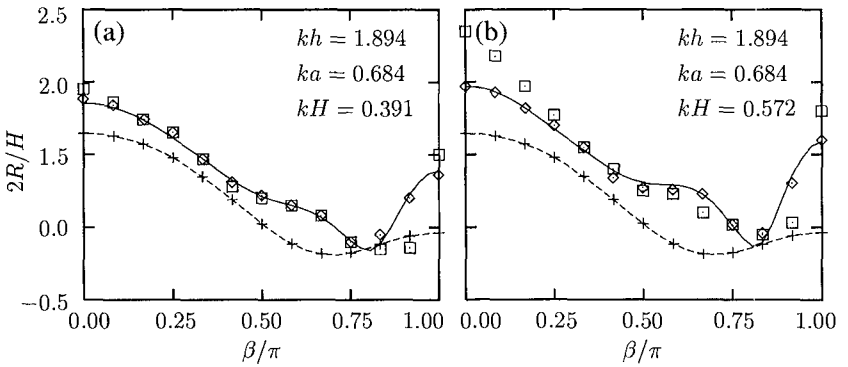

Figure 7: Run-up, R, as function of the angle, β, around a cylinder for $kh = 1.894$ and $ka = 0.684$. Legend: see Fig. 6 above.

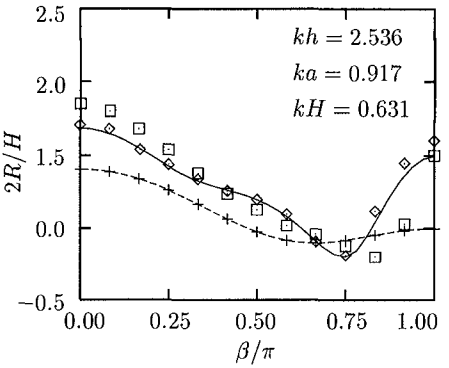

Figure 8: Run-up, R, as function of the angle, β, around a cylinder for $kh = 2.536$ and $ka = 0.917$. Numerical results to first order (---) and to second order (—). Analytical results by MacCamy and Fuchs (1954) (+). Semi-analytical results (◇) and experimental results (□) by Kriebel (1992).

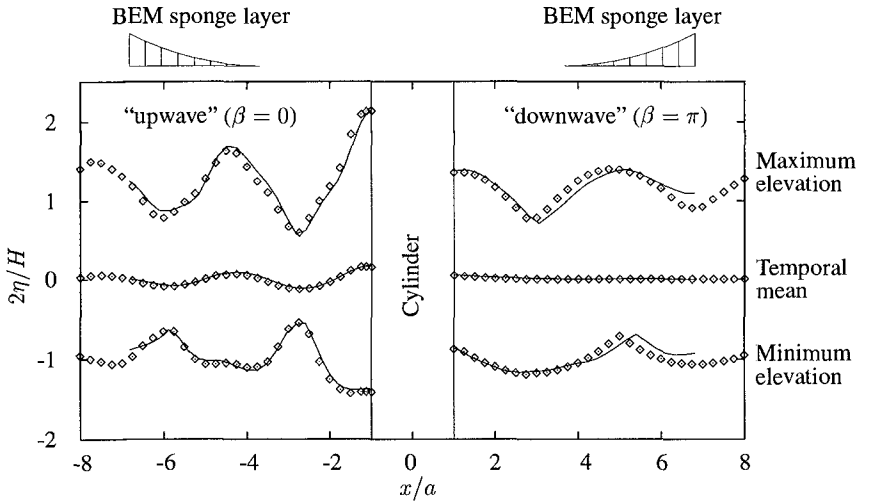

Figure 9: Vertical cross-section of wave envelope in the direction of wave propagation consistent to second order with $ka = 1.00$, $kh = 1.57$ and $kH = 0.50$. Numerical results using the BEM (—) and semi-analytical results by Kriebel (1990) (◇). The spatial extent of the BEM is indicated by the sponge layers.

ON THE EFFECT OF 2-LAYER THICKNESS BY HIGH-SPECIFIC GRAVITY ARMOR BLOCKS ON WAVE REFLECTION

Masahiro ITO [1], Yuitch IWAGAKI [2], Hiroshi MURAKAMI [3], Kenji NEMOTO [4], Masato YAMAMOTO [4] and Minoru HANZAWA [4]

Abstract

High-specific gravity (HSG) armor blocks have high stability for waves compared with the same size blocks made with normal concrete. Since an armor layer constructed with HSG armor blocks is thinner than the equivalent layer built with normal concrete, it is expected that it will produce significantly higher wave reflection. The goal of the present study is to investigate experimentally the effect of a double layer of HSG tetrapods (referred to as 2-tetrapod layer) on wave reflection. During the tests, regular waves were generated against a breakwater covered with the 2-tetrapod layer, and wave reflection was recorded for several layer thicknesses. Six sizes of tetrapod models were used ranging from 3.1 to 16.6 cm in vertical height, i.e., the 2-tetrapod layer thickness varied from 5.2 to 22.5 cm. Based on the laboratory test data, the effect of the layer thickness on wave reflection was examined using dimensionless factors derived from dimensional analysis. It was concluded that wave reflection increases as the specific gravity of armor blocks becomes larger, in a manner that depends on the deep water wave steepness.

Introduction

Normal concrete armor blocks have been widely used in many countries as armor units or construction units for wave absorbing works, detached breakwaters, artificial reefs, and so on. Armor blocks stable weight against wave action has been usually evaluated by Hudson's formula. Yet the use of armor blocks is a difficult technique associated with a number of typical problems and weak points. Here are some of them :

1. Armor blocks positioning vs wave action :
① Armor blocks are subjected to the combined action of waves and wave-induced currents on the seaward slope and at the crest of breakwaters, groins, wave absorbing works, submerged breakwaters, and artificial reefs. Corners at the sea side front of reclaimed lands also experience complex wave actions.
② In the swash zone, in front of breakwaters, armor blocks may be entrained due to the multiple effect of wave breaking, runup and backwash.

1 Professor, Department of Civil Engineering, Meijo University, Shiogamaguchi 1-501, Tempaku-ku, Nagoya 468-8502, JAPAN
2 Professor Emeritus of Meijo University and Kyoto University
3 Toyokuni Shrine, Nagoya, JAPAN
4 Tetra Co. Ltd., JAPAN

2. Use in construction :
③ The construction area for the armor blocks casting yard and for the armor layer is usually limited in size.
④ Large scale manufacturing devices are difficult to transport in remote places such as distant detached islands.

3. Sea-landscape and coastal structures :
⑤ Harmony between natural beaches and coastal structures requires a good balance between armor block size and natural beach scale.

High-specific gravity (HSG) armor blocks can provide very effective solutions to these problems compared with normal concrete blocks {unit weight: 22.54kN/m^3 (2.3tf/m^3)}. Given the design wave height and the angle of the armor layer slope relative to the horizontal, coastal structures made with HSG concrete blocks are more compact and smaller in size.

Authors (1994) analyzed the effect of a change of specific gravity on the stability of armor blocks relative to wave action. Results are based on a series of laboratory tests conducted with tetrapod models. It was found that a scaling effect prevails in tests carried out at small or medium scale, which is not accounted for by Hudson's formula. Yet, once corrected for this effect, the formula can be applied to evaluate the stable weight of HSG armor blocks. If the same wave acts against both normal concrete blocks and HSG concrete blocks, the latter can be smaller in size. Thus, at the scale of the incident waves, the thickness of a layer of HSG concrete blocks appears relatively thin. Indeed, the change of relative armor layer thickness has a considerable influence on wave reflection from armored coastal structures.

About ten years ago, Chevalier at SOGREAH Co. Ltd. in France (1994) developed the Accropod, not only aimed at protecting the slope-surface of breakwaters made with rubble stones and at absorbing the waves, but also designed to present high stability for waves when used in single armor layers. Turk and Melby (1994) at CERC, USA developed the Core-Loc that has also high stability for wave action under a single armor layer. Thus, new types of armor blocks are successively developed by seeking stability for waves, economical efficiency and ease of construction. These high-performance armor blocks are designed to be used in a single layer. Therefore, wave reflection and wave runup cannot be neglected when these blocks are made out of HSG concrete, because the absorption of incident wave energy becomes increasingly worse as the layer thickness decreases.

However, current investigations in this field are incomplete. It is the goal of this study to measure experimentally wave reflection from 2-tetrapod layers under the action of regular waves. The effect of a change of layer thickness is examined by using tetrapods of different sizes. Dimensionless hydraulic parameters such as relative water depth at the toe of the structure, deep water wave steepness, and relative 2-tetrapod layer thickness are used to analyze the data and to discuss the characteristics of wave reflection.

Dimensional Analysis on Wave Reflection

(1) Dimensional Analysis

We examine the effect of a change of specific gravity of armor blocks on wave reflection from an armor layer by means of dimensional analysis. Considering the 2-D case of a wave striking perpendicularly a seawall covered with a 2-tetrapod armor block layer, wave reflection from the seawall is expected to be dependent on the following hydraulic parameters.

a) Armor blocks characteristics

B_{2h} ; 2-tetrapod layer thickness

B_r ; methods of placement

B_ε ; porosity

B_u ; under layer roughness (crushed stone or smooth surface)

θ ; angle of armor layer slope, measured from the horizontal

b) Properties of Waves

h ; water depth at the toe of the structure covered with armor blocks

H ; wave height

T ; wave period

ρ ; mass density of water

μ ; viscosity of water

g ; gravitational acceleration

The reflection coefficient K_r is expected to be a function of these eleven hydraulic parameters :

$$K_r = f_1(h, H, T, \mu, \rho, g, B_\varepsilon, B_{2h}, B_T, B_u, \tan\theta) \tag{1}$$

In dimensionless form, this equation becomes

$$K_r = f_2\left[\frac{h}{H}, \frac{T}{\sqrt{H/g}}, \frac{\sqrt{gh}\cdot H}{\nu}, \frac{B_{2h}}{H}, B_\varepsilon, B_T, B_u, \tan\theta\right] \tag{2}$$

The right hand second term in Eq.(2), $T/\sqrt{H/g}$, is rewritten as L/H, using the relationship, $L=\sqrt{gH}\cdot T$. This dimensionless parameter s/H represents the deep water wave steepness. The right-hand second term, divided by the fourth term, becomes

$$\frac{T}{\sqrt{H/g}} \propto \frac{\sqrt{gH}\cdot T}{B_{2h}} \tag{3}$$

which can be rewritten as UT/B_{2h} is possible to rewrite as UT/B_{2h}, because the term $\sqrt{gh}$ has the dimension of a velocity and is a direct function of the particle

velocity U induced by the waves. This term has the form of a KC number, which is a dimensionless number relating to the generation and separation of eddies. More precisely, the right-hand second term of Eq. (2) can be considered as the KC number based on wave characteristics and layer thickness. Also, multiplying the third term by the fourth term, we obtain

$$\frac{\sqrt{gh}\cdot H}{\nu} = \frac{\sqrt{gH}\cdot B_{2h}}{\nu} \tag{4}$$

which is the Reynolds number based on wave celerity and layer thickness. So far, we can see that several choices of dimensionless parameters are permitted and Eq. (2) may take the equivalent form:

$$K_r = f_3\left\{\frac{h}{L}, \frac{L}{H}\left(or\ \frac{\sqrt{gH}\cdot T}{B_{2h}}\right), \frac{B_{2h}}{L}, \frac{\sqrt{gH}\cdot B_{2h}}{\nu}, B_T, B_\varepsilon, B_\alpha, \tan\theta\right\} \tag{5}$$

In these laboratory tests, tetrapods are randomly placed and the under layer is made out of crushed stone. Therefore, B_α and B_α may be considered as constant and disregarded. The porosity rate B_ε is measured by a submerging method. A box-type basin (90cm wide x 100cm long x 50cm high) is used for this purpose. The method consists of filling the basin with water up to the top level of the tetrapods placed randomly on its base. This test is performed with a series of tetrapod models ranging from 3.0 to 16.0cm in vertical height. Porosity values are summarized in Table 1. They vary from 53% to 63% but only tetrapods of 3.1cm height have a porosity of 53%. Taking into account the size of the tetrapods and the accuracy of the present method, we may consider that the scattering of porosity is small and that the porosity term in Eq. (2) can be omitted. Furthermore all tests are carried out with the same breakwater slope: $\tan\theta = 3/4$, so that this term can also be neglected. Taking wave characteristic parameters in deep water as a reference, the dimensionless expression of the reflection coefficient reduces to

Table 1 Characteristics of tetrapods used for the tests and figure reference marks

Classification type No.	Vertical block hight l (cm)	Two tetrapod leyers thickness B2h(cm)	Procity rete B ε (%)	Total number of tetrapod	Marks
C-1	3.1	5.2	53	1800	✡
E-1	5.7	8.3	61	1048	▽
E-2	7.8	12.0	57	572	◇
E-3	10.4	14.6	63	287	□
E-4	14.2	18.5	61	223	⊙
D-5	16.6	22.5	59	108	△

$$K_r = f_4\left\{\frac{h}{L_0}, \frac{H_0}{L_0}(or\ KC), \frac{B_{2h}}{L_0}(or\ \frac{B_{2h}}{H_0}), \frac{\sqrt{gH_0}\cdot B_{2h}}{\nu}\right\} \quad (6)$$

From Eq. (6) we can see that the reflection coefficient is governed by four factors only : the relative water depth h/L_0, the deep water wave steepness H_0/L_0, the relative armor layer thickness B_{2h}/H_0 and the Reynolds number $\sqrt{gH_0}\cdot B_{2h}/\nu$.

Laboratory Tests

The laboratory tests for wave reflection were performed in the same basin that was already used for stability tests (Ito et al. 1994). This wave basin is divided into seven flumes by separating walls. The breakwater models which were set to measure wave reflection were constructed within every other flume. They were covered with two layers of tetrapods (referred to as 2-tetrapod layer), placed randomly over an underlayer of crushed stone. The sea-side slope was set to 1V:4/3H. During the laboratory tests, tetrapods were covered by a steel net to prevent accidental displacement due to wave action. Recall that the purpose of the tests is to measure wave reflection in terms of the 2-tetrapod layer thickness only, not including any entrainment by the waves. In order to absorb multiple wave reflections between breakwaters and wave paddle, a slope of 1V:10H was constructed with wave absorbing net-mats within every intermediate flume, i.e. in those flumes where no breakwaters were installed. With this method, stable wave conditions could be sustained for long durations in the flumes with breakwaters, and it is there that wave reflection was recorded Test conditions are summarized in Table 2. As shown in this table, six sizes of tetrapod models were investigated: 3.1, 5.8, 7.8, 10.5, 14.2 and 16.6cm in vertical height. Time histories of the wave profile, in which the incident wave and the wave reflected from the 2-tetrapod layer overlap, were recorded by a wave meter at the toe of the slope of the breakwater. These analog data were converted to numerical data by an A to D board converter connected to a personal computer. The reflection coefficient was computed from the incident reflected waves separation method proposed by Goda et al. (1976). During the entire duration of the tests, flow characteristics such as nonbreaking waves,

Table 2 Test conditions and characteristics of breakwater model

Regular waves	Water depth at the toe of breakwater slope	h(cm)	50					
	Wave height	H(cm)	5 ~ 30					
	Wave period	T(sec)	1.0 ~ 3.0 (interval 0.5 sec)					
	Wave steepness in deep water	Ho/Lo	0.002 ~ 0.12					
Breakwater covered with 2-tetra layer	Sea bed slope		horizon					
	Slope angle	tan θ	1:4/3					
	Armor block model		Tetrapod					
	Tetrapod vertical height	B_h(cm)	3.1	5.7	7.84	10.4	14.2	16.6
	Tetrapod 2-layer thickness	B_{2h}(cm)	5.2	8.3	12.0	14.6	18.5	22.5

collapsing or surging breakers, as well as plunging breakers were also recorded visually along the slope of the 2-tetrapod layer.

Relationship between Relative Layer Thickness and Specific Gravity

(1) Armor block size

Hudson (1959) made comprehensive investigations and proposed a formula to determine the stability of armor units on rubble structures. The stability formula resulted from extensive model testing, in the form:

$$W = \frac{w_r H^3}{K_D (S_r - 1)^3 \cot\theta} \tag{7}$$

where

W: weight of an individual armor unit

w_r : unit weight of armor unit

H: design wave height

S_r: specific gravity of armor unit to water ($=w_r/w_w$)

w_w : unit weight of water

θ : angle of the breakwater slope measured from the horizontal, in degrees

K_D : stability coefficient of an armor unit

Given H, K_D, and tan θ , we shall consider the relationship between the weight of an armor block, W, and its characteristic height l. Without loss of generality, this relationship may be expressed as

$$W = kl^3 w_r \tag{8}$$

Where, k is a constant. Using Eq. (8) , Eq.(7) becomes

$$l^3 k = \frac{H^3}{K_D (S_r - 1)^3 \cot\theta} \tag{9}$$

Now, let's denote l_n and l_h, S_n and S_h the characteristic heights and the specific gravities of blocks made out of HSG concrete and normal concrete, respectively. Eq. (9) can be rewritten, for each type of block, as:

$$l_n^3 k = \frac{H^3}{K_D (S_n - 1)^3 \cot\theta} \tag{10}$$

$$l_h^3 k = \frac{H^3}{K_D (S_h - 1)^3 \cot\theta} \tag{11}$$

From Eq. (10) and Eq. (11), assuming the design wave height to be a constant and taking a value of S_n=2.3 for the specific gravity of normal concrete, the size of any HSG block relative to a normal concrete block, l_h/l_n, can be expressed as

$$\frac{l_h}{l_n} = \frac{S_n - 1}{S_h - 1} = \frac{1.3}{S_h - 1} \tag{12}$$

It can be seen from that equation that the block size ratio l_h/l_n is inversely proportional to the high-specific gravity of concrete in water, S-1. The block size ratio is indicated by a thick solid line in Fig. 1. The case of sea water is also considered and represented by a dashed line. As can be deduced from this figure, the difference between fresh water and sea water is very small. The ratio of the stability weights W_h/W_n is also sketched in this figure by a solid line and a dashed line, for fresh water and sea water, respectively. This ratio decreases as the 3rd-power of the specific gravity in water as can be deduced from Eq. (7).

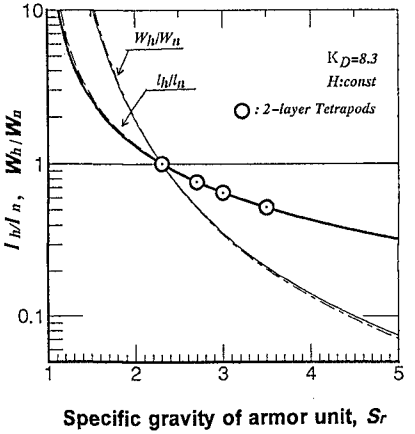

Fig. 1 Armor block size ratio, l_h/l_n, and stable weight ratio, W_h/W_n, in terms of specific gravity

(2) Relative Armor Layer Thickness

As discussed in the previous section, the relationship between the size of the armor blocks and their specific gravity was derived from Hudson's formula. We shall now examine the relationship between the 2-tetrapod layer thickness and the specific gravity of armor units. Let's define the relative layer thickness by the ratio of the 2-tetrapod layer thickness to the design wave height. From Eqs.(10) and (11), the following relationship is obtained

$$\frac{l^3}{H^3} k = \frac{1}{K_D (S_r - 1)^3 \cot\theta} \tag{13}$$

The relative armor layer thickness B_h/H may be assumed to be proportional to l/H, where l is the height of a single armor block. Then,

$$\frac{B_{2h}}{H} \propto \frac{l}{H} \tag{14}$$

From Eqs. (13) and (14),

$$\frac{B_{2h}}{H} \propto \frac{1}{(K_D \cot\theta)^{1/3}(S_r - 1)} \tag{15}$$

K_D and tan θ being usually constant, it can be seen from Eq(15) that the relative layer thickness is inversely proportional to the specific gravity in water, S_r-1. Given the design wave height, it is possible to evaluate the stability weight of tetrapod (K_D=8.3), for various specific gravities, by using Hudson's formula. From the specific gravity and the stability weight, the 2-tetrapod layer thickness B_{2h} can be estimated; it is commonly taken as 4/3 of the tetrapod height. Define the relative layer thickness B_{2h}/H_c as the ratio of the 2-tetrapod layer thickness to the design wave height. B_{2h}/H_c can be considered as the relative layer thickness under critical conditions. It is interesting to derive the critical layer thickness, B_{2h}/H_c, for several sizes of tetrapods. Results are summarized in Table 3 which indicates, for each size of tetrapod, the design wave height and the relative layer thickness, for four values of the specific gravity S_r=2.3, 2.7, 3.0 and 3.5, respectively. In this table, the designed wave height is derived from Hudson's formula, and the relative layer thickness is obtained from the design manual published by TETRAPOD Co., Ltd. Note, from this table, that the relative layer thickness is nearly independent on the tetrapod size. As listed in Table 3, the values of B_{2h}/H_c = 0.70, 0.54, 0.45 and 0.36 depend only on the specific gravity S_r. Block size ratios are indicated with circle marks in Fig.1. As can be seen in this figure, for a high-specific gravity of S_r=3.5, block size is reduced by a factor of two compared to normal blocks (S_r=2.3). As expected, values of the relative layer thickness derived in Table 3 are in the same ratio.

Table 3 Tetrapod weights, design wave heights and relative 2-tetrapod layer thicknesses. for different values of the specific gravity

Specific gravity		2.3		2.7		3.0		3.5	
Weight (tf)	2-layer thickness (m)	Hc (m)	B2h/Hc	Hc (m)	B2h/Hc	Hc (m)	B2h/Hc	Hc (m)	B2h/Hc
0.46	1.2	1.7	0.71	2.2	0.54	2.6	0.46	3.3	0.36
0.92	1.5	2.1	0.71	2.8	0.53	3.3	0.45	4.1	0.36
9.20	3.2	4.6	0.69	6.0	0.53	7.1	0.45	8.8	0.36
46.00	5.5	7.9	0.69	10.3	0.53	12.1	0.45	15.1	0.36
80.00	6.7	9.5	0.71	12.4	0.54	14.6	0.46	18.2	0.37

H : Design wave height (based on K_D =8.3)
B2h/Hc : Relative two tetrapods layers thickness

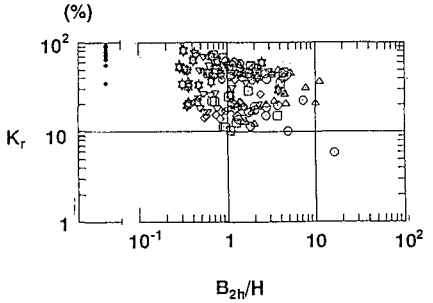

Fig. 2 Relationship between wave reflection and relative 2-tetrapod layer thickness

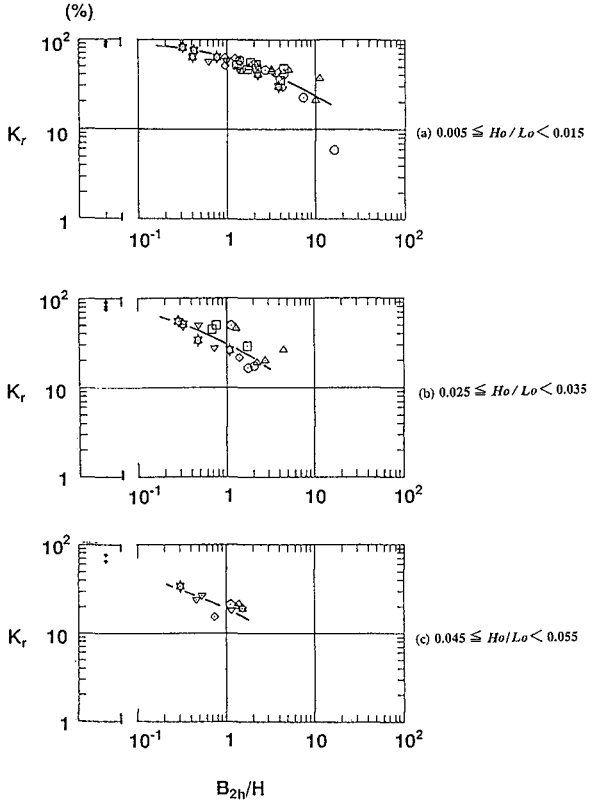

Fig. 3 Effect of deep water wave steepness on the relationship between wave reflection and relative 2-tetrapod layer thickness

Relative Armor Layer Thickness and Wave Reflection

(1) Wave Reflection

We classified the data according to the ratio of the 2-tetrapod layer thickness to the wave height at the toe of the seawall, B_{2h}/H, corresponding to the term B_{2h}/H_b in Eq. (6), and plotted them in Fig. 2. As shown in this figure, the relationship between the reflection coefficient K_r and the relative layer thickness B_{2h}/H scatters widely. In this figure, dark circles denote reflection from a smooth slope. Data points were obtained by covering the sea-side slope of the seawall with a steel plate; this corresponds to the case where both armor layer thickness and underlayer porosity are zero. We investigated the effect of the relative water depth d/L_o on the relationship between K_r and B_{2h}/H, by plotting data according to the parameter d/L_o. The effect of d/L_o, however, couldn't be found : data points remain widely scattered. In a similar way, we examined the effect of the Reynolds number, $\sqrt{gH_0}\cdot B_{2h}/\nu$: the effect of the Reynolds number couldn't be found either. Then, by separating the data into seven range-values of the deep water wave steepness, H_b/L_o= ~ 0.005, $0.005 \sim 0.015$, $0.015 \sim 0.025$, $0.025 \sim 0.035$, $0.035 \sim 0.045$, $0.045 \sim 0.055$ and $0.055 \sim$, the relationship between the reflection coefficient and the relative layer thickness was rearranged, as displayed in Fig. 3 (for the sake of clarity, only three values of H_b/L_o have been represented). It can be deduced, from this figure, that the deep water wave steepness strongly affects the relationship between K_r and B_{2h}/H. Here again, reflection from a smooth slope is indicated with dark circles, as a reference. In each subfigure, Fig. 3(a) to Fig. 3(c), the trend of the reflection coefficient is shown by fitting the data with a solid curve. The relationship between K_r and B_{2h}/H is rearranged in Fig. 4 by plotting all solid curves together in the same graph, based on the parameter H_b/L_o. Each value of H_b/L_o is the mean value of another range of wave steepnesses examined. Dashed lines stand for estimates of the reflection coefficient there where experimental data couldn't be obtained. It can be seen in this figure that the relationship between K_r and B_{2h}/H changes considerably depending on H_b/L_o.

(2) Wave reflection for storm waves

From this diagram, characteristics of wave reflection, when the design wave acts on the 2-tetrapod layer, can be analyzed. Since the relative layer thickness B_{2h}/H, which depends on the specific gravity of armor units only, is already given in Table 3, Fig. 4 can be used directly to derive the reflection coefficient from the wave steepness. For this purpose, values of the relative layer thickness B_{2h}/H have been represented with vertical dashed lines in Fig. 4. The reflection coefficient is easily obtained by reading the K_r values at the intersection between these vertical lines and the solid curves of wave steepness H_b/L_o. From these K_r-values, it is possible to evaluate the increasing rate of wave reflection $(K_r)_{hc}/(K_r)_{nc}$ when HSG tetrapods are used rather than normal concrete tetrapods. Fig. 5(a) indicates the relationship between $(K_r)_{hc}/(K_r)_{nc}$ and the specific gravity in water, S-1, according to the parameter H_b/L_o. As can be seen in this figure, for armor blocks designed to sustain the same critical wave height, wave reflection becomes bigger as tetrapod

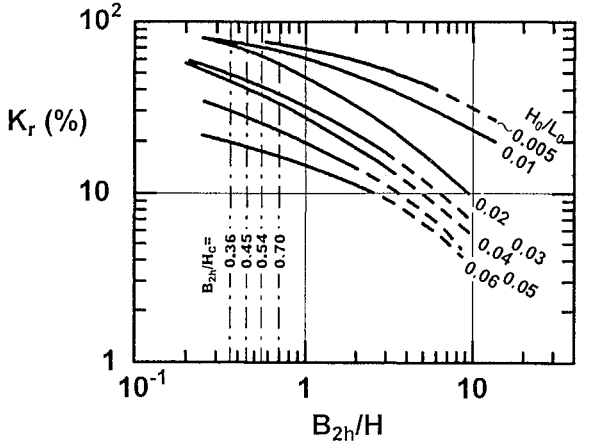

Fig. 4 Relationship between wave reflection and relative 2-tetrapod layer thickness, based on the deep water wave steepness

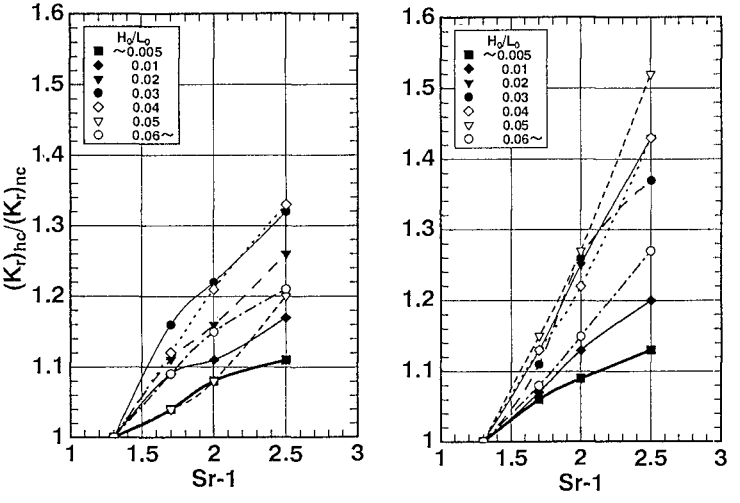

(a) In case of the design wave height (b) In case of half of the design wave height

Fig. 5 Increase of relative wave reflection for increasing values of specific gravity

specific gravity gets larger. Fig. 5(a) also shows that this increase is proportional to specific gravity, with a rate that depends strongly on the parameter H_b/L_o.

(3) Wave reflection for mild waves

As mentioned in the previous section, the effect of HSG tetrapods on wave reflection was analyzed using the design wave height, which corresponds to the strongest waves the tetrapods are able to resist and which may, in practice, represent storm waves. Now we shall also examine the increase of wave reflection under the condition of mild waves. This condition is set by taking half of the design wave height for the estimate of the reflection coefficient from Fig. 4. The same graphical method is used with values of the relative thickness B_{2h}/H simply doubled. As for the previous case, the rate of wave reflection, $(K_r)_{hc}/(K_r)_{nc}$ is plotted in terms of the specific gravity of tetrapod in water, in Fig. 5(b). From this figure, it can be seen that for mild waves too, the rate of reflection increases proportionally to the specific gravity of the blocks.

For both storm waves, Fig. 5(a), and mild waves, Fig. 5(b), the amount of reflection tends to increase with the specific gravity of the tetrapods. Yet, the rate of increase is strongly affected by the deep water wave steepness. As the wave becomes steeper, and as long as the wave steepness remains within the range $0.005<H_b/L_o<0.04$ (storm waves) and $0.005<H_b/L_o<0.05$ (mild waves), the rate of increase tends to become larger. Above these values, i.e. for steeper waves, it shows the opposite tendency and drops. In the case of blocks of HSG S=3, the reflection coefficient for storm waves is from 1.07 to 1.22 times bigger than the reflection coefficient for normal concrete (from 1.09 to 1.27 times bigger for mild waves), depending on the wave steepness.

Conclusions

This study was intended to investigate experimentally the effect of a change of specific gravity of armor blocks on wave reflection using tetrapod units. From the results of this work, the following conclusions can be drawn:

(1) Given the specific gravity of armor units in water, the relative 2-tetrapod layer thickness, B_{2h}/H, is a constant, regardless of the tetrapod weight and of the design wave height.
(2) Given the design wave height, the relative layer thickness, B_{2h}/H, is inversely proportional to the specific gravity of armor units in water.
(3) The relationship between the reflection coefficient and the relative layer thickness is considerably affected by the deep water wave steepness.
(4) The reflection coefficient for high-specific gravity concrete blocks relative to the reflection coefficient for normal concrete blocks increases proportionally to the specific gravity, in a manner that depends on the deep water wave steepness.
(5) For both storm waves and mild waves, the larger the specific gravity of the blocks, the bigger the reflection coefficient.

Acknowledgments

Part of this study was supported by the Specified Research Grant at Meijo University.

References

Goda, Y. and Suzuki, Y.(1976) "Estimation of incident and reflected waves in random wave experiment, " *Proc. of 15th Conf. on Coastal Engrg., ASCE, Vol.1, 828–845.*

Hudson, R. Y.(1959) "Laboratory investigation of rubble-mound breakwaters," *Journal of the Waterways and Harbors Division, ASCE, Vol. 85, No. WW3, 93–121.*

Ito, M., Iwagaki, Y., Murakami, H., Nemoto, K., Yamamoto, H., and Hanzawa, M. (1994) "Stability of high–specific gravity armor blocks, " *Proc. of 24th Conf. on Coastal Engrg., ASCE, Vol. 1, 1143–1156.*

Ito, M., Murakami, H., Iwagaki, Y., Nemoto, K., Yamamoto, H., and Hanzawa, M. (1994) "Wave reflection due to high–specific gravity armor blocks, "*Proc. of Coastal Engineering, JSCE, Vol. 42, 736–740* (in Japanese)

Melby, J. A. and Turk, G.F. (1994) "The core-loc: optimized concrete armor," *Proc. of 24th Conf. on Coastal Engrg., ASCE, Vol. 2, 1426–1438.*

SOGREAH Co. (1994) "ACCROPOD, --Efficient and economical protection of breakwaters--," *Pamphlet of SOGREAH, 9p.*

DEVELOPMENT OF TWO-DIMENSIONAL NUMERICAL WAVE FLUME FOR WAVE INTERACTION WITH RUBBLE MOUND BREAKWATERS

Peter Troch[1], Julien De Rouck[2]

Abstract

The numerical wave flume VOFbreak² for simulation of wave interaction with a rubble mound breakwater is presented. The key innovations are a porous flow model and wave boundary conditions. The porous flow is implemented using a Forchheimer model. At the boundaries waves are generated using a combined wave generation-absorption technique and are absorped using a numerical sponge layer.

1 Introduction

A 2D numerical model for the simulation of free surface breaking waves at permeable coastal structures is developed at the Department. This numerical wave flume VOFbreak² aims at a better description of the wave-induced flows and pressures at porous structures, resulting in a better design (tool) of coastal structures. Special attention is paid to the application of the model to wave interaction with a rubble-mound breakwater. Fig. 1 shows a snapshot of the simulation of a typical numerical wave flume set-up where waves interact with the porous breakwater.

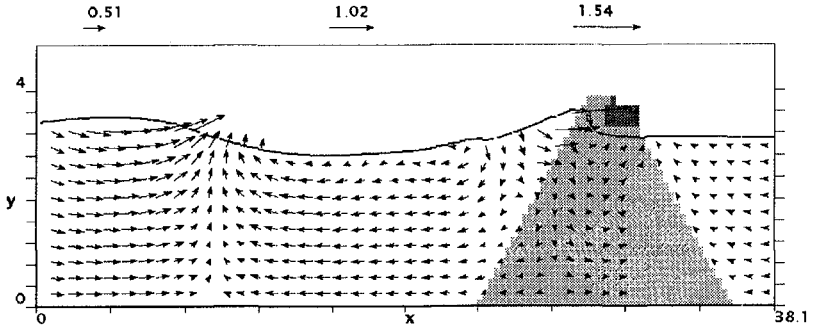

Fig. 1. Snapshot of a typical numerical simulation of wave interaction with a rubble mound breakwater using VOFbreak².

[1] Research Assistant, Dept. Of Civil Engineering, University of Gent, Technologiepark 9, B-9052 Gent, Belgium. Email: PeterB.Troch@rug.ac.be.
[2] Professor, Dept. Of Civil Eng., University of Gent, Technologiepark 9, B-9052 Gent, Belgium.

First the underlying mathematical and numerical models of VOFbreak² are presented briefly. Secondly the key innovations in the numerical wave flume that are necessary for simulation of wave interaction with permeable rubble mound structures are discussed in more detail: a porous flow model and wave boundary conditions. Finally an example application illustrates the model features.

2 Numerical wave flume VOFbreak²

2.1 Mathematical model

The numerical wave flume VOFbreak², VOF-algorithm for breaking waves on breakwaters, is based on the original SOLA-VOF code (Nichols et al., 1980) capable to compute free surface flow when the fluid domain becomes multiply connected. Incompressible Newtonian fluid with uniform density is assumed in the vertical plane (two-dimensional), governed by the Navier-Stokes equations:

$$\frac{\partial u}{\partial t} + u\frac{\partial u}{\partial x} + v\frac{\partial u}{\partial y} = -\frac{1}{\rho}\frac{\partial p}{\partial x} + \nu\left(\frac{\partial^2 u}{\partial x^2} + \frac{\partial^2 u}{\partial y^2}\right) + g_x \qquad (1)$$

$$\frac{\partial v}{\partial t} + u\frac{\partial v}{\partial x} + v\frac{\partial v}{\partial y} = -\frac{1}{\rho}\frac{\partial p}{\partial y} + \nu\left(\frac{\partial^2 v}{\partial x^2} + \frac{\partial^2 v}{\partial y^2}\right) + g_y \qquad (2)$$

and the continuity equation:

$$\frac{\partial u}{\partial x} + \frac{\partial v}{\partial y} = 0 \qquad (3)$$

where t (s) is time, u and v (m/s) are the velocity components in x and y direction respectively., p (N/m²) is pressure, and g_x, g_y (m/s²) are horizontal and vertical gravity components respectively, ρ (kg/m³) is the density of the water, ν (m²/s) is the kinematic coefficient of viscosity.

The free surface is described by introducing a function F(x, y, t) that represents the fractional volume of fluid in the mesh cells. The volume of fluid evolution equation (4) expresses that the volume fraction F moves with the fluid:

$$\frac{\partial F}{\partial t} + u\frac{\partial F}{\partial x} + v\frac{\partial F}{\partial y} = 0 \qquad (4)$$

2.2 Numerical model

Finite difference solutions of the four unknowns u, v, p and F, are obtained on an Eulerian rectangular mesh in a Cartesian co-ordinate system (x,y).

The Navier-Stokes equations (1)-(2) are discretised using a combined FTCS/upwind scheme. As a result, explicit approximations of the Navier-Stokes equations are used to compute the first guess for new-time-level velocities.

To satisfy the continuity equation (3), i.e. to obtain a divergence free velocity field, the pressure-velocity iteration is used. It is a variant of the Newton-Raphson relaxation technique applied to the pressure Poisson equation for incompressible flow. Using this method, pressures are iteratively adjusted in each cell and velocity changes induced by each pressure change are added to the velocities computed out of the Navier-Stokes equations.

Finally, the volume of fluid function F, defining the fluid regions, is updated using the donor-acceptor flux approximation for the calculation of fluxes from a donor cell to an acceptor cell. A unit value of F corresponds to a full cell, while a zero value indicates an empty cell. Cells with values between zero and one and having at least one empty neighbour cell contain a free surface. A line is constructed in each surface cell with the correct calculated surface slope and correct amount of fluid lying on the fluid size, and is used as an approximation to the actual free surface.

2.3 Code portability

The code VOFbreak[2] is based on SOLA-VOF (Nichols et al., 1980) and includes some selected improvements from its successor code NASA-VOF2D (Torrey et al., 1985). These are mainly a numerical defoamer technique preventing non-physical voids inside the fluid to appear, and fixes in the donor-acceptor algorithm.

The code is implemented on a UNIX workstation using ANSI C, providing general computer compatibility, and providing a flexible code structure for adaptations with little effort. A series of post-processing tools has been developed, using Tcl/Tk (Ousterhout, 1994), for the visualisation, processing and interpretation of the computed results. Numerical instrumentation for the acquisition of relevant phenomena (wave height, run-up level, pore pressure, surface elevation, ...) is included for easy access to calculated data.

3 Porous flow model

A breakwater is composed of a porous core, and porous filter and armour layers, which are made using coarse granular material. For a simulation of wave induced porous flow, this material is considered homogeneous and isotropic within areas where one characteristic porosity n and one characteristic diameter d are assigned. Following assumptions are used for porous flow:

- The discharge (or filter) velocity u, in x direction, is replaced by the pore (seepage) velocity $u_p = u/n$; regarded as a macroscopic quantity, i.e. the discharge velocity is averaged over a cross sectional area consisting of a mixture of material and voids. The porosity n of the cell material is defined as the ratio between the volume of the pores and the total volume.

- The F-function is now considered as the fraction of maximum volume of fluid in a cell.

- The Forchheimer resistance terms replace the viscosity terms in the Navier-Stokes equations, these are expressed by the hydraulic gradient I (-), e.g. in x direction (Burcharth et al., 1995):

$$I = -\frac{1}{\rho g}\frac{\partial p}{\partial x} = au + bu|u| + c\frac{\partial u}{\partial t} \tag{5}$$

where the Forchheimer coefficients a and b take the form:

$$a = \alpha \frac{(1-n)^2}{n^3}\frac{\nu}{gd^2} \tag{6}$$

$$b = \beta \frac{1-n}{n^3}\frac{1}{gd} \tag{7}$$

and the inertia coefficient c takes the form:

$$c = \frac{n + (1-n)C_m}{g}, \text{ where } C_m = 1 + C_A \tag{8}$$

where α and β are dimensionless constants, ν (m^2/s) is the kinematic coefficient of viscosity, g (m/s^2) is the gravitational acceleration, n (-) is the porosity, d (m) is a characteristic stone diameter, C_A(-) is the added mass coefficient.

The linear term au in equation (5) constitutes the contribution from the laminar flow. The non-linear term, $bu|u|$, represents the fully turbulent flow contribution. The term $c\partial u/\partial t$, taking into account the inertia forces connected with the local accelerations $\partial u/\partial t$, represents the resistance of the porous medium to accelerate the water.

A verification of the implementation of the one-dimensional porous flow in steady state flow conditions has been carried out by comparing numerical calculated results to experimental measurements (Troch, 1997).

4 Wave Boundary Conditions

4.1 Introduction

In Fig. 2 a conventional numerical wave flume set-up is given. Waves are generated at the left boundary of the computational domain and propagate towards a rubble mound breakwater positioned near the other boundary. The incident waves interact with the porous breakwater causing transmitted and reflected waves to propagate towards the boundaries. At the boundaries, an 'open boundary' or 'absorbing boundary' condition is required, allowing the transmitted and reflected waves to leave the computational domain without disturbing the interaction of the incident waves with the breakwater.

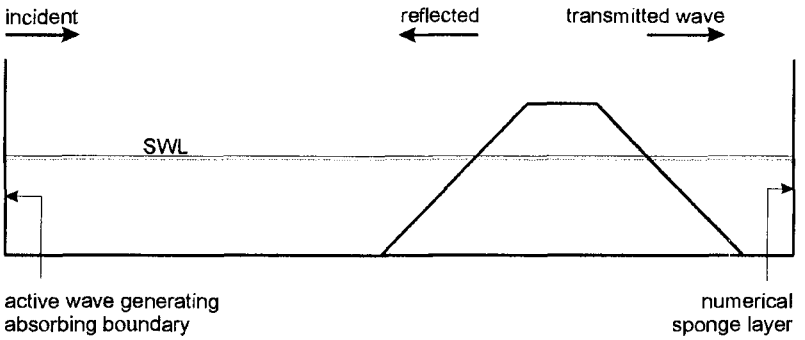

Fig. 2. Conventional numerical wave flume set-up with boundary conditions for the study of wave interaction with porous rubble mound breakwater.

The numerical problem is similar to the wave absorption problems in a physical wave flume. Therefore in principle the same solutions could be applied in the numerical flume. Schäffer and Klopman (1997) give an overview of the basic concepts of wave absorption in physical wave flumes.

However in order to increase the computational efficiency of the calculations a number of constraints are present. These are very important in the final choice of the numerical wave boundary conditions. A very important constraint is that the length of the numerical wave flume should be as short as possible for reasonable CPU time. Therefore the numerical wave flume requires a relatively short foreshore (1 or 2 wavelengths), and a very short lee-side (maximum 1 wavelength). The wave absorption techniques need to perform in these conditions. Also an efficient and simple technique that absorbs waves numerically might be more favourable than the numerical simulation of the physical behaviour of e.g. a progressive wave absorber.

The generation of incident waves is implemented in VOFbreak² using boundary generation. Any wave theory can be used to provide the surface elevation $\eta(x_0, t)$ and the velocity components $u(x_0, z, t)$ and $v(x_0, z, t)$ at the left boundary ($x_0=0$). For the simulations in this paper linear wave theory is used. Another efficient wave generation technique is source generation (Brorsen and Larsen, 1987) where the volume from the incident wave is added inside the computational domain. The advantage of this latter method is that the generation of the incident waves is not disturbed by the reflected waves. The disadvantage is that the length of the computational domain is considerably increased because a relatively long absorption layer is required for absorption of the reflected waves at the boundaries. Iwata et al. (1996) have successfully implemented the source generation technique in a SOLA-VOF model. The absorption layers required up to 6 wavelengths for sufficient wave absorption.

The wave absorption generally is divided into active systems and passive systems. An active system provides an active response to the waves; a passive system damps (mostly by energy dissipation) the wave motion. For this application, the transmitted waves are passively absorbed using an efficient numerical sponge layer technique

from Larsen and Dancy (1983). This passive absorption system is discussed in more detail in the next section.The reflected waves are actively absorbed at the wave-generating boundary using an active wave absorption technique. A detailed discussion of the active system performance in the VOFbreak² model is described in Troch and De Rouck (1998).

4.2 Numerical Sponge Layer

Larsen and Dancy (1983) presented an efficient numerical passive wave absorber for use in short wave models. This technique is implemented into the VOFbreak² model. It has been chosen because of its very elegant and simple use. An absorption function a(x) is applied on velocities and elevation in a numerical sponge layer with length x_s, Fig. 3. The absorption function at the start of the sponge layer equals 1 and gradually decreases to 0 near the end of the sponge layer. The sponge layer is located at the closed end of the wave flume. Only a limited number of grid cells is required for absorption of the wave.

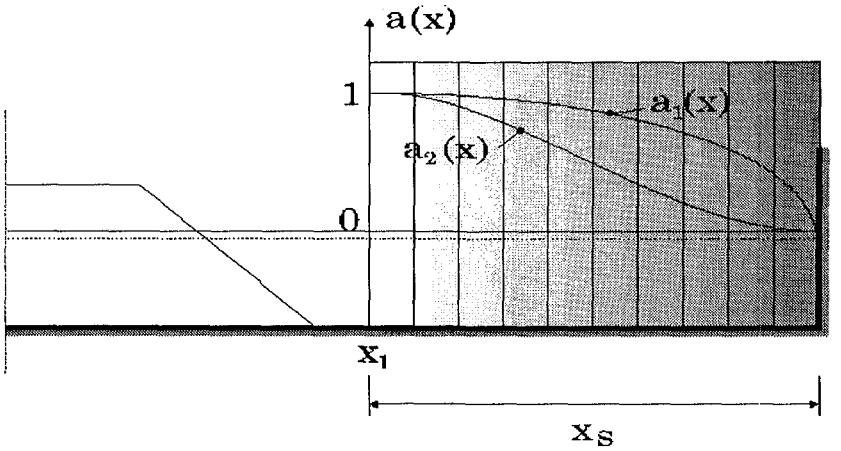

Fig. 3. Numerical sponge layer with width x_s placed at the end of the numerical wave flume. The two absorption functions a(x) are plotted inside the sponge layer.

Two simple absorption functions have been used for testing the performance of the sponge layer technique: an elliptic function $a_1(x)$ (equation (9)) and a cosine function $a_2(x)$ (equation (10)):

$$a_1(x) = \sqrt{1 - \left(\frac{x - x_1}{x_s}\right)^2} \tag{9}$$

$$a_2(x) = 0.5\left(1 + \cos\left(\frac{\pi}{x_s}(x - x_1)\right)\right) \tag{10}$$

The absorption function is applied on the calculated velocity components in the cells of the sponge layer after each time step calculation. In the present simulations no attempt has been made to apply the absorption function on surface elevations. The surface elevation is not a direct unknown of the system of differential equations (1)-(4), but is derived from the F function in each column of cells. A damping of the surface elevation means deleting volume fractions and doing this without adjusting the pressure consequently in each cell would lead to non-converging solutions.

The performance of the two types of sponge layer has been tested by deriving reflection (K_r) and transmission (K_t) coefficients from a sponge layer located inside the numerical wave flume. The water depth d = 0.40 m, the wave height H = 0.02 m, the wave period T = 1.60 s. The width of the sponge layer varied between 40% and 60% of the wavelength L = 2.84m. The results are summarized in Table 1.

	x_s/L [-]	K_r [%]	K_t [%]
a1	0.40	27	7
a1	0.60	21	3
a2	0.60	33	1

Table 1. *Reflection (K_r) and transmission (K_t) coefficients from sponge layer performance tests.*

The elliptic absorption function a_1 with a length x_s = 0.40L still has a considerable reflection coefficient of 27% and transmission coefficient of 7 %. Increasing the sponge layer width to 0.60L decreases reflection to about 20% and almost no transmission (3%). In comparison the cosine absorption function with a width of 0.60L still shows 33% reflection but no transmission.

It is concluded from these simple performance tests that the elliptic a_1 type function performs better than the cosine a_2 type. A slightly larger width x_s of the sponge layer would be required for practical purposes: it is suggested to use a width between 0.60L and 1.0L. It is noted that the absorption function not necessarilly should equal 0 at the end of the sponge layer, it is more important to have a gradually decrease causing least reflection of the waves. In order to decrease the number of cells in the sponge layer it might be preferable to increase gradually the cell width towards the boundary.

There are other solutions available to obtain an open boundary.

- The well-known radiation boundary (also referred to as the Sommerfeld or the weakly reflecting boundary (used e.g. in the SKYLLA model, van der Meer et al., 1992) is another efficient solution. This method might become elaborate when working with irregular waves.

- Modelling of a spending beach with a mild slope (1:10 or more) would require a long distance to be modelled. This solution is not efficient for use in a numerical flume.

- Modelling of a physical progressive passive wave absorber with decreasing porosity would need a comprehensive description of geometry, porous flow characteristics, etc. Also for the physical performance of this solution it is required to go through the full model equations resulting in a longer calculation time.

- An active wave absorption system (see next section for more details) provides an active response at the boundary to the transmitted wave leaving the domain. It generally is used at the wave generating boundary in combined wave generating-absorbing mode, but the system is usable for wave absorption only. This solution is very elegant, but more complicated to implement in the numerical model than the sponge layer.

4.3 Active wave absorption system

The active wave generating-absorbing system implemented in the numerical wave flume is based on the AWASYS system (Frigaard and Christensen, 1994) from Aalborg University. The AWASYS system originally is a surface elevation based system to be used in a physical wave flume with two conventional wave height meters. The system for VOFbreak² is based on a velocity meter based system because velocities are readily (or computationally cheap) available from the computations. Hald and Frigaard (1996) show that the performance (i.e. the absorption characteristics) of both elevations and velocities systems is similar.

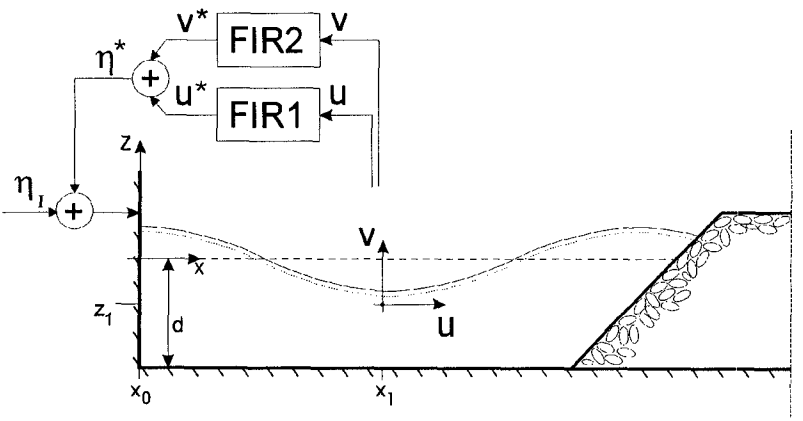

Fig 4. Definition sketch of the numerical wave flume set-up and the principle of the active wave generating-absorbing boundary condition.

The principle of the active wave generating-absorbing system requires two steps. First an on-line detection of the reflected wave field is performed using a set of spatially co-located velocities (u, v). Secondly the wave generator has to generate the incident wave and an additional wave which cancels out the reflected wave propagating towards the boundary. Fig. 4 shows schematically the principle of the system. The correction signal η^* that cancels out the reflected wave, is determined from superposition of the two filtered velocity signals u^*+v^*. The digital Finite Impulse Response (FIR) filters are operated using a time-domain discrete convolution of the velocities (u, v) and the impulse response h^i, where i = u or v; e.g. for the u velocity component:

$$u^*[n] = \sum_{j=0}^{J-1} h^u[j] \cdot u[n-j] \qquad (11)$$

where J is the number of filter coefficients, and $u^*[n] = u^*(n \cdot \Delta t_f)$ is the filter output at time $t = n \cdot \Delta t_f$, where Δt_f is the filter time interval.

Having outlined the principle of the active wave generation-absorption, the only task remains the design of the corresponding frequency response function H(f) of the filters from where the impulse response function h(t) is easily derived using inverse Fourier Transform. The theoretical and practical design of the frequency response function for use in a numerical wave flume is described in Troch and De Rouck, 1998.

5 Example application

To demonstrate the possibilities of the VOFbreak² model for coastal engineering applications, a simulation of regular waves attacking a conventional rubble mound breakwater with permeable homogeneous core, is given. Fig. 5 is a snapshot during wave run-up and wave run-down respectively, and shows the induced velocity field in front of the breakwater and inside the breakwater core. From the zoomed slope area (Fig. 6) it is seen clearly that the occurring flow pattern cannot be reduced to one dimension. Both infiltration and seepage of pore water arise simultaneously along the slope.

Therefor this type of 2D model is better equipped to simulate wave-structure interaction than one-dimensional models. The model also gives a better insight in the wave interaction dynamics at the breakwater and may be helpful to assist to improve design guidelines.

The numerical model is verified with both physical model data and prototype data. This latter validation is unique world-wide by using the Zeebrugge breakwater (Belgium) prototype wave and pressure data (Troch et al., 1996). Validation results will help to improve further developments of the numerical wave flume.

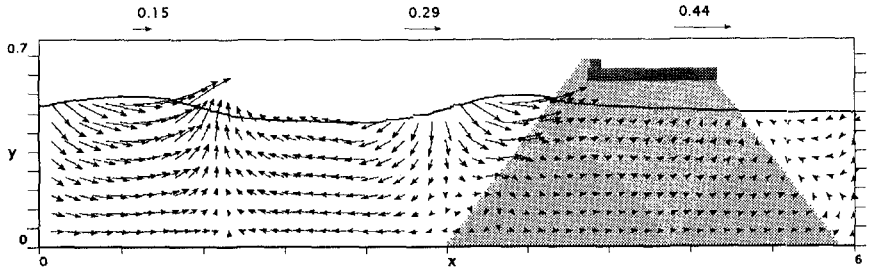

(a) wave run-up

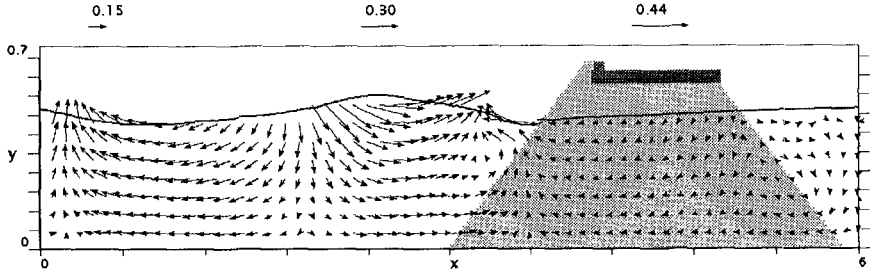

(b) wave run-down

Fig. 5. *Regular incident waves on and in permeable breakwater. Snapshot of calculated free surface location and velocity field during wave run-up (a - top) and run-down (b - bottom).*

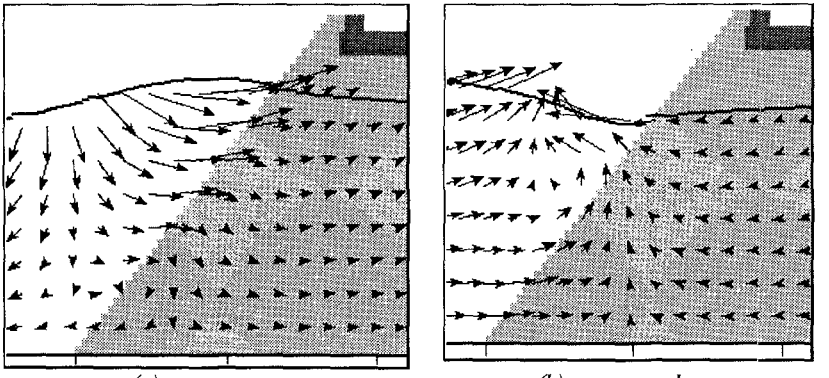

(a) wave run-up *(b) wave run-down*

Fig. 6. *Zoom of calculated free surface location and velocity field at the breakwater slope during wave run-up (a - left) and run-down (b - right).*

Acknowledgements

The development of this work originated during the EC MAST2 project MAS02-CT92-0023. The financial support of EC is greatly acknowledged. Discussions with Ass. Prof. Michael Brorsen and Ass. Prof. Peter Frigaard from Aalborg University, Denmark, on wave boundary modelling are very much appreciated.

References

Brorsen M. and Larsen J., 1987. Source Generation of nonlinear gravity waves with boundary integral equation method. Coastal Eng., Vol 11, pp. 93-113.

Burcharth H.F., Andersen O.H., 1995. On the one-dimensional steady and unsteady porous flow equations. Coastal Eng., 24: 233-257.

Frigaard P. and Christensen M., 1994. An absorbing wave-maker based on digital filters. In: Proceedings, 24th International Conference on Coastal Engineering, Kobe, Japan, Vol.1, pp. 168-180.

Hald T. and Frigaard P., 1996. Performance of active wave absorption systems – comparison of wave gauge and velocity meter based systems. In: Proceedings 2nd International Conference on Coastal, Ports and Marine Structures. ICOPMAS, Tehran, Iran.

Iwata K., Kawasaki K., Kim D., 1996. Breaking limit, breaking and post-breaking wave deformation due to submerged structrures. In: Proceedings 25th International Conference on Coastal Engineering, Orlando, USA, Vol.3, pp. 2338-2351.

Larsen J. and Dancy H., 1983. Open boundaries in short wave simulations -- a new approach. Coastal Eng., Vol. 7, pp. 285-297.

Nichols B.D., Hirt C.W., Hotchkiss R.S, 1980. SOLA-VOF: a solution algorithm for transient fluid flow with multiple free boundaries. Report LA-8355, Los Alamos, California, USA.

Ousterhout J.K., 1994. Tcl and the Tk Toolkit. ISBN 0-201-63337-X, Addison-Wesley, USA.

Schäffer H. A. and Klopman G., 1997. Review of multidirectional active wave absorption methods. In: Proceedings of the I.A.H.R. seminar on multidirectional waves and their interaction with structures, 27th I.A.H.R. congress, San Francisco, USA, pp.159-182.

Torrey M.D., Cloutman L.D., Mjolsness R.C., Hirt C.W., 1985. NASA-VOF2D: a computer program for incompressible flows with free surfaces. Report LA-10612-MS, Los Alamos Scientific Report, Los Alamos, New Mexico, USA.

Troch P., 1997. VOFbreak², a numerical model for simulation of wave interaction with rubble mound breakwaters. In: Proceedings 27th IAHR Congress, San Francisco, USA, pp. 1366-1371.

Troch P. and De Rouck J., 1998. An Active Wave Generating-Absorbing Boundary Condition for VOF type numerical model. Submitted for Coastal Engineering.

Troch P., De Somer M., De Rouck J., Van Damme L., Vermeir D., Martens J.P., 1996. Wave attenuation inside a rubble mound breakwater based on full scale measurements. Proc. ICCE '96, Orlando, USA.

van der Meer J.W., Petit H.A.H., van den Bosch P., Klopman G., Broekens R.D., 1992. Numerical simulation of wave motion on and in coastal structures. In: Proceedings 23rd International Conference on Coastal Engineering, Venice, Italy, Vol.2, pp. 1772-1784.

Nonlinear Wave Forces on a Rubble Covered Pipeline

William G. McDougal[1]
Norimi Mizutani[2]
Ayman M. Mostafa[3]

Abstract

A nonlinear numerical model is developed for the interaction of waves with a pipeline covered with rubble. The wave field utilizes a fully nonlinear potential formulation while the porous medium is governed by modified Navier-Stokes equations. The model employs the BEM in the water column and the FEM in the rubble layer. Wave forces on the pipeline are calculated by integrating pressure around the pipeline perimeter. The numerical and experimental results for the wave kinematics in the pipeline vicinity are found to be in reasonable agreement. Numerical analyse indicate that the horizontal wave force is larger than the vertical force for all tested wave and rubble conditions. Forces increase with increasing wave height and decreasing depth. However, for the cases examined there is an intemediate water depth at $h/L \approx 1/6$ for which the forces are largest. The armor stone size and rubble layer pososity have little influence on the magnitudes of the forces. The horizontal force is nearly independent of the depth of rubble cover over the pipeline. However, the vertical force increases significantly as the depth of cover decreases. Also, for partial pipeline cover, the maximum horizontal and vertical forces are more in phase, which combined with the larger vertical force, results in a substantially less stable condition.

[1] Professor, Department of Civil Engineering, Oregon State University, OR 97331, USA
[2] Associate Professor, Department of Civil Engineering, Nagoya University, Nagoya 464-8603, Japan
[3] Assistant Professor, Department of Civil Engineering, Nagoya University, Nagoya 464-8603, Japan

Background

Marine pipelines in nearshore water are often either buried or covered with an armor layer. This reduces the wave forces on the pipeline and the possibility of seabed scour around the pipeline. This may also protect the pipeline from mechanical damage due to anchor drag or fishing nets. In the case of armor protection, little design information is available for estimating the magnitude of wave forces on the pipeline. As a result, designs for large projects are often verified with physical models. During the past few years, several such model studies have been conducted at the O.H. Hinsdale Wave Research Laboratory at Oregon State University. Typical conditions are shown in Figure 1. These pipelines are all outfalls with pipe diameters that range from 1.1m to 3.7m. The protective armor stone diameter ranges from 0.4m to 1.1m. These conditions are representative of outfall conditions on the west coast of the United States. In the physical model tests, typical design concerns include the following: Is the armor stone stable? What is the minimum stable cross-section for the armor? If the pipeline loses weight due to air or gas in the line, is the ballast sufficient to maintain stability? Will the flow around the pipeline and armor induce seabed scour? The objective of the present study is to develop a numerical model to begin to address these issues. At this point in the model development, the intent is not to replace physical model testing, but rather to narrow the range of conditions tested in the laboratory to the most promising alternatives. The numerical model can also be used to provide fast results prior to the experiment at low cost.

The proposed model is a direct extension of previous work by the authors. Mizutani, et al. (1996) developed a coupled BEM-FEM model to study the nonlinear interaction between waves and a submerged breakwater. This model was successful in predicting 2-D wave transformations over a submerged breakwater. Next, Mizutani, et al. (1998) developed a coupled BEM-FEM model for wave, submerged breakwater, and seabed nonlinear interaction. This model incorporated the seabed and the porewater flow. The validity of the BEM-FEM model was demonstrated in comparisons with experimental measurements for a submerged breakwater on a sand seabed. This progression of model development lends itself well to the inclusion of a pipeline within the rubble structure. The objectives of the paper are to develop a numerical model for wave-rubble interaction and wave forces on a marine pipeline.

Figure 2 shows different armor configurations. The pipeline may be wholly buried within the armor layer, partially exposed or heavily exposed. All three are used in practice. The fully covered alternative provides greater protection and stability, but is also more costly. How much the armor section can be reduced is a major consideration in the design. Figure 3 shows nomenclature used to describe the geometry of the armor protection.

Numerical Formulation

The model domain is shown in Figure 4. The free surface is S_f, the mudline along the bottom is S_B, the surface of the armor is S_s, and the pipe surface is S_C. In the water column, the fluid is assumed to be inviscid and incompressible and the flow is irrotational. This leads to a formulation based on a velocity potential. Since this is a potential flow formulation, vortex shedding or other dissipation mechanisms are not included in the water column. The governing equations for the wave field are conservation of mass (Laplace Equation) with pressure recovered from the energy equation. The flow in the porous rubble is modeled by conservation of mass and momentum. The porewater is assumed to be viscous and incompressible and the resistance terms in the momentum equation are based on the Forchheimer equation.

Wave Field:

Governing equation:

$$\frac{\partial^2\phi}{\partial X^2}+\frac{\partial^2\phi}{\partial Z^2}=q, \qquad q(X,Z,t)=U_o(Z,t)\delta X \tag{1}$$

Boundary Conditions:

$$\frac{\partial\phi}{\partial n}=n_z\frac{\partial\phi}{\partial t} \qquad (\text{on } S_f) \tag{2}$$

$$\frac{\partial\phi}{\partial n}=0 \qquad (\text{on } S_B) \tag{3}$$

$$\frac{\partial\phi}{\partial n}=V_n \qquad (\text{on } S_s) \tag{4}$$

$$\frac{\partial\phi}{\partial n}+\frac{1}{2}(\nabla\phi)^2+g\eta+\mu\phi-\int_{X_1}^{X}\frac{\partial\mu}{\partial X}\phi dX=0 \qquad (\text{on } S_f) \tag{5}$$

$$\frac{\partial\phi}{\partial X}=\frac{1}{\sqrt{gh}}\left(\frac{\partial\phi}{\partial t}+\mu\phi+\int_{X_2}^{X_3}\frac{\partial\mu}{\partial X}\phi dX\right) \qquad (\text{on } S_L) \tag{6}$$

$$\frac{\partial\phi}{\partial X}=-\frac{1}{\sqrt{gh}}\left(\frac{\partial\phi}{\partial t}+\mu\phi-\int_{X_3}^{X_{14}}\frac{\partial\mu}{\partial X}\phi dX\right) \qquad (\text{on } S_R) \tag{7}$$

$$\mu_{\max}=(0.25\sim 0.50)\sqrt{\frac{g}{h}} \tag{8}$$

in which ϕ = velocity potential, η = water surface elevation wrt SWL, n_z = outward normal with respect to the Z axis, V_n = velocity component normal to the boundary, μ = damping factor, h = still water depth, X, Z = horizontal and vertical coordinates, and t = time. An idealized wave tank similar to that of Ohyama and Nadaoka (1991) is adapted to simulate the nonlinear deformations over a marine pipeline.

The numerical solution technique used for the wave field is the boundary element method (BEM). The BEM formulation maps the 2-D problem onto the 1-D boundary. The boundary is discritized using linear elements at a spacing of approximately 20 elements per wave length in the horizontal and 8 elements along the vertical boundaries at the ends of the domain. Typically about 150 boundary elements were employed.

Porous Flow:

Governing equations:

$$\frac{\partial U}{\partial X}+\frac{\partial W}{\partial Z}=0 \tag{9}$$

$$A\frac{\partial U}{\partial t}+B(U\frac{\partial U}{\partial X}+W\frac{\partial U}{\partial Z})+C\frac{\partial P}{\partial X}+EU+FU\sqrt{U^2+W^2}=0 \tag{10}$$

$$A\frac{\partial W}{\partial t}+B(U\frac{\partial W}{\partial X}+W\frac{\partial W}{\partial Z})+C\frac{\partial P}{\partial Z}+EW+FW\sqrt{U^2+W^2}=0 \tag{11}$$

$$A=\left(1+\frac{1-\varepsilon}{\varepsilon}C_a\right)/\varepsilon g,\ B=1/\varepsilon^2 g,\ C=1/\gamma,\ E=\frac{6(1-\varepsilon)\upsilon C_{D2}}{g\varepsilon^2 D^2}$$

$$F=\frac{C_{D1}(1-\varepsilon)}{2gD\varepsilon^3},\ P=p-\gamma Z \qquad \text{(Mizutani et al., 1996)}$$

Boundary conditions:

$$P = -\rho\frac{\partial\phi}{\partial t} - \frac{\rho}{2}\left\{\left(\frac{V_n}{\varepsilon}\right)^2 + V_s^2\right\} - \gamma Z \qquad \text{(on } S_S\text{)} \qquad (12)$$

$$V_n = W\cos\theta \pm U\sin\theta \qquad \text{(on } S_S\text{)} \qquad (13)$$

$$V_s = \frac{\partial\phi}{\partial S} \qquad \text{(on } S_S\text{)} \qquad (14)$$

$$V_n = 0 \qquad \text{(on } S_C\text{)} \qquad (15)$$

in which U, W = horizontal and vertical seepage velocities, P = total pressure, p = dynamic pore pressure, ε = porosity, C_a = added mass coefficient, g = acceleration of gravity, υ = kinematic viscosity of water, γ = unit weight of water, D = stone diameter, θ = side slope angle, C_{D1} , C_{D2} = drag coefficients, and A, B, C, D, E, F are notational constants.

The rubble flow model is solved using the finite element method (FEM). Since there are internal variations in the flow properties and dissipation, the rubble problem does not conveniently map to a boundary and must be solved in 2-D. The fundamental unknowns are U, W, and P. These are approximated using isoparametric finite elements. The flow in the rubble includes nonlinear dissipation through the Forchheimer resistance terms.

On the surface of the pipeline, the normal component of velocity is zero. The forces are calculated by integrating the pressure around the pipeline. The force does not include drag. As a result, the solution is most appropriate for large diameter pipelines in which the forces are diffraction dominated. On the surface of the rubble, the pressure and normal fluid flux from the BEM and FEM solutions are required to match. This matching couples the two solution domains. This leads to a large matrix in which the upper left corner is densely populated (the BEM part), the lower right part is sparsely populated (the FEM part) and the off diagonal corners are zero. The form of this matrix allows the use of efficient matrix algorithms. The equations are integrated in time by explicit finite difference. The time step varies from T/24 to T/144 depending upon the degree of nonlinearity in the problem.

This formulation is well suited for the present application. It is reasonably efficient, but includes nonlinear terms at the free surface and in the rubble matrix. The formulation is less suitable for breaking waves, but the application of the model is intended for pipelines outside of the surf zone where breaking is less significant. The model can also be modified to include the influence of wave angle. In this paper, only waves which have crests parallel to the pipeline are considered. In practice, there are many cases where the wave crests are nearly perpendicular to the pipeline.

Physical Model Tests

Several pipeline stability tests have been conducted at the Oregon State University Wave Research Laboratory. Tests were conducted in the large wave flume which is 104m long, 3.7m wide, and 4.6m wide. Simple periodic, random, nonbreaking, and breaking wave conditions have been examined. The model is typically placed near the center of the flume at an orentation to simulate the prototype conditions. Figure 2 gave examples of three tested configurations. Incident and reflected waves are determined using a Goda wave gage arrary. The transmitted wave height and fluid velocities in the vicinity of the structure are also measured. The stability of the armor is monitored with underwater video. A variety of parameters are varied including the wave conditons, stone size, rubble geometery, and bouyancy of the pipeline.

Table 1 gives several predicted and measured results for the horizontal velocity. Laboratory results are for an 11.4 cm diameter pipe in 158 cm of water armored with 2cm stone. Two wave height conditions are given which differ by approximately a factor of 2; 25.3cm and 54.3cm. Figure 5 shows numerical model results for the horizontal velocity computed for these conditions. These two cases span a range from nearly linear to nonlinear wave conditions. In general, the agreement is reasonable; but as indicated by these examples, the variation can be as much as 30%.

Table 1 *Measured and computed horizontal velocities near a rubble covered pipeline.*

	Run A180101 H=25.3cm, T=3.65s, h=158cm		**Run A1830209** H=54.3cm, T=4.95s, h=158cm	
	Numerical	Measured	Numerical	Measured
U_{max}(cm/s) Offshore	28.0	28.5	109.5	83.2
U_{min}(cm/s) Offshore	-26.0	-25.4	-57.9	-51.8
U_{max} (cm/s) Above pipe	30.0	25.3	65.8	65.2
U_{min}(cm/s) Above pipe	-29.0	-21.3	-36.5	-35.4

Results

Figure 6 shows the horizontal and vertical forces for a fully buried pipeline and a partially exposed pipeline. The gap at the beginning of the runs is the time required for the waves to propagate from the generation boundary to the pipeline. Result are shown for time durations of 6 and 8 wave periods. The numerical computations remained stable beyond this time. The horizontal force is much less

than the vertical force and is approximately 90° out of phase for the fully buried case. For the partially exposed case, the horizontal force has increased slightly, but the vertical force has increased significantly. The phase difference between the two forces is approximately 60°. For the partially exposed case, there is an increase in the magnitude of the vertical force and the maximum horizontal and vertical forces are closer in phase. As a result, the partially exposed pipeline is much less stable.

Figure 7 shows the pressure field in the rubble around the pipeline and Figure 8 shows the porewater velocity. At this phase, the pressure gradient drives a flow in the direction of wave propagation. The resulting flow is accelerated around the pipeline and may be constricted beneath the pipeline if the clearance above the seabed is small.

The numerical model provides an opportunity to efficiently determine the sensitivity of the pipeline force to wave and rubble conditions. The base conditions for this sensitivity analysis are given in Table 2. First the wave height, period, and depth are considered. Figure 9 shows the dimensionless horizontal and vertical forces on the pipeline as a function of the wave height. The forces are scaled by the weight density of the water, the wave height, and the pipeline diameter. It is seen that this linear scaling captures the wave height dependency over a range of conditions. Figure 10 shows the influence of the wave period on the pipeline forces. There is an intermediate period for which the forces are a maximum. This period corresponds to a dimensionless water depth of $h/L \approx 1/6$ for this particular rubble geometry. The figure shows both the positive and negative forces. The horizontal forces are generally larger in the direction of wave propagation and this difference increases as the waves become more nonlinear. The upward vertical forces are larger than the downward forces. The influence of the water depth is shown in Figure 11 and is as anticipated, the deeper the water, the smaller the forces. The horizontal forces scale as approximately $1/h$ for these shallow to intermediate depth conditions.

Three rubble parameters are examined, the porosity of the rubble matrix, the stone diameter, and the depth of burial of the pipeline. Porosities from $\varepsilon = 0.24$ to 0.40 were examined and found to have little influence on the magnitude of the forces. The stone diameter also has very little influence on the forces on the pipeline. The influence of depth of burial is shown in Figure 12. The results indicate that the horizontal force is not strongly influenced by the depth of cover. The vertical force increases as the depth of cover decreases. The case with the center of the pipe at the top of the armor ($s / D_p = 0$) corresponds to half of the pipe being exposed. For this case the vertical force is much larger; nearly as large as the horizontal force. It was noted in Figure 6 that the phase of the maximum vertical force is closer to the maximum horizontal force which leads to a larger total force. The numerical model does not include friction or dissipation in the water

***Table 2** Base conditions f sensitivity analysis.*

H	1.0m
T	9.0s
h	8.0m
D_p	1.0m
D	0.25m
s	1.0m
ε	0.4
B	3.0m

column and these results may be suspect. However, the calculated value is in agreement with the trend of the covered pipeline cases.

Figure 13 shows the influence of the pipe diameter. The dimensionless horizontal force increases nearly linearly with the pipe diameter. Since the forces are calculated based on diffraction theory, this is an anticipated result. The vertical force also increases slightly with the pipeline diameter.

Conclusions

A nonlinear numerical model using BEM in the water column and FEM in the porous rubble has been developed. The numerical model results compared reasonably well with model test results and can adequately simulate the nonlinear interaction between waves and a pipeline covered with rubble protection. It was observed that the horizontal wave force is larger than the vertical force for all wave conditions and rubble configurations examined in this paper. The dimensionless wave forces on a buried pipeline generally decrease as the depth increases. However, there is a wave period dependency that yields a maximum wave force corresponding to $h/L \approx 1/6$. The armor stone size and armor layer porosity have little influence on the magnitudes of the forces. The depth of pipeline burial has little influence on the magnitude of the horizontal force. However, the vertical force on a partially exposed pipeline is much larger than for a fully covered pipeline and is closer to being in phase with the horizontal force. As a result, the partially buried case is much less stable.

References

Bailey, S.B. (1992) ***Goleta Sewer Outfall Stability Tests***, Masters of Science Project, Ocean Engineering Program, Civil Engineering Department, Oregon State University, Corvallis, OR, 138 pp.

Freeman, P. (1994) ***South Bay Tunnel Outfall Stability Tests***, Masters of Science Project, Ocean Engineering Program, Civil Engineering Department, Oregon State University, Corvallis, OR, 177 pp.

Mizutani, M., W.G. McDougal, and A.M. Mostafa (1996) BEM-FEM analysis of nonlinear interaction between wave and submerged breakwater, ***Proceedings of ICCE***, Orlando, Florida, 2377-2390.

Ohyama, T. and K. Nadaoka (1991) Development of a numerical wave tank for analysis of non-linear and irregular wave field, ***Fluid Dynamics Research***, 8:231-251.

Mizutani, N., A. Mostafa and K. Iwata (1998) Nonlinear regular wave, submerged breakwater and seabed dynamic interaction, ***Coastal Engineering***, 33:177-202.

Ruggiero, P. (1993) ***Point Loma Sewer Outfall Stability Tests***, Masters of Science Project, Ocean Engineering Program, Civil Engineering Department, Oregon State University, Corvallis, OR, 177 pp.

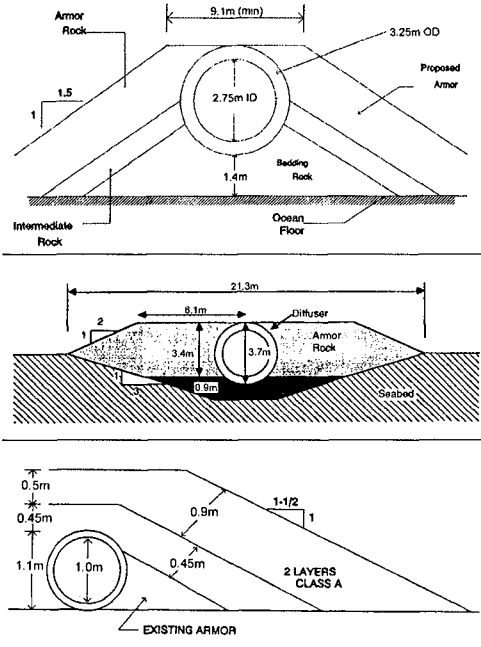

Point Loma Outfall
$H = 8.5$m, $h = 70$m
$L_p = 3{,}350$m, $D_p = 3.25$m
$D = 1.1$m
(*after* Ruggiero, 1993)

South Bay Tunnel Outfall
$H = 18.4$m, $h = 28$m
$L_p = 6{,}100$m, $D_p = 3.7$m
$D = 0.7$m
(*after* Freeman, 1994)

Goleta Outfall
$H = 3.7$m, $h = 26$m
$L_p = 1{,}770$m, $D_p = 1.1$m
$D = 0.39$m
(*after* Bailey, 1992)

Figure 1 *Examples of pipeline stability tests.*

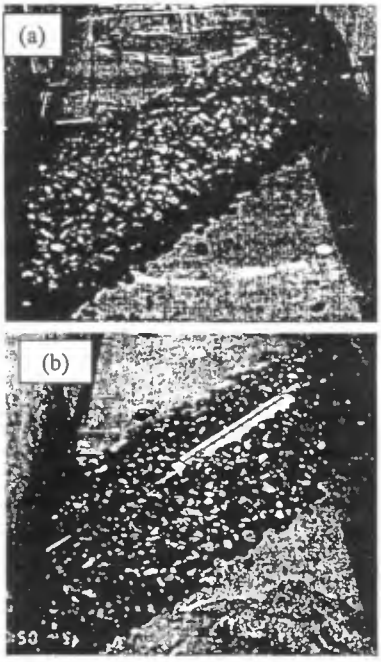

Figure 2 Examples of (a) fully covered, (b) partially covered, and (c) fully exposed pipelines.

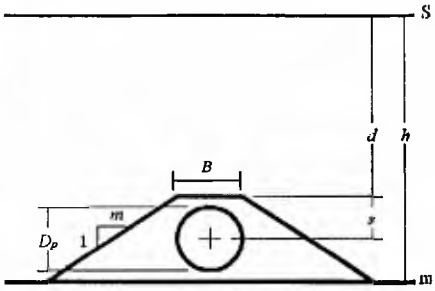

Figure 3 Definition sketch.

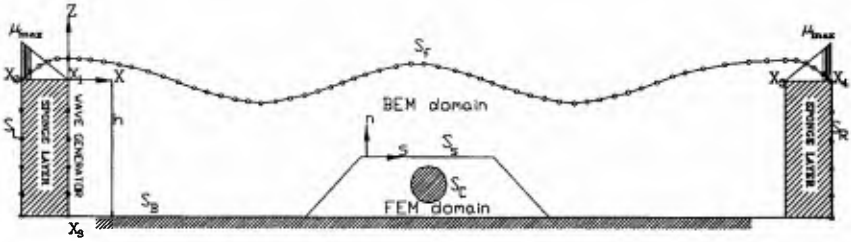

Figure 4 Model domain.

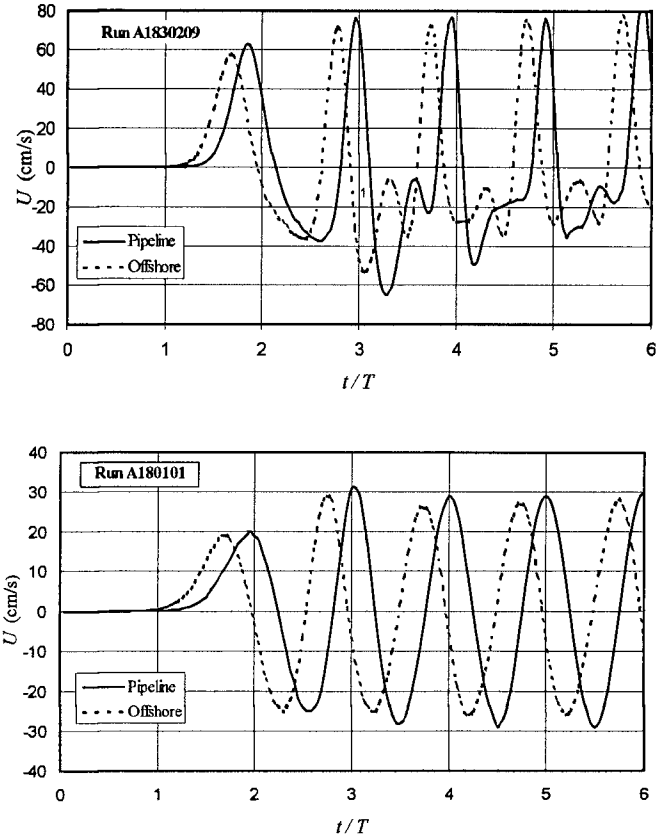

Figure 5 Computed horizontal velocities for two physical model cases.

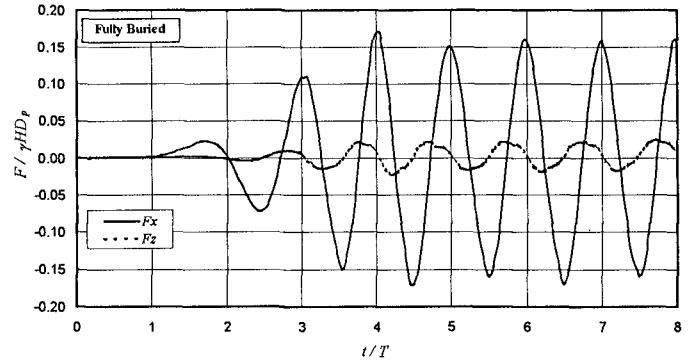

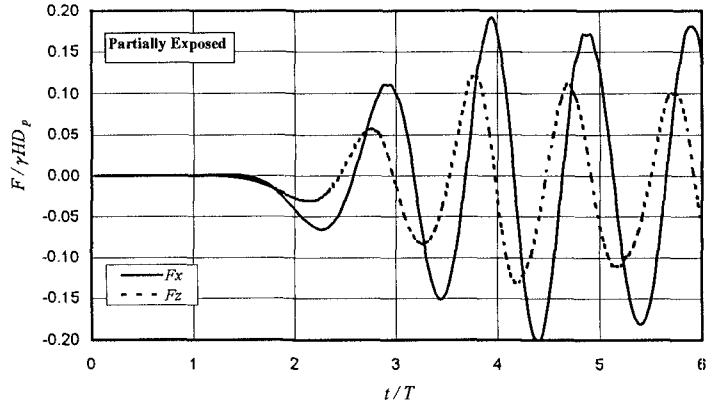

Figure 6 Time history of wave forces acting a fully buried and a partially exposed pipeline.

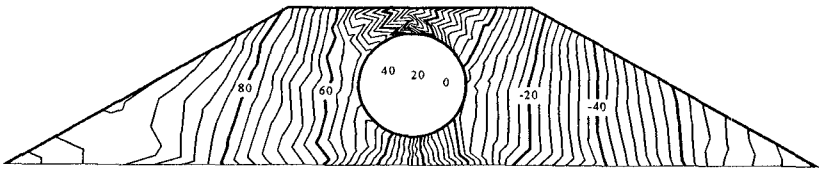

Figure 7 *Pore pressure around a fully buried pipeline at t/T=6.0.*

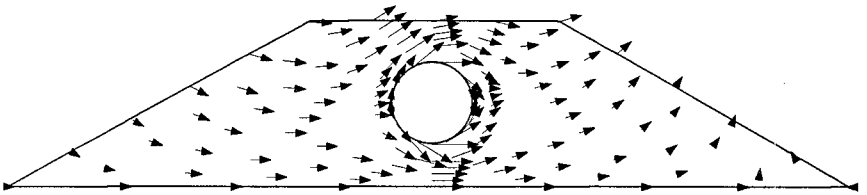

Figure 8 *Porewater velocity around a fully buried pipeline at t/T=6.0.*

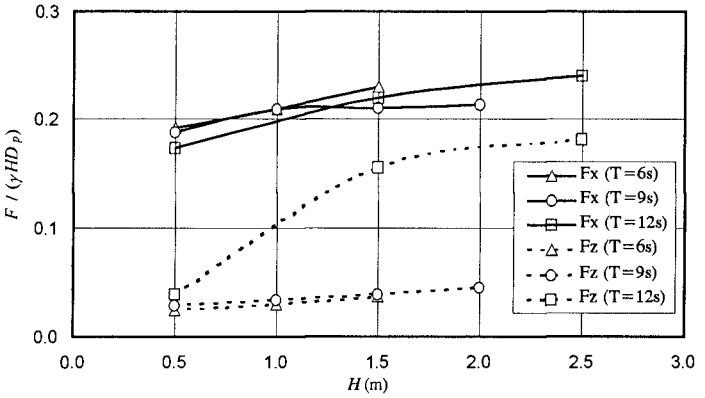

Figure 9 *Influence of wave height on dimensionless force.*

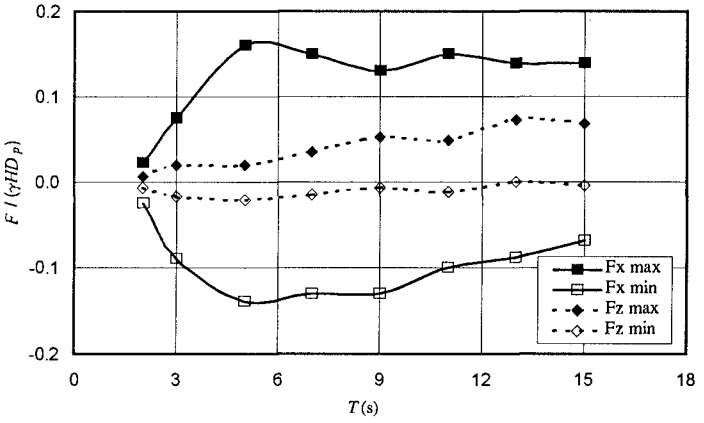

Figure 10 *Influence of wave period on dimensionless force.*

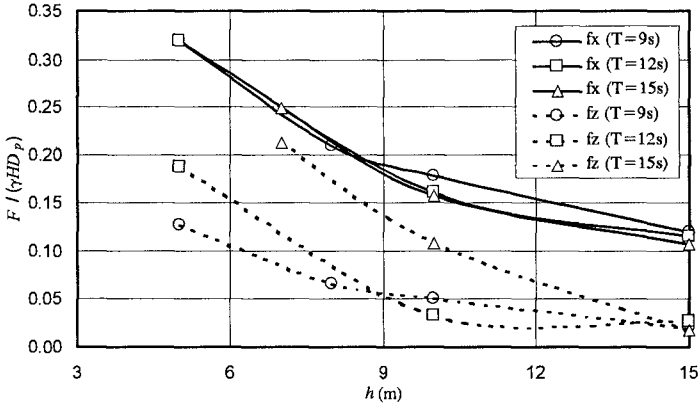

Figure 11 *Influence of water depth on dimensionless force.*

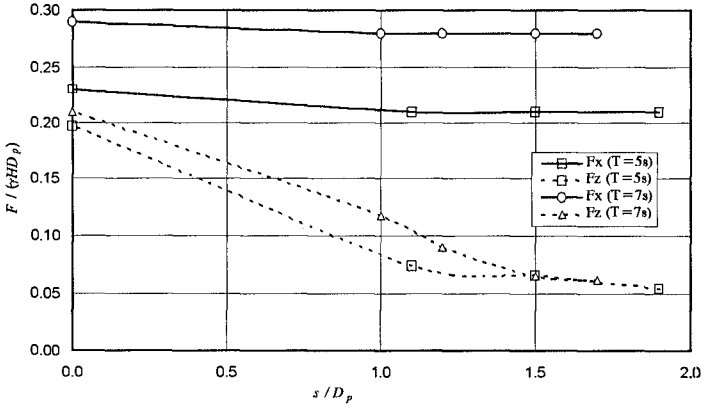

Figure 12 *Influence of burial depth on dimensionless force.*

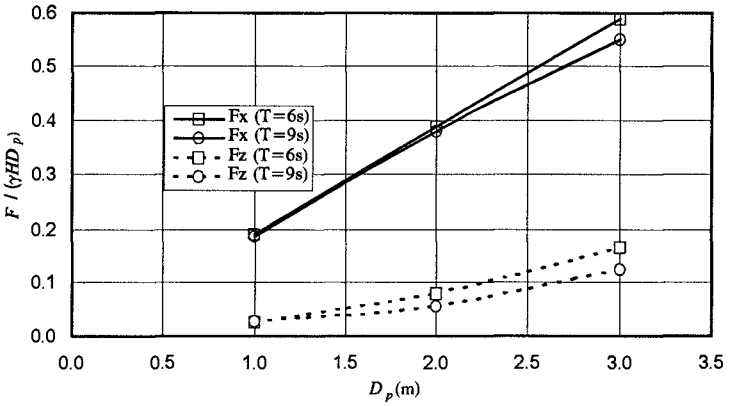

Figure 13 *Influence of pipe diameter on dimensionless force.*

SEA LEVEL SET-UP BEHIND DETACHED BREAKWATERS

J. H Loveless[1] , D. Debski[2] & A B MacLeod[3]

ABSTRACT

This paper reports some of the results of a theoretical and experimental study of submerged, detached, segmented, trapezoidal rubble mound breakwaters. It focuses on the phenomenon of sea level set-up which occurs at these structures. A theoretical analysis is presented which gives an explanation for the occurrence of set-up and the experimental results so far confirm the proposed relationship, which is given by Equation 4. Various other checks are presented in the paper, such as a demonstration that the set-up can be eliminated by pumping out from behind the breakwater and the measurement of a net drift velocity offshore in the core of the breakwater.

INTRODUCTION

Any detached breakwater where the waves are able to pass over or through the structure will experience a rise in the mean sea level on the shoreward side. This "set-up" can have a significant effect on the performance of the structure, but it has been very little researched and is still not well understood. It is created because the wave inflow or overflow is greater than the backwash. The means of restoring equilibrium to the situation is either for the sea level to rise behind the breakwater in order to create more backflow or for a transverse current behind the breakwater to be created, if this is possible.

The results of our research into this set-up have shown, so far, that the magnitude of the set up is a maximum when the freeboard, R_c is zero i.e. when the breakwater's crest is at mean sea level. However we have not yet tested any impermeable breakwaters and these will exhibit slightly different behaviour displacing the maximum set-up position.

[1]Senior Lecturer & [3]Research Assistant, Department of Civil Engineering, University of Bristol, Bristol BS8 1TR, United Kingdom
[2]Engineer, Sir William Halcrow & Partners Ltd., Burdcrop Park, Swindon SN4 0QD, United Kingdom

Detached breakwaters are now widely accepted as one of the three main methods of protecting eroding coastlines; the other methods being groynes and shoreline armouring. Detached breakwaters have greatly increased in popularity in recent years and many papers on their design have been reported at recent coastal engineering conferences. Few if any of them have discussed the phenomenon of (breakwater created) set-up. Yet we believe that an understanding of this set-up and the other effects it produces is essential to the correct design of detached breakwater schemes. Furthermore, as designs of detached rubble mound breakwaters have evolved, designers have tried to use lower crested breakwaters. This is because since the cost of the breakwater system is proportional to the volume of rock per km. of coastline it probably follows that the cheapest rubble mound scheme will minimise the crest height and width and maximise the side slopes. Indeed the first author recommended nearly 12 years ago (Loveless 1986) "From the evidence available it can be argued that a crest level over one metre below the MHWS level would be sufficient for many cases of coast and beach protection.".

Unfortunately, the recent experience of researchers (Murphy 1996) (Van der Biezen 1998) and practising engineers (Browder et. al 1997) when investigating or designing low crested or submerged detached breakwaters, has been that they produce large longshore currents which can result in more beach erosion instead of less. Some of these researchers are now advising against the use of detached breakwaters altogether. It is our view however that these longshore currents are mainly due to the phenomenon of set-up. Once all the mechanisms governing the creation of set-up have been identified it will be possible to produce designs which minimise it and so eliminate its adverse consequences on beach erosion and minimise overtopping of the final sea defences.

This paper reports on a 2-D flume study of detached trapezoidal rubble mound breakwaters which was carried out to investigate the nature of the set-up. In most detached breakwater schemes the potentially very large levels of set-up do not in fact occur because they are relieved by 3-D current circulations. However, in this study, a way of transferring the data obtained from the 2-D flume research was devised so that the advantages of control and increased scale offered by the 2-D flume research could be retained. The new technique enabled the applicability of these 2-D results to be extended very simply so that they could be used to predict the performance of the kind of 3-D installations common in the field. The method used was simply to install a pump behind the breakwater in the flume so that a relationship between the pumping rate and the reduction of set-up could be obtained. The paper also reports briefly on some 3-D experiments in the UK's National Coastal Research Facility at HR Wallingford.

A detailed report of the original research is obtainable from the Department of Civil Engineering at the University of Bristol (Debski & Loveless 1997) and a previous paper (Loveless & Debski 1997) presents the findings with respect to wave transmission which were found to be generally as predicted by earlier researchers.

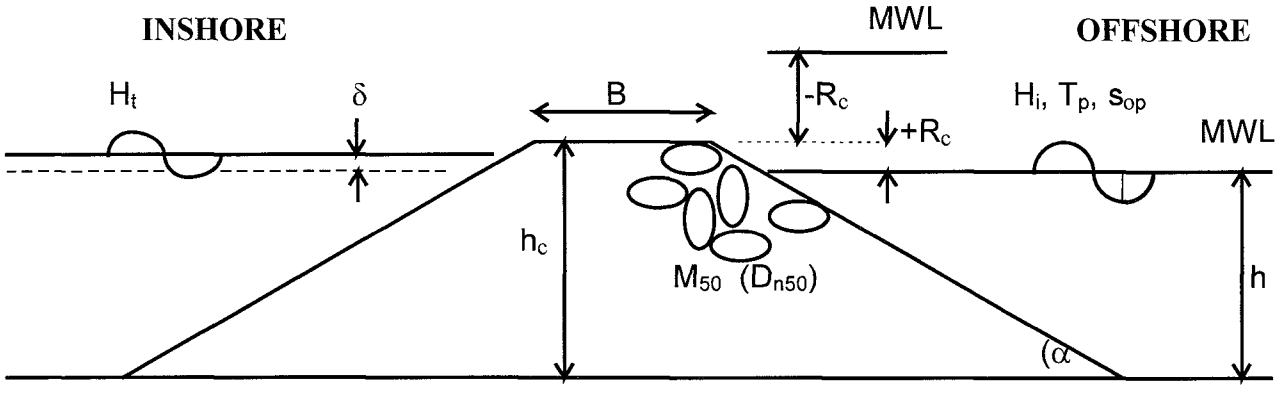

Variable	*Definition*	*Units*	*Variable*	*Definition*	*Units*
B	Breakwater crest width	m	H_i	Incident wave height (H, H_s, H_{rms})	m
R_c	Breakwater freeboard, - when $R_c<0$, referred to as the submergence of the breakwater	m	H_t	Transmitted wave height (H, H_s, H_{rms})	m
			H_r	Reflected wave height (H, H_s, H_{rms})	m
h_c	Breakwater crest height	m	H_s	Significant wave height	m
h	Water depth at offshore toe	m	H_{rms}	Root-mean-square wave height	m
α	Offshore slope angle	degrees	K_t	Transmission coefficient, $K_t=H_t/H_i$	-
M_{50}	50% value of rock mass distribution curve	kg	K_r	Reflection coefficient, $K_r=H_r/H_i$	-
ξ	Surf similarity number, $\xi=\tan\alpha/\sqrt{(2\pi H_i/gT^2)}$	-	T	Wave period (regular monochromatic waves)	s
δ	Inshore water level set-up	m	T_p	Peak wave energy period (wave spectra)	s
L	Local incident wavelength	m	s_{op}	Deep water wave steepness, $s_{op}=2\pi H_i/gT_p^2$	-

Figure 1 : Definition sketch and major variables for breakwater cross-section and analysis

PROBLEM DEFINITION

The problem studied in the research was the performance and design of submerged, detached, (trapezoidal) rubble mound breakwaters. A definition sketch, which also shows the major variables involved in the problem, is shown in Figure 1. The freeboard, R_c, which is a key variable in the problem, is negative when the crest is submerged.

The main purpose of a detached breakwater is to reduce the wave energy between it and the shoreline. The incident waves transfer quantities of water inshore over and through the breakwater. Since the waves inshore are smaller and the return flow resistance is generally greater, the return velocities over and through the breakwater are less than the inshore velocities and this results in a net transfer of water to the inshore zone at the breakwater. However, the shoreline behind the breakwater is usually relatively impermeable so there can be no net flux of water inshore. The excess flow must therefore be driven back offshore either through the breakwater (if it is permeable) or over the breakwater (if it is submerged) or around the ends of the breakwater (if it has gaps) or by a combination of these three flow paths. All three routes offer resistance to a flow of water and require a head difference to drive the flow. Therefore a rise in water level will occur inshore to maintain a zero net flux of water transfer in the near shore zone.

It can be shown that the volume of flow backwards and forwards in half wave period of a progressive wave is $HL/\pi T$. At a breakwater (or other bar like structure) there is greater resistance to the return flow than the overflow. Therefore there is a net inflow which must be balanced (in 2-D) by a set-up of the water surface behind the breakwater (or inshore of the bar).

If the resistance is dominantly turbulent (which it is for both bars and breakwaters) then the set-up, δ should be proportional to u_o^2, where u_o is the mean offshore set-up driven velocity. If h is the water depth then it follows that

$$\delta \quad \alpha \quad \left[\frac{H_i L}{hT}\right]^2 \qquad \text{Eq. 1}$$

and this was found to be true in the experimental results.

Because the resistance to flow is dramatically reduced when the breakwater is submerged it is also likely that the relative submergence R_c/h_c will be an important variable and since the resistance to flow within the breakwater is a function of D_{n50} the stone size (or permeability of the breakwater) will also affect the set-up.

If the set-up height is non-dimensionalised using the crest width, B we have a hydraulic gradient δ / B which is related to u_o by means of the Forcheimer equation.

Hence,

$$\frac{\delta}{B} = f\left[\left(\frac{H_i L}{hT}\right)^2, \frac{R_c}{h_c}, D_{n50}\right] \qquad \text{Eq. 2}$$

or alternatively

$$\frac{\delta}{B} = f\left[\frac{(H_i L/hT)^2}{8gD_{n50}}, \frac{R_c}{h_c}\right] \qquad \text{Eq. 3}$$

So far we have found that for our admittedly limited range of tests that

$$\frac{\delta}{B} = \frac{(H_i L/hT)^2}{8gD_{n50}} \cdot e^{-20(R_C/h_C)} \qquad \text{Eq. 4}$$

best describes the results.

DESCRIPTION OF THE 2-D MODELS

The experiments were performed in a large random wave flume, 15m long, 1.5m wide and 1.1m high with a 5m long, 0.5m wide test section. A total of six different model breakwater cross-sections were tested utilising three different sizes of carefully graded rock. A schematic layout of the flume showing the position of the breakwater models is shown in Figure 2 and a picture showing the three rock sizes used is presented in Figure 3. All the breakwaters were 500 mm high, but the crest widths varied from 200 to 600 mm. A range of wave and water level conditions were tested with incident waves ranging from 50 to 200 mm height and water depths being varied between 400 and 650 mm giving both submerged and emergent conditions. Both random and regular waves were tested.

As can be seen in Figure 2 a submersible pump was located behind the wave absorber at the end of the flume so that the set-up could be artificially lowered in order to simulate 3-D conditions and investigate the nature of set-up.

RESULTS FOR SET-UP IN 2-D MODELS

An example of the results obtained is given in Figure 4 where the set-up for one of the breakwater models is plotted against the incident wave height for various water levels. The set-up was found to be a maximum when the water level is just below the crest of the breakwater.

As can be seen from Figure 4 when $R_c = 0$, the set up is greatest. For a regular wave of height 3.0 m the maximum (unrelieved) set-up was found to be 1.0 m. The results for random waves were found to given equivalent amounts of set up provided that the mean wave height rather than the significant wave height was used. Figure 5 shows

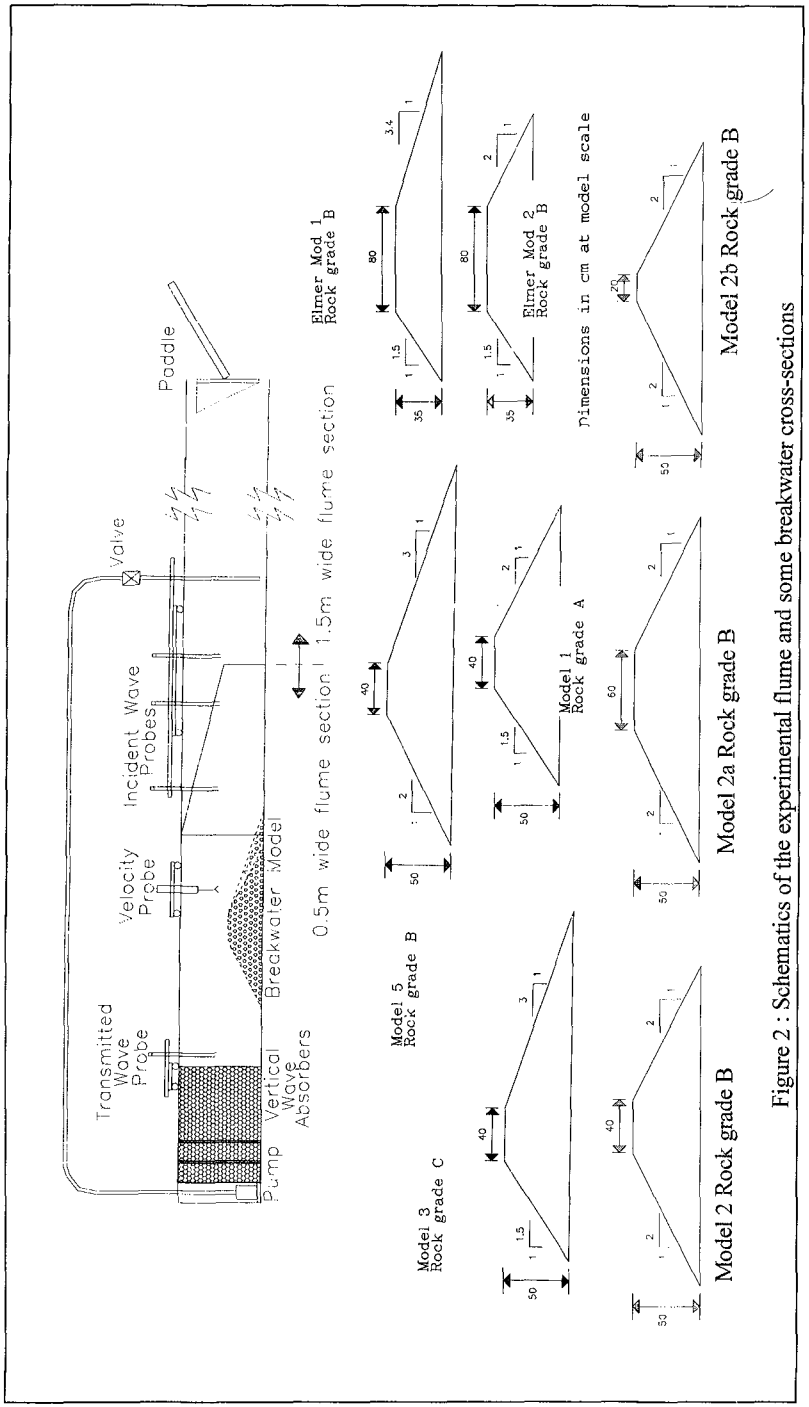

Figure 2 : Schematics of the experimental flume and some breakwater cross-sections

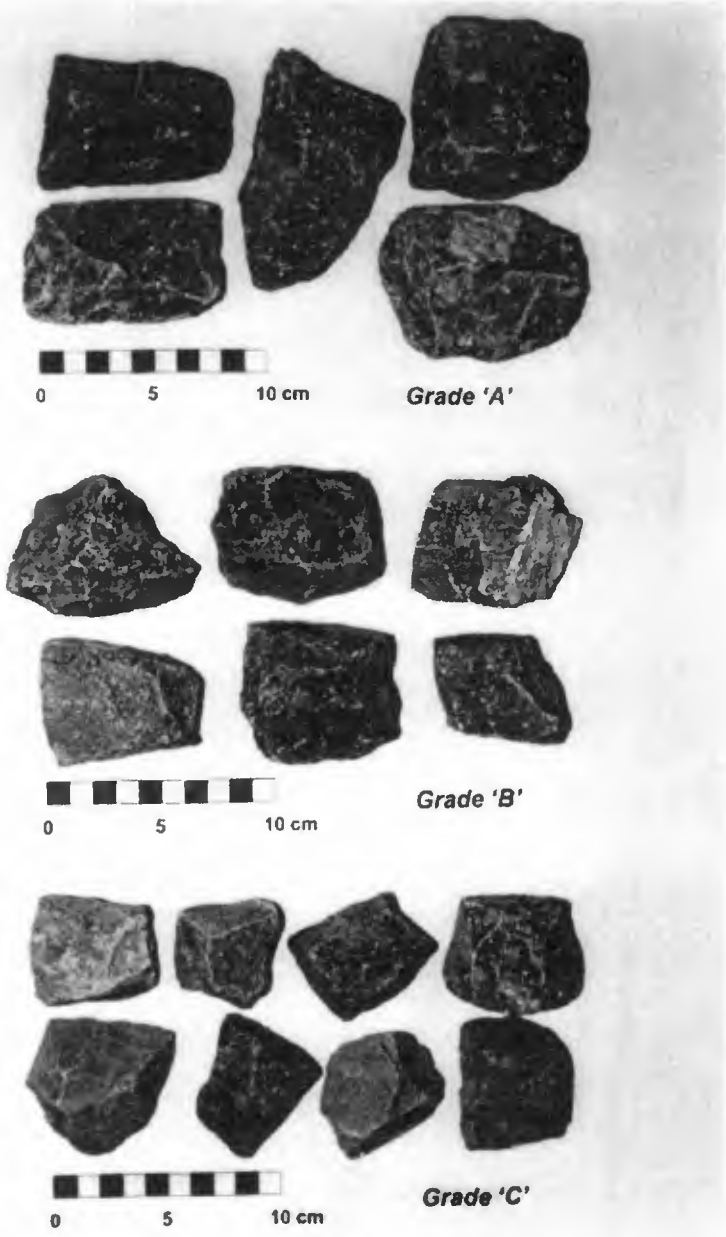

Figure 3 : The three grades of rocks used in the breakwater models

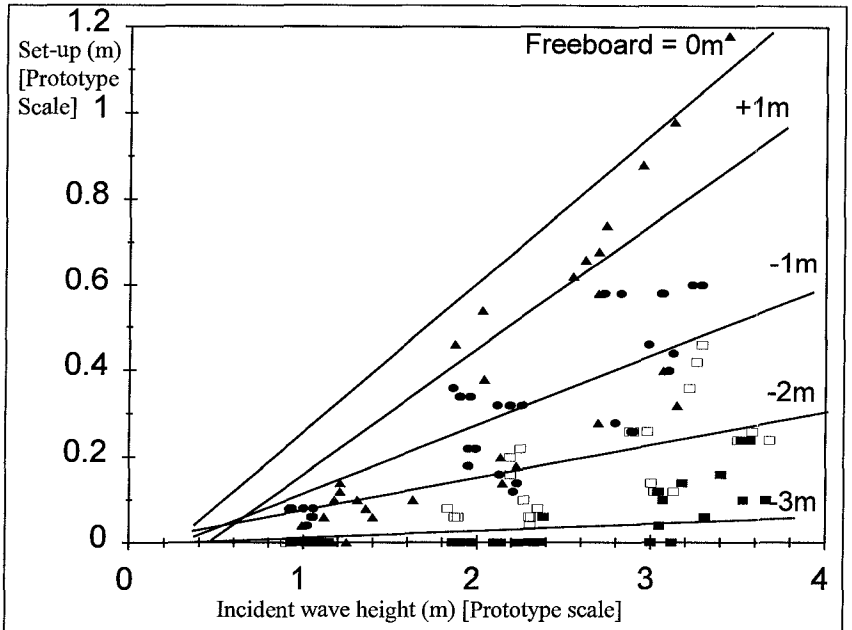

Figure 4 : Set-up inshore of breakwater at prototype scale (averaged for three different models: 2; 2a; 2b for T = 11.2s)

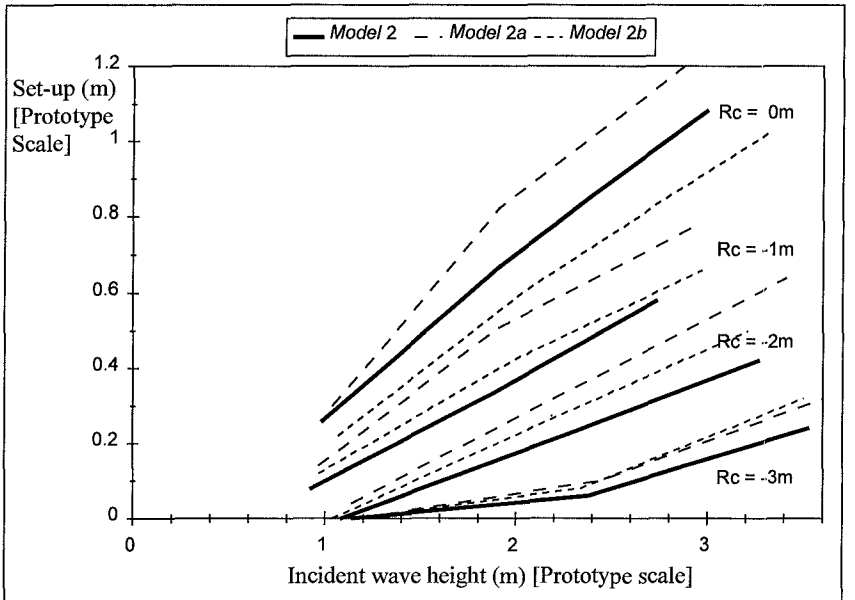

Figure 5 : Set-up inshore of breakwater at prototype scale for T = 11.2s (Models 2, 2a, 2b shown separately)

how set-up is affected by the crest width. Model 2b has the narrowest crest and 2a has the widest. It can be seen that set-up generally increases with crest width.

The only previous study of set-up at a trapezoidal rubble mound breakwater was that of (Diskin 1970). However, the results of our experiments, which are shown against Diskin's curve on Figure 6 gave much lower results. This was attributed to the fact that we had used a larger stone size in our tests. From all the results we have obtained so far the best fit curve is that given by Equation 4 which, as explained earlier, also has a firm theoretical basis.

PUMPING TESTS AND VELOCITIES

Besides the measurement of set-up the research in the 2-D flume provided accurate data on the quantity of flow necessary to suppress it. Thus, by reference to Figure 7, it may be seen that, with model 5, a set-up of 0.5 m could be reduced to zero with a rate of pumping of 1.8 $m^3/s/m$ width of breakwater.

Velocities both within and around the model breakwaters were measured using an ADV velocity probe. Figure 8 shows an example of the net velocity vectors obtained. From this figure it is possible to identify clearly both the circulation cell just beyond the crest of the breakwater and the presence of a horizontal jet in front of the breakwater. Figure 9 shows the velocity vectors at the four key points of the wave cycle and clearly shows that the velocities within the core of the breakwater are subject to a net drift velocity offshore due to the set-up. In fact the magnitude of the drift velocity in the core of the various breakwaters was found to be as predicted by the Forcheimer equation and this result is shown in Figure 10.

SET-UP IN 3-D

All these flume measurements of set-up are those that would occur where it is not possible to relieve the very large rises in mean sea level by transverse currents or some other means. i.e. the pure 2-D situation. In 3-D the set-up is frequently dissipated by being converted into strong transverse currents so that, in many 3-D configurations, only a very small amount will occur. Nevertheless all the set-up drivers are still present and when converted into these strong currents may result in beach erosion and scour at the ends of the breakwaters. These unwanted results, as mentioned earlier, have been reported by a number of researchers and practitioners. We have also observed them in our own 3-D studies in the UK's National Coastal Research Facility. Figure 11 shows that the maximum set-up that we measured in one test was only 70mm (prototype scale) ,but the current measurements taken indicated, as expected, strong transverse flows. It is our view though that they can be eliminated once appropriate remedial action has been taken by the more appropriate design of submerged breakwaters.

CONCLUSIONS

We believe that coastal engineers in their search for cheaper forms of coastal defence will increasingly seek to deploy segmented detached trapezoidal rubble mound breakwaters with lowered crest elevations.

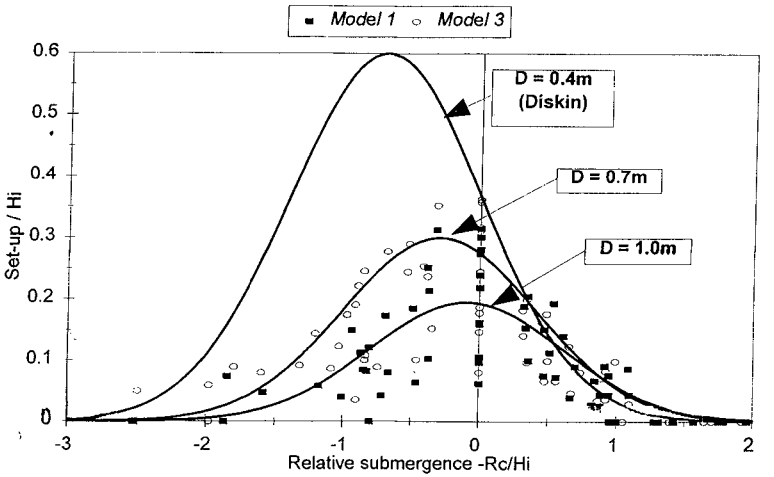

Figure 6 Diskin's curve for set-up compared to the new results

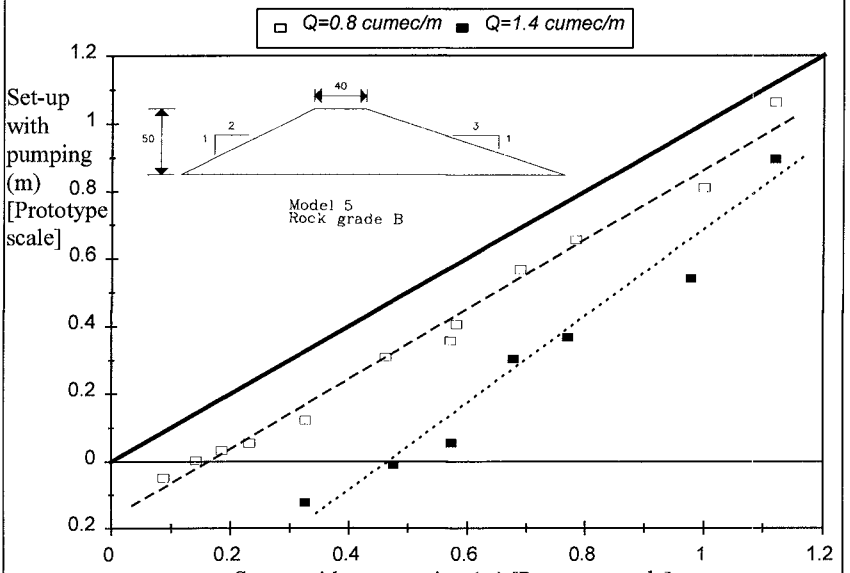

Figure 7 Reduction in set-up by pumping for Model 5 : R_c = 0m

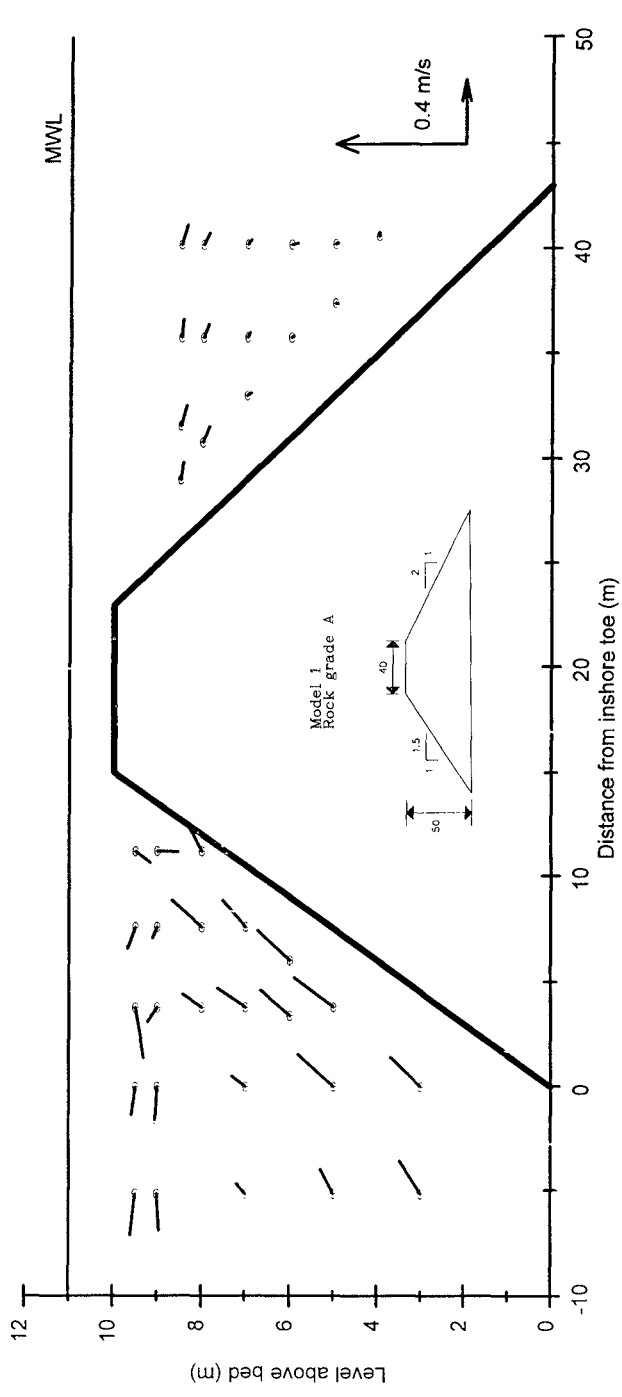

Figure 8 : Net velocity vectors for Model 1, T=6.4s, H_i=2.0m, R_c=-1m (K_t=0.55, δ=0.22m)

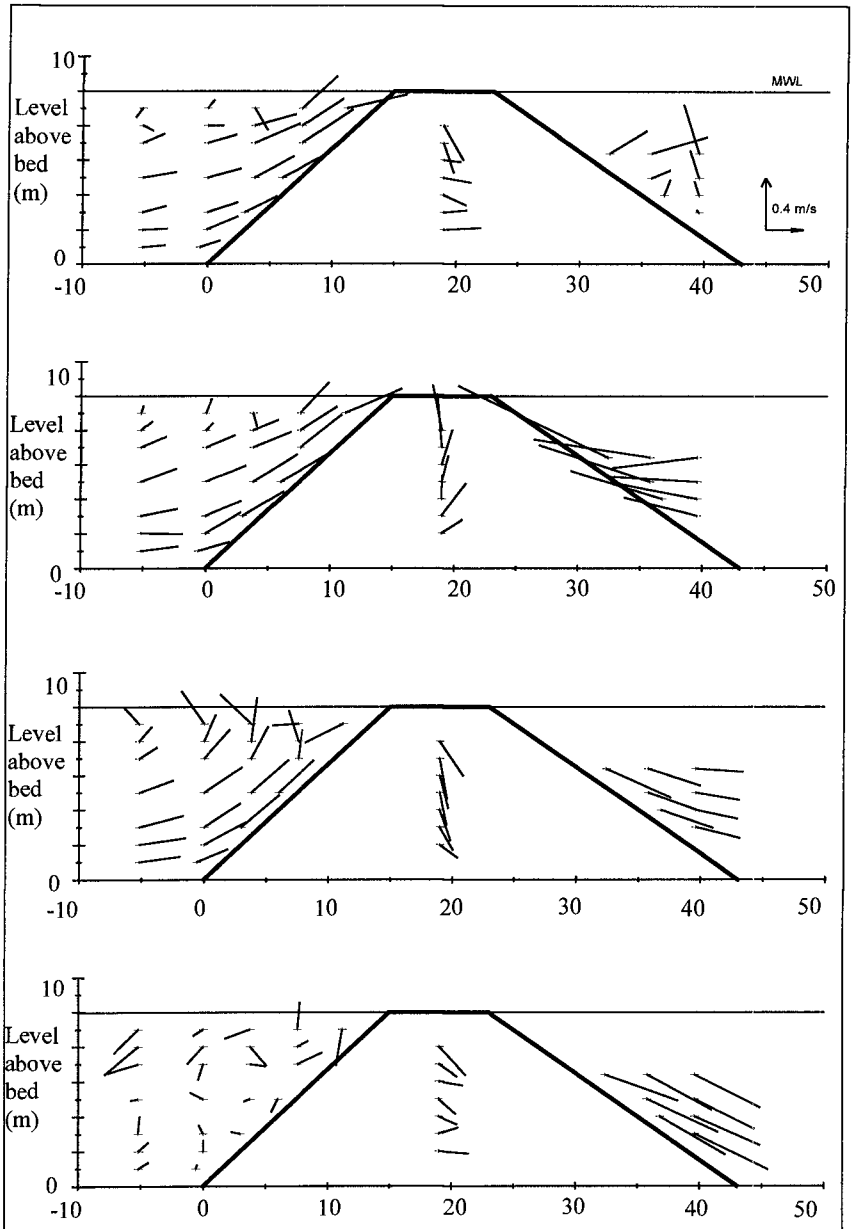

Figure 9 Velocity vectors at t=0, T/4, T/2, 3T/4 for Model 1, T=11.2s, Hi=3.2m, Rc=0m (Kt=0.45, δ=0.96m), Rock grade A

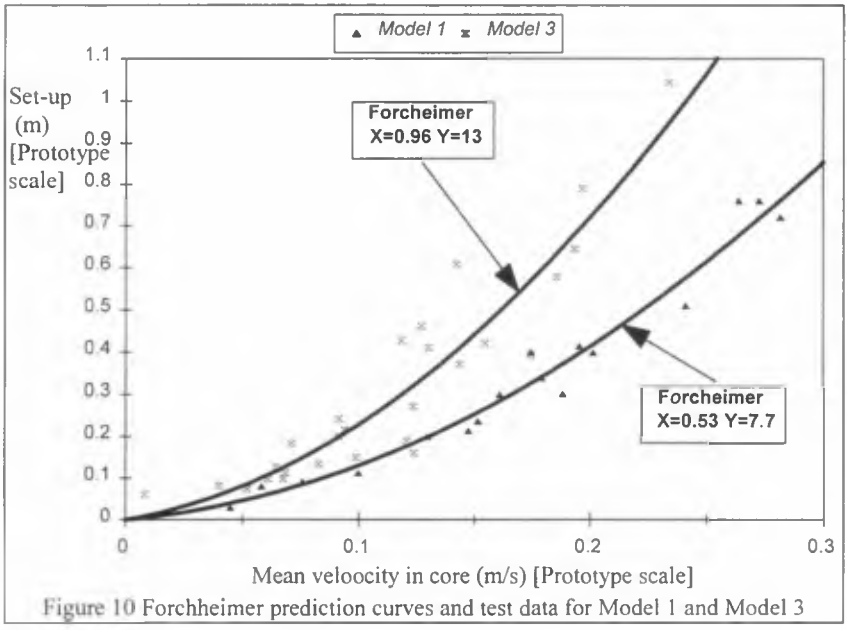

Figure 10 Forchheimer prediction curves and test data for Model 1 and Model 3

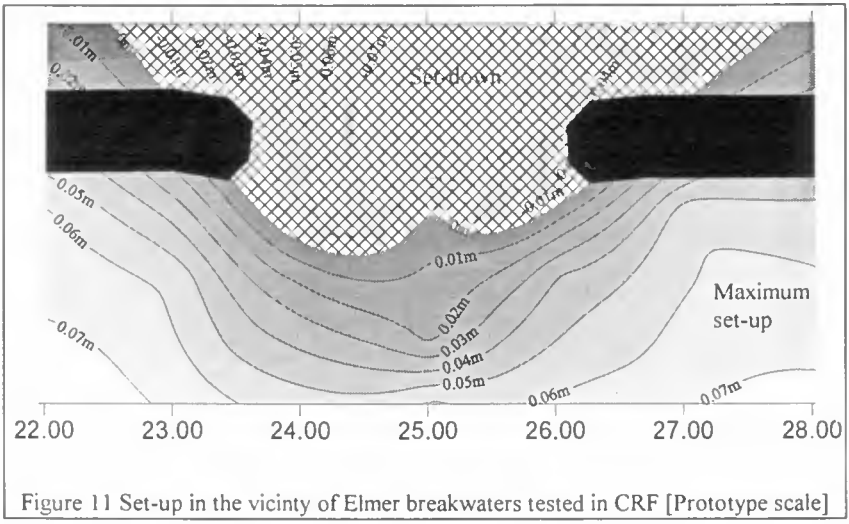

Figure 11 Set-up in the vicinty of Elmer breakwaters tested in CRF [Prototype scale]

In this paper we have shown that these designs are subject to the phenomenon of set-up of the sea level inshore and we have gone a long way towards defining exactly how this set-up is created.

In breakwater configurations where transverse currents are constricted or prevented the set-up can be very large. In most 3-D configurations however it is not readily observable, but the forcing elements are still present and they create instead strong currents which are capable of eroding the beach.

Further research, it is confidently expected, will lead to improved designs which will minimise these unwanted effects and make the use of detached breakwaters still more advantageous.

ACKNOWLEDGMENTS

This work was carried out under a Research and Development contract for the UK Ministry of Agriculture Fisheries and Food, Flood and Coastal Defence Division.

REFERENCES

Van der Biezen, S et al. "2DH numerical modelling of the effects of submerged breakwaters on nearshore morphology." 26th Intl. Conf. on Coastal Engineering. Book of Abstracts. 1998. p.148.

Browder, A E et al. "Performance of a submerged breakwater for shore protection." 25th Intl. Conf. on Coastal Engineering 1997.

Debski, D & Loveless, J H. "The design and performance of submerged breakwaters." University of Bristol. Research Report. 1997.

Diskin, M H et al. "Piling-up behind low and submerged permeable breakwaters." Journal, Waterways & Harbours Division, ASCE. 1970.

Loveless, J H. "Offshore breakwaters: Some new design considerations". Vol 40 No. 6. (JIWES) Journ. Inst. of Water Engnrs. & Scientists. Dec. 1986.

Loveless, J H & Debski, D. "Wave transmission and set-up at detached breakwaters." Coastal Dynamics. Plymouth 1997 ASCE.

Murphy, J et al. "Submerged breakwater research in the EU human capital and mobility programme." 31st MAFF Conference of River and Coastal Engineers. July 1996, Keele. UK.

Coastal Erosion Caused by Construction of an Artificial Island and Performance of Beach Nourishment

Ryuichiro Nishi[1], Takaaki Uda[2], Michio Sato[1],
Masakazu Wakita[3], Yasuro Ohtani[4] and Takahiro Horiguchi[4]

ABSTRACT

It is well known that the littoral drift carries much sand into a sheltered area caused by the presence of coastal structures such as detached breakwaters. As a result, the shoreline in the sheltered area advances, whereas the shoreline of the neighboring coast recedes to balance a sand budget of the coast. An artificial island for storage of crude oil was constructed off the Kashiwabara coast, Shibushi, Kagoshima Prefecture, Japan since 1985. The island has a rectangular shape roughly 1.5 km long and 1.5 km wide. This paper describes coastal processes related to the construction of the artificial island, and proposes a new dredging and beach fill scheme including a groin to decrease the coastal erosion due to the sheltering effect by the artificial island.

INTRODUCTION

When coastal structures such as detached breakwaters and artificial reefs are constructed, sheltered areas are created. The littoral drift carries much sand into these sheltered areas. As a result, the shoreline in the sheltered area advances, whereas the shoreline of the neighboring coast recedes. The sand from the neighboring shoreline becomes the sediment source for the sheltered area. A plan view of the shoreline configuration changes significantly after the construction of sheltering coastal structures in a nearshore region. These kinds of engineering issues in Japan are documented by Uda (1997) in detail. To overcome this problem, it is proposed that a single groin should be set at the boundary of the sheltered and non-sheltered beaches to block the excess longshore sediment transport into the sheltered area. This scheme will also ideally prevent additional coastal erosion along the non-sheltered beach.

An artificial island for storage of crude oil was constructed off the Kashiwabara coast, Shibushi, Kagoshima Prefecture, Japan since 1985 (see Figure 1). The construction of outer facility of the island was completed in 1987 and then the island was reclaimed by dredged material from the nearshore area in front of the island. The island has a rectangular shape roughly 1.5 km long, 1.5 km wide, and the size of

[1] Dept. of Ocean Civil Engineering, Kagoshima University, 1-21-40 Korimoto, Kagoshimashi-shi Japan 890 Tel. (Fax. ditto.) +81-99-285-8483, Email: sediment@oce.eng.kagsohima-u.ac.jp

[2] River Department, PWRI, Ministry of Construction, Asahi 1, Tsukuba 305, Japan

[3] Dept. of Civil Engineering, Kagoshima Prefectural Government Office, Kamoike, Kagoshima-shi, Japan

[4] Coastal Environment Division, INA Co., Ltd., 1-44-10 Sekiguchi, Bunkyoku, Tokyo, Japan

the island is 192 ha. The length of the island is nearly eighteen times longer than the wave length of mean energy wave and 3.8 times longer than the observed longest significant wave length, respectively in this area of the Pacific Ocean. The refraction and diffraction patterns are modified by the shape of the borrow site for reclamation and the presence of the island to cause an uneven wave height distribution along the shoreline. Because of its size, this artificial island generated a large sheltered area as shown in Photograph 1 and caused significant beach and dune erosion on the neighboring coasts. Thus, monitoring projects in terms of a shoreline configuration, bathymetry, dune and beach scarp, and incident wave climate have been conducted since the construction of the island at the Kashiwabara coast. This study aims at the investigation of coastal processes related to the construction of the artificial island and a beach nourishment scheme involving a single groin based mainly on the monitoring data.

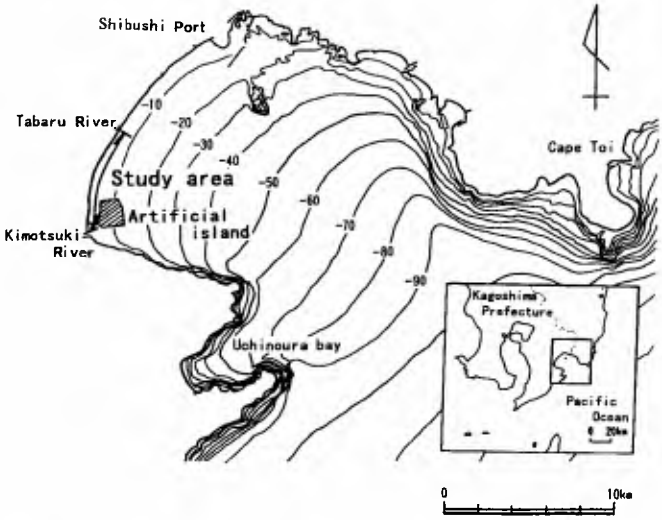

Figure 1 Location of study area.

Photograph 1. Aerial view of the artificial island.

SUMMARY OF STUDY AREA

Location of study area

The Kashiwabara coast is located on the south side of Shibushi Bay which opens to the southeast direction as shown in Figure 1. Shibushi Bay is 16.8 km long and faces to the Pacific Ocean. Shibushi Port and the artificial island lie on the northeast and southwest sides of the bay, respectively. The sandy beach extends nearly 14.2 km along the coast. Five rivers, i.e. Mae, Anraku, Hishida, Tabaru and Kimotsuki Rivers, run into the coast and supply the sediment to the beach. However, the length of each of these rivers is only 14.5, 27.1, 49.3, 14.7 and 34.0 km, respectively, therefore the sand discharge from the river mouths are probably minimal. For instance, the annual mean water discharge of the Kimotsuki River is only 35.12 m^3/sec. The Kimotsuki and Tabaru Rivers run into the southwest and northeast side of the study area, respectively.

Wave climate

The entire coast in the bay opens to southeast direction and both sides of the coast are surrounded by the capes as shown in Figure 1. Therefore, the incident wave direction is limited nearly to the southeast direction with some seasonal fluctuation. The incident wave conditions have been monitored by an ultrasonic type of wave gauge which is installed at the -35m water depth and located just off the Birou island. The monthly mean energy wave conditions is shown in Table 1, where as of the highest significant wave since 1980 are shown in Table 2. The incident angles are positive to clockwise from southeast. As can be seen in Table 1, the mean energy wave height during the winter season (December to February) is smaller than that in summer season (July to September). In addition, mean incident wave angle in June, July and August is slightly southward compared to that during the period from September to May, because the mean wind directions in winter and summer are from landward and seaward, respectively. Moreover, high waves generated by typhoons approach to the coast in the summer season.

Table 1. Mean energy wave conditions obtained at Birou wave station from Jan. 1992 to Dec. 1996. (h = -35m)

Month	$H_{1/3}$ (m)	$T_{1/3}$ (sec)	Angle (° SE=0)	Deviation (°)
Jan.	0.45	6.48	1.8	-1.54
Feb.	0.54	6.40	2.7	-0.64
March	0.70	6.99	2.6	-0.74
April	0.69	6.64	1.6	-1.74
May	0.77	6.87	-1.4	-4.74
June	0.68	6.65	5.5	2.16
July	1.01	7.40	8.8	5.46
Aug.	1.45	7.98	6.8	3.46
Sep.	1.17	8.24	2.4	-0.94
Oct.	0.92	8.14	2.5	-0.84
Nov.	0.90	8.30	2.7	-0.64
Dec.	0.53	7.17	4.1	0.76
Mean	0.89	7.29	3.34	

Table 2. The highest significant wave conditions

Date	$H_{1/3}$ (m)	$T_{1/3}$ (sec)	Climate
2:00 Sep. 11, 1980	7.39	13.1	Typhoon 8013
10:00 Oct. 22, 1981	3.73	14.0	Typhoon 8124
22:00 Aug. 26, 1982	7.88	12.3	Typhoon 8213
14:00 Aug. 14, 1983	3.65	12.8	Typhoon 8305
0:00 Aug. 19, 1984	3.54	9.9	Typhoon 8410
2:00 Aug. 31, 1985	4.70	12.1	Typhoon 8512,8513
0:00 Aug. 26, 1986	4.59	13.2	Typhoon 8613
0:00 Aug. 31, 1987	3.86	8.8	Typhoon 8712, Depression
18:00 June 2, 1988	2.64	7.5	Combined depression
18:00 July 27, 1989	4.28	13.1	Typhoon 8911
2:00 Sep. 18, 1990	7.48	13.8	Typhoon 9019
10:00 Sep. 23, 1991	5.91	11.9	Typhoon 9119
8:00 Aug. 8, 1992	4.99	11.3	Typhoon 9210
2:00 Aug. 10, 1993	8.30	12.8	Typhoon 9307
12:00 Aug. 13, 1994	6.52	12.2	Typhoon 9414
16:00 Sep. 16, 1995	5.24	15.9	Typhoon 9512
14:00 July 18, 1996	6.02	10.5	Typhoon 9606
14:00 July 18, 1997	7.17	13.1	Typhoon 9719

Characteristics of bed material

Sediment samples were taken from the beach face to the nearshore. A transect for the sediment sampling was set in the middle of the eroded coast where shoreline recession by the presence of island was the most significant. The median diameter of the sediment on a beach during the summer season is of the order of 0.5 mm and is larger than that during the winter season, whereas the median diameter in the shallow water area is of the order of 0.19 mm. The average density of sediment is nearly 2.55 g/cm^3 with a variation between 2.35 and 2.7 g/cm^3.

OVERVIEW OF THE COASTAL PROCESSES BY AERIAL PHOTOGRAPHS

Aerial photographs have been regularly taken at Kashiwabara Coast since 1984. An overview of coastal processes will be given first based on these photographs. Photograph 2 taken in 1984 shows the natural condition of the Kashiwabara coast before the construction of the island. The mouth of the Kimotsuki River and parallel jetties can be seen on the left side of photograph. The curved breaker line in front of the river mouth shows that there is a shallow water area. This river mouth terrace was generated by the sediment deposition discharged from the Kimotsuki River. In addition, the shorelines during a high and a low water levels are easily recognized as dry and wet beaches, respectively. The width of wet beach near the north jetty is narrow implying that the beach face is steep compared to the northern beach, because this area is highly depositional.

The outer facility of the island was completed in 1987. After that, a large tombolo was formed in the sheltered area by the refracted and diffracted waves. The major sediment source for the depositional features are neighboring northern sandy beach. The shoreline retreated nearly 80 m compared to the shoreline before the construction of island (in November 1984). The steepening and narrowing of beach face caused pronounced dune and beach scarps. The highest dune scarp attained to

Photo 2. Kashiwabara coast in natural condition (1984).

Photo 3. Plan view before the beach nourishment (Sept. 27, 1992).

Photo 4. Plan view after the beach nourishment (May 13, 1993).

Photo 5. Coastal damage after the first typhoon season (Feb. 16, 1994).

nearly 7 m at that time. To prevent further coastal erosion and shoreline recession, a beach nourishment project with single groin was carried out. Photograph 3 dated on May 27, 1992 is the situation just before the beach nourishment.

Photograph 4 shows the plan view just after the beach nourishment. The sand for the nourishment had been taken from two borrow sites between a groin and Hami fishery harbor. Therefore the sandy beach behind the island is somewhat uniform. The non-sheltered beach north to the groin was filled by the sand from the sheltered area, and thus the beach was widened nearly 80 m offshore. As a result, the shoreline configuration became more straight. In addition, a T-shaped single groin was installed between the sheltered and non-sheltered beaches to block the excess southern longshore sediment transport.

Photograph 5 shows the shoreline configuration of nourished beach just after one typhoon season. As seen in the photograph, the shoreline in the entire nourished beach receded and scarp generation had initiated. The profile adjustment after the beach nourishment is accelerated by two of the largest typhoon since 1980. It was observed that foot of scarp exists at an elevation of berm height at that time. So it is expected that the scarp generation can be avoided if the elevation of nourished beach is kept to be the natural berm height in the design.

LONGSHORE PROCESSES

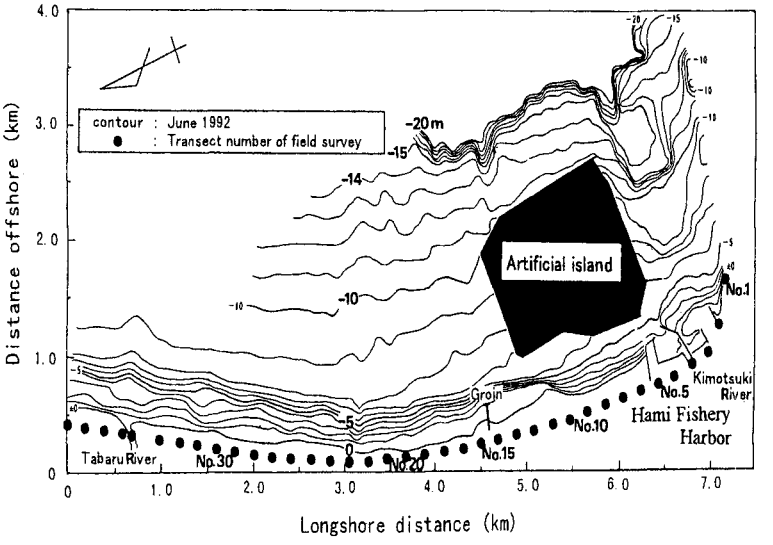

Figure 2. The orientation of coastal structures and transects.

The orientation of artificial island, groin, fishery harbor is shown in Figure 2. The incoming waves are refracted and diffracted by the island and tend to transport much sediment into the sheltered area located just behind the island. The bathymetry and shoreline data have been collected twice a year since 1984, and wave data is collected since 1980. The bathemetry survey covers the region from the southwest end of the bay, where the Kimotsuki River runs into, to beyond the Tabaru River.

The length of this study area extends to 7.5 km. The origin of the x-coordinate for a survey is set to the northeast end of the study area. The number of survey transects increases from the Kimotsuki River to the Tabaru River as shown in Figure 2. The borrow sites for the reclamation sand were in front of the island and te Kimotsuki River mouth.

Shoreline Change (Plan View) after the Construction of Artificial Island

Shoreline configurations of the Kashiwabara coast after the construction of artificial island are shown in Figure 3. The reference shoreline is set to be the shoreline in July 1985. As seen in the shoreline in June 1986, when an outlying facility of the artificial island was being constructed, the wave sheltering effect on the sandy beach had initiated especially in further south area than x = 4.3 km. It is clearly seen that sediment had been deposited in the sheltered area, and the shoreline configuration showed quasi-double-tombolo features. The peaks in the shoreline were located at x = 4.9 km and x = 6.3 km in June 1987. The migration of southern quasi-tombolo along a shore was blocked by an outer facility of the Hami fishery harbor, but the size of this depositional area had continued to grow. The sediment supply from the Kimotsuki River partially contributed to the generation of the south depositional feature. The north tombolo had shifted south along shore and the size of the tombolo had enlarged year by year.

Regarding the growth of the north tombolo, where significant amount of sand had been deposited, the offshore distance of peak of the tombolo had advanced from 40 m in June 1986 to 170 m in June 1992. The maximum shoreline advance in this period was 130 m, resulting the mean advance speed 21.7 m/yr of the shoreline. In addition, the peak of the tombolo was migrated from x = 4.75 km in 1986 to x = 5.25 km in 1992 to south direction, hence the tombolo had been shifted 500 m in this period. The mean migration speed was 83 m/yr after the construction of island. Once the tombolo generation was initiated by the diffracted waves in the sheltered area, the water depth at the tip of the tombolo was getting deeper according to its offshore growth. As a result, more diffracted waves with higher wave energy flux tend to act toward south direction in the sheltered area. Therefore, the peak of the tombolo migrated southwards while the size of tombolo was increasing in the sheltered area. As seen in the figure, the boundary of northern tombolo and southern quasi-tombolo had been also shifted 270 m to south with an annual mean speed of 45 m/yr. In accordance with the migration of tombolo behind the island, the boundary of depositional and erosional areas of this coast shifted 132 m toward the sheltered area.

The sandy beach in the sheltered area had widened, but the neighboring sandy beach in non-sheltered area had suffered severe coastal erosion after the construction of artificial island. As can be seen in the first and second rows of the figure, there is little shoreline recession in 1988 and 1989. The shoreline recession in non-sheltered area seems to be delayed two years compared to the quick shoreline advance in sheltered area. The shoreline started to retreat over 1360 m stretch from 1988, and then the total length of shoreline recession had become nearly 2.5 km by June 1992. The maximum shoreline recession was nearly 100 m at that time. The northern boundary of erosional area had shifted from x = 2.8 km to x = 1.8 km in June 1992, while the peak of erosion has shifted from x = 4.1 km to x = 3.2 km with an annual speed of 200-250 m/yr. The shoreline recession triggered the dune erosion and scarp generation as well. Because the shoreline is located closed to the upper beach face and dune face, the steeper the cross-shore profile, avalanching tends to occur on the steep slope to cause the scarp. Following the severe dune and beach erosion, a beach nourishment project with single groin had been carried out to prevent further coastal erosion. The project was completed in May 1993.

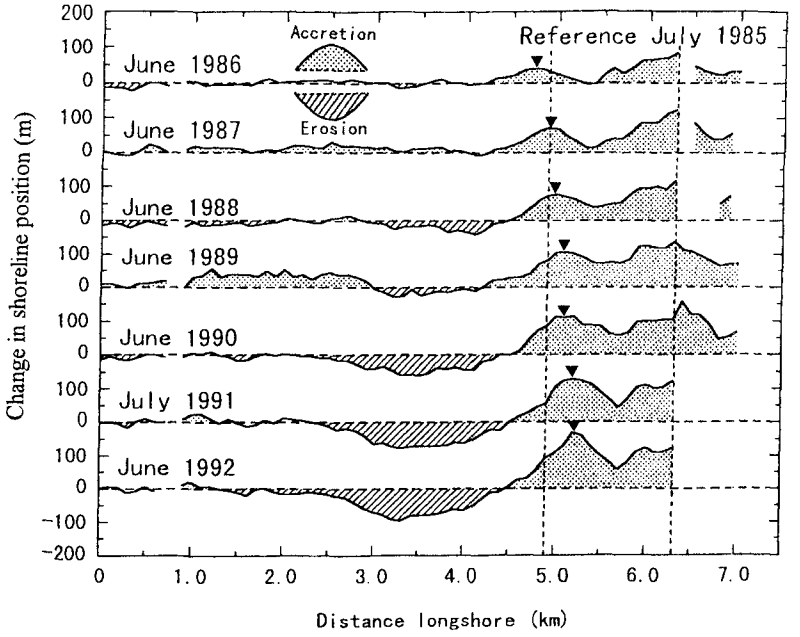

Figure 3. Shoreline change after the construction of the island.

Shoreline Change after the Beach Nourishment

A volume of 1.15 x 10^6 m^3 of sand was dredged from two borrow sites just behind the island and filled into the eroded beach. The two borrow sites for the beach nourishment were deployed between x = 5.3 km and x = 6.24 km, respectively. The shoreline changes after the beach nourishment is shown in Figure 4. The reference shoreline is set to be the shoreline in June 1992 when the nourishment project had conducted thereafter. As seen in the figure, the shoreline advanced in a region from x = 4.94 to 6.3 km (= 1.36 km extension) in June 1992. The maximum shoreline advance was 152 m at x = 5.34 km. On the other hand, the shoreline receded in the region from x = 1.43 to 4.75 km (= 3.32 km extension) with a convex plan view in June 1992 before the beach nourishment. This maximum shoreline retreat in November 1992 was nearly 80m at x = 3.74 km.

To prevent further erosion and property damage, sand was filled in the non-sheltered area in May, 1993 as shown by the shoreline in Nov. 1993. The nourished shoreline around x = 2.63 km was smoothly connected to the natural shoreline at x = 2.43 km. The shoreline was advanced 80 to 100 m in the eroded section of the beach by the beach nourishment.

A single T-shaped groin 230 m long was extended from the beach face to the water depth of -2.3 m at x = 4.6 km. The function of this groin is to block the excess longshore sediment transport into the sheltered area from the northern neighboring beach. In addition, beach and dune scarps were scraped by bulldozers to guarantee

safe accessibility and utilization of the beach. Then a mild-slope revetment with 200 m extension was installed at x = 3.5 km.

Following the beach fill project in May 1993, the largest typhoon since 1980 generated a maximum significant wave with $H_{1/3}$ = 8.3 m and $T_{1/3}$ = 12.8 sec period on August 10, 1993. Then unfortunately the third largest significant wave caused by Typhoon 9313 approached the shore with 7.72 m wave height and 11.2 sec wave period on September 3, 1993. As a result, the filled shoreline quickly receded nearly 50 m in the first six months just after the beach fill project as shown by solid line in Nov. 1993. Following this shoreline recession in the first six months, successive shoreline recession including a crescentic shoreline configuration between x = 3.27 km and x = 4.68 km occurred until 1995. In contrast, the shoreline in the non-sheltered area was advanced in Nov. 1996, because the Typhoon wave condition in this year was smaller than previous years. However, Typhoon 9713 which lasted three days (in terms of the significant wave height condition higher than 3.0 m) and Typhoon 9719 caused the shoreline recession in the entire region except the river mouth of the Tabaru River and the sheltered area. Finally, the shoreline configuration became as shown by the solid line in December 1997.

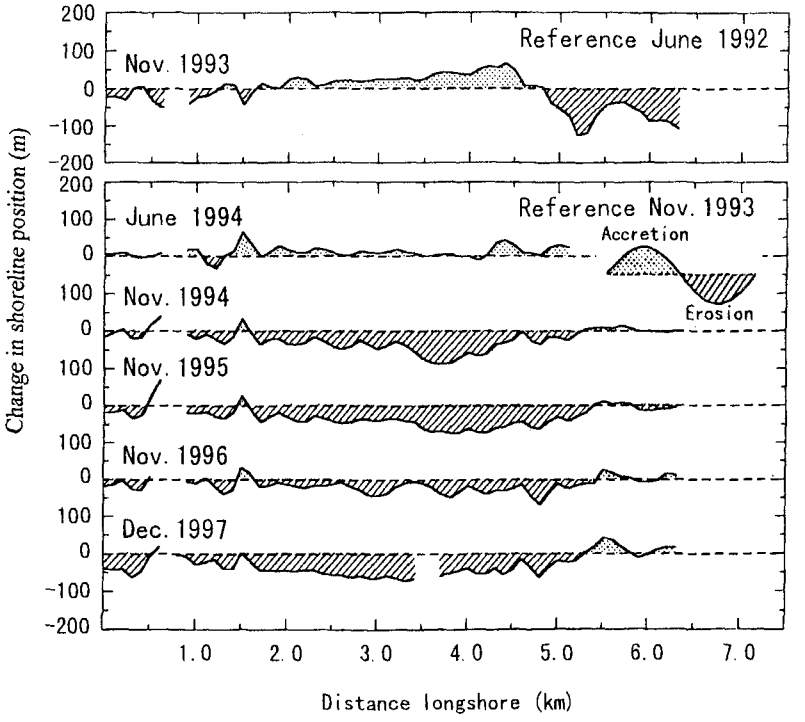

Figure 4. Shoreline change after the beach nourishment.

Figs. 5 (a), and (b) show the time series of shoreline position at representative transects. The mean shoreline changes at x = 5.34 km and x = 3.74 km were nearly +19.3 m/yr and -10.5 m/yr, respectively. In contrast, the shoreline

changes in the sheltered area after the beach nourishment show either small positive trend or stabilization.

The shoreline changes on the nourished beach were accelerated during the first 2.5 years after the nourishment due to attack of two of the three largest typhoons in the wave record in 1993 and profile adjustment relating to the overfill. For instance, an annual rate of shoreline change at transect x = 3.74 km was 60.2 m/yr. Following this period, the shoreline change seems to have stabilized or shows some positive trend except the shoreline position in Dec. 1997.

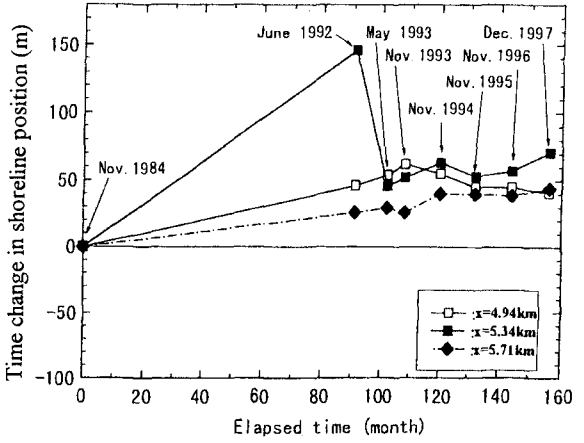

(a) Time change in shoreline position in the sheltered area.

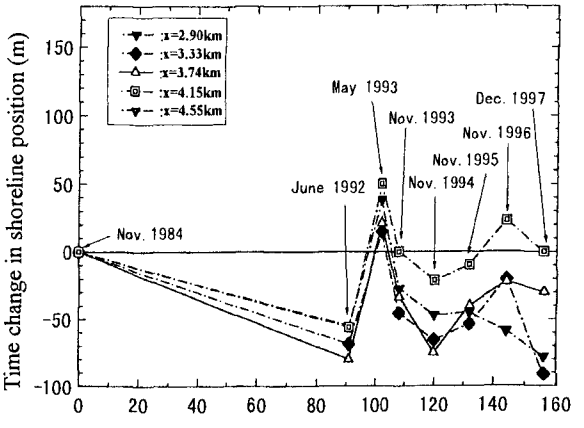

(b) Time change in shoreline position in the non-sheltered area.

Figure 5. Shoreline changes of each transect.

The inverse exponential behavior of the shoreline changes on the nourished beach (on non-sheltered beach) clearly means that a single groin installed between sheltered and non-sheltered beaches functions to block an excess longshore sediment transport into the sheltered area.

SAND BUDGET ALONG THE COAST

A time series of the change in sand volume over the entire Kashiwabara coast is shown in Figure 6. The change in sand volume along the shore is calculated by multiplying the cross-sectional change by the transect spacing. The volumetric change beyond the -9 m water depth was not taken into account for the estimation, since the sounding survey was conducted to this water depth. The profile analysis which will be shown later and the cross-shore distribution of sediment diameter show that the critical water depth for profile change in this study area is nearly -8 m. Therefore the change in sand volume in Figure 6 can be used as the first approximation. The change in total sand volume in the sheltered area x=4.55 to 6.30 km was nearly 600 x 10^3 m^3, thus the annual depositional rate in this area was 160 x 10^3 m^3/yr after the construction of the island (June 1986 to November 1990). On the other hand the change in total sand volume in the erosional area from x = 2.68 to 4.55 km was roughly 970 x 10^3 m^3. Thus, the annual erosional rate in this area was –220 x 10^3 m^3/yr.

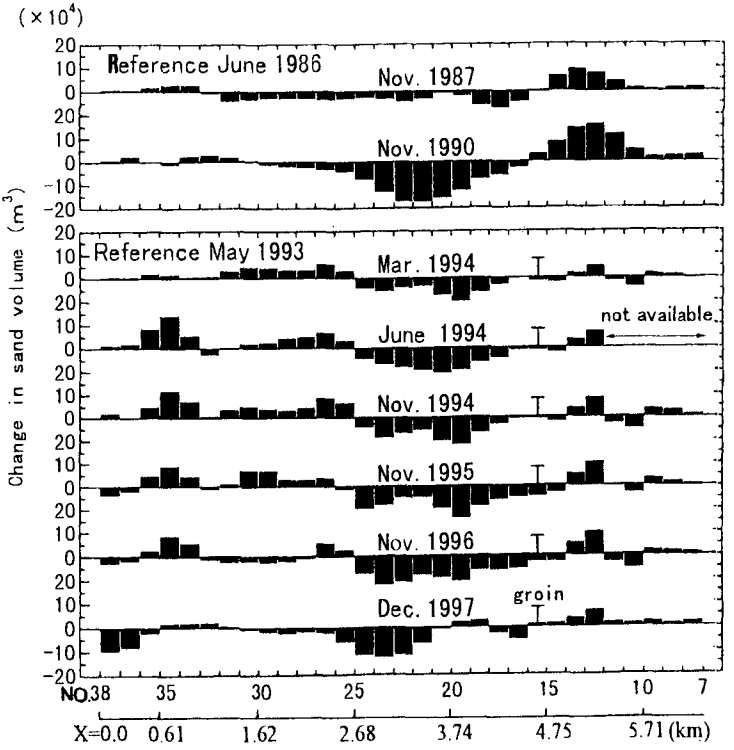

Figure 6. Change in sand volume in the study area.

The beach nourishment project with the single groin was completed in May 1993. The change in sand volume in the area from x = 4.75 to 5.71 km was +220 x 10^3 m^3 after the beach nourishment, and thus the annual depositional rate in this area is 50x10^3 m^3/yr. This means that the transmission rate of this groin for longshore sediment transport is estimated by comparison of depositional rate before and after the beach nourishment as follows;

$$P_{er} = \frac{50 \times 10^3 (m^3/yr)}{130 \times 10^3 (m^3/yr)} \times 100(\%) = 38\%$$

Volumetric change in the northern area from the groin after the beach nourishment was –830 x 10^3 m^3, thus the annual erosion volume was -200 x 10^3 m^3/yr.

CROSS-SHORE PROCESSES

The profile variations in space during the post-construction period, beach nourishment period, and post-nourishment period are examined here. Figure 7 shows the change in profile along shore from November 1984 to June 1992. The coordinate x = 4.94 km is located in the sheltered area and x = 3.53 km is located in the middle of erosional area. In addition, an entire profile at x = 3.53 km is lowered by more than 1.4 m.

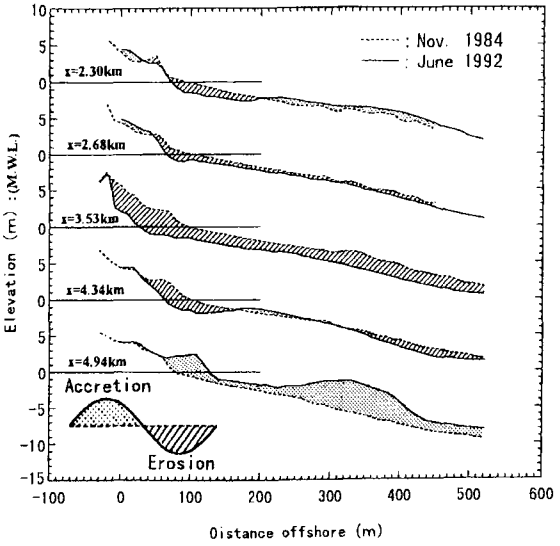

Figure 7. Profile change along the shore after the construction of the island.

Figure 8 shows the profile change along the coast before and after the beach nourishment. The nourished sand was filled from a landward boundary of erosional area to –4 m water depth. As can be seen in the figure, the profile was designed to have composite slopes. The beach slopes higher than 1m elevation are 1/25, 1/29, 1/27 and the offshore slopes are 1/60, 1/59 and 1/51 at x = 2.68, 3.53 and 4.34 km, respectively.

Figure 9 shows that the profile changes along the coast in the first typhoon season after the beach nourishment. Because two of the three largest typhoons since 1980

struck on the shore during this period, the nourished beach had been extensively damaged and scarp generation has commenced again. Typhoons 9307 and 9313 produced 8.3 m and 7.72 m significant wave height, respectively. The elevation of the scarp base is nearly 2 m along the shore.

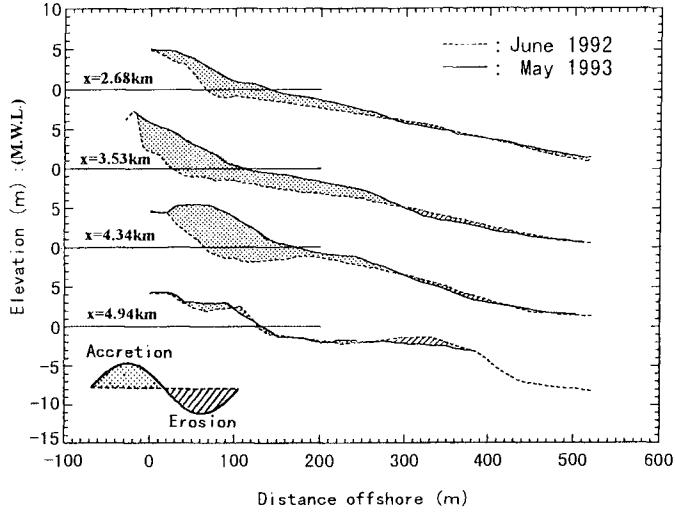

Figure 8. Profile change along the shore during the beach nourishment.

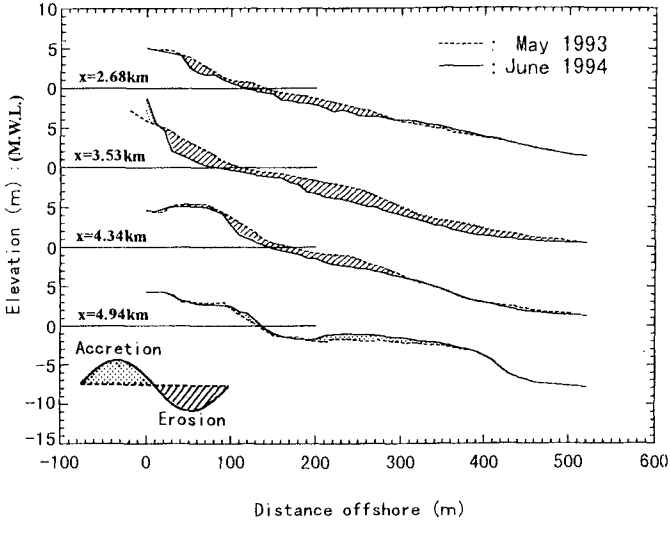

Figure 9. Profile change along the shore after the beach nourishment

CONCLUSIONS

Field observations were carried out to study the mechanism of coastal erosion due to the presence of artificial island, and to access the performance of new beach nourishment scheme as well as develop database for future numerical work. The main conclusions are as follows;

(1) A quasi-double-tombolo feature was generated by the sheltering effect of the artificial island at the Kashiwabara coast. The northern tombolo moved into the sheltered area with the speed of 75m/year due to the wave refraction and diffraction. Sediment was supplied from the northern neighboring coast. As a result, the neighboring coast eroded over a 2.0km stretch.

(2) A single groin, which was set between the sheltered and non-sheltered areas, decreased the southward longshore sediment transport. The transmission rate of the groin is estimated to be 38% in terms of annual transport rate. Despite rapid shoreline recession due to profile adjustment and severe typhoon conditions during the first 2.5-year period after the beach nourishment, shoreline position tends to be stabilized or slightly progressed in the last few years. It can be concluded that the nourished beach close to the groin tends to be partially stabilized.

(3) Part of the nourished sand has been transported still beyond the single groin, because the water depth at the tip of groin was set to be -4m and thus it is shallower than the depth of closure which is roughly -8m in this area. In addition, a large amount of nourished sand, which exceeded the equilibrium berm height has been transported to north direction due to the excess longshore slope of nourished beach, and partially to offshore beyond a typical closure depth due to severe typhoons.

ACKNOWLEDGEMENT

The authors would like to express their special thanks to Mr. Nishihara, former Chief of River Section, Kagoshima Prefectural Government Office, for his kind permission to release the field data. The author also wishes to extend special thanks to Dr. Nicholas C. Kraus at the Coastal and Hydraulic Laboratory, US Army Engineer Waterways Experiment Station for his kind proofreading.

REFERENCES

Takaaki Uda (1997): *Beach erosion in Japan*, SankaidoShuppan, p.442 (in Japanese)

ON THE DESIGN OF SHORE-PARALLEL BREAKWATERS

J.A. Zyserman[1], I. Brøker[1], H.K. Johnson[2], K. Mangor[1] and K. Jørgensen[1]

Abstract

The morphological aspects of the design of shore-parallel breakwaters are investigated through a series of tests using a two-dimensional (in the horizontal plane) morphological modelling system. The analysis focuses on the optimisation of the breakwater length and its distance to shore in order to achieve the desired type of response. The results obtained are compared to empirical formulas from the literature and observations from the field.

Introduction

Shore-parallel breakwaters are frequently used in coastal protection and restoration schemes. An important aspect of the design of these structures is the prediction of the morphological response (i.e. the type of planform that will develop) in their vicinity. Depending on the intended purpose of the structure, a tombolo may be desired in some cases, whereas a stable salient behind the breakwater, without significant down-drift erosion, may be the preferred solution in other cases.

In this paper we concern ourselves only with the morphological aspects of the design of shore-parallel breakwaters. From this perspective, the design of the breakwater consists of defining appropriate dimensions for the length of the structure and its location in the nearshore area, in order to obtain the desired morphological response.

A coastal area morphological modelling system is applied to systematically investigate the morphological response behind a detached breakwater subjected to wave action. Tests are made with various combinations of breakwater length and distance from shoreline for given incident wave conditions, beach characteristics and sediment properties. The results of these tests are analysed to derive practical guidelines for the design of the structures.

---

1 Coastal Engineering Department, Danish Hydraulic Institute, Agern Allé 5, DK-2970 Hørsholm, Denmark
2 Dr. Nik & Associates, 20-2 Jalan 10/55 A, Taman Setiawangsa, 54200 Kuala-Lumpur, Malaysia

The following aspects of the study are discussed in the ensuing sections:

- the phenomena leading to the special planforms that are observed in the vicinity of detached breakwaters.
- the modelling system used to simulate the morphological evolution in the vicinity of shore-parallel breakwaters
- the test matrix defined on the basis of the findings from the dimensional analysis of the parameters controlling the morphological response
- presentation and discussion of the results

Processes in the vicinity of a detached breakwater

At a macro-scale level, the presence of the shore-parallel breakwater shelters the coast immediately behind the structure and the adjacent areas from the incoming waves. This means that the wave height at breaking will be smaller in the sheltered areas than elsewhere, which in turn will result in larger wave-induced set-up along the exposed beaches than in the sheltered areas.

The longshore variability in the wave set-up results in gradients of the mean water surface. These gradients tend to accelerate the longshore current flowing towards the sheltered area behind the structure and to change the direction of the current which is driven away from the breakwater by the breaking waves in the region immediately downdrift of the breakwater. The two current systems merge behind the structure, giving raise to complex circulation patterns.

The acceleration of the littoral current that takes place updrift of the shore-parallel breakwater causes initial erosion of the beach in that area. The same occurs in the area immediately downdrift of the structure. The currents carry the eroded material towards the sheltered area, where it deposits. These mechanisms cause the pattern of deposition behind the breakwater and erosion on either side of it that can be observed in nature.

The 2DH Morphological Modelling System

The coastal-area morphological modelling system applied in the present analysis was described in detail by Johnson et al. (1994). At that moment, the emphasis was placed on the selection of the wave model, the description of the bed roughness under combined waves and current, etc.

Briefly, the morphological modelling system is based on an explicit forward-time integration scheme for the evolution of the bathymetry. The system consists of a number of modules capable of reproducing the governing processes that were discussed in the previous section:

(i) a wave module, MIKE 21 PMS, based on the parabolic approximation to the mild-slope equation, used to calculate wave parameters as well as radiation stresses over

the model area. MIKE 21 PMS accounts for the effects of shoaling, refraction, diffraction, breaking, directional spreading and bed friction on the incident waves

(ii) a hydrodynamic module, MIKE 21 HD, in which the flow field is found from the solution of the depth-intcgrated continuity and momentum equations. The currents driven by the breaking waves and the gradients in mean water level are calculated on a mobile bed evolving at the rate of dz/dt calculated by the sediment transport module

(iii) an intra-wave sediment transport module, MIKE 21 ST, accounting for the combined influence of waves and current on the transport rates of graded sediment

(iv) a bed level update scheme using an improved second-order Lax-Wendroff scheme

Further details on the morphological modelling system can be found in Johnson et al. (1994, 1995).

Dimensional Analysis and Test Matrix

Using dimensional analysis, Johnson et al. (1995) showed that the morphological response behind shore-parallcl breakwaters on an initially plane beach can be expressed as a function of the dimensionless numbers ϕ_1 and ϕ_2 according to

$$\text{Morphological Response} = f(\phi_1 * \phi_2) \quad (1)$$

with

$$\phi_1 = \phi_1(H_b/L_0, \theta_b, m/(H_b/L_0)^{0.5}, H_b/d_{50}) \quad (2)$$

and

$$\phi_2 = \phi_2(t/T, X/X_{80}, L/X_{80}) \quad (3)$$

where H_b is the wave height at breaking, L_0 is the deep-water wave length, θ_b is the direction of wave propagation at breaking, m is the beach slope, t is time, T is wave period, d_{50} is the median grain size, L is the length of the structure, X is its distance to the coast, and X_{80} is the distance from shore within which 80% of the undisturbed littoral transport takes place. Therefore, X_{80} can be seen as a measure of the width of the surf zone.

ϕ_1 and ϕ_2 in (1) can be interpreted as being dimensionless parameters that describe the dependence of the morphological response on the magnitude of the sediment transport and the geomctry of the structure, respectively.

In order to systematically investigate the dimensions of the detached breakwater that are required to obtain the desired response, tests in which the morphological

response obtained by varying X/X_{80} and L/X_{80} in (3) while keeping constant the dimensionless parameters in (2) have to be defined. Therefore, 8 tests in which X/X_{80} and L/X_{80} were systematically varied while keeping the incident wave characteristics, the initial beach slope and the sediment properties unchanged were defined for the present analysis, as detailed in Table 1 below.

Table 1. Definition of test cases (X_{80} = 240m)

Test	X (m)	L (m)	X/X_{80}	L/X_{80}	L/X
KM1	120	312	0.50	1.30	2.60
KM2	240	312	1.00	1.30	1.30
KM3	360	312	1.50	1.30	0.87
KM4	480	312	2.00	1.30	0.65
KM5	600	312	2.50	1.30	0.52
KM6	360	192	1.50	0.80	0.53
KM7	360	432	1.50	1.80	1.20
KM8	360	552	1.50	2.30	1.53

Tests KM1 to KM5 were aimed to investigating the influence of the location of the structure with respect to the coast on the morphological response. Tests KM3, KM6, KM7 and KM8, in turn, were defined to investigate the influence of the length of the structure on this response.

In all the tests, irregular unidirectional waves were applied. The root-mean-square wave height H_{RMS}, peak wave period T_p and direction of wave propagation θ at a water depth of 10m were defined as equal to 2m, 8s and 10°, respectively. The initial beach slope m was kept as 1:50 in all tests, and a sediment with median grain size d_{50} = 0.25mm and geometrical standard deviation $\sigma_g = (d_{84}/d_{16})^{0.5} = 1.1$ was used over the whole model area. With this definition of parameters, a value of X_{80} = 240m was found.

Each morphological simulation test was carried out for a minimum period of nine days, after which the results were analysed. Even though it can be argued that the "final" morphological response of a natural beach to the local wave conditions will arise after a number of years, it must be kept in mind that this response will be mainly dictated by some significant (from a sediment-transport point of view) events. Normally, these events will have a limited persistence over an average year. Since the same (relatively rough) wave conditions were kept during the entire morphological simulation period reported here, it can be reasonably expected that the time scale required for the bathymetry to adapt itself to the incident waves will be much shorter in the model tests than in nature.

Presentation and discussion of results

Fig 1 shows the initial model bathymetry for tests KM3, KM5 and KM8. The area shown is 720m wide and 1800m long. The length of the structure is the same in tests KM3 and KM5, but the breakwater is located further away from the shore in KM5. On the other hand, the two breakwaters are located at the same position with respect to the

coast in tests KM3 and KM8, but the length of the structure is almost double for the case of tests KM8, see table 1 for additional details.

Figs 2, 3 and 4 show the initial wave, current and sediment transport fields calculated over the same area as shown in Fig 1 for the three tests. Inspection of the figures shows how the dimension and location of the structure influence the nearshore hydrographic and transport conditions.

For example, it can be seen that placement of the structure further away from the coast for test KM5 permits more penetration of wave energy in the area behind the structure, cf. Fig 2. On the other hand, the sheltered area created by the structure along the coast is largest for this case (KM5), as shown by the extension of the recirculation area downstream of the breakwater in Fig 3. For test KM8, the penetration of wave energy behind the relatively long structure is so limited that two independent regions (from a sediment-transport point of view) exist in the vicinity of the tips of the structure, cf. Fig 4.

Fig 5 shows the bathymetry predicted by the morphological model after 10 days. All bed levels above –2m have been shown in black in order to facilitate interpretation of the results.

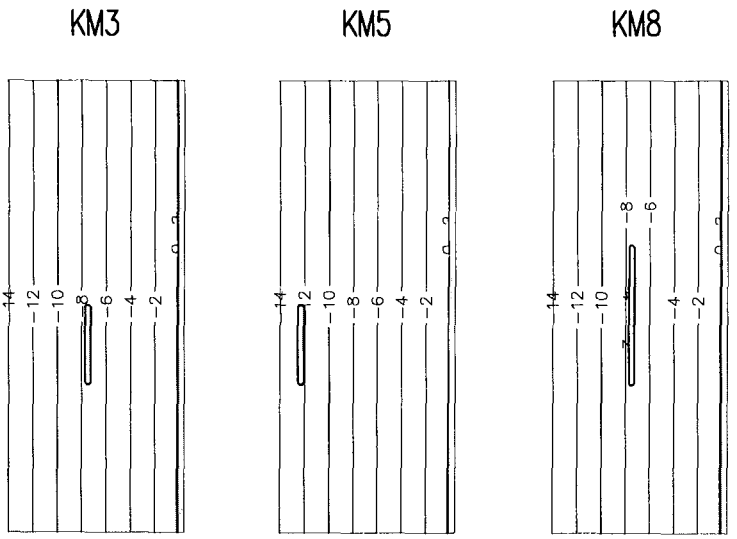

Figure 1. Initial model bathymetry

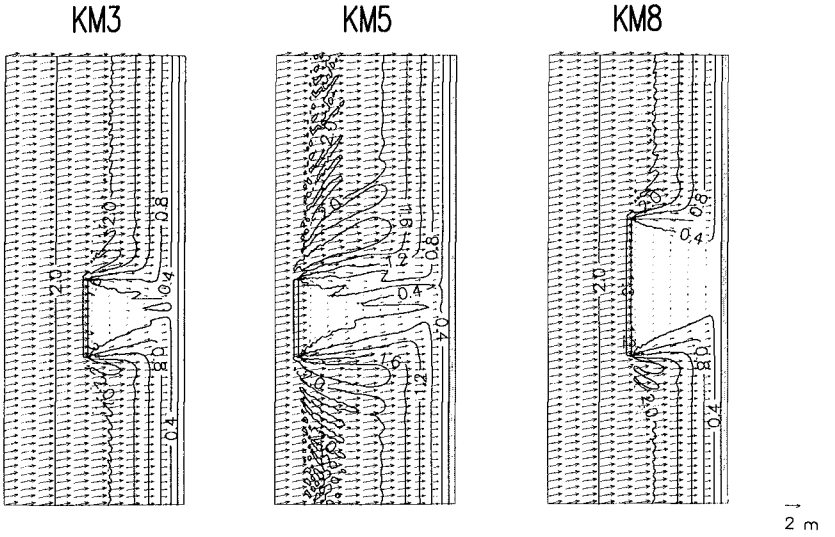

Figure 2. Initial wave fields

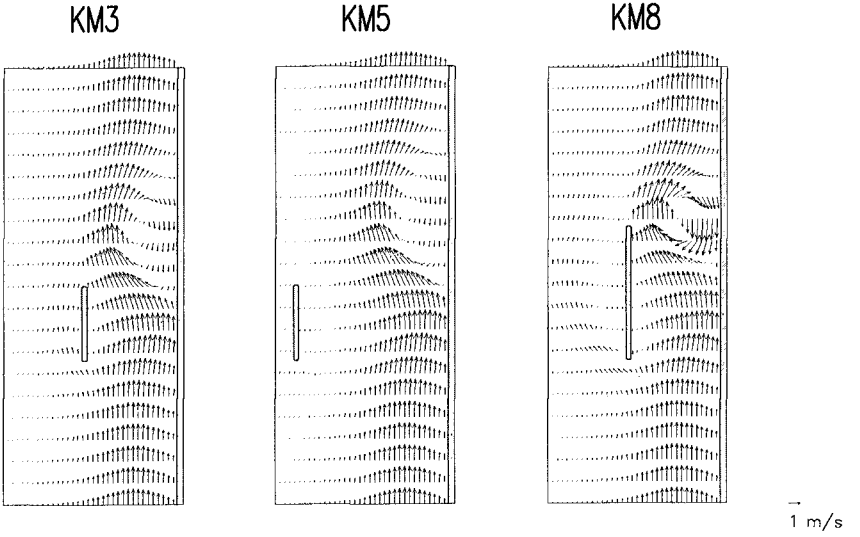

Figure 3. Initial wave-driven current fields

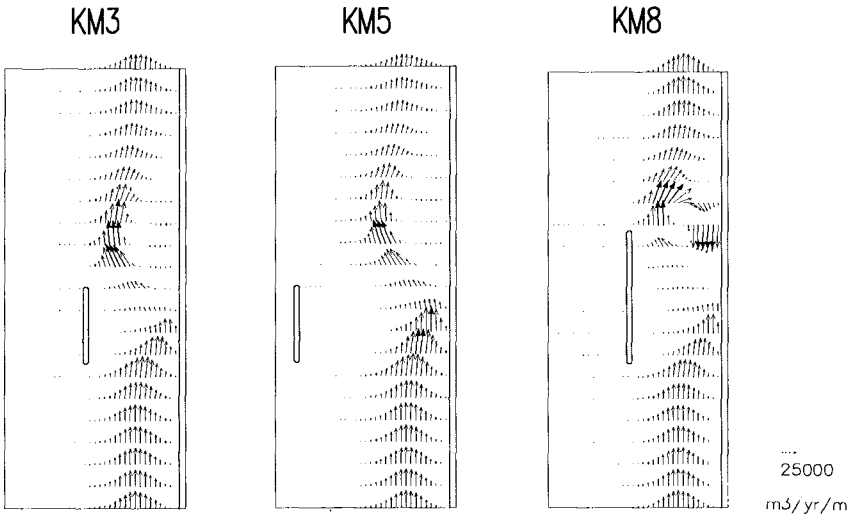

Figure 4. Initial sediment transport rates

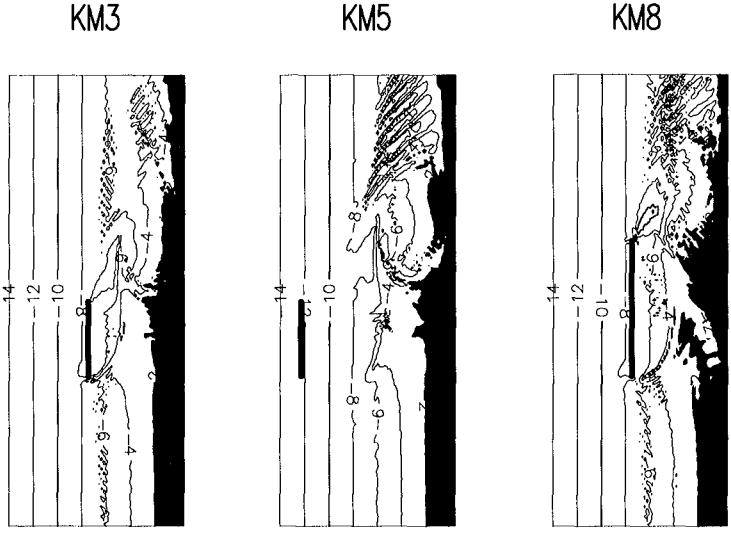

Figure 5. Predicted bathymetry after 10 days of simulation

The bathymetry predicted by the morphological modelling system at the end of each test was inspected and classified. The predicted planform was either classified as tombolo (for those cases in which the structure had become connected to the shore), or salient (if a widening of the beach had occurred without significant changes of the bathymetry beyond the shallower area) or salient/tombolo (if a significant salient not attached to the structure had developed at the end of the test).

The predicted response was compared to empirical formulas from the literature. The results of this comparison have been summarised in Table 2. It is observed that the predicted morphological response is generally in good agreement with the predictions from the empirical formulations.

The results obtained are summarised in graphical form in Fig 6 as a function of L/X_{80} and X/X_{80}. The empirical relationship $L/X = 1$, proposed among others by Herbich (1989) and Suh and Dalrymple (1987) to identify the occurrence of tombolo or not, has also been indicated. Points located above the line ($L/X > 1$) will correspond to tombolo formation, whereas points below the line ($L/X < 1$) will indicate salient formation, and points close to or right on the line will correspond to the case of unstable tombolo formation.

It is observed that the response predicted by the morphological modelling system is in good agreement with this empirical criterion.

Table 2. Comparison of Calculated Response to Empirical Formulas

Test	Herbich	Ahrens & Cox	Dally & Pope	Suh & Dalrymple	Mangor	Morphol. Modelling
KM1	Tombolo	Periodic tombolo	Tombolo	Tombolo		Tombolo
KM2	Tombolo	Well-developed salient		Tombolo	Salient	Tombolo
KM3	Salient	Subdued salient			Tombolo	Salient/ tombolo
KM4	Salient	Subdued salient	Salient		Salient	Salient
KM5	Salient	Limited accretion	Salient		Salient	Salient
KM6	Salient	Subdued salient	Salient		Salient	Salient
KM7	Tombolo	Well-developed salient		Tombolo	Tombolo	Tombolo
KM8	Tombolo	Well-developed salient	Tombolo	Tombolo	Tombolo	Tombolo

The coastal features observed behind three breakwaters located respectively on the West coast of Jutland, Denmark (stable tombolo), SW coast of Sri Lanka (unstable tombolo) and Sergipe (Brazil) have also been included in the figure. Again, good agreement between the model predictions and the observed response in the field is found.

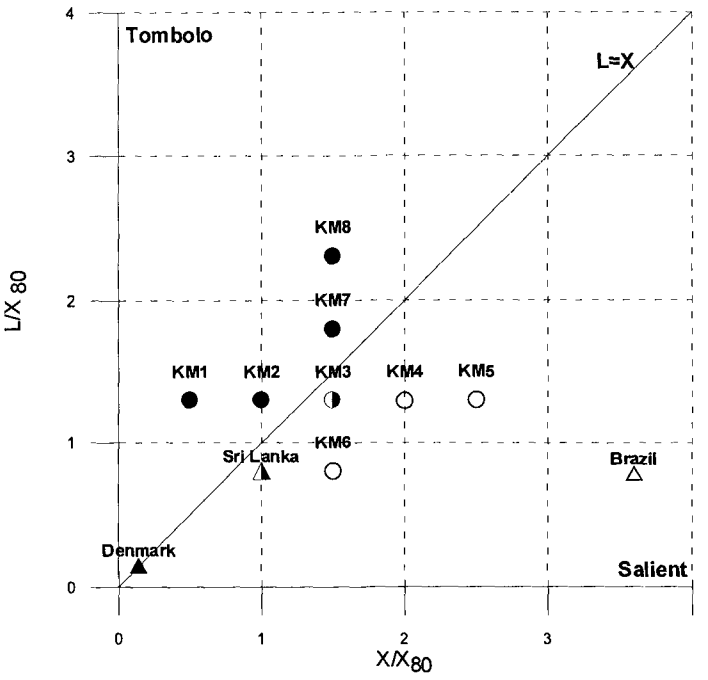

Figure 6. Calculated morphological response as a function of the length and location of the detached breakwater. Triangles: field data. Circles: model results. Open symbols: salient. Filled symbols: tombolo.

The dependence of the modelling results on the dimensions and the position of the breakwater were investigated through the total volume of sediment deposited on the initial bathymetry after 9 days of simulation.

The results have been plotted in Fig. 7 as a function of the distance from the coast to the structure for breakwaters of constant length (tests KM1 to KM5) and in Fig. 8 as a function of the length of the breakwater for breakwaters with constant distance to the coast (tests KM3, KM6, KM7 and KM8). The labels close to the symbols in both figures indicate the corresponding ratio L/X for the breakwater.

Fig 7 shows that for a detached breakwater of given length, there is an optimal location from the point of view of the amount of sediment that the structure will trap. In the extremes, a breakwater located very close to the coast will trap small amounts of sediment, as it will only marginally interfere with the surf zone.

On the other hand, a breakwater located too far away from the coast will also trap moderate amounts of sediment, since there will be space enough behind the structure for wave energy to penetrate and for the waves to reform before reaching the outer edge of the surf zone.

Fig 8 shows that for a breakwater located at a certain distance from the shore, a limiting length exists beyond which the amount of sediment trapped by the structure will not increase with its length. This is due to the fact that no penetration at all of wave energy behind the structure is possible due to its length, and therefore the transport processes at both ends of the structure occur independently of each other.

Figs 7 and 8 can be used in combination to optimise the design of a shore-parallel breakwater from the point of view of the desired morphological response. If the length of the breakwater has been defined beforehand, or if it is restricted by external requirements, then Fig 7 can be used to determine the location of the structure that will yield the maximum deposited volume (if desired). The morphological modelling system will in turn predict the type of planform that will be created behind the structure.

If the position of the breakwater with respect to the coast is fixed, then Fig. 8 can be used to optimise its length, and the morphological modelling results (or, alternatively, Fig 6) to verify the type of morphological feature that will be generated.

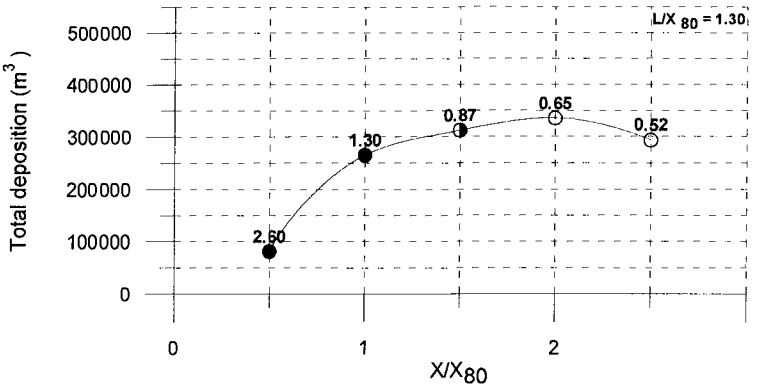

Figure 7 Influence of distance to coast on the amount of sediment deposited on the initial bathymetry. All breakwaters have L = 312m. Figures on the plot correspond to values of L/X. Symbols as in Fig 6.

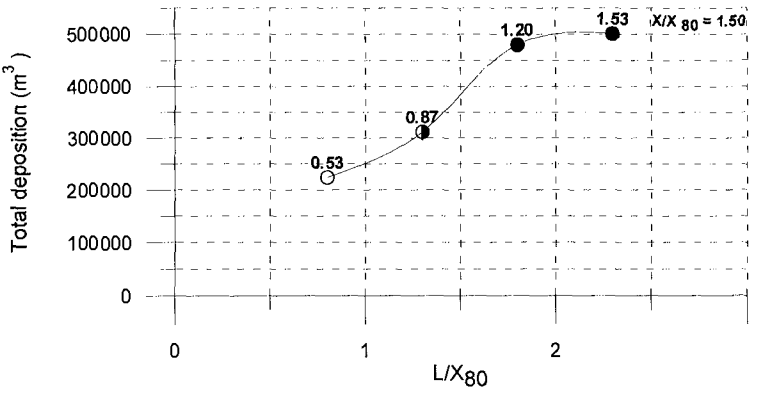

Figure 8 Influence of structure length on the amount of sediment deposited on the initial bathymetry. All breakwaters have X = 360m. Figures on the plot correspond to values of L/X. Symbols as in Fig 6.

It is important to keep in mind that Figs 7 and 8 are not general design curves, but have been created for a particular wave climate and beach profile. Application of the morphological modelling system as described in the previous sections to the particular hydrographic and sedimentological conditions found at a given study site will therefore allow the optimisation of the dimensions of shore-parallel breakwaters from the point of view of the associated morphological response.

Currents generated in the vicinity of shore-parallel breakwaters

Shore-parallel breakwaters are frequently used as coastal structures in connection with recreational beaches, either to stabilise the coastline or to provide swimming areas that are sheltered from the incoming waves.

Since complex current patterns are generated in the vicinity of detached breakwaters, the sheltered areas may prove hazardous for inexperienced swimmers, who will be attracted to the apparently calm areas where they may be trapped by the current and be dragged offshore.

In order to quantify the magnitude of these currents, the maximum current speed predicted by the hydrodynamic model on the initial bathymetry for each of the eight tests has been listed in Table 3 below. These strong currents always take place shoreward or close to the tips of the breakwater.

The figures in Table 3 may be compared to the maximum value of 1.33 m/s attained by the wave-driven current along the open stretch upstream of the breakwater.

Table 3. Magnitude of the currents in the vicinity of the breakwater

Test	Max. speed on initial bathymetry
KM1	1.50
KM2	1.70
KM3	1.68
KM4	1.66
KM5	1.63
KM6	1.53
KM7	1.95
KM8	1.89

It can be seen that the currents generated by the presence of the shore-parallel breakwater can be up to 40% stronger than the maximum value of the wave-driven current.

Conclusions

The application of the coastal morphological modelling system to the design of shore-parallel breakwaters allows determining the optimal geometry of an isolated structure for given wave conditions and characteristics of the beach profile and the bed material.

The morphological response predicted by the modelling system is in good agreement with observations from the field and the guidelines provided by commonly used empirical formulas.

Even though the results obtained indicate that depth-integrated currents are the dominating mechanism from the point of view of the morphological response, there is a number of additional effects, the significance of which is not fully understood yet, and should therefore be the subject of future investigations. Among them, the vertical structure of the wave-driven currents and the suspended sediment transport, bed-slope and space-lag (non-equilibrium suspended load transport) effects on sediment transport may be mentioned.

References

Dally, W.R., and Pope, J. (1986). "Detached Breakwaters for Shore Protection". Technical Report CERC-86-1, Coastal Eng. Res. Center, US Army Corps of Engineers.

Herbich, J.B (1989). "Shoreline Changes due to Offshore Breakwaters". Proceedings XXIII Congress, IAHR, Ottawa, Canada.Vol. C, pp. 317-327.

Johnson, H.K., Brøker, I., and Zyserman J.A. (1994). "Identification of Some Relevant Processes in Coastal Morphological Modelling". Proceedings of the 24th International Conference on Coastal Engineering, Kobe, Japan, pp. 2871-2885.

Johnson, H.K., Brøker, I., Zyserman J.A., and Mangor K. (1995). "Morphological Response in the Vicinity of Offshore Breakwaters". Proceedings of the IV COPEDEC Conference, Rio de Janeiro, Brazil.

Mangor, K., Godage, D., Amarasinghe, S., and Anderskov, U. (1991). "Coast Conservation Scheme Combining Beach Nourishment and Offshore Breakwaters – Testing, Design and Performance". Proceedings of the III COPEDEC Conference, Mombasa, Kenya.

Mohr, M.C., and Ippolito, M. (1991). "Initial Shoreline Response at the Presque Isle Erosion Control Project". Proceedings Coastal Sediments'91, pp. 1740-1754.

Suh, K., and Dalrymple, R.A. (1987). "Offshore Breakwaters in Laboratory and Field". Journal of Waterway, Port, Coastal, and Ocean Eng. Vol. 113, No. 2, pp. 105-121.

Acknowledgement

This study was carried out as a part of the MAST3-SASME project (Surf and Swash Zone Mechanics), supported financially by the Commission of the European Communities, Directorate General for Science, Research and Development under contract no. MAS3-CT97-0018. Financing was also provided by the Danish Technical Research Council (STVF) within the frame of the "Marin Teknik" research programme.

Shore Parallel Breakwaters & Beach Nourishments

Jan van de Graaff[1]
Henk Steetzel[2]
Bram Bliek[3]
Hans de Vroeg[4]

Abstract

The application of shore parallel offshore breakwaters in coastal engineering is discussed. Four well-defined practical coastal engineering problems are the starting point of discussion. The possibilities of a new morphological model and a design support model are indicated.

1 Introduction

Within the CUR-framework (CUR: Centre for Civil Engineering Research, Codes and Specifications), many Dutch partners (Governmental institutes, Consulting firms, Contractors and Universities) recently participated in a joint Dutch research project concerning the application of shore parallel detached breakwaters in combination with beach nourishments.

Shore parallel detached breakwaters are increasingly used as a tool in coastal engineering practice. All over the world series of detached breakwaters have been constructed. In the Netherlands, however, shore parallel breakwaters have not yet been applied in the open sea. Whether this is wise or not is an almost ever lasting debate amongst experts in the Netherlands. The CUR project was partly initiated with the aim to provide the debaters with some joint background information. A second aim was of course to enhance the knowledge concerning this intriguing tool in coastal

[1]Delft University of Technology, Stevinweg 1, 2628 CN Delft, the Netherlands

[2]Alkyon Hydraulic Consultancy & Research, p.o. box 248, 8300 AE Emmeloord, the Netherlands

[3]Ingenieursbureau Svašek, p.o. box 91, 3000 AB Rotterdam, the Netherlands

[4]WL | DELFT HYDRAULICS, p.o. box 177, 2600 GA Delft, the Netherlands

engineering practice.

Many series of shore parallel breakwaters have been built along many coasts all over the world. To build detached breakwaters calls generally for huge investment costs. Thus consequently serious problems had apparently to be resolved with the help of detached breakwaters. It is striking that in the overwhelming number of books, papers and reports which appeared concerning the detached breakwaters topic, often the very reason to apply this tool is hardly discussed. In literature often great successes of the application of series of offshore breakwaters are reported. But, what was the problem which had to be resolved with the help of offshore breakwaters? Often this very basic question is not dealt with in the papers.

In the study a slightly different approach was followed. First four well-defined practical coastal engineering problems were stated and next the possible application of shore parallel breakwaters to resolve these four problems was investigated. (Of course realizing that the use of shore parallel breakwaters is only one tool out of many other tools, and realizing that in more cases than the restricted number of four defined problems, shore parallel breakwaters can be used.) In the investigation it was analyzed how the use of breakwaters could resolve the problem. Special attention was paid to possible additional effects of the application of shore parallel structures. The study was restricted to the application of shore parallel (rock) structures, whether in combination with artificial nourishments or not.

2 Outline of study

The entire study was divided in three phases. In Phase I 'Introduction and inventory' amongst others four well-defined practical coastal engineering problems were outlined; one case was subdivided in two alternatives, viz.:

- A Erosion of a continuous coastline;
- B1 Coastline with interrupted sediment transport: near harbour breakwaters;
- B2 Coastline with interrupted sediment transport: near a tidal inlet;
- C Artificial beaches along coastlines with a lack of natural sediments (recreational beaches);
- D Seaward shifted coastline of a large-scale land reclamation project.

The several cases were defined and the possible use of shore parallel breakwaters was indicated. Typical design problems were pointed out concerning each of the cases. In the Phase I report (CUR, 1997a) also a brief summary was given of more than 100 papers related to the application of shore parallel breakwaters.

In Phase II 'Modelling of sand transport' of the study a method was developed to quantify the effect with time, of (series of) shore parallel breakwaters on coastal morphology in the vicinity of the breakwaters. An existing multi-layer computational model was adapted to a large extent. New formulations were derived. The effect of diffraction behind the breakwaters was taken into account.
One case of the four cases, Case A 'Erosion of a continuous coastline' was studied in detail.

The use of shore parallel breakwaters is often an alternative for the application of artificial (beach) nourishments. The application of breakwaters will often only reduce the erosion rate in the area under consideration; a real zero erosion rate, however, is difficult to achieve. It must be stressed that any reduction of the erosion rate in the area under consideration is often at the spent of the lee-side area. In that area increased erosion rates are to be expected.

The efficiency of an applied shore parallel system of breakwaters was defined in the model as the ratio between the savings in erosion rate and the original erosion rate **in the area to be protected**. The expected increased erosion rates in the lee-side area are not taken into account in the efficiency to be determined. An essential feature of the model is the easy way in which the efficiency of a given (arbitrary) series of breakwaters can be determined. The results of the study in Phase II are summarized in (CUR, 1997b).

With the help of the model developed in Phase III 'Evaluation by a design support model' (CUR, 1997c), the consequences of the application of shore parallel structures related to costs and several other aspects, can easily be evaluated. By filling out some Menu's, the user defines the problem to be studied and the characteristics of the solution with offshore breakwaters in mind. Alternative offshore structures schemes are easily to be generated by the user; the model next calculates the costs.

The basic comparison parameter to evaluate different alternatives is the net present value (NPV) of an alternative. Interest rate and assumed lifetime of a project are to be defined by the user. Also for the zero option (compensation of the observed erosion rate in the area to be protected by artificial nourishments) NPV calculations are made.

The models as developed in Phase II and III of the study are further discussed in Paragraph 4 and 5. In Paragraph 3 the four basic coastal engineering problems where shore parallel breakwaters might be used, are discussed in more detail.

3 Basic problems and the application of shore parallel breakwaters

General

Coastal erosion is in fact a tricky notion. Erosion of the part of the coast which is often considered to be the most valuable part, viz.: beach and dunes (or mainland), can be because of two fundamentally different processes:

i) erosion during a severe storm surge;
ii) structural erosion.

To a first approximation process i) can be considered as a typical (temporary) cross-shore redistribution phenomenon. Sand from the dunes and upper part of the beach is transported during the storm surge to deeper water and settles there. (Under common weather conditions the sand will return to its pre-storm position.) The total volume of sand between some fixed limits in a cross-shore profile [m^3/m] does not essentially change because of the storm surge.

Process ii), structural erosion, is quite different from erosion due to a storm surge. Because of the structural erosion process the volume of sand within a cross-shore profile reduces gradually with time. Sooner or later also the upper part of the profile (dune area) is lost permanently.

If erosion control is required, both types of erosion call for quite different solutions. In the present study structural erosion problems are mainly considered. If in the following **erosion** is mentioned, the erosion is meant to originate from structural erosion processes. When, however, an erosion control scheme to a structural erosion problem is designed, one always needs to take into account the consequences of the selected alternative for the erosion process during storm surges.

Case A: Erosion of a continuous coastline

The present, more or less autonomous, behaviour of many stretches of coast is often annoying the coastal zone managers involved. E.g. structural erosion of a part of the coast calls often for adequate countermeasures. Artificial nourishments have proven to be a good solution for this type of problems, despite the fact that this solution does not resolve the basic cause of the erosion problem. The gradual erosion still continues; only the detrimental effects of the erosion process (e.g. the final loss of beaches) is ultimately prevented. The occurring losses are replenished at a regular basis. (Say every 5 till 10 years.) Application of artificial nourishments in this case can be considered as a **curing-the-symptoms** approach.

With the application of structures (either groynes or shore parallel breakwaters) the coastal zone manager intends to interfere in such a manner in the present sediment transport processes in the erosion area, that the gradual erosion stops or at least is reduced. This approach may be characterized with a **curing-the-disease** approach.

Because many structural erosion problems are due to gradients in longshore sediment transport, it means in fact that often the longshore transports have to be reduced along some parts of the eroding coast. An effective application of structures to stop or to reduce the gradual erosion in the area under consideration, always results in a reduced input of sediments to the lee-side area. Often this reduced input leads to (increased) erosion in the lee-side area compared to the previous situation. Whether this is acceptable or not depends on the particular case. The lee-side consequences must always be taken into account properly in studying solutions for erosion problems.

The unavoidable lee-side consequences of a for the rest even perfect protection scheme, are a serious draw-back of this type of shore protection. Nevertheless in some cases the (extra) lee-side erosion might be acceptable. E.g. in cases where the lee-side area is considered to be less valuable than the protected area, or in cases where artificial nourishments can be better (cheaper) carried out in the lee-side area than in the area to be protected. If the erosion area concerns for instance an important recreation area, artificial nourishments on a regular basis may yield extra costs with respect to economic losses.

A structural erosion problem can be characterized with several parameters, e.g.:

i) length of area to be protected;
ii) rate of autonomous erosion in that area;
iii) longshore sediment transports passing the boundaries of the erosion area;
iv) boundary conditions with respect to wave climate and tide characteristics;
v) 'value' of the lee-side area with increased erosion.

With the actual values of these parameters as starting point, different schemes of shore parallel breakwaters provide an equal number of solutions, each with its own related costs. The main emphasis of the study was to acquire facts to judge the quality of different alternatives. That means that one should be able to quantify in sufficient detail the morphological impact of a chosen system of shore parallel breakwaters. Although some rules of thumb exist, it is generally felt that our knowledge of this topic is far from sufficient. A quote from the US Corps of Engineers Technical Report (Chasten *et al.*, 1993) may illustrate this:

> *'Although numerous references exist for functional design of U.S. detached breakwater projects, the predictive ability for much of this guidance is limited. Knowledge of coastal processes at the project site, experience from other prototype projects, and a significant amount of engineering judgement must be incorporated in the functional design of a breakwater project.'*

(Page 10 of Chasten *et al.*, 1993.)

Within the study in Phase II an important step forward has been made towards our ability to model (and thus to quantify) the effects of arbitrary breakwater schemes properly. (See Section 4.)

Case B: Coastline with interrupted sediment transport

The classical example of a port, built along a sandy coast with a significant longshore sediment transport, shows large morphological changes at both sides of that port. Because of the interruption of the sediment transport by the breakwaters, at the up-drift side of the port continuous accumulation of sediment is observed. Erosion occurs at the down-drift side. (Lee-side erosion.) Although eventually also the accumulation of sediments will yield serious problems for a smooth operation of the port (sediment transport along the up-drift breakwater and sedimentation in the approach channel to the port), in the first years after the construction of the port the gain of new areas is often considered as advantageous. The lee-side erosion, however, is in most cases a serious detrimental side effect of the new port. If this lee-side erosion is not accepted, series of offshore breakwaters might be helpful to mitigate the erosion problem. As long as the breakwaters entirely interrupt the longshore sediment transport, the sediment input into the erosion area remains zero. In order to avoid continuous erosion in the down-drift area the only and best solution with the use of structures is to achieve resulting zero longshore sediment transports in the down-drift area to be protected. At the very end of the protection scheme the lee-side erosion (again) will take place. Indeed only a shift of the local erosion problem can be achieved. Whether this is acceptable or not depends on the particular case. With a well-designed shore parallel offshore breakwater scheme this goal can be achieved in principle.

Although an artificial sand by-pass system with a capacity equal to the full interrupted transport would resolve most of the morphological problems, in practice often under-designed systems are applied (if a system is applied at all). If only a part of the required volume is by-passed (say 75 %), still some lee-side erosion can be expected. Mitigating the remaining erosion with the help of an offshore breakwater scheme to an area further down-drift, puts quite different requirements to the scheme than compared to the zero sediment transport option. Now the scheme should be designed allowing to pass continuously 75 % of the original sediment transport. Undoubtedly quite different design characteristics of the protection scheme are required than in the zero transport case.

The coastlines of the stretches of coast near tidal inlets often show continuous erosion. A tidal basin which is out of equilibrium (e.g. by land reclamation projects in the basin area) continuously 'calls' for sediment imports in order to reach a new equilibrium state. Often the required import of material is at the spent of the sediment volumes in the ebb tidal delta in the initial phase, but eventually also at the spent of the adjacent stretches of coast. This results in a gradual erosion of the coast for a rather long time. This erosion can be prevented by application of an offshore breakwater scheme; a proper design is, however, complicated because the erosion is often (partly) due to effects of tidal currents at deeper water.

If a proper design of the protection scheme is achieved, one has to take into account that less material will reach the tidal basin. The 'demand' of the tidal basin for sediments in order to reach a new equilibrium has then to be fulfilled by other sources.

Case C: Artificial beaches along coastlines with a lack of natural sediments (recreational beaches)

Coastal areas which rely heavily on recreational use of their beaches are often faced with a lack of natural sediments. Consequently small and poor beaches are only available. (E.g. many beaches along the Mediterranean.) Improving the beaches in a restricted area will have large economical benefits for these areas. Since often only in a small area improvements are required and to restrict the volume of sand, artificial nourishment schemes call for additional projects in order to keep the nourishments in place. Shore parallel breakwaters, probably in combination with end-groynes, serve this goal. Wide beaches and a rather long waterline can be achieved in this way. Behind the breakwater segments often tombolo's are designed and constructed.

In order to be able to make a proper design, one should know what is the equilibrium position of the bay-shape behind the gaps between the breakwater segments in relation to the breakwater lay-out and boundary conditions. Sometimes also the case of a non-equilibrium position of the bay-shape (seaward shifted bay-shape in comparison with the equilibrium shape), but with some yearly maintenance nourishments, might be a proper solution. In order to apply this possibility one should have a proper insight in the (yearly) losses as a function of the deviation from the equilibrium position of the bay-shape.

Because of variations (within a year) of the predominant wave direction in fact a real equilibrium position of a bay-shape does not exist. What are the expected variations in this position in a particular case? For a coastal zone manager and the users of the beaches a clear answer to this question is important.

An equilibrium position of a bay-shape under (yearly averaged) common conditions might be a proper notion. However, for a total judgement of an applied scheme, also the behaviour of the scheme under severe storm conditions should be known. Probably irreversible losses of sediments through the gaps will occur. Quantifying these losses as a function of the particular conditions is a difficult design task.

Case D: Seaward shifted coastline of a large-scale land reclamation project

A large land reclamation project in front of a (straight) coastline in open sea calls for huge volumes of sediment. Provided that the new situation calls again for a beach as sea front, a zero option would be to shift all depth contours with the required distance (say two kilometers) in seaward direction. In this case the shape of the cross-shore profile is after the reclamation project the same as before the project. To a first approximation the coastal processes (longshore and cross-shore sediment transports) are expected to change only slightly by the reclamation project.
Shifting all depth contours (say from Datum +5 m to Datum -17 m) means that for each m^2 of new land 22 m^3 of sand is required. Indeed a huge total volume of sand is thus needed for a large reclamation project. Much of the eventual required volume is stored in deeper water in the 'toe' of the cross-shore profile. If one would be able to avoid the fill of the toe, large savings can be achieved.

Shore parallel submerged breakwaters could be used to 'support' the upper part of the cross-shore profile, while the toe can be omitted (a 'perched beach'). In the present example (2000 m seaward shift and 22 m^3 sand for each m^2 new area) 44,000 m^3 sand is required per running meter alongshore. A submerged breakwater supporting the upper part of the profile above Datum -8 m which is situated in the original profile at Datum -13 m yields a reduction with approximately 13,000 m^3 sand per running meter (approximately 30 % reduction). In this application 1 m^3 of stone 'saves' approximately 130 m^3 of sand; in other cases slightly different values are found.

The savings figures as given seem promising. Before the application of submerged breakwaters will be considered as a real alternative, however, various problems have to be resolved (and quantified). What are the losses of sand from the upper part of the profile over and across the submerged breakwater? Is the equilibrium shape of the supported part of the profile still the same as in the shifted case? What are the details of the transition between submerged breakwater and supported profile? Is the transition at crest level of the breakwater or at some distance below the crest?

Comparable to the application as discussed under Case C also a series of emerged shore parallel breakwaters could be considered as a seaward boundary of a large land reclamation project. Instead of a straight new coastline, now a series of bay-shapes serves as sea front. Equilibrium shapes as well as non-equilibrium shapes (but then with some additional maintenance nourishments) are to be considered. Each

alternative has advantages and disadvantages. Before real applications are considered, quantification of the morphological consequences is necessary.

Discussion of possible applications of shore parallel breakwaters in some coastal engineering problems

In the discussion of the possible application of shore parallel breakwaters for Cases A to D it became clear that these breakwaters have to be considered as promising alternatives for the problems as indicated. However, it also became clear that before application still some fundamental problems have to be resolved. One should e.g. be able to quantify, as reliable as possible the morphological impact of a proposed scheme. It is felt that no standard methods are yet available to do so. Different boundary conditions only already yield quite different morphological responses and hence quite different protection schemes are to be applied.

Taking some clearly defined real life coastal engineering problems as a guide, has turned out to be a good starting point in notifying the required complex design process of a shore parallel breakwater scheme. Sediment transports play a leading part in the morphological behaviour. Phase II of the study was meant to reveal some of the needed sediment transport quantification aspects of a possible application of shore parallel breakwater schemes. (See Section 4.)

4 Model of Phase II

In Phase II of the project an existing multi-layer computation model is adapted and extended in order to cope with the complicated processes occurring near (especially landward of) offshore breakwaters. In the multi-layer concept distinction is made between longshore transports and cross-shore transports.

In the multi-layer concept the cross-shore profile is schematized in a series of horizontal (rectangular) layers. (See Fig.1.) After schematization the cross-shore profile looks like a staircase. Cross-shore transport occurs from one layer to another; along each vertical part of the staircase a part of the total longshore transport takes place.

The present mutual distance between two adjoining layers $a_{pres.}$ (the present length of a step) is compared with the mutual distance of these layers under equilibrium conditions $a_{eq.}$ (equilibrium distance of a step). The rate of cross-shore transport S_y is assumed to be proportional to the difference between $a_{eq.}$ and $a_{pres.}$.

$$S_y = s_y (a_{eq.} - a_{pres.})$$

where s_y is the cross-shore transport constant. The values of s_y depend amongst others on the depth in the profile. In this approach a cross-shore profile which is out of equilibrium, 'returns' because of cross-shore profile adjustments to equilibrium again after some time. Based on many calculations with a detailed cross-shore morphological computation model (UNIBEST-TC developed by DELFT HYDRAULICS) a distribution over depth of s_y is determined.

Fig.2 shows the well-known distribution of the longshore sediment transport over a cross-shore profile because of an obliquely approaching wave field for a uniform coast in longshore direction. If this distribution is plotted as a function of depth, a (remarkable) triangular distribution is found (see also Fig.2). Such a triangular distribution was found for many different cases (different cross-shore profiles; different wave conditions; different particle sizes). The characteristic water depths d_{top} and d_{zero} (see Fig.2) appeared to be simple functions of the significant wave height H_s. ($d_{top} = \alpha H_s$; $\alpha \approx 1.4$; $d_{zero} = \beta H_s$; $\beta \approx 3.0$.)
Also in cases with a combination of waves and currents typical distributions of the longshore sediment transport over depth have been derived. (See CUR 1997b.)

Reliable distributions of the longshore sediment transport over the horizontal layers are required in the multi-layer model. In the model the orientation of a horizontal layer determines the rate of longshore transport in the part of the profile which is schematized by the layer.

With the existing multi-layer concept the morphological behaviour of large coastal stretches, however, without structures could be simulated with time. To be able to handle also offshore breakwaters in the model, did require serious adaptations of the model. A typical effect of shore parallel breakwaters (either submerged or emerged) is the reduction of the wave height in the 'shadow' zone of the breakwater. Since the wave height is an important determining parameter in the sediment transports, these wave height reductions have to be quantified as a function of breakwater layout (e.g. position with respect to waterline; gap width; length of breakwater segments; crest height) and boundary conditions (e.g. wave height; wave direction; tidal currents).

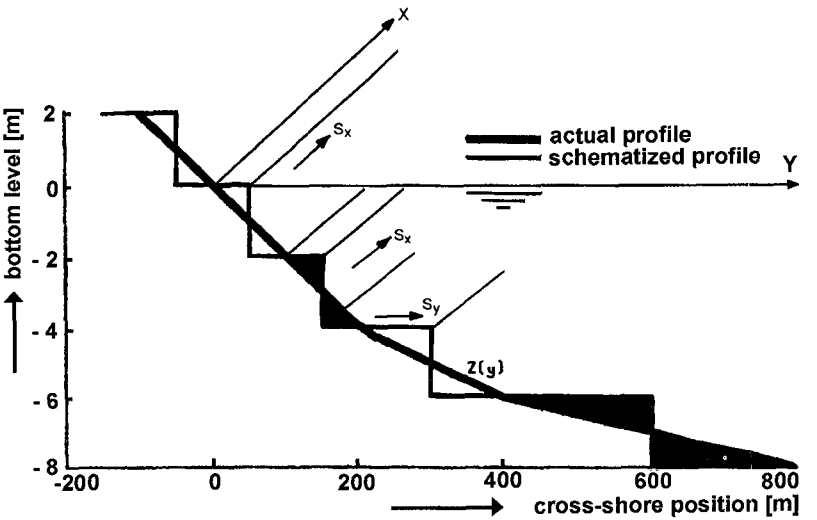

Fig.1 Schematized cross-shore profile.
(Cross-shore transport S_y occurs at different levels; longshore transport S_x is distributed over profile.)

Taking wave transmission and wave diffraction into account, the wave height adaptation has been quantified for some general cases.

The adapted model has been applied in a typical Case A problem with a series of different shore parallel breakwater schemes. The morphological development with time after inserting a breakwater scheme in the model, could be simulated. Some test cases showed reliable results; at least showed a behaviour as qualitatively expected.

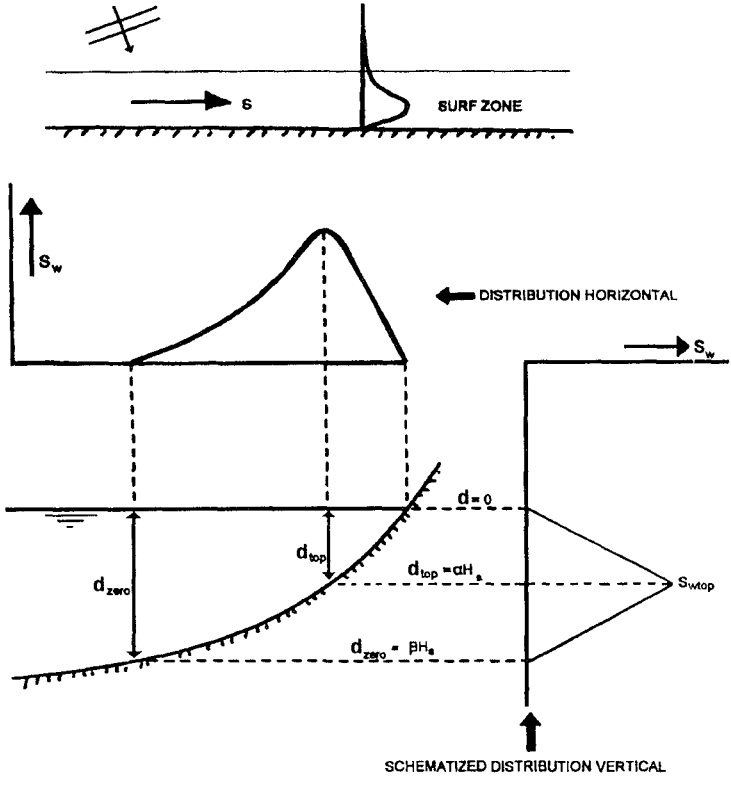

Fig.2 Longshore sediment transport distribution because of obliquely approaching waves.
(Upper panel: top view; lower panel: horizontal and vertical distribution of longshore transport.)

The efficiency of a given breakwater scheme is an important parameter in a design process. The efficiency of a scheme is defined as the ratio between the savings in erosion volume and the original erosion volumes **strictly in the area to be protected**. The model is provided with a very useful 'auto-nourishment' option. With that option the efficiency of a given scheme can be directly determined. Assume that the policy is to keep the waterline at least seaward of a limit position. If somewhere in the area to be protected at any time the waterline surpasses the limit position in landward direction, the computational model adds the required volume of sand in order to restore the position of the waterline to the limit position. Comparing the volumes still to be added in a case with a shore parallel protection scheme, with the volumes to be added in the unprotected case, yields the efficiency of that scheme. (See Figs.3 and 4 for examples.)

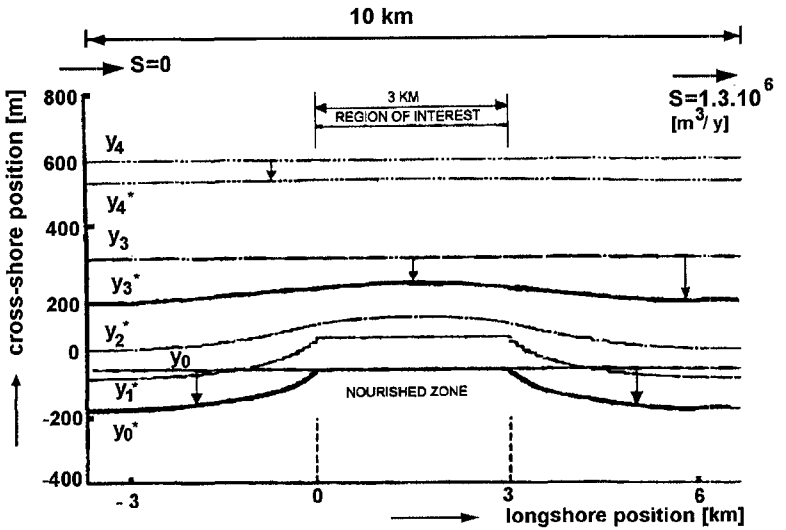

Fig.3 Development of eroding coast after 10 years with auto-nourishments.
(A stretch of coast of 10 km shows a large gradient in longshore sediment transport; dS_x/dx = 130 m^3/m per year. The waterline of the middle part is kept at position with the auto-nourishment option. The figure shows the development of 5 different layers.)

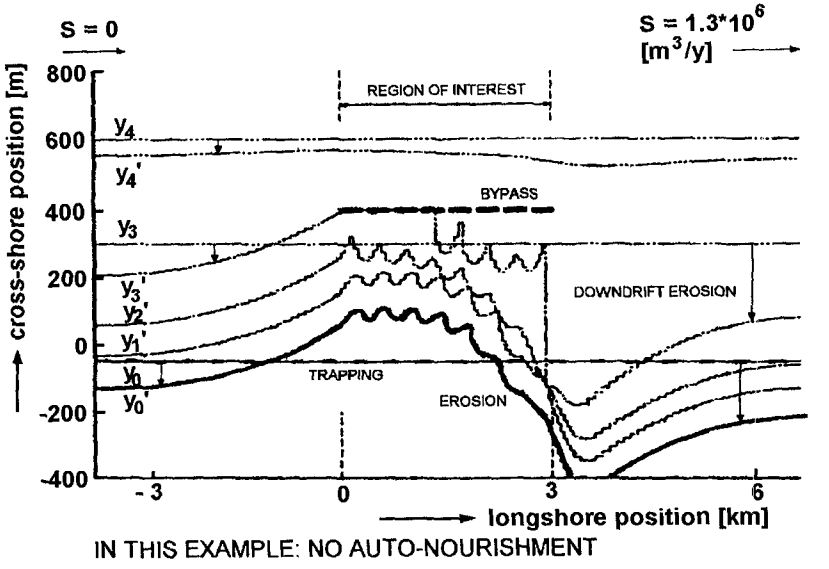

Fig.4 Development of eroding coast protected by a series of offshore breakwaters after 10 years.
(Same stretch of coast of Fig.3. In this case protected by a series of shore parallel offshore breakwaters. Notice the accumulation of sediments at the up-drift side behind the breakwaters and the lee-side erosion.)

The Phase II model has been applied in only a restricted number of cases. The model has shown its abilities. The model is still a research version; it will be upgraded in future to a general applicable model. (See Steetzel *et al.*, 1998.)

Applying a multi-layer model to simulate the very complex morphodynamical processes in the vicinity of offshore breakwaters is in fact a sign of weakness. Applying process-based morphological models would be strongly preferred. Although this type of models is improving very fast, the present versions are not yet able to simulate the development of the coast over a longer time for offshore breakwater cases satisfactorily. As a part of the studies in Phase II of the project some simulations of a few basic lay-outs of offshore breakwaters have been made with the Delft 2D morphological model of DELFT HYDRAULICS. The results are promising, but further research is necessary before this approach can be used in general applications. It is expected that as a result of the EU sponsored SASME project (SASME: Surf and Swash zone MEchanics), much progress will be made in the morphological modelling abilities.

5 Model of Phase III

A design support model was developed in Phase III of the project. It has proven to be a useful tool during the first phases of a design process. Different alternatives can be fast and easily evaluated. The model is Menu-oriented; the user has to fill out the basic characteristics of the design in mind. The model is available in a LOTUS 123 release 3.4, and in an Excel version.

The problem, indicated as Case A (erosion of a continuous coastline) has been studied in detail. The autonomous behaviour of the stretch of coast under consideration yields erosion. The detrimental effects because of the retreat of the coast can be mitigated by regular beach nourishments. This solution is considered as zero option. Also with different shore parallel breakwater schemes the erosion problem can be (partly) resolved. Often the problem is indeed only partly resolved, because the scheme does not prevent the erosion entirely. Some additional (but reduced) regular artificial nourishments are still required to keep the coastline at the prescribed position. Four sets of input data are required to run the design support model. These four sets of data can be generated with the Phase II model. Consequently a strong link exists between the Phase II and the Phase III model. Based on experience, rules of thumb or engineering judgement these four sets of data can of course be simply changed.

The model thus requires the input of a (restricted) number of efficiency values as a function of characteristic breakwater lay-out parameters like:

(i) the position of the offshore breakwaters from the coastline;
(ii) the relationship between offshore distance and length of the breakwater segments;
(iii) the ratio between gap width and length of the breakwater segments;
(iv) the crest height of the segments relative to the mean water level.

Within the program some basic dimensions of a breakwater scheme and some boundary conditions have to be specified by the user; next 'automatically' a simple static stable cross-section is calculated (Hudson formula). With (freely to select) fixed costs and unit prices for primary layers, secondary layers and core material, the construction costs of the breakwater scheme are determined.

The model is primarily developed for the use of rock structures as breakwaters. If for instance the use of geocontainers (large bags of geotextiles filled with sand) is considered as construction material for the offshore breakwaters, the user can 'simulate' this application by simply using appropriate unit prices.

The basic comparison parameter to evaluate different alternatives (including the zero option) is the net present value (NPV) of an alternative. Interest rate and assumed lifetime of a project are to be defined by the user.

If along a continuous eroding stretch of coast an offshore breakwater protection scheme is applied, the reduction in erosion in the protected area is always at the spent of the lee-side area. If at the end of the day also the (increased) erosion problem in the lee-side area has to be resolved, a shore parallel breakwater scheme ean never be

an adequate solution. In some special cases, however, this firm statement might be relaxed. If, for example, regular nourishments in an area to be protected yield huge additional cost (e.g. economic losses in an important recreation area), concentrated nourishments in the lee-side area could be ultimately cheaper. The design support model has been provided with opportunities to take such cases into account.

6 Concluding remarks and recommendations

Concluding remarks

Although many day to day coastal engineering problems can be properly resolved with 'soft' methods (artificial nourishments), the application of shore parallel structures ('hard' method) could be a promising alternative in some cases. [Often a combination of 'hard' and (additional) 'soft' seems a good solution.]

Although the project has not resolved all problems, and not all aims have been achieved, the study has certainly increased the knowledge concerning the possible application of shore parallel structures. The project has served as a fruitful starting point for further studies. A promising approach to resolve the remaining problems has been found.

Recommendations

The Phase II part of the study has revealed that a promising modelling tool has been developed. It is recommended to extend and to generalize the use of this computation model. See e.g. Steetzel *et al.*, 1998.

Process-based morphodynamic modelling of complex cases (like offshore breakwaters applications) is developing very fast. It is recommended to spend additional efforts in attempts to model some typical cases with this type of morphodynamic models.

7 References

Chasten, M.A., J.D. Rosati and J.W. McCormick (1993)
Engineering Design Guidance for Detached Breakwaters as Shoreline Stabilization Structures.
US Army Corps of Engineers, WES, Technical Report CERC-93-19.

CUR, 1997a
Beach Nourishments and Shore Parallel Structures, Phase I: Introduction and inventory.
CUR, Gouda, the Netherlands.

CUR, 1997b
Beach Nourishments and Shore Parallel Structures, Phase II: Modelling of sand transport.
CUR, Gouda, the Netherlands.

CUR, 1997c
Beach Nourishments and Shore Parallel Structures, Phase III: Evaluation by a design support model.
CUR, Gouda, the Netherlands.

Steeztel, H.J., J.H. de Vroeg, L.C. van Rijn and J.M.T. Stam (1998)
Morphological modelling using a multi-layer approach.
Proceedings 26th Int. Conf. on Coastal Engineering, Copenhagen, Denmark.

Sediment Transport Around a Mound Breakwater: the Toe Erosion Problem

Asunción Baquerizo[1] and Miguel A. Losada[2]

Abstract

The combined action of waves (incident and reflected) and the alongbreakwater current driven by wave energy dissipation inside an infinitely long porous breakwater under oblique wave attack (Baquerizo and Losada, 1998), is taken into account to study the formation of bars in front of the structure and the sediment transport at the toe of it. The main features of the bars are explained in terms of the incident wave characteristics, remarking the wave incidence angle dependence, and the structural and hydrodynamic properties of the breakwater. Results may explain the existence of erosion/deposition patterns at the toe of the structure.

Introduction

Some coastal structures, designed to protect an area from wave action are built with quarry or rip-rap. Generally speaking, they reflect part of the incident energy modifying the wave field in the neighborhood of the structure. Moreover, part of the energy is dissipated inside the porous medium due to pore friction.

On sandy beds, it is known that wave action may induce the erosion of the toe of the breakwater, producing the failure of the structure. However, sometimes it is found that sand accumulates at the toe, filling up the structure and reducing its functionality as a wave dissipator.

Dalrymple et al. (1991) obtained the wave field in front of and inside a porous vertical structure when a monochromatic wave impinges obliquely on it. On the other hand, Baquerizo and Losada (1998) showed that for waves approaching obliquely an infinitely long porous structure, wave energy dissipation inside the pores drives an alongbreakwater current inside the structure that is transferred to the water regions by

[1]Research Associate, Department of Hydraulic Engineering. Faculty of Civil Engineering. Delft University of Technology. Stevinweg 1. 2628 CN Delft. The Netherlands.

[2]Professor, Department of Civil Engineering. E.T.S. de Ingenieros de Caminos, Canales y Puertos. Universidad de Granada. Campus de Cartuja s/n. 18071 Granada. Spain.

turbulent diffusion. Moreover, they studied the combined action of waves and the current to study the sediment transport patterns in front of the porous structure showing that these mechanisms explain the formation of bars parallel to the breakwater, producing in some cases the erosion of the toe of the structure.

In this paper, the shape of the bars and the conditions under which erosion/deposition occurs at the toe of the structure are analyzed in terms of the characteristics of the incident wave and the structural properties of the breakwater. The reflection coefficient and the phase lag between the incident and reflected waves is presented first, next the drift velocity and the alongbreakwater current profiles are analyzed, finally the sediment transport patterns are obtained and the tendency of the bed is studied.

Theoretical Background

Let us consider an infinitely long vertical porous structure of width b, in water of constant depth, h, and a monochromatic wave train that impinges obliquely on it with an angle of incidence θ. The origin of the reference frame is in the seaward face of the

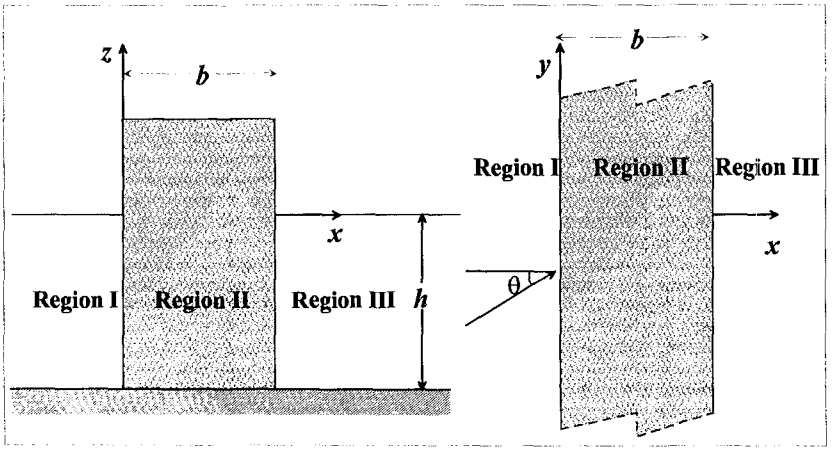

structure with the x-axis normal to it, the y-axis lying along the breakwater and the z-axis pointing upwards (see Fig. 1).

Figure 1. Definition sketch showing waves approaching an infinitely long vertical porous breakwater at an oblique angle.

The presence of the breakwater modifies the incident wave field. In the first region, part of the incident wave energy is returned in the seaward direction. Some of the remaining energy, transmitted to the porous structure is dissipated because of friction losses within the pores. Inside the breakwater, part of the wave energy is reflected

because of the discontinuity at the leeward face of the structure and some is transmitted to the third region.

Wave field inside and outside the structure

Under plane wave assumption, Dalrymple et al. (1991) obtained the velocity potentials in each region. The corresponding water surface elevation can be expressed as:

$$\eta_\alpha(x,y,t) = a_\alpha(x)e^{-i(\vec{k}_\alpha\cdot\vec{x}-\sigma t)} \quad \alpha=I,II,III \tag{1}$$

where the amplitude of the oscillations, $a_\alpha(x)$, in each region $\alpha = I,II,III$ is constant along lines parallel to the breakwater.

Seawards of the structure, the amplitude of the water surface elevation is:

$$\begin{aligned} a_I(x) &= \left(|A_1|^2+|B_1|^2+2|A_1||B_1|\cos(2k_a\cos\theta x+\varphi)\right)^{1/2} \\ &= |A_1|\left(1+|R|^2+2|R|\cos(2k_a\cos\theta x+\varphi)\right)^{1/2} \end{aligned} \tag{2}$$

where A_1 is the amplitude of the incident wave, $R=|R|e^{i\Phi}$ is the reflection coefficient of the structure and $B_1=A_1R$ is the amplitude of the wave reflected at the seaward face of the structure. $a_I(x)$ varies periodically with x, with a characteristic wavelength $L_b=L/2\cos(\theta)$, showing lines of maximum (quasi antinodes) and minimum (quasi nodes) amplitude, whose distance to the breakwater depends on the phase lag between the incident and the reflected trains.

Inside the structure, the amplitude is:

$$a_{II}(x)=|s-if|\left(|A_2|^2e^{2q_Ix}+|B_2|^2e^{-2q_I(x-b)}+2|A_2||B_2|e^{q_Ib}\cos(q_R(2x-b)+\varphi_{A_2}-\varphi_{B_2})\right)^{1/2} \tag{3}$$

where $A_2=|A_2|e^{i\varphi_{A_2}}$ is the amplitude of the wave transmitted to the structure and $B_2=|B_2|e^{i\varphi_{B_2}}$ is the amplitude of the wave reflected at the leeward face of the breakwater. s and and f are parameters describing the porous medium and q_R, q_I are, respectively, the real and imaginary parts of the wave number inside the coastal structure (see Dalrymple et al.,1991; Losada et al.,1993 for details). The waves transmitted at $x=0$ and reflected at $x=b$ are dissipated as they propagate inside the structure and consequently, the oscillations of the amplitude of the water surface elevation inside the porous medium decrease with x. As the characteristic length of the oscillations is again $L_b=L/2\cos(\theta)$, they can be observed only for breakwater widths larger than L_b.

Alongbreakwater current

Wave energy dissipation inside the pores produces a variation, in the acrossbreakwater direction, of the radiation stress, S_{xy}, inside the porous medium (Méndez, 1997) driving a current, $V(x)$, that flows parallel to the structure (Baquerizo and Losada, 1998). Due to the turbulence induced by temporal and spatial fluctuations of the velocity flow inside the pores, the current is transferred to the water regions.

The velocity profile shows a maximum inside the structure, close to the seaward face of it, and decreases towards 0 far from the structure. The magnitude of the velocity profile depends on the structural properties of the breakwater and on the characteristics on the incident wave.

Summarizing, in the proximity of the structure, particularly at the toe of the structure, there are the combined action of waves and the alongbreakwater current, which may provide an efficient mechanism for initiating and transporting the sediment.

Sediment transport

Using Bailard's formula (1981), the sediment transport patterns under the influence of waves and currents are obtained in terms of the total velocity, $\vec{u}_t$, at the bottom, which results from the superposition of the orbital velocity, $\vec{u}_o$, and a small perturbation which does not depend on time, $\vec{U}$. Notice that the orbital velocity is due to the incident and the reflected waves.

Far from the structure, $\vec{U}$ is the drift velocity, $\vec{U}_d$, at the top of the bottom boundary layer. Close to the structure, both alongbreakwater current, $V(x)\hat{j}$, and drift velocity have to be considered. Although V may modify the mean motion of the boundary layer, in a first approach, as $|U_d|$ and V are both very small compared to the orbital motion, they may be linearly superimposed without significant error.

Bed morphology in front of the coastal structure

Dalrymple et al. (1991) showed that the reflection coefficient on a porous structure depends on the angle of incidence and that there is a value, called the Brewster angle, for which the modulus of the reflection coefficient is minimum. That means that the same breakwater may behave as a highly reflective or as a low reflective structure depending on the angle of wave attack. Baquerizo and Losada (1998) showed that the drift velocity patterns in front of the structure and the alongbreakwater current also depend on the breakwater reflectivity. This property justifies the choice of two case studies representing a moderately permeable and dissipative breakwater, and an almost impermeable and fully reflective one, with special attention in the effect of the angle of incidence. Table 1 summarizes the principal characteristics of the breakwater and wave conditions for the two cases, which will be referred to Structure A and Strueture B, respectively.

	A_1(m)	h(m)	T(s)	b(m)	f^1	ε^2
Structure A:	0.5	5	10	10	0.8	0.45
Structure B:	0.5	5	10	10	50	0.25

[1] friction factor of the porous medium
[2] porosity of the porous medium

Table 1. Incident wave and breakwater characteristics

For Structure A, the reflection coefficient varies from to R=53 at θ=0° to R=0.04 at the Brewster angle, θ_B=70°, then it increases. The phase lag between the incident and the reflected trains is very small for $\theta<\theta_B$. At θ_B it changes rapidly until it achieves a constant value $\phi=\pi$ for angles larger than θ_B (Fig.2 a). This means that for angles smaller than θ_B the antinodal lines will be at $x_n=-nL_b$, n=0,1,2,... whereas for higher values they will be at $x_n=-nL_b-L_b/2$, n=0,1,2,.... For the almost impermeable breakwater (Case B), the structure behaves always like a highly reflective structure and the Brewster angle converges asymptotically to $\theta=\pi/2$. The phase lag is close to 2π and therefore, the antinodal lines will be at $x_n=-nL_b$, n=0,1,2,...

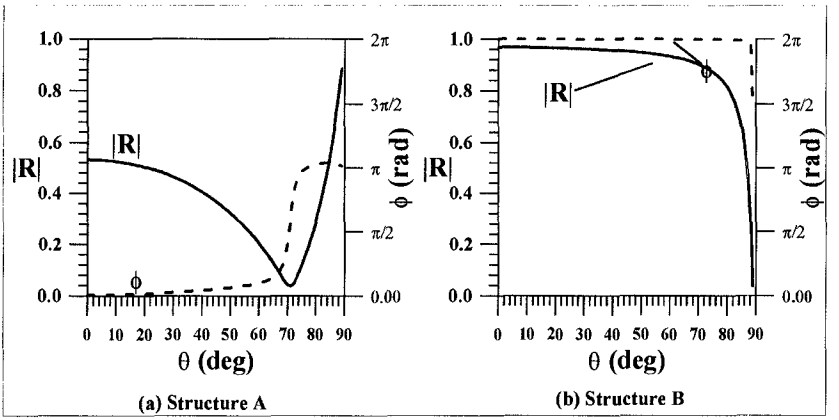

Figure 2. Magnitude and phase of the reflection coefficient

The drift velocity $\vec{U}_d=U_d\hat{i}+V_d\hat{j}$ at the top of the boundary layer in a three-dimensional small-amplitude oscillatory flow was obtained by Hunt and Johns (1963) and applied later by Carter et al. (1973) to a field resulting from the superposition of an incident wave and a reflected wave with normal incidence. For the wave field in front of the structure, $\vec{U}_d$ is a function uniform in y, varying periodically with the distance to the breakwater. The velocity component in the y- direction, V_d, is in phase with the wave amplitude, that is, it is maximum at, $x_n=-nL_b-\phi L_b/(2\pi)$, n=0,1,2,3,... The component in the x- direction, U_d, has a lag of $-L_b/4$ with respect to V_d with maximum values at $x_n-L_b/4$. V_d is always a positive function, whereas U_d changes the sign for values of the reflection coefficient above a threshold value which is about R_t=0.82.

Fig. 3 shows, for Cases A and B, the x- and the y- component of the drift velocity as well as the alongbreakwater current profile obtained for θ=45°. For Case A and small angles of incidence, U_d and V_d are of the same order of magnitude, and as θ increases, the y-component of the drift velocity dominates over the x-component. The resulting sediment transport patterns (Fig. 4 a) are essentially in the direction of propagation of the incident wave, except at the antinodes where the angle with respect to the x-axis increases slightly. For Case B, the drift velocity in the y-direction is larger

than U_d and, because it corresponds to a highly reflective structure with reflection coefficients above R_t, U_d changes the sign. The resulting sediment transport converge towards the antinodes and diverges at the nodes (Fig 4 b).

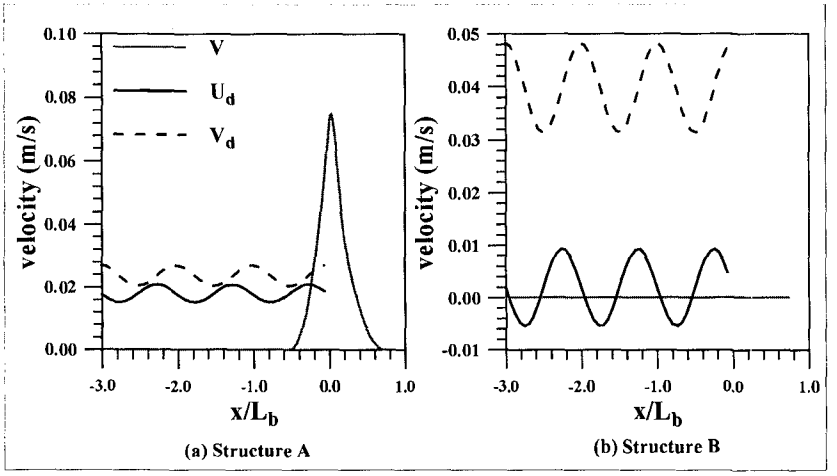

Figure 3. Drift velocity and alongbreakwater current profiles

For Structure A, the alongbreakwater current at the face of the structure is of the same order of magnitude than the drift velocity (see Fig. 3 a), and the maximum values of the alongbreakwater current profile are achieved for $\theta \approx 50°$. For structure B the alongbreakwater current is negligible compared to the drift velocity.

Fig. (5) shows, for Cases A and B, the evolution with the angle of incidence of the local time variation of the bed. For Case A, it can be seen that the tendency of the bed is to form bars parallel to the breakwater almost sinusoidal in shape, with a distance between crests of L_b, and a distance from the first crest to the structure of $L_b/4$. The higher bars are expected to develop for small angles of incidence. As the angle of incidence increases, the height of the bars decreases and the effect of alongbreakwater current becomes more important. Consequently, it is expected that the bed erodes at the toe of the breakwater.

For Case B the bed develops bars with double peak crests and deep troughs. Again, the higher bars are expected to be for small angles of incidence. The distance between troughs is L_b and the first bar through is $L_b/2$ away from the structure. For all angles of incidence, sediment accumulates at the toe of thc structure.

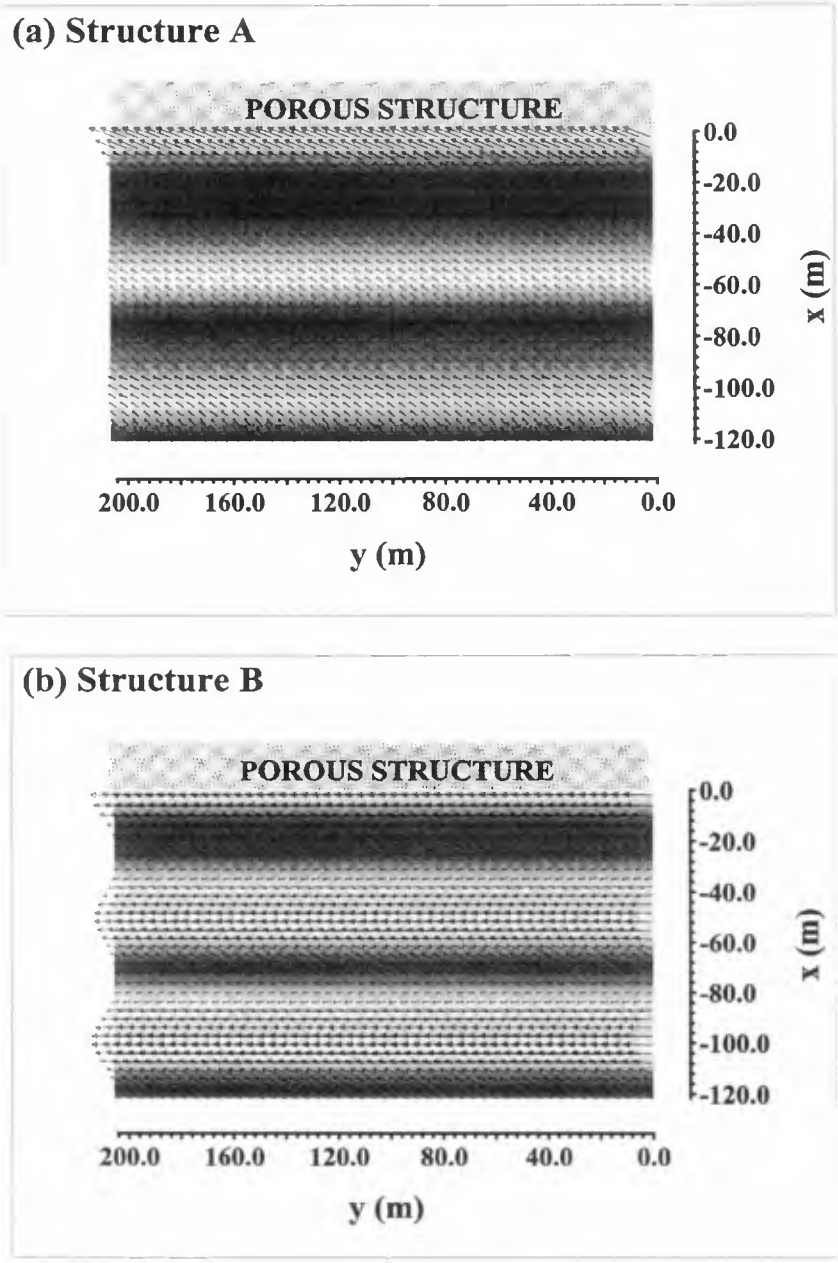

Figure 4. Sediment transport patterns in front of the breakwater

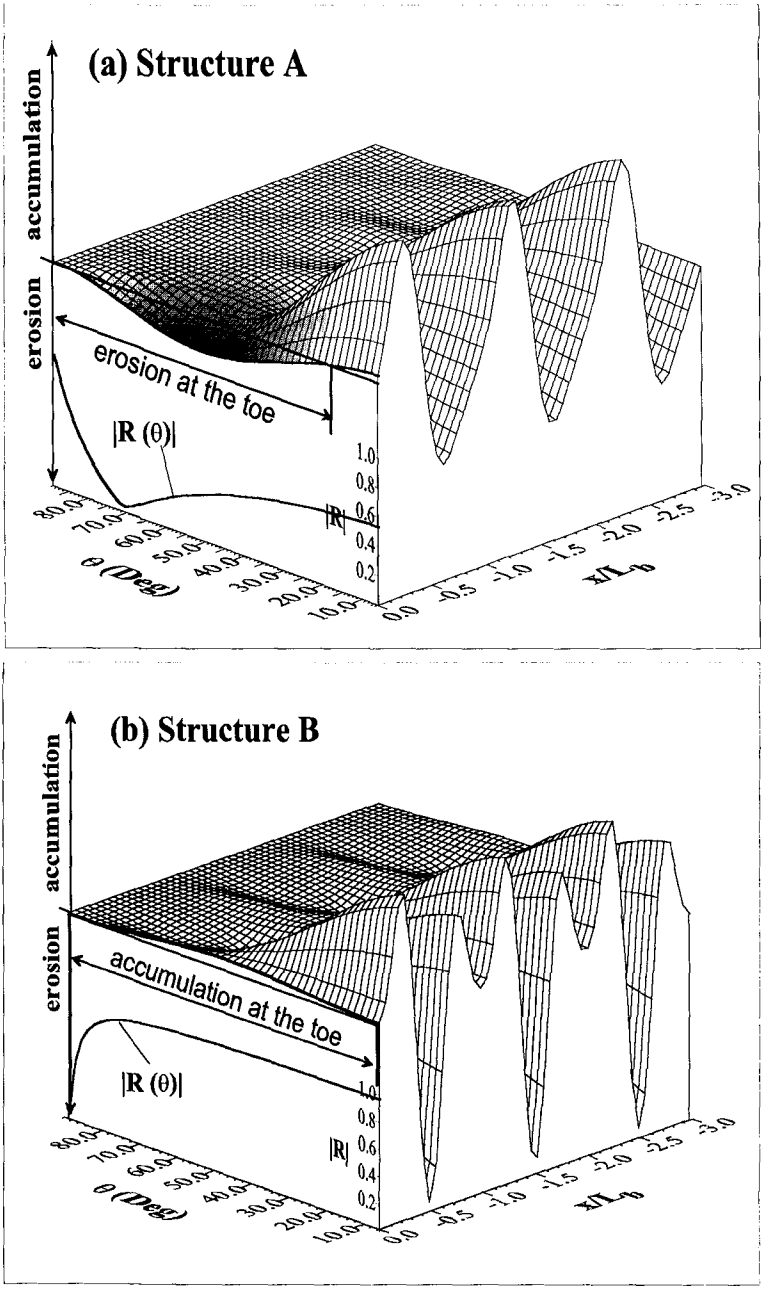

Figure 5. Local time variation of the bed in front of the breakwater

Conclusions

The combined action of waves (incident and reflected) and the alongbreakwater current, driven by wave energy dissipation inside a porous structure, is considered to study the sediment transport patterns and the associated local time variation of the bed in front of an infinitely long porous breakwater of finite width when a monochromatic wave train impinges obliquely on it.

The modulation of the $x-$ and the $y-$ components of the drift velocity with the distance to the breakwater is found to produce sediment transport patterns that explain the formation of bars parallel to the breakwater whose characteristics depend on the characteristic of the incident wave train (wave number and angle of wave attack) and on the reflection coefficient of the structure. Moreover, the alongbreakwater current modifies the sediment transport in the neighborhood of the breakwater.

For a moderately permeable and dissipative structure, the reflectivity depends strongly on the angle of incidence and the bars are expected to be almost sinusoidal in shape, with a distance between crests of $L_b = L/(2\cos\theta)$. For small angles of incidence, the effect of the alongbreakwater current is negligible and the first bar crest is likely to be $L_b/4$ away from the structure. For larger angles of incidence, the alongbreakwater erodes the bed in the vicinity of the breakwater; this effect is maximum at $\theta \approx 50°$.

For an almost impermeable and fully reflective structure, the alongbreakwater current is negligible compared to the drift velocity and has no significant effect on the sediment transport patterns. The $x-$component of the drift velocity changes the sign, and as a result, the sediment transport converges towards the antinodes and diverges at the nodes. The tendency of the bed is to form bars with two peaks and deep troughs, with a distance between troughs of L_b and the first through located $L_b/2$ away from the structure. It is expected that sand accumulates at the toe of the structure.

Acknowledgements

A.B. was funded by the Commission of the European Communities in the framework of the Training and Mobility Researchers Programme (TMR) under contract no. ERBMBICT961598. M.A.L. is indebted to the Commission of the European Communities in the framework of the Marine Science and Technology Programme (MAST) under contract no. MAS3970081 (Sasme Project). Furthermore, motivation and development of this work have been stimulated in the context of Scarcost Project.

References

Bailard , J. A. (1981). "An energetic total load sediment transport model for a plane sloping beach". Journal of Geophysical Research, 86: 10938-10954.

Baquerizo, A. and M. A. Losada (1998). "Longitudinal Current Induced by Oblique Waves along Coastal Structures". Submitted to the Journal Coastal Engineering.

Carter, T. J., P. L. F. Liu and C. C. Mei (1973). "Mass transport by waves and offshore sand bedforms". J. Waterways, Harbours Coastal Eng. Div ASCE 99: 165-184.

Dalrymple, R. A., M. A. Losada and P. Martin (1991). "Reflection and transmission from porous structures under oblique wave attack". Journal of Fluids Mechanics. Vol.

224, pp. 625-644.

Hunt, J. N. and B. Johns, (1963). "Currents induced by tides and gravity waves". Tellus XV, No. 4, pp

Losada, I. J., M. A. Losada and A. Baquerizo (1993). "An analytical method to evaluate the efficiency of porous screens as wave dampers". Applied Ocean Research. No 15, pp. 207-215.

Méndez, F. J., (1997). "Flujos medios inducidos por las ondas de gravedad en medios reflejantes y disipativos naturales o artificiales". Ph.D. Dissertation, Universidad de Cantabria, Santander, Spain, 344pp..343-351.

STABILITY OF NEAR-BED RUBBLE-MOUND STRUCTURES

César Vidal [1], Íñigo J. Losada , Associate Member, ASCE[1]
[1]and Francisco L. Martín [2]

Abstract

This paper describes the experimental and theoretical analysis carried out to improve our knowledge of the stability of near-bed rubble-mound structures. Laboratory tests have been performed to improve the data base on the stability of this kind of structure. The experimental results are compared with the results of three different approaches to stability: dimensional analysis, Morison forces and forces derived from bed shear stresses. In all cases considered, the influence of the geometry of the structure has not been taken into account, and the characteristics of the flow around the structures have been obtained from linear wave theory. The analysis of the data shows that the mobility parameter, a non-dimensional form of the bed shear stress, gives the best representation of the damage in these structures. From the analysis it can also be concluded that inertia forces are not relevant in the representation of the damage using Morison forces. Based on these approaches, some formulations of damage are presented. These formulations indicate that, for the first stages of damage, damage varies almost linearly with force (Morison or bed shear stress).

Introduction.

Near-bed structures are those whose height is low compared with water depth. The depth of submergence of these structures is enough to assume that wave breaking does not affect the hydrodynamics around the structure. This definition separates them from the low-crested or submerged breakwaters. Rubble-mound, near bed structures are used in coastal engineering for the protection of other structures such as pipelines or outfalls, for scour protection, as toe or lateral beach support or for the construction of artificial reefs for marine life. Stability under wave action and currents is usually the

[1] Associate Professor. Ocean and Coastal Research Group. Universidad de Cantabria. Avda. de los Castros s/n, 39005 Santander, Spain.

[2] Assistant Professor. Ocean and Coastal Research Group. Universidad de Cantabria. Avda. de los Castros s/n, 39005 Santander, Spain.

design condition while other loads such as those induced by anchors or fishing nets may be of secondary importance.

In recent years, experimental and theoretical efforts have been undertaken to fill the lack of information on the stability of submerged rubble-mound structures. Much of the experimental work has been directed towards low crested or submerged breakwaters, Vidal et al. (1992), van der Meer (1993) and today, some guidelines for the design of these structures are available. In the field of near-bed structures, experimental information is scarce, Lomónaco (1994), Levit et al. (1997), and mostly dedicated to assess the transport of rubble units. Therefore, most engineers are using sediment transport formulas developed for horizontal bottom to determine the stone size.

The approaches that scientists and engineers apply to assess the damage of rubble-mound structures are based on one of the following general methodologies:

- Dimensional analysis: Using the methods of dimensional analysis, the damage is expressed as a function of some non-dimensional parameters. The experimental data are used to obtain the function that gives the better fit between the calculated and the measured damage. This approach is the most widely used in the assessment of damage of rubble-mound breakwaters. This functional will vary any time the geometry of the structure or the type of the armor units changes the hydrodynamics, gravity or interlocking forces involved in the movement of the units.

- Quasi-empirical approach: This approach makes use of the knowledge of the flow around and inside the structure which is possible due to the continuous improvement of the flow models. With a flow model and a formulation for the hydrodynamic forces (similar to those of the dynamical analysis) the quasi-empirical model is based on the assumption that the damage should be a functional of some non-dimensional parameters that represent the hydrodynamic forces acting on the units. This functional will be general for all structures with similar interlocking and gravity forces, that have not been taken into account in the force formulation.

- Dynamic analysis: This approach makes use of some analytical model of the flow around and inside the porous structure. Once the flow is known, the vector forces over the units are expressed, including the interlocking forces. This approach allows the study of the dynamics of the armour stones in real time. As a result, the deformed profile of the structure after the wave attack can be obtained. Although this approach is improving as more knowledge on the flow and interlocking forces is achieved, the state of the art does not allow its use for the design of structures.

In this paper, some work in the frame of the first and second approaches to the stability problem of near-bed rubble-mound structures, carried out at the Universidad de Cantabria is presented. First, some model experimentation has been done to improve the

existing data sets on stability, paying special attention to the initial stages of damage. After that, the data analysis is compared with two different parameters for the quasi-empirical model; one based on the Morison drag forces (*drag parameter*) and the other based on a bed shear stress parameter (*mobility parameter*). These two approaches are also compared with a conventional non-dimensional approach using two parameters, the stability number and the relative submergence, that have been found to be the most relevant for the assessment of the damage.

Methodology

Detached near-bed rubble-mound structures are usually very flat, and are deployed in relatively deep waters. Typical ratios of crest height/structure width, are in the range $0.1<h_c/B<0.2$ while the ratios of crest height/water depth are in the range $0.1<h_c/h<0.5$. Waves propagate over these structures with little transformation and reflection is very low. In the case of very steep waves, the breaking takes place after the waves have overtaken the structure and the perturbation of the breaking wave does not affect the flow over the structure. This means that flow around the structure can, in a first approximation, be described by wave theory.

For the implementation of a fully quasi-empirical model of damage, a model of the flow around and in the porous structure will be necessary. But before that, an appropriate flow-force parameter should be chosen in order to relate damage with forces. If enough experimental data is obtained with only one geometry and rubble type, the geometry and porous characteristics of the rubble will not affect the results, and the suitability of different flow-force parameters could be studied using a simple wave theory to describe the flow around the structure. To do this, the next steps will be followed:

1- Stability model tests of a single near-bed rubble-mound structure using regular waves.
2- Dimensional analysis of the experimental data and formulation of damage in terms of the most relevant non-dimensional parameters.
3- Analysis of the relative importance of the drag and inertia terms in the description of the structure's measured damage. Definition of a proper flow-force parameter based on Morison-type forces.
4- Analysis of the observed damage in terms of the Morison drag parameter.
5- Definition of an appropriate bed shear stress flow-force parameter.
6- Analysis of the observed damage in terms of the bed shear stress parameter.
7- Comparison between the three different approaches to damage analysis.

Stability model tests

Experimental set-up

In the wave tank of the laboratory of the Ocean and Coastal Research Group of the Universidad de Cantabria 167 stability tests have been carried out. Regular wave trains of 230 waves have been used to test the stability of a single low-crested, rubble-

mound structure. Figure 1 shows the general layout in the wave tank and the geometric properties of the structure. The structure is a detached protection, 150 cm long, 42 cm wide and 6 cm high. The crest width is 6 cm and the slopes are 3/1. The rubble is composed of uniform angular marble stones, with the following characteristics: W_{15} = 0.18 g, W_{50} = 0.23 g, W_{90} = 0.37 g, ρ_s = 2675 Kg/m^3 and n = 0.47, where ρ_s is the density of the stones and n is the porosity of the rubble. With these data, the following cube-equivalent nominal diameters can be calculated: D_{n15} = 4.1 mm, D_{n50} = 4.4 mm and D_{n90} = 5.2 mm.

The structure was installed in the bottom of the wave tank, over a rigid steel plate that can be lifted with the laboratory crane to assess the damage without draining the tank. Between the structure and the wave board there is a mild slope, 32/1, that shoals the waves. Behind the structure, a rubble beach, with a slope 15/1 dissipates the generated waves.

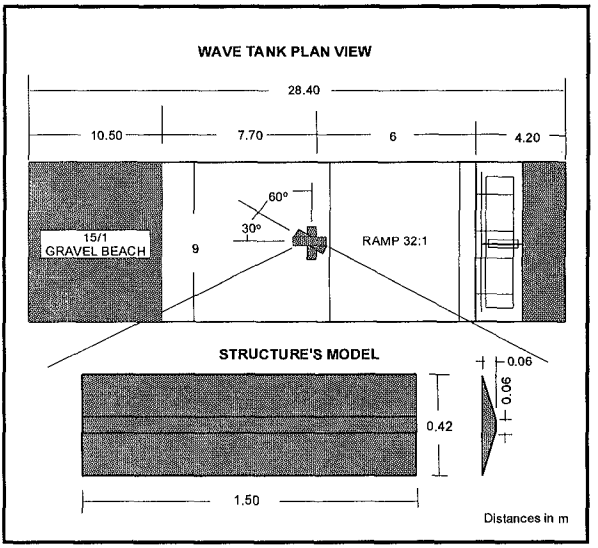

Fig- 1. General layout of the experimental work

For the experiments, three different orientations of the structure axis with respect the wave rays have been considered: 90° (normal incidence), 30° (oblique incidence) and 0° (parallel incidence). In this paper, only the results of the 62 tests carried out with normal incidence will be considered. Three water depths and three wave periods have been selected for the tests. The number of wave heights tested for each water depth and period is variable, depending on the measured damage. Free surface has been measured in four locations, three resistive wave gauges were installed in front of the structure in order to separate incident and reflected waves. Another wave gauge was installed in the rear of the structure, to measure the transmitted waves.

Test methodology.

For each test, the model was rebuilt over the steel plate, outside the water tank. The model shape was obtained using a steel plate that glided longitudinally over two rails, see Figure 2-a. A gap at the top of the plate allowed the input of more stones, if necessary. When the model was finished, no single stone of the model touched the gliding plate. With the laboratory crane, the steel plate that supported the model was lifted to its position in the wave tank. The model was moved carefully to avoid any movement of stones when the model was submerged in the water, Figure 2-b. Each test was defined by the wave incidence angle, water depth, wave period and wave height. After the wave run, the model was carefully lifted again and moved to a working table to assess the damage, which was measured counting the number of stones in the accreted area of the structure and those removed from the structure. The test area of the model was a section 50 cm long, that in the case of normal incidence was located in the center of the model. To obtain the accreted stones, the gliding plate is moved along the model. All the stones of the test area touching the gliding plate were collected and added to those stones removed from the test area.

Fig. 2- Experimental methodology. (a) Model over steel plate. (b) Submerging the model.

Test results

The wave gauge data were analyzed to obtain incident, reflected and transmitted wave trains. Due to the low h_c/h ratio, wave reflection from the structure was very low, less than 5%. For the longer periods, wave reflection from the dissipating beach was higher (about 10%) than the reflection from the structure. Conventional up-crossing analysis of the incident waves was carried out to determine the statistical properties of the waves.

The measured water depth, incident wave period and wave height as well as the number of displaced stones are presented in table 1.

Water depth (m)	**Wave period (s)**	**Measured incident wave heights** (mm)-Number of displaced stones
0.2	1.2	**54**-15 **63**-51 **90**-96 **110**-356 **143**-630
	2.0	**61**-31 **83**-55 **110**-131 **129**-301 **149**-1293
	2.8	**49**-33 **68**-65 **89**-151 **120**-391 **124**-857
0.4	1.2	**95**-21 **118**-42 **139**-117 **163**-99 **172**-109 **186**-143 **207**-196 **212**-209
	2.0	**83**-31 **100**-34 **118**-56 **135**-72 **155**-122 **175**-236 **192**-334 **222**-848 **241**-1996
	2.8	**82**-22 **97**-25 **118**-66 **132**-70 **151**-124 **178**-228 **220**-361 **242**-729 **263**-1984
0.61	1.2	**183**-59 **210**-69 **217**-52 **235**-50 **236**-62
	2.0	**116**-12 **143**-32 **159**-49 **181**-41 **201**-46 **221**-70 **250**-177 **278**-562 **290**-1457
	2.8	**113**-26 **154**-44 **190**-66 **211**-127 **236**-234 **267**-602 **334**-1814

Table 1. Measured wave parameters and number of displaced stones for normal incidence

Although the waves are regular there are always slight differences in wave heights that have to be taken into account in the statistical analysis. The average of the 100 biggest waves, H_{100}, of the incident wave train has been used as the wave height parameter for the following stability analysis.

Data analysis

As stated earlier, the objective of this research is the comparison between the suitability of two flow/force parameters (Morison forces and bed shear stress forces) to explain the observed damage. A conventional non-dimensional approach will be used as a reference.

Dimensional analysis of stability

The number of stones in the accreted area is the measured damage. In a conventional dimensional analysis, this damage should be a functional of all the flow and geometry parameters involved:

$$N = f(H, T, \theta, h, h_c, B, \alpha, D, \rho_s, \rho, \mu) \quad (1)$$

where:

-H: Wave height
-T: Wave period
-θ: Angle between wave ray and the structure axis
-h: Water depth

-h_c: Crest height of the rubble protection
-B: Width of the rubble protection
-α: Slope angle of the rubble protection
-D_{n50}: Nominal diameter corresponding to the W_{50} stones of the rubble
-ρ_s: Density of the rubble stones
-ρ: Density of the water
-μ: Dynamic viscosity of water.

In this work the geometrical characteristics of the structure will be held constant, and only normal incidence results will be used, so the expression (1) can be simplified to:

$$N = f(H, T, h, h_c, D, \rho_s, \rho, \mu) \quad (2)$$

The measured damage is defined as the number of stones, N, counted in the accreted area. This accreted area is assumed to be the same as the eroded area, so N is also the number of stones lost in the eroded area. Once N and the mound porosity is known, the average eroded area, A_e, in a section of length X, can be estimated using the non-dimensional parameter S expressed as:

$$S = \frac{A_e}{D_{n50}} = \frac{ND_{n50}}{(1-n)X} \quad (3)$$

It is well-known that the non-dimensional parameter that relates the stone size and density with the wave height is the stability number or Hudson number:

$$N_s = \frac{H_s}{\Delta D_{n50}}; \quad where\ \Delta = \frac{\rho_s}{\rho} - 1 \quad (4)$$

The freeboard of the structure has a great influence on the damage. Its influence can be taken into account using the non-dimensional parameter h_c/h. Other non-dimensional parameters that could be important for the damage are the relative water depth, h/L and the wave stcepness, H/L, whcre L is the wave length.

The viscosity of the water affects the flow around the stones. This influence is taken into account using the Reynolds number. In the hypothesis that model tests are such that the flow above the rubble is rough turbulent, the Reynolds number would not affect the drag over the stones and the influence of the water viscosity on the resulting damage can be neglected. After the previous statements, eq. (3) can be simplified to the following non-dimensional form:

$$S = f(N_s, \frac{h_c}{h}, \frac{h}{L}, \frac{H}{L}) \quad (5)$$

Figure 3 shows the influence of N_s on damage. The points clearly show the exponential increase of damage with N_s. It is also clear from the figure that damage is decreased when the crest submergence, h_c/h, decreases. Although the general trend is an

exponential growth of damage with N_s, if only low values of S are taken into account, S<2, the growth of S with N_s can be considered to be linear.

The influence of wave steepness and relative water depth is not that clear. Following the results shown in Figure 3, for a water depth of 0.2 m and a period of 1.2 s, damage increases slightly faster than for a period of 2.0 s. However, for a period of 2.8 s the evolution of damage is similar again to that of the former period of 1.2 s. This behavior is different for the two other water depths considered, indicating that the influence of these two parameters is small and that it cannot be easily evaluated with independent potential fits of any of them. For this reason, and as a first approach, the influence of these two parameters is discarded in the analysis, and only the two main parameters will be taken into account:

$$S = f(N_s, \frac{h_c}{h}) \tag{6}$$

Figure 3 shows also the best fit lines for the function f(), using an exponential form for the influence of N_s and a potential form for the influence of h_c/h.

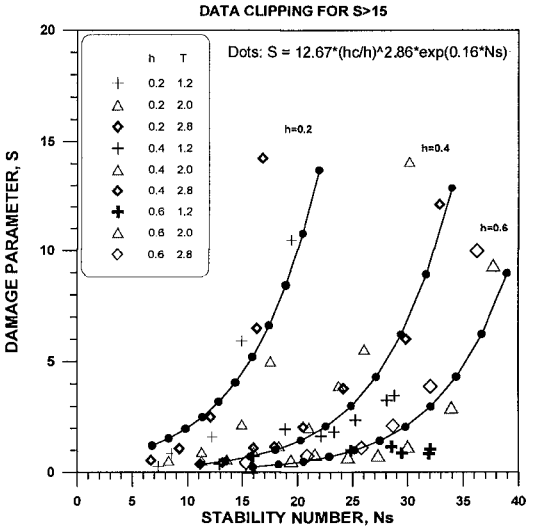

Fig. 3. Damage parameter, S, versus stability number, Ns and crest sumergence h_c/h. Experimental data and best fit lines.

Morison forces analysis

The Morison equation relates the flow properties with the parallel and normal forces generated by that flow above a solid object:

$$F_D = \frac{1}{2} \rho C_D D_{n50}^2 \bar{u}|\bar{u}| + \rho C_M D_{n50}^3 \frac{D\bar{u}}{Dt} \tag{7}$$

$$F_L = \frac{1}{2}\rho\, C_L D_{n50}^2\, \bar{u}|\bar{u}| \qquad (8)$$

where $\bar{u}$ is the velocity vector and C_D, C_M and C_L are drag, inertia and lift coefficients, respectively, that depend on the shape of the solid and on the characteristics of the flow. These coefficients should be obtained experimentally.

Tørum (1994) measured forces over individual armour units of a rubble- mound breakwater laboratory model and determined the drag, inertia and lift coefficients. Among other conclusions, two are enhanced here:

- Maximum parallel (to the slope) forces are in phase with maximum velocities. This implies that maximum parallel forces are dominated by drag.
- Maximum normal forces are a combination of drag, lift and inertia forces. Their magnitude is less than half the maximum parallel forces.

In the threshold of initiation of damage, the armor units will be displaced only by the maximum forces, that are dominated by drag. If that is true, damage will only be a function of the maximum parallel velocities affecting the units. Maximum parallel forces over the crest of the rubble protection can be represented as a function of the oscillatory velocity amplitude at the crest level, U_c, by the following non-dimensional drag force parameter:

$$F_{dp} = \frac{\rho_w U_c^2}{\rho_s g D_{n50}} \qquad (9)$$

where,

$$U_c = \frac{\pi H}{T}\frac{\cosh kh_c}{\sinh kh} \qquad (10)$$

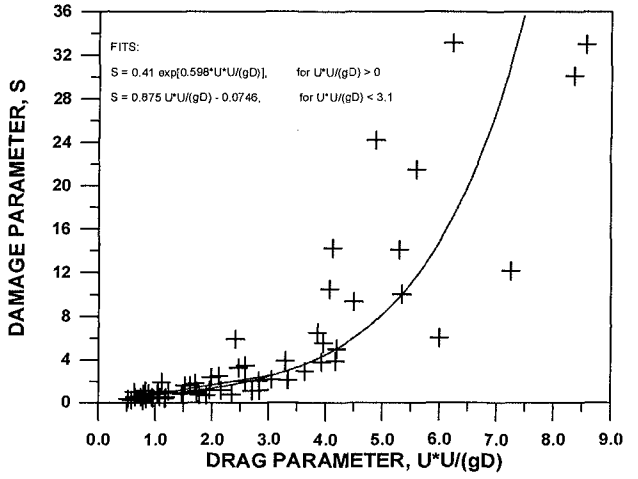

Fig. 4. Damage parameter vs. drag parameter. Data and best fit.

Figure 4 shows the damage data as a function of the drag force parameter (9) with the best exponential fit. As can be seen, the fit for low levels of damage, S<4, is fairly good, but the spread increases above that value of S, indicating that above that level, transport of stones is not well related with drag forces.

Figure 5 shows a zoom of the data below S=4. As can be seen the data trends for different periods and water depths can still be separated, indicating that there should be more flow information in the force parameter. Also shown in the figure is that, for S<2, a linear relation between the drag force parameter and damage is nearly as good as the exponential fit.

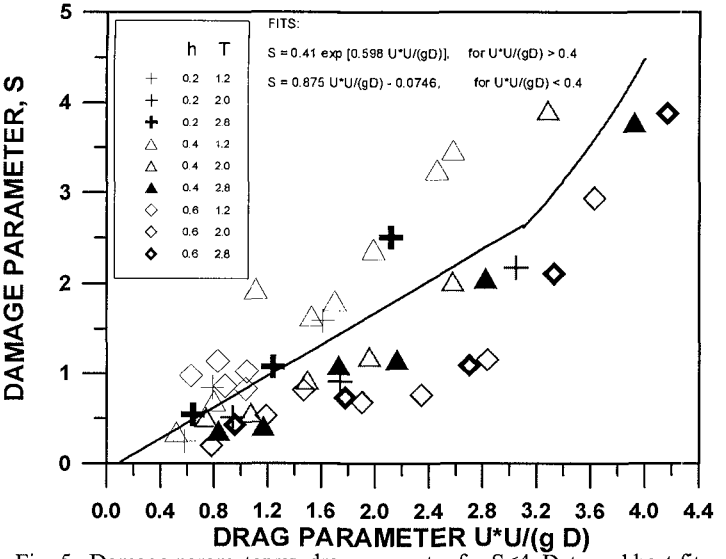

Fig. 5. Damage parameter vs. drag parameter for S<4. Data and best fit.

Bed shear stress forces analysis.

Formulations of sediment transport make use of the Shields parameter or mobility parameter, M_p, that relates the shear stress at the crest, τ_{cw}, with the submerged weight of the sediment grains:

$$M_p = \frac{\tau_{cw}}{\Delta g D_{n50}} \tag{11}$$

The shear stress over the crest due to the oscillatory motion of waves can be expressed as a function of the oscillatory velocity amplitude at the crest level, U_b, using the following quadratic expression:

$$\tau_{bw} = 0.5\rho f_w U_c^2 \tag{12}$$

where f_w is a wave friction factor, that can be expressed following Swart (1976) as follows:

$$f_w = \exp\left[-6 + 5.2\left(\frac{A_c}{k_s}\right)^{-0.19}\right], \quad for \frac{A_c}{k_s} > 1.57 \tag{13}$$

$$f_w = 3, \quad for \frac{A_c}{k_s} \leq 1.57 \tag{14}$$

where A_c is the amplitude of the oscillatory horizontal displacement of the water particles under the wave motion at the crest level that for linear wave theory is given by:

$$A_c = \frac{H}{2}\frac{\cosh kh_c}{\sinh kh_c} \tag{15}$$

and k_s is the bed roughness that can be related to the stone size trough the expression given by Kamphuis (1975):

$$k_s = 2D_{90} \tag{16}$$

In Figure 6 the damage results as a function of the mobility parameter is presented. Again, for damage levels S>4, the dispersion increases, indicating that the mobility parameter alone is not appropriate to explain high levels of damage, where formulations of transport could be more suitable. Figure 7 shows a zoom of the damage data in the range S<4. It can be seen that dispersion is lower than for the drag force parameter case. Again, in the first stages of damage, the evolution of damage with the mobility parameter is very linear; in particular in the range of S<1. For damages S>1, dispersion increases, giving some information about when transport starts.

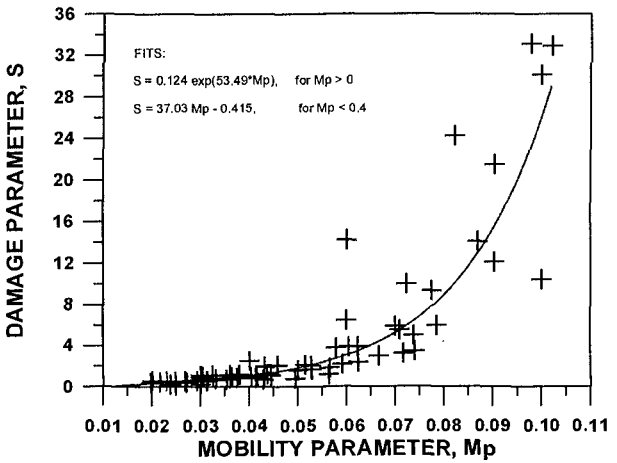

Fig. 6. Damage parameter vs. mobility parameter. Data and best fit.

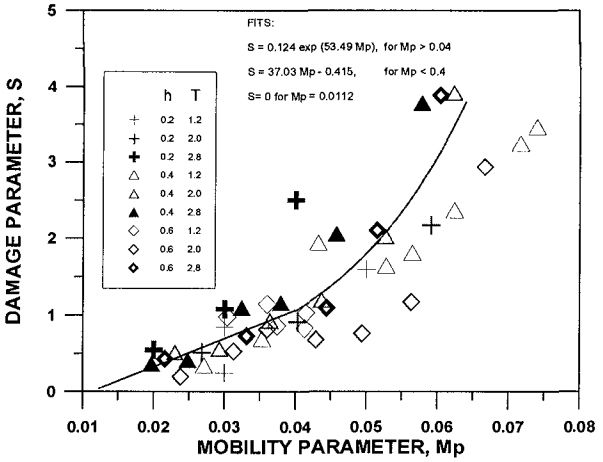

Fig. 7. Damage parameter vs. mobility parameter for S<5. Data and best fit.

Comparison between the three approaches.

Figure 8 is a plot of the measured damage parameter against the calculated one, using the three approaches and fits indicated above: non-dimensional with two parameters, drag force parameter and mobility parameter. Only damage data in the range S<4 have been taken into account. S calculated versus S measured has been also drawn in the figure. In the legend, the mean square error (*mse*) between the measured and the calculated damage is also shown. As can be seen from Figure 8, the mobility parameter gives the lowest *mse*, while the drag force parameter and the biparametric formulas give similar results for the *mse*. For S<1, the suitability of the mobility parameter is still better than the other approaches.

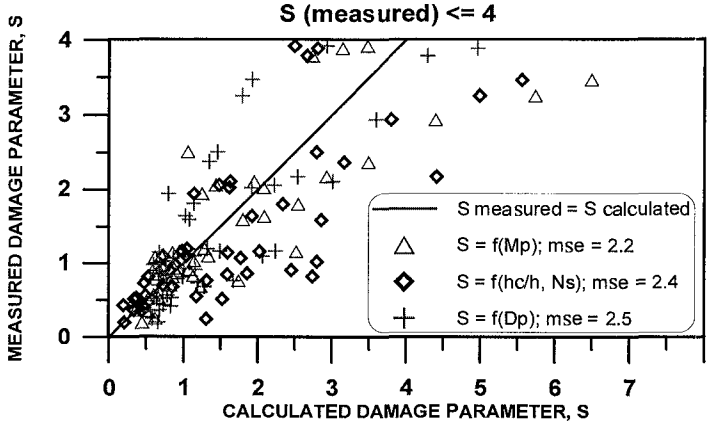

Fig. 8. Measured vs. calculated damage parameter.

The sharp increase of dispersion between the calculated and the observed damage parameters could be an indication of a change in the transport modes: for S<1 the stone jumps or rolls once until a more stable position in the mound is achieved. In this case, only the least stable units are affected and the number of waves (regular waves) should not influence the measured damage. For 1<S<2, units can be moved many times until they find a stable position on the rubble. In that case the number of waves necessary for the stabilization of damage increases with the damage level but the damage continues its linear increase with the mobility parameter. If the total number of waves is maintained, dispersion increases. For S>2 stones are not able to find a stable position in the rubble and can be transported away. In that case, damage never stabilizes and depends on the number of waves. As the transport is not well described by the mobility parameter alone, dispersion increases again. The change from linear to exponential in the relation between the damage and the mobility parameter is a clear indication that new parameters should be added to describe the influence of the transported stones.

Engineers are not comfortable with the idea of having the stones of their protection rolling away (and perhaps appearing in the nearby beach). For that reason, it seems reasonable to design these structures for damages in the S<1 region.

Conclusions.

The results of the analysis show that the approach considering the forces generated by the bed shear stresses gives a better agreement between the observed and the calculated damage than the conventional approach using Morison forces on the units. If dimensional formulas of damage are restricted to a maximum of two parameters, the more relevant parameters for damage are the stability number and the relative submergence of the structure. In that case, the bed shear stress gives a better fit to damage than the dimensional approach.

In the first stages of damage, for damage parameters in the range S<1, the evolution of damage with the mobility parameter is very linear. In the range 1<S<2, the evolution of damage with the mobility parameter is also linear, but dispersion increases. In the range S>2, the evolution of damage with the mobility parameter is exponential, with dispersion increasing as the mobility parameter increases.

The sharp increase of dispersion between the calculated and the observed damage parameters could be an indication of a change in the transport modes: for S<1 the stone jumps or rolls once until a more stable position in the mound is achieved. In that case, only the least stable units are affected and the number of waves (regular waves) should not influence the measured damage after the first tenths of waves have stabilized the damage. For 1<S<2, units can be moved many times until they find a stable position on the rubble and the number of waves necessary for the stabilization of the damage increases with the damage level. If the total number of waves is maintained, dispersion is increased. For S>2 stones are not able to find a stable position in the rubble and can be transported away. In that case, damage never stabilizes and depends on the number of waves. As the transport is not well described by the mobility parameter alone, dispersion

increases again. The change from linear to exponential in the relation between the damage and the mobility parameter is a clear indication that new parameters should be added to describe the transported stones.

It can be concluded that it seems reasonable to design near-bed rubble mound structures considering damages in the S<1 region.

Acknowledgements

This work is part of the Research Project MAR96-1833 funded by the Spanish Comisión Interministerial de Ciencia y Tecnología (CICYT). Undergraduate student Román Gutierrez carried out the stability laboratory tests and the wave data analysis. Also the help of PhD student Rafael Diez in part of the data analysis is acknowledged.

References

Kamphuis, J.W., (1975). Friction factors under oscillatory waves. Proc. A.S.C.E. J. Waterw. Harbors Coastal Eng. Div. 101, (WW2): 135-144.

Levit, M., van Gent, M.R.A. and Massie, W.W, (1997). Stability of pipeline covers under waves and currents. Proc. of the 8th Int. Conf. on the Behaviour of Offshore Structures (BOSS'97). Vol. 1 pp. 195-210.

Lomónaco, P. (1994). Design of rock cover for underwater pipelines. Master of Science Thesis HH 197. International Institute for Infrastructural, Hydraulic and Environmental Engineering. Delft.

van der Meer, J.W. (1993). Conceptual design of rubble mound breakwaters. Delft Hydraulics Publication, no. 483.

Swart, D.H. (1976). Coastal sediment transport. Computation of longshore transport. Delft Hydraulics Laboratory. Rep. R968, Part I.

Tørum, A. (1993). Wave-induced forces on armour unit on berm breakwaters. J. of Waterw., Port, Coastal and Ocean Eng., Vol 120, No. 3, May/June, 1994, pp251-267.

Vidal, C., Losada, M.A., Medina, R., Mansard, E.P.D and Gómez-Pina, G. (1992). A universal analysis for the stability of both low-crested and submerged breakwaters. Proc. 23th Int. Conf. on Coastal Eng. ASCE. Vol. 2, pp. 1679-1692.

COASTAL DEFENCE STRUCTURES IN NSW, AUSTRALIA

S.J. Wyllie, Section Engineer, Manly Hydraulics Laboratory[1]
D.B. Lord, Consultant Engineer, Manly Hydraulics Laboratory[1]
I.F.W. Jayewardene, Consultant Engineer, Manly Hydraulics Laboratory[1]
T. Young, Department of Land and Water Conservation[2]

ABSTRACT - 100 Years of Experience In a High Energy Wave Climate
This paper uses the examples of Coffs Harbour breakwaters and the training wall head on the Richmond River at Ballina to outline some of the developments in coastal engineering design and construction over the last century. Most of the 63 major structures along the New South Wales (NSW) coastline are similar. Recent developments in data collection and analysis as well as the evolution of physical modelling techniques used for coastal structure design at the NSW Department of Public Works and Services' Manly Hydraulics Laboratory (MHL) are discussed using these two projects. The use of computational models in conjunction with physical models and the introduction of new variables such as wave obliquity and groupiness into breakwater design are discussed. The need to evaluate the performance of artificial units such as Accropodes, concrete cubes and Hanbars for primary armour at breakwater heads due to restrictions on the availability of quarry armour and available construction techniques is briefly addressed.

1. Introduction

The first European settlement of NSW at Sydney in 1788 was by sea. The first public works in the new colony included landing steps and wharves constructed in Sydney Cove. The involvement of Public Works in coastal engineering extended along the coastline with the growth of the new colony. To a very large extent, the need for these works to improve navigation and trade formed the basis for the development of coastal engineering practice in NSW.

[1] NSW Department of Public Works and Services, Manly Hydraulics Laboratory, 110B King Street, Manly Vale, NSW, Australia, 2093
[2] Department of Land and Water Conservation, 10 Valentine Avenue, Parramatta, NSW, Australia, 2150

Coastal engineering in NSW has gone through a series of stages which are identifiable in the public (coastal engineering) works and government programs of the time. These included:

- From 1788 to the 1950s the emphasis on coastal engineering was for the improvement of navigation for the coastal trade, including the development of major ports, construction of wharves, dredging of navigation channels and construction of shipbuilding and repair facilities. By the 1950s the coastal trade had all but ceased to exist and could not compete with the expanded rail and road network. The major ports of Newcastle, Sydney, Port Kembla and Botany Bay were established and have continued to develop the capacity to handle larger ships and containers.
- From the 1950s to the present there has been an emphasis on the use of all but the major ports for the fishing industry. From 1959 to 1966 Public Works constructed nine fishing ports under the fishing ports program. This program was augmented in 1976 and further works included wharves, facilities, entrance works, breakwaters, boat harbours and mini-ports.
- From the mid-1970s to the present there has been an increasing awareness of the coastal environment and its fragile nature and the need to preserve the natural environment and the recreational amenity it provides. This increased awareness has coincided with a boom in the tourist industry, together with an unparalleled increase in coastal development. The number of registered vessels in NSW increased from 12,000 in 1979 to 90,000 in 1989 and 160,000 in 1997 (NSW Waterways pers. comm.) Coastal engineering focus has changed to beach protection works, beach regeneration and the provision of tourist and recreational infrastructure. These works have been supported by government programs since the mid-1970s.

2. The Coastal Structure as an Asset

The NSW Government recently undertook an asset appraisal of breakwaters and river entrance training walls, including aspects on the history of design, construction and performance over a period of nearly 100 years. A total of 63 structures which are 22,600 m in length (Figure 1) were appraised. The figure also shows the location of 12 rock quarries from which armour was obtained for construction. The study (MHL648 1993) placed the value of the structures at $550 million.

MHL has been closely linked with many of the designs of the structures on the NSW coastline through its data collection and physical modelling capabilities which have been built up over a period of nearly 40 years. Some of the original designs as constructed (with irregular maintenance) have withstood wave energy over the last 100 years. In designing a coastal structure a number of different factors have to be considered by the engineer. These include the practicalities of construction, the short- and long-term requirements of the construction, the availability of materials, environmental factors and the hydraulic criteria. After arriving at a prelirninary design or, more commonly, a number of options the design is usually optimised using either a physical or numerical model or both.

3. Some Examples of Historical Developments in Coastal Engineering Structures
For over three decades both numerical and physical modelling have been found to complement each other and have been used in investigations such as on the Coffs Harbour breakwater layout (MHL110, 1966). To illustrate the evolution in design philosophy examples of the training walls at Ballina on the Richmond River (Figure 2) and Coffs Harbour eastern breakwater (Figure 3) are discussed. These two structures are examples of a training wall and a breakwater at a harbour. Most of the 63 major structures along the NSW coastline are in these two categories. This section also describes recent developments in data collection and analysis as well as the evolution of physical modelling techniques used for coastal structure design at MHL. The paper also traces the rationale for using computational models in conjunction with these physical models.

3.1 Richmond River Entrance
The Richmond River entrance was charted by Captain Henry Rous in August 1828 while inspecting the coast between Brisbane and Port Macquarie. His records include a note on manoeuvres for getting inside the tricky entrance bar.

"*The sandbar at the entrance to the Richmond River was notorious - it shifted across the 6,000 ft wide entrance sculpting mazes of sand which discouraged ships*" (Coltheart 1997). The bar was regularly dredged from 1878. By the turn of the century the Public Works Department maintained a fleet of 39 dredges working along the NSW coast.

A plan to train the entrance was drawn up by the Chief Engineer of Public Works, Sir John Coode. In 1889 the entrance was completely blocked by natural sand shoals so that produce had to be carted overland to the Clarence River to the south. Work on the entrance training was commenced that year comprising internal training walls and the southern breakwater. Figure 2 shows a design cross-section developed and presented for the Richmond River breakwaters. The design consisted essentially of the placement of a pile of rocks to form the structure, as shown on this original design drawing.

Rock for the northern breakwater was quarried locally at Pilot Point while rock for the southern breakwater was punted from a quarry at Rileys Hill, 19 miles upstream.

In the spring of 1891 it is reported that "*the channel again broke through the southern spit, moving in one day a distance of nearly 3,000 feet.*" (Coltheart 1997). A training wall was under construction at west Ballina on the north arm upstream. A larger training wall on the southern side was added, enclosing a reclamation site of 63 acres. Dynamite was used to break up the shoals and two dredges were deployed working 16 hours a day to clear the shoals. This was unsuccessful as the southerly weather continued to wash sand around the southern breakwater and into the entrance. Work on the northern breakwater was stopped in 1899 and for more than two years the total workforce of 200 men was deployed night and day on the southern breakwater to try to stop the sand ingress.

By May 1901 the southern breakwater had reached a length of 7,542 feet and the night force recommenced work on the northern breakwater. By mid-1902 the

southern breakwater was 800 feet short of the design length and the northern breakwater 1,000 feet short. Several time the ends had to be restored as they were flattened by storms. A new quarry was opened to provide larger armour stone. A locomotive was used to haul the blocks along the northern wall while four horses hauled the tip trucks carrying rock from 1 ton to 20 tons along one mile of track to the ends of the breakwater.

The entrance works had totally reformed the entrance, reconfiguring the channels with the dredges reclaiming swamps and tidal flats and creating new channels. Dredging and bank protection works were ongoing to maintain the navigability of the river. Vessels with a draft of 10 feet could steam 63 miles up river and, in 1904, 300 steamers and two schooners crossed the Richmond River bar.

In the 1930s the storm damage required constant repairs and unemployment relief funds were used in setting 30 ton concrete blocks onto the southern wall. Five dredges worked regularly in the river during the 1930s. The northern breakwater was damaged and repaired in 1947 and the southern wall again in 1949.

By the 1960s dredging was only used to maintain a 6 foot minimum depth over the bar for smaller vessels.

In contrast, the upgrading of the Richmond River entrance training walls today included intensive numerical assessment, modelling to determine inshore wave conditions, and physical model testing of various primary armour materials in a random wave basin at MHL. The modern design is based on one of the most thorough and longest wave databases used anywhere in the world.

3.2 Coffs Harbour

Coffs Harbour is situated on the mid-north coast of NSW approximately 600 kilometres north of Sydney. The area was settled in the 1840s by timber loggers and the harbour developed as a timber trading port.

The Coffs Harbour jetty was completed and opened to shipping in August 1892. It was severely damaged in storms two years later. The port had the highest net tonnage in NSW and was the busiest on the north coast averaging 399 ships per year between 1909 and 1924. Ship visits reduced to 26 in 1960 and to seven by 1970. The last freighter to use the jetty was in 1973. The jetty has been subsequently shortened to its original length and restored, primarily as a tourist feature. Figure 3 indicates the period in time that construction at Coffs Harbour took place. It is seen that construction of the breakwater took place from 1918 to 1974.

In 1912 the decision was taken to construct an artificial harbour by constructing breakwaters at Coffs Harbour to protect the jetty. Work began immediately on the causeway connecting the mainland to South Coffs Island and this effectively intersected the alongshore drift past the islands and to the northern beaches. A quarry was established on the island to provide rock for the proposed eastern and northern breakwaters which enclosed a harbour of 217 acres. Construction of the breakwater private contract commenced in 1915 and the contract was cancelled and taken over by Public Works in 1917.

Work on the eastern breakwater which commenced in 1918 was washed away by heavy storms in 1919 and 1920. The northern wall was two thirds complete when heavy storms in 1921 destroyed the end and washed away five tipping wagons leaving the railway track suspended in mid air. The northern wall was finally connected to Muttonbird Island in 1924. Continual maintenance was required as the wall was low enough to be overtopped in storms. In 1925 storms levelled 400 feet of the northern wall which had to be reconstructed.

Storm damage was a major cost factor on the eastern wall construction. Following major damage in 1925 it was noted that "*the quarry could not provide stone big enough to withstand the seas*" (Coltheart 1997) and use of concrete blocks with a toe of 100 tonne blocks was recommended for the seaward face. In gales during 1937, 110 feet of the wall was demolished and had to be replaced. The wall was completed in 1939 and the concrete capping in 1943. Major repairs required upgrading of the railway line and carriages in 1953.

Major impacts on the coastal processes in the study area have resulted from the harbour construction. The breakwaters have intersected the estimated south to north littoral drift of 75,000 m^3/annum resulting in accretion of Boambee Beach to the south and Jetty Beach within the harbour. At the present time, following many years of lower than average wave energy conditions the beaches north of Coffs Harbour are still in a depleted condition.

4. Historic Aspects of Data Collection for Coastal Engineering Design

The necessity to use accurate site specific data for coastal engineering construction has been acknowledged for over a century. Data has also been used to evaluate the performance of a structure after it was constructed and to refine and improve coastal engineering design. Some of the first evidence available on the collation of wave data for Coffs Harbour is the documentation of wave heights at the seaward end of the wharf (Figure 3) during rough seas on six occasions from December 1936 to July 1954 (MHL186 1974).

An example of continuous wave data recording prior to the use of data buoys is obtained from wave pole records as reported by White (MHL109 1966) taken half a mile from the coast at Nobbys Head, Newcastle in 1965 (Figure 4). A significant step in wave data analysis on the NSW coastline was taken when wave hindcasts were calculated for Port Kembla for the years 1950 to 1964 by Stone and Foster (MHL109 1966). The results of these analyses are indicated in Figure 5 and compare well with present day hindcast wave data. Long-term continuous offshore wave measurements were begun in Sydney in 1974 and have continued since, using a network of seven wave data buoys. Increased accuracy in extreme wave height (Goda et al 1988) and storm duration (Sobey 1997) analysis are of interest to the coastal engineer. Analysis techniques have been developed over the last three decades to make maximum use of short time series. The relevance of long-term wave measurement is seen in the variations obtained for the 100-year wave height for Port Kembla (Figure 6). Presently, MHL measures wave height and directions using a number of methods such as a network of wave data buoys (Kulmar 1995). These include a directional buoy in Sydney (Figure 6); radar imagery; aerial photography; electromagnetic current meters; hindcasting and satellite imagery. Whilst the data buoy network is a

continuous measurement program, the other methods of measurement were used for specific projects. The NSW measured wave climate represents one of the longest continuous measured wave data sets anywhere in the world.

4.1 An Example in the Change in Requirements for Data

The requirements for data to aid coastal engineering design projects have changed over the last few decades. This can be illustrated by the equation used to obtain armour size. Many design equations have been developed to obtain armour size. Of these equations those suggested by Irribarren (1938), Hudson (1958) and Van der Meer (1987) have been the most accepted and utilised.

Iribarren's equation for stability (1938):

$$\frac{H}{\Delta D_{n50}} = \frac{\cos\alpha - \sin\alpha}{K^{1/3}} \qquad (1)$$

Hudson's equation for stability (1958):

$$\frac{Hs}{\Delta D_{n50}} = \left(K_D \cot\alpha\right)^{1/3} \qquad (2)$$

Van der Meer's equations for stability (1987):

For plunging waves:
$$\frac{H_s}{\Delta D_{n50}} * \sqrt{\xi_z} = 6.2P^{0.18}\frac{S}{\sqrt{N}}^{0.2} \qquad (3A)$$

For surging waves:
$$\frac{H_s}{\Delta D_{n50}} = 1.0P^{-0.13}\frac{S}{\sqrt{N}}^{0.2}\sqrt{\cot\alpha\xi^P} \qquad (3B)$$

where:

ξz	=	surf similarity parameter	P	=	permeability coefficient of structure
α	=	slope angle	$S = A/D^2_{n50}$	=	damage level
Δ	=	relative mass density	A	=	erosion level in cross-section
Dn_{50}	=	nominal diameter of a stone	N	=	number of waves
W_{50}	=	50 percentile value of mass distribution	$H_i H_s$	=	wave height
			$K_i K_D$	=	coefficient of damage

Variables such as storm duration or number of waves (N), permeability coefficient of the structure (P) and surf similarity parameter (ξ) have been included in design criteria to obtain the mass of primary armour over the last decade. Water level and therefore the influence of breaking waves was included in Hudson's physical modelling regime though not in his formulae. Variables such as wave obliquity (Galland 1994) and wave groupiness (Funke 1979), though not included in the design formulae, have to be considered in the finalisation of designs when using physical models. To this end MHL has included the analysis of wave groups during storm and

calm conditions (Jayewardene 1993) and the influence of wave obliquity on primary armour (Jayewardene 1997) in its research and development programs.

5. A Short History of Physically Modelling Coffs Harbour Breakwaters

Two physical models were carried out on Coffs Harbour, one in 1966 and the most recent investigation in 1998. The main aims of the 1966 model were to provide improved berthing at the existing jetty (Figure 3) and improved anchorage conditions for the existing fishing fleet. The 1998 model attempted to simulate damage conditions to the eastern breakwater head where thirteen 40 tonne blocks were displaced during a storm in May 1997. Although the aims of the two investigations were different, it is instructive to compare the techniques of wave generation and data collection used in these models to obtain an understanding of the material changes that have taken place in coastal engineering design.

5.1 Wave Data

Hindcast wave data was used to obtain the deep water design wave for the 1966 model (MHL 109 1966). Extreme wave analysis was carried out to obtain design wave data for the 1998 model (MHL 914 1997). Regular waves were used in the early model whereas long crested irregular waves were used in the more recent model. Irregular waves have been used in physical models since the late 1970s and the advantages over regular wave modelling are well documented in the literature (Graveson 1974). In the mid-1980s the importance of wave grouping in harbour layout and the importance of correct reproduction of these groups particularly for ship movement investigations was established (Sand 1983, Bowers 1988). This is probably the reason for the observation made at the conclusion of the 1966 study that *"Reproduction of the surge motion by detailed observation of the prototype were not successful in the model"* (MHL110 1966). Accurate wave height (Figure 7) and wave direction (Figure 8) data during the May 1997 storm in conjunction with numerical modelling (Figure 9) aided in establishing that relatively long period waves (15-17s) of relatively low return period (1-2 year) resulted in the damage of the head. This damage was reproduced accurately in the physical model (Figure 10).

5.2 Water Level Data

Table 1 indicates some water levels used in physical model investigations carried out at MHL for previous projects. In addition to the 90 years of tidal data recorded at Fort Denison, Sydney a network of tide recorders established in 1984 has enabled MHL to predict tides utilising 69 tidal constituents (MHL591 1991). The ability to predict tides has in turn enabled MHL to estimate anomalies accurately and, hence, obtain accurate return periods for extreme water level statistics (MHL591 1991). The water level recorder at Coffs Harbour was able to record the extreme water levels during the May 1997 storm and helped to accurately simulate storm conditions in the physical model. The database generated by the MHL network has monitored some extreme storms such as the one that occurred in May 1974 when waves up to 12 metres associated with large tides and storm surges affected the NSW coastline over several days. A decade ago this storm was adopted as a design storm. With improved tools for extreme event analysis (AWACS 1992) it has been shown by Monte Carlo simulation techniques (Goda 1988) that this storm was more extreme than the 100-year event. This resulted in considerable lowering of crest heights of

structures such as the Sydney parallel runway (AWACS 1992) that have been constructed recently.

MHL Report No.	Year	Site	Design Wave Height/Period	Design Water (Low Water)	Head Slope	Recommended Size	Comment
110	1966	Coffs Harbour	18 ft/10 s	6 ft		10.5 to 12 tonne	Physical 3D model
112	1966	Wollongong Harbour	25 ft/10 s	6 ft		15 tonne	Physical 3D model
256	1978	Bellambi	2 m/7 and 10 s	2.5 m	1:1.5	10.5 to 12 tonne	Physical 3D model
261	1979	Port Kembla revetment	5.4 to 7.1 m/10 s	3.5 m and 4 m	1:1.5	15 tonne	Physical 2D model
272	1979	Port Kembla sea wall	5.5 m/10 and 14 s	4 m	1:2	12 tonne Hanbars 7 tonne dolos	Physical 2D model
301	1980	Eden breakwater	4 to 6 m/6 to 15 secs	to 3.2 m	1:1.5	15 tonne Hanbars	Physical 2D model
782	1996	Oblique wave tests	6.3 m/12 s	2.4 m	1:1.5	10 tonne rock	Physical 3D model
795	1996	Ballina	6.3 m/12 s	2.4 m	1:2.2	suggested to 57 tonne 15 tonne Accropode	Physical 2D model
860	1997	Ballina	6.3 m/12 s	2.4 m	composite		Physical 3D model
897	1997	Ballina	6.3 m/12 s	2.4 m	composite	15 tonne Accropode, antifer cubes, Hanbars	Physical 3D model
941	1998	Coffs Harbour eastern breakwater	7.4 m/12 s 5.4 m/15 s	2.4 m	composite	40 tonne cubes 28 tonne Hanbars 22 tonne Accropodes	Physical 3D model

Table 1 Design Data - Physical Models

6. Physical Model of Ballina Training Wall Head

Historical records indicate that 30 tonne artificial concrete cubes were used instead of rock armour in the early 1930s on the Ballina Heads. Recent physical modelling carried out at MHL (MHL860 1997) compared the performance of artificial armour units such as Accropodes, Antifer cubes and Hanbars (a NSW patented unit) with that of rock armour. Table 2 indicates the values for the mass of primary armour using a coefficient of damage (K_d) obtained from testing carried out by Foster and Gordon (1973). Their tests were conducted using regular waves, whereas present day (MHL) tests use Pierson Moskowitz spectra with spectral peak period and wave height associated with extreme event analysis. Reflection analysis (Mansard 1980) carried out in the flume to accurately assess the incident wave height and numerical modelling using REFDIF (a numerical refraction/diffraction model) was utilised to obtain inshore wave conditions which were replicated in the physical model.

7. Numerical Modelling Used in Conjunction with Physical Models

Constant updating and improvement of short and long wave computational models in the last three decades has significantly extended the design situations for which they can be used. These include the use of directional wave spectra, bed friction, flow separation and recirculation near jetties, radiation damping near harbour entrances and diffraction through breakwater gaps. However, in cases such as the simulation of the May 1997 storm at Coffs Harbour, nearly all the damage was caused by wave overtopping and instabilities caused by flows in the secondary armour. These are

better simulated in a properly scaled physical model with gravitational and inertial forces dominating frictional forces (Cornett 1995). Conditions at the water depth corresponding to the long crested irregular wave generator were obtained for the 100-year event by using the numerical model REFDIF. A similar approach was used when comparing the performance of artificial armour units such as Hanbars, Accropodes and Antifer cubes (MHL897 1997).

	Hudson's Method			Oblique Wave Results				
Chainage (m)	Wave Height (m)	Damage (%)	Armour Size M50 (tonnes)	Kd 30°	Kd 60°	Armour Size (single layer) 30°	Armour Size (single layer) 60°	Actual Placed Contract
325	4	5-10	7.6	4	5.5	7.1	5.1	5
		10-15	5.7	5.5	8.5	5.1	3.2	
								↓
390	4.5	5-10	10.8	4	5.5	10.1	7.3	7.5
		10-15	8	5.5	8.5	7.3	4.7	
								↓
440	5	5-10	14.9	4	5.5	13.8	10.1	10
		10-15	11.1	5.5	8.5	10.1	6.4	
								↓
490	5.5	5-10	19.8	4	5.5	18.	13	10
		10-15	14.8	5.5	8.5	13	8	↓
								Ch520
540	6	5-10	25.7	4	5.5	23.8	17.3	15-18
		10-15	19.2	5.5	8.5	17.3	11.2	
								↓
590	6.5	5-10	32.6	4	5.5	30.3	22	Head
		10-15	24.4	5.5	8.5	22	14.2	

Table 2 Comparison of armour size on Ballina breakwater using Hudson's method, oblique wave testing and actual placed armour

Table 2 indicates values for the mass of primary armour using coefficient of damage (K_d) values obtained from testing carried out by Foster and Gordon (1973). These values were compared with those obtained by using Van der Meer's breakwater design criteria (Van der Meer 1988). The results obtained from Hudson's formula and from oblique wave testing are shown in Table 2.

8. Methods of Construction and Quarrying

Up to the mid-1970s the construction methods used at both Ballina and Coffs Harbour generally involved the sourcing of local armour rock and random placement by tipping. Natural armour stone was sourced on site from adjacent coastal headlands and nearby purpose quarries. In most instances these stones were tipped from specially constructed tipping frames on rail wagons and later from modified truck bodies. To increase the primary armour mass, concrete armour units ranging from 10 to 38 tons were cast and then tipped on training wall slopes. Smaller units up to 2 tons were frequently cast on top of the wall and pushed over the crest by bulldozers. The lack of control resulted in haphazard positioning of the units and poor interlocking. Where rail systems were adopted for armour placement (at Ballina and Coffs east breakwater) the crests were capped with concrete to support the loads

imposed by the construction plant and armour unit. The concrete caps often deteriorated as the structure settled. Current construction techniques have emphasised the need to optimise armour size by careful design utilising both single layer and double layer, placed and tipped primary armour (MHL860, MHL897 1997). Cost considerations have also favoured single layer placement of even rock armour as tipping of rock results in significantly increased material costs. Other factors relevant to single layer placement of rock are a reduction in environmental cost of quarry utilisation, difficulty in sourcing large armour and the increasing distance and cost of material transport.

Physical modelling has enabled the designer to evaluate the influence of wave grouping, wave obliquity and permeability of the structure. It has also aided in comparing the performance of the single layered Accropode unit with units that have already been placed on structures on the NSW coastline such as the Hanbar, dolos and rectangular cube.

Many of the NSW coastal structures are located adjacent to popular holiday towns and villages and hence provide waterway recreational facilities. Presently construction and repair is regulated from the planning approval stage to the on-site placement of material, and must fulfil the mandatory requirements of NSW occupational health and safety legislation.

9. Conclusions

Manly Hydraulics Laboratory has been closely linked with many of the designs of the structures on the NSW coastline through its data collection and physical modelling capabilities which have been built up over a period of nearly 40 years. Some of the original designs as constructed have withstood wave energy over the last 100 years which, by design standards, should have failed. However recently introduced design variables such as wave obliqueness offer quantitative explanations for this stability. This paper has used the examples of Coffs Harbour breakwaters and the Ballina training wall head construction and repair to outline some of the developments in coastal engineering design and construction in NSW over the last century. An example of the design equations for primary armour size was used to indicate the influence of new variables such as permeability, storm duration and wave obliqueness on training wall construction at Ballina. The present day focus on the awareness of and need to care for a fragile environment which provides many recreational amenities is emphasised. The establishment and maintenance of extensive water level and wave databases is shown to increase design wave height and wave periods used in physical model investigations. The return period for design water levels has been established. The paper highlights the shortcomings of physical modelling when tools such as the proper generation and control of wave groupiness were unavailable.

10. Acknowledgments

The authors acknowledge the approval of the NSW Department of Public Works and Services and the Department of Land and Water Conservation to present this information. The historical development of the NSW coast is based on information contained in the book *Between Wind and Water* which was prepared by Lenore Coltheart. The assistance of Rob Jacobs and Mark Kulmar from MHL and Helmutt Rangger from DLWC in preparation of information for the paper is also gratefully acknowledged.

11. References

Australian Water and Coastal Studies 1992, *Parallel Runway Combined Probability of Occurrence of Water Levels and Waves,* AWACS Report No. 92/20.

Bowers E.C, *Wave Grouping and Harbour Design*, NATO ASI Series 1988, Lisbon Portugal, pp 391-416

Coltheart, L. 1997 *Between Wind and Water,* Hale & Iremonger

Cornett, A 1995 PhD Thesis, Technical Report HYD-TR-005, National Research Council, Canada

Department of Public Works N.S.W. Head Office File No. R 1017/7, *Coffs Harbour Jetty Range 1948 -1963.*

Foster D.N., A.D. Gordon 1973, *Stability of Armour Units Against Breaking Waves,* Proc 1st Australian Conference on Coastal and Ocean Engineering Sydney, Australia

Funke E.R, Mansard E.P.D, 1979 *On the Synthesis of Realistic Sea States in a Laboratory Flume,* Report LTR-HY-66-1979 National Research Council Canada pp 1-54

Galland J.C 1994, *Rubble Mound Breakwater Stability Under Oblique Waves*, Proc ICCE 1994

Goda Y 1988, *On the Methodology of Selecting Design Wave Height,* Proc 21st ICCE, Malaga, Spain, 1988.

Graveson, H. 1974, *Model Tests with Directly Reproduced Nature Wave Trains,* 14th ICCE Copenhagen, Denmark

Jayewardene, I.F.W. *et al* 1993, *Analysis of Wave Groupiness,* 11th Australasian Conference on Coastal and Ocean Engineering, Queensland, Australia, pp 99-103

Jayewardene, I.F.W. 1997, Young, T *Laboratory Measurement of Oblique Irregular Waves on a Rubble Mound Breakwater,* 13th Australasian Conference on Coastal and Ocean Engineering, Christchurch, New Zealand, pp 197-202

Kulmar, M. 1995, *Wave Direction Distributions off Sydney, New South Wales,* 12th Australasian Conference on Coastal and Ocean Engineering, Melbourne, Australia, pp 197-202

Manly Hydraulics Laboratory 1966, *Report on Wave Conditions at Shellharbour*, MHL109

Manly Hydraulics Laboratory 1966, *Coffs Harbour Model Investigation*, MHL110

Manly Hydraulics Laboratory 1974, *Coffs Harbour Historical Data Review* MHL186

Manly Hydraulics Laboratory 1991, *Storm Surges Monitored Along the NSW Coast* MHL591

Manly Hydraulics Laboratory 1992, *NSW Breakwater Asset Appraisal Pilot Study*, MHL636.

Manly Hydraulics Laboratory 1993, *Breakwater Asset Appraisal*, MHL648

Manly Hydraulics Laboratory 1996, *Laboratory Measurement of Oblique Irregular Waves on a Rubble Mound Breakwater,* MHL Report No. 782 (draft).

Manly Hydraulics Laboratory 1997, *Ballina Accropode Breakwater 3D Basin Testing* MHL860

Manly Hydraulics Laboratory 1997, *Coffs Harbour Eastern Breakwater Historical Storm Analysis*, MHL914

Mansard. E, 1980, *The Measurement of Incident and Reflected Spectra Using a Least Square Method,* Proc 17th Int. Conf on Coastal Engineering pp 154-172

Sand S.E. et al, 1983, *Group Bounded Long Waves In Physical Models*, Ocean Engineering Vol 10, pp 261-294

Sobey, R.J. and Orloff L.S. 1995, *Triple Annual Maximum Series in Wave Climate Analysis,* Coastal Engineering 26 (1995) pp135-151

Van der Meer, J.W 1988, *Deterministic and Probabilistic Design of Breakwater Armour Layers,* Journal of Waterway Port and Coastal Engineering Jan 1988

	No	Length (m)	Present Value A$
Rubble mound structures	63	22.600	$550 million (approx)

Figure 1 Asset Appraisal Study indicating Location of Rubble Mound Structures on the NSW Coast (MHL648)

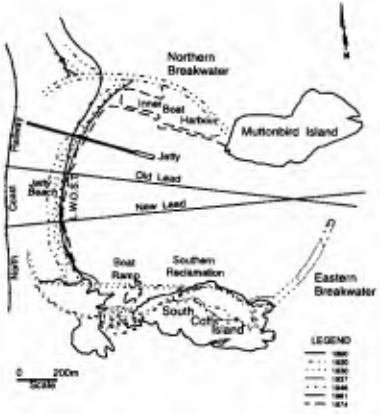

Figure 3 Sequence of Coffs Harbour Construction from Survey Plans and Aerial Photography (MHL186)

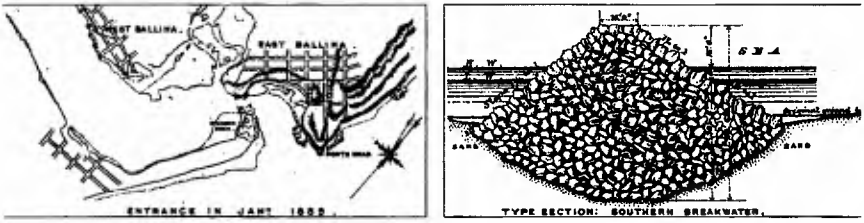

Figure 2 Sketches of the Richmond River Entrance Southern Breakwater Structure (Burrows 1904-05) (Coltheart 1997)

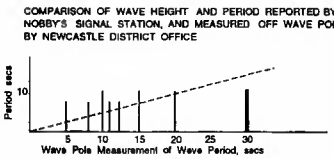

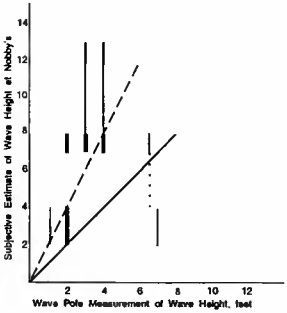

Figure 4 Visual Estimates vs Wave Pole Estimates (1965) (MHL 109)

	Extreme Wave Height Analysis Port Kembla (m)		
Years	10 yr event	20 yr event	100 yr event
1975-77	6.20	7.30	7.75
1975-80	7.05	8.35	8.95
1975-83	7.10	8.60	9.20
1975-86	6.80	8.05	8.55
1975-89	7.20	8.50	9.10
1975-92	7.55	8.95	9.60
1975-97	7.30	8.60	9.20

Figure 6 NSW Offshore Wave Climate Measurement

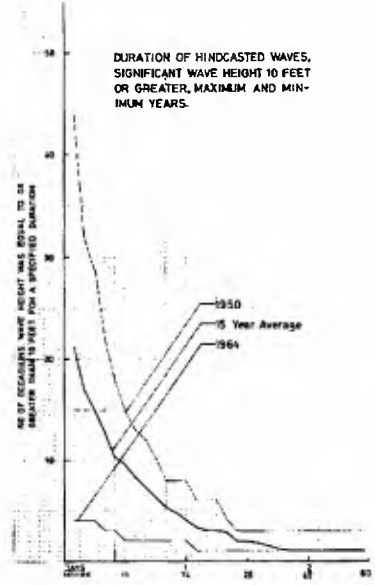

Figure 5 Return Periods for Hindcast Waves (1965) (MHL109)

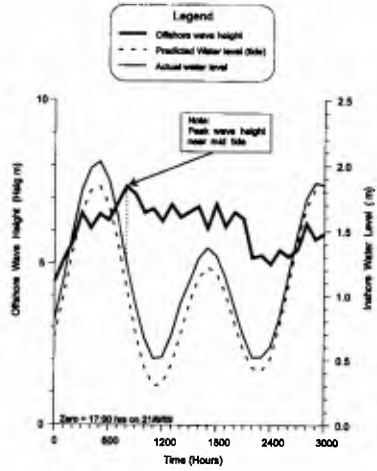

Figure 7 Coffs Harbour Water Level and Offshore Wave Height Data) (May 1997 Storm) (MHL914)

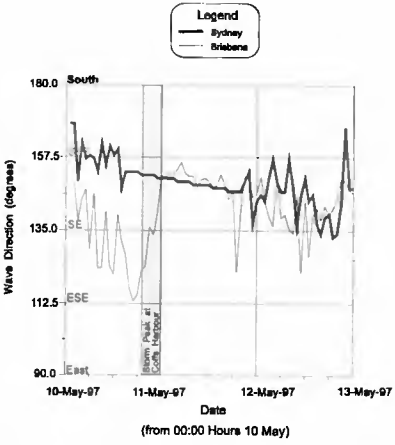

Figure 8 Coffs Harbour Offshore Wave Direction Data (May 1997 Storm) (MHL914)

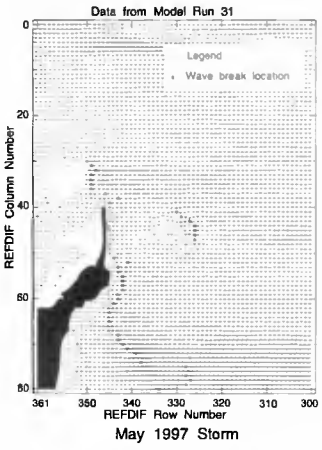

Figure 9 Numerical Modelling of Coffs Harbour Breakwater (MHL 914)

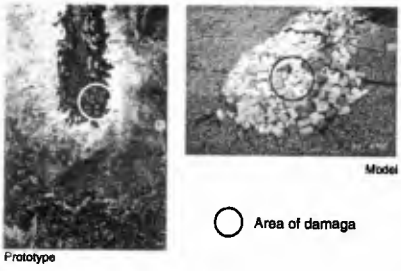

Figure 10 Replicating May 1997 Storm Damage in a Physical Model

ALDERNEY BREAKWATER - SCHEME EVOLUTION

Paul B Sayers[1], N William H Allsop[1] and Alan A Hill[2]

[1]Coastal Group, HR Wallingford, Howbery Park, Wallingford, OX10 8BA, UK
Tel: +00 44(0)1491 835381 email: pbs@hrwallingford.co.uk
[2]Principal Engineer, States of Guernsey, Sir Charles Frossard House, Guernsey

Abstract

Alderney is the northernmost of the Channel Islands, lying 13km off the Normandy coast. The main breakwater at Alderney, known as the Admiralty Breakwater, provides essential shelter to the commercial and fishing quays and swing moorings for fishing boats and visiting yachts. It also provides protection to the shoreline around Braye Bay.

Wave conditions at Alderney are frequently severe. In response to this severe wave attack the Admiralty Breakwater (constructed between 1847 and 1864) has required continual maintenance (costing £447,000 in 1998). Even with this level of investment, however, the long-term decay of the structure and occasional breaches continue.

This paper explores the history to the Admiralty Breakwater, why there is a need for works and how a range of disparate designs have evolved over time leading ultimately to a small number of viable solutions.

Introduction

Alderney Breakwater has been the subject of many studies since Vernon Harcourt gave an account of the construction of the Breakwater at the Institute of Civil Engineers in 1873 (Vernon Harcourt, 1873). In more recent times, HR Wallingford have been employed by successive owners of the Admiralty Breakwater to investigate its structural behaviour (see for example HR Wallingford 1963 and Allsop et al 1990) and latterly to propose an appropriate long-term solution for the protection of Alderney Harbour (Sayers et al, 1996a).

The complex history and structural of the Admiralty Breakwater combined with the severe wave climate at Alderney provides an interesting topic for study. This paper brings together some of the recent studies and discusses some of the options for

solving the significant problems associated with providing a long-term solution at Alderney.

The history of Alderney Harbour

At the start of the last century Napoleon threatened to invade England. In response, the Royal Navy conceived the idea of a deep-water naval anchorage on Alderney, the northernmost of the Channel Islands, close to France (Figure 1).

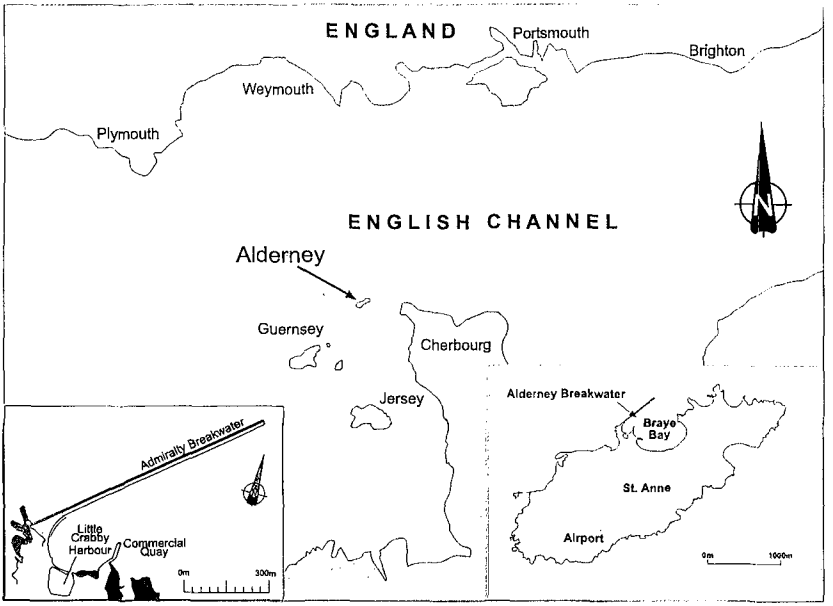

Figure 1 Location Plan

From here, the Admiralty claimed, they would be able to watch and, if necessary, blockade the French Port of Cherbourg and so repel French aggression. The Admiralty's original proposal was an ambitious plan enclosing all of Braye Bay (Figure 2). With a receding threat of invasion and escalating project costs however, construction of the planned second (east) breakwater was never realised.

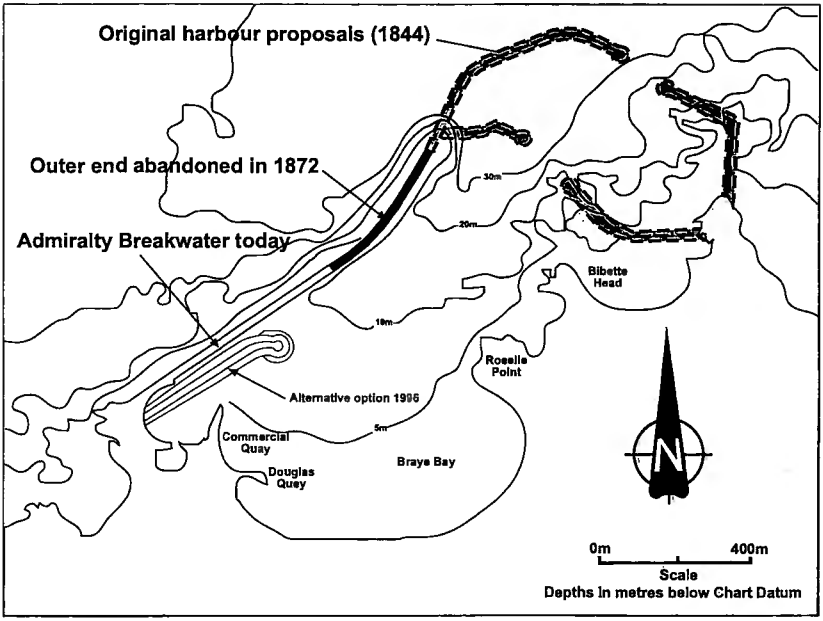

Figure 2 Alderney Harbour: The original harbour proposals

The overall length of the Admiralty Breakwater at completion in 1864 was 1430m. By 1872, however, continual storm damage, in some instances complete breaches, had led to unsustainable maintenance costs. To limit their financial commitment, the Admiralty abandoned the outer end of the Breakwater and chose to maintain only the first 871m where a temporary head, which had served to protect the 'scar end' of a seasons work during construction, formed a suitable point for termination. It is this remaining length that continues to provide shelter to Alderney Harbour today (Plate1).

Plate 1 The existing Admiralty Breakwater

The existing structure

A review of the original construction method reveals the Admiralty Breakwater to consist of two distinct sections: a rubble mound foundation which had been placed on the seabed (in water depths frequently greater than 40m) to a formation level near low water (+0.8mCD); and a masonry superstructure constructed on top of the rubble mound to +12.1mCD (Figure 3).

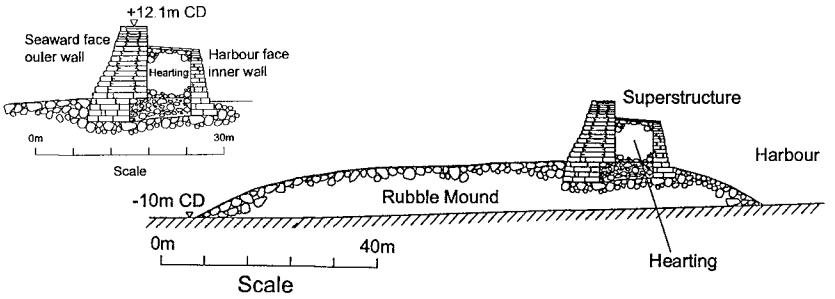

Figure 3 Section through the existing breakwater

The failure mechanisms of the existing structure have been analysed by a number of authors (Hall J et al (1995), Allsop et al (1990)). Based on this analysis, an event tree of the likely failure mechanisms was developed (Figure 4). From this analysis it is clear that any attempt to rehabilitate the existing structure will need to ensure stability of the masonry superstructure and protect it from aggressive abrasion by the highly mobile rubble mound and undermining of its toe.

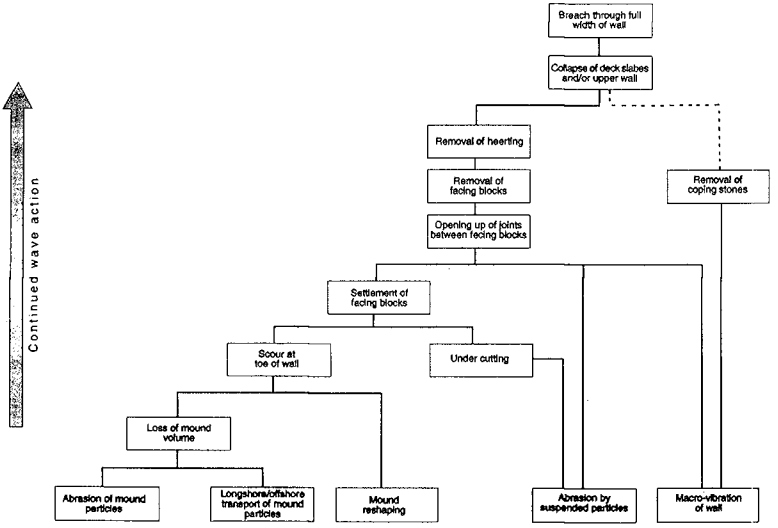

Figure 4 Likely failure mechanisms of the Admiralty Breakwater

The severe wave and tidal climate

Wave and tidal conditions at Alderney are frequently severe. The large open fetch to the north-west of the island exposes the island to the full force of Atlantic swell and the large tidal range drives notoriously strong tidal currents through The Swinge and the Alderney Race (5.5m tidal range on Mean Spring Tides and tidal currents up to 3.0m/s – see Table 1).

Table 1 Indicative tidal current speeds (measured by HR Wallingford, 1989a)

1km offshore	Upto 3.0 m/s
In the Harbour Approaches	Upto 1.0 m/s
Adjacent to the Admiralty Breakwater	Upto 0.5 m/s

Swell is an important component of the wave climate at Alderney and needs to be included in prediction of the design wave conditions. Therefore, the extreme offshore wave climate has been derived using data from the Meteorological Office Wave Model[1] of the Atlantic Ocean. Using a wave refraction model (PORTRAY, HR Wallingford, 1995) which includes the refracting effects of the strong tidal currents at Alderney, the predicted offshore waves were propagated inshore to the -10mCD contour close to the face of the Admiralty Breakwater (Table 2).

Table 2 Wave conditions at the –10mCD contour

Inshore Return Period (years)	H_s(m) (offshore wave direction 330°N)	T_m(s)	Still water level SWL(mCD)
0.1	4.0	9.6	3.6 (mid ebb)[2]
1	5.2	10.7	3.6
10	6.2	11.8	3.6
100	7.6	12.8	3.6
2000	9.5	14.2	3.6

Why is there a need for rehabilitation or replace works

The States of Guernsey, Board of Administration (the body responsible for the maintenance of the Breakwater since 1987) currently spend approximately £500k per annum (£447,000 in 1998) on maintenance of the superstructure. Even with this level of investment however, the long-term decay of the structure and occasional breaches continue (Plate 2).

[1] This data has the distinct advantage over the more usual method of deriving an offshore wave climate from a wind-wave prediction model based on local winds in that it includes the effects of swell.

[2] Interestingly, the most severe waves impact on the Breakwater at approximately normal incidence, and originate from the 255°-285° N offshore sector; not the expected north-west direction (the largest fetch). The reason for this is the strong wave-current interactions that cause significant wave refraction. It was also found that wave-current interactions cause the largest waves occur at the ebb mid tide condition.

Plate 2 Storm attack and damage - 1962

Studies by HR Wallingford in 1990 (Allsop et al, 1990 and 1991) and more recent analysis (Sayers et al, 1996b) confirms that the rubble mound upon which the superstructure is founded continues to erode. If this trend continues, future maintenance costs are likely to increase as toe support to the super-structure is lost and breaches become more frequent.

In addition to these long-term changes in the level of the mound the level at the toe of the super-structure is highly volatile in the short-term (Figure 5). In combination the long term processes and short-term volatility of the toe level lead to considerable uncertainty as to when the mound will reach a level that critically undermines the super-structure.

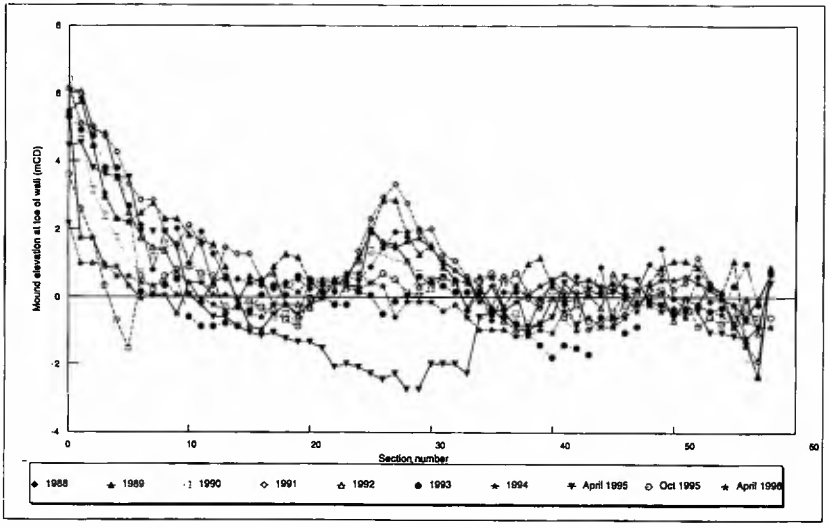

Figure 5 Toe level of the Admiralty Breakwater superstructure from dip measurement

Evolving a solution: Study terms of reference

In 1995 the States of Guernsey Department of Engineering on behalf of the Board of Administration, commissioned HR Wallingford to undertake studies to assess and design in outline the most appropriate long term solution for providing shelter to Alderney. The Terms of Reference for this study were:

"To assess the viability of alternative solutions for replacing or upgrading the Admiralty Breakwater based on the need to satisfy the following requirements:

- Minimise maintenance commitment
- Maintain access to a commercial quay
- Maintain mooring facilities for fish storage
- Maintain small craft moorings
- Limit impact on the coastline
- Minimise financial risk"

It should be noted here however, that the States of Guernsey have responsibility for protecting a harbour on the Island of Alderney and providing the financial backing (subject to financial constraints) for any capital project undertaken (if and when necessary). Therefore, not surprisingly, their objective is to minimise expenditure without compromising (but not necessarily improving) existing operations in Alderney Harbour. The objective of the States of Alderney however, is to seek an improved Harbour facility and one that provides potential for future development. These are somewhat disparate viewpoints and are not easily reconciled by a single solution.

This paper largely addresses the needs and solutions based on the Terms of Reference set out by the States of Guernsey (the Client). The arguments developed in terms of structural performance, navigation and other operational issues for the various options are however, generic to any solution proposed.

Design criteria

An important precursor to any study to propose remedial or replacement works is to understand the design criteria against which the 'solutions' are to be judged. Below is an outline of the main design criteria set for this study.

Cost limits

For the construction of a new breakwater to be viable it will need to be justified in economic terms. For the States of Guernsey this means that the primary cost of any given solution should be justified based on reduced maintenance of the Admiralty Breakwater. Based on an annual present expenditure by the States of Guernsey on maintenance of £0.5 million and a 50 year design life the capital expenditure that may be directly justified is approximately £8 million (based on a discount rate of 6%). Continued loss in the volume of the rubble mound and the known volatility of its level at the toe of the super-structure are expected to increase the frequency of major breaches in the Admiralty Breakwater. Hence, the annual maintenance cost may be expected to rise. To avoid the repair and maintenance becoming uneconomical and

unsustainable it is, therefore, appropriate to consider options for rehabilitation or replacement of the Admiralty Breakwater with present day values in excess of £8 million.

Navigation issues
At present the largest vessel conducting commercial operations at Alderney is the Ariante (79.15m LOA x 13.1m beam). It is noteworthy that although there is a marked trend for smaller vessels (such as the Ariante) to be difficult to source, as they become increasingly uneconomic to operate, the Ariante has been defined as the 'design vessel' for a number of locally applicable reasons. For all designs therefore a nominal navigation channel of about 60m in width has been set (based on five times the beam of the Ariante). (Note: If it does become necessary then it is accepted that any design developed using the Ariante may require significant alteration.)

Wave disturbance at the Commercial Quay
Wave disturbance at the Commercial Quay is a function of wave transmission through the Harbour entrance and over/through the breakwater. The wave disturbance criterion adopted is that any proposed solution should provide the same standard of shelter at the Commercial Quay as is afforded at present. Based on more detailed study of the operational limitations at the Commercial Quay the limiting wave height for safe mooring at the Commercial Quay has been set as approximately 0.45m (Thoresen (1988), PIANC (1995), Iceland Harbour Authorities (1987), Brattleland (1974) and 3-dimensional physical model tests by Sayers et al, 1996a). This wave height is expected to cause total horizontal movements in the Ariante of up to 1.5m in surge and in sway, and angular movements of 2 to 5 degrees.

Small craft moorings
A total of 135 multi-point moorings are laid and maintained in Braye Bay by the Harbour Authorities. If some or all of the facilities for small craft moorings in the lee of the Admiralty Breakwater are lost a small craft marina may be required as an integral part of any solution considered.
Wave overtopping
No limit on wave overtopping for serviceability in terms of safety of access has been imposed. When overtopping is expected to represent a high risk to persons on the breakwater an overtopping hazard warning will be issued and access to the breakwater prevented. The design criterion in terms of wave overtopping was, therefore, based only on the protection afforded against wave disturbance. The criteria was set such that wave heights in the lee of the structure should be no more than that experienced at present.

Armour layer stability
Any solution proposed is likely to involve the use of rock or concrete armouring. The required performance of any armour layer is to:

- Require no more than limited maintenance in the aftermath of a 1:100 year return period storm (i.e. a storm that has a 63% chance of being exceeded during any 100 year period).

- Be able to resist `failure` (defined as a total breakdown of the form of the design) during a 1:2000 year return period storm (i.e. a storm that has a 5% chance of being exceeded during any 100 year period).

Impact on coast protection in Braye Bay and swing moorings
Wave activity in Braye Bay will be an issue when selecting the most acceptable option. The acceptability of the design proposals in terms of the impact on wave activity within Braye Bay has been based on the relative increase when compared to the existing situation and the significance of that increase. A prescriptive criterion has not, therefore, been set.

Scheme options and design

A number of solutions have been proposed:

- Rehabilitation/protection of the existing structure
  - Improved maintenance
  - Rock / concrete armouring, **Option A**
  - Grouting
- Offshore breakwaters
- Abandonment and construction of a new breakwater in the lee of Admiralty Breakwater, **Option B**

Some of the above form part of the studies undertaken by HR Wallingford and others have been investigated by independent consultants and those employed by the States of Alderney. This paper focuses on the detailed studies undertaken in the investigation of the performance of two of these options: Option A and Option B.

Option A

Option A consists of a shortened length of the existing Admiralty Breakwater armoured using a composite structure of concrete armour units (Accropodes) and rock. A 'spur' breakwater is then 'returned' through the superstructure of the Admiralty Breakwater to afford protection against wave penetration up to the Commercial Quay (Figure 5 and 6).

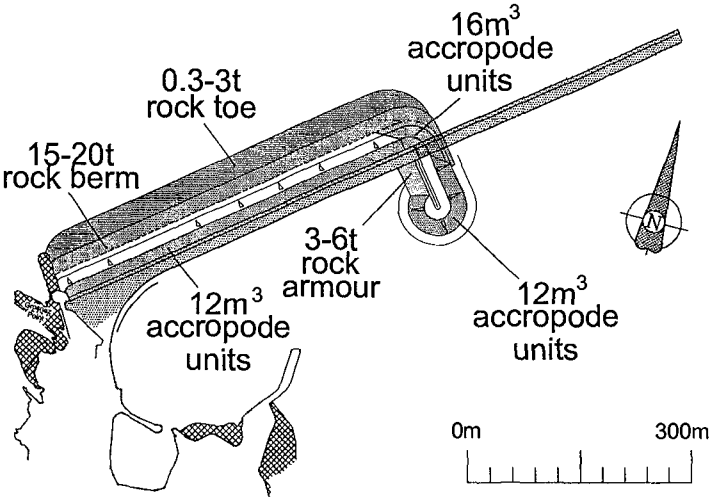

Figure 5 Plan view: Option A

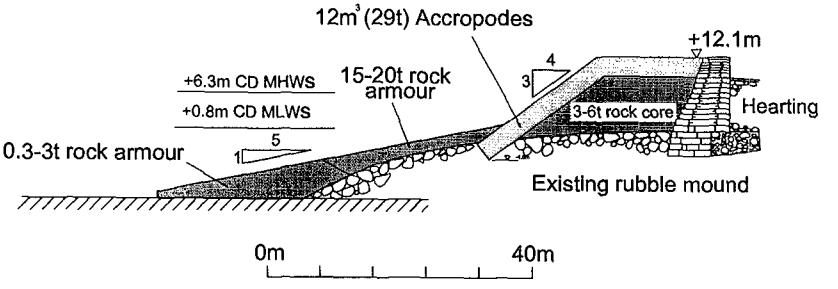

Figure 6 A typical cross-section: Option A

Option B

This option abandons the Admiralty Breakwater and proposes the construction of a new breakwater within Alderney Harbour. The new breakwater is set back 70m landwards of the Admiralty Breakwater. Its construction uses concrete armour units (Accropodes) and rock armour (Figures 7 and 8).

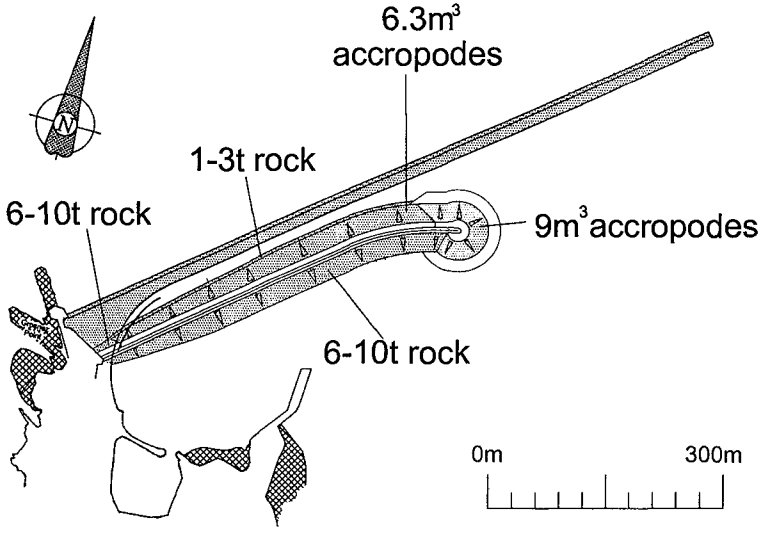

Figure 7 Plan view: Option B

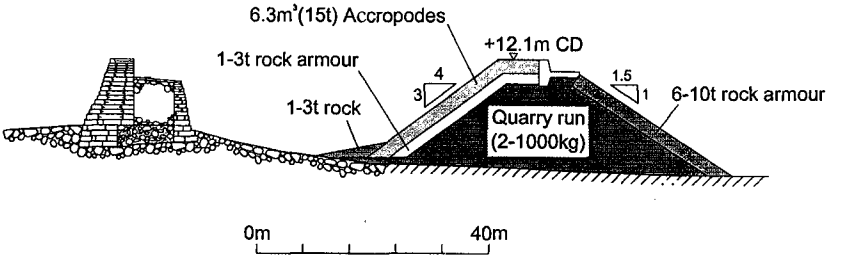

Figure 8 A typical cross-section: Option B

Comparing Options A and B

Based on detailed 2 and 3-dimensional physical modelling, numerical modelling of waves and currents, engineering design, investigation of construction risks and cost estimates it has been possible to compare the performance of Options A and B and comment on their ability to satisfy the study terms of reference. A discussion of this comparison is given below.

Impact on the coastline of Braye Bay
Physical model tests suggest that when the Admiralty Breakwater is replaced with either Option A or B wave activity within the Bay is increased. This will adversely impact on the tenability of present swing moorings within the Bay and can be expected to accelerate coast erosion in the east of the Bay. Increased coastal erosion will, in the medium term, result in the need for remedial measures. There is, however, no significant difference between the two Options A and B in terms of their likely impact on the coastline of Braye Bay.

Impact on navigation
Navigation simulations were undertaken to establish the feasibility of continuing to navigate into Alderney Harbour using the Ariante following construction of the proposed breakwater Option B.

Prior to these studies two principal concerns regarding the approach and berthing of a ship if the Alderney Breakwater was shortened were raised. These were:

- The ability of the ship to counter the strong cross currents in the existing approach.

- The ability of the design ship to slow its approach to a near zero speed in a controlled manner in the distance from the end of a new breakwater to the Commercial Quay.

To investigate the validity of these concerns comprehensive navigation simulations were undertaken in the HR Wallingford simulator[3] (Sayers et al, 1996a).

[3] The mathematical model used in the HR Wallingford simulator is of a standard type, using Newtonian equations in three degrees of freedom, and having a modular structure. The effects on the hull of all the influences due to the hydrodynamic, effect or and disturbance forces are added, and the accelerations found in three degrees of freedom, i.e. in the surge, sway and yaw directions. Integration and transformation will yield the position of the ship in the playing area. Once the ship position is known, this position can be used to access the databases for current and depth, so as to produce new currents and depths for use in the next iteration of the model equations. The outputs of the model are the position and heading of the ship as a function of time, taking account of the effects of wind, current, depth of water and tugs (as necessary). The mathematical models used to represent the Ariante must also behave in such a way that the position, swept path and heading of the simulated ship are always representative of real behaviour (including the combined influence of wind, waves and currents).

Prior to undertaking the simulations it was important to reliably predict the strong tidal currents and include them in the simulations. To obtain the required variable resolution, with a finer mesh in the area of the Admiralty Breakwater and a coarser grid further away, the numerical model TELEMAC-2D (developed by LNH, Paris and HR Wallingford) was selected as the most suitable.

Once calibrated (against various existing sources of current data and specially commissioned surveys) TELEMAC-2D was used to predict in detail the existing flow regime and the likely future changes if the Admiralty Breakwater was abandoned and Option B constructed (Figure 9).

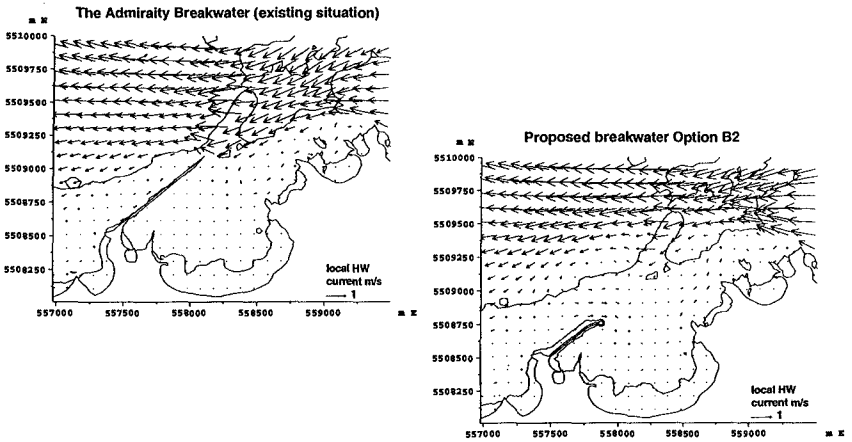

Figure 9 Tidal flows: Existing and future conditions

It can be observed that in the existing situation an eddy current is generated offshore of the Admiralty Breakwater during the late flood (generated as the strong tidal currents in the Swinge flow past the Admiralty Breakwater). This leads to a strong cross current at the head of the Admiralty Breakwater. This current flows westward at about 1 m/s causing difficult for vessels approaching the existing harbour.

With Option B the eddy is affected by changed breakwater location and is generally significantly reduced with the proposed scheme when compared with the existing condition[4].

[4] For most of the runs it was assumed that the existing Breakwater had totally collapsed, so that there was no protection beyond the head of the Option B breakwater. For many years this is unlikely to be the case, and the entrance channel will be afforded some additional protection from waves, particularly for winds from north through to west. The condition of an Admiralty Breakwater in a partially collapsed condition was not considered.

The simulations confirmed that at present it is not practicable to start to slow the ship significantly from its approach speed of about six knots until the ship is in the shelter of the Admiralty Breakwater. Once in shelter, the Ariante at present needs around five ship lengths to slow in a controlled manner. However, when the Admiralty Breakwater is replaced, the improved tidal conditions in the approach to the Harbour facilitate a slower approach speed past the head of the new breakwater. Consequently, the distance required for the ship to slow once inside the shelter of the breakwater is reduced.

In summary the navigation simulations concluded that the adopted position of the head of the proposed breakwater, Option B2, is an optimum compromise between the two conflicting requirements, of shelter and ease of approach, given above. When combined with approach navigation aids Option B allows satisfactory access to Commercial Quay.

Provisions for small craft moorings
The disadvantage both Options A and B is loss of harbour space and the restricted flexibility for future harbour.

To minimise encroachment into the existing harbour space of Option B concrete armour units (15t Accropode units) are used as the primary armour layer. This enables a steep seaward face of 3 in 4 to be used to minimise the breakwater footprint without compromising structural stability. Even so, in the case of Option B seventy moorings are lost, including twenty local, service and store box moorings. A slightly reduced number are lost if Option A is constructed.

To offset the loss of moorings it was shown that it would be possible to relocate the majority of moorings in to the space just outside of Little Crabby Harbour. (Further details of the proposed new anchorage / marina development may be found in Sayers et al, 1996a)

Interaction with a decaying Admiralty Breakwater
The unpredictable decay of the Admiralty Breakwater may adversely affect the performance of Option B. However, the physical model investigations allay many of the early concerns. The potential for wave energy to be focused through breaches in the Admiralty Breakwater causing structural damage to Option B has been explored and discarded. In addition, fouling of the navigation approaches by mound material and abrasion of the Accropode units by mound material carried landwards by incoming waves have both been considered and discounted as a significant risk.

Construction risks and costs
The novel idea of constructing a new breakwater 'set-back' in the lee of the Admiralty Breakwater (Option B) has two distinct advantages over construction on the seaward side of the Admiralty Breakwater (Option A). Firstly, the existing breakwater could be used as shelter to the construction, significantly reducing construction risk and lengthening the safe construction working period. Secondly, it is predicted that the rubble mound foundation of the Admiralty Breakwater will remain in place in the long-term, albeit at a reduced level, providing partial shelter to the completed works

during the worst of the Alderney storms. In-turn this eliminates the need for the very heavy armour rock required if construction were to take place on the seaward face of the Admiralty Breakwater, material that is often difficult to source.

For each of the main breakwater Options A and B the estimated construction costs are given below in Figure 10.

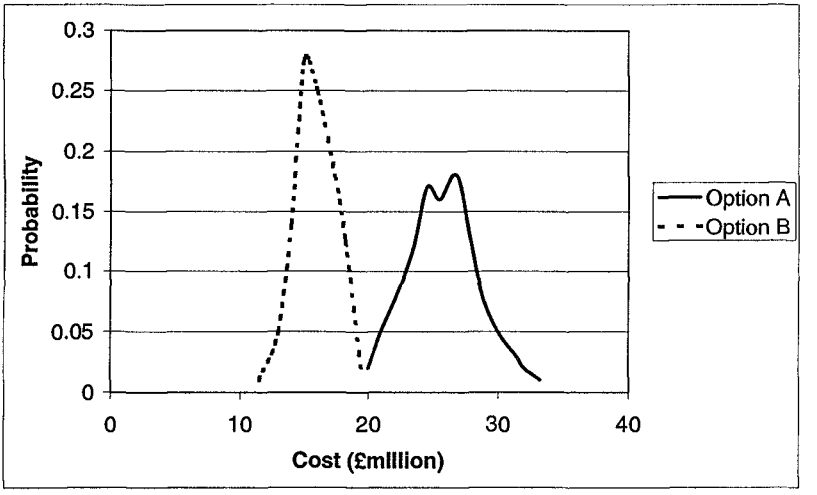

Figure 10 Estimate construction costs: Options A and B

These cost estimates have been developed based on detailed dialogue with would-be contractors and reflect the higher construction risks associated with Option A. For example, potential future increases in price of rock would add considerable cost to Option A due to the large quantities of large armour rock required (an increase of £10/m^3 placed would add £0.9 million to the total construction cost). Option A is further disadvantaged by severe construction risks; heavy downtime during a necessarily long construction period spread over several seasons is also expected to add considerable cost to the project. The difficulty in excavating the existing mound to secure the toe of the Accropode slope and the susceptibility of part-completed structures to storm damage will add further risk, and hence cost, to the project. In addition, Option A requires large volumes of heavy armour rock (87056m^3 of 15 to 20t rock). This will be difficult to source and may have a slow rate of supply.

Option B however is less sensitive to fluctuations in the price of large amour rock and has no significant risk attached to construction due to its sheltered position in the lee of the Admiralty Breakwater (giving a high degree of certainty to the cost estimates). It can also be constructed in one year (assuming sufficient lead in time is given to facilitate pre-casting and stockpiling of the Accropode units and rock).

To over-come some of these issues a procurement route involving a design and construct package is recommended.

Summary: Options A and B

Option A partially retains the visual appearance of the Admiralty Breakwater from the Harbour side and maintains an area for swing moorings to the north of the 'Safety Fairway' (albeit for a reduced number of vessels). In addition, existing access to Little Crabby Harbour is maintained. However, Option A involves the abandonment of the outer 365m of Admiralty Breakwater. Therefore, a considerable number of swing moorings will be lost.

Following the demise of the Admiralty Breakwater and the construction of Option B, it is predicted that the tidal current regime in the approaches to the new Harbour will be generally improved over that experienced at present. This facilitates access to the Commercial Quay under similar environmental restricts to those applied at present. In addition, access to Little Crabby Harbour is also maintained. the historic value and appearance of the Admiralty Breakwater is, however, lost..

Both Options A and B lead to the loss of protection to majority of swing moorings currently available in Braye Bay and Harbour space. Most of these, could, however to relocated. Effective protection to the east coastline of Braye Bay is also lost together and the likely erosion will have to be management appropriately.

What are the alternatives to Options A and B

The rehabilitation or replacement of Alderney Breakwater has caused considerable interest; both in Alderney and Guernsey. As a result, various consultants have been engaged by the States of Alderney to propose ameliorative works that attempt to address the Terms of Reference as given by Alderney (as opposed to those defined by the States of Guernsey). The "solutions" proposed range from armouring the full length of the Admiralty Breakwater (at an estimated cost of at least £40million) to the use of salvaged ship hulls as offshore reefs.

Some of the "solutions" proposed by the various consultants offer little in the detailed understanding of the existing Breakwater and how any future works may perform. Others, however, are more interesting and worth of further investigation. Due to the present status of this project (currently in the hands of the Board of Administration, States of Guernsey) it is, unfortunately, outside the scope of this paper to discuss the details of these "alternative" proposals.

Conclusions

Options A and B provide well-engineered and robust solutions to the problems perceived by Guernsey. The costing exercise associated with Options A and B has however, demonstrated that due to the harsh physical environment at Alderney the cost of construction is sensitive to the method adopted and the availability of the required sizes and volumes of rock. In particular the construction risks associated with undertaking works on the seaward side of the Admiralty Breakwater (for example Option A) are vast.

This study has clearly demonstrated that if different questions are posed different solutions will result. At present the States of Guernsey (would-be funders of any scheme) have differing requirements to the States of Alderney (would-be users of any

scheme). It is clear therefore, that until consensus is achieved on the ultimate objectives of the project there will be continued debate over the selection of the most appropriate solution for rehabilitating or replacing the Admiralty Breakwater.

Acknowledgements

The authors are grateful for advice and assistance received from the colleagues at HR Wallingford, in particular Jim Hall and Jonathan Simm. The cooperation of Mr Stephen Shaw (the Harbour Master at Alderney), Captain Tim Spencer (the Harbour Master at Guernsey) and Mr Keith Webster, the Breakwater Supervisor, is also gratefully acknowledged.

References

Allsop N W H et al (1990). Alderney Breakwater: Phase 3 hydraulic model studies. HR Wallingford Report EX2231, December 1990.

Allsop N W H, Briggs M G, Densiloe T and Skinner A E (1991). Alderney Breakwater: The quest for a final solution. ICE Proceeding Coastal Structures and Breakwater November 1991

Bratteland, E (1974). A survey on acceptable ship movements in harbours. The Dock and Harbour Authority. Vol 55 No.647.

Bridgestone (1994). Marine Fender Design Manual, F100E-1

Hall J et al (1995). Alderney Breakwater - Phase IV, Engineering Feasibility studies, HR Wallingford Report EX 3169 - Revised December 1995.

HR Wallingford (1963). Alderney Breakwater - Report on a model investigation. Report EX 217, Hydraulics Research Station, September 1963.

HR Wallingford (1989a). Prediction of the extreme wave climate at the Admiralty Breakwater, Alderney, HR Wallingford Report EX1983, August 1989

HR Wallingford (1995). Alderney Harbour - Wave disturbance modelling. Report EX3239.

Sayers P B et al (1996a). The Admiralty Breakwater, Alderney: Phase IV, Further studies on changes to the Breakwater mound 1990-1996, HR Wallingford Report EX 3536.

Sayers P B et al (1996b). The Alderney Breakwater, Alderney: Phase IV, Engineering Feasibility and Physical Model Studies, HR Wallingford Report EX 3536.

Iceland Harbour Authorities (1987). Ship movements in harbours. Report of the joint research project in the Nordic countries.

PIANC (1995). Criteria for movements of moored ships in harbours. A practical guide. Report of Working Group No. 24. Supplement to Bulletin No.88.

Thoresen, C A (1988). Port Design. Guidelines and recommendations. Tapir Pub. Trondheim Norway.

Vernon Harcourt LF, 1873 Account of the construction and maintenance of the harbour at Braye Bay, Alderney. Proceedings ICE Vol XXX VII Part 1, 1873

BREAKWATER REPAIR: MONITORING, MODELLING, AND CONSTRUCTION

S Pillay[1], D Phelp[2] and A Bartels[3]

Abstract

*The trunk section of the **south breakwater**, at the entrance to the **Port of Richards Bay**, has suffered some damage since its construction which was completed in 1976. This paper briefly discusses the changes in the design conditions as a result of sand-trap dredging off the breakwater, the annual photographic monitoring results showing the excessive rates of damage, and the model testing of various repair options, using 20t and 30t dolosse. Both 2D flume and 3D basin model tests were carried out at various scales, with fixed and movable bed models. Finally the construction of the optimal repair, carried out in 1997/98, using a heavy duty mobile crane (with 48m boom reach) and DGPS positioning, is described.*

Introduction

The Port of Richards Bay, on the east coast of South Africa, has two dolos breakwaters, a shorter straight breakwater on the northern side of the harbour entrance channel and a longer curved breakwater on the southern side. The south breakwater consists of an "S" shaped rubble mound structure (Figure 1), constructed between 1973 and 1976, which stretches for approximately 1km, almost perpendicular to the coastline. The original armouring on this breakwater consists mainly of 20t dolosse on both sides of the trunk (Figure 2), but includes 30t dolosse on the roundhead. The south breakwater forms the main protection of the Richards Bay harbour entrance channel, against dominant southerly storms and the nett littoral drift, which is from south to north.

Annual photographic monitoring of the south breakwater has shown a gradual increase in damage to localised areas on the southern side of the trunk, despite spot repairs using 20t dolosse, carried out by Portnet in 1985. A detailed evaluation of the

[1] Portnet, Port of Richards Bay, P O Box 464, Richards Bay 3600 (SA)
[2] Environmentek, CSIR, P O Box 320, Stellenbosch 7600 South Africa
[3] Entech Consultants (Pty) Ltd, P O Box 752, Stellenbosch 7600 (SA)

damage was undertaken by Zwamborn in 1988 (CSIR, 1988) which lead Portnet to commission the CSIR in 1991 to carry out investigatory model tests in an existing 3D 1:100 scale model of the entrance to the Port of Richards Bay. These tests were to check different repair options, taking into account the position of a dredged sand-trap along the seaward side of the breakwater. The original idea was to use 20t and 30t dolosse, available from a stockpile of spare dolosse at the root of the south breakwater.

Figure 1: Aerial View of South Breakwater

Due to delays in the commissioning of a suitable crane, and the use of most of the spare dolosse on repairs to the north breakwater head (Phelp, 1996), the construction of the repairs to the south breakwater were delayed until 1997/98. This also required the casting of 1000 additional 30t dolosse. Between 1991 and 1996, additional 2D flume tests were carried out at a 1:40 scale to check the stability of the rock toe of the repair slope. These tests were carried out with a movable (sand) bed to model the effects of toe scour. Before the commencement of the repair work it was found that, due to a gap in the dredging programme, there was a buildup of sand along the breakwater toe. Final model tests were therefor carried out to re-check the toe stability at this shallower depth.

Monitoring Results

The crane/helicopter photographic survey method (Phelp, 1994) has been used to annually monitor the breakwater since 1979 on an ad-hoc basis, but regularly since 1987, and crane and ball profiling surveys have been carried out since 1981. The photographic survey stations are spaced at 25m, and the ball profiles at 5m intervals. Figure 2 shows the position of the survey stations and Figure 3 the rate of damage increase since 1987.

The original breakwater construction used a total of 13 400 20t dolosse on the trunk, and 2 200 30t dolosse on the roundhead, which amounts to approximately 10 dolosse per metre of breakwater. The original depth at the head was -18m and -14m along the outer curve of the trunk. The worst damage prior to the repair, located at station C8, was 17% dolosse displaced or broken (Figure 2).

Ad-hoc spot repair work was carried out in this area in 1985, when 52 new 20t dolossse were placed. Although this showed a significant improvement in the measured profiles, the photo survey showed that half of these dolosse were broken and/or lost by 1987. This type of spot repair, which was not model tested, with non-reinforced dolosse in a single layer not interlocking with the surrounding dolosse, proved to be ineffective.

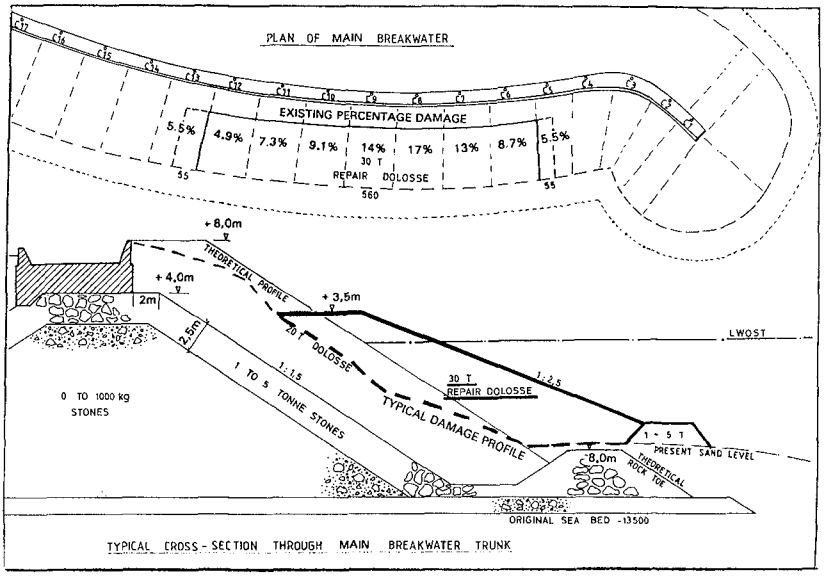

Figure 2: Plan View of South Breakwater and Cross-Section through trunk.

Factors Contributing to the High Damage

The occurrence of low pressure cyclonic storms (cyclones Demoina and Emboa in 1984) subjected the breakwater to wave heights exceeding the 7,9m 1:50 year design H_{mo}. Storm wave set-up and low atmospheric pressure associated with these storms also had the effect of raising the water level, thereby raising the depth limited wave heights reaching the breakwater. There have also been a number of lesser, but still powerful storms with wave heights in excess of 6m - the latest being experienced in 1990. The rates of damage are shown in Figure 3 for the worst stations on the trunk section.

A nett littoral drift of up to 800 000m^3 northwards has necessitated the dredging of a sand-trap against the outside of the south breakwater. Bathymetric surveys carried out regularly by Portnet in the sand-trap area have shown that dredging has taken place

much closer to the breakwater than originally anticipated (up to 60m closer). The depth of the sand-trap has reached -24m and the side slope as steep as 1:4,7. Figure 4 shows the dredger and Figure 5 the average position and sections through the sand-trap.

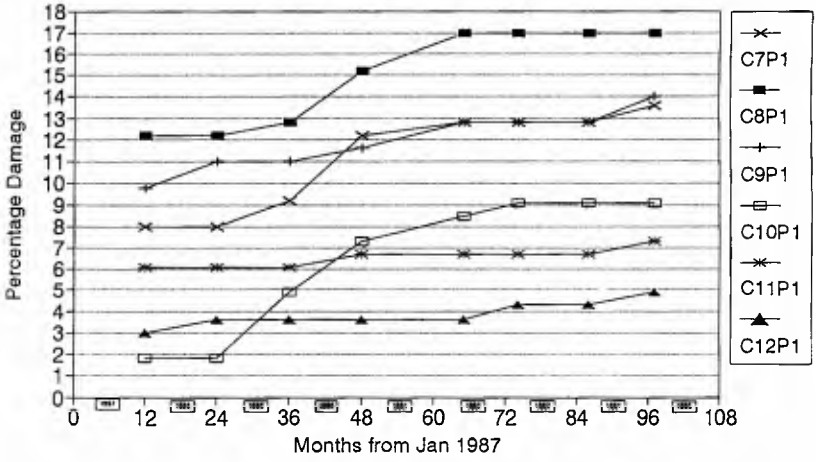

Figure 3: Rates of Damage to Worst Stations since 1987

Besides the deeper trap and steep side slopes, there has also been scour at the toe of the original breakwater (seismic surveys carried out by CSIR in 1993 confirmed the toe erosion (CSIR,1994)). The damage profile along the breakwater (shown in Figure 2) matched the plan of the sand-trap, with the highest damage area aligning with the deepest parts of the trap. The 3D basin model tests, which modelled various trap layouts, confirmed that the sand-trap allowed higher depth limited waves to reach the breakwater.

Figure 4 : Portnet Dredger Trail Dredging in the Sand-trap

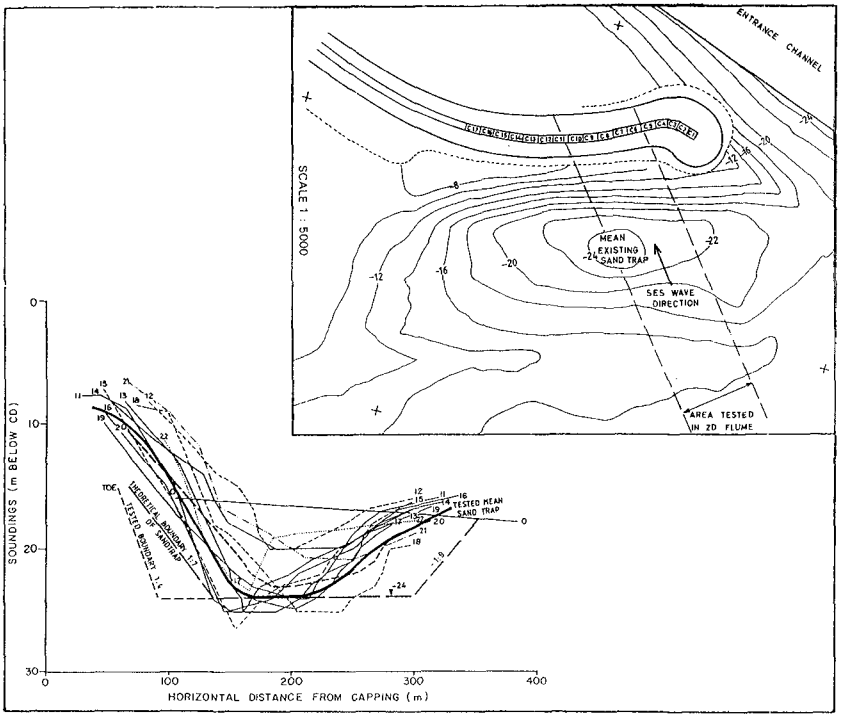

Figure 5: Plan and Cross-Sections showing Average Sand-trap Position.

Constraints to the Repair Design

Model tests were carried out in an existing 3D model of Richards Bay, to save both time and costs. This original model was built at a scale of **1:100** and covered the harbour entrance and part of the inner channel. The model test options were also originally restricted to using available 20t and 30t dolosse from a stockpile near the southern breakwater. A number of repair options were tested using either the 20t or 30t dolosse, with different repair slopes between 1:1,5 and 1:2,5, both with and without a rock toe.

The removal of rubble and pre-repair slope preparation was limited due to poor underwater visibility and rough sea conditions normally experienced along the outer breakwater. Contour plots of the outer slope, drawn from crane and ball profile surveys, were used to locate damage cusps below water and guide the filling of these holes at the toe of the armour slope. A double layer repair slope was then designed to cover the worst damaged areas. The top and sides of the repair are then tied into the original breakwater slope by tapering the repair. The width of the repair was limited to 40m from the splash wall, which was the limit for the boom of the crane lifting a 30t dolos. This mobile crane (Figure 10) was specially designed to fit onto the 6,7m wide mass-concrete capping.

Choice of Model Scale

The scale of 1:100 used for the tests gives a Reynolds number of approximately $1x10^4$, which is just within the minimum range recommended by Van der Meer (Van der Meer, 1988). Some scale effects were expected, but have been found to make the model results more conservative. The scale effects, being similar for all the test runs, allowed for comparisons to be made between the repair options tested. The calibration test showed that the hind-cast of the damage which occurred in the cyclonic storms of 1984, is in qualitative agreement with the observed prototype damage confirming the validity of the physical model. Details of the chosen repair section were confirmed at larger scales (1:63) in a 3m wide flume with a fixed bed and at 1:40 in a 2m wide flume with a movable bed. Figure 5 shows the section through the sand-trap and breakwater which was modelled in the 2D flume tests.

Wave Generation and Measurement

Up to 14 standard wire resistance wave probes were used which were coupled so that measurements could be carried out over prescribed areas. A hinged paddle wave generator bank for the 3D tests was 30m long situated approximately 30m seawards of the breakwater (representing 3km by 3km in prototype). Based on a review of existing wave data and analysis of the cyclonic storm data as recorded by a waverider buoy off the breakwater, the following **main test conditions** were chosen:

- Wave direction, harbour entrance area (12s) **140°**
- Storm input, **Richards Bay Spectrum**, $\gamma = 2{,}74$ with the following 1.5 m steps H_{mo} = **2.5, 4, 5.5, 7, 8.5 m** with wave periods T_p = **12 s to 16s**. This is above the design wave height of 7,9 m and cyclone wave recording of 8,4 m.
- Water level MHWS = **+2,0 m CD** which resulted in the highest damage.

The above conditions were considered applicable to reproduce the damage on the breakwater which has been subjected to a minimum of one 1:1 year storms (H_{mo}>5m) per year, three 1:10 year storms (H_{mo}>6m) and one storm exceeding a 1:50 year storm (H_{mo}>7.9m) during the lifetime of the breakwater.

Test Procedure

In order to calibrate the physical model, a calibration test was carried out in which the prototype damage resulting from the storm history was reproduced in the 3D model (Figure 6). A number of repair options were then investigated, starting with the simplest option, and extending the repair until a stable solution was found. Before each repair was constructed, the original damage was replicated in the model. The repaired breakwater was than exposed to the conditions described above.

After each test, the repair was removed and the original damage reconstructed, after which the next repair option was implemented. The optimum repair option chosen from the 3D tests was then reproduced at a larger scale in the 2D flume tests, initially with a fixed bed and then with a movable sand bed. These larger scale flume tests were used to give special attention to the ability of the breakwater to withstand some toe scour resulting from sand-trap dredging.

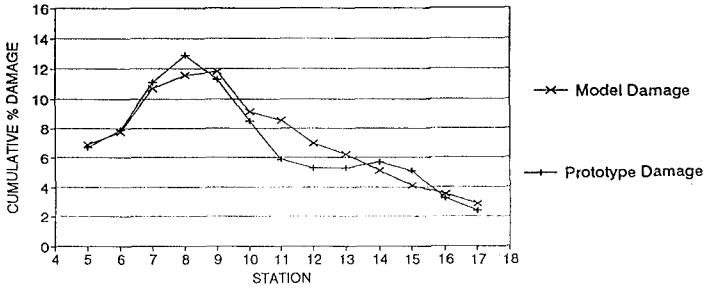

Figure 6: Prototype versus Calibrated Model Damage

Measurement of Damage

Prototype damage is assessed by counting the broken or lost dolos units and adding the units which have been displaced more than ½ h (dolos height). A number of swing tests were carried out on full-scale 9t dolosse to determine the degree of movement these dolosse could sustain without breakage (Zwamborn and Phelp, 1989). Based on the results of these tests it was recommended that all movements greater than half the height of a dolos be included as damage. This damage is then expressed as a percentage of the total number of dolos in a particular section of breakwater (Figures 2 and 3).

In the model, the number of dolos movements was determined by the digital analysis of video images taken before and after each run. In addition, the number of dolosse which were rocking was recorded visually and by cine camera during each test. However due to the difficulty in observing movements over the whole test area, it was decided to use the video measurement of small movements (< h), as an estimation of rocking dolosse. This was then calibrated against the recorded prototype damage to give a calibration factor of 0.4(<h) + (>h), which gave an accurate simulation of the prototype damage profile along the trunk of the breakwater between stations 5 and 17 (Figure 6).

Figure 6 also shows, both in model and prototype results, that the worst damage occurred between stations 7 and 9. Hydrographic surveys of the sand-trap between 1977 and 1991 have shown that, almost since completion of the breakwater, the deepest area of the sand-trap was located opposite stations 7 to 9 (Figure 5). This also coincided with the area where the sides of the sand-trap were steepest and closest to the toe of the breakwater. One model test which was carried out with a larger deeper sand-trap resulted in an increase in damage proportional to the extension of the sand-trap, which indicated that the increased breakwater damage could be linked to the sand-trap dredging.

Discussion on the Repair Strategy Followed

Static tests on dolosse have shown that a dolos can carry 4 to 6 times its own weight without breaking; this implies that a number of layers can be constructed without breakage under static load. Thus it was considered feasible to place a 1 to 2 layer thick 20t to 30t dolos strengthening layer, safely on top of the existing damaged 20t dolosse.

Although the quality of the underlying 20t dolosse is questionable, the dynamic loading over the past 20 years has caused the weaker dolosse to break, and careful placing of new dolosse should not result in significant further breakages, besides the initial "shake down damage". However, since most parts of the repair sections will consist of a number of already broken units, the repair itself was designed as well interlocked armour, finished to a uniform slope, which should be able to stand on its own. Although stresses cannot be modelled, extensive prototype observations and structural tests on full size dolosse support the above conclusions.

Repair Options Tested in 3D Basin

Comparative tests were first carried out using the same wave conditions and sand-trap configuration. Later tests included the option of extending and deepening the sand-trap. The **first repair option** tested involved covering only the worst stations (C7 and C8) with a double layer of 30t dolosse, with 20t dolosse on either side to tie into the existing slope. A total of 150 30t and 250 20t dolosse were used for repair option 1, placed at 1:1,5 slope with no rock toe. After this proved unsuccessful, **repair option 2** was tried, with 30t dolosse and a rock toe stretching from stations C5 to C12. A total of 504 dolosse were placed covering a distance of 165m. Although repair option 2 showed less damage, it was still unacceptably high. **Repair option 3** was similar to option 2 but with a flatter 1:2,5 slope from +3,5m. A total of 670 30t dolosse were used. This repair 1:2,5 slope option was repeated unsuccessfully with 950 20t dolosse and then with 785 30t dolosse but without a rock berm.

Repair Options Tested in 2D Flume

Repair option 3 was then repeated in a larger 1:63 scale 2D flume (3m wide). The effect of extending and deepening the sand-trap was also re-tested in the 2D flume. The latter test confirmed the relationship between high damage and the deepest part of the sand-trap (Figure 5). Because of the vulnerability of the breakwater toe to scour resulting from sand-trap dredging, it was decided to optimise the size and position of the rock toe by running some tests at an even larger 1:40 scale in a 2m movable bed flume. This was done to check stability of the toe at low tide, and its ability to accommodate settlement and erosion, but still maintain support for the bottom row of repair dolosse. The movement of the rock and change in profile of the toe were carefully monitored. These tests showed the need for the rock toe and first two rows of dolosse to be placed first, and allowed to settle, before the rest of the repair dolosse were placed.

Change in design conditions

After acceptance of the above repair design, a total of 1000 new 30t dolosse were cast near the root of the south breakwater (Figure 7). The start of construction of the repairs was however delayed for more than a year because the Portnet crane that was to be used for the repair at Richards Bay was unavailable. In this time there was substantial accretion, (of up to 3m) especially along the trunk of the breakwater (Figure 8). The breakwater repair section was again tested in the 2 D flume with the reduced depth. The depth at the toe at some sections was as shallow as -5m CD. During the re-testing of the

model it was found that the proposed rock toe was unstable, with the rocks being displaced into the dolos slope. The dolosse would have sustained more damage and become clogged (lower porosity) in such a scenario. Various options were then investigated to solve this problem, such as dredging a trench in front of the breakwater to lower the toe, or to use heavier rock (> 5t), or to do away with the rock altogether.

Figure 7: Casting Yard for New Dolosse

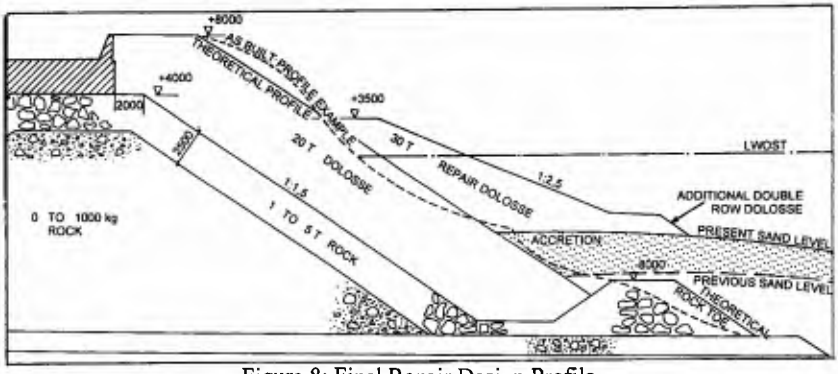

Figure 8: Final Repair Design Profile

Implementation of Model Test Results

A comparison of the damage at the end of each test run in the 3D basin showed that option 3, with the 30t repair dolosse at a flatter 1:2,5 slope was clearly the best option, although some "shake down" damage was expected from the repair settling into the existing dolosse, from the pre-settlement of the first rows of repair dolosse and from possible future toe scour. Research by the CSIR (Zwamborn and Phelp, 1989 and Luger, 1994) has shown that armour unit strength can be enhanced by rail reinforcing and by increasing the size of the dolos fillet between the fluke and shank. For this reason, the new dolos shape with large curved fillets was used and one third of the repair dolosse were rail reinforced for use in potentially high damage areas.

The solution that was eventually found to provide a stable repair at the shallower toe depth was to replace the rock toe with an additional three rows of "sacrificial" dolosse. There would ultimately thus be 5 rows of dolos lying on the accreted seabed. These dolos were allowed to pre-settle into the sand over a length of time, before placing the rest of the repair slope. In the model, the maximum settlement was recorded at 2-3m at the toe (Figure 9). It was also found that the dolos had to be placed at a packing density of 0,75 for the maximum pre-settlement to occur. The rest of the breakwater repair was then placed at a packing density of 0,85.

In reality the dolos would settle 2-3m or until they reached the previous rock toe, or the remnants thereof. The pre-settlement dolosse placed directly onto the sand were all to be rail reinforced for additional strength, and their settlement was monitored by ball surveys. Figure 9 gives a typical profile before and after placing the first 5 rows of dolosse, which shows the dolos 2m above the sand, indicating a settlement of about 2m. The results of the crane and ball survey were analysed and contours plotted of the data. These contours were then analysed and large holes were identified where additional dolosse were placed to ensure a smoother profile before placement of the new double layer repair. Each dolos was given a fixed co-ordinate (Figure 10), calculated to achieve the desired packing density and final repair profile.

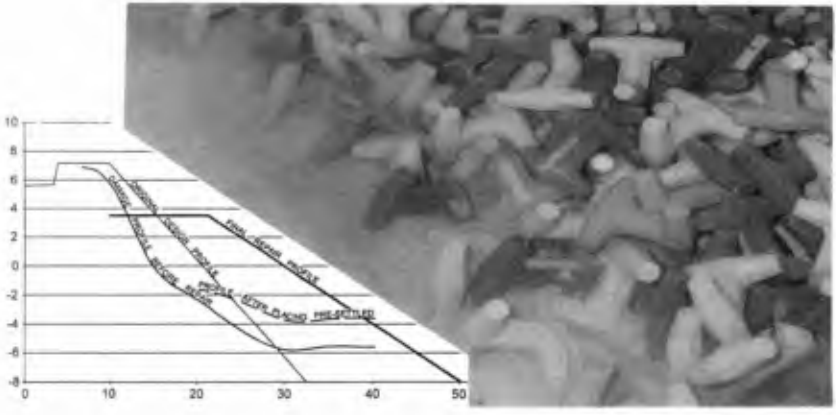

Figure 9: Pre-settlement of Toe Dolosse - Prototype and Model

Construction Methods

Based on the results of the model tests, only 30t dolosse were to be used for the repair. These dolosse were brought from the casting yard (1001 new 30t units) and old stockpile (37 old 20t and 88 old 30t units left over from the original breakwater construction) on the south side of the entrance channel directly onto the breakwater. Three double direction trailers were then used to transport the dolosse, but as these trailers could only pass when unloaded, it meant that only one 30t dolos could be brought onto the breakwater at any one time (Figure 11). A portal crane was used to handle the dolosse from the casting yard onto the stockplie and from there onto the trailers.

Initial crane and ball surveys were done with 5m profile intervals over the damaged areas. Repair dolos placing grids were then calculated and the pre-settlement dolosse were placed. Another ball survey was then carried out to check the pre-settlement, from which the final repair dolos placing grid could be re-calculated if necessary. The smoother the under-layer profile, the easier it was to set placing grids for uniform packing density.

The crane hook was fitted with a 15m sling (to ensure the hook and pulley remained out of the seawater), a quick release hook and a double cable sling. The double slings which support the dolosse were hand spliced (instead of swage joined) to allow easy removal of the slings once the dolos was in position. The quick release hook was hung from a swivel and fitted with two torque bars, which allowed easy rotation of the dolosse to ensure good interlocking. The torque bars were attached to 10mm nylon (light and water resistant) ropes, which were pulled perpendicularly from the mass capping to orientate the dolosse. The front row of toe dolosse were placed with the vertical fluke facing seawards.

It was found that to ensure correct packing density, the dolos placing must be kept as close as possible to the grid coordinates. The final orientation and positioning of the dolos is then done by eye to ensure good interlocking. Dolosse are placed with a minimum of three contact points to reduce the chance of rocking under wave action. After all the grid positions were full, it was found that up to 5% additional dolosse (using old 20t and 30t units from the stockpile) had to be placed "in holes" to ensure a well interlocked uniform profile. To identify these "holes" an aerial view of the slope was studied from a helicopter.

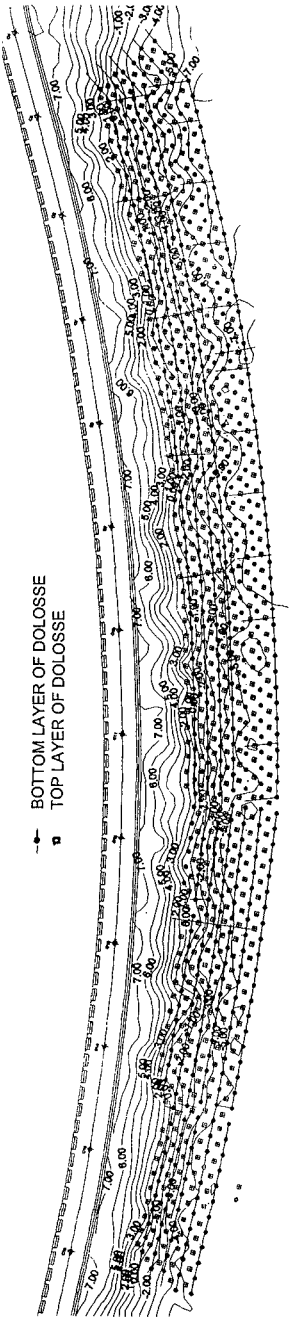

Figure 10: Pre-repair Contour Plot and Dolos Placing Grid

Figure 11: Portnet Crane Offloading Dolosse from Trailor

DGPS for Crane Positioning

For both the crane and ball surveys of the slope profiles, and the correct placing of the dolosse, there was a need to accurately position the hook of the crane. A differential GPS system was introduced using satellite positioning linked to a portable computer onboard the crane. The satellite receiver is positioned on top of the crane boom, directly above the position of the hook. The pre-determined positions are entered into AutoCAD software on the computer, and standard survey software enters the real time navigation parameters which indicate the position of the boom. By entering the standing position of the crane along the breakwater, the boom reach and safety circle can also be indicated on the screen. The crane operator can then immediately see which dolosse can be placed from the present position of the crane. The AutoCAD dolos placing grid is shown in Figure 10.

The positioning software includes the following useful features:

- Zoom in and out, and centring the cranes position on the screen.
- The entry of up to 20 predetermined crane standing positions on the breakwater, including facility to orientate and offset.
- The entry of up to 1000 top and bottom layer dolosse, including an indication of size and numbering (colour options)

- The facility to import and do editing of an AutoCAD or other CAD drawing of the breakwater eg: the "as-built" layout.
- Indication and editing of the safe radius of the cranes reach.
- The input and storage of the placed positions of the dolosse.
- A backup system where the polar coordinates can be entered to position the crane, should the DGPS signal fail.

The dolosse were numbered as per their sequence of placement. A top layer dolos was always placed centred between 4 under-layer dolos. The sequence thus entailed the placing of alternate bottom and top rows of dolos, moving up the slope. The placing of the pre-settlement under-layer dolosse started at the root of the breakwater and progressed towards the head. The crane then returned to the root to place the rest of the repair dolosse after the lower dolosse had had a chance to settle. The end of the repair was always left tapered at 45° up the slope, thus ensuring no unstable units which might be displaced before the repair could be completed (during storm conditions or breaks in construction). The limiting operating conditions for the crane were wind speeds of 50kph or swell heights above 2m.

Figure 11: Successfully Completed South Breakwater Repair

Conclusions

Close cooperation was maintained between Portnet, the Client/Port Authority who also partook in the model tests and constructed the repairs, the CSIR Research Laboratory which undertakes the annual breakwater surveys and who carried out the model studies, and Entech Coastal Consulting Engineers who assisted with parts of the design and construction. This ensured problems encountered could be quickly investigated and amendments incorporated into the final design. The early warning provided by the annual breakwater monitoring also meant that there was sufficient time to carry out the model tests and come up with an optimum repair design.

The completed repair can be seen in Figure 12, which shows the uniform profile and good integration with the original structure. A final ball survey of the repair showed that for most profiles, there was a perfect match between the design and surveyed profile. This was achieved by accurate dolos placing with the aid of DGPS on the crane. This repair which was completed in June 1998, has already withstood two storms in excess of the 1:1yr design wave height above 4m. A photographic aerial survey done after these storms showed less than 1% damage resulting from the initial "shake down". Annual surveys will be continued, to monitor the performance of the new shaped 30t dolosse.

Acknowledgements

The authors would like to thank those concerned for the team spirit which prevailed between Portnet, the CSIR and Entech for the successful completion of this project and for the contributions made to this paper.

References

CSIR (1988). Richards Bay South Breakwater, Evaluation of Damage and Proposals for Repair. CSIR report EMAS-C 88114, Stellenbosch, South Africa.

Van der Meer J (1988). Rock slopes and gravel beaches under wave attack. Doctoral thesis. Delft University of Technology.

Zwamborn J A and Phelp D (1989). Structural tests on dolosse. Seminar on stresses in concrete armour units. Vicksburg, USA.

CSIR (1992). Port of Richards Bay: Model Study to Optimise Breakwater Repairs. CSIR report EMAS-C 93049, Stellenbosch, South Africa.

Luger *et al* (1994). Increased Dolos Strength by Shape Modification. 24 ICCE 1994, Kobe, Japan.

Phelp *et al* (1994). Results of Field Monitoring of Dolos Breakwaters. ICCE 1994, Kobe.

Phelp *et al* (1996). Richards Bay North Breakwater - Repair of a Roundhead. 25 ICCE 1996, Orlando, Florida.

DIGITAL IMAGING PROCESSING TECHNIQUES FOR THE AERIAL FIELD MONITORING OF HARBOUR BREAKWATERS

Gavin Hough[1]& David Phelp[2]

Abstract

The entrances to the six largest ports in South Africa are protected by rubble mound breakwaters, which have Dolos armouring. PORTNET, the national Port Authority, have commissioned the CSIR to conduct detailed monitoring of existing rubble mound breakwaters including records of the wave conditions to which they are subjected in service. This paper presents the image processing techniques used to monitor breakwater damage as well as the wave field causing the damage. Wider applications of these techniques have been commissioned during pipeline outfall construction as well as during the design & modelling stage of a proposed new harbour. The image processing techniques have been used to measure both breakwater settling and damage as well as moored ship motion for competing breakwater designs constructed as in scale models, of proposed harbours at the CSIR's physical modelling facilities in Stellenbosch.. The image processing techniques developed by TECHTRIX International are reported here.

Context and Background

Recent trends highlighting the increased use of global satellite mosaics are impacting on the research, infotainment, and animation industries. National Geographic Television have for example, in a joint effort with Jet Propulsion Laboratory, taken over 500 satellite images and stitched them together digitally covering the entire globe at 1km resolution. Cloudy areas are replaced with cloud free data, colours are balanced, and the infrared channels converted from infrared (for vegetation) to natural hues.

This process is now recurring on smaller scales, with image mosaics, recorded from helicopters, aircraft and balloons using GPS to log viewing positions. These images are then projected onto digital terrain models of the area of interest. By repeating flybys at well-chosen intervals, changes, which would otherwise be too slow or subtle for the human eye, are clearly resolved.

In the United States, highway surveys from slow flying helicopters are used for road maintenance programs, and in South Africa annual harbour breakwater surveys use helicopters with differential GPS for imaging. Both digital and analogue images are recorded on pre-determined flight paths. The video sequence is digitised to supplement

[1] Director, TECHTRIX International, Innovation Foundation, University of Natal, PO Box 1493, Kloof 3640, South Africa. E-mail: hough@innov.und.ac.za

[2] Manager –Ports & Coastal Structures, CSIR, PO Box 320, Stellenbosch 7599, South Africa. E-mail: dphelp@csir.co.za

the image sequence recorded using a digital camera. This *current* image sequence can then be compared with archived reference photographs, which are scanned or digitised using a CCD camera. These image sequences are analysed to monitor storm damage and movement of Dolos and more recently Core-loc armour units. A significant data archive, spanning a decade of wave damage to South African breakwaters, can now be analysed using these new image-processing techniques.

Breakwater Imaging

The primary goal of this ongoing breakwater-monitoring project is to quantify damage to breakwaters protecting all major harbours along South Africa's 3000km coastline. Broken and missing armour units, as well as individual displacements of these units are quantified on an annual basis, or more frequently in the case of major storm damage.

Flight paths following GPS stored way stations are flown annually with images typically recorded at 25m intervals along the breakwater from a position, which is normal to the plane, defined by the bank of armour units. Figure 1 illustrates a typical imaging configuration and the position of the photographer on the outrigger

Movement Logging

This image sequence is digitised and stored as the *digital reference breakwater*. This image sequence defines the reference frame against which future breakwater images are compared. Where the flight paths differ despite the deployment of differential GPS, the images are warped in such away as to optimise the fit between the earlier "reference breakwater" images and the more current images. The imaging system then flicks between these two images (the reference and the registered current image) allowing small movements (<10cm) to become immediately apparent to the operator who logs the displacement, damage and disappearance of armour units with a few simple mouse clicks.

Figure 1 illustrating the positioning of the photographer for breakwater imaging. Images are recorded at 25m intervals.

Figure 2a: Model breakwater view with ripples on right hand side barely visible.

In Figure 2a and b the movement of a single armour unit cluster is illustrated using simple image subtraction techniques. Note the barely visible ripples being resolved in this 1:100 scale model. Outdoor harbour surveys often require edge detection techniques in order to resolve small movements despite differing lighting conditions. Typical images as well as the program for illustrating these techniques can be downloaded from http://flyer.ph.und.ac.za/~techtrix/.

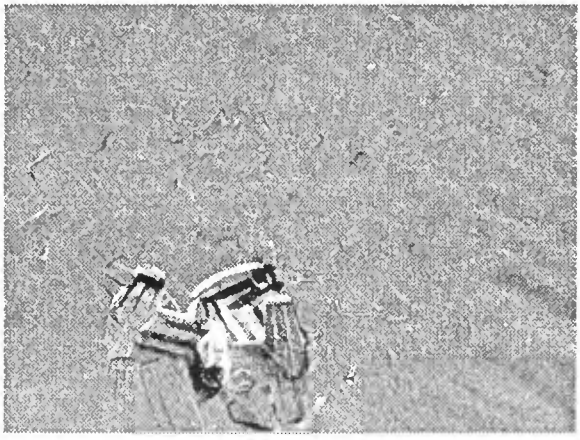

Figure 2b illustrating the registered image subtraction technique which is applied in real-time for identifying significant breakwater movement.

Figure 2c highlight recorded movements during a series of design storm tests in this model application.

Scope of Application

This *Breakwater Monitoring* System is focussed on four specific areas of application:

- Rapid recovery of quantitative breakwater damage from existing photographic archives. In this case a live video digitising station is used to allow freehand movement of the current image until it overlays[3] the reference image (already digitised). The ergonomics of this operation are significantly better than having to pair up common reference positions in every image pair before applying the appropriate image transform. It is however important that the before-and-after image pairs differ only in position and orientation. Should the images differ in size then the zoom has to be adjusted which slows the process down, making it as slow as the cursor controlled "drag and stretch" operation performed on scanned images.
- Real-time multi-camera system for model applications. Both systems, (a 4 CCD camera system for B&W imaging and a 3 camera system for colour imaging) are

[3] This is achieved using either of two methods:
[1] the "blink-comparator" method traditionally used by astronomers when scanning for commits by blinking between two images of a given star fields where fixed stars have been used to register the images or
[2] the "flicker optics" method (South African patent No 94/10303) which interlaces the live video of the current image with the fixed reference image.

used for logging breakwater damage in scale model applications where design storms expose the strengths and weaknesses of different harbour breakwater designs. This kind of work has been labour intensive in the past and has not resolved the details of the breakwater settling process, as well as the myriad of smaller displacements which will propagate over considerable distances from a racking armour unit. The current set-up in the CSIR's model hall in Stellenbosch, SOUTH AFRICA allows for a 10-fold saving in data sampling and processing, making the systematic study of multiple large scale design variations more feasible.

- Off-line digital image archive analysis. When analysing an existing digital image database sampling stations, scanners and digital frame grabbers are not required. These systems are typically run in parallel with the multi-camera sampling systems during a run. In this way several personnel can analyse images pairs as current breakwater image sequences are sampled by running both systems on a common LAN.
- Remote surveillance and environmental monitoring systems. Cameras located on coastal high-points are able to monitor breakwaters and surrounding wave fields during daylight hours. These cameras running at full video frame rates can measure wave orientation and period by continuously sampling video intensities along lines parallel to and at right angles to the nominal direction of wave propagation. Breakwater images can be triggered by wave drawback ensuring image sampling when the bulk of the breakwater is exposed. The research objective here is to log all significant armour movements by time and position and then analyse the statistics as a function of different sea states. The sea-state system has been deployed and a feasibility study undertaken for PORTNET on their Durban Bluff Signal tower – one of the few land based high points with a view of the exposed side of a harbour breakwater. Both modem dial-up for downloading processed data, and microwave links for transmitting live video between camera and frame grabber, have been deployed with reliable performance for environmental monitoring contracts ranging from 2 months[4] to 2 years[5].

Daytime Wave Field Monitoring in the Vicinity of Breakwaters

The *WaveWatch©* system developed by TECHTRIX International is set up during good seeing conditions when the horizon is well resolved. The calibration procedure automatically locates the horizon, and asks the operator to click on the positions of several locations with known GPS co-ordinates within the field of view. This information is used to set up a mapping locating any part of the picture in real-word co-ordinates, allowing any sampling line to resolve true bearing and length. The operator will then position a sampling line, which is roughly orientated along a wave front. Intensity profiles along this wave front are then sampled 25 times a second (using the PAL video standard) and the phase lag between intensity modulations at opposite ends of the sampling line, used to track wave bearing in real-time on an ongoing basis during daylight hours.

---

[4] Sappi-Saiccor 6.5km outfall pipeline construction which required pipe-flooding in the event of design storms (1-in-1 year storm from 60° and a 1-100 year storm from 170°) to avoid pipeline displacement on the seabed.

[5] Multi-camera systems using remote cameras on pan-tilt platforms linked by microwave to a central operations centre where digital image processing techniques are used for forest fire detection in forest plantation environments.

Figure 3a illustrates the horizon fix, GPS landmark selection and video sampling line placement. The keograms which follow illustrate the time stack output of the intensity profiles extracted from the sampling line at the full TV frame rate and averaged in order to focus on the phenomena of interest. (For details see the appendix at the end of the chapter.

This time stack is compiled from 576 video images. A fixed video intensity profile running along the shore-line is extracted form each video image and "stacked" from left to right in sequence.

This particular view was selected to illustrate the effect of a rip current near the base of Durban's south breakwater. Surface water is shown converging (through time) on the rip channel. The inset bottom right is 1 (of he 576 profiles) displayed as a plot of intensity for the vertical sampling line passing through the cursor.

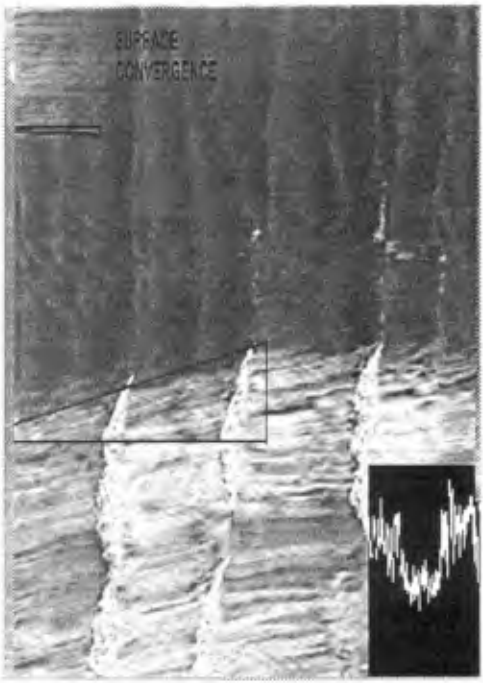

Figure 3b is a time-stack illustrating along shore movements in the vicinity of an off shore ri current near the base of a breakwater in the surf zone.

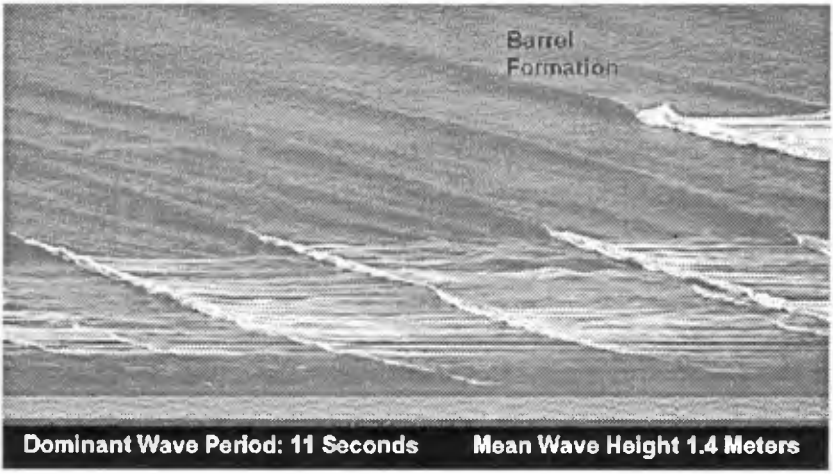

Figure 3c: In contrast to the previous time-stack sampled along a fixed line parallel to the shore, this time stack is sampled from the beach at the base of the breakwater straight out through the surf zone. The shoreward propagation of the swells and the gradual sea-ward drift of the white water is illustrated here. One can clearly make out larger swells "overtaking" smaller swells en route to the beach visible at the base of this video mosaic. On the opposite side of the breakwater ships entering and leaving the harbour can be tracked in this format keeping a record of their arrival and departure times through the harbour mouth.

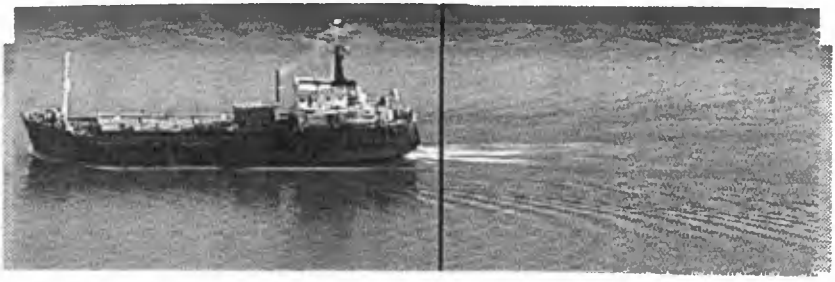

Figure 3d displays the digital video record (in time stack mosaic form) of ships entering and leaving the harbour.

Decision Support for Harbour Breakwater Management

Breakwater movement after the settling stage following construction is required when compiling a set of practical management directives supported by the emerging trends in breakwater damage (when is it best to repair the breakwater?). Early repairs may be too frequent and therefor expensive while late repairs stand the risk of having to repair runaway damage events like leading to total breakwater failure. The current directive is for immediate repairs when displacement, loss and breakage approach 30% of armour units along any given section. Historical records do however include results where these directives were not applied in the past ensuring that management evaluation data is available over a wide range of management regimes (*CSIR reports .....1987-1997).*

Once the repair has gone ahead, its implementation can be significantly improved with the used of GPS assisted armour placement cranes, streamlining the process from movement detection to the physical positioning of the replacement armour unit (*Phelp et al 1998*).

Ship Dynamics in the Vicinity of Breakwaters

The recent advent of wave field monitoring with view to highlighting the risks associated with specific storms on a more quantitative bases, has been focussed on developing operational criteria for storm related port closure to shipping. The narrow Durban harbour entrance, which only exceeds the large ship beam by a factor of three, is monitored for wave sea conditions impacting on the safety of the ships approaching the harbour entrance. As vessels enter the lee of the south breakwater strong yawing motion as well current shear have been measured. The figure below is a time-stack montage illustrating the cross-current in the vicinity of the harbour entrance displacing the ship's wake from the path followed by the ship's bow through the water.

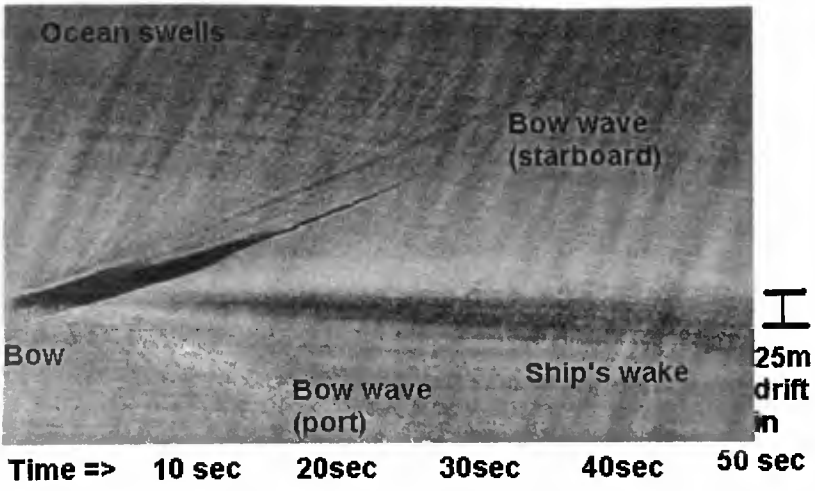

Figure 4: This remarkable keogram of a ship approaching the harbour entrance from a distance of 2 nautical miles. The cross-current in the surface layer is evidenced by the gradual sideways drift of the wake (by 25m over 50 seconds) resolved here at progressively lower positions towards the right hand side of this time stack mosaic.

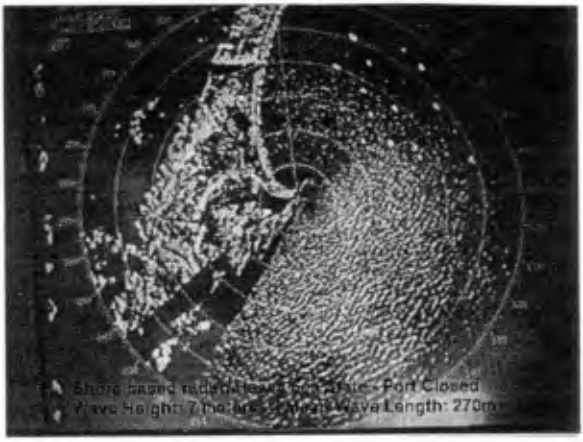

Figure 5a displays a single sweep of the radar field. This is digitised and analysed over any portion of the wave field for wave propagation speeds, wavelengths and periodicity. Qualitative wave amplitude estimates can also be made.

24 Hour Monitoring of Wave Fields in the Vicinity of Breakwaters

Machine vision based ship tracking and wave field sampling are limited to daylight hours and can be effected during heavy sea conditions when visibility can deteriorate. For this reason radar data have been digitised enabling around the clock monitoring of storm-time wave fields up to a distance of 6 nautical miles from the bluff signal station. The radar field is digitised in time series allowing for accurate wave celerity, wavelength, period and *qualitative wave height variation* measurements to be made. The radar image mosaic below illustrates in space-time (or time-stack) format, how wave length and period as well as phase velocity can be measured. It is interesting to note that the "envelope" modulating the amplitude propagates at close to half the phase velocity. This allows one to estimate the group velocity, which is effected by both the surface current and bottom topography.

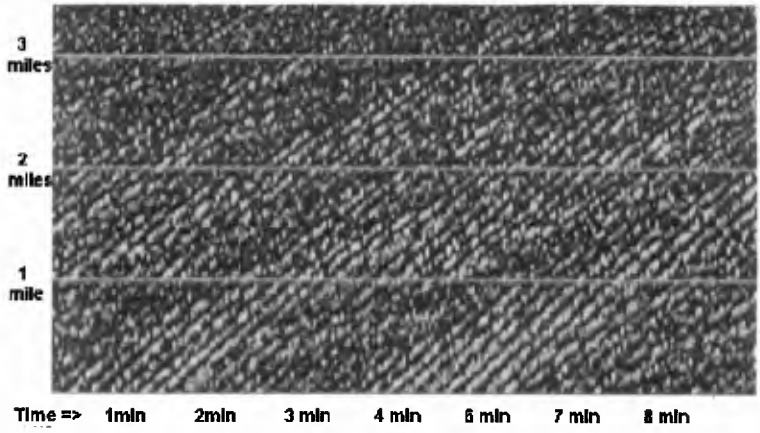

Figure 5b illustrates the propagation of individual wave fronts during heavy sea conditions which necessitated the closure of the Durban port during May 1998.

Breakwater Design and Moored Ship Dynamics

Remote measurement of moored ship movements is illustrated below allowing for the quantitative comparison of different design storms and breakwater designs in the model environment, as well as useful information for harbour records and container loading availability on a daily basis in the port environment. The most recent system can measure all 6 degrees of freedom with a single camera in the model environment.

Figure 6a showing the model ship with all the attachments required for performing conventional measurements of model ship dynamics. This is contrasted with the techniques deployed here where images are analysed and displacement profiles are

measured at 25 or 30Hz. These techniques have been scaled up to field trials with change in hardware or increase in cost.

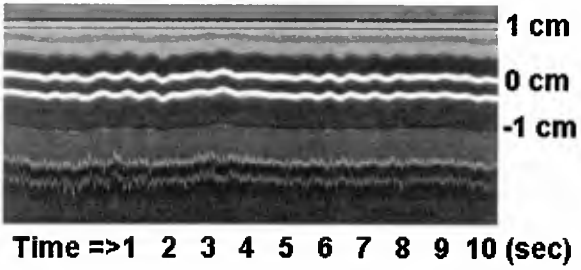

Figure 6b showing a typical feature trace, which is automatically tracked when extracting displacement time series data. One or more sets of data can be sampled for each degree of freedom.

References

Hough G., M. J. Kosch & M. W. J. Scourfield, *First observations of superfast auroral waves*, Geophysical Reearch Letters **19**, No 24, Dec 24 1992.

Hough G., N. Nishitani & M. W. J. Scourfield, *Spatial and temporal characteristics of Giant Undulations*, Geophysical Reearch Letters **21**, No 24, Dec 1 1994.

Phelp D., S. Luger, A. van Tonder & A. Holtzhausen, *Results of extensive field monitoring of dolos breakwaters*, PIANC 1996, Proceedings, 1996a.

Phelp D. & G. Hough, *Advanced video techniques for aerrial field monitoring of dolos breakwaters*, PIANC Bulletin (PIC) 1996b.

Design of Rock Armoured Single Layer Rubble Mound Breakwaters

T. Hald [1], A. Tørum[2], T. Holm–Karlsen[3]

ABSTRACT

There have been several investigations on the stability of site specific single layer breakwaters, e.g. for Søvær Fishing Port, Bratteland and Tørum (1971) and for Berlevaag Harbour, Kjelstrup (1977). However, despite the frequent use of the single layer design only little systematic investigations of the stability have been conducted until now. During the winter/spring 1997 a series of physical model tests have been conducted at SINTEF with focus on the hydraulic stability of the single layer rubble mound breakwater armour layer and the wave induced loading (Hald and Tørum (1997)). The present paper describes the results of these tests.

1. INTRODUCTION

Along the Norwegian coastline more than 600 breakwaters have been build since 1866. Some of these breakwaters are located on severely exposed locations with significant wave heights up to 6.5 m. The present value of these breakwaters is estimated to approximately 4.000 mil. NKr. The far most build breakwater type is the socalled single layer rubble mound breakwater utilizing only one layer of rock in the armour layer. This type of breakwater has developed from the time when heavy equipment was not easily available and the armour layer was constructed by dumping the stones from the breakwater crest.

Obviously the use of one layer rock in the armour layer requires fewer blocks than the traditional two–layer rubble mound breakwater. Despite the fact that heavier blocks are required for the single layer breakwater there is normally a better balance in quarry yields between large armour blocks and the smaller fractions used in the core for the single layer than for the two–layer breakwater.

[1]Hydraulics & Coastal Engineering Laboratory, Aalborg University, Denmark.
[2]SINTEF Civil and Environmental Eng., Dep. of Coastal and Ocean Engineering, Norway.
[3]Norwegian Coast Directorate, Oslo, Norway.

The use of one layer rock in the armour layer is in most countries not allowed because of apparent weaknesses in the construction. However, the Norwegian experience with respect to low maintenance cost is fairly good. The total maintenance budget is normally 2 – 4 mil. NKr. per year and in extreme winters the maintenance budget may occasionally raise to approximately 15 mil. NKr, c.f. Holm–Karlsen and Tørum (1998).

Thus, regarding both construction and maintenance the single layer breakwater has been considered to be a cost effective structure in Norway.

1.1 Construction of a single layer breakwater

Many of the older breakwaters in Norway were designed and built before any good knowledge of wave climate and on breakwater hydraulics was available, i.e. before the sixties. Thus experience and subsequent trial–and–error procedures were used.

Traditionally, the armour layer was constructed by dumping the armour stones from the breakwater crest from rail wagons or trucks. This dumping of the stones has to some extent been an art and the result depended also on the skills of the foreman. If an armour stone did not come into its right position it was necessary to use dynamite to blow it away before any new stones were placed. During the construction it was aimed at placing the stones orderly with the longest side almost perpendicular to the filter layer and the smallest area facing the waves, but often the result was a random placement. In order to make the stones roll in position the slope needed to be fairly steep and typical breakwaters were constructed with a slope of 1:1.25 to 1:1.5.

The period of construction was frequently over several years with longer breaks during winter and autumn due to hard weather. The winter storms have settled the unfinished breakwater incurred small damages to it. Possible damages were subsequently repaired during the following construction period and the net result was an improved stability of the finished breakwater.

In some cases today backhoes have been used to place the stones orderly in the armour layer. This method can only be applied from a level of approximately 2 m below LWL because of the limited range of the backhoe. Below this level the armour stones are placed traditionally by dumping from crest. This calls for special attention paid to the lower part in order to secure a safe foundation for the orderly placed upper part. Recently some of the newer build breakwaters built this way have suffered heavy damage.

2. MODEL TEST SETUP

Based on investigations of cross sectional parameters and armour stone characteristics of the Svartnes, Årviksand and Sørvær breakwaters a 3D scale model of 1:30 – 1:40 has been designed. Characteristics of the armour stones are given in Tab. 1.

Armour layer	W_{50}	ρ_m [g/cm^3]	$\frac{W_{85}}{W_{15}}$ [–]	L_{50} [mm]	B_{50} [mm]	T_{50} [mm]	$\frac{W_{50}}{\rho_m T B L}$ [–]
Årviksand	11.7 t	2.8	2.5	-	-	-	0.40
Sørvær	22.0 t	-	1.7	-	-	-	-
Svartnes	18.0 t	-	1.6	-	-	-	-
Stone type A	152 g	2.7	1.8	80.5	54.1	33.3	0.40
Stone type B	306 g	2.7	1.9	96.2	67.5	42.0	0.41

Table 1: Armour stone characteristics.

The breakwater scale model was composed of a core with stones of 4–8 mm, a toe of 118 g stones, a filter layer of 6.4 g stones and a superstructure. The filter layer stone size has been designed according CIRIA–CUR (1991) and with a thickness of 50 mm corresponding to 3–4 stone diameters. On the filter layer the armour layer was constructed with a constant slope of 1:1.5. Two types of armour stones with different weight but similar grading and shape characteristics were used, see Tab. 1, type A and B. The toe has been designed to withstand the most severe waves in order to avoid reconstruction after every test. In Fig. 1 the model cross section is shown.

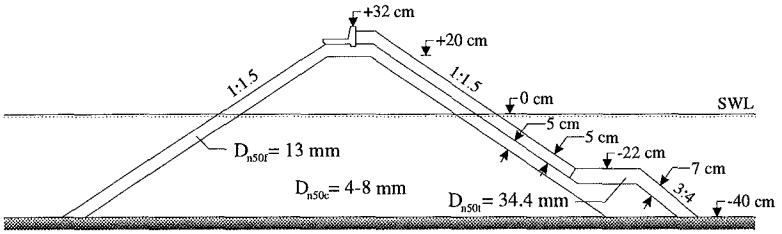

Figure 1: Model test cross section.

The model was installed on a slope of 1:30 in a 54 m long and 5 m wide basin approximately 25 m from the wave generator, see Fig. 2. The breakwater head was constructed by rotating the cross section for the trunk 180° around a vertical axis through the centerline of the model. Opposite the wave generator waves were absorbed on a parabolic shaped beach. To damp eventual cross modes perforated steel boxes were installed along both basin walls behind the breakwater model and in the gap between the model and the wall.

Five resistance type wave gauges were used to measure the incident wave, see Fig. 2. Three gauges were placed offshore on a constant water depth of 0.8 m and two gauges were placed in the gap between the breakwater model and the basin wall on a water

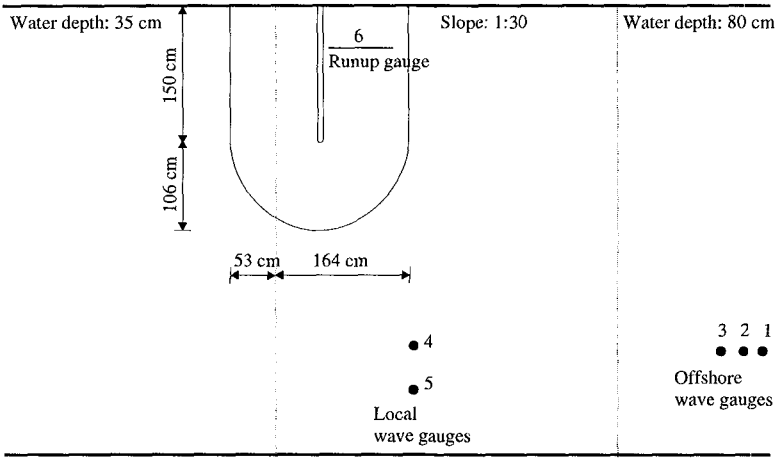

Figure 2: Model test layout.

depth of 0.4 m corresponding to the water depth at the toe. To measure the up– and downrush a resistance type gauge was placed on the slope. The sampling frequency was kept constant at 20.0 Hz.

3. STABILITY OF ARMOUR LAYER

3.1. Damage registration

The damage was registered by counting the accumulated number of moved stones N_m and by measuring the average eroded area A_e after each sea state run. The stones included in N_m were defined as the stones moved more than one D_{n50} from their original position and the stones that does not have a stabilizing effect. With respect to the average eroded area profiles were measured by laser for every 10 cm over the width of the breakwater. On the trunk 10 profiles, corresponding to a measurable width of 0.9 m, were averaged to obtain the average profile $\overline{z}_i(x)$. The vertical difference between two individual profiles was calculated so erosion becomes negative, i.e.

$$\Delta\overline{z}(x) = \overline{z}_{i+1}(x) - \overline{z}_i(x) \tag{1}$$

Followingly, the average eroded area was calculated by integration of negative values of $\Delta\overline{z}(x)$ between the toe and the breakwater crest.

$$A_e = \int_{x_{toe}}^{x_{crest}} (\overline{z}_{i+1}(x) - \overline{z}_i(x))\, dx \tag{2}$$

The damage level S was then calculated by

$$S = \frac{A_e}{D_{n50}^2} \tag{3}$$

Physically S can be interpreted as the number of squares with the length D_{n50} that fits into the average eroded area.

As a comparison between the two damage measures, the equivalent number of stones moved N_{mS} corresponding to the measured damage level S was calculated.

$$N_{mS} = \frac{Sl(1-n)}{D_{n50}} \tag{4}$$

where

l : Length of measurable part of trunk section, i.e. 0.9 m
n : Porosity of armour layer, $n = 0.4$

For small degrees of damage the counting method is considered the most reliable since the profiling also includes settling while profiling is considered better for larger degrees of damage when counting is more difficult.

Corresponding to the accumulated number of moved stones after each sea state the percentage damage $N_{\%D}$ and N_d that represents the number of stones moved in a down–slope row with the diameter D_{n50} were calculated.

The reason for using two damage measures is that the total number of stones in the armour layer is different for tested cross sections. E.g. when comparing the orderly and the randomly placed armour layers the same percentage damage corresponds to the same amount of erosion, but a different number of displaced stones. Same N_d gives same number of displaced stones but different eroded area.

3.2. Test programme

The tests were performed according to the test programme in Tab. 2.

Test identifier	Test runs	s_m	Armour layer characteristics	Cross section
A	3 3	3% 5%	1–layer orderly, stone type A	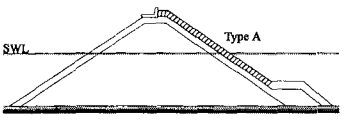
B	3 3	3% 5%	1–layer randomly, stone type B	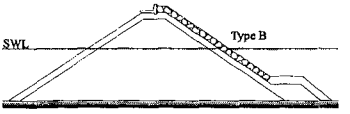
Ca	1	5%	1–layer orderly above level –7 cm stone type A 2–layer randomly below level –7 cm stone type A	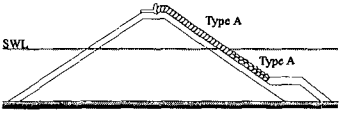
Cb	3	5%	1–layer orderly above SWL stone type A 2–layer randomly below SWL stone type B	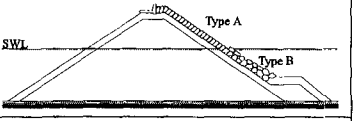
D	3	3%	1–layer orderly above level –7 cm stone type A 1–layer randomly below level –7 cm stone type B	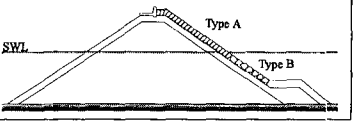

Table 2: Test programme for stability investigations.

In each test the steepness s_m was kept constant and the wave height was increased by 1.5 cm until failure was reached. The waves were generated according to a JONSWAP spectrum with $\gamma = 3.0$. Each sea state was run for app. 2000 waves.

Due to the stochastic nature of the waves and the constructed model all tests were repeated up to 3 times in order to provide some statistical sound data.

3.3. Stability of orderly placed stones

The damage begins above SWL by displacement of single stones from the armour layer followed by down-slope rolling of the stones. When the wave height increases the damage develops by displacement of more and more stones from the armour layer. As the stones are moved from the armour layer the remaining stones in the armour layer begin to turn downwards. In some cases the armour stones are hindered from turning by a high degree of interlocking and support from neighbouring stones. When sufficient stones have been displaced or turned downwards the high degree of support decreases and failure is inevitable.

In more quantitative terms the damage development for orderly placed stones on the trunk is shown in Fig. 3 the for the wave steepness of 3% and the wave steepness of 5%, respectively.

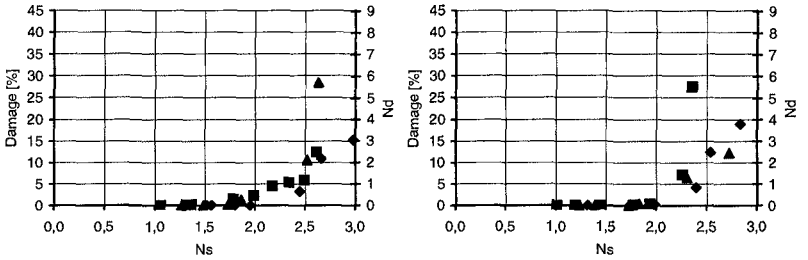

Figure 3: Damage development for orderly placed stones on trunk, s_m = 3% (left) and s_m = 5% (right).

From Fig. 3 only little spreading between repeated tests and no or only little influence of wave steepness is observed. Furthermore, the damage develops slowly. Considering a damage level of 5% the stability number is approximately 2.3 which corresponds to a stability coefficient K_D in the Hudson formulae of 8.1.

3.4. Stability of randomly placed stones

For a randomly placed armour layer the damage begins around SWL as a result of large settlements of the armour layer below water level. In single tests a long transverse fissure just above SWL with a width of 2–4 cm was observed. An increase in wave height resulted in displacement of more and more stones in the area around SWL.

In Fig. 4 the damage development for randomly placed stones on the trunk is shown for the wave steepness of 3% and the wave steepness of 5%, respectively.

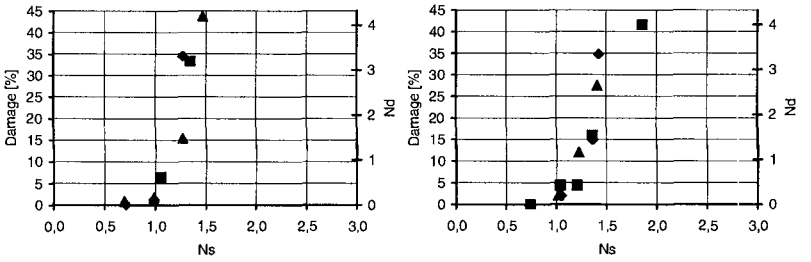

Figure 4: Damage development for randomly placed stones on trunk, s_m = 3% (left) and s_m = 5% (right).

From Fig. 4 only little spreading between repeated tests and only little influence of wave steepness is observed. Opposite the orderly placed armour layer the damage development for the randomly placed armour layer is very rapid. Considering a damage level of 5% the stability number is approximately 1.05 for a steepness of 3% and 1.1 for a steepness of 5% which corresponds to a stability coefficient K_D in the Hudson formulae of 0.8 and 0.9, respectively.

3.5. Stability of armour with combined placement methods

Fig. 5–6 depicts the damage development for the tests with orderly placed armour stones on top of an armour layer constructed by randomly placed stones. For a more complete description of the combined placement methods it is referred to Tab. 2.

In Fig. 5 the damage development for the construction type Ca (left) and Cb (right) is shown for a wave steepness of 5%.

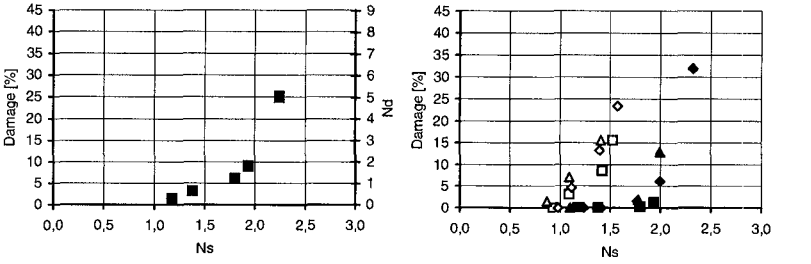

Figure 5: Damage development for combined placement methods, type Ca (left) and Cb (right), closed = stone type A, open = stone type B.

For the construction type Ca the stone type A have been used in both the orderly and in the randomly placed armour layer. In Fig. 5 (left) a slow damage development is seen. However, this is not a true picture of the behaviour since only stones in the lower randomly placed armour layer are moved up till a certain damage level. Above

this level the orderly placed part starts to slide. At a damage level of 5% the stability number is 1.6 corresponding to a stability coefficient of 2.7.

For the construction type Cb the stone type B have replaced stones type A in the randomly placed lower part of the armour layer in type Ca. The damage development for type Cb is shown in Fig. 5 (right). Compared to the Ca–type the behaviour of the armour layer is similar: Almost same slow damage development of the lower randomly placed armour layer followed by a rapid damage development of the upper orderly placed armour layer. At a damage level of 5% the stability number is 1.2 corresponding to a stability coefficient of 1.2. This level is significantly lower than for type Ca since the transition between the two methods of placement is at a higher level, see Tab. 2.

In Fig. 6 the damage development for the construction method D is shown for a wave steepness of 3%.

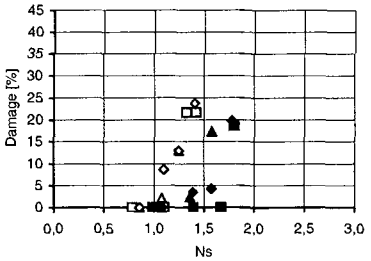

Figure 6: Damage development for combined placement method, type D, closed = stone type A, open = stone type B.

The construction method D differs from the C–types by the use of only one layer of stones in the randomly placed lower part of the armour layer and when comparing the way damage develops a more rapid damage development for the randomly placed part and a more slowly developed damage for the orderly placed part is observed. This is due to the larger settlements related to the single layer randomly placed armour layer. Corresponding to 5% damage the stability number is more or less similar with the Cb–type.

4. WAVE INDUCED FORCES

4.1. Wave force registration

For measuring forces a single stone was selected and a reprint was made in coated plastic foam and succeedingly mounted on a load transducer able to measure two force directions. The load transducer was designed and manufactured by MARINTEK A/S, SINTEF. The principle of the transducer is measuring shear strain in different cross sections enabling measurements of the force both parallel and normal to the slope. To avoid any contact with neighbouring stones a chicken wire was wrapped around the mounted stone with a distance of approximately 1 cm.

The load transducer with mounted stone was placed in four positions over the slope as shown in Fig. 7. Also the definition of force directions is shown. Before positioning, the load transducer was calibrated in dry conditions up to 500 g.

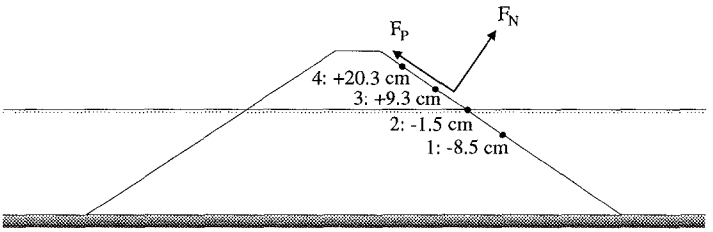

Figure 7: Position of load transducer and positive direction of forces.

Both tests with regular waves and irregular waves were conducted with the transducer positioned in all four positions but only results for regular waves are treated herein, see Hald and Tørum (1997) for full reference. For regular waves a wave steepness of 3% and of 5% was tested by increasing the wave height in three steps: 9.0 cm, 12.0 cm and 15.0 cm. Forces were sampled at 500.0 Hz and subsequently lowpass filtered with a cutoff frequency of 250.0 Hz.

In the measured force time series maxima and minima peaks have been determined by zerocrossing analyses of the time derivative of the measured force time series. In order to determine only independent peaks, registered peaks within a desired filter width are sorted out leaving only one peak within one wave period.

4.2. Wave force characteristics

Measured force characteristics are shown in Fig. 8. Generally, force characteristics are almost invariante with varying wave height and wave steepness why only $H = 15\,\mathrm{cm}$ and $s_m = 3\%$ is presented. Notice that the largest forces occur 10 cm below and 10 cm above SWL (in position 1 and 3) despite that the waves break directly upon the stone positioned in SWL (in position 2).

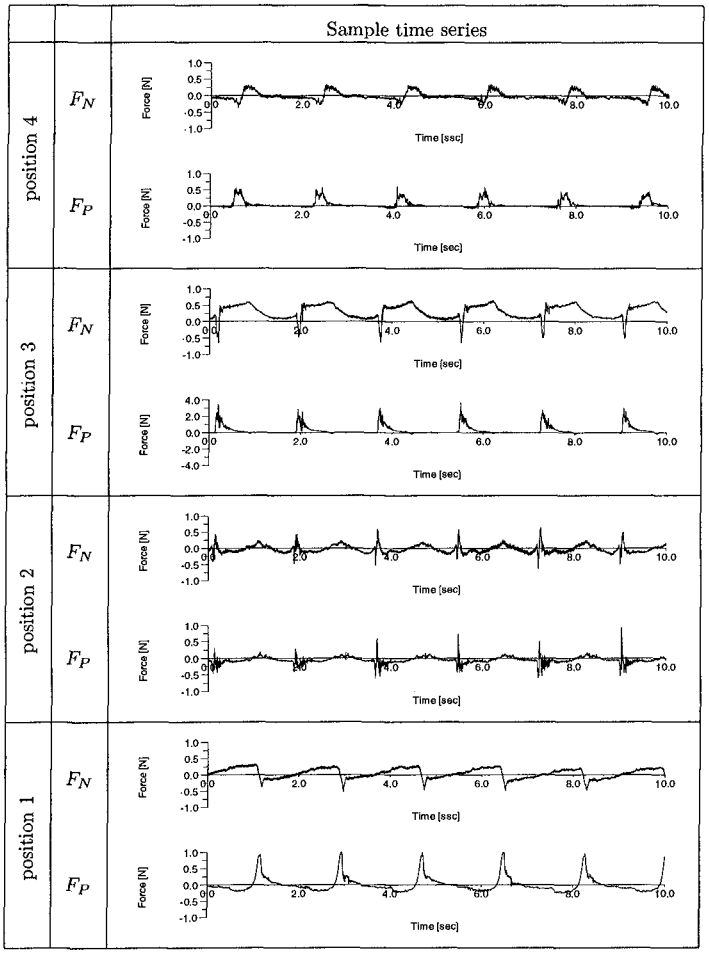

Figure 8: Sample normal and parallel force time series for $s_m = 3\%$, $H = 15$ cm.

4.3. Regular wave induced forces

To illustrate how the total force and corresponding direction varies down the slope all combinations of normal and parallel force within one test are plotted in a (x,y)–coordinate system – a socalled hodograph. As the total force varies in each direction, the average force F_m within intervals of 5° was calculated. In Fig. 9 hodographs for each position and each combination of wave height and period are shown.

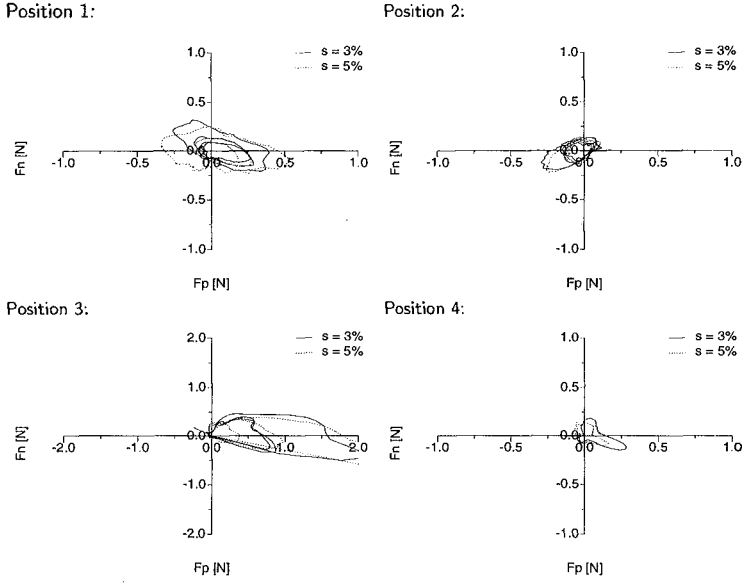

Figure 9: Hodographs based on F_m at position 1–4 for regular waves.

Generally, the shape of each hodograph for all combinations of wave height and period within each position is very similar, c.f. Fig. 9. The largest forces occur below and above SWL in position 1 and 3. In position 1 the dominating forces are either directed outwards and down–slope or inwards and up–slope. In position 2 the forces are smaller and of more or less the same magnitude in all directions. Further up–slope in position 3 the largest forces occur in up slope direction and mainly parallel to the slope. In position 4 the force is of the same character as in position 3 but only smaller.

The most interesting forces are the destabilizing forces in outward directions and in order to get an impression of the vertical distribution along the slope three outward directions are selected: 45° down–slope, 90° slope normal and 45° up–slope, see Fig. 10.

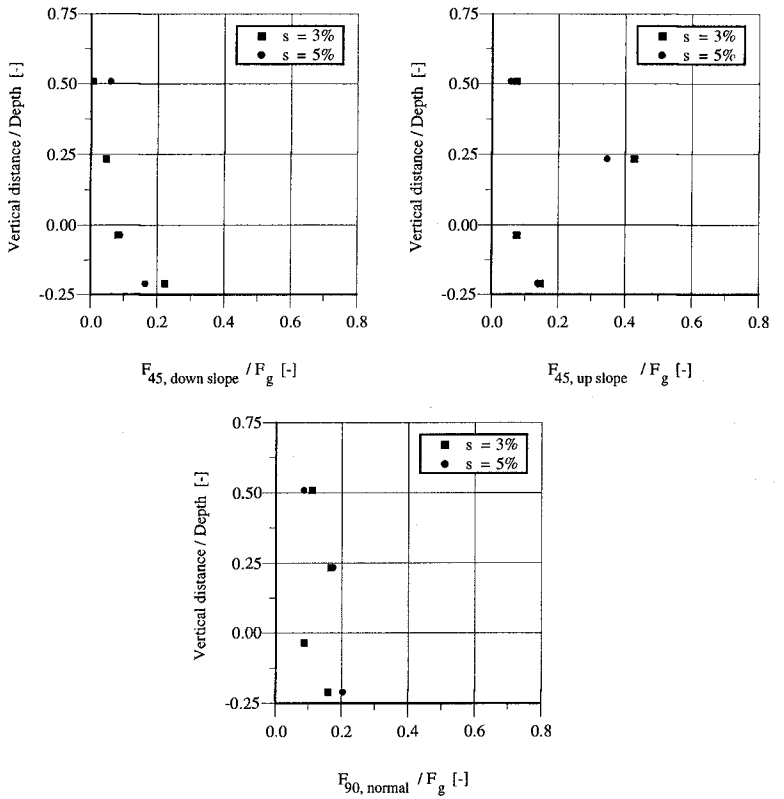

Figure 10: Vertical distribution of outward directed mean force F_m normalized to the stone gravity F_G of one stone based on regular wave tests, $H = 15$ cm.

Considering Fig. 10 it is observed that each position except 0.25 times the water depth above SWL, i.e. position 3, the force magnitude is of the same order of magnitude for all directions. In position 3 the force increases as the direction becomes more upward directed.

4.5. Comparison with stability

Comparing video recordings from the model tests it is observed that for the randomly placed stones, damage is initiated below SWL. However, for the orderly placed stones damage is initiated above SWL.

Relating the stability observations to the force measurements it is interesting to see that only in the case of random placements, the downward directed force is able to remove the individual stones from their original position. This downward directed force is not sufficient to remove any stones when placed orderly because of the higher degree of

interlocking and support from neighbouring stones. In this case high normal/upward forces are required to remove any stone. These forces are present above SWL in position 3, especially in the 45° upslope direction.

5. CONCLUSIONS

The stability of different types of single layer rubble mound breakwaters have been investigated in a scale model for two characteristic wave steepnesses. The scale model and the sea states correspond to typical Norwegian breakwaters in scale 1:30 to 1:40 and typical prevailing storm situations in the Norwegian Sea.

Different methods of placing the armour stones in the armour layer have been investigated, see Tab. 2 and the stability performance is presented in individual damage curves. The highest degree of stability is obtained by placing the stones orderly. This placement method more than doubles the stability in terms of the Hudson–type stability coefficient compared to the conventional random placement method in two layers. Placing the stones randomly in one layer a very low stability of one third of the stability obtained by the conventional method is found. Generally, no influence of steepness was observed.

With respect to the wave induced forces on single armour stones the normal and the parallel force have been measured in 4 positions over the slope. Tests with regular waves have been conducted with two wave steepnesses. Large destabilizing forces were identified both above and below SWL. The influence of wave period was little as was the case for the stability tests whereas the influence of wave height was significant in some cases, especially in the positions above and below SWL.

ACKNOWLEDGEMENTS

The work is jointly supported by the Danish Technical Research Council under the frame programme Marin Teknik 2 and the Norwegian Coast Directorate.

REFERENCES

Bratteland, E., Tørum, A., *Stability tests on a rubble mound breakwater head in regular and irregular waves. Sørvær fishing port, Norway*, In: Proc. of the 1st Int. Conf. on Port and Ocean Engineering under Arctic Conditions, Trondheim, Norway, 1971.

Hald, T., Tørum, A., *Stability investigations of single layer rubble mound breakwaters* (in Danish), SINTEF NHL report STF22 A97252, 1997.

Holm–Karlsen, T., Tørum, A., *Single layer quarry stone rubble mound breakwaters, The Norwegian practice and experience*, Abstract for 29th Int. Navigation Congress of PIANC, The Netherlands, 1998.

Kjelstrup, Sv., *Berlevaag Harbour on the Norwegian Arctic Coast*, In: Proc. of the 4th Int. Conf. on Polar and Ocean Engineering under Arctic Conditions, Memorial University at St. Johns, New Foundland, 1977.

Tørum, A., *Reliability of Norwegian breakwaters* (in Norwegian), SINTEF NHL report STF60 F93057, 1993.

Tørum, A., Mathiesen, M., Vold, S., *Årviksand harbour, Wave penetration and breakwater stability* (in Norwegian), SINTEF NHL report STF60 F90057, 1990.

The form of the mound of rubble dumped by a barge

Prof. Drs. Ir. J.K. Vrijling[1] and Ir. G. van Oord[1]

Introduction

In coastal engineering many structures are (partly) made of rubble or concrete blocks. The usual way of construction is by gradually discharging a specified amount of rubble from a stone dumping barge. The stone dumping barge is steadily repositioned along the structure.To ascertain a geometry as designed in case of a breakwater, a specified evenness in case of a caisson foundation or an acceptable coverage in case of a scour protection a reliable prediction model of the deposition mound of the rubble is needed. Such a model can be helpful in designing and in calculating the cost of the structure. First a model to describe the process af a single stone falling through water, the single stone model (SSM) is given. A mathematical model that describes the dumping from a point source was developed based on the SSM. By integration this model is extended to a description of a line dump as executed by a stationary dumping barge. Finally using the same principle the model is adapted to describe a dump by a laterally translating dumping barge, the area dumping model. In order the verify and to calibrate the SSM a number of experiments were carried out in the Hydualic Laboratory of Delft University of Technology.

The mathematical model

The model divides the gradual deposition of rubble or blocks in three stages. In the first stage the deposition of rubble is governed by a random walk of many independant steps with zero mean. If the rubble is dumped from a single point the diffusion to a cross section of the mound of rubble shaped like a two-dimensional Gaussian p.d.f.. From first physical principles it is derived that the standard deviation should be gouverned by:

$$\sigma_N = \alpha \bullet \sqrt{h \bullet D_{n50}}$$

[1] Delft University of Technology, Faculty of Civil Engineering, P.O. Box 5048, 2600 GA Delft, The Netherlands, E-mail: H.Vrijling@ct.tudelft.nl

in which α = constant depending on the mass density and the shape of the rubble particles
h = water depth
D_{n50} = nominal diameter of the rubble particles.

A detailed derivation of this single stone model (SSM) is given by Vrijling et al. For regularly shaped blocks the random walk consists of one single step and consequently the deposition mound has a circular pattern with a radius proportional to the waterdepth. The cross-section of the ring is gaussian shaped and the standard deviation increases linearly with the waterdepth.

During the first stage the slope of the cross section increases with the amount of rubble dumped, until it exceeds the angle of repose of the rubble at the inflection of the Gaussian shaped mound. This second stage of the build up ends, when in every point of the slopes of the mound the angle of equilibrium is reached. In the third stage the shape of the mound of rubble can then be described by a triangle. If dumping continues the mound maintains its triangular shape. The triangle can also be characterized by its radius of inertia or standard deviation:

$$\sigma_N = \sqrt{\frac{A}{6 \bullet \tan(\varphi)}}$$

in which t_Δ = radius of inertia of the triangle
A = area of the cross section of the mound
φ = angle of repose of the rubble

It should be noted that in the third stage the radius of inertia of the cross section depends only on the dumped volume of rubble and the angle of equilibrium. The second stage, when the Gaussian cross section is reshaped into a triangular form, can be treated as a transition stage of lesser importance.

The deposition from a single point leads for reasons of symmetry to a bi-Gaussian shaped mound: the Point Dumping Model (PDM). To find the theoretical shape of the mound of rubble formed by a side-dumping barge with deck-length L moored at a fixed point with a constant heading is found by the integration of an infinite number of single point dumps along the length-axis Y of the barge. The Line Dumping Model (LDM):

$$z(x,y) = \frac{V}{L\sqrt{2\pi}\,\sigma_G} e^{-0.5\left(\frac{x}{\sigma_G}\right)^2} \int \frac{1}{\sqrt{2\pi}\,\sigma_G} e^{-0.5\left(\frac{y-Y}{\sigma_G}\right)^2} dY$$

Solving the integral leads to a slightly simpler form containing the standard normal distribution $\Phi_N(x)$:

$$z(x,y) = \frac{V}{L\sqrt{2\pi}\,\sigma_G} e^{-0.5(\frac{x}{\sigma_G})^2} \cdot [\,\Phi_N(\frac{Y_1 - y}{\sigma_N}) - \Phi_N(\frac{Y_0 - y}{\sigma_N})]$$

It should be noted that the endpoints of the line dump are described by the standard normal distribution, while the cross-section is given by the normal p.d.f. The center-line of the mound shows a offset with reference to the board of the barge. This offsett is not included in the mathematical model.

If the barge is translated perpendicular on it's length axis along the X-axis during dumping, to cover an area with rubble the theoretical form of the deposition mound is found by a double integration over the area covered by the dumping edge of the deck of the barge. The Area Dumping Model (ADM):

$$z(x,y) = \frac{V}{(X_1 - X_0)(Y_1 - Y_0)} \int \frac{1}{\sqrt{2\pi}\,\sigma_G} e^{-0.5(\frac{x-X}{\sigma_G})^2} dX \int \frac{1}{\sqrt{2\pi}\,\sigma_G} e^{-0.5(\frac{y-Y}{\sigma_G})^2} dY$$

Now the four edges of the dumped area are described by a normal distribution:

$$z(x,y) = \frac{V}{(X_1 - X_0)\,L} \cdot [\,\Phi_N(\frac{X_1 - x}{\sigma_N}) - \Phi_N(\frac{X_0 - x}{\sigma_N})] \cdot [\,\Phi_N(\frac{Y_1 - y}{\sigma_N}) - \Phi_N(\frac{Y_0 - y}{\sigma_N})]$$

The constant thickness of the layer is equal to the volume V divided by the area covered by the edge of the translating barge.

Experimental verification

In order to validate the mathematical model and to find values for the constant α and for the angle of equilibrium of the rubble, model tests (see appendix) were carried out at the laboratories of Delft Hydraulics and the Delft University of Technology in a tank of 2 x 2.5 x 2.5 m. An extra aluminum bottom was installed to facilitate experiments at (four) different waterdepth. Two sides were made of 60 mm thick glass.

To validate the SSM stones were dumped individually from a fixed point in the center of the tank. The dumping of single stones was continued untill the stones started to fall on top of each other thus making the positioning less accurate. After the dumping the tank was drained and digital pictures were taken to produce a top view. From the picture the radius from the center of the tank to every individual stone was determined. Afterwards the cumulative distribution function of the measured radii was compared to the Rayleigh-distribution, which gives the theoretical distribution of radii for bi-normally distributed points (SSM,PDM).

In other tests small amounts of rubble were dumped, taking pictures through the glass sides of the two cross sections of the build up of the rubble mound at regular

intervals to follow the forming of the Gaussian profile and the gradual tansition to the triangular profile, when the angle of repose was exceeded.

The test results will be discussed in three categories: natural stone, cubes and spheres and thin shapes.

For broken rubble the agreement between the experiment and the theoretical Rayleigh distribution was quite good (Fig.1). The difference might in part be explained by the fact that the size of the rubble follows a sieve curve.

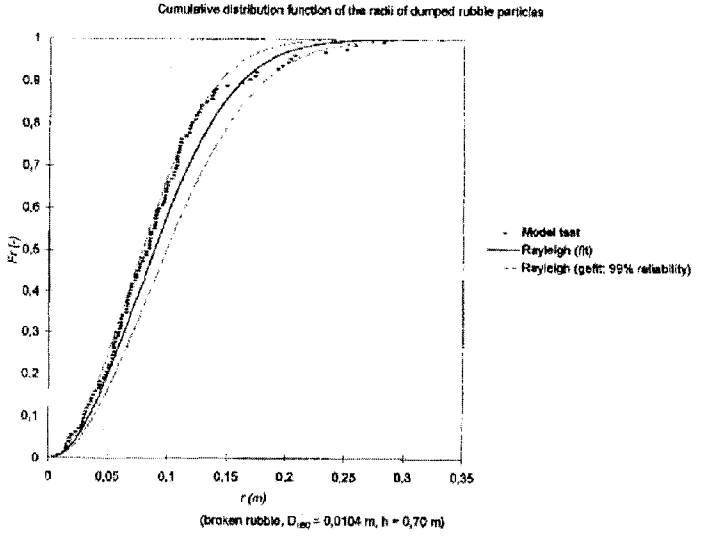

Figure 1.

Also the relation between the horizontal displacement and the square root of the waterdepth was confirmed by the tests (Fig.2). The value of the constant α was 0.72 on average with a standard deviation of 0.09. If the rubble is dumped simultaneously the average value of α increases by 6%

The gradual transition from the Gaussian profile with a width dependant of the waterdepth to a triangular profile with a width dependant of the volume dumped was experimentally verified. In Fig.3 the depth and the volume dependant models are drawn together with the experimental results.

For rounded rubble the value of the constant α was 0.60 on average with a standard deviation of 0.012. If the rounded rubble is dumped simultaneously the average value of α increases by 22%.

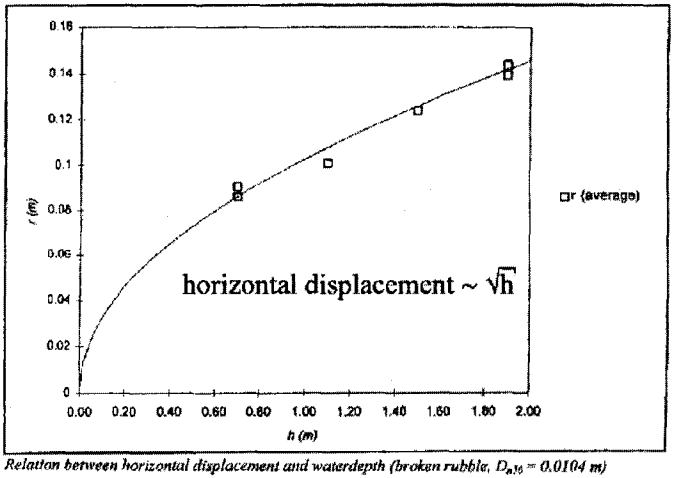

Relation between horizontal displacement and waterdepth (broken rubble, D_{n16} = 0.0104 m)

Figure 2.

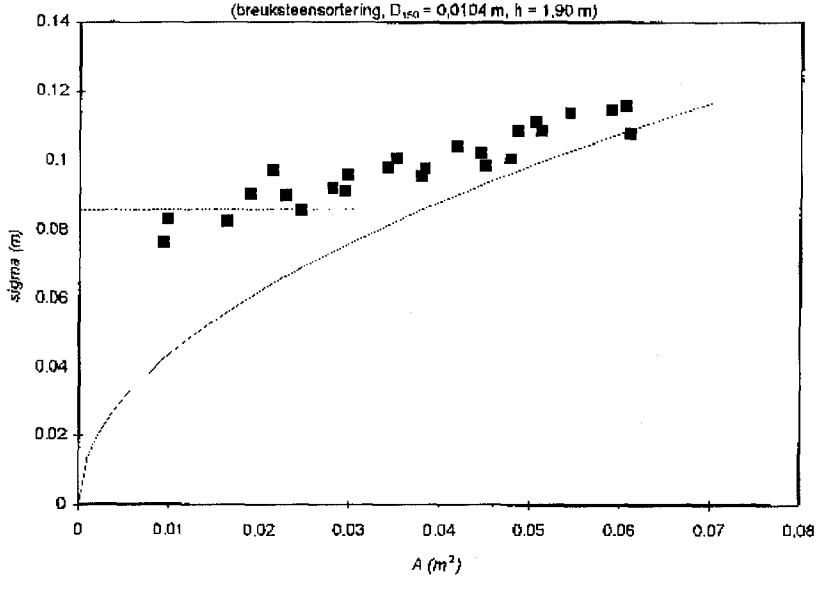

Figure 3.

Surprisingly aluminum cubes formed a ring when dumped. It appeared that the regular sharp edged cubes started rotating after falling over 8 to 15 D. So the formation of the ring may be attributed to the Magnus-effect, which results in an randomly directed, extra and stable horizontal force causing a ring shaped deviation from the center. The cumulative distribution function of the radii of the dumped cubes is not Rayleigh but normal (Fig.4). The total horizontal displacement is not the result of many independant steps with zero mean but of one single with a distinct mean. It appears that the mean radius increases proportionally with the waterdepth irrelevant of the size of the cubes (Fig.5). The previously found relation for the broken rubble is also depicted in this graph.

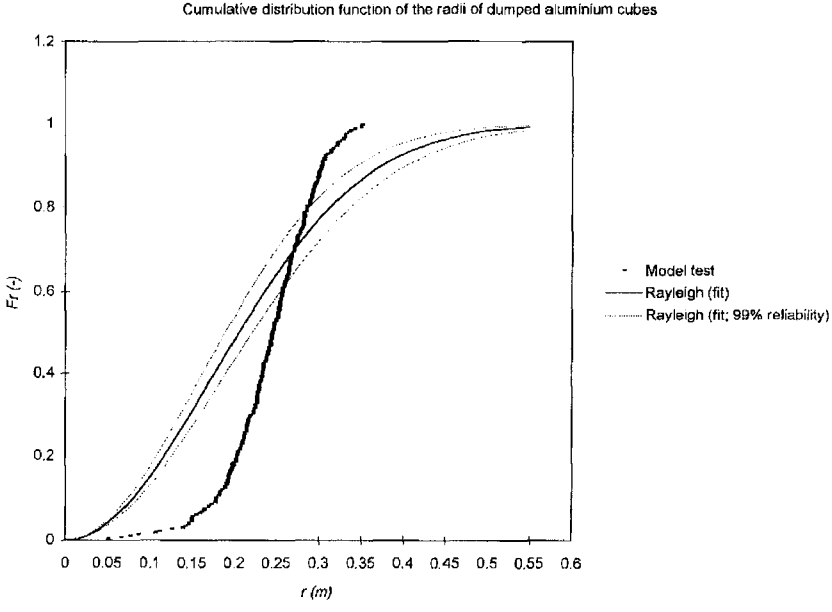

Figure 4: Aluminium cubes with D_{n50}=0.0145m and h=1.10m.

The result for concrete cubes with a diameter of 0.015m was strikingly similar. Also for glass balls (D=0.0156m) the same behaviour was found. The average deviation for the balls was exactly equal to that of the cubes, but the standard deviation around the ring was slightly bigger.

For reasons of comparison also some experiments were performed with square plates 0.05m thick with the same size as the cubes. Here the falling motion was very stable and the horzizontal deviation of the center was almost zero. However experiments with Dutch guilders (D=0.025m), which have approximately the same size, behaved quite differently. A guilder falls with loopings leading to considerable deviations of the center. The c.d.f. of the radii conforms exactly with the Rayleigh distribution (Fig.6). Dutch rijksdaalders (D=0.029m) show exactly the same behaviour but with a bigger

standard deviation around the center. The strikingly different behaviour of falling objects depending on form and mass is also reported by Field et al and earlier by Stringham et al.

Tests were carried out to verify the theoretical shape of the mound of rubble formed by a side-dumping barge. An amount of gravel was shoved off a board with a length of 0.70 m, mounted on top of the tank. the form of the mound was analysed and compared with the theory (LDM). A reasonable agreement was found, but not all differences are yet well understood.

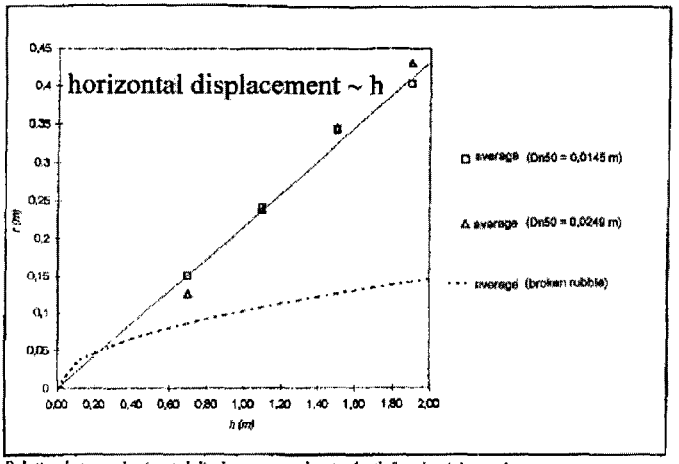

Relation between horizontal displacement and waterdepth for aluminium cubes

Figure 5.

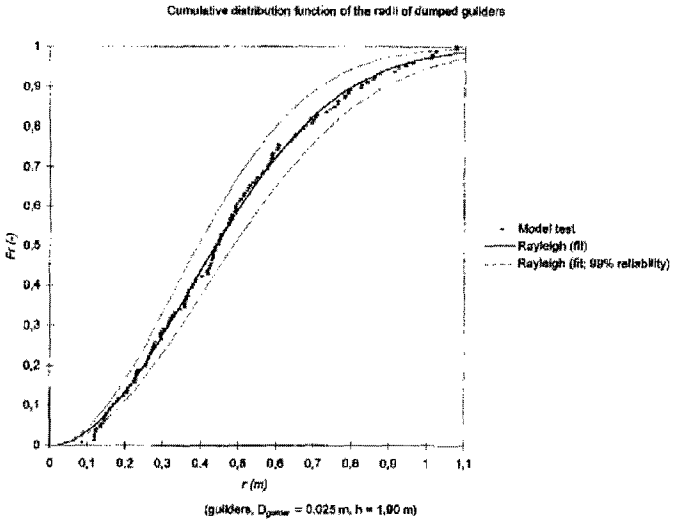

Figure 6.

Conclusion

A practical model to predict the deposition of rubble dumped from a stone dumping barge was developed and validated in principal form. The model shows that three phases have to be discerned in which different variables gouvern the width and the form of the deposition.

The model is extended to describe the dumping process of a side dumping barge. With this model the form of the mound and the evenness of the resulting surface can be predicted.

The single stone model (SSM) gives a good description of the falling motion of rubble in water. Also the further build up when the angle of repose is exceeded is confirmed.

The horizontal displacement of the falling motion measured at the bottom is proportional to the quare root of the waterdepth as found in the SSM. The influence of the diameter D_{n50} of the rubble needs however further verification.

The development of the Gaussian profile into a triangle after the angle of repose has been exceeded was also confirmed for rubble.

Due to rotation the SSM does not give a good description of the falling of cubes and spheres. Here a ring is formed with a radius proportional to the waterdepth irrespective of the size of the particles.

The SSM gives a good description of platelike objects. However due to stronger lift-forces the horizontal displacement is far greater than for rubble.

In view of the good agreement for rubble, the model has shown to be of great practical value in the construction of rubble mound structures.

References

Oda K. (1990): Studies on deposition-mound configurations of rubble discharged from a split-hull barge, *Abstracts 22nd Inter. Conf. on Coastal Engg.* (ASCE), pp. 481-482, Paper no. 241.

Matsumi Y., Kimura A. (1992): Hydraulic approach to determining optimum interval of discharge sites of barge in constructing rubble foundation of deep water breakwater, *23rd Inter. Conf. on Coastal Engg.* (ASCE), pp. 3149-3162.

Cregten,H.J., The use of probabilistic methods in judging the dumped mound of a side dumping barge (in dutch),*MSc thesis*, Delft 1995

J.K.Vrijling et alt.,Prediction of the deposition-mound of dumped rubble, *Proceedings of COPEDEC IV*, Rio de Janeiro, 1995

Oord, G.van, The spreading of stone in the dumping process of side dumping barges (in dutch),*MSc thesis*, Delft 1996

Stuckrath,T.,Volker,G. en Meng,J., *Untersuchungen zum Fallverhalten würfelförmiger Einzelkörper in Wasser*, T.U.Berlin,1996

Field,S.B. et al.,Chaotic dynamics of falling disks, *Nature*,Vol.388, 17 july 1997

Stringham,G.E. et al.,The behaviour of falling particles in quiesquent liquids, *Prof. Pap. US Geol. Surv.* 562-c,1969

Appendix

Dumping material	Mass density	Characteristic dimension	Description of the form	Water depth
Crushed basalt	3000 kg / m^3	D_{n50} = 10.4 mm	Irregular, sharply edged	0.70 m 1.10 m 1.50 m 1.90 m
River pebbles	2500 kg / m^3	D_{n50} = 12.7 mm	Irregular, rounded	1.90 m
Aluminium cubes	2700 kg / m^3	D_{n50} = 14.5 mm D_{n50} = 24.9 mm	Regular, sharply edged	0.70 m 1.10 m 1.50 m 1.90 m 0.70 m 1.10 m 1.50 m 1.90 m
Concrete cubes	2400 kg / m^3	D_{n50} = 15.0 mm	Regular, rounded edges	0.70 m 1.10 m 1.50 m 1.90 m
Glass marbles	2500 kg / $M3$	D_{n50} = 12.6 mm D_s = 15.6 mm	Regular, spherical	0.70 m 1.10 m 1.50 m 1.90 m
Al. plates, d_p = 2,5 mm Guilders, d_d = 1,5 mm Rijksdaalders, d_d = 2,0 mm	2700 kg / m^3 ≈ 7000 kg / m^3 ≈ 7000 kg / m^3	D_p = 25.0 mm D_d = 25.0 mm D_d = 29.0 mm	Regular, square, flat Regular, circular, flat Regular, circular, flat	1.90 m 1.90 m 1.90 m

HYDRAULIC MODEL TEST OF STABILITY OF AMENITY-ORIENTED BREAKWATER

Shoji Kunitomi[1], Hajime Mase[2], M. ASCE, and Tomotsuka Takayama[3]

ABSTRACT: A slit caisson breakwater has now been under construction at Takamatsu Harbor, Kagawa Prefecture, Japan, as an amenity-oriented breakwater (that is, a human friendly breakwater opened for citizen). However, wave pressures and forces acting on the slit caisson have not been evaluated. Hydraulic experiments are carried out to examine the stability of the slit caisson breakwater and uplift forces on a upper board, and to investigate a desired type of upper board of the breakwater.

INTRODUCTION

This paper examines the stability of an Amenity-Oriented Breakwater against sea waves. Here the term of amenity-oriented breakwater is defined as a human friendly breakwater opened for public.

A main function of breakwater is to protect harbors against sea waves and keep them calm. Recently, because of small amenity space near urban area, there has been an increasing demand for breakwaters to be served as a recreation space for citizen. From the view point of amenity, breakwaters should be surrounded by clear water and allow easy water exchange.

A slit caisson breakwater is now under construction at Takamatsu Harbor, Kagawa Prefecture, Japan, as an amenity-oriented breakwater. Initially, this breakwater was designed only for protecting waves. However, as one of city plans of Takamatsu City, this breakwater was determined to be opened for amenity space. However, wave pressures and forces acting on such slit caisson have not been evaluated adequately. Here, we examine the stability of slit caisson breakwater by hydraulic model tests in order to propose a desired type of upper board of the caisson.

Photo.1 shows a view of the slit caisson breakwater now being constructed at Takamatsu Harbor, and Fig.1 shows an image view of the breakwater.

[1] Graduate Student, Disaster Prev. Res. Inst., Kyoto University, Gokasho, Uji, 611-0011, Japan
[2] Assoc. Prof., Disaster Prev. Res. Inst., Kyoto University, Gokasho, Uji, 611-0011, Japan
[3] Prof., Disaster Prev. Res. Inst., Kyoto University, Gokasho, Uji, 611-0011, Japan

Photo.1 View of slit caisson under construction

Fig.1 Image view of slit caisson

HYDRAULIC MODEL EXPERIMENTS

The breakwater will have parapets, handrails, boardwalk, footlights and stand-lights, as shown in Fig.1. One of problems is to determine what kind of boardwalk we should employ from the viewpoint of uplift forces and stability of the breakwater. We adopted three kinds of upper board for experiments: 1) boardwalk, 2) boardwalk on a slab, and 3) boardwalk on a slit slab. In actual, boardwalk is made by wood.

We carried out hydraulic experiments of sliding stability of the slit caisson and uplift forces on three kinds of the upper board due to wave motion inside the caisson. Photo.2 shows the model caisson made by transparent acrylic, and Fig.2 shows the size of cross section of the model. The model scale of the caisson is 1/30. The slit opening ratio is 30.1 % on the front side and 4.3 % on the rear side. The experimental wave flume was

Photo.2 View of model caisson

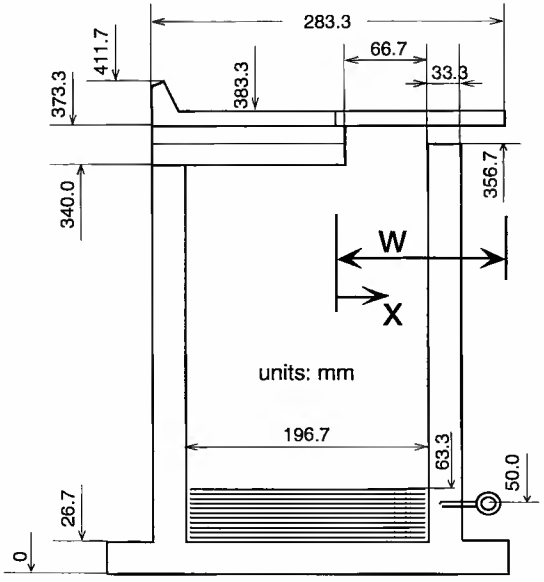

Fig.2 Size of cross section of model caisson

70 cm deep, 70 cm wide, and 40 m long. The model caisson was installed at 27 m far from the wave paddle.

The design wave height and period are 1.9 m and 5.5 s, respectively, as a fifty-years return period wave in the field. We carried out experiments by using regular and random waves. In the case of regular waves, the wave period was fixed as 1.1 s. Wave heights were changed from 6 cm to 13 cm so as to include the design wave height of 6.3 cm in the experiment. The water depth was set constant at 38 cm corresponding to the high water level. Concerning random waves, the significant wave height and period were 6.3 cm, and 1.1 s, respectively. The water depth was 38 cm (high water level) and 41 cm (highest high water level).

EXPERIMENTAL RESULTS AND DISCUSSION

Regular Wave Tests

Figure 3 shows the results of sliding stability tests for the caisson with three kinds of upper board against a parameter of wave height. The friction factor between the caisson and rubble mound was measured and found to be 0.51 on average. The displacements of the caisson under wave action were measured by two displacement gages installed at back side of the caisson. The vertical axis of the figure indicates the mean displacement per one wave. The horizontal axis indicates the sliding resistance force defined as the product of friction factor and caisson weight in water. From the results, we can obtain

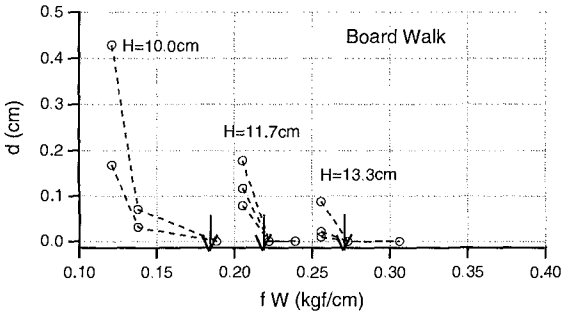

(a) Board walk

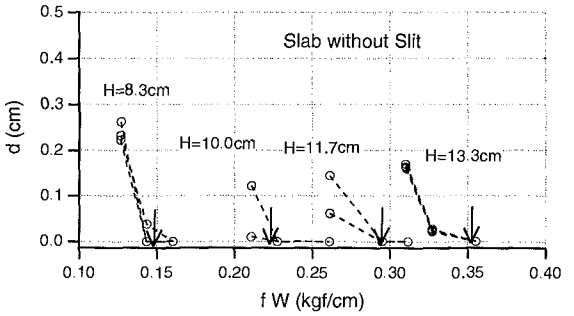

(b) Slab without slit

Fig.3 Relation between sliding resistance force and caisson displacement

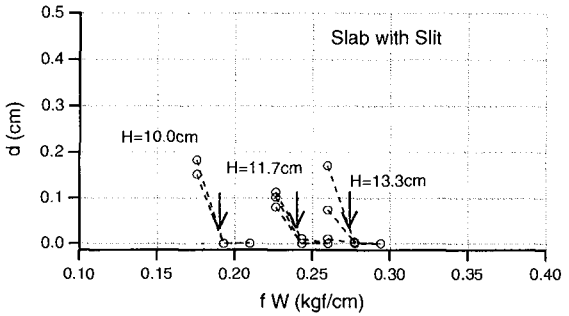

(c) Slab with slit

Fig.3 Continued

the critical resistance force for different wave height conditions as shown by arrows in the figures.

Figure 4 summarizes the non-dimensional critical resistance forces. The horizontal axis is the non-dimensional wave height normalized by the design wave height and the vertical axis is the critical resistance force nondimensioned by w_0Hd (w_0: the weight of water per unit volume; H: the wave height; d: the water depth). The circles, triangles and squares denote the results for the cases of the slab without slit, the slit slab, and the

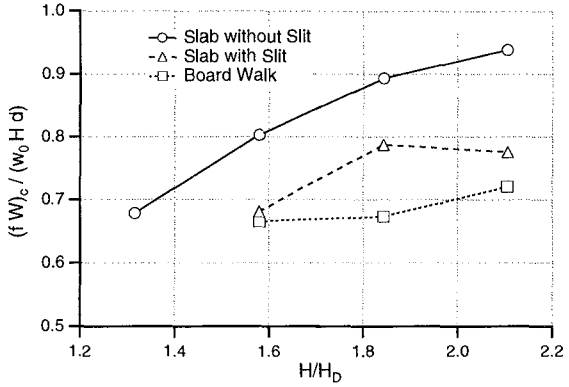

Fig.4 Critical sliding resistance force and caisson displacement

boardwalk, respectively. This figure shows that the critical resistance force becomes smaller as the slit opening ratio of the upper slab becomes larger.

Figure 5 shows the modification factor against the wave height. Here the modification factor is defined as the ratio of measured critical resistance force to the predicted one by Goda's formula (1985). This figure shows that, in the case of the slab without slit, the modification factor becomes largest, and its value is about 1.0 at H/H_D=1.85 (corresponding to the maximum wave height of random waves). The maximum modification factor is about 0.9 for the slit slab, and about 0.8 for the boardwalk. By formu-

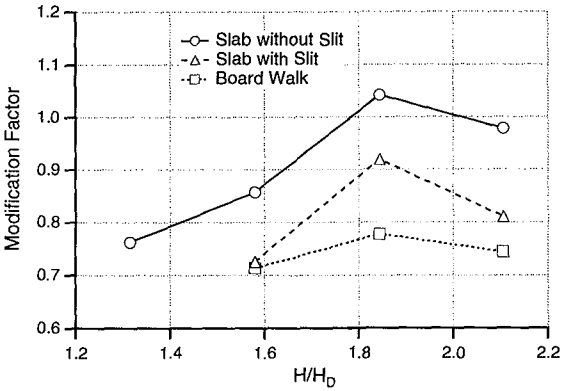

Fig.5 Critical sliding resistance force and caisson displacement

lating the modification factor for the slit caissons generally, we can estimate the resistance force by utilizing the Goda's formula (1985).

After the sliding stability tests, we measured wave pressures and uplift forces on upper boards by using five wave pressure gages and by utilizing strain gages.

Figure 6 shows the spatial distribution of wave pressures on upper board. The x is the distance from the edge of the slab, and w is the width of the slab, shown in Fig.2. The vertical axis is wave pressure normalized by w_0H. Normalized wave pressures become the maximum around x/w=0.45 ~ 0.5 (in front of the rear wall of caisson). Wave pressures decrease to be zero towards the rear end of the caisson. We also see that wave pressures depend on the incident wave heights for the case of the slab.

Figure 7 shows the normalized uplift force per unit length against normalized wave height. The uplift force coincides with the integrated value of wave pressures as a whole. Figure 7 shows that uplift force is proportional to the wave height in the rage of this experimental condition. Besides, we can see that uplift force on the slab without slit is larger than that on boardwalk. From the viewpoint of hydrodynamics, employment of boardwalk is preferable for small resistance sliding force and small uplift force. However, it is dangerous to walk on the boardwalk when the water splashes out of slits at wave attack on the boardwalk, and how to set wooden boardwalk to the caisson against local wave pressure, shown in Fig.6, is a remaining problem.

Random Wave Tests

Total record time was 20 minutes. We analyzed 700 individual waves excluding first 100 waves from the start of wave making. Figure 8 shows the measured and target wave spectra which are represented by solid and dash lines respectively. Random waves were well generated in the flume.

From random wave experiments, we obtained the critical sliding forces as 0.21 kgf/cm for the boardwalk, 0.25 kgf/cm for the slab, 0.21 kgf/cm for the slit slab. These critical sliding resistance force correspond to those by regular waves of H/H_D=1.58. This means that we can estimate the sliding resistance force of random waves from regular wave experiments by employing the regular wave smaller than the maximum wave (H/H_D=1.8).

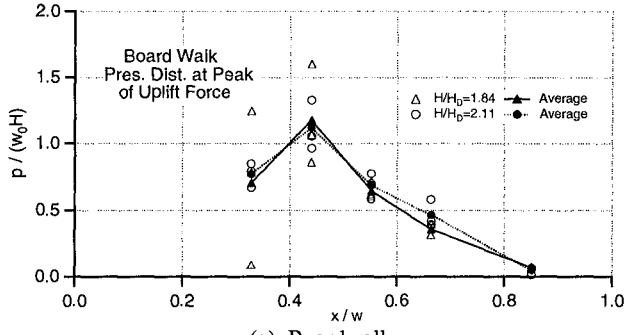

(a) Boardwalk

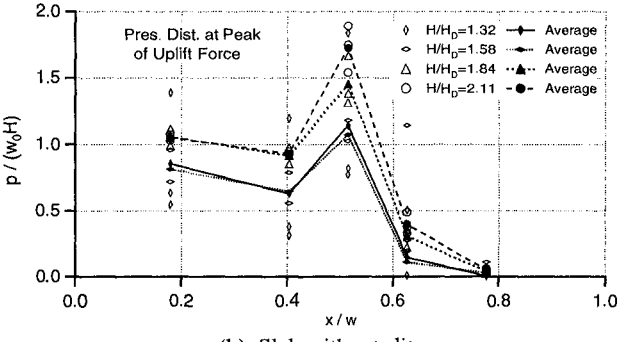

(b) Slab without slits

Fig.6 Horizontal distribution of wave pressures on upper board

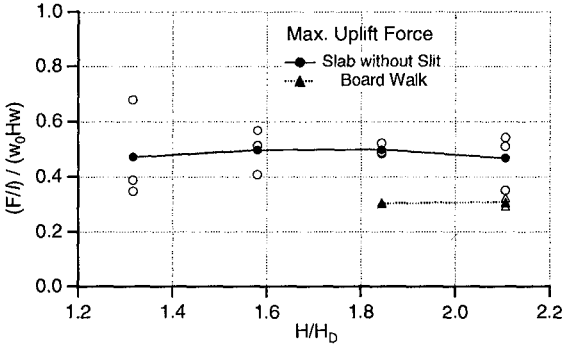

Fig.7 Horizontal distribution of wave pressures on upper board

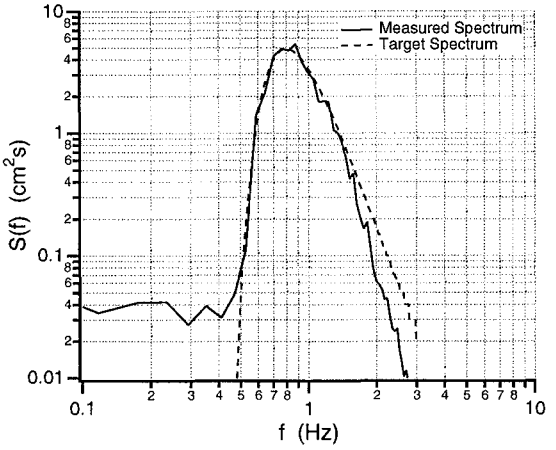

Fig.8 measured and target wave spectra

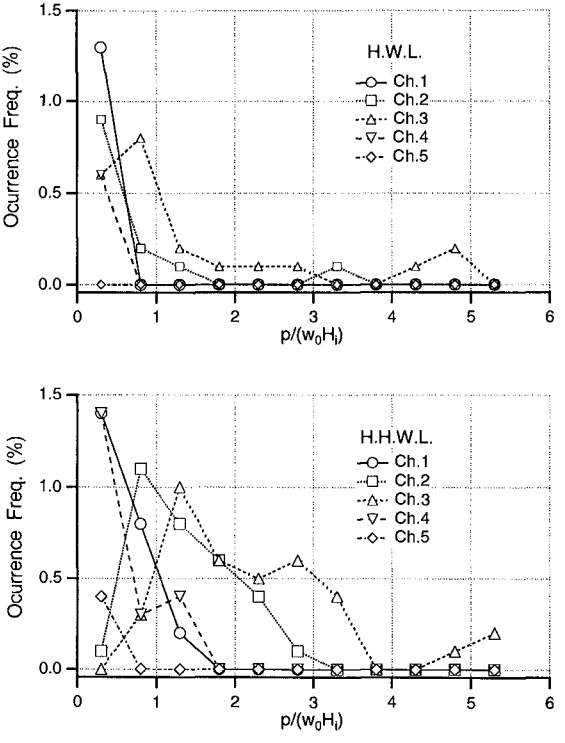

Fig.9 Horizontal distribution of occurrence frquency of wave pressures on upper board

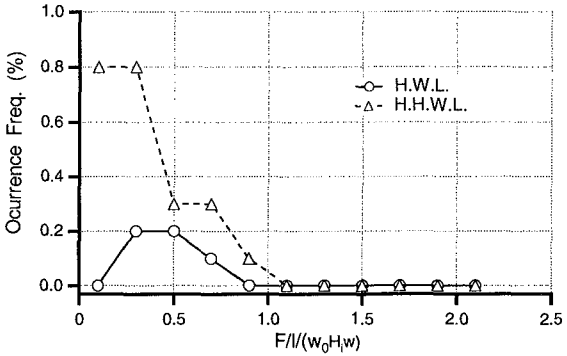

Fig.10 Horizontal distribution of occurrence frequency of wave force on upper board

Figure 9 shows the occurrence frequency of wave pressure at each pressure gage. The water depth was set at high (H.W.L.) and highest high water level (H.H.W.L.). Maximum pressure occurs at the location of Ch.3. This location is just in front of rear wall and same as in the case of regular wave experiments.

Figure 10 shows the occurrence frequency of uplift force. The occurrence frequency of uplift force at H.H.W.L. becomes larger than that at H.W.L.; however, the occurrence frequency itself is small.

CONCLUSIONS

Main results of this study are summarized as follows:

1) From experiments of regular waves, the critical sliding resistance force becomes smaller as the slit opening ratio of the upper board increase.
2) Wave pressures and uplift forces on the upper board decrese as the slit opening ratio becomes larger.
3) However, the problem is how to fix wooden boardwalk to the crown against wave pressures which locally become strong.
4) From experiments of random waves, critical resistance forces are found to be estimated from regular wave experiments by using waves of which wave height is a little smaller than the maximum wave height.
5) Besides, we can find the occurrence of large wave pressures and uplift forces is infrequent. But the boardwalk should withstand against large wave pressures even if it rarely occur.

From the results we proposed a type of upper board such as boardwalk installed on a slit slab by taking into account its leif time.

Refencres

Goda, Y. (1985): Random seas and design of naritime structures, Univ. of Tpkyo Press, Tokyo, p.323.

Stability of mound breakwaters: dependence on wave reflection.

Cristina López [1], Miguel A. Losada [2], Member, ASCE
and Nobuhisa Kobayashi [3], Member, ASCE

Abstract

Since the work by Ahrens and McCartney (1975) and Bruun and Johannesson (1976), it has been accepted that, for given slope, unit type and damage level, the stability number, N_s, and the so called K_d factor depend on Iribarren number, I_r, and that the worst stable conditions are related to collapsing wave breakers. The plotted values of N_s and K_d from laboratory tests, as a function of I_r, show a large scatter. This scatter is larger for large values of I_r. It is shown here that the scatter almost disappears once the data are plotted against kh, or I_{rt}, using the total wave height at the toe of the structure instead of the incident wave height. The total wave height, H_t, results from the interaction of the incident and reflected wave trains on the slope and depends not only on the magnitude of the reflection coefficient but also on its phase.

Introduction

The weight of the armor unit of a rubble mound breakwater depends on the geometry of the mound, the type of units, the characteristics of the incoming wave train represented by the wave height and period, and on the level of damage. One of the early formulas to calculate the weight of the armor units, W, of a mound breakwater was given by Castro (1933). Iribarren (1938, 1965) and Iribarren and Nogales (1950, 1954) based on this former work, proposed a more general formula, which was tested under monochromatic waves. Hudson (1959) proposed a simplified formula using the so called K_d factor or stability coefficient. These formulas based on monochromatic wave tests are still being used in many countries. All of them can be written as follows (Losada and

[1] Ocean & Coastal Research Group. University of Cantabria.
E.T.S.I. de Caminos, C. y P. Avda. de los Castros, s/n. 39005 Santander, Spain.
[2] E.T.S.I. de Caminos, C. y P. University of Granada. Campus " La Cartuja". Granada, Spain.
[3] Center for Applied Coastal Research. University of Delaware. Newark, Delaware 19716, USA.

Giménez-Curto, 1979):

$$W = \gamma_w \cdot \Psi \cdot S \cdot H^3 \tag{1}$$

with,

$$S = \frac{\frac{\gamma_s}{\gamma_w}}{\left(\frac{\gamma_s}{\gamma_w} - 1\right)^3} \tag{2}$$

where H is the incident wave height, H_i, which will be used later to differentiate H_i from H_t, γ_s and γ_w are the unit weight of armor unit and water, respectively. Ψ is the stability function, which is related to the K_d factor by,

$$K_d = \frac{1}{\Psi \cdot \cot\alpha} \tag{3}$$

where α is the angle of the structure slope. The stability number is given by

$$N_s = \left(K_d \cot\alpha\right)^{1/3} \tag{4}$$

For given slope, unit type and damage level, K_d, N_s and Ψ depend on Iribarren number, I_r, defined as follows:

$$I_r = \frac{\mathrm{tg}\,\alpha}{\sqrt{\frac{H}{L_0}}} \tag{5}$$

where L_0 is the linear wave length in deep water and H is the characteristic wave height, H_i or H_t.

For irregular waves there is no unique characteristic wave height. Van der Meer (1988) recommends to use the significant wave height, H_s; The Shore Protection Manual (1984) recommends to use higher wave heights such as $H_{1/10}$ or $H_{1/20}$. In order to consider the influence on the damage level of the number of waves in the train higher than a certain height, Vidal et al. (1995) examined characteristic wave height statistics and recommended $H_{1/20}$.

Moreover, K_d, N_s and Ψ, based on the experiments using any of those characteristic

wave heights, and plotted against Iribarren number, showed a considerable scatter. Figure 1 shows Ψ versus I_r obtained from the experiments carried out by Iribarren and Nogales (1965) for several slopes. Furthermore, the best fit curve to the data points was given by Losada and Giménez-Curto (1979). The data points scattered about the best fit curve by a factor of about 3. This empirical scatter exists for both monochromatic and irregular waves. Figure 2 shows the stability number versus I_r for quarry stones given by Van der Meer (1988). The data were plotted in terms of the nominal diameter of the unit, that is proportional to the 1/3 power of the weight. The scatter appears to be reduced because of the use of $W^{1/3}$, but is still apparent.

Figure 3 summarizes the scatter of the experimental results depending on Iribarren number, where $\Delta\Psi$ and Ψ_{min} are the range and minimum value of Ψ, respectively, in each range of I_r. The largest scatter occurs under collapsing and surging waves. For these types of waves, mound breakwaters reflect a considerable potion of the incident energy: more than 60% of the incoming wave energy may be reflected.

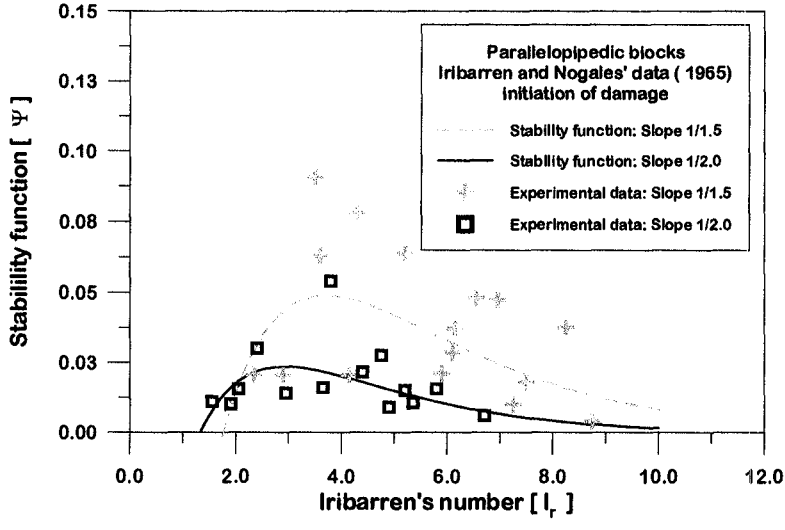

Figure 1. Stability function of parallelopipedic blocks versus I_r for monochromatic wave test.(Losada and Giménez_Curto, 1979)

The interaction of the incident and reflected wave trains leads to a partial standing wave in front of the structure. Flow kinematics and dynamics on the slope depends on this partial standing wave pattern.

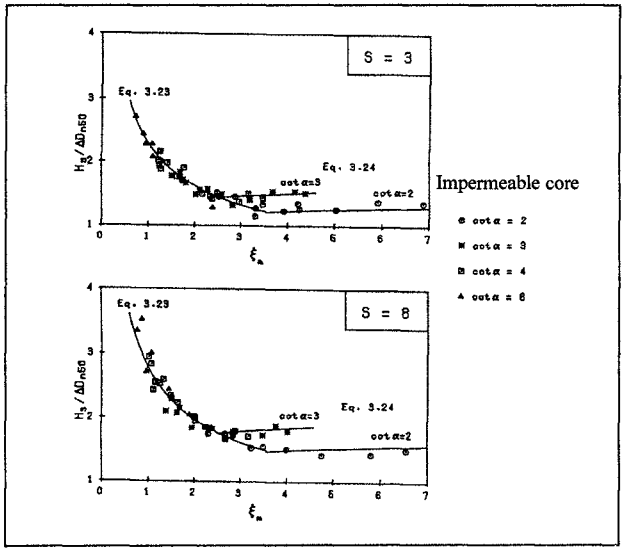

Figure 2. Stability results for irregular waves. (Van der Meer, 1988)

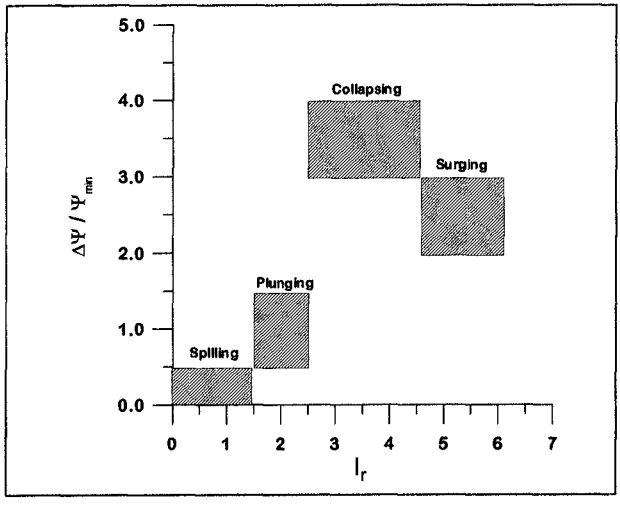

Figure 3. Scatter of monochromatic wave data depending on Iribarren number.

In this paper, the connection between the partial standing wave and the stability of the units of the cover layer is analyzed. First, the reflection process is considered and the magnitude and phase of the reflection coefficient are evaluated. Next, the total wave height of the incident and reflected wave trains at the toe of the structure is calculated. Finally, this total wave height is used to calculate the stability function, Ψ_t, for the experiments by Iribarren and Nogales (1965) and the new tests conducted in the flume of the University of Cantabria. It is concluded that, for plunging-collapsing, collapsing and surging waves, the stability function, Ψ_t, does not depend on Iribarren number, but only on the breakwater slope, unit type and damage level. Furthermore, the use of Ψ_t based on the total wave height at the structure toe is shown to reduce the data scatter.

Wave Reflection from Porous Structures

Wave reflection from permeable rubble mound breakwaters were examinated by Ahrens and McCartney (1975), Losada and Giménez-Curto (1979), van der Meer (1988), Wurjanto and Kobayashi (1992) and Seelig and Ahrens (1995), who showed the dependence of the reflection coefficient on Iribarren number. More recently, Hughes and Fowler (1995), and Sutherland and O'Donoghue (1998), analyzed the phase shift of the reflected wave train at the toe of coastal structures. The modulus, R, and the phase, ε, of the reflection coefficient as a function of the structure geometry and the hydraulic properties of the porous medium were discussed only partially.

For vertical porous medium the dependence of the reflection coefficient on those factors can be analyzed theoretically following the work by Dalrymple et al. (1991) and Méndez (1997). Figure 4 shows the modulus and phase of the reflection coefficient versus kh, were k is the wave number in front of the structure and h is the water depth, for a breakwater located at a certain distance from the flume end wall. Several values of the breakwater width, b, are considered, where the porosity $P = 0.45$ and the median diameter $D_{50} = 0.03$ m. for the porous material. This figure clearly shows that the reflection coefficient modulus and phase depend strongly on the experimental setup.

If the breakwater is sloped, waves breaking may occur, but similar patterns may be found. Figure 5 shows the modulus, R, of the reflection coefficient versus the width and porosity of the cover layer, and Figure 6 shows the dependence of R on the slope angle, α. Both figures are obtained by the numerical computation using PBREAK (Wurjanto and Kobayashi, 1992).

Figure 7 shows the envelope of the wave crest on the slope and in front of the breakwater. The data points were recorded by Iribarren and Nogales (1965), and the curve was obtained by the best fit of the wave envelope to the experimental data points. Two different cases of kh for $\cot \alpha = 2.0$ are shown, where h is the water depth at the structure toe. In Figure 7a, for kh=0.47, the underwater slope is under the node of the standing wave. For the second case, kh=1.26 in Figure 7b, the underwater slope is under the antinode of the standing wave.

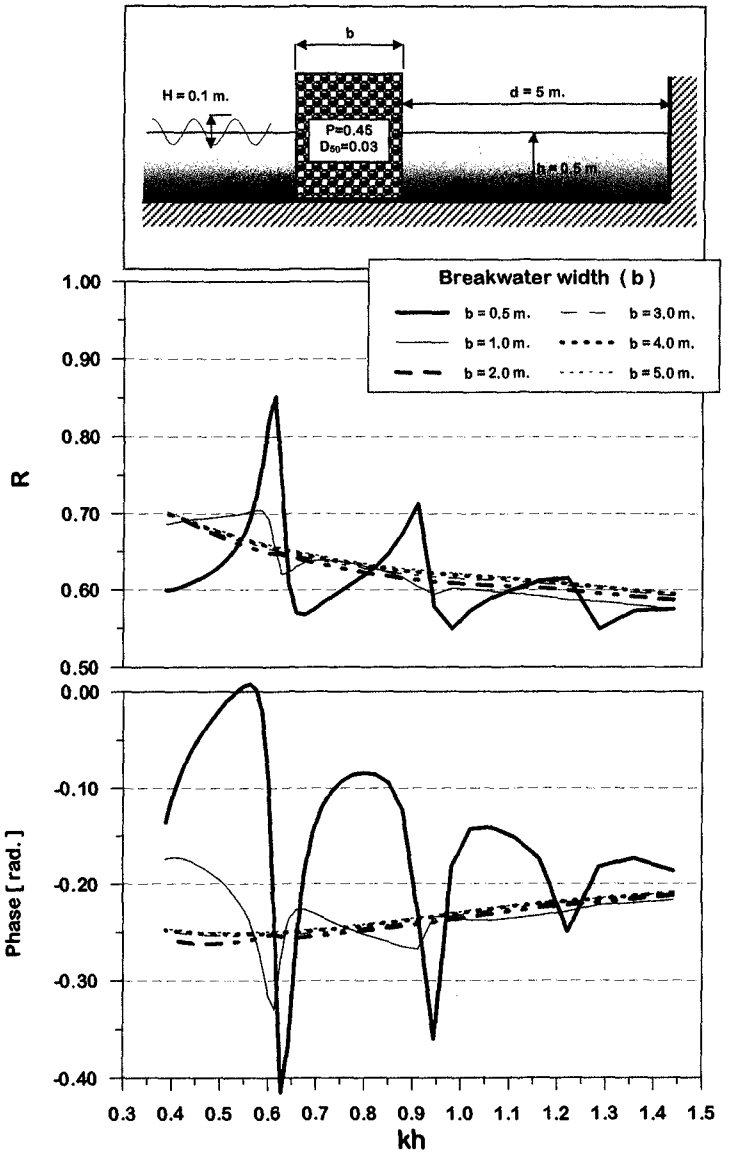

Figure 4. Modulus and phase of reflection coefficient versus *kh* for breakwater located at 5 m. from the flume end wall.

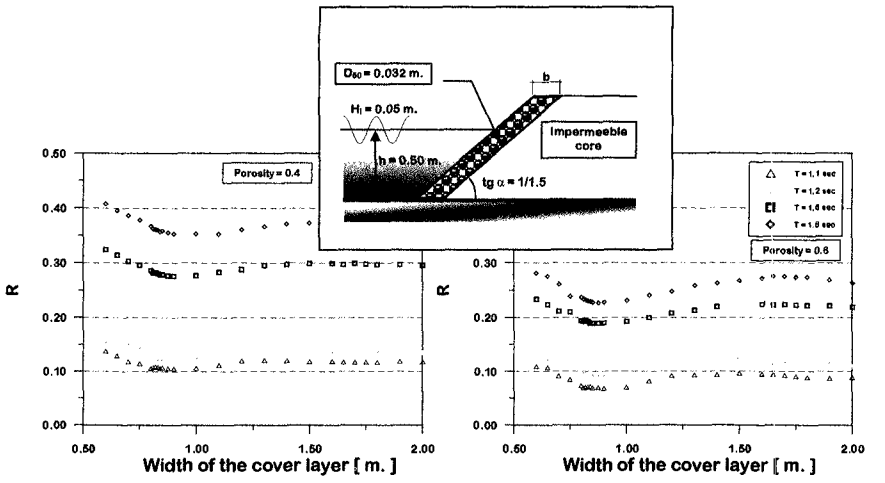

Figure 5. Modulus, *R,* of the reflection coefficient, computed using PBREAK, versus the width and the porosity of the cover layer.

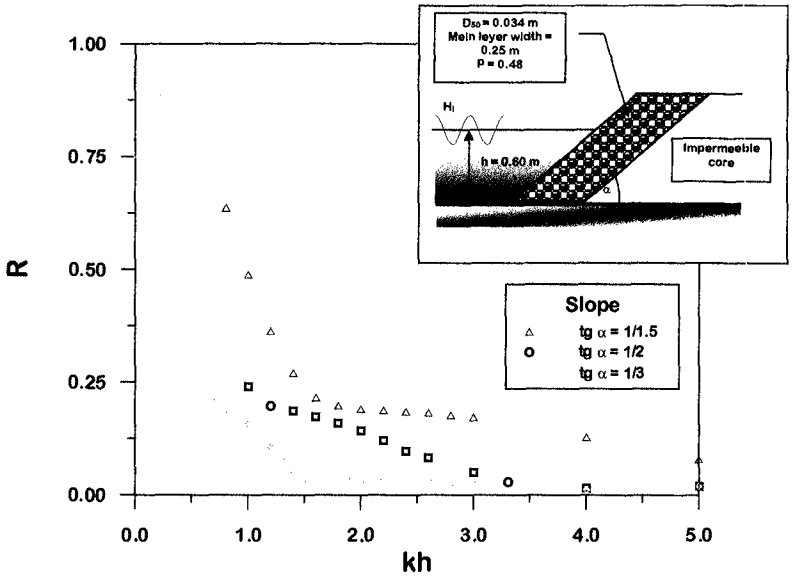

Figure 6. Modulus, *R*, of the reflection coefficient, computed using PBREAK, versus *kh* for different slopes.

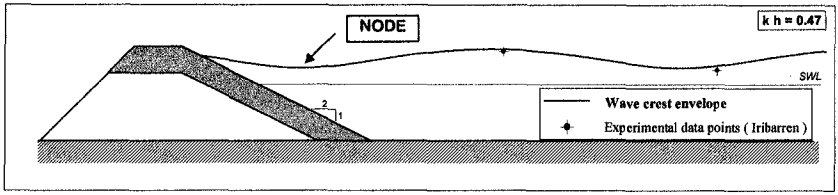

Figure 7a. Envelope of the wave crest on the slope and in front of the breakwater for kh=0.47 with node on underwater slope.

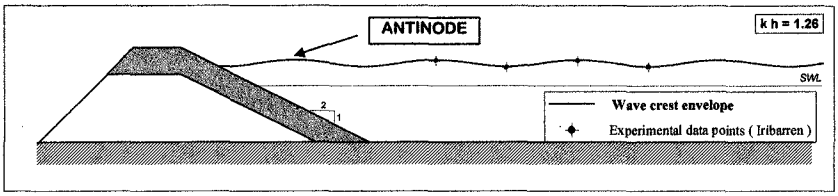

Figure 7b. Envelope of the wave crest on the slope and in front of the breakwater for kh=1.26 with antinode on underwater slope.

From these results it can be concluded that the characteristics of the reflected waves depend strongly on the structure geometry, materials properties and experimental setup. Once the modulus and phase of the reflection coefficient is known, the total wave height, H_t, at the toe of the structure can be evaluated as follows:

$$H_t = H_i\left(1 + R^2 + 2R\cos(2kx + \varepsilon)\right)^{1/2} \tag{6}$$

where H_i is the incident wave height and R is the reflection coefficient modulus

$$R = \frac{H_r}{H_i} \tag{7}$$

where H_r is the reflected wave height, ε is the phase shift obtained from the experimental data and x is the cross-shore coordinate with x=0 at the toe of the structure.

In the following, if the K_d factor, the stability number, N_s or the stability function, Ψ, are calculated using H_t as the characteristics wave height, the empirical scatter shown in Figure 1 turns out to be reduced significantly.

Stability Analysis

The stability of armor units placed on the cover layer is analyzed using both incident and total wave heights. First, the experimental data of Iribarren and Nogales (1965) on the stability of uniform quarry stones for four slopes, *cot* α = 1.25, 1.50, 2.0 and 3.0 are re-analyzed. The K_d factor and the stability function, Ψ, are computed using the incident wave height, H_i, and the total wave height, H_t.

Figure 8 shows the values of the stability function,Ψ, given by (1), plotted as a function of *kh*, using the incident wave height, in Figure 8a, and the total wave height, in Figure 8b. Figure 8b, shows that the experimental points for each slope follow approximately a straight line. The value of the stability function decreases with the decrease of the slope, *tan* α. The dependence of the stability function on *kh* is very weak. For slopes *cot* $\alpha \geq 1.5$ and the range $kh < 2.5$, Ψ is practically constant for each slope and independent of the wave period.

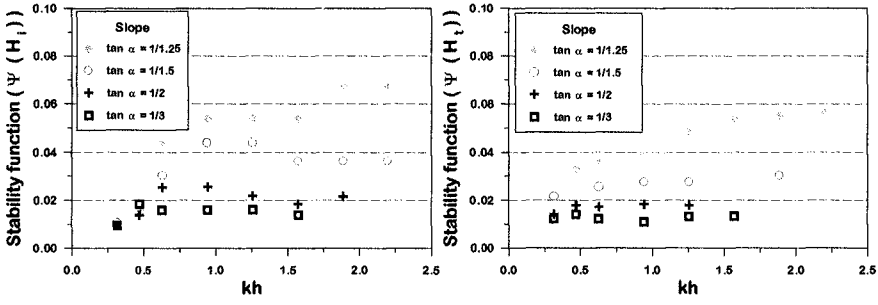

Figure 8. Stability function versus *kh* for the data of Iribarren and Nogales (1965): (a) using the incident wave height and (b) using the total wave height.

New experiments at the University of Cantabria

Additional experimental tests were performed in the flume of the University of Cantabria. The experimental setup is summarized in Table 1.

Table 1 – Characteristics of the flume.

Length	68.5 m.
Width	2 m.
Depth	2 m.
Wave board	Piston

- Experimental technique and damage criteria.

A burst of waves were generated, ensuring that the re-reflected waves from the paddle did not impinge on the slope. After the water surface calmed, a new burst of the same number of waves was generated. Damage was evaluated by counting the number of units displaced by a nominal diameter from its placed position. The test was repeated with the same burst until no unit was displaced by the burst. The slope was not repaired after the burst. Two levels of damage were considered: (1) *Iribarren damage*, defined by the number of displaced units at the time when the second layer of the cover layer was attacked by the waves, and (2) *initiation of damage*, defined as 5% of the number of units corresponding the Iribarren damage were displaced, as explained in detail by López (1998).

- Characteristic of tests.

The monochromatic waves characteristics are given in Table 2. The characteristics of the mound breakwater are summarized in Table 3.

Table 2 – Characteristics of monochromatic waves.

TEST	DEPTH (m.)	PERIOD (sec.)	*kh*
ES1	0.50	1.05	1.90
ES2	0.50	1.07	1.845
ES3	0.50	1.20	1.533
ES4	0.50	1.35	1.28
ES5	0.50	2.0	0.77

Table 3 – Characteristics of mound breakwater.

Slope (sea side)	Slope (lee side)	Height	Crown width	Main layer	Core (D_{50})
1/1.5	1/1.25	0.90 m	0.50 m.	Cubic units 3.2 x 3.2 cm 0.07 kg.	1-3 cm.

Results

Figure 9a shows the stability functions, Ψ_i and Ψ_t, versus *kh* for the new monochromatic wave tests using the incident wave height and the total wave height, respectively, for the initiation of damage. The values of Ψ_i are in the wide range 0.04-0.14, while Ψ_t is in the narrow range 0.06-0.075. The same trend is found for the stability functions plotted versus Iribarren numbers, $I_{r,i}$ and $I_{r,t}$, calculated using the incident and total wave heights as shown in Figure 9b.

For the Iribarren damage, as defined above, the values of Ψ_t plotted versus *kh* are in the narrower range 0.038-0.043.

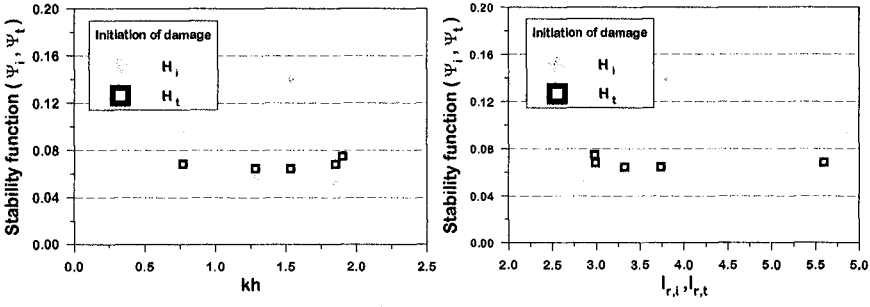

Figure 9. Stability function using the incident wave height and using the total wave height: (a) versus *kh* and (b) versus Iribarren number's. for new monochromatic wave test at the University of Cantabria.

Conclusions

From this research it may be concluded that:

(1) Wave reflection from the breakwater modifies the incident wave characteristics such that the flow velocities and accelerations on the slope are produced by the interaction of the incoming and reflected wave trains.

(2) The values of the K_d factor and the stability function, Ψ, depend on the total wave height, H_t. The scatter of the experimental data points can be reduced significantly by the use of H_t. The reduction is greater for larger damage.

(3) For the practical application of this method, the reflection coefficient modulus, *R*, and its phase shift, ε, produced by the reflection process on the breakwater need to be evaluated in advance. *R* and ε depend on the geometry and the hydraulic properties of the coastal structure as well as the boundary condictions on the landward side of the

structure.

(4) The extension of this method to irregular waves is being examined to clarify the connection between the irregular wave reflection and armor stability.

References

- Ahrens, J.P and McCarney, B.L., 1975. *Wave period effect on the stability of rip-rap.* Proc. of the 3rd Civil Engineering in the Oceans Conference. Vol. 11, pp. 1019-1034.

- Bruun, P. and Johannesson, P., 1976. *Parameters affecting stability of rubble mounds.* Journal of Waterway, Port, Coastal and Ocean Division, ASCE, Vol. 102 (2), pp. 141-164.

- Castro (de), E., 1933. *Diques de escollera.* Revista de Obras Púbilcas, pp.183-185.

- Dalrymple, R.A., Losada, M.A. and Martin, P., 1991. *Reflection and transmission from porous structures under oblique wave attack.* Journal of Fluid Mechanics, Vol. 224, pp. 625-644.

- Hudson, R.Y., 1959. *Laboratory investigation of rubble mound breakwaters.* Journal of Waterway, Port, Coastal and Ocean Engineering, ASCE, Vol. 85 (3): pp. 93-121.

- Hughes, S.A. and Fowler, J.E., 1995. *Estimating wave-induced kinematics at sloping structures.* Journal of Waterway, Port, Coastal and Ocean Division, ASCE, Vol. 121(4), pp. 209-215.

- Iribarren, R., 1938. *Una fórmula para el cálculo de los diques de escollera.* M. Bermejillo Usabiaga, Pasajes, Guipuzcoa, Spain.

- Iribarren, R., 1965. *Formulae pour le calcul des diques en enrochements naturels ou elements artificiels.* XXI International Navigation Congress, Stockholm, Section II-1.

- Iribarren, R. and Nogales, C., 1950. *Generalización de la fórmula para el cálculo de los diques de escollera y comprobación de sus coeficientes.* Revista de Obras Públicas, pp. 277-289.

- Iribarren, R. and Nogales, C., 1954. *Otras comprobaciones de la fórmula para el cálculo de los diques de escollera y comprobación de sus coedicientes.* Revista de Obras Públicas, pp. 275-285.

- López Arias, C., 1998. *Influencia de la reflexión del oleaje en la estabilidad de diques en talud.* Thesis in partial fulfillment of the Ph. D. Degree, University of Cantabria, Spain (in Spanish).

- Losada , M.A. and Gimenez -Curto, L., 1979. *The joint effect of the wave height and period on the stability of rubble-mound breakwaters using Iribarren's Number.* Coastal Engineering, Vol. 3, pp. 77-96.

- Méndez, F. J., 1997. *Flujos medios inducidos por las ondas de gravedad en medios reflejantes y disipativos naturales y artificiales.* Thesis in partial fulfillment of the Ph. D. Degree. University of Cantabria, Spain (in Spanish).

- Seelig, W. N. and Ahrens, J.P., 1995. *Wave reflection and energy dissipation by coastal structures.* Wave forces on inclined and vertical wall structures, ASCE, pp. 28-55.

- Shore Protection Manual, 1984. U.S. Army Coastal Engineering Research Center, U.S. Goverment Printing Office, Washington, D.C.

- Sutherland, J. and O'Donoghue, T., 1988. *Wave phase shift at coastal structures.* Journal of Waterways, Harbors and Coastal Engineering, ASCE, Vol. 124(2), pp. 90-98.

- Van der Meer, 1988. *Deterministic and probabilistic design of breakwater armor layer.* Journal of Waterway, Port, Coastal and Ocean Engineering, ASCE, Vol. 114 (1), pp.66-80.

- Vidal, C., Losada, M.A. and Mansard, P.D., 1995. *Suitable wave-height parameter for characterizing breakwater stability.* Journal of Waterway, Port, Coastal and Ocean Engineering, ASCE, Vol. 121 (2), pp. 88-97.

- Wurjanto, A. and Kobayashi, N., 1992. *Numerical model for random waves on permeable structures. Research Report No. CACR-92-02, Center for Applied Coastal Research, University of Delaware.*

IMPACT STRUCTURAL RESPONSE OF CORE-LOC®

George F. Turk[1], Member and Jeffrey A. Melby[1], Member

ABSTRACT

In 1996, the U.S. Army Corps of Engineers, Waterways Experiment Station, Coastal and Hydraulics Laboratory in conjuction with Oregon State University and Concrete Technology Corporation, Tacoma WA, conducted the first structural response experiments of the new concrete armor unit, CORE-LOC®. Large scale 32-kg and prototype 9.2-tonne core-loc units, were molded, cast, and fitted with surface-mounted strain gages. The units were subjected to repeated impact loads generated during drop tests. In addition to the CORE-LOC® drop test, similiar tests were conducted on 26-kg and 10.9-tonne dolosse. The structural response to these loads were recorded and analyzed. Measured maximum tensile stresses in CORE-LOC® were approximately half those in similiar size dolosse.

INTRODUCTION

The CORE-LOC® (heretofore referred to as Core-Loc), invented and developed at the U.S. Army Engineer Waterways Experiment Station, is a new-generation optimized breakwater concrete armor unit for protecting shoreline and navigation structures (Figure 1). The versatile unit can be used for a wide range of coastal armoring applications including the repair and rehabilitation of dolos armor layers. Until recently the majority of experiments on Core-Loc focussed on hydraulic stability. Because of the very difficult construction, in-service, and repair conditions associated with high energy wave environments, a need was identified to characterize the dynamic impact structural response of Core-Loc. The most common method of accomplishing this is the drop test. In the past

[1] U.S. Army Engineer Waterways Experiment Station, Coastal and Hydraulics Laboratory, Vicksbur MS, USA

two decades, these types of tests have been conducted on other types of concrete armor units. Nishigori et al (1989), Zwamborn and Phelp (1989), Burcharth (1981), and others have tested both dolosse and tetrapod to destruction using drop tests.

Figure 1. The first 9.2-tonne prototype CORE-LOC™ units

DEVELOPING CORE-LOC® DROP TESTS

Drop tests are used to evaluate the structural performance of an armor unit when exposed to impact loads. In 1996, the U.S. Army Corps of Engineers, Waterways Experiment Station, Coastal and Hydraulics Laboratory in conjuction with Oregon State University and Concrete Technology Corporation, Tacoma WA, conducted the first structural response experiments of the new concrete armor unit, Core-Loc. In the experiment described herein, two sizes of Core-Loc were tested, 32-kg and the 9.2-tonne. Also, 26-kg and 10.9-tonne dolosse were tested for comparison. The test configurations were essentially the same except for scale. The experiment involved measuring impact strains with surface-mounted strain gages, as the armor units were dropped from incrementally increasing heights onto a rigid concrete base. The units were tested to failure where the unit completely broke apart. For the smaller units, shims of various thicknesses were pulled from under the unit allowing it to freely drop to the concrete base pad. For the prototype, a crane was used to lift the unit to the pre-determined drop height. A quick-release mechanism attached to slings was used to release the unit, dropping it onto the one meter thick concrete base. The drop height was then increased and the unit dropped again.

The Core-Loc units cast at CTC were the first prototypes ever built. A rational decision had to be made as to standard drop test configurations. One aim of the experiment was to compare results with past drop test experiments of other popular types of concrete armor units. In order to best accomplish this, several types of drops were performed. To best compare Core-Loc to dolos, the "hammer drop" was chosen. These two drops are shown in Figure 2. Tetrapods are typically dropped by lifting the unit completely off the concrete base. The Core-Loc drop configuration, dubbed "anvil drop" is similiar to the tetrapod drop in that it also is completely lifted off the base. These are shown in Figure 3. A third Core-Loc drop configuration (Figure 4), unlike any other armor unit drop test, was needed to emulate the typical manner by which a non-interlocked Core-Loc rocks on slope or how a Core-Loc can fall over due to handling mishaps. This drop is called a "tipping drop." Each of these three drop configurations were performed during the experiment at CTC.

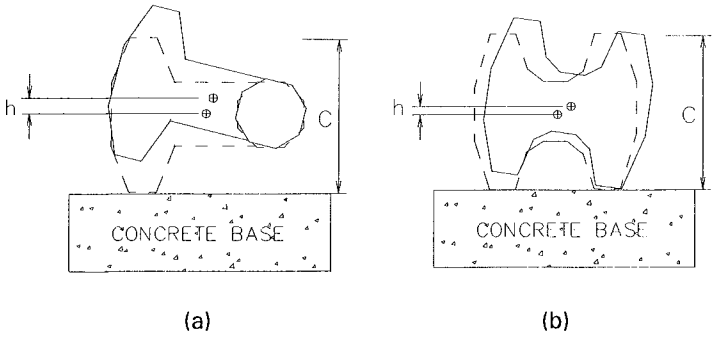

Figure 2. Drop Tests, (a) standard dolosse, (b) hammer drop

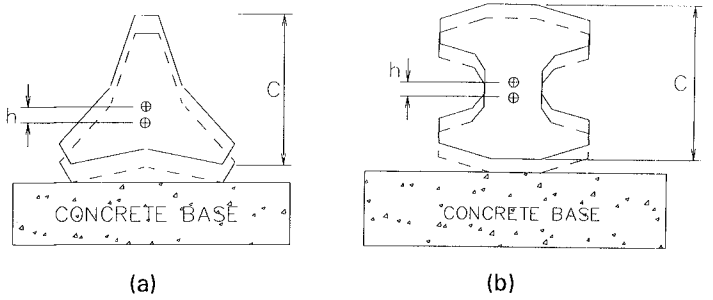

Figure 3. Drop Tests, (a) standard tetrapod, (b) anvil drop

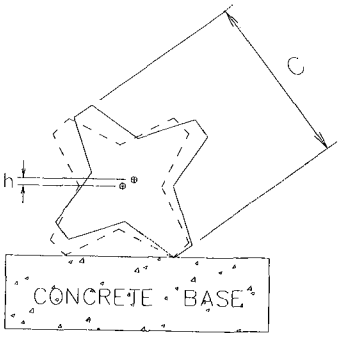

Figure 4. CORE-LOC® tipping drop test

PREPARATION FOR EXPERIMENT

The preparation for the experiment consisted of making molds, fabricating, and instrumenting a single 32-kg Core-Loc and four 9.2-tonne Core-Loc. In addition, three two-year old surplus 10.9-tonne dolosse were fitted with strain gages for measurement of strain in the unit's shank section. The drop tests of 26-kg dolosse, referred to in this report, were conducted in 1994 during the Large Scale Dolos Flume Study (Melby and Turk, 1994).

The first major task in preparing for the experiment was to build molds for both the 32-kg and 9.2-tonne Core-Loc units. For the smaller units, a two-piece fiberglass mold was fabricated. A sophisticated four-part steel "clamshell" mold (Figure 5) was constructed and used to cast four 9.2-tonne units. This unique mold design simplified the difficult casting and mold stripping process usually associated with concrete armor units.

The 32-kg model Core-Loc unit and the 26-kg dolos were cast using concrete with prototype properties. The properties of the large scale model units were as follows:

Property	Core-Loc	Dolos
Concrete Type	Type I Portland Cement	Type I Portland Cement
Aggregate	Coarse Sand	Coarse Sand
Specific Weight, γ	2170 kgf/m^3	2180 kgf/m^3
Modulus of Elasticity, E	21 Gpa	26 GPa
Poisson Ratio, υ	0.43	0.46
Compressive Strength, f_c	45 Mpa	54 MPa
Appox. Tensile Strength, f_t	$\approx$ 4.5 Mpa	$\approx$ 4.5 MPa
Armor Unit Mass, M_a	32-kg	26-kg
Characteristic Length, C	40.6 cm	43.2 cm

The mix design used to cast the 9.2-tonne Core-Loc units, was the same mix designed used two years prior to cast the 10.9-tonne dolos, as follows:

a) Concrete Type	Type III Portland Cement
b) Coarse Aggregate	16 mm Gravel
c) Fine Aggregate	Paving Sand
d) Water-to-Cement Ratio, W/C	39% (max)
e) Cement Content, C_C	390 kg/m^3
f) Water-Reducing Admixture	Conforming to ASTM-C494
g) Superplasticizing Admixture	Meets the requirement for Type F, W-R admixture
h) Air-entraining Admixture	Complies with ASTM C-260.

Figure 5. Four-piece "clamshell" mold

After the concrete was poured in the mold, it was cured for 24 hours. It had been CTC'c experience that accelerated curing is not required to achieve high release strength for this type of concrete product. Insulated "curing houses" were placed over the forms to control heat loss during curing. This system effectively forms a heated envelope with a uniform, controlled temperature gain of 4-7^0 C/hr. This curing method has a long history of successfully attaining transfer strength requirements within a daily production cycle.

The high strength concrete mix allowed the molds to be stripped after 24 hours and the drop tests to be performed after seven days. During each casting, test cylinders and beams were made so the compressive and modulus of rupture strength, along with the modulus of elasticity, could be determined. The concrete used for the Core-Loc units cured for one week before the drop tests were conducted. The 10.9-tonne dolosse tested were two years old. Core samples were taken from the concrete used in the three dolosse and tested immediately prior to the drop tests. Like the Core-Loc, the dolos concrete compressive and tensile strength, and modulus of elasticity were determined. The

specimens for a given Core-Loc or dolos were tested on the day of its drop test. The mean properties of the concrete and prototype units were as follows:

Property	9.2-tonne Core-Loc	10.9-tonne dolosse
Specific Weight, γ	2400 kgf/m^3	2400 kgf/m^3
Compressive Strength, f_c	43 Mpa	81.2 Mpa
Splitting tensile strength, f_{st}	3.2 Mpa	4.2 Mpa
Modulus of Rupture, f_{MR}	5.1 Mpa	N/A
Modulus of Elasticity, E	33.4 Kpa	35.9 Kpa
Armor Unit Mass, M_a	9.2-t	10.9-t
Characteristic Length, C	259 cm	293 cm

INSTRUMENTATION AND DATA ACQUISTION

For most drop tests in the past, failure was characterized by some arbitrary crack width. Thus results were subject to interpretation. Melby and Turk (1994) first collected drop test data with a sophisticated Data Acquistion System (DAS) attached to 26-kg dolosse. Sensitive surface-mounted strain gages were applied directly to the concrete surface. With this technique, direct precise measurements of strain and rate of strain were obtained. This same system and strain gaging technique was used on the 32-kg and 9.2-tonne Core-Loc, and the 10.9-tonne dolosse.

The new strain gaging technique and data acquisition technologies increased signal-to-noise ratio and range such that accurate impact measurements could be made. The waterproofed 350 Ω polyester-backed gages were capable of detecting minute strains on the surface of the concrete Core-Loc with a variable range of around 1000 $\mu\epsilon$, depending on the gain and sampling rate. The strain gages were sensitive enough to respond to small changes in strain with a resolution of $\pm$ 2 $\mu\epsilon$ (a change in length of 2E10^{-6} cm per cm). The gages proved extremely sensitive yet robust enough to survive repeated impacts. They were repeatedly checked for integrity, and except for the anvil drop performed flawlessly throughout the experiment.

The strain gaging for the dolosse was different than that used on the Core-Loc. With the principle stress direction well defined for the dolosse drop test, single gages were placed longitudinally along the axis of dolosse shank, near the intersection of the vertical fluke (Figure 6a). This is the primary gage location used for both the 26-kg and 10.9-tonne dolosse. The 26-kg dolos had additional gages placed on the fluke For the dolosse, strain was converted to stress by application of Hooke's Law, $\sigma_T = E\epsilon_T$, where σ_T is tensile stress, E is modulus of elasticity, and ϵ_T is tensile strain.

The stress state for the Core-Loc is more complex, and principal stress direction ill-defined. Thus for the 32-kg and the 9.2-tonne Core-Loc, five critical stress locations on the surface of the units (Figure 6b) were selected from finite element analyses of computer simulated drop tests. Instead of the single gage quarter bridge configuration

used on the dolosse, strain gage rosettes (three gages per rosette) were used for the Core-Loc. Each time an instrumented Core-Loc impacted against the hard concrete base surface with enough force to trigger any one of the 15 individual gages in the five rosettes, strain data were recorded. The individual strains measured by the three gages in the rectangular rosette were converted to principal tensile stress by:

$$\sigma_T = E\left[\frac{\epsilon_A+\epsilon_C}{2(1-\nu)} + \frac{1}{2(1+\nu)}\sqrt{(\epsilon_A-\epsilon_C)^2+(2\epsilon_B-\epsilon_A-\epsilon_C)^2}\right] \quad (1)$$

where

ν = Poisson's Ratio
$\epsilon_A, \epsilon_B, \epsilon_C$ = strains from three gage rosette

The 15 channels of raw data were decimated and reduced by selecting the peak or maximum impact stress for each individual triggered impact. Therefore, for example, if a single impact duration lasted one second, the 150,000 data points collected (10 kHZ x 15 channels) would be reduced to five data points representing the maximum principal tensile stress at the five locations on the Core-Loc for a single impact.

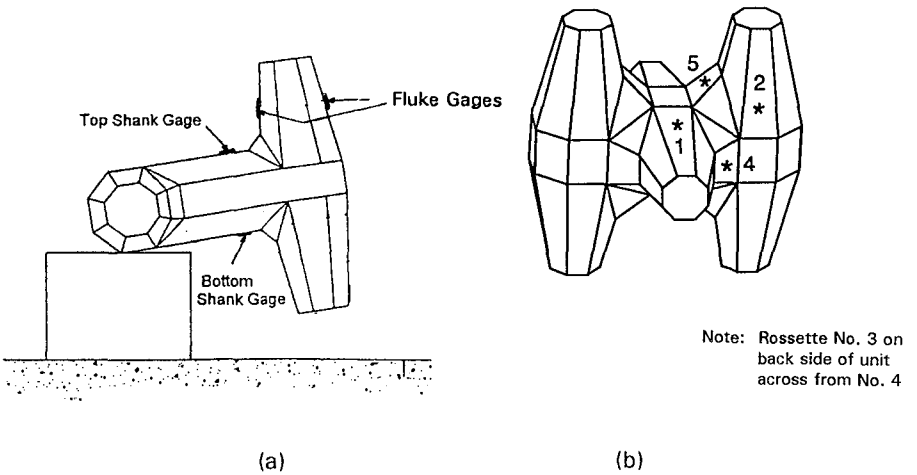

Figure 6. (a) Dolos gage locations, (b) CORE-LOC® gage locations

LARGE SCALE AND PROTOTYPE DROP TEST RESULTS

For all the results presented herein, the maximum tensile stress or the mean of the maximum tensile stresses (for multiple drops at the same height), σ_T, was expressed as a non-dimensional tensile stress, $\sigma_T/(E\gamma C)^{1/2}$. These stress values are plotted as a function of the centroidal drop height, expressed as the non-dimensional parameter $(h/C)^{1/2}$, where h is the drop distance between the centroid of the armor unit at rest and lifted off the concrete base the predetermined drop height distance. By expressing results in these terms, it becomes simpler to compare results between different types and different sizes of units.

The drop tests for Core-Loc and dolos are similar but not directly comparable. When dropping the dolos, almost 1/3 to 1/2 of the total weight of the dolos is supported on a pedestal, whereas the full weight of the Core-Loc is unsupported at impact. The first set of drop test results compares the 32-kg Core-Loc to the 26-kg dolos. Figure 7 shows the stresses generated in the similar size Core-Loc and dolos units. For the dolos, the plot shows stresses in both the shank and fluke sections (Figure 6a). For the Core-Loc, the maximum tensile stresses produced during the hammer and tipping drops are compared to the dolos stresses. The highest stresses in the dolos are in the shank where dolosse typically fail. Fluke stresses are approximately 75% of the shank stresses. The hammer drop and tipping drop stresses are 48% and 31%, respectively, of the dolos shank stresses. And the hammer drop and tipping drop stresses are 68% and 41%, respectively, of the dolos fluke stresses.

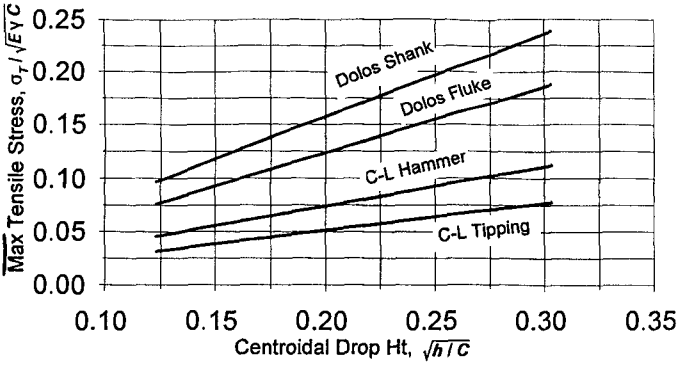

Figure 7. Drop test results from 26-kg dolos and 32-kg CORE-LOC®

A complimentary data set to the 32-kg Core-Loc and dolos drop test compares the prototype 10.9-tonne dolosse to the 9.2-tonne Core-Loc. It is to be noted that the prototype dolosse were only instrumented in the shank section. Figure 8 shows the same divergent trends between the prototype dolosse and Core-Loc as found for the smaller units. In this case, the Core-Loc hammer drop test is compared to the standard dolos

drop. As in Figure 7, the same trends emerge for the prototype tests. In this case, the Core-Loc stresses are 55% that of the dolosse. Figure 9 shows the results of the prototype tipping drop test for the 9.2-tonne Core-Loc. In comparing these results to the dolosse, the mean stresses are 52% of the dolos stresses. The anvil drop test was also conducted. In this test the Core-Loc was lifted completely off the concrete base before being dropped. Figure 10 shows the results. Only a single Core-Loc was used for the anvil drop, and the test was conducted in stormy weather. The data show lower stresses than either the tipping or hammer drop, which appears suspect. Some problems were encountered with collecting data as some of the strain gages started to malfunction during inclement weather.

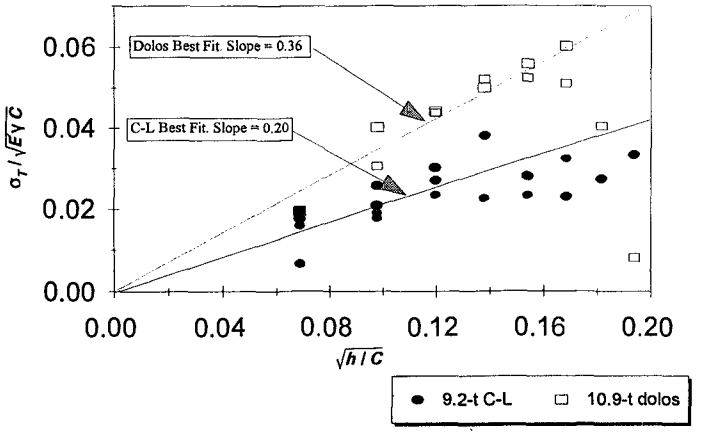

Figure 8. Drop test results for 10.9-t dolos and 9.2-t CORE-LOC®

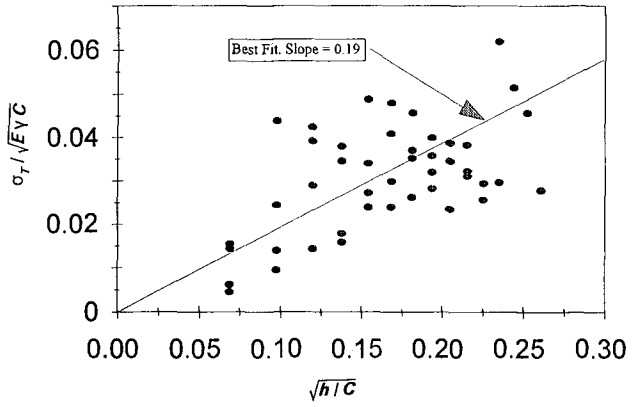

Figure 9. 9.2-t CORE-LOC® tipping drop test

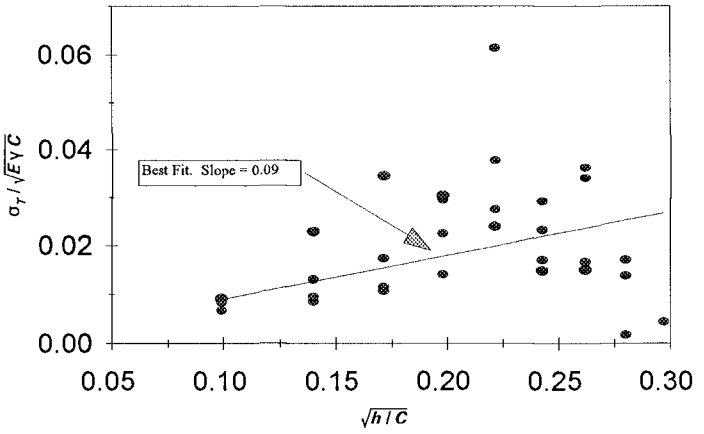

Figure 10. 9.2-t CORE-LOC® anvil drop test

DISCUSSION OF DROP TEST RESULTS

All the drop tests conducted at CTC used a very stiff base over a meter in thickness. Dropping units on this type of base creates one of the most severe impacts that can occur. Defining impact strength in itself is very difficult. There is no definite or unique relationship between the static strength of concrete and impact strength; but Neville and Brooks (1987) reported that, in general, the higher the compressive strength of the concrete the lower the energy absorbed per blow before cracking. Thus the impact strength and total energy absorbed by the concrete increases with compressive strength and age. It can be surmised that older units would have more impact resistance. However, in comparing drop test results, the two-week old Core-Loc consistently showed more impact resistance than the two-year old dolosse. Also, when dropping dolosse in the "standard" configuration, 1/3 to 1/2 of the weight of the dolos is supported on a pedestal, whereas the full weight of the Core-Loc is unsupported at impact.

For the prototype armor units tested, the mean flexural tensile strength of the dolosse was 140% of the Core-Loc and the mean compressive strength of the dolos was 188% the Core-Loc. The modulus of rupture for the Core-Loc was approximately 12% of the compressive strength and it is expected that it would be similiar for the dolos since the mix design was the same for the two types of units. Thus the dolos concrete was nearly twice as strong as that of the Core-Loc. The modulus of elasticity was minimumly higher for the dolosse (107% of the Core-Loc). But repeatly, the Core-Loc significantly outperformed the dolosse either in drop height and/or number of repeated blows to failure.

The data sets collected during the drop test experiment were relatively limited and warrant significant expansion. The prototype drop tests were conducted with four Core-Loc units of one size and the same type concrete. As with all experiments concerning

tensile strength of unreinforced concrete, there is fair amount of scatter in the data. Definitive trends are difficult to ascertain.

CONCLUSIONS

For the prototype drop tests conducted at CTC, the Core-Loc proved more robust than the dolosse tested. In the dolosse armor units tested, the tensile strength of the concrete was 140% of the Core-Loc and the compressive strength of the dolos concrete 188% of the Core-Loc. Young's Modulus was minimumly higher for the dolos (107% of the Core-Loc). In comparing drop test results, the two-week old Core-Loc consistently showed more impact resistance than the two-year old dolosse. Stresses generated in the Core-Loc are approximately half of those generated in similiar size dolos. Repeatly, the Core-Loc outperformed the dolos either in drop height and/or number of repeated blows to failure.

ACKNOWLEDGEMENT

The work described herein was conducted as part of the Repair, Evaluation, Maintenance, and Rehabilitation Research Program of the US Army Waterways Experiment Station, Vicksburg, MS. Permission to publish this paper was granted by the Chief of Engineers.

REFERENCES

Burcharth, H.F., (1981). "Full-scale dynamic testing of dolosse to destruction." Coastal Engr. Vol. 4

Melby, J.A. and G.F Turk, (1994). "Scale and modeling effects in concrete armor experiments," *ASCE Proc. 1st Int. Conf. on Role of L.S. Exp in Coas. Res.*, ASCE, New York, NY. pp. 686-700

Neville, A.M. and J.J. Brooks, (1987). Concrete Technology. John Wiley & Sons, Inc. New York, NY.

Nishigori, W., Endo, T., Nemoto, K., Noguchi, Y., Yamamoto, M., 1989. "Similarity law of impact between model and prototype tetrapods." *ASCE Proc. Seminar on stresses in concrete armor units*, ASCE, New York, NY pp 107-122

Zwamborn, J.A. and Phelp, D.T., (1989). "Structural tests on dolosse." *ASCE Proc. Seminar on stresses in concrete armor units*, ASCE, New York, NY. pp. 40-60

RESULTS OF FIELD MONITORING OF THE NEW CORE-LOC BREAKWATER at PORT ST FRANCES - SOUTH AFRICA

D Phelp [1], A Holtzhausen [2], J Melby [3]

Abstract

The newly completed fishing and recreational harbour at Port St Francis, on the south-east coast of South Africa, has a 220m outer rubble mound breakwater and an inner revetment, both protected by Core-loc® armour units. This paper briefly discusses the breakwater layout and armouring design, the effect of severe storm conditions during construction, and the performance of the Core-loc armouring, as based on the results of photographic monitoring, crane-and-ball profile surveys, visual observations and diver surveys below water.

Introduction

The first prototype application of a Core-loc armoured breakwater was constructed for the small craft harbour of Port St Francis, South Africa in 1996/97. Port St Francis is a small coastal town situated on the south-east coast of South Africa, on the northern side of the Cape St Francis peninsula, adjacent to the Krom River estuary (Figure 1). In the past the squid fishing industry has used the estuary for anchorage and access to the sea. Using the unprotected river mouth for access to and from the sea is dangerous and conditions are often unsafe resulting in accidents and loss of life and fishing vessels. The dangerous conditions, together with the growth squid fishing

[1] ENVIRONMENTEK, CSIR, P O Box 320, Stellenbosch 7599, South Africa

[2] WATERMEYER, PRESTEDGE and RETIEF, P O Box 50023, Waterfront, 8002

[3] CERC, WATERWAYS EXPERIMENT STATION, P O Box 631, Vicksburg, USA

industry and urban recreational developments highlighted the need to establish a small craft harbour on the east coast to support the squid fishing industry as well as recreational sport fishing and yachting. It was decided to construct a small craft harbour at the Port St Francis condominium resort to serve these needs. Construction of the harbour breakwater, marina and luxury resort facilities started in February 1996 and was completed in November 1997. The port is the first privately developed small craft harbour in South Africa.

The Core-loc armour unit was developed by the Waterways Experimental Station, Coastal Engineering Research Center (CERC) in the United States of America (Melby and Turk, 1994,1995). CERC participated in the design, testing and monitoring of the breakwater together with the South African consulting engineers AR Wijnberg Inc. Design and testing included full 3D model tests at a scale of 1:60 undertaken at the laboratories of the CSIR in Stellenbosch, South Africa. Initial baseline and subsequent breakwater surveys have been undertaken by the CSIR to monitor the performance of concrete Core-loc armour units. The use of the South African developed dolos units was also investigated, with the Core-loc units proving to be a more economic solution.

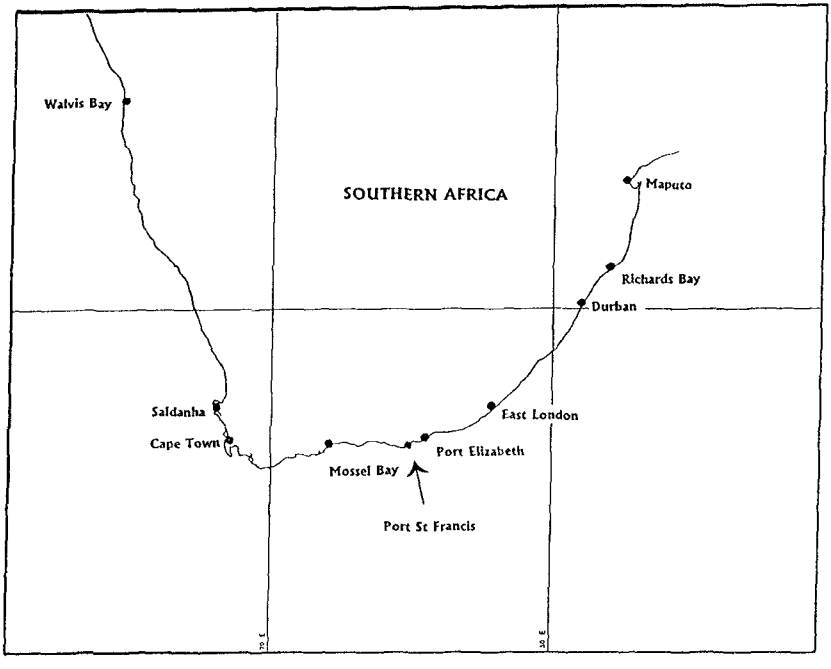

Figure 1: Location of Port St Francis

Location and Design Details of Main Breakwater and Peninsula Protection

The harbour is located on the east coast of South Africa, south of Port Elizabeth. The shoreline in the vicinity of the harbour consist of a rocky beach with a sandy beach and Krom River mouth to the south and Cape St Francis peninsula to the north (see Figure 2).

Figure 2: Rocky beach to the north of Port St Francis and

The total protective structures include a main outer breakwater and an inner peninsula revetment, both protected by 15 ton Core-locs. The breakwater consists of a rubble mound at a slope of 1:1,5 with 1,5 ton median under-layer rock and a concrete mass capping. A total number of 800 Core-loc units were used plus 20 spare units cast (approximately 560 for the breakwater and 260 for the revetment). The finish level of the mass capping is +4,4 m MSL and splash wall at +6,5 m MSL. The inner slope of the main breakwater is rock protected towards the head (Figures 3 and 4) and abuts directly onto the main harbour quay wall.

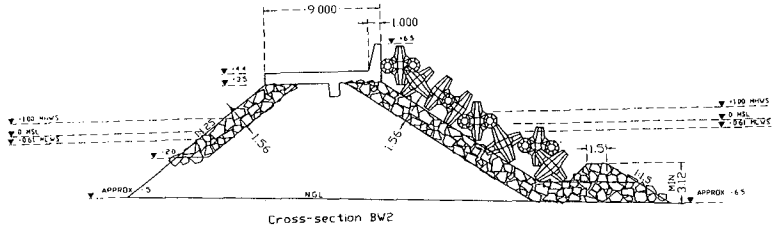

Figure 3: Cross section of the breakwater

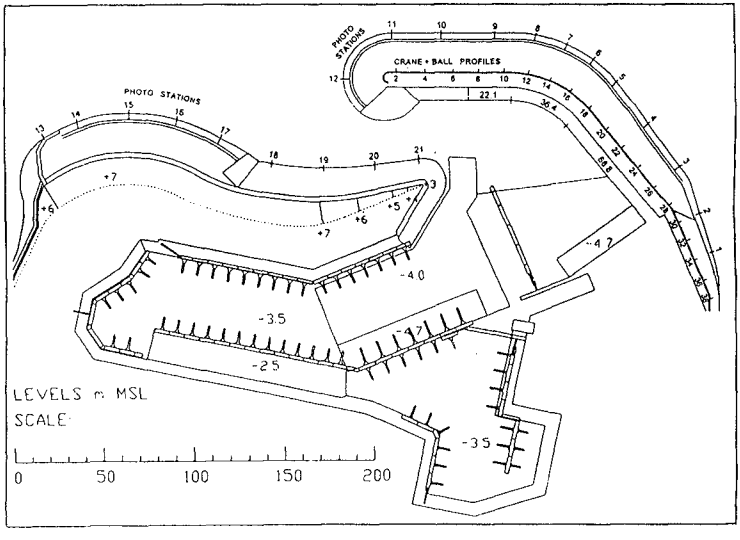

Figure 4: Layout of small craft harbour of Port St Francis -showing the positions of the photo stations and crane and ball profile positions

Sea Conditions

Although the bathymetry off the harbour causes depth limited wave conditions, four near design storms were experienced during construction (i.e. when the breakwater was uncapped and at +3,5m MSL working level). This resulted in overtopping and breaching of the uncompleted breakwater. As a result several Core-loc units required replacement and re-packing. One design storm has also been experienced after completion of the construction of the breakwater and the first baseline survey in October 1997. This caused little further damage to the well compacted (shaken down) slope.

The initial Core-loc design was base on Melby and Turk (1995). Maximum design depths of 8 m can be expected for the main breakwater, which means that the design is depth limited. With a foreshore slope of 1:50 and peak wave periods of up to 16 s, the maximum wave height at the structure is estimated to be approximately 7,2 m. using Hudson K_d factor of 16, a unit mass of 15 t was selected as a preliminary design. Further details of the design and construction of the breakwater see the ICCE '98 paper "The First Core-loc Breakwater" by Holtzhausen.

Construction Problems

To ensure sound breakwater concrete armour protection, it is imperative that good interlocking is achieved, especially when placing a single layer armouring system such as with Core-loc. This is done by accurately placing the individual units on a prescribed grid. This grid must be correct, right from the toe units which then form the foundation for the upper rows to lock onto. On the main breakwater it was apparent from diving surveys that some Core-loc were incorrectly placed seawards of the design toe.

Unfortunately at Port St Francis, the extreme storms experienced during early stages of construction also contributed to the displacement of many Core-loc units out of their allocated positions. This gave rise to poor interlocking in some areas and resulted in a non-uniform slope, especially on the bend of the breakwater. Additional Core-loc units were needed to fill gaps in the armouring, sometimes resulting in a semi-double layer. Up to 20 loose or damaged units were also removed from the toe and re-used on the breakwater.

These problems experienced during the construction phase of the breakwater, contributed to the majority of damage (displaced and broken Core-loc units) found on the breakwater. During this phase the low crest (+3,5 m MSL) working level was unprotected against wave overtopping, resulting in the displacement of a number of units during the near design storms that were experienced before construction of the mass-capping. During one of the storms, overtopping caused a breach of the core material and the displacement of Core-loc units into the harbour. Most of these units were recovered and re-packed on the front slope. Some grading problems with the under-layer rock also caused an irregular profile. Figure 5 shows the breakwater, revetment and marina still under construction.

Figure 5: Breakwater, revetment and marina under construction

Initial placement problems were largely overcome during the construction of the revetment as this was constructed after the breakwater. This lead to a better constructed armour protection in this area, with good interlocking and a uniform slope (Figure 9). The revetment was also partially protected by the main breakwater and the working level during construction was higher, so that there were no serious overtopping problems.

Breakwater Monitoring Methods

The baseline survey of the breakwater and revetment included an aerial photographic survey, a "crane and ball" survey (Phelp, 1994), a visual inspection and a diving inspection. These were used to provide as-built data (against which future monitoring could be compared) and document the breakage type, providing a count and location of damaged Core-loc armour units. The baseline surveys were carried out in October 1997 to capture the damage which occurred during construction, while follow-up surveys were done in May 1998.

Visual Inspection

A visual inspection was carried out to record the location and type of Core-loc breakage. This was done by climbing over the Core-loc slope during low spring tide and relating the positions to the ball survey lines. The recorded damage was later correlated with that seen in the aerial photographs taken by the CSIR.

Photographic Survey

A "Robinson 44" 4-seater helicopter, was used for the photographic survey. It allowed the camera to be elevated to a position perpendicular to the slope of the Core-loc armouring. Pre-determined coordinates were chosen to give good coverage, with photo stations spaced at 26m centres on the straight sections of breakwater and 13m over the curved sections. Figure 4 shows the layout of the survey stations on both the outer breakwater and inner revetment.

Navigation of the helicopter was carried out with the aid of a "Landstar" Differential Global Positioning System (DGPS) which was fitted to the helicopter (Figure 6). DGPS is a satellite-based positioning system which achieves high accuracies by utilizing real time radio transmitted corrections from a reference station, placed at a known location. This then provides dynamic positioning of the survey camera, to an accuracy of plus/minus 0,5 m. The altitude of the helicopter was kept at 65 m above the breakwater slope.

Figure 6: DGPS system fitted to helicopter for position fixing.

The photographs were taken with a Nikon FM 35 mm camera with a 50 mm lens and using 200 ISO colour film. The photo stations were marked on the breakwater and the revetment and numbered 1 to 12 and 13 to 21 respectively (Figure 4) and were positioned at the centre of each photograph. This allowed for each station to include approximately 50 Core-loc units per photograph. By careful observation of the approaching waves, the photographs were taken at maximum wave draw-down to ensure the maximum area of Core-locs (approximately 90%) exposed, including those toe units located below the still-water line.

Crane and Ball Survey

A mobile crane with an 18 m reach was used for the "crane and ball survey". The radius of the ball used for the survey was 1 metre. The survey was carried out by positioning that crane at each station (Figure 7) with the boom perpendicular to the breakwater. The profile of the Core-loc armour units was then measured by suspending the ball from the boom by a calibrated staff. Starting from the splash wall the levels were measured at 3 m intervals, horizontally along the boom.

A DGPS satellite system was mounted on the top of the boom to fix the positions at which the levels were taken. The level of the ball were recorded by dumpy level from the capping and related back to the top of the splash wall at a level of +6,5 m. At each position the ball was lowered until it touched the Core-locs. The levels were then plotted with Figure 8 showing the plot for stations 1 to 5.

The ball survey gave a profile generally 1 metre higher than the design profile. The latter was closer to the levelling survey taken by holding a staff on the centroid of each Core-loc, as carried out by A.R. Wijnberg Inc. (Figure 8).

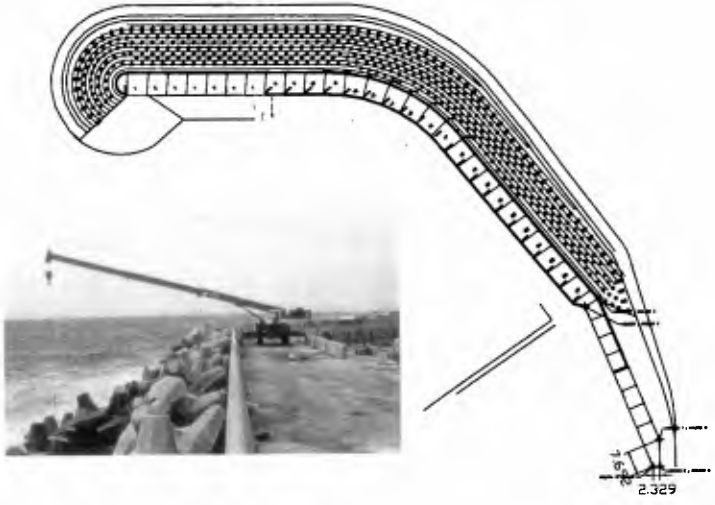

Figure 7: Crane and ball survey stations

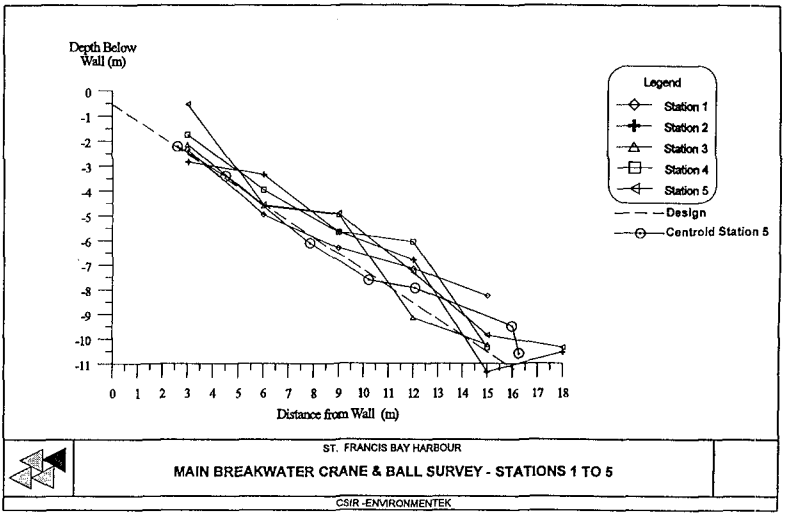

Figure 8: Main Breakwater crane and ball survey - stations 1 to 5

Diving Inspection

A diving inspection was undertaken by a diver in the water and one assistant on the breakwater to record the position and state of the underwater part of the breakwater. The diver swam along the toe of the main breakwater from the inner roundhead, along the outer slope to the root. The inner revetment was not included in the diving survey, as the toe was mostly exposed during low spring tide, and could be monitored by the aerial photographic survey.

Poor visibility reduced the effectiveness of the main breakwater diving survey to counting broken units and recording those units which had moved away from the breakwater toe. The latter were no longer interlocked with the rest of the armour slope, and therefor not contributing to the stability of the structure. Some of these units, displaced by the storm, were recovered and re-used higher up the slope. The diving inspection also confirmed the buildup of sand along the toe which had completely covered the rock berm and the first row of Core-loc. This buildup occurred within the fist year after completion of the breakwater.

The diving inspection also revealed the importance of the manner in which the first row of Core-locs are placed behind the toe berm. Where good toe placement was achieved, such as on the revetment, it provided a stable foundation on which to build the rest of the slope. Areas where the toe units were loose, the armour slope had become flattened (e.g. storm damage around the bend in the main breakwater) resulted in looser packing and poorer interlocking of the Core-loc above. The slope of the revetment was more uniform with each row of Core-loc anchored by the row above, resulting in a strong well interlocked slope (Figure 9).

Figure 9: Revetment and main breakwater

Analysis of Damage

In October 1997 the first detailed "as-built" survey was undertaken of the first Core-Loc armoured breakwater. A visual inspection of the breakwater was conducted by CERC while the CSIR carried out an aerial photographic survey to record the location and type of breakages. As discussed above, most of the damage recorded can be attributed to difficulties arising from several design storms experienced during construction of the breakwater, and to the placement of Core-loc units too far in front of the design toe. The type and position of the breakages were categorised as H-tip breaks, double H-tip breaks, nose-tip breaks, middle breaks and multiple breaks (Figure 11).

It was noted from the analysis of the photographs that almost double the damage was recorded than that recorded from the visual survey alone. This is possibly because it was difficult to reach the lower units due to wave action, whereas the helicopter could

hover while waiting for wave draw-down, before taking the photograph. The broken Core-loc units were indicated by highlighting them on the photographic records.

Although there was unusual storm damage during construction, the normal "shake down" or "settling in" damage (for dolos breakwaters this was found to be more than double the average annual damage - Phelp, 1994) took place before the baseline survey. Additional Core-loc units were also placed on the upper slope of the breakwater, after completion of the mass capping, to complete the armour slope up to the top of the splash wall. Without a complete re-pack of the entire slope, it proved difficult to fit additional units in the open spaces. Minor further damage to the breakwater occurred after shake down, as shown by the follow-up survey in May 1998. The repairs to the bend in the breakwater have resulted in an "S" shaped cross-section similar to a dynamically stable rock berm.

The revetment was built to a final height of +7 m MSL, whereas the main breakwater was built to an interim height of +3,5 m before the mass-capping was cast. The revetment was also built after the main breakwater, which meant that, besides being partially in the lee of the main breakwater, the construction crew had more experience with handling the single layer Core-loc units. The underlying rock layer also appeared to be more uniform which allowed for easier placing of the Core-loc units, correctly positioned right from the toe of the slope. The free Core-loc units at the northern end of the revetment were secured by a concrete buttress / caissons anchored to the sea-bed, which proved very successful. In general, the revetment has shown minimum shake down damage.

Figure 10: View of completed small craft harbour

Of the total 800 Core-loc used for the breakwater and the revetment, a total of 35 units were damaged during the construction of the harbour, ie. before the baseline survey. The majority of the damaged units being on the main breakwater (30 on the breakwater and 5 on the revetment). The reasons for the high construction damage have been discussed above.

A follow-up aerial photographic survey done in May 1998, showed very little further damage to the breakwater (**and no further damage to the revetment**), despite the occurrence of another near-design storm after the baseline survey. Only 3 Core-loc units were recorded as new damage resulting from extreme storm conditions between October 1997 and May 1998. Two of the previously damaged units, which were already weakened, were found to have broken further. This low damage figure represents the true performance of the new Core-loc breakwater, excluding the problems experienced during construction.

It was however felt that it would be useful to classify the different types of breaks which took place during construction (see Figure 11). These were identified for each damaged Core-loc unit and totals were calculated accordingly. The percentages of the various breakage categories is indicated in the table below:

Breakage Type (during construction)	**% Breakage**
H-tip breaks (one tip only) = 5% wt. Loss	61%
Double H-tip breaks = 10% wt. Loss	5%
Nose-tip breaks = 5% wt. Loss	13%
Middle breaks (unit broken in half)	13%
Multiple breaks (more than 2 pieces)	8%

Of the breakage that did occur, 13% were located towards the top of the breakwater slope, 47% in the middle and 40% at the bottom. Some of these broken units were however re-used during remedial work and are no longer located at the position where they were originally damaged. Large Core-loc movements (> 3H, where H is the height of a Core-loc unit) were recorded without breakage, especially at the section that was breached during the construction phase. Breakages that were noted at the breached section may have resulted from the tumbling that occurred as a result of the erosion of the lee side of the breakwater. Several Core-locs displayed signs of impact (spalling) without breakage.

It is important to note that the units that experienced the H-tip and double H-tip breakages still retain 90% of their original weight allowing them to adequately provide the necessary protection. Furthermore, the majority of these units still appear to be well interlocked with the surrounding units. Other types of breakages recorded may also have occurred as a result of poor quality control during the making and placing of the units in the construction phase.

Figure 8 gives an example of the results of the "crane and ball" survey. Included on the figure is a plot of the design slope. The "S" shape damage apparent in the cross-sections nearest the bend in the breakwater was most likely caused by breaching during storm conditions and by poor placement.

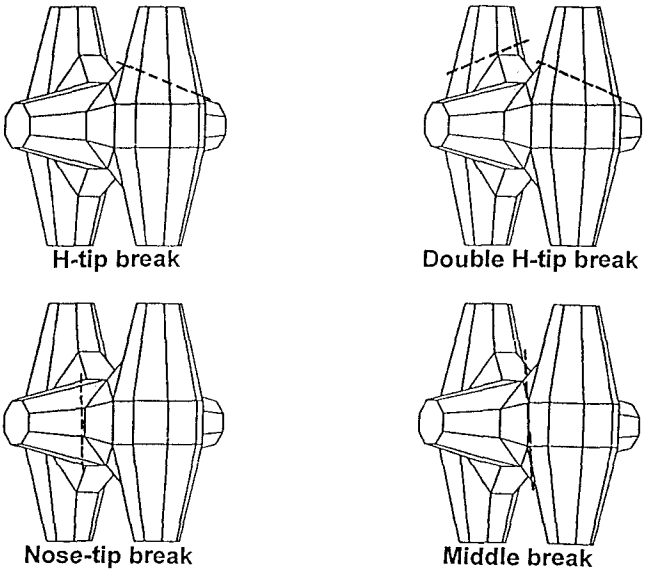

Figure 11: Types of breakages of Core-loc unit

Some loose Core-locs were found in front of the rock toe of the breakwater during the diving inspection. These units were mostly placed too far seawards of the designed position of the toe, but were also subject to displacement due to poor interlocking. The interlocking also appears to be less effective where the slope of the toe is flatter. Most loose Core-locs were recovered and re-used on the breakwater - where a toe unit could be removed without affecting the stability of the slope, it was re-used elsewhere on the slope. This accounted for up to 15 of the damaged units. Since the baseline survey it was also evident that sand has built up along the main breakwater toe, thus making it more stable and resulting in reduced wave heights

The toe of the revetment showed no displacement damage compared to the breakwater. This was due to better placing allowing for the effective interlocking achieved for most of these units.

Conclusions

- The Core-loc breakwater armour unit, as used for the first time at Port St Francis, has proved successful, despite some difficulties during construction.
- Excluding the damage recorded during the breakwater construction, the damage recorded by a follow-up survey was 3 broken units, which is less than 0,5% of the total of 800 units, despite the occurrence of further design storm sea conditions.
- Minimal as-built damage was found on the revetment, and no additional damage was recorded by the follow-up survey. This was no doubt due to the good packing and interlocking achieved on this part of the protection structure.
- CERC research showing improved structural stability (over other slender units) has proved itself in the field, with less breakage under extreme conditions. This allows recovery and re-use of displaced units (> 3H displacement recorded without breakage).
- Despite the high damage during construction, almost 80% of the total number of breaks consisted of either single "H-tip" fluke breaks, "nose-tip" breaks or double "H-tip" breaks, which still leaves 90% of the original unit weight allowing the units to remain well interlocked and functional. This will reduce the maintenance required during the lifetime of the structure.
- Good interlocking (as achieved on the revetment) is especially important for single layer armour units such as Core-loc. A well placed toe and a uniform slope are essential to achieve this, as is accurate placement of the armour units on a pre-determined grid.
- The stability of the toe units is especially important for a "shallow water" breakwater, such as is the case at Port St Francis, where the waves break directly onto the toe of the structure.

References

PHELP *et al.* (1994). Results of Extensive Field Monitoring of Dolos Breakwaters, 24th ICCE 1994, Kobe, Japan.

MELBY J A and TURK G F, 1995, The Core-loc: Optimised Concrete Armour, 24th ICCE 1994, Kobe, Japan.

TURK G F and MELBY J A, 1995a, Repair of Dolos Armoured Breakwater Slopes Using Core-loc, Proceedings COPEDEC IV, Rio de Janeiro, Brazil.

MELBY J A and TURK G F, 1995b, "Core-loc: Optimised Concrete Armour Units", PIANC Bulletin No. 89, p. 5 - 21.

THE FIRST CORE-LOC BREAKWATER

Anton H Holtzhausen[1]

Abstract

The first project in which Core-Locs were used as the main breakwater armour unit, is a small craft harbour on the south east coast of South Africa named Port St Francis. The Core-Loc was selected based on economic advantages over other units. Stability of 15 t units was confirmed in a full three-dimensional model study. Construction of the harbour commenced in early 1996 and was successfully completed towards the end of 1997. Practical construction issues are discussed in detail. Core-Loc performance under construction stage storms was excellent and virtually no damage has taken place under design storm conditions subsequent to the completion of the structure.

Background

The Core-Loc was developed at the Waterways Experiment Station (WES) Coastal and Hydraulics Laboratory (CHL) in 1992 and patented in 1995 (Melby and Turk 1995). During the initial stages of breakwater design for Port St Francis in 1995, the advantages of the Core-Loc over the commonly used dolos unit became apparent.

Figure 1 shows an aerial view of Port St Francis where Core-Locs were used

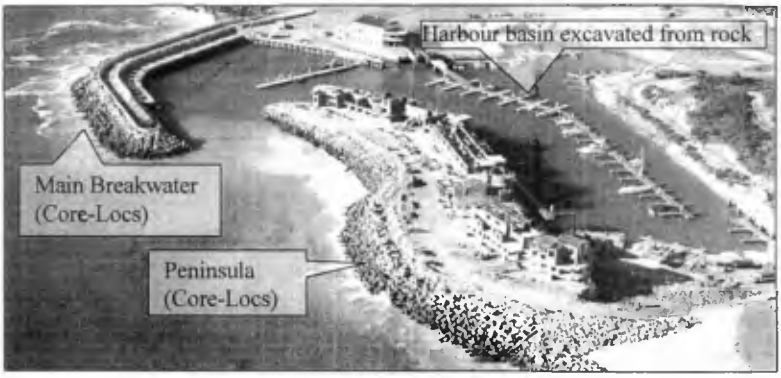

Figure 1. Port St Francis small craft harbour and marina development.

[1]Associate, Watermeyer Prestedge Retief, Marina Centre, West Quay Road, Victoria & Alfred Waterfront, 8001 South Africa (Previously A R Wijnberg Inc).

on the main breakwater and peninsula. Previous attempts to develop a small craft harbour at St Francis Bay were unsuccessful. One of the main reasons for the viability of the present project is minimization of harbour costs. Since the breakwaters make up a large component of these costs, the savings achieved by using Core-Locs as the primary armour, were substantial.

A further significant saving was achieved by optimizing the layout with regard to rock excavation and fill. The harbour basin was positioned to produce sufficient rock excavation for use as breakwater core and armour rock, as well as rock fill required for reclamation of the peninsula as shown in Figure 1.

Core-Loc Design

The initial Core-Loc design was based on Melby and Turk (1995). Maximum design depths of 8 m can be expected for the main breakwater, which means that the design is depth limited. With a foreshore slope of 1:50 and peak wave periods of up to 16 s, the maximum wave height at the structure is estimated to be approximately 7.2 m. Using a Hudson K_d factor of 16, a unit mass of 15 t was selected as a preliminary design.

A three dimensional model study of the proposed design was conducted at a scale of 1:60 in the CSIR hydraulics laboratory in Stellenbosch. The Core-Loc proved to be very stable and even on the breakwater head zero percent damage was achieved. Together with a representative of CERC, Mr J A Melby, who attended part of the model study, the design was finalized as shown in Figure 2.

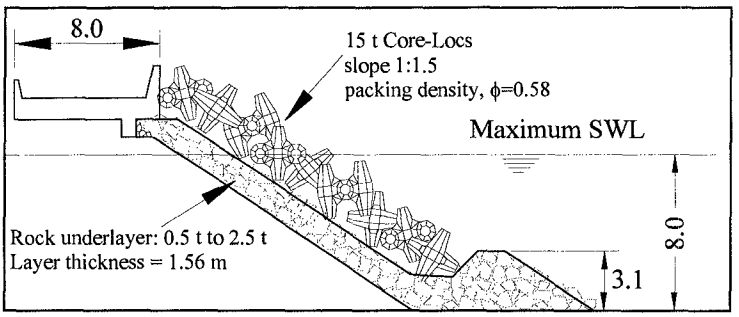

Figure 2. Design cross section for Port St Francis

The rock toe shown in the figure was included to allow for settlement in the case of scour. Probing results indicated that scour would be limited to a depth of approximately 1.5 m by a rock layer underlying the sand on which the breakwater and peninsula was to be constructed.

The packing density and placing grid for the Core-Locs were determined by experimentation since there were no set guidelines established at the time of the study.

A final packing density of ϕ=0.58 was used, where ϕ is defined as the number of units per area D_n^2, with:

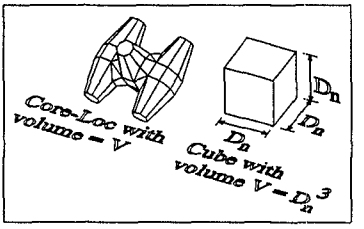

$D_n = V^{1/3}$

V = Volume of one armour unit

The equivalent solid concrete layer thickness, t, for a given armour size and packing density is given as:

$$t = \phi D_n \quad \text{..... (1)}$$

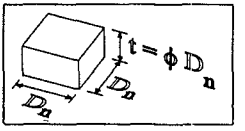

The total volume of concrete, V_{total}, required to cover a given area of slope, A, is:

$$V_{total} = t\,A \quad \text{..... (2)}$$

The packing density ϕ, can therefore also be expressed as:

$$\phi = t/D_n$$

The number of Core-Locs per area is given by:

$$N = \phi / D_n^2 \quad \text{..... (3)}$$

For a 15 t Core-Loc with a concrete density of 2.4 t/m^3 the volume is 6.25 m^3, and D_n = 1.842 m. The number of Core-Locs per area is:

$$N = 0.58 / 1.842^2$$
$$= 0.1709 \text{ units/m}^2$$

The total slope area that had to be protected was 4 680 m^2, which required 800 Core-Locs for both the breakwater and peninsula, with a total volume of concrete of 5 000 m^3. The equivalent solid concrete layer thickness, t was:

$$5\,000 / 4\,680 = 1.068 \text{ m}$$

The only displacements of Core-Locs in the model took place in shallow areas under angular wave attack. This was especially the case at the root of the peninsula where severe plunging breakers caused some displacements of toe units in

cases where they were not interlocked with units behind them. Dolosse with a unit mass of 15 t were also tested and showed the same instability along the toe as that found with the Core-Locs. Since this problem only existed in shallow areas, it would be possible to construct these areas carefully with toe units being visible at low tides. A number of repeat tests were conducted to investigate the probability of toe displacements. These tests confirmed good stability if toe units are placed with reasonable care.

Comparison of Core-Locs with dolosse

Although the focus of the model study was to confirm and refine the Core-Loc design, some tests were conducted with dolosse that allow a comparison of the two units. In general the stability of the two units, both with a mass of 15 t, was good and appeared to be similar (a more rigorous testing program would be required to allow a good estimate of the relative stability of the two units). Dolosse are traditionally placed at a packing density of ϕ=1 in South Africa which implies a 72 percent increase in both the volume of concrete and the number of units to be placed relative to the Core-Locs (packing density of ϕ=0.58). CERC (1984) indicates a packing density of ϕ=0.83 for dolosse, which would bring the 72 percent increase in concrete down to 43 percent, but this is still a very large difference. The minimum packing density that can be used for dolosse is probably ϕ=0.8, which still implies a 38 percent saving if Core-Locs are used.

Due to the larger packing density of a dolos structure, it can withstand more damage than lower packing densities, without exposing the rock under layers. Another aspect that makes it difficult to directly compare the two units, is that a dolos is more likely to break than a Core-Loc when being displaced by wave action. Since a comparison of units with the same unit mass contains a certain degree of subjectivity, the comparison was also done for equal volumes of concrete. In Table 1, dolos options that have the same total volume of concrete are compared to the 800 Core-Locs with a total volume of concrete of 5 000 m^3. Options with equivalent volumes of concrete have the same equivalent solid concrete layer thickness (Equation 1):

$$\phi \, D_n = 1.068 \text{ m}$$

Using this relationship, dolos options with packing densities of 1.0, 0.83 and 0.8 are compared with the 15 t Core-Locs in Table 1.

Table 1. Comparison of dolos options with Core-Locs that require a total volume of concrete of 5 000 m^3 (12 000 t concrete at a density of 2.4 t/m^3).

Packing Density, ϕ	Cube Dimension (m)	Unit Mass (t)	Total Number of Units
0.58	1.842	15	800
0.80	1.336	5.7	2 100
0.83	1.287	5.1	2 344
1.00	1.068	2.9	4 100

This table indicates the sensitivity of unit mass to packing density if the same total volume of concrete is specified. A graphical illustration of this comparison is shown in Figure 3.

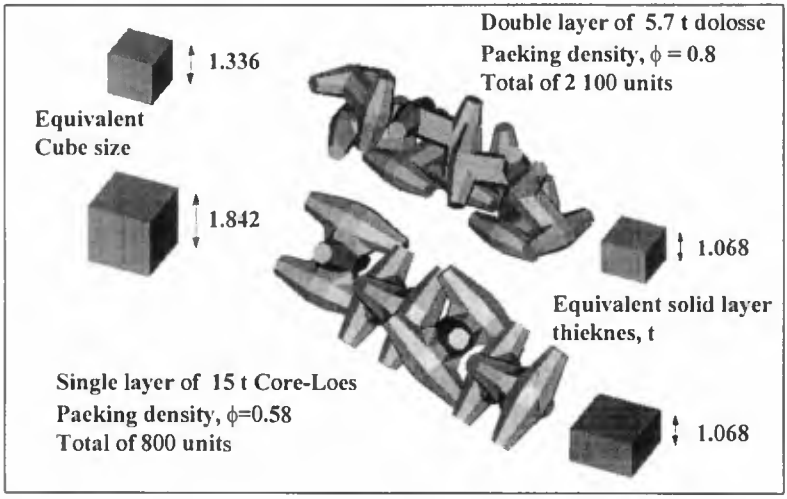

Figure 3. Comparison of dolosse with Core-Locs for equal concrete volumes

The best dolos option is obviously a packing density of 0.8, however the unit mass of 5.7 t is more than 2.5 times lighter than the 15 t Core-Loc and would undoubtedly sustain significantly more damage than the Core-Locs under design wave conditions. This would result in increased maintenance that once again makes the Core-Loc option less expensive. Also, the number of dolosse to manufacture and place is more than 2.5 times the number of Core-Locs. In terms of handling and time for construction, this would tend to make the dolos option more expensive than the Core-Locs.

Construction

The developers of Port St Francis decided against an open tender. A contracting company was formed and a negotiated contract was accepted after a number of modifications to further optimize costs and layout. The contractor had no in-house experience of breakwater construction. Since it was also the first time that Core-Locs would be used, a test section was built in the dry to check the tolerances that would be achieved with the type of construction proposed by the contractor.

The rock toe and under layer were dumped from a skip. Tolerances achieved with this method were checked by measuring rock profiles. It also provided an opportunity to check the toe placement proposed for shallow areas of the breakwater. Figure 4 shows an example of this type of placement and Figure 5

Figure 4. Toe placement used for shallow areas

Figure 5. Completed test section

shows the completed test section in which toe units were placed according to this orientation. In general the rock profiles and Core-Loc placement achieved on the

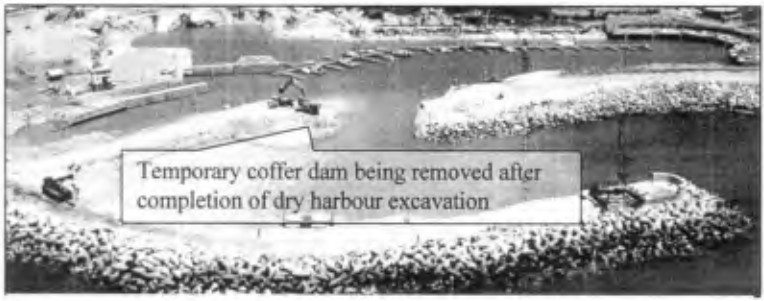

Figure 6. Temporary coffer dam built to allow dry excavation and construction of slipway, mooring piles and quay walls

test section was found to be acceptable. This, together with a specification based on CIRIA (1991), would form the basis for approving actual breakwater sections.

Excavation of the harbour basin commenced in January 1996. It was possible to excavate this area in the dry by constructing a temporary coffer dam as shown in Figure 6. Figure 7 shows the construction site before the harbour basin was excavated. The rock appeared to be good quality sandstone and it was estimated that this quarry would yield approximately 15 percent armour rock based on results obtained from a trial blast and excavation.

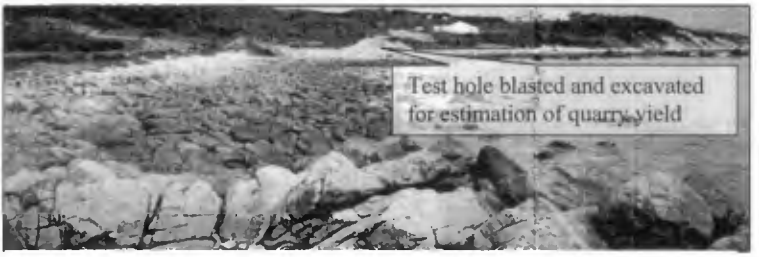

Figure 7. Harbour basin before excavation with location of test hole

Figure 8 shows the excavated harbour basin (quarry) which only yielded approximately 6 percent armour rock. This required the opening of a new quarry some 11 km away from the site, causing extensive delays to the breakwater construction.

In addition to the low yield in armour rock, the basin excavation also produced fines and clay that fell outside specifications for breakwater core material and fill material for the peninsula. In spite of the specification, some of this material was used for breakwater construction, leading to the rejection of these sections of breakwater. A compromise was reached where areas containing fines were excavated and sluiced before being replaced.

Figure 8. Harbour basin ater excavation. Armour rock yielded ~ 6%

Storms during Construction

At least 3 severe storms hit the breakwater during construction while a number of smaller storm events caused delays due to the breakwater being inaccessible for the crane. The first major storm hit without any warning. Luckily the waves only started picking up around mid-morning, allowing some time for emergency rock dumping on the breakwater crest. Figure 9 shows the last truck leaving the breakwater just in time. Surprisingly, the Core-Locs sustained almost

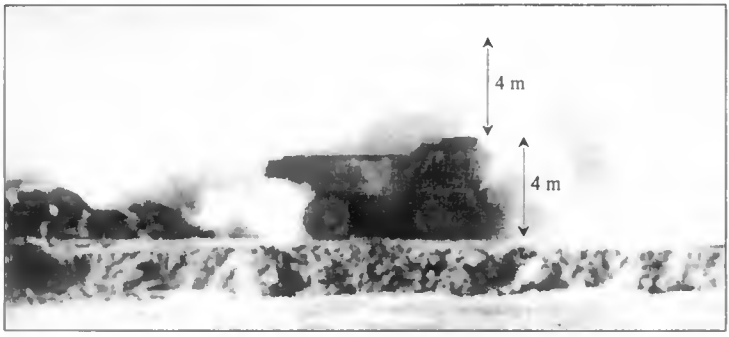

Figure 9. Emergency rock dumping during the first major construction storm. The Core-Locs sustained virtually no damage.

Figure 10. Largest storm that hit the breakwater during construction

no damage during this storm and only the unprotected head of the breakwater was eroded by some 15 to 20 m.

The breakwater was constructed all the way to the head at the level corresponding to the foundation level of the crown wall. Crown wall sections were then cast from the head towards the root of the breakwater (Figure 6 shows the first section of crown wall that was cast on the head). The crown wall construction had just reached the bend in the breakwater when the biggest storm during construction hit the breakwater. Figure 10 shows a wave photographed during this storm with a crane on the completed section of crown wall. Apart from some broken windows the crane was not seriously damaged but the breakwater experienced significant

Figure 11. Construction stage damage mainly due to erosion of breakwater crest. Some Core-Locs rolled further than 10 m without any breakage.

damage along sections where the crown wall had not yet been constructed.

Over the section where the crown wall had been completed, almost no damage took place. However, the section from the bend in the breakwater to the root sustained significant damage. The damage was caused mainly by erosion of the breakwater crest to a level that caused top row Core-Locs to roll toward the lee of the breakwater. This is illustrated in Figure 11 where some Core-Locs rolled over a distance of more than 10 m without breaking.

Figure 12. Crane and ball survey equipment

Engineering Evaluation

Construction of the first section of breakwater in relatively shallow water, proceeded without many problems. However, the crane and ball survey method that was used for surveying core and underlayer rock, had obvious limitations that gave rise to differences between the Contractor and Engineer. The survey was done using the breakwater crane shown in Figure 12. The height of the crane coupled with wave action made horizontal

positioning of the ball very difficult so that surveys often took very long to complete. This was especially frustrating when rising wave conditions made it urgent to protect breakwater sections where under layers had been placed. Before placement of Core-Locs could proceed, under layers had to be surveyed, plotted and approved by the engineer.

When the breakwater reached the bend it appeared that some problem was experienced with the positioning system since a number of Core-Locs were placed too far seaward, resulting in units that were isolated from the rest of the slope. This presented a problem since the isolated units could not interlock and were obviously rolled during some of the storms, as revealed by diving inspections during periods when underwater visibility was sufficient to evaluate the toe of the structure.

In some instances underwater inspections also revealed gaps between Core-Locs that were outside the placing specification. To resolve a differences between the Contractor and Engineer regarding these issues, an accurate survey of the structure was undertaken. A survey system was specificaly made up for this purpose that could measure accurately and quickly. It consisted of a measuring staff that slid vertically within a pipe fixed to a crane. The pipe was fixed vertically so that the horizontal position of the staff was always directly below the pipe. The entire breakwater was surveyed in one day, with both the Engineer's representative and the Contractor's site agent agreeing on each point that was measured.

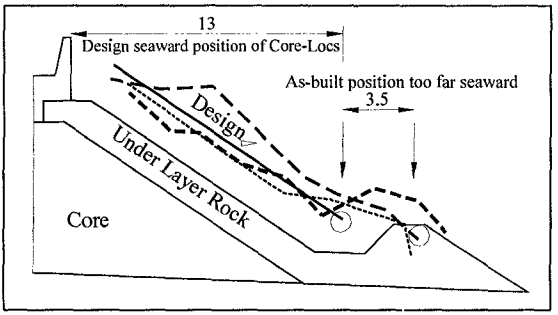

Figure 12. Design versus as built Core-Loc profiles

The survey results showed that some sections of the breakwater did not conform to the contract specifications. Figure 12 shows 3 profiles spaced at 7 m intervals approximately 50 m from the breakwater head. In some instances the toe Core-Loc was more than 3 m too far seaward. Areas were identified where remedial work was required. This mainly entailed removal of toe units that were positioned

away (seaward) of the slope. Approximately 20 units were removed underwater and re-positioned on other areas of the breakwater.

In one area (approximately 15 m length of breakwater) Core-Locs had to be removed to enable rectification of underlayer profiles (placing additional underlayer rock) before replacing the Core-Locs. Removing units from the slope was easy, even underwater, and the remedial work could be completed in less than one week.

Figure 13 shows some typical breaks that occurred during storm conditions on uncompleted sections of the breakwater and on units that were placed incorrectly (mostly seaward of the toe). In most cases the percentage loss in mass is as low as 5 percent. It was therefore decided not to reject Core-Locs with such minor breaks, especially where a displacement causing the break resulted in the unit moving into a more stable position.

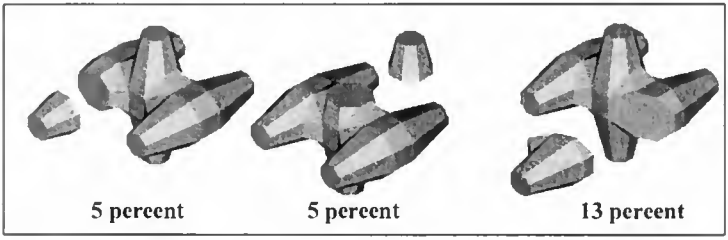

Figure 13. Percentage loss in mass for different types of breakages

Placement of Core-Locs on the peninsula was done after the majority of Core-Locs had been placed on the main breakwater. The experience gained on the breakwater lead to much improved work on the peninsula. Also, no major storm hit the peninsula before the structure had largely been completed. The final Core-Loc protection on the peninsula was of a high standard and was accepted without qualification in terms of the contract specification.

Figure 14 shows parts of the Core-Loc structures that were accepted in terms of the contract specifications, with one section of the breakwater being accepted subject to reduced payment. The acceptance of this part of the breakwater was qualified since it was not built to the original contract specification. However, the relatively minor deviations from the design profile was evaluated as possibly resulting in increased maintenance rather than causing major damage during the design storm event. An amount relating to the estimated increase in maintenance was used as the basis for reducing payment on this section of the breakwater.

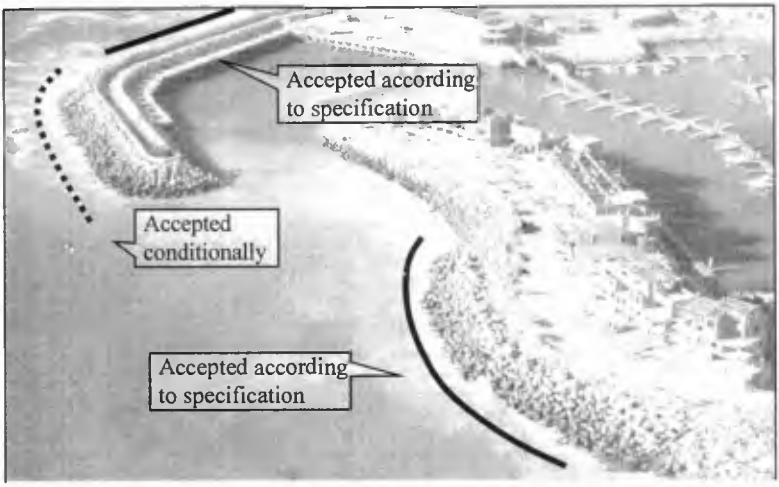

Figure 14. Contractual acceptance of Core-Loc structures

Conclusions

The first Core-Loc breakwater has been successfully completed. It played a significant role in the viability of the Port St Francis development by saving an estimated 30 percent on the cost of the breakwater armouring, compared to the traditional dolos protection used on most South African breakwaters.

Three storms,that approached the breaking wave design condition, were experienced during the approximately 2 year construction period. Core-Loc stability on the uncompleted structure was excellent under these conditions. During one storm, the breakwater crest and core was eroded by overtopping waves, causing some of the top row Core-Locs to roll on to the eroded area. Some units rolled up to 10 m and more without any breakage, clearly illustrating superior structural characteristics.

Post construction performance has been good so far and very little maintenance is expected in future. The structure will be monitored on a yearly basis by the CSIR as part of their research work on prototype breakwater performance.

Acknowledgement

The author wishes to thank the U. S. Army Coastal Engineering Research Center, and specificaly the designers of the Core-Loc, Mr J A Melby and Mr G Turk, for their co-operation and assistance with the project.

References

CIRIA (1991). Manual on the use of rock in coastal and shoreline engineering. Construction Industry Research and Information Association, Special Publication 83, 1991. CIRIA, 6 Storey's Gate, London SW1P 3AU, UK.

Melby, J.A., and Turk, G.F. (1995). "CORE-LOC: Optimized concrete armor units," PIANC Bul. N. 87-5, 5-21.

DAMAGE PROGRESSION ON BREAKWATERS

J. A. Melby[1], M. ASCE, and N. Kobayashi[2], M. ASCE

Abstract

An experiment is described consisting of seven relatively long-duration breakwater damage test series. The test series were conducted in a flume using irregular waves. New damage measurement techniques were developed and damage development data were acquired for breaking wave conditions. Wave height, wave period, water depth, storm duration, storm sequencing, and stone gradation were all varied systematically. The experiment yielded relationships for both temporal and spatial damage development. The relations by Melby and Kobayashi (1998a,b) for predicting temporal variations of mean damage with wave height and period varying with time in steps are shown to describe damage reasonably well (within one standard deviation) for new test series, although damage initiation is consistently underpredicted by more than a standard deviation. The prediction is shown to improve significantly if the initial profile adjustment is accounted for in the test series with relatively small cumulative damage.

1 INTRODUCTION

Contemporary breakwater armor stability design is founded on the well known work of Iribarren and Hudson. Much work has been done to extend these stability models for no-damage design conditions; but little work has been done to quantify damage progression. With only limited knowledge of damage progression, it is difficult to rationally determine life cycle costs or to evaluate and prioritize maintenance requirements for various projects. Further, determining the reliability with adequate accuracy for a particular design is impossible without prediction models for damage progression.

Existing stability formulas are limited to constant wave conditions [e.g. Hudson(1959) and van der Meer (1988)]. They are primarily intended to give a stable armor layer for a design level storm. These existing formulas can be used to design a new armor layer, but are not sufficient to predict life-cycle costs or to determine maintenance requirements for

[1] Res. Engineer, USAE Waterways Experiment Station, CERC, 3909 Halls Ferry Rd., Vicksburg, MS, 39180

[2] Professor and Assoc. Dir., Center for Applied Coastal Research, University of Delaware, Newark, Delaware, 19716

damaged rubble mounds. Additionally, existing formulas only predict the average damage, where damage is characterized by eroded area or number of displaced units. Melby and Kobayashi (1998a,b) showed that the damage variability along the structure is significant. Van der Meer (1988) showed that the shape of the eroded profile may be important in assessing the remaining capacity of an armor layer. Mansard et al. (1996) utilized the minimum cover layer thickness to describe failure of an armor layer. Melby and Kobayashi (1998a,b), hereafter referrred to as M&K, showed that this cover layer thickness as well as the depth and extent of erosion can be used to characterize the profile and all are quite variable along the slope. Existing stability formulas give no predictive capabilities for these profile parameters. Thus, existing stability prediction techniques cannot fulfill the need for predicting the future performance of existing structures.

2 PHYSICAL MODEL EXPERIMENT

A small-scale physical model experiment was designed to provide the hasis for an empirical model for spatial and temporal breakwater damage development. The experimental design was focused on quantifying damage for long duration tests composed of sequences of storms. The objectives of the experiment were as follows:

1. Quantify the progression of damage for multiple storm events, with water level, breaking wave height at toe, and storm duration being the primary variables of interest. Wave period and stone gradation were also varied systematically.
2. Quantify the uncertainty or scatter in damage due to natural variahility.
3. Determine whether the ordering of storm events effects the ultimate damage level.
4. Promote laboratory experimental standards for hreakwater damage progression.

The experiment utilized two small-scale ruhble mound breakwater sections in a wave flume. Figure 1 shows the flume profile and Figure 2 shows a typical structure cross section. A total of seven irregular wave test series were conducted as shown in Table 1. M&K describe the first three series. This paper summarizes results from all seven series. Each series was composed of a sequence of storms of varying wave height and water level. Parameters varied systematically from series to series were storm duration, storm ordering, wave height, water depth, wave period, and armor gradation. The structures were profiled using a newly developed automated profiler (Winkelman 1998). The profiles were used to determine the eroded cross sectional area and profile characteristics. The experimental setup, instrumentation, and initial tests are described in detail in M&K and will only be summarized herein.

Table 1
Summary of Test Series

Test Series	Test Type	Armor Type	Water Level Order	Test Duration (hr)
A′	Deterioration to Failure	Uniform	Low - High	28.5
B′	Storm Ordering	Uniform	Low - High	8.5
C′	Storm Ordering	Uniform	High - Low	9.0
D′	Wave Period	Uniform	Low-High	8.5
E′	Wave Period	Uniform	Low-High	8.5
F′	Gradation	Riprap	Low-High	8.5
G′	Gradation	Riprap	Low-High	8.5

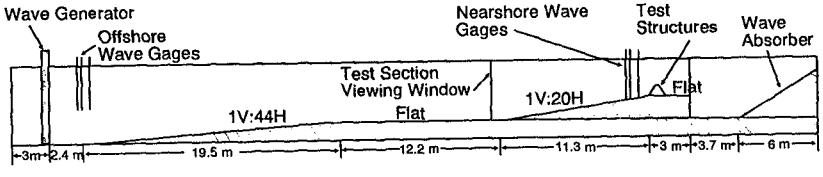

Figure 1. Flume Profile

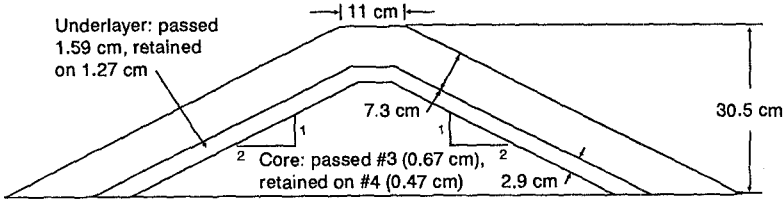

Figure 2. Model structure cross section

The experiment was conducted in a 61 m long by 1.5 m wide by 2 m deep flume, with a beach slope of 1V:20H. Two side-by-side identical conventional rubble mound cross sections were constructed with seaward slopes 1V:2H, crest heights 30.5 cm, and angular armor stone. Irregular waves corresponding to the TMA spectrum were run in bursts of 15 min. The undamaged underlayer and armor layer for the two identical structures were profiled before each series. Then both structures were profiled after each 30 min of irregular waves.

The seven series, summarized in Table 1, were designed to define spatial and temporal damage development under irregular depth limited breaking wave conditions. Series A′, lasting a total of 28.5 hr, was run until failure of the armor layer occurred, where failure was defined as exposure of the underlayer through a hole of diameter of at least D_{n50}. This series was intended to define the long term response of a structure. Series A′ was run once yielding 16 alongshore profiles every 30 min. Series B′, C′, D′, E′, F′, and G′, each lasting approximately 9 hr, were run twice producing 32 alongshore profiles per 30 min. These latter series were not run to failure but were intended to define the damage development for various conditions. Series B′ and C′ were designed to investigate storm sequencing by running low water first then high water in B′, and then reversing the water levels in C′. Series B′, D′, and E′ investigated period effects, each having a different peak period. Series F′ and G′ investigated stone gradation effects. The average damage $\bar{S}$ and the standard deviation of damage, σ_S, were computed using the 16 or 32 profiles after each 30 min of waves.

Two very different armor stone gradations were utilized. The armor stone for Series A′, B′, C′, D′, and E′ was uniformly sized with a median mass M_{50} = 128 g, nominal diameter $D_{n50} = (M_{50}/\rho_a)^{1/3}$ = 3.64 cm, stone density ρ_a = 2.66 g/cm^3, and D_{85}/D_{15} = 1.05, where D_{85} and D_{15} are the nominal diameters corresponding to 85 and 15 percent finer for the stone mass distribution, respectively. The armor stone for Series F′ and G′ was widely graded riprap with a median mass M_{50} = 256 g, nominal diameter $D_{n50} = (M_{50}/\rho_a)^{1/3}$ = 4.58 cm, stone density ρ_a = 2.66 g/cm^3, and D_{85}/D_{15} = 1.53. The riprap followed the widest recommendation of the SPM (1984) of approximately $0.125M_{50} < M < 4M_{50}$. For all series, the underlayer had a gradation of D_{85}/D_{15} = 1.32 and was sized such that $(M_{50})_{armor} / (M_{50})_{filter}$ = 25 and $(D_{50})_{armor} / (D_{50})_{filter}$ = 2.9.

Damage can be defined according to Broderick and Ahrens (1982) as

$$S = \frac{A_e}{(M_{50}/\rho_a)^{2/3}} = \frac{A_e}{D_{n50}^2} \qquad (1)$$

where A_e = eroded volume per unit length or cross-sectional eroded area. The eroded area was measured using a profiler composed of eight rods which spanned a width on one structure of 35 cm. The alongshore profiler rod spacing was 5 cm. The width of one structure was 0.76 m so the profiled section did not include the side wall effect. The profiler

design was similar to that used by Davies et al. (1994). Each profile rod had a sphere of diameter 3.64 cm at the profiling end that followed the slope as the profiler was moved along the flume. The position of each sphere was determined from digital measurements of the angular rotation of each profile rod and translational position of the profile carriage. This technique provided an accurate and complete profile as the cross-shore spatial sampling interval was less than 1 mm. The eroded area, shown in Figure 3, was defined as the area between the undamaged profile and the damaged profile, but limited to the eroded region. The profile points were averaged over a small cross-shore spatial interval in order to eliminate contributions to the eroded area from minor downslope shifting of the armor layer.

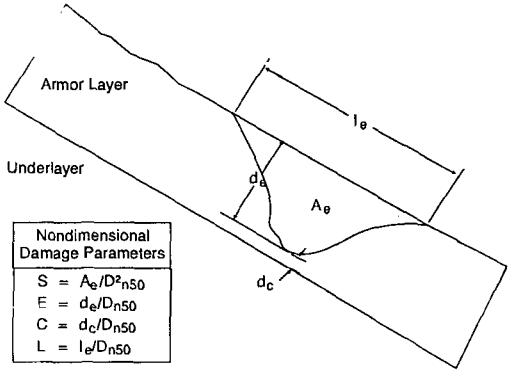

Figure 3. Sketch of breakwater profile with definition of damage parameters

As stated above, the eroded depth d_e, eroded length l_e, and cover depth d_c, shown in Figure 3, were used to define the profile shape. d_e was computed for each profile as the maximum distance between the eroded profile and the undamaged profile, measured normal to the structure slope. Similarly, d_c was computed as the minimum slope-normal difference between the undamaged underlayer slope and the damaged profile. Note that $d_e \neq (t_a - d_c)$ where t_a is the undamaged armor layer thickness, due to irregularities in the original armor layer thickness. The eroded length was defined as $l_e \approx 2A_e/d_e$ corresponding to a roughly triangular shaped region along slope. These three profile parameters were normalized by M&K, in order to generalize the test results, as $E = d_e/D_{n50}$, $C = d_c/D_{n50}$, and $L = l_e/D_{n50}$. The mean values were computed and denoted as $\bar{E}$, $\bar{C}$, and $\bar{L}$ while their standard deviations along the slope were σ_E, σ_C, σ_L. These statistical representations will be used throughout the remainder of this paper.

Incident wave statistics for all series are listed in Table 2. For all tests, the structure toe water depths were limited to h_t = 11.9 and 15.8 cm. The combination of wave periods and water depths produced low depth-to-wavelength ratios which resulted in severely breaking waves at the toe of the structure, which is typical of design conditions on most U.S. coastlines and represents the worst case for stability. In Table 2, T_p = spectral peak period, H_{mo} = spectral significant wave height defined as $H_{mo} = 4m_o^{1/2}$ with m_o = zero moment of the

incident wave spectrum, $R = [(m_o)_r/m_o]^{1/2}$ = average reflection coefficient, with $(m_o)_r$ = zero moment of the reflected wave spectrum, T_m = mean wave period, H_s = average height of the highest 1/3 of waves, $H_{1/10}$ = average height of the highest 1/10 of waves, and $H_{2\%}$ = wave height exceeded by 2 percent of the waves in the wave height distribution. Time domain statistics T_m, H_s, $H_{1/10}$, and $H_{2\%}$ were all computed from a zero-upcrossing analysis.

Table 2
Summary of Incident Wave Characteristics

Series	Wave	Dura-tion hr	ht cm	Tp sec	Hmo cm	R	Tm sec	Hs cm	H1/10 cm	H2% cm
A'	1	1.5	11.9	2.48	9.78	0.46	1.76	9.38	11.50	12.80
	2	1.5	11.9	2.48	12.40	0.47	1.69	11.60	13.80	15.37
	3	7.5	11.9	2.48	14.20	0.48	1.74	13.20	15.70	17.30
	4	1.0	15.8	2.59	10.50	0.52	1.73	10.10	12.72	14.30
	5	6.0	15.8	2.59	13.60	0.51	1.67	13.00	15.97	17.80
	6	11.0	15.8	2.59	15.80	0.51	1.66	14.90	18.00	19.30
B'	1	0.5	11.9	2.48	9.78	0.46	1.76	9.38	11.50	12.80
	2	2.0	11.9	2.48	12.40	0.47	1.69	11.60	13.80	15.37
	3	2.0	11.9	2.48	14.20	0.48	1.74	13.20	15.70	17.30
	5	2.0	15.8	2.59	13.60	0.51	1.67	13.00	15.97	17.80
	6	2.0	15.8	2.59	15.80	0.51	1.66	14.90	18.00	19.30
C'	4	1.0	15.8	2.59	10.50	0.52	1.73	10.10	12.72	14.30
	5	2.0	15.8	2.59	13.60	0.51	1.67	13.00	15.97	17.80
	6	2.0	15.8	2.59	15.80	0.51	1.66	14.90	18.00	19.30
	2	2.0	11.9	2.48	12.40	0.47	1.69	11.60	13.80	15.37
	3	2.0	11.9	2.48	14.20	0.48	1.74	13.20	15.70	17.30
D'	7	0.5	11.9	1.97	6.13	0.44	1.64	6.05	7.62	8.36
	8	2.0	11.9	1.97	9.88	0.38	1.54	9.88	12.48	13.59
	9	2.0	11.9	1.97	13.11	0.33	1.44	13.18	16.14	17.11
	10	2.0	15.8	2.02	9.62	0.38	1.61	9.74	12.48	14.00
	11	2.0	15.8	2.02	12.83	0.34	1.55	13.21	16.80	17.87
E'	12	0.5	11.9	1.53	5.05	0.38	1.29	5.05	6.72	7.75
	13	2.0	11.9	1.53	7.13	0.35	1.29	7.26	9.70	11.11
	14	2.0	11.9	1.53	9.93	0.31	1.23	10.19	13.38	14.90
	15	2.0	15.8	1.48	6.60	0.34	1.30	6.58	8.15	8.78
	16	2.0	15.8	1.48	9.41	0.32	1.26	9.53	12.03	13.34
F'	17	0.5	11.9	2.48	7.21	0.49	1.72	6.96	8.68	9.61
	18	2.0	11.9	2.48	11.68	0.42	1.56	11.51	14.39	15.63
	19	2.0	11.9	2.48	15.33	0.37	1.39	14.95	18.09	19.39
	20	2.0	15.8	2.59	6.43	0.47	1.80	6.18	7.78	8.58
	21	2.0	15.8	2.59	8.82	0.44	1.72	8.54	10.95	12.45
G'	22	0.5	11.9	1.97	7.62	0.42	1.50	7.53	9.53	10.62
	23	2.0	11.9	1.97	12.07	0.37	1.36	11.99	14.93	16.22
	24	2.0	11.9	1.97	15.42	0.35	1.30	15.21	17.95	18.99
	25	2.0	15.8	2.02	11.92	0.37	1.44	11.98	15.06	16.67
	26	2.0	15.8	2.02	15.34	0.35	1.34	15.36	18.64	20.03

3 PREDICTIVE EQUATIONS

M&K showed that the normalized damage was in the range $-2.7 \le S^* \le 3.0$, where $S^* = (S - \bar{S})/\sigma_S$. This relation can be used to predict the range of damage on the armor layer. For instance, the damage at failure of Series A′ was $\bar{S} = 13$ and $\sigma_S = 2.65$ yielding a range of $6 \le S \le 21$. This clearly shows that the variability of damage on this short section of structure was significant, especially considering that the waves were uniform alongshore. $E^* = (E - \bar{E})/\sigma_E$ and $C^* = (C - \bar{C})/\sigma_C$ were shown to have similar ranges with S^*, E^* and C^* all in the range from -3 to 3. The standard deviation of damage was shown to be a function of the mean damage, following the relation $\sigma_S = 0.5\bar{S}^{0.65}$. This relation indicates that the variability in damage increases with mean damage. Figure 4 shows σ_S for the four new series (D′, E′, F′, G′) plotted as a function of $\bar{S}$, where Series B′ is included for reference in this and the following figures. This figure indicates that the previously derived relation slightly underpredicts damage variability for the new series. The greater variability in damage for the wider gradation (Series F′ and G′) is expected; but the reason for the greater damage variability for shorter wave periods is not clear.

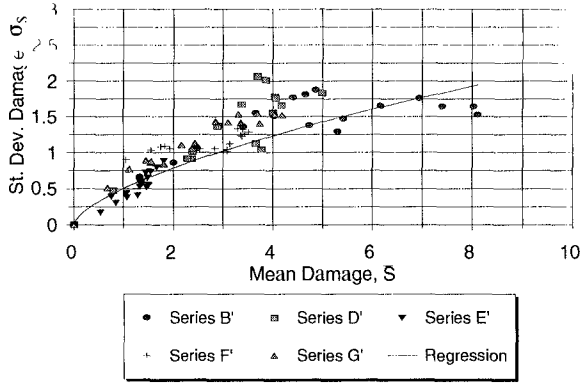

Figure 4. Standard deviation of damage as a function of the mean

M&K also showed that the number of variables could be reduced because the mean and standard deviation of the profile parameters were a function of the mean damage. The relation for the eroded depth was $\bar{E} = 0.44\bar{S}^{0.52}$ indicating that the shape of the eroded area remained geometrically similar during damage progression. Figure 5 shows $\bar{E}$ for the four new series as a function of $\bar{S}$. It is clear that the relation for $\bar{E}$ based on Series A′, B′, and C′ describes the new data well. Similarly M&K showed that the normalized eroded length followed $\bar{L} = 4.6\bar{S}^{0.48}$. This relation along with data from the four new series are shown in Figure 6. Again, the previously derived relation provides an excellent fit to the new data. Finally, the mean cover depth was shown to be described by the relation $(\bar{C}_0 - \bar{C}) = 0.1\bar{S}$, where the subscript 0 indicates the initial value at $\bar{S} = 0$. This relation also provides a good fit to the new data, as shown in Figure 7. In addition, the standard deviations for maximum eroded depth and remaining minimum cover depth were shown to be described by the relations $\sigma_E = [0.26 - 0.00007\,(\bar{S} - 7.8)^4]$ and $\sigma_C = [\sigma_{C_0} + 0.098 - 0.002\,(\bar{S} - 7)^2]$, respectively.

The agreement of these relationships for the four new series is similar to that shown in Figure 4. The above relations in this paragraph were developed using only profile data without regard to incident wave conditions or water levels.

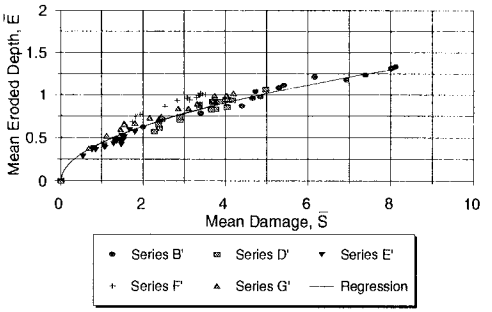

Figure 5. Mean normalized eroded depth as a function of mean damage

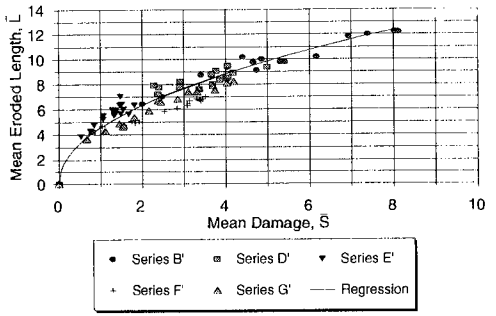

Figure 6. Mean normalized eroded length as a function of mean damage

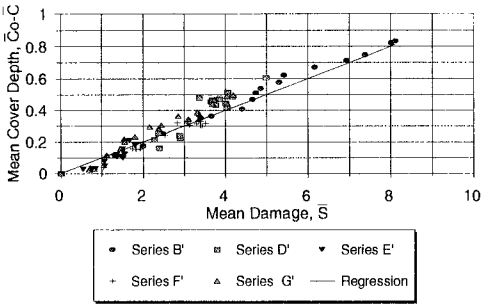

Figure 7. Mean normalized cover depth as a function of mean damage

The relations for the damage variables as a function of mean damage allow prediction of profile shape and alongshore variability of damage. A preliminary empirical equation was

also proposed by M&K for predicting the temporal progression of mean eroded area as a function of time domain wave statistics as

$$\bar{S}(t) = \bar{S}(t_n) + a_s \frac{(N_s)_n^5}{(T_m)_n^b}(t^b - t_n^b) \quad for \quad t_n \le t \le t_{n+1} \tag{2}$$

where $\bar{S}(t)$ and $\bar{S}(t_n)$ are predicted and known mean damages at times t and t_n, respectively, with $t > t_n$. $N_s = H_s / (\Delta D_{n50})$ is the stability number based on the average of the highest one-third wave heights from a zero-upcrossing analysis, $\Delta = S_r - 1$ where S_r is the specific gravity, T_m is the mean period, and a_s, and b are empirical constants. A similar equation relating mean damage to spectral wave characteristics was given as

$$\bar{S}(t) = \bar{S}(t_n) + a_p \frac{(N_{mo})_n^5}{(T_p)_n^b}(t^b - t_n^b) \quad for \quad t_n \le t \le t_{n+1} \tag{3}$$

where a_p and b are again empirical coefficients and $N_{mo} = H_{mo} / (\Delta D_{n50})$. The empirical coefficients in (2) and (3) will be a function of structure slope, wave period, beach slope, structure permeability, and armor gradation. Figures 8 and 9 show (2) and (3) fitted to the profile data of Series A′, which is characterized as the mean damage from 16 profiles. M&K showed that the generalized formulas (2) and (3) with $a_s = 0.025$, $a_p = 0.022$ and $b = 0.25$, for wave conditions during multiple storm events, predicted the progression of damage quite well for the first three series in Tables 1 and 2. Figures 10 and 11 show (2) plotted along with data from Series B′ and C′. The fit of (3) for Series B′ and C′ with coefficients given above is similar to that shown in Figure 9 for Series A′. It is noted that the final damage was similar for both series consisting of different sequences of storms of similar cumulative wave action.

Figures 12 through 15 show (2) plotted against data from Series D′, E′, F′, and G′. Although (3) is not shown, the fits look very similar to those shown for (2). Series D′ and E′ were similar to Series B′ except that the peak wave period was changed for the three series. Series F′ and G′ were again similar except that the uniform armor was replaced with riprap. Two different peak wave periods were tested in Series F′ and G′. It can be seen that the damage progression equations predict overall damage reasonably well for Series D′ through G′ using $a_s = 0.025$, $a_p = 0.022$, and $b = 0.25$, although there are noted discrepancies. For example, it can be seen that damage initiation is underpredicted in all series. Equations (2) and (3) significantly underpredict damage initiation, if only 1 or 2 stones are displaced at the beginning of each test series. This underprediction appears to be produced by the variability in damage initiation. Thus, a second prediction curve has been added to Figures 12 through 15 which starts at the first measured damage point. As can be seen, the prediction is much better for this advanced damage. Figures 12 through 15 indicate that the empirical coefficients in (2) and (3) may vary somewhat with wave period and stone gradation for the

range of experimental conditions described herein.

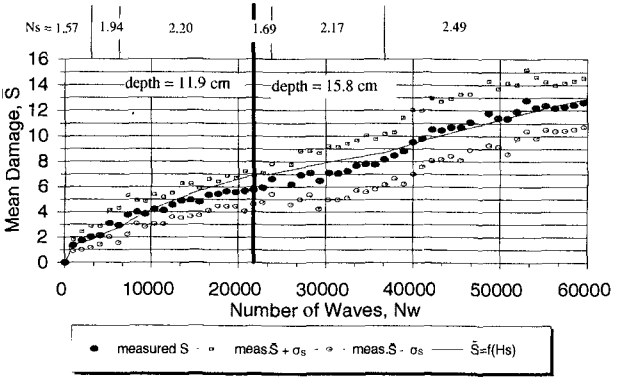

Figure 8. Measured damage and (2) as a function of number of waves for Series A'

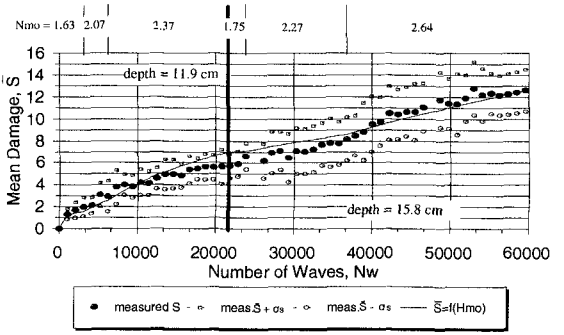

Figure 9. Measured damage and (3) as a function of number of waves for Series A'

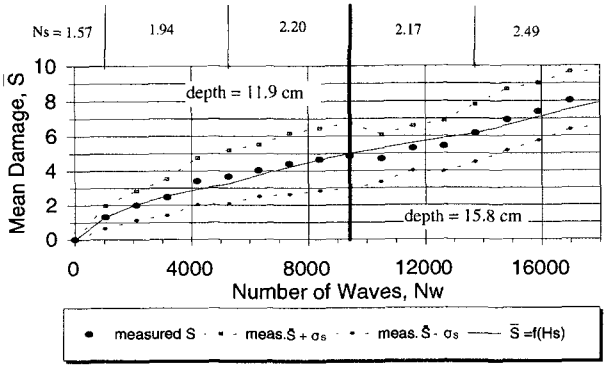

Figure 10. Measured damage and (2) as a function of number of waves for Series B'

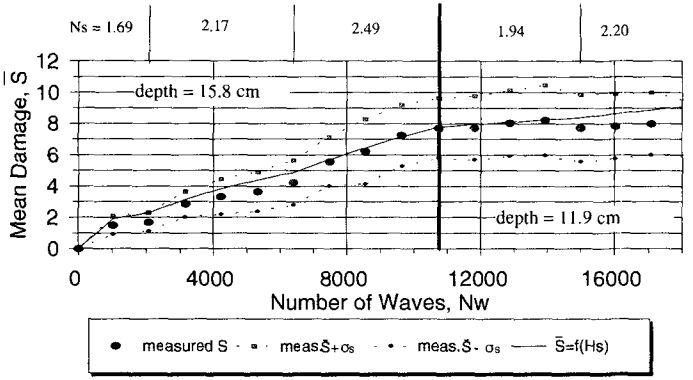

Figure 11. Measured damage and (2) as a function of number of waves for Series C′

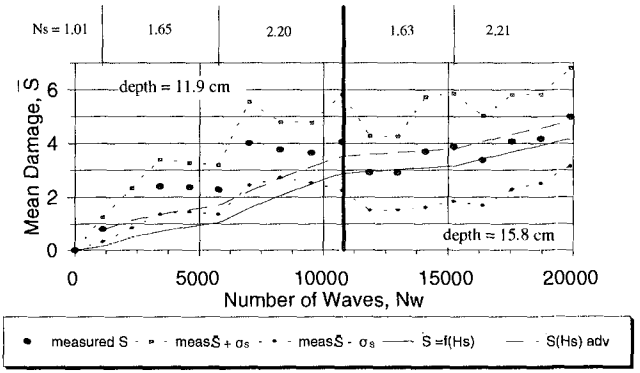

Figure 12. Measured damage and (2) as a function of number of waves for Series D′

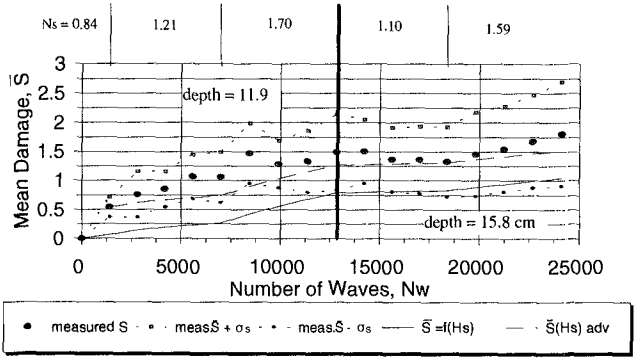

Figure 13. Measured damage and (2) as a function of number of waves for Series E′

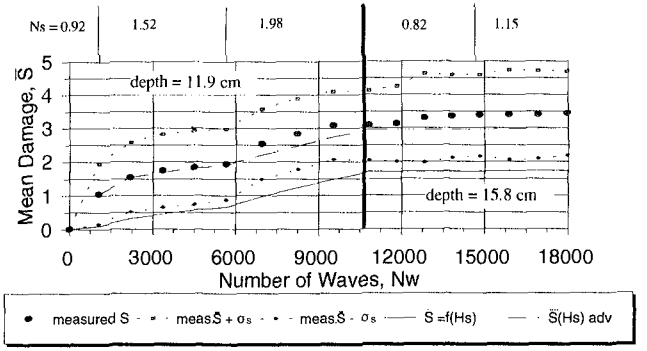

Figure 14. Measured damage and (2) as a function of number of waves for Series F′

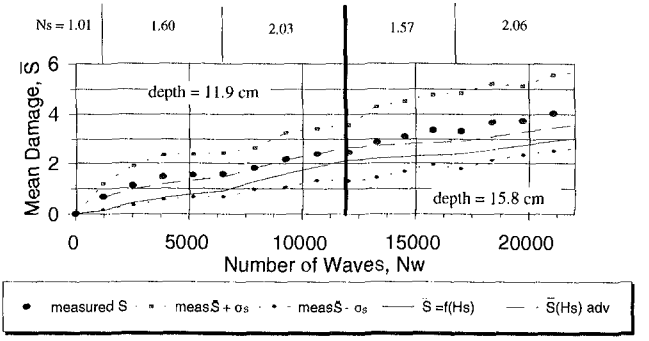

Figure 15. Measured damage and (2) as a function of number of waves for Series G′

4 CONCLUSIONS

An experiment is described consisting of seven relatively long-duration breakwater damage test series. The test series were conducted in a flume using irregular waves. New damage measurement techniques were developed and damage development data were acquired for breaking wave conditions. Wave height, wave period, water depth, storm duration, storm sequencing, and stone gradation were all varied systematically. The experiment yielded relationships for both temporal and spatial damage development.

It is shown that the damaged profile can be described by the eroded area A_e, maximum eroded depth d_e, minimum cover depth d_c, and maximum eroded length l_e. These parameters

are normalized as $S = A_e/D^2_{n50}$, $E = d_e/D_{n50}$, $C = d_c/D_{n50}$, and $L = l_e/D_{n50}$ and the mean and standard deviation of each are shown to be a function of the mean damage $\bar{S}$. Relations are given for the standard deviation of S as a function of the mean as well as the mean and standard deviation of E, C, and L. Using these relations, the statistical variability of the profile and S can be quantified, which is a necessary step in a modern minimum cost analysis.

The relations by Melby and Kobayashi (1998a,b) for predicting temporal variations of mean damage with wave height and period varying with time in steps are shown to describe damage reasonably well (within one standard deviation) for four new test series, although damage initiation, where only 1 or 2 stones have moved, is consistently underpredicted by more than a standard deviation. This appears to be due to the variability in damage initiation. It is shown that the prediction is significantly improved if the damage progression is predicted immediately after the initial profile adjustment lasting 30 min. The initial profile adjustment may need to be accounted for in test series with relatively small cumulative damage. These relations are a reasonable first step in developing a damage prediction technique for predicting life-cycle costs and assessing maintenance needs. The empirical parameters in these equations may need to be varied somewhat with wave period and armor gradation. Employment of a critical stability number for measurable damage may be necessary to reduce the number of storms required in a life-cycle analysis.

ACKNOWLEDGEMENTS

This work was funded by the Coastal Structures Evaluation and Design Civil Works Research Program, Headquarters, U.S. Army Corps of Engineers. Permission was granted by the Office, Chief of Engineers, to publish this information. The first author gratefully acknowledges Mr. John Winkelman of the San Francisco, CA Corps District for developing the automated breakwater profiler and assisting with the initial stages of the experiment.

REFERENCES

Broderick, L., and Ahrens, J.P. (1982). "Rip-rap stability scale effects," Tech. Paper 82-3, U.S. Army Engineer Waterways Experiment Station, Coastal Engineering Research Center, Vicksburg, MS.

Davies, M.H., Mansard, E.P.D., and Cornett,A.M., (1994). "Damage analysis for rubble mound breakwaters" *Proc. of the 24th Intl. Conf. On Coastal Engineering*, V. 1, pp 1001-1015.

Hudson, R.Y. (1959). "Laboratory investigation of rubble-mound breakwaters," *Jour. of Waterways and Harbors Div.*, American Society of Civil Engineers, V. 85, N. WW3, pp 93-121.

Mansard, E. P. D., Davies, M. H., and Caron, O. (1996) "Model Study of reservoir riprap stability." *Proc. 25th Coast. Enrgr. Conf.*, ASCE, New York, NY, 2, 1748-1761.

Melby, J. A., and Kobayashi, N. (1998a). "Damage progression on rubble mound breakwaters," Technical Report in press. Coastal and Hydraulics Laboratory, USAE Waterways Experiment Station, Vicksburg, MS.

Melby, J. A., and Kobayashi, N. (1998b). "Progression and variability of damage on rubble mound breakwaters," *Jour. Of Waterway, Port, Coastal, and Ocean Engineering,* Vol 124, No. 6.

SPM (1984). Shore Protection Manual, U.S. Army Engineer Waterways Experiment Station, Coastal and Hydraulics Laboratory, USAE Waterways Experiment Station, Vicksburg, MS.

Van der Meer, J. (1988). *Rock slopes and gravel beaches under wave attack,* Delft Hydraulics Communication No. 396, Delft Hydrulics Laboratory, Emmeloord, The Netherlands.

Winkleman, J. (1997). *Rubble mound damage measurement,* Master's thesis, Univ of Rhode Island, Kingston, R.I.

The Influence of Pressure Fluctuations on the Flow Between Armour Elements

Robert Booij [1], Wim S.J. Uijttewaal [1], Patrick van Os [1],
Harry L. Fontijn [1], Jurjen A. Battjes [1]

Abstract

To reduce the high expenses of armour layers for the protection of sandy beds in rivers and coastal areas around structures a so called geometrically open armouring, consisting of a single layer of large rocks, is often tried nowadays. In most models it is assumed that the mean flow (and shear stress) above the armour layer penetrates in the pores between the armour elements and that this penetrated flow is responsible for the erosion of the sand bed below the armour layer. However, the relatively thin armour layer these models predict does not always suffice for a safe armouring of the sand bed in practice. Measurements of the flow velocities in the pores between armour elements in a flume using the laser-Doppler technique suggest a completely different erosion mechanism. Erosion appears not to be caused by the mean pore flow. Instead small-scale locally generated velocity fluctuations in the pores lift the sand particles from the bed; large-scale fluctuations, due to large-scale turbulence in the main flow, transport the sand particles through the armour layer into the flow above.

Introduction

In coastal areas and rivers, cover layers consisting of rocks or other armour elements are applied locally to protect the underlying sandy bed from erosion. Armour layers are used:

- as bed defense in rivers
- around piers and other structures
- around breakwaters and groynes
- downstream of sluices

[1] Fluid Mechanics Section, Faculty of Civil Engineering, Delft University of Technology, P.O. Box 5048, 2600 GA Delft, The Netherlands.

- at the toe of dikes and banks
- as "falling aprons"

The dimensions of the rocks used and the thickness of the cover layer are chosen such that the underlying sand bed is shielded from the eroding currents and waves. A relatively safe armouring, so-called geometrically closed armouring, consists of several layers of rocks of different dimensions, such that the rocks in a layer cannot escape through the holes between the rocks in the next higher layer, see figure 1. To reduce the very high expenses of this way of armouring a single layer of large rocks, so-called geometrically open armouring, is often tried nowadays, however with at best varying success.

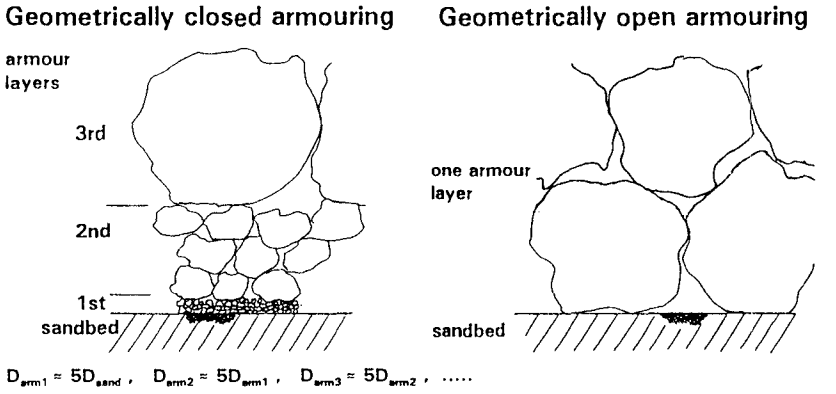

Figure 1. Geometrically closed and open armouring.

In most models that are used for the design of rock beds it is assumed that a direct coupling exists between the mean flow above the bed and the flow through the porous bed. The mean velocity profile is supposed to penetrate a certain distance into the bed and the turbulent fluctuations in the bed to be generated locally by the flow between the rocks. Beyond this distance only a small depth-independent pore velocity, v_p, remains, driven by the same pressure gradient (or slope) as drives the main flow above the armour layer, see figure 2. This pore velocity leads to a very small shear stress at the sand bed below the rocks and a supposedly small erosion. This suggests that in general a relatively thin single rock layer would suffice for a safe armouring.

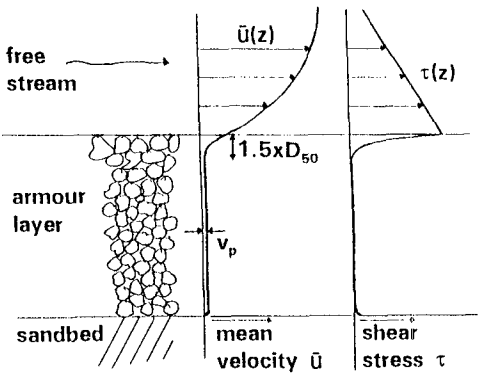

Figure 2. Penetration of main flow.

From a fluid mechanical point of view, however, one can expect that the turbulence present in the main flow above the armour layer generates pressure fluctuations that in their turn lead to a fluctuating flow through the pores of the armour layer. These flow fluctuations may have an important influence on the erosion of the sand bed. Introductory measurements of the fluid velocity and its fluctuations inside the armour layer were executed in order to find out which erosion mechanism is predominant.

Experimental setup

The fluid velocity and its fluctuations inside the armour layer were measured in a flume of the Laboratory of Fluid Mechanics of the Delft University of Technology, using the well-established laser-Doppler (LDA) technique. The typical diameter of the rocks used for the armour layer in the experiments was $D_{r50} = 21$ mm, and of the sand below this rock bed $D_{b50} = 0.10$ mm. The ratio of over 200 between the two diameters makes this a case of geometrically open armouring. Optical access to a cavity in the rock bed was established by guiding the laser beams through the bed using small tubes that have negligible effect on the flow (see figure 3). Special care was taken to avoid distortion of the natural rock configuration around the location of measurement. Doing so it was possible to measure the horizontal velocity component between the rocks of the armour layer. The measurements reveal the mechanism of flow generation in the porous bed.

Figure 4 shows an example of a histogram of instantaneous velocities from a time series of 200 seconds, measured 5 cm beneath the bed-stream interface for a 30 cm deep free surface flow. It shows that the mean velocity is small (in this example ≈ 0.6 cm/s), whereas the standard deviation of the velocity fluctuations is rather large (≈ 0.9 cm/s). This velocity distribution suggests that the fluctuating velocities do not stem from the mean flow through the bed. Instead they might be related more directly to the turbulence of the flow over the bed in the following way: The large turbulence scales in the main flow lead to pressure fluctuations at the bed-stream interface. The fluctuating pressure gradients, which can be much larger than the pressure gradient associated with the mean flow, induce a fluctuating flow through the rock bed.

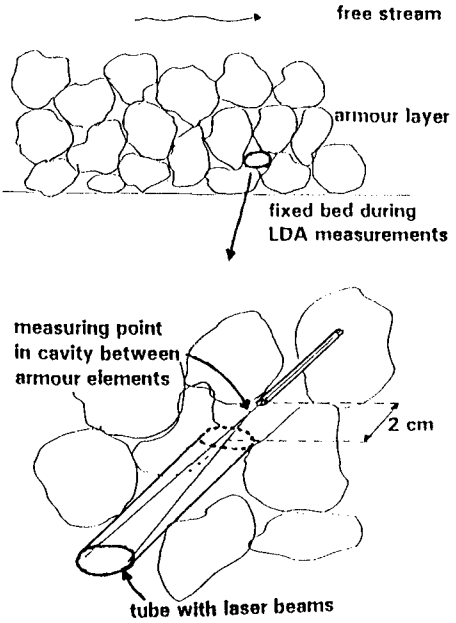

Figure 3. Schematic side view of the laser-Doppler velocimeter set-up.

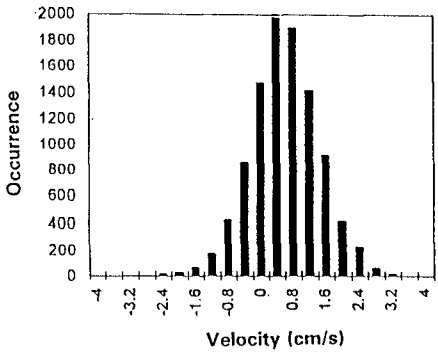

Figure 4. Histogram of pore velocity.

To investigate the consequences for the erosion of the sand bed, part of the flume was covered by a caisson acting as a lid over the water flow, see figure 5. In the resulting slit both the large turbulence scales and the flow velocity could be varied by adjusting the height of the slit S and the water level difference upstream and downstream from the caisson (or the hydraulic gradient in the slit).

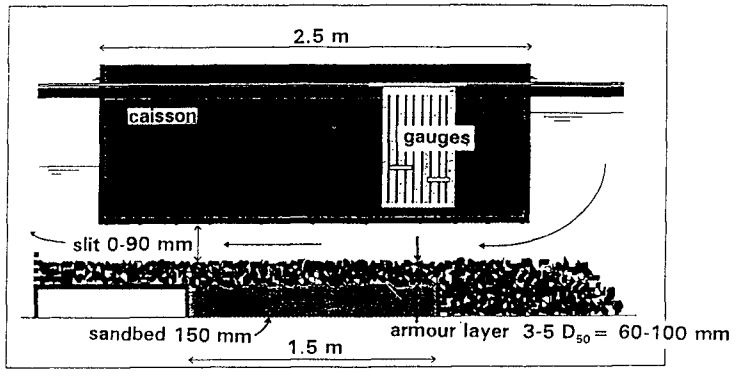

Figure 5. Experimental setup.

The measurements were all executed at a value of the hydraulic gradient just below the critical valuc at which the sand bed starts to erode. This critical value was well-defined as the rate of erosion started abruptly to grow with increasing hydraulic gradient, see figure 6. As LDA measurements require transparent water the sand bed was replaced by a fixed bed during those measurements. The LDA measurements were executed directly above the fixed bottom beneath a 10.5 cm thick armour layer and at the critical hydraulic gradient, i_{cr}, determined in advance in experiments with a sand bed.

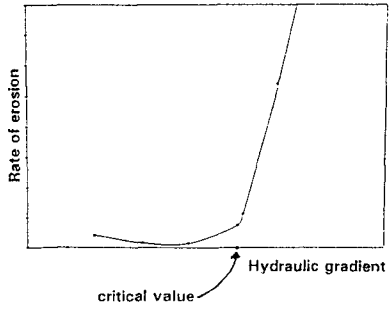

Figure 6. Determination of the critical hydraulic gradient.

Results of the measurements in the armour layer

The LDA measurements yielded mean values and fluctuations of the longitudinal velocity component of the pore flow at the measuring volume in the cavity. Table 1 gives the dependence of the mean pore velocity v_p on the height of the slit. Considering that all measurements were at the critical hydraulic gradient, the results in table 1 show that the mean pore flow is not the cause of the erosion of the sand bed below an armour layer. If that was the case an equal mean pore velocity was to be expected as only the flow condition changes, whereas all other conditions of cavity and bed remain unchanged. Moreover the magnitude of the mean pore flow appears not to be sufficient to lead to erosion. (The critical bed shear velocity of the sand according to the Shields condition is $u_{*cr} \approx 0.6$ cm/s).

S (cm)	i_{cr} (%)	v_p (cm/s)
2.0	4.9	3.91
3.0	4.4	3.61
5.0	3.9	2.50
7.0	3.4	2.15
9.0	3.0	2.28

Table 1. Mean pore velocity.

The cause of the erosion has to be found in flow fluctuations. To investigate this, the autocorrelation functions of the velocity fluctuation were determined. Figure 7 gives an example. Two time-scales are apparent, a large time-scale (of the order of half a second) and a small time-scale of less than 20 ms. (The sample rate used does not allow resolution of the small-scale autocorrelation.) Thus, two kinds of flow fluctuations are present: the small-scale fluctuations, due to locally generated turbulence or small eddies behind flow separations at irregularities in the pore walls, which may be carried away by the mean pore flow, and large-scale fluctuations, caused by the free stream turbulence in the main flow above the armour layer.

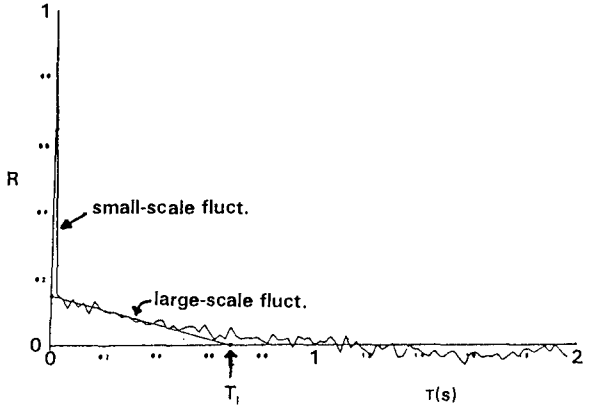

Figure 7. Example of an autocorrelation function, R(τ).

Measured values for both kinds of fluctuations in a series of experiments with different slit heights S are combined in table 2. The columns give respectively S and the measured values for the standard deviation of the small-scale velocity fluctuations σ_h, the standard deviation of the large-scale fluctuations σ_l, the longest time-scale of the fluctuations observable in the correlations T_l and the estimated vertical distance L over which the sand particles move (see below).

S (cm)	σ_h (cm/s)	σ_l (cm/s)	T_l (s)	L (mm)
2.0	1.65	0.65	.18	40
3.0	1.44	0.72	.14	35
5.0	1.30	0.46	.27	39
7.0	1.18	0.40	.26	32
9.0	1.21	0.38	.31	36

Table 2. Measured characteristics of the velocity fluctuations.

From the results in table 2 the following picture of the erosion of the sand bed below a geometrically open armour layer emerges. The very short time scales of the small-scale fluctuations mean that in the flow between the armour elements strong accelerations occur. These accelerations are caused by strong pressure gradients in the flow. The forces on the sand grains by these pressure gradients initiate the lifting of the sand grains from the sand bed. However these pressure gradients last too short to displace the grains through the armour layer. The large-scale fluctuations, which are too slow to generate strong enough pressure gradients to do the initial lifting, move the grains through and out of the armour layer into the free stream.

The estimated distance L over which the sand grains are displaced by the large-scale fluctuations is taken proportional to the standard deviation σ_l and the time-scale measured. For the beginning of erosion the strongest and longest lasting fluctuations are important. Fluctuations of 4 or more times the standard deviation σ_l are present and a few fluctuations lasting about 10 times the time-scale T_l were observed in the executed flow measurements, see figure 8 (which is taken from a different measurement). This is taken into account in the estimated value for L:

$$L = (4 \cdot \sigma_l) \cdot (10 \cdot T_l)$$

Considering the large uncertainty in the measurement of T_l, the valuc for the displacement distance L estimated in this way (see table 2) is a consistent fraction of the total thickness of the armour layer, more or less independent of the slit height. This is what is to be expected as all measurements are executed at the same erosion condition. The time-scale and the standard deviation of the large-scale fluctuations appear to determine thc erosion.

The small-scale fluctuations are generally strong enough to perform the initial lifting.

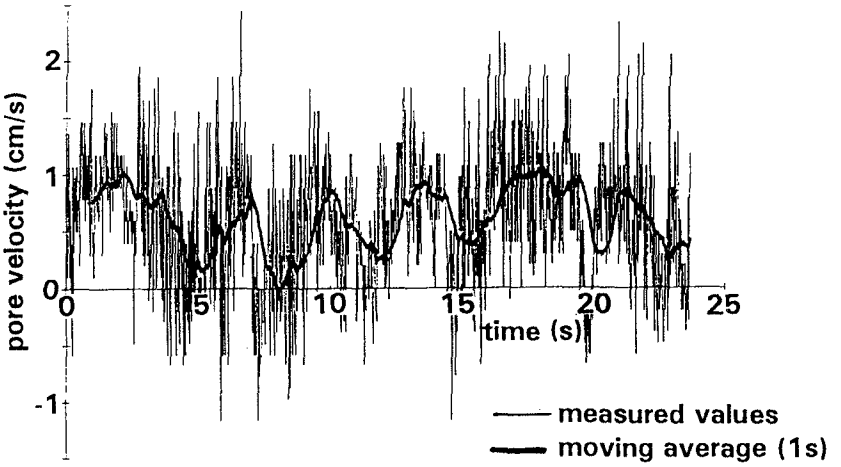

Figure 8. Presence of very large time scales.

Conclusions

In the flow between the armour elements several contributions can be distinguished:

- Mean pore flow. In the upper part of the armour layer it concerns penetrated main flow; deeper in the armour layer the mean pore flow is driven by the hydraulic gradient which also drives the main flow above the armour layer.
- Small-scale fluctuations: locally generated turbulence or small eddies behind flow separations at irregularities in the pore walls, which may be carried away by the mean pore flow.
- Large-scale fluctuations due to turbulence in the main flow.

Based on the magnitudes and characteristics of the different flow contributions between the armour elements the following erosion mechanism is derived:

- Contrary to the assumption used in most models erosion is not caused by the mean pore flow.
- The small-scale fluctuations lift the sand particles from the bed.
- The large-scale fluctuations transport the sand over the armour layer into the flow above.
- The erosion appears to be determined by the time-scale and standard deviation of the large-scale fluctuations. The small-scale fluctuations are generally strong enough to perform the initial lifting.

The conclusions above mean that the design of geometrically open armouring requires knowledge of the large-scale turbulence in the main flow and on the large-scale fluctuations

it brings about in the armour layer.

Analogous processes can be observed with pressure fluctuations under waves due to the wave motion itself or associated with the turbulence under the waves. Knowledge concerning the erosion processes due to the large turbulent fluctuations above the bed as well as the fluctuations under waves are of key importance for the design of the armouring for the protection of erodible beds.

To give the conclusions reached above a firmer base, further research is suggested:
To check the description of the erosion process:
- measurements of correlations of velocities and pressures in and above the armour layer,
- check on the presence of very large-scale turbulence in the main flow above the armour layer,
- high frequency velocity measurements,
- measurements at more places in one cavity,
- measurements with larger slit height (or free flow depth).

To be able to predict the erosion for armouring design:
- measurements with different armour elements (e.g. size, form or stacking),
- measurements in armour layers below a free surface flow,
- measurements under different turbulence conditions (e.g. in wake flow or the flow behind a sill or pier).

Wave Kinematics on Breakwater Heads and Stability of Armour Layers under Multidirectional Waves

Yoshiharu Matsumi [1], Akira Kimura [2] and Kenichi Ohno [3]

Abstract

This study complements the wave kinematical investigation on the performance of rubble mound breakwater under uni and multidirectional waves. The measurements of wave kinematics over the head and trunk sections were undertaken to achieve an improved understanding of the influence of wave directionality on the stability of armour layers. The directionality and magnitude of velocity vectors over the head and trunk sections under 3D waves were assessed by comparing them with the measurements under 2D waves. The sensitive zones of the initial damage in the head and trunk were evaluated by linking the velocity measurements with the stability formulas for armour stone movement.

Introduction

Recently there have been studies published, which have examined breakwater stability under uni and multidirectional waves. Unfortunately those studies still may not have established trends for whether or not the influence of wave directionality in multidirectional seas leads to more loads on the breakwater. The staple reason of limited understanding is that the characteristics of the structure such as the slope, the type of armour layer and the breakwater geometry may contribute to different types of breakwater damage. Therefore, a better approach to achieving a comprehensive understanding of the influence of multidirectional waves on breakwater stability is to make the kinematics of the various multidirectional waves over the breakwater, which are concerned in the damage, clear.

In our previous experimental study (1996), the spatial characteristics in correlation of the magnitude of measured velocity vectors over the head were

1 Associate Professor, D. Eng., Dept. of Social Systems Eng., Tottori University, Tottori 680-8552, Japan.
2 M. ASCE, Professor, D. Eng., Dept. of Social Systems Eng., Tottori University
3 Graduate Student, M. Eng., Dept. of Social Systems Eng., Tottori University

investigated. In the case of multidirectional waves, the correlation in the middle and back head was very poor regardless of the mean direction of waves and peak periods. From those results, possibility of oblique wave attacking directly the heads due to the directional spread in multidirectional seas could be supported. When relating the initial damage in the head and trunk sections to those oblique waves in the multidirectional seas, those direct wave attacks may lead to higher loads on the armour stones at some local position in the head and trunk. Namely, the location of the sensitive zones where the initial damage occurred under multidirectional waves is deemed to be stronger than the case of unidirectional waves.

The main objective of the present study is to compare wave kinematics under the effect of uni and multidirectional waves in terms of measured magnitudes and directions of velocity vectors over the breakwater. Furthermore, the direct unexpected oblique wave attacks, which are associated with the directional spread of multidirectional waves may cause more damage to the armour layers at some local position in the breakwater. Therefore, the difference in the sensitive damage zones under 2D and 3D waves is also evaluated by linking the velocity measurements with the stability formula for armour stone movement on the slope, which was proposed by authors (1996).

Experimental Setup

Layout of breakwater model

Physical model tests were carried out, at the Tottori University, in the multidirectional wave basin that had a length of 14m and a width of 8.4m. Figure 1 shows a plan view of the experimental setup. A fourteen-segment snake generator is located along one of the 8.4m sides of the basin. Expanded polystyrene absorbers with permeability, capable of limiting wave reflections to 20% for most frequencies of interest, are installed along the two sides of the basin. The slope of 1:5 and 1:30 is placed on the side opposite the wave generator, in order to ensure an efficient dissipation of wave energy.

The layout of the breakwater model had to be designed carefully to ensure homogeneous sea states on the breakwater. For this purpose, the numerical model (Isaacson; 1992) which was based on the diffraction theory and used the boundary integral equation was adopted in this study. This model can predict the water surface elevation and kinematics of the sea states prevailing at different locations in the basin. A sample output resulting from this numerical model is shown in Figure 2. It illustrates the spatial distribution of wave heights under a multidirectional sea state (mean angle of incidence (α); $\alpha=0^\circ$) in the basin without the breakwater model in place. The expected wave heights presented in this figure were normalized with respect to the target wave height. The useful test area, over which the sea state is homogeneous, is limited by a triangular boundary. According to this figure, the best location for the model would be close to the paddle. However, since this wave basin was not yet equipped with active absorption, in order to minimize re-reflections from

the paddles, the model was placed with its longitudinal axis rotated 20 ° with respect to the paddles, as shown in Figure 1.

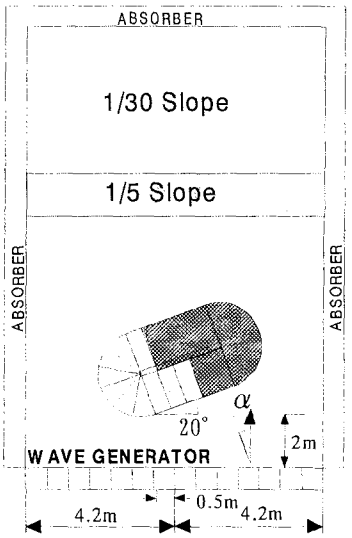

Figure 1 Plan view of the experimental setup.

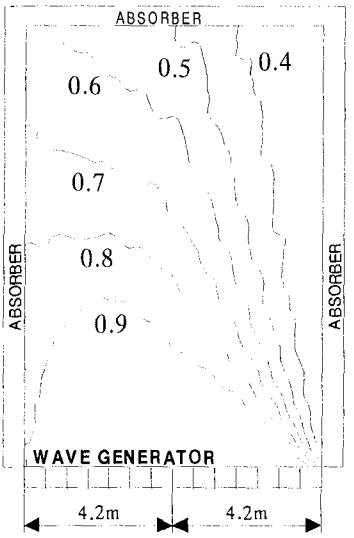

Figure 2 Spatial distribution of wave heights in the basin without the model.

Breakwater model

Figure 3 shows both plan and profile views of the breakwater model adopted in this study. The three dimensional rubble-mound breakwater consisted of two outer layers of armour stones and a relatively porous core, and was built with a slope of 1:2. Its height was 50cm and it performed as a non-overtopping structure in a water depth of 30cm, which was adopted in this experiment. Since the purpose of this study was to investigate the wave velocity field over the head and trunk sections without any damage, the whole surface of the breakwater was covered with a hard nylon mesh in order to restrain the armour stones. The reflection characteristics of the breakwater were estimated under unidirectional waves of normal incidence in the preliminary experiments. The resulting reflection coefficient was about 25%.

The characteristics of the armour and core stones used in this study are presented in Table 1. The weight of armour stones, W_{50}, was 42 gf, this value was 1.5 times the weight estimated by Van der Meer's formula (1987) with damage

parameter S=2 against the targeted significant wave height, H_{m0}=6cm, and peak wave period, Tp=1.4s. The gradations of the armour stones were meticulously checked and the resulting D_{n85}/D_{n15} ratio for the armour was 1.1.

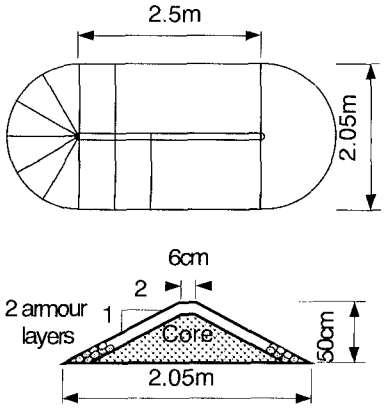

Figure 3 Plan and profile view of the breakwater model.

Table 1 Summary of the breakwater characteristics.

W_{50} weight of armour	42gf
W_{a50} weight of core	3.75gf
D_{n50} nominal diameter of armour	2.51cm
Porosity of armour layers	0.45
D_L Length of head	205cm
T_L Length of trunk	250cm
Crest breadth	6cm
Height of breakwater	50cm

$D_{n50}=(W_{50}/\rho_s)^{1/3}$

ρ_s : unit weight of armour stone

Layout of current meters and wave gauges

The velocity field over the head and trunk sections was measured using 6 bi-axial electromagnetic current meters at 124 different locations indicated by dotes in Figure 4. The measuring points in the head sections were located at 10° intervals from the top of front head in a clockwise direction (θp). In the trunk section, these points are located at 10cm intervals. The water surface elevations of the sea states in the proximity of the model were measured using 8 wave gauges at 8 different locations indicated by circles in Figure 4.

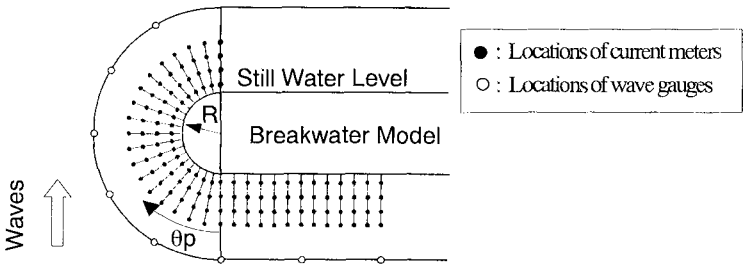

Figure 4 Measuring points of velocity components over the breakwater.

Test series

Table 2 indicates the characteristics of the incident waves adopted in these experiments. The spectra were the JONSWAP type with two different peak periods (Tp=1.0s, 1.4s). The peak enhancement factor (γ) was chosen to be equal to 3.3. The multidirectional waves were simulated by using the well-known Single Summation Method. For the directional spreading function, the Mitsuyasu-type (1975) was chosen, the spreading parameter (s) was given by the following form (Goda 1985):

$$s = \begin{cases} S_{max} \cdot (f/f_p)^5 & : f \le f_p \\ S_{max} \cdot (f/f_p)^{-2.5} & : f \ge f_p \end{cases}$$

Here f_p denotes the frequency at the spectral peak. Values of S_{max}=5 and $S_{max} = \infty$ were applied to simulate multi and unidirectional waves respectively. In order to assess the influence of obliqueness, two different mean angles of incidence α=0° and α=−15° were used, ensuring at the same time homogeneity of the sea state at the head and trunk sections.

In order to minimize statistical variability associated with short wave record lengths, a recycling period (T_R) of 20 minutes in model scale was used in the synthesis. This storm duration corresponded to about 1400 waves when Tp=1.0s and about 1000 for Tp=1.4s. The ratios of diameter of the head (D_L) over wave length and length of trunk (T_L) over wave length are indicated in Table 2. In each test series, the sea states were pre-calibrated in the basin without the structure in position, while keeping all wave gauges in place. The water depth was 30cm uniformity.

Table 2 Characteristics of incident waves in experiments.

Spectrum	Tp (s)	γ	Hm0 (cm)	α (deg.)	Smax	T_R (min.)	N	D_L/L	T_L/L
JONSWAP	1.0	3.3	6, 8.5	0, -15	5,∞	20	1440	1.49	1.82
JONSWAP	1.4	3.3	6, 8.5	0, -15	5,∞	20	1028	0.95	1.16

Directional Distribution of Velocity Vectors over the Head

This study has discussed the velocity vectors, which pass a magnitude above the highest 1/10 of those magnitudes evaluated from time series data of the velocity measurements. Because, the armour stones of breakwater may be strongly prone to move under conditions of faster flow velocities.

Figures 5(a)-(d) show examples of the distribution of the relative

frequencies in directionality of the individual velocity vectors in the time series data of the measurements at four difference positions in the head section for uni ($S_{max}=\infty$) and multidirectional waves ($S_{max}=5$) under normal incidence. Line of 180-0 in every figure is normal to the trunk, bold solid lines (ex. line 60-240 in figure (a)) indicate a line tangent to the horizontal curve of the head at four positions respectively, as shown in figure (e).

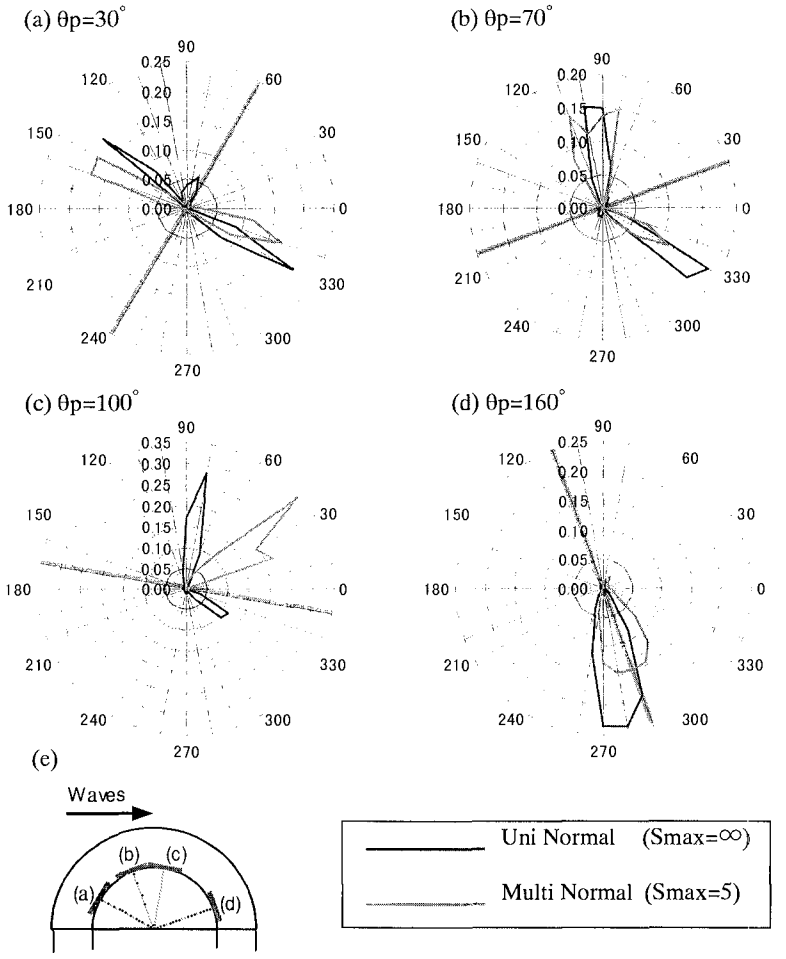

Figure 5 Distribution of directionality of velocity vectors over the head.

From these figures, the directionality of the velocity vectors under 3D waves is wider than that under 2D waves due to the directional spreading of waves. In figures (a) and (b), the characteristics of the velocity field from the front head section to the top of middle head section are mainly dominated by flow of the runup and rundown of waves on the slope. The center of middle section as seen in figure (c), demonstrates the flow towards down-slop of the head. And the prevailing direction of velocity vectors under 3D waves is different from that of 2D waves. This phenomenon may be generated by reflected waves, which are generated by the oblique wave attacks due to directional spread of 3D waves. In the back head section of figure (d), the flow towards the rear surface of breakwater only exists under both 3D and 2D waves. The difference in the direction of velocity vectors over the head section under 2D and 3D waves remarkably occurs in middle head section by the directional spread of 3D waves. Therefore, in the next section, the influence of this difference on the stability of head and trunk is investigated by linking the stability formulas for armour stones with the measurements of velocity over the breakwater.

Stability of Armour Stones in Head and Trunk

In this section, the sensitive zones of the initial damage in the head and trunk sections will be evaluated by linking the velocity measurements with the stability formulas for armour stone movement. These formulas have been derived by taking account of tangential slope of the breakwater with respect to the direction of velocity vectors.

(a) Case of Head (b) Case of Trunk

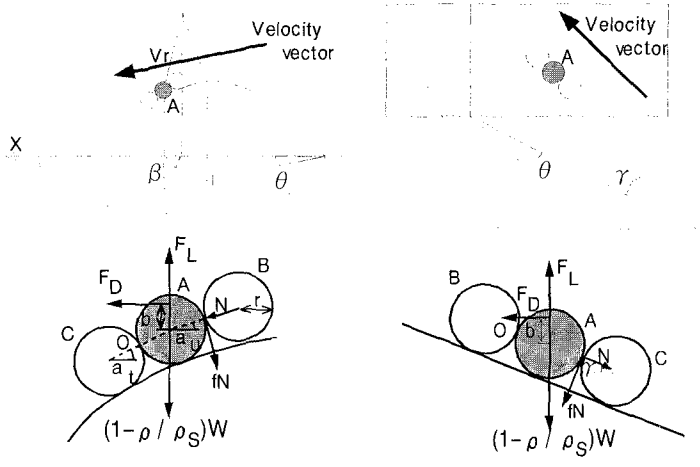

Figure 6 Attacking velocity and hydrodynamics forces on armour stone in head and trunk.

Critical velocity for stability of armour stones in head and trunk

In Figure 6(a), the armour sphere (A) is placed on the head with the horizontal angle (β) for the velocity vector (V_r) with horizontal angle (θ). By assuming the shape of the head is a circular cone, the curve of intersection between the vertical plane and the cone becomes a hyperbola. In this study, the both drag and lift forces were considered as hydrodynamic forces acting on the armour stones. Then, the equilibrium equations between the armour weight and the hydrodynamic forces can be derived by balancing the moment about point O in these figures:

(a) Case of Head

$$\left(1-\frac{\rho}{\rho_S}\right)W[\cos a_t + f\sin a_u\{1+\cos(a_t - a_u)\}] = F_D\left(\sin a_t + \frac{b}{r}\right) + F_L\cos a_t \qquad (1)$$

(b) Case of Trunk

$$\left(1-\frac{\rho}{\rho_S}\right)W[\cos\gamma + 2f\sin\gamma] = F_D\left(-\sin\gamma + \frac{b}{r}\right) + F_L\cos\gamma \qquad (2)$$

where W and r are weight and diameter of armour stone, ρ_s and ρ are unit weight of stone and water, F_D and F_L are drag and lift forces, f is friction coefficient between stones, b is distance between the center of stone and drag force acting point. The parameters a_u and a_t in Eq. (1) are respectively the angle of elevation of armour sphere (A) from (C), and (B) from (A) as shown in Figure 6(a). The parameter γ in Eq. (2) is the angle of slope of the trunk section against the attacking velocity vector as shown in Figure 6(b). In this study, the drag and lift forces are described by the following formulas, respectively:

$$F_D = m'\rho\pi r^2 V_r^2 \qquad (3)$$

$$F_L = \frac{1}{2}\varepsilon C_L\rho\pi r^2 V_r^2 \qquad (4)$$

where m' and C_L are drag and lift coefficients respectively, ε is sheltering coefficient of armour stone against the velocity. In Eqs. (1)-(4), f, m', C_L, ε and b are unknown parameters, a_u, a_t and γ can be derived from tangential slope of the breakwater with respect to the velocity vector. Assuming that a_t is equal to a_u for simplicity in this study, they are given by following equation after the simple mathematical analysis.

$$a_t = a_u = \tan^{-1}\left\{\frac{1}{2}\cos(\beta-\theta)\right\} \qquad (5)$$

$$\gamma = \tan^{-1}\left(\frac{1}{2}\cos\theta\right) \tag{6}$$

Finally, the critical velocities (V_{rcH}, V_{rcT}) for armour stone movement in the head and trunk sections are respectively expressed as:

$$\frac{V_{rcH}^2}{gr} = \frac{\left(1-\frac{\rho}{\rho_S}\right)\{1 \pm f\cos(\beta-\theta)\}}{\frac{3}{4}\frac{\rho}{\rho_S}\left[m'\left\{\frac{\cos(\beta-\theta)}{2}+\frac{b}{r}\sqrt{1+\left\{\frac{\cos(\beta-\theta)}{2}\right\}^2}\right\}+\frac{\varepsilon C_L}{2}\right]} \tag{7}$$

$$\frac{V_{rcT}^2}{gr} = \frac{\left(1-\frac{\rho}{\rho_S}\right)(1 \mp f\cos\theta)}{\frac{3}{4}\frac{\rho}{\rho_S}\left[m'\left\{-\frac{\cos\theta}{2}+\frac{b}{r}\sqrt{1+\left(\frac{\cos\theta}{2}\right)^2}\right\}+\frac{\varepsilon C_L}{2}\right]} \tag{8}$$

When the tangential slope with respect to attacking velocity vector becomes positive, in Eqs. (7) and (8), the plus and minus sign before the friction coefficient are replaced by minus and plus sign, respectively. The unknown parameters m', C_L, b, f and ε in Eqs. (7) and (8) were considered as m'=1, C_L=0.5, b=0.5r, f=0.4 and ε=0.4 for simplicity in this paper.

Influence of wave directionality on sensitive zones for damage

In order to investigate the influence of the aforementioned difference in the directional spread of the velocity vectors under 2D and 3D waves on the stability of breakwater head and trunk, the spatial occurrence frequencies for armour stone movement in the head and trunk sections are estimated by linking Eqs. (7), (8) and the velocity vectors which have been measured at 124 points shown in Figure 4.

Figures 7(a) and (b) show the spatial distribution of the calculated occurrence frequencies for armour stone movement in the head and trunk sections under normal 3D and 2D waves conditions, where Tp=1.4s and H_{m0}=6cm. R is the distance in the radial direction from the center of head as shown in Figure 4. In these figures, the contour lines of relative occurrence frequencies which are normalized with respect to the total number of velocities measured for 20 minutes, are indicated with interval every 0.004.

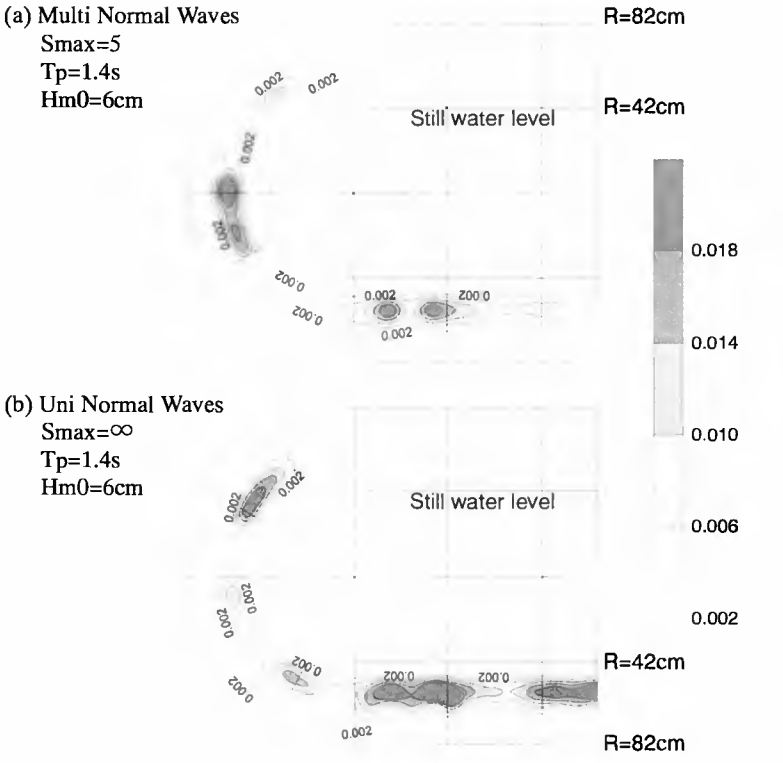

Figure 7 Spatial distributions of occurrence frequencies for armour stone movements.

It can be found that the sensitive zones for armour stone movement in the head section appear typically at three locations; the front, middle and back head sections, respectively. There is obviously a difference between the values of both occurrence frequencies under 3D and 2D waves. Namely, under unidirectional waves (Figure 7(b)), a more sensitive zone for armour stone movement appears in the back head section. Under unidirectional waves attack, it could be observed in the damage tests (Matsumi et al, 1994) that the damage in the back head section was caused to plunge of the strong current with the high velocities generated by the refraction, shoaling and diffraction processes. On the other hand, under multidirectional waves (Figure 7(a)), the middle section is more sensitive parts for the initial damage. The reason for this phenomenon may be the oblique waves directly attacking that section due to the directional spread associated with the multidirectional seas, which have been mentioned in the direction of velocity vectors (Figure 5(c)). For the trunk

section, the sensitive zone for armour stone movements under 2D waves appears at the whole section. In the case of 3D waves, the existence of the oblique waves has resulted in remarkable spot sensitive zone.

Under oblique incidence, the sensitive zones for armour stone movement in the case of 2D waves were shifted to the rear direction of breakwater with near angle of incidence. In the case of 3D waves, there is no difference between the locations of sensitive zones under normal and oblique incidence, as shown in Figure 8. The reasons for it are unclear, but are possibly due to the wide directional spreading value (Smax=5) adopted in this study.

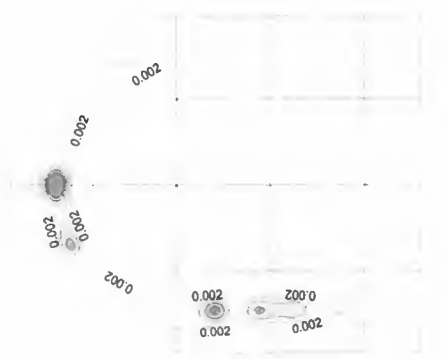

Figure 8 Spatial distributions of occurrence frequencies for armour stone movements under oblique 3D waves (Smax=5, Tp=1.4s, Hm0=6cm, α=-15°).

In order to investigate the reliability of these calculations, initial damage tests of armour stones in the head and trunk sections were carried out under the same incident wave conditions as those in the velocity measuring tests. It can be presumed that the repeatability in the damage tests is not good, because the interlocking force of individual stones placed on the breakwater model may be different in every testing case. Then, in this study, the damage tests under the same wave condition were repeated five times. The resulting initial damage zones where the second armour layer was clearly exposed due to the displacement of the first armour layer under 3D and 2D waves attack are shown in Figures 9(a) and 9(b), respectively. The damage areas shown in these figures indicate parts where the initial damage in the same position on the breakwater occurred more than three times in five tests. By comparing these initial damage patterns with the spatial distributions of occurrence frequencies for armour stone movements shown in Figure 7, it can be seen that the calculated results of the sensitive zones for damage of stones in the head and trunk sections are fairly close to the experimental locations.

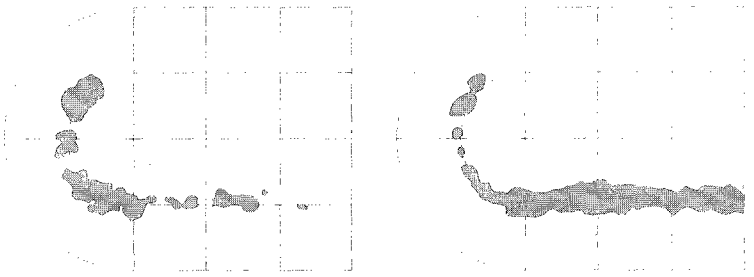

(a) Multi Normal Waves (Smax=5) (b) Uni Normal Waves (Smax=∞)

Figure 9 Initial damage zones in the experiments.

Magnitude of velocities over head

Figures 10(a) and 10(b) show the spatial distribution of occurrence frequencies for velocities (V_r) beyond the critical velocity (V_{rcH}) at the head section. The contour lines of relative occurrence frequencies are normalized with respect to the total number of velocities measured in 20 minutes.

In the case of 3D waves (Figure 10(a)), the maximum magnitude of velocities acting on the middle head section becomes nearly 3.5 times the value of critical velocity. This phenomenon may be pointed out to depend on the direct oblique wave attacks, which are associated with the directional spread of 3D waves. On the other hand, in the case of 2D waves, the high velocities with higher occurrence frequencies than those of 3D waves appear especially in the back head section. It has been observed in the damage tests that the reason for it depends on plunge of the strong current generated by refraction, shoaling and diffraction processes on the front and middle head sections

Conclusion

The prevailing velocity vectors in the middle head section under 3D waves flow towards the down-slop of the head. This occurrence may be generated by the reflected waves which are produced by the oblique waves directly attacking the front head section.

The presented equations of the critical velocity for armour stone movement in the head and trunk sections could satisfactorily explain the initial damage zones in the damage tests. The middle head section under 3D waves is the most sensitive zone for the initial damage. Under 2D waves, a more sensitive zone appears in back head section. For the trunk section, the sensitive zone for the initial damage under 2D

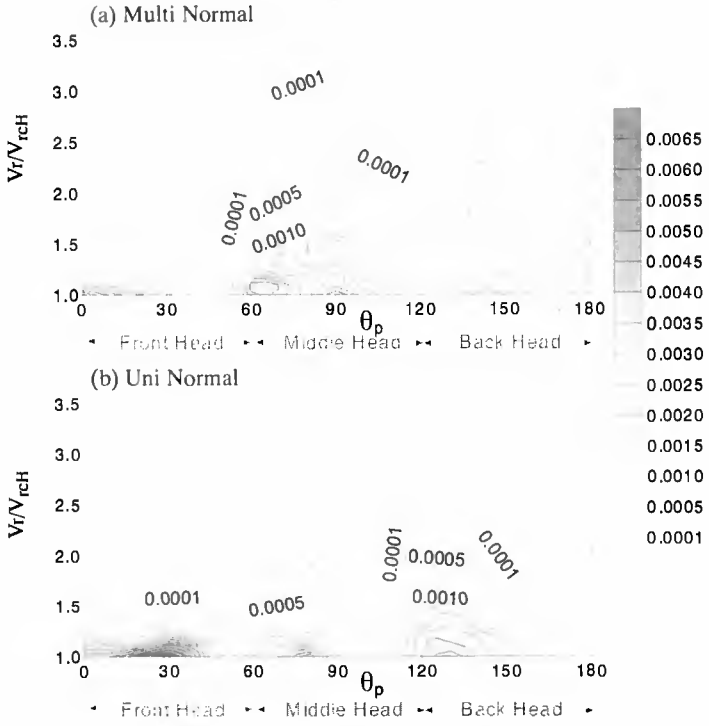

Figure 10 Spatial distribution of occurrence frequencies for velocities beyond critical velocity (V_{rcH}).

waves appears at the whole section. In the case of 3D waves, the sensitive damage zones become spot patterns because of the existence of the oblique waves.

The maximum magnitude of velocities acting on the middle head section under 3D waves becomes nearly 3.5 times the value of critical velocity for armour stone movement. In the case of 2D waves, the high velocities with higher occurrence frequencies than those of 3D waves appear in the back head section due to plunge of the strong current generated on the front and middle head sections.

Further numerical analysis of wave kinematics over the heads and trunks as a continuation of this study is expected to make the weight of stable armour units under 3D waves clear.

References

Isaacson, M. (1992), "Diffraction model of directional wave generation in a basin with partially reflecting boundaries", Report prepared for National Research Council of Canada.

Matsumi, Y., Mansard, E.P.D. and Rutledge, J. (1994), "Influence of wave directionality on stability of breakwater heads", Proc. 24th Int. Conf. on Coastal Engineering, ASCE, 1397-1411.

Matsumi, Y., Kimura, A. and Ohno, K. (1996), "Velocity field measurements over breakwater heads under 3D waves", Proc. 25th Int. Conf. on Coastal Engineering, ASCE, 1776-1788.

Mitsuyasu, H. et al (1975), "Observation of the directional spectrum of ocean waves using a cloverleaf buoy", Jour. Physical Oceanography, Vol.5, 750-760.

Van der Meer, J.W. (1987), "Stability of breakwater armour layers - design formulae", Coastal Engineering, 219-239.

Goda, Y. (1985), Random seas and design of maritime structures, University of Tokyo Press, Japan.

"A STATISTICAL TOOL FOR BREAKWATER DESIGN"

Rodolfo Silva[1], Georges Govaere[2] & Francisco Martin[3]

Abstract

This article presents a methodology for the design of breakwater dikes which includes wave estimation, evaluation of the runup at the dike, calculation of the dynamic and pseudohidrostatic forces operating on the crown wall and finally the estimation of the stability of the armour units in the main layer.

The methodology presented is a development of existing experience in the evaluation of the effects produced by regular or monochromatic waves on structures (stability of pieces, induced forces and flow on the slope). This experience is extended to irregular or spectral waves via statistical distribution of waves, taking account of parameters such as root mean square or significant wave height, mean or peak period and water depth.

The application of the methodology described here has given satisfactory results compared with those of other methodologies and experimental data from various researchers.

INTRODUCTION

The function of a breakwater is to provide a sheltered area, to allow certain port activities on the quay and/or to protect against sediment transport in the coastal area. Breakwaters have an outer layer that has to be stable under the wave action, it is constructed with armour units of either natural or artificial material. A core provides the support for the

[1] Dr., Instituto de Ingeniería, National University of Mexico. Cd. Universitaria. Apdo. Postal 70-472. 04510, México, D.F. Email : rodo@quetzal.iingen.unam.mx. Tel. (5) 6.22.33.26, Fax. (5) 6.16.21.64
[2] PhD. Student, Instituto de Ingeniería, UNAM. Apdo. Postal 70-472. 04510, México, D.F.
[3]Dr., Grupo de Ingeniería Oceanográfica y de Costas. Universidad de Cantabria. Av. de los Castros s/n. 39005 Santander, Spain. Email : martin@puer.unican.es. Tel. (42) 20.18.07, Fax. (42) 20.18.60.

main layer. In between, there are several layers, forming a transition between the core and main layer. It is common practice, for economic or functional reasons, to construct a crown wall that reduces the extension of the main layer, the most expensive part of the dike.

Wave estimation is perhaps the most important calculation in the design of breakwaters. It is very easy to arrive at erroneous conclusions which can result in badly designed structures. The best way to determine the sea state is undoubtedly through measurements made in situ, preferably over a period of years. However this is not always possible due to the high cost of measuring equipment, its maintenance and operation as well as lack of time.

Where this information is unavailable it is possible to estimate parameters such as root mean square or significant height and its associate mean period by different means. Green (1994) compared different theoretical distributions with several of wave series. His conclusion was that Tayfun's statistical distribution for wave heights best describes the different states of the sea.

Figure 1 shows an example of best fit for different distributions of wave heights to waves corresponding to a TMA spectrum in shallow waters. As can be seen, the Tayfun's distribution offers the best fit.

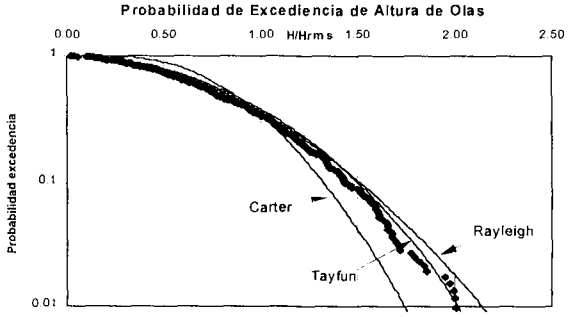

Figure 1. Probability of exceedance of irregular wave against three statistical distributions.

ESTIMATION OF RUNUP

As regards the geometric design of coastal protection structures, such as mound breakwaters, the estimation of runup is particularly important in determining the crest elevation for structures allowing overtopping and those which do not.

Based on experimental results of his own and other researchers, Losada et al (1981) developed a mathematical model to estimate runup. The original method, which only be applied to regular waves, is given by

$$Ru = H\,[Au(1 - e^{-Bu\,Ir})] \tag{1}$$

where Ir is the Iribarren number defined as,

$$Ir = \frac{\tan\alpha}{\sqrt{H / L_o}} \tag{2}$$

H is the wave height
L_0 is the wave length in deep water
α is the slope angle

The coefficients Au and Bu depend on the type of material of which the main layer of the dike is made.

Ahrens (1988) proposes another formula for the estimation of runup

$$\frac{Ru}{H} = \frac{a\ Ir}{1 + b\ Ir} \tag{3}$$

where the coefficients a and b are obtained by a regression analysis.

Through a last square method the values of Au and Bu corresponding to various materials have been found. Table 1 gives the values found for two types of breakwater, firstly homogeneous in which there is no core, and then one with two armour units on its main layer and an impermeable core. Van der Meer (1988) defined a "porosity parameter P", that for the case of a homogeneous rubble mound breakwater corresponds to value of 0.6, and for the case of a rubble mound breakwater with two pieces in its main layer and impermeable core, P = 0.1.

		HOMOGENEOUS			IMPERMEABLE CORE		
Material	Porosity	Au	Bu	Reference	Au	Bu	Reference
Rip-rap	0.31	1.80	0.46	Ahrens, 1975*	2.00	0.32	Ahrens, 1968
Rubble	0.40	1.37	0.60	Gumbak, 1976*	1.89	0.40	Seeling, 1980
Cubes	0.47	1.05	0.72	Jackson, 1968*			
Tetrapods	0.50	0.93	0.75	Jackson, 1968*	1.40	0.45	Dai & Kamel, 1969
Dolosse	0.56	0.70	0.82	Wallingford, 1970*	1.19	0.53	Wallingford, 1970

Table 1 Au and Bu for different homogeneous breakwaters and breakwaters with impermeable core. * Compiled by Losada (1991)

In figures 2 and 3 the linear relation between the Au and Bu parameters versus the porosity of the main layer of the dike can be seen. In order to find the runup produced by a dike the parameters for that type of main layer material are evaluated and Losada's exponential model is applied. If the core of the dike is neither homogeneous nor impermeable the values of Au and Bu can be estimated through an interpolation of the two extreme cases.

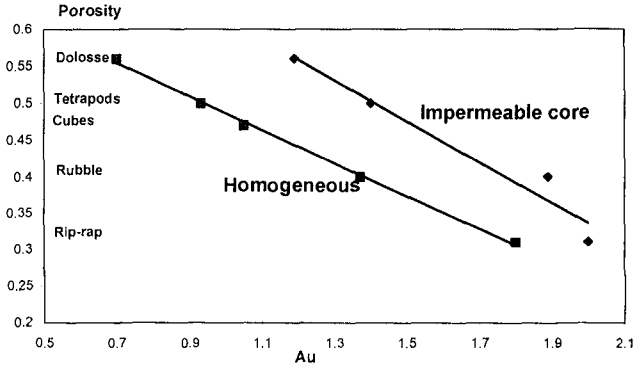

Figure 2. Variation in the parameter Au related to porosity of the main layer

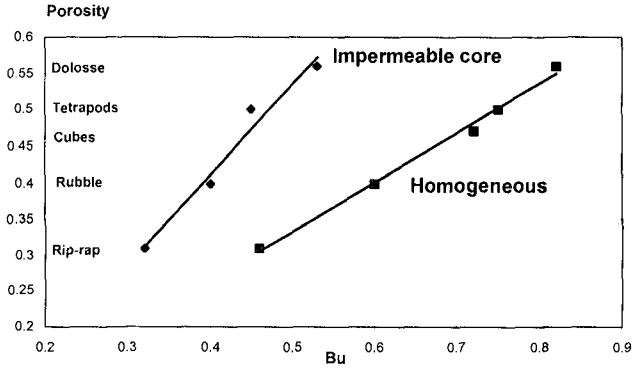

Figure 3. Variation in the parameter Bu related to porosity of the main layer

For homogenous dikes, the Au and Bu coefficients can be found through

$$Au = -4.706 \cdot n + 3.293 \tag{4}$$

$$Bu = -1.569 \cdot n + 0.038 \quad (5)$$

For dikes with impermeable core, the Au and Bu coefficients can be found through

$$Au = -3.825 \cdot n + 3.344 \quad (6)$$
$$Bu = -1.179 \cdot n + 0.081 \quad (7)$$

where n is the porosity.

Applying the formulas of Losada et al. (1981) and Ahrens (1988), the results obtained are practically the same. This can be seen in figure 4, which shows Ru/H against Ir for the case of a homogeneous dike composed of rip rap. Based on these characteristics, the parameters a and b of the Ahrens formula for different main layers was evaluated using the previous values of Au and Bu. These results are shown in figures 5 and 6. The latter gives the relation a/b against the porosity of the main layer. The relation shows a linear tendency between parameters a/b and b versus porosity.

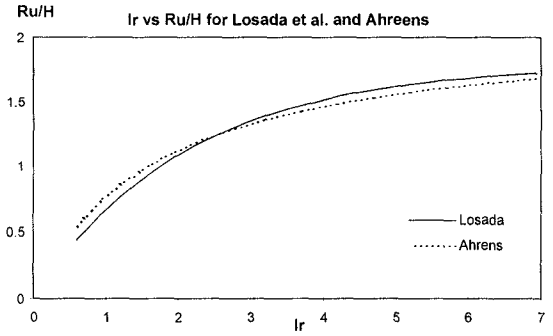

Figure 4. Ru/H versus Ir for the Losada et al. (1981) and Ahrens (1988) formulas Ir for the case of a homogeneous dike composed of rip rap.

In order to obtain the parameters a and b the following equations are used:

For homogeneous dikes

$$a = b\ (-5.5589 \cdot n + 3.7954) \quad (8)$$
$$b = 3.9753 \cdot n - 0.6774 \quad (9)$$

For dikes with impermeable core

$$a = b\ (-3.6922 \cdot n + 3.5785) \quad (10)$$
$$b = 1.3971 \cdot n + 0.0501 \quad (11)$$

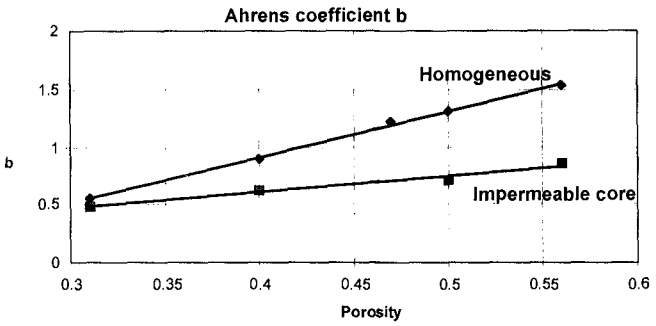

Figure 5. Ahrens coefficient b versus porosity of the main layer.

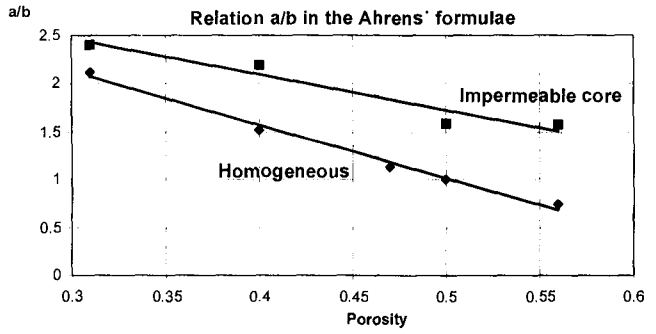

Figure 6. Relation a/b of the Ahrens formula versus main layer porosity.

To extrapolate the results of regular wave criteria to irregular wave criteria Silva et al. (1997b) and Govaere (1997) proposed a method in which the distribution of runup is considered as the same type as that of the wave height. The wave height distribution presented by Tayfun (1981) was used, a probability distribution which takes into account wave period, root mean square wave height and local water depth at the toe of the breakwater among other parameters.

The methodology is as follows:

- Depending on the mechanical characteristics of the breakwater and the formula selected, Losada et al (1981) or Ahrens (1988), Au and Bu (figures 2 and 3) or a and b (figures 5 and 6) are chosen.

- An Ru_{rms}, representative of the mean characteristics of the flow, is evaluated,

  using the formula of Losada et al (1981)

$$Ru_{rms} = H_{rms}[Au(1 - e^{Bu\,Ir_{rms}})] \tag{12}$$

  or using Ahrens (1988) formula

$$Ru = H_{rms}\frac{a\ Ir_{rms}}{1 + b\ Ir_{rms}} \tag{13}$$

  where,

$$Ir_{rms} = \frac{\tan\alpha}{\sqrt{H_{rms} / L_{o_{med}}}} \tag{14}$$

$$Lo_{med} = \frac{g\overline{T}^2}{2\pi} \tag{15}$$

$$H_{rms} = \left[\frac{1}{N}\sum_{i=1}^{N} H_i^2\right]^{1/2} = \sqrt{8\,m_o} \tag{16}$$

  $\overline{T}$ is the mean period

- Tayfun's statistical distribution function (1981), modified to generate a runup distribution, is applied:

$$p(\xi, N) = \xi\int_0^{\infty}\left[u\,J_o^N\left(\frac{u}{N^{1/2}}\right)J_o(\xi\ u)\right]du \qquad 0 \le \xi \le N^{1/2}$$

$$p(\xi, N) = \xi\left[1 - \frac{4}{\pi}\cos^{-1}\left(\frac{N^{1/2}}{\xi}\right)\right]\int_0^{\infty}\left[u\,J_o^N\left(\frac{u}{N^{1/2}}\right)J_o(\xi\ u)\right]du \qquad N^{1/2} \le \xi \le (2N)^{1/2} \tag{17}$$

  where N is the parameter defined by Tayfun as:

$$N = \left(\frac{\pi}{7\sqrt{2}}\frac{\tanh(k_o h)}{k_o\sqrt{2\,m_o}}\right) \tag{18}$$

  and $\xi = Ru\ /\ Ru_{rms}$

Using this methodology it is possible to evaluate the runup for all types of main layers and for different core porosities under irregular wave attack and for whatever probability of exceedance.

Figure 7 shows a comparison of this methodology with that of van der Meer (1988), which was developed for irregular wave criteria and gives very good results but unfortunately can be applied to very few cases. As can be seen, the proposed method gives good results for whatever probability of exceedance.

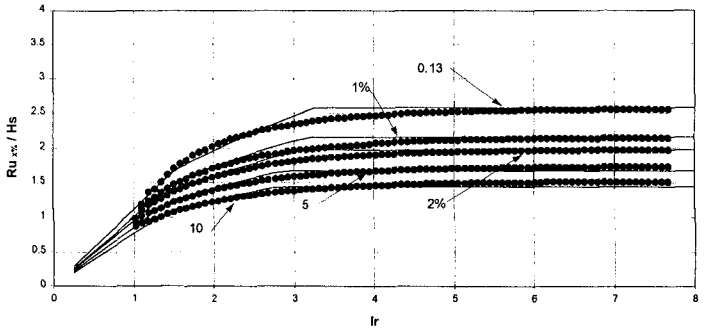

Figure 7 Comparison of Ru/Hs versus Iribarren's parameter with the suggested method (•••) and van der Meer (1988) formula (——) for different probabilities of exceedance.

CROWN WALL DESIGN

A conventional breakwater is generally composed of two structures which are very different in their behaviour and response to wave action, figure 8. First, there is the body of the breakwater composed of a core of loose material protected by a series of layers of larger pieces. The second is a structure embedded into the top of the former, usually a crown wall of concrete, where services are installed. Being made of loose materials the body of the breakwater is more easily deformed and the damage is ductile in nature; generally taking place over a period of time, after storms. On the other hand, the crown wall is a rigid structure; damage here is of a fragile nature; usually the result of the action of just one sufficiently large wave.

There are numerous methods to calculate the forces acting upon a crown wall, all of which are based on laboratory experiments. Martin et al. (1995) proposed a model which separates the pressures of dynamic origin from those of pseudohydrostatic origin, since these pressure are presented at different times. Figure 9 shows the forces affecting a crown wall according to this method.

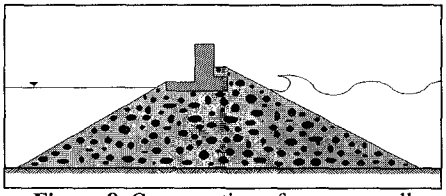

Figure 8. Cross section of a crown wall

Martin's method was originally developed under regular wave criteria. The extension to the case of irregular wave criteria was made by Silva et al. (1997a) and can be summarised as follows:

Dynamic pressure

The law of dynamic pressures, P_d, on the breakwater can be evaluated as:

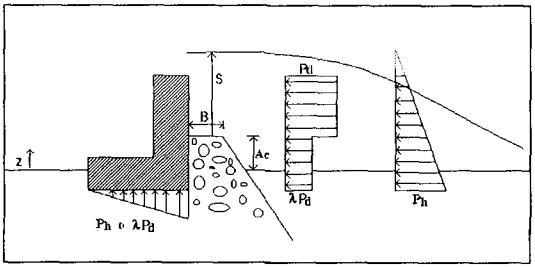

Figure 9. Laws of pressure affecting a crown wall

$$P_d = \beta \rho g S \qquad \text{for } A_c < z < A_c + S \qquad (20)$$

$$P_{d'} = \lambda P_d = \lambda \beta \rho g S \qquad \text{for the crown wall foundation } < z < A_c \qquad (21)$$

With the runup, Ru_x, for the probability of exceedance chosen, equation (12) o (13), the parameters α and λ are calculated from the following expressions:

$$\beta = 2\, Ru_x / H \cos^2 \alpha \cos \theta \qquad (22)$$

where,

$$S = H (1 - A_c / Ru_x) \qquad (23)$$

$$\lambda = 0.8\, e^{(-10.9B/Lmed)} \qquad (24)$$

θ is the angle of incidence

Pseudohydrostatic pressure

Martin et al. (1995) proved that the law of pseudohydrostatic pressure is linear and proportional to $\mu\rho g$, where μ is a factor of 1 or less, shown by them.

$$P_h(z) = \mu\rho g\,(S+A_c) \tag{25}$$

Comparison of the suggested method was made with measurements of Burcharth et al. (1995) and experiments carried out by Pedersen (1996). The proposed method gives very good results and has the advantage that it can be applied to a wide variety of crown walls of different configurations. More details can be seen in Silva et al. (1997a) and Martin et al. (1995).

ARMOUR STABILITY

Nowadays the methodologies most used to evaluate the stability of the main layer of a dike are those of Hudson (Shore Protection Manual, SPM (1984), the formula of Losada et al. (1979) and the van der Meer formulas (1988). The first two were developed under regular wave criteria and numerous investigations have been carried out with the idea of extrapolating these formulas to irregular wave criteria, such as that of van der Meer (1988).

After some experimental work in a laboratory, Jensen et al. (1996), suggested that when using formulas of SPM (1984) the wave height H_{250} be taken(the mean of the 250 highest waves in a sea state) to obtain the same result as with irregular wave. Vidal et al. (1995) suggest using H_{100} (the mean of the 100 highest waves in a sea state) when Losada's formula is used. Using the H_n concept is better than that of a probability of exceedance or of $H_{1/n}$, in that using the mean of a given number of large waves implicitly takes into account the length of the storm.

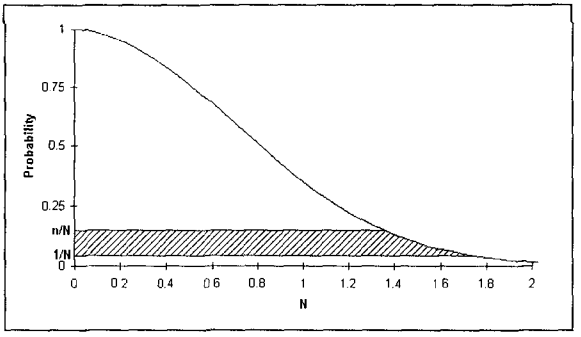

Figure 10. Example of wave height probability of exceedance.

Where the wave height distribution is unknown Tayfun's formula (1981) ean be applied, and results as presented in figure 10 are obtained. The minimum probability of exceedance given for a sea state defined by N waves is 1/N. H_n would be the mean wave height found within the probability of exceedance n/N and N, as follows,

$$H_n = \frac{N}{n-1} \int_{1/N}^{n/N} H \, dp \tag{26}$$

Normally, using Hudson's formula with the K_D parameter presented in the SPM (1984) gives very conservative armour sizes, as if the uses H_{100} and H_{250}. The number of stability, Ns, used in Hudson's formula and the function of stability Ψ used in the Losada's formula are related by the relation $Ns^3 = 1/\Psi$.

Figures 10 and 11 compare the methods of van der Meer (1988), Losada et al. (1979) using H_{100}, as suggested by Vidal el al. (1995), and SPM (1984) using H_{250}, again as suggested by Vidal el al. (1995) versus van der Meer's experimental results (1988). A sea state of 1000 and 3000 individual waves, respectively was considered for levels of damage, S, between 1.5 and 2.5, mass density of the rock ρ_s = 2650 kg/m^3, mass density of the water ρ_w = 1025 kg/m^3. The rest of the parameters are presented in table 2. In the first case, 1000 waves, the root mean square errors are: van der Meer (0.0031), Losada (0.0029) and SPM (0.0039), and for the second case, 3000 waves, the root mean square errors are: Van der Meer (0.0061), Losada (0.0075) SPM (0.0064).

Method	Parameters
Van der Meer (1988)	K_D= 4.0
SPM (1984)	P = 0.4
Losada et al. (1979)	For cot α = 3.0: Ir_0 = 0.88, A_w = 0.04697, B_w = -0.8084
(Values compiled in	For cot α = 2.0: Ir_0 = 1.33, A_w = 0.05698, B_w = -0.6627
Losada , 1991)	For cot α = 1.5: Ir_0 = 1.77, A_w = 0.09035, B_w = -0.5879

Table 2. Parameters used to evaluatc figures 10 and 11, for each method.

The extension of Losada et al (1979) to irregular wave criteria and van der Meer metho take into account the wave period effect, Losada's formula in the calculation of th stability function Ψ and van der Meer's in the calculation of the stability Ns. Bot methods produce results of similar dispersion. The SPM method however does not tak into account the wave period, even so the root mean square error is similar to those c Losada and van der Meer.

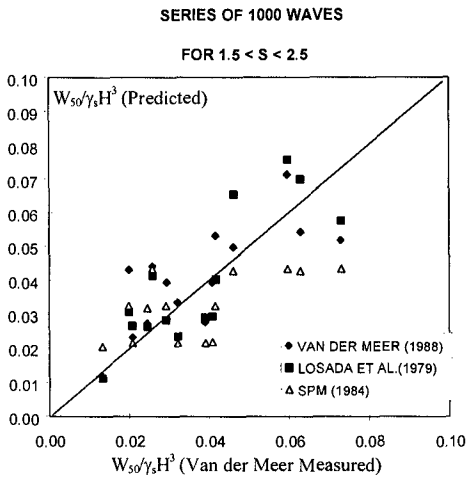

Figure 10. SPM (1984), Losada et al. (1979) and van der Meer (1988) methods versus experimental data of van der Meer (1988) for dimensionless weight of the main layer.

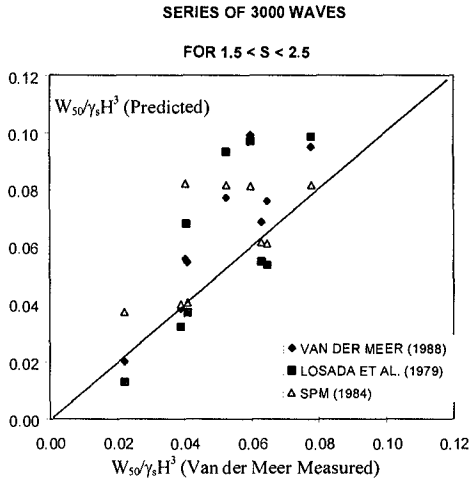

Figure 11. SPM (1984), Losada et al. (1979) and van der Meer (1988) methods versus experimental data of van der Meer (1988) for dimensionless weight of the main layer.

CONCLUSIONS

The statistical distribution for wave height presented by Tayfun (1981) correctly represents different sea states, having the advantage of considering wave breaking in shallow waters.

The method of Losada et al. (1981) and Ahrens (1988) can be used to estimate runup for regular waves for whatever type of armour unit used in the main layer of a dike and for different porosities of the core. The extension to the case of irregular wave criteria via the Tayfun distribution is simple and gives very good results.

Crown wall design using the methodology for irregular wave criteria given by Silva et al. (1997a) gives good results and is easy to apply.

If it is used the wave height of H_{250} is used, as suggested by Jensen et al. (1996), in Hudson's formula, or the wave height of H_{100}, as suggested by Vidal et al. (1995), in Losada's formula for the evaluation of the weight of the pieces in the main layer, almost the same results as for the van der Meer's formula.

For shallow waters, using the Tayfun distribution along with the stability function given by Losada et al. (1979) gives a significant reduction of the weight of pieces in the main layer related to those results given by the van der Meer (1988) formula.

The methodology described in this article has given very good results and presents a tremendous advantage in being applicable to many cases, which is not true of the formulas conceived under the irregular wave criteria.

ACKNOWLEDGEMENTS

This research was funded by the Mexican Consejo de Ciencia y Tecnología, CONACYT, project *Estabilidad de estructuras permeables bajo la acción del oleaje* under contract 25114-A.

REFERENCES

1. Ahrens, J.P. Heimbaugh, M.S. 1988. " Irregular wave run up on revetments". J. of Waterway, Port, Coastal and Ocean Eng., Vol. 114, No. 4, pp 524-530.
2. Ahrens, J.P. and Mc Cartney, B.L., 1975. "Wave period effect on the stability of rip rap". Proc. Civ. Eng. Oceans, III, vol. 2, pp. 1019-1034.
3. Burcharth, H.F., Frigaard, P., et al. 1995. "Design of the Ciervana Breakwater, Bilbao." P.I.A.N.C., London.
4. Dai, Y.B. and Kamel, A.M., 1969. "Scale-effects tests for rubble-mound breakwaters: Hydraulic model investigation". Res. Report H-69-2, U.S. Army Eng. Waterways Exp. Station.

5. Govaere, G. A. 1997. " Acción del oleaje sobre estructuras marítimas no rebasables". Thesis for M.Sc. UNAM, Mexico, pp. 164. (In Spanish).
6. Green M.O. 1994. "Wave height distribution in storm seas: Effect of wave breaking" Journal of Port, Coastal and Ocean Engineering. Vol 120 No 3 pp 283-301.
7. Günbak, A.R. 1976. "The stability of rubble mound breakwaters in relation to wave breaking and runup characteristics and to the ξ number". Div. Port and Ocean Eng., The Norwegian Institute of Technology, Trondheim, Norway. Rep. 1-1976.
8. Jackson, R.A., 1968. "Design of cover layers for rubble-mound breakwater subjected to non-breaking waves". U.S. Army Eng. Waterways Exp. Station, Res. Report 2-11.
9. Jensen, T., Andersen, H., Gronbech, J. Mansard, E.P.D. and Davis, M.H. 1996. "Breakwater stability under regular and irregular wave attack". ICCE, Orlando, Fl. Pp. 1679-1692.
10. Losada, M.A. and Gimenez-Curto, L.A. 1979. "The joint effect of the wave height and period on the stability of rubble-mound breakwaters using Iribarren's number". Coastal Eng. 3:77-96.
11. Losada, M.A. and Gimenez-Curto, L.A. 1976. "Flow characteristics on rough, permeable slopes under wave action". Coastal Eng. 4:187-206.
12. Losada, M.A. 1991. " Recent developments in the design of mound breakwaters". Gulf publishing. Handbook of Ocean Eng., pp.939-1050.
13. Martin, F.L., Vidal. C., Losada, M.A. & Medina, R., 1995. "Un método para el cálculo de las acciones del oleaje sobre los espaldones de los diques rompeolas." Revista de Ingeniería del Agua, Vol. 2, N° 3. Universidad Politécnica de Valencia. Spain. (In Spanish) pp. 37-52.
14. Pedersen, J. 1996. "Wave forces and overtopping on crown walls of rouble mound breakwaters." Dep. of Civil Eng., Alborg University. Series paper No. 12, pp. 140.
15. Seelig, W.N., 1980. "Two-dimensional test of wave transmission and reflection characteristics of laboratory breakwaters". C.E.R.C. Technical report no. 80-1.
16. Shore Protection Manual, 1984, 4thEd., Army Corp. of Engr., Coast. Engrg. Res. Ctr., Washington,D.C.
17. Silva R., Martín F. and Govaere G. 1997a "An approach for the forces on crown walls due to irregular waves" WAVES'97, ASCE, Virginia,USA.
18. Silva R., Govaere G. and Losada M. 1997b "Evaluación del runup en taludes rugosos para cualquier probabilidad de excedencia." IV Jornadas Españolas de Ingeniería de Puertos y Costas, Cádiz, Spain. (In Spanish)
19. Tayfun A.A.,1981 "Breaking-limited wave heights" J. Wat., Port, Coastal and Ocean Eng., Vol 107.
20. van der Meer, J.W. 1988. "Rock slopes and gravel beaches under wave attack. Doctoral Thesis, Delf Technical University.
21. Vidal C. Losada, M.A. and Mansard, E.P.D. 1995 "Suitable wave height parameters for characterising breakwater stability". J. Wat., Port, Coastal and Ocean Eng., Vol.107, No.2.
22. Wallingford, 1970. (Consulted in Günbak, AR 1979. "Rubble mound breakwaters". Div. Port and Ocean Eng., The Norwegian Institute of Technology, Trondheim, Norway. Rep. 1-1979).

COST COMPARISON OF BREAKWATER TYPES

W.H. Tutuarima[1] and K. d'Angremond[1]

Abstract

A cost comparison have been made between various types of breakwaters for a fictitious situation in waterdepths to a local maximum of -15 m and an adopted sea climate. The comparison is based on optimal total project costs, being the sum of costs of construction and capitalized damage during the service period. For these selected conditions the caisson breakwater and the rubble mound type provided with a single concrete armour layer appear most attractive. Composite type of breakwaters seem advantageous for water depths approximately below -20 m.

Introduction

It is remarkable that caisson breakwaters are widely found in coastal areas of Japan and Italy and far less elsewhere. Conventional rubble mound breakwaters, provided occasionally with concrete armour top layers, are far more numerous in western industrial countries. It may be questioned whether the selected type may also result from a rational design approach.

The aim of this paper is to provide a brief review of various types of breakwater which are most fit for a location on the basis of economical considerations with regard to the type of harbour, the site conditions and the service time of the construction.

Approach

For a fixed layout the costs of following breakwaters are compared:

* Conventional rubble mound breakwater
* Bermbreakwater
* Rubble mound b.w. + toplayer of concrete units: Cubes, Tetrapods and Accropods
* Caissons breakwater
* Composite breakwater

[1] Delft University of Technology, Faculty of Civil Engineering and Geosciences, P.O.Box 5048, 2600 GA Delft, The Netherlands

The conventional rubble mound breakwater and the bermbreakwater had previously been compared for a fictitious layout by Hauer (et al,1995). The same conditions have been used for caisson and composite breakwaters (Schols, 1997) and for conventional breakwaters provided with concrete armour units (Schepers, 1998). In all cases similar site conditions are applied. Costs taken into account are construction costs and capitalized maintenance during the lifetime of the construction.

Layout and site conditions

There are two breakwaters in the adopted layout: a northern mole of 1 km and a southern of 3 km length. Both are subdivided in sections with a specific average depth (figure 1). In all solutions the shallow sections in the breaker zone (approx. -6.0 m) are designed as conventional breakwaters. Therefore cost comparisons are due to differences in the deeper sections. The depth at the northern head is at -10 m, at the southern head at -15 m. Depth contours of the sandy seabed, D_{50} = 200 micron, are parallel to the coast, sloping 1:100 down to deep water.

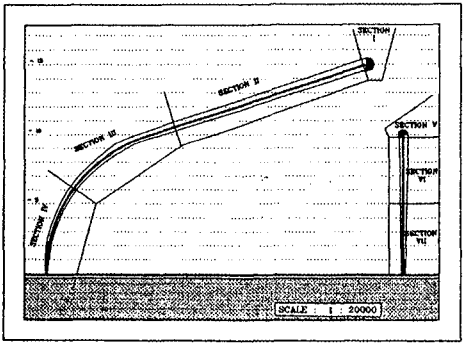

SECTION	length	av. depth
I	-	15.0
II	1500	12.9
III	950	8.95
IV	550	2.95
V	-	10.0
VI	500	8.10
VII	500	2.80

Figure 1 Layout of breakwaters and water depth

Wave climate at deepwater (H_{so}) and setup of waterlevels (h) above MSL are expressed in terms of probability of exceedance of these values (figure 2). The storm duration is set at 6 hours. For the deep water conditions the mean wave period T_z is related to H_{so} according (Allersma and Massie, 1973):

$$T_z = 3.94 * H_{so}^{0.376} \quad (1)$$

The wave direction is pependicular to the coastline. In view of the shallow area near the coastline the maximum significant waveheight H_s is limited by the local waterdepth h according to $H_s/h = 0.55$. The tidal amplitude is 1.0 m.

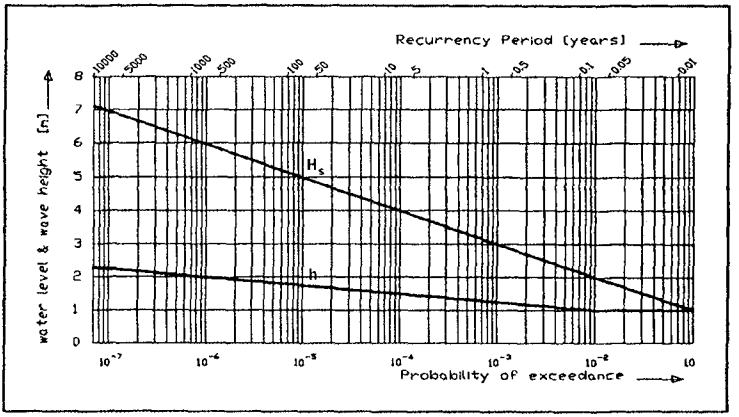

Figure 2 Wave and sea climate

Two yield curves A and B of the quarry are adopted (figure 3), which are similar to ordinary existing curves. The more gentle curve A is applied to the conventional breakwater (without concrete armour units) and to the caisson types, curve B to the breakwater types with concrete armour toplayers.

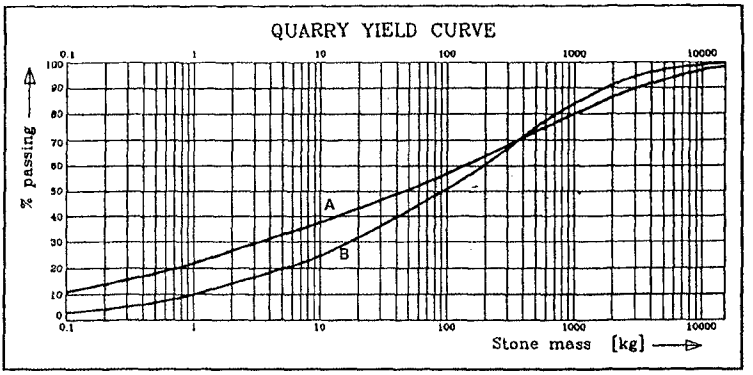

Figure 3 Quarry yield curves

Stability requirements

Design calculations for the rubble mound breakwater, including the stability of the concrete armour units, are based on methods developed by Van der Meer (1993), applied in the program Breakwat. The design of the caisson type of breakwaters are

mainly based on the method of Goda (1985). In all cases crest levels are high enough so as to achieve a transmitted wave height $H_T < 0.5$ m. Cross sections of the various types of breakwaters from the main layout section (II) are given in figure 4 to figure 8.

Rubble mound breakwaters

*** Conventional breakwater**

For each section of the layout the slopes have been varied so as to achieve optimum total costs given the quarry yield curve A as boundary condition. With the resulting slope 1:3.5 costs of repair are rather low but construction costs increased. The cross section is drawn in figure 4. Heaviest armour gradation is 8-15 tons. The efficiency of quarry production was just 24% .

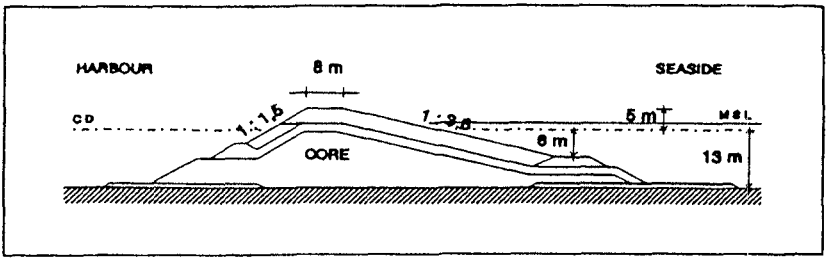

Figure 4 Conventional breakwater, optimal design section II

*** Bermbreakwater**

In order to limit costs of damage the bermbreakwater had been designed rather conservatively using the arbitrary selected return period of 500 years for H_s to size the rocks of the berm. Optimization of the waveheight in view of berm stability and the littoral transport by wave action had not been carried out. The cross section is drawn on figure 5. The quarry efficiency was 78% .

*** Conventional breakwater + armour units: Cubes, Tetrapods or Accropods**

The design method is similar to the conventional type. By replacing the heavy armour rock (8-15 tons, curve B) by concrete armour units (tetrapods, cubes and accropods), the design may be subject to potential cost savings in rock supply. Moreover much effort was given to optimize the quarry efficiency (64%); part of the heavy rocks were crushed for use as armour in the shallow parts of the layout (bedlevels -3 to -6 m). Though the applied steeper slopes (1:1.5 to 1: 4/3) will require higher crest levels to match tranquility in the port basin, rock volumes needed were remarkebly reduced. On figure 6 the cross section of the accropod is drawn.

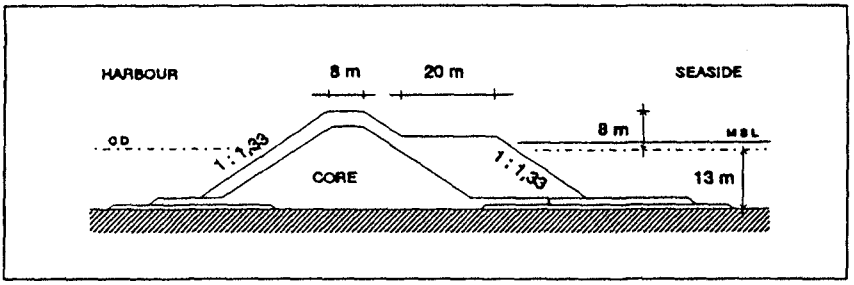

Figure 5 Bermbreakwater, section II

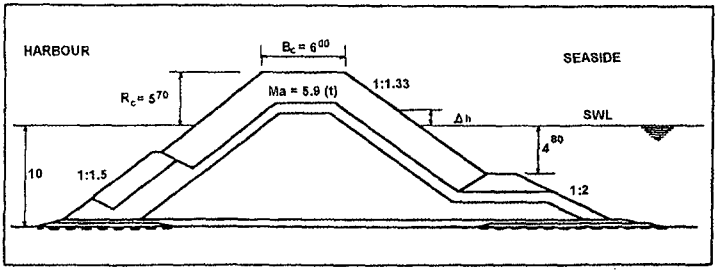

Figure 6 Section II rubble mound + Accropod armour units

Caisson breakwater and composite breakwater

Again the same layout and climate conditions (figure 2) have been used to analyse an optimum design of the two types vertical breakwaters. In both cases the concrete caissons are filled with sand. Minimum freeboard is set by transmission requirements. By variation of the freeboard total costs of material could be reduced. Increasing freeboards may contribute to more structural mass from the caisson above design waterlevel and increase stability to sliding and reduction of the required width of the structure so as to avoid risks of tilting. By limited sailing distances for rock transport (< 150 km) construction costs of the composite breakwater appear lower than of the caisson type. Fragmentation curve A is used for the substructures of rubble mound. Overproduction could be reduced by crushing production of too large rocks down to required grades. Rock production efficiencies are for caisson type 64% and composite type 68% .

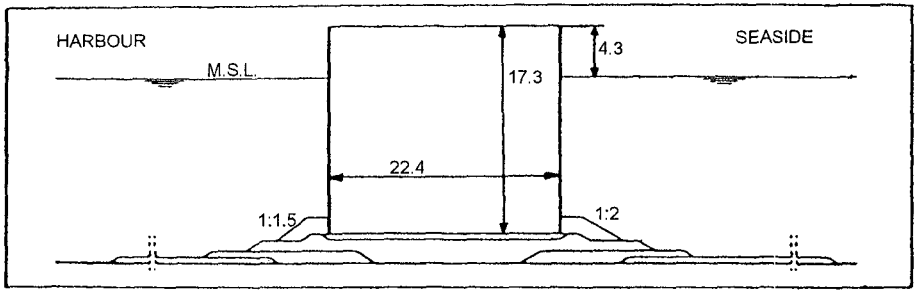

Figure 7 Cross section caisson breakwater

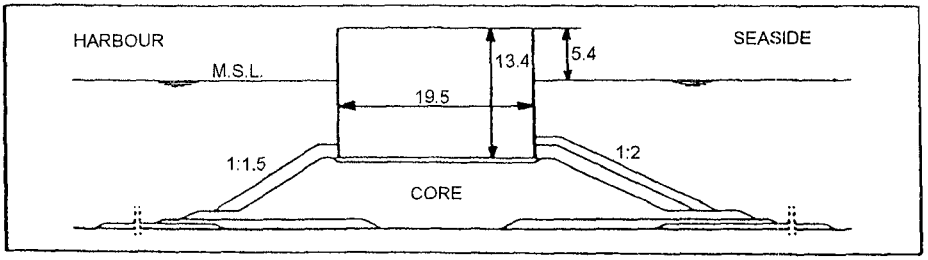

Figure 8 Cross section composite breakwater

Cost calculations

The aim is to base the design on minimum total project costs (TPC), i.e. the lowest sum of costs of construction (CC) and the capitalized costs of damage during the lifetime of the construction. The costs of damage are the sum of direct costs of repair (DC) and indirect costs (IC) due to consequential losses (e.g loss of port operations) multiplied with the present worth factor (pwf). The consequential losses are related to the amount of industrial investments in the port area. The rate of interest used is 4% and the currency is the Dutch guilder (DGL, 1997).

$$TPC = CC + pwf*(DC+IC) \quad (2)$$

Direct costs of repair are related to the yearly risk of damage due to wave action. The method is illustrated for concrete armour units in figure 9 following the damage ranges of N_{od} of Van der Meer (1993).

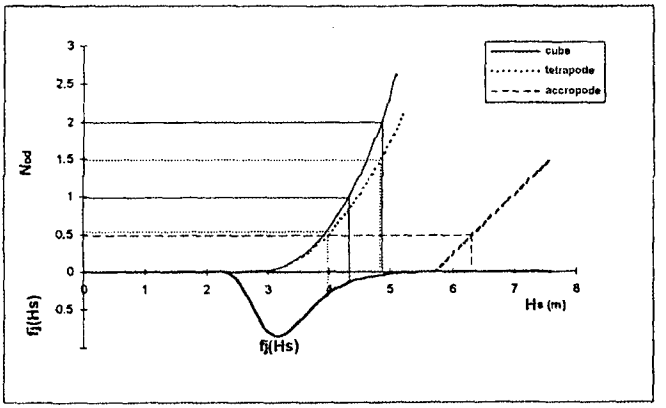

Figure 9 Risk of damage to concrete armour units

Characteristic volumes per m' breakwater

To illustrate characteristics differences in volumes of material applied in the various types, typical volumes for the main layout section II are mentioned in table 1. The remarkable low volume of concrete in the Accropod solution is due to the applied single unit armour layer, as recommended by the supplier. Also clear are the relative high amount of rock of the bermbreakwater and the reduced rock volumes in the types with concrete armour units, when compared with the conventional breakwater, as the result of steeper slopes applied.

TYPE OF BREAKWATER	ROCK (t)	CONCRETE (m^3)	SAND (m^3)	GEOTXT (m^2)
Conventional rubble mound	1700	-	-	35
Bermbreakwater	2200	-	-	-
Rubble mound + cubes	1400	80	-	35
Rubble mound + tetrapods	1400	65	-	35
Rubble mound + accropods	1400	30	-	35
Caisson breakwater	500	90	305	130
Composite breakwater	700	70	245	120

Table 1 Typical volumes/m' section II layout

Conditions for comparison

The applied optimum conditions as bases for the cost comparison between the various types of breakwater are summarized below:

* Varying frequency of hydraulic loads
  (25 to > 100 years return period)
* Transmitted wave height inside port basin: $H_T > 0.5$ m
  less than 10 times per year
* Distance of quarry 75 km

* Basic costs according Table 2
* Repair costs acceptable damage = 1.5 * basic costs
* Repair costs of failure = 2 * basic costs

Basic costs of production, transport and construction

Activities	Unit costs
Quarry production (all gradings)	DGL 15.00 / ton
Transport of rocks (over land)	
< 300 kg	DGL 0.25 / tonkm
> 300 kg	DGL 0.40 / tonkm
Construction costs	
Bedprotection	DGL 15.00 / ton
Core	DGL 10.00 / ton
Rock armour and filter layers	DGL 15.00 / ton
Concrete armour units (all in)	
- cubes	DGL 300.00 / m^3
- tetrapods	DGL 325.00 / m^3
- accropods	DGL 400.00 / m^3
Concrete caissons (all in)	DGL 500.00 / m^3
Mobilization & demobilization	DGL 2.0 million

Table 2 List of basic costs

Results

Total project costs have been calculated with increasing return periods of design wave heights (25, 50, etc. years). Clearly these costs decrease with increasing level of design wave heights, due to the rapidly decreasing sum of capitalized direct and indirect damage costs and the relatively small increase of construction costs. Table 3 illustrates the results for the concrete cubes solution. In this case the optimum is reached at a design $H_s = 5.4$ m, return period 500 years.

ITEM	Costs			
Return period	25 years	50 years	100 years	500 years
Design H_s	4.2 m	4.6 m	4.8 m	5.4
Construction costs Capit.dam. costs	225 230	230 105	237 48	250 10
Total project costs	455	335	285	260

Table 3 Costs for breakwater with cube toplayer (mill.DGL)

The indirect damage costs resulting from the level of investments and the economical value of harbour operations appear to have a great influence on the optimum return period of H_s. Reduction thereof will allow for smaller design values. Similar results have been attained with other designs.

Moreover, in the points of optimum return periods for lowest total project costs, the capitalized damage costs are minimal and a clear distinction can be made between the various designs on the bases of the construction costs in those points. The results thereof are summarized in table 4.

TYPE OF BREAKWATER	CONSTRUCTION COSTS (million DGL)
Conventional rubble mound Bermbreakwater	480 270
Rubble mound + Cube units Rubble mound + Tetrapods Rubble mound + Accropods	250 245 195
Caisson breakwater Composite breakwater	205 215

Table 4 Construction costs of breakwater types

The high costlevel of the conventional type is mainly due to inevitable overproduction of lighter quarry material (quarry efficiency 24%). Costs can be reduced drastically if these volumes can be utilized elsewhere. Although higher volumes are involved, the bermbreakwater yields lower costlevels, mainly due to a higher efficiency (78%). However with increasing transport distances, the savings due to the bermbreakwater decrease (Hauer et al.1995).

The use of concrete units so as to replace heavy armour rocks over e.g. 10 tons have limited advantages to the costs when unit weights and volumes involved are close to the yield curve of the quarry. However, remarkable savings are reached with a single unit layer of Accropods; this might be the result of a single heavy rock layer as well, provided properly placed. The influence of transport costs of rock will decrease in that case.

The caisson breakwater appears more favourable than the composite type. For deeper bedlevels (> 15 m) this may be the opposite due to higher rock volumes required for the base structure.

Most favourable solutions for the ficitious layout and conditions are the accropode and the caisson breakwater. However transport costs and unit concrete costs may change the results. Larger transport distances may reduce the difference and may even result in an advantage for the caisson solution.

Increased waterdepths

For average coastal conditions some interesting results are found with varying water depths. Though expected, it is remarkable that as from water depths larger than 8 to 10 m the caisson types of breakwaters already seem to have cost savings compared to the rubble mound breakwater types, obviously due to increasing volumes of rocks at the base. However, with depths increasing to more than 20 m the composite breakwater appears to be a more cost saving solution, as the increasing heights of the caissons alone require additional widths. The study has been extended to foundation depths of 30 m (Schols, 1997), indicative values are mentioned in table 5.

Conventional type	Caisson type	Composite type
0 - 8 m	8 - 20 m	20 - 30 m
Waterdepth		

Table 5 Indicative range of favourable breakwater type

However, for real situations specific site conditions may alter the results drastically. Construction costs depend strongly on the rate of down time due to wave climate and tidal height conditions, if offshore located breakwaters are considered. Production of accurate placing of heavy concrete armour units from floating crane barges, may vary quite differently from the speed of placing caissons in full height or as composite type, in the presence of ocean swell and local wind waves. Moreover, the feasibility of a caisson solution depends largely on the stability of the foundation, and in particular the sensivity of the subsoil to liquefaction

Conclusions

For conditions similar to the case following can be concluded:
- The rubblemound breakwater + Accropod toplayer is most attractive, due to less rock volumes (steeper slopes) and the application of a single unit toplayer.
- The caisson breakwater appears to be a good alternative and may even become favourable if costs of required rock transport for a conventional type are increased.
- The high costlevel of the conventional type is mainly due to inevitable overproduction of lighter quarry material. In cases lower design wave heights are applicable, lighter quarry material and higher level of quarry efficiency will reduce related construction costs.
- Although large volumes of rocks are required, the bermbreakwater yields lower costlevels, mainly due to higher efficiency of quarry production.
- In case high wave heights require heavy armour units, a conventional rubble mound breakwater provided with a toplayer of concrete elements will soon become favourable. A stable single unit toplayer (armour) may increase this advantage.
- Caisson types of breakwater seem to become advantageous with waterdepths exceeding approx. 10 m. For composite breakwaters the advantage may start at waterdepths exceeding 20 m.

References

Allersma, E and W.W. Massie, Statistical Description of Ocean Waves, Coastal Engineering Group, Faculty of Civil Engineering, Delft University of Technology (1973)

CUR/CIRIA (various authors), Manual on the use of rock in coastal and shoreline engineering, Ciria special publication 83/Cur report 154, Balkema, Rotterdam, 1991.

Goda, Y. Random seas and Design of Marine Structures, Univers. Tokyo Press 1985.

Goda, Y. The design of upright breakwaters. In: Proc.short course on design and reliability of coastal structures, 23rd ICCS Venice, Tecnoprint, Bologna, 1992

Hauer, M., W. op den Velde, J.K. Vrijling, K. d'Angremond, Comparison construction costs conventional rubblemound breakwaters / bermbreakwaters, Proc. 3rd Seminar on Ports and Inland Waterways, Goa 1995, Publ. by PIANC/PCDC, Brussels.

Meer, J.W. van der, Conceptual design of rubble mound breakwaters Delft Hydraulics, 1993.

Schepers, M.R. Cost of breakwaters with concrete elements (in Dutch). MSc thesis Delft University of Technology (1998)

Schols, N.N.E. Considerations on construction costs of monolitic breakwaters (in Dutch). MSc thesis Delft University of Technology (1997)

WAVE FORCES ON SOLID AND PERFORATED CAISSON BREAKWATERS: COMPARISON OF FIELD AND LABORATORY MEASUREMENTS

L. Franco[1], M. de Gerloni[2], G. Passoni[3], D. Zacconi[2].

Abstract

Following an old Italian tradition of prototype measurements of wave pressures at vertical breakwaters (Franco, 1994), a new twin recording station was set up and operated in 1992-1994 at Porto Torres (Sardinia, Italy) industrial harbour breakwater. In the framework of the MAST3-PROVERBS project an extensive analysis of the available data has been carried out.

Within the same project 2D model tests have also been performed in order to investigate the relation between pressure distribution and overall forces on and under both plain and perforated (multichamber) caissons. The results have been compared with the available design formulae like Goda's (1985). Statistical distributions of the horizontal and uplift forces for both structure types have also been derived. The scope of the study has been to assess the reliability of the present design methods and to outline a more physically based approach especially for the perforated structure type.

Introduction

The prototype structure is a vertical composite breakwater subjected to nonbreaking wave conditions. Two caissons (20.5x13.9 m), one with plain (solid) wall and one perforated, 62 m apart, based at –15 m on rubble footing in 20 m water depth, were instrumented with ultrasonic wave gauges and pressure sensors along the caisson's base, on the vertical face and also in the internal chambers as described by De Girolamo et al. (1995). The operating time of the instrumentation was 1992-1994, in which 10 significant storms ($2 \leq H_s \leq 3.5$ m, $6 \leq T_p \leq 9.2$ s) have been recorded. A directional wave gauge has been installed 700 m away from the breakwater at the same depth (20 m). Water levels at the wall, front and uplift pressures have been recorded with a sampling frequency of 20 Hz, except for deep sensors (2 Hz).

[1] Dept. Civil Engineering - 3rd University, via C. Segre 60, 00146 Roma (Italy)
[2] Hydraulic Laboratory - ENEL-PIS, via Pozzobonelli 6, 20162 Milano (Italy)
[3] DIIAR - Politecnico di Milano, Piazza Leonardo da Vinci 32, 20133 Milano (Italy)

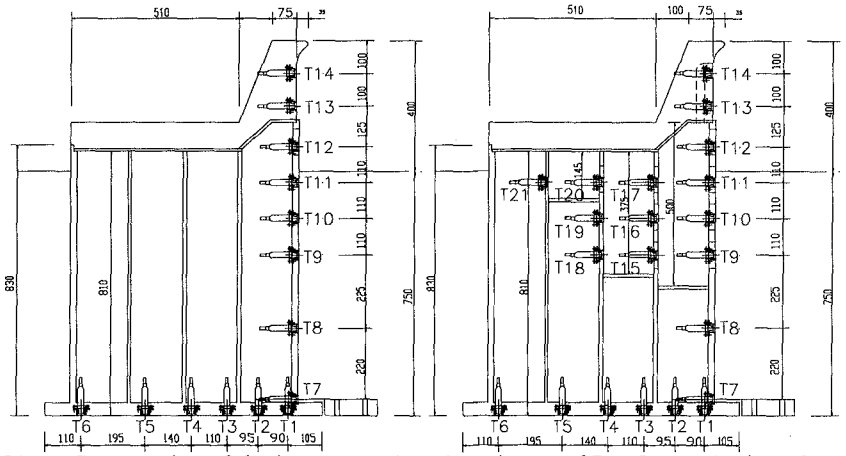

Fig. 1 Cross section of the instrumented model caissons of P.to Torres (plain wall at lef and perforated at right, dimensions in mm)

Experimental conditions identical to prototype have been reproduced in the ENEL random wave flume (but just 2D homogeneous wave field) where the model caisson was equipped with the same number of pressure transducers as in the prototype (Fig. 1) and also with a dynamometer for simultaneous recording of global forces and pressures. The same wave frequency spectra were reproduced in the lab according to the prototype water levels recorded at the wall. Some synthetic Jonswap spectra have been simulated as well.

Prototype data

Parameters describing the loading signal shape of the most severe events of all recorded storms, together with all the other data relative to wave measurements, are collected in a database compiled according to MAST3/PROVERBS notations and confirming the single-peak shape for the pulsating (non-breaking) wave conditions.
A further statistical analysis of wave loads proved a good fitting with 2-parameters Weibull statistical distribution for both front and uplift forces on plain caisson and for uplift forces on perforated caisson. With regards to perforated caisson, the trapezoidal integration method cannot be applied, because of geometrical complexity, to calculate horizontal forces from pressure measurements: the Kriebel (1992) method was used instead, and it has proven to give approximation of +-20% in laboratory, not much bigger than values obtained from statistical analysis of front and back pressures.

Out of the ten storms recorded in field (Franco, 1996) the three largest ones in terms of significant wave height were chosen. A transfer function between the incident spectral densities and the ones measured at the wall was applied and spectra reproduction was good enough to allow a consistent comparison of pressure

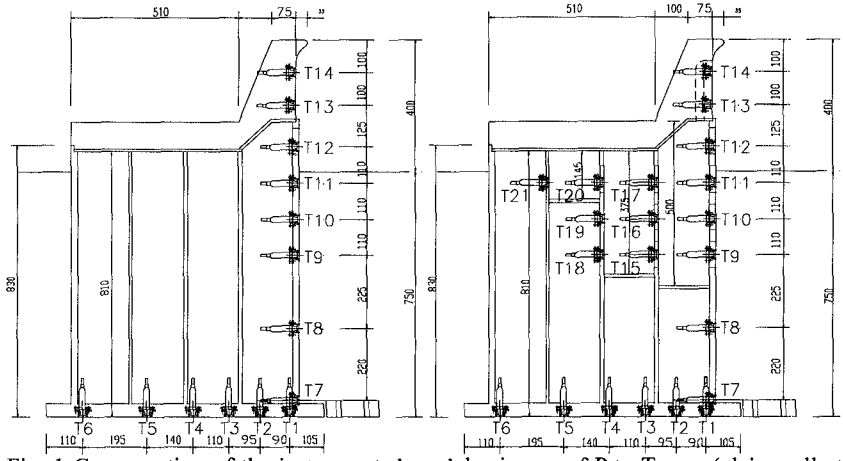

Fig. 1 Cross section of the instrumented model caissons of P.to Torres (plain wall at left and perforated at right, dimensions in mm)

Experimental conditions identical to prototype have been reproduced in the ENEL random wave flume (but just 2D homogeneous wave field) where the model caisson was equipped with the same number of pressure transducers as in the prototype (Fig. 1) and also with a dynamometer for simultaneous recording of global forces and pressures. The same wave frequency spectra were reproduced in the lab according to the prototype water levels recorded at the wall. Some synthetic Jonswap spectra have been simulated as well.

Prototype data

Parameters describing the loading signal shape of the most severe events of all recorded storms, together with all the other data relative to wave measurements, are collected in a database compiled according to MAST3/PROVERBS notations and confirming the single-peak shape for the pulsating (non-breaking) wave conditions.
A further statistical analysis of wave loads proved a good fitting with 2-parameters Weibull statistical distribution for both front and uplift forces on plain caisson and for horizontal forces on perforated caisson. With regards to perforated caisson, the trapezoidal integration method cannot be applied, because of geometrical complexity, to calculate horizontal forces from pressure measurements: the Kriebel (1992) method was used instead, and it has proven to give approximation of +-20% in laboratory, not much bigger than values obtained from statistical analysis of front and back pressures.

Out of the ten storms recorded in field (Franco, 1996) the three largest ones in terms of significant wave height were chosen. A transfer function between the incident spectral densities and the ones measured at the wall was applied and spectra reproduction was good enough to allow a consistent comparison of pressure

measurements. Details on the sea storms parameters are given in de Gerloni (1997 et al.).

Uplift pressure model and scale effects

Both plain and perforated caissons and their foundation were accurately reproduced in the lab with a geometric reduction scale of 1/20. The tests were carried out in a 43 m long wave flume equipped with a wedge type generator and with a system of porous walls and lateral channels intended to absorb reflected waves. The rubble foundation grain size simulation was studied in a particular set of tests with a simplified superstructure. In order to ensure the test repeatability, the rubble base set up in the flume was accurately controlled and the rubble foundation material was deposited by means of the so called "pluvial deposition" method, which ensures the maximum density of the deposited material (Pedroni et al., 1992). A 5 mm thick sheet of tender and waterproof rubber mousse, with holes for six pressure transducers, was applied on the caisson bottom in order to avoid the water to find preferential paths between the caisson bottom and the top layer of the rubble foundation (see Fig. 2).

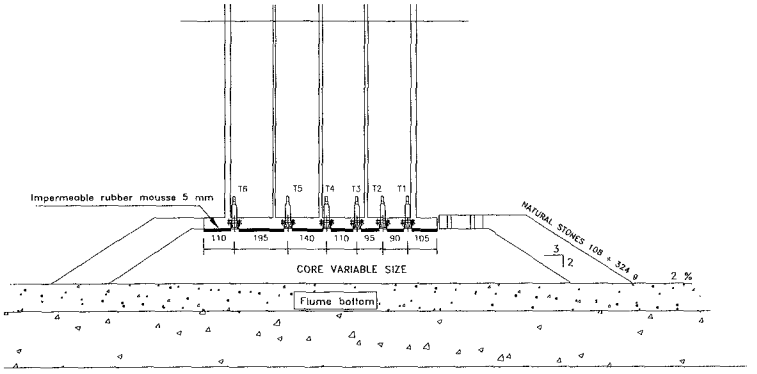

Fig. 2 Model set-up for rubble foundation material tests.

A sensitivity analysis has been conducted on the scale effect of the grain size distribution of the rubble mound foundation in terms of uplift pressures. Three grain size curves of the rubble mound foundation with different density and gradation have been tested (cores A, B, C). Limestone rock was used with diameter D_{10} varying from 1.8 to 20 mm and diameter D_{50} varying from 3 to 23 mm. The average grain size has been scaled with respect with the Froude number. Further details are given in de Gerloni et al. (1997). Prototype and model data were analysed in terms of time-sequences values and statistical parameters associated to pressure waves, obtained after zero-down-crossing analysis. A first comparison with prototype data was done by looking at comparable runup time sequences in the model and prototype (Fig. 3).

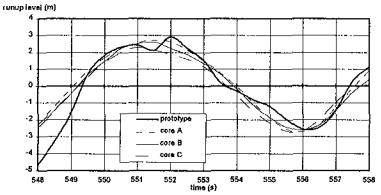

Fig. 3 Storm 1 - Prototype and model runup levels at the vertical wall

Such comparison doesn't take into account the influence of runup history previous to the selected sequences, which has been proven to be negligible. A strong difference between prototype and model wave uplift pressure on the caisson base (the latter beeing twice as large) is apparent especially at the seaward edge (Fig. 4 right), but when approaching the harbour edge wave effects get smaller and they cannot be distinguished from the "noise". It is also shown that the grain size has little influence.

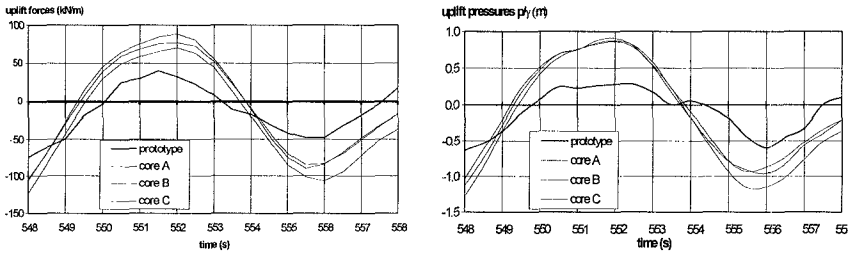

Fig. 4 Storm 1-Prototype and model uplift forces (left) and pressure (right) at 2.1m back from seaward edge

Also the triangular pressure diagram recorded in the model at the moment of maximum uplift force (Fig. 5) appears not to be affected by the model grain size, or conversely the prototype is characterized by a non uniform transversal transmissivity which may be explained by cyclic tilting loading at the edges, as reported by Van Hoven (1997). In fact, neither Le Mehauté (1965) theory (suggesting a grain size scale from 1/16 to 1/11, close to core C scale 1/10) nor Jensen & Klinting's (1983) studies (suggesting a scale 1/18 close to core B scale 1/20) seem able to justify the differences found. Similar uniform diagram shapes are observed in the troughs of pressure waves, too. Alike conditions had also been noticed in previous prototype measurements at Molo Cornigliano of Genoa Harbour, in 1975 (possibly with the foundation silted up on the harbour side), in small and large-scale model tests (Marchi et al., 1975; Kortenhaus et al., 1994) and in prototype measurements at Dieppe caisson (ULH Group, 1998).

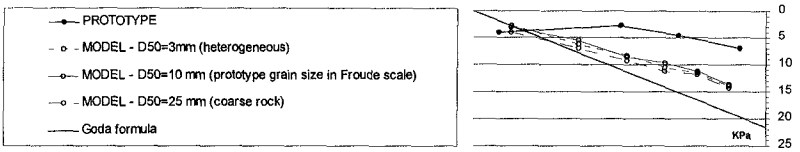

Fig. 5 Prototype, model and design formula for underpressures at max. uplift force. (storm1)

In order to verify directly the actual conditions of the caisson foundation at Porto Torres a scubadiving inspection was carried out by the first author in October 1997. Observation was made along some 150 m of breakwater at the instrumented sections in the transition trunk between plain and perforated caissons on both sides. The outer apron slabs at toe were found to be placed very carefully/regularly one to each other with no more than 2 cm distance from caisson toe. No sand or fine material was observed at toe either sides. Gravel and small stones were found beneath the armour slabs. Info from construction divers confirms that the rubble foundation top was levelled with some 20 cm of gravel before accurate and smooth caisson placement.

The actual non-triangular shape of the uplift pressure diagram can be also explained by the obliquity and shortcrestedness of the real incident waves (recorded storm waves showed a mean attack angle up to 30° to the normal to the breakwater axis). As shown by Franco et al.(1996) after a systematic 3D model study on plain and perforated caissons, the uplift pressure diagrams under 3D waves can have a concavity that shifts the resultant towards the seaward toe (increasing the overturning moment) and the total uplift force is generally overstimated by Goda. This is also consistent with storm 1 records where the Goda design formula describes the triangular model diagram but overestimates uplift pressure values especially near the seaward edge.

Horizontal loads on plain walls

With the same method as for uplift pressures, the horizontal pressure time-series on the vertical wall have been compared between prototype and model for specific time intervals in which runup levels were in satisfactory agreement. In Fig. 7 (left) two different prototype time intervals having the same peak elevation and one model time interval in good agreement with them are plotted; the corresponding model and prototype (seq. a) time sequences of front pressure at -2.90 m M.S.L. during storm 1 are shown in Fig. 6 (right) and all the pressure data recorded at each sampling time in the model are compared with those in the prototype in Fig. 7. They show that with similar runup sequences, model pressures are on average larger than the prototype ones (≈+50% in wave troughs, ≈+20% in wave crests).

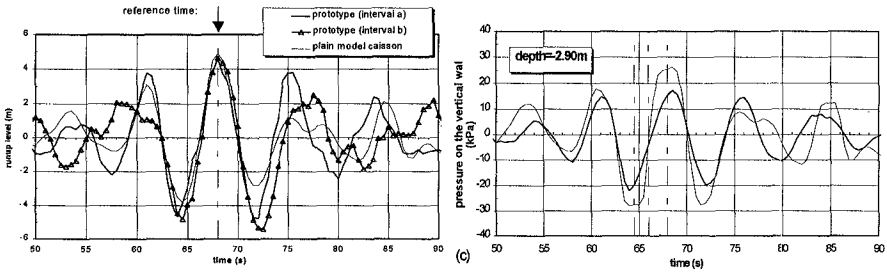

Fig. 6 Model compared with two prototype water levels (left) and model compared with prototype pressure time series (right).

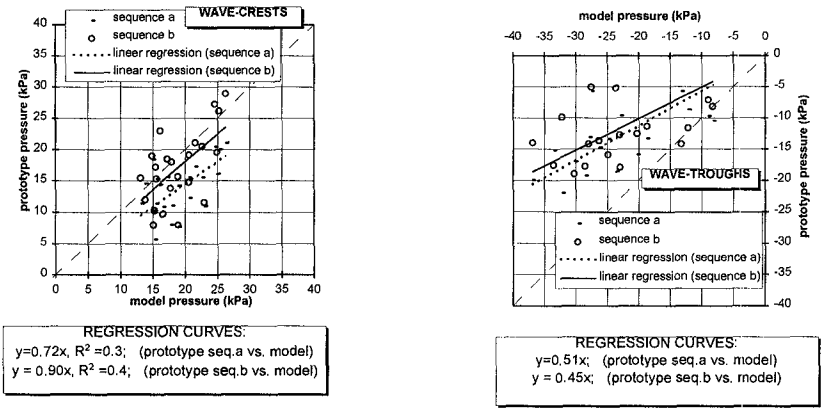

Fig. 7 Model and prototype pressure measurements under similar wave runup crests (left) and troughs (right)

The overall actions on the model and prototype caissons at comparable runup sequences are plotted in Fig 8: differences are evident in both pressure gradients (uplift pressures and around the peak of the front pressure diagram) and in absolute values; under wave crests the differences are reduced.

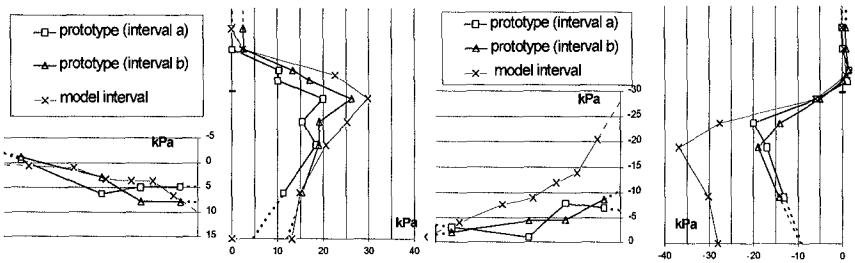

Fig. 8 Uplift and horizontal pressure diagrams under wave crests (left) and wave troughs (right) as in Fig. 6 for the plain wall caisson.

The pressure diagrams proposed by Goda formula are compared in Fig. 9 with the corresponding model and field measurements at the different instants of maximum horizontal and uplift force: Goda method is further "conservative" because it assumes simultaneously the max values of horizontal and uplift forces.

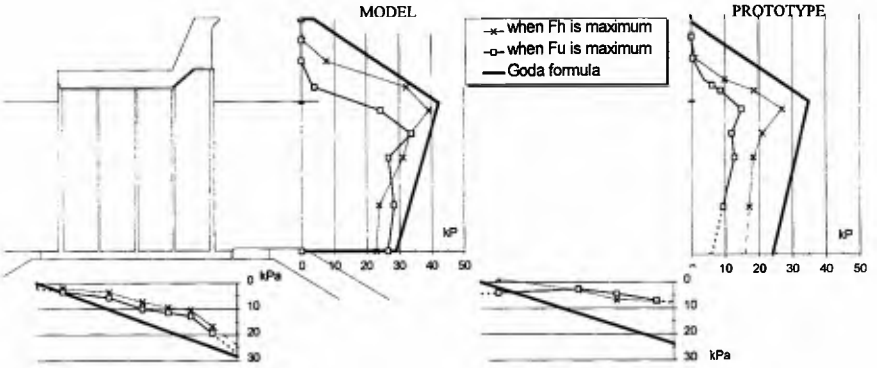

Fig. 9 Maximum forces diagram compared with Goda prediction (left: model tests; right: prototype measurements).

Both model and prototype pressure data were integrated with linear interpolation over the vertical face and along the bottom; crests extracted with the zero-down crossing method are well fitted by the 2-parameters Weibull distribution (Fig. 10). Prototype shape parameter (α) relative to horizontal forces F_h is well reproduced in the model but the corresponding scale parameter (β) is in the average 72% smaller, which means that the F_h distribution is the same but shifted towards higher values in the model; F_u distributions have both different shape and scale parameters.

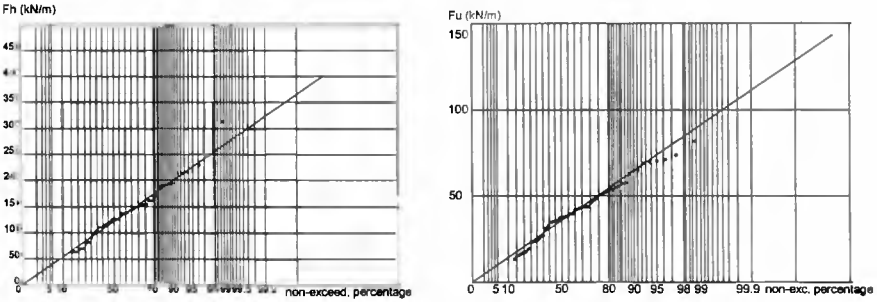

Fig. 10 Prototype F_h (left) and F_u (right): Weibull distribution of upper 85% (Storm 1)

Statistical estimates of horizontal and uplift forces (P=95%, 98%, 99%, 99.6%, 99.85%, 99.9%) have been compared with the corresponding model ones and also with the extreme estimates (P=99.85%) according to the Goda method. Forces calculated with Goda formula are on average higher than the corresponding estimated ones, especially prototype F_h (Fig. 11). The lab force data are, on the average, 35%

and 40% larger than those of the prototype respectively for F_h and F_u as shown in Fig. 12.

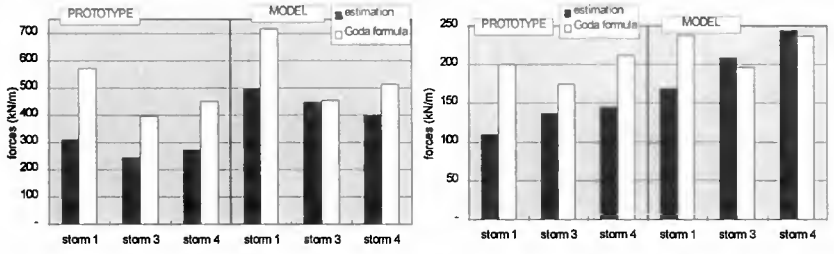

Fig. 11 Comparison of estimates of F_h (left) and F_u (right) forces from 99.85 % Weibull estimates and Goda formula.

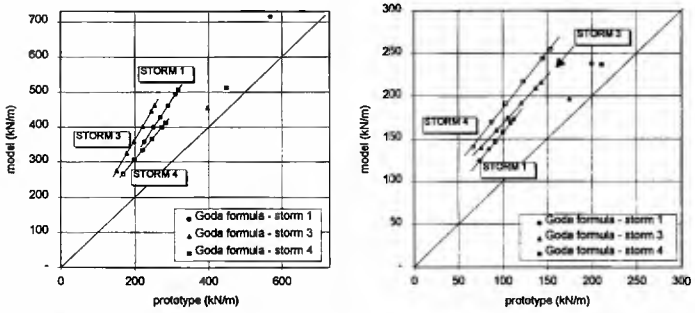

Fig. 12 Extreme horizontal (left) and uplift (right) forces: model and prototype.

Horizontal loads on perforated wall

In the same way as for the plain caisson, the perforated wall caisson was instrumented with pressure transducers on the bottom slab and on each vertical wall, and also with a dynamometer for global horizontal forces measurements. In order to investigate the pressures on the internal walls, the tests were repeated by turning backwards the pressure transducers placed on the perforated walls (Fig. 13).

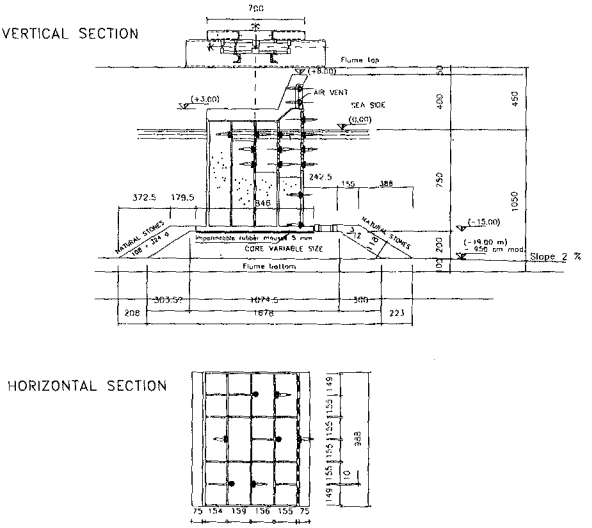

Fig. 13 Setup of perforated caisson model with pressure transducers turned backwards

The model pressure data, recorded in the external and internal walls, have been integrated over the vertical face using the Kriebel (1992) and the Canel (1995) method. Both results exhibit non negligible discrepancies when compared with the lab dynamometer data (Fig. 14). This may be explained both by the intrinsic overestimate of the Goda distribution also on plain walls (up to 20%) and by the lack of knowledge about the true pressure distribution on the perforated walls.

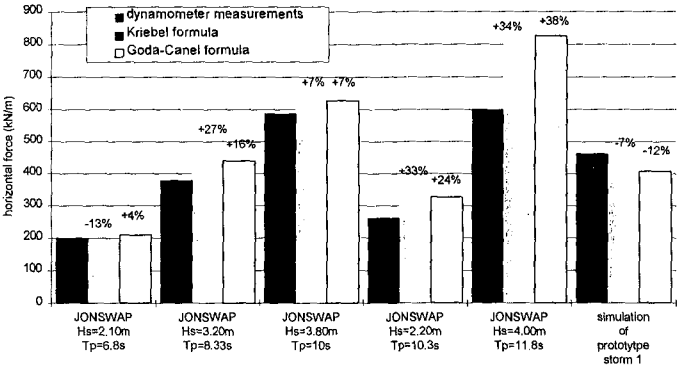

Fig. 14 Comparison between lab data, Goda and Kriebel estimates.

The model test results, in terms of statistical distributions, also indicate that the perforated caissons can be subjected to larger horizontal loads than the plain ones when extreme waves attack the structure (Fig. 15 left). This appears different when

looking at the negative forces (Fig. 15 right) for which the perforated caisson behaves efficiently and more consistently in the load reduction.

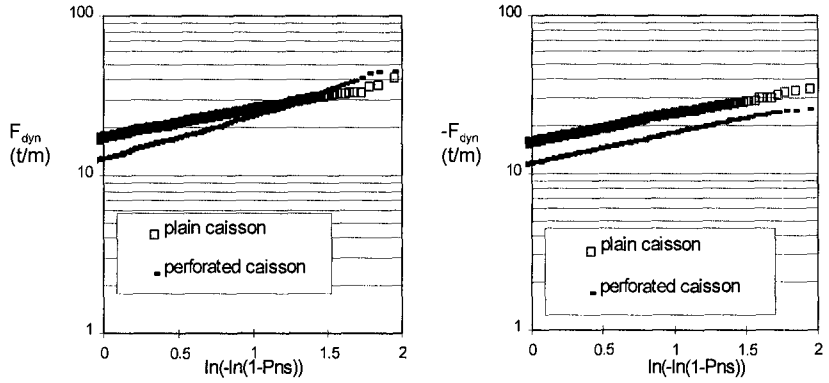

Fig. 15 Force PdFs at wave crests (left), troughs (right).

A simple formula was looked for to calculate wave forces on perforated caissons as an improvement of Canel's (1995) one that is a modified version of Goda formula itself. By Canel method the hydrodynamic load due to an incoming wave of height H on a partially reflecting structure is estimated by the Goda model with a suitably corrected design wave

$$\left\{\left(\frac{1+Cr}{2}\right)*H\right\} \qquad (1)$$

in which Cr is the expected reflection coefficient. This approach was suggested by the observation of Goda model that establishes a linear relation between the hydrodynamic effects of waves and their height in most hydraulic situations. Values of Cr around 0.5 were measured in the flume for the specific caisson with wall porosity of 0.31.

In order to give an input as general as possible to that formula, a simple modification of the design wave height involving only the dimensionless parameter B/L (where B is the chamber width and L the wavelength), instead of the reflection coefficient C_r was found. The total horizontal force F_h by Goda model was worked out and compared with the corresponding measured values for each available perforated structure data set, coming from different experimental set-ups (University of Le Havre ULH, Leichtweiss Inst. Braunschweig LWI, as reported in MASTIII-PROVERBS 2nd Overall Project Workshop). Fig. 16 shows the comparison of the experimental data with the corresponding Goda values; as expected all the data are below the matching line.

The difference in percentage

$$\left\{\frac{\left(F_{h\,GODA} - F_{h\,MEAS}\right)}{F_{h\,GODA}}\right\} \qquad (2)$$

with respect to the Goda calculation resulted on average equal to 30 % for ENEL and PM/DH 3D random wave tests (Franco et al., 1996) and 24 % for ULH regular wave tests.

A reduction coefficient was calculated for each experimental datum in order to make the measured and calculated force coincident. Fig. 17 shows the coefficient trend as a function of the dimensionless parameter B/L. A linear model to describe the relationship between the reduction coefficient of the Goda's H_{max} and B/L parameter was found. The equation of the fitted model is:

$$reduction\ coefficient = 1 + a * (B/L) \qquad (3)$$

where:

$a = -1.43$
$\sigma_a = 0.08$
$R^2 = 0.52$

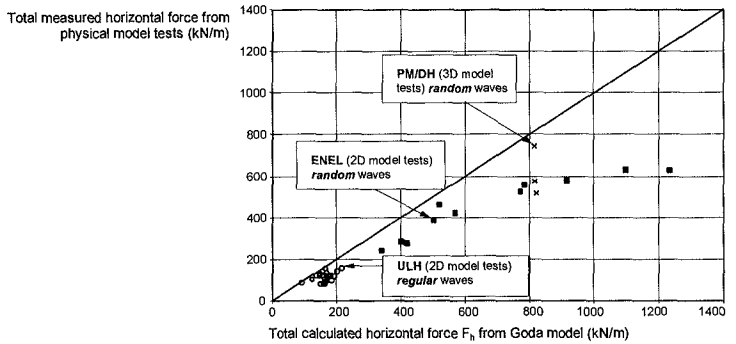

Fig. 16 Comparison between measured vs calculated forces

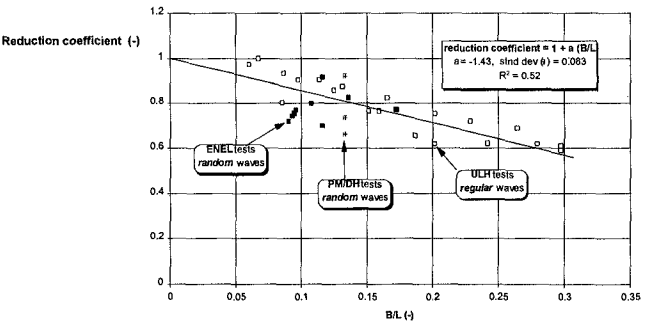

Fig. 17 Reduction coefficient trend as a function of the dimensionless B/L parameter

The reflection (C_r) and the reduction coefficient [(1+Cr)/2] trends are shown in Fig. 18 as a function of the dimensionless parameter B/L. The linear model adopted for the reduction coefficient is therefore conservative for a total chamber width B less than about a quarter of wave length, while it gives lower wave heights (and then forces) for greater values (though the more B/L increases, taking B constant, the less becomes the force).

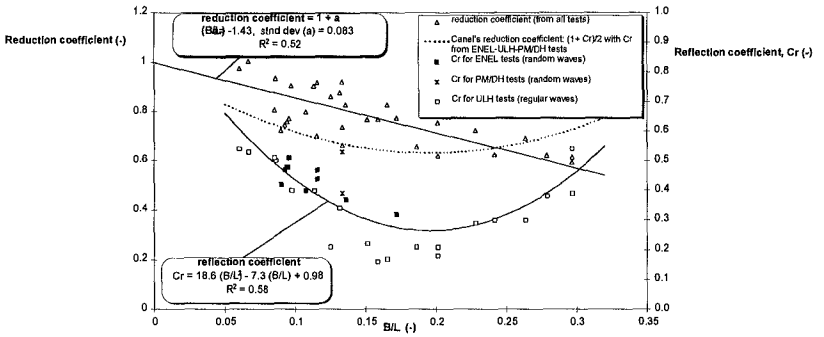

Fig. 18 Force reduction and reflection coefficient as a function of B/L

For such analysis both field and lab data were used, but in the prototype caisson the actual total horizontal force is unknown while in the lab the total horizontal force have been measured.

Conclusions

The behaviour of caisson type breakwaters is generally less severe than predicted by the Goda method both with respect to the horizontal and vertical loads. The real uplift pressure distribution is not triangular as conventionally assumed, but a trapezoidal diagram is more reasonable. With respect to the perforated caissons, the global forces are not well described by the standard design methods. The overall performance of this structure types is effective in the reduction of water levels and negative forces, but they can show an opposite tendency for the horizontal forces at the highest wave crests. A new simplified formula for the preliminary design of multichamber perforated caissons is also proposed.

Acknowledgements

This research has been supported by the EU Commission under the project MASTIII-PROVERBS (contract MAS3-CT95-0041). The authors express their gratitude to Dr. D.Colombo and Dr. S.Meucci for their kind help in the analysis of the experimental data. The fruitful cooperation of the European PROVERBS partners, especially H.Bergmann (LWI), H.Tabet (ULH) and M.Belorgey (ULH) is acknowledged.

References

Canel, M. (1995) *Dissipative Monolithic Breakwaters - Some Aspects of Hydrodynamics*. MASTII-MCS, Final Project Workshop, Alderney Island (GB), May 1995.

de Gerloni, M., Colombo, D., Franco, L., Passoni, G, Zacconi, D. (1997) *Scale effects in uplift pressure measurements on caisson breakwaters* 2nd Overall Workshop, MAST III / PROVERBS, Las Palmas 1997.

De Girolamo, P., Noli, A., Spina, D. (1995) *Field Measurements of Loads acting on smooth and perforated vertical Walls*. Proc. ICE Breakwater Conf., London (GB), T.Telford Ed.

Franco C.,Van der Meer J.W., Franco L.(1996) *Multidirectional wave loads on caisson breakwaters*, Proc. 25th ICCE, Orlando, ASCE, NY, vol.2, pp.2008-2021.

Franco, L. (1994) *Vertical Breakwaters: the Italian experience.* Coastal Engineering, 22, 31-55.

Franco, L. (1996) *Analysis of wave pressure measurements on plain and perforated caisson at Porto Torres breakwater.* MAST III / PROVERBS, Belfast 4-5 July 1996.

Goda, Y. (1985) *Random Seas and Design of Maritime Structures.* University of Tokyo Press.

Jensen, J., Klinting, P. (1983) *Evaluation of scale effects in hydraulic models by analysis of laminar and turbulent flows*. Coastal Engineering, 7.

Kriebel, D. (1992) *Vertical Wave Barriers: Wave Transmission and wave Forces.* Proc. 23rd ICCE, Venice (I), Sept. 1992, ASCE Ed.

Le Mehauté, B. (1965) W*ave absorbers in harbours.* Report n° 2-122, US Army Waterways Experiment Station, Vicksburg, June 1965.

MASTIII-PROVERBS (1998) Proceedings 2nd Overall Project Workshop, Naples, Feb. 1998.

Pedroni, S., Crippa, V., Lo Presti, D. (1992) *Maximum dry density of cohesionless soils by pluviation and by ASTM D4253 - 83: a comparative study. ENEL/CRIS*

ULH Group (1998) Group Field Work Report, MASTIII-PROVERBS 2nd Overall Project Workshop, Naples (I), February 1998.

Van Hoven, A. (1997) *Hindcast of Pore Pressures underneath Porto Torres Breakwater.* MAST3- PROVERBS, Task 1 Tech. Workshop, Edinburgh (GB), July 1997.

Wave Impacts on Caisson Breakwaters situated in Multidirectionally Breaking Seas

Frigaard, P., Burcharth, H. F. & Kofoed, J. P.

1. Abstract

The paper concerns horizontal wave forces on caisson breakwaters in multidirectional breaking seas. It is based on model tests performed in a 3D wave tank at Hydraulics and Coastal Engineering Laboratory, Aalborg University. The measured horizontal wave forces are compared to the Goda force. Good agreement with the Goda formula is found for waves not breaking directly on the structure, while increasing degree of breaking on the structure results in forces of up to 50 % higher than the Goda force. Furthermore, the reduction of the horizontal wave force on long structures due to the non full correlation of the wave pressure along the structure is investigated. A formula for the force reduction factor based on cross correlation coefficients is given as a function of the mean wave direction and the wave spreading.

2. Introduction

In the design of caisson breakwaters it is common to use the rather simplified but well documented (Goda, 1974), equation for calculation of the wave forces. Alternatively, equations from (Takahashi et al., 1994), (Allsop & Vicinanza, 1996), deals with effects from impulsive forces. However, these models do not at the same time take into account both wave impacts and wave directionality.

The effects of wave breaking and impact forces on vertical structures have been investigated by several researchers in the past. However, the research on impact loading has mainly been based on 2D breaking waves, (Takahashi et al., 1994), (Oumeraci et al., 1995), (Allsop & Vicinanza, 1996), (McKenna & Allsop, 1998).

Hydraulics and Coastal Engineering Laboratory, Dept. of Civil Engineering, Aalborg University, Sohngaardsholmsvej 57, DK-9000, Aalborg, Denmark, Fax. +45 98142555, E-mail: peter.frigaard@civil.auc.dk

Attention has also been addressed to the effects of wave obliquity and multidirectionality on the wave loads on vertical caisson breakwaters situated in non breaking seas. Battjes (1982) gave a theoretical description of effects of short-crestedness on wave loads on long structures. Within the joint European (MAST-LIP-TAW) research project, a 3D model investigation was carried out at Delft Hydraulics to assess these effects. The results have been published by several researchers, among them Franco et al. (1995).

Few researchers (Grønbech et al., 1997), (Calabrese & Allsop, 1998), described the effect of obliquity on wave load. These studies included effects from impact forces.

So far, little attention has been paid to the effects of wave obliquity and mulitidirectionality on the reduction in the wave loads on long caisson breakwaters placed in deep water breaking seas. To assess these effects, a physical model study has been carried out (Hydraulics and Coastal Engineering Laboratory, Aalborg University, 1997 and 1998).

In addition ongoing research will in the near future focus further on this topic. Late autumn 1998 a joint European TMS research project entitled Coherence of impact pressures at vertical wall in multidirectional seas lead by Prof. Alberto Lamberti, University of Bologna, Italy, will be performed at HR Wallingford.

3. Experimental setup

The physical model tests were carried out in the 3D wave basin. A caisson breakwater model constructed in plywood was used in the tests. The model was placed on a one layer smooth foundation constructed in concrete. The idea of this foundation was to provocate wave breaking in front of the caisson or even to introduce wave breaking on the caisson. The cross section and a plan view of one of the models are seen in Figure 1.

The size of the model did not refer to any particular prototype structure, however, a Froude scaling of 1:20 - 1:25 seems appropriate for this type of structures.

Two different crest freeboards corresponding to dimensionless crest freeboards in the range 1.17 – 1.90 were applied in the tests.

Two different model layouts were used, obliquity of the model relative to the wave paddles where 15° and 30°, respectively. The reason for these two model layouts was the fact that model influence given by the layouts should be extracted.

To assess the effects of wave obliquity and multidirectionality of the waves, the wave induced pressures were measured on a 2.4 m wide test section, giving the opportunity to study these effects on a single vertical element of the test section as well as on the total width of the test section.

To eliminate the disturbance from wave diffraction at the two ends of the model, the model were extended beyond the test section.

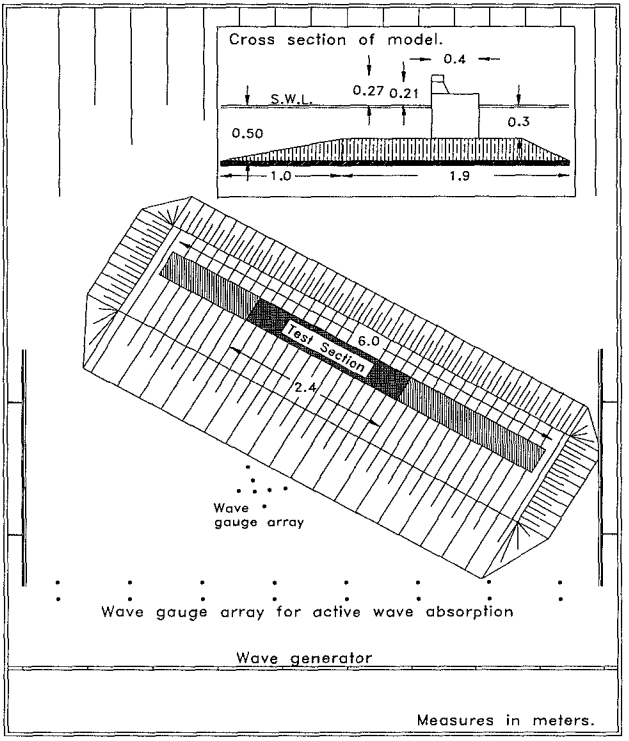

Figure 1 - Model setup.

Preliminary to the tests a numerical study was performed in order to evaluate the diffraction effect from the two ends of the caisson. A consequence of this study was a non-symmetrical placing of the test section in the whole structure, see Figure 1. Even though much effort during planning and model changes were done trying to minimize effects from diffraction it must be concluded that variations in the order of +/- 5 % of the incident wave height along the structure within the test section could be expected in a test. Consideration of this variation is rather important for the analysis of lateral force distribution.

In order to control the incident waves the basin were equipped with a full 3D active absorption system, see (Hald & Frigaard, 1997).

As the main objective of the study was to assess the effect of wave obliquity and multidirectionality in breaking seas, the changes on test conditions were mainly the incident mean direction of the waves and the directional spreading of the waves. The wave parameters are summarized in table 1.

Wave spectrum	JONSWAP, γ= 3.3
Peak period T_P	1.2 sec
Significant wave height H_S	0.14 - 0.18 m
Crest freeboard R_c	0.21 and 0.27
Water depth near caisson h	0.3 m
Mean wave direction θ	0° to 48°
Spreading of waves	Cosine squared, σ = 0° - 25°

Table 1 - Wave parameters.

To obtain an adequately statistically validity of the test results, rather long time series were performed with no test series having less than 1800 waves, and on certain occasions up to 2500 waves.

4. Wave analysis

Wave height is the most important parameter in the description of the wave forces. Due to high amount of reflection from the caisson and thereby the relatively confused sea, high priority were given to calculation of the incident wave height.

Wave elevations were measured by a wave gauges array consisting of 7 wave gauges located on deep water, see Figure 1. Using the Bayesian Directional Method, see Hashimoto & Kobune (1988), the wave field were separated into incident and reflected wave fields. Mean wave directions, spreading of the waves, significant wave heights and reflection coefficients at deep water were calculated from this incident wave field.

As the waves approached the more shallow water near the caisson they shoaled, refracted and started to break. Therefore, deep water wave parameters could not describe the waves sufficient in shallow water near the structure. Due to the wave reflection wave breaking and the rapid chances in the sea state shallow water wave parameters like wave direction, spreading of energy and wave height could not be calculated with high accuracy. Therefore, the front of the caissons was equipped with up to 4 wave gauges.

Using measured reflection coefficients of approximately 95 % an estimate of the shallow water significant wave height were calculated from $H_S = 4/1{,}95\ \sqrt{m_0}$, with m_0 = total amount of energy.

Mean wave directions and energy spreading of the waves referred to in the following were all calculated from the deep water incident wave field.

5. Statistical distribution of forces

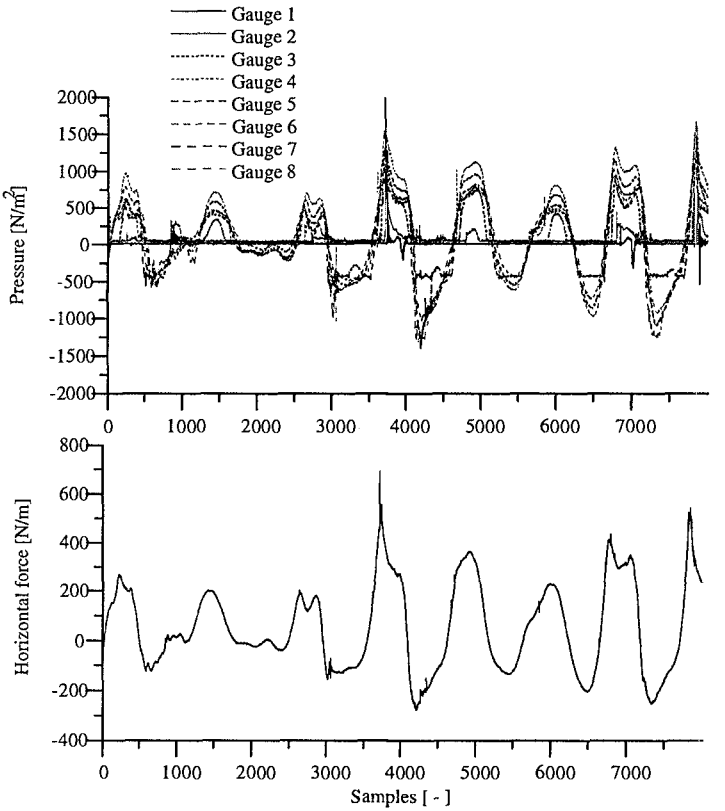

Figure 2 – Example of time series with a duration of 10 seconds showing sampled pressures in one section and the corresponding integrated horizontal force.

The forces in the sections were determined by integrating the measured pressures over the height of the model. In Figure 2, a time series of measured pressures in eight different levels and corresponding integrated horizontal force are shown. The pressures were sampled at 800 Hz. In order to compare the results of the tests with the prediction formula of Goda and to compare the results of tests with different wave heights, the measured forces were expressed in terms of the statistical force parameter $F_{1/250}$ which is average of the force peaks occurring with a probability less than 0.4 %. Wave heights input into the Goda formula were measured at the structure exactly where the forces were measured.

In the design of the model layout for non braking and breaking conditions approximately 0 % of the waves and 8 % of the waves were assumed to break on the ramp or at the caisson, respectively. Figure 2 show that some impulsive loading from the breaking waves were measured but only some deviations relative to pulsating forces were seen.

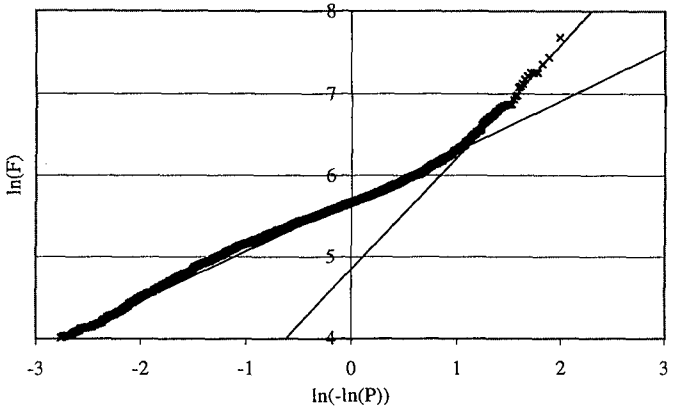

Figure 3 – Example of statistical distribution of horizontal force peaks.

McKenna & Allsop (1998), stated that the statistical distribution of the pulsating force peaks may be described well by the Weibull distribution, and that a change in the gradient of the Weibull plot indicates the onset of impulsive wave impacts.

Figure 3 show that this deviation happened for force peaks with a probability of exceedence P less than approximately 3 - 4 % which corresponds rather well to the observed number of waves breaking near the caisson or at the caisson.

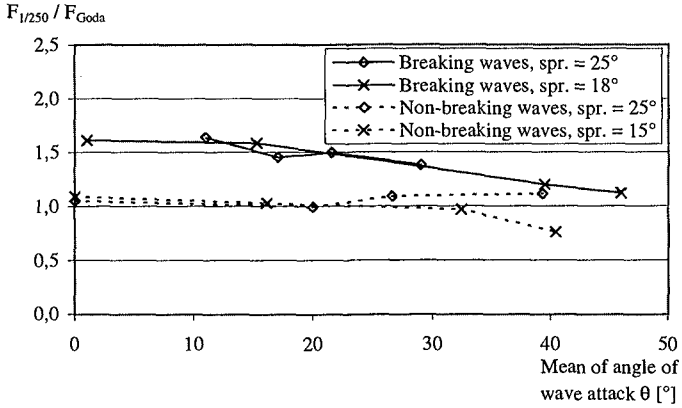

Figure 4 - Force comparisons.

Figure 4 show that measured forces corresponds very well to forces predicted by the Goda equation. As long as the waves were non breaking this was the case for all tests no matter wave direction and wave spreading. Other researchers, (Franco et al. 1995) and (Grønbech et al., 1997), found poorly agreement between measurements and the Goda force. They reported deviations up to 20 %. This is because they calculated the Goda force from the deep water parameters where the present study uses shallow water wave parameters.

The measured force for the breaking waves deviate approximately 50 % from the forces predicted by the formula of Goda. Apparently, the Goda formula underestimates the forces from the breaking waves. Though, here it must be remembered that the test conditions for the breaking waves present somewhat the most severe possible sea condition, which in practice is the upper limit for the number of breaking waves. Such conditions were never meant to be covered by the Goda formula. Goda (1984), described how to avoid such a condition in the design.

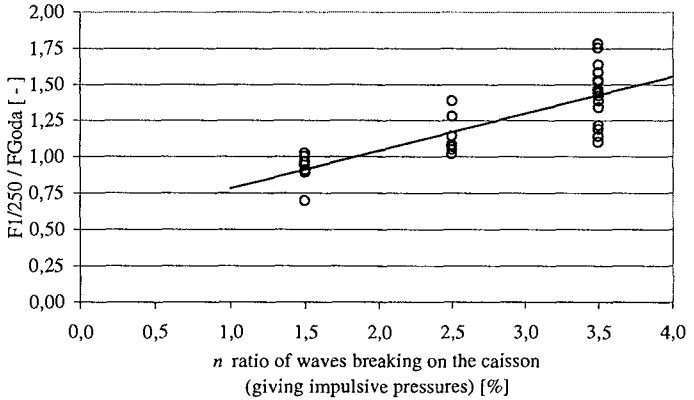

Figure 5 – Measured forces compared to the Goda force for different degrees of wave breaking on the caisson.

Allsop et al. (1996), also found that the Goda equation underestimated impact loadings from breaking waves and they demonstrated very good correlation with the equation originally proposed by Allsop & Vicinanza (1996):

$$F_{1/250} / \left(\rho_w g h^2\right) = 15\left(H_S/d\right)^{3.134} \quad \text{for } 0.35 < H_S/h < 0.6 \tag{1}$$

In the present study relatively good agreement to the Allsop & Vicinanza equation were found but the equation seemed to overestimate the measured forces. For the test cases the Allsop & Vicinanza equation estimate forces approximately double the estimates from the Goda equation.

Figure 5 shows that force ratio as a function of the number of waves breaking on the caission. From plots like the one shown in Figure 3 it is possible to find the number of waves breaking on the caisson.

The performed tests were divided in three groups, non breaking waves, moderate breaking waves and breaking waves, respectively. In Figure 5 all force ratios are plotted relative to the average number of waves breaking on the structure in the whole group of wave conditions. A clear trend described by the following equation is found.

$$F_{1/250} / F_{Goda} = 0.6 + 25n \tag{2}$$

6. Lateral distribution of forces

The horizontal wave load over a length of caisson will be reduced relative to forces measured in one section due to the non full correlation of the wave pressures along the structure.

By measuring the vertical distributions in nine sections spaced by 0.3 m and one section 0.1 m wide, the lateral distribution of the horizontal forces was studied. This is important due to the unknown correlation between the lateral distribution of the horizontal pressure and the lateral distribution of the horizontal force. The wave pressures were measured by a set of pressure transducers placed in the test section as shown below.

Figure 6 indicates 10 sections with 8 - 9 pressure transducers in each section. Never the less due to a restriction of 50 available pressure transducers only measurements in four sections were done simultaneously.

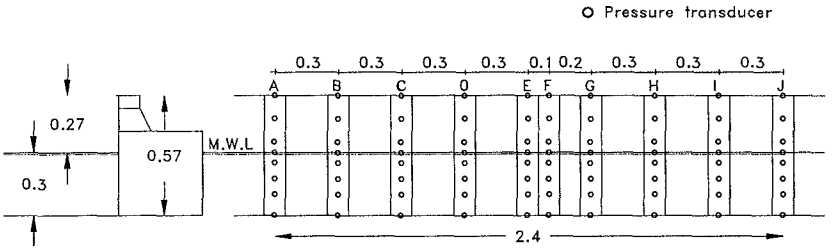

Figure 6 - Pressure transducer placement. Measures in meter.

From simultaneous measurements of force time series in different sections the reduction factor r_F can be calculated (actually r_F describes the non reduction in the force). Given a structure with length l_S the reduction factor is traditionally calculated as:

$$r_F(l_S,P)=\frac{\int_0^{l_S} F(x,t)dx}{l_S \cdot F_P(t)} \tag{3}$$

Notice that the reduction factor might be depending on the probability level P for the calculation.

Calabrese & Allsop (1997) and Burcharth (1998), calculated force reduction coefficients simply by doing statistical analysis of lateral integrated force time series, and then take r_F as the ratio between $F_{1/250}$ from the lateral integrated force time series and $F_{1/250}$ from the force times series measured in one section.

Though, such a method for calculating the force reduction will be influenced by diffraction patterns along the structure leading to too low reduction factors, which is unsafe. Furthermore, it is impossible to perform tests with high spatial resolution, so results will be based on a coarse resolution. Generally this effect will result in too high reduction factors. It is not possible assess these effects.

In the present study the spatial correlation coefficient used as the basis for calculation of the force reduction factor is calculated as:

$$\rho\left(\left|x_1 - x_2\right|\right) = \frac{\frac{1}{\Gamma}\sum_{i}^{\Gamma} F(x = x_1, t_i) F(x = x_2, t_i) \Delta t}{\sigma^{\Gamma}_{F(x=x_1)} \sigma^{\Gamma}_{F(x=x_2)}} \tag{4}$$

Here Γ is the part of the time series that the spatial correlation coefficient is based on (Γ can consist of disconnected parts of the time series). x_1 and x_2 are coordinates of the sections where the time series are measured along the structure. σ^{Γ}_F is the variance of the Γ part of the time series.

The advantages of using the cross correlation coefficients are that diffraction effects are removed from the measurements, and it is possible to get a very high spatial resolution by repeating the tests with different distances between the sections. Results will not be affected by smaller changes in the seastates.

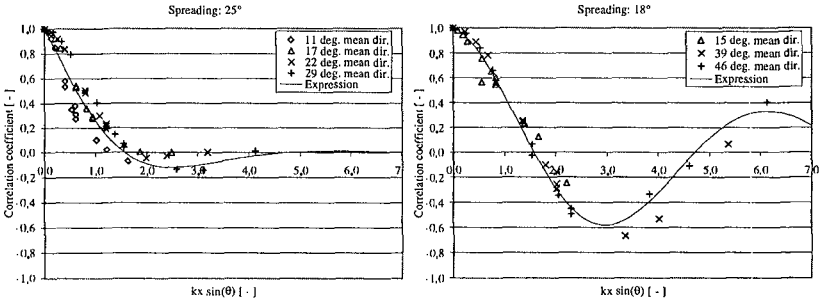

Figure 7 – Spatial correlation coefficients and fitted spatial correlation function $\rho_1 = \rho_1(kx\ sin(\theta))$ based on all data points in the time series.

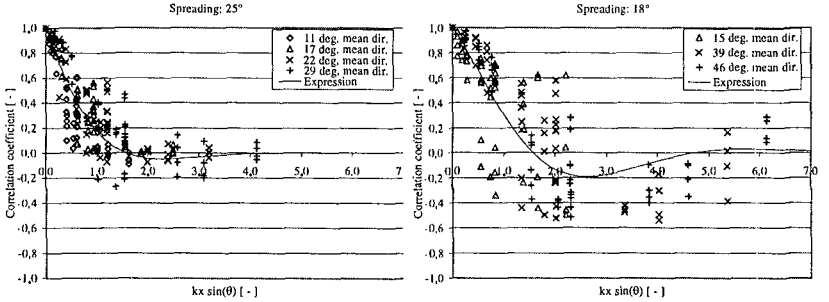

Figure 8 – Spatial correlation coefficients and fitted spatial correlation function $\rho_2 = \rho_2(kx\ sin(\theta))$ based on all force peaks in the time series.

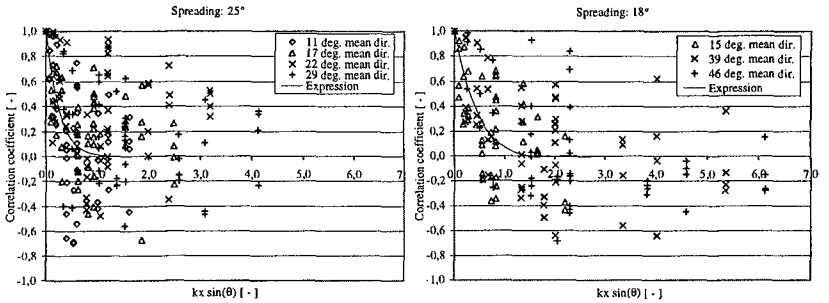

Figure 9 – Spatial correlation coefficients and fitted spatial correlation function $\rho_3 = \rho_3(kx\ sin(\theta))$ based on force peaks with a probability of occurrence less than 0.4 %.

Spatial correlation coefficients between the measured integrated pressures in sections with varying lateral distance have been calculated in three different ways, see Figure 7 – 9.

First spatial correlation function ρ_1 were calculated from the whole of the forces, i.e. using all data points. Second spatial correlation function ρ_2 were calculated from the parts of the force time series were the peaks of the forces were situated. Finally, the third spatial correlation function ρ_3 were calculated only from the parts of the force time series were the highest peaks (peaks with a probability of occurrence lower than 0.4 %) were situated. k is the wave number based on the peak period of the waves at shallow water.

It is obvious that the calculated spatial correlation coefficients show increasingly scatter when they are calculated from fewer data points. Also the figures indicates that the spatial correlation for the highest forces is lower than the spatial correlation for the whole time series. This means that the reduction factor for the highest peaks is lower than the reduction factors for the whole time series.

The reduction coefficients for the design forces were calculated using the spatial correlation function ρ_3:

$$r_F = \frac{1}{l_S^2} \int_{\frac{-l_S}{2}}^{\frac{l_S}{2}} \int_{\frac{-l_S}{2}+\xi}^{\frac{l_S}{2}+\xi} \rho_3 dx \; d\xi \tag{5}$$

It is assumed that the force peak will hit anywhere along the caisson with even probability. This means that the caisson in the calculation is placed randomly relative to the spatial correlation function.

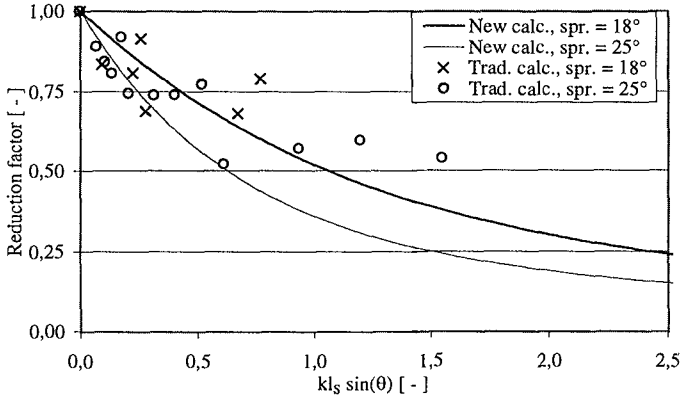

Figure 10 – Reduction factors for the horizontal wave loads.

Figure 10 show calculated reduction factors based on spatial correlation functions (eqn. (4)) compared to reduction factors based on a traditional method of calculation (eqn. (3)). For low values of the dimensionless structure length $kl_S\ sin(\theta)$ it is seen that a traditional calculation will underestimate the reduction factor where as for high values of the dimensionless structure length the traditional calculation will overestimate the reduction factor.

The calculated reduction factors can be described by the following equation:

$$r_F = \frac{1}{1 + a\left(kl_s \sin(\theta)\right)^{1.2}} \quad \begin{cases} for\ \sigma = 18°, a = 1.0 \\ for\ \sigma = 25°, a = 1.8 \end{cases} \quad for\ \theta > 5° \tag{6}$$

7. Conclusion

Regarding the effect of wave breaking on vertical caisson breakwaters, an increase compared to non-breaking waves and the predictions by the Goda formula of the wave forces was seen. It was found that the ratio of the waves breaking on the caisson controls the amplification of the force relative to the Goda force.

Because no full correlation exists between measured horizontal forces in sections with varying lateral distance, a force reduction for wide caisson sections are found. It has been shown that force reduction coefficients must be based on measured cross correlation coefficients. Expressions for reduction factors as function of wave angle and wave spreading are given.

8. Acknowledgements

This work has been carried with support from the framework programme *Dynamics of Structures* of the Danish Technical Research Council and the EU Commission MAST III project *Probabilistic Design Tools for Vertical Breakwaters*.

9. References

Aalborg University, Denmark, Hydraulics and Coastal Engineering Laboratory (1998). *An overview of performed laboratory tests related to the investigation of wave overtopping and harizontal wave forces acting on vertical breakwaters in non-breaking and breaking multidirectional seas.* Proc. EU MAST III project PROVERBS, 2nd Overall Project Workshop, Naples, 1998.

Aalborg University, Hydraulics and Coastal Engineering Laboratory (1997): *Results of Caisson Breakwater Tests in Multidirectional Breaking Seas (Internal Laboratory Test Report).*, Aalborg University, Dept. of Civil Engineering, Denmark, December 1997.

Allsop, N. W. H. & Vicinanza, D. (1996): *Wave impact loadings on vertical breakwaters: development of new prediction formulae.* 11th Int. Harbour Congress. Antwerp.

Allsop, N. W. H., McKenna, J. E., Vicinanza, D. & Whittaker, T. T. J (1996): *New design methods for wave impact loadings on vertical breakwaters and seawalls.* Proc. of teh 25th int. conf., Florida, ASCE.

Battjes, J. A. (1982): *Effects of short-crestedness on wave loads on long structures*, Applied Ocean Research, Vol. 4, No. 3.

Burcharth, H. F. (1998): *Identification and Evaluation of Design Tools, Report of Sub-Group A.* PIANC PTCII WG 28 on Breakwaters with Vertical and Inclined Concrete Walls, Aalborg University, 1998.

Calabrese, M. & Allsop, N. W. H. (1997): *Impact loadings on vertical walls in directional seas.* Proc. Task 1 Technical Workshop, Edingburg, EU MAST III project PROVERBS.

Franco, C., Franco, L., Passoni, G., Restano, C., van der Meer, J.W. (1995). *The effect of wave obliquity and short-crestedness on the horizontal and uplift forces on caisson breakwaters.* In: Final proceedings, MAST II, (MAS2-CT92-0047), MCS-Project: Monolithic (Vertical) Coastal Structures, Paper 4.8, 22 pp.

Goda, Y. (1974): *A new method of wave pressure calculation for the design of composite breakwaters.* Report Port and Harbour Research Institute, Vol. 12, No. 3 (in Japanese) or Proc. 14th Conf. Coastal Eng., Copenhagen, 1974, pp. 1702 – 1720.

Grønbech J., Hald T., Frigaard P. and Burcharth H. F. (1997) *Wave Loading and Overtopping on Caisson Breakwaters in multidirectional breaking seas.* IAHR seminar on Multidirectional Waves and their interaction with Structures, San Francisco, 1997.

Hald, T. & Frigaard, P. (1997): *Alternative method for active absorption in multidrectional waves.* IAHR Seminar Multidirectional waves and their Interaction with Structures, San Francisco, ISBN 0-660-17093-0.

Hashimoto, N., and Kobune, K. (1988): *Directional spectrum estimation from a Bayesian approach.* In Proc. 21st International Conference on Coastal Engineering, Malaga, Spain, 1988, pp. 62 – 76, ASCE.

McKenna, J. & Allsop, W. (1998): *Statistical distribution of horizontal wave forces on vertical breakwaters*, 26th International Conference on Coastal Engineering, Copenhagen, 1998.

Oumeraci, H., Hewson, P., Juhl, J. and van der Meer, J.W. (1995). MCS-Project: *Multi-Disciplinary Research on Monolithic Coastal Structures*, Final proceedings, MAST II, (MAS2-CT92-0047), MCS-project: Monolithic (Vertical) Coastal Structures. Papers Task 1-2.

Takahashi, S., Tanimoto, K. and Shimosako, K. (1994): *A proposal of impulsive pressure coefficient for design of composite breakwaters*. Proc. of Int. Conf. on Hydro-technical Eng. for Port and Harbour Construction. Port and Harbour Research Institute, Yokosuka, Japan.

Prototype Measurements of the Dynamic Response of Caisson Breakwaters

Alberto LAMBERTI[1] and Luca MARTINELLI[1]

Abstract

Prototype tests, aiming to describe the dynamics of caisson breakwater oscillations, were carried out at Genoa Voltri and at Brindisi Punta Riso. The rigid body natural frequencies and modes of oscillation of the caissons were evaluated as well as the rate of damping. The effect of the longitudinal array structure, never tested in physical models, was found extremely relevant; the Mass Spring Dash-pot model for an isolated caisson of Oumeraci & Kortenhaus (1994) was then conveniently updated in order to represent an array structure, showing finally good agreement with the recorded signals.

1. Introduction

When vertical breakwaters are subject to breaking waves, the plane front wall is hit by impulsive pressure loading, which, provided the wall resists the load, will accelerate the caisson causing its oscillation. In these conditions only part of the applied load will be transferred to the foundation and may cause failure, normally by displacing the caisson (Franco, 1994).

Several models were proposed in literature in order to simulate the caisson dynamics: Petrashen (1956), Loginov (1958), Hayashi (1965), Benassai (1975), Smirnov & Moroz (1983), Marinski & Oumeraci (1992), Goda (1994), Oumaraci & Kortenhaus (1994). The last two provide calibrations based on physical models that do not consider the effects of the longitudinal structure of the breakwater. Prototype measurements were carried out only by Muraki (1966), who identified a single system eigenfrequency ($\approx$0.2 Hz) but apparently the identified oscillations were not coherent with the wave force that was generating them.

Given the overall lack of knowledge of the response of a vertical caisson subjected to impulsive waves, the EU has financed a project, PROVERBS, with the aim of providing information and tools to allow the design of vertical breakwaters with a desired probability of failure, accounting for the mentioned dynamic behaviour. University of Bologna, within the project, was charged of exciting artificially some prototype caissons and measuring their dynamic response, in order to verify existing models of caisson dynamics and to check errors in the estimate of soil parameters.

In this paper the prototype tests and analysis will be briefly described (chapter 2); the analysis of the movements of the excited caisson showed the presence of natural modes of oscillation that could not be interpreted through the simple models present in literature (chapter 3), based on the dynamic description of an isolated caisson. The analysis of movements of the caissons adjacent to the excited ones suggested that these dynamic models should be adapted in order to represent the caisson array structure (chapter 4). In particular the model by Oumeraci & Kortenhaus (1994) was updated and calibrated, resulting suitable for the simulation of all the observed modes of oscillation (chapter 5).

[1] Università di Bologna, DISTART Idraulica, viale Risorgimento 2, I-40136 Bologna, Italy
E-mail: lamberti@idraulica.ing.unibo.it

Fig. 1 2 tons sand sac used for caisson excitation.

Fig. 2 100 tons tug-boat hitting the caisson

2. Description of the tests

The prototype tests were performed in Genoa Voltri and Brindisi, during 1997. The tests were carried out hitting a vertical breakwater with a sac and/or with a tug-boat in order to produce a significant dynamic response.

The sac, half filled with sand and weighting 2 tons, see Fig. 1, could fall completely free from a height of 5 m (or partially slowed down from a greater height) and it hit the caisson in proximity of the harbour edge, i.e. with a strong eccentricity. One accelerometer was installed on a "buoy" right into the sac on the sand surface, in order to give information on the applied force.

Fig. 2 shows the excitation due to a tug boat displacing 100 tons and hitting a caisson in Genoa Voltri (a 500 tons tug boat was used in Brindisi). The speed before the contact was close to 0.3 m/sec, varying on the occasions, and the impact force lasting about 0.5 sec for the smaller tug (1.0 sec for the bigger one) was evaluated by one accelerometer fixed on the tug-boat in the longitudinal direction.

The accelerations of the excited caisson and of the two adjacent ones were measured by 15 accelerometers placed as shown in Fig. 3. 9 accelerometers are placed on the central caissons, 1 describing the movements in the longitudinal direction and 8 describing the movements in the perpendicular plane. The adjacent caissons were monitored with 3 accelerometers each. In total, seven groups of three adjacent caissons were monitored, belonging to three vertical breakwaters (main breakwater in Voltri, western lee breakwater in Voltri and main breakwater in Brindisi, see Fig. 4) similar in shape but different in size ($3\ 10^7$ kg, $1\ 10^7$ kg and $2\ 10^7$ kg respectively). The joints between adjacent caissons are wide (5-10 cm) only for the case of the main breakwater in Genoa, but in all cases the superstructure has joints at the ends of each caissons. The rubble mound height vary from 2 m to 15 m for the different cases, and the foundation has a first layer of clayey-silty sand over a more fine material and rock below. A detailed description of the hydrodynamic conditions, caisson geometry, structural and foundation aspects are given in Lamberti et al (1998) and Lamberti & Archetti (1998).

In order to reduce the high frequency vibrations produced by sharp impacts, and thus avoid amplifier saturation, the accelerometers of the central caisson were fixed on a concrete cubes acting as mechanical filters. Since vibrations are greatly reduced passing from the central excited caissons to the adjacent ones, only the instruments placed on the central caissons needed to be mechanically filtered.

The filter (See Fig. 5) is formed by a concrete cube (side of 20 cm) glued to the superstructure through 4 round rubber disks. The response of this filter to an impulse is shown in Fig. 6. Note that the natural frequency of oscillation (≈20 Hz) is out of the range of interest ([1÷8] Hz) and that the damping is rather strong.

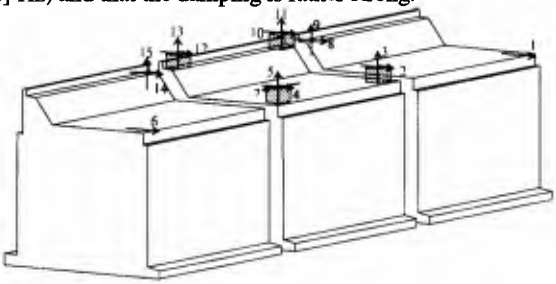

Fig. 3 Position of accelerometers.

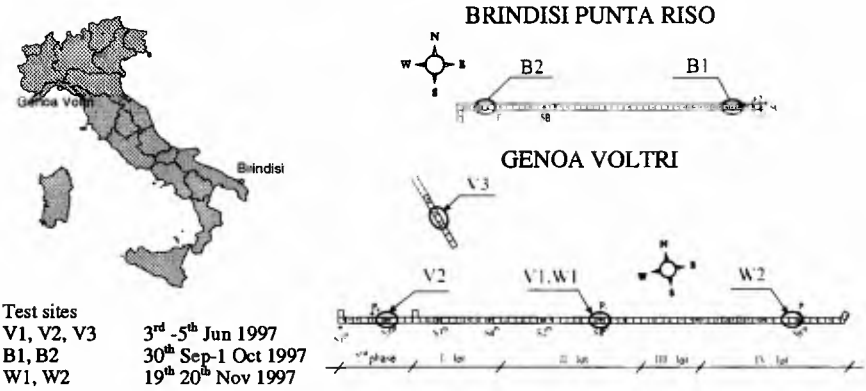

Fig. 4 Position of tested caisson in tested breakwaters. Symbols starting with letters S,P or F are relative to several geotechnical drillings, analysed in Lamberti & Archetti (1998) and Lamberti et al. (1998)

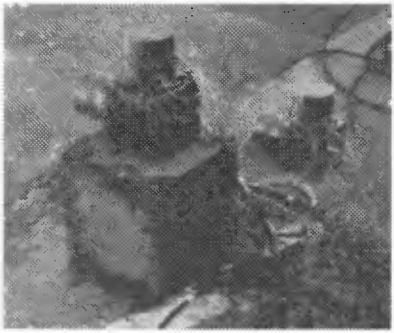

Fig. 5 The accelerometers of the central caissons were fixed on a concrete cube

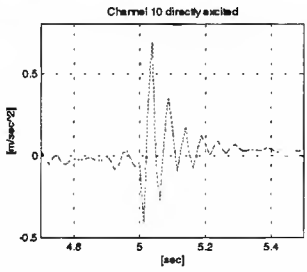

Fig. 6 The concrete block was excited by a hammer, and this is the response of one of the accelerometers fixed on the block. The eigenfrequency of the mechanical filter is about 20 Hz and the damping is high: amplitude is halved in one cycle.

3. Analysis of tests results relative to the hit caisson

The analysis started with the quantitative definition of the original applied force signal. For the sand sac exciting case the accelerometer direction was controlled fixing the accelerometer to a round and flat disk inserted into the sac, that could 'float' over the sand. The sac is not rigid and the average acceleration could not be measured; the signal was used for the evaluation of the length of the impact and for the force-response synchronisation. The force history was then defined assuming an anelastic behaviour, knowing the sac weight, the velocity before the impact and its duration. For the tug-boat excitation, the acceleration during the contact is actually proportional to the real applied force (a 10% hydraulic added mass was considered).

All the 16 channel registrations of the same type (same caisson, same kind of excitation) were cut 2 seconds before the impact and 8 seconds after it, analysed in the frequency domain and bandpass filtered (in Tab. 1 the range for the different tests is given), and pasted into a unique *sequence* in order to have data in a single file. Furthermore, *phase averaged signals* were created averaging each channel for the same kind of excitation. The records were synchronised maximising the cross correlation.

The interpretation scheme at the base of the analysis is that caissons can be considered as rigid bodies. Oumeraci & Kortenhaus (1994) described a Mass, Spring and Dash-pot (MSD) model where contributions to mass, stiffness and damping are due to rubble mound and foundation and to seawater. Such a system has three natural oscillation modes (see Fig. 7):

1. the *sway mode* (m_1): an almost horizontal translation (or rotation around a low centre);
2. the *roll mode* (m_2): a rotation around a higher centre;
3. the *heave mode* (m_3): an almost vertical translation.

In order to describe caisson movements a reference system was defined, the origin being in proximity of the instrumentation in order to reduce the overall error; components are:

1. *sway*, or harbour directed translation (ξ_o),
2. *heave*, or vertical translation (η_o),
3. *roll*, or rotation around a longitudinal axis (θ).

The choice of the pole 'O' (points of which displacements ξ_o and η_o are given) is arbitrary and the relation between any other pole position $\{x_o^c, y_o^c\}$ and its displacement is trivial (see Fig. 8):

$$\xi_c=\xi_o+\theta_o\, y_o^c$$
$$\eta_c=\eta_o-\theta_o\, x_o^c \qquad (1)$$
$$\theta_c=\theta_o \text{ (index is then usually omitted for rotations)}$$

The rigid body movements of the central caisson were extracted combining the eight horizontal and vertical accelerations of the central caissons with a best fit procedure: the sway signal is approximately obtained by averaging the four original horizontal signals; the heave is approximately the average of the vertical signals and the roll is similar to the difference between the upper and lower horizontal and vertical accelerations divided by the respective distance of the instruments.

A similar procedure was applied to the adjacent caissons, whose rigid movements have been averaged over the two caissons.

The following analysis consisted in assessing the Power Spectral Density of the responses and the Transfer Functions between force and response, both for phase averaged signal and sequence of tests. The

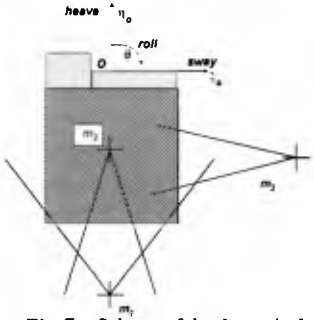

Fig. 7 Scheme of the theoretical oscillation modes of an isolated caisson and reference origin adopted for system identification.

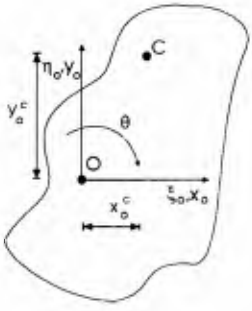

Fig. 8

power peaks coherent with the force for each signal were then evaluated, see Fig. 9 for instance. Since the force showed a rather flat spectrum in correspondence of peaks of the signals, their frequencies were interpreted as the natural frequencies of oscillation.

Signals were then band-pass filtered around the natural frequency.

Vibrations are only partially filtered out from the rigid body signal, they are finally recognised comparing the single and fitted rigid body signals in the appropriate frequency range.

The damping of the natural oscillations was assessed measuring, for each mode, the rate of amplitude decrease of the *phase averaged signals* after the impact. Similarly, comparing for each mode the acceleration amplitude and phase of the central and adjacent caissons, the amount of energy that travels along the breakwater was evaluated.

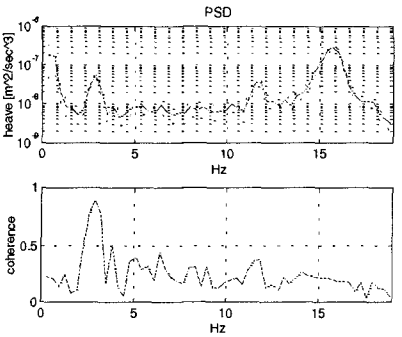

Fig. 9 PSD (with confidence interval 95%) of th fitted vertical acceleration of the central caisson and coherence with the force in case of sand sac impact (the recorded signal saturated, the reconstructed force signal is not well reliable at high frequencies, and this explains the low coherence of the two peaks above 10 Hz).

The upper graph of Fig. 10 shows the acceleration at quay level (precisely the phase averaged sway signal) induced in Brindisi by the tug-boat. It is possible to note immediately the presence of two different harmonics. The harmonics are presented in the lower graph of the same figure, and they are obtained bandpass filtering the signal around [0.5-1.8 Hz] and [1.8-6 Hz] (e.g. around the frequency peaks observed in the roll and sway signals, see Tab. 1).

The sum of this two harmonics reproduces almost exactly the original signal (almost undistinguished dotted line in upper graph). The same two harmonics are present in the 'roll signal' describing two rigid body rotations, i.e. two modes.

The rotation centre can be assessed band-pass filtering the *average signal* around the rigid mode frequencies and evaluating the ratio between sway and roll, and/or, for the central caissons, evaluating the acceleration directions at the four corners.

The power of the horizontal acceleration at any point can be easily evaluated combining sway and roll signals: the power of the horizontal acceleration is minimum if the pole is placed at the height of the rotation centre (Eq.1 governs the affect of changing the reference system).

Fig. 11 shows the relative power of the horizontal acceleration at different heights for the two different frequency bands: it is clear that the minimum of the curve, i.e. the position of the rotation centre, is placed below the caisson base.

Similar results are found for the cases of Voltri: this means that two modes have two low rotation centres, in total disagreement with the assumed mathematical model described in Fig. 7, according to which the higher frequency mode (present in the sway

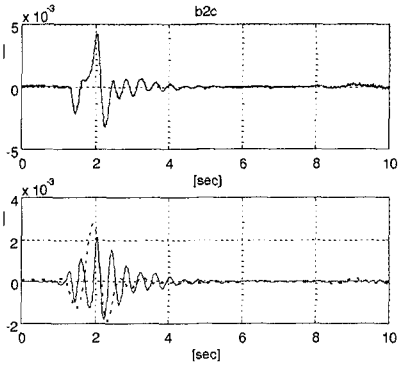

Fig. 10 The sway acceleration induced in Brindisi by the tug-boat (upper graph), is the sum of two harmonics, presented in the lower graph, and they are obtained bandpass filtering the signal around [0.5-1.8 Hz], dotted line, and [1.8-6 Hz], full line). The sum of this two harmonics reproduces almost exactly the origina sway signal (dotted line in upper graph).

and roll signal) should have a high rotation centre.

Fig. 12 represents, maybe more clearly, the same effect: within the frequency range of the 2nd observed frequency, the corners of the caissons move in the directions shown by the two graphs, obtained plotting the horizontal vs vertical acceleration. The rotation centre is located at the intersection of the two radii orthogonal to the displacement or acceleration: evidently a rotation around a very low centre is taking place.

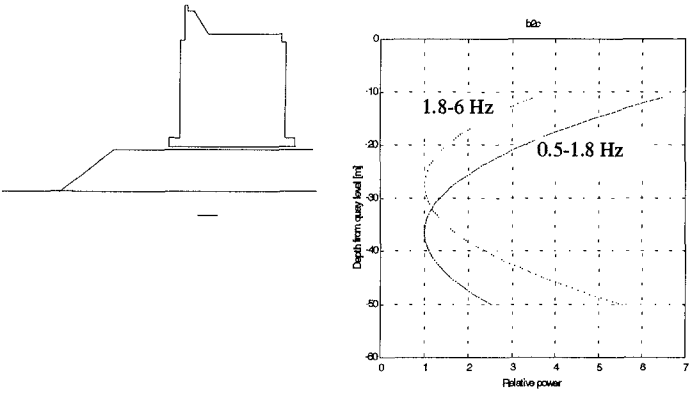

Fig. 11 The horizontal acceleration power (divided by its minimum value) in the two frequency bands (see Fig. 10) is presented as function of the distance from quay level. The minimum value of the acceleration power is considered as a good estimation of the height of the rotation centre. The rotation centre is placed well below the caisson base (caisson height = 21.7 m).

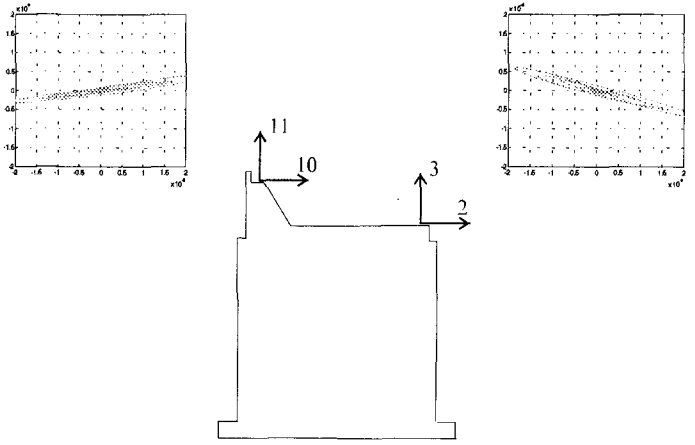

Fig. 12 The accelerations of the corners of the caissons describe a rotation around a very low centre. The graphs are obtained plotting the horizontal vs vertical acceleration in the higher frequency band [1.8-6 Hz], which according to the single caisson model is instead associated to a mode with a high rotation centre.

Tab. 1 The natural periods of oscillation were assessed as well as the associated rigid movements: for the almost horizontal oscillation, which are rotations around low centres, the actual depth below the base of rotation centre (R.C.) could be identified comparing the sway and the roll signal. Superstructure vibrations (v) are present only in case of sharp impacts and if the band of frequency, given in the rightmost column, is large enough. Non accurate data are given in square brackets.

Test Type	1st Frequency Sway/Roll signal [Hz]	R.C. below base [m]	2nd Frequency Sway/Roll signal [Hz]	R.C. below base [m]	Frequency present in Heave signal [Hz]	Vibrations [Hz]	Band of frequencies considered [Hz]
V1A	not evident		not evident		not evident		0.5-9
V1B	[2.3]		[3.2]		not evident		0.5-9
V1C	1.4		[2.3]		not excited		0.5-9
V2A	[1.2]		2.5		3.0		0.5-9
V2B	1.4		2.7		not evident		0.5-9
V2C	1.4		2.5		not excited		0.5-9
V3A	1.8		3.6		4.3		0.5-9
V3C	1.8		3.6		not excited		0.5-9
B1A		-	2.4	-	2.5	10	0.2-19
B1C	1.4	10	2.4	7	not excited	not excited	0.2-19
B2A			2.5	[0]	2.7	10	0.2-19
B2C	1.4	17	2.4	8	not excited	not excited	0.2-19
W1A			2.7	[0]	2.5	15	0.2-19
W2A			2.7	[0]	2.7	15	0.2-19
W2C	1.3	10	2.7	6	not excited	not excited	0.2-19

Tab 1 summarises the results of the analysis: the identified frequencies and modes. Two natural frequencies of oscillation were identified in the sway and roll signals plus one in the heave signal (see Fig. 9). The two modes recognised in the roll and sway signals represent rotations around low centres.

Even disregarding the position of the rotation centres, a 3 DOF model for isolated caisson could not be calibrated interpreting the observed oscillations as modes m_1 and m_2; the ratio between the measured eigenfrequencies was lower than foreseen by the model for any value of rotational and horizontal stiffness. Also using the model of the foundation suggested by Goda (1994), it was impossible to obtain a calibration without assuming an irrealistic anisotropy of the foundation.

In conclusion the test analysis pointed out three main modes, two of which are rotations around low centres (two m_1 modes, in disagreement with the system described in Fig. 7) and one is a vertical displacement (m_3).

4. Effect of adjacent caissons and interpretation of the identified modes of oscillation

The oscillation amplitudes of the caissons adjacent to the central one were almost one third compared the central one and significantly delayed; a large amount of energy is then subtracted from the central caisson by waves propagating along the breakwater. The effect of this wave can not be completely described by the considered single caisson model.

Comparing the horizontal oscillation of the central and adjacent caissons in a single frequency band (see Fig. 13), it was possible to observe that the oscillations were almost in phase in the frequency band [0.5-1.8 Hz] (around 1st observed frequency) and almost in opposition of phase in the frequency band [1.8-6 Hz] (around 2nd observed frequency).

A possible interpretation of the two identified sway modes involves then the longitudinal dimension: the 1st observed mode is given by a movement of all the caisson in phase, the 2nd observed mode is given by an alternate movement of these.

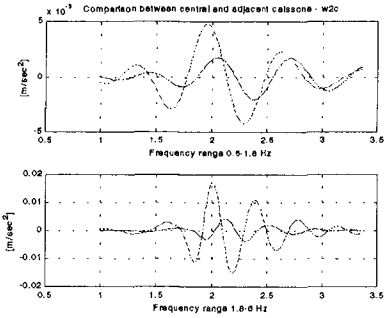

Fig. 13 Horizontal accelerations induced by the tug at Brindisi on the central and adjacent caissons: the oscillations are almost in phase in the frequency band around the 1st observed frequency (upper graph) and nearly in opposition of phase in the frequency band around the 2nd observed frequency (lower graph).

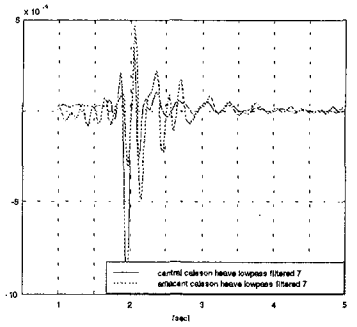

Fig. 14 7 Hz lowpass filtered heave for central and adjacent caissons. The frequency peak in the heave signal describes in phase movements of the central and adjacent caisson. Any other combination of vertical modes was not identified, probably due to the high environmental noise.

The MSD model was then modified considering an array of caissons, formed by several MSD modules connected one another by spring and dash-pot elements. The added stiffness was estimated as a fraction of the stiffness between caisson and foundation, and the proportionality coefficient was calibrated so that the adjacent caisson accelerations do fit the actually measured ones. Damping coefficients were not calibrated directly, since the model describes damping effects directly on the uncoupled modes.

Since the system is symmetric and it was excited symmetrically, only the symmetric movements were considered in the model.

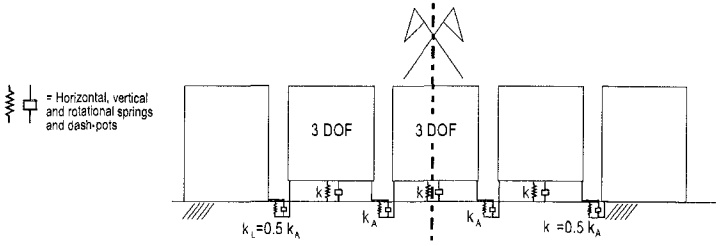

Fig. 15 6 DOF model considering the 3 DOF of the central caisson and 3 symmetrical DOF of the adjacent caisson on the plane perpendicular to the longitudinal direction of the breakwater.

A boundary condition must be inserted if the represented array of caissons is shorter than the actual one. If it is assumed that the last caisson is fixed and the stiffness between the end caissons and the adjacent ones (K_L) is equal to the stiffness between any two other caissons (K_A), the system results more stiff than it actually is; the opposite case is found if the last caissons are supposed to be free to move, i.e. K_L=0. The assumed lateral condition was then a compromise, consisting of a reduction of the last stiffness coefficient to 50 % of the others (K_L/K_A=0.5). The effect of this assumption is reduced if

more caissons are considered, and for an array of 7 caissons the two limit cases do not affect significantly the acceleration of the central caisson.

Let's consider, for simplicity, a model of just three caissons: the output is not totally satisfactory, but it is possible to highlight the most important characteristics. The system has 6 DOF (three movements of the central caisson and three symmetrical movements of the two adjacent ones) and thus 6 eigenmodes. Fig. 16 shows that two of these eigenmodes are actually formed by rotations around low centres: one is due to all the caisson moving together and the other to a movement in opposition of phase. The observed natural oscillations (Tab. 1) can be interpreted along this line.

When the adjacent caissons move in phase with the central caisson (superscript +), the geodynamic added mass is reasonably bigger than in case of a movement in opposition of phase (superscript -), since in the second case part of the foundation between adjacent caissons is resting (not moving). This effect explains different heights of the 'm_1' rotation centres (see Fig. 11). Such difference is less important for the case of Voltri, where the longitudinal dimension of the caisson is bigger (the caisson length is 30.1 m in Voltri, 21.0 m, in Brindisi). A small mixed term in the geodynamic added mass matrix was considered (only 1/3 of the geodynamic added mass is considered for an opposition of phase) in all the simulations.

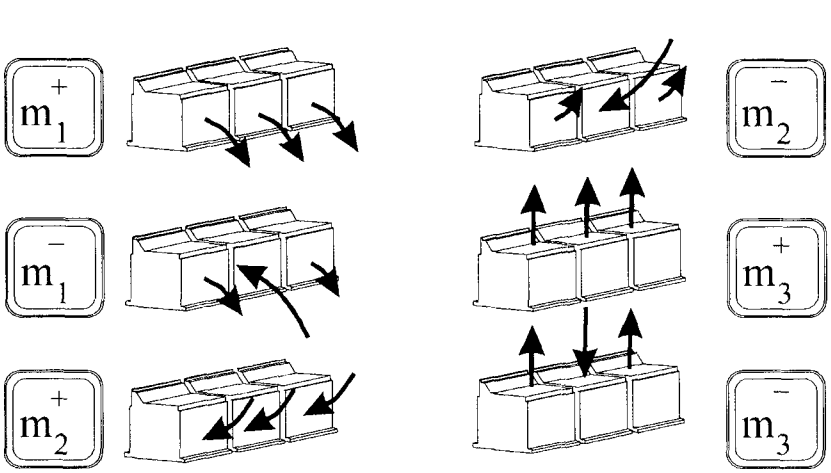

Fig. 16 If the two adjacent caissons are considered in the dynamic system, each eigenmode described in Fig. 7 appears twice: the mode due to all the caisson moving together (superscript +) and the mode due to a movement of the caissons in opposition of phase (superscript -).

In heave oscillations just one frequency peak was clearly identifiable, which was apparently associated to an 'in phase' motions of the caissons (see Fig. 14) and it was thus interpreted as mode m_3^+. Mode m_3^- and of type 'm_2' were not identified, probably due to the low signal/noise. In the next chapter Tab. 2 shows that modes 'm_2' are almost not excited by the tug, while for the falling sac excitation case in Fig. 22 a comparison between simulated and measured PSD of the roll signals is presented, showing that computed 'm_2' frequency peaks in the range 3.9-7.9 Hz could be hidden by the environmental noise.

5. Numerical simulations and calibration of the final model

The final simulations were performed considering a 12 DOF model presenting an array of 7 caissons.
The horizontal, vertical and rotational stiffness between caisson and foundation depend on the shear modulus G, and, secondarily, on the Poisson coefficient (=0.4). G was evaluated assuming E_o=320 MPa (Young modulus for average pressure = 100 kPa);

$E \propto \sqrt{\sigma_v \frac{1+2K_o}{3}}$, vertical pressure σ_v=350 kPa, coefficient of lateral confinement K_o= 1.

The horizontal and rotational stiffness between central and adjacent caisson (K_A) was calibrated (in a preliminary way) as 40 % of the stiffness between caissons and foundation (K_C) given by the elastic homogeneous half space theory. For vertical oscillations, the stiffness of the link with the adjacent caissons was calibrated as 60 % of the stiffness with the foundation.
Fig. 17 shows the simulation of the horizontal acceleration at quay level for the case of Voltri (W2). The exciting force due to the tug boat is presented in the upper graph. The simulation is compared with phase averaged sway signal of the central caisson.
Also the recorded rotational oscillations were found to be well simulated.

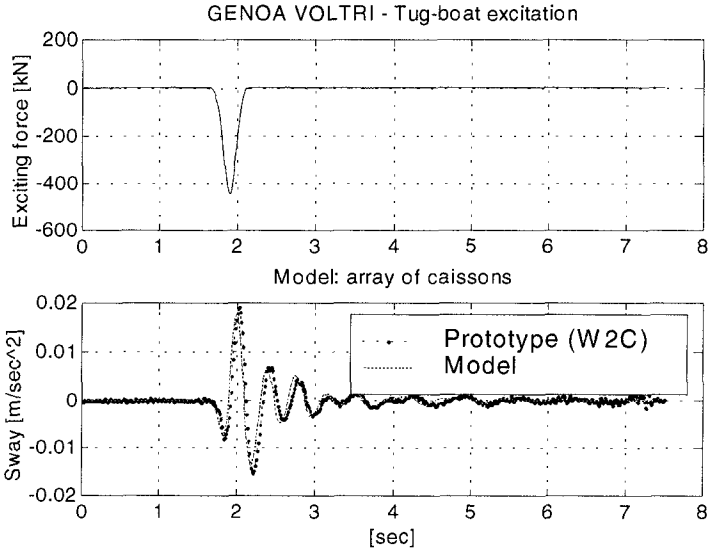

Fig. 17 Simulation of horizontal acceleration at quay level for the case of Voltri, induced by the tug-boat excitation.

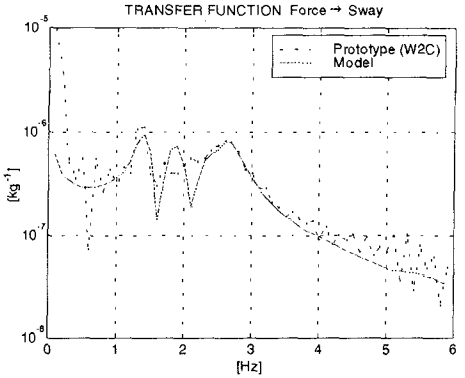

Fig. 18 Transfer Function between exciting force and accelerations shown in Fig. 17

Comparison between the model and experimental transfer function between such acceleration and the applied force, presented in Fig. 18, is extremely relevant. The first peak of the TF is placed at 1.4 Hz and it is relative to a sway mode of all the caissons in phase (m_1^{+++}). The last peak is placed at 2.7 Hz and is relative to a sway mode of the caissons in opposition of phase (m_1^{+-}). Since the model represent 7 caissons (the central one plus 3 couples) there are in total 4 sway modes, which are modes m_1^{+++}, m_1^{+-}, and the two modes m_1^{+--} and m_1^{--+} with intermediate eigenfrequency (1.9 Hz and 2.4 Hz, in the simulation). The horizontal force applied by the tug does not excite the four heave modes, and also the four rocking ones are weakly excited. The tug-boat impact excited only the rotations around low centres mainly for two reasons:
1. the point where the force is applied is very close to the rocking centre and
2. the length of the impact is not short compared to all 'm_2' eigenfrequencies.
Tab. 2 shows the relative power of the excited modes (in terms of rotations).

Tab. 2 Computed eigenmodes for Voltri main breakwater, excited by the tug boat. The damping coefficients (reduction of the oscillation equal to 40% per cycle) were globally calibrated on the basis of the transfer function. The vertical positions of the computed rotation centres, R.C., are given.

Mode	Eigen-frequency [Hz]	Relative power [%]	Computed R.C. [m above base]	Mode	Eigen-frequency [Hz]	Relative power [%]	Computed R.C. [m above base]
m_1^{+++}	1.4	45.1	-7.5	m_2^{+++}	3.9	0.3	17.6
m_1^{+-}	1.9	26.9	-7.7	m_2^{+-}	5.2	0.1	16.9
m_1^{--+}	2.4	10.5	-7.8	m_2^{--+}	6.8	0.1	16.2
m_1^{+-}	2.7	17.2	-8.0	m_2^{+-}	7.9	0.1	15.8

In prototype, the breakwater is formed by many caissons and thus many modes are placed between mode m_1^{all+} and $m_1^{alternate+-}$, i.e. a continuum spectrum of modes is present.

The vertical oscillations induced by the sand sac impacts are not perfectly simulated (see Fig. 19) probably because the applied force, as explained in chapter 3, was reconstructed and since the impact is not really impulsive (the impact lasts about .15 sec), the time history has some importance. The simulated response could reproduce only the first cycles of the recorded acceleration oscillation. Since the impact strongly excites superstructure vibrations, identified at 10-15 Hz, the rigid body oscillations in Fig. 19 were assessed by filtering below 10 Hz the recorded signal.

In the records of the vertical accelerometers 9 and 15 placed in the adjacent caissons (the position is shown in Fig. 3) there is much less noise. Since the main

breakwater caissons in Voltri have large longitudinal joints, the superstructure vibrations excited in the central caissons do not pass to the adjacent ones. The low-pass filtering at 10 Hz is then not necessary for these signals (presented in Fig. 20); they are similar between them for symmetry reasons and they describe the vertical acceleration of the seaward corner of the adjacent caissons. Such acceleration was simulated and presented in Fig. 21.

Comparing Fig. 20 and Fig. 21, it can be seen that the first three oscillations are very well defined with regard to maximum values and wave lengths, while a 4 Hz component seems to be unsufficiently damped in the model (a constant damping was applied to every vertical mode, resulting in a reduction of the oscillations of 47% per cycle)

Tab. 3 shows how the sand sac impact excite the various simulated modes in terms of displacements. In general the 'all in phase' and the 'alternate' motions are the most excited modes in terms of accelerations, the former more than the latter.

Note that all the modes are excited, even the 'm_2' modes that were not identified.

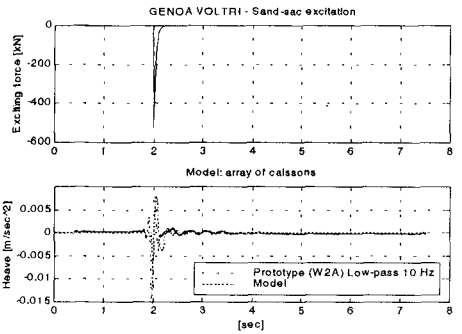

Fig. 19 Comparison between simulated and measured vertical accelerations induced by the falling sand-sac. The vibrations induced by the sharp impact are filtered out (lowpass 10 Hz) for a better comparison.

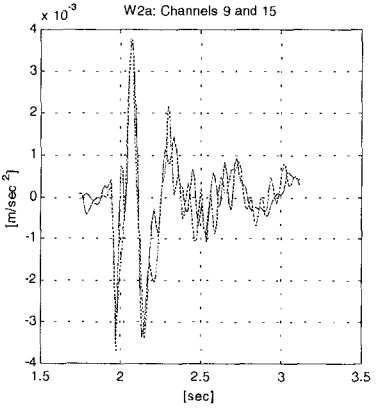

Fig. 20 Mean acceleration averaged over the W2A tests. Channels n° 9 and n° 15 (placed on the adjacent caissons, see Fig. 4)

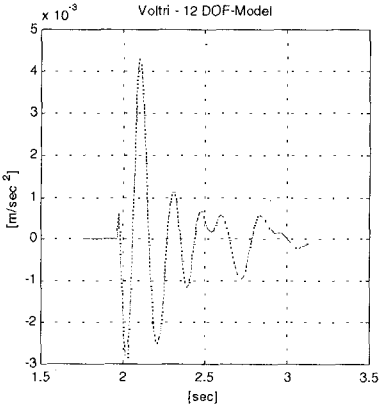

Fig. 21 Simulation of the vertical accelerations of the seaward corner of Voltri main breakwater caisson, induced by the sand sac falling in the adjacent caisson.

Fig. 22 presents PSD of the simulated roll induced by the sand sac excitation, compared to the recorded case: at 2.5 Hz an experimental peak is present, much higher than the simulated one, which might be effect of the vertical oscillation motion having almost the same frequency that was not perfectly identified by the combination of signals that described the rigid body 'roll', or it could be induced by resonance between the two modes with same frequency. Above 10 Hz a lot of energy is present, relative to

superstructure vibration. It is evident that in between the electronic noise can hide the peaks of the simulated signal.

Tab. 3 The falling sand sac eccentric impact excites not only the heave modes but also and the rocking and sway modes. The relative power of each mode is given below (for a meaningful comparison, the rotational oscillations were multiplied by the lever arm of the force, i.e. the eccentricity of the falling sac). The applied reduction per cycle was globally calibrated as 47% for the vertical modes, 40% for the rotational modes.

Mode	Eigen-frequency [Hz]	Relative power [%]	Mode	Eigen-frequency [Hz]	Relative power [%]	Mode	Eigen-frequency [Hz]	Relative power [%]
m_1^{+++}	1.4	12.7	m_2^{+++}	3.9	21.1	m_3^{+++}	2.5	9.8
m_1^{+-}	1.9	9.3	m_2^{+-}	5.2	13.0	m_3^{+-}	3.8	3.9
m_1^{-+}	2.4	4.6	m_2^{-+}	6.8	5.8	m_3^{-+}	5.0	1.4
m_1^{--}	2.7	9.0	m_2^{--}	7.9	7.5	m_3^{--}	5.7	2.1

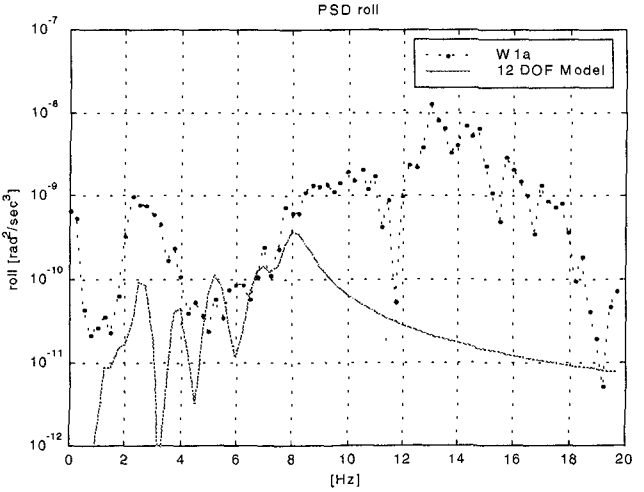

Fig. 22 PSD of computed roll, solid line, and PSD of roll derived from tests W1a: the simulated modes 'm_2 type' (frequencies in [3.9-7.9 Hz], solid line) might be present but hidden by the environmental noise

6. Conclusions

Due to the interaction of all the breakwater caissons, the eigenmodes of caisson system are many. The most excited modes in case of a horizontal force applied at the sea-level (as for the tug-boat or a breaker hitting the breakwater) are all sway oscillations (rotational oscillations around centres placed below the caissons base). The relative eigenfrequencies were measured for the cases of both Genoa Voltri and Brindisi breakwaters and shown in Tab. 1: they are in the range 1.3-3.6 Hz

The heave and rocking oscillations (vertical oscillations and rotation around high centres) were excited only by the falling sand sac load, which induced also high vibration of the superstructure; consequently much more noise was present in the records. The most excited heave mode (apparently the 'all in phase' mode) had frequency around 2.5 Hz.

Unfortunately the rocking modes were not identified with certainty, probably due to the high noise present: Fig. 22 shows that the noise is higher than the model simulated signal.

The superstructure vibrations of the analysed caissons were assessed and found in the range 10-15 Hz.

A MSD model combined to an elastic half space foundation model (Oumeraci and Kortenhaus) can describe the system dynamics only if the movements of at least three adjacent caissons are represented. A very good description (see Fig. 17) of the system dynamics was obtained simulating the movements of an array of 7 caissons. The calibrated parameters were 5: the foundation stiffness for isolated caissons, the stiffness between central and adjacent caisson (40% of the stiffness with foundation for modes 'm1' and 60% for modes 'm3') and the damping of the 'm1' and 'm3' modes (reduction per cycle of 40% and 47%, respectively).

The calibration of the foundation stiffness was obtained considering the relation between the Young modulus and the confining stress (the assumed Poisson coefficient being 0.4 and not yet better investigated). The calibration for both Brindisi and Genoa Voltri suggested a Young modulus of 320 MPa relative to a nominal average pressure of 100 kPa.

Acknowledgements

The partial support of European Community within project "Probabilistic design tools for vertical breakwaters (PROVERBS)" under contract MAS3-CT95-0041 is gratefully acknowledged.

References

E. Benassai (1975). *The stability against sliding of breakwaters under action of breaking waves.* PIANC, Vol II, n°21

L. Franco (1994) *Analysis of the dynamic response of caisson breakwaters.* Coastal Engineering, vol. 22, nos 1-2, pp. 31-55.

Y. Goda (1994). Coastal Engineering, vol. 22, nos 1-2, pp. 31-55.

T. Hayashi (1965) *Virtual mass and the damping factor of the breakwater during rocking, and the modifications by their effect on the expression of the thrusts exerted upon breakwater by the action of breaking waves.* Coastal Eng. Jpn., 8, pp. 105-117.

A. Lamberti & L. Martinelli (1997) *Detailed design of prototype tests and analysis.* PROVERBS 2nd Project Workshop, Las Palmas, 18-22 February 1997

A. Lamberti, L. De Angelis & L. Martinelli (1998) *The Port of Genoa Voltri.* PROVERBS 3nd Project Workshop, Napoli, 25-27 February 1998.

A. Lamberti & R. Archetti (1998) *The Port of Brindisi.* PROVERBS 3nd Project Workshop, Napoli, 25-27 February 1998.

V.N. Loginov (1958): *Dynamic analysis of the stability of harbour protective structures under the action of wave impacts.* Tr. SNIIMF, vol. 19, pp. 58-68 (in Russian)

J.G. Marinski & H. Oumeraci (1992): *Dynamic response of vertical structures to breaking wave forces - review of the CIS design experience.* Proceedings International Conference Coastal Engineering (ICCE), ASCE, vol. 23, Part 2, pp. 1357-1370.

Y. Muraki (1966): *Field observation of wave pressure, wave run-up, and oscillation of breakwater.* Proceedings International Conference Coastal Engineering (ICCE), ASCE, Tokyo, Japan, vol. 10, pp. 302-321.

H. Oumeraci & A. Kortenhaus (1994) *Analysis of the dynamic response of caisson breakwaters.* Coastal Engineering, vol. 22, nos 1-2, pp. 159-183.

V.I. Petrashen (1956) *Action of breaking waves on vertical structures.* Sbornik trudov VNIIGs, 7, pp. 75-110 (In russian)

G.N. Smirnov & L.R. Moroz (1983) *Oscillation of gravity protective structures of a vertical wall type.* IAHR, Proc. 20th Congress, Vol. 7, pp. 216-219

Experimental and FEM Simulation of the Dynamic Response of a Caisson Wall Against Breaking Wave Impulsive Pressures

Shigeo Takahashi [1], Muneo Tsuda [2], Kojiro Suzuki [3], and Ken-ichiro Shimosako [4]

Abstract

After presenting a summary of field survey-observed damage incurred over the past 20 years by caisson walls of Japanese breakwaters, this study describes a series of model experiments and three-dimensional FEM simulations performed to evaluate the dynamic response of a caisson wall subjected to breaking wave impulsive pressure. The important roles played by "elastic" and "inertia" soil pressures are subsequently clarified, and good agreement is obtained between measured and calculated results. The proposed calculation method, which applies the Goda pressure formulae in conjunction with the impulsive pressure coefficient α_I, is expected to provide a practical design method against impulsive pressures.

1. INTRODUCTION

Caisson walls seldom fail even when acted upon by impulsive wave pressures that are large relative to normal design wave pressures, *i.e.*, the strain in the wall is reduced by the static and dynamic response of the filling soil and water contained within the caisson chambers. While these responses tend to stabilize a caisson, they have not yet been specifically considered in the design evaluation process. Moreover, if the impulsive pressures are quite large and act at very high frequency, a caisson breakwater can suffer failure (Tanimoto *et al.*, 1975).

Such effects led to the present study whose main objective is to establish a design method against wave pressures, especially impulsive ones, such that wave action failures can be prevented. We consider a caisson wall containing filling sand in the caisson chambers, and focus our attention on its dynamic response, which includes both "inertia" and "elastic" effects, against impulsive wave pressure.

After conducting a field survey of Japanese breakwaters—to determine damage

[1] Chief, Maritime Structures Lab., Port and Harbor Research Institute (PHRI), MOT, 3-1-1 Nagase, Yokosuka 239, Japan.

[2] Research Engineer, Technical Research Institute, TOA Corporation, 1-3 Anzen-cho, Tsurumi-ku, Yokohama 230, Japan.

[3] Research Engineer, Maritime Structures Lab., PHRI, MOT, Japan.

[4] Senior Research Engineer, Hydraulics Div., PHRI, MOT, Japan.

that has occurred in caisson walls over the past 20 years—a box-shape model caisson was used to perform a series of experiments in which soil pressures and wall strain were measured, *i.e.*, impulsive pressures were applied after filling the model caisson with sand and water or only with water. We also carried out three-dimensional FEM calculations to simulate the strains generated by impulsive wave pressures, and then compared measured and calculated results such that the applicability of the simulations could be evaluated. Finally, the employed FEM simulation is used to investigate the failure of caisson walls of a prototype built at Mutsu-Ogawara Port.

2. CAISSON WALL FAILURES

Current Design Method of Caisson Wall against Wave Actions

Figure 1 shows a diagram of a breakwater caisson, *i.e.*, a large, reinforced concrete box in which chambers separated by inner walls are filled with sand and water. The outer and inner walls have a thickness of 40–60 and 20–30 cm, respectively. The caisson's front wall is designed against wave pressures, static soil pressure of filling sand, and static water pressure (Fig. 2). The wave pressure distribution at the wave crest is determined by the Goda pressure formulae (Goda, 1974), while that of the wave trough by the relation $0.5\ w_0H$.

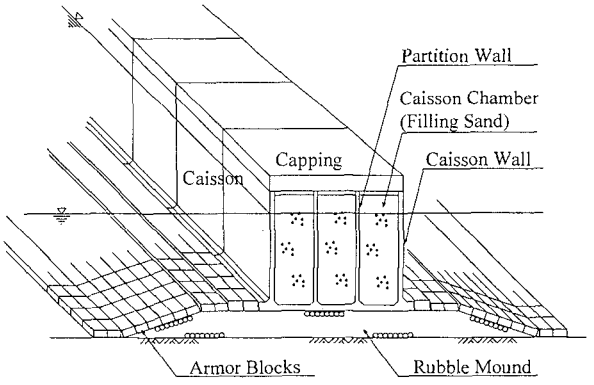

Fig. 1 Diagram of caisson breakwater.

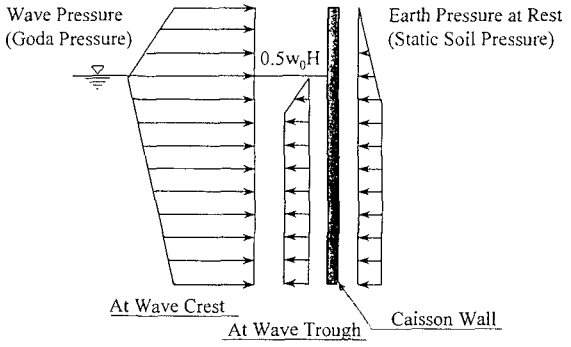

Fig. 2 Current design method.

Table 1 Summary of caisson wall failures over past 20 years.

PORT	TYPE OF BREAK WATER	DATE OF FAILURE	FAILURE FEATURES OF CAISSON WALL	CAUSE OF FAILURE
MASHIKE	Composite type	1977/04	Caisson wall damage (cracks) filling sand flow-out	Impulsive wave pressure due to abrupt water depth change
KUSHIRO	Horizontally composite type	1981/08	1m hole on wall	Collision of blocks at the end of covering blocks (under construction)
ONAHAMA	Composite type	1981/08	Caisson wall damage (cracks) filling sand flow-out	Impulsive wave pressure due to high rubble mound
OMAEZAKI	Horizontally composite type	1981/08	1m hole (not peneterated)	Collision of blocks at the end of covering blocks (under construction)
SINNGU	Composite type	1982/09	Caisson wall damage (cracks) filling sand flow-out	Impulsive wave pressure due to abrupt water depth change
A	Horizontally composite type	1987/02	1 caisson almost destroyed	Impulsive wave pressure due to insufficient block-covering (under construction)
B	Horizontally composite type	1987/12	Cracks and 3m hole, and Concrete crown damage	Impulsive wave pressure at the end of covering blocks around breakwater head
KATADOMARI	Composite type	1987/08	1 caisson almost destroyed	Impulsive wave pressure due to the settlement and scttering of covering blocks
UDONO	Composite type	1990/11	Caisson wall damage (Cracks and holes)	Impulsive wave pressure due to high rubble mound cuased by sea bottom profile change
KASHIMA	Composite type	1990/11	1 caisson almost destroyed	Impulsive wave pressure due to high rubble mound
MUTSU-OGAWARA	Horizontally composite type	1991/02	1 caisson almost destroyed, 4 caissons damaged	Impulsive wave pressure due to end of covering wave dissipating blocks
OMOTO	Horizontally composite type	1991/02	3 caissons damaged	Impulsive wave pressure due to settlement and scttering of covering blocks
MINAMINOHAMA	Composite type (Jetty)	1991/09	1 caisson almost destroyed	Impulsive wave pressure due to steep sea bottom, Failure of breakwater head caisson
K	Horizontally composite type	1996/09	Holes on walls in several caissons	Collision of covering blocks
H	Horizontally composite type	-1996	Holes and cracks on 18 caissons in 129 caissons	Collision of covering blocks
M	Horizontally composite type	96/8,97/9	Holes on walls in 3 caissons	Collision of covering blocks
W	Composite type	1997/08	1 caisson almost destroyed,	Impulsive wave pressure due to steep sea bottom, Failure of breakwater head caisson

Caisson Wall Failures in Japan

Table 1 presents a summary of field survey-observed damages incurred over the past 20 years by caisson walls of Japanese breakwaters (Hattori *et al.*, 1984; Miyai *et al.*, 1993), where 12 cases due to impulsive wave pressure are indicated. Although failures at fishery ports are not included, the number of failures is still quite small relative to the total number of caissons in Japanese ports (> 16,000). Table 2 summarizes the main reasons for caisson wall failures, with each reason being discussed next using a typical case.

Table 2 Summary of main reasons for caisson wall failures.

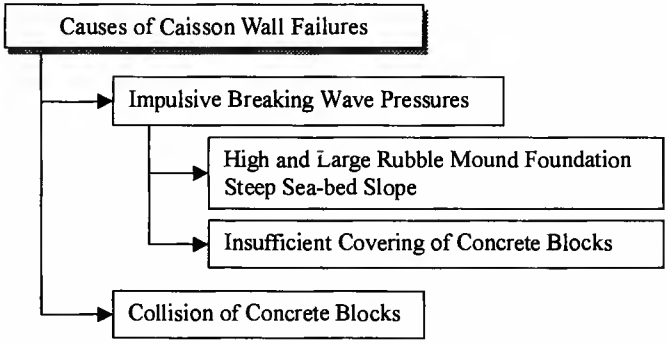

Udono Port Case

Photo 1 shows a caisson wall failure at Udono Port, being damage caused by impulsive breaking wave pressures produced due to the presence of a high, large rubble mound foundation. Note that four caissons slid and one suffered caisson wall damage. Such failures seldom occur nowadays because the generation of impulsive pressure due to this type of rubble mound is common knowledge among breakwater design engineers. In this particular failure, the mound was not originally high, but due to substantial movement of a sandbed situated near the breakwater, the water depth in front of the breakwater increased such that the relative height of the mound became high.

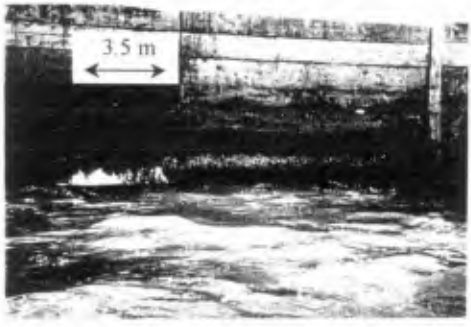

Photo 1 Damaged caisson wall.

Mutsu-Ogawara Port Case

Impulsive pressures can also be generated when caisson walls are not sufficiently covered by concrete blocks. This situation especially applies to horizontally composite type breakwaters, where the caisson is covered by concrete blocks that dissipate wave energy. Unfortunately, the covering can sometimes become insufficient due to settlement or scattering of the blocks, or it might be insufficient at

the transition part from the horizontally composite type to ordinary composite type.

Photo 2 shows damage to a breakwater at Mutsu-Ogawara Port following a severe storm equivalent to its design conditions (Hitachi, 1994). Caisson No. 7 was nearly destroyed by impulsive pressures from waves breaking on concrete blocks which were scattered and settled.

Figure 3 shows the breakwater's plane view and cross section. While the upper part of caisson No. 7 was completely destroyed, caisson No. 8 moved only 0.4 m and its wall was not damaged. As caisson No.8 was designed to be located at the transition part, such impulsive pressures were considered in the design. Caisson No. 7 was covered sufficiently by blocks, but due to scattering the transition part was extended such that it reached caisson No. 7. In fact, it had a wall thickness of 70 cm compared to that of No. 7 which was only 45 cm. As will be discussed later, a thicker wall led to differences in resulting damage.

Photo 2 Damaged caisson No. 7.

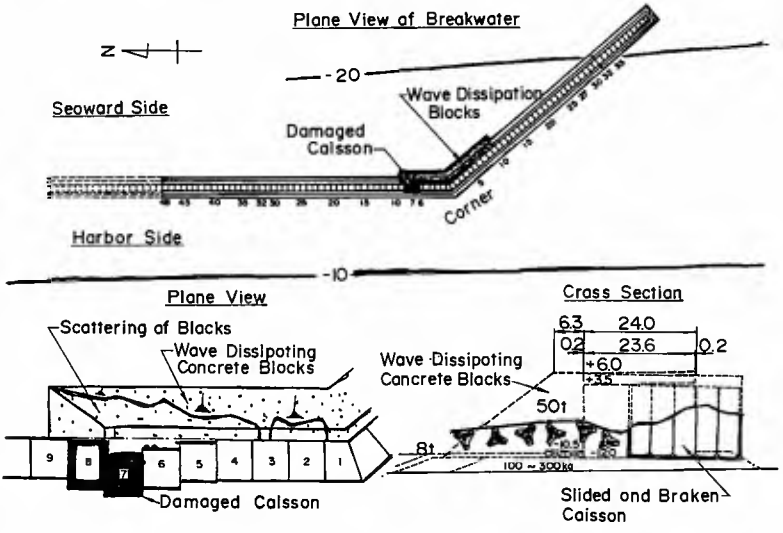

Fig. 3 Plain view and cross section of the breakwater.

Collision with Concrete Blocks

Photo 3 shows a horizontally composite type breakwater whose caisson wall suffered damage due to concrete blocks colliding with it. When a breakwater is located in rough seas, the blocks are usually large and can hit the wall making holes due to shear failure of the wall. Since impulsive breaking wave pressures are typically responsible for producing damage, here we focus our attention on this type of failure and do not consider in detail those due to collisions with concrete blocks.

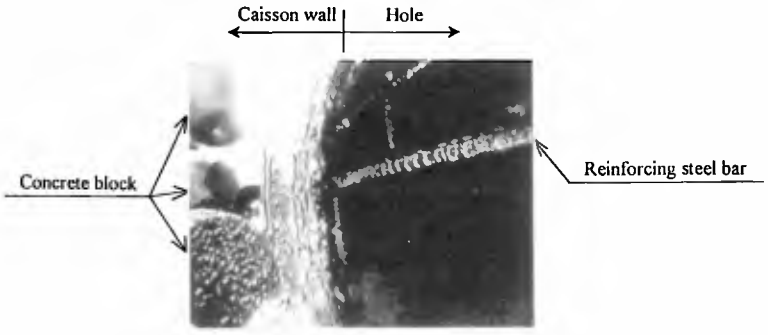

Photo 3 Damaged caisson.

3. MODEL EXPERIMENTS

Experimental Setup

Figure 4 shows a cross section of the box-shape model caisson and locations of instrumentation for measuring pressure, strain, and acceleration. The walls are made from acrylic plates, with the front wall having a thickness of either 10 or 15 mm. Regular waves were applied. The shallow water concrete blocks situated directly in front of the caisson generated wave breaking such that impulsive wave pressures impact the front wall. Note that in order to clearly see the effect of soil pressures due to wall acceleration and the resultant wall deformation, we deliberately used a single

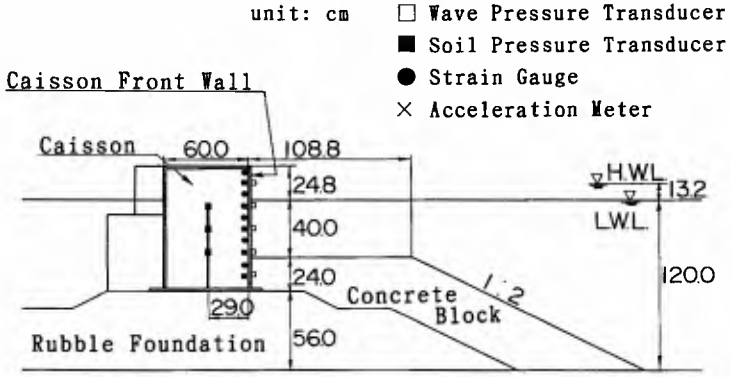

Fig. 4 Experimental setup and instrument locations.

caisson model in which the width of the wall is quite long compared to that of a standard caisson.

The natural frequency of the model caisson wall was measured to be 38.5 Hz in air but only 6.3 Hz in water with filling sand present; values that are nearly the same as theoretical ones. The reduction in frequency is due to the added mass effect of water and sand surrounding the wall.

Elastic Soil Pressure and Inertia Soil Pressure

We consider two types of internal soil pressure:
(1) elastic soil pressure due to soil acceleration and
(2) inertia soil pressure due to soil deflection.
The former is mainly discussed based on experiments using non-breaking waves, while the latter using impulsive breaking waves. Static soil pressure, *i.e.*, earth pressure at rest, is also considered.

Caisson Wall Strain Against Non-Breaking Waves

Figure 5 shows the strain and internal soil pressure generated in a sand-filled caisson when a non-breaking wave hits the front wall. Since the internal soil pressure is nearly proportional to wall displacement, we term this as "elastic" soil pressure.

The wave pressure and elastic soil pressure are compared in Fig. 6, where the elastic soil pressure shows a peak value ≈ 70% of the standing wave pressure. This elastic soil pressure assuredly reduces the strain significantly, and therefore resultant pressure (p–q) acting on the wall is greatly reduced.

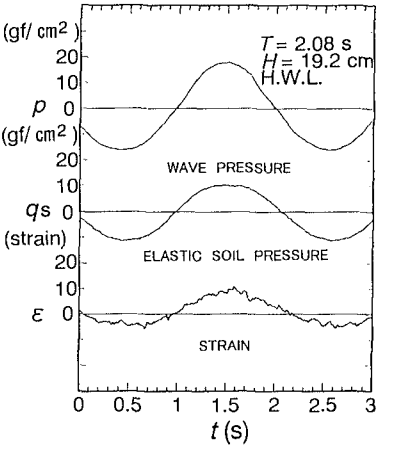

Fig. 5 Caisson wall strain due to non-breaking waves.

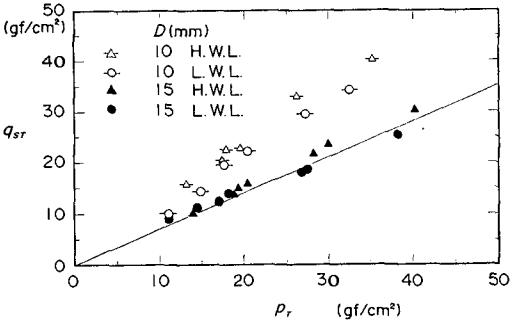

Fig. 6 Soil pressure vs. wave pressure.

Dynamic Response of Caisson Wall Against Impulsive Breaking Waves

Figure 7 shows the soil pressure q, strain ε, and acceleration α after a wave with impulsive pressure p impacts the front wall. The resultant pressure acting on the wall (p–q) is also shown. Acceleration data indicates that the wall vibrates strongly, and that the soil pressure due to the "added mass effect" is proportional to acceleration. We term the internal soil pressure due to the added mass effect as "inertia" soil pressure, q_{sp}."The dynamic response of the front wall and associated pressures can be described using two phases (Fig. 7), namely, phases I and II represented in Fig. 8. In phase I, p shows a positive peak coinciding with positive peaks in α and q; and, due to q_{sp}, (p–q) and accordingly ε show no peak. In Phase II, ε and (p–q) contrastively show nearly coincident peaks while α shows a negative peak. Note that even though q is reduced below its peak value, ε and (p–q) nevertheless increase due to the negative inertia soil pressure. However, due to the coincidently acting positive elastic soil pressure, (p–q) decreases. In other words, in this case the dynamic response of the caisson wall reduces the peak in ε by about 50%.

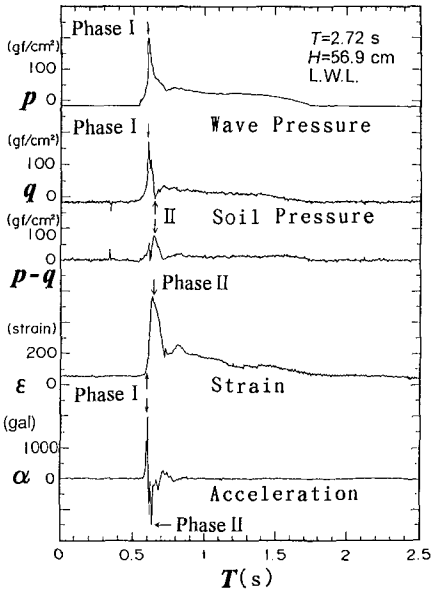

Fig. 7 Dynamic response of a caisson wall against impulsive breaking waves.

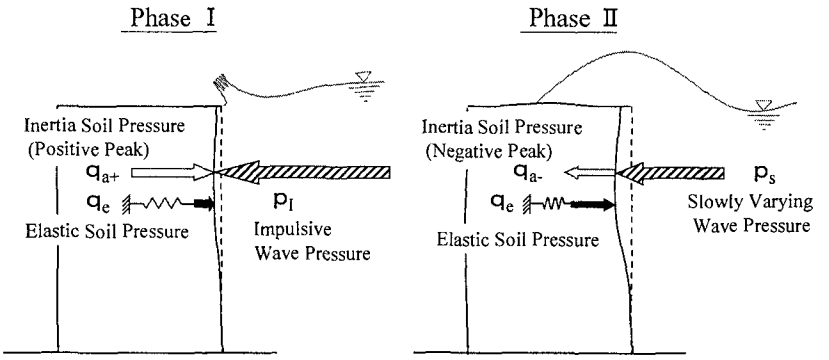

Fig. 8 Diagramatic representation of the dynamic response.

Figure 9 shows the peaks of impulsive wave pressure and inertia soil pressure in Phase 1, and Fig. 10 shows the peaks of wave pressure and wall strain. The inertia soil pressure is 70 – 90% of the impact wave pressure, which indicates that the strain at Phase I is greatly reduced due to soil pressure, making the strain at Phase II more

significant. By comparing the peak strains for the sand-filled and water-filled caissons due to the soil pressure the peak strain is reduced 40 – 80%.

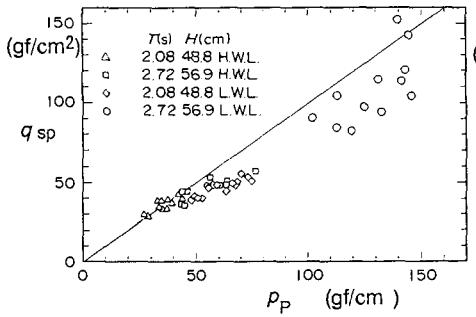

Fig. 9 Impulsive pressure vs. inertia soil pressure.

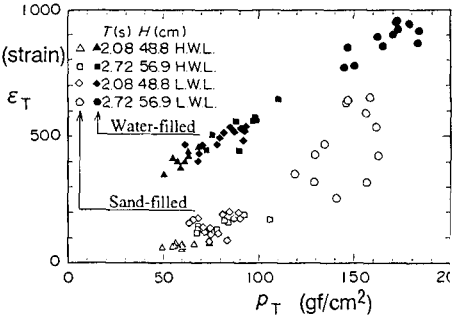

Fig. 10 Impulsive pressure vs. wall strain.

4. FEM SIMULATION

FEM Model

Figure 11 shows the mesh system used to carry out time-dependent, three-dimensional FEM numerical calculations simulating the dynamic response of a caisson wall.

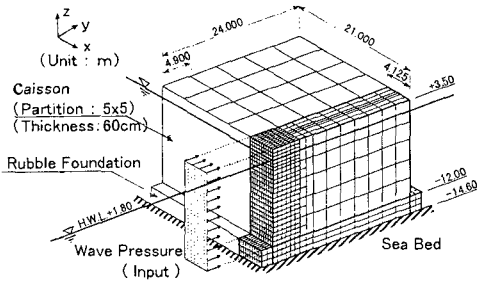

Fig. 11 Mesh system used for FEM simulation.

Experiments vs. Calculations

Figure 12 compares measured and calculated profiles of p, α, q, and ε, where the apparent good agreement between them indicates that employed FEM simulation is suitable for approximating the caisson's dynamic response.

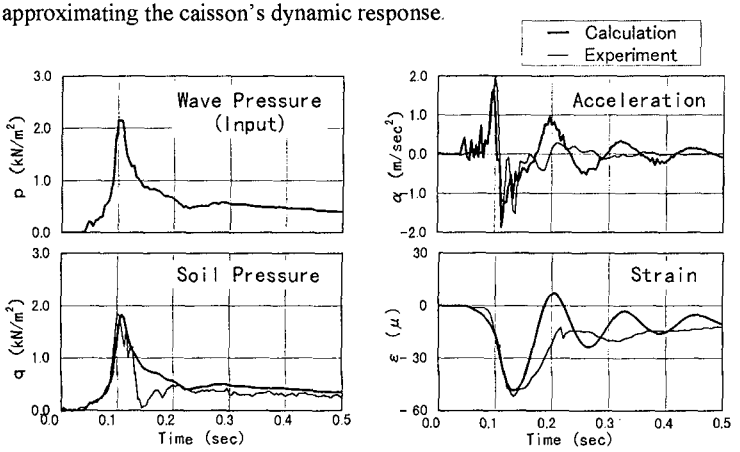

Fig. 12 Measured vs. calculated results.

Dynamic Response of a Prototype Caisson Wall

Figure 13 shows simulated profiles for a prototype caisson (height, 15.5 m; chamber width, 4.125 m; wall thickness, 60 cm) located at Mutsu-Ogawara Port, where results are indicated for an input wave pressure profile with an impact duration τ of 0.01 or 0.06 s. At $\tau = 0.01$ s, the inertia effect is the same as that of the model caisson, *i.e.*, it delays the peak in wall displacement and reduces its value by about 30%. At $\tau = 0.06$ s, however, the wall displacement peak almost coincides with the peak in wave pressure, with its peak value being the same as the static value. In other words, the effect of the inertia soil pressure is limited only when the impact duration is short.

It should be noted, however, that wall deformation δ_{st} includes the effect of elastic soil pressure, which is about one third of input wave pressure; and therefore the resultant wall deformation is in turn reduced by one third.

Figure 14 shows the effect of τ on the inertia effect for a wall with filling sand and water; *i.e.*, the caisson's internal soil pressure, displacement, and deflection

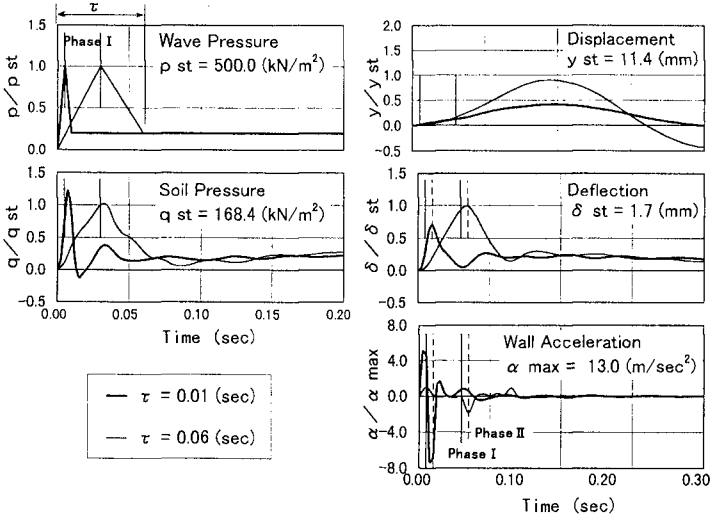

Fig. 13 Dynamic response of a prototype caisson wall.

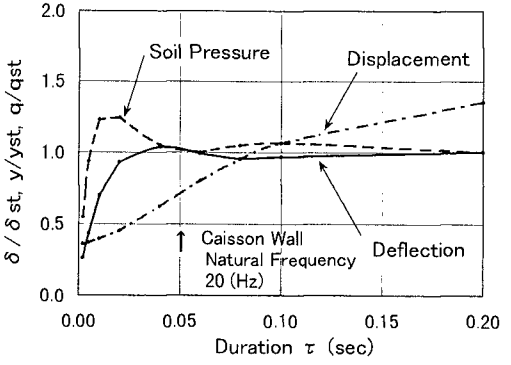

Fig. 14 Duration and inertia effect.

which are all non-dimensionalized by static values. As can be seen, the reduction in deflection, namely strain, due to the inertia effect appears when the duration of impact is much less than the wall's natural period (20 Hz).

The natural frequency of the wall in air is 40 Hz, whereas in water it is 20 Hz for a sand-filled caisson; being slightly higher than standard frequencies because the considered wall thickness of 60 cm is slightly larger than the standard value. These results indicate that the reduction in strain due to the dynamic response, especially that due to the inertia effect, appears when τ is short, *i.e.*, around 40 ms.

Rubble Mound Stiffness and Dynamic Response

The above simulation considered a relatively stiff rubble mound foundation that is lower and wider than standard ones. Therefore, to determine if rubble mound stiffness affects the dynamic response, the value of stiffness was reduced to 1/10th the original value. Figure 15 compares the simulations, where it should be noted that no marked differences appear during the duration of impact, which results clearly indicate that the dynamic response effect of the caisson wall is not affected by the rubble mound foundation.

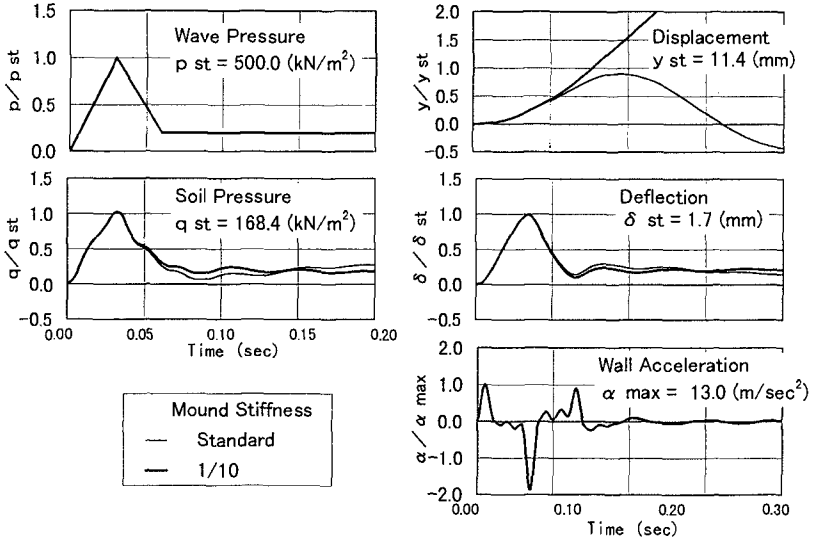

Fig. 15 Effect of stiffness of ruble mound on dynamic response.

Bending Moment

Figure 16 shows the horizontal and vertical bending moments of the caisson wall with $\tau = 0.06$ s, where the sand filling markedly reduces both bending moments by ≈ 30%. Also shown are corresponding profiles calculated using the conventional design method in which a reinforced concrete plate is fixed along three edges and no filling sand is considered. Note that the horizontal moment is overestimated and the vertical moment underestimated, especially around S.W.L where huge impulsive wave pressure are present.

Figure 17 shows the effect of wall thickness and partition distance on wall compressive stress due to bending moment, where these results clarify that increasing wall thickness is much more effective than decreasing partition distance.

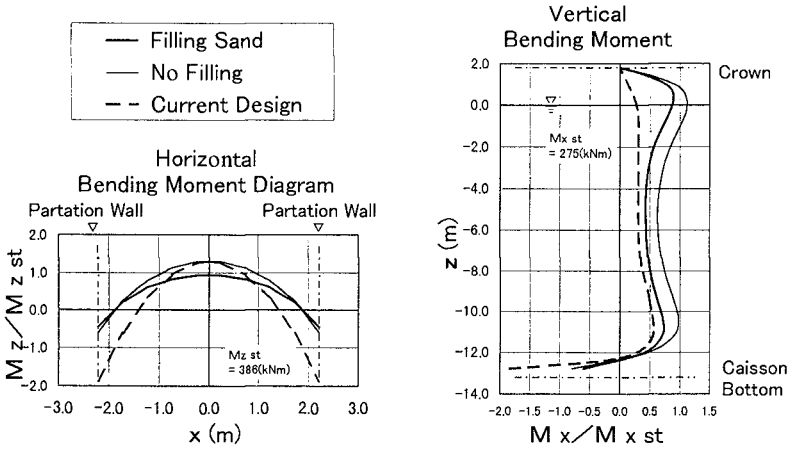

Fig. 16 Effect of filling sand on bending moment.

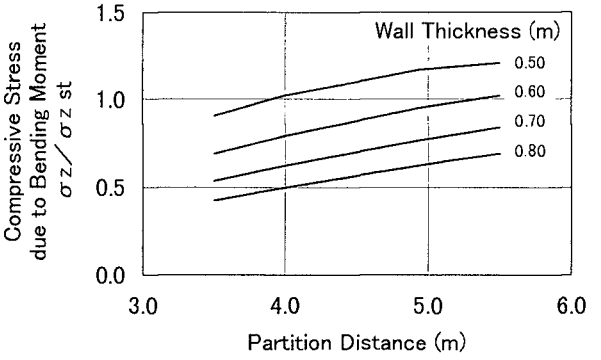

Fig. 17 Effect of wall thickness and partition distance on wall compressive stress.

Mutsu-Ogawara Case

Table 3 summarizes the results of applying our 3D, time-dependent FEM model to simulate the actual effects of a strong, 1991 winter storm on the No. 7 (damaged) and adjoining No. 8 (undamaged) caissons of the Mutsu-Ogawara breakwater. From previous work (Takahashi *et al.*, 1994), if we apply the modified Goda formulae (Goda, 1974) assuming an impulsive pressure coefficient of α_I, then the predicted value of the impulsive wave pressure impacting the breakwater would be about 2.8 w_0H, *i.e.*, since maximum incident wave height during the storm was 14.88 m, the breakwater was hit by an impulsive pressure of 500 kN/m^2.

As indicated, the 45-cm-thick wall of the No. 7 caisson was subjected to a bending moment of 315 kNm, which is much higher than the allowable value of 240 kNm. On the other hand, the 70-cm-thick wall of the No. 8 caisson was subjected to a resultant bending moment of 421 kNm, which is much lower than the allowable bending moment of 540 kNm. Such correspondence with field survey observations points towards the suitability of using our model to establish a practical design method against impulsive pressures.

Table 3 FEM simulation results applied to the caisson walls at Mutsu-Ogawara Port.

Caisson No.	No.7	No.8
Thickness of Caisson Wall (m)	0.45	0.70
Allowable Bending Moment (kNm)	240	540
Calculated Bending Moment (kNm)	315	421
Judgement	Failure	No Failure

* Input

Maximum wave height : Hmax = 14.88 (m)

Impulsive wave pressure coefficient : $\alpha_I = 1.10$

Maximum wave pressure : $p = 2.8w_0H$

5. CONCLUSIONS

Main results are summarized as follows:

1) Although failures of caisson walls rarely occur, they are possible if the impulsive pressure is quite large and the thickness of the caisson wall is insufficient.
2) Model experiments successfully demonstrated the dynamic response of the caisson wall against impulsive breaking wave pressures.
3) Based on measured and calculated results showing good agreement, the employed 3D, time-dependent FEM model is considered to effectively simulate the dynamic response of a wall of a sand/water-filled caisson.
4) Internal soil pressures, namely, elastic and inertia soil pressures, play important roles in reducing the strain in a caisson wall, *i.e.*, the strain in the caisson wall due to the elastic soil pressure is dependent on wall stiffness and can reduce the bending moment by as much as 30%.
5) Wall strain due to the inertia effect appears when the impact duration time of

impulsive pressure is shorter than the natural period of the wall, *i.e.*, around 40 ms.

6) The wall's dynamic response is not affected by the stiffness of the rubble mound foundation.
7) Our simulation model is expected to provide a good foundation for continued analysis of caisson wall failures such that a practical design method can be effectively established against impulsive pressures. The ultimate design method will be based on applying the Goda pressure formulae (Goda,1974) in conjunction with the impulsive pressure coefficient α_I(Takahashi *et al.*, 1994).

ACKNOWLEDGEMENTS

We wish to thank Dr. O. Kiyomiya, Professor, Waseda University, and Dr. H. Yokota, Chief, PHRI Structure Laboratory, for their valuable assistance in conducting FEM simulations.

REFERENCE

Goda, Y. (1974): New Wave Pressure Formulae for composite Breakwaters, Proc. of 14th Coastal Engineering Conference, ASCE, pp. 1702–1720.

Hitachi, S. (1994): Case Study of Breakwater Damages - Mutsu-Ogawara Port -, Proc. of Int. Workshop on Wave Barriers in Deepwaters, Port and Harbor Research Institute, pp. 308–331.

Hattori, C., K. Shibata, and K. Ohori (1984): Disasters of Breakwaters by Wave Action (Part 3), Technical Note of Port and Harbor Research Institute, No. 485, 281 p (in Japanese).

Miyai, S., K. Ohira, and M. Shiomi (1993): Disasters of Breakwaters by Wave Action (Part 4), Technical Note of Port and Harbor Research Institute, No. 765, 248 p (in Japanese).

Shimosako, K. and S. Takahashi (1995): Numerical Calculations of Dynamic Response of Breakwater Caisson and Foundation against Impulsive Wave Forces, Proc. XXVI IAHR Congress, London.

Shimosako, K., S. Takahashi, and K. Tanimoto (1994): Estimating the Sliding Distance of Composite Breakwaters due to Wave Forces Inclusive of Impulsive Forces, Proc. of 24th ICCE, pp. 1580–1594, Kobe.

Takahashi, S., K. Tanimoto, and K. Shimosako (1994): A Proposal of impulsive pressure coefficient for design of composite breakwaters, Proc. of Int. Conf. On Hydro-Technical Eng. for Port and Harbor Research Institute.

Tanimoto, K., K. Kobune, and M. Osato (1975): Wave Forces on a Caisson Wall and Stress Analysis of the Caisson Wall for Prototype Breakwaters, Technical Note of Port and Harbor Research Institute, No. 224, 39 p (in Japanese).

Wave Transmission at Submerged Rubblemound Breakwaters

Stuart R. Seabrook[1] and Kevin R. Hall[2]

Abstract

Submerged rubblemound breakwaters are becoming more popular as a potential alternative to coastal protection measures where a moderate degree of energy transmission is acceptable. Such situations include areas where vegetative shore protection is existing or proposed or in the event that an existing shore protection structure has become damaged or under designed and a method is needed to reduce the incident wave energy. Although there have been previous investigations on the performance of submerged rubblemound breakwaters, there are only a few design equations available to the design engineer. Those available are based on a limited range of input design variables and as a result are insufficient in some cases.

Physical model studies were performed at the Queen's University Coastal Engineering Research Laboratory (QUCERL) in Kingston, Canada to assess the performance of submerged rubblemound breakwaters under a wide range of design conditions in two-dimensional (2-D) and three-dimensional (3-D) settings. The tests include a number of wide crested structures to provide data where previous investigations have not. The results show that the relative submergence, incident wave height and structure crest width are the most important design variables.

A number of potential design equations were evaluated by statistical analysis methods. The proposed design equation fits the 2-D test data well and provides moderate agreement with the 3-D test results. Although physical testing is suggested for all design applications due to the complexity of site specific considerations, the proposed equation does provide a good preliminary design tool for submerged rubblemound breakwaters.

---

[1] Department of Civil Engineering, Queen's University, Kingston, Ont. K7L 3N6

[2] Professor, Department of Civil Engineering, Queen's University, Kingston, Ont. K7L 3N6

1.0 Introduction

Submerged rubblemound breakwaters are simply rubblemound structures constructed with a crest elevation below the local water level. Although they are well suited to situations where minimal visual intrusion is desired and where it is desirable to maintain a moderate degree of energy transfer between the shoreline and the offshore region for environmental reasons, their performance is sensitive to water level changes and it is not practical to expect transmission coefficients as low as those achievable with conventional surface piercing structures. However, there are benefits associated with the potentially smaller material requirements for stable submerged structures and the ability to rehabilitate existing structures by simply reducing the incident wave conditions with a submerged breakwater.

Numerous physical and numerical investigations have been performed for various submerged structure configurations and materials. In general, the physical processes at submerged rubblemound breakwaters can be defined for three regions in the vicinity of the structure as indicated in Figure 1. Relevant nomenclature is also indicated.

In Region 1, the incident wave shoals on the rising face of the breakwater, considerable non-linear wave transformations take place as bound waves are developed (Beji and Battjes, 1993) and some wave breaking is initiated. A portion of the incident energy is also reflected from the front breakwater face. Wave breaking continues into Region 2 where significant non-linear interactions occur between the various wave phases. Harmonic generation occurs as energy is transferred from the fundamental wave frequency to higher harmonic frequencies (Driscoll, Dalrymple and Grilli, 1993). Some wave energy is also dissipated on the breakwater crest through friction and air entrainment as well as within the breakwater structure. In Region 3, the free and bound transmitted waves dissociate as they travel into the deeper water. This generally results in a broadening energy spectra as the various wave components travel with their own celerity.

Numerical modeling efforts have met with some success in representing the transformation of weakly non-linear incident waves (Ohyama and Nadaoka, 1993; Driscoll, Dalrymple and Grilli, 1993; Beji and Battjes, 1994; Losada, Silva and Losada, 1996). Although all models are reported to reflect some of the physical modeling data well, none of the approaches can fully model the breaking and non-linear decomposition process on a theoretical basis. Therefore, given the uncertainties associated with the present state-of-the-art in numerical modeling, it may be most appropriate for the design engineer to consider more general design equations based on physical modeling results.

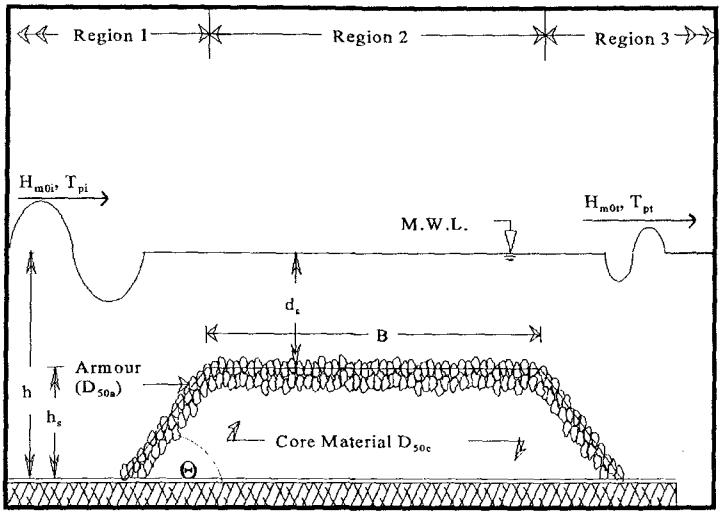

Figure 1 : Submerged Breakwater Nomenclature

Relatively few design equations have been developed to date for submerged rubblemound breakwaters. Those available have been developed by Seelig (1980) for surface piercing and submerged permeable breakwaters, by Ahrens (1987) for reef-type breakwaters and by Van der Meer (1991) for low crested and submerged rubblemound structures. Seelig's equation was developed with very little submerged breakwater data and Ahren's equation is not directly applicable to conventional submerged rubblemound breakwaters given the reshaping nature of reef breakwaters. Van der Meer's equation was developed from a considerable volume of test data from a number of authors but some variables were not varied to a large degree; a limited variation in crest width was perhaps the most important shortcoming of this research. As a result, none of the existing equations are sufficient for application over a wide range of design conditions.

The objectives of the research presented in this paper are therefore as follows:

1. To test a sufficiently wide range of submerged breakwater geometries, ensuring a broad range of crest widths, under a relatively large range of incident wave conditions in a 2-D setting to assess the validity of the existing design equations.
2. To extend and modify the existing design equations as necessary to provide some physical basis for the dimensionless parameters utilized.
3. To perform 3-D testing for a number of conditions similar to those tested in the 2-D apparatus to assess the validity of the proposed equations for application in more realistic 3-D environments.

2.0 Experimental Setup

The majority of the physical tests were 2-D in nature and were performed in a 1 meter wave flume at QUCERL. These test results provided the data for development of the proposed design equations. Subsequent 3-D testing was carried out in the wave basin at QUCERL using a smaller set of test variables. The results of these tests were used in the evaluation of alternative design equations.

2-D Testing

The testing setup for the 2-D tests is shown in Figure 2. The wave flume is 47.0 m long, 1.2 m deep and 1.0 m wide and is equipped with a flapper type wave generator. A plywood beach was constructed in the flume, upon which the test breakwaters were constructed. The beach permits testing of the submerged breakwaters in relatively large incident waves. The submerged breakwater cross section consisted of a core of relatively course core material (D_{50c} = 0.017 m) and two layers of primary armour (D_{50a} = 0.059 m). A second armour size (D_{50a} = 0.037 m) was used in some tests. The armour size was determined such that the breakwater remained stable during testing. The stone size required for the most severe testing condition was determined using the stability equation of Vidal et al. (1993). The stone size recommended for the "total slope" section was used for the entire breakwater.

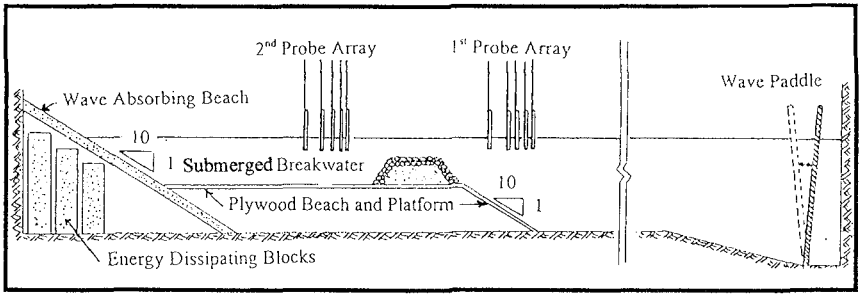

Figure 2 : 2-D Testing Configuration

Incident and transmitted waves were measured by two wave probe arrays, located in front and rear of the breakwater respectively. The probes were capacitive type water level gauges, sampling the water surface at 20 Hz. Reflection from the rear wall of the wave flume was minimized using a 1:10 beach of rubberized hair in front of a porous matrix of concrete blocks.

In total, approximately 800 tests were performed with irregular waves. A number of tests were also performed with regular waves in order to confirm the presence of physical phenomenon observed by previous authors. The testing program involved 13 submerged breakwater geometries tested under 5 different water levels with a number of incident

wave characteristics.

All irregular wave spectra tested were Jonswap with $\alpha = 0.0081$ and $\gamma = 3.3$. The signals were gencrated using the National Research Council of Canada's (NRC), GEDAP wave generation and analysis package. Given the physical characteristics of the flume and the mechanical response of the paddle to the input signal, the generated wave spectral characteristics may vary from the target characteristics by 5% to 10%. A summary of the irregular wave characteristics tested is provided in Table 1.

Table 1 : Irregular Wave Characteristics in 2-D Tests

Wave Set	W01	W02	W03	W04	W05	W06	W07	W08	W09	W10	W11
Hmo (m) *	0.05	0.05	0.05	0.10	0.10	0.10	0.15	0.15	0.15	0.20	0.20
Tp (s)*	1.2	1.5	2.0	1.2	1.5	2.0	1.2	1.5	2.0	1.5	2.0

* Note: Wave characteristics are target values - those measured in flume may vary to some degree.

3-D Testing

The wave basin at QUCERL is approximately 30 m by 25 m by 1.2 m deep and is equipped with a piston-type wave paddle 10.5 m long. All dimensions for the 3-D tests were scaled at 0.63 times those of the 2-D tests and the submerged breakwater structure was constructed on the floor of the basin. A concrete beach was constructed behind the breakwater and covered with sand to minimize the reflection and provide a qualitative assessment of beach development. A subset of testing parameters was used in the 3-D tests, with 3 breakwater geometries and 3 water depths, all tested at incident angles of 90 ° and 60°. The general testing configuration is shown in Figure 3 below.

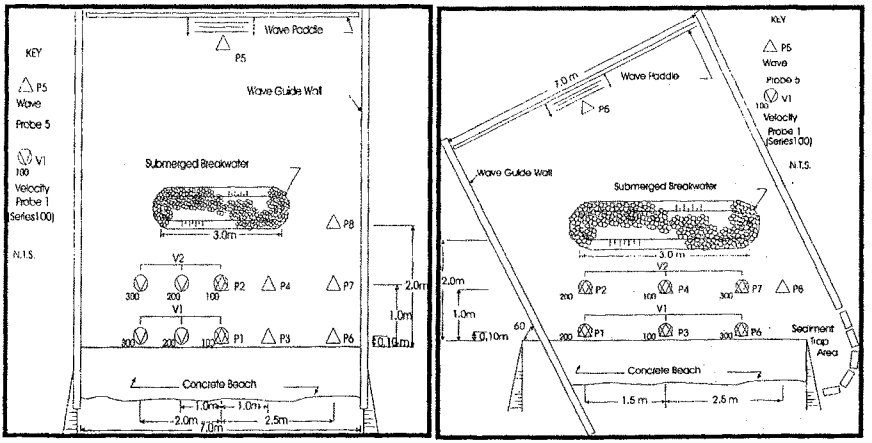

(a) 3-D Testing at 90°

(b) 3-D Testing at 60°

Figure 3: 3-D Testing Configurations

The submerged breakwaters used in the 3-D tests were constructed using a relatively fine core material (D_{50c} = 0.004 m) and the smallest armour tested in the flume (D_{50a}=0.037 m). The wave signals were generated from Jonswap spectra. Because the breakwater for the 3-D tests was not constructed on an elevated platform, it was not possible to generate waves as large as those used in the 2-D tests. A summary of the irregular wave characteristics used in the 3-D tests is provided in Table 4.

Table 2 : Irregular Wave Characteristics in 3-D Tests

Wave Set	W01	W02	W03	W04	W05	W06	W07	W08	W09	W10	W11
Hmo (m)*	0.032	0.032	0.032	0.032	0.063	0.063	0.063	0.063	0.095	0.095	0.095
Tp (s)*	0.95	1.19	1.59	1.98	0.95	1.19	1.59	1.98	0.95	1.19	1.59

* Note: Wave characteristics are approximate - those measured in basin may vary to some degree.

Water level probes were placed throughout the area behind the submerged breakwater, and one probe was located near the paddle to provide an indication of the incident wave height. Two velocity probes were also moved throughout the area behind the submerged breakwater to provide a qualitative indication of the general velocity patterns. The locations of the various probes are shown in Figure 3 above.

Data Sampling and Analysis

Sampling for each test was performed at 20 Hz over a period of 100 waves. Full reflection analysis was undertaken for the 2-D data to separate the incident and reflected spectra. The reflection analysis was performed using a least squares analysis of 3 probes of the 5 probe array (Mansard and Funke, 1987). The incident wave characteristics at probe arrays 1 and 2 were used to define the transmission coefficient K_t such that:

$$K_t = \frac{H_t}{H_i} \tag{1}$$

where H_t and H_i are the incident H_{m0} values at probe arrays 2 and 1 respectively.

The significant wave height (H_s) at individual probes was used to define the transmission coefficient for the 3-D tests. The incident wave was defined by Probe 5 and the transmission coefficient was computed at various locations behind the submerged breakwater. Although the use of H_s instead of H_{m0i} to define K_t is not consistent with the analysis of the 2-D data, it reduces the effect of energy that has leaked into the testing area or been reflected into the lee of the breakwater, on the characteristic wave height estimate.

The transmission coefficient values were analyzed with respect to the various incident wave and structure characteristics. This analysis involved a simple graphical trend analysis of the data, followed by a comprehensive statistical analysis of alternative design equations relating K_t to the most important design variables. The trend analysis was conducted with

dimensional and dimensionless variables considered to be important to the transmission process. The most important dimensionless variables were ascertained by dimensional analysis of the transmission process.

It is generally accepted that the transmitted wave at a submerged breakwater is a function of a number of variables.

$$H_t = f(\rho, g, \mu, D_{50a}, n, H_i, L, d_s, \theta, B, h_s, h) \quad (2)$$

where ρ, g and μ are density, gravitational acceleration and dynamic fluid viscosity respectively and the other variables are defined in Figure 1. A dimensionless form of this expression can be developed using ρ, g and H_i as basic or repeating variables such that:

$$K_t = \frac{H_t}{H_i} = \varphi\left(\frac{\rho H_i \sqrt{H_i g}}{\mu}, \frac{D_{50_a}}{H_i}, n, \frac{L}{H_i}, \frac{d_s}{H_i}, \theta, \frac{B}{H_i}, \frac{h_s}{H_i}, \frac{h}{H_i}\right) \quad (3$$

These basic dimensionless variables were used to develop alternative dimensionless variables which are more relevant to the physical processes affecting transmission at submerged breakwaters. Dimensional and statistical analysis of these relevant variables was undertaken to develop a design equation for transmission at submerged rubblemound breakwaters.

3.0 Results

The observations made during testing were generally consistent with observations noted from previous investigations. The incident wave spectra were broadened with a shift of energy to higher frequencies as the waves passed the breakwater and there was evidence of harmonic generation and subsequent dispersion as individual waves passed over the structure. The most obvious process affecting K_t was wave breaking. Inspection of the general trends defined by the 2-D test data indicate that K_t is most sensitive to the depth c submergence d_s, the incident wave height H_i and the crest width B. To a lesser degree, K is influenced by the period of the incident wave (T_p), the breakwater armour dimensions (D_{50a}) and the breakwater slopes (θ).

Typical trends observed during the 2-D tests are summarized in Figures 4 through 8. It i evident that the transmission increases with increased d_s, increased H_i and increased B. I is also shown that a small increase in K_t is observed with increasing T_p, increasing D_{50a} an steeper slopes (increasing Tan θ).

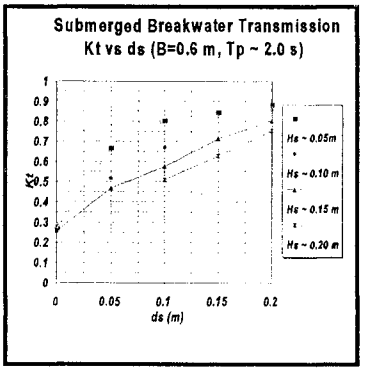

Figure 4
Effect of d_s and H_s on K_t

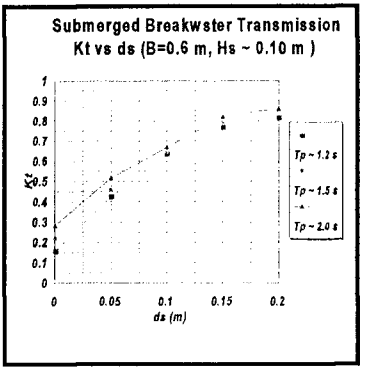

Figure 5
Effect of d_s and T_p on K_t

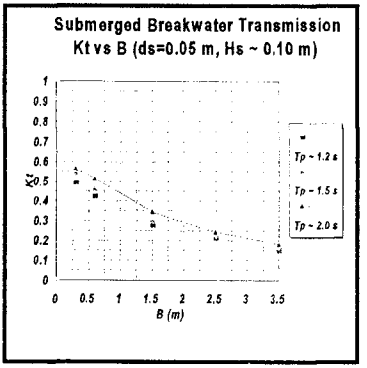

Figure 6
Effect of B and T_p on K_t

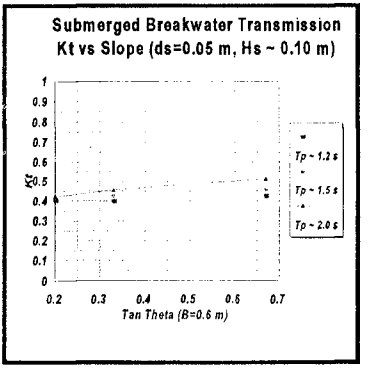

Figure 7
Effect of θ and T_p on K_t

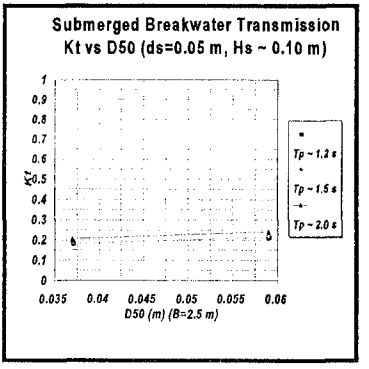

Figure 8
Effect of D_{50} and T_p on K_t

Three dimensional test data showed similar trends in general but the scatter in the data was much more evident. The transmission coefficients were generally higher in the 3-D tests: this is attributed to a number of factors including diffraction of wave energy into the lee of the breakwater and reflection of wave energy from the testing apparatus. The results show that the relative submergence is the most influential factor under low submergence conditions while crest width is important under higher submergence conditions.

The effects of submergence depth, incident wave height and crest width are shown in Figure 9. This figure is based on the transmission coefficient immediately behind the mid-point of the breakwater with incident waves perpendicular to the structure.

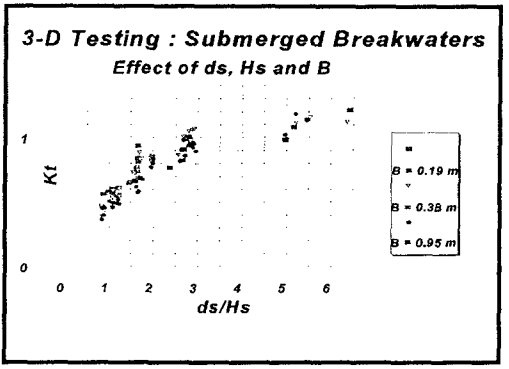

Figure 9 : Typical 3-D Testing Results

The predicted values of the transmission coefficient for the 2-D test variables were generated using van der Meer's Equation for submerged and low crested breakwaters and Ahren's Equation for reef breakwaters, and are shown in Figures 10 and 11.

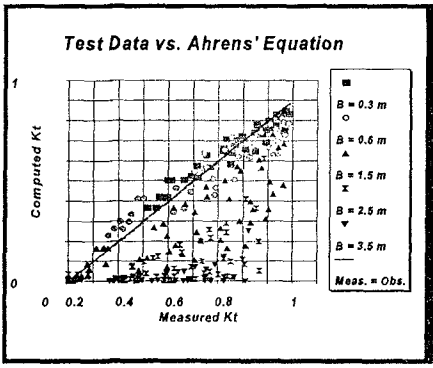

Figure 10 : Predicted K_t - Ahrens' Eqn.

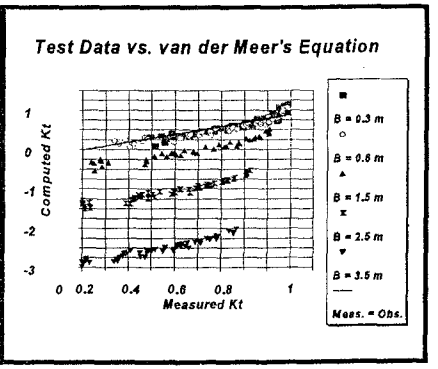

Figure 11 : Predicted K_t -Van der Meer's Eqn.

The results show that these equations are not suitable to represent transmission for structures tested in this study, particularly when the crest width is large. The inability of the existing design equations to predict suitable transmission coefficients for the tested conditions indicates that there is a need for an improved design equation.

4.0 Development of an Improved Design Equation

Previous investigations have indicated that d_s/H_{m0i} is the most important dimensionless variable affecting transmission. This observation was supported by these tests. Numerous dimensionless variables considered, including variables discussed in previous authors works. Only those found to be significant in defining the transmission process are discussed here.

Dimensionless variables representing wave breaking, overtopping, frictional losses and internal flow losses were found to be important in defining the transmission process. These variables are discussed below.

i. The wave breaking process is considered to be represented by the dimensionless variable d_s/H_{m0i} (relative submergence). The relationship between K_t and d_s/H_{m0i} for all of the 2-D test data is shown in Figure 12. The effect of relative submergence is very evident when d_s/H_{m0i} is small. This is expected since the majority of waves are breaking and under breaking wave conditions, the unbroken wave (transmitted) has been found to be closely related to the water depth (d_s). Given the scatter, there are obviously other factors playing an important role in the process as well.

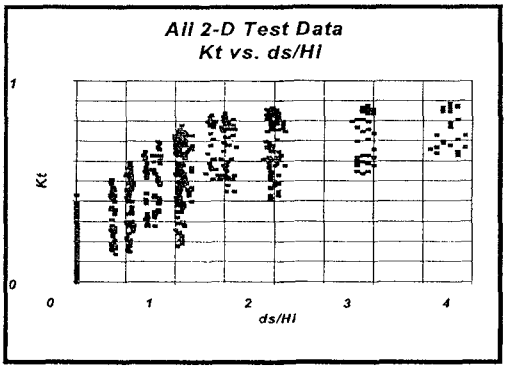

Figure 12 : Effect of Relative Submergence

As the relative submergence increases, its influence is reduced substantially. This is expected as the relative portion of the incident waves which would break is reduced as the submergence depth increases.

ii. The effect of overtopping is expected to be relatively important in defining the transmission coefficient at submerged breakwaters, especially under wave breaking conditions. As the relative submergence approaches zero, transmission at the submerged breakwater was observed to become a function of the potential for overtopping as well as transmission through the breakwater structure, in particular, the large armour crest material.

Typically, overtopping rates are a function of the wave steepness and structure geometry. A dimensionless form of the structure crest width and the local wave height (H_{m0i}/B) was found to be representative of the overtopping effect.

iii. As the wave passes over the breakwater, some energy is lost to frictional dissipation on the surface of the structure. The dimensionless variable representing this process was loosely based on the empirical Darcy-Weisbach expression for head loss. This requires the assumption that the flow velocity can be represented by the velocity of a gravity wave and results in the dimensionless variable $d_s H_{m0i}/BD_{50a}$.

iv. Flow within the breakwater structure will also result in some energy loss as a wave travels over a submerged breakwater. Given the relatively high porosity of the armour layer, the effect of the wavelength on the fluid velocity, the effect of submergence depth on the portion of flow within the armour layer and the effect of the crest width on the overall drag losses, the dimensionless variable selected to represent drag losses was Bd_s/LD_{50a}.

On the basis of these dimensionless variables, statistical fitting was used to develop a suitable design equation. A number of alternative equations were considered in an effort to develop a design equation which provided:

- a good statistical fit (R^2),
- a normal distribution of residuals,
- predictions which are well bounded (ie. $0.0 \le K_t \le 1.0$),
- physically relevant variables with a minimum number of fitted parametcrs

Through trial and error, a finalized form of the design equation was developed such that these criteria were generally satisfied for the 2-D test data.

$$K_t = 1 - \left(e^{-0.65\left(\frac{d_s}{H_i}\right) - 1.09\left(\frac{H_i}{B}\right)^2} + 0.047\left(\frac{B}{L}\frac{d_s}{D_{50_a}}\right) - 0.067\left(\frac{d_s}{B}\frac{H_i}{D_{50_a}}\right)\right) \quad (4)$$

The proposed equation fits the 2-D test data well, resulting in an R^2 value of 0.914. Given thc uncertainty associated with the fitting of statistical parameters, all of the parameters of the proposed design equation were adjusted to their upper or lower 95% confidence

interval values such the change in predicted K_t value was maximized. The results, as shown in Figure 13 show that the prediction is not very sensitive to these changes and as a result, the prediction is relatively robust in its relation to the physical variables affecting the transmission phenomenon.

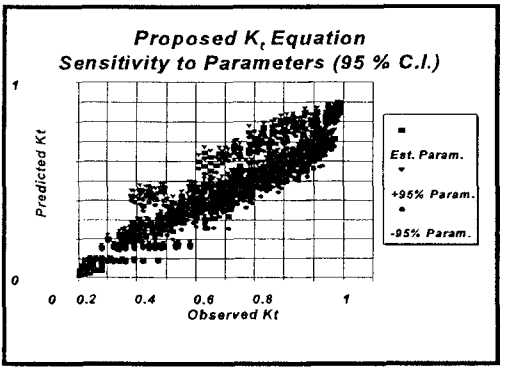

Figure 13 : Sensitivity to Parameter Estimates

Although the proposed equation does not fit the 3-D data as well, the prediction is still relatively good at low to moderate transmission coefficients (Figure 14).

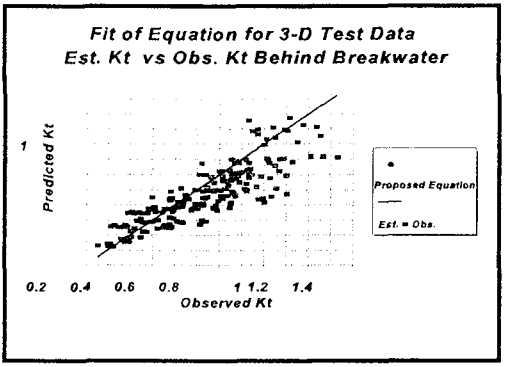

Figure 14 : Observed vs Predicted K_t - 3-D Tests

5.0 Conclusions

Based on an extensive set of 2-D and 3-D tests of wave transmission at submerged breakwaters, a number of conclusions can be drawn.

i. The transmission coefficient at submerged breakwaters is most sensitive to the

relative submergence (d_s/H_i).

ii. The relative crest width is another very important factor which has not been adequately accounted for in previous design equations.

iii. An improved design equation for transmission at submerged breakwaters would be:

$$K_t = 1 - \left(e^{-0.65\left(\frac{d_s}{H_i}\right)-1.09\left(\frac{H_i}{B}\right)} + 0.047\left(\frac{B\ d_s}{L\ D_{50}}\right) - 0.067\left(\frac{d_s\ H_i}{B\ D_{50}}\right)\right) \quad (4)$$

iv. The proposed equation represents the comprehensive set of test data well (R^2=0.914) and is robust in its relation to the physical variables which significantly affect the transmission process.

v. The equation is well bounded over the range of test data, which is considered to be representative of typical design conditions. The equation does, however, become unbounded when B becomes very large or very small due to the size of the 3rd and 4th terms. Therefore, it is recommended that caution be used when applying the equation outside of the following variable ranges.

$$0 \le \frac{B\ d_s}{L\ D_{50_a}} \le 7.08$$
$$0 \le \frac{d_s\ H_i}{B\ D_{50_a}} \le 2.14 \quad (5)$$

References:

Ahrens, J.P. "Characteristics of Reef Breakwaters". CERC Technical Report 87-17, 1987.

Beji, S. and Battjes, J.A. "Experimental Investigation of Wave Propagation Over a Bar", Coastal Engineering, 19:1-2, 1993, pp. 151-162.

Beji, S. and Battjes, J.A. "Numerical Simulation of Nonlinear Wave Propagation Over a Bar", Coastal Engineering, 23:1-2, 1994, pp. 1-16.

Driscoll, A.M., Dalrymple, R.A. and Grilli, S.T. "Harmonic Generation and Transmission Past a Submerged Rectangular Obstacle", 23rd International Conference in Coastal Engineering, American Society of Civil Engineers, New York, Vol. 1, 1993, pp. 1142-1160.

Losada, I.J., Silva, R. and Losada, M.A. "3-D Non-Breaking Regular Wave Interaction with Submerged Breakwaters", Coastal Engineering, 28, 1996, pp. 229-248.

Mansard,E.P.D. and Funke, E.R. "On the Reflection Analysis of Irregular Waves", Technical Report No. TR-HY-017, National Research Council of Canada, Ottawa, 1987.

Ohyama, T. and Nadaoka, K. "Modelling the Transformation of Nonlinear Waves Passing over a Submerged Dyke", 23rd International Conference on Coastal Engineering, American Society of Civil Engineers , New York, Vol. 1, 1993, pp. 526-539.

Seabrook, S.R. "Investigation of the Performance of Submerged Rubblemound Breakwaters", M.Sc. Thesis, Queen's University, Kingston, 1997.

Seelig, W.N. "Estimation of Wave Transmission Coefficients for Overtopping of Impermeable Breakwaters", CERC Coastal Engineering Technical Aid 80-7, 1980.

Van der Meer, J.W. "Stability and Transmission at Low-Crested Structures", Delft Hydraulics Publication 453, 1991.

Vidal, C., Losanda, M.A., Medina, R., Mansard, E.P.D. and Gomez-Pina, G. "Universal Analysis for the Stability of Both Low Crested and Submerged Breakwaters", 23rd International Conference on Coastal Engineering, American Society of Civil Engineers , New York, Vol. 2, 1993, pp. 1679-1692.

VERTICAL CIRCULATION INDUCED BY A SUBMERGED BREAKWATER

Sánchez-Arcilla, A.[1], Rivero, F.[2], Gironella, X.[3], Vergés, D.[3] and Tomé, M.[3]

Introduction: The concept of submerged breakwaters

Submerged breakwaters are structures whose crest height is below the main water level. From a hydrodynamic standpoint this type of structures show significant differences in behaviour with respect to the emerged ones. As an illustration (figure 1), it is well known that the wave height field in the lee of a structure is significantly different for emerged or submerged breakwaters or even the way it varies with the wave height to free-board, H to F, ratio. Also from a hydrodynamic standpoint, the enhanced mass flux over the submerged breakwater may lead to erosion on the lee-side instead of the conventional accretion and resulting tombolo formation.

From a morphodynamic standpoint, submerged breakwaters induce lower profile mobilities in addition to helping building a perched beach. In general terms, since a submerged structure exerts a smaller barrier effect, the morphodynamic impact should also be smaller (see for some additional discussion the papers by Van de Graaf and Sánchez-Arcilla and others dealing with the results of the DYNBEACH research project as presented in the Coastal Dynamics 95 and 97 conferences).

Finally, this type of submerged structures are normally associated to smaller impacts (e.g. smaller visual impacts, smaller ecological impacts associated to an enhanced water renovation which is essential for a tideless sea as the Mediterranean, etc.)

To understand and model the hydrodynamic behaviour of submerged breakwaters a 3D nearshore circulation model (see e.g. (Svendsen and Putrevu, 1994), (Sánchez-Arcilla et al, 1992),etc) is required in combination with a wave

[1] Head, Laboratori d'Enginyeria Marítima (LIM/UPC), Universitat Politècnica de Catalunya, c/ Jordi Girona, 1-3, Campus Nord-UPC, Edif. D-1, 08034 Barcelona, Spain. (http://www.upc.es/lim)
[2] Engineer, Alatec Haskoning S.A., c/ Roselló 205, 08008 Barcelona, Spain
[3] Engineer, Laboratori d'Enginyeria Marítima (LIM/UPC), Universitat Politècnica de Catalunya, c/ Jordi Girona, 1-3, Campus Nord-UPC, Edif. D-1, 08034 Barcelona, Spain. (http://www.upc.es/lim)

propagation model able to deal with depth induced breaking and the geometry and porosity of the submerged breakwater. There is nowadays a number of nearshore circulation models, featuring relatively sophisticated "effects" such as the transition zone (Nairn et al, 1990) (Dally and Brown, 1995) the full matrix of wave induced shear stresses $\langle \tilde{u}_i \tilde{u}_j \rangle$ (Rivero and Sánchez-Arcilla, 1993, 1996) or the mixing associated to vertical dispersion of the current -UV-terms (see e.g. Svendsen et Putrevu, 1994)-. However, these models cannot fully reproduce the experimentally observed hydrodynamic behaviour over a submerged breakwater. Some of the observational (Okayasu, 1989) (Rivero et al, 1997) features which these models cannot reproduce are: i) The mean water level gradient above the submerged breakwater, ii) The recirculation cell over the front slope of the submerged breakwater, and iii) The wave current interaction in front and above the submerged breakwater.

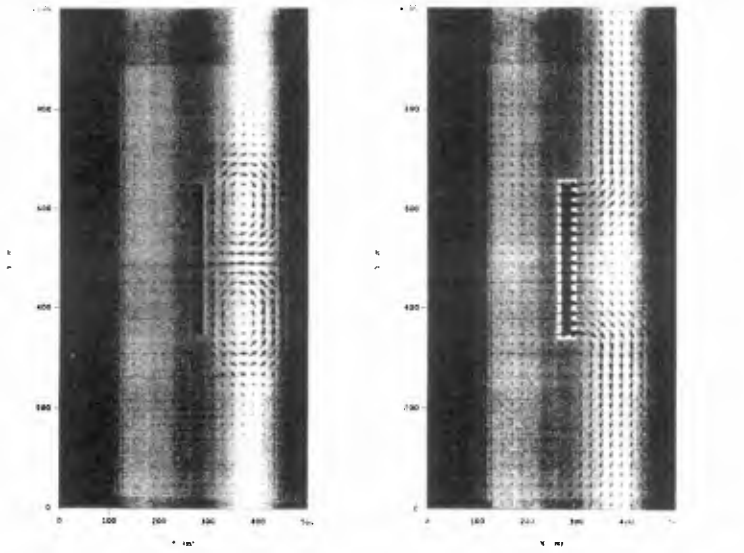

Figure 1. The differences in the vertically averaged circulation field induced by breaking waves in the presence of a shore parallel breakwater depending on whether it is an emerged or a submerged structure

The aim of this paper is to present the on-going development of a 2DV circulation model and a phase-averaged wave model to better understand the hydrodynamic behaviour of a submerged structure. The experimental information derived from previous research projects and the plans for a new set of mobile-bed tests with a submerged breakwater will also be presented.

Numerical modelling: the waves and currents around a submerged breakwater

i) THE WAVES

The wave model developed for the submerged breakwater case is an energetics one, based on the following equation:

$$\nabla\left[\left(C_g+U\right)\frac{E}{\sigma}\right]+\frac{D_b}{\sigma}+\frac{D_f}{\sigma}+\frac{D_p}{\sigma}=0 \qquad (1)$$

which states the conservation of wave action (due to the existence of strong currents above and in front of the submerged breakwater) considering the rates of "action loss" due to wave breaking, D_b (occurring on the up-slope of the submerged breakwater) bottom friction, D_f (because of the drag exerted by the submerged breakwater main armour units) and porous flow, D_p (due to the permeable flow inside the submerged breakwater).

The D_b term is evaluated using the (Battjes and Janssen, 1978) formulation for irregular wave tests and the (Dally et al, 1985) formulation for regular waves. Even though these formulae are intended for purely depth-induced breaking, all parameters are set to standard values. The maximum wave-height, Hm, in (Battjes and Janssen '78) is calculated using (Tomé, 1997):

$$Hm=\frac{2\pi\gamma_d}{k}tanh\frac{\gamma_s}{\gamma_d}\frac{kh_b}{2\pi} \qquad (2)$$

where γ_d,γ_s, are the deep and shallow water breaker indexes, to account for breaking waves of different frequencies (i.e. different h/L ratios).

The D_f term is evaluated according to (see e.g. Tolman, 1992)

$$D_f=\frac{2\rho}{3\pi}f_w U_{orb}^3 \qquad (3)$$

This term, although expected to be important above the submerged breakwater section, has not been analysed in any detail in this work. The friction coefficient used is a standard wave friction factor (see e.g. (Nielsen, 1992)).

The loss of energy (action) due to the existence of a permeable submerged breakwater is evaluated using (Sawaragi et Deguchi, 1992):

$$D_p=\frac{\rho}{4}\beta_p C_g H^2 \qquad (4)$$

where β_p corresponds to the imaginary part of the wave number and is a function (see (Sawaragi and Deguchi, 1992)) of:

$$\beta_p = \mathrm{f}\left(\frac{d_{porous}}{h}, \frac{K_p \sigma}{\nu}, Cg \right) \tag{5}$$

with d_{porous} the thickness of the porous layer (the lab tests described in next section use an impermeable core) and K_p the permeability of such a layer.

The introduction of reflection in the proposed phased-averaged model -given essentially by equation (1) plus the corresponding dispersion relationship, including the current Doppler-shift- is accomplished using "external" linear superposition.

$$\eta = \mathrm{Re}\left(a \cdot e^{i(\theta - \Delta\theta)} + R \cdot a \cdot e^{i\theta} \right) \tag{6}$$

where Re means "real part", $ae^{i(\theta-\Delta\theta)}$ is the incident (regular) wave train, and $\Delta\theta$ is the phase lag between incident and reflected waves due to their travel above a bottom with variable slope (figure 2):

$$\Delta\theta = 2 \int_{x}^{xl} K dx \tag{7}$$

This expression coincides, for a plane sloping bottom, with the ones proposed by other authors (see e.g. (Méndez, 1997), (Sutherland and O'Donoghue, 1998)).

The reflection coefficient R is written in terms of a modulus and a phase (the former expressing the ratio between reflected and incident wave heights and the latter the uncertainty about the exact point where reflection starts.)

Within this framework it is relatively straight forward, although cumbersome, to derive other wave properties such as (Méndez, 1997):

$$U = \mathrm{Re}\left[-\frac{g}{w} a \cdot k \cdot f(z) \left[e^{i(\theta - \Delta\theta)} + \mathrm{Re}^{i\theta} \right] \right] \tag{8}$$

$$Mf = E \frac{K}{w} \left(1 - R \quad R^* \right) \tag{9}$$

$$Sxx = E \left[\left(1 + R_R^2 + R_I^2 \right) \cdot \left(2 \cdot n - \frac{1}{2} \right) - R_R \cdot \cos\Delta\theta + R_I \cdot \mathrm{sen}\,\Delta\theta \right] \tag{10}$$

$$\text{where } n = \frac{1}{2} \left(1 + \frac{2 \cdot k \cdot h}{\mathrm{senh}(2 \cdot k \cdot h)} \right)$$

and where M_f is the wave-induced mass flux and R* is the complex conjugate of R (all other variables having their usual meaning in this context).

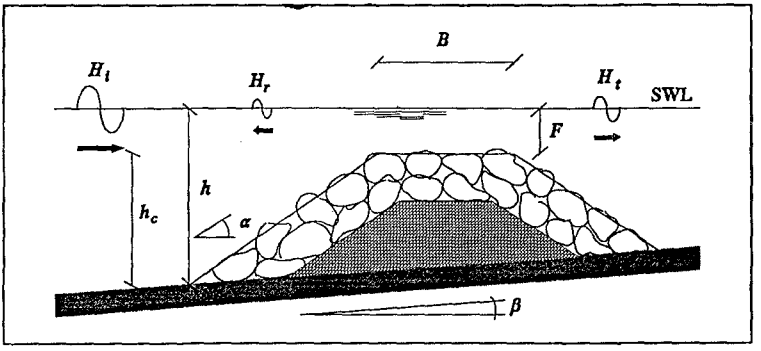

Figure 2. Schematization of the geometry and coordinates for a submerged breakwater under waves

ii) THE DEPTH-AVERAGED CURRENTS

The mean water level variations, $\langle\eta(x)\rangle$ are derived from the vertically-averaged x-momentum equation:

$$\frac{\partial}{\partial x}\langle\int_{-h}^{\eta_{cr}} u^2 dz\rangle + \frac{\partial S_{xx}}{\partial x} + \rho g(h+\langle\eta\rangle)\frac{\partial\langle\eta\rangle}{\partial x} = \langle\tau_s\rangle - \langle\tau_b\rangle \qquad (11)$$

Where $U = I + \bar{u}$, η_{cr} is the crest level and the rest of variables are as usual in surf zone analyses. The S_{xx} term has two contributions: S_{xx}=S_{xx}, waves +S_{xx}, roller (see e.g. (Tomé, 1997)).

The conventional approach to evaluate $\langle\eta\rangle$ in beach surf-zones is to neglect the convective term $\langle u^2\rangle$ and the τ_s and τ_b so that the x-momentum equation becomes:

$$\frac{\partial S_{xx}}{\partial x} + \rho g(h+\langle\eta\rangle)\frac{\partial\langle\eta\rangle}{\partial x} = 0 \qquad (12)$$

However, in front and above the submerged breakwater, according to the (laboratory) experimental evidence the u^2 terms cannot be neglected, since U is large near the submerged breakwater and the $\frac{\partial}{\partial x}$ of u is also large. This term is thus

retained, assuming a uniform undertow distribution below $\langle\eta\rangle$ and a 1DV local mass balance (i.e. the mass flux above $\langle\eta\rangle$ cancels the undetow). With this, the convective term can be evaluated as:

$$\langle\int_{-h}^{\eta_{cr}} \rho u^2 dz\rangle = \int_{-h}^{\langle\eta\rangle} \rho U^2 dz + \int_{\langle\eta\rangle}^{\eta_{cr}} \rho u^2 dz = \frac{Mf^2}{\rho(h+\langle\eta\rangle)} + aMf^2 \quad (13)$$

$$\text{with } a = \frac{64}{3\pi\rho H}$$

iii) SOME RESULTS

A sample of the wave and mean water level results so obtained is shown in figure 3 for regular waves. The wave-height variation appearing in figure 3a) shows the oscillatory behaviour typically associated to the superposition of an incident and a reflected wave. The $\langle\eta\rangle$ variation with x follows reasonably the experimental results although under-estimating the set-up in the downward slope of the submerged breakwater.

The results "without" reflection appear in figure 4 and show that the model without reflected waves is not able to predict the spatial oscillations of H in front of the submerged breakwater.

The mean water level predictions, although comparable, also tend to improve "with" reflection in the sense that an enhanced set-up is predicted (by the "full" model) in the downward slope.

The effects of the convective term (figure 5) affect basically the $\langle\eta\rangle$ predictions. The introduction of the u^2 term allows a deeper "trough" in $\langle\eta\rangle$ right at the beginning of the submerged breakwater crest just as it appears in the observations. The increased set-up right after the submerged breakwater is however not fully reproduced.

The same trends in results are obtained for irregular waves although in this case the H and $\langle\eta\rangle$ predictions are far better than the Q_b results. It should be, however, remarked that the fraction of breaking waves (determined visually from video recording of the experiments) is being used far beyond its intended original applicability. The overall agreement between observations and predictions for H and $\langle\eta\rangle$ is however satisfactory.

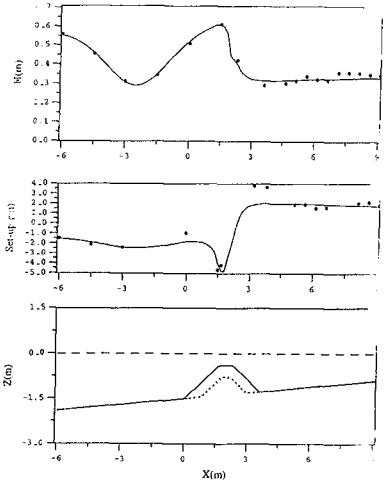

Figure 3. Sample results of the wave-height field and associated MWL for the "full" model presented in section 2 and the geometry depicted in the figure

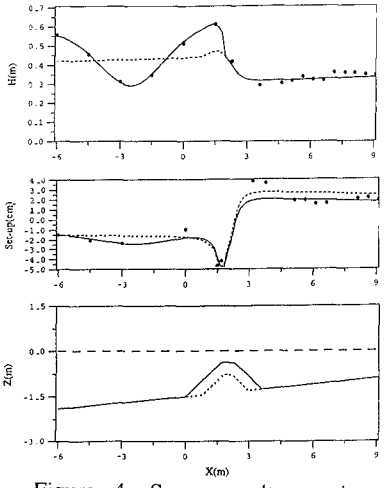

Figure 4. Same results as in figure 3 but without the reflection mechanism for the wave model (dashed line)

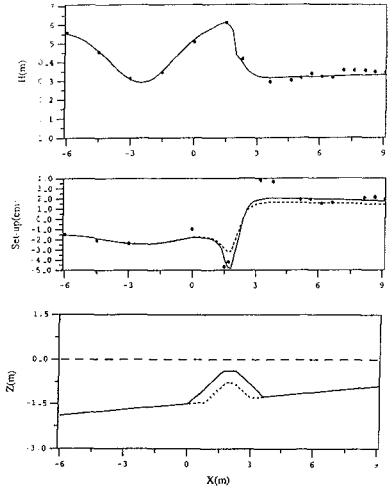

Figure 5. Same results as in figure 3 but without the convection terms in the $\langle \eta \rangle$ equation (dashed line)

iv) SOME REMARKS ON THE 2DV CURRENT FIELD

The 2DV current problem is being solved with the corresponding mass and momentum equations, using σ-co-ordinates so as to have the same vertical resolution for all water depths (i.e. well in front of the submerged breakwater or right above it).

The preliminary obtained results are based on the following x-momentum equation:

$$u\frac{\partial u}{\partial x}+w\frac{\partial w}{\partial z}+\frac{1}{\rho}\frac{\partial P}{\partial x}=-\frac{\partial}{\partial x}\langle\tilde{u}^2\rangle-\frac{\partial}{\partial z}\langle\tilde{u}\tilde{w}\rangle+\frac{\partial}{\partial z}\left(\upsilon_T\frac{\partial u}{\partial z}\right) \tag{14}$$

where the pressure is evaluated by

$$\mathrm{P}=\rho g(\eta-z)-\rho\langle\tilde{w}^2\rangle \tag{15}$$

and the x-derivative mixing term has been neglected (due to the expected greater vertical variations in flow properties).

The obtained results show a relatively high sensitivity to the bottom and mean water level boundary conditions, given by the corresponding shear stresses at $\langle\eta\rangle$ (associated essentially to the wave decay due to breaking, see e.g. (Sánchez-Arcilla et al., 1992), (Sánchez-Arcilla et al., 1994)) and at z_b (associated to the experienced bed friction due to the drag exerted by the submerged breakwater plus the flow inside of it). These preliminary results appear also to be quite sensitive to the $\langle\tilde{u}_i\tilde{u}_j\rangle$ wave shear stresses, in the sense that the resulting circulation field could feature or not a recirculation cell in front of the structure.

Because of this, the focus here will be exclusively on the evaluation of the wave stresses for the case of a sloping bottom with a submerged structure.

In general, the wave shear stresses, for the x-momentum equation, WSS_x, are given by:

$$WSS_x=-\frac{\partial}{\partial x}\langle\tilde{u}^2\rangle-\frac{\partial}{\partial z}\langle\tilde{u}\tilde{w}\rangle \tag{16}$$

There will be a non-zero contribution to WSS_x whenever there is a spatial variation of the wave-height field . Far the case of a sloping-bottom with a submerged structure there are two physical origins for these H variations:

a) The shoaling/breaking processes, for which

$$\frac{\partial\langle\tilde{u}\tilde{w}\rangle}{\partial z}=\langle\tilde{u}\tilde{\omega}\rangle-\frac{1}{2}\left[\frac{\partial}{\partial x}\left(\langle\tilde{u}^2\rangle-\langle\tilde{w}^2\rangle\right)\right]\approx-\frac{1}{2}\left[\frac{\partial}{\partial x}\left(\langle\tilde{u}^2\rangle-\langle\tilde{w}^2\rangle\right)\right] \tag{17}$$

according to (Rivero and Sánchez-Arcilla, 1995) and assuming that the oscillating motion has no vorticity, $\tilde{\omega}$ (even for the breaking wave case).

With this, the resulting shear stresses, WSS_{S-B}, are given by:

$$WSS_{S-B} = -\frac{1}{2}\left[\frac{\partial}{\partial x}\left(\frac{H}{2}\frac{gT}{L}\right)^2 \frac{ch(2kz)}{ch^2(kh)}\right] \qquad (18)$$

The order of magnitude of WSS_{S-B} is -0.1 m/sec^2 for shoaling waves and $+0.1$ m/s^2 or greater for breaking waves (governed by a saturation law of the type $H_b = \gamma h$). For more details see (Vergés and Sánchez-Arcilla, 1998).

b) The reflection processes for which (assuming a horizontal bottom), the corresponding shear stresses, WSS_{I-R}, are given by:

$$WSS_{I-R} = -\frac{1}{4}kH^2w^2\frac{sin\,2kx}{sh^2(kh)} \qquad (19)$$

This term turns out to be, thus, a function of 2kx which represents the phase-lag between reflected and incident waves (Vergés and Sánchez-Arcilla, 1998). It is due to the fact that the correlations between incident and reflected wave velocities need not be necessarily 0:

$$\langle \tilde{w}_i \tilde{u}_r \rangle \neq 0 \neq \langle \tilde{u}_i \tilde{u}_r \rangle$$
$$\langle \tilde{w}_i \tilde{w}_r \rangle \neq 0 \neq \langle \tilde{u}_i \tilde{w}_r \rangle \qquad (20)$$

The order of magnitude of the modulus of this term is around 0.5 m/s^2.

The WSS_x term for the general case of sloping bottom with submerged breakwater can therefore be written as (Vergés and Sánchez-Arcilla, 1998):

$$WSS_x = \left(1 + K_R^2\right)WSS_{S-B} + K_R WSS_{I-R} \qquad (21)$$

where $K_R = \frac{H_R}{H_I}$ is the reflection coefficient.

Model testing: The fixed and mobile bed experiments.

i) RIGID-BED TESTS

A set of hydrodynamic tests to analyse the submerged breakwater hydrodynamic performance and "impact" have been performed in a number of recent research projects carried out at the LIM/UPC. The tests, which are now beginning to be fully processed, cover a range of H/L_0 (wave steepnesses) and F/H (relative freeboard) values (figure 6). For most of the tests twelve "verticals" were obtained (figure 7). Each vertical was instrumented with 5 electromagnetic currentmeters and 6 pressure sensors.

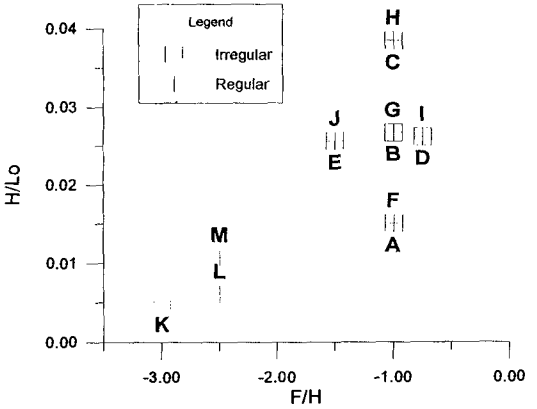

Figure 6. Schematization of the range of wave steepnesses (H/L_0) and freeboards (F/H) covered in the "hydrodynamic" experiments

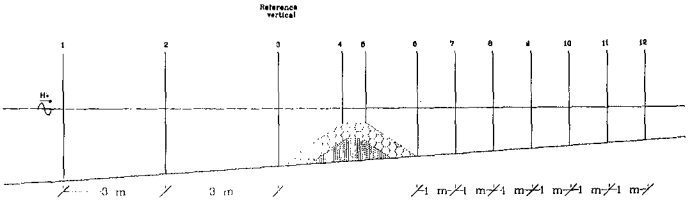

Figure 7. Distribution of "instrumented" verticals (with current-meters and pressure sensors) in the experiments

The preliminary results show transmission coefficients, K_T, in close agreement with state of art predictions (see e.g. (Van der Meer, 1990)). The dependence of K_T on F/L_0 (freeboard over the deep-water wavelength) rather than on F/H_{m0} (as is usual in the state of art) allows improved predictions and a "clearer" variation with the wave steepness H/L_0 (figure 8). From this type of analysis it is

possible to derive engineering formulae for the design of submerged breakwaters such as:

$$K_T = K_T(I_r)\big|_{F=0} + f(I_r)\,{}^{F}\!/_{L_0} \tag{22}$$

This expression shows that K_T starts -for F=0- with a value (a function of Iribarren's parameter) for submerged breakwaters reaching the mean water level, and then K_T increases linearly with F/L_0, the slope being also a function of

Irribarren's parameter, Ir. The same type of analysis can be applied to e.g. the reflection coefficient or, in general, the hydrodynamic behaviour of the structure.

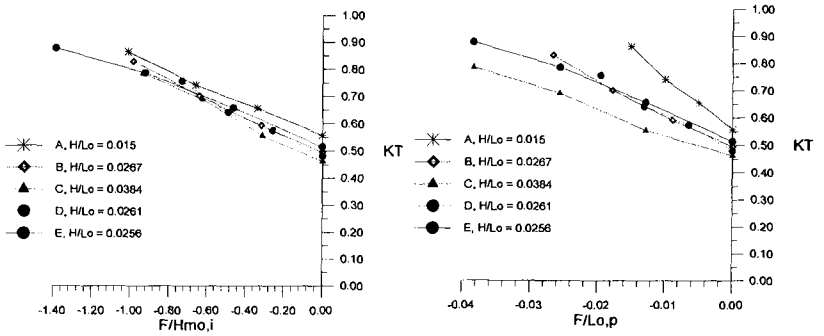

Figure 8. Free-board, F, dependence on wave-steepness for two possible ways to make F dimensionless

The observed circulation fields also display the expected features (e.g. a strong return flow over the crest of the structure, enhanced with respect to a real submerged breakwater since in the flume there must be 1DV mass flux compensation) plus some less "obvious" characteristics, such as the vortex in the up-ward slope of the structure.

ii) MOBILE BED TESTS

The mobile bed tests will be carried out as part of the MAST-III SCARCOST project whose main aim is, in this context, to analyse the hydrodynamic behaviour of the submerged breakwater and, in particular, the scouring in front of it.

The tests, scheduled for the 2nd term of 1999, will "repeat" the geometry, wave and "free-board" conditions tested for a rigid bed. This will allow to concentrate on the hydrodynamics in front of the structure and the associated bed evolution (figure 9). The observations include, as shown in the figure, free-surface elevations in front and over the structure, the current field in front and on the upward slope and pore pressures in the sand in front of the submerged breakwater. A PIV system, recently implemented in the CIEM flume of the LIM/UPC, will also be used to record the spatial velocity field in front of the structure and, in particular, in the vicinity of the scouring section.

Each of the mobile bed tests will have a minimum of 15,000 waves so as to allow for a "reasonable" development of the scouring in front of the structure (see e.g. (Herbich et al, 1984)).

The expected results will allow a characterisation of scouring as a function of hydrodynamic conditions and also the derivation of practical recommendations for the design of submerged breakwaters.

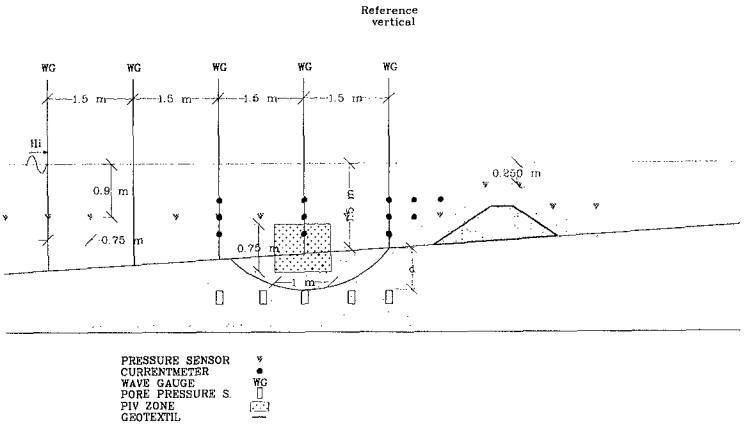

Figure 9. Mobile bed test arrangement, showing the hydrodynamic measurements, the PIV area and the pore pressure sensors

Conclusions: what has been done and remains to be done.

The following conclusions must be considered as on-going remarks since a large part of the experimental work is still to be processed and parts of it (mobile bed tests) even to be done. The numerical simulations are in a similar position since the adaptation of existing models for the submerged breakwater case is still very much under development.

Within this frame, the main on-going conclusions are the following:

i) The hydrodynamic performance of submerged breakwaters is quite sensitive to the design parameters. This requires careful selection and analysis since otherwise the submerged breakwater may not behave as expected (e.g. it could hardly affect the incoming waves) or even have contrary effects (e.g. enhanced erosion in the lee-area due to enhanced mass flux over the structure).

ii) The wave modelling with the submerged breakwater geometry appears to require a reflection coefficient "modulus" (to account for the decrease in H_r) and a reflection coefficient "phase" (to account for the exact origin of reflection). The same (i.e. real and imaginary parts) happens with the wave number, whose imaginary part is required to account for the energy loss in the porous (granular) layer.

iii) The current modelling appears to require the convective terms for the accurate predictions of set-up variations and the full "wave" stresses (due to the sloping bottom and the co-existence of incident and reflected wave fields) for the correct simulation of the current pattern.

Acknowledgements.

The authors would like to acknowledge the Spanish CICYT for sponsoring part of the rigid bed tests. The SCARCOST (Mast III) project partly supports the mobile bed tests and the COAST-3D (Mast IIII) project partly supports the theoretical development for the wave modelling. The authors also want to acknowledge the discussions and exchange of ideas with researchers from the Escuela de Caminos de Santander and, in particular, Drs. I. Losada and F. Mendez.

References

Battjes, J.A. and Jansen, J.P.F.M. (1978). "Energy loss and set-up due to breaking of random waves". *Proceedings of the 16th International Conference on Coastal Engineering*, Hamburg, Vol. Y. ASCE, New York.

Dally, W.R., Dean, R.G. and Dalrymple, R.A. (1985). "Wave height variation across beaches of arbitrary profile". *Journal of Geophysical Research*, 90(C6), pp. 11917-27.

Herbich, B.J., Schiller, R.E. and Dunlap, W. (1984). "Seafloor Scour". *Marcel Dekker, Inc.* USA.

Méndez, F.J. (1997). "Flujos medios inducidos por las ondas de gravedad en medios rflejantes y disipativos naturales o artificiales". PhD Thesis. ETSICCP, Universidad de Cantabria.

Nairn, R.B., Roelvink, J.A. and Southgate, H.N. (1990). "Transition zone width and applications for modelling surfzone hydrodynamics", *Proc. 22nd. Int. Conf. on Coastal Engineering*, ASCE, pp.68-81.

Nielsen, P. (1992). "Coastal bottom boundary layers and sediment transport". World Scientific, Singapore, 324 pp.

Okayasu, A. (1989). "Characteristics of turbulence structure and undertow in the surf zone". *Ph.D. thesis*, University of Tokio, Japan.

Rivero, F.J. and Sánchez-Arcilla, A. (1993). "On the vertical distribution of<*uw*>", Coastal Engineering, 25, pp. 137-152.

Rivero, F.J. and Sánchez-Arcilla, A. (1996) "The role of wave-induced shear stresses in the momentum balance equations", Coastal Engineering, pp. 1168-1177.

Rivero, F.J., Sánchez-Arcilla, A., Gironella, X. and Corrons, A. (1997). "Large-scale hydrodynamic experiments on submerged breakwaters". *Coastal Dynamics'97*, ASCE, pp. 754-763.

Sánchez-Arcilla, A., Collado, F. and Rodriguez, A. (1992). "Vertically varying velocity field in Q-3D nearshore circulation". *Proc. 23th. Coastal Eng. Conf.*, ASCE, pp. 2811-2824.

Sawaragi, T. and Deguchi, Y. (1992). "Waves on permeable breakwaters". *Proc. 23th. Coast. Eng. Conf.*, ASCE, pp. 1531-1544.

Sutherland, J. and O'Donoghue (1998). "Wave phase shift at coastal structures". *Journal of Waterway, Port, Coastal and Ocean Engineering*, March-April, ASCE.

Svendsen, Ib A. and Putrevu, U. (1994). "Nearshore mixing and dispersion". *Proc. Royal Society London*, A, 445, pp. 561-576.

Tolman, H.L. (1992). "An evaluation of expressions for wave energy dissipation due to bottom friction in the presence of currents". Coastal Engineering, 16, pp. 165-179.

Tomé, M. (1997). "Modelado matemático de la circulación 2DH inducida por el oleaje en presencia de diques sumergidos". *Master Thesis*, ETSICCPB, Universitat Politècnica de Catalunya.

Van der Meer, J.W. (1990). "Data on wave transmission due to overlaping". Report H-986, Delft Hydraulics, The Netherlands.

Verges, D. and Sanchez-Arcilla, A. (1998) "Wave-induced currents in front of sea structures" (under preparation).

2DH Morphological Modelling of Submerged Breakwaters

S.C. van der Biezen[1], J.A. Roelvink[1,2], J. van de Graaff[1], J. Schaap[3] and L. Torrini[3]

Abstract

The results are presented of 2DH numerical modelling of morphological effects of submerged breakwaters. In particular, segmented configurations are focussed upon, since segmented submerged breakwaters induce interesting and important current circulations in the horizontal plane.

In a previous study, a module that calculates a phase-averaged stationary wave field was used to compute wave forces. These forces were next used to calculate current patterns. In the present study, waves are introduced via a harmonic boundary condition in a phase-resolving module, based on the nonlinear shallow water equations. The advantage of this approach is that the current patterns are directly calculated, the disadvantage is that it requires more computation time.

The first results of morphodynamic computations with submerged breakwaters, in intra-wave mode, are promising. The most important mechanisms are reproduced rather well. Some of the shortcomings of the previous model study with a stationary wave model have been overcome. However, a lot of fine tuning still needs to be done.

1. Introduction

Submerged breakwaters are detached, mostly shore parallel, structures with their crest below water level. Their purpose is twofold. Firstly, submerged breakwaters 'filter' waves, by causing larger waves to break and leaving smaller waves more or less undisturbed. Secondly, they block offshore transport of sediment.

In Italy, submerged breakwaters have been used at various locations (Lamberti and Mancinelli, 1996; Tomasicchio, 1996). Their economic and aesthetic (Liberatore, 1992; Ozaki and Mitushashi, 1993) advantages compared to emerging breakwaters make submerged breakwaters an attractive tool for coastal management.

However, specially in case of the segmented configuration, one should be prepared for large sediment losses through the gaps due to concentrated offshore flow (Browder et al., 1996). A special (and expensive?) design of the structure may solve

[1] Faculty of Civil Engineering and Geosciences, Delft University of Technology, Stevinweg 1, 2628 CN, Delft, The Netherlands, J.vandeGraaff@ct.tudelft.nl
[2] Delft Hydraulics, Delft, The Netherlands, Dano.Roelvink@wldelft.nl
[3] M.Sc. student, Delft University of Technology

this problem (Nobuoka et al., 1996). In any case, extensive numerical and physical modelling are recommended for a proper implementation (Smith et al., 1995).

2. Basin experiments

At the Laboratory of Fluid Mechanics of Delft University of Technology, small scale 3D basin experiments with segmented submerged breakwaters were carried out (De Later, 1996; Van der Biezen et al., 1996). Aim of the experiments was to obtain a data-base for numerical modelling studies. A movable bed was used to include morphological effects of the structures. The measurements focussed on morphology rather than on hydrodynamics. Apart form Delft University of Technology, five other universities participated in this research project, which was funded by the Human Capital and Mobility Programme of the EU.

At the Hydraulic and Maritime Research Centre in Cork, Ireland, hydrodynamic parameters were measured in similar tests with a fixed bottom (Murphy et al.,1996). Apart from these basin tests, flume experiments were carried out as well by other universities. Detailed information on the project is included in the Test Definition Report (Høgedal et al., 1994).

2.1 Experimental setup

In the wave basin (length = 28 m, width = 14 m, depth = 0.60 m), three series of test were carried out: one series without structures, one series with three separate breakwaters of 6 m length each (two gaps of 3 m in between) and one with two breakwater segments of 12 m and 6 m length with only one gap of 3 m in between. In each series three different wave heights were generated: 0.08 m, 0.10 m and 0.12 m. The generated wave field was regular and normal incident to the beach, with a wave period of 1.55 s. The initial beach slope for each test was 1:15. Figure 1 shows a plan view of the wave basin for the configuration with three submerged breakwaters (all measures in meters).

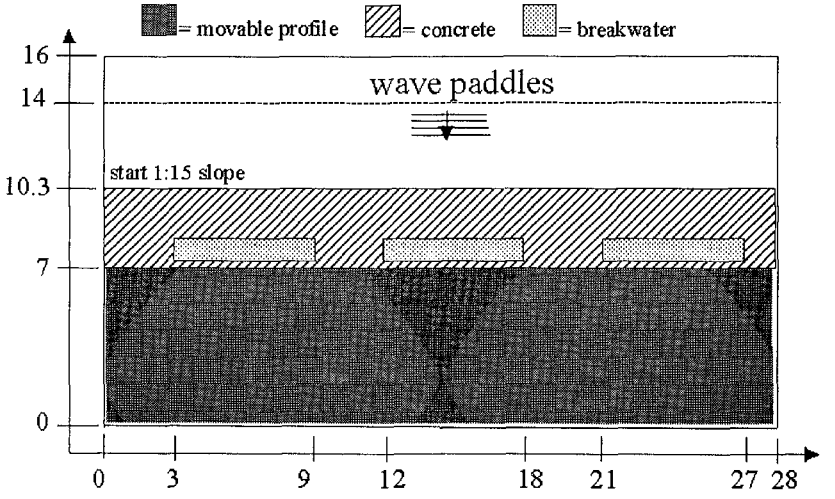

Figure 1. Plan view of the wave basin with three submerged breakwater segments.

All experiments were conducted with a rubble mound breakwater with an impermeable core and 2:3 slopes on both sides. The armour layer of the prototype breakwater consisted of two layers of rock stones, D_{50} = 0.812 m. The crest width was chosen as $3D_{50}$ and the thickness of the armour layer as $2D_{50}$. The water depth at the seaward toe of the breakwater equals 6 m and the breakwater submergence equals 1.5 m.

Scaling the prototype breakwater with a 1:15 ratio yields the measures given in Figure 2. The submergence of the breakwater crest is constant for all tests.

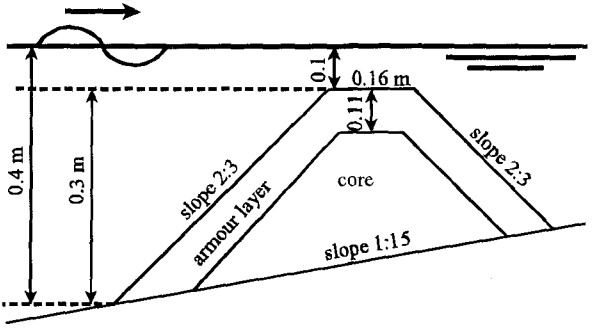

Figure 2. Submerged breakwater design

The structure is placed on a concrete slope. The profile landward of the structure consists of sediment with a grain size D_{50} of 95μm.

2.2 Measured parameters

The experiments lasted 7:30 h each, interrupted by several profile measurements. The first profile measurement is at t = 0:00 h, the initial profile. The next measurements are at t = 0:30 h, t = 1:30 h, t = 3:30 h and, finally, at t = 7:30 h. During the profile measurements the wave generator was stopped.

Apart from the profile height, velocities in the horizontal plane and free surface elevations were measured. The time series were taken at different cross-sections. For more details, reference is made to Van der Biezen et al. (1996).

2.3 Measurement results

The measurement results presented here only intend to illustrate the measurement data used for the numerical study. For each measured parameter a short explanation is given.

Figure 3 shows two examples of measured wave heights, for a generated wave height of 0.12 m. The left plot shows wave height measurements for an experiment without submerged breakwaters, and the right plot shows measurements in a cross-section with a submerged breakwater.

Free surface elevation was measured at four cross-shore locations. From the time series, an average wave height was calculated using the standard deviation of all samples. Although the hydrodynamic measurements are not detailed, the influence of the submerged structure on the wave heights is clearly visible.

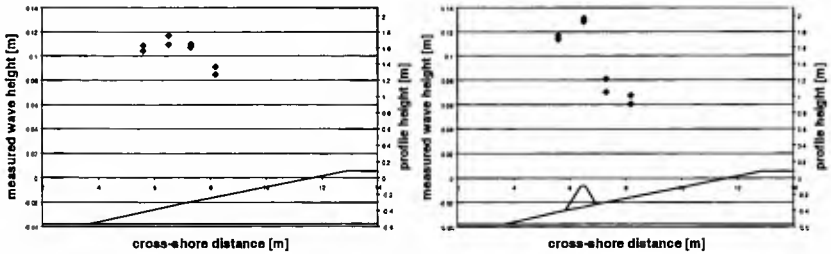

Figure 3. Measured wave heights with and without a submerged breakwater

Current velocities in the horizontal plane were measured at several cross-shore locations. Figure 4 shows depth averaged currents, averaged in time over the first 1:30 h of the experiment to obtain the overall current pattern. The waves propagate top-down in this figure.

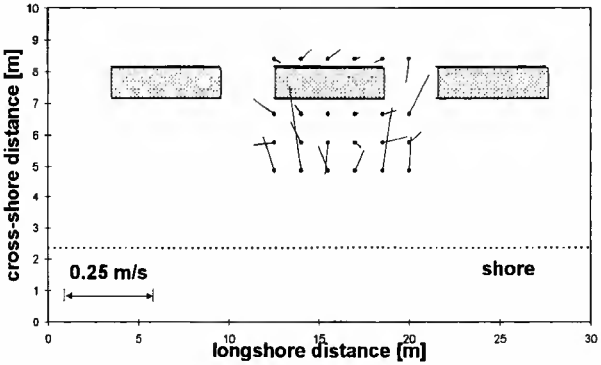

Figure 4. Measured currents, magnitude and direction

The velocity measurements show offshore directed currents towards and through the gaps between the breakwater segments. This leads to significant sediment losses, as illustrated by Figure 5 which shows the bathymetry of the basin with three breakwater segments after 7:30 h of wave action.

Figure 5. Measured bathymetry after 7:30 h of wave action

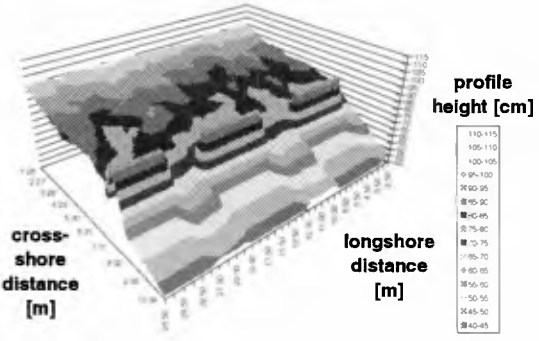

3. 2DH Morphological Modelling, phase averaged

In 1997, a first attempt was made to reproduce the experiments with a numerical model (Schaap 1997, Torrini 1997, Van der Biezen et al. 1997). The package used for this study was Delft3D, developed by Delft Hydraulics. Delft3D consists of several modules, which can be combined so that it suits the case of interest. Only a few aspects of this previous study are mentioned, more details can be found in the given references.

3.1 The model system

Without going into detail (details on Delft3D can be found in the Manual, 1996) the combination of modules applied in this first study is given in Figure 6.

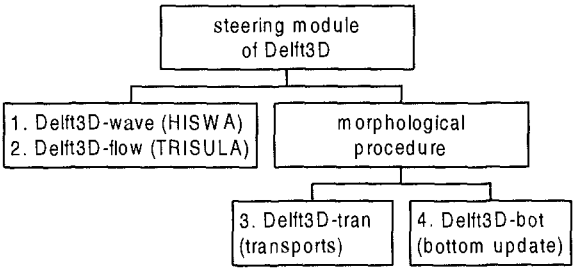

Figure 6. Model system including a wave field module

The computation starts with the calculation of the stationary wave field (module 1) for the given boundary conditions and initial bathymetry. Wave diffraction, which is not included in this module, is represented by directional spreading. Relevant output of module 1 (e.g. wave forces) is written to a communication file. Secondly, the currents are calculated by module 2, which needs information from the communication file. The current field is again written to the communication file. Module 2 takes most of the computation time.

Next the morphological procedure can be run. Module 3 calculates a velocity field from the discharge data in the communication file, with a correction of the total flux velocity for the mass flux by waves. Sediment transports are calculated using the Bijker formula with wave effect. Module 4 updates the bathymetry and adds the new bathymetry to the communication file.

From a stability consideration, the allowed morphological timestep can be determined. Several morphological timesteps can be processed (sequence of modules 3 and 4) without the need to update the current field (and to run module 1 and 2). In this case new velocities corresponding to the updated bottom are calculated from the last discharge data using a continuity relation.

3.2 Waves

The Delft3D-wave module calculates a stationary wave field, which includes wave heights, setup, energy dissipation etc. Figure 7 shows the calculated wave setup for a two-breakwater-segments case. Setup behind the structures is a consequence of energy dissipation by friction and by wave breaking. The resulting setup gradients,

together with the level increase due to mass transport of water over the breakwater crests, are the driving mechanisms for the return flow through the gaps as illustrated in Figure 8.

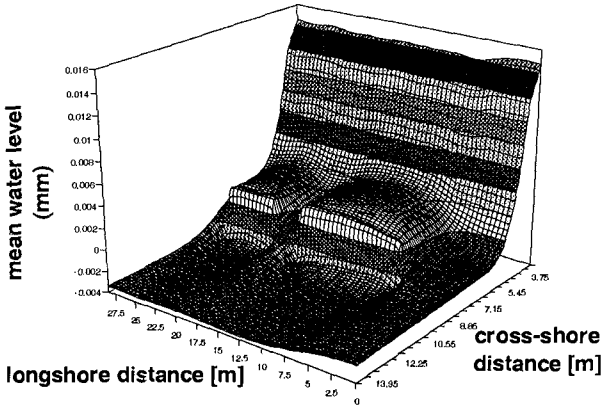

Figure 7. Wave set-up calculated by Delft3D-wave

3.3 Currents

The wave forces in the communication file are used to calculate currents. The measured horizontal current pattern, see Figure 4, appears to be well reproduced by the pattern calculated by module 2, see Figure 8. Waves propagate top down; the circulation cells with offshore directed flow through the gaps are clearly present.

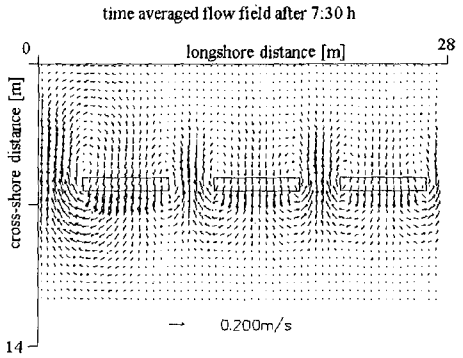

Figure 8. Calculated horizontal current pattern

3.4 Morphology

The calculated morphologic changes are, to some extent, in accordance with the measurements. The sediment loss through the gaps between the breakwater segments is well reproduced. However, there are also large discrepancies.

Figure 9 gives the calculated bottom after 3:30 h (approximately half of the experiment duration) which shows large local scour at the waterline and at the landward toe of the structure.

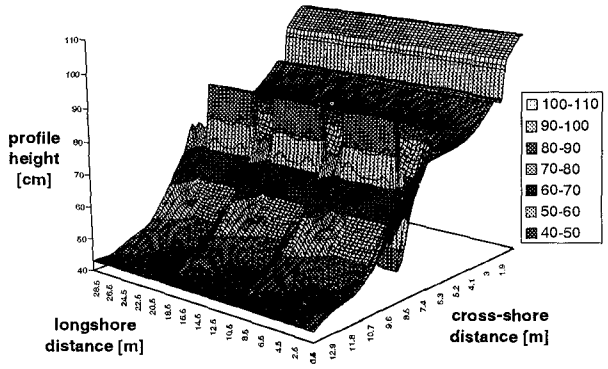

Figure 9. Calculated bathymetry after 3:30 h wave action

The local scour landward of the submerged breakwater follows from a peak in energy dissipation calculated by the wave module. In the experiments, energy was dissipated over a longer distance by spilling breakers. Furthermore, the wave module was not specifically developed to handle a regular wave field.

The unrealistic (computed) scour at the waterline is due to the inability of the model to change 'dry' grid points into 'wet' gridpoints. Since the initial slope is quite steep, this shortcoming has important consequences.

4. 2DH Morphological Modelling, phase resolving

Since the above shortcomings are related to the use of the wave module, and since the experiments are carried out with regular waves, it was decided to try the harmonic boundary option in the flow module for wave generation instead of the wave module. Normally, this option is used to introduce the tide in a simulation.

Delft3D–flow solves the non-linear shallow water (NSW) equations. This implies, amongst others, that a hydrostatic pressure is assumed, which is correct in case of tidal waves. In case of short waves this is usually not so, since vertical accelerations in the water column disturb the hydrostatic pressure.

The waves generated in the basin, however, approximate shallow water waves to a large extent. In the deepest part of the wave basin, the wave celerity that follows from the linear wave theory (with hyperbolic functions) equals 1.99 m/s. The shallow water wave celerity, calculated by the model, equals 2.36 m/s which is only 19% too high. This percentage will even be less in the area of interest, near the structures.

An alternative to the nonlinear shallow water equations, solved in this study, are the Boussinesq equations which can be applied to a larger part of the coastal region. An advanced model based on these equations is discussed by Madsen et al. (1997). In the present study, however, a NSW approach was chosen for the reason that sediment transports and morphology needed to be included.

4.1 The model system

The model system as described in section 3.1 is now changed, since the wave module will not be used during computation. The new model system is given in Figure 10.

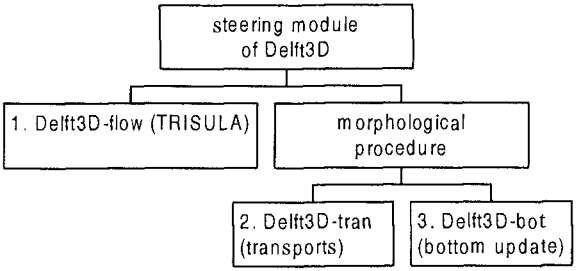

Figure 10. Model system without wave module

In the sections below, the output of each module will be discussed according to their computational sequence during a model run.

4.2 Waves

The simulation starts with the calculation of the wave propagation in the basin (with initial bathymetry) induced by a harmonic boundary condition. In contrast with the previous study, the output does not consist of one stationary wave field. Instead, for each grid point now a time series containing water levels and current data is written to the communication file.

Consequently, the flow in the basin is not calculated separately, like in the previous study, but follows directly from the time-averaged velocity fields stored in the communication file. The same holds for the setup (time averaged water levels).

The calculation of wave propagation is continued until any start-up effects have disappeared. Figure 11 gives an example of calculated water levels in a particular cross-section at different time steps just after the start of a simulation.

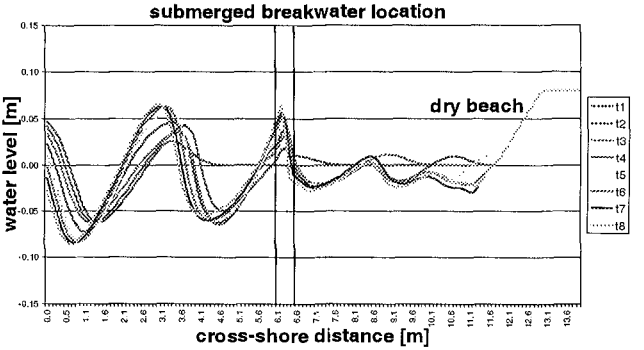

Figure 11. Calculated water levels for different time steps

The influence of the submerged breakwater on the wave height is clearly visible in Figure 11. It is remarked that this approach also includes wave reflection, wave diffraction and, most important, wave runup. Wave runup is responsible for erosion of the dry beach.

The front of the waves tends to become steeper during their propagation towards the breakwaters. To ensure that the wave, once it reaches the structure, has a proper shape, the incoming wave at the boundary was modified to anticipate for the steepening of the wave front. Furthermore, a discharge boundary instead of a water level boundary was chosen since it corresponds more to the motion of the wave paddles.

The parameters used for calibration are the horizontal viscosity and the roughness length. The viscosity was found to be smaller than the default value and the roughness length needed to be enlarged: $\nu_H = 0.01$ m^2/s and $k_s = 0.5$ m, where k_s is the Nikuradse roughness length used in White Colebrook's friction formulation. Specially k_s is large, to obtain enough wave decay. Figure 12 shows some calibration results for a section with and a section without a submerged breakwater.

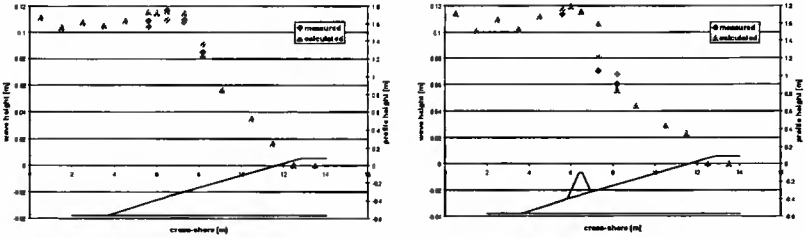

Figure 12. Measured and calculated wave heights

Figure 12 shows that the measured wave heights are reproduced quite well; the calibration parameters are somewhat out of range, though. Some wave height variation seewards of the submerged structure can be seen. This is due to reflection of wave energy. The calculated wave set-up shows the presence of interfering waves, both in cross-shore and in longshore direction, see Figure 13. The waves propagate from left to right in this figure and two submerged breakwater segments are present.

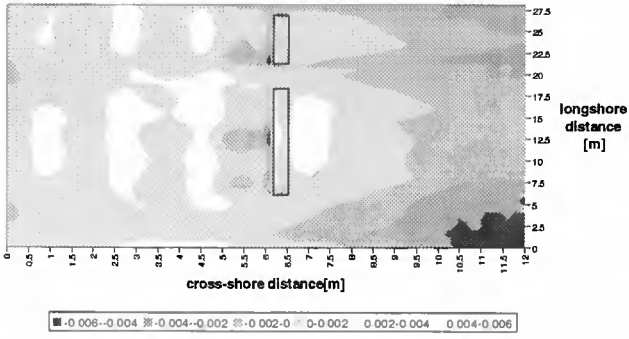

Figure 13. Wave setup [m] calculated from water level time series

Figure 13 also shows a wave setup landwards of the submerged breakwaters, which is in accordance with the output of the wave module in the previous study, see Figure 7 in section 3.2.

4.3 Currents

As mentioned before, the net current pattern as well as the setup can be obtained by averaging respectively the velocity and water level time series over a number of wave periods. The resulting net current pattern looks similar to Figure 8.

4.4 Transports

The sediment transports are computed from discharge fields, stored in the communication file. With use of the bathymetry, first time varying velocity fields are computed from which time varying sediment transports can be calculated. To obtain the net sediment transports, again a time average over a number of wave periods is taken.

The Bijker sediment transport formula is used to calculate sediment transports from the velocity components. However, since the wave module is not used, no wave effect could be included. This reduces the Bijker transport formula to a combination of the Kalinske-Frijlink formula for bed load transport, the Rouse-Einstein expression for the sediment concentration distribution and the Einstein expression for the suspended sediment transport. Since this combined formula is applied within the wave periods (intra-wave), the wave effect is more or less included via the individual discharge fields.

An example of an intra-wave sediment transport field is given in Figure 14.

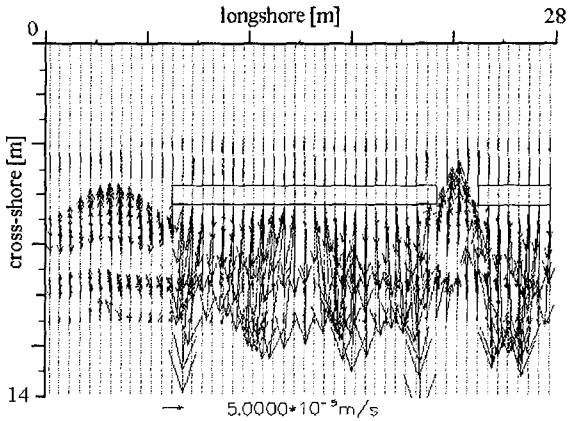

Figure 14. An individual intra-wave sediment transport field

The waves propagate top-down in this figure. Large onshore sediment transports can be seen at the lee side of the structures and offshore transports through the gaps. Other sediment transport fields show a similar pattern.

4.5 Morphology

As mentioned before, one of the advantages of the present NSW approach is the calculation of wave runup. This opens a way to include erosion near and above the waterline.

The transport module uses a parameter that influences the downslope transport by gravity. A higher parameter value yields a smoother profile. Also, a high value increases the transport of sediment from dry to wet grid points near the water line, because at the water line steep slopes tend to occur. As soon as the begin and end grid point of a local slope are both wet, downslope sediment transport takes place. For one cross-section, the profile development including the calculated behaviour near the waterline is given in Figure 15.

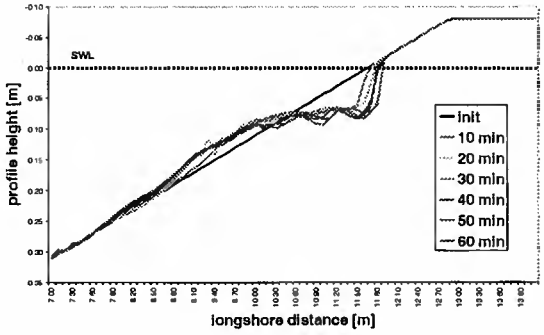

Figure 15. Calculated profile development

With the adjusted parameter for downslope sediment transport, full morphologic runs were made. Since the required computation time is large, only the first 3:30 h of the total duration of the experiments was computed. The runs presented here all have an initial wave height of 0.12 m.

Figure 16 shows the calculated erosion and accretion during a 3:30 h simulation with two submerged breakwaters.

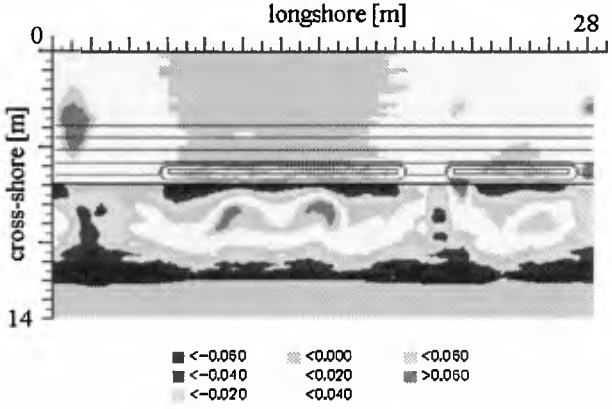

Figure 16. Calculated erosion and sedimentation after 3:30 h

In this figure, erosion is negative and accretion is positive. The figure shows erosion at the waterline and at the landward toe of the submerged breakwaters. Accretion occurs in the area between the structures and the waterline, because of the 'flattening' of the initial profile which is quite steep (1:15). Furthermore, sediment is deposited seawards of the gaps.

Figure 17 shows a 3D image of the calculated bathymetry after 3:30 h wave action with two submerged breakwaters.

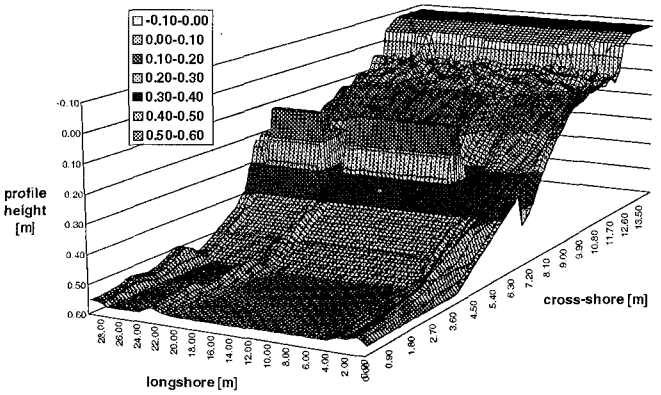

Figure 17. Calculated bathymetry after 3:30 h for two submerged breakwaters

Comparing Figure 17 to Figure 9, it can be seen that the results have improved, specially near the water line and near the landward toe of the structures. The large scouring at these locations, pictured in figure 9, does not occur for the new model system with the shallow water approach. Furthermore, the longshore bed variations, which were absent in the previous study, see Figure 9, are now reproduced.

Finally, the Figures 18a and 18b compare the measured profile, the calculated profile from the previous study and the calculated profile from the present study for two cross-sections. One section is with a submerged breakwater and one section is without a submerged breakwater. The simulated time is 3:30 h.

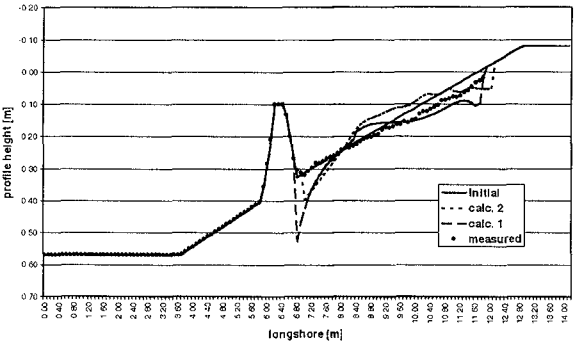

Figure 18a. Comparison for a section with submerged breakwater

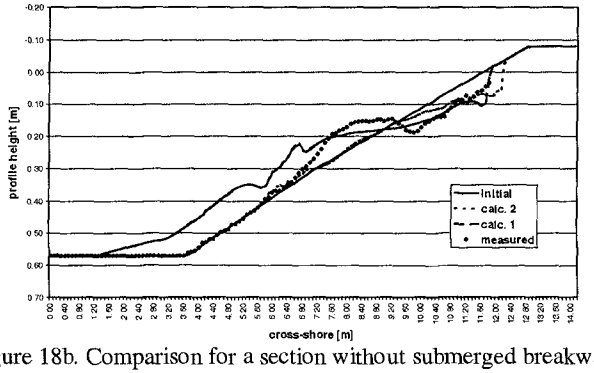

Figure 18b. Comparison for a section without submerged breakwater

Specially at the waterline and at the landward toe of the structure, the shallow water approach seems to be more accurate.

5. Conclusions and Recommendations

From the above presented numerical study on segmented submerged breakwaters, the following conclusions can be drawn:

- Numerical modelling of submerged breakwaters describing waves with the non-linear shallow water equations yields promising results.
  The calculation time, however, increases compared to simulations which use a stationary wave field.
- The measured wave height decay over a submerged breakwater is predicted well when using the shallow water approach, although somewhat unusual values have to be used for bottom roughness and horizontal viscosity.
- When modelling morphology around submerged breakwaters, it is of importance to describe the erosion near the water line correctly. The study shows that the intra-wave approach is more accurate on this aspect. However, both approaches require further study.

The shallow water assumption opens new possibilities regarding morphological modelling of submerged breakwaters. The present research has been a pilot study into this field. A lot of fine tuning still needs to be done. Other sediment transport formulas should be tried, and the description of the transport processes near the water line needs more attention. Furthermore, extra measurement data bases would be useful for calibration purposes.

6. Acknowledgements

The author wishes to acknowledge Delft Hydraulics for the use of the Delft3D package. The experiments were carried out in the scope of the 'Dynamics of Beaches' project, funded by the Human Capital and Mobility Programme of the Commission of the European Communities (contract CHRX-CT93-0392). The numerical study was partly funded by the MaST-3 project "Surf and swash zone mechanics" (SASME).

7. References

Browder, A.E., R.G. Dean and R. Chen (1996), *Performance of a submerged breakwater for shore protection*, Proc. ICCE'96, Chapter 179.

De Later, J. (1996), *Effect of submerged breakwaters on a beach profile exposed to regular waves in a wave basin*, Delft University of Technology, Msc.Thesis.

Høgedal, M. et al. (1994), *Dynamics of Beaches,* Test Definition Report for the Human Capital and Mobility Programme.

Lamberti, A. and A. Mancinelli (1996), *Italian experience on submerged barriers as beach defence structures*, Proc. ICCE'96, Chapter 182.

Liberatore, G. (1992), *Detached breakwaters and their use in Italy,* Proc. of the Short Course on Design and Reliability of Coastal Structures, Venice, pp. 373 - 395.

Madsen, P.A., O.R. Sørensen, H.A. Schäffer (1997), *Surf zone dynamics simulated by a Boussinesq type model. Part II: surf beat and swash oscillations for wave groups and irregular waves*, Coastal Engineering 32, pp. 289 – 319.

Manual (1996), *An introduction to Delft2D-Mor*, Release 2.07, Delft Hydraulics.

Murphy, J., A.W. Lewis, C. Wall, J. van de Graaff and S.C. van der Biezen (1996), *Submerged breakwaters research in the EU Human Capital and Mobility Programme,* Proc. of the Maff Conf. on River and Coastal Eng., Hydraulic and Maritime Research Centre Cork.

Nobuoka, H., I. Irie, K. Hajime and N. Mimura (1996), *Regulation of nearshore circulation by submerged breakwater for shore protection*, Proc.ICCE'96, Chapter 185.

Ozaki, T. and K. Mitushashi (1993), *Ecology conscious submerged breakwater*, Proc. of the Symp. on coastal and ocean management, ASCE, pp. 265 – 279.

Schaap, J. (1997), *Modelling the effects of submerged breakwaters in a wave basin*, Delft University of Technology, Msc.Thesis.

Smith, D.A.Y, P.S. Warner, R.M. Sorensen, L.A. Nurse and K.A. Atherley (1995), *Submerged-crest breakwater design*, Proc. 1995 Coastal Struct. Conf., London.

Tomasicchio, U.(1996), *Submerged breakwaters for the defence of the shoreline at Ostia, field experiences, comparison*, Proc. ICCE'96, Chapter 186.

Torrini, L. (1997), *Nearshore effects of submerged breakwaters*, Delft University of Technology, Msc.Thesis.

Van der Biezen, S.C., J. van de Graaff and J. de Later (1996), *3D model tests of the influence of submerged breakwaters on a beach profile exposed to regular waves*, Proc. PECS'96, The Hague.

Van der Biezen, S.C., J. van de Graaff, J. Schaap and L. Torrini (1997), *Small scale tests and numerical modelling of the hydrodynamic and morphological effects of submerged breakwaters*, Proc. Pacific Coasts and Ports, pp. 219 – 224.

WAVE PRESSURE DISTRIBUTION ON PERMEABLE VERTICAL WALLS

Hendrik Bergmann[1], Hocine Oumeraci[2]

Abstract

The pressure distribution at permeable vertical walls is investigated within a comprehensive large-scale test programme considering experiments with a variation of wave parameters and structure porosities. Monochromatic non breaking and slightly breaking waves on such structures are examined and results are compared to the GODA formula for impermeable vertical walls and a modified GODA method which has been developed here for permeable walls. Two parameters involving the structure porosity are introduced to account for the nonlinear processes at permeable walls. Using these parameters new prediction formulae have been derived for the pressure distribution at the wall.

1. Introduction

The advantages of permeable vertical wave barriers are obvious in terms of wave damping performance, reduction of wave reflection, overtopping and forces. Wave damping is of fundamental importance for the protection of harbours and marinas. Rubble mound structures can be used if there are no limitations in space and in case of shallow water depth, otherwise vertical structures may be favoured. However, impermeable vertical structures result in considerable wave reflection which can cause navigation problems in harbour entrances for smaller vessels. Therefore, it might be advisable to use perforated structures which allow to better control wave transmission and reflection. In this case reliable information on wave loads and pressure distribution on the permeable wall is needed for stability analysis and design.

The most widely used pressure formulae for the design of coastal structures with vertical walls under breaking and non breaking wave conditions are the GODA

[1] Dipl.-Ing., Research Assistant, Leichtweiss-Institut, TU Braunschweig, Beethovenstr. 51a, 38106 Braunschweig, Germany, e-mail: h.bergmann@tu-bs.de

[2] Prof. Dr.-Ing., University Professor, Managing Director of Leichtweiss-Institut, TU Braunschweig

formulae (1985). However, these formulae do not account for a wall porosity so that reduction coefficients can only be estimated by engineering experience or obtained from hydraulic model tests. Therefore, the hydraulic performance and the pressure distribution of single permeable vertical walls was investigated within a comprehensive large-scale test programme. The extension of the existing formulae in terms of structure permeability was performed considering experiments in intermediate water depth with different wave conditions and structure porosities. For this paper only non breaking and slightly breaking waves on such structures were examined and results are compared to the GODA method for impermeable walls. Two dimensionless parameters involving the structure porosity were introduced to account for the nonlinear processes at permeable walls.

2. Experimental Set-up and Test Conditions

The tests were conducted in the Large Wave Flume (GWK) of the Coastal Research Centre, a joint institution of the University of Hannover and the Technical University of Braunschweig. The flume has a length of 320m, a width of 5m and a depth of 7m (Fig. 1). A sand beach with a slope of 1:6 was installed about 220m from the wave paddle for the dissipation of transmitted wave energy. The vertical permeable wall, made of horizontal steel bars was located about 100m from the wave paddle.

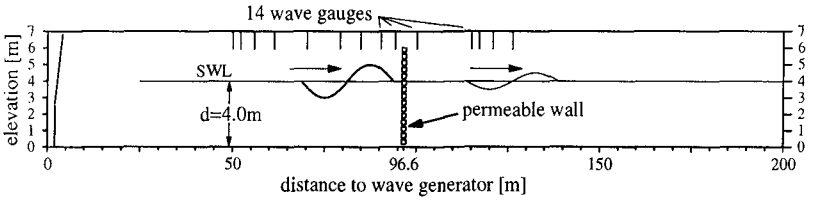

Figure 1: Cross Section of the Large Wave Flume (GWK) with Positions of Permeable Wall and Wave Gauges.

The incident waves, wave transmission and wave reflection were analyzed by wave gauges which were grouped in three harps (one in the far field, one in front and one behind the structure) with 4 wave gauges each. Additional wave gauges were installed to measure the water surface elevation and the waterlevel gradient directly at the permeable wall.

The tests were carried out with regular waves (H=0.5-1.5m and T=4.5-12s), random waves (H_s=0.5-1.25m, T_p=4.5-12s), solitary waves (H=0.5-1.0m) and transient wave packets. The water depth was kept constant (d=4.0m) in the test phase with permeable walls but was varied between 3.25 and 4.75m for the impermeable wall tests (P=0%). Due to the structure height of approximately 6m, overtopping is negligible.

The structure porosity P=s/e, with gap spacing s and distance e between two ad-

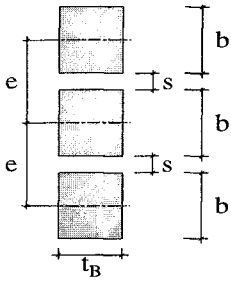

Figure 2: Definition of Structure Porosity P=s/e.

jacent element axis' (Fig. 2), was varied in five steps: P=0.0% (impermeable wall), 11%, 20%, 26.5% and 40.5%. A permeable wall consists of up to 29 horizontal elements which were built of quadratic steel pipes (t_B×b: 180×180mm, Fig. 2). The tested structures had an overall weight of up to eight tons depending on their porosity.

In order to analyze the resulting wave loads pressure transducers of type NATEC SCHULTHEISS PDCR 830 were installed at 10 positions at the front and rear side of the structure. Fig. 3 shows the front view of the wall (porosity P=26.5%) with locations of the pressure transducers over the structure height. The resultant pressures were calculated by adding the two pressure components on both sides of the wall elements which were equipped with pressure cells (Fig. 4). Data were recorded at 200Hz logging frequency.

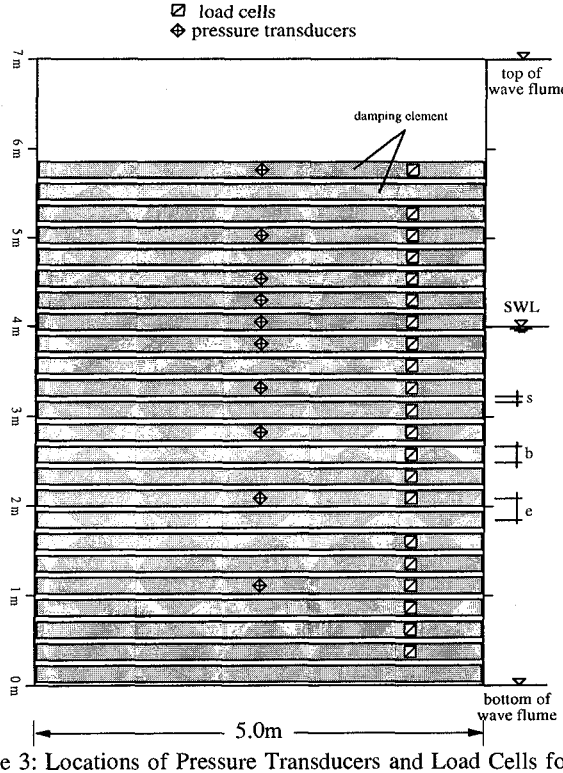

Figure 3: Locations of Pressure Transducers and Load Cells for a Permeable Wall with Porosity P=26.5%.

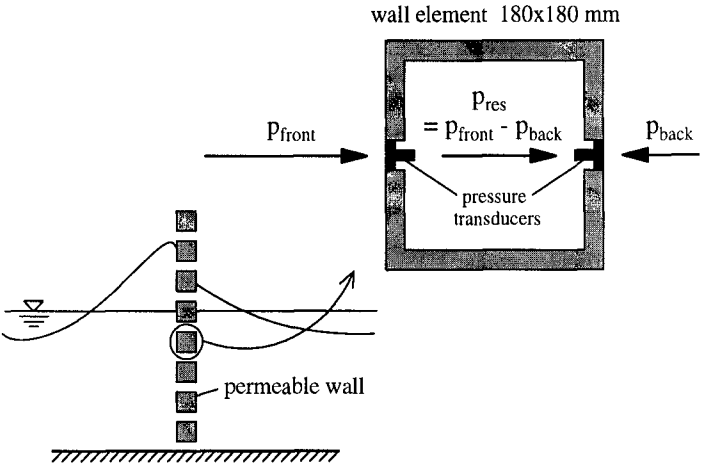

Figure 4: Calculation of Resultant Pressures p_{res}.

3. Experimental Results and Discussion

The hydrodynamic pressure distribution under wave attack at the front of a vertical impermeable structure can be described by the water surface elevation η^* above still water level, the pressure p_1 at still water level (SWL) and the pressure p_2 at the toe of the structure (GODA, 1985). For the vertical walls tested in the GWK (2D-case, normal incidence of waves, no berm) the equations for the characteristic values (Fig. 5) described by GODA can be simplified to:

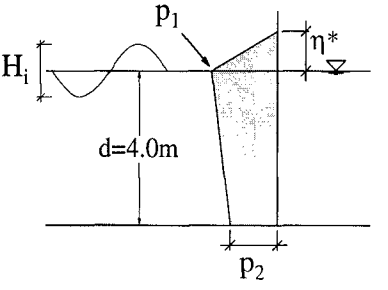

Figure 5: Definition Sketch for Pressure Distribution according to GODA's Method.

$$\eta^* = 1.5 \cdot H_i \tag{1}$$

$$p_1 = \alpha_1 \cdot \rho \cdot g \cdot H_i \tag{2}$$

$$\text{with } \alpha_1 = 0.6 + 0.5 \cdot \left(\frac{(4\pi d/L)}{\sinh(4\pi d/L)} \right)^2 \tag{3}$$

$$p_2 = \frac{1}{\cosh(2\pi d/L)} \cdot p_1 \tag{4}$$

The tests considered in this paper were run with monochromatic waves. The wave height H_i describes the mean incident wave height and L is the local wave length at the structure.

Fig. 6 shows the measured pressure heads at the front and at the rear side for different structure porosities. Results are shown exemplarily for an incident wave height of H_i=0.80m and a wave period of T=8s for all porosities investigated. In addition, the calculated pressures (Eq. (1) - Eq. (4)) on an impermeable wall are also plotted. The graph represents a) the pressure distribution acting simultaneously on the front face of the wall and on the rear side of the wall (left side) and b) the resultant pressures (right side) for the time step where the maximum total force on the structure occurred (wave crest). The total horizontal force was obtained by integration of measured resultant pressures over the structure height for every time step.

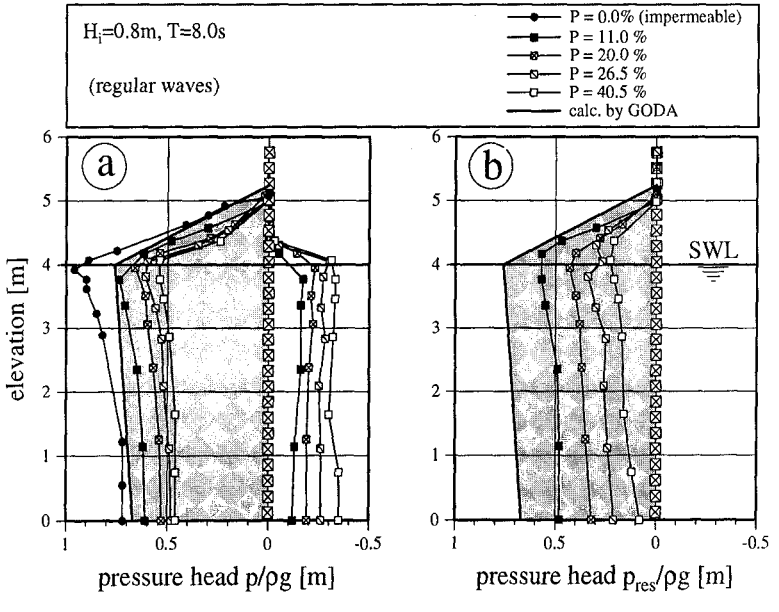

Figure 6: Simultaneous Pressure Distribution on Front and Back Side (a) and Resulting Pressure Distribution (b).

Generally, all measurements show a similar profile compared to the GODA distribution, but the influence of the wall porosity is obvious. At the structure front

face higher pressures p_1 are observed for low structure porosities (P=11%), whereas on the rear side of the structure the higher pressures occur for large values of structure porosity (P=40.5%). Due to the reduction of pressure at the structure face and the increase of pressure at the rear side of the structure the resulting pressure values are even more reduced when compared to the calculated pressures for an impermeable wall (Fig. 6, right). Hence, in the case of a permeable wall the resulting pressure values $p_{1,res}$ and $p_{2,res}$ are the governing pressures for the calculation of the total loading of the structure. The resulting pressure values are calculated as described above (see also Fig. 4) and used for further analysis. In addition it is apparent from Fig. 6 that the wave run-up at the structure is overestimated by Eq. (1). In the following the aforementioned characteristic values will be discussed in terms of the porosity of the wall.

3.1 Maximum Surface Elevation at Structure Front η^*

The linear relationship between run-up height and wave height (Eq. (1)) is not appropriate for the description of the physical processes at the structure face. In fact, ratios η^*/H_i measured in the Large Wave Flume varied between 0.56 and 1.32 for P=40.5% to P=0.0%, respectively. The maximum wave run-up at the structure front (η^*) is governed by the influence of shallow water depth (function of d/L) and the reflection properties of the structure which is directly related to the reflection coefficient C_r and the structure porosity P. The influence of the structure porosity P is considered by the reduction parameter Ψ_e. The surface elevation at the structure face can be determined as:

$$\eta^* = \Psi_e \cdot \left[2 - \tanh\left(\frac{4\pi d}{L}\right)\right] \cdot H_i \tag{5}$$

where the reduction parameter Ψ_e is defined as a function of the wall porosity P:

$$\Psi_e = \left(1 - 0.5 \cdot \sqrt{P}\right) \tag{6}$$

The correlation between measured and calculated η^*-values is relatively good, although the wave run-up at the structure is slightly overestimated for small waves but underestimated for large waves (Fig. 7). This nonlinear process in terms of the wave height and the influence of the reduction parameter Ψ_e will be discussed more thoroughly under Section 3.2.2.

3.2 Pressure Distribution at Structure

In Fig. 8 all measured resultant pressure values $p_{1,res}$ (at SWL) under different wave conditions (regular waves) are shown in comparison with results using the GODA formula for impermeable walls. The influence of the structure porosity is significant, resulting in twice the $p_{1,res}$-values for the porous wall with a porosity P=11% as

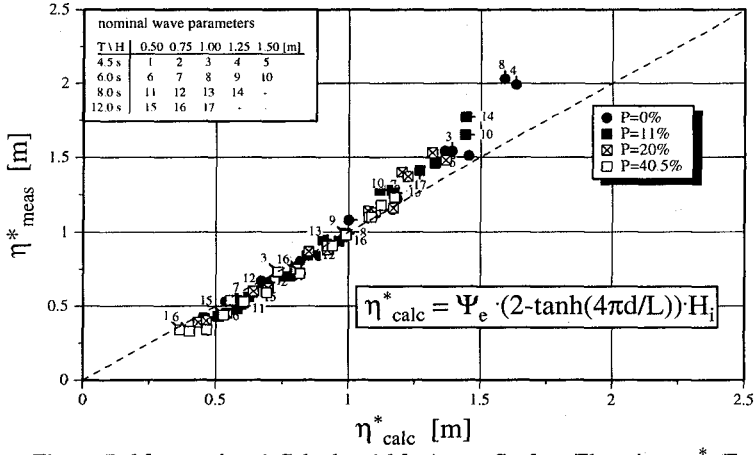

Figure 7: Measured and Calculated Maximum Surface Elevations η^* (Eq.(5)) at the Front Face of the Structure.

compared to a wall with porosity P=40.5%. The GODA formula overestimates the measured pressure values, mainly due to the influence of structure porosity.

It is also seen from Fig. 8 that the results for the impermeable wall tested in the GWK are not well predicted by the GODA formula. The measured pressures at SWL are underestimated, particularly for the longer waves (i.e. no. 11 - 17).

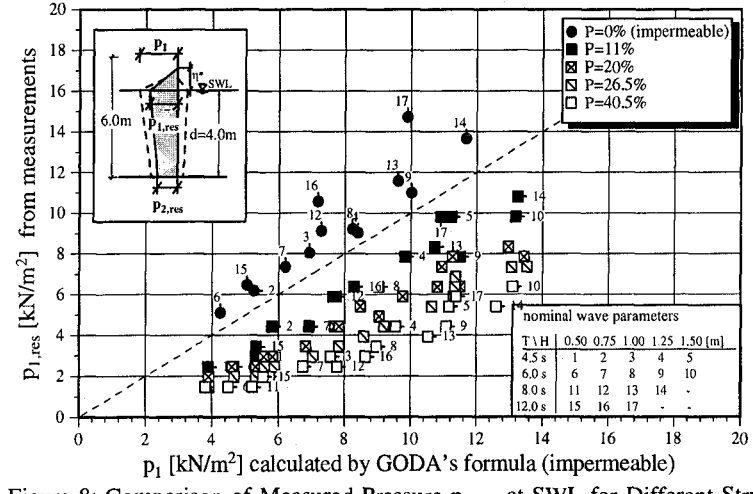

Figure 8: Comparison of Measured Pressure $p_{1,res}$ at SWL for Different Structure Porosities and Calculated Pressure p_1 for Impermeable Walls.

Applying a linear correction factor which accounts for the structure porosity of the permeable wall did not show satisfactory results. Smaller pressures $p_{1,res}$ are described accurately with this linear correction method while higher pressures are underestimated.

Hence, a correction procedure accounting for the load reduction due to porosity for vertical breakwaters in the GODA method has to consider nonlinear effects due to shallow water conditions and large wave heights. Consequently, the extension of the existing formulae has to be performed in two successive steps:

1. Modification of the GODA formula (Eqs. (2) and (3)) to predict the measured pressures in the reference case (impermeable wall).
2. Introduction of reduction factors considering the porosity of the structure.

3.2.1 Modification of the α_1-Value in the GODA Formula for the Impermeable Case

The normalised pressure p_1 at still water level in the simplified GODA formula (Eq. (2)) is controlled by α_1 which accounts for the maximum surface elevation at the structure

$$\alpha_1 = \frac{p_1}{\rho \cdot g \cdot H} = \left[0.6 + 0.5 \cdot \left(\frac{(4\pi d/L)}{\sinh(4\pi d/L)}\right)^2\right] \tag{7}$$

Plotting α_1 as calculated by Eq.(7) over the relative water depth d/L, it becomes apparent that Eq.(7) does not represent the measured normalized pressures (Fig. 9).

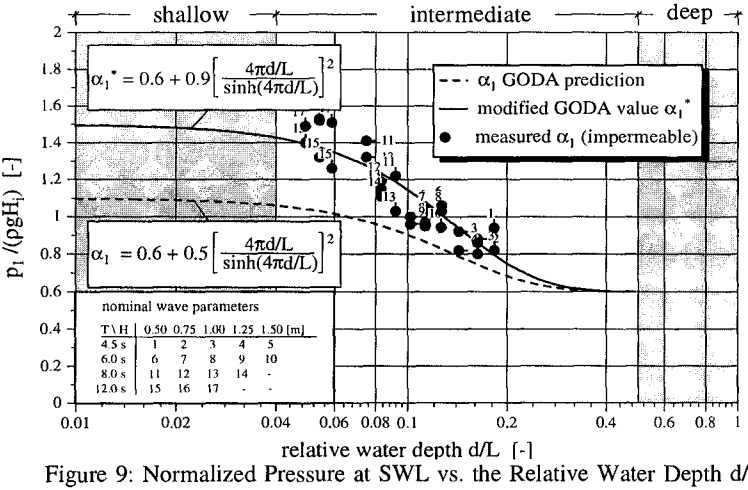

Figure 9: Normalized Pressure at SWL vs. the Relative Water Depth d/L.

Increasing the second coefficient for calculating α_1 from 0.5 to 0.9 allows a much better prediction of the data measured at the impermeable wall. This result seems to be acceptable as a first attempt to consider the influence of shallow water depth (tests performed in the region of shallow water to intermediate water depth, $0.04< d/L <0.5$, see Fig. 9). This modification has to be considered for the calculation of the resultant pressure at the structure toe $p_{2,res}$ which is described in Section 3.2.3.

3.2.2 Reduction Factors for Resultant Pressure at Still Water Level (SWL)

Moreover, besides modifying the GODA formula in terms of prediction of maximum pressures at impermeable structures the next step is to consider the force reduction due to the structure porosity. The reduction factors Ψ_p is introduced which describes the influence of the surface elevation at the rear side of the structure. The whole set of extended formulae regarding to maximum resultant pressure at SWL ($p_{1,res}$) are given as follows:

$$p_{1,res} = \rho \cdot g \cdot H^* \tag{8}$$

with

$$H^* = \alpha_1^* \cdot \Psi_e \cdot \Psi_p \cdot H_i \tag{9}$$

The resultant pressure head $p_{1,res}$ is controlled by the pressure gradient at the structure which is affected by the following factors

- the modified α_1-value in the GODA formula

$$\alpha_1^* = 0.6 + 0.9 \cdot \left(\frac{(4\pi d/L)}{\sinh(4\pi d/L)} \right)^2 \tag{10}$$

- reduction of wave run-up due to structure porosity (Ψ_e, Eq. (6))
- reduction of resulting pressure due to surface elevation at the back side of the structure

$$\Psi_p = \left(1 - \sqrt{P}\right)^a \qquad \text{with } a = \sqrt{\frac{1}{6}\frac{d}{H_i}} \tag{11}$$

The coefficient Ψ_e (Eq. (6)) is dependent on the structural porosity and describes the influence of the permeability on the wave run-up at the structure face. Ψ_p estimates the decrease in resulting pressure due to surface elevation at the back side of the structure (see also Fig. 6). Ψ_p is strongly influenced by the transmission of wave energy through the structure gaps which depends on the flow resistance induced by the velocity in the apertures. The schematic flow pattern is illustrated in Fig. 10. High waves and thus large horizontal velocity components increase the flow resistance due to large velocities in the structure gaps. Hence, for large wave heights the transmission of wave energy through the structure openings is much more limited compared

to small wave heights. The parameter Ψ_p describes therefore a kind of "dynamic porosity" of the structure. The expected influence of the wave period on wave transmission and flow resistance could not confirmed by the data.

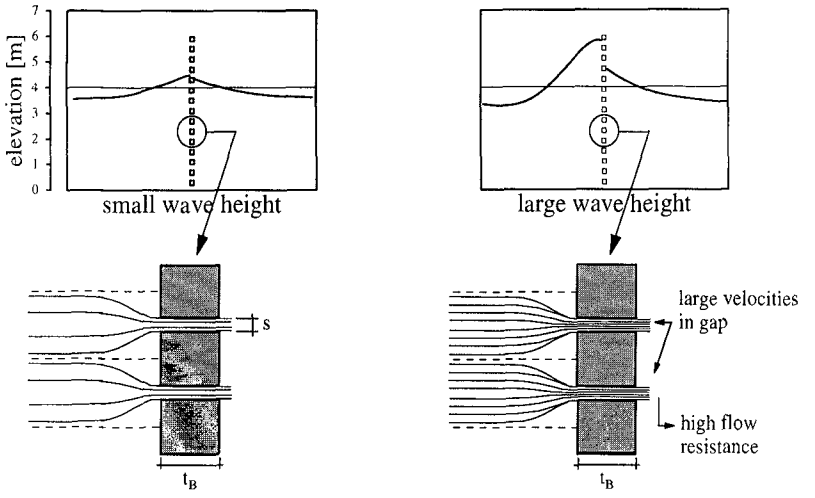

Figure 10: Flow Resistance for Small- (left) and Large Wave Heigths (right), Induced by the Velocity Gradients in the Structure Gaps.

In Fig. 11 the product of the two coefficients Ψ_e and Ψ_p is shown as a function of the wave height H_i for various structure porosities. For an impermeable wall no reduction of pressure values results from the equations given ($\Psi_e \cdot \Psi_p = 1$). In this case only the modification of the $\alpha_t{}^*$-value should be considered for the prediction of the maximum resulting pressures at still water level. The reduction factors decrease significantly with increasing structure porosity which is even more relevant for smaller wave heights H_i.

3.2.3 Reduction Factors for the Resultant Pressure at the Structure Toe

Compared to impermeable walls, the pressure reduction at the structure toe is larger for permeable structures. This is due to the almost constant pressure over the water depth on the rear side of the structure (see Fig. 6). The main influencing parameter is the "dynamic porosity" (Ψ_p) which is therefore included in the depth dependent term of the GODA formula (see Eq.(4)). This will decrease the pressure $p_{2,res}$ at the structure toe. Additionally, a further reduction factor (85%) was necessary to fit the measured data (Eq.(12)). The following relation for $p_{2,res}$ was found:

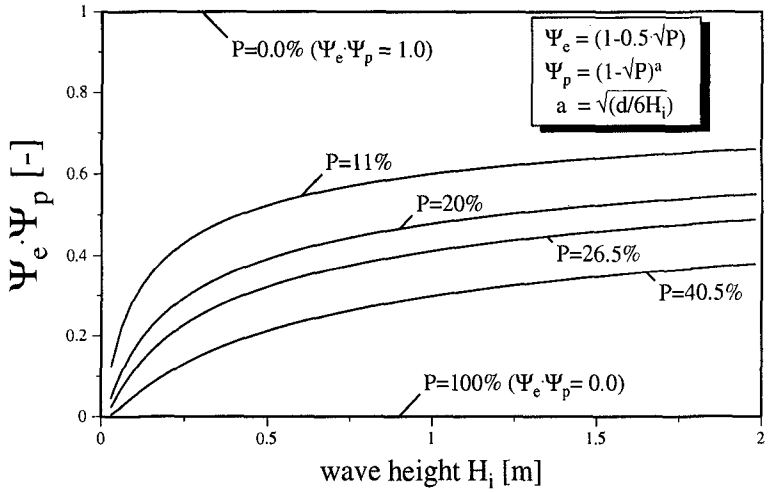

Figure 11: Total Reduction Coefficients Ψ_e and Ψ_p versus Incident Wave Height.

$$p_{2,res} = 0.85 \cdot \frac{1}{\cosh\left(\frac{2\pi d}{L} \cdot \frac{1}{\Psi_p}\right)} \cdot p_{1,res} \qquad (12)$$

Taking into account the modified α_1^* value and the reduction coefficients Ψ_e and Ψ_p the comparison of measured and calculated characteristic resulting pressure values $p_{1,res}$ and $p_{2,res}$ is shown in Fig. 12 and Fig. 13, respectively.

The results confirm the proposed formulae for the prediction of characteristic pressure values at permeable walls for maximum horizontal forces under wave crests.

3.3 Relation between Wave Elevation and Pressure Distribution at Permeable Walls

For the impermeable wall the wave elevation at the structure front η^* should result in the same value as the wave height H^* used for the calculation of resultant pressures. This is more or less verified by the data (Fig. 14, P=0%). For permeable vertical walls the ratio H^*/η^* is influenced by the surface elevation at the rear side of the structure and can be described by a factor $(1-P^{0.5})$.

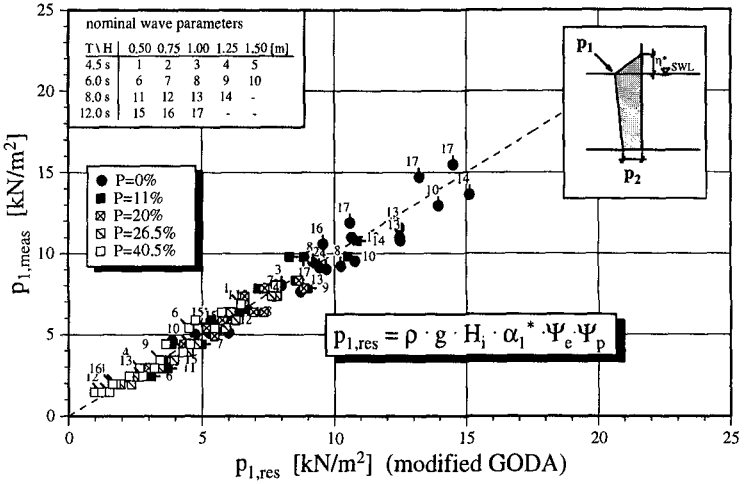

Figure 12: Measured and Calculated Resultant Pressures $p_{1,res}$ at SWL Considering the Nonlinear Influence of the Structure Porosity.

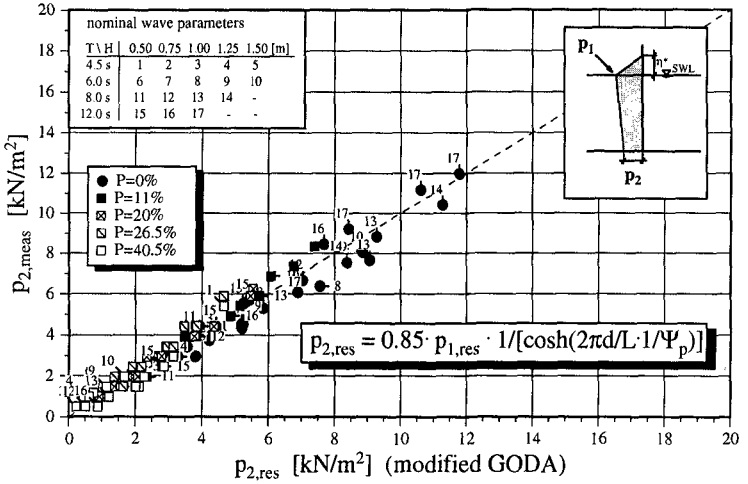

Figure 13: Measured and Calculated Resultant Pressures $p_{2,res}$ at Structure Toe Considering the Nonlinear Influence of the Structure Porosity.

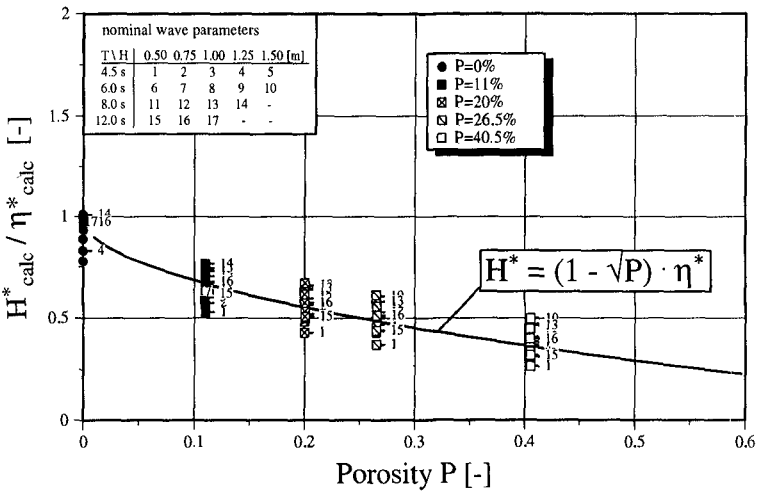

Figure 14: Ratio of Calculated Parameters for the Pressure Head at SWL (H^*) and Wave Elevation (η^*) as a Function of Structure Porosity.

The elevation of the nonlinear wave crest is described for the wave run-up by Eq. (5) and for the pressure distribution by Eq. (10). This should be done in a more consistent way by one equation. As a first attempt the resultant pressures on permeable walls should be calculated by the modified formulae (Eq. (6) -(12)). The elevation above still water level η^* estimated by Eq. (5) can be used as the upper limit of pressure integration for the calculation of horizontal forces.

It will be the objective of further studies to relate the resultant pressures directly to the nonlinear wave elevation at the structure front.

4. Conclusions and Future Work

For the design of permeable structures reliable information on wave loads and pressure distribution is needed. The influence of the incident wave height H_i, described by the "dynamic porosity" has to be considered for the analysis of wave damping processes at the porous wall. The resultant pressure distribution at vertical wave screens under non breaking and slightly breaking waves is dominantly governed by:

- the non-linear wave profile (section 3.2.1)
- reduction of wave run-up due to "structural porosity" (section 3.2.2)
- reduction of resulting pressure due to "dynamic porosity" (section 3.2.2)

The nonlinear extension of the GODA formulae for calculating the resultant pressure distribution at permeable vertical walls as proposed in this paper gives accurate results for wall porosities between 0% and 40.5%, as compared to data obtained from hydraulic model tests in the Large Wave Flume (GWK) of the Coastal Research Centre, Germany.

The future work will resolve the following main objectives:

- Pressure distribution under wave troughs
- Wave spectra (random conditions at front and rear side of the structure!)
- Chamber systems (combinations of different permeable walls followed by an impermeable wall).

5. Acknowledgements

This study has been supported by the Federal Ministry of Education, Science, Research and Technology (BMBF), Bonn, Germany, within the joint project "Optimisation of Vertical Wave Absorbers for Coastal Protection and Wave Damping in Harbours and Waterways", jointly performed by the Technical Universities of Berlin and Braunschweig.

6. References

GODA, Y. (1985) Random Seas and Design of Maritime Structures. University of Tokyo Press.

IMPACT LOADINGS ON VERTICAL WALLS IN DIRECTIONAL SEAS

N.W.H. Allsop & M. Calabrese *

ABSTRACT

Recent research under PROVERBS has demonstrated that wave impact loads can cause damage or failure of caisson or blockwork breakwaters. Research studies of wave loadings, pulsating or impact, have generally used only 2 - dimensional wave flume experiments, and so most design methods are strongly biased towards 2-d .

This paper describes results from 3-dimensional wave basin tests by Universities of Naples, Sheffield, and HR Wallingford in the UK Coastal Research Facility (CRF). The aim of the study was to quantify effects on wave pressures or forces of oblique or short-crested wave conditions on simple vertical or composite breakwaters.

This analysis has focussed particularly on wave impact loadings as earlier 2-d tests at Wallingford showed them to be potentially severe for some combinations of foundation level and relative wave conditions. New reduction factors are presented.

1. INTRODUCTION

Hydro-dynamic wave loads constitute the main design loading for overall stability of a vertical breakwater. Many wave loads are slow-acting or pulsating, but wave impact loads can be very intense. Research in the UK with support from the EU MAST project PROVERBS has demonstrated that wave impact loads, despite their short durations, can cause failure of caisson or blockwork breakwaters.

Design wave forces on caisson breakwaters and related structures are usually derived as quasi-static loads using methods by Goda (1985) which calculate equivalent loads for sliding. Recent studies on failures of vertical breakwaters by Oumeraci et al.

* Professor (associate) University of Sheffield, c/o HR Wallingford, Howbery Park, Wallingford, Oxon OX10 8BA, U.K. e-mail: w.allsop@sheffield.ac.uk

Assist. Prof. Dr.-Ing., Dipt. di Ing. Idraulica ed Ambientale, Università di Napoli Federico II, Via Claudio 21, 80123 Napoli, Italy, e-mail: calabres@cds.unina.it

(1995) Allsop & Vicinanza (1996), Allsop et al (1996a, b) and others have demonstrated that damage or failure can be caused by wave impacts. These may be triggered by particular combinations of waves and water levels, bed slope, berm and wall geometries, some of which have been identified in studies by Allsop et al. (1996b), Allsop & Vicinanza (1996) or Calabrese et al. (1996).

Most studies of wave loadings, pulsating or impact, have used 2-dimensional (2-d) wave flume experiments as it has been assumed that long-crested normal wave attack is most damaging. Design methods are therefore strongly biased towards 2-d wave attack, and relatively little information is available on 3-dimensional effects. There are however strong reasons to review this, and to investigate the stability of such structures under 3-d wave conditions:

a) Real waves are highly irregular in space and time, so along particular lengths of wall, the instantaneous widths of wave fronts are often relatively short.
b) Main breakwaters are often orientated oblique to the largest waves so that the worst wave forces act over only a short length of the structure at any one time.
c) Wave impact pressures are limited spatially, even under long-crested waves, but reduction of effective force with length of element has not been quantified.

Methods to evaluate wave forces under oblique and/or short-crested waves have been suggested by the empirical methods of Goda (1985) or theoretical methods of Battjes (1982). Battjes' method estimates wave force reduction coefficients in relation to: angle of attack, β; directional dispersion index, n; and relative length of caisson or wall element L_c/L, where the element length is L_c and wavelength is L. Experiments by Franco et al. (1996), measured effects of long- and short-crested waves with $\beta \leq 60°$ and standard deviation of spreading $\leq 30°$, but did not record impact loads.

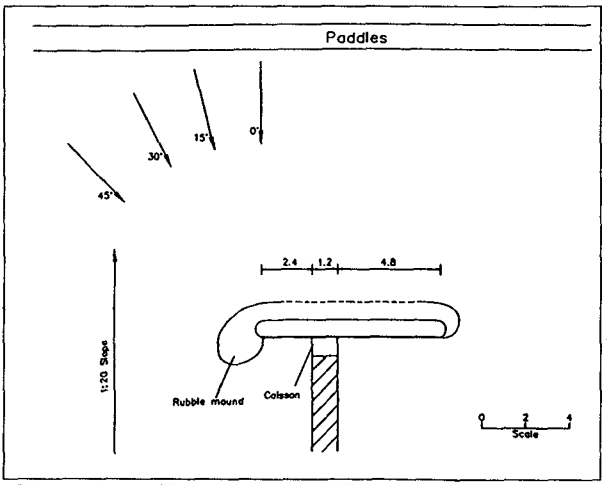

Figure 1 Test set-up in CRF

In contrast, important objectives of the studies summarised here, were to:
a) Identify conditions which lead to impulsive loads on vertical breakwaters under oblique or short-crested waves;
b) Evaluate the influence of wave obliquity, β, and of directional dispersion, n, on the intensity of the wave load;
c) Assess the influence of multi-directionality on the distribution of loads along the wall under pulsating and impact wave conditions.

2 EXPERIMENTAL STUDY

2.1 Test facilities

These experiments were conducted in the UK Coastal Research Facility (CRF), a large wave and current basin 54m by 27m equipped with 72 paddles to give oblique long-crested or short-crested waves. The model caisson sections were placed in a line in the basin, parallel to the paddles, and on a 1:20 bed slope, see Figure 1.

Oblique or short-crested random waves were produced by adjusting the wave paddle control signals. Absorbing beaches behind the structures reduced wave reflections, and extension walls reduced diffraction distortions. Four different breakwater types were tested: Structure 0 was a simple vertical wall and Structures 1-3 were composite walls with mounds of different geometry. The structures were closely based on those tested by Allsop et al (1996) and McKenna (1997), and used the same measurement caisson, but fitted with eighteen pressure transducers in 3 vertical rows, see Figure 2.

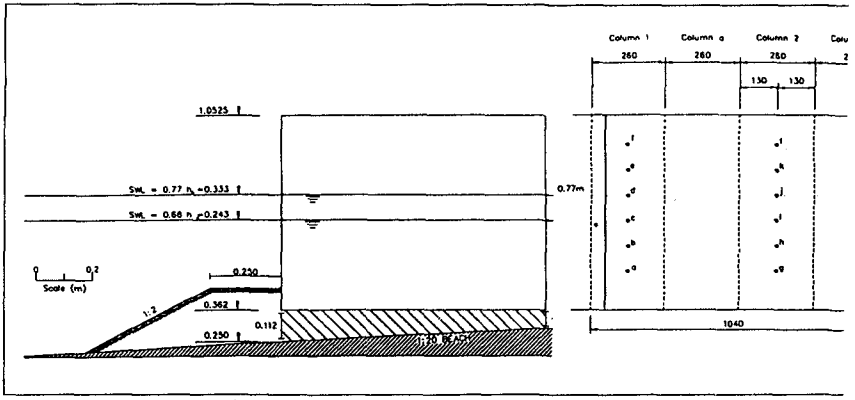

Figure 2 Test caisson and pressure transducers

Most tests were run for 500 waves, but some were repeated for 2000 waves. For Structures 1-3, three different relative height / depth of rock armoured berm in front of the caisson were studied. Test conditions for Structure 0 covered the range tabled below, but restrictions on basin availability limited tests for other structures:

	$s_m = 0.02$	$s_m = 0.04$	$s_m = 0.06$
H_s (m)	T_m (s)	T_m (s)	T_m (s)
0.10	1.8	1.3	1.0
0.20	2.5	1.8	1.5
0.25	2.8	2.0	1.6

2.2. Test Programme

Tests on each structure were conducted in three phases:

a) long-crested waves with $\beta = 0°$;

b) long-crested oblique waves with $\beta = 15°$, 30° and 45°;

c) short-crested waves, β=0° and directional dispersion index of n = 2 or n = 6.

2.3 Pressure Signal Analysis

Pressures were summed by trapezium rule to give horizontal forces on each column, F_h at each timestep (at 400 Hz). The time signal of pressures at static water level was divided into "events" using parameter and threshold definitions developed within PROVERBS, and analysis methods by Calabrese et al (1997) and Allsop et al (1996). Forces and moments were calculated at each timestep. Fictional pressures or forces on imaginary column "a" were interpolated between columns 1 and 2.

Maximum wave forces on each column ("1", "a", "2", "3") were found for each event. Individual column forces were considered as representative of wave loads, $F_h(0)$, acting on an infinitesimal segment, $L_c=\delta l$, of the wall. To simulate longer caissons, average wave forces were calculated for combinations of columns ("2+3"; "1+a+2"; "a+2+3"; "1+a+2+3") giving wave loads, $F_h(n)$, for each caisson length, L_c:

F_h (n)	Caisson length, L_c (m)	Adjacent column combinations
F_h (0)	δl	1; 2; or 3
F_h (1)	0.260	2+3
F_h (2)	0.520	1+a+2; or a+2+3
F_h (3)	0.780	1+a+2+3

For each caisson length, forces, $F_h(n)$, were ranked in magnitude and the average of the 1/250 highest forces, $F_{h1/250}(n)$, was evaluated. For the overall analysis of forces, values of $F_{h1/250}(n)$ for n = 0, 1, or 2 were calculated by averaging across the columns used. This average has been used in the analysis below, except when relative peak to average values are discussed in section 3.2.

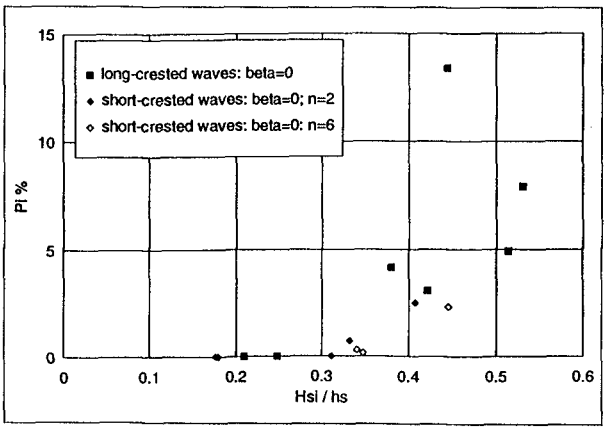

Figure 3 Effect of short-crested waves on impacts

3. RESULTS

3.1 Occurrence of impacts

The aim of the initial analysis was to identify conditions which lead to impulsive loads and to evaluate their occurrence P_i. Work by Allsop et al (1996) and McKenna (1997), distinguished between "pulsating" and "impact" loadings using probability distributions of wave forces. Individual forces were ranked and plotted on Weibull axes, and any significant departure above the Weibull line was taken as indicating an impact. The probability level at which forces started to diverge from the Weibull line gave percentage of impacts P_i (%) for each column of transducers.

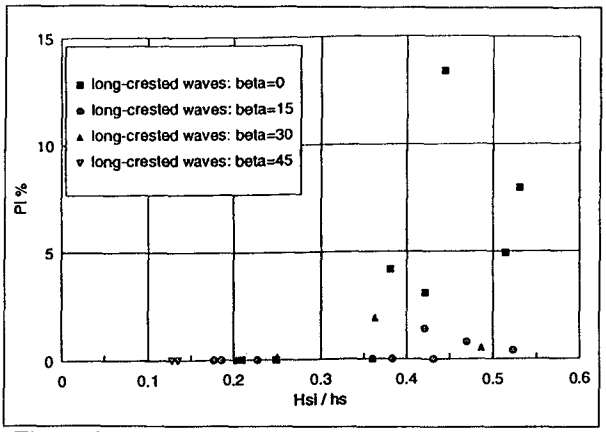

Figure 4 Effect of oblique wave attack on impacts

This paper generally discusses average values of P_i across three columns. Evaluations of P_i were checked by evaluating impacts from video recordings of the experiments.

Simple vertical wall

Impacts under long-crested normal waves were compared with results from 2-d tests by Allsop et al (1996) with only slight variation. The onset of impacts was reached at about $H_{si}/h_s = 0.35$ in both experiments for long-crested waves at β=0°. For short-crested waves at β=0°, P_i again showed no changes in comparison with long-crested waves. Again, impacts begin at conditions close to $H_{si}/h_s = 0.35$, although there are some indications in Figure 3 that impacts do not increase as rapidly with increasing H_{si}/h_s in short-crested waves as for long-crested waves.

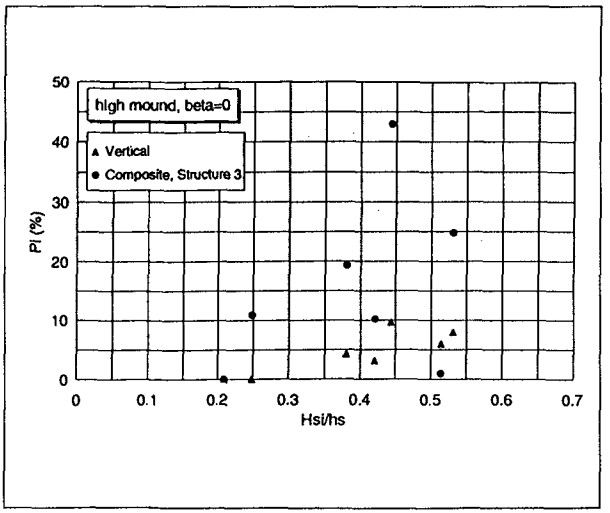

Figure 5 Effect of H_{si}/d on P_i, high mound

Lower steepnesses, $s_p = 0.02$, showed no impacts.

For oblique long-crested waves, β = 15°, 30° and 45°, there were much fewer impacts than for normal long-crested waves, Figure 4. For larger waves, $H_{si}/h_s > 0.35$, impacts were less frequent with oblique waves than for normal attack, β=0°.

These tests were in intermediate depths: $0.05 \le h_s/L_{pi} \le 0.18$. Conditions which gave impacts fell in $0.03 \le s_p \le 0.06$.

Composite walls, low and high mounds

Addition of even a small rock berm or slope in front of a simple wall has been shown to increase substantially the number and severity of impacts. In the previous 2-d study, Allsop et al (1996) argued that the onset of impacting for low mounds, $0.3<h_b/h_s<0.6$, occurred at $H_{si}/h_s = 0.35$, but that P_i increases rapidly at higher values of H_{si}/h_s. Results from long-crested waves at $\beta=0°$ from these tests support the earlier conclusions, , but suggest that impacts for low mounds might start to occur at lower relative wave heights than suggested previously, perhaps $H_{si}/h_s \leq 0.30$.

The 2-d tests by Allsop et al (1996) showed that impacts increase further with high mounds, $0.6<h_b/h_s<0.9$. Impacts start at smaller values of H_{si}/h_s, and become much more frequent with increasing relative wave height. Tests on high mound composite walls in the CRF at $\beta=0°$ substantially confirmed this, with impacts starting at values of H_{si}/h_s as low as 0.25. These are shown against H_{si}/d in Figure 5. Whilst there are substantially fewer results than in the 2-d tests, and the general trend is very similar, it may be noted that the % of impacts in the 3-d tests all fall below the outer limit of the results for the 2-d tests. This confirms the expectation that, even when using nominally perpendicular and long-crested waves, inherent perturbations and instabilities are likely to develop, and these will reduce the level of wave impacts from those predicted from 2-d wave flume tests.

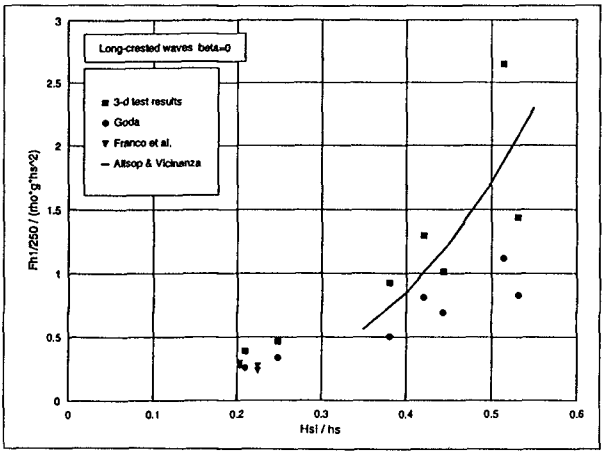

Figure 6 Dimensionless wave force for vertical walls, normal wave attack

3.2 Horizontal forces

Values of $F_{h1/250}$ are compared in Figure 6 with results from earlier 2-d tests, and predictions using Goda's method. The predictions do not take account of caisson length, L_c, so measurements used in this analysis were those of $F_{h1/250}(0)$, thus giving three sets of measurements representative of wave forces over a narrow vertical strip, $L_c=\delta l$.

Forces for long-crested normal waves in Figure 6 have been non-dimensionalised as $F_{h1/250}/\rho g h_s^2$, and plotted against relative wave height H_{si}/h_s. Summary results from the 3-d tests by Franco et al (1996), are included, for which $H_{si}/h_s = 0.20$. These forces are very similar to those measured here for the lower values of H_{si}/h_s where there are no impacts, only pulsating loads. Comparisons with Goda predictions show relatively good agreement over the pulsating zone, but use of Goda's method seems

inappropriate in the impact zone ($0.35 < H_{si}/h_s < 0.55$) where Goda's method would not be expected to match the measured wave loads.

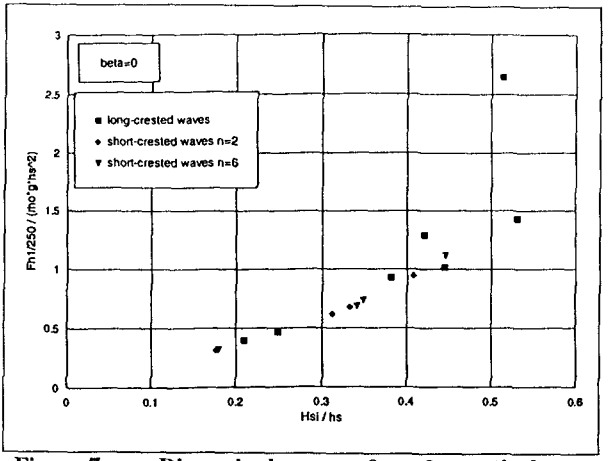

Figure 7 Dimensionless wave force for vertical walls, short-crested wave attack

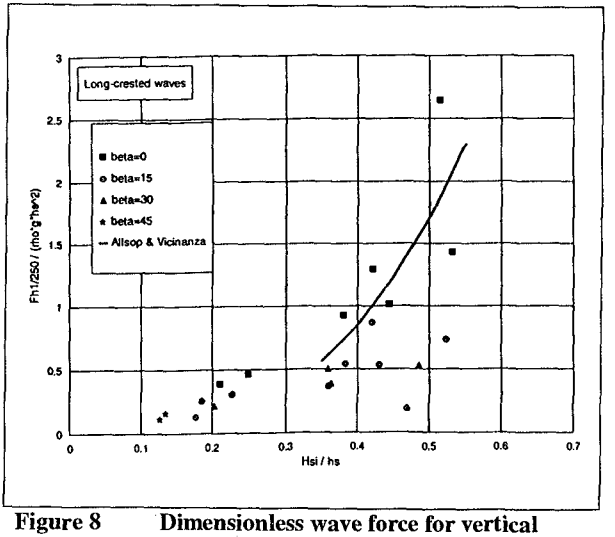

Figure 8 Dimensionless wave force for vertical walls, oblique wave attack

The simple prediction line by Allsop & Vicinanza (1996) in Figure 6 indicates an upper limit, with a few results above the line. This may be due to the greater possibility of extreme loads under impacting conditions, particularly when sampled by more than one column of transducers, and illustrates the essential variablity of impact loads, even under similar hydro-dynamic and geometric conditions.

For short-crested waves, values of $F_{h1/250}/\rho g h_s^2$ are again plotted against relative wave height H_{si}/h_s in Figure 7. The results appear to show no significant change in local force for the range of conditions tested, dispersion index (n = 2 or 6), compared with loads generated by long-crested waves of the same height.

The influences of oblique long-crested waves on forces on any narrow strip of the caisson are more significant in Figure 8. Over the pulsating zone, $H_{si}/h_s \leq 0.35$, forces are very similar to those for normal approach, even though the component of force perpendicular to the caisson might have been expected to reduce. In the impact region however, wave loadings diminish considerably under oblique attack.

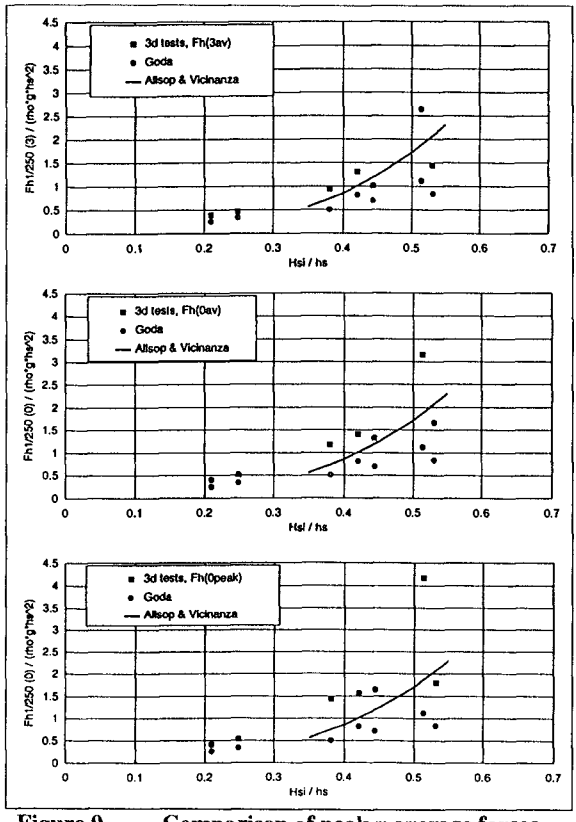

Figure 9 Comparison of peak v average forces

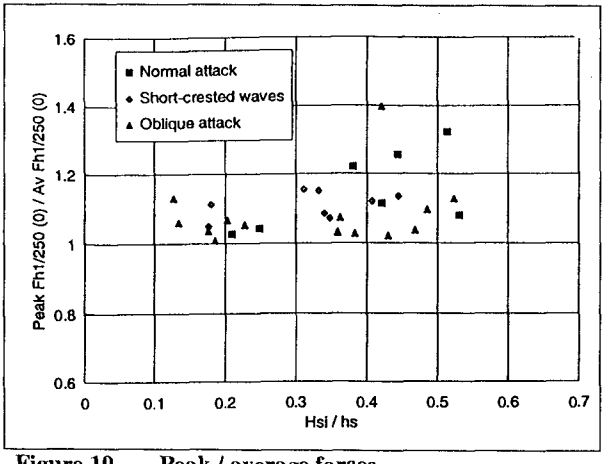

Figure 10 Peak / average forces

3.3 Variability of forces

With these data, it is possible to estimate variations of peak force by comparing results from the 3 columns of transducers. Values of F_h, including the "Goda" force ($F_{h1/250}$) can be calculated using three alternative methods, giving successively less averaged values:

a) from the average force calculated at each timestep across all three columns;

b) from peak forces on each column, averaged event by event, but not neccesarily at the same point in time;

c) from peak forces on any individual column, irrespective of event or timestep.

Most analysis has been based on averages by methods a) or b). These are necessarily smaller than the peak values calculated using method c). Some estimates of increase in "local" force may therefore be derived from comparison of these values, plotted as dimensionless forces in Figure 9a)-c).

These comparisons show consistent increases in $F_{h1/250}$, with reduced averaging, methods a) –

c). Allsop & Vicinanza's simple formula gives a reasonable representation of forces averaged over typical caisson widths of 10-20m, but under-estimates the "local" force over a single narrow strip, even for normal and long-crested wave attack.

Peak valucs in c) have been compared with average forces in a) as $F_{h(peak)} / F_{h(av)}$ plotted against H_{si}/h_s in Figure 10. Values of $F_{h(peak)} / F_{h(av)}$ reached 1.2-1.3 for normal long-crested attack. Under long-crested oblique attack, most results were much lower, not exceeding $F_{h(peak)} / F_{h(av)} = 1.15$, but with a single test giving 1.4. Under short-crested waves the ratio $F_{h(peak)} / F_{h(av)}$ never exceeded 1.15, suggesting that peak forces are unlikely to exceed those analysed in this research by any substantial margin, except under conditions of normal attack.

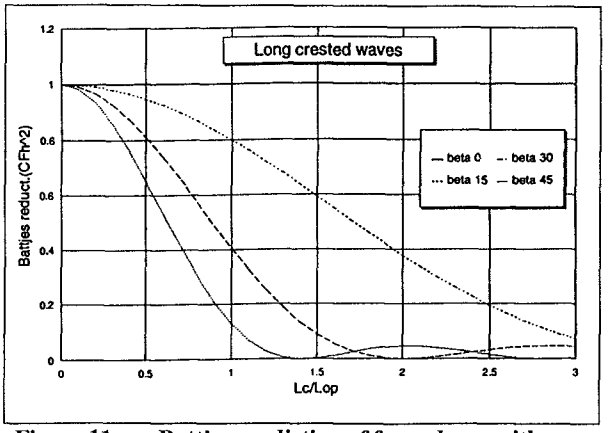

Figure 11 Battjes prediction of force decay with wave obliquity

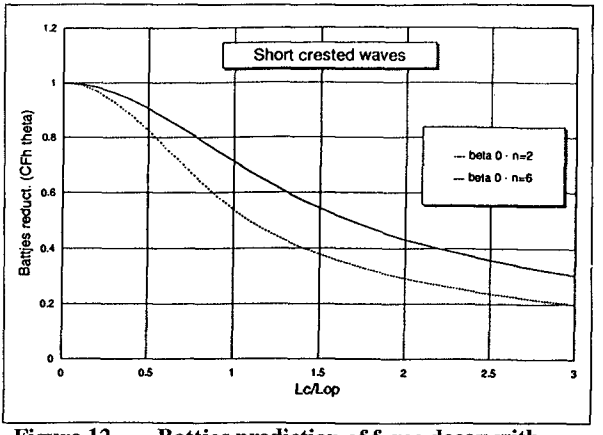

Figure 12 Battjes prediction of force decay with short-crested waves

3.4 Effect of caisson length

Battjes (1982) argued that oblique or short-crested wave attack on caisson of length L_c will give further reductions in effective force relative to normal and/or long-crested attack, and relative to loads on a narrow strip (modelled here as a single column of transducers.

These reductions are illustrated in Figures 11 and 12 where Battjes methods give prediction curves of the decay coefficient, C_{Fh} in relation to relative caisson length, L_c/L_{op}. These curves, show that these theoretical considerations predict only small reductions in effective force over caisson lengths around 10-25m, the largest caisson constructed to date

being a single example in Japan of 100m long. In contrast waves of T_p=7-15s would cover wave lengths of L_{op}=80-350m.

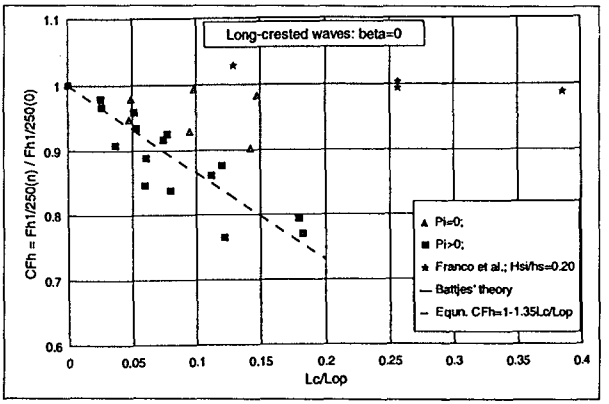

Figure 13 Force decay for long-crested / normal waves

Battjes methods were developed for simple vertical walls, so the comparisons here are based on tests with Structure 0, the simple vertical wall. The first results considered here are therefore for normal, long-crested waves in Figure 13. Results from these tests have been combined with results from Franco et al (1996), which show little decay over caisson lengths L_c/L_{op} up to 0.4. Measurements from the CRF however show up to 10% decay, ie C_{Fh} down to 0.9 for non-impact conditions for relative caisson lengths up to L_c/L_{op}=0.15. Wave impact conditions (H_{si}/h_s>0.35), however, gave substantially greater reductions in the effective force, even over short caisson lengths, 0.005 <L_c/L_{op} <0.2. A simple regression line gives the reduction factor C_{Fh} in terms of relative caisson length with a coefficient B = 1.35 for long-crested waves and $\beta = 0°$:

$$C_{Fh} = 1 - B\,(L_c/L_{op}) \qquad (1)$$

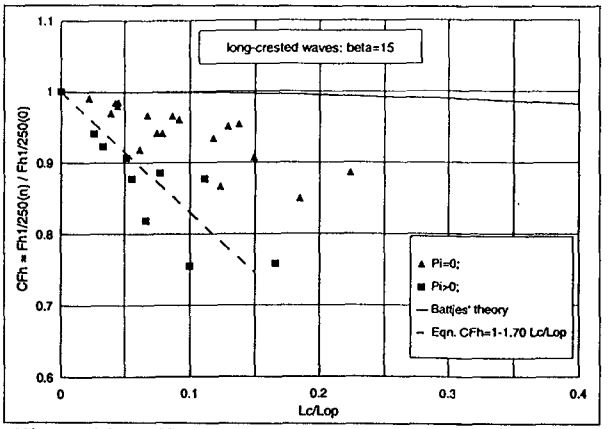

Figure 14 Force decay for long-crested waves and oblique attack, β = 15°

Under slightly oblique attack, β = 15°, forces in Figure 14 for non-impacting conditions show more significant reductions than for β = 0°, but there is only slightly greater change for impact conditions. The same simple form of regression line gives C_{Fh} in terms of L_c/L_{op}: for β = 15°, yielding B = 1.70:

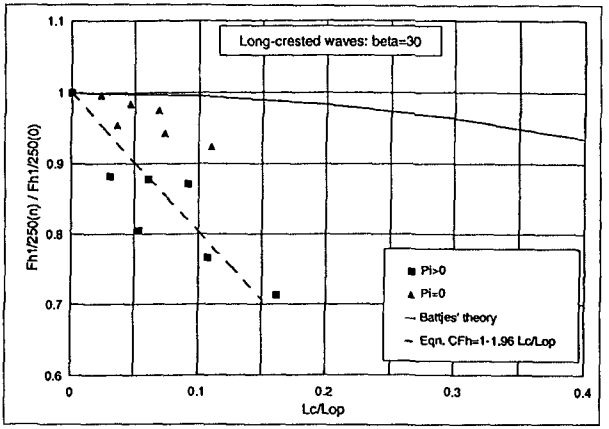

Figure 15 Force decay for long-crested waves and oblique attack, β = 30°

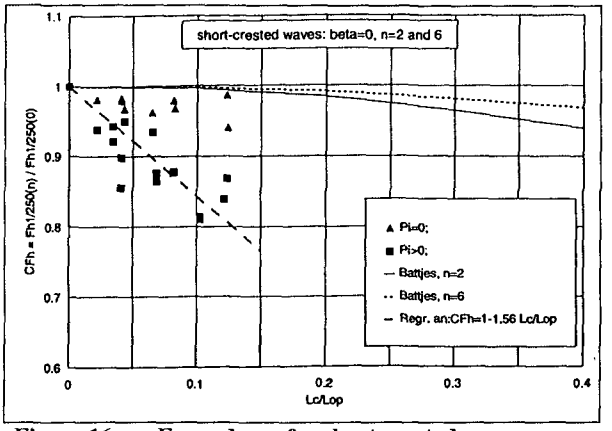

Figure 16 Force decay for short-crested waves

At greater obliquities, the force reduction is more marked for pulsating conditions. Measurements at β= 30° in Figure 15 also show slightly greater reduction for impacts.

Effects of short-crested waves in Figure 16 show no significant effect of spreading between n=2 and n=6. The regression for β = 0° gives B = 1.56, steeper than for long-crested waves at β = 0°, but less severe than for long-crested waves and β = 15°.

These results suggest that Battjes' model may be used to give conservative predictions in the pulsating zone, but that force reductions under impacts are much more significant than predicted by linear methods. Calculations of the mean decay function on F_h for impacting conditions can be summarised by the simple equation relating decay to relative caisson width, L_c/L_{op} given in equation (1) where coefficient B is defined for each test case below.

Impact force reduction coefficients

Wave condition	Coefficient B	Coef. Varn. (%)	Correlation r^2
Long-crested, β = 0°,	1.35	6.6	0.82
Long-crested, β = 15°,	1.69	9.2	0.77
Long-crested, β = 30°,	1.96	10.4	0.79
Short-crested, n= 2,	1.55	10.6	0.76
Short-crested, n= 6	1.58	9.3	0.77
Short-crested, n= 2, 6	1.56	6.8	0.77

4. CONCLUSIONS

Initial conclusions from these studies may be summarised:

a) There is good agreement between results from 2-d tests in 1994 with 1:50 approach bed slope, and results from tests with normal long-crested waves in the CRF with 1:20 approach bed slope.

b) Impacts on composite walls follow trends identified previously at Wallingford. There are however indications that impacts might start at slightly lower relative wave heights, perhaps $H_s/h_s \leq 0.30$,. The data also suggest that higher levels of impacts for some configurations may be reduced under 3-d conditions, even if only normal wave attack is used.

c) Under oblique long-crested waves, the occurrence of wave impacts on vertical walls are substantially reduced at β=15°, 30° and 45°. This is repeated for high mounds at β=15°, 30° and 45°, and low mounds for β=30° and 45°.

d) Effects of short-crested waves of dispersion index 2 or more do not appear to vary significantly with increased spreading.

e) Under oblique or short-crested waves, the variation of peak forces relative to those averaged over a short length equivalent to a single caisson of about 20m are relatively small, not exceeding a ratio of 1.2.

f) The variation of peak force on a single narrow strip under normal wave attack is more substantial, with peak forces up to 1.3 times greater than the average.

g) Battjes' method for estimating the decay of average force with longer caissons gives very small reductions for most practical caisson lengths. The tests with pulsating conditions show that Battjes' predictions are generally conservative.

h) For impact conditions, average forces reduce significantly with caisson length, giving reductions of 25% or so over relative caisson lengths of only 0.2.

i) A simple reduction factor for F_h under impacting conditions as a function of L_c/L_{op} has been developed. Values of a coefficient B have been presented here in Table 1 for long-crested waves at different obliquities, and for short-crested waves.

The results of these studies also suggest the following initial conclusions on spatial correlation of impact forces under oblique / short-crested waves:

j) For heavy impacts ($F_{Impact}/F_{Goda} >> 2.5$), and small obliquity or spreading: - assume a typical coherence length $\leq L/16$;

k) For light impacts ($F_{Impact}/F_{Goda} < 2$), normal wave attack ($\beta = 0°$) and little spreading: - assume a typical coherence length $\leq L/4$;

ACKNOWLEDGEMENTS

This paper is based on studies by the Department of Hydraulic and Environmental Engineering of University of Naples, the Coastal Group of HR Wallingford, and Department of Civil Engineering of University of Sheffield. Tests and analysis were supported by the Construction Sponsorship Directorate of the UK Department of Environment under contract CI 39/5/96, and by the EU's MAST project PROVERBS under MAS3-CT95-0041.

Additional support was given by the "Programme for International Exchange of Researchers" of University of Naples Federico II, with further funding for visiting researchers at Wallingford from the National Council for Research in Italy, CNR, and by University of Sheffield and HR Wallingford.

The authors gratefully acknowledge assistance in testing at Wallingford by Adrian Channel, Rob Jones, Diego Vicinanza, and Alberto Bracci-Laudiero; and in processing data by Lawrence Banyard, Kirsty McConnell, and Rob Jones.

REFERENCES

Allsop N.W.H., Calabrese M., Vicinanza D. & Jones R.J. (1996a) "Wave impact loads on vertical and composite breakwaters" Proc. 10th Congress of the Asia and Pacific Division of IAHR, 26-29 August 1996, Langkawi Island, Malaysia

Allsop NWH, Vicinanza D, & McKenna JE (1996b) "Wave forces on vertical and composite breakwaters" Research Report SR 443, HR Wallingford, Wallingford.

Allsop N.W.H. & Vicinanza D. (1996) "Wave impact loadings on vertical breakwaters: development of new prediction formulae " Proc. 11th Int. Harbour Congress, pp 275-284, Royal Flemish Society of Engineers, Antwerp, Belgium.

Battjes J.A. (1982) "Effects of short-crestedness on wave loads on long structures" Applied Ocean Research, Vol.4, No.3, pp.165-172.

Calabrese M., Vicinanza D. & Allsop N.W.H. (1996) "Azioni idrodinamiche su dighe marittime a parete verticale - Influenza della geometria dell'imbasamento", XXV Convegno di Idraulica e Costruzioni Idrauliche, Torino, Settembre 1996.

Franco C., Meer J.W. van der, & Franco L (1996) "Multi-directional wave loads on vertical breakwaters" Proc 25th Int. Conf. on Coastal Eng., Orlando, publn. ASCE, New York.

Goda Y. (1985) "Random seas and maritime structures", University of Tokyo Press, Tokyo.

McKenna J.E (1997) "Wave forces on caissons and breakwater crown walls" PhD thesis, Department of Civil & Struct. Eng., Queen's University of Belfast, Belfast.

Oumeraci H. (1994) "Review and analysis of vertical breakwater failures - lessons learned" Coastal Engineering, Special Issue on Vertical Breakwaters Vol. 22, pp. 3-29, Elsevier Science BV, Amsterdam.

Tanimoto K. & Takahashi S. (1994) "Design and construction of caisson breakwaters - the Japanese experience" Coastal Engineering, Vol 22, pp57-78, Elsevier Science BV, Amsterdam.

WAVE FORCES ON A VERTICAL WAVE BARRIER

David Kriebel[1], Charles Sollitt[2], and William Gerken[3]

Abstract

This paper presents a comparison of measured and predicted wave forces on a vertical wave barrier, defined here as a thin impermeable vertical wall extending from above the water surface down to near mid-depth. Theoretical wave loads are computed using the eigenfunction expansion method. Measured wave loads are obtained from two sets of laboratory experiments, one conducted at the U.S. Naval Academy and the other conducted at the Oregon State University in a large wave flume. Results of this study suggest that the eigenfunction theory can predict wave loads to within 10% to 20% accuracy for a wide range of wave conditions, water depths, and wave barrier drafts.

Introduction

Existing methods of predicting forces on vertical wave barriers, as contained in the Army Corps of Engineers *Shore Protection Manual* (1984) or the Naval Facilities Engineering Command *Design Manual 26.2* (1982), appear to be overly-conservative. Both design manuals adopt the Sainflou or Miche-Rungren solutions for wave forces on a full-depth vertical wall, and then modify these with an *ad hoc* reduction factor to account for the limited draft of the wave barrier. Both manuals also state that the maximum wave force should be computed under the assumption that a wave crest occurs on one side of the wall while a wave trough occurs on the other side. In general, however, neither assumption is valid; and, as a result, predicted wave loads may far exceed actual wave loads for a typical wave barrier.

[1] U. S. Naval Academy, Ocean Engineering Program, Annapolis, MD 21402 USA

[2] Oregon State University, Dept. of Civil Engineering, Corvallis, OR 97331 USA

[3] Peratrovich, Nottingham, and Drage, Inc., 811 First Ave., Seattle, WA 98104 USA

In the present paper, a more rigorous method of computing wave loading on a wave barrier, based on the eigenfunction expansion theory, will be reviewed. Results of this theory will then be compared to measured wave forces obtained from two recent laboratory experiments. The experimental portion of this study is itself unique in that tests were conducted independently at two different scales in two different laboratories, with small-scale tests conducted at the U.S. Naval Academy and large-scale tests conducted at the Oregon State University.

Background

An illustration of a vertical wave barrier is shown in Figure 1. The wave barrier consists of an thin impermeable vertical wall with a draft or penetration, w, in water of depth d. The wave field consists of incident waves with height H_i, transmitted waves of height $H_t = K_t H_i$, and reflected waves of height $H_r = K_r H_i$, where K_t and K_r are the transmission and reflection coefficients. As waves interact with the barrier, each side of the barrier experiences fluctuating dynamic pressures and, because these pressures differ on the up-wave and down-wave sides, the barrier experiences time-varying wave forces.

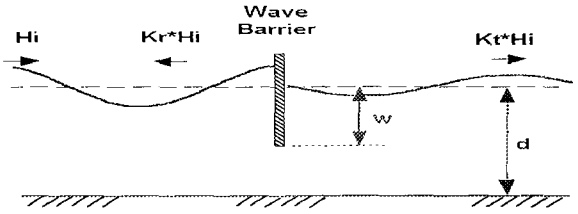

Figure 1. Definition sketch of wave interaction with a vertical wave barrier.

It does not appear, however, that these wave forces have been widely studied. For design purposes, the most widely used method of computing wave loads on a wave barrier is that outlined in the Army Corps of Engineers *Shore Protection Manual* (SPM) and in the Navy *Design Manual 26.2* (DM26.2). However, as noted above, this procedure has been adapted from experience with wave loading on full-depth vertical walls; and, to the authors' knowledge, it has never been verified against measured wave loads on a partial-depth vertical wave barrier. From discussions with design engineers,[4] it appears that the procedure outlined in the SPM or in DM26.2 is overly conservative, and one goal of the present study is to evaluate the predictive skill of this method.

[4] Based on discussions at a Wave Barrier Design workshop, held by Peratrovich, Nottingham & Drage, Inc. in Seattle, Washington, on April 24-25, 1995

A second goal of this study is to evaluate a more rigorous method of estimating the wave loads on wave barriers. Two theoretical methods have been proposed for computing the linear or first-order wave forces on these structures: (1) the boundary integral equation method of Liu and Abbaspour (1982) and (2) the eigenfunction expansion method of Losada, Losada, and Roldan (1992). With these theories, the interaction of the incident waves with the barrier is determined based on a solution of the appropriate boundary value problem for linear waves. The wave force per unit length on the barrier, f, is then computed as

$$f = \int_{-w}^{0} (P_{up} - P_{dn}) \, dz \qquad (1)$$

where P_{up} and P_{dn} are the dynamic pressures on either side of the wave barrier as obtained from the theoretical solution. In this paper, we compute these pressures using the eigenfunction theory. For given incident waves, this theory determines the reflected and transmitted progressive waves, as well as the evanescent wave modes, all of which contribute to the pressures on the face of the barrier. To date, however, the eigenfunction theory has not been widely accepted for design; and, it is the goal of the present paper is to evaluate its validity relative to the design methods now adopted in the SPM or in DM26.2.

Description of Experiments

Laboratory measurements of wave forces on vertical wave barriers were conducted independently in two facilities at two different scales. In the summer of 1996, a series of experiments were conducted at the Naval Academy Hydromechanics Laboratory (NAHL) using regular waves in a wave tank 37 m long and 1.5 m deep. In the summer of 1997, experiments were conducted at the Oregon State University (OSU), using both regular and irregular waves, in a wave tank which is 104 m long. The water depth in the OSU tests was fixed at 3.0 m so that tests could be conducted at twice the scale used in the NAHL tests. In each set of tests, four values of the wave barrier draft, w, were tested, producing four values of the dimensionless draft, w/d, of 0.4, 0.5, 0.6, and 0.7.

In both tanks, an extensive set of regular waves were tested with a wide range of relative depths, ranging from near shallow conditions, with d/L of about 0.10, to deep water conditions, with d/L exceeding 0.50. For each relative depth, two values of wave steepness were tested, with target values 1/40 and 1/30. In the OSU tests, irregular waves were also used. These were generated from target JONSWAP spectra, most with peak enhancement factors of 3.3. Peak wave periods were in the range of 2 to 6 seconds and were selected to produce a range of relative depths, d/L_p, (where L_p is the wavelength associated with the peak period) similar to regular wave values. Zero-moment significant wave heights, H_{mo}, were in the range of 0.3 to 0.7 m and were similarly selected to produce values of the spectral steepness, H_{mo}/L_p, similar to the steepness used for regular wave tests.

One difference between the two test programs involved the way that forces were measured. In the NAHL tests, a rigid frame was installed across the 2.4 m tank width and the wave barrier was attached to this frame in three sections. The two outer sections, each 1.05m wide, were rigidly attached to the supporting frame and forces on these sections were not measured. The center section, 0.30m wide, was then attached to two modular force gages (one near the top and one near the bottom) which were, in turn, attached to the supporting frame. The center section was separated from the outer sections by gaps 1 to 2 mm in width, thus permitting the wave load on the center panel to be isolated and measured. In the OSU tests, in contrast, the wave barrier was constructed as a single rectangular panel that spanned the entire 3.3 m tank width. This panel was attached to the side walls at four points (top and bottom on each side of the tank) by load beams that were instrumented with strain gages.

For regular waves, the forces analyzed in this paper are based on an average of force amplitudes in the positive (down-wave) and negative (up-wave) directions. Most wave heights were small enough that mean forces on the wave barrier were small and difficult to resolve. The force amplitudes were, however, sometimes skewed so that the amplitude in one direction (either the up- or down-wave direction) was somewhat larger than that in the opposing direction. These amplitudes typically differed by only a few percent and, as a result, the two force amplitudes could be averaged with little loss of information. For irregular waves, the significant force amplitude was determined from the force spectrum. In this case, the zero-moment of the spectrum, m_o, was determined, and the significant force amplitude was determined as $F_{mo}=2*(m_o)^{½}$. It is noted that the factor of two is used here, instead of four, in order to determine the force amplitude.

Evaluation of SPM and DM26.2 Design Method

One of the primary goals of the experiments was to provide data that could be used to evaluate the existing design practice as summarized in the SPM or DM26.2. Figure 2 presents results of this evaluation in which measured wave loads from the laboratory tests are compared to those predicted using the SPM approach. Figure 2a shows the results in dimensional form (force per unit width across the tank) while Figure 2b shows the same results in dimensionless form. In this case, the measured and predicted wave loads are normalized by the force associated with a linear wave on a full depth vertical wall as

$$F_o = \rho g H_i \frac{1}{k} \frac{\sinh kd}{\cosh kd} \qquad (2)$$

In Figure 2a, it is apparent that the wave loads predicted using the SPM or DM26.2 procedure are generally more than twice as large as those that were measured. In some case, predicted forces were three or four times as large as those measured. The scales of the two test series are also apparent as the OSU data extends the range of measured values to forces that are about eight times as large as those measured in the NAHL tests. When the same data are plotted in dimensionless form, it is apparent that the NAHL and OSU

data follow the same trends and cover nearly the same dimensionless range of conditions. It is still clear, however, that the predicted values are generally more than twice as large as those measured. Some predicted forces are more than 2.5 times F_o while none of the measured forces exceeded F_o.

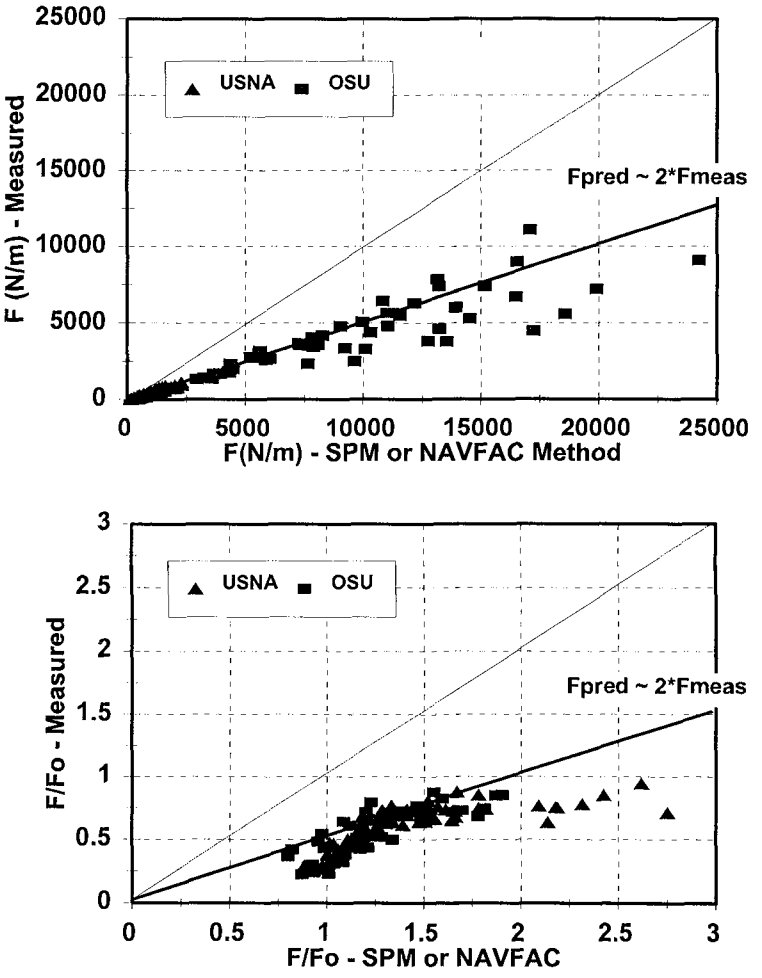

Figure 2. Comparison of measured forces to forces predicted using SPM or DM26.2 design method, for regular waves.

Review of Eigenfunction Theory

In order to obtain more accurate theoretical predictions of the wave forces, the eigenfunction expansion theory of Losada et al. (1992) and Abul Azm (1993) was implemented. Kriebel and Bollmann (1996) applied this method to the prediction of wave transmission past vertical wave barriers and their solution is repeated here.

The eigenfunction theory involves solution of the velocity potentials on the up-wave (incident wave) and down-wave (transmitted wave) sides of the wave barrier. These up-wave and down-wave solutions must then be appropriately matched at the location of the wave barrier ($x=0$). Following Losada et al. (1992), these potentials can be selected to automatically satisfies the requirement that the velocities must be matched at all elevations below the barrier at $x=0$. As a result, the velocity potentials must have a spatial dependence (in x and z) given by

$$\Phi_{up} = Z_1 e^{i(k_1 x - \sigma t)} + \sum_{n=1}^{N} R_n Z_n e^{-i(k_n x + \sigma t)} \qquad \Phi_{dn} = Z_1 e^{i(k_1 x - \sigma t)} - \sum_{n=1}^{N} R_n Z_n e^{i(k_n x - \sigma t)} \tag{3}$$

where R_n are complex coefficients describing the dimensionless amplitude and phase of the progressive ($n=1$) and evanescent ($n>1$) wave modes and where other terms are defined below. In this form, the first term in each velocity potential is the incident progressive wave mode while the terms in the summation includes both the scattered progressive wave ($n=1$), and the evanescent wave modes ($n>1$).

The functions Z_n in equation (3) describe the depth-dependence of the wave modes and are given by

$$Z_n = -i \frac{g H_i}{2 \sigma} \frac{\cosh k_n(d+z)}{\cosh k_n d} \tag{4}$$

The wavenumbers k_n are given by the solution of the dispersion equation

$$\sigma^2 = g k_n \tanh k_n d \tag{5}$$

where the first root is the linear progressive wavenumber, $k_1 = k$, and where there are then an infinite set of imaginary roots for $n>1$.

The solution for the complex amplitudes R_n must satisfy two additional physical requirements: (a) the horizontal velocities must be zero on both sides of the barrier in the upper region where $-w<z<0$, and (b) the dynamic pressures must match in the gap below the barrier where $-d<z<-w$. As a result, two sets of matrix equations are obtained as follows.

The first boundary condition, in the upper region, is satisfied by setting the horizontal velocities ($u=\partial\Phi/\partial x$) equal to zero at the barrier ($x=0$), by multiplying by the orthogonal eigenfunctions, and by depth integrating over the immersed length of the wall ($-w<z<0$), giving

$$\sum_{n=1}^{N} R_n k_n Y_{nm} = k_1 Y_{1m} \tag{6}$$

where the function Y_{nm} is the same as that defined by Losada et al. (1992)

$$Y_{nm} = \int_{-w}^{0} Z_n Z_m \, dz \tag{7}$$

The second boundary condition in the lower region involves matching dynamic pressures or, equivalently, matching the up and down-wave potentials from equation (3) under the wall ($x=0$). As shown by Losada et al. (1992), this yields a second set of matrix equations for the unknown amplitudes R_n as

$$2 \sum_{n=1}^{N} R_n X_{nm} = 0 \tag{8}$$

where X_{nm} is given by

$$X_{nm} = \int_{-d}^{-w} Z_n Z_m \, dz \tag{9}$$

The unknowns R_n can be readily obtained by solving a single set of equations which result by adding the two matrices in equations (6) and (8) as

$$\sum_{n=1}^{N} R_n (2 X_{nm} + k_n Y_{nm}) = k_1 Y_{1m} \tag{10}$$

Once the solution is obtained for the unknowns R_n, the wave forces on the wave barrier may be determined from equation (1). Based on linear wave theory, the dynamic pressures are related to the velocity potentials as $p = i\rho\sigma\Phi$, and the linear wave force per unit width (at $x=0$) is given by

$$F = i \rho \sigma \int_{-w}^{0} (\Phi_{up} - \Phi_{dn}) \, dz = 2 i \rho \sigma \sum R_n \int_{-w}^{0} Z_n \, dz \tag{11}$$

Substitution of equation (4) gives the following expression for forces on a vertical wave barrier

$$F = \rho g H_i \sum_{n=1}^{N} \frac{R_n}{k_n} \frac{\sinh k_n d - \sinh k_n (d-w)}{\cosh k_n d} \quad (12)$$

For a full-depth wall ($w = d$) with perfect reflection, $R_1 = 1$, and all other values of $R_n = 0$ for $n > 1$, such that equation (12) gives the force associated with linear standing waves, denoted F_o, in equation (2). This value provides a convenient normalizing parameter for the forces on a partial-depth wave barrier, and experimental results can be compared to theory on the basis of the ratio, F/F_o.

Comparison of Theory and Data

Regular Waves

Forces computed using equation (12) are compared to selected results of the regular wave tests in Figure 3 for values of $d/L = 0.12$ to 0.50. As may be seen in these comparisons, the predicted loads essentially agree with the measured values for each relative depth and for each of the four values of wall penetration, w/d, tested. In the top of Figure 3, for relatively shallow water depths, the agreement is particularly good. For deeper water depths, at the bottom of Figure 3, there is more scatter in the data and the eigenfunction solution tends to form an upper bound to the data. In all cases, measured and predicted wave loads range from about 20% to 90% of the value F_o associated with a linear wave reflecting from a full-depth vertical wall.

A summary of all of the regular wave results obtained in this study is shown in Figure 4 where the measured force (dimensionless) is compared to that predicted from the eigenfunction theory. From this comparison, it is clear that the eigenfunction theory predicts the force amplitude to within about 10% to 20% for all cases tested. The eigenfunction solution forms nearly an upper bound to the data and, on average, it tends to overestimate the measured wave loads by just a few percent.

In comparison to the SPM or DM26.2 methods discussed earlier, the eigenfunction solution is clearly superior. It can be shown that the eigenfunction method provides improved predictive capabilities for two reasons. First, it more accurately models the vertical distribution of pressure on the wall without *ad hoc* reduction factors, especially near the base of the wall where the pressures on the two sides of the wall must match. Second, it correctly models the phase shifts between incident, reflected, and transmitted waves, and between the various evanescent wave components. While the SPM and DM26.2 method assumes a 180° phase shift in the water levels across the wall, observations show that the phase shift is closer to 90° under most conditions. While not shown here, measured values of the phase shift are well-predicted by the eigenfunction theory.

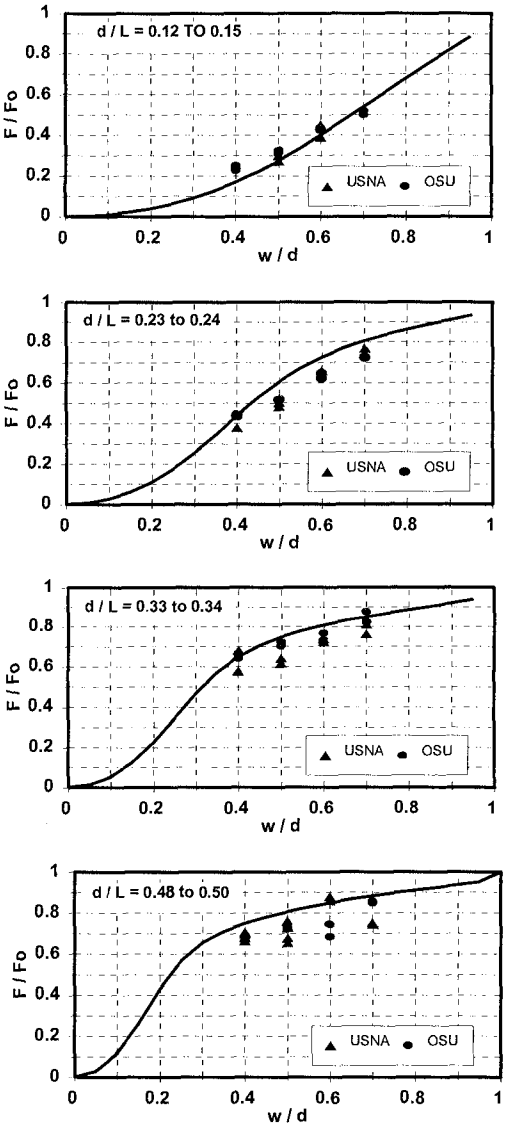

Figures 3. Comparisons of measured and predicted wave forces for regular waves, for selected values of relative depth *d/L*.

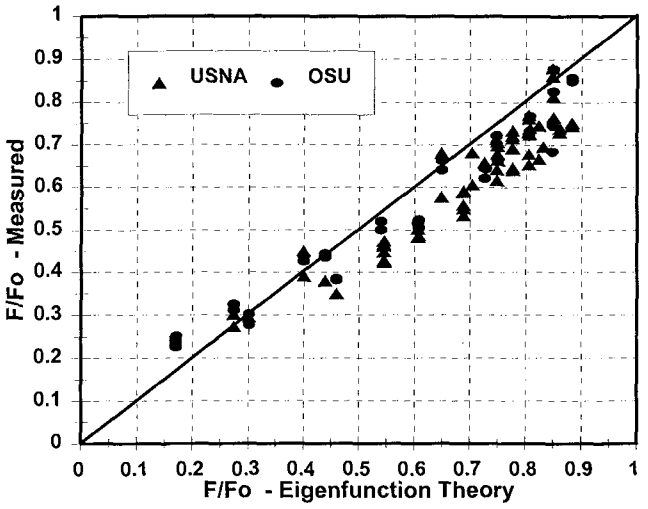

Figure 4. Comparison of measured wave loads to those predicted by the eigenfunction theory, for all regular wave tests.

Irregular Waves

Selected results of tests using irregular waves are shown in Figure 5. In these comparisons, the measured data consist of the zero-moment or significant force amplitude, derived from the force spectrum as described earlier. The predicted wave loads are determined as follows. Starting with a JONSWAP wave energy spectrum, equation (12) is used to compute a transfer function between wave amplitude and force amplitude at each frequency in the spectrum. The squared value of this transfer function is then multiplied by the JONSWAP wave spectrum at each frequency to obtain the force spectrum. The significant force amplitude is then derived as two times the square-root of the area under the force spectrum. Both the measured and predicted significant force amplitudes are then normalized by the force on a full depth vertical wall as computed from the zero-moment significant wave height, H_{mo}, as

$$F_o = \rho g H_{mo} \frac{1}{k_p} \frac{\sinh k_p d}{\cosh k_p d} \qquad \textbf{(13)}$$

where k_p is the wavenumber associated with the wave period at the peak of the spectrum.

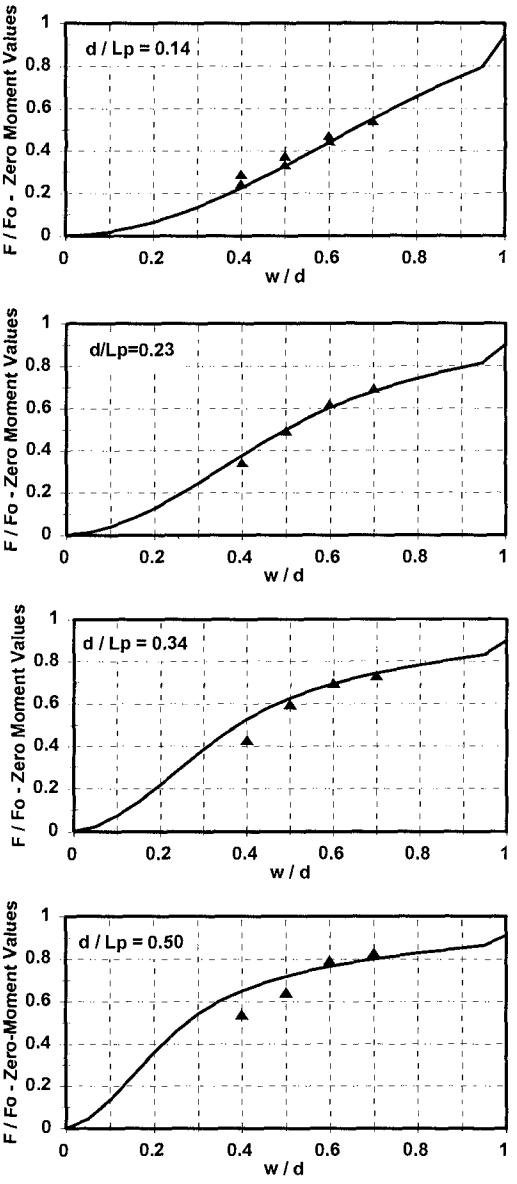

Figures 5. Comparisons of measured and predicted wave forces for irregular waves, for selected values of relative depth d/L_p.

Results in Figure 5 suggest that the eigenfunction solution, applied on a frequency-by-frequency basis in the frequency domain, can provide very robust predictions of wave loads across a wide range of relative water depths. Figure 6 presents a comparison of the measured and predicted significant force amplitudes for all of the irregular wave tests conducted at OSU. As may be seen, the predictions appear to be even more accurate for random waves than for regular waves, as all but five points are predicted to within a 10% error.

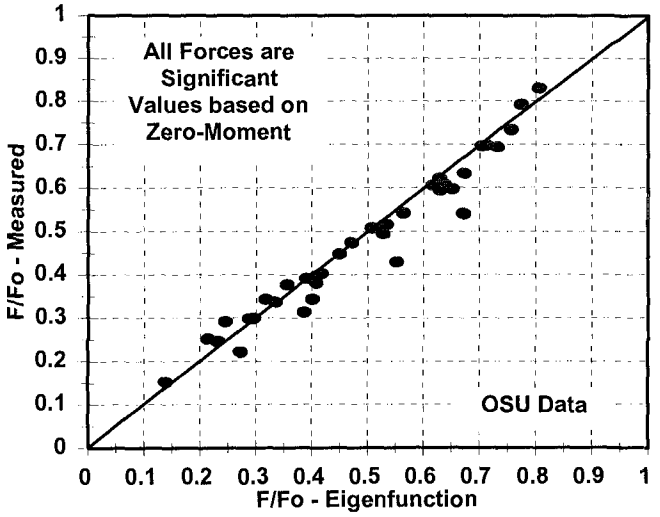

Figure 6. Comparison of measured wave loads to those predicted by the eigenfunction theory, for all irregular wave tests.

Summary and Conclusion

Results presented in this paper indicate that for a wide range of relative water depths, and for wave barrier drafts near mid-depth, the eigenfunction expansion theory is capable of predicting wave loads to within 10% to 20%, with somewhat more accurate predictions for irregular waves than for regular waves. This is considerably more accurate than the predictions obtained from the SPM or DM26.2, which were often more than twice as larger as the measured wave loads.

It is interesting to contrast these findings to those of Kriebel and Bollmann (1996) who found that the eigenfunction theory generally over-predicted wave transmission by a larger percentage. They found that viscous dissipation in a large vortex at the base of the wall acts to reduce the size of the transmitted wave from that predicted by the eigenfunction theory. This is of little concern for the prediction of wave forces, however, because of the nearly 90° phase shift found between water levels across the wave barrier. Wave forces are maximum at the time when the incident and reflected waves form a partial standing wave crest (or trough) on the up-wave side of the barrier, but when the water level on the down-wave side is near the still water level. At this instant, the magnitude of the transmitted wave is of little consequence.

Finally, it is noted that the eigenfunction solution presented here is consistent with linear wave theory with pressures only integrated up to the still water level. Inclusion of pressures above the still water level, up to the instantaneous wave crest, did not improve the solution but tended to cause the eigenfunction solution to over-predict by a larger margin. As a result, it may be inferred that dynamic pressures predicted by the eigenfunction theory below the still water level must be somewhat larger than those that would be measured if a wave barrier were instrumented with pressure transducers. This could be the subject of future research.

Acknowledgements

This work has been supported by the National Science Foundation and by the Alaska Science and Technology Foundation.

References

Abul-Azm, A.G., 1993, "Wave Diffraction Through Submerged Breakwaters," J. of Waterway, Port, Coastal, and Ocean Engineering, Vol. 119, No. 6, pp. 587-605.

Kriebel, D., and Bollmann, C., 1996, " Wave Transmission Past Vertical Wave Barriers," Proc. of 25th Intl. Conf. on Coastal Engineering, Orlando.

Liu, P.L-F., and Abbaspour, M., 1982, "Wave Scattering by a Rigid Thin Barrier," J. of Waterway, Port, Coastal, and Ocean Engineering, Vol. 108, WW4, pp. 479-491.

Losada, I., Losada, M., and Roldan, A., 1992, "Propagation of Oblique Incident Waves Past Rigid Vertical Thin Barriers," Applied Ocean Res., Vol. 14, pp. 191-199.

Naval Facilities Engineering Command, 1984, *Coastal Protection Design Manual 26.2*, U.S. Government Printing Office, Washington, D.C.

U.S. Army Corps of Engineers, 1984, "*Shore Protection Manual*," 4th edition, U.S. Government Printing Office, Washington, D.C.

STATISTICAL DISTRIBUTION OF HORIZONTAL WAVE FORCES ON VERTICAL BREAKWATERS

Janice McKENNA[1] and William ALLSOP[2]

ABSTRACT

This paper discusses the statistical distribution of wave impact forces on vertical wall structures. It describes new analysis carried out based on the distribution type to identify the parameter combinations that lead to wave impacts.

Comprehensive 2-dimensional random wave model tests were carried out to measure wave pressures on a range of structure types. Initial analysis of these tests showed that the Weibull distribution could be used to describe non-breaking wave forces.

For some structural configurations however the wave forces were found to give a poor fit with the Weibull distribution. These data had been excluded from the initial analysis. The new analysis described in this paper has resulted in a revised parameter map to summarise the risk of wave impact, derived from the full data set and based on the distribution type.

1. INTRODUCTION

Vertical wall structures were widely used in the UK as seawalls and breakwaters before rubble mound breakwaters and rip-rap revetments gained popularity in the 1900's. In Japan and Italy, caissons continue to be favoured for breakwater construction. A thorough understanding of the relationship between wave forces on vertical walls and overall structure geometry is necessary to enable the design of a suitable, cost-effective structure, with an acceptably low risk of failure. It is also desirable to minimise the risk of severe exposure to large breaking wave impact forces, so that future maintenance costs are not unduly high.

Vertical walls in the marine environment are subjected to highly variable wave loads, yet existing design methods are deterministic. The main design method for caissons, developed by Goda (1974, 1985), provides a good estimate of non-breaking wave forces (McKenna, 1997). For wave impacts however, the predicted forces using Goda's

[1] Assistant Engineer, Babtie Group Ltd., 95 Bothwell Street, Glasgow, G2 7HX, UK
[2] Visiting Professor, The Queen's University of Belfast, University Road, Belfast, BT7 1NN, UK
Manager Coastal Structures, HR Wallingford, Howbery Park, Wallingford, Oxon OX10 8BA, UK

method are 'effective' values, damped by the response of the structure and foundation, rather than actual impact loads. These wave impact loads were previously thought to be unimportant for the stability of massive structures such as caissons, but Oumeraci et al (1995) have shown that repeated wave impacts can cause incremental displacements.

It is necessary to recognise the wide variation in force type and magnitude, and to incorporate a measure of their probability of occurrence, in order to develop improved design methods. Work within MAST III-PROVERBS has been directed towards this aim.

Identification of a suitable statistical distribution for wave forces on vertical wall structures is particularly important for the development of probabilistic design tools. Previous work on the statistics of wave forces has concentrated on establishing the extreme distribution of a series of (theoretically) regular waves, see for instance Kirkgöz (1995), but these results cannot be applied to real (random) seas.

The Weibull distribution can be used to describe pulsating wave forces measured in model tests on caisson breakwaters using random waves. Allsop et al (1996a) have shown that the onset of wave impacts can be defined as a change in gradient of the probability plot where wave forces start to increase rapidly above those predicted by the simple Weibull distribution.

The design load for many structures will however be due to wave impact forces rather than non-breaking waves. It is therefore important to be able to establish the statistical distribution of wave impact forces, and to know the relative proportions of pulsating and impact forces for a given structural configuration.

2. MODEL TESTS

Comprehensive parametric model tests were conducted in a random wave flume at HR Wallingford during 1994. These tests were designed to investigate the influence of structure geometry on wave pressures and forces, using random waves. Over 200 tests were carried out in all, to explore the effects of varying the following parameters:

a) Significant offshore and inshore wave heights, H_{so} and H_{si};
b) Water depth in front of structure, h_s; and crest freeboard R_c;
c) Wave steepness, s_{mo}, and peak wavelength at structure toe, L_{pi};
d) Water depth over mound in front of wall, d; and berm height, h_b;
e) Berm width, B_b;
f) Front slope of mound, α;
g) Depth of embedment of caisson into mound, h_b-h_c;

The caisson was instrumented with 8 pressure transducers on the front face and 4 on the underside as shown in Figure 1. Pressure data were acquired on all transducers simultaneously at 400Hz for 500 waves in each test. These tests have been described previously by Allsop et al (1996b).

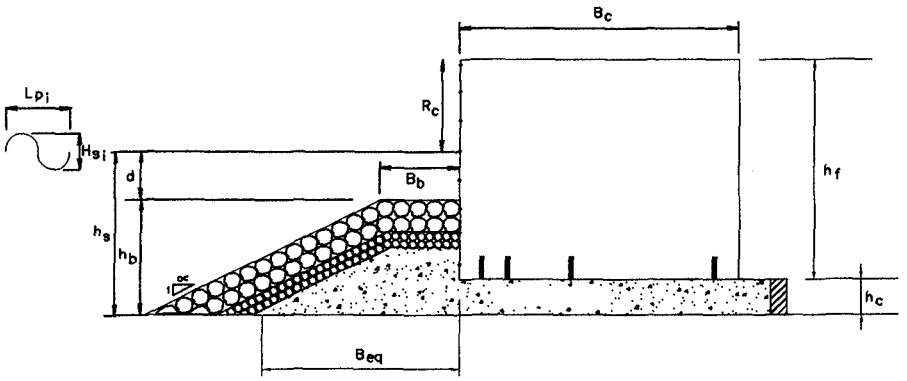

Figure 1 Instrumented Model Caisson

3. DATA ANALYSIS

A data analysis program was developed to carry out the initial analysis of the pressure data acquired from these model tests. The pressure data were spatially integrated at each time-step to give horizontal and uplift force time histories. In order to study the statistics of the data set, information regarding the force maxima was required for each wave event. An event was defined from the beginning of each rapid pressure rise on the transducer at still water level, and the analysis program was configured to search for the required information within each 'event'.

As horizontal and uplift pressure and force maxima do not necessarily occur at the same time, a number of output files were written, so that each phenomenon could be studied separately.

The next stage of the data analysis was to rank the pressure and force maxima contained in the output files in order of magnitude to enable their statistics to be explored. This paper concentrates on the results of the further analysis of the horizontal forces.

4. STATISTICS OF WAVE FORCES

Wave impact forces on coastal structures are extremely variable, and are therefore better described by their statistics than by any single deterministic value. In selecting an appropriate statistical distribution for wave forces, it is an advantage to maintain any association between wave heights and wave forces. If a narrow band process is assumed, wave heights can be approximated by the Rayleigh distribution, which is a special form of the more generic 3-parameter Weibull distribution.

Analysis of the pressure data from these model tests by Allsop et al (1996a,b) showed that the Weibull distribution could be used to give a good description of wave forces from non-breaking waves (referred to here as pulsating wave forces), as shown in Figure 2. It was also found that the onset of wave impacts could be defined by a change in the gradient of the Weibull plot, where the wave forces start increasing more rapidly with non-exceedance level, Figure 3.

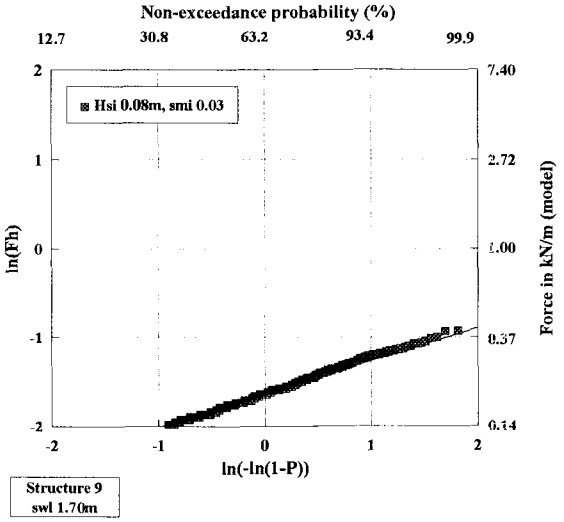

Figure 2 Weibull distribution of pulsating wave forces

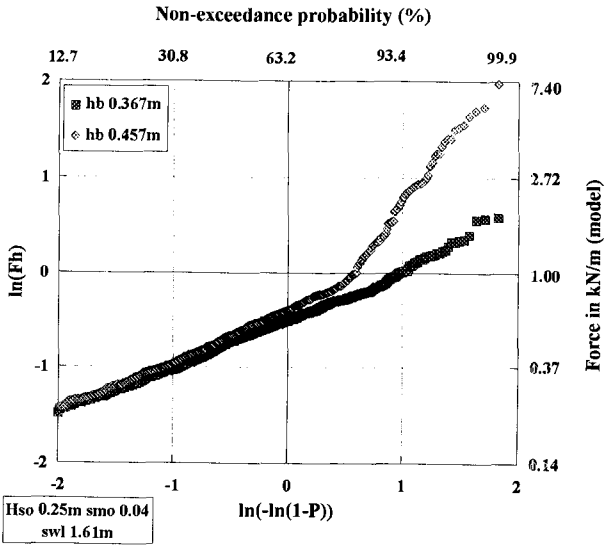

Figure 3 Transition from pulsating forces to impact forces

This method of estimating the percentage of impacts was applied to each test, and was found to give good agreement with observations from the flume testing and with analytical considerations of the physical processes involved. This analysis led to the development of a parameter map, Allsop et al (1996a,b) that could be used to estimate the risk of wave impacts on a particular structure.

Further analysis by McKenna (1997) revealed that the Weibull distribution could also be used to describe wave impact forces in some instances, Figure 4. It was also noted that for other cases the percentage of impacts could be difficult to determine, as the change in the gradient of the distribution was not distinct. These cases were selected for further investigation, and it was found that the data points plotted as a gradual curve on Weibull axes, rather than a straight line with a sharp change in gradient, Figure 5.

The structural configurations corresponding to these curved distributions were investigated and a common link was found in the relationship between the offshore wave conditions and the local water depth at the structure. Limiting values of H_{so}/h_s = 0.425 and L_{mo}/h_s =17 were identified, beyond which wave forces no longer fit the Weibull distribution, Figure 6. The distortion of the distribution is caused by shallow water wave transformations. The smallest waves reach the structure relatively unchanged, but there is a gradual increasc in the amount of modification of the wave shape as the wave heights and lengths increase. The incident wave height distribution was found to be non-Rayleigh for these cases, Figure 7.

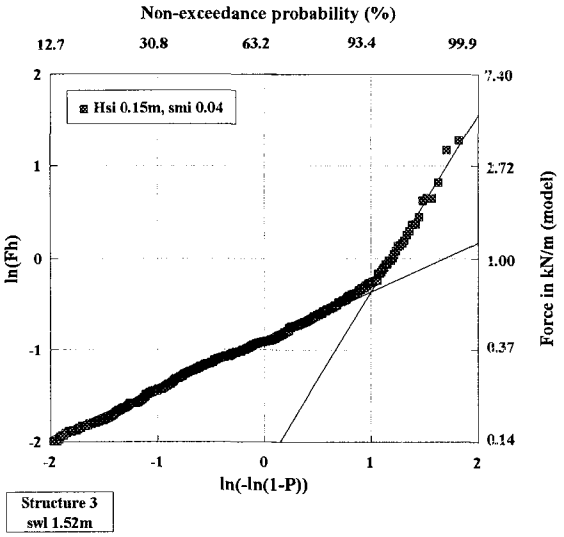

Figure 4 Weibull Distribution of horizontal wave impact forces

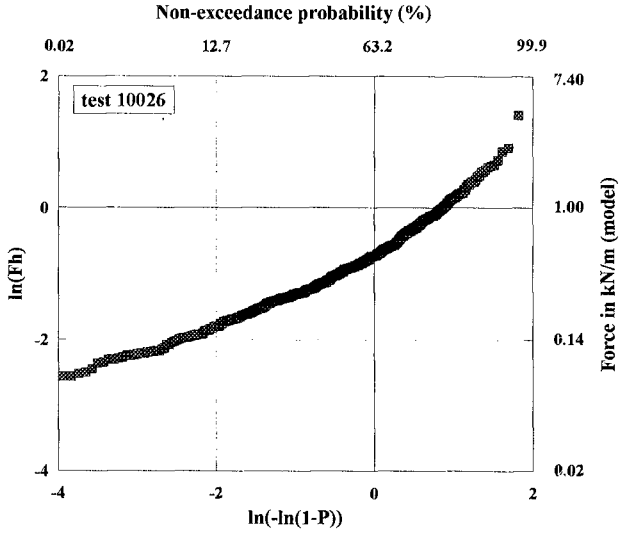

Figure 5 Non-Weibull distribution

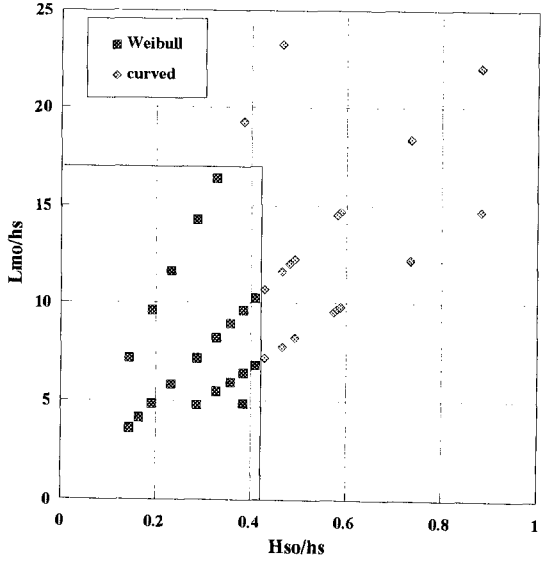

Figure 6 Parameter ranges for Weibull distributed forces

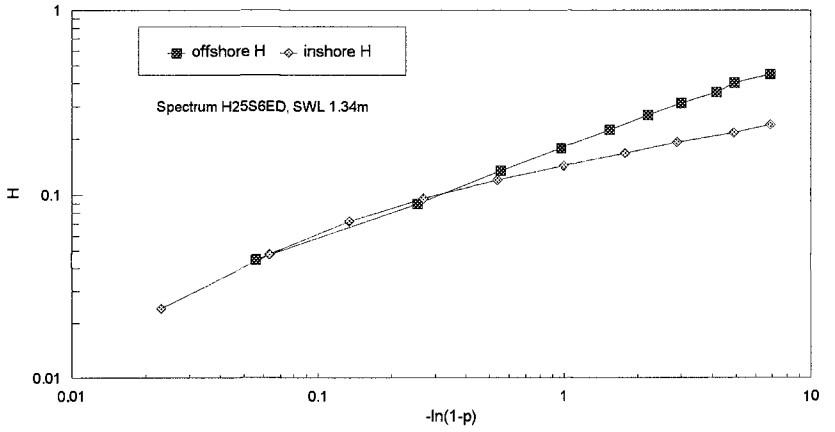

Figure 7 Modified inshore wave height distribution

5. DEVELOPMENT OF PARAMETER MAP

Attempts to analyse the full data set by Allsop et al (1996b) had highlighted the need to separate the data into regions of similar response characteristics. The dimensionless parameters that influenced wave forces were identified as:

- Relative mound height, h_b/h_s;
- Relative wave height, H_{si}/d;
- Relative berm length, B_{eq}/L_{pi}.

The effects of these parameters were summarised in the parameter map presented by Allsop et al (1996a,b). The derivation of that parameter map had concentrated on a central core of data, where the water depth over the rubble mound berm, d, was greater than twice the significant inshore waveheight, H_{si}. Cases where the water level was close to or below the top of the rubble mound were excluded.

Potential weaknesses had been recognised in that derivation, both in excluding of a set of data from the analysis, and in using the dimensionless parameter H_{si}/d, which tends to infinity as the water depth over the rubble mound tends to zero. It was concluded that, if possible, this parameter should not be used in further work to extend the parameter map to include the full data set.

The approach used in this further work to include the full data set in the parameter map considered the effects of the non-Weibull distributed forces, and included additional parameters to describe the effects of transformation from the offshore wave climate to the inshore wave climate. The dimensionless parameters used in the new parameter map (Figure 8) are:

- Relative offshore wave height,H_{so}/h_s;
- Relative offshore wave length, L_{mo}/h_s;

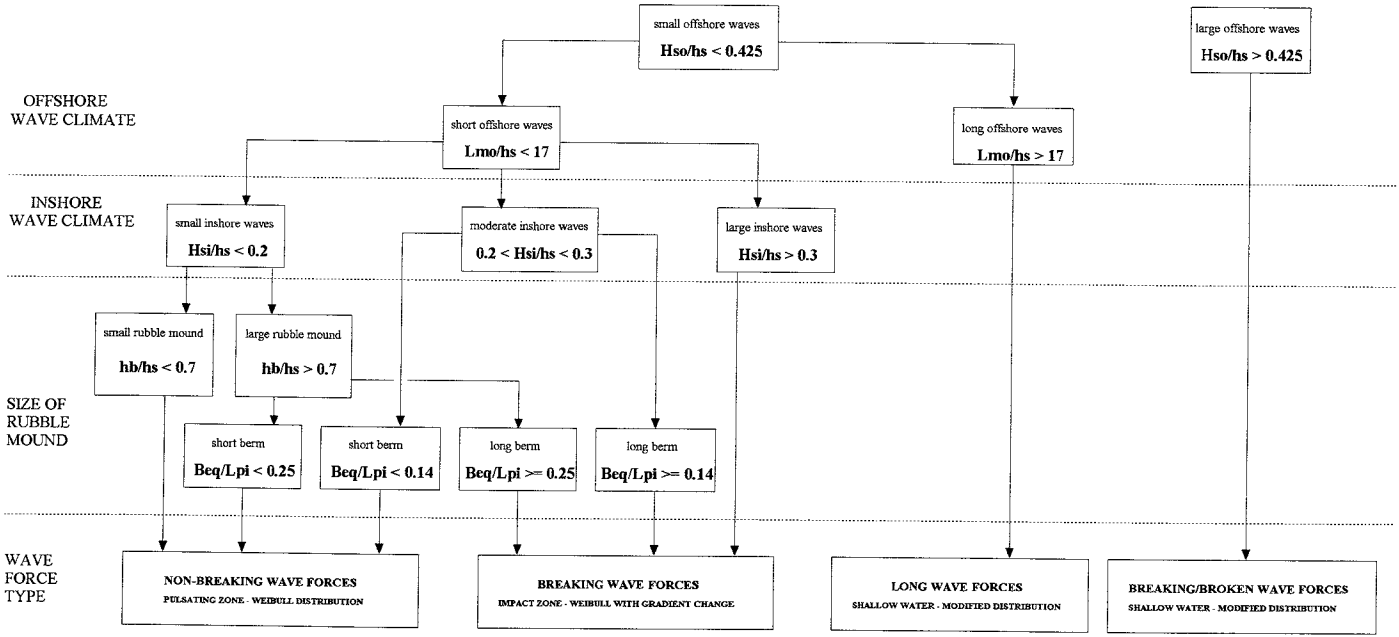

Figure 8 **Parameter map showing critical parameter ranges for wave impacts on vertical and composite breakwaters**

- Relative inshore wave height, H_{si}/h_s;
- Relative berm height, h_b/h_s;
- Relative berm length, B_{eq}/L_{pi}.

The significance of each of these parameters, and their contribution to the description of the overall physical processes are described below.

5.1 Degree of Wave Breaking (H_{so}/h_s and L_{mo}/h_s)

In order to represent the effects of structural geometry properly, it is first necessary to identify those tests where the seabed causes wave breaking on the approach to the structure. These tests must be identified at the beginning of the analysis, as they would distort any conclusions about the overall response to the structure itself. These tests were easily identified by the curved distribution of data when plotted on Weibull axes, as described previously.

Further work is required to identify the parameter influences in cases for which the data are not Weibull distributed. A suitable statistical distribution must be established for these tests and the response to the structure geometry may then be identified from this new analysis.

It is not possible at this stage to speculate on effects of individual parameters in these cases, but it is certain that structures in shallow water are at risk of exposure to breaking wave forces. The overall level of forces on the structure may however be low, as the incident waves may be substantially broken (and aerated) before reaching the structure. Blackmore and Hewson (1984) have shown that wave forces due to highly aerated waves are significantly lower than corresponding 'deep water' waves.

Configurations that fall into this category should be treated as though they will be subjected to high impact forces, and designed accordingly, until further work has been carried out in this region of the parameter map. This is particularly important for structures in areas with high tidal ranges.

5.2 Wave regime at structure (H_{si}/h_s)

The most significant parameter affecting the onset of wave impacts for Weibull distributed data was found to be the relative incident wave height, H_{si}/h_s. This parameter represents the likelihood of wave breaking at the toe of the structure, before any significant interaction with the structure has taken place. The critical value of H_{si}/h_s to cause the onset of impacts was investigated by plotting the percentage of impacts, Pi%, for each test against H_{si}/h_s.

Initial investigations using Weibull distributed data from structures 0, 1, and 2 suggested that if the value of H_{si}/h_s was less than a critical value of 0.2, there would be no wave breaking, and the resulting forces would therefore be pulsating, see Figure 9.

Extension of this analysis to include all structures showed that impacts did occur for some configurations where $H_{si}/h_s < 0.2$ (Figure 10), but that all these structures had very high rubble mounds in comparison to the local water depth. This effect is described in section 5.3. The limit of $H_{si}/h_s = 0.2$ was therefore accepted as the impact indicator for

vertical wall structures and structures with low rubble mounds. A second limit of H_{si}/h_s = 0.3 was identified as the point beyond which some impacts were recorded in all tests, also illustrated in Figure 10.

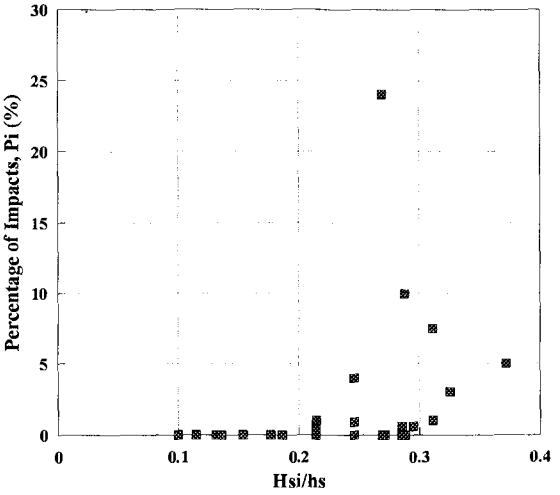

Figure 9 Variation in percentage of impacts with H_{si}/h_s (structures 0, 1 and 2)

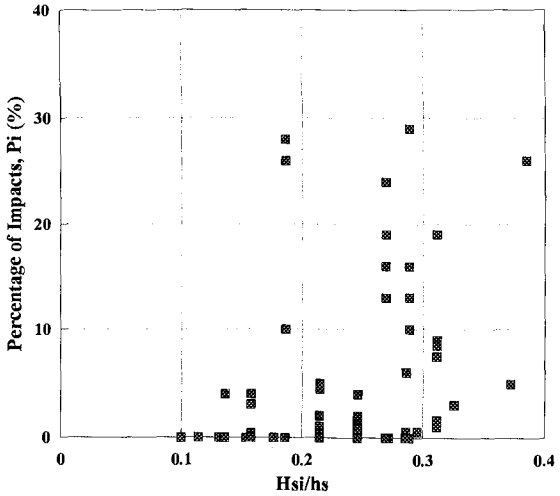

Figure 10 Variation in percentage of impacts with H_{si}/h_s (all structures)

In the zone between these limits, ie $0.2 < H_{si}/h_s < 0.3$, a mixture of pulsating and impact conditions was observed. In this region, the occurrence of wave impact forces was later found to be dependent on the relative berm length, B_{eq}/L_{pi}, as described in section 5.4.

The effects of relative incident wave height, H_{si}/h_s, may be summarised as follows:

- $H_{si}/h_s < 0.2$ pulsating wave forces except for structures with high mounds and long berms;
- $0.2 < H_{si}/h_s < 0.3$ pulsating wave forces except for structures with long berms;
- $H_{si}/h_s > 0.3$ high probability of impacts on all structure types.

5.3 Height of rubble mound berm (h_b/h_s)

The relative height of the rubble mound berm was found to be significant in cases where $H_{si}/h_s < 0.2$, ie the relative incident wave height was low. In this region, no impacts were observed for cases where $h_b/h_s < 0.7$, defined here as 'low mounds', as shown in Figure 11. A mixture of pulsating and impact forces was observed in tests on structures with $h_b/h_s \geq 0.7$, defined here as 'high mounds'. The relative berm length, B_{eq}/L_{pi}, was found to be important in these cases, as described in section 5.4.

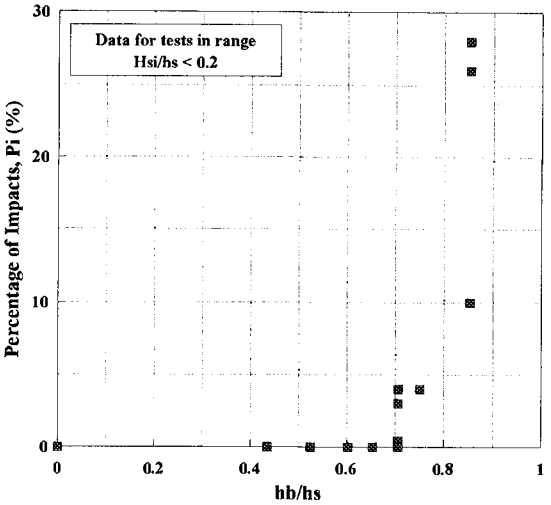

Figure 11 Influence of relative berm height, h_b/h_s (structures with small relative incident wave height)

The relative berm height, h_b/h_s, is a much less significant parameter than the relative incident wave height, H_{si}/h_s. It plays an important role however in causing impacts for those configurations with small values of H_{si}/h_s, and may therefore be particularly important for structures in areas with high tidal ranges. The parameter h_b/h_s describes the effect of a small water depth on top of the rubble mound on the breaking process, identified as important by Allsop et al (1996a,b). The relative berm height replaces H_{si}/d to describe this effect. It is a much more stable parameter, as it tends to infinity only if

the water depth at the toe of the structure is zero, and may therefore be used over the range of practical structures.

The effect of h_b/h_s is markedly less significant than the effect of H_{si}/h_s over the parameter ranges considered here. It is however an important part of the overall physical processes involved, and further investigations concentrated in the region $H_{si}/h_s < 0.2$ with various berm configurations may well uncover potentially damaging cases related to the berm height. In addition, further work covering the whole region of the parameter space might indicate that h_b/h_s is important in other instances, for example when combined with the relative berm length.

5.4 Length of rubble mound berm (B_{eq}/L_{pi})

The relative berm length, B_{eq}/L_{pi}, was found to be important in the regions $H_{si}/h_s < 0.2$ and $0.2 < H_{si}/h_s < 0.3$ (small and intermediate relative wave heights).

A mixture of impacting and non-impacting cases occurred for high mounds ($h_b/h_s \geq 0.7$) in the region $H_{si}/h_s < 0.2$, as stated previously in 5.2. Configurations with relative berm lengths, B_{eq}/L_{pi}, of at least 0.25 were found to experience wave impacts, as shown in Figure 12.

In the region $0.2 < H_{si}/h_s < 0.3$, a similar analysis showed that impacts occurred in those tests with relative berm lengths, $B_{eq}/L_{pi} \geq 0.14$ as shown in Figure 13.

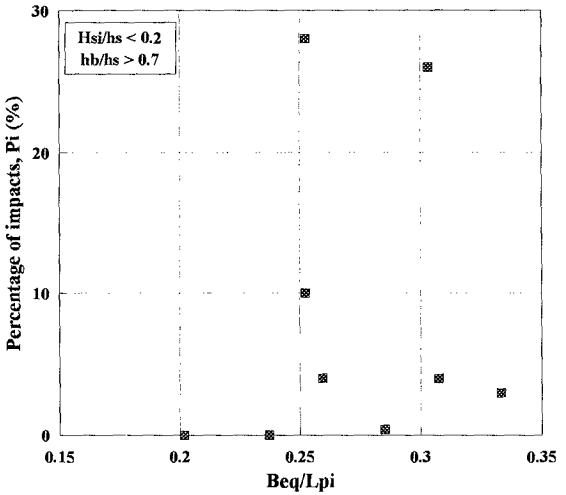

Figure 12 Influence of relative berm length B_{eq}/L_{pi} (Structures with high mounds and small relative incident wave height)

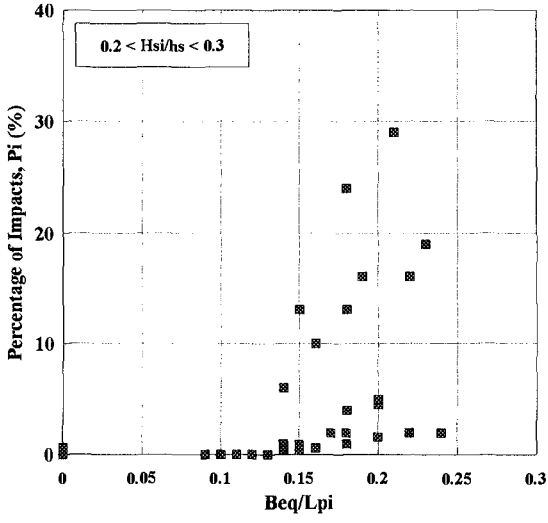

Figure 13 Influence of relative berm length, B_{eq}/L_{pi} (Structures in the range 0.2 < H_{si}/h_s < 0.3)

6. CONCLUSIONS

Random wave forces on vertical walls may be described well by the Weibull distribution, both in the pulsating and impact zones. In these cases, the onset of impacts can be identified by a sharp change in the gradient of the probability plot.

If significant shallow water wave transformations have occurred, the resulting wave forces plot as a curve on Weibull axes. Critical values of relative offshore wave height and wave length have been identified, to determine whether the Weibull distribution may be used to describe wave forces.

The parameter map presented by Allsop et al (1996a,b) has been improved following new analysis and the identification of non-Weibull distributed data.

A revised parameter map for determining the risk of wave impacts is presented, which includes data for structures where the water depth over the rubble mound berm is small.

ACKNOWLEDGEMENTS

This paper is based on results of research for the UK Department of Environment under contracts PECD 7/6/263 and 7/6/312; and of the EC MAST III programme under MAS3-CT95-0041. Additional support has been given by The Queen's University of Belfast, by the Universities of Sheffield and Naples, and by the Department of Education, Northern Ireland.

The authors also wish to thank all the staff and visiting researchers at HR Wallingford and at The Queen's University of Belfast who assisted with the model testing and data analysis, and to acknowledge the continuing support of Babtie Group Ltd and HR Wallingford for the preparation of this paper.

REFERENCES

Allsop N.W.H., McKenna J.E. Vicinanza D & Whittaker T.J.T. (1996a) "New design methods for wave impact loadings on vertical breakwaters and seawalls", Proceedings of 25th International Conference on Coastal Engineering, Orlando, Florida.

Allsop N.W.H., Vicinanza D. & McKenna J.E. (1996b) "Wave forces on vertical and composite breakwaters", Report SR443, HR Wallingford, Oxfordshire.

Blackmore P.A. & Hewson P. (1984) "Experiments on full-scale impact pressures", Coastal Engineering, Vol 8, pp 331-346, Elsevier Science B.V., Amsterdam.

Goda Y. (1974) "New wave pressure formulae for composite breakwaters"; Proceedings of 14th International Conference on Coastal Engineering, Copenhagen, Denmark, pp 1702-1720.

Goda Y. (1985) "Random Seas and Design of Maritime Structures"; University of Tokyo Press, Japan

Kirkgöz M.S. (1995) "Breaking wave impact on vertical and sloping coastal structures", Ocean Engineering, Vol 22, No 1, pp 35-48, Elsevier Science, Oxford.

McKenna J.E. (1997) "Wave forces on caissons and breakwater crown walls", PhD Thesis, The Queen's University of Belfast, Northern Ireland.

Oumeraci H., Kortenhaus A. & Klammer P. (1995) "Displacement of caisson breakwaters induced by breaking wave impacts" Advances in Coastal Structures and Breakwaters – Proceedings of the International Conference held at The Institution of Civil Engineers in London, UK, pp50-63.

NEURAL NETWORK MODELLING OF FORCES ON VERTICAL STRUCTURES

Marcel R.A. van Gent[1] and Henk F.P. van den Boogaard[1]

ABSTRACT: For the design of vertical breakwaters, reliable predictions of the horizontal forces are required. Through physical modelling useful predictions can be made but, due to the very complex interaction between waves and structures, the derivation of reliable empirical relations based on such tests can still be rather difficult. Here, based on a large data-set from physical model tests, use is made of Neural Network modelling to predict horizontal forces on vertical structures. In addition, a method is developed to estimate the reliability-intervals around the predictions. The resulting tool is a complementary design-tool for predicting forces on vertical breakwaters and also a suitable tool for application in probabilistic design methods.

1. INTRODUCTION

Horizontal forces on the upright seaward section of vertical structures often form the most important wave load. Due to the complexity of the phenomena, it is difficult to describe the effects of all relevant parameters in design formulae. For such processes in which the interrelationship of parameters is unclear while sufficient experimental data are available, Neural Network (NN) modelling may be a suitable alternative. Mase *et al.* (1995) showed that this technique is valuable for the stability analysis of rubble-mound breakwaters. Here, an NN is developed for predicting wave forces on vertical structures where nine different parameters are considered important as the main factors that determine the total horizontal force. First the parameters that were used to determine the horizontal forces are discussed.

1) WL | DELFT HYDRAULICS, P.O. Box 177, 2600 MH Delft, The Netherlands.

Then the actual development of the NN is described, followed by a comparison with traditional design formulae. In addition, a method to assess the reliability of the NN-predictions is presented. More detailed information concerning this paper can be found in Van Gent and Van den Boogaard (1998).

2. NEURAL NETWORK MODELLING

2.1 PARAMETERS INVOLVED IN FORCE PREDICTION

The total horizontal force on a vertical breakwater is the result of the interaction between the wave field, the foreshore and the structure itself. Here perpendicular wave attack is considered. In order to describe the wave field two parameters are applied: The significant wave height in deep water (H_s) and the corresponding peak wave period (T_p). The effect of the foreshore is described by the slope of the foreshore ($tan\ \theta$) and the water depth in front of the structure (h_s). The structure is characterised by the height of the vertical wall below and above the water level (h' and R_c), the water depth above the rubble-mound foundation (d), the width of the berm (B_b) and the shape of the superstructure (φ). Figure 1 shows the nine parameters on which the NN was based.

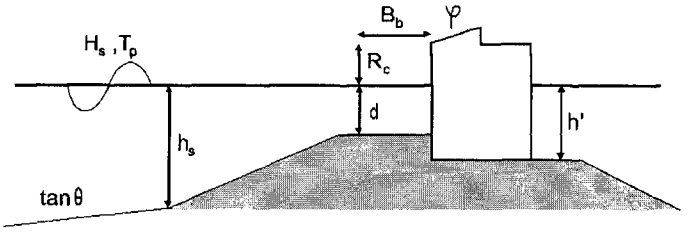

Fig. 1 Parameters used for NN-modelling of horizontal forces on vertical structures.

In particular, the crest shape factor (φ) was introduced to account for the differences in crest shapes of the structure, such as inclined or curved crests. Measured forces obtained under similar wave conditions and similar structures but with different crest shapes (vertical and non-vertical) were compared by computing the ratio of the corresponding horizontal forces. The average of the computed ratios was taken as the crest shape factor for that shape. The values were in the range from 0.8 to 1.0 (1.0 corresponds to a vertical crest). This approach was adopted in view of the fact that wave overtopping was not significant in those tests where the crest elements differ considerably from a simple rectangular caisson.

2.2 DESCRIPTION OF DATA-SET

Data on total horizontal forces on vertical structures are collected from physical-model tests performed at several laboratories. The applied measurement techniques and analysis methods differ from institute to institute. Based on published data the parameter corresponding to the total horizontal force that is exceeded by 99.6% of the waves has been derived. For some cases this parameter was not directly measured but has been obtained by interpolating between for instance the 99% and 99.8% values. For one data-set an extrapolation has been applied by using a Weibull-fit through the 90%, 95% and 98% values; the fit gave good predictions of the measured 99%-values and therefore has been applied to predict the corresponding 99.6% values. Nevertheless, inaccuracies may have been introduced by these interpolations and extrapolations.

The data is described in detail in the following publications: Van der Meer and Juhl (1992), Allsop et al (1996), Kortenhaus and Oumeraci (1997) and Madrigal and Wei (1997). In total 612 data-patterns have been used: 68 from DELFT HYDRAULICS (The Netherlands), 59 from DHI (Denmark), 97 from CEDEX (Spain), 215 from HR Wallingford (UK) and 173 from Leightweiss Institute (Germany).

As will be discussed, an analysis concerning the consistency of the data-set has been performed. It occurred that some data-sets, especially the relatively large data-sets, show significant variations in output for data-patterns with similar input-patterns. The inconsistencies in the data-set do not necessarily lead to incorrect predictions by the NN if these measurement errors can be considered as a random white noise, i.e. no 'systematic errors'.

One of the sources of inconsistencies in the data-set is that the data includes several types of wave forces. The data-set contains conditions that lead to pulsating wave forces but also conditions that lead to impact forces. Especially tests leading to impacts with a relatively low number of waves lead to relatively weak repeatability and therefore input-patterns with a less reliable output. However, if conditions are divided into classes of 'pulsating forces', 'impact forces' and 'transitional' according to the diagram by Kortenhaus and Oumeraci (1997), 244 patterns are identified as 'pulsating forces', 362 as 'impact forces' and 12 as 'transitional'. Inconsistencies such as large differences between output for similar input-patterns are not restricted to one of these classes (inconsistencies occur for 'impact forces' and for 'pulsating forces').

The accuracy of the NN-modelling depends strongly on the quality of the data-set. Therefore, for this application it is even of greater importance that a method is available to quantify the reliability of the NN-output. The consequence of the applied method is that the accuracy of the NN predictions can be further improved if more reliable data-patterns become available,.

2.3 NEURAL NETWORK TRAINING

General

Here, NN-modelling will be briefly discussed. For a more detailed but still general introduction a well written review on NN included in ACM (1994) is recommended, as well as the book of Beale and Jackson (1990). For further details on the technical background, examples, and applications the book of Haykin (1994) is very suitable.

NN can be seen as a sophisticated data-oriented modelling technique to find relations between input- and output-patterns without using process-knowledge. Here, the applied input-pattern is $[H_s, T_p, tan\theta, h_s, h', R_c, d, \varphi, B_h]$ and the output is a single parameter $[F_{h\text{-}99.6\%}]$. For the preparation of an NN model a sufficiently large set of input-output patterns is required.

The configuration of an NN-model can vary. The NN is organised in the form of layers and within each layer there are one or more processing elements called 'neurons'. The first layer is the input layer and the number of neurons in this layer is equal to the number of input-parameters. The last layer is the output layer and the number of neurons in this layer is equal to the number of output parameters. The layers between the input and output layer are the so-called 'hidden layers'. Here, a configuration with only one hidden layer is chosen and information goes from the input-layer, via the hidden layer, to the output-layer ('feed-forward' configuration). Figure 2 shows an example of such a configuration.

Each neuron receives inputs from all neurons of the preceding layer via the connectivities. To each connectivity a weight is assigned. The total input of a neuron then consists of a weighted sum of the outputs of the preceding layer. The output of the neuron is generated using a 'non-linear activation function' with a sigmoid shaped form. This procedure is followed for each neuron; the output neuron generates the final prediction of the NN.

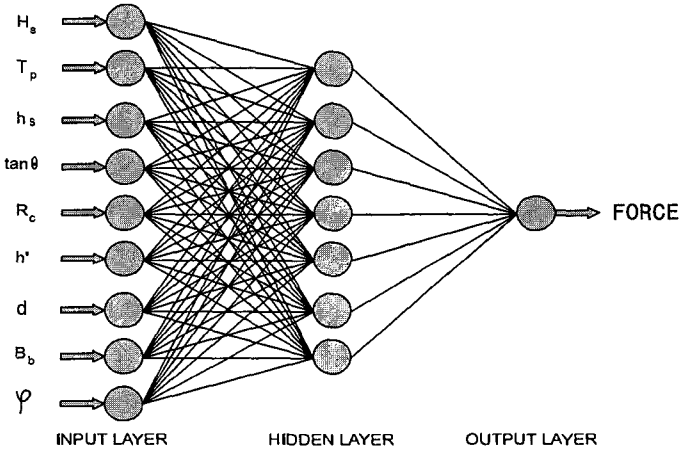

Fig. 2 NN-configuration.

Before the NN can be used the weight-factors need to be calibrated for which a part of the data-set is used (here: a 'training-set' of 500 of the 612 tests). This is the so-called 'training' of the NN using some 'learning' procedure. After that the NN need to be validated by using the remaining part of the data-set (here: a 'testing-set' of 112 of the 612 tests).

Training and testing

The calibration of the weight-factors is performed by using data for which both the input and the output are fed to the NN. Starting with an initial guess for the weights the procedure is that the inputs of this 'training-set' are fed to the NN and the NN's outputs are compared to the observed outputs (measured output). On the basis of the differences between both, the weights are adjusted in such a way that in the next step when the inputs are again fed to the NN, a better prediction is found. This procedure is repeated until no further improvements can be made. This iterative adjustment of the weights is called 'training' of the NN and usually this is done by minimisation of some cost function (or error function) that quantifies the differences of predicted outputs and the desired output (measured), often called 'targets'. A common form of cost function is a superposition of the squared differences. For the minimisation of the cost function, gradient based methods turn out to be most efficient and for the computation of gradient the well known 'error back propagation rule' is used. Here, for calibration the root-mean-square error is defined as:

$$RMS_{train} = \sqrt{\frac{1}{N_{train}} \sum_{n=1}^{N_{train}} \left(\left(F^{obs}_{H\text{-}0.4\%}\right)_n - \left(F^{NN}_{H\text{-}0.4\%}\right)_n \right)^2} \quad (1)$$

An important step in the NN-modelling is to find the optimal number of neurons in the hidden layer. By increasing the number of hidden neurons the differences between the NN-output and the desired output (measured) of the data used for calibration will decrease because more hidden neurons lead to more degrees of freedom (more weight-factors). However, there is a certain optimum because at a certain number of hidden neurons, the NN also starts to model 'noisy fluctuations' in the data-set which is unfavourable for the accuracy of the real predictions. At that moment the NN-model is 'overtrained'. To prevent such an overtraining of the NN not all available data is used for training; a part is reserved for verification. In this partition the 'training-set' and 'testing-set' must be equivalent in statistical sense (i.e. representative for the whole data-set). The optimal number of neurons can be found by training the NN for a range of numbers of neurons in the hidden layer and each time comparing the NN's performance (root-mean square error) on the training and testing-set. Figure 3 shows the performance of NN with various numbers of hidden neurons. More neurons lead to a better performance of the NN for the data used for training but at some stage the predictions of the remaining data (testing-set) become worse. This is an indication that at this stage, NNs with more hidden neurons are not suitable for generalisation and do not provide optimal predictions. This is shown in Figure 3 and in this case a configuration with 8 hidden neurons was chosen as the optimal NN.

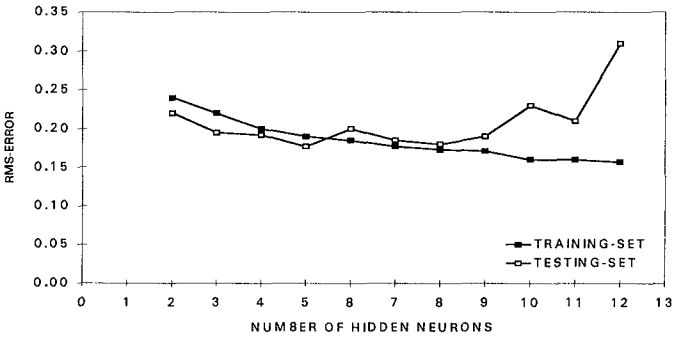

Fig. 3 NN-performance with configurations with various numbers of neurons in hidden layer.

Application

The aim of the NN is to be applied both for small-scale tests and for proto-type situations. Here the basic data-set is based on small-scale tests, however. Therefore a treatment to predict correct proto-type situations needs to be included. If for a certain input-pattern [H_s, T_p, $tan\theta$, h_s, h', R_c, d, φ, B_b] a prediction is required, this input-pattern is scaled by using the Froude-scaling law to an input-pattern with a wave height on which the NN is trained (here all patterns are scaled to a wave height of H_s=*0.1 m*). This also reduces the number input-parameters for the actual NN-configuration from 9 to 8 (here the configuration 8-8-1 is used which means 8 input parameters, 8 hidden neuron and 1 output parameter). The prediction by the NN ($F_{h-99.6\%}$) is then again scaled back to the actual wave height. This procedure where physical knowledge is incorporated in the NN, allows for predictions on different scales. However, this also introduces overpredictions for situations with wave impacts where the Froude-scaling law is not strictly valid.

Using the above described scaling of the data, the data-set can be statistically summarised as shown in Table 1. It must be taken into account that the input components of data-set are not uniformly distributed within the ranges of the parameters given in Table 1. This non-uniformity cannot be recognised from the univariate statistics of Table 1 and a more advanced approach must be followed to obtain an 'accurate' description of the input domain. This, as well as a method to obtain reliability-intervals for NN-predictions of the forces, will be addressed in the following section.

parameter	*mean*	*standard deviation*	*lower extreme*	*upper extreme*
H_s	*0.1*	*0.0*	*0.1*	*0.1*
T_p	*1.672*	*0.526*	*0.8208*	*4.208*
$tan\ \theta$	*0.0133*	*0.0090*	*0.0*	*0.025*
h_s	*0.300*	*0.147*	*0.046*	*0.8276*
h'	*0.206*	*0.110*	*0.0192*	*0.6557*
R_c	*0.221*	*0.136*	*0.0*	*0.8571*
d	*0.152*	*0.111*	*-0.0585*	*0.7000*
φ	*0.989*	*0.0387*	*0.8*	*1.0*
B_b	*0.221*	*0.224*	*0.0*	*1.221*

Table 1 *Statistical parameters of the scaled input-patterns of the data-set used for calibration/training.*

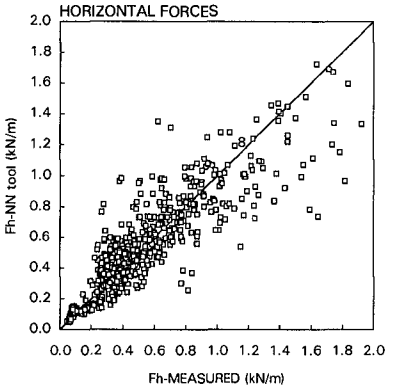

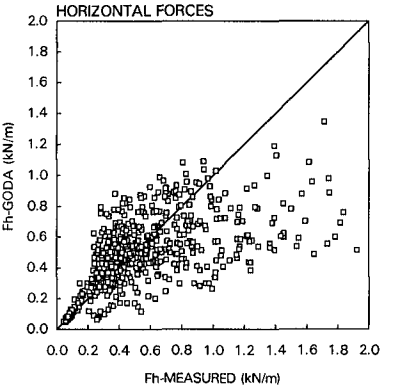

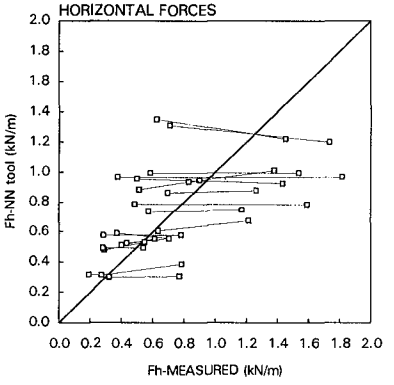

Fig.4 Comparison of measured and predicted (NN) horizontal forces.

Fig.5 Comparison of measured and predicted (Goda) horizontal forces.

Fig.6 Data-points with similar input but large differences in measured properties.

Fig.7 Comparison of measured and predicted (NN) horizontal forces (2 data-sets).

Fig.8 Comparison of measured and predicted (Goda) horizontal forces (2 data-sets).

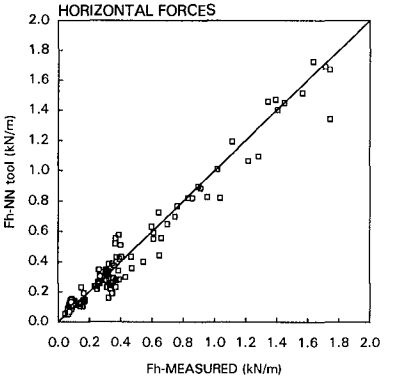

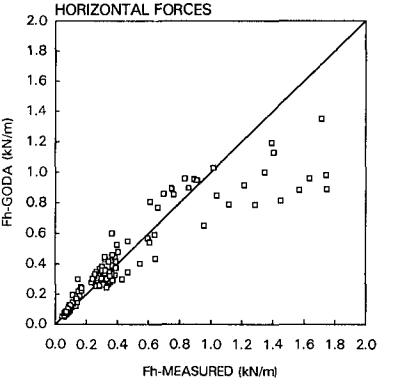

Comparison with Goda-method

Figure 4 shows a comparison between the measured horizontal forces and the predictions by the NN for all 612 data-patterns. Figure 5 shows a comparison between the same measured forces and the well-known Goda-method (Goda, 1985). For this data-set the scatter is large for both prediction methods. For this data-set the NN-output shows a better agreement than the Goda-method. The large scatter is not due to the prediction methods but mainly the result of inconsistencies in the data-set (see also Van Gent and Van den Boogaard, 1998).

In Figure 6 some data-patterns from Figure 4 which have the same, or nearly the same, input-pattern are connected with lines. This figure shows that for nearly identical input-patterns considerable deviations are observed in the measured output. For such input-patterns the NN-output shows nearly the same output, however this is consistent in contrast to the measured data which show rather large inconsistencies. Since the accuracy of the NN-predictions depends largely on the quality of the data-set, the observed inconsistencies in the data-set induce the necessity for information concerning the reliability of the NN-predictions. Although the NN is developed with data of all five data-sources, two data-sources do not show these inconsistencies. For those two data-sets Figure 7 and Figure 8 show the same comparison between measured data and predictions by the NN-tool and the Goda-method. The comparison between measured and by the NN-tool predicted forces shows a good agreement. For a relatively large part of the data-set, the Goda-method underpredicts the forces. The comparisons indicates that the NN-tool can serve as a complementary design-tool. In the following section, a method to quantify the reliability of the predictions is discussed.

3. RELIABILITY INTERVALS

Here, a tool is described to obtain reliability-intervals for the horizontal force predictions of the NN. Since the NN is calibrated with a data-set that does not uniformly cover all possible situations, the NN in fact interpolates between certain measured data-patterns or extrapolates from a region with measured data-patterns. The NN-tool, like other 'fit-procedures' is more suitable for interpolation than for extrapolation. The tool to quantify the reliability is based on information of the distribution of the data-set, hereafter the *training-set*, over the range of the parameter-domain covered by the measured parameter combinations. It is noted that the here developed approach is quite general and is not restricted to the NN-

modelling of forces on vertical breakwaters (more details can be found in Van Gent and Van den Boogaard, 1998).

Three steps are distinguished in this approach: First it is studied how the input-parameters of the training-set are distributed over their domain; then a method is developed to decide whether or not a prediction by the NN can be accepted or not, and finally a method to quantify the reliability of an NN-prediction is described.

In the first step the parameter-domain spanned by the input-patterns of the training-set is determined by means of a probability density function (PDF) $f(\cdot)$. In particular the PDF can be used to determine which parts of the input parameter-domain are densely represented by the training-set (and where the NN will generate the most accurate predictions) and which parts are sparse, or even absent (and where the NN is used for extrapolation rather than interpolation).

Following the approach suggested by Van den Boogaard *et al* (1993) a very suitable and accurate way to find an estimate of the PDF $f(\cdot)$ is to place a basis function $\varphi(\cdot)$ at every input-pattern of the training-set and then take the superposition of all these basis functions. In this way the basis function $\varphi(\cdot)$ spreads each point over its neighbourhood and for this reason $\varphi(\cdot)$ is called a *Point Spread Function* (PSF). Often a (multivariate) Gaussian profile is chosen for the PSF and a copy of this Gaussian functions is centred at each input-pattern. Gaussian functions have (multivariate) ellipsoids as iso-lines and the form of these ellipsoids (i.e. the directions and lengths of the principal axes) is uniquely determined by the covariance matrix within the formula of a Gaussian function. For the PSF $\varphi(\cdot)$ this covariance matrix Σ_p cannot be chosen arbitrarily but must be derived from the N input-patterns within the training-set. This is done in such a way that the superposition of all the Gaussian Point Spread Functions provides the most accurate estimate of the PDF $f(\cdot)$. From the derivation of this 'optimal' covariance function it also follows that the PSF $\varphi(\cdot)$ is centred at 0. All this leads to:

$$f(\vec{x}) = \frac{1}{N}\sum_{n=1}^{N}\varphi\left(\vec{x}-\vec{X}_n\right) \quad \text{with} \quad \varphi(\vec{\xi}) := \frac{1}{\left(\sqrt{2\pi}\right)^{D}\cdot\sqrt{|\Sigma_p|}}\exp\left[-\tfrac{1}{2}\vec{\xi}^{T}\cdot\Sigma_p^{-1}\cdot\vec{\xi}\right] \qquad (2)$$

where D is the number of input-parameters (dimensions), N is the number of input-patterns, Σ_p is a covariance matrix, $\vec{X}_n$ denotes the n-th input-pattern, and $\vec{x}$ is the vector of the input-pattern for which the prediction by the NN is required. This provides the density-function for a certain input-pattern for which the NN is applied. If this density-function exceeds a certain minimal threshold value δ, one can say that

the input-pattern is close to input-patterns of the training-set, and thus the NN can provide a relatively accurate result. The remaining problems are first to define a proper threshold-value δ for which the prediction of the NN can still be accepted and secondly, if a prediction can be made, to quantify the reliability of the predictions.

To illustrate the above described technique Figure 9 shows the principle for data with two parameters (x,y) only. The basic-data (i.e. the training-set) is non-uniformly spread over the parameter-domain. For predictions within the range of the basic-data (Data-point 1), a relatively reliable prediction will be obtained. For a prediction outside the range of the basic data the predictions are based on extrapolation and will be less reliable. When extrapolating in a direction with basic-data, a relatively reliable extrapolation might still be obtained (Data-point 3). For extrapolations in a direction with low spread, the reliability of the extrapolation (and thus the prediction of the NN) will be unreliable (Data-point 2) (ellipsoids in Figure 9 denote iso-lines of the PSF $\varphi(\cdot)$ centred at the measured input-patterns; the PDF $f(\cdot)$ is the superposition of these PSFs and provides the density of the input data-set).

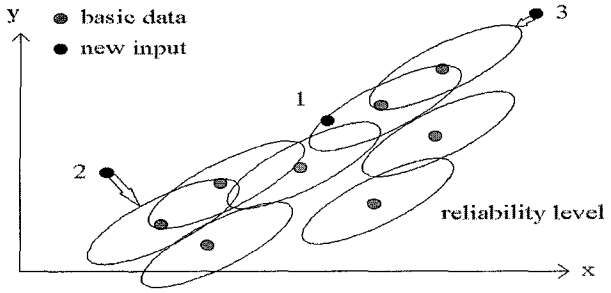

Fig. 9 Principle of applied technique for obtaining reliability intervals.

To obtain a proper threshold-value δ for which a prediction by the NN can be accepted, a 'level of significance α' is introduced. Then the PSF $\varphi(\cdot)$ is used to define an ellipsoid (forming an iso-line of the PSF) that is placed around the input-pattern $\vec{x}$ for which an NN-prediction is required. The 'radius' of this ellipsoid is R_α and it depends on the significance level α. R_α is such that the volume of the ellipsoid is a fraction $\beta := 1-\alpha$ of the total volume of the PSF. It can be shown that for a given α this radius must satisfy the equation $\gamma(\tfrac{1}{2}D, \tfrac{1}{2}R_\alpha^2)=1-\alpha$ where $\gamma(\bullet,\bullet)$ is the incomplete gamma-function. The relation between the threshold-value δ and the radius R_α is then as follows:

$$\delta = \varphi(\xi_\alpha) = \frac{1}{N\left(\sqrt{2\pi}\right)^D \cdot \sqrt{|\Sigma_p|}} \exp\left[-\tfrac{1}{2} R_\alpha^2\right] \tag{3}$$

Then all input-patterns $\vec{X}_n$ of the training-set are selected that are within the ellipsoid of the radius R_α around the new input $\vec{x}$. These patterns of the training-set are used to derive the 95% reliability interval for the NN's prediction of the total horizontal force for the new input $\vec{x}$. The number of the so selected input-patterns depends on the value that is chosen for the significance level α. From a sensitivity analysis a value $\alpha=0.05$ turned out to be very suitable in practice. If no input-patterns of the training-set are within the ellipsoid, the corresponding NN-prediction will be considered as unreliable and no reliability-interval is defined. If a number of K input-patterns (with $K \geq 1$) of the training-set are within the ellipsoid, the reliability-interval around the prediction for the new input-pattern $\vec{x}$ is determined based on the measured outputs T_k ($F_{h\text{-}99.6\%}$) belonging to the input-patterns $\vec{X}_n$ within the ellipsoid. The mean and variance of the outputs of T_k can be estimated by:

$$\langle T_k \rangle = \frac{1}{K} \sum_{k=1}^{K} T_k \quad , \quad \sigma^2_{\langle T \rangle} = \frac{1}{K \cdot (K-1)} \sum_{k=1}^{K} \left(T_k - \langle T \rangle \right)^2 \tag{4}$$

Assuming that the mean of the K outputs satisfy a Gaussian distribution, the 95%-reliability-interval is:

$$\left(\langle T_k \rangle - 1.96 \cdot \sigma_{\langle T \rangle}, \langle T_k \rangle + 1.96 \cdot \sigma_{\langle T \rangle} \right) \tag{5}$$

The mean of the outputs $\langle T_k \rangle$ is in general not equal to the prediction by the NN. The reliability-interval however, is considered as a useful measure for the reliability of the prediction. Therefore, for the final reliability-interval around a prediction by the NN, i.e. $NN(\vec{x})$, the following measure is used:

$$\left(NN(\vec{x}) - 1.96 \cdot \sigma_{\langle T \rangle}, NN(\vec{x}) + 1.96 \cdot \sigma_{\langle T \rangle} \right) \tag{6}$$

Inaccurate test-results that are used for training the NN, such as those with observed inconsistencies leading to the relatively large scatter (Figure 4), affect the prediction of the NN but this also leads to a wider reliability-interval around the prediction. This justifies that also these tests are used for the NN; the user of the NN-tool is given a prediction but in regions with relatively unreliable basic-data, this prediction will involve a wider reliability-interval.

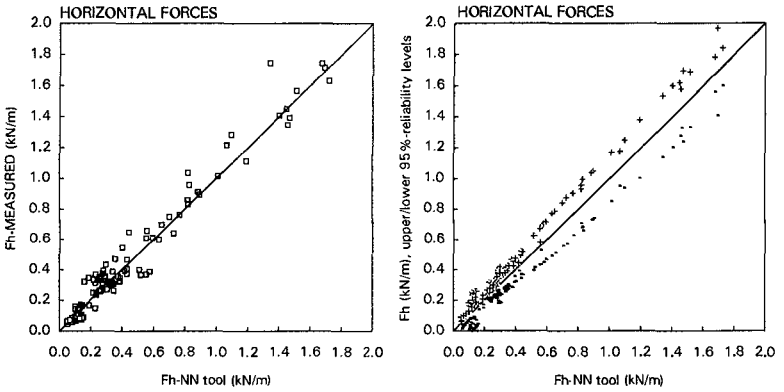

Fig. 10 Predictions by NN-tool (left) and reliability-intervals (right).

As an example of the above described approach the predictions by the NN-tool are shown in the left graph of Figure 10 (as in Figure 7) while the right graph shows the upper limits and the lower limits of the 95%-reliability-intervals for these predictions. This approach which yields insight in the accuracy of the predictions prevents application of the NN for situations where no basic-data is available (significant extrapolation) and also provides a measure for the reliability of the predictions for situations where sufficient tests in the applied data-set are available.

4. CONCLUSIONS

The presented results show that Neural Network modelling can well be used for the prediction of horizontal forces on vertical structures. A tool has been developed to obtain a reliability-interval for the Neural Network predictions. Still, the accuracy of the Neural Network is largely determined by the quality of the data-set. It has been shown that the differences between the Neural Network predictions and the measured values are to a large extend caused by inconsistencies in the data-set. For the data-sets that show none of the observed inconsistencies the comparison between the NN-output and the measured forces is good and the agreement is such that the tool can be used as a complementary design tool. For the present data-set the predictions by the NN-tool show a better comparison with the measured data than the Goda-method.

ACKNOWLEDGEMENTS

This study was co-sponsored by the Commission of the European Communities within the framework of the MAST-PROVERBS project (contract MAS3-CT95-0041). Mr. M.D. Sánchez (IHE/DELFT HYDRAULICS) is acknowledged for his preliminary study which led to valuable insight in applications of NN-modelling for the present subject.

REFERENCES

ACM (1994), *Communications of the ACM: Artificial Intelligence*, Volume 37, Number 3, March 1994.

Allsop, N.W.H., D. Vicinanza and J.E. McKenna (1996), *Forces on vertical breakwaters and related structures*, Research report SR443, HR Wallingford, (revised version).

Beale, R,, T. Jackson (1992), *Neural Computing: An Introduction*, Institute of Physics Publishing Ltd, London.

Goda, Y. (1985), *Random seas and design of maritime structures*, University of Tokyo Press, Tokyo.

Haykin, S. (1994), *Neural Networks. A comprehensive Foundation*, Macmillan College Publishing Company, New York, 1994.

Kortenhaus, A and H. Oumeraci (1997), *Supplementary data for response map*, MAST-PROVERBS proceedings, Overall workshop 18-22 February 1997, Las Palmas, Spain.

Kreyszig, E. (1970), *Introductory Mathematical Statistics. Principles and Methods*, Wiley&Sons, New York.

Madrigal, B.G. and C. Wei (1997), *Analysis of pressure measurements on composite breakwater from 2D tank tests performed during the MCS-Project, MAST-II*, MAST-PROVERBS proceedings, Overall workshop 18-22 February 1997, Las Palmas, Spain.

Mase, H., Sakamoto, M. and Sakai, T. (1995), *Neural network for stability analysis of rubble-mound breakwaters*, J. of Waterway, Port, Coastal and Ocean Engrg, ASCE, nov/dec 1995, pp. 294-299.

Van den Boogaard, H.F.P, M.J.J. Hoogkamer, and A.W. Heemink (1993), *Parameter identification in particle models. Stochastic Hydrology and Hydraulics*, Vol. 7, No. 2, pp. 109-130.

Van der Meer, J.W. and J. Juhl (1992), *Quasi-static wave forces on vertical structures, re-analysis of data at the Danish Hydraulic Institute and Delft Hydraulics*, Project Report 2, prepared for MAST G6-S Coastal Structures.

Van Gent, M.R.A. and H.F.P. van den Boogaard (1998), *Neural network and numerical modelling of forces on vertical structures*, Proc. of 2nd Overall Project Workshop MAST-PROVERBS, Chapter 1.9, February-1998, Naples.

Pore pressures in vertical breakwater foundations

C. Zwanenburg[1]
M.B. de Groot[1]
T.J. Kvalstad[2]
A. van Hoven[1]

Abstract

When calculating the stability of a breakwater foundation information on the pore pressures directly underneath the caisson in the bedding layer and in the sand layer is needed. In this paper easy to handle calculation techniques are presented to derive the pore pressures underneath the caisson. A quasi-stationary calculation technique has been verified for the situation of a caisson breakwater, by a hindcast of laboratory tests. The differences between the quasi-stationary calculations and the laboratory measurements appear to be small and can be explained by non-stationary effects. The pore pressure distribution in real cases may considerably deviate from the traditionally assumed triangular distribution, due to several effects. Non-stationary effects are only relevant if the rubble is relatively fine and wave impact occurs. The pore pressures in the sand layer have been studied by centrifuge tests. Two types of pore pressure development can be distinguished, the instantaneous pore pressures, which follow the wave action at sea and the residual pore pressures, which gradually develop under repetition of loading. The residual pore pressures may lead to liquefaction if silt or fine sand is present in the subsoil.

Introduction

In the past many vertical breakwaters have been built. Several have been collapsed or suffered severe damage, see [Oumeraci, 1994]. When judging the stability of the foundation of a vertical breakwater the strength of the subsoil is important. Until recently only little was known about the strength of the vertical breakwater foundation and the strength development during wave attack. In this paper a study on the influence of the pore pressures on the strength of the rubble mound and the subsoil is presented.

[1] Delft Geotechnics, Stieltjesweg 2 P.O. Box 69 2600 AB DELFT, The Netherlands
[2] Norwegian Geotechnical Institute, P.O. Box 3930 Ullevaal Hageby N-0806 OSLO, Norway

In the following only vertical, caisson breakwaters are considered. The results, however, can also be applied to block walls. The caissons are assumed to be placed on a rubble mound. Underneath the rubble the original subsoil is present. Pore pressures in the subsoil will only be explicitly predicted if the subsoil consists of sandy material.

The water pressures in the rubble and in the subsoil, in the following referred to as pore pressures, are fluctuating by the wave action at sea. The pore pressures fluctuate around an average pressure level, corresponding to mean sea level. The wave-induced deviations in pore pressures are referred to as excess pore pressures. So the actual pore pressures are a summation of the average pore pressures and the excess pore pressures. In this paper only the excess pore pressures will be discussed. The resultant of these pressures along the caisson bottom is referred to as uplift force.

The total stress in the rubble and the subsoil consists of two components the pore pressure and the effective stress. When the total stress remains constant and the pore pressure increases as a result of wave action the normal effective stress decreases and the shear resistance, being the product of normal effective stress and the tangent of the friction angle, decreases proportionally.

Three main failure modes of a caisson foundation can be distinguished:

- Sliding over the foundation
- Bearing capacity failure of the rubble
- Bearing capacity failure of the subsoil

The three failure modes are depicted in figure 1. In reality a number of combinations of the above mentioned failure modes can be observed. In all the failure modes the pore pressures play an important role. They determine the uplift force relevant for the first mode, the reduction of the shear resistance in the mound, relevant for the second mode and the reduction of the shear resistance in the subsoil relevant for the last mode.

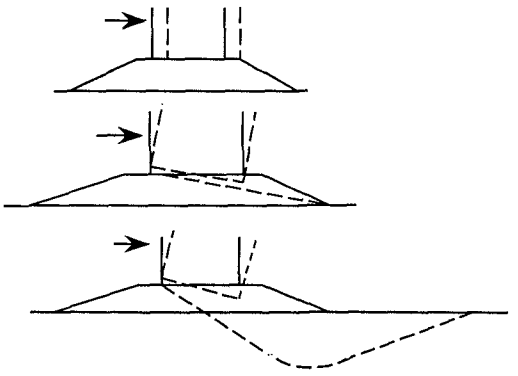

Figure 1 Failure modes

Pore pressures in rubble

Linear pressure distribution

Traditionally, the pore pressures along the caisson bottom are estimated by a triangular shaped distribution. The water pressure at the front edge of the caisson bottom can be calculated by an analytical equation, e.q. the Goda formula. Since at the harbour side of the caisson no wave action is assumed to be present, the excess pore pressures at the harbour side toe of the rubble are negligible. Linear interpolation between the two points leads to the previous mentioned triangular shaped water pressure distribution underneath the caisson bottom.

Validation of a stationary numerical model

The linear pressure distribution is valid for a homogeneous bedding layer with a constant small thickness. When considering other cases a more sophisticated model is needed. In soil mechanics laminar flow models are used to simulate a stationary ground water flow situation. These models are based on Darcy's law in combination of the continuity equation. When applying these equations, only the permeability and the layout of the rubble and subsoil need to prescribed. This limited amount of information makes these models easy to be used.

These models however imply a number of restrictions.

- Stationary flow: the non-stationary effects will be discussed below
- Laminar flow: in coarse rubble the flow will usually be turbulent, however, corrections can be made by an adaptation of the permeability distribution.
- Incompressible water: this not a serious restriction for this situation.

The validity of the application of such a model (MSEEP) for calculating the pore pressure development in the rubble layer underneath a caisson is studied with a hindcast of large-scale laboratory tests.

The laboratory tests have been carried in the large wave flume of Hannover, see [Kortenhaus et el, 1994]. In this wave flume a test caisson has been constructed. The caisson height was about 2,76 m and the caisson width 3.0 m. The caisson was placed on a rubble mound with a thickness underneath the caisson of 0.60 m, a height at the front of 1.02 m and 0.77 m at the backside. Below the mound and separated by a geotextile a sand layer with a thickness of about 2 m was present. This sand layer was placed on the concrete floor of the flume.

The water pressures have been measured at several locations in the model. Directly underneath the caisson 6 rows of pore pressure transducers were located. The first row on top of the rubble, directly below the caisson bottom. The next row in the middle of the rubble layer. The following rows were located in the sand layer.

Four water pressure transducers have been placed in the front slope of the rubble. The readings of these transducers are used to determine the boundary conditions for the numerical model calculations. The pressures measured underneath the caisson are used to validate the calculation results.

A large number of waves have been applied on the test model. Two regular waves have been selected for this hindcast. First a smooth non-breaking wave, $H = 0.7$ m and $T_p = 6.5$ s, has been selected, secondly a breaking wave including wave impacts, $H = 0.9$ m and $T_p = 3.5$ s. Despite differences in wave characteristics, the maximum wave induced pressures in the rubble at the front of the caisson were nearly equal for both waves.

For the validation of the quasi-stationary calculation technique four moments in time have been selected from the continuously measured time-series. The moments are indicated by the water level at the front of the caisson:

- wave crest
- falling water level, passing still water level
- wave trough
- rising water level, passing still water level

The exact moments in time are selected from the reading of the pore pressure transducer, closest to the caisson front.

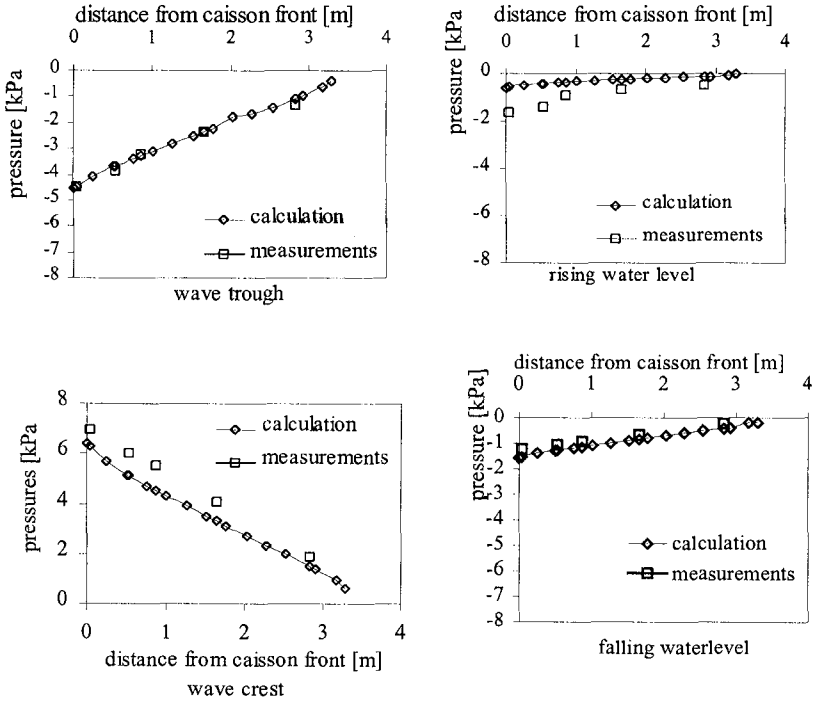

Figure 2 Comparison between the measured and calculated pore pressures

In figure 2 the validation results for the breaking wave are presented for each of the four conditions. From these graphs the following can be notified:

- Differences between the measured and calculated pore pressures in the rubble are found to be negligible for wave trough conditions.
- Differences are found for the situation at which the water level at the front passes still water level. For the rising water level more difference is found then for the falling water level.
- For the wave crest differences up to 20 % are found.

The calculations of the non-breaking wave show similar tendencies. Except that the differences for the wave crest are negligible, like for the wave trough.

Non-stationary effects can explain the differences between the measured and calculated pore pressures for the rising and the falling water level. When the water level passes still water level, the acceleration of the water flow reaches it's peak value and the time-depending effects of inertia and elastic storage become important.

The differences in pore pressures found for the wave crest with its temporarily high peak forces during the wave impact can also be explained by non-stationary effects, as will be discussed below.

In the scale model a homogeneous rubble layer with constant thickness has been applied. Consequently, an almost triangular shaped distribution is found for the wave crest as well as for the wave trough.

Stationary model applied in practice

No triangular pressure distribution is found, however, if the grainsize distribution of the rubble is non-homogeneous. When at one side of the caisson finer material is used more flow resistance and larger pore pressure gradients are found in the region of the finer material. An example is presented in figure 3. That such a pore pressure distribution may be realistic was demonstrated by measurements underneath the Porto Torres breakwater [Franco, 1996].

Not only the deviation in grainsize distribution leads to a deviation of the triangular shaped pore pressure distribution underneath the caisson. Other causes for deviation from the linear distribution may be:

- All kinds of natural activities, like animals or plants, may block the pores in the rubble. This leads to a gradual reduction of the permeability of the rubble.
- The presence of impermeable, tightly placed apron slabs in front of the breakwater.
- Flow concentration around the edges in combination with the effect of turbulence, especially with high mounds.
- When the caisson bottom does not connect perfectly to the top of the rubble some space is present larger then the average pore volume.

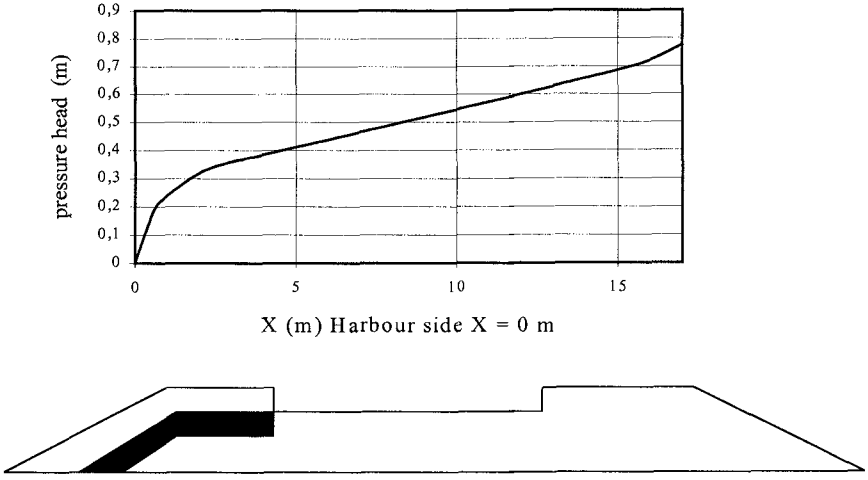

Figure 3 Pressure head distribution along the caisson floor at wave crest with non-homogeneous rubble (black represents fines of quarry run at harbourside)

Non-stationary effects

The quasi-stationary calculations approximate the actual pressures until a certain level of accuracy. For a more accurate approximation of the pressures the non-stationary effects need to be included.

In this study it is assumed that the non-stationary effects can simply be added to the results of the quasi-stationary calculations. Furthermore the non-stationary effects are split into two different components. First the effect of the (pressure) wave passing the caisson foundation is studied. For this situation the caisson is assumed to be completely fixed. This is referred to as the direct component. The second component is the indirect component. For this situation the movement of the caisson is studied independently from the wave action at sea. The water level at the front of the caisson is assumed at still water level. The excess pore pressures underneath the caisson are caused by the rocking and uplift motions of the caisson. Both components are presented in figure 4. In the following it is assumed that these phenomena can be studied individually from each other and that superposition of these components is allowed.

The non-stationary effects will be discussed for the situation of wave crest with wave impact, as this is the most relevant situation for the stability of the foundation.

Direct component

The first approximation of the direct component is a quasi-stationary pore pressure distribution, as can be found from the numerical calculations. According to this approximation all pore pressure-time curves in the bedding layer would have the

same shape as the pressure-time curve at the front of the caisson and the variations would also be simultaneous. All pressures need only be reduced with a factor, which is constant for each location and can be found from quasi-stationary calculations or, even more simplified, with a linear distribution, as proposed by Goda and many others.

Inertia and elastic compressibility, however, influence the direct component during wave impacts with short duration: the pressure wave induced at the seaside needs some time to pass through the bedding layer. The combination of inertia, elastic compressibility in the two phases (soil skeleton and water, which is compressible due to small air bubbles) makes analytical solutions rather complicated. Before trying to find such analytical solution, two approximations of the direct component are presented:

- Approximation for one-phase material: "acoustical wave"
- Approximation without inertia: "elastic storage".

Both approximations will be studied in the next sections in order to find formulations for the relevant corrections to the quasi-stationary approach.

Acoustical wave in direct component

The propagation of the wave impact pressure variation through the rubble mound can be described as an acoustical wave if inertia and compression of the rubble-water mixture are modelled and

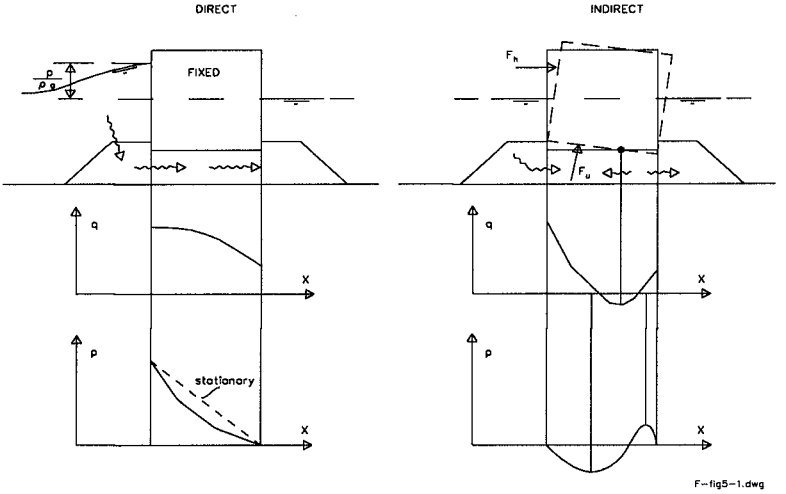

Figure 4 Distinction between direct and indirect component

if the mixture can be considered as a one-phase material. Last condition is met either if both phases move together ("no drainage"), as occurs with fine grained material, or if the water phase moves alone, hardly hindered by the rubble ("complete drainage"), as occurs with very coarse rubble.

Equations for both cases have been developed [MAST III / PROVERBS 1999] in order to quantify the influence on the uplift force during wave crest. This influence depends on the duration of the wave impact, the width of the caisson and the stiffness of the rubble skeleton and pore water. A maximum increase of the uplift force of 30 %, of the static situation, may only occur if the duration and stiffness are very small, where as the width is very large. Otherwise, the influence is negligible.

Elastic storage in direct component

According to the assumption used for the "acoustical wave", no energy loss, thus no damping occurs with the acoustical wave transmitted through the mound. For the completely undrained case it is assumed that the pore pressure variation at the seaside is transferred from the water to the skeleton without relative movement of the water through the skeleton. For the completely drained case, it is assumed that the fluid moves freely through the skeleton, without any stress transfer ("friction") to the skeleton. Both extremes are rather unlikely with the grainsizes usually applied in a mound.

There will be some relative movement of the water with respect to the skeleton together with friction and, consequently, energy loss. This effect in combination with the compression of the water, but without inertia, can be modelled with the one dimensional storage equation for elastic compression of the pore water.

The solutions of this equation yield an equation for the characteristic length for elastic storage, L_{esp}, a function of impact duration, pore water stiffness and permeability of the rubble, [MAST III/ PROVERBS, 1999]. This characteristic length should be compared with the caisson width, B_c. The characteristic length can be determined with equation 1.

$$L_{esp} = \sqrt{\frac{Tc_v}{\pi}} \qquad (1)$$

Where;

$$c_v = \frac{k \times K_w}{n\gamma_w}$$

T	= wave period
c_v	= consolidation coefficient
k	= permeability
K_w	= compressibility of the pore water
n	= porosity
γ_w	= unit weight of water

The progress is now largely determined by the parameter L_{esp}. If $L_{esp} >> B_c$ the elastic storage is not relevant and the pore pressure distribution may be quasi-stationary. With $L_{esp} < B_c$, the uplift force, $F_{u,max}$, will be reduced, as illustrated in figure 4.

Indirect component

The effect of the indirect component can be found by considering the case where the "external" forces, together with caisson inertia, cause uplift and rotation of the caisson, whereas the pressure heads at both outer ends of the caisson remain equal to the mean sea level, defined to be zero. (right hand side of figure 4).

The "external" forces are F_h and F_u. Where F_u is the resultant of the excess pore pressures along the caisson floor. In this case, however, these pore pressures are not considered explicitly. The pore pressures found below, are those which should be added to the quasi-stationary pore pressures to find the final value of F_u.

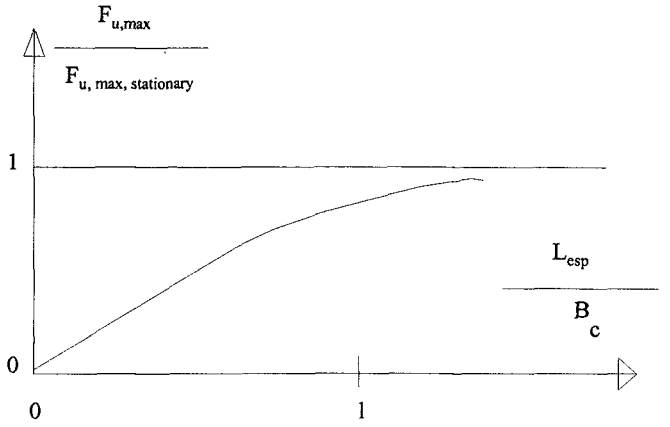

Figure 5 Influence of elastic storage on uplift force

Uplift causes an increase in pore volume; rotation causes an increase and a decrease in pore volume. Uplift and rotation together cause a change in pore volume, which is linearly distributed in x-direction, as illustrated at the right hand part of figure 4. The mass balance requires a flow velocity q, which will vary more or less parabolically in x-direction. This flow causes friction resistance, which is compensated by a pressure head gradient to meet the impulse balance. With the given zero pressure head at both ends of the caisson, a pore pressure decrease where the caisson rises and an increase where it descends.
An analytical equation has been developed to estimate the influence of the indirect effect [MAST III/ PROVERBS, 1999], i.e. the reduction of the uplift force during wave crest. Relevant parameters appear to be the impact duration, the caisson width, the skeleton stiffness and the permeability. The reduction appears to be significant for short impact duration, large caisson width, small skeleton stiffness and low permeability. Usually this is not the case.

By extended Finite Element calculations the effects of direct and indirect component have been studied separately, in the framework of the hindcast of the above mentioned large-scale tests in Hannover. For the calculations in which the caisson

was completely fixed the calculated pore pressures did not differ from the pore pressures calculated for the free moving caisson. From these results the indirect component is considered of minor importance during these tests.

Pore pressures in the sandy subsoil

The influence of the wave action on the pore pressure development is among other things studied by centrifuge tests [van der Poel and de Groot, 1998]. These tests were carried out in the centrifuge of Delft Geotechnics in Delft. For these tests the 13 m (prototype) wide caisson was directly placed on the sand layer. The model was enclosed by a gravel layer, which covered the sandy subsoil. A lay-out of the prototype caisson is presented in figure 6. The figure shows two displacement meters on top of the model. Below the caisson pore pressure transducers were placed. First a row is placed in the caisson floor. Secondly a row of pore pressure transducers was placed at 2,70 m, prototype measures, below the bottom of the caisson.

A typical reading of the transducer indicated in figure 6 by a circle is presented in figure 7. From this figure two types of pore pressure development can be distinguished.

First type is the instantaneous pore pressures. These pore pressures follow the wave action at sea directly. This type of pore pressure development can be distinguished from the reading by the sharp high rise peaks.

The instantaneous pore pressures are caused by the deformation of the skeleton of the sand layer. The movements of the caisson cause compression, decompression and shear deformation of the skeleton of the sandy subsoil. At locations where compression occurs the pore volume decreases, leading to an increase of the pore pressures. At locations of decompression and shear deformation the pore volume increases, leading to a decrease of pore pressures. These fluctuations occur rapidly in time. For this reason the instantaneous pore pressures are hardly influenced by drainage effects. Only in a small top layer some drainage influences the pore pressures.

The second type of pore pressure development, the residual pore pressures, can be distinguished from the reading. These pore pressures induce a gradual increase of average pore pressure. Under a repetition of loading, the wave attack, the grains of the sand layer will show a tendency of re-arrangement. For many situations the subsoil will densify or show the tendency of densification. For these conditions the pore volume will decrease. This pore volume decrease leads to extra pore pressures. When by consolidation the excess pore pressures can not be completely drained off during the passage of one wave some residual pore pressures are left leading to an increase of average pore pressures.

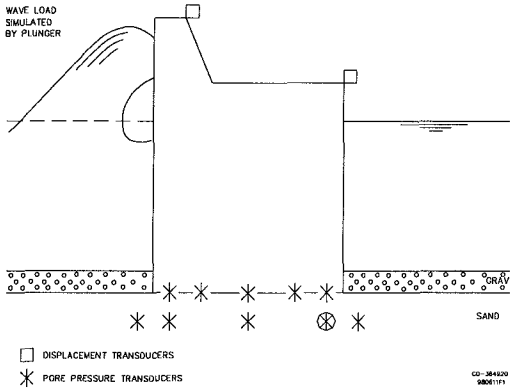

Figure 6 Model lay-out

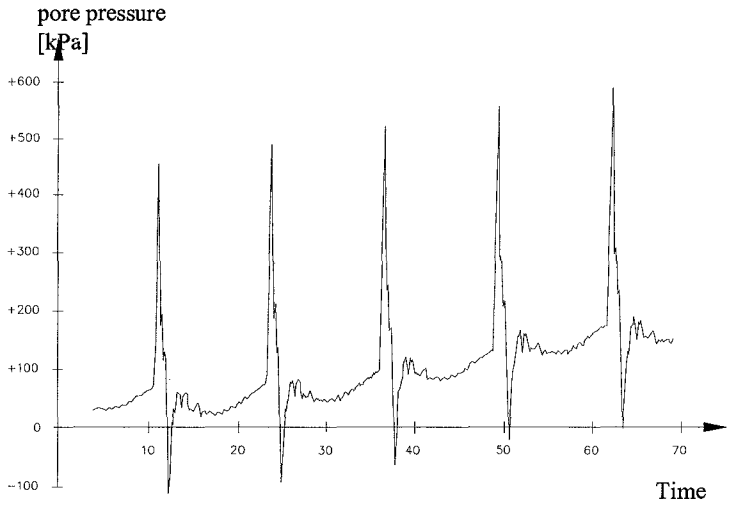

Figure 7 Pore pressure development

When full drainage occurs during a wave train or during a storm, the subsoil will densify and even the residual pore pressures will not remain. This might lead to deformations of the subsoil and to settlements at the surface. Where no drainage occurs the pore pressures will increase. A continuous increase of pore pressures will lead to liquefaction of the sandy subsoil. To judge whether this increase might lead to liquefaction the following rule of thumb is presented. When drainage period $T_{drainage}$

is smaller than 100 times the wave period T no significant pore pressure can be expected. When drainage period is longer the possibility of liquefaction should be considered. The parameter $T_{drainage}$ is a function of caisson width B_c and consolidation coefficient of the subsoil c_v.

$$\frac{T_{drainage}}{T} < 100 \qquad (2)$$

$$\text{Where} \qquad T_{drainage} = \frac{B_c^2}{c_v}$$

Application to a practical example

The above presented theories and equations have been applied to real existing structures. In this paper the results of the calculations for the breakwater Genoa Voltri, Italy, are presented.

The breakwater is located on a rubble layer with a thickness of up to 15 m. Below this rubble several soil layers can be distinguished. On top there is a silt layer with a thickness of 13 m. Below the silt layer there is a sand layer of 8.5 m of thickness. Underneath the sand layer there is a stiff clay layer with a strongly variable thickness. For the calculations a thickness of 9.5 m is applied. These soil layers are based on a rock foundation. The characteristic soil parameters are presented in table 1.

material type	unit weight	angle of internal friction	undrained shear strength	thickness of layer
	γ [kN/m^3]	φ [°]	c_u [kPa]	D [m]
Rubble	20	38	-	15
Silt	18.05	25-30	variable	13
Sand	19.62	29-35	variable	8.5
Clay	18.64	-	450	9.5

Table 1 Applied soil parameters

The following wave characteristics are applied

- significant wave height 8.3 m
- design wave height 13.2 m
- wave period 11.5 s

First the influence of the non-stationary effects are considered. For the acoustical wave approach it is found that the influence of these effects on the uplift force are negligible.

For the elastic storage approach L_{esp}/B_c is found to be equal to 4. From figure 5 it can be seen that for the elastic storage approach the uplift force equals to the stationary found uplift force.

Also the influence of the indirect component of the non-stationary effects appeared to be of minor importance.

From both simulations it can be concluded that the non-stationary effects are not relevant for the Genoa situation. The uplift force during wave crest can be calculated by stationary calculation techniques.

For the pore pressures in the subsoil the possibility of occurrence of liquefaction can be judged according to the equation 2. The results are presented in table 2.

	c_v [m^2/s]	$T_{drainage}$ [s]	$T_{drainage}/T$ [-]
sand	1	506	44
silt	0.01	50 600	4 360

Table 2 Results of liquefaction judgement

For the sand layer the drainage period is short enough to prevent the occurrence of liquefaction. For the silt layer however it is possible for liquefaction to occur. For designing purposes for this situation a study focussed on liquefaction needs to be carried out.

With this information the stability can be calculated. Applying the stationary pore pressure distribution underneath the caisson in the rubble the factor of safety can be calculated for each of the earlier mentioned failure modes. The following safety factor are found:

- Sliding over the foundation $\mu = 1.73$
- Bearing capacity failure in the rubble $\mu = 1.27$
- Bearing capacity failure of the subsoil $\mu = 1.16$

According to the calculations the bearing capacity failure of the subsoil is the dominant failure mode. Sliding of the caisson over the rubble is found to be unlikely.

Conclusions

Pore pressures influence the stability of breakwater foundation. For preliminary design an easy to handle stationary flow model can be used to calculate the pore pressure underneath the caisson. Uneven distribution of the grain sizes in the rubble, a non-flat seabed and apron slabs may cause a significant deviation from the traditionally assumed triangular pressure distribution. To estimate the importance of non-stationary effects analytical equations and graphs can be used. The residual pore pressures in the sandy subsoil might lead to liquefaction if the drainage period is 100 times smaller then the wave period, which may be the case with silt or fine sand in the subsoil.

Acknowledgements

This study is performed in the framework of the MAST III / PROVERBS project, under joint funding of the European Union, The Dutch government (Rijkswaterstaat), Delft Geotechnics and the Norwegian Geotechnical Institute.

References

de Groot, M.B., K.H. Andersen, H.F. Burcharth, L.B. Ibsen, A. Kortenhaus, H.Lundgren, W. Magda, H. Oumeraci, W. Richwien, (1996). Foundation design of caisson breakwaters.

Franco, L. (1996). Analysis on of wave pressure measurements on plain and perforated caisson at Porto Torres Breakweter. MAST III/ PROVERBS, Las Palmas 1997.

van Hoven, A. (1998).Hindcast of pore pressures underneath Porto Torres breakwater van Hoven A., MAST III / Technical University Delft, Faculty of Civil Engineering and Delft Geotechnics CO-364920

Kortenhaus A., Oumeraci H., Kohlhase S., Klammer P. (1994).Wave –induced uplift loading of caisson breakwaters, ICCE '94, Kobe Chapter 94, pp 1297-1131

MAST III/PROVERBS (1999). Final report, Geotechnical Aspects, Volume IIb Leichtweiss institute, Technical University Braunsweig Germany 1999

Oumeraci H., (1994) Review and analysis of vertical breakwater failures and lessons learned. Coastal Engineering, volume 22 January 1994, ISSN 0378-3839.

van der Poel, J.T. and de Groot, M.B. (1998). Cyclic load tests on a caisson breakwater placed on sand. Centrifuge 98.

Economic Optimal Design of Vertical Breakwaters

H.G. Voortman[1], H.K.T. Kuijper[2], J.K. Vrijling[3]

Abstract

In the design of coastal structures, the choice of the safety level for which the structure has to be designed is a major problem. This is also the case for vertical breakwaters. This paper applies the concept of economic optimisation to derive the appropriate safety level and at the same time the optimal geometry. Application to a design case shows that it can be economically optimal not to distribute the acceptable failure probability equally over all failure modes, but rather let one or two failure modes determine the total probability of failure.

Introduction

In Europe the interest in and the importance of vertical breakwaters is growing. A central point is the optimal geometry, e.g a ratio of the width and height of a vertical breakwater in the sense that the total lifetime costs are minimised. For a given safety level it is possible to choose the width and height of the breakwater in such a way that the construction costs are minimised. In practice however one has to determine the optimal level of safety.

In general there are two boundary conditions for the acceptable safety level:

- The individual acceptable risk. The probability accepted by an individual to die in case of collapse of a structure;
- The societal acceptable risk. The probability of occurrence of a certain number of casualties in case of collapse of a structure.

In addition to these limits, it is possible in some cases to derive the optimal probability of failure based on an economic analysis. In the case of a breakwater without amenities the probability of loss of life due to failure is very small, but the economic losses can be severe. Therefore an economical point of view for optimising the structures design is suitable and sufficient.

In this paper the concept of economic optimisation is applied to a fictitious design case of a vertical (caisson) breakwater. The relation between a full probabilistic optimisation procedure and the simpler approach of minimising the construction costs for a given safety level is shown. It is also shown that the system probability of failure of an optimal designed breakwater is largely determined by only

[1] Research assistant
[2] Associate Professor
[3] Professor
Delft University of Technology, Hydraulic and Offshore Engineering Section
Stevinweg 1, NL-2628 CN Delft, The Netherlands
Homepage: http://hydr.ct.tudelft.nl/wbk/

one or two failure modes. Wave transmission imposes a constraint on the caisson height.

Van Dantzig (1956) was the first to apply economic optimisation for the determination of the optimal safety level. He applied the method to derive the optimal height of the dike protecting the central part of the Netherlands. A wide variety of applications is found nowadays, primarily in engineering and economics. However, the only application to vertical breakwaters known to the authors is by Burcharth et al (1995). In the paper by Burcharth a vertical breakwater is optimised using an objective function which assumes the caisson costs proportional to the caisson weight. The only design variable considered in Burcharth's paper is the caisson width.

In this paper, a more realistic caisson cross-section consisting of a concrete floor and cap and a mixed sand/concrete body is used. The objective function consists of a part that describes the construction costs and a part that describes the expected costs of failure. The construction costs are described as a function of the volumes of sand, concrete and rubble stone in the breakwater cross section. The risk part contains a part that describes damage due to serviceability limit states (SLS) and a part that describes damage due to ultimate limit states (ULS). As design variables the caisson height, the caisson width and the height of the rubble foundation are chosen in order to find the optimal breakwater geometry.

Practical experience shows that very often the system probability of failure of a structure is determined by a single failure mode (weak link). This paper will show that it is economically optimal to have such weak links in the design of a vertical breakwater.

Economic Optimisation

An economic optimal design is defined as the design for which the total lifetime costs are minimal. The total lifetime costs consist of the construction costs and the expected value of the damage costs. In case of a vertical breakwater the total lifetime costs are a function of:

- The vector of design variables ($\vec{x}$)
- Initial costs, not depending on the design variables (I_0);
- Construction costs as a function of the design variables ($I(\vec{x})$);
- Costs per day in case of serviceability failure (C_{SLS});
- The probability of serviceability failure per day ($P_{f;SLS}(\vec{x})$)
- Costs per event in case of ultimate limit state failure (C_{ULS});
- The probability of ultimate limit state failure per year ($P_{f;ULS}(\vec{x})$)
- Maintenance costs for the breakwater per year (C_{maint});
- The net interest rate per year (r');
- The yearly rate of economical growth, expressing growth and development of the harbour (g);
- The lifetime of the structure in years (N).

In this paper the maintenance costs have been neglected.

The optimal set of design variables is found by minimising the cost function:

$$I(\vec{x}) = I_0 + I(\vec{x}) + \sum_{n=1}^{N} \left(\frac{365 C_{SLS} P_{f;SLS}(\vec{x}) + C_{ULS} P_{f;ULS}(\vec{x})}{(1+r'-g)^n} + \frac{C_{maint}}{(1+r')^n} \right) \quad (1)$$

Several minimisation procedures have been developed which can be used to minimise function (1) (Press et al, 1990). For the calculation of the failure probabilities also several methods exist (Ditlevsen and Madsen,1996). Some points to consider in the choice of the algorithms are mentioned in the remainder of this paper.

The Design Case

In this paper, a fictitious design case has been considered. A caisson breakwater has to be designed for a water depth of 25 m with respect to mean sea level (MSL). The subsoil consists of sand. An overview of the conceptual design cross section is given in Figure 1. The exact sizing of all elements in this design cross section will be derived by economic optimisation.

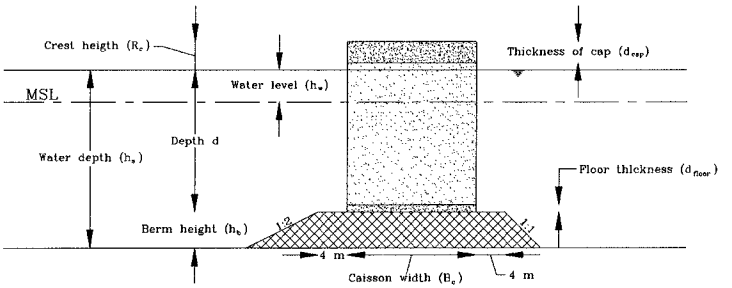

Figure 1: Overview of breakwater cross section

The total length of the breakwater is assumed to be 6000 meters. The height and width of the caisson as well as the berm height are chosen as design variables. The height of the concrete cap and floor are kept constant. The cap and floor consist of concrete only. The zone between cap and floor consists of filling sand and concrete. In the optimisation procedure the number of walls inside the caisson is unknown. A fixed percentage of concrete of 10 % has been used in the weight and cost calculations. The costs of concrete, filling sand and rubble are estimated by practising engineers. An overview is given in Table 1.

Material	Costs [$/m^3]
Concrete	250
Filling sand	5
Rubble	70

Table 1: Overview of material costs

Due to these cost figures and the properties of the breakwater cross section, it is more expensive to increase the width of the caisson then the height of the caisson. Increasing the caisson width results in a larger volume of the concrete cap and floor

which results in a faster increase of the concrete volume in comparison to an increase of the caisson height.

In case of failure of the breakwater, the damage will consist of structural damage to the breakwater itself and economical damage due to the interruption of harbour processes. In this study for the damage in monetary terms, figures have been used which originate from a similar study for a rubble mound breakwater (Delft University of Technology, 1995).

Failure type	Damage description	Damage amount (US $)
SLS	Economic damage per day	750,000
ULS	Structural damage per event	9,000,000 + 20 % of construction costs of breakwater
	Economic damage per event	555,000,000

Table 2: Overview of damage costs

All damage is considered from the viewpoint of the harbour authorities. Economic damage denotes the economic damage due to interruption of harbour operations, loss of port dues, claims and costs of alternative transport. Structural damage consists of a (fixed) part that denotes damage to harbour inventory and a (variable) part denoting the damage to the breakwater itself.

Boundary Conditions and Wave Force Model

The boundary conditions for the breakwater consist of hydraulic boundary conditions (wave height, water levels) as well as of geotechnical boundary conditions (friction angles and densities). An overview of the relevant boundary conditions and the assumed distributions is given below.

Variable	Description	Distribution type	Shift	Scale	Shape	Power
Yearly hydraulic conditions						
H_s	Significant wave height	Gumbel	3 m	0.25 m	-	1
s	Wave steepness	Normal	5 %	1 %	-	1
R	Ratio between significant wave height and maximum wave height	Rayleigh	-	1	2	3000
h_w	Water level with respect to MSL	Weibull	2.2 m	0.8 m	2	1
Daily hydraulic conditions						
H_s	Significant wave height	Gumbel	1.5 m	0.25 m	-	1
h_w		Normal	0 m	1 m	-	1
Subsoil properties						
$\varphi_{subsoil}$	Friction angle of subsoil	Normal	35°	1.8°	-	1
δ	Friction angle between rubble and caisson bottom	Normal	30°	1.5°	-	1
φ_{rubble}	Friction angle of rubble	Normal	40°	2°	-	1
γ_{rubble}	Density of rubble	Deterministic	21 kN/m^3	-	-	-
$\gamma_{subsoil}$	Density of subsoil	Deterministic	21 kN/m^3	-	-	-
Properties of caisson cross section						
γ_{fill}	Density of caisson fill	Normal	18 kN/m^3	1.8 kN/m^3	-	1
γ_{concr}	Density of concrete	Deterministic	24 kN/m^3	-	-	-

Table 3: Overview of boundary conditions

The wave loading on the caisson is calculated by means of the method of Goda (1985) which is extended by Takahashi (1996) to include impact conditions.

Failure Modes

In this study a total of six failure modes have been implemented in the optimisation procedure. These six failure modes are:

- Wave transmission (SLS);
- Sliding of the caisson over the rubble foundation (ULS);
- Exceedance of the maximum allowable eccentricity of the resultant vertical force (ULS). The eccentricity has to be limited to ensure sufficient rotation capacity for the other ULS failure modes to be valid;
- Straight sliding plane through the rubble foundation (ULS);
- Sliding of rubble foundation over the subsoil (ULS);
- Failure of the subsoil (ULS).

Wave transmission effectively describes the functionality of the breakwater. It is included by applying the transmission model of Goda (1969) and providing an acceptable significant wave height in the harbour basin.

The last five failure modes describe different forms of foundation failure. These models are taken from a report written under the European Marine Science and Technology program (de Groot et al, 1996). In the report two sets of "feasibility level models" are given. One set is applicable to caissons placed on low rubble mounds and the other is applicable to caissons placed on high rubble mounds. De Groot provides no clear definition of low and high rubble mounds. Furthermore, in an optimisation process all options are open and therefore the behaviour of all alternatives should be accurately described. Therefore, the set of failure modes in this study consists of the union of the two sets given in de Groot.

Observation of the list of failure modes and the cost function shows that there are two main sources of damage, i.e. damage due to excessive wave transmission and damage due to instability of the caisson. Instability of the caisson is the result of a series system containing all the ULS failure modes mentioned above. In a fault tree, instability of the caisson is described as in Figure 2.

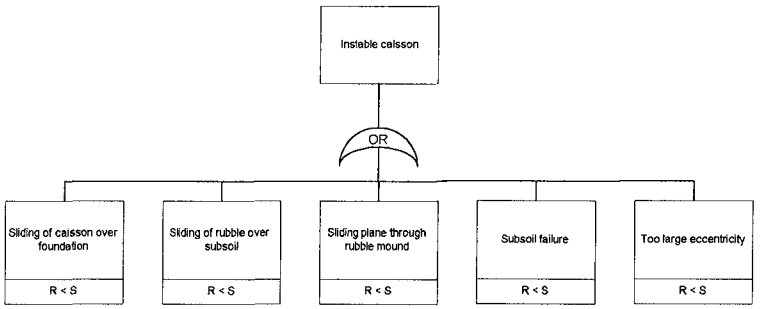

Figure 2: Fault tree for ultimate limit states

Several methods are available to provide reliability estimates for this kind of systems of failure modes. The choice of the algorithm is not an arbitrary one, as will be seen later.

Deterministic Optimisation of the Caisson Design

If all input is treated deterministically, it is possible to derive the required width of the caisson as a function of the crest height of the caisson. Since the construction costs are a function of the height and width of the caisson, the construction costs can be minimised for a given design wave height and water depth, resulting in optimal caisson dimensions. Analysis of this case is useful since it is an integral part of the full probabilistic optimisation, as will be shown later. The disadvantage of this procedure is that the optimal design is still dependent on the choice of the (deterministic) design conditions and is therefore in fact still open.

The deterministic optimisation procedure has been applied to a breakwater design according to Figure 1, using design wave heights of H_s = 3.74 m for SLS and H_d = 9.64 m for ULS. The design variable berm height has been fixed to 6 m. The required caisson width is expressed as a function of the caisson height for each limit state. The construction costs have been calculated for every design alternative, resulting in Figure 3.

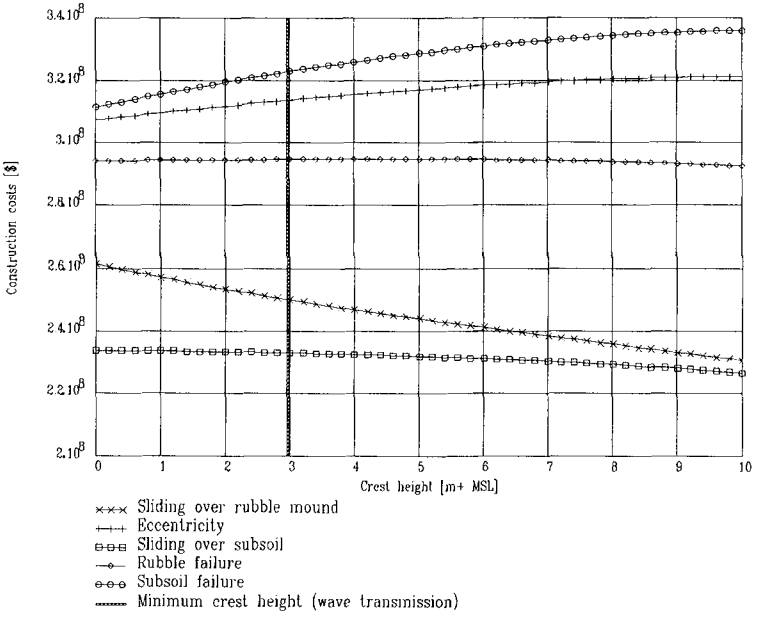

Figure 3: Construction costs as a function of the crest height of the breakwater (berm height 6 m)

Subsoil failure requires the largest caisson width in all cases and thus decides the construction costs. Assuming an acceptable significant wave height behind the breakwater of 0.50 m, wave transmission imposes a constraint on the crest height. This constraint is shown in Figure 3 by the vertical line. This shows that the function of the breakwater (in this case described by wave transmission) is an essential part of the optimisation of the breakwater design.

Probabilistic Optimisation and its Relation to Deterministic Optimisation

In the previous section the optimal breakwater design was determined for chosen design wave heights. However, also the design wave heights (significant wave height for SLS and design wave height for ULS) can be made subject to economic optimisation by specifying them as distribution functions (all other input is still treated deterministically). This approach can be considered an intermediate step between the deterministic optimisation of the previous section and the full probabilistic approach of the next section.

Using the fault tree (figure 2) it is possible to calculate the probability of caisson instability due to any of the given failure modes. Wave transmission is treated separately, resulting in an ultimate significant wave height which indicates when excessive wave transmission occurs. Since in this case the daily and extreme wave heights are the only random variables, substitution of the ultimate wave heights in their respective distributions results in estimates of the failure probabilities. The failure probabilities are used in equation (1) to derive the expected value of the damage costs. Following this procedure for several caisson height and width combinations provides the total lifetime costs as a function of the caisson dimensions. Figure 4 shows a contour plot of the total lifetime costs for a breakwater using a berm height of 6 m.

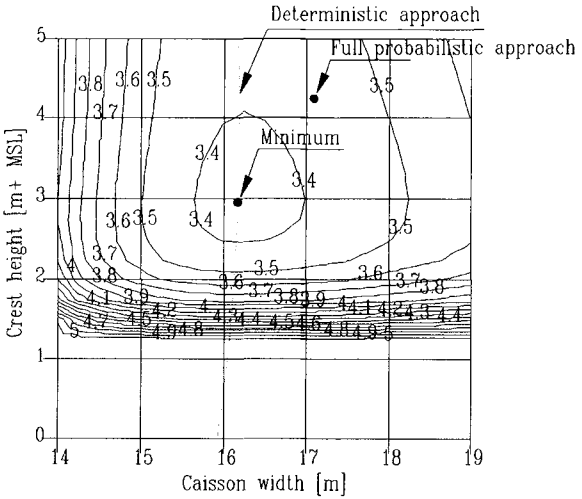

Figure 4: Contour plot of total lifetime costs (random wave height only, costs in 10^8 US $)

In the previous section it was shown that for fixed values of the berm height, water depth and design wave heights, it is possible to derive the required caisson width as a function of the caisson height. The result of this deterministic approach is also shown in Figure 4 as the dotted line. The optimal design found in the probabilistic procedure lies exactly on this curve. This shows that minimisation of the construction costs for a fixed probability of failure is included in the probabilistic optimisation procedure. In figure 4 the point "full probabilistic approach" denotes the result of the full probabilistic optimisation, decribed in the next setion.

In the probabilistic procedure, wave transmission causes a sharp increase of the lifetime costs with decreasing crest height, rather than a fixed constraint. This effect is also visible in Figure 4.

A Procedure for Full Probabilistic Optimisation

In the previous section the probability of failure of the breakwater was considered equal to the probability of exceedance of a certain wave height. In practice however the failure probability depends on several parameters which might show random behaviour. Optimising a breakwater design taking into account several uncertainties requires a numerical optimisation procedure, which consists of the following components:

- An algorithm for the minimisation of functions in several dimensions;
- A numerical description of the cost function;
- A procedure for the calculation of the system probability of ULS failure;
- A procedure for the calculation of the probability of SLS failure.

Figure 5 shows a scheme of the co-operation between the main components.

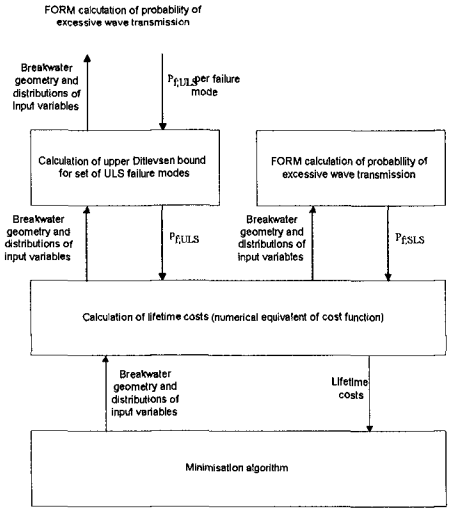

Figure 5: Structure of optimisation process

Minimisation algorithms can with advantage be obtained from several sources (See for instance: Press et al, 1990). The choice of the algorithm should be made with care. In general, algorithms that use derivatives of the function are the most efficient. Application of such an algorithm requires the function to be continuously differentiable. In this case the deterministic optimisation has shown that in most cases the optimal design is found exactly in the intersection point of two failure modes. Therefore, the derivatives can be expected to be discontinuous and the use of them in the minimisation procedure has therefore been avoided. The direction set method developed by Powell and implemented by Press et al (1990) has been used. The minimisation procedure is the central part of the optimisation procedure since it controls all the calls made to the cost function and therefore also all the calls to the probabilistic method.

The numerical description of the objective function is the equivalent of formula (1) expressed in programming language. The cost function needs the failure probabilities as input. To obtain the failure probabilities the procedure makes a call to a probabilistic algorithm and passes all relevant input to this procedure.

Several methods for the calculation of the system probability of failure exist (See for instance: Ditlevsen and Madsen, 1996). For application in an optimisation program the algorithm has to fulfil two requirements:

- The algorithm should provide reliability estimates in a relatively short time;
- The resulting estimates of the failure probabilities have to be stable, meaning that recalculation of the failure probability for the same geometry should yield a result that only differs in the range of numerical inaccuracies.

The first requirement is important because of the large number of reliability calculations that are to be made in the course of the optimisation procedure (typically 100 to 500). A probabilistic procedure that takes long calculation times will slow down the optimisation too much.

The second requirement is necessary because of the co-operation between a minimisation procedure and a probabilistic procedure. Especially Monte Carlo methods provide reliability estimates that slightly vary from calculation to calculation, even for the same dimensions of the breakwater. This variation is inherent to the Monte Carlo method and presents no problem if the reliability estimates are not used in an optimisation procedure. When using Monte Carlo estimates in an optimisation, the slightly varying failure probabilities cause variations of the cost function, which cause convergence problems for the minimisation procedure.

In this paper first order reliability methods have been used to calculate the Ditlevsen bounds of the system probability of failure (Hasofer and Lind, 1974; Ditlevsen, 1979; Hohenbichler, 1983). The upper bound of the failure probability according to Ditlevsen is used in the cost function as the system probability of ULS failure. The probability of serviceability failure is calculated by means of a first order reliability method.

Results of Full Probabilistic Optimisation

The procedure described in the previous section has been used to derive optimal caisson dimensions for several berm heights using all input given in Table 3. The results have been used to determine an overall optimal breakwater cross section, i.e. a breakwater cross section with an optimal berm height, crest height and caisson width. Figure 6 shows the optimal total caisson height and the caisson width for several berm heights. For a berm height of 6 m the optimal width and height are 17.20 m and 23.25 m respectively. This is larger then in the case with only random wave heights due to the added uncertainty in the subsoil properties and the water level (see also figure 4).

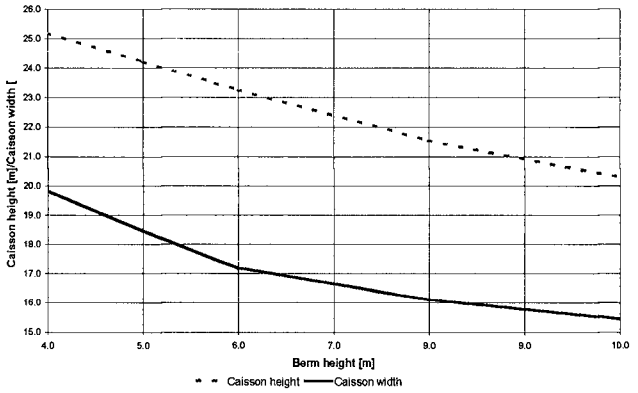

Figure 6: Optimal caisson dimensions as a function of the berm height

Figure 7 shows three alternative breakwater designs with different berm heights and corresponding optimal caisson dimensions.

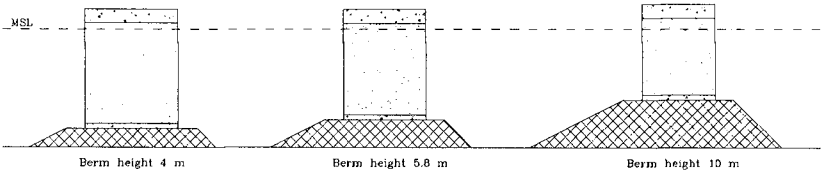

Figure 7: Optimal designs for three berm heights

Both Figure 6 and Figure 7 show that up to a berm height of approximately 6 m there is a strong decrease of the caisson width with increasing berm height. For higher berms this reduction is considerably less.

Figure 8 shows the failure probability per failure mode as well as the overall probability of ULS failure for every calculated alternative.

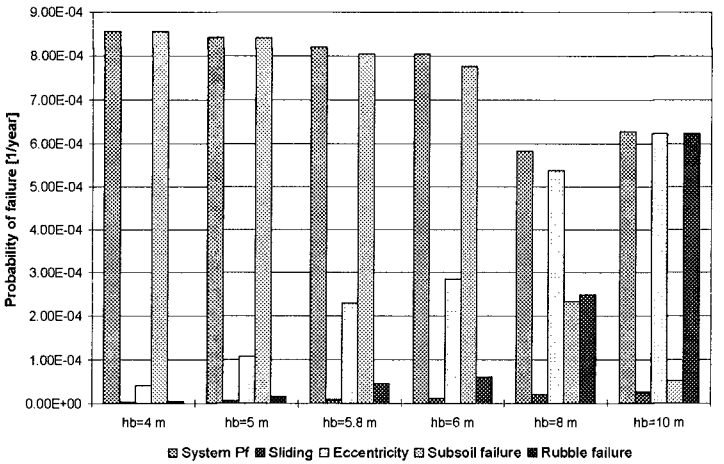

Figure 8: Overview of failure probabilities for alternative designs

Figure 8 shows that in most cases the system probability of failure is determined by one failure mode only (subsoil failure). In these cases the height is governed by wave transmission, in the way shown in Figure 4. Since there is a clearly dominant failure mode, the system probability of failure can also be accurately calculated by taking the fundamental upper bound of the failure probability instead of the Ditlevsen bound.

Figure 9 gives an overview of total lifetime costs as a function of the berm height. It should be noted that every point denotes the costs of an optimal caisson corresponding to that berm height.

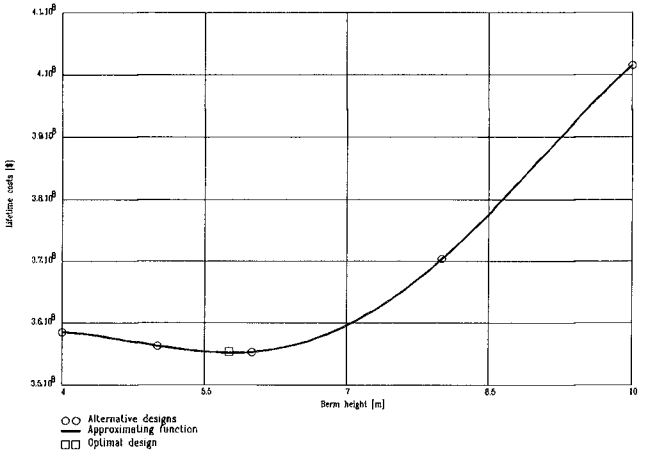

Figure 9: Lifetime costs as a function of the berm height

Apparently, the optimal design is found in the vicinity of the point in Figure 6 where the large width reduction due to higher berms is virtually over. This leads to the conclusion that in this case the only (economical) justification of the rubble foundation is a reduction of the loading on the subsoil.

The calculation results lead to the following conclusions regarding the optimal breakwater geometry for the design case:

1. The optimal design consists of a berm with a height of 5.8 m with respect to the sea bottom and a caisson with a total height of 23.5 m (crest height MSL +4.3 m) and a width of 17.5 m;
2. The optimal geometry is decided by wave transmission (SLS) and subsoil failure (ULS);
3. The system probability of ULS failure of the optimal design virtually equals the probability of subsoil failure. This indicates that subsoil failure is a very clear "weak link" in the design;
4. Due to the presence of a weak link, the system probability of failure can be accurately calculated by taking the fundamental upper bound instead of the Ditlevsen bound.

Conclusions

This paper considers the application of economic optimisation to the design of vertical breakwaters. Regarding the procedure itself the following conclusions can be drawn:

- The concept of economic optimisation provides a rational way of supporting the choice of the optimal safety level;
- Minimisation of the construction costs of a breakwater for a given safety level is an integral part of the full probabilistic optimisation procedure.

Regarding the optimal geometry for the design case, the following conclusions are justified:

- The crest height of the optimally designed caisson breakwater is determined by wave transmission;
- The system probability of ULS failure virtually equals the probability of subsoil failure. Subsoil failure is therefore a very clear "weak link" in the optimal design. The optimisation procedure shows that it is not economical to distribute the acceptable probability of failure equally over all failure modes;
- The only (economical) justification of a rubble berm in this case is reduction of the loading of the subsoil, thus decreasing the probability of failure of the structure.

Regarding the implementation of the procedure in programming language, the following points are important:

- Ready-at-hand minimisation algorithms can with advantage be used;
- Minimisation algorithms which use derivatives of the cost function should be avoided;

- The probabilistic algorithms to be implemented in the optimisation procedures should provide stable estimates of the failure probabilities, in order to avoid convergence problems of the minimisation algorithm. Stability in this case meaning that a repeated calculation for the same geometry should provide a result for the probability of failure that only differs within the range of numerical accuracy.

Acknowledgement

This work was partially funded by the Marine Science and Technology program of the European Union under contract MAS3-CT95-0041.

References

Burcharth, H.F; Dalsgaard Sørensen, J; Christiani, E.
Application of reliability analysis for optimal design of monolithic vertical wall breakwaters
Proceedings of the International Conference on Coastal and Port Engineering in Developing Countries, pg 1321-1336
Rio de Janeiro, 1995

Dantzig, D. van
Economic Decision Problems for Flood Prevention
Econometrica nr. 24, pg. 276-287
New Haven, 1956

Delft University of Technology
Ennore Coal Project, India. Risk Analysis and Probabilistic Modelling
Delft, 1995

Ditlevsen, O.
Narrow Reliability Bounds for Structural Systems
Journal of Structural Mechanics, pg. 453-
1979

Ditlevsen, O; Madsen, H.O.
Structural Reliability Methods
John Wiley and Sons
Chichester, 1996

Goda, Y.
Re-analysis of Laboratory Data on Wave Transmission over Breakwaters
Report of the Port and Harbour Research Institute, Vol. 8 no. 3
1969

Goda, Y.
Random Seas and Design of Maritime Structures
University of Tokyo Press
Tokyo, 1985

Groot, M.B. de; Andersen, K.H; Burcharth, H.F; Ibsen, L.B; Kortenhaus, A; Lundgren, H; Magda, W; Oumeraci, H; Richwien, W.
Foundation Design of Caisson Breakwaters
Prepared for: MAST-II Monolithic Coastal Structures
Oslo, 1996

Hasofer, A.M; Lind, N.C.
An Exact and Invariant First-order Reliability Format
Journal of the Engineering Mechanics Division ASCE, pg. 111-121
1974

Hohenbichler, M; Rackwitz, R.
First-order Concepts in System Reliability
Structural Safety, pg. 177-188
Amsterdam, 1983

Press, W.H; Flannery, B.P; Teukolsky, S.A; Vetterling, W.T.
Numerical Recipes in Pascal, The Art of Scientific Computing
Cambridge University Press
Cambridge, 1990

Takahashi, S.
Design of Vertical Breakwaters
Reference Document No. 34
Port and Harbour Research Institute, Ministry of Transport
Yokosuka, 1996

Design of Vertical Wall Caisson Breakwaters Using Partial Safety Factors

Hans F. Burcharth* and John Dalsgaard Sørensen**

1. Abstract

The paper presents a new system for implementation of target reliability in caisson breakwater designs by means of partial safety factors. The development of the system is explained, and tables of partial safety factors are presented for important overall stability failure modes related to caisson structures placed on bedding layers and high rubble mound foundations with underlaying sand and clay subsoils.

2. Introduction

Given the stochastic nature of wave loads it is important to deal with the involved uncertainties in a rational way when designing breakwaters. Application of the partial safety factor concept is generally accepted as a rational solution to implementation of safety in designs, and is adopted in many national codes as well as in the EUROCODE. The partial safety factors are in existing codes calibrated against experience with the performance of numerous civil engineering structures in which way it is assured that a conventional structure, such as a house, will obtain the usual safety when designed using the prescribed safety factors. However, the actual safety in terms of probability of a certain damage within a certain span of years is unknown. For breakwaters this seems not to be a suitable concept because extensive experience with existing structures is not available. Moreover, it is deciable to know the actual safety of a design also because rational comparisons of alternative designs have to be performed on the basis of equal safety levels. Reliability analysis, f.ex. using a level 2 First Order Reliability Method (FORM), can of course be done for any structure by means of computer programs. However, it is regarded a help to the designers to make a partial safety factor system available which in an easy way makes it possible to design a breakwater to any target reliability level.

Such a system was introduced and developed by the PIANC PTC II Working Group 12 on Rubble Mound Breakwaters (Burcharth 1991 and 1993) and has now been further developed to cover caisson breakwaters by the PIANC PTC II Working Group 28 on Vertical Wall Breakwaters.

The partial safety factor system is developed on the basis of the validity of the Goda (1985) wave load formula. This formula is not valid for design cases where frequent wave breaking directly on the caisson wall takes place. This causes very large short-duration impulsive loads for which design tools are hardly developed. Steep seabed slopes or semi-high rubble slopes in front of the structure can trigger such unfavorable wave conditions. Goda (1985 pp 132-138) provides advice as how to avoid such excessive impact loadings.

---

*Prof. Dr.Techn. Hydraulics and Coastal Engineering Laboratory, Inst. of Civil Eng., Aalborg University
**Associate prof. Ph.D. Inst. of Building Technology and Structural Engineering, Aalborg University

The overall procedure in development of the partial safety factor system comprises the following steps:

- Identification of failure modes
- Formulation of limit state equations for the failure modes
- Modelling of uncertainties related to loads (waves), strengths (soils, concrete) and limit state equations
- Selection of format for the partial safety factor system
- Calibration of the partial safety factors
- Verification

3. Failure modes

All possible failure modes must be considered in the design. The present paper deals with the overall stability failure modes illustrated in Fig.1. A more complete discussion of failure modes is given in Burcharth (1998).

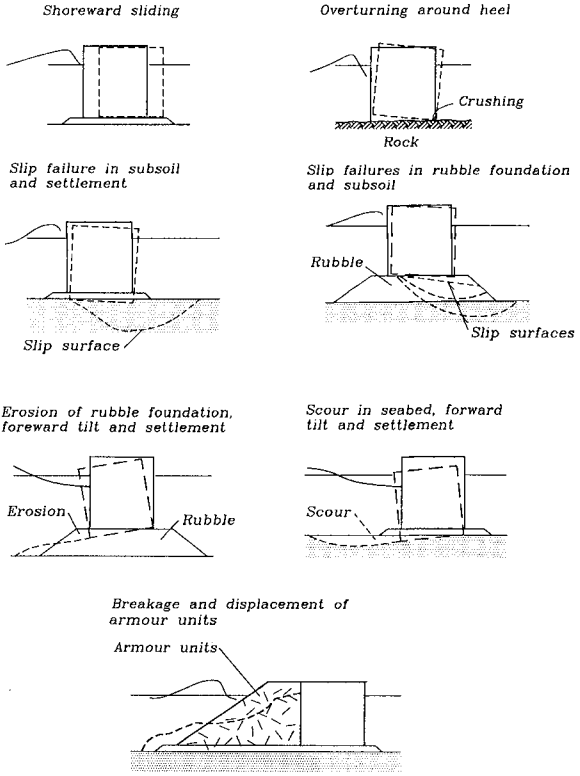

Fig.1. Important overall stability failure modes.

4. Wave modelling

For calibration of partial safety factors the maximum significant wave height in T years is denoted H_S^T and is modelled by the extreme Weibull distribution function:

$$F_{H_S^T}(h_S) = \left[1 - exp\left(-\left(\frac{h_S - H_S'}{\beta}\right)^{\alpha}\right)\right]^{\lambda T} \tag{1}$$

Wave data from 4 quite different geographical locations are selected, see table 1 where h_s is the water depth, N is number of samples and λ is the number of observations per year.

	N	λ	α	β	H_S'	h_s
Bilbao	50	4.17	1.39	1.06	4.9	29
Sines	15	1.25	1.78	2.53	7.1	35
Tripoli	15	0.75	1.83	3.24	2.9	27
Follonica	46	5.94	1.14	0.58	2.69	10

Table 1. Wave data from different locations fitted to a Weibull distribution. β, H_S' and h_s are in meters.

The wave data from Bilbao, Sines and Tripoli correspond to deep water waves while the wave data from Follonica correspond to shallow water waves. In order to model the statistical uncertainty α and β are modelled as Normal distributed variables.

The model uncertainty related to the quality of the measured wave data is modelled by a multiplicative stochastic variable Z_{H_S} which is assumed to be normal distributed with expected value 1 and standard deviation $\sigma'_{Z_{H_S}}$. Good and poor wave data could be represented by $\sigma'_{Z_{H_S}} = 0.05$ and 0.2, corresponding to accelerometer bouy and fetch diagram estimates, respectively.

5. Soil strength modelling

The undrained shear strength of clay is modelled by a log-Gaussian distributed stochastic field $\{c_u(x,z)\}$ where z and x are vertical and horisontal coordinates, respectively. The expected value function $E[c_u(x,z)]$ and the covariance function $Cov[c_u(x_1,z_1), c_u(x_2,z_2)]$ is written

$$E[c_u(x,z)] = E[c_u(z)] \tag{2}$$

$$Cov[c_u(x_1,z_1), c_u(x_2,z_2)] = Cov[c_u(x_1 - x_2, z_1 - z_2)] \tag{3}$$

where (x_1,z_1) and (x_2,z_2) are two points in the soil. $E[c_u(x,z)]$ gives the expected value in depth z of the undrained shear strength of clay. $Cov[c_u(x_1,z_1), c_u(x_2,z_2)]$ gives the covariance between c_u at position (x_1,z_1) and c_u at position (x_2,z_2). $Var[c_u(x_1,z_1)] = Cov[c_u(x_1,z_1), c_u(x_1,z_1)]$ is the variance of c_u at position (x_1,z_1).

It is seen that the expected value depends on the depth and the covariance depends on the vertical and horisontal distances. Generally the correlation lengths in horisontal and vertical direction will be different due to the soil stratification.

The mean value function and covariance function are assumed to be modelled by

$$E[c_u(x,z)] = c_{u0} + c_{u1}z$$
$$Cov[c_u(x_1,z_1), c_u(x_2,z_2)] = \sigma_{c_u}^2 \exp\Big(-|\alpha(z_1 - z_2)|\Big) \exp\Big(-\big(\beta(x_1 - x_2)\big)^2\Big)$$

where c_{u0} and c_{u1} model the expected value, σ_{c_u} is the standard deviation and α and β model the correlation.

Since the breakwater foundation is made of friction material and it is assumed that foundation failure modes can develope both in the rubble mound and in sand subsoil, statistical models for the effective friction angle and the angle of dilation are needed for the rubble material and the sand subsoil. These angles are modelled by Lognormal stochastic variables.

6. Estimation of partial safety factors for one failure mode

In code calibration based on first order reliability methods (FORM) it is assumed that the limit state function can be written

$$g(\mathbf{x}, \mathbf{z}) = 0 \tag{4}$$

where $\mathbf{x} = (x_1, \ldots, x_n)$ is a realization of $\mathbf{X} = (X_1, \ldots, X_n)$. External loads (e.g. wave), strength parameters and model uncertainty variables are examples of uncertain quantities. $\mathbf{z} = (z_1, \ldots, z_N)$ are N design variables which are used to design the actual structure. Realizations $\mathbf{x}$ of $\mathbf{X}$ where $g(\mathbf{x}, \mathbf{z}) \leq 0$ corresponds to failure states, while $g(\mathbf{x}, \mathbf{z}) > 0$ corresponds to safe states.

If the number of design variables is $N = 1$ then the design (modelled by z) can be determined from the **design equation**

$$G(\mathbf{x}^c, z, \boldsymbol{\gamma}) \geq 0 \tag{5}$$

$\mathbf{x}^c = (x_1^c, \ldots, x_n^c)$ are characteristic values corresponding to the stochastic variables $\mathbf{X}$. $\boldsymbol{\gamma} = (\gamma_1, \ldots, \gamma_m)$ are m partial safety factors. The partial safety factors $\boldsymbol{\gamma}$ are usually defined such that $\gamma_i \geq 1, i = 1, ..., m$. In the most simple case $m = n$.

The design equation is closely connected to the limit state function (4). In most cases the only difference is that the variables $\mathbf{x}$ are exchanged by design values $\mathbf{x}^d$ obtained from the characteristic values $\mathbf{x}^c$ and the partial safety factors $\boldsymbol{\gamma}$.

The characteristic values are for variable load variables usually the 98 % fractile of the distribution function of the stochastic variables. For the significant wave height the characteristic value $\hat{H}_S^{T_L}$ is chosen as the central estimate of the significant wave height which in average is exceeded once every T_L years. The design values for load variables are then obtained from

$$x_i^d = x_i^c \gamma_i \tag{6}$$

The characteristic values are for strength variables usually the 5 % or 50 % fractiles of the distribution function of the stochastic variables. Here the 50 % fractile is

used in order to obtain partial safety factors larger than or equal to 1. The design values are then obtained from

$$x_i^d = \frac{x_i^c}{\gamma_i} \tag{7}$$

The limit state / design equations are formulated either as a force balance or, in case of foundation failure modes, as work equations using the upper bound theory of plasticity related to kinematically admissible rupture failures. Figure 2 illustrates two typical cases.

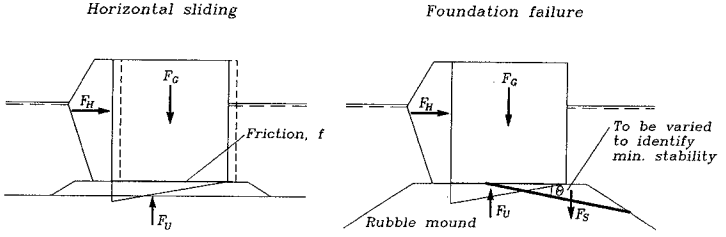

Figure 2. Illustration of failure modes for formulation of limit state design equations.

For sliding failure the limit state function can be written

$$g = (F_G - Z_{F_V} F_U(Z_{H_S} H_D))f - Z_{F_H} F_H(Z_{H_S} H_D) \tag{8}$$

where

F_G	reduced weight of caisson under water
F_U	wave induced uplift force
F_H	horisontal wave force
H_D	design wave height
Z_{H_S}	model uncertainty related to the significant wave height H_S
ρ_c	density of the caisson
Z_{F_H}	model uncertainty on horisontal wave load
Z_{F_V}	model uncertainty on vertical wave load
f	friction coefficient

The design equation corresponding to (8) is written

$$G = \frac{1}{\gamma_Z}(F_G^c - 0.77F_U^c)f^c - 0.90F_H^c \tag{9}$$

where

f^c mean of base friction coefficient

γ_Z partial safety factor on f^c

F_G^c mean value of reduced weight of caisson under water

F_U^c and F_H^c wave induced uplift force and horisontal wave force calculated by Goda formulae using $\gamma_H \hat{H}_D^{T_L}$ as wave height, where γ_H is the partial safety factor and $\hat{H}_D^{T_L}$ is the expected maximum wave height in a storm with T_L-years return period (often taken as $1.8\hat{H}_S^{T_L}$). The factors $Z_{F_V}^c$=0.77 and $Z_{F_H}^c$=0.90 compensates for the bias (safety) implemented in the Goda formulae.

For foundation failure the limit state function can be written

$$g = (F_S + F_G - Z_{F_V} F_U(Z_{H_S} H_D))\omega_V - Z_{F_H} F_H(Z_{H_S} H_D)\omega_H \tag{10}$$

where

F_S boyancy reduced gravitational force on the sliding soil element

ω_V displacement vector, $\omega_V = sin(\varphi_d - \theta)/cos\varphi_d$

ω_H displacement vector. $\omega_H = cos(\varphi_d - \theta)/cos\varphi_d$

The reduced effective angle of friction is calculated from

$$\tan\varphi_d = \frac{\sin\varphi_r' \cos\psi_r}{1 - \sin\varphi_r' \sin\psi_r}$$

where φ_r' is the effective angle of friction and ψ_r is the dilation.

The design equation is written

$$G = (F_S^c + F_G^c - 0.77F_U^c)\omega_V^c - 0.90F_H^c\omega_H^c \tag{11}$$

where F_S^c is the mean value of F_S. ω_V^c and ω_V^c are obtained using the the design value of $\tan\varphi_d^c$ determined from

$$\gamma_Z \tan\varphi_d^c = \frac{\sin\varphi_r^c \cos\psi_r^c}{1 - \sin\varphi_r^c \sin\psi_r^c} \tag{12}$$

where γ_Z is the partial safety factor on $\tan\varphi_d^c$.

The application area for the code is described by a number, L of different typical structures. The partial safety factors γ are calibrated such that the reliability indices corresponding to the L structures are as close as possible to the target reliability index $\beta_t = -\Phi^{-1}(P_f^t)$, where P_f^t is the target probability of failure. This is formulated by the following optimization problem

$$\min_{\gamma} \quad W(\gamma) = \sum_{j=1}^{L} w_j(\beta_j(\gamma) - \beta_t)^2 \tag{13}$$

where $w_j, j = 1, \ldots, L$ are weighting factors ($\sum_{j=1}^{L} w_j = 1$) indicating the relative frequency of appearance of the different design situations. $\beta_j(\gamma)$ is the reliability index for structure no. j

7. Format for partial safety factors

Partial safety factors are calibrated with the following code entries:

- the design lifetime T_L (= 20, 50 or 100 years)
- the acceptable probability of failure P_f (= 0.01, 0.05, 0.10, 0.20 or 0,40) corresponding to the target reliability indices β_T (= 2.33, 1.65, 1.28, 0.84 or 0.25)
- the coefficient of variation $\sigma'_{Z_{H_S}}$ = (0.05 and 0.20).
- Deep or shallow water conditions.
- Hydraulic model test or not.

The partial safety factors are:

- a load partial safety factor $\gamma_P = 1$ to be multiplied to the permanent load.
- a load partial safety factor γ_H to be multiplied to $\hat{H}_S^{T_L}$ (the central estimate of the significant wave height which in average is exceeded once every T_L years). The design wave height is to be taken as a multiplum of $\hat{H}_S^{T_L}$.
- a safety factor γ_Z to be used with friction materials in rubble mound and/or subsoil (tangent to the mean value of the friction angle is divided by γ_Z).
- a safety factor γ_C to be used with the undrained shear strength of clay materials in the subsoil (the mean value of the undrained shear strength is divided by γ_C).

8. Limit state functions and design equations

For calibration of the partial safety factors the parameters for the stochastic variables shown in table 2 are used. The correlation coefficient between Z_{F_H} and Z_{M_H} and between Z_{F_V} and Z_{M_V} are estimated roughly to 0.9. In table 2 D denotes a deterministic variable, N(μ, σ) denotes a normal distribution with expected value μ and standard deviation σ and LN(μ, σ) denotes a lognormal distribution.

The tidal elevation ζ is modelled as a stochastic variable with distribution function $F_\zeta(\zeta) = \frac{1}{\pi} \arccos\left(-\frac{\zeta}{\zeta_0}\right)$ where ζ_0 is the maximum tidal height. $\zeta_0 = 0.75$ m is used.

	distribution	reference
ρ_c	N(2.1, 0.1075)	Burcharth (1992)
Z_{F_H}	N(0.90, 0.25)	Bruining (1994)
Z_{F_V}	N(0.77, 0.25)	Bruining (1994)
Z_{M_H}	N(0.81, 0.40)	Bruining (1994)
Z_{M_V}	N(0.72, 0.37)	Bruining (1994)
ψ_r	LN(0.43, 0.043)	
φ'_r	LN(0.61, 0.061)	
ψ_s	LN(0.35, 0.035)	
φ'_s	LN(0.52, 0.052)	
U_{c_u}	N(0, 1)	
c_{u0}	150 kPa	
c_{u1}	0	
σ_{c_u}	D(37.5 kPa)	
α	D(0.33)	
β	D(0.033)	
Z	N(1, 0.1)	
f	N(0.636, 0.0954)	Takayama (1992)
ζ	see eq. (14)	Takayama (1992)
H_S	ex Weibull	
Z_{H_S}	$N(1, \sigma'_{Z_{H_S}})$	

Table 2. Statistical parameters for calibration of partial safety factors for foundation failure with sand subsoil.

If model tests have been performed to estimate the wave forces the model uncertainties shown in table 3 can be used.

	distribution	reference
Z_{F_H}	N(0.90, 0.05)	Van der Meer et al. (1994)
Z_{F_V}	N(0.77, 0.05)	Van der Meer et al. (1994)
Z_{M_H}	N(0.81, 0.10)	Van der Meer et al. (1994)
Z_{M_V}	N(0.72, 0.10)	Van der Meer et al. (1994)

Table 3. Statistical parameters for model uncertainties when wave forces are determined on the basis of model tests.

8.1 Horizontal sliding

Equations are given in section 6.

8.2 Scour failure for circular roundheads on sand

The design equation is written, see Sumer et al. (1996) (no rubble foundation):

$$G = \frac{1}{\gamma_Z}\frac{S^c}{B^c} - 0.5\left(1 - \exp\left(-0.175\left(KC\left(\gamma_H \hat{H}_S^{T_L}\right) - 1\right)\right)\right)$$

where s_p is the wave steepness and

$$KC = \frac{U_m T_p}{B_r} \qquad U_m = \frac{\pi Z_{H_S} H_S}{T_p}\frac{1}{\sinh(2\pi h'_s/L_p)}$$

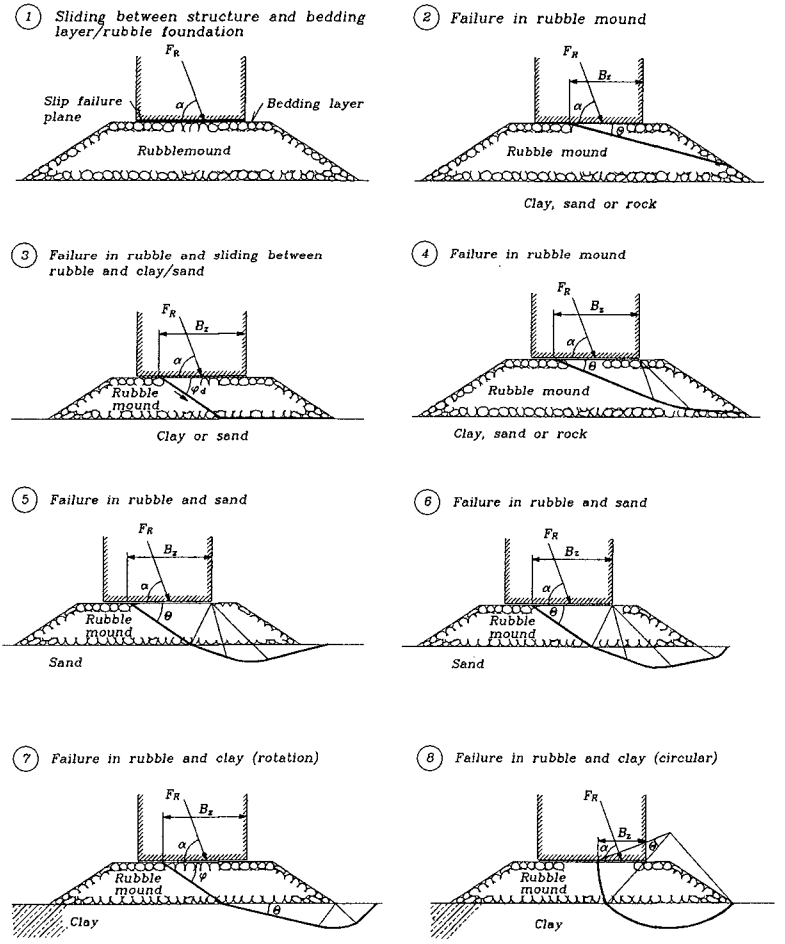

Figure 3. Foundation failure modes.

$$T_p' = \sqrt{\frac{Z_{H_S} H_S}{s_p} \frac{2\pi}{g}}$$

and the wave length L_p is determined from

$$L_p = g\frac{T_p^2}{2\pi}\tanh(2\pi h_s'/L_p)$$

8.3 Hydraulic instability of foundation rubble mound armour layer

The design equation is written, see Madrigal et al. (1995) :

$$G = \frac{1}{\gamma_Z}\Delta^c D_n^c (5.8\frac{h'}{h_s} - 0.60)N_{od}^{0.19} - \gamma_H \hat{H}_S^{T_L}$$

8.4 Foundation failure modes

Figure 3 shows the investigated foundation failure modes. The complete sets of design equations can be found in Burcharth (1998) and J.D. Sørensen et al. (1998).

9. Partial Safety Factors

Below is shown the results of the probabilistic calibration of partial safety factors. In deterministic design of the breakwater the following bias values for the forces and moments are to be used:

	value
$\hat{Z}_{F_H}$	0.90
$\hat{Z}_{F_V}$	0.77
$\hat{Z}_{M_H}$	0.81
$\hat{Z}_{M_V}$	0.72

Table 4. Values of model uncertainties to be used in deterministic design.

Foundation failure - sand subsoil:

	$\sigma'_{Z_{H_S}} = 0.05$		$\sigma'_{Z_{H_S}} = 0.2$	
$P_f(\beta_t)$	γ_H	γ_Z	γ_H	γ_Z
0.01	1.4	1.4	1.4	1.4
0.05	1.3	1.3	1.3	1.4
0.10	1.2	1.3	1.2	1.3
0.20	1.1	1.2	1.1	1.2
0.40	1.1	1.1	1.1	1.1

Table 5. Partial safety factors for *foundation failure - sand subsoil - deep water - no model tests performed.*

	$\sigma'_{Z_{H_S}} = 0.05$		$\sigma'_{Z_{H_S}} = 0.2$	
P_f	γ_H	γ_Z	γ_H	γ_Z
0.01	1.3	1.3	1.4	1.3
0.05	1.3	1.2	1.4	1.2
0.10	1.2	1.2	1.3	1.2
0.20	1.1	1.2	1.1	1.2
0.40	1.1	1.1	1.1	1.1

Table 6. Partial safety factors for *foundation failure - sand subsoil - deep water - model tests performed.*

	$\sigma'_{Z_{H_S}} = 0.05$		$\sigma'_{Z_{H_S}} = 0.2$	
P_f	γ_H	γ_Z	γ_H	γ_Z
0.01	1.5	1.4	1.3	1.5
0.05	1.4	1.3	1.3	1.4
0.10	1.3	1.2	1.2	1.3
0.20	1.2	1.1	1.1	1.3
0.40	1.1	1.0	1.1	1.1

Table 7. Partial safety factors for *foundation failure - sand subsoil - shallow water - no model tests performed.*

	$\sigma'_{Z_{H_S}} = 0.05$		$\sigma'_{Z_{H_S}} = 0.2$	
P_f	γ_H	γ_Z	γ_H	γ_Z
0.01	1.3	1.3	1.4	1.3
0.05	1.3	1.3	1.4	1.3
0.10	1.2	1.2	1.3	1.2
0.20	1.1	1.1	1.1	1.1
0.40	1.1	1.1	1.1	1.1

Table 8. Partial safety factors for *foundation failure - sand subsoil - shallow water - model tests performed.*

Foundation failure - clay subsoil:

	$\sigma'_{Z_{H_S}} = 0.05$			$\sigma'_{Z_{H_S}} = 0.2$		
P_f	γ_H	γ_Z	γ_C	γ_H	γ_Z	γ_C
0.01	1.3	1.4	1.4	1.4	1.4	1.4
0.05	1.2	1.3	1.3	1.3	1.3	1.3
0.10	1.1	1.2	1.3	1.2	1.2	1.3
0.20	1.0	1.1	1.2	1.0	1.1	1.2
0.40	1.0	1.1	1.1	1.0	1.0	1.1

Table 9. Partial safety factors for *foundation failure - clay subsoil - deep water - no model tests performed.*

	$\sigma'_{Z_{H_S}} = 0.05$			$\sigma'_{Z_{H_S}} = 0.2$		
P_f	γ_H	γ_Z	γ_C	γ_H	γ_Z	γ_C
0.01	1.2	1.4	1.4	1.3	1.4	1.4
0.05	1.1	1.3	1.3	1.2	1.3	1.3
0.10	1.0	1.2	1.2	1.1	1.2	1.3
0.20	1.0	1.1	1.1	1.0	1.1	1.2
0.40	1.0	1.0	1.1	1.0	1.0	1.1

Table 10. Partial safety factors for *foundation failure - clay subsoil - deep water - model tests performed.*

	$\sigma'_{Z_{H_S}} = 0.05$			$\sigma'_{Z_{H_S}} = 0.2$		
P_f	γ_H	γ_Z	γ_C	γ_H	γ_Z	γ_C
0.01	1.2	1.7	1.5	1.3	1.7	1.5
0.05	1.1	1.5	1.4	1.2	1.5	1.4
0.10	1.1	1.4	1.3	1.2	1.4	1.4
0.20	1.0	1.3	1.2	1.1	1.3	1.3
0.40	1.0	1.2	1.2	1.1	1.2	1.2

Table 11. Partial safety factors for *foundation failure - clay subsoil - shallow water - no model tests performed.*

	$\sigma'_{Z_{H_S}} = 0.05$			$\sigma'_{Z_{H_S}} = 0.2$		
P_f	γ_H	γ_Z	γ_C	γ_H	γ_Z	γ_C
0.01	1.2	1.5	1.4	1.3	1.5	1.4
0.05	1.1	1.4	1.3	1.2	1.4	1.3
0.10	1.1	1.3	1.3	1.1	1.3	1.3
0.20	1.0	1.2	1.2	1.1	1.2	1.2
0.40	1.0	1.1	1.1	1.1	1.1	1.1

Table 12. Partial safety factors for *foundation failure - clay subsoil - shallow water - model tests performed.*

Sliding failure:

	$\sigma'_{Z_{H_S}} = 0.05$		$\sigma'_{Z_{H_S}} = 0.2$	
P_f	γ_H	γ_Z	γ_H	γ_Z
0.01	1.4	2.0	1.5	2.0
0.05	1.3	1.7	1.4	1.7
0.10	1.3	1.5	1.4	1.5
0.20	1.3	1.2	1.3	1.2
0.40	1.1	1.1	1.1	1.1

Table 13. Partial safety factors for *sliding failure - deep water - no model tests performed.*

	$\sigma'_{Z_{H_S}} = 0.05$		$\sigma'_{Z_{H_S}} = 0.2$	
P_f	γ_H	γ_Z	γ_H	γ_Z
0.01	1.3	1.7	1.4	1.7
0.05	1.2	1.6	1.3	1.6
0.10	1.2	1.4	1.3	1.4
0.20	1.2	1.2	1.2	1.2
0.40	1.1	1.2	1.1	1.1

Table 14. Partial safety factors for *sliding failure - deep water - model tests performed.*

	$\sigma'_{Z_{H_S}} = 0.05$		$\sigma'_{Z_{H_S}} = 0.2$	
P_f	γ_H	γ_Z	γ_H	γ_Z
0.01	1.3	2.2	1.4	2.2
0.05	1.2	1.9	1.3	1.9
0.10	1.2	1.7	1.3	1.7
0.20	1.2	1.3	1.2	1.3
0.40	1.0	1.2	1.0	1.2

Table 15. Partial safety factors for *sliding failure - shallow water - no model tests performed.*

	$\sigma'_{Z_{H_S}} = 0.05$		$\sigma'_{Z_{H_S}} = 0.2$	
P_f	γ_H	γ_Z	γ_H	γ_Z
0.01	1.2	1.7	1.3	1.6
0.05	1.1	1.5	1.2	1.5
0.10	1.1	1.3	1.2	1.3
0.20	1.1	1.2	1.1	1.2
0.40	1.0	1.1	1.0	1.1

Table 16. Partial safety factors for *sliding failure - shallow water - model tests performed.*

Scour failure:

	$\sigma'_{Z_{H_S}} = 0.05$		$\sigma'_{Z_{H_S}} = 0.2$	
P_f	γ_H	γ_Z	γ_H	γ_Z
0.01	2.0	2.4	2.0	2.4
0.05	2.0	2.0	2.0	2.0
0.10	2.0	1.8	2.0	1.8
0.20	2.0	1.5	2.0	1.5
0.40	2.0	1.2	2.0	1.2

Table 17. Partial safety factors for *scour failure for circular roundheads - deep water.*

	$\sigma'_{Z_{H_S}} = 0.05$		$\sigma'_{Z_{H_S}} = 0.2$	
P_f	γ_H	γ_Z	γ_H	γ_Z
0.01	2.0	2.4	2.0	2.4
0.05	2.0	2.0	2.0	2.0
0.10	2.0	1.8	2.0	1.8
0.20	2.0	1.5	2.0	1.5
0.40	2.0	1.2	2.0	1.2

Table 18. Partial safety factors for *scour failure for circular roundheads - shallow water.*

Armour layer failure:

	$\sigma'_{Z_{H_S}} = 0.05$		$\sigma'_{Z_{H_S}} = 0.2$	
P_f	γ_H	γ_Z	γ_H	γ_Z
0.01	1.6	1.3	1.7	1.3
0.05	1.4	1.2	1.5	1.2
0.10	1.3	1.2	1.4	1.2
0.20	1.2	1.1	1.3	1.1
0.40	1.1	1.0	1.2	1.0

Table 19. Partial safety factors for *armour layer failure - deep water.*

	$\sigma'_{Z_{H_S}} = 0.05$		$\sigma'_{Z_{H_S}} = 0.2$	
P_f	γ_H	γ_Z	γ_H	γ_Z
0.01	1.5	1.5	1.6	1.5
0.05	1.3	1.3	1.4	1.3
0.10	1.2	1.2	1.3	1.2
0.20	1.1	1.2	1.2	1.2
0.40	1.1	1.0	1.2	1.0

Table 20. Partial safety factors for *armour layer failure - shallow water.*

10. References

Burcharth H.F.: Introduction of partial coefficient in the design of rubble mound breakwaters. Conference on Coastal Structures and Breakwaters, ICE (Inst. of Civil Engineers), London, Nov. (1991).

Burcharth H.F.: Reliability-based design of coastal structures. ICCE92, Short course, Venice, Italy, (1992).

Burcharth H.F.: Development of a partial coefficient system for the design of rubble mound breakwaters. PIANC PTC II Working Group 12, Subgroup-F, final report, December 1991. Published by PIANC in (1993).

Bruining J.W. : Wave forces on vertical breakwaters. Reliability of design formula. Delft Hydraulics Report H 1903, MAST II contract MAS2-CT92-0047, (1994).

Burcharth H.F.: Identification of design tools for vertical wall breakwaters. PIANC PTC II Working Group 28, Report by Sub-Group A. (1998).

Madrigal B.G. and J.M. Valds: Results on stability tests for rubble foundation of a composite vertical breakwater. MAST II/MCS, CEPYC-CEDEX, Madrid, (1995).

Sumer B.M. & J. Fredsøe : Scour at the head of a vertical-wall breakwater. Coastal Engineering, (1996).

Sørensen J.D. and Burcharth H.F.: Implementation of safety in the design. PIANC PTC II Working Group 28, Report by Sub-Group D. (1998).

Takayama T.: Estimation of sliding failure probability of present breakwaters for probabilistic design. Report of Port and Harbour Research Institute, Yokosuka, Japan, Vol. 31, No. 5, (1992).

Van der Meer J., K. d'Angremond and J. Juhl: Probabilistic calculations of wave forces on vertical structures. Proc. Coatal Engineering, Kobe, Japan, pp. 1754-1767 (1994).

LATERAL VERSUS LONGITUDINAL ARTIFICIAL REEF SYSTEMS

Yoshimi Goda[1] and Hiroshi Takagi[2]

Abstract

A new submerged breakwater structure for shore protection is proposed and called the longitudinal reef system. It is efficient in dissipating wave energy by increasing wave heights at the front through wave refraction effect and by enhancing wave breaking. Comparison is made between the new longitudinal reef system and the conventional broad-crested reef system through model experiments and numerical computation. The superiority of the longitudinal system to the conventional system is confirmed through the comparison.

Introduction

Shore-parallel, detached breakwaters have been used in many countries to protect beaches from erosion. As their emerged crests obstruct the aesthetic view of the sea from beach areas, however, they are sometimes rejected by local residents and visitors. Thus, submerged breakwaters with broad crests are developed and built at several coasts around Japan; they are called artificial reefs.

Artificial reefs dissipate incoming wave energy by forcing them to break on top of the crests because of shallow depth there. Energy dissipation could be enhanced if the wave refraction effect is mobilized to increase wave heights before breaking. This can be done by building a number of slender artificial reefs arranged longitudinally as shown in Fig. 1. Goda (1995) named such a system as a longitudinal reef system. The conventional artificial reefs with crests extended alongshore are called the lateral artificial reefs in the present paper.

In the previous paper by Goda (1995), wave transmission characteristics over a longitudinal reef system were presented, based on wave flume tests and numerical computations. The present paper discusses the results of 3-D tests in a wave

[1] Professor, [2] Graduate Student, Yokohama National University, Department of Civil Engineering, 79-5 Tokiwadai, Hodogaya-ku, Yokohama 240-8501, Japan

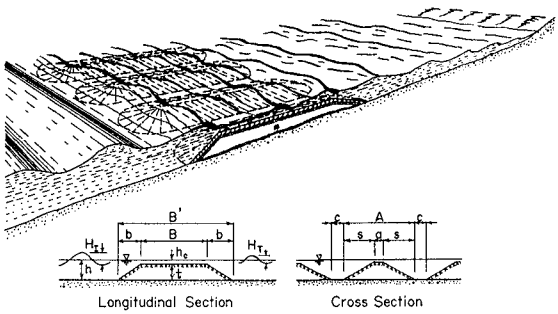

Fig. 1 Sketch of longitudinal artificial reef system.

basin for wave heights and wave-induced currents around both lateral and longitudinal reef systems, and compares their performances by means of numerical computations.

Models of Longitudinal and Lateral Reef Systems for Tests

Volume of Reef Unit

With the notations listed in Fig. 1, the volume of one unit of reefs is approximately calculated by Eq. 1.

$$V = t[b(a + \pi s/3) + (a + s)B] \tag{1}$$

The above equation applies for both lateral and longitudinal reef systems; *i.e.*, the former has the crest width a greater than the crest length B, while the latter has a smaller than B.

In the comparison between the lateral and longitudinal reef systems, their construction cost is an important factor together with their hydrodynamic characteristics. As the construction cost is primarily controlled by the total volume of reef units, model reefs of longitudinal and lateral units were built with the same total volume to make a fair comparison of their performance.

Wave Basin for Model Tests

An outdoor wave basin with the size of 9.0 m by 13.0 m was employed in the present study. A planar slope with the inclination of 1/20 was built with mortar in a slant angle of 15° to the wave paddles as shown in Fig. 2. The initial section of 0.52 m was made with the inclination of 1/10.

All the tests were carried out with the water depth of 0.30 m in front of the wave paddles. The grid lines of the x and y coordinates were drawn on the slope with the interval of 0.5 m with the origin at the upper left corner. The shoreline

was located at the line of $x = 6.0$ m. Two wave guide walls were placed at the both sides along the lines of refracted wave propagation; their locations were determined after several trials so as to insure smooth wave propagation along them.

Model Reef Units

Three longitudinal reef units were placed in the basin as shown in Fig. 2. The submergence depth was h_c =0.03 m, the crest length was $B = 1.50$ m, and the crest width was $a = 0.10$ m. They were built with crushed stones with the diameters ranging from 30 to 50 mm. The front and rear slopes were 1/2, and the side slope was 1/2.5.

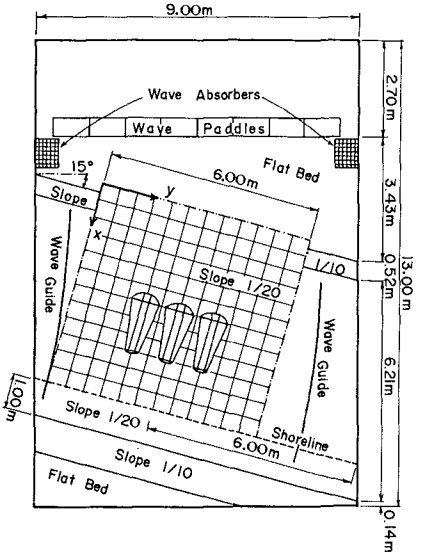

Fig. 2 Wave basin with longitudinal reefs.

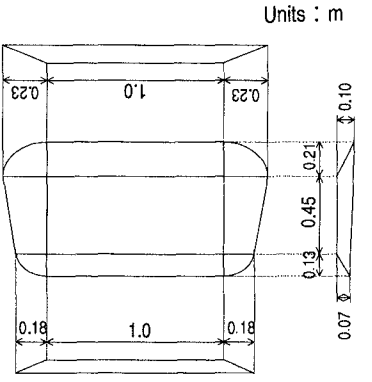

Fig. 3 Sketch of a lateral reef unit.

These three longitudinal reef units were placed at the location of $x = 3.0$ to 4.5 m (crest position) with the separation of 1.0 m between the central axes which were located at y =2.0, 3.0, and 4.0 m, respectively.

A lateral reef system was made with two units with h_c =0.03 m, B =0.45 m, and $a = 1.00$ m. Figure 3 provides a sketch of the lateral unit built on a slope of 1/20. The total volumes of the longitudinal and lateral reef systems were about 0.127 m^3 for both cases. The front line of the crests of two units were placed at the location of $x = 3.5$ m, and their central axes were set at the lines of $y = 2.1$ and 3.9 m.

Test Waves

Two trains of irregular waves with $H_{1/3}$ =7.5 cm and $T_{1/3}$ = 1.2 s and those with $H_{1/3}$ =5.5 cm and $T_{1/3}$ = 1.6 s were used in the tests. The offshore incident wave angle was 15°. Wave profiles were recorded with capacitance gauges at the sampling frequency of 20 Hz. The wave records were analyzed by the zero-downcrossing method, and the highest one-third wave height $H_{1/3}$ and period $T_{1/3}$ were computed. The data shown in the present paper refer to the significant wave height and period. Current velocities were measured with bi-axis ultrasonic current meters. Though the instrument could output instantaneous velocity data, only the mean currents averaged over 200 s were utilized for analysis of wave-induced currents.

Numerical Analysis of Wave Heights and Radiation Stresses

Governing Equation

Numerical simulation of wave deformation around the reef was made by using the parabolic equation based on the numerical scheme by Hirakuchi and Maruyama (1986). According to their scheme, the governing equation for the complex amplitude of the velocity potential, ϕ, is given as follows:

$$\frac{\partial \phi}{\partial x} = \left\{ i\left(k_x + \frac{k_y^2}{2k_x}\right) - \frac{1}{2k_x cc_g}\frac{\partial}{\partial x}(k_x cc_g)\right\}\phi + \frac{1}{2k_x cc_g}\frac{\partial}{\partial y}\left(cc_g\frac{\partial \phi}{\partial y}\right) - f_D'\phi \quad (2)$$

where k_x and k_y denotes the wave numbers in the x and y directions, respectively, c the wave celerity, c_g the group velocity, i the imaginary number. The term f_D' is a function which represents the effect of wave breaking on amplitude attenuation, and it is hereby called the wave attenuation function for brevity.

As the wave amplitude is proportional to the absolute amplitude of velocity potential, its spatial distribution is obtained by solving Eq. 2 with a forward difference scheme. Numerical computation was carried out for an area corresponding to physical model tests shown in Fig. 2: the grid size was set at $\Delta x = \Delta y = 0.10$ m.

Modification of Wave Celerity and Wave Number

Observations of breaking wave fronts running over a submerged mound reveal that the part of wave front on top of the crest moves faster than the neighboring part of wave front on the side slopes, even though the water depth is shallower at the crest than on the side. The increase of wave speed is caused by the fact that the wave celerity is not only governed by the water depth but also affected by the wave amplitude; *i.e.*, a finite amplitude effect. Because the wave refraction by local topography is controlled by the spatial variation of wave celerity, a correct representation of wave celerity is required for appropriate evaluation of wave transformations. The finite amplitude effect on wave celerity was approximated by Goda (1995) as in the following empirical formulation:

$$c = \begin{cases} c_A \left[1 + \frac{3}{8}\left(\frac{H}{h}\right)^2\right]^{1/2} & : H < 2h \\ c_A \left[1 + \frac{3}{4}\left(\frac{H}{h}\right)\right]^{1/2} & : H \geq 2h \end{cases} \tag{3}$$

where c_A denotes the wave celerity by the small amplitude wave theory, H the wave height, and h the local water depth.

The upper expression in the right-hand side of Eq. 3 was formulated in analogy of the phase velocity of the 3rd order Stokes waves. The lower expression was set to make a smooth transition across the boundary of $H = 2h$. The wave numbers k_x and k_y have been adjusted by dividing them with this rate of wave celerity increase. However, the group velocity c_g has been kept the same as that given by the small amplitude wave theory

Formulation of Wave Attenuation Function

The wave attenuation function f'_D was given the following form as discussed by Goda (1995):

$$f'_D = \begin{cases} 0 & : H < \gamma h \\ \frac{K}{2h}\left[\left(\frac{H}{\gamma h}\right)^2 - 1\right]^{1/2} & : H \geq \gamma h \end{cases} \tag{4}$$

The constant K in Eq. 4 represents the relative rate of wave energy decay by breaking. It was given the value of $K = 0.125$ which yielded best agreement with the results of previous model tests. As for γ, which is the ratio of wave height to water depth at breaking, the present study sets its value according to the following breaker index by Goda (1974):

$$\gamma = 0.17\frac{L_0}{h}\left\{1 - \exp\left[-\frac{1.5\pi h}{L_0}(1 + 15\tan^{4/3}\theta)\right]\right\} \tag{5}$$

where L_0 is the deepwater wavelength and θ represents the angle of inclination of bottom slope from the horizon. In the present study, the $\tan\theta$ was set at 1/30 throughout the computational area inclusive of the submerged crests of reef systems, for the sake of simplicity.

Computation of Irregular Wave Heights

Though the numerical scheme of the parabolic equation has been developed for regular waves, the effect of wave irregularity can be taken into account by superposing the results of regular wave analysis for multiple levels of wave heights but with the same wave period. Individual wave heights are assumed to follow the Rayleigh distribution, and the range of wave height distribution is divided into N segments with the equal probability of appearance. The wave height representing

each segment is assigned as

$$H_m = 0.706(H_{1/3})_I \left[\ln \frac{2N}{2m-1}\right]^{1/2} \tag{6}$$

where N is the number of representative wave components and m is an integer from 1 to N ($m = 1$ yields the largest height and $m = 30$ the smallest). In the present study, $N = 30$ was employed. The results of the computations of N components at a given grid point were summed up to calculate the representative heights of irregular waves. By summing up the upper one-third components and multiplying it with the probability of appearance, the significant height $H_{1/3}$ is obtained, while the summation of the whole components yields the mean height $\overline{H}$.

Computation of Radiation Stresses

For each component of regular waves, the radiation stresses S_{xx}, S_{xy}, and S_{yy} are computed at each grid point from the results of wave amplitude and direction. The results of the 30 components are summed up to yield the overall radiation stresses, which provide the steady state input for computation of wave setup and wave-induced currents. As the radiation stress is proportional to the wave energy density, the overall radiation stress in the present study is an energy-averaged one.

Numerical Analysis of Wave Setup and Wave-Induced Currents

Governing Equations

The wave-induced currents and water level change are simulated by solving the continuity and momentum equations for long waves with the input of radiation stresses computed from the wave deformation analysis. The continuity equation is expressed as

$$\frac{\partial \zeta}{\partial t} + \frac{\partial U(h+\zeta)}{\partial x} + \frac{\partial V(h+\zeta)}{\partial y} = 0 \tag{7}$$

where ζ denotes the amount of water level change, and U and V represent the cross-shore and longshore components of depth-integrated current speeds, respectively. The equations of motions are described as

$$\frac{\partial U}{\partial t} + U\frac{\partial U}{\partial x} + V\frac{\partial U}{\partial y} + F_x - M_x + R_x + g\frac{\partial \zeta}{\partial x} = 0 \tag{8}$$

$$\frac{\partial V}{\partial t} + U\frac{\partial V}{\partial x} + V\frac{\partial V}{\partial y} + F_y - M_y + R_y + g\frac{\partial \zeta}{\partial y} = 0 \tag{9}$$

where F represents the friction terms, M the horizontal mixing terms, R the gradients of radiation stresses, and g the acceleration of gravity.

The friction terms are evaluated with the friction coefficient $C_f = 0.01$ by using the vector-sum velocity of wave-induced currents and orbital velocity at the bottom. The horizontal mixing terms are calculated with the dimensionless

constant $N = 0.016$ after Longuet-Higgins (1970).

Computational Procedures

The governing equations are solved with the finite difference scheme. The central difference is employed for spatial grids and the forward differences are used for time steps. The grid size is the same as that for wave field, and the time step was set at $\Delta t = 0.01$s.

Computation starts from the condition of rest with the input of spatially-distributed radiation stresses, which are adjusted to increase gradually to the full magnitude to avoid computational instability. As computation progresses, the changes in water level and wave-induced currents approach to the equilibrium state. In the present study, the computation was stopped when the maximum value, throughout the computation area, of the velocity difference from the preceding time step became equal to 0.001 cm/s or less. Because this condition was quite strict compared with conventional computations of wave-induced currents, one run of computation required 5,000 to 10,000 time steps to yield the final results.

Examples of Wave-Induced Current Computation

Figure 4 exhibits the computed results of wave-induced currents around the reef systems for irregular waves with $H_{1/3}$ =7.5 cm and $T_{1/3}$ =1.2 for both the longitudinal and lateral reefs. Strong onshore currents are generated on top of reef units as expected. Rip currents between reef units are stronger for the lateral reef than for the longitudinal reef. Counterclockwise vortices at the left sides of both figures are probably the results of insufficient calibration of side boundary conditions in numerical works.

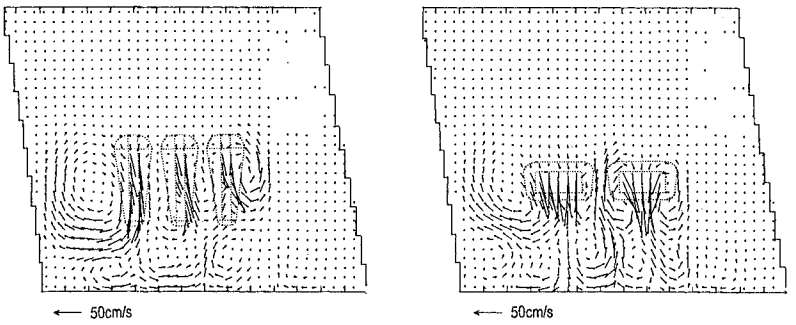

(a) Longitudinal reef (b) Lateral reef

Fig. 4 Computed currents around longitudinal and lateral artificial reefs: $H_{1/3}$ =7.5 cm and $T_{1/3}$ = 1.2 s.

Wave Heights and Currents around Longitudinal Reef System

Significant wave heights measured in the physical models are compared with the results of numerical computations in Figs. 5 and 6. The former is for waves $H_{1/3}$ =5.5 cm and $T_{1/3}$ = 1.6 s, and the latter is for waves $H_{1/3}$ =7.5 cm and $T_{1/3}$ = 1.2 s. The left drawings show the cross-shore variations of wave heights along the line y =2.5 m (middle line between the first and second reef units), while the right drawings depict the longshore variations along the line x =4.75 m (just behind the reef units).

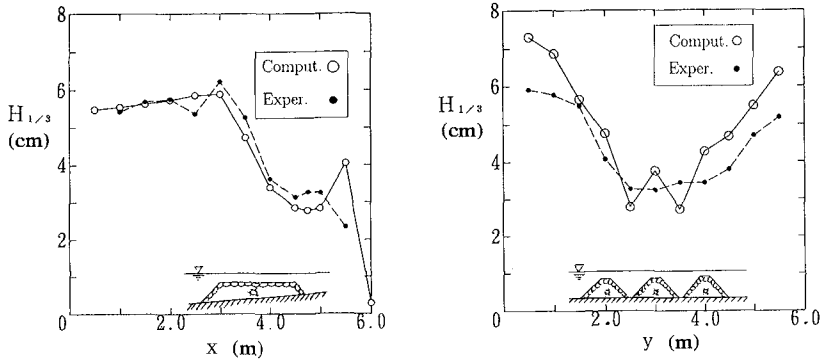

Fig. 5 Comparison of measured and computed wave heights around the longitudinal reef system for waves of $H_{1/3}$ =5.5 cm and $T_{1/3}$ = 1.6 s: the cross-shore variation along y =2.5 m in the left and the longshore variation along x =4.75 m in the right.

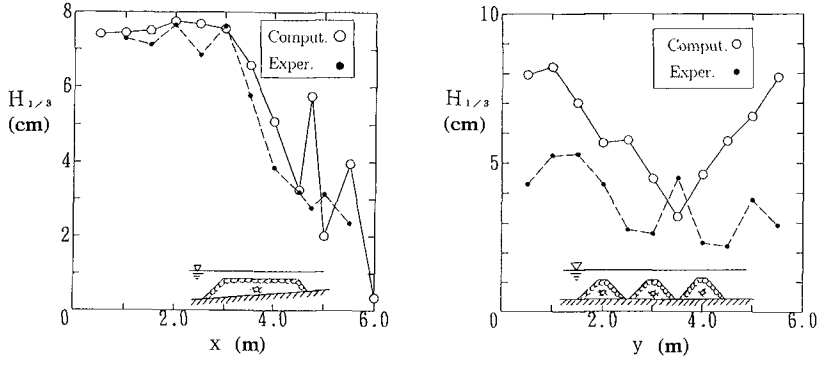

Fig. 6 Comparison of measured and computed wave heights around the longitudinal reef system for waves of $H_{1/3}$ =7.5 cm and $T_{1/3}$ = 1.2 s: the cross-shore variation along y =2.5 m in the left and the longshore variation along x =4.75 m in the right.

Numerical computation generally yields the wave heights almost in agreement with the measurements. Exception is the longshore variation of Fig. 6 in the left drawing, in which numerical computation overpredicts wave heights. Because the local water depth along the line x =4.75 m is h =6.25 cm, the significant wave height by random wave breaking should be about 5.3 cm according to the random wave breaking model by Goda (1975). However, computation predicts the wave height up to 8 cm.

The discrepancy is due to the use of a simple technique of representing irregular waves with segments of wave heights as determined by Eq. 6. Each component of waves is treated as regular waves, and the wave height after breaking eventually becomes $H = \gamma h$ regardless of incident wave heights. The original Rayleigh distribution of wave heights is transformed to have an upper cutoff at $H = \gamma h$. Thus the wave height in very shallow water approaches to the breaker height of regular waves.

Comparison of the measured and computed wave-induced currents are shown in Fig. 7. On top of the reef crests, strong onshore currents were visually observed, but they could not be confirmed by measurements, because the current meter emerged at the troughs of large waves and could not produce reliable records. The current patterns and velocities of measurements and computations are quite similar except for the counterclockwise vortices in the left which are predicted by computation but not observed in the measurements.

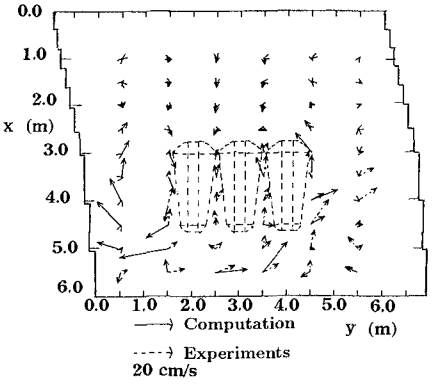

$H_{1/3}$ =7.5 cm and $T_{1/3}$ = 1.2 s

Fig. 7 Measured and computed wave-induced currents around the longitudinal reef.

Wave Heights and Currents around Lateral Reef System

The distributions of wave heights around the lateral reef system are exhibited in Figs. 8 and 9. The cross-shore wave height variations are shown in Fig. 8 for waves with $H_{1/3}$ =5.5 cm and $T_{1/3}$ = 1.6 s. The line y =3.0 m at the middle of the two reef units and the line y =4.0 m being off the central axis of the

second unit by 0.1 m were chosen for demonstration and shown in the left and right drawings, respectively. In the area between the reef units, the computed and measured significant wave heights are in good agreement. On top of the reef crest, wave heights decrease rapidly and the computation can simulate the wave decay quite well. However, in the area behind the reef along this section, the computation gives the wave height much higher than the measurement. This height corresponds to the breaker height of regular waves, owing to the use of a simple representation of irregular waves by Eq. 6 as discussed earlier.

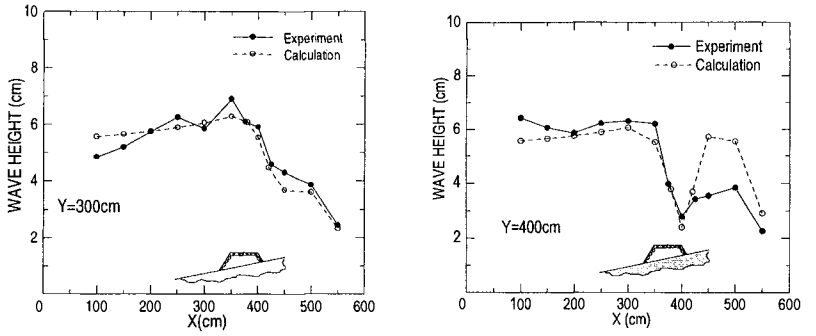

(a) Cross section at y =3.0 m (b) Cross section at y =4.0m

Fig. 8 Cross-shore wave height variations around the lateral reef system: $H_{1/3}$ =5.5 cm and $T_{1/3}$ = 1.6 s.

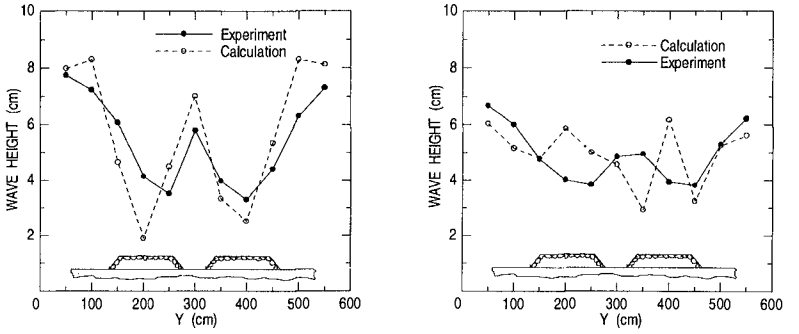

(a) Line along x = 4.0 m (b) Line along x =4.5 m

Fig. 9 Longshore wave height variations around the lateral reef system: $H_{1/3}$ =7.5 cm and $T_{1/3}$ = 1.2 s.

The longshore variations of wave heights are shown in Fig. 9 for waves with $H_{1/3}$ =7.5 cm and $T_{1/3}$ = 1.2 s. The line along x =4.0 m in the left is located slightly behind the rear tip of the crest, and the line along x =4.5 m in the right is located in the area of planar slope. Though computed wave heights exhibit

wider variations than the measured ones, they are approximately in agreement.

The strength of wave-induced currents around the lateral reef system is compared with that of the longitudinal system in Tables 1 and 2. Examples of currents by computation have been shown in Fig. 4. The maximum rip currents through the gap of reef units by model tests and numerical computation are listed in Table 1, and those of the maximum longshore currents are listed in Table 2.

Table 1 Maximum Rip Currents at the Gaps of Reef Units

$H_{1/3}$	$T_{1/3}$	Lateral Reefs		Longitudinal Reefs	
		experiments	computation	experiments	computation
5.5 cm	1.6 s	8.5 cm/s	13.2 cm	8.3 cm/s	10.5 cm/s
7.5 cm	1.2 s	12.0 cm/s	28.5 cm	11.4 cm/s	15.0 cm/s

Table 2 Maximum Longshore Currents behind the Reef Units

$H_{1/3}$	$T_{1/3}$	Lateral Reefs		Longitudinal Reefs	
		experiments	computation	experiments	computation
5.5 cm	1.6 s	10.1 cm/s	14.7 cm	11.8 cm/s	25.0 cm/s
7.5 cm	1.2 s	9.6 cm/s	19.8 cm	11.3 cm/s	22.5 cm/s

Numerical computation predicts stronger rip currents for lateral reefs and weaker longshore currents for a lateral reef system than for a longitudinal reef system. However, measurements did not record velocities as strong as those by computation, and differences between the two reef systems were not significant. A relatively small number of current measurement points might have been a reason that measurements could not detect the largest velocities around the reef system.

Discussion on Numerical Computation for Artificial Reef System

Figures 4 through 9 provide the basis for judging the accuracy and reliability of the numerical computation method employed in the present analysis. Admittedly it has several shortcomings, such as false current patterns and locally large wave heights in the area sheltered by the reef units.

One problem inherent to the numerical analysis around reef systems is the steep gradients at the front, sides, and rear slopes of reef units. Application of the mild slope equation as well as the parabolic equation to such a bathymetry violates the assumption of gradual variations of the physical quantities involved. Nevertheless, the parabolic equation by Hirakuchi and Maruyama (1986) can predict the wave height distribution relatively well. Wave irregularity has been incorporated simply by summing up the computational results for multiple levels of wave heights.

The merit of the parabolic equation is the fast speed in computation, because the spatial distribution of wave amplitude is directly solved. Computations of various reef layouts are done quickly and a best layout can be selected. A weak point in the present analysis is the difficulty in an appropriate evaluation of the wave decay function f_D' which would well behave on top of reef units as well as

in the rear area. The assessment of f'_D needs a calibration with laboratory data. The scale effect is a problem in model tests of artificial reefs, because the water depth at the reef crest is often quite small. Goda and Morinobu (1997) reported that a minimum water depth of 10 cm is required to correctly reproduce the wave breaking phenomenon on a trapezoidal step; a smaller water depth results in a smaller height-to-depth ratio at breaking.

Comparison of Prototype Lateral and Longitudinal Reef Systems

As the foregoing discussions were limited to the model reef systems, an examination of prototype structures is presented in the following.

A prototype situation is postulated as shown in Fig. 10. The sea bottom has the gradient of 1/20 from the shoreline to the depth h =2 m, 1/50 from the depth h = 2 to 10 m, and 0 beyond 10 m. A lateral artificial reef system of two units (a = 150 m and B = 40 m) with the gap 50 m (at the crest level) is set at the location of x = 280 to 320 m in the water depth from h = 4.5 to 3.7 m. For comparison, a longitudinal artificial reef system with seven units (a = 20 m and B = 65 m) is set at the location of x = 280 to 345 m in the water depth from h = 4.5 to 3.2 m. The submergence depth is h_c = 1.5 m, the front and rear slopes have the gradient of 1/2, and the side slopes has the gradient of 3/10 for both the systems. The approximate volume of the lateral system is 64,000 m^3, while the latter is 62,000 m^3.

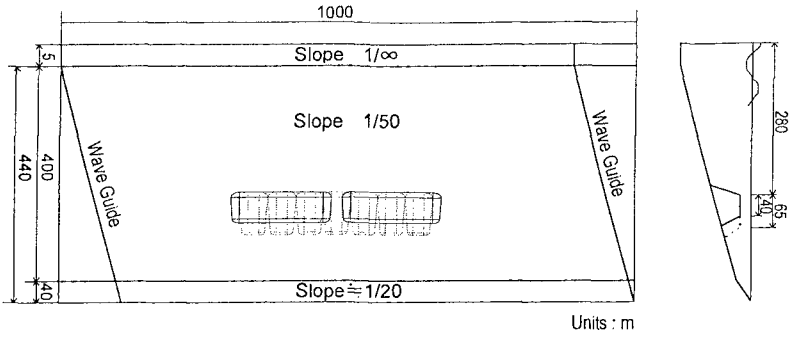

Fig. 10 Setup of computational area for lateral and longitudinal reef systems.

Figure 11 shows examples of computation of wave height distributions. The incident waves are unidirectional irregular waves with the height $H_{1/3}$ = 1.0 and 3.0 m, the period $T_{1/3}$ = 8 s, and the incident angle of 15°. The top figures show the wave heights along the front edges of the both reef systems (h = 4.5 m), the center figures are for those along the middle line of the reefs (h = 3.5 m), and the bottom figures correspond to those along the rear edge of the longitudinal reef (h =2.5 m).

As seen in Fig. 11, wave heights behind the longitudinal reef system are found to be lower than those behind the lateral system. Difference is prominent in the case of the small wave height $H_{1/3} = 1.0\,\mathrm{m}$. It is owing to the acceleration of wave breaking process by increase of wave height owing to the wave refraction effect at the heads of longitudinal reefs. Thus a longitudinal reef system is judged superior to a lateral reef system in the efficiency of energy dissipation when the crest submergence depth is the same.

In construction of prototype structures, a lateral reef system requires a minimum depth of 2 m or so owing to the limitation of the draft of working vessels. On the other hand, a longitudinal reef system can be constructed with the zero crest depth, because the crest width is small and a working vessel can reach out the crane arm to any location on the crest while mooring along the side slopes. Wave damping capacity of a longitudinal reef system can be further enhanced by setting the crest elevation as close to the low water level.

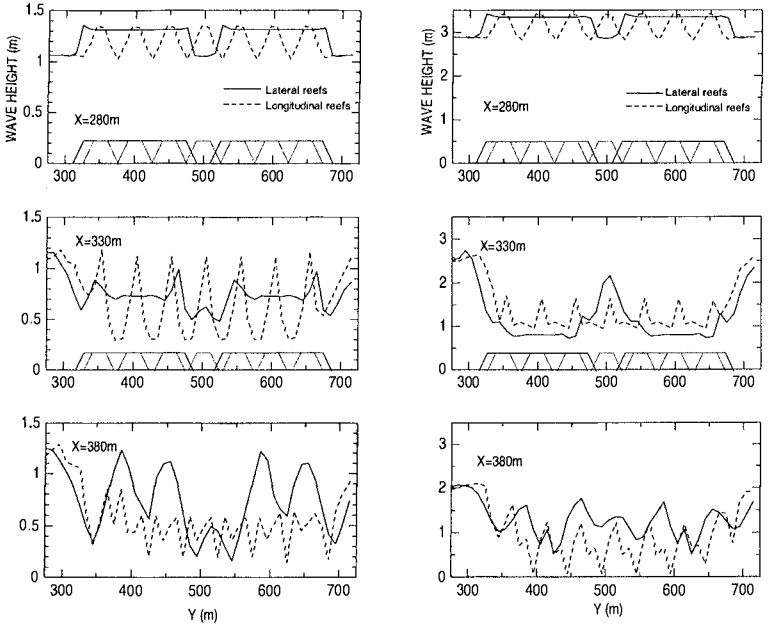

(a) $H_{1/3} = 1.0\,\mathrm{m}$, $T_{1/3} = 8\,\mathrm{s}$ (b) $H_{1/3} = 3.0\,\mathrm{m}$, $T_{1/3} = 8\,\mathrm{s}$

Fig. 11 Computed wave heights around the lateral and longitudinal reef systems

Conclusions

Major findings in the present studies are summarized as in the following:

1. A numerical scheme based on the parabolic equation for irregular waves demonstrated its capability to simulate the wave height distribution around

the lateral and longitudinal artificial reef systems. The capability was confirmed through comparison with 3-D model test data.

2. Wave-induced currents around the artificial reefs were approximately simulated by numerical computation, though further refinements are needed.

3. The newly-proposed longitudinal reef system has been shown more efficient in dissipating wave energy than the conventional lateral artificial reef system, because of incorporation of wave refraction effect.

4. Strong rip currents between the gap between the lateral units were predicted by computation, but model tests did not yield appreciable differences in current speeds between the longitudinal and lateral reef systems.

References

Goda, Y. (1974): New wave pressure formulae for composite breakwater, *Proc. 14th Int. Conf. on Coastal Engrg.*, Copenhagen, pp.1702-1720.

Goda, Y. (1975): Irregular wave deformation in the surf zone, *Coastal Engrg. in Japan*, JSCE, Vol.18, pp.13-26.

Goda, Y. (1995): Wave damping characteristics of longitudinal reef system, *Advances in Coastal Structures and Breakwaters (Proc. of Conf.)* edited by J.E.Clifford, Thomas Telford Pub., London, pp.192-203.

Goda, Y. and K.Morinobu (1997): Breaking wave height on horizontal bed, *Proc. Combined Australasian Coastal Engrg. and Ports Conf.*, Christchurch, New Zealand, pp.953-958.

Hirakuchi, H. and K.Maruyama (1986): An extension of the parabolic equation for application to obliquely incident waves, *Proc. 33th Japanese Conf. on Coastal Engrg.*, pp.114-118 (*in Japanese*).

Longuet-Higgins, M.S. (1970): Longshore currents generated by obliquely incident sea waves, 2, *J. Geophys. Res.*, Vol.75, No.33, pp.6790-6801.

Development of a New Type of Reef Breakwater, Theoretical and Experimental Study

Shohachi KAKUNO*[1], Masao ENDOH*[2], Yiming ZHONG*[3], Takaaki SHIGEMATSU*[1], and Kazuki ODA*[1], Member of ASCE

Abstract

The concept of a horizontal perforated plate placed in water, with a method for implementing the concept in a real sea as a new type of reef breakwater, is proposed in the present paper. The feasibility and superiority of the proposed breakwater in hydraulic characteristics in comparison with conventional reef breakwaters has been shown by theoretical and experimental study.

1. Introduction

Wave height reduction with reef breakwaters is caused by energy dissipation from waves breaking over the crests of the breakwaters. Mass transport caused by the wave breaking, however, may generate offshore flow at the gaps between two adjacent breakwaters and, hence scouring at the bottoms of the gaps. Also, the massive structural body of the breakwater may interfere with existing currents on the beach. As an alternative breakwater, an impermeable plate placed horizontally in the water does not interfere with currents. However, strong wave forces may be exerted on the plate, causing problems. If perforations are made in the horizontal plate, much wave energy dissipation at the perforations due to flow separation and reduced wave forces may be anticipated. The perforations could also encourage vertical flow with vertical oxygen transport. The region under the perforated plate could become good shelter for aquatic creatures.

The objective of this study is to propose the concept of a horizontal perforated plate placed in water, with a method for implementing the concept in a real sea as a new type of reef breakwater, and to investigate the hydraulic characteristics of the breakwater theoretically and experimentally.

*1: Dept. Civil Engrg., Osaka City Univ., Sugimoto, Sumiyoshi-Ku, Osaka 558-8585, Japan

*2: Toyo Suiken Co. Ltd., Tokyo, Japan

*3: Shusei Consultant Co. Ltd., Osaka, Japan

2. Theoretical Study

2-1. A boundary-value analysis

A theoretical study to search for an optimum opening ratio for the plate was performed as a boundary-value problem for small amplitude waves (Kakuno & Zhong 1993). A plate having slits as perforations was considered. To analyze the problem, the whole region was divided into five regions, as shown in **Fig.1**. In each region except that which holds the plate, a velocity potential which satisfies the boundary conditions at the sea surface and/or the sea bottom was assumed, with unknown coefficients. Evanescent waves which may occur near the plate were neglected. The waves over and under the plate were assumed to have the same wave number because of the continuity of flow through the slits. In the region which holds the slitted plate, a velocity potential for flow through a slitted plate that has been obtained theoretically is assumed (Kakuno & Liu 1993). The unknown coefficients included in each velocity potential can be determined after matching the potentials at the boundaries.

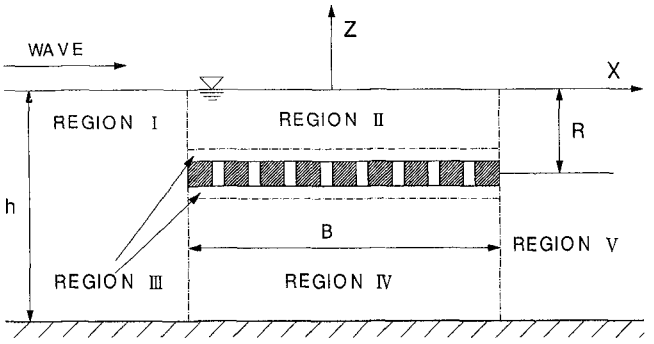

Fig.1 A boundary-value problem

2-2. An Energy Dissipation Model

The effect of the energy dissipation due to flow separation at slits can be included by introducing a complex wave number in the regions over and under the plate. The imaginary part of that wave number can be determined by equating the energy flux difference between plate ends evaluated linearly using the imaginary part to that evaluated using quadratic resistance at the slits. The same value, f=1.5, was assigned as for vertical slits (Kakuno & Liu 1993), where f is the value of the energy dissipation coefficient included in the quadratic resistance.

2-3. Preliminary experiments to verify the theory

To verify the theory, preliminary experiments to measure the reflection and transmission coefficients were performed using a horizontal slitted plate placed in water of constant depth, h=0.3m, in a wave tank 20m long, 0.5m wide, and 0.6m high. The thickness, the width in the direction of wave propagation, the opening ratio, and the submerged depth of the plate were b=6mm, B=60m, r=0.089, and R=6cm,

respectively.

Fig. 2 (a) and **(b)** show comparisons of the theoretical transmission and reflection coefficients, γ_T and γ_R, with laboratory data as a function of B/L, where L is the wave length, under the conditions of the wave steepness H/L=0.01 and 0.02, where H is the wave height. The agreement between the theoretical results, in which the effect of the energy dissipation is taken into consideration, and the laboratory data is good overall; hence the validity of the theory has been shown.

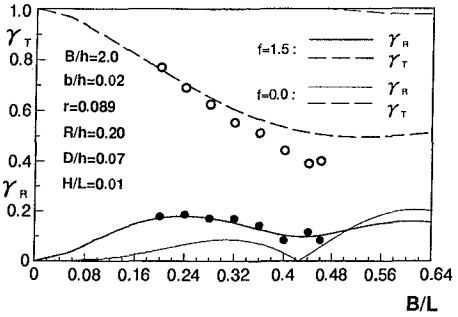

(a)

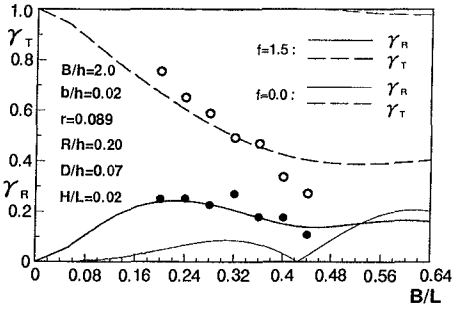

(b)

Fig.2 Comparison of transmission coefficients between theory and experiment

2-4. Comparison with impermeable horizontal plate

To examine the difference between the perforated horizontal plate and the solid horizontal plate, laboratory data for an impermeable plate (Aoyama et al. 1988) were compared with calculated results for the perforated plate under the same conditions (**Fig.3**). As shown in the figure, the characteristics of the two types of plate are remarkably different. Lower transmission and reflection may be attained by the perforated plate over a wide range of B/L, indicating more effective energy dissipation by the perforated plate.

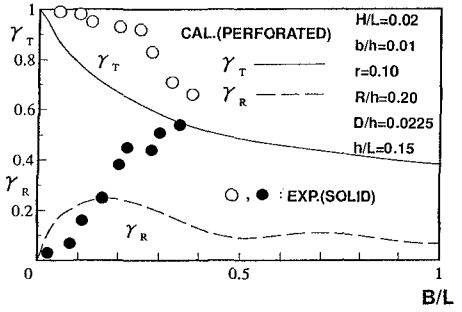

Fig.3 Comparison of transmission and reflection coefficients with those of an impermeable horizontal plate

2-5. Optimum opening ratio

Fig.4 shows calculated results for the perforated plate for a varied opening ratio. As shown in the figure, a smaller ratio leads to less transmission and greater reflection. An opening ratio of r=0.1 may be concluded to be the optimum which minimizes transmission and reflection.

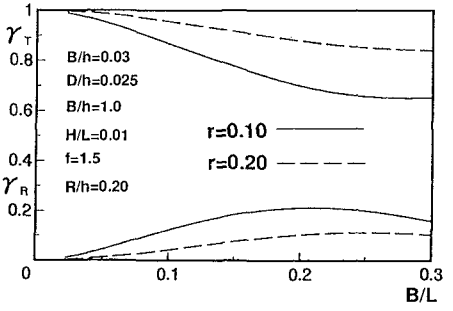

Fig.4 Transmission and reflection coefficients as a function of opening ratio

3. Proposal of a New Type of Reef Breakwater

To implement the concept of the horizontal perforated plate in the sea, concrete units, whose schematic diagram is shown in **Fig.5**, were conceived. Each unit is principally composed of a horizontal perforated upper slab which plays a principal role in wave energy dissipation, and columns to support the slab from the bottom. The dimensions and weight of a typical unit in the sea are 3m×3m×3m and Wa=16tf, respectively. The opening ratio of a unit will be about r=0.1, which was determined to be the optimum in the theoretical study. The units will be placed in a single layer on a rubble mound with a crest depth of 0m - 2m in the sea, as shown in **Fig.6**.

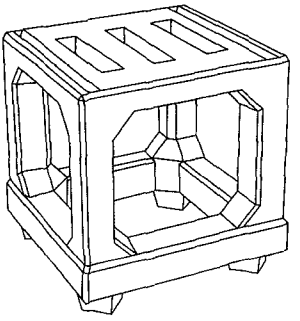

Fig.5 A concrete unit to make up a new type of reef breakwater

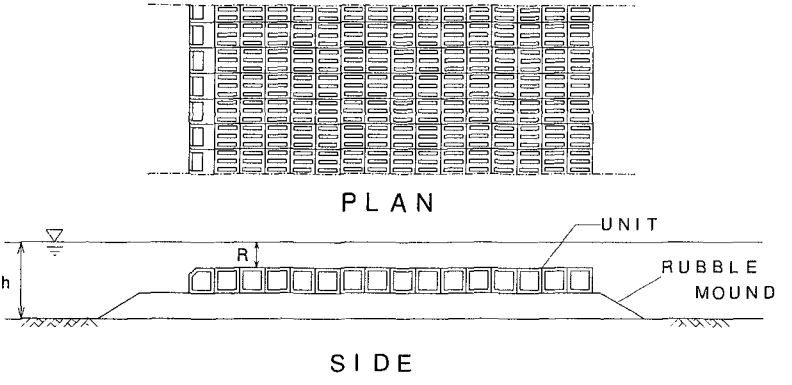

Fig.6 A new type of reef breakwater

4. Experimental Studies

A series of experimental studies was performed using 1/20 scale models of the units in a wave tank 50 m long, 1 m wide, and 1.50 m high, to measure the transmission and reflection coefficients. Experiments to measure water level rise and wave height attenuation over the breakwater, and to examine the stability of the units, were also performed using the same wave tank. The waves were regular in all experiments. The model units were placed on a 15 cm-thick rubble mound on a horizontal floor in the wave tank. The breakwater width tested was primarily B=2.4m, 16 rows of units, but in the experiments to measure the transmission and reflection coefficients, breakwaters with widths B=1.2m, 8 rows of units, and 0.6m, 4 rows of units, were also tested. The water depths (crest water depth) tested were h=30cm (R=0cm), 35cm (5cm), 40cm (10cm), and 45cm (15cm). **Fig.7** shows a picture of waves over the crest of the breakwater model (B=2.4m, R=0cm, T=3s, H=15.5cm).

The experiments to examine the stability of the units were performed by using breakwater models which were placed on a horizontal floor raiscd from the wave tank floor. The berm widths tested were 30cm and 75cm, with the length from the rubble mound end to the offshore edge of the units, L_M, 55cm and 100cm, respectively. Four wave periods within the range from 1.5s to 3.15s were used, and the wave heights were increased till instability was observed, keeping the period constant. Because instability was observed in the row at the very offshore side edge only, modifications were made for the row. One of the modifications was made by using units made of high density material, and the other was made by modifying the cross section of the units. **Fig.8** shows a unit with the modified cross section, and **Fig.6** shows a breakwater with the units at the offshore edge. It was found that the units with the modified cross section were most stable. This is because that the larger opening in the upper slab may reduce wave forces exerted on a unit. The degree of stability was determined on the basis of the criteria shown in **Table 1**.

Table 1 A criterion used to judge stability

STABILITY	CRITERION
STABLE	STATIONARY OR ROCKING≦5mm
UNSTABLE	ROCKING>5mm OR FLOATING

5. Results

5-1. Comparison of transmission coefficient with that of a conventional reef breakwater

Fig.9 (a) and **(b)** show examples of comparisons of experimental data for the transmission coefficients of the present breakwater with those of a conventional reef breakwater (Uda et al. 1988) as a function of B/L_0, where L_0 is the deep water wave length, with relative crest depth, R/H_0', as a parameter, where H_0' is the wave height in deep water if the wave is not refracted. In transmission wave records, the effect of bi-frequency components was found to be small, and hence these were not included in the figures. As shown in the figures, the transmission coefficients of the present breakwater are much smaller than those of conventional breakwaters, implying effective energy dissipation over the breakwater. The difference between the two types of breakwaters becomes large when relative crest depth, R/H_0', becomes large, which implies that, at deeper crest depths, effective energy dissipation caused by separation can still be expected in the present breakwater, while breaking waves of large scale may not occur in conventional reef breakwater. A flat water surface with no waves nor any disturbances was observed under the condition $R/H_0'=0$ and $B/L_0>0.75$, shown in **Fig.9 (b)**. The slits were aligned with the direction of wave incidence in all experiments. But the same results were obtained in an experiment in which the slits were changed to be perpendicular to the wave incidence,.

Fig.7 Waves over the crest of the breakwater model

The transmission and reflection coefficients were obtained from transmitted and reflected wave heights behind and in front of the model by using Goda's method (Goda et al. 1976). The period and the wave height were varied from 1s to 3s, and from 0.01m to 0.16m, with the wave steepness H/L=0.01-0.05.

The water level rise and the wave height attenuation over the breakwater were measured at 13 points over the crest, including the offshore edge and lee edge. Water level fluctuations were recorded for 60s with sampling period 0.04s, from the time that the first wave arrived at the wave gauge at the offshore side. The water level records were then averaged for the duration, excluding the first 20s and the last several waves, to obtain averaged water level rise from the still water surface. The wave heights over the breakwater were determined by using the zero-up crossing method.

Fig.8 A concrete unit with modified cross section for the offshore side edge

The reflection coefficients were confirmed to be small. The maximum value obtained was γ_R=30 % when R=0cm, and the coefficients tended to decrease with increasing crest depth up to γ_R=10 % when R=15cm.

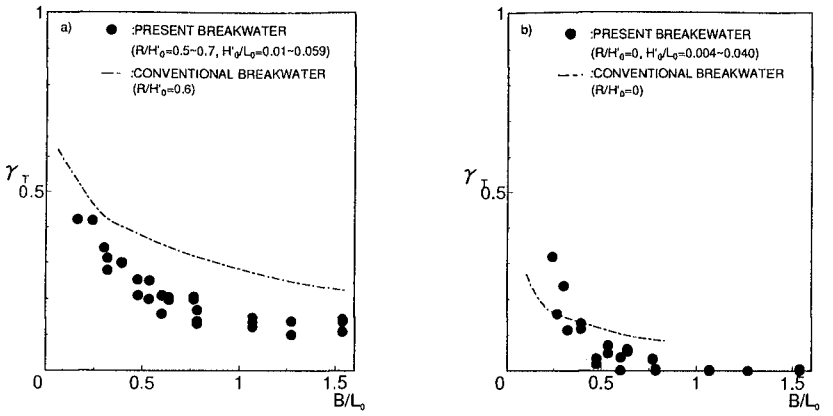

Fig.9 Comparison of transmission coefficients with those of a conventional reef breakwater

5-2. Water level rise distribution over the breakwater

Fig.10 shows relative water level rise distribution over the crest of the present breakwater, η/H_0', when R=5cm. As shown in the figure, the water level rise gradually increases as waves propagate over the crest from the offshore side to the lee side, showing the same tendency as with a conventional breakwater, and becoming maximum at the point just before the lee side edge. Smaller R/H_0' tends to be associated with larger η/H_0', a trend which can also be seen in conventional reef breakwaters.

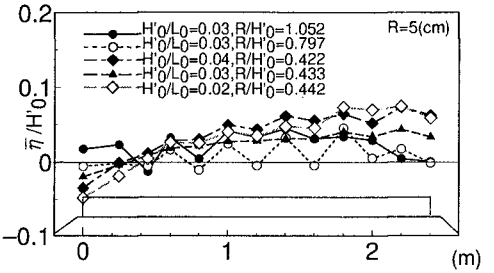

Fig.10 Water level rise over the present reef breakwater

5-3. Comparison of the water level rise with that of a conventional reef breakwater

As mentioned earlier, water level rise over the crest of the reef breakwater may cause scouring at the gap between two adjacent breakwaters. Hence, scouring characteristics should be investigated and compared with those of conventional

breakwaters. In **Fig.11**, a comparison of the water level rise at the lee edge of the present breakwater as a function of R/H_0' with that of a conventional breakwater is shown. Much smaller water level rises than those from conventional breakwaters, especially for the range $R/H_0'<2$, can be seen. In addition, the present breakwater presents no massive body obstructing the flow, so that scouring at the gap between two adjacent breakwaters would not become a problem.

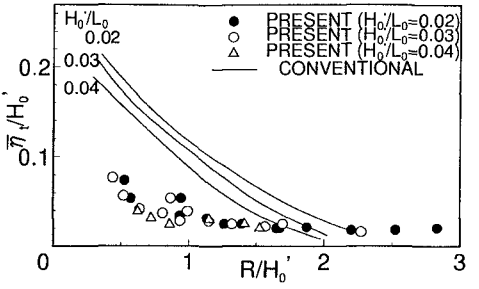

Fig.11 Comparison of water level rise at the lee side edge with that of a conventional reef breakwater

5-4. Wave height distribution over the breakwater

Fig.12 shows a wave height distribution over the crest of the breakwater. In contrast to conventional reef breakwaters, where wave height dissipates rapidly because of waves breaking over the crest, wave height reduces gradually over the crest because of the energy dissipation due to flow separation.

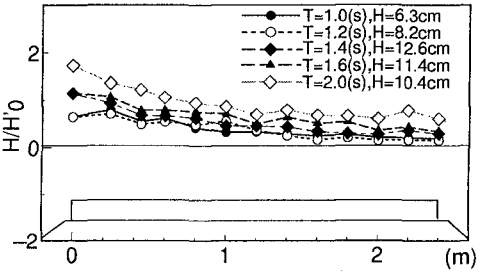

Fig.12 Wave height distribution over the breakwater

5-5. Stability

The present unit is characterized by an upper slab with perforations and a large vacant volume underneath. This configuration leads to concern for the stability of the units under severe wave conditions. Also, as mentioned earlier, the units will be placed in a single layer on a rubble mound, so the instability of the units will be caused by a different mechanism from that for conventional reef breakwaters, which

feature sloping units with waves running up and down the slopes. Therefore, characterization of the stability of the present breakwater design should be carried out using a different approach from that for conventional breakwaters.

Experiments to examine the stability showed that waves which were incident upon the breakwater attacked the offshore side edge first, then traveled over the crest, reducing the wave height by energy dissipation. Because of this mechanism, the instability occurred in the row at the very offshore side edge only. Moreover, the instability was observed to be due to incipient motion with large waves, and not due to drag force, which plays a role in conventional breakwaters which have side slopes (see **Fig.13**).

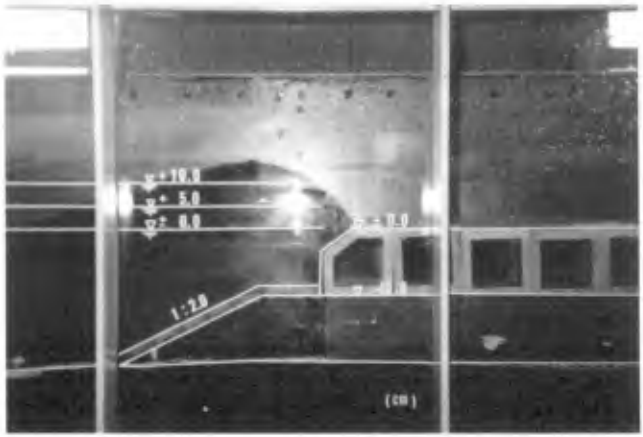

Fig.13 A large wave at the offshore edge of the breakwater

The experiments showed that the units became unstable as the wave period became longer, and as the crest depth became shallower, as anticipated.

5-6. Required weight of the unit

Assuming that the unstable motion occurring in the row at the very offshore side edge is caused mainly by the inertia force, a theoretical formula with an empirical coefficient to examine the stability of the breakwater in the sea was created. This examination was carried out for a unit with the modified cross section which has a greater opening ratio, shown in **Fig.8**, than the regular units which will be placed behind the offshore side row.

The concept of the formula was as follows. The inertial component in the wave force exerted on a plate, which has slits as perforations, is expressed as (Kakuno & Liu 1993)

$$\Delta P = 2\rho C\dot{w} \tag{1}$$

where ρ is the fluid density, C is the blockage coefficient determined theoretically and corresponding to the inertial resistance, and $\dot{w}$ is the acceleration which acts on the plate in the normal direction. Because the wave force of Eq.(1) is per unit area, the force exerted on the upper slab is

$$F = \Delta P L_B^2 \tag{2}$$

letting L_B denote the side length of the upper slab.

The acceleration $\dot{w}$ in Eq.(1) was assumed to be proportional to the convective term, that is

$$\dot{w} \propto w(\partial w / \partial z) \tag{3}$$

where w is the vertical component of water particle velocity passing through the slits. Moreover, it was assumed that $\partial w / \partial z$ could be evaluated as

$$\partial w / \partial z \propto \alpha(w / b) \tag{4}$$

where b is the thickness of the upper plate, and α is a constant to be determined experimentally. Consequently, the acceleration may be evaluated as

$$\dot{w} = \alpha(w^2 / b) \tag{5}$$

If we substitute the vertical water particle velocity at the depth of the upper slab calculated by the small amplitude theory for w, then the wave force exerted on the plate can be expressed as

$$F = 2\rho\alpha \left(\frac{C}{A}\right)\left(\frac{A}{b}\right) \frac{\pi^2 H^2 \sinh^2 k(h-R)}{T^2 \sinh^2 kh} L_B^2 \tag{6}$$

where A is half the spacing of adjacent slits of the upper slab. The coefficient α can be determined using Eq.(6) and the minimum unstable weight of the unit obtained in the experiments. **Fig. 14** shows a graph of α against L_M/L_0, for various types of breakwater model. As shown in the figure, α has a strong and unique relationship with L_M/L_0 regardless of the type of the unit, the type of the berm width, the crest depth, etc. A regression curve which best fits the data, shown as a broken line in the figure, is expressed as

$$\alpha = 0.078 \, (L_M / L_0)^{-1.20} \tag{7}$$

For simplicity in the derivation of a design formula for the stability of the units, however, we will use

$$\alpha = 0.15 \, (L_M / L_0)^{-1} \tag{8}$$

instead of Eq.(7), which is shown as a solid line in the figure.

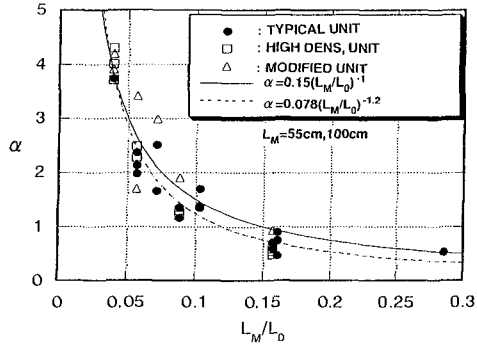

Fig.14 The relationship between α and L_M/L_0

Since we can have C/A=0.4805 and A/b=3.75 for the modified unit, the minimum required weight in water of the modified unit, which is equivalent to the value from Eq.(6), is

$$W_w = 0.85\,\gamma_w \frac{H^2 \sinh^2 k(h-R)}{L_M \sinh^2 kh} L_B^2 \tag{9}$$

where γ_w is the unit weight of sea water, and the relation $L_0 = gT^2/2\pi$ was used in the derivation from Eq.(6) to Eq.(9). From the above expression, the required weight in air of the unit with modified cross section can be obtained readily as

$$W_a = 0.85\,\gamma_w \frac{S_r}{S_r - 1} \frac{H^2 \sinh^2 k(h-R)}{L_M \sinh^2 kh} L_B^2 \tag{10}$$

where $S_r = \gamma_c / \gamma_w$, and γ_c is the unit weight of the unit.

The most significant discrepancy from conventional formulae, for example the Hudson formula, is that the required weight is proportional to the square of the wave height, not to the third power of the wave height, as in conventional formulae. This is mainly because the water particle velocity is assumed to be proportional to the wave height in the present derivation, while it is assumed to be proportional to the square root of the wave height in the conventional formulae. Another reason is that a representative length scale of armor unit is treated as the side length of the upper slab, L_B, in the present derivation, while it is assumed to be proportional to the cube root of the wave height in the conventional formulae.

6. Concluding remarks

The present theoretical and experimental study has shown the feasibility and superiority of the proposed breakwater. The characteristics of the proposed reef breakwater may be summarized as follows:

- invisible
- less transmission and reflection
- does not generate current
- does not interfere with existing currents
- reduced wave forces
- good shelter for aquatic creatures and hence,
- totally environment-friendly breakwater.

Acknowledgment

We are grateful to Dr. Douglas B. Moog for his critical reading of the manuscript, and to Tetsuya Tatekawa for his help in preparing the manuscript.

References

Goda, Y. and Suzuki, Y., 1976, Estimation of incident and reflected waves in random wave experiments, *Proc. ICCE*, 828-562.

Kakuno, S. and Liu, P.L.-F., 1993, Scattering of Water Waves by Vertical Cylinders, *J. Port, Coastal, and Ocean Engrg.*, **119**, (3), 302-322.

Kakuno, S. and Zhong, Y., 1993, A basic study on wave height reduction by a perforated horizontal plate placed in water, *Proc. Coastal Engrg., JSCE*, **40**, 666-670, in Japanese.

Uda et al., 1988, "A function and a design method of the reef breakwaters," *Report of the Public Works Research Institute*, **2696**, 79p., in Japanese.

Aoyama, T., Izumiya, T., Isobe, M., and Watanabe A., 1988, A basic study on wave height reduction by a horizontal plate placed in water, *Proc. 35th Japanese Conf. on Coastal Engrg., JSCE,* **35**, 507-511, in Japanese.

Performance of Submerged Active Breakwaters in a Hydraulic Model

K. R. Hall [1] and M.P. Fischer [2]

Abstract

A submerged active breakwater consists of a large buoyant cylinder that is held horizontal beneath the free surface of the water, by a spring and damper restraint system. The cylinder will be forced to oscillate in a certain mode, in response to an incident wave train. If properly "tuned", the cylinder can absorb a considerable fraction of the incident wave energy. Utilization of this concept may provide a number of potential benefits including; 1) a no loss to fish habitat; 2) a depth-independent materials cost; 3) a scheme easily adaptable to long term water level changes (such as those which occur naturally in the Great Lakes and those which are anticipated with sea level rise); and 4) the capability of adequately protecting a coastal area while maintaining boat access and water circulation. Knowledge of these devices however, is currently limited to performance in; 1) regular wave trains of narrow frequency bands, 2) zero angle of incidence between the wave crest and the structure, and 3) waves of small amplitude.

Research evaluating the performance of submerged active breakwaters was performed in a two-dimensional wave flume in the Queen's University Coastal Engineering Research Laboratory (QUCERL). Both single cylinders and multi-cylinders placed in series were evaluated. Transmission coefficients in the range of 0.3 to 0.7 were measured over a broad range of conditions, indicating the possibility of these devices being used in prototype situations to achieve the benefits described above.

INTRODUCTION

In the field of coastal zone protection, with a general trend of global sea level rise, the design and implementation of coastal defense structures is becoming significantly more complex. In response to the detrimental effects of conventional breakwaters, such as elimination of fish habitat and water stagnation, a variety of new breeds of breakwaters are emerging in an effort to meet the new demands and restrictions of coastal protection.

[1] Professor, Centre for the Aquatic Environment, Queens University, Kingston, ON, Canada
[2] Project Engineer, Aquafor Beech, Kingston, ON, Canada

A submerged active breakwater is one such variety. Consisting primarily of a large circular cylinder, this type of breakwater is designed to remove a large portion of incident wave energy while maintaining fish habitat and remaining fully submerged.

In order to investigate these devices, a series of experiments was performed at the Centre for the Aquatic Environment (CAE), Queen's University, Canada. The testing program was completed to broaden the existing experimental data base, evaluate the performance of these devices subject to irregular waves, evaluate the influence of the depth of submergence and to examine the performance of a multi-cylinder array of submerged active breakwaters. Specifically, tests were focused on determining the performance of a specific type of submerged active breakwater by examining the effects of wave height, wave period, the degree of randomness of the waves and the depth of submergence. In addition, a significant portion of the testing was aimed at observing the attenuation abilities of a system of two such devices placed in parallel.

BACKGROUND

The type of submerged active breakwater under consideration has been previously studied by Evans *et* al[2] and Davis[4, 5] and was referred to as the "Submerged Cylinder Wave Energy Device" or the "Bristol Cylinder". Figure 1 shows a typical setup for a submergcd active breakwater. Essentially, the device consists of a large buoyant cylinder that is submerged to a desired depth by a system of cables, springs and some damping mechanism. As the on-coming wave motion interacts with the cylinder, it is forced to oscillate, typically in circular orbits in some phase related to that of the water particle orbits. By adjusting the stiffness of the springs and degree of damping in the restraining system, the device can be "tuned" to the incoming wave frequency and wave energy. When this tuning condition is satisfied, the device is capable of absorbing a considerable portion of the incident wave energy. As the cylinder oscillates in a circular orbit beneath the free surface, the damping mechanism absorbs the energy of the waves, causing little or no reflection and in certain cases, virtually eliminating the transmitted wave.

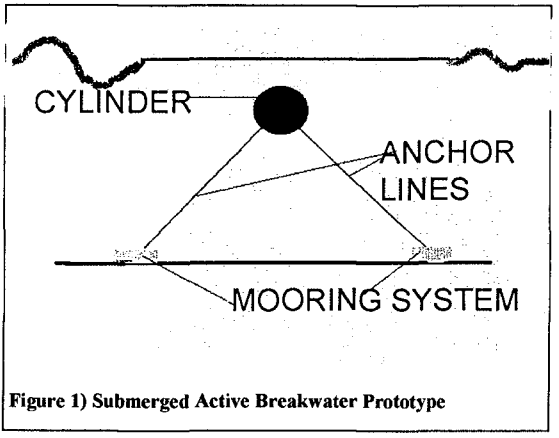

Figure 1) Submerged Active Breakwater Prototype

The concept for this type of submerged active breakwater was first studied on a theoretical basis by Evans[1] who built on the early work on submerged cylinders by Dean[6],

Ursell[7] and Ogilvie[8]. From all of the work presented by Evans and Davis, the primary goal of the Bristol Cylinder was the conversion of readily available wave power to usable electrical energy.

Several benefits and drawbacks are immediately apparent; others become more apparent when one considers the previous studies and experiment of Evans[1], Evans *et al*[2] and Davis[3,4]. Benefits for such devices at the prototype scale include:

- No loss to fish habitat.
- A material cost that is virtually independent of the depth of water.
- A scheme that is potentially adaptable to long-term water level changes, such as those apparent in the Great Lakes and also those anticipated with global sea level rise.
- The adequate protection of a coastal region while maintaining more than sufficient water circulation to prohibit stagnation.
- The suitability for use in conjunction with newer bio-engineered shore protection methods which are capable of withstanding some degree of wave energy.
- The ability to maintain boat access across the breakwater.

Some of the current fundamental shortcomings include the following:

- Previous testing and theory has shown adequate performance of submerged active breakwaters in wave attenuation only for regular waves of small amplitude over narrow frequency bands.
- Progressive wave crests are limited in angle to a direct wave attack, an incident angle of zero degrees.
- Devising a robust spring and damping unit that can be used in a prototype scenario may prove to be a challenging task.

RESEARCH GOALS

In an effort to broaden the experimental background of submerged active breakwaters, a few key shortcomings were to be addressed. Initially, since most, if not all published experimental data is based on device performance with regular sinusoidal wave trains, the experiments were to be conducted using random wave signals as well. Developing seas, indicative of Great Lakes conditions, were to be modelled by using Jonswap spectra with a specified significant wave height, H_s, and a peak period, T_p.

Secondly, a single device in operation produces a typical performance curve that is narrow in bandwidth over which it provides adequate wave attenuation. In an effort to improve the frequency range, two devices, tuned to different conditions, were to be tested in parallel. This was meant to partially validate the "n" cylinder theory presented by Evans *et al*[3]. This dual-cylinder system was also to be examined under random wave conditions.

The devices would then be reversed in order to observe the potential benefits of having a smaller period-tuned device in front versus behind.

Thirdly, the performance of individual and dual systems is to be examined in four different depths of submergence using irregular wave conditions.

NUMERICAL MODEL

A numerical model to be used to provide a comparison between the theoretical efficiency (or ability to reduce the height of the transmitted waves) with experimental data was developed based primarily on the underlying assumptions of irrotational flow around the cylinder and first-order small amplitude wave theory. From an external force balance equating the oscillatory wave forces to the resistive forces of the cylinder, including added mass and hydrodynamic damping terms related to the cylinder motion, and the spring and damper effects, the efficiency can be calculated as,

$$E = \frac{4\omega^2 db}{\left\{k - (m+a)\omega^2\right\}^2 + \omega^2 (b+d)^2} \qquad [1]$$

where ω = angular wave frequency (2π/T), rads/s, d = damper constant, Ns/m,
b = hydrodynamic damping, Ns/m, k = spring constant, N/m,
m = cylinder mass per unit length, N/m, a = added mass, N/m.

From this relationship, it can be seen that to maximize the efficiency of the system, the spring rate and damper constant must be adjustable such that the following conditions can be met,

$$d = b \qquad \text{and} \qquad k = (m+a)\omega^2 . \qquad [2]$$

The added mass term, *a*, is representative of the additional mass of water that is moved in conjunction with the motion of the cylinder. The hydrodynamic damping term, *b*, can be thought of as the wave-making ability of the cylinder. Curves of the variation of these two parameters with wave number can be found in McIver[9]. By using the efficiency equation, we can essentially choose a desirable tuned wave period and then examine the predicted performance of a cylinder over a wide range of frequencies subjected to small amplitude waves. This results in the typical theoretical performance curves shown in Figures 2 and 3 in terms of wave height reduction (transmission coefficient) and energy removal (power absorption efficiency). Since the added mass and hydrodynamic damping terms vary to a large extent with wave frequency and depth of submergence, so do the predicted efficiency curves. Since this paper deals primarily with breakwater transmission, only transmission curves will be discussed.

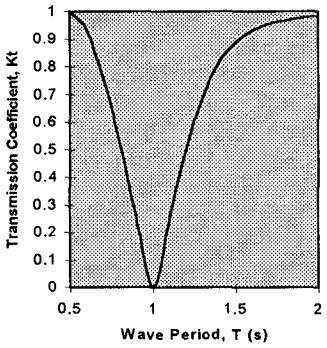

Figure 1. A typical cylinder response curve - wave transmission versus period

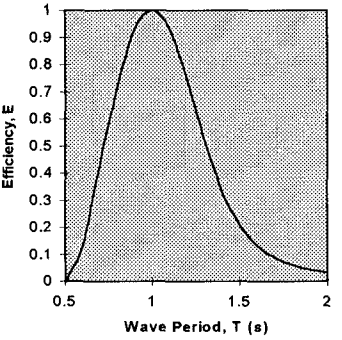

Figure 2. A typical cylinder response curve - power absorption efficiency versus period

Additional parameters that affect these curves are the cylinder's specific gravity and the spring and damper rates. Figures 4, 5, 6 and 7 show the variation in cylinder performance as a function of these parameters.

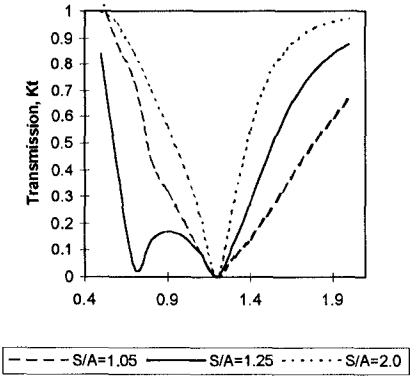

Figure 4. Variation in transmission with cylinder specific gravity

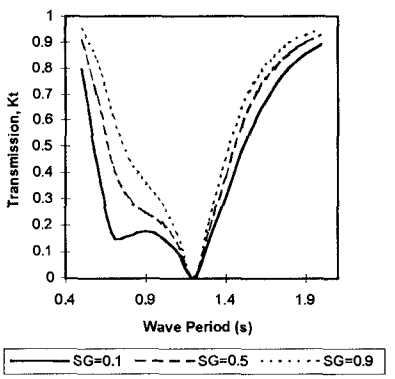

Figure 5. Variation in transmission with depth of submergence

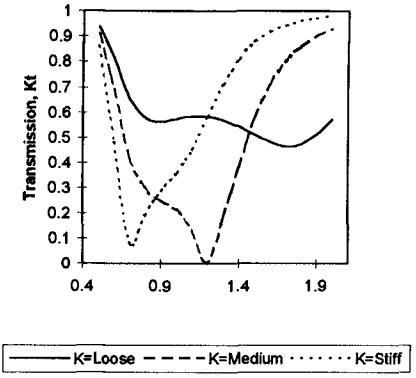

Figure 6. Variation in transmission with spring stiffness

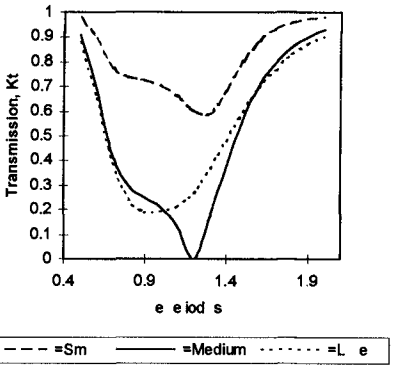

Figure 7. Variation in transmission with damping rate

From the experimental work of Davis[4, 5], it was shown that the numerical model can predict the performance of a single cylinder quite accurately provided the modeller has a good estimate of the spring and damper rates being used.

Further theoretical work carried out by Evans *et al*[3] demonstrated mathematically that any number of devices could be used in parallel with no destructive interference. The performance of a system of "n" cylinders could thus be predicted using superposition of the individual performance curves for each cylinder. Since the addition of any device could only cause additional reduction of the transmitted wave, an "n" cylinder system could only be an improvement over an "n-1" cylinder system. The outcome of this work showed that any degree of wave attenuation could be achieved over a wider frequency band by adding additional devices in parallel.

This effect can be seen in Figures 8 and 9 in terms of wave transmission and power absorption efficiency. In addition to this broadened frequency band, the system would be capable of performing satisfactorily in progressively larger waves due to the subsequent attenuation by successive cylinders.

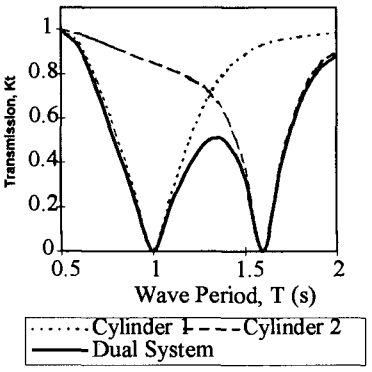

Figure 8. Wave transmission past a system of two cylinders in parallel, tuned to 1.0 s and 1.5 s

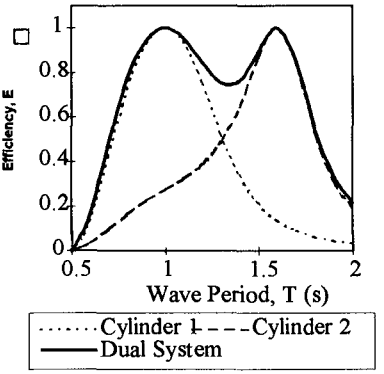

Figure 9. Power absorption efficiency of a two cylinder system, tuned to 1.0 s and 1.5 s

For the dual-cylinder system, Evans *et al*[3] expresses the power absorption efficiency as a function of the individual cylinder efficiencies,

$$E(T) = 1 - [1 - E_1(T)] \cdot [1 - E_2(T)] \qquad [3]$$

where E is shown as a direct function of the incident wave period, T. In addition, assuming the reflection is truly zero, the transmission coefficient of the dual-cylinder system can be expressed as,

$$K_T = K_{T_1} \cdot K_{T_2} \qquad [4]$$

The creation of this "n" cylinder model is restricted by the linear simplification that the transmitted wave is restricted to the fundamental harmonic.

EXPERIMENTAL SETUP

Tests were performed in a two-dimensional wave flume in the Queen's University Coastal Engineering Research Laboratory. The flume is 1.2 m deep and is approximately 50 m long. The water depth was maintained at 86.0 cm for all tests described in this paper. Both regular and irregular waves were utilized in the testing program. In order to determine the performance of a device for all conditions tested, a sweep of wave periods with a constant wave height was performed. Waves of 2.0, 3.0 and 5.0 cm were used with periods of 0.7 s to 2.0 s at 0.1 s intervals. Although this setup allows a conversion to any scale, the anticipated scale of 1:60 would project performance of a 12 m diameter cylinder in 1.2 m, 1.8 m and 3 m waves with periods ranging from 5.4 s to 15.5 s.

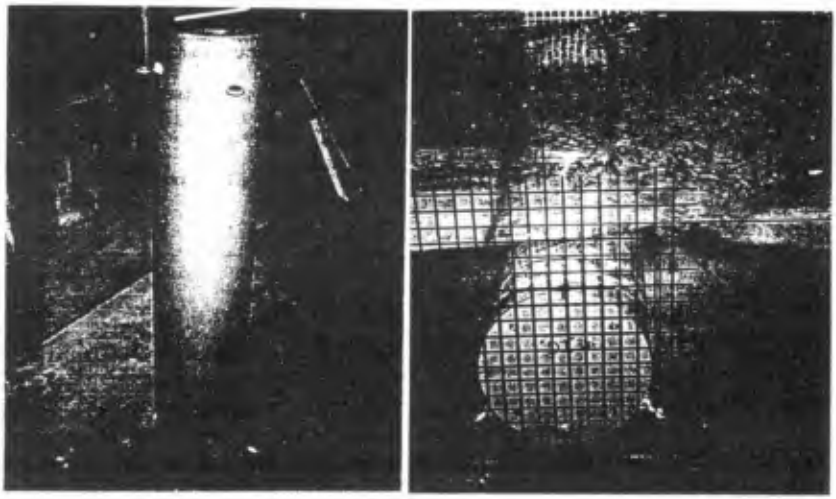

Figure 10. Test Cylinder

Figure 10 shows one of the test cylinders in the dry and in the wave flume. Both cylinders, 1.08 m long with a 10.6 cm (4") radius, were constructed using ABS pipe and symmetrically weighted to give a specific gravity of 0.3. Two 8.0 m long parallel tracks were installed on the flume bottom and equipped with stainless steel, double sealed bearings at the desired anchor points. Two cables at each side, attached at 90° to each other, passed down underneath the bearings and vertically up towards the springs that were located above the water surface.

The springs were automotive leaf springs attached to provide an upward force on the cables. Damping was not added because preliminary tests tended to indicate that there was too much damping already inherent with this cable system.

The wave flume was equipped with ten capacitance wave probes of which eight were sampled during each run. The signals were generated by the GEDAP wave generation and analysis package, developed by the NRC Canadian Hydraulics Center. Sampling was done at 20 Hz. The samples were then analysed by the GEDAP package by zero-crossing analysis and variance spectral density for a number of parameters including incident and transmitted significant wave height, incident and transmitted periods, incident and transmitted wave power and reflection from the device(s). The zero-moment wave height was not used due to the irregular nature of the transmitted spectra.

After the analysis of the wave signal, the efficiency, E, could be expressed as the fraction of the incident wave power absorbed by the cylinder,

$$E = \frac{P - P - P_T}{P} \qquad [6]$$

where P is the wave power of the incident (i), reflected (r) and the transmitted (t) components. The power is calculated as per small amplitude wave theory as,

$$P = \frac{\rho g^2 T H^2}{32\pi} \cdot \tanh(kd) \cdot \left\{1 + \frac{2kd}{\sinh(2kd)}\right\} \qquad [7]$$

where P = wave power , W/m
ρ = density of water, Kg/m^3
g = acceleration by gravity, m/s^2
T = wave period, s
H = wave height, m
d = water depth, m
k = wave number (2π/L), dimensionless.

Note that with this equation, the efficiency could also be determined easily by the measured wave heights thus knowing the values of the reflection coefficient, K_R, and the transmission coefficient, K_T,

$$E = 1 - K^2 - K_T^2 \qquad [8]$$

where

$$K = \frac{H}{H} \quad \text{and} \quad K_T = \frac{H_T}{H} \qquad [9]$$

since the wave power is a function of H squared. This efficiency equation could only be used if the transmitted wave was truly locked to the fundamental, since the power is a function of the wave period, T. As will be discussed later, wave scattering to higher harmonics is common and thus expressing E in terms of K_R and K_T alone is invalid.

RESULTS

The notation for the devices and systems of devices tested is shown in Table 1. To tune the devices to the desired frequency, the spring and damper rates require adjustment. The intent was to determine a suitable spring rate and then add damping to maximize the efficiency of the devices by the addition of a rubbing strip or "brake" on the cables. This was tested but any addition of frictional damping caused a decrease in the performance.

Device Number	Desired Tuned Period	Location
Device 1	1.0s	Cylinder by itself
Device 2	1.5s	Cylinder by itself
System 3	1.0s , 1.5s	Device 1 in Front, Device 2 in Back
System 6	1.5s , 1.0s	Device 2 in Front, Device 1 in Back

Table 1 Device descriptions

Reflection from the cylinders rarely exceeded 5%. Even reflection of up to 10% would cause no more than 1% error in the determination of the efficiency, which is certainly less than the accuracy of the probe sampling and analysis routines combined. The reflection from the cylinders could thus be neglected as well. Measurements of significant wave height and wave power in front and behind the cylinder could therefore directly represent incident and transmitted components.

Regular Wave Results

The results of extensive testing using regular waves are shown in Figures 12, 13, 14, and 15. Device 1 shows trends in good agreement with the theoretical optimum although a certain degree of difference is expected as the optimum is based on infinitely small waves. The shape of the observed curve is quite consistent with the theory, indicating that the inherent damping is close to the required damping. The theoretical drop in efficiency on the other side of the peak cannot be examined due the limitations in wave generation at periods less than 0.7 s. During the higher frequency waves (T<1.1 s), transmission was typically 40% to 70% but increased to 80% to 100% at lower frequencies. The data supports the trend that an increase in incident wave height will generally cause a decrease in efficiency. Device 1 transmission peaked with the attenuation of 2 cm waves at 0.7 s to a K_T of 28%.

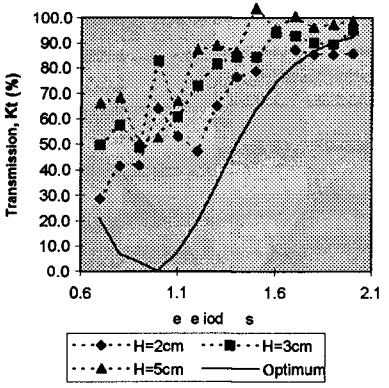

Figure 12. Device 1 transmission in regular waves

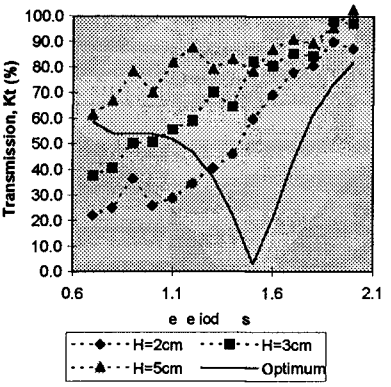

Figure 13. Device 2 transmission in regular waves

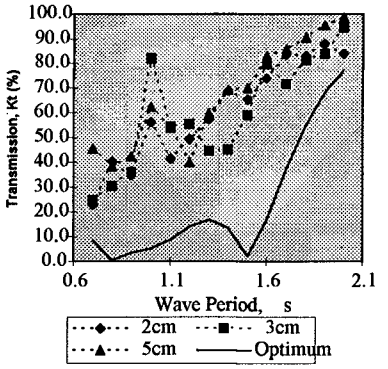

Figure 14. System 3 transmission in regular waves

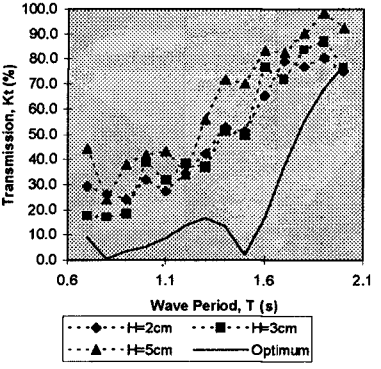

Figure 15. System 6 transmission in regular waves

Experiments with Device 2 were significantly different than the desired optimum. Since the same bearing/cable mechanism was used as with Device 1, inherent damping of was significantly greater than required. This caused skew of the peak to significantly lower wave periods than the desired 1.5 s peak. Despite this problem, Device 2 provided better wave attenuation for 2 cm and 3cm waves than Device 1 with K_T values typically 10% less. Wave attenuation for Device 2 peaked again at 0.7 s for 2 cm waves with a K_T of 22%. It should be noted that the performance curves show a rather broad frequency band over which they perform satisfactorily. The peaks are broad for two reasons, the first being the low specific gravity of the cylinders tested (see Figure 4) and secondly, the excessive damping inherent in the test setup (see Figure 7).

System 3 performed worse than anticipated. Firstly, with the first cylinder performing satisfactorily, scattering of the 0.8 s to 1.2 s to the second harmonic proved to be of too high a frequency for the second device to provide any attenuation of its own. It actually had a detrimental effect, especially with the smaller waves. Possible reasons for include the fact that the inherent damping and friction in the system did not permit the rear cylinder to oscillate in the typical circular orbit and for the most part, the cylinder did not move. The small wave forces generated by the reduced wave were insufficient to cause any motion. Additionally, the smaller period scattered waves of 0.4 s to 0.6 s are believed to experience additional shoaling and their energy tends to pass primarily over the top of the cylinder. In one case, a transmission of 31% occurred across the first cylinder and 133% across the second which resulted in an overall system transmission of 42%. It's unfortunate that the wave generator used could not properly generate waves of such high frequencies such that the performance of single devices under very small period waves could be tested. Wave attenuation peaked at 0.7 s with a K_T of 23% for 2 cm waves and tapered off almost linearly at higher periods.

When the position of the cylinders was reversed, the performance of the system improved. For System 6, the greatest attenuation resulted in K_T values of 17% to 18% for wave periods of 0.7 s, 0.8 s and 0.9 s for 3 cm waves. The data tends to approximate the theoretical optimum better with a typical improvement greater than 5% across the entire spectrum. Overall, transmissions of 50% and less were achieved over 0.7 s to 1.2 s for all wave heights tested, providing better results than system 3 and both cylinders individually. Again, the wave attenuation for the larger waves improved significantly while the 2 cm wave attenuation improved to a lesser degree. The main beneficial effect of a dual-cylinder system is that the performance curves of the larger 3 cm and 5 cm waves are significantly improved. No significant widening of the performance curves was achieved primarily due to the lack of difference between the individual devices' peak periods.

Irregular Wave Results

The results with irregular waves are shown in Figures 17, 18, 19 and 20. The response curves are significantly smoother as no standing waves develop. In comparing these results with those of regular tests, observation shows that larger wave heights cause less drop in efficiency than with regular waves, for all devices tested. Wave attenuation of 5 cm waves always improved, for 3 cm waves it usually improved mildly while for 2 cm

performance was rarely improved. All devices tend to perform significantly better at longer periods with irregular waves.

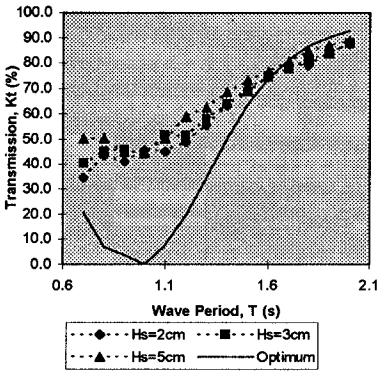

Figure 17. Device 1 transmission in irregular waves

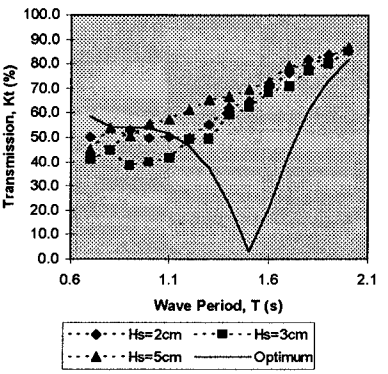

Figure 18. Device 2 transmission in irregular waves

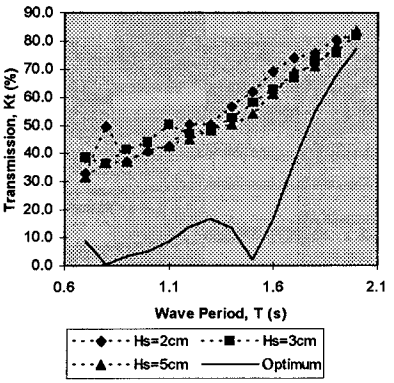

Figure 19. System 3 transmission in irregular waves

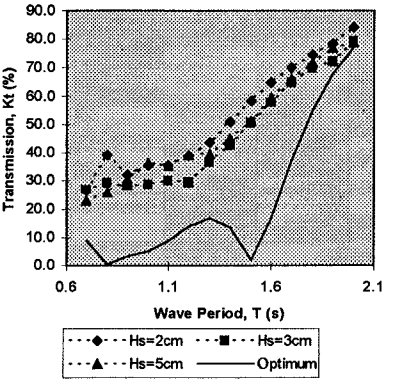

Figure 20. System 6 transmission in irregular waves

These two latter points are likely due to the nature of a Jonswap spectrum. First, the x-ordinate on the graphs indicates the peak period of the spectrum. With regular waves, the peak period is also equal to the average period. However, with irregular wave spectra, the average period is less than the peak period, such that the overall device performance may reflect response to the average period as opposed to the peak period. Second, we are using the significant wave height as the governing wave height parameter. For regular waves, it is more representative of the average wave height, as opposed to irregular wave signals, where the average wave height is significantly less than the significant wave height. The typical drop in efficiency in 2 cm significant waves can be attributed to this as

well, since the average height of the 2 cm irregular waves was likely insufficient to generate the required oscillatory forces to create ideal movement of the cylinder.

The peak attenuation of Devices 1 and 2 in random seas is quite consistent with the regular wave tests. It can be seen more clearly with this data, that the peak period of Device 2 is approximately 1.0 s whereas the peak of Device 1 may be 0.7 s or less. The only significant difference in performance is for waves of larger periods, where Device 2 causes 5% to 10% more attenuation than Device 1. Device 1 peaked at 0.7 s with 2 cm waves with a K_T of 34%. Device 2 peaked with a K_T of 39% at 0.9 s with 3 cm waves.

The difference in performance based on which device is in front can also be observed easier with the irregular waves. The wave attenuation is up to 15% more for System 6 than System 3. System 3 peaked at 0.7 s with 5 cm waves with a K_T of 32%, while system 6 peaked at 0.7 s with 5 cm waves with a K_T of 23%.

Essentially, the efficiency of these breakwaters was only very slightly worse in random developing seas than in regular sinusoidal waves. The linear theory is also clearly capable of predicting trends in their performance under random waves. This is very beneficial since the numerical model could therefore be used for prototype design with relative confidence that it will perform as intended in random wave conditions.

SUMMARY

A variety of very general, conservative conclusions can be drawn from these results.

1. Wave transmission of less than 50% can be obtained by a single breakwater over a relatively large frequency range for waves less than 0.3A, where A represents the radius of the cylinder. This broad frequency envelope can be attributed primarily to the use of cylinders with a low specific gravity.
2. Wave transmission of less than 50% can be obtained by a dual-breakwater system over a slightly larger frequency range for waves less than 0.5A.
3. A general trend exists whereby the efficiency of the breakwater drops when subjected to waves of increasing size.
4. The spring rate and degree of damping are crucial in tuning a cylinder to the intended design conditions. Over-damping tends to broaden the performance curve and drop the theoretical peak efficiency slightly.
5. The numerical model, which predicted this test data satisfactorily, is sufficient to predict trends in the performance of submerged active breakwaters. It also shows that a wider performance envelope can be achieved when placing two devices in parallel, tuned to different wave periods. The test data cannot confirm the widened envelop, but it shows that even with devices tuned to approximately the same peak period, an overall improvement in efficiency can be obtained.
6. The order in which the individual tuned cylinders are placed appears to have some effect on the dual-breakwater system performance curves. Positioning the cylinder tuned to the longer periods in front and shorter periods behind provided better results

when examining the combined systems. Designing and positioning cylinders with the second device tuned to the second harmonic would likely have some practical advantages. Unfortunately, the numerical model and experimental data cannot fully support this hypothesis at this time.

7. A two-cylinder system can cause wave attenuation of larger waves to a level that may be acceptable relative to the attenuation caused by a single cylinder.
8. Current testing is being performed to observe the effects of varying the depth of submergence on a breakwater with pre-set tuned conditions. A comparison will be made to the numerical model.

References

[1] Evans, D.V. 1976. *A Theory for Wave-Power Absorption by Oscillating Bodies.* Journal of Fluid Mechanics, vol. 77, part 1, pp. 1-25.

[2] Evans, D.V., D.C. Jeffery, S.H. Salter and J.R.M Taylor. 1979. *Submerged Cylinder Wave Energy Device: Theory and Experiment.* Applied Ocean Research, vol. 1, pp. 3-12.

[3] Evans, D.V., J.P. Davis and M.A. Srokosz. 1979. *A System of Efficient Wave-Energy Absorbers.* Mechanics of Wave-Induced Forces on Cylinders. T.L. Shaw. Pitman Publishing Limited, London. pp. 673-683.

[4] Davis, J.P. 1986. *The Submerged Cylinder Wave Energy Device.* PhD Thesis. University of Bristol, UK.

[5] Davis, J.P. 1990. *Wave Energy Absorption by the Bristol Cylinder - Linear and Non-Linear Effects.* Proceedings of the Institution of Civil Engineers, Part 2, vol. 89, pp. 317-340.

[6] Dean, W.R. 1948. *On the Reflexion of Surface Waves by a Submerged Circular Cylinder.* Proceedings of the Cambridge Philosophical Society, vol. 44, pp. 483-491.

[7] Ursell, F. 1950. *Surface Waves on Deep Water in the Presence of a Submerged Circular Cylinder.* Proceedings of the Cambridge Philosophical Society, vol. 46, pp. 141-158.

[8] Ogilvie, T.F. 1963. *First- and Second-Order Forces on a Cylinder Submerged under a Free Surface.* Journal of Fluid Mechanics, vol. 16, pp. 451-472.

[9] McIver, P. and D.V. Evans. 1983. *The Occurrence of Negative Added Mass in Free Surface Problems involving Submerged Oscillating Bodies.* Journal of Engineering Mathematics, vol. 18, pp. 7-22.

WAVE FORCE AND STABILITY OF ARMOR UNITS FOR COMPOSITE BREAKWATERS

Katsutoshi KIMURA*, Yuzo MIZUNO and Michifumi HAYASHI*****

Abstract

The stability of armor units for composite breakwaters was studied by two- and three-dimensional model tests and prototype failure analyses. The wave force on armor blocks was cleared for different relative mound depths and berm widths. The stable weight of armor blocks is proposed in which the block shape factor is used as a parameter. The necessary thickness of foot-protection blocks is formulated as a function of the relative mound depth for the breakwater trunk and head.

Introduction

Rubble mounds for composite breakwaters are usually protected by armor blocks and foot-protection blocks. These blocks are conventionally designed according to the knowledge obtained through past experience. However, due to a recent increase in the construction of breakwaters at deeper locations with a higher design wave height, a number of cases have occurred in which such experience-based methods are no longer effective. In addition, the armor stability for three-dimensional conditions, such as oblique incident waves and wave action around breakwater heads, remains unknown and damage under such conditions has been increasing.

In this study, the stability of armor blocks and foot-protection blocks was

* **Civil Engineering Research Institute, Hokkaido Development Bureau, Hiragishi, Sapporo 062, JAPAN**

** **Hokkaido Institute of Technology, Maeda 7-15, Sapporo 006, JAPAN**

*** **Cold Region Port and Harbor Engineering Research Center,Kita-7, Nishi-2, Sapporo 060, J APAN**

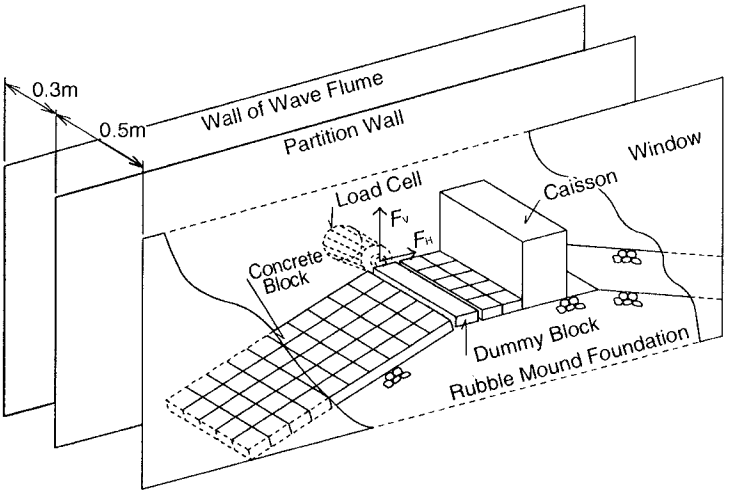

Figure 1 Breakwater model for measuring wave forces

examined by two- and three-dimensional model tests. From these results, methods to calculate the necessary armor units for composite breakwaters are proposed, and their applicability for practical design is verified by data analyses of previous damage.

Wave forces on armor blocks

A two-dimensional wave flume (24m × 0.8m × 1.0m) was divided into two parts. The horizontal and vertical wave forces acting on the dummy block (48cm × 10cm ×

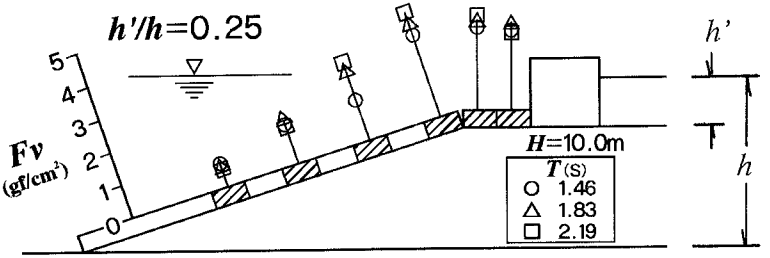

Figure 2 Wave force distribution

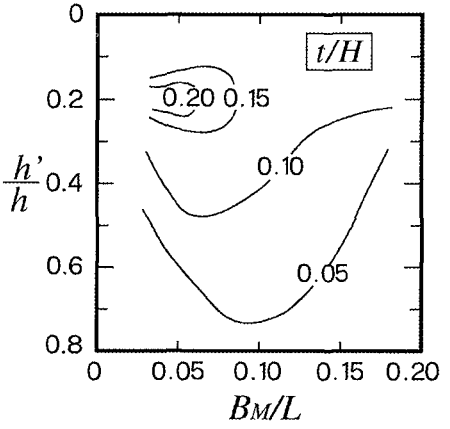

Figure 3 Contour diagram for wave force acting on blocks

5cm) were obtained using a load cell (**Figure 1**). The structural conditions were: water depth h was set at 50 cm and the depth of the mound h' and mound berm width B_M were altered. The wave force experiment was made with regular waves and the wave conditions were altered using three types of wave period, T, and a wave height, H, of 2 to 14 cm. In addition to the wave forces, the water levels above the dummy block were also measured

Figure 2 shows the vertical wave force at each location of the mound when the relative mound depth h'/h was 0.25. The wave force reached its maximum at the mound shoulder and decreased as the water depth increased. The wave force at the front of the caisson was slightly smaller compared with that of the shoulder.

Figure 3 shows the vertical wave forcc acting on the block at various values of relative berm width B_M/L (L: wave length for the water depth h) and relative mound depth h'/h, which was obtained by dividing t, or the required thickness of blocks to resist the vertical wave force, by the wave height H. The maximum wave force acting on the block was at $h'/h = 0.2$, with the corresponding required block thickness t/H being about 0.2. Under the usual mound conditions of $h'/h = 0.6$ to 0.8, the maximum wave force occurs when B_M/L is at or around 0.1.

Stability Formula for Armor Blocks

The following Hudson's formula gives the stable weight of an armor block,

$$W = \frac{\gamma_d H_{1/3}^3}{N_S^3 (S_r - 1)^3} \tag{1}$$

where, $H_{1/3}$ is the significant wave height needed for designing, γ_d is the unit weight of the block, and S_r is the relative density of concrete in the sea water. The stability number N_S was formulated by Tanimoto et.al.(1982) and was extended for armor stones by Kimura et.al.(1994). For armor blocks, the following equations were modified to separate the block shape factor and mound shape conditions of composite breakwaters,

$$N_S = N_{SO} \cdot \max\{1.0, A\frac{(1-\kappa)}{\kappa^{1/2}}\frac{h'}{H_{1/3}} + \exp[-0.9\frac{(1-\kappa)^2}{\kappa^{1/2}}\frac{h'}{H_{1/3}}]\} \tag{2}$$

where, h' is the water depth of the mound foundation, N_{SO} is the standard stability number of each armor unit, and is determined by stability tests for the high mound conditions. The coefficient A was decided from the results of the stability tests. The non-dimensional flow parameter κ is expressed as,

$$\kappa = \begin{cases} \dfrac{4\pi h'/L'}{\sinh 4\pi h'/L'} \cdot \sin^2 kB_M & (B_M/L' < 0.15\ ) \\ \dfrac{4\pi h'/L'}{\sinh 4\pi h'/L'}\{2\sin^2(0.15 \cdot 2\pi) - \sin^2(2\pi B_M/L')\} & (0.15 < B_M/L' < 0.25) \end{cases} \tag{3}$$

where L' is the wave length of the design significant wave period where the water depth is h'.

Two-dimensional model tests for armor blocks

The stability tests were made for three types of blocks, A, B and C, using irregular waves. The number of waves was 500 and the stability number, N_S, was calculated by using the critical stability weight corresponding to the damage ratio of 1%. The relative mound depth, h'/h, was altered within the range of 0.25 to 0.75. The high

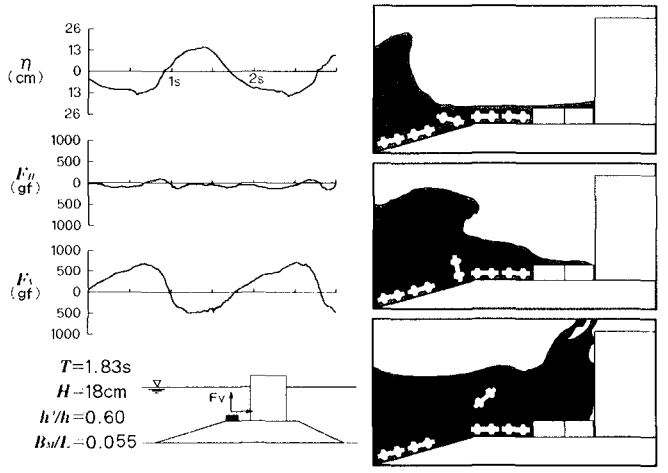

Figure 4 Wave action and block motion

mound condition of h'/h= 0.2 represents the hardest condition for the stability of the armor block, and the stability number at this time was defined as the critical stability number N_{SO}.

Figure 4 shows the motion of blocks together with time-series describing wave forces obtained by load cells when the wave period T was 1.83 s, wave height H was 18 cm, h'/h was 0.6 and B_M/L' was 0.055. The vertical wave force, F_V, was larger than the horizontal wave force, F_H. Considering the block motion, the peak of the vertical wave force coincided with the time when the block was uplifted. The uplifted block was then rolled by the wave-induced flow. Predominance of the vertical wave force is characteristic of the wave force acting on armor blocks. After the uplift motion, the blocks are overturned by the wave-induced flow. The stability number N_S was obtained for blocks A, B and C under various structural and wave conditions. The coefficient A in Eq.(2) was found to be 0.525.

Figure 5 shows the relationship between $h'/H_{1/3}$ and the dimensionless stability number N_S/N_{SO}, when κ is from 0.06 to 0.40. The values of N_S/N_{SO} for blocks A, B

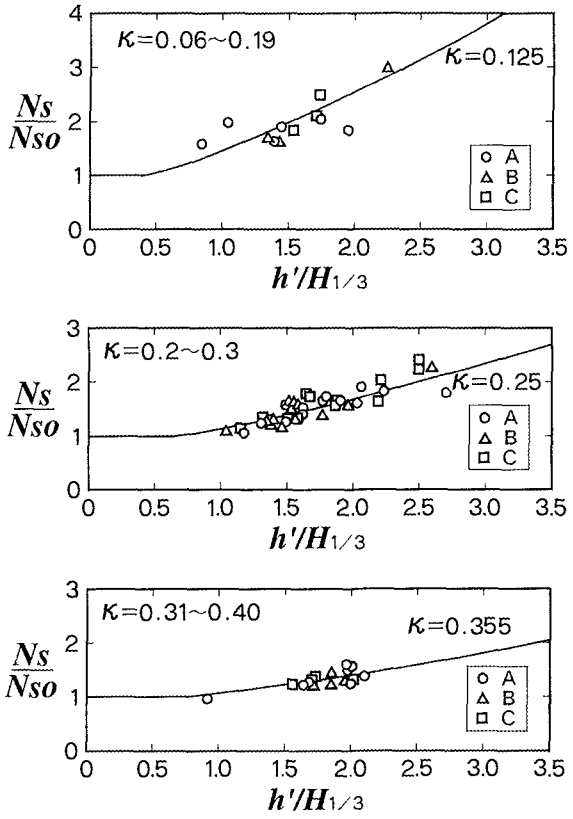

Figure 5 Stability number

and C are indicated by different marks, but each mark corresponds well with the calculated values (solid line), thus verifying the calculation method. N_{SO} was found to be 2.0 for all blocks used.

Three-dimensional model tests for armor blocks

The three-dimensional test was made in a wave basin 33 m wide and 20 m long.

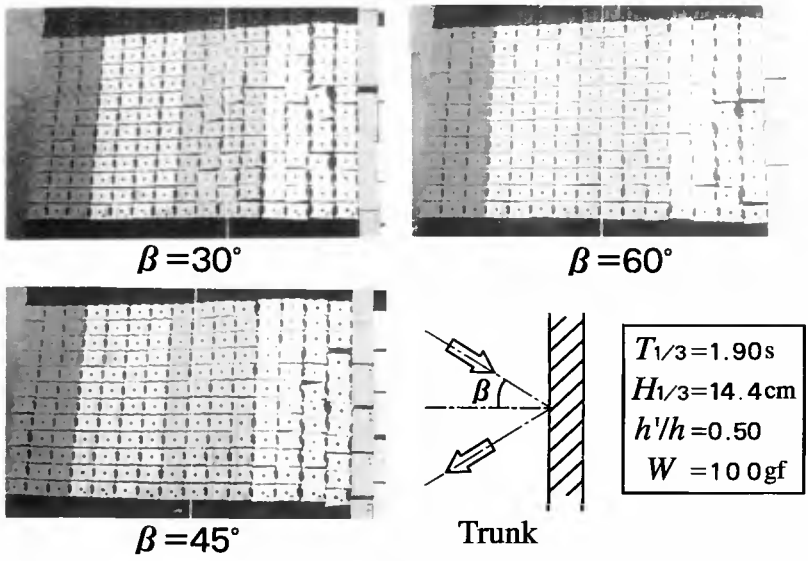

Photo 1 Damage patterns for oblique wave attack

By changing the breakwater alignment, the wave incident angle was altered in four cases to 0, 30, 45 and 60deg. The length of the island breakwater was 8.4 m for normal incidence and 7.2 m for oblique incidence. The water depth was set constant at 46.8 cm and the mound depth was altered. Long-crested irregular waves were used for the stability test with a D-block of three weights (66gf, 100gf and 140gf). The mound condition of h'/h was set at 0.5, the wave period $T_{1/3}$ was constant at 1.90s and wave height $H_{1/3}$ was varied in a range of 5 to 25 cm.

Photo 1 shows the movement of blocks under oblique incident conditions of $H_{1/3}$=14.4cm, $T_{1/3}$=1.90s, with β = 30, 45 and 60 deg. The damage of armor blocks occurred mostly at the berm of the mound for oblique wave conditions. This compares with normal incident conditions when damage starts from the slope of the mound.

Figure 6 shows the effect of the incident wave angle for a stable block weight for the wave condition of $T_{1/3}$=1.90s and $H_{1/3}$=18.0cm. The stable weight for oblique waves was smaller than that for normal incidence.

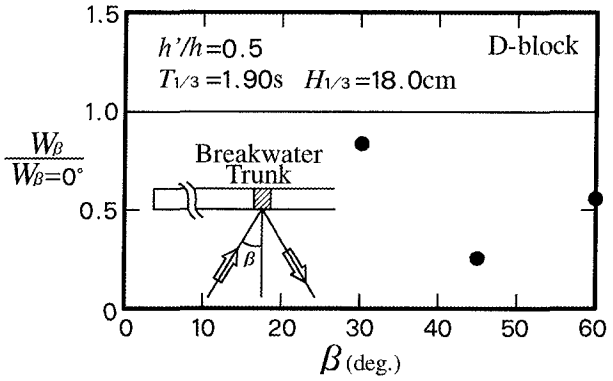

Figure 6 Armor block stability for oblique wave attack

Required thickness of foot-protection blocks

The two-dimensional experiments were made to identify the stability of foot-protection blocks using a wave flume (28 m × 0.6 m × 1.0 m) and irregular waves. Water depth h was constant at 46.8 cm, and three different mound depth h' were used. The foot-protection blocks used were of a uniform plane shape (10cm in length × 5cm in width), with their thickness t varied between 1.6cm, 2.4cm and 3.2cm. The specific gravity of the block model mortar was adjusted in accordance with the specific gravity of seawater. The foot-protection blocks were laid side by side in two rows, with the longer side facing the upright section.

The three-dimensional experiments were made using the wave basin mentioned previously. The model's cross section was the same shape as in the two-dimensional experiments. Using four different incident angles β (0, 30, 45 and 60 deg.), the breakwater trunk and head were analyzed for their respective required thicknesses. The breakwater head, in particular, was checked both forward and backward in relation to the direction of the waves.

Table 1 shows the standard dimensions of foot-protection blocks commonly used in Japan. The thickness of foot-protection block t was formulated as a function of relative mound height

Table 1 Standard dimension of foot-protection blocks

Required Thickness t (m)	Size of F-P Block $l \times b \times t$ (m) (m) (m)
~0.8	2.5×1.5×0.8
~1.0	3.0×2.5×1.0
~1.2	4.0×2.5×1.2
~1.4	5.0×2.5×1.4
~1.6	5.0×2.5×1.6
~1.8	5.0×2.5×1.8
~2.0	5.0×2.5×2.0
~2.2	5.0×2.5×2.2

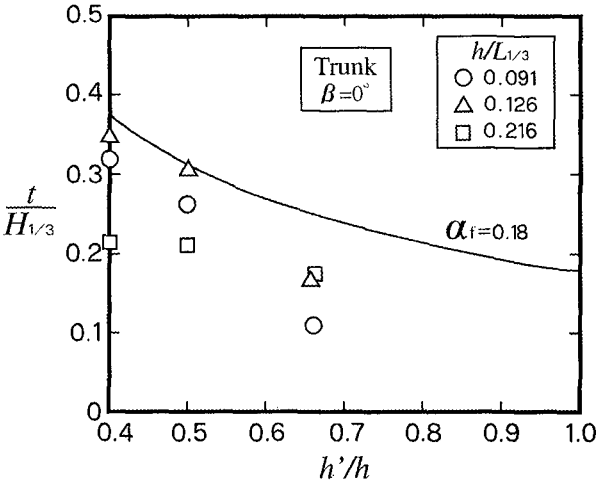

Figure 7 Necessary thickness for trunk section

h'/h as follows;.

$$t/H_{1/3} = \alpha_f (h'/h)^{-0.787} \qquad (h'/h \geq 0.4\ ) \qquad (4)$$

Here α_f is a parameter showing the differences in breakwater trunk and head.

Figure 7 shows the results of the stability test at the breakwater trunk. In this figure, the horizontal axis represents the relative mound depth, h'/h, and the vertical axis represents the thickness of the foot-protection block, t, which was made non-dimensional by the wave height $H_{1/3}$. The necessary thickness was greater when the period was shorter. By focusing on the condition of the safe side, the necessary thickness was formulated as shown with the dotted line in this figure (α_f = 0.18) for the breakwater trunk.

Figure 8 shows the effect of incident wave angles. In the case of oblique wave attack at the breakwater trunk, relative mound depth, h'/h, was limited to 0.5. When the oblique incident angle was within 60 deg, the difference in necessary thickness was smaller compared with the normal incident condition.

Figure 9 shows the results of the experiments on the breakwater head. Unlike

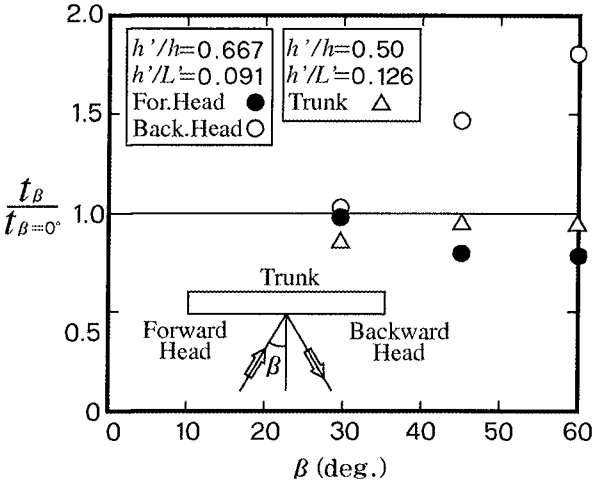

Figure 8 Effect of oblique wave attack

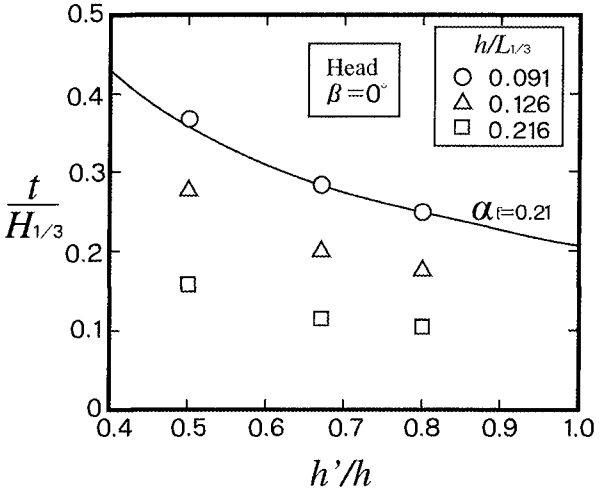

Figure 9 Necessary thickness for head section

the breakwater trunk, the required thickness increased as the wave period increased, which is due to local flows generated at the breakwater head. From the values on the safe side of the experiment range, a_f for the breakwater head corresponds to 0.21. According to **Figure 8**, which shows the influence of the direction of waves when the relative mound depth $h'/h = 0.667$ at the breakwater head, the required thickness at the forward head is maintained at about the same level by the incident angle β, while at the backward head the required thickness increases when β is 45 deg. or more. This is because of the rapid flow around the corner and the increasing standing wave height at the backward head of the island breakwaters.

Table 2 Prototype failures of foot-protection block

Name of Port	Year and Mon.	Head or Trunk	Structural Conditions		Storm Wave Conditions			F-P Block	
			h (m)	h' (m)	$H_{1/3}$ (m)	$T_{1/3}$ (s)	β (deg.)	t_p (m)	W (tf)
A	66.01	H	8.0	5.5	5.8	–	5.0	1.5	21.6
B	67.03	T	16.5	10.0	5.5	–	18.0	1.5	13.8
C	70.01	H	11.5	9.5	6.8	13.0	17.5	1.5	38.8
D	70.01	H	9.0	6.0	5.5	14.1	0.0	1.5	21.6
E	70.01	H	17.0	8.0	5.0	8.1	0.0	1.0	17.3
F	70.01	T	8.0	6.5	6.8	13.0	17.5	1.5	38.8
G	71.08	H	14.0	6.7	4.5	–	–	1.0	–
H	71.01	H	15.5	8.5	4.6	11.0	0.0	1.0	11.5
I	71.09	H	5.7	4.0	4.7	15.0	19.0	1.0	23.0
J	72.01	T	15.5	10.0	7.0	14.0	0.0	1.5	31.1
K	72.02	T	6.0	4.0	5.8	15.0	19.0	1.0	23.0
L	76.10	H	19.0	14.0	7.5	12.3	31.0	1.5	38.8
M	76.10	T	15.5	13.5	7.1	13.6	31.0	1.5	38.8
N	78.01	H	11.0	8.5	6.2	–	7.0	1.5	41.1
O	78.01	H	17.5	11.0	6.3	–	0.0	1.5	41.1
P	78.01	H	17.0	11.0	6.3	–	0.0	1.5	41.1
Q	79.12	H	18.0	11.8	10.8	–	26.3	2.0	47.6
R	79.12	H	18.0	11.8	10.8	–	26.3	1.5	46.6
S	80.01	H	16.5	13.0	7.0	–	15.0	1.5	41.4
T	80.09	T	11.5	8.5	5.6	10.0	14.0	1.2	34.5
U	80.10	T	8.0	5.0	5.7	13.0	45.7	1.5	31.1
V	80.10	H	13.7	8.5	5.9	9.4	–	1.0	–
W	81.08	H	24.0	16.5	9.2	11.0	0.0	1.5	41.4
X	85.01	H	11.6	8.0	5.6	10.1	66.0	1.2	27.6

Analysis of disaster damage regarding foot-protection blocks

Table 2 summarizing the disasters (1966 to 1991) related to destruction of foot-protection blocks of composite breakwaters in Japan. In 18 cases out of 25, breakwater heads experienced disaster damage, this indicating that breakwater heads suffer more damage than breakwater trunks. The details show that foot-protection blocks on the breakwater trunk experience less displacement. In this case, the damage was limited merely to foot-protection block displacement. In contrast, on the breakwater head, in many cases, foot-protection block displacement is followed by rubble foundation scouring. The incident wave angle β in most disasters was within 30° .

Figure 10 shows a typical example of the disaster condition at the breakwater head in S-Port. The details of the storm wave are assumed to be: $H_{1/3}$ =7.0 m, $T_{1/3}$ =13.5 s, incident wave angle β =15 deg. Foot-protection blocks on the harbor side (40 tf) were scattered, and 150 m^3 of material at the corner of the rubble mound foundation (0.2～0.3tf) below the caisson was scoured. When the wave incidence was almost normal, the damage started from the harbor side corner of the head caisson.

In X-Port, the island breakwater tail suffered greatest damage from the β =66° of oblique incident waves (**Figure 11**). The wave condition was: $H_{1/3}$ =5.6m, $T_{1/3}$ =10.1s. The damage was concentrated at the breakwater tail, and the foot-protection blocks (28tf) were displaced and partly broken by the shock of the displacement. Such damage to the breakwater head was caused by the rapid flow around corners. It corresponds well with the numerical calculation results shown by Kimura et al. (1994) in terms of the flow speed around the mound. The required thickness expected for the foot-protection block to prevent disaster damage in **Table 2** is given by Eq.(4).

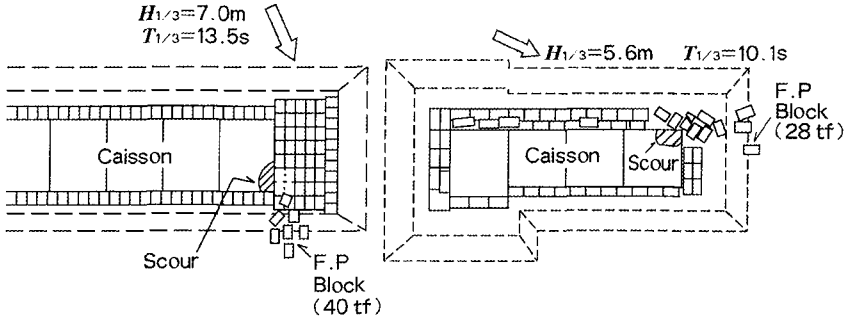

Figure 10 Damage at S-Port

Figure 11 Damage at X-Port

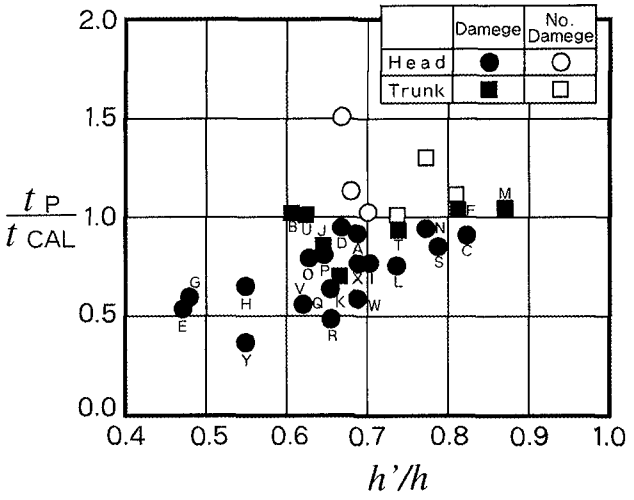

Figure 12 Comparison with prototype failures

Figure 12 shows on the axis of the ordinates that the ratio of required thickness of foot-protection blocks used t_p to t_{cal}, which contrasts with the relative mound depth h'/h on the axis of the abscissa. Most of the damage to foot-protection blocks occurred under the condition of t_p/t_{cal} =1 on both the breakwater head and trunk, which verifies the adequacy of the calculation method.

Conclusions

The calculation method of the stable weight for composite breakwater armor blocks and the required thickness of foot-protection blocks are discussed. The major conclusions are as follows;

- Armor blocks:
  - A calculation method for the stability number using a block form factor as a parameter is proposed.
  - For oblique incident waves, the weight required for stability is likely to be less than for normal incident waves.
  - The stability number for wide mound berm conditions is formulated.

- Foot-protection blocks:

- The required thickness for breakwater head and trunk are formulated by using the ratio of the relative mound depth as a major parameter.
- The wave direction effect on the breakwater trunk was found to be small..
- The necessary thickness at the breakwater head needs to be increased depending on the wave direction.
- The adequacy of the required thickness calculation method was verified from field damage data.

Acknowledgments

We would like to thank Dr. Shigeo Takahashi, Port and Harbour Research Institute, Ministry of Transport, Japan, for his valuable overall suggestions concerning this study. The great contribution of Mr. Takanobu Suzuki of Hokkaido Development Bureau and Mr. Yoshikazu Doi of North Japan Port Consultants is also deeply appreciated.

References

Kimura, K., S. Takahashi and K. Tanimoto (1994): Stability of Rubble Mound Foundations of Composite Breakwaters under Oblique Wave Attack, Proc. of 24th ICCE, pp. 1227-1240.

Tanimoto, K., T. Yagtu and Y. Goda (1982): Irregular Wave Tests for Composite Breakwaters Foundations, Proc. of 18th ICCE, pp.2144-2163.

HYDRAULIC PERFORMANCE OF A HIGH MOUND COMPOSITE BREAKWATER

Muttray, M.[1]; Oumeraci H.[2]; Shimosako, K.[3]; Takahashi, S.[4]

Abstract

The hydraulic performance of an innovative structure based on the concept of a high mound composite breakwater has been investigated in large-scale hydraulic model tests in the Large Wave Flume (GWK) of the Coastal Research Center (FZK), Germany. The experimental results concerning wave breaking, wave transmission and wave reflection are presented.

1 Introduction

The development of effective and economic protective structures (sea walls, breakwaters etc.) still remains one of the main tasks in coastal engineering. Due to increasing requirements (structural integrity, multipurpose use, environmental aspects etc.) the complexity of these structures is also growing. It is therefore necessary i) to better understand the hydraulic processes at, on and inside these structures and, based on this understanding, ii) to develop rational design formulas.

A new type of breakwater called 'high mound composite breakwater' (HMCB) has been developed at the Port and Harbour Research Institute (PHRI), Japan. It will be applied for the protection of artificial islands along the Japanese coast. This new structure appears to be more effective in terms of hydraulic performance and stability than traditional breakwaters.

Within a joint research project between Port and Harbour Research Institute (PHRI), Yokosuka/Japan and Leichtweiß-Institute (LWI) of the Technical University Braunschweig/Germany the wave load on a HMCB has been investigated in

[1]Dipl.-Ing., Research Assistant, Leichtweiß-Institute, TU Braunschweig, Beethovenstr. 51a, 38106 Braunschweig, Germany, e-mail: m.muttray@tu-bs.de

[2]Prof. Dr.-Ing., University Professor, Managing Director of Leichtweiß-Institute, TU Braunschweig

[3]Senior Research Engineer, Hydraulic Engineering Division, Port and Harbour Research Institute, 3-1-1 Nagase Yokosuka, Japan 239, e-mail: shimosako@cc.phri.go.jp

[4]Dr. Engg., Chief of Maritime Structures Lab., Hydraulic Engineering Division, Port and Harbour Research Institute

1996. In a second Japanese-German research project between Civil Engineering Research Institute (CERI), Hokkaido, Japan and LWI wave overtopping and splash on a HMCB has been studied in 1998. This paper is intended to summarize and discuss the main results concerning the hydraulic performance for this new type of breakwater mainly using results from the first project.

(a) Historical Background

A traditional high mound breakwater consists of a rubble foundation which is larger than the foundation of a caisson breakwater but smaller than a normal rubble mound breakwater. A monolithic superstructure which is much smaller than a caisson but larger than the crown wall on a rubble mound breakwater is placed on top of this foundation (Fig. 1).

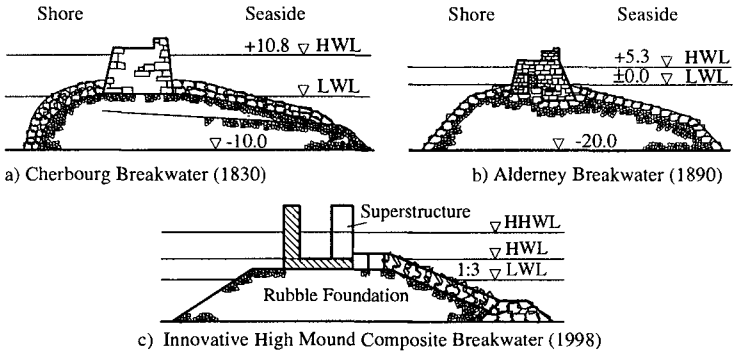

a) Cherbourg Breakwater (1830)

b) Alderney Breakwater (1890)

c) Innovative High Mound Composite Breakwater (1998)

Figure 1: High Mound Composite Breakwater Concept (HMCB-Concept)

The high mound breakwater concept is very old *(Takahashi, 1997)*. The Cherbourg breakwater, originally a rubble mound breakwater, was reconstructed in 1830. Its height was increased, a superstructure was placed on top and it became a high mound breakwater (Fig. 1a). The Alderney breakwater, built in 1890, is another example for an early high mound breakwater (Fig. 1b).

The advantages of high mound breakwaters are as follows:

- the volume of the rubble material is smaller than for a traditional rubble mound breakwater.
- all armour units are placed below still water level, therefore a smaller block weight is required than for a rubble mound breakwater.
- the superstructure is much smaller than a traditional caisson breakwater.

Since armour units, mound and superstructure are smaller than for traditional breakwaters the construction is easier and the costs are lower. However, stability problems may arise from breaking wave impact loads on the monolithic superstructure. The waves start breaking on the seaward slope of the rubble foundation and

cause impact loads which may be critical for the stability of the comparatively small superstructure. Consequently, the breakwater development has moved from the high mound towards low mound composite breakwaters which became the standard type of composite breakwater.

(b) Concept of the High Mound Composite Breakwater (HMCB-Concept)

The breaking wave forces on the superstructure have to be controlled to make use of the aforementioned advantages of the HMCB. The new idea consists in a perforated superstructure to decrease breaking wave impact loads and thus the stability without increasing the mass of the superstructure.

The superstructure of the new HMCB consists of a permeable front wall (pillars resulting in a porosity of ca. 28%) and an impermeable back wall. It is placed on a rubble foundation with a relatively flat seaward slope. The height of the rubble foundation is about 50% of the height of the total structure (Fig. 2).

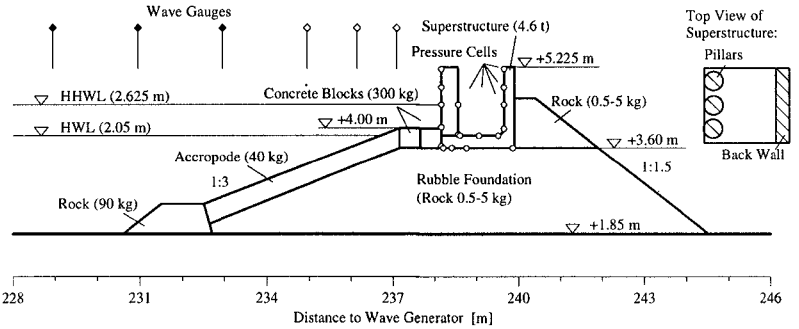

Figure 2: Cross Section of the HMCB Model in the GWK with Measuring Devices

The wave load on a HMCB is qualitatively different for different wave heights. Very small waves, which do not break, will not be critical for the stability of the superstructure. Larger waves which will break close to the superstructure will cause impact loads on the superstructure. However, these impacts are very local at the pillars of the slit front wall and therefore not critical for the stability. Further increasing the wave height will move the breaking point seaward. These very large waves will be already broken when they reach the superstructure and the load will remain almost constant even for increasing wave heights.

The concept behind the HMCB consists in the following two effects:

i. Temporal and spatial separation of the total wave load into 3 components which will occur at different times:
   - wave load on the seaward slope of the rubble foundation;
   - wave load on the slit front wall of the superstructure;
   - wave load on the impermeable back wall of the superstructure.

ii. Reduction of wave load by increasing the amount of dissipated wave energy due to breaking.

The mechanism which is responsible for the wave breaking at this structure will necessarily limit the maximum wave load on the superstructure which can not be exceeded even for very large waves. This is the governing characteristic of the HMCB. The maximum load for a properly designed HMCB is significantly smaller than the maximum load for a low mound vertical breakwater. Therefore, the HMCB might become a promising alternative for conventional breakwaters in shallow water; i.e. a fourth standard type of breakwater besides rubble mound breakwaters, berm breakwaters and low mound caisson breakwaters.

2 Experimental Set-up and Test Procedure

The model in the Large Wave Flume (GWK) of the Coastal Research Center (FZK), a joint institution of the University of Hannover and the Technical University of Braunschweig, Germany consists of a mound and a monolithic superstructure (Fig. 2). The rubble mound which is 1.75 m high and made of coarse rock material (0.5-5 kg) is placed on a sand layer of 1.85 m with a 1:75 foreshore slope. The armour layer on the seaward 1:3 slope is covered by a single layer of Accropodes (40 kg). The toe is protected with rock material (90 kg). The berm is covered with concrete blocks of 300 kg with holes (opening ratio of 10%). The superstructure is divided into 3 instrumented concrete units across the 5 m flume width. Each unit has a width of 1.75 m, a height of 1.63 m and a total weight of 4.6 t. The front side of each unit consists of 3 cylindrical pillars with a diameter of 40 cm and a distance of 56 cm from centerline to centerline (porosity of 28%). The back wall is impermeable. By turning the superstructure the impermeable back wall became a front wall and a traditional high mound breakwater alternative has been tested comparatively.

19 wave gauges have been used to record the wave motion in front of, at, inside and behind the breakwater (Fig. 3). To measure the wave load 18 pressure transducers have been placed in and outside the superstructure. The structural response of the superstructure has also been measured using strain gauges, displacement meters and accelerometers.

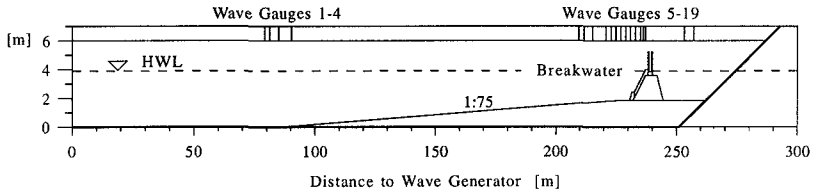

Figure 3: Cross Section of the Breakwater Model in the Large Wave Flume

A total of 133 tests have been performed with regular and irregular waves (PM spectra with 200 waves/wave train) at 3 different water levels (h = 2.05 m, 2.625 m and 2.875 m in front of the breakwater) and with 3 different wave periods

(T_p = 3.6 s, 5.0 s and 7.0 s). For each water depth and wave period the wave height has been increased stepwise until the wave load reached a maximum and started decreasing due to wave breaking.

3 Experimental Results

(a) Wave Breaking

Wave breaking is the most relevant hydrodynamic process for a HMCB. The incident waves are expected to break on the seaward slope of the rubble foundation. Only very small waves ($H < d_b$) will reach the wall without breaking (Fig. 4). These waves will cause only small wave loads and are therefore not critical for the stability of the superstructure. All the larger waves ($H > d_b$) will break at or in front of the breakwater. To predict breaking wave impact loads on the superstructure it is therefore necessary to know the breaking point:

- for small waves (slightly breaking) the breaking point is close to the superstructure;
- for larger waves the wave breaking becomes more pronounced but at the same time the breaking point moves seawards. Therefore, smaller waves might break against the superstructure whereas larger waves break on the seaward slope or at the toe of the rubble foundation; i.e. they are already broken when they reach the superstructure.

Two critical wave heights at the breakwater toe have been defined to describe the transition from non-breaking to breaking waves (H_{min}) and from breaking to broken waves (H_{max}). For each wave height and water level the first critical wave height H_{min} occurs just when waves start breaking against the superstructure and the second critical wave height H_{max} when the waves are already broken when they reach the superstructure.

The breaking criteria available have essentially been developed either for beaches or for traditional vertical breakwaters. Both can not be used to describe the range of critical wave heights for a HMCB. Therefore, an engineering approach has been developed to predict wave breaking for high mound breakwaters within the range of wave and structural parameters tested.

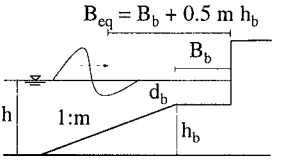

Figure 4: Definition Sketch of the Main Parameters for Wave Breaking

The critical wave heights H_{min} and H_{max} are influenced by the following parameters which are drawn in Fig. 4: (i) the geometry of the rubble foundation (equivalent berm length B_{eq} and height of the rubble foundation h_b), (ii) the local wave length L and (iii) the water depth (at the toe of the rubble foundation h and on the berm d_b).

To describe the wave breaking process in front of a HMCB three dimensionless parameters have been used:

- *relative wave height* on the berm H/d_b ("breaking criterion");

- *relative berm length* B_{eq}/L (geometry of the rubble foundation in horizontal direction);
- *relative berm height* h_b/h (geometry of the rubble foundation in vertical direction).

These ratios have been combined in a dimensionless breaker number I_b:

$$I_b = \frac{2\pi}{L} B_{eq} \left(\frac{h}{h_b} \right)^{3/2} \quad (1)$$

An empirical formula has been developed to calculate the critical wave heights $H_{crit} = H_{min}$ and $H_{crit} = H_{max}$:

$$\frac{H_{crit}}{d_b} = a + b\cos(c \cdot I_b) \quad (2)$$

where a, b and c are empirical coefficients and are to be determined for H_{min} and H_{max}.

For traditional vertical breakwaters H_{min} is an important design parameter because larger waves will cause a significant increase of the wave forces (wave impact loads). For a HMCB the critical wave height H_{max} is a more relevant design parameter because this wave height will cause the maximum load. Larger waves will increase the wave energy dissipation but will not increase the load.

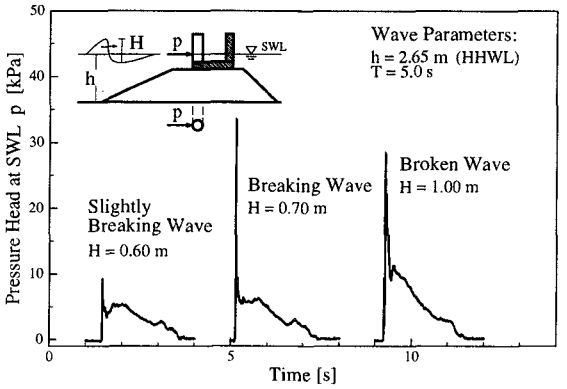

Figure 5: Typical Time Series of the Pressure Head Measured at the Perforated Front Wall for Slightly Breaking, Breaking and Broken Waves

The breaker types have been identified by three different procedures: (i) visual observation during the tests and analysis of video records, (ii) analysis of time series of pressure measurements at the front wall at SWL (Fig. 5) and (iii) analysis of time series of the total horizontal force on the front wall.

Pressure time series (at SWL) of different breaker types are plotted in Fig. 5. Three typical time series of regular waves (T = 5 s, HHWL) are shown. By increasing the incident wave height the signal is continuously changing from a typical slightly breaking wave to a breaking and broken wave. Even at the slit front wall large impact pressures have been observed. But these high pressures are very local and therefore result in comparatively small forces.

The transition from non breaking to breaking and broken waves with increasing wave height is shown in Fig. 6. The pressure head p/ρg measured at the front side of the pillar (perforated front wall) is plotted against the incident wave height H for regular waves of T = 5 s (HHWL). For non-breaking and slightly breaking waves the pressure head increases linearly with the wave height whereas for breaking waves the relationship becomes exponential. For broken waves the pressure head is decreasing in most cases with increasing wave height. In some cases with long waves the pressure head was slightly increasing even for broken waves.

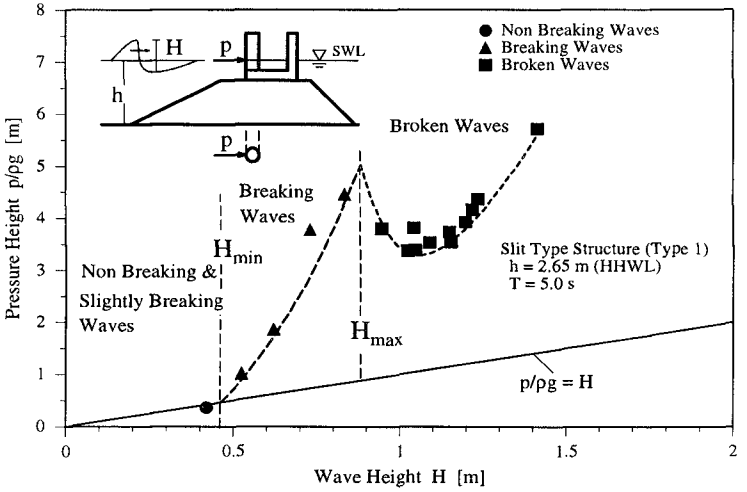

Figure 6: Pressure Head at the Perforated Front Wall vs. Wave Height for Different Breaker Types

It is obvious that errors in the prediction of wave breaking of more than 10% of the incident wave height may result in large uncertainties for the wave load prediction. Thus an accurate method for the load type classification is needed.

The critical wave heights H_{min} and H_{max} as a function of I_b are shown in Fig. 7. These wave heights can be determined using the simple approach given by Eq. (2).

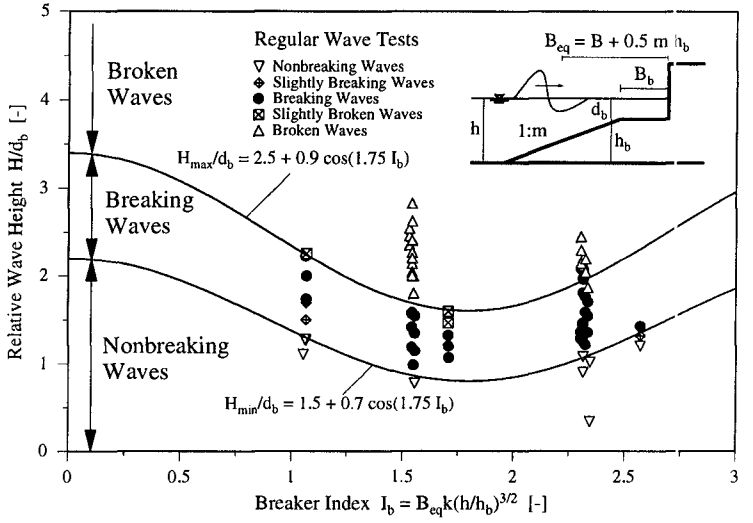

Figure 7: Breaking Criterion for the HMCB for Regular Waves

$$\frac{H_{min}}{d_b} = 1.5 + 0.7\cos(1.75\,I_b)$$
$$\frac{H_{max}}{d_b} = 2.5 + 0.9\cos(1.75\,I_b) \qquad (3)$$

(b) Wave Transmission

The wave transmission has been analysed by two wave gauges located behind the breakwater (WG 18 and 19 in Fig. 3). The average wave height measured by these gauges has been used to estimate the transmitted wave height. Due to resonance effects (wave reflection at the 1:6 slope at the end of the wave flume and re-reflection at the rear side of the breakwater) the transmission of regular wave tests was significantly higher than for irregular waves (essentially model effects). Therefore, the irregular wave results should be used for design purposes.

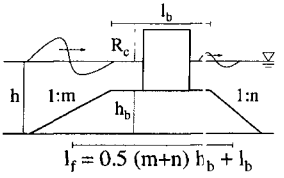

Figure 8: Definition Sketch of the Main Parameters for Wave Transmission

For the transmission analysis the tests have been divided into two groups: (i) "non overtopping" conditions ($H < R_c$) and (ii) "overtopping" conditions ($H > R_c$). The relevant parameters for the wave transmission are defined in Fig. 8.

For "non overtopping" cases the following dimensionless parameters were used to describe the wave transmission:

- *relative length of the rubble foundation* l_f/L (l_f = average length of the rubble foundation = 7.68 m (1996) resp. 10.18 m (1998)) which is relevant for the wave energy dissipation due to friction inside the foundation;
- *wave steepness* H/L which influences the wave breaking process and the subsequent wave energy dissipation;
- *relative water depth* in front of the breakwater h/H which may represent the dynamic porosity of the rubble foundation (hydraulic conductivity decreases with increasing wave height).

These parameters have been combined to yield a dimensionless transmission number M:

$$M = \left(\frac{L}{l_f}\right)^{3/2} \left(\frac{H}{L}\right)^{1/2} \left(\frac{h}{H}\right)^{3/4} \tag{4}$$

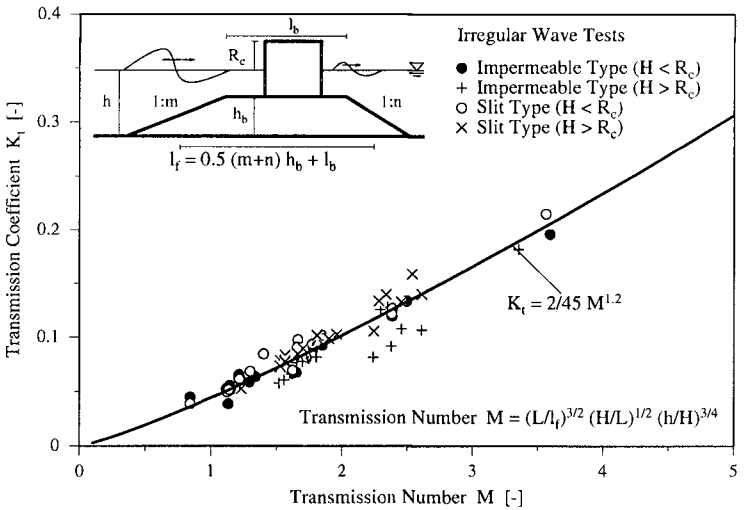

Figure 9: Wave Transmission for "Non Overtopping" ($H < R_c$) and "Overtopping" ($H > R_c$) Conditions vs. Transmission Number M for Irregular Waves

The wave transmission K_t for "non overtopping" conditions ($H < R_c$) of impermeable and slit type structure can be described by the following empirical formula:

$$K_t = a M^b \tag{5}$$

regular waves: a = 0.033 b = 2.0
irregular waves: a = 0.044 b = 1.2

In Fig. 9 the transmission coefficient K_t for irregular waves is plotted against the transmission number M for both types of superstructure. For "non overtopping" conditions the transmission past the rubble foundation is independent of the geometry of the superstructure. For the slit type superstructure the same transmission has been observed as for the impermeable superstructure. For "overtopping" conditions it was found that wave transmission does not substantially increase due to wave overtopping for irregular waves. Transmission for "overtopping" conditions shows more scatter without any clear tendency for higher values. Therefore, wave transmission should be calculated for "non overtopping" and "overtopping" conditions by Eq. (5).

(c) Wave Reflection

The partial standing wave field in front of the breakwater has to be analysed to determine: (i) the incident wave parameters as input parameters for the wave load of the structure and (ii) the wave reflection and thus the wave energy dissipation at the structure.

The reflection analysis has been performed by two different procedures using wave records of the first 4 wave gauges (WG 1 to 4) which were located about 140 m in front of the breakwater (Fig. 3):

- the 3-gauge-procedure *(Mansard & Funke, 1980)*: This standard procedure was used for the analysis of regular and irregular wave tests in the frequency domain;
- a new reflection analysis which has been developed at LWI *(Oumeraci & Muttray, 1997)*: This procedure was used for the re-analysis of the regular wave tests in the time domain.

In Fig. 10 the wave reflection at the breakwater is plotted against the surf similarity parameter ξ for both structure types and for regular and irregular waves. The scatter in Fig. 10 shows that ξ is not a very appropriate parameter to describe wave reflection. Therefore, a new reflection number has tentatively been developed.

The wave reflection depends on the wave length L, the water depth h and the wave height H at the toe of the breakwater as well as on a number of structural parameters like: steepness and roughness of the seaward slope, porosity of the rubble foundation, height and length of the berm, reflection properties of the superstructure etc.. The reflection performance is also affected by wave overtopping. The following dimensionless parameters which are defined in Fig. 4 were found to be most relevant for wave reflection:

- *wave steepness* H/L (breaking process and subsequent wave energy dissipation);
- *relative berm length* B_{eq}/L (horizontal geometry of the foundation);
- *relative berm height* h_b/h (vertical geometry of the foundation).

The wave reflection for regular and irregular waves is qualitatively different for this type of breakwater. The reflection process at the complex front face of the HMCB generates higher harmonic free waves which are propagating slower than the reflected waves. Therefore, only the first waves in the reflected wave train are not disturbed by free waves. The regular wave reflection analysis has been performed for these first waves and does not consider the higher harmonic free waves. The irregular wave reflection analysis has been performed for a complete wave train of about 200 waves and it includes the transfer of wave energy towards higher frequencies. The physical processes in the wave reflection will be described in detail in a forthcoming paper.

Two different reflection numbers are used to describe the wave reflection for regular waves (R) and for irregular waves (R^*) where the former describes a linear reflection process and the latter also covers nonlinear effects. The regular wave reflection is mainly influenced by the wave length L whereas the wave steepness H/L is predominant for the irregular wave reflection.

The wave steepness H/L and the relative berm length B_{eq}/L are combined to yield the regular wave reflection number R:

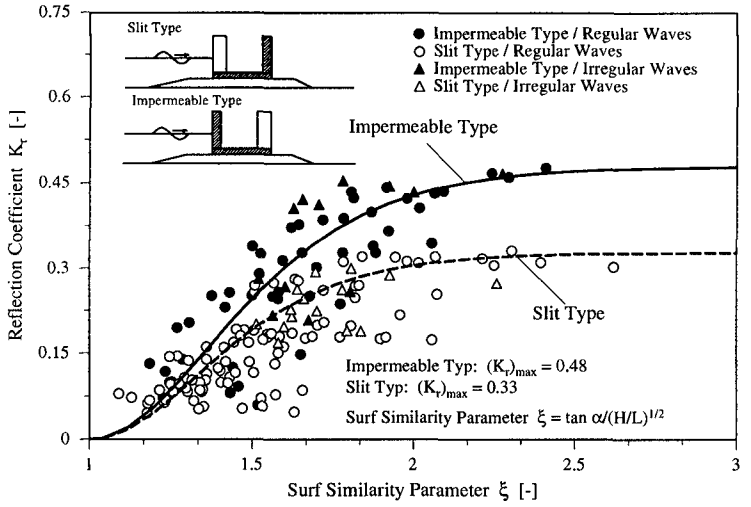

Figure 10: Wave Reflection for Regular and Irregular Waves vs. Surf Similarity Parameter

$$R = \left(B_{eq} \frac{2\pi}{L} \right)^{-2} \frac{1}{\sqrt{H/L}} \tag{6}$$

Other structural parameters like slope of the mound, roughness and porosity of the rubble foundation are constant and their influence may be included in empirical coefficients. The relation between reflection number R and reflection coefficient K_r can be calculated by the following empirical formula:

$$K_r = a \tanh^b(R/c) \tag{7}$$

slit type wall:	a = 0.32	b = 1.5	c = 5.2
impermeable wall:	a = 0.45	b = 1.5	c = 4.3

The results of the reflection analysis are plotted in Fig. 11 for regular waves and irregular waves.

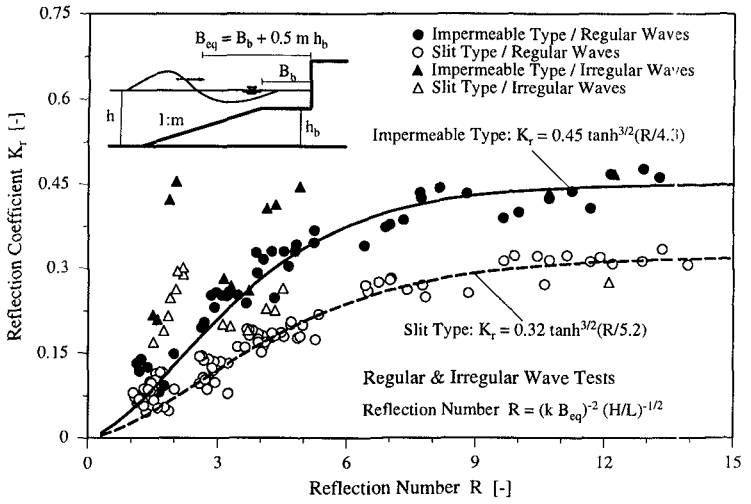

Figure 11: Reflection Coefficient vs. Regular Wave Reflection Number for Regular and Irregular Waves

The regular wave reflection is increasing with increasing reflection number R. This plot shows significantly less scatter for regular waves than the relation between reflection coefficient K_r and surf similarity parameter ξ in Fig. 10. The maximum reflection is about 45% for the impermeable type and about 32% for the slit type.

The reflection coefficients for irregular waves are much larger for small reflection numbers ($R < 5$) and are more scattering than those of regular waves (Fig. 11). Therefore, a new reflection number R^* has been developed for irregular

waves which takes into account the wave steepness H/L and the relative berm height h_b/h:

$$R^* = \left(\frac{h}{h_b}\right)^2 \frac{1}{\sqrt{H/L}} \tag{8}$$

The wave reflection for irregular waves is shown in Fig. 12 against the irregular wave reflection number R^*. The maximum wave reflection is about 50% for the impermeable type and 30% for the slit type. To calculate the reflection coefficient for irregular waves R^* has to be used together with Eq. (7) and the following coefficients:

impermeable type:	a = 0.5	b = 2.0	c = 4.5
slit type:	a = 0.3	b = 2.0	c = 4.5

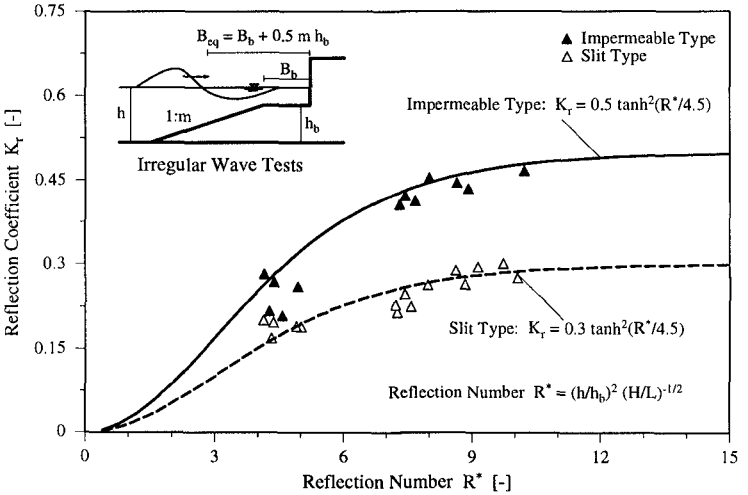

Figure 12: Reflection Coefficient vs. Irregular Wave Reflection Number R^* for Irregular Waves

4 Conclusions

The hydraulic performance of an innovative structure based on the concept of HMCB has been investigated in the Large Wave Flume (GWK), Hannover, Germany using regular and irregular waves. The following key results have been achieved:

The breaking process has been analysed for regular waves. Two critical wave heights H_{min} and H_{max} have been defined (Eq. (3)). H_{max} is most critical for the stability of the superstructure. An engineering approach has been developed taking

into account the geometry of the front face of the breakwater and the incident wave parameters to predict these critical wave heights.

Wave transmission past the HMCB has been investigated for regular and irregular waves. The main parameters for the wave transmission have been combined in a dimensionless transmission number M (Eq. (4)). Wave overtopping does not contribute significantly to the wave transmission.

Wave reflection has been analysed for regular and irregular waves. The main parameters for the wave reflection were used to build two dimensionless reflection numbers: R describing the linear reflection of regular waves (Eq. (6)) and R^* for nonlinear reflection of irregular waves (Eq. (8)). For a high mound breakwater with an impermeable type superstructure the maximum reflection coefficient is about 50% and significantly smaller than the maximum reflection for a vertical breakwater. The slit type superstructure will reduce the maximum reflection to about 30%.

Future research work is needed to extend the results to the prediction of breaker types under irregular wave conditions. The empirical formulae for the prediction of wave transmission and reflection should be replaced by more general formulae.

5 Acknowledgements

This project has been supported by the Science and Technology Agency of Japan and the 5th Port Construction Bureau of Ministry of Transport (MOT)/Japan. However, without the basic research project 'Design Wave Parameters in Front of Structures with Different Reflection Properties' (OU 1/3-1) founded by the German Research Council (DFG) these results would not have been achieved. Those supports are gratefully acknowledged.

6 References

MANSARD, E.P.D.; FUNKE, E.R. (1980): The measurement of incident and reflected spectra using a least square method. Proceedings International Conference Coastal Engineering (ICCE); ASCE; Vol. 17; pp. 154-172; Sydney.

OUMERACI, H.; MUTTRAY, M. (1997): Large scale model tests on a high mound composite type breakwater - final report; Leichtweiß-Institute; Technical University Braunschweig; Report No. 818, pp. 115 and Annexes; Braunschweig.

OUMERACI, H.; MUTTRAY, M. (1997): Bemessungswellenparameter vor Strukturen mit unterschiedlichen Reflexionseigenschaften (Design wave parameters in front of structures with different reflection properties). Zwischenbericht; Leichtweiß-Institut; Technical University Braunschweig; pp. 47 and Annexes; Braunschweig (in German).

TAKAHASHI, S. (1997): Breakwater Design, Chapter 10 in Handbook of Port and Harbor Engineering edited by G. P. Tsinker, Chapman and Hall, pp.951-1043.

DOUBLE WALLED, LOW REFLECTION WAVE BARRIERS

R J Cox[1], P R Horton[2] and S H Bettington[3]

Abstract

The effectiveness of a second perforated barrier seaward of a solid wave barrier in significantly reducing wave reflections and simultaneously improving wave protection is demonstrated in the paper. The indicated optimum seaward wall porosities and overall widths can be readily incorporated into practical structural designs for small craft facilities in relatively sheltered waters with limited wave periods. Results of an extended laboratory testing program and specific application to a recently designed and constructed structure are presented.

Introduction

Wave barriers (screens, curtains or skirts) have been found to offer cost effective and space efficient means of providing wave protection for small craft facilities in sheltered waterways where wave periods are restricted to locally wind generated seas.

The resultant wave reflections from a vertical barrier (as from other structures such as rubble mounds and floating breakwaters) often adversely impact on surrounding areas. Li (1995) demonstrated the significant reductions in wave reflection that may be achieved (for a full depth vertical seawall) by the seaward addition of a second perforated wall.

[1] Assoc Prof Civil and Environmental Engineering, Director, Water Research Laboratory, University of New South Wales, King Street, Manly Vale NSW 2093, Australia.
[2] Projects Engineer, Unisearch, Water Research Laboratory, King Street, Manly Vale NSW 2093, Australia.
[3] Senior Engineer, Queensland Government Hydraulics Laboratory, Department of Environment, Quinlan Street, Deagon, Queensland 4017, Australia.

In this paper, the design and effectiveness of a double wave barrier (with perforated seaward wall) in simultaneously satisfying low wave reflection and transmission requirements has been investigated in scaled laboratory wave flume and basin testing. Under design storm situations such structures experience significant wave overtopping and turbulent energy losses, conditions which are not conducive to analytical nor numerical solution.

Single Vertical Wave Barrier

Kriebel and Bollmann (1996) modified the original power transmission theory of Wiegel (1960) in obtaining an improved yet simple solution for estimating wave transmission for a single vertical wave barrier of the type shown in Figure 1.

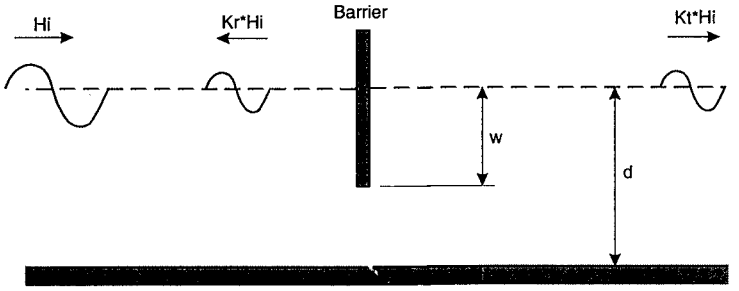

Figure 1. Definition sketch for single vertical wave barrier.

The Kriebel and Bollmann solution for wave transmission (H_t/H_i) is given by,

$$K_{ts} = 2\,T_F / (1 + T_F) \tag{1}$$

where $$T_F = \frac{2\,k\,(d-w) + \sinh 2k\,(d-w)}{2\,kd + \sinh 2\,kd} \tag{2}$$

and the wavenumber $k = 2\pi / L$

Kriebel and Bollmann favourably compared predictions from the above solution with a range of test data and the mathematically derived eigenfunction expansion methods of Losada et al (1992).

Kriebel and Bollmann confirmed the findings of Peirson and Cox (1989) in that the Wiegel theory overestimated wave transmission in deepwater conditions whilst underestimating in shallow water. Peirson and Cox noted that the method of predicting forces on a single wave barrier as contained in the US Army Corps of

Engineers Shore Protection Manual (1984) was overly conservative due to the assumption that the transmitted wave is 180° out of phase with that of the incident wave – a restricted series of wave flume experiments resulted in phase lags not exceeding 60°. Over an extended range of conditions, Kriebel et al (1998) utilising eigenfunction expansion solutions and near prototype scale laboratory tests have found the phase lag to vary with wave period and be generally less than 90°. The eigenfunction predictions of wave forces were validated against the experimental data and found to provide a reasonable upper-bound solution – the Shore Protection Manual (1984) method of estimating forces again shown to be overly conservative.

Double Walled Low Reflection Wave Barrier

A double walled structure is effective at reducing the reflection coefficient because waves reflecting off the front barrier are out of phase with those reflecting off the rear barrier. The theoretical ideal separation between front and rear barriers can be readily shown to be *L/4, 3L/4 or 5L/4* where *L* is the wavelength. For a separation of *L/2* there would be little to no effective reduction in wave reflection.

For many small craft facilities even a separation of *L/4* can be cost prohibitive. The introduction of porosity in the front barrier has been found to assist in reducing wave reflections with separations significantly less than the theoretical optimum *L/4*. In studying a full depth solid rear wall with porous front wall structure, Li (1995) indicated that the optimum separation could be as low as *0·18L*. *For many small craft facilities* the concept of a double wave barrier structure as shown in Figure 2 is most appealing. Major benefits include: (i) little impact on water circulation which can continue below the penetration depth; (ii) the horizontal deck connecting the two barriers can be utilised for pedestrian and/or vehicular traffic; and (iii) control of wave reflections (optimised by incorporation of porosity in the front wall) and reduction of adverse impacts on surrounding areas.

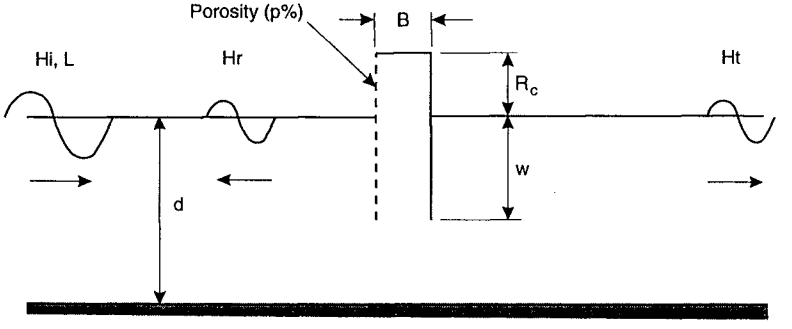

Figure 2. Definition sketch for double walled low reflection wave barrier.

Testing Program

To examine the behaviour of low reflection double wave barrier structures, an extensive experimental testing program was undertaken in the random wave flume at Water Research Laboratory, School of Civil and Environmental Engineering, University of New South Wales. The flume is 32 m long, 1 m wide and 1·2 m deep. Waves are generated by a single paddle hydraulic wave actuator at the upwave end. Wave energy absorption at the downstream end is achieved with porous plates and a sloping mat of synthetic hair. Double barrier structures for testing were mounted in a specially constructed force measurement rig located 24 metres away from the wave generator. The test rig with load cell arrangement is shown in Figure 7. Model double wave barriers were constructed from marine ply or transparent rigid acrylic for a range of vertical heights, widths/separations between front and rear walls and perforation porosities of the front wall.

The testing program examined transmitted and reflected wave behaviour for varying water depth (d), wavelength (L), incident wave height (H_i), barrier penetration (w), double barrier separation (B), and front wall porosity (p%). The above water crest level (R_c) was initially set above wave runup level to eliminate any overtopping.

Wave heights were measured with twin wire capacitance wave probes at various locations upwave and downwave of the test rig to determine incident (H_i) transmitted (H_t) and reflected (H_r) wave heights and thus the dependent parameters of wave transmission ($K_t = H_t / H_i$) and reflection ($K_r = H_r / H_i$) coefficients.

The range of the governing independent non-dimensional terms examined in the testing was:

porosity of front wall	p%	10% to 30%
water depth to wavelength ratio	d/L	0.2 to 0.6
barrier penetration to depth ratio	w/d	0.2 to 0.6
barrier separation to wavelength	B/L	0.1 to 0.3
wave steepness	H/L	0.02 to 0.10

More than 250 independent conditions were tested for wave transmission and reflection behaviour. Force measurements were restricted to the reduced set of conditions directly related to the Royal Prince Alfred Yacht Club structure in which significant wave breaking and overtopping of the structure occurred due to the low deck crest level required.

Test Results

Preliminary testing for a selected range of *d/L*, *w/d* and *B/L* confirmed the results of Li (1995) in that reflections were minimised for an optimum front wall porosity of about 20%. A 20% porosity was also found to be optimum for practical construction and operational purposes such as incorporation of reinforcing steel in concrete panelled porous walls and minimising effects of marine growth. The majority of testing was subsequently carried out for front barrier porosity of 20%.

As indicated in Figure 3, wave steepness was found to have little effect on wave transmission and reflection coefficients.

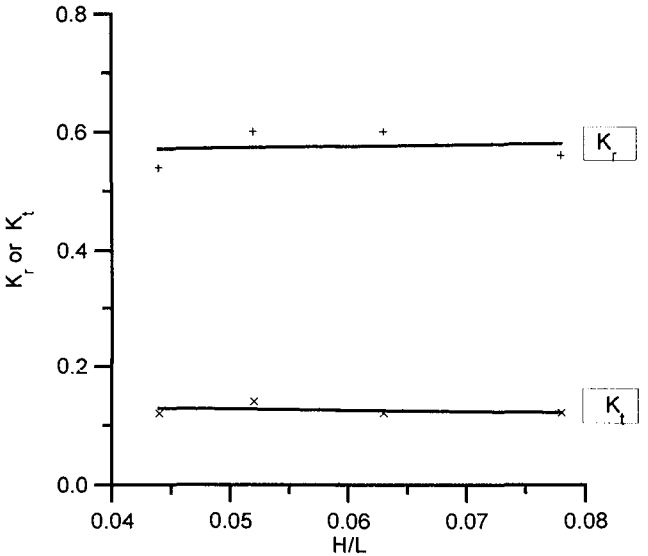

Figure 3: Double barrier transmission (K_t) and reflection (K_r) coefficients, varying H/L (porosity = 20%, d/L = 0.5, w/d = 0.5 and B/L = 0.21)

As indicated in Figures 4 and 5, wave reflections were minimised for barrier separations *B* less than 0·20*L*. The sensitivity of reflection coefficient to barrier separation was found to increase for reduced barrier penetrations in deeper water - conditions generally giving rise to increased wave transmission. In most applications *B/L* may be reduced to a suggested practical (and near optimum) value of 0·15 with little increase in reflected wave energy above the measured minimums. With near optimum 20% front wall porosity and double wall separation of 0.15*L*, reflection coefficients less than 0.3 were achievable for penetration ratios *w/d* less than 0.5.

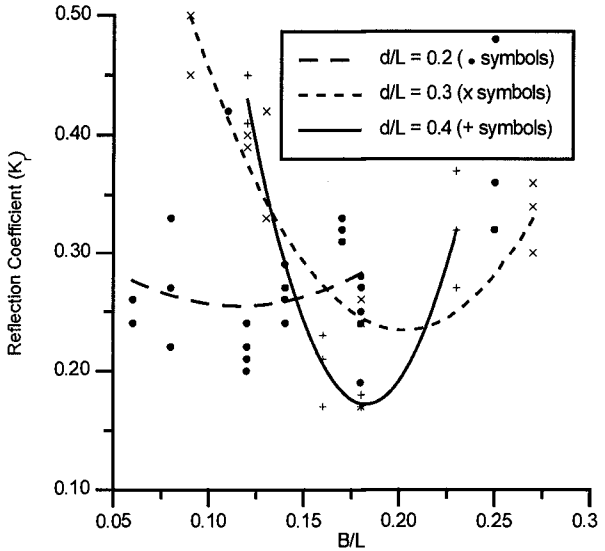

Figure 4: Double barrier, K_r variation with B/L and d/L (porosity = 20% and w/d = 0.3)

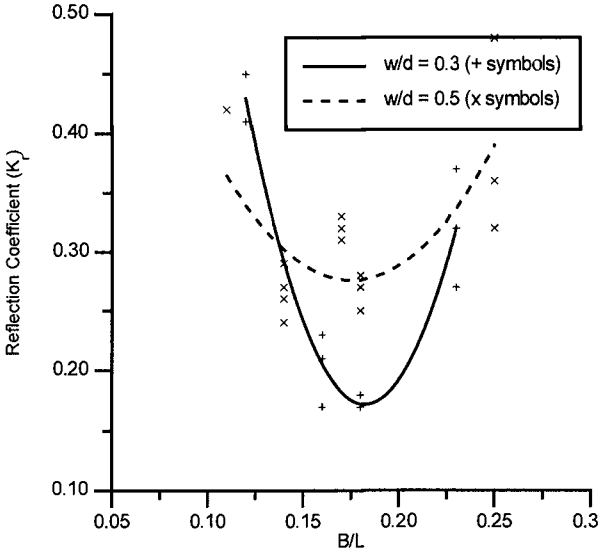

Figure 5: Double barrier, K_r variation with B/L and w/d (porosity = 20% and d/L = 0.4)

In Figure 6 the measured transmission coefficient K_t is compared to the value K_{ts} given by Kriebel and Bollmann (1996) in equation (1) for a single wave barrier. Over a wide range of *H/L*, *d/L*, *w/d* values the Kriebel and Bollman method was found to reasonably predict the wave transmission even for the porous front double barrier structures provided the barrier separation was less than the suggested optimum of 0·15*L*. With increasing barrier separations above 0·15*L* the double barrier can significantly further reduce wave transmissions below values achievable with a single barrier. It is, however, more efficient to achieve lower wave transmissions by increasing the penetration rather than widening the separation of the double barrier structure.

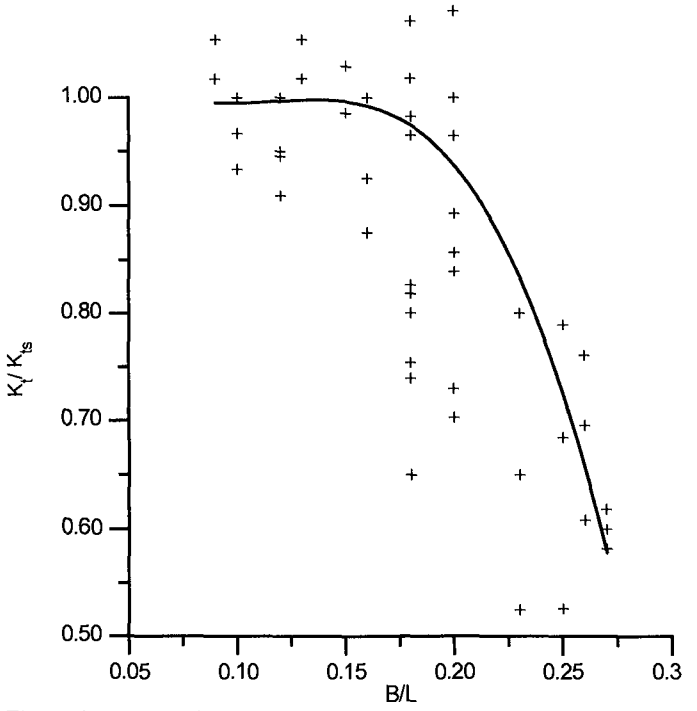

Figure 6: Ratio of double barrier transmission coefficient (K_t) to single barrier transmission coefficient of Kriebel and Bollmann (K_{ts}), versus B/L

The experimental test program clearly indicated the ability of a porous front walled double wave barrier in providing low wave reflections concurrent with

adequate wave protection (low wave transmission). The concept has been recently utilised at Royal Prince Alfred Yacht Club.

Royal Prince Alfred Yacht Club – double walled low reflection wave barrier

Royal Prince Alfred Yacht Club (RPAYC) on Pittwater in Sydney's north required a new breakwater as part of an upgrade of its marina facilities. The breakwater was to provide protection for a system of floating marina units and replaces an aging slatted timber structure. To gain construction approval the structure had to meet the requirements of Pittwater Council. These included minimisation of wave reflections, visual impact (structure crest to be not more than 1.25 m above Mean Sea Level) and impact on current or sediment flows. Waves at the site are boat wakes or locally generated short period wind waves, with the longest fetch being at an angle of 55° to the required breakwater alignment. For the established design wave conditions (significant height 1 m and period 2.8 seconds), both the wave transmission and reflection coefficients were required to be less than 0.3. Bed materials consist of sands and silts over rock. Water depths range up to 11 m.

Following a design process that considered a number of options a double walled low reflection wave barrier was chosen as the best solution. The basic concept described above was refined for the particular application with detailed 2D wave flume and 3D wave basin modelling at Water Research Laboratory. The 2D testing was used to optimise the configuration of the double wave barrier - specifically the front wall porosity, the penetration depth and separation width. 2D detailed wave loading measurements by load cells incorporated hydrostatic and dynamic impact force components acting on both the seaward porous and rear solid barrier walls. The 3D testing was carried out to determine wave attenuation and reflection characteristics of the structure under angled wave attack. 3D wave induced forces (perpendicular and axial load components) on an instrumented 5 metre double barrier panel were measured under angled wave attack. The force testing arrangements of load cells are shown in Figure 7.

The adopted design double wave barrier is shown in Figure 8. The double barrier structure is supported by raking piles capped with concrete blocks at 5 m spacings. Panels (5 m long x 3.12 m deep) and decking (2 m wide) straddle the space between the supports. The total length of the structure is approximately 200 m. The front (seaward) wall panel is perforated with thirteen 500 mm holes, resulting in 17% porosity. This arrangement was arrived at after consideration of marine growth as well as code requirements for reinforcing steel and concrete cover. Two small holes are located in the rear wall at about the high water level to reduce buildup of floating debris.

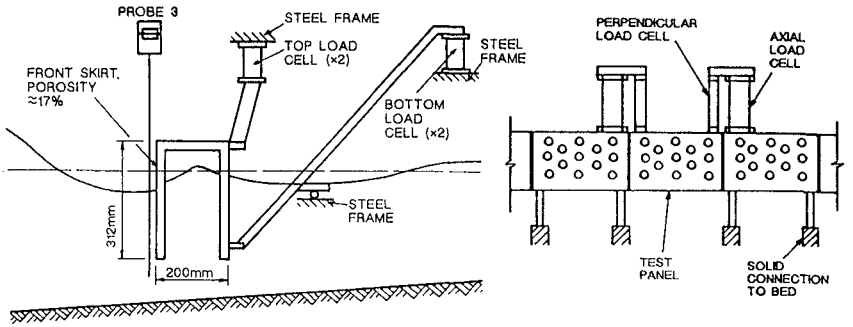

Figure 7. 2D force testing rig (scale 1:10) 3D force testing rig (scale 1:30)

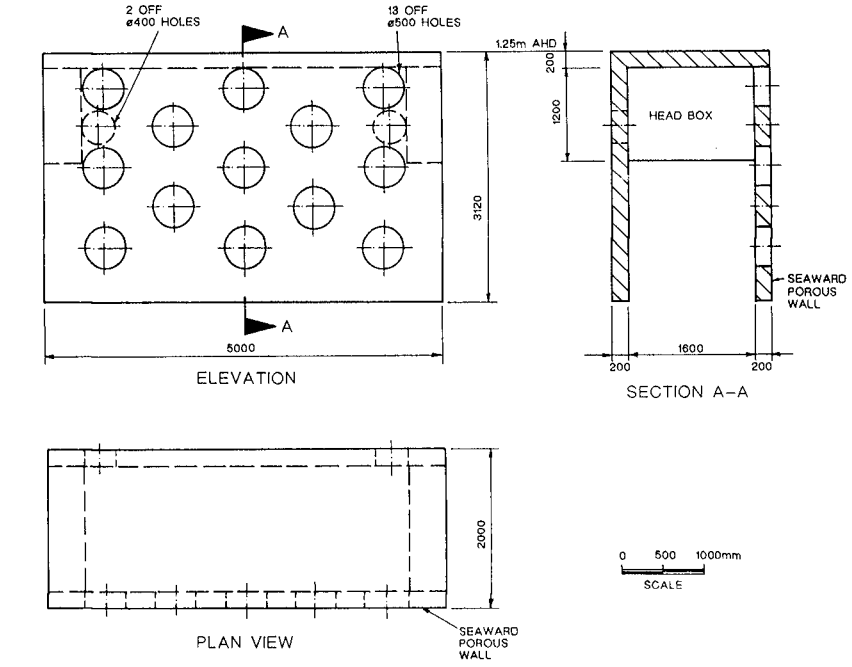

Figure 8. Royal Prince Alfred Yacht Club adopted double barrier structure.

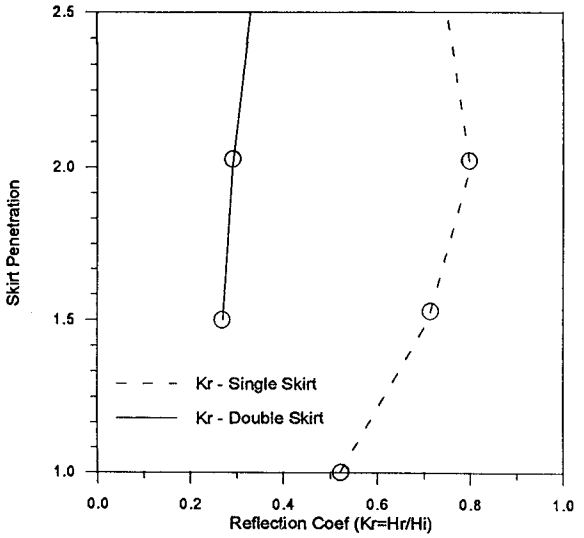

Figure 9. Impact of double barrier/skirt on reflections (H=1m, T=2.8s, 90°)

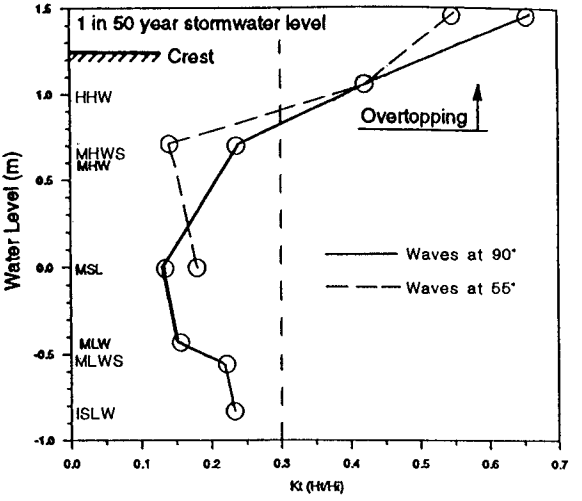

Figure 10. Wave transmission vs water level (H=1m, T=2.8s)

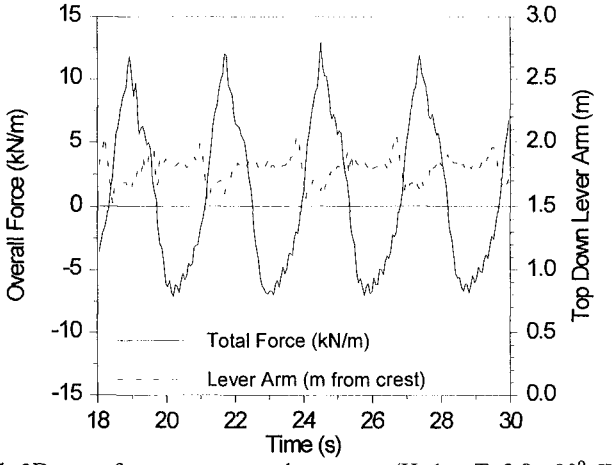

Figure 11. 2D wave force trace on total structure (H=1m, T=2.8s, 90°, WL=0m)

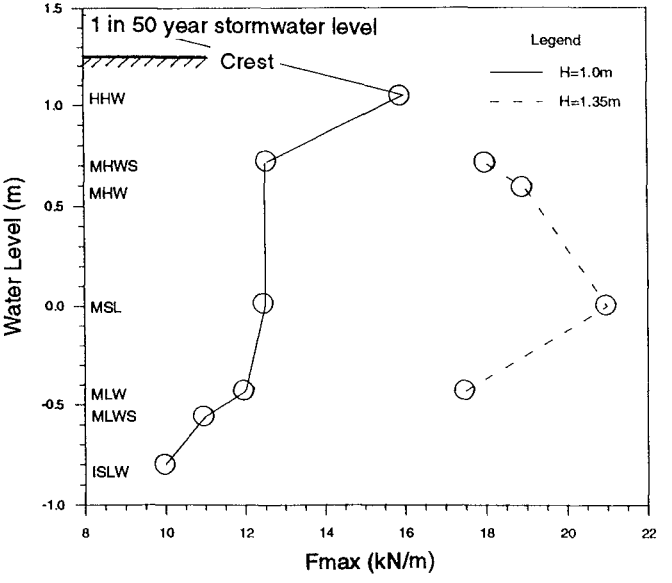

Figure 12. Maximum wave force vs water level (T=2.8s, 90°)

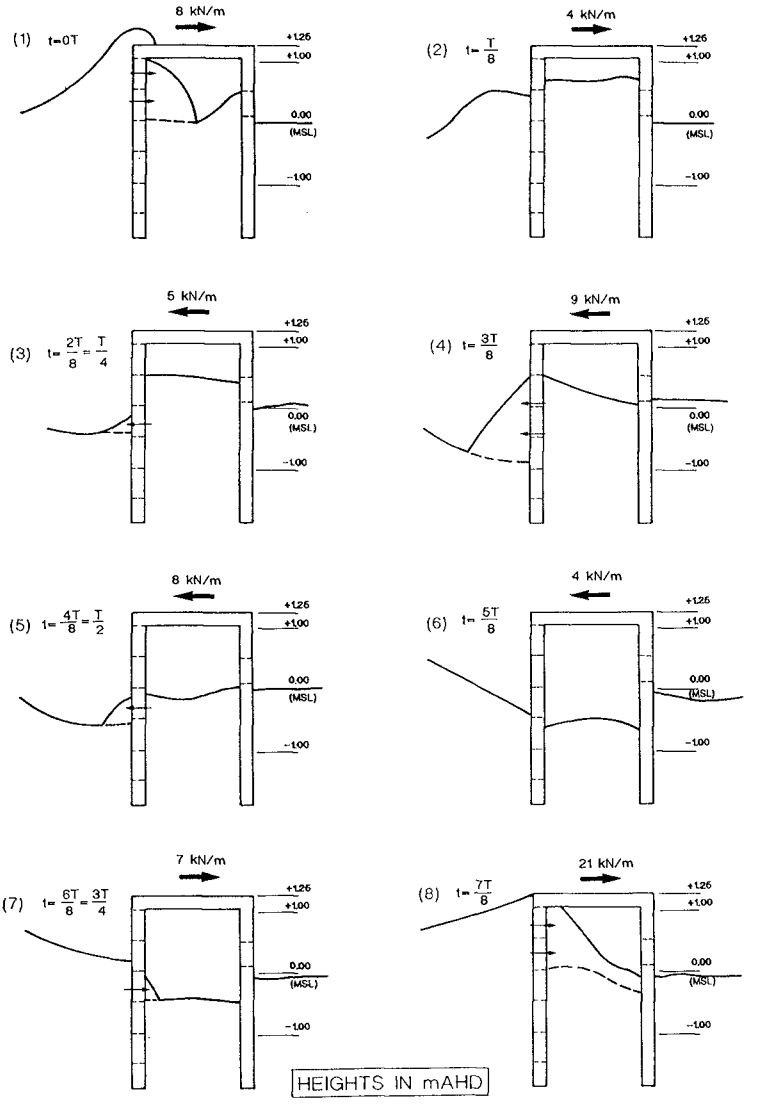

NOTES: → Refers to water passing through front skirt above receiving water level.

Figure13. Wave forces within a wave period (H=1.35m, T=2.8s, 90°, WL=0m)
Selected T/8 time steps do not necessarily coincide with peak forces

In Figure 9 the single solid barrier/skirt reflection coefficients of 0.7 to 0.8 were reduced to 0.3 by the addition of a second barrier/skirt (porosity 17% placed L/6 seaward in 10m water depth). As indicated in Figure 9, wave reflection was relatively insensitive to the water level/penetration depth. In contrast, as indicated in Figure 10, wave transmission varied markedly with water level. The transmission coefficient Kt was maintained at less than the design required value of 0.3 for water levels within the spring tide range and for approach wave angles from 55 to 90 (orthogonal) degrees. The increased wave transmission at water levels above High High Water resulted from overtopping of the deck at the imposed low crest level of 1.25m MSL.

An example 2D total force test trace under monchromatic waves is given in Figure 11. The variation of total force with water level is shown in Figure 12. Under design wave conditions the recorded maximum shoreward force (water levels between MLWS and MHWS) was 12 to 13 kN/m whilst the seaward forces (not shown) peaked at 8 kN/m. Sensitivity testing for waves more extreme than the design 1m was undertaken. The resulting total 2D forces and distribution of wave forces on the double barrier structure are included for 1.35m wave conditions in Figures 12 and 13.

Conclusions

The effectiveness of a second perforated barrier seaward of a solid wave barrier in reducing wave reflections and simultaneously improving wave protection has been demonstrated. The resulting indicated optimum seaward wall porosities and overall widths can be readily incorporated into practical structural designs for small craft facilities in relatively sheltered waters with limited wave periods. For longer wave periods the width required to provide low wave reflections (as well as low transmission) will generally become structurally and cost prohibitive.

The ability to reduce wave reflections to low levels was paramount in the acceptance and success of the recently constructed double walled low reflection wave barrier structure at Royal Prince Alfred Yacht Club.

The double walled wave barrier structure is clearly suited to reinforced concrete fabrication techniques similar to those already widely used in precasting of culverts. In addition to vessels being able to berth at the structure, the connecting deck can be readily utilised for pedestrian and/or vehicular traffic.

References

Kriebel, D.L., and Bollmann, C.A., (1996), "An Assessment of Power Transmission Theory for Vertical Wave Barriers", ICCE96, Orlando, Florida, pp.2470-2483.

Kriebel, D.L., Sollitt, C., and Gerken, W., 1998, "Wave Forces on a Vertical Wave Barrier", ICCE98, Copenhagen, In Press.

Li, R., 1995, "Hydraulic Design Method of Wave Dissipating Structure with Partially Perforated Front Wall", China Ocean Engineering, Vol. 9, No. 1, pp.73-82.

Losada, I., Losada, M., and Roldan, A., 1992, "Propagation of Oblique Incident Waves past Rigid Vertical Thin Barriers", Applied Ocean Research, Vol. 14, pp.191-199.

Peirson, W.L., and Cox, R.J, 1989, "Practical Design Procedures for Skirt Breakwaters", 9th Australasian Conference on Coastal and Ocean Engineering, December 1989, pp.103-107.

Shore Protection Manual, (1984), US Army Corps of Engineers, 4th Edition, US Govt, Washington, D.C.

Wiegel, R.L., 1960, "Transmission of Waves past a Rigid Vertical Thin Barrier", Journal Waterways and Harbours Division, ASCE, Vol. 86, No. WW1, pp.1-12.

WAVE OVERTOPPING OF RUBBLE MOUND BREAKWATERS

Mogens Hebsgaard[1], Peter Sloth[1], and Jørgen Juhl[2]

Abstract

A general expression for the overtopping discharge of a rubble mound breakwater has been derived utilising the general experience on this subject found in the bibliography and from the results of comprehensive series of model tests carried out at Danish Hydraulic Institute (DHI). The expression includes the important breakwater parameters (geometry of the breakwater profile) and the environmental parameters, and has been derived for applications with non-breaking waves in front of the structure. In research studies, model test series were carried out on pure rubble mound breakwater profiles with quarry rock as armour layer. Through results from projects carried out at DHI, the expression was extended to include different armour types and to describe the influence of a superstructure.

The aim has been to set-up a reliable expression, which is simple, general and easy to use. Previously, predictions of overtopping discharges have been based either on expressions including empirical constants for different shapes of the breakwater profile, on very complicated expressions or on diagrams giving the overtopping discharges as function of the layout of the breakwater profile and the environmental conditions.

[1] Danish Hydraulic Institute, Agern Allé 5, DK-2970 Hørsholm, Denmark, e-mail: mhe@dhi.dk, prs@dhi.dk, Fax: +45 45 179 186

[2] COWI, Parallelvej 15, DK-2800 Lyngby, Denmark, e-mail: jju@cowi.dk, Fax: +45 45 97 21 14

Introduction

Research on overtopping of rubble mound breakwaters has been undertaken at DHI during the last couple of decades. Since 1993, a large number of tests have been carried out as part of a research study on overtopping with the aim to determine the overtopping discharge as a function of the geometry of the breakwater profile and of the environmental parameters. On the basis of the test results, an expression on the functional relationship between the overtopping discharge and the breakwater parameters and the environmental parameters has been derived.

All research tests were carried out with quarry rock as armour, but the derived expression has been extended also to include artificial blocks as armour layer by using the test results from projects carried out in the past.

The overtopping discharges measured in the model have been transformed to prototype values in order to get the results as easily accessible and understandable as possible. It has been the intention to focus on overtopping discharges in the range where there will be a risk of damage to structures, vehicles, installations and persons behind the breakwater. According to for instance reference 1, limited damage may occur for an average overtopping discharge of 10^{-6} m^3/s per metre run of the breakwater, but serious damage may take place if the average discharge exceeds 10^{-5} m^3/s per meter run. If the average overtopping discharge exceeds 10^{-3} to 10^{-2} m^3/ms, the discharge will be so large that the damage to possible installations behind the breakwater will be severe. In case of such large overtopping discharges, the exact discharge is not interesting, but only the stability of the crest and the rear side. Accordingly, the present paper has focused on average overtopping discharges from 10^{-6} m^3/ms to 10^{-2} m^3/ms.

Model Set-up and Test Programme

Physical model tests have been carried out partly in a wave flume partly in a wave basin at DHI with the purpose to measure the average overtopping per metre run of the breakwater. All tests were carried out with long-crested waves generated on the basis of a Pierson-Moscowitz wave spectrum. The modelled profile and the definition of the breakwater parameters are shown in Figure 1.

The investigated profiles were traditional rubble mound profiles with core, filter and armour layer and without superstructure. The armour layer was quarry rock. The size of the rocks was so large that significant damage to the structure for the investigated wave conditions could be avoided during testing. The tests were all carried out with horizontal seabed in front of the profile.

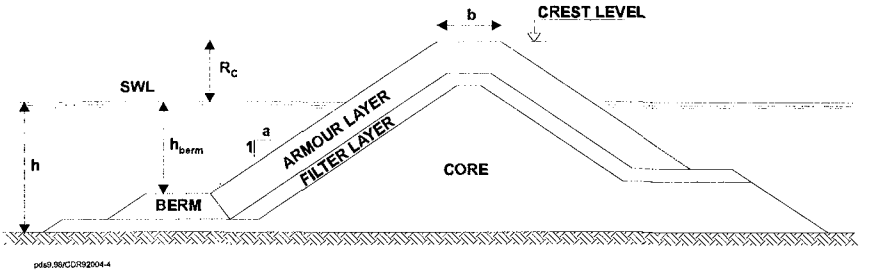

Figure 1 Definition of breakwater parameters

The overtopping discharge was defined as the average amount of water passing the rear side edge of the breakwater crest.

The tests were carried out with different wave conditions and different breakwater parameters. The following parameters were varied.

Wave Conditions:

- Significant Wave Height H_s (m)
- Peak Wave Period T_p (s)
- Wave Steepness $s_p \left(= H_s \cdot 2 \cdot \pi \,/\, g \cdot T_p^2\right)$
- Wave Direction β (°)

Breakwater Parameters:

- Water Depth h (m)
- Crest Freeboard R_c (m)
- Crest Width b (m)
- Seaside Slope Angle a
- Type of Armour

The following ranges of parameters were investigated in the model studies. The values are given in model measures. The values in brackets being the model values interpreted at a linear scale of 1:40.

Investigated Wave Conditions:

- H_s = 0.05 to 0.11 m (2.0 to 4.4 m)
- T_p = 1.0 to 2.0 s (6.3 to 12.6 s)
- s_p = 0.018, 0.025, 0.030 and 0.045
- β= 0°, 10°, 20°, 30°, 40° and 50°

All tests were carried out with irregular, long-crested waves. Most of the tests were carried out with wave steepness of s_p=0.018 and 0.030 and with perpendicular wave attack (β= 0°).

Investigated Breakwater Parameters:

- h = 0.350, 0.375 and 0.400 m (h = 14.0, 15.0 and 16.0 m)
- R_c = 0.100, 0.075 and 0.050 m (R_c = 4.0, 3.0 and 2.0 m)
- b = 0.16, 0.21 and 0.26 m (b = 6.4, 8.4 and 10.4 m)
- a = 1.5, 2.0 and 2.5
- Quarry rocks (100 - 180 g) (6400 – 11500 kg)

Formulation of the Overtopping Expression

The expression for the average overtopping of rubble mound breakwaters given in this paper is derived from the results of the model tests described above, but the evaluation of the expression has been inspired by previously developed overtopping formulae given in the literature. Owen, 1980 (see for instance references 1, 3, 5 and 7), has formulated one of the best known expressions. Various authors have elaborated on the formula to include different types of armour, different roughness of the layer, etc.

Owens formula expresses the overtopping Q (m^3/ms) as:

$$Q = Q^* \cdot (g \cdot T_m \cdot H_s) \qquad [1]$$

where

Q* is a dimensionless expression for the overtopping discharge

$$Q^* = A \cdot \exp(-B \cdot R^* / r)$$

A and B are constants depending on the geometry of the profile such as the slope of the seaside armour and elevation and width of the berm

R* is a dimensionless expression for the freeboard, ie the vertical distance between the still water level and the crest level

$$R^* = \frac{R_c}{T_m \sqrt{H_s \cdot g}}$$

R_c is the freeboard of the breakwater (m)

T_m is the mean wave period (s) of the incoming wave train

H_s is the significant wave height (m) of the incoming wave train

g is the acceleration of gravity (m/s^2)

r is a 'run-up reduction factor' or a description of the roughness of the armour layer

The formula includes the effect of different slopes of the seaside armour through the constants A and B, which however, are difficult to understand physically. The run-up reduction factor is a measure of the run-up level relative to a smooth impermeable slope.

Goda presents design diagrams for the overtopping discharges at block mounded seawalls covering different wave steepness and seabed slopes in front of the seawall (reference 2).

Jensen et al tried to include the geometry of the profile through a representative 'width' of the breakwater (reference 10). This 'width' was defined as the distance from the point where the profile intersects with the still water level to the position from where the overtopping was measured. In this way, both the slope of the breakwater and the crest width were taken into consideration.

Van der Meer et al give formulae which can be used to determine overtopping discharges at dikes, sloping revetments and seawalls (reference 4).

Juhl and Sloth present an expression for estimating the overtopping discharges of breakwater profiles armoured with quarry rocks (reference 9). The expression was based on some of the model test results, included in this present paper, and considers both the geometry of the profile, the wave height and wave period.

$$Q = Q^* \sqrt{g \cdot H_s^3}$$

$$Q^* = \exp\left[\left(-17.505 - 4.20\ln(s_p)\right) + \left(1.869 + 1.198\ln(s_p)\right)\left(\frac{a^{0.3}(2R_c + 0.35b)}{H_s}\right)\right] \quad [3]$$

a is the slope of the armour layer
b is the width of the crest (m)

The expression includes the actual shape of the breakwater, ie the slope of the armour layer, the width of the crest and the freeboard, but does not include, for instance, the type of armour.

For $[\ a^{0.3}(2R_c + 0.35b)/H_s > \sim 4\ ]$, ie for small values of the wave height compared to the freeboard, expression [3] gives larger overtopping for larger wave steepness. For smaller values of this factor, the overtopping discharge will increase with decreasing wave steepness. Whether this assumption is correct is difficult to tell from the test results, as no clear tendency was found.

In the evaluation of the new expression, both Owens formulae and Juhl and Sloth's formulation were considered. With the basis in the model tests, Juhl and Sloth found a representative dimension, which could describe the influence of the geometry of the profile [3],

$$C = a^{0.3}(2R_c + 0.35b)$$

This dimension, which can be taken as a representative 'width' and/or as a representative crest 'freeboard' of the breakwater, was included in the new expression. It was investigated if an expression in the following form would fit the model test data.

$$Q = Q^* \sqrt{g \cdot H_s^3}$$

$$Q^* = k_1 \cdot \ln(s_p)^{c1} \cdot \exp\left(\frac{k_2 \cdot C \cdot (s_p)^{c2}}{H_s}\right) \qquad [4]$$

where k_1, k_2, c1 and c2 are constants.

The best fit to the data was obtained with k_1=-0.3, k_2=-2.9, c1=1 and c2=0. The derived expression has then the following form

$$Q = Q^* \sqrt{g \cdot H_s^3}$$

$$Q^* = k_1 \cdot \ln(s_p) \cdot \exp\left(\frac{k_2 \cdot C}{H_s}\right) \qquad [5]$$

with k_1=-0.3 and k_2=-2.9. Applying a roughness factor or a wave run-up reduction factor for the armour layer of r=0.55, which is a recognised value for quarry rock slopes in two layers (see for instance reference 1), the expression will be as follows.

$$Q^* = k_1 \cdot \ln(s_p) \cdot \exp\left(\frac{k_2 \cdot C}{rH_s}\right) \qquad [5a]$$

k_1 = -0.3, k_2 = -1.6, $C = a^{0.3} \cdot (2 \cdot R_c + 0.35 \cdot b)$

Verification of the Expression, Quarry Rock Slope

Figure 2 shows the results of all tests, which were carried out in the wave flume compared to the results obtained by using expression [5].

As previously mentioned, the overtopping discharges are given in 'nature' values assuming a linear scale of 1:40. These tests were carried out with wave steepness of 0.018 and 0.030, R_c= 2, 3 and 4 m, and a = 1.5, 2.0 and 2.5.

Figure 3 shows the influence of the crest freeboard for an armour layer slope of 1:2, Figure 4 shows the influence of the slope (all tests) and Figure 5 shows the influence of the wave steepness (all tests).

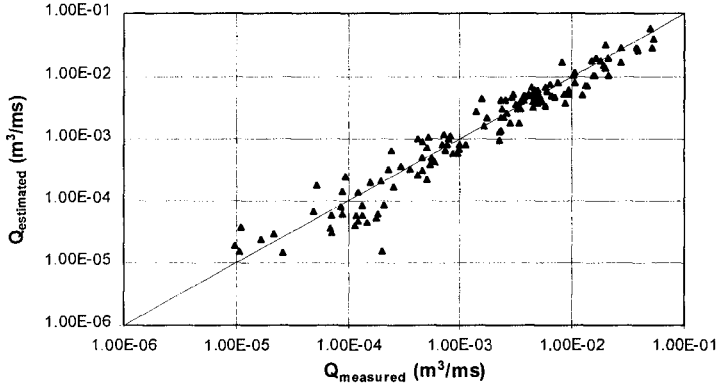

Figure 2 Comparison of measured and computed overtopping discharges, all data from flume tests

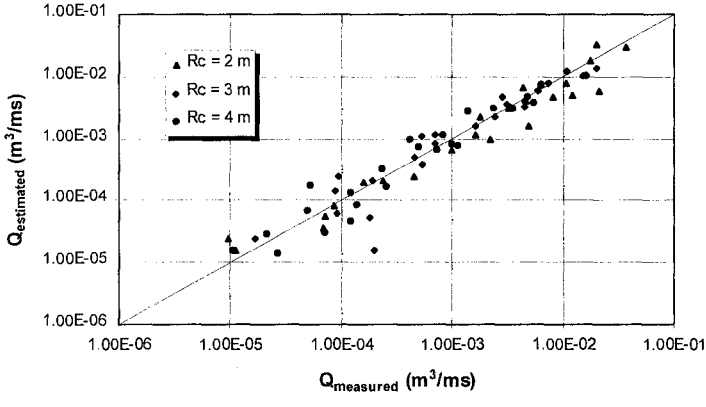

Figure 3 Comparison of measured and computed overtopping discharges, influence of crest freeboard, a=2

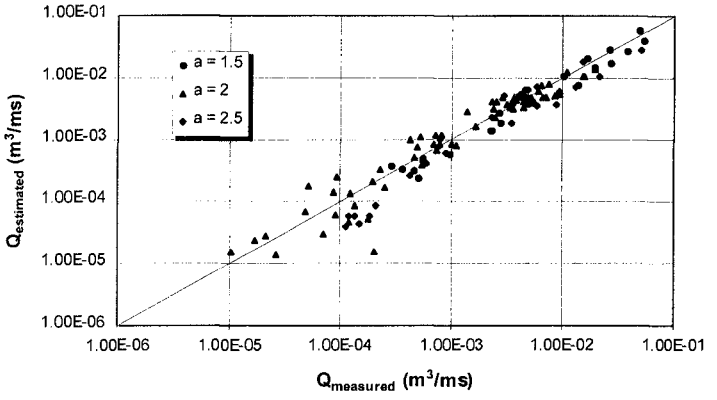

Figure 4 Comparison of measured and computed overtopping discharges, influence of seaside slope

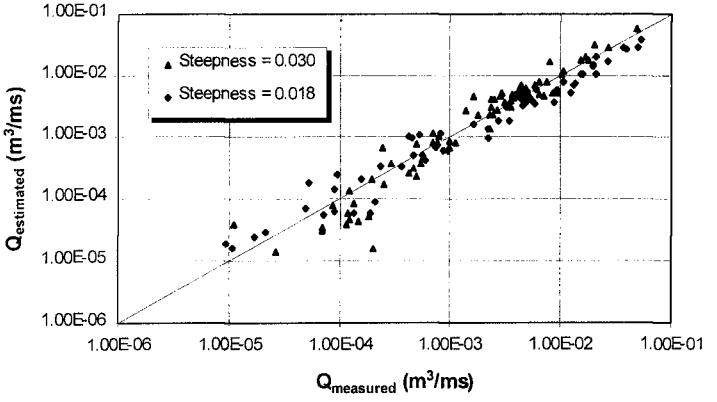

Figure 5 Comparison of measured and computed overtopping discharges, influence of wave steepness

It is seen that the measured and the computed overtopping discharges in most cases are in good agreement with each other.

Overtopping under Oblique Wave Attack, Quarry Rock Slope

The tests carried out with different wave directions relative to the breakwater alignment have been analysed, and the influence of wave direction on the overtopping discharge has been fitted into the formula [5]. Generally, the tests showed that the overtopping discharges for a wave obliqueness of 10^{o} are almost the same as for head-on waves, and that the discharges are reduced significantly for wave obliqueness larger than 20^{o}. The influence of the wave obliqueness has been included in the overtopping expression as shown in [6].

$$Q^{*} = k_1 \cdot \ln(s_p) \cdot \exp\left(\frac{k_2 \cdot C}{rH_s\sqrt{\cos\theta}}\right) \qquad [6]$$

where

$k_1 = -0.3$, $k_2 = -1.6$, $C = a^{0.3}(2R_c+0.35b)$

θ is the oblique angle (relative to head-on wave direction)

Figures 6 and 7 show the results of all tests carried out in the wave basin. Figure 6 shows the results of the tests carried out with a crest freeboard of 2 m, and Figure 7 shows the results of the tests carried out with crest freeboards of 3 and 4 m.

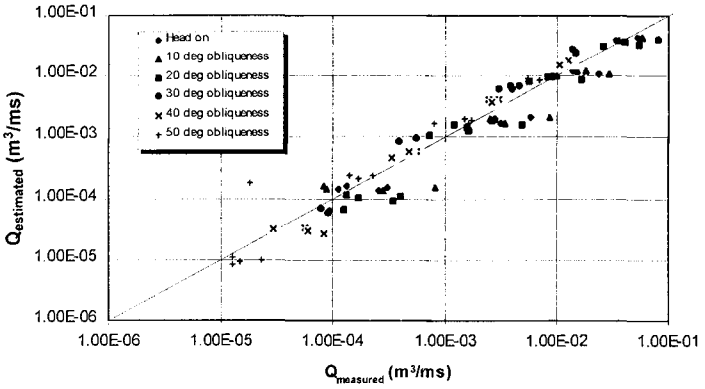

Figure 6 Comparison of measured and computed overtopping discharges, influence of wave direction, R_c =2 m, s_p = 0.018, 0.025, 0.030 and 0.045

From Figure 6, it is seen that the expression gives a very good description of the overtopping discharges for the lowest crest freeboard, whereas the results presented in Figure 7 for the two other investigated freeboards give too low, respectively too high, estimated overtopping discharges.

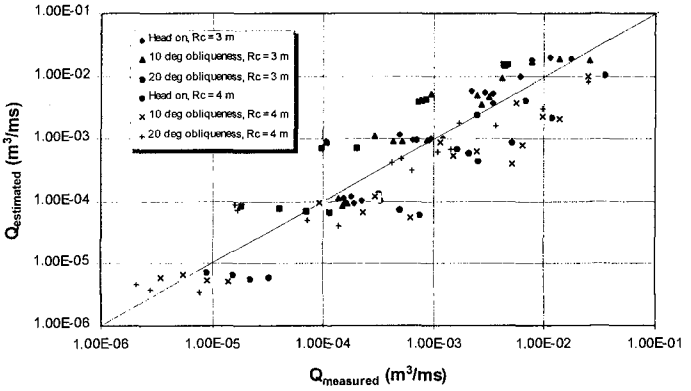

Figure 7 Comparison of measured and computed overtopping discharges, influence of wave direction, R_c =3 and 4 m, s_p = 0.018, 0.025, 0.030 and 0.045

Overtopping for Different Types of Armour

Results from overtopping tests, which have been carried out as part of projects at DHI, have been used in order to test the expression on different armour layer stones/blocks.

Results from four different projects with different armour types are shown in Figure 8. It should also be noted that the models in all four regarded projects were constructed with a sloping seabed in front of the breakwater.

The wave and breakwater parameters for the four projects are given in Table 1.

The results from the tests show that the run-up reduction coefficients (r) to be applied should be ~0.65 for grooved cubes, ~0.60 for quarry rock/grooved cubes, ~0.65 for rounded stones, and 0.55 for Accropodes in one layer.

Considering the deviations in test set-up for the different projects, it is found that there is rather good agreement between the measured and the estimated overtopping discharges. This indicates that the expression will give reasonably good results for other armour types when applying reasonable values of the run-up reduction factors.

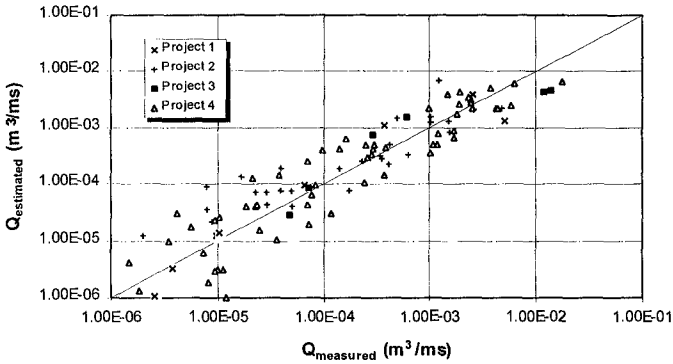

Figure 8 Comparison of measured and computed overtopping discharges, influence of armour layer type

Table 1 Wave and breakwater parameters, projects 1-4

Project	Armour	R_c (m)	a	b (m)	H_s (m)	s_{op}
1	Rounded stones	3–5	2	4	1.3-2.8	0.009-0.025
2	Quarry rocks/ Grooved cubes *)	13–15	2	7	5.5-8.6	0.014-0.036
3	Grooved cubes	6.5–7.5	2	12	4.1-6.2	0.021-0.026
4	Accropodes	2-5	1.33	6.6	1.2-4.0	0.010-0.045

*) Quarry rocks at the crest and down to 3-3.5 m below the crest at the seaside

Influence of Superstructure at the Crest

On the basis of the results from projects carried out at DHI, expression [6] has been extended to include breakwater profiles with a superstructure at the crest. Two different layouts were included in the measured data, a 'low' respectively 'high' crested structure, see Figure 9.

It was found that the overtopping discharges for both 'low' and 'high' superstructures could be described by the expression

$$Q^* = k_1 \cdot \ln(s_p) \cdot \exp\left(\frac{k_2 \cdot C}{rH_s\sqrt{\cos\theta}}\right) \qquad [7]$$

$k_1 = -0.01$, $k_2 = -1.0$, $C = a^{0.3} \cdot (2 \cdot R_c + 0.35 \cdot b)$

θ is the oblique angle (relative to head on wave direction)

The expression is apart from the constants k_1 and k_2 identical to the expression for pure rubble mound breakwaters.

Results from the tests with different types of armour layers show that the run-up reduction coefficient (r) to be applied should be ~0.65 for grooved cubes, ~0.55 for quarry rock, ~0.65 for rounded stones, and 0.45 for Dolos in two layers.

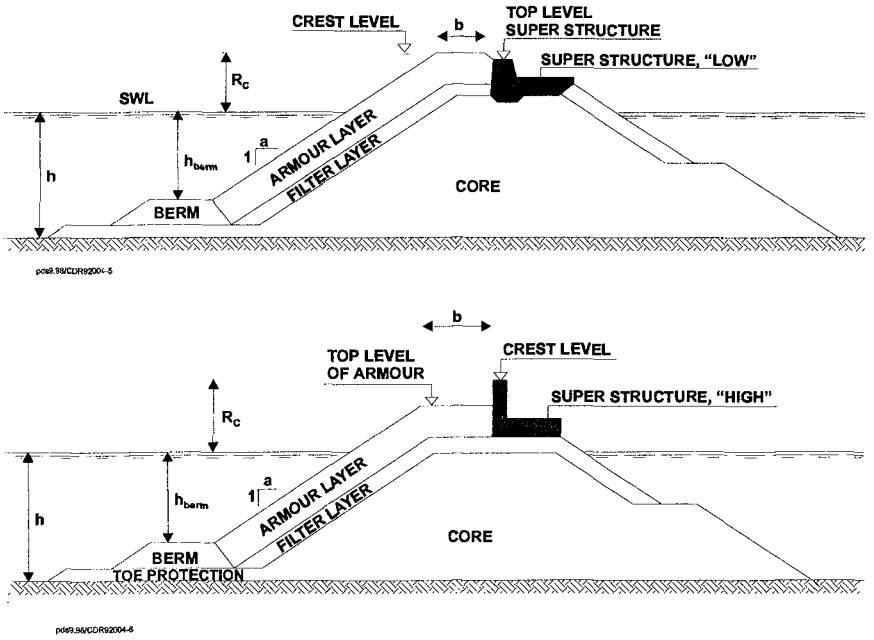

Figure 9 Layout of 'low' respectively 'high' superstructure

Concluding Remarks

A general expression for the overtopping discharge of rubble mound breakwaters has been proposed. It includes the influence of wave obliqueness and different types of armour. The expression is valid for rubble mound breakwaters both with and without superstructures.

$$\left.\begin{aligned} Q &= Q^* \sqrt{g \cdot H_s^3} \\ Q^* &= k_1 \cdot \ln(s_{op}) \cdot \exp\left(\frac{k_2 \cdot C}{r H_s \sqrt{\cos\theta}}\right) \\ C &= \left(a^{0.3} \cdot (2R_c + 0.35 \cdot b)\right) \end{aligned}\right\} \quad [8]$$

The following values for k_1, k_2 and r are recommended:

k_1 = -0.3, k_2 = -1.6 for pure rubble mound structure
k_1 = -0.01, k_2 = -1.0 for rubble mound structure with superstructure

r = 0.65 for an armour layer of rounded stones in two layers
r = 0.65 for an armour layer of grooved cubes (Antifer units) in two layers
r = 0.55 for an armour layer of quarry rock in two layers
r = 0.55 for an armour layer of Accropodes in one layer
r = 0.45 for an armour layer of Dolos units in two layers

It should be realised that the expression for other types of armour than quarry rock has been verified through model tests with different model set-ups, with sloping seabeds, different model scales, etc, than used in the research study. In spite of this, the results of the verifications show that [8] gives good estimates on the overtopping discharges.

It is, however, found that further research will be needed to obtain an understanding of the importance of

- Breaking waves in front of the structure
- Seabed slope in front of the structure
- Berm structures
- Influence of wind on the overtopping discharge.

Acknowledgement

The Danish Technical Research Council (STVF) under the program Marine Technique financed the study.

References

/1/ *Manual on the Use of Rock in Coastal and Shoreline Engineering*, CIRIA Special Publication 83, CUR report 154, 1991

/2/ Yoshimi Goda: *Random Seas and Design of Maritime Structures*, University of Tokyo Press, 1984
/3/ Allsop et al: *Analysis of Practical Rubble Mounds*, Chapter 67, Coastal Engineering 1994
/4/ JP de Wall and JW van der Meer: *Wave Run-up and Overtopping on Coastal Structures*, Chapter 134, Coastal Engineering 1992
/5/ NWH Allsop and AP Bradbury: *Hydraulic Effect of Breakwater Crown Walls*, Breakwaters '88.
/6/ F Zuang et al: *Modelling of Wave Overtopping over Breakwater*, Chapter 122, Coastal Engineering 1994
/7/ Randa M Hassan: *Planning and Engineering Aspects of a Small Craft Harbour in the Arabian Gulf*, International Conference on Coastal and Port Engineering in Developing Countries, 1995
/8/ Ole Juul Jensen and Jørgen Juhl: *Wave Overtopping on Breakwaters and Sea Dikes*, Second International Conference on Coastal and Port Engineering in Developing Countries, 1987
/9/ J Juhl and P Sloth: *Wave overtopping of Breakwaters under Oblique Waves*, Chapter 86, Coastal Engineering 1994
/10/ Juul Jensen, O and Sørensen, T: *Overspilling/Overtopping of Rubble Mound Breakwaters*, Coastal Engineering 3: pp 51-65, 1979.

Directional Wave Overtopping Estimation Model and Experimental Verification

Tetsuya Hiraishi and Haruhiro Maruyama [1]

Abstract

The accurate estimation of wave overtopping quantity is of great importance for the design of seawalls to protect artificial islands constructed offshore. The estimation model for overtopping rate in multi-directional waves is proposed and it is experimentally verified. The numerical results demonstrate that the overtopping rate in multi-directional waves becomes smaller than in uni-directional waves when the incident principal wave angles are near to the normal to sea wall face. The result becomes reverse when the wave angle is more than 30°.

Introduction

Artificial islands are widely under construction and plan to create a new area for the human-conscious space like a promenade, marina and recreational parks as well as the residential and commercial area. An artificial island is surrounded by sea walls which need a specified crown height to prevent serious wave overtopping. When the wave overtopping volumes become very large, the human conscious space like a promenade and a green belt are heavily damaged. Meanwhile, a high barrier may cause the disconnection between the water front and inner land. The lower crown height is more beneficial to make a wide human conscious space. Therefore, the crown heights of sea walls in an artificial island to reduce the wave overtopping rate under the appropriate allowable levels should be determined with high accuracy (Franco, et.al.,1994).

Wave overtopping rates have been studied on the basis of the results in the two dimensional channel test (Goda, et.al.,1975). They proposed a practical formula estimating the wave overtopping rate on the vertical and block-armored

[1] Wave Laboratory, Port and Harbour Research Institute, Nagase 3-1-1, Yokosuka, Japan 239-0826

sea walls in shallow water rigion with an uniform slope. Uni-directional waves have been employed in the experimental study for wave overtopping mainly because of the lack of the facility generating multi-directional waves in a laboratory. The laboratory works employing multi-directional waves are strongly desired as real sea waves have characteristics of directional random waves of which energy propagates to various directions. In the paper, we discuss the applocability of estimation model of directional wave overtopping rate at vertical sea walls in deep water area.

Numerical Simulation for Directional Wave Overtopping

A new approach to estimate the wave overtopping rate is needed for the design of seawalls in deep water area where the wave directionality appears remarkably. To estimate the wave overtopping rate in multi-directional waves, the evaluation of that for waves propagating obliquely to the sea wall face is needed. Takayama et.al.(1982) suggest that the wave overtopping rate of oblique incident waves may become smaller than that of the normal incident waves. We assume that an infinite vertical sea wall is arranged on the x-axis and that the incident waves are perfectly reflected at the sea wall. **Figure 1** shows the imaginary seawall model for numerical simulation. The water surface elevation at the front of sea wall is expressed in the single summation method (Takayama and Hiraishi,1989) as follows ;

$$\zeta(x,t) = K \sum_{n=1}^{Ns} 2a_n \cos(k_n \sin\theta_n + \sigma_n t + \varepsilon_n) \qquad (1)$$

where, $\zeta(x,t)$ is the water surface elevation at the point x and time t. The subscript n denotes the value for the n-th component wave. In the eq.(1), a_n, k_n, θ_n, σ_n and ε_n represents the amplitude, wave number, wave angle, angular frequency and random phase respectively. The wave angle is measured clockwise from the normal line to seawall face. The number Ns is the total number of the synthesized component waves. The indication K is the coefficient for the consideration of wave non-linearity and breaking introduced by Goda et.al.(1975). In this study, assuming that the water depth in front of the sea wall is enough deep, we employ the following expression ;

$$K = \zeta/H = \min \{ [1.0 + a_b H_{1/3}/h], c_b \} \qquad (2)$$

where, 'min' means that the minimum value in { } is adopted. In the vertical sea wall, we employ a_b=1.0 and c_b=10.

Figure 2 shows the image of wave overtopping. When the water surface elevation becomes higher than the crown height, the wave overtopping occurs.

The wave overtopping rate q is calculated as follows ;

$$q = \begin{cases} C(\zeta - h_c^*)^{3/2} & (\zeta \geqq h_c^*) \\ 0 & (\zeta < h_c^*) \end{cases} \tag{3}$$

where C is the wave overtopping coefficient given by $C_o\sqrt{2g}$. The value of C_o

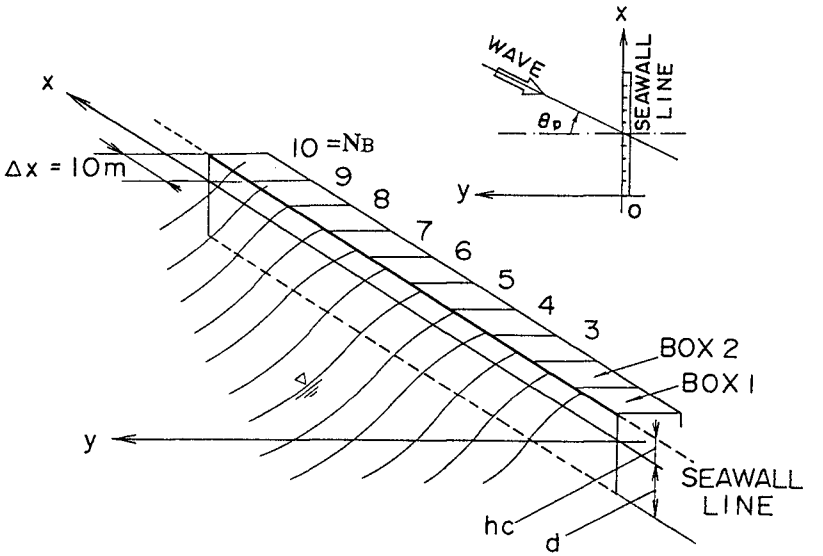

Figure 1 Sketch of sea wall model in numerical simulation

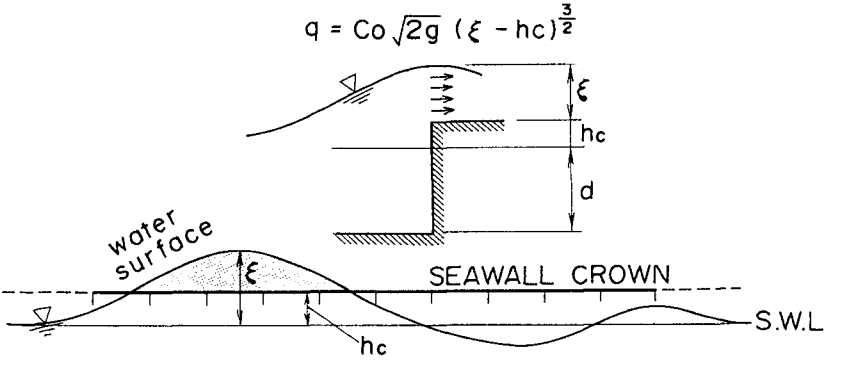

Figure 2 Wave overtopping image at vertical wall

is determined as the estimated q agrees with the measured q. The consideration for the value of C_O is done in the later chapter. The symbol h_c^* represents the virtual crown height for oblique component waves. The virtual crown height h_c^* is evaluated as the linear superposition of the function λ_n standing for the variation of uni-directional wave overtopping rate for the incident angle.

$$h_c^* = \left[\sum_{n=1}^{NS} \frac{S(f_n)\Delta f_n}{m_O} \lambda_n \right] \tag{4}$$

$$\lambda_n = \frac{h_{co}}{\beta_n} \tag{5}$$

where, f, $S(f)$, Δf and m_O denotes the frequency, spectrum density, interval of representative frequency and total wave energy. The symbol h_{co} represents the original crown height of sea wall.

The function β_n is the dimensionless modification factor of crown height for n-th component waves. It corresponds to the ratio of crown height in oblique incident wave giving a specified overtopping volumes to that gives the same volume in normal incident waves. The factor is determined later according to the variation of overtopping rate in uni-directional waves.

The amplitude of n-th component wave is given by

$$a_n = \sqrt{2S(f_n)\Delta f_n \Delta\theta_n} \tag{6}$$

where $\Delta\theta_n$ represents and the angle band of n-th component. The directional spectrum is the product of the frequency spectrum and directional function. The modified Bretschneider-Mitsuyasu type spectrum (Goda,1987) and Mitsuyasu-type directional function modified for engineering simplification (Goda and Suzuki,1975) were employed as the wave energy spectrum and directional spreading function respectively. The modified frequency spectrum is expressed as,

$$S(f) = 0.205 H_{1/3}^2 T_{1/3}^2 (T_{1/3} f)^{-5} \exp\left[-0.75 (T_{1/3} f)^{-4}\right] \tag{7}$$

where $H_{1/3}$ and $T_{1/3}$ represents the significant wave height and period. The modified Mitsuyasu-type directional function is given by,

$$G(\theta; f) = G_o \cos^{2s}\left(\frac{\theta - \theta_p}{2}\right) \quad (-90^\circ < \theta < 90^\circ) \tag{8}$$

where θ_p is the principal direction and G_o the normalized coefficient expressed as ;

$$G_0 = \frac{1}{\int_{-\pi/2+\theta_p}^{\pi/2+\theta_p} G(\theta;f)d\theta} \tag{9}$$

The parameter s is the angular spreading coefficient determined as follows;

$$s = \begin{cases} (f/f_p)^5 S_{max} & : f \leqq f_p \\ (f/f_p)^{-2.5} S_{max} & : f > f_p \end{cases} \tag{10}$$

where S_{max} denotes the angular spreading parameter representing directionality of wave energy, and f_p the peak frequency of wave spectrum. In the simulation, we assume the wave overtopping volumes are measured in the measurement boxes with the width of Δx behind the sea wall as shown in Fig.1. The total overtopped water volume Q_i in the i-th box is evaluated as,

$$Q_i = q(t)t_0 \Delta x \tag{11}$$

The component value q_i is caluculated in eq.(3). The averaged wave overtopping rate q for a sea wall is estimated as,

$$q = \frac{1}{N} \sum_{i=1}^{NB} \frac{Q_i}{t_0 \Delta x} \tag{12}$$

where N_B is the total number of the boxes. Compared with the several computation results with different condition, the following number are adopted in the computation;

$$\Delta x = 10\text{m}, \quad N_B = 10, \quad N_S = 300, \quad t_0 = 20\text{min} \tag{13}$$

Experimental Setup

Figure 3 shows the arrangements of experimental models in a directional wave basin. Along a side, a directional random wave generator with 60 paddles each 50cm wide is installed. The generator is possible to reproduce oblique regular waves, oblique uni-directional waves and directional random waves with the principal wave direction normal to the gerateor face. A continuous vertical wall to represent an offshore vertical breakwater is installed parallel to the generator face with the distance of 6.4m. The total length of the vertical wall is 18m and the both of edge sides are slightly bent to protect the effects of diffracted waves. A measurement box for wave overtopping volumes is attached at the backside of center part of seawall to obtain the total overtopped volume Q. In the

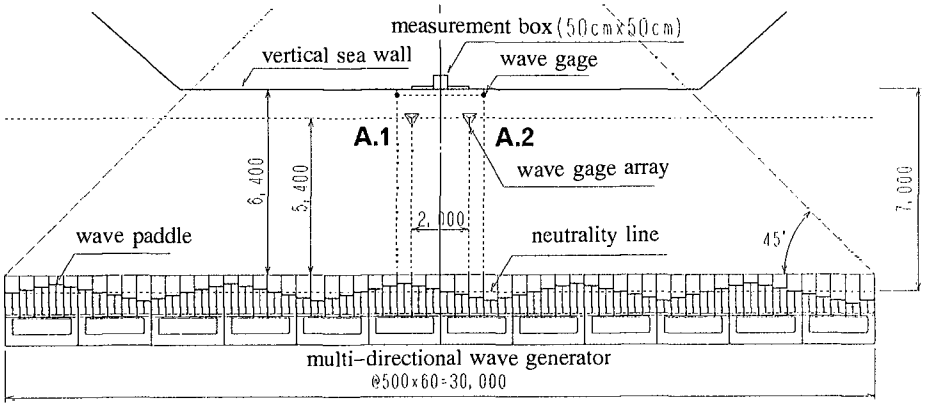

Figure 3 Arrangement of wave generator and sea wall model

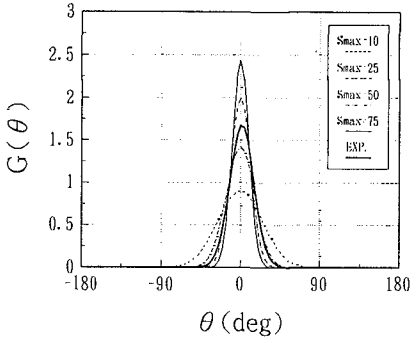

Figure 4 Analysed directional function

experiments, the wave overtopping rates are analysed for the case of (i) uni-directional waves with oblique incident angle and (ii) multi-directional waves with normal principal wave direction. The single summation method is employed to synthesize the wave signal to generator.

In the experiment, the scale is 1/100 and the water depth is fixed to be 38m in the prototype. The crown height h_c are 6 and 8m. The significant wave height $H_{1/3}$ of incident uni- and multi-directional waves is 6 and 8m. The significant wave periods are changed from 11.3 to 14.1s. In the case (i) uni-directional waves, the incident wave angle varies from 0 to 45°. In the case (ii) multi-directional waves, the principal angle is 0° and the target S_{max} is changed from 10 to 100. **Figure 4** shows the example of wave directional function measured at the wave gage array located at the measurement box without seawall model. The Extende Maximum Entoropy Method (Hashimoto et. al., 1994) was employed to analyze the directional spectrum. The experimental wave represented in the solid line is generated with the target of S_{max}=100. However, the peak height of directional function in the experimental waves is not as tall as the theoretical peak height for case of S_{max}=50. The reduction of angular concentration may be caused by the finite length of generator.

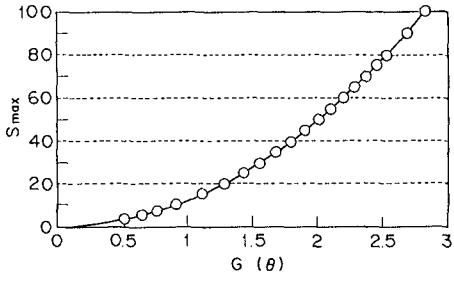

Figure 5 Correlation of S_{max} and $G(\theta_p)$

So, the angular spreading in the experiment is evaluated accoring to the peak value of directional function measured in the wave basin. **Figure 5** shows the correlation of the parameter S_{max} and the measured $G(\theta_p)$. The values of S_{max} are evaluated employing Fig.5 after the values of $G(\theta_p)$ is obtained in the spectral analysis.

Determination of Experimental Coefficient

In the numerical simulation model, the overtopping coeffficient C_o and the crown height modification factor β_n should be evaluated in the experiment. Those value is derived from the comaprison between the measured and estimated results in uni-directional wave condition. **Figure 6** shows the variation of the error between the estimated and measured wave overtopping rates in uni-directional waves with the normal incident angle for the value of C_o. The ratio of wave overtopping rate becomes about 1 for both cases of $T_{1/3}$=11.3 and 14.1sec when C_o becomes 0.3. Therefore, in the simulation model, C_o=0.3 is adopted. This value is smaller than the value proposed by Goda et.al.(1976).

Figure 7 shows the ratio of overtopping rates in oblique uni-directional waves to those in the uni-directional waves with the incident angle normal to wall face. The ratio becomes more than 1.0 in case of oblique incident waves with 7.5°. When the angle becomes larger than 7.5° the overtopping rate decreases as the incident angle increases. When the angle becomes 45°, the rate becomes

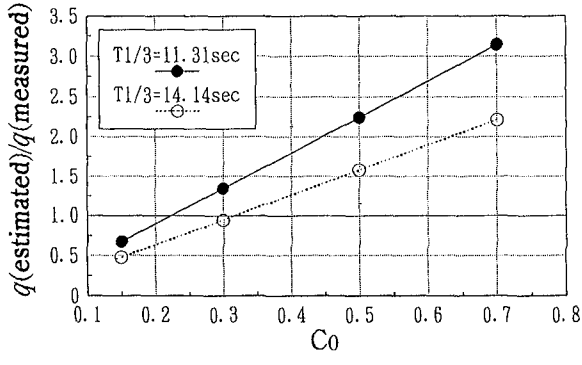

Figure 6 Error ratio of esimated to measured wave overtopping rate

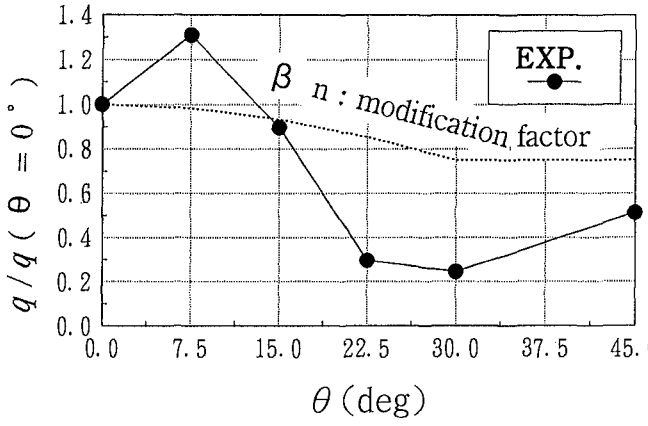

Figure 7 Variation of uni-directional wave overtopping rate and crown height modification factor for incident wave angle

slightly larger than those in case of θ =30° . The reason why the overtopping rate becomes maximum at the angle slightly apart from the normal is not clear. However, our results demonstrate that the overtopping wave rate has tendency to become large when the incident angle becomes slightly defferent from the normal. The mofification factor for crown height is determined so that it represents the effects of oblique wave components to reduce the wave overtopping rates.

In Fig.7, the overtopping rate decreases rapidly as the angle increases in the range of θ <30° . Meanwhile, the variation of wave overtopping rate becomes small for the range of θ >30° . Therefore, the modification factor is asuumed as follows;

$$\beta_n = \begin{cases} 1-\sin^2\theta_n & (|\theta| \leqq 30^\circ) \\ 1-\sin^2 30^\circ & (|\theta| > 30^\circ) \end{cases} \tag{14}$$

The broken line in Fig.7 indicates the profile of modification factor.

Verification of Numerical Model

Figure 8 shows the comparison between the measured and estimated wave overtopping rate in uni-directional waves. In the following figures, q^* represents the dimensionless overtopping rate given by,

$$q^* = q \,/\, \sqrt{2gH_o'^3} \tag{15}$$

where H_o' represents the equivalent offshore wave height. The comparison is done for the various cases for different incident angles. The estimated wave

overtopping rates agree well with measured ones. The good agreement between the estimated and measured wave overtopping rates demonstrates that the numerical model with the coefficient of C_O=0.3 is suitable for the estimation of uni-directional wave cases.

Figure 9 shows the range of estimation error for uni-directional wave condition. The estimated q are plotted within the range for 50% error of measured values. The estimated error for analytical caluculation model proposed Goda(1975) included the estimation error of 100-200% for wave overtopping rates. Therefore, the error in the present simulation model is small and allowable to be employed in the sea wall design.

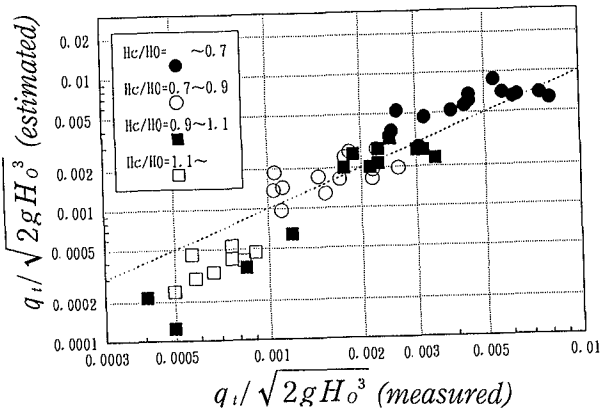

Figure 8 Comparison of estimated and measured ectional overtopping rate in uni-directional wave condition with oblique incident angles

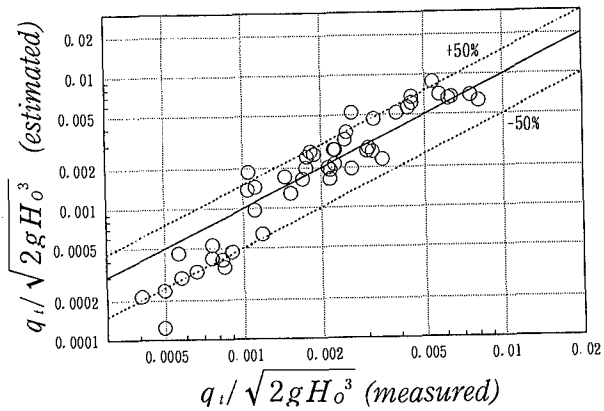

Figure 9 estimation error range for uni-directional wave overtopping rate

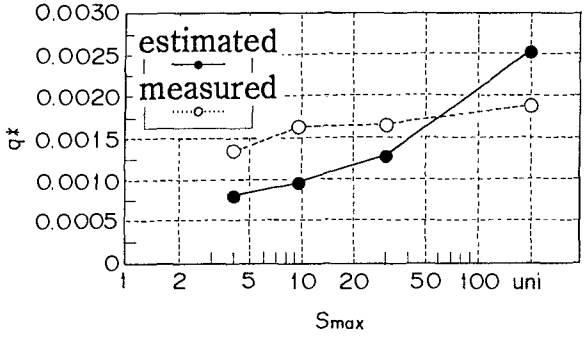

(1) in case of $H_{1/3}$=6m, $T_{1/3}$=11s, h_c=6m

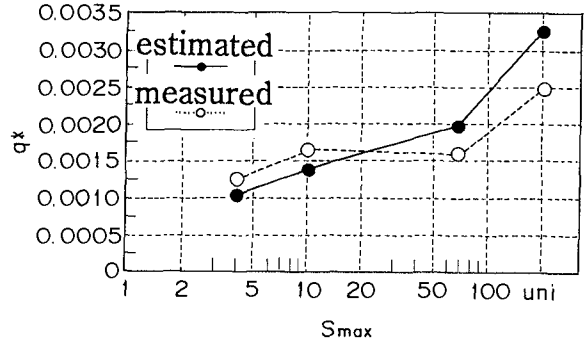

(2) in case of $H_{1/3}$=8m, $T_{1/3}$=11s, h_c=8m

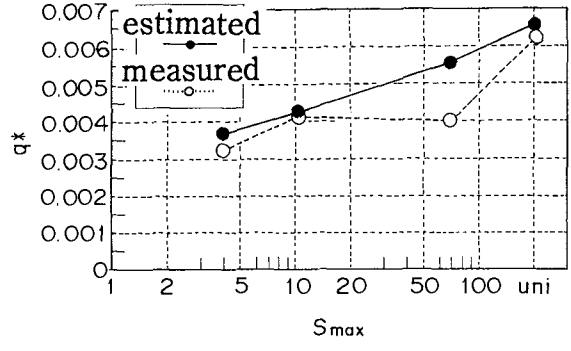

(3) in case of $H_{1/3}$=8m, $T_{1/3}$=14s, h_c=6m

Figure 10 Comparison of estimated and measured q^* in multi-directional waves

Figure 10 shows the variation of computed and measured wave overtopping rate in multi-directional waves with different angular spreading parameters. The figures represent the comparison between the estimated and measured wave overtopping rate for the various wave height and period conditions. The indication "uni" in the figures shows the case for uni-directional waves. In Fig.10(1), the measured wave overtopping rate gradually increases as the value of S_{max} increases. The estimated wave overtopping ratea are smaller than the measured ones by about 50%. In case of uni-directional waves, the estimated wave overtopping rate becomes larger than the measured one by 25%. The error is small and allowable for the sea wall design metod. The numerical model gives good agreemnet between the estimated and measured overtopping rate.

In Fig.10(2), the differences between the estimated and measured wave overtopping rates are small at the various angular spreading parameter. The estimated values agree well with the measured ones. In Fig.10(3) for the case of $T_{1/3}$=14.1s, the agreement between the estimated and measured wave overtopping rate is good except the case of S_{max}=75. For the case of S_{max}=75, the error between the estimated values is about 30%. Therefore, the simulation model is applicable to estimate the wave overtopping rate of directional random waves with different angular spreading parameter.

The good agreemnet in the cases for multi-directional waves shown in Fig.10 demonstrates that the simulation model is applicable to estimate the wave overtopping characteristics in directional sea conditions.

Wave Overtopping Characteristics in Directional Seas

Figure 11 shows the numerical results for the variation of directional wave overtopping rate for angular spreading parameter in the various crown height. The principal wave direction is normal in the cases. For any crown height cases, the wave overtopping rate becomes large as the S_{max} becomes large. In the normal principal wave dierection, the case of uni-directional waves becomes critical. If the wave directionality is obtained in a construction site, the employment of multi-directional waves may give reduction of the design crown height of sea walls.

Figure 12 shows the variation of multi-directional wave overtopping rates for principal wave direction θ p. In both cases of uni- and multi-directional waves, the wave overtopping rate decreases as the the incident angle increases. The variation ratio, however, is different between the uni- and multi-directional waves. The wave overtopping rate changes more gradually in case of multi-directional waves. Therefore, the wave overtopping rate in multi-directional waves is smaller than in uni-directional wave conditions for the case of θ_p=0 and 15°. Meanwhile, for the case of θ_p=30°, the wave overtopping rate in multi-directional waves is larger than in the uni-directional wave conditions. The

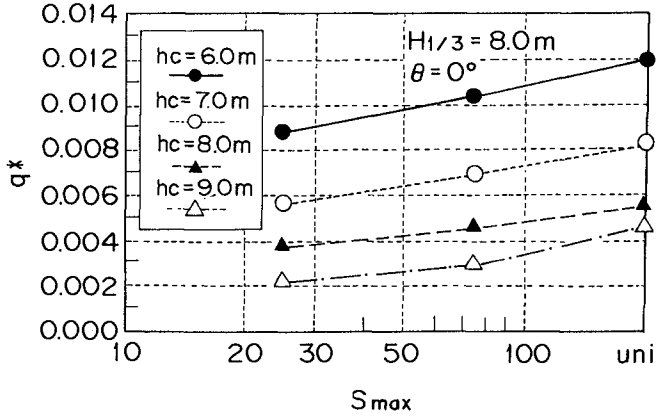

Figure 11 Esimated variation of q^* for sea wall crown height

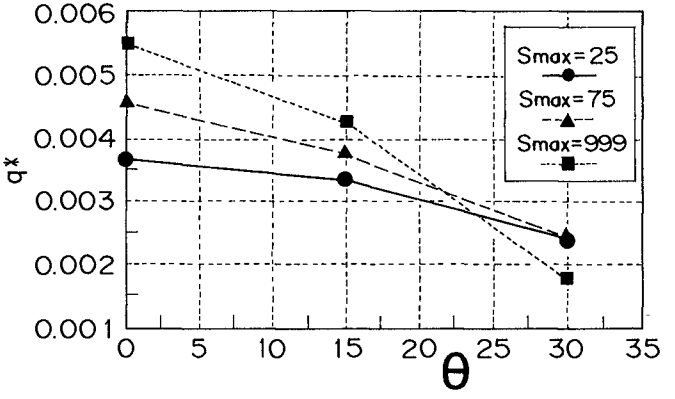

Figure 12 Variation of q^* for principale wave angle θ_p

multi-directional wave condition gives the critical condition to the design. Therefore, in case that the principal wave direction θ_p becomes larger than 30°, the multi-directional waves should be considered in the design of seawall.

Conclusions

A numerical model for directional wave overtopping is proposed. The following conclusions are derived from the comparison of numerical and experimental results;

(1) The numerical model is applicable to estimate the wave overtopping rates in the both cases of oblique uni-directional waves and of multi-directional waves with the normal principal direction when the overtopping flow coefficients and modified crown height coefficient.

(2) The wave overtopping rates in multi-directional waves become larger than in uni-directional waves in case of the principal wave direction θ p more than 30° meanwhile the former ones become smaller than the later one in case of normal and small incident principal angle.

REFERENCES

Franco, L., M. de Gerloni, J.W. van der Meer (1994) : Wave overtopping on vertical and composite breakwaters, *24th ICCE*, pp.1030-1045.

Goda,Y., Y.Kishira and Y.Kamiyama (1975) : Laboratory investigation on the overtopping rate of seawalls by irregular waves, *Rept.Port and Harbour Res. Inst.*, Vol.14, No.4, pp.3-44.

Goda,Y. and Y.Suzuki (1975) : Computation of refraction and diffraction of sea waves with Mitsuyasu's directional spectrum, *Tech.Note Port and Harbour Res. Inst.,* No.230, 45p.

Goda,Y. (1987) : Standard spectra and statistics of sea waves derived by numerical simulation, *Proc.34th Japanese Conf. Coastal Engi.*,pp.131-134.

Hashimoto, N., N. Nagai and T. Asai (1994) : Extension of the maximum entoropy principle method for directional wave spectrum estimation, *24th ICCE*, pp.232-246.

Takayama,T., T.Nagai, K.Nishida and T.Sekiguchi (1984) : Experiments on oblique random wave overtopping rates over sea walls, *31st Japanese Conf. Coastal Engi.*, pp.542-546.

Takayama,T. and T.Hiraishi (1989) : Reproducibility of directional random waves in laboratory wave simulation, *Rept. of Port and Harbour Res. Inst.*,Vol.28, No.4, pp.3-24.

Part IV: Coastal Processes and Sediment Transport

Rubjerg Knude (Cliff at Lønstrup)

Tombolo Formation, Liseleje, Zealand

THE MORPHOLOGICAL CHANGES ALONG THE NORTHERN COAST OF THE NILE DELTA

John B. Herbich[1], Fellow and Life Member ASCE, Abdel-Fattah Elfiky[2] and Gamal H. Elsaeed[3], Member ASCE

Abstract

Major beach erosion has been occurring along the Nile Delta shoreline. The erosion is primarily caused by diminished sediment transport in the River Nile due to construction of the Aswan high dam.

Egyption and foreign experts have evaluated various shore protection methods since 1983.

A summary of alternative shore protection methods, including offshore breakwaters, beach sand replenishment, groins, inlet training jetties, etc. is presented.

Introduction

The objective of this study was to investigate a variety of coastal erosion problems occurring along the Nile Delta Shoreline.

The erosion started after constructing the first dam at Aswan, the development of other dams and barrages, and the increased diversion of river water for irrigation purposes.

1 W.H. Bauer Professor Emeritus, Coastal and Ocean Division, Department of Civil Engineering, Texas A&M University, College Station, TX 77843-3136 USA.
2 Ain Shams University, Cairo, Egypt.
3 Ain Shams University, Cairo, Egypt.

After completion of the Aswan high dam in 1966, erosion along the Delta coastline accelerated considerably, resulting in the loss of several beaches and blockage of estuaries and navigation channels by sediment, as well as flooding of coastal villages.

Nile Delta Coastal Erosion Problems

Due to the resulting economic losses and the great importance of this national problem, the Egyptian Government conducted several studies since 1960 through several Egyptian and international consultants.

The areas in which erosion problems are critical along the Nile Delta Coast between Port Said City east and Alexandria City west are:

1) Alexandria Beach,
2) Baltim Beach,
3) Burullos,
4) Elgamil Strip,
5) Ras-Elbar Beach, and
6) Rosetta Promontory.

Field Data For The Egyptian Northern Delta Coastline

Most recent data were collected by the Egyptian Academy for Scientific Research and Technology, Suez Canal Research Center, The United Nations Development Program (UNDP), Coastal Research Institute and the Egyptian Shore Protection Authority.

Several shoreline changes from 1895 to 1988 at the Rosetta and Damietta promontories were recorded. Shoreline survey studies were based on data available from two aerial photographs taken in 1955 and 1983. The old shoreline was obtained from topographic maps, admiralty charts, satellite photographs and the Egyptian Survey Department maps.

Shore Protection Plans

In order to develop a shore protection plan, the Egyptian Government awarded a contract for the protection of the Rosetta area to a French consulting firm in 1983. In 1985 the Egyptian Government awarded a contract to an American consulting firm to prepare a General Master Plan for the protection of the Nile Delta Coast. In 1987 the Bilateral Panel for the Nile Delta Coastal Zone Management appointed a Dutch consulting firm to investigate the feasibility of protecting the Ras-Elbar area. Table 1 indicates several shore protection alternatives.

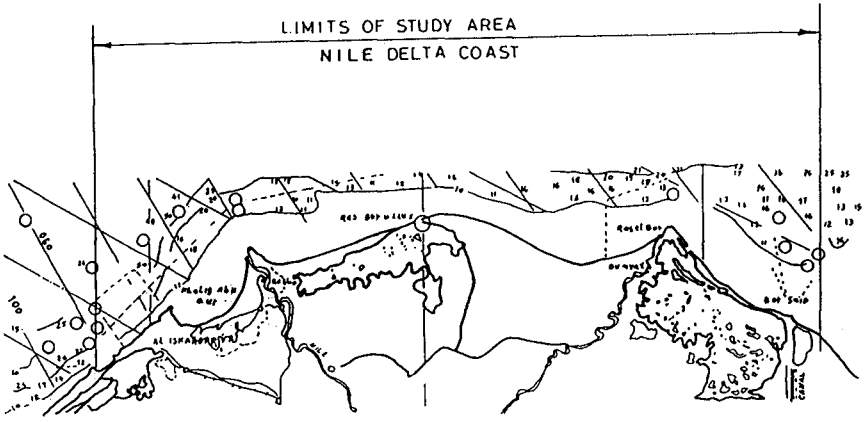

a) Shore protection study area

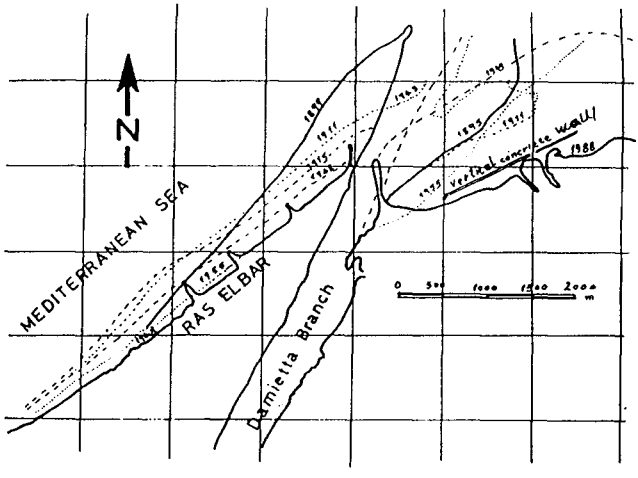

b) Shoreline retreat at Ras-Elbar

Figure 1. The shore protection study area and shoreline retreat at Ras-Elbar

Table 1. Conceptual Shore Protection Alternatives

Location	Alternative
1. Alexandria Eastern	a) Detached offshore breakwater b) interior breakwater
2. Alexandria Area Beaches	a) Offshore breakwaters and beach restoration at Chatby and Ibrahymiya beaches b) Groin field and beach restoration
3. Abou Quir (Mohamed Ali Seawall)	a) Monitoring of rehabilitated and old section. b) Add 2 tons modified cubes at damaged areas.
4. Lake Idku Inlet	Only monitoring is recommended
5. Rosetta Promontory	a) Dolosse seawall and breakwater 4.7 km revetment and breakwater section. b) Other alternatives discussed in SOGREAH (1984)
6. Burullos	a) Inlet training jetty b) Maintenance dredging as required c) Seawall (monitoring only)
7. Baltim Resort Area	a) Groin field and sand nourishment b) Offshore breakwater and sand nourishment c) Construction setback guidelines

(from Tetra Tech Report)

Conclusions

The study concluded that:

a. Planning for the whole region is more realistic and will create an interactive plan for the whole coast.

b. Further studies are recommended to cover all problem areas along the Nile Delta coast.

c. It is strongly recommended to develop and to improve the record-keeping procedures in a standard uniform format.

d. Evaluating the existing shore protection measures by analyzing the field data and comparing it with the calculated data.

References

Arafa, F. (1981) "Coastal Protection Structures Effect on Northern Coast of Egypt," Report number 1 – Cairo University/MIT.

Delft Hydraulics (1987) "Ras-Elbar Shore Protection," Report.

Elsaeed, Gamal H. (1996) "Study of Protection of the Northern Coast of Nile Delta Using Mathematical Models," Ph.D. Dissertation, Faculty of Engineering, Ain Shams University, Cairo.

Fanos, A., Khafagy, A. and Sharaf-Eldin, S. (1989) "Coastal Changes Along the Egyptian Mediterranean Coast," International Seminar.

Frihy, O., Fanos, A., Khafagy, A. and Komar, P. (1991) "Patterns of Nearshore Sediment Transport along the Nile Delta Egypt," *International Journal of Coastal Engineering*, Volume 15, The Netherlands, pp. 409-429.

Inman, D., Golik, A. and Carmel, Z. (1984) "transport of Nile Sand Along Southeastern Mediterranean Coast," *Proceedings of the Coastal Engineering Conference*, ASCE, pp. 1282-1290.

Kadib, A., Shak, A., Mazen, A. and Nadar, A. (1986) "shore Protection Plan for the Nile Delta Coastline," *Proceedings of the Coastal Engineering Conference*, ASCE, pp. 2530-2544.

SOGREAH (1984) "Coastal Protection of the Rosetta Shoreline," Technical Report.

Tetra Tech Inc. (1984-1985) "Shore Protection Masterplan for the Nile Delta Coast," Report 1, 2.

UNDP (1973) "Coastal Erosion Studies," Technical Report.

Modelling the Morphological Sensitivity of Large Nontidal Coastal Areas to Climatological Changes

H. Weilbeer and W. Zielke[1]

Abstract

This paper deals with two–dimensional hydrodynamical and morphological modelling of a large nontidal coastal area located at the German coast of the Baltic Sea. This work has been carried out in order to consider the morphological response of this region caused by climatological changes. The morphological processes in this region are mainly wave–dominated, hence a shallow water wave model was coupled with a vertical integrated flow model. Stationary simulations for waves, currents and sediment transport are carried out for a large range of meteorological situations, which were defined due to a statistical analysis of the output fields of a coupled ocean – atmosphere global circulation model. The wave parameters of this surface wave model are used as input to coastal area models.

The calculated morphological trends obtained for different meteorological situations show good agreement with the morphological changes observed in this area. By combining and weighting the individual situations the resulting flow field and sediment transport for known meteorological events can be found. The morphological sensitivity to climatological changes of the coastal area is investigated by applying this methodology to different climate scenarios.

Introduction

The prediction of the morphological behaviour of a coastal zone, for present or future environmental conditions, is a task for a coastal area morphodynamic modelling system. A system of this kind consists of coupled wave, flow and sediment transport components, which are able to describe the dynamical behaviour of the simulated area due to the feedback of morphological changes to the hydrodynamical conditions (de Vriend et al., 1993a, Nicholson et al. 1997).

In the coastal area presented in this paper, a quantification of sediment transport and of the morphological behaviour under changed environmental conditions is carried out. The

[1] Institut für Strömungsmechanik, Universität Hannover, Appelstr. 9A, 30167 Hannover, FRG

investigated domain covers an area of about 90 km by 60 km, and is located at the German coast of the Baltic Sea (Figure 1). Attention is concentrated on the morphological behaviour of the outer coast formed by the peninsula Fischland, Darß and Zingst. Observations have shown that the Western coast of Fischland and the Northern coast of Zingst are erosion zones. At Darßer Ort, which is found between these erosion zones, accretion is observed. It is important to note that this area is located at a coast nearly without any tidal movements. Thus the definition of boundary conditions for the hydrodynamical models is very difficult due to the absence of periodical water level oscillations.

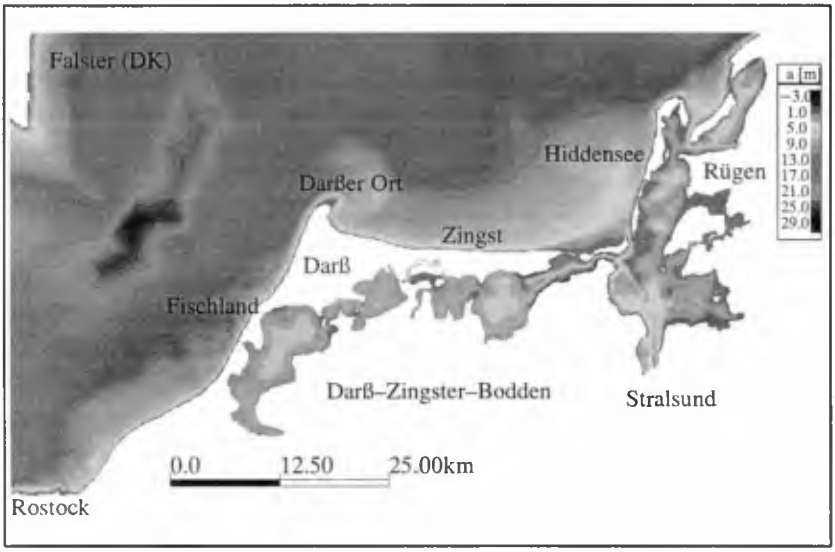

Figure 1: Domain of investigation

Waves and wave–driven currents are highly important for the sediment transport processes in this region, so emphasis was laid on the simulation of the hydrodynamical conditions in the coastal area, especially in the nearshore zone. For that purpose, a coupling of the free surface model *TELEMAC–2D* (Hervouet, 1993) and the wave model *HISWA* (Holthuijsen and Booij, 1989, 1995) due to wave–induced forces has been carried out.

The idea is to discern the effect of hydrodynamical forces on various coast sections for specific wind situations by wave and flow modelling on a large scale. The results calculated by the wave and the flow model are suitable for sediment transport calculations with regard to erosion as well as accretion zones. By combining calculated typical situations it is intended to develop scenarios which are to show the morphological sensitivity of any particular coast section to changing conditions.

In the following text, hydrodynamical simulations and sediment transport calculations will be described and scenario results will be presented and discussed with regard to their sensitivity to climatological changes.

Hydrodynamical Simulations

Flow and wave conditions in the area under research must be thoroughly understood, since the results will be decisive for the qualitative and quantitative representation of the sediment transport results, which in turn are required for the morphological findings. In order to obtain experience in the use of coupled models and in the spatial resolution required in the models, initial studies for a schematic test case have been carried out (Weilbeer, 1998).

2D–Momentum–Equation:

$$\frac{\partial v}{\partial t} + \vec{u}grad(v) + g \cdot \frac{\partial h}{\partial y} - h \cdot div\left(\nu_T \cdot grad(\vec{u})\right) = S_y - g \cdot \frac{\partial Z_f}{\partial y}$$

$$\frac{\partial u}{\partial t} + \vec{u}grad(u) + g \cdot \frac{\partial h}{\partial x} - h \cdot div\left(\nu_T \cdot grad(\vec{u})\right) = S_x - g \cdot \frac{\partial Z_f}{\partial x}$$

Source Terms:

Waves $\longrightarrow$ $S_i = \frac{1}{\rho \cdot h} \cdot \frac{D \cdot T}{L} \cdot k_i$

Bottom Friction (WCI) $\longrightarrow$ $S_i = \frac{1}{\rho \cdot h} \cdot Y \cdot (\tau_c + \tau_w)$

Wind $\longrightarrow$ $S_i = \frac{1}{\rho \cdot h} \cdot \rho_{air} \cdot c_D \cdot u_i|\vec{u}|$

Eddy Viscosity: $\longrightarrow$ $\nu_T = M \cdot h \cdot \left(\frac{D}{\rho}\right)^{\frac{1}{3}}$

Figure 2: Coupling of Models

A significant influence of grid–scale on the diversity of the hydrodynamic results was evident in these coupled wave and flow computations. The flow model as well as the wave model requires a spatial resolution of at least 10 m in order to reproduce satisfactory results. This resolution is vital since the waves, particularly in nearshore regions, undergo a number of transformations and have a high spatial variability. Furthermore, it was evident that more reliable results were obtained, if the wave–driving forces were calculated using the dissipation formulation (Dingemans et al., 1987). Wave–Current–Interaction is also considered due to an enhanced bottom friction using the parameterization of Soulsby et al. (1993), the wind stress is considered due to a coupling with an atmospheric model (Hinneburg et al., 1998) and the eddy viscosity is expressed in terms of the dissipation rate D (Battjes, 1975) (Figure 2). The most relevant processes for a wave–driven coastal area model are considered (Johnson et al., 1994, Péchon et al., 1997).

These findings were the basis for the developement of the model of the outer coast. For the wave model, high resolution is necessary in the nearshore region and demands a nesting of the area. Consequently, an elaborate nested grid system for the wave model has been developed (Figure 3) and also the FE–mesh of the flow model has been highly resolved along the shoreline in order to meet all requirements.

First the wave model is run for the entire area with a spatial resolution of approximately $\Delta x/\Delta y$ = 125/250. The boundary conditions for the eight nested grids defined in advance are retrieved from the model. Next the nested grids are calculated with a spatial resolution of approximately $\Delta x/\Delta y$ =10/25. The wave parameters (wave height, period, wave length, dissipation etc.) required for the successive models are interpolated onto the nodes of the FE–mesh.

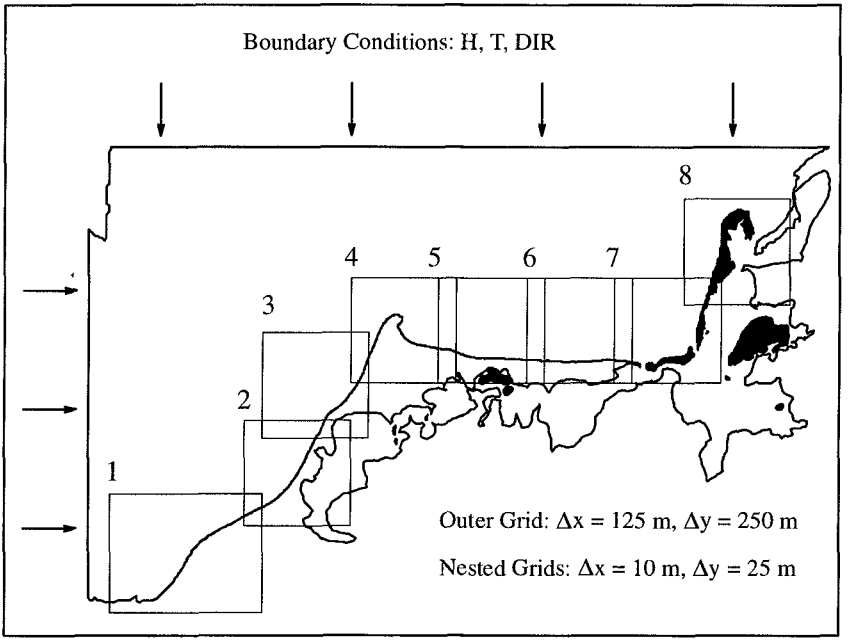

Figure 3: Nested grid system used for wave modelling

Defining the boundary conditions for the wave and the flow model presented a considerable problem for the region under consideration. The flow model requires boundary conditions at two open boundaries. It has been mentioned above that there is no periodicity as in tidal areas. Consequently, the boundary conditions have to be interpolated either by water levels measured in the area, or from a larger scale hydrodynamic model of the Baltic Sea.

However in this particular application the free surface elevation at the open boundaries in the flow model were kept constant, since noticeable water level elevations will only occur during an extreme storm event. It is true that such events will affect the bottom morphology of the area, but they cannot be completely represented by applying a method like the one used here. Instead, attention was paid to the definition of boundary conditions, i.e. wave heights H, wave periods T and incident wave direction DIR along the open boundary of the wave model.

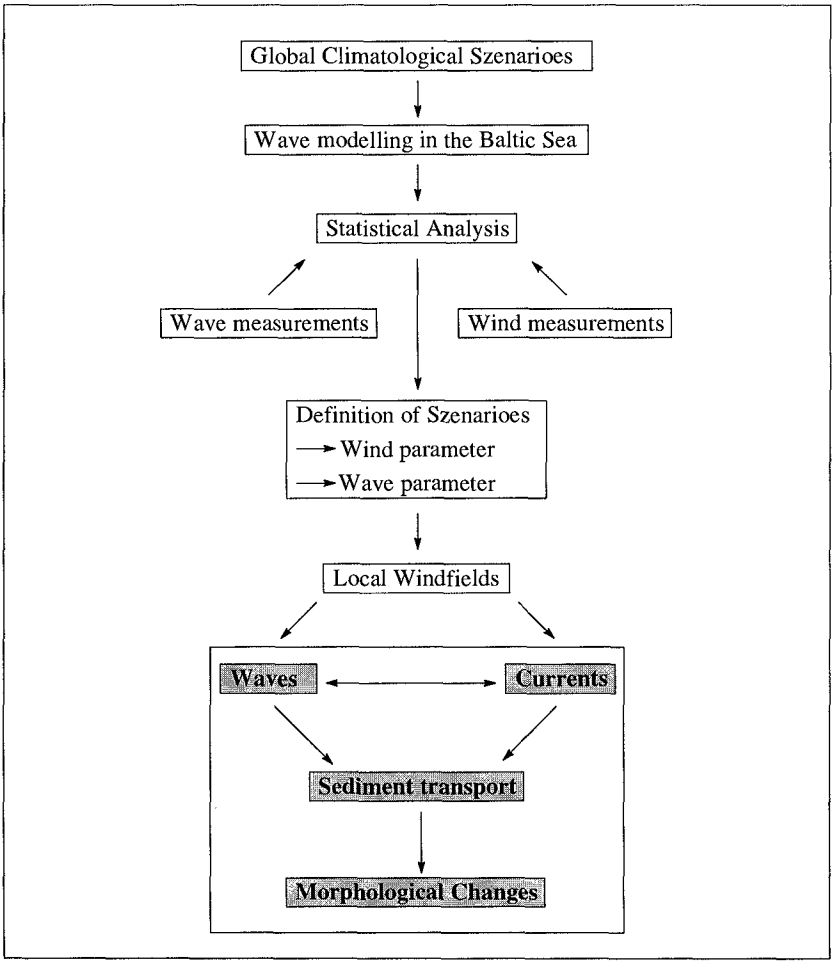

Figure 4: Modelling concept to assess the climatological impact on local coastal zones

Figure 4 presents the procedure for the compled model application. The climate input comes from global climate computations carried out at the German Climate Computation Centre (DKRZ). Wind fields calculated for a span of 13 years (1981 – 1994) were ex-

tracted and taken as input data for a sea motion model of the Baltic Sea (*HYPAS*, Günther et al., 1979, Kolax, 1998). The wave data output from this model are used as basis for defining typical situations.

First, the events were classified into 8 wind velocity classes and 12 wind velocity directions. A reduction of the input data is required in order to simplify the hydrodynamic input conditions (Steijn, 1992, de Vriend, 1991, 1993b). For the required values H/T/DIR the above hindcast results, considering regional wave measurements, were used as boundary conditions for the wave model (*HISWA*). In addition, variable wind fields were used corresponding to the direction and the velocity classes.

As a consequence of the geometry, the waves can be included only in half the number of direction classes, reaching from the Southwest to the Northeast section. Since, however, the predominant wind direction in the region is West, the main directions are accounted for. The other flow fields are generated exclusively by wind–induced forces.

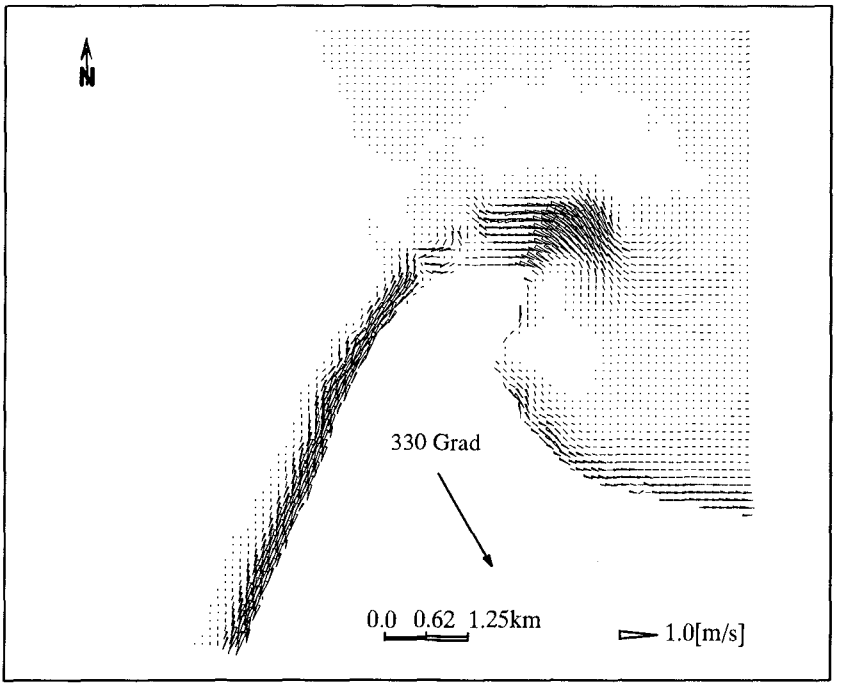

Figure 5: Current pattern near Darßer Ort (Northwest)

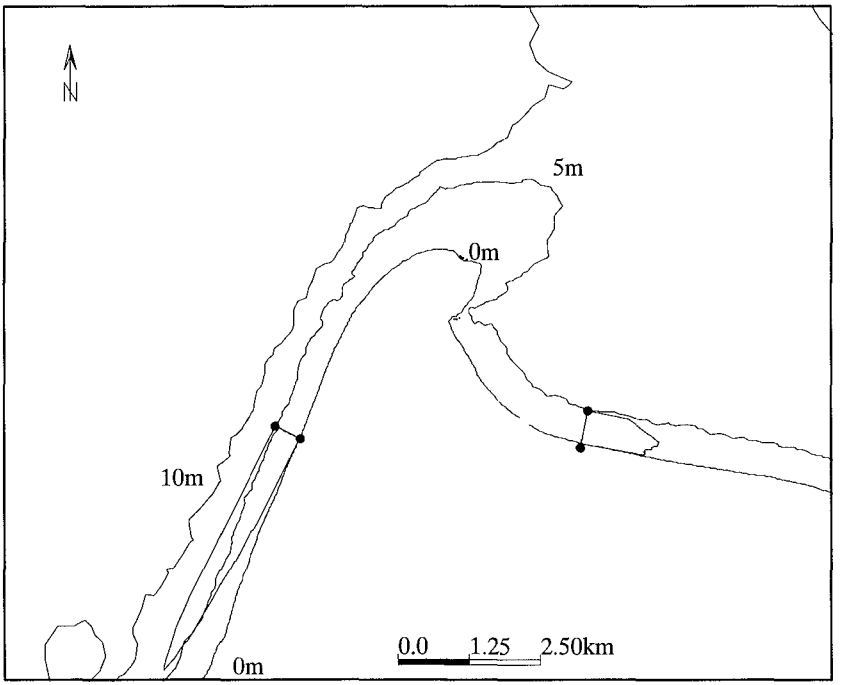

Figure 6: Typical sediment transport pattern near Darßer Ort (Northwest)

The computation times necessary for the high–resolution models limit their applicability. Continuous simulations cannot be carried out with these coupled models. A recoupling of calculated water levels and current velocities – and so a real interaction between currents and waves – is equally difficult to realize. Instead, boundary conditions and driving forces were kept constant for each situation, until stationary flow conditions had been established.

Figures 5 and 6 show as an example the current and sediment transport patterns near Darßer Ort, which are created when the wind and wave direction is from Northwest at a wind velocity of 12.3 m/s and a wave height of approximately 1.5 m. The strong longshore currents in front of Fischland as well as the protecting effect of Darßer Ort are clearly visible.

Measured time series of wind data or data obtained from climate models can be used to form statistical wind distributions in accordance with the above classification. The number of occurences (described by a Weibull distribution) leads to calculations of factors for the weighting of typical meteorological situations. As long as no changes of bathymetry are taken into account, the individual results can be combined, thus helping to find the resulting flow and sediment transport.

This procedure was carried out with a wind data series gathered over 20 years (Beckmann, 1998). Figure 7 shows the weighting factors for the average distribution of the time range 1970 – 1990. Climate scenarioes are represented by such a wind distribution, for example by a distribution for one year with extremely much Western wind, or a contrasting year (1976) with extremely little Western wind (Weilbeer, 1998). Other wind distributions could be found from measured wind data series, or else extracted from model calculations for different climate scenarios (e.g. doubling or tripling the carbone dioxide (CO_2) content in the atmosphere).

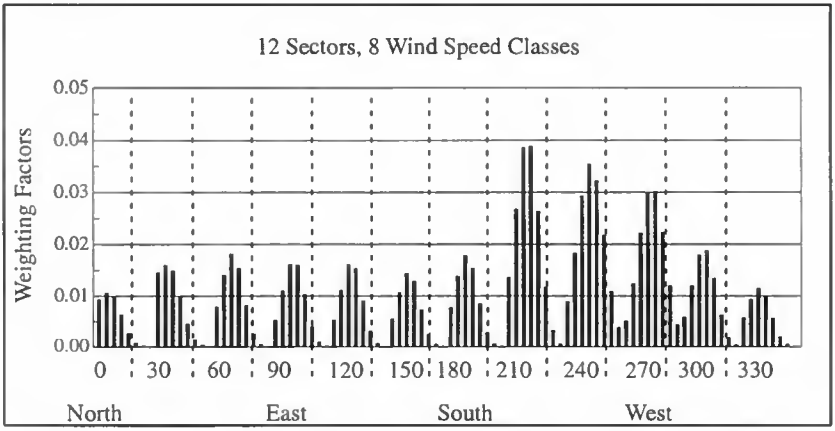

Figure 7: Weighting factors for a mean wind distribution

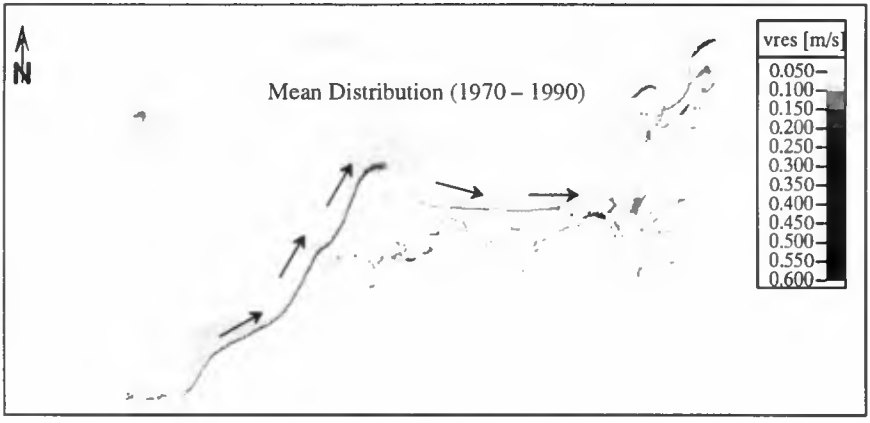

Figure 8: Resulting current pattern for a mean wind distribution

The flow resulting from this distribution is shown in Figure 8. The flow direction (represented by the arrows) is always East, as can be observed in nature. The varying flow velo-

cities are clearly recognizable. It is particularly satisfying that the highest velocities, and consequently the probably highest hydrodynamical forces are found in those regions which are known to be erosion zones. This is due to the location of the coast line of Fischland, which is oriented nearly perpendicular to the main wind direction (West) and to the steep slope of the bathymetrie in front of Fischland. The dissipation of the wave energy offshore this coast section is rather small.

This interpretation regarding the hydrodynamical forces is a rather positive evidence. Further analyses of the hydrodynamic results, e.g. regarding bottom shear stresses, could be carried out.

Sediment transport:

This method was used for the calculation of the net potential sediment transport as well. It is practicable, in this case, to use a so–called ISE–Model (*Initial–Sedimentation–Erosion*) (de Vriend et al., 1993b). Starting from the wave and flow conditions already found, the sediment transport can be calculated in a separate run completely decoupled from the hydrodynamics. The formulations of Bijker and Van Rijn (van Rijn, 1989) on potential sediment transport due to currents and waves are used for the calculations. Then, by weighting the individual events in the way already described above, the possible resulting sediment transport is calculated.

The calculations led to annually averaged rates of sediment transport which are distinctively different. If the rates of sediment transport which arise from average conditions are taken as reference values, the rate of transport in front of Fischland is reduced up to 40% at the scenario with a weaker west wind and amplified up to 40% at the scenario with a strong west wind. The differences are not as big at the locations Westdarß and Darßer Ort. A bigger rate of sediment transport already at the medium wind conditions led to smaller differences (+–25%) at the other scenarios.

Another system behavior can be recognized east of Darßer Ort. The resulting capacities of sediment transport are growing towards the east in front of Zingst, but the differences between the scenarios are not as clear as on the west coast.

It is noteworthy that if one compares the different formulations of transport then the fuzziness in the quantitative description of sediment transport only effects the absolute rates. The percentage changes of different wind scenarioes are in general very small, although comparisons of certain events lead to bigger differences in the rates of transport. It follows that this technique can produce realistic statements on the sensitivity of this coastal area for climatic fluctuations if the present conditions are modeled accurately.

Unfortunately there are hardly any clues about how to asses the reliability of the model results at this time. Therefore they could only be checked for plausibility up to now. The growth of area at Darßer Ort suggests the order of magnitude, but can not directly be used for a model validation.

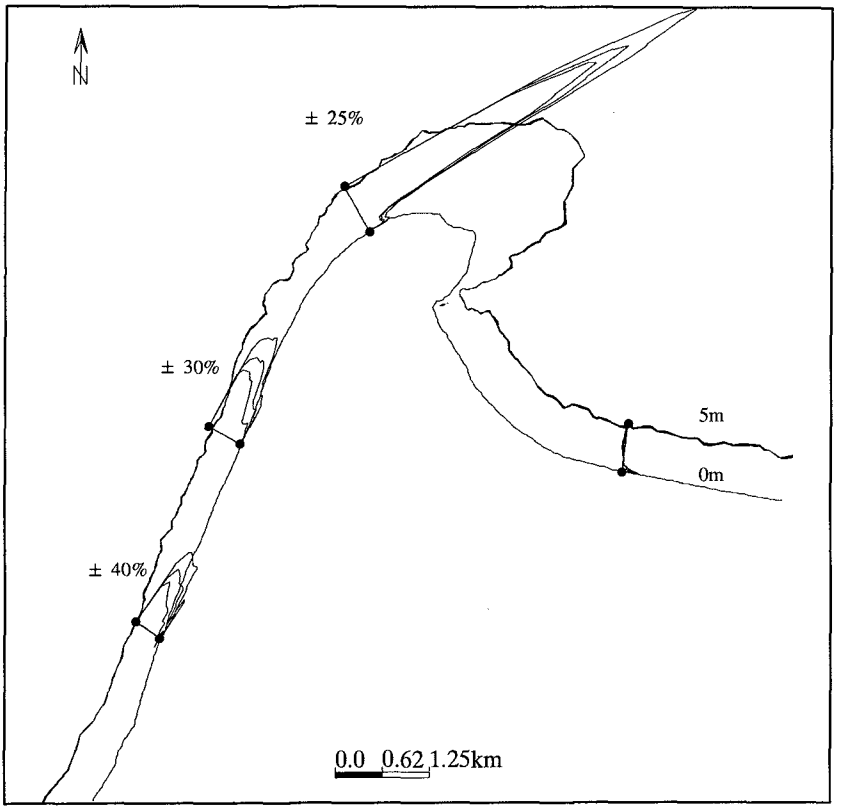

Figure 9: Resulting sediment transport for three different climate scenarioes. Potential sediment transport is calculated using the formula of van Rijn (1989)

It would, generally speaking, be possible to carry out morphodynamic calculations, but in reality they would not be feasible due to the size of the area. Application of models of this kind is limited regarding time scale and spatial scale. Succesfull calculations have been carried out in small coastal areas only, in order to find out, for example, about the changes in the bathymetry, due to constructions, such as breakwaters or groynes (Nicholson et al., 1997). The boundary conditions again are to be considered, since the effect of wave chronology, e.g. the succession of events may be decisive for a morphological development (Southgate, 1995).

Therefore, the described way was used to show the sensitivity of this coastal area to changing environmental conditions. The techniques presented here have potentials which are not at all exploited yet. Further principle and sensitivity studies can be conducted easily by using different transport formulations with more detailed approaches concerning for example suspended sediment or total load formulas.

Conclusions

A method for carrying out two–dimensional hydrodynamical numerical simulations in a large non–tidal area has been presented, with the intention to give forecasts on possible morphological trends due to changed environmental conditions. By coupling a wave model with a flow model with (wave–) boundary conditions coming from a larger numerical model, the hydrodynamical situation and the resulting sediment transport for single events can be calculated. By combining such situations, scenarioes can be developed which can be used for investigating the morphological sensitivity of this particular section of the coast.

Acknowledgements

This work has been undertaken as part of the project "Klimawirkung und Boddenlandschaft" which is part of the project "Klimaänderung und Küste" funded by the BMBF.

References

Battjes, J.A.: Modeling of turbulence in the surf zone. International Conference on Modeling Technology, ASCE, New York, 1975.

Beckmann, B., Tetzlaff, G.: Veränderungen in der Häufigkeit von Sturmhochwassern an der Ostseeküste von Mecklenburg–Vorpommern und deren Ursachen. To appear in: *Die Küste*, Heft 61, 1998.

Dingemans, M.W., Radder, A.C., de Vriend, H.J.: Computation of the driving forces of wave–induced currents, *Coastal Engineering 11*, 1987.

Günther, H., Rosenthal, W., Weare, T.W., Worthington, B.A., Hasselmann, K., Ewing, J.A.: A hybrid parametrical wave prediction model. *Journal of Physical Oceanography*, Vol. 84, p. 5727 – 5738, 1979.

Hervouet, J.–M.: TELEMAC–2D Version 2.0, Principle Note, Rapport EDF HE–43/92/13, 1993.

Hinneburg, D., Raabe, A., Tetzlaff, G.: Die Berechnung von Windfeldern und Schubspannungsgeschwindigkeiten an der Wasseroberfläche. To appear in: *Die Küste*, Heft 61, 1998.

Holthuijsen, L.H., Booij, N., Herbers, T.H.C.: A Prediction Model for Stationary, Short–Crested Waves in Shallow Water with Ambient Currents, *Coastal Engineering 13*, 1989.

Holthuijsen, L.H., Booij, N.: Hiswa User Manual, Delft University, 1995.

Johnson, H., Brøker, I., Zyserman, J.: Identification of some relevant processes in coastal morphological modelling. Proceedings of the 24th International Conference of Coastal Engineering, ASCE, pp. 2871–2885, 1994.

Kolax, M., Hupfer, P.: Die Seegangsparameter in den Gewässern vor der deutschen Ostseeküste und ihre Variabilität in Abhängigkeit von Klima– und Zirkulationsschwankungen. To appear in: *Die Küste*, Heft 61, 1998.

Nicholson, J., Brøker, I., Roelvink, J.A., Price, J.A., Tanguy, J.M., Moreno, L.: Intercomparison of coastal area morphodynamic models, *Coastal Engineering 31*, 1997.

Péchon, P., Rivero, F., Johnson, H., Chesher, T., O'Connor, B., Tanguy, J.M., Karambas, T., Mory, M., Hamm, L.: Intercomparison of wave–driven current models, *Coastal Engineering 31*, 1997.

van Rijn, L.C.: Sediment transport by currents and waves, Report H 461, Delft Hydraulics, 1989

Soulsby, R.L., Hamm, L., Klopman, G., Myrhaug, D., Simons, R.R., Thomas, G.P.: Wave–current interaction within and outside the bottom boundary layer. *Coastal Engineering 21*, 1993.

H. N. Southgate: The effects of wave chronology on medium and long term coastal morphology, *Coastal Engineering 26*, 1995.

Steijn, R.C.: Input filtering techniques for complex morphological models. Report H 824, Delft Hydraulics, 1992.

H. J. de Vriend: Mathematical Modelling and large–scale coastal behavior–Physical processes and Predictive Models, *Journal of Hydraulic Research*, Vol. 29, No.6, 1991.

de Vriend, H. J., Zyserman, J., Nicholson, J., Roelvink, J.A., Péchon, P., Southgate, H.N.: Medium–term 2DH coastal area modelling. *Coastal Engineering 21*, 1993.

de Vriend, H. J., Capobianco, M., Chesher, T., de Swart, H.E., Latteux, B., Stive, M.J.F.: Approaches to long–term modelling of coastal morphology: a review. *Coastal Engineering 21*, 1993.

Weilbeer, H., Zielke, W.: Hydrodynamical modelling of nontidal coastal areas assessing the morphological behaviour. In Spaulding, M.L. and Cheng, R.T., Editors, Estuarine and Coastal Modeling, Proceedings of the 5th International Conference, 1998.

North-Coast of Texel: A Comparison between Reality and Prediction

Rob Steijn[1]
Dano Roelvink[2]
Dick Rakhorst[3]
Jan Ribberink[4]
Jan van Overeem[1]

Abstract

For an efficient protection of the north coast of the Dutch Waddensea island Texel, a long dam was constructed in 1995. The position of this dam is on the southern swash platform of the ebb tidal delta of the Eijerlandse Gat: the tidal inlet between the two Waddensea islands Texel and Vlieland. The long dam changed the hydro-morphological conditions in this tidal inlet. The changes in the inlet's morphology have been monitored through regular bathymetry surveys. This paper describes some of the most remarkable changes that occurred in the inlet after the construction of the long dam. The impact of the long dam on the inlet's morphology and the adjacent shoreline stability has been examined with the use of a medium-term morphodynamic model. From a comparison between the observed and predicted morphological changes it followed that the model was able to simulate the large scale morphological response of the inlet system. However, on a smaller scale there were still important discrepancies between the observations and the predictions.

Introduction

The Dutch Government decided in 1990 to maintain the coastline at its 1990-position by means of artificial sand nourishments. However, at certain coastal sections, where nourishments appear to be less effective, alternative coastal protection methods could be considered. The north-coast of Texel (Figure 1) appeared to be such a coastal section.

Over a distance of some 6 km, the north-coast of Texel has lost in the last decades on average about 0.5 million m^3 sand per year. Before 1995 the maximum coastline retreat was 5 - 10 m/year at the most severely eroded northern sections. According to the formalised Dutch Coastal Defence Policy (Rijkswaterstaat, 1990), this erosion was combatted through regular sand nourishments. However, these nourishments became less and less effective. Alternative coastal protection measures were considered for this coast, like groynes, offshore breakwaters, long dam(s), revetments; most of them in combination with initial beach nourishment. Detailed numerical model studies were

1 Alkyon Hydraulic Consultancy & Research, P.O. Box 248, 8300 AE Emmeloord, The Netherlands; fax: +31 527 610020
2 WLIDelft Hydraulics, P.O Box 177, 2600 MH Delft, The Netherlands; fax: +31 15 2858582
3 Ministry of Public Works, Rijkswaterstaat, regional Directorate North Holland, P.O. Box 3119, 2001 DC Haarlem, The Netherlands; fax: +31 23 5301752
4 University of Twente, P.O.Box 217, 7500 AE Enschede, The Netherlands; fax: +31 53 4894040

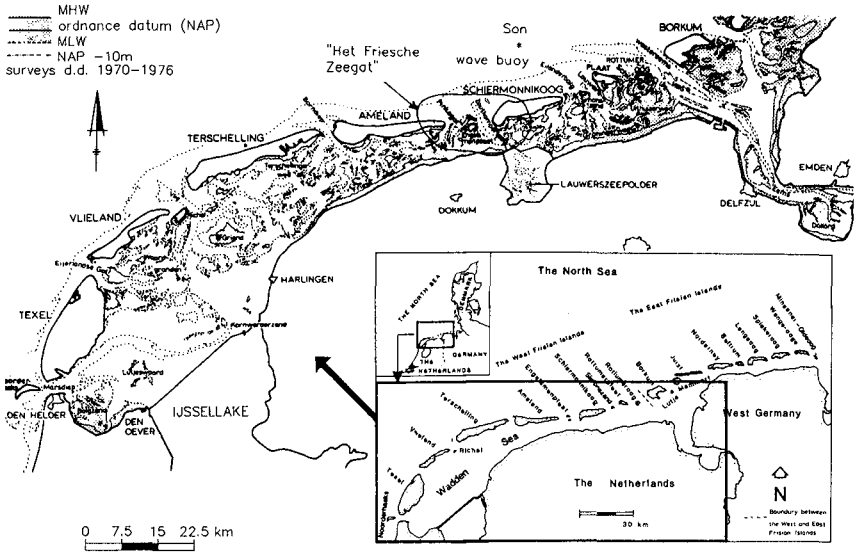

Figure 1 Geographical setting

carried out to investigate the effect of the alternative measures and their cost-efficiency to combat the erosion. A long dam (700 m from the MLW-line) was finally chosen (Rakhorst, De Wilde and Schot, 1997).

The long dam was constructed in 1995 at the northern end of the north coast of Texel (at RSP 30.5 km), in combination with nourishment and dredging works. The morphological changes that took place afterwards were monitored, which gave valuable data for a comparison between predicted and actually observed morphological tidal inlet responses.

In recent years, process-based morpho-dynamical modelling has developed rapidly. In the present study the available dataset for the long dam case has been used to check and validate the model. The model parameters were set as much as possible identical as the ones in the "old model" from 1993; however this time with the latest versions of the applied software DELFT3D (Roelvink, Boutmy and Stam, 1998). A comparison between the renewed predictions (improved hindcast) and the field observations was made and valuable information was obtained on how to set up and operate similar models and to know their weak and strong points.

The tidal inlet "Eijerlandse Gat"

The ebb tidal delta, the inlet throat and the flood tidal basin are shown in Figure 2 (situation as in 1993; before the dam construction). On the ebb tidal delta, the pattern of tidal channels can clearly be recognised, as well as the presence of shallow areas and delta bars. The ebb-dominant inlet throat channel "Robbengat" will be of special

importance for the present study. The flood tidal basin is, in contrast to the other Waddensea flood tidal basins, a closed basin: only during storms, exchange of water takes place across the watersheds.

Figure 2 The tidal inlet "Eijerlandse Gat"

The particles size of the seabed and the beach sediments ranges between 150 and 350 μm: coarser in the tidal channels than on top of the shallow areas or on the beaches.

The tide is semi-diurnal with neap, mean and spring tidal ranges of, respectively, 1.35 m, 1.70 m and 1.90 m. Tidal wave propagation is from south to north. Waves are moderate, with a mean annual wave height (at deep water) of H_s = 1.2 m. The yearly average wind speed is 7 m/s from south-southwesterly directions. Storms (larger than 7 Beaufort) mainly come from northwesterly directions.

What has been done in the last decades?

The southward migration of the Robbengat was stopped succesfully in 1948 and 1956 with the construction of two slope-protection schemes on the north-side of Texel (inside the inlet throat). Ongoing erosion of the north coast of Texel (south of the above-mentioned slope-protection works) was combatted in 1979, 1985 and 1990 by artificial sand nourishments of 2.5 to 3 million m^3, each time. The actual lifetime of the last nourishment was shorter than what was expected beforehand.

In the period 1990 - 1993 different studies were carried out to find more efficient methods to protect the north-coast of Texel (e.g. Negen, 1993, Ribberink and de Vroeg, 1991, 1992, Hartsuiker, 1991, Ribberink, de Vroeg and van Overeem, 1993, Rakhorst and Pwa, 1993 - all of them in Dutch and Ribberink, Negen and Hartsuiker, 1995). A first attempt for a full morpho-dynamic simulation of the tidal inlet, including a long dam alternative, was made by Negen (1993). Based on these effect-studies, which also included ecological and cost-benefits studies, it was concluded that a long dam at the northern end of Texel would be the most cost-effective for maintaining the north-coast of Texel.

In 1994 a 1.3 million m^3 sand nourishment was carried out on the north coast of Texel. This was necessary as the 1994-position of the coastline had already receded behind the reference 1990-position. The sand for this nourishment was reclaimed from a borrow area below the MSL -20 m depth contour (i.e. below the closure depth, so from outside the active coastal system).

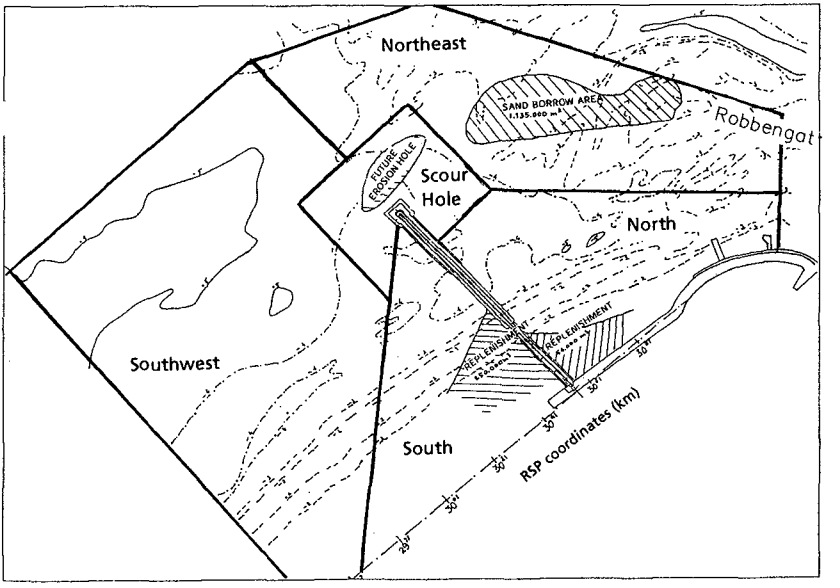

Figure 3 Drawing of the long dam and dredging works

Construction of the long dam at position RSP 30.5 km (Figure 2) commenced in April 1995. By July 1995, the dam had reached its most seaward tip at 700 m from the most seaward MLW-line; or 800 m from the dunefoot. Also in early 1995, an additional 0.7 million m^3 sand was replenished along the north coast of Texel. Another 0.4 million m^3 sand was placed in the neck of the dam (Figure 3), also to make the construction site better accessible for construction equipment. This 1.1 million m^3 sand was borrowed by a cutter suction dredger from an area between the expected scour hole and the inlet channel Robbengat (Figure 3). The idea behind this was to initiate the

development of a new ebb tidal channel in southward direction, and consequently to let the ebb tidal delta develop more in front of the north coast of Texel, which on the longer term could also benefit the sand balance of the north-coast of Texel.

Observations

The long dam and dredging works changed the tidal flow regime and wave conditions around and in the immediate vicinity of the dam. It also affected the tidal flow to and from the flood basin. Figure 4 shows for the area around the dam, the observed pattern of erosion and sedimentation between 1995 and 1997 (two-years period).

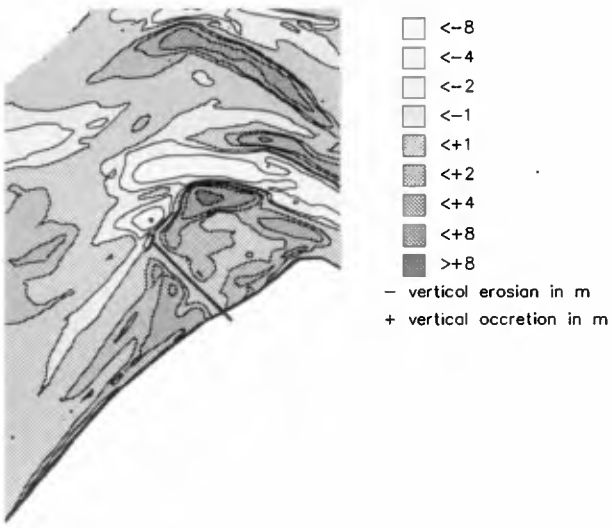

Figure 4 Observed sedimentation and erosion 1995 – 1997

The figure shows areas with significant erosion (such as in front of the tip of the dam, and to the north of the dredged borrow area), as well as areas with significant accretion (such as in the dredged borrow area and to the southwest of the ebb tidal delta). The figure also clearly shows the accretion along the coastlines on both sides of the dam. Below, some details of the observations are given:

Scour hole

The scour hole in front of the tip of the dam developed more rapidly than expected. The maximum depth reached MSL -18 m already in september 1995, that is only two months after the dam was finished (note that the local depths at this point were only MSL -5 m). The slopes on the dam-side of the scour hole are very steep, namely 1:2 to 1:3 (vert:hor), which led to the placement of an extra rubble layer after completion of the dam and later again in December 1996 (Rakhorst, De Wilde and Schot, 1997). The wet volume of the scour hole in m^3 below MSL -5m is given in Table 1.

Wet volume below MSL -5 m (m^3)	Time after dam construction (months)	Max. depth (MSL - m)
0	0	-5
250,000	2.5	-18
350,000	8	-16
300,000	14	-15
300,000	20	-13

Table 1 Development of the scour hole.

The maximum depth reduced considerably in the winter of 1996 / 1997, where it is noted that the winter of 1995 / 1996 hardly had any westerly storms (which is an anomaly). Without the occurrence of high waves, the scour hole apparently developed first in vertical direction, before it widened in horizontal direction.

Dredged hole

The borrow area north of the dam (Figure 3), which was intended to develop into a tidal ebb-channel, indeed changed in that direction. The maximum dredged depths down to MSL -15 m reduced rapidly to not deeper than MSL -10 m two years later. While the MSL -7 m depth contour of the dredged borrow area and that of the inlet channel Robbengat were not connected in June 1995, they were in March 1997 (see Figure 5). Once the borrow area stretched in east-west directions and became "connected" with the inlet channel Robbengat and with the scour hole, it migrated in northward direction under the influence of the eastward resultant sediment transport and the west-to-east tidal wave propagation.

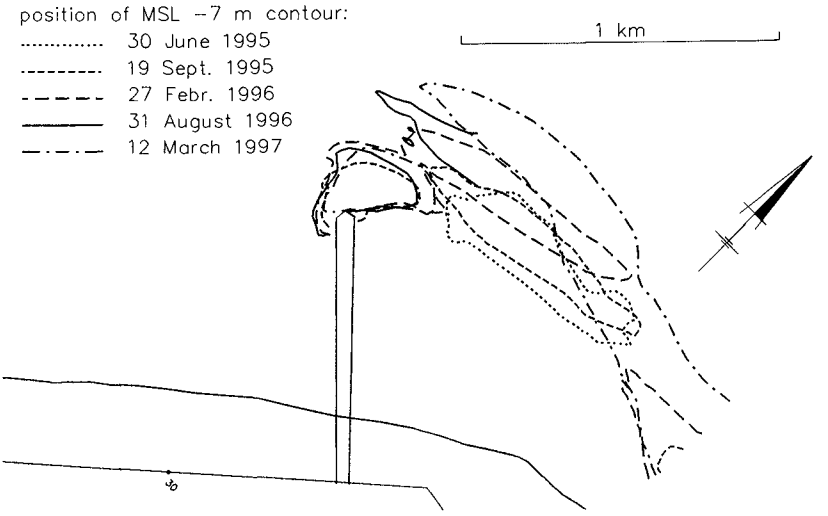

Figure 5 Movements of the MSL –7 m depth contour

Coastal area north of the dam
Immediately after the dam construction, significant accretion rates were found in the area to the north of the dam. This area continued to accumulate sand (Figure 4), albeit at a steadily slower rate. In the period July - September 1995 a resultant sand accumulation of more than 70,000 m^3 per month was found in an area of some 0.4 km^2. About one year later this accretion rate had reduced to some 30,000 m^3 per month. Between the coastline of Texel, the dam and this accretion area, a small shortcut gully was present till early 1998, when it silted up.

Coastal area south of the dam
If we consider an area from the dunefoot to a shore-parallel line through the tip of the dam, and from the dam to a position 2.5 km south of the dam (Figure 4), then the total sand accumulation in this area in the period 1995 - 1997 is 475,000 m^3 per year. This accretion can be attributed to the effect of the long dam; nourishments have not been carried out in that period.

If we disregard the upper part of the profiles, above MSL -1.5 m, then the observations show that initially erosion took place (70,000 m^3 in the period July - September 1995). In volumetric sense not much changed in the foreshore area in the winter of 1995 / 1996. But after the winter of 1996 / 1997, when westerly storms had occurred, accretion of more than 300,000 m^3 was observed. This demonstrates the importance of higher waves for the shoreward transport of sand from greater depths.

Model predictions

A numerical model of the entire tidal inlet system including the long dam and dredging works (Figure 3) was set up. The model is based on the DELFT3D software package, which is described in more detail elsewhere in these proceedings (Roelvink, Boutmy and Stam, 1998). The model computes the tidal wave propagation, the tide-, wave- and wind generated flow conditions, the short wave conditions, sediment transport and seabed changes. The model is of the medium term morphodynamic type (MTM-model: De Vriend, e.a., 1993). A limited number of input conditions (waves, tides, wind) have been selected in such a way that they represent the annual sediment transports.

Figure 6 shows, as an example, the computed tide-averaged sediment transports in the vicinity of the dam for one of the selected wave conditions "West-High" (at deep water: H_s = 3.1 m, T_p = 7.6 s, from 268° N). These transports follow after one year of morphodynamic simulation, so when the deepest portion of the dredged borrow area have already largely silted up.

An interesting detail in the resultant sediment transport patterns was observed near the dredged borrow area. Here, the resultant sediment transport at the start of the morphodynamic simulation is directed from two sides towards the center of the borrow area, leading to a steady siltation of the center of the dredged hole. The flood-dominance on the west-side of the borrow area is due to relaxation effects: during flood the incoming concentration vertical is over-saturated while during eb the incoming concentration vertical is under-saturated.

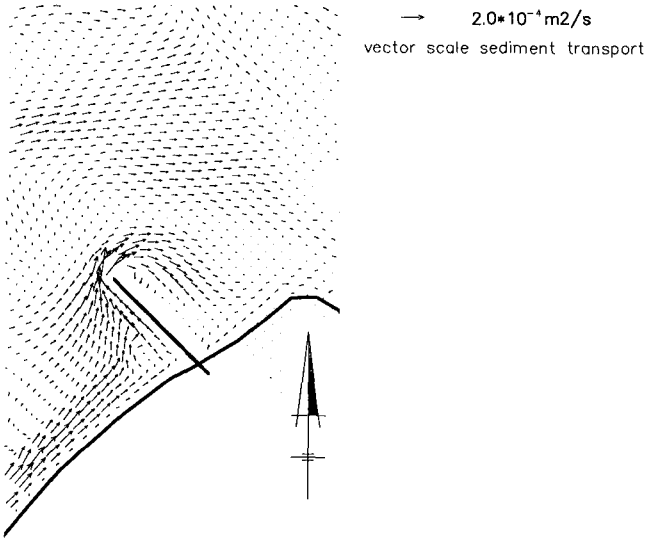

Figure 6 Tide-averaged sediment transport

A direct confrontation between the model predictions and the observations is given in Table 2 below. It gives the volumetric changes over a period of two years (1995 - 1997) for the five areas as indicated in Figure 3. It is noted that this table is not the only source for comparison: for that it lacks too much information on details of smaller scale phenomena

Area (Figure 3)	Surface (m^2)	Reference computation			Observations (Rakhorst, 1997)		
		Sedimentation (m^3)	Erosion (m^3)	Volumetric changes (m^3)	Sedimentation (m^3)	Erosion (m^3)	Volumetric changes (m^3)
South	510,000	169,000	-25,000	144,000	354,000	0	354,000
Scour hole	172,000	16,000	-115,000	-99,000	0	-466,000	-466,000
North	485,000	32,000	-323,000	-291,000	972,000	0	972,000
Southwest	1,278,000	260,000	-600,000	-340,000	987,000	-48,000	939,000
Northeast	785,000	156,000	-2,237,000	-2,081,000	15,000	-1,040,000	-1,025,000

Table 2: Computed and observed volumetric changes (1995 – 1997)

From the confrontation of the predictions with the observations it follows that:

- The predicted volume of the scour hole is much smaller than observed. Especially the maximum depth of the scour hole was not predicted (MSL - 7 m in stead of MSL -18 m).
- The dredged borrow area north of the dam also stretched and aligned with the inlet's channel Robbengat in the computations. It even showed a tendency for a northward migration although not at the same rate as in the observations. A weak point is that the computed total volumetric changes in the large area NorthWest does not correspond with the observations.

- The accumulation of sand north of the dam was not predicted by the model. This could be related to the smaller scour hole (less sand available) or could be due to a too much restricted horizontal eddy exchange just behind the dam.
- The computed accretion south of the dam is almost half the observed accretion. Apparently, too much of the longshore sediment transport is directed in seaward direction along the dam, in stead of being stopped. This may also be one of the reasons why the computed scour near the tip of the dam remains so limited.

The conclusion that follows is that predictions with a state-of-the-art numerical morpho-dynamical model using "standard model settings", may still differ considerably from actual developments. This is even more true when looking at smaller-scale morphological developments.

Sensitivity computations

The following series of sensitivity computations with the numerical model were carried out to get a better understanding of the behaviour of the model and to improve our knowledge on how these type of models should be designed and operated for the current type of applications:

- Computation with a one-week storm-condition;
- Computation not with a full harmonic analysis of the tide, but by only applying the A0, M2 and M4 tidal constituents. The phases of these constituents were then varied to study the sensitivity of the tide-averaged sediment transport on the modelled phase difference between the M2 and M4 constituents;
- Computation with another tidal schematization;
- Computation with a different model boundary at the tidal flood basin;
- Computations with different values for the dispersion coefficient in the flow and sediment transport modules;
- Computation including a schematised reproduction of spiral flow;
- Computation with an adjusted bed roughness. The spatial differences in the bed roughness have been determined in such a way that it reflects the influence of larger-scale horizontal eddies on the bed shear stress. The applied method can only be regarded as a first attempt to schematise the complex influence of large-scale turbulence on the sediment transport capacities behind structures like the long dam;
- Computation with a different chronology in the wave and tidal conditions.

It goes beyond the scope of this paper to present the findings from the above set of model computations. Details can be found in Roelvink, van Holland and Steijn (1998). Yet, the following recommendations followed for improving the model:

- Take into account the actual chronology in the wave conditions for the simulated period. As stated before, the season 1995 / 1996 was completely different in terms of westerly heavy winds, than the 1996 / 1997 season. In the improved model hindcast (see below), it was therefore decided to run the model for its first year with no waves, and for its second year with a schematisation of the actually occurring wave

conditions. This appeared to be especially important for the rapid development of the scour hole.

- Take into account the effect of spiral flow. This phenomenon appeared to be important for the curving of the new channel through the dredged borrow area. Spiral flow also appeared to be important for additional sand movement towards the inner bend of the curved channel, that is towards the accretion zone north of the dam.
- Use spatially varying bed roughnesses, in such a way that they represent the effect of increased turbulence behind the long dam.

Results from the improved model hindcast

With the improved model a new hindcast was made of the morphological developments in the period 1995 - 1997. Table 3 summarises for the same areas as in Table 2, the computed and observed volumetric changes after one year (1996) and after two years (1997).

Area (Figure 3)	Improved hindcast			Observations (Rakhorst, 1997)		
	Sedimentation (m^3)	Erosion (m^3)	Volumetric changes (m^3)	Sedimentation (m^3)	Erosion (m^3)	Volumetric changes (m^3)
South	11,000	-31,000	-20,000	12,000	-31,000	-19,000
Scour hole	22,000	-310,000	-288,000	0	-497,000	-497,000
North	147,000	-63,000	84,000	572,000	-96,000	476,000
Southwest	945,000	-46,000	899,000	641,000	-109,000	532,000
Northeast	232,000	-906,000	-675,000	127,000	-495,000	-368,000

a) After 1 year (1995-1996): no waves

Area (Figure 3)	Improved hindcast			Observations (Rakhorst, 1997)		
	Sedimentation (m^3)	Erosion (m^3)	Volumetric changes (m^3)	Sedimentation (m^3)	Erosion (m^3)	Volumetric changes (m^3)
South	227,000	-281,000	-53,000	354,000	0	354,000
Scour hole	116,000	-271,000	-155,000	0	-446,000	-446,000
North	363,000	-121,000	241,000	972,000	0	972,000
Southwest	538,000	-882,000	-344,000	987,000	-48,000	939,000
Northeast	299,000	-2,515,000	-2,216,000	15,000	-1,040,000	-1,025,000

b) After 2 years (1995-1996)

Table 3: Comparison between predicted and observed volumetric changes

Figures 7 and 8 further show the computed sedimentation and erosion patterns in the vicinity of the long dam, respectively after one and two years of morphodynamic simulation. Figure 8 can be compared with Figure 4, which was based on the observations.

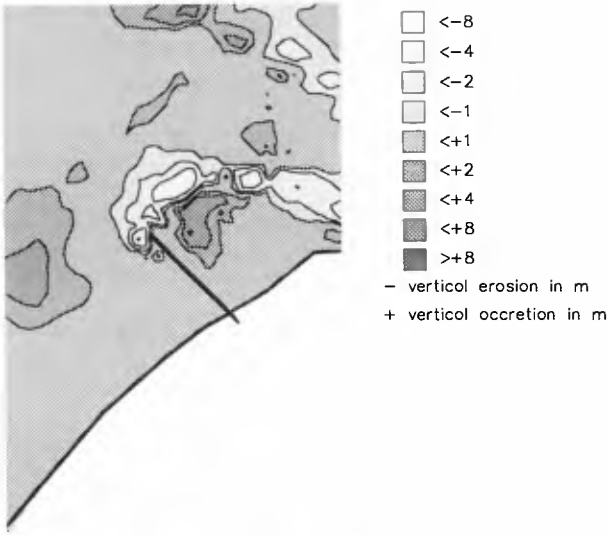

Figure 7 Computed sedimentation and erosion 1995 – 1996 (no waves)

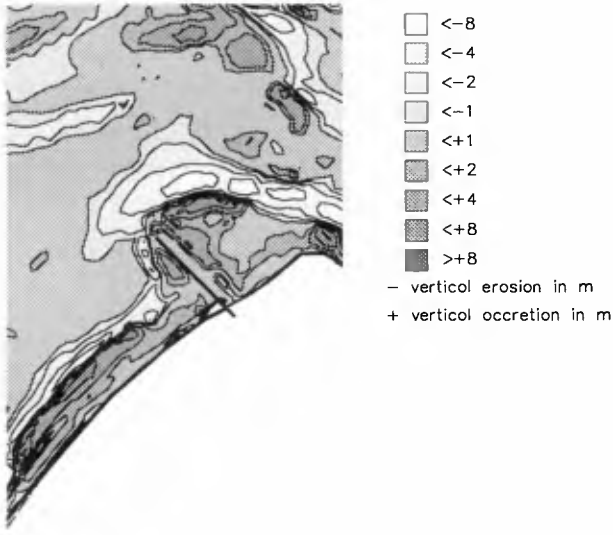

Figure 8 Computed sedimentation and erosion 1995 – 1997

Conclusions

From a comparison of the results of the improved hindcast with the observations it follows that:

- The maximum depth in the scour hole now is computed at MSL -14 m after six months of simulated time, which is not far from the observed maximum depth of 18 m;
- In the first simulated year there is hardly any accretion south of the dam, which corresponds with the observations. In the next year, when waves are considered in the computations, there is significant accretion, which also fits with the observations.
- The coastal zone north of the dam now also accretes (contrary to the reference computation), which agrees with the observations. In absolute sense, however, there are still discrepancies between the computed accretion rates and the observed ones.
- The model shows that the dredged borrow area quickly develops into a tidal channel (in line with the Robbengat in the inlet throat), which starts to migrate in northward direction. This corresponds with the oservations, albeit that the curvature of the channel as well as the migration speed differ.
- The coastal profiles in front of the north-coast of Texel (south of the dam) develop into unrealistic profiles, which would be corrected if cross-shore transport effects by waves were taken into account.

In summary, it can be concluded that the improved model simulates most of the observed morphological changes. The largest uncertainties are the modelling of the turbulence effects around the dam and the modelling of the effect of waves and turbulence on the sediment transport. For a correct representation of the morphological developments, the *behaviour* of the applied sediment transport formula as a function of the combined flow, turbulence and orbital velocities, is of special importance.

Final remarks

The long dam has been effective in the protection of the north coast of Texel. Contrary to the predictions it has not worsened the situation directly north of the dam. Possible negative consequences for the sand balance of the downdrift island Vlieland have not yet been recorded, but that is probably a matter of time. The morphological response have largely been restricted to the immediate surroundings of the works. But again, this may be a matter of time. After all, the new elongated tidal channel Robbengat has proven to play an important role in the filling and emptying of the flood basin.

Rijkswaterstaat will continue to monitor the situation in the tidal inlet and around the dam. We expect that after some time this data set will form a very valuable source for experimental testing of existing and new model concepts.

Acknowledgements

The work is carried out as part of the Coast*2000 programme of the Dutch Ministry of Transport and Public Works (Rijkswaterstaat). The authors further want to acknowledge the staff of the Regional Directorate North-Netherlands of Rijkswaterstaat for visualising the data sets of the Eijerlandse Gat.

References

De Vriend, H.J., J. Zyserman, J. Nicholson, J.A. Roelvink, P. Pechon and H.N. Southgate, 1993. Medium-term 2DH coastal area modelling. Coastal Engineering, 21 (1993) pp. 193-224

Hartsuiker, G., 1991. Coastal Defence Eijerland- hydraulic morphologic effect-study; phase 1. Delft Hydraulics report number H1241, Delft, June 1991 (in Dutch)

Negen, E.H., 1993 Morphologic investigations using 2DH numerical models at Eijerland (Texel). M.Sc. Thesis Delft University of Technology. Also: Delft Hydraulics report number H1887, Delft, The Netherlands (in Dutch).

Rakhorst, D. 1997. Morphological evaluation Dam at Eijerland (third report). Rijkswaterstaat, Regional Directorate North Holland, december 1997 (in Dutch).

Rakhorst, D., D. De Wilde and C. Schot, 1997. Seaward Coastal Defence Scheme Eijerland. Terra et Aqua - number 67 - june 1997, pp. 3-13.

Ribberink, J.S. and J.H. De Vroeg, 1992. Coastal Defence Eijerland - hydraulic morphologic effect-study phase II. Delft Hydraulics report number H1241, May 1992

Ribberink, J.S., E.H. Negen and G. Hartsuiker, 1995. Mathematical Modeling of coastal morphodynamics near a tidal inlet system. Coastal Dynamics '95, ASCE, Gdanks, Poland.

Roelvink, J.A., A.E.G. Boutmy and J.M.T Stam, 1998. A simple method to predict long-term morphological changes using complex model results. These Proceedings.

Roelvink, J.A., G. van Holland and R.C. Steijn, 1998. Sensitivity computations Eijerland and SW-Texel - phase 1 Eijerland. Report jointly prepared by Alkyon (number A266) and Delft Hydraulics (number Z2430), May 1998, (in Dutch)

Rijkswaterstaat, 1990 A new coastal defence policy for the Netherlands. Ministry of Public Works, the Netherlands

Littoral Processes in a Prograding Coast: the Case Study of the Atlantic Ocean Coast of Uruguay

Luis Teixeira[1], Juan Montaña[2], Miguel Losada[3], ASCE Member

Abstract

The Atlantic Ocean coast of Uruguay extends from Punta del Este outer limit of the Rio de la Plata Estuary, to the Brazilian border, over 220 kms. This case study applies to a homogeneous coastal stretch of 80 kms long, north of Punta del Este. The main coastal features are three littoral lagoons, Jose Ignacio, Garzón and Rocha, whose mouths open and close by natural or antropic actions every year. The coastline is formed by 1-2 mm coarse sand on highly reflective beaches. Beach berm is overwashed by the SE storm waves. Landward there is a dune system. This beach-dune structure is approximately 100 m wide. At least three similar morphological structures may be landward identified, which were developed during a period of time when the sea level was about 5 m higher than today's sea level (approximately 5000 years BP). ^{14}C technique applied to chalk samples shows a relative decrease of the sea level in the last 5000 years. Furthermore, gravimetric data shows that there is an anomaly, which supports the existence of an isostatic rise of the continental shelf. As a result, the Atlantic Ocean Coast of Uruguay is prograding. The beach coarse material is provided by the wave action from the continental shelf, while the fine dune material seems to be obtained from the erosion of the land weathered granite.

1 Introduction

The Atlantic Ocean Coast of Uruguay is part of the eastern coast of South America. It extends over 220 km, from Punta del Este, outer limit of the Rio de la Plata estuary to the Brazilian border, at the NE. The case study refers to a part of about 80 km of this coast,

[1] Instituto de Mecánica de los Fluidos e Ingeniería Ambiental, Facultad de Ingeniería, J. Herrera y Reissig 565, Montevideo, Uruguay. FAX: 5982 7115277, E-mail: luistei@fing.edu.uy
[2] Departamento de Geología, Facultad de Agronomía, Uruguay. FAX: 5982 393004, E-mail: geologia@suelos.edu.uy
[3] Universidad de Granada, España. FAX: 3458 248951, E-mail: mlosada@platon.ugr.es

from Punta del Este to Cabo Santa María (La Paloma) (Figure 1). It is an homogeneous and almost straight coastline, oriented perpendicular to the SSE (N 65° E) and whose middle point is at the coordinates 34°45' S and 54°30' W (Figure 2).

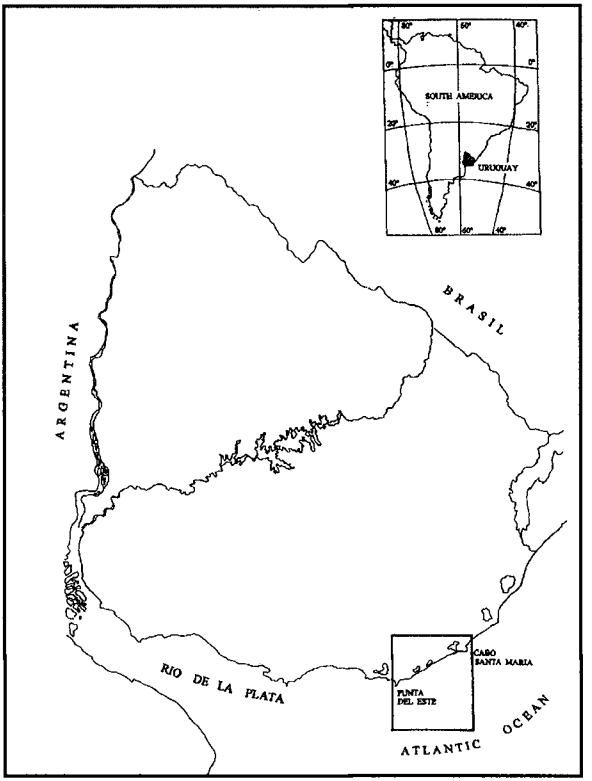

Figure 1. Zone of interest

The main coastal features are three littoral lagoons, José Ignacio, Garzón and Rocha whose mouths open and close intermittently, each year, by antropic or natural actions. These lagoons constitute a rich and sensitive ecosystem, that has to be preserved, as the remaining coastline, which is still almost unexploited by the tourist trade.

East of Punta del Este, the outlet of the Maldonado River, and 30 km eastern, about in the middle of the studied stretch, José Ignacio rocky point, are located.

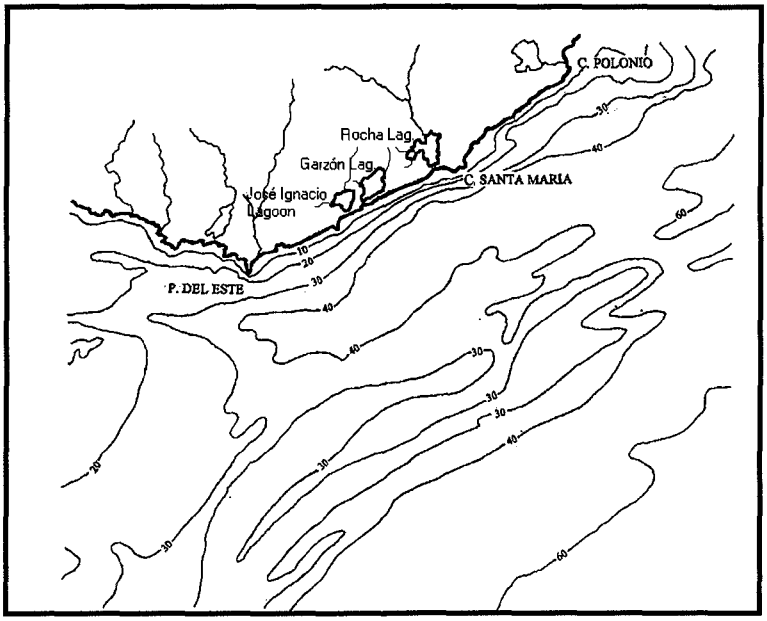

Figure 2. Studied coastal stretch and bed contours

To establish the bases for a management plan of this coast, today non-existent, but urgently needed, the long term evolution pattern has to be determined. It must be considered that Punta del Este is one of the main summer tourist resort in South America, and La Paloma placed in Cabo Santa Maria, can be considered the second one in Uruguay.

In this paper the main geological and morphological features of this coastline are considered, as well as the main hydrodynamic variables. The existent gravimetric data and mollusk samples analyzed with the ^{14}C technique, as well as the recognition of lines of previous coasts, sustain the hypothesis of the prograding character of the studied stretch.

2 Geological and morphological data

This zone of the Uruguayan coast presents a crystalline rock substratum from 500 to 660 million years, which is exposed in some areas and in other is covered by deposits from the cenozoic and quaternary (UNDP, URU.73.007 1980).

The crystalline rocks that crop out in the immediate zone at the east of the José Ignacio Lagoon are intrusive granites, porphyries, with phenocrysts of up to 8 to 10 cm. The

quaternary deposits include clays, sands and mudstones, from the pleistocene, which provide large quantities of detritus sediments to the coastal environment through gullies and ravines.

In the vicinity of Garzon and Rocha lagoons, series of coastal dunes, formed by coarse and very coarse moderately sorted sand, belonging to the recent, can be found (UNDP, URU.73.007 1980). Beaches have steep slopes (about 12%) and coarse sand as large as 2 mm. For example in Las Garzas beach, located approximately in the middle of the stretch, indicative grain diameters are D_{90}=1.62 mm and a D_{50}=0.96 mm. These are immature sands, both texturally and mineralogically, with evidences of little transportation by rolling.

Behind these beaches there is an eolian dune system of fine sands. That beach-dune structure is approximately 100 m wide. Landwards, it can be easily recognized three similar geomorphologic structures, which were formed in the past (5000 years B.P), when the sea level was about 5.0 m above the present sea level

Large sandy spits separate the three coastal lagoons from the ocean. These spits are formed by sand provided by the ocean. Their natural opening and closure are produced by the dynamic ocean action over the coast.

3 Hydrodynamics and wave energy flux

The mean sea level

This coast stretch has a semidiurnal astronomical tide regime with diurnal inequality. The difference among the mean high water level and the mean low water level is 0.45 m in La Paloma and 0.54 m in Punta del Este (east and west borders of the studied stretch, respectively). On the other hand the meteorological tide, associated with strong southeastern winds, provokes higher mean sea level. For example in Punta del Este the average of annual maximum levels recorded in this century is 1.41 m and the highest record is 2.15 m. In Cabo Santa Maria the average of annual maximum levels is 1.22 m.

Wave climate

Deep water wave climate was established on the basis of data from the UK Met. Office's Main Global Marine Data Bank, for the area limited by coordinates 34.0° S, 36.0° S and 55.0° W, 53.0° W. These data were obtained by merchant ships during the period from 01/1949 to 06/1996 and constitute a total of 5558 records of significant wave height, period and direction, grouped at sectors of 30°. Furthermore, the significant wave height exceedence curve obtained by the U.S. Navy GEOSAT with records from November 1986 to March 1989, for a 4° by 4° area (Young I. R., 1996) was used.

These data were compared to the significant wave height satellite records for the region between 35°S to 36°S and 53° W to 56° W, provided by the Global Real Near Real –Time

Significant Wave Height Visualization Program, sponsored by the Colorado Center for Astrodynamics Research at the University of Colorado were recorded by ERS and TOPEX/POSEIDON satellites for a period of 15 months starting in July 1996.

On the other hand wave records obtained during some months between 1976 and 1978, by a non-directional Datawell type buoy which was installed close to Punta del Este were analyzed.

Wave propagation based on the obtained wave climate was computed with a refraction-diffraction model. This parabolic weakly non-linear wave propagation model, named OLUCA-RD, was developed at the Oceanographic and Coastal Engineering Group of University of Cantabria, Spain. Bed contours are given schematically in Figure 2.

Wave propagation with periods in the range 6 and 12 seconds and all the directions which arrive to the studied stretch was computed. In this way, wave direction and wave height at the coast (10 m water depth), that is coastline wave climate was established. Moreover, the net percentage of the annual energy flux arriving to the coast, corresponding to each direction, was determined. The results obtained are shown in Figure 3.

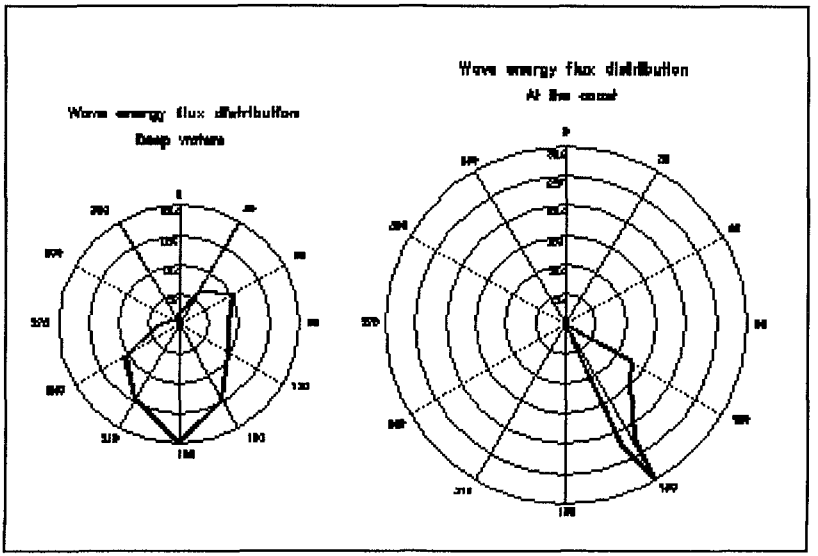

Figure 3. Wave energy flux in deep water and at the coast

Even though in deep water the net annual energy flux spreads in a wide direction range, the effects of the wave propagation over the existing bed contours determine that at the coast the net flux of energy is concentrated on the direction perpendicular to the coast. The vector sum of these results shows that the net annual energy flux over the 10 m depth bed contour is esentially perpendicular to the coastline (Figure 4).

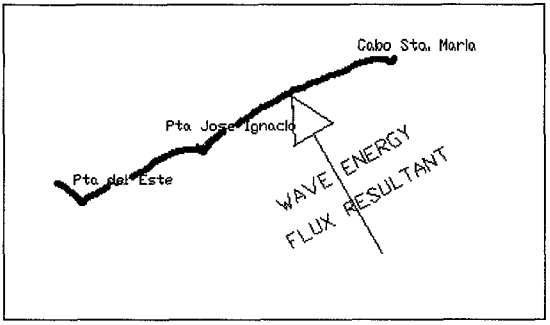

Figure 4. Resultant annual net energy flux

On the basis of this result it becomes apparent that the net longshore sediment transport is minimum in this stretch of coast. That is verified by the comparative analysis of sand characteristics of the neighboring beaches.

4 Relative sea level changes

It is well known that the relative sea level is the result of the balance between the isostasy, determined by the tectonic activity, and the eustasy or modifications of the sea level due to the changing volume of ocean water or the capacity of ocean basins.

At a global scale it is accepted that the eustatic level in the last 5000 years has been growing. Between 5000 and 3000 years B.P there was a growth of 20 to 30 cm each 1000 years, and during the last 3000 years the sea level has been oscillating or growing with a lower rate. Summing up it can be said that the eustatic level during the last 5000 years has been growing with a rate of 0.01 cm per year.

In the zone under study there exists evidence of the fact that during the last holocenic transgression the sea level had reached a level of +5.0 m relative to today's sea level. As it will be shown in the next paragraph, from those days up the present, a relative decrease of the sea level up to the current sea level was produced. This statement implies that during the last 5000 years the isostatic change rate was greater than the eustatic change rate.

5 Verification of descendant sea level: prograding coast

Martin and Suguio (Martin, M. and Suguio K., 1989) determined a curve of sea level fluctuation in the holocenic period, for three different zones of Brazil. This curve establishes an increase of the relative sea level up to a maximum transgression 5000 years BP, a regression 4000 years BP and successive variations up to present level, with a negative rate of 1 mm per year. Moreover, Bracco and Ures (Bracco et al 1997), (Bracco and Ures, 1998) through ^{14}C technique applied to mollusk samples confirmed the results from Martin and Suguio (Figure 5).

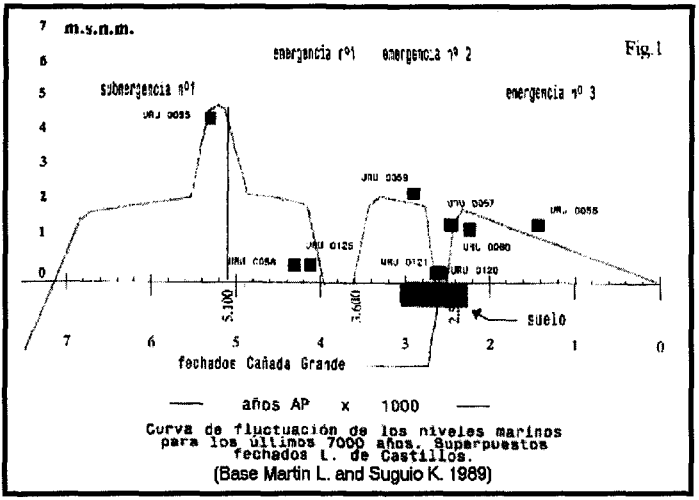

Figure 5. Sea level fluctuation curve and data from ^{14}C

Furthermore gravimetric data show the presence of a strong anomaly in the zone. The interpretation of this data supports the hypothesis of an isostatic rise for this stretch of the SE coast of Uruguay.

The Figure 6 reproduces an aerial photograph of Garzon lagoon, in which many different paleocoasts can be observed.

Thus, it may be established the hypothesis of a relative sea level decrease, with a medium rate of 1 mm per year, for this stretch of Uruguayan coast. This fact allows to forecast a progression of the coastline in parallel lines to the actual one and perpendicular to the annual net energy flux.

6 Conclusions

In this paper the long term evolution of the Uruguayan coastline between Punta del Este and Cabo Santa María (La Paloma) is analyzed. Based on the existing information the following conclusions may be drawn:

- Gravimetric anomalies show that SE Uruguayan earth's crust is rising.
- Eustatic world sea level is rising.
- Relative sea level change in this stretch of coast is decreasing.
- The Uruguayan Atlantic stretch of coast between Punta del Este and Cabo Santa María is prograding.
- The progression of the coast is in parallel lines perpendicular to the annual net energy flux.

Figure 6. Garzón Lagoon

Acknowlodgement
The third author thanks the Uruguayan organization PROBIDES the support given during the visit to the studied area, their help is appreciated.

References

Bracco, R., Navarro, R. and Ures, M. (1997). "Primeros resultados geocronológicos y paleogeográficos de la Cuenca de la Laguna de Castillos (Rocha, Uruguay". In print.

Bracco, R., and Ures, M. (1998). "Las variaciones del nivel del mar y el desarrollo de las culturas prehistóricas del Uruguay". *Actas del II Congreso Uruguayo de Geología.* Sociedad Uruguaya de Geología Punta del Este, Uruguay. 16-20.

Martin, M. And Suguio, K., (1989). *International Symposium on Global Changes in South Africa during the Quaternary*, Special Publication N°2, Sao Paulo, Brasil, 8-12.

UNDP/URU/73/007 (1980). *Conservación y mejora de playas* Informe técnico. UNESCO, Uruguay.

Young Ian R., 1996. *Atlas of the Oceans: Wind and Wave Climate*, CD-ROM Version 1.0, Elsevier Science.

TURBIDIMETRIC MEASURING OF THE SUSPENDED SEDIMENT CONCENTRATION IN THE COASTAL ZONE

Prof. Dr. Ruben D. Kos'yan[1], Dr. Igor S. Podymov[2],
Dr. Sergey Yu. Kuznetsov[3]

Abstract

The construction peculiarities of the new model of turbidimeter for measurement of instantaneous values of suspended sediment concentration are described in this paper. The presence of optic negative feed back is the basic feature of this turbidimeter, which allows to eliminate practically completely the temperature instability of light source and of its electronic units. A new model of turbidimeter has given a possibility to create a three-dimensional lattice for the investigations of suspended particle spatial shift. One turbidimeter of the lattice cell is recording continuously the background transparency of examined liquid in a real scale. It gives possibility of continuous controlling not only of the light radiation flux attenuation by suspended particles but and of a ratio between the light flux absorption in researched water column with suspended particles and the light flux absorption in "clean" water. During the field experiments with the help of turbidimeters new data about physical mechanisms of sediment suspension above a smooth and rippled bottom were received.

Introduction

Till now there is no strict mathematical description of regularities of two-phase flux motion. Determination of empirical dependencies describing a process of sediment transport is not possible without instrumental measurements of the suspended sediment concentration. That's why a selection of a reliable method of measuring of instantaneous values of suspended sediment concentration is one of the most urgent tasks.

[1]Director, the Southern Branch of the P. P. Shirshov Institute of Oceanology, Russian Academy of Sciences, Gelendzhik-7, 353470 RUSSIA.
[2]Head Scientific Researcher, the Southern Branch of the P. P. Shirshov Institute of Oceanology, Russian Academy of Sciences, Gelendzhik-7, 353470 RUSSIA.
[3]Senior Researcher, P. P. Shirshov Institute of Oceanology, Russian Academy of Sciences, 36 the Nahimov prospectus, Moscow, 117851 RUSSIA.

Optical methods which are the most quick-acting ones afford to research high-frequency non-stationary processes within the bottom layer where the concentration of sufficiently large particles of inorganic origin are rather high (> 10 g/dm^3).

There are two basic methods of determination of suspended material concentration in water which are based on the optical principle: measurements of attenuation of the light flux radiation (turbidimetry) and measurements of light energy scattered by particles under angles different from zero ones with respect to the direction of incident light (nephelometry). Nephelometers are seldom applicable for the measurements in the coastal zone since calibration characteristics of nephelometers depend greatly on the size of particles suspended in water. For this reason nephelometers are used, as a rule, for measurements of low concentration of homogeneous particles at comparatively large depth.

Brief theory of turbidimetry

Bugger's law is in the basis of turbidimetry. In compliance with it the initial flux of Φ_0 radiation passes the distance l in a certain medium and is attenuated by this medium to Φ level according to formula:

$$\Phi = \Phi_0 \exp(-\varepsilon l), \tag{1}$$

where ε is the index of light flux attenuation by given medium.

And the fundamental equation of turbidimetry can be written (Onishchenko, Kos'yan, 1989) as:

$$S = bA\frac{1}{l}\ln\frac{I_0}{I}, \tag{2}$$

where $b = \frac{2}{3}\rho_s$;

S - weight concentration;

A is a parameter defining the suspended sediment composition;

I_0 and I are output signals for «clean» water and water with suspended sediment consecutively.

And linear dependence between suspended sediment concentration and measured value of $\ln\left(I_0/I\right)$ remains only when the following parameters keep to be invariable in the course of measuring and meet the calibration conditions: suspended sediment composition (parameter A); density of grains ρ_s; base of instrument l; parameter I_0, that characterizes optical properties of clean water. When designing

turbidimeter, only measuring base l is strictly controlled parameter from four mentioned ones. Suspended sediment composition and density of grains ρ_s causes a methodical error of turbidimetric method, the value of which can be estimated on experimental data and results of calibration. In general case the parameter I_0 can also lead to additional methodical error. But if an additional channel which gives an information about optical properties of water will be provided in the construction of measuring system, methodical error caused by the change of I_0 parameter can be considerably diminished.

To control I_0 parameter it is necessary to define precisely the term «optical properties of water». In our case under optical properties of water we mean the transparency not a clean water but water with such a part of suspended sediments which do not settle and are transported together with water flow. It is known that particles with diameter less than 100 mkm form the transported part of suspended matter. That's to say, to record I_0 it is necessary to create such an additional zone of measurements where only suspended particles with diameter < 100 mkm are present.

Two turbidimeters were worked out and constructed for experimental turbidimetric research (Kos'yan et al., 1995). When designing these turbidimeters a task to restrict in size of construction was not raised. That's why turbidimeters turned out to be bulky and heavy.

Results of field research important for turbidimetry

The turbidimeters were used in several field experiments. In the course of the Russian field experiment «Novomikhailovka-93» a strongly pronounced interrelation between fluctuations of suspended sand concentration and kinetic turbulent energy were revealed in the bottom layer of the surf zone (Pykhov et al., 1995). According to obtained measuring data temporal and spatial scales of turbulent vortexes which have been formed when waves are breaking were also calculated and estimated.

The Russian-German experiment «Norderney-94» confirmed the existence of turbulent mechanism of sand suspension and afforded to determine the scales of variability of turbulent kinetic energy and concentration of suspended sand (Kos'yan et al., 1997).

The analysis of recordings has shown the presence of a sharp increase of suspended sand concentration which coincide in time with corresponding turbulent fluctuations of cross-shore and along-shore velocities.

A typical example of solid particle suspension is given in Figure 1. Wave breaking with the crest spilling occurred at the depth of $\bar{h}$= 2.36 m. Increase of turbulent fluctuations of velocity and splash of concentration may be provoked by horizontal advection of turbulent vortexes with captured sand to thc region of the gauge installation.

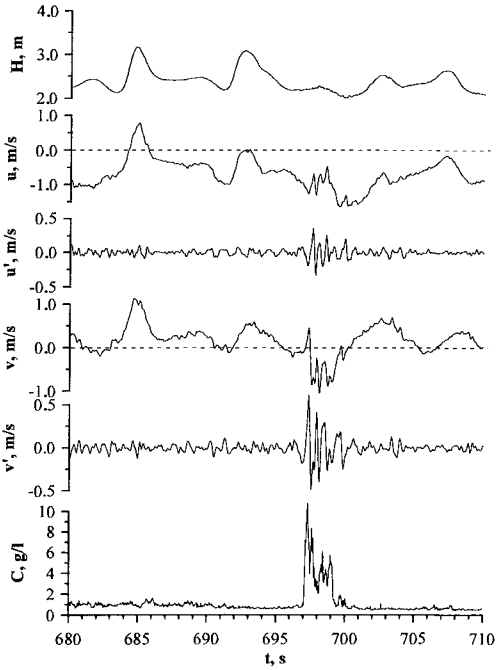

Figure 1. An example of a single moment of suspension. Recording 6a.

H(t) is the height of free surface oscillations; *u(t)* and *u'(t)* is cross-shore velocity and its turbulent component; *v(t)* and *v'(t)* is along-shore velocity and its turbulent component; *C(t)* is concentration of suspended sand. Recording was made when wind wave parameters were: H_s = 1.07 m, T_p = 8.7 s, $\bar{h}$ = 1.53 m, Sp.

Figure 2 shows a chronogram of turbulent pulsations of velocity and their hodograph for the case which is demonstrated in Figure1. An end of vector of turbulent component of velocity shown on the hodograph describes two complete cycles during one second. This indicates the passing of the chain of four vortexes through the gauges, as it is shown in the right lower part of Figure 2. Then neighbor vortexes rotate in opposite direction.

The assess of spatial scales of turbulence afforded to reveal vortex structures from 1 to 10 m. Passing of vortex structure through the measuring point corresponded to the cases of intensive sand suspension. Linear dimensions of some vortexes varied from 0.3 m to 1.5 m, and they were different within one vortex structure. Maximum but not mean values of the vortex dimension were used for the determination of interrelations between vortex dimensions and a distance from the bottom to the surface, because it was not possible to define whether the turbulent vortex had passed through the gauge area by its central or marginal part. The dependence between dimensions of the largest vortex in series and the distance between the bottom and the surface is presented in Figure 3. It demonstrates how vortex diameter grows with the increase of the distance between the bottom and the surface. Such a dependence confirms a classic idea about the proportionality between vortex dimensions and flux parameters.

One can determine precisely the dimensions of turbulent sandy vortexes by using for measurements of three-dimensional grating, in which the distance between gauges may be roughly selected from the diagram shown in Figure 3. Thus, for

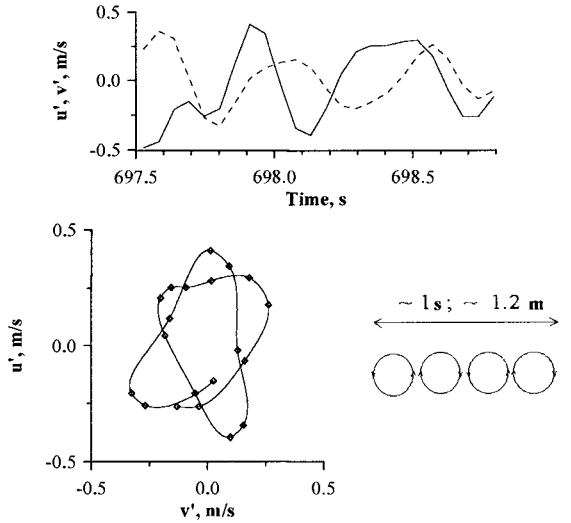

Figure 2. Time scales of turbulent vortexes.

example, when measuring in the coastal zone where the distance between the bottom and the surface was 2 m, the largest diameter of vortex was 1.1 m (see Figure 3). Therefore, in order to record extreme values of vortexes of turbulence and concentration, the length of each side of measuring grating must be not less than a half of the largest vortex diameter for coherent conditions of research. In given case it must be not less than 0.55 m. Then the distance between gauges on every side must be 0.275 m, if there are three gauges on this side. Roughly calculated dimensions of grating demand rather rigid requirements for the size of measuring instruments installed on it. It should be added also that the vortex size within one vortex structure may be different.

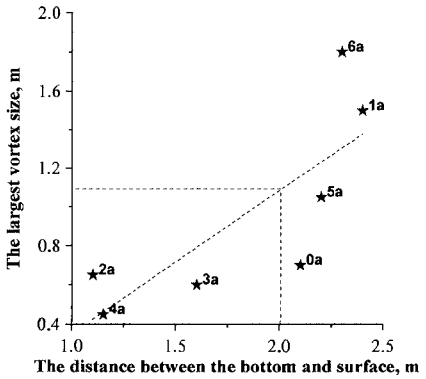

Figure 3. Relation between the vortex dimensions and a mean depth.

After complex estimation of the results of field data processing it became clear that turbidimeters of old construction are useless for investigations of spatial-temporal characteristics of vortex structures. Overall dimensions of turbidimeter of old construction allow to place not more

than two gauges in calculated volume of measuring grating. This was the reason for working out a new construction of turbidimeters of less size.

Structural block-diagram of the turbidimeter

To be more demonstrative, the structural block-diagram of the turbidimeter is divided into two basic parts (Figure 4): underwater block and above water unit. Underwater block includes: a source of reference voltage, comparator (differential amplifier of error signal), coordinating amplifier, modulator, generator, hardly stabilized current amplifier with a loop of negative feed-back, two light sources with the length of radiated light wave being $\lambda = 0.67$ mkm, optical negative feed-back channel and measuring channel. Each of channels includes photoreceiver, photocurrent amplifier and demodulator with filter. Measuring channel differs from optical negative feed-back channel only by presence of the current amplifier with a loop of negative feed-back that is necessary for matching with communication line.

The formation of a beam of light occurs in the following way. Reference voltage formed by the source comes to modulator through the comparator. The modulator makes the modulation of this voltage with the frequency of internal generator. Ripple (pulsating) voltage controls two identical light sources, the role of which is played by luminous radiating diodes with built-in mirror and narrow radiation pattern. Introduced modulation of the light flux eliminates completely the influence of flare spot when working at the shallow depth and thereby considerably decreases an instrument error.

The beam of light from the source 1 passing through investigated water column is attenuated in accordance with the law of light absorption and is perceived by photoreceiver 1. A signal from photoreceiver is amplified by precise photocurrent amplifier, is demodulated, is filtered and in analog form (as a current) comes to the above water unit by communication line. Silicon photodiode serves as photoreceiver. Its dimensions are small, its sensitivity is high. It has temperature stability and a small non-linearity. An angle of registration of a light beam in the receiver is reduced with the help of diaphragm (membrane). Time constant of the measuring channel does not exceed 0.01 s.

The channel of optical negative feed-back is destined for a hard stabilization of measuring parameters of the turbidimeter under the influence of different disturbing factors. Its structure is similar to that one of the measuring channel. Photoreceiver of this channel takes the light from its light source not through the investigated volume of water but by a special light channel. Output signal of the channel of optical negative feed-back is transmitted to the second input of comparator (differential amplifier of error signal) which controls emissive power. As a result, the emissive power is set in such a way, that output current of photoreceiver of the feed-back channel is stabilized.

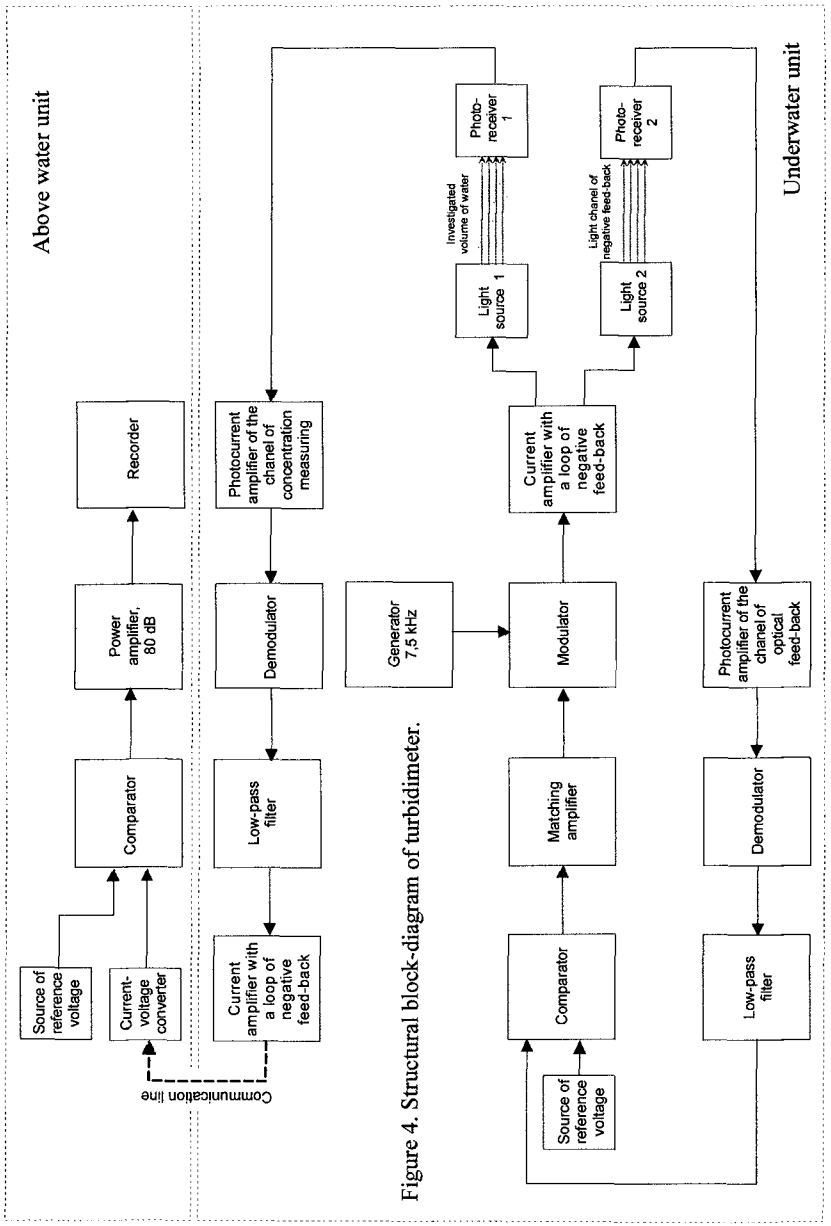

Figure 4. Structural block-diagram of turbidimeter.

The impact of any disturbing factor (temperature, aging, etc.) provokes the change of output signal of feed-back channel. In its turn the change of this signal leads to the change of error signal, the phase of which is displaced for 180°. As a result, the units of automatic control of initial current of photoreceiver change the power of luminous radiation. An initial value of photoreceiver current of the channel of optical negative feed-back is restabilized in new conditions. Since the channels (measuring and feed-back) are identical, the regularities of current stabilization of photoreceivers also concur in them. Here, a possible dispersion of parameters of light sources and photoreceivers is the factor of instability. And this demands rather strict requirements for the selection of identical pairs. The difference of this construction of turbidimeter from tbe previous one is the presence of a special (additional) source of light for the feed-back channel. Stability of characteristics of such a structure is somewhat less (Kos'yan et al., 1998). But the technological effectiveness and reliability of the construction is higher, and the cost of turbidimeter is sizably less.

Figure 5. The turbidimeter.

The turbidimeter is connected with the above water unit by the four-core cable. Supply voltage ±15V and midpoint (centroid) is transmitted by three cable lines. lnformation signal (as a current) functionally connected with suspended matter concentration is transmitted by a separate line. Electronic unit forming the current is made as a self-tuning loop with negative feed-back, the parameters of which (to a certain degree) do not depend on the cable resistance.

In above water unit information signal is transformed into voltage. Then a direct component is removed from the information signal with the help of comparator and reference voltage source. Information signal on the output of comparator of above water unit exists as a voltage functionally connected with the suspended matter concentration. Comparator is built in such a way that in it besides the compensation of a direct component of a signal there is a possibility to change the conversion conductance of the information signal. This simplifies the matching of calibration functions of different specimens of turbidimeters to a single type. (Providing that the linear interrelation is kept between suspended matter concentration and the

attenuation index, as it was mentioned before). And, finally, an information signal passes through the amplifier, which has voltage transmission factor equal to 1, and power amplification factor being 80 dB. Such a power isolation allows to use recorders with different input impedance without distortion of transmitting function of turbidimeter. And the range of input impedance may vary within very broad limits: from 10 to 10^7 Ohms.

Appearance of the underwater block of turbidimeter is shown in Figure 5.

Laboratory study

Laboratory research was carried out with the view to calibrate the turbidimeter and to assess the influence of different disturbing factors upon the precision of instrument reading.

Sand collected in the course of «Ebro-delta-96» experiment was used for this research. Its granulometric composition is given in Figure 6.

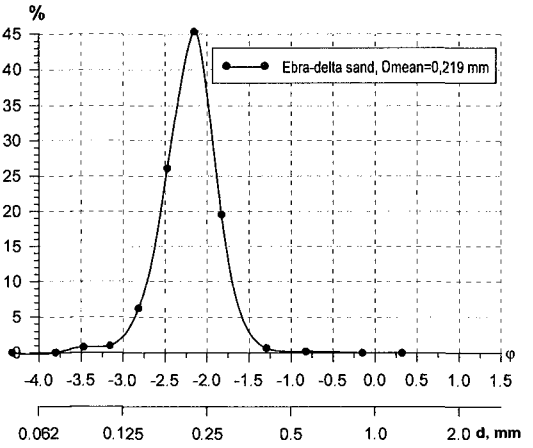

Figure 6. Curve of granulometric composition of sand used for laboratory study.

Testing of turbidimeter was fulfilled in the tank of 50 liters. The diagram of the installation for these investigations is presented in Figure 7. Two turbidimeters (2 and 3), propeller (4) connected through a drive (5) with electric engine (6), tube for sampling water with suspended sediments were placed into the tank simultaneously.

The electric engine was connected with the power source by the rpm governor (7). A signal from the turbidimeters was loaded into computer through multy-channel

analog-to-digital converter. Sand was poured to the tank bottom. Fluctuations of suspended particle concentration were created by the change of the rotation velocity of the propeller and the change of sand amount. The distance between the water surface and turbidimeter sensors was 21 cm. The thickness of the water column was 37 cm.

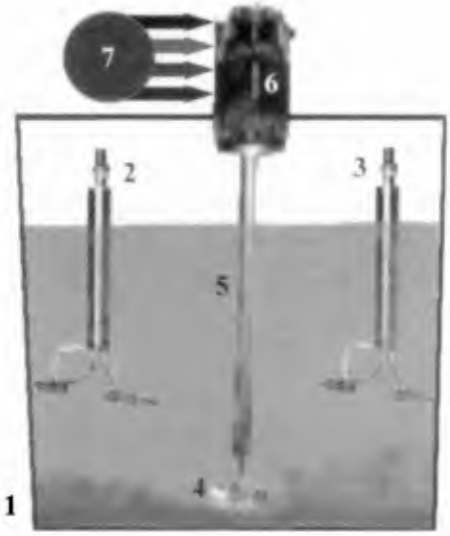

Figure 7. Diagram of installation for laboratory study:

1 - tank, 2 - turbidimeter 1, 3 - turbidimeter 2, 4 - propeller, 5 - drive, 6 - engine, 7 - revolutions-per-minute (rpm) governor.

A signal from the turbidimeter was recorded continuously. Sampling of suspended sand was done with the help of siphon roughly during one minute. Values of concentration in codes were averaged during the period of sampling. Before the start of measuring turbidimeter readings were recorded for clean water.

Figure 8 shows a calibration characteristics of turbidimeter for sand with above mentioned granulometric composition.

Figure 9 demonstrates a diagram of fluctuations of suspended particle concentration near the sensors of turbidimeter in the course of calibration. Digits on the diagram show values of concentration obtained by sampling with the help of

siphon. The position of the digits on the diagram corresponds to the time moments when sampling was performed.

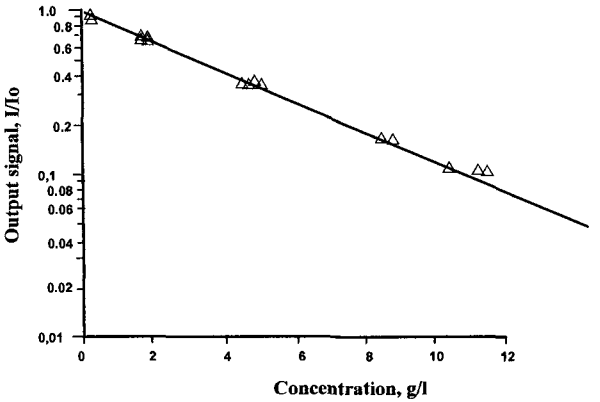

Figure 8. Calibration characteristics of turbidimeter.

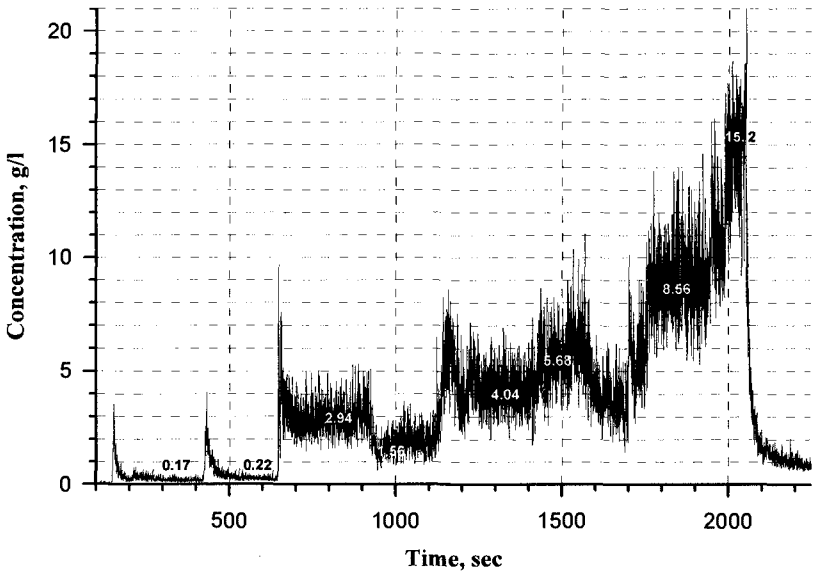

Figure 9. Diagram of fluctuations of suspended particle concentration near the sensors of turbidimeter in the course of calibration.

Figure 10 shows the change of suspended particle concentration in different places of the laboratory tank. Measurements were performed synchronously by two turbidimeters. These diagrams give an ides of the uniformity of suspended matter distribution in the whole tank space, and allow to judge about the replication of the transmission characteristics of different copies of measuring instrument. In concrete case one equation for two turbidimeters was used for the calculation of concentration. With the help of operating means the coefficients of the turbidimeter transmission functions are made equal ones.

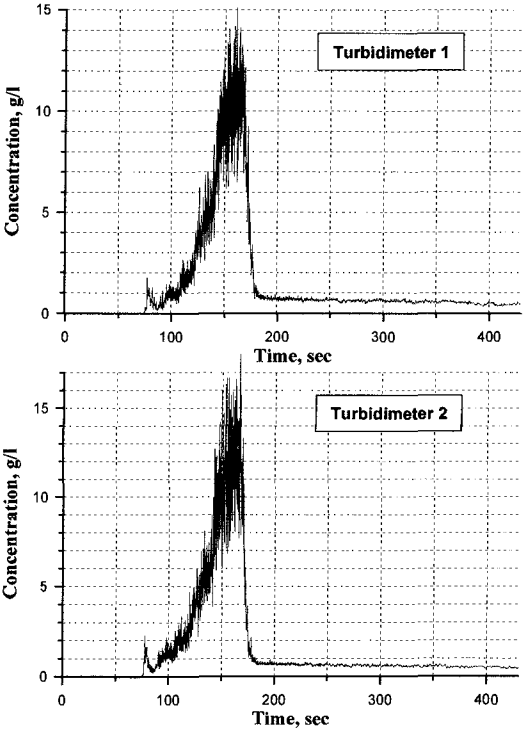

Figure 10. Synchronous change of suspended particle concentration in different zones of the laboratory tank.

It is evident that particles with grain size being <0.1 mm settle in the flux much longer than larger particles. This affords us to consider suspension with particles <0.1 mm as non-settling one, and in such a way to determine optical properties of «clean water», i.e. background. Measuring zone of one turbidimeter must be protected with filter with cell being 0.1 mm. A device that continuously

records values of the background must be additional one to the total number of gauges.

Appearance of the turbidimeter measuring head with filter is given in Figure 11.

Figure 11. Turbidimeter measuring head with filter.

Conclusions

During the field experiments with the help of turbidimeters new data about physical mechanisms of sediment suspension above a smooth and rippled bottom were received. On its base the contribution of different wave frequency into the formation of sedimentary flux was assessed. The origin of some components of the sedimentary flux was revealed.

Laboratory testing has demonstrated that turbidimeters of proposed structure ensure precise measurements of suspended sediment concentration in a broad range of temperature fluctuations of the environment.

The construction of turbidimeter gives the possibility to build three-dimensional grating for the research of suspended particle spatial shift.

These features makes the turbidimeter an effective instrument when studying sediment transport in the coastal zone.

Acknowledgement

This research was supported by a grant 98-05-64460 from the Russian Foundation for Basic Research.

References

Kos'yan R.D., Kuznetsov S.Yu., Podymov I.S., Pykhov N.V., Pushkarev O.V., Grishin N.N., Harizomenov D.A. (1995). *Optical Instrument for Measuring of Suspended Sediment Concentration during Storm in the Coastal Zone.* // Okeanologiya (Oceanology). 1995. vol. 35. № 3. P.463-469 (in Russian).

Kos'yan R.D., Kunz H., Kuznetsov S. Yu., Pykhov N.V., Krylenko M.V. (1997). *Sand Suspension and Intermittence of Turbulence in the Surf Zone.* // Proc. of the 25th International Conference on Coastal Engineering, "COASTAL ENGINEERING' 96". American Society of Civil Engineering. New York. P.4111-4119.

Kos'yan R.D., Kuznetsov S.Yu., Podymov I.S., Pushkarev O.V., Pykhov N.V. (1998). *Turbidimeter.* // Russian Patent of Invention # 6241 (96121755).

Onishchenko E.L., Kos'yan R.D. (1989). *About Use of Optical Method of Determination of Suspended Sediment Concentration in Natural Basins.* // M.: Vodnye resursy (Water resources). 1989. № 3. P. 94-101 (in Russian).

Pykhov N.V., Kos'yan R.D., Kuznetsov S.Yu. (1995). *Time scales of sand suspending by irregular waves.* // Proc. of the Second International Conference on the Mediterranean Coastal Environment "MEDCOAST'95". Tarragona, Spain. P.1073-1092.

Characteristics of Suspended Sediment Transport in the Surf Zone of Irregular Waves and their Reproduction by a Cross-Shore Beach Deformation Model

M. Ikeno[1] and T. Shimizu[1]

Abstract

Suspended sediment flux and cross-shore beach deformation in the breaker zone are elucidated experimentally with the CRIEPI's irregular wave flumes of large and middle sizes. Effects of long waves on suspended sediment transport are also investigated with a new experimental system for correct reproduction of infragravity waves bounded by irregular wave groups. Based on the experimental results, the pick up rate from sea bed and convection and diffusion of suspended sediment are modelled, and a new numerical model is developed for cross-shore beach deformation due to irregular waves. This numerical model can well reproduce wave deformation, suspended concentration, undertow, sediment flux and beach topography change.

1. INTRODUCTION

In the surf zone, sea bed sands are picked up violently and suspended sediment transports are more signifficant. A numerical model for beach deformation due to ramdom waves should be developed by taking irregular time variation of suspended sediment flux into account..

In this paper, first, suspended sediment flux and cross-shore beach deformation in the breaker zone are elucidated experimentally with the CRIEPI's irregular wave flumes of large and middle sizes. Scale effects on beach deformation are also investigated, and a new similarity law of the grain size of beach sediment is applied to irregular waves. Effects of long wave components on suspended sediment transport are also investigated with a new experimental system for correct reproduction of infragravity waves bounded by irregular wave groups.

Secondly, based on the experimental results, the pick up rate from the sea bed and vertical convection and diffusion of suspended sediment are modelled, and a new numerical model is developed for cross-shore beach deformation due to irregular waves. Nonlinear wave deformation, suspended concentration, undertow, sediment flux, and beach topography change in experiments are reproduced by this numerical model.

2. EXPERIMENT

2.1 Experimental condition

Beach deformation tests were performed with two different scales of wave flumes

[1] Hydraulics Dept., Central Res. Inst. of Electric Power Industry, 1646 Abiko, Abiko-shi, Chiba, Japan

and compared. One is a large wave flume (205m long, 3.4m wide and 6m deep). The median grain size of sand used is 1mm. Initial beach slopes are changed from 1/10 to 1/50. Incident waves are irregular with JONSWAP spectrum. Significant wave heights and periods are 0.5～1.2m and 3～8s. Sharpness parameter γ are 1 or 7 (experimental cases L1～L7; Shimizu and Ikeno, 1996). The other is a middle wave flume (50m long, 0.9m wide and 1.2m deep). The scale of beach deformation tests corresponds to one-fifth the scale of those with the above large wave flume by the Froude similitude. Initial beach slope, significant wave height, period and parameter γ are similar values to those with the above large wave flume. Significant wave heights and periods are 0.1～0.24m and 1.35～3.58s (experimental cases M1～M8).

However, using the sand size according to the Froude similitude, the scale effects on beach deformation will occur between the middle and large sizes of tests, as you know. In this paper, the sand size is determined by a new similarity law of the grain size of beach sediment (see Fig.1 ; Shimizu, 1995), based on many different scales of beach deformation tests in regular waves. According to Fig.1, the median grain size of sand is determined to 0.6 mm, which corresponds to one half the scale of sand in the above large wave flume. Comparing both experimental results, the validity of this similarity law is verified subject to irregular waves.

Fig.2 shows the grain size distribution of sands used in the large and middle scale tests. In these experiments, vertical distribution of suspended sediment transport flux in the surf zone are measured simultaneously by optical turbidimeters, electromagnetic current meters and capacitance type wave gauges.

2.2 Verification of a new similarity law of sand grain size

Fig.3 shows the comparison between beach deformation results by large and middle wave flumes. Beach deformation of these cases is erosion type by plunging breaking waves. One is the case L6: H_s=1.2m, T_s=3s, tan β =1/10, and the other is the case M7: H_s=0.24m, T_s=1.35s, tan β =1/10. The formation points of bar and the erosional regions in the large scale test show good agreement with those of the middle

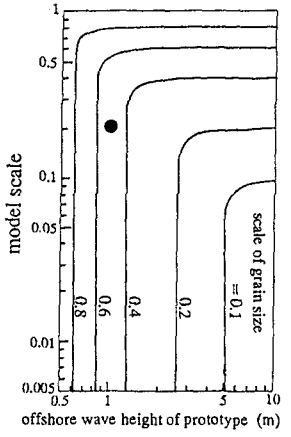

Fig.1 Model scale and grain size considering the scale effect (Shimizu, 1995)

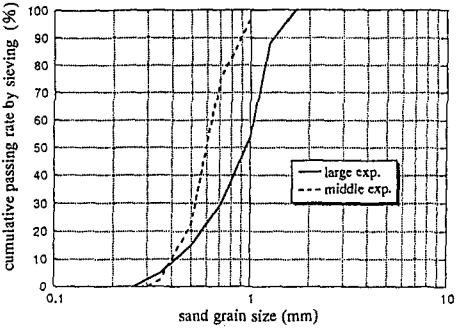

Fig.2 Grain size distribution of sands used in the large and middle size tests

case L6: H_o=1.2m, T_o=3s, γ =7, tan β =1/10, BLOWRES

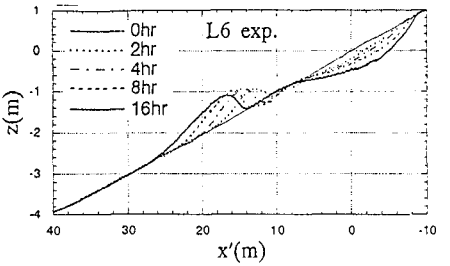

case M7: H_o=0.24m, T_o=1.35s, γ =7, tan β =1/10, BLOWRES

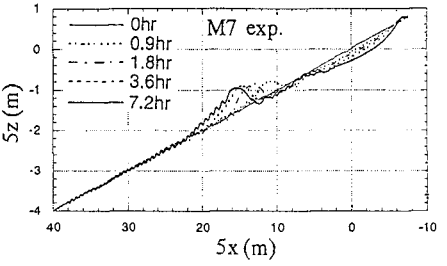

Fig.3 Comparison between beach deformation results by large and middle wave flumes

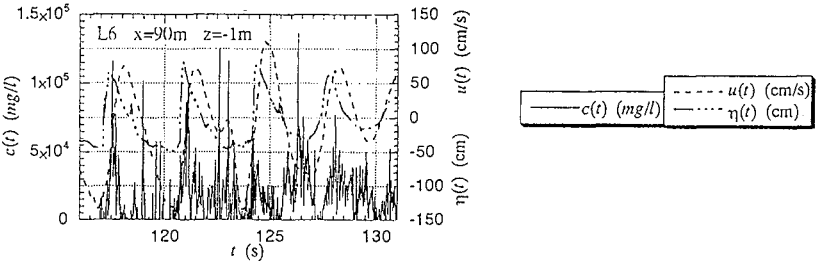

Fig.4 Time variation of suspended concentration and horizontal velocity in the surf zone of irregular waves (case L6 of large scale test)

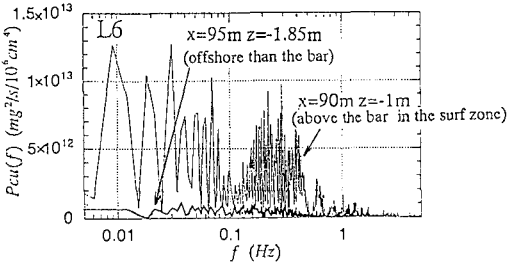

Fig.5 Power spectra of the suspended sediment flux c(t)u(t) at the vertical height 20cm above the sea bottom in the case L6 of large scale tests

test. And the velocity of beach changes in the large test also shows good agreement with that according to the Froude similitude in the middle test. And thus, the application of this new similarity law of the grain size (Shimizu, 1995) to random waves is verified.

2.3 Effects of long waves on suspended sediment

Fig.4 shows time variation of suspended concentration and horizontal velocity near the sea bottom and water surface elevation in the surf zone of irregular waves. According to Fig.4, the sea bed sand can be seen to be significantly picked up when the horizontal velocity changes not only from onshore to offshore, but also from offshore to onshore.

Effects of long waves on suspended sediment flux are also investigated with a new experimental system, which can correctly reproduce bounded long waves in irregular wave groups by eliminating free long waves generated by a wave maker (BLOWRES ; Ikeno and Tanaka, 1996).

Fig.5 shows the power spectra of the suspended sediment flux c(t)u(t) at the vertical height 20cm above the sea bottom in the case L6 of large scale tests. In this figure, a fine solid line corresponds to the formation point of bar in the surf zone, and a bold solid line corresponds to the offshore side than it. From Fig.5, the suspended sediment flux can be seen to be separated into the the higher and the lower frequency components as the boundary of 0.07Hz. Especially, the long wave components of the suspended flux above the bar in the surf zone are much greater than the short components of it. According to these experimental results, three kinds of components such as the steady: $\dot{c}\dot{u}$, the shorter waves: $\overline{cu}_s$, the longer waves: $\overline{cu}_l$ as the boundaries of 0.16Hz: middle tests and 0.07Hz: large tests, are included in the suspended sediment flux due to random waves. So, each component of the suspended flux is evaluated as the time-averaged (net) values of c(t)u(t) obtained by the inverse FFT after cutting the flux except the remarkable frequency region.

Fig.6 shows the vertical distribution of three kinds of the flux components in the middle scale tests. This corresponds to th-

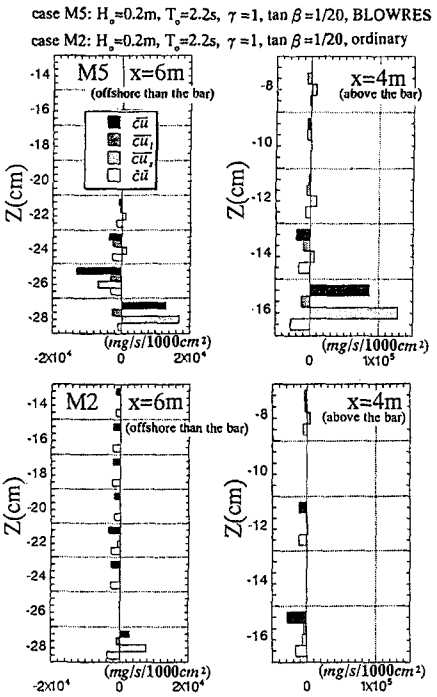

Fig.6 Vertical distribution of three kinds of the flux components in the middle scale tests
(tan β =1/20, spilling wave breaking and wider surf zone)

e case of the sea bed slope 1/20, the spilling wave breaking and the wider surf zone. In this figure, the upper figures are the results with the new experimental system for correct reproduction of infragravity waves; BLOWRES. And the lower figures are those without using it; ordinary.

Comparing between the upper and the lower figures, specially, the difference can be seen between the direction and the quantities of long wave components of the suspended sediment flux in the tests with and wthout eliminating free long waves. This difference becomes more significant in the case of the wider surf zone.

The long period and steady components of suspended sediment flux in the surf zone are generally offshore direction while the short period components of suspended sediment flux are onshore direction. Its steady components increase more than the short and long period components with shoaling and breaking.

3. NUMERICAL MODEL

A numerical model is developed for cross-shore beach deformation due to nonlinear irregular waves. This numerical model consists of the following sub-models.

3.1 Irregular wave deformation

The improved Boussinesq equation (Madsen et al.,1991) with a breaker-induced energy dissipation term (Sato and Kabiling,1994) is adopted as follows:

$$\frac{\partial \eta}{\partial t}+\frac{\partial Q}{\partial x}=0 \tag{1a}$$

$$\frac{\partial Q}{\partial t}+\frac{\partial}{\partial x}\left(\frac{Q^2}{D}\right)+gD\frac{\partial \eta}{\partial x} =\left(B+\frac{1}{3}\right)h^2\frac{\partial}{\partial t}\left(\frac{\partial^2 Q}{\partial x^2}\right)+Bgh^3\frac{\partial^3 \eta}{\partial x^3}+\nu_e\frac{\partial^2 Q}{\partial x^2} \tag{1b}$$

where η is the water surface elevation, Q is the depth-integrated flow rate in the horizontal ditrection, h is the still water depth, D is the total water depth (=h+ η), g is the acceleration due to gravity, B is a parameter for improving linear dispersion and equal to be 1/21 (Madsen et al.,1991), ν_e is the eddy viscosity for momentum mixing exchange due to turbulence by wave breaking (Sato and Kabiling,1994).

3.2 Vertical distribution of velocity in the surf zone of irregular waves

Relationship between the horizontal velocity **u** at the arbitrary vertical position **z** and vertically averaged velocity $\tilde{u}$ is derived by Nwogu (1993) as follows:

$$u(z,t)=\tilde{u}(t)+\left\{\frac{h^2}{6}-\frac{(h+z)^2}{2}\right\}\frac{\partial^2 \tilde{u}(t)}{\partial x^2} \tag{2a}$$

where $\tilde{u}(t)=Q(t)/(h+\eta)$, z is the vertical position positive above the still water level.

In the above Eq.(2a) based on the Boussines type equation , undertow caused by wave breaking can't be taken into account. So, the vertical distribution of undertow must be added to the above Eq.(2a) by using the another method. In this paper, the vertical distribution of undertow is added as time-averaged velocity based on the eddy viscosity model. The regular wave undertow formula (Rattanapitikon and

Shibayama,1996) proposed by Okayasu et al. (1990) is modified to apply to irregular wave undertow obtained by the large and middle scale of cross-shore beach deformation tests.

As results, the vertical distribution $\bar{u}(z)$ of undertow of irregular waves is proposed by taking into account the energy dissipation D_B due to wave breaking on the basis of the bore model (Thornton and Guza, 1983) as follows:

$$D_B=\rho g H_s^3/4T_s h \tag{2b}$$

$$\bar{u}(z) = \rho^{1/3} D_B^{1/3}\left[(z+h)/h - 0.5 - 0.22\cdot ln\{(z+h)/h\}\right] - 0.1\frac{\sqrt{gh}H_s}{h} \tag{2c}$$

where H_s is the significant wave height, ρ is fluid density, T_s is the significant wave period.

3.3 Suspended sediment concentration

The time variation of sediment concentration due to combined convection-diffusion is calculated by using the following equation :

$$\frac{\partial c}{\partial t} = w_s\frac{\partial c}{\partial z} + \varepsilon_s\frac{\partial^2 c}{\partial z^2} + \frac{1}{w_c}\exp\left(-\frac{z+h}{L_s}\right)p\left(t-\frac{z+h}{w_c}\right) + \frac{1}{L_s}p\left(t-\frac{z+h}{w_c}\right)\exp\left(-\frac{z+h}{L_s}\right) \tag{3a}$$

where, c is the sediment concentration, p is the pick up rate from sea bed, w_s is the settling velocity (sand grain size 1mm; 0.095m/s).

L_s is the scale of suspended sediment distribution (Nielsen ,1992) as follows:

$$L_s = \begin{cases} 0.15\pi af/w_s & for\ 2\pi af/w_s \le 18 \\ 1.4\zeta & for\ 2\pi af/w_s \ge 18 \end{cases} \tag{3b}$$

where ζ is the sand ripple height (0.15m from large experiments), f is the significant wave frequency, a is the significant wave amplitude.

ε_s is the sediment diffusivity (Nielsen,1988) as follows:

$$\varepsilon_s = w_s\zeta\left[1.24\exp\left\{-40\left(w_s/\hat{u}_b\right)^2\right\} + 0.2\right] \tag{3c}$$

where $\hat{u}$ is the amplitude in a half period by zero-crossing the horizontal velocity nearthe sea bottom.

w_c is the vertical convection velocity of sediment by Sleath (1987) as follows:

$$w_c \approx 2\pi f\delta_{.05}/2.27 \tag{3d}$$

where $\delta_{.05}$ is the thickness of boundary layer as follows:

$$\delta_{.05} = 0.26r(a/r)^{0.7} \tag{3e}$$

where r is the roughness (=d), d is the sand grain size.

w_c, ε_s and L_s are time-varying, corresponding to the zero-crossing amplitude of velocity u near the sea bottom.

Boundary condition at the sea bottom is as follows:

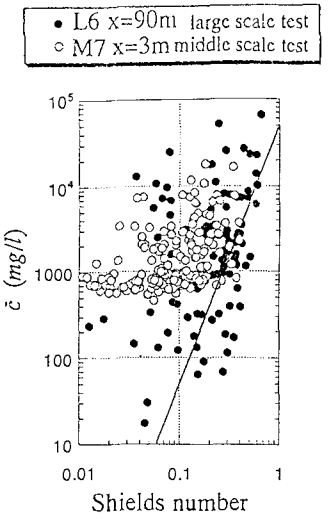

Fig.7 Relationship between the time-averaged suspended concentration in a half period by zero-crossing the horizontal velocity near the sea bottom and the Shields number corresponding to a half period just before it

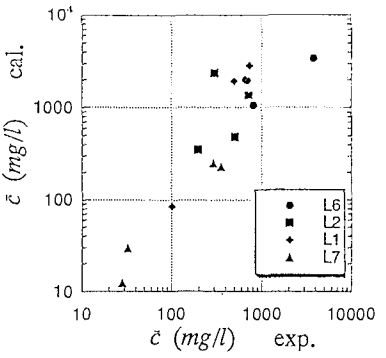

Fig.8 Comparison between the time-averaged suspended concentration computed and measured at the height of 20cm above the sea bottom in the large scale cases of L1～L7

$$-\varepsilon_s \frac{\partial c}{\partial z} = 0 \qquad at\ z = -h \qquad (3f)$$

Fig.7 shows the relationship between the time-averaged suspended concentration in a half period by zero-crossing the horizontal velocity near the sea bottom and the Shields number corresponding to a half period just before it. These data are measured near the sea bottm formating the bar in the surf zone, where the concentration is the highest in the large and middle scale tests. According to Fig.7, high correlation can be seen between the suspended concentration and the Shields number just before it. Especially, heigher concentration in the large scale tests, which means the pick up rate is much, can be also seen to be proportional to the 1.5th power of the Shields number just before it.

Based on the above experimental results, the pick up rate p(t) is newly modelled as follows:

$$p(t) = \alpha_s w_s \rho_s (\psi_{i-1} - \psi_c)^{1.5} \delta(t - t_i) \qquad (3g)$$

where ρ_s is sediment density (=2.65), $\delta(t-t_i)$ is the delta function, and t_i is the zero-crossing time of velocity u near the sea bottom.

α_s is a parameter proposed based on experimental results as follows:

$$\alpha_s = \begin{cases} \left(H_o/L_o\right)\left(-\lambda + 2.3\right) & for\ \lambda \geq 1.3 \\ \left(H_o/L_o\right)\left(0.62\lambda + 0.2\right) & for\ \lambda \leq 1.3 \end{cases} \qquad (3h)$$

$$\alpha_s = \max\left\{\alpha_s' , 0.01\right\} \tag{3i}$$

where $\lambda = h/(H_0 \tan\beta)$, H_0 and L_0 are the offshore significant wave height and the wave length, **tan** β is the sea bed slope. ψ_c is the critical Shields number, ψ_{i-1} means the Shields number of the 'i-1' th zero-crossing wave in a half period. Eq.(3h) and (3i) are based on the experimental results in the cases of $H_0/L_0 \geqq 0.02$.

Fig.8 shows the comparison between the time-averaged suspended concentration computed and measured at the height of 20cm above the sea bottom in the large scale cases of L1～L7. The computed values show good agreements with the experimental values.

3.4 Sediment transport rate and sediment conservation equation

The suspended sediment transport rate is estimated by integrating the sediment flux **cu** in the vertical section as follows:

$$q_s(t) = \int_{-h}^{0} c(z,t)\, u(z,t) dz \tag{4a}$$

The bed load transport rate is estimated by the following formula proposed by Sato and Kabiling (1994).

$$q_b(t) = \sqrt{\left(\rho_s/\rho_w - 1\right) g d^3}\, \alpha_b \left|\psi(t)\right|^{0.5} \max\left\{\psi(t) - \psi_c, 0\right\} u_b(t) \Big/ \left|u_b(t)\right| \tag{4b}$$

where α_b is a parameter (=1), ψ_c is the critical Shields number.

Therefore, the total sediment transport rate is as follows:

$$q(t) = q_s(t) + q_b(t) \tag{4c}$$

Finally, the sea bed topography is updated by using the following sediment conservation equation.

$$\frac{\partial z_b}{\partial t} = -\frac{\partial h}{\partial t} = -\frac{\partial}{\partial x}\left\{\bar{q} - \varepsilon_b \left|\bar{q}\right| \frac{\partial z_b}{\partial x}\right\} \tag{4d}$$

where z_b is the vertical height of sea bed, $\bar{q}$ is the time-averaged (net) total sediment transport rate, ε_b is a coefficient that reflects the effect of local bottom slope on the sediment transport (=2.0).

During the offshore rush in the swash zone, the total water depth is less than that during the onshore rush so larger velocities will result during the offshore rush. In order to avoid unrealistic erosion, the net total sediment transport rate in the swash zone is linearly interpolated between the zero sediment transport corresponding to the maximum beach run-up height, and the sediment transport at the most onshore side position computing the suspended sediment and bed load rates actually, where the still water depth is equal to $\triangle z$ divided vertically in combined convection-diffusion computation of suspended concentration (Larson, 1994).

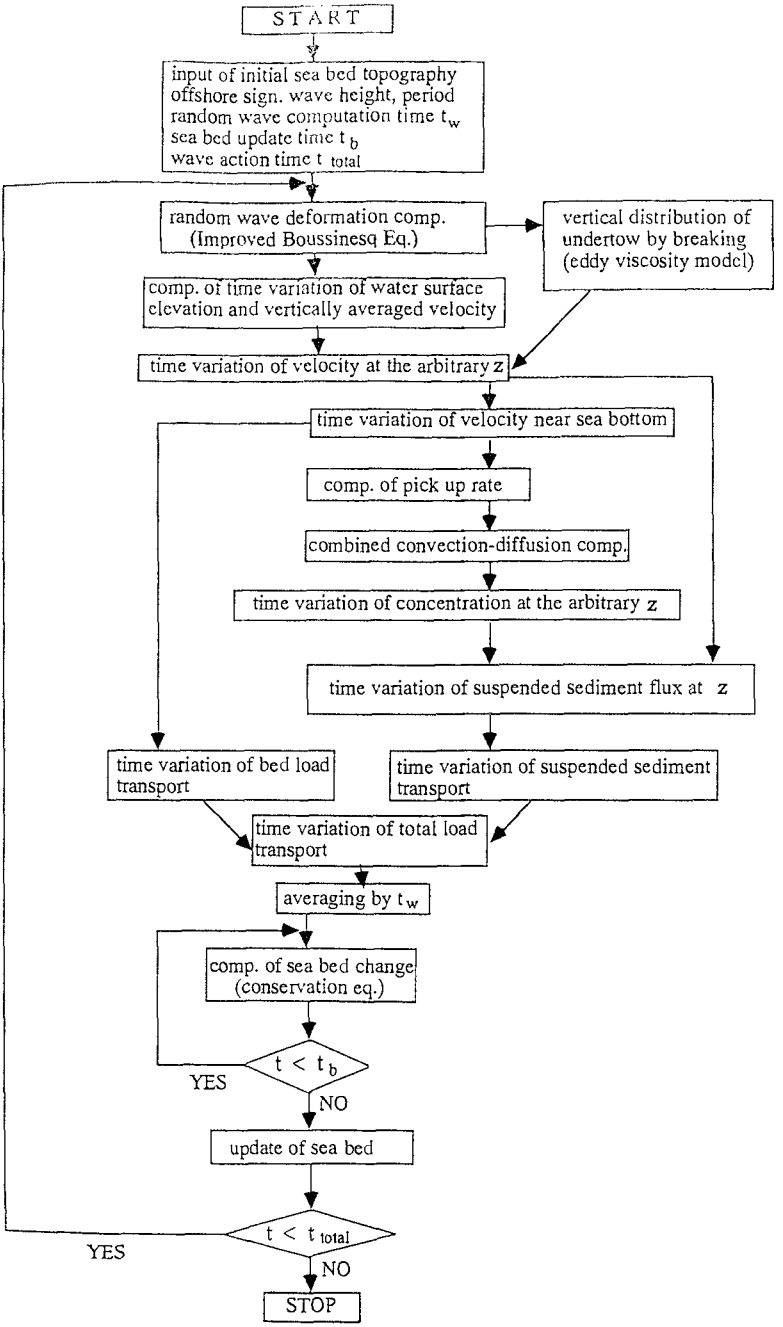

Fig.9 Computation flow of this new cross-shore beach deformation model

Fig.9 explains the computation flow of this new cross-shore beach deformation model. In this numerical model, first, the irregularly varying physical quantities such as the wave deformation, the suspended concentration, the coss-shore bed load and suspended sediment transport rates, are computed in the interval of the random wave computation time t_w, corresponding to one hundred waves' time. If required, the vertical distribution of undertow by wave breaking is added as the time-averaged values to the time variation of the horizontal velocity at the arbitrary position z obtained by the improved Boussinesq equation. Next, the net total sediment rate averaged by t_w is computed, and input on the sediment conservation equation. This sediment conservation equation continues to be computed until the sea bed update time t_b. After passing t_b, the sea bed topography is updated. After that, using a new sea bed topography, the above physical quantities are computed in the same interval of t_w and repeated.

4. REPRODUCTION BY THIS NUMERICAL MODEL

4.1 Reproduction of the vertical distribution of suspended concentration, flux and velocity in the surf zone of irregular waves

Figs.10 and 11 show the comparison between the vertical distribution of time-averaged velocity in the surf zone by computation and experiments. In the computation, the vertical distribution of irregular wave undertow is added to that of velocity by the improved Boussinesq equation. Fig.10 corresponds to the large size tests, and Fig.11 corresponds to the middle size tests. According to these figures, computation results with the undertow formula can well reproduce the vertical distribution of time-averaged velocity in the surf zone of irregular waves.

Figs.12 and 13 show the comparison between the time variation and the vertical distribution of suspended concentration in the surf zone of irregular waves by computation and experiments. In Figs.12 and 13, computation results include those by pure diffusion without convection and by combined convection-diffusion. According to these figures, suspended concentration by the pure diffusion computation can't reach into the upper area near the water surface and underestimates the experimental suspended concentration. However, the computation results by combined convection-diffusion can well reproduce the irregular time variation and the vertical distribution of experimental results, where suspended sediment with higher concentration reaches near the water surface. Fig.14 shows the comparison between the vertical distribution of time-averaged suspended sediment flux by computation with combined convection-diffusion and experiments. According to Fig.14, the computation results can well reproduce the vertical distribution of time-averaged suspended sediment flux.

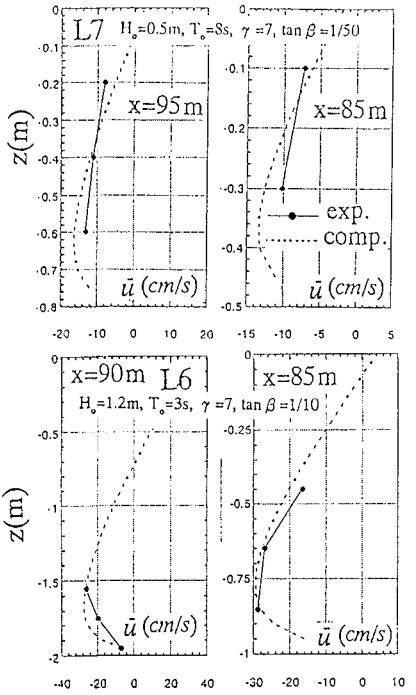

Fig.10 Comparison between the vertical distribution of time-averaged velocity in the surf zone by computation and large scale tests

4.2 Reproduction of wave deformation, beach change and sediment transport rate

Figs.15 and 16 show the comparison between sea bed changes, wave height deformation and sediment transport rates by computation and large size experiments. Computation results include the cases

H_0=0.24m, T_0=1.35s, γ=7, tan β=1/10

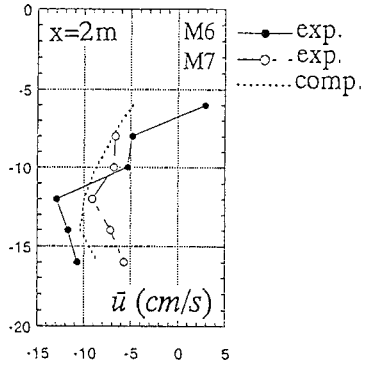

Fig.11 Comparison between the vertical distribution of time-averaged velocity in the surf zone by computation and middle scale tests

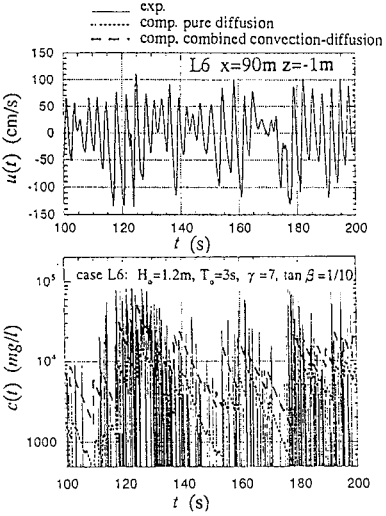

Fig.12 Comparison between the time variation of suspended concentration in the surf zone of irregular waves by computation and experiments

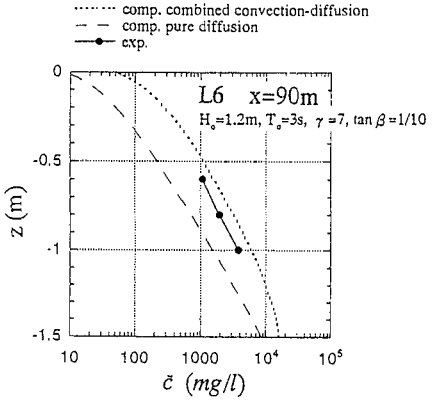

Fig.13 Comparison between the vertical distribution of time-averaged suspended concentration by computation and experiments

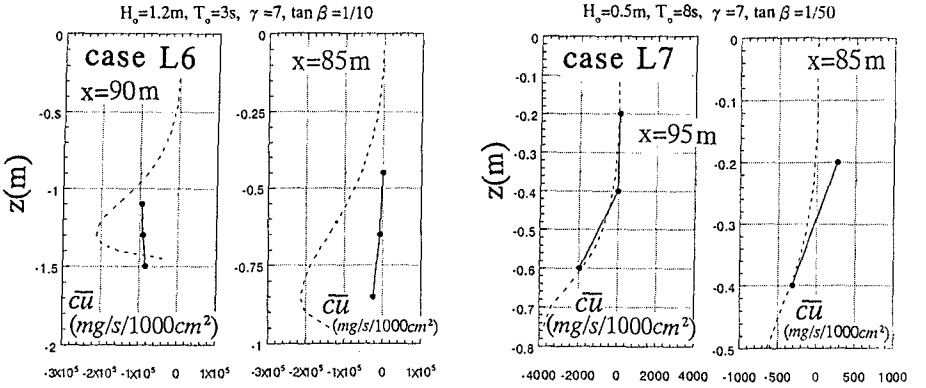

Fig.14 Comparison between the vertical distribution of time-averaged suspended sediment flux by computation with combined convection-diffusion and experiments

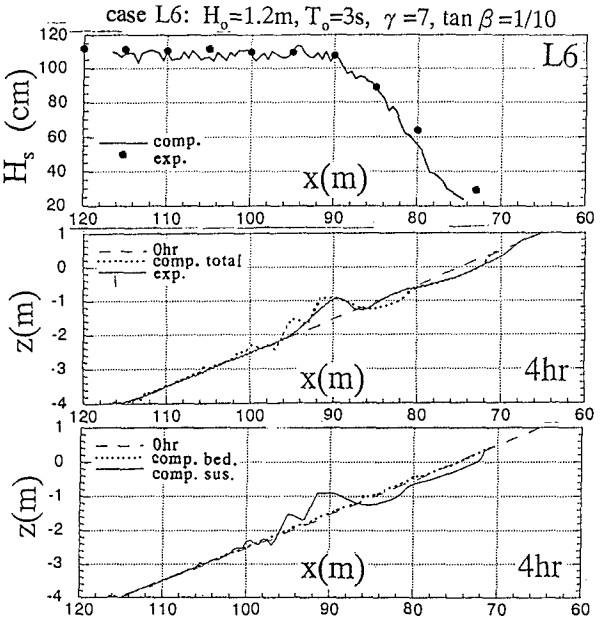

Fig.15 Comparison between irregular wave deformation and sea bed changes by computation and large size experiments

taking into account the suspended sediment alone, the bed load alone and the total sediment transport. According to thesefigures, the computation results can well reproduce the experimental sea bed changes, wave height deformation and total sediment transport rate. The suspended sediment transport rate is much greater than the bed load transport rate in the case L6 with larger wave height.

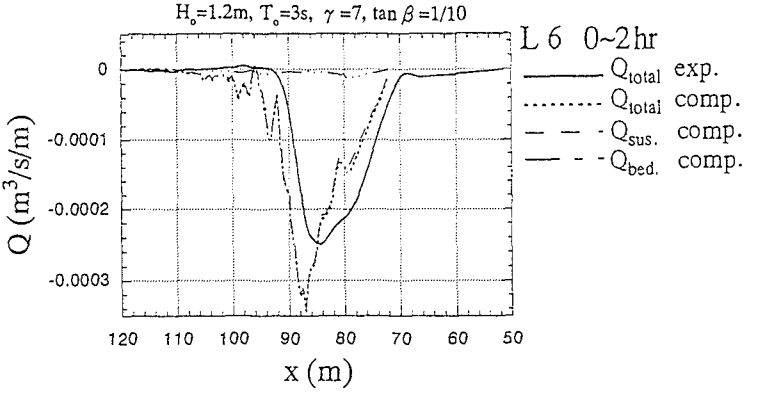

Fig.16 Comparison between sediment transport rates by computation and large size experiment

CONCLUSIONS AND REMARKS

1) Beach deformation and suspended sediment flux in the large scale tests showed good agreement with those in the middle scale tests. And thus, the application of this new similarity law of sand grain size (Shimizu, 1995) to random waves is verified.

2) In all cases, the difference can be seen between long period components of suspended sediment flux in the tests with and without eliminating free long waves. This difference becomes more significant in the case of the wider surf zone.

3) The long period and steady components of suspended sediment flux in the surf zone are generally offshore direction while the short period components of suspended sediment flux are onshore direction. Its steady components increase more than the short and long period components with shoaling and breaking.

4) This numerical model can well reproduce irregular time variation such as nonlinear wave deformation, suspended concentration, velocity and sediment flux and beach topography change.

5) Suspended load is much greater than bed load in the case of large wave height.

REFERENCES

Ikeno, M. and H.Tanaka (1996) : A New Experimental System for Reproduction of Infragravity Waves Bounded by Irregular Wave Groups and their Wave Deformation, CRIEPI Abiko Res. Lab. Rep. No.U95042 (in Japanese).

Ikeno, M. and T. Shimizu (1997) : Characteristics of Suspended Sediment Transport in the Surf Zone of Irregular Waves and their Reproduction by a Cross-Shore Beach Deformation Model, CRIEPI Abiko Res. Lab. Rep. No.U96037 (in Japanese).

Larson, M. (1994) : Predictive Beach Profile Change at Mesoscale under Random

Waves, Proc. 24th Int. Conf. on Coastal Eng., pp.2252-2266.

Madsen, P. A., R. Murrary and O. R. Sorensen (1991) : A new form of the Boussinesq equations with improved linear dispersion characteristics, Coastal Eng., Vol.15, pp.371-388.

Nielsen, P. (1984) : Field measurements of time-averaged suspended sediment concentrations under waves, Coastal Eng., Vol.8, pp.51-72.

Nielsen, P. (1988) : Three simple models of wave sediment transport, Coastal Eng., Vol.12,pp.43-62.

Nielsen, P. (1992) : Coastal Bottom Boundary Layers and Sediment Transport, Advanced Series on Ocean Engineering, Vol.4, World Scientific, pp.201-262.

Nwogu, O. (1993) : Alternative Form of Boussinesq Equations for Nearshore Wave Propagation, J. of Waterway, Port, Coastal, and Ocean Engineering, Vol.119, No.6, ASCE, pp.618-628.

Okayasu, A., A.Watanabe and M.Isobe (1990) : Modeling of Energy Transfer and Undertow in the Surf Zone, Proc. 22th Int. Conf. on Coastal Eng., ASCE, pp.123-135.

Rattanapitikon, W. and T.Shibayama (1996) : Cross-shore Sediment Transport and Beach Deformation Model, Proc. 25th Int. Conf. on Coastal Eng., ASCE, pp.3062-3075.

Sato, S. and M.B.Kabiling (1994) : A Numerical Simulation of Beach Evolution Based on a Nonlinear Dispersive Wave-Current Model, Proc. 24th Int. Conf. on Coastal Eng., ASCE, pp.2557-2570.

Shimizu, T. (1995) : Derivation of an Experimental Method for Beach Change Considering Scale Effect and Applicability of the Method, Proc. Japanese Coastal Eng., Vol.42, JSCE, pp.621-625 (in Japanese).

Shimizu, T. (1988) : Similarity of Model Experiments on Onshore-offshore Beach Profile Change, CRIEPI Abiko Res. Lab. Rep. No.U87059 (in Japanese).

Shimizu, T. and M.Ikeno (1996) : Experimental Study on Sediment Transport in Surf and Swash Zones Using Large Wave Flume, Proc. 25th Int. Conf. on Coastal Eng., ASCE, pp.3076-3089.

Sleath, J.F.A. (1987) : Turbulent Oscillatory Flow over Rough Beds, J. of Fluid Mech., Vol.182, pp.369-409.

Sunamura, T. (1984) : Quantitative Predictions of Beach-Face Slopes, Geol. Soc. Am. Bull., Vol.95, pp.242-245.

Thornton, E.B. and R.T. Guza (1983) : Transformation of Wave Height Distribution, J. Geophys. Res., Vol.88, pp.5925-5938.

CROSS-SHORE SEDIMENT TRANSPORT: A FIELD TEST OF THE BAILARD ENERGETICS MODEL.

Troels Aagaard[1], Brian Greenwood[2] and Jørgen Nielsen[1].

ABSTRACT: This paper reports on the results from a field test of the Bailard energetics sediment transport model. Model predictions agreed well with observed and measured volumetric change in the inner surf zone under erosional as well as accretionary conditions, occurring over a 72 h long storm event. The observed formation of a nearshore bar was reproduced by the model; bar formation was predicted to be due to a sediment transport convergence generated by seaward directed undertow and landward directed incident wave asymmetry.

INTRODUCTION

Attempts to model cross-shore sediment transport and profile evolution under varying energy conditions has been a major concern within coastal science and engineering and a fairly large number of sediment transport/morphodynamic models exist (e.g. Roelvink and Brøker, 1993). These models have generally been tested using laboratory data as sufficiently detailed high-quality field data are scarce.

An exeption to this has been the energetics model (Bagnold, 1966) and derivations thereof (Bowen, 1980; Bailard, 1981). The Bailard model which uses measured velocity moments as input has been tested in the field by e.g. Guza and Thornton (1985), Russell et al. (1995), Thornton et al. (1996) and Gallagher et al. (1998).

This model generally predicts offshore sediment transport events fairly well; these events occur as a response to mean currents and low-frequency waves during high-energy conditions. Onshore directed transport due to incident waves associated with beach recovery is generally poorly reproduced by the model (Russell et al., 1995; Thornton et al., 1996). A major reason is that the model does not consider phase-changes between velocity and sediment concentration which occur during oscillatory wave motions over

[1]Institute of Geography, University of Copenhagen, Øster Voldgade 10, DK-1350 Copenhagen K., Denmark. e-mail: taa@geogr.ku.dk.

[2]Scarborough College Coastal Research Group, The University of Toronto at Scarborough, 1265 Military Trail, Scarborough Ontario M1C 1A4, Canada.

a rippled bed; ripples mainly occur during low and moderate energy conditions.

In this paper, we test the Bailard energetics model using a data set which was collected during a 3½-day moderate storm event at Skallingen on the Danish North Sea coast. During this event, the inner nearshore was subjected to fairly large morphological changes involving an initial onshore bar migration followed by renewed bar formation and finally onshore migration of the newly formed bar. The model was capable of reproducing these morphological changes. Model predictions are also compared quantitatively with measured volumetric changes as well as with suspended sediment flux which was measured during the event.

THE MODEL

Predicted sediment transport was computed from the Bailard-model following the methodology of Thornton et al. (1996), where cross-shore sediment transport is predicted by

$$\langle q_x(t)\rangle = K_b(\langle |u_t|^2 u'\rangle + \langle |u_t|^2 \bar{u}\rangle) - K_{bg}\langle |u_t|^3\rangle + K_s(\langle |u_t|^3 u'\rangle + \langle |u_t|^3 \bar{u}\rangle) - K_{sg}\langle |u_t|^5\rangle \quad (1)$$

where

$$u_t = (u'^2+v'^2+\bar{u}^2+\bar{v}^2+2(u'\bar{u}+v'\bar{v}))^{1/2} \quad (2)$$

and

$K_b = (\rho/\rho_s-\rho)c_f g a'(e_b/\tan\phi);$
$K_{bg} = K_b(\tan\beta/\tan\phi);$
$K_s = (\rho/\rho_s-\rho)c_f g a'(e_s/w_s);$
$K_{sg} = K_s(e_s/w_s)\tan\beta$

$\bar{u},\bar{v}$ are the mean cross-shore and longshore velocities, respectively, u',v' are the oscillatory cross-shore and longshore velocity components, β is beach slope, w_s is sediment fall velocity and $\tan\phi$ the angle of repose; a' is the pore space factor = 0.6. The bedload and suspended load efficiency factors e_b, e_s were set at 0.21, 0.025 (Bailard, 1981). c_f was determined from $c_f = f_w/2$ with $f_w = \exp(5.213(k_s/A)^{.194}-5.977)$, where bed roughness k_s was set to $5D_{50}$ for a flat mobile bed and A is the oscillatory velocity amplitude; $A = u_{max}T/2\pi$ with T being the peak spectral density. c_f was on the order of 0.003-0.004 depending upon location within the profile. These parameters were kept constant at all times; no further adjustments were undertaken.

In eq.(1), the first two terms are the bedload transport terms due to oscillatory and mean cross-shore currents, respectively; terms four and five are the corresponding suspended load terms while the final two terms are due to gravity. u' was further subdivided into incident wave and infragravity wave components using Fourier-filtering.

THE FIELD EXPERIMENT

The field experiment was conducted during October 1995 in the shallow inner surf zone

at Skallingen. Four instrument stations, termed S1-S4, spanned the inner nearshore bar and two additional stations (S5-S6) were deployed on the beach and only submerged during high tides and/or storm surges (Figure 1). The instrument stations were each equipped with one Marsh-McBirney OEM512 electromagnetic current meter, initially installed at 0.23-0.34 m above the bed and vertically adjusted at each low tide (if possible) to compensate for bed level changes. The sensors were oriented to record positive flows landward and to the north; errors in orientation are estimated to be within +/- 3 degrees. Sensor offsets which were on the order of < 0.02 m/s were removed prior to data analysis while sensor gains were computed according to the manufacturer's specifications.

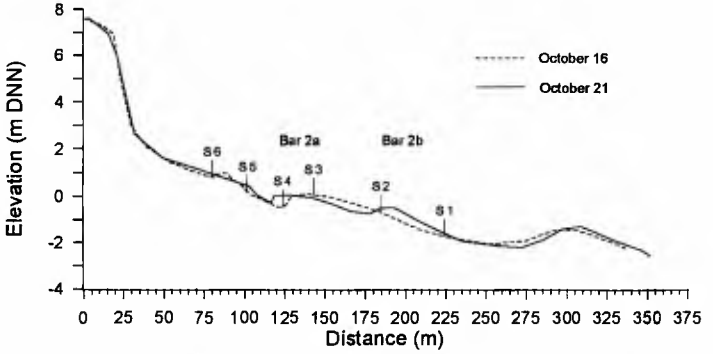

Figure 1. The cross-shore profile of the instrument transect surveyed prior to (Oct.16) and after (Oct.21) the storm event. Locations of the instrument stations as well as bar designations are indicated.

The stations were also each equipped with 3 OBS 1-P optical backscatter sensors (installed at nominal elevations of 0.05, 0.10 and 0.20 m above the bed) while pressure sensors were deployed at S1 and S5. All sensors were sampled at 4 Hz for periods of 34 minutes each 1-1½ hours during the event.

Bed elevation and hence morphological changes were recorded at each low tide through the experiment using a cross-shore array of twenty-eight ½-inch steel rods, spaced at 5 m increments along the instrument transect from x=50-185 m (Figures 1 and 2). The distance from the top of the rods to the sand was measured using a graduated rod fitted with an endplate. As the bed was always flat and tightly packed at low tide, survey errors were small and estimated as +/- 0.5 cm. Potential cumulative errors across the survey section are thus +/- 0.7 m^3/m.

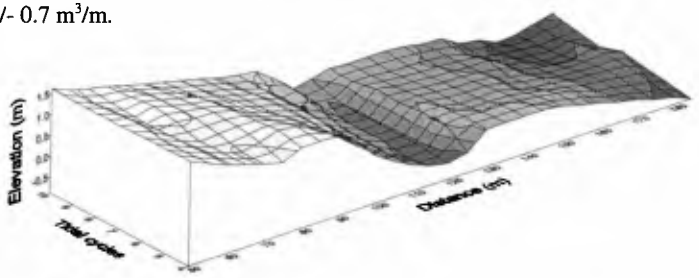

Figure 2. Time-distance diagram of the morphological evolution of the beach/inner surf zone during the experiment (tidal cycles 5-10). Note the trough formation at x = 170 m and the onshore migration of bar 2b into the survey area during tidal cycle 10.

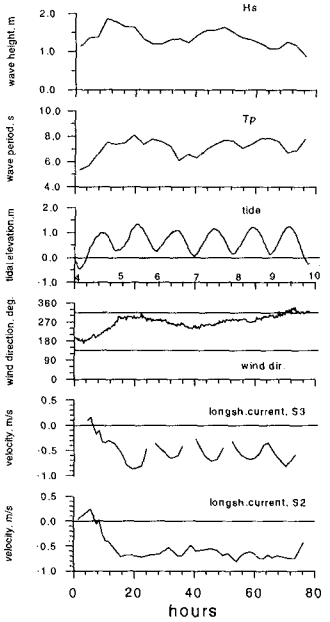

Figure 3. Offshore wave characteristics, tidal elevation, wind direction and longshore current velocities during the storm event. Negative longshore currents are directed to the south.

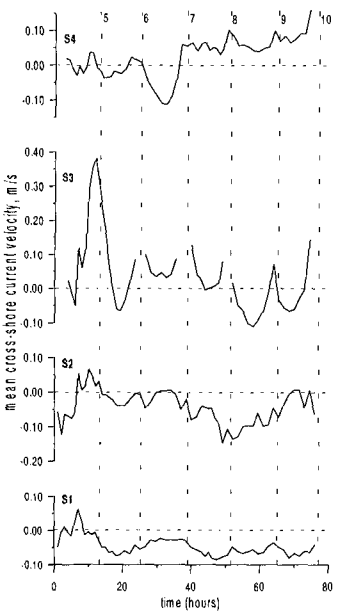

Figure 4. Mean cross-shore current velocities measured at S1-S4. The vertical dashed lines indicate times of low tide. Onshore currents are positive.

The storm event was characterized by moderate wave energy with a maximum significant wave height of H_s = 1.9 m seaward of the surf zone (Figure 3). Depending upon tidal stage, waves broke between stations S1 and S2. Wave periods were 7-8 seconds and the winds which were oblique to the shoreline generated relatively strong southward directed longshore currents, on the order of 0.7-0.9 m/s. The longshore currents were tidally modulated with maximum currents occurring at high tide when local wave energy level (radiation stress) was at a maximum.

Measured cross-shore mean currents were initially directed landward across the nearshore bar (Figure 4). At this time, cross-shore currents at the bar crest (S3) were also tidally modulated but in this case with maximum currents at low tide when incident wave dissipation was large and the breaking waves assumed a roller-like shape. Also, the sensors were relatively higher in the water column. Current velocities reached +0.38 m/s at the bar crest, and these landward directed flows are interpreted as being due to onshore wave- and bore-induced mass transports forming the onshore-directed limb of a rip circulation cell feeding the rip current south of the instrument transect (Aagaard et al., 1998). During the second half of the event, cross-shore currents at S3 (and S2) as well as the tidal modulation of these currents reversed; at this time the maximum currents at S3 occurred at high tide with velocities on the order of -0.05-0.1 m/s. The rip circulation was locally replaced by an undertow (Aagaard et al., 1998).

RESULTS AND DISCUSSION

Bed elevation changes in the beach/inner surf zone region are shown in Figures 2 and 5. The morphological evolution can be separated into three phases: Initially, the inner nearshore bar (bar 2a) migrated onshore during tidal cycles 5-7. Sediment was eroded from the crest of the bar and deposited in the trough and on the beach face. The second phase somewhat overlapped the first (tidal cycles 7-9) and was associated with trough excavation on the seaward slope of the bar (around x = 170 m) with renewed bar formation (bar 2b) seaward of the survey area (Figure 1). The final phase occurred during cycle 10 and was associated with onshore transport of sediment. The inner trough infilled and bar 2b migrated into the survey area. In plan view, the inner bar was initially slightly convex to the shoreline, with the instrument transect (located at y = 0 m) crossing the highest point of the bar (Figure 6). At the termination of the event, bar 2a had merged with the shoreline slightly updrift of the instrument transect and it was oriented obliquely to the shore. Note that the rip channels located at y = +/- 175 m (Figure 6) remained stable in position. The main areas of erosion/accretion were located at the updrift and downdrift ends of the bars.

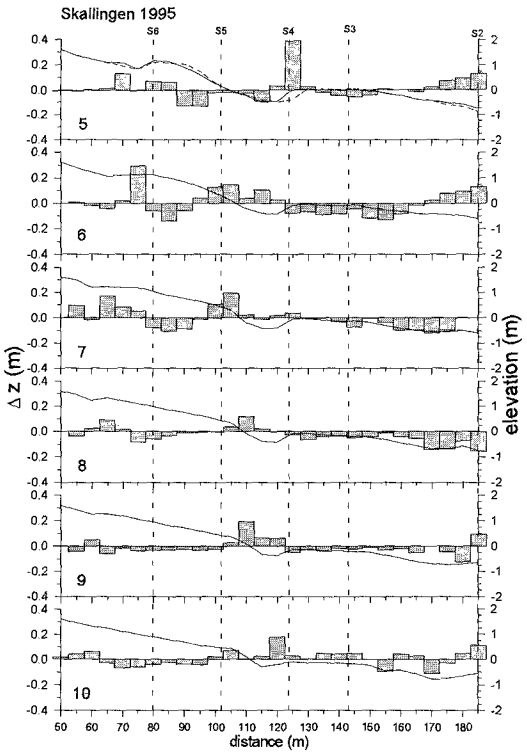

Figure 5. Changes in bed elevation at survey rods (Δz), and the cross-shore profile over tidal cycles 5-10. The left-hand ordinate refers to Δz, while the one on the right refers to elevation above Ordnance Datum. The dashed line in the upper panel is the profile at the termination of tidal cycle 4.

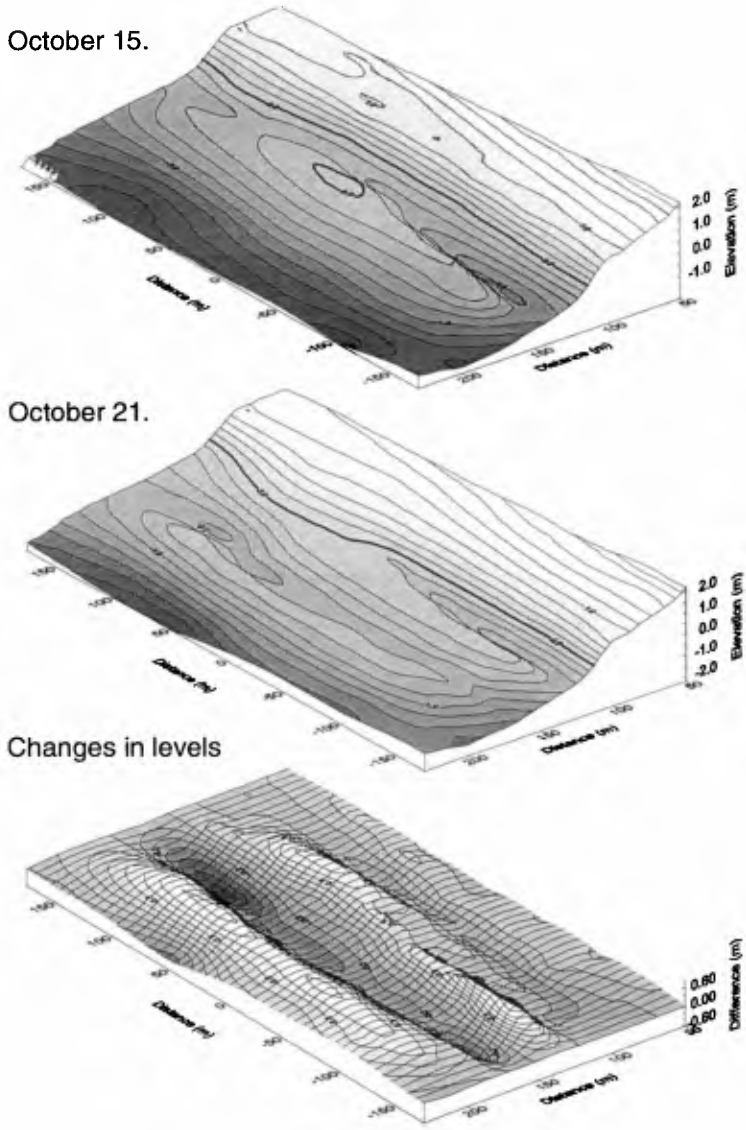

Figure 6. Three-dimensional views of the topography at the field site prior to (October 15) and after (October 21) the storm event. The bottom graph shows positive and negative bed elevation changes. The instrument transect was located at y = 0 m.

Predicted sediment transport

Figure 7 shows model-predicted sediment transport rate at stations S1-S4. Computed sediment transport rates and directions are in qualitative agreement with the observed morphological changes. During cycles 5-7, sediment transport was directed landward at all stations; transports at S4 were, however, very small as this station was located in the trough where sediment concentrations were small due to decreasing incident wave energy. During cycles 7-9, a transport divergence existed between S2 and S3 corresponding to the trough formation at this location. Simultaneously, there was a transport convergence between S1 and S2 resulting in the formation of bar 2b. Finally, tidal cycle 10 was characterized by a reversal to the initial transport conditions with onshore transport across the bar(s). Transport rates at S4 gradually increased as bar 2a migrated through this station and sediment concentrations increased. According to the model, suspended load was significantly more important than bedload, on average ranging from a high of 88% of the total load at S2 where incident wave energy was at a maximum, to 68% at S4.

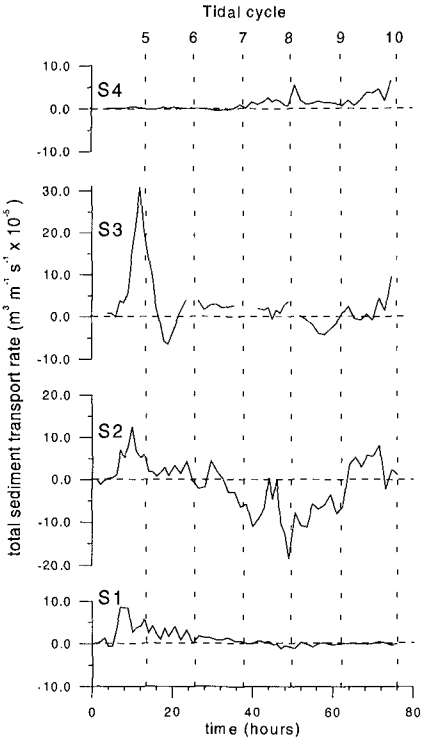

Figure 7. Predicted sediment transport rates at stations S1-S4. Vertical dashed lines indicate times of low tide. Positive values signify onshore directed transport.

Bed elevation changes at the inner edge of the survey area were almost consistently nil (Figure 5). Assuming a closed landward boundary to the profile and assuming a lack of longshore sediment transport gradients (which appears not unreasonable; Figure 6), net volumetric change within the survey area should match the sediment transport rate at the seaward edge of the area, i.e. at S2. In Table 1, predicted net volumetric transport at S2 over individual tidal cycles (ΔQ) is compared with volumetric change landward of S2 (ΔV). In the table, the agreement between predicted and measured volumetric change was excellent in 4 out of 6 cases. During cycles 6 and 9, the model overpredicted the volumetric transport by a factor of 1.7 and 2.4, respectively, resulting in a factor 2 overprediction of the sediment loss over the entire event. Examining the patterns of cut and fill (Figure 6), it is not evident that the overprediction should be mainly due to longshore sediment transport gradients.

Table 1 also compares the sediment balance over bar 2a (bounded by S2 and S4) with predicted sediment transport balance between these two stations. In this case, the correlation was excellent in 3 cases. During cycles 6 and 7, the model underpredicted the loss from the section, associated with onshore sediment transport at S4. This was at least

partly due to the current meter at S4 being very close to the bed (< 0.1 m) as the bar migrated onshore and almost buried this station. The model again overpredicted the sediment loss during cycle 9.

	S2-beach		S2-S4	
Tidal cycle no.	ΔV	ΔQ	ΔV	ΔQ
5	+1.85	+1.79	+1.55	+1.71
6	+0.48	+0.82	-2.09	+0.77
7	-0.56	-0.52	-2.79	-0.50
8	-3.74	-3.78	-3.95	-4.36
9	-1.51	-3.62	-1.78	-4.48
10	+1.65	+1.71	+0.44	+0.36
Total	-1.83	-3.60	-8.62	-6.50

Table 1. Volumetric change (ΔV) between S2 and the most landward survey rod, and between stations S2 and S4, as well as predicted net sediment transport (ΔQ) onshore/into (+) and offshore/out of (-) these sections. Values are in m^3/m shoreline.

Predicted transport vs. measured flux.

Predicted suspended sediment transport rates at S2 and S3 were compared with the sediment flux measurements using the backscatter sensors (Figure 8). Net sediment flux was estimated from these sensors by linearly integrating individual flux estimates from (nominal) elevations z = 0.025-0.275 m. True elevations changed when the bed eroded/accreted. Obviously, such a comparison can not validate quantitatively any of the two methods; a large part of the suspended sediment transport is expected to occur at elevations below the lowermost OBS-sensor and the concentration profiles are not linear. Nevertheless, within the inner surf zone where bores predominate, vertical sediment concentration gradients are expected to be relatively small due to the high levels of turbulence (Yu et al., 1993). Therefore, it should be possible to assess the qualitative performance of the two methods relative to each other.

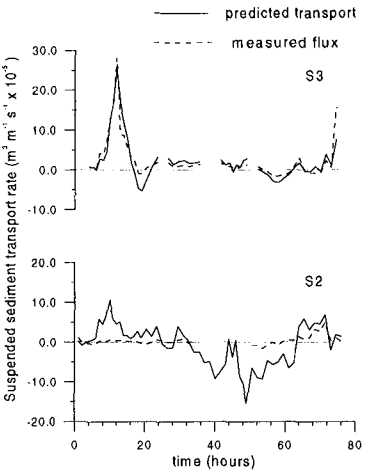

Figure 8. Model-predicted suspended sediment transport versus measured suspended sediment flux at stations S2 and S3. Positive values are directed onshore.

At S3, where measured vertical sediment concentration gradients were generally small, the correspondance between the predicted transport and the measured flux was very good. Data gaps at this station indicate instrument exposure; at S2 the gap represents a period when the OBS-sensors became dislodged and buried. At S2, measured vertical sediment concentration gradients were generally quite large and the correspondance between predicted transport and measured flux was poor except towards the end of the event.

The discrepancy between these stations may have been due to a number of factors. First, vertical mixing appears to have been stronger at S3. Furthermore, bed elevation changes at this station were relatively small (Figure 5) and the sensors were adjusted vertically at each low tide. This was not the case at S2 where bed elevation changes were larger and it was difficult to access this station at low tide. E.g. when the sensors were reinstalled around hour 50 (Figure 8), they could not be deployed sufficiently close to the bed. At this time, the lowermost sensor was at z ~ 0.12 m. As the bed gradually accreted, the correspondance between measurements and predictions improved significantly.

Sediment transport mechanisms

In Figure 9, the predicted suspended sediment transport has been separated into contributions from mean flows and oscillatory incident and infragravity wave components. The Figure illustrates transport rates at stations S1-S4 on three occasions representing the three morphological stages identified earlier. The first example (hour 10) represents the phase when bar 2a migrated landwards. According to the model, this was mainly accomplished by incident wave asymmetry accompanied by onshore directed mean flows on the bar crest. The second phase (hour 49.5) occurred when a trough was excavated between S2 and S3 and bar 2b formed between S1 and S2. This evolution appears to have been mainly due to the reversal of the mean flows which became offshore directed seaward of S3, representing an undertow. The result was a transport divergence between S3 and S2, and a convergence between S2 and S1. At the latter, mean transport became weak and increasingly opposed by incident wave asymmetry. The final example (hour 72) is taken from the time when both bars migrated onshore. At this stage, mean currents had decreased and consequently, onshore directed incident wave asymmetry dominated the inner surf zone.

Figure 9 illustrates a number of important points. First of all, predicted incident wave transport became offshore directed at S2 during tidal cycles 8 and 9 (represented by hour 49.5). This was not a response to an overall reversed incident-wave asymmetry. During the sample run at hour 49.5, velocity asymmetry at high frequencies (computed from $u^3/(u^2)^{0.5}$ and using high-pass filtered time series) was small (+0.071) but positive, i.e. onshore directed. At the preceding high tide (hour 44) incident wave asymmetry was +0.22. Thus, incident wave asymmetry was tidally modulated as would have been expected as asymmetry has been found to decrease into the surf zone (Thornton and Guza, 1989), and at low tide, S2 was further from the breakpoint. The asymmetry was, however, always onshore directed. The reason for the predicted offshore directed transport at wind wave frequencies was that u_f (Eq. 2) tended to be maximum under incident wave troughs at S2.

The waves were incident north of the shore-normal, generating southerly (negative) longshore currents. Figure 10 shows an example of longshore and high-pass filtered cross-

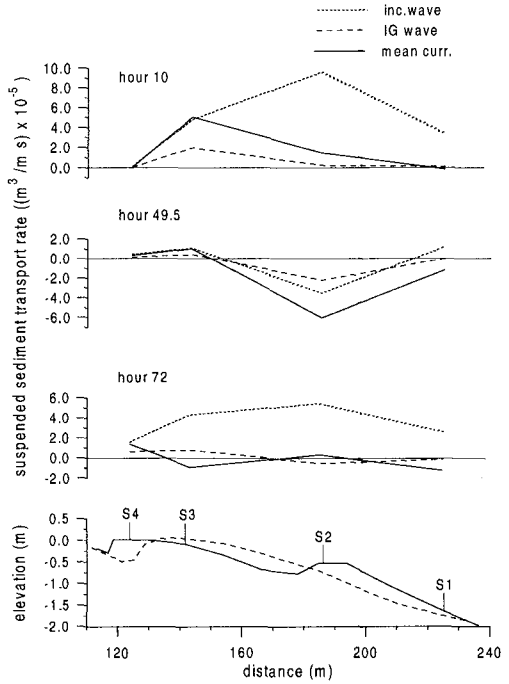

Figure 9. Predicted sediment transport rates due to incident waves (dotted lines), infragravity waves (dashed lines) and mean currents (solid lines) across the nearshore, at representative times. In the lower panel, the dashed line is the profile prior to the storm and the solid line is the profile after the event. Hours 10 and 49.5 represent runs close to low tide whereas hour 72 was a high-tide run.

shore velocity time series at S1 and S2 during hour 49.5. At S1, the velocity field behaved as expected: Maximum onshore velocities occurring under incident wave crests were generally in phase with maximum longshore (southerly) velocities. This was not the case at S2 where the incident waves in many cases appears to have been propagating against the longshore current leading to maximum values of u, in wave troughs. Between S1 and S2, the incident waves appear to have been refracted against the current at this time. The reasons for this are not known, however.

Returning to Figure 9, net sediment transport at oscillatory infragravity wave frequencies tended to be relatively small even though a transport divergence was consistently located between S2 and S3 with onshore directed transport in the innermost surf zone, and more offshore trending transport further seaward.

Finally, as already noted, the mean currents were depth-dependent with respect to directionality. At bar crests (bars 2a and 2b), and particularly at low tide (Figures 4 and 9), the currents were directed onshore while they were directed offshore in larger water depths. This indicates a presence of feed-back mechanisms between topography and mean

current circulation, implying that on gently sloping beaches and in cases when the bar is close to the water surface, e.g. in the intertidal or upper subtidal zones, there will be a tendency towards a generation of rip cell circulation as the water brought onshore by mass

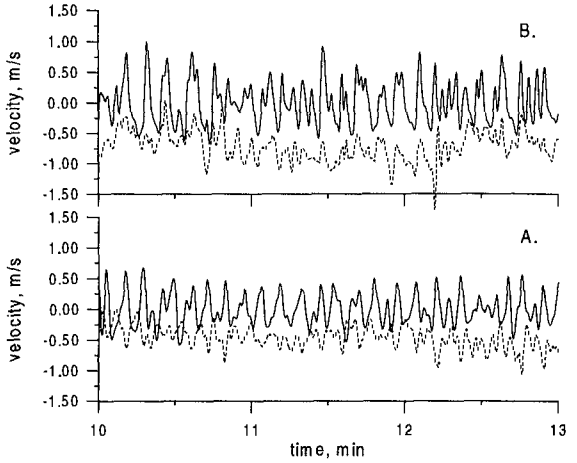

Figure 10. Example time series of longshore velocities (dashed lines) and high-passed cross-shore velocities (solid lines) at stations S1 (A) and S2 (B); runs 292_12 (hour 49.5).

transport cannot escape seaward as an undertow. At Skallingen, rips channels are rarely absent from the inner surf zone.

DISCUSSION AND CONCLUSIONS

In the present study, a vertically homogeneous cross-shore velocity field has been assumed in the sediment transport computations. This might seem inappropriate as most models as well as several laboratory and field studies have demonstrated a tendency for vertically segregated flows, with onshore directed mass transport in the upper part of the water column (generally above trough level) and seaward directed flows in the lower parts. At first glance, the tidally modulated cross-shore current observed at S3 during tidal cycles 5-8 might suggest this scenario as the current sensor was relatively high in the water column at low tide, and vice versa. However, a number of points contradict this interpretation. First, predicted sediment transport rates and directions agreed well qualitatively with the observed volumetric changes, and in most cases quantitatively as well. Second, around low tide rips were visually observed approximately 175 m south (and north) of the instrument transect throughout the event. Third, an undertow did develop at S3 during cycles 9 and 10 (Figure 4) due to reversed longshore pressure gradients (Aagaard et al., 1998). It is not evident why this shift would occur if current direction depended upon sensor elevation as maximum and minimum tidal elevations were relatively constant during all tidal cycles (Figure 3). Finally, the tidally-modulated flow at S2 was far from systematic, suggesting that a simple velocity response to relative sensor elevation did not exist, at least at this station.

Therefore it is concluded that the energetics model is potentially capable of predicting sediment transport rates under high-energy field conditions in the inner surf zone, to within a factor of 2 or 3, provided that longshore velocity components are included in the sediment stirring term. The model appears quite robust as no adjustment of free parameters occurred. On most occasions, there was a close agreement between predicted and measured volumetric change, particularly considering the potential survey errors. While this is probably fortuitous, the model only failed significantly during one tidal cycle.

Previous field tests of the model (e.g. Russell et al., 1995; Thornton et al., 1996) have indicated problems with predicting transport due to incident waves, particularly during onshore sediment transport conditions, and the model has generally been incapable of simulating beach recovery. This was not the case here, probably because the bed in these shallow water depths was generally flat; no evidence of bedforms was observed. The energetics model assumes a zero phase-shift between velocity and sediment concentration; this assumption is violated in the case when the bed is rippled.

The data presented here provide strong support for the concept of nearshore bar formation due to undertow. Approximately half-way through the event, an undertow developed locally at S2 (and later at S3), probably because of reversed longshore pressure gradients (Aagaard et al., 1998). The undertow weakened and became opposed by incident wave asymmetry at S1, resulting in the development of bar 2b.

Finally, this study has suggested an existence of morphodynamic interactions in the nearshore, involving feedbacks between hydrodynamics and topography, exemplified by the dependency between bar topography/water depth and mean flow directions. Apart from the presence or absence of longshore pressure gradients which are intimately linked to longshore (non-)uniform bar topography, the mean flow pattern, i.e. offshore-directed undertow versus onshore-directed rip feeders, seems to be constrained by water depth. In shallow water (bar crests and/or low tide), there was a tendency towards onshore directed mean currents over the bar while offshore directed mean flows prevailed in larger water depths (in troughs, during high tide and at S1).

ACKNOWLEDGEMENTS

This research was supported by the Danish Natural Sciences Research Council, grant no. 11-0925. Superb field assistance was rendered by Ulf Thomas, Rasmus Nielsen, Carlo Sørensen and Torsten Christensen.

REFERENCES

Aagaard, T., Nielsen, J. and Greenwood, B., 1998. Suspended sediment transport and nearshore bar formation on a shallow intermediate-state beach. *Marine Geology*, 148, 203-225.

Bagnold, R.A., 1966. An approach to the sediment transport problem from general physics. *Geological Survey Professional Paper 422-I*. U.S. Government Printing Office, Washington.

Bailard, J.A., 1981. An energetics total load sediment transport model for a plane sloping beach. *Journal of Geophysical Research*, 86, 10938-10954.

Bowen, A.J., 1980. Simple models of nearshore sedimentation; beach profiles and longshore bars. In: S.B.McCann (ed) *The Coastline of Canada*. Geological Survey of Canada, Paper 80-10, 1-11.

Gallagher, E.L., Elgar, S. and Guza, R.T., 1998. Observations of sand bar evolution on a natural beach. *Journal of Geophysical Research*, 103, 3203-3215.

Guza, R.T. and Thornton, E.B., 1985. Velocity moments in nearshore. *Journal of Waterway, Port, Coastal and Ocean Engineering*, ASCE, 111, 235-256.

Roelvink, J.A. and Brøker, I., 1993. Cross-shore profile models. *Coastal Engineering*, 21, 163-191.

Russell, P., Foote, Y. and Huntley, D.A., 1995. An energetics approach to sand transport on beaches. *Proceedings Coastal Dynamics '95*, ASCE, 829-840.

Thornton, E.B., Humiston, R.T. and Birkemeier, W., 1996. Bar/trough generation on a natural beach. *Journal of Geophysical Research*, 101, 12097-12110.

Thornton, E.B. and Guza, R.T., 1989. Wind wave transformation. In: R.J.Seymour (ed) *Nearshore Sediment Transport*, Plenum Press, New York, 137-171.

Yu, Y., Sternberg, R.W. and Beach, R.A., 1993. Kinematics of breaking waves and associated suspended sediment in the nearshore zone. *Continental Shelf Research*, 13, 1219-1242.

Field Observations of Small Scale Sedimentation Processes

Daniel M. Hanes[1] (member, ASCE), Eric D. Thosteson[1], Yeon-Sihk Chang[1], Craig Conner[1], and Chris E. Vincent[2]

Abstract

A series of field experiments have been conducted to investigate small-scale sediment dynamics near the seabed in the nearshore region. The experiments took place at the U.S. Army Corps of Engineers Field Research Facility, in Duck, North Carolina, U.S.A., where the seabed typically consists of fine to medium sized sand. An array of instrumentation was deployed at various locations across the surf zone and nearshore region between depths ranging from 1 to 5 meters. Examples of suspended sediment measurements are presented along with examples of observed bedforms. We observed that the suspension of sand tends to occur at low frequencies that correspond to the time scale of wave groups. Small wave ripples are also found to evolve over similar time scales. We explore the linkages between the suspension of sediment and the evolution of small wave ripples, and show that the size of the ripples plays a significant role in determining the amount and distribution of suspended sediment.

Introduction

Small-scale sedimentation processes are responsible for the movement of sediment grains in the coastal zone. We use the term "small-scale" to describe those processes affecting the sediment dynamics and hydrodynamics on spatial scales ranging from the size of the sediment grain up to approximately 1 meter. This range of spatial

[1] Department of Coastal and Oceanographic Engineering, University of Florida, Box 116590, Gainesville, FL 32611, U.S.A., email: hanes@coastal.ufl.edu

[2] School of Environmental Sciences, University of East Anglia, Norwich NR4 7TJ, United Kingdom, email: C.Vincent@uea.ac.uk

scales typically covers the thickness of the turbulent wave boundary layer, as well as small wave ripples that often are found on the seabed.

A series of field experiments have been conducted to investigate small-scale sediment dynamics near the seabed in the nearshore region. The experiments took place at the U.S. Army Corps of Engineers Field Research Facility, in Duck, North Carolina, U.S.A., where the seabed typically consists of fine to medium sized sand. An array of instrumentation was deployed at various locations across the surf zone and nearshore region between depths ranging from 1 to 5 meters. The instruments measured the local hydrodynamics using a pressure sensor and 3 axis Acoustic Doppler Velocimeter (ADV). The suspended sediment concentration was measured with a three frequency Acoustic Concentration Profiler (ACP), and the local bedforms were measured with a Multi-Transducer Array (MTA). Surficial sediment samples were also obtained at most sites, as well as water temperature, turbidity, and video images when the water wasn't too turbid. A schematic of the instrumentation is shown in Figure 1.

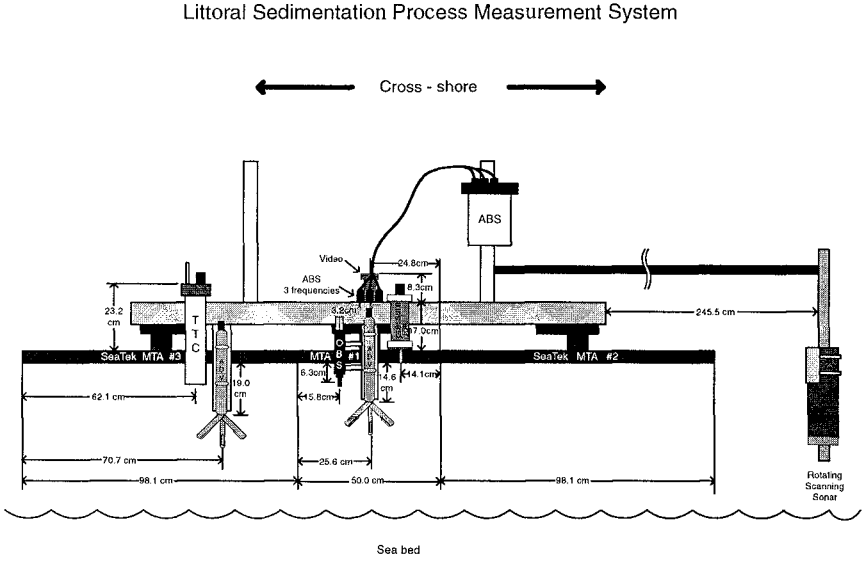

Figure 1: Instrumentation Schematic

The data were obtained over a variety of wave and current conditions, and exhibit high variability in both the suspended sediment concentration and the bedform geometry. This paper will focus on the scales of variability. In particular, we will examine the temporal variability in the concentration of suspended sediment near the seabed, and the variability in the spatial scale of the bedforms.

Background

In steady, unidirectional flow, suspended sediment flux is calculated at a fixed depth from the product of the water velocity and the suspended sediment concentration. In the presence of waves the concentration of suspended sediment and the velocity of the water are generally not in phase, but a phase relation exists between the two quantities. This results in a component of sediment flux that depends explicitly on the time varying components of velocity and concentration. Several investigators have shown that because of this coherent transport component, significant sediment transport can occur in a direction different from that of the mean water velocity (Jaffe et al., 1985; Hanes, 1988; Vincent et al, 1991). Furthermore, this coherent transport has been shown to be frequency-dependent by using the cospectrum of measured velocities and concentrations (Hanes and Huntley, 1987). In view of the importance of this coherent transport component, accurate modeling of the transport of sediment in the presence of waves requires instantaneous time series of both water velocity and of suspended sediment concentration.

The importance of this intermittent sediment suspension on the time scale of waves has been parameterized for monochromatic waves in the surf zone by use of the Dean number (Dean, 1973).

$$D = \frac{H_b}{wT} \tag{1}$$

In eq. 1, H_b is the breaking wave height, w is the sediment fall velocity, and T is the wave period. For low values of the Dean number, sediment movement is onshore, but at some critical value, the direction becomes offshore. Basically, the parameterization is based upon the assumption that sediment is elevated to some height at the phase corresponding to the passage of the wave crest. The quantity and direction of net sediment transport then depends on the fraction of the suspended sediment which settles before flow reversal occurs - which introduces the importance of the settling velocity of the sediment and the period of oscillation. As an instantaneous predictive model, use of the Dean number is complicated too extensively by the frequency interactions of random seas. As a conceptual model, the Dean number parameterization illustrates the 'memory' or 'history' effect of the sediment suspension process that results in the above mentioned concentration phase lag. It also illustrates some parameters important in its characterization: height of suspension, sediment fall velocity, and wave period.

Suspended Sediment Observations

Previous research has indicated that significant variation in suspended sediment concentration occurs at frequencies below those of the incident waves, particularly at those frequencies associated with wave groups (Hanes, 1991). More recent work outside the surf zone has verified this result, showing concentration variation at wave group frequencies - even when no infragravity energy was present in the wave power spectrum.

Such a case is shown in figure 2, which shows the frequency spectrum of the concentration time series measured 1 cm above the seabed. Note in this figure the high representation at low frequencies, despite the lack of energy at these frequencies in the bottom velocity spectrum, shown in figure 3. The same study showed that these low-frequency variations in suspended sediment concentration can actually dominate the concentration spectrum (Thostéson, 1997). Moreover, the coherence between the squared magnitude of the bed velocity (chosen for the envelope or group detection properties) and the concentration is very high at these frequencies (as is apparent in figure 2), with the peak in concentration lagging slightly behind the peak in the envelope time series. These results are interpreted, as in the Dean number parameterization, to be a consequence of the history effect of sediment suspension, but on a much longer time scale. Interestingly, it is not difficult to conceptualize additional mechanisms that vary substantially on the time-scales of wave groups and that could contribute to this history effect of sediment suspension. Such mechanisms include variation in turbulence intensity, fluidization and consolidation of sand beds (which could enhance the erosion potential of the bed), bedform geometry, boundary layer stability, etc.

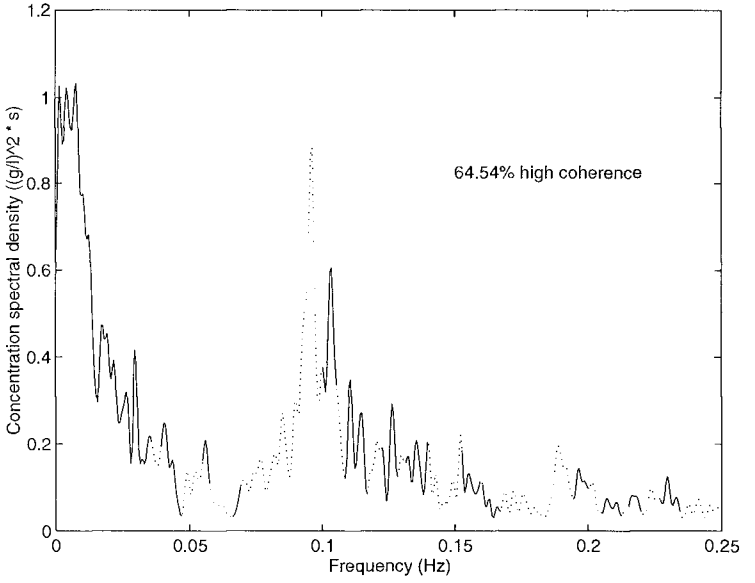

Figure 2: Frequency spectrum of concentration time series measured 1 cm above the bed. Solid line indicates coherence with square of bottom velocity magnitude > 0.60.

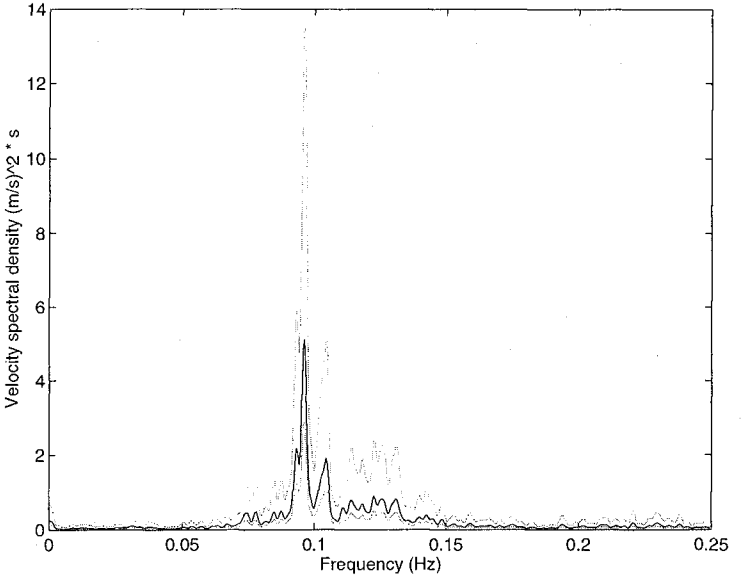

Figure 3: Frequency spectrum of bottom velocity with 80% confidence limits.

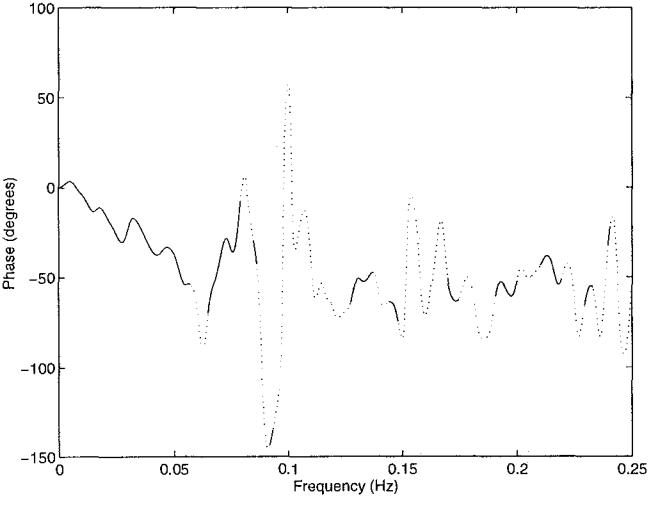

Figure 4: Phase of transfer function between near bed concentration and square of bottom velocity (envelope).

Figure 4 shows the phase of the transfer function between near bed concentration and the square of the bottom velocity (the envelope at low frequencies in absence of infragravity motion). As seen from examination of figure 4, the low-frequency phase of the transfer function could be well approximated by a linear fit. This is significant, because a linear phase response in the frequency domain corresponds to a constant time lag in the time domain.

Bedform Observations

Bedforms consisted mainly of two different types. Wave formed ripples were measured with heights up to 2 cm and lengths from 10 to 15 cm. Mega-ripples, with heights of 5 to 10 cm and lengths of 75 to 150 cm were also measured. Each of these bedform types sometimes occurred alone, and other times both types were superimposed. For example, Figure 5 illustrates the bedforms when both types were present. The center section of the MTA has higher resolution, and is blown up in the lower plot to show the smaller scale bedforms. The lines in this figure represent a sequence of scans (bedform measurement) separated in time by 1 minute; the lines have been displaced vertically by 1 mm in order to better see them. These measurements were obtained outside the surf zone in a depth of 3.9 m with a surficial sand size D_{50} = .19 mm, under conditions with H_{mo} = 0.50 m, T_p = 10.7 sec.

Interestingly, under very similar conditions, but closer to the breaker zone, the smaller scale ripples were not present, as seen in Figure 6. These mega-ripples were observed in a depth of 1.6 m, just outside the surf, with a surficial sand size D_{50}=.19 mm, under conditions with H_{mo} = 0.53 m, T_p = 9.8 sec. It would appear that the threshold for sheet flow has probably been exceeded in this case.

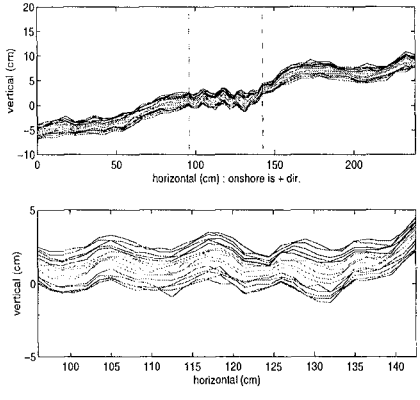

Figure 5: Small and mega-ripples

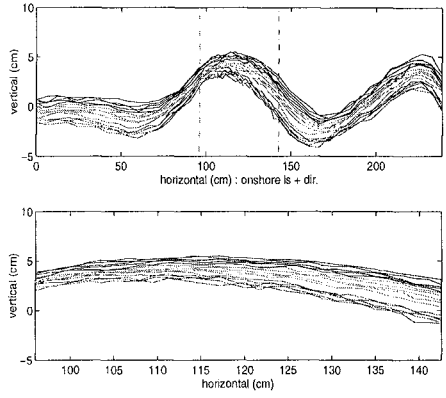

Figure 6: Only mega-ripples

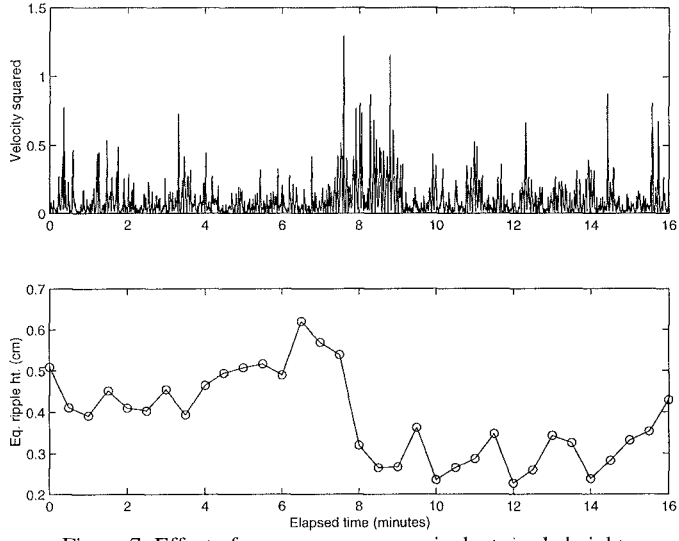

Figure 7: Effect of wave groups on equivalent ripple height

Bedform-suspended sediment interactions

For examination of the temporal variability of the bedforms, the equivalent ripple height is utilized. The equivalent ripple height is defined as the height of a sinusoidal bedform with the same standard deviation as measured by the linear array. The lower plot in Figure 7 shows the variation of the equivalent ripple height for 16 minutes during

a run with a significant wave height of 0.55 meters and 9 second waves. In the upper plot of Figure 7 is the velocity magnitude squared, again used to make the passing wave groups apparent. It is interesting to note the decrease in equivalent ripple height each time a group passes, particularly the large group occurring within the 7 to 9 minute range of the plot.

Shown in Figure 8 is the time series of concentration profiles collected during the same 16 minutes presented in Figure 7. The darkest areas in the plot represent the highest concentrations, while the lighter areas show the lowest concentrations. The concentration is seen to increase with passing groups, as discussed previously, but the most dramatic concentration event occurs at nearly the same instant as the reduction in ripple height.

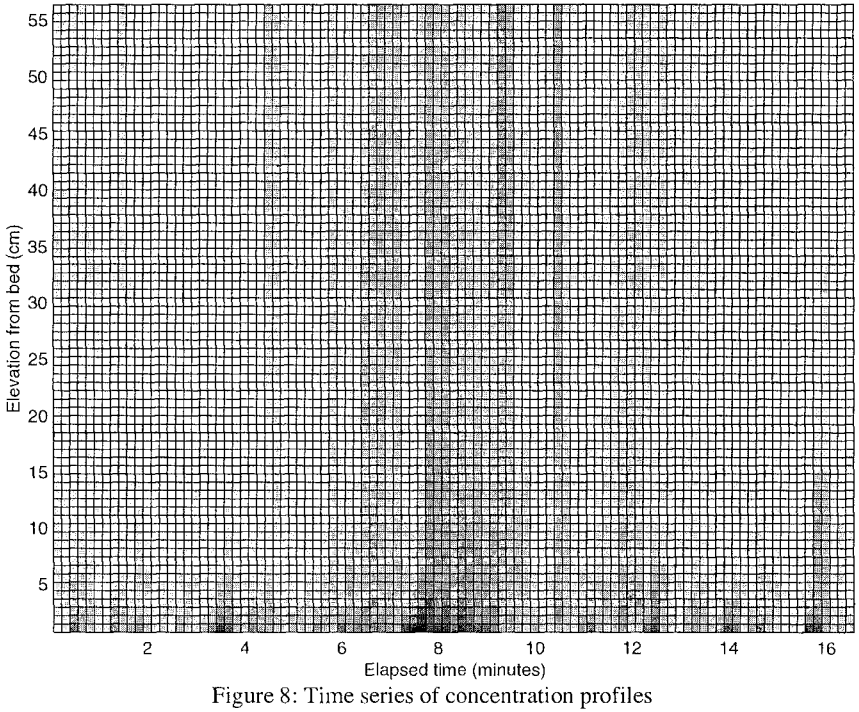

Figure 8: Time series of concentration profiles

Summary

Suspended sediment concentration has been shown to vary most significantly on the temporal scale of wave groups. Bedforms of various spatial scales and geometries are seen to be similarly dynamic, often reduced in amplitude or wiped clean during wave group passage. In addition, the variability of suspended sediment concentration and

bedform geometry are seen to be linked to one another. Continuing and future research of these processes with increasingly more advanced instrumentation, improved methods of data analysis, and measurements higher in resolution will improve our understanding of these processes and their roles in the process of sediment transport.

Acknowledgements

The authors wish to acknowledge the generous support of the Coastal Sciences Program of the Office of Naval research and would also like to express their appreciation to those at the Field Research Facility in Duck, North Carolina for use of the facilities.

References

Beach, R.A. and R.W. Sternberg (1991): Infragravity driven suspended sediment transport in the swash, inner and outer-surf zone, Coastal Sediments '91, 114-128.

Dean, R.G. (1973): Heuristic models of sand transport in the surf zone, Technical report UF/COEL-73/26, University of Florida

Hanes, D.M. (1988): Intermittent sediment suspension and its implications to sand tracer dispersal in wave-dominated environments, Marine Geology, Vol. 81, 175-183.

Hanes, D.M. (1991): Suspension of sand due to wave groups, Journal of Geophysical Research, Vol. 96, No. C5, 8911-8915.

Hanes, D.M. and D.A. Huntley (1987): Direct measurement of suspended sediment transport, Coastal Sediments '87, ASCE, New York, 723-737.

Jaffe, B.E., R.W. Sternberg, and A.H. Sallenger (1985): The role of suspended sediment in shore-normal beach profile changes, Proceedings of the 19th Coastal Engineering Conference, ASCE, NewYork, 1983-1996.

Osborne, P.D. and G.A. Rooker (1997): Surf zone and swash zone sediment dynamics on high energy beaches: West Auckland, New Zealand, Coastal Dynamics '97, 814-823.

Thosteson, E.D. (1997): Development and field application of a littoral processes monitoring system for examination of the relevant time scales of sediment suspension processes, Ph.D. dissertation, University of Florida.

Vincent, C.E., D.M Hanes, and A.J. Bowen (1991): Acoustic measurements of suspended sand on the shoreface and the control of concentration by bed roughness, Marine Geology, Vol. 96, 1-18.

LITTORAL TRANSPORT UNDER COMPLEX WAVE FIELDS: PECÉM, NORTH EAST BRAZIL

Berry Elfrink[1], Domenico Accetta[2], Berenice Motta Vargas[2] and Wagner Santos Scisinio Dias[2]

Abstract

In connection with the design of new marine facilities a hydraulic study was carried out at Pecém, NE Brazil. The project comprised mathematical modeling of waves, nearshore hydrodynamics and sediment transport before and after the construction of the offshore harbor in front of Ponta do Pecém. The wave conditions are characterized by the simultaneous occurrence of sea and swell from different directions. The littoral current generated by the sea becomes detached at the headland. A shore-connected spit develops under these circumstances. During periods of predominant swell the spit erodes. The main impact of the harbor is a further reduction of the littoral drift W of the headland, which causes increased sediment accumulation immediately W of the headland and coastal erosion W of the city of Pecém.

Introduction

Presently an offshore harbor is being constructed in front of the city of Pecém, approximately 40 km west of Fortaleza in NE Brazil, see Fig 1. The harbor is located approximately 2 km offshore. In connection with the design of the new marine facilities, a coastal impact assessment was carried out (Danish Hydraulic Institute 1997). The location of the harbor is shown in Fig 2

The coastline of Ceará is characterized by curved sandy beaches, interrupted by small rocky headlands. The beach material consists of medium to fine sand with a median grain size of the order 0.25-mm. Since several years the coastline in front of Pecém is subject to

[1] Danish Hydraulic Institute, Agern Allé 5, DK-2970 Hørsholm, Denmark
[2] Instituto de Pesquisas Hidroviárias, Rua General Gurjão 166, Caju - Rio de Janeiro, CEP: 20-931-040 Brazil

erosion. An analysis of aerial photographs has revealed that the coastline in front of the city has retreated with approximately 50 meters during the last 25 years. The coastline erosion is not homogeneous along the coast but varies from approximately 4 m/year at the western edge of Pecém to approximately 2m/year at its eastern boundary. Approximately 500 m further towards west, a slight beach accretion was observed locally.

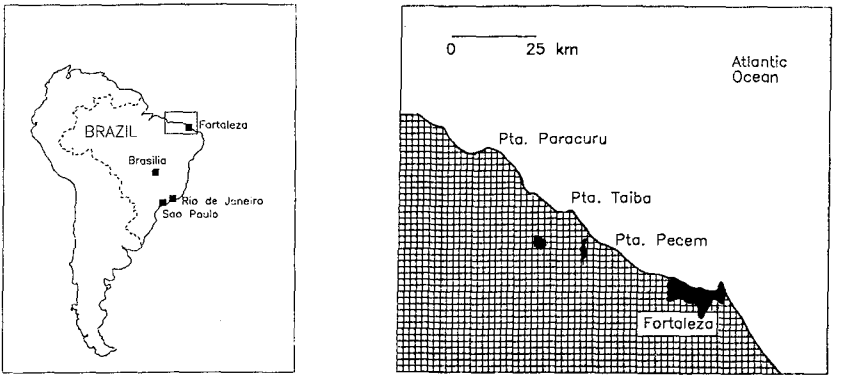

Fig. 1 Location of the project site

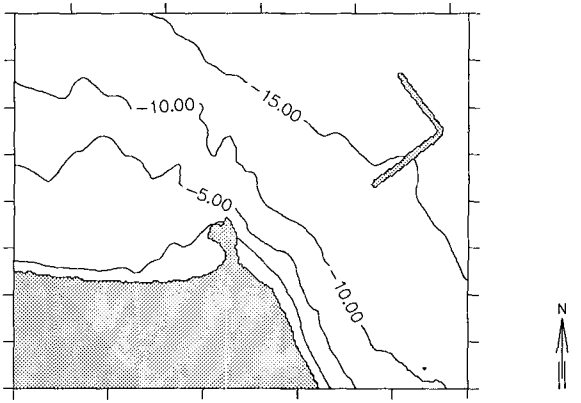

Fig. 2 Location of the new offshore harbor of Pecém scale 1: 60,000.

Variations in the coastline position occur during the year. In the period from November until April, beach erosion occurs due to swell coming from the Northern Hemisphere. During this period rock is exposed at many locations at the beach. From May until November, the wave conditions are dominated by sea waves.

The project site is characterized by a stable wind climate. The wind speed and directions are fairly constant through the year. The main wind direction is E-ESE. The most frequent wind speed is 6 - 8 m/s from E.

Along the entire coastline, high eolian dunes extend to several kilometers away from the coast and form a dominant morphological feature of the landscape. The height of the dunes exceeds 30 m in some locations. Their orientation corresponds to the prevailing wind direction, which is approximately 95° N. The dunes consist of marine sand with a slightly better sorting than the beach sand. Close to the shoreline, the dunes are active. Aerial photographs show that the dunes migrate with an average speed of approximately 6 to 7 m/year. The older dunes further away from the coastline are fixed by vegetation. Depending on the coastline orientation, the coastal dunes act as a sink of sediment in the coastal sediment balance. Due to the dominating winds from easterly directions and the coastline configuration at Pecém, sediment loss due to wind transport is only of importance at the eastern side of Ponta do Pecém.

The wave conditions are characterized by the simultaneous occurrence of swell and sea from different directions. Sea approaches the coast at Pecém under large angles. Due to refraction and diffraction around the headland, a part of the wave energy reaches the shore. The area E of Ponta do Pecém is considerably more exposed to the action of sea waves than the western side.

Although the tidal range is approximately 3 meters, tidal currents are very weak, of the order 0.1 m/s. These currents are of minor importance for the nearshore sediment transport. The main effect of the tides is the cross-shore shift of the sediment transport patterns, which is dictated by the water levels. During ebb, wave breaking occurs on the shoals in front of the city of Pecém at a distance of several hundred meters off the coast. During flood, the headland becomes partly inundated.

Wave conditions

Between 1991 and 1995 INPH has carried out wave measurements in Fortaleza by means of a Wave rider located at a distance of approximately 1 km offshore of the port of Mucuripe. The wave buoy was located at a water depth of 15 m. (INPH 1986a).

Since March 1997 wave data has been recorded with a directional Wave-Rider, which is located approximately 4 km offshore of Pecém in a water depth of 17m. These measurements provide detailed information about the spectral characteristics of the wave conditions. In order to obtain reliable statistics, measurements carried out over several years are necessary. However, the wind conditions at the present site are fairly constant

throughout the year. The measured wave height statistics showed good agreement with the data from Mucuripe and were assumed representative for the present site.

Fig. 3 shows an example of a measured wave spectrum at Pecém. A clear bimodal distribution of the wave energy distribution can be noticed. The first peak occurs at frequencies of approximately 0.06 to 0.1 s^{-1} corresponding to wave periods of 10 to 16 s. The mean direction of the waves with these frequencies varies between approximately 20° N and 45° N. These waves represent the swell originating from the Northern Hemisphere. The second peak represents sea, with frequencies typically in the order of 0.12 to 0.3 s^{-1}, corresponding to wave periods of 3 to 8 s. The direction varies between approximately 75° N and 120° N.

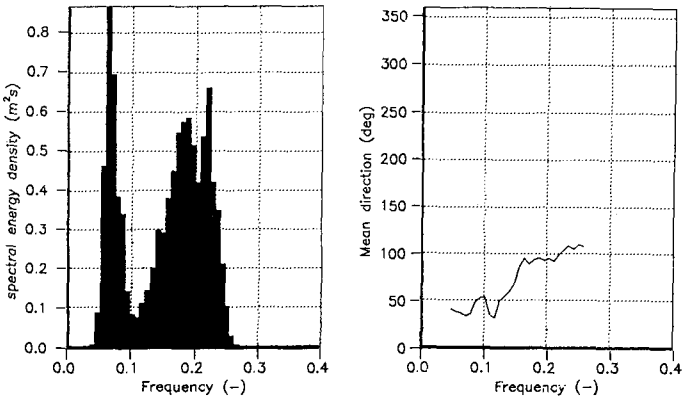

Fig. 3 *Typical wave spectrum at Pecém. Two distinct peaks can be observed with frequencies of approximately 0.08 and 0.12 s-1 representing swell and wind waves (sea) respectively. The wave directions of the two dominant wave components are varying from approximately 30° N for the swell to approximately 120° N for the sea waves.*

The usual way to apply the wave data in coastal studies is to represent the wave spectrum by a few statistical parameters. Typically the significant wave height H_s and the peak period T_p are used in sediment transport studies. If these parameters were used to characterize the wave conditions, information about the structure of the spectrum would be lost. The use of the peak wave period would only represent sea, as the short wave components usually are predominant in the spectrum. Further, the calculated mean wave direction would not resemble the observed direction from neither the swell nor the sea waves, but instead some average angle, which does not represent the natural conditions. The littoral sediment transport is very sensitive to parameters such as the wave height, period and especially the wave direction. Small errors in these parameters may lead to considerable errors in the calculated sediment transport rates. The sediment transport mechanisms under swell waves are quite different from those under short period waves

and thus care must be taken in the representation of complex sea states as in Pecém by these assumptions. Therefore, it is important to distinguish the swell from the sea and treat them separately in the sediment transport calculations.

In order to distinguish between sea and swell an analysis was made of the measured wave energy spectra. Each spectrum was subdivided in a discrete number of frequency intervals. For each interval a wave height was calculated according to the measured energy density in the respective interval. In this way, the wave energy spectrum was transformed to a number of individual wave events characterized by a wave height, period and direction. A statistical analysis was performed on all investigated spectra. From this analysis wave climates for each month of the year were derived. A dominance of sea is observed for the period from July to October. From December to April swell is dominant. The intermediate months show the occurrence of both wave types simultaneously. Fig. 4 shows the derived climates for January and July with a predominance of swell and sea respectively.

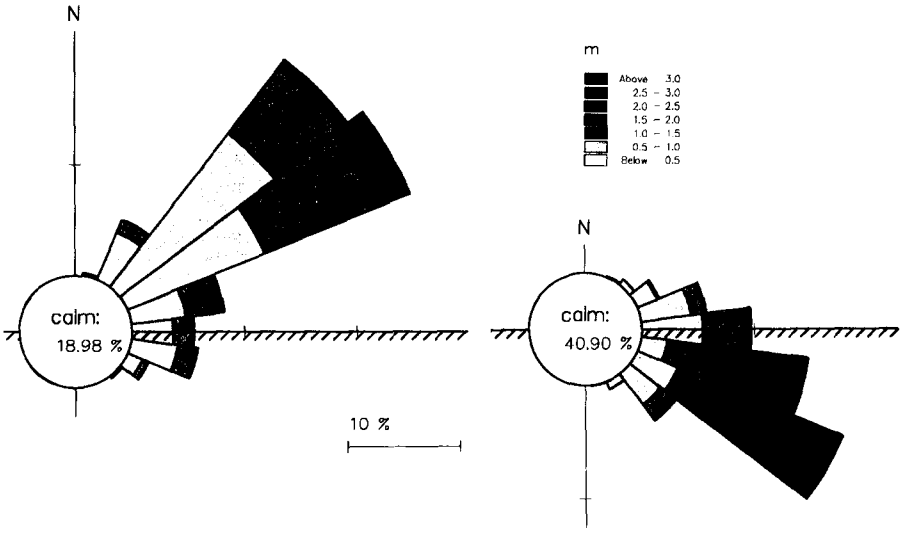

Fig. 4 *Observed wave conditions at Pecém.*
Left: January (Swell dominated) Right: July (sea dominated)

A number of characteristic wave conditions were simulated with a 2D wave model developed by DHI. The model is based on the parabolic approximation of the elliptic mild slope equations and includes dominant wave transformation phenomena such as refraction, shoaling, reflection, bottom friction and breaking. In these simulations, sea and swell were treated separately

Figs 5 shows simulated wave fields for an offshore wave height $H_{s\ of}$ 1.75 m, a peak period of 7 s and a mean offshore wave direction of 82.5°. These wave conditions occur frequently in the area and contribute significantly to the net annual drift. Simulations for the present situation and the situation after establishment of the marine facilities are shown. East of Ponta do Pecém, the bathymetry is quite regular and the wave field is seen to be more or less uniform along this part of the coast. At the breaking point, the angle between the wave crests and the coastline is large, of the order of 45 degrees. This causes strong longshore currents that are able to transport large amounts of sediment along the coast.

At the western side of the headland, the wave field is rather complex due to the irregular bathymetry. The waves refract around the headland and approach the coast under a large angle. The area immediately W of Ponta do Pecém is sheltered by the headland. In front of the city of Pecém, wave breaking occurs far away from the beach due to the shoal that is located here. However, the shoal in front of the city does not provide much shelter for the incoming waves due to the large angles of incidence. Waves from these directions propagate between the headland and the shoal and reach the coast at Pecém under large angles.

The new harbor has a strong sheltering effect on the waves coming from easterly directions e.g. sea waves. The area of influence covers the entire area between the headland and the city of Pecém.

Fig. 6 shows the wave fields in the vicinity of Ponta do Pecém for swell. The convergence of the wave crests towards the headland is clearly seen. Immediately W of the headland, the coast is sheltered from wave action due to the headland. However, the shadow area is much smaller for swell waves than for sea waves.

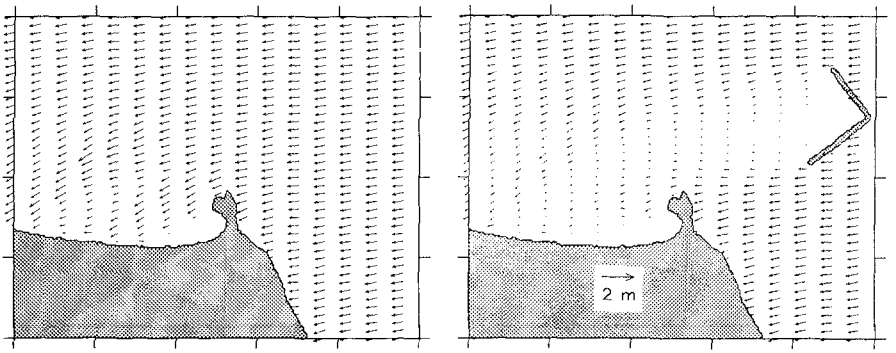

Fig. 5 *Simulated wave field (Sea). Hs=1.75m, Tp=7s, MWD=82.5 °*
Scale 1:70,000 Left: present situation, Right: including new harbor

The propagation of swell towards Pecém is not drastically affected by the harbor. Swell approaches the shore from offshore angles between approximately 20° to 45° N. The area where the sheltering by the harbor is maximal is located approximately 1.5 km E of Ponta do Pecém

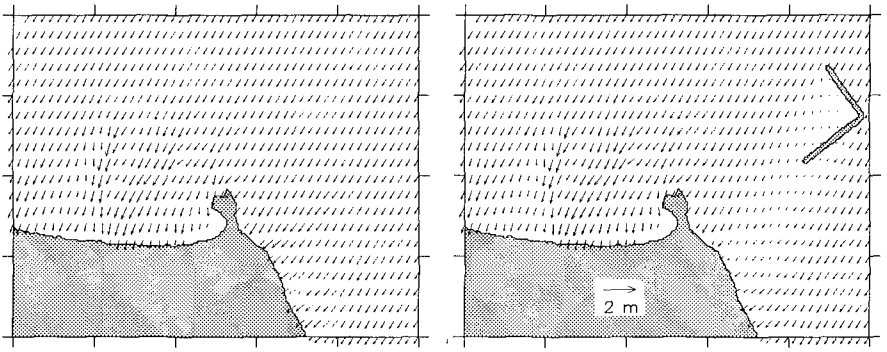

Fig. 6 Simulated wave field (Swell). Hs=0.5m, Tp=14s, MWD=30°
Scale 1:70,000 Left: present situation, Right: including new harbor

Nearshore hydrodynamics

In order to study the 2D wave driven currents, a number of hydrodynamic simulations were carried out with DHI's hydrodynamic model MIKE 21 HD. This is a general modeling system for the simulation of water levels and flows in estuaries, bays and coastal areas. The model solves the unsteady depth integrated flow equations. The driving force in the present simulations originates from the radiation stress field calculated with the wave model as described in the previous section.

The wave-driven current pattern for the present situation and after establishment of the harbor is shown in Fig. 7. The wave conditions correspond to sea (H_s = 1.75 m, T_p = 7s, MWD = 82.5° N).

The littoral currents are considerably stronger at the eastern side of Ponta do Pecém than on the western side. This is due to the more exposed character of the beaches on the eastern side. The littoral current follows the shoreline until it reaches the head of Ponta do Pecém. Close to the headland, the flow is slightly accelerating due to a local convergence of the depth contours. West of the headland, the current becomes detached from the shoreline. The flow velocities are highly reduced in this area. At a distance of

approximately 1 km W of the headland, the current reattaches to the shore and its strength gradually increases towards W. Due to the irregular bathymetry in front of Pecém, complex nearshore current patterns can develop.

The presence of the harbor strongly reduces the littoral current velocities W of Ponta do Pecém. The harbor induces a large-scale eddy at the offshore edge of the headland. The littoral current becomes partly directed into the harbor basin, which may cause additional sedimentation problems inside the harbor.

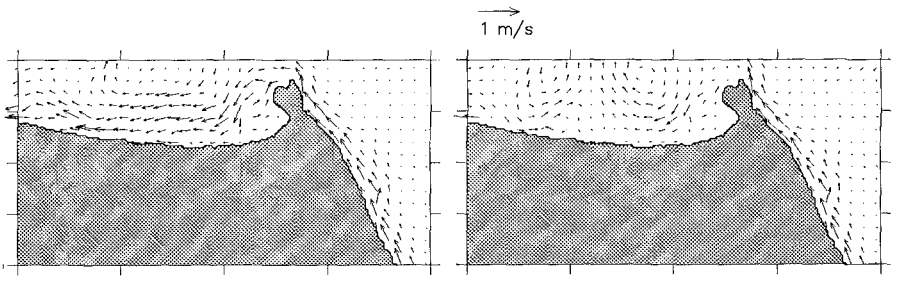

Fig. 7 *Wave driven current fields for the present situation (Sea). Offshore wave conditions: Hs = 1.75, Ts = 7s, MWD = 82.5° N Scale 1:55,000. Left: Present situation, Right: including new harbor*

Simulated wave driven flow fields due to swell are shown in Fig. 8. At both sides the currents are directed away from the headland.

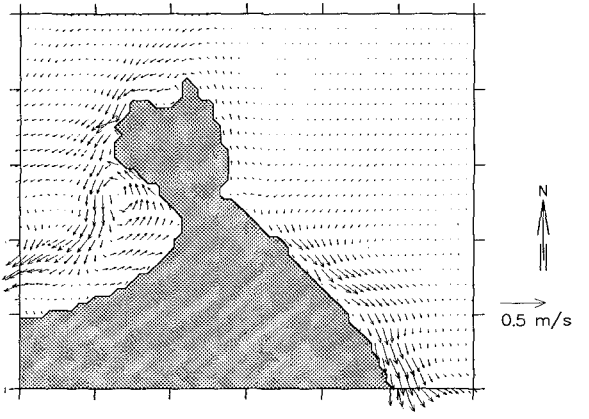

Fig. 8 *Wave driven current around the headland for the present situation (Swell). Scale 1:15,000. Offshore wave conditions: Hs=0.5m, Tp=14s, MWD=30°*

The flow velocities W of Ponta do Pecém are not significantly affected by the presence of the harbor. At the eastern side, the flow is slightly reduced due to the sheltering of the harbor. The maximal differences occur at a distance of approximately 1.5 km E of Ponta do Pecém.

Nearshore sediment transport

The complex sediment transport patterns for the present site were simulated with DHI's 2D sediment transport model MIKE 21 ST (Sand Transport). This model calculates the sediment transport of non-cohesive sediment due the combined action of currents and waves. Model calibration was performed upon available data of the Port of Mucuripe-CE, (see INPH 1986b). For a detailed description of sediment transport mechanisms in currents and waves, the reader is referred to Fredsøe and Deigaard (1992).

The results of the wave and current simulations were used as input for the sediment transport calculations.

During predominant sea relative large transport rates occur E of Ponta do Pecém. The harbor does not affect the littoral transport rates significantly in this area. Along this coastal stretch, at a distance of approximately 1 km E of the headland, the littoral transport is locally directed offshore.

At the western side of the headland, the littoral transport becomes detached from the shoreline. The sediment transport rates are reduced significantly for the new situation due to the decreased wave action and the associated strength of the wave driven current. The magnitude of the sediment transport is reduced considerably by the sheltering effect of the harbor on the nearshore hydrodynamic conditions in this area. With the presence of the harbor, the littoral transport at Ponta do Pecém continues further offshore than for the present situation without harbor and less, if any, sediment is passing Ponta do Pecém.

For swell waves, the littoral sediment transport pattern looks quite different. The coastline orientation in the area of Pecém varies from approximately 355 degrees N in front of the city to approximately 55 degrees N along the coastal stretch E of Ponta do Pecém. Due to this coastline configuration, the littoral current is directed towards E at the eastern side of the headland and towards W at the western side. The resulting littoral drift is therefore always directed away from Ponta do Pecém; towards E at the eastern side and towards W at the western side.

In this way, swell counteracts the sediment accumulations due to sea. East of Ponta do Pecém, swell reduces the net littoral transport rates towards the headland. On the western side of the headland, a part of the accumulated material is transported towards the shore by cross-shore transport mechanisms. Further towards West, swell gives rise to an additional westward drift.

During periods with prevailing swell, the spit developed during periods with predominant sea erodes. If the swell domination lasts for sufficiently long time, the coastline in front of Pecém erodes because the westward littoral drift due to combined sea and swell exceeds the sediment bypass around Ponta do Pecém, which is reduced due to the action of the swell.

Cross-shore sediment transport

In the calculations of littoral sediment transport the wave orbital motion was assumed described by one single wave with a constant height, period and direction. In case of longshore sediment transport this assumption is justified as the longshore transport is dominated by the longshore current and to lesser degree by the wave orbital motion, which is almost perpendicular to the coast in the surf zone.

However, the wave motion and the resulting shear stress are important for the calculation of the cross-shore sediment transport. The net cross-shore transport is determined by factors such as the strength of the undertow, the asymmetry of the wave orbital motion and the mass transport under progressive waves. In the present case the wave conditions are characterized by the simultaneous occurrence of sea and swell from different directions. In order to estimate the onshore sediment transport immediately W of the headland, an existing model for non-cohesive sediment transport was extended to include the effect of simultaneous occurrence of sea and swell. The basis for the model is DHI's sediment transport modeling system LITPACK. This model calculates the bedload and suspended load due to combined wave/current motion. The bedload is calculated from the sediment characteristics and the instantaneous bed shear stress, which was calculated from the solution of the turbulent wave boundary layer (Fredsøe 1984). The suspended load is calculated from the diffusion equation for suspended sediment (Fredsøe et al. 1985). Here the sediment exchange factor is taken equal to the eddy viscosity, which contains contributions of the wave boundary layer, the mean flow and the turbulence due to wave breaking (Deigaard et al 1986). The mean flow is calculated from the force balance across the water column (Deigaard 1993 and Elfrink et al 1996).

For the present application, the wave orbital motion was described by a linear superposition of a short wave component and a long wave component with different directions. Both components were assumed to occur as groups. The respective contributions to the total orbital velocity were calculated from 5^{th} order Stokes' or Cnoidal theory, depending on the local Ursell number. Fig. 9 shows an example of the wave orbital velocity composed of 2 wave groups with mean periods of 6 and 11 seconds. The angle between the short waves and the long waves was 60 degrees.

The orbital velocities were used to calculate the bottom boundary layer under the complex wave field. Fig. 10 shows the shear velocities, U_f, derived from the boundary layer solution

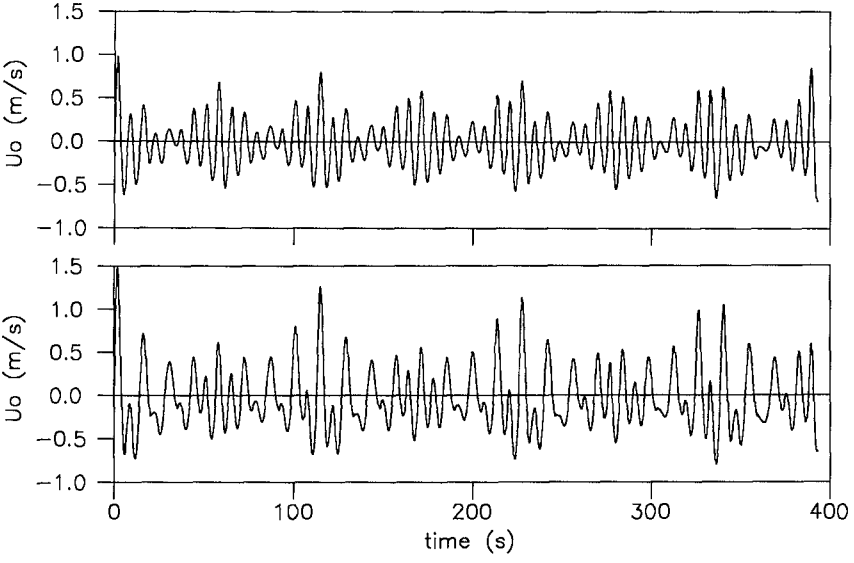

Fig. 9 *Instantaneous bed orbital velocities due to different wave groups. Top: Longshore component, Bottom: Cross-shore component*

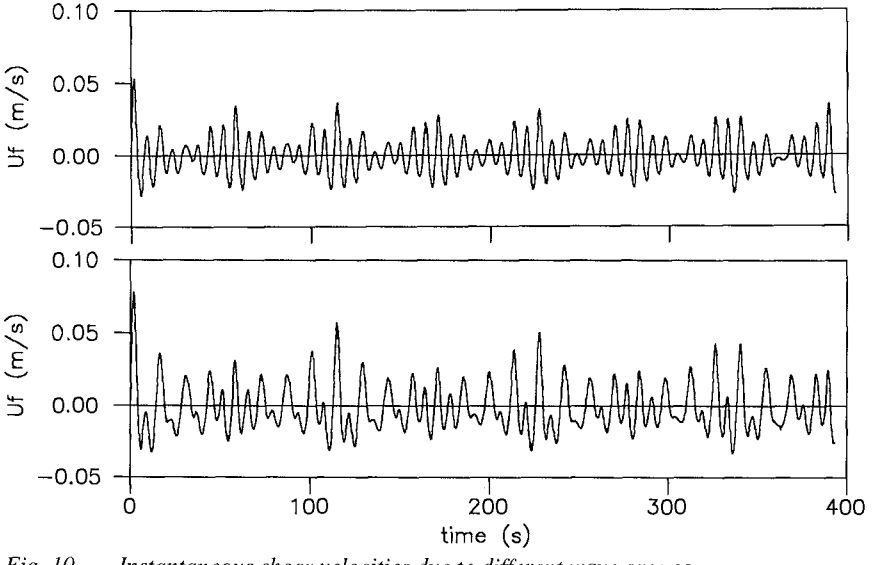

Fig. 10 *Instantaneous shear velocities due to different wave groups. Top: Longshore component, Bottom: Cross-shore component*

The resulting sediment flux, Q_t, in the cross-shore and longshore direction is shown in Fig.11.

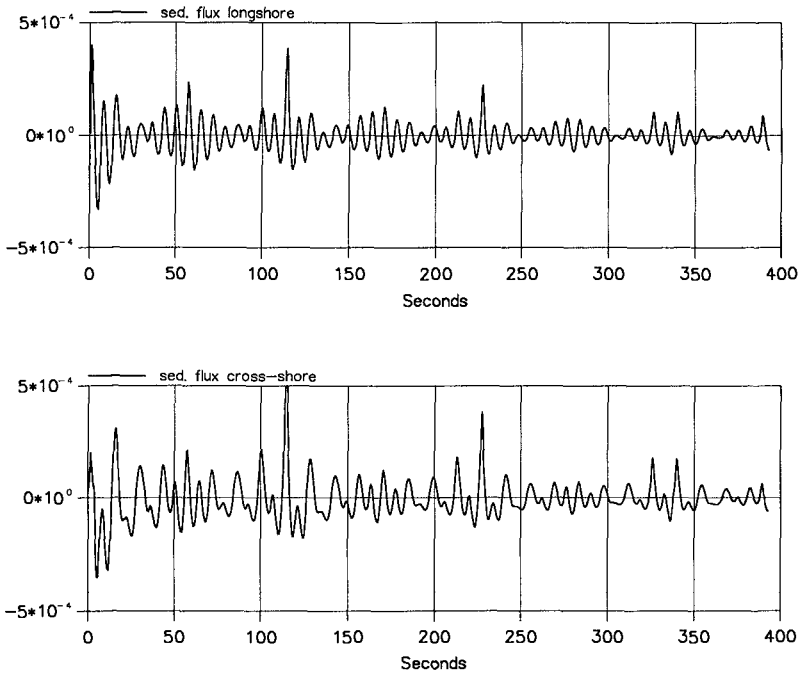

Fig. 11 Instantaneous sediment flux due to different wave groups. Top: Longshore component, Bottom: Cross-shore component

The model was applied to estimate the onshore transport of sediment from the headland to the coastline W of it. It was found that the transport capacity under swell waves was increased due to the presence of short waves and vice versa. Even in cases were the two wave groups were taken perpendicular to each other.

The coastal sediment budget and future coastline evolution

The 2D simulations and the wave statistics were used to calculate the annual sediment balance.

Present situation

Along the beaches E of Ponta do Pecém a net littoral drift of the order of 350,000 m^3/year is transported towards W. The headland causes the littoral current to become detached

from the shoreline. A total volume of approximately 90,000 m^3/year is transported offshore of Ponta do Pecém.

West of Ponta do Pecém, net onshore directed sediment transport occurs due to the reattachment of the littoral current and the net onshore sediment transport in (Non-breaking) swell waves.

West of the headland, the littoral transport is of the same order of magnitude as along the eastern side. The drift due to the sea waves is reduced due to the orientation of the beach and the sheltering of the headland. However, the importance of the drift due to the swell has increased, due to the larger angle between the swell waves and the coastline.

In the area immediately E of the city of Pecém, local gradients in the wave heights exist due to the irregular bathymetry. Here the littoral drift is reduced which gives rise to small accumulations. Further towards W, the littoral drift increases which causes erosion at the western edge of Pecém. This erosion/sedimentation pattern is confirmed by field observations.

Situation after establishment of the harbor
The main effect of the harbor is a strong reduction of the potential sediment transport rates due to sea waves in front of Ponta do Pecém and westwards, which results in increased sediment accumulations in front of and immediately W of the headland. A total sediment volume of the order of 115,000 m^3/year will initially accumulate in this area.

The flow velocities of the detached littoral current are strongly reduced due to the presence of the harbor. However, the transporting capacity of the swell is not affected in the immediate vicinity of the headland. A net onshore transport rate under swell waves of the order of 30,000 m^3/year was calculated. Approximately 85,000 m^3 sand will accumulate in front of Ponta do Pecém by means of a shore-connected spit.

Further West, the net littoral drift rates are reduced due to the sheltering of sea by the harbor. However, the combination of the reduced sediment supply and the reduced transport capacity of the littoral currents gives rise to erosion rates of the same order of magnitude, although slightly smaller, as for the present situation.

Further towards W, the effect of the harbor will vanish, which means that the littoral drift gradually increases from Pecém towards west. This leads to erosion between Pecém and Taiba.

From the calculated erosion/ sedimentation rates the annual coastline movements were estimated. East of Ponta do Pecém, the coastline is fairly stable. The accumulation of sediment due to the gradients in the littoral drift is of the same order of magnitude but slightly smaller than the net loss of sediment due to the wind. This gives rise to a slight coastline erosion of the order of 1 - 2 m/year. Variations occur during the year due to seasonal variations in the wave and wind conditions. The presence of the harbor does not

affect the coastline dynamics in this area. However, in the long run the accumulations in front of the headland will change the coastline orientation in this area. This will cause coastal sedimentation. This coastline progress will start immediately E of the headland and proceed gradually in eastern direction.

After establishment of the harbor a shore-connected spit will start to develop from the headland. The spit will grow both in the offshore- and western direction. A part of the accumulated sediment will be transported by the action of swell. The total accumulation in the offshore region is of the order of 85,000 m^3/year. The presence of the spit itself will have an impact on the wave and current conditions along the beach W of Ponta do Pecém. Wave diffraction around the spit may cause a local divergence of the littoral current and the resulting sediment drift. This may lead to temporary coastline erosion immediately W of the projection of the spit on the coastline. This erosion process will proceed along the coastline as the spit develops. The erosion stops when the spit becomes attached to the coastline.

After establishment of the harbor the coastline erosion rates west of Ponta do Pecém, are of the same order of magnitude as for the present situation. A general coastline retreat of approximately 2 - 3 m/year must be expected due to the decrease of sediment bypass around ponta do Pecém.

Conclusions

A net annual littoral transport of the order of 350,000 m^3/year occurs along the entire coastline. Seasonal variations in the coastline position occur due to dominance of sea or swell during different periods of the year. Net erosion along the entire coast was observed.

Sea and swell have different effects on the net littoral sediment transport. Sea initiates strong littoral currents and relatively high transport rates along the coast E of Ponta do Pecém. Along the western side of the headland, the littoral drift is strongly reduced due to the sheltering provided by Ponta do Pecém and the different orientation of the coastline. The headland acts as a bottleneck for the littoral transport. This is of crucial importance for the stability of the coastline in front of the city. The topography of Ponta do Pecém forces the littoral current to become detached from the shoreline W of the headland. The sudden reduction in potential transport rates causes sediment accumulations around Ponta do Pecém.

The swell causes a sediment transport directed towards E at the eastern side of Ponta do Pecém and towards W at the western side. This transport pattern counteracts the accumulation of sediment around Ponta do Pecém due to sea. Sediment transport towards the shoreline occurs due to the sediment transport mechanisms associated with non-linear wave motion. During periods of predominant swell the sediment supply around the headland is strongly reduced. This causes beach erosion at the western side of Ponta do Pecém during the southern summer.

The main effect of the new harbor on the littoral transport is a general reduction of the potential sediment transport from Ponta do Pecém towards West. The littoral drift along the eastern side of the headland is initially not significantly affected by the harbor. The sediment bypass around Ponta do Pecém becomes heavily reduced. The reduced transport capacities W of Ponta do Pecém cause the development of a permanent shore-connected spit in the lee side of the headland. This accumulation will proceed in both northern (offshore) and western (longshore) directions. A net accumulation of the order of 85,000 m^3/year is estimated.

Further W of the headland the littoral drift will be reduced due the presence of the harbor. However, the gradients in the littoral drift along the shore are more or less the same as for the present situation. West of the city of Pecém, the sheltering effect of the harbor will vanish. This causes a gradual increase of the littoral drift rates between Pecém and Taiba and will give rise to increased coastal erosion in this area.

References

Danish Hydraulic Institute (1997) Coastal impact assessment of new marine facilites at Pecém, NE brazil. DHI report no 97-5144.

Deigaard, R., J. Fredsøe and I.B. Hedegaard (1986) Suspended sediment in the surf zone. Journal of the Waterway, Port, Harbor, Coastal and Ocean Engineering, ASCE, Vol. 112. no 1. pp115 - 128

Deigaard, R. (1993) A note on the three-dimensional shear stress distribution in the surf zone. Coastal Engineering, 20. pp 157 - 171

Elfrink, B., R. Deigaard, I.Brøker, E. A. Hansen and P. Justesen. Modeling of 3D sediment transport in the surf zone. Proc. Int. Conference on Coastal Engineering, Orlando. USA.

Fredsøe. J. (1984) Turbulent bounday layers in wave-current motion. Journal of HydraulicEngineering, ASCE, vol. 110 (HY8), pp 1103 – 1120

Fredsøe, J. and R. Deigaard, (1992) Mechanics of Coastal Sediment Transport. Advanced Series on Ocean Engineering, Vol. 3.World Scientific Singapore,369p

Fredsøe, J., O.H. Andersen and S. Silberg, (1985) Distribution of suspended sediment in large waves. Journal of the Waterway, Port, Harbor, Coastal and Ocean Engineering, ASCE, vol. 3, no. 6 pp. 1041 - 1059

Instituto de Pesquisas Hidroviarias (1996a) Relatório Final das medições de Ondas ao Largo de Mucuripe-CE periodo 19/02/91 à 22/07/95 no 68/96 Fortaleza –130/18.

Instituto de Pesquisas Hidroviarias (1996b) Projeto Pecém-CE Relatório de Medições Ambientais (Correntes, Temperatura, Salinidade e Sólido em Suspensão. No 24/96 Fortaleza

Morphological Modelling using a Modified Multi-layer Approach

Henk J. Steetzel [1], *Hans de Vroeg* [2],
Leo C. van Rijn [2 3] *and Jean-Marie Stam* [4]

Abstract

*One of the topics of the National Dutch research program COAST*2000 focuses on the long-term (50-100 years) and large-scale (1-100 km) morphological problems of the Dutch coast and the implications for coastal management. Examples of such problems are the effects of climate change and sea-level rise on a partly protected coastline, the long-term effects of on-going sand nourishments, the far-field effects of large-scale land reclamation and of the required sand-mining etc. Within this framework a pilot version of a conceptual model (the so-called PONTOS-model) has been developed, basically capable of simulating the morphological evolution of the Dutch coast at the above-mentioned spatial and temporal scales.*
This present paper focuses on the theoretical background of the model. The results of a preliminary application of the model for the closed coastal section of the Dutch coast between Hoek van Holland and Den Helder are also presented.
The actual PONTOS-model is based on the multi-layer concept, in which the cross-shore profile is schematised as a number of mutually coupled layers, defined between fixed profile depths. These layers interact through cross-shore transport. In longshore direction the layers respond to gradients in the longshore transport generated at the profile regions they represent. The main input of the model, to be provided by the user, are the characteristics of the coastal stretch to be studied, including the initial positions of the various layers and offshore hydraulic conditions in terms of wave and tidal climate tables. On the basis of these data the yearly-averaged sediment transport pattern is computed and finally used for the assessment of the coastal evolution.

Introduction

For national decisions regarding coastal management it is important to understand the long-term (50-100 years) effects and large-scale (1-100 km) implications of both natural processes and major coastal engineering projects. Examples of natural processes are the effects of climate change and sea-level rise on the sandy coast partly protected by groins or sea-walls and, in relation to this, the long-term effects of coastline maintenance by on-going sand nourishments. Problems related to major

[1] Alkyon Hydraulic Consultancy & Research, P.O. Box 248, 8300 AE Emmeloord, The Netherlands (Steetzel@Alkyon.nl)
[2] WL Delft Hydraulics, Delft, The Netherlands
[3] Utrecht University, Utrecht, The Netherlands
[4] National Institute for Coastal and Marine management/RIKZ, The Netherlands

coastal engineering projects are the far-field effects of large-scale land reclamation and the effects of the large-scale sand-mining necessary for such projects.
One of the topics of the national research program COAST*2000 focuses on understanding these long-term large-scale morphological effects and on developing tools to quantify them. Within this framework, a model is being developed, capable of simulating the morphological evolution of the Dutch coast at the required spatial and temporal scales.
Morphological characteristics of complicated coastal systems can be described using different modelling approaches. One such an approach is process-based modelling where the physical processes involved are described mathematically, combining a detailed fluid-flow model with a sediment-transport model. By successive iteration the dynamical evolution of an area can be simulated. For the analysis of the predominant processes and circulation patterns, wave, current and sediment transport, process-based models appear to be useful. However, they are less suitable for simulating long time periods, as they require large computation effort and the numerous iterations and accumulation of rounding-off errors may lead to unrealistic results. PonTos uses a different approach, which is more behaviour-oriented [Steetzel et al., 1998]. The physical processes (i.e. cross- and long-shore transport) are parametrized in simple relationships which respond to input conditions of wave and tidal climate and sea-level. The combined effects of the processes result in the morphological evolution of the coastal system. The resolution of simulations is smaller than would be available with a process based model, but the results in terms of the distribution of erosion and sedimentation after, e.g. a 50 year-period, seem more realistic. Moreover, because of its approach, this model is easier accessible more user-friendly than most process-based models. The results of the pilot version of this model (the so-called PONTOS-model) indicate that it is a promising tool to simulate and quantify the morphological implications of the problems just described.

The multi-layer model

The model is based on the multi-layer concept, in which the cross-shore profile is schematised as a number of mutually coupled layers, defined between fixed profile depths, see Figure 1.

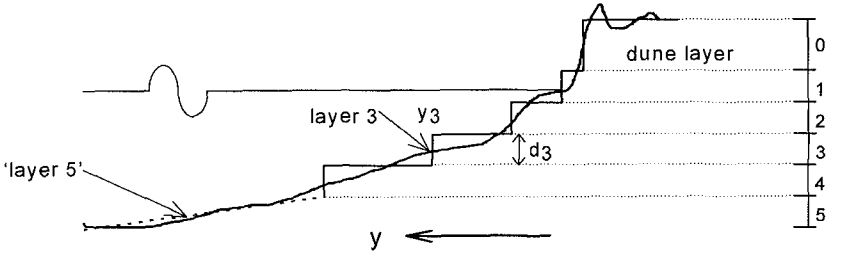

Figure 1: Layer schematization used in the model

These layers interact through cross-shore transport. In longshore direction the layers respond to gradients in the longshore transport generated at the profile regions they represent. The present model uses a rectangular grid, with the x-axis in longshore direction, whereas the y-axis in the seaward direction. The z-axis is directed upward with the zero level at the reference level. As a consequence of the definition of the y-axis, a positive cross-shore transport implies movement of material in seaward/downward direction. In the present model, the cross-shore profile is schematised into five horizontal layers and two additional zones. Each individual layer is denoted with an index j, ranging from j = -1 to j = 5, in which layer j = 0 to 4 refer to physical layers. The first physical layer, with index j = 0, refers to the dune layer. Subsequent layers refer to layers positioned further seaward, as shown in Figure 1. The actual position of a layer has to be assessed from the sediment balance of the cross-shore profile. The characteristic layer position y_j for a layer with thickness d_j between lower level Z_{j+1} and upper level Z_j is the average position computed from:

$$y_j = \frac{1}{d_j} \int_{Z_{j+1}}^{Z_j} y(z)\, dz$$

Depending on the actual shape of the local cross-shore profile, the characteristic layer position is located between the position of the depth contours of the boundaries.

Governing equations

For a specific computational cell with width ΔX_i ($= X_i - X_{i-1}$) the increase of volume $\Delta Vol_{j,i}$, is computed from:

$$\frac{\Delta Vol_{j,i}}{\Delta t} = (Q_{x,j,i-1} - Q_{x,j,i}) - (Q_{y,j,i} - Q_{y,j+1,i}) + \frac{\Delta S_{j,i}}{\Delta t}$$

in which $Q_{x,j,i}$ refers to the (total) longshore transport in layer j at position X_i, $Q_{y,j,i}$ refers to the cross-shore transport at level Z_j in the interval $X_{i-1} \ldots X_i$ and $\Delta S_{j,i}$ corresponds to a source or sink term in cell (j,i).

Using the concept of a layer-approach, the volume in a specific cell or layer is represented by the specific position of the layer in cross-shore direction. A change in a cell's volume, $\Delta Vol_{j,i}$ in layer j and cell with index i yields a cross-shore shift in the characteristic position of layer j, denoted as $\Delta y_{j,i}$ according to:

$$\Delta y_{j,i} = \frac{\Delta Vol_{j,i}}{d_{j,i}\, \Delta X_i}$$

in which $d_{j,i}$ denotes the thickness of layer j in the interval $X_{i-1} \ldots X_i$.

Substitution of this translation yields:

$$\frac{\Delta y_{j,i}}{\Delta t} = \frac{(Q_{x,j,i-1} - Q_{x,j,i})}{d_{j,i}\, \Delta X_i} - \frac{(Q_{y,j,i} - Q_{y,j+1,i})}{d_{j,i}\, \Delta X_i} + \frac{\Delta S_{j,i}}{d_{j,i}\, \Delta X_i\, \Delta t}$$

In this equation Q_y refers to the longshore integrated magnitude, viz. taken into account the width of the cell ΔX_i. Using q_y (expressed in $m^3/m^1/yr$) instead of Q_y (expressed in m^3/yr) yields:

$$\frac{\Delta y_{j,i}}{\Delta t} = \frac{(Q_{x,j,i-1} - Q_{x,j,i})}{d_{j,i}\,\Delta X_i} - \frac{(q_{y,j,i} - q_{y,j+1,i})}{d_{j,i}} + \frac{\Delta S_{j,i}}{d_{j,i}\,\Delta X_i\,\Delta t}$$

The assessment of the longshore transport for each individual layer and the cross-shore transport rate at each intersection is discussed in the next.

New formulations

Earlier versions of this model [Steetzel, 1995] had the drawback that the interaction between the layers and their response in the longshore direction was determined by a series of pre-defined constants, which had to be determined by the users based on process-based models or on empirical data, see e.g. [Bakker et al., 1988]. This puts considerable restraints on the practical use of the concept. In the present set-up of the model these pre-defined constants have been replaced by formulations to compute cross-shore and longshore sediment transports directly within the model on the basis of external conditions such as wave climate, tidal conditions, bathymetry and sediment characteristics. In this way a very user-friendly behaviour-oriented model has been formulated. As such, the multi-layer concept is now more suitable for the evaluation of changes in a coastal system [Steetzel, 1997c, 1998].

Climate schematization

The model uses yearly mean wave climates at the seaward boundary as input. Specifically, wave conditions must be described on the Z_5-depth contour (e.g. at NAP-20m for the Dutch coast). This climate schematization forms the main driving force of the model.

Wave climates

A local wave climate is schematised as a set of individual conditions. These individual conditions are described by a number of parameters, namely:

- the significant wave height H_s (at the deep water boundary);
- the accompanying peak wave period T_p;
- the angle of wave approach θ_o;
- the storm-related set-up h_s;
- the fraction of occurrence of the combination of previous four parameters.

The wave climate consists of a distinct number of individual conditions for which the total fraction of occurrence equals 1. The longshore variation of the yearly wave climate is taken into account by relating a specific wave climate to a specific longshore position.

Using the yearly-mean wave climates as starting-point, the effect of long-term changes in the governing parameters such as wave heights and wave direction, can be taken into account by a correction of some of the parameters.

Tidal climates

The astronomical conditions are schematised using the mean features of the astronomical climate, viz. the vertical and horizontal tide. A local tidal climate is schematised as a limited number of individual tidal conditions, each having a specific percentage of occurrence. These individual conditions are described by:

- the astronomical water level elevation h_a;
- the accompanying longshore tidal velocity v_a;
- the reference depth d_a for which v_a is specified;
- the fraction of occurrence of the combination of former three parameters.

The tidal climate consists of a number individual conditions for which the total fraction of occurrence equals 1.

The local vertical tide is described by an overall fluctuation of the water level, denoted as $h_a(t)$ with respect of the reference level. During a year, a large range of individual h_a-values will be present. For schematization purposes however, only a limited number of them will be used. The distribution of the tidal velocities over the profile is computed with the Chézy-equation.

The longshore variation of these time-averaged climates is taken into account by relating a specific tidal climate (viz. a tidal climate table with a specific index as discussed later) to a specific longshore position. Using the yearly-mean tidal climates as starting-point, the effect of long-term changes in the governing parameters such as:

- mean water level,
- tidal range and
- tidal velocities,

are taken into account by a specific corrections of the parameters. E.g. a gradual sea level rise is taken into account by adding the absolute change in the mean water level, denoted as $\Delta h_0(t)$, to the astronomical elevation h_a.

Transport formulations

Processes that have been schematised up to an acceptable level for the present version of the PONTOS-model are:

- the rate and distribution of the wave-induced cross-shore sediment transport;
- the rate and distribution of the wave-induced longshore sediment transport;
- the rate and distribution of the tide-induced longshore sediment transport;
- the effect of groynes on the longshore transport rate,

although some of these formulations will need some further improvement during a later stage of the model development.

The following processes have been conceptually developed and will be implemented in a later stage of the model development:

- refraction and shoaling of waves;
- diffraction around structures;
- flow contraction around structures like cross-shore dams.

In the following the main characteristics of both the cross-shore interaction and the longshore transport assessment is discussed briefly.

Cross-shore transport

The cross-shore interaction between the layers is based on the principle of a wave-based equilibrium profile. Deviations from this equilibrium slope result in a cross-shore exchange of sand between the layers. The rate of adjustment depends, amongst others, on relative water depth and local sediment characteristics. For both the equilibrium slope and the transport rates, formulations have been derived, partly based on empirical formulae and partly based on the results of a series of computations carried out with a process-based model. The process-based computations involved the main processes determining the cross-shore transport i.e. wave asymmetry, gravity and the undertow compensating for the mass-flux above the wave troughs. Relevant input parameters are wave climate and sediment characteristics [Steetzel, 1997a/b].
In the PONTOS-model, the wave-induced cross-shore transport $q_{y,w}$, for a specific hydraulic condition (water level and waves) at a certain depth is computed from:

$$q_{y,w} = q_o \, F_b \left(\frac{s}{s_e} - 1 \right) \left| \frac{s}{s_e} - 1 \right|^{\beta - 1}$$

in which the s denotes the actual local bed slope and s_e refers to the local equilibrium slope and β equals 2.0. Due to the terms on the right-hand side, a relatively too steep slope, viz. $s > s_e$, yield offshore directed, viz. positive transport.
The F_b-function describes the relative transport rate as a function of the d / H_s-ratio according to:

$$F_b = \exp\left[\frac{-d}{\alpha \, H_s} \right]$$

in which α equals 1.5. The coefficient q_o was used for calibration.
In the following the equation for the term s / s_e will be derived.
In the model, the equilibrium slope s_e is expressed in terms of the offshore hydraulic conditions and the characteristics of the bed material.
For a concave cross-shore profile as a starting point, this function is schematised as:

$$s_e(d) = s_o \, F_s$$

in which s_o refers to the bottom slope at the water level and $F_s(d)$ describes the vertical variation assessed from:

$$F_s(d) = \left(1 + d / \alpha_s H_s \right)^{-\gamma}$$

The slope in the model at layer boundary Z_j denoted as s_j is assessed using the mutual distances between the two layers, according to:

$$s_j = \frac{Y_j - Y_{j-1}}{\left(d_{j-1} + d_j \right) / 2}$$

If for the equilibrium profile this mutual distance is denoted as W_j, the characteristic equilibrium slope $s_{e,j}$ can be assessed from:

$$s_{e,j} = \frac{2\,W_j}{\left(d_{j-1} + d_j\right)}$$

Consequently, the relative slope in the transport formulation is computed from:

$$\frac{s_j}{s_{e,j}} = \frac{Y_j - Y_{j-1}}{W_j}$$

yielding the source term for the assessment of the cross-shore transport rate $q_{y,j}$ as discussed before.

Longshore transport

Formulations for both the wave-induced and the tide-induced longshore transport are implemented in the model. These formulations are also based on series of computations carried out with a process-based model. Relevant input parameters are wave climate, horizontal and vertical tide and sediment characteristics.

The wave-induced longshore transport, denoted as $q_{x,w}$ (expressed in $m^3/m^1/yr$) is generated by oblique incident waves which generate an longshore current in the breaker zone mainly. The wave-induced transport rate mainly depends on the incoming wave energy and the direction of wave propagation relative to the coastline. For the assessment of the wave direction the offshore direction is used in the present set-up of the model. An approach to account for the effects of wave refraction will be taken into account in the next version of the model.

The total, viz. cross-shore integrated wave-induced longshore transport $Q_{x,w}$ for a specific wave condition and grid cell, is computed from:

$$Q_{x,w,j,i} = F_z\, c_{w,0} \left(H_s^{2.8} / D_{50}\right) (\phi_c - \phi_w) \exp\left(-c_2 (\phi_c - \phi_w)^2\right)$$

in which ϕ_c denotes the orientation of a specific layer, ϕ_w the direction of the incoming waves and c_2 a constant. The coefficient $c_{w,0}$ is used for calibration.

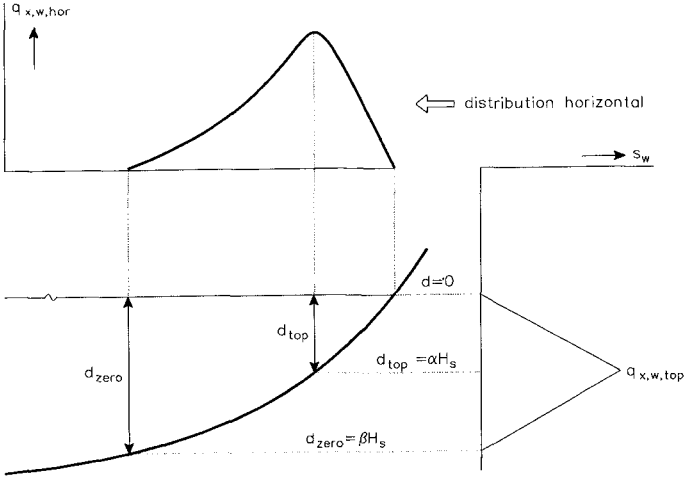

Figure 2: Shematization of wave-induced longshore transport

The above equation accounts for the total wave-induced long-shore sediment transport, which then has to be distributed over the different layers. In the present version of the model, this is schematised as a triangle, as illustrated in Figure 2. The fraction of the total transport present in a specific layer is defined by the factor F_z, with $0 \leq F_z \leq 1$. This factor is derived from the triangle schematization, depending on the level of the upper and lower boundary of the layer relative to the water level.

The distribution of this transport over the various layers is schematised as a triangle in the present version of the model, as illustrated in Figure 2 .
Depending on the level of the upper and lower boundary of the layer relative to the water level, the magnitude of the fraction F_z can be assessed.

The tide-induced transport, denoted as $q_{x,t}$, is determined by the tidal currents, and is furthermore affected by the water depth, the sediment characteristics, and the presence of waves (stirring up the sediment).
In the PONTOS-model, the tide-induced longshore transport $q_{x,t}$ for a specific hydraulic condition (water level, wave and tidal current) is computed from:

$$q_{x,t,j,i} = c_{t,0} \left(D_{50}\right)^{-2.2} \left(v_a\right)^4 \left[1 + 2\frac{H_s^{1.5} T_p}{d\, v_a^2}\right] \left(\frac{\Delta y}{\Delta z}\right)$$

in which the term in between squared brackets accounts for the effect of additional stirring due to the presence of waves and the coefficient $c_{t,0}$ is used for calibration..
The $\Delta y / \Delta z$ -term on the right-hand side is needed to transform the transport rate per m^1 in cross-shore direction to a rate per m^1 in vertical direction needed for the layer-concept. To assess the transport in a specific layer, the computed rate has to be multiplied by the height of the layer (to be derived from the width in cross-shore direction).

A simple formulation for wave diffraction has been defined to account for the modified wave field around structures. In a later stage it is envisaged to also defined and include the effect of flow contraction around structures [Steetzel and de Vroeg, 1997].

Conceptual validation

The present model has been conceptually validated for a large number of theoretic cases, specifically to check the mathematical implementation of the developed formulations. In addition, the following cases have been studied in more detail:

- the evolution of a cross-shore profile for individual waves and wave climates;
- the impact of changing tidal conditions (sea-level rise);
- the behaviour of a closed coastal section for perpendicular, oblique and spatially varying wave conditions;
- the effect of a single groyne;
- the effect of nourishments.

In Figure 3 as an illustration, the cross-shore evolution is given for an initially steep cross-shore profile using one single wave condition as a forcing agent.

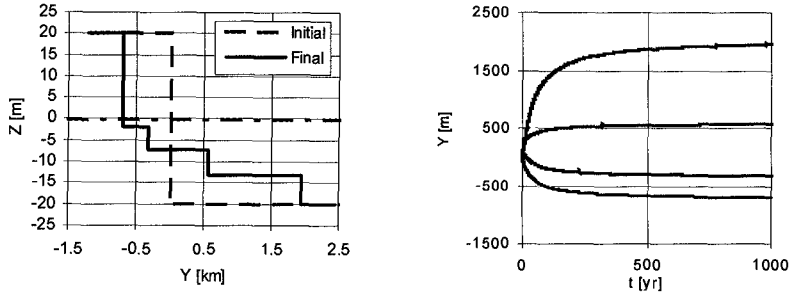

Figure 3: Cross-shore profile development

As can be seen from the right-hand panel, the final equilibrium profile is reached asymptotically in time. In addition to this relatively simple example the effects of wave climates, additional tidal climates, large-scale nourishments and sand mining, climate change and sea level rise have been studied in more detail.

Application of the pilot-version

The PONTOS-model is designed in such a way that it is generally applicable. A specific application has been carried out for a part of the Dutch coast. This application focuses on the uninterrupted coast, excluding therefore the delta coast in the south and the tidal inlets in the north of the Dutch coast. The goal of this application was to show the ability of the model to simulate the large-scale transport patterns along the Holland coast, taking into account the non-uniform wave and tidal climate [Steetzel et al., 1998].

Set-up

For the study of the Dutch coast using a multi-layer model, the overall contour of the whole Dutch coastline was schematised using a series of straight and curved lines.
The position and orientation of the coastline contours have been transferred to this new co-ordinate system, using this reference line and resulting in a stretched coastline.
For the present application, the central Dutch coast (i.e. the Holland coast) was modelled in more detail, with the southern boundary at X_m = 98 km and the northern boundary at X_m = 208 km, resulting in a stretch of 110 km.
The layer positions were derived on the basis of the JARKUS data-set (dataset with results of yearly nearshore surveys with fixed rays). For this first model set-up the layer positions were determined for a number of specific JARKUS profiles (year 1990) in order to implement the main bathymetrical features of the Dutch coast in the model (See Figure 4).

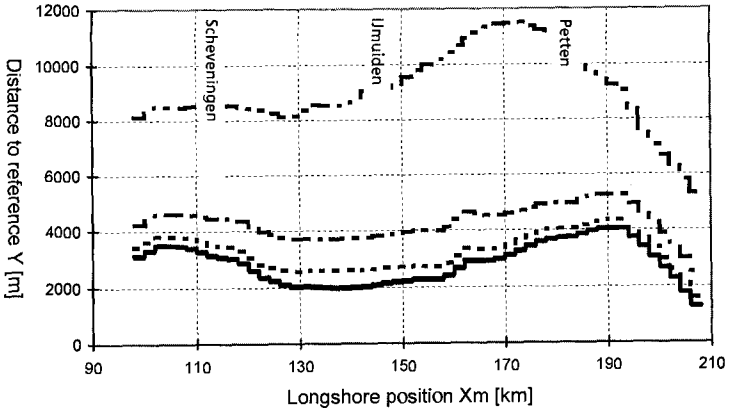

Figure 4: Overview of layer positions for the Holland coast.

The long-term wavc data from the stations Light Vessel Goeree, Noordwijk and Eierland werc used to schematise the along-coast varying wave climate.
The tidal climate along the coast was characterised by a "morphological tide". This is a tide which is considered to be representative for the neap-spring tidal cycle. In order to account for the non-linear relationship between the sediment transport and the flow velocities the tidal range of the morphological tide is somewhat larger than the mean tidal range. For this first application of the PONTOS-model for the Dutch coast, the basic computations were carried out with one representative tide for the entire central coast, as derived on a depth of NAP-8m near Noordwijk.

Calibration and verification

The simplified representation of the coastal structures does not allow for a detailed verification of the sediment balance and coastline development in the region next to these structures. For this reason both long groynes and harbour breakwaters have not yet been included in the verification of the model for the Dutch coast.

Verification and calibration of the model has been carried out in 4 steps:
- step 1 : Verification of the wave-induced longshore transports
- step 2 : Verification of the tide-induced longshore transports
- step 3 : Verification of the cross-shore transports
- step 4 : Verification of the sediment balance

Results

The basic runs for the longshore transports show promising results. Without any fine-tuning or calibration, the results show a fair similarity with the more detailed computations based on computations with a process-based model as presented by van Rijn (1995, 1997), see Figure 5. The transports in the upper part of the profile are

based on the wave-induced transports only. If the tide is included in the upper part of the profile, the net northward transports are somewhat larger.
If the effect of wave refraction between the seaward boundary and the breaker zone is included in the model, the resulting transports can be expected to change somewhat.

In the regions with the relatively gentle profile in the central section of the model area, the computed cross-shore transports are rather high. This can be expected on the basis of the cross-shore concept which is based on an equilibrium slope. The relatively small variations in the wave-climate along the coast do not justify the relatively large variations in the profile slope. It is expected that some calibration of the equilibrium

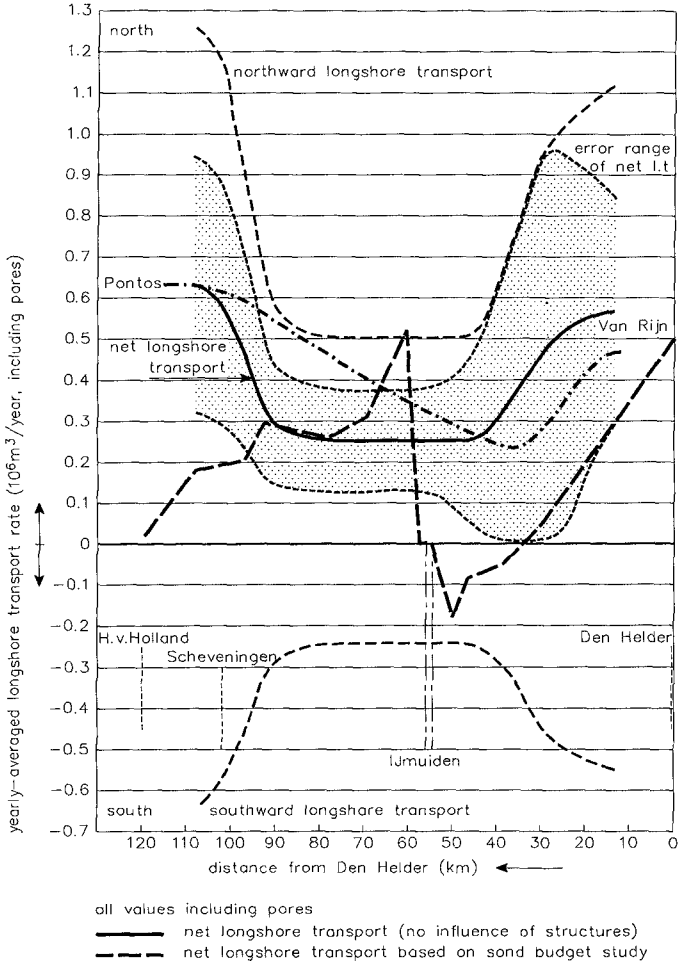

Figure 5: Comparison of computed wave-induced longshore transport [Van Rijn, 1995,1997].

slopes in some regions along the coast will be necessary for a fine-tuning of the model. Variations of the sediment size should be taken into account in a detailed verification.

The response of the model is as can be expected on the basis of the modelled processes. Considerable improvement is possible if the effect of structures is modelled in more detail. The results presented in Figure 6 give the impression that in that case fine-tuning of the model is very well possible.

Conclusions regarding the application

The first application of the pilot-version of the PONTOS-model for the central Dutch coast yields promising results. On the basis of simple schematization procedures for the wave- and tidal climate the direction and magnitude of the net yearly transports show a fair agreement with the results of the more in-depth study of van Rijn (1995, 1997).
For this first application of the model, attention has been focused mainly on the sediment transports. Detailed calibration of the model on the basis of the sediment balance was not yet possible, since some important effects were not yet included in the model. These are:

- the effect of wave diffraction around large structures;
- the effect of flow contraction around large structures;
- the effect of wave refraction;
- the interaction between tide- and wave-induced currents in the surf zone.

The above processes do partly affect the magnitude of the sediment transports and they all affect the sediment balances on a scale of kilometres to tens of kilometres. Implementation of the above mentioned effects is therefore necessary in order to be able to fine-tune the model on the basis of the detailed balances.

General conclusions

From the trial applications performed with the pilot-version of the model it was concluded that:

- the rather simple and straight-forward formulations of both the wave-induced as tide-driven longshore transport proved to be able to 'simulate' to a large extent the results of more complicated models;
- the way the cross-shore transport is taken into account in the model and specifically the explicit formulation of an equilibrium profile proved to have an advantage compared to standard approaches (especially for applications in which the interaction between cross-shore and longshore transport is complicated);
- the method of representing spatial and temporal climates seems to be an effective way to characterise the main driving forces of the model;
- the first application of the model for the Dutch coast yielded promising results;

on the basis of a simple schematization procedure for the wave- and tidal climate, both the direction and magnitude of net yearly transports showed a fair agreement with the results of a more in-depth study [Van Rijn, 1995];
- the behaviour-oriented multi-layer model provides a conceptual tool which seems to be able to 'model' to a large extent the evolution of a coastal system.

With respect to the conceptual approach it was concluded that:
- since both the longshore and the cross-shore transport processes are linked to the offshore hydraulic conditions, the effect of changing conditions (e.g. sea level rise) will be taken directly into account in the model and no other assumptions (e.g. Bruun-rule) have to be made;
- the use of more layers (compared to a single line-model) has the advantage that processes such as the bypass of sediment around the seaward tip of a groyne can be taken into account in a more correct way. However, the impact of structures for a case with more layers becomes far more complicated; in order to model this correctly, additional processes have to be accounted for);
- in a simple way both the effects of 'soft' and 'hard' management strategies can be taken into account, is an important advantage of the model as most of the natural coastal systems are influenced by human intervention; This makes it a useful tool for coastal management decisions;
- the auto-nourishment option (used to maintain at least a specific minimum shore line position by computational nourishments) proved to be a valuable tool to estimate the relative effect of structures and other human interference on the nourishment needs.

Future work

In order to update the present pilot-version of the PONTOS-model to a version that can be applied for practical cases, the following extensions are foreseen:
- to improve the input and assessment of the hydraulic conditions, the link between cross-shore profiles and layer schematization as well as the model output;
- to incorporate the processes which have been conceptually developed until now in an update of the mathematical model, yielding a version capable of simulating coastal evolution at a higher level of reliability;
- to improve the formulations for the interaction between tide- and wave-induced currents in the surf zone;
- to extend the model in seaward direction by adding one layer as a characterisation of the behaviour of the shelf, this in order to incorporate the effect of withdrawal of large quantities of sediment for land reclamation purposes;
- to perform a more integrated validation of the model concept.

Acknowledgements

The research described in this paper was carried out by a joint venture of Alkyon Hydraulic Consultancy & Research and WL Delft Hydraulics in the framework of the COAST*2000-research program of the Dutch Ministry of Transport, Public Works and Water Management, Directorate General of Public Works and Water Management (Rijkswaterstaat), National Institute for Coastal and Marine Management/RIKZ, under contract no. RKZ-370. The concept of the model was initially based on research on behalf of the Centre for Civil Engineering Research, Codes and Specifications (CUR) in the Netherlands.
It was co-sponsored by Alkyon Hydraulic Consultancy & Research and is partly based on work carried out in both the PACE- and SAFE-project in the framework of the EU-sponsored Marine Science and Technology Programme (MAST-III) under contract no. MAS3-CT95-0002 and MAS3-CT95-0057 respectively.

References

Bakker, W. Th., C. van de Kerk and J. H. de Vroeg, 1988, *Determination of coastal constants in mathematical line models*, Second European workshop on coastal zones, Loutraki, Greece.
Graaff, J. van de , H.J. Steetzel, A. Bliek and J.H. de Vroeg, 1998. *Shore parallel breakwaters and nourishment schemes,* Proceedings 26th International Conference on Coastal Engineering, Copenhagen, Denmark.
Rijn, L.C. van, 1995. *Yearly-averaged sand transport at the -20m and -8m NAP depth contours of the JARKUS profiles 12, 40, 76 and 103,* Delft Hydraulics, Report H1887.
Rijn, L.C. van, 1997. *Sediment transport and budget of the central coastal zone of Holland,* Coastal Engineering No. 32, pp.61-90.
Steetzel, H.J., 1995 *Prediction of development coastline and outer deltas Wadden coast for the period 1990-2040,* Delft Hydraulics, report H1887 (in Dutch).
Steetzel, H.J., 1997a. *Behaviour-oriented cross-shore transport modelling*, Abstract Overall Workshop PACE-project, Barcelona, Spain.
Steetzel, H.J., 1997b. *Parametric modelling of short-term profile development*, Abstract Overall Workshop SAFE-project, Thessaloniki, Greece.
Steetzel, H.J. ,1997c. *Using a multi-layer model for the assessment of nourishment schemes*, Abstract overall Workshop SAFE-project, Thessaloniki, Greece.
Steetzel, H.J., 1998, *Using a Modified Multi-layer model for the assessment of large-scale coastal evolution.* Abstract second overall workshop PACE-project, London, The United Kingdom.
Steetzel, H.J. and J.H. de Vroeg, 1997. *Beach nourishments & Rock structures - Behaviour-oriented modelling of the combination of nourishments and rigid shore parallel structures*, Centre for Civil Engineering Research, Codes and Specifications, The Netherlands.
Steetzel, H.J., J.H. de Vroeg and L.C. van Rijn, 1998. *Pilot-version of the PONTOS-model - Definition and preliminary elaboration of a behaviour-oriented model for the assessment of the large-scale development of the Dutch coast.* Joint venture Alkyon Hydraulic Consultancy & Research - Delft Hydraulics, Report A066/H3159.

Parameterizing Beach Erosion/Accretion Conditions

John P. Ahrens[1], affiliate member and Edward B. Hands[2]

Abstract

A simple method to parameterize beach erosion and accretion processes is presented. The parameterization is accomplished by combining important findings from two studies on the initiation of sediment movement, with near-bottom velocities estimated from nonlinear wave theory. This synthesis allows the development of a simple schematization or model based on only two variables that provides considerable insight on cross-shore sediment movement. Once calibrated, the model shows surprising skill (0.94) in predicting erosional or accretionary profile changes on sand beaches and is general enough to predict observed onshore movement of gravel during storms. If linear wave theory is used, the ability to discriminate between erosional and accretionary events declines.

Introduction and Background

Analysis by Ahrens and Hands (1998) showed clearly that shoreline erosion or accretion could be predicted quite well using the ratio of two velocities. Symbolically, we have:

$$U = u_{-d\,max}/u_{crit} \tag{1}$$

where $u_{-d\,max}$ is the maximum near-bottom orbital velocity of the wave and u_{crit} is the critical velocity required to initiate sediment movement under the wave. Two versions of U were developed, denoted U_c and U_t, for the maximum near-bottom velocity under the crest and trough respectively. Near-bottom maximum velocities under waves were calculated using Dean's (1974) Stream Function Wave Theory (SFWT). Critical velocities for the initiation of sediment movement are calculated as follows:

$$u_{crit} = \sqrt{8\Delta g d_{50}}\ ,\ for\ d_{50} = \leq 2.0\,mm \tag{2}$$

---

[1] Coastal Consultant, 6702 Springfield Drive, Mason Neck, Virginia 22079, USA
[2] Research Physical Scientist, USAE Waterways Experiment Station, CHL, 3909 Halls Ferry Road, Vicksburg, Mississippi 39180, USA

$$u_{crit} = [0.46\Delta g T^{1/4}(\pi d_{50})^{3/4}]^{4/7}, \text{ for } d_{50} > 2.0 \text{ mm} \quad (3)$$

where g is the acceleration of gravity, d_{50} is the median sediment diameter, T is the wave period, and $\Delta = (\rho_s - \rho)/\rho$, where ρ_s is the density of the sediment and ρ is the density of water. Eqs. 2 and 3 are based on research by Hallermeier (1980) and Komar and Miller (1974), respectively.

Although not developed in Ahrens and Hands (1998), their analysis indicated that it was possible to make good approximations of U using only two variables. This was accomplished by generating an extensive synthetic data set using SFWT and Eqs. 2 and 3 above. Regression analysis and dimensional analysis were used to obtain the following equations:

$$U_c = 0.132 N_s^{0.466}(d/L_o)^{-0.0506}exp[-3.523(d/L_o)] \quad (4)$$

$R^2 = 0.970$, N =392,
max. % error = 36.1%,
rms % error = 22.2%,

and for the trough:

$$U_t = -0.519 N_s^{0.447}(d/L_o)^{0.569}exp[-5.049(d/L_o)] \quad (5)$$

$R^2 = 0.993$, N = 392,
max. % error = 29.4%,
rms % error = 16.3%,

where N_s is the stability number commonly used to measure the stability of rubble structures, d is the water depth and L_o is the deep-water wave length. The negative sign in Eq. 5 is used to indicate an offshore directed velocity.

Hudson, et al. (1979) shows how the stability number evolves from dynamic and dimensional considerations from a combination of a Froude Number and a density ratio. The combination accounts for the most important forces on an armor unit, i.e., form drag and submersed weight. An investigation of rubble-mound stability might involve stability numbers in the range of 1.0 to 3.0, but for this study the range was about 1 to 60,000. For investigating sediment movement under waves, it is more appropriate to refer to N_s as a mobility number. The mobility number is defined:

$$N_s \equiv H/(\Delta d_{50}). \quad (6)$$

Madsen (1998) notes the similarity between the mobility number for shallow water wave conditions and the Shields parameter, i.e.,

$$N_s \equiv H/\Delta d_{50} = gH/g\Delta d_{50} \propto u^2_{-d\max}/\Delta g d_{50}$$

The Shields parameter is the ratio of the drag forces that initiates sediment movement and the resisting force of the submerged weight.

The ranges of variables in the synthetic data set were:

$0.002 \leq d/L_o \leq 0.2$

$H_b/4 \leq H \leq H_b$

$0.1 \leq d_{50} \leq 100$ mm, $\rho_s = 2.65$ gr/cm^3

$\rho = 1.000$ gr/cm^3 (fresh water) and $\rho = 1.025$ gr/cm^3 (sea water).

Eqs. 4 and 5 have captured, in a simple formulation, some of the essential information about sediment movement under waves from three important studies, Dean (1974), Komar and Miller (1974) and Hallermeier (1980). The equations are a function of just two dimensionless variables which in turn are a function of six dimensional variables. None of the dimensional variables appears in both dimensionless variables, i.e. the dimensionless variables are independent and unusually effective in describing erosional and accretionary processes. The profile adjustment variables used here are the height and period of the wave, size and density of the sediment, and depth and density of the water. These variables seem like the minimum set required to predict profile response to waves and at the same time in many situations they may well be all the information available. This discussion is quite simplified because it assumes that sediment movement responds only to the near-bottom velocity produced by wave motion. Obviously, many other variables could be important at the selected site of application, such as the slope of the bed, the presence of other currents, and the bedform.

Findings

a. The Big Picture

Fig. 1 provides perspective on the implications of Eqs. 4 and 5. Fig. 1 shows U_c and U_t for three values of relative depth as a function of mobility number. The following features of Fig. 1 are noted:

1.) U_c and U_t are small for small mobility numbers and large for large mobility numbers, indicating increasing sediment movement under waves with increasing mobility numbers.

2.) U_c and U_t are quite asymmetrical about $U = 0$ for $d/L_o = 0.02$ and 0.002, suggesting the accretional properties of long waves, i.e. because for a given mobility number the absolute value of U_c is much greater than U_t.

3.) U_c and U_t are almost symmetrical about $U = 0$ for deeper water, e.g., $d/L_o \geq 0.2$, suggesting the erosional characteristics of short-period waves because the absolute values of U_c and U_t are about the same, but the offshore flow under the trough lasts longer than the landward directed flow under the crest.

4.) Because sediment characteristics are contained only in the mobility number, the figure shows how wave conditions that might be erosive for fine-grained sediment could be accretive for large sediment: e.g. sediment with a high mobility

could move shoreward under the crest and offshore under the trough, whereas sediment with a lower mobility number could be below the threshold for offshore movement and be constrained to move shoreward under the crest.

All of .the characteristics noted above are consistent with current understanding of sediment movement under waves.

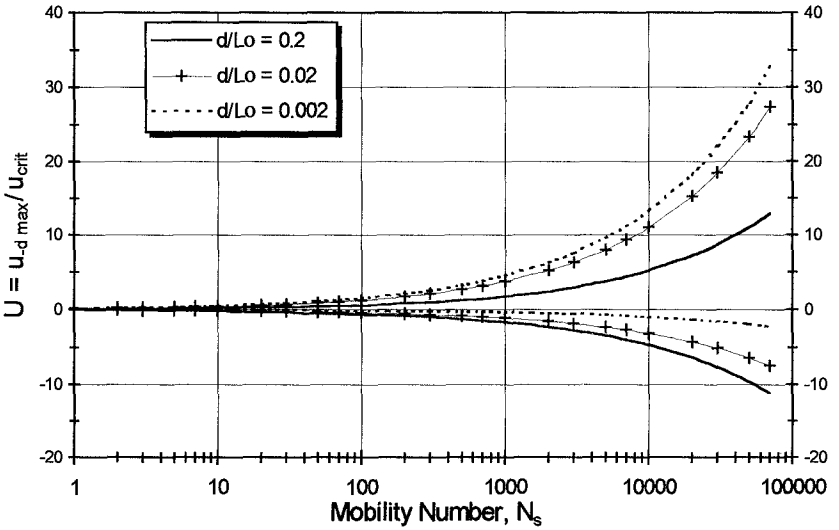

Fig. 1 U_c and U_t as functions of mobility number, for three values of relative depth, from Eqs. 4 and 5.

b. Depth of Breaking Calculations

In order to test the ability of Eqs. 4 and 5 to predict erosional or accretional events on beaches, it is necessary to select a depth of application. The following procedure is used to select this depth:
The maximum or breaking wave height, H_b, consistent with SFWT can be estimated by:

$$H_b/d \approx 0.171(L_o/d)\{\tanh[0.73(2\pi d/L_o)]\} \quad (7)$$

$R^2 = 0.9997$, N = 10
max. % error = 1.16%
rms % error = 0.72%
over the range, $0.002 \leq d/L_o \leq 2.0$

Eq. 7 was developed using regression analysis. To estimate H_b from deep water conditions the breaker height index formula of Kaminski and Kraus (1993), is used:

$$H_b/H_o = 0.46(H_o/L_o)^{-0.28} . \quad (8)$$

Combining Eqs. 7 and 8 gives a relative depth of breaking as:

$$d_b/L_o = 0.109\ln[(1+x)/(1-x)] , \quad (9)$$

where $x = 2.69(H_o/L_o)^{0.72}$.

Fig. 2 shows a plot of Eq. 9 with the relative depth at breaking as a function of deep-water wave steepness. The figure indicates that almost any deep-water steepness will yield a relative depth at breaking within the range required for Eqs. 4 and 5, i.e. $0.002 \le d/L_o \le 0.2$. For convenience, the relative depth at breaking calculated using Eq. 9 will be referred to as the reference depth.

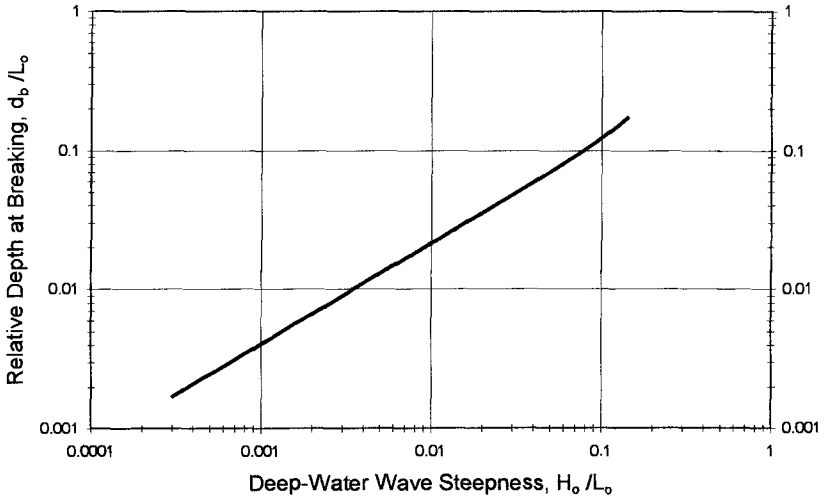

Fig. 2 Relative depth at breaking as a function of deep-water wave steepness

c. Field Beach Profiles

Kraus, et al. (1991) used a field data set to develop criteria to discriminate between erosional and accretionary type beach profiles; these data are tabulated in Kraus and Mason (1991). Data are from beaches all over the world, collected by many researchers, and include observations of 99 distinct wave conditions. Deep-water significant wave heights were in the range $0.08 \le H_o \le 7.90$ m, wave periods were in the range $2.0 \le T \le 15.3$ sec, and sediment sizes were in the range $0.17 \le d_{50} \le 3.5$ mm for

these observations. Wave periods are associated with either the deep-water significant wave height or deep-water spectral peak. For the field data set, the deep-water significant wave height is used in Eqs. 8 and 9; this approach is used to adapt equations developed for monochromatic waves to the irregular wave conditions of nature. The procedure yields relative depths (reference depth) near the seaward limit of the surf zone. Erosional profiles were defined as having no berm and at least one pronounced bar; accretionary profiles were defined as having a prominent berm and no bar formations.

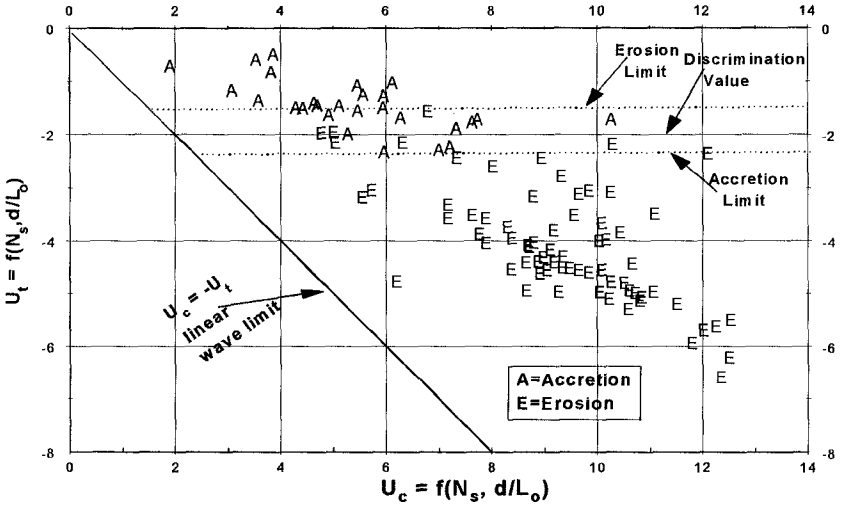

Fig. 3 Field beach data of Kraus and Mason (1991)

Accretionary or erosional type profiles are denoted in Fig. 3 as functions of U_c and U_t, calculated using Eqs. 4 and 5 respectively. Surprisingly, U_t discriminates well between erosional and accretionary profiles, without the need to use U_c, at a value around -2. Interestingly if $U_t \leq$ -2 erosion profiles will occur even if U_c is quite large. If a value of U_t = -2.0 is used as a threshold level, see Fig. 3, then there are three miscategorized erosion and three miscategorized accretion observations in a data set of 99, for a prediction skill of 0.94. Skill is the ratio of correct predictions to total observations, Seymour and Castel (1989). If linear wave theory is used to calculate $u_{d\,max}$, the ability to predict erosional and accretionary beach conditions declines to a skill of 0.88. The difference in skill may not seem great, but consider that the U_t approach corrects 6 of the 12 miscategorized observations using linear theory.

Fig. 3 shows a line for U_t = -2.0, as the best discrimination value between erosional and accretionary conditions. Above the discrimination line is a line given by U_t = -1.51, which is the smallest value which has only accretionary conditions above it, i.e. it is the limit for erosion. There is also a line for U_t = -2.27, which is the smallest

value which has only erosional conditions below it, i.e. it is the limit for accretion. These lines have been transferred to Fig. 4, using Eq. 5, which shows erosion/accretion conditions as a function of N_s and d_b/L_o. Above the upper limit curve is a region on the plane where erosion would be expected, below the lower limit curve is a region where accretion would be expected, and between the two is a transition region where both accretionary and erosional profiles are observed. The transition region is somewhat weighted toward accretionary profiles with 10 observations, as opposed to 6 observations of erosional profiles. If linear wave theory is used to establish a transition region, for the data of Kraus and Mason (1991), it contains 42 observations, 26 erosional and 16 accretionary. Clearly, the U_t approach is more effective in defining a transition region.

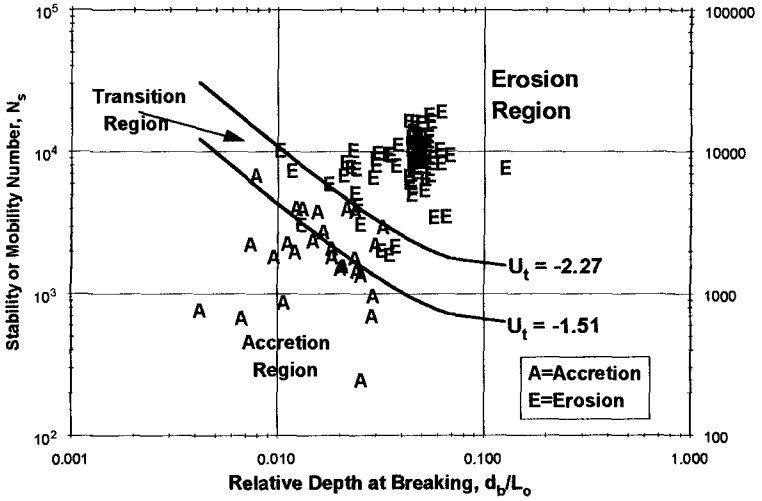

Fig. 4 N_s vs. d_b/L_o plane showing beach condition regions defined by U_t values

Another perspective on the information shown in Fig. 4 can be obtained by using Eq. 9 to transform the relative depth at breaking to deep-water wave steepness. This transformation is shown in Fig. 5 for the limit curves and a curve for the approximate limit of sediment movement. The limit for sediment movement was calculated by setting $U_c = 1.0$ in Eq. 4; this limit helps add scale to the figure.

d. Offshore Dumping of Gravel for Beach Nourishment

Zenkovich and Schwartz (1987) discuss offshore dumping of gravel in the Black Sea. Gravel was dumped by barge in depths of 4 to 6 m and storm wave conditions brought this material up to the shoreline over the next year or so to provide effective

beach nourishment and shore protection. Findings of Zenkovich and Schwartz were consistent with a limited number of wave tank tests at CERC (Ahrens and Camfield 1989).

Typically the deep-water wave steepness in a storm is in the range, $0.03 \leq H_o/L_o \leq 0.06$. Eqs. 7 and 8 can be used to calculate breaker heights, which for this range of steepness is $H_b/d \approx 0.76$ and in these water depths give $3.04 \leq H_b \leq 4.56$ m. The size of the gravel was not given in Zenkovich and Schwartz (1987), but sediment with median diameters in the range of $5 \leq d_{50} \leq 76$ mm is normally regarded as gravel. This range of breaker heights and sediment sizes gives mobility numbers in the range $24 \leq N_s \leq 553$. Fig. 5 shows that this range of mobility numbers and wave steepness generally fall into the accretionar region, which is consistent with the on-shore movement of the gravel observed by Zenkovich and Schwartz. The curve for the limit to sediment movement suggests that coarse gravel might have remained at depths of 4-6 m rather than move onshore. If find sand, say $d_{50} = 0.2$ mm, had been dumped at these depths mobility numbers in the range $9{,}152 \leq N_s \leq 13{,}818$ would have been obtained and Fig. 5 indicates this is an erosional condition; i.e., the sand would have moved offshore during

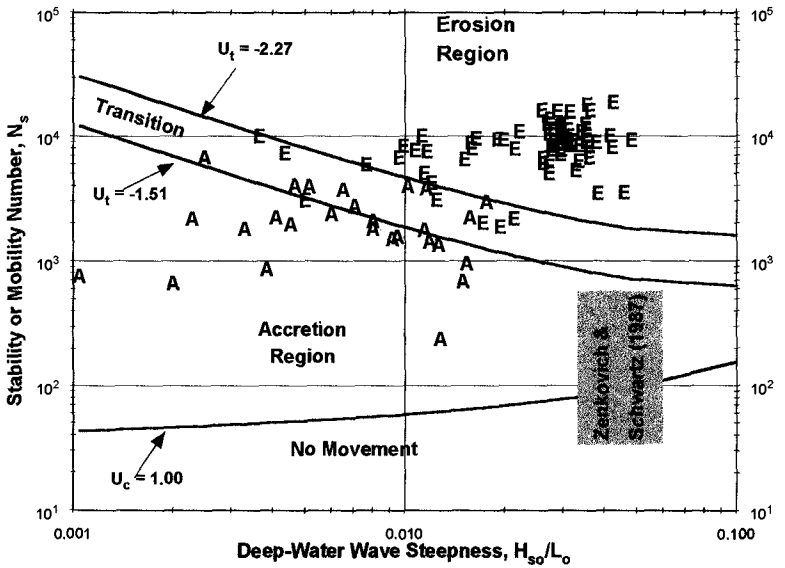

Fig. 5 N_s vs. H_{so}/L_o plane with beach condition regions defined by U_t and U_c

storms.

Fig. 5 provides a rather comprehensive view of erosion/accretion processes on beaches and is easier to interpret than Fig. 4. Fig. 5 shows that when the deep-water waves are steep, erosional conditions dominate, but there is a window of accretional conditions for gravel that was confirmed by the research of Zenkovich and Schwartz (1987). When deep-water steepness is quite small, say $H_o/L_o = 0.001$, accretional conditions dominate. At this steepness erosion will occur only for median sediment diameters smaller than used in the development of this model, i.e., $d_{50} = 0.1$ mm.

e. A Further Simplification and Application

Fig. 5 suggests that a further simplification could be made in predicting erosional and accretionary conditions by determining the equations of the discrimination curve, the accretion limit curve, erosion limit curve, and the limit of movement curve directly as $N_s = f(H_{so}/L_o)$. This functional relation was determined using regression analysis, with the following results:

for $U_c = 1.00$, approximate limit of movement,

$$N_s = 93.2(H_{so}/L_o)^{0.113} exp[7.89(H_{so}/L_o)] \quad (10)$$

$R^2 = 0.9998$, N = 99, $0.1 \le H_{so}/L_o \le 0.001$

and for U_t,

$$N_s = C_o(H_{so}/L_o)^{-0.854} exp[10.1(H_{so}/L_o)] \quad (11)$$

$R^2 = 0.9999$, N = 99, $0.1 \le H_{so}/L_o \le 0.001$
and where: $C_o = 30.8$, $U_t = -1.51$, erosion limit
$C_o = 62.1$, $U_t = -2.00$, best discrimination value
$C_o = 83.0$, $U_t = -2.27$, accretion limit

Eq. 11 discriminates between erosional and accretionary conditions exactly the same way as Eq. 5 and has exactly the same 16 observations in the transition region as Eq. 5. However, Eq. 11 is easier to use than Eq. 5 because there is a direct link between the mobility number and wave steepness. Fig. 6 illustrates an application of Eq. 11.

In Fig. 6, beach condition regions are shown as a function of H_{so} and T for two beaches, one with $d_{50} = 0.2$ mm and one with $d_{50} = 0.3$ mm, and using $\Delta = 1.65$. Using the 0.2 mm beach as a reference, it can be seen that the transition region moves up for the 0.3 mm beach expanding the accretion region and reducing the erosion region. The figure provides a very clear idea of what wave conditions cause erosion or accretion and provides a simple way to compare the response of beaches with different size sand to various wave conditions. Fig. 6 could be used to assess the value of nourishing a 0.2 mm beach with somewhat coarser sand. The limit on wave steepness is $H_{so}/L_o = 0.08$.

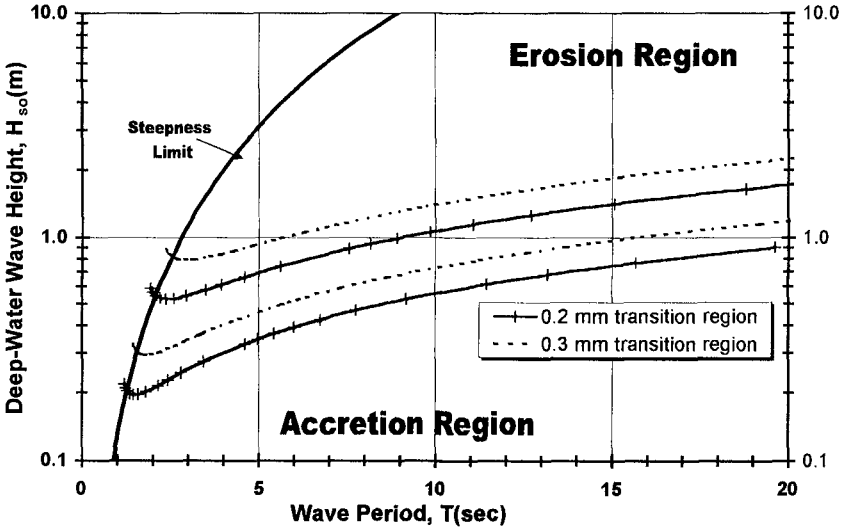

Fig. 6 Beach condition regions for 0.2 and 0.3 mm sand as a function of H_{so} and T

A question and a comment made at the conference can be addressed in this section. The question in essence was, can this model predict erosion of gravel beaches? The related comment observed, in part, that gravel beaches do in fact suffer erosion, however, they recover very quickly, Nicholls (1998). Fig. 7 shows the beach condition regions for a beach composed of small gravel, i.e., $d_{50} = 5$ mm. The figure indicates that small gravel will erode, but that H_{so}'s would probably have to be in the range of 10 – 15 m. There is a very large accretion region in Fig. 7 indicating that most wave conditions are accretionary for a 5 mm beach and supporting Nicholl's observation that gravel beaches recover from erosion very quickly. Fig. 7 also shows a small region where no onshore/offshore sediment movement would be expected. For the 0.2 mm and 0.3 mm beaches shown in Fig. 6, there is no region of no movement shown because wave heights for this region were always less then 0.1 m.

Summary and Conclusions

This paper uses nonlinear wave theory to predict cross-shore sediment movement under waves in shallow water. This synthesis of wave theory and sediment movement initiation criteria allows much of the present understanding of cross-shore sediment movement to be schematized or modeled using only two dimensionless variables, i.e., a mobility number and relative depth. When calibrated, the model shows surprising skill (0.94) in predicting erosional or accretionary beach profiles. The model is sensitive enough to distinguish between strong and weak erosional/accretionary tendencies. A wide range of sediment sizes was included in the development, which allows consideration of not only sand, but also gravel-sized particles. The model also provides

an interesting and useful perspective on cross-shore sediment movement under waves as functions of a mobility number and relative depth or a mobility number and deep-water wave steepness.

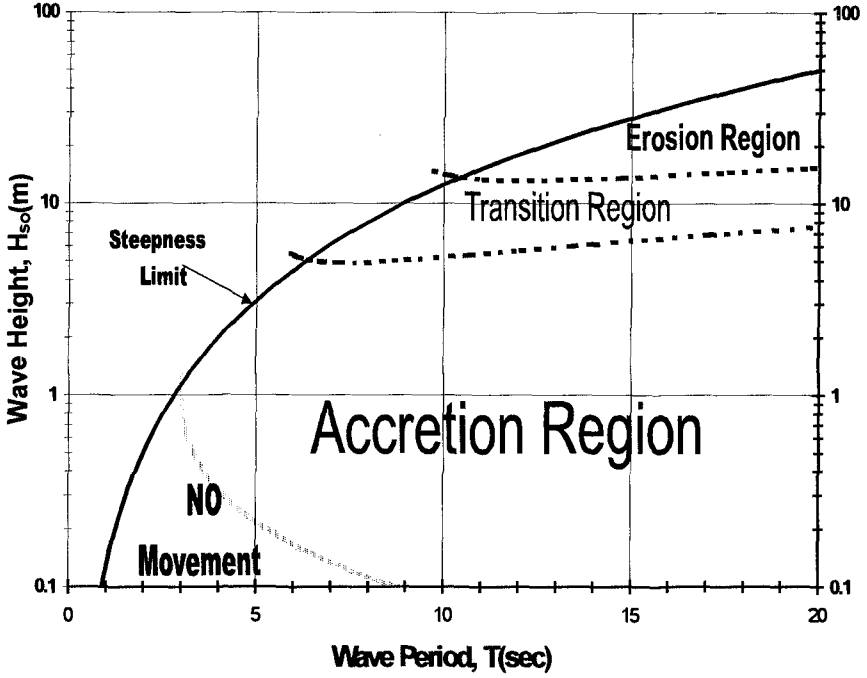

Fig. 7 Beach conditions for d_{50} = 5.0 mm as a function of H_{so} and T

It is the characteristics of nonlinear waves and specifically, the near-bottom velocities under the troughs, that accounts for the high skill of the model in predicting erosion/accretionary beach conditions. If linear wave theory is used to predict near-bottom velocities, the ability of the model to discriminate between erosional and accretionary beach events declines from a skill of 0.94 to 0.88.

The reference depth used to apply the model is near the outer limit of the surf zone. Surprisingly, the dimensionless version of the reference depth is easy to calculate, Eq. 9, as function of only deep-water wave steepness. When near-bottom velocities under a trough are more than twice the velocity required to initiate sediment movement, at this depth, the beach experiences erosion. If this ratio of velocities is less than two, then accretionary or possibly static profile conditions exist on the beach. Prediction of erosion or accretion is not improved by knowledge of the near-bottom fluid movement under the crest.

Simplifications were possible at three stages in the development of this model: First, the recognition that much of the physics of sediment movement under waves in shallow water could be summarized using only two variables, i.e., a mobility number and either relative depth or deep-water wave steepness. Second, the discovery that erosional or accretionary conditions, or a transition region could be discriminated using only Eq. 5, related to movement under the trough. Third, that a direct relationship between the mobility number and deep-water wave steepness could be developed, Eq. 11, that could be used to define beach conditions.

Appendix, Definition of Symbols

d - water depth
d_b - water depth at wave breaking
d_{50} - median grain diameter
d_b/L_o - relative depth at breaking, referred to as reference depth
g - acceleration of gravity
H - wave height
H_o - deep-water monochromatic wave height or significant deep-water wave height for field wave conditions, depending on context
H_b - maximum or breaking wave height
L_o - deep water wave length = $gT^2/2\pi$
N_s - mobility number, Eq. 6
% error = [(predicted - observed)/observed]*100
rms - root mean square
SFWT - Stream Function Wave Theory
T - momochromatic wave period or characteristic wave period for field wave conditions, depending on context
$u_{d\,max}$ - maximum near bottom velocity due to waves
u_{crit} - critical velocity required to initiate sediment movement
U - ratio $u_{d\,max}/u_{crit}$, in general
U_c - value of U under crest
U_t - value of U under trough
ρ_s - density of sediment
ρ - density of water
Δ - $(\rho_s-\rho)/\rho$

References

Ahrens, J.P., and Camfield, F. (1989). "Dynamic Revetments," The CERCular, Information Exchange Bulletin, Vol. CERC-89-2, Coastal Engineering Research Center, Vicksburg, MS.

Ahrens, J.P. and Hands, E.B., (1998). "Velocity Parameters for Predicting Cross-Shore Sediment Movement," ASCE Jour. of Waterway, Port, Coastal and Ocean Engineering, Vol.124, No.1, 16-20.

Dean, R.G.(1974). "Evaluation and Development of Water Wave Theories for Engineering Application; Volume I - Presentation of Research Results; Volume II - Tabulation of Dimensionless Stream-Function Variables," Coastal Engineering Research Center Special Report No. 1, Fort Belvoir, VA.

Dean, R.G. (1987). "Coastal Sediment Processes: Toward Engineering Solutions," Proc. Coastal Sediments '87, ASCE, 1-24.

Hallermeier, R.J.(1980). "Sand Motion Initiation by Water Waves: Two Asymptotes," ASCE Jour. of Waterway, Port, Coastal, and Ocean Engineering, Vol. 106, No. WW3, 299-318.

Hudson, R.Y., Herrmann, F..A., Sager, R.A., Whalen, R.W., Keulegan, G.H., Chatham Jr., C.E., and Hales, L.Z., (1979). "Coastal Hydraulic Models," Coastal Engineering Research Center Special Report No. 5, Ft. Belvoir, VA.

Kaminski, G.M., and Kraus, N.C.(1993). "Evaluation of Depth-Limited Wave Breaking Criteria," ASCE Proceedings Ocean Wave Measurement and Analysis Conf., ASCE, New Orleans, LA, 180 - 193.

Komar, P.D., and Miller, M.C.(1974). "Sediment Threshold under Oscillatory Waves," Proc.14th International Conference Coastal Engineering, ASCE, Copenhagen, Denmark, 756-775.

Kraus, N.C., Larson, M., and Kriebel, D.L.(1991). "Evaluation of Beach Erosion and Accretion Predictors," Proceedings Coastal Sediments '91, ASCE, Seattle, WA, 572-587.

Kraus N.C., and Mason, J.M.(1991). "Field Data Set for Testing Beach Erosion and Accretion Predictive Criteria," Memorandum for Record, Coastal Engineering Research Center, U.S. Army Eng. Waterways Experiment Station, Vicksburg, MS, 28 May 1991.

Madsen, O.S. (1998) personal communication.

Nicholls, R.J. (1998) personal communication.

Seymour, R.J., and Castel, D.(1989). "Modeling Cross-Shore Transport", in *Nearshore Sediment Transport*, R.J. Seymour, Editor, Plenum Press, New York.

Zenkovich, V.P. and Schwartz, M.L.(1987). "Protecting the Black Sea-Georgian S.S.R. Gravel Coast," J. of Coastal Research, 3 (2), 201-211.

DETERMINING DEPTH FROM REMOTELY-SENSED IMAGES

Robert A. Dalrymple, F. ASCE, Andrew B. Kennedy,
James T. Kirby, M. ASCE, and Qin Chen, M. ASCE[1]

Abstract *Remotely-sensed images can provide synoptic or nearly synoptic data for large areas of the sea surface. Photographic and, more recently, radar measurement techniques can resolve the pattern of waves on the water surface and can provide a very dense sampling of kinematical variables of interest, ranging from a complete picture of the wave phase (in the case of single photographs) to horizontal velocity components at the water surface resulting from wind, tides, or waves (in the case of advanced radar techniques). When applied in the coastal zone, these images contain surface waves that are propagating over a complex bottom bathymetry and current field, and that are affected by a combination of shoaling, refraction, diffraction and nonlinear processes. This paper examines two methods to determine bathymetry from surface elevation information. The first is to examine the ability of linear dispersion relationship models to determine bathymetry, in cases with refraction and diffraction, and the second, based on lagged correlation method (and several images), is more generally useful for application.*

Introduction

Remote sensing of the ocean surface can provide a great deal of information about the sea. Since World War II, it has been desirable to make use of images of the sea surface to deduce the bathymetry and nearshore current structure of a region of interest. The advantages of remote sensing systems for bathymetric and current surveys are that they can be more rapid than ground based methods, the cost per survey is lower, and it is less hazardous (in terms of exposure to the elements or hostile activity).

There are a variety of possible remote sensing systems. Satellites now provide wind speed and wave heights by altimetry. Aircraft with radars: synthetic aperature radar (SAR) and interferrometric SAR (INSAR) provide the ability to measure waves and currents. Some bathymetric data is being gleaned from the modulation of currents by the bottom from SAR data now, such as the ARGOSS BAS system in the Netherlands. LIDAR, using lasers from helicopters, such as the U.S. Army Corps of Engineers' SHOALS system (Lillycrop, Parson, and Irish, 1996), can provide bathymetric information at a rate of 5 km^2 per hour, with accuracies of ± 3 m horizontally

[1]all at the Center for Applied Coastal Research, University of Delaware, Newark, DE 19716 USA

and ±15 cm vertically in water depths of 40 m or less–provided that the water is reasonably clear. Turbidity affects the depths to which this methodology can be used.

An image of the water surface will contain information about the wave length of the surface waves, $L(x,y)$, which may vary with position, denoted by the horizontal coordinates x and y. Methods based on simple approaches (such as using the linear wave dispersion relationship to estimate local water depth from local estimates of wave length and period) provide an initial indication of the variation of depth in intermediate water depths, where nonlinearity is weak and currents typically are not the leading order factor in determining wave properties. The usual linear wave theory dispersion relationship is $\sigma^2 = gk\tanh kh$, where the wave angular frequency $\sigma = 2\pi/T$, where T is the wave period and the wave number k is $2\pi/L$. The wave period, assumed to be constant over the image, is determined from assuming a deep water wave length in a portion of the image or some other means.

Rearranging the dispersion relationship,

$$h(x,y) = \frac{1}{k(x,y)}\tanh^{-1}(\sigma^2/g)$$

Gleaning the wave length, $L(x,y)$, from an image, however, is not without error. There may be errors in the measurement technique and there may also be errors in how the wave period is determined.

Taking the derivative of the above equation and then dividing by $h(x,y)$, we have the relative error in depth as a function of the relative error in the wave angular frequency and the wave number.

$$\left(\frac{dh}{h}\right) = 2\left(\frac{\sinh 2kh}{2kh}\right)\left(\frac{d\sigma}{\sigma}\right) - \left(1+\frac{\sinh 2kh}{2kh}\right)\left(\frac{dk}{k}\right) = f(kh)\left(\frac{d\sigma}{\sigma}\right) - g(kh)\left(\frac{dk}{k}\right), \tag{1}$$

which defines two functions, $f(kh)$ and $g(kh)$, which determine the relative contributions of the percentage errors in angular frequency and wave number to the percentage error in the depth. These error terms are equal to two in shallow water, meaning that any errors in wave length determination are multiplied by this factor of two. What is worse is that these terms grow exponentially with kh. (Errors in wave length lead to the same size errors in wave number, as $dk/k = -dL/L$.) Figure 1 shows how $f(kh)$ and $g(kh)$ grow with depth. Clearly, the relative depth becomes far more sensitive to error as the depth increases.

Close to shore, nonlinearity can become a dominating factor in determining wave properties. Further, since waves are rapidly evolving and do not correspond well to any particular permanent form solution, it is likely to be difficult to parameterise nonlinear effects in a useful form. (Grilli and Skourup (1998, this proceedings) have examined the depth inversion of nonlinear periodic waves using a fully nonlinear boundary element method.)

This paper reports on bathymetry determination from "remotely sensed" (actually synthetically generated) images using two different methods. First, we determine the ability of the linear wave theory to determine the bathymetry from water surface elevations obtained by wave models over given bathymetry. Then we utilize a maximum

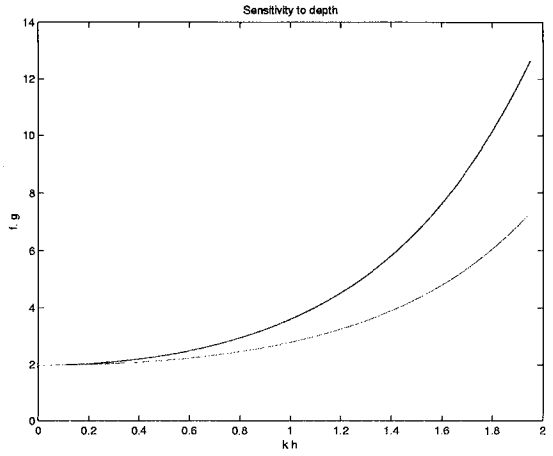

Figure 1: Plot of $f(kh)$ and $g(kh)$ versus kh. Upper line is $g(kh)$.

entropy method with a time series of synthetic images taken over a short period of time (comparable to a wave period).

Hilbert Transform

REF/DIF 1 is a forward scattering parabolic wave model (Kirby and Dalrymple, 1983, 1984, 1992) that predicts refraction and diffraction. This model was run with a simple idealized geometry (the Berkhoff, Booij, and Radder (1982) basin test, denoted BBR, which includes oblique wave incidence on a 1:50 planar beach with an elliptical shoal), using the BBR wave conditions, and surface elevations were computed by the model on a 200 by 200 grid (each grid is 0.125m x 0.125 m). These surface elevations (which have been shown to agree with measurements extremely well) were then used as the "remotely sensed" data and analysed for bathymetry.

To obtain the phase of the waves within the "image," a Hilbert transform was used along the 200 onshore grid lines. The Hilbert transform converts real time series into complex series from which the phase may be obtained. [In Matlab, this involves three steps: unwrap(phase(hilbert(data))). The unwrap command ensures that the phase increases monotonically, instead of staying in the range $-\pi$ to π]. The horizontal gradient of the phase over the image then provides the local wave numbers, from which the depths are determined using the linear theory dispersion relationship and the given wave period (T=1 s).

Figure 2 shows the results for the BBR data set. Note that the depth inversion (using a linear dispersion relationship in **REF/DIF 1**) gives quite good results except in the focussing/diffraction region behind the shoal, where very sharp ridges of unreal channels and bars occur. This is due to the fact that the wave length determination

is difficult where waves are short-crested and diffraction is strong.

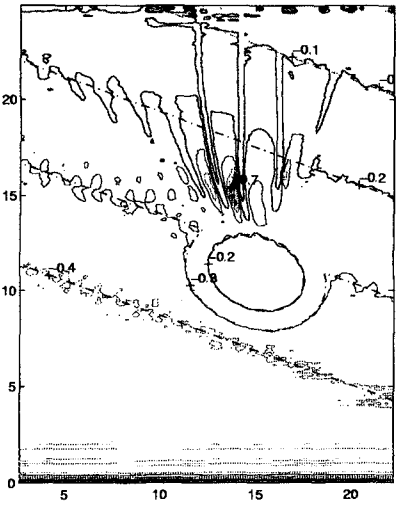

Figure 2: Depth inversion of **REF/DIF 1** output for BBR data set, showing the actual bathymetry (dashed lines) and the determined bathymetry (solid lines).

Applying a 2-D Fourier smoothing algorithm to the determined depths removes the sharp changes in depth produced by the focussing, as shown in Figure 3. (Note that we do introduce boundary effects due to the assumed spatial periodicity required by the Fourier filtering.) However, in the middle of the figure, the shoal is clearly and accurately picked out by the depth-inversion algorithm.

No remotely-sensed image will be as free of noise as model output. Variations in the field data will occur due to spectral sea effects, wind, capillary waves, specular reflections, etc. Therefore we introduced random noise to model output to determine the effect on the inversion algorithm. Figure 5 shows the bathymetry deduced by surface elevation data which have a 10% normally distributed random variation added. While the results are not as good as the no-noise case, the depths are reasonably well delineated. More noise results in seriously degraded bathymetry.

Additional examinations of the method included determining the errors involved with increasing the random noise and using the incorrect wave period. Further these comparisons were carried out with data from the linear **REF/DIF 1** run along with a nonlinear model computation (using a composite dispersion relationship that fits the deep water Stokes relationship to a shallow water form). The variation of error introduced by these noise and period effects are shown in Figures 7 and 8.

While comparisons of linear and nonlinear versions of REF/DIF to the laboratory data show important differences, the bathymetry obtained from linear and nonlinear

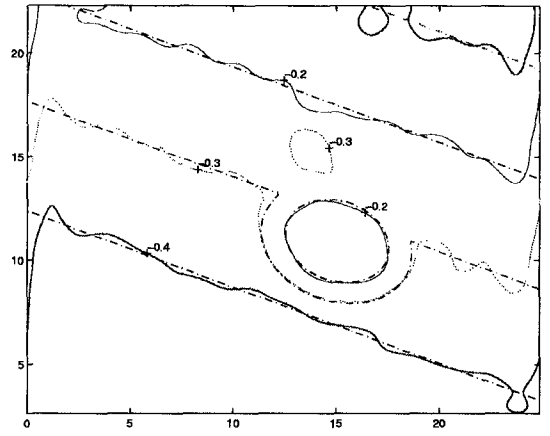

Figure 3: 2-D smoothed depth inversion of **REF/DIF 1** output for BBR data set, showing the actual bathymetry (dashed lines) and the smoothed bathymetry (solid lines).

synthesized surface data using the linear dispersion relationship for both cases show no real differences over the shoal and that the shoal is accurately found, even in the presence of noise introduced into the surface wave image. This method is extremely sensitive to the wave period, however.

All tests here have been done with a single frequency incident wave. A spectral sea state is best treated by the next method, which requires a sequence of images in time to determine wave frequencies.

Lag-Correlation Methods

Sequential images of a water surface taken at reasonably short time intervals show waves of varying directions and wave numbers propagating through space at their characteristic phase speeds. This is the basis of the lag-correlation methods, where the sequential images are used to determine a relationship between wave number and frequency, and thus to estimate depth. For large spatial records where the wave number spectrum is constant over the image and sequential images are available, wave number spectra and the associated phase speeds may be easily determined using standard Fourier techniques. However, in coastal regions, wave lengths and directions may change significantly over several wave lengths, making direct methods like this impossible. In this case, different methods must be used to estimate the wave number spectrum and associated phase speeds. Note that here the spectrum is characterised

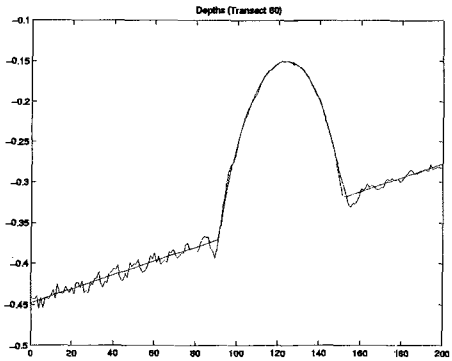

Figure 4: 2-D smoothed depth inversion of **REF/DIF** 1 output for BBR data set, along on/offshore transect 80, showing the actual bathymetry and the inferred bathymetry (wavey line).

in terms of wave number rather than frequency, which is much more natural given the form of the data. The methods used here will make the assumption that the the wave field is approximately stationary over a window of about two peak wave lengths. Although this assumption becomes invalid near the shore, and in areas with strong changes in bottom topography, it remains reasonable for many situations.

To aid analysis, the surface elevation data contained in the windows of interest is transformed into auto and cross correlation functions (e.g. Bendat and Piersol, 1986, Balakrishnan, 1995). Auto correlation functions of some window of data show the correlation of an image with itself at different spatial lags. If sequential images of the same window are compared, a cross-correlation function results. Autocorrelation functions contain information about the wave number spectrum to within a 180 degree directional ambiguity, while the addition of cross-correlation functions resolves this ambiguity and provides information about phase speed. Auto and cross correlation functions may also be easily constructed from a given wave number spectrum and dispersion relationship. For full and accurate records of auto and cross correlation functions, the wave number spectrum and dispersion relationship may be easily found, and the depth may be deduced from this. However, window sizes are assumed to be only about two peak wave lengths, and because of way they were constructed from data, correlation functions with high lags become unreliable. Therefore, since full records are unavailable, more approximate methods must be used to find the wave number spectrum and, more importantly, the dispersion relationship and therefore the depth.

One Horizontal Dimension

As a first test, the lag-correlation method was tested for one horizontal dimension. Spatial images of the water surface were generated using a fully nonlinear extended

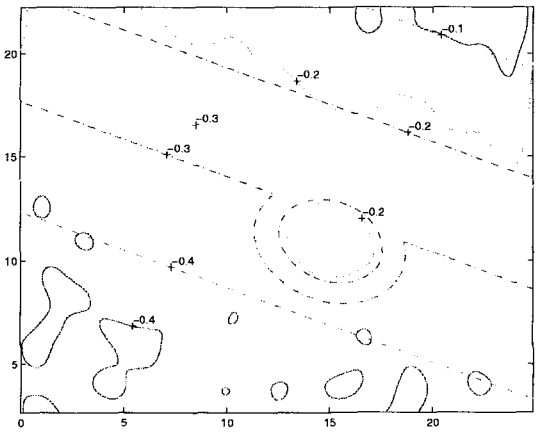

Figure 5: 2-D Smoothed Depth inversion of **REF/DIF 1** output for BBR data set, showing the actual bathymetry (dashed lines) and the smoothed bathymetry (solid lines).

Boussinesq model (Wei et al., 1995) over a bar-trough topography (Figure 9). The surface was then divided into overlapping windows with a length of about two peak wave lengths. Unbiased auto and cross correlations, which include a factor to correct for finite record length, were then computed in these windows. Ten sequential images were used to provide data; multiple auto and cross correlations were thus averaged to reduce error. However, there remained significant error for high spatial lags, and all correlations for lags greater than 2/3 of the window size were considered unreliable and discarded.

The inverse problem was then solved on a window by window basis. In each window, the measured auto and cross correlations were assumed to come from a spectrum that had either a JONSWAP or TMA type form (results were almost identical for both). The unit spectrum of this form was defined by a peak wave number, k_p, and a peak enhancement factor, γ. In order to specify the dispersion relationship for calculating cross correlations, a depth h also needed to be specified. Initially, of course, none of these were known, although a reasonable estimate could be made for the peak wave number. Initial guesses were made for each which were then iterated until the squared error between the measured and estimated auto and cross correlations was at a minimum. The depth at this minimum was then assumed to be the inversion depth.

Figure 9 shows actual and estimated depths for an incident spectrum with peak $T_p = 7$s and height $H_{RMS} = 0.025$m. The time lag between sequential images was 2s. Agreement is quite good, although small scale features cannot be reproduced.

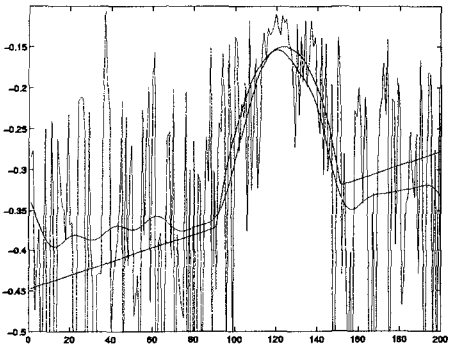

Figure 6: 2-D smoothed depth inversion of **REF/DIF 1** output for BBR data set, along transect 80, showing the actual bathymetry, the inferred bathymetry (no smooothing (very wavy line), and the smoothed bathymetry.

Furthermore, some scatter is clearly visible. This is likely due to a finite record length, and the resulting error in the correlation functions. Errors are greatest for deeper depths because here, the dependence of phase speed on depth is small. Thus, small errors in estimating phase speed or wave number will be magnified.

Figures 10-11 show inversions performed over the same topography as RMS wave heights increase. The time series of input waves to the Boussinesq model remained identical except for a multiplicative factor. Nonlinearities would, of course become evident as waves evolved. The main effect of this nonlinearity is to overestimate water depth wherever wave heights are large. This is because of amplitude dispersion, which increases with phase speed. Evidently, as shown by Grilli and Skourup (1998), using a nonlinear celerity would increase accuracy.

Two Horizontal Dimensions

For two horizontal dimensions the general problem remains the same: find a wave number spectrum and associated depth to best match the measured auto and cross correlation functions. However, it is more difficult to define a two dimensional wave number spectrum in terms of a few parameters - particularly if the spectrum has more than one dominant wave number or direction.

Accordingly, a more general technique was used to estimate the wave number spectrum in each window. The maximum entropy technique of Lim and Malik (1981) has been shown to be useful for finding the maximum entropy spectrum for two dimensional wave number problems from incomplete autocorrelation data. This technique uses two dimensional FFT's to transform between autocorrelation and wave number space, and again between wave number space and constraint space until a maximum entropy spectrum is reached that satisfies the measured constraints on the autocorrelation function. A variant of this method was used to compute the wave number

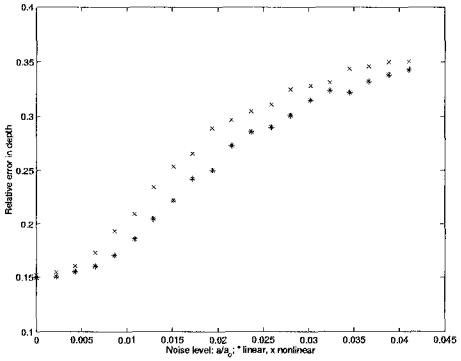

Figure 7: Relative errors introduced by uniform random noise for linear and nonlinear REF/DIF results.

spectrum directly from the autocorrelation function. In some cases, the method may be slow to completely converge, but it was found that complete convergence was not necessary to accurately invert depths. As long as the peak of the wave number spectrum was in the correct location, results continued to be accurate.

Once the wave number spectrum had been computed, the depth in each window was iterated until the cross correlation function resulting from the maximum entropy spectrum best matched the measured function. A 180 degree ambiguity with respect to the wave number spectrum had to be specified, but this was a minor concern. Figure 12 shows estimated and actual depths for the Berkhoff, Booij and Radder (1982) experiment described earlier. Once again, agreement is quite good, although the depth at the top of the shoal is overestimated, due to nonlinearities and/or a finite window size. Figure 13 gives a one dimensional slice through the shoal, and clearly shows the overprediction of depth on top of the shoal. This is almost certainly because depth is asumed to be constant throughout the analysis windows, an assumption that is violated in the region of the shoal.

Next, to test the effect of inaccuracies in the measurements, Gaussian noise with a standard deviation of 10 percent of the wave height was added to the data. Depths were then estimated as before. Figure 14 shows the computed and measured depths. These are virtually identical to those computed earlier. This insensitivity is because the maximum entropy technique transforms white noise in the data into a noise floor in the wave number spectrum. This noise has no strong correlation with depth and thus does not affect greatly estimates of depth. Figure 15 shows a slice through the shoal and again the results are almost identical to the no noise case.

Appendix: References

Alpers, W., and Hennings, I., "A Theory of the imaging of underwater bottom topography by real and synthetic aperture radar," *Journal of Geophysical Research*,

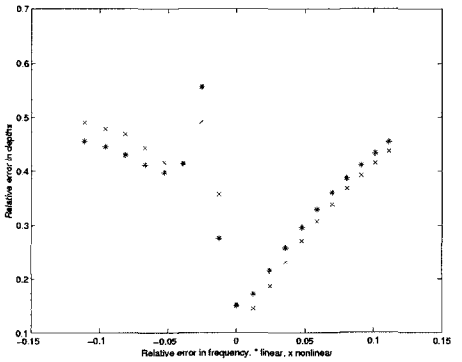

Figure 8: Relative errors introduced by relative errors in angular frequency for linear and nonlinear REF/DIF results.

89, C6, 10,529-10,546, November 20, 1984.

Balakrishnan, A.V., 1995, "Introduction to random processes in engineering", Wiley-Interscience, New York.

Bendat, J.C, and Piersol, A.G., "Random data: analysis and measurement procedures", Wiley-Interscience, New York, 1986.

Berkhoff, J.C.W., N. Booij, and A.C. Radder, "Verification of numerical wave propagation models for simple harmonic linear water waves," *Coastal Engrg.*, 6, 255-279, 1982.

Grilli, S.T. and Skourup, J., "Depth inversion in shallow water based on properties of nonlinear shoaling waves", *Proc. 26th Int. Conf. Coastal Eng.*, Copenhagen, 1998.

Kirby, J.T. and R.A. Dalrymple, "A Parabolic Equation for the Combined Refraction-Diffraction of Stokes Waves by Mildly Varying Topography," *J. Fluid Mechanics,* 136, 453-466, 1983.

Kirby, J.T. and R.A. Dalrymple, "Verification of a parabolic equation for propagation of weakly-nonlinear waves," *Coastal Engrg.*, 9, 219-232, 1984.

Kirby, J.T. and R.A. Dalrymple, " Combined Refraction/Diffraction Model–**REF/DIF 1**, Version 2.5," Center for Applied Coastal Research, Res. Rpt. CACR-94-22, 1994.

Lillycrop, W.J., L.E. Parson, and J.L. Irish, "Development and Operation of the SHOALS Airborne Lidar Hydrographic Survey System," *SPIE Laser Remote Sensing of Natural Waters: From Theory to Practice*, 2964, 26-37, 1996

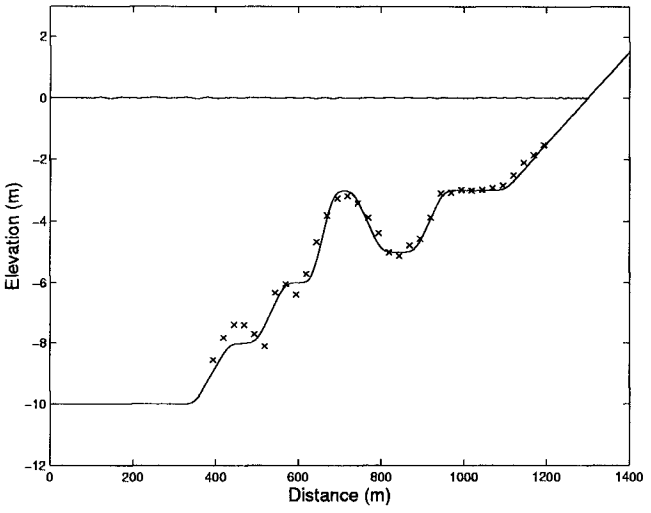

Figure 9: Estimated (×) and actual (–) depths over a bar-trough topography, $H_{RMS} = 0.025$ m

Lim, J.S. and Malik, N.A., 1981, "A new algorithm for two-dimensional maximum entropy power spectrum estimation",*IEEE Trans. Acoust., Speech, Signal Processing*, **29**, 401-413.

Schuchman, R.A., Lyzenga, D.R., and G.A. Meadows, "Synthetic aperture radar imaging of ocean-bottom topography via tidal current interactions: Theory and observations, *Int. J. of Remote Sensing*, 6, 1179-1200, 1985.

Wei, G., Kirby, J. T., Grilli, S. T. and Subramanya, R., 1995, "A fully nonlinear Boussinesq model for surface waves. I. Highly nonlinear, unsteady waves", *Journal of Fluid Mechanics*, **294**, 71-92.

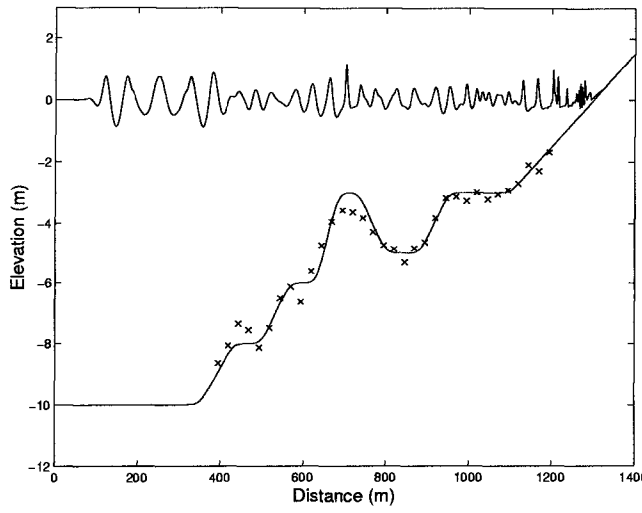

Figure 10: Estimated (×) and actual (–) depths over a bar-trough topography, $H_{RMS} = 1$ m

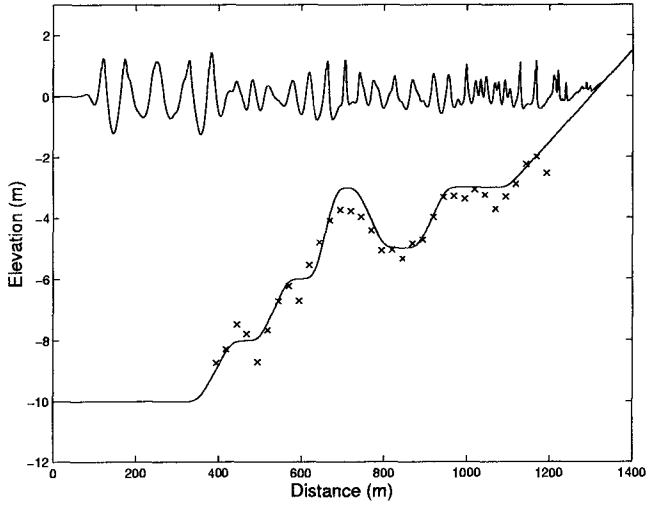

Figure 11: Estimated (×) and actual (–) depths over a bar-trough topography, $H_{RMS} = 1.5$ m

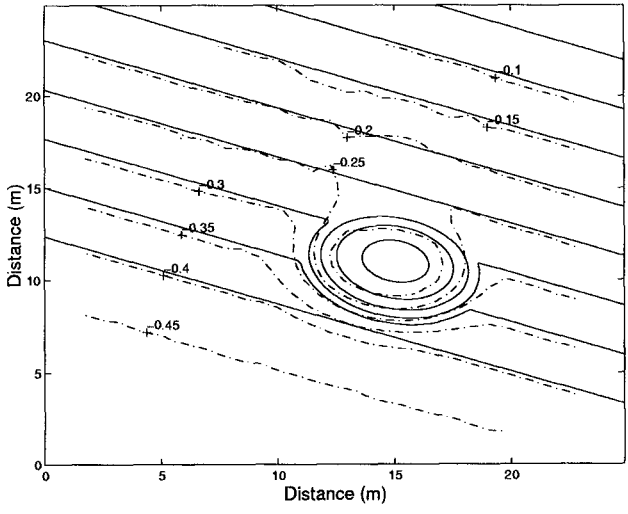

Figure 12: Depth contours over the BBR shoal (–) actual; (– · –) estimated

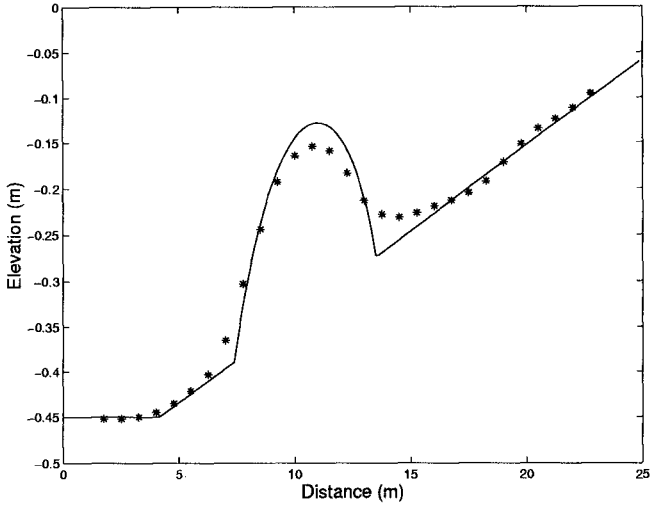

Figure 13: Cross section of depth through the BBR shoal, (–) actual; (*) estimated

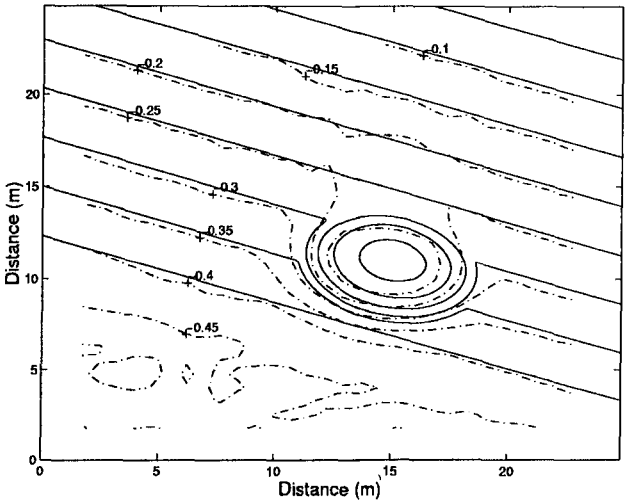

Figure 14: Depth contours over the BBR shoal (–) actual; (– · –) estimated from noisy data

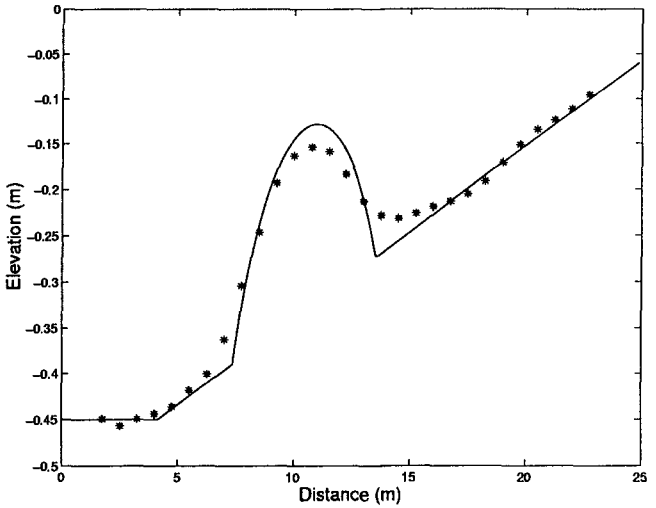

Figure 15: Cross section of depth through the BBR shoal, (–) actual; (*) estimated from noisy data

COASTAL ENGINEERING 1998

Volume 3

CONFERENCE PROCEEDINGS

June 22-26, 1998
Falconer Hotel
Copenhagen, Denmark

EDITED BY
Billy L. Edge

ASCE American Society of Civil Engineers
1801 ALEXANDER BELL DRIVE
RESTON, VIRGINIA 20191–4400

Abstract: This proceedings, *Coastal Engineering 1998*, contains over 270 papers presented at the 26th International Conference on Coastal Engineering which was held in Copenhagen, Denmark, June 22-26, 1998. The proceedings is divided into five parts: 1) characteristics of coastal waves and currents; 2) long waves and storm surges; 3) coastal structures; 4) coastal processes and sediment transport; and 5) coastal, estuarine, and environmental problems. The individual papers include such topics as the effects of wind, waves, storms, and currents as well as the study of sedimentation, erosion, and beach nourishment. Special emphasis is given to case studies of completed engineering projects. With the inclusion of both theoretical and practical information, these papers provide the civil engineer and professionals in related fields with a broad range of information on coastal engineering and coastal processes affecting design and operations in the coastal zone.

Cover photo and all photos on section breaker pages 71, 1153, 1393, 2263, and 3373 provided by Danish Hydraulic Institute.

Library of Congress Cataloging-in-Publication Data

Coastal engineering 1998: proceedings of the twenty-sixth international conference: 22-26 June 1998, Falconer Hotel, Copenhagen, Denmark / edited by Billy L. Edge.
p. cm.
"Held under the auspices of the Coastal Engineering Research Council of the American Society of Civil Engineers."
Includes bibliographical references and index.
ISBN 0-7844-0411-9
1. Coastal engineering–Congresses. 2. Ocean waves–Congresses. 3. Shore protection –Congresses. I. Edge, Billy L. II. Coastal Engineering Research Council (U.S.)
III. International Conference on Coastal Engineering (26th: 1998: Copenhagen, Denmark)
TC203.5.C6184 1999 98-55126
627'.58–dc21 CIP

Any statements expressed in these materials are those of the individual authors and do not necessarily represent the views of ASCE, which takes no responsibility for any statement made herein. No reference made in this publication to any specific method, product, process or service constitutes or implies an endorsement, recommendation, or warranty thereof by ASCE. The materials are for general information only and do not represent a standard of ASCE, nor are they intended as a reference in purchase specifications, contracts, regulations, statutes, or any other legal document.
ASCE makes no representation or warranty of any kind, whether express or implied, concerning the accuracy, completeness, suitability, or utility of any information, apparatus, product, or process discussed in this publication, and assumes no liability therefore. This information should not be used without first securing competent advice with respect to its suitability for any general or specific application. Anyone utilizing this information assumes all liability arising from such use, including but not limited to infringement of any patent or patents.
Photocopies. Authorization to photocopy material for internal or personal use under circumstances not falling within the fair use provisions of the Copyright Act is granted by ASCE to libraries and other users registered with the Copyright Clearance Center (CCC) Transactional Reporting Service, provided that the base fee of $8.00 per chapter plus $.50 per page is paid directly to CCC, 222 Rosewood Drive, Danvers, MA 01923. The identification for ASCE Books is 0-7844-0411-9/99/ $8.00 + $.50 per page. Requests for special permission or bulk copying should be addressed to Permissions & Copyright Dept., ASCE.

Copyright © 1999 by the American Society of Civil Engineers, All Rights Reserved.
Library of Congress Catalog Card No: 98-55126 ISBN 0-7844-0411-9
Manufactured in the United States of America.

Contents

VOLUME 1

Keynote Presentations

The Art of Coastal Engineering 1
Torben Sorensen

The European Research Programmes in Coastal Engineering 15
Hans-Werner Partenscky

Beach Nourishment: A Limited Review and Some Recent Results 45
Robert G. Dean

Part I: Characteristics of Coastal Waves and Currents

The Modelling of a Spilling Breaker: Strong Turbulence at a Free Surface 72
M. Brocchini and D.H. Peregrine

Time-Dependent Depth-Integrated Turbulence Modeling of Breaking Waves 86
Kazuo Nadaoka and Osafumi Ono

Wave Crest Interaction in Water of Intermediate Depth 98
C.C. Bird and D.H. Peregrine

Energy Dissipation Model for Irregular Breaking Waves 112
Winyu Rattanapitikon and Tomoya Shibayama

Stochastic Modelling of Nonlinear Waves in Shallow Water 126
Henrik Kofoed-Hansen and Jørgen H. Rasmussen

Comparing First, Second, and Third Generation Coastal Wave Modelling 140
L.H. Holthuijsen, N. Booij, and I.J.G. Haagsma

Wave Transformation near a Quasi-1D Coast 150
J.H. Andorka Gal, L.H. Holthuijsen, J.C.M. de Jong, and
A.T.M.M. Kieftenburg

A New Formulation of Deterministic and Stochastic Evolution Equations for Three-Wave Interactions Involving Fully Dispersive Waves 161
Per A. Madsen and Yasser Eldeberky

The Horizontal Eddies in the Offshore Zone 175
Li Li and Robert A. Dalrymple

Nonlinear Distribution of Nearshore Free Surface and Velocity 189
Nobuhito Mori and Nobuhisa Kobayashi

Evolution Equations for Edge Waves and Shear Waves on Longshore Uniform Beaches 203
James T. Kirby, Uday Putrevu, and H. Tuba Özkan-Haller

On the Viscous Destabilization of Longshore Currents 217
Uday Putrevu, James T. Kirby, Joan Oltman-Shay, and H. Tuba Özkan-Haller

Shear Waves over Longshore Nonuniform Barred Beaches 230
F.E. Sancho and I.A. Svendsen

Trapped and Free-Wave Propagation in Channels and Harbours 244
João A. Santos and D.H. Peregrine

A Boussinesq Model for Breaking Waves: Comparisons with Experiments 258
Jayaram Veeramony and Ib A. Svendsen

Nearshore Wave Dynamics Simulated by Boussinesq Type Models 272
Ole R. Sørensen, Per A. Madsen, and Hemming A. Schäffer

A 2D Model of Waves and Undertow in the Surf Zone 286
Brian A. O'Connor, Shunqi Pan, John Nicholson, Neil MacDonald, and David A. Huntley

Field Measurements of Undertow on Longshore Bars 297
Yoshiaki Kuriyama

Application of an Undertow Model to Irregular Waves on Barred Beaches 311
Douglas L. Kennedy, Daniel T. Cox, and Nobuhisa Kobayashi

Wake Wash of High-Speed Craft in Coastal Areas 325
Jens Kirkegaard, Henrik Kofoed-Hansen, and Berry Elfrink

Wave Propagation Directions under Real Sea State Conditions 338
Joachim Grüne

On the Accuracy of Parabolic Wave Models 352
Hakeem K. Johnson and Sanne Poulin

A Refraction-Diffraction Model for Irregular Waves 366
Q. Gao and A.C. Radder

Calculation of Velocity Field in 3-D Random Waves 380
Yu-xiu Yu and Ning-chuan Zhang

On the Reflection of Short-Crested Waves in Numerical Models 394
Michael Brorsen and Jacob Helm-Petersen

Breaking Waves and Induced Currents on Coastal Structures 408
Entin A. Karjadi and Nobuhisa Kobayashi

ALES Shallow-Water Flow Solver with Non-Hydrostatic Pressure: Wave Applications 422
J.G. Zhou and P.K. Stansby

Linear and Nonlinear Modeling of Long Waves Propagating around Channel Bends 433
Aimin Shi and Michelle H. Teng

Mass Transport of Progressive Edge Waves: A Comparison between the Full and Shallow-Water Wave Theories 443
K.M. Mok and Harry Yeh

Coherent Motions in the Bottom Boundary Layer under Shoaling and Breaking Waves 457
Daniel T. Cox and Nobuhisa Kobayashi

Experimental Study on Non-Linear Wave Boundary Layers 471
Hitoshi Tanaka, Hiroto Yamaji, and Ahmad Sana

A 2-DV Numerical Solution for the Turbulent Wave Boundary Layer under Breaking Waves 484
Nguyen The Duy, Tomoya Shibayama, and Akio Okayasu

Wave Modelling in the WISE Group 498
L. Cavaleri and L.H. Holthuijsen

A Long Term Wave Hindcast System Using ECMWF Winds 509
Yoshio Hatada and Masataka Yamaguchi

Numerical Simulations of Directionally Spread Shoaling Surface Gravity Waves 523
Françoise Becq, Michel Benoit, and Philippe Forget

Effects of Wave Reflection and Dissipation on Wave-Induced Second Order Magnitudes 537
Fernando J. Méndez, Iñigo J. Losada, Robert A. Dalrymple, and M.A. Losada

Green-Function Analysis of a Wave Field over Arbitrary Bathymetry 551
Hitoshi Nishimura and Moon-Su Kwak

Wave Propagation over a Bar and Wave Induced Bed Pressure Gradients 562
Øivind A. Arntsen

A Multi-Level Model for Nonlinear Dispersive Water Waves 576
Susumu Kanayama, Hitoshi Tanaka, and Nobuo Shuto

Recent Extensions to Local Polynomial Approximation Models 589
Andrew B. Kennedy

Depth Inversion for Nonlinear Waves Shoaling over a Barred-Beach 603
Stéphan T. Grilli and Jesper Skourup

Numerical Model of Fully-Nonlinear Wave Refraction and Diffraction 617
Masahiko Isobe and Samir Abohadima

A Comparison of Higher-Order Boussinesq and Local Polynomial Approximation Models 631
Maurício F. Gobbi, Andrew B. Kennedy, and James T. Kirby

Experiments on Nonlinear Wave Groups Shoaling in a Tank 645
L. Shemer, Haiying Jiao, and E. Kit

Modulation of Bichromatic Wave Train in a Wave Tank 656
Motohiko Umeyama

Simulation of Nonlinear Wave Deformation by a Shoal in 3D 670
Paul de Haas and Maarten Dingemans

Variations in Nonlinearly Evolved Nearshore Spectra and Their Significance in the Estimation of Wave Forces 682
Serdar Beji and Kazuo Nadaoka

Wave Refraction across a Current with Strong Horizontal Shearing 692
Richard R. Simons and Ruairi D. Maciver

Random Waves on a Vertically-Sheared Current 706
C. Swan and R.L. James

Wave Setup and Other Tidal Anomalies in Coastal Rivers 720
Eko Santoso, David Hanslow, Peter Nielsen, and Kevin Hibbert

3D Wave-Current Interactions in Wave-Current Channels 732
Jacco Groeneweg and Jurjen A. Battjes

Vorticity and Surf Zone Currents 745
D.H. Peregrine and O. Bokhove

Experimental Study of Wave Breaking and Blocking on Opposing Currents 759
Arun Chawla and James T. Kirby

Tidal Ellipses in the Nearshore Zone (-3 to -10m): Modelling and Observations 773
Klaas T. Houwman and Piet Hoekstra

ADCP Observation of Nearshore Current Structure in the Surf Zone 787
Takao Yamashita, Hiroshi Yoshioka, Shigeru Kato, Lu Ming, and Chikara Shimoda

Numerical Modeling of Nearshore Circulation on a Barred Beach with Rip Channels 801
K.A. Haas, I. A. Svendsen, and M.C. Haller

Applicability of a Quasi-Three Dimensional Numerical Model to Nearshore Currents 815
Masamitsu Kuroiwa, Hideaki Noda, and Yuhei Matsubara

Three-Dimensional Nearshore Currents Model Based on Vertical Distribution of Radiation Stress 829
Hisamachi Nobuoka, Nobuo Mimura, and Hajime Kato

Numerical Simulation of Wave Fields around the Submerged Breakwater with SOLA-SURF Method 843
Norio Hayakawa, Tokuzo Hosoyamada, Shigeru Yoshida, Gozo Tsujimoto

Numerical Analysis of Wave Breaking Due to Submerged Breakwater in a Three-Dimensional Wave Field 853
Koji Kawasaki and Koichiro Iwata

Classification of Wave Loading on Monolithic Coastal Structures 867
Andreas Kortenhaus and Hocine Oumeraci

Lagrangian Measurements of Accelerations in the Crests of Breaking and Broken Waves 881
Søren Peter Kjeldsen, Pierre Bonmarin, Michael G. Skafel, and William M. Drennan

Numerical Simulation of Breaking Waves by Large Eddy Simulation and VOF Method 892
Qun Zhao and Katsutoshi Tanimoto

Influence of Steep Seabed Slopes on Breaking Waves for Structure Design 906
N.W.H. Allsop, N. Durand, and D.P. Hurdle

Influence of False Waves on Wave Records Statistics 920
Marcos H. Giménez, Carlos R. Sánchez-Carratalá, and Josep R. Medina

Changing of Local Wave Climate Due to Ebb Delta Migration 934
Ralf Kaiser and Hanz D. Niemeyer

Sensitivity of Wind Wave Simulation to Coupling with a Tide/Surge Model with Application to the Southern North Sea 945
J. Monbaliu, C.S. Yu, and P. Osuna

Probability Distribution of Wave Height in Finite Water Depth 958
Michel K. Ochi

Increase of Wave Height in the North Pacific Ocean 972
Kozo Okada, Yasushi Suzuki, Yoshihiro Utsunomiya, and Yoshihiro Watanabe

Analysis of Wave Data at Sines 985
Carlos Pita and Fernando Abecasis

On the Statistical Variability of Wave Height and Period Parameters 999
Carlos R. Sánchez-Carratalá and Marcos H. Giménez

Duration in Wave Climate Analysis 1013
Rodney J. Sobey and Leah S. Orloff

Encounter Probability of Individual Wave Height 1027
Zhou Liu and Hans F. Burcharth

Wave Run-up and Overtopping: Prototype Versus Scale Models 1039
Julien De Rouck, Raf Verdonck, Peter Troch, Luc Van Damme, Flemming Schlütter, and John De Ronde

Wave Run-up and Reflection on Coastal Structures in Depth-Limited Conditions 1053
Joel R. Rathbun, Daniel T. Cox, and Billy L. Edge

Wind Effects on Run-up and Breakwater Crest Design 1068
Josep R. Medina

Some Design Aspects of an Absorbing 3D Wavemaker 1082
Hemming A. Schäffer

Generation of Double Peak Directional Wave by Dual Mode Snake-Type Wave Maker 1096
Tetsuya Hiraishi and Katsuya Hirayama

Extreme Multi-Directional Waves 1110
T.B. Johannessen and C. Swan

Low Frequency Surf Zone Response to Wave Groups 1124
Merrick C. Haller, Uday Putrevu, Joan Oltman-Shay, and Robert A. Dalrymple

Wave Dynamics and Revetment Design on a Natural Reef 1138
Thomas Jensen, Peter Sloth, and Vagner Jacobsen

VOLUME 2

Part II: Long Period Waves, Storm Surges, and Wave Groups

Long Waves in Flume Experiments 1154
J. William Kamphuis

Probabilistic Model for Tsunami-Wave Elevation along the Alborán Seacoast 1168
M. González and R. Medina

Long-Period Wave Responses in a Harbor with a Narrow Mouth 1182
Weon Mu Jeong, Kil Seong Lee, and Woo Sun Park

Application of Computer Modeling for Harbor Resonance Studies of Long Beach and Los Angeles Harbor Basins 1196
Jiin-Jen Lee, Ching-Piau Lai, and Yigong Li

Attenuation of Very Long Waves by a Large Resonator as an Outer Harbor 1210
Takayuki Nakamura and Satoshi Morita

Application of Physical Model in Long Wave Studies for the Port of Long Beach 1222
Ying-Keung Poon, Frederic Raichlen, and James (Kimo) Walker

Nautical Design Studies: Haifa Port Extensions 1236
J.A. Zwamborn, F. Di Castro, M. Radomir, and J.T.M. van Doorn

Wave Propagation Modeling for Pusan New Harbor 1250
Jang-Won Chae and Weon Mu Jeong

The Studies for the Resonance of Hwa-Lian Harbour Agitated by Typhoon Waves 1263
Chien-Kee Chang, Chung-Ching Chien, and Hsiang-Maw Tzeng

Application of Mathematical Modeling in Optimizing Layout of a Large Industrial Fishery Harbour 1276
P.P. Gunaratna, P. Justesen, D.S. Abeysirigunawardena, and H.-J. Scheffer

Characteristics of Long-Period Flow Velocity Fluctuations around Tomakomai Harbor 1290
Hiroya Kinoshita, Hideki Hoshi, Youichi Atsumi, Shin-ichiro Sekiguchi, and Toshihiko Yamashita

Transformation of Wave Groups and Accompanying Long Waves in Shallow Water 1299
M. Mizuguchi and H. Matsutate

Observation and Simulation of Low-Frequency Waves on Two Natural Beaches 1313
Satoshi Nakamura and Nicholas Dodd

Quasi 3-D Effects in Infragravity Waves 1323
A.R. Van Dongeren, I.A. Svendsen, and U. Putrevu

Numerical Modelling of Long Wave Ship Motions 1337
John R. Headland and Ying-Keung Poon

Response of Moored Vessels in Buffington Harbour 1350
E.P.D. Mansard, T. Faure, and K. MacIntosh

Statistical Wave Forecasting through Kalman Filtering Combined with Principal Component Analysis 1364
Noriaki Hashimoto, Toshihiko Nagai, and Masanobu Kudaka

Data Assimilation and Nested Hydrodynamic Modelling in Storm Surge Forecasting 1378
Rafael Cañizares and Henrik Madsen

Part III: Coastal Structures

Berm Breakwaters: Influence of Stone Gradation, Permeability, and Armouring 1394
Jørgen Juhl and Peter Sloth

Berm Breakwaters: Fifteen Years Experience 1407
Sigurdur Sigurdarson, Gisli Viggosson, Sigtryggur Benediktssson, Sigurdur Einarsson, and Omar Bjarki Smarason

The First Berm Breakwater in Hong Kong 1421
K.C. Ander Chow, Charles P. Fournier, P.F. Ma, and W.Y. Shiu

On the Stability of Berm Breakwaters in Shallow and Deep Water 1435
Alf Tørum

The Economic Analysis of "Soft" Versus "Hard" Solutions for Shore Protection: An Example 1449
David R. Basco

Uncertainty Analysis of Coastal Projects 1461
Jim W. Hall, John P. Davis, and David I. Blockley

Preventing Natural Breaching of the Major Sand Spit Protecting the Port of Walvis Bay 1475
J.S. Schoonees, L. Lenhoff, and A.J. Raw

Phenomena in Standing Wave Impact on a Horizontal Plate 1489
Piotr Wilde, Kazimierz Szmidt, and Eugeniusz Sobierajski

Two and Three-Dimensional Pressure-Impulse Models of Wave Impact on Structures 1502
Deborah J. Wood and D. Howell Peregrine

Thyborøn Barriers: A Master Case of Coastal Engineering 1516
Per Roed Jakobsen, Ida Brøker, Jesper Holt Jensen, Ann Skou, and Sanne Poulin

Application of Shore Protection Schemes in Hornbæk 1530
Mads Peder Jørgensen, Peer Skaarup, Karsten Mangor, and Jørgen Juhl

Design and Construction of Seawater Exchange Breakwaters 1539
Sadamitsu Akeda, Yasushi Yamamoto, Katsutoshi Kimura, and Kenji Yano

Application of Overtopping Models to Vertical Walls against Storm Surges 1553
Holger Schüttrumpf, Andreas Kortenhaus, and Hocine Oumeraci

Advanced Assessing of the Stability of Existing Placed Block Revetments 1567
Adam Bezuijen and Gerard A.M. Kruse

Design of Revetments in the Öresund Link: Reclaimed Artificial Island and Peninsula 1576
Jeppe Blak-Nielsen, Helge Gravesen, and Niels Lykkeberg

Design of Alternative Revetments 1587
M. Klein Breteler, K.W. Pilarczyk, and T. Stoutjesdijk

Inventory of the Stability of Existing Placed Block Revetments in the Netherlands 1601
Theo Stoutjesdijk, Mark Klein Breteler, and Hans Johanson

Second Order Wave Interaction with a Large Structure 1613
Bjarne Büchmann, Jesper Skourup, and David L. Kriebel

On the Effect of Two-Layer Thickness by High-Specific Gravity Armor Blocks on Wave Reflection 1625
Masahiro Ito, Yuitch Iwagaki, Hiroshi Murakami, Kenji Nemoto, Masato Yamamoto, and Minoru Hanzawa

Development of Two-Dimensional Numerical Wave Flume for Wave Interaction with Rubble Mound Breakwaters 1638
Peter Troch and Julien De Rouck

Nonlinear Wave Forces on a Rubble Covered Pipeline 1650
William G. McDougal, Norimi Mizutani, and Ayman M. Mostafa

Sea Level Set-up Behind Detached Breakwaters 1665
J.H. Loveless, D. Debski, and A.B. MacLeod

Coastal Erosion Caused by Construction of an Artificial Island and Performance of Beach Nourishment 1679
Ryuichiro Nishi, Takaaki Uda, Michio Sato, Masakazu Wakita, Yasuro Ohtani, and Takahiro Horiguchi

On the Design of Shore-Parallel Breakwaters 1693
J.A. Zyserman, I. Brøker, H.K. Johnson, K. Mangor, and K. Jørgensen

Shore Parallel Breakwaters and Beach Nourishments 1706
Jan van de Graaff, Henk Steetzel, Bram Bliek, and Hans de Vroeg

Sediment Transport around a Mound Breakwater: The Toe Erosion Problem 1720
Asunción Baquerizo and Miguel A. Losada

Stability of Near-Bed Rubble-Mound Structures 1730
César Vidal, Íñigo J. Losada, and Francisco L. Martín

Coastal Defense Structures in NSW, Australia 1744
S.J. Wyllie, D.B. Lord, I.F.W. Jayewardene, and T. Young

Alderney Breakwater: Scheme Evolution 1758
Paul B. Sayers, N. William H. Allsop, and Alan A. Hill

Breakwater Repair: Monitoring, Modelling, and Construction 1775
S. Pillay, D. Phelp, and A. Bartels

Digital Imaging Processing Techniques for the Aerial Field Monitoring of Harbour Breakwaters 1789
Gavin Hough and David Phelp

Design of Rock Armoured Single Layer Rubble Mound Breakwaters 1800
T. Hald, A. Tørum , and T. Holm-Karlsen

The Form of the Mound of Rubble Dumped by a Barge 1814
J.K. Vrijling and G. van Oord

Hydraulic Model Test of Stability of Amenity-Oriented Breakwater 1824
Shoji Kunitomi, Hajime Mase, and Tomotsuka Takayama

Stability of Mound Breakwaters: Dependence on Wave Reflection 1833
Cristina López, Miguel A. Losada, and Nobuhisa Kobayashi

Impact Structural Response of Core-Loc 1846
George F. Turk and Jeffrey A. Melby

Results of Field Monitoring of the New Core-Loc Breakwater at Port St. Frances, South Africa 1857
D. Phelp, A. Holtzhausen, and J. Melby

The First Core-Loc Breakwater 1871
Anton H. Holtzhausen

Damage Progression on Breakwaters 1884
J. A. Melby and N. Kobayashi

The Influence of Pressure Fluctuations on the Flow between Armour Elements 1898
Robert Booij, Wim S.J. Uijttewaal, Patrick van Os, Harry L. Fontijn, and Jurjen A. Battjes

Wave Kinematics on Breakwater Heads and Stability of Armour Layers under Multidirectional Waves 1906
Yoshiharu Matsumi, Akira Kimura, and Kenichi Ohno

A Statistical Tool for Breakwater Design 1920
Rodolfo Silva, Georges Govaere, and Francisco Martin

Cost Comparison of Breakwater Types 1934
W.H. Tutuarima and K. d'Angremond

Wave Forces on Solid and Perforated Caisson Breakwaters: Comparison of Field and Laboratory Measurements 1945
L. Franco, M. de Gerloni, G. Passoni, and D. Zacconi

Wave Impacts on Caisson Breakwaters Situated in Multidirectionally Breaking Seas 1959
P. Frigaard, H.F. Burcharth, and J.P. Kofoed

Prototype Measurements of the Dynamic Response of Caisson Breakwaters 1972
Alberto Lamberti and Luca Martinelli

Experimental and FEM Simulation of the Dynamic Response of a Caisson Wall against Breaking Wave Impulsive Pressures 1986
Shigeo Takahashi, Muneo Tsuda, Kojiro Suzuki, and Ken-ichiro Shimosako

Wave Transmission at Submerged Rubblemound Breakwaters 2000
Stuart R. Seabrook and Kevin R. Hall

Vertical Circulation Induced by a Submerged Breakwater 2014
A. Sánchez-Arcilla, F. Rivero, X. Gironella, D. Vergés, and M. Tomé

2DH Morphological Modelling of Submerged Breakwaters 2028
S.C. van der Biezen, J.A. Roelvink, J. van de Graaff, J. Schaap, and L. Torrini

Wave Pressure Distribution on Permeable Vertical Walls 2042
Hendrik Bergmann and Hocine Oumeraci

Impact Loadings on Vertical Walls in Directional Seas 2056
N.W.H. Allsop and M. Calabrese

Wave Forces on a Vertical Wave Barrier 2069
David Kriebel, Charles Sollitt, and William Gerken

Statistical Distribution of Horizontal Wave Forces on Vertical Breakwaters 2082
Janice McKenna and William Allsop

Neural Network Modelling of Forces on Vertical Structures 2096
Marcel R. A. van Gent, and Henk F. P. van den Boogaard

Pore Pressures in Vertical Breakwater Foundations 2110
C. Zwanenburg, M.B. de Groot, T. J. Kvalstad, and A. van Hoven

Economic Optimal Design of Vertical Breakwaters 2124
H. G. Voortman, H.K.T. Kuijper, and J.K. Vrijling

Design of Vertical Wall Caisson Breakwaters Using Partial Safety Factors 2138
Hans F. Burcharth and John Dalsgaard Sørensen

Lateral Versus Longitudinal Artificial Reef Systems 2152
Yoshimi Goda and Hiroshi Takagi

Development of a New Type of Reef Breakwater: Theoretical and Experimental Study 2166
Shohachi Kakuno, Masao Endoh, Yiming Zhong, Takaaki Shigematsu, and Kazuki Oda

Performance of Submerged Active Breakwaters in a Hydraulic Model 2179
K.R. Hall and M.P. Fischer

Wave Force and Stability of Armor Units for Composite Breakwaters 2193
Katsutoshi Kimura, Yuzo Mizuno, and Michifumi Hayashi

Hydraulic Performance of a High Mound Composite Breakwater **2207**
M. Muttray, H. Oumeraci, K. Shimosako, and S. Takahashi

Double Walled, Low Reflection Wave Barriers **2221**
R.J. Cox, P.R. Horton, and S.H. Bettington

Wave Overtopping of Rubble Mound Breakwaters **2235**
Mogens Hebsgaard, Peter Sloth, and Jørgen Juhl

Directional Wave Overtopping Estimation Model and Experimental Verification **2249**
Tetsuya Hiraishi and Haruhiro Maruyama

Part IV: Coastal Processes and Sediment Transport

The Morphological Changes along the Northern Coast of the Nile Delta **2264**
John B. Herbich, Abdel-Fattah Elfiky, and Gamal H. Elsaeed

Modelling the Morphological Sensitivity of Large Nontidal Coastal Areas to Climatological Changes **2269**
H. Weilbeer and W. Zielke

North-Coast of Texel: A Comparison between Reality and Prediction **2281**
Rob Steijn, Dano Roelvink, Dick Rakhorst, Jan Ribberink, and Jan van Overeem

Littoral Processes in a Prograding Coast: The Case Study of the Atlantic Ocean Coast of Uruguay **2294**
Luis Teixeira, Juan Montaña, and Miguel Losada

Turbidimetric Measuring of Suspended Sediment Concentration in the Coastal Zone **2303**
Ruben D. Kos'yan, Igor S. Podymov, and Sergey Yu. Kuznetsov

Characteristics of Suspended Sediment Transport in the Surf Zone of Irregular Waves and Their Reproduction by a Cross-Shore Beach Deformation Model **2317**
M. Ikeno and T. Shimizu

Cross-Shore Sediment Transport: A Field Test of the Bailard Energetics Model **2331**
Troels Aagaard, Brian Greenwood, and Jørgen Nielsen

Field Observations of Small Scale Sedimentation Processes **2344**
Daniel M. Hanes, Eric D. Thosteson, Yeon-Sihk Chang, Craig Conner, and Chris E. Vincent

Littoral Transport under Complex Wave Fields: Pecém, Northeast Brazil **2353**
Berry Elfrink, Domenico Accetta, Berenice Motta Vargas, and Wagner Santos Scisinio Dias

Morphological Modelling Using a Modified Multi-Layer Approach **2368**
Henk J. Steetzel, Hans de Vroeg, Leo C. van Rijn, and Jean-Marie Stam

Parameterizing Beach Erosion/Accretion Conditions **2382**
John P. Ahrens and Edward B. Hands

Determining Depth from Remotely-Sensed Images **2395**
Robert A. Dalrymple, Andrew B. Kennedy, James T. Kirby, and Qin Chen

VOLUME 3

On the Predictability of Nearshore Bar Behaviour 2409
Stefan Aarninkhof, Claire Hinton, and Kathelijne Wijnberg

Laboratory Evaluation of Instrumentation Used in Field Studies of Wave-Sediment Interactions 2423
J.J. Williams, P. Bell, L.E. Coates, A.E. Davies, P.J. Hardcastle, J.D. Humphery, S.P. Moores, L.C. van Rijn, P.D. Thorne, and K. Trouw

Size Gradation Effects in Sediment Transport 2435
Y. Chatelus, I. Katopodi, M. Dohmen-Janssen, J.S. Ribberink, P. Samothrakis, B. Cloin, J.C. Savioli, J. Bosboom, B.A. O'Connor, R. Hein, and L. Hamm

Phase-Lag Effects in Oscillatory Sheet Flow 2449
C. Marjolein Dohmen-Janssen, Gizella van der Hout, and Jan S. Ribberink

Cross-Shore Graded Sediment Transport: Grain Size and Density Effects 2463
R.L. Koomans, R.J. de Meijer, and L.B. Venema

Cross-Shore Sediment Transports on a Cut Profile for Large Scale Land Reclamations 2475
Martijn Onderwater, Dano Roelvink, and Jan van de Graaff

Optimum Size of Distorted Ripple Train for the Control of Cross-Shore Sediment Transport 2489
Satoshi Takewaka, Isao Irie, Masahiro Uchida, Hirokazu Sakamoto, and Nobuyuki Ono

The Effect of Sediment Composition on Cross-Shore Bed Profiles 2495
Leo C. van Rijn

The Breaching of Sand Investigated in Large-Scale Model Tests 2509
Cees van Rhee and Adam Bezuijen

A Dimensionless Parameter Describing Sea Cliff Erosion 2520
Akira Mano and Shigenori Suzuki

The Sand Trapping Trench as a Countermeasure To Control Wind-Blown Sand on Beaches 2534
Shintaro Hotta, Katsumori Hatanaka, Hiroyoshi Tanaka, and Kiyoshi Horikawa

Coastal Sediment Transport: The COAST3D Project 2548
R.L. Soulsby

Modelling of a Three-Layer Sediment Transport System in Oscillatory Flow 2559
Leszek M. Kaczmarek and Rafal Ostrowski

Analytical Model for Wave-Related Transport 2573
Judith Bosboom, Gert Klopman, Ad Reniers, and Marcel J.F. Stive

Vertical Length Scales of Nearshore Suspension Events 2587
D.L. Foster, A.J. Bowen, and A.E. Hay

Sediment Resuspension under Non-Breaking Waves: Predicting Sediment "Pulses" as a Function of Groupiness 2595
José A. Jiménez, Agustín Sánchez-Arcilla, and German Rodríguez

Coherent Doppler Sonar: Sediment Flux and Turbulent Velocities in a Wave Flume 2607
Len Zedel and Alex Hay

Eddy Viscosity Models for Wave Boundary Layers 2615
Ole Secher Madsen and Paulo Salles

Measurement of Shear Stress on a Moveable Bed 2628
Kelly L. Rankin, Michael S. Bruno, and Richard I. Hires

Evaluation of Longshore Sediment Transport Models on Coarse Grained Beaches Using Field Data: A Preliminary Investigation 2640
Erik van Wellen, Andrew J. Chadwick, Mark Lee, Brian Baily, and John Morfett

Motions of Pebbles on Pebble Beach 2654
Ichiro Deguchi, Masanobu Ono, Susumu Araki, and Toru Sawaragi

ONELINE: A Numerical Model for Shoreline Change 2668
Mohamed Dabees and J. William Kamphuis

Seasonal Shoreline Variations by Cross-Shore Transport in a One-Line Model under Random Waves 2682
Hans Hanson and Magnus Larson

Coastline Evolution in Response to a Major Mine Sediment Discharge on the Namibian Coastline 2696
G.G. Smith and G.P. Mocke

Longshore Patterns of the Sea Bottom Morphology 2710
Giovanna Vittori, Huib de Swart, and Paolo Blondeaux

Simple Models for Equilibrium Profiles under Breaking and Non-Breaking Waves 2722
Magnus Larson and Randall A. Wise

Equilibrium Terraced and Barred Beaches 2736
Mark D. Orzech and Nobuhisa Kobayashi

Breaker Bar Formation and Migration 2750
Bart T. Grasmeijer and Leo C. van Rijn

Beach Evolution on the Southern North Sea Coast 2759
Daniel J. Leggett, Jeremy P. Lowe, and Nicholas J. Cooper

Extracting Morphologic Information from Field Data 2773
Nathaniel G. Plant and Rob A. Holman

Nonlinear Time-Averaged Model in Surf and Swash Zones 2785
Bradley D. Johnson and Nobuhisa Kobayashi

Swash Zone Morphodynamics and Sediment Transport Processes 2799
K. Todd Holland, Asbury H. Sallenger, Britt Raubenheimer, and Steve Elgar

Field Measurements of Swash Induced Pressures within a Sandy Beach 2812
D.P. Horn, T.E. Baldock, A.J. Baird, and T.E. Mason

Flow Structures in Swash Zone 2826
H.H. Hwung, K.S. Hwang, W.S. Chiang, and C.F. Lai

Modelling Large-Scale Dynamics of Hel Peninsula, Poland 2837
Marek Szmytkiewicz, Ryszard B. Zeidler, Grzegorz Różyński, and Marek Skaja

Morphodynamics of Shoreface-Connected Ridges 2851
A. Falques, D. Calvete, H.E. de Swart, and N. Dodd

The Spatial Variability of Large Scale Sand Bars 2865
C.R. Worley, T.C. Lippmann, J.W. Haines, and A.H. Sallenger

Modeling the Dynamics of a Bar System at Duck, North Carolina, USA 2877
B. Boczar-Karakiewicz, W. Romańczyk, J.L. Bona, and E.B. Thornton

Depth of Closure: Improving Understanding and Prediction 2888
Robert J. Nicholls, Magnus Larson, Michele Capobianco, and William A. Birkemeier

Short-Term Relatively Deep Sedimentation on the Ebro Delta Coast: Opening the Closure Depth 2902
Vicente Gracia, José A. Jiménez, Agustín Sánchez-Arcilla, Jorge Guillén, and Albert Palanques

Spatial and Temporal Behavior of Depth of Closure along the Holland Coast 2913
Claire Hinton and Robert J. Nicholls

Depth of Closure and Seabed Variability Patterns 2926
Grzegorz Różyński, Zbigniew Pruszak, Tomasz Okrój, and Ryszard Zeidler

2DH Non-Linear Dispersive Wave Modelling and Sediment Transport in the Nearshore Zone 2940
Theofanis V. Karambas

Comparison of Storm Longshore Transport Rates to Predictions 2954
Herman C. Miller

Depth of Erosion under Storm Conditions 2968
John F.A. Sleath

Numerical Investigation of Sediment Transport for Combined Waves and Currents 2980
Juan Savioli

A Morphodynamic Model for River and Estuary Management 2992
Volker Barthel and Ulrich Zanke

Random Wave Modelling Approach Included in a Beach Deformation Model 3008
Ioan Nistor and Tomoya Shibayama

Geomorphological Modelling in Coastal Waters 3022
Morteza Kolahdoozan, Roger A. Falconer, and Yiping Chen

Beach Recharge Design and Bi-Modal Wave Spectra 3036
T.T. Coates and P.J. Hawkes

Management of Beach Nourishment in an Open Sand System 3046
Hans H. Dette

Beach Fills in Europe: Projects, Practices, and Objectives 3060
L. Hamm, H. Hanson, M. Capobianco, H.H. Dette, A. Lechuga, and R. Spanhoff

Evaluation of the Effect of 20 Years of Nourishment 3074
Christian Laustrup and Holger Toxvig Madsen

Zurriola Beach Evolution Two Years after Nourishment 3086
José C. Santas, José M. Medina, Alejandro Caballero, Adolfo Uriarte, and Vicente Esteban

Model Tests for Evaluating Beach Nourishment Performance 3096
Massimo Tondello, Piero Ruol, Mauro Sclavo, and Michele Capobianco

Assessment of Depth of Closure on a Nourished Beach: Terschelling, The Netherlands 3110
S.W. Marsh, R.J. Nicholls, A. Kroon, and P. Hoekstra

Post-Stabilization Morphology of Oregon Inlet, North Carolina 3124
Brian P. Joyner, Margery F. Overton, and John S.Fisher

Predictive Model of Three-Dimensional Development and Deformation of a River Mouth Delta by Applying Contour Line Change Model 3138
Takaaki Uda, Hiroshi Yamagata, Ken-ichi Katoh, and Naohiro Akamatsu

Field Investigation on Sediment Transport into the Submarine Canyon in the Fuji Coast with the New Type Tracers 3151
Shigenobu Tanaka, Koji Yamamoto, Hitoshi Ito, Toshiharu Arisawa, and Toshimitsu Takagi

Sea Breeze Climatology and Nearshore Processes along the Perth Metropolitan Coastline, Western Australia 3165
G. Masselink and C.B. Pattiaratchi

Field Observation of Erosion and Accretion Waves on Shizuoka and Shimizu Coasts in Suruga Bay in Japan 3178
Naoki Itabashi and Takaaki Uda

Coastal Erosion at Keta Lagoon, Ghana: Large Scale Solution to a Large Scale Problem 3192
R.B. Nairn, K.J. MacIntosh, M.O. Hayes, G. Nai, S.L. Anthonio, and W.S. Valley

Morphological Vulnerability Index: A Simple Way of Determining Beach Behavior 3206
Óscar Ferreira, Rui Taborda, and J. Alveirinho Dias

Homogeneity Aspects in Statistical Analysis of Coastal Engineering Data 3215
P.H.A.J.M. van Gelder and J.K. Vrijling

A Simple Method To Predict Long-Term Morphological Changes 3224
Dano Roelvink, Alain Boutmy, and Jean-Marie Stam

Coastal Morphologic Variability of High Energy Dissipative Beaches 3238
Peter Ruggiero, George Kaminsky, and Nathaniel Plant

Effect Resonance on Morphology of Tidal Channels 3252
Willem T. Bakker

Inlet Cross-Sectional Area Calculated by Process-Based Model 3265
Nicholas C. Kraus

Stabilisation of the Tidal Entrance at Hornafjordur, Iceland 3279
Gisli Viggosson, Sigurdur Sigurdarson, and Bjorn Kristjansson

Application of a Long-Term Evolution Model of Tidal Inlets to the Design of a Navigation Channel, The Navia Inlet Case 3293
R. Medina, M.A. Losada, P. Lomónaco, and A. Baquerizo

Change of Mean Tidal Peaks and Range Due to Estuarine Waterway Deepening 3307
Hanz D. Niemeyer

Inlet Dynamics from Semi-Annual Surveys 3318
Owen W. Callard, William R. Dally, and Kathy FitzPatrick

Nearshore Coastal Processes Adjacent to a Tidal Inlet 3331
Thomas O. Herrington, Michael S. Bruno, Majid Yavary, and Kelly L. Rankin

Inlet Impacts on Local Coastal Processes 3345
Rajesh Srinivas and R. Bruce Taylor

Long-Term Morphological Development of the Accumer Ee Tidal Inlet and Its Impact on Island Beaches and Engineering Responses 3359
U. Abels, H. Kunz, G. Ragutzki, and H.-J. Stephan

Part V: Coastal, Estuarine, and Environmental Problems

Integrated Design Optimization for a Tropical Land Reclamation: Bali Turtle Island Development 3374
Andrew M. Driscoll, Tom Foster, Claus Pedersen, Palle Mikkelsen, and Yukimitsu Tateishi

The Influence of Marina Construction in Beach Stability: El Milagro Case Study 3388
J. Galofré, F.J. Montoya, and R. Medina

Man Made Beaches Balancing Nature and Recreation 3401
Ulf Anderskouv, Hanne Bach, Dan B Hasløv, and Karsten Mangor

Environmentally Friendly Coastal Protection: The ECOPRO Project 3412
Brendan Dollard

Coastal Restoration Considerations 3425
Karsten Mangor

Integrated Approach on the Safety of Dikes along the Great Dutch Lakes 3439
Jentsje van der Meer, Harry de Looff, and Peter C.G. Glas

Maintenance Dredging Required after Port Extensions at Walvis Bay 3453
R.C. Coppoolse and J.S. Schoonees

Accuracy in Spill Monitoring: Turbidity Distribution and Conversion Factors 3466
Klavs Høgh, Iris Buxborn, and Trine Borum Bojsen

Defining an Unusual Littoral Regime To Optimize Dredging at East London 3479
A.K. Theron and J.S. Schoonees

The Development of Sand Waves and the Maintenance of Navigation Channels in the Bisanseto Sea 3490
Kazumasa Katoh, Hidetoshi Kume, Keiji Kuroki, and Junzo Hasegawa

Coastal Disaster Prevention Works in Japan 3503
Ichio Motono and Susumu Naruse

Breach Erosion in Sand-Dikes 3516
Paul J. Visser

Bayesian Estimation of Quantiles for the Purpose of Flood Prevention 3529
J.M. van Noortwijk, and P.H.A.J.M. van Gelder

Flood Protection in the Danish Wadden Sea Area 3542
Jens Otto Andersen

Dispersion of Wave Action 3553
James M. Buick and Tariq S. Durrani

Predicting and Evaluating Turbidity Caused by Dredging in the Environmentally Sensitive Saldanha Bay 3561
S.A. Luger, J.S. Schoonees, G.P. Mocke, and F. Smit

Simulation of the Behavior of Oxygen-Deficit Water in Tokyo Bay by Three-Dimensional Water Quality Model 3575
Nobuo Mimura, Mitsuhiro Tsukada, and Masaharu Suzuki

Watertable Fluctuations in a Sandy Ocean Beach 3588
B. Raubenheimer, R.T. Guza, and Steve Elgar

Seepage Effects on Sediment Transport by Waves and Currents 3601
T.E. Baldock and P. Holmes

The Settlement, Hardness and Liquefaction of Sand Beds Due to Fluctuating Water Pressure 3615
Takaaki Minamimura, Masaki Niiyama, Takao Akutu, Kenji Yano, and Toshihiko Yamashita

A Method for Estimating the Bed Velocities Produced by a Ship's Propeller Wash Influenced by a Rudder 3624
G.A. Hamill, J.A. McGarvey, and P.A. Mackinnon

Design of Scour Protection for the Bridge Piers of the Øresund Link 3634
Lars Kirkegaard, Mogens Hebsgaard, and Ole Juul Jensen

Experimental Analysis of Wave-Induced Liquefaction in a Fine Sandbed 3643
Kojiro Suzuki, Shigeo Takahashi, and Yoon-Koo Kang

Long-Period Oscillations in a Harbor with a Fluid Mud Bottom **3655**
Wataru Kioka, M. Akter Hossain, and Kenji Kashihara

Non-Uniformity in the Wind Generated Gravity Waves Phase Distribution **3668**
Germán Rodríguez, C. Guedes Soares, E. Pérez Martell, and J.C. Nieto

Subject Index **3681**

Author Index **3691**

On the predictability of nearshore bar behaviour

Stefan Aarninkhof[1], Claire Hinton[2] and Kathelijne Wijnberg[3]

Abstract

The analysis of field observations of surf zone dynamics has revealed some 'unexpected' behaviour of the coastal system, generally referred to as 'free behaviour', which is behaviour that is unrelated to similar patterns in the external forcing. Present-day process-based modeling concepts are not capable to deal with these free modes of behaviour. In order to assess the validity of model-based predictions of bar dynamics, the relative importance of free behaviour versus forced response in the surf zone needs to be addressed. This work aims to contribute to the debate, by investigating the sensitivity of breaker bar behaviour to chronology effects from coastal profile modeling at a multiple-barred beach, with probabilistic forcing conditions. The results show chronology effects merely affect the predicted height of the bars, rather than their location which is remarkably consistent over the various runs. The latter observation has raised the question up to what extent predicted bar behaviour is controlled by model characteristics (concept, parameter settings), rather than system and forcing characteristics.

Introduction

Over the years, nearshore sand bar behaviour was believed to show a rather consistent pattern of delayed response to the wave energy input, featuring a rapid straightening of the outer bar during storms, and a gradual development of a crescentic bar pattern via some intermediate stages during subsequent periods of low-energy exposure (e.g. Wright and Short, 1984; Lippmann and Holman, 1990). However, another field observation of bar behaviour has been presented by Southgate and Möller (1998). They applied a fractal

[1] Netherlands Centre for Coastal Research, Delft University of Technology, c/o WLIDELFT HYDRAULICS, p.o. box 177, 2600 MH Delft, The Netherlands
[2] Flood Hazard Research Centre, Middlesex University, Queensway, Enfield, London, EN3 4SF, UK
[3] Netherlands Centre for Coastal Research, Institute for Marine and Atmospheric Research, Utrecht University, p.o. box 80115, 3508 TC Utrecht, The Netherlands

analysis technique to the Duck, NC, data base (10.5 years of monthly cross-shore surveys) to indicate the existence of self-organized (or free) behaviour in a coastal system. They arrive at the conclusion that the profile behaviour has a fractal structure and is uncorrelated to the input variations, but only within a certain time window. The width of this time window varies with the cross-shore location, featuring a maximum of 30-40 months well inside the surf zone. Within these time windows, the process of self-organization seems to be dominant, while outside, the profile behaviour is well-correlated to the forcing factors.

Considering the vast amount of plans for human interference in coastal systems (like large-scale land reclamations, artificial islands in sea and beach nourishments), the need for model-based predictions of coastal behaviour on the time scale of years to decades is evident. It would be interesting to see how the present generation of process-based profile models predict bar behaviour on these time scales, and up to what extend they are be able to deal with the types of 'unexpected' behaviour as given above. In the end a model-based investigation of bar dynamics might contribute to our understanding of the balance of free versus forced behaviour in coastal systems. This study is a first start to addressing these questions.

Concepts in relation to morphodynamics of breaker bar systems

Bed dynamics in the coastal zone occur at various time scales. At the smallest scale bedforms like ripples and mega ripples evolve (minutes to hours). Moving up, the evolution of features like nearshore bars becomes apparent (days to years). Channels on ebb deltas may evolve over decadal time scales, while at a time scale of centuries, we may for instance observe the steepening of the shore face, or changes in the global shoreline orientation. In this paper, the ripple scale is referred to as 'micro-scale', the nearshore bar scale (and tidal channel scale) as 'meso-scale', and the larger scales as 'macro-scale'.

Physical processes at a certain scale level will be in dynamic interaction with coastal behaviour of a similar scale. This is what is called the primary-scale relationship (De Vriend, 1991), see Figure 1.

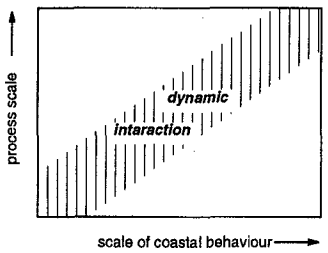

Fig. 1: Primary-scale relationship (after De Vriend, 1991)

A physical process at a certain scale acts as an extrinsic condition (or constraint) for dynamics at a lower scale level, whilst it is just noise for dynamics at a higher level. Within one scale level, a feedback between response and forcing is observed. For example, for the nearshore bars, wave energy input generates a flow field (FF) in the nearshore zone, causing sediment transport (ST) gradients across the bars and hence morphologic changes (MC), which again affect the nearshore flow field, see Figure 2. Furthermore, a coastal system is stochastically forced, dissipative and features various components which are highly non-linear (like transport rates). It is because of these characteristics that a coastal system might easily allow for unpredictable behaviour in a deterministic sense (De Vriend, 1998), i.e. the system develops very complex patterns that could be modeled in detail, however, without being able to predict when and where they occur (cf. turbulence).

These considerations allow us to schematize the coastal system of consideration, viz. that of nearshore bars. The morphodynamics at this scale level are supposed to be in dynamic interaction with the incoming wave energy and tide-induced variations in water level elevation. Larger scale phenomena like sea level rise and variations in the tidal current pattern act on the system as a constraint via the macro level, as they are affected by features at this higher level. Also, physical constraints like jetties are considered as a macro-level induced constraints, while a weak constraint might result from the lower level by means of bed-form induced friction. Besides forced response, possibly represented by the consistent tendency of bars to straighten during storm conditions, free behaviour needs to be taken into account. This results in the schematization as given in Figure 2. Though the meso-level breaker bar system also affects the lower and higher scales, these relations have been ignored in Figure 2.

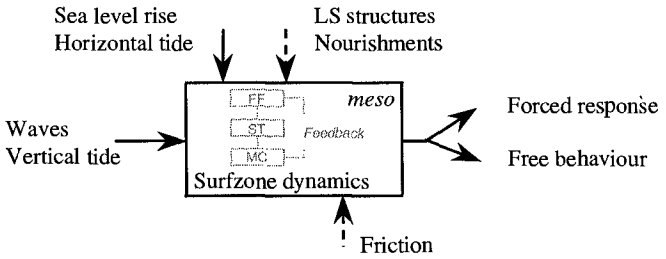

Fig. 2: Schematization of a meso-scale coastal system

In order to assess the predictive skills of profile models, the relative importance of forced response versus free behaviour needs to be determined, which requires the analysis of bar behaviour from both field observations and model simulations.

Positioning of present study

As stated, the predictability of breaker bar behaviour needs be assessed along two different ways:

1. By analyzing bar dynamics from field observations, in relation to the forcing conditions. This requires long time series of bar morphology, with high resolution in time. ARGUS-stations, which collect hourly video observations of the nearshore zone (Holman *et al*, 1993), provide such type of data. Different techniques to quantify bathymetry from video observations are presently under development, based on the inverse modeling of wave dissipation patterns (Aarninkhof *et al*, 1997) or wave celerities (Stockdon, 1997).
2. By investigating breaker bar behaviour from simulations with a process-based coastal profile model, both in terms of the sensitivity to various model parameters, as well as regarding the effect of different forcing sequences with similar statistics.

On the longer term, we aim at a comparison of both approaches, however, the present paper only discusses an initial step into the second approach. It concerns a model-based investigation of bar dynamics at Noordwijk, The Netherlands. Multiple model runs have been made, using different time series of hydrodynamic conditions with nevertheless similar statistical characteristics. If a considerable variability in final profile evolution over the various runs is observed (indicating the importance of chronology effects), the system's response is interpreted to be forced. Alternately, the dynamical quantities of the system might show fractal statistics (in space or time), indicating self-organized response or free behaviour.

The present work treats the sensitivity of model-predicted bar behaviour to chronology effects. To that end a model regarding a multiple-barred coastal system has been set up and calibrated, which will be the subject of the next sections.

1DV-model simulations of bar dynamics at Noordwijk, The Netherlands

Description of model concept

To do the model simulations, WL|DELFT HYDRAULICS' 1DV coastal profile model UNIBEST-TC has been applied. The UNIBEST-TC model consists of a wave, flow, transport and bed level change module, for which the initial formulations are given in Roelvink and Stive (1989). Although they arrive at a satisfactory calibration of the hydrodynamics in terms of wave height, wave set-up and flow moments, the Bailard transport formulation did not result in a correct description of transport rates, despite an extension of the original Bailard formulation to account for additional stirring of sediment by surface breaking-induced turbulence which penetrates toward the bottom. Consequently, the development and migration of the outer bar were (amongst others) simulated insufficiently.

Later on, the formulation for the breaking-induced turbulence was replaced by the roller concept after Svendsen (1984), and, for heuristic reasons, a breaker delay function was introduced (Roelvink *et al*, (1995)). Moreover, the transport formulations were modified according to Ribberink and Van Rijn (see Van Rijn *et al*, 1995) without however, significantly changing the basic concept of the quasi-steady transport model. These new formulations allowed for the modification of transport rates by means of breaker delay and slope effects (Bosboom *et al*, 1997), that finally resulted in the mimicking of cyclic bar behaviour. However, a robust validation of these formulations has not been performed yet.

Model set-up

The numerical model has been set up for a characteristic profile along the Central Dutch coast. Bed elevations along this coast have been surveyed yearly since 1963, which makes its long-term behaviour relatively well understood. A profile at Noordwijk was chosen because this site is also monitored with ARGUS cameras, which gives a reference to short- and medium-term behaviour. The actual profile applied was surveyed in 1980 and extends to 2500 m off-shore; it features 3 bars, which exhibit cyclic behaviour over about a 4 year time span (Wijnberg, 1995).

Time series for the off-shore hydrodynamic conditions have been generated from a wave-climate, measured 6 km off-shore of Noordwijk in 18 m water depth, at 3-hour intervals during a 12-year period of time. The statistics of the wave heights and angles of incidence that occur in the time series obey the frequencies of occurrence as prescribed by the measured wave climate. The adjoining wave period and mean water level elevation have been chosen accordingly, depending on the randomly selected wave height and angle of incidence. At presence, tidal variations are not accounted for, which allows for a simplification of the problem by means of a reduction of the number of independent variables.

The computational grid extends from 2500 m off-shore (14.9 m water depth) to the dune foot; wave conditions measured at 6 km off-shore are translated to the seaward boundary of the model, taking into account the effects of shoaling and refraction. The horizontal grid spacing decreases towards the shore so that a higher resolution is obtained in the active zone, yielding a total of 147 grid points. The time step characteristically amounts 0.25 days for short term runs (180 days).

Sensitivity of bar behaviour to model parameters

Three model parameters are of particular importance in view of bar behaviour, viz. the breaker parameter γ, the breaker delay parameter λ and the subaquous angle of natural repose $\tan(\varphi)$. γ merely affects the migration of bars, while λ and $\tan(\varphi)$ are important with respect to the growth, maintenance, and damping of bars. Their role in the model formulations, as well as their effect on final profile evolution is shortly discussed here.

The wave breaking parameter γ stems from the Battjes-Janssen wave propagation model and affects the maximum local wave height H_{max}, which is determined as a function of local water depth h and wave steepness, according to

$$H_{max} = \frac{0.88}{k}\tanh\left(\frac{\gamma kh}{0.88}\right) \qquad \text{(Eq. 1)}$$

where k is the wave number. Waves smaller than H_{max} are assumed to be non-breaking and Rayleigh distributed, while all waves higher than H_{max} are breaking. An increase of γ allows for higher wave heights at a certain depth, hence shifting the process of wave dissipation to more shallow water. Consequently, an increase of undertow-induced off-shore directed transport rates is induced, yielding a faster off-shore migration of the breaker bars. Figure 3 illustrates this, showing the final profile evolution after 50 days in case of a constant wave height H_{rms} = 1.5 m.

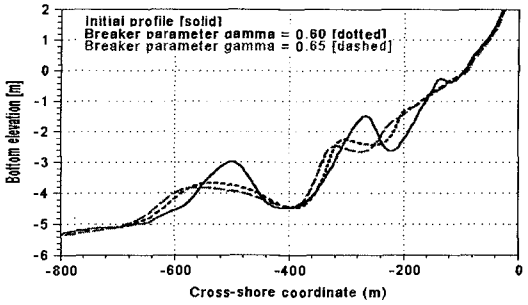

Fig. 3: Effect of breaker parameter γ on final profile evolution

The concept of breaker delay (Roelvink *et al*, 1995) was introduced based on field observations of breaking waves, which showed that waves – having inertia – need a distance of the order of one wave length to actually start or stop breaking. Roelvink *et al.* accounted for this by replacing the local water depth h in Eq. 1 with a seaward weighted reference depth h_r. Consequently, slightly higher waves are allowed at the seaward flank of breaker bars while the concept also allows for ongoing wave breaking in the trough – because of the seaward weighted water depth - hence shifting the undertow currents somewhat towards the trough. The latter allows for offshore-directed sediment transport towards the bar crest, which originally suffered from heavy erosion in the concept without breaker delay. In this way some sediment accumulates in the region close to the bar crest, yielding a better-preserved bar shape. Figure 4 shows the effect of breaker delay after 50 days of constant forcing conditions with H_{rms} = 1.5 m.

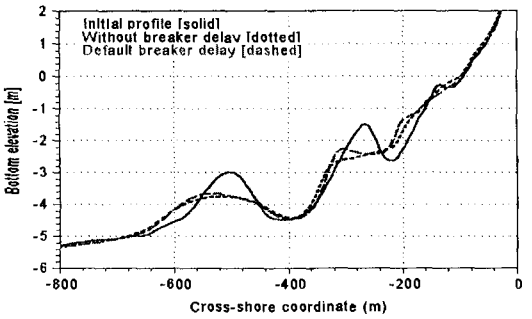

Fig. 4: Effect of breaker delay on final profile evolution

The subaquous angle of natural repose tan(φ) accounts for slope effects (Bosboom *et al.*, 1997) and affects the computed transport rates in two ways. First, the threshold criterion for the initiation of motion is adapted using the Schoklitsch factor. With increasing tan(φ), the non-dimensional critical shear stress θ_{cr} (according to Shields) decreases in case of upslope transport, and increases for downslope transport. In other words, upslope transport is stimulated with increasing tan(φ), downslope transport hindered. Second, bed load transport rates are affected by means of a Bagnold multiplication factor β_s, which increases with increasing tan(φ) in case of upslope transport, and decreases in conditions of downslope transport. Again, upslope transport rates are facilitated by increasing values of tan(φ), downslope rates hampered. Both modifications to the computed transport rates result in the same effect: a higher value of tan(φ) stimulates accumulation of sediment around the bar crest, hence bar development, a lower value causes the damping of bars.

Figure 5 shows the effect of different subaquous angles of natural repose on the final profile evolution after 50 days in case of a constant wave height H_{rms} = 1.5 m. The values of tan(φ) are constant along the beach profile, though generally, they are set to decrease somewhat in off-shore direction, to facilitate the damping of bars at deeper water.

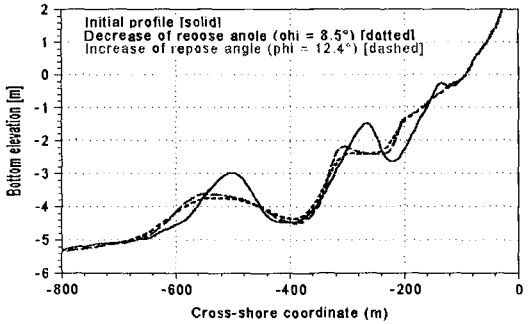

Fig. 5: The effect of tan(φ) on final profile evolution

Selection of appropriate model settings

As a robust validation of the modified transport module has not been performed yet, the present model can be considered as a (for heuristic reasons) modified version of the original model according to Roelvink and Stive (1989). The heuristic element lies in the transport formulation, and is dealt with by adopting appropriate settings of the wave breaking parameters and the slope effect. Though this might enable a satisfactory representation of cyclic bar behaviour, it does not guarantee that the morphodynamic concept of the model is fully correct.

Lacking local field data on surf zone hydrodynamics, the model has been tuned by carefully choosing the parameters of relevance as mentioned above, such that it represents medium-term bar behaviour reasonably well. Whenever possible, default settings have been applied. In order to obtain sufficient damping of bars at deeper water, the value of φ needed to be lowered to 9.1° at deeper water as compared to 12.4° at the waterline. The resulting bar behaviour is shown in Figure 6.

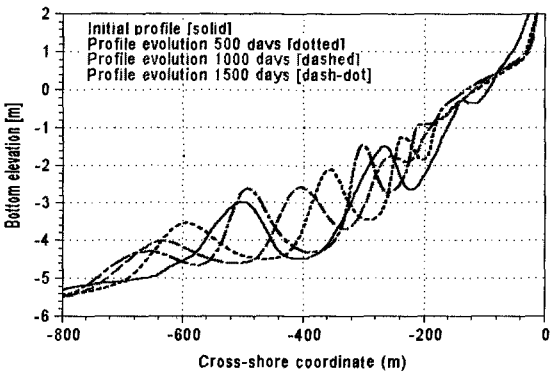

Fig. 6: Bar behaviour in calibrated model

Clearly, the erosion and formation of the steep berm around the waterline are not realistic. This might be attributed to the absence of tidal variations, cf. Southgate (1995). However, in view of bar behaviour, the 4-year bar cycle is clearly recognized while a new bar is being generated in the upper part of the profile.

Overview of model runs

In order to test model-predicted bar behaviour on its sensitivity to chronology effects, multiple model runs have been made with statistically similar input conditions. The sequence of wave events was randomly generated as described above. The statistics of each time series were determined by means of its mean wave height, the standard deviation around the mean and the lowest respectively highest wave of the series.

Statistics of various series show good comparison, as can be seen from 5 representative cases in the table below.

	Statistics of wave height H_{rms}			
Series	Mean	SD	Min	Max
# 01	0.91	0.57	0.23	4.04
# 02	0.89	0.57	0.23	3.51
# 03	0.88	0.54	0.23	4.04
# 04	0.88	0.53	0.23	3.56
# 05	0.89	0.54	0.23	4.04

Table 1: *Wave height statistics of generated time series*

25 Randomly generated time series at 3 hour intervals have been generated for use in the short-term computations, yielding 25 different profile evolutions after 180 days. Each of the 25 time series were then sorted based on wave height, both ascending and descending. This again yielded 25 different realizations of bathymetry after 180 days for both sortings.

Results of short-term (180 days) tests on chronology

In case of the random wave input, general bar behaviour seems to be consistent throughout the 25 cases. All of the three bars migrate seaward, over rather similar distances of about 75 m. Figure 7 shows the mean profile evolution after 180 days, averaged over 25 runs (lower panel), as well as the cross-shore variability in final profile evolution by means of the standard deviation of final bottom elevation over 25 runs and its extreme realizations (upper panel). Maximum variability occurs around the initial location of the bars and their final positions, indicating that the system has not run through a full cycle yet. Moreover, it points out that the horizontal variability (i.e. the variability in the final location of the bars) is rather weak, whereas the vertical variability is more significant: the standard deviation amounts up to 10-15% of the absolute changes of bottom elevation, which is in good correspondence with values found by Southgate (1995). Vertical variability slightly decreases towards the shore.

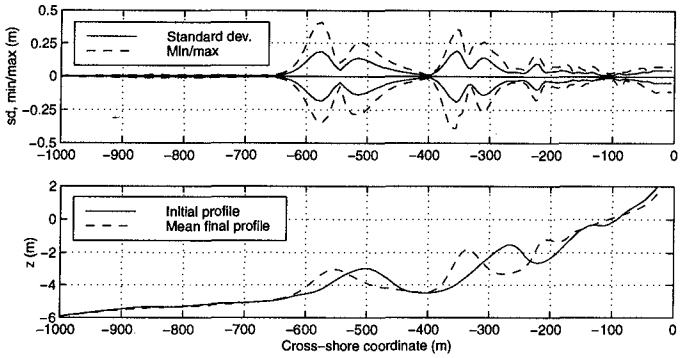

Fig. 7: Variability in final profile evolution (180 days) over 25 runs, random waves

The results of the runs with sorted input conditions are given in Figure 8. Analogous to the upper panel of Figure 7, the upper and middle panel of Figure 8 show the cross-shore variability in final profile evolution expressed in terms of the standard deviation and extreme realization over 25 runs, for the cases of ascending and descending wave heights respectively. The lower panel visualizes the mean profile evolution for both cases, averaged over 25 runs.

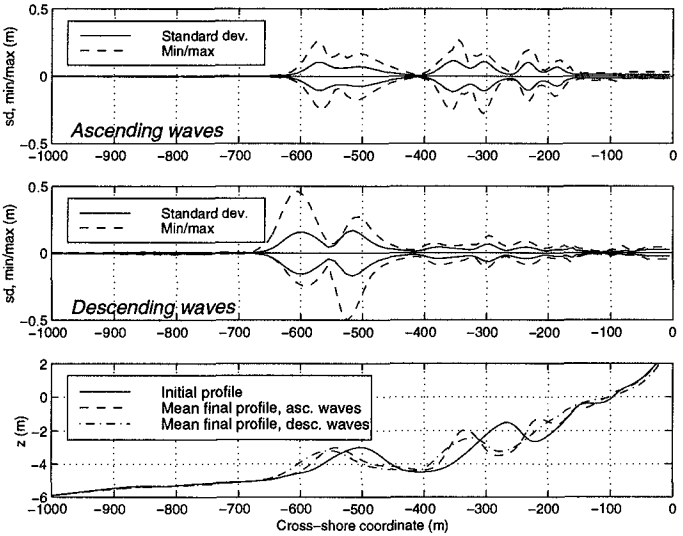

Fig. 8: Variability in final profile evolution in case of sorted wave height input

Again, the observed mean bar behaviour is remarkably consistent: after 180 days, all bars have migrated off-shore over a distance of about 75 m, though the bar-shape tends to be

better preserved in the case of ascending wave heights. The variability in final profile evolution clearly differs amongst the 2 cases: the system exposed by ascending wave heights shows moderate variability over 25 runs, which is rather constant along the profile, featuring relatively minor extremes around the initial and final locations of the bars. The case of descending wave heights, on the other hand, shows large variability around the outer bar which drops to almost zero through the central and inner surf zone, indicating very consistent behaviour of the middle and inner bar over the 25 runs.

Discussion

The results described above generally show a decrease of vertical variability in bottom elevation towards the shore, indicating a weaker response of inner surf zone morphodynamics to chronology-related variations in the input conditions. This can be explained from the presence of the outer bar, which filters the wave climate for the central and inner region of the surf zone with respect to high waves, hence reducing the temporal variations in the central and inner surf zone wave conditions. Apparently, the behaviour of the inner bars is not only controlled by the forcing conditions, but also by internal parameters like the height of the outer bar, which might more easily allow for free behaviour in this region. This observation is in accordance with Southgate (1998) who states that 'generally, fractal responses are found at locations ... where the temporal variations of wave forcing conditions are relatively weak'.

The important role of the outer bar in view of central and inner surf zone morphodynamics is also observed from the runs with sorted wave height input. Significant changes of the outer bar are assumed to be induced by the highest waves of the input time series, therefore the outer bar, in case of descending wave heights, is affected at the very beginning of the simulated time period, whilst in the case of ascending waves, this occurs only at the end of the 180-days period. Consequently, the height of the inner bars after 180 days is more reduced in case of descending wave heights, as they are exposed to more energetic wave conditions during the simulation period. This again stresses the importance of internal system parameters like the height of the outer bar in view of the morphodynamics of the central and inner region of the surf zone.

Nevertheless, though it seems like the observed vertical variability in bottom elevation along the cross-shore profile can be explained reasonably well, the absence of variability in the final position of the bars has not been explained yet. Particularly, the close correspondence between the position of the outer bar resulting from runs with ascending and descending waves respectively - suggesting that bar migration depends on the cumulative amount of energy input rather than the sequence of events – would indicate that chronology is of hardly any importance to the morphodynamics of the outer bar at Noordwijk. This seems counter-intuitive since bars are expected to migrate onshore during periods of low-energetic conditions, and off-shore during storms. Hence the question is raised up to what extend predicted bar behaviour is controlled by model characteristics (concept, parameter settings), rather than system and forcing characteristics.

Apparently, this might be not the only source of unpredictability that arises when addressing the possibility of model-based predictability of long-term bar behaviour. Generally, we can identify 4 possible sources of unpredictability:

1. The limited time horizon of predictability of wave conditions.
2. The numerical discretization of model equations.
3. The model concept, i.e. the dimension of the concept (1DV in the present case) and the schematization of real-world physics in terms of model equations.
4. The complexity or 'irregularity' of natural beach behaviour.

The first source is related to the limited horizon of predictability of weather conditions (characteristically up to 10 days), hence wave conditions, and forms a fundamental limitation to the deterministic predictability of bar behaviour, both from model runs and field observations. However, knowing statistics on the wave climate from long-term field measurements, the probabilistic approach based on randomly generated, realistic time series of wave events seems the best way to cope with this problem.

Also the second source is fundamentally related to the application of a process-based modeling approach. Even in case of a 'perfect' model concept, small errors, caused by the inevitable discretization of model equations, tend to accumulate to become significant in case longer-term computations, justifying the question which part of the model prediction is realistic behaviour and which part can be considered to be error-induced noise. The unrealistic damping of bars after 1 cycle can be attributed to this accumulation of errors, either concept- or discretization-related. Given a certain model-concept, the application of sufficiently small computational steps and the careful selection of parameter settings are ways to reduce this source of unpredictability as much as possible.

The third source of unpredictability seems to play an important role in the present study. Although the model predicts the 4-year bar cycle reasonably well, some essential characteristics of bar behaviour as observed in the field are clearly missing in the present model. The absence of onshore migration (and adjoining growth) of bars during periods of low-energetic conditions and the weak sensitivity of the behaviour of the outer bar to chronology effects can be mentioned in this respect. Further investigation of the present model concept and parameter settings in terms of bar behaviour is necessary to improve acceptability of a model-based approach to assess the predictability of bar behaviour. Questions to be addressed in this respect are: What are the governing processes causing the consistent off-shore movement of sand bars? What is the effect of the initial profile? Would long-period swell affect the predicted bar behaviour? Would the same behaviour be observed at different sites?

Regarding the fourth aspect, it might be questioned whether process-based numerical models will ever be capable to predict natural 'irregular' behaviour, commonly referred to as free behaviour of coastal systems. Nevertheless, a fundamental understanding of the relative importance of forced response versus free behaviour will help to assess the validity of model-based predictions of coastal morphodynamics. Both the analysis of

ARGUS video-based obser vations of bar behaviour and the investigation of model-based predictions are expected to attribute to the assessment of this balance.

Conclusion

The present study has attempted to contribute to our understanding of sand bar dynamics by means of coastal profile modeling of a multiple-barred beach with probabilistic forcing conditions. In the case of 180-days simulations, chronology effects turn out to play a role throughout the surf zone, the importance of which increases with distance offshore. Chronology effects merely affect the predicted height of the bars, rather than their final location which is remarkably consistent over the various runs. Moreover, the onshore migration of bars during periods of low-energetic wave conditions was not clearly observed. These observations raise the question up to what extent predicted bar behaviour is controlled by model characteristics (concept, parameter settings), rather than system and forcing characteristics. Further investigation of the model concept and a sensitivity analysis, more extensively than the one presented in this paper, are needed to address this problem.

Acknowledgements

The present study has been performed in the PACE project, in the framework of the EU-sponsored Marine Science and Technology Programme (MAST-III), under contractno. MAS3-CT95-0002. It was cosponsored by the NICOP fund, DELFT HYDRAULICS and Utrecht University. The ARGUS video technique has been developed with funds generated by the Coastal Imaging Lab, Oregon State University.

References

Aarninkhof, S.G.J, Janssen, P.C. and Plant, N.G. (1997). Quantitative estimations of bar dynamics from video images. *Proc. of Coastal Dyn. Conf.*, Plymouth, UK, 1997

Battjes, J.A. and Janssen, J.P.F.M. (1978). Energy loss and set-up due to breaking in random waves. *Proc. of 16th Conf. on Coastal Eng.*, ASCE, pp. 569-587

Bosboom, J., Aarninkhof, S.G.J., Reniers, A.J.H.M., Roelvink, J.A. and Walstra, D.J.R. (1997). Unibest-TC 2.0. Overview of model formulations. Delft Hydraulics report H2305.42

Holman, R.A., Sallenger Jr, A.H., Lippmann, T.C. and Haines, J.W. (1993). The application of video image processing to the study of nearshore processes. *Oceanography*, Vol. 6, No 3.

Lippmann, T.C. and Holman, R.A. (1990). The spatial and temporal variability of sand bar morphology. *J. Geoph. Res.*, 95(C7): 11575-11590.

Lippmann, T.C, Holman, R.A. and Hathaway, K.K. (1993). Episodic, nonstationary behavior of a double bar system at Duck, North Carolina, USA, 1986-1991. J.Coastal Res., 15(SI): 49-75.

Rijn, L.C. van, Reniers, A.J.H.M., Zitman, T. and Ribberink, J.S. (1995). Yearly-averaged sand transport at the -20 m and -8 m NAP depth contours of the Jarkus-profiles 14,40,76 and 103. Delft Hydraulics report H1887.

Roelvink, J.A., Meijer, Th.J.G.P., Houwman, K., Bakker, R. and Spanhoff, R. (1995). Field validation and application of a coastal profile model. *Proc. Conf. Coastal Dynamics*, ASCE, pp. 818-828.

Roelvink J.A., and Stive, M.J.F. (1989). Bar generating cross-shore flow mechanisms on a beach. *J. of Geophysical Research*, 94: 4785-4800.

Southgate, H.N. (1995). The effects of wave chronology on medium and long term coastal morphology. Coastal Engineering 26:251-270

Southgate, H.N. and Möller, I. (1998). Fractal properties of beach profile evolution at Duck, North Carolina. Submitted to *JGR Oceans*.

Stockdon, H. (1997). Estimations of wave phase speed and nearshore bathymetry using video techniques. M.Sc. Thesis, Oregon State University, College of Oceanic Atmospheric Sciences, Augst 1997.

Svendsen, I.A. (1984). Wave heights and set-up in a surf zone. *Coastal Eng.*, 8:303-329

Vriend, H.J. de (1991). Mathematical modelling and large-scale coastal behaviour, Part 1: Physical processes. *Journal of Hydraulic Research* 29, pp. 727-740.

Vriend, H.J. de (1998). On the predictability of coastal morphology. In: Proc. 3rd Marine Science and Technology Conf., Lisbon, 1998.

Wijnberg, K.M.(1995). Morphologic behaviour of a barred coast over a period of decades. Ph.D. Thesis, Utrecht University, Utrecht, The Netherlands, Netherlands Geographical Studies 195, KNAG, 245 pp.

Wright, L.D. and Short, A.D. (1984). Morphodynamic variability of surf zones and beaches: a synthesis. *Marine Geology* 56, 93-118.

Laboratory Evaluation of Instrumentation used in Field Studies of Wave-Sediment Interactions

J. J. Williams[1], P. Bell[1], L. E. Coates[2], A. E. Davies[3], P. J. Hardcastle[1], J. D.Humphery[1], S. P. Moores[1], L. C. van Rijn[4], P. D. Thorne[1] & K. Trouw[5]

Abstract

Restrictions imposed by the physical size of testing facilities has limited the range of trials undertaken on field instruments and little is known about interactions between the observed processes and large frames used to deploy equipment in the sea. Further, limited information on the physical processes from the field leads to ambiguity in interpretation of field data. This paper describes tests of the autonomous multi-sensor instrument STABLE, and process studies conducted in the Deltaflume (230 m long, 5 m wide and 7 m deep) of the Delft Hydraulics Laboratory. Regular and random waves with a specified time history and height up to 1.5 m, were used to test instrument performance and to examine sediment processes under waves on beds of medium (D_{50} = 0.329 mm) and fine sand (D_{50} = 0.162 mm). Selected results from studies of hydrodynamics, bedforms and suspended sediments are presented.

Introduction

Instruments used to measure near-bed hydrodynamic conditions and sediment dynamics in field situations are usually tested and calibrated in relatively 'small-scale' laboratory facilities where it is not always possible to simulate natural processes accurately. In many instances the physical size of these calibration facilities has restricted the range of trials undertaken and frequently little is known about the interactions between the observed processes, the instruments, and the bulky frames used to deploy instrumentation in the sea. Further, instrumentation frequently provides only limited information on the processes under investigation leading to ambiguity in some aspects of field data interpretation. Whilst some of these deficiencies can be addressed through recourse to numerical modelling, recent field experiments have highlighted an urgent requirement to examine critically the performance of

1 *Proudman Oceanographic Laboratory*, Bidston Observatory, Birkenhead, Merseyside L43 7RA, UK, (*jjw@pol.ac.uk*).

2 *School of Civil Engineering*, University of Birmingham, Edgbaston, Birmingham B15 2TT, UK.

3 *Marine Science Laboratory*, University College of North Wales, Menai Bridge, Gwynedd LL59 5EY, UK.

4 *Delft Hydraulics*, P.O. Box 177, 2600 MH Delft, The Netherlands.

5 *Laboratorium voor Hydraulica*, Burgerlijke Bouwkunde, KU Leuven, De Croylaan 2, 3001 Haverlee, Belgium.

state-of-the-art field instrumentation in a range of controlled experimental conditions at full-scale.

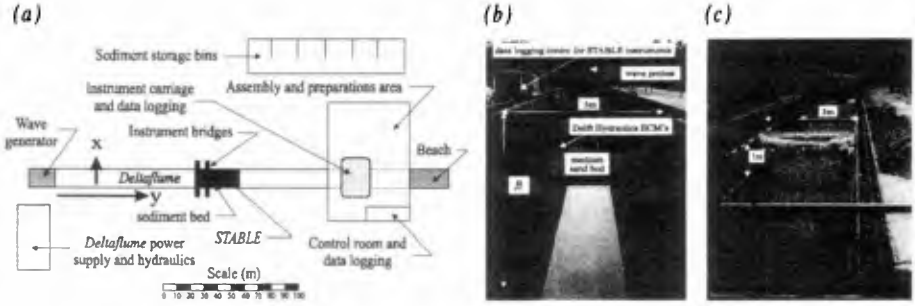

Figure 1 *(a)* Schematic plan of the *Deltaflume* research facility; *(b) Deltaflume* before filling showing the medium sand bed *in situ*; *(c)* 1 m regular waves in the *Deltaflume*, *test A4b*.

This paper describes research undertaken in the large *Deltaflume* facility, *Figure 1*, of Delft Hydraulics during a six-week period in July and August 1997. The work aimed to evaluate the performance of the autonomous multi-sensor frame *STABLE* (Sediment Transport And Boundary Layer Equipment, *Humphery & Moores, 1994*), *Figure 2*, and to measure in detail, bed sediment response to forcing by waves.

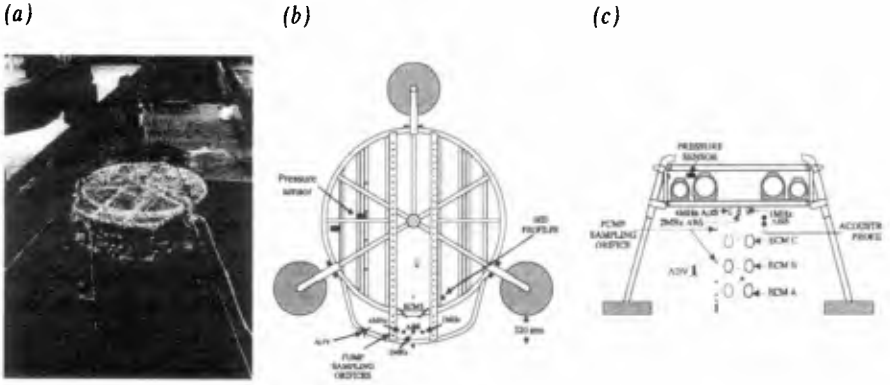

Figure 2 *STABLE*: *(a)* deployment in the *Deltaflume*; *(b)* plan view; and *(c)* side view

During tests, *in situ* measurements of wave characteristics, flow turbulence, bedforms and vertical suspended sediment concentration profiles were obtained in regular and irregular waves conforming to the JONSWAP spectrum. Hydrodynamic conditions below, approximating to and exceeding the threshold for resuspension of the bed material were examined. Independent measurements of wave-induced flow and vertical suspended sediment concentration profiles were obtained from locations adjacent to the side-wall of the *Deltaflume*.

Equipment and Methods

The *Deltaflume*

The Delft Hydraulics Laboratory *Deltaflume* is 230 m long, 5 m wide and 7 m deep, *Figure 1*. Regular and irregular waves with a height up to 2 m can be generated according to a required time history. During the present tests, 10 cm discus-shaped electromagnetic current meters were fitted to the side-wall of the flume at heights z = 25 cm, 50 cm, 100 cm, 150 cm and 250 cm above the bed at a distance y = 120.9 m from the wave generator. Two resistive wave measurement probes positioned at y = 117.9 m and at 120.9 m (*Figure 1a*) were used to measure wave height, H. Data from these instruments were logged at 25 Hz. Delft software was used to calculate a number of wave parameters including wave period, T, and in the case of random waves, significant wave height, H_s and peak wave period, T_p.

Samples of suspended sediment were obtained at 10 heights above the sand bed using a pump-sampling device deployed using vertical guide rails at y = 121.5 m. The sampling device consisted of 10 intake nozzles (diameter 4 mm) orientated at 90° to the wave orbital motion. Each nozzle in the array was connected to a plastic pipe through which a mixture of water and sediment was drawn to the surface by means of a peristaltic pump. The resulting water/sand mixture from each sampling position in a given array was collected in 10 litre buckets.

Sediment beds

Two sandy test beds were studied: *(a)* medium sand (median grain diameter, D_{50} = 0.329 mm); and *(b)* fine sand (D_{50} = 0.162 mm). The sandy beds were approximately 30 m long, 5 m wide and 0.5 m deep, and were placed at y = 105 m in the *Deltaflume*, (*Figure 1*). Both ends of the test beds were tapered to reduce erosion. To minimise bed disturbance, drainage was laid beneath the sediment bed to allow the free passage of water during filling of the *Deltaflume*. The sandy beds were compacted by mechanical vibration. After filling and prior to taking any acoustic measurements, large waves were generated for approximately 4 hours to force remaining air out of the bed and to develop equilibrium bedforms.

STABLE

Instrumentation on *STABLE* measured waves, flow turbulence and suspended sediment concentrations. A *Digiquartz* pressure sensor with integral pressure housing was used to measure the water-depth at wave frequencies at z ≈ 170 cm. Near-bed fluid motion induced by waves was measured using *Valeport Series 800* electromagnetic current meters (*ECM*'s) with a diameter of 10 cm and a resolution of ±0.1 cm/s. *ECM* sensors were arranged in pairs set at 90° to each other at $z \approx 30$ cm, 60 cm, and 91 cm. Horizontal separation between each *ECM* sensor was 20 cm. Measurements of flow turbulence were also obtained at $z \approx 30$ cm using a SonTec acoustic Doppler velocimeter, *ADV*, Ocean Probe operating at approximately 5.0 MHz. Measurements of horizontal and vertical wave induced fluid motion were measured using *POL* coherent Doppler sensors.

Bedforms beneath *STABLE* were measured using an acoustic ripple profiler (*ABP*) and a sector scanning sonar (*SSS*) device (*Bell & Thorne, 1997*). Acoustic backscatter, *ABS*, instruments (*Thorne & Hardcastle, 1997*) operating at 1.0 MHz, 2.0 MHz, and 4.0 MHz, were located 15 cm in front of the *ECM* sensors at $z \approx 128$ cm. These instruments measured the vertical suspended sediment concentration profiles, $\overline{C}$ *profiles*, from the bed to $z \approx 120$ cm at intervals of 1 cm. A vertical array of pump sampling nozzles was also fixed to the *STABLE* frame. A calibrated volume meter was then used to determine approximately, the suspended sediment concentration at each sampling height, (*Bosman et al., 1987; Havinga, 1992*). Subsequent analysis of samples in the laboratory gave dry weight sediment concentration values and the suspended sediment grain size at each sampling height. *ECM* and *PS1* data were sampled at 8.0 Hz and *ABS1, ABS2* and *ABS3* data were sampled at 4.0 Hz over a period of approximately 19 minutes. *ADV* data were sampled at 25.76 Hz during the same period. A schematic illustration of the experimental set-up is given in *Figure 3* and a summary of all hydrodynamic and morphodynamic variables measured during *Deltaflume* tests is given in *Table 1.* Further details of *STABLE* and the *Deltaflume* are given by *Williams et al., (1998a).*

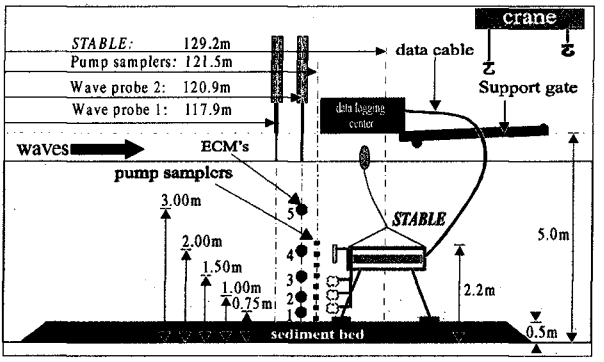

Figure 3 Schematic of experiment layout showing *Deltaflume* and *STABLE*

Variables	Instrumentation	Accuracy	Sampling frequency
Water temperature	Thermistor	± 0.05°C	0.016Hz
Water (dynamic) pressure	Pressure sensors	± 0.15%	8Hz
Water velocity	*ECM*'s	± 0.2cm/s	8Hz
Turbulence	*ECM*'s	± 0.2cm/s	8Hz
Turbulence	SonTec *ADV*	± 0.1cm/s	25Hz
Vertical flow component	Coherent Doppler	± 0.1cm/s	8Hz
Horizontal flow cross-correlation	Coherent Doppler	± 0.1cm/s	8Hz
Horizontal flow component	Coherent Doppler	± 0.1cm/s	8Hz
Free surface elevation	Surface following gauge	± 2.5cm	10Hz
Free surface elevation	Resistance type gauge	± 1cm	10Hz
Suspended sediment	*ABS* (1.0; 2.0; 4.0MHz)	0.001g/l	4Hz
Suspended sediment	Pump sampling	± 20%	-
Bed morphology	*DH* ripple profiler	± 2mm	1cm grid
Bed morphology	Sector scanning sonar	± 2mm	0.016Hz
Bed morphology	Acoustic ripple profiler	± 2mm	0.032Hz
Orientation of *STABLE*	Compass & inclinometers	± 1°	0.016Hz

Table 1 Hydrodynamic and morphodynamic variables measured during *Deltaflume* tests

Measurements programme

The sequence of experimental conditions was chosen to run from low to high wave conditions so that erosion of the bed was minimised. Surveys showed that the depth of sediment either side of the *STABLE* deployment site remained approximately constant throughout the tests. Six separate synchronised data logging systems were needed to handle the diverse and extensive data from the various sensors deployed on *STABLE* and in the *Deltaflume*. All data sets were time and date stamped to allow easy cross-referencing. *Table 2* summarises the range of wave conditions in the *Deltaflume* during tests on the medium and fine sand beds.

	regular waves		irregular waves	
Wave height (m)	**medium sand**	**fine sand**	**medium**	**fine sand**
0.50	$\tau_c < \tau_t$	*f03a*	$\tau_c < \tau_t$	*f04a*
0.75	*A08a*	*f11a*	*A09a*	*f07a*
1.00	*A05b*	*f08a*	*A10a*	*f10a*
1.25	*A11a*	*Not tested*	*A12a*	*f12a*

Table 2 Approximate wave conditions for tests on the medium (*A*) and fine (*f*) sand beds (wave period ≈ 5 seconds in all cases)

Results and discussion

In this section only selected results from the experiments in the *Deltaflume* are presented in order to illustrate the breadth and detail of the present study. The range of data acquired during the experiments was very extensive and it is possible here only to present a fraction of the results currently obtained. Since the main thrust of the work has been to assess the performance of sensors on the *STABLE* frame at approximately field-scale, attention here is

focussed primarily upon results that aid in this assessment exercise. Work examining $\overline{C}$ *profiles* is currently in review (*Williams et al., 1998b*).

Hydrodynamics

In order to assess instrument performance, comparisons have been made between the *STABLE ECM*'s and the *ADV*. *ECM* data were calibrated and despiked and corrected for misalignment using a modified form of the method described by *Soulsby et al. (1991)*. Values for the zero-mean orthogonal flow components u, v and w were calculated using the method described by *Williams et al. (1997)*. In the case of the *ADV*, values for u, v and w were also corrected for misalignment using the rotation angles determined for the *ECM*'s and knowledge of the position of the instrument on the *STABLE* frame.

Figure 4 shows power spectra on log-log axes derived using a fast Fourier transform for u and w components measured above the fine sediment bed by the *ECM*'s and by the *ADV* during: (*i*) test *f08a* (regular waves, H = 1.0 m, T = 5.0 s); and (*ii*) test *f10a* (irregular waves, H_s = 1.0 m, T_p = 5.3 s). In the case of regular waves, u spectra show peaks at approximately wave, half wave and quarter wave frequencies. A broad peak in u spectra spanning the frequency range 0.1 Hz to 0.3 Hz is measured for the irregular waves. In contrast, spectra for the w component are much flatter. However, there are peaks in energy corresponding to those in the u spectra. These are attributed to wave asymmetry.

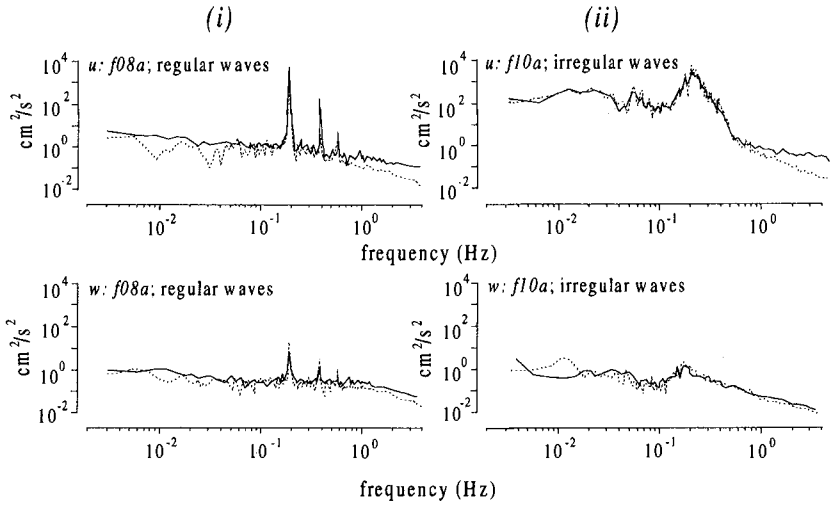

Figure 4 Typical u and w power spectra for 1.0 m regular and irregular waves: —— *ECM* spectra; ····· *ADV* spectra.

In all cases the spectra derived from *ECM* and *ADV* time-series are broadly similar over the frequency, *f*, range 0 001 Hz to 0 3 Hz At frequency values greater than 0 7 Hz, *ECM* and *ADV* spectra diverge significantly, demonstrating the high frequency cut-off attributable to the larger sampling volume and lower sampling frequency of the *STABLE ECM* system These results demonstrate that broadly speaking, the *ADV* and the *ECM*'s give comparable results across a wide frequency band

If one considers the implication of these results in the context of current-only or wave-current situations, then failure of the *ECM*'s to measure all the high frequency energy has consequences when *ECM* data are used to derived estimates of the bed shear stress, τ using the eddy correlation, *EC*, turbulent kinetic energy, *TKE*, or inertial dissipation, *ID*, approaches Specifically, the present *ECM*'s system will always underestimate τ However, since the total amount of energy missing from the *ECM* spectra is estimated to be less than 3% of the total, estimates of τ are unlikely to be seriously in error The relative importance of these errors in the context of sediment transport in the marine environment is almost insignificant when one considers the imprecision with which entrainment threshold, settling velocity and bedform dimensions are known

Bedforms

Figure 5 shows long-crested vortex ripples on the medium sand bed measured using the *SSS* The side-walls of the *Deltaflume* and imprints left in the sand by *STABLE* feet are clearly visible Of particular relevance to the present study is the proof provided by *Figure 5* and other images, that ripple geometry is unaffected by the presence of the rig This result confirms unequivocally that *STABLE* has no detectable influence upon the process of ripple formation in wave-only conditions

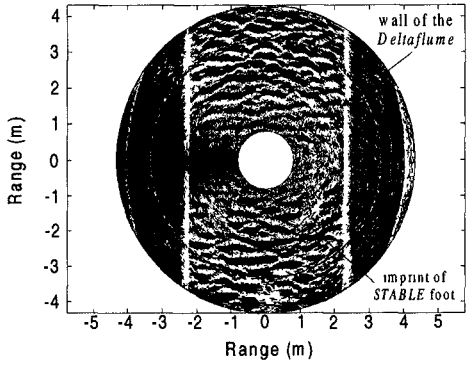

Figure 5 SSS image of long-crested vortex ripples on the medium sand bed

Temporal changes in ripples on the medium sand bed measured during test *A13a* and *A14a* using the *ARP*, (H = 1.0 m, T = 5 0 s), are illustrated in *Figure 6* This figure shows vortex ripples migrating up the flume towards the wave generator a distance of approximately 1 0 m in 80 minutes

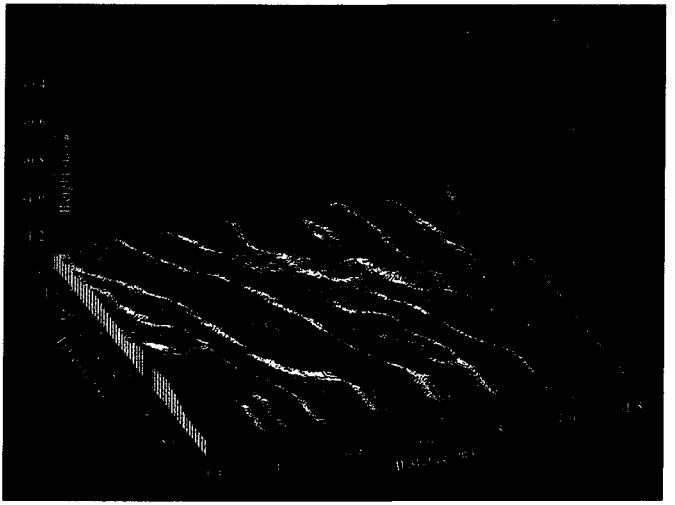

Figure 6 Temporal and spatial variation in h_r and λ_r measured by the *ARP*

Values for ripple height, h_r, and wavelength, λ_r, measured using the *ARP* are found to be in good agreement with predicted vortex ripple dimensions in regular wave conditions (*Nielsen, 1992*) Whilst some of the temporal variability in ripple geometry may be attributed to random wave conditions during the tests, the migration of ripples shown in *Figure 6* probably results from a compensating current near the bed and from wave asymmetry The ability to monitor continuously the bed geometry directly beneath *STABLE* is clearly demonstrated by *Figure 6* It is considered that in future field deployments of *STABLE*, measurements from the *ARP* and the *SSS* will prove to be invaluable in characterising the local micro-morphology of the sea bed

Suspended sediments

Typical $\overline{C}$ *profiles* measured from *STABLE* and from the *Deltaflume* using the pump-sampling equipment on are shown using log-log axes in *Figure 7a* for. *(a)* regular waves above the medium and fine sand beds [*tests A11a* and *f11a*], and *(b)* for irregular waves above the medium and fine sand beds [*tests A10a* and *f07a*] For the $\overline{C}$ *profiles* considered here, time - averaged suspended sediment concentration, $\overline{C}$, values measured at the sampling

position closest to the bed span a range from approximately 0.01 g/l to 10.0 g/l. In most cases, $\overline{C}$ values measured during the experiments by the volume method and in the laboratory differ by less than 50%. However, at a given height above the bed, differences between $\overline{C}$ values measured from *STABLE* and from the *Deltaflume* frequently exceed 100%. These differences are thought to arise owing to the combined effect of different sampling locations relative to bedforms, side-wall effects, zero datum errors and flow turbulence generated by *STABLE*.

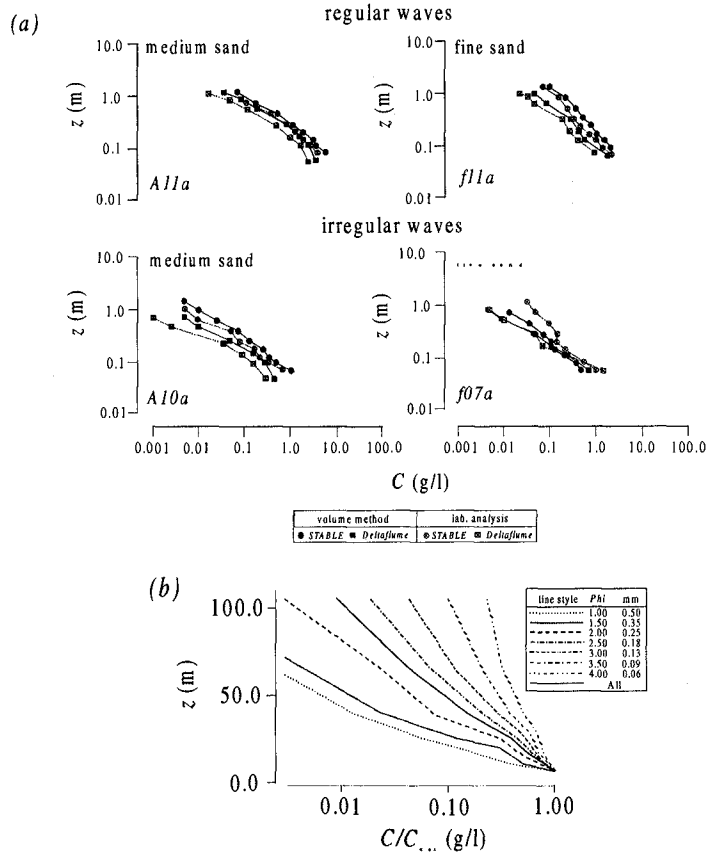

Figure 7 *(a)* $\overline{C}$ *profiles* measured above bed of medium and fine sand in regular and irregular wave conditions; and *(b)* $\overline{C}$ *profiles* for separate grain size fractions, *test A11a.*

Figure 7b shows normalised $\overline{C}$ *profiles* for separate grain size fractions measured during *test A11a* on the medium sand bed In common with other published data, $\overline{C}$ values at any given height increase with decreasing grain size and demonstrate that suspended sediments are composed principally of the fine fraction of sediments comprising the bed Detailed study and modelling of $\overline{C}$ *profiles* has been undertaken by *Williams et al , (1998b)*

An example of data from the 2 0 MHz *ABS* instrument is shown in *Figure 8* This figure shows the response of the medium sand bed to a group of 8 waves during random wave conditions and is typical of other results Modulation at approximately the wave frequency is evident as is a general increase in the average suspended sediment concentration It is also seen that by the passage of the fifth wave appreciable quantities of suspended sediment are present at $z = 0\,6$ m Also evident is a parcel of suspended sediment in the region $0\,4\text{ m} < z < 1\,0$ m under wave 7 in the group This suspended sediment is surrounded by fluid containing little in suspension and may be the manifestation of vortex detachment from ripples on the bed A similar but much smaller volume of suspended sediment is also evident under wave 8 It is considered that both suspension structures are related where the structure beneath wave 7 is the remnant of the first structure These data provide a fascinating insight into the intricacies of inter-wave period sediment resuspension processes and a major study to quantify these mechanisms is currently underway

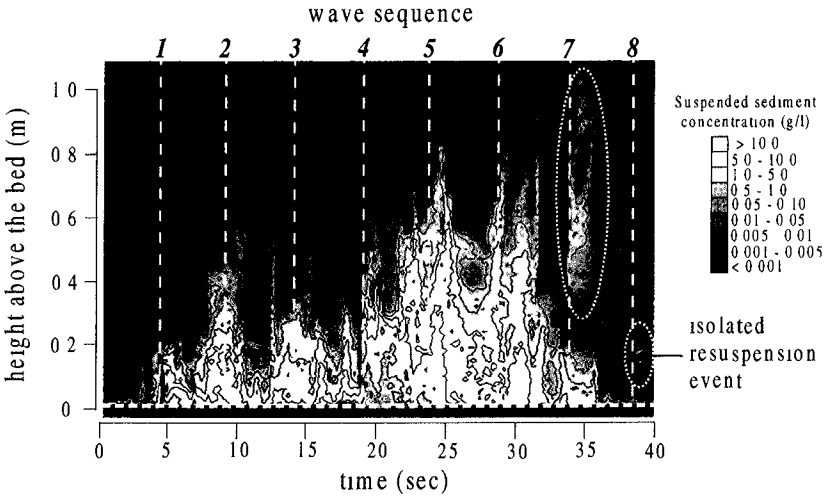

Figure 8 Example of data from the 2 0 MHz *ABS* instrument showing resuspension by a wave group

Summary

This paper describes experiments conducted in the *Deltaflume* of Delft Hydraulics to evaluate the performance of field instrumentation used to measure near bed hydrodynamic conditions and sediment dynamics from the large tripod frame *STABLE*. Tests were conducted on beds of medium (D_{50} = 0.329mm) and fine (D_{50} = 0.162mm) sand under regular and irregular waves of sufficient size to re-suspend the bed material. Measurements of waves, turbulence, vertical suspended sediment concentration profiles and bed morphology were obtained using a comprehensive suite of state-of-the-art acoustic and electromagnetic sensors and *in situ* samples of sediment in suspension were obtained by pump sampling.

In order to illustrate the nature and quality of the measurements, selected results from the experiments pertaining to bedforms (vortex ripples), to hydrodynamic conditions close to the bed and to suspended sediments have been presented. These data will make possible critical evaluation of the performance of field instruments and will aid interpretation of existing data sets from past deployments in the field. Furthermore, the data will aid the study of the detailed processes leading to the mobilisation and resuspension of sandy sediments in wave conditions and provide a rigorous test case for existing and future numerical models of sediment entrainment and suspension. Exploitation of the *Deltaflume* data set is already underway through the European MAST 3 project *INDIA* and the UK EPSRC Programme COSMOD. In the future it is also planned to make these data available to researchers through the publication of a CD-ROM .

Acknowledgements

The work was jointly supported by the European Communities through the TMR Programme "*Access to Large Scale Facilities*" by the MAST 3 project '*Inlet Dynamics Initiative: Algarve*' (*INDIA*) contract MAS3-CT97-0106 and by the UK *NERC*.

References

BELL P. S., THORNE P. D. (1997) Measurements of sea bed ripple evolution in an estuarine environment using a high resolution acoustic sand ripple profiling system. *Oceans '97*, Volume 1, MTS/IEEE, Washington D.C., pp 339-343.

BOSMAN, J. J., VELDEN, E. T. J. M. VAN DER, HULSBERGEN C. H. (1987) Sediment concentration measurements by transverse suction. *Coastal Engineering*, **11**, 353-370.

HAVINGA, F. J. (1992) Sediment concentrations and sediment transport in case of irregular non-breaking waves with a current, Report **H840** *Parts E, F & G*, Delft Hydraulics, Delft University of Technology, Delft, The Netherlands.

HUMPHERY, J. D. & MOORES, S. P. (1994) STABLE *II* - An improved benthic lander for the study of turbulent wave-current-bed interactions and associated sediment transport. *Electronic Engineering in Oceanography*, IEE Conference Publication No. **394**, 170-174.

NIELSEN, P. (1992) *Coastal bottom boundary layers and sediment transport.* World Scientific Publishing Co., River Edge, N.J., USA, ISBN-981-02-0472-8, 324pp.

SOULSBY R. L., GOLDBERG D. G. & STEVENSON E. C. (1991) *Norfolk Sand Banks. Analysis of STABLE data.* HR Wallingford, Report Number **EX 2345**, 18 pp.

THORNE, P. D. & HARDCASTLE, P. J. (1997) Acoustic measurements of suspended sediments in turbulent currents and comparison with *in-situ* samples. *Journal of the Acoustic Society of America*, **101**(5), 2603-2614.

WILLIAMS, J. J., ROSE, C. P., THORNE, P. D., COATES, L. E., WEST, J. R., HARDCASTLE, P. J., HUMPHERY, J. D., MOORES, S. P. & WILSON, D. J. (1997) Observed suspended sediments in storm conditions. *Proceedings ICCE'96,* ASCE, Volume **3**, 3257-3269.

WILLIAMS, J. J., BELL, P. S., COATES, L. E., HARDCASTLE, P. J., HUMPHERY, J. D., MOORES, S. P., THORNE, P. D. & TROUW, K. (1998a) Evaluation of field equipment used in studies of sediment dynamics. *POL Report* **53**, 45pp.

WILLIAMS, J. J., BELL, P. S., THORNE, P. D., TROUW, K., HARDCASTLE, P. J. & HUMPHERY, J. D. (1998b) Vertical suspended sediment concentration profiles and bedforms in oscillatory-only flow. *Coastal Engineering* (*submitted*).

Size Gradation Effects in Sediment Transport

Chatelus,Y.[1], I. Katopodi[2], M. Dohmen-Janssen[3], J.S. Ribberink[3], P. Samothrakis[2], B. Cloin[4], J.C. Savioli[5], J. Bosboom[4,6], B.A. O'Connor[7], R. Hein[7] and L. Hamm[1]

Abstract

This paper presents the experimental results obtained at prototype scale in the Large Oscillating Water Tunnel (LOWT) facility of WL | Delft Hydraulics with graded sediment subjected to non-linear waves and linear waves plus current flows. The objective of this experiment is to increase our present understanding and physical insight of the basic mechanisms of bed-load and suspended load transport in oscillatory flow conditions when graded sediments are present in the bed. The sediment bed consists of a mixture of two well sorted sands (two fractions) that have been used before in the tunnel in order to make comparisons possible. Net sediment transport rates, time averaged suspended sediment profiles, time dependent concentrations in the suspension and sheet flow layers as well as time dependent velocity profiles are measured. Moreover, the sediment bed composition before and after each test is recorded in order to calculate the transport rate of each sediment fraction. Selected results are presented here. Full details are included in the data report (Hamm et al, 1998). The data will be used for the development of mathematical model formulations for graded sediment transport.

Introduction

The Large Oscillating Water Tunnel (LOWT) facility of WL | Delft Hydraulics in de Voorst, The Netherlands enables experiments at full scale including horizontal oscillatory flows with superimposed currents. The test section is 14 m long, 1.1 m high and 0.3 m wide. Most of the research in the tunnel during the last decade was carried out using unsieved dune sand with a median diameter of 0.21 mm and a narrow size distribution (Ribberink and Al-Salem,1994 and 1995, Ribberink et al., 1994, Katopodi

[1] SOGREAH Ingénierie - BP 172 - 3B042 Grenoble Cedex 9 - Fronce -
[2] Dept of Civil Engineering - Democritus university of Throce - 67100 Xonthi - Greece -
[3] University of Twente (NCK) - Civil Engineering ond Monogement - PO Box 217 - 7500 AE Enschede - The Netherlonds
[4] Dept of Civil Engineering - Delft University of Technology (NCK) - PO Box 504B 2600 GA Delft - The Netherlonds
[5] Donish Hydraulic Institute - Agern Alle 5 - DK-2970 Horsholm - Denmork -
[6] WL|Delft Hydroulics - PO Box 177 - 2600 MH Delft - The Netherlonds
[7] University of Liverpool - Dept of Civil Engineering - PO Box 147 - L69 3BX Liverpool - U. K. -

et al., 1994). Two types of oscillatory flow conditions were generally used, namely regular second-order Stokes waves and sinusoidal waves with superimposed net currents. In the majority of the experiments the plane-bed regime with sheet-flow conditions was observed.

Since three years, specific attention is paid to the influence of the grain size in combined wave-current conditions. Experimental programmes were carried out with median diameters of 0.13 mm and 0.32 mm keeping the geometric standard deviation unchanged (Janssen and Ribberink, 1996, Dohmen - Janssen et al., 1998).

The flume is now also used to study sediment transport with sands containing heavy minerals with a density >2.9 kg/l which are naturally found in the field. These tests show that these heavy minerals, have clearly different transport properties than light minerals and induce armouring effects (Tánczos et al., 1997).

The present experiments actually include two Series named K and L. In Series L, the previous experiments of Tánczos et al. (1997) were completed by using mixtures of light sand and zircon with the same grain size but distinctly different density. These tests are reported by Manso et al.(1998). In Series K described in the present paper, a mixture of two sand types with median diameters of 0.13 mm and 0.32 mm has been used and the hydrodynamic conditions have been chosen in close connection with previous experimental series in the tunnel. This makes comparisons with available data possible and increases the scope and possibilities of the present work.

Experimental set-up and programme

Hydraulic conditions

The experimental programme consisted of 3 asymmetric wave conditions and 2 sinusoidal waves/net current conditions, which are summarised in Table 1. Two 2nd-order Stokes waves conditions were chosen with different root-mean square velocities, u_{rms} (K1 and K2). The 2nd order Stokes wave can be described with

(1) $u(t) = u_1\cos(\omega t) + u_2\cos(2\omega t)$,

the root-mean square velocity yields:

(2) $u_{rms} = \sqrt{0.5 * (u_1^2 + u_2^2)}$

Where u_1 and u_2 are the first- and second-order components of the horizontal velocity, respectively. ω is the angular frequency of the wave ($=2\pi/T$). The wave period T=6.5 s was the same for both conditions. The degree of asymmetry R, defined as $(u_1+u_2)/2u_1$ was 0.66.

Also a different asymmetric wave was used called the sawtooth wave (K3). The only difference between the sawtooth and the 2nd-order Stokes wave is a 90 degree phase shift of the second harmonic component. The sawtooth wave can be described by:

(3) $u(t) = u_1\cos(\omega t) + u_2\cos(2\omega t+\pi/2)$

Even when the values of u_1 and u_2 are the same, the third order velocity moment is very different, i.e. zero for the sawtooth wave and non-zero for the 2nd-order Stokes wave. It is therefore interesting to investigate the difference in net transport rates caused by a sawtooth wave and by a 2nd-order Stokes wave, with the same period and the same root-mean square velocity.

The last two conditions were combined sinusoidal waves/current conditions (K5 and K6). The net current velocity at 10 cm above the bed <u> and the amplitude of the sinusoidal velocity û were different for each condition. The oscillation period T=7.2 s. was the same for both conditions. All conditions correspond to the sheet flow regime and lie within the constrictions of the tunnel.

Table 1. Hydraulic conditions

Cond	type	mean oscillatory flow (1)	mean net current (1)		number of runs	
		U_{rms} (m/s)	T (s)	<U> (m/s)	net sediment transport rate	detailed measurements
K1	2nd order Stokes	0.84	6.5	0.04	7	
K2	2nd order Stokes	0.59	6.5	0.02	3	8
K3	sawtooth	0.70	6.4	0.01	3	
		û (m/s)	T (s)			
K5	sinusoidal	1.47	7.2	0.25	3	15
K6	sinusoidal	0.95	7.2	0.45	3	2

(1) measured at 0.10 m above the initial bed

Sediment properties

The sand used in the present experiments consisted of a 50%-50% mixture of the fine (D_{50} = 0.13 mm) and the coarse sand (D_{50} = 0.32 mm) with hardly any overlap as can be seen from the D_{90} of the fine sand (0.182 mm) and the D_{10} of the coarse sand (0.217 mm). The characteristics of the mixture derived from sieve-analyses (figure 1) are D_{10}= 0.097 mm, D_{50}= 0.194 mm, D_{90}= 0.406 mm with a density of 2650 kg/m^3. Analysis of the sand in the Visual Accumulation Tube (VAT) gives a median fall velocity of $W_{s,50}$ = 20.3 mm/s for the mixture.

Measurement programme and instruments

The measurement programme was designed as comprehensively as possible making use of several kind of instruments to measure time-averaged as well as time-dependent quantities. In order to achieve that goal, it was necessary to repeat the hydraulic conditions several times, each run being devoted to a particular instrument.

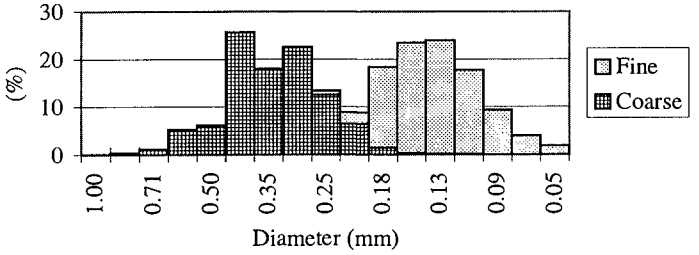

Figure 1. Grain-size distribution of the mixture

The measurements were especially delicate and more time consuming compared with previous measurements with uniform sand. For graded sand, the bed composition changes with time and thus replacement of the bed was necessary to restore the designed bed composition for the next runs. Thus, the upper layer of the sand bed (~5 cm) had to be removed from the tunnel and replaced with new sand every few tunnel runs. Considerable effort was also required for the extraction of the bed samples and their analysis in the settling tube.

The measurements required to obtain the net, time-averaged transport rates (global and per fraction) were performed first for the five hydraulic conditions. Then, the suction system was installed to measure the vertical profile of time-averaged concentrations in suspension for three hydraulic conditions (K2, K5 and K6). Finally, detailed time-dependent measurements over the the vertical were performed for two hydraulic conditions (K2 and K5) by installing successivelly four instruments described below.

Bed levels along the tunnel were measured before and after each run using a bed level profiling system. Additionally, the weight of the sand collected in the traps was measured underwater.

The upper layer of the sand bed in the test section was sampled using a siphoning system. A perspex cylinder (height about 12 cm) with a diameter of 100 mm was stuck into the sand bed for about 5 cm. Next the sand-water mixture within the cylinder was siphoned out of the tunnel, and the sand water mixture was collected in buckets. The grain size distribution and the percentage of the fine and the coarse fraction, present in each sample

was determined by using a settling tube (Visual Accumulation Tube, VAT). Samples from the sand collected in the traps were also subjected to the same analysis.

The time-averaged concentration $\langle c(z,t) \rangle$ in the suspension layer was measured using a transverse suction system able to extract samples of a mixture of sand and water at ten locations over a vertical simultaneously. The concentration was determined and the sample was then put into the VAT to get the grain-size distribution of the suspended sediment.

Time-dependent sediment concentration c(z,t) was measured over the vertical both in the suspension layer (for $z > 0.01$ m) using an optical concentration meter (OPCON) and in the sheet flow layer using a conductivity concentration meter (CCM). The OPCON is based on the extinction of the infra-red light when concentrations are in the range 0.1-50 g/l. The CCM is able to measure large sand concentrations in the range 100-1500 g/l on a sensing volume with a height of 1 mm.

Finally, time-dependent flow velocity components over the vertical were measured thanks to an acoustic doppler velocity meter (ADV) able to work even in high concentrations of sediment and a laser doppler flow meter (LDFM). In total, 41 runs were performed to achieve the measurement programme. The number of runs per hydraulic condition is provided in table 1.

Experimental results

Net sediment transport rate

The net sediment transport rates were measured for all five flow conditions. The sediment continuity equation was solved twice (starting either from the left or the right-hand-side) using as boundary conditions the sand volumes collected in the sand traps (given the sand porosity). This gives two estimates of the actual occurring transport rate in the middle of the tunnel for a specific test and the mean value is used. Figure 2 gives an example of such a result for test K5. In table 2, the net transport rates averaged over several runs are presented. Moreover, the standard deviation and the relative error are provided. They are comparable to the previous experiments (see i.e. Katopodi et al., 1994).

Table 2. Net sediment transport rate, averaged over all tests per condition

Test	$\langle q_{savg} \rangle$ (10^{-6} m^2/s)	σ (10^{-6} m^2/s)	$r=\sigma/\langle q_{savg} \rangle$ (%)	$\frac{r}{\sqrt{N}}$ (%)
K1	34.53	2.87	8.30	4.79
K2	17.03	0.17	1.00	0.58
K3	18.03	1.82	10.07	5.81
K5	78.80	9.03	11.46	6.61
K6	72.70	5.20	7.15	5.06

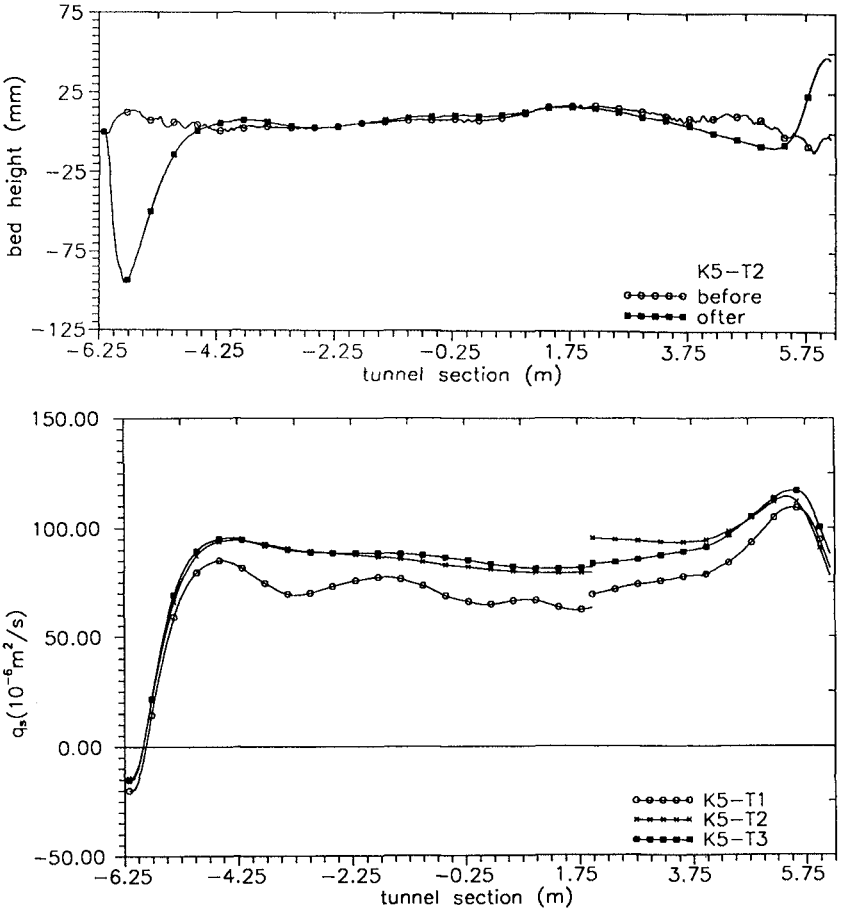

Figure 2. up: bed level before and after run K5-T2
down: net sediment transport along the test section for the three runs of test K5.

Cloin (1998) compared these results with available previous experiments performed with uniform sand (Katopodi et al., 1994, Janssen and Ribberink,1996 and Dohmen-Janssen et al., 1998) and with similar hydraulic conditions (see figure 3). She also performed an analysis of the sediment transport per fraction, which is presented hereafter, in order to understand the main features of this comparison.

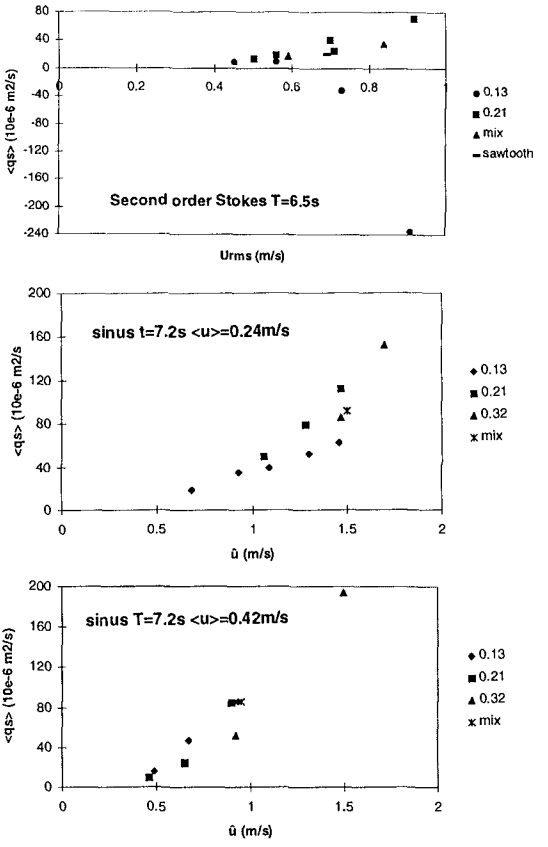

Figure 3. Comparison of the net sediment transport rate with previous experiments using uniform sediment. up: test K1, K2 and K3, middle: test K5 and down: test K6

Bed composition

An important part of the experiment was the estimation of the bed composition before and after each test. This information was necessary to estimate the transport rate per fraction and also explain the suspended sediment behaviour. Unfortunately, large scatter was observed in the bed composition data. The bed composition before the test was not completely uniform along the tunnel owing either to non uniform mixing of the two sand fractions or to inaccuracies of the sampling method. The bed composition after the tests did not show the same trends for all the tests of each condition. This might be

again due to the sampling method or due to the fact that the upper layer of the bed was not changed after each test.

A detailed analysis of the bed composition data as well as an evaluation of the sampling method can be found in Cloin (1998). Despite of the large scatter of the data, she was able to calculate the transport rate per sediment fraction for all flow conditions. Figure 4 shows the result obtained for test K5.

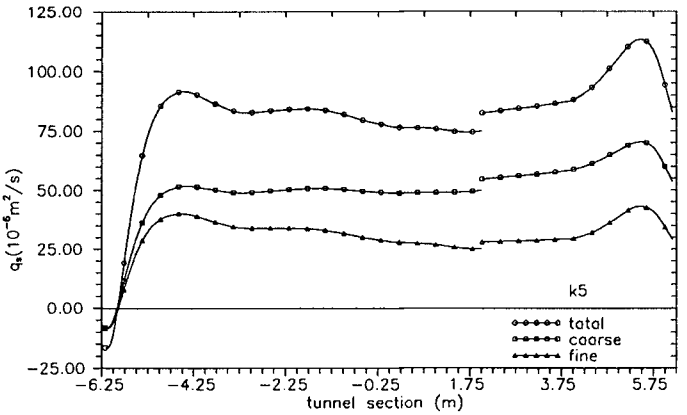

Figure 4: Net sediment transport per fraction along the test section for the test K5.

Then, she compared the measured sediment transport per fraction with the previous measurements with uniform sand (figure 3) by attaching to each fraction an estimated , uniform-based sediment transport. This estimation was computed by multiplying the volume percentage of occurence of the fraction considered in bed material with the transport rate of the fraction assumed to be alone, this transport being derived from the measurements with uniform sands. She was thus able to show that for sinusoidal waves with a net current, the fine fraction is hidden by the coarse fraction and the coarse fraction is more easily transported than in the case of uniform coarse bed material. The hiding is larger in case of higher mean velocity and smaller oscillating velocity. For second-order wave conditions, the fine fraction is also hintered by the coarse fraction for the strongest case (K1) but the coarse fraction is not influenced by the fine fraction in both cases.

Vertical sorting of the grain sizes

The sand samples extracted from the flow (suspension layer) with transverse suction present a strong reduction of the median diameter with elevation for all three conditions

examined (K2, K5 and K6). The coarsest sand found near the bed has a D_{50} of only 0.13mm while the D_{50} of the original sand in the bed was 0.21 mm. This shows that only sand belonging to the finer fraction was set into suspension. The median diameter for all conditions decreases with elevation reaching a minimum of 0.08mm. The two tests per condition give similar results, except for K2 where the two tests are considerably different for elevations higher than 2 cm. The sand of the first test is much finer than of the second. It is clear that for the two tests the bed composition was not the same.

Sediment concentrations

a) Time-averaged concentrations

Time-averaged suspended sediment concentrations were measured with transverse suction for K2, K5 and K6. The concentrations for all conditions follow a power law (straight best fit lines), as has been found for all previous measurements in the tunnel under sheet flow conditions. For all cases the concentrations are larger than the concentrations measured previously with well sorted sand of D_{50}= 0.21mm for the same flow conditions. Time-averaged suspended sediment concentrations were also computed from the time dependent OPCON signal for K2 and K5. The two tests of K2 give somewhat different results, with the first test showing larger concentrations than the second. This indicates different bed composition during the two tests. For K5 the different tests show a rather good agreement. Comparison with transverse suction concentrations shows a satisfactory agreement for K5, differences for K2. Again, the rather variable bed composition for K2 may have played a role. The time-averaged concentrations computed from the CCM time dependent signal show an almost constant value of about 1350 g/l in the pick-up layer below the bed level. Above the bed the concentration decays rapidly to values less than 100 g/l in a distance of 3-5 mm (thickness of the sheet flow layer).

The vertical profile of the concentrations measured with the three instruments spans a distance from ~ 1cm below the bed up to ~ 25 cm above the bed and covers the pick-up, the sheet flow and the suspension layers. For both conditions (K2 and K5) the concentration profile shows a transition from a convex shape (pick-up layer) to a concave shape (suspension layer), reflecting the presence of different mechanisms in the mixing process. The profile obtained during test K5 is shown on figure 5.

b) time-dependent concentrations

The time-dependent concentration was measured at different elevations with OPCON (suspension layer) and CCM (sheet flow and pick-up layers) for K2 and K5. In the sheet flow layer the concentration is in phase with the free stream velocity. The same also holds for the suspension layer although a phase shift growing with elevation can be

observed. In the pick-up layer the concentration follows the opposite behaviour (i.e. min concentrations at max velocities and max concentrations at zero velocities). The concentration in the sheet flow layer shows sharp peaks at the moments of the flow reversal a feature found before in measurements with uniform sand. In general the shape of the time dependent concentrations was the same as with well sorted sand with the same D_{50} . Figures 6 and 7 show the results obtained for test K5.

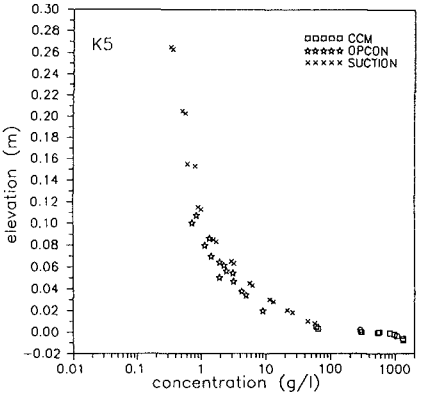

Figure 5: Time-averaged concentration profiles - test K5

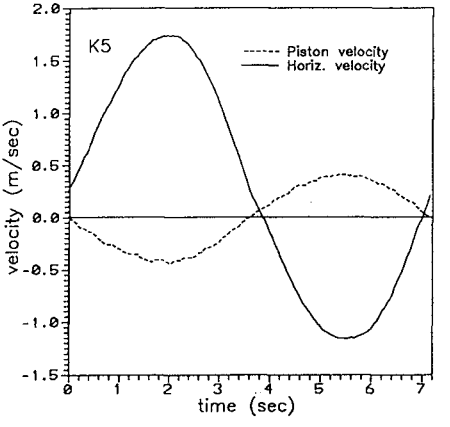

Figure 6: Time-dependent horizontal velocity at 10 cm above the initial bed (test K5)

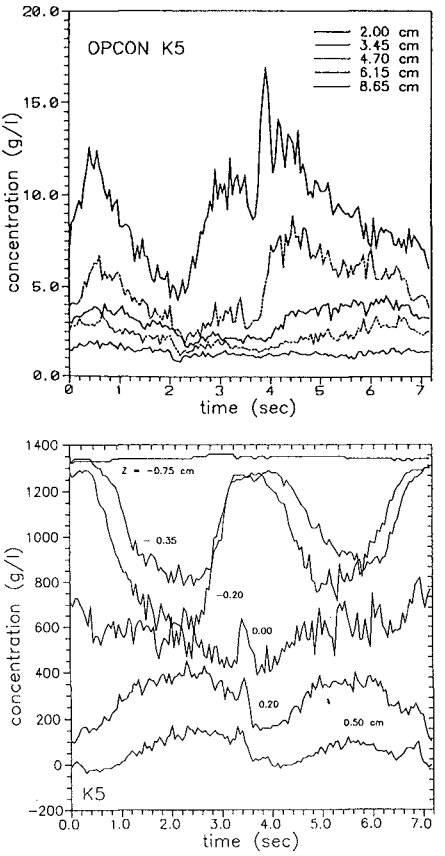

Figure 7: Time-dependent measurement of concentration - test K5. up: OPCON measurement and down: CCM measurement.

Flow velocities

Time dependent velocities were measured at different elevations for K2 and K5 with ADV and laser (LDFM). Velocity profiles could not be measured satisfactorily with laser for condition K5 because the suspended concentration was large and was blocking the laser beams almost for the entire depth.

The ADV signal in general was disturbed but we could measure close to the bottom (see figure 8 illustrating a typical result). Although the net ADV profile data present

The ADV signal in general was disturbed but we could measure close to the bottom (see figure 8 illustrating a typical result). Although the net ADV profile data present much scatter, for the second order Stokes condition K2 a small net current in the crest direction was distinguished as well as the asymmetry induced boundary layer streaming in the opposite direction. For the wave and current condition K5 the profile was logarithmic. These findings are in accordance with previous measurements in the tunnel.

Comparison of ADV and laser measurements for K2 showed a systematic difference which is small in the time dependent values but significant when averaged over the wave period. In Katopodi et al (1994), a similar mismatch was found when comparing laser and EMF (electromagnetic flow meter) measurements for waves and currents. Although the two cases are not directly comparable, they both concern asymmetric flows (K2 second order Stokes, series E current and sinusoidal waves).

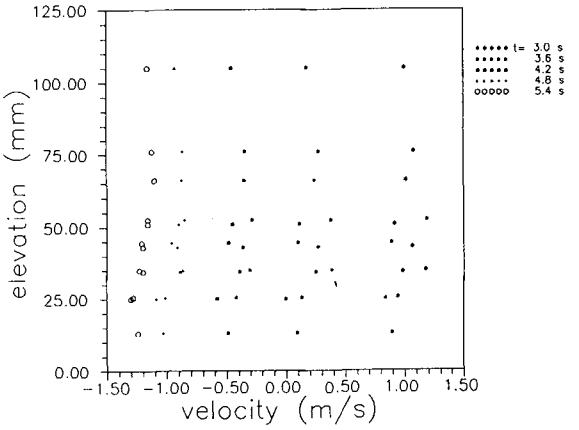

Figure 8: Time dependent velocity profiles measured by ADV test K5 between 3.0 and 5.4 secs.

Conclusions

An experimental investigation of graded sediment transport was conducted in the Large Oscillating Water Tunnel of WL | Delft Hydraulics under various hydraulic conditions with plane bed. The sediment bed consisted of a mixture of two well sorted sands (two fractions) that have been used before in the tunnel. The experiment concerned measurements of net sediment transport rates, bed composition change, time averaged suspended sediment profiles, time dependent concentrations in the suspension and sheet

flow layers and time dependent velocity profiles. A detailed presentation of the measurements and results is presented in the data report (Hamm et al, 1998).
Furthermore, net transport rates per sediment fraction were calculated by Cloin (1998) based on the bed composition data.

The data set has then been used by Cloin (1998) to compare with previous experiments using uniform sands. She also used it for the experimental verification of various transport formulae as well as time dependent models of sediment transport of graded sediment in sheet-flow conditions. This work is being extended to enlighten the influence of size and density in selective transport mechanisms. The examination of the gradation characteristics of the suspended sand samples and their linking with the characteristics of the bed samples is also scheduled (Katopodi et al., 1999).

As seen from the bed composition results, the used bed sampling technique did not prove very accurate and should be improved, possibly by taking cores out of the bed or colouring one of the fractions. Moreover, it would be very useful if the measurements concerning the two well sorted sands that constitute the sediment mixture of this experiment were completed such that all the quantities measured for series K could be compared with measurements of sand consisting out of one fraction only (see Hamm et al, 1998).

Acknowledgements

The experiments were part of the project « Access to the experimental facilities of WL | DELFT HYDRAULICS in the framework of the EU programme « Training and Mobility of Researchers », contract n° ERBFMGECT950045. The analysis of the data has been performed in the framework of the SAFE project carried out as part of the MAST III programme, partly funded by the European Commission/ Directorate of Science, Research and Development (DG-XII), contract MAS3-CT95-0004 and by national bodies including Sogreah Ingénierie, Ministère de l'Equipement, des Transports et du Logement/Direction de la Recherche et des Affaires Scientifiques et Techniques/Service Technique des Ports Maritimes et des Voies Navigables (France), subvention N° 97 M/3 and the Netherlands Centre for Coastal Research (NCK).

References

Cloin, B. (1998): Gradation effects on sediment transport in oscillatory sheet-flow. M.Sc. Thesis, Delft University of Technology, Report H2305, March 1998, WL | Delft Hydraulics, The Netherlands.

Dohmen-Janssen, C.M., G. van der Hout and J.S. Ribberink (1998). Phase-lag effects in oscillatory sheet flow. Proc. 26th Int. Conf. on Coastal Engng., Copenhagen, Denmark, ASCE, in press.

Hamm L., I. Katopodi, C.M. Dohmen-Janssen, J.S. Ribberink, P. Samothrakis, B. Cloin, J.C. Savioli, Y. Chatelus, J. Bosboom, J. Nicholson, R. Hein (1998): Grain Size, Gradation and Density effects on Sediment Transport Processes in Oscillatory flow conditions. Data Report Z2153, Part I: The effects of grain size gradation (Series K), WL | Delft Hydraulics, The Netherlands.

Janssen, C.M. and J.S. Ribberink (1996). Grain-size influence on sand transport in oscillatory sheet flow. Proc. 25th Int. Conf. on Coastal Engng., Orlando, FL, USA, ASCE, 4779-4792

Katopodi, I., J.S. Ribberink, P. Ruol and C. Lodahl (1994). Sediment transport measurements in combined wave-current flows. Proc. Coastal Dynamics'94 conf., Barcelona, Spain, ASCE, 837-851.

Katopodi, I., J.S. Ribberink, L. Hamm, P. Samothrakis, N. Kitou, C.M. Dohmen-Janssen and J.C. Savioli (1999). Comparison of concentrations measured in an oscillating tunnel with well-sorted and bimodal sand. Accepted for Coastal Sediments'99 Conference, Long Island, USA, ASCE.

Manso, F., R.L. Koomans, R.J. de Meijer and F. Vilas(1998). The effect of density gradation in oscillatory sediment transport. Proc. 26th Int. Conf. on Coastal Engng., Copenhagen, Denmark, ASCE, in press.

Ribberink, J.S. and A.A. Al-Salem (1994). Sediment transport in oscillatory boundary layers in cases of rippled beds and sheet-flow. J. Geophys. Res., vol.99, n°C6, 12,707-12,727

Ribberink, J.S. and A.A. Al-Salem (1995). Sheet-flow and suspension of sand in oscillatory boundary layers. Coastal Engineering, 25, 205-225.

Ribberink, J.S., I. Katopodi, K.A.H. Ramadan, R. Koelewijn and S. Longo (1994). Sediment transport under (non)-linear waves and currents. Proc. 24th Int. Conf. on Coastal Engng., Kobe, Japan, ASCE, 2527-2541.

Tánczos, I.C., de Meijer, R.J., Ribberink, J.S., Janssen, C.M. (1997). Selective transport of heavy and light minerals under asymmetric waves, Submitted to Sedimentology.

Phase-lag effects in oscillatory sheet flow

C. Marjolein Dohmen-Janssen[1], Gizella van der Hout[1], Jan S. Ribberink[2]

Abstract

It is often assumed that in sheet flow conditions the transport rate in oscillatory flow behaves quasi-steady, i.e. showing a direct relation with the instantaneous flow velocity (e.g. Ribberink et al., 1994). In this paper it will be shown that this assumption is not always valid.

Therefore a new semi-unsteady sand transport model is developed which takes into account phase-lag effects of the sediment on the net transport rate. In order to verify this new semi-unsteady model and two existing quasi-steady models, new experiments were performed in the Large Oscillating Water Tunnel (LOWT) of WL | DELFT HYDRAULICS. Together with earlier experiments these measurements form a data set of net sand transport rates of uniform sand for three different grain sizes (D_{50} = 0.13; 0.21 and 0.32 mm) in combined wave-current sheet flow conditions.

The verification shows that phase-lag effects become important for a combination of fine sand, large flow velocities and small wave periods. Under these conditions the quasi-steady models cannot predict the behaviour of the net transport rates correctly and the predictions of the new semi-unsteady model show much better agreement.

Introduction

Sheet flow corresponds to conditions of high velocities when ripples are washed out and the bed becomes flat. In those conditions the majority of the sand transport takes place in a thin, high-concentrated layer close to the bed, i.e. the sheet flow layer.

Because of the small thickness of this layer it is generally assumed that the response time of the sand transport process to changes in flow conditions is small compared to the wave period. If that is the case, it can be expected that the time-dependent sediment transport rate depends directly on the instantaneous flow velocity or bed shear stress. This assumption is applied in all quasi-steady models.

[1] Delft University of Technology, Hydraulics & Offshore Eng. Section. p/a University of Twente, Section of Civil Eng. & Management, PO Box 217, 7500 AE Enschede, The Netherlands, phone: 31 53 4892831, fax 31 53 4894040, email: c.m.dohmen-janssen@sms.utwente.nl

[2] University of Twente, Section of Civil Eng. & Management, PO Box 217, 7500 AE Enschede, The Netherlands, phone: 31 53 4892767, fax 31 53 4894040, email: j.s.ribberink@sms.utwente.nl

If the response time of sediment particles is not small compared to the wave period, the sediment concentration may lag behind the velocity. This will be caused by the fact that both the sediment entrainment from the bed into the flow and the settling of the particles back to the bed takes time. The latter depends on the settling time of a particle and on the height to which the particle is entrained, which is expected to be determined by the flow velocity.

Therefore it is expected that phase-lags will become important if sediment is entrained relatively high into the flow (large oscillatory velocities) and slowly settles down to the bed (fine sand) while the available fall time is short (small wave period). Moreover, it is expected that if phase-lags occur, the net transport rates are reduced. This can be explained as follows: If the transport behaves quasi-steady, the net (wave-averaged) transport rate under asymmetric oscillatory flow will always be in direction of the largest velocity, due to the non-linear relation between velocity and sand transport rate. If the sediment concentration lags behind the flow velocity, part of the sediment that is picked-up under a certain half wave cycle, may still be entrained into the flow and transported in opposite direction during the successive half wave cycle.

A new semi-unsteady model is developed to take into account the effect of phase-lags on the net transport rates. The model is called semi-unsteady, because it accounts for phase-lag effects, without describing the complete time-dependent velocity and concentration profiles. Apart from the new *semi-unsteady* model, also two existing *quasi-steady* models are presented, in order to compare the differences between these two types of models. The three transport models are verified against experimental data.

The set-up of the experiments and the measured net transport rates are presented first. Next the two existing quasi-steady models are described shortly and the new semi-unsteady model is presented. Finally, the behaviour of the measured net transport rates is discussed in relation with the predictions of the three transport models.

New experiments

Two new sets of sand transport experiments were carried out with uniform sand of different grain sizes. The experiments were performed in the Large Oscillating Water Tunnel (LOWT) at WL | DELFT HYDRAULICS from October 1996 to January 1997. The mean grain sizes of the two sands were 0.32 and 0.21 mm for series I and J respectively. The experiments are a follow up of the previous experimental series with 0.21 mm sand (Series E: Katopodi et al., 1994) and 0.13 mm sand (Series H: Janssen and Ribberink, 1996 and Janssen et al., 1997). The measurements of these four series can be considered as one consistent data set on sediment transport under combined wave-current flow in the sheet flow regime.

The LOWT of WL | DELFT HYDRAULICS is a large-scale facility that allows experiments to be performed at full scale (1:1). It consists of a large U-shaped tube, with a long horizontal test section and two vertical cylindrical risers. One of them is open to the air; the other riser contains a steel piston. The piston sets the water in motion and induces an oscillating water motion in the test section. The test section is 14 m long, 0.3 m wide and 1.1 m high. A 0.3 m thick sand bed can be brought into the test section, leaving 0.8 m for the oscillating water flow above the bed.

Underneath both risers a sand trap is constructed. The range of oscillatory velocities is 0.2-1.8 m/s; the range of periods is 4-15 s.

A recirculation flow system for the generation of a net current is connected to both cylindrical risers. The maximum superimposed net current velocity in the test section is about 0.5 m/s. A third sand trap is constructed in this recirculation system. A picture of the LOWT is given in Figure 1.

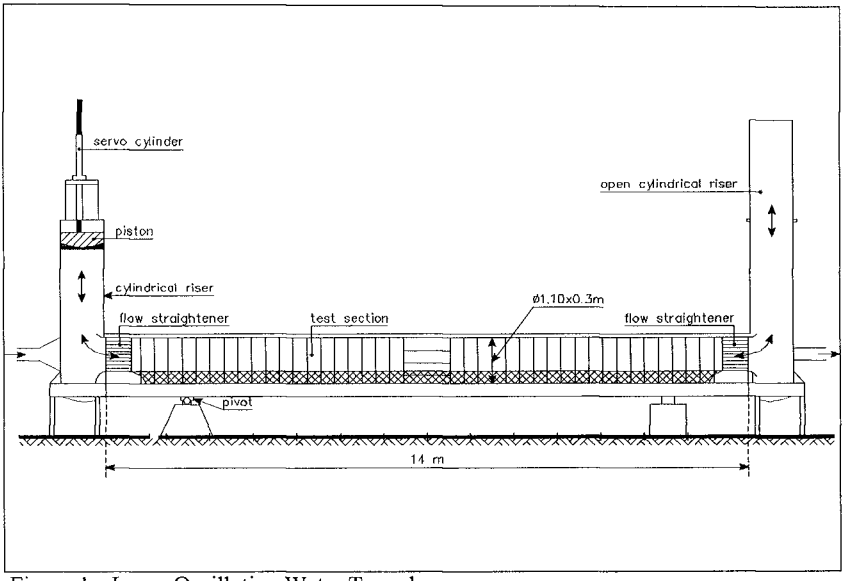

Figure 1: Large Oscillating Water Tunnel

The characteristics of the three sands, used in the experimental series are:

Series H:	D_{10} = 0.10 mm,	D_{50} = 0.13 mm,	D_{90} = 0.18 mm
Series E/J:	D_{10} = 0.15 mm,	D_{50} = 0.21 mm,	D_{90} = 0.32 mm
Series I:	D_{10} = 0.22 mm,	D_{50} = 0.32 mm,	D_{90} = 0.46 mm

The test conditions consisted of different combinations of a sinusoidal oscillatory flow and a net current. A condition is characterised by the wave period T (s), the velocity amplitude u_a (m/s) and the mean current velocity u_m (m/s) measured at 10 cm above the bed. For the present series I and J the conditions are mainly the same as in the previous experimental series with unsieved dune sand with D_{50}= 0.21 mm (Series E) and fine sand with D_{50}= 0.13 mm (Series H).

For every condition net (wave-averaged) transport rates were measured, together with the flow velocity at 10 cm above the bed. Net transport rates were derived from measured bed level changes and the weight of the sand, collected in the traps.

The measured net transport rates are based on measurements over the full width of the tunnel. However, the velocities are measured in the centreline of the tunnel. Due to boundary layer effects the net current velocities in the centreline are somewhat

higher than the width-averaged values. Therefore the net transport rates are corrected such that they correspond to the measured velocities in the centreline of the tunnel (see e.g. Van der Hout, 1997). Table 1 presents the measured wave periods and flow velocities, together with the corresponding net transport rates, expressed in m^2/s, i.e. volume of sand per unit width per second.

Table 1: Measured wave periods, flow velocities and net transport rates

Test	D_{50} (mm)	T (s)	u_a (m/s)	u_m (m/s)	$\langle q_s \rangle$ (10^{-6} m^2/s)
H2	0.13	7.2	0.68	0.23	18.8
H3	0.13	7.2	0.93	0.24	34.9
H4	0.13	7.2	1.09	0.25	40.0
H5	0.13	7.2	1.30	0.24	51.7
H6	0.13	7.2	1.47	0.24	65.5
H7	0.13	7.2	0.49	0.42	15.6
H8	0.13	7.2	0.67	0.43	47.4
H9	0.13	7.2	0.94	0.43	85.7
H24	0.13	4.0	0.68	0.24	12.8
H44	0.13	4.0	1.06	0.25	9.0
H212	0.13	12.0	0.68	0.23	19.9
H412	0.13	12.0	1.09	0.24	97.1
J1	0.21	7.20	1.06	0.24	46.3
J2	0.21	7.20	1.28	0.25	74.4
E2	0.21	7.22	1.47	0.23	111.8
J3	0.21	7.20	0.46	0.41	9.0
J4	0.21	7.20	0.65	0.41	25.3
E4	0.21	7.23	0.95	0.44	84.4
J5	0.21	4.00	1.04	0.24	29.2
J6	0.21	12.0	1.09	0.23	49.2
I1	0.32	7.2	1.47	0.26	94.0
I2	0.32	7.2	1.70	0.25	152.3
I3	0.32	7.2	0.65	0.42	23.6
I4	0.32	7.2	0.92	0.42	53.3
I5	0.32	7.2	1.50	0.45	193.7

For conditions E1–E4, H6, H9, and I1 also time-dependent measurements were carried out: During the wave cycle both flow velocities and sediment concentrations at different levels above the sand bed were measured. Moreover, video recording were taken to determine the bed level variation during the wave cycle. These time-dependent measurements are not included in this paper (see e.g. Katopodi et al., 1994; Ribberink et al. 1994; Janssen et al., 1997 and Janssen and Van der Hout, 1997).

Quasi-steady model of Bailard (1981)

Bailard applied the theoretical energy consideration of Bagnold (1963) to determine the sand transport rate. He assumed that the sediment transport rate is proportional to the available fluid power, which is equal to the work done by the fluid, i.e. the absolute value of the fluid shear stress times the velocity.

The model consists of a bed load and a suspended load component. Each component includes a term that depends on the bed slope. The bed slope terms are not included here, because the sand bed in the experiments is horizontal. The equation reads:

$$q_s(t) = \frac{c_f}{(s-1)g}\left(\frac{\varepsilon_b u^3(t)}{\tan\varphi} + \frac{\varepsilon_s \left|u^3(t)\right| u(t)}{w_{fall}}\right) \quad (1)$$

Here q_s is the sediment transport rate, t is time, c_f is a friction factor, s is the relative density ($s = \rho_s/\rho$ with ρ_s the density of the sediment and ρ the density of water), g is the gravity acceleration, u is the horizontal velocity, φ is the angle of internal friction and w_{fall} is the fall velocity. The coefficients ε_b (= 0.1) and ε_s (= 0.02) are efficiency factors for the bed load and the suspended load transport.

In the present study the friction factor is calculated as a combined wave-current friction factor, as described by Ribberink (1998). The bed roughness height is considered to be equal to the grain diameter, i.e. $k_s = D_{50}$.

Quasi-steady model of Ribberink (1998)

The quasi-steady model of Ribberink is a bed load model. However, Ribberink considers all transport in the sheet flow layer as bed load. In sheet flow conditions the majority of the transport is transported inside the sheet flow layer, which means that the total transport will only be slightly larger than the bed load component, defined in this way.

Ribberink assumed the sand transport rate to be proportional to the difference between the actual time-dependent bed shear stress and the critical bed shear stress. The bed shear stress is expressed in terms of the (dimensionless) Shields parameter:

$$\theta(t) = \frac{\tau_b(t)}{\rho(s-1)gD_{50}} \quad (2)$$

Here τ_b is the time-dependent bed shear stress and D_{50} is the mean grain diameter. The sand transport rate is normalised by the parameter $\sqrt{(s-1)gD_{50}^3}$. This gives the following expression for the sand transport rate:

$$q_s(t) = m\sqrt{(s-1)gD_{50}^3}\left(\left|\theta(t)\right| - \theta_{cr}\right)^n \frac{\theta(t)}{\left|\theta(t)\right|} \quad (3)$$

The values of the coefficients m and n are based on many data from laboratory and field experiments with steady and oscillatory flows: m = 11, n = 1.65.

New semi-unsteady model

As mentioned in the introduction, phase-lag effects are expected for fine sand, large oscillatory velocities and small wave periods. Moreover, phase-lag effects are expected to reduce the net transport rate. Therefore a new-semi unsteady model is developed which predicts the same net transport rates as the quasi-steady model of Ribberink if phase-lag effects are small and smaller net transport rates if phase-lag effects become important.

This is realised by introducing a correction factor r to the calculated net transport rates of the model of Ribberink. The correction factor r is equal to 1.0 if no phase-lag effects occur and decreases for increasing phase-lag effects.

The correction factor r is defined as the ratio of the net sand transport rate, including phase-lag effects (*real* net transport rate) to the net sand transport rate when phase-lag effects are neglected (*equilibrium* net transport rate). These transport rates are calculated as follows:

$$q_s(t) = \int_0^h u_\infty(t) * c(z,t)\, dz \qquad (4)$$

Here h is the water depth, $u_\infty(t)$ is the periodic velocity outside the wave boundary layer, (free-stream velocity) and c is the sediment concentration. The time-dependent sediment concentration profile c(z,t) is derived from an advection-diffusion equation. Nielsen (1979) showed that this equation can be solved analytically if a constant sediment mixing coefficient ε_s is used. The advection-diffusion equation reads:

$$\frac{\partial c}{\partial t} = \frac{\partial}{\partial z}\left[w_{fall} c + \varepsilon_s \frac{\partial c}{\partial z} \right] \qquad (5)$$

The *equilibrium* sand transport rate is equal to the product of the free-stream velocity and the equilibrium concentration profile, while the *real* sand transport rate is equal to the product of the free-stream velocity and the real concentration profile.

To derive the time-dependent *equilibrium* concentration profile, it is assumed that the concentration profile adjusts itself instantaneously to changes in flow velocity. This corresponds to a solution of the advection-diffusion equation for which the term $\partial c/\partial t$ is set zero. The time-dependent *real* concentration profile is derived without this assumption, which corresponds to the solution of the complete advection-diffusion equation, i.e. including the term $\partial c/\partial t$.

The bottom boundary condition for the equilibrium concentration profiles is based on the assumption that the bottom concentration is instantaneously related to the flow velocity. Using a coefficient a and exponent b this can be expressed as follows:

$$c(0,t) = a\left|u(t)^b\right| \qquad (6)$$

For the real concentration profiles the bottom boundary condition is based on the assumption that the *pick-up rate* of sediment is directly related to the instantaneously velocity. This implies that the concentration *gradient* is instantaneously related to the flow velocity:

$$\left.\frac{\partial c}{\partial z}\right|_{z=0} = -\frac{w_{fall}}{\varepsilon_s} a \left| u(t)^b \right| \tag{7}$$

The advection-diffusion equation only has an analytical solution if b is even. In the present study b = 2 is chosen, giving a transport rate proportional to u^3. This is close to the value of 3.3 in the model of Ribberink (1998), which results for negligible values of the critical Shields parameter, as is the case in sheet flow conditions.

Applying all these considerations results in the following expressions for the real and the equilibrium sand transport rate, i.e. $q_{s,r}$ and $q_{s,eq}$, respectively:

$$q_{s,r}(t) = \left[\sum_{k=0}^{N} u_k \cos(k\omega t)\right]\left[\sum_{k=0}^{2N} \frac{\varepsilon_s}{w_{fall}} \frac{\hat{c}_{bk}}{\left(P_k^2 + Q_k^2\right)^{\frac{3}{2}}}\left[P_k \cos(k\omega t + \varphi_k) + Q_k \sin(k\omega t + \varphi_k)\right]\right] \tag{8}$$

$$q_{s,eq}(t) = \left[\sum_{k=0}^{N} u_k \cos(k\omega t)\right]\left[\sum_{k=0}^{2N} \frac{\varepsilon_s}{w_{fall}} \hat{c}_{bk} \cos(k\omega t)\right] \tag{9}$$

With:

$$\hat{c}_{b0} = a\left(u_0^2 + \tfrac{1}{2}u_1^2\right) \tag{10}$$

$$\hat{c}_{b1} = a\left(2u_1 u_0\right) \tag{11}$$

$$\hat{c}_{b2} = a\left(\tfrac{1}{2}u_1^2\right) \tag{12}$$

$$P_k = \frac{1}{2} + \left[\frac{1}{16} + \left(\frac{k\varepsilon_s\omega}{w_{fall}^2}\right)^2\right]^{\frac{1}{4}} \cos\left(\tfrac{1}{2}\alpha_k\right) \tag{13}$$

$$Q_k = \left[\frac{1}{16} + \left(\frac{k\varepsilon_s\omega}{w_{fall}^2}\right)^2\right]^{\frac{1}{4}} \sin\left(\tfrac{1}{2}\alpha_k\right) \tag{14}$$

$$\alpha_k = \arctan\left(\frac{4k\varepsilon_s\omega}{w_{fall}^2}\right) \tag{15}$$

$$\varphi_k = \arctan\left(-\frac{Q_k}{P_k}\right) \tag{16}$$

Here ω is the angular frequency of the wave (= $2\pi/T$, with T the wave period) and u_k is the k^{th} harmonic of the horizontal velocity. In the present analysis only u_0 and u_1 are considered (sinusoidal oscillatory flow plus a net current), because all experimental conditions consist of sinusoidal oscillatory flow combined with a net current.

As mentioned before, the correction factor r is defined as the ratio of the *net* real sand transport rate to the *net* equilibrium sand transport rate. These net sand transport rates can be determined by averaging Eqs.(8) and (9) over time.

From these equations it can be seen that the difference between the equilibrium and the real transport rate (and thus the value of the correction factor) is fully determined by $\varepsilon_s\omega/w^2_{fall}$, called the phase-lag parameter p. The ratio of sediment mixing coefficient to fall velocity ε_s/w_{fall} can be considered as a characteristic length δ to which particles are entrained. Therefore the phase-lag parameter can be written as:

$$p = \frac{\varepsilon_s \omega}{w_{fall}^2} = \frac{\delta \omega}{w_{fall}} = 2\pi \frac{\delta}{w_{fall} T} \tag{17}$$

In order to calculate the phase-lag parameter p and thus the real and equilibrium sand transport rates and the correction factor r, either the value of the sediment mixing coefficient (ε_s) or the characteristic height to which particles are entrained (δ) must be known.

In the present study δ is assumed to be equal to the thickness of the sheet flow layer δ_s. The latter is defined as the distance between the top of the non-moving sand bed during the wave cycle and the level where the time-averaged concentration is equal to 8 vol%. Values of δ_s were derived from concentration profiles, as measured in the LOWT of WL | DELFT HYDRAULICS (e.g. Katopodi et al., 1994; Janssen et al., 1997; Janssen and Van der Hout, 1997).

It was found that the fine sand (D_{50} = 0.13 mm) behaved systematically different than the two coarser sands (D_{50} = 0.21 and 0.32 mm sand). Therefore two equations have been derived for the sheet flow layer thickness as a function of the maximum Shields parameter:

$$\frac{\delta_s}{D_{50}} = 4.5\,(7.5\theta_{max} + 0.90) \qquad \text{for } D_{50} = 0.13\,\text{mm}$$

$$\frac{\delta_s}{D_{50}} = 2.9\,(4.5\theta_{max} + 0.065) \qquad \text{for } D_{50} \geq 0.21\,\text{mm} \tag{18}$$

The maximum Shields parameter θ_{max} is based on the amplitude of the oscillatory velocity and a wave friction factor, using $k_s = D_{50}$.

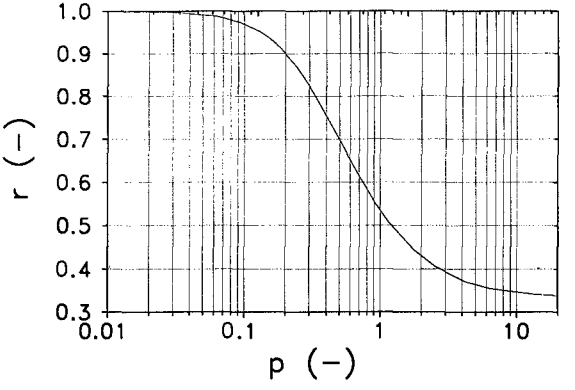

Figure 2: Reduction factor of equilibrium sand transport (r) as a function of phase-lag parameter (p) for a situation of sinusoidal oscillatory flow and a net current

Figure 2 shows the value of the reduction factor r as a function of the phase-lag parameter p for a situation of a sinusoidal oscillatory velocity and a net current, i.e. for $u(t) = u_0 + u_1\cos(\omega t)$. This figure shows that the reduction factor decreases for increasing values of p, which means that the difference between the real and the equilibrium net transport rates is large for large values of p. This can be explained as follows: The value of p is large for large values of the height to which particles are entrained (δ) and small values of the fall velocity (w_{fall}) and the wave period (T). As explained in the introduction, this corresponds to large phase-lag effects.

Behaviour of measured net transport rate and verification of sand transport models

In order to study the behaviour of the measured net transport rates and to verify the predictions of the three sand transport models, the measured and computed net transport rates are plotted as function of the grain size, the amplitude of oscillatory velocity and the wave period.

Grain size influence

Figure 3 shows the net sand transport rate as a function of the grain size for the following flow condition (H6, E2, I1):

$T = 7.2$ s
$u_a = 1.5$ m/s
$u_m = 0.25$ m/s

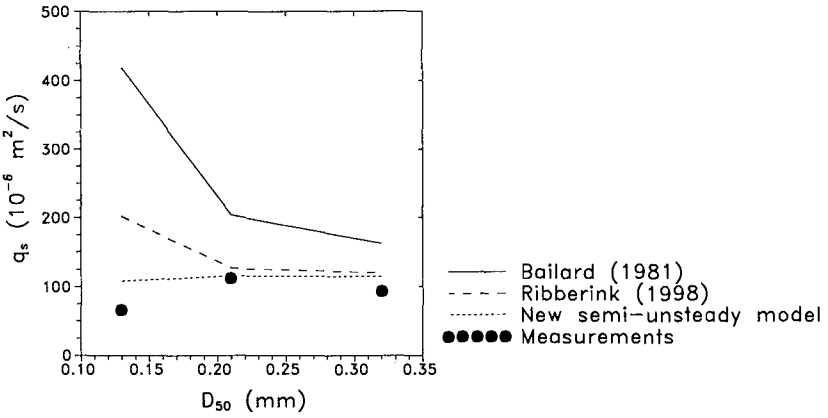

Figure 3: Measured and computed net sand transport rate as a function of grain size

The figure shows that the two quasi-steady models predict increasing net transport rates for decreasing grain size. This is in qualitative agreement with the measurements for medium and coarse sand. The magnitudes of the net transport rates for medium and coarse sand are predicted quite well by the model of Ribberink (1998) and overpredicted by the model of Bailard (1981).

The situation for fine sand is very different: The measurements show decreasing net transport rates for a grain size decrease from 0.21 to 0.13 mm. This may be explained by relatively large phase-lag effects due to the small settling velocity of the fine sand and the large oscillatory velocity, resulting in relatively large entrainment heights of the sediment particles.

In the new-semi unsteady model the small settling velocity and large oscillatory velocity result in a large value of the phase-lag parameter p, corresponding to a small value of the reduction factor r. That is why the net transport rate for the fine sand, predicted by the new semi-unsteady model is much smaller than for the model of Ribberink. Consequently, the new semi-unsteady model agrees much better with the measured net transport rate of fine sand.

For the medium and the coarse sand the predicted net transport rates of the new semi-unsteady model are almost equal to those of the quasi-steady model of Ribberink, indicating that phase-lag effects are small.

Flow velocity influence

The three panels of Figure 4 show the net sand transport rate as a function of the amplitude of the oscillatory velocity for three different grain sizes. In all cases the wave period is equal to 7.2 s and the net current velocity is equal to 0.25 m/s.

This figure shows that the two quasi-steady models predict increasing net transport rates for increasing oscillatory velocities. Again this is in qualitative agreement with the measurements for medium and coarse sand. For these two sand types the magnitudes of the measured net trans-

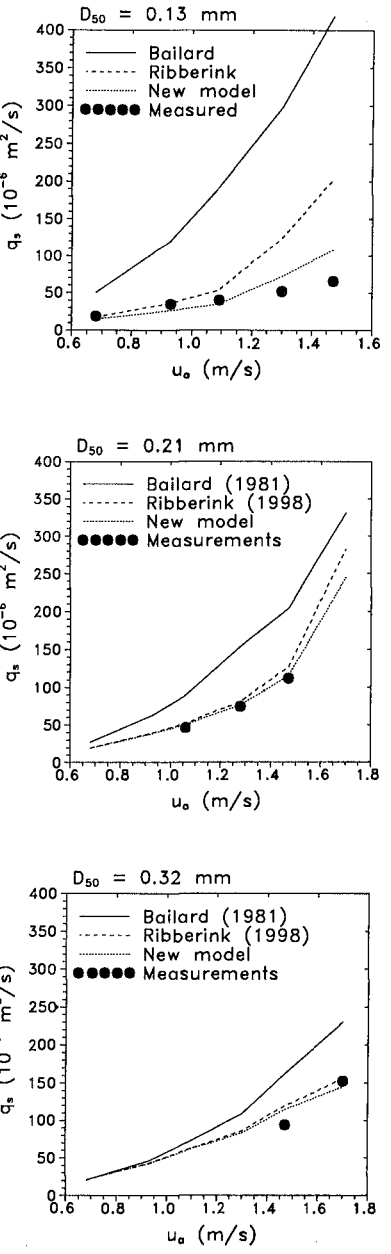

Figure 4: Measured and computed net sand transport rate as a function of amplitude of oscillatory velocity.

port rates are again overpredicted by the model of Bailard and predicted quite well by the model of Ribberink. Moreover, the semi-unsteady model gives almost the same results as the model of Ribberink for these two cases, indicating that phase-lag effects are not very important.

Again the situation is different for the fine sand: For small oscillatory velocities, the model of Ribberink predicts the measured net transport rates quite well. The model of Bailard largely overpredicts the measured net transport rates. The new semi-unsteady model gives almost the same results as the model of Ribberink, indicating that phase-lag effects are small. This can be explained by the fact that particles are not entrained very high into the flow for these low velocities.

However, for increasing oscillatory velocities, the increase in measured net transport rates is much smaller than predicted by the quasi-steady models, which may again be explained by increasing phase-lag effects. This is confirmed by the fact that the difference between the predictions of the new semi-unsteady model and the model of Ribberink increases for increasing oscillatory velocities, indicating that phase-lag effects become indeed more important. The predictions are thus again improved by including phase-lag effects.

Wave period influence

Figure 5 shows the net sand transport rate as a function of the wave period:

- The upper panel shows the results for *fine* sand and a relatively *low* oscillatory velocity of 0.7 m/s.
- The middle panel shows the results for *fine* sand and a relatively *large* oscillatory velocity of 1.1 m/s.
- The lower panel shows the results for *medium* sand and a relatively *large* oscillatory velocity of 1.1 m/s.

The net current velocity is equal to 0.25 m/s in all cases. All figures are plotted at the same scale to allow intercomparison between the three plots.

Figure 5 shows that the two quasi-steady models predict slightly increasing net transport rates for decreasing wave periods, due to the increase in wave friction factor. This is in qualitative agreement with the measurements for:

- Fine sand, $u_a = 0.7$ m/s, $T \geq 7.2$ s
- Medium sand, $u_a = 1.1$ m/s, $T \geq 7.2$ s

For these conditions the magnitudes are overpredicted by the model of Bailard and predicted quite well by the model of Ribberink.

For the other conditions the measurements show decreasing net transport rates for decreasing wave periods. This may again be explained by phase-lag effects, which become larger for shorter wave periods.

For fine sand with an oscillatory velocity of 0.7 m/s (upper panel) the measurements show that a decrease in wave period from 7.2 to 4 s leads to a decrease in net transport rate of about 30%. This can be explained by phase-lag effects: despite the relatively small oscillatory velocity, the wave period is so small and the sand so fine that phase-lag effects still occur.

The new semi-unsteady model predicts a similar phase-lag effect, which therefore results in improved predictions, compared to the model of Ribberink.

A phase-lag effect also seems to be present in the measurements for medium sand with an oscillatory velocity of 1.1 m/s and a wave period of 4 s (lower panel). The new semi-unsteady model predicts a much smaller phase-lag effect than observed in the measurements, indicated by the very small reduction in net transport rate, compared to the model of Ribberink.

For the conditions with fine sand and an oscillatory velocity of 1.1 m/s (middle panel) the measured net transport rate for a wave period of 7.2 s is predicted somewhat better by the new semi-unsteady model than by the model of Ribberink. Apparently phase-lag effects do occur for this condition.

For a wave period of 4 s the measured net transport rate is strongly reduced, compared to the transport rate for a wave period of 7.2 s. This can be explained by large phase-lag effects. The new semi-unsteady model agrees indeed much better with the measurement than the model of Ribberink. However, the measured net transport rate is still overpredicted, indicating that the phase-lag effects are somewhat larger than predicted by this model. This may be partly caused by the fact that the quasi-steady model predicts increasing net transport rates for decreasing wave periods, due to the increase in wave friction factor. It is not clear whether this is true. Only for the condition with a wave period of 12 s the predicted net transport rate does not agree at all with the measurement.

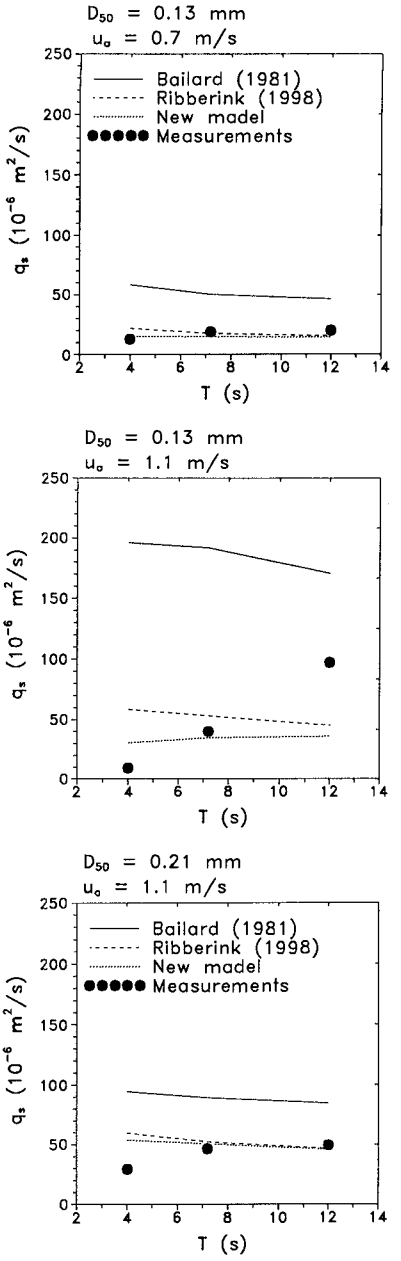

Figure 5: Measured and computed net sand transport rate as a function of wave period.

A different mechanism, which has not received any attention yet, may be responsible for this strong overprediction of the model, i.e. the limited pick-up rate of sand from the bed.

Video recordings of the bed level variation during the wave cycle show that several layers of sand grains are eroded from the bed. The thickness of the total eroded layer appears to be larger for increasing wave periods. Also, the concentration measurements in the sheet flow layer show that the sheet flow layer thickness is larger for a longer wave period. Existing expressions for the thickness of the sheet flow layer (e.g. Wilson, 1989; Sumer et al., 1996), as well as the formulae used in this study (Eq.(18)), assume that the thickness of the sheet flow layer only depends on the Shields parameter, which slightly *decreases* for increasing wave periods, due to the decrease in wave friction factor.

Both observations indicate that, at least for large velocities and fine sand, the amount of sand entrained into the flow and thus the sand transport rate depends on the wave period. The phenomenon of limited pick-up rate is not included in the presently used quasi-steady and unsteady sand transport models and needs further experimental investigation.

Conclusions

It is often assumed that in sheet flow conditions the response time of sediment particles is small with respect to the wave period, because the majority of the sand is transported in the thin sheet flow layer, close to the bed. This quick sediment response would result in a quasi-steady behaviour of the sand transport rate, i.e. a direct relation between the instantaneous sand transport rate and the instantaneous flow velocity.

However, measurements in a LOWT show that for fine sand, large oscillatory velocities and small wave periods the net transport rate is smaller than what could be expected from a quasi-steady behaviour. This may be explained by the presence of phase-lag effects: For large oscillatory velocities the sediment is entrained relatively high into the flow. If the entrained sand is very fine it settles down to the bed slowly and if the wave period is small this will result in a relatively large phase-lag between velocity and concentration. This means that sediment, which is entrained during the positive half wave cycle, can be transported in opposite direction during the successive half wave cycle, resulting in a reduction in *net* sand transport rate.

The fact that even in sheet flow conditions phase-lags effects can occur is explained by a new semi-unsteady model. This new model was developed using the bed load model of Ribberink and a phase-lag correction factor, which was based on an analytical solution of the advection diffusion equation for sediment concentration (Nielsen, 1979).

The phase-lag effects can be characterised by a phase-lag parameter p, defined as:

$$p = \frac{\varepsilon_s \omega}{w_{fall}^2} = \frac{\delta_s \omega}{w_{fall}} = 2\pi \frac{\delta_s}{w_{fall} T} \qquad (19)$$

Here ε_s is the sediment mixing coefficient, ω is the angular frequency of the wave ($=2\pi/T$, with T the wave period), δ_s is the sheet flow layer thickness and w_{fall} is the fall velocity of the sediment. It turned out that for $p > 0.8$ phase-lag effects become

significant (i.e. reductions in net transport rates, compared to the quasi-steady behaviour, of 40% or more).

In general the quasi-steady model of Ribberink (1998) agrees quite well with the measurements. The model of Bailard overpredicts the measured net transport rates. However, generally the behaviour is predicted qualitatively correctly.

Only for fine sand, large oscillatory velocities and small wave periods the behaviour is different than predicted by the two quasi-steady models and both the model of Bailard and the one of Ribberink overpredict the measured net transport rates. For these conditions the new semi-unsteady model shows a better agreement with the measurements.

Acknowledgements

The authors want to thank the Dutch Ministry of Transport and Public Works (RIKZ), for the financial support to perform the experiments. The first author also wants to thank the Technology Foundation (STW) for their financial support during the complete research project.

References

Bagnold, R.A. (1963). Mechanics of marine sedimentation. *In: The Sea, Vol. 3, ed. M.N. Hill, Interscience, New York.*

Bailard, J.A. (1981). An energetics total load sediment transport model for a plane sloping beach. *J. Geoph. Res., Vol. 86, No. C11, pp. 10938-10954.*

Hout, G. van der (1997). Grain size and gradation effects on sediment transport under sheet flow conditions. *M.Sc. Thesis, Delft University of Technology.*

Janssen, C.M., J.S. Ribberink (1996). Grain size influence on sand transport in oscillatory sheet flow. *Proc. 25th ICCE, Orlando, Florida, pp. 4779-4792.*

Janssen, C.M., W.N. Hassan, R. van der Wal, J.S. Ribberink (1997). Grain size influence on sand transport mechanisms. *Proc. Coast. Dyn.'97, Plymouth.*

Janssen, C.M. and G. van der Hout (1997). Sediment transport for two sands with different grain diameters under combined wave-current sheet flow conditions. *Data report Z2137, Part 1, April 1997, Delft Hydraulics.*

Katopodi, I., J.S. Ribberink, P. Ruol & C. Lodahl (1994). Sediment transport measurements in combined wave-current flows. *Proc. Coast. Dyn.'94, Spain.*

Nielsen, P. (1979). Some basic concepts of wave sediment transport. *Inst. of Hydrodyn. and Hydr. Eng., Tech. Univ. of Denmark, series Paper no. 20.*

Ribberink, J.S., I. Katopodi, K.A.H. Ramadan, R. Koelewijn and S. Longo, (1994). Sediment transport under (non)linear waves and currents. *Proc. 24th Int. Conf. on Coast. Eng., Kobe, Japan, pp. 2527-2541.*

Ribberink, J.S. (1998). Bed-load transport for steady flows and unsteady oscillatory flows, *Coastal Eng., Vol.34, pp. 59-82.*

Sumer, B.M., A. Kozakiewicz, J. Fredsøe and R. Deigaard (1996). Velocity and concentration profiles in sheet-flow layer of movable bed. *J. Hydr. Eng., ASCE, Vol. 122, No. 10, pp. 549-558.*

Wilson, K.C. (1989). Mobile bed friction at high shear stress. *J. Hydr. Eng., ASCE, Vol. 115, No. 6, pp. 825-830.*

CROSS-SHORE GRADED SEDIMENT TRANSPORT: GRAIN SIZE AND DENSITY EFFECTS

R.L. Koomans[1)], R.J. de Meijer[1)], and L.B. Venema[1)]

Abstract

Sediment sorting processes (sorting on grain size and density) are the result of local hydrodynamic conditions. In this paper two measuring techniques are described which derive *in situ* time dependent and time averaged distributions of sediment sorted on grain size and density. The technique on measuring grain size of the sediment is described in more detail. The sediment distributions give information on the local hydrodynamic conditions on different time scales. Measurements from the field serve as a test case of describing the depth of closure from measurements of sediment composition.

Introduction

Coastal sediments are rarely composed of one type of sediment. Grain sizes may vary from cobbles, gravel and coarse sand to fine sand, silt and clay; densities show variations from about 1.6 kg l^{-1} for certain carbonates to heavy minerals as dense as cassiterite (7.4 kg l^{-1}). Seldomly however, one observes all varieties mixed at one localised spot. Variations in currents, waves and/or wind tend to concentrate certain sediments at specific locations according to the hydrodynamic properties of a sediment. In turn the variations (gradation) in grain size and density reflect the changes in transport conditions.

Sorting occurs due to differences in settling and pick up of grains with different size, density and shape. In settling the fall velocity of grains is determined by an equilibrium between gravity and friction forces, depending on the size, density and shape of the grain. In entrainment, sorting is due to differences in the exposure of the grain to the fluid and gravity acting on the grain.

Figure 1 presents fall and entrainment velocities as function of grain size and density. The upper part of Figure 1 shows that with small grain sizes, density

[1] Nuclear Geophysics Division, KVI, University of Groningen, Zernikelaan 25, 9747 AA Groningen, The Netherlands

variations have little impact on the fall velocity of a grain (Cheng, 1997) but with increasing grain size, density effects become more important. The lower part shows the critical peak value of the orbital velocity near the bed needed to entrain a grain as a function of density and grain size, based on the formula given by Komar and Miller (1975). For small grain sizes, changes in the entrainment velocity are small with varying density, but for larger grain sizes (>100 μm) density is the most important parameter determining the entrainment velocity.

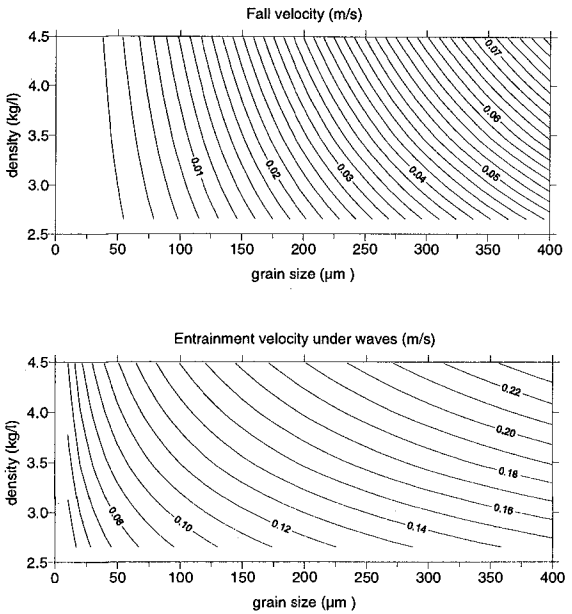

Figure 1: Settling velocity and entrainment velocity (m s^{-1}) as function of grain size and density.

A comparison between both figures shows that settling and entrainment processes are affected differently by grain size and density variations. Whilst grain-size variations will have a larger effect on the settling velocity, variations in density will have relatively larger effects in the entrainment velocity.

Already in 1949, Inman pointed out that the effects of sorting, reflected in the median grain diameter of the sediment may give information on the conditions under which the sediment was transported and deposited. Also other studies have been conducted describing hydrodynamic conditions based on sediment distributions. Veenstra and Winkelmolen (1976) describe size, shape and density sorting patterns of sediments of the coast of Dutch the barrier island of Ameland, which is also object of study in this paper. Their data show that in the offshore area (deeper than 12m) a coarse sediment population is the result of an earlier high-energy situation during the post-glacial transgression and can not been transported under present hydrodynamic processes. The sediments between this offshore area and the beach show a rather narrow size spectrum and sorting occurs mainly on density and shape.

Studies on the relation between size gradation and hydrodynamics were carried out by various authors (e.g. Guillén and Hoekstra, 1996, Swift *et al.*, 1971).

Guillén and Hoekstra describe a model of the equilibrium distribution of grain-size classes across the cross-shore coastal profile of the Dutch barrier island Terschelling (adjacent to Ameland). They state that the shape of the grain-size distribution curve depends on the hydrodynamic processes acting on the profile and serves as a fingerprint of the system. They observed that the median grain size of the sediment and the distribution of grain-size fractions show a break in their cross-shore distribution at approximately 6m depth across the shore face of Terschelling. This depth is considered to be the closure depth of the profile because it corresponds to the seaward limit of the shallowest and high mobility part of the littoral profile during the studied period.

Hallermeier (1981) extensively describes the expected maximum water depth for significant effect on the sand bottom by surface waves (later referred to as closure depth). In his description, he takes account of sand characteristics and wave parameters to calculate a seaward limit of intense sediment transport and extreme bottom changes. The concept is based on the observation that cross-shore sediment transport decreases seaward and becomes almost negligible beneath a certain depth (closure depth). Since this depth of closure is dependent on the movement of sediment, the position of the depth of closure along the cross-shore profile is a function of density, grain size, shape and time. Figure 2 schematically indicates the shore profile and the border of initiation of motion (depth of closure) as function of grain size and density. Large, heavy grains are harder to transport than small, light grains and, for equal wave conditions, the initiation of motion occurs at a shallower water depth, higher on the profile. Similarly heavier grains have a shallower closure depth than light grains of the same diameter. Investigations of selective transport processes of heavy minerals under shoaling waves (Tánczos (1996), May (1973), Stapor (1973)) showed that selective transport processes are rather rule than exception and start directly at the initiation of motion of sediments. Therefore, measurements of changes in sediment gradation provide information on the initiation of motion.

Measurements of sediment characteristics in the field to determine hydrodynamic conditions have been conducted since 1949 (Inman, 1949). However, these measurements lacked high spatial resolution and were too time consuming for regular measurement campaigns. With the techniques described in this paper, high-resolution *in situ* measurements can be conducted and makes an approach of describing hydrodynamic conditions from sediment characteristics fruitful.

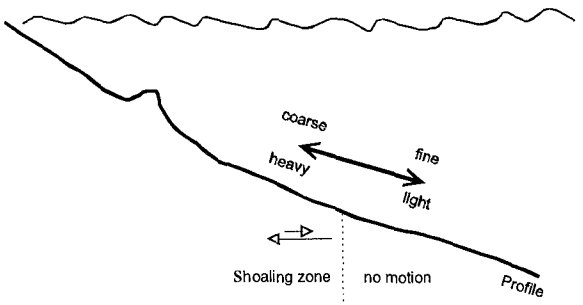

Figure 2: The seaward limit of significant sediment transport is dependent on grain size *and density.*

This paper presents variations of grain size and density along profiles in the field and in the laboratory. The data consist of high density, *in-situ* measurements of grain size and density using a towable seabed detector MEDUSA (de Meijer *et al*, 1996 and de Meijer, 1998). The grain size and density variations are derived from the intensity of friction sound and natural radioactivity. The sensor that utilises the relation between friction-sound and grain size will be explained in more detail. Data is collected on the foreshore of the Dutch Frisian Island of Ameland and in the Großer Wellenkanal (GWK) in Hannover, Germany. The aim of the present study is to measure sediment distributions to extract information on the local hydrodynamic conditions on different time scales. Measurements from the field serve as a test case of describing the depth of closure from measurements of sediment composition.

Experimental techniques

The heavy mineral concentration of the sediments in the field survey is determined from the concentrations of the naturally occurring radionuclides of the decay series of ^{238}U and ^{232}Th. In heavy minerals, the concentrations of ^{238}U and ^{232}Th are two orders of magnitude higher than in light minerals. Although the actual concentrations of ^{238}U and ^{232}Th depends on the mineral composition of the heavy mineral suite, it was found that the heavy minerals near the Dutch Frisian Islands have a quite constant radiometric fingerprint (de Meijer *et al*, 1990, de Meijer and Donoghue, 1995). The total concentration of heavy minerals (THM) is hence calculated from the values listed in de Meijer *et al* (1990). The radiometric variations in the sand of the flume at GWK are not related to the heavy mineral concentration only, but also to grain-size variations (Figure 3). Figure 3 shows a decreasing activity concentration of ^{40}K as function of grain size whereas there is no clear difference in the average activity concentration of ^{40}K in the light and heavy fraction. The $^{238}U+^{232}Th$ activity concentration also decreases with increasing grain-size, but here the light and heavy fractions differ two orders of magnitude in the $^{238}U+^{232}Th$ concentration. The grain size dependence of the $^{238}U+^{232}Th$ concentration may also reflect the grain size distribution of the heavy fraction.

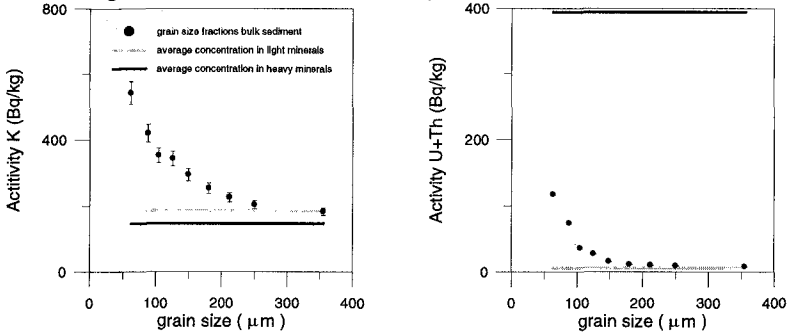

Figure 3: Activity concentrations of 40K, 238U and 232Th as a function of grain-size compared to the average concentrations in the light and heavy mineral fractions.

Measurements with the MEDUSA detector system were carried out at GWK, Hannover and the seafloor near the Island of Ameland. Natural radioactivity is measured with a highly sensitive gamma-ray detector in the standard set-up as described in de Meijer (1998) and the system yields activity concentrations of the three nuclides as long as it is in contact with the bed.

The measurements of friction-sound were carried out with a microphone inside the detector casing. The microphone records noise that the detector generates when the casing slides over the sediment. It was originally included in the detector system together with the water depth sensor to monitor the contact of the detector with the sediment, but the signal variations proved to be consistent with grain size variations and reproducible during several surveys. This triggered the question which variations caused the changes in sound level. Part of this paper deals with the interpretation of the friction-sound measurements and the data of the experiments in the GWK will show that the friction sound level is indeed a quantitative indicator of grain-size variations on the bed.

The experiments in the Large-scale Wave Flume (300x5x7 m^3) (Grosser Wellenkanal Hannover) in Germany were conducted as part of the EU MAST-III-program SAFE. In these experiments, profile development and sediment transport under storm conditions were studied. The sediment was rather coarse (d_{50}=280μm) and not well sorted (d_{10}/d_{90}=3). For the wave conditions, a TMA –wave spectrum with H_m=0.9 m and T_m=6 s was used that was repeated after every 0.5h. The experiments started with a smooth-bed profile with a slope 1:20 and with a water depth of 5m.

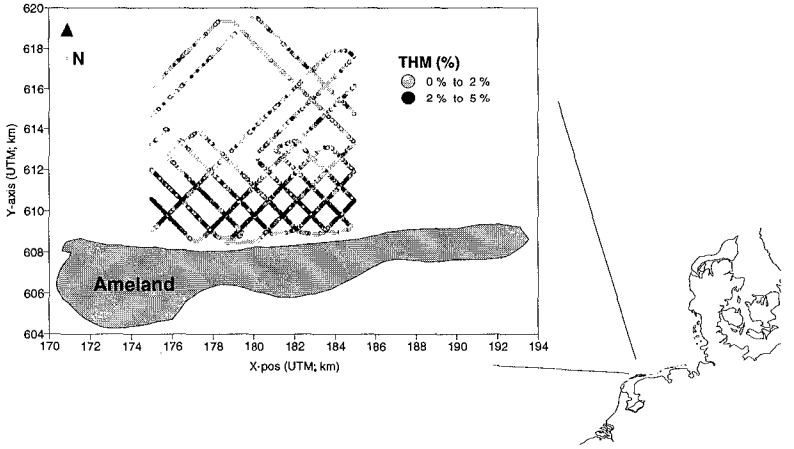

Figure 4: Geographical location of Ameland and an overview of lines towed near Ameland and of the concentrations of total heavy minerals (THM) along these lines. The map is given in UTM co-ordinates.

Results

Seafloor mapping

In June-July 1995, a survey was carried out using a MEDUSA- detector system towed by a vessel of Rijkswaterstaat. During this survey lines were towed between position RSP18 (beach pole 18) on Terschelling and the eastern tip of Ameland at depths of 1-25m. The barrier island Ameland is located in the northern part of the Netherlands just north of the Dutch Wadden Sea and flanked on both sides by a tidal inlet (Figure 4). The near-shore zone of Ameland is characterised by the presence of a bar system with an overall slope between the high water line and the off shore of about 1:400.

This paper presents the data collected in an area between the two ebb-tidal deltas in front of the coast of Ameland.

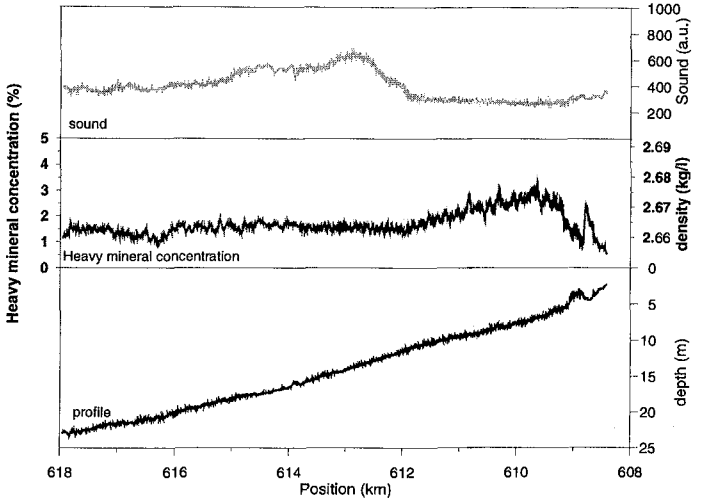

Figure 5: Average profile, heavy-mineral concentration and sound-level variations as function of distance to the coast of Ameland.

Figure 4 shows the distribution of total heavy mineral concentrations (THM) along the towed lines. A coast-parallel region of high concentrations of heavy minerals (up to 5% by mass) is visible a few kilometres off the coast. Seawards of this region the heavy mineral content of the sediment decreases. The heavy-mineral concentration seems to be constant in long shore direction. This distribution triggers the question if the concentration of heavy minerals is solely the result of cross-shore processes.

The mean of all survey data is presented as a cross-shore distribution in Figure 5. In the lower part of the figure, profile data show the position of a breaker bar at a water depth of 2.5-5m and a rather concave seaward slope with a slight convex "bump" between 610 and 613 km. At a position of 611.5 km, the slope steepness seems to increase. The heavy-mineral concentration (middle figure) shows an increased concentration just landwards of the breaker bar, a steep decrease on the breaker bar and again an increase up to position 609.8 km. From this position, the heavy-mineral concentration shows a decreasing trend to position 612 km, where it remains constant towards deeper water. The sound level shows a rather low, constant signal from the breaker bar towards position 612 km. From hereon the sound level doubles in intensity towards position 613 km, followed by a decreasing trend further seawards.

In the case of the heavy minerals of Ameland the density and grain-size distributions were measured by Tánczos (1996): $\rho_{50} = 3.5$ kg/l and $d_{50} = 110$ μm. Taking the density of quartz sand to be $\rho_q = 2.65$ kg/l, the heavy-mineral concentrations are converted to bulk densities. The corresponding values are indicated in the right-hand scale. From the figure one notices that small changes in density can be measured.

It is remarkable that large variations in sound level and heavy mineral concentrations occur in the region of convex bump in the profile. Seawards from this position, the heavy mineral concentration remains constant, while the recorded sound levels show an increase.

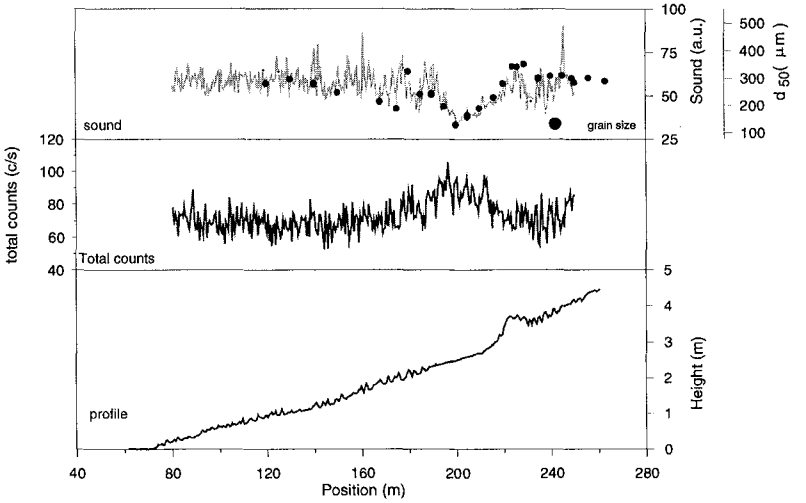

Figure 6: Profile, heavy mineral concentration and sound level distribution after 17h of storm conditions in the laboratory experiments at GWK, Hannover.

Laboratory experiments

The wave conditions of the experiments in the GWK were planned to be erosive at the beach face and during the experiment, a breaker bar developed at x=220m and at a water depth of 1-2m (Figure 6). "Seawards" of the breaker bar, the morphology is characterised by a smooth region without ripple structures, followed by a region with relatively large ripple structures. Again, MEDUSA is used to derive sediment characteristics along the profile.

For the sand in the flume the activity concentrations are very low and the total count rate rather than the individual radionuclide distribution is presented. The total count rate on the breaker bar is lower compared to other parts of the profile. Seawards from the breaker bar, the total count rate increases. In the smooth region, where the ripple structures are absent, the total count rate shows a maximum. In the region with ripple structures, "seawards" from the "flat zone" the count rate remain constant. The sound level shows variations that are almost opposite to the heavy-mineral concentration pattern. The sound level is high on the breaker bar, shows a decrease in the region where the ripple structures are absent, increases and remains constant towards deeper water. It is remarkable that the scatter in sound level is low in the

region where ripples are absent.

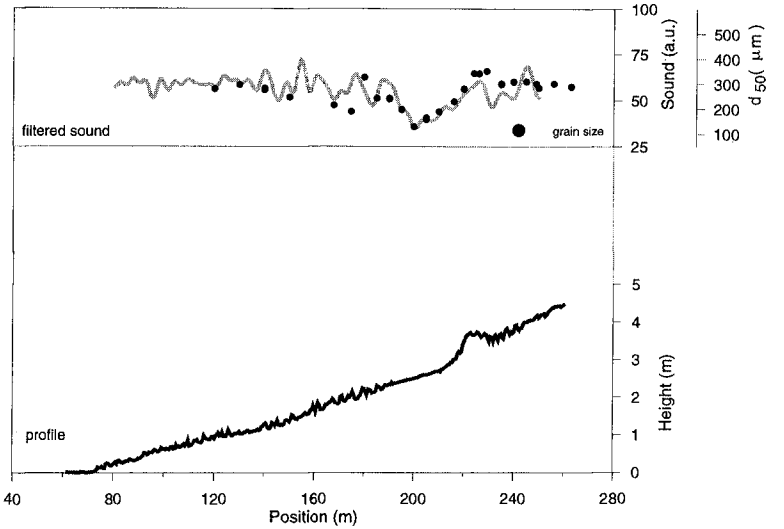

Figure 7: Profile, filtered sound level and median grain size *(d_{50}) after 17hrs of storm conditions in the laboratory experiments.*

Assessment of the relation between friction-sound and grain size

To investigate a possible relation between sound level and grain size of sediment, samples of the sediment top layer were collected at various locations of the bed after the water was drained from the flume. After drying and sieving, the grain-size distribution was derived. The d_{50} values are presented in the top part of Figure 6 together with the sound-intensity level. The two data sets show a remarkable correspondence in behaviour; the more because the sound level is likely produced by the upper grains of the sediment whilst, even in careful scooping of sediment, layers of several millimetres thick are collected.

A statistical analysis of the correlation between grain-size and sound level measurements of three different datasets from the wave flume experiments, show a significant correlation (r^2=0.7, with 41 degrees of freedom). To test the importance of grain size in the measured sound levels, two samples of sediment from the profile, with different sound-level characteristics, were glued on a wooden plate over which the detector was towed. Since the measurements with the calibration plate were conducted out off the water and the acoustic properties of the plate and natural sediment are different, only relative values may be compared. This small experiment confirms that larger grain sizes show larger sound levels than smaller grain sizes.

Table1: Sound levels of two types of sediment with different grain size. *Statistical uncertainties, 1 STD, are given in brackets.*

Grain size (µm)	Sound level wooden plate (a.u.)	Sound level sediment (a.u.)
265	167 (18)	53 (4)
380	210 (20)	69 (3)

The sound level exhibits a spiky behaviour, mainly, in the region of the ripples; in the smooth region and on the "seaward" part of the breaker bar such spikes are hardly present. A fourier transform was applied to filter small scale variations in the sound level (<5 metres) from the signal, testing the hypothesis that small scale variations are correlated to ripple structures. Figure 7 shows the filtered signal in comparison with the d_{50} value. Apparently, the small-scale variations on the sound level do not have an influence on the large-scale trend of sound level. It seems that the large-scale trend in sound level reflects the grain-size variations of the bed while sound level variations correlated with small-scale changes in morphology (like ripple structures) are superimposed on this trend. Whether these small-scale variations are directly the result of "bumping" on morphologic features or arise from the grain-size variations due to sorting within ripple structures is not clear.

Synthesis

It is remarkable that on the coast of Ameland large variations in radiometry and sound level occur in the region of the convex bump in the profile. Seawards from this position, the heavy mineral concentration becomes constant, while the sound level shows an increase. These changes in sound, which are related to grain size, and THM are probably caused by a difference in sediment population compared to the sediments near shore. During the fast sea level rise after the last glacial period, the barrier islands showed a fast landward retreat and part of the profile was "overstepped". This lower part of the profile shows sediments that are sorted by hydrodynamic conditions that are different from present day hydrodynamics. Since the transgression slowed down, the sediment distribution could come in equilibrium with present day hydrodynamic conditions (Veentra and Winkelmolen, 1976; Guillén and Hoekstra, 1996) and sediments could be sorted by grain size, density and shape. The change in slope steepness of the profile reflects the change between the relict profile from the transgressive phase and the "recently" reworked part of the coastal rofile (Swift, 1971).

During the process of coastal retreat, the recently reworked part of the profile eroded older sediments and heavy minerals remained as a lag deposit. The increase in heavy mineral content from the concave bump up to the breaker bar is probably the result of sorting of these lag deposits by processes due to wave shoaling (Tánczos, 1996; May, 1973). The constant sound level shows that the grain size is rather constant in this region and sorting will mainly occur on density and shape. Landward of the bar system the heavy mineral content increases while the breaker bar itself is depleted of heavy minerals. Here light sediments are transported and build the breaker bar, while heavy minerals remain in the eroding parts as lag deposits.

To compare the sediment distributions on the profile of the field measurements and the laboratory experiments, the sediment characteristics are plotted as a function of a scaled dimensionless waterdepth in Figure 8. The dimensionless waterdepth is derived by dividing the waterdepth by the maximum wave height. In the upper left part of Figure 8, a clear change in heavy-mineral grading occurs at a $d/H_{max} \sim 2$. Seaward from this location, the heavy-mineral concentration is constant, while the concentration shows a landward increase. It is remarkable that this depth (11m) coincides with the long-term closure depth (9-11m) for this region calculated from wave data (Westlake, 1995).

Experiments on graded sediment transport showed that sorting occurs at the initiation of motion. At a water depth >11m, sediment is not transported and sorting does not occur, while at shallower waterdepths, light minerals start to move and heavy minerals remain as a lag deposit or are transported at smaller transport rates. A this location where light minerals start to be transported, sorting is initiated. In the lower left part of Figure 8, a similar behaviour of sediment sorting can be observed. At a d/H_{max} >2 sediment composition is constant, while at shallower depths sediment sorting is initiated. The sorting pattern from the laboratory experiments is solely generated by cross-shore sediment transport processes. Since this pattern is comparable with the measurements of the seafloor, it seems that the sediment distribution on the seafloor is predominantly the result of cross-shore processes.

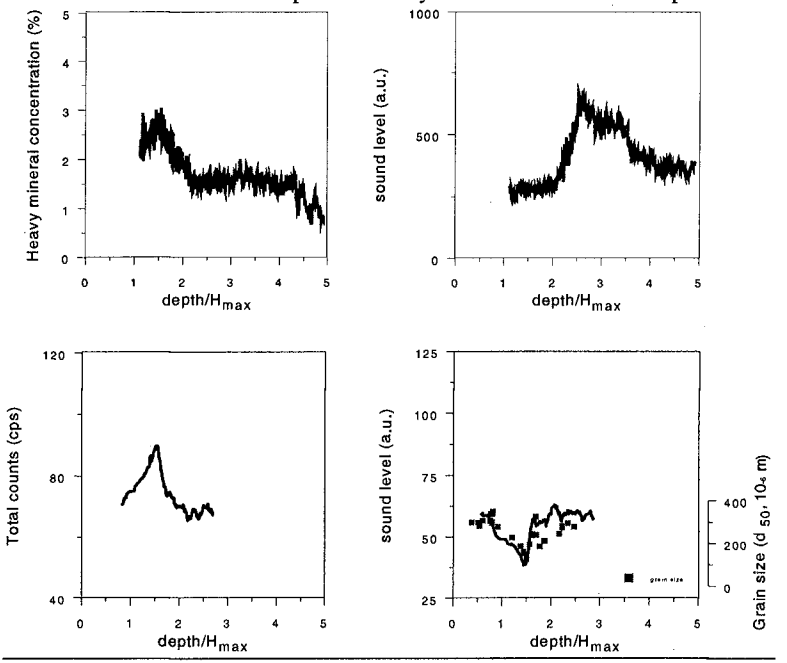

Figure 8: Heavy-mineral concentration and sound level variation as a function of depth/H_{max} from the Ameland survey (upper graphs) and total count rate, sound level and grain-size distribution (squares) as a function of depth/H_{max} from the laboratory study (lower graphs). The lines represent a running average fit trough the data points.

For the GWK measurements a major change in sound level can be observed at a d/H_{max} ~2. This depth was indicative for the depth of initiation of motion. However, sound level variations for the field survey are somewhat different from the sorting patterns measured with radiometry. Here, the large sound levels at d/H_{max} >2 are the coarse relict sediments of the transgressive phase while the lower sound levels at d/H_{max} <2 reflect sediments that are sorted by present day processes.

Both measuring techniques give different information on the depth where significant sorting processes start. The radiometric measurements comprise the upper 20 to 30cm of the sediment bed (maximum penetration depth of γ-radiation in sand)

and will therefore describe time scales of at least a few weeks, while the measurements of sound level only describe the upper grains of the sediment bed. The results of the laboratory study have shown that sorting of the upper layer of the sediment reach equilibrium for the specific wave conditions in a few hours. Therefore, the sound level measurements reflect only a local closure depth on a very small time scale.

Conclusions

Measurements on the seafloor near Ameland and measurements in the flume at GWK, Hannover show corresponding (scalable) distribution patterns of sediment sorting by density and grain size. The wave-flume experiments indicate that these distributions can be predominantly the result of cross-shore hydrodynamic processes. Heavy minerals tend to be concentrated seawards of the bar system in a region of fine-grained sediments just landward from where sediment motion is initiated.

The technique of deriving grain size by measuring the friction noise of the MEDUSA detector seems promising and would allow a synoptical, in-situ measurement of grain-size parameters. Together with the measurement of heavy-mineral content by means of natural radioactivity, MEDUSA allows the measurement of as well density and grain size. These two sedimentological parameters play an important role in sediment transport processes. Applying these techniques both in the field and the laboratory offers a handle to study these in more detail in laboratory experiments and in the field.

The results from the present investigation suggest that by the applied methodology the depth of initiation of motion can be measured in the field for different time scales.

Outlook

Further research on the correlation between friction-sound measurements and grain size will focus on frequency dependent sound measurements. At the moment, friction-sound measurements comprise a summation of all the sound frequencies. A sensor for measuring frequency specific friction-sound will be tested. For a refining of the sediment distributions in the radiometric measurements of the wave flume, a refinement of the fingerprint of the sediments will be conducted to allow a clear distinction between heavy mineral and grain-size distribution. Therefore the heavy and light sediment fractions will be split into separate grain-size fractions and measured for its radionuclide content.

Acknowledgements

The present investigation is part of the research programme of the Nuclear Geophysics Division of the KVI. The experiments in the Grosser Wellenkanal, Hannover were conducted as part of the MAST-III project SAFE. The measurements on the seafloor near Ameland were partly financed by the KUST*2000 programme of Rijkswaterstaat (the Dutch Ministry of Transport, Water Management and Public Works).

References

Cheng, N. S. (1997) *Simplified settling velocity formula for sediment particles.* Journal of Hydraulic engineering, **123**(2), pp. 149-152

Guillén, J. and Hoekstra, P. (1996) *The "equilibrium" distribution of* grain-size *fractions and its implications for cross-shore sediment transport: a conceptual model.* Marine Geology, **135**, pp. 15-33

Hallermeier, R. J. (1981) *A profile zonation for seasonal sand beaches from wave climate.* Coastal engineering, **4**, pp. 253-277

Inman, D. L. (1949) *Sorting of sediments in the light of fluid mechanics.* Journal of Sedimentary Petrology, **19**(2), pp. 51-60

Komar, P. D. and Wang, C. (1984) *Processes of selective grain transport and the formation of placers on beaches.* Journal of Geology, **92**, pp. 637-655

May, J. P. (1973) *Selective transport of heavy minerals by shoaling waves.* Sedimentology, **20**, pp. 203-211

de Meijer, R. J. (1998) *Heavy minerals: from 'Edelstein' to Einstein.* Journal of Geochemical Exploration, **62**(1-3), pp. 81-103

de Meijer, R. J. and Donoghue, J. F. (1995) *Radiometric fingerprinting of sediments on the Dutch, German and Danish coasts.* Quaternary International, **26**, pp. 43-47

de Meijer, R. J., Lesscher, H. M. E., Schuiling, R. D. and Elburg, R. D. (1990) *Estimate of the Heavy Mineral Content in Sand and its Provenance by Radiometric Methods.* Nuclear Geophysics, **4**(4), pp. 455-460

de Meijer, R. J., Tánczos, I. C. and Stapel, C., (1996), *Radiometry as a technique for use in coastal research.* In: Geological Society Special Publication No. 117 Geology of Siliciclastic Shelf Seas (Ed. by M. De Batist and P. Jacobs), pp. 289-297.

Stapor, F. W. j. (1973) *Heavy mineral concentrating processes and density/shape/size equilibria in the marine and coastal dune sands of the Apalachicola, Florida, region.* Journal of sedimentary petrology, **43**(2), pp. 396-407

Swift, D. J. P., Sanford, R. B., Dill Jr., C. E. and Avignone, N. F. (1971) *Textural differentiation on a shoreface during erosional retreat of an unconsolidated coast, Cape Henry to Cape Hatteras, western North Atlantic shelf.* Sedimentology, **16**, pp. 221-250

Tánczos, I. C. (1996) *Selective transport phenomena in coastal sands.* Ph. D., University of Groningen, Groningen, the Netherlands, ISBN 90-367-0669-6.

Veenstra, H. J. and Winkelmolen, A. M. (1976) *Size, shape and density sorting around two barrier islands along the north coast of Holland.* Geologie en Mijnbouw, **55**, pp. 87-104

Cross-shore sediment transports on a cut profile for large scale land reclamations

Martijn Onderwater[1]
Dano Roelvink[2]
Jan van de Graaff[3]

Abstract

When building a large scale land reclamation, the safest way is to shift the existing profile over the required distance of the reclamation project, up to a depth of say 20 m. This way the profile in cross-shore direction does not change and therefore also cross-shore sediment transports will be the same as before the land reclamation was made. A large disadvantage however is that a very large amount of material is needed for realising the reclamation. This makes the reclamation very costly.
To reduce the amount of material a cut profile can be applied. Above a certain depth (say CD -8 m) the cross-shore profile will be the same as the existing profile, but below this depth a relatively steep profile (say 1:50) is constructed. By doing this, material saving up to 40% can be achieved. A disadvantage of this cut profile is that a relatively steep profile has been made, which will effect the sediment transports.
In this study the effect of a cut profile are investigated by using the numerical model UNIBEST-TC of DELFT HYDRAULICS *for the computation of wave energy dissipation and cross-shore sediment transports. As an example the 'Plan Waterman', a plan for a land reclamation between Hook of Holland and Scheveningen, is used in this study. Various different cut profiles have been studied and it is found that especially relatively large waves, which break at the edge of the cut-off, have large influence on the cross-shore sediment transports. It is concluded, that the cut-off should at least be applied at CD-12 m if large changes in the coastal system are not desired.*

Introduction

People often want to live near water and all over the world the areas near the sea get more and more occupied by structures. For this reason there is a trend to reclaim land by making an artificial island near the existing coast or a peninsula against the existing coast. Examples are the recently opened airport in Hong Kong and the 'Plan Waterman', a plan to extend the Dutch coastline between Hook of Holland and Scheveningen. This plan is also known as the 'Plan New Holland'.

In most cases an extension of the coastline is made by dredging material from relatively deep water near the coast and dumping the material in the nearshore section. The safest way is to shift the existing cross-shore profile over the distance of the land

1 Alkyon Hydraulic Consultancy & Research, De Deel 21, 8302 EK Emmeloord, The Netherlands (formerly MSc student Delft University of Technology)
2 WL|Delft Hydraulics, Rotterdamseweg 185, 2629 HD Delft, The Netherlands
3 Delft University of Technology, Stevinweg 1, 2628 CN Delft, The Netherlands

reclamation. This way large changes in cross-shore sediment transports are avoided because the beach profile keeps the same shape. However, to make a land reclamation this way, a lot of material has to be dredged, which makes the land reclamation project expensive.

There is also another way to construct the land reclamation. On a certain level beneath mean sea level (is Chart Datum; CD) a cut-off can be applied. This means, that the cross-shore profile will not be shifted completely over the distance needed for the reclamation.
In the near shore area the design profile will have the same shape as the existing beach profile. Then, from a certain level beneath CD, the design profile will have a constant and relatively steep slope until it reaches the existing beach profile. By doing this, a lot of material is saved when making the land reclamation. In Figure 1 a cut profile is shown with the definitions as used in this paper..

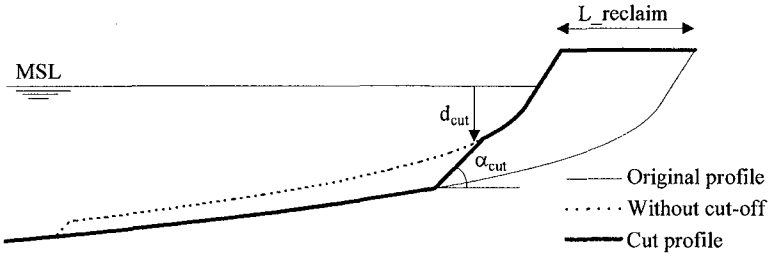

Figure 1. Two methods of making a large scale land reclamation

When a cut profile is applied, wave heights and sediment transports will change in comparison with the situation where no cut profile is applied. When a cut profile is being applied, one of three mechanisms will occur:

- there will be erosion;
- the cross-shore profile will stay stable;
- there will be accretion.

Without any study, the most likely mechanism will be erosion in the nearshore section until a profile shape is reached, which comes close to the profile before the land reclamation. This means eventually a retreat of the waterline, which is, in case of the Dutch policy, not desired.

During this study the numerical model UNIBEST-TC of DELFT HYDRAULICS is used for investigating the influence of a cut profile. To make computations as realistic as possible, the "Plan Waterman" is used as a practical example. In order to get realistic results, the numerical model has been calibrated for the existing situation without the land reclamation before computations on a cut profile are carried out.

Then various computations are done for investigating the influence of a cut profile on the sediment transports and the development of the cross-shore profile. These

computations have been subdivided into two parts:

- Initial computations;
- Morphological computations.

Initial computations are used for investigating the effects of a cut profile on the way waves approach the shoreline and the resulting cross-shore sediment transports along the profile.

Morphological computations are done over a period of 10 years. These computations are done by using measured wave conditions from a station near Hook of Holland.

In this study cross-shore transports are only considered; changes in shore parallel sediment transports are not taken into account

The 'Plan Waterman'

In the western part of The Netherlands there is a large need for more land, especially for housing and recreation. Besides the reshuffle of existing areas, also the possibility to create new land in the North Sea is still open. This plan of land reclamation is known as the 'Plan Waterman'.

The 'Plan Waterman' is a plan for extending the Dutch coast between Hook of Holland and Scheveningen over an average distance of about 2 km, varying from 1500 m at Scheveningen to about 3 km at Hook of Holland and with a total area of 3000 hectares (see Figure 2).

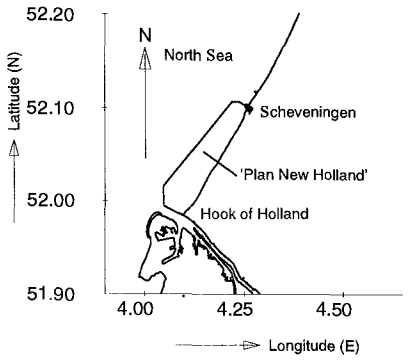

Figure 2. Overview of the 'Plan Wateman'.

The total volume, which has to be nourished for the realisation of the 'Plan Waterman' can roughly be estimated by assuming 25 m^3 necessary for 1 m^2 of the reclamation (from CD -20 m to CD +5 m). For the 'Plan Waterman' the total volume is then estimated at $750*10^6$ m^3.

When applying a cut-off in this situation, a lot of material and therefore money can be

saved. As a reference profile, a shifted profile is chosen, which coincides at a depth of CD -20 m with the existing profile. The beach profile of the land reclamation is continued up to CD +5 m.

In Table 1 is shown how much (in %) is saved by applying a cut profile.

Cut-off depth [m-CD]	Slope of the cut-off			
	1/25	1/50	1/100	1/150
12.0	26%	26%	25%	24%
10.0	32%	31%	30%	28%
8.0	37%	36%	33%	31%
6.0	41%	39%	36%	32%

Table 1. Savings to achieve by applying a cut-off.

From this table it is obvious, that most savings are achieved when the cut-off is made steep and on small depth. On large depths less savings can be achieved by making a steep slope. This is because the slope of the cut-off is shorter at larger depth.

Environmental conditions

To be able to make realistic computations with the UNIBEST model, it is necessary to describe the real situation properly. In this chapter the environmental conditions, as used in the numerical model are discussed shortly.

Cross-shore profiles

Since 1964, every year profile measurements are taken along the Dutch coast to determine the position of beach profiles perpendicular to the shoreline. These profiles are called the 'JARKUS' profiles. The location of these profiles are marked by bench marks along the whole coast of Holland. The area of this study starts near Scheveningen at km 102 and ends at Hook of Holland at km 118.

Grain sizes

For this study, the average value of grain-sizes measured along the coast between Hook of Holland and Scheveningen is used (Table 2).

Parameter	Value
d_{50}	220 μm
d_{90}	290 μm
porosity	0.4

Table 2. Sediment parameters.

Waves

Wave conditions from the nearby EURO-0 platform were used for model

computations. A time series with measured waves and water levels from 1979 to 1991 was analysed and a time series, which represents the average wave climate of these 13 years of measurements was assembled. The measured wave climate from the EURO-0 platform is shown in Figure 3.

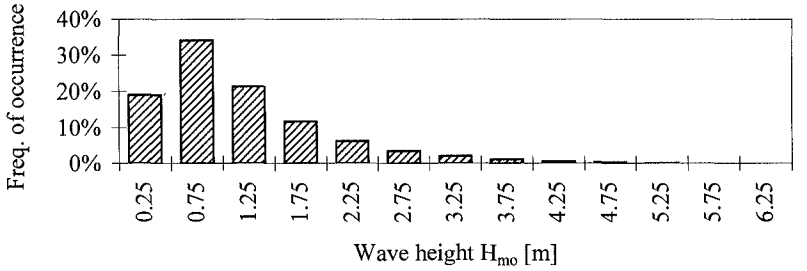

Figure 3. Wave climate as measured at the EURO-0 platform.

Tide levels

The tidal range along the part of the Dutch coast as considered is in the order of 1.5 m during neap tide and 2.0 m during spring tide conditions. Water levels as measured at EURO-0 were taken into account.

At the EURO-0-platform the water level is measured in combination with wave heights. These water levels contain the astronomical tide and also water level changes, caused by wind. Because of storm set up the water level tends to be higher with larger wave heights.

Currents

Because currents are mainly present in the longshore direction and not in cross-shore direction as investigated in this study, currents are not be taken into account during the calculations.

Model calibration

Before any transport computations on a cut profile can be made, the model has to be calibrated. By slightly changing the models parameters, the model is tuned.

For the calibration of the numerical model, the morphological behaviour of an existing beach profile along the coast between Scheveningen and Hook of Holland is used. In this profile a longshore bar is present at about 450 m from the reference point. The bar moves in seaward direction with a speed of approximately 40 m/yr. This bar behaviour is used to compare the outcomes of the numerical model with the measured profiles, because the speed and shape of the bar are easily to be compared. The quality of the calibration is judged by:

- The movement of the sand bar;

- The bed level changes near the waterline;
- Global volume changes along the profile.

By changing parameters such as bed roughness, internal friction angle and wave parameters the model has been adjusted in a way that it represents the existing profile development in a satisfying way. Figure 4 shows the results of the calibration of the profile as chosen.

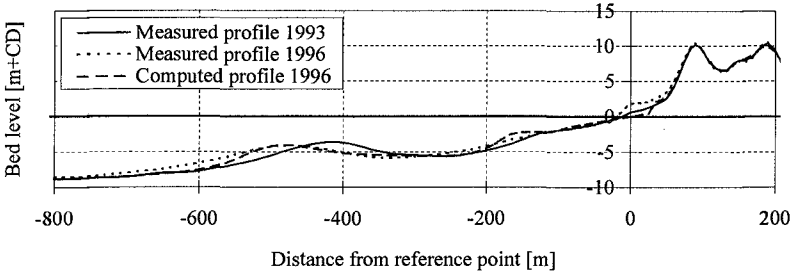

Figure 4. Results of the calibration of the UNIBEST-TC model.

Initial effects of a cut profile

Before the effect of a cut profile on a morphological time scale can be understood, it is worthwhile to investigate the most important processes. Therefore initial computations are performed. For various different wave conditions and cut profiles the distribution of wave height, wave energy dissipation and cross-shore sediment transports are determined. In this chapter some of the results are shown. The results are compared to a profile without a cut-off, which is used as the zero-alternative.

It was found, that especially the location of breaking waves has large effect on the occurring processes. Relatively high waves will suddenly break on the edge of the cut-off, which then leads to large energy dissipation over a small distance. Waves which break onshore of the cut-off, show a more gradual energy dissipation.

For explaining the most important processes in more detail results of computations on a cut profile with d_{cut} = CD -6 m and α_{cut} = 1:50 are discussed. First a wave height distribution with H_{m0} = 1.75 m is discussed, which does hardly result in wave breaking on the edge of the cut-off. Secondly a wave height distribution with H_{m0} = 2.75 m is discussed. This wave height gives breaking on the edge of the cut-off. The results are compared to the zero-alternative.

No breaking waves on the edge of the cut-off

The results of initial computation for deep water wave conditions of H_{m0} =1.75 m are shown in Figure 5. In this figure the wave height, energy dissipation and sediment transport distributions along the cross-shore profile are shown.

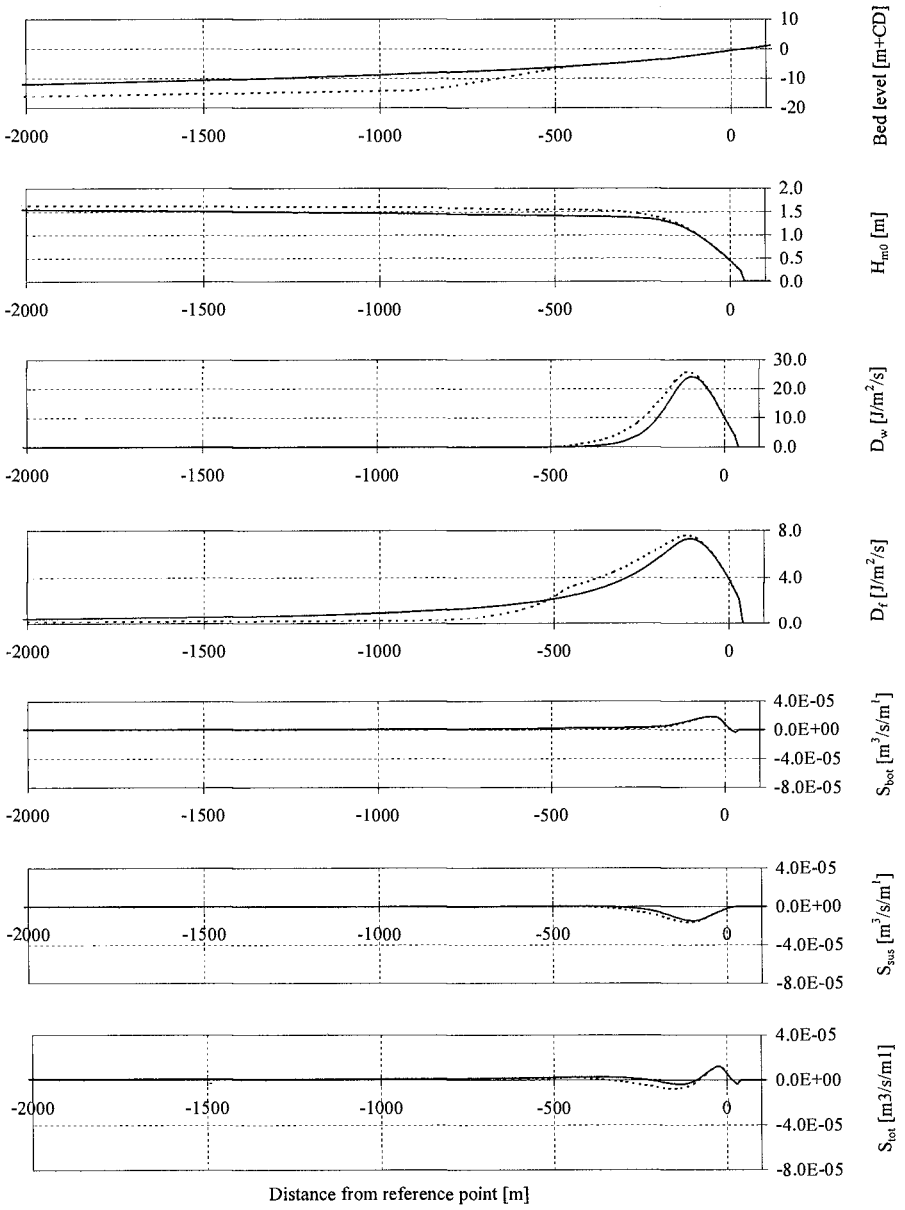

Figure 5. Results of initial computations without wave breaking on the edge of the cut-off.

The wave height H_{m0} distribution

Because the water depth offshore of the cut-off is larger than the depth at the same location along the profile of the zero-alternative, also the wavc height is still larger along the cut-profile. Differences are however small.

In the breaker zone more breaking waves and more dissipation due to bottom friction occur in case of the cut profile. Closer to the shoreline the differences between the wave heights in the two profiles vanish. Notice, that the difference between the two profiles is notable up to approximately 150 from the waterline (that is 350 m onshore of the cut-off).

Energy dissipation

Wave energy dissipation as used in the UNIBEST-TC model is based on Battjes & Janssen (1978).

Offshore of the cut-off water depths are still relatively large in both cases and energy dissipation due to wave breaking hardly occurs here. Onshore of the cut-off larger wave heights are present in case of the cut profile. This leads to larger energy dissipation for the same water depth. Wave breaking also starts at larger distance from the shoreline.

Also the dissipation due to bottom friction, D_f, is affected by the cut-off. Because of the larger depth offshore of the cut-off the energy dissipation due to bottom friction is smaller here. Along the slope of the cut-off the water depth decreases relatively fast. Together with larger wave heights this leads to an increased dissipation due to bottom friction onshore of the cut-off.

Bottom sediment transport

For bed-load transport computations thc formula of Ribberink (see Van Rijn et al., 1995) is used in the UNIBEST-TC model.

Only a very small increase in wave energy dissipation occurs and therefore also the difference in bottom transport along both profiles is very small. Just onshore of the cut-off the onshore directed bottom transport tends to be slightly smaller in case of the cut profile.

Suspended sediment transport

Suspended transport is formulated with the velocity times concentration concept. Sediment concentrations are modelled following Van Rijn, 1993.

In case of the cut profile energy dissipation because of breaking waves is slightly higher than if the zero-alternative profile is applied. This yields a larger sediment concentration. Because of the higher waves also the offshore directed flow velocities increase. This results in an increased offshore directed suspended transport.

Differences in wave heights and energy dissipation are however small, so also the increase of the suspended transport is small.

Total sediment transport

Because of the smaller onshore directed bottom transport and the larger offshore directed suspended transport, the total sediment transport in case of a cut profile is more offshore directed. Even in this case, where hardly any wave breaking on the edge of the cut-off takes, the difference with the zero-alternative is relatively large.

Breaking waves on the edge of the cut-off

When waves break due to the sudden change of the depth at the edge of the cut-off, other effects occur than described in the previous section. In Figure 6 results are shown from computations with a cut profile where large wave breaking occurs at the edge of the cut-off (H_{m0} = 2.75 m).

The wave height H_{m0} distribution

Offshore of the cut-off the water depth is larger than at the same location in the zero-alternative profile. Because of smaller bottom influence, wave heights are here also slightly larger. At the edge of the cut-off the wave height suddenly decreases. In case of the cut profile the wave height at this location is significantly larger and wave breaking occurs. Onshore of the cut-off the wave height further decreases up to approximately 150 m from the waterline. Here wave heights are the same in both cases.

Energy dissipation

Where the wave height along the profile increases, the energy dissipation due to breaking, D_w, suddenly increases as well and D_w is relatively high along the whole profile onshore of the cut-off. Along this part of the profile a large amount of breaking occurs and finally the wave height decreases to a height which is similar to the wave height distribution in case of the zero-alternative.

Offshore of the cut-off the water depth is still relatively large in relation to the wave height. Therefore also energy dissipation is much smaller in case of the cut profile. Along the slope of the cut-off the energy dissipation due to bottom friction, D_f, suddenly increases. Compared to the local water depth the waves are relatively high and this results in a large energy dissipation. Also onshore of the cut-off waves are higher than in the zero-alternative. This also results in larger D_f values

Bottom sediment transport

Along the profile the bottom transports are more or less similar in both cases. In case of the cut profile the onshore directed bottom transports are slightly smaller. Seaward of the cut-off this is because of smaller bottom friction (or larger water depth). At the edge of the cut-off large energy dissipation due to wave breaking causes a near bottom velocity which is offshore directed. Because of this, also the bottom transport becomes

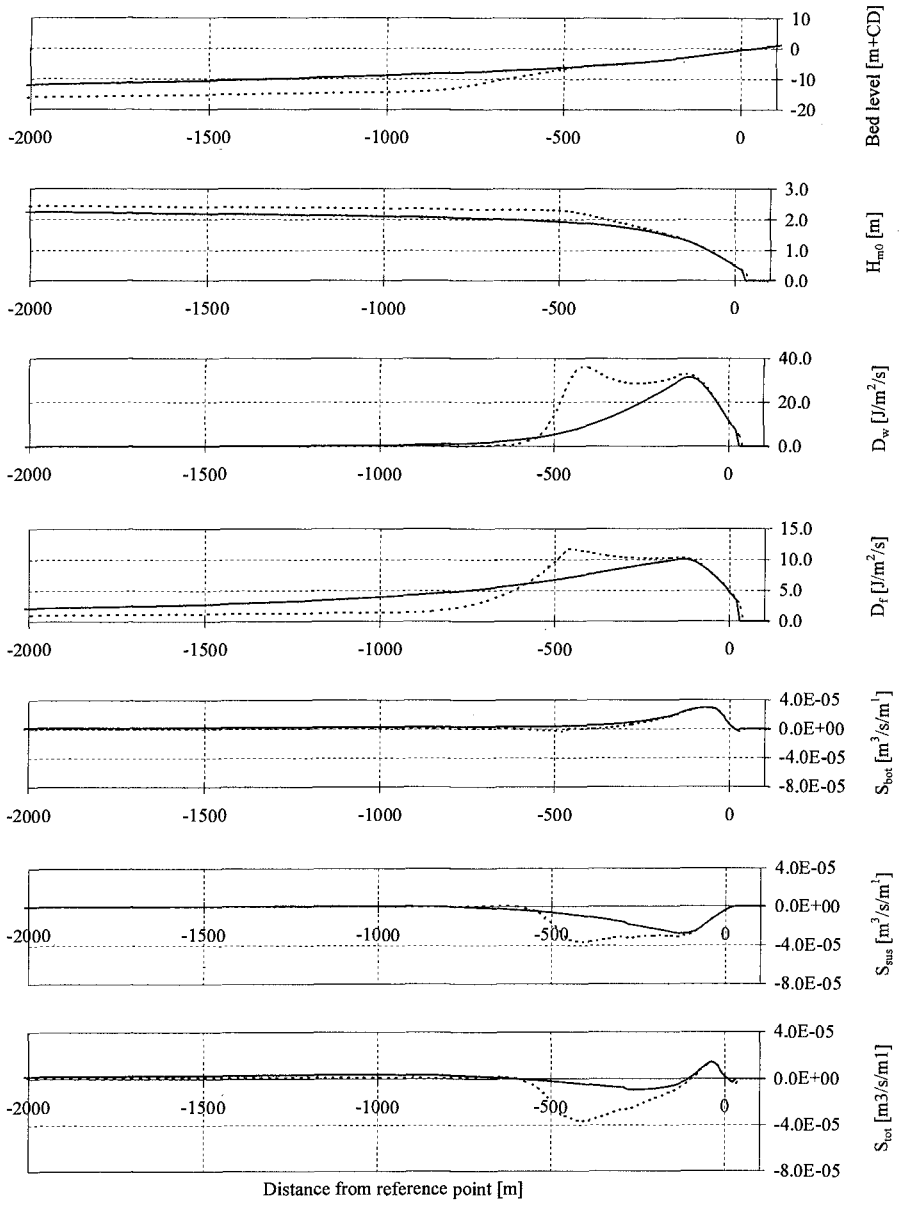

Figure 6. Results of initial computations with large wave breaking on the edge of the cut-off.

offshore directed along the edge of the cut-off.

Suspended sediment transport

The effect of the sudden breaking of waves at the edge of the cut-off can also be seen in the suspended transport along the profile. At this point large turbulence because of breaking causes larger sediment concentrations and with a larger offshore directed flow this results in a larger offshore suspended transport.

Total sediment transport

Especially the suspended transport is largely influenced by the cut-off. This can also be seen in the total sediment transport distribution. Up to approximately 150 m from the waterline the difference in offshore directed transport is relatively large compared to the zero-alternative.

Morphological effects of a cut profile

In order to investigate the morphological effects of a cut profile close to the coast, computations were carried out over a period of 10 years. For these computations a wave scenario based on measured waves at the EURO-0 platform are used. Computations were performed for various cut-off depths and cut-off slopes and the results are again compared with the zero-alternative. As an example the profile changes of a cut profile with a cut-off at CD -6 m is shown in Figure 7.

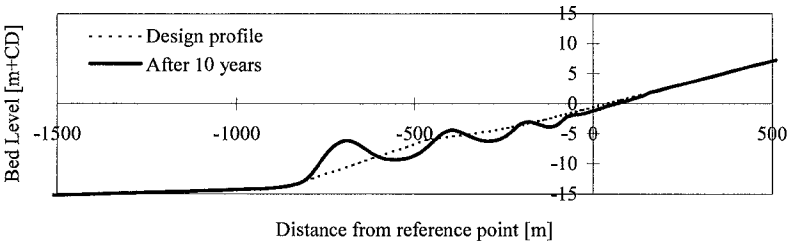

Figure 7. Computed profile with d_{cut} = CD -6 m after 10 years.

As can be seen, large erosion occurs in the nearshore area and the waterline retreats.

If the cut-off is placed at larger depth, less waves break because of the sudden change of depth and therefore also the amount of erosion is smaller. In Figure 8 profile changes after 10 years are shown for a design profile with d_{cut} = CD -14 m. As can be seen, the profile is quite stable and there is even some accretion near the waterline.

In order to make a quantitative comparison between different cut profiles, the yearly averaged transports through depth contours is computed. This is discussed in the next sections.

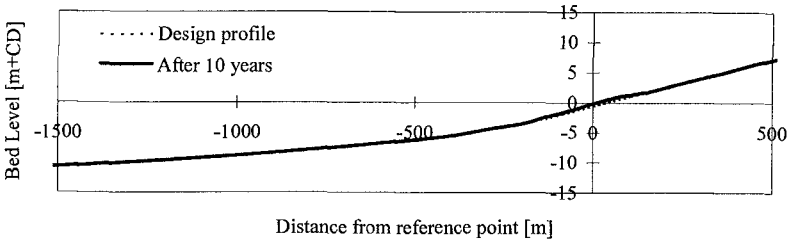

Figure 8. Computed profile with d_{cut} = CD -14 m after 10 years.

Influence of the cut-off depth d_{cut}

As can be seen in the results of the initial computations especially the application of relatively high waves, which lead to wave breaking on the edge of the cut-off, results in a large effect on the sediment transports. It is obvious that the effect of the cut-off will decrease when the cut-off is applied at larger depth. Wave breaking on the edge of the cut-off then hardly occurs and therefore also differences in the sediment transports in comparison with the zero-alternative will be smaller. For investigating the influence of the cut-off depth on a morphological time scale, computations over a period of 10 years are made. The yearly average cross-shore transports are shown in Figure 9. In this figure the horizontal axis shows the depth contours along the profile and the vertical axis gives the yearly amount of sediment which is transported through that depth contour. This is done for cut-profiles with d_{cut} = CD -6 m, -10 m and -14 m Results are compared with the zero-alternative. As can be seen from this figure, a cut-off at CD -6 m results in large offshore directed transport up to large depth.

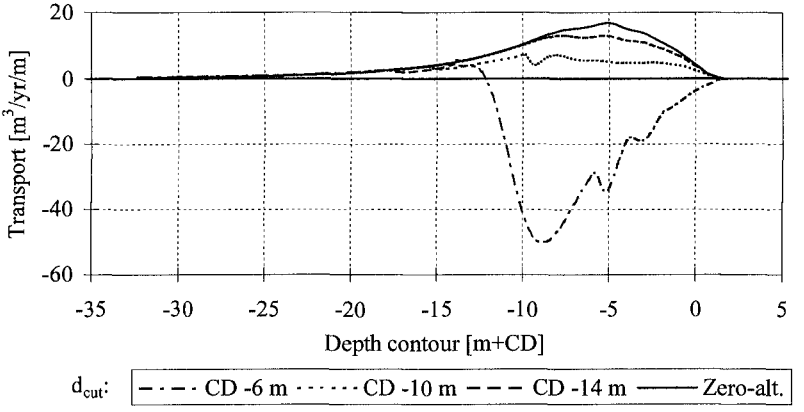

Figure 9. Influence of the cut-off depth on the yearly average cross-shore transports.

From Figure 9 it can also be seen that the initial cross-shore profile of the zero-alternative as applied is apparently not a fully stable (equilibrium) profile

Influence of the cut-off slope d_{cut}

From the previous section it was seen that the cut-off depth has large influence on the yearly average transports along the profile. In Figure 9 however a very steep slope of 1:50 was used. A more gentle slope will result in a more gradual wave breaking. This will then result in smaller offshore directed transports. As an example results of morphological computations on a cut profile with d_{cut} = CD - 8 m are done for various cut-off slopes. Results are shown in Figure 10. As it can be seen from this figure, the cut-off slope indeed affects the yearly average transports in the nearshore section. However, even with a cut-off slope of 1:150 differences are still large compared to the zero-alternative.

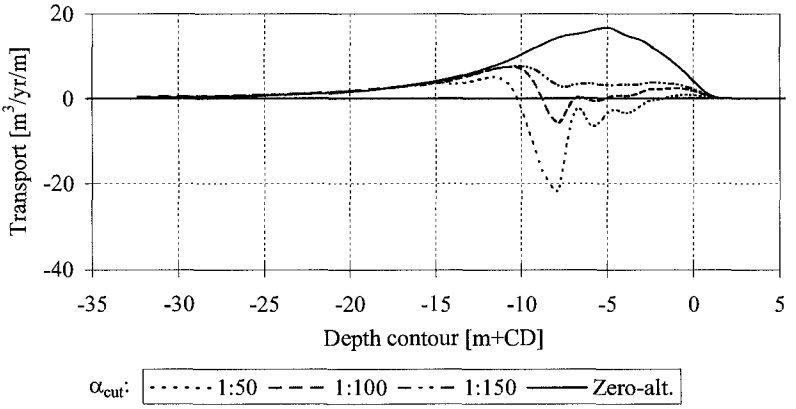

Figure 10. Influence of the cut-off slope on the yearly average transports.

Conclusions

For a large scale land reclamation project as the 'Plan Waterman' a huge amount of material is needed, which makes a project like this very expensive. When applying a cut-profile instead of shifting the whole beach profile over the distance needed for the reclamation, a lot of material can be saved. Material savings up to 40 % are possible.

During this study computations are made with the numerical model UNIBEST-TC, developed by DELFT HYDRAULICS. Especially the effects of a cut profile in cross-shore direction are investigated. Before computations on cut profiles were made, the model has been calibrated for the situation along the coast of between Hook of Holland and Scheveningen.

Computations have been subdivided in initial and morphological computations. From the initial computations it is concluded, that especially the location where waves break is of large influence on the energy dissipation and sediment transports. If waves start breaking onshore of the cut-off the processes are similar to the processes as occur on a profile without a cut-off. Relatively large waves start breaking due to the sudden

change of depth at the edge of the cut-off. This sudden breaking of waves results in large energy dissipation over a small distance which results in large offshore directed suspended transports.

From morphological computations it is concluded, that even a cut-off at large depth still has influence on the sediment transports in the nearshore section of the beach profile. During normal wave conditions differences in sediment transports along a cut profile are very small in comparison with a profile where no cut-off has been applied. When however looking at the yearly average cross-shore transports through specific depth contours, it can be seen that these small differences still have large influence on the coastal development in cross-shore direction. When applying a cut-off at relatively small depth (CD -8 m) a less steep cut-off slope can reduce the seaward directed transports. On the more gentle slope waves break more gradual and the more gradual energy dissipation leads to small offshore directed suspended transports.

In case of the Dutch policy for the coastline protection the coastline is not allowed to retreat due to erosion. In that case there are mainly two options:

- Placing the cut-off at large depth (at least CD -12 m) and do small extra maintenance nourishments;
- Placing the cut-off at small depth and do a lot of extra maintenance nourishments in order to prevent ongoing erosion.

Since the cross-shore profile will eventually develop to an equilibrium profile. At the end the volumes needed for the zero-alternative and the volumes, needed for a cut profile and maintenance nourishments together, are the same. In the first case this volume is already needed during construction. In the latter case the volume is spread over time. This might result in economical advantages.

References

Battjes, J.A. and Janssen, J.P.F.M., 1978, Energy loss and set-up due to breaking in random waves, Proc. 16th Int. Conf. on Coastal Eng, p. 569-587

Rijn, L.C. van , 1993, Principles of sediment transport in rivers, estuaries and coastal seas. Aqua Publ.. (The Netherlands)

Rijn, L.C. van, Reniers A., Zitman, T., Ribberink J.S., 1995, Yearly-averaged sand transport at the 20 m and 8 m NAP depth contours of the JARKUS-profiles 14, 40, 76 and 103, Report H1887, DELFT HYDRAULICS

Optimum Size of Distorted Ripple Train for the Control of Cross-shore Sediment Transport

Satoshi Takewaka[1], Isao Irie[2], Masahiro Uchida[3], Hirokazu Sakamoto[4] and Nobuyuki Ono[5]

Abstract

The Distorted Ripple Train System, which is aimed to control the cross-shore sediment transport, is proposed. The concept and basic functions of the artificial ripple system are introduced in the study and a detailed discussion is given on the determination of the optimum size of the individual ripple which enhance the effect of control.

Introduction

This study examines the basic function and determines the optimum size of the Distorted Ripple Train System (**Fig.1**), which is developed to control the flow and sediment movement near the bottom. The form of the individual artificial ripple resembles to a natural ripple, but its asymmetry is exaggerated and the steep side faces offshore. The difference of the scale and strength of the detached vortices which are formed behind the ripple crest during one wave cycle, being large when the water particle travels offshore, is the agency for the emergence of onshore directed steady flow and sediment transport.

One possible application of the Distorted Ripple Train System is its installation in front of a nourished beach which will endure the effect the nourishment (**Fig.2**). Offshore directed sediment, which becomes active just after the nourishment, will be trapped and transported shorewards on the Distorted Ripple Train System.

[1]Assistant Prof., Inst. of Engineering Mechanics, Univ. of Tsukuba, Japan 305–8573.
[2]Prof., Department of Civil Engineering, Kyushu Univ., Japan 812-8581.
[3]Engineer, Japan Railway Construction Company.
[4]Graduate Student, Department of Civil Engineering, Kyushu Univ.
[5]Research Assistant, Department of Civil Engineering, Kyushu Univ.

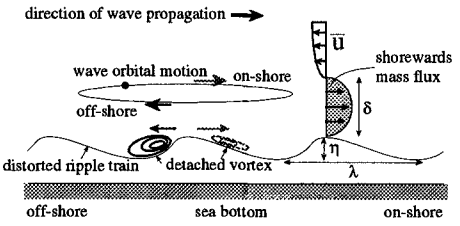

Figure 1 Conception of Distorted Ripple Train System

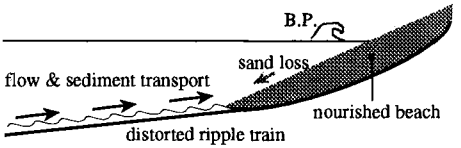

Figure 2 Idea of an application of the Distorted Ripple Train System

Part of this study is originated from the idea of Inman and Tunstall (1972) who have studied basic functions of asymmetrical ripple-like roughness element. No succeeding research, however, was reported to the author's knowledge.

While the general result obtained thus far by our research group is reported by Irie et al. (1998), this study concentrates on how the size of the individual ripple in the train system should be determined to maximize the performance of the sediment control. To this aim, results of laboratory experiments and numerical computations are presented in this paper .

Laboratory tests

The length λ ($= 0.055m$) and height η ($= 0.01m$) of the individual ripple in the train system were set as a trial equal to the length and height of a natural ripple formed in a movable bed experiment with water depth $h = 0.35m$, wave period $T = 1.5s$, wave height $H = 0.08m$ and sand diameter $= 0.16mm$. The horizontal asymmetry is fixed tentatively to 1 : 3. Another train with ripples of same configuration but enlarged two times in dimensions ($\lambda = 0.11m$, $\eta = 0.02m$) was also prepared. The train of the distorted ripple was set in the bottom of the wave flume extending $6m$ in length.

Experiments were conducted by changing the wave condition ($0.05m < H < 0.09m$, $0.8s < T < 2.0s$). Vertical distributions of horizontal velocity u above the ripple crest were measured with laser-doppler velocimeter. **Fig.3** shows an example of the measurement, which indicates that the steady flow U

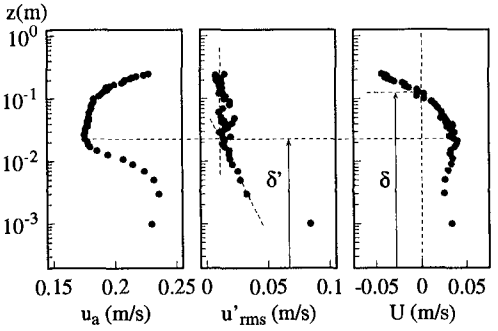

Figure 3 Velocity distribution above ripple crest.
u_a : wave velocity amplitude, u'_{rms} : turbulent intensity, U : steady flow.
Experimental condition : T=1.5s, H=0.08m, h=0.35m.

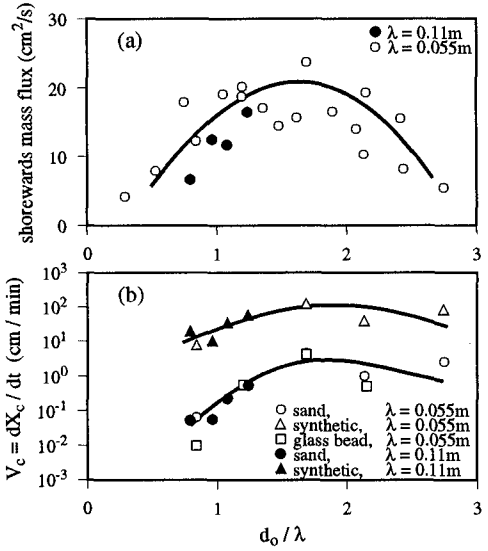

Figure 4 Results of the experiment :
(a) Shorewards mass flux Q, and (b) speed of the particle movement V_c, versus d_o/λ.

near the bottom is directed shorewards extending to the height δ. The amount of the onshore directed steady flow = shorewards mass flux $Q = \int^{\delta} U$ varied

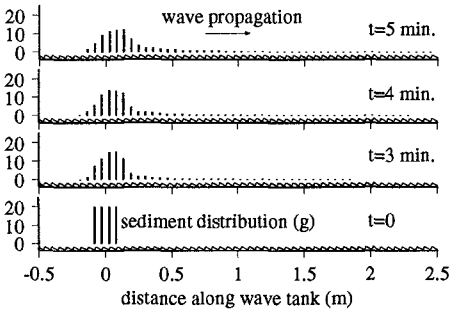

Figure 5 Movement of particle(fine sand) above distorted ripple train. Experimental condition : T=1.5s, H=0.08m, h=0.35m.

in accordance with the wave condition. This variation is depicted in **Fig.4(a)** with the horizontal axis being the ratio of water particle orbital diameter d_o to ripple length λ. The flow becomes intense when d_o/λ approaches 1.7, which is equivalent to the wave condition of the movable bed experiment mentioned before.

Movements of particles above the train were observed and their speed was measured. Three types of particles were used in the tests : glass bead (diameter : 0.08mm, specific gravity : 2.6), fine sand (0.16mm, 2.6) and synthetic particle (0.32mm, 1.6). Particles of 20g in weight were placed above the trough of the ripple at the rest. Particles moved and scattered shorewards as a whole after the wave action in all experiments (**Fig.5**). On and offshore distributions of scattered particles were measured and the variation of their centroid position X_c and dispersion width were recorded. **Fig.4(b)** shows the result of experiments, where the vertical axis is the variation of centroid in time V_c=dX_c/dt. The movement of particles shows a tendency to become intense when d_o/λ approaches 1.7, which agrees well with the characteristics of steady bottom flow variation described before.

The result of the experiments suggests that an effective sediment control is achieved when the ratio of the orbital diameter of the wave motion to ripple length d_o/λ approaches 1.7, which suggests that the size of the individual ripple in the train should be set identical to the size of the natural ripple. This finding will help the determination of the size of the ripple in practical application.

Numerical computation

System of equations for stream function ψ and vorticity ω was solved numerically introducing turbulent diffusion coefficient. Curvilinear grid system and finite difference method were employed. There is a limitation in the nu-

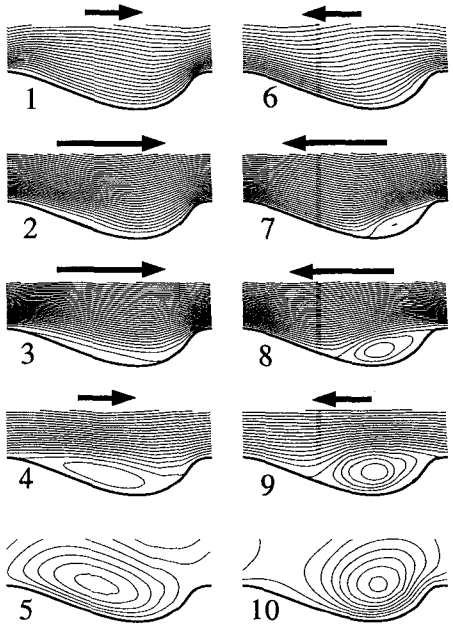

Figure 6 Variation of ψ during one oscillatory flow cycle

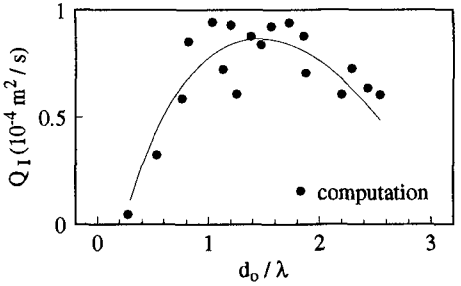

Figure 7 Variation of Q versus d_o/λ

merical work : the computation is conducted under oscillatory flow condition, where the real phenomenon occurs under wave motion. This restricts the direct comparison between the experimental and computational results, however,

our primary concern in the computational work is to catch the change of vortex shedding pattern and shorewards mass flux according to the external flow condition variation.

Figure 6 shows a typical result of the computation. The stream function distribution are depicted with contour lines. The vortex shedding from the ripple crest is observed, being asymmetric in one oscillatory flow cycle. The magnitude of the vortex can be estimated roughly by counting the number of isolines and it is evident that the vortex formed above the steep slope is more energetic.

A large number of computation was conducted by varying the oscillatory flow condition, the oscillatory period and excursion length. **Figure 7** shows the variation of the amount of shorewards mass flux according to external flow condition change. The steady mass flux reaches a maximum when d_o/λ approaches 1.6, which is the same tendency with the experiment.

There remains some points to be refined in the computational work, however, the potential of the numerical approach have been demonstrated.

Conclusion

The performance of the Distorted Ripple Train System, which is aimed to control the bottom flow field and sediment transport, have been demonstrated through laboratory experiments and numerical computations. The optimum size of the individual ripple was determined from the experimental results. The flow and sediment control become effective when the wave condition approaches $d_o/\lambda \sim 1.7$, which suggests that the optimum size of the individual ripple should be set identical to the size of the natural ripple.

References

Inman, D.L. and Tunstall, E.B. (1972) : Phase dependent roughness control of sand movement, Proc. 13th ICCE, pp.1155–1171.

Irie I., S. Takewaka, N. Ono, K. Murakami, H. Sakamoto and O. Shimada (1998) : Retaining beach sand by a distorted ripple mat, Int. Conf. on Coastlines, Structures and Breakwaters, The Institution of Civil Engineers, London.

THE EFFECT OF SEDIMENT COMPOSITION ON CROSS-SHORE BED PROFILES

Leo C. van Rijn[1]

Abstract

This paper provides information on the effect of sediment (sand) composition on cross-shore sand transport and cross-shore bed profile evolution, based on computational results of a mathematical cross-shore profile model (CROSMOR) and data from flume and field experiments (Egmond beach, The Netherlands and Duck beach, USA). The model has also been applied to study longshore sand transport along a sand-gravel beach. Finally, the effect of sediment size on shoreface nourishment is discussed.

Introduction

The sediment bed of the coastal zone may exhibit a large variation of sediment sizes. Generally, cross-shore sorting due to selective transport processes will occur in nature, yielding coarser sediment just beyond the waterline (wave plunging zone) and fining of sediment size in seaward direction. These effects can only represented by taking into account the full size composition of the bed material, which may vary across the profile. At present stage of research, mathematical modeling of sand transport and morphology generally is based on a single representative sediment fraction ($d=d_{50}$ and fraction size= 100%). A method is presented to compute the sand transport rate based on a multi-sediment fraction approach in cross-shore direction. The method is implemented as a submodule in a cross-shore model for wave propagation and wave-induced currents using a multi-wave (wave by wave) approach. The computational results of hydrodynamics and morphodynamics are compared to flume and field data. Model applications for sand-gravel beach and shoreface nourishment are given.

Model description

The details of the model (CROSMOR) are described by Van Rijn (1997b, 1998). Herein, a short summary is given.

[1]Delft Hydraulics and Dep. of Phys. Geography, Univ. of Utrecht
Delft Hydraulics, P.O. Box 177, 2600 MH Delft, The Netherlands
Email: Leo.vanRijn@wldelft.nl

The propagation, transformation (shoaling) and breaking of individual waves are described by a probabilistic model. The individual waves shoal until an empirical criterion for breaking is satisfied. Wave height decay due to bottom friction and breaking is modelled by using an energy dissipation method. Wave-induced set-up and set-down and breaking-associated longshore and cross-shore currents are also modelled (Van Rijn and Wijnberg, 1996). The near-bed orbital velocities of the high-frequency waves (low-frequency effects are neglected) are described by second order Stokes theory and by linear wave theory in combination with an empirical correction factor. The depth-averaged return current (U_r) under the wave trough of each individual wave (summation over wave classes) is derived from linear mass transport and the water depth (h_t) under the trough. Streaming in the wave boundary layer due to viscous and turbulent diffusion of fluid momentum is taken into account. The streaming (u_b) in the wave boundary layer is of the order of 5% of the peak orbital velocity and generally onshore-directed in deeper water (symmetric waves).

To show the performance of the probabilistic model with respect to the computation of wave height and longshore velocity, a recent laboratory experiment (Reniers and Battjes, 1997) was simulated. Measurements of wave height and longshore velocity across a barred beach profile in a laboratory basin were performed. Herein, the test (S0-014) with random waves is considered. The deep-water boundary conditions are: depth=0.55 m, H_{rms}=0.07 m, T_p=1.3 s and wave incidence angle= 30°. The bed roughness of the cement floor was k_s=0.0005 m. Figure 1 shows computed and measured wave heights and longshore velocities. The breaking coefficient was taken to be 0.6. The horizontal mixing coefficient E was used as a fit parameter for the longshore current. Good results were obtained for E=0.05 m^2/s in the surf zone (depth<0.1 m).

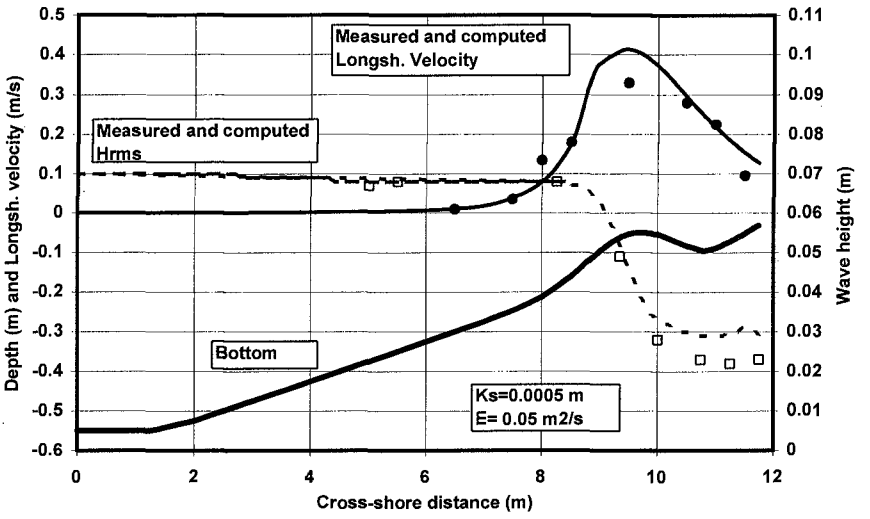

Figure 1. Measured and computed wave height and longshore velocity for basin experiment

The sand transport rate of the model is determined for each wave (or wave class), based on the computed wave height, depth-averaged cross-shore and longshore velocities, orbital velocities, friction factors and sediment parameters. The net (averaged over the wave period) total sediment transport is obtained as the sum of the net bed load (q_b) and net suspended load (q_s) transport rates. The net bed-load transport rate is obtained by time-averaging (over the wave period) of the instantaneous transport rate using a formula-type of approach.

The net suspended load transport is obtained as the sum ($q_s = q_{s,c} + q_{s,w}$) of the current-related and the wave-related transport components (Van Rijn, 1993). The current-related suspended load transport ($q_{s,c}$) is defined as the transport of sediment particles by the time-averaged (mean) current velocities (longshore currents, rip currents, undertow currents). The wave-related suspended sediment transport ($q_{s,w}$) is defined as the transport of sediment particles by the oscillating fluid components (cross-shore orbital motion). The oscillatory or wave-related suspended load transport ($q_{s,w}$) has been implemented in the model, using the approach given by Houwman and Ruessink (1996). The method is described by Van Rijn (1997a). The modelling of the $q_{s,w}$-component includes a calibration coefficient γ in the range between 0.3 and 0.7. Computation of the wave-related and current-related suspended load transport components requires information of the time-averaged current velocity profile and sediment concentration profile.

The current velocity profile is represented as a two-layer system to account for the wave effects in the near-bed layer (Van Rijn, 1993). The convection-diffusion equation is applied to compute the equilibrium time-averaged sediment concentration profile for current-related and wave-related mixing. The effect of the local cross-shore bed slope on the transport rate is taken into account (Van Rijn, 1993, 1997a).

In the multi-fraction mode the bed material is divided in a number of size fractions and the sand transport rate of each size fraction is computed using an existing single fraction method (replacing the mean diameter of the bed material by the mean diameter of each fraction) with a correction factor to account for the non-uniformity effects (Van Rijn, 1993, 1997). This corrrection is necessary because the coarser particles are more exposed to the near-bed current and wave motion than the finer particles which are somewhat sheltered by the coarser particles (hiding effect). The interaction of the size fractions can be represented by increasing the critical shear stress of the finer particles and decreasing the critical shear stress of the coarser particles.

The total sand transport rate for all size fractions can be obtained by summation of the transport rates per fraction taking the probability of occurrence of each size fraction into account, as follows: $q_b = \Sigma p_i\, q_{b,i}$ and $q_s = \Sigma p_i\, q_{s,i}$ in which: p_i = probability of occurrence of size fraction i, N= number of size fractions

Bed level changes per fraction i are described by: $\rho_s(1-e)\partial z_{b,i}/\partial t + \partial(p_i q_{t,i})/\partial x = 0$ with: z_b= bed level to datum, $q_{t,i} = q_{b,i} + q_{s,i}$= volumetric total load (bed load plus suspended load) transport per fraction i, p_i= value of fraction i, ρ_s= sediment density, e= porosity factor. The total bed level change is obtained by summation of fractional bed level changes over all fractions. The bed material composition is computed in a thin surface mixing layer of thickness δ (order of 0.1 m) applying a one-layer approach. The thickness of the surfaee layer is assumed to be constant in space and time and is moving in vertical direction with the bed surface in response to bed level changes (deposition upwards and erosion downwards). Thus, the surface layer is always at the top layer of the bed. The mixing of sediment within the surface layer is assumed to be effectuated within each time step (instantaneous mixing) through small-scale bed form migration processes

in the lower regime or by wave-induced vortices in the sheet flow regime. The bed material composition of the subsoil below the surface layer is assumed to be uniform (no layered structure) and equal to the initially specified fraction values.

Model results of bar behaviour for Egmond, The Netherlands and Duck , USA

Computations using the single and multi-sediment fraction methods have been made for a sloping coastal profile with multiple bars along microtidal (Duck beach, USA) and mesotidal coasts (Egmond beach, The Netherlands).

Egmond beach, The Netherlands

The model has been applied to simulate nearshore bar behaviour at Egmond in The Netherlands (Wolf, 1997). The case considered is an onshore, accretive event (15 October to 26 October 1992) during which accretive hydrodynamic conditions are present, resulting in significant bar growth and onshore bar migration. As no cross-shore distributions of the hydrodynamic and transport parameters are available, the model is mainly evaluated based on measured profile developments.
The field site is a coastal area of about 1 kilometre alongshore and about 1 kilometre offshore. It is situated south of the village of Egmond aan Zee along the Holland coast. Longshore differences in the offshore wave climate are small due to the relatively uniform orientation of this section of the Dutch coast. The wave climate is dominated by wind waves related to low pressure areas moving from west (Atlantic) to east (European Continent). The tidal range near Egmond varies between 1.2 m (neap tide) and 2.1 m (spring tide). At the site, the flood tide has a duration of 4 hours and the ebb tide of 8 hours. The horizontal tide runs ahead of the vertical tide by about 45 minutes. The semi-diurnal tide induces asymmetrical surface currents which may reach values of 0.6 to 1.0 m/s.
Because of the absence of man-made structures in the area, the coast can be characterised as a natural coast. The sequence of (usually) three bars in the cross-shore profile is representative for a large part of the central Dutch coastal region.
Wave data were collected at Pole 3 (Profile No. 39500), located 545 m offshore at a water depth of about 4 m. The available data comprises time series of water level, wave height, wave period and direction. A sea-sledge (Sub-Aquatic Profiler, SAP) was used to monitor the inner bar. The SAP is pulled back and forth through the surf zone by a capstan (attached to a tractor) and a cable in a closed loop between the capstan and two pulleys, one of which is attached to a beach pole and the other to a pole in the surfzone.
The boundary conditions (over 11 days) of the accretive event are: wave heights (H_{rms}) between 0.5 and 2.5 m, wave period between 4.5 and 10 s, wave angle between 50° and -50° to coast normal, water levels between 1.25 m and -1 m (to MSL).
As the wave model is based on a probabilistic approach, the number of wave classes has to be prescribed. Generally, three to five wave classes are sufficient to give accurate results. One base run was made using ten wave classes. The computed bed profiles were almost identical to those of the run with four wave classes.
The initial bed profile, the measured and computed bed profiles after 11 days for the base run (no oscillatory suspended transport or gamma= 0, median sand size d_{50}= 0.3 mm, bed roughness= 0.016 m) are given in Figure 2.

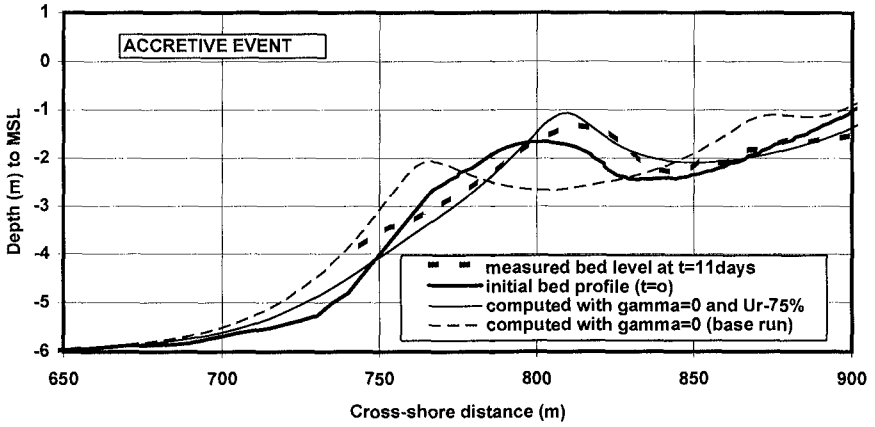

Figure 2. Base run and effect of undertow velocity on bar behaviour, Egmond

The computed profile shows offshore migration of the nearshore bar, whereas the measured profile shows weak onshore migration of the bar. The model produces minor bars in the swash zone near the beach, probably as a result of tide level variations modifying the location of the breaker zone.

The results of a series of sensitivity runs showed that the most sensitive parameters are: undertow velocity, bed roughness, oscillatory suspended transport (gamma-factor) and bed material composition.

The bed roughness was increased from 0.016 m to 0.05 m to better simulate the presence of vortex ripples on the bed, which may be present during accretive conditions. Increase of the bed roughness leads to reduced wave heights and reduced near-bed cross-shore velocities and hence to a relatively large decrease of offshore transport components.

Several gamma factors have been used to increase the onshore-directed suspended transport. Onshore bar migration was obtained for gamma values larger than about 0.3.

The undertow velocity (Ur) was by trial and error reduced to obtain reasonable agrreement between computed and observed bar behaviour. The reduction factor was found to be 75%. Results are given in Fig. 2. The measured bed profile is reasonably well represented for x>775 m. The erosion is overpredicted for x between 740 and 775 m.

The effect of sand fractions was studied by a run using the multi-fraction method with 4 fractions; the d_{50}-value of 0.29 mm was kept the same. The bed roughness was k_s=0.016 m in both runs.

The results are presented in Figure 3. The bed profile after 11 days shows a lower crest level without significant offshore migration of the crest. The undulations landward of the bar crest are somewhat larger. The cross-shore distribution of the d_{50} is changed after 11 days (constant value of d_{50}=0.29 mm at t=0). The nearshore sediment becomes coarser, because the fines are eroded in larger quantities and are carried in seaward direction.

The best agreement between measured and computed bed evolution (with onshore bar migration) was obtained by using four sand fractions, gamma= 0.3, k_s= 0.05 m, and a 20%-reduction of the undertow velocities. Results are shown in Figure 4.

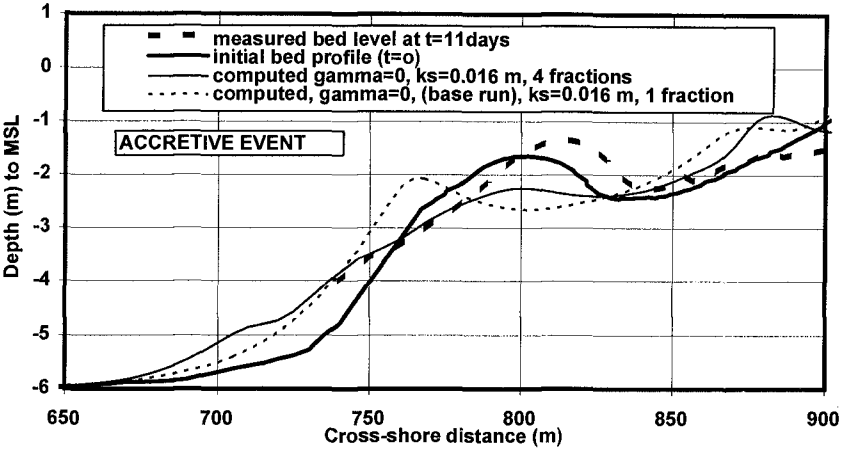

Figure 3. Effect of bed material distribution on bar behaviour, Egmond beach

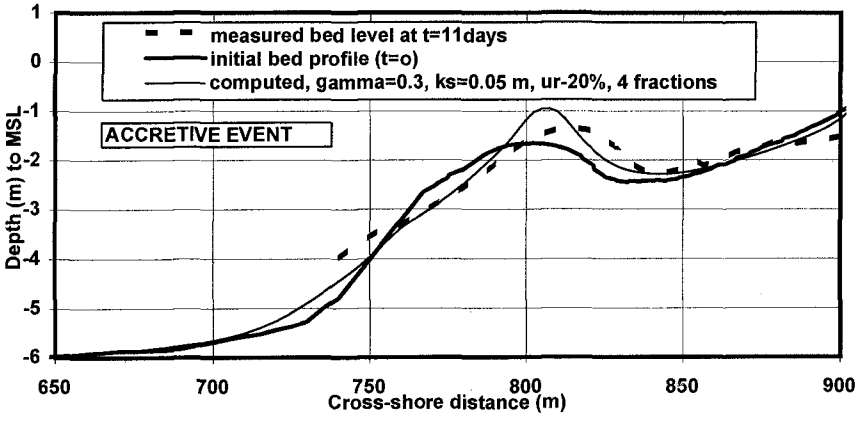

Figure 4. Optimum parameter setting for accretive event, Egmond beach

Duck beach, USA

The CROSMOR profile model has been applied to the cross-shore profile data measured at the Duck beach (USA) during the year 1982 (Mason et al., 1984). The Duck site is exposed to waves coming from the Atlantic Ocean. The tidal range is about 1 m; the tidal currents are weak. The winter period is dominated by storm waves; offshore wave heights can be as high as 6 m. The summer period is dominated by long-period swell. The bed profile generally shows a single bar in the surf zone; sometimes a low outer bar is present. The swash zone near the shoreline consists of relatively coarse material (1 to 2

mm); the sediment is fining down in landward direction to about 0.5 mm on the upper beach and in seaward direction to about 0.2 mm in the outer surf zone (Richmond and Sallenger, 1984). Two cases are considered: storm event 9-12 Oct. 1982 (inner bar moved offshore) and calm event 24 Feb.-24 Aug. 1982 (outer bar moved onshore; beach profile accreted and gained about 50 m^3/m due to 3D effects).

Basic input data of *Storm event, 9-12 Oct. 1982* : $H_{s,0}$= 2.4 m (3 wave classes), T= 11 s, wave angle= 20°, time step= 300 s. The gamma-factor of the wave-related suspended transport was set to 0.35. The thickness of the mixing layer was set to 0.1 m. The bed roughness was set to 0.01 m.

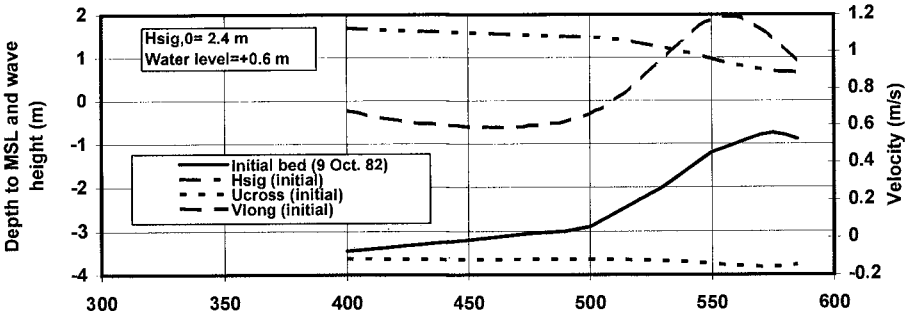

Figure 5. Computed significant wave height, depth-averaged cross-shore undertow velocity (below wave trough), and depth-averaged longshore velocity for storm event 9-12 Oct. 1982, Duck beach, USA

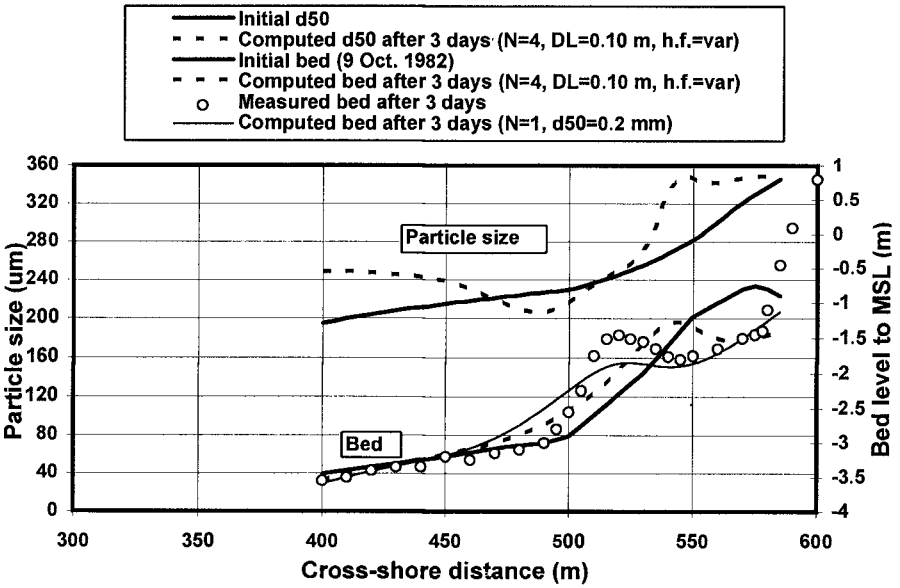

Figure 6. Effect of particle size distribution on bed profile evolution for storm event 9-12 Oct, 1982, Duck beach, USA

The computed hydrodynamic parameters (wave heights and currents) along the profile are shown in Figure 5. The wave height at the bar crest is reduced to about 0.8 m. The longshore current is maximum (about 1.2 m/s) near the bar crest. The maximum cross-shore return current is about 0.15 m/s near the bar crest.
The effect of particle size distribution on bed profile evolution using the multi-fraction method (N=4) instead of the single-fraction method (N=1) is shown in Figure 6.
The initial median particle size is assumed to vary between 0.2 mm at x=400 m and 0.35 mm at x=585 m for the run with N=4 fractions; the initial sediment size is taken constant along the profile for N= 1 fraction. Using N=1 fraction instead of N=4 fractions results in a more seaward position of the bar after 3 days; thus the bar position is significantly affected taking selective transport processes into account.

Basic input data of *Calm event, 24 Feb.- 24 Aug. 1982* are: $H_{s,0}$= 0.9 m (3 wave classes), T= 9 s, wave angle= 10°, time step= 21600 s. The gamma-factor of the wave-related suspended transport was set to 0.7. The thickness of the mixing layer was set to 0.1 m. The bed roughness was set to 0.01 m. The computed hydrodynamic parameters (wave heights and currents) along the profile are shown in Figure 7. The wave height in deep water is 0.9 m, which increases to about 0.95 m at the bar crest due to shoaling. The depth-averaged longshore current is zero up to the bar crest, after which it increases to about 0.15 m/s near the shoreline due to oblique wave breaking. The maximum depth-averaged (below wave trough) cross-shore return current is about 0.05 m/s near the shoreline. The effect of particle size on bed profile evolution using the multi-fracttion method (N=4 fractions) instead of the single-fraction method (N=1) is shown in Figure 8. The initial median particle size is assumed to vary between d_{50}=0.14 mm at x= 200 m and 0.35 mm at x= 635 m for N= 4 fractions; the median sediment size is constant (d_{50}= 0.2 mm) for N= 1. The computed sand transport rates and bed profile evolutions for N= 1 and N= 4 fractions are shown in Figure 8. Using N=1 fraction instead of N=4 fractions, results in a significant decrease of the onshore migration distance of the bar after 6 months (Figure 8); thus the bar position is significantly affected taking selective transport processes into account. Using N=1 fraction instead of N=4 fractions, results in a significant increase of the suspended transport close to the shore (x>600 m); this is an initial effect which hardly influences the bed level close to the shore after 6 months.

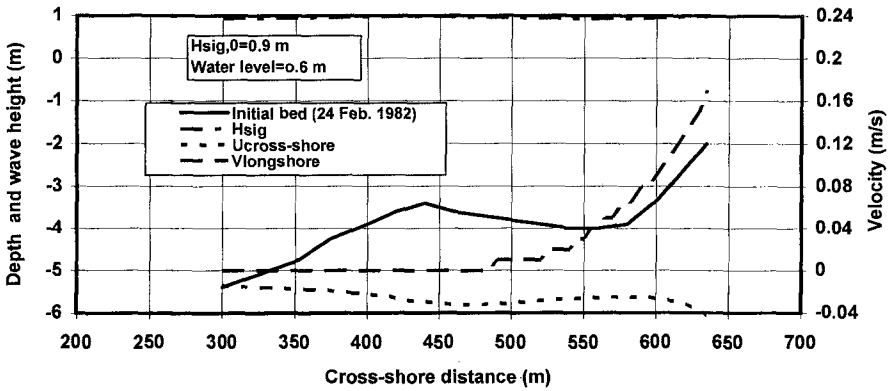

Figure 7. Computed significant wave height, cross-shore undertow velocity, and longshore velocity for calm event 24 Feb.-24 Aug. 1982, Duck, USA

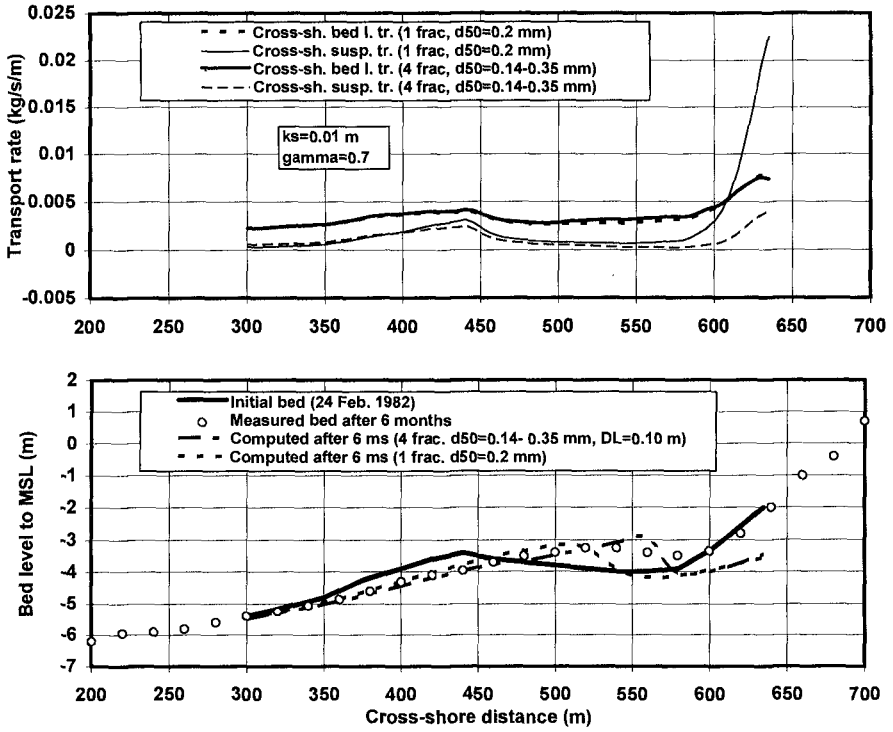

Figure 8. Effect of particle size distribution on computed sand transport distribution and bed profile evolution for calm event 24 Feb.-24 Aug. 1982, Duck beach, USA

Model results for sand-gravel beach

The model has been used to compute the cross-shore distribution of the longshore transport rate for a sand-gravel beach. The (hypothetical) beach profile consists of: slope of 1 to 20 between -10 and -3 m, slope of 1 to 10 between -3 and -2 m and slope of 1 to 5 landward of -2 m (Fig. 9). The model has been calibrated for gravel (taking sizes of 5 and 20 mm), using the available data of Chadwick (1989) and Nicholls and Wright (1991). The cross-shore distributions of significant wave height, wave-induced longshore current and sediment transport (bed load and suspended load) for sand-gravel in the range between 0.2 and 5 mm due to storm waves ($H_{s,0}$= 2.8 m) are given in Figure 9. The profile consists of uniform sand (d_{50}= 0.2 mm) seaward of x= 180 m, uniform gravel (d_{50}= 5 mm) landward of x= 190 m and a bimodal sand-gravel mixture between 180 and 190 m, see Figure 9. Results for a pure gravel beach (no sand) are also shown. Suspended sand transport is dominant, if the bed seaward of the -3 m line consists of fine sand (0.2 mm). The width of the active littoral zone is about 100 m for a sand-gravel beach and about 50 m for a pure gravel beach.

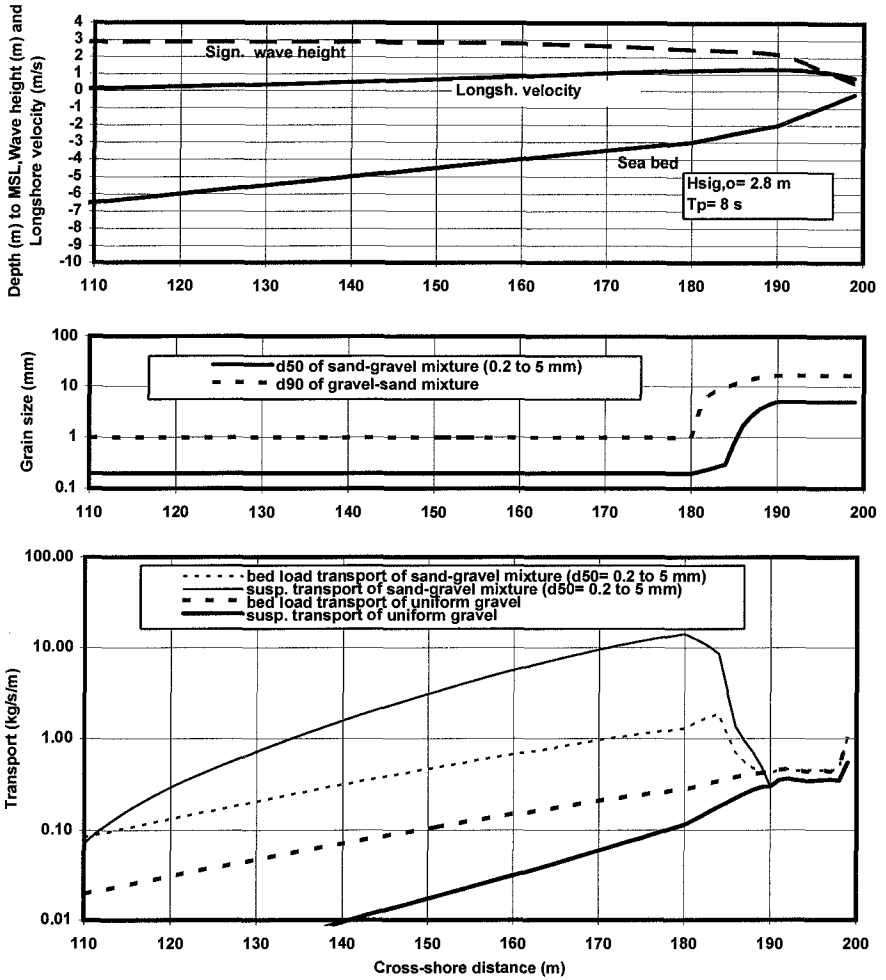

Figure 9. Cross-shore distribution of wave, current and transport parameters
$H_{s,0}$= 2.8 m, T_p= 8 s, wave angle= 30°
Top: Bed profile, wave height and longshore velocity
Middle: Grain size values (d_{50} and d_{90}) of sand-gravel mixture
Bottom: Longshore bed load and suspended load transport for uniform gravel (5 mm) and sand-gravel mixture (0.2-5 mm)

Results for a minor storm with $H_{s,0}$= 1.4 m are given in Fig. 10. The bed load transport is dominant in the gravel zone; the suspended load transport is dominant in the fine sand zone seaward of the -3 m line. The active sand zone has a width of about 30 m. The active gravel zone extends over about 10 m. Details are given by Van Rijn (1998).

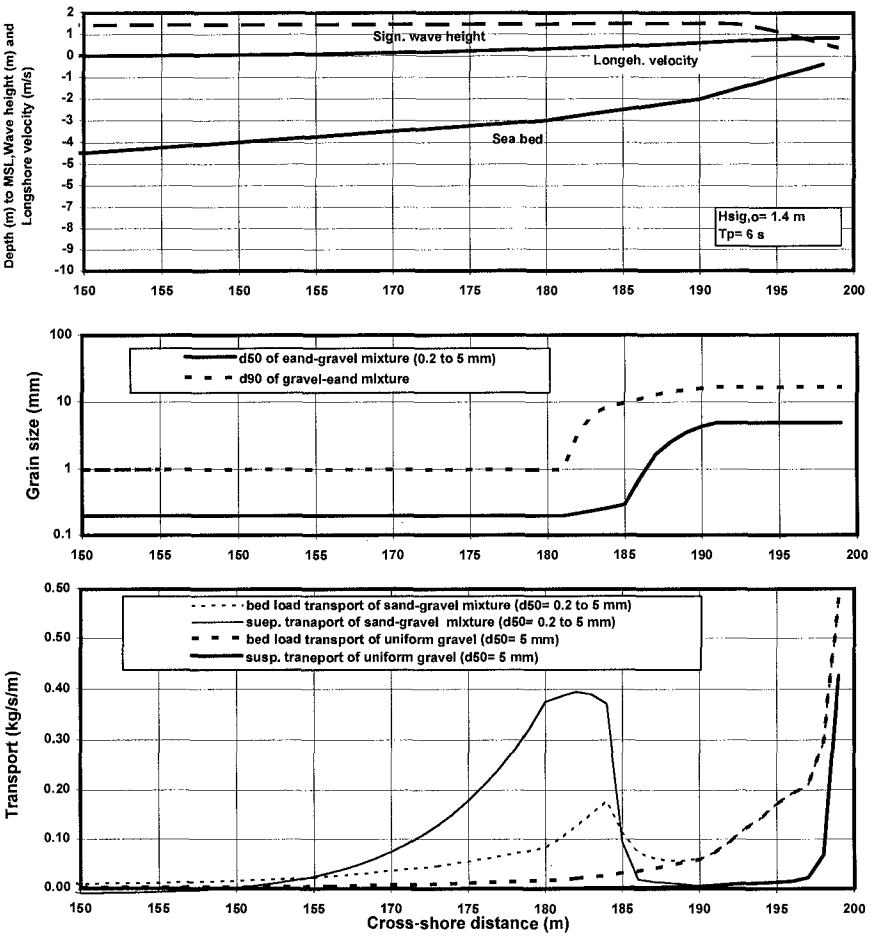

Figure 10. Cross-shore distribution of wave, current and transport parameters
$H_{s,0}$= 1.4 m, T_p= 6 s, wave angle= 30°
Top: Bed profile, wave height and longshore velocity
Middle: Grain size values (d_{50} and d_{90}) of sand-gravel mixture
Bottom: Longshore bed load and suspended load transport for uniform gravel (5 mm) and sand-gravel mixture (0.2-5 mm).

Model results for shoreface nourishment

The model was applied to a hypothetical case consisting of shoreface nourishment on a sloping cross-shore profile. The cross-shore profile is assumed to be plane, consisting of four sections: slope of 1:200 up to -6 m, slope of 1:70 between -6 and -3 m, slope of 1:50 between -3 and 0 m and slope of 1:30 on the beach (see Figure 11). The bed material consists of uniform sand with d_{50}= 0.3 mm. Two types of sand (d_{50}= 0.2 mm and d_{50}= 0.4 mm) are assumed to be available for shoreface nourishment.

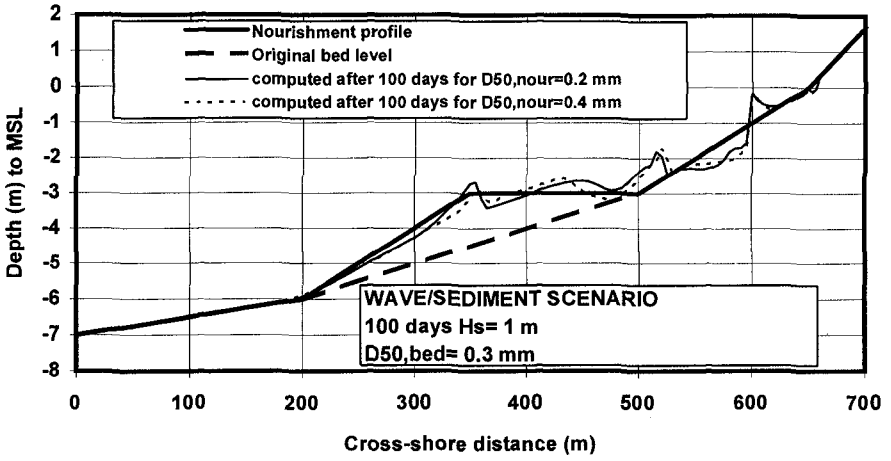

Figure 11. Effect of sediment size on shoreface nourishment for period of 100 days with low waves ($H_{s,0}$= 1 m)

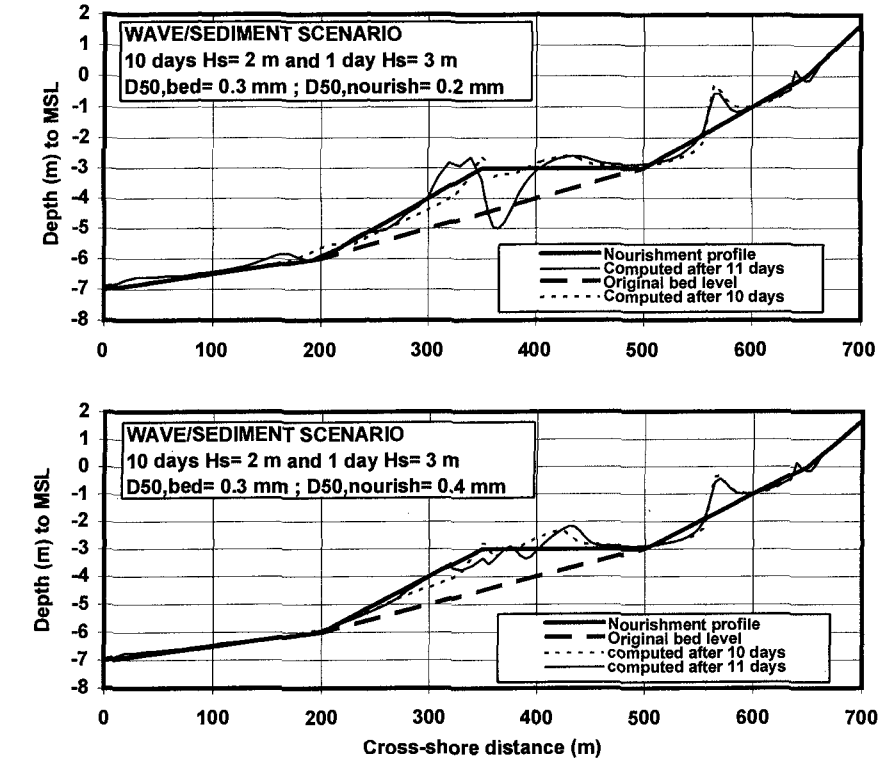

Figure 12. Effect of sediment size on shoreface nourishment for period of 11days with high waves ($H_{s,0}$= 2 and 3 m)

After nourishment the profile is assumed to be triangular with a slope of 1:50 over its seaward section of 150 m and a horizontal profile over its landward section of 150 m (see Figure 11). The water level is constant (no tide). Two wave scenarios are considered: calm period with H_s= 1 m during 100 days (T=7 s α= 30^o); storm period with H_s= 2 m during 10 days (T=7 s, α= 30^o) and H_s= 3 m during 1 day (T=7 s, α= 30^o).
The computed evolutions of the nourishment profiles with 0.2 and 0.4 mm sediment for the calm period (100 days) are shown in Figure 11. The bed profiles after 100 days are almost similar, showing no clear effect of particle size for low waves.
The computed evolutions of the nourishment profiles with 0.2 and 0.4 mm sediment for the storm period (10 days with $H_{s,0}$= 2 m and 1 day with $H_{s,0}$= 3 m) are shown in Figure 12. The nourishment profile of 0.2 mm sediment is moulded into a relatively large sand bar with a deep trough during conditions with $H_{s,0}$= 3 m (1 day). Furthermore, minor offshore sand transport can be observed for the case with 0.2 mm sediment; about 5% of the nourishment volume is carried offshore after 11 days of storm waves. The nourishment profile of 0.4 mm sediment shows considerably less variability and no offshore transport. The profile development landward of the nourishment is not much affected by the sediment size on the short term time scale of storms.

Conclusions

The most sensitive model parameters are: undertow velocity, bed roughness, wave-related suspended transport (velocity asymmetry) and sand composition. The presence of graded sand leads to flatter and wider bars; uniform sand leads to more peaked bars. The wave-related suspended transport due to velocity asymmetry can not be neglected; it is essential for onshore bar migration/growth.
The modelling of selective transport depends on hiding factor and effect of particle size on bed and suspended load transport. The model results show that: (1) coarser sediment is carried shorewards as bed load during calm periods, (2) finer sediment is carried seawards as suspended load and is deposited in bar trough zones and in offshore zone during periods with storm waves and (3) coarser sediment is eroded from outer bar and is carried landwards as bed load to swash/beach zone during periods with storm waves.
Longshore suspended sand transport is dominant along sand-gravel beach under storm waves. The width of active littoral zone may be as large as 100 m for storm wave conditions.
Sand size between 0.2 and 0.4 mm has almost no effect on shoreface nourishment during periods with low waves (calm period). The use of fine sand of 0.2 mm for shoreface nourishment results in offshore loss (about 5% of nourishment volume) during storm conditions and more variability of the profile due to the generation of relatively large sand bars during storm waves.

References

Chadwick, A.J., 1989. *Field measurements and numerical model verification of coastal shingle transport, p. 381-402. BHRA, Fluid Engineering Centre, Bedford, England*
Houwman, K.T. and Ruessink, B.G., 1996. *Sediment transport in the vicinity of the shoreface nourishment of Terschelling. Dep. of Physical Geography. Univ. of Utrecht*

Mason, C. et al., 1984. *Duck82-a coastal storm processes experiment, p. 1913-1927, 19th ICCE, Houston, USA*

Nicholls, R.J. and Wright, P., 1991. *Longshore transport of pebbles: experimental estimates of K-factor, p. 920-933. Coastal Sediments, Seattle, USA*

Reniers, A.J. and Battjes, J.A., 1997. *Laboratory study of longshore currents over barred and non-barred beaches. Coastal Engineering, Vol. 30, p. 1-22*

Richmond, B.M. and Sallenger, A.H., 1984. *Cross-shore transport of bimodal sands. 19th ICCE, Houston, USA, p. 1997-2007.*

Van Rijn, L.C., 1993. *Principles of sediment transport in rivers, estuaries and coastal seas. Aqua Publications, Amsterdam, The Netherlands.*

Van Rijn, L.C., 1997a. *Cross-shore modelling of graded sediments. Delft Hydraulics, Report Z2174. Delft, The Netherlands*

Van Rijn, L.C., 1997b. *Sand transport and bed composition along cross-shore profile. Coastal Dynamics, Plymouth, England*

Van Rijn, L.C., 1998. *Principles of coastal morphology. Aqua Publications, Amsterdam, The Netherlands.*

Van Rijn, L.C. and Wijnberg, K.M., 1996. *One-dimensional modelling of individual waves and wave-induced longshore curents in the surf zone. Coastal Engineering, Vol. 28, p. 121-145*

Wolf, F.C.J., 1997. *Hydrodynamics, sediment transport and daily morphological development of a bar-beach system. Doc. Thesis, Dep. of Phys. Geography, Univ. of Utrecht, The Netherlands*

THE BREACHING OF SAND INVESTIGATED IN LARGE-SCALE MODEL TESTS

Cees van Rhee* and Adam Bezuijen**

Abstract

The physical principles, which govern the breaching process, are analysed. It will be shown that this process involves both geotechnical and hydraulic phenomena. The stability of the surface of the slope and the internal stability are studied. The theories are compared with results from a large-scale experimental programme. Results show that the propagation velocity of the breach is influenced by the permeability and that the resulting slope is gentler as the breach height increases. The breaching process can even become unstable which can lead to failure of a slope over a very large distance.

Introduction

Suction of sand several metres below the original bottom will lead to breaching of sand. The sand will form a steep slope in front of the suction-mouth. The steep slope is not stable and will propagate from the suction-mouth, producing a sand water mixture that flows in the suction-mouth. Breaching of sand is an important process in the dredging industry. The steepness and propagation velocity of the slope determines the sand production that can be achieved. A research programme has been performed to investigate the mechanisms that govern the breaching of sand. This programme included large-scale model tests and theoretical modelling of the mechanism.

Theory

Erosion theories

When a suction pipe is moved forward with constant velocity v_z in a two dimensional situation, the so-called pit production P follows from continuity:

$$P = v_z B \tag{1}$$

The thickness of the sand layer or the physical limitations of the dredge mostly restrict the depth of the pit B, therefore the velocity v_z determined the slope production. However, the forward velocity is limited by the behaviour of the soil body in front of the suction pipe.

* Ham Int. Dredging Contractors, P.O. Box 8574, 3009 AN Rotterdam, The Netherlands during this research: WL | Delft Hydraulics, Product Group Dredging Technology
** Delft Geotechnics, P.O. Box 69, 2600 AB Delft, The Netherlands

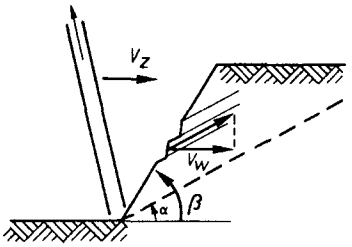

Figure 1: Slope in front of suction mouth.

The slope can be very steep due to the shear dilatancy effect of compacted sand. Dilatancy is the effect that the pore volumes of dense sand tend to increase during shear deformation as result from increased shear stresses. When the sand is saturated with water, this will lead to water under-pressure in the pores. The under-pressure will result in an increased effective pressure and hence increased shear resistance.

In the seventies, the behaviour in front of a dredger was studied at Delft Hydraulics using small-scale two-dimensional experiments. A suction tube was moved forward at the bottom of a flume and the developing slope in front of the suction mouth was studied. From a stability analysis of the surface of the slope the following relation between the forward velocity and slope angle β was derived (Breusers, 1977):

$$\frac{\cot\beta}{\cot\phi} = 1 - \frac{v_z}{v_w} \tag{2}$$

In which v_w was defined as the active wall velocity:

$$v_w = \frac{k_l}{\Delta n} \cdot \Delta \cdot (1 - n_0) \cot\phi \tag{3}$$

In which ϕ, Δn, n0, Δ, and k_l are the internal friction angle, relative porosity increase, initial porosity, relative grain density and permeability respectively. From Eq. (2) follows that at very low velocity the angle of the front slope will be equal to the internal friction angle. The limit speed follows from $v_z=v_w$. In that case the front slope will be vertical. The relative porosity increase is calculated with:

$$\Delta n = \frac{n_l - n_0}{1 - n_l} \tag{4}$$

The active wall velocity (v_w) can be seen as the propagation speed of a vertical disturbance on the slope. By moving a suction mouth downwards a sudden disturbance is created in the soil. The initial steep slope will not be stable in the long term. Fig. 2 gives an impression of the development of a slope after some time. The vertical "wall" will move sideways. The sand from this collapsing front will flow towards the suction mouth. The slope angle below the producing wall is drawn rather steep in Fig. 2. Indeed at relative low production (i.e. small-scale test) this will be the case and a slope angle equal to the natural angle of repose will develop.

In practice however, it was experienced many times that the resulting slope angles were often more gentle. It was suggested that this was due to the erosion caused by a sand-water mixture (acting like a density current) running down the slope

(Koning, 1981), although this hypothesis was not proven. Some years later the influence of the flowing sand-water mixture on the slope development (hydraulic filling) was studied in 1988 by Delft Hydraulics and Delft Geotechnics in the dredging flume of Delft Hydraulics. (Mastbergen and Bezuijen, 1988 and Bezuijen and Mastbergen 1988).

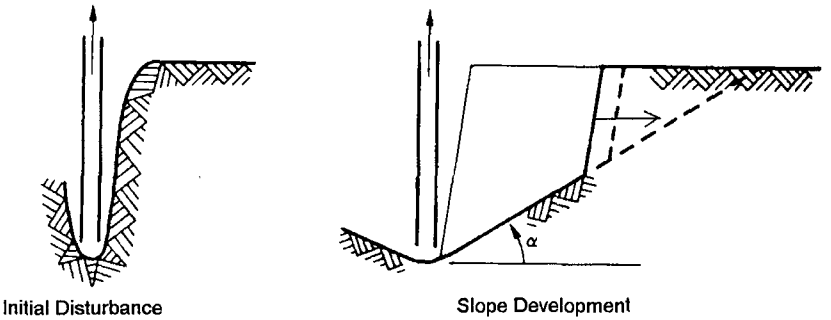

Figure 2: Slope development resulting after sudden disturbance.

It was found that at small production rate, the grain flow on the slope was laminar and slope angles were close to the natural angle of repose. When the sand production increased, the grain flow became turbulent and the slope angle decreased with increased sand flux s [kg/(ms)]. The other important factor was the grain diameter. Coarse sand resulted in steeper angles. The following empirical relation was found:

$$i = \tan(\beta) = 0.0049\, D_{50}^{0.92} s^{-0.39} \qquad (D_{50} \text{ in } [\mu m],\ s \text{ in } [kgm^{-1}s^{-1}]) \qquad (5)$$

The sand production from the slope equals:

$$s = v_w B (1 - n_0) \rho_s \qquad (6)$$

The permeability can be calculated with the following equation:

$$k = \frac{g}{160\nu} d_{15}^2 \frac{n^3}{(1-n)^2} \qquad (7)$$

Combining the equations above, the slope angle of an active wall at a certain depth can be calculated as a function of height. Since the production increases going down the slope, the slope angle will also decrease. Fig. 3 shows the results for two different dense sands. In this figure, it can be seen that at the lower end of a large breaching slope the slope angle will be small. In this example the slope is even gentler for the

coarser sand than for the fine sand because permeability (and therefore v_w en s) dominates over the grain size.

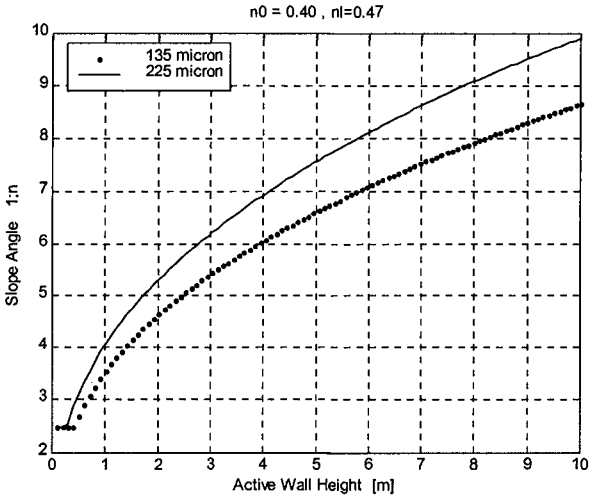

Figure 3: Slope angle at toe of breach as function of breach height.

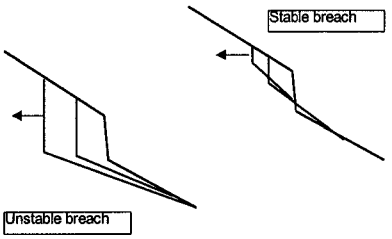

Figure 4: Stable and Unstable breaching.

When an active wall runs up an existing slope as sketched in Fig. 4, the breaching process can become unstable when the slope angle below the active wall is smaller than the existing slope. In that case, the active wall height and thus production will increase. This will lead to an even gentler slope at the toe, which again accelerates the growth of the breach height. This mechanism will go on until the bottom of the active wall reaches the sea bottom. It must be noted that this mechanism can be present in very dense sands. Therefore, it is very likely that this mechanism can be responsible for unexplained "slope liquefaction" in areas where sand was not in a loose state. The mechanism agrees with slope failures observed at the riverbanks of the Mississippi River (Torry, 1995).

Stability of slope

At large propagation velocity of the suction mouth and for a limited breach height, the slope of the breach will be steeper than the slope corresponding to the friction angle of the sand. A slope of saturated fine sand will be stable as long as the angle of the slope α_0 is smaller than the friction angle ϕ of the sand. Above the water line capillary forces can lead to steeper slopes below the water line this is not possible. If therefore the slope is below the waterline and it is steeper then the friction angle, this will always lead to instability. This is not an instantaneous instability. The unstable slope will lead to plastic deformation of the sand and dilatancy (an increase in volume of the sand due to an increase of the pore volume, caused by a different arrangement of the grains, see Fig. 5). Such a dilantancy is only possible if water flows into the sand. Therefore a temporarily stable position is possible for slopes steeper than the friction angle of the sand. In such slopes, there will be dilatancy of the sand leading to a decrease in pore pressure and a water flow into the sand and to a temporarily stable slope. When maximum possible dilatancy is reached, there will be a collapse of the slope.

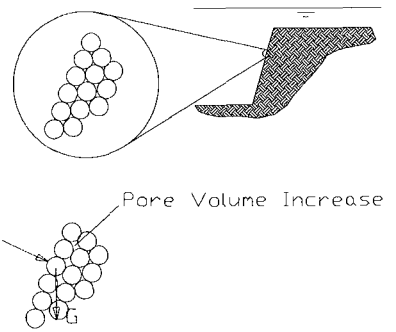

Figure 5: Dilatant behaviour of dense sands.

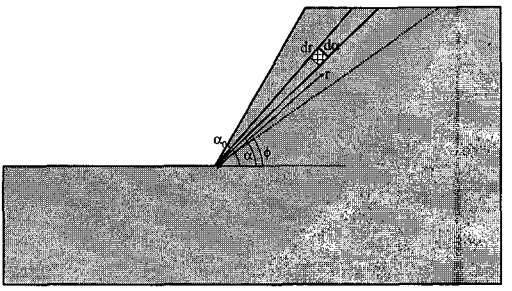

Figure 6: Definition sketch for the calculation of pore pressures in a breach.

If the sand is in this temporarily stable situation, which means that the gradients generated by the dilatancy are just enough to stabilise the soil, the decrease in pore pressure can be calculated. A simplified calculation, neglecting the influence of the groundwater flow, is presented below. Assume that the sand mass within the triangle with a slope angle between ϕ and α_0 (see Fig. 6) is just stable. In that case all particles in that sand mass should be just stable. With the notation presented in Fig. 6, this leads to the following equilibrium equation:

$$\tan\phi = \frac{\gamma' r \sin\alpha.\partial\alpha.\partial r + \partial p/\partial r.r.\partial\alpha.\partial r}{\gamma' r \cos\alpha.\partial\alpha.\partial r + \partial p/\partial\alpha.\partial\alpha.\partial r} \qquad (8)$$

Integration over the angle α and reworking leads to the equation:

$$\frac{\partial p}{\partial r} - \frac{A}{r} p = B \tag{9}$$

with:

$$A = \frac{\tan\phi}{\phi - \alpha_0} \quad \text{and} \quad B = \frac{\gamma}{\phi - \alpha_0}\{\cos\phi - \sin\alpha_0 + \tan\phi.(\sin\phi - \sin\alpha_0)\} \tag{10}$$

Integration over r leads to the minimum pressure (p) that can be expected in the breach:

$$p = \frac{-\gamma.r\{(\cos\phi - \cos\alpha_0)/\tan\phi + \sin\phi - \sin\alpha_0\}}{1 + (\alpha_0 - \phi)/\tan\phi} \tag{11}$$

The pressure drop increases with the slope angle and is linearly proportional with the height of the breach. This equation will be compared with the results of measurements in the section Results.

As long as dilatancy of the sand can provide this minimum pressure, the slope will be temporarily stable. When the maximum porosity of the sand is reached, instability will occur.

Large scale model tests

Two dimensional model tests have been performed in a flume of 32 m length, 1 m width and 2.5 m high at Delft Hydraulics. The flume was filled with fine (135μm) or medium fine (225μm) saturated sand. The density of the sand was controlled by a vibration procedure. In various tests the porosity varied between 38 and 47%. During the experiments a suction mouth was moved through the flume with a constant velocity, varying between 2 and 9 mm/s in the different tests. The suction mouth was moved forward over the bottom of the flume between 0.10 and 0.70 m above the bottom. The resulting breach height varied between 1.50 and 2.2 m

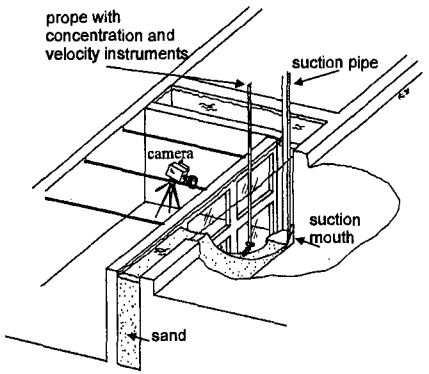

Figure 7: Set-up of the model experiments.

During a test the production, the density and discharge was measured using an EMF and radioactive concentration meter. The pore pressures in the sand and the porosity of the sand were measured by means of a measurement panel that was placed in one of the walls of the flume.

It was expected that during the tests a steep slope angle would develop and that the slope would move constantly forward. This complicated the measurements in the density current on

the slope. It was decided to place the instruments on a carriage that could move over the flume in the same direction as the suction mouth. Close to the instruments, a pressure sensor was placed and the carriage was moved forward automatically until the sensor "felt" the slope. At that moment the carriage stopped and started the measurements. If the process was stationary a concentration and velocity vertical could be obtained because the slope moved away from the instruments. Using this device, the thickness, concentration and velocity of the sand-water mixture could be measured. The process was monitored also by video, through the sidewalls of the flume. The set-up of the experiments is sketched in Fig. 7.

Measurements

Slope angles

Since the tests were two-dimensional, only the slope in front of the suction mouth could be investigated. From the video recordings, the development of the slope angle was followed. It became clear that the description of the active wall velocity according to eq. (3) was not valid at large breach height due to:

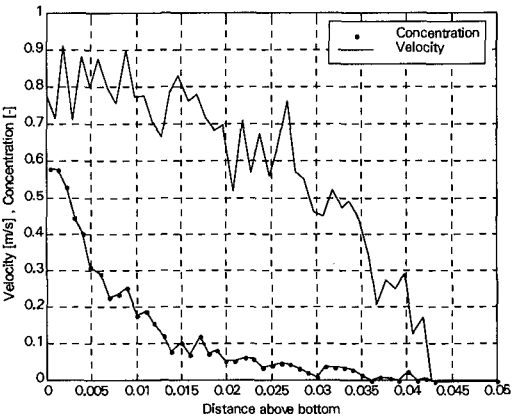

Figure 8: Velocity and concentration profile.

- The presence of a turbulent density current that eroded the sand surface at the toe of the breach leading to a gentler slope which was in accordance with the analysis of section Theory.
- Failure of lumps of sand that was noticed instead of raining of single grains, which occurred at small breach heights.

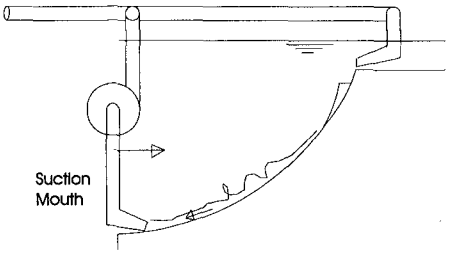

Figure 9: Backfilling at top of the slope.

The effect of the density current on the slope angle

Fig. 8 shows one of the large numbers of concentration and velocity that were measured during the tests. Velocities up to 1 m/s were measured in the density current. It will be clear that this is sufficient to erode the surface of the slope. The influence of the density current on the slope can be investigated by varying

the slope height at a constant forward velocity of the suction mouth. As explained in the theoretical section, the sand-mixture flow must be turbulent to get sufficient erosion. This will only be the case above a certain production level and hence breach height. The sand level in the test flume was limited to 2.3 m.

To simulate the situation for a higher breach, a part of the mixture sucked from the toe of the breach was backfilled at the top of the slope, see Fig 8. The apparent extra height created with this method was approximately 1-1.5 m. During the test, the forward velocity of the suction mouth was 6 mm/s. At a breach height of 2.3 m the slope angle was between 52^0-55^0. During backfilling the apparent slope increased to 3.5 m and the slope angle decreased to below 40^0 as can be seen in the figure below.

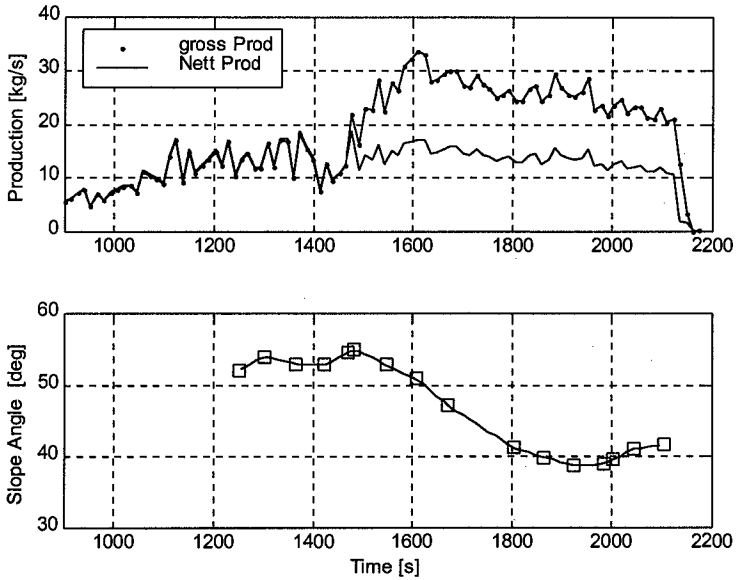

Figure 10: Influence of density current on slope angle

In Fig. 10 it can be seen that at t=1500 s. backfilling at the top of the slope starts. From this moment the gross production increased (part of the mixture is circulating). The net production, which is the amount of soil being removed from the flume, maintains almost the same level. It can be seen clearly however that the large production fluctuations diminish soon after backfilling is started. This is a result from the eroding work of the current at the slope. Before backfilling started, the production was dominated by the sliding of sand lumps from the slope. This is a more irregular process than the erosion process. When the slope angle in Fig. 10 is compared with the theory (Fig. 3) it is clear that the slopes during the tests were steeper. This can be explained by the fact that the slope angles of Fig.3 are derived for a situation were sedimentation dominates, while at the experiments every part of the slope was eroding, due to the forward velocity of the suction mouth. However, both figures show the same tendency.

Porosity and pore pressures

Breaching of sand will lead to a reduction of the pore pressure in the remaining

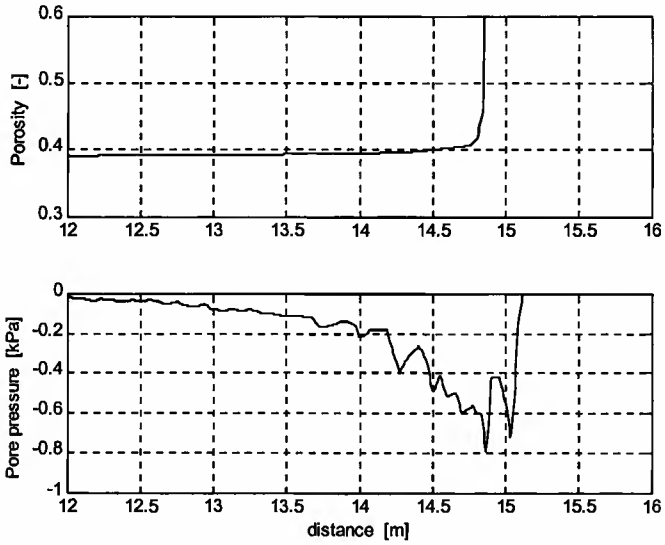

Figure 11: Measured Porosity and porosity changes.

sand, as was explained in the chapter on theory. An example of this reduction is shown in Fig. 11. This figure shows the measured pore pressure and porosity changes on a horizontal plane. The surface of the slope was at that moment situated at x=15.1 m. At this location the reduction in pore pressure disappears.

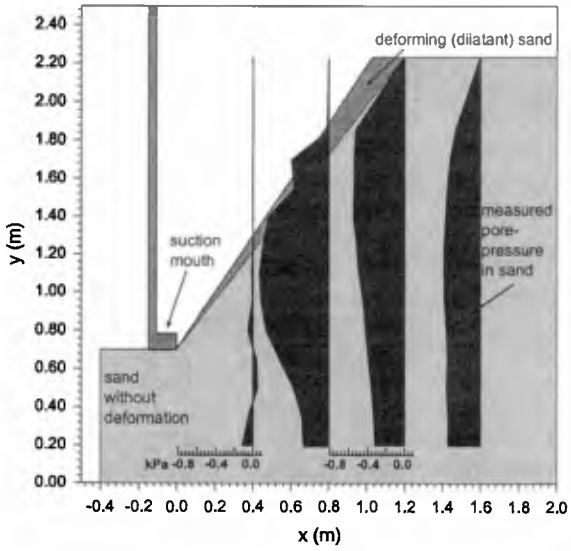

Figure 12: Pore pressure changes in front of suction mouth.

It appears from this figure that the pore pressure reduction is measured more than a metre from the suction mouth. This pore pressure reduction is caused by dilatancy in the sand before it runs

of the slope. However, the electrical density measurements show Fig. 11) that is only limited to a small layer of sand, as is also indicated in Fig. 12. Dilatancy is measured as a decrease of electrical resistance due to the increased porosity. The area indicated functions as a sink. Groundwater flow causes the reduction of pore pressures in the non-dilating part of the sand body. This corresponds with theory.

The measured maximum pore pressure reduction is compared with the results of Eq. (11) in Fig. 13. It appears that using the friction angle of the sand as measured in a triaxial test (35 degrees), Eq. (11) overestimates the pore pressure reduction. However, in densified sand the peak value is always larger than the residual value presented as result of a standard triaxial test. The peak value can be up to 45 degrees. Using this value there is good agreement between measurements and theory for slope angles up to 70 degrees. For larger slope angles the pore pressure reduction is overestimated by theory. This can be caused by density currents that are not taken into account for this model, but lead to an increase of pore pressure.

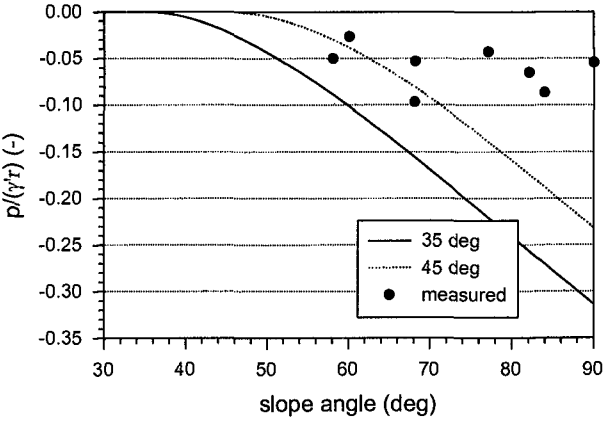

Figure13: Measured pore pressure reduction compared with theory.

Conclusions

Measured pore pressure reduction in the sand is caused by groundwater flow to the limited zone of dilatant sand.

The slope angle developing during the suction of sand and therefore the maximum forward velocity and hence production does not only depend on the sand characteristics. Also the height of the breach as well the effect of the density current are of importance. At a high breach this can lead to very small slope angles, and even to unstable breaching. This effect has been reported in literature from field experience and has now been proved by experiments and theory.

Acknowledgement

F. M. Grootenboer performed the experiments for this study. The research reported in this paper was sponsored by the Dredging Research Association, which includes Amsterdam Ballast Dredging, Royal Boskalis Westminster Dredging BV, HAM Dredging, and the Dutch Department of Public Works.

References:

Bezuijen A., Mastbergen D.R. (1988) "On the construction of sand fill dam – Part 2: Soil mechanical aspects", Proc. Modelling Soil-Water-Structure Interactions, Kolkman et al. (eds.), Balkema, Rotterdam, ISBN 90 6191 8154.

Breusers, H.N.C. (1977),"Hydraulic Excavation of Sand",Proc. Int. Course on Modern Dredging", Post Graduate courses in Civil Engineering", The Hague.

Koning, J. de, (1981) "Developments in Hydraulic Deep Dredging", IVth Latin American Dredging Congress, Mexico.

Masbergen D.R., Bezuijen A. and Winterwerp J.C. (1988) "On the construction of sand fill dam – Part 2: Soil mechanical aspects", Proc. Modelling Soil-Water-Structure Interactions, Kolkman et al. (eds.), Balkema, Rotterdam, ISBN 90 6191 8154.

Torrey III, V.H. (1995) Retrogressive Failures in Sand Deposits of the Mississippi River, US Waterways Experiment Station, Vicksburg
Chapter 22 in:
River, Coastal and Shoreline Protection: Erosion Control Using Riprap
and Armourstone, Edited by C. R. Thomas, S. R. Abt, F. B. J. Barends and
K. W. Pilarczyk, 1995 John Wiley & Sons Ltd.

A Dimensionless Parameter Describing Sea Cliff Erosion

Akira Mano [1]and Shigenori Suzuki [2]

Abstract

Macroscopic analysis based on the energy conservation on sea cliff erosion gives a dimensionless parameter including recession rate of the cliff, wave energy flux at the breaking point, Young's modulus of rocks composing the cliff, and cliff height. This parameter was examined through field data on the Fukushima Coast where a series of soft rock cliffs extends about 50 km. The modulus was obtained by the measurement of the propagation velocity of elastic waves in the rocks and the energy flux was evaluated by the wave ray method. The long-term recession rate had been obtained from the aerial photographs. The recession rate is shown to be proportional to the wave energy flux and inversely proportional to Young's modulus. These quantities prove that the dimensionless parameter has the constant value of 0.082.

1 Introduction

It is a common sense from the physical point of view that the rate of sea cliff erosion depends on both of the intensity of incoming waves and the strength of the rocks composing the cliff. However quantitative relationship to connect these parameters in the field was still unknown. This comes mainly from the difficulty of the observation. Significant cliff erosion occurs in the storm condition, often associated with massive collapse of the cliff. We cannot approach such site during the storm. Furthermore individual collapse may not represent the recession characteristics at the site, because the structural cracks would determine the position of the failure. Debris produced by the collapsed cliff would also affect the recession rate.

Thus we have only limited data on the sea cliff erosion in spite of the significant requirements on the protection works. To develop physical model on the recession characteristics at this stage, macroscopic approach using the energy conservation relationship would be appropriate.

[1]Disaster Control Research Center, Tohoku University, Aobayama 06, Sendai 980-8579, Japan
[2]Electric Power Development Co. Ltd., 6-15-1 Ginza, Tokyo, 104-0061, Japan

2 Energy Conservation Analysis

For the high cliffs made of soft rock, the erosion would take the following process: (1) erosion of the cliff base, (2) collapse of the overhanging, (3) successive fragmentation from large rocks into sands or mud, (4) longshore transport of the fine materials. However since the knowledge of (1) and (2) is unsatisfactory and the both process produce the debris, we will simplify them as one process. Let us consider a two dimensional configuration of the cliff erosion as illustrated in Fig. 1. Taking unit width in the longshore direction and denoting the cliff height and recession rate by L and q respectively, we have volume rate of the debris production from the continuity of the cliff material,

$$\dot{V}_1 = Lq. \tag{1}$$

Furthermore steady state assumption gives the volume rate of the debris removal equal to the production rate.

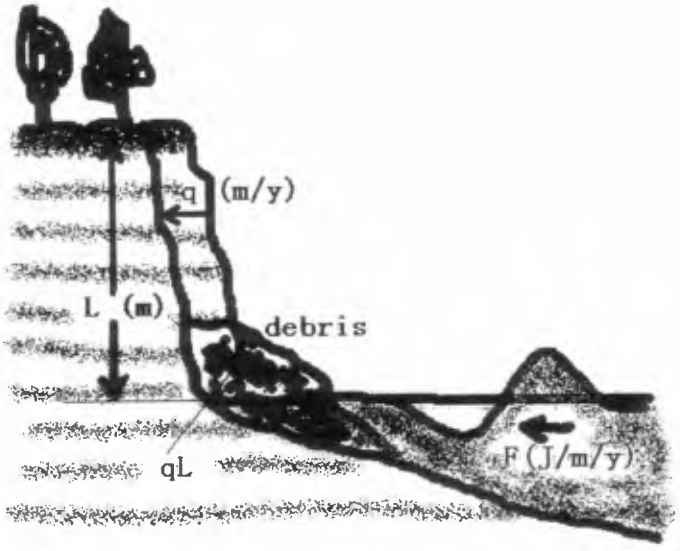

Fig. 1: Definition sketch.

The energy conservation equation for the cliff erosion could be written as,

$$F = \dot{W}_1 + \dot{W}_2 + \dot{W}_3 + \dot{R}. \tag{2}$$

Where F is the energy supply rate and represented by the onshore component of the wave energy flux in unit longshore length at the breaking point as,

$$F = E_b C_{gb} \cos^2 \theta_b. \tag{3}$$

Here subscript b denoting the breaking point, E_b is the wave energy density, C_{gb} group velocity, and θ_b wave angle. The powers $\dot{W}_1$, $\dot{W}_2$, and $\dot{W}_3$ are the rate of the work to detach the large rocks from the cliff, to fragmentize the large rocks of debris into sand or mud, and to transport these fine sediments in the longshore direction. The power $\dot{R}$ is the remainder such as energy dissipation rate in the surf zone.

The first two terms of $\dot{W}_1$,$\dot{W}_2$ are modeled by the elastic theory. If external force is applied to compress the rock sample with unit length and unit cross section from zero to the yield stress, the work done by the force is given by

$$w = \frac{1}{2}\sigma_y \epsilon_y = \frac{1}{2}\frac{\sigma_y^2}{E}. \tag{4}$$

Where σ and ϵ are the stress and strain respectively, E is Young's modulus, and the subscript y indicates yield point. Among various kinds of metals, the yield stresses of the materials are directly proportional to their Young's moduli as stated in Kobayashi (1993). This corresponds to the physical state that fracture occurs when the relative dislocation of atoms exceeds a certain time of the interatomic distance. Introducing this relationship also for rocks, we can rewrite the above equation as,

$$w \propto E. \tag{5}$$

Thus the maximum strain energy that the rock of unit volume can hold is proportional to its Young's modulus. Then if cracks generate in the rock, a part of the strain energy transforms into the surface energy of the newly generated cracks. Therefore the energy consumed in the processes from the erosion to the fragmentation could be interpreted to change the surface energy. Thus, with coefficient C_1

$$\dot{W}_1 + \dot{W}_2 = C_1 L q E. \tag{6}$$

The third term is modeled by employing Komar and Inman(1970) with the coefficient K,

$$\dot{W}_3 = KF \tan\theta_b. \tag{7}$$

The last term is expressed by the efficiency factor β as,

$$\dot{R} = (1-\beta)F. \tag{8}$$

By substituting all these model into Eq.(2) and dividing by F, it follows,

$$1 = C_1 \Pi_c + K \tan\theta + (1-\beta). \tag{9}$$

Where

$$\Pi_c \equiv \frac{qEL}{F}. \tag{10}$$

Equation (9) indicates the dimensionless parameter, Π_c is constant if the wave angle θ_b is small and the efficiency coefficient β is constant.

$$\Pi_c = const. \tag{11}$$

In the following sections, we will examine this parameter by collecting field data on the Fukushima Coast.

3 Outline of the Coast

The Fukushima Coast locates in the East of the main land of Japan and faces directly toward the Pacific Ocean as shown in Fig.2. The coast extends about 50 km in the north direction and is composed of a series of cliffs and pocket beaches. The coast had suffered from serious erosion, reaching 10 m/y at most. The geographical situation that the coast is subject to high wave attack is one reason of the severe erosion.

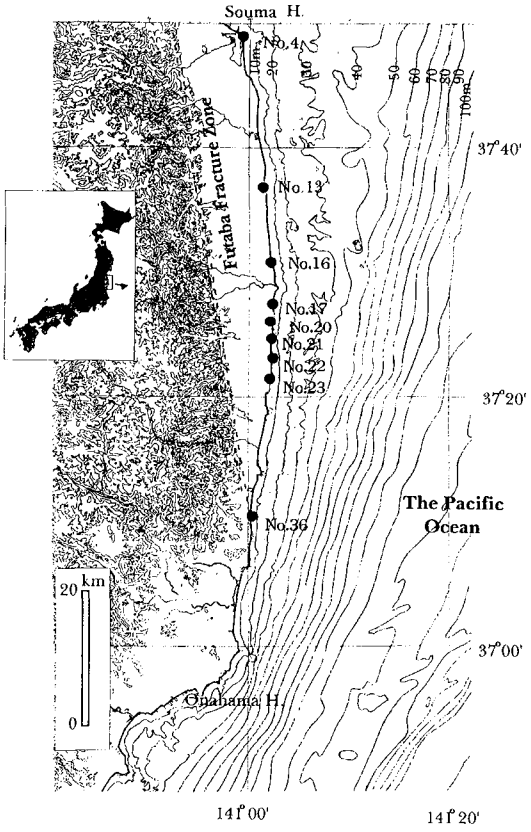

Fig. 2: Topography of the Fukushima Coast and sampling points.

The other reason comes from geological condition. The coastal area together with the hinter land and offshore region is subject to the uplift, the rate of which is estimated by Oka et al. (1981) as 0.2 to 1.6mm/y , varying temporary and spatially. The bed layer of the cliff in the northern part of the coast is marine mudstone or sandstone, formed in the Upper Pliocene, while the southern part is widely covered with green tuff formed in the Miocene, the Tertiary. Weakly

consolidated rocks of geologically young age are easily eroded by wave attacks.

In the West of the coastline, Futaba Fracture zone parallels the coast. The West of the fracture zone uplifted about 200 m relative to the East in the Lower Pleistocene and is now called Abukuma Plateau. Many rivers originated in the plateau run east by eroding the Pliocene sediments on the bed layer and made pocket beaches at the coast. The submarine contour lines of 20 to 40m are significantly winding in the northern part. It is also estimated that the submarine valleys were made by the fluvial erosion during the regression of seawater in the Pliocene. The valleys would affect the refraction of incident waves and then the distribution of wave energy.

Nine sampling points for the examinations of the rock and wave properties described in the next section were selected so as to cover the wide area of the coast and to include wide range of the recession rate. Fig.2 illustrates also the points by the gray circles with numbers.

Figure 3 shows the cliff at No.4 point. The headland is eroded vertically at the tip and has a hollow near the base at the side. In order to mitigate the erosion, numbers of concrete block were put at the shoreline and demonstrated to mitigate the erosion. The other places on the coast are also in the similar circumstances. To guard the railway, roads, and houses in the hinterland from the erosion, protection works were done in 1960s and 1970s. Now the protection works such as the block at the shoreline or detached breakwater has covered major part of the coast.

Figure 4 shows the cliff at No.20. The cliff surface exhibits many layers stretching horizontally. At the base of the cliff, there scatter numerous large rocks of debris. The cliff height is about 18 m. Fig. 5 shows the cliff at point No. 36, which is formed by the hardest rocks in our study. The layers run nearly vertically. Thus, nine samples were taken from various conditions of cliff.

Fig. 3: Photograph at the cliff, No.4.

Fig. 4: Photograph at the cliff, No.20.

Fig. 5: Photograph at the cliff, No.36.

4 Evaluation of the Parameters

Young's modulus E of the rock composing cliffs was evaluated by the measurement of the propagation velocity of the elastic wave. First, we collected rock samples of the size of about 30cm by detaching them from cliffs near the sea water level. Then, after cutting them into the rectangular solids and drying them in the electric furnace at 200°C for 24 hours, we measured the propagation velocity of the elastic primary wave, V_p by attaching transducers on the surface of the formed samples. Young's modulus is given by the following equation,

$$E = \rho V_p^2 \frac{(1+\nu)(1-2\nu)}{1-\nu}. \tag{12}$$

Where ν is Poisson's ratio and the standard value 0.25 was used. The obtained values of Young's modulus together with the other quantities are listed in Table 1.

Table 1 Parameters for the sampled cliffs.

Cliff point	Recession rate q (m/y)	Young's modulus $E(10^9\times$ N/m^2)	Cliff height L (m)	Energy flux $F(10^{11}\times$ J/m/y)	$1/E$	$1/L$
4	0.35	1.08	20	1.55	0.93	0.0050
13	2.12	0.56	18	2.43	1.79	0.0056
16	1.56	0.65	20	3.44	1.54	0.0050
17	3.22	0.74	20	4.79	1.35	0.0050
20	1.86	0.56	18	2.75	1.79	0.0056
21	1.08	0.97	20	2.09	1.03	0.0050
22	0.92	0.92	20	2.81	1.09	0.0050
23	2.06	0.53	25	2.83	1.89	0.0040
36	1.03	2.31	30	3.55	0.43	0.0330
Mean $\bar{z}$				2.92	1.31	0.048
Standard deviation Sd				0.883	0.457	0.00677
Relative range $Sd/\bar{z}$				0.303	0.348	0.140

Energy flux was obtained by the wave ray method of Mano and Sawamoto (1997). That is, the wave ray equation of Mei(1983) and wave ray density equation of Munk and Arthur(1952) together with the dispersion relation are solved on the sea bottom topography approximated as a set of triangular panels. The breaking points are determined by Goda's criterion (1974).

Examples of wave rays are shown in Figs. 6 and 7 for respective wave directions ENE and ESE of wave period, 12.0s. The numbers and vertical lines at the bottom of the figures indicate the sample numbers of cliffs specified in Fig. 2 and cliff extension respectively. Wave rays refract remarkably by the submarine valleys and then result in the periodic distribution of energy concentration and dispersion. In order to evaluate the wave energy flux from wave rays that include crossing, the

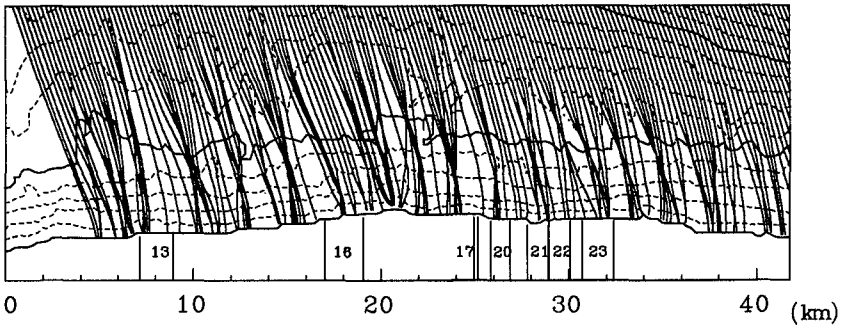

Fig. 6: Wave rays for the incident waves with the period, 12s, and direction, ENE.

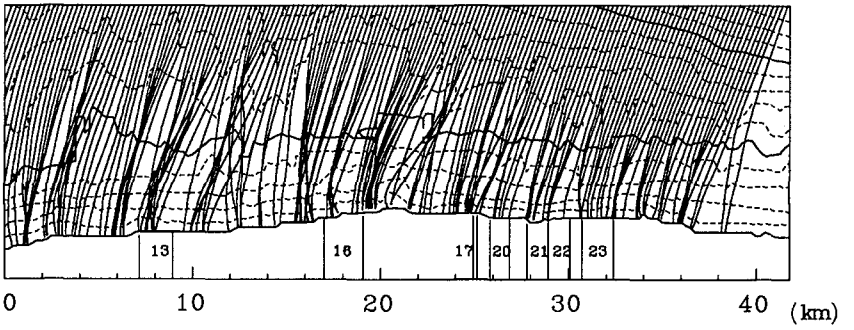

Fig. 7: Wave rays for the incident waves with the period, 12s, and direction, ESE.

following definitions were adopted,

$$F = \frac{1}{N}\sum_{j=1}^{N}\frac{f_j}{n_j}\sum_{i=1}^{n_j}(E_b C_{gb} cos^2\alpha_b)_i. \tag{13}$$

where N is the number of the data sets in a year, $f_j = n_j \Delta S/\ell$, ΔS is the ray ejection spacing in the offshore boundary, n_j is the number of wave rays approaching the cliff, ℓ is the cliff extension projected to the offshore boundary. The coefficient f_j is introduced to take into account of the wave ray gathering. Here we adopted the data sets of daily mean values of the significant wave height, period and direction observed in 1991 off the Souma Harbor located at the north end of the coast with the total days, $N = 364$.

The Fukushima Prefecture(1993) had performed comprehensive research on the coastal erosion, including the recession rate evaluation of all cliffs on the Fukushima Coast and histories of the protection works. The aerial photographs taken in 1963 to 1991 were used for the evaluation. Thus the rate is the mean values in time span of 15 to 30 years. We took these values but modified them by assuming no recession after the protection works. The cliff height is obtained also in the same report.

5 Results and Discussion

Equation (11) for the dimensionless parameter Π_c constituted by four quantities deduces further several relations with the additional conditions that two quantities among four are chosen with keeping the other quantities constant;

$$q \propto F, \tag{14}$$

$$q \propto 1/E, \tag{15}$$

$$q \propto 1/L. \tag{16}$$

Before getting into the individual relationship, let us examine the characteristics of our data set in Table 1. The lowest three rows of the table indicate the mean values, standard deviation and relative range, which is defined by the standard deviation normalized by the mean value, among samples. In the three quantities, F, $1/E$, and $1/L$, the first two quantities have wide range, while the last quantity narrow. In other words, our data set is appropriate to examine Eqs. (14) and (15), and is rather poor to Eq.(16).

Figure 8 examines the relationship between the recession rate q and the wave energy flux F. The recession rate is linearly proportional to the energy flux as shown by the regression line but with a certain data scatter. This corresponds to Eq. (14). Similar relationship has been obtained by Gelinas and Quigley (1973) on the cliff erosion of the north shore of the Great Lake, Erie. As the parameter of wave intensity, they used the total energy flux, not the onshore component, however the difference is generally small, because waves approach perpendicularly to the shore. They made $q-F$ plot and got the regression line but without passing the origin. If we ignore the intercept, which is not so unnatural judging from the scatter of their data, it also becomes Eq. (14).

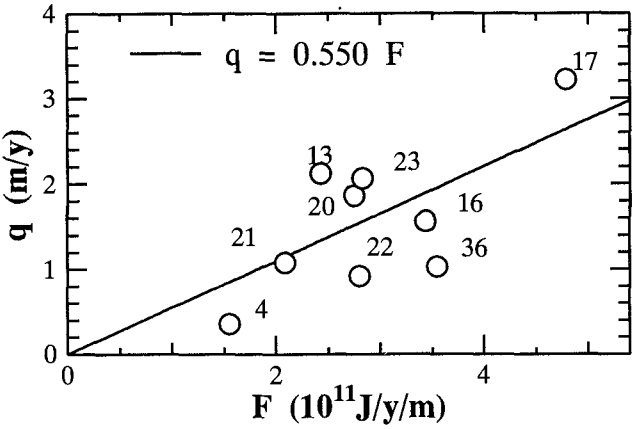

Fig. 8: Relationship between the recession rate and the wave energy flux.

Figure 9 examines the relationship between the recession rate and Young's modulus. The recession rate is inversely proportional to Young's modulus. Although there is also data scatter, referring to the previous figure, we could find some reasons for the scatter. For example, No 17 far above the regression line indicating excessive erosion for the strength of the rock is reasoned by the high energy flux shown in Fig.8. Therefore the data scatter of these figures does not always mean the poorness of the models (14) and (15). Fig. 9 is also supporting Eq.(15).

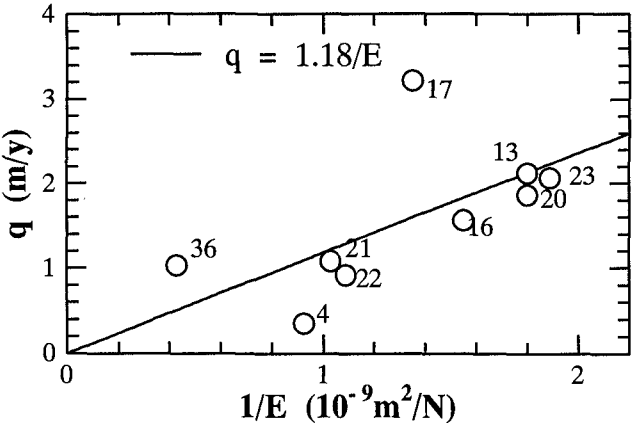

Fig. 9: Relationship between the recession rate and the inverse of Young's modulus.

Sunamura (1992) examined the relationship between the recession rate and compressible yield stress, by collecting related data on the Fukushima Coast by

three researchers. He plotted these two parameters in the log-linear scale plane and got regression relationship by the logarithmic function. However, recalling the relationship used in Section 2 that the yield stresses are linearly proportional to Young's moduli, we can expect inversely linear relationship between the two quantities with the help of Eq. (15). Fig.10 is the modification of Sunamura (1992)'s Fig. 5.13, by taking the linear scale for the inverse of the yield stress. Here the numbers by the circle indicate different sites. The expectation is realized with small data scatter in this figure.

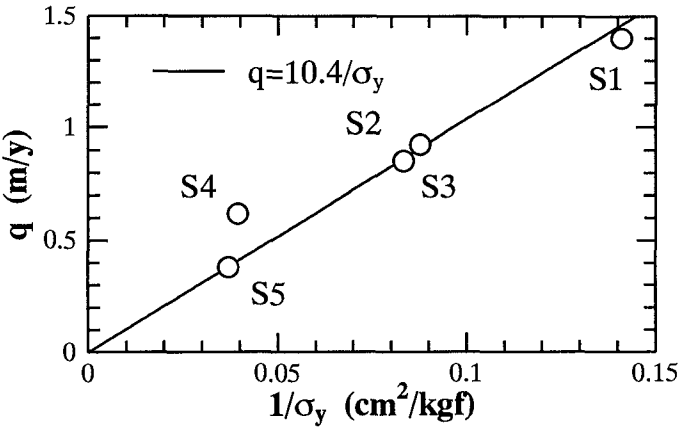

Fig. 10: Relationship between the recession rate and inverse of the yield stress, obtained by modifying Sunamura (1992)'s Fig. 5.13.

Figure 11 shows the correlation between the recession rate and cliff height. The largest data scatter would come from the narrowness of the relative range of $1/L$. We have shown the significant effects of the energy flux and Young's modulus on the recession rate, which was enabled by the wideness of the relative range of these parameters and the narrowness of the remaining parameter, because Eqs. (14) to (16) require the constancy of the other parameters when one parameter among $F, 1/E$ and $1/L$ is chosen.

As for the effect of the cliff height on the recession rate of the sea cliff, there have been conflicting arguments that high cliff is effective to retard the erosion in the short time span but ineffective in the long time span in Sunamura (1992). Detailed analysis on the effect of cliff height and discussions on the above arguments will appear in Mano and Suzuki.

Figure 12 shows the correlation between the recession rate and the combined parameter F/EL. The recession rate is proportional to the parameter with small data scatter. We have the regression line,

$$q = 0.082F/EL, \tag{17}$$

identically,

$$\Pi_c = 0.082 = const. \tag{18}$$

Thus, Eq.(11) is proofed.

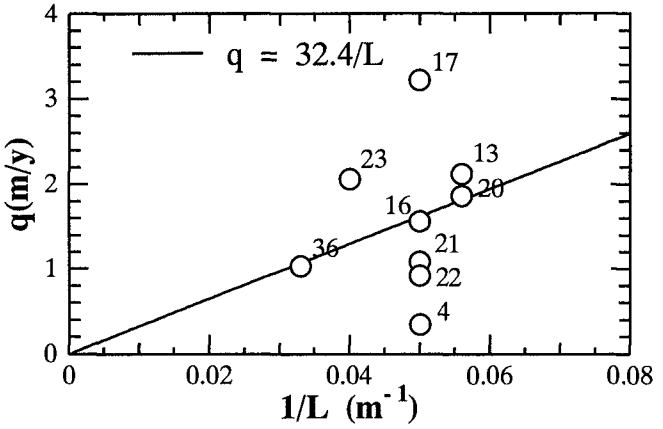

Fig. 11: Relationship between the recession rate and the inverse of cliff height.

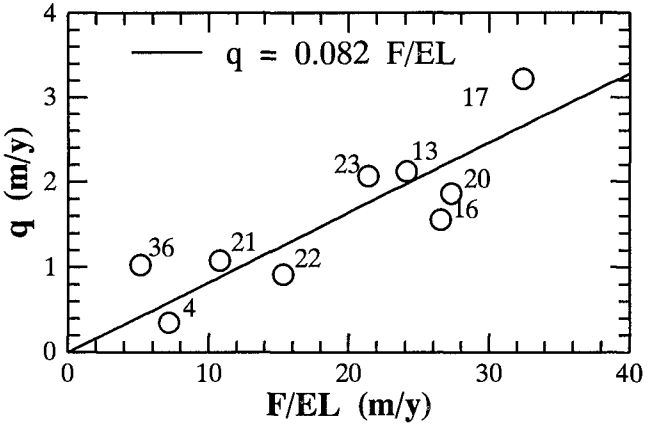

Fig. 12: Relationship between the recession rate and the combined parameter F/EL.

6 Conclusions

The macroscopic analysis based on the energy conservation relation on the sea cliff erosion produces a dimensionless parameter $\Pi_c \equiv qEL/F$ and expects this parameter is constant in the first approximation. Four quantities constituting the dimensionless parameter were evaluated and collected on the Fukushima Coast which had been suffered from severe erosion through the dual reasons of the high wave attack and weakly consolidated rocks. Young's modulus was evaluated by the measurement of the propagation velocity of the elastic waves, while the energy flux through the wave ray analysis. The recession rate and the cliff height had been evaluated through the measurement by the aerial photographs and by the geographical maps, respectively, by Fukushima Prefecture.

Equation (11) on the constancy of the dimensionless parameter includes Eqs. (14) to (16) as special cases. Eq. (14) on the dependency of the recession rate on the energy flux and Eq. (15) on Young's modulus are satisfied by our data set and are shown to be consistent with the foregoing studies by Gelinas et al (1973) and Sunamura (1992). However for the last quantity, the cliff height, our data set is poor to proof Eq. (16), directly. Finally, as for the whole four quantities, our data set gives the relationship $q = 0.082F/EL$ with small data scatter. This is equivalent to $\Pi_c = 0.082$ and the constancy of the dimensionless parameter is proofed.

Acknowledgements
The authors are indebted to Professors Masaki Sawamoto, who introduced us this exciting subject, Tsuguo Sunamura, whose comprehensive review guided us to the important problems on this subject, Shigeru Niizeki, who allowed us to use the measurement system of the elastic wave, and Satoshi Kanisawa, who helped us to study the geological circumstance on the Fukusima Coast. Thanks are also due to Fukushima Prefecture for the permission to use the data and to the Ministry of Education, Science, Sports and Culture in Japan for the Grant-in-Aid.

References

[1] Fukushima Prefecture(1993):Research on the Coastal Erosion in 1993 – Reading from the aerial photograph, as referendum, 62p.(in Japanese).

[2] Gelinas,P.J. and R.M.Quigley(1973):The influence of geology on erosion rates along the north shore of Lake Erie, Proc. 16th Conference Great Lakes Research, pp.421-430.

[3] Goda, Y. (1974): New wave pressure formulae for composite breakwater, 14 th Int. Conf. Coastal Engineering, pp.1702-1720.

[4] Kobayashi, H. (1993): Fracture Mechanics, Kyoritu Publishing Co., 193p.(in Japanese).

[5] Komar, P. D. and D. L. Inman(1970): Longshore sand transport on beaches, Journal of Geophysical Research, Vol. 75, No. 20, pp.5914-5927.

[6] Mano A. and M. Sawamoto(1997): Interactions between a sand barrier and flood terrace at the Abukuma river mouth, Proc. 25th Inter. Conf. Coastal Engineering, pp.4505-4516.

[7] Mano A. and S. Suzuki: Erosion characteristics of sea cliff on the Fukushima Coast, Coastal Engineering Journal, (to be published).

[8] Mei, C.C.(1983):The Applied Dynamics of Ocean Waves, John Wiley & Sons, 740p.

[9] Munk, W.H. and R.S. Arthur (1952):Wave intensity along a refracted ray, Natl. Bur. Stand., U.S. , Circ., 521, Gravity Waves, pp.95-108.

[10] Oka, S., S. Katsurajima, T. Kakimi, T. Aihara and A. Unosawa (1981): Deformatio of a terrace plain along the eastern coast of Fukushima Prefecture,Bulletin of the Geological Survey of Japan, Vol. 32, pp.275-292(in Japanese).

[11] Sunamura, T.(1992): Geomorphology of Rocky Coasts, John Wiley & Sons, 302p.

The Sand Trapping Trench As A Countermeasure to Control Wind-Blown Sand on Beaches

Shintaro Hotta [1] Katsumori Hatanaka[1],
Hiroyoshi Tanaka [2] and Kiyoshi Horikawa [3]

Abstract

The sand trapping trench for controlling wind-blown sand is proposed and general functioning, evaluation of sand trapping efficiency, process of trench development, and usage methods are descrived.

1 Introduction

One of the important problems in the beach stabilization and the effective utilization of beaches is how to control wind-blown sand. Different types of countermeasures are employed in different parts of the world depending on the local conditions at the beach, such as weather, sea, and geographical conditions as well as the economical importance of the region. At the latest ICCE (25th), Hotta and Horikawa (1996) proposed a new type of prevention work, a sand trapping trench, for controlling wind-blown sand. The trench is given a rectangular shape with a depth of more than 1 m and a width of around 5 or 6 m by excavating the backshore of the beach (see Fig. 1). However, the details of trench could not be described in the paper since the main focus of the paper was not to discuss the trench itself. The purpose of this paper is to report the design and use of the trench in more detail.

2 Procedure

2.1 Background and Process of Trench Development

The idea of a sand trapping trench for controlling wind-blown sand stems from the results of several previous studies.

Inspiration to the trench came from an early paper that described a case where cultivated land close to a sandy beach was protected from wind-blown sand by excavating a stream upwind the beach, letting sand grains fall into the stream, and then returning the sand to the sea (Iwagaki, 1950).

Considering this case, Horikawa et al. (1983, 1984) tried to measure the sand transport rate in the field by using trenches those were 1 m deep and several meters wide. Figure 2 shows examples of the sand accumulation process in the

[1]Dept. of Const. Eng., Nihon Univ., 7-24-1, Narashino-dai, Funabashi, Chiba 274-8501, Japan
[2]Central Research Institute of Electric Power Industry, Abiko, Chiba, Japan
[3]Musashi Institute of Technology, Tokyo, Japan

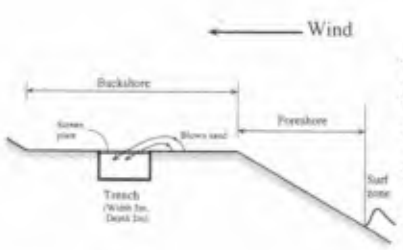

Fig. 1 Conceptional sketch of trench trap.

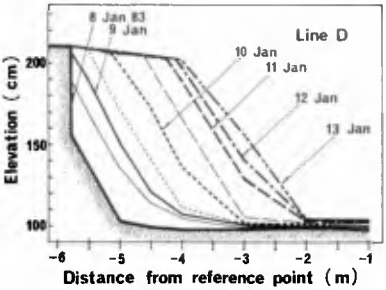

Fig. 2 Sand accumulation process in the trench. (copied from Horikawa et al., 1984)

(a) Begining of the observation.

(b) After 5 days.

Photo 1 Trench trap used on a real beach.

trench and Photo 1 shows the trench (a) at the beginning of the observation., and (b) at the same location after 5 days. Figure 2 and Photo 1 show that the blown sand that fell into the trench was deposited at the upstream edge of trench with the deposition progressing in the downstream direction. The same level was maintained with respect to the beach surface and the rest angle of dry sand determined the downwind slope. This form of accumulation can be understood when we realize that a portion of the blown sand moves with the surface creep motion and that the flying distance of sand grains in saltation is rather short. Horikawa et al. (1983, 1984) also reported that no significant amount of sand was transported beyond the trench and they concluded that the trench could trap almost 100 % of the blown sand.

Using a large wind tunnel, Hotta and Horikawa (1993) measured the flying distance of blown sand in saltation motion. Figure 3 shows examples of observed distributions of falling sand grains. The falling rate was measured by a horizontal distribution-type trap that was 1 m long in the wind direction.

At the downwind end of the trap, a stainless wire net with a mesh of 75 μm was stretched vertically to a height of 30 cm. In Fig. 3, the solid curves are predictions obtained from the modified equation of the vertical distribution of sand transport rate by wind derived by Kawamura (1951). A large amount of sand grains falls a distance of 20 cm downwind from the end of the sand bed. The falling rates at locations 80 cm and 90 cm somewhat increase compared to the value at location 70 cm and deviate upwards from the predicted curve when the shear velocity becomes larger. This was caused by the fact that the flying sand grains hit the end-net and fell into the trap. Sand grains associated with this increase in amount are probably those that would fly beyond 1 m in the horizontal direction if not trapped. Therefore, we must recognize the fact that some amount of sand grains fly beyond 1 m in the horizontal direction. However, considering the fact that over 90 % of the total amount of wind-blown sand is transported below the elevation of 15 cm in a range of the shear velocity from 30 cm/s to 100 cm/s, we can safely assess that the flying distance for an amount of over 90 % of the total transported sand will be smaller than 1 m.

Using a horizontal distribution-type trap similar to the trap used by Hotta and Horikawa (1993), but enlarged to be 50 cm wide and 2 m long, Shiozawa et al. (1993) measured the flying distance of blown sand at a real beach. The result of the measurements is shown in Fig. 4. Figure 4 shows that the theoretical curve of flying distance of blown sand grains modified from Kawamura's equation can predict the observed data well and that the flying distance is smaller than 1 m in the horizontal direction for a shear velocity of about 29 cm/s. In the field measurements, a trench was used that was 1.5 m deep and 5.0 m wide. Shiozawa et al (1993) also reported that sand was transported beyond the trench for strong winds but the amount transported was negligible small compared to the amount trapped in the trench. The values of the transported and trapped sand and the wind speed were not given in the original paper.

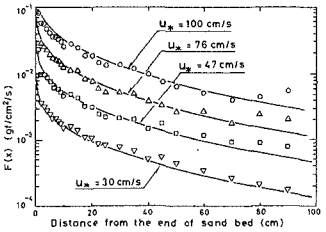

Fig. 3 Examples of horizontal distribution of falling sand grains. (copied from Hotta and Horikawa, 1993)

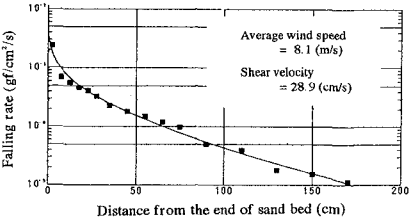

Fig. 4 Flying distance of blown sand grains observed in the field. (redrawn from Shiozawa et al., 1993)

Based on the investigations discussed above, the present authors concluded that the trench could be employed as a prevention work for wind-blown sand and proposed to use the trench practically in the field.

2.2 Remaining Problems and Study Subject

It is highly probable that over 90 % of blown sand will be trapped in the trench, if the trench has a length of about 2 m in the wind direction (hereafter we refer to the length as the width of trench), for shear velocities lower than 100 cm/s on sand surfaces with a grain size of around 0.3 mm. However, the field experiments carried out by Horikawa et al. (1983) also showed that the wind rushed onto the downwind edge of the trench and a violent disturbance of the flow field was generated in the case of a trench wider than 7 m. Thus, it was found that a trench too wide would not be good for stabilizing trapped sand. To solve this problem, the present authors carried out a wind tunnel experiments together with numerical simulations to determine a suitable width of the trench from the flow conditions in an open cavity (of similar shape). The main objective of this work was to find a suitable aspect ratio of the open cavity, where the aspect ratio is defined by the ratio of width to height of the open cavity. In the following sections, the wind tunnel and numerical experiments will be described.

3 Wind Tunnel Experiment

The wind tunnel experiments consisted of two parts, namely one part that was a tracer experiment to visualize the flow pattern inside the trench and an other part that encompassed measurements of wind speed to determine the wind speed field.

3.1 Facilities

The wind tunnel used in the experiments was a blow-off type with a test section having dimensions of 1.1 m high, 1.0 m wide, and 20 m long. To provide an open cavity (trench), the tunnel floor was fixed by wooden boards as shown in Fig. 5. An arbitrary aspect ratio could be selected by changing the width of the cavity.

Wind speed was measured with an array of hot-film anemometers consisting of twelve anemometers. The output from the amplifier unit of the anemometers was recorded and analyzed on a personal computer. The sampling interval of data was 1 Hz. The hot-film anemometer was omni-directional. Therefore, it was not possible to detect the wind direction.

For the tracer experiment, four 8 mm video cameras, including two digital-type and two high grade conventional-type cameras, were employed. The num-

ber of cameras used depended on the width of the cavity and the spatial range photographed by a camera varied from 20 cm to 60 cm.

Styrofoam particles with diameters ranging from 0.1 mm to 0.3 mm were employed as tracers. The specific gravity of the particles was about 0.02.

3.2 Experimental Procedures

The tracer experiment was carried out first. While blowing the wind and operating the cameras, the tracer was injected at different elevations through a pipe with an inner diameter of 25 mm that was lowered from the ceiling into the tunnel at a location 1 m upwind from the upwind edge of the cavity. The elevations of injection varied from the bottom to near the ceiling. A run continued until we could roughly sketch the flow pattern using visual observations. For one aspect ratio, tracer experiment was done for three reference wind speeds around 5 m/s, 10 m/s, and 15 m/s. The employed aspect ratios were 2, 4, 5, 6, 8, 10, and infinity (step down).

After finishing the tracer experiment, the vertical distribution of the wind speed was measured at locations where we judged that it was needed based on the tracer experiment. The measuring period of wind speed was 2 min at a location and data series encompassing 120 values was taken. The average of the wind speed at the point was then calculated. The complete wind field was also measured for three reference wind speeds.

3.3 Results and Discussions

Before discussing the results, we should keep in mind the limitations of this experiment.

The wind speeds employed, 5, 10, and 15 m/s, are prototype-scale. However, the floor surface consisted of a wooden board and the roughness of the surface

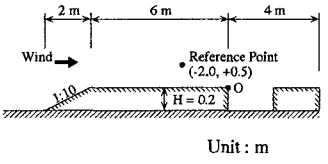

Fig. 5 Floor configuration for experiments.

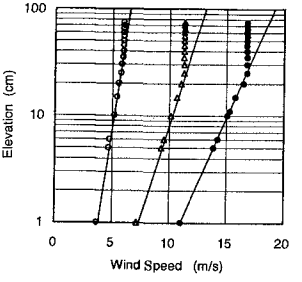

Fig. 6 Vertical distribution of wind speed.

was smaller than that at real beaches. The length scale becomes 1/5 or smaller than 1/5 if we assume that a trench will be employed in the field that has a depth of 1 m or more. The model experiment was carried out at a distorted scale, making it difficult to define a characteristic Reynolds number for the experiment. If we choose the depth of the trench, 0.2 m, as the characteristic dimension, Reynolds number becomes about 6.7×10^4, 1.3×10^5, and 2.0×10^5, for wind speeds of 5, 10, and 15 m/s, respectively, where the kinematic viscosity is taken as $1.5\times10^{-5}m^2/s$.

The tracer employed was light but still had some weight; therefore, the tracer tended to fall down to the floor. However, the flow patterns drawn from scattered tracers were almost the same for the three reference wind speeds, although the figures are not shown here because of space limitations.

The aim was to use a constant wind speed during the experiment. However, the wind speed fluctuated on the average about ±3.0 % due to the mechanical characteristics of the tunnel. Figure 6 shows the vertical distribution of the averaged wind speed above the wooden board floor. The logarithmic law is satisfied under an elevation of about 30 cm and the wind speed becomes constant at elevations higher than 30 cm. The reference wind speeds, 5, 10, 15 m/s are the wind speeds measured at the reference point (-2.0 m, +0.5 m) in Fig. 5 in the constant wind speed region. The wind speed measured was normalized by these reference speeds. The vertical distribution of the normalized wind speed at each location was the same for three of the reference wind speeds within the experimental error. Based on the above observations, the following discussion of the results is presented with reference to the flow patterns and the normalized wind speed field averaged for three of the reference wind speeds.

Figure 7 shows the flow patterns and the wind speed profiles. Allows showing the flow pattern are loci of tracers and do not mean wind velocity vectors. Attention is draw to Fig. 7 (b) showing the tests with aspect ratios of 6, 8, and 10 and the back step flow. The horizontal distance is reduced with a scale of 1/2 in these tests differentiating them from what is presented in Fig. 7 (a) . In the back step flow the stagnation point appeared at a location of about 7.2H downwind the upwind edge of the cavity (from the origin). Many previous wind tunnel experiments or numerical simulations show that the stagnation point appears in a region about 7.0H to 7.5H. Therefore, it is considered that the present experiment provided reliable results in agreement with previous studies. The stagnation point shifts upwind to 6.8H for B/H = 10.0, to 5.8H for B/H = 8.0, and to 5.2H for B/H = 6 in the presence of a downstream wall so that an open cavity is formed. No stagnation point appears for B/H = 4.0, and for B/H = 5.0 it was difficult to establish the existence of a stagnation point in the visual observations during the experiment or on the video movie analysis. Considering these observation and looking closer at the flow patterns we can conclude that the main flow lowered downward due to the cavity touches

the bottom of the cavity and rushes onto the downwind wall of the cavity for aspect ratios larger than 6.0. The return flow from the downwind wall probably generates a violent disturbance in the cavity, and this result agrees with our field experience. A circulation cell exists for aspect ratios smaller than 5.0.

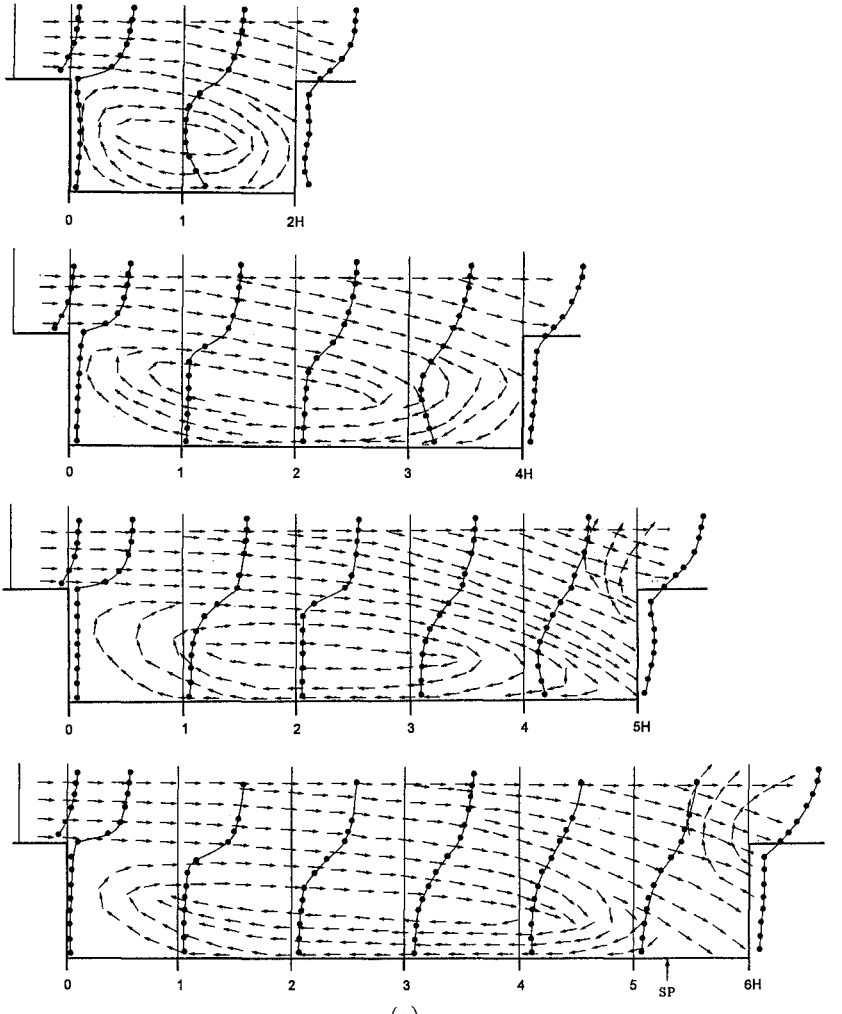

(a)

Fig. 7 Flow patterns and wind speed profiles. (SP : stagnation point)

At a first glance on the wind speed profiles it is difficult to directly find any particular features of the flow. However, careful investigations of the profiles together with the overall flow pattern allowed us to quantitatively establish the

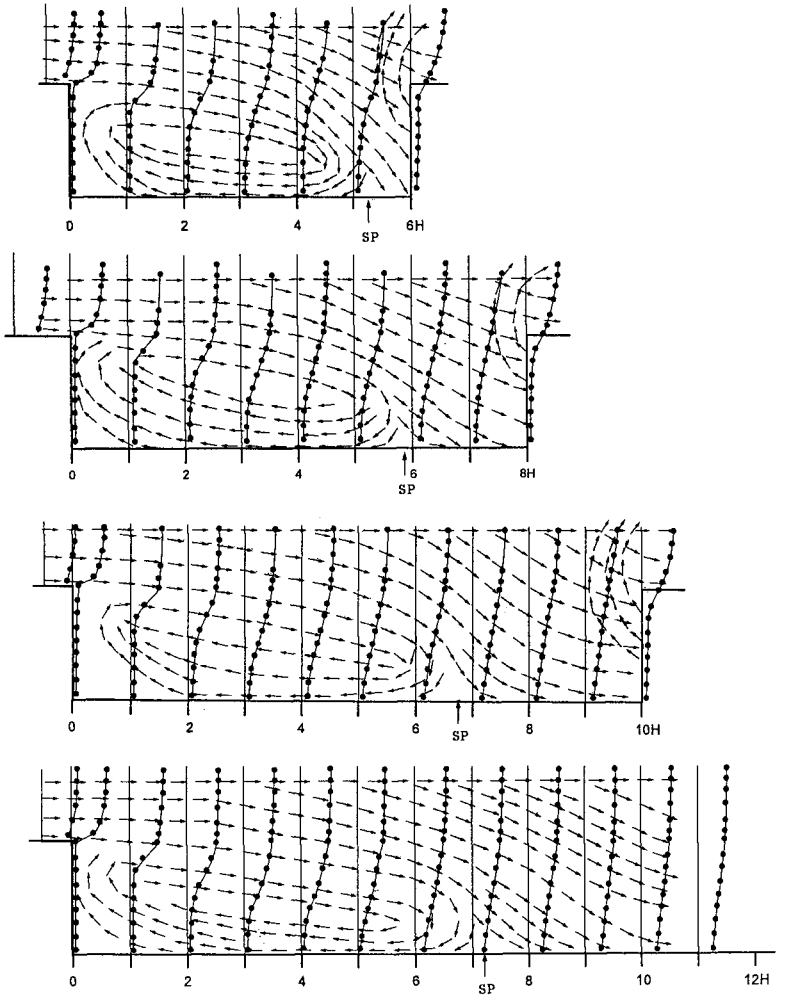

(b)

Fig. 7 Flow patterns and wind speed profiles. (SP : stagnation point)

flow characteristics. Figure 8 shows curves of equal wind speed in the cavities. From Fig. 8 we can perceive that the wind speed inside the cavity becomes stronger when the aspect ratio increases. To evaluate the wind speed conditions, we focus on the curves that have a value of 0.5 for equal wind speed. It is seen that the lowering of the curve valued at 0.5 into the cavity becomes larger when the aspect ratio becomes larger than 5.0. Based on the above discussion of the results, the present authors conclude that the aspect ratio should be smaller than 5.0 to keep low-disturbance conditions inside the cavity.

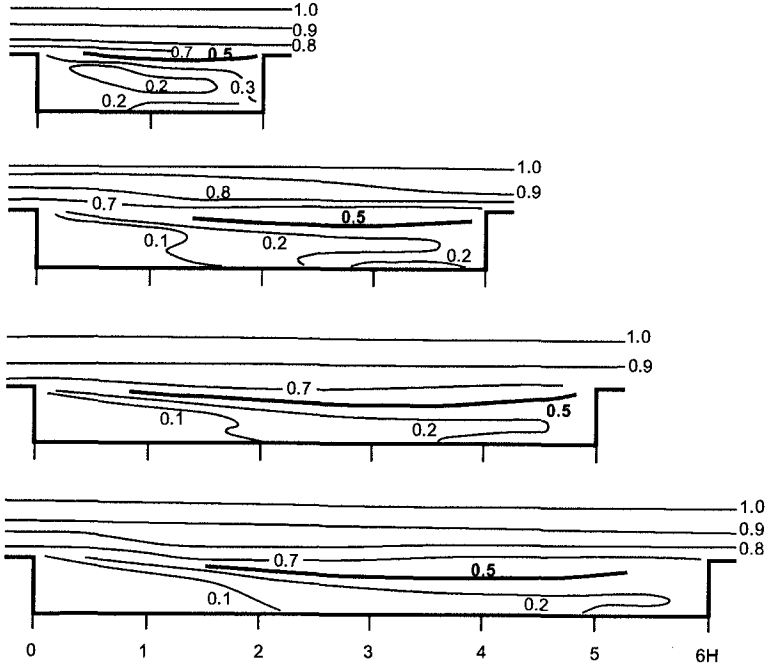

(a)

Fig. 8 Equal wind speed curves in the cavities.

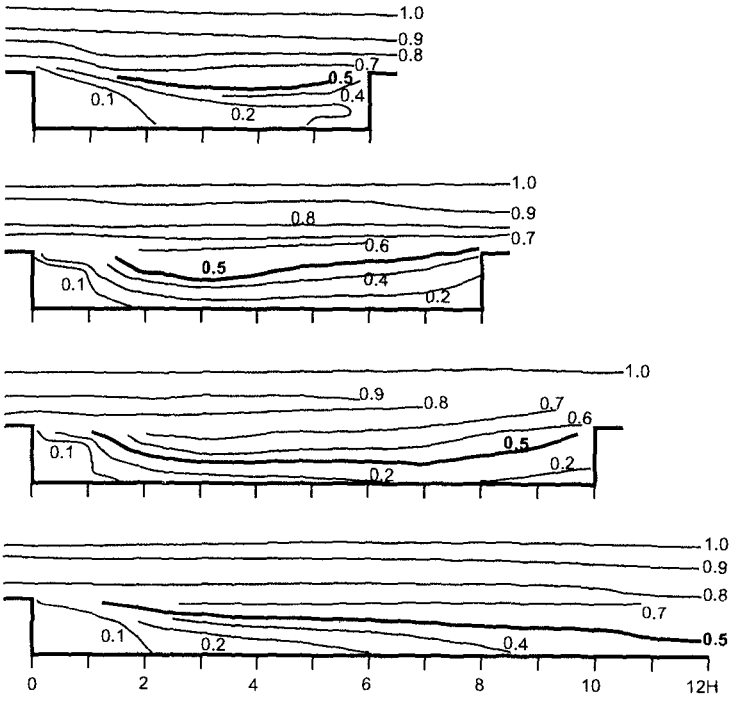

(b)

Fig. 8 Equal wind speed curves in the cavities.

4 Numerical Experiment

4.1 Basic Equations

In order to theoretically examine the results obtained in the experiments, we performed numerical simulation of the air flow in the trench trap. Since the fluid under consideration can be treated as an incompressible viscous fluid and the flow is a fully developed trubulent flow, the time-dependent Reynolds-averaged Naview-Strokes equation were selected together with the $k-\varepsilon$ modeling equations as the basic equations of the simulation. The equations can be written in

the following form.

$$\frac{\partial U_i}{\partial x_i} = 0 \tag{1}$$

$$\frac{\partial U_i}{\partial t} + U_j \frac{\partial U_i}{\partial x_j} = -\frac{1}{\rho}\frac{\partial P}{\partial x_i} + \frac{\partial}{\partial x_j}\left\{(\nu + \nu_t)\left(\frac{\partial U_i}{\partial x_j} + \frac{\partial U_j}{\partial x_i}\right)\right\} \tag{2}$$

$$\frac{\partial k}{\partial t} + U_j \frac{\partial k}{\partial x_j} = \frac{\partial}{\partial x_j}\left\{\left(\nu + \frac{\nu_t}{\sigma_k}\right)\frac{\partial k}{\partial x_j}\right\} + G - \varepsilon \tag{3}$$

$$\frac{\partial \varepsilon}{\partial t} + U_j \frac{\partial \varepsilon}{\partial x_j} = \frac{\partial}{\partial x_j}\left\{\left(\nu + \frac{\nu_t}{\sigma_\varepsilon}\right)\frac{\partial \varepsilon}{\partial x_j}\right\} + \frac{\varepsilon}{k}(C_{\varepsilon 1} G - C_{\varepsilon 2}\varepsilon) \tag{4}$$

$$\nu_t = C_\mu \frac{k^2}{\varepsilon} \tag{5}$$

$$G = \nu_t \left(\frac{\partial U_i}{\partial x_j} + \frac{\partial U_j}{\partial x_i}\right)\frac{\partial U_i}{\partial x_j} \tag{6}$$

Here, U_i and is the local time-averaged velocity components and P is the pressure, k and ε are the turbulent kinetic energy and its dissipation rate, respectively. ν is the kinematic viscosity, ν_t is the turbulent eddy viscosity, and G in the k and ε equations is the turbulence production term. The values of the constants $C_\mu, C_{\varepsilon 1}, C_{\varepsilon 2}, \sigma_k, \sigma_\varepsilon$ used in the turbulence model are $0.09, 1.44, 1.92, 1.0, 1.3$, respectively.

This formulation, however, is known to give poor predictions of turbulent characteristics when excessive generation of turbulent energy leads to a too high turbulent viscosity. To overcome this, Kato and Launder have presented a modified $k-\varepsilon$ model. Let the dimensionless strain parameter S and vorticity parameter Ω be defined according to :

$$S = \sqrt{\frac{1}{2}\left(\frac{\partial U_i}{\partial x_j} + \frac{\partial U_j}{\partial x_i}\right)^2} \tag{7}$$

$$\Omega = \sqrt{\frac{1}{2}\left(\frac{\partial U_i}{\partial x_j} - \frac{\partial U_j}{\partial x_i}\right)^2} \tag{8}$$

From eq.(6), it is easily verified that the energy production term may be rewritten :

$$G = \nu_t S^2 \tag{9}$$

Near a stagnation point, the very high value of S leads to the excessive levels of G. However, the vorticity parameter Ω near a stagnation point becomes nearly equal to zero since the deformation is nearly irrotational. Thus the replacement,

$$G = \nu_t S \Omega \tag{10}$$

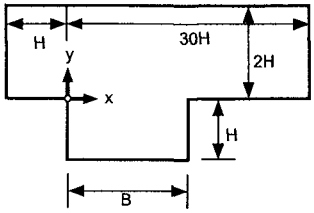

Fig. 9 Definition sketch of the computational domain.

gives a substantial reduction of G in the region around the stagnation point. This method has been found to give satisfactory predictions in the computation of turbulent flows. The modification is no remedy for the weakness in the Bousinessq stress-strain hypothesis, but it does greatly improve the behavior in some flows.

The discretization strategy used in this study is the three-step Taylor/Galerkin method. The discretized formulations of the basic equations are omitted here due to the limited space. One can find more details about this strategy in the referencies Hatanaka et al. (1998) and Jiang. et al. (1993).

4.2 Results and Discussions

In the numerical simulations, the Reynolds number was fixed to 10^5 and simulations for two aspect ratios, $B/H = 4$ and 6,were carried out. Figure 9 shows a definition sketch of the computational domain. The computational domain is discretized using bi-linear isotropic quadratic finite elements. The finite element mesh used in both cases had 8,365 nodes and 8,160 elements.

Figure 10 shows the stream lines of the flow field for the case $B/H = 4$ and for the case $B/H = 6$. In the case $B/H = 4$, one can see that the primary vortex in the trench is large and that the main stream dose not flow into the trench. However, in the case $B/H = 6$, the primary vortex move upstream in the trench and the main stream flows into the trench trap. Moreover, a stagnation point can be observed in the case $B/H = 6$ whereas no stagnation point can be observed in the case $B/H = 4$. These are the same results as were obtained in the experiments and therefore it can be said that the observations made in experiments were verified by the numerical model.

5 Concluding Remarks

The dimensions that the newly proposed sand trapping trench needs to function well as a controlling device for wind-blown sand are a width of 2 m (at

least in proto-type) and an aspect ratio of width to depth (B/H) smaller than 5.0. However, for engineering use, when solving problems on real beaches, we must also consider the storage capacity for trapping sand and the removal of the trapped sand. The optimal width and depth of the trench depend on the maximum allowable volume of trapped sand and the frequency of removal of the trapped sand during the windy season. The sand volume that will be trapped can be calculated by using the Kawamura or Bagnold formulas with a reasonable accuracy for engineering purposes, if we can estimate the wind conditions at the site. Then, a suitable width and depth of trench can be chosen. In addition, we must consider the removal method of the trapped sand. It is reasonable to assume that trapped and stored sand will be removed by earthmoving construction machines such as power shovels and bulldozers. The dimensions and effectiveness of the earthmoving machines will be one of the factors that determines the width and depth of the trench. To preserve a safe environment for various activities on the beach, a cover made of screen or mesh plate should be placed on top of the trench. The opening ratio, defined as the ratio of the open space to the total project area of the plate, is also one of factors that determines the width of the trench; (this problem has not been studied yet). There are many problems to be solved in the practical use of trenches on beaches. The authors believe, however, that well-educated engineers can deal with them.

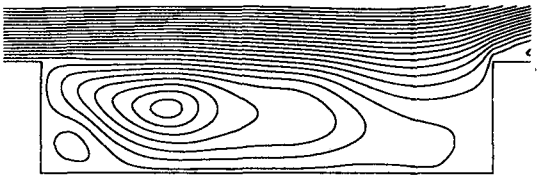

(a) B/H=4.0

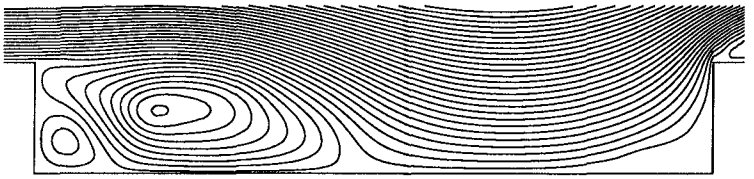

(b) B/H=6.0

Fig. 10 Stream lines of mean velocity field ($Re = 10^5$)

References

Hatanaka, K. and S. Hotta (1998) : Finite element analysis of air flow around permeable sand fences, Int. J. Num. Meth. Fluids, Vol. 24, pp. 1291-1306.

Horikawa, K., S. Hotta, S. Kubota and S. Katori (1983) : On the sand transport rate by wind on a beach, Coastal Eng. in Japan, Vol. 26, JSCE, pp. 101-120.

Horikawa, K., S. Hotta, S. Kubota and S. Katori (1984): Field measurement of blown sand transport rate by trench trap, Coastal Eng. in Japan, JSCE, Vol. 27, pp. 213-232.

Hotta, S. and K. Horikawa (1993) : Vertical distribution of sand transport rate by wind, Coastal Eng. in Japan, JSCE, Vol. 36, pp. 91-110.

Hotta, S. and K. Horikawa (1996) : Countermeasures against wind-blown sand on beaches, Proc. 25th, Coastal Eng. Conf., ASCE, pp. 4188-4199.

Iwagaki, Y. (1950): Sand drift by wind on the coast, Bulletin of the Disaster Prevention Research Institute, Kyoto University, No. 3, pp. 31-35. (in Japanese)

Jiang, C.B., K.Hatanaka, M.Kawahara and K.Kashiyama (1993), A Three-Step Finite Element Method for Convection Dominated Incompressible Flow, Computational Fluid Dynamics Journal, Vol.1, No.4, pp.447–466.

Kato, M. and B.E. Launder (1993) : The modeling of turbulent flow around stationary and vibrating square cylinder, Proc. of 9th Symp. On Turbulent Shear Flows, pp. 10-4-1 - 10-4-6.

Kawamura, R. (1951) : Study on blown sand by wind, Rep. of the Inst. of Science and Technology, Univ. of Tokyo, Vol. 5 (3/4) : pp.95-112 (in Japanese), English translation available in : Research Tech. Rep. HEL-2- 8, Hydraulic Eng. Lab., Univ. of Calif., Berkeley, 1964, pp. 38 (I.Nagahama and H. Hiraoka, translators).

Launder, B.E. and D.B. Spalding (1974) : The numerical computation of turbulent flow , Comput. Meth. Appl. Mech. Eng., Vol. 3, pp. 269-289.

Shiozawa, T., S. Nakayauchi, M. Akazawa, S. Tamashiro and K. Kuroki (1993) : Observation of the sand transport rate by wind at Niigata West Beach, Proc. of Coastal Eng., Vol. 40, JSCE, pp. 281-285. (in Japanese)

Coastal Sediment Transport: the COAST3D Project

R L Soulsby[1]

Abstract

The MAST-III RTD project COAST3D started in October 1997. A consortium of 11 partners including hydraulic laboratories, universities and national regulatory authorities from five EU states (UK, Netherlands, France, Spain and Belgium) will undertake this three-and-a-half year project. The project will make field measurements of waves, currents, sediment transport and morphodynamics at two contrasting sites. The results will be used to valid existing morphodynamic computational models, and lead to coastal zone management tools.

Introduction

Coastal management and engineering decisions rely increasingly heavily on predictions made by computational numerical models of hydrodynamic and sediment-dynamic processes and the resulting morphodynamic changes to the coastline and sea bed. Yet such models are rarely tested adequately against real data from coastal field measurements. This is largely because the many field experiments made to date have been designed to elucidate the physical processes rather than to evaluate numerical models. In addition, the most detailed data-sets are from North American sites, which are fundamentally different to European conditions. Evaluation of numerical models makes special requirements of the data, such as detailed measurement at the boundaries, and a dense spatial coverage of measurements within the modelled area. At the same time, improvements to numerical models are mainly made through improved understanding of the processes, so it is important to measure and interpret these also. The knowledge and models also need to be taken beyond the domain of the scientist, and put into a framework of guidelines and methodologies to be of direct value for coastal zone management.

[1] Manager, Marine Sediments Group
HR Wallingford, Howbery Park, Wallingford, OX10 8BA, UK

Sandy coasts can be classified as 2-dimensional (uniform in the coastwise direction), 2.5-dimensional (as 2D, but with natural non-uniformities such as rip-channels), and 3-dimensional (with irregular features such as headlands and tidal inlets). One of the best ways of gaining insights into the complex 2- or 3-dimensional development and behaviour of sandy coastal systems is by simulating their structure, organisation and functioning by using numerical models. Nowadays, morphodynamic models especially have become important tools for coastal zone management to predict and evaluate the evolution in coastal morphology in response to environmental change and engineering works.

Numerical morphodynamic models are generally of two types: Coastal Profile (CP) Models, suitable for 2D coasts, and Coastal Area (CA) Models, suitable for 3D coasts, with certain variants of both being applicable to 2.5D coasts. The understanding and modelling of notionally 2D coasts is reasonably well advanced, but the question is being raised whether any natural coast is sufficiently uniform to enable 2D modelling techniques to make successful predictions. Hence the focus is now turning to understanding the three-dimensional aspects.

Objectives

The purpose of the COAST3D project is

- to improve understanding of the physics of coastal sand transport and morphodynamics
- to remedy the present lack of validation data of sand transport and morphology suitable for testing numerical models of coastal processes
- to test a representative sample of numerical models for predicting coastal sand transport and morphodynamics against this data
- to develop validated modelling tools, and methodologies for their use, in a form suitable for coastal zone management

This will be achieved by making field measurements purpose-designed for numerical model evaluation, with adequate boundary conditions and a dense horizontal array of measurement points, in conditions typical of the European coastline. Previous coastal experiments in Europe and elsewhere have placed their main emphasis on hydrodynamics; an innovative feature of the present project is that the emphasis throughout is on sand transport and morphodynamics.

Another distinctive feature is that the focus is on non-uniform (3D) coasts, rather than on the relatively well understood (but possibly unrealistic) uniform 2D case. Experiments will be performed at two contrasting sites: a quasi-uniform (2.5D) stretch of the Dutch coastline, and a fully 3D site on the UK coast. This phased

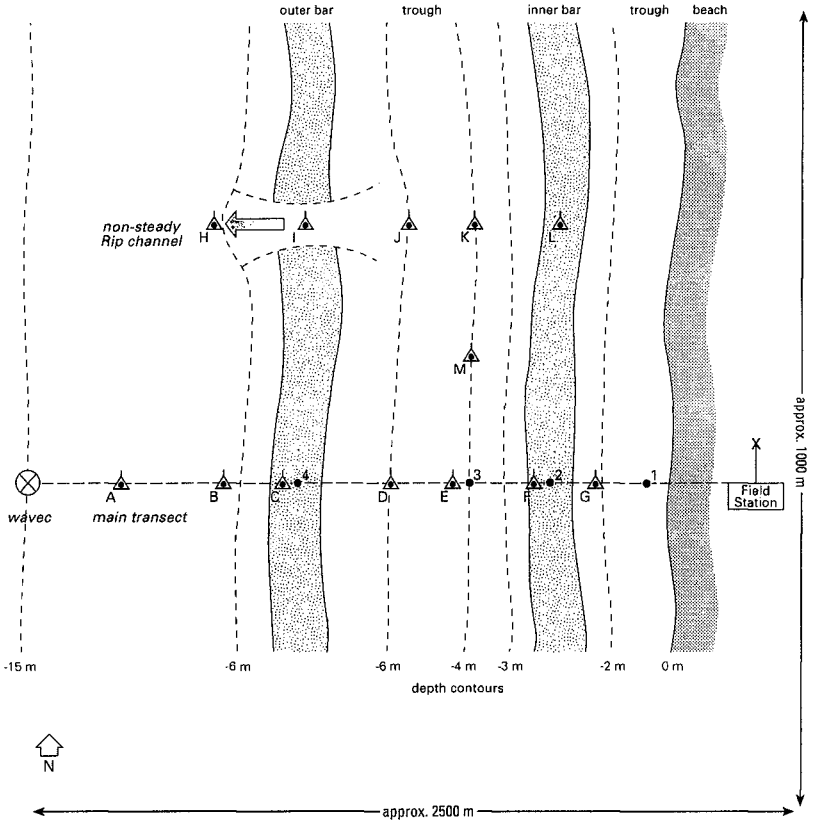

Figure 1. Schematic layout of instruments for Egmond experiment

approach will allow both the process information and the performance of the numerical models to be more easily interpreted.

Innovative techniques will be used in the experiments. Numerical modellers will work interactively with the experimenters, at the planning, experiment, and evaluation phases. Participants from national regulatory authorities will ensure that the project is focused on practical tools for coastal zone management.

Sites have been chosen in:

- the Netherlands for the 2.5D case, which is typical of the quasi-uniform sandy beaches dominated by breaker bars found on much of the coastlines of northeast France, Belgium, the Netherlands, western Germany, western Denmark, and eastern England.

- the UK for the 3D case, which is typical of the irregular coastlines featuring tidal inlets, river and estuary mouths, headlands, and coastal structures, often without breaker bars, found in western and southern Britain, Ireland, northern and western France, northern Spain, Portugal, and Norway.

A large proportion of the coastline of Europe falls into these two categories. The remainder comprise the micro-tidal coasts of the Mediterranean and the Baltic. These latter seas fall within the remit of the ongoing MAST-3 FANS project, based on an experiment in the Mediterranean to measure water, sediment and nutrient fluxes in three domains: the nearshore, the shelf and the continental slope. Another complementary MAST-3 project, INDIA, will study the morphodynamic behaviour of tidal inlet entrances and adjacent coastlines at a site in Portugal. Links will be forged between COAST3D, INDIA and FANS, through the presence of common partners, so that a wide variety of different European environments will be covered by these three projects.

Experiments

The first experiment will take place at Egmond on a quasi-uniform stretch of the Dutch coast (Fig.1), starting with a pilot experiment in spring 1998 followed by the main experiment in autumn 1998. Although the coastline and bathymetric contours appear on charts to be nearly straight, it is known from earlier work that the natural three-dimensionality produced by rip-channels intersecting a bar system has a major effect on the hydrodynamics and sediment dynamics of the coast. The site is regarded as "2.5–dimensional" as a result of these sedimentary non-uniformities, and the departures from 2-dimensionality are an important aspect of this experiment.

The second experiment, scheduled for 1999, will take place at Teignmouth on the south coast of England (Fig.2), where a rocky headland and a river mouth provide a

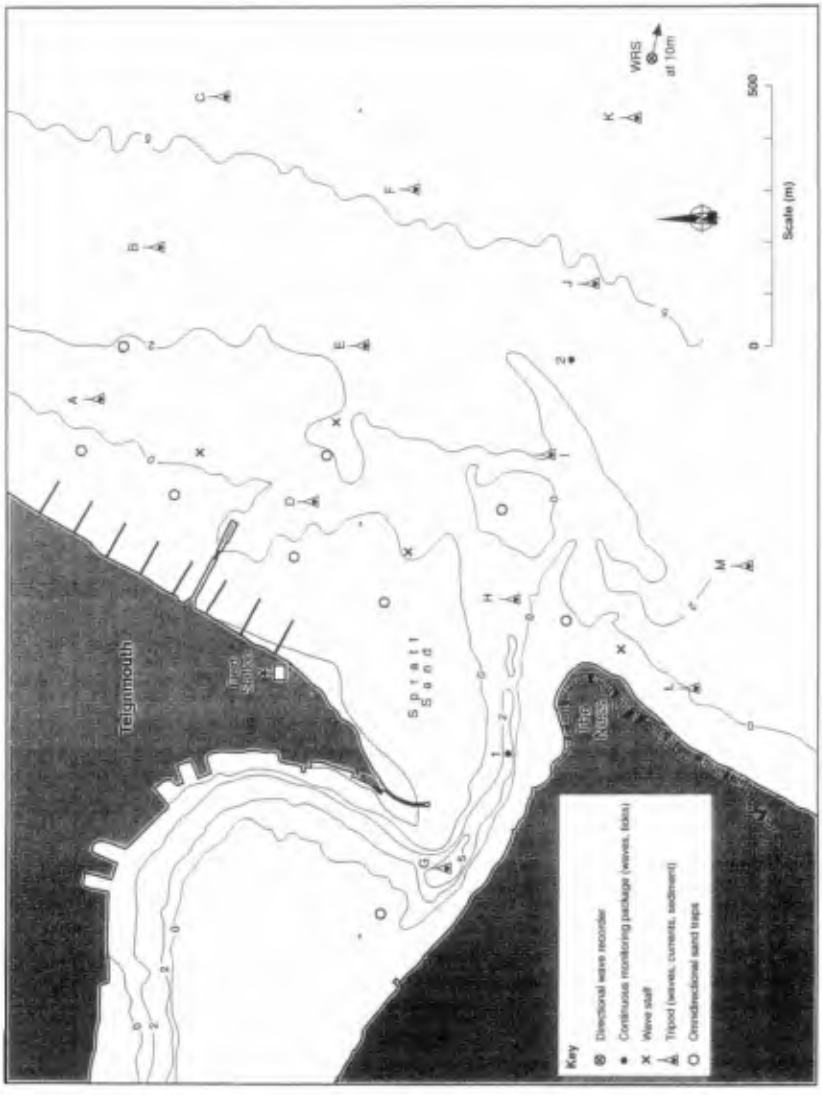

Figure 2. Schematic layout of instruments for Teignmouth experiment

strong three-dimensionality. A complicated re-curving spit is very active morphodynamically. This site, which additionally has a wide range of grain-sizes, will stretch the capabilities of present day coastal morphodynamic numerical models to their limits, and will provide a very exacting test of these and future models.

At each site a small number of permanent instruments will monitor conditions over at least 12 months. The main experimental work, however, will take place over an approximately 6 week period in the autumn (when beach conditions change most rapidly) at first the Dutch, and then the UK, site. The vast majority of the instruments are already owned by the partners, and will be deployed at both sites in succession, thereby making optimum use of the instruments, the logistics, the cooperative working practices, and the data management scheme. Instruments will be deployed in an array designed to meet the needs of numerical model evaluation, and to provide the more detailed process information. A pilot experiment of about two weeks duration will take place in the spring preceding each main experiment, to maximise the chances of success in the autumn.

The use of the innovative devices WESP and CRIS, which have been recently designed and constructed specifically for coastal experiments, is an important aspect of the implementation of the research programme. The WESP is a 10m high motorised tripod on wheels with a platform at the top supporting the engine and a cabin with facilities. Surveys can be conducted from the beach out to water depths of 6m in wave heights up to 2m (moderate storms). The WESP will tow a sledge (CRIS) carrying an intensive array of instruments wired in to the WESP cabin. This arrangement will ensure that the flow disturbance around the WESP does not influence the instruments.

The WESP is valuable for the collection of sand transport data, because it allows on-line measurements of short duration (30 min), and simultaneous collection of calibration samples by pumping systems. The availability of the WESP will allow a greater flexibility during the measurements by increasing the number of operational hours, by reducing ship time and the reaction time after an event and by deploying instruments at sites which are otherwise difficult to reach. The WESP will be used for measuring the 3-dimensional bathymetry of the nearshore zone, for placing and relocating instruments and for taking samples. The WESP can be dismantled to be able to carry it to various sites in Europe.

A crucial aspect of the experiments is the large number of instruments which will be deployed. In many ways this is what distinguishes COAST3D from previous field campaigns, and makes the resulting data-set of so much value for evaluating numerical models. Most of the instruments are already owned and used by the participants, and in many cases have been specially developed by them.

Modelling

A representative selection of numerical models of coastal hydrodynamics, sediment dynamics, and morphodynamics developed by the partners will be used at various stages throughout the project, most particularly for:

- preliminary runs to aid the design of the experiment. The models will be set up for the study area and run with representative inputs. Areas with strong spatial variations of the modelled parameters (waves, currents, sediment transport), and those areas where the models markedly disagree among themselves, will be identified for intensive instrumentation

- on-site modelling at a "modellers' week" midway through each experiment. Deficiencies in the experimental set-up can be remedied for the remainder of the experiment, and initial indications of the performance of the models obtained. The modellers' weeks will be open to modellers from outside the project to participate

- evaluation of the models after the full data validation, calibration and reduction. This will be the largest modelling effort, and will contribute towards the validation and accreditation of the models used.

The models used range from research models exploring the detailed physical processes (mainly at the universities) to fully operational models used routinely for consultancy applications (mainly at the hydraulic institutes).

Comparisons of the models with the data will be made in two distinct ways, by two distinct groups.

A diagnostic modelling group, made up of the university partners, will compare the measurements of individual physical processes with their representation by the models. It will identify: which models include the important processes, which of these give the best agreement with the data, how they can be improved, and how the improved algorithms can be included in the other models.

A practical modelling group, made up of the hydraulic institutes and regulatory authority partners, will test the overall capability of the models to reproduce the main trends in the data. They will address issues such as ease of setting up and driving the models, computational speed, stability and robustness, ease of plotting and interpreting results, as well as establishing an objective measure of "skill" in the models' performance against data. Best features will be further improved and included in all the models. Further, the group will decide on recommended procedures for the use of numerical models in coastal applications, and embody these in guidelines for use in coastal zone management.

Process Interpretation

The use of the data to further the understanding of the processes taking place in the coastal zone is every bit as important as the use for model validation. Accordingly, the experiments have been designed to accommodate both uses of the data.

For the 2.5D experiment one of the major questions which will be addressed is the growth, development and migration of nearshore bars in the surfzone and its impact on the behaviour of the coast, as well as the role of rip channels on bar behaviour. In many surfzones nearshore bars are the main morphological phenomena and their behaviour is still only partly understood and forms a good test case for the models. To measure the different processes and parameters a main cross-shore array of instruments will be installed covering the entire shoreface from a depth of about 20 m to the high tide levels on the beach. A number of instruments will be mounted to one side of the main line, to quantify the effects of rip channels on longshore nonuniformity (Figure 1).

For the 3D experiment the main emphasis is on the variations in the measured parameters in the two horizontal dimensions, particularly identifying horizontal circulation patterns of currents and sediments. A wide range of depths is necessary to identify the differing processes which re-distribute sediment in offshore areas and in the surf-zone. Some emphasis on the vertical distributions is also necessary. To measure the different processes and parameters a main array of instruments will be installed along intersecting cross-shore and longshore transects as shown schematically in Figure 2. Instruments will be located at the offshore and lateral boundaries of the studied region, to provide boundary conditions for the numerical models.

In both cases, it must be emphasised that the layout of instruments in the figures are schematic, and the exact layout will be determined by consultation between all the partners at an early stage of the project, after initial runs of the numerical models have been made.

Data Management and Availability

Good data management is a vital part of the project. A Data Management Group will oversee and specify:

- the synchronisation, record lengths and file formats of the logged data,
- the validation, calibration and basic analysis of the data,
- the design of a suitable data-base system,
- the storing of the data in the data-base,
- the public dissemination of the data through the Internet and CD-ROMs.

This will ensure uniformity of procedures between partners.

The data will be publicly available six months after the end of the project in two distinct forms:

(a) the complete data-set for study of physical processes,
(b) a condensed data-set of the basic variables for running and evaluating numerical models.

Coastal Zone Management

One of the most important products of the project is a set of tools and guidelines for practical coastal zone management (CZM). The production of these CZM tools will be guided particularly by the Rijkswaterstaat and Environment Agency partners, having regard to the following considerations.

Tools available to the coastal zone manager for solving problems are:

- data analysis
- measurement and monitoring
- (numerical) modelling.

Guidelines for using these tools should answer the following basic questions:

- WHEN to use,
- WHAT tools, and
- HOW to use these.

Answering the WHEN question first of all, requires an analysis of the CZM problem(s), leading to the definition of measurable:

- CZM objective(s), [eg maintenance of the coastline over a well defined length and for a well defined period of time],
- CZM parameter(s), [eg sand content of a well defined control volume],

and on this basis the definition of the most important

- temporal and spatial scale(s), and
- physical parameters.

Then, the answer to the question WHAT tools to use is depending on

- the availability of data,
- the possibilities for monitoring and measurements,
- the availability and (more important) the validity of numerical models, considering the spatial and temporal scales of interest.

Finally, the question HOW to use the tools may lead to guidelines for each individual tool, eg

- statistical analysis techniques (minimum data demands etc),
- monitoring and measurement schemes (parameters, instrumentation, frequency and spatial distribution, accuracy etc),
- methodology and procedures for applying individual numerical models.

For practical use however, it is just as important to develop guidelines on the combined use of the tools, answering:

- how to interpret measurement data,
- how to interpret model results, and
- how to draw conclusions in relation to the CZM problems.

Partners

The partners and contact names for further information are as follows:

Partner	Country	Contact	Email
HR Wallingford (Coordinator)	UK	RL Soulsby	rls@hrwallingford.co.uk
Univ. of Utrecht	NL	P Hoekstra	p.hoekstra@frw.ruu.nl
Rijkswaterstaat	NL	R Spanhoff	R.Spanhoff@rikz.rws.minvenw.nl
Delft Hydraulics	NL	LC van Rijn	Leo.vanRijn@wldelft.nl
Plymouth Univ.	UK	DA Huntley	D.Huntley@plymouth.ac.uk
Liverpool Univ.	UK	BA O'Connor	price@liverpool.ac.uk
Proudman O Lab	UK	P Thorne	pdt@pol.ac.uk
Université de Caen	FR	F Levoy	levoy@neptune.msh.unicaen.fr
CIIRC, Barcelona	ES	A S-Arcilla	arcilla@etseccpb.upc.es
MAGELAS	BE	J Lankneus	jean.lankneus@skynet.be
Environment Agency	UK	M W Owen c/o M Smalls	martin.smalls@environment-agency.gov.uk

Up to date news can be found on the project web-site:
http://www.hrwallingford.co.uk/projects/COAST3D

The EU responsible scientific officer is C. Fragakis (christos.fragakis@dg12.cec.be).

Conclusions

The COAST3D project will

- make measurements at two contrasting sites, one typical of 2.5D and one of 3D conditions

- store the data in a properly managed data-base, and make them publicly available in two forms:

  (a) the complete data-set for study of physical processes, and

  (b) a condensed data-set of the basic variables needed for running numerical models, to provide definitive test-cases against which present and future models can be evaluated

- interpret the data to provide an increased understanding of the physical processes operating in the coastal zone

- make an evaluation of a representative sample of present-day European morphodynamic numerical models, in terms of both their ability to represent individual processes (diagnostic), and their overall usability and performance (practical)

- present the models and methods in a form suitable for coastal zone management, for example by providing a series of guidelines.

Acknowledgements

The COAST3D project is funded partly by the European Commission's research programme MAST under Contract Number MAS3-CT97-0086, and partly through national funding from the UK Ministry of Agriculture, Fisheries and Food under research project FD0803, the UK Environment Agency's Research and Development programme, the UK Natural Environment Research Council, and the Netherlands Rijkswaterstaat. This paper is written on behalf of all the partners in the project. Much of the material in the paper was published previously by the European Commission, DG XII, Third European Marine Science and Technology Conference, Project Synopses Vol.II, 1998.

MODELLING OF A THREE-LAYER SEDIMENT TRANSPORT SYSTEM IN OSCILLATORY FLOW

Leszek M. Kaczmarek & Rafał Ostrowski[1]

Abstract

An extension of the bedload model of Kaczmarek & Ostrowski (1996), taking account of suspended sediment, is proposed for the calculation of sediment transport features, such as the transport rate and thickness. The paper is focused on the transition region (named as a contact load layer) between the outer region (suspension layer) and the bedload layer within the proposed three-layer sediment transport model.

Theoretical background

Formulation of the problem

A typical vertical distribution of velocity at a rough bed is supposed to be characterised by a sub-bottom flow and a main or outer flow, as shown in Fig. 1. The figure provides an explanatory drawing with velocities and concentrations. The collision-dominated granular-fluid region stretches below the nominal static bed while the wall-bounded turbulent fluid region extends above it. The outer region of pure suspension is characterised by very small concentration, where the process of sediment distribution may be considered as a convective and (or) diffusive process. In contrast, the granular-fluid region below the nominal bed is characterised by very high concentrations, where the intergranular resistance is predominant.

Since both water and grains are assumed to move in both regions, there must be a certain transition zone between these two regions, in which the velocity and stress profiles merge and preserve continuity of shape. The transition zone, called a contact load layer, is a central topic of the present study. The velocity profile in the contact load layer is assumed to be continuous. Its intersection with nominal seabed is the

[1] Snr. Research Associates, Polish Academy of Sciences' Institute of Hydro-Engineering *IBW PAN*, 7 Kościerska, 80-953 Gdańsk, Poland

apparent slip velocity u_b which can be identified as a characteristic velocity of sediment moving in the form of bedload. The downward extension of the velocity distribution in the outer zone of the main flow yields a fictitious slip velocity u_0 of the fluid at the nominal static bed level. Clearly, the fluid velocity u_0 is greater than the sediment velocity u_b.

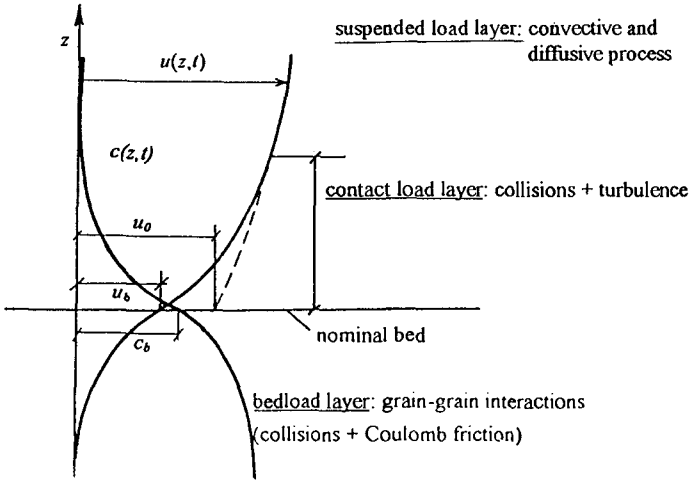

Fig. 1. Definition sketch

The above three-layer system of the momentum exchange has recently been observed in the measurements of concentrations carried out by Ribberink & Al-Salem (1995).

Physical bases

It is traditionally assumed, see for instance Wilson (1987), that the contact load layer consists of several layers of grains in motion, and in these layers the applied shear stress τ is resisted by the sum of a granular component τ_s and a fluid component τ_f. As demonstrated by Bagnold (1956), τ_s is associated with the intergranular stresses due to particle collisions. The sheared layer extends down to a certain level (say nominal bed) at which the intergranular resistance τ_s equals the applied shear stress τ. Further down towards the non-moving bed the intergranular resistance is predominant and it can be assumed that the particle interactions in the bedload layer produce two distinct types of behaviour. The particle collisions give rise to viscous-type stresses, while further down towards the non-moving bed, Coulomb friction between particles (which remain in contact with each other) give rise to plastic-type stresses.

Because the intergranular resistance is predominant in the bedload layer, it is postulated that the weight of moving sediment is transferred to the grain skeleton in the non-moving bed.

In contrast, the sediment in the contact load layer is transported partially as a bedload and partially as a suspended load. This means that the sediment is carried both by the dispersive stresses and by the fluid. When the suspended sediment is carried by

the fluid, its weight causes an increase in the pressure above the hydrostatic. Hence, it can not be assumed that the stress transferred to the bedload layer from the contact load layer corresponds exactly to the weight of the load. This was illustrated by Deigaard (1993) who considered a grain jumping in fluid.

Grain-grain-water interactions in the contact load layer are assumed to produce three distinct types of behaviour. The random motion of the sediment grains, which is the basis for the diffusion process, is caused by a combination of turbulence and the collisions between the grains in the contact load layer. These two effects give rise to skin friction τ'. Aside from the skin friction, a particle exposed to a turbulent flow will additionally feel a drag due to a pressure difference on the up- and downstream sides of the grain because of flow separation. Thus, the residual part of the total shear stress τ-τ' is carried as a drag on the moving bed particles. This drag gives rise to a convective sediment exchange rather than to turbulent diffusion.

The above shows that the two layers, e.g. bedload and contact load, differ considerably in momentum exchange. Hence, the interface between them, i.e. the level at which the intergranular resistance equals the applied total shear stress, can be expected as a very distinct one. This is supported by the recent measurements of concentration carried out by Ribberink & Al-Salem (1995). The detailed concentration measurements showed a three-layer system with a lower and upper sheet flow layer and a suspension layer. The lower and upper sheet flow layer can be identified as bedload and contact load layers, respectively. Sediment was picked up from the lower sheet flow layer at the two phases of maximum velocity during the wave cycle, resulting in two concentration dips in the lower sheet flow layer and two concentration peaks in the upper sheet flow layer.

Solution procedure

It is next proposed that the downward extension of the velocity distribution from the suspension layer to the bedload layer is described by the logarithmic distribution and is controlled by effective bed roughness k_e. The logarithmic velocity profile extrapolated from the suspension region is positioned at $z_0=k_e/30$, the height where the velocity profile approaches zero. Further, the flow at the top of the contact load layer is assumed to be unaffected by the transition phenomena.

These assumptions allow to solve the problem of nearbed sediment motion within two steps, schematically shown in Fig. 2. Within the first step, the problem is reduced to bedload transport (Fig. 2a) the solution of which was proposed in a series of papers by Kaczmarek et al. (1994), Kaczmarek et al. (1995) and Kaczmarek & Ostrowski (1996), who used a theoretical approach based on grain-grain interaction ideas in analogy to the flow of dry, cohesionless materials. The iterative procedure was employed to match the velocity and shear stress profiles in both regions (Fig. 2a) using a theoretical bed level for the outer wave-induced flow of δ_{sx}, which was taken as an arbitrary fraction of the thickness of the moving, collision-dominated bed layer δ_n.

The motion of sediment inside the contact load layer is proposed to be solved within the second step (Fig. 2b). In this case the problem is focused on finding of skin effective roughness k_e' with determination of the thickness δ_c of the contact load layer. As a boundary condition it is proposed to use the instantaneous (during wave period) sediment velocity $u_b(t)$ and concentration c_b (assumed to be constant and equal to 0.32) at the top of bedload layer, found from the bedload model with δ_{sx}/δ_n=0.50.

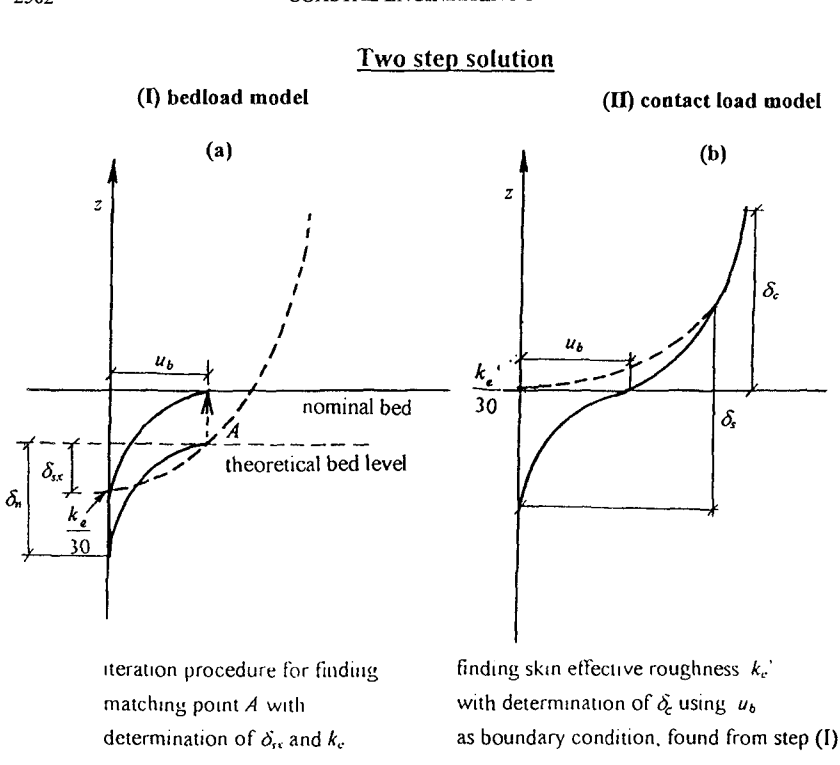

Fig. 2. Solution procedure

Basic equations and solution

Bedload layer

The bedload sediment transport model is based on a collision-dominant drag concept and uses a single parameter, δ_{sx}, to define the theoretical level of the top of the moving bedload layer in relation to the effective roughness height, k_e, of the above-bed wave-induced flow.

Previous comparison of model results with experimental data for sediment transport rates and thicknesses, presented by Kaczmarek et al. (1995) and Kaczmarek & Ostrowski (1996), had suggested a value of δ_{sx}/δ_n=0.5. The use of the single constant parameter δ_{sx}/δ_n=0.5 yields the effective roughness height decreasing with the increase of the grain roughness Shields parameter $\theta_{2.5}$, the definition of which is given by Nielsen (1992). This decreasing trend is related to the constant value of δ_{sx}/δ_n ratio kept for the entire range of $\theta_{2.5}$, see Fig. 3.

It is possible, however, to determine the variation of δ_{sx}/δ_n with $\theta_{2.5}$ (see Fig. 4) so that the model reproduces the variation in apparent roughness k_a observed by Nielsen (1992) for (artificially) flat beds, see Fig. 3.

Next, using the variable δ_{sx}/δ_n values, calculations were made to find bedload properties such as bedload thickness and transport rate. These calculations have been

carried out for a wide range of wave heights and for two sets of depth and period values, i.e. h=5 m, T=3.6 s and h=10 m, T=8.39 s, with grain diameter d=0.2 mm for both sets of parameters and additionally d=0.7 mm for the long-period data set. The results of computations shown in Fig. 5 reveal that the present approach with the fitting parameter k_e given by Nielsen (1992) provides a good approximation of bedload thickness $L_{B,max}$ for (artificially) flat beds at low flow intensities ($\theta_{2.5} \leq 0.4$). In the range of relative effective roughness values with $\theta_{2.5} > 0.4$ the theoretical results overestimate the experimental data. It seems that, for this range of $\theta_{2.5}$, the present approach with the fitting parameter k_e resulting from constant ratio δ_{sx}/δ_n=0.5, provides a better estimation of bedload thickness. The same conclusions can be drawn from the calculations of bedload rate carried out for both fixed and variable values of δ_{sx}/δ_n.

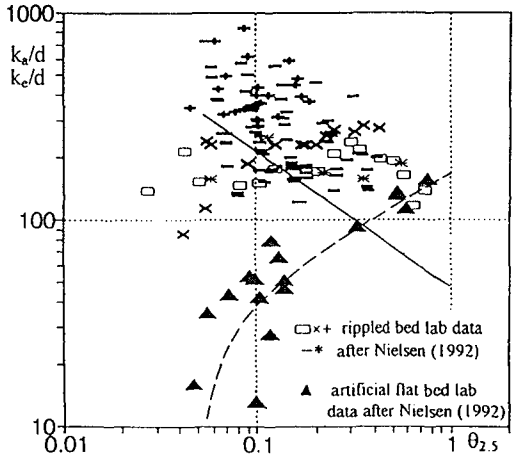

Fig. 3. Comparison of an apparent roughness found from friction and dissipation lab. data (k_a) with computed effective roughness (k_e) for δ_{sx}/δ_n=0.5 (solid line) and for variable δ_{sx}/δ_n (dashed line)

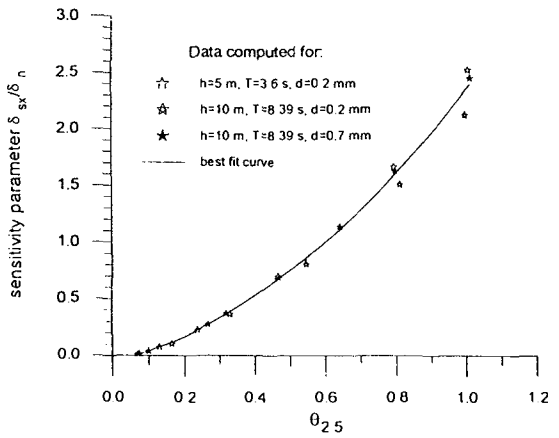

Fig. 4. Variation of sensitivity parameter δ_{sx}/δ_n with $\theta_{2.5}$

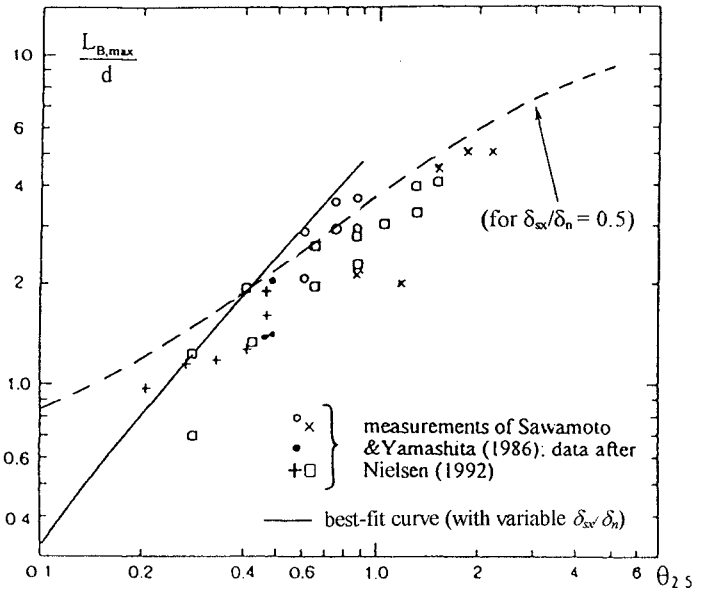

Fig. 5. Model bedload thickness $L_{B,max}$ (with variable δ_{sx}/δ_n) vs. lab. measurements of Sawamoto & Yamashita, data and definition of $L_{B,max}$ after Nielsen (1992)

Contact load layer

Following Fernández Luque's, after Fredsøe & Deigaard (1992), and Engelund & Fredsøe's (1976) ideas, the momentum transfer in the contact load layer can be described by the equation:

$$\tau = \overbrace{\tau_f + \tau_s}^{\tau'} + nF_D \qquad (1)$$

where F_D is the average drag on a single moving particle, while n is the number of moving particles per unit area.

It is assumed that the moving particles in the contact load layer reduce the fluid shear stress τ_f by exerting an average reaction force on the surrounding fluid. This reduction, however, is not so drastic as it is inside the bedload layer, where the intergranular resistance is predominant. Further, it is proposed that the velocity gradient inside the contact load layer is affected by the presence of sediment.

A new formulation for skin friction, which is considered as a combination of turbulence and the collisions between the grains, is proposed. A new model of sheet flow is developed, incorporating the diffusion concept presented by Deigaard (1993).

By assuming that the settling of sediment balances the vertical exchange, and that the momentum exchange balances the shear stress, Deigaard (1993) proposed two coupled differential equations to determine the mean concentration profile and the velocity profile:

$$\left[\frac{3}{2}\left(\alpha\frac{d}{w_s}\frac{du}{dz}\frac{2}{3}\frac{s+c_m}{c_d}+\beta\right)^2 d^2c^2(s+c_m)+l^2\right]\left(\frac{du}{dz}\right)^2 = u_f'^2 \tag{2}$$

$$\left[3\left(\alpha\frac{d}{w_s}\frac{du}{dz}\frac{2}{3}\frac{s+c_m}{c_d}+\beta\right)^2 d^2\frac{du}{dz}c+l^2\frac{du}{dz}\right]\frac{dc}{dz} = -w_s c \tag{3}$$

in which w_s denotes settling velocity of grains, s is a relative sediment density, c_m and c_d are the added mass and drag coefficients, respectively, and l is a mixing length defined as $l=\kappa z$.

In general, two coefficients α and β have to be determined, e.g. by calibration. For simplicity, equal values of α and β have been assumed in further considerations. The boundary conditions for these equations are that the sediment velocity u and concentration c are given at the top of bedload layer positioned in the model at $k_e'/30$. In the calculations the sediment concentration at $z=k_e'/30$ was assumed as 0.32 (in agreement with the bedload model). It was further assumed that $(s+c_m)=3.0$ and $c_d=1.0$.

It is still unclear how to evaluate the drag due to moving sand particles. It is possible, however, to overcome these difficulties making an additional assumption that the sediment velocity distribution in the contact load layer is controlled by the effective skin roughness k_e' and that the sediment velocity profile attains a logarithmic shape at a certain distance from the nominal bed. Making use of the above, sediment motion in the contact load layer is determined by Eqs. (2) and (3) and by the following relationship:

$$\tau' = \tau - nF_D = \rho u_f'^2 \tag{4}$$

in which u_f' is the skin friction velocity, proposed to be found using Fredsøe's (1984) integral momentum model with k_e' specified as a fixed constant value. Following Nielsen (1992) a value of $2.5d$ was adopted for the effective skin roughness k_e' of the moveable flat bed.

Knowing the instantaneous (during the wave period) skin shear stress $\rho u_f'^2(t)$ it is possible to calculate sediment concentration $c(z,t)$ and velocity $u(z,t)$ in the contact load layer using Eqs. (2) and (3) with the boundary conditions u_b (t) and c_b given at $z=k_e'/30$ from the bedload solution with $\delta_{sx}/\delta_n=0.50$. The proposed solution depends on the coefficient α $(=\beta)$. Making use of the fact that the velocity attains a logarithmic shape at a certain distance from the bed and that the roughness corresponding to this logarithmic profile depends on α, an iterative procedure is postulated to find α $(=\beta)$. The sought value of α $(=\beta)$ must provide the match of velocity profile yielded by Eqs. (2) and (3) with the logarithmic profile described by the skin friction parameters (k_e' and u_f'). The match is found at the moment corresponding to the maximum skin shear stress.

The model solution is restricted by a number of simplifying assumptions. Therefore, the determination of the layer thickness δ_c identified as the solution validity limit plays a very important role. The selection criterion for δ_c can be based on the degree of fit to experimental data comprising sediment concentrations and transport rate within the contact load layer. In the next section, two values for the upper limit of the contact load layer are tested against laboratory data, namely $\delta_l/4$ and $\delta_l/2$, where δ_l is the thickness of the bed boundary layer $\delta(t)$ calculated from Fredsøe's (1984)

model at the moment corresponding to maximum free stream velocity. The quantity $\delta_1/2$ can be identified as the conventional bottom boundary layer thickness while $\delta_1/4$ denotes upper limit of the region where the logarithmic velocity profile is observed.

Finally, it is worthwhile noting that the turbulence damping by the suspended particles is represented in the model by the following relationships:

$$\varepsilon_s = \beta_1 \cdot \varepsilon = \beta_1 \cdot \kappa \cdot u_f \cdot z \tag{5}$$

$$\varepsilon_s = \kappa \cdot z \cdot (\beta \cdot u_f) = \kappa \cdot z \cdot u_f' \tag{6}$$

in which ε_s is the mixing coefficient for solid material, κ is von Karman's constant (=0.4) and β_1 is a factor which, according to Deigaard, after Fredsøe & Deigaard (1992), is always smaller than the turbulent momentum exchange coefficient ε, with difference proportional to w_s/u_f.

Comparison with experimental data

Reference concentration and sheet flow layer thickness

The model has been run for two sets of water depth and wave period (h=10 m, T=8.39 s and h=5 m, T=3.6 s) and for the grain diameter d=0.2 mm. In addition, the first set of depth and period values has been run for the grain diameter d=0.7 mm. The wave height has been changed in each run so that a wide range of sediment transport intensities has been analysed. The model results for concentration at z=1.5d has been compared with the experimental data of Guy et al., as interpreted by Zyserman & Fredsøe (1994). The comparison, shown in Fig. 6, yields quite good agreement.

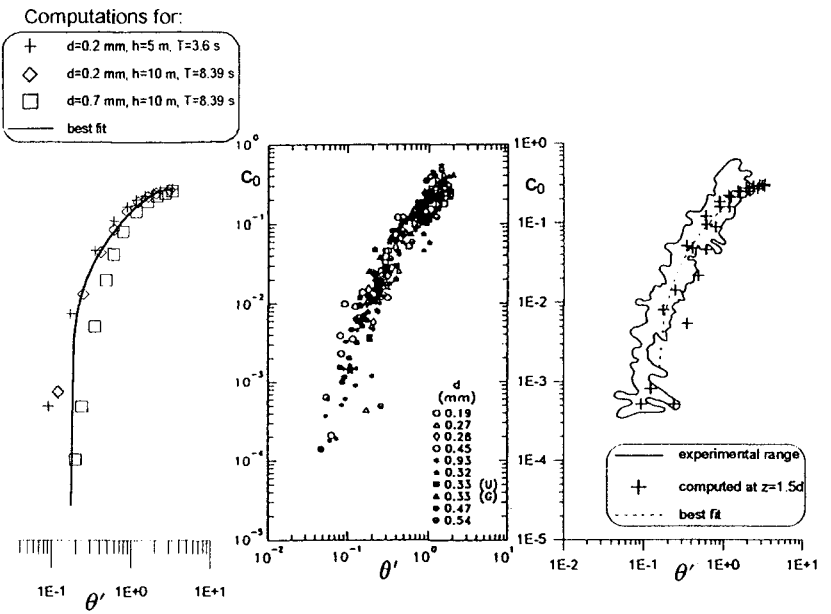

Fig. 6. Reference concentration c_0: model results vs. experimental data of Guy et al. as interpreted by Zyserman & Fredsøe (1994)

The same sets of computational parameters have been used in the modelling of the sheet flow layer thickness δ_s. The upper limit of this layer has been interpreted as the level at which the model result for velocity at the moment corresponding to the maximum skin shear stress attains the logarithmic velocity distribution with the accuracy of 99%. The distance between the above defined level and $z=k_e'/30$, summed up with the bedload layer thickness, yields the sheet flow layer thickness and is shown in Fig. 7 as a function of dimensionless maximum skin shear stress, i.e. $\theta'=u_f'^2/[(s-1)gd]$. It can be seen that the sheet flow layer thickness, even in very severe storm conditions, does not exceed 20 grain diameters. Good agreement between theoretical findings for the sheet flow layer thickness from the present model and the experimental data of Sumer et al. (1996) has also been found, see Fig. 7.

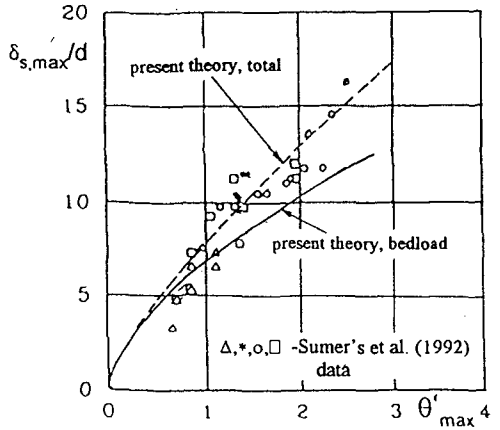

Fig. 7. Sheet flow layer thickness: model results vs. experimental data of Sumer et al. (1996)

Time-dependent and mean concentration

The data used in the present comparisons were obtained by Ribberink & Al-Salem (1994, 1995) for regular symmetric and asymmetric waves. The experiments were carried out in the Large Oscillating Water Tunnel (LOFT) at Delft Hydraulics. All the data were obtained above plane sand beds, corresponding to very vigorous conditions in nature, with median grain diameter $d=d_{50}=0.21$ mm. Suspended sediment concentrations were measured principally with an optical concentration meter (OPCON) while concentrations in the sheet flow layer were measured using a conductivity concentration meter (CCM), see Al-Salem (1993) for details.

In the comparisons discussed below the aim has been to compare the model predictions with emphasis on time-variation in sediment concentration $c(z,t)$ at different heights (z) above the bed. The data sets used for this purpose are the series „C" experiments: Conditions 1 and 2 for asymmetric waves, with $U_{rms}=0.6$ m/s, $T=6.5$ s and $U_{rms}=0.6$ m/s and $T=9.1$ s, respectively, and Condition 3 for sinusoidal wave, with $U_{rms}=1.2$ m/s and $T=7.2$ s.

In Fig. 8 the exemplary model predictions for Condition 2 are compared with time-varying sediment concentrations $c(z,t)$ measured at two representative ordinates with respect to the original bed level z=0 (i.e. the undisturbed bed level prior to the start of the experiment, identified as $z=k_s'/30$ in the model). The curve for z=-1 mm has been produced (for the time sectors in which the sediment movement occurs) using the bedload model while for z=+1 mm the concentration has been computed by the present contact load model. At both levels the prediction shows satisfactory agreement with the data. The concentration at z=0 is assumed as c_b=0.32=848 g/l (with grain density of 2650 kg/m^3).

At higher levels, however, the measured time series of $c(z,t)$ develops a more complicated structure, and agreement in phase between the model and the data is lost. The reason for the failure of the model to predict the phase angle of the time-dependent concentration is the appearance, at around the time of flow reversal in the free stream between wave crest and trough, of an additional peak in sediment concentration, identified by Davies et al. (1997) as a convection peak. Near the bed (roughly up to $z=\delta_1/4$) this peak is very small and the time series of concentration is dominated by the main diffusion peak associated with the maximum velocity, and hence maximum bed shear stress, during the wave cycle. With increasing height, the additional peak grows in relative importance, becoming larger than the diffusion peak and dominating the concentration time series.

Hence, the ordinate of $\delta_1/4$ (which corresponds to z=0.5 cm for Condition 2) determines the upper limit of the region where the phase agreement exists between the model and data concentrations. This value can be recommended as the upper boundary of the contact load layer for the purpose of net sediment transport calculations.

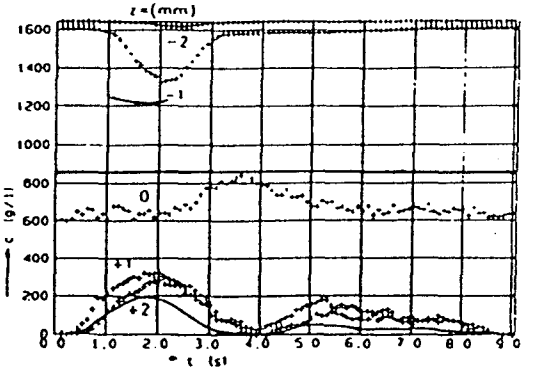

Fig. 8. Time-dependent concentrations: model results for z=-1, 0, +1 mm (solid lines) vs. measurements of Condition 2 (symbols), experimental data after Al-Salem (1993)

The model also provides reasonably accurate vertical profile of time-averaged concentration $\langle c \rangle$ up to the level of $\delta_1/2$, as shown in Fig. 9 for Condition 2 of Al-Salem's (1993) laboratory experiments.

Further evidence of good model predictions in the context of time-averaged concentration is depicted in Fig. 10 where the model results for z=1 cm are compared with experimental data of 10 wave series B and 3 series C of measurements of Ribberink & Al-Salem (1994, 1995).

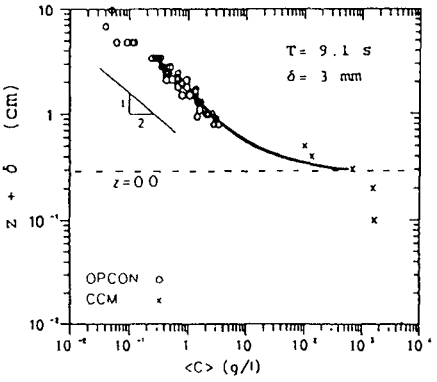

Fig. 9. Time-averaged concentration profiles: model results (solid line) vs. measurements of Condition 2 (symbols), experimental data after Al-Salem (1993)

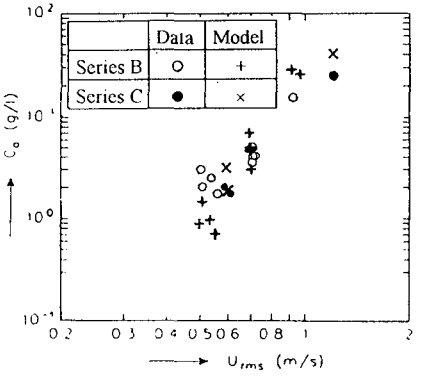

Fig. 10. Time-averaged concentrations at z=1 cm: model results ("+" and "×" for series B and C, respectively) vs. measurements ("o" and "•" for series B and C, respectively) of Ribberink & Al-Salem (1994, 1995)

Half-period averaged and net sediment transport

The same sets of computational parameters as used for determination of the sheet flow layer thickness has been assumed as the model input in the computations of sediment transport rate averaged over half wave period. In accordance to the discussion of the contact load layer thickness, the computations comprise the layer up to $\delta_1/2$. The model results can be presented as a function of $\theta_{2.5}$, the definition of which has been given by Nielsen (1992).

The model results are successfully compared in Fig. 11 with laboratory half-period sediment transport measurements. As one could have expected, for low shear stresses sediment transport consists mainly of bedload while for higher shear stresses it is dominated by suspended load. The contribution of suspended load is obviously bigger for fine sediments. It has been found out that this contribution at low shear stresses is a bit more pronounced for short wave period while at high shear stresses

suspended load is slightly bigger for long wave period. The above results from bigger values of maximum shear stress and - on the other hand - smaller values of δ_1 for short periods. The value of δ_1 plays more important role in the regime of suspended load, thus bigger suspended load contribution is achieved at high $\theta_{2.5}$ for long wave periods. Since the differences between long and short wave period results are not very significant, one approximation for long and short wave period, for d=0.2 mm, is given in Fig. 11.

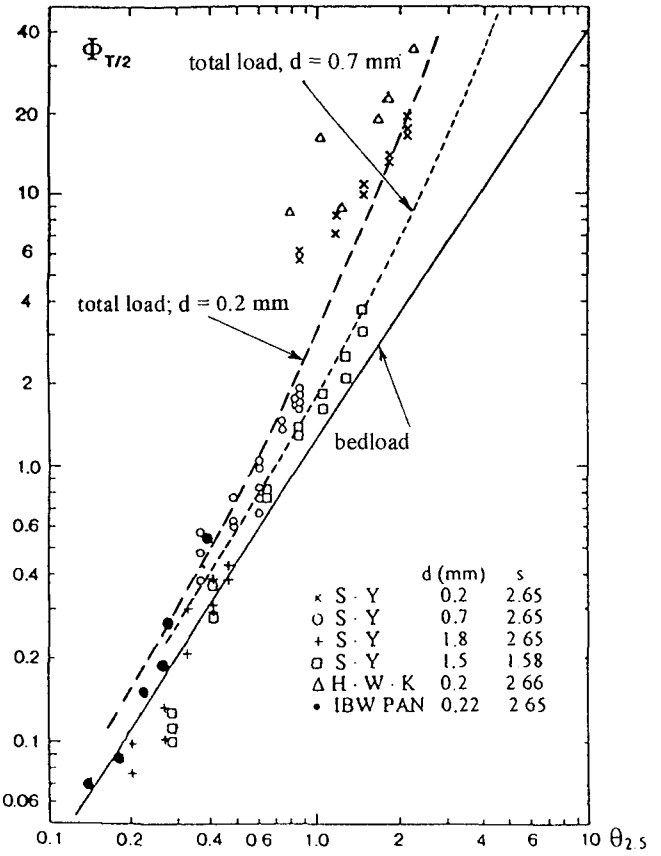

Fig. 11. Sediment transport rate averaged over half wave period model results vs. laboratory data of Sawamoto & Yamashita and Horikawa et al., definition of $\phi_{T/2}$ and experimental data as given by Nielsen (1992), and IBW PAN laboratory data

Finally, the comparison between predicted and observed net sediment transport rates for Ribberink & Al-Salem's (1994) experiments is presented in Fig. 12. Here, following the discussion on the upper validity limit for net transport determination, the computations have been carried out up to the level of z=δ_1/4 only. Except for one experiment, the compliance between calculated and measured values is good.

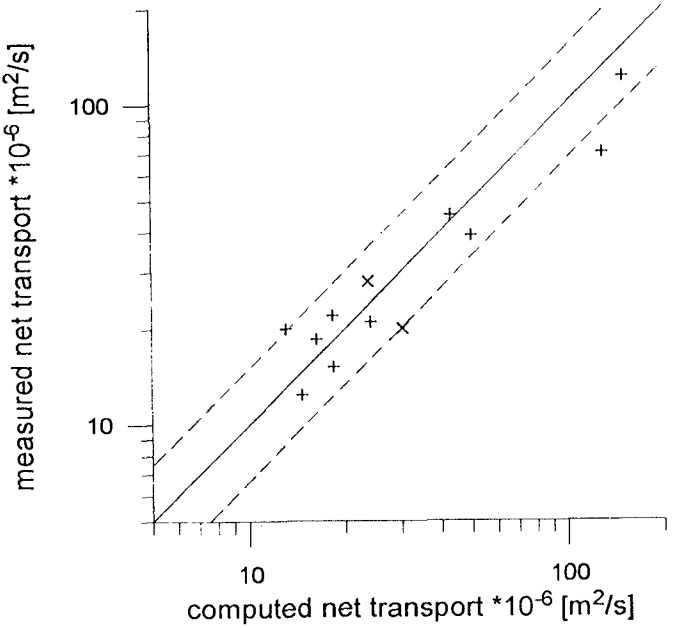

Fig. 12. Comparison between predicted and observed net sediment transport rates for 10 of Ribberink & Al-Salem's (1994) series B experiments ("+") and for 2 of the series C ("×"); the dashed lines indicate factor ±1.5

Conclusions

The contact load layer model, being an extension of the bedload model, is proposed for the calculation of sediment transport features, such as sheet flow layer thickness, sediment concentration and velocity distributions under sinusoidal and asymmetric waves. The bedload model is a basis of the proposed approach as it provides the boundary conditions for the solution of the contact load layer which makes use of the equations proposed by Deigaard (1993). The iterative procedure has been developed to determine two calibration coefficients, basically unknown in the Deigaard's (1993) proposal.

The comparisons made between the model results and available laboratory data in all analysed cases yield at least satisfactory agreement. Significant discrepancies between the model results and the experimental data, in the context of time-dependent concentrations, are found at higher levels of the contact load layer. They are most probably linked to convective events in flow reversal. Now, there is a need to carry out further studies in order to include the description of convective terms in the present model.

References

Al-Salem, A. (1993). Sediment transport in oscillatory boundary layers under sheet-flow conditions, *Ph.D. Thesis,* Delft Hydraulics.

Bagnold, R.A. (1956). The Flow of Cohesionless Grains in Fluids, *Phil. Trans. Roy. Soc.*, London, Ser. A, Vol. 249, 235-297.

Davies, A.G., J.S. Ribberink, A. Temperville & J.A. Zyserman (1997). Comparisons between sediment transport models and observations made in wave and current flows above plane beds, *Coastal Engineering* 31, 163-198.

Deigaard, R. (1993). Modelling of sheet flow: dispersion stresses vs. the diffusion concept, *Prog. Rep.* 74, Inst. Hydrodyn. and Hydraulic Eng., Tech. Univ. Denmark, 65-81.

Engelund, F. & J. Fredsøe (1976). A sediment transport model for straight alluvial channel, *Nordic Hydrology*, Vol. 7.

Fredsøe, J. (1984). Turbulent boundary layer in combined wave-current motion, *J. Hydraulic Eng.*, ASCE, Vol. 110, No. HY8, 1103-1120.

Fredsøe, J. & R. Deigaard (1992). Mechanics of coastal sediment transport, *Advanced Series on Ocean* Engineering, Vol. 3, World Scientific, Singapore..

Kaczmarek, L.M., J.M. Harris & B.A. O'Connor (1994). Modelling Moveable Bed Roughness and Friction for Spectral Waves, *Proceedings of 24th International Conference on Coastal Engineering*, ASCE, 300-314.

Kaczmarek, L.M., R. Ostrowski & R.B. Zeidler (1995). Boundary Layer Theory and Field Bedload, *Proc. International Conference on Coastal Research in Terms of Large Scale Experiments (Coastal Dynamics '95)*, ASCE, 664-675.

Kaczmarek, L.M. & R. Ostrowski (1996). Asymmetric and Irregular Wave Effects on Bedload: Theory versus Laboratory and Field Experiments, *Proc. 25th ICCE*, ASCE, 3467-3480.

Nielsen, P. (1992). Coastal bottom boundary layers and sediment transport. *Advanced Series on Ocean* Engineering, Vol. 4, World Scientific, Singapore.

Ribberink, J.S. & A. Al-Salem (1994). Sediment transport in oscillatory boundary layers in cases of rippled beds and sheet flow, *Journal Geoph. Res.*, Vol. 99, No. C6, 12,707-12,727.

Ribberink, J.S. & A. Al-Salem (1995). Sheet flow and suspension of sand in oscillatory boundary layers, *Coastal Engineering*, No. 25, 205-225.

Sumer, B.M., A. Kozakiewicz, J. Fredsøe & R. Deigaard (1996). Velocity and concentration profiles in sheet-flow layer of movable bed, *J. Hydraulic Eng.*, Vol. 122, No. 10.

Wilson, K.C. (1987). Analysis of Bed-Load Motion at High Shear Stress, *J. Hydraulic Eng.*, Vol. 113, No. 1, 97-103

Zyserman, J.A. & J. Fredsøe (1994). Data analysis of bed concentration of suspended sediment, *J. Hydraul. Res.*, Vol. 120, No. 9, 1021-1042.

Acknowledgements

This study contributes to the research project *INDIA* carried out under the EU Environment and Marine Science and Technology (MAST III) programme and is sponsored by KBN, Poland, under SPUB and programme 2 *IBW PAN*.

Analytical model for wave-related transport

Judith Bosboom[1,2], Gert Klopman[3,2], Ad Reniers[1,2], Marcel J.F. Stive[1,2]

Abstract

A computationally efficient, analytical model to determine net sediment transport rates in oscillatory flow is presented. The model is based on (approximate) analytical solutions to the 1DV momentum and advection-diffusion equations and on the subsequent analytical integration of the sediment flux over time and depth. The model is validated against measurements of sediment concentrations and net transport rates performed in WL|DELFT HYDRAULICS' Large Oscillating Water Tunnel (LOWT). Further, comparisons are made with the predictions of numerical 1DV models and sediment transport formulae. The model gives accurate estimates of the net transport rates for medium sand. For finer sand, although qualitatively correct, the model fails to predict the strong offshore sediment transport rates at higher velocities, mainly due to limitations of the diffusion approach for the upward transport of sediment.

Introduction

A variety of concepts is used in morphodynamic models to describe the wave-related transport, i.e. the transport related to the correlation between sediment concentration and long wave motions as well as to wave asymmetry and time lag effects between wave orbital velocity and concentration within the wave cycle.

In quasi-steady models, instantaneous adaptation of the concentration to the time-varying near-bed velocity (or bed shear stress) is assumed such that the total load is directly related to some power of the instantaneous velocity. Assuming in addition that the velocity profile is reasonably uniform over the vertical, the vertically integrated flux can be schematised as the product of the velocity at some reference level and the total load, typically resulting in a formula in which the transport is proportional to some power of the instantaneous velocity, e.g. the Bagnold model (Bowen, 1980; Bailard, 1981). Although the neglect of phase-lag effects between velocity and concentration is potentially inaccurate, quasi-steady formulae are popular amongst morphodynamic modellers thanks to their simplicity and possibility to combine processes acting on different time-scales.

Experiments of Ribberink and Chen (1993) and Janssen et al. (1996) demonstrate that in asymmetric oscillatory sheet flow conditions, the net transport rates for fine sand decrease for increasing oscillatory velocities and ultimately even reverse. In contrast with the Bailard formula, the semi-unsteady formulation according to Dibajnia and Watanabe (1992)

[1] WL|DELFT HYDRAULICS (mailing adress), P.O. Box 177, 2600 MH Delft, The Netherlands. Judith.Bosboom@wldelft.nl

[2] Netherlands Centre for Coastal Research (NCK), Department of Civil Engineering and Geosciences, Delft University of Technology, Delft, The Netherlands

[3] Albatros Flow Research, P.O. Box 85, 8325 ZH Vollenhove, The Netherlands

qualitatively reproduces these unsteady effects (Janssen et al., 1996). The latter formulation combines an essentially quasi-steady approach with a schematised time lag effect. It was found that for coarse sand the results obtained with both formulae are almost identical.

A more general modelling approach requires the intra-wave-period modelling of the velocity and concentration fields using for instance 1DV models (e.g. Fredsøe et al., 1985; Davies et al., 1997). The direct use of such a detailed intra-wave transport model in a morphodynamic model is time-consuming from a computational point of view, especially when used to study the effects of irregularity of the waves and wave groups. This disadvantage is partly removed by making an initial effort of tabulating the results of the intra-wave model for a specific situation, after which the morphodynamic model is run at relatively low costs (Rakha et al., 1997). An alternative way to reduce the computational costs is to apply (semi-) analytical methods to account for the intra-wave effects on the net transport rates while still capturing the essential features of the unsteady transport, i.e. the strong vertical gradients in the near-bottom time-varying flow and concentration including the non-instantaneous response of the sediment.

The purpose of this work is to present an analytical model based on the equations underlying the 1DV unsteady models. By finding (approximate) analytical solutions for the oscillatory velocity $\tilde{u}(z,t)$ and the oscillatory concentration $\tilde{c}(z,t)$ in the near-bed wave boundary layer and analytically integrating over time and depth, the net transport rate $q_{wave} = \frac{1}{t_2-t_1}\int_{t_1}^{t_2}\int_z \tilde{u}\tilde{c}\,\mathrm{d}z\mathrm{d}t$ as a function of the depth is obtained. A similar approach has been taken by Nielsen (1988), who however assumes a depth-invariant oscillatory velocity, therewith neglecting one of the essential features, viz. the strong vertical variation of the oscillatory velocity close to the bed.

The oscillatory boundary layer structure is taken into account by using an (approximate) analytical solution to the wave boundary layer momentum equation using a time-invariant eddy viscosity approach. For the computation of the bed shear stress, the time-variation of the eddy viscosity is accounted for. The time- and depth-dependency of the concentration field is resolved by analytically solving the advection-diffusion equation using a time-invariant sediment diffusivity and a bottom boundary condition which is a function of the instantaneous bed shear stress. In this way we expect to account for the majority of the transport near the bed; the bed load transport is assumed to be small as compared to the suspended load contribution.

Although in principle the model can be applied for an arbitrary input series of the oscillatory near-bed velocity, the validation of the model as presented in this paper focuses on second order Stokes conditions in the absence of a mean current. Measurements in WL|DELFT HYDRAULICS' Large Oscillating Water Tunnel (LOWT) by Ribberink and Al-Salem (1994) and Ribberink and Chen (1993) are used for model validation. In addition, comparisons are made with 1DV numerical models and the transport formulae of Bailard (1981) and Dibajnia and Watanabe (1992).

Oscillatory boundary layer model

Equation of motion and boundary conditions

After Reynolds-averaging, the wave boundary layer approximation to the momentum equation, for a rough, fully turbulent wave boundary layer flow, reads:

$$\frac{\partial u - u_\infty}{\partial t} = \frac{\partial u_d}{\partial t} = -\frac{\partial \langle u'w' \rangle}{\partial z}, \tag{1}$$

in which $u = u(z,t)$ is the Reynolds-averaged horizontal velocity, $u_\infty = u_\infty(t)$ the free stream velocity outside the boundary layer and $u_d = u - u_\infty$ the deficit velocity. Note that only a

purely oscillatory motion is considered in this paper. Further, $-\langle u'w' \rangle = \tau_{zx}/\rho$ is the Reynolds shear stress representing the vertical flux of fluid momentum. Here ρ is the fluid density, u' and w' are the instantaneous velocity fluctuations in horizontal and vertical direction respectively, and the brackets denote averaging over the turbulence time-scale.

The turbulence fluxes are modelled according to the Boussinesq hypothesis as:

$$-\langle u'w' \rangle = \nu_{t,f} \frac{\partial u}{\partial z}, \tag{2}$$

where $\nu_{t,f}$ is the eddy viscosity or turbulence eddy diffusivity of fluid momentum which we assume is not influenced by the presence of suspended sediment.

The wave boundary layer equation (1) is solved subject to the no-slip boundary condition and the boundary condition of the wave velocity approaching the quasi-constant $(\partial/\partial z \approx 0)$ velocity prescribed by e.g. an irrotational theory at the edge of the wave boundary layer:

$$\begin{aligned} &u = 0 \qquad \text{at} \qquad z = z_0 = \frac{k_n}{30}; \\ &u \to u_\infty \ \text{for} \qquad z \to \infty, \end{aligned} \tag{3}$$

where z_0 is the effective position of the bottom depending on the equivalent Nikuradse sand grain roughness k_n and where ∞ implies a distance far from the bed compared to the boundary layer thickness, but close to the bed compared to the water depth.

Eddy viscosity model

Using the Prandtl mixing-length hypothesis and assuming that in the immediate vicinity of the bed the mixing length l is proportional to the distance above the bottom, $l = \kappa z$, yields for the bed shear stress:

$$\tau_b(t) = \lim_{z \to 0} \left(\rho (kz)^2 \left| \frac{\partial u}{\partial z} \right| \frac{\partial u}{\partial z} \right) \tag{4}$$

Using the Boussinesq hypothesis and realising that $\tau_b(t) = \rho |u_*(t)| u_*(t)$ gives for the eddy viscosity close to the bed $\nu_{t,n} = \kappa |u_*| z$. Trowbridge and Madsen (1984) demonstrated that the solution to the wave boundary layer equation (1) depends only slightly on time variation in the eddy viscosity and is more sensitive to a proper treatment of the vertical distribution; the third harmonic of the velocity, present in the velocity field due the time-varying nature of the eddy viscosity, was found to be only a few percent of the first harmonic. In order to avoid the complex mathematics involved when using a time-varying eddy viscosity, the eddy viscosity close to the bed can be simplified by replacing $|u_*|$ by a characteristic constant $u_{*,\mathrm{char}}$.

On the contrary, the third harmonic of the bed shear stress was found to be 20-25% of the first harmonic. The lack of higher harmonics in the predictions of a linear model with time-invariant eddy viscosity may significantly underestimate the asymmetry of the bed shear stress and therewith the asymmetry in sediment concentrations and transport. For that reason, in the determination of the bed shear stress a time-variant eddy viscosity will be used as will be addressed later.

Based on the above considerations, for the determination of analytical solutions to Equation (1), the viscosity close to the bed is often taken to increase linearly away from the

bed. Grant and Madsen (1979) used $\nu_{t,f} = \kappa u_{*,\max} z$ over the entire wave boundary layer thickness where $\kappa = 0.4$ is the von Karman's constant and $u_{*,\max}$ is the maximum bed friction velocity which is related to the maximum bed shear stress $\tau_{b,\max}$ via $u_{*,\max} = \sqrt{\tau_{b,\max}/\rho}$. A two layer model was used by Brevik (1981) who combined the Grant and Madsen model close to the bed with a constant eddy viscosity in the outer layer. The two-layer concept is adopted here since it provides the best compromise between accuracy and simplicity; the constant eddy viscosity in the outer layer is not only more realistic than a linearly increasing eddy viscosity but results in simple analytical solutions as well, whereas close to the bed the linearly increasing eddy viscosity is essential for a good representation of velocity and shear stress. The following two-layer model is used:

$$\begin{aligned} \nu_{t,f} &= \kappa u_{*,\mathrm{char}} z \qquad && z_0 < z \le \delta, \\ \nu_{t,f} &= \kappa u_{*,\mathrm{char}} \delta \qquad && \delta < z, \end{aligned} \tag{5}$$

in which the transition level δ between the two profiles is modelled as:

$$\delta = m \frac{\kappa u_{*,\mathrm{char}}}{\omega}, \tag{6}$$

where ω is the wave cyclic frequency and $u_{*,\mathrm{char}}$ is a characteristic time-invariant shear velocity representing the time-variant turbulence level in the flow. The choices for the characteristic shear velocity and the coefficient m are discussed later. Note that δ directly determines the magnitude of the eddy viscosity in the relatively large outer layer.

Oscillatory velocity solution

Analytical solutions to (1) using the above specified two-layer eddy viscosity profile (5) are in terms of simple exponential functions of z in the outer layer where a height-invariant viscosity is assumed. In the lower layer however, the linearly varying viscosity results in an analytical solution in terms of Kelvin function of zeroth order (e.g. Grant and Madsen, 1979; Brevik, 1981), which are not only time-consuming from a computational point of view but complicate the depth-integration of the sediment fluxes. For small values of $z\omega/\kappa u_{*,\mathrm{char}}$ and $z_0\omega/\kappa u_{*,\mathrm{char}}$ or equivalently close to the bottom and for large values of a_∞/k_b, asymptotic expressions for the zeroth order Kelvin functions may be used to simplify the velocity profile. These assumptions result in a logarithmic velocity profile and a depth-invariant shear stress and were seen to be valid up to $z = \frac{1}{10}\kappa u_{*,\mathrm{char}}/\omega$. Here we use the equivalent assumption that the shear stress is constant to obtain the velocity profile in the lower layer.

Inserting Equation (2) in (1), using the constant stress assumption in the lower layer and the viscosity profile defined by (5), results in the following set of equations:

$$\begin{aligned} \frac{\partial}{\partial z} \kappa u_{*,\mathrm{char}} z \frac{\partial u}{\partial z} &= 0 \qquad && z_0 < z \le \delta, \\ \frac{\partial u - u_\infty}{\partial t} &= \kappa u_{*,\mathrm{char}} \delta \frac{\partial^2 u}{\partial z^2} \qquad && \delta < z, \end{aligned} \tag{7}$$

In addition to the two boundary conditions (3), we require the velocity and the velocity gradient to be continuous at the transition level δ between lower and outer layer.

Solving the momentum equations (7) proceeds assuming a harmonie time-dependent wave motion specified by its near-bottom velocity:

$$u_\infty(t) = \sum_{n=1}^{n=N} U_{\infty,n} e^{i\omega_n t} + c.c., \tag{8}$$

where $\omega_n = 2\pi/T_n$ is the angular frequency, T_n the harmonic period, N the number of components under consideration, and $i = \sqrt{-1}$. Note that the coefficients $U_{\infty,n}$ are complex which means that phase differences may exist between the various harmonics in the near-bottom velocity and that *c.c.* denotes the complex conjugates to the terms in the series since the resulting quantities must be real-valued.

The complete solution for the velocity profile in the wave boundary layer as a function of time becomes in the lower layer ($z_0 < z \le \delta$):

$$u(z,t) = \frac{\ln\frac{z}{z_0}}{\ln\frac{\delta}{z_0}} \sum_{n=1}^{n=N} U_n(\delta) e^{i\omega_n t} + c.c. = \ln\frac{z}{z_0} \sum_{n=1}^{n=N} \frac{2U_{\infty,n}}{\left[2\ln\frac{\delta}{z_0} + \frac{\delta}{\delta_n}(1-i)\right]} e^{i\omega_n t} + c.c \tag{9}$$

and in the outer layer ($z < \delta$):

$$u(z,t) = \sum_{n=1}^{n=N} \left[U_{\infty,n} + \left\{U_n(\delta) - U_{\infty,n}\right\} e^{-(1+i)\frac{z-\delta}{\delta_n}} \right] e^{i\omega_n t} + c.c \tag{10}$$

where:

$$\delta_n = \sqrt{\frac{2\kappa u_{*,\mathrm{char}}\delta}{\omega_n}} \tag{11}$$

Comparison of velocity predictions of analytical and numerical model

The velocity predictions were compared with the results of the IDV NEREUS wave boundary layer model (Klopman, see Ribberink and Al-Salem, 1995) in which a mixing length approach (see previous section) is used to derive a time-varying eddy viscosity. For the coefficient m and the characteristic shear velocity $u_{*,\mathrm{char}}$ in Equation (11) we used $m = 1/4$ and $u_{*,\mathrm{char}} = u_{*,\mathrm{mean}}$ based on representation of the mean bed shear stress. For a purely sinusoidal shear velocity, we would have $u_{*,\mathrm{mean}} = 1/\sqrt{2}\, u_{*,\mathrm{max}}$. Generally, the characteristic shear velocity $u_{*,\mathrm{char}}$ is chosen to represent the maximum bed shear stress ($u_{*,\mathrm{char}} = u_{*,\mathrm{max}}$) in order to avoid underestimation of the eddy viscosity during the high-velocity portion of the wave cycle when most of the turbulence is generated (Grant and Madsen, 1979). For the predictions of the maximum velocity profile however, we found that $u_{*,\mathrm{char}} = u_{*,\mathrm{mean}}$ gave the best results in the analytical model. The coefficient m can be expected to be in the range of $1/10$ to $1/4$. The value of $1/8$ corresponds to Kajiura's (1964) transition level to the outer layer, whereas the value of $1/4$ corresponds to the optimal level as found by Brevik (1981) which is half the boundary thickness as defined by Jonsson and Carlsen (1976). The latter value of $m = 1/4$ is adopted here as the standard value for m and has been applied in all computations shown in this paper. Somewhat better velocity predictions can be obtained using a smaller

value for m. Note that the assumption of constant shear stress can formally not be expected to be valid up above $z = 1/10\,\kappa u_{*,\mathrm{char}}/\omega$.

A second order Stokes condition is used in the comparison corresponding to the conditions of LOWT test C1 (see Table 1). We determine $u_{*,\max} = \sqrt{f_w/2}\hat{u}_1$ using Swart's (1974) explicit approximation for the wave friction factor to Jonsson's implicit, semi-empirical formula. The influence of the use of $\hat{u}_1$, the amplitude of the first harmonic, rather than the root-mean-square velocity was negligible and more appropriate in the wave tunnel situation used in the net transport model validation.

Figure 1 shows the velocity at different phases with zero phase corresponding to the maximum 'onshore' velocity as well as the amplitudes of the two harmonic components and the root-mean-square velocity. It can be seen that the predictions of the velocity amplitudes by the analytical model are somewhat smaller than the NEREUS predictions. The velocity predictions with the analytical model are quite reasonable, especially when considering the use of this velocity profile for sediment transport predictions.

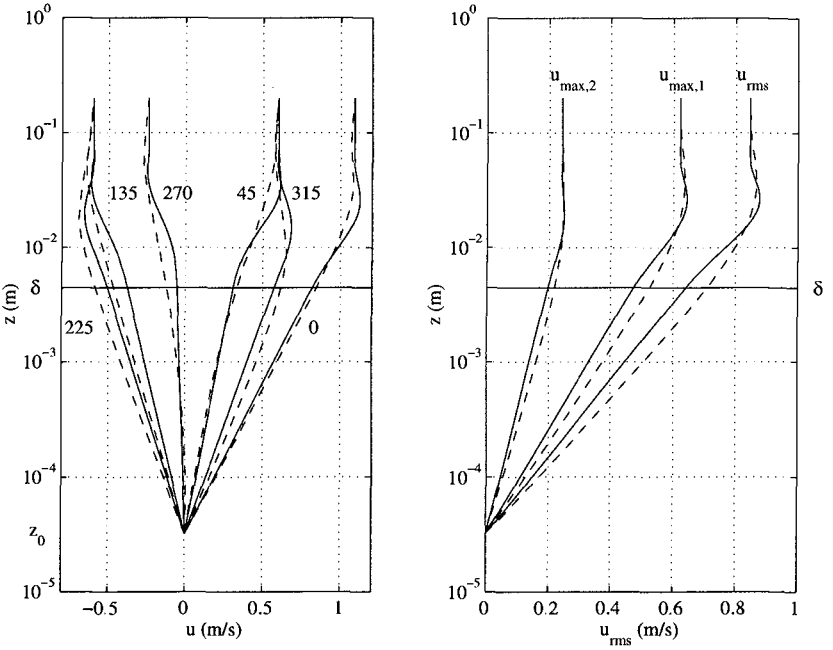

Figure 1 Velocity predictions at different phases and velocity amplitudes (NEREUS dashed lines; analytical model drawn lines). Conditions correspond to test C1 (see Table 1)

Bed shear stress

The bed shear stress resulting from the time-invariant eddy viscosity model is given by:

$$\tau_{b,1} = \lim_{z\to 0}\left(\rho\kappa u_{*,\mathrm{char}} z\frac{\partial u}{\partial z}\right) = \rho\kappa u_{*,\mathrm{char}}\frac{1}{\ln\dfrac{\delta}{z_0}}\sum_{n=1}^{n=N} U_n(\delta)e^{i\omega_n t} + c.c., \qquad (12)$$

from which it can be seen that a linear model with a time-invariant eddy viscosity is obviously not able to predict any higher harmonics in the shear stress field. By choosing $u_{*,\mathrm{char}} = u_{*,\max}$ in a time-invariant model, the maximum bed shear stress can be predicted quite accurately. Trowbridge and Madsen (1984) suggested that a simple way to reproduce in a theoretical model the potentially important third harmonic of the bed shear stress while ignoring the small third harmonic of the velocity would be to compute the velocity field by using a time-invariant eddy viscosity and then compute the bed shear stress by combining the velocity prediction with a time-varying eddy viscosity proportional to a shear velocity based on the instantaneous bed shear stress predicted by the time-invariant model.

This concept is adopted by using the bed shear stress definition (4) which corresponds to a time-variant eddy viscosity model:

$$\tau_{b,2} = \lim_{z\to 0}\left(\rho\kappa|u_*(t)|z\frac{\partial u}{\partial z}\right) = \lim_{z\to 0}\left(\rho(\kappa z)^2\left|\frac{\partial u}{\partial z}\right|\frac{\partial u}{\partial z}\right) = \rho\frac{\kappa^2}{\left(\ln\frac{\delta}{z_0}\right)^2}|u(\delta,t)|u(\delta,t), \tag{13}$$

in which the velocity field is obtained using the time-invariant eddy viscosity model (see Equation (9)).

Comparison of shear stress predictions of analytical and numerical model

Figure 2 shows the bed shear stress for both the time-variant and time-invariant eddy viscosity model using $\delta = \frac{1}{4}\kappa u_{*,\mathrm{mean}}/\omega$ as well as $\delta = \frac{1}{8}\kappa u_{*,\max}/\omega$ in comparison with the bed shear stress as computed by NEREUS.

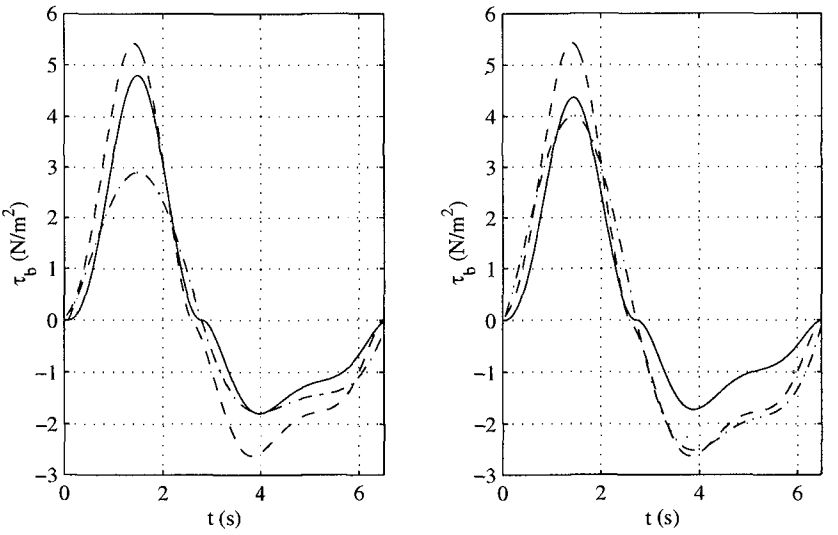

Figure 2 Comparison of bed shear stress for $\delta = \frac{1}{4}\kappa u_{*,\mathrm{mean}}/\omega$ (left) and $\delta = \frac{1}{8}\kappa u_{*,\max}/\omega$ (right) for NEREUS (dashed), time-invariant model (dashed-dot) and time-variant model (drawn)

From Figure 2, it can be seen that for the predictions of the linear model with the time-invariant eddy viscosity, the maximum shear velocity must be used to adequately predict the shear stress amplitude. This could be expected since the shear stress in the linear model is directly proportional to the characteristic shear velocity $u_{*,\mathrm{char}}$, whereas the velocity gradient is less sensitive to the value of $u_{*,\mathrm{char}}$. The predictions using the time-variant model, which are governed by the velocity gradient, are relatively insensitive to $u_{*,\mathrm{char}}$. The most important feature in the predictions of the time-invariant model, is the presence of third and higher harmonics such that the asymmetry of the bed shear stress is in better accordance with NEREUS than the relatively symmetrical bed shear stress as predicted using the time-invariant model. This was found to be extremely important to predict the asymmetry in the sediment concentration at the bed.

Sediment concentration model

Advection-diffusion equation

Conservation of mass is applied to the sediment and the resulting equation is Reynolds averaged. Assuming that the Reynolds averaged vertical water velocity is negligible compared to the fall velocity of the sediment, using the boundary layer approximation and introducing the mass balance for the fluid, yields:

$$\frac{\partial c}{\partial t} + w_s \frac{\partial c}{\partial z} + \frac{\partial \langle c'w' \rangle}{\partial z} = 0, \tag{14}$$

in which c denotes the turbulence averaged concentration, w_s the particle fall velocity (assumed constant) and $-\langle c'w' \rangle$ the turbulence upward sediment flux, where the brackets denote averaging over the turbulence time-scale. In order to model the turbulence sediment flux, we make the assumption of upward transport due to turbulence diffusion as for the fluid, see Equation (2):

$$-\langle c'w' \rangle = \rho \nu_{t,s} \frac{\partial c}{\partial z} \tag{15}$$

in which $\nu_{t,s}$ is the turbulence diffusivity of sediment mass.

The solution to Equation (14) requires two boundary conditions in z. At the water surface the vertical flux is zero which due to the limited extent of the wave boundary layer is normally equivalent to $c \to 0$ for $z \to \infty$. The second boundary condition is related to the bed concentration of the suspended sediment taken at a specified level above the mean bed level. Here we use the reference concentration of Zyserman and Fredsøe (1994) which has the advantage of an upper cut-off for the sediment concentration at large values of the bed shear stress. The sediment concentration is prescribed at a reference level $z_a = 2D_{50}$:

$$c(z_a, t) = c_b(t), \tag{16}$$

Besides, we apply the above boundary condition as a pick-up type boundary condition in which it is the upward diffusive flux from the bed $-\nu_{t,s}\,\partial c/\partial z$ and therefore the concentration gradient rather than the concentration itself which is prescribed:

$$\left(\frac{\partial c}{\partial z}\right)_{z=z_a} = -\frac{w_s}{(\nu_{t,s})_{z=z_a}} c_b(t) \tag{17}$$

Diffusivity model

The diffusivity of sediment mass is in principle assumed to follow the same distribution as the diffusivity of fluid momentum, Equations (5). The exact solution in case of a linearly varying diffusivity in the lower layer is in terms of higher order Kelvin functions (Smith, 1977) which are time-consuming to compute and not easily approximated. Therefore, a representative constant diffusivity in the lower layer is used which is determined by requiring the mean concentration at $z = \delta$ to be equal to the mean concentration when using the linearly varying diffusivity. We now have:

$$\begin{aligned} \nu_{t,s} &= \nu_{t,s,1} = \beta \kappa u_{*,\mathrm{char}} \delta \qquad && z_0 < z \le \delta \\ \nu_{t,s} &= \nu_{t,s,2} = \kappa u_{*,\mathrm{char}} \delta \qquad && \delta < z \end{aligned} \tag{18}$$

in which β follows from the above requirement.

In addition, we allow the settling velocity to be different in the two layers. In the lower layer we have $w_s = w_{s,1}$ which is taken as the settling velocity corresponding to the D_{50} of the bed material. In the outer layer, the settling velocity $w_s = w_{s,2}$ can be expected to be smaller, corresponding to $0.7 D_{50} - 0.9 D_{50}$.

Solution

Solving the advection-diffusion equation (14) proceeds assuming a harmonic time-dependent wave motion specified and using complex variables. The general solution in case of a constant diffusivity reads:

$$c(z,t) = \sum_{m=-M}^{m=M} C_m \exp\left(-\alpha_m \frac{w_s}{\nu_{t,s}} z\right) e^{i\omega_m t}, \tag{19}$$

with

$$\alpha_m = \frac{1}{2} + \sqrt{\frac{1}{4} + i\omega_m \frac{\nu_{t,s}}{w_s^2}}, \tag{20}$$

and $M > N$ is the number of harmonic components in the bed concentration. The complex coefficients C_m are determined by the bed boundary condition. With $c_b(z,t) = \sum_{m=-M}^{m=M} C_{b,m} e^{i\omega_m t}$, we find $C_m = C_{b,m}$ and $C_m = C_{b,m}/\alpha_m$ for the concentration-type and gradient-type boundary condition, respectively. At the transition of the lower and outer layer, the concentration is required to be continuous.

Wave-related sediment transport model

Writing the previously found expressions for oscillatory velocity and concentration as $\tilde{u}(z,t) = \sum_{n=1}^{n=N} \zeta_{u,n}(z) e^{i\omega_n t} + cc.$ and $\tilde{c}(z,t) = \sum_{m=1}^{m=M} \zeta_{c,m}(z) e^{i\omega_m t} + cc.$, integration of the

instantaneous flux $\varphi(z,t)=uc$ over time and depth yields for the net wave-related sediment transport:

$$q_{wave}=\frac{1}{t_2-t_1}\int_{t_1}^{t_2}\int_{z_a}^{\infty}\varphi(z,t)\mathrm{d}z\mathrm{d}t=\int_{z_a}^{\infty}\langle\varphi(z)\rangle\mathrm{d}z=\int_{z_a}^{\infty}\left\{\sum_n\zeta_{u,n}(z)\zeta_{c,-n}(z)+cc.\right\}\mathrm{d}z \qquad (22)$$

In the outer layer with a constant diffusivity of fluid momentum and sediment mass, the solutions $\zeta_{u,n}(z)$ and $\zeta_{c,n}(z)$ are in terms of exponential functions such that the integration of the time-averaged flux $\langle\varphi(z)\rangle$ over depth is easily carried out analytically. The linearly increasing diffusivity close to the bed yields a logarithmic profile for $\zeta_{u,n}(z)$ which complicates the analytical integration of $\langle\varphi(z)\rangle$. Therefore a polynomial approximation valid for small values of z is used to approximate the integral.

Herewith we have arrived at a computationally efficient method to account for the wave-related suspended sediment transport taking into account the strong vertical variations in the near-bottom time-varying flow and concentration including the non-instantaneous response of the sediment. With the present time-domain formulation of the bed boundary condition for the sediment, the determination of the net transport rate requires a transformation from frequency to time-domain and vice versa. Compared to using a numerical finite difference scheme however, we have at least a two orders of magnitude reduction in the computational effort.

Comparison with LOWT experiments and results of various models

Description of LOWT experiments

The data used for model validation were obtained by Ribberink and Al-Salem (1994) for dune sand with $D_{50}=210\mu m$ and by Ribberink and Chen (1993) for finer sand with a $D_{50}=130\mu m$. The experiments were carried out in the Large Oscillating Water Tunnel. The experiments used here were performed above a plane sand bed for regular asymmetric (2nd order Stokes) waves in the absence of a mean current. The set of experiments covered a range of wave periods, flow velocity and asymmetry (see Table 1). For C1 and D13 (bold in Table 1) detailed time-dependent measurements were performed. For all tests net transport rates were derived using a mass-conservation technique. Time-averaged concentration were measured using a suction system, whereas time-dependent concentrations were measured using a conductivity concentration meter (CCM) in the sheet flow layer and an optical concentration meter (OPCON) in the suspension layer.

The comparison with the experiments was carried out on sediment concentration and time-averaged sediment fluxes for the tests C1 and D13 and on net transport rates for all tests in the respective series. For all tests, the model was run using the standard settings of $\delta=0.25\kappa u_{*,\mathrm{mean}}/\omega$ and $k_n=3D_{90}$ and with a fall velocity in the outer layer corresponding to a grain diameter of $0.75D_{50}$ based on grain-size data collected during the experiments. Both the concentration-type and pick-up type concentration boundary conditions were used. Only for D13, a significant difference could be observed in the results of the two boundary conditions.

Series B and C ($D_{50}=210\mu m$)

In Figure 3, the prediction of the analytical model is compared with the time-varying sediment concentrations at four heights above the original bed level and with the time-

	Tp (s)	u_{rms} (m/s)	$<u^3>$ m^3/s^3		Tp (s)	u_{rms} (m/s)	$<u^3>$ m^3/s^3
B7	6.5	0.5	0.102	D11	6.5	0.56	0.096
B8	6.5	0.7	0.256	D12	6.5	0.91	0.537
B9	6.5	0.92	0.562	D13	6.5	0.73	0.220
B10	9.1	0.54	0.104	D14	6.5	0.45	0.044
B11	9.1	0.70	0.220				
B12	9.1	0.97	0.574				
B13	6.5	0.70	0.114				
B14	9.1	0.71	0.094				
B15	5.0	0.51	0.103				
B16	12.0	0.56	0.101				
C1	6.5	0.59	0.124				

Table 1 Test conditions for B- and C-series (Ribberink and Al-Salem, 1994) and D-series (Ribberink and Chen, 1993).

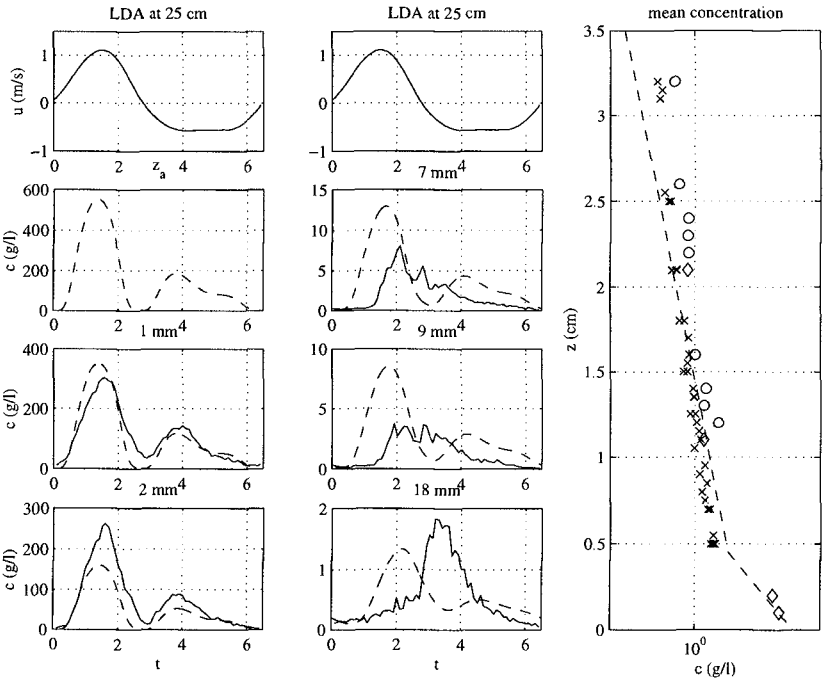

Figure 3 Comparison of measured (drawn) and computed (dashed) sediment concentrations for C1

averaged sediment concentration profile. At the lower levels the predictions are in good agreement regarding amplitude and phase. With distance from the bed especially the phase between the model and data increases. Further, the data show a single-peaked concentration, whereas a second peak is still present in the model predictions. The time-averaged concentration profile is reasonably well predicted. Qualitatively, these features are in agreement with model predictions discussed in a MAST2 G8-M intercomparison study comparing four numerical 1DV models with LOWT data (Davies et al.,1997). In Figure 4 (upper left plot), the predicted time-averaged flux profiles are compared with the data and the

predictions of the Danish STP model based on an eddy viscosity approach (Fredsøe et al., 1985) and a turbulent kinetic energy model (Davies, 1995). The results of the latter two models were taken from the aforementioned paper and were obtained without any fine-tuning of the respective models. Note that for the lower five points measured values for the concentration were combined with estimated values of the velocity, since no velocity measurements were available here. All models and the data show an 'onshore' transport in the near-bed layer and an 'offshore' transport in the outer suspension layer. All models give comparable results and significantly overestimate the height of zero flux and is a direct result of the underestimation of the phase differences between velocity and concentration in the models which are all based on a diffusion approach for the upward transport of sediment.

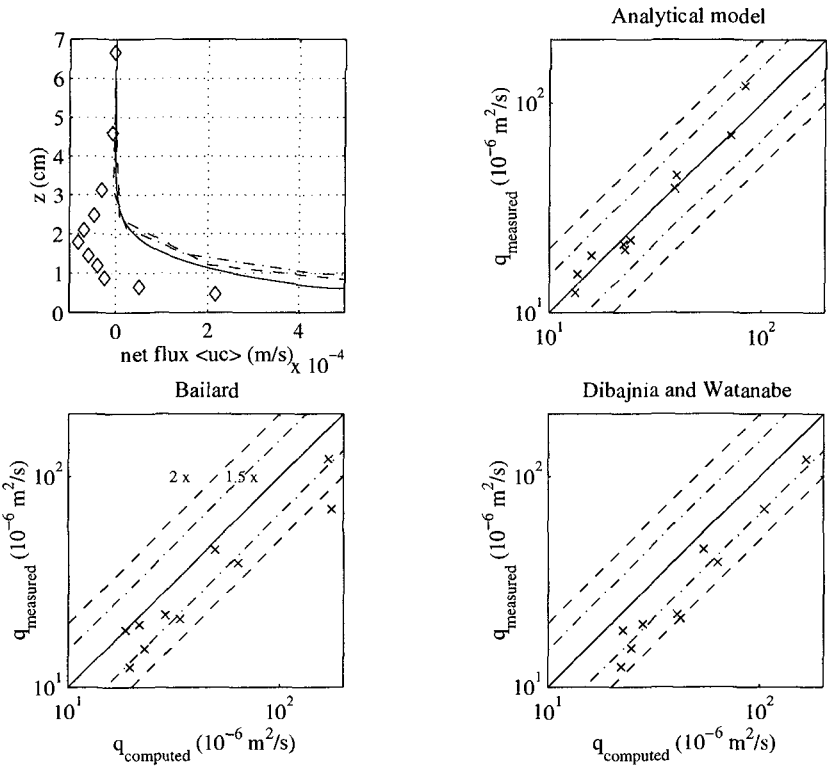

Figure 4 Comparison of measured and computed time-averaged fluxes (upper left plot, STP: dashed, t.k.e.: dashed-dot; analytical: drawn) and comparison of measured and computed net transport rates for various models for the B- and C-series.

The net sediment transport is dominated by the flux in the near-bed layer such that the mismatch between model and data further from the bed can be expected to be relatively unimportant for the net transport predictions. This can be seen in Figure 4, which compares the net transport predictions of the analytical model with the data. Besides, the performance of the Bailard (1981) and Dibajnia and Watanabe (1992) is shown. The latter model results are taken from Janssen et al. (1996). In this figure, perfect agreement corresponds with the 45° line. Also shown are the lines indicating a factor 1.5 and 2 around the line of perfect

agreement. It can be seen that the predictions of the analytical model, the Bailard model and the Dibajnia and Watanabe model are within a factor 2 from the data for 100%, 90 % and 100 % of the tests considered, respectively. Within the band of factor 1.5 we have 100%, 60% and 50% respectively. Also compared to the predictions in Davies et al. (1997), the analytical model gives favourable results.

Series D ($D_{50} = 130\mu m$)

A comparison of the predicted and measured time-varying and time-averaged sediment concentrations, not shown here for brevity, showed many of the features as reported above for test C1. An important difference is the relatively large concentration in the outer layer, such that the predictions in the outer layer are more important to the net sediment transport rate predictions than for the coarser sand.

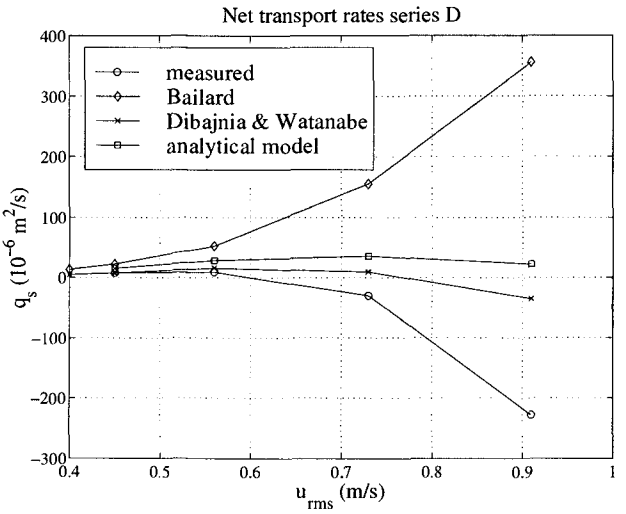

Figure 5 Comparison of measured and computed net transport rates for various models for the D-series

In Figure 5, these net transport rate predictions are compared with the data, together with the predictions of the Bailard and the Dibajnia and Watanabe model (from Janssen et al., 1996). The data show a decreasing and eventually reversing transport rate for increasing root-mean-square velocities. Due to its assumption of quasi-steadiness, the Bailard model cannot follow this trend. Both the analytical model and the Dibajnia and Watanabe model qualitatively follow the observed behaviour, although neither of them predicts the right order of magnitude of the transport rates. The Dibajnia and Watanabe model gives somewhat better results.

Conclusions

The sediment fluxes and net transport rates predicted by the analytical model are comparable to results of numerical 1DV models. However, a considerable reduction of computational effort is obtained. The model gives accurate estimates of the net transport rates for medium sand. For finer sand, although qualitatively correct, the model fails to predict the strong offshore sediment transport rates at higher velocities, mainly due to the diffusion approach.

Acknowledgements

This work is undertaken in the SAFE, FANS and SEDMOC projects, in the framework of the EU-sponsored Marine Science and Technology Programme (MAST-III), under contractno.

MAS3-CT95-0004, MAS3-CT95-0037 and MAS3-CT97-0115, respectively. It is cosponsored by the Dutch Ministry of Transport and Public Works (Rijkswaterstaat) and WL|DELFT HYDRAULICS in the framework of the Netherlands Centre for Coastal Research (NCK).

References

Bailard, J.A, 1981. An energetics total load sediment transport model for a plane sloping beach. *J. of Geophys. Res.*, Vol. 86: C11: 10,938-10,954

Bowen, A.J., 1980. Simple models of nearshore sedimentation; beach profiles and longshore bars. *The Coastline of Canada*, edited by S.B. Cann, pp.1-11, Geological Survey of Canada, Ottawa, 1980

Brevik, I. ,1981. Oscillatory rough turbulent boundary layers. *J. of WatWays, Port, Coastal Ocean Div. Am. Soc. Civ. Engrs*, 107, WW3: 175-188.

Davies, A.G., 1995. Effects of unsteadiness on the suspended sediment flux in co-linear wae-current flow. *Continental Shelf Research*, 15, 8: 949-979.

Davies, A.G., J.S. Ribberink, A. Temperville and J.A. Zyserman, 1997. Comparisons between sediment transport models and observations in wave and current flows above plane beds. *Coastal Engineering*, 31: 163-198.

Dibajnia, M. and A. Watanabe, 1992. Sheet flow under nonlinear waves and currents. *Proc. 23rd Int. Coastal Eng. Conf.*, ASCE, pp. 2015-2028

Fredsøe, J., O.H. Andersen, and S. Silberg, 1985. Distribution of suspended sediment in large waves. *J. of Waterway, Port, Coastal and Ocean Engineering*, 111, 6: 1041-1059.

Grant, W.D. and O.D. Madsen, 1979. Combined wave and current interaction with a rough bottom. *Journal of Geophysical Research*, 84,C4: 1797-1808.

Janssen, C.M. and J.S. Ribberink, 1996. Grain-size influence on sand transport in oscillatory sheet flow. *Proc. 25rd Int. Coastal Eng. Conf.*, ASCE, pp. 4779-4792.

Jonsson, I.G. and N.A. Carlsen, 1976. Experimental and theoretical investigations in an oscillatory sheet flow. *Journal of Hydraulic Research*, 14:45-60.

Kajiura, K., 1964. On the bottom friction in an oscillatory current. *Bull. Earthquake Res. Inst. Uniiv. Tokyo*, 42: 147-174.

Nielsen, P. (1988). Three simple models of wave sediment transport. *Coastal Engineering*, 12: 34-62.

Rakha, K.A., R. Deigaard and I. Brøker, (1997). A phase-resolving cross shore sediment transport model for beach profile evolution. *Coastal Engineering*, 31: 231-261.

Ribberink, J.S. and Z. Chen, 1993. Sediment transport of fine sand under asymmetric oscillatory flow. Data Report H840.20, Part VII, January 1993, WL|DELFT HYDRAULICS, Delft, The Netherlands.

Ribberink, J.S. and A.A. Al-Salem, 1994. Sediment transport in oscillatory boundary layers in cases of rippled beds and sheet flow. *Journal of Geophysical Research*, 99,C6: 12707-12727.

Ribberink, J.S. and A.A. Al-Salem, 1995. Sheet flow and suspension of sand in oscillatory boundary layers. *Coastal Engineering*, 25, 205-225.

Smith, J.D., 1977. Modelling of sediment transport on continental shelves, in *The Sea*, Vol. 6, edited by E.D. Goldberg, I.N. McCave, J.J. O;Brien and J.H. Steele. Pp. 539-577, Interscience, New York, 1977.

Swart, D.H., 1974. Offshore sediment transport and equilibrium beach profiles. WL|DELFT HYDRAULICS, Publ. No. 131.

Trowbridge, J. and O.S. Madsen, 1984. Turbulent wave boundary layers, 1. Model formulation and first-order solution. *Journal of Geophysical Research*, 89,C5: 7989-7997.

Zyserman, J.A. and J. Fredsøe, 1994. Data analysis of bed concentration of suspended sediment. Proc. Am. Soc. Civ. Eng., *Journal of Hydraulic Engineering*, 120(9):1021-1042.

Vertical Length Scales of Nearshore Suspension Events

D. L. Foster, A. J. Bowen, and A.E. Hay [1]

Abstract

Most commonly, nearshore suspended sediment time series are characterized by distinct high concentration events. These events are coherent structures which should have lengths scales that are dependent on the length scale of the near bed turbulence. Possible generation mechanisms for coherent turbulent structures include bed shear, vortex shedding from bed forms, shear instabilities of oscillatory boundary layers, and surficial wave breaking. For turbulence mechanisms other than wave breaking, the characteristic length scale should be governed by the thickness of the bottom boundary layer. The objective of this investigation is to characterize the observed vertical length scales of suspended sediment plumes over the course of a single evolving storm and to compare these length scale estimates with the thickness of the displacement WBBL.

Field observations were made at Queensland Beach on the east coast of Nova Scotia in 1995. This steep planar beach faces a restricted opening, with incoming waves approaching normal to the shore and has a 1 m tidal range. The instruments were located in an intermediate water depth of 3.2 m where the median grain size was 0.02 cm. Sediment suspension was measured with a 2.25 MHz acoustic sounder looking downward and the bed geometry was measure with a rotary sonar.

Over the course of a relatively short lived storm event within a 24 hour period, the wave height ranged from .35 m to 1.4 m and the bed geometry underwent multiple transitions. During this event, the sediment suspension observations showed that while the the relatively infrequent large suspension events increase with increasing storm intensity, the mean suspension event length scale shows little variability. The suspended sediment length scales were compared with an estimate of the displacement thickness of the wave bottom boundary layer. Although the two estimates showed an order of magnitude agreement, the displacement thickness estimates increased slightly with increasing storm intensity. The rms deviation between the estimated boundary layer thickness and the mean length scale of the suspended sediment vertical excursion was 1.2 cm.

[1]Department of Oceanography, Dalhousie University,Halifax, Nova Scotia, Canada, B3H 4J1.

Introduction

Nearshore suspended sediment observation time series are dominated by distinct high concentration events. Recent observations have shown these events to be spatially-discrete coherent structures (Hay and Bowen, 1994) with horizontal lengths scales ranging two orders of magnitude from 5 cm to 1 m. The length scale of the coherent plumes should be dependent on the length scale of the near bed turbulence, indicating the near bed turbulence also exhibits a coherent, spatially discrete structure. Possible generation mechanisms for these turbulent structures include bed shear, vortex shedding from bed forms, shear instabilities of the oscillatory boundary layers, and surficial wave breaking. The turbulence length scale should be governed by the wave bottom boundary layer (WBBL) thickness for these mechanisms, other than wave breaking.

The objective of this investigation is to characterize the observed vertical length scales of suspended sediment plumes over the course of a single evolving storm. Furthermore, we will compare these length scale estimates of the suspended sediment with an estimate thickness of the displacement WBBL.

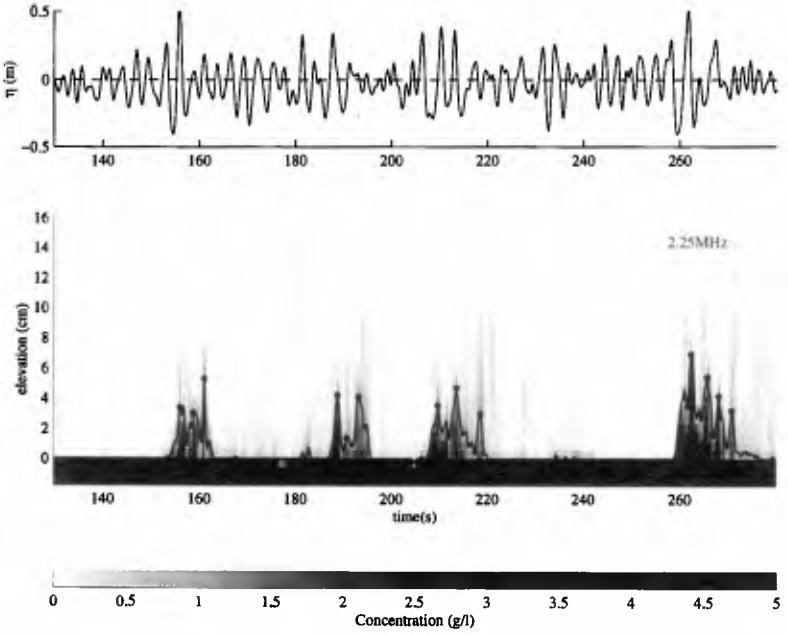

Figure 1: Sea surface elevation, η, as a function of time (top) and suspended sediment concentration, c, as a function of time and elevation (bottom). the solid black line indicates the elevation of the $1g/l$ contour line and the circles indicate the elevation of individual suspension events.

Observations

Field observations were made at Queensland Beach on the southeast coast of Nova Scotia in 1995. This steep planar beach faces a restricted opening, with incoming waves approaching normal to the shore and has a 1 m tidal range. The instruments were located 80 m offshore in an intermediate water depth of 3.2 m. The median grain size was 0.02 cm.

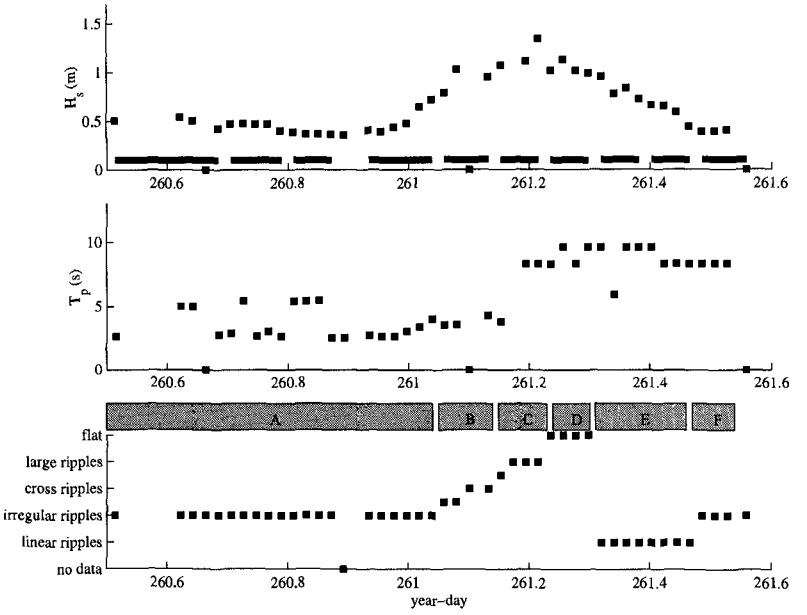

Figure 2: Significant wave height (top), H_s, peak wave period (middle),T_p, and bed form geometry (bottom) over consecutive 500 second runs during year- day 260-261.

For this investigation, sediment suspension and bed elevation were measured with an acoustic sounder operating at 2.25 MHz. The backscatter profile from the sounder spanned a vertical range of about 1 m divided into 0.6 cm range bins and was acquired at 8 Hz. Surface elevation was measured with an upward looking acoustic sounder. A sample time series of sea surface elevation and suspended sediment concentration is given in Figure 1. The concentration and sea surface elevation observations were recorded for 500 seconds every 30 minutes. Bed form geometry was determined over a 5 m radius at each 30 minute interval with a rotary sidescan and rotary pencil beam sonar.

This investigation will focus on the evolving storm during year-days 260 and 261. During the course of this storm the significant wave height, H_s, varied from .35 m to 1.4

m, and the peak wave period, T_p, varied from 2.5 s to 8.3 s. The bed varied between rippled and flat bed, Figure 2.

Results and Discussion

This section is divided into three parts. First, we determine the vertical distribution of suspension excursion. Secondly, we estimate the displacement boundary layer thickness with an empirical model. Finally, we compare the boundary layer thickness estimate with the vertical excursion length scale of the suspended sediment.

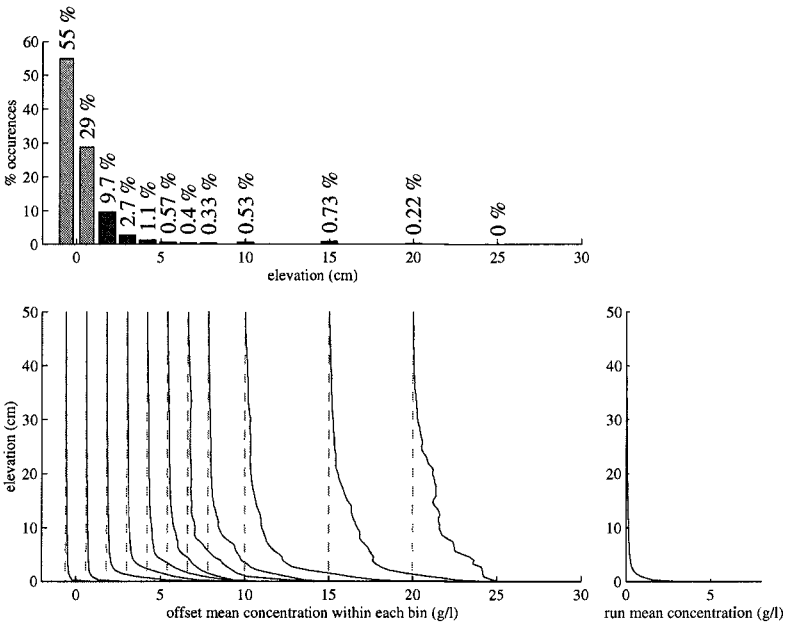

Figure 3: Histogram of the 1 g/l contour elevation of the 2.25 MHz sounder (top panel) and the offset mean profile of observations contained within each histogram bin (bottom panel). The frequency of occurence in each bin are given directly above each bar.

The upper boundary of the sediment laden water was defined with the 1 g/l elevation computed over consecutive 30 second windows, Figure 1. This example shows the 1 g/l contour elevation mostly remains on the bed and has occasional short duration excursions to elevations ranging from 2 to 7 cm. The histogram of the 1 g/l contour elevation time series for this record (Figure 3) shows that 84% of the elevations are less than 2 range bins (1.2 cm) from the bed but there are occasional occurrences where the elevation reaches 15 to 20 cm above the bed. The histogram can be used isolate the mean profile of the suspension events by conditionally sampling the observations based on the elevation of the 1 g/l contour elevation. This is accomplished by calculating the mean vertical profile

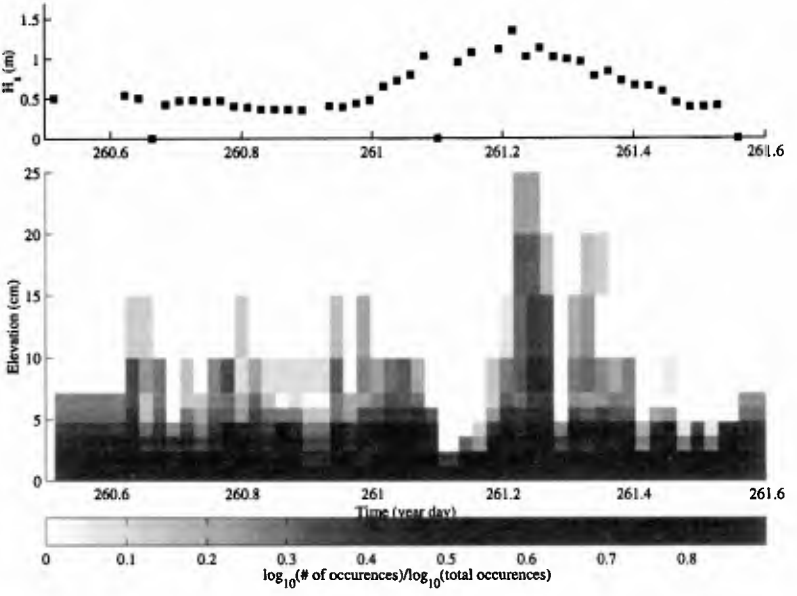

Figure 4: The significant wave height (top), and log_{10} of the fraction of events in each histogram bin. Note that an intensity corresponding to a value of 1 would indicate 100% of the events would be in the single bin and an intensity corresponding to a value of .5 indicates 50% of the events would be contained in the single histogram bin.

of the observations for the set of observations within each histogram bin. The confidence of each profile will be directly dependent on the number of samples in each histogram bin. The sample shows a significant deviation between the complete record mean profile and the mean profile within the individual bins at the higher contour elevations (see the mean profiles for the histogram bins greater than 5 cm from the bed). This sample shows the mean concentration profile of the record is strongly biased towards the large percentage of occurrences when insignificant levels of sediment are in suspension.

The histogram for each of the records over the 24 hour period are shown in Figure 4. In general, as the significant wave height increases larger suspension excursions are reached. Under the storm peak, the sediment suspension reaches elevations of at least 25 cm above the bed.

For this investigation, a displacement thickness was chosen as the characteristic length scale of the WBBL. The displacement WBBL thickness, δ, was estimated following an empirical formulation outlined in Nielsen (1992),

$$\delta_w = c_d A \tag{1}$$

where $A(= u_o/\omega)$ is the wave orbital excursion amplitude and the drag coefficient, c_d, is defined with (Swart, 1974)

$$c_d = 0.5e^{5.2r^{0.2}-6.0}. \tag{2}$$

This formulation is based on numerous laboratory experiments and relies on an accurate estimate of the bed geometry. For these observations on a restricted opening beach with normally incident waves, the excursion amplitude is dominated by onshore and offshore motions. The relative roughness, r, was assumed to be a function of the bed geometry and grain roughness (Nielsen, 1992)

$$r = \frac{\frac{8\eta_b^2}{\lambda_b} + 170(\theta_{2.5} - 0.05)^{0.5}}{A} \tag{3}$$

where η_b is the bed form amplitude, λ_b is the bed form wavelength, and $\theta_{2.5}$ is the grain roughness Shields parameter. The bed form amplitude and wave length were quantified with a rotary pencil beam sonar (Hay and Mudge, in preparation). The grain roughness shields parameter is defined with

$$\theta_{2.5} = c_{d_{2.5}}\psi \tag{4}$$

where $c_{d_{2.5}}$ is the grain roughness drag coefficient and ψ is sediment mobility number (Swart, 1974). The grain roughness drag coefficient is defined with

$$c_{d_{2.5}} = \frac{1}{2}e^{5.213(\frac{2.5d_{50}}{A})^{0.194}-5.977} \tag{5}$$

and the mobility number is defined with

$$\psi = \frac{(A\omega)^2}{(s-1)gd_{50}} \tag{6}$$

where d_{50} is the median grain size diameter, ω is the peak frequency, s is the relative sediment density, and g is gravity.

The relative roughness varies over an order of magnitude throughout the experiment, Table 1. There also exists a significant variation in the drag coefficient over the 24 hour period, Figure 5. Prior to the storm, the existing bed geometry and low excursion amplitude yields a large relative roughness. As the wave height increases and wave period decreases, the orbital excursion amplitude increases and the bed begins to plane off resulting in a significant decrease in the drag coefficient. The resulting boundary layer thickness increases by a factor of 2 as the storm intensity increases.

The mean vertical length-scale, L_z,was estimated by calculating the mean of the individual event vertical intrusion heights in each record. Individual events were identified by searching for local maxima greater than 2 range bins (1.2 cm) away from the bed of the 1 g/l contour elevation sampled at 8 Hz and smoothed with a 1/2 second boxcar win-

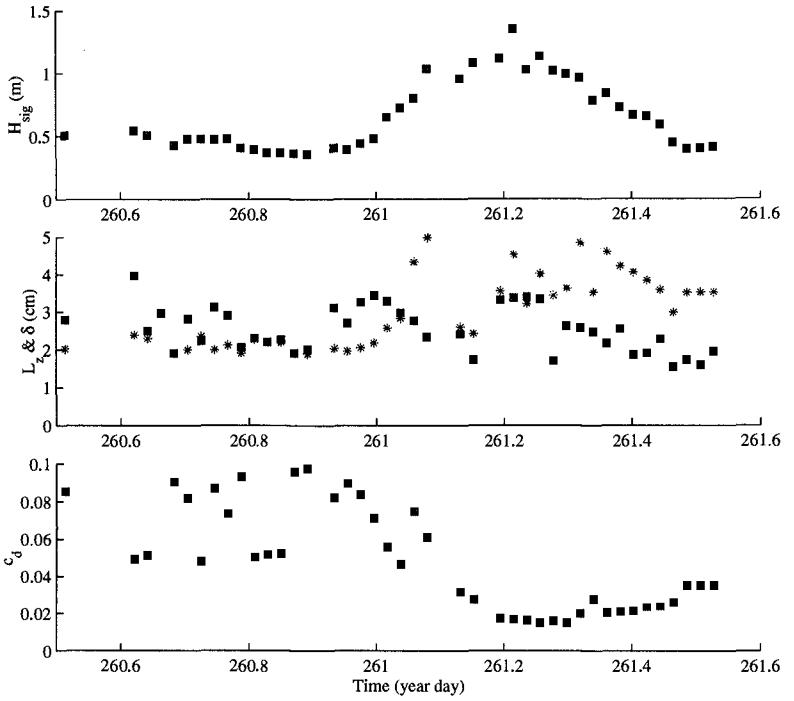

Figure 5: The significant wave height (top), mean vertical excursion length scale, L_z, (middle panel), estimated displacement WBBL thickness, δ, (middle panel), and the drag coefficient, c_d, (bottom) as a function of time.

dow. The darkened circles in Figure 1 show the time and elevation of the defined events for this example. The mean vertical intrusion height is compared with the estimated displacement WBBL thickness in Figure 5. Unlike the extreme event envelope (Figure 4), the mean vertical excursion length scale remains remarkably uniform over the period. The mean vertical length scale remains relatively uniform because the statistic is dominated by the relatively high number of small events. The rms deviation between the mean vertical length scale and estimated displacement WBBL thickness is 1.2 cm over the 24 hour record.

Summary

These results showed that while the relatively infrequent large suspension events increase with increasing storm intensity, the mean suspension event length scale shows little variability. The estimated displacement WBBL thickness increased with increasing storm intensity. The rms deviation between the estimated boundary layer thickness and the mean

	Bed Forms	η_b cm	λ_b cm	A cm	r
A	irregular	3	13	20-50	.38-.16
B	cross	2-4	50	60-80	.28-.08
C	large	3	100	90-270	.07-.03
D	flat	-	-	200-240	.02
E	linear	3	13	125-225	.07-.04
F	irregular	3	13	20-50	.1

Table 1: The bed form classification, bed form amplitude, η_b, bed form wavelength, λ_b, excursion amplitude, A, and relative roughness, r, for the duration of the storm (A-F). The six intervals are shown in the bottom panel of Figure 2.

length scale of the suspended sediment vertical excursion was 1.2 cm. Further investigations of these observations will include similar evaluations of the horizontal length-scales and temporal evolution of events. Also, vertical lengths scales as measured by 2 other sounders will be compared.

Acknowledgments

This work was funded by the Andrew Mellon Foundation and Natural Science and Engineering Research Council of Canada.

References

Hay, A.E., and Bowen, A.J., (1994),*Coherence scales of wave induced suspended sand concentration fluctuations*, J of Geophys. Res.

Nielsen, P (1992),*Coastal bottom boundary layers and sediment transport*, World Scientific, Singapore.

Swart, DH (1974), *Offshore sediment transport and equilibrium profiles*, Delft Hydraulics Lab Publ No 131.

Sediment Resuspension under Non-Breaking Waves. Predicting Sediment "Pulses" as a Function of Groupiness

José A. Jiménez[1], Agustín Sánchez-Arcilla[1] (M.ASCE) and German Rodríguez[2]

Abstract

Near-bottom sediment suspension reacts to non-breaking random wave-induced velocity field showing a pulsating structure (high concentration discrete events) lagged with respect to the actual velocity field. A coefficient of variation, GF_{Cfil}, has been applied to low pass filtered concentration time series to characterise these pulses. The use of simple parameters based on the actual velocity field such as the shear stress (e.g. using the velocity squared) is not enough to fully explain the sediment response. To take into account the apparent relationship between groups and sediment pulses, several parameters characterising groupiness have been analysed: (i) the groupiness factor, GF, derived from SIWKEH; (ii) the mean run length, j_1, and mean total run, j_2, based on the use of the envelope; and (iii) the spectral correlation coefficient between successive waves, ρ. The best predictor for the pulsating structure of the sediment response was found to be GF, with a linear relationship for similar energetic wave states ($u_{*,rms}/u_{*,cr})^2 > 1$), i.e. the larger the GF is, the larger GF_{Cfil} the will be. When the time lag in the sediment response is analysed, the parameters retaining information about the temporal structure of the groups such as j_1 or ρ are the only able to predict it. Thus, a linear relationship was found between the time lag and the mean run length and ρ, i.e. the longer the group is, the longer the lag in the sediment response will be.

1. Introduction

It is reasonably well known that in natural conditions, sediment resuspension from the bottom is a more or less intermittent process, in which large sediment concentrations are picked-up from the bed and released to the water column as "pulses" (*e.g.* Hanes, 1990). These pulses are generally related with the presence of wave groups and their associated long waves (*e.g.* Shi and Larsen, 1984; Sato, 1992) (figure 1).

[1] Laboratori d'Enginyeria Marítima, ETSECCPB, Catalonia University of Technology, c/Jordi Girona 1-3, Campus Nord, Ed. D1, 08034 Barcelona, Spain (e-mail: jimenez@etseccpb.upc.es).
[2] Department of Physics, Universidad de Las Palmas de Gran Canaria, Campus Universitario de Tafira, 35017 Las Palmas, Spain.

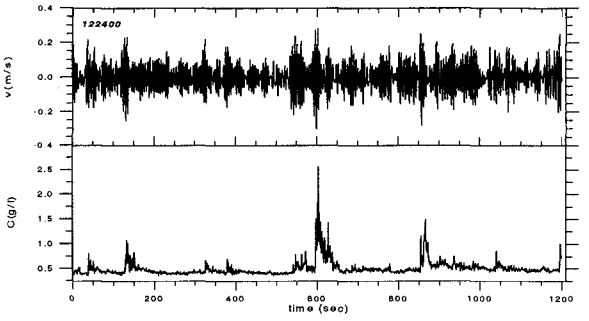

Figure 1. Near-bottom (0.11 m) velocity (top) and suspended sediment concentration (0.12 m a.b., bottom) measured in the Ebro delta shoreface (8.5 m depth).

However, although conceptually this is generally accepted, there is no model able to predict this sediment pulsing structure as a function of the level of groupiness of a determined wave-energetic state. Most of existing studies recognise the influence of groupiness (*e.g.* Shi and Larsen, 1984; Hanes, 1990, Shibayama *et al.* 1992) or estimate the increase in the integrated suspended sediment concentration within a wave state (Sato, 1992, Lee *et al.* 1994) but without details on how to predict frequency and magnitude of sediment pulses.

It is the aim of this paper to analyse the relationship between wave groups and induced suspended sediment pulses and to find wave groups related parameters able to predict/characterise the pulsing structure.

2. Field data

Data used in this study were acquired in the inner shelf (8.5 m depth) of the Ebro delta (Spanish Mediterranean coast). The data were obtained by using an instrumented tripod supporting 3 ECM's, 3 OBS's, 1 pressure sensor and 1 compass. The system worked in burst mode, with a burst duration of 20 min every 3 hours and with a data acquisition frequency of 1 Hz. All the data were taken under non-breaking wave conditions. A description in depth about the governing conditions during the survey period can be seen in Jiménez et al. (1998).

All the data analysed in this work correspond to the measurements taken at the lowest position, 10 cm above the bottom.

3. Sediment resuspension and incident velocity field

Since sediment resuspension depends on the characteristics of the near-bottom flow, a first approach is to directly relate sediment suspension with near-bottom velocity. Following earlier works of Smith (1977) and Smith and McLean (1977), suspended sediment concentration, C, can be expressed as a function of the excess of shear stress, τ_b, above a critical value τ_{cr}, as

$$C = C_b \gamma \frac{s'}{(1+\gamma s')} \qquad s' = \frac{\tau_b}{\tau_{cr}} - 1 \tag{1}$$

where C_b is the reference concentration at the bottom and γ is the resuspension factor. Eq. (1) can be simplified assuming that the actual shear stress is much higher than the critical one as

$$C(t) \propto \frac{|\tau_b(t)|}{\tau_{cr}} \propto U(t)^2 \tag{2}$$

Following this approach figure 2 shows the relationship between near-bottom sediment concentration and velocity squared in the time and frequency domains. As it can be seen, although cross-correlation gives a different from zero value (indicating the existence of a relationship between them), the calculated coefficient of correlation is relatively low.

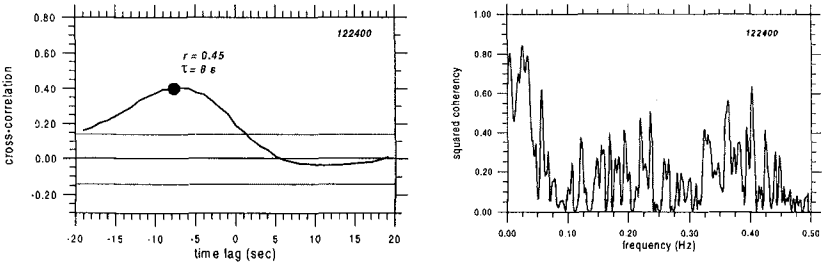

Figure 2. Relationship between near-bottom sediment concentration and near-bottom velocity squared. Left: cross-correlation (lines show limits for different from zero correlation). Right: squared coherence from cross-spectral analysis using both variables.

If this is done in the frequency domain through cross-spectral analysis similar results are found. Thus, results show that the squared coherency at low frequencies is much higher than the calculated for at high frequencies (peak frequency -0.19 Hz- corresponding to u or first harmonic -0.38 Hz- corresponding to u^2, figure 2). This should indicate that a large part of the sediment suspension would be related to the existence of low frequency motions such as those induced by the presence of wave groups.

Figure 2 also shows the existence of a time lag between the sediment response (suspension) and the incident velocity field as it has been demonstrated in earlier works (e.g. Jaffe et al. 1994). Two dimensionless parameters have been selected to look for a simple relationship between the lag in the sediment response and the incident velocity field. These dimensionless parameters retain both velocity field and sediment characteristics and they are (i) a kind of excess of bottom shear stress, $(u_{*,rms})^2$ above the critical shear stress for initation of sediment motion, $(u_{*,cr})^2$, i.e. $(u_{*,rms}/u_{*,cr})^2$ and (ii) the shear velocity adimensionalised with the fall velocity of the sediment, w_s, i.e. $u_{*,rms}/w_s$. The first parameter gives an idea about the capacity of sediment mobilisation of the incident velocity field, the larger this parameter is, the larger the mobilisation will be. On the other hand, the second one gives an idea about

and the ability of the sediment to be in suspension in the water column. Thus, assuming that the suspended sediment concentration is a function of the $-w_s/u_{*,rms}$ power (e.g. Nielsen, 1992), this would imply that the larger the $u_{*,rms}/w_s$ is, the longer the "resident" time of the sediment in the water column will be.

Figure 3 shows the time lag adimensionalised with the actual peak period versus both parameters. As it can be seen no simple relationship can be found. The only aspect arising from the figures is that velocity fields with a relatively low capacity of mobilisation - $(u_{*,rms}/u_{*,cr})^2 \approx 0.5$ - show a trend to present longer time lags.

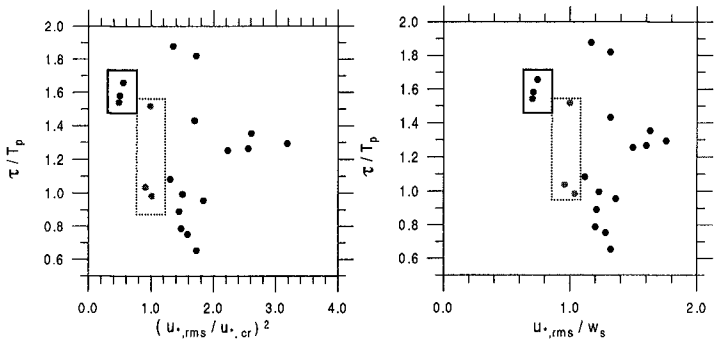

Figure 3. Normalised time lag versus excess of shear stress (left) and normalised shear velocity (right).

On the other hand, for velocity fields with a relatively high capacity of mobilisation - $(u_{*,rms}/u_{*,cr})^2 > 1$ - and inducing a relatively long residence time, there seems to exist a trend for longer time lags as both parameters increase. However, this trend is not uniform since there are some cases not showing this behaviour.

As a summary, although the near-bottom velocity squared and related parameters are able to qualitatively predict some aspects of the near-bottom suspended sediment concentration, their predictability skill is relatively low as it has been pointed out by Jaffe et al. (1994) among others, i.e. some hydrodynamic aspects are missed.

4. Sediment resuspension and groupiness

To account the apparent effect of wave groups in sediment resuspension (figure 1), the incident velocity field was manipulated to characterise its degree of groupiness. To do this several methods have been investigated: two in the time domain -SIWEH and the run length (derived from the envelope)- and one in the frequency domain -the spectral correlation coefficient between successive waves-. In all the cases, the selected parameter is related to the suspended sediment time series to analyse its ability to characterise the pulsing structure and the observed time lag between velocity and concentration.

The *SIWEH method* (Funke and Mansard, 1979) was applied to near-bottom velocities projected on the mean wave direction (SIWKEH, where K means kinetic) to characterise velocity groupiness (eq. 3). Moreover, to remark the sediment pulsing

behaviour, suspended sediment concentration time series were also filtered using a Barlett window similar to SIWEH but with a linear gain (eq. 4). Figure 4 shows the effect of applying such technique on the original time series.

$$E_u(t) = \frac{1}{T_p} \int_{-\infty}^{\infty} u^2(t+\tau) Q(\tau) d\tau \tag{3}$$

$$C_{fil}(t) = \frac{1}{T_p} \int_{-\infty}^{\infty} c(t+\tau) Q(\tau) d\tau \tag{4}$$

where $Q(\tau)$ is a Barlett filter given by

$$Q(\tau) = \begin{cases} 1 - \dfrac{|\tau|}{T_p} & |\tau| < T_p \\ 0 & |\tau| \geq T_p \end{cases} \tag{5}$$

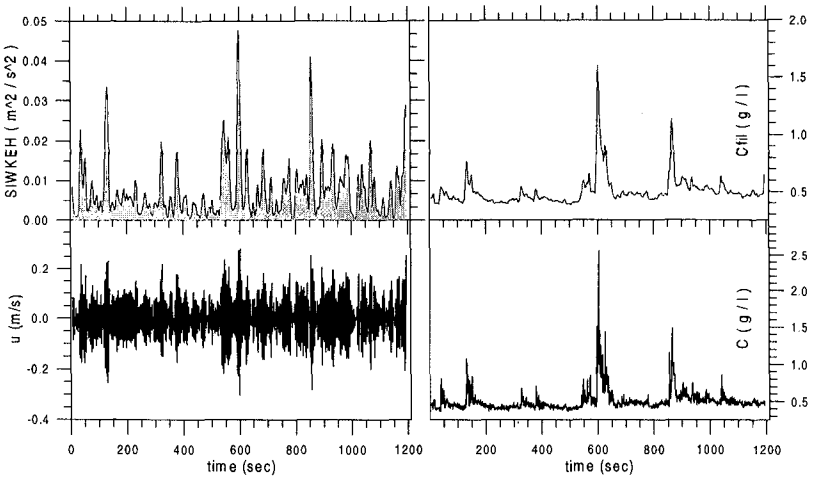

Figure 4. Bottom: original time series of velocity (left) and concentration (right). Upper: filtered time series -SIWKEH (left)- and concentration (right).

Figure 5 shows the results of a cross-correlation analysis between SIWKEH and the bottom filtered concentration, where a significantly different from zero correlation at the 95% level was found. This correlation amounts to 0.65 which is larger to the obtained with u^2, and it should imply that when groupiness is taking into account, the suspended sediment response can be better explained. As in the previous analysis, a time lag between velocity and suspended sediment concentration was also found with the same value (figure 5). In a simple manner, with regards the "magnitude", the larger the SIWKEH is, the stronger the sediment pulse will be and, with respect to the temporal structure, sediment pulses appear to be retarded with respect to the group.

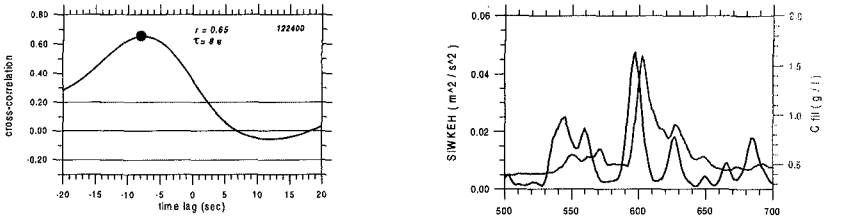

Figure 6. Relationship between filtered concentration time series and SIWKEH (same case than in figure 3). Left: cross-correlation. Right: zoom of time series illustrating the time lag.

To characterise wave groupiness, the groupiness factor *GF* (Funke and Mansard, 1979) was used, which in essence is a coefficient of variation given by

$$GF = \frac{1}{\overline{E_u}} \sqrt{\frac{1}{T_n} \int_0^{T_n} (E_u(t) - \overline{E_u})^2 \, dt} \tag{6}$$

$$\overline{E_u} = \frac{1}{T_n} \int_0^{T_n} E_u(t) \, dt \tag{7}$$

This *GF* was also applied to the filtered suspended sediment time series, C_{fil}, to obtain a measure of the pulsing structure, GF_{Cfil}. Large values of GF_{Cfil} would imply a strong pulsing structure.

Figure 6 shows GF_{Cfil} versus the wave groupiness factor, *GF*. As it can be seen, the larger the wave groupiness factor is, the stronger the pulsing structure will be. In numerical terms, this linear relationship is highly significant with a coefficient of determination, $r^2 = 0.7$. However, there exist some cases with similar GF_{Cfil} values for different *GF* ones. These cases correspond to wave states with very different energetic contents. Thus, points in the shadow area of figure 6 were taken under relatively low energetic conditions, i.e. $(u_{*,rms}/u_{*,cr})^2 \approx 0.5$, and as GF is a measure of the variance of the SIWKEH, a large GF can be obtained for small waves but grouped. On the other hand, as GF_{Cfil} is a coefficient of variation, relatively high values can be obtained for time series with a low mean value (see figure 6 right). Thus, similar GF_{Cfil} values for different energetic conditions have different implications. For low energy conditions, few pulses give a larger than expected GF_{Cfil} value due to the actual low mean concentration.

All of this indicates that although *GF* obtained from SIWKEH is a good "predictor" of the pulsing structure, a *GF* larger than others will not necessarily imply a larger sediment pulsing, GF_{Cfil}, unless wave states with similar energetic contents are compared. In this sense, it is recommended restricting the comparative analysis to wave states with $(u_{*,rms}/u_{*,cr})^2 \geq 1$.

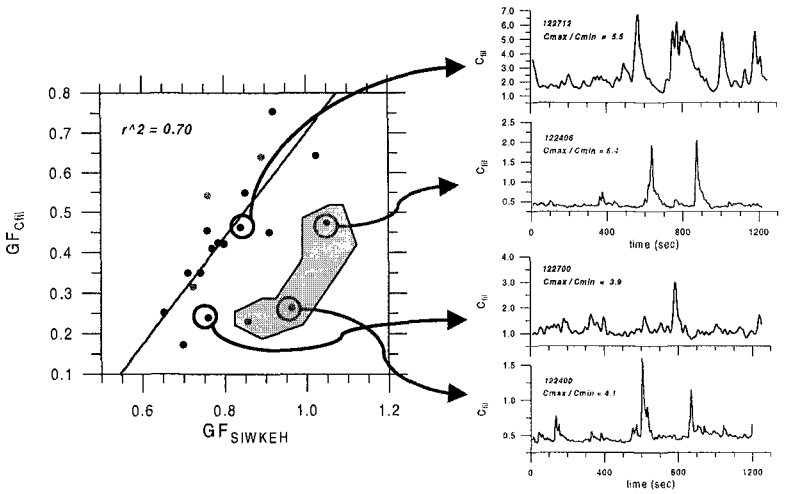

Figure 6. Suspended sediment pulsing structure, GF_{Cfil}, versus wave groupiness factor, GF. Cases in the shadow area correspond to time series with $(u_{*,rms}/u_{*,cr})^2 \approx 0.5$. Right: selected filtered suspended sediment concentration time series.

Figure 7 shows the time lag in the sediment response adimensionalised with the peak period of the incident waves versus the groupiness factor, GF. As it can be seen, there is no relationship between both, i.e. GF is not a good parameter to predict such lag.

The different behaviour of GF to measure pulsing and time lag can be explained taking into account that SIWKEH gives a measure of the variability of the energy packets within a wave state but it does not measure the temporal distribution of the groups. A large GF indicates that many packets exist (and in consequence the probability to have sediment pulses will be larger) but it does not include any information about the energy content, so only wave states with similar contents can be compared.

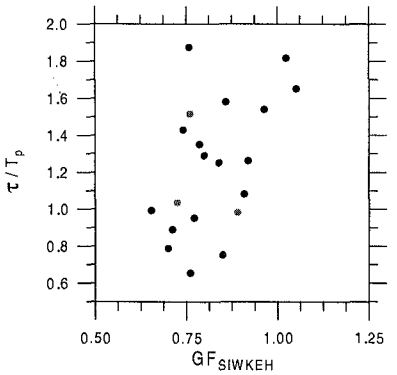

Figure 7. Normalised time lag versus wave groupiness factor, GF.

The *Run Length method* (Goda, 1970) was applied to near-bottom velocities projected on the mean wave direction using the envelope method. Thus, the envelope of the incident velocity field was calculated by using the Hilbert transform. Once the envelope was obtained, the groups were defined using a threshold value characteristic of the analysed problem. Since we are studying the sediment response, the treshold value was selected to be the critical velocity for initiation of motion, obtained by assuming the Shields criterium to be valid for oscillatory flow. Once this value was obtained, the run length of each group is calculated in a continuous manner, i.e. the time during which the envelope exceeds the threshold, with a minimum duration of the peak period (see figure 8).

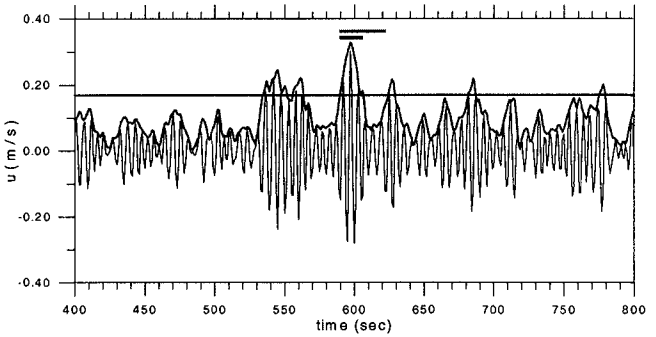

Figure 8. Run length and total run definition using the envelope method (line is the threshold velocity for initiation of sediment motion calculated by using Shields criterium).

Figure 9 shows the sediment pulsing intensity, GF_{Cfil}, and the normalised time lag versus dimensionless mean run length, j_1/T_p, and dimensionless mean total run, j_2/T_p. As it can be seen, no relationship between GF_{Cfil}, and mean run length or mean total run was found. On the other hand, a linear relationship between normalised time lag and normalised mean run lengths and mean total run was found. In the case of the use of the run length, if low energetic wave states are removed, i.e. $(u_{*,rms}/u_{*,cr})^2 \approx 0.5\text{-}1.0$, the larger the duration of the group (run length) is the longer the time lag will be. Similarly, a linear relationship between time lag and mean total run was also found with about the same coefficient of correlation and also taking out the low energetic states (figure 9). This implies that for similar energetic states and for the same threshold, the longer the time between groups is, the longer the time lag will be.

This different behaviour of j_1/T_p and j_2/T_p to measure pulsing and time lag can be explained taking into account that in opposite to SIWKEH, these parameters give a measure of the temporal structure of the groups. However, they do not give too much information about the energy content (only that each group exceeds the selected threshold). A possible improve of its predictive skill could be the application of an approach similar to the proposed by Medina *et al.* (1990), the envelope exceedance coefficient, in which not only the duration of the group is considered but also its energy content.

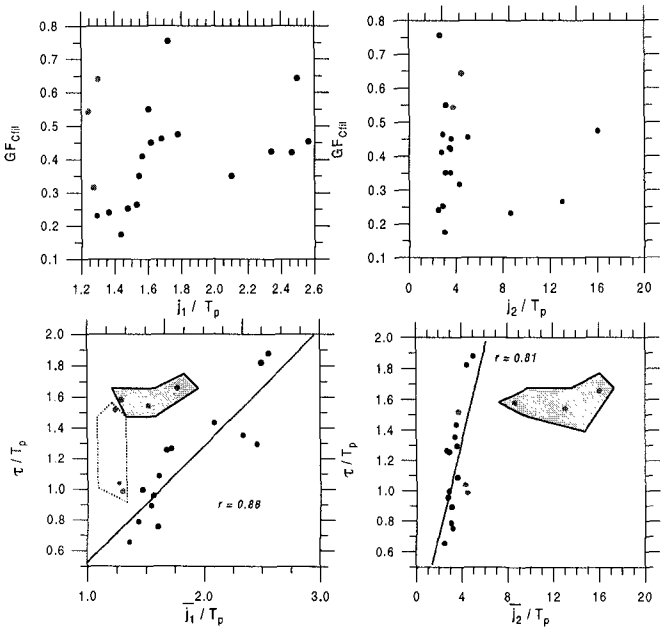

Figure 9. Sediment pulsing intensity, GF_{Cfil}, (top) and normalised time lag (bottom) versus dimensionless mean run length, j_1/T_p, and dimensionless mean total run, j_2/T_p. Cases in the shadow area correspond to time series with $(u_{*,rms}/u_{*,cr})^2 \approx 0.5$ and cases in the dashed area to time series with $(u_{*,rms}/u_{*,cr})^2 \approx 0.9\text{-}1.0$.

Kimura (1980) proposed the *correlation coefficient between successive waves* as a way to predict the mean and standard deviation of the run lengths and the total runs of a wave state. This method was originally derived to work in the time domain (i.e. using the zero crossing analysis) and, in consequence, it does not include not too much advantage in comparison with the direct determination as presented above (see e.g. Mansard and Sand, 1994).

However, Battjes and van Vledder (1984) derived such correlation parameter directly from the spectral density of the waves, which implies that most information on wave groups is contained in the spectrum itself. In this work, an improved correlation coefficient in the way proposed by van Vledder (1992) is used to characterise wave groupiness. This correlation coefficient is given by

$$\hat{\rho}_t = \frac{\rho_f(\frac{1}{2}\hat{T}) + 2\,\rho_f(\hat{T}) + \rho_f(\frac{3}{2}\hat{T})}{2 + 2\,\rho_f(\frac{1}{2}\hat{T})} \tag{8}$$

where

$$\hat{T} = T_{m02}\,(1-\frac{1}{2}\nu^2) \tag{9}$$

Figure 10 shows the sediment pulsing intensity, GF_{Cfil}, and the normalised time lag versus the spectral correlation coefficient between successive waves. As expected, since this coefficient is related to the mean run length, it presents a similar behaviour than j_1. Thus, no relationship between GF_{Cfil}, and ρ was found. On the other hand, a linear relationship between normalised time lag and ρ was also found, with a similar coefficient of correlation, $r=0.84$, although there is no need to consider the energetic content of each cases (as it was done with the mean run length).

The different behaviour to measure pulsing and time lag can be explained in the same way that was done in the case of the mean run length, since they are related. The advantage of this method is that can be applied directly to the recorded spectra without identifying the groups in the time series.

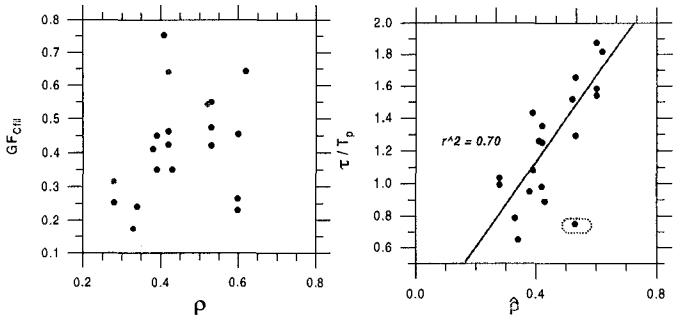

Figure 10. Sediment pulsing intensity, GF_{Cfil}, (left) and normalised time lag (right) versus spectral correlation coefficient between successive waves.

Summary and discussion

Near-bottom sediment suspension reacts to non-breaking random wave-induced velocity field showing a pulsating structure, i.e. high concentration discrete events, that it is lagged with respect to the actual velocity field. This pulsating structure was characterised via a coefficient of variation similar to the groupiness factor, GF_{Cfil}, applied to a low pass filtered concentration time series (eq. 4).

The use of a simple parameter based on the actual velocity field such as the shear stress (e.g. using the velocity squared) is not enough to fully explain the sediment response. To solve this and taking into account the apparent relationship between groups and sediment pulses, several parameters characterising groupiness have been analysed: (i) the groupiness factor derived from SIWKEH (using the actual velocity instead of the wave height), GF; (ii) the mean run length, j_1, and mean total run, j_2, based on the use of the envelope; and (iii) the spectral correlation coefficient between successive waves, ρ.

When the *pulsating structure* of the sediment response, GF_{Cfil}, is analysed, the best predictor of the tested parameter was found to be the groupiness factor derived from SIWKEH, GF. Thus, for similar energetic wave states (with $(u_{*,rms}/u_{*,cr})^2 > 1$), a linear

relationship was found, i.e. the larger the *GF* is, the larger GF_{Cfil} the will be. The other two tested parameters are not useful to predict the pulsating structure, i.e. no relationship was found.

When *the time lag in the sediment response* is analysed, the parameters retaining information about the temporal structure of the groups such as j_1 or ρ are the only able to predict it. Thus, a linear relationship was found between the time lag and the mean run length and ρ, i.e. the longer the group is, the longer the lag in the sediment response will be. From both parameters, that directly obtained from the spectrum, ρ, is recommended because there is no need to account its energetic content as it is the case of the use of j_1. In this last case, the groups have been defined using a threshold selected as a function of the analysed problem, the critical velocity for initiation of sediment motion.

These results seem to suggest that instantaneous sediment transport models have to account grouping-induced sediment response (sediment pulses and time lags) to make realistic predictions.

Present on-going analysis is being directed to include an intensity-oriented parameter (to take into account the magnitude of the pulse) and to analyse the possibility of the existence of a relationship between the time lag and the wave group-induced bound long wave.

Acknowledgements

This work has been done in the framework of the *FANS* and *PACE* projects (EC MAST-III, MAS3-CT95-0037 and MAS3-CT95-0002) and *TRASEDVE* (MAR98-0691-C02-01). First author thanks to DPTOP (Generalitat de Catalunya) for a grant given through the Faculty of Civil Engineering.

References

Battjes, J. & van Vledder, G.Ph. 1984. Verification of Kimura's theory for wave group statistics. *Proc. 19th ICCE*, ASCE, 642-648.

Funke, E.R. & Mansard, E.P.D.1979. On the synthesis of realistic sea states in a laboratory flume. Rep. LTR-HY-66.

Goda, Y. 1970. Numerical experiments on wave statistics with spectral simulation. *Rep. Port Harbour Res. Inst.*, 9, 3.

Hanes, D.M. 1990. The structure of events of intermittent suspension of sand due to shoaling waves. *The Sea*, Vol. 10, 941-952.

Jaffe, B.E.; Rubin, D.M. K. & Sallenger, A.1994. How much velocity information is necessary to predict sediment suspension in the surf zone. *Proc. 24th ICCE*, ASCE, 2085-2099.

Jiménez, J.A.; Guillén, J.; Gracia, V.; Palanques, A.; García, M.A.; S-Arcilla, A.; Puig, P.; Puigdefábregas, J. & Rodríguez, G. 1998. Water and sediment fluxes on the Ebro delta shoreface: On the role of low frequency currents. *Mar. Geol.*, (in press).

Kimura, A. 1980. Statistical properties of random wave groups. *Proc. 17th ICCE*, ASCE, 2955-2973.

Lee, J.; O'Neil, S.; Bedford, K. & van Evra, R. 1994. A bottom boundary layer sediment response to wave groups. *Proc. 24th ICCE*, ASCE, 1827-1836.

Mansard, E.P.D. & Sand, S.E. 1994. Evaluation of wave grouping measures. *Proc. 24th ICCE*, ASCE, 832-846.

Medina, J.R.; Fassardi, C. & Huspeth, R.T. 1990. Effects of wave groups on the stability of rubble-mound breakwaters. *Proc. 22nd ICCE*, ASCE, 1552-1563.

Nielsen, P. 1992. *Coastal Boundary Layers and Sediment Transport.* World Scientific Press.

Sato, S. 1992. Sand transport under grouping waves. *Proc. 23rd ICCE*, ASCE, 2411-2423.

Shi, N.C. & Larsen, L.H. 1984. Reverse sediment transport induced by amplitude-modulated waves. *Mar. Geol.*, 54, 181-200.

Shibayama, T.; Okayasu, A. & Kashiwagi, M. 1992. Long period wave and suspended sand transport in the surf zone. *Proc. 23rd ICCE*, ASCE, 2411-2423.

Smith, J.D. Modeling of sediment transport on continental shelves. *The Sea*, Vol. 6, 539-577.

Smith, J.D. & McLean, S.R. 1977. Spatially averaged flow over a wavy surface. *J. Geophys. Res.*, 1735-1746.

van Vledder, G.Ph. 1992. Statistics of wave group parameters. *Proc. 23rd ICCE*, ASCE, 946-959.

Coherent Doppler Sonar: Sediment Flux and Turbulent Velocities in a Wave Flume

Len Zedel[1] and Alex Hay[2]

1 ABSTRACT

Observations of vertical sediment flux and velocity structure are made under prototype scale waves in the Wave Research Flume at the National Research Council (NRC) in Ottawa. Observations were made under regular waves of 3.5 s period with heights ranging from 20 to 70 cm. Direct measurement of sediment flux is made possible using 1.7 MHz pulse-to-pulse coherent sonar which determines concentration from acoustic backscatter levels and velocity using acoustic Doppler. Operating over a 0.8 m range, velocity profiles with 1.4 cm range resolution and a 0.5 cm s^{-1} vertical velocity accuracy can be made at a rate of 30 profiles per second. We find that there is an apparent balance between the mean downward flux of sediment and the upward flux due to turbulent motions. The component of (upward) vertical flux caused by wave action is small compared to the turbulent and mean components. Profiles of turbulence intensity are provided by the vertical velocity fluctuations, these profiles show a rapid rise to a peak value within 5 cm of the bottom and then a subsequent decrease. The (near bottom) peak value of root-mean-square vertical velocity fluctuations are equal to the friction velocity characteristic of the bottom boundary layer. The decrease in turbulence with height above the bottom shows behavior consistent with the decrease in grid generated turbulence but appears sensitive to the length scales of the bed-forms rather than sand grain roughness.

2 INTRODUCTION

Knowledge of the vertical distribution of suspended sediment is required to model the transport of sediment due to wave action. In order to better understand the contributions of turbulent motions to the sediment suspension process coincident measurements of suspended particle concentration and velocity must be made. Such observations are lacking and are particularly needed for comparison with model predictions.

[1] Assistant Professor, Department of Physics and Physical Oceanography, Memorial University of Newfoundland, St. John's, Nf, A1B 3X7 Canada.

[2] Professor, Department of Oceanography, Dalhousie University, Halifax, NS, Canada, B3H 4J1.

We present acoustic measurements of vertical velocity and suspended sediment concentration using a coherent Doppler sonar (Zedel et al. 1996). The 1.7 MHz, Dopbeam system was configured to provide velocity profiles with 1.4 cm range resolution and a 0.5 $cm\,s^{-1}$ vertical velocity accuracy at a rate of 30 profiles per second. Concentration measurements are acquired at the same time and location through calibration of the acoustic backscatter levels to absolute concentrations for the sediment samples used. The Dopbeam system has been calibrated using a sediment laden turbulent jet as described by (Hay 1991).

The measurements were made in the Wave Research Flume at the National Research Council (Ottawa), Canada. This facility has a length of 100 m, a width of 2.0 m and was filled to a water depth of 1.8 m. A 10 cm thick layer of 150 μm (sorted) sand was deposited through a 20 m long test section. Observations were made with regular and irregular waves with nominal heights of 20 to 70 cm.

3 VERTICAL FLUX

The vertical flux of sediment can be expressed as;

$$F = < \bar{w}\bar{c} + \tilde{w}\tilde{c} + w'c' > \qquad (1)$$

where w is the vertical component of velocity, c is the concentration, the tilde and prime refer to wave and turbulent components respectively, $<>$ indicates a time average. The three terms on the right hand side of Equation (1) represent mean, wave induced, and turbulent vertical flux respectively: each of these terms are evaluated from the amplitude and Doppler shift of the backscattered signal as a function of height above the bed.

The mean component of flux results from the mean settling velocity and the concentration structure. In general, the mean flux component will depend on changes in concentration and velocity. One approach to modeling this component is to assume that the mean velocity is fixed at the free descent velocity of the particles (Nielsen 1992). For the present observations, where the particles have uniform size, we might expect mean velocities to be constant with height. Fig. 1 shows concentration profiles (Fig. 1a) and mean vertical velocities (Fig. 1b) for the present observations. The concentration profiles show the expected logarithmic form decreasing with height above the bottom. The velocities however are notable in that the mean downward velocity is not constant with height. In particular, there is a consistent trend for the mean velocity to decrease with proximity to the bottom in a region extending to within 5 cm of the bottom. Based on these observations, the assumption of a uniform mean velocity is not appropriate.

Wave components were isolated by selectively averaging data according to the wave phase, the turbulent components were then determined as the residual after mean and wave components were removed. We find that the sum of these flux terms is approximately balanced as is shown by the example in Fig. 2. The averaged mean flux is downward (settling) with the wave and turbulent flux being in an upward direction. The wave component of flux is relatively small and thus an approximate balance exists between the turbulent upward flux and the mean downward settling flux.

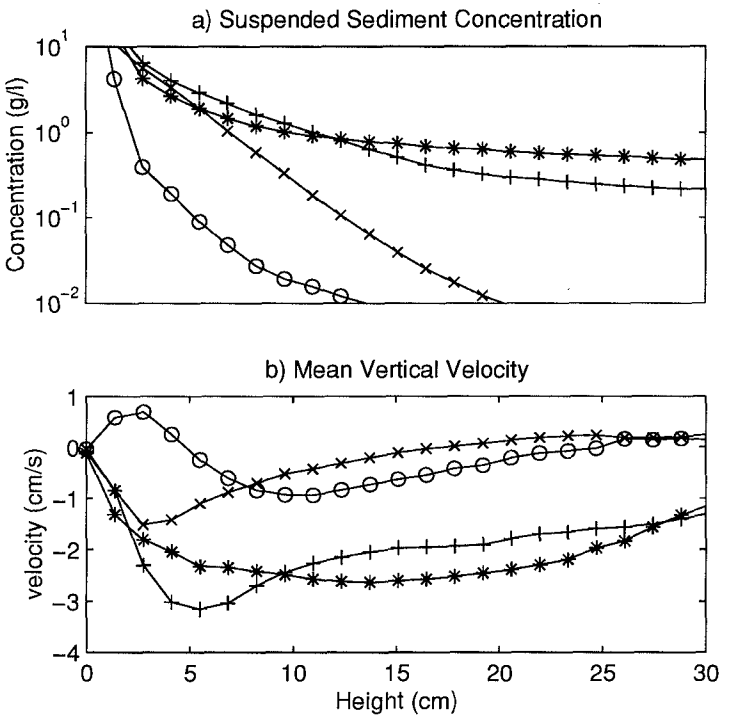

Figure 1: Mean profiles of a) suspended sediment concentration and b) vertical velocity for observations of 3.5 s period regular waves with heights of 20, 40, 60 and 70 cm indicated by ∘, ×, +, and ∗ respectively.

4 TURBULENCE INTENSITY

The energy driving sediment upward from the bottom is derived from turbulent fluid motions. This energy can be parameterized in terms of the friction velocity u_*. A parametric estimate of friction velocity can be determined from sand grain roughness, wave amplitude and frequency (Nielson 1992),

$$u_* = \sqrt{f_w/2}\, A\omega \tag{2}$$

where $\omega = 2\pi/T$, $T = 3.5\,\mathrm{s}$ is the wave period, A is the wave orbital excursion and f_w is the friction factor computed as,

$$f_w = exp(5.5(r/A)^{.2} - 6.3) \tag{3}$$

with $r = 150\,\mu$ m the sand particle diameter. Values for this parametric estimate of friction velocity are listed under u_* in Table 1 along with bed form characteristics and wave heights.

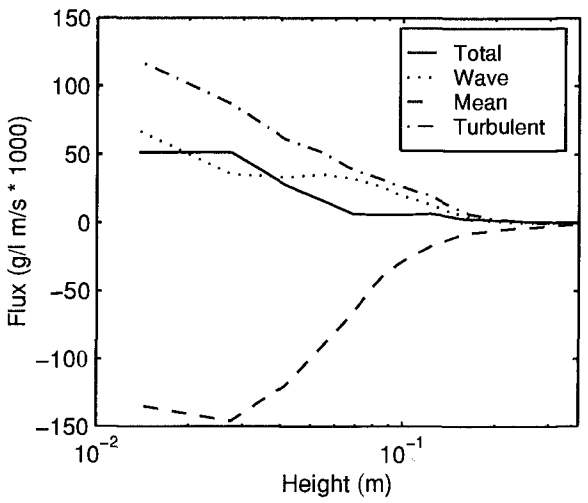

Figure 2: Profiles of mean, wave, turbulent and total sediment flux. Profiles are based on a 6 minute data sample under regular, 3.5 s period waves of 60 cm height.

H cm	Bed Form	u_* cm s^{-1}	u_*(sediment) cm s^{-1}	w'_{max} cm s^{-1}	b(parametric) s/m^2	b(observed) s/m^2
20	R_l	1.5	2.2	2.3	3200	920
30	R_s	2.3	2.5	2.5	1330	440
40	R_s	3.1	3.2	2.9	660	560
50	X	3.4	3.9	3.5	430	460
60	X	4.2	7.0	5.6	240	340
70	F	4.9	5.0	4.4	150	80

Table 1: Summary of trials under 3.5 s period waves with heights indicated as H; u_* is the friction velocity computed from parameterizations of wave height, u_*(sediment) is based on the near bottom profile of suspended sediment (Sheng and Hay, 1995), w'_{max} refers to the maximum observed variance in vertical velocity observations. Bedforms are indicated by R_l, R_s, X, and F for long crested, short crested, cross ripples, and flat bed respectively, b(parametric) and b(observed) are the predicted (see 5) and observed slope in $1/ < w'_{rms} >$ profiles.

Values of u_* can also be estimated from the observations through the slope of the suspended sediment concentration following the approach used by Sheng and Hay (1995). Table 1 compares the values of u_* derived from this technique ($u_*(sediment)$ in Table 1) with parameterizations based on the waves

and grain roughness (Nielson, 1992) (u_* in Table 1).

An independent indicator of the turbulence characteristics of the boundary layer is provided in the present observations by profiles of $< w'_{rms} >$: example profiles are shown in Fig. 3a. Nielsen (1992, p. 72) reports that peak values of $< w'_{rms} >= 0.5u_*$ occurring at a height approximately equal to the top of the roughness elements. Similar relations are also seen in unidirectional boundary layer flow (Tennekes and Lumley, 1972 p. 162). The peak values of $< w'_{rms} >$ in the present observations are very close to the parametric estimates of friction velocity as well as those based on concentration profiles (see the values listed as w'_{max} in Table 1).

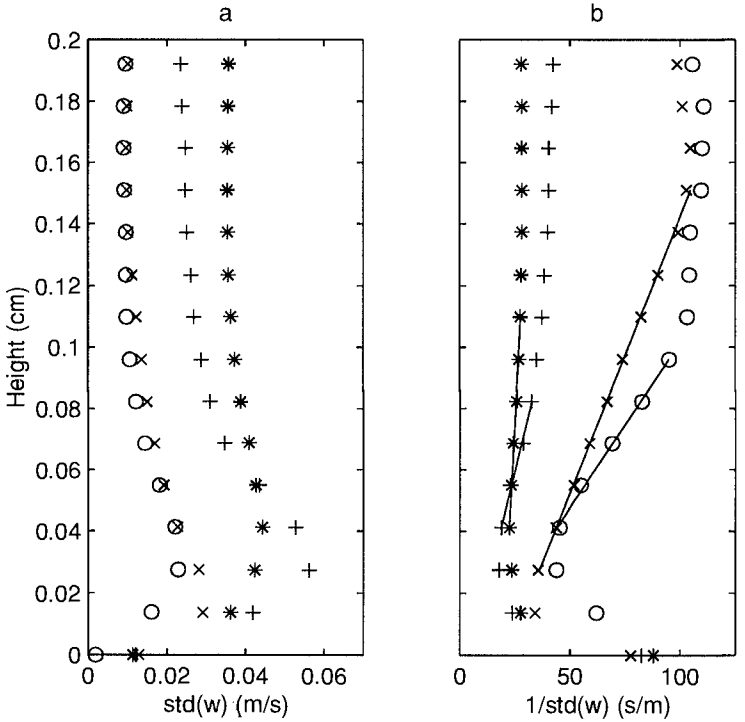

Figure 3: a) Profiles of $< w'_{rms} >$ and b) $1/ < w'_{rms} >$ as observed under 3.5 s period waves of height 20, 40, 60 and 70 cm indicated by $\circ$, $\times$, $+$, and $*$ respectively.

An important aspect of the data summarized in Table 1 is the apparent response to changing bedforms. In particular, the decrease in the observed indicators of friction velocity (u_*(sediment), and w'_{max} in Table 1), that occurs between 60 and 70 cm wave heights coincides with the disappearance of small scale bedforms. The associated change in roughness is not accounted for in the

parametric estimate of friction velocity but it is clearly important to regulating the turbulent contribution to sediment flux.

5 TURBULENCE DECAY

Sleath (1991) suggests that oscillatory boundary layers can be modeled after the turbulence generated by an oscillating grid. Such a model is qualitatively consistent with the present observations where $< w'_{rms} >$ decreases with height beyond a point of maximum value near the bottom. Following Sleath's model, the turbulent intensity should decrease with distance from the bottom according to the relation (Sleath, 1991),

$$1/ < w'_{rms} >= bz \tag{4}$$

with

$$b = KA^{-3/2}r^{-1/2}T \tag{5}$$

where A is the wave orbital excursion, r is the bottom roughness (here we have set $r = \lambda_r$ because use of the sand grain roughness gave extremely inconsistent results), and $K \approx 6.29$ is a constant. Values for the expected slopes from (5) are indicated as b(parametric) in Table 1. Figure 3b shows observed values of $1/ < w'_{rms} >$ plotted as a function of height above the bottom for trials under wave heights of 20, 40, 60 and 70 cm. There is a well defined section where a straight line fit to the data is achieved. The slope from linear regression fits to this region (indicated by straight line segments in Fig. 3b), are identified in Table 1 as b(observed). Approximate agreement between predictions of (5) and the observations is seen for some of the trials, but in general, there are significant differences. In particular, at low wave energies, the value of b predicted by (5) is larger than the observations by a factor of 3 indicating that turbulence does not decay with height as rapidly as expected based on the grid turbulence model.

6 DISCUSSION

Doppler velocity estimates represent a backscatter strength weighted average over the velocity of any scatterers present in the sample volume. When Doppler sonar is used to measure water velocities, it is necessary to assume that the motion of the scattering particles is representative of the water motion as a whole. For the present application, the velocities observed will be those of the uniformly sized (150 μm diameter) sand particles added to the tank. Only when the concentration of these particles is extremely low will the small bubbles and dust particles in the tank provide an estimate of the water velocity itself. As a result, the mean vertical velocities shown in Fig. 1 are a direct measure of the in-situ settling velocity of the suspended sand particles.

The settling velocity for spherical particles can be calculated using Stokes law,

$$w_s = \frac{(s-1)gd^2}{18\nu} \tag{6}$$

where $s = 2.7$ is the relative density of the particle, d is the particle diameter (d =150 μm for the present sand particles), g is the acceleration of gravity and ν is the viscosity ($\nu = 1.0 \times 10^{-6}$ $\mathrm{m^2 s^{-1}}$). For the present d =150 μm sand particles, $w_s \simeq 2.0$ $\mathrm{cm\,s^{-1}}$.

Settling velocities of 2 to 3 $\mathrm{cm\,s^{-1}}$ were observed at heights of between 10 and 20 cm for the 60 and 70 cm height wave runs (Fig. 1b). These values are consistent with the prediction of the Stokes settling velocity given by (6). The low velocities seen in this depth range for lower wave heights are most likely caused by the low particle concentrations ($\approx 10^{-2}$ $\mathrm{g\,l^{-1}}$) that occur (see Fig. 1). Under such circumstances, the backscatter from small contaminants in the water would provide an adequate signal such that the true water velocity would be obtained.

In all cases, the mean velocity goes to zero as the bottom is approached. These decreased settling velocities clearly have a significant impact on the concentration profiles. The cause of the reduced velocities is not obvious but some disturbance is expected due to the presence of bedforms. These bedforms could not however account for the gradual transition to zero velocity that is observed. It is very likely that these near bottom reduced settling velocities are related to the presence of turbulence as described by Murray (1970).

Profiles of mean turbulent intensities based on values of $< w'_{rms} >$ demonstrate a rapid increase from 0 at the bottom to a peak value within 5 cm of the bottom and then an asymptotic decrease with greater height. In the present observations, $max(< w'_{rms} >)$ is clearly proportional to friction velocity, but it appears to vary as an equality; that is $max(< w'_{rms} >) = u_\star$ (see Table 1). It is possible that the present observations do not resolve velocities close enough to the bottom to recover the true peak values. If this were the case, one would expect that the proportion of the fluctuations seen would change with the bed-form dimensions. No such dependence is seen and so we feel that we are sampling a consistent maximum in velocity fluctuations. It is also possible that the sonar system does not resolve the total turbulent spectrum. We consider this explanation unlikely as well because the 'red' nature of turbulent spectra places most of the energy at lower frequencies, (and larger scale structures) which the Dopbeam system does resolve.

7 CONCLUSIONS

Through the use of combined Doppler sonar and acoustic backscatter measurements it has been possible to make simultaneous estimates of particle velocity and concentration. This combination of measurements allows for direct observation of particle flux. Phase averaging under regular waves (possible in the tow tank test facility) allows the discrimination of both turbulent and wave components of flux ($w'c' + \tilde{w}\tilde{c}$) in addition to the mean (downward) flux.

The assumption of a balance between the upward wave and turbulence induced flux with the mean downward flux is fundamental to most models of vertical sediment transport (see for example Lee and Hanes, 1996). We have demonstrated that such a balance does exist in the present data. Previous estimates of the downward flux term have been made from independent measurements of particle descent rate and concentration: a common assumption is that the particle descent rate is given by the free descent rate of the particles (Sheng and Hay, 1995). This assumption appears to hold for most of the water column but breaks down within 5 cm of the bottom in the present observations.

The turbulent velocity represented by $< w'_{rms} >$ peaks a small distance above the bed (within 5 cm in the present observations). At heights above the peak value, $< w'_{rms} >$ decays as 1/height, consistent with Sleath (1991).

The near bottom peak values of $< w'_{rms} >$ are equal to the friction velocity characteristic of the bottom boundary layer (as estimated parametrically and from the concentration profile). We conclude that the direct observation of $< w'_{rms} >$ possible with the coherent Doppler system is an effective means of estimating friction velocity.

The three separate estimates of friction velocity (based on the sediment diffusivity, the wave parameters, and the $< w'_{rms} >$ measurements) are all consistent. The slight decrease in friction velocity occurring in the diffusivity and $< w'_{rms} >$ based estimates when going from the 60 cm to 70 cm wave height at first appears inconsistent. However, the fact that both of these direct observations show the same behavior supports their accuracy. The bed-form observations for these two wave conditions show that they correspond to the transition from cross ripples to 'mega-ripples'. The 'mega-ripples' result in a much reduced mean bottom slope and associated with this reduced bottom slope we would expect a reduced efficiency in turbulence generation. While the data is clearly limited, we believe that the reduced friction velocity is accurately being observed and is associated with the changing bed-forms. The parametric estimate of friction velocity (which ignores bed-forms) matches the observations reasonably well. This close agreement indicates that (in the present case), while bedforms effect the turbulence generation they do not account for a large contribution to turbulence important to sediment suspension.

8 REFERENCES

Hay, A.E., 1991: Sound scattering from a particle-laden jet. J. Acoust. Soc. Am., 90, 2055-2074.

Lee, T.H. and D.M. Hanes, 1996: Comparison of field observations of the vertical distribution of suspended sand and its prediction by models. J. Geophys. Res., 101, 3561-3572.

Murray, S.P., 1970: Settling velocities and vertical diffusion of particles in turbulent water, J. Geophys. Res., 75, 9, 1647-1654.

Nielsen, P., 1992: Coastal bottom boundary layers and sediment transport. World Scientific. Singapore, 324 pp.

Sheng, J., and A.E. Hay, 1995: Sediment eddy diffusivities in the nearshore zone, from multifrequency acoustic backscatter. Cont. Shelf Res., 15, 2/3, 129-147.

Sleath, J.F.A., 1991: Velocities and shear stresses in wave-current flows. J. Geophys. Res. 96, C8, 15237-15244.

Tennekes, H. and J.L. Lumley, 1972: A first course in turbulence. MIT Press, Cambridge, 300 pp.

Zedel, L., A.E. Hay, R. Cabrera, and A. Lohrmann, 1996: Performance of a single beam, pulse-to-pulse coherent Doppler profiler. IEEE Journal of Oceanic Technology, 21, 290-297.

Eddy Viscosity Models for Wave Boundary Layers

Ole Secher Madsen[1], M. ASCE, and Paulo Salles[2]

Abstract

Motivated by recent experimental results on wave, current and combined wave-current flows over an artificially rippled bed, the boundary resistance experienced by waves over two-dimensional bottom roughness elements is formulated in terms of a drag law. The resulting empirical relationship for the drag coefficient suggests a flow resistance that is similar in nature to one obtained from a constant, pseudo-laminar eddy viscosity model for the wave boundary layer flow. Analysis of available experimental data on energy dissipation for oscillatory flow over movable rippled beds leads to a constant eddy viscosity model for wave boundary layers above naturally rippled beds. The constant eddy viscosity model is modified to include a near-bottom linear transition to make it zero at the bed. This hybrid eddy viscosity model is shown to capture the essential features of wave boundary layer flows for the full range of bottom roughnesses encountered, i.e. from sand grains to ripples. Application of the hybrid model requires knowledge of the equivalent bottom roughness for which empirical expressions are derived. The implication of the results, obtained here for waves, for combined wave-current boundary layer flows suggests modifications of the Grant-Madsen model that greatly improve this model's ability to predict observed current velocity profiles over rippled bottoms in the presence of waves.

Introduction

In recent papers Mathisen and Madsen (1996a and b, hereafter referred to as MM) reported results from laboratory experiments on currents and waves, separately as well as combined, over a bottom covered by fixed equally spaced 1.5-cm-high triangular two dimensional roughness elements. The major result of their study was that waves and

[1] Professor and [2] Graduate Student, R. M. Parsons Laboratory, Department of Civil and Environmental Engineering, Massachusetts Institute of Technology, Cambridge, MA 02139, USA

currents perpendicular to the axes of their artificial ripples experience the same equivalent bottom roughness, i.e., the equivalent bottom roughness, k_N, was shown to be a function of the bottom roughness characteristics only and independent of the flow. Besides being limited to the particular flow conditions of their experiments, i.e. wave, current and combined co-directional wave-current flows perpendicular to fixed two-dimensional roughness elements, their conclusion of k_N's single-valuedness is limited to analyses of these flows based on a modified version of the Grant-Madsen model (Grant and Madsen, 1979 and 1986; hereafter referred to as GM) since this model was used by MM in their analysis of experimental data.

To make this latter limitation more explicit, and also to introduce concepts and notation to be used in subsequent sections, MM obtained experimental values for the average rate of energy dissipation per unit bottom area, D, from measurements of wave attenuation and expressed D in terms of turbulent wave bottom boundary layer theory,

$$D = \frac{1}{4}\rho\, f_w \cos\varphi\, u_{bm}^3 = \frac{1}{4}\rho\, f_e\, u_{bm}^3 \tag{1}$$

in which ρ denotes the fluid density; f_w is the wave friction factor defined by

$$\frac{\tau_{bm}}{\rho} = u_{*m}^2 = \frac{1}{2} f_w\, u_{bm}^2 \tag{2}$$

where τ_{bm} is the maximum bottom shear stress; and φ is the phase lead of the bottom shear stress relative to the periodic near-bottom wave orbital velocity

$$u_b = u_{bm} \cos\omega t \tag{3}$$

Thus, from their experiments MM obtained values for the energy dissipation factor, $f_e = f_w \cos\varphi$, which, in turn, may be related to the relative bottom roughness, $u_{bm}/(k_N\omega)$, through the use of a theoretical model for turbulent wave boundary layer flows over a rough bottom. In taking this last step, which leads to the determination of the equivalent bottom roughness, k_N, MM found it necessary to modify the GM model in order to obtain the k_N–values that were in agreement with the values obtained from analysis of measured current velocity profiles over the same bottom roughness configuration. This modified version of the original GM-model has been presented by Madsen (1994) and consists of the determination of the wave friction factor, f_w, and the phase lead, φ, by evaluating the bottom shear stress at $z = z_0 = k_N/30$, where z is the vertical distance above the theoretical bed level, instead of in the limit $z \to 0$.

However, when the modified GM-model is used to predict the structure of the wave orbital velocity profile within the wave boundary layer this is found to be in poor agreement with measurements. In particular, the GM-model's prediction of the wave boundary layer thickness

$$\delta_w = A\frac{\kappa u_{*m}}{\omega} \tag{4}$$

in which κ is von Karman's constant (=*0.4*) and A is a scaling factor given the value of 1 to 2 by GM, is found to be too small by a factor of 2 to 3 when compared with measurements. This disturbing observation has profound implications for the GM-model's ability to predict the velocity profile of currents in the presence of waves, since $z=\delta_w$ is the location where the eddy viscosity is assumed to change from being scaled by the wave-current shear velocity, u_{*m}, to being scaled by the generally much smaller current shear velocity, u_{*c}. Thus, in order to obtain a reasonable agreement between predicted and observed current velocity profiles in the presence of waves, MM found it necessary to introduce an artificially "enhanced" wave boundary layer thickness. This apparent inability of the GM-model to predict the velocity structure as well as the thickness of the wave boundary layer for flows over a rippled bottom motivated the present study.

Drag Law Formulation and its Implications

In an attempt to break with the conventional treatment of wave boundary layer flows based on an eddy viscosity formulation, we express the flow resistance experienced by an oscillatory flow over a bottom covered by two-dimensional ripples in terms of the drag force exerted on the flow by the individual roughness elements. Formally, we may write this drag force per unit length

$$F_D = \frac{1}{2}\rho C_D \eta |u_b| u_b \tag{5}$$

in which η is the height of the ripple, u_b is the wave orbital velocity given by (3), and C_D is a drag coefficient. Assuming this drag force to dominate the flow resistance, i.e. neglecting the contribution of skin friction shear stress acting directly on the bottom between roughness elements (ripple crests), the rate of energy dissipation associated with this drag force is given by $F_D\, u_b$. Since this represents the rate of energy dissipation per roughness element, we obtain the time average rate of energy dissipation per unit area

$$D = \frac{\overline{F_D u_b}}{\lambda} = \frac{2}{3\pi}\rho C_D \frac{\eta}{\lambda} u_{bm}^3 \tag{6}$$

where "overbar" denotes time-averaging and λ the ripple spacing (length). In passing it is noted that the neglect of a potential inertia force has no effect on the calculated average energy dissipation rate since this force would be proportional to $\partial u_b/\partial t$ and hence time-average to zero.

Comparison of the expressions obtained from conventional boundary layer theory, (1), and drag law formulation, (6), shows that

$$C_D = \frac{3\pi}{8}(\lambda/\eta) f_e \tag{7}$$

Thus, the experiments on wave attenuation performed by MM, which provide values of f_e for given λ (10 or 20 cm) and η (1.5 cm), may be used directly in (7) to obtain

experimental values for the drag coefficient, C_D, for waves over the artificially rippled bed. In analogy with drag coefficients for circular cylinders, e.g. Sarpkaya and Isaacson (1981), one would expect the drag coefficient to be a function of a Reynolds number, *Re*, and a Keulegan-Carpenter number, *KC*. Recognizing that the roughness elements in the experiments performed by MM were 90° angle iron bars placed on the glass bottom of a flume, i.e. effectively corresponding to half cylinders, the equivalent "diameters" of their two-dimensional roughness elements is 2η. Therefore, one would be seeking an empirical expression of the form

$$C_D = C_D\left(Re = \frac{2\eta u_{bm}}{\nu}, KC = \frac{u_{bm}T}{2\eta} = \pi\frac{A_b}{\eta} \right) \tag{8}$$

where ν is the kinematic viscosity of water and $A_b = u_{bm}/\omega = u_{bm}T/(2\pi)$ is the near-bottom wave orbital excursion amplitude.

For the experiments performed by MM the range of Reynolds Numbers is (3 to 6).10^3, i.e. a range for which *Re*-dependency is expected to be weak. As seen from the values of C_D plotted against η/A_b in Figure 1, the excellent correlation supports this anticipation and results in the empirical drag coefficient relationship given by

$$C_D = C_{Do}\frac{\eta}{A_b} = 9.0\frac{\eta}{A_b} \tag{9}$$

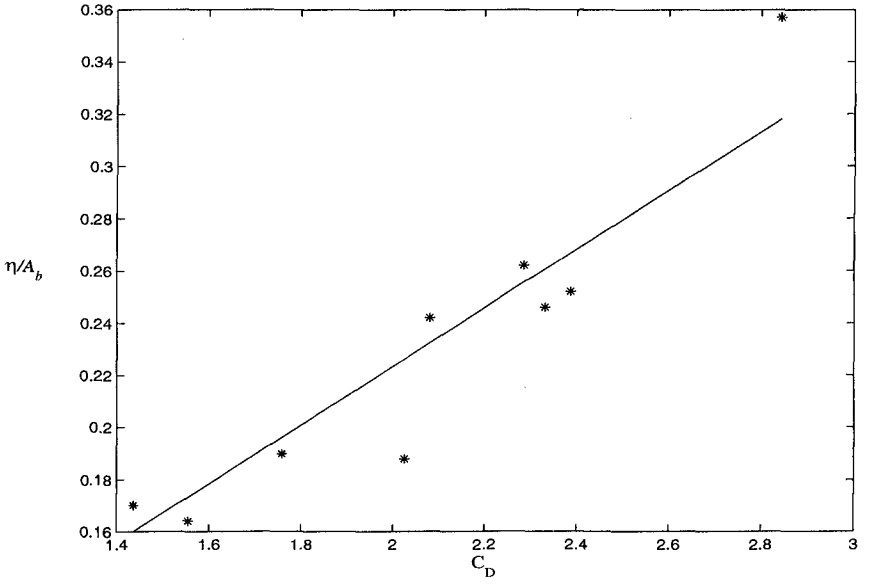

Figure 1: Ratio of the ripple height over the bottom excursion amplitude, η/A_b, as a function of the drag coefficient, C_D. Experimental values (*stars*) and linear fitting (*solid line*). The coefficient of determination is $r^2 = 0.87$.

The limitation of this relationship to the experimental range of η/A_b values from which it is obtained should be kept in mind. Extension beyond this range leads to obvious errors, e.g. $C_D \rightarrow 0$ or ∞ as $\eta/A_b \rightarrow 0$ or ∞. However, for the range covered by (9) the dependency of C_D on η/A_b is similar to the dependency on Keulegan-Carpenter number for circular cylinders and $Re = 10^4$ (Sarpkaya and Isaacson, 1981, Figure 3.15; Salles, 1997).

A Pseudo-Laminar Eddy Viscosity Model

When the empirical drag coefficient relationship, (9), is introduced in the drag law expression for the rate of energy dissipation, (6), and $u_{bm} = A_b\omega$ is utilized one obtains

$$D = \rho\left(\frac{2}{3\pi} C_{Do} \frac{\eta^2}{\lambda}\right)\omega u_{bm}^2 \tag{10}$$

This form of the average dissipation rate, in particular, its proportionality to the square of the wave orbital velocity, resembles the expression obtained from a laminar or constant eddy viscosity model of oscillatory boundary layers, e.g. Jonsson (1966)

$$D = \rho\left(\frac{1}{4}\sqrt{2\nu_c/\omega}\right)\omega u_{bm}^2 \tag{11}$$

in which ν_c denotes the value of the constant viscosity.

Equating (10) and (11) leads to a functional relationship for an equivalent constant, pseudo-laminar eddy viscosity

$$\nu_c = \left(\frac{8}{3\pi} C_{Do}\right)^2 \pi \frac{\eta^4}{\lambda^2 T} \cong 180 \frac{\eta^4}{\lambda^2 T} \tag{12}$$

where C_{Do} = 9.0, obtained from MM's experiments, was introduced. With a constant eddy viscosity, the classical solution of Stokes gives the wave orbital velocity profile as the real part of the complex expression (i^2 = -1)

$$u_w = \left(1 - e^{-(1+i)z/\delta}\right) u_{bm} e^{i\omega t} \tag{13}$$

with

$$\delta = \sqrt{2\nu_c/\omega} \tag{14}$$

denoting the boundary layer scale.

The wave boundary layer thickness, δ_w, is obtained by requiring the orbital velocity to approach the free stream velocity to within a small, but finite, fraction, ε, of the free stream velocity. Defining δ_w in this manner and making use of (13) and (14) results in

$$\delta_w = (-\ln \varepsilon)\delta = \begin{Bmatrix} 3.0 \\ 4.6 \end{Bmatrix}\delta \quad \text{for} \quad \varepsilon = \begin{Bmatrix} 5\% \\ 1\% \end{Bmatrix} \tag{15}$$

Figure 2 demonstrates that the pseudo-laminar wave orbital velocity profile obtained from (13) and (14) with ν_c given by (12) is in excellent agreement with the measurements obtained in MM's experiment "a". This agreement includes the prediction of the wave boundary layer thickness, the scale of which is obtained from (14) with ν_c given by (12) ($\delta = 7.6\ \eta^2/\lambda = 1.7$ cm). From (15) it follows that δ_w is of the order of 5.1 to 7.8 cm for the $\lambda = 10$ cm spacing of the individual roughness elements, in agreement with MM's "enhanced" wave boundary layer thickness of 6.0 cm.

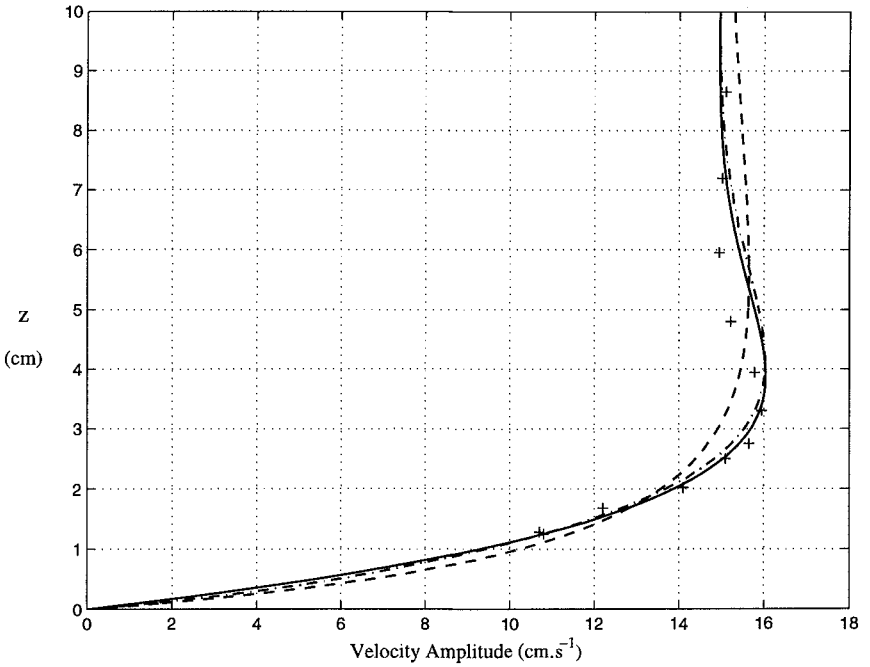

Figure 2: Velocity amplitude profiles obtained from 1) the pseudo-laminar model (*solid line*), 2) the hybrid model (*dash-dotted line*), 3) the GM-modified model (*dashed line*), and 4) MM's experiment "a" measurements above the trough of the ripples (*pluses*).

Thus, the pseudo-laminar model is capable of not only predicting the observed wave attenuation – an ability that is, of course, assured since ν_c was derived to produce exactly this result – but also the detailed velocity structure within and the thickness of the wave boundary layer.

Mathisen and Madsen (1996a and b) chose the geometry of their artificial ripples, $\eta = 1.5$ cm and $\lambda = 10$ cm, in accordance with observed ripple geometry for similar wave conditions to those in their experiments. Differences between the detailed geometry of natural and MM's artificial ripples may, however, prevent the success of the pseudo-

laminar model to be transferred to naturally rippled beds. Guided by our results from analysis of MM's data, equating the expressions for the rate of energy dissipation given by (1) and (11), with ν_c depending on ripple geometry as suggested by (12), we obtain

$$\nu_c = \nu_{co} \frac{\eta^4}{\lambda^2 T} = \frac{1}{4\pi} T f_e^2 u_{bm}^2 \tag{16}$$

Following the suggestion of (16) we plot experimental values of ripple geometry and energy dissipation for experiments with waves over naturally rippled beds in Figure 3, from which we obtain a best fit value of the constant $\nu_{co} = 95$ in (16), with a standard deviation of 53. Not surprisingly, the eddy viscosity for naturally rippled beds is not as well defined as the one obtained for the artificial ripples. Nevertheless, the result that ν_{co} is smaller for natural ripples than for artificial ripples is statistically significant and does make physical sense since one would expect the more rounded crests of the natural ripples to result in a smaller rate of energy dissipation and hence a smaller eddy viscosity.

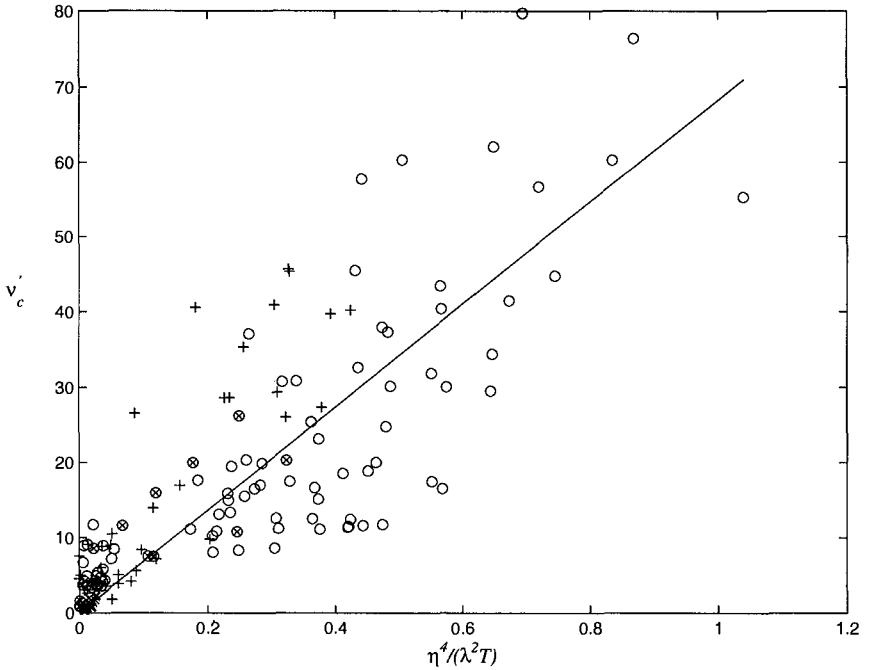

Figure 3: Eddy viscosity $\nu_c' = (8/3\pi)^2 \nu_c$ as a function of $\eta^4/(\lambda^2 T)$. Both quantities are in $(cm^2.s^{-1})$. Experimental data from Carstens et al. (1969) (*pluses*), Lofquist (1986) (*circles*), Rosengaus (1987) and Mathisen (1989) (*crosses*). The linear fitting (*solid line*) has a coefficient of determination $r^2 = 0.70$.

From a practical point of view, the difference between the values of ν_c for artificial and natural ripples may be less significant, when one considers the fact that the data plotted in

Figure 3 used observed ripple geometry. For application, one would have to use predicted values of η and λ in the empirical expression for ν_c, (16). Our current ability to predict geometry of wave generated ripples is unfortunately such that a potential factor of 2 variability in ν_{co} in (16) is overshadowed by the uncertainty associated with the prediction of η^4/λ^2.

Detailed velocity profile measurements are not available within the wave boundary layers over naturally rippled beds. The similarity of the expressions obtained for ν_c suggests, however, that one may expect the pseudo-laminar eddy viscosity model to afford reasonably accurate predictions of the velocity structure within the wave boundary layer over naturally rippled beds.

A Hybrid Eddy Viscosity Model

The constant eddy viscosity model presented in the preceding section can be considered valid only for the very large bottom roughness values corresponding to rippled beds. It will neither predict a phase lead of the bottom shear stress different from $\pi/4$ or a near-bottom logarithmic wave orbital velocity profile, both of which are experimentally observed features for wave boundary layer flows for smaller values of the relative roughness. These features are, however, predicted by simple wave boundary layer models that employ an eddy viscosity that, near the bottom, increases linearly with distance above the theoretical bottom, e.g. Hsu and Jan (1998).

A hybrid eddy viscosity model that captures the observed features of wave boundary layer flows for small as well as large relative bottom roughness values is chosen as

$$\nu_t = \begin{cases} \kappa u_{*m}(z + z_0), & 0 \le z \le z_m \\ \kappa u_{*m}(z_m + z_0), & z > z_m \end{cases} \tag{17}$$

in which $z_0 = k_N/30$ is the hydraulic bottom roughness, and u_{*m} is defined by (2). In (17) the value of z_m, the elevation above which the eddy viscosity is considered constant, is chosen as

$$z_m = 0.5\frac{\kappa u_{*m}}{\omega} \tag{18}$$

For this choice of z_m the constant value of the eddy viscosity given by (17) is roughly the same as the pseudo-laminar viscosity given by (12) for the experiments of MM. Furthermore, this value of z_m coincides with value chosen by Madsen and Wikramanayake (1991) who showed this choice to lead to acceptable agreement between predicted and observed velocity structures within the wave boundary layer for relative roughness, k_N / A_b, smaller than $O(10^{-1})$.

Solving the linearized boundary layer equation with the eddy viscosity prescribed by (17) and evaluating the maximum bottom shear stress at $z = 0$ determines the relationship between wave friction factor and the relative bottom roughness. Approximating this

relationship in a manner analogous to that utilized by Madsen (1994) we obtain explicit expressions for the wave friction factor f_w and the phase angle φ (in degrees)

$$f_w = \exp\left\{8.89(A_b/k_N)^{-0.059} - 10.68\right\}$$
$$\varphi = 38 - 8.3\log\frac{A_b}{k_N} \tag{19}$$

valid for the range $0.2 < A_b/k_N < 10^2$. For larger values of A_b/k_N the formulas given by Madsen (1994) may be used.

From the experimental value of $f_e = f_w \cos\varphi$ obtained by MM the equivalent bottom roughness, k_N, is obtained from (19). The predicted wave orbital velocity profile obtained from the hybrid eddy viscosity model, given by (17) is shown in Figure 2, and is virtually indistinguishable from the velocity profile predicted by the pseudo-laminar model.

The hybrid eddy viscosity model requires knowledge of the equivalent bottom roughness in order to be applied. Thus, to make the model applicable for the prediction of wave boundary layer flows over naturally rippled beds, an empirical relationship for k_N is required. Such a relationship is obtained by assuming it to be of the form

$$k_N = \begin{cases} \alpha\eta \\ \beta(\eta/\lambda)\eta \end{cases} \tag{20}$$

and determine the best fit values of α and β by fitting the experimental data on rate of energy dissipation over naturally rippled beds using the experimentally measured ripple characteristics. This exercise results in values of α=12 and β=78, with both formulations providing a fit of equal goodness to the data used.

The experimentally obtained values for f_e are plotted against A_b/k_N, with $k_N = 12\ \eta$, in Figure 4. The relationship, $f_e(A_b/k_N)$, obtained from (19) is shown for comparison, and represents the experimental data with a coefficient of variation of 28%. This accuracy of the hybrid eddy viscosity model is similar to that of the pseudo-laminar model. For the pseudo-laminar model we obtained a coefficient of variation for ν_c of 53/95 = 0.56 which is roughly twice the coefficient of variation for the prediction of f_e since $f_e \propto \sqrt{\nu_c}$ for the pseudo-laminar model. Again, it is emphasized that the accuracy of 28% for the prediction of the energy dissipation factor when k_N is obtained from (20) is likely to be an optimistic value when η is predicted rather than measured. Finally, it should be pointed out that the seemingly very large value of $\alpha = 12$ is obtained as a result of using (19), which is the friction factor relationship obtained by evaluation of the bottom shear stress at $z+z_0 = z_0$. For a model that uses a near-bottom eddy viscosity proportional to z instead of $(z+z_0)$ this corresponds to evaluation of the shear stress at $z=z_0$ instead of in the limit $z\to 0$. The original GM-model, if applied to the data shown in Figure 4 would therefore lead to different best fit constants in (20). In fact, for the GM-model with the shear stress evaluated in the limit $z\to 0$, one obtains values of $\alpha = 4$ and $\beta = 25$, i.e. roughly a factor of three lower than the best fit values obtained for the hybrid eddy viscosity model.

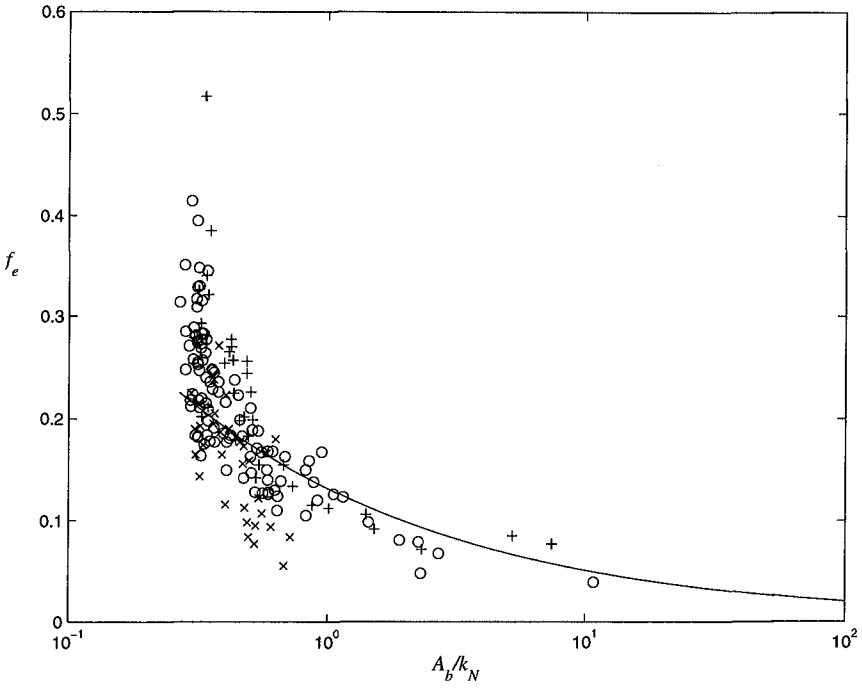

Figure 4: Measured and predicted energy dissipation factors, f_e, as a function of relative roughness, A_b/k_N. Theoretical values using (19) with $k_N = 12\,\eta$ (*solid line*); data from Carstens et al. (1969) (*pluses*), Lofquist (1986) (*circles*), Rosengaus (1987) and Mathisen (1989) (*crosses*).

Modified Grant-Madsen Wave-Current Interaction Model

If one is willing to sacrifice a little accuracy in the prediction of the velocity structure within the wave boundary layer for the sake of simplicity, one may adopt a linearly increasing eddy viscosity throughout the wave boundary layer. In this case the eddy viscosity reduces to the first expression given by (17) and the wave orbital velocity within the wave boundary layer is simply that predicted by Madsen (1994) with the origin of z taken a distance z_0 below his theoretical bed elevation. This effectively changes Madsen's (1994) eddy viscosity length scale from his "z" to the value $z+z_0$ used in (17). Except for this change, all formulas obtained by Madsen (1994) are still valid. To achieve a measure of the accuracy one sacrifices if adopting this simplification, the predicted wave orbital velocity profile of this modified GM-model is show in Figure 2. Obviously, either the pseudo-laminar or the hybrid eddy viscosity models provide a better fit to the experimental data shown in Figure 2 than does the modified GM-model. However, the GM-model does provide a reasonably accurate (better than 10% error) representaion of observations for this large bottom roughness.

Given the modified GM-model's ability to represent the velocity structure within the wave boundary layer, it is extremely surprising that the model's prediction of the wave boundary layer thickness is as poor as it is for the experiments by MM involving artificial ripples. This inability of the modified GM-model was discussed in the Introduction, where it was mentioned that the GM-model estimated the wave boundary layer thickness from (4) with a scaling factor A between 1 and 2, which for MM's experiment "a" shown in Figure 2 gives $\delta_w \approx 2.5$ cm – clearly a value much lower than the wave boundary layer thickness suggested by the data.

This inability of the GM-model to afford an accurate estimate of δ_w and hence, for combined wave-current flows, the elevation at which the current profile exhibits a discontinuous slope in the presence of waves, is actually not an inability of the model but the result of an unfortunate oversight on the part of the model's authors. The estimate of the scaling factor A in (4) being of the order of 1 to 2 was originally derived by Grant and Madsen by considering the elevation above the bottom where the wave orbital velocity had reached the free stream velocity within a relative error of roughly 5%. This, of course, is a completely legitimate criterion to use for the definition of a wave boundary layer thickness. However, GM failed to recognize that their value of A, which they obtained for a relative roughness $k_N / A_b \approx 0.01$, should be considered a function of the relative roughness and not be treated as a generally valid constant. When one corrects this oversight by defining the wave boundary layer thickness as the value of z for which the velocity magnitude is within 5% of the free stream velocity, the resulting value of the scaling factor in (4) may be expressed as

$$A = exp\left\{2.96\left(A_b/k_N\right)^{-0.071} - 1.45\right\} \tag{21}$$

For $A_b/k_N = 100$ this formula gives $A = 2.0$ in agreement with the original GM-value. However, for $A_b/k_N = 0.35$, which is representative of the relative roughness values in the MM experiments over artificially rippled beds, $A = 5.7$ is obtained from (21), i.e. an increase by a factor of roughly 2.8 over the value obtained if $A = 2.0$ is assumed independent of the relative roughness.

Use of (21) in conjunction with (4) to obtain the wave boundary layer thickness and modifying the GM-model's prediction of current velocity profiles in the presence of waves accordingly completely removes the need for the artificially "enhanced" wave boundary layer thickness introduced by Mathisen and Madsen. The modified GM-model can be used directly to explain and analyze observations for combined co-directional wave-current flows over a rippled bed so long as it is corrected to account for the wave boundary layer scaling factor's dependency on relative roughness.

Conclusions

From a drag law formulation of the boundary resistance experienced by waves over an artificially rippled bottom, we were led to the establishment of a constant pseudo-laminar eddy viscosity formulation for wave boundary layer flows over rippled bottoms. For naturally rippled bottom, analysis of available experimental data suggests the adoption of a pseudo-laminar eddy viscosity given by

$$\nu_c = \nu_{co} \frac{\eta^4}{\lambda^2 T} \tag{22}$$

in which $\nu_{co} = O(100)$, η and λ are the ripple height and length, respectively, and T is the wave period.

The pseudo-laminar model should be considered limited to the flow conditions corresponding to the existence of two dimensional wave-generated ripples covering the bottom. To establish a model that could be considered generally valid for the range of bottom roughness encountered by waves over a movable bottom, a hybrid eddy viscosity model was developed. For this model, given by (17), the constant eddy viscosity was reduced towards zero through a linear transition immediately above the bottom. The velocity structure within the wave boundary layer predicted by the hybrid eddy viscosity model was shown to be virtually identical to the predictions of the pseudo-laminar model for rippled beds. However, the hybrid model is, in contrast to the pseudo-laminar model, capable of predicting observed velocity features for small values of the bottom roughness. For wave boundary layer flows over naturally rippled bottoms , the bottom roughness, k_N, needed to apply the hybrid eddy viscosity model was found, from laboratory experiments with simple periodic wave motions, to be related to the ripple height through

$$k_N = 12\eta \tag{23}$$

Both the pseudo-laminar and the hybrid eddy viscosity models gave estimates of the wave boundary layer thickness that were in good agreement with observations for artificially rippled beds. An unfortunate oversight in the development and application of the Grant-Madsen model for combined wave-current flows over very rough bottoms was corrected by introducing a roughness-dependent scaling factor, A, given by (21). Following this correction, the artificially "enhanced" wave boundary layer thickness introduced by Mathisen and Madsen (1996b) to explain and analyze their experimental results for combined co-directional wave-current flows over artificially rippled bottoms, was found to be entirely unnecessary. Thus, the applicability of the corrected Grant-Madsen wave-current interaction model to the prediction of current profiles in the presence of waves over very rough, rippled, bottoms was established. For a rippled bed, it is emphasized, however, that application of the modified GM-model is limited to co-directional wave-current flows. The reason for this limitation is that the bottom roughness has been shown to be the same for waves and currents only for this type of combined flows over two-dimensional roughness elements.

Acknowledgement

The research leading to the results presented here was supported by a grant: 9314366-OCE from the Marine Geology and Geophysics Program, Ocean Sciences, of the National Science Foundation, and by a fellowship from the National Autonomous University of Mexico.

References

Carstens, M. R., Neilson F. M. and Altinbilek, H. D. (1969). Bedforms generated in the laboratory under an oscillatory flow. *Technical Report TM-28.* U. S. Army Corps of Engineers. Coastal Engineering Research Center.

Grant, W. D. and Madsen, O. S. (1979). Combined wave and current interaction with a rough bottom, *Journal of Geophysical Research* **84**(C4): 1797-1808.

Grant, W. D. and Madsen, O. S. (1986). The continental shelf bottom boundary layer. *Annual Review of Fluid Mechanics* **18**: 265-305.

Hsu, T. W. and Jan, C. D. (1998). Calibration of a Businger-Arya type of eddy viscosity model's parameters, *J. WPCOE,* ASCE, **124**(5): 281-284.

Jonsson, I. G. (1966). Wave boundary layer and friction factors, *Proceedings of the 10th Conference on Coastal Engineering,* ASCE, Tokyo, Japan, pp. 127-148.

Lofquist, K. E. B. (1986). Drag on naturally rippled beds under oscillatory flows, *Technical Report MP-86-13,* U.S. Army Corps of Engineers, Coastal Engineering Research Center.

Madsen, O. S. (1994). Spectral wave-current bottom boundary layer flows, *Proceedings of the 24th International Conference on Coastal Engineering,* ASCE, Kobe, Japan, pp. 384-398.

Madsen, O. S. and Wikramanayake, P. N. (1991). Simple models for turbulent wave-current bottom boundary layer flow, *Technical Report DRP-91-1,* U.S. Army Corps of Engineers, Coastal Engineering Research Center.

Mathisen, P. P. (1989). *Experimental Study on the Response of Fine Sediments to Wave Agitation and Associated Wave Attenuation,* MSc thesis, Massachusetts Institute of Technology, Cambridge, MA.

Mathisen, P. P. and Madsen, O. S. (1996a). Waves and currents over a fixed rippled bed (1), Bottom roughness experienced by waves in the presence and absence of currents, *Journal of Geophysical Research* **101**(C7): 16533-16542.

Mathisen, P. P. and Madsen, O. S. (1996b). Waves and currents over a fixed rippled bed (2), Bottom and apparent roughness experienced by currents in the presence of waves, *Journal of Geophysical Research* **101**(C7): 16543-16550.

Rosengaus, M. (1987). *Experimental Study on Wave Generated Bedforms and Resulting Wave Attenuation,* ScD dissertation, Massachusetts Institute of Technology, Cambridge, MA.

Salles A. de A., P. (1997). *Eddy Viscosity Models for Pure Waves Over Large Roughness Elements.* MSc thesis, Massachusetts Institute of Technology, Cambridge, MA.

Sarpkaya, T. and Isaacson, M. (1981). *Mechanics of Wave Forces on Offshore Structures,* Van Nostrand Reinhold Co., New York, NY.

Measurement of Shear Stress on a Moveable Bed

Kelly L. Rankin[1], Michael S. Bruno[2], member ASCE, Richard I. Hires[3]

Abstract

A shear plate has been developed to obtain direct measurements of bottom shear stress under non-breaking surface gravity waves on a movable sand bed. The shear plate provides a direct measurement of the bottom shear stress on a sand bend under complex flow conditions particularly over bottom roughnesses. It was designed for use under laboratory oscillatory flow conditions where the periods of motion range from 1.5 to 6 seconds and the range of shear forces are from 0.08 Nm^{-2} to 84 Nm^{-2}. The spatially averaged bottom shear stress was determined and the quadratic drag law was used to convert measurements of bottom shear stress to values of wave friction factor. The apparent roughness of the bed was specified using four times the sum of the mean and standard deviation of the sediment profile on the shear plate. Values of wave friction factor compared well with both theory and data obtained through previous laboratory studies.

Introduction

The accurate measurement of bottom shear stress over moveable sand beds is critical to our understanding of nearshore processes, including sediment transport and

[1] Research Assistant Professor, Department of Civil, Environmental and Ocean Engineering, Stevens Institute of Technology, Castle Point on the Hudson, Hoboken, New Jersey 07030 USA

[2] Professor, Department of Civil, Environmental and Ocean Engineering, Stevens Institute of Technology, Castle Point on the Hudson, Hoboken, New Jersey 07030 USA

[3] Professor, Department of Civil, Environmental and Ocean Engineering, Stevens Institute of Technology, Castle Point on the Hudson, Hoboken, New Jersey 07030 USA

shallow water wave attenuation. Although indirect techniques for estimating bottom shear stress including the use of bottom boundary layer velocity profiles, wave energy dissipation, and the measurement of Reynolds stresses have been used successfully in previous experiments, these techniques can be problematic in complex flow regimes particularly in the presence of bedforms. A shear plate, designed using the same principles as those employed in the field of naval architecture for measurement of the resisting force on a towed vessel, avoids these problems. The shear plate provides a non-intrusive, direct measurement of the tangential force on the sand bed and can resolve temporal changes in the bottom stress caused by variable wave-generated bedforms.

As part of a development effort pointed at designing a shear plate for use in the open ocean environment, a shear plate has been constructed for use in a laboratory wave tank. This enabled the evaluation of a number of design issues pertinent to long-term deployments in the field. It also permitted the testing of the apparatus under carefully controlled conditions, and the comparison of results to previous theoretical and experimental investigations of moveable bed dynamics.

Shear Plate Design and Tests

The shear plate design and experimental methodology are outlined in Rankin and Hires (submitted to J. Geophys. Res., 1998). The original experimental design was modified slightly during the present study. These modifications included the use of an aluminum plate mounted on top of an existing drag balance and the reduction of the gaps between the shear plate and the false bottom from 1.5 cm to 0.6 cm.

The shear plate was designed for use under laboratory oscillatory flow conditions where the periods of motion range from 1.5 to 6 seconds and the range of shear forces are from 0.08 Nm^{-2} to 84 Nm^{-2}. The shear plate was 0.875 m long by 0.620 m wide (0.543 m^2 area) and was constructed by mounting a 0.63 cm thick aluminum plate on top of a drag balance (fig. 1). The drag balance was instrumented with a waterproofed linear variable differential transformer (LVDT) which produced linearly increasing voltage with the horizontal deflection of the plate. Resolution was to ± 0.08 Nm^{-2}.

The shear plate was tested for moveable bed conditions under waves in Davidson Laboratory's Large Wave Tank. The wave tank is 95m long, 3.7 m wide and can accommodate water depths up to 1.8 m. It is equipped with a double flap wavemaker that is designed to simulate both regular and irregular waves. It can produce wave heights to 46 cm and wave periods to 6 seconds.

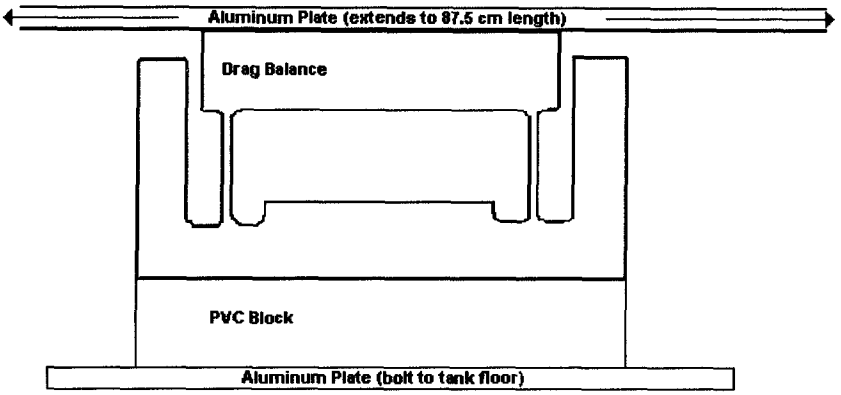

Figure 1. Schematic of Shear Plate Design

The shear plate was bolted to the concrete floor of the wave tank (fig. 2). A false bottom was constructed to surround the plate. The gap between the shear plate and the false bottom was fixed conservatively at 0.6 cm to ensure that sediment grains would not become trapped or wedged in the gap. A 1.0 to 2.5 cm thick layer of cohesionless quartz sand (d_{50} = 0.23mm) was placed on top of the shear plate and the surrounding false bottom. The shear stress on the sand bed was measured under waves ranging in height from 11 to 38 cm and periods from 1.75 to 6 seconds.

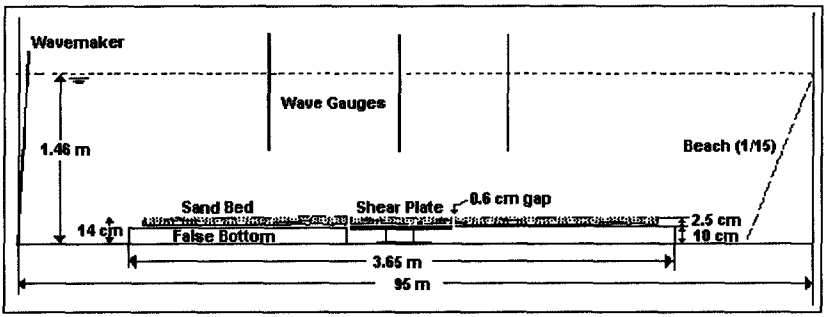

Figure 2. Experimental Set-up (not to scale)

Surface elevation records were obtained using three resistance-type gauges mounted on the sill of the wave tank. The gauges were installed 17.50 m, 28.17 m (over the center of the shear plate) and 38.84 m from the wavemaker, respectively. The gauges

resolve ± 1 mm changes in the surface elevation and were calibrated over a range of 15.24 cm.

Profiles of the sediment bed were taken according to the procedure outlined in Rankin and Hires (submitted to J. Geophys. Res., 1998). Table 1 summarizes the test matrix.

Results

Figure 3 represents sample time histories for the resistance on the shear plate with sand, resistance on the shear plate without sand, and the surface elevation.

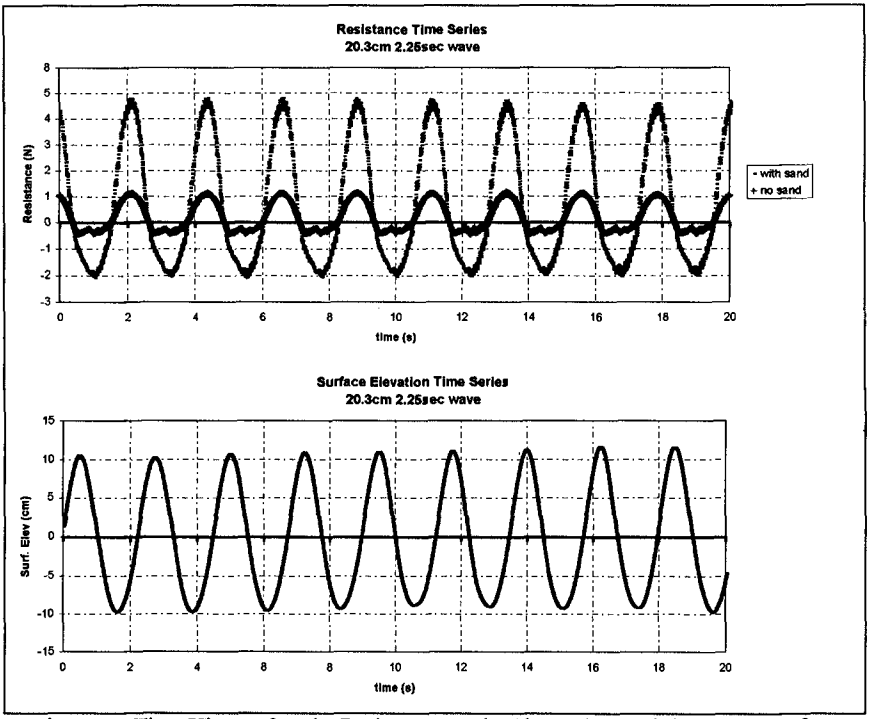

Figure 3. Time History for the Resistance on the Shear Plate and the Water Surface Elevation

The time history for the resistance on the shear plate without sand contains a conspicuous departure from a sine wave due to a relatively large second order harmonic signal. What is not immediately apparent is that this signal is also present in the time history for the resistance on the shear plate with sand; in this case the amplitude of the first order harmonic is over two orders of magnitude larger than the amplitude for the second order harmonic and therefore the non-linearity is not easily discerned.

Harmonic analysis was performed on the resistance and surface elevation time histories to determine the amplitude and phase of the harmonic components of the signal. The analysis program reads the input file and determines the fundamental period by counting the number of zero crossings. Next, it estimates the amplitude and phase of the signal by using a least squares method. The analysis assumes that the signal is of the form

$$y_i(t) = A_{i0} + \sum_{n=1}^{NH} A_{in} \cos(n\frac{2\pi}{T}t) + \sum_{n=1}^{NH} B_{in} \sin(n\frac{2\pi}{T}t) \qquad (1)$$

where

$n = 1,2,3, \ldots$

A_{i0}: mean of the time series

A_{in}: harmonic coefficient

B_{in}: harmonic coefficient

T : fundamental period

NH: order of harmonics

The program calculates the harmonic coefficients, A_{in} and B_{in} to minimize the sum of the squares of the difference between the recorded value and the estimate. The cosine and sine coefficients, A_{in} and B_{in}, were changed to the amplitude and phase as,

$$y_i(t) = C_{i0} + \sum_{n=1}^{NH} C_{in} \cos(n\frac{2\pi}{T}t - \phi_{in}) \qquad (2)$$

where

C_{i0}: mean of the time series

C_{in}: amplitude of the nth harmonic of the time series

ϕ_{in}: phase of the nth harmonic of the time series

Amplitudes of the first order harmonics are reported in Table 1. The amplitudes of the second order harmonics were nearly identical for runs with sand and without sand and had relatively small magnitudes that ranged from 0.05 to 0.20 N. It is believed that the second harmonics are related to the mechanical properties of the instrumentation.

The elimination of secondary forces to obtain the force on the shear plate due to the resistance associated with the sand bed alone, F_{res}, through the subtraction of the first order amplitude of the resistance on the shear plate without sand from the first order amplitude of the resistance on the shear plate with sand, and the calculation of the spatially averaged bottom shear stress, $\overline{\tau_{bm}}$, are reviewed in Rankin and Hires (submitted to J. Geophys. Res., 1998). These data are summarized in Table 1.

Analysis

apparent roughness

The apparent roughness, k_n, was specified initially as $k_n = 4 * \eta$ as suggested by Wikramanayake and Madsen (1994). After their extensive review and analysis of field and laboratory studies, they suggest that the ripple length does not appear to have a significant

influence on the apparent bottom roughness. It has been concluded by Wiberg and Harris (1994) that for wave dominated environments, the ripple length scales with wave excursion amplitude ($\lambda \cong 0.75A_b$) where A_b is the bottom excursion amplitude and the ripple steepness, η/λ, is nearly constant between 0.15 and 0.17 for equilibrium conditions. The results presented here are in close agreement with Wiberg and Harris (1994) with ripple steepnesses between 0.11 and 0.15 and an average wave steepness of 0.13 indicating that equilibrium conditions were achieved (Table 1).

Figure 4 illustrates the profile of the rippled sand bed and represents a general example of the bottom roughness.

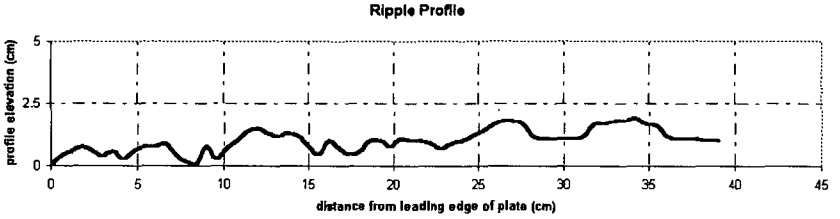

Figure 4. Sample of a Sediment Profile on the Shear Plate

Since the excursion amplitude of a section of the flow extended from the false bottom, across the gap and onto the shear plate, the ripple height alone was not sufficient to specify the apparent roughness (fig.5).

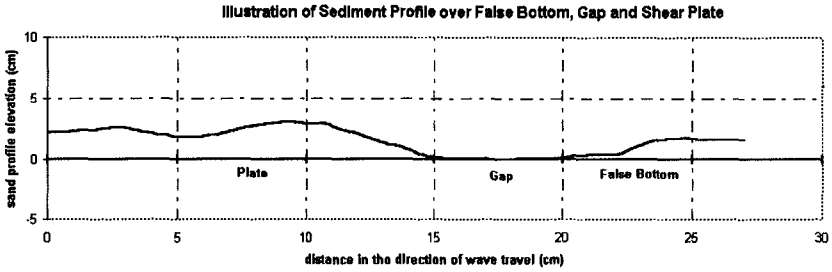

Figure 5. Sediment Profile from the False Bottom, across Gap and onto Shear Plate

The thickness of the sand bed itself made a significant contribution to the bottom roughness. The sand bed on the plate was therefore treated as a large ripple ($\eta \cong 2.5$cm and $\lambda \cong 91.5$cm where η is the ripple height and λ is the ripple length) with smaller surface ripples superimposed ($\eta \cong 0.3$cm and $\lambda \cong 10.0$cm). The apparent roughness was finally specified using the mean and standard deviation of the sand bed profile by $k_n = 4 * (mean + s.d.)$ (Table 1; fig. 6)

friction factor

The quadratic drag law was used to convert measurements of bottom shear stress to values of wave friction factor using a spatially integrated version of Jonsson's (1966) equation

$$\overline{\tau_{bm}} = 1/2 f_w \rho \overline{u_{bm}^2} \qquad (3)$$

where $\overline{\tau_{bm}}$ is the maximum spatially integrated shear stress on the bed over the area of the shear plate, f_w is a wave friction factor to be experimentally determined, ρ is the density of the water and $\overline{u_{bm}^2}$ is the spatially integrated maximum of the squared near-bottom velocities on the plate at one instant in time.

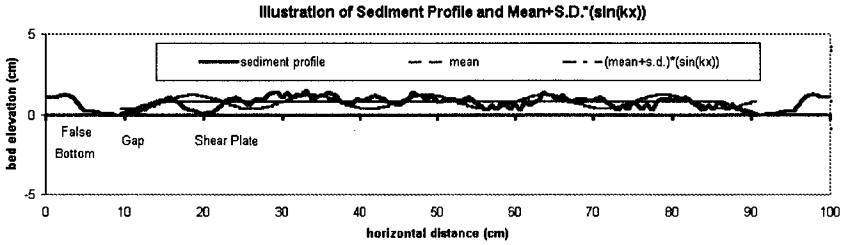

Figure 6. Specification of the Apparent Roughness of the Bed using the Mean and Std. Dev. of the sediment profile

Our values of wave friction factor were compared with Jonsson's (1966) semi-empirical theory,

$$\frac{1}{4\sqrt{f_w}} + \log_{10}\left[\frac{1}{4\sqrt{f_w}}\right] = \log_{10}\left[\frac{A_b}{k_n}\right] - 0.08 \qquad (4)$$

(where k_n / A_b is a measure of relative roughness), and Grant and Madsen's (1979) theory,

$$f_w = \frac{0.08}{\ker^2 2\sqrt{\varsigma_o} + i\,kei^2 2\sqrt{\varsigma_o}} \qquad (5)$$

(where ζ_o is a non-dimensional distance from the boundary) (figs. 7 and 8). Our values were also compared to values of wave energy dissipation factor, f_e, from previous studies using moveable beds, assuming that $f_w = f_e$.

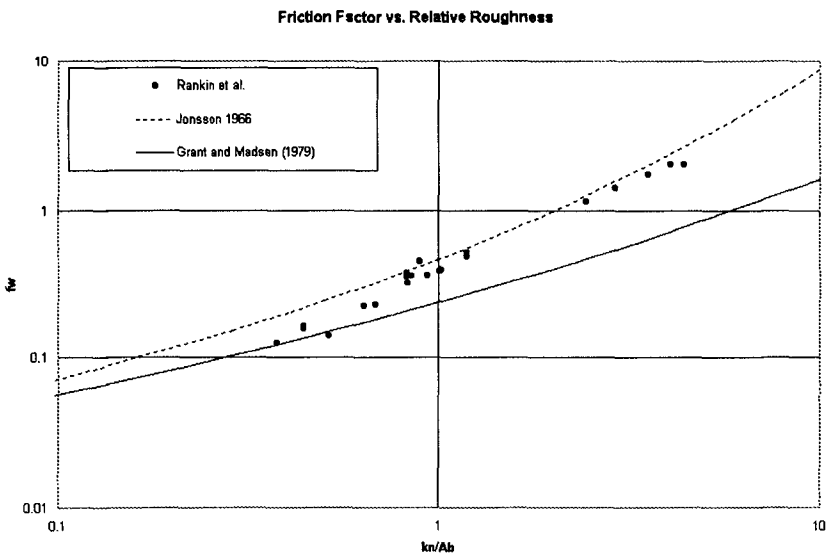

Figure 7. Comparison of f_w with Jonsson's (1966) and Grant and Madsen's (1979) theories (u_b is specified by linear wave theory)

These data compared well with those obtained from previous studies; values of the wave friction factor derived from the shear plate were as accurate as those derived from the energy dissipation method. The data also suggest that the value for the wave friction factor may be predicted using Jonsson's (1966) theory (fig. 8) for values of relative roughness greater than unity. Simons et al. (1996) also found agreement for this range of relative roughness.

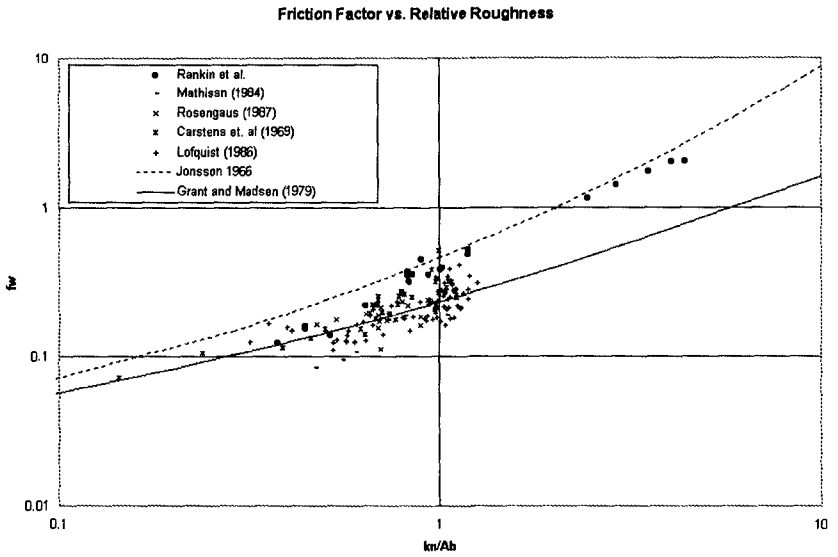

Figure 8. Comparison of f_w with previous studies

Conclusions

A shear plate has been designed and constructed for use in the laboratory measurement of bottom shear stress over moveable beds. The device has been tested in a large wave tank under a range of wave conditions that offers the opportunity of comparing the results to the findings of previous investigators. The values of wave friction factor obtained here compare well with both theory and the data obtained through former laboratory experiments. These comparisons have proven the utility of the device. Discretion must be exercised in the specification of the apparent bottom roughness; for this study, the bed thickness as well as the ripple height significantly contributed to the bottom roughness. The wave friction factor does not reach a constant value for values of relative roughness exceeding unity. Instead, data in this region were in reasonable agreement with Jonsson's (1966) theory. A new configuration of the shear plate will include an attempt to eliminate the gap between the plate and the false bottom by introducing a layer of latex between the plate and the sand bed. In addition, the dimensions of the shear plate will be greatly reduced.

Appendix

TABLE 1: Measured Wave Parameters, Ripple Geometry and Residual Force on the Shear Plate

Runs with Sand									Runs with no Sand							
H	T	F	k_n		η	λ	η/λ	Re_b	H	T	F	F_{res}	τ_b	u_b	k_n/A_b	f_w
cm	s	N	cm	cm	cm	cm			cm	s	N	N	N/m^2	cm/s		
			4*mean	4*s.d.	mean	mean										
27.9	3.00	3.83	5.2	1.6	1.2	11.0	0.11	3.7E+04	26.9	3.00	0.93	2.89	5.33	27.9	0.5	0.14
27.9	3.00	3.51	4.4	0.8	no ripples			3.7E+04	26.9	3.00	0.93	2.58	4.76	27.9	0.4	0.13
35.1	2.25	4.23	2.8	1.2	0.7	6.7	0.11	2.6E+04	35.1	2.25	1.16	3.07	5.46	27.1	0.4	0.16
35.1	2.25	4.09	4.0	0.4	no ripples			2.6E+04	35.1	2.25	1.16	2.94	5.41	27.1	0.4	0.16
21.8	3.00	3.51	4.8	2.4	1.6	13.0	0.12	2.2E+04	21.6	3.00	0.71	2.80	5.17	21.7	0.7	0.23
20.3	3.00	3.11	5.6	0.4	no ripples			1.9E+04	21.6	3.00	0.71	2.40	4.43	20.1	0.6	0.22
21.1	2.25	3.25	4.4	0.4	no ripples			9.2E+03	21.6	2.25	0.76	2.49	4.59	16.0	0.8	0.38
20.8	2.25	3.25	4.0	1.6	1.0	7.5	0.13	8.9E+03	21.6	2.25	0.76	2.49	4.59	15.8	1.0	0.38
29.0	1.75	3.20	3.6	1.2	0.6	4.8	0.13	5.5E+03	28.7	1.75	0.67	2.54	4.67	14.0	1.2	0.53
29.0	1.75	2.85	2.8	0.8	no ripples			5.5E+03	28.7	1.75	0.67	2.18	4.02	14.0	0.9	0.46
40.7	2.25	12.32	9.2	1.6	1.3	10.0	0.13	3.6E+04	41.6	2.25	2.76	9.56	17.63	31.7	0.9	0.37
27.3	3.00	8.45	9.2	1.6	1.3	10.7	0.12	3.5E+04	27.8	3.00	2.18	6.27	11.56	27.2	0.8	0.32
22.3	3.00	6.85	9.2	1.6	1.2	10.7	0.11	2.3E+04	22.8	3.00	1.69	5.16	9.51	22.1	1.0	0.40
32.5	2.25	10.14	9.2	1.6	0.9	6.0	0.15	2.2E+04	31.9	2.25	2.31	7.83	14.43	25.0	1.2	0.49
13.9	5.02	3.42	9.2	1.6	1.3	10.0	0.13	2.1E+04	14.4	5.02	0.85	2.58	4.76	16.4	0.8	0.36
11.4	5.98	2.45	9.2	1.6	0.8	7.0	0.11	1.7E+04	11.1	5.98	0.67	1.78	3.28	13.5	0.8	0.36
32.0	1.75	8.50	9.2	1.6	0.7	5.0	0.13	6.8E+03	31.5	1.75	1.51	6.98	12.87	15.7	2.5	1.16
27.4	1.75	7.29	9.2	1.6	0.7	5.0	0.13	4.8E+03	27.2	1.75	1.29	6.00	11.07	13.2	2.9	1.42
22.9	1.75	6.05	9.2	1.6	0.7	5.0	0.13	3.3E+03	22.4	1.75	1.11	4.94	9.10	10.8	3.6	1.74
20.1	1.75	5.34	9.2	1.6	0.7	5.0	0.13	2.5E+03	20.5	1.75	0.98	4.36	8.04	9.4	4.1	2.03
18.6	1.75	4.67	9.2	1.6	0.7	5.0	0.13	2.1E+03	18.3	1.75	0.93	3.74	6.88	8.7	4.4	2.04

Acknowledgements

This work was sponsored by the National Science Foundation under Grant No. OCE-9753174.

References

Carstens, M.R., Neilson, F.M., and H.D. Altinbilek. (1969). Bed forms generated in the laboratory under an oscillatory flow: analytical and experimental study. *TM-28,* U.S. Army Corps of Engineers, Coastal Engineering Research Center.

Grant, W.D. and O.S. Madsen. (1979). Combined wave and current interaction with a rough bottom. *J. Geophys. Res.*, 84, no. C4, pp. 1797-1808.

_____, (1982). Movable bed roughness in unsteady oscillatory flow. *J. Geophys. Res.*, 87, no. C1, pp. 469-481.

Jonsson, I.G. (1966). Wave boundary layers and friction factors. *Proc. Coastal Eng. Conf., 10th,* Tokyo, pp. 127-148.

Lofquist, K.E.B. (1986). Drag on naturally rippled beds under oscillatory flows. *MP-86-13.*, U.S. Army Corps of Engineers, Coastal Engineering Research Center.

Mathisen, P.P. (1989). Experimental study on the response of fine sediments to wave agitation and associated wave attenuation. *M.S. thesis,* Massachusetts Institute of Technology.

Mathisen, P.P. and O.S. Madsen. (1996). Waves and currents over a fixed rippled bed 1. Bottom roughness experienced by waves in the presence and absence of currents. *J. Geophys. Res.* vol. 101, no. C7, pp 16,533-16,542.

Rankin, K.L. (1997). Development and implementation of a shear plate for the direct measurement of bottom shear stress in moveable bed environments. Ph.D. thesis, Stevens Institute of Technology, Hoboken, New Jersey.

Rosengaus, M. (1987). Experimental study on wave generated bedforms and resulting wave attenuation. *Ph.D. thesis,* Massachusetts Institute of Technology, Cambridge, Massachusetts.

Simons, R.R., Grass, T.J. and Mansour-Tehranj, M. (1996). Bottom shear stresses in the boundary layers under waves and currents crossing at right angles. Proc. 23rd Coast. Engrg. Conf. ASCE, 604-617.

Wiberg and Harris. (1994). Ripple geometry in wave-dominated environments. *J. Geophys. Res.* vol. 99, no. C1, pp 773-789.

Evaluation of Longshore Sediment Transport Models on Coarse Grained Beaches Using Field Data: A Preliminary Investigation

Erik Van Wellen[1], Andrew J. Chadwick[1], Mark Lee[2],
Brian Baily[3] and John Morfett[4]

Abstract

This paper evaluates a number of widely used predictive transport equations and the use of tracers and GPS in the measurement of longshore transport for the validation of such equations. It also addresses the inconsistencies which can sometimes be introduced as a result of these techniques. The analysis shows that most of the equations examined tend to over-predict the expected transport by a factor of 1.5 to 4. The use of tracers on macro-tidal coarse grained beaches is found to be a viable method for obtaining reliable transport rate measurements of which the confidence levels are expected to increase as present day calculation techniques are adapted for use on macro-tidal shingle and mixed beaches. DGPS appears to be an economical way of data collection but needs to be used with the highest possible accuracy level settings if it is to be used in quantifiable sediment transport calculations.

Introduction

The management of beaches has become an important and effective engineering tool for protecting coastal areas. Increasing research efforts in this field have been aimed mostly at trying to understand and quantify the elements which govern the morphodynamics of beaches over both long- and short-term time scales. One of the key elements in improving the engineer's understanding of beach morphodynamics and sediment budgeting along a coastline is the search for a better determination of the net longshore movement of the sediment. The formulation of a reliable estimate of the total longshore transport (TLT) rate is paramount in coastal engineering problems such as feasibility studies of port extensions, derivation of

[1] School of Civil & Structural Engineering, University of Plymouth, Palace Court, Palace Street, Plymouth, PL1 2DE, Devon, United Kingdom
[2] Department of Oceanography, University of Southampton
[3] Department of Geography, University of Portsmouth
[4] Department of Civil Engineering, University of Brighton

sediment budgets for coastal areas and the appraisal of long term beach stability. Such estimates should be based only on the use of reliable sediment transport models underpinned by accurate transport measurements. To date, sand beaches have received the bulk of the attention. The number of documented studies and available data on sand beaches is, therefore, considerable and ranges from analytical/numerical models and laboratory tests to large scale field experiments. In strong contrast is the moderate attention which coarser grained (*i.e.* shingle) beaches have received. Studies of the processes governing shingle beaches have been limited mainly to empirical models based on laboratory studies, such as those by Pilarczyk and den Boer (1983) and Powell (1990). The prediction of longshore transport rates on shingle beaches has been mainly limited to the use of variations of the CERC formula from the US Army Corps of Engineers (1984), combined with laboratory studies.

Approximately one third of the UK's coastline is protected by shingle and mixed beaches (Fuller and Randall, 1988). Some of the areas protected by these beaches have a considerable economic importance attached to them. Coarser grained (*i.e.* shingle) beaches therefore warrant the attention of British researchers. The Shingle Beach Project (Van Wellen *et al.*, 1997) funded by the UK Ministry of Agriculture, Fisheries and Food (MAFF) and the Environment Agency (EA) was designed to go some way towards this. To date, two large scale field deployments have been carried out by the authors and their institutions in partnership with HR Wallingford. The 1996 deployment concentrated upon shingle transport on an open section of beach at Shoreham-by-Sea whilst the 1997 work was carried out on an adjacent groyned beach at Lancing. These two major field deployments have produced an extensive database of high quality field data. The present paper concentrates on the longshore transport rates as measured during the 1996 Shoreham open beach experiments and the evaluation of existing TLT equations using this field data.

Field Site

The field site at Shoreham-by-Sea, West Sussex, is an open stretch of beach consisting predominately of shingle. The beach is open towards the West and is in a natural state over an alongshore distance of 1500m. To the East, the beach is confined by a long harbour breakwater which extends approximately 200m. The prevailing wave direction is from the SW and SSW and the site is exposed fully to storm waves generated within the English Channel. A more detailed description of the field site is given in Van Wellen *et al.* (1997).

Historical Analysis of Net Longshore Transport and Annual Wave Climate

The Southern Water Authority (SWA) has been carrying out annual aerial surveys of the coastline in the area since 1973. The records also contain a statistical analysis of the trends of beach line movements and the changes in cross sectional area. In his analysis of this data, Chadwick (1989) assumed no longshore transport moving past the harbour breakwater. This assumption appears to be reasonable since the most seaward cross shore position of the toe of the shingle beach extends only half way along the breakwater. Chadwick estimated a mean sediment volume accretion of 14,539m^3 per year. This figure is supported by the volumes obtained from sediment

bypassing around the harbour breakwater which suggest that sediment accumulates against the breakwater at a mean rate of 15,000-20,000m^3/a (Wilson, 1996).

The mean annual hydrodynamic conditions *i.e.* wave height, period, direction and frequency of occurrence within a representative year were obtained using hindcast offshore wave data based on a wind data set covering a four year period between May 1980 and August 1984 (Chadwick, 1991). This period is also covered by the SWA beach surveys, which increases the level of confidence with regards to the comparison of the predicted and measured transport rates.

Data Collection and Methods

One of the key objectives during the 1996 field work was to undertake a comprehensive series of field measurements of hydrodynamic conditions and concurrent sediment transport. This data has been used to evaluate the performance of existing analytical TLT equations and to make an intercomparison between independent techniques for measuring the longshore transport.

The first method of measuring the sediment transport at the field site was the use of tracers. Three types of shingle tracer were used within the project as a whole: painted indigenous pebbles (Caldwell, 1981); aluminium tracers (Wright *et al.*, 1978) and electronic tracers (Workman *et al.*, 1994). The comparatively low cost of the painted and aluminium tracers made them ideal for use in pilot studies in the early stages of the two deployments, when the least was known about the behaviour of the indigenous material and tracer losses were likely to be at a maximum. The highest quality tracer data (*i.e.* those studies with the highest recovery rates, the most frequent searches and the most complete supporting wave, current and sedimentological data) were those using the electronic tracer system. The main advantage of the electronic system was the ability to detect buried tracers at depths of up to 100cm as compared to 35-40cm with the aluminium system and 0-10cm with the painted tracers.

A wide range of tracer sizes and shapes were used within the study; the sieve diameters of the electronic tracers ranged from 23.9mm to 66.8mm and the shapes from 0.93 Maximum Projection Sphericity (MPS) to 0.621 MPS. These electronic tracers represent between 9.5 and 44.5% of the size range of the indigenous material. This is an advantage over the standard aluminium tracers which represented a smaller size and shape range throughout the majority of the study. The number of tracers deployed was relatively small (60-147) due to the labour intensive nature of tracer recovery and the logistical limitations of the study.

Tracer injection was at three cross-shore sites, chosen according to the expected active beach width at the time of deployment. Between 1 and 3 layers of tracers were placed at each cross-shore site to ensure that possible variations in tracer movement with depth were represented. The depths chosen were governed by the expected hydrodynamic conditions. The individually identifiable tracers were located by means of specially designed detectors and their depth and position surveyed in. Each of the electronic tracer studies lasted for four low waters in total. Tracer injection was carried out on the first low water, tracers were located but left in position during the two following low waters and were recovered on the fourth low water. Recovery rates of the electronic tracers lay usually around 90%.

From the tracer experiments, drift rates (Q_{ls}) were calculated using the method of Nicholls and Wright (1991) which has its basis in the work of Komar and Inman (1970). Three parameters are needed for this calculation: the velocity of movement of the tracer centroid (centre of mass) (U_s), the width of the active beach (m) and the thickness of the moving sediment layer (depth of disturbance) (n).

$$Q_{ls} = U_s mn \quad (1)$$

The recorded co-ordinates of the pebbles in the horizontal plane were used to calculate the tracer centroid (centre of mass) position on the beach. The velocity of the tracer centroid was given by the average longshore distance travelled by the moving tracers and the average duration of coverage. The average duration of tidal inundation of each tracer was determined by means of the height at which it was found on the beach and by using the measured beach profile data and Admiralty tidal predictions for the site. The thickness of the moving sediment layer was taken as the depth of the boundary between moving and non-moving tracers (Voulgaris *et al.*, 1998). If an event occurred in which more than 90% of the tracers were in transport, then the thickness of the moving sediment layer was taken as the depth above which 95% of the moving tracers were present. Active beach width was taken from the measured topographic profile at the site *i.e.* the distance between the high water mark and the sand/shingle border.

The second method of obtaining measurements of the transport rate is by means of calculating the volume changes of the beach based on topographic surveys in the vicinity of a structure (for example the harbour breakwater) which is assumed to stop all longshore transport. Traditional surveying allows constant high accuracy surveys to be carried out. However, using traditional surveying techniques, relatively few points can be captured over large areas within a short time period. Whilst the collection of a large number of points may not be relevant on simple topographic features, on more complex morphological surfaces there is a need for a system that can capture large amounts of data in relatively short time intervals. One answer to this problem is the use of DGPS (Differential Global Positioning Systems) to monitor beach morphological changes and the use of GPS technology is becoming more widespread by those concerned with obtaining and recording geographic information (Cornelius *et al.*, 1994). The most important features of GPS are its high positional accuracy and velocity determination in three dimensions, all weather capability, accurate timing capacity and global coverage (Leick, 1995). Importantly, from the point of view of the coastal geomorphologist, the ability of GPS kinematic surveying to record measurements rapidly and accurately over relatively large areas can be seen to be potentially invaluable in such a dynamic environment. Morton *et al.* (1993), discuss the use of GPS surveying techniques to monitor beach changes and state that GPS beach monitoring provides a way of understanding beach dynamics and the factors that influence volumetric gains and losses.

Typical surveys recorded between 3,500 and 5,000 points in a four hour time interval. These data points are then used as the input for a topographic modelling system to create a DEM (Digital Elevation Model) from the irregularly spaced data. This in turn allows subsequent volumetric analysis of the GPS data. For this purpose, individual blanking files for five different areas were set up (blanking files allow a particular section of the beach to be separated from a larger grid file). The volumetric differences were then fed into a finite difference scheme which allows calculation of

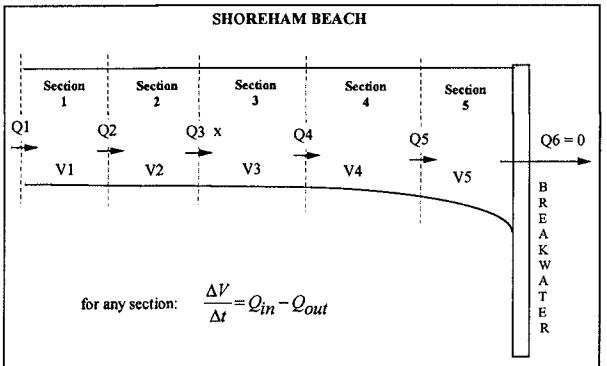

Figure 1 Schematic of finite difference scheme for the volumetric survey data.

the TLT rate tracer at the location where the tracer experiments took place (x on Figure 1).

The nearshore waves were recorded using the Inshore Wave Climate Monitor (IWCM; Chadwick *et al.*, 1995). This device consists of a star array of four 6m resistive sensors mounted on a 6m sided triangular aluminium tubular frame. This device measures the waves acting on the beach directly rather than measuring them offshore and having to refract them in by computational means at a later stage.

Sediment size distribution data were obtained from extensive sampling during the tracer experiments. Concurrently with each tracer experiment, sediment samples of approximately 70kg each were collected at each low water during a tracer study. Samples were taken at three cross shore positions close to the original injection sites for the tracers. The samples were then subjected to sieve analysis at half ϕ intervals.

Analytical Models Used

Numerous analytical expressions have been developed for the prediction of the TLT rate. A selection of seven equations representing the current approaches to longshore transport calculation is used here. They have been selected based on either their long standing use, their new approach to the analytical prediction of the TLT or the fact that they have been developed specifically for the transport of coarse grain material. The selected equations are:

- The energetics based CERC formula (CERC, 1984) calibrated for shingle size sediment comparable to that found during the field experiments (Chadwick, 1989)

CERCF
$$Q_{ls} = K\left(\frac{1+e}{\rho_s - \rho}\right)\left(\frac{1}{16}\rho g H_{sb}^2 C_{nb} \sin 2\theta_b\right) \quad (2)$$

where K is a proportionality coefficient equal to 0.0527, e is the void ratio, ρ is the fluid density, ρ_s is the sediment density, g is the gravitational acceleration, H_{sb} is the significant wave height at breaking, C_{nb} is the wave group velocity at breaking and θ_b is the angle of the breaker line relative to the shoreline.

- A physics based analytical equation for the longshore bedload transport ($Q_{b,ls}$) of shingle (Damgaard and Soulsby, 1996)

DS96
$$Q_{b,ls} = sign\{\theta_b\} \max\{|Q_{x1}|, |Q_{x2}|\} \quad (3)$$

where Q_{x1} is the longshore transport under current dominated conditions and Q_{x2} is the sediment transport under wave dominated conditions. Expressions for both of these can be found in Damgaard and Soulsby (1996). This equation explores a new path in analytical TLT prediction by means of using a force-balance approach to quantify the TLT rate.

- Two empirical formulae developed by Kamphuis (Kamphuis *et al.*, 1986 and Kamphuis 1991)

KAM86
$$Q_{ls} = \frac{1.28}{(1-n)(\rho_s - \rho)} \frac{\tan\alpha \, H_{sb}^{7/2}}{D} \sin 2\theta_b \tag{4}$$

where *tan* α is the representative bed slope, D is the representative grain diameter and n is the porosity. With additional laboratory study and further data analysis Kamphuis (1991) modified Equation (4) and included the influence of the peak wave period, T_p:

KAM91
$$Q_S = \frac{2.27}{(1-n)(\rho_S - \rho)} H_{sb}^2 \, T_p^{1.5} \tan\alpha^{0.75} \, D^{-0.25} \sin^{0.6} 2\theta_b \tag{5}$$

This equation has been found to be the most accurate transport equation (Schoonees and Theron, 1996).

- Two improved versions of the Kamphuis 1991 equation as suggested by Schoonees and Theron (1996)

SCHA
$$Q = \frac{63433}{365 \cdot 24 \cdot 60 \cdot 60} x_{Kamphuis} \tag{6}$$

recommended for use on exposed sites where the sediment is of a finer nature; and

SCHB
$$Q = \frac{50000}{365 \cdot 24 \cdot 60 \cdot 60} x_{Kamphuis} \tag{7}$$

recommended for use at sites where calm conditions prevail and/or where the sediment is coarser.

$$x_{Kamphuis} = \frac{1}{(1-n)\rho_s} \frac{\rho}{T_p} L_0^{1.25} H_{sb}^2 (\tan\alpha)^{0.75} \left(\frac{1}{D_{50}}\right)^{0.25} (\sin 2\theta_b)^{0.6} \tag{8}$$

where L_0 is the deep water wave length.

- An empirical formula developed specifically for the transport of coarse grain material by van der Meer (1990)

VDM90
$$Q_{ls} = 0.0012 g D_{50} T_p H_{sb} \sqrt{\cos\theta_b} \left(\frac{H_{sb}\sqrt{\cos\theta_b}}{D_{50}} - 11 \right) \sin\theta_b \tag{9}$$

Evaluation and Findings

Using the long term average wave climate as input, the predicted TLT was calculated using the seven analytical models and compared to the expected net annual longshore transport. From Figure 2 it can be seen that CERCF and DS96 give the most accurate prediction for the sediment transport in the study area. This was not altogether unexpected since both of these equations have been calibrated against transport measurements for sediment of similar size to that at Shoreham beach. VDM90 scores rather poorly by giving the highest estimate of all despite being derived specifically for coarse gained sediment. KAM86 scores reasonably well and even out-performs the KAM91, which gives an estimate that is nearly three times as high as the one from KAM86. The improved versions of KAM91 (SCHA and SCHB)

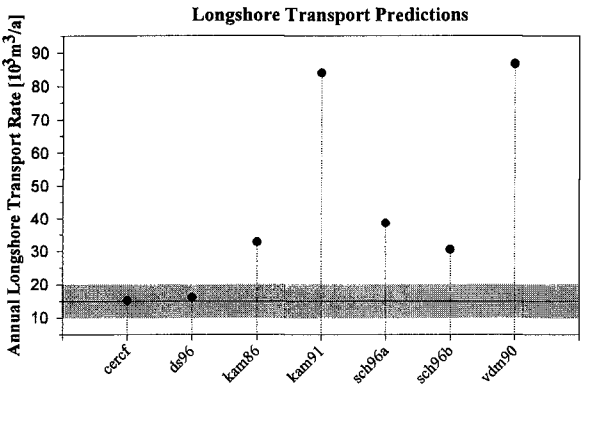

Figure 2 Expected (grey band) and predicted TLT at Shoreham.

give estimates which are closer to the one initially put forward by the KAM86 equation. Most equations appear to have a tendency to over-predict the TLT.

As part of the analysis, an extensive sensitivity analysis of the equations to the different parameters was undertaken. From this analysis two interesting plots are shown in Figure 3 and Figure 4. The TLT rates (Q) predicted by each equation have been divided by a reference TLT rate (Q_{ref}) obtained using that same equation with a fixed set of input parameters.

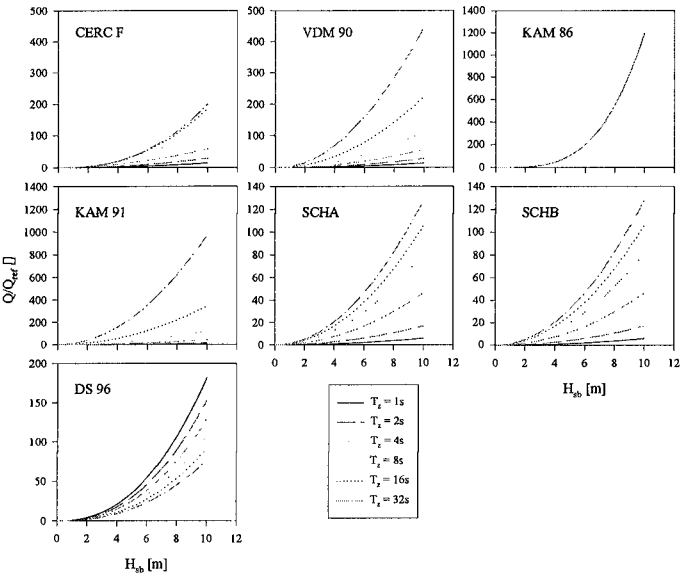

Figure 3 Sensitivity analysis for H_{sb}.

Figure 3 illustrates the power-law-like growth in predicted transport rate with an increase in wave height for each of the transport equations. The main difference is the magnitude with which the transport rate is increased. This is to be expected since all formulae incorporate the influence of the wave height on the transport by raising the wave height to a certain power larger than unity *e.g.* CERC-like equations have H^2. Apart from KAM 86 which does not take wave period into account, different transport rates are predicted for different wave periods. In general, all equations predict a larger TLT rate for larger wave periods. This appears to be a logical trend in transitional water depths were larger periods mean larger orbital velocities. Conversely, DS 96 shows an opposite trend, predicting larger transport rates for smaller wave periods. Since this equation assumes shallow water conditions the TLT becomes independent of the wave period but increases with wave steepness.

When looking at the influence of the D_{50} on the predicted transport rate (Figure 4) a similar anomaly is shown. Apart from the CERC equation (which does not take grain size into account) all equations predict lower transport rates for larger grain sizes. Again the exception is DS 96 which, under wave dominating conditions, predicts larger TLT rates for coarser sediment. This property of the DS 96 equation can be explained by the underlying assumptions of the model where an increase in D_{50} means an increase in the roughness influencing the wave boundary-layer and an increase in the wave related bottom shear stress resulting, in turn, in an increase in TLT (Damgaard and Soulsby, 1996).

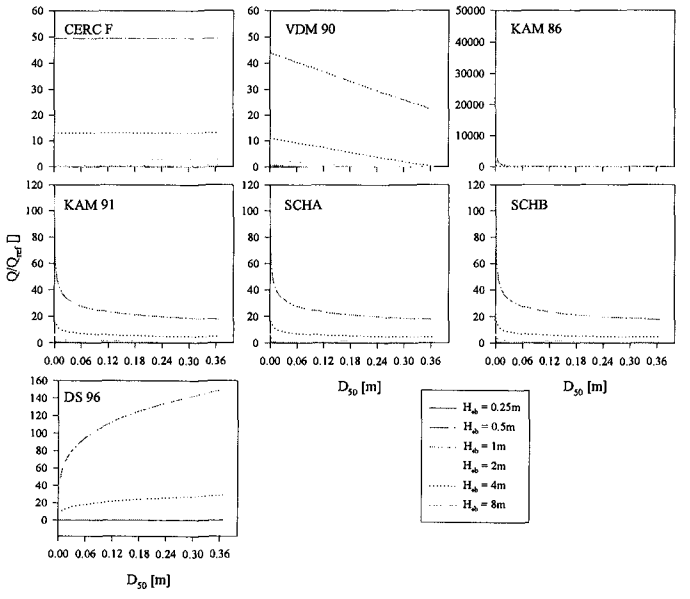

Figure 4 Sensitivity analysis for D_{50}.

With regard to sensitivity to θ_b, all the equations included in this paper showed a similar trend differing only in magnitude. Shoreham is characterised by a fairly stable wave climate with waves breaking at about 2 to 3° relative to the beach orthogonal and hence any variation in θ_b is unlikely to be an important factor in the comparison of measured and predicted TLT. Nevertheless, the sensitivity analysis showed the importance of an accurate determination of θ_b when predicting TLT.

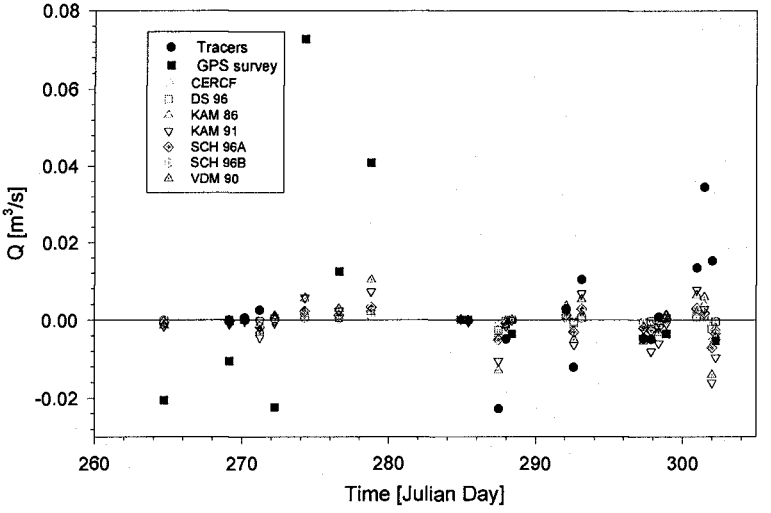

Figure 5 Measured (filled symbols) and modelled (open symbols) TLT for the 1996 fieldwork.

Using the wave data as recorded at the field site, Figure 5 shows a temporal plot of both the measured and the modelled TLT rates. It can be seen that there is a significant difference between the measured and the modelled rates.

To quantify the discrepancy between the measured and the predicted transport rates, a discrepancy ratio equal to $Q_{predicted}/Q_{measured}$ was introduced. Figure 6 and Figure 7 are histograms giving the percentage of occurrence that the discrepancy ratio from a certain formula can be placed in a preset interval. Combining these two figures with Figure 5, shows that for the tracer data most transport predictions made by the equations are characterised by a discrepancy ratio lower than 4 whilst for the GPS measurements nearly all fall in the bin for discrepancy ratios larger than 10. Since Figure 2 suggested that most models were likely to over-predict the transport measurements made during the experiment these discrepancy ratio's are likely to be underestimates. Calculation of the Relative Standard Error of Estimate (RSEE) for the GPS data suggests an average RSEE of about 1.4. This is a very high value and can be

only partially explained by the relatively small sample size. Kamphuis (1986) and Schoonees and Theron (1996) using large samples, found RSEE values of below 0.4.

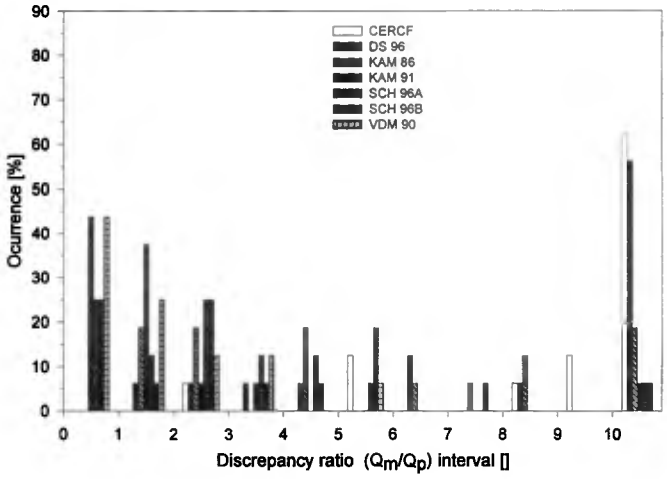

Figure 6 Discrepancy ratio of the predicted over the TLT rates measured by tracers.

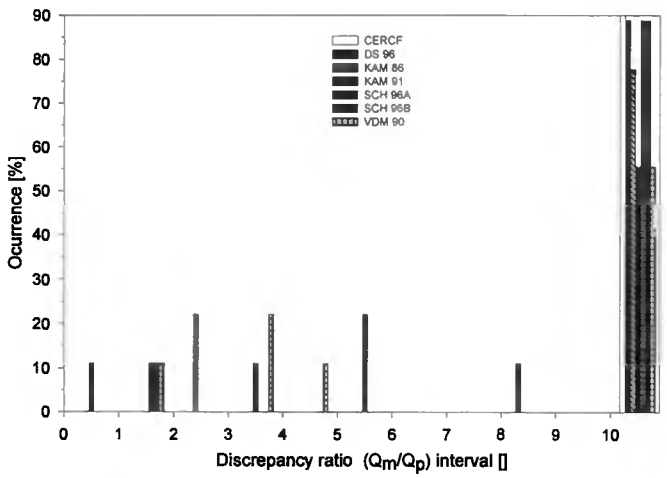

Figure 7 Discrepancy ratio of the predicted over the TLT rates measured by GPS.

One of the most widely accepted assumptions is that the TLT rate is proportional to the alongshore energy flux, *P*. The validity of this assumption has been underpinned by several studies and data sets (Kamphuis *et al.*, 1986, Kamphuis 1991 and Wang *et al.*, 1998). It is fair to say that this assumption holds true for shingle transport, although the importance of a threshold of motion criteria for sediment transport to occur is far greater than for sand. However, there is no consistent proportionality between the alongshore energy flux and the TLT rates measured by the tracers and GPS (Figure 8). The graph shows a significant amount of scatter and a particularly low correlation coefficient (r^2 = 52%) for the GPS measurements.

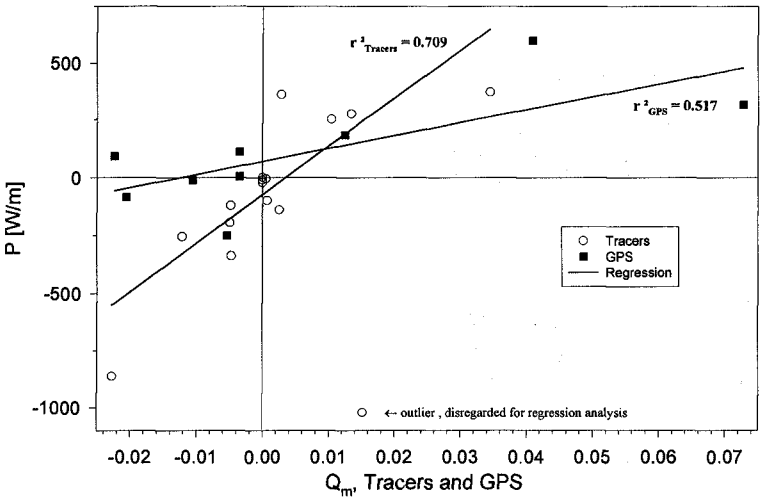

Figure 8 Correlation between the measured TLT rates (using Tracers & GPS) and the alongshore energy flux (P).

The significant difference in measured transport rates between the two systems was not expected, neither was the low correlation between the predicted transport rates and those obtained from the GPS measurements. The latter discrepancy is potentially more significant since GPS technology is starting to take over from the more classical surveying techniques in coastal management applications. Bodge and Kraus (1991) found their TLT estimates obtained from sediment impoundment combined with classic survey techniques to be more accurate than those obtained from tracer experiments. They stated that spurious trapping unrelated to the TLT and survey inaccuracies could each account for up to 100% of the TLT. Most of the erratic TLT measurements obtained from the GPS measurements are probably a result of the poor vertical accuracy accepted on the measurements made using the GPS when operating in kinematic mode in this study.

Some of the scatter in the data obtained from the tracers can be explained by the limitations of present day tracer theory. Often the main uncertainty lies in how representative the tracer is of the resident sediment, both in size distribution and quantity of the tracers. Bodge and Kraus (1991) stated that TLT estimates derived from tracers can be in error by a factor of 4 due purely to limitations in sampling methodology (or recovery rate, when dealing with individually identifiable tracers). However, problems such as recovery rates needed for reliable TLT measurements and differences in cross-shore distribution of the TLT have been minimised in this study by means of high recovery rates and by simultaneous injection of the tracer at different cross-shore locations. It is believed that the main uncertainty in the measured transport rate using the tracers is introduced through the calculation technique, which was originally developed for fine grain sediment on beaches characterised by a small tidal range.

Conclusions and Recommendations

This paper has examined a selection of today's most widely used predictive total longshore transport equations and two commonly used methods of obtaining estimates of the longshore transport under field conditions.

The CERC equation and Damgaard and Soulsby (1996) equation, calibrated for shingle of similar size to those found on Shoreham beach, appear to produce good estimates of the average annual TLT rate in the study area. The other equations tend to over-predict the expected annual TLT by a factor ranging from 1.5 to 4. This is perhaps not surprising since the Kamphuis equations and the Schoonees and Theron equations have been developed as general purpose transport equations rather than being specifically aimed at shingle and mixed sediment transport. The fact that they give predictions which are of the right order of magnitude gives a very encouraging signal for their future development to incorporate the coarser spectrum of the grain size scale, whilst maintaining their robustness by means of using only a limited number of environmental input parameters. The Damgaard and Soulsby equation shows promise in that it is based on the physically meaningful principle of force-balance. Unfortunately the resultant expression is significantly more complex. However, the sensitivity analysis has shown that it predicts opposite trends to all the other equations suggesting that further research is required. The van der Meer (1990) equation which was specifically developed for the prediction of TLT on gravel beaches did not perform well against the Shoreham long term transport data.

The use of tracers on macro-tidal shingle and mixed beaches shows promise in producing reliable transport rates. Care needs to be taken, however, since it appears that the present calculation techniques for obtaining sediment transport rates from the raw tracer data (*i.e.* the methods traditionally used for sand beaches and beaches with a small tidal range) may not be valid for the field conditions as described here. In general, the tracers appear to give higher transport rates than would be expected over the duration of a tracer experiment. This needs to be taken into account when extrapolating the results from tracer experiments to annual TLT values. Work is presently being undertaken within the MAFF Shingle Beach Project to improve the techniques for extracting transport rates from tracer data. It is expected that this will lead to an increase in confidence level on the measured values.

The method of obtaining estimates of the TLT rate from the volumetric change between topographic surveys using GPS was proven to be a fast and relatively inexpensive way of data collection. However, the potential error introduced by a low preset level in acceptable accuracy means that although more data points are collected, these do not necessarily give an accurate representation of the true beach volume. Ideally, real-time DGPS with a preset accuracy of 1cm in the vertical should be used if the data are to be used for construction of accurate morphological DEMs. This, in turn, will lead to a higher degree of confidence in the transport rates inferred from the changes in volume. This is especially important if the resultant transport rates are used by shoreline managers as part of a predictive tool over a wider range of time scales. Volumetric surveys, either from DGPS or more traditional methods using a Total Station or Level form a proven technique which should work irrespective of the type of beach or sediment. The fact that both short and long times between surveys can potentially smooth out the individual link between specific hydrodynamic conditions and the corresponding TLT but may lead to more stable predictions for the TLT.

Acknowledgements

The authors wish to acknowledge the financial support of the UK MAFF and EA. J. Damgaard and T. Mason are thanked for their invaluable discussions. The authors also extend special thanks to L. van Rijn, W. Kamphuis and J. Schoonees for their positive encouragement and comments after the presentation at the conference. We also thank C. Walker of Shoreham Port Authority for his assistance.

References

Bodge K. R. and Kraus N. C., Critical examination of longshore transport rate magnitude, *Coastal Sediments '91 Conference*, ASCE pp 139-155, 1991

Caldwell N. E., The relationship between tracers and the background material, *Journal of sedimentary petrology*, 51, pp 1163-1168, 1981

CERC, Shore Protection Manual, Coastal Eng. Research Centre, US Army Corps of Eng., Washington, 1984

Chadwick A. J., Field measurements and numerical model verification of coastal shingle transport, *Advances in Water Modelling and Measurement*, BHRA, The Fluid Engineering Centre, Chapter 27, pp 381-402, 1989

Chadwick A.J., An unsteady flow bore model for sediment transport in broken waves. Part 1 & 2, *Proc. Inst. Civ. Engrs*, Part 2, pp 719-793, 1991

Chadwick A. J., Pope D.J., Borges J. and Ilic S., Shoreline directional wave spectra Part 2. Instrumentation and field measurements, *Proc. Instn Civ. Engrs Wat., Marit. & Energy*, 112, pp 209-214, 1995

Cornelius S. C., Sear D. A., Carver S. J. and Heywood D. I. GPS, GIS and Geomorphological Field Work. *Earth Surface Processes and Landforms*, 19, pp 777-787, 1994

Damgaard J. S. and Soulsby R. L., Longshore bed-load transport. *Proc. 25th Int. Conf. on Coastal Eng., Orlando, ASCE,* pp 3614-3627, 1996

Fuller R. M. and Randall R. E., The Oxford Shingles, Suffolk, UK, Classic Conflicts in Coastline Management, *Biological Conservation*, 46, pp 95-114, 1988

Kamphuis J. W., Alongshore sediment transport rate. *J. Waterway, Port, Coastal and Ocean Engineering, ASCE*, Vol. 117; pp 624-640, 1991

Kamphuis J. W., Davies M. H., Nairn R. B. and Sayo O. J., Calculation of littoral sand transport rate. *Coastal Eng.*, Vol. 10; pp 1-21, 1986

Komar P.D. and Inman D.L., Longshore sand transport on beaches, *Journal of Geophysical Research*, 75, pp 5914-5927, 1970

Leick A., *GPS Satellite Surveying*. Wiley, New York, 1995

Morton R. A., Leach M. P., Paine J. G. and Cardoza A., Monitoring beach changes using GPS surveying techniques. *Journal of Coastal Research*, 9, pp 702-720, 1993

Nicholls R. J. and Wright P., Longshore transport of pebbles: Experimental estimates of k, *Coastal Sediments '91 Conference*, pp 920..933, 1991

Pilarczyk K.W. and den Boer K., Stability and profile development of coarse materials and their application in coastal engineering. Delft, Holland, *Delft Hydraulics, publication No. 293*, 1983

Powell K.A., Predicting short term profile response for shingle beaches, *Report 219, HR Wallingford*, February 1990

Schoonees J. S. and Theron A. K., Improvement of the most accurate longshore transport formula. *Proc. 25th Int. Conf. on Coastal Eng., Orlando, ASCE*; pp 3652-3665, 1996

van de Meer J. W., Static and dynamic stability of loose material. *Coastal protection, Balkema/Pilarczyk (Ed)*, ISBN 90 6191 1273; pp 157-195, 1990

Van Wellen E., Chadwick A. J., Bird P. A. D., Bray M., Lee M and Morfett J., Coastal sediment transport on shingle beaches, *Proceedings of Coastal Dynamics'97, Plymouth, ASCE*, pp 38-47, 1997

Voulgaris G., Workman M. and Collins M. B., New techniques for the measurement of shingle transport in the nearshore zone, *Journal of Coastal Research* (in press), 1998.

Wang P., Kraus N. C. and Davis A. D., Total longshore transport rate in the surf zone: field measurements and empirical predictions, *Journal of Coastal Research*, Vol. 14, pp 269-282, 1998

Wilson S. F., Shoreham and Lancing Sea Defence Strategy Plan., *Final Report to National Rivers Authority*, Southern Region, 1996

Workman M., Smith J., Boyce P., Collins M.B. and Coates T.T., Development of the Electronic Pebble System. *HR Report SR 405, HR Wallingford Ltd.*, 70p., 1994

Wright P., Cross J. S. and Webber N. B., Aluminium pebbles: A new type of tracer for flint and chert pebble beaches, *Marine Geology*, 27, pp 9-17, 1978

MOTIONS OF PEBBLES ON PEBBLE BEACH

Ichiro Deguchi[1], Masanobu ONO[1], Susumu ARAKI[1] and Toru SAWARAGI[2]

ABSTRACT

Motions of pebbles on an artificial pebble beach were measured by tracking tracers. After the beach profile reached equilibrium, pebbles moved mainly in the longshore direction parallel to the shore line under the condition of oblique wave incidence. Intensive motions of pebbles were observed in the swash zone and the maximum displacement reached 30m during one week. The authors proposed a numerical procedure for analyzing pebble motion. The motion of pebble up to the maximum wave set-up point can be predicted numerically when the time and spatial variation of water particle velocity and fluid force on pebbles are given.

INTRODUCTION

The authors have been carrying out series of field studies on an artificial pebble beach constructed as a seawall of the reclamation. The sea wall was originally designed as a usual vertical seawall with wave energy absorbing blocks in front of it. However it was altered to be a permeable gentle slope seawall constructed by using pebbles of marble. The reason was that the mild slope permeable seawalls has little influence on the surrounding coast. The accessibility to the shoreline is also greatly improved when compared with the impermeable seawalls with armor blocks.

A gentle slope seawall is usually constructed by using rubble stones with a cover layer. Therefore any significant deformation of the cover layer is not permitted in the design because the deformation may cause fatal destruction of the seawall. The artificial pebble beach was constructed without cover layer and the deformation in the profile is permitted as far as it maintains the initially designed hydraulic function as is the case of the artificial sandy beach. Therefore it is necessary to know the deformation pattern of the beach and the change in the hydraulic function caused by the deformation. Although a number of research has already been done about the deformation of sandy beach, only a few have been done on the pebble beach.

In this paper movement of pebbles on the artificial pebble beach is investigated through field measurement of the motion of pebbles. Numerical model for analyzing the movement of pebbles is constructed to know the influence of the geometry of the beach, diameter of the pebble and characteristics of incident waves on the pebble motion.

1 Prof., Lecturer and Student of Graduate School, Dept. of Civil Eng., Osaka University, Yamada-oka, Suita-city , Osaka 565, Japan
2 Prof., Dept. of Civil Eng., Osaka Sangyo University, Daito-city Osaka, Japan

FIELD MEASUREMENT OF PEBBLE MOTION

Figure 1 shows the location and plane view of the artificial pebble beach. The total length of the beach is about 3 km and the slope of the beach is 1/15. A representative cross section of the beach is schematically illustrated in Fig.2. The beach was constructed by rubbles of a mean diameter about 6 cm and covered by the pebble of marble of the diameter 4 to 8cm. The thickness of marble layer is about 1m. The beach is divided into some portions by groins of the length about 80m. The length of the beach of one portion is 300m.

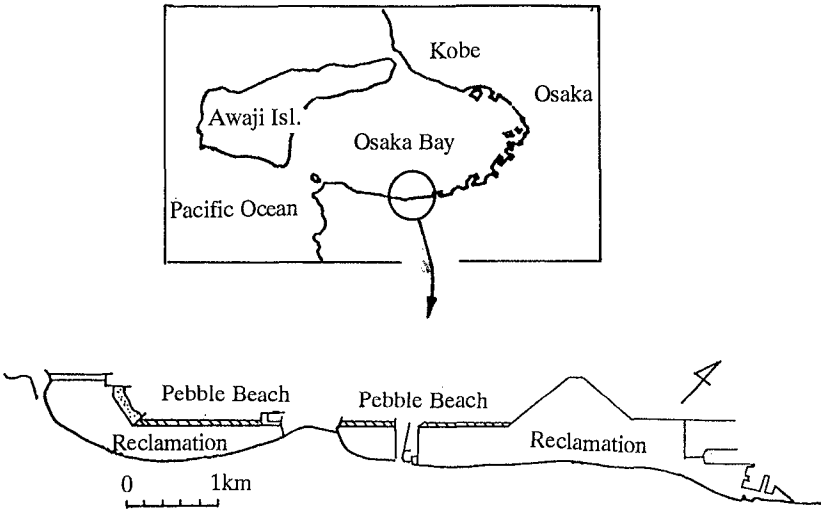

Fig. 1 Location and plane view of the artificial pebble beach

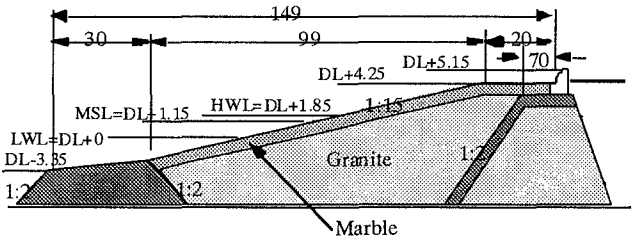

Fig 2 Representative cross-section of the pebble beach

Figure 3 is the bottom topography of the objective beach measured on November 1996. The predominant wave direction is found to be vary from season to season but waves from north and northwest predominant all through the year. The cross-shore profile reached equilibrium relatively shortly after the completion and longshore movement of the pebble from SW to NE. As a result, contour lines advanced more than 15m around measuring lines Nos. 13 and 15. (Deguchi et al, 1996)

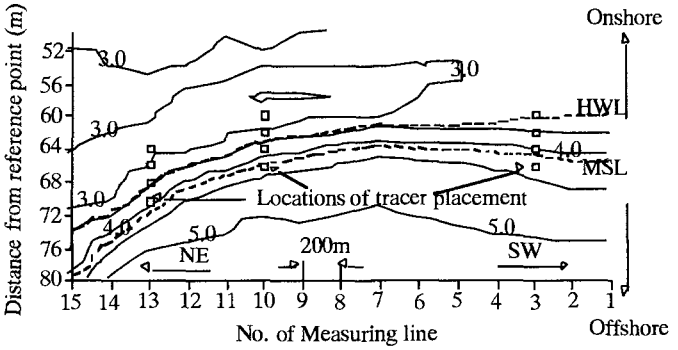

Fig.3 Bottom profile of the objective beach (Nov., 1997)

Until 1997 we carried out four times measurements of the pebble motion on the beach. Here the results of the first two measurements are analyzed. In the measurement, pebble motions were measured by tracking pebbles to which running number were given. 10 to 20 numbered pebbles were placed at four locations at the distance of 2 m along the three measuring lines perpendicular to the initial shoreline. The displacements of pebbles were measured one week after the placements.

The first measurement was conducted during 21st and 28th of November 1996. Tracers were placed along the measuring lines Nos.3, 10 and 13 as shown in Fig.3. The south groin shades a region around the measuring line No.3 from the predominant incident waves. The longshore pebble transport due to the predominant incident waves becomes the maximum around measuring lines Nos.9 to 10 and the measuring line No.13 locates in the accretion area by the longshore pebble transport (Deguchi et al. 1996).

Figure 4 is the cross-section along the measuring line Nos.3, 10 and 13 where the tracers were placed at the first measurement. The most of tracers were placed above the MWL.

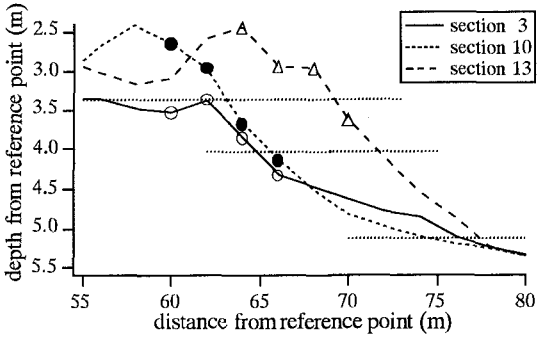

Fig. 4 Cross sections of tracer placement (First measurement)

The second measurement was carried out during 28th February and 7th March, 1997 just after finishing the maintenance reshape of the beach. The beach profile was reshaped to be an almost initial profile. Tracers were place along the measuring line Nos.5, 9 and 13.

The most of tracers except for the measuring line No.5 were placed between HWL and MWL as shown in Fig. 5.

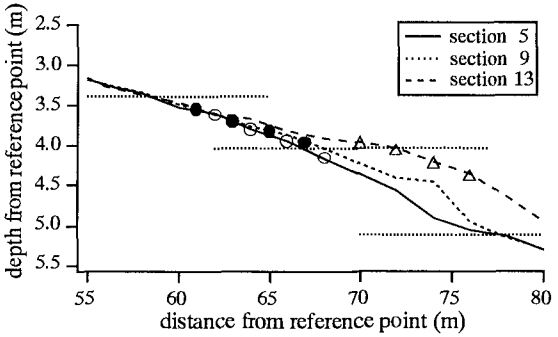

Fig. 5 Cross section of tracer placement (Second measurement)

CHARACTERISTICS OF INCIDENT WAVES AND MEADURED PEBBLE MOTIONS

First measurement:

Along the measuring line No.3 any movement of tracers could not be found and the tracers placed in the region higher than 2.8m along the measuring lines Nos.9 and 13 did not move. Figure 6 shows the measure displacements of tracer pebbles. More than 60% of the tracers placed along the measuring line No.9 were found.

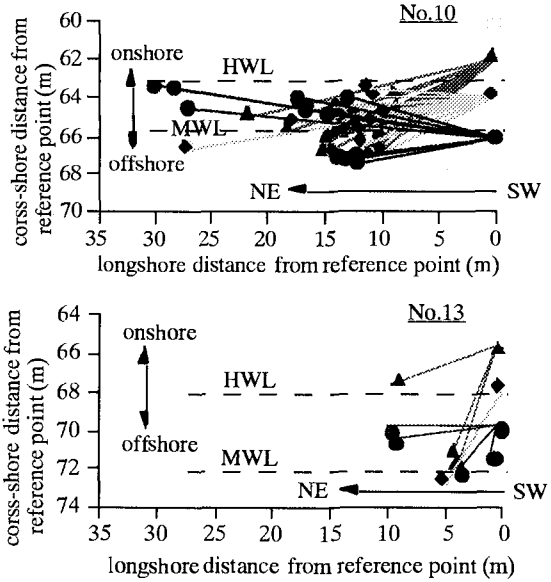

Fig. 6 Measured displacement of tracers along measuring line Nos.10 and 13 (first measurement)

All tracers moved in the longshore direction toward NE and the maximum longshore displacement is more than 30m. While the cross shore displacement was 4m at the maximum. As was already explained, the longshore pebble movement became the maximum around the measuring line Nos.9 and 10.

Only a few tracers placed along the measuring line No.13 were found They also moved in the longshore direction toward NE with the offshore displacement. The bottom profile was almost equilibrium around measuring line No.13 and the longshore pebble transport decreased to a large extent. It seemed that the a large part of tracers were covered by the pebbles transported in a steady stream from SW.

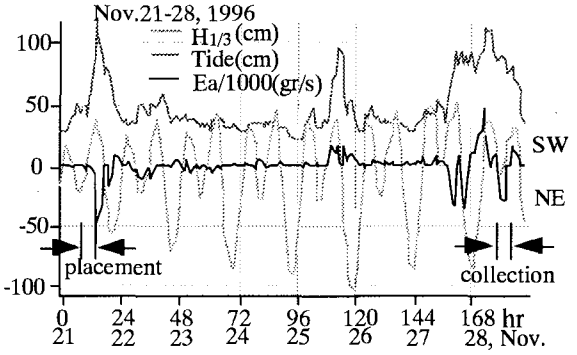

Fig.7 Incident waves and tidal level during the first measurement

Figure 7 is the time history of the incident waves and tidal level during the first measurement. A so-called E_a parameter that is usually used to relate incident waves and longshore sediment transport rate and is calculated from Eq.(1) are also shown.

$$E_a = \frac{1}{8}\rho g H^2 C_g \sin\theta \cos\theta \qquad (1)$$

Just after the placement of the tracers, height of incident waves increased rapidly and finally it became more than 1 m. The direction of incident wave energy flux was from SW to NE. Active motion of tracers were observed under these waves. Another high waves of significant wave height more than 0.5m were measured in 25, 27 and 28 of November. Especially, during 27 and 28 high waves continued for more than 24 hrs and direction of incident wave energy in the period changed from NE to SW. In average incident wave energy flux from SW to NE was predominant in this period.

Second measurement:

In the second measurement, tracers placed in the deeper region along the measuring line No.5 did not move. Someone threw tracers in the shallower region. So, we could not judge whether the tracers were moved by waves or not.

Figure 8 is the measured displacements of the tracers along measuring lines Nos.9 and 13. Tracers placed in the deeper region than MWL moved longshore direction from NE to SW. However, the displacement was only 2m at the maximum. Tracers in the shallower region along measuring line No.9 moved little and tracers in shallower region along No.13 moved toward NE. The maximum displacement was 1m. More than 80% of the tracers were collected.

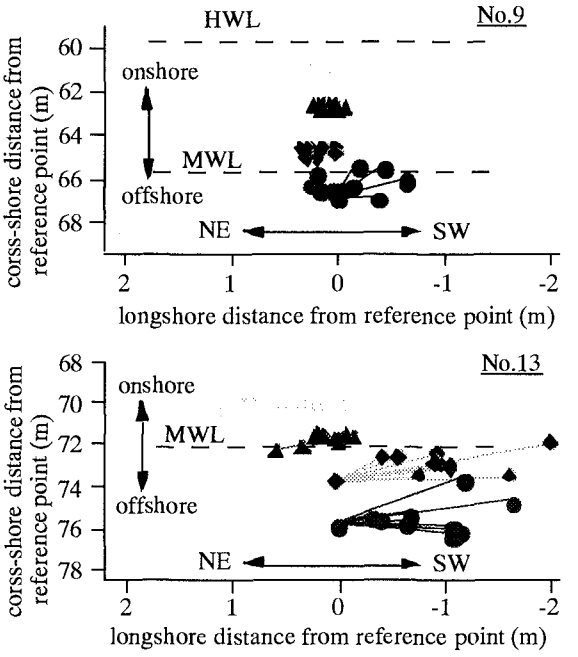

Fig. 8 Measured displacement of tracers along measuring line No.9 and 13 (Second measurement)

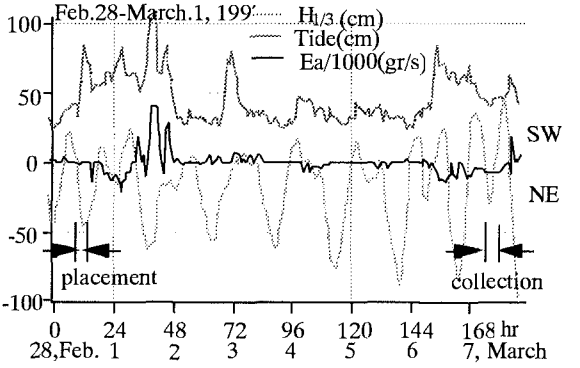

Fig.9 Incident waves and tidal level during the second measurement

Figure 9 is the time variation of significant incident waves, tidal level and value of E_a parameter. Large waves of wave height higher than 1m appeared only once when the tide was low. The energy flux was in the direction of SW. The movements of pebbles in the deeper region along Nos.9 and 13 were caused by these waves. Pebble motion in the shallower region might be caused by the waves of wave height higher than 0.5m and tide was high, i.e. 1 March and 6 March.

ANALYSIS OF PEBBLE MOTION

Modeling of pebble motion:

Currently there are two methods for analyzing pebble motion. One is a so-called discrete element method where the motions of all pebbles in an objected region are solved simultaneously (for example Araki et al.,1997). The other is the usual way to solve equations of motion for sliding and rotation of projected pebbles on the bottom. In this paper, the motion of pebble is analyzed by the latter method.

Here we focus on the motion of the projected pebble on the bottom. Figure 10 is the rough flow of our procedure for calculating motion of pebbles on the pebble beach. First of all we have to evaluate spatial and temporal variation of fluid motion in the objective region. This is done by calculating wave transformation and wave-induced current. Then fluid force on the projected pebble is estimated to determine the mode of motion and displacement of pebble. The loop is iterated during the desired time. The mode of the pebble motion and displacement of the pebble is determined by the equations of motion for rotation and sliding of pebble.

Spatial and temporal variation of fluid motion

⇩

Evaluation of fluid force on pebble

⇩

Determination of mode of pebble motion

⇩

Calculation of pebble displacement

⇩

Determination of mode of pebble motion

⇩

Calculation of pebble displacement

Fig. 10 Flow of calculation

Definition of the forces on the model pebble C whose diameter is a, mass in the air is W is shown in Fig.11 where X and Z are the displacements in the cross-shore and upward directions, v is the speed of the motion and ϕ is the mean bottom slope.

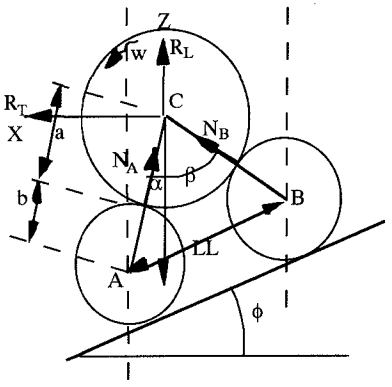

Fig.11 Definition of the forces on projected pebble

Horizontal and vertical fluid force are expressed by R_T and R_L and reactive forces from pebble A and B of diameter b are N_A and N_B. These forces are expressed by the following equations.

$$N_A = \frac{\left(W_g - R_L\right)\tan\beta + R_T}{\sin\alpha + \tan\beta\cos\alpha} \tag{2}$$

$$N_B = \frac{\left(W_g - R_L\right)\tan\beta + R_T}{\sin\beta + \tan\alpha\cos\beta} \tag{3}$$

When both N_A and N_B are positive, C dose not move. When N_A is positive and N_B is less than or equal to zero, pebble C moves toward left hand side and so on.

When the pebble moves toward left hand side as shown in Fig.12, the equations of motion are expressed by Eqs.(4)-(6).

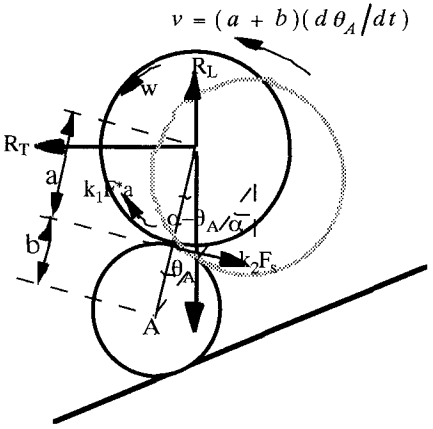

Fig.12 Motion of pebble to left hand side caused by rotation and sliding

Equation of motion in the horizontal direction:

$$M\frac{dv}{dt} = R_T\cos\left(\alpha - \theta_A\right) + \left(R_L - W_g\right)\sin\left(\alpha - \theta_A\right) + k_2F_S \tag{4}$$

Equation of motion in the upward direction:

$$M\frac{v^2}{a+b} = -R_T\sin\left(\alpha - \theta_A\right) + \left(R_L - W_g\right)\cos\left(\alpha - \theta_A\right) + N_A \tag{5}$$

Equation of motion of rotation:

$$I\frac{dw}{dt} = k_1F^*a - k_2F_Sa \tag{6}$$

where $I = \frac{2}{5}Ma^2$, M is the immersed mass of pebble C, θ_A is the displacement angle defined in Fig12 and the values of k_1 and k_2 are determined according to the direction of pebble motion as follows:

$$w \geq 0 : k_1 = 1, w \leq 0 : k_1 = -1 \tag{7}$$

$$v \geq 0 : k_2 = -1, v \leq 0 : k_2 = 1 \tag{8}$$

In this case, the speed of pebble motion v is expressed by Eq.(9)

$$v = (a+b)\frac{d\theta_A}{dt} \tag{9}$$

Using Eq. (9), Eqs.(4) to (6) are rewritten as follows:

$$M(a+b)\frac{d^2\theta_A}{dt^2} = R_T \cos(\alpha - \theta_A) + (R_L - W_g)\sin(\alpha - \theta_A) + k_2 F_S \tag{10}$$

$$M(a+b)\left(\frac{d\theta_A}{dt}\right)^2 = -R_T \sin(\alpha - \theta_A) + (R_L - W_g)\cos(\alpha - \theta_A) + N_A \tag{11}$$

$$\frac{2}{5}Ma^2\frac{dw}{dt} = k_1 F^* a - k_2 F_S a \tag{12}$$

$$f(t, \theta_A, F_S),\ g(t, \theta_A, N_A),\ h(t, w)$$

There are six unknowns in these equations, i.e.., N_A, θ_A, v, F_S, F* and w. However, there are only five equations, i.e.., Eqs.(2), (9), (10), (11) and (12). Another one equation is determined through the mode of the pebble motion.

Motion caused by rotation

When the motion is caused by purely rotation, then Eq.(13) relating θ_A, and w is used.

$$(a+b)\frac{d\theta_A}{dt} = aw \tag{13}$$

Equations (10) to (12) are also simplified as follows:

$$\frac{2}{5}M(a+b)\frac{d^2\theta_A}{dt^2} = k_1 F^* - k_2 F_S \tag{14}$$

$$\frac{d^2\theta_A}{dt^2} = \frac{5}{7M(a+b)}\left\{R_T \cos(\alpha - \theta_A) + (R_L - W_g)\sin(\alpha - \theta_A) + k_1 F^*\right\} \tag{15}$$

$$k_2 F_S = k_1 F^* - \frac{2}{5}M(a+b)\frac{d^2\theta_A}{dt^2} \tag{16}$$

When F_S is smaller than μN_A, the motion due to rotation takes place. This condition is expressed by Eq.(17).

$$F_S \leq \mu N_A \tag{17}$$

Motion caused by rotation and sliding

When the pebble moves by rotation and sliding, F_S is expressed by Eq.(18).

$$F_s = \mu' N_a \tag{18}$$

where μ' is the friction factor in motion.

In this case, equations of motion in horizontal and vertical direction are rewritten as follows:

$$\frac{d^2\theta_A}{dt^2} = \frac{1}{M(a+b)}\left\{R_T\cos(\alpha-\theta_A)+(R_L-Wg)\sin(\alpha-\theta_A)+k_2\mu' N_A\right\} \quad (19)$$

$$N_A = M(a+b)\left(\frac{d\theta_A}{dt}\right)^2 + R_T\sin(\alpha-\theta_A)-(R_L-Wg)\cos(\alpha-\theta_A) \quad (20)$$

The condition for the occurrence of motion due to rotation and sliding to take place is expressed as shown here.

$$F_S \le \mu N_A \ , \ (a+b)\frac{d\theta_A}{dt} \ne aw \quad (21)$$

When N_A becomes less than 0, the pebble leaps out.

These equations of motion are solved step by step by 4th-order Runge-Kutter method to obtain θ_A, v, w and so on. Before calculating these values, the mode of the motion are judged. In this case, there are 5 modes of the motion. That is, motion to left hand side and to right hand side, and the motion caused by purely rotation and that caused by rotation and sliding and no movement.

Using calculated values of θ_A and so on, variables concerning the pebble motion such as the horizontal displacement X, speed of displacement v and angular velocity ω are calculated according to the mode of motion.

Displacement caused by rotation:

$$X = (a+b)\left\{\sin\alpha-\sin(\alpha-\theta_A)\right\} \quad (22)$$

$$w = \frac{a+b}{a}\frac{d\theta_A}{dt} \quad (23)$$

$$v = (a+b)\frac{d\theta_A}{dt} \quad (24)$$

Displacement caused by rotation and sliding:

$$X = (a+b)\left\{\sin\alpha-\sin(\alpha-\theta_A)\right\} \quad (25)$$

$$w_n = \frac{5(k_1\mu^*-k_2\mu')}{2Ma}N_A h + w_{n-1} \quad (25)$$

$$v = (a+b)\frac{d\theta_A}{dt} \quad (25)$$

where subscript n and n-1 are the time steps of calculation.

When the pebble moves to the right hand side, the same modeling as shown above is done.

Evaluation of fluid force:

Figure 13 is the procedure for evaluating fluid force on the projective pebble. At first, wave field is determined by solving an equation of wave energy conservation, where

the effect of bottom permeability is taken into account. Then the wave-induced current is calculated by solving depth and time averaged shallow water equations. Spatial and temporal variation of fluid motion caused by waves is assumed to be sinusoidal.

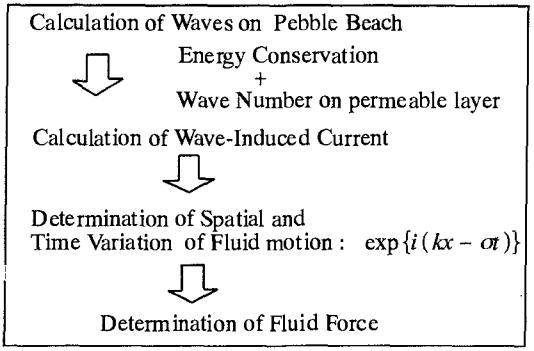

Fig. 13 Flow for determining fluid force

Finally the spatial and temporal variation of fluid force on pebble are determined by Eq.(26) where C_D is the drag coefficient and is evaluated by Eq.(27), C_M is the added mass coefficient and $\mathbf{u}_f$ is the velocity vector due to waves and wave-induced current.

$$R_T = \frac{\rho_f C_D}{2}\frac{\pi D^2}{4}\left|u_f - u_s\right|\left(u_f - u_s\right) + \frac{\rho_f C_M}{2}\frac{\pi D^3}{6}\frac{d}{dt}\left(u_f - u_s\right) \qquad (26)$$

$$C_D = 2 + 24/R_e, R_e = \left|u_f - u_s\right| D/\nu \qquad (27)$$

In the following calculation, the vertical force is assumed to be negligibly small.

CALCULATED PEBBLE MOTION ON INITIAL PROFILE

These equations are extended to three-dimensional motion. In the actual beach, there are various arrangement of projected pebble. For simplicity, we assume the situation where the pebble is on uniformly arranged pebble layer. Then there are two initial arrangements of projected pebble as shown in Fig.14. We carried out calculations of the motion on these two initial conditions.

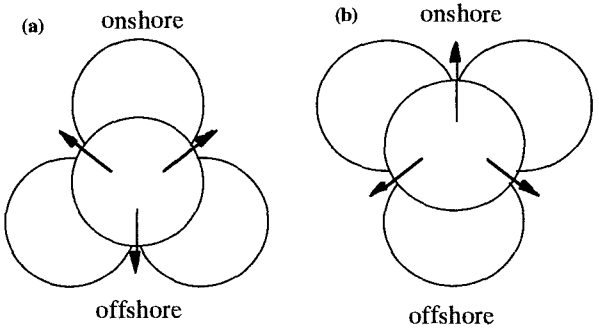

Fig. 14 Initial arrangement of projected pebble

As the first step of the application of these procedure, we calculated pebble motion on the initial beach with the straight parallel bottom contours. Figure 15 is an example of calculated wave field and wave-induced current under the condition of incident wave height is 1.2m , period is 4.5s and wave direction is 150°.

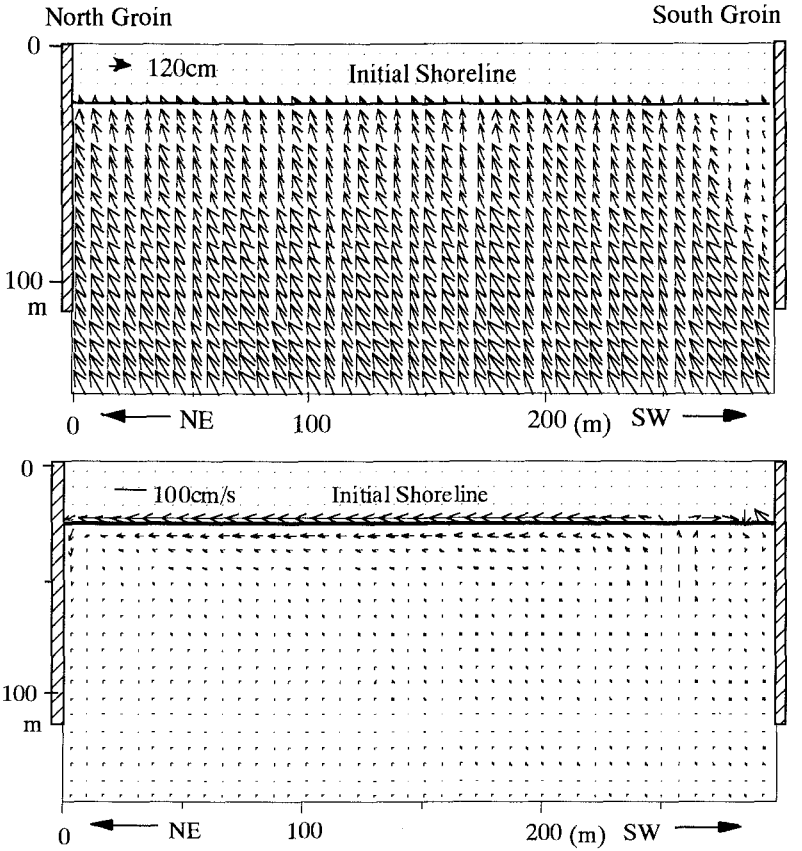

Fig. 15 Waves and wave-induced current on initial profile
(H_i=1.2m, T=4.5s, θ=150°)

Figure 16 is the examples of the calculated displacement of pebbles of diameter 6 cm during one wave period under the condition of fluid motion shown in Fig.15. The results shown by the thick line thin line correspond to the initial condition of the cases(a) and (b), respectively. Figure 17 is the result calculated under the small wave incidence.

Calculated results shown in Fig.16 indicates that the pebbles of diameter 6cm moves in the longshore direction toward NE. The maximum displacement takes place around the midpoint between shoreline and wave breaking point at the depth between 40cm and 60cm regardless of the initial condition. The maximum speed is 8cm/1cycle. When this

waves continue for one half hour, the displacement of the pebble reaches almost 30m. The order of the displacement corresponds to the measured maximum displacement.

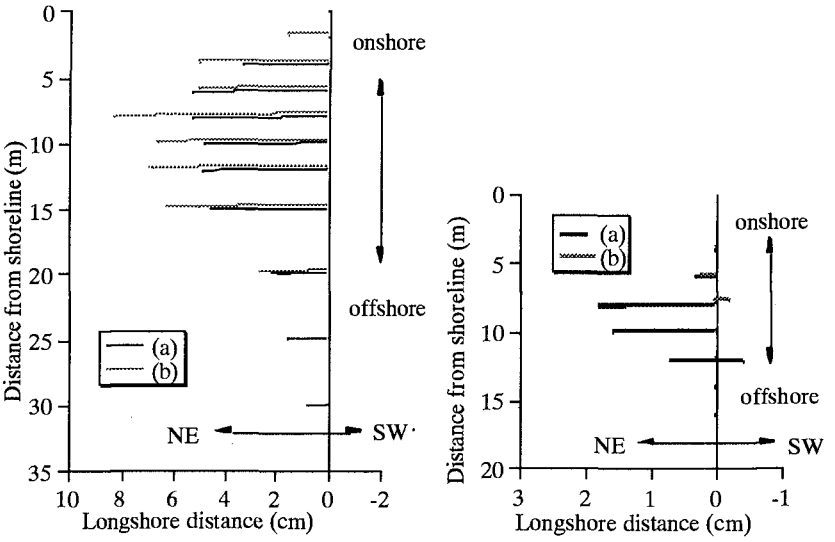

(a) H_i=1.2m, T=4.5s, θ=150^o (b) H_i=0.8m, T=4.5s, θ=150^o

Fig.14 Calculated displacement of pebbles during one period

The calculated speed of the same pebble at the same depth under the incident wave condition of wave height 80cm, period 4.5s and incident angle 150^o decreases significantly to 1cm/1cycle at the maximum. Any significant residual displacement is not calculated when wave height is 50cm.

By carrying out series of calculations of the movement of pebbles, we evaluated the rate of longshore pebble transport. It is found that the longshore pebble transport rate is not directly proportional to the longshore component of the incident wave energy flux at wave breaking point as is the case of the longshore sediment transport rate. The reason is explained by the difference of the characteristics of the movements of sand and pebble. The pebble usually moves intermittently during one wave period even under the condition of large wave incidence. While sand moves constantly over a whole wave period and is easily transported by wave-induced current when it is brought into suspension.

The movement of pebbles in the swash zone can not be reproduced by the numerical model because the model is based on the linear wave theory.

CONCLUSIONS

The main results obtained in this study are summarized as follows:

Pebbles on the surface of the beach of almost equilibrium profile move mainly in the longshore direction under obliquely incident waves.

The motion of pebble up to the maximum wave set-up point can be predicted numerically when the time and spatial variation of water particle velocity and fluid force on pebbles are given.

To evaluate the motion of pebbles in the swash zone, we have to solve a nonlinear wave equation including swash oscillation exactly.

REFERENCE

Araki S., S. Ito and I. Deguchi (1996): Equilibrium profile of rubble mound breakwater from the view point of dynamic response, Proc. Coastal Engineering, JSCE, Vol.43(2), pp.826-830.

Deguchi, I., M. Ono and T. Sawaragi (1996) :Wave on pebble beach and deformation of pebble beach, Proc. 25th Conf. Coastal Engineering, ASCE, Vol.3, pp.3349-3362.

Sawaragi, T. and I. Deguchi (1992) : Waves on permeable layer, Proc. 23 ICCE, ASCE, Vol.2, pp.1531-1544.

ONELINE, A NUMERICAL MODEL FOR SHORELINE CHANGE

Mohamed Dabees and J. William Kamphuis, M.ASCE[1]

Abstract

This paper describes the latest revision of the Queen's University coastal morphology model ONELINE. The model provides practical and reliable full, time-dependent simulations of shoreline change for coasts controlled by structures and complex boundary conditions. ONELINE calculates shoreline change due to longshore sediment differentials as well as on-offshore sediment movements. Model tests and case studies from around the world were conducted to test ONELINE's capabilities. Two case studies for Sea Isle City beach, New Jersey, and along the Nile Delta Coast in Egypt are discussed in this paper. Results are compared with observed field measurements to examine the model capabilities.

Introduction

The increasing development of coastal areas is faced with persisting erosion and flooding problems. Almost two-thirds of the world's population reside within 200 km of the coast, and continuous engineering activities are needed to safeguard coastal areas from erosion and flooding. Comprehensive coastal zone management and erosion/flood control requires a reliable and practical tool for predicting shoreline evolution to optimize shore protection measures.

One-dimensional coastal morphology models (one-line models) have demonstrated practical capability in predicting long-term shoreline change. However, most one-line models suffer from various constraints that limit their wide applicability. Work is currently in progress at Queen's University on upgrading ONELINE, a shoreline morphology model developed earlier, to create a practical shoreline change model with wide applicability for complex beach system configurations. The main objective is to provide accurate predictions that match the quality of available input data and knowledge of sediment transport processes

ONELINE is based on the one-line theory of shoreline change, but does not make any small angle assumption with respect to the incident wave angle and the shoreline

[1] Department of Civil Engineering, Queen's University, Kingston, Ontario, Canada K7L 3N6
Email: dabees@civil.queensu.ca; kamphuis@civil.queensu.ca

direction. The work on ONELINE was started in 1988 and was followed by several refinements to improve the model's capabilities. The latest upgrades include the cross-shore sediment transport contribution to shoreline change, the capability to simulate shoreline response to any combination of off-shore or shore-connected structures, improved formulation of the lateral boundary conditions, and provision of a Windows-based user interface that renders a user-friendly environment.

This paper provides a brief description of the ONELINE modeling system and demonstrates its capabilities through model tests and case studies. Two case studies are described in which complex beach system configurations are simulated. The first one features a groin field at Sea Isle City, New Jersey along the East Coast of the United States. The second is along the Nile Delta Coast in Egypt and includes detached breakwaters, groins, seawall, and a river mouth boundary. Simulation results are compared with measured shorelines to examine the model's capability of predicting shoreline change.

Model Description

Following the one-line assumption that the beach profile moves parallel to itself out to a limiting depth of closure (d_C), conservation of sediment for an infinitely small length of shoreline, Δx, can be expressed as follows (Figure 1):

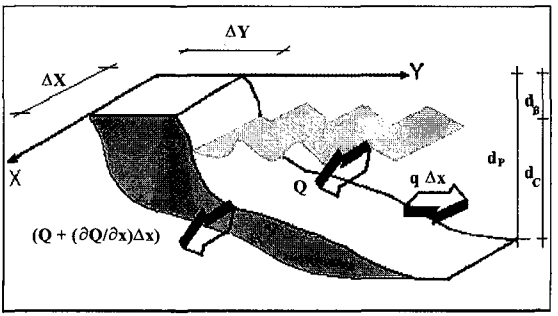

Figure 1. Definition sketch of conservation of sediment

$$\frac{\partial y}{\partial t} = -\frac{1}{d_p}\left(\frac{\partial Q}{\partial x} + q\right) \tag{1}$$

where y is the shoreline position, x is the longshore coordinate, t is the time, Q is the longshore sediment transport, q represents the average on-offshore transport rate, and d_P is the profile depth which equals the closure depth d_C plus the beach berm height d_B. The present model uses the Kamphuis formula (Kamphuis, 1991) modified to include transport by wave height gradient (Hanson and Kraus, 1989) to calculate longshore sediment transport (Equation 2).

$$Q = CKH_b^2T^{1.5}\beta^{0.75}D^{-0.25}\left[\sin^{0.6}(2\alpha_b) - \frac{2}{\beta}\cos\alpha_b\frac{\partial H_b}{\partial x}\right] \tag{2}$$

where Q is the alongshore sediment transport rate, C is a constant that is 7.3 when Q is expressed in m^3/hr., K is the ratio of actual over potential sediment transport rate (used as

an empirical factor for model calibration), H_b is the breaking wave height, T is the wave period, β is the beach slope in the breaking zone, α_b is the breaking wave angle, and D is the nominal grain size. Cross-shore sediment transport is calculated using Bailard's 1982 model (Equation 3).

$$q = k_s \frac{\rho C_f u_b^3}{(\rho_s - \rho) g p} \left\{ \frac{\varepsilon_B}{\tan\phi} \left(\psi_1 + \frac{2}{3}\delta_u - \frac{\tan\beta}{\tan\phi} u_3^* \right) + \frac{u_b}{\omega_s} \varepsilon_S \left[\psi_2 + \delta_u u_3^* - \frac{u_o}{\omega_s} \varepsilon_S \tan\beta u_5^* \right] \right\} \quad .....(3)$$

In which δ_u, ψ_1, ψ_2, u^*_3, and u^*_5 are cross-shore velocity moments defined by Bailard (1982) as functions of wave height; ϕ is the angle of internal friction; ε_B and ε_S are the coefficients of bed load and suspended load efficiency; C_f is the drag coefficient, u_b is the fluid bottom velocity, ρ and ρ_s are the fluid and sediment densities respectively, p is the sediment concentration, ω_s is the fall velocity, and k_s is an empirical factor used for calibration.

The basic ONELINE model structure is illustrated in Figure 2. The modeled shoreline is discretized into a finite grid and the simulation time is divided into time steps. For each time step wave shoaling, refraction, diffraction and the resulting sediment transport are calculated at each grid point. Then, the governing equations are solved simultaneously in the form of a matrix to determine the new shoreline.

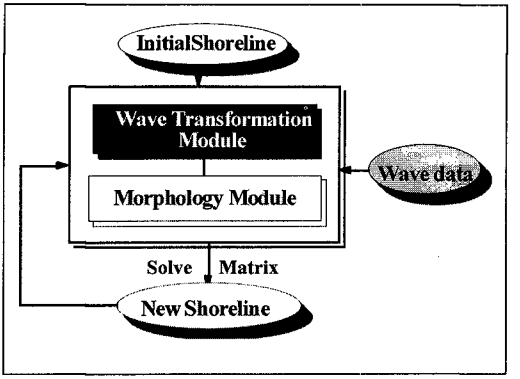

Figure 2. ONELINE model structure

The updated version of ONELINE includes improved mathematical formulation of boundary conditions and internal constraints. The new lateral boundary conditions give the modeler greater control in defining complex conditions near the boundaries. User-specified inflow and outflow factors at each boundary are used to define the sediment transport gradients at the boundaries. Boundary conditions can be properly formulated through sensitivity analysis and model calibration with observed shorelines. These highly adaptable boundary conditions provide the capability to simulate a wide range of complex beach system configurations with various sources or sinks near the boundaries. For example, sources such as river sediment discharges, updrift feeder beaches where nourishment occurs outside the modeled area, and sinks such as tidal inlets, or submarines canyons can all be modeled. Likewise, the representation of internal constraints such as groins or breakwaters was significantly improved to provide accurate response of shoreline to nearshore structures. The mathematical formulation of the influence of various structures on wave transformation and morphological changes was

refined, tested, and calibrated with various model runs and case studies from around the world.

Model Tests

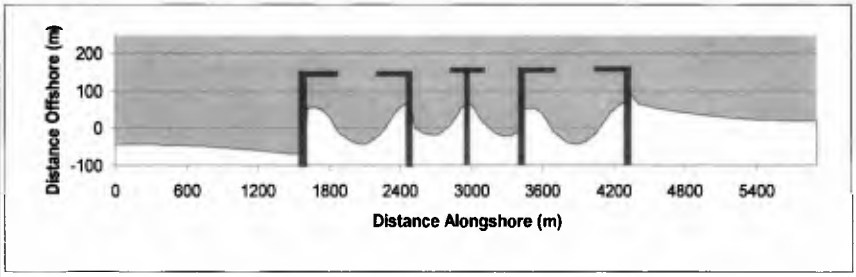

Figure 3a. Shoreline response to coastal structures

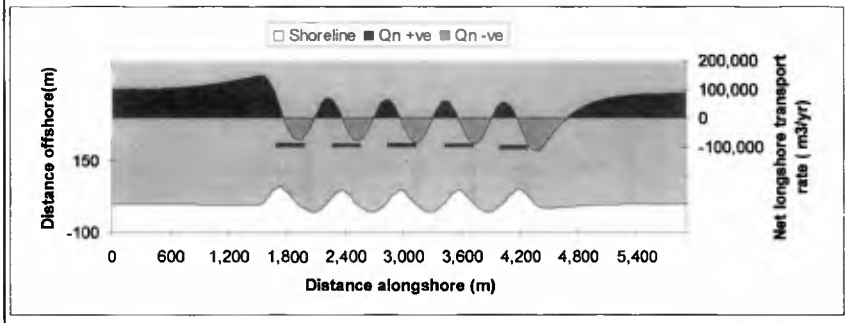

Figure 3b. Shoreline response and longshore transport patterns near breakwaters

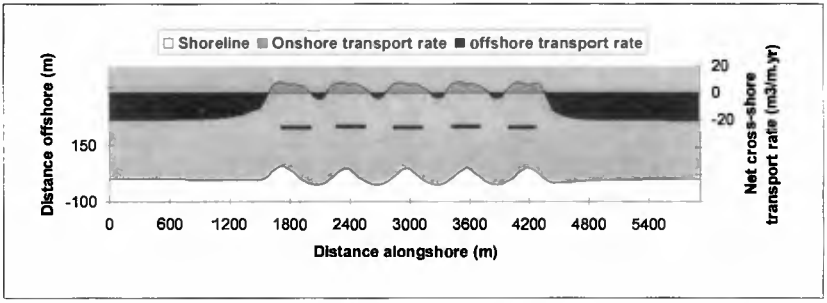

Figure 3c. Shoreline response and cross-shore transport pattern near breakwaters

Figure 3. Model test results

Several model tests were performed to examine ONELINE's new formulations. Figure 3a shows the result of a 5-year simulation on a straight beach with various coastal structures subjected to an annual wave time series with 4-hour time step. Figure 3b shows simulation results of the net longshore transport rate distribution near a series of detached breakwaters subjected to measured wave time series. Figure 3c indicates simulated cross-shore transport patterns near breakwaters subjected to big waves. The breakwaters reduce wave heights behind them yielding on-shore sediment movement unlike the open coast areas where larger waves produce net offshore sediment losses. The results reflect ONELINE's realistic simulation of the influence of coastal structures on wave transformation, sediment transport and shoreline change.

Two cases are discussed in this paper to demonstrate the capability of ONELINE The cases were selected along Sea Isle City beach, New Jersey, USA, and the Nile delta coastline in Egypt.

Sea Isle City Model

The first case study is a 15-year simulation of a groin field at Sea Isle City, New Jersey. Sea Isle City faces the Atlantic and is located at the south end of Ludlam Island, a barrier island in southern New Jersey, USA (Figure 4).

Background

Sea Isle City coastline is a fine sandy beach backed by sand dunes. The predominant waves come from northeast direction producing an average net longshore transport of about 300,000 m^3/yr to the south (Everts 1979). To stabilize the beach and reduce erosion rates along Ludlam Island, several groins have been constructed to form a groin field. Early groins were built at the northern part of the Ludlam Island by the turn of this century. The groins were low in profile and relatively short so that they would not produce large shoreline offset across them. The groin system along with periodic nourishment maintained a wider, more stable beach within the groin compartments. However, erosion was shifted to the beach downdrift of the southermost groin. Thus, over the years, the groin field was extended southward to cover most of the island shoreline.

Figure 4. Sea Isle City location

Model Setup

The Sea Isle City model covers 2.6 km between a groin field at the northern boundary and a tidal inlet at the southern boundary (Figure 5). ONELINE modeled this shoreline reach by 75 grid cells 35 m long each. The input wave data were determined from measured wave gauges near Sea Isle City. The simulations were carried out in two phases for the period between November 1980 and March 1995 with a 4-hour time step, generating a total of 11,406 time steps. The first simulation phase from 1980 to 1986 was used for model calibration. During that simulation period 4 groins were added in 1983. Calibration involved the determination of the sediment transport calibration constants, and appropriate representation of the lateral boundary conditions and internal constraints. The fast execution time of ONELINE simulations allowed sensitivity analyses for each of those controlling parameters. Thus, several runs were performed: first to estimate the sediment transport factors to give average transport rates close to the estimated or measured rates; then the lateral boundaries were adjusted so that the observed sediment losses or gains for the area were correct, and finally, the internal

Figure 5. Sea Isle City model setup

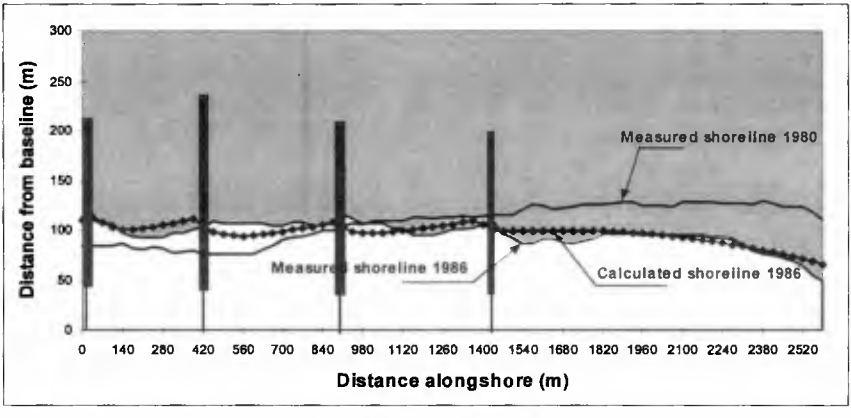

Figure 6. Model calibration results

constraints (structures on the grid) were adjusted by changing groin permeability to provide good agreement between predicted and measured shorelines near the structures.

Figure 6 shows the calibration results. The averaged prediction error (E_P) for the calibration phase was 10%, where E_P is the average of all the absolute values of the error of calculated shoreline change at each grid point. Following calibration, the second simulation phase from January 1986 to March 1995 verified the calibrated model. During that period two more groins and two major beach fills were added and still verification showed close agreement of measured and predicted shorelines of 1995 with E_P = 9% (Figure 7).

The Simulations of Sea Isle City beach showed the effectiveness of ONELINE's improved features. Of particular concern was the simulation of the southern boundary formed by the tidal inlet. The beach morphology close to that inlet is greatly affected by the inlet processes and realistic simulation of the sand influx across the boundary was crucial to the reliability of the predictions. The adaptable formulation of the lateral boundary conditions in ONELINE enabled a reasonable presentation of that complex boundary condition. The improved formulation of internal groins also provided accurate shoreline response within the groin field of Sea Isle city over a 15 year simulation period as shown in Figure 7. The top part of Figure 7 shows the net shoreline change along the modeled area where 6 groins and half a million cubic meters of sand were added over a period of 15 years. ONELINE succeeded in identifying locations and magnitudes of erosion and accretion along the modeled region.

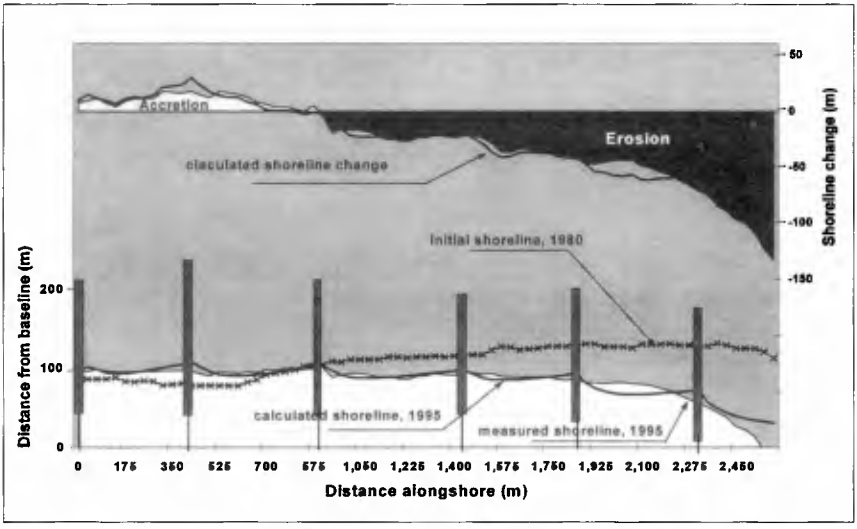

Figure 7. Sea Isle City model verification and final results

Ras-El-Bar Model

The second case study is of a rather complex beach system along the Nile Delta Coast in Egypt. The Nile Delta was formed by the Nile river sediment discharges into the Mediterranean Sea over thousands of year. Human intervention with the natural system of the Nile has profoundly modified the geological processes in the northern delta. Since completion of the Aswan High Dam in 1964, fluvial sediments are no longer transported to the coast, and the balance between fluvial and marine processes has been completely modified. The Nile Delta is not an active delta anymore, but an entirely wave-dominated coastal plain. Widespread erosion along the Nile delta coastline became a persisting problem and large-scale coastal projects have been implemented to combat coastal erosion. Ras-El-Bar is a site along the Nile delta west of the Damietta Nile branch (Figure 8). The Nile Delta coastline runs generally west to east, while local orientation of Ras-El-Bar shore is southwest to northeast. Thus only waves coming from west to northeast can reach the nearshore zone of Ras-El-Bar. The predominant wind directions offshore of Ras-El-Bar are from NW and WNW (Delft,1987). Wave records from 1985 to 1990 near Ras-El-bar indicate that the maximum and average offshore wave heights were 4.5m and 0.6 m respectively (Coastal Research Institute Alexandria, 1996).

Figure 8. Ras-El-Bar location

Ras-El-Bar beach is composed of very fine sand with average median diameter of about 0.12 millimeters. Several studies along the Egyptian coast provide sufficient description of sediment transport at Ras-El-Bar (Inman and Jenkins, 1984; Frihy and Komar, 1991). The general net longshore transport is eastward, but due to local shoreline orientation near the Damietta mouth, the local net transport is to the west. Although Ras-El-Bar represents a littoral-drift convergence zone, the accretion is small and secondary to offshore losses caused by cross-shore transport. Longshore transport at Ras El Bar is small in both directions and the net transport is minimal. Cross-shore transport plays a significant role in the shoreline change at Ras-El-Bar. Shoreline recession due to cross-shore transport was estimated in Delft Hydraulics (1987) to be about 3 to 5 m/year.

Several erosion control measures have been taken to stabilize the beaches of Ras-El-Bar (Figure 9) after the construction of the Aswan Dam. Three groins were constructed in 1970 in an attempt to eliminate the erosion of Ras-El-Bar peninsula. The groin system was not successful because the cross-shore sediment transport dominates. A dolos and riprap revetment was placed within the groin field to protect a nearby highway. Erosion was maximum at the western end-groin and diminished to the west. The erosion threatened Ras-El-Bar resort community, and further shore protection was needed to

restore its eroding beach. A system of detached breakwaters was constructed in 1990, west of the groin field. The breakwaters were placed 400 meters offshore such that they would restore the recreational beach while being far enough offshore to prevent tombolo formation. In 1994, the beach area east of the breakwaters was nourished with two hundred thousands cubic meter of sand.

Model Setup

A complete time dependent simulation of shoreline changes over a 9-year period for Ras-El-Bar beach was carried out using ONELINE. The modeled area embodied a number of coastal protection works and rather complex boundary conditions. The modeled region covers 4 kilometers of beach west from the Damietta Nile mouth. This shoreline reach was modeled in ONELINE by 200 grid cells 20 m long each. The focal point of the model is the four detached breakwaters built in 1991. The breakwater system covers 1.4 km of beach; however the modeled region was extended far enough to include all the nearby littoral barriers affecting the hydro-sedimentological regime in the area. Figure 9 shows the model location and coordinate system and Figure 10 shows the modeled region schematically. Measured shorelines of 1986, 1993, and 1995 were digitized from the surveying and contour maps and transformed to the model coordinate system. Input wave data were generated using measured time series at Ras El Bar (Coastal Research Institute Alexandria, 1996). The wave gauge was located at the eastern side of Damietta promontory at 7-meter depth of water. The simulation runs covered the period from June 1986 to September 1995 on two phases. Phase one was from 1986 to 1993 during which

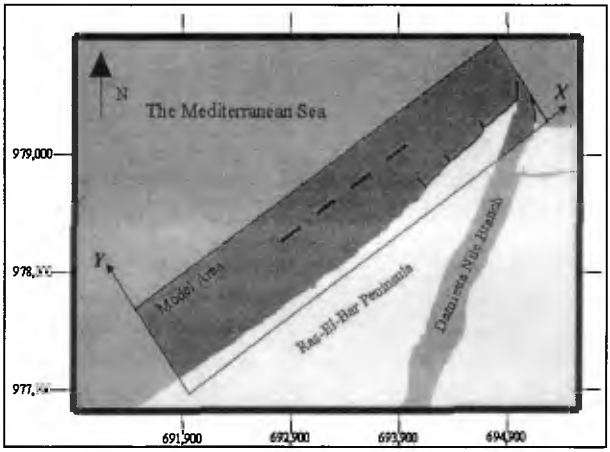

Figure 9. Model location and coordinate system

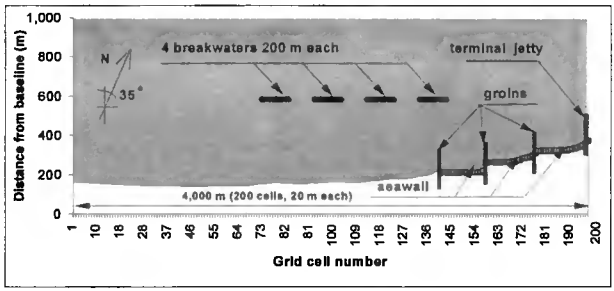

Figure 10. Schematic diagram of the modeled region

the 4 breakwaters where built in 1991, while phase two was from 1993 to 1995. A time step of 2 hours was used in all simulations, yielding a total of 40,500 time steps.

Model Calibration and Verification

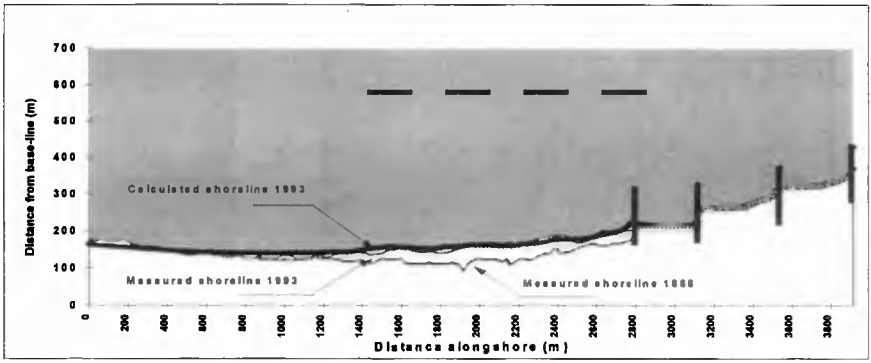

Figure 11. Ras-El-Bar model calibration results

The model was calibrated and verified with measured shorelines of 1993 and 1995 respectively. During the calibration process, first the calibration coefficient for longshore and cross-shore transports were adjusted to provide values within reasonable ranges of measurements and observations; then the lateral boundaries were set to match the inflow and outflow of sediment through both boundaries with the prototype

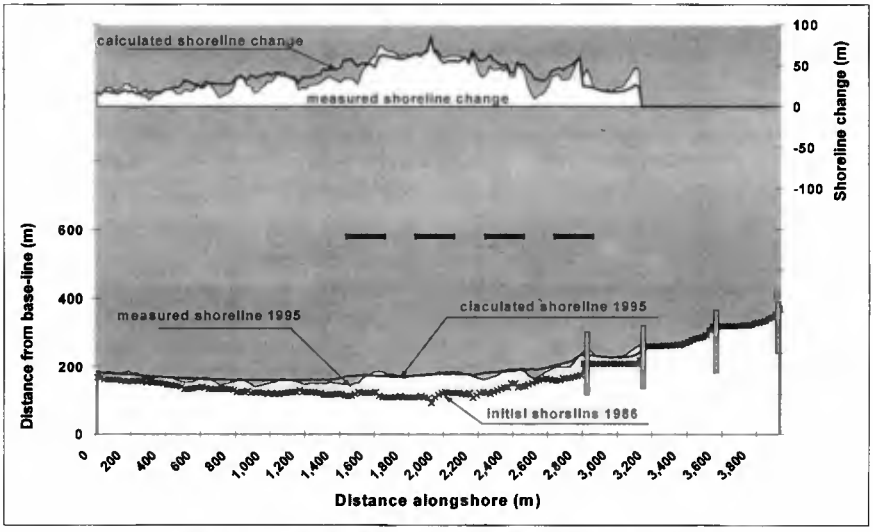

Figure 12. Ras-El-Bar model verification and final results

conditions; and finally the internal constrains such as the properties of the jetty, groins, and breakwaters were set to fine tune the calculated shoreline to match the measured shoreline.

Figure 11 shows the model calibration results. The averaged prediction error (E_p) on calibration was 13%, while for the verification was E_p =12%. Figure 12 shows the model verification and final results. A plot of the net shoreline change over the nine-year simulation period is also shown in Figure 12. ONELINE has successfully calculated the shoreline buildup behind the breakwaters due to the combined effect of longshore and cross-shore sediment transport. The results also indicate success in calculating sand bypassing and buildup seaward of the revetment in the westerly groin compartment.

Model Results

Figures 13 to 16 show samples of Ras-El-Bar model results and demonstrate the realistic simulations of coastal processes in the vicinity of various coastal structures.

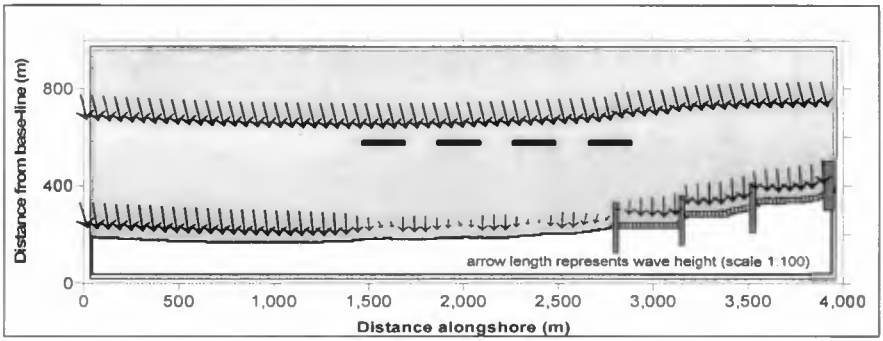

Figure 13. Wave transformation patterns

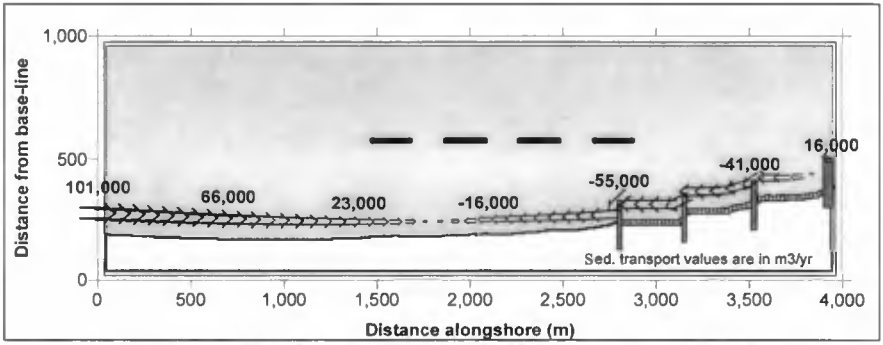

Figure 14. Net annual longshore transport rates along the modeled area

Figure 13 shows the calculated wave transformation patterns for a particular incident wave along the modeled area. ONELINE wave transformation calculations take into account the influence of wave shoaling, refraction, and diffraction for each wave

event. The spatial change in wave heights and directions along the modeled region reflects clearly the diffraction patterns from different structures. The calculated longshore and cross-shore transport rates are shown in Figures 14 and 15 respectively. The model results correspond well with the field measurements and observations. The

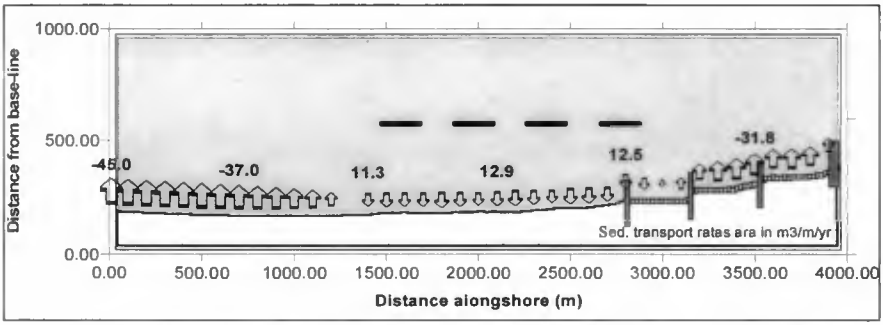

Figure 15. Net annual cross-shore sediment transport along the modeled area

model results show how the breakwaters reduce the wave energy and consequently the sediment transport in the shadow zones. The smaller waves in the shadow zones move sediment on-shore, unlike outside the breakwater protected area where the cross-shore transport produces substantial offshore losses.

Sediment Budget

Sediment budget analyses based on model results were conducted before and after the placement of the breakwaters. Figure 16 demonstrates the effects of the breakwater system on the sediment regime at Ras-El-Bar. The sediment transport rate entering the region from western boundary was around 100,000 m^3/yr. while only 16,000 m^3/yr. bypass the terminal jetty at the eastern boundary. The breakwater system reduced the offshore losses from 167,000 m^3/yr. to 42,000 m^3/yr. The sediment budget analyses indicate that before the construction of the breakwaters, a net loss of 83,000 m^3/yr (equivalent to shoreline erosion of an average 2.3m/yr) while after the construction a gain of 42,000 m^3/yr. is attained (equivalent to a shoreline gain of an average 1.4m/yr.).

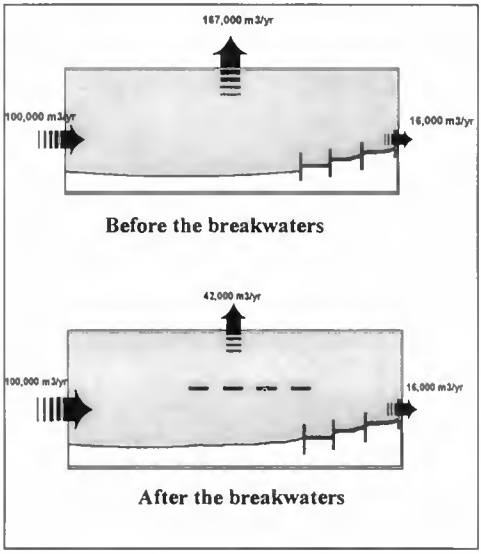

Figure 16. Sediment budget results

Conclusion

This paper describes, ONELINE, a shoreline change modeling system, and demonstrates its capabilities through model tests and case studies. ONELINE's recent improvements boosted its practical applicability to simulate more complex beach system configurations. Model tests indicated ONELINE's credible predictions of sediment transport and shoreline response to various combinations of coastal structures. Two case studies were simulated to verify the model capabilities. A 15-year simulation of a 2.6-km shoreline reach at the southern part of Sea Isle City, New Jersey, proved the effectiveness of ONELINE to simulate shoreline response to permeable groins and complex boundary conditions. The refined formulation of lateral boundary conditions enabled reasonable presentation of the tidal inlet boundary of Sea Isle City model. ONELINE was also used to model Ras-El-Bar, a beach resort area along the rapidly eroding Nile delta. Several erosion control measures were built over the years such as breakwaters, groins, seawall, and river mouth jetties. A 9-year simulation of a 4 km-long beach at Ras-El-Bar was successful. The adaptable boundary conditions of ONELINE enabled simulation of the sediment flow patterns at the jettied river mouth of the eastern boundary as well as longshore transport gradients at the western boundary. Cross-shore sediment transport plays a large role in the shoreline change at Ras-El-Bar. ONELINE's ability to simulate cross-shore sediment transport as well as longshore transport in the vicinity of different coastal structures allowed a successful modeling of these complex beach systems. The model results corresponded with the field measurements and hence provided quantitative results and a well-verified prediction capability of the region. The consistently small prediction error on calibration and verification of these widely varying cases demonstrates the robustness of ONELINE. The modeling system, ONELINE, is still under development. Future improvements include upgrading ONELINE to contour lines model to enable predictions of profile changes as well.

Acknowledgments

This study is supported by the Natural Science and Engineering Research Council of Canada, and by funds from the School of Graduate Studies, Queen's University. Thanks to Dr. J. Richard Weggel for providing us with necessary data for the Sea Isle City beaches, and to the Egyptian Shore Protection Authority for the Ras-El-Bar data.

References

Bailard J. A. (1982). Modeling on-offshore sediment transport in the surf zone. *Proc., Int. Conf. on Coastal Eng., ASCE,*. CapeTown, RSA. pp. 1419-1438

Coastal Research Institute Alexandria (1996), "Wave Climate along the Mediterranean Egyptian coast." *Progress Report No. W1, Ministry of Public Works and Water Resources*, Egypt. 62 pp.

Dabees, M. A., and Kamphuis, J.W. (1997). "Numerical Modeling and Coastal Processes: Overview of a Modeling System for Simulating Shoreline Change" *Proc., Canadian Coastal Conf. '97*, Guelph, Canada, pp 161-176.

Delft Hydraulics, (1987), "Ras-El-Bar Shore Protection: Feasibility study on a detached breakwater system as a coastal defense measure." *Delft, H 500*, 44 pp.

Everts, C. H. (1979). "Beach behavior in the vicinity of groins - Two New Jersey Field Examples." *Proc., Specialty Conf., Coastal Structures '79, ASCE,* Alexandria, VA, pp 853-867

Everts, C.H., Wall, A. E., and Czerniak, M. T. (1980). "Beach and inlet changes at Ludlam Beach, New Jersey." Misc. Rep., MR-80-3, *U.S. Army Corps of Eng., Coastal Engineering Research Center*, Fort Belvoir, VA.

Frihy, O.E., and Komar, P. D. (1991). "Patterns of beach-sand sorting and shoreline erosion on the Nile Delta." *J. Sed. Petrol*, Vol 61, pp 544-550.

Frihy, O.E., Fanos, A.M., Khafagy, A.A., and Komar P.D. (1991). "Patterns of nearshore sediment transport along the Nile Delta, Egypt." *Coastal Eng.*, Vol. 15, pp. 409-429.

Inman, D.L. and Jenkins, S.A., (1984). "The Nile littoral cell and man's impact on the coastal zone of the southeastern Mediterranean." Proc., *19th Int. Conf. Coastal Eng., ASCE*, pp. 1600-1617.

Hanson, H. and Kraus, N.C. (1989), "GENESIS: Generalized Model for Simulating Shoreline Change", CERC Rep. 89-19, US Corps of Eng., Vicksburg, 185 pp

Kamphuis, J.W. (1991). "Alongshore sediment transport rate", *J. of Waterway, Port, Coastal, and Ocean Eng., ASCE*, Vol. 117, pp 624-640.

SEASONAL SHORELINE VARIATIONS BY CROSS-SHORE TRANSPORT IN A ONE-LINE MODEL UNDER RANDOM WAVES

Hans Hanson[1] and Magnus Larson[1]

ABSTRACT: *An algorithm for representing seasonal variations in shoreline position as caused by on-offshore sediment transport in a one-line model is presented. The study was based on an analysis of an 11-year long time series of waves and shoreline location obtained at Duck, North Carolina. Two different approaches were used: one was based on wave steepness and dimensionless fall speed and the other on ratio of the maximum near-bottom orbital velocity to the critical velocity required to initiate sediment movement. Both applications showed that it is possible to reproduce the overall spatial and temporal behavior of seasonal cross-shore transport related shoreline variation using two simple one-line model compatible approaches. Preliminary calculations show that the method may be used for analyzing the seasonal behavior of a beach. At the same time, the impact of individual storms are not represented to any significant degree.*

INTRODUCTION

One-line models of shoreline response have demonstrated their predictive capabilities in numerous projects (Hanson *et al.* 1988). This class of models calculates shoreline position changes that occur over a period of years to decades. Changes in shoreline position are assumed to be produced by spatial and temporal differences in the **longshore** sand transport rate (Hanson 1989, Hanson and Kraus 1989). Thus, this type of model is best suited to situations where there is a systematic trend in long-term change in shoreline position, such as recession down-drift of a groin. Cross-shore transport effects, such as storm-induced erosion and cyclical movement of shoreline position associated with seasonal variation in wave climate, are assumed to cancel over a long enough simulation period or are accounted for through external calculation.

[1]Assoc. Prof., Dept. of Water Res. Engrg., Univ. of Lund, Box 118, S-22100 Lund, Sweden. Fax +46 46 222 8987. Email Hans.Hanson@tvrl.lth.se, Magnus.Larson@tvrl.lth.se.

Cross-shore models, on the other hand, typically predict beach change as a result of **cross-shore** transport produced by storms (Larson and Kraus 1989). This type of models is simplified by omitting longshore transport processes. Although these models have been relatively successful in reproducing short-term profile response to individual storm, they have been less suitable for long-term predictions. In principle, the two types of models could be combined to obtain both long- and short-time changes in shoreline position. Such attempts have been done (e.g. Bakker 1969, Perlin and Dean 1979, Larson *et al.* 1990), but these approaches have not yet found their way into engineering practice.

Nevertheless, it is recognized that seasonal variations can play a significant role in the long-term evolution of the shoreline. Therefore, it would be a significant step forward if, at least in a schematic way, the main features of cross-shore related seasonal shoreline variations could be represented in one-line shoreline response models. If successful, it would constitute a model for simulating long-term cross-shore related coastal evolution for engineering use and at the same time eliminate one of the main constraints of the use of one-line models.

An important criterion for the formulation of the cross-shore contribution was that it should be compatible with the one-line formulation in terms of independent variables and level of sophistication. This may seem like a paradox because numerous studies (e.g. Larson and Kraus 1989) have shown that the profile shape is a key parameter for the cross-shore transport magnitude and direction. At the same time, it is recognized that one-line models does not provide any information about the profile shape. Thus, the relatively simple one-line model cannot be expected to represent the complex impact of individual storms, but rather to capture the more long-term effects. Consequently, the objective of this study was to represent seasonal variation due to cross-shore transport using a one-line model.

PROCEDURE

Transport Magnitude

Because the one-line model does not require or provide any information about the actual shape of the bottom profile, the cross-shore transport magnitude must be calculated using a relation that is independent of the profile shape. Numerous formulae for the cross-shore sand transport rate may be found in the literature (Horikawa 1988, p. 196 ff.). Many of these may be written in the generic form

$$\frac{q_o}{wd} = K_q \, (\Psi - \Psi_c)^a \tag{1}$$

where q_o = cross-shore sediment transport rate per unit width, w = sediment fall speed, d = median grain size, K_q = transport coefficient, (Ψ_c) Ψ = (critical) Shields parameter, and a = exponent. The value of the exponent a varies from 1 to 3 in the different proposed

relationships. In the present study a value of 1.5 was selected in accordance with Watanabe (1982). For simplicity, the value of the critical Shields parameter was set to zero. Thus the expression may be written:

$$\frac{q_o}{wd} = K_q \, \Psi^{1.5} \tag{2}$$

Recognizing that the Shields parameter may be expressed in the form (using shallow water approximations),

$$\Psi = \frac{f_w \, u_{b,m}^2}{2sgd} = K_\Psi \, \frac{u_{b,m}^2}{gd} \approx K_\Psi \, \frac{gH}{gd} = K_\Psi \, \frac{H}{d} \tag{3}$$

where f_w = Jonsson's (1966) wave friction factor, $u_{b,m}$ = the maximum horizontal near-bottom orbital fluid velocity, s = sediment specific density in water, g = acceleration due to gravity, K_Ψ = coefficient, H = the local wave height. In order to be consistent with the one-line theory, it is presumed that the conditions at the break point may be used to compute the overall cross-shore sediment transport, i.e., a fixed transport distribution is assumed that scales with the breaker height. Thus, the cross-shore sediment transport rate per unit length alongshore, q_o, here regarded as a potential rate, may be calculated, with $K \equiv K_q \, K_\Psi^{1.5}$:

$$q_o = wd \, K_q \left(K_\Psi \, \frac{H_b}{d} \right)^{1.5} = w \, K \left(\frac{H_b^3}{d} \right)^{0.5} \tag{4}$$

where H_b is the breaking wave height. This relationship will be used in the following application of a numerical model with K used as a calibration parameter. However, because this relation does not give a transport direction, this will have to be resolved separately.

Transport Direction using Fall Speed

Kraus *et al.* (1991) presented several criteria for discriminating between erosive and accretive conditions on the basis of a classification of profile response to breaking waves in large wave tank (LWT) model tests as well as from the field. The LWT data consisted of two data sets. One was from US Army Corps of Engineers, compiled by Kraus and Larson (1988) and referred to in the following as the CERC data. The other set was from the Central Research Institute for Electric Power Industry (CRIEPI) in Japan (Kajima *et al.* 1982) and referred to here as the CRIEPI data. The field data set (Kraus and Mason 1991) consisted of observations of well-documented responses to small and large storms.

In the present study, on the basis of shoreline (MSL) movement alone, the results from the LWT and field tests were re-evaluated in terms of erosion and accretion. Figure 1 shows

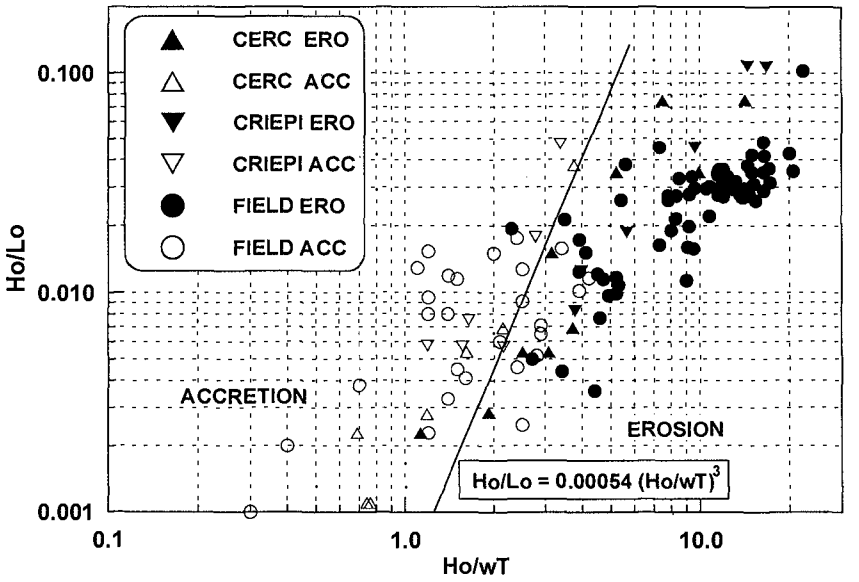

Figure 1. Discriminating erosive and accretive shoreline conditions on the basis of wave steepness and dimensionless fall speed (modified from Kraus *et al.* 1991).

the data plotted on wave steepness H_o/L_o versus dimensionless wave steepness H_o/wT, where H_o = deep-water wave height, L_o = deep-water wavelength, w = fall speed, and T = wave period. The proposed criteria,

$$\frac{H_o}{L_o} = M_1 \left(\frac{H_o}{wT}\right)^3 = 0.00054 \left(\frac{H_o}{wT}\right)^3 \tag{5}$$

where M_1 = discriminator coefficient, discriminates between erosion and accretion with a skill of 0.92, defined as the ratio of correct predictions to total observations (Seymour and Castel 1989).

By assuming a Rayleigh probability distribution function (pdf) for the wave height, the smallest (critical) erosional deep-water wave height H_{oc} may be derived from Eq. (5) as (Larson 1996):

$$H_{oc} = \sqrt{\frac{1}{M_1}\frac{(wT)^3}{L_o}} \tag{6}$$

At a location x, a certain portion δ_e of the broken waves will be erosional:

$$\delta_e = \frac{e^{-(\frac{H_{oc}}{H_{rmso}})^2}}{e^{-(\frac{H_{bo}}{H_{rmso}})^2}} \qquad \delta_e \le 1 \tag{7}$$

Thus, if evaluated at the shoreline where $H_{bo} = 0$, the portion will be

$$\delta_e = e^{-(\frac{H_{oc}}{H_{rmso}})^2} \qquad \delta_e \le 1 \tag{8}$$

By substituting Eq. (6) into Eq. (8) we obtain

$$\delta_e = e^{-\frac{1}{M}\frac{H_{rmso}}{L_o}(\frac{wT}{H_{rmso}})^3} \qquad \delta_e \le 1 \tag{9}$$

If a portion δ_e of the broken waves are erosional the rest δ_a=1-δ_e of the waves must be accretionary. Giving each single wave equal weight when summing up to determine the net direction yields,

$$\xi = \delta_a - \delta_e = 1 - 2\delta_e \qquad -1 \le \xi \le 1 \tag{10}$$

where ξ gives the net direction and a weight that includes the variability in wave height defined by the Rayleigh pdf. Substituting Eq. (9) into Eq. (10) gives the net transport direction as:

$$\xi = 1 - 2e^{-\frac{1}{M}\frac{H_{rmso}}{L_o}(\frac{wT}{H_{rmso}})^3} \qquad -1 \le \xi \le 1 \tag{11}$$

Transport Direction using Velocity Ratios

Based on the same field data as above, Ahrens and Hands (1998) parameterizes beach erosion and accretion processes on the basis of the ratio of the maximum near-bottom orbital fluid velocity $u_{b,m}$ to the critical velocity u_{crit} required to initiate sediment movement under the wave. Whereas Ahrens and Hands (1998) use stream function wave theory, the present study will focus on linear wave theory, again to be consistent with traditional one-line modeling procedures. The critical velocity u_{crit} was defined as (Hallermeier 1980),

$$u_{crit} = \sqrt{8\Delta g d} \tag{12}$$

where $\Delta = (\rho_s - \rho)/\rho$, ρ_s (ρ) is the density of the sediment (water).

Figure 2 shows the data plotted on wave steepness H_o/L_o versus relative velocity $u_{b,m}/u_{crit}$. The horizontal full line is given by $u_{b,m}/u_{crit} = 9.85$ and represents the criterion that separates most of the accretion and erosion events. Thus, in this analysis the discriminating criterion may be written as

$$u_{b,m} = M_2 u_{crit} = 9.85\, u_{crit} \tag{13}$$

where M_2 = discriminator coefficient, that discriminates with a skill of 0.92 if only field data are considered and 0.85 if all data are considered. The application of the random wave concept leads to relationships quite similar to Eqs. (6) to (11) in the previous section and will not be discussed here.

Slope Effects

Because the proposed Eq. (4) gives the transport magnitude for a horizontal bottom, it has to be corrected for slope effects on an inclined bottom. Madsen (1993) presents a relationship,

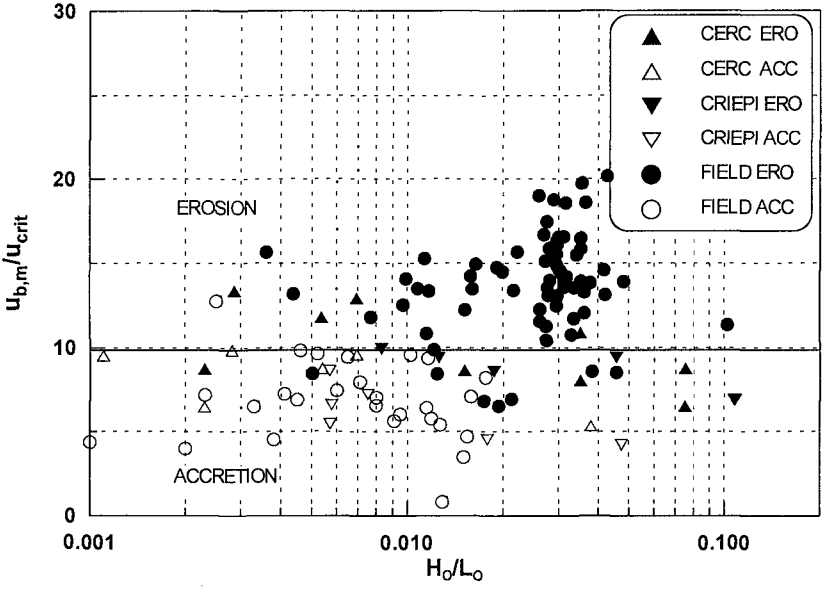

Figure 2. Discriminating erosive and accretive shoreline conditions on the basis of wave steepness and velocity ratios.

$$q_\beta = q \frac{1}{1 + \frac{\tan\beta}{\tan\theta_m}} = q\, k_\beta \tag{14}$$

where β = bottom slope (positive for upward slope in transport direction), θ_m = angle of moving friction (here set to 30° according to King (1991)), and k_β = slope coefficient.

Actual Transport Rate

With the transport potential q_o, the net direction and magnitude of transport ξ, and the slope coefficient k_β all determined, the actual transport rate q is given by:

$$q = q_o\, \xi\, k_\beta \tag{15}$$

Shoreline Change

Following the one-line theory, the shoreline location y is calculated based on the continuity equation:

$$\frac{\partial y}{\partial t} + \frac{1}{D_c}\left(\frac{\partial Q}{\partial x} - q\right) = 0 \tag{16}$$

where y = shoreline position, t = time, D_c = vertical extension of the active profile, Q = the longshore sediment transport rate, and x = the alongshore coordinate. By assuming no longshore transport gradients ($\partial Q/\partial x = 0$), the shoreline change Δy during a time step Δt is given by:

$$\Delta y = \pm\, q \frac{\Delta t}{D_c} \tag{17}$$

where a positive sign corresponds to onshore transport.

FIELD APPLICATION

Field Data

As an application of the proposed procedure, simultaneously collected data on waves and beach profiles from the US Army Field Research Facility at Duck, North Carolina (Figure 3) (Howd and Birkemeier 1987, Lee and Birkemeier 1993) were analyzed to investigate the relationship between the incident waves and the seasonal shoreline variations over a longer

time period. The data set comprised shoreline positions extracted from surveys taken bi-weekly in profile line 188 during 11 years (Figure 4). Spectral wave properties (significant height and peak period), recorded at least every 6 hours, were available for the same period.

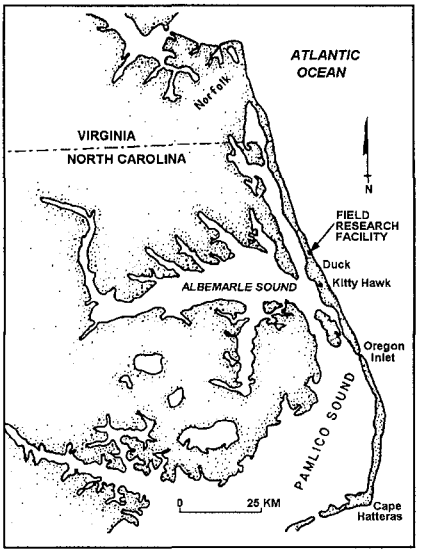

Figure 3. Field site at US Army Field Research Facility at Duck, North Carolina.

The beach at Duck is one of the most well-documented field sites in the world with collected time series on waves and profiles that are unique in their length and quality. Thus, it was a natural choice to employ data from Duck in the development and validation of the cross-shore transport algorithm. However, coarse material is often found around the shoreline at Duck (Larson 1991) creating a steep beach face and an armoring effect that could significantly reduce the shoreline response to changes in the wave conditions. Because of this the beach response at Duck might not be as well-behaved as on other beaches. In spite of this, the Duck data was chosen. The long-term variation of different contour lines was extracted by linear interpolation from the measured profiles. For this study, the MSL (+0.08 m NGVD) of profile line 188 was analyzed.

In order to investigate the temporal scale in the shoreline (defined as MSL) variation, an FFT analysis was performed on the data series after a linear trend was removed. Figure 5 (solid line) shows that there is a strong annual variation with a frequency of 1 year, that most likely is associated with seasonal variations in the wave climate. The long-term trend in the shoreline signal was assumed to be associated with alongshore processes and was, therefore, removed from the continued analysis. For simplicity, the long-term trend was assumed to be linear, although the FFT analysis indicates that there are other low-frequency oscillations in the signal.

Model Simulation using Fall Speed

Based on the wave time series, the cross-shore sediment transport rate was calculated at each time step according to Eq. (15). In the calibration procedure, a best fit value of the discriminator coefficient M_1, that separates onshore from offshore transport, was determined to minimize the difference between measured and calculated shoreline positions on the basis of visual evaluation. The shoreline change and the corresponding shoreline location associated with the cross-shore sediment transport was calculated based on Eq. (17). A best fit

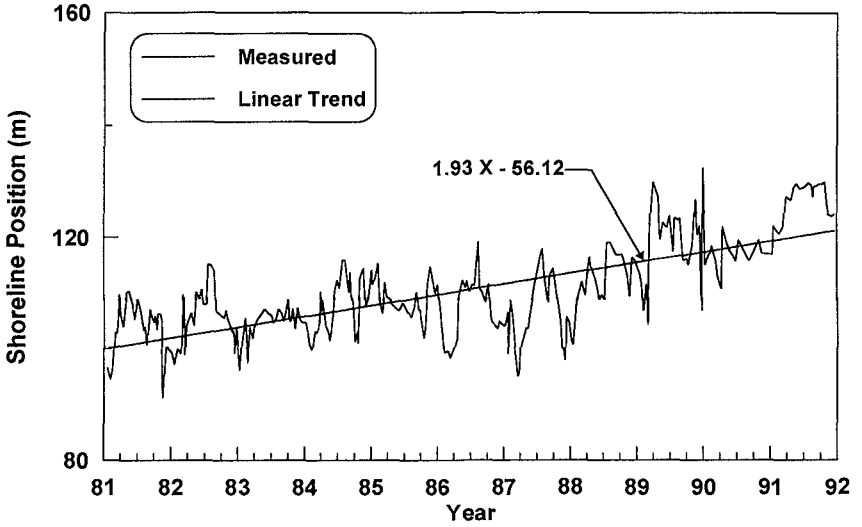

Figure 4: Temporal variation of MSL in profile line 188.

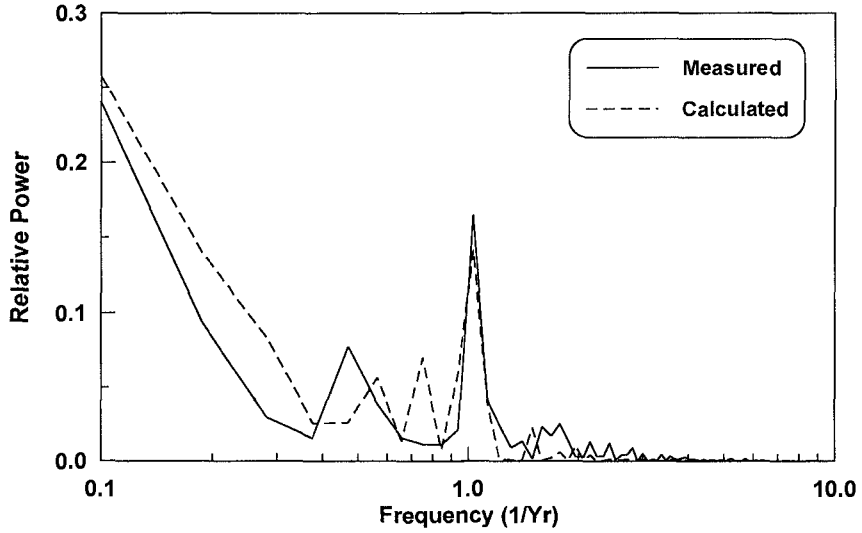

Figure 5: FFT analysis of periodicity in shoreline fluctuations.

value of M_1 = 0.00056 was obtained (Figure 6), which is only marginally greater than the value obtained from the comparison with laboratory model tests (Figure 1). As for the actual shoreline change, the calculated shoreline variation was analyzed by FFT. The temporal behavior of the oscillations is shown in Figure 5 (dashed line). Similar to the measured variations the calculated ones show a strong annual signal indicating that there is a pronounced seasonal variation in addition to a low-frequency variation associated with interannual changes in the wave climate. It is also worth noticing that there are virtually no higher frequencies represented. Thus, the calculations show that, although the seasonal behavior of the shoreline is clearly expressed, the impact of individual storms are not represented to any significant degree. In addition, a comparison between measured and calculated shoreline changes (Figure 6) indicates that he excursion around the mean value is of the right order of magnitude. Hence, the overall temporal and spatial properties seem to be well represented in the model. However, there does not seem to be a coherent instantaneous behavior of the two signals. The phase difference is generally quite significant.

Model Simulation using Relative Velocities

Using the same data as in the above section, the shoreline change was determined using the criterion based on the velocity ratio. Figure 7 shows the result of a simulation with a best fit value of M_2 = 8.0, which is somewhat smaller than the value obtained from the comparison with the LWT and field data sets (Figure 2), but still with a skill of 0.85, i.e., as

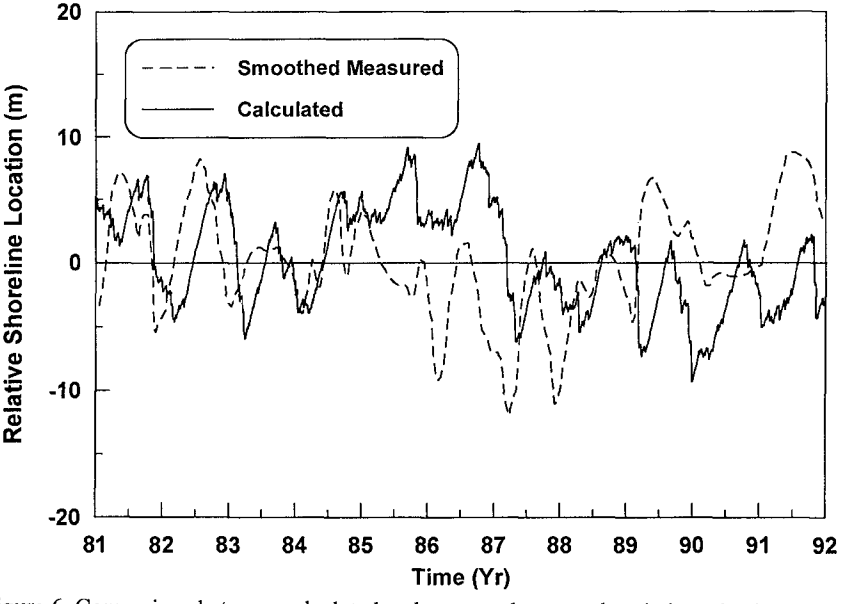

Figure 6. Comparison between calculated and measured temporal variation of MSL.

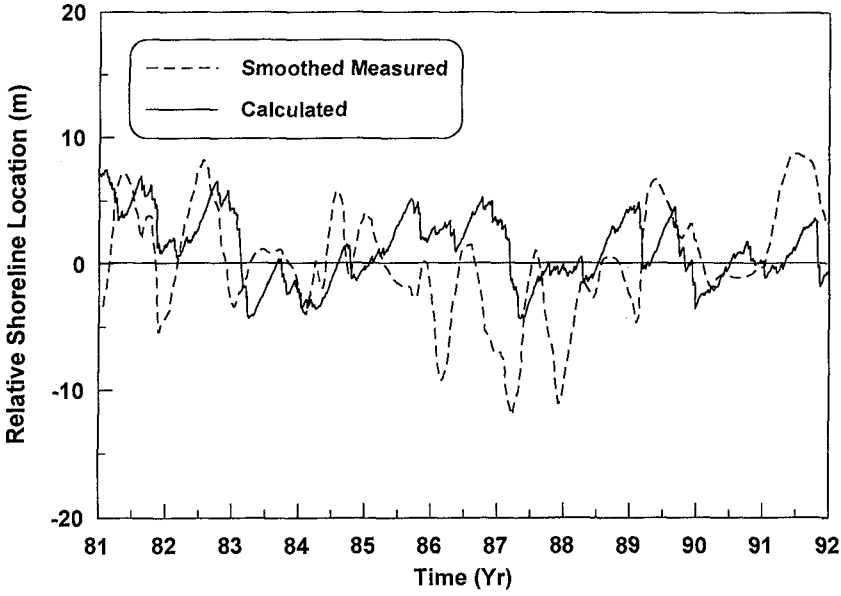

Figure 7. Comparison between calculated and measured temporal variation of MSL.

good as the proposed value of 9.85. A visual evaluation seems to suggest that this method reproduces the actual shoreline change slightly better than the previous method based on fall speed. Like in the previous application, the seasonal behavior is quite well represented.

CONCLUSIONS

The present analysis showed that it is possible to reproduce the overall spatial and temporal behavior of seasonal cross-shore transport related shoreline variation using two simple one-line model compatible approaches. Similar to measured shoreline changes at Duck, N.C., model calculations over 20 years showed clear seasonal variations. FFT analysis of measured and calculated shoreline changes also showed strong similarities for more long-term variations. As expected, the impact of individual storms that are present in the measurements, are not represented in the simulated shoreline behavior to any significant degree. More work is still needed to represent the instantaneous changes correctly with the proposed methods.

The reason for the limited success of the proposed methods could be that the selected parameters are more related to bar behavior than to shoreline behavior and that the lag represents an intrinsic phase shift between the shoreline response and the bar movement as documented in Hanson et al. (1997). Another, more pessimistic, explanation could be that

the approach is too simplified to be able to represent such a complex process as cross-shore transport under breaking waves. It is not totally clear, at present, which of he two hypothetical reasons is true even though the former is our working hypothesis.

The predictive capability of the proposed method is still not demonstrated. In this respect, it will have to be shown that the criteria cannot only be used to determine the direction of the transport but also the magnitude. For this reason, further applications will be made with field data from other well-documented sites.

ACKNOWLEDGMENTS

The research in this paper was conducted under the PACE and SAFE projects of the European Commission/Directorate of Science, Research and Development (DG-XII) under the MAST program (Contracts No. MAS3-CT95-0002 and MAS3-CT95-0004, respectively).

REFERENCES

Ahrens, J.P. and Hands, E.B. 1998. "Parameterizing Beach Erosion/Accretion Conditions," *Proc. 26th Conf. on Coastal Engrg.*, ASCE. (in press)

Bakker, W.T. 1969. "The Dynamics of a Coast with a Groin System," *Proc. 11th Coast. Engrg. Conf.*, ASCE, 492-517.

Hallermeier, R.J. 1980. "Sand Motion Initiation by Water Waves: Two Asymptotes," *J. Wtrwys., Port, Harbor, and Coastal Engrg.*, Vol. 106, No. WW3, ASCE, 299-318.

Hanson, H. 1989. "GENESIS - A Generalized Shoreline Change Numerical Model," *Journal of Coastal Research*, Vol 5(1), pp. 1-27.

Hanson, H., Gravens, M. B., and Kraus, N. C. 1988. "Prototype applications of a generalized shoreline change numerical model," *Proc. 21st Coast. Engrg. Conf.*, ASCE, 1265-1279.

Hanson, H. and Kraus, N. C. 1989. "GENESIS - Generalized model for simulating shoreline change," Vol. 1: Reference Manual and Users Guide, *Tech. Rep. CERC-89-19*, US Army Eng. Wtrwy. Exp. Sta., Coast. Engrg. Res. Ctr.

Hanson, H., Larson, M., Kraus, N.C., and Capobianco, M. 1997. "Modeling of Seasonal Variations by Cross-shore Transport Using One-line Compatible Methods," *Proc. Coastal Dynamics '97*, ASCE, 893-902.

Howd, P.A. and Birkemeier, W.A. 1987. "Beach and Nearshore Survey Data: 1981-1984 CERC Field Research Facility," *Tech. Rep. CERC-87-9*, US Army Eng. Wtrwy. Exp. Sta., Coast. Engrg. Res. Ctr.

Horikawa, K. 1988. "*Nearshore Dynamics and Coastal Processes,*" Univ. of Tokyo Press, Tokyo.

Jonsson, I.G. 1966. "Wave Boundary Layers and Friction Factors," *Proc. 11th Coast. Engrg. Conf.*, ASCE, 492-517.

Kajima, R., Shimizu, T., Maruyama, K., and Saito, S. 1982. "Experiments of Beach Profile Change with a Large Wave Flume," *Proc. 18th Coast. Engrg. Conf.*, ASCE, 194-210.

King, D.B., Jr. 1991. "The Effect on Slope on Oscillatory Flow Bedload Transport," *Proc. Coastal Sediments '91*, ASCE, 734-744.

Kraus, N.C. and Larson, M. 1988. "Beach Profile Change Measured in the Tank for Large Waves, 1956-1957 and 1962," *Tech. Rep. CERC-88-6*, US Army Eng. Wtrwy. Exp. Sta., Coast. Engrg. Res. Ctr.

Kraus, N.C., Larson, M., and Kriebel, D.L. 1991. "Evaluation of Beach Erosion and Accretion Predictors.," *Proc. Coastal Sediments'91*, ASCE, 572-587.

Kraus, N.C. and Mason, J.M. 1991. "Field Data Set for Testing Beach Erosion and Accretion Predictors," *Memorandum for Record*, US Army Eng. Wtrwy. Exp. Sta., Coast. Engrg. Res. Ctr.

Larson, M. 1996. "Model of Beach Profile Change under Random Waves," *J. Wtrwys., Port, Harbor, and Coastal Engrg.*, Vol. 122, No. 4, ASCE, 172-181.

Larson, M. and Kraus, N. C. 1989. "SBEACH: Numerical Model for Simulating Storm-Induced Beach Change," Report 1: Empirical Foundation and Model Development, *Tech. Rep. CERC-89-9*, US Army Eng. Wtrwy. Exp. Sta., Coast. Engrg. Res. Ctr.

Larson, M., Kraus, N.C., and Hanson, H. 1990. "Decoupled Numerical Model of Three-Dimensional Beach Change," *Proc. 22nd Int. Conf. on Coastal Eng.*, ASCE. pp. 2173-2185.

Lee, G. and Birkemeier, W.A. 1993. "Beach and Nearshore Survey Data: 1985-1991 CERC Field Research Facility," *Tech. Rep. CERC-93-3*, US Army Eng. Wtrwy. Exp. Sta., Coast. Engrg. Res. Ctr.

Madsen, O.S. 1993. "Sediment Transport on the Shelf," *Sediment Transport Workshop DRP TA1*, 8-9 June, US Army Eng. Wtrwy. Exp. Sta., Coast. Engrg. Res. Ctr.

Perlin, M. and Dean, R.G. 1979. "Prediction of Beach Planforms with Littoral Controls," *Proc. 16th Coast. Engrg. Conf.,* ASCE, 1818-1838.

Seymour, R.J. and Castel, D. 1989. "Modeling Cross-Shore Transport," in *Nearshore Sediment Transport*, R.J. Seymour, Ed., Plenum Press, New York, NY.

Watanabe, A. 1982. "Numerical Models of Nearshore Currents and Beach Deformation," *Coastal Engrg. in Japan*, Vol. 25, 147-161.

COASTLINE EVOLUTION IN RESPONSE TO A MAJOR MINE SEDIMENT DISCHARGE ON THE NAMIBIAN COASTLINE

G G Smith and G P Mocke[1]

Abstract

The measurement, monitoring and modelling of the impacts of a major sedimentary discharge to the highly dynamic coastline of southern Namibia is described. Some 27 million m³ of sediment will be discharged over a 5 year period as a result of a novel diamond mining technique employing an inland dredger. The study demonstrates that mathematical modelling, supported by comprehensive monitoring information, constitutes an important tool for mining optimization and impact prediction and management.

Introduction

A major diamond mining operation at Oranjemund in Namibia (Figure 1) which commenced in April 1997 involves the dredging and processing of overburden material (CSIR, 1996; Smith *et al*, 1996). This overburden sediment overlays rich diamond deposits located primarily in gravel layers on the bedrock. Typical overburden thicknesses are from 5 to 20 m. As an alternative to historical "dry" mining techniques, calling for massive dewatering operations, the present mining uses a dredger floating in excavated ponds. Water-levels in the ponds are controlled by a balance between seepage from the sea, a wellfield on the beach, and extraction pumping.

The sediment resulting from the dredging process is then discharged onto the beach (Figure 2 and Figure 3) on a highly dynamic coastline (median wave height ≈ 1.9 m). A total of some 27 million m³ is to be discharged onto the beach over a period of about 5 years. This massive amount of sediment is comparable with the total quantities supplied for beach nourishment in some European countries (Hamm *et al*, 1998). The shoreline accretion which results from the discharge will have a significant effect on the **safety** of mining operations and in the protection of beach wellfield installations from wave action. In addition, the shoreline behaviour affects the rate of **water seepage** to the inland dredge pond, and accordingly affects pumping requirements to maintain the required water-level.

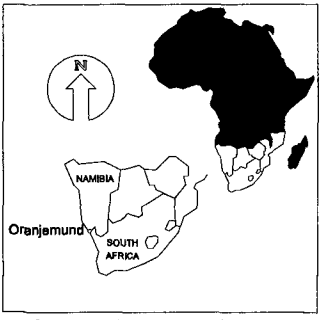

Figure 1: *Location map*

Furthermore, accretion of the shoreline will facilitate **land reclamation** and consequent additional

[1] Research Engineers, CSIR, P O Box 320, Stellenbosch, 7599 South Africa
(Fax: +27 21-8882693; e-mail: gsmith@csir.co.za; gmocke@csir.co.za)

exploitation of mining terrain. Thus, accurate predictions of the shoreline evolution, both in the short-term and long-term, are essential for the mine to plan these aspects.

Figure 2: Dredger tailings discharge

A delicate balance exists, with regard to water seepage, as is schematically illustrated in Figure 4. In Figure 4 (top) the situation at the start of dredging is shown. At this stage the dredger was situated on an existing pond created from a previously mined-out area. By means of pumping from a wellfield close to the shoreline, the water-level was maintained just above mean sea level (MSL). As dredging progresses, the pond water-level is progressively lowered, as indicated in Figure 4 (bottom). The advantage of this is that the bedrock, which is inclined towards the sea, will be accordingly exposed, thus allowing mining to continue. As the water-level drops, seepage will tend to increase. However, by optimising the beach accretion the seepage during the later stages of dredging can be minimised. This optimisation of accretion was evaluated at the feasibility stage of the project by adapting the sediment discharge locations.

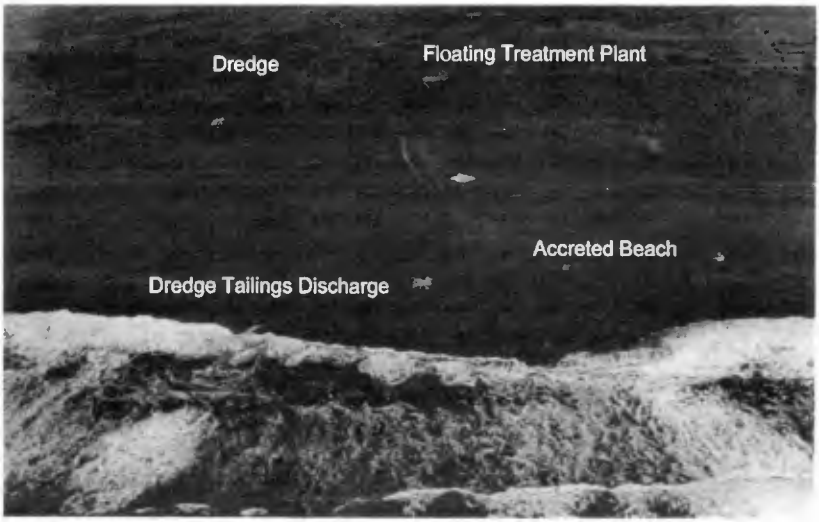

Figure 3: Aerial oblique view of the study site

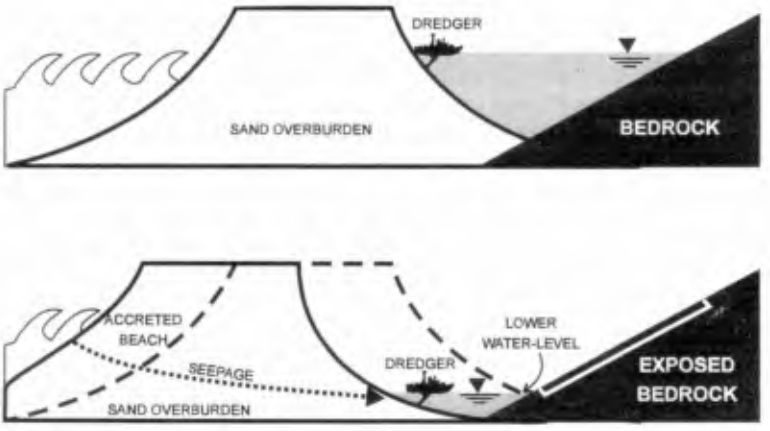

Figure 4: Water-levels and seepage at the commencement (top) and during dredging operations (bottom)

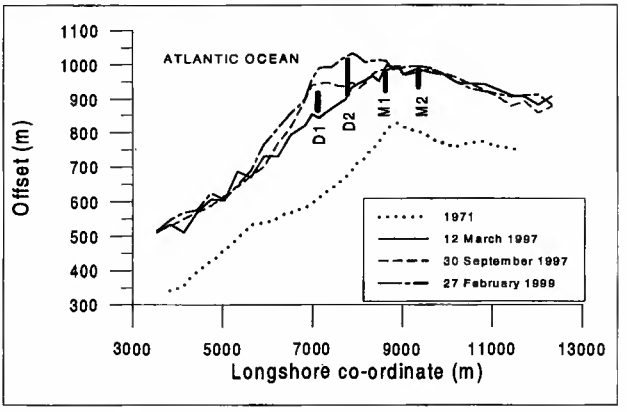

Figure 5: Shorelines at the study site

An interesting aspect is that the coast in the project region is already in an extremely accreted condition. This is due to the discharge in the region of some 80 million m^3 of sand onto the beach between 1971 and 1997. About 60% of this quantity was in the form of hydraulically discharged mine tailings, while 40% was in the form of direct nourishment of overburden sand to massive sand seawalls used for protection from wave action and in some cases for land reclamation (Smith *et al*, 1996). This sand input to the shoreline caused accretion of up to about 250 m in places (Figure 5). With the use of survey data in regions relatively unaffected by sand input, the assumed beach profile of 1971 was reconstructed, and is plotted together with the pre-dredging profile of 1996 in Figure 6. It may be noted that the recently measured profile is steeper on average. Utilising profile information together with shoreline data, the total volume of accretion between 1971 and 1997 could be estimated. Taking into account losses of sediment as a result of longshore transport, it was estimated that some 6% of material comprised fines lost offshore.

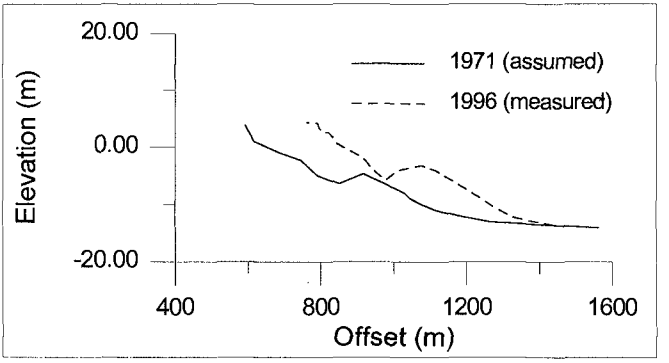

Figure 6: *Nearshore profiles prior to mine discharges (1971) and subsequently (1996)*

In sum, both the massive quantity of sediment to be discharged on a high-energy coastline during the dredging project and the extremely accreted condition of the beach result in a unique shoreline evolution study. In order to attain quality shoreline predictions, the long-term (months/years) shoreline behaviour is assessed by means of monitoring data analyses in combination with employment of a one-dimensional shoreline model. Superimposed on these results, short-term (hours/days) shoreline fluctuations are investigated by means of data analyses and cross-shore profile modelling.

Monitoring Data Analysis

The comprehensive monitoring programme at the study site incorporates wave measurements, sediment measurements, measurement of beach topography and nearshore bathymetry, photography and debris-line recordings.

Waves

Directional wave measurements were conducted offshore of the project site in 16 m to 20 m water depth. In the first few months of measurement, two SEAPAC current meters, utilising an electromagnetic current meter and a pressure sensor to resolve directional waves, were situated 4 km offshore. A directional wave buoy operating on a dual-frequency differential GPS system (CSIR, 1997) was situated 2 km offshore. The measurement by three instruments allows some comparison and data quality checks. In Figure 7(a) it may be noted that the time series of significant wave height for SEAPACs and the GPS buoy are remarkably similar, despite being some 2 km apart. Directions are also reasonably similar (Figure 7(b)) considering instrument accuracy and the separation between the instruments. More recently, only a single instrument has been deployed. A total of 14 months of measurements has been recorded since October 1996. It is intended to obtain a further 10 months of measurements.

An energetic wave climate is reflected in the exceedance plot (Figure 8) which indicates a median significant wave height of 1.9 m and significant wave heights of up to 6 m. The nearshore waves (in 20 m depth) approach the project site from a fairly narrow band of directions, with waves approaching from the south-westerly and south-south-westerly sectors 89% of the time (Figure 9). Since the coastline extends from south-east to north-west, this results in a net northerly-directed longshore sediment transport, varying from

0.4 to 1.6 million m^3/year. Wave periods are relatively long, with 80% of these being between 8 and 14 seconds.

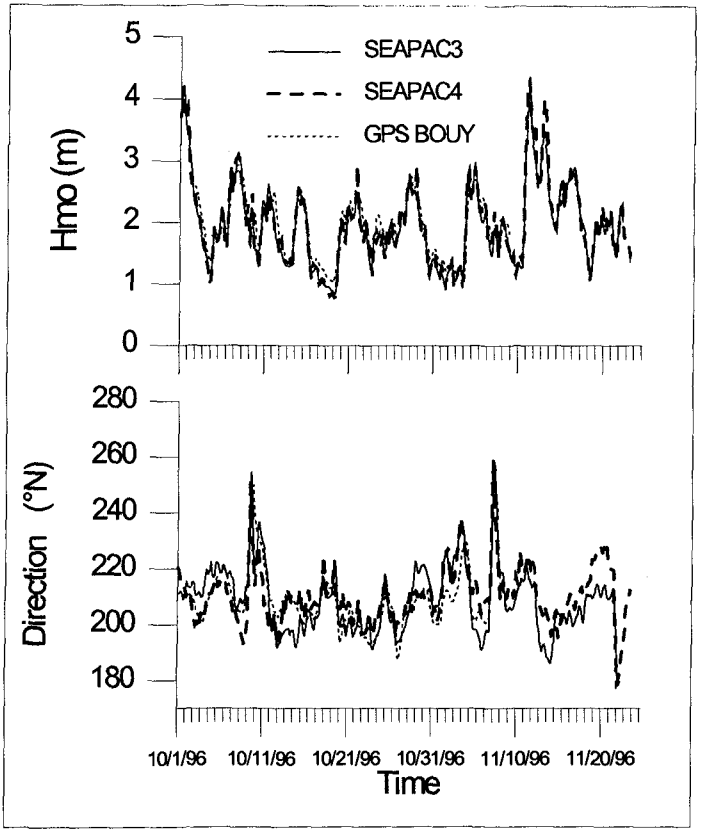

Figure 7: *A comparison of wave heights (top) and wave direction recordings by 3 different instruments*

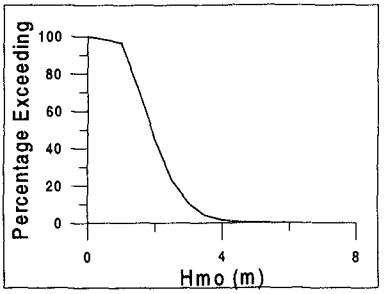

Figure 8: *Wave height exceedence graph*

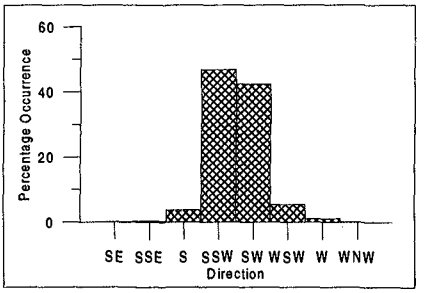

Figure 9: *Histogram of wave directions (measured in 20 m depth)*

Sediment

The beach sediment at the project site is fairly coarse, a composite median grain size of 611 μm being recorded prior to the commencement of dredging in April 1997. Extensive sampling of the beach 4 months after dredging had commenced indicated a somewhat finer composite median grain size of 447 μm, seemingly in response to the discharge of material of median grain size 495 μm. This occurred despite the winnowing effect of winter waves on a steep beach. It is recognized, however, that as the sampling is limited to the intertidal beach (spring tidal range≈1.6 m) the sediment sizes are not representative of the entire cross-shore profile.

Morphology

An analysis of surveyed beach topography and nearshore bathymetry reveal a dynamic hydro-sedimentary regime at the study site. Vertical variations in the profile of up to 4 m over a period of a few months are also not uncommon, with a profile closure depth of up to 18 m.

Figure 5 illustrates the shoreline evolution since commencement of the dredging project in April 97. The details of quantities discharged are as indicated in Table 1. A total of 3.766 million m^3 of dredger tailings was discharged in a period of 16 months. During this period, a quantity of 0.832 million m^3 (in the form of a finer tailings discharge from a mine processing plant) was discharged via positions M1 and M2. This slightly finer sediment seems to have a limited impact on shoreline evolution (Figure 5). However, the effect of the dredge discharge, which shifts (for the most part) from position D1 to D2 to D3, on the shoreline evolution is clearly evident. By July 1998, the maximum measured seaward shoreline excursion (as represented by the MSL+2m contour) relative to the pre-dredging shoreline of 12 March 1997 is about 130 m.

Table 1: Dredge Discharge Volumes

Discharge Position (as per Figure 5)	Start date	End date	Vol. of sediment pumped onto the beach (m^3)
D1	4 April 1997	28 Nov 1997	1 814 000
D2	28 Nov 1997	14 Jan 1998	488 000
D1	14 Jan 1998	13 Feb 1998	174 000
D2	13 Feb 1998	19 Feb 1998	43 000
Dredger testing	19 Feb 1998	10 Mar 1998	
D2	10 Mar 1998	29 April 1998	479 000
D3	29 April 1998	31 July 1998	768 000
TOTAL			3 766 000

A survey of the beach topography and nearshore bathymetry was conducted in September 1997, after 1.107 million m^3 had been discharged onto the beach from discharge point D1. With the use of GIS overlay techniques whereby the September 1997 survey is superimposed on a pre-dredging survey, the fate of this material could be assessed. At that stage material was evenly distributed, with 0.57 million m^3 calculated to have accumulated to the north-west of D1, while 0.55 million m^3 was deposited to the south-east. The slightly higher accretion to the north-west is likely due to the discharge of finer mine tailings at positions M1 and M2, although the morphology suggested that most of this material is transported north-westwards away from the dredge discharge region.

The surveys also revealed that at that stage about half of the accreted material was situated above MSL, while some 45% of the material accumulated between the MSL-6m and MSL.

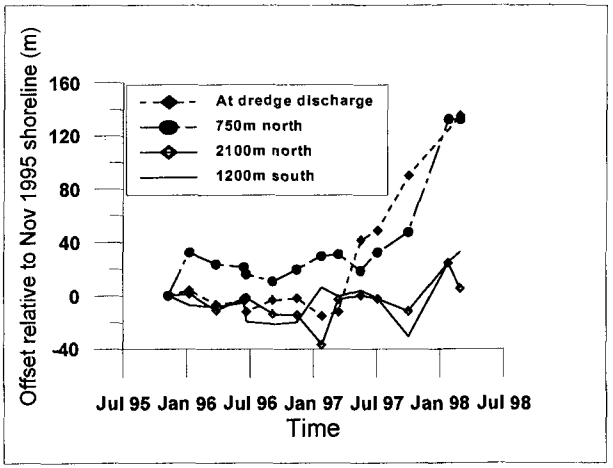

Figure 10: *Contour excursions relative to November 1995*

The above information provides valuable insights for shoreline modelling to estimate the long-term shoreline evolution. Superimposed on this, an understanding of the short-term variability of the shoreline is also required. Figure 10 shows the on/offshore excursions of the MSL+2m contour, relative to the situation as measured in November 1995. In some cases a classical summer/winter variability occurs, such as 1200 m south of the discharge location, where a shoreward shift is seen around and after July, while a seaward shift is seen around January. This trend does not always occur, however. For example, the data from 2100 m north (Figure 10) indicate a retreat of the MSL+2m contour in January 1997. Such deviations from seasonal trends are likely due to the formation of localised giant cusps, as observed frequently on the study coastline. Also evident in Figure 10 is the accretion as a result of dredge discharge. A steady build-out of the shoreline is evident from about April 1997 at the dredge discharge position (D1), while 750 m to the north, the response of the shoreline is delayed but extremely rapid. This is likely the result of relatively rapid distribution of sand by longshore transport.

Also evident in Figure 10 is a rapid retreat of the shoreline just prior to July 1996 (except for the 2100 m north case, since data was not available). This retreat occurred as a result

of a major storm (of estimated recurrence interval of 2 years) during which significant wave heights of up to 5.9 m were recorded, while high waves (mostly over 4 m) persisted for four days. The result of this storm was an average retreat along the 9 km study coastline of 5 m, while a maximum retreat of 20 m was recorded.

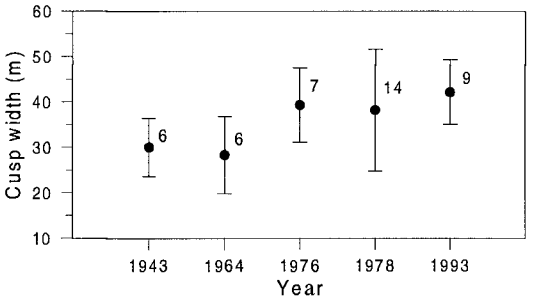

Figure 11: *Average widths of cusp embayment. The number of samples are shown as well as the standard deviation (error bars)*

A detailed analysis of the variability of the shoreline was conducted, utilizing 9 surveys of 38 beach profiles along some 9 km along the study site. These indicated a maximum shoreline (MSL+2m) accretion (relative to the average of the shorelines) of 29 m, while a maximum shoreline retreat of 35 m was measured. Since the major variations of the shoreline are the result of giant cusp formations, a study was focussed on these. A coastal section of some 20 km at the study site was investigated, with the use of photographs taken prior to the commencement of any significant mine sediment discharges (i.e. in 1943 and 1964) as well as later (1976, 1978 and 1993). In Figure 11, the average width of cusp (i.e.shore perpendicular extent) are indicated, while numbers indicate total cusps recorded in the study region and the error bars provide the standard deviation of the width. A definite increase in cusp width is evident after the commencement of discharge of mine sediment onto the beach in the early '70's. The pre-mining cusps average about 30 m width, while the later cusps average about 40 m width. The number of cusps observed also increases. The average cusp length for all the measurements is 383 m, with a standard deviation of 115 m.

Additional measurements

The "more conventional" measurements of waves, sediments and bathymetry/topography are supplemented with regular photographs and measurements (from a series of fixed beacons) of the debris line. The photographs provide a useful qualitative assessment of cusps, beach slopes and wave conditions, while the debris-line measurements provide an indication of the maximum extent of wave runup. The latter is useful for verifying wave runup calculations and for assessing safe setback distances.

Trials are in progress to improve measurement techniques. A system of digital video recording is being tested. Analysis of the digital images will ultimately provide more comprehensive data on intertidal topography, wave runup, and some indication of nearshore bathymetry. In addition, it is intended to improve measurement of bathymetry through the surf zone through the deployment of a helicopter-borne survey. This method

is the obvious choice in a region to which rapid access is difficult, calm days are limited, and where a mine helicopter is readily available. Referring to trial surveys conducted in 1990 (Coppoolse *et al*, 1992) and the technique of Pollock (1994) improved survey techniques have been explored. In Figure 12(a), the method involving deployment of a stand is illustrated. Using ranging rods or a differential geographical positioning system (DGPS) with a graphical display, the helicopter is positioned. The 5 m high stand is lowered onto the sea bed. The elevation and distance to the prism cluster are obtained by means of a shore-based total station. This method is practical provided conditions are reasonably calm. Preliminary tests indicate that the method is functional in wave heights of over 1 m.

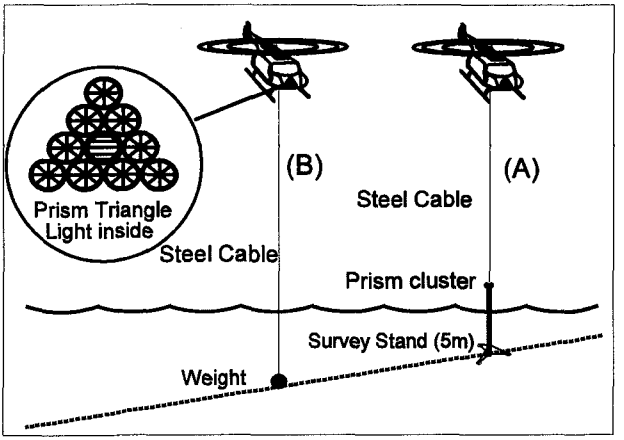

Figure 12: *Helicopter survey techniques for (a) the near-beach region and (b) further offshore*

Although not yet tested, figure 12(b) provides a possible method for surveying in deeper water. As for the above, the helicopter would be positioned by means of ranging rods or DGPS. The weight at the end of the steel cable is then lowered and carefully observed by the flight engineer. At the instant that the weight touches the sea bed, the flight engineer depresses a light switch. Until this time a prism triangle would have been tracked from the shore-station, from which the position of the helicopter prism is logged as the light is switched on. Since the line has a predetermined length, the position of the bed can be recorded.

Predictive Modelling

Shoreline model predictions

The measured wave data were synthesized into 7 offshore swell conditions (representing 94% of the measured swell conditions) and 5 offshore sea conditions (representing 80% of the sea conditions). Wave refraction for these conditions was computed with the HISWA model. With the use of the resulting nearshore wave data, an extensive set of survey data (incorporating 17 measured shorelines) and historical records of sediment

inputs to the beach (from mine plant tailings discharges and from nourishment of sand seawalls), the shoreline model UNIBEST was set up over a coastal extent of 16 km. The relatively featureless coastline is ideal for a shoreline model application, and the "fixed sediment transport" boundaries were situated far enough from the region of interest to have any impact. Figure 13 illustrates the result of the shoreline model validation. As can be seen measured shorelines, which display on/offshore excursions of up to some 200 m over a 21 year period, are well predicted.

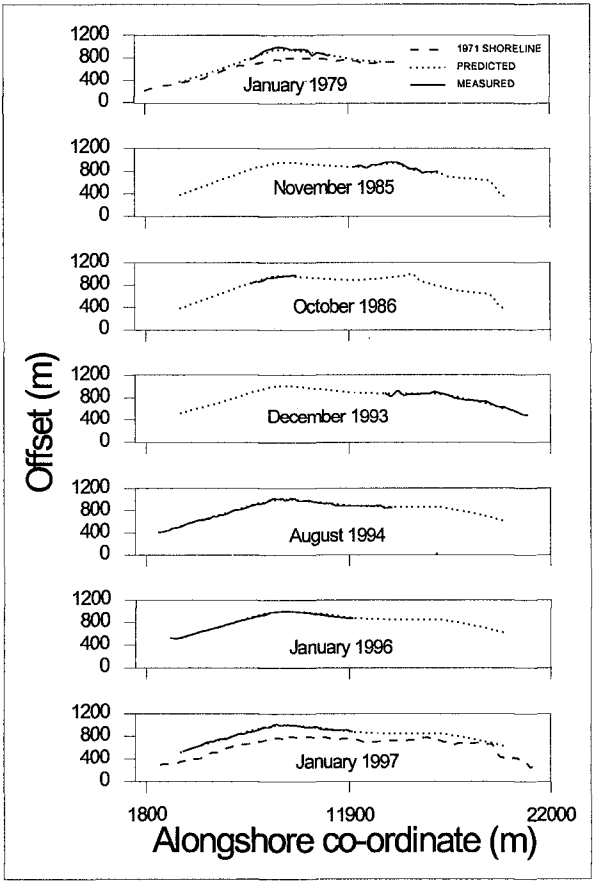

Figure 13: Shoreline model predictions against measured data (pre-dredging)

This validation of the shoreline model provided a firm basis for the prediction of shoreline evolution as a result of dredger tailings discharge along part of the shoreline. Extensive data on discharges and shorelines (6 surveys extending up to 9 km along the study coast) available since commencement of dredging in April 1997 allowed an updated validation of the model, some of the results of which are depicted in Figure 14. Here the model generally predicts the shoreline evolution well within 20 m of measured shorelines, while at isolated points the accuracy is within 30 m. This accuracy margin is within the limits of short-term shoreline changes, such as due to cusps and storms.

Although the shoreline model is well verified, a considerable degree of uncertainty exists for predictions of shoreline evolution as a result of the massive sediment input proposed for the next few years. A key question in this regard is how longshore transport and offshore loss of finer material will be affected by the rapid steepening of the beach and corresponding increase in wave breaking intensity. Violent plunging breakers observed on site will certainly be extremely effective in suspending and transporting sediment. An additional uncertainty is the exact rate and volume of sediment to be discharged from the dredging operation. These uncertainties were accommodated by simulating several scenarios which test the sensitivity to wave conditions, grain size, sediment discharge rates and sediment discharge volumes. For example, Figure 15 illustrates shoreline model sensitivity to the volume of sediment discharged. A standard case was run, with the model based on the boundary conditions as for the model verification, and the volume of sediment as is anticipated at present. The result at the end of dredging in January 2004 is depicted in the figure. If the total volume discharged is 25% more, but at the same rate of discharge, the coastline is predicted to be some 30 m to 40 m seaward (in July 2005). On the other hand, 25% less material results in a predicted shoreline of some 40 m to 50 m shoreward of the standard case.

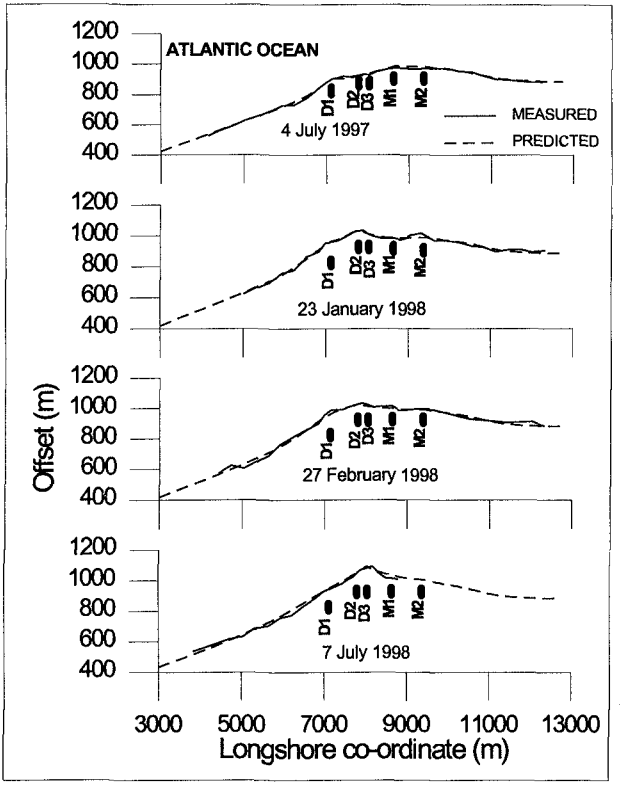

Figure 14: *Shoreline model predictions against measured data (during dredger discharge)*

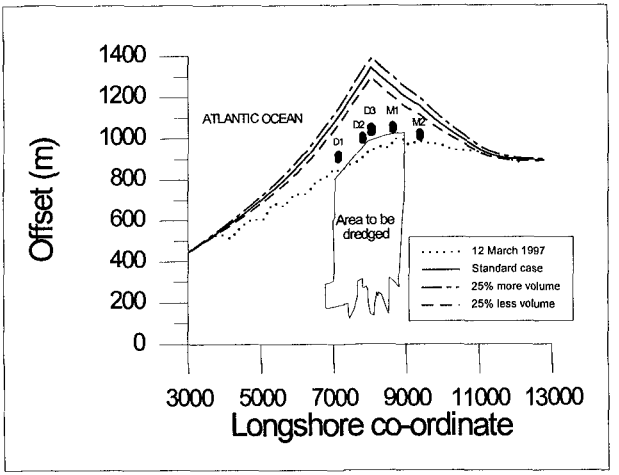

Figure 15: Predicted shoreline evolution sensitivity to the volume of material discharged

A notable feature of the predicted shorelines is that the accretion occurs opposite the dredging area. This has been carefully planned to ensure that seepage to the area, which will have a lowered water level near the end of dredging, is limited. This facilitates minimal pumping to maintain an area of exposed bedrock to be mined (as in Figure 4(b))

Table 2 indicates the results of further sensitivity tests. In each case, the condition of the shoreline at the end of dredging is compared to the standard case, and the maximum shoreline variation relative to the standard case is indicated. In general the scenarios tested were "pessimistic", in order to explore worst cases for the mine.

Table 2: Shoreline model sensitivity test results

SCENARIO	Max. Shoreline variation from the Standard Case (m)
1. 5% higher waves, 5 degrees more southerly	-52
2. Sediment size decreased by 100 μm	-34
3. Sediment size decreased by 170 μm	-58
4. Decreased discharge rate by 25%	-52
5. 25% more material discharged	+35
6. 25% less material discharged	-46

As may be noted, considerable variations in the wave, grain size and sediment discharge conditions cause variations in the shoreline of the same order of magnitude (i.e. approximately 50 m).

Cross-shore profile model predictions

In order to obtain comprehensive shoreline predictions, short-term shoreline variations must be superimposed on the long-term shoreline model predictions. In addition to the insights obtained from empirical data, cross-shore profile modelling provides an assessment of erosion during episodic events such as storms. Figure 16(a) shows a validation of the SBEACH profile model predictions against beach profile measurements made over a storm event (i.e. the 1 in 2 years storm as described above). Unfortunately nearshore data were not available for a full calibration of the profile. Nevertheless, the "dry" beach profile behaves approximately as would be expected, i.e. material is eroded from the upper beach and deposited on the lower profile. Based on this calibration, the response to more severe storm action can be explored. Figures 16(b) and 16(c) depict predicted profile changes under storms of return periods 1:10 and 1:50 years respectively. The effect of these storms on the shoreline (MSL+2m contour) are recorded in Table 3.

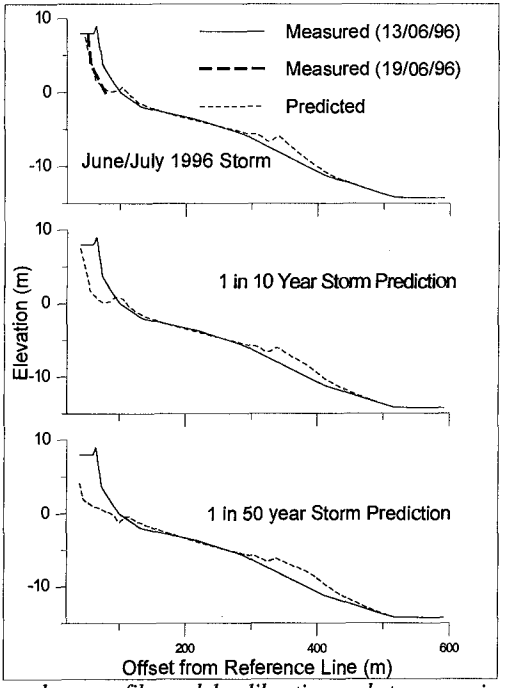

Figure 16: *Cross-shore profile model calibration and storm erosion prediction*

Table 3: Predicted shoreline retreat as a result of storms

Storm return period	Predicted retreat of the MSL+2m contour (m)
1:2 years	20
1:10 years	37
1:50 years	43

Based on these results, together with results of cusp analysis and wave runup calculations, a safe setback of 90 m was recommended for mining operations. This is however provided that protection against waves overtopping the beach berm is in place, and does not take account of longer-term erosion due to longshore transport. A maximum erosion of 40 m, and intrusion of wave runup by a further 30 m, was recorded prior to dredging. As short-term erosion of a temporarily accreted shoreline is likely to be more extreme, the above-mentioned setback estimate is considered reasonable.

Conclusion

The accreted condition of over shoreline in combination with the massive quantity of sediment to be discharged some 5 years set the scene for a totally unique project. An open, relatively straight coast, together with large sediment inputs and significant coastline changes, provide ideal conditions for the application of a one-dimensional shoreline model. With the availability of extensive data, a reliable validation of the model was possible. Together with model sensitivity tests, reasonable predictions of future long-term shoreline evolution scenarios were made.

Further analyses of survey and aerial photograph data facilitated, together with the application of a cross-shore profile model, an understanding of the short-term shoreline fluctuations. Combining these with the long-term predictions results in the provision of essential input to mining operations.

Acknowledgments

The authors wish to thank Christoph Soltau and Christopher Peter for their contributions to the work presented in this publication.

References

Coppoolse, R.C., Schoonees, J.S., Smith, G.G. and Mocke, G.P. (1992). Hydrodynamics and sediment concentrations at Walker Bay, *Proc of the 23rd International Conf. on Coastal Engineering*, ASCE.

CSIR (1996). Coastal evolution due to the disposal of dredger tailings in thhe G68-G90 region. CSIR Report EMAS-C 96022.

CSIR (1997) The development of a 3D directional wave buoy making use of differential global positioning technology. CSIR Report ENV/S - I 97017.

Pollock, C.B. (1995) Helicopter-borne nearshore survey system, a valuable tool in difficult survey areas. Journal of Coastal Research, Vol 11, No 3, pp 959-966.

Smith, G.G., Mocke, G.P. and Swart, D.H. (1994) Modelling and analysis techniques to aid mining operations on the Namibian coastline. Proc. of the 24th Coastal Eng. Conf., ASCE.

Hamm, L., Hanson, H., Capobianco, M. Dette, H.H., Lechuge, A, Spanhoff, R (1998) Beach fills in Europe - projects, practices and objectives. Proc. Of the 26th Coastal Eng Conf, ASCE, *In press.*

LONGSHORE PATTERNS OF THE SEA BOTTOM MORPHOLOGY

Giovanna Vittori[1], Huib de Swart[2], Paolo Blondeaux[3]

Abstract

It is shown that the two-dimensional flow field and the bottom configuration induced by a wave of small amplitude normally approaching a straigth beach may be unstable with respect to infinitesimal perturbations. The time development of the bottom perturbation leads to the formation of crescentic forms periodic in the longshore direction. The growth of the perturbation is due to a positive feedback mechanism, involving the incoming wave, synchronous edge waves and the bedforms. In particular the growth is related to the presence of steady currents caused by the interaction of the incoming wave with synchronous edge waves which in turn are excited by the incoming wave moving over the wavy bed. For natural beaches the model predicts two maxima in the amplification rate; the former is related to incoming waves of low-frequency, the latter to wind waves. Thus two bedforms of different wavelengths can coexist in the nearshore region, the longshore spacing of which is few hundreds and few decades of metres respectively. To illustrate the potential validity of the model, its results are compared with field data.

1 INTRODUCTION

Field surveys of the morphology of the coastal region show the existence of periodic longshore patterns. These patterns are characterized by different length scales in the range between 1 meter to 1 kilometer. Previous studies on the process originating these coastal forms assume that edge waves are the driving mechanism. However in these models bottom topography does not enter in the mechanism originating bottom forms since the dynamics of the sea bottom is not considered and sediment motion is assumed to be passively driven by the water flow.

Recently Vittori et al. (1998) have shown that rhythmic longshore patterns may be due to a feedback between water flow and the erodible bottom. In their paper it is demonstrated that crescentic forms in the coastal area, far away from the breaker line, can be produced by the time development of

[1]Assistant Professor, Hydraulic Institute, University of Genoa, via Montallegro, 1 - 16145 Genova, Italy

[2]Professor, Institute for Marine and Atmospheric Research, Utrecht University, P.O. Box 80.005, 35 TA Utrecht, The Netherlands

[3]Professor, Hydraulic Institute, University of Genoa, Via Montallegro, 1 - 16145 Genoa, Italy

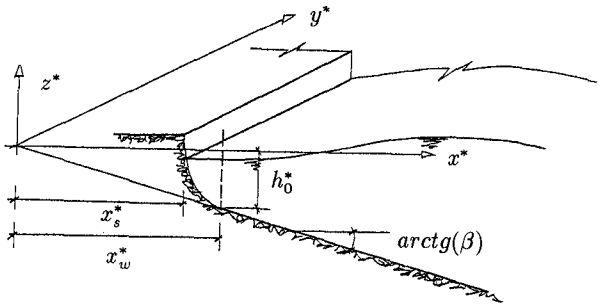

Figure 1: Sketch of the beach geometry.

small random perturbations both of the sea bottom and of the water motion which interact with a monochromatic wave which approaches the beach. The basic mechanism is that the incoming wave interacts with a small bottom perturbation (periodic in the longshore direction) and produces a synchronous edge wave. This wave subsequently interacts with the incoming wave and leads to the generation of steady currents. These currents induce a net sediment transport, the convergence pattern of which is in phase with the bedforms. Hence there is a positive feedback between the water motion and the erodible bottom which gives rise to an exponential growth of both the free surface and bottom morphology perturbations.

In the present paper the analysis of Vittori et al. (1998) is briefly outlined and their results are summarized. Then a comparison is performed between their theoretical results and field data. In particular the observations of Homma & Sonu (1963) and Pruszak et al. (1997) are considered.

2 THE THEORETICAL MODEL

In the theoretical model of Vittori et al. (1998) a simplified beach profile is used (see figure 1) which consists of two regions. In the outer region ($x^* > x_w^*$) the local water depth increases in the offshore direction with a constant slope β, starting from a finite value h_0^* at $x^* = x_w^*$. The inner region ($x_s^* < x^* < x_w^*$) is characterized by a slope which rapidly increases when moving towards the beach. The variables (x^*, y^*, z^*) denote an orthogonal coordinate system with the x^* and y^* axes lying on the still water level. The x^*-axis points offshore, while the y^*-axis is parallel to the straight beach and the z^*-axis is vertical.

The water motion in the outer region is described by the shallow water

equations which read

$$\frac{\partial(h^*+\eta^*)}{\partial t^*}+\frac{\partial[h^*+\eta^*)u^*]}{\partial x^*}+\frac{\partial[(h^*+\eta^*)v^*]}{\partial y^*}=0 \tag{1}$$

$$\frac{\partial u^*}{\partial t^*}+u^*\frac{\partial u^*}{\partial x^*}+v^*\frac{\partial u^*}{\partial y^*}=-g^*\frac{\partial \eta^*}{\partial x^*} \tag{2}$$

$$\frac{\partial v^*}{\partial t^*}+u^*\frac{\partial v^*}{\partial x^*}+v^*\frac{\partial v^*}{\partial y^*}=-g^*\frac{\partial \eta^*}{\partial y^*} \tag{3}$$

The forcing is due to a prescribed surface gravity wave which normally approaches the straight beach and is partially reflected. This yields the matching condition (see Mei, 1989)

$$\lim_{x^*\to\infty}\eta^*=\lim_{h^*\to 0}\frac{a_x^*(x)}{2}\left[\exp(i\int \ell^* dx^*)+\hat{K}\exp(-i\int \ell^* dx^*)\right]e^{i\omega^* t^*}+c.c. \tag{4}$$

In (1), (4) h^* is the water depth, η^* is the water surface displacement, (u^*, v^*) are the depth-averaged velocity components in the cross- and long-shore directions respectively. Furthermore a_x^*, ℓ^* and ω^* are the amplitude, the wavenumber and the angular frequency of the incoming wave and $\hat{K}$ is the complex reflection coefficient of the beach. Finally c.c. denotes the complex conjugate of a complex quantity.

By assuming that $x_w^*-x_s^*$ is much smaller than the horizontal length scale of the problem, the dynamics of the flow in the inner region is neglected and all the phenomena which take place between x_s^* and x_w^* are described by means of an appropriate boundary condition at x_w^*:

$$u^*(h^*+\eta^*)=\chi^*\eta^* \tag{5}$$

Relationship (5) simply forces a mass balance within the inner region and the constant χ^* depends on the reflection coefficient of the beach and the characteristics of the wave.

The problem is then closed by Exner equation, which forces the sediment balance, and by a constitutive relationship relating the sediment transport rate per unit width (q_x^*, q_y^*) and the water motion

$$\frac{\partial h^*}{\partial t^*}=\frac{1}{(1-p)}\left[\frac{\partial q_x^*}{\partial x^*}+\frac{\partial q_y^*}{\partial y^*}\right] \tag{6}$$

$$(q_x^*, q_y^*)=h_0^*\tilde{Q}\alpha(x)(\overline{u^*}, \overline{v^*}) \quad \alpha=\overline{|u_w^*/\sqrt{g^* h_0^*}|^{b-1}} \tag{7}$$

In (5), (6) p is sediment porosity, an overbar denotes the time average over a wave cycle, α is a wave stirring coefficient which depends on the dimensionless

periodic component $u_w^*/\sqrt{g^*h_0^*}$ of the wave field, $\tilde{Q}$ is a dimensionless constant which depends on sediment characteristics and b is assumed to be equal to 4.

The basic wave field, which is uniform in the longshore direction, can be easily determined by expanding the solution in terms of the small parameter $a = a^*/h_0^*$ (a^* denotes the wave amplitude at $x^* = x_w^*$)

$$u = \frac{u^*}{\sqrt{g^*h_0^*}} = aU_1 + O(a^2) \tag{8}$$

$$\eta = \frac{\eta^*}{h_0^*} = aE_1 + O(a^2) \tag{9}$$

$$h = \frac{h^*}{h_0^*} = \frac{x}{x_w} + O(a^2) \tag{10}$$

In (10) x is the dimensionless cross-shore coordinate ($x = x^*\omega^*/\sqrt{gh_0^*}$) and $x_w = x_w^*\omega^*/\sqrt{gh_0^*}$ is a dimensionless frequency parameter. Moreover because of the matching (4) with the deep water solution, the wave amplitude a^* is related to the wave amplitude a_∞^* of the incoming wave far from the coast ($a^* = a_\infty^*\sqrt{2\pi/\beta}$). Both the dimensionless free surface E_1 and the velocity U_1 turn out to be periodic in time with angular frequency ω^* and characterized by a cross- shore structure described by Hankel functions.

$$E_1(x,t) = \frac{1}{2}\left\{H_0^{(1)}(2\sqrt{xx_w}) + \hat{K}H_0^{(2)}(2\sqrt{xx_w})\right\}e^{it} + c.c. \tag{11}$$

$$U_1(x,t) = \frac{i}{2}\sqrt{\frac{x_w}{x}}\left\{H_1^{(1)}(2\sqrt{xx_w}) + \hat{K}H_1^{(2)}(2\sqrt{xx_w})\right\}e^{it} + c.c. \tag{12}$$

where $t = \omega^*t^*$ is the dimensionless time.

Then small perturbations of the free surface and of the bottom configuration are considered

$$\frac{\eta^*}{h_0^*} = aE_1 + \epsilon\left\{A^{\pm}(\tau)\hat{\eta}_0(x)e^{i(k^*y^* \pm \sigma^*t^*)} + c.c. + O(a)\right\} \tag{13}$$

$$\frac{h^*}{h_0^*} = \frac{x}{x_w} + \epsilon\left\{B^{\pm}(\tau)\hat{h}_0^{\pm}(x)e^{ik^*y^*} + c.c. + O(a)\right\} \tag{14}$$

where ϵ is a parameter much smaller than one (strictly infinitesimal) and τ a slow time scale defined by $\tau = a\omega^*t^*$. Of course perturbations of similar form are induced in the velocity field.

At order ϵ equations (1), (3) provide the structure of $\hat{\eta}_0(x)$

$$\hat{\eta}_0(x) = e^{-k^*x^*}U(d, 1, 2k^*x^*) \tag{15}$$

where d is equal to $(k^* - \sigma^{*2}x_w^*/(g^*h_0^*))/2k^*$ and U indicates one of the Kummer functions (Abramowitz & Stegun, 1964). Then the boundary condition (5)

yields the dispersion relation

$$d = -\frac{U(d,1,2k^*x_w^*)}{2U(d+1,2,2k^*x_w^*)} \tag{16}$$

which shows that different modes are possible. Moreover at order ϵ, $\hat{h}_0^{\pm}(x)$ turns out to be arbitrary as well as $A^{\pm}(\tau)$ and $B^{\pm}(\tau)$.

In order to determine $\hat{h}_0^{\pm}$ and the time behaviour of $A^{\pm}$ and $B^{\pm}$, it is necessary to study the interaction between the perturbations and the incoming wave which is described by the problem at order ϵa. In nonresonant cases a solution of the problem forced by the interactions of the perturbation with the basic wave field can be found and it gives rise to a slight modification of the original perturbation. However, as discussed by Guza & Davis (1974) who considered only perturbations in the water motion, many resonanting cases exist and in particular resonance is present when the interaction between subharmonic edge waves (frequency σ^* equal to $\omega^*/2$) and the incoming wave is considered.

When bottom perturbations are included, it can be seen that their presence induces extra forcing terms. These terms can give rise to a secular growth of the solution if h^* is characterized by a periodic longshore dependence characterized by a wavenumber k^* equal to that of a synchronous edge wave.

In order to prevent the solution from growing unbounded on the fast time scale, a solvability condition must be imposed which leads to

$$\frac{dA^{\pm}}{d\tau} = \gamma_1^{\pm} B^{+} + \gamma_2^{\pm} B^{-} \tag{17}$$

where the coefficients $\gamma_1^{\pm}, \gamma_2^{\pm}$ depend on the characteristics of the incoming wave. These equations describe the growth of the amplitude of synchronous edge waves due to their interaction with the incoming wave propagating on a wavy bottom. A further link between $A^{\pm}$ and $B^{\pm}$ is found by considering the bottom time development forced by the steady part of the $O(\epsilon a)$ flow. This is because the interaction of synchronous edge waves with the incoming wave generates steady currents, which cause the movement of sediment and thereby result in the formation of bedforms. Sediment continuity equation and the sediment transport rate relationship yield

$$\hat{h}_0^{\pm}(x) = \frac{d}{dx}\left[\overline{|U_1|^{b-1}u_1^{\pm}}\right] + ik\overline{|U_1|^{b-1}}v_1^{\pm} \tag{18}$$

$$\frac{dB^{\pm}}{d\tau} = QA^{\pm} \tag{19}$$

where the steady velocity field described by $u_1^{\pm}, v_1^{\pm}$ can be derived by means of the variation of the parameter method and the constant Q, which turns out to be $\tilde{Q}a^{b-1}/(1-p)$, is much smaller than one.

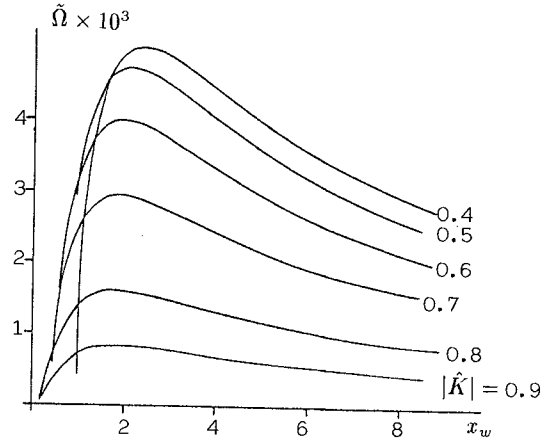

Figure 2: Maximum value of the growth rate $\tilde{\Omega}$ plotted versus x_w for different values of $|\hat{K}|$ and $n = 1$.

The solution of the amplitude equations is of exponential type

$$B^{\pm} \sim \exp(a^{(b+1)/2}\tilde{\Omega}\tilde{t}) \tag{20}$$

where

$$\tilde{t} = t^* \sqrt{\frac{\tilde{Q}gh_0^*}{(1-p)(x_w^*)^2}} \tag{21}$$

is a dimensionless time coordinate obtained using a morphodynamic time scale which does not depend on wave characteristics. Of course the amplification rate $\tilde{\Omega}$ appearing in (20) depends on the parameters of the problem, i.e. $x_w = x_w^*\omega^*/\sqrt{gh_0^*}$ and $\hat{K}$.

3 THE RESULTS

The theoretical analysis, briefly summarized in the previous section, shows that crescentic forms may appear when A and B tend to grow. Figure 2 shows the maximum value of amplification rate $\tilde{\Omega}$ versus the frequency parameter x_w for different values of $|\hat{K}|$ and for the first mode ($n = 1$). Note that $|\hat{K}|$ indicates the modulus of the reflection coefficient of the beach and its phase ϑ is determined by means of the simple model described in (Vittori & al., 1998). The results indicate that bedforms periodic in the longshore direction tend to form when the incoming wave has an angular frequency ω^* such that x_w takes values close to 4.5. However the first mode is not always the most unstable as

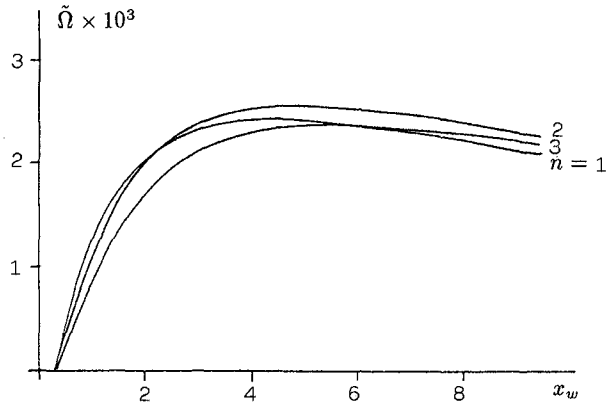

Figure 3: Maximum value of the growth rate $\tilde{\Omega}$ plotted versus x_w for different mode numbers n and $|\hat{K}| = 0.8$.

it can be seen from figure 3, where $\tilde{\Omega}$ is plotted versus x_w for $|\hat{K}| = 0.8$ and different mode numbers. In this case the second mode is the most unstable and crescentic forms appear when forced by incoming waves characterized by an angular frequency such that $x_w \cong 4.75$. By considering the behaviour of $\tilde{\Omega}$ for different values of n, x_w and $\hat{K}$ it is possible to single out the most unstable conditions, i.e. to evaluate the frequency ω^* of the incoming wave triggering the instability of the bottom configuration and the wavelength of the most unstable mode.

Let us now compare the theoretical findings with some field data. First of all this requires the determination of the values of x_w^* and h_0^* which are representative for the actual beach profiles. Figure 4 shows one of the bottom

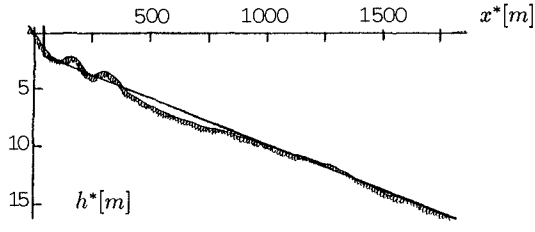

Figure 4: Bottom profile measured along Niigata beach in 1958 (Hom-ma & Sonu, 1963) and the model beach geometry.

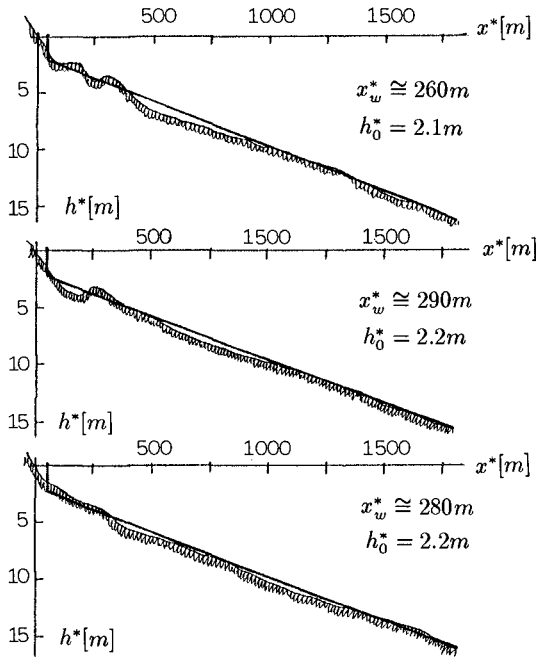

Figure 5: Bottom profiles measured along Niigata beach in 1958 (Hom-ma & Sonu, 1963) at different longshore locations along with the model beach geometry.

profiles measured by Hom-ma & Sonu (1963) at Niigata beach during 1958 along with our simplified beach profile in such a way that the differences between the two geometries are minimized in a least square sense. In this case our best fitting procedure yields $x_w^* = 260$ m and $h_0^* = 2.1$ m. However it turns out that x_w^* and h_0^* depend on the longshore coordinate as it follows from figure 5 where the beach profiles detected at different longshore locations along the Niigata coast during 1958 are shown together with the values of x_w^* and h_0^*. Hence in order to apply the theory, it is necessary to average x_w^* and h_0^* along the longshore coordinate. The data described in the paper by Hom-ma & Sonu (1963) provide the beach profiles at Niigata site at 6 longshore locations only and the average values of x_w^* and h_0^* can be determined with some uncertainty. It turns out that x_w^* and h_0^* fall within a small range around 280 m and 2.2 m respectively. The same procedure applied to the data obtained by Hom-ma & Sonu (1963) in August 1957 at Tokai beach provides values of x_w^* and h_0^* which are somewhat larger, i.e. 310 m and 2.9 m respectively. However it is necessary to point out that different wave climates make x_w^* and h_0^* to change. Indeed

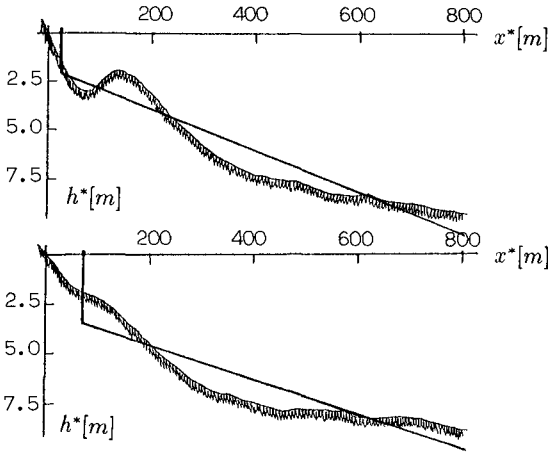

Figure 6: Bottom profiles measured along Tokai beach (Hom-ma & Sonu, 1963) along with the model beach geometry. (a) December 1956, (b) August 1957.

figure 6 shows that beach profiles detected at the same longshore location but at different times are characterized by large differences. The changes observed in the values of x_w^* and h_0^* are significant and hence the theoretical analysis should be used to indicate the range of wavelengths of possible crescentic forms rather than to predict an exact value.

Because the maximum value of the amplification rate $\tilde{\Omega}$ is around $x_w = 4.75$, the incoming waves which are most likely to give rise to the appearance of crescentic forms are those characterized by a period equal to about 80 s and 85 s for the Niigata and Tokai sites, respectively. Then the dispersion relation yields a value of the longshore wavelength of the bottom forms. For Niigata site the predicted length is around 600 m while for Tokai beach it appears that the most unstable crescentic forms are characterized by a wavelength of about 700 m. If a comparison is performed with the observed values a fair agreement is found taking into account that, at this stage, the analysis is linear and that a highly idealized model has been used. From figure 7, which shows bottom morphology measured in front of Niigata beach in 1958, it can be seen that bottom forms periodic in the longshore direction are present, which have wavelengths larger than 500 m. Likewise figure 8 clearly shows a longshore periodic pattern in the offshore bar at Tokai beach, with a wavelength which ranges between 1000 and 1500 m depending on the wave climate. The field surveys show also the presence of much shorther crescentic forms, with wavelengths of about 50 m. These bottom forms are also predicted by the theory since the total

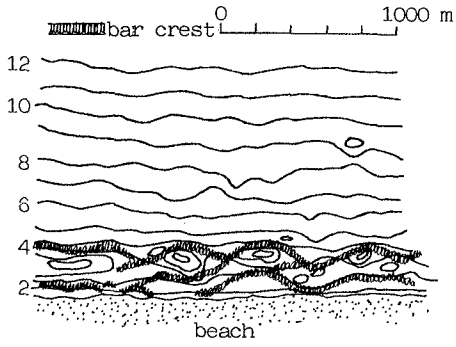

Figure 7: Bottom topography showing bar position in 1958 at Niigata beach (adapted from Hom-ma & Sonu, 1963).

amplification rate of the bottom perturbations (see (20)) is characterized by two maxima. The former is due to the maximum of $\tilde{\Omega}$, the latter is caused by maximum of the amplitude a of the incoming wave which of course depends on the frequency parameter x_w. The prediction of the smaller bottom forms would require accurate measurements of the spetrum of the inconing wave field outside the breaker zone. These data are not available for Niigata and Tokai beaches. However it can be certainly assumed that the wave spectrum is characterized by a maximum for wind waves which have periods around 10 s. With these data, the theory predicts bedforms with a longshore wavelength of about 50 m, a value which is very close to the observed one. Good agreement is also found when comparing the theoretical findings with the field survey performed at Lubiatowa (Poland) by Pruszak et al. (1997). The presence of longshore crescentic forms can be seen in figure 9 which is an adaptation of the data described in Pruszak et al.'s (1997) paper. The wavelength of these crescentic forms is approximately 800 m even though the presence of only two bars and three pools does not allow a precise evaluation. By analysing the beach profile measured by Pruszak et al. (1997) during august 1996 it turns out that the values of x_w^* and h_0^* are 370 m and 2.1 m respectively. Using these input values in the theoretical model, the predicted wavelength is close to 850 m. In determining this value it has been assumed that it is caused by the maximum in the growth rate induced by the curve $\tilde{\Omega}$ versus the frequency parameter x_w. The bottom forms induced by wind waves which give rise to a maximum in $a(x_w)$ have not been observed by Pruszak et al. (1997). This may be due to the reflection coefficient of the beach. Indeed the theory predicts the appearance of crescentic forms only when the incoming waves are somewhat reflected by the beach. At Lubiatowa site the presence of a system

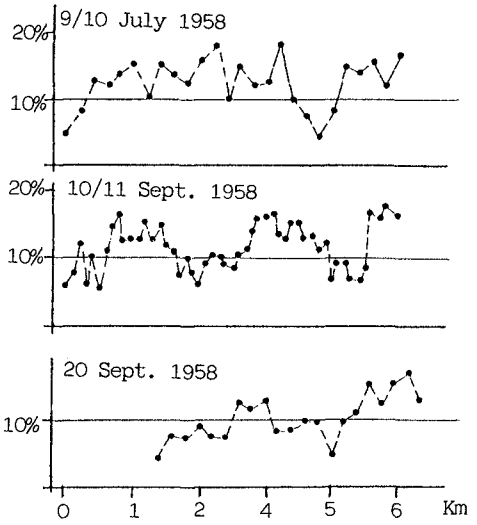

Figure 8: Shoreface slope along Tokai beach in different months of 1958 (adapted from Hom-ma & Sonu, 1963).

of longshore parallel bars induces the breaking of short waves and makes the reflection coefficient of the beach very small.

4 CONCLUSIONS

The comparison between the theoretical findings and field data described in the previous section seems to indicate that the main ingredients of the process leading to the formation of crescentic forms are captured by the simplified model formulated by Vittori et al. (1998). Of course in order to obtain more refined predictions of the characteristics of the bottom forms it would be necessary to improve the model by removing some of the assumptions introduced to work out the solution by analytical means. In particular the geometry of the beach should allow for the presence of bars and the wave model should include the description of breaking, since quite often the surf zone is not small when compared with the length of the incoming wave. Such a refined model would require a numerical approach to determine both the basic wave field and the time development of bottom perturbations.

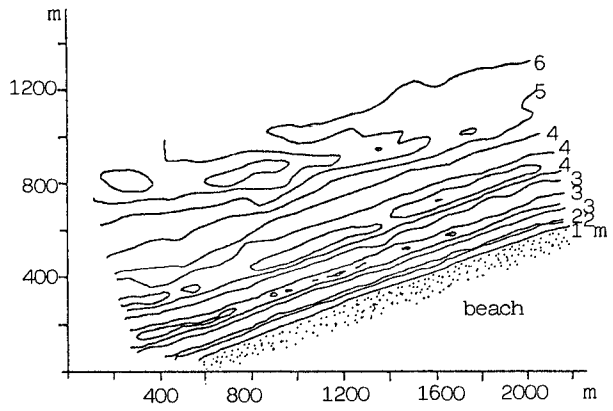

Figure 9: Bottom topography measured by Pruszak & al. (1997) at Lubiatowa beach (adapted from Pruszak et al., 1997).

Acknowledgement

This paper is partly based on work in the PACE- research project supported by EU under contract n. MAS3-CT95-0002 in the framework of the Marine Science and Technology Programme (MAST-III). The financial support of the Office of Naval Research (O.N.R.), U.S.A., under contract N. 00014-97-0790 and of the Ministero dell'Università e della Ricerca Scientifica e Tecnologica (Italy) is gratefully acknowledged.

Appendix I. References

Abramowitz, M., and Stegun, I.A. (1964). *Handbook of mathematical functions.* Dover Publication.

Guza R.T., and Davis, R.E. (1974). "Excitation of edge waves by waves incident on a beach". *J. Geophys. Res.*, 79(9), 1285-1291.

Hom-ma, M., and Sonu, C. (1963). "Rhythmic pattern of longshore bars related to sediment characteristics". *8th Coastal Eng. Conference*, Mexico City, November 1962, 248-278.

Mei, C.C. (1989). *The Applied Dynamics of Ocean Surface Waves.* World Scientific.

Pruszak, Z., Rozynsky G., and Zeidler, R.B. (1997). "Statistical properties of multiple bars". *Coastal Eng.*, 31, 263-280.

Vittori, G., De Swart, H.E., and Blondeaux P. (1998). "Crescentic bed forms in the nearshore region". Submitted for publication.

SIMPLE MODELS FOR EQUILIBRIUM PROFILES UNDER BREAKING AND NON-BREAKING WAVES

Magnus Larson[1] and Randall A. Wise[2]

ABSTRACT: *Simple theoretical models are presented to calculate the equilibrium profile shape under breaking and non-breaking waves. For the case of breaking waves the seaward transport in the undertow at equilibrium is locally balanced by a net vertical sedimentation so that no bottom changes occur. The parameterization of the water and sediment flux in the surf zone yields a power curve for the equilibrium profile with a power of 2/3. Three different models are developed to derive the profile shape under non-breaking waves, namely (1) a variational formulation where the wave energy dissipation in the bottom boundary layer is minimized over the part of the profile affected by non-breaking waves, (2) an integration of a small-scale sediment transport formula over a wave period where the slope conditions that yield zero net transport determine equilibrium, and (3) a conceptual formulation of mechanisms for onshore and offshore sediment transport where a balance between the mechanisms defines equilibrium conditions. All three models produce equilibrium profile shapes of power-type with the power typically in the range 0.15-0.30. Comparisons with laboratory and field data support the results obtained indicating different powers for the equilibrium profile shape in the surf zone and offshore zone.*

INTRODUCTION

The concept of an equilibrium profile (EP) is of central importance to coastal engineers because it provides a basis for assessing a characteristic shape to a beach in design and analysis situations. A beach of a specific grain size, if exposed to constant forcing conditions (monochromatic waves or random waves with constant statistical properties), normally assumed to be short-period breaking waves, will develop a profile shape that displays no net change in time, although sediment will be in motion. The validity of this concept has been verified through a large number of laboratory

[1] Associate Professor, Department of Water Resources Engineering, University of Lund, Box 118, S-221 00 Lund, SWEDEN (Email: magnus.larson@tvrl.lth.se).
[2]Coastal and Hydraulics Laboratory, U.S. Army Corps of Engineers, 3909 Halls Ferry Road, Vicksburg, MS 39180-6199, USA.

experiments on beach-profile change (e.g., Saville 1957, Kajima et al. 1982, Kraus and Smith 1994, Dette et al. 1998). On a natural beach, however, the forcing conditions are never constant and changes in the beach topography occur at all times. In spite of this, the beach profile in the field exhibits a remarkably persistent concave shape (Bruun 1954, Dean 1977), where changes may be taken as perturbations upon the main profile configuration. Such changes in beach profile shape can be regarded as adjustment of the profile from the course of one equilibrium state to another as the forcing conditions change (for example, during a storm). With this view the equilibrium concept is valid not only for the long-term average forcing conditions but for varying forcing conditions over different time scales.

The conditions for equilibrium on a beach and associated slopes and profile shapes have been a topic of research since the 1950's. Bruun (1954) proposed a power law to describe the profile depth as a function of distance from the shoreline based on field data from the Danish West coast and from California (a power of 2/3 provided the best fit). Dean (1977) analyzed an extensive data set consisting of beach profiles measured along the Atlantic and Gulf coasts of United States. He also found that a power law with a power of 2/3 provided the best overall fit to the measured profile shapes. Furthermore, Dean (1977) theoretically motivated this power law by assuming that equilibrium occurred for constant wave energy dissipation per unit water volume along the profile. This constant is known as the equilibrium energy dissipation and has been shown to be a function of grain size (Moore 1982) or fall speed (Dean 1987).

Bowen (1980) derived EP shapes by analysis of the sediment transport formulas proposed by Bagnold (1963). Analytical expressions for the profile shape were obtained for the cases of a steady drift due to wave mass transport in the boundary layer and wave asymmetry, producing powers of 2/3 and 2/5, respectively. Larson and Kraus (1989) generalized the derivation by Dean (1977) to include the effect of gravity leading to a planar beach slope at the shoreline. Inman et al. (1993) divided the profile into two portions, an inner and outer region, which corresponded to the regions with breaking and non-breaking waves, respectively. Both portions were successfully approximated with power curves matched at the break point and the optimum values of the power was 0.4 for both curves. In fitting the power curve to the inner portion of the profile the height of the berm was employed as the base elevation; this differs from previous studies where typically the mean sea level was used as vertical datum.

Although a number of studies have been carried out regarding EPs, as indicated above, there are presently no general, physically based theories to derive the EP shape under both breaking and non-breaking waves that produce a realistic EP shape over the entire active profile. Thus, the main objective of this study is to develop theories for the EP shape under breaking and non-breaking waves. It is assumed that the region where wave breaking prevails may be treated separately from the offshore zone where mainly non-breaking waves control the profile shape. This separation is conceptually justified because intense turbulence exists in the surf zone, making both bedload and suspended load significant, whereas bottom-boundary layer processes and bedload transport are

expected to be dominant in the deeper and less turbulent water offshore under non-breaking waves. First, the EP shape in the surf zone will be discussed, where wave breaking controls the profile development. Then, the EP under non-breaking waves is treated where oscillatory waves determine the profile shape. The derived EP formulas were validated through comparisons with laboratory and field data.

THEORETICAL CONSIDERATIONS

EP Shape Under Breaking Waves (Surf Zone)

Although the theoretical model proposed by Dean (1977) for EPs produces a shape that is in agreement with field data, the physical justification for the equilibrium condition is not clear and the assumptions made are rather *ad hoc.* Also, a profile that is close to equilibrium may still produce a significant net sediment transport in the undertow that is difficult to explain within the framework of the Dean model. Here, an alternative model is derived that relies on certain assumptions about the circulation of water and sediment in the surf zone. In this sense the model is non-local as opposed to the Dean model where the equilibrium conditions are established from a local criterion of zero transport. A beach subject to waves experiences a return flow across the profile that carries sediment stirred up by the waves offshore in the undertow. Even at equilibrium conditions, when no net change in the profile shape occurs, this transport should take place implying that material has to come onshore above the undertow layer to compensate for the offshore transport. When the undertow reaches the break point the transported sediment has to be resuspended up into the water column and pushed onshore to ensure an equilibrium situation where no material goes offshore. Thus, such a simplified picture yields a surf zone with sediment moving, but with no net changes in time of the profile depths, and the break point acts almost as a singularity. Fig. 1 schematically illustrates the water and sediment flow in the surf zone at equilibrium conditions (note that the size of the arrows is exaggerated in the figure).

To arrive at an EP shape it is assumed that the change in the sediment transport in the undertow is balanced by sedimentation through the water column. This sedimentation represents the net effect from sediment being resuspended locally by the waves and the settling of the material. If it is assumed that the transport in the undertow is the product between the flow q and a characteristic bottom concentration c, and that the gradient in this transport is balanced by a net sedimentation (μwc), the following equation for the EP profile may be derived (Larson et al. 1998),

$$\frac{d}{dx}\left(\lambda_u \sqrt{gh}\gamma h^2\right) = \mu w h \tag{1}$$

where h is the water depth, w the sediment fall speed, g the acceleration of gravity, and λ_u, γ and μ constants (referring to the undertow flow, wave height-depth ratio, and net sedimentation, respectively). The undertow flow was set proportional to the mass transport in the breaking waves, c was derived from a balance between the work needed

to keep grains in suspension in the bottom layer and the energy dissipation in the bottom boundary layer (Larson et al. 1998), and the vertical sediment transport was parameterized in terms of c. Integrating the above equation with $h=0$ when $x=0$ yields:

$$h = \left(\frac{3}{5} \frac{\mu w}{\lambda_u \sqrt{g\gamma}} \right)^{2/3} x^{2/3} \tag{2}$$

This is the same EP shape as Dean derived with a similar functional dependence on w for the constant in front of $x^{2/3}$ as what Kriebel et al. (1991) obtained (c.f., Bowen 1980).

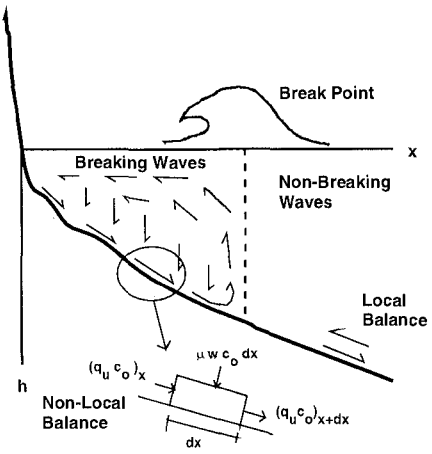

Figure 1. Schematic picture of assumed sediment transport pattern in the surf zone for deriving an EP shape.

EP Shape Under Non-Breaking Waves (Offshore Zone)

Three different approaches were employed to derive the EP shape under non-breaking waves. The first approach was based on the heuristic assumption that the profile shape seaward of the break point at equilibrium is such that the waves dissipate a minimum of energy when traveling across the profile. In the second approach a detailed sediment transport formula proposed by Madsen (1991) was integrated over a wave period, and an equilibrium slope is determined that produces zero net transport. Finally, a conceptual model was formulated that assumed a balance at equilibrium between onshore transport due to wave asymmetry and offshore transport due to gravity.

Variational Formulation

Many systems in nature strive towards equilibrium in such a way that some energy quantity attains a minimum. Thus, it seems reasonable to assume that a beach profile is in equilibrium with the forcing conditions when an appropriate energy quantity reaches its minimum value. The basic assumption employed in the present formulation is that the total wave energy dissipation per unit beach width and time along the profile exposed to non-breaking waves attains a minimum at equilibrium. This implies that the waves loose minimum energy as they propagate across the profile, experiencing the least reduction in wave height for all possible profile shapes. Using the Euler-Lagrange approach from variational calculus to determine the optimal profile shape that minimizes the integral expressing the total wave energy dissipation gives the following equation to solve for the EP shape,

$$C_1 h^{9/4}\sqrt{1+(dh/dx)^2} = -1 \tag{3}$$

where C_1 is a constant. However, this equation does not have a general solution that satisfies the boundary conditions $h=h_b$ for $x=x_b$ and $h=h_c$ for $x=x_c$, where subscripts b and c denote break point and closure depth, respectively (dissipation is assumed to occur between x_b and x_c). Instead, by assuming a general power shape for the EP, that is, $h=(h_b^{1/n}+(h_c^{1/n}-h_b^{1/n})(x-x_b)/(x_c-x_b))^n$, the following integral should be minimized to obtain the optimal power n,

$$I=\int_0^1 \frac{\sqrt{1+\left(\dfrac{Z^{1/n}-1}{W}\right)^2 n^2\left(1+(Z^2-1)\xi\right)^{2(n-1)}}}{\left(1+(Z^{1/n}-1)\xi\right)^{9n/4}}d\xi \tag{4}$$

where $Z=h_c/h_b$, $W=(x_c-x_b)/h_b$, and $\xi=(x-x_b)/(x_c-x_b)$. The optimal value of n (n_o) is a function of h_c/h_b and $(x_c-x_b)/h_b$ and may be found from solving the equation $dI/dn=0$. Thus, the EP shape depends on the location of the boundaries and these have to be specified before the shape can be predicted. The breakpoint location can be calculated from the incident wave height, whereas the seaward limit of the profile experiencing significant dissipation is more difficult to estimate. Fig. 2 displays how n_o varies with h_c/h_b and the mean offshore slope $\tan\beta=(h_c-h_b)/(x_c-x_b)$. In all cases with realistic values on these parameters, n_o is markedly lower than the value 2/3 that is often found for the surf zone. Thus, the predicted EP shape under non-breaking waves has a lower curvature than the EP shape under breaking waves.

Microscale Formulation

Madsen (1991) derived a formula for the instantaneous bedload sediment transport rate based on a detailed description of the physical processes controlling the transport in the offshore zone. Under certain conditions this formula will produce zero net transport

over a wave period which implies that the beach does not experience any changes because of the transport. Only the wave motion will be considered here and there will be no attempt to include a steady current, although it is possible if the current speed can be specified. The Madsen formula always produces offshore transport for a sloping bed under purely sinusoidal waves (gravity promotes down-slope transport); thus, it is necessary to include the asymmetry of the velocity field so that a realistic balance is obtained between the tendency of onshore transport in shoaling waves and offshore transport due to gravity. The local condition for equilibrium may be expressed as (Larson et al. 1998),

$$\int_{h_b}^{h} \frac{I_p + I_n}{I_p - I_n} dh = \tan\phi_m (x - x_b) \tag{5}$$

where I is an integral over the bottom shear stress, ϕn the friction angle for a moving grain, and subscripts p and n denote the periods when the shear stress is positive and negative, respectively. The EP shape can only be obtained if the shear stress integrals I_p and I_n are calculated which require a detailed solution of the flow in the bottom boundary layer. However, using a number of approximations a simple analytical solution can be derived from the above exact equation.

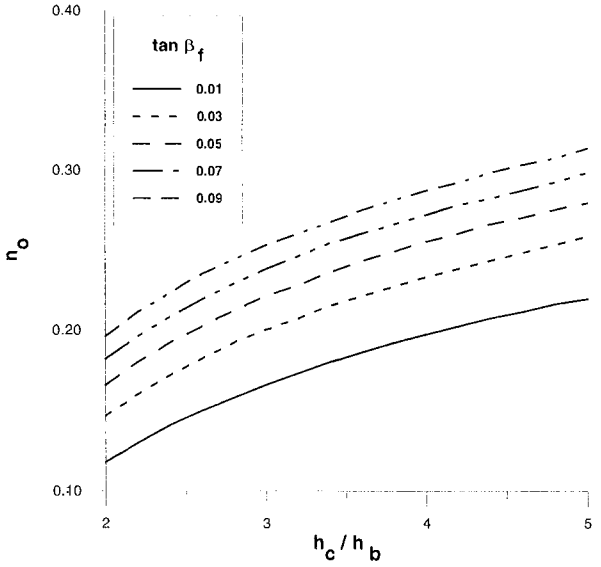

Figure 2. Dependence of the optimal power in the EP equation for the offshore on the geometric parameters.

Cnoidal wave theory was used to describe the asymmetric properties of the waves and an empirical equation was fitted to the theory to allow straight-forward calculation of these properties. Furthermore, the effect of the initiation of motion was neglected and the asymmetric waves were schematized using two sinusoidals to describe the periods when the shear stress is positive and negative. These assumptions together with a nonlinear shoaling law for the wave height yield the following EP shape for larger values of h/h_b (Larson et al. 1998),

$$\frac{h}{h_b} = \left(1 + \frac{1}{K_1} + \frac{\tan\theta_m}{K_1}\frac{x - x_b}{h_b}\right)^{\frac{1}{1+(2+p)m}} \tag{6}$$

where K_1 is a constant, p the power in the nonlinear shoaling law, and m an empirical power (about 7/5) originating from the empirical fit to cnoidal wave theory. Realistic values on p and m yields a power in the EP equation of about 0.25.

Conceptual Formulation

Instead of starting from a detailed sediment transport formula (e.g., Madsen) a conceptual approach was taken to derive the EP shape. It is assumed that the two main mechanisms that govern the profile shape in the offshore are the onshore transport due to the shoaling waves and the offshore transport due to gravity (compare Niedoroda et al. 1995). At equilibrium these two mechanisms produce equal amounts of transport and there will be no local net transport. The mean cross-shore transport rate q_c is often related to the bottom Shields stress ψ_m to a power k. To include the effect of wave asymmetry on the transport rate, a dependence on the Ursell number U_r was introduced,

$$\frac{q_c}{wd} = C\psi_m^k U_r^m \tag{7}$$

where d is the grain size and C a constant. The U_r-dependence (including the power m) is the same as was used in the previous section. The transport q_c should be balanced by the offshore transport due to gravity, which is estimated from a sediment layer with a characteristic concentration c moving offshore at the speed wdh/dx (c is estimated in a similar manner to what was done in the surf zone; see Larson et al. 1998). Equating the two types of transport and introducing shallow-water approximations yields the following EP shape,

$$\frac{h}{h_b} = \left(1 + rK_2\frac{x - x_b}{h_b}\right)^{1/r} \tag{8}$$

where $r=1+3/2k+9/4(m-1)$ and K_2 is a constant. Again, an EP shape is derived that follows a power law. The coefficient k is typically in the range 3/2 to 3, and $m=7/5$

provided a good fit to cnoidal wave theory. Thus, for $k=3/2$ the equation gives the power a value of 0.24, whereas $k=3$ produces a value of 0.15.

COMPARISONS WITH LABORATORY AND FIELD DATA

In summary, the previously derived EP shapes under breaking and non-breaking waves may be written, respectively,

$$h = Ax^m, \qquad 0 \le x \le x_b \tag{9}$$

$$h = \left(h_b^{1/n} + B(x - x_b)\right)^n, \qquad x \ge x_b \tag{10}$$

where A and B are shape parameters, and subscript b denotes the break point. The values of the powers were determined to be m=2/3 (compare Bruun 1954 and Dean 1977), whereas n was in the range 0.15-0.30, depending on the mechanisms assumed to control profile equilibrium. The shape parameter A has been related to grain size (or fall speed), whereas B is a function of the sediment characteristics as well as the offshore wave conditions (in the general case). Descriptions of beach profiles that involve regions governed by different predictive relationships have previously been proposed by Everts (1978) and Inman et al. (1993).

Eqs. 9 and 10 were least-square fitted towards measured profiles in the laboratory and the field to evaluate how well they are able to characterize the profile shape in the surf zone and offshore zone. The distinction between these two zones was typically made based on the presence of a nearshore bar (compare Inman et al. 1993). Only the shape parameters A and B were optimized in the fitting procedure, whereas x_b and h_b were visually determined based on the observed profiles introducing an element of subjectivity in the calculations. The value of the power n was also varied, but n=0.3 provided the best overall fit. This value is somewhat larger than what was typically found from the theoretical analysis, although it still within the range of realistic values. The theoretical EP models were essentially based on monochromatic (or representative) wave conditions and the effects of wave randomness were not explicitly addressed. In the following, the least-square fit was carried out some distance away from the bar region, where the effects of randomness are expected to be most pronounced. Thus, seaward of the bar mostly non-breaking waves prevail and shoreward of the bar fully broken waves dominate, implying that a monochromatic wave description should be appropriate as a first approximation.

Laboratory Data

Data obtained in the German Large Wave Tank were employed to evaluate how well the derived EPs could describe measured profile shapes at near-equilibrium conditions (Dette et al. 1998). The tests used here for comparison involved random waves according to a TMA spectrum with an H_{mo}=1.2 m and T_m=5 sec. In total data from three tests were used and the experimental conditions were similar in all tests except for the foreshore slope. In all cases, both in the surf zone and offshore zone, it

was possible to obtain a close fit between the equations and the data (one example given in Fig. 3). The estimated A-value in the surf zone (A=0.12 $m^{1/3}$) was in good agreement with what is to be expected for the grain size employed (median grain size 0.33 mm). The B-values varied somewhat more (0.44-0.78 $m^{7/3}$), which partly depended on the amount of material deposited in the bar area. A larger amount implied a steeper seaward bar face and the need for a larger B-value to properly fit both the steep bar face and the more gently sloping profile seaward of the bar.

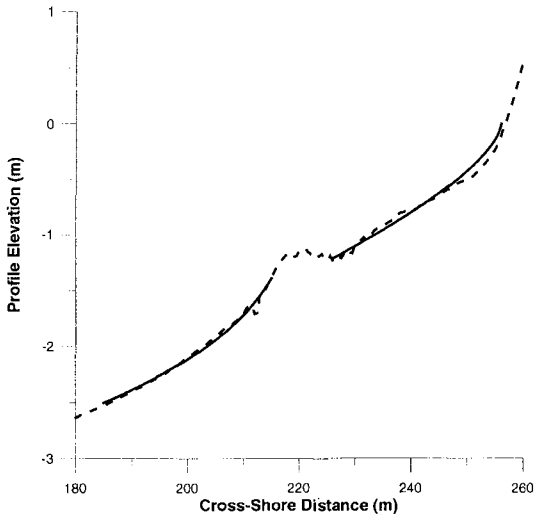

Figure 3. Comparison between theoretical and measured EPs from Test B2 in the German Large Wave Tank.

Field Data

Profile measurements from several locations around the United States were employed to test the derived EP shapes for field conditions. Data sets from Ocean City, Long Island (Fire Island, Westhampton Beach, and Ponds), Cocoa Beach, and Silver Strand were employed in this comparison representing a wide variety of wave and beach conditions. In most cases a more or less clear breakpoint bar was present along the profiles that provided a natural separation point between the surf zone and offshore zone. As an example, Fig. 4 displays a fit towards a profile measured at Silver Strand (Larson and Kraus 1992), where the estimated parameter values were A=0.21 $m^{1/3}$ and B=12.3 $m^{7/3}$. The obtained A-parameter value is somewhat high considering the grain size at the site; however, the profile shape near the shoreline reveals a feature indicative of accretion that complicates the picture.

In Fig. 4 the bar feature was quite suppressed and the two EPs eould be joined at a matching point without too mueh deviation from the measured profile around this point. This was not always the case, but frequently a pronounced bar feature appeared that produced a region where it was not possible to obtain an acceptable fit. Fig. 5 illustrates one sueh example from Ocean City (Stauble et al. 1993), where a large bar was present creating a region where the composite EPs fail to deseribe the shape. On the contrary, extrapolating the EPs so that they intersect at a match point eould be a useful way of defining the bar feature. The shape parameters for the fit deseribed in Fig. 5 were A=0.14 $m^{1/3}$ and B=3.7 $m^{7/3}$.

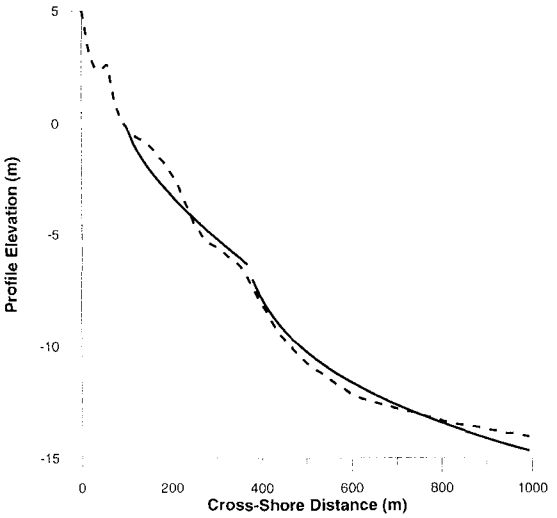

Figure 4. Comparison between theoretical and measured EPs from Silver Strand, USA.

As indicated by the profile fits presented in Figs. 3-5 the optimal value of the shape parameter B varied substantially between the studied surveys. In order to usefully employ the eomposite EP for predictive purposes, a formula is needed that will yield B as a funetion of the governing factors (A is predieted from grain size aceording to Moore (1982) or Dean (1987)). A closer examination revealed a distinet eorrelation between h_b and B (see Fig. 6), implying that knowledge of the depth at the location where wave breaking typically oeeurs can be used to eompute B. Several different empirieal relationships were developed, encompassing both linear and power-type funetions (see Fig. 6), each explaining about 70% of the variation in the data (in total 41 profiles from the above-mentioned sites were used in the fit). The following equation is dimensionally eonsistent and results if the EPs (Eqs. 9 and 10) are scaled with h_b:

$$B = 0.142 h_b^{7/3} \tag{11}$$

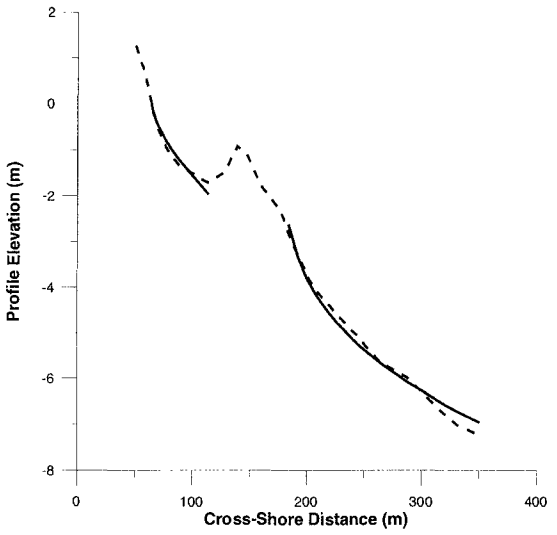

Figure 5. Comparison between theoretical and measured EPs from Ocean City, USA.

The rational between Eq. 11 is that the typical breaking wave height (and, thus, water depth at breaking) is the main quantity that scales profile behavior allowing for intercomparison between profile shapes at different sites. Eq. 11 may be regarded as a first-order approximation to compute the shape parameter controlling the EP in the offshore for profiles with one more or less well-developed bar. It should be pointed out that the analysis presented here of the field profiles contains some amount of uncertainty, not only concerning objectively determining the fitting parameters, but also regarding how close the measured profiles were to equilibrium conditions at the time of survey.

CONCLUDING REMARKS

One theoretical model to calculate the EP under breaking waves and three models to calculate the EP under non-breaking waves were briefly discussed in this paper. The theoretical models were derived based on descriptions of wave and sediment transport processes, providing physical justification for the equilibrium conditions. The approach for breaking waves resulted in a power function with a value on the power of 2/3, which is in accordance with existing field data and Dean's formulation of equilibrium based on constant energy dissipation per unit water volume across the profile. The first formulation of equilibrium for non-breaking waves was based on an assumption about the overall behavior of the offshore profile shape regarding the dissipation of wave

energy, whereas the other two formulations relied on assumptions about the predominant sediment transport mechanisms controlling the EP shape. For the two latter models, one approach started from a micro-scale sediment transport formula, whereas the other approach encompassed a conceptual description of the processes governing sediment transport in the offshore. A power function was obtained for all three approaches with the value of the power being around 0.25. Thus, these models confirm the common observations that the EP shape in the offshore has a lower curvature than in the surf zone.

Comparisons with field data showed that the theoretically derived composite EP could well describe the measured profiles over a wide range of water depths. However, in some cases, when a marked bar was present along the profile, the composite EP failed to accurately describe the shape in the bar region. The simple theoretical EP models derived here were not designed to resolve the complex flow and sediment transport conditions in the bar region, but mainly to describe the profile behavior under a steady bore propagating shoreward or a purely oscillatory wave in the offshore. It might be possible to heuristically include the bar region by some additional assumptions regarding the equilibrium conditions in this region.

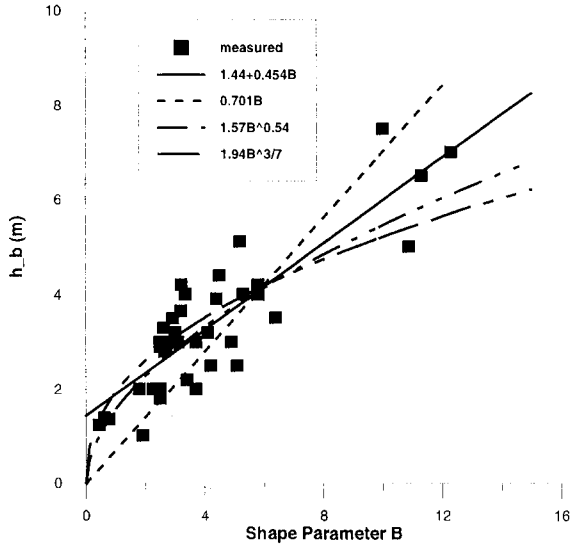

Figure 6. Relationship between the shape parameter for the EP in the offshore and the depth at breaking.

Two of the approaches to calculate the EP shape under non-breaking waves were based on balances between the onshore and offshore transport. If this balance is not fulfilled there will be a net sediment transport and the magnitude of this transport is determined

as the difference between the onshore or offshore rate. Although the calculation of the net transport is straight-forward, it might be advantageous to formulate the local transport rate in terms of a deviation from the equilibrium shape. In the case such a formulation is employed, EP shapes obtained from laboratory and field data can be used to determine some of the unknown coefficients in the transport formulas (or eliminate the coefficients completely from the formulas).

ACKNOWLEDGEMENTS

This work was partly carried out in the framework of the PACE and SAFE research programs. It was funded by the Commission of the European Communities, Directorate General for Science, Research and Development, under Contracts No. MAS3-CT95-0002 and MAS3-CT95-0004, respectively. The work was also funded by the Coastal Research Program of the U.S. Army Corps of Engineers. Permission was granted by the Chief of Engineers to publish this information.

REFERENCES

Bagnold, R.A. (1963). "Mechanics of marine sedimentation." In: *The Sea Vol 3*, Editor M.N. Hill, Interscience, New York, pp 507-528.

Bowen, A.J. (1980). "Simple models of nearshore sedimentation: Beach profiles and longshore bars." In: *The coastline of Canada*, editor S.B. McCann, Geological Survey of Canada, 80-10, pp 1-11.

Bruun, P. (1954). "Coast erosion and the development of beach profiles." Technical Memorandum No. 44, Beach Erosion Board, U.S. Army Corps of Engineers.

Dean, R.G. (1977). "Equilibrium beach profiles: U.S. Atlantic and Gulf coasts." Department of Civil Engineering, Ocean Engineering Report No. 12, University of Delaware, Newark, DE.

Dean, R.G. (1987). "Coastal sediment processes: Toward engineering solutions." *Proceedings of Coastal Sediments '87,* American Society of Civil Engineers, pp 1-24.

Dette, H., Newe, J., and Peters, K. (1998). "Data documentation: LWF experiments '96/97." Report No. 825, Leichtweiss- Institute, Technical University of Braunschweig, Braunschweig, Germany.

Everts, C.H. (1978). "Geometry of profiles across the inner continental shelves of the Atlantic and Gulf Coasts of the United States." Technical Paper No. 78-4, Coastal Engineering Research Center, U.S. Army Corps of Engineers, Fort Belvoir, VA.

Inman, D.L., Elwany, M.H.S., and Jenkins, S.A. (1993). "Shorèrise and bar-berm profiles on ocean beaches." *Journal of Geophysical Research*, Vol 98, No. C10, pp 18,181-18,199.

Kajima, R., Shimizu, T., Maruyama, K., and Saito, S. (1982). "Experiments of beach profile change with a large wave flume." *Proceedings of the 18th Coastal Engineering Conference*, American Society of Civil Engineers, pp 1385-1404.

Kraus, N.C. and Smith, J.M. (1994). "SUPERTANK laboratory data collection project. Volume I: Main text." Technical Report CERC-94-3, Coastal Engineering Research Center, U.S. Army Engineer Waterways Experiment Station, Vicksburg, MS.

Kriebel, D.L., Kraus, N.C., and Larson, M. (1991). "Engineering methods for predicting beach profile response." *Proceedings of Coastal Sediments '91,* ASCE, pp 557-571.

Larson, M. and Kraus, N.C. (1989). "SBEACH: numerical model for simulating storm-induced beach change. Report 1, empirical foundation and model development." Technical Report CERC-89-9, Coastal Engineering Research Center, U.S. Army Engineer Waterways Experiment Station, Vicksburg, MS.

Larson, M. and Kraus, N.C. (1992). "Analysis of cross-shore movement of natural longshore bars and material placed to create longshore bars." Technical Report DRP-92-5, Coastal Engineering Research Center, U.S. Army Engineer Waterways Experiment Station, Vicksburg, MS.

Larson, M., Kraus, N.C., and Wise, R.A. (1998). "Equilibrium beach profiles under breaking and non-breaking waves." *Coastal Engineering*, (under revision).

Madsen, O.S. (1991). "Mechanics of cohesionless sediment transport in coastal waters." *Proceedings of Coastal Sediments '91,* ASCE, pp 15-27.

Moore, B.D. (1982). "Beach profile evolution in response to changes in water level and wave height." unpublished M.S. thesis, University of Delaware, Newark, DE.

Niedoroda, A.W., Reed, C.W., Swift, D.J.P, Arato, H., and Hoyanagi, K. (1995). "Modeling shore-normal large-scale coastal evolution." *Marine Geology*, Vol 126, pp 181-199.

Saville, T. (1957). "Scale effects in two dimensional beach studies." *Transactions from the 7th General Meeting of the International Association of Hydraulic Research,* Vol. 1, pp A3-1-A3-10.

Stauble, D.K., Garcia, A.W., Kraus, N.C., Grosskopf, W.G., and Bass, G.P. (1993). "Beach nourishment project response and design evaluation: Ocean City, Maryland. Report I. 1988-1992," Technical Report CERC-93-13, Coastal Engineering Research Center, U.S. Army Engineer Waterways Experiment Station, Vicksburg, MS.

EQUILIBRIUM TERRACED AND BARRED BEACHES

Mark D. Orzech[1] and Nobuhisa Kobayashi[2]

ABSTRACT

The results of two sediment transport models based on the sheet flow approach and the energetics approach are compared with experimental data of random waves over fine sand beaches in equilibrium in a wave flume. Two tests were conducted with a terraced profile (test 1) and a barred profile (test 2). The energetics-based model predicts the equilibrium profile better than the sheet flow model for both tests. However, the energetics model predicts offshore sediment transport and bar migration, whereas the sheet flow model predicts onshore sediment transport and bar migration. These models cannot predict zero net sediment transport rate on these equilibrium profiles with negligible profile changes, whereas the standard equilibrium profile cannot explain the existence of the terrace and bar.

INTRODUCTION

At the present time, there are no models capable of accurately predicting the development and final shape of terraced and barred equilibrium beach profiles. A profile of the form $d = Ay^{2/3}$, with d = still water depth, y = seaward distance from the shoreline, and A = sediment scale parameter, has been shown to represent typical profiles of natural beaches [*e.g.*, Dean (1991)]. Perturbations on the simple equilibrium profile in the form of barred and terraced beaches have also been observed. However, the processes involved in the creation of these perturbed beach profiles are not presently well understood. Trowbridge and Young (1989) developed a sheet flow sand transport model based on the time-averaged bottom shear stress and showed that this model could explain the measured onshore movement of a nearshore bar in Duck, North Carolina during the mild wave conditions between February and August, 1982. Thornton *et al.* (1996) and Gallagher *et al.* (1998) used an energetics-based sediment transport model to explain the offshore movement of a bar on the same beach during storms in 1990 and 1994, respectively. Yet no existing model can predict both onshore and offshore bar migrations satisfactorily.

[1]General Engineer, Dept. of Oceanography, Naval Postgraduate School, Monterey, CA 93943, (408)656-1012 [Fax: (408)656-2712].

[2]Prof. and Assoc. Dir., Ctr. for Appl. Coastal Res., Univ. of Delaware, Newark, DE 19716.

This study conducted two detailed tests with a concave fine-sand beach in a laboratory wave tank, on one barred and one terraced profile in quasi-equilibrium. This ensured that the net cross-shore sediment transport rate on these profiles would be zero. The velocity and surface elevation measurements made during these tests were used to calculate bottom elevation changes predicted by the sheet flow and energetics-based models. These tests will help to identify the cross-shore sediment transport processes that take place on these quasi-equilibrium profiles and to suggest effects that have been neglected by existing transport models.

EXPERIMENT

The two tests were conducted in a wave tank that was 30 m long, 2.44 m wide, and 1.5 m high with a constant water depth of 61.0 cm. Repeatable irregular waves, based on the TMA spectrum (Bouws *et al.* 1985) using linear wave theory and random phases, were generated with a piston-type wave paddle. The beach was composed of fairly uniform fine sand with an initial slope of 1:12. For the random waves chosen for tests 1 and 2, the incident wave spectral peak periods were T_p = 2.8 s and 1.6 s, respectively, and the spectral significant wave heights were H_{mo} = 0.203 m and 0.182 m, respectively. The experimental setup is shown in Figure 1. Quasi-equilibrium profiles were obtained after repeatedly running the selected waves in bursts of 400 s for several days.

Ten capacitance wave gauges were used to measure the temporal variations of free surface elevations. Velocity statistics were measured in multiple cross-shore positions using a single Acoustic-Doppler Velocimeter (ADV) (Kraus *et al.* 1994). After equilibrium had been established for each test, the corresponding random wave burst was run 21 times over the stable profile, repositioning the velocimeter and several wave gauges between runs. The wave paddle motion, controlled by a computer, was approximately identical for all the runs in each test. The sampling rate for the free surface and fluid velocity measurements was 20 Hz. The measurement positions for the wave gauges and the ADV are shown in Figure 2. At two of its positions (x = 7.35 m and x = 9.85 m) the 2D probe was adjusted vertically to obtain three-point profiles of the cross-shore velocity over depth. At the remaining positions the velocity was measured as close as possible to mid-depth. Longshore velocities associated with three-dimensional turbulence were small compared with cross-shore velocities, and thus only cross-shore velocities were analyzed in these tests. The duration of each run was 400 s, from which the initial transient duration of 75 s was removed before the following analysis.

Preceding the experiment, a grain size analysis showed the beach sand to be relatively uniform, with mean diameter d_{50} = 0.18 mm. The average fall velocity for a spherical particle of diameter d_{50} was calculated to be w = 1.89 cm/s and the measured fall velocity was 1.9 cm/s. During each of the two tests detailed measurements were made of the beach profile using a manual vernier pointer in the swash zone and a Panametrics 22DLHP ultrasonic depth gauge in deeper water. In both tests fairly uniform ripples (approximately 1–3 cm in height and 10–15 cm in length) were established in the regions offshore of the bar and along the terrace between the bar and the

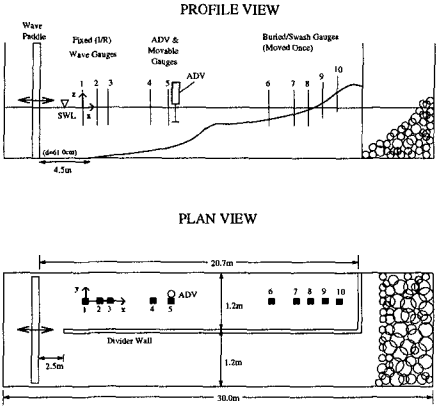

Figure 1: Wave Tank Experimental Setup

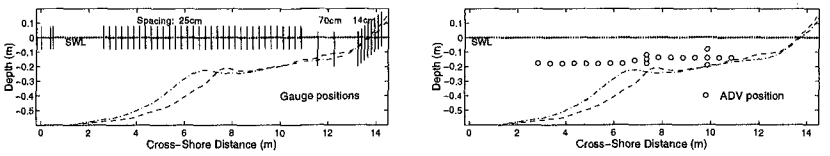

Figure 2: Cross-Shore Positions of Wave Gauge and ADV Measurements Over Final Profiles (- - Test 1, -.- Test 2)

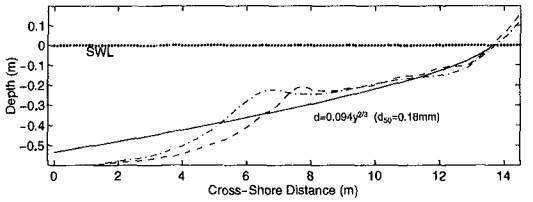

Figure 3: Final Equilibrium Profiles (- - Test 1; -.- Test 2) and $d = Ay^{2/3}$

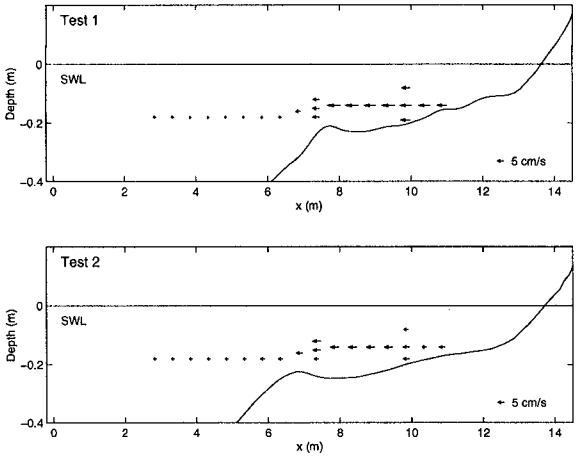

Figure 4: Undertow Velocity Fields for Tests 1 and 2

swash zone. The waves in test 1 plunged intensely in a small region slightly shoreward of the terrace edge, creating a large amount of suspended sediment. Spilling breakers were more common in test 2, and breaking occurred more continuously over the bar and in shallower water up to the swash zone. Figure 3 shows the measured equilibrium profiles for tests 1 and 2 in comparison with the equilibrium profile $d = Ay^{2/3}$ with $A = 0.09\text{m}^{1/3}$ estimated for this sand using the empirical formula given by Dean (1991). The standard equilibrium profile represents the profile inside the surf zone fairly well, but there are significant deviations from the profile in the region of the terrace edge (test 1) or the bar crest (test 2) where the incident random waves broke intensively. The terraced and barred beaches for tests 1 and 2 are similar to beach profiles measured in Duck, except that the offshore slope in these laboratory tests was much steeper (*e.g.*, Thornton *et al.* 1996).

Free Surface and Velocity Statistics

Measured wave statistics were presented in detail by Kobayashi *et al.* (1997), and in comparison with the corresponding results for a 1:16 slope by Kobayashi *et al.* (1998). The wave setup, $\overline{\eta}$, gradually increased as waves moved shoreward in shallower water, becoming tangential to the beach slope in the swash zone in both tests. The measured values of H_{rms} were approximately constant in the region seaward of the bar/terrace. They reached a slight peak after passing onto the terrace, then decreased steadily in the surf zone and more rapidly in the swash zone. The measured values of $H_{\text{rms}}/\overline{h}$ reflected the beach profile fairly strongly in deeper water, then began to rise rapidly as they approached the still water shoreline. Undertow

was strong over most of the terrace region in both tests, indicating the existence of other mechanisms required to maintain the equilibrium profile against undertow. The measured undertow velocity fields are shown over the corresponding profiles in Figure 4.

Figure 5 shows profiles of velocity statistics measured at two locations ($x = 7.35$ m and 9.85 m) for the two tests. In general, the mean velocity, $\overline{u}$, and standard deviation, σ_u, remain relatively constant over the depth ranges measured. The measured undertow was within 20% of its mid-depth value for all profiles. The vertical variation of $\overline{u}$ for irregular waves appears to be less than that for regular waves (Cox and Kobayashi 1998a). The standard deviation remains within 5% of the value calculated at mid-depth for both tests. The figures also show relative uniformity of values for the skewness, s_u, and the kurtosis, K_u, over the depth. The greater variability in these results at $x = 9.85$ m for test 1 may be explained as a consequence of the intense wave breaking. This uniformity of the cross-shore velocity and its moments over depth provides support for our decision to calculate cross-shore sediment transport using a mid-depth velocity at each cross-shore location.

SHEET FLOW MODEL FOR ONSHORE BAR MOVEMENT

The sheet flow model proposed by Trowbridge and Young (1989) is presently the only existing model that attempts to explain onshore bar movement outside the surf zone in the absence of undertow. While application of this model has been limited to plane beds without ripples, the profiles obtained in these experiments did include rippled sand beds in the offshore and surf zones for both tests. However, both profiles were free of ripples in the region over the bar with the most intense wave breaking and in the swash zone. The following comparison should be interpreted in light of these limitations.

Theory

The measured cross-shore velocity is represented here by $u(t)$, with t = time. The overbar is used to indicate time averaging. The time-averaged rate of onshore sediment transport, q, is assumed to be expressible as

$$\overline{q} = K \frac{w \overline{\tau}_b}{\rho g (s-1)} \tag{1}$$

where w = sand fall velocity, ρ = density of fluid, $s = \rho_s/\rho$ = specific gravity of sand with ρ_s = sand density, $\overline{\tau}_b$ = time-averaged bottom shear stress, g = gravitational acceleration, and K = an empirical coefficient. Trowbridge and Young (1989) analyzed the wave boundary layer and derived the following expression for the mean bottom shear stress, $\overline{\tau}_b$:

$$\overline{\tau}_b = +\frac{\rho f_w}{2} \frac{\overline{|\tilde{u}|^3}}{\sqrt{g\bar{h}}} \tag{2}$$

where f_w = friction coefficient and $\tilde{u} = (u - \overline{u})$ = oscillatory part of first-order wave velocity. Their wave boundary layer analysis did not account for undertow, which was

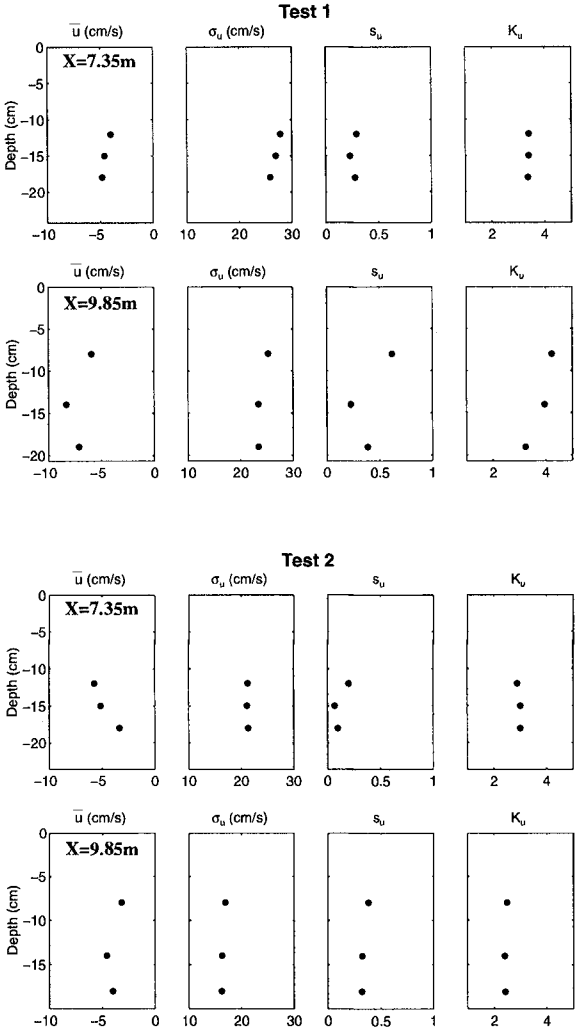

Figure 5: Depth variations of $\overline{u}$, σ_u, s_u, and K_u at x=7.35 and 9.85 m

significant in the present experiment. Note that while Trowbridge and Young defined the x-axis as positive offshore, the present analysis defines x as positive onshore. Substituting (2) into (1):

$$\overline{q}_u = \left(\frac{Kf_w}{2}\right) \frac{w\overline{|\tilde{u}|^3}}{g(s-1)\sqrt{g\overline{h}}} \tag{3}$$

Trowbridge and Young calibrated the value of Kf_w for $d \simeq 0.2$ mm and recommended $Kf_w = 0.5$. In the present tests, $d_{50} = 0.18$ mm and $Kf_w = 0.5$ is adopted as well. For sheet flow conditions, (3) may be used to predict the time-averaged cross-shore transport rate, $\overline{q}_u$, based on the velocity data as indicated by the subscript u.

Trowbridge and Young used linear long wave theory to relate $\tilde{u}$ to $\tilde{\eta} = (\eta - \overline{\eta})$, with the assumption that $\tilde{\eta}$ is Gaussian. Since the velocity data is available here, it is assumed instead that $\tilde{u}$ is Gaussian. This assumption yields

$$\overline{|\tilde{u}|^3} \simeq \sqrt{\frac{8}{\pi}}(\overline{|\tilde{u}|^2})^{1.5} \tag{4}$$

which is better than the result of Trowbridge and Young because the skewness, s_u, of the velocity is generally smaller than the skewness, s, of the free surface (Kobayashi *et al.* 1997, 1998). Linear long wave theory is then assumed to obtain

$$\overline{|\tilde{u}|^2} = \overline{|(u-\overline{u})|^2} \simeq \overline{|\sqrt{\frac{g}{\overline{h}}}(\eta-\overline{\eta})|^2} = \frac{g}{\overline{h}}\overline{|\tilde{\eta}|^2} \tag{5}$$

Combining (4) and (5), one obtains

$$\overline{|\tilde{u}|^3} \simeq \sqrt{\frac{8}{\pi}}\left(\frac{g}{\overline{h}}\overline{|\tilde{\eta}|^2}\right)^{1.5} = \sqrt{\frac{8}{\pi}}\frac{g}{\overline{h}}\sqrt{\frac{g}{\overline{h}}}\sigma^3 \tag{6}$$

where σ is the standard deviation of the free surface elevation. Substitution of (6) into (3) yields

$$\overline{q}_\eta = \frac{Kf_w}{16\sqrt{\pi}} \frac{wH_{\rm rms}}{(s-1)} \left(\frac{H_{\rm rms}}{\overline{h}}\right)^2 \tag{7}$$

where the root-mean-square wave height $H_{\rm rms}$ is defined as $H_{\rm rms} = \sqrt{8}\sigma$. Eq. (7) may be used to predict the time-averaged cross-shore transport rate, $\overline{q}_\eta$, using free surface data as indicated by the subscript η.

An expression for the predicted rate of change of the sand bottom elevation is derived by applying the conservation equation of sediment. This yields an expression for the erosion (negative) or accretion (positive) rate $\partial z_b/\partial t$ in terms of the gradient of the cross-shore transport rate $\overline{q}$:

$$\frac{\partial z_b}{\partial t} = \frac{-1}{(1-n_p)}\frac{\partial \overline{q}}{\partial x} \tag{8}$$

in which the porosity n_p was 0.4 in this experiment. Eq. (8) is combined with (3) or (7) to determine the erosion/accretion rate based on the velocity data or free surface data, respectively, where $(\partial z_b/\partial t)_u$ and $(\partial z_b/\partial t)_\eta$ are used for the computed values of $(\partial z_b/\partial t)$ corresponding to $\overline{q}_u$ and $\overline{q}_\eta$, respectively. In addition, $\overline{q}_u \simeq 0$ and $\overline{q}_\eta \simeq 0$ for the quasi-equilibrium profiles if the sheet flow model is applicable to these tests.

Analysis of Experimental Results

The velocity and free surface data from tests 1 and 2 were analyzed to obtain the quantities necessary for the evaluation of (3) and (7) at the 17 cross-shore measurement locations. At the locations of the three point velocity profiles the time series from only the middle position were used. A cubic spline interpolation was performed on each set of $\overline{q}$ values to obtain the corresponding derivatives, $\partial\overline{q}/\partial x$. Eq. (8) was then used to calculate $\partial z_b/\partial t$ at each location. The results of these calculations are displayed graphically in Figure 6 and detailed in Orzech and Kobayashi (1997).

The sheet flow model predicts large onshore transport rates and rapid profile change in the surf zone, especially for test 1. For perfectly equilibrium profiles, $\overline{q} = 0$ and $\partial z_b/\partial t = 0$, but the measured equilibrium profiles for test 1 and 2 had uncertainties on the order of 1 cm/hr. For test 2, $\partial z_b/\partial t$ based on u is somewhat smaller than $\partial z_b/\partial t$ based on η, though still greater than 1.0 cm/hr over the bar. For both tests the bar is predicted to move further shoreward. Change of this magnitude was of course not observed in any part of either profile.

ENERGETICS-BASED MODEL FOR OFFSHORE BAR MOVEMENT

Unlike the sheet flow model, the energetics-based model developed by Bowen (1980) and Bailard (1981) attempts to account for both onshore/offshore transport due to wave asymmetry and offshore transport due to undertow, as well as slope effects due to gravity. This model separates sediment transport into bed load and suspended load components, including separate terms for each of the above transport mechanisms. Because these experiments were conducted in a wave flume there was no longshore current to contribute to sediment transport. This model does not account for the initiation of sediment movement, although the fine sand particles were observed to move constantly during this experiment.

Theory

In the energetics model, the time-averaged cross-shore sediment transport rate per unit width can generally be expressed by equation (2) in Thornton *et al.* (1996). For the present analysis with zero longshore velocity, however, the net onshore sediment transport rate $\overline{q}$ is simplified as:

$$\begin{aligned}\overline{q} &= K_b\left(\overline{|u(t)|^2\tilde{u}(t)}\right) + K_b\left(\overline{|u(t)|^2}\overline{u}\right) - K_{bg}\left(\overline{|u(t)|^3}\right) \\ &\quad + K_s\left(\overline{|u(t)|^3\tilde{u}(t)}\right) + K_s\left(\overline{|u(t)|^3}\overline{u}\right) - K_{sg}\left(\overline{|u(t)|^5}\right) \\ &\equiv \overline{q}_{bw} + \overline{q}_{bu} + \overline{q}_{bg} + \overline{q}_{sw} + \overline{q}_{su} + \overline{q}_{sg}\end{aligned} \tag{9}$$

where $u(t)$ = cross-shore horizontal velocity, which is positive shoreward in this analysis. In (9), the first three terms represent bed load (subscript b) produced by wave asymmetry (subscript w), undertow (subscript u), and the effects of gravity (subscript g) on the bottom slope, respectively. The final three terms represent suspended load (subscript s) produced by the same three respective effects. The coefficients in (9)

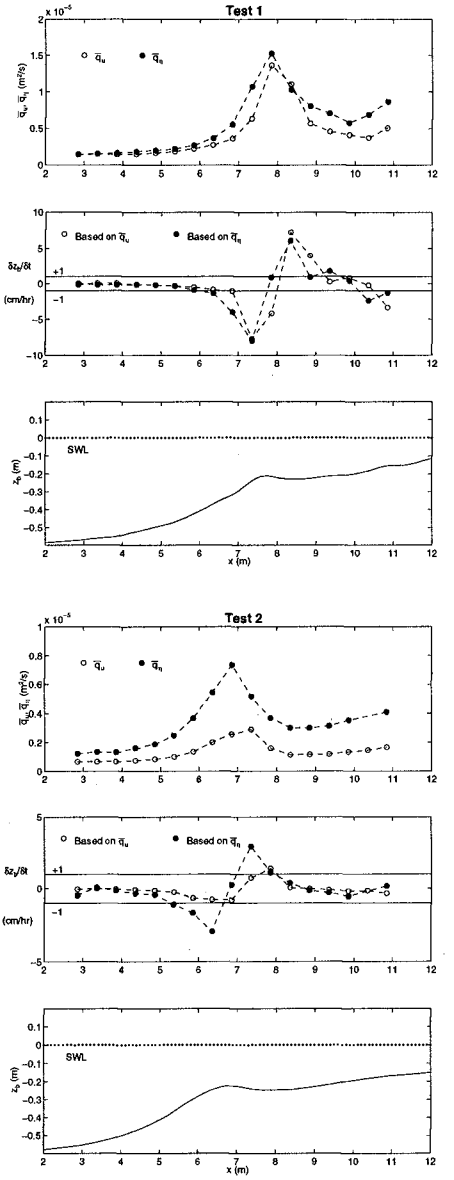

Figure 6: Net Transport Rates $\overline{q}_u$, $\overline{q}_\eta$ and Bottom Elevation Change Rates $(\partial z_b/\partial t)_u$, $(\partial z_b/\partial t)_\eta$, Over Test 1 and 2 Profiles (Sheet Flow Model)

are expressed as

$$K_b = \frac{1}{(s-1)g} C_f \frac{\varepsilon_b}{\tan(\phi)} \quad ; \quad K_{bg} = K_b \frac{\tan(\beta)}{\tan(\phi)}$$

$$K_s = \frac{1}{(s-1)g} C_f \frac{\varepsilon_s}{w} \quad ; \quad K_{sg} = K_s \frac{\varepsilon_s}{w} \tan(\beta)$$

where $s = \rho_s/\rho$ = specific gravity of sand, C_f = drag coefficient, ϕ = internal friction angle of sand, ε_b = bed load efficiency factor, ε_s = suspended load efficiency factor, $\tan(\beta)$ = local bed slope, and w = fall velocity. In this experiment, $s = 2.66$ and $w = 1.9$ cm/s, while the other parameters are given the same values as those used in Thornton *et al.* (1996): $C_f = 0.003$, $\tan(\phi) = 0.63$, $\varepsilon_b = 0.135$, and $\varepsilon_s = 0.015$. The local slope, $\tan(\beta) = dz_b/dx$, is computed using the equilibrium bottom profile, $z_b(x)$, for each test.

After $\overline{q}$ is obtained using (9), the predicted erosion or accretion rate, $\partial z_b/\partial t$, for the profile at given locations is found by use of (8). This corresponds to equation (1) in Thornton *et al.*, except that here the value of $\mu = (1 - n_p)$ is taken as 0.6 rather than 0.7 because the measured porosity $n_p = 0.4$ in this experiment.

Analysis of Experimental Results

Each of the time-averaged velocity expressions in (9) was evaluated for the 17 velocity locations, with the middle position again selected from the two three-point velocity profiles. The values of the six sediment load components are plotted over the test 1 and test 2 equilibrium profiles in Figure 7 (tabulated in Orzech and Kobayashi (1997)). In both tests the largest values predicted for all the terms in (9) occur around the location of the bar or terrace edge, in the vicinity of $x \simeq 7$–8 m. The more intense breaking of test 1 is clearly visible from the comparison of sediment loads in this region. At $x = 7.85$ m in this test, a large volume of sediment is transported seaward by both wave asymmetry and undertow effects; however, just 0.5 m shoreward at $x = 8.35$ m, the wave asymmetry suspended load $\overline{q}_{sw}$ suddenly reverses and becomes strongly positive onshore. In general, the predicted suspended load values are larger than the corresponding bed load terms, as would be expected from the relatively large waves and fine sand used in the experiment.

For the two velocity profile locations, the cross-shore sediment transport rate $\overline{q}$ in (9) was found to be largely insensitive to the elevation of the cross-shore velocity, $u(t)$, used for its prediction. Predicted sediment loads due to undertow and bottom slope remained nearly constant over the depth, while predictions of wave-asymmetry-induced loads $\overline{q}_{sw}$ and $\overline{q}_{bw}$ varied somewhat more, especially for test 1. It may thus be reasonable to predict the sediment load due to undertow and bottom effects by measuring velocities at mid-depth (as done in this study) instead of immediately outside the bottom boundary layer as specified by the theory of Bailard (1981).

The total sediment loads and rates of profile change predicted by the energetics model at each cross-shore location are plotted over the equilibrium profiles in Figure 8 (tabulated in Orzech and Kobayashi (1997)). Unlike Thornton *et al.* (1996), the

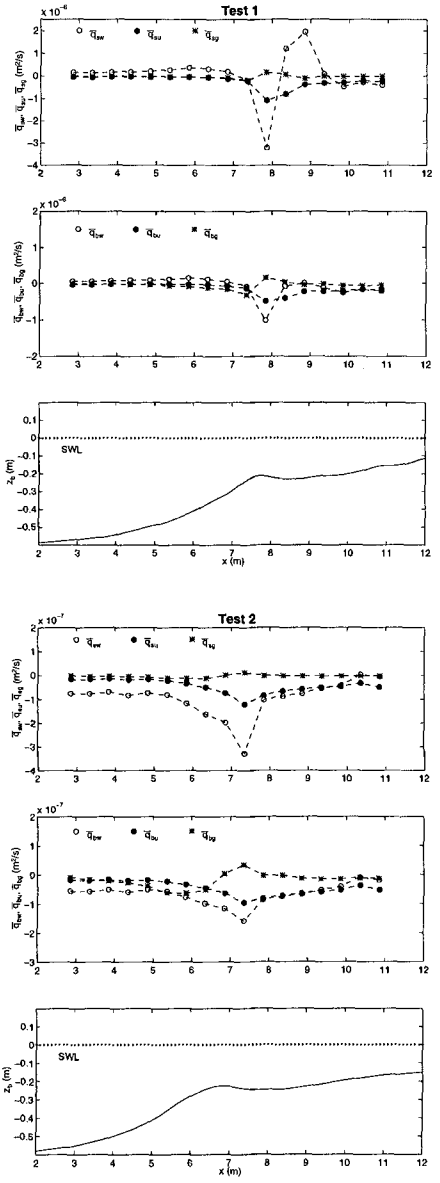

Figure 7: Cross-Shore Variation of Suspended Load and Bed Load Quantities Over Test 1 and 2 Profiles (Energetics Model)

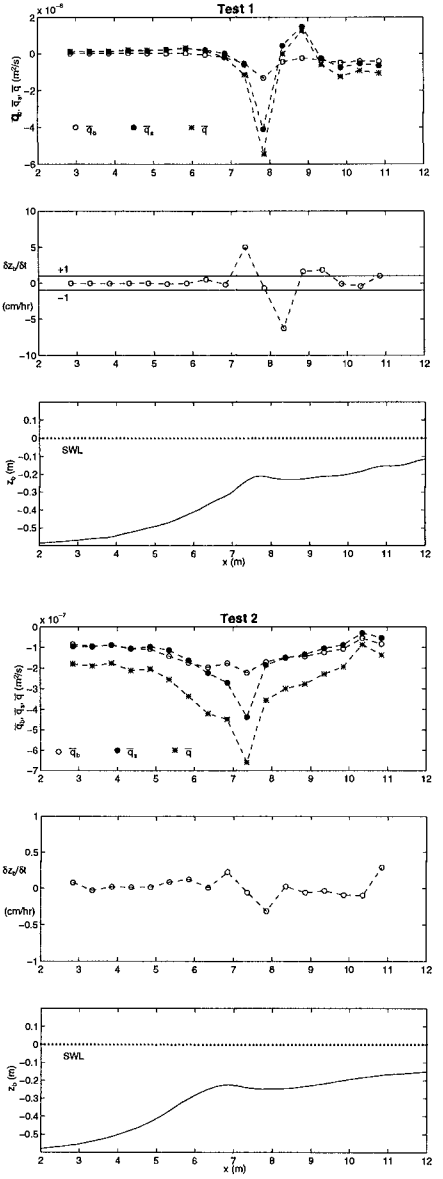

Figure 8: Predicted Bed Load $\overline{q}_b$, Suspended Load $\overline{q}_s$, and Total Load $\overline{q}$ with $\partial z_b/\partial t$ Over Test 1 and 2 Profiles (Energetics Model)

suspended load, $\overline{q}_s$, is rarely an entire order of magnitude larger than the bed load, $\overline{q}_b$, in this laboratory experiment. In test 2, the total bed load $\overline{q}_b$ is actually comparable to the total suspended load, $\overline{q}_s$, at most locations. This may be reasonable under the milder wave conditions of this test. If the energetics model could predict the existence of these equilibrium profiles, one would expect that the net sediment transport $\overline{q} = 0$. In test 1, $\overline{q}$ is predicted to be very weakly onshore at locations seaward of the breaker zone but strongly offshore at almost all locations on the terrace. The magnitude of the parameter $\partial z_b/\partial t$ is not greater than 1 cm/hr except in the region of intense breaking. In test 2, all locations are predicted to have a weak offshore transport, with $\partial z_b/\partial t$ consistently small and within measurement errors of 1 cm/hr. These values are smaller than those in test 1 because waves broke less intensely, leading to slower profile changes. For both tests the energetics model predicts the growth and offshore movement of a bar near $x = 7$ m and the deepening of a trough near $x = 8$ m. The energetics model is unable to predict quasi-equilibrium profiles with no net sediment transport, although it predicts the bottom profile change within 1 cm/hr for test 2.

CONCLUSIONS

The general failure of state-of-the-art sediment transport models to predict the equilibrium profiles illustrates the limitations on such models at the present time. While the sheet flow model predicted onshore sediment transport and bar migration, the energetics model predicted offshore sediment transport and bar migration. The energetics model, which attempts to account for effects of wave asymmetry, undertow, and bottom slope, predicted smaller profile change than the sheet flow model, which did not include the effects of wave breaking and undertow. The standard $Ay^{2/3}$ equilibrium profile represents the profile inside the surf zone fairly well, although it does not predict the existence of a bar and terrace.

An improved sediment transport model will need to account for the combined onshore and offshore transport effects of the above two models. In this study, the energetics model was more accurate than the sheet flow model in both tests 1 and 2, very likely because of the inclusion of a greater number of sediment transport mechanisms. The assumptions involved in simulating each transport mechanism must also be carefully reviewed and questioned. In this experiment, both models assume the instantaneous response of bed load *and* suspended load particles to the horizontal velocity immediately outside the bottom boundary layer. However, the water was observed to be consistently very cloudy during both tests; thus the assumption of the instantaneous response of suspended load appears to be questionable. A better model of sediment suspension might need to consider the instantaneous vertical velocity associated with the coherent intermittent fluid motion, as suggested in Cox and Kobayashi (1998b).

ACKNOWLEDGEMENT

This work was supported by the NOAA Office of Sea Grant, Department of Commerce, under Grant No. NA85AA-D-SG033 (Project SG 97 P/OE-22).

REFERENCES

Bailard, J.A. (1981). "An energetics total load sediment transport model for a plane sloping beach," *J. Geophys. Res.*, 86(C11), 10,938–10,954.

Bouws, E., Gunther, H., Rosenthal, W., and Vincent, C.L. (1985). "Similarity of the wind wave spectrum in finite depth water. 1: Spectral form." *J. Geophys. Res.*, 90(C1), 975–986.

Bowen, A.J. (1980). "Simple models of nearshore sedimentation; beach profiles and longshore bars," *The Coastline of Canada*, Geological Survey of Canada, Paper 80-10, 1–11.

Cox, D.T., and Kobayashi, N. (1998a). "A kinematic undertow model with a logarithmic boundary layer," *J. Waterway, Port, Coast. and Oc. Engrg.*, ASCE, 123(6), 354–360.

Cox, D.T., and Kobayashi, N. (1998b). "Coherent motions in the bottom boundary layer under shoaling and breaking waves," *Proc., 26th Coast. Engrg. Conf.*, ASCE.

Dean, R.G. (1991). "Equilibrium beach profiles: characteristics and applications," *J. Coast. Res.*, 7(1), 53–84.

Gallagher, E.L., Elgar, S., and Guza, R.T (1998). "Observations of sand bar evolution on a natural beach," *J. Geophys. Res.*, 103(C2), 3203–3215.

Kobayashi, N., Herrman, M., Johnson, B.D., and Orzech, M.D. (1998). "Probabilistic distribution of surface elevation in surf and swash zones," *J. Waterway, Port, Coast. and Oc. Engrg.*, ASCE, 124(3), 99–107.

Kobayashi, N., Orzech, M.D., Johnson, B.D., and Herrman, M. (1997). "Probabilistic modeling of surf zone and swash dynamics," *Proc., Waves '97*, ASCE, 107–121.

Kraus, N.C., Lohrmann, A., and Cabrera, R. (1994). "New acoustic meter for measuring 3D laboratory flows." *J. Hydraulic Engrg.*, ASCE, 120(3), 406–412.

Orzech, M.D., and Kobayashi, N. (1997). "Random wave transformation and sediment transport across barred and terraced sand beaches." Res. Rpt. No. CACR-97-06, Ctr. for Appl. Coast. Res., Univ. of Delaware, Newark, Del.

Thornton, E.B., Humiston, R.T., and Birkemeier, W. (1996). "Bar/trough generation on a natural beach," *J. Geophys. Res.*, 94(C8), 10,971-10,991.

Trowbridge, J., and Young, D. (1989). "Sand transport by unbroken water waves under sheet flow conditions," *J. Geophys. Res.*, 94(C8), 10,971-10,991.

BREAKER BAR FORMATION AND MIGRATION

Bart T. Grasmeijer[1] and Leo C. van Rijn[1, 2]

Abstract

The formulation of Isobe and Horikawa (1982) is modified and adapted for use in a probabilistic cross-shore transport model (CROSMOR). Computed changes of wave height, peak near-bed orbital velocity and depth-averaged return flow are compared to laboratory measurements. A comparison is made between computed and measured bed profile changes for a large scale laboratory experiment.

Introduction

The generation and maintenance of longshore bars is commonly associated with the shoaling and breaking of high-frequency waves and the generation of low-frequency wave effects in the surf zone. Breaker bars may be generated and maintained by a combination of spilling and shoaling waves; the latter producing landward sediment transport due to wave asymmetry and increasing toward the break point, thereafter reducing and grading into seaward transport by undertow currents associated with spilling breakers leading to build up of the bar. Although formation and maintenance of bars may also be related to low-frequency waves, in this paper attention will be focused on the convergent pattern of sediment fluxes due to wave asymmetry and undertow. Model calculations are compared to a small and a large scale laboratory tests.

Model description

The cross-shore transport model is based on a wave by wave approach (Wijnberg and Van Rijn, 1996). The probability density function of the deep water wave height is schematised into a discrete series of wave height classes and corresponding periods. Each wave height class is assumed to propagate independently of the other classes by solving the wave energy balance separately. The waves shoal until an empirical criterion for breaking is satisfied. Wave height decay after breaking is modelled by dissipation of energy in a breaking wave and a bore. Tide, wave, and storm induced water level variations and tide, wind and wave driven longshore currents are also included in the model.

The high-frequency near-bed orbital velocities (low-frequency effects are neglected) are computed using a modification of the method of Isobe and Horikawa (1982). The method of Isobe and Horikawa method is a parameterisation of fifth-order Stokes wave theory and third-order cnoidal wave theory which can be used over a wide range

[1] Dep. of Phys. Geography, Univ. of Utrecht, P.O. Box 80.115, 3508 TC, Utrecht, The Netherlands, e-mail: B.Grasmeijer@geog.uu.nl

[2] Delft Hydraulics, P.O.Box 177, 2600 MH, Delft, The Netherlands, e-mail: Leo.vanRijn@wldelft.nl

of wave conditions. In the original formulation the near-bed value of û (defined as: u_{on} + u_{off}) is derived from deep water wave conditions as follows:

$$\hat{u} = 2.r.u_{linear} \tag{1}$$

with:

$$r_3 = -27.3 \log_{10}\left(\frac{H_0}{L_0}\right) - 16.3 \tag{2}$$

$$r_2 = 1.28 \tag{3}$$

$$r_1 = 1 \tag{4}$$

$$r = r_1 - r_2 \exp\left\{-r_3 \frac{h}{L_0}\right\} \tag{5}$$

u_{linear} = peak near-bed velocity computed using linear wave theory (m/s), H_0 = deep water wave height (m), L_0 = deep water wave length (m), h = local water depth (m).

Hamm (1996) tested the formulation from Isobe and Horikawa and the formulation from Swart and Crowley (1988) against laboratory measurements. He found that the Isobe and Horikawa formulation can be used over a large range of wave conditions except in the surf zone when monochromatic waves are considered. Although the covocoïdal theory from Swart and Crowley provides a more comprehensive description of wave properties, abnormal results were observed in a few cases. The use of one representative wave height and period in random waves may lead to an underestimation of velocity moments with low steepness waves.

Stripling and Damgaard (1997) adapted the method from Isobe and Horikawa for use in a model for morphodynamic predictions. They compared the results with vocoidal theory (Swart, 1978). Although vocoidal theory consistently over-predicted the values of the odd bottom velocity moments and the method of Isobe and Horikawa consistently under-predicted them by a similar order, the most important aspect of their comparison was not so much in the values of the moments but rather the direction in which the methods predict the moments to be in. Vocoidal theory occasionally predicted the odd moments in the opposite direction to the measurements, which was not so with the method of Isobe and Horikawa (1982). Compared to vocoidal theory the method of Isobe and Horikawa led to greater accuracy in the morphodynamic prediction capability of the profile model.

In the present modified formulation the near-bed value of û is derived from the local wave conditions as follows:

$$r = 1 - 3.2\left(\frac{H}{L}\right)^{065}\left(\frac{H}{L}\right)^{3.4\frac{h}{L}} \tag{6}$$

with: H = local wave height (m), L = local wave length (m), u_{linear} = near-bed velocity computed using linear waves theory.

The r factor was found by calibration using laboratory and field data with random waves. Basic data are given in Table 1.

Description	Testnumber	h (m)	H_{m0} (m)	T_p (s)
Field: Terschelling, The Netherlands	Fop05330	9.0	1.89	8.0
	Fop17352	9.4	0.37	17.1
	Fop17576	10.5	4.20	10.2
	Fra05330	5.6	1.87	8.0
	Fra17576	7.7	3.42	9.7
	Fre05330	4.1	1.70	8.1
	Fre17352	5.4	0.37	16.5
Field: Egmond aan Zee, The Netherlands	1B_04430	1.9	0.76	6.1
Lab: small scale flume Delft Univ. of Techn.	TUDB2_01	0.60	0.18	2.2
	TUDB2_05	0.31	0.17	2.2
	TUDB2_07	0.51	0.15	2.2
Field: Muriwai, New Zealand	Muriwai2	1.83	0.92	19.7
Field: Skallingen, Denmark	Sk304_08	1.8	0.80	11.0
	Sk310_01	2.6	1.49	8.8
Lab: Delta Flume Lip11D WL Delft Hydraulics	1A0203_02	2.31	0.92	5.0
	1A0203_07	0.91	0.62	5.0
	1B0213_02	2.30	1.19	5.0
	1B0213_07	0.89	0.57	5.0
	1C0204_02	2.25	0.63	8.0
	1C0204_03	1.77	0.63	8.0
	1C0204_05	1.16	0.63	8.0
	1C0204_11	1.59	0.63	8.0

Table 1. Basic data of measurements used in calibration of r factor.

Measured signals of surface elevation and horizontal orbital velocity near the bed were analysed using spectral analysis. High- and low-frequency oscillations were separated (by filtering) at a period of 2 times the wave spectrum peak period, T_p. The high-frequency signals were separated into shorter time series each containing 10-15 individual waves. Each of the short time series was defined as one single wave class with one representative wave height, wave period, crest velocity near the bed, and trough velocity near the bed. The mean values were chosen to represent the wave class. A comparison between measured and computed values of $\hat{u}$ is presented in Figure 2. The broken lines indicate a 20% error band.

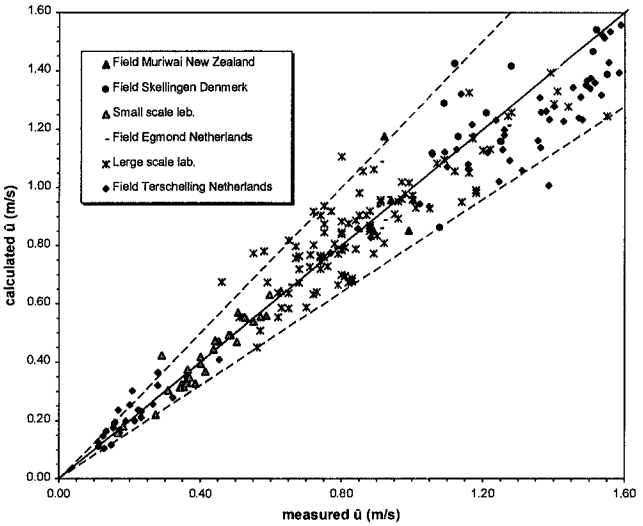

Figure 1. Comparison between measured and computed values of near-bed orbital velocity û defined as $u_{on} + u_{off}$.

The following formulae, Eq.(7)-Eq.(14), were derived to account for the asymmetry of the velocity profile (Isobe and Horikawa, 1982). Eq.(7)-Eq.(12) is a parameterisation of fifth-order Stokes wave theory and third-order cnoidal wave theory. Eq.(13) and Eq.(14) were introduced to take into account the deformation of the velocity profile due to bottom slope.

$$\left(\frac{u_{on}}{\hat{u}}\right)_a = \lambda_1 + \lambda_2\left(\frac{\hat{u}}{\sqrt{gh}}\right) + \lambda_3 \exp\left(-\lambda_4\left(\frac{\hat{u}}{\sqrt{gh}}\right)\right) \tag{7}$$

with:

$$\lambda_1 = 0.5 - \lambda_3 \tag{8}$$

$$\lambda_2 = \lambda_3\lambda_4 + \lambda_5 \tag{9}$$

$$\lambda_3 = \frac{(0.5 - \lambda_5)}{\lambda_4 - 1 + \exp(-\lambda_4)} \tag{10}$$

$$\lambda_4 = \begin{cases} -15 + 1.35\left(T\sqrt{\frac{g}{h}}\right), & T\sqrt{\frac{g}{h}} \le 15 \\ -2.7 + 0.53\left(T\sqrt{\frac{g}{h}}\right), & T\sqrt{\frac{g}{h}} > 15 \end{cases} \tag{11}$$

$$\lambda_5 = \begin{cases} 0.0032\left(T\sqrt{\frac{g}{h}}\right)^2 + 0.000080\left(T\sqrt{\frac{g}{h}}\right)^3, & T\sqrt{\frac{g}{h}} \le 30 \\ 0.0056\left(T\sqrt{\frac{g}{h}}\right)^2 - 0.000040\left(T\sqrt{\frac{g}{h}}\right)^3, & T\sqrt{\frac{g}{h}} > 30 \end{cases} \quad (12)$$

$$\left(\frac{u_{on}}{\hat{u}}\right)_{modified} = 0.5 + \left(\left(\frac{u_{on}}{\hat{u}}\right)_{max} - 0.5\right)\tanh\left(\frac{\left(\frac{u_{on}}{\hat{u}}\right)_a - 0.5}{\left(\frac{u_{on}}{\hat{u}}\right)_{max} - 0.5}\right) \quad (13)$$

with:

$$\left(\frac{u_{on}}{\hat{u}}\right)_{max} = 0.62 + \frac{0.003}{\text{bed slope}} \quad (14)$$

A comparison between preliminary computations using the present probabilistic model and laboratory tests showed that the influence of the bed slope might be less pronounced. The following relation gave more realistic results:

$$\left(\frac{u_{on}}{\hat{u}}\right)_{max} = 0.62 + \frac{0.001}{\text{bed slope}} \quad (15)$$

The present model includes a sinusoidal distribution of the instantaneous velocities during the forward and backward phase of the wave cycle. The duration period of each phase is corrected to obtain zero net flow over the full cycle. This is in contrast to the original approach of Isobe and Horikawa.

The depth-averaged return current under the wave trough of each individual wave (summation over wave classes) is approximated with the following expression:

$$U_{mean,return} = 0.125\sqrt{\frac{g}{h}}\frac{H_{rms}^2}{h_t} \quad (16)$$

in which H_{rms} = root-mean-square wave height, h = mean water depth, averaged over half a wave length seawards, h_t = water depth below wave trough level defined as h-½H_{rms}. Equation (16) is based on linear mass flux ($q = U_{mean}\, h_t = 0.125\, g\, H^2/c$), an effective depth equal to h_t (=depth below wave trough) and $c=(gh)^{0.5}$ = wave propagation speed in shallow water.

The sand transport rate of the model is determined for each wave (or wave class), based on the computed wave height, depth-averaged cross-shore and longshore velocities, orbital velocities, friction factors and sediment parameters. Net transport rates are obtained after time-averaging of instantaneous values over the wave period. The sediment transport model is local and horizontal advection of sediment clouds due to mean currents and long period oscillations is not considered. The net (averaged over the wave period) total sediment transport is obtained as the sum of the net bed load (q_b) and net suspended load (q_s) transport rates.

Small Scale Laboratory Test

The cross-shore transport model was used to compute the hydrodynamics measured during a small scale laboratory test. The tests were conducted in the Large Research

Flume of the Laboratory of Fluid Mechanics of the Faculty of Civil Engineering (Delft University of Technology).

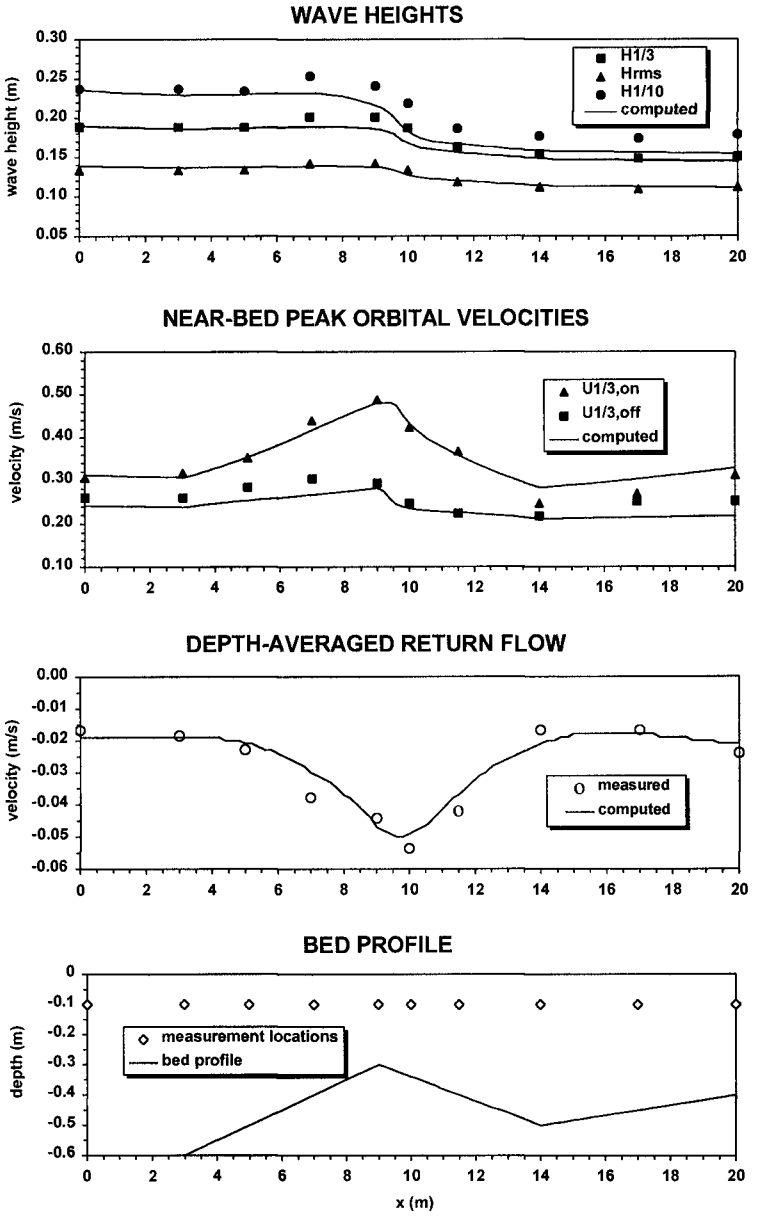

Figure 2. Measured and computed wave heights, peak orbital velocities and depth-averaged return flows for small scale laboratory test.

The flume has a length of 45 m, a width of 0.8 m and a depth of 1.0 m. Irregular waves (following a Jonswap spectrum) were generated with a peak spectral period of, T_p = 2.3 s (± 0.2 s). A nearshore bar of the form shown in Figure 2 was generated in the flume. The bed profile varies in depth from 0.60 m seawards of the bar to 0.30 m at the bar crest (Figure 2). The water depth in the trough landward of the bar crest is 0.50 m. The nearshore bar has a steep seaward slope of 1 to 20 and a steep landward slope of 1 to 25. The bed slope landward of the bar trough is 1 to 63. Measurements were performed at 10 different locations across the nearshore bar. Herein the test with an initial wave height of 0.19 m (B2) is considered. Figure 2 shows the measured and computed wave heights, peak orbital velocities and depth-averaged return flows. It can be observed that in the region near the bar crest the computed $H_{1/3}$ and $H_{1/10}$ values are about 10% too small, which may be caused by the use of linear wave theory. Better agreement between measured and computed wave heights may be obtained by using non-linear shoaling. The computed and measured return flow values show reasonably good agreement. From Figure 2 it can be observed that the significant values of the near-bed peak orbital velocities can be predicted with reasonable accuracy using the modified Isobe and Horikawa formulation. The depth-averaged return flow is rather accurately predicted by the model.

Large Scale Laboratory Tests

The model has been applied to compute the hydrodynamics and morphodynamics measured during large scale laboratory tests (Roelvink and Reniers, 1995). The tests were conducted in the Delta Flume of Delft Hydraulics. The Delta Flume is a large flume with the following dimensions: length = 200 m, width = 5 m and depth = 7 m. Three different test conditions were simulated: slightly erosive wave conditions, highly erosive wave conditions and strongly accretive wave conditions. The bed consisted of fine to medium coarse sand (D_{50} = 200 μm and D_{90} = 400 μm). Before and after each test the bed levels were measured in three longitudinal sections. Irregular waves (following a Jonswap spectrum) were generated. The wave board driving system was compensated for the reflection of long waves in the flume. Water level variations were measured by pressure sensors and by resistance type wave gauge at various locations in the flume. Herein, the test with highly erosive wave conditions (test 1b) is considered. The incident wave conditions are: H_{m0} = 1.40 m, T_p = 5.0 s, duration = 6 hours. Figure 3 shows the computed and measured wave heights, peak orbital velocities and depth-averaged return flows. The computed wave heights show fairly good agreement with the measurements with exception of an overestimation of H_{rms} in the region near the bar crest. It can be observed from Figure 3 that in the region seaward of the bar the significant values of the near-bed peak orbital velocities ($U_{1/3,on}$ and $U_{1/3,off}$) are reasonably well represented by the modified formulation of Isobe and Horikawa. Near the bar crest the onshore directed velocity is overestimated by the model while landward of the bar the offshore directed near-bed orbital velocity is slightly underestimated. The computed depth-averaged return flow shows good agreement with the measured values, except in the shallow surf zone (x > 160 m) where the depth-averaged return flow is significantly overestimated.

The initial bed profile and the measured and computed bed profiles after 6 hours of wave action are given in Figure 4. The measured profile shows an offshore migration of the bar, with erosion between 140 m and 160 m and accretion between 125 m and 140 m. The predicted profile also shows an offshore migration of the bar, however, this is too far seaward, with erosion between 138 m and 150 m and accretion between 110 m and 138 m.

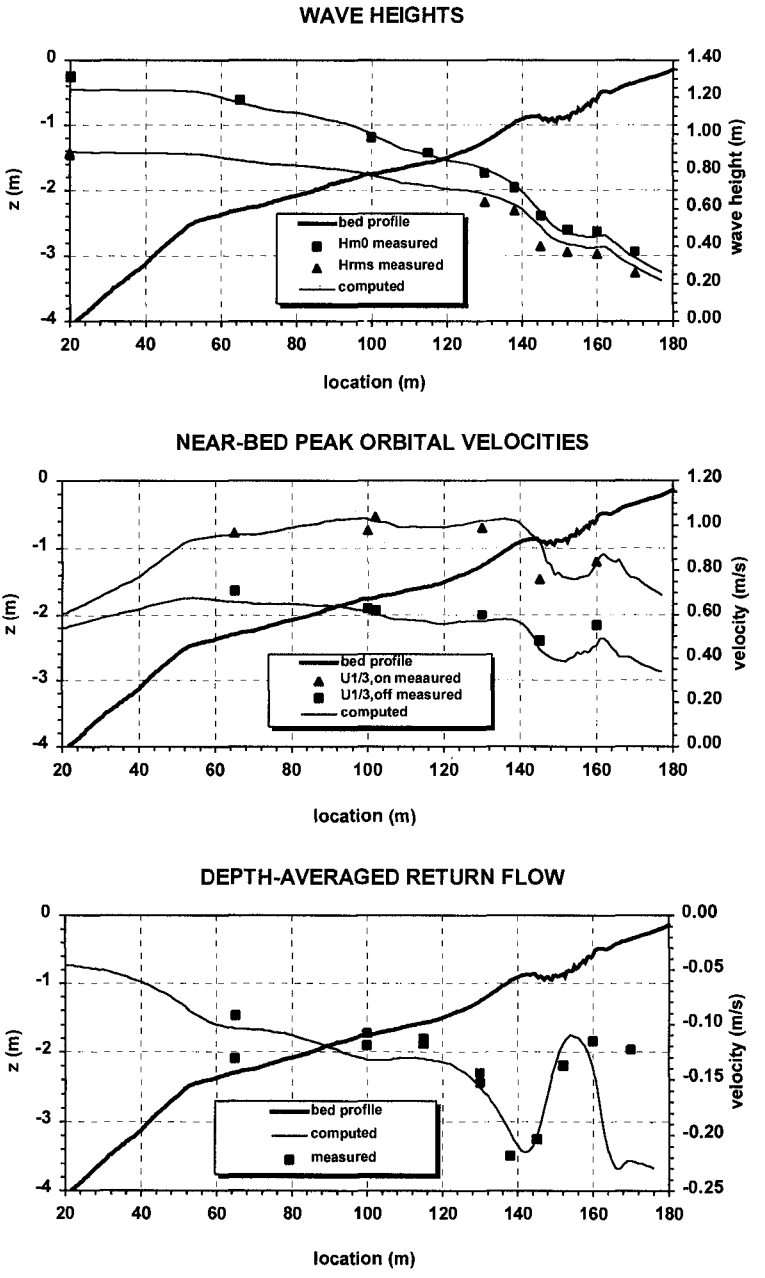

Figure 3. Measured and computed wave heights, peak orbital velocities and depth-averaged return flows for large-scale laboratory test.

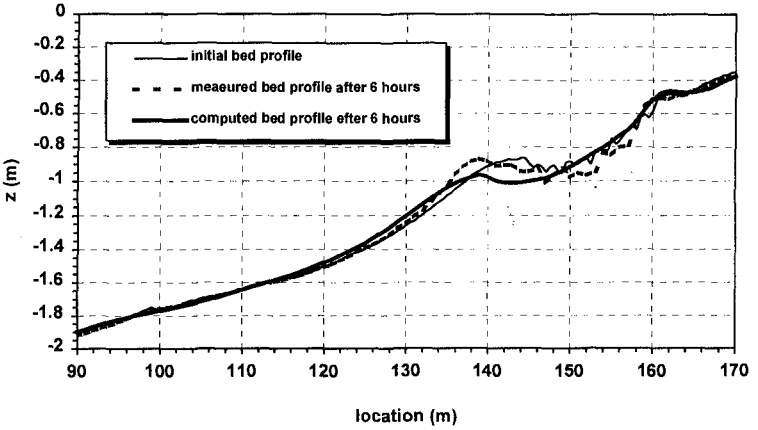

Figure 4. Measured and predicted bed profile change.

Conclusions

The formulation of Isobe and Horikawa (1982) was modified and adapted for use in a probabilistic cross-shore transport model. Comparison of model calculations and laboratory measurement showed that the near-bed orbital velocities could be predicted with reasonable accuracy using the method of Isobe and Horikawa (1982). However, the asymmetry of the orbital velocity was overestimated landward of the breakpoint. The depth-averaged mean return flow could reasonably well be represented using a simple formulation based on linear mass transport, except in the shallow surf zone where the depth-averaged mean return flow was significantly overestimated by the model. Further work is required to improve the morphodynamic predictions of the probabilistic cross-shore transport model.

References

Hamm, L., 1996. *Computation of near-bottom kinematics of shoaling waves, Proc. Int. Conf. on Coastal Engineering 1996, pp. 537-550.*

Isobe, M. and Horikawa, K., 1982. *Study on water particle velocities of shoaling and breaking waves, Coastal Engineering in Japan, Vol.25, 1982.*

Roelvink, J.A. and Reniers, A.J.H.M., 1995. *Lip11D Delta Flume Experiments, a profile dataset for profile model validation. Report H2130, January 1995, Delft Hydraulics, The Netherlands.*

Stripling, S. and Damgaard, J.S., 1997. *Improvement of morphodymamic predictions in COSMOS-2D, Report IT 443, March 1997, HR Wallingford, England.*

Swart, D.H., 1978. *Vocoidal water wave theory, Volume 1: Derivation, Nat. Res. Inst. for Oceanology, CSIR Report 357, Stellenbosch.*

Swart, D.H. and Crowley, J.B., 1988. *Generalised wave theory for a sloping bed, Proc. Int. Conf. on Coastal Engineering 1988, pp.181-203.*

Van Rijn, L.C. and Wijnberg, K.M., 1996. *One-dimensional modelling of individual waves and wave-induced longshore currents in the surf zone. Coast Engineering, Vol. 28, p.121-145*

Beach Evolution on the Southern North Sea Coast.

Daniel J Leggett[1], Jeremy P Lowe[2] and Nicholas J Cooper[2]

Abstract

A monitoring programme has been established for the 351km of the UK Southern North Sea Coast (between the Humber and Thames estuaries). This has produced over 3300 beach profiles captured to a clear specification at 1km intervals in summer and winter since 1991. The analysis of this data has been previously linked to specific flood defence and coastal protection engineering schemes. The first analysis on a region wide basis has now been undertaken to provide some strategic insight into how the coast is evolving on an Integrated Scale. The analysis provides quantification of the change at the coast, and demonstrates that simple analytical tools combined with geomorphological interpretation can provide meaningful information for coastal management.

1. Introduction

The increased awareness of natural processes in the management of the coast has led to renewed efforts in the monitoring of the UK coastline. Such monitoring has been carried out in an ad-hoc fashion over the last 50-100 years with local grids and datums being employed. The purpose of such monitoring is to provide information on long term (decade - century) changes in the coast and intelligence on what is happening with the highly complex and dynamic coastal processes in the short term (month - year). Monitoring considers both the forces affecting the coastline and the response of the coast to these forces, in many cases a symbiotic relationship.

One of the core data sets in monitoring is beach profiles (for the purpose of this paper beaches may be of any sediment type, including fine-grained silt and mud). Beach profiles provide indicators of coastal change in the most important area to coastal managers, the inter-tidal zone (Davis, 1971; Pethick, 1984). However the offshore bathymetry should also not be overlooked in their importance to the inter-tidal profile (Leggett, 1995). Beach profiles provide qualitative and quantitative information on how a coastline is reacting to the forces upon it. Over time the pattern of reaction enables trends, cycles, or the impact of distinct events to be identified.

---

[1] Head of Water Engineering, CIRIA, 6 Storey's Gate, Westminster, London, England, SW1P 3AU.

[2] Centre for Coastal Management, University of Newcastle Upon Tyne, England, NE1 7RU.

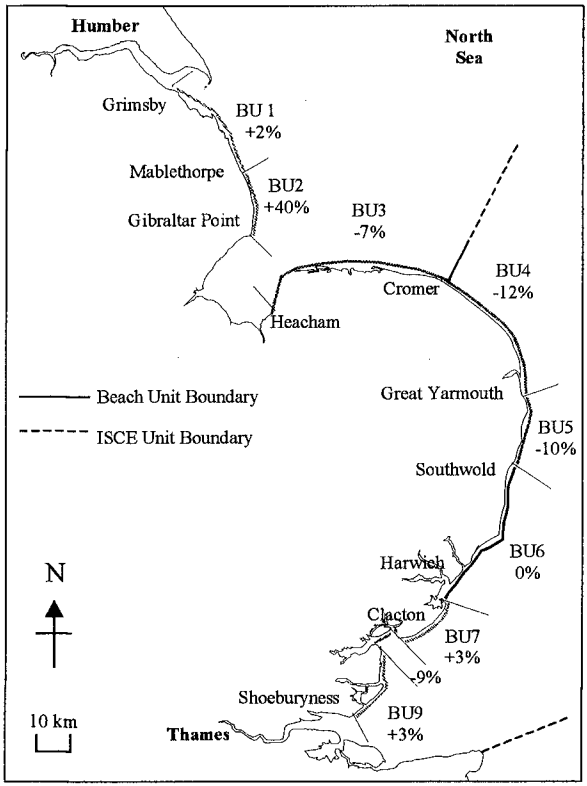

Figure 1. Location of the Southern North Sea Coast with Average Change in Profile Volume, 1991 to 1996

The Southern North Sea Coast of the United Kingdom (figure 1) has had a structured monitoring programme since 1991 (Child and Leggett, 1991). This paper reports on the first five years of this programme with particular reference to beach profiles.

2. Coastal Scale

The Southern North Sea Coast has 5,400km^2 of low lying land which alternates with soft rock cliffs (Leggett, 1993). This means it is vulnerable to flooding and coastal erosion. The management of this coast involves a number of approaches but almost all of the open coast has some form of man-made defence along it. Defence includes hard sea walls, clay embankments, groynes, nearshore reefs, and beach recharge. To be able to take effective management decisions a fundamental question is: What is the change of the beaches over medium to long time scales and how best can this be evaluated? To be able to answer such a question for over 351km of coastline there is a need to consider the philosophical approach to take.

The approach has been derived from the Coastal Evolution work in the Netherlands (Stive *et al.*, 1990). This approach considers the relationships that exist

between the spatial scale of the coastal feature and the temporal scale over which its behaviour is manifested. Changes on the temporal scale of a tidal cycle that link to profile shape and landforms over (say) a hundred meters are Small Scale Coastal Evolutions (SSCE). Changes over about a kilometre, that take a year to form, can be considered as Medium Scale Coastal Evolution (MSCE). Large Scale Coastal Evolution (LSCE) happens over tens of kilometres and form over decades. This approach has been further developed to create the Integrated Scale Coastal Evolution or ISCE (Pethick and Leggett, 1993).

The ISCE integrates the MSCE and LSCE as critical parts of coastal evolution. It also extends the temporal frame to include high magnitude - low frequency events such as 1:250 year return period storms. The approach also extends the longshore scale to hundred of kilometres and, importantly, integrates offshore processes to changes at the beach. The ISCE is an important philosophical approach to coastal management problems and has influenced the approach to monitoring the coast on a Regional scale.

3. Coastal Forcing Parameters

Beach surveys in themselves yield valuable information on changes at a particular site; this can be greatly enhanced if they form a carefully co-ordinated component of a broader monitoring programme. Wave, water level, wind and (estuary) tidal prism measurements all provide invaluable information to aid the interpretation of beach profile changes. The Southern North Sea Coast monitoring programme measures all these coastal forcing parameters (Townend and Leggett, 1992), however, this paper focuses on the use of beach profiles.

As analytical methods continue to become easier to apply, are better understood by managers, and become more sophisticated, it will be the paucity of data that will be a limiting factor. These long-term records are an invaluable benchmark for any future monitoring and analytical activities.

4. Strategic Beach Monitoring

The apparent ease of collecting beach profiles is very attractive in a subject area where field measurements may be highly specialised and costly. The ease of collection provides a source of valuable information that, with geomorphic interpretation, provides extremely good value for money. The ease of collection has, however, spawned a proliferation of approaches, which often means that modelling analysis cannot directly compare data sets together, limiting the value of time series information. Data capture in the past has varied from location to location meaning that spatial analysis of information is equally problematic.

To answer the main management questions it is suggested that a beach monitoring programme has, as its goal, the collection of beach survey and coastal forcing parameters in order to facilitate:

- The development of a holistic understanding of coastal processes along the coastline to guide the development of coastal defence and coastal zone management strategies.
- The provision of coastal engineering design data for the design of coastal defence.
- The monitoring of beaches to guide beach recharge and recycling programmes.

The focus of the Regional survey is not on the extreme event but on the envelopes of beach change from year to year.

5. Beach Profile Measurement Methods

There are a variety of techniques for monitoring beach profiles. These range from traditional survey techniques, to laser and active aircraft remote sensing (Cracknell and Hayes, 1991), to video imaging. These techniques all provide the same basic information, beach level. Some provide highly detailed (but less accurate) images of the beach surface whilst others provide an accurate cross section.

Collecting data and analysing it regularly requires rigorous and repeatable techniques. New techniques are always under investigation and when suitably developed may replace existing methods or provide a useful additional data set; they may in time also be able to provide suitably accurate profiles that would negate the need for direct land survey. Most remote methods provide accuracy in +/- hundreds to thousands of millimetres. This accuracy would provide considerable error over the length of Southern North Sea Coast. Until methods are proven (such as kinematic global positioning) the risk of missing a time step in the data set is too critical to contemplate embracing new techniques.

There are merits and drawbacks in all approaches but certain issues are important for any long-term monitoring activity:

- Repeatability.
- Accuracy.
- Comparability.

These principles should affect the decision of monitoring approach, rather than just following the latest technology. Repeatability is vital if any meaningful analysis is to be achieved. This requires both spatial and measurement accuracy to be well defined. If this is the case then the best approach at present is considered to be measurement of beach profiles using land based survey techniques.

5.1 Cross Section Specification

The beach profile survey lines of the UK Southern North Sea Coast monitoring programme run from the landward toe of the defence line or 200m inland of a cliff edge to MLWS as a minimum. Spot heights are taken on section lines at all breaks of slope, at a maximum of 20m intervals, and at all changes in beach material. Changes in beach material (sediment and vegetation) are recorded qualitatively against each profile.

All levels are taken to Ordnance Datum Newlyn at +/- 3mm accuracy for spot height. The corresponding plan position accuracy specification is +/- 20mm. These values correspond fairly closely to the recommendations made from analysis of annual data captured over 30 years on the Lincolnshire coast (HR Wallingford, 1990).

5.2 Ground Control

Lack of ground control in beach survey has led to errors in the repeatability of some surveys and invalidated time-series data. At worst it may yield erroneous answers and false information on which to base decisions. A sound ground control and permanent marking is considered essential for any repetitive survey work.

Survey section lines, each with their own co-ordinated reference monuments have been established along the Southern North Sea Coast at 1km intervals to determine regional beach changes. All surveys are tied to OSGB 1936 as a common co-ordinate system; being the most commonly used in the UK (Pos, 1994). This enables re-location of profiles in the event of loss during defence works or through

erosion and also instant utilisation of data transferred between coastal authorities and passed to consultants. The monuments are established from the national grid network at 1:20,000 accuracy and their existence aids the identification of profile location by surveyors.

Each profile data point has a chainage calculated for it. Zero chainage represents the original profile marker position which is normally at the first line of sea defence, or inland from a cliffline (the current position could be landward, and in a few cases seaward, of this original position). This chainage system does not change if the marker is re-established, instead the marker has a positive or negative value. Chainage is positive to seaward and negative to landward of this original position.

5.3 Frequency and Timing of Surveys

Twice-yearly surveys are a recommended minimum requirement for beach surveys. However, additional site specific surveys should be carried out at particularly volatile locations to monitor the maximum negative (or positive) beach conditions. It may also be necessary to monitor more frequently for beach recharge purposes.

Whilst profiles after storms may show the most extreme condition of the beach it is difficult to capture *the* most extreme profile each year along the 351km of coastline. The volatility of beaches under storms leads to daily change in beach profile and high spatial variability. For specific defence schemes such detail may be feasible to collect, and indeed critical for structural design and stability. In order to represent more 'typical' beach conditions and to determine long term change in beaches it is more suitable to survey the coast at times of reduced beach volatility. The timing must, however, still capture the key beach change between the winter (storm) and summer (swell) beach profiles (Komar, 1998). For this reason survey is undertaken in January and July where perturbation in the beach is reduced but the gross pattern of change is still represented. This reduction in perturbation also provides a wider time window to measure profiles, for the Regional beach survey, and helps to provide consistency in information from one year to the next.

5.4 Integrating Land, Aerial, and Bathymetric Surveys

The Southern North Sea Coast monitoring programme has many sources of data including:

- Historic shoreline positions (high water mark, low water mark and coastline) have been taken from Ordnance Survey maps dating back to 1880.
- Over 9000 aerial photographs, using stereo-photography methods at a scale of 1:5000 with forward motion compensation have been taken between 1991 and 1996. They are suitable for photogrammetry, timed to coincide with beach profile measurement, and cover the whole coastline.
- 3399 beach profiles and 509 bathymetric profiles were measured between 1991 and 1996.

The costs of different survey approaches are comparable but aerial techniques allow the plan form of the coast to be mapped and the movement of important geomorphic indicators (such a spits, nesses, or bars) to be quantified. The aerial technique requires suitable ground control, which can be provided by the land based survey operations. It is suggested that for consistency (and maximum necessary accuracy) profiling is best delivered through the land based survey technique with plan form being delivered from aerial or video methods (rectified using the land based

survey data). Such an approach provides high quality data on a consistent basis across all coastal types and gives a three dimensional view of coastal changes. In inaccessible or dangerous locations (such as on wide mudflats) photogrammetry can be used to extend beach profiles across the inter-tidal area. However, the different errors generated in this need to be considered and accounted for in any analysis and interpretation.

Beach surveys are undertaken in conjunction with bathymetric survey (extending the profiles offshore). These surveys extend to at least 10km offshore, or to at least 20m depth of water, which is a nominal closure depth (Hallermeier, 1981; Birkemeier, 1985). The inclusion of bathymetric profiling is on a five year rolling programme due to expense and the initial consideration that change offshore was not as volatile, or as critical, as beach change. This view has been challenged by some of the results of this work.

5.5. Data Quality

The accuracy of the survey technique, accuracy of data capture, and accuracy of data recording all effect quality. To be confident of subsequent analysis, and to generate a credible data archive, it is essential to check the data. For the Southern North Sea Coast specification checks need to be undertaken by the surveyor to identify erroneous or spurious data and consider:

- Data outside the limits of the sensor(s).
- Rates of change between data points.
- Gaps in data.
- Timing of data points within a data set.

The editing of data is restricted to deletion of clearly spurious data points. The validity of the data is checked upon receipt from the field. In 1991 this was undertaken manually using hard copy output, but this is now done automatically by checking the digital data through computer programmes. These routines check the data files for errors or changes in key data elements, for example, beach profile marker positions and level, beach profile orientation, maximum and minimum beach levels. The routines compare the new data to the previous data, and to predefined tolerances (such as 4m change in beach elevation). In some instances large change may be real, but where there is an error this approach helps to ensure it is identified quickly (within 24 hours) and if necessary re-survey of a profile can be undertaken.

Spot checks are also employed to give an independent assesment of the quality and accuracy of data capture. Where possible any errors found are corrected. Where it is not possible to correct an error the data is not used for analysis.

5.6 Data Storage and Databases

For the Southern North Sea Coast storage of data is undertaken using a Geographic Information System (GIS). The GIS (Intergraph MGE) is used to update, manipulate and supply information and data to coastal managers. This provides a consistent dataset and rapid access to information (Leggett and Jones, 1996). The development of the GIS to handle the data more efficiently, and provide analysis of data, has been recognised as an ongoing need (Leggett and Dowie, 1993). This is essential where such large volumes of information are being handled.

The quality control, visualisation and analysis software has been developed separately by the Centre for Coastal Management, University of Newcastle to allow

easy access to this data for non-specialist users. Such management tools are essential if the monitoring process is not to become just a data capture exercise.

6. Analytical Methods

A considerable number and range of analytical techniques exist for the manipulation and interpretation of beach profile data. However, the type of analysis undertaken depends upon two important factors, namely: the questions that the monitoring programme is intending to answer, and the type, quality and format of the data that are available.

Temporal analysis techniques can be employed at a specific location to identify both short-term variations in beach profile (often storm related), and the longer-term trends at that site. This can be of use when identifying the standard of defence provided by a particular beach profile. Spatial analysis techniques can be employed to determine changes in beach profiles along the coastline and to identify areas of material gain and loss on the ISCE scale.

6.1 Beach Volume Comparison

The data from the 1991 to 1996 monitoring has been analysed to determine the volume of the beach and the position of a fixed contour level. This is an initial analysis and the limits of integration and choice of fixed contour level have been chosen to be as wide as possible. There are a large number of different limits that could be used, dependent upon the use of the results; further analysis with different limits and levels is part of the on-going work to be undertaken.

Each survey yields a different total profile length because of natural changes, the tidal state at the time of survey (although all are undertaken on spring low tides), and the safe working area for the surveyor. The method of analysis must allow for this variability whilst providing a consistent spatial area for consideration. The elevation of the defined shoreline position will vary from profile line to profile line. The method allows maximum use of the available data and takes account of the varying nature of the coastal morphology (Lowe, 1997).

The analysis provides a comparative measure of beach volume, not the total beach volume surveyed for each survey campaign. This comparison is vital for coastal managers to be able to objectively consider the state of beaches. The area of beach represents the width over which energy may be dissipated, the change in volume of material within fixed bounds, and a means of comparing different geomorphological features that may have different coastal dynamics. This means that mudflat areas can be compared to sand beaches or gravel ridges in terms of their relative percentage change, rather than absolute change. This approach helps to determine whether change is independent of the type of coastline or not.

6.2 Expert interpretation

A major part of the analysis of the profiles is qualitative rather than quantitative. The ability to easily view the profiles and to determine their relation with other profiles in both time and space (through the GIS and bespoke software) allows a much greater depth of understanding of beach behaviour. Using this data in combination with information on the coastal processes and sediments helps the interpretation of the changes and to develop management advice.

7. Results and Analysis

This study is a first overview of the beach profile behaviour for the Southern North Sea Coast. Characteristic closure depths, eigenvalues, and other more recent methods of analysis have not been applied to this data yet. The analytical techniques are relatively simple but yield interesting results for comparison of change on an Integrated Scale (ISCE).

7.1 Beach Volume Results

Representative beach volumes and shoreline positions for each profile are dependent upon the nature of the morphology. It is, therefore, unwise to compare the absolute figures of change (mean and standard deviation) for the whole coast. The focus for management information is therefore the relative changes in volume and position of beaches between 1991 and 1996.

The cumulative percentage change in profile volume and the calculated shoreline position between 1991 and 1996 demonstrate the trend of beach evolution over the five-year period (figure 2).

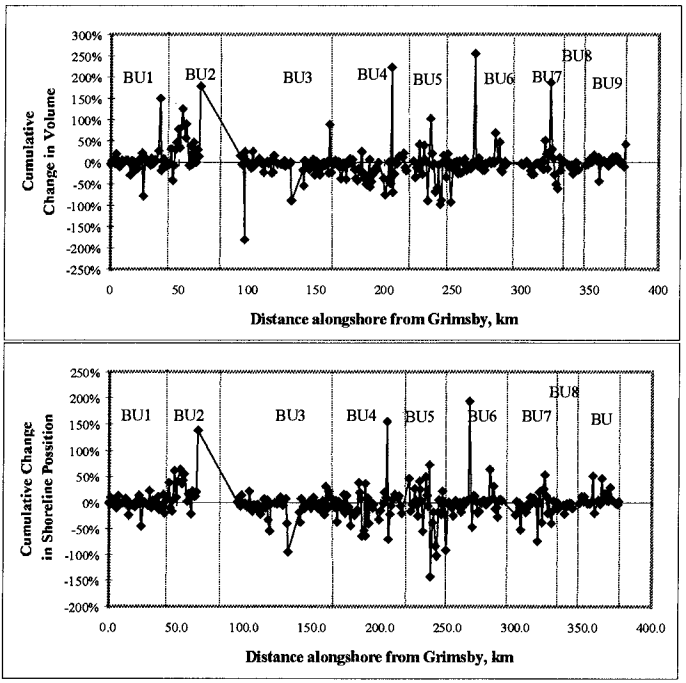

Figure 2. Cumulative Change in Profile Volume and Shoreline Position, 1991 to 1996

These have been plotted against the distance along the shore from Grimsby; the northern limit of the study area (this was calculated from the straight-line distance between the zero chainage of neighbouring profile lines; this is therefore slightly longer than the actual length of the coastline).

The results indicate that the Southern North Sea Coast can be split into a number of distinctive coastal evolution areas. The boundaries of these represent statistical divisions where profile evolution has a fundamental change along-shore. Change may be from gross erosion to accretion, a step in the magnitude of change, or the degree of intra-variability along the coast. The divisions have been indicated on figure 2 and can be considered as LSCE Beach Units. This analysis provides some indication of the broad behaviour of the whole coast, it also serves as an important starting point for any future analysis.

The average change within each LSCE Beach Unit is presented in figure 1. A total of nine units have been identified. The recent beach profile evolution in each of these areas can be explained by both natural and anthropogenic influences; each is briefly discussed below:

Beach Unit 1 – Unit 1 is at the northern end of the region from the Humber Estuary to Mablethorpe and appears to show overall stability. Here 2.4% accretion has been recorded over the study period. This area has a variety of profiles ranging from sand beaches in front of sea walls to wide sand flats and mud flats which are relatively stable. This gain in sediment links to protective offshore banks and a seaward extension of the profile. There is also a significant sediment supply from the Holderness coast via the Humber Estuary (NRA and SWHP, 1991).

Beach Unit 2 - This runs between Mablethorpe and Gibraltar Point. There is a consistent gain in beach volume within this Unit. The effect of large beach renourishment can be clearly seen along this 23km stretch of coast. The average beach volume has been increased by nearly 40% since 1991. The impact of the individual renourishments can be clearly seen in the temporal record. The on-going monitoring will be able to evaluate loss of sediment from this scheme but historic data shows a 15% loss over the five years prior to replenishment.

Beach Units 3 and 4 – These Units demonstrate that not all beach variation is due to anthropogenic impacts. The variation in the orientation of the shoreline along the Norfolk coast and the degree of protection afforded by the offshore banks can clearly be seen in the profile results. There is an increase in erosion of the beaches from Heacham eastwards to Cromer. The average loss of volume is about 10% over the past five years, although this can reach up to 50% in the southern half of this area. The gross pattern appears to be related to the continuing long-term reorientation of this coast since the last ice age.

Beach Units 5 and 6 – The reverse of the trend of Units 3 and 4 is found here, with erosion decreasing to the south from the critical ISCE divide at Cromer (Pethick and Leggett, 1993). Sea defence schemes designed to stabilise parts of this coast are starting to have an impact on this larger, longer-term pattern, with clear steps in the data from one scheme to another. This section also sees the linkage of the beach profile change to change offshore in the sandbanks. It is believed there is a large-scale sediment circulation spanning Units 3, 4, 5, and 6, this is subject to further investigation under the Southern North Sea Sediment Transport Study (ABP, 1996).

Beach Unit 7 – Unit 7 has a 3% increase in average volume since 1991. This masks a consistent spatial pattern of stability, accretion, then erosion as one moves southwards. The maintenance of high beach levels along the Clacton frontage, by the use of beach control structures, quite clearly starves the downdrift beaches. This starvation has led

to reduced beach levels (and standards of protection) and the requirement for beach nourishment, and re-design of the structures.

Beach Unit 8 – This Unit is on Mersea Island and is treated separately due to its geographical position. The profiles show an average loss of 9.1% since 1991. This is related to a lowering of the foreshore during this period which appears to be associated with a widening of the mouth of the adjacent estuary.

Beach Unit 9 – This shows stable areas that are accreting. Along the Essex coast, between Dengie and Shoeburyness, the average profile has gained about 3% in volume since 1991. This is an area of wide mud and sand flats that appears to be responding well to the high relative sea level rise. These are complicated profiles that show profiles evolving around an upper 'hinge'. Seaward variations of the profiles tend to be greater than the landward end of the profiles where vegetation helps stabilise the profile.

The nine Beach Units above support the two ISCE Units (figure 1) by demonstrating the critical evolutionary divide at Cromer and the general trends of change away from that point (Pethick and Leggett, 1993). The analysis has provided a more detailed view that allows the impact of defence schemes along the coast to be identified. The fact that the Beach Units are nested into the ISCE Units demonstrates that coastal management can have considerable affect upon the wider coastline.

7.2 Expert Interpretation

The analysis of the data has led to some fundamental understanding of the coast. The qualitative interpretation of the data sets has provided insight into a number of issues that merit more detailed and in-depth consideration. The following sections briefly describe some of the observations made when undertaking the analysis of individual profiles.

Orientation and Exposure - The role of beach orientation appears to have fundamental importance, particularly in Beach Units 3 to 6, which have a systematic change in profile bearing. This is illustrated where the profile bearing is plotted against the cumulative change in volume (figure 3).

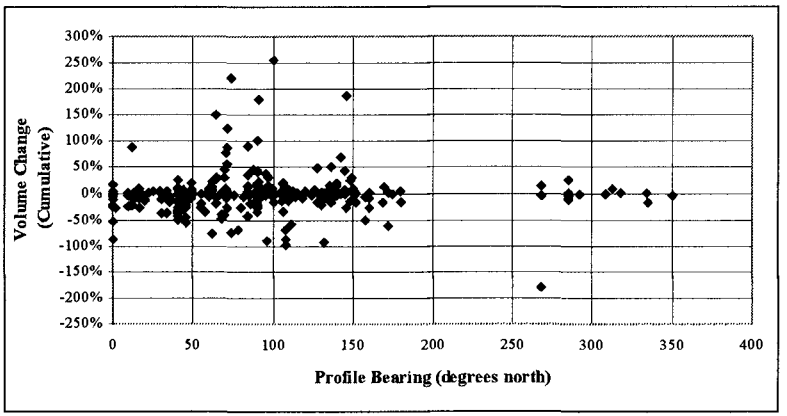

Figure 3. Profile Orientation vs. Cumulative Change in Beach Volume, 1991 to 1996

There are some indications that the volatility of the profiles is greatest between 60^0 and 100^0N with another band around 120^0 and 150^0N. These two groups, again, support the ISCE divisions. The degree of exposure to storm waves varies with orientation and the banding represent the northern ISCE beaches which are exposed to north-easterly and easterly storms, and the southerly ISCE beaches which are more exposed to the south-easterly storms (Pethick and Leggett, 1993).

Offshore Profile - Beach evolution is intimately related to the offshore bathymetry both in terms of the exchange of material and the dissipation of wave energy. The evolution of the offshore can be quite clearly seen in many of the longer profiles. Figure 4 is an example of the exchange of material between the offshore and the beach at Sea Palling (Beach Unit 4). Material appears to have been removed from the seaward side of the offshore bar and placed on the beach. Changes up to 1.2m in elevation are shown in 15m depth of water.

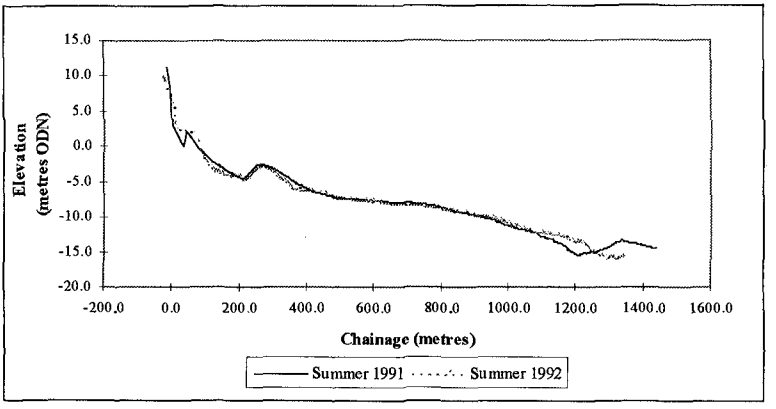

Figure 4. Evolution of Offshore Bathymetry, 1991 to 1996

The role of offshore bars (banks) in protecting the shoreline is illustrated at Orford Ness (Beach Unit 6) where profiles have distinctive bathymetric changes over a longshore distance of 4km. The northernmost profile has a large offshore bar that helps stabilise the beach profile (2% accretion 1991-1996). Further to the south the same orientation of the beach exists but no offshore bar, here 18% loss of volume occurred over the same period.

Trends of Profile Change - A number of different trends can be identified in the profile data (figure 5). Simple trends are shown in cliff profiles at Covehithe (figure 5a) where the cliff line can only retreat. The retreat of the cliff at Covehithe (Beach Unit 5) is a relatively simple process of parallel retreat - a constant form translates landwards.

Figure 5b shows nearshore bar movement at Cleethorpes (Beach Unit 1). The full time series shows the progressive movement onshore of this bar over the last five years. Clearly there are trends in the nearshore behaviour that will have an impact on shoreline management in the long term. These need to be identified before action is taken to stabilise the coastline.

A more complex response is shown at the Ray Sand at Dengie (Beach Unit 9). Here the saltmarsh has been accreting vertically since 1991 (figure 5c). The saltmarsh

cliff has, however, not moved. Seaward of the cliff the mudflat is also accreting but the rate increases offshore. The net result is a reduction of the slope of the mudflat, with the surface hinging around the toe of the cliff. This profile behaviour is characteristic along this stretch of the coast.

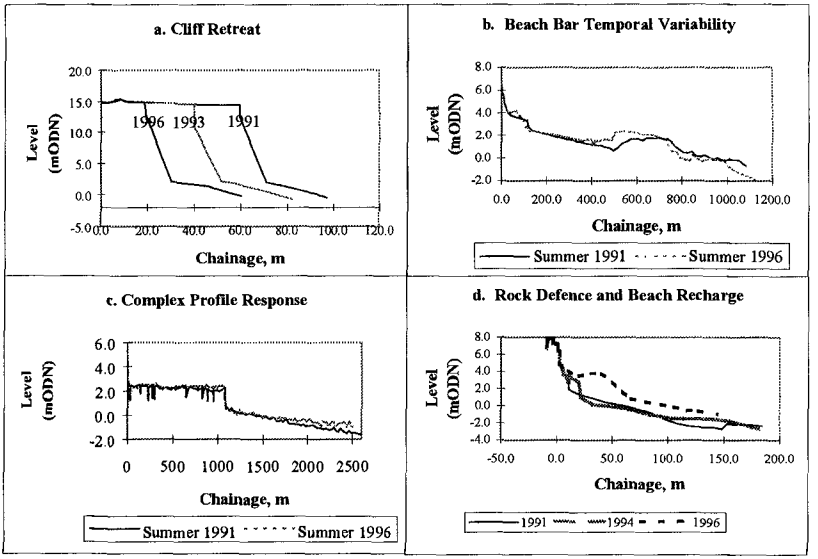

Figure 5. Examples of Profile Responses on the Southern North Sea Coast

Profile History - Knowledge of the history of each profile line (constructions, renourishments, etc) is increasingly important. This is illustrated at Chapel St Leonards in Beach Unit 1 (figure 5d). The low beach in 1991 caused sufficient problems to require the construction of a rock revetment which appears as 'accretion' of the upper profile. Beach levels at the toe of the rock revetment remained low so by the end of 1995 the beach was recharged, to completely cover the revetment. About 280m^3 of sand was placed per metre run of the beach of which 26% was lost in the following six months (73m^3 per metre). This history is based on the evidence in the profiles and the detailed local knowledge of relevant coastal engineers. Without that knowledge mis-interpretation of coastal change would be common place.

8. Conclusions and Recommendations

The analysis of 3399 beach profiles and 509 bathymetric profiles has provided a broad picture of beach evolution along the whole length of the Southern North Sea Coast. These results indicate some general trends and highlight specific challenges for some methods of sea defence. A re-analysis of the profiles following further survey work should be a relatively simple matter and provide more insight to coastal changes. The results presented, and those generated in the future will always be of an interim nature.

There is a definite need to integrate the profile data more closely with the forcing data (wind, wave and tides) which are also available. This integration will increase the value of the data that has already been collected and will help explain

some of the patterns and trends that have been observed. The ISCE approach has helped to define the data and information needs for the coast and helped in the conceptual approach to interpreting the analytical outputs. The critical divide for evolution of the Southern North Sea Coast at Cromer has been confirmed, this helps coastal managers to understand the evolution of the coast and to place individual schemes into context with the surrounding coastline, nearshore and offshore area.

The effect of large beach renourishment schemes undertaken for flood defence purposes can be clearly seen in Unit 2 (Lincolnshire) along a 23km stretch of coast. The average beach volume has been increased by nearly 40% since 1991. The impact of the individual renourishments can be clearly seen in the temporal record. It is too early to determine the long term stability of these schemes; however envelopes of expected change can be constructed.

Not all the variation in beach volume is due to anthropogenic impacts. The variation in the orientation of the shoreline from Units 3 to 6 (the Norfolk and Suffolk coast) and in the degree of protection afforded by the offshore banks can clearly be seen in the profile results. The gross pattern appears to be related to the long-term reorientation of this coast (certainly since 1880 and probably throughout the Holocene). Sea defence schemes designed to stabilise the coast are starting to have an impact on this larger, longer-term pattern.

Further to the south in Unit 7, (the Essex coast) at Clacton, the negative impacts of sea defence can be seen in the spatial distribution of erosion and accretion. Here the overall picture of relative change is fairly stable (a 3% increase in average volume since 1991) but this masks a spatial pattern of downdrift erosion. The maintenance of high beach levels along the Clacton frontage, by the use of beach control structures, quite clearly starves the downdrift beaches. This starvation has led to both reduced beach levels and reduced standards of coastal protection.

There are also stable areas that are showing accretion. Along the Unit 9 coast, between Dengie and Shoeburyness, the average profile has gained about 3% in volume since 1991. This is an area of wide mud and sand flats that appears to be responding well to the high relative sea level rise. A similar picture can also be found at the northern end of the region in Unit 1, from Humber to Mablethorpe. Here an average of 2% accretion has been recorded over a similar period.

These gross figures provide an overview and, combined with the analysis of individual profiles, better understanding of the evolutionary behaviour of the Southern North Sea Coast. The relationship of the beach behaviour to the offshore bathymetry, to the orientation of the coastline and to sediment pathways and their local interruption is very evident. For the first time coastal managers of the Southern North Sea Coast have an overview of the contemporary evolution of their coastline and the impact that their interventions have along a 351km shoreline. Monitoring continues on a twice-yearly basis and it is anticipated that the analysis will be repeated and refined at regular intervals. In the long term this will improve not only our understanding of how this coast behaves but also improve management decisions.

References

ABP Research and Consultancy, 1996. *Southern North Sea Sediment Transport Study – Phase I: Literature review and conceptual sediment transport model.* Anglian Coastal Authorities Group (UK) Report 1996.

Birkemeier W.A., 1985. Field data on seaward limit of profile change. *Journal of Waterway, Port, Coastal & Ocean Engineering*, ASCE, 111 (3), 598-602.

Child M.W. and Leggett D.J., 1991. The Anglian Coastal Management Study. *Proceedings of the MAFF Conference on Coastal & River Engineering*, No.26 Loughborough, UK, July 1991, 17 pp.

Cracknell A.P. and Hayes L.W.B., 1991. *Introduction to Remote Sensing*. Taylor & Francis, 293pp.

Davis R.A., 1971. *Coastal Sedimentary Environments*. Springer Verlag, 238-247.

Hallermeier R J, 1981. *Seaward Limit of Significant Sand Transport by Waves: An Annual Zonation for Seasonal Profiles.* US Army Corps of Engineers, Coastal Engineering Research Center, Technical Aid No.81-2, January 1981.

HR Wallingford, 1990. Monitoring Guidelines - Annex II Assessment of Beach Survey Methods. *Sea Defence Management Study, Stage III.* NRA (Environment Agency) Anglian Region, UK.

Komar P.D., 1998. *Beach Processes and Sedimentation*. Second Edition, Prentice-Hall, Inc, 270-335.

Leggett D.J., 1993. Geology and geomorphology of the North Sea coastal margin. In: Doody P., Johnston C. and Smith B. (eds.). *Directory of the North Sea Coastal Margin,* Joint Nature Conservation Committee, Peterborough, UK, 17-33.

Leggett D.J. and Dowie P.J., 1993. Avoiding deep water - Getting the job done with GIS. *Association of Geographic Information Yearbook*, AGI, 21pp.

Leggett D.J., 1995. Bathymetric Monitoring: It's contribution to Shoreline Management in the Anglian Region. *Proceedings of the Hydrographic Society*, November 1995, 69-78.

Leggett D.J. and Jones A., 1996. The application of GIS for flood defence in the Anglian Region. *International Journal of Geographical Information Systems,* **10**, (1), 103-116.

Lowe J.P., 1997. *Anglian Region Beach Profile Analysis 1991 to 1996*. Environment Agency Anglian Region, UK, Report 1, 37pp.

NRA and SWHP, 1991. *The Future of Shoreline Management: Conference papers.* ICE London, October 1991, NRA (Environment Agency), 116pp.

Pethick J.S., 1984. *An Introduction to Coastal Geomorphology*. Arnold, 91-107.

Pethick J.S. and Leggett D.J., 1993. The morphology of the Anglian coast. In: Hillen, R. and jan Verhagen, H. (eds.). *Coastlines of the Southern North Sea*. American Society of Civil Engineers, New York, 52-64.

Pos J., 1994. *National Database for Monitoring Phase I - Beach Monitoring Questionnaire Survey of Existing Practice and Guidelines for the Monitoring of Natural and Recharges Beaches,* NRA (Environment Agency), PR 441/3/A.

Stive M.J.F. *et al.*, 1990. Large Scale Coastal Evolution. In Louisse C.J., Stive M.J.F. and Wiersma (eds), *22nd International Conference on Coastal Engineering,* Delft Hydraulics 9.1-9.13.

Townend I.H. and Leggett D.J., 1992. Shoreline Management in the Anglian Region. *Proceedings of the International Coastal Congress,* Kiel, Germany, September 1992, 505-518.

Extracting Morphologic Information From Field Data

Nathaniel G. Plant[1] and Rob A. Holman[2]

Abstract

We quantified the strengths and weaknesses of two sources of morphologic data available from Duck, NC, utilizing an objective definition of nearshore morphology (Gaussian curves added to a plane slope). Directly surveyed bathymetry provided the most complete estimate of the morphologic state of the nearshore bathymetry. That is, all of the parameters of the morphologic model could be estimated from these data. Oblique video images were used to estimate the position of inner bars. This information represented only a subset of the morphologic parameters defined in the morphologic model. However, the image data were collected frequently (daily) and, thus, resolved a wide range of temporal scales. Bar crest positions estimated from the video images were well correlated with estimates extracted from the bathymetric surveys ($R^2 = 0.8$). Differences between the two estimates of bar position depended on both wave height and on the bar amplitude.

1. Introduction

Field observations of nearshore sand bar systems (Figure 1) have provided a great deal of information about the morphologic evolution (often called morphodynamics) resulting from the complicated interaction between morphology, hydrodynamics, and sediment transport (Sonu, 1973; Short, 1975, Wright and Short, 1984, and many others). Two types of measurements are commonly available to study sand bar systems. One type is visual observations, which can be made with the human eye and are a bit subjective

[1] University of Twente, PO Box 217, WB-building, 7500 AE Enschede, The Netherlands

[2] College of Oceanic and Atmospheric Sciences, Oregon State University, Corvallis OR 97330, USA

A. Duck, 11 Oct. 1994

B. Duck, 20 Oct. 1994

C. Noordwijk, 10 Oct. 1996

D. Agate Beach, 11 Feb. 1996

E. Palm Beach, 21 May 1997

F. Waimea, 29 Mar. 1995

Figure 1. Time exposure images of beaches from around the world, including the US East Coast (A,B), Dutch Coast (C), US West Coast (D), South Australian Coast (E), Hawaii (F). Sand bars and the shoreline may be identified by light, often shore parallel bands that correspond to shallow regions where waves tend to break.

(Short, 1975). Visual observations made with video cameras are also available (Figure 1) and these can be used more quantitatively (Lippmann and Holman, 1990). The main advantages of the video observations are that they can be made frequently (several times per day), over long time periods (decades), and they span large distances alongshore (O(km)). The primary disadvantage of visual observation methods is that, in most cases, they do not give a direct estimate of actual beach elevations.

The other technique for sampling nearshore morphology is direct bathymetric surveying. This technique gives high precision estimates of beach elevations. The primary constraint here is time, which, under the best circumstances, allows sampling of a region spanning 1 km in the cross-shore and 1 km alongshore in about 1 day (Birkemeier and Mason, 1984).

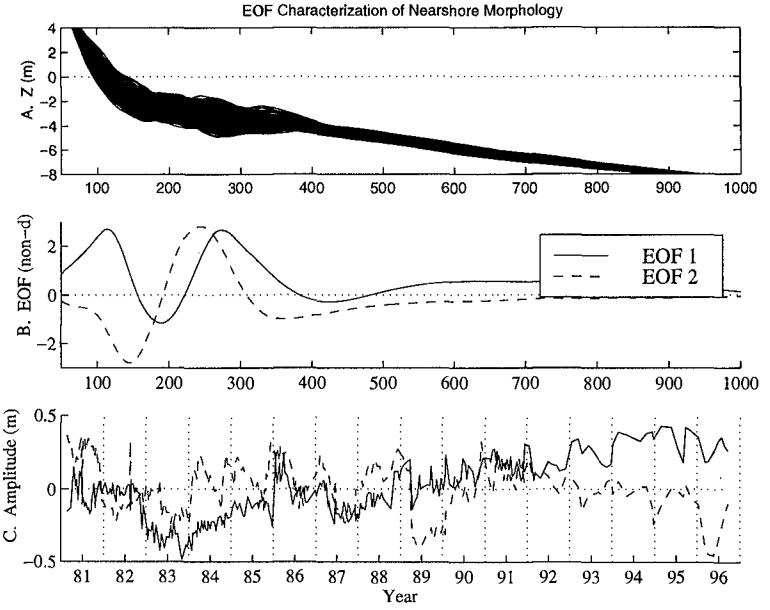

Figure 2. Analysis of beach profiles (A) using EOFs (B). The EOFs are spatial patterns describing correlated or anti-correlated beach variations. The EOFs clearly suggest the presence of sand bars. The EOF amplitudes (C) indicate the correlation of the actual profile at a particular time to each the EOF. The movement of the bars is not readily apparent from inspection of the amplitude time series.

Because of the complexity of some morphologic patterns (Figure 1d), it has been difficult to objectively define what we mean by morphology and treat the morphologic observations quantitatively. Several attempts to quantify morphology have used empirical orthogonal functions (EOFs) to represent, for example, surveyed profile data (Winant et al., 1975, and many others) and alongshore arrays of profile data (Wijnberg and Terwindt, 1995). The EOFs typically aide the analysis of morphologic variability by reducing the dimensionality of the bathymetric data (which contain observations at many spatial locations). Dimensionality is reduced by projecting observed beach elevations onto a small number of basis functions (i.e. morphologic patterns).

However, morphologic evolution described in terms of EOFs is often hard to interpret (Figure 2), since the EOFs may not have any clear physical interpretation. One example where they have been successfully interpreted is on the Dutch coast, where temporally periodic behavior was identified (Wijnberg and Terwindt, 1995). The ability to interpret the morphologic parameterization may be important when trying to constrain the morphology using two different data types. For example, video image data have been used to locate the position of surf zone sand bars (Lippmann and Holman, 1989; Lippmann and Holman, 1990; Lippmann et al., 1993). It is not clear how this information could be used to constrain any part of the morphologic patterns identified by an EOF model.

Both directly surveyed bathymetry and remotely sensed video images have different sampling strengths and weaknesses. We wish to combine the strengths of these data via an objective morphologic model. The goal of this paper is to evaluate whether the two data sources constrain a particular morphologic model in an identical manner. In section 2.1, a morphologic model for a nearshore sand bar system is defined. In section 2.2, the methods used to project the observations on the model are described. In section 3, sand bar crest position estimates (the only parameter estimated from the video data) are extracted from both surveyed bathymetry and video images. These estimates are compared and the differences analyzed. Section 4 contains both the discussion and conclusions.

2. Methods

2.1 morphologic model

We use a morphologic model that describes an alongshore-uniform, barred beach. The model consists of several Gaussian shaped sand bars superimposed upon a plane sloping beach (Figure 3). The bathymetry as a function of time (t) and cross-shore location (x) is expressed as

$$Z(x,t) = \beta_1(t) + \beta_2(t)\,x + A_1(t)\exp[-\{\frac{x - X_1(t)}{L_1}\}^2] + A_2(t)\exp[-\{\frac{x - X_2(t)}{L_2}\}^2] + A_s(t)\exp[-\{\frac{x - X_s}{L_s(t)}\}^2], \quad (1)$$

where $\beta_1(t) + \beta_2(t)\,x$ describes a plane slope component, $A_1(t)\exp[-\{\frac{x - X_1(t)}{L_1}\}^2]$ describes a Gaussian shaped sand bar located at $X_1(t)$, having a characteristic length of L_1 and amplitude $A_1(t)$. The subscript 1 refers to an inner bar and 2 to an outer bar. The subscript "s" refers to a half-Gaussian located at the shoreline, which accommodates the shape of the subaerial beach. This model allows the true sand bars (bars 1 and 2) to change amplitude and migrate, but undergo no changes in length. The "shoreline bar" is fixed in space, but may vary its amplitude and wavelength.

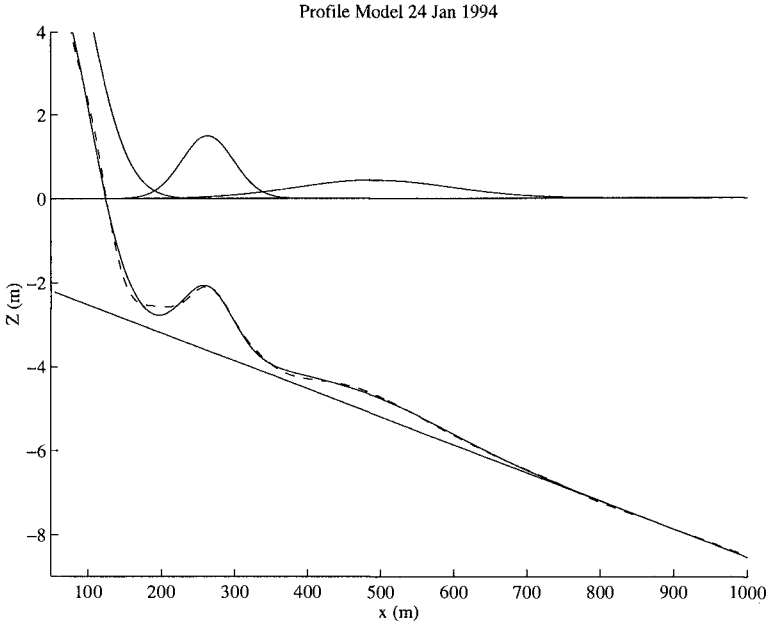

Figure 3. Example of the morphologic model (solid line), applied to FRF bathymetry (dashed line). The morphologic components of the model are shown as well.

2.2 Estimation of morphologic parameters

The model (1) described well the temporal and spatial variability of the bathymetric surveys obtained from the Army Corps of Engineers Field Research Facility (FRF, Figure 4). Surveys were conducted at bi-weekly and monthly intervals. The model was fit to a region north of the research pier in order to avoid inclusion of pier effects on the morphology (Figure 4). The data within a 300 m wide (alongshore) region (from y=776 m to 1096 m) were alongshore-averaged and then fit to the morphologic model in order to extract the following 8 parameters $\beta_1(t), \beta_2(t), A_1(t), X_1(t), A_2(t), X_2(t)$,

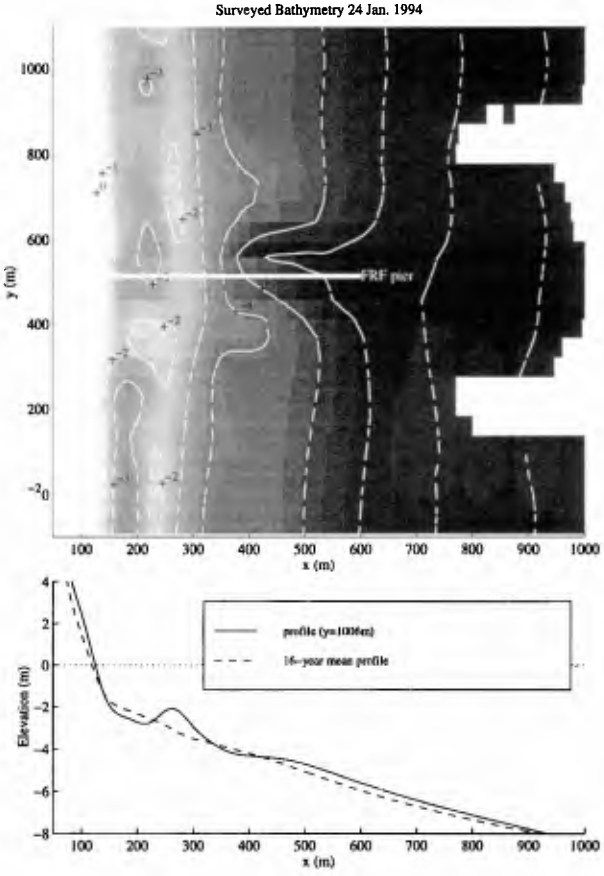

Figure 4. Contour map of the FRF bathymetry and example profile. Contour interval is 1 m.

$A_S(t), L_S(t)$. L_1 and L_2 were fixed at 50 m and 150 m, while X_s was fixed at 50 m. The model was fit to the alongshore averaged bathymetry using a nonlinear least squares algorithm. A typical rms error was less than 0.1 m. The rms elevation explained by the Gaussian parts of the model typically exceeded 1 m.

Since it was designed to represent bathymetric data, the model (1) could not be employed directly on video images. Instead, we assumed that the bar crest term in the model corresponded to the bar crest determined from an analysis of time exposure, video images (Lippmann and Holman, 1989 – hereafter LH89). Bar crest positions are revealed in the images by bright bands (Figure 1) that are associated foam generated in regions of wave breaking. The bar crest position data that we used are described in detail in Lippmann et al. (1993). We discuss only the estimated position of the inner bar of the commonly double-barred FRF site. We will test the correlation of the bar crest positions identified in the video images with estimates made from the bathymetric survey data.

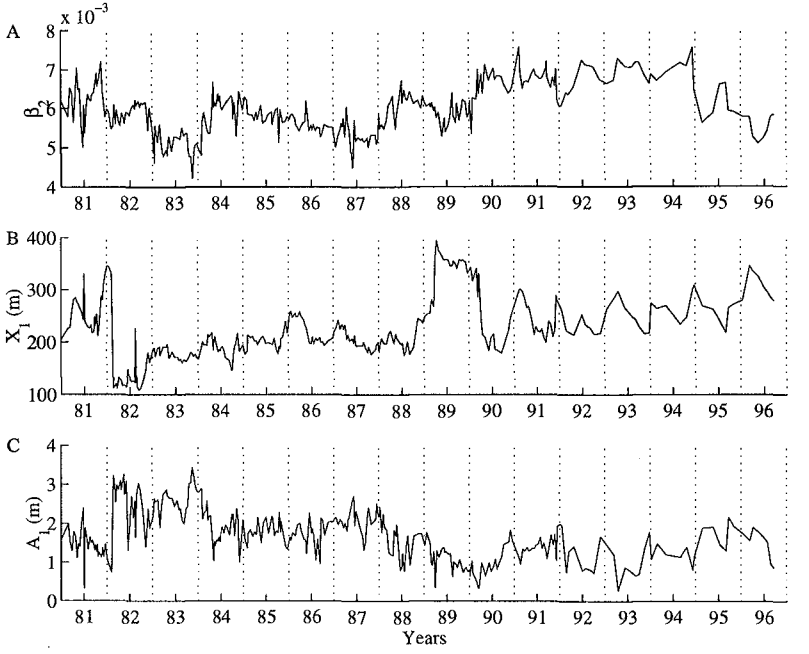

Figure 5. Time series of slope component of morphology (A), inner bar position (B), and inner bar amplitude (C). Morphologic components were extracted from the bathymetric surveys.

3. Results

Figure 5 shows a time series of several morphologic parameters extracted from the FRF bathymetry. In Figure 5a, a time series of the slope parameter, β_2, is shown. Variation of beach slope occurred on a variety of time scales. Interestingly, there is no evidence for a long term trend. Temporal aliasing is apparent in a comparison of the time series prior to 1992 with the time series following 1992, when the sample interval changed from 0.5 months to 1 month.

Figure 5b shows a time series of the inner bar position. Rapid offshore migration occurred in Dec. 1982 and Feb. 1989. These periods correspond to offshore migration of the inner bar, followed by the generation of a new inner bar near the shoreline (apparent rapid onshore migration). These periods are marked by minimum sand bar amplitudes (Figure 5c).

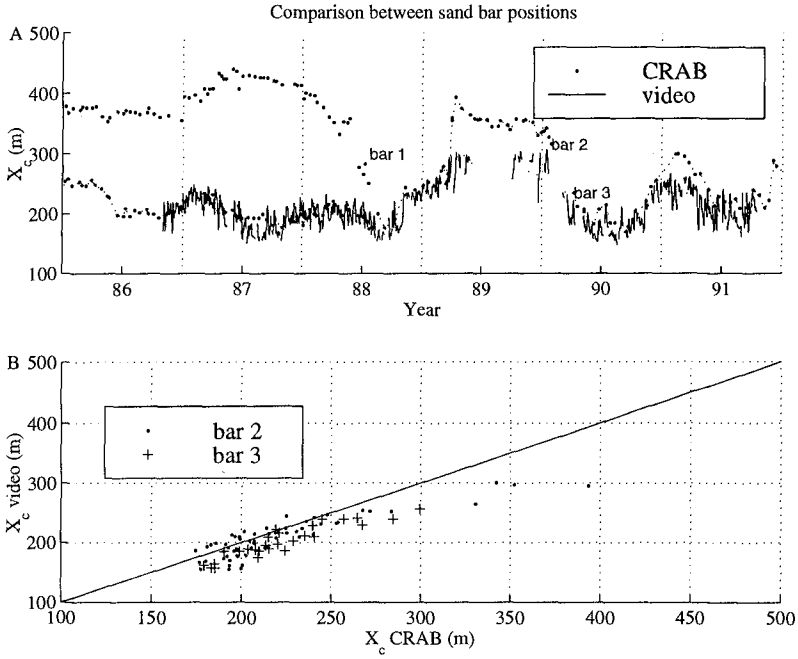

Figure 6. Time series of bar crest positions (A) from both the surveyed data sets (labeled "CRAB") and video estimates. Sand bars are labeled in order of their appearance at the FRF site. Panel B shows the correlation between survey- and video-based bar position estimates.

Figure 6 shows a time series of bar positions that were extracted from the video image time series, plotted together with time series extracted from the bathymetric data. The two time series generally correspond well with each other and clearly capture the same interannual variations of the inner bar at Duck. The image data resolve high frequency fluctuations, which may record actual variations in the bar crest position. Alternatively, the high frequency fluctuations may be related to high frequency fluctuations in the wave height, since patterns of wave breaking are used to visually identify bars in the video images.

The correlation between the time series generated from the two data sources is described in Figure 6b. The data are divided into two categories, one for bar 2 (the inner bar that formed prior to 1989, Figure 6a) and one for bar 3 (which formed after bar 2 migrated offshore to become an outer bar). The correlation, mean difference and standard deviation of the difference are shown in Table 1. The bar position identified in the video images tended to be onshore of the bar position extracted from the bathymetric surveys. This is consistent with the observations made by LH89, who attributed the shoreward bias to the persistence of foam shoreward of the bar crest. The difference in bar positions tended to increase as the bars moved farther offshore, which was not predicted by LH89.

Table 1. Statistics for bar position differences

Bar	N	R^2	Avg. Difference ($X_{video} - X_{bathy}$)	Std.
2	60	0.78	-13 m	21 m
3	27	0.85	-22 m	12 m

Figure 7a shows a comparison of the bar position differences plotted against wave height. There was a slight tendency for the difference in bar positions to decrease as the wave height increased. The relationship is more clearly seen if the discrepancy between bar positions is plotted as a function of both wave height and bar amplitude (Figure 7b). The contours are of the mean discrepancy within 0.25 m by 0.25m ranges of wave height and bar amplitude. Only means having 95% confidence regions less than 5 m wide are shown. The mean discrepancy is smallest when both wave height and bar amplitude are high. The discrepancy increases as bar amplitude decreases and increases as wave height decreases if the bar amplitude is large. If the bar amplitude is small, the discrepancy remains large and is relatively insensitive to changes in wave height.

The difference between the two bar position estimates may simply result from the definition of a bar in terms of a deviation from the background slope, as opposed to depth minimum. In all cases, the depth minimum (if it exists) occurs where the slope of the Gaussian shaped bar is equal to, but opposite of the plane beach slope. This point is onshore of the Gaussian bar position. The fractional (relative to a bar length, L) difference between the two choices of bar position is approximately $-(\beta_2 L)/(2 A)$. For the Duck case, this difference was typically less than 10%, which is within the error of the estimated differences.

4. Discussion and Conclusions

Typically, changes in the form of nearshore bathymetry involve the evolution of a number of characteristic shapes. Ideally, it is possible to describe the bathymetry in terms of a morphologic model having only a few parameters. In addition to providing an

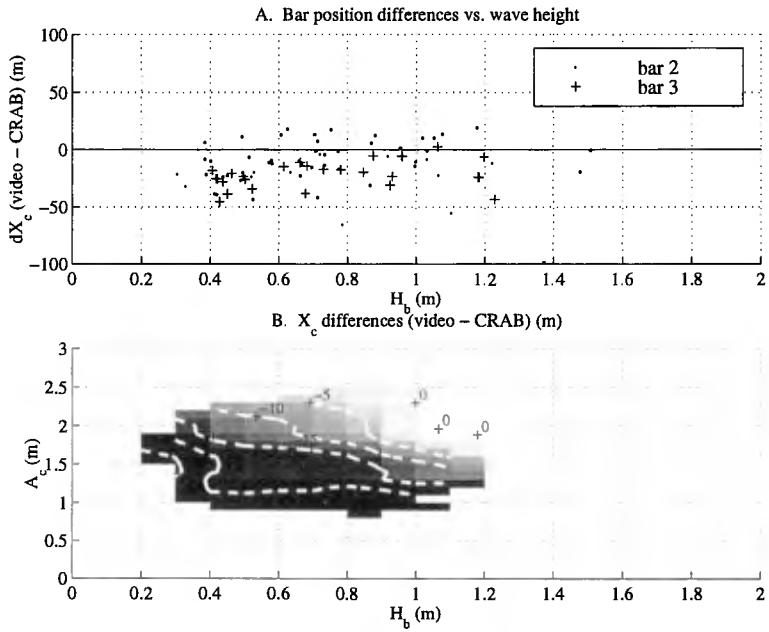

Figure 7. Analysis of discrepancy between survey and video estimates of bar crest positions. In panel A, the differences are plotted against the expected wave height at breaking (wave heights were transformed from observed wave heights using linear wave theory). Contours of the discrepancy are plotted in panel B as a function of bar amplitude and wave height.

objective definition of morphology, this step greatly reduces the dimensionality of the problem, aiding in the statistical analysis and physical interpretation of nearshore beach response.

We utilized an objective definition of nearshore morphology (Gaussian functions and a plane slope) to quantify and compare the morphologic information contained in two sources of morphologic data available from Duck, NC. Directly surveyed bathymetry provided the most complete definition of the morphologic state of the nearshore bathymetry. That is, all of the parameters of the morphologic model could be estimated from these data. Oblique video images were used to estimate the position of inner bars. This information represented only a subset of the morphologic parameters defined in the morphologic model. However, the image data were collected frequently (daily) and, thus, resolved morphologic variability over a wide range of time scales.

In a comparison, the bar positions extracted from the video images were well correlated ($R^2 = 0.8$) with positions extracted from the direct surveys. Deviations between the two different estimates of bar position depended on both wave height (consistent with observations reported by LH89) and, most strongly, on the bar amplitude. An explanation for the bar amplitude dependence could be an increasing dominance of the slope morphology on the wave breaking process as bar amplitudes approached zero. LH89 point out that, even on a plane beach, a "bar" would be identified due to the presence of a maximum in wave energy dissipation. The foam generated provides the visual signal used to identify bars. The differences in the bar position estimates made from the different data sets may need to be reconciled either empirically or, perhaps, using process-based models (LH89 or Aarninkhof et al., 1998).

5. Acknowledgements

The video image data were graciously provided by Tom Lippmann and were published previously in Lippmann et al., 1993. The bathymetric data were provided by the Army Corps of Engineers Field Research Facility. Many different analyses of these data have been published by many other people.

6. References

Aarninkhof, S. G. J., Janssen, P. C., and N. G. Plant, Quantitative estimations of bar dynamics from video images, *Proc. Coastal Dynamics '97, Plymouth*, pp.365-374, 1998.

Birkemeier, W. A. and C. Mason, The CRAB: A unique nearshore surveying vehicle, *Journal of Survey Engineering, 110*, 1-7, 1984.

Lippmann, T. C. and R. A. Holman, Quantification of sand bar morphology: A video technique based on wave dissipation, *Journal of Geophysical Research, 94*(C1), 995-1011, 1989.

Lippmann, T. C. and R. A. Holman, The spatial and temporal variability of sand bar morphology, *Journal of Geophysical Research, 95*(C7), 11,575-11,590, 1990.

Lippmann, T. C., R. A. Holman and K. K. Hathaway, Episodic, non-stationary behavior of a two sand bar system at Duck, NC, USA, *Journal of Coastal Research, SI*(15), 49-75, 1993.

Short, A. D., Three-dimensional beach stage model, *Journal of Geology, 87*, 553-571, 1975.

Sonu, C. J., Three-dimensional beach changes, *Journal of Geology, 81*, 42-64, 1973.

Wijnberg, K. M. and J. H. J. Terwindt, Extracting decadal morphological behavior from high-resolution, long-term bathymetric surveys along the Holland coast using eigenfunction analysis, *Marine Geology, 126*, 301-330, 1995.

Winant, C. D., D. L. Inman and C. E. Nordstrom, Description of seasonal beach changes using empirical eigenfunctions, *Journal of Geophysical Research, 80*(15), 1979-1986, 1975.

Wright, L. D. and A. D. Short, Morphodynamic variability of surf zones and beaches: A synthesis, *Marine Geology, 56*, 93-118, 1984.

Nonlinear Time-Averaged Model in Surf and Swash Zones

Bradley D. Johnson[1] and Nobuhisa Kobayashi, Member, ASCE[2]

Abstract

A time-averaged model is developed to predict the cross-shore variations of the mean and standard deviation of the free surface elevation from outside the surf zone to the lower swash zone on beaches. This new model includes nonlinear correction terms in the cross-shore radiation stress and energy flux that become important in very shallow water. Empirical formulas are proposed for the skewness and kurtosis as well as the ratio of the root-mean-square wave height to the mean water depth which increases rapidly near the still water shoreline. The developed model is shown to be in agreement with three irregular wave tests on a 1:16 smooth impermeable slope and two tests of quasi-equilibrium terraced and barred beaches. The model can predict the observed large increase of wave setup near the still water shoreline. The developed model and empirical formulas will need to be verified using additional experiments.

Introduction

The need for a simple model for the wave motion in the swash zone on a beach has been pointed out in relation to the prediction of beach erosion and recovery near the shoreline [e.g., Hedegaard et al. (1992)]. The time-dependent numerical model based on the finite-amplitude shallow-water equations (Kobayashi and Wurjanto 1992) has been shown to be capable of predicting the swash characteristics on natural beaches (Raubenheimer et al. 1995; Raubenheimer and Guza 1996). However, the time-dependent numerical model requires significant computation time and is hard to incorporate in beach profile models. The time-averaged models for random waves represented by the root-mean-square wave height [e.g., Battjes and Janssen (1978)] or expressed as the superposition of regular waves [e.g., Dally (1992)] are much more efficient computationally but do not predict the wave conditions in the swash zone (Cox et al. 1994).

A nonlinear time-averaged model is developed here to predict the cross-shore variations of the wave setup, $\overline{\eta}$, and the root-mean-square wave height, H_{rms}, from outside the surf zone to the lower swash zone where H_{rms} is defined as $H_{rms} = \sqrt{8}\,\sigma$ with σ

[1]Ph.D. Student, Dept. of Civ. & Envir. Engrg., Univ. of Delaware, Newark, DE 19716, USA
[2]Professor & Assoc. Director, Center for Applied Coastal Research, University of Delaware, Newark, DE 19716.

= standard deviation of the free surface elevation. This model is based on the time-averaged continuity, momentum, and energy equations derived by time-averaging the nonlinear equations used in the time-dependent model of Kobayashi and Wurjanto (1992). The time-averaged equations can be solved numerically with much less computation time but require empirical relationships to close the problem. The time-averaged rate of energy dissipation due to random wave breaking is estimated by modifying the empirical formula of Battjes and Stive (1985) to account for the landward increase of $H_{rms}/\overline{h}$ near the shoreline where $\overline{h}$ = mean water depth. The skewness s and the kurtosis K of the free surface elevation included in the time-averaged momentum and energy equations are expressed empirically as a function of $H_{rms}/\overline{h}$.

The developed model is compared with three tests conducted on a 1:16 smooth impermeable slope and two tests on quasi-equilibrium terraced and barred beaches consisting of fine sand. This new time-averaged model is shown to be capable of predicting the cross-shore variations of $\overline{\eta}$ and H_{rms} of the free surface elevation from outside the surf zone to the lower swash zone of frequent wave uprush and downrush. The model of Battjes and Stive (1985) considerably underpredicts $\overline{\eta}$ and H_{rms} near the still water shoreline. The new model will need to be verified using additional experiments because the empirical formulas adopted in the model are developed using the same five tests.

New Time-Averaged Model

The assumptions of alongshore uniformity and normally incident irregular waves are made in the following. To account for nonlinear effects in very shallow water, use is made of the time-averaged equations derived from the finite-amplitude shallow-water equations. Assuming that the beach is impermeable, the time-averaged continuity equation with the overbar denoting time-averaging is expressed as

$$\overline{hU} = 0 \tag{1}$$

where h = instantaneous water depth; and U = instantaneous depth-averaged horizontal velocity. The time-averaged cross-shore momentum equation is written as (Kobayashi et al. 1989)

$$\frac{dS_{xx}}{dx} = -\rho g \overline{h}\ \frac{d\overline{\eta}}{dx} \tag{2}$$

with

$$S_{xx} = \rho\left[\overline{hU^2} + \frac{1}{2}g\overline{(\eta-\overline{\eta})^2}\right] \tag{3}$$

in which x = cross-shore coordinate taken to be positive landward; S_{xx} = cross-shore radiation stress; ρ = fluid density; g = gravitational acceleration; and η = instantaneous free surface elevation above the still water level (SWL). The time-averaged bottom shear stress may be neglected in (2) as explained by Kobayashi and Johnson (1998). The bottom elevation z_b given by $z_b = (\eta - h)$ is assumed to depend on x only. The time-averaged energy equation corresponding to (1) and (2) may be expressed as (Kobayashi and Wurjanto 1992)

$$\frac{d}{dx}\left(\overline{E_F}\right) = -\overline{D_B} \tag{4}$$

with

$$\overline{E_F} = \frac{1}{2}\,\rho\,\overline{hU^3} + \rho g\overline{\eta h U} \tag{5}$$

in which $\overline{E_F}$ = energy flux per unit width; and $\overline{D_B}$ = energy dissipation rate due to wave breaking which needs to be estimated empirically in this time-averaged model.

To simplify (1), (2), and (4), the instantaneous free surface elevation η is expressed as

$$\eta = \overline{\eta} + \sigma\eta_* \tag{6}$$

where $\overline{\eta}$ and σ = mean and standard deviation of η; and η_* = normalized free surface elevation with $\overline{\eta_*} = 0$ and $\overline{\eta_*^2} = 1$. If wave reflection is negligible, linear long wave theory may be used locally to relate the oscillatory components $(\eta - \overline{\eta})$ and $(U - \overline{U})$ inside and outside the surf zone (Guza and Thornton 1980; Kobayashi et al. 1998). This relationship together with (6) yields

$$U = \overline{U} + \sqrt{\frac{g}{\overline{h}}}\,\sigma\eta_* \tag{7}$$

Eq. (7) is necessary to reduce the number of unknown variables in the time-averaged model although the local reflection coefficient may not be small near the still water shoreline on beaches (Baquerizo et al. 1997). Substitution of (6) and (7) into (1) with $h = (\eta - z_b)$ and $\overline{h} = (\overline{\eta} - z_b)$ yields

$$\overline{U} = -\sigma_*^2\sqrt{g\overline{h}} \quad ; \quad \sigma_* = \frac{\sigma}{\overline{h}} \tag{8}$$

which indicates that $\overline{U}$ is negative and represents return current (Kobayashi et al. 1989). Although (8) does not account for the landward mass flux due to a surface roller, it predicted the undertow measured at the mid-depth below SWL fairly accurately (Kobayashi et al. 1997, 1998).

Substitution of (6) and (7) with (8) into (3) yields

$$S_{xx} = \frac{1}{8}\,\rho\,g\,H_{rms}^2\left[\left(2n - \frac{1}{2}\right) + C_s\right] \quad ; \quad H_{rms} = \sqrt{8}\,\sigma \tag{9}$$

with

$$C_s = \sigma_* s - \sigma_*^2 \tag{10}$$

where s = skewness of η and η_* with $\overline{\eta_*^3} = s$; n = finite-depth adjustment parameter with $n = 1$ in shallow water; and C_s = nonlinear correction term for S_{xx}. For linear progressive waves in finite depth, n is normally expressed as [e.g., Battjes and Stive (1985)]

$$n = \frac{1}{2}\left[1 + \frac{2k_p\overline{h}}{\sinh\left(2k_p\overline{h}\right)}\right] \tag{11}$$

where k_p = linear wave number corresponding to the spectral peak period T_p outside the surf zone. The cross-shore variation of T_p may be neglected in (11) because $n = 1$ in shallow water for any reasonable representative wave period used to calculate k_p. The cross-shore radiation stress S_{xx} based on linear wave theory is given by (9) with

$C_s = 0$. C_s is on the order of unity near the still water shoreline and can not be neglected in the swash zone (Kobayashi and Johnson 1998).

Substitution of (6) and (7) with (8) into (5) yields

$$\overline{E}_F = \frac{1}{8}\,\rho\, g\, H_{rms}^2\, n\, C_p(1 + C_F) \tag{12}$$

with

$$C_F = \frac{3}{2}\, s\, \sigma_* \left(1 - \sigma_*^2\right) + \frac{1}{2}\, \sigma_*^2\, (K - 5) + \sigma_*^4 \tag{13}$$

where C_p = phase velocity based on T_p with $C_p = \sqrt{g\overline{h}}$ in shallow water; C_F = nonlinear correction term for $\overline{E}_F$; and K = kurtosis of η and η_* with $\overline{\eta_*^4} = K$. The finite-depth adjustment is included in (12) in the same way as (9) where $n\, C_p$ in (12) is the group velocity based on T_p. The cross-shore energy flux $\overline{E}_F$ based on linear wave theory is given by (12) with $C_F = 0$ where C_F is on the order of unity near the still water shoreline (Kobayashi and Johnson 1998).

The momentum equation (2) with (9) and the energy equation (4) with (12) need to be solved numerically to predict the cross-shore variations of the wave setup $\overline{\eta} = (\overline{h} + z_b)$ and the root-mean-square wave height $H_{rms} = \sqrt{8}\,\sigma$. These equations reduce to those used in the existing time-averaged models [e.g., Battjes and Stive (1985)] if $C_s = 0$ and $C_F = 0$. To estimate the nonlinear correction terms C_s and C_F using (10) and (13) with $\sigma_* = \sigma/\overline{h}$, the skewness s and the kurtosis K are assumed to be expressed in the following empirical forms

$$s = f_s\left(H_{rms}/\overline{h}\right) \quad ; \quad K = f_K(s) \tag{14}$$

where f_s and f_K = empirical functions which will be obtained using the five tests discussed later.

Finally, the energy dissipation rate $\overline{D}_B$ due to wave breaking in the energy equation (4) needs to be estimated. The empirical formula proposed by Battjes and Janssen (1978) and calibrated by Battjes and Stive (1985) is adopted here for its simplicity. The formula proposed by Thornton and Guza (1983) may predict the distributions of breaking and nonbreaking wave heights more accurately but requires additional empirical parameters. In the present formulation, the exponential gamma function may be used to describe the probability density function of η instead of wave heights after the cross-shore variations of $\overline{\eta}$, σ, and s are predicted (Kobayashi et al. 1997, 1998).

The calibrated formula by Battjes and Stive (1985) is given by

$$\overline{D_B} = \frac{\alpha}{4}\,\rho\, g\, f_p\, Q\, H_m^2 \tag{15}$$

with

$$\frac{Q - 1}{\ln Q} = \left(\frac{H_{rms}}{H_m}\right)^2 \tag{16}$$

$$H_m = \frac{0.88}{k_p} \tanh\left(\frac{\gamma\, k_p\, \overline{h}}{0.88}\right) \tag{17}$$

$$\gamma = 0.5 + 0.4 \tanh\left(33\, \frac{H_{rmso}}{L_o}\right) \quad ; \quad L_o = \frac{g\, T_p^2}{2\pi} \tag{18}$$

where α = empirical coefficient recommended as $\alpha = 1$; f_p = spectral peak frequency given by $f_p = T_p^{-1}$; Q = local fraction of breaking waves in the range $0 \le Q \le 1$; H_m = local depth-limited wave height; k_p = linear wave number calculated using f_p and $\overline{h}$; γ = empirical parameter determining $H_m = \gamma \overline{h}$ in shallow water; L_o = deep-water wavelength based on T_p; and H_{rmso} = deep-water value of H_{rms} calculated using linear wave shoaling theory with T_p, $\overline{h}$ and H_{rms} specified at the seaward boundary of the numerical model.

The empirical parameter γ is uncertain in light of the field data by Raubenheimer et al. (1996) but is estimated using (18) without any additional calibration. Relatedly, Battjes and Janssen (1978) indicated that $\overline{D}_B$ given by (15) would underestimate the actual energy dissipation rate and produce $H_{rms} > H_m$ near the shoreline, although (16) with $Q \le 1$ requires $H_{rms} \le H_m$. They recommended use of a cutoff of $H_{rms} = H_m$ when $H_{rms} > H_m$. This adjustment leads to $H_{rms} = \gamma \overline{h}$ near the shoreline. However, $H_{rms}/\overline{h}$ is not constant and increases landward where $H_{rms}/\overline{h} \simeq 2$ at the still water shoreline for the SUPERTANK data of Kriebel (1994). As a result, (15) with (16)–(18) is assumed to be valid only in the outer zone $x < x_i$ with x_i = cross-shore location where Q computed by (16) becomes unity and the still water depth decreases landward in the region $x > x_i$. The latter condition is required for a barred beach to allow $Q < 1$ landward of the bar crest where $Q = 1$ may occur. For the inner zone $x > x_i$, the ratio $H_* = H_{rms}/\overline{h}$ is assumed to be expressed as

$$H_* = \gamma + (\gamma_s - \gamma)\, x_*^{\beta} \quad ; \quad x_* = \frac{x - x_i}{x_s - x_i} > 0 \tag{19}$$

where γ_s = value of H_* on the order of two at the still water shoreline located at $x = x_s$; and β = empirical parameter. The values of γ_s and β will be calibrated using the five tests discussed later. Eq. (19) describes the landward increase of H_* from $H_* = \gamma$ at $x = x_i$ to $H_* = \gamma_s$ at $x = x_s > x_i$. For the inner zone $x > x_i$, the momentum equation (2) and (19) are used to predict the cross-shore variations of $\overline{h}$ and H_{rms}, whereas the energy equation (4) is used to estimate $\overline{D_B}$ which must be positive or zero.

The numerical model called CSHORE (Kobayashi and Johnson 1998) is developed to solve (2) and (4) with (9)–(19) where CSHORE includes the option to include the bottom friction effects neglected in (2) and (4). The seaward boundary of CSHORE is located at $x = 0$ where the values of T_p, H_{rms} and $\overline{\eta}$ at $x = 0$ are specified as input. The bottom elevation $z_b(x)$ in the region $x \ge 0$ is also specified as input and the location x_s of the still water shoreline is found using $z_b(x = x_s) = 0$. First-order finite-difference approximations of (2) and (4) are expressed as

$$\overline{\eta}_{j+1} = \overline{\eta}_j - \left[\rho\, g \left(\overline{h}_{j+1} + \overline{h}_j\right)\right]^{-1} \left\{2\left[(S_{xx})_{j+1} - (S_{xx})_j\right]\right\} \tag{20}$$

$$\left(\overline{E}_F\right)_{j+1} = \left(\overline{E}_F\right)_j - \frac{\Delta x}{2}\left[\left(\overline{D}_B\right)_{j+1} + \left(\overline{D}_B\right)_j\right] \tag{21}$$

where the subscripts $(j+1)$ and j indicate the quantities at nodes located at x_{j+1} and x_j, respectively, with $\Delta x = (x_{j+1} - x_j)$ being the nodal spacing. In the subsequent computations for the laboratory data, use is made of $\Delta x \simeq 10$ cm. For the known quantities at node j, the unknown quantities at node $(j+1)$ are computed by solving (20) and (21) using an iteration method starting from σ_{j+1}^2 computed using (21) with $(\overline{D}_B)_{j+1} = (\overline{D}_B)_j$. The adopted iteration method is found to converge within several iterations. The convergency is based on the differences between the iterated values of σ_{j+1} and $\overline{h}_{j+1}$ being less than the specified small value ϵ, where $\epsilon = 0.01$ mm is used in the subsequent computations. If $Q_{j+1} = 1$ and $(dz_b/dx) > 0$ for $x \geq x_{j+1}$, the inner zone is reached and $x_i = x_{j+1}$ is set.

For the nodes located in the inner zone $x > x_i$, (19) is used to obtain $H_* = H_{rms}/\overline{h}$ and $\sigma_* = H_*/\sqrt{8}$. Since the mean water depth $\overline{h}$ can become very small in the inner zone, (2) with (9) is rewritten as

$$(2P+1)\frac{d\overline{h}}{dx} = -\overline{h}\frac{dP}{dx} - \frac{dz_b}{dx} \qquad \text{for} \quad x > x_i \tag{22}$$

with

$$P = \sigma_*^2\left[\left(2n - \frac{1}{2}\right) + \sigma_* s - \sigma_*^2\right] \tag{23}$$

A first-order finite difference approximation of (22) between nodes j and $(j+1)$ yields

$$\overline{h}_{j+1} = (3P_{j+1} + P_j + 2)^{-1}\left\{(P_{j+1} + 3P_j + 2)\,\overline{h}_j - 2\left[(z_b)_{j+1} - (z_b)_j\right]\right\} \tag{24}$$

Eq. (24) is solved using an iteration method starting from the value of n_{j+1} involved in P_{j+1} calculated using $\overline{h}_j$ where $(\sigma_*)_{j+1}$ and s_{j+1} are known using (19) and (14), respectively. Since n given by (11) is essentially unity in shallow water, this interaction method converges rapidly. After $\overline{h}_{j+1}$ is computed, the energy equation (4) is used to obtain $(\overline{D}_B)_{j+1}$. The computation is marched landward until $\overline{h}_{j+1} < \epsilon$.

EXPERIMENTS AND EMPIRICAL FORMULAS

Two different experiments were conducted in a wave tank that was 30 m long, 2.4 m wide, and 1.5 m high. These experiments were explained in detail by Kobayashi et al. (1997, 1998). Irregular waves based on the TMA spectrum were generated with a piston-type wave paddle. Three tests were conducted with a plywood beach of a 1:16 slope. The water depth in the tank was 76.2 cm. For each test, 17 runs were performed to measure free surface elevations using eight capacitance wave gages. Wave gages partially immersed in gage wells were used for the free surface measurements near the still water shoreline. In addition, two tests were conducted with a fine sand beach whose initial slope was 1:12. The sand was well-sorted and its median diameter was 0.18 mm. These two tests with specified random waves were conducted after the sand beach was exposed to the specified wave action for several days and became quasi-equilibrium with the bottom elevation changes less than about 1 cm/hr. For each of the two tests, 21 runs were performed to measure free surface elevations using ten wave gages. Wave gages near the still water shoreline were partially buried in the sand. The duration of each run in these five tests was 400 s and the initial transient duration of 75 s was removed. The sampling rate was 20 Hz.

Table 1: Wave Conditions at Seaward Boundary and Breaker Parameter γ for Five Tests

Test (1)	d (cm) (2)	$\overline{\eta}$ (cm) (3)	T_p (s) (4)	H_{rms} (cm) (5)	H_{inc} (cm) (6)	R (7)	γ (8)	x_i (m) (9)	x_s (m) (10)
1	75.0	0.03	1.5	12.4	12.2	0.14	0.84	11.1	12.0
2	75.0	-0.32	2.8	16.9	15.8	0.15	0.67	9.0	12.0
3	76.2	-0.24	4.7	18.4	18.4	0.17	0.56	8.3	13.0
4	60.0	-0.15	1.6	12.8	12.9	0.19	0.83	13.3	13.8
5	60.0	-0.12	2.8	14.6	14.3	0.25	0.65	12.4	13.7

Table 1 lists the wave conditions at the seaward boundary located at $x = 0$ for each of the five tests where d = still water depth; $\overline{\eta}$ = wave setup or set-down; T_p = spectral peak period; and H_{rms} = root-mean-square wave height defined as $H_{rms} = \sqrt{8}\,\sigma$ with σ = standard deviation of the measured free surface oscillation. Tests 1, 2 and 3 are the 1:16 slope tests described by Kobayashi et al. (1998), whereas tests 4 and 5 correspond to the sand beach tests explained by Kobayashi et al. (1997). The wave setup or set-down is very small at $x = 0$ outside the surf zone. The measured wave conditions at $x = 0$ include the slight effects of reflected waves. The incident and reflected waves at $x = 0$ were estimated using a three-gage method by Kobayashi et al. (1997, 1998). Table 1 lists the estimated values of the spectral root-mean-square wave height, $H_{inc} = \sqrt{8m_{oi}}$, with m_{oi} = zero-moment of the incident wave spectrum at $x = 0$, and the average reflection coefficient, $R = \sqrt{m_{or}/m_{oi}}$, with m_{or} = zero-moment of the reflected wave spectrum at $x = 0$. The difference between H_{rms} and H_{inc} is negligible except for test 2 with $(H_{rms} - H_{inc})/H_{rms} = 0.065$. The reflection coefficient was in the narrow range $0.14 \leq R \leq 0.25$ and slightly larger for tests 4 and 5 with the foreshore slope of about 1:5 at the still water shoreline.

The measured values of $\overline{\eta}$, T_p, and H_{rms} at $x = 0$ listed in Table 1 are specified as input to CSHORE. The measured bottom elevation $z_b(x)$ in the region $x \geq 0$ is also specified as input where Table 1 lists the cross-shore location x_s of the still water shoreline for each test. The bottom profile $z_b(x)$ will be presented in conjunction with the measured and predicted cross-shore variations of $\overline{\eta}$ and H_{rms}. The breaker parameter γ calculated using (18) and the cross-shore location x_i at the seaward limit of the inner zone computed by CSHORE are listed in Table 1.

The measured values of $H_* = H_{rms}/\overline{h}$ in the inner zone $x > x_i$ are used to calibrate the new empirical parameters γ_s and β in (19) for the five tests. Fig. 1 shows the

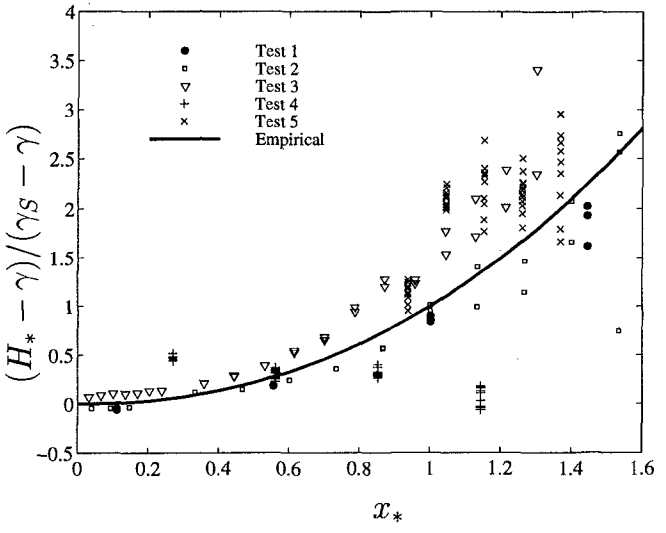

Figure 1: Empirical Formula for $H_* = H_{rms}/\overline{h}$ in Inner Zone $x > x_i$.

measured values of $(H_* - \gamma)/(\gamma_s - \gamma)$ with $\gamma_s = 2$ as a function of $x_* = (x - x_i)/(x_s - x_i)$ where the values of γ, x_i, and x_s for each test are listed in Table 1. The trend of the scattered data points for the five tests may be represented by (19) with $\gamma_s = 2$ and $\beta = 2.2$. Fig. 1 shows that H_* increases gradually from $H_* = \gamma$ at $x_* = 0$ and more rapidly above the still water shoreline located at $x_* = 1$. It is noted that the large scatter in the region $x_* > 1$ is caused partly by the scatter of data points obtained in repeated runs due to the difficulty in measuring $\overline{h}$ and H_{rms} accurately in the swash zone.

The measured values of H_*, s, and K in the entire region $x \geq 0$ for the five tests are analyzed to obtain the empirical relationships expressed by (14). Fig. 2 shows the skewness s as a function of $H_* = H_{rms}/\overline{h}$. The trend of the scattered data points in Fig. 2 are simply represented by three straight lines

$$\begin{aligned} s &= 2H_* && \text{for} \quad 0.1 < H_* \leq 0.5 \\ s &= 1.5 - H_* && \text{for} \quad 0.5 \leq H_* \leq 1.0 \\ s &= 0.7H_* - 0.2 && \text{for} \quad 1.0 \leq H_* \lesssim 5 \end{aligned} \tag{25}$$

The skewness s increases initially with the increase of H_* due to wave shoaling but decreases after wave breaking. Both s and H_* increase rapidly near and beyond the still water shoreline. Fig. 3 shows the relationship between the kurtosis K and the skewness s which may be expressed as

$$K = 3 + s^{2.2} \qquad \text{for} \quad 0.2 < s \lesssim 3 \tag{26}$$

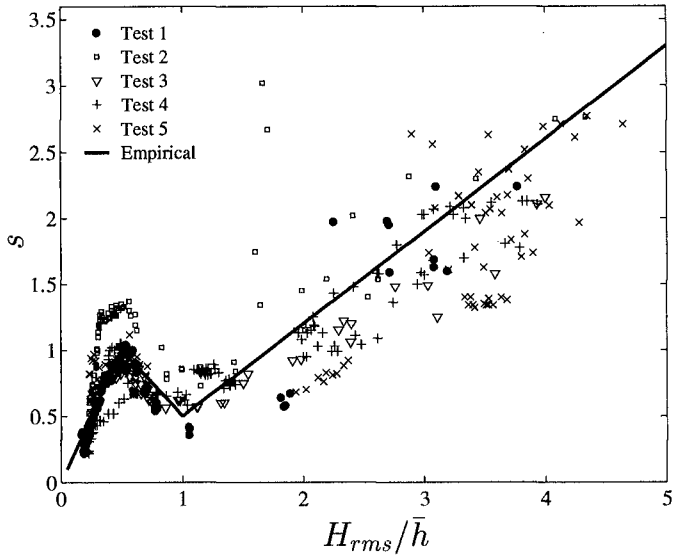

Figure 2: Empirical Formula for Skewness s as a Function of H_*.

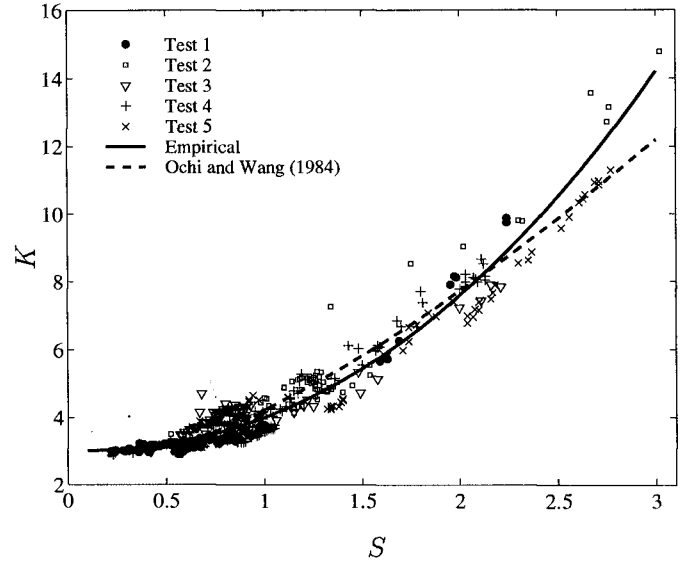

Figure 3: Empirical Formula for Kurtosis K as a Function of Skewness s.

The empirical relationship between K and s proposed by Ochi and Wang (1984) yields similar agreement as shown in Fig. 3. However, their expression is more complicated and (26) is adopted here for its simplicity.

COMPARISONS WITH FIVE TESTS

The numerical model CSHORE is compared with the five tests listed in Table 1 and used to develop the empirical formulas (25) and (26) as well as (19) with $\gamma_s = 2$ and $\beta = 2.2$. Figs. 4–8 compare the measured and computed cross-shore variations of $\overline{\eta}$ and H_{rms} for tests 1–5, respectively. The variations of $\overline{\eta}$ and H_{rms} computed by the model of Battjes and Stive (BJS hereafter) are also plotted in these figures. The bottom elevation $z_b(x)$ above and below SWL is shown in the first and second panels, respectively, in Figs. 4–8 to show the effects of the beach profile on the wave setup $\overline{\eta}$ and the root-mean-square wave height H_{rms}. The data points from repeated runs in each test are presented without averaging to indicate the degree of the data scatter which was apparent in the swash zone because of the difficulty in measuring small water depth accurately (Kobayashi et al. 1997, 1998).

For tests 1–3 shown in Figs. 4–6, breaker types on the 1:16 smooth slope varied from mostly spilling breakers for test 1 to predominantly plunging breakers for test 3. Correspondingly, the inner zone became wider from test 1 to test 3 where $(x_s - x_i)$ = 0.9, 3.0 and 4.7 m for tests 1, 2, and 3, respectively, in Table 1. Comparing CSHORE and the BJS model, the computed variations of $\overline{\eta}$ and H_{rms} in the outer zone $x < x_i$ are practically the same in view of the larger uncertainty associated with the empirical formula (15) with (16)–(18). No attempt is made to calibrate γ to improve the agreement for H_{rms} in the outer zone for test 2. In the inner zone $x > x_i$, CSHORE is capable of predicting the larger increase of the wave setup $\overline{\eta}$ and the more gradual decrease of the wave height H_{rms} in the inner zone.

For tests 4 and 5 shown in Figs. 7 and 8, incident waves shoaled and broke on the small bar at the edge of the terrace. Plunging breakers at the terrace edge were intense in test 5. Wave breaking was reduced on the terrace before incident waves broke again in the swash zone. The BJS model is capable of predicting this wave transformation across the terrace except for the detailed variations of H_{rms} at the terrace edge. The differences between CSHORE and BJS model are limited essentially in the narrow inner zone where $(x_s - x_i) = 0.5$ and 1.3 m for tests 4 and 5, respectively, in Table 1. CSHORE allows the extension of BJS model into the lower swash zone.

CONCLUSIONS

A time-averaged model is developed to predict the cross-shore variations of the mean and standard deviation of the free surface elevation from outside the surf zone to the lower swash zone. This time-averaged model derived from the time-dependent continuity, momentum, and energy equations which were used successfully to predict irregular wave runup on beaches includes nonlinear corrections terms in the cross-shore radiation stress and energy flux. The correction terms involving the skewness and kurtosis are important in very shallow water. The time-averaging of the time-dependent equations reduces computation time considerably but creates a closure problem. The energy dissipation rate due to wave breaking is estimated using an

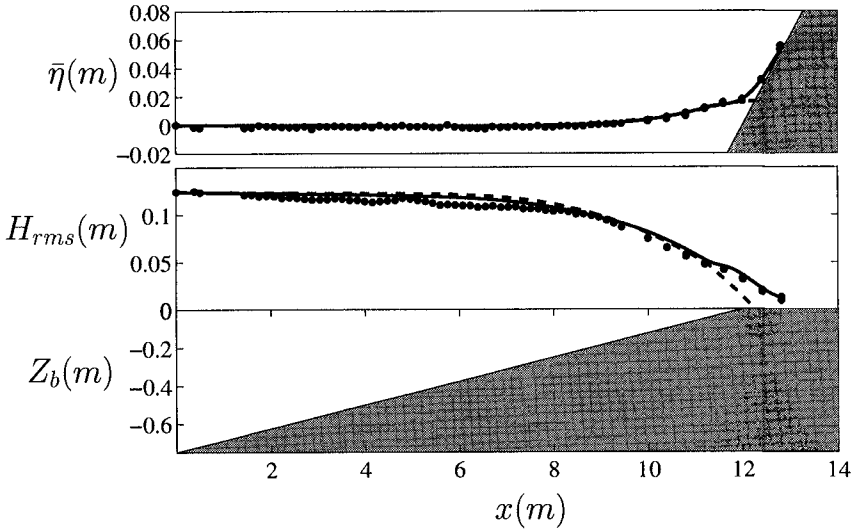

Figure 4: Measured and Computed Setup $\overline{\eta}$, and Height H_{rms} for Test 1.

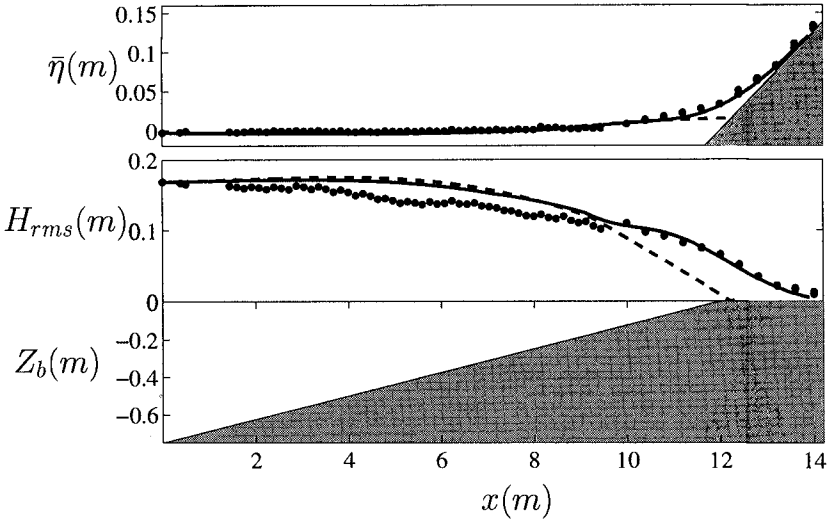

Figure 5: Measured and Computed Setup $\overline{\eta}$, and Height H_{rms} for Test 2.

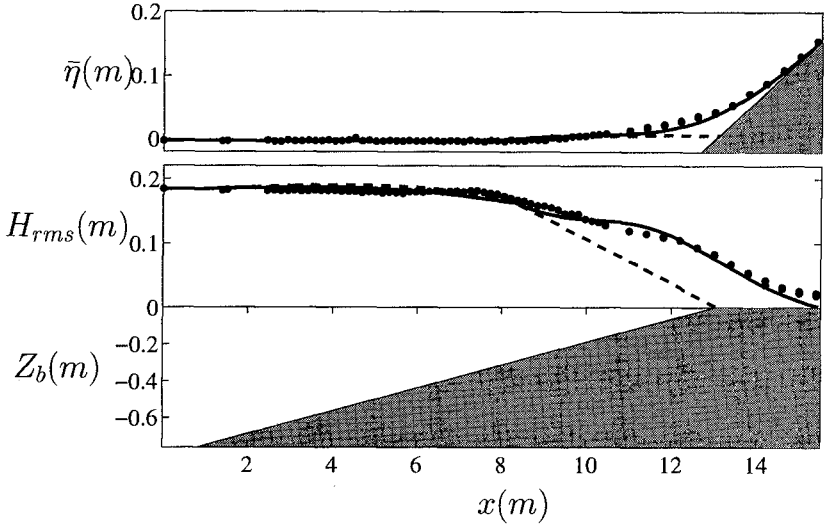

Figure 6: Measured and Computed Setup $\overline{\eta}$, and Height H_{rms} for Test 3.

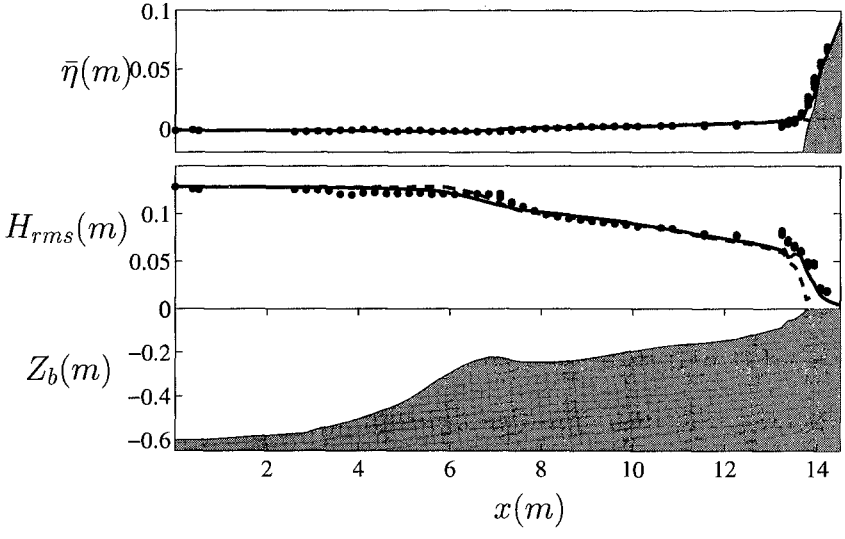

Figure 7: Measured and Computed Setup $\overline{\eta}$, and Height H_{rms} for Test 4.

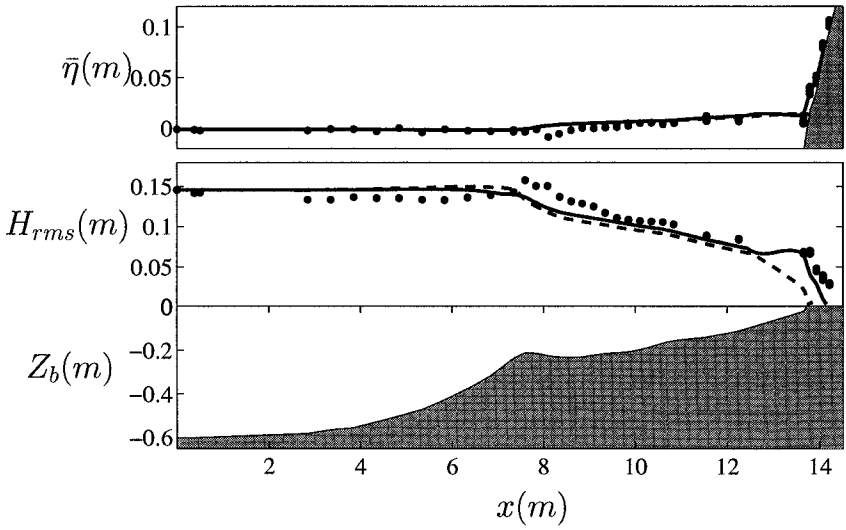

Figure 8: Measured and Computed Setup $\overline{\eta}$, and Height H_{rms} for Test 5.

existing empirical formula in the outer zone. In the inner zone near the still water shoreline, a new empirical formula for $H_* = H_{rms}/\overline{h}$ is proposed to describe the landward increase of H_*. In addition, simple empirical formulas are proposed to express the skewness and kurtosis as a function of H_*.

The developed model is compared with three irregular wave tests on a 1:16 smooth impermeable slope and two tests on quasi-equilibrium terraced and barred beaches. The major improvements of the new model in comparison to existing models are that it is capable of predicting the wave setup and root-mean-square wave height near the still water shoreline. Since the new empirical formulas are developed using the same five tests, the new model will need to be verified using additional tests. Coupling of the new wave model with a cross-shore sediment transport model may make it feasible to predict the erosion and recovery near the still water shoreline.

ACKNOWLEDGMENT

This work was supported by the NOAA Office of Sea Grant, Department of Commerce, under Grant No. NA85AA-D-SG033 (Project SG97 R/OE-22).

APPENDIX. REFERENCES

Baquerizo, A., Losada, M.A., Smith, J.M., and Kobayashi, N. (1997). "Cross-shore

variation of wave reflection from beaches." *J. Wtrwy., Port, Coast. and Oc. Engrg.*, ASCE, 123(5), 274–279.

Battjes, J.A., and Janssen, J.P.F.M. (1978). "Energy loss and set-up due to breaking of random waves." *Proc., 16th Coast. Engrg. Conf.*, ASCE, New York, N.Y., 1, 569–587.

Battjes, J.A., and Stive, M.J.F. (1985). "Calibration and verification of a dissipation model for random breaking waves." *J. Geophys. Res.*, 90(C5), 9159–9167.

Cox, D.T., Kobayashi, N., and Kriebel, D.L. (1994). "Numerical model verification using SUPERTANK data in surf and swash zones." *Proc., Coast. Dynamics '94*, ASCE, New York, N.Y., 248–262.

Dally, W.R. (1992). "Random breaking waves: Field verification of a wave-by-wave algorithm for engineering application." *Coast. Engrg.*, 16, 369–397.

Guza, R.T., and Thornton, E.B. (1980). "Local and shoaled comparisons of sea surface elevations, pressures, and velocities." *J. Geophys. Res.*, 85(C3), 1524–1530.

Hedegaard, I.B., Roelvink, J.A., Southgate, H., Pechon, P., Nicholson, J., and Hamm, L. (1992). "Intercomparison of coastal profile models." *Proc., 23rd Coast. Engrg. Conf.*, ASCE, New York, N.Y., 2, 2108–2121.

Kobayashi, N., DeSilva, G.S., and Watson, K.D. (1989). "Wave transformation and swash oscillation on gentle and steep slopes." *J. Geophys. Res.*, 94(C1), 951–966.

Kobayashi, N., Herrman, M.N., Johnson, B.D., and Orzech, M.D. (1998). "Probability distribution of surface elevation in surf and swash zones." *J. Wtrwy., Port, Coast. and Oc. Engrg.*, ASCE, 124(3), 99–107.

Kobayashi, N., and Johnson, B.D. (1998). "Computer program CSHORE for predicting cross-shore transformation of irregular breaking waves." *Res. Rep. CACR-98-04*, Ctr. for Appl. Coast. Res., Univ. of Delaware, Newark, Del.

Kobayashi, N., Orzech, M.D., Johnson, B.D., and Herrman, M.N. (1997). "Probability modeling of surf zone and swash dynamics." *Proc., Waves '97*, ASCE, Reston, Va., 107–121.

Kobayashi, N., and Wurjanto, A. (1992). "Irregular wave setup and run-up on beaches." *J. Wtrwy., Port, Coast. and Oc. Engrg.*, ASCE, 118(4), 368–386.

Kriebel, D.L. (1994). "Swash zone wave characteristic from SUPERTANK." *Proc., 24th Coast. Engrg. Conf.*, ASCE, New York, N.Y., 2, 2207–2221.

Ochi, M.K., and Wang, W.C. (1984). "Non-Gaussian characteristics of coastal waves." *Proc., 19th Coast. Engrg. Conf.*, ASCE, New York, N.Y., 1, 516–531.

Raubenheimer, B., and Guza, R.T. (1996). "Observations and predictions of run-up." *J. Geophys. Res.*, 101(C10), 25575–25587.

Raubenheimer, B., Guza, R.T., and Elgar, S. (1996). "Wave transformation across the inner surf zone." *J. Geophys. Res.*, 101(C10), 25589–25597.

Raubenheimer, B., Guza, R.T., Elgar, S., and Kobayashi, N. (1995). "Swash on a gently sloping beach." *J. Geophys. Res.*, 100(C5), 8751–8760.

Thornton, E.B., and Guza, R.T. (1983). "Transformation of wave height distribution." *J. Geophys. Res.*, 88(C10), 5925–5938.

Swash Zone Morphodynamics and Sediment Transport Processes

K. Todd Holland[1], Asbury H. Sallenger, Jr.[2], Britt Raubenheimer[3], and Steve Elgar[3]

Abstract

Observations of foreshore morphologic change and swash flow velocities were made at Duck, NC in an effort to estimate cross-shore sediment flux magnitudes. The three-dimensional foreshore surface over an approximately 10 x 20m study area was determined repeatedly to roughly centimeter accuracy using a stereometric video method. Sediment flux magnitudes derived from the temporal gradient of these data showed erosion rates of over 25 cm/hr. Near-bed, cross-shore swash velocities were measured at multiple cross-shore locations using a separate video technique. Swash velocities estimated using this method were found to be consistent with current measurements obtained using acoustic Doppler and ducted impeller current meters. The swash zone profile observations and velocity estimates were used to test an energetics–based total load sediment transport model. Although the trends of both the model and the observations were qualitatively consistent, the magnitudes and positioning of observed sediment fluxes did not match the transport model predictions. This discrepancy implies that other factors, such as water depth variations, infiltration, or sediment advection, may be important.

Introduction

It is generally recognized that gradients of sediment flux across the swash zone contribute significantly to beach morphological change. However, the present understanding of sediment transport mechanisms in this region is poor, partially owing to the complexity of foreshore processes. Nonlinearity and feedback between forcing and response are common. Yet even more problematic is the fact that measurements of fluid motions and sediment concentrations are difficult to obtain in this dynamic region. Swash flows move in a Lagrangian sense requiring either very dense arrays of in-situ sensors, dual-resistance runup wires (Guza and Thornton 1982; Raubenheimer et al. 1995), or

[1]Naval Research Laboratory, Code 7442, Stennis Space Center, MS 39529-5004
[2]USGS Center for Coastal Geology, 600 4th St. S, St. Petersburg, FL 33071
[3]Washinton State University, EECS 2752, Pullman, WA 99164

remote sensing methods (Holland et al. 1995). In addition, the foreshore surface itself may change rapidly making estimation of the measurement elevation complicated.

In previous studies of swash zone morphology and associated sediment transport, coarsely sampled changes in bed elevation have been used to infer total load sediment transport rates (Duncan 1964; Howd and Holman 1987; Sallenger and Richmond 1984; Waddell 1976); and either optical sensors or traps have been used to monitor suspended and bedload concentrations (Beach and Sternberg 1992; Horn and Mason 1994; Osborne and Rooker 1997; and others). Although much is known about fluid motions in the swash zone and the above studies give glimpses of relative sediment concentration magnitudes, there is a great need for simultaneous measurement of hydrodynamic forcing and morphodynamic response to advance foreshore sediment transport modeling. This deficiency is even more pronounced with respect to relatively large temporal and spatial scales (hours to days and 10s to 100s of meters, respectively).

This paper presents new swash observations collected at Duck NC with a recently developed stereometric video system and a video-based current meter method that show great promise in overcoming the difficulties mentioned above. The observations of profile change and cross-shore swash velocity are used to develop and validate a simple model of swash zone sediment transport. The correlation between model estimates and observations is then discussed.

Study Site and Field Methods

Data were obtained at the US Army Corps of Engineers' Field Research Facility (FRF) at Duck, NC. Duck is multi-barred, intermediate to reflective beach with a tidal range of approximately 2 m. The foreshore slope is roughly 1:12. A large number of experiments have taken place at the FRF field site with many swash observations indicating infragravity dominated motions at the shoreline, especially during storms.

To quantify net sediment transport and morphologic change in the swash zone, foreshore surface measurements were made over a study region of dimensions 10 m in the cross-shore and 20 m in the alongshore during the DUCK94 experiment. Three-dimensional (3-D) foreshore topography was determined to roughly centimeter accuracy by using a stereometric video method (described fully in Holland and Holman 1997). By monitoring the progression of the swash line using edge detection algorithms, multiple views of the foreshore study area allow determination of point object positions (x,y,z) for each pixel along the swash edge. Repeating the process for each subsequent edge over the swash cycle results in several thousand estimates of the foreshore surface per wave. Although observations were made over a much larger time interval, the data presented in this paper were obtained during a particularly dynamic period of erosion on October 10, 1994. A burst sampling mode was employed to measure swash excursions and elevations over the foreshore region approximately once every 15 minutes at a rate of 6 Hz [Figure 1].

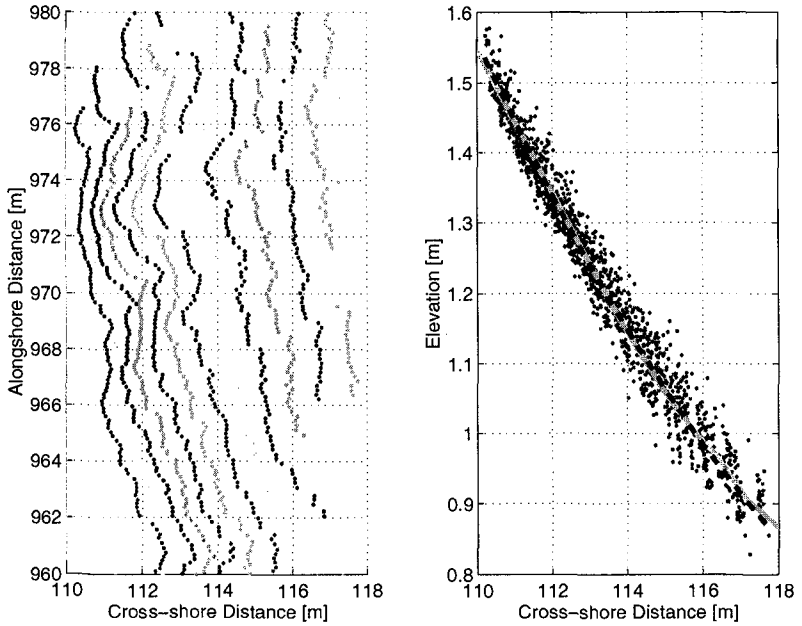

Figure 1: Left panel shows stereo-estimated swash edge positions intensity coded by time (temporal separation interval of 0.33 s). Right panel shows elevation versus cross-shore distance as determined by the stereo method (dots) and GPS surveying methods (dashed). Optimal interpolation of the nearly 7000 stereo estimates (solid) yields a cross-shore profile with a root-mean-square deviation from the surveyed profile of 1.4 cm.

Corresponding cross-shore swash velocities were estimated using a new application of an existing video method known as a timestack (Holland et al. 1995). Since timestacks [Figure 2] represent the temporal variation in pixel intensity along a given cross-shore profile, Lagrangian estimates of the swash edge speed can be calculated as the time derivative of the measured cross-shore swash position. In contrast, Eulerian estimates of cross-shore currents, $u(x)$, were calculated at specific cross-shore distances using the edge speeds during uprush and backwash derived from timestacks (sampled at 10 Hz). In doing so we assumed that fluid particles immediately behind the bore front move at the speed of the bore and that a constant velocity gradient exists from the moment the swash bore reaches the video sensor till the time of maximum backwash. Velocities were set to zero for times during which the virtual sensor was dry. Using this method, saw-toothed, swash velocity time series were computed at eleven locations spaced by one meter along the cross-shore transect in the center of the study area. Figure 3 exemplifies the differences in velocities at two cross-shore positions.

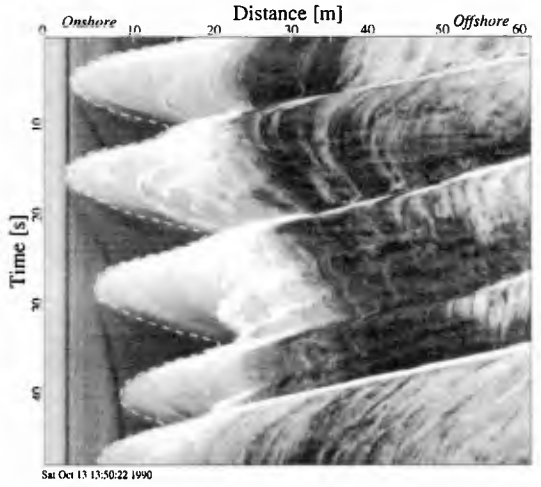

Figure 2: Video timestack showing swash edge position (dashed) as a function of time and cross-shore position (from Holland and Holman 1993).

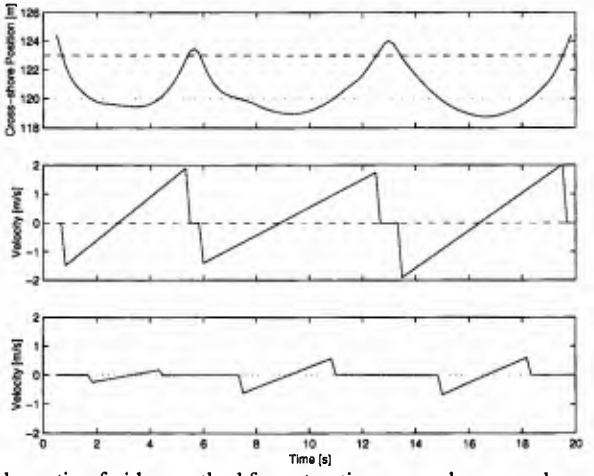

Figure 3: Schematic of video method for extracting cross-shore swash currents at two cross-shore (x=123 and x=120, middle and bottom respectively) locations from position time series (top). Position decreases landward and negative velocities correspond to onshore flow.

To determine the validity of this video method for deriving cross-shore currents in the swash zone, measurements made using this technique were compared to velocity measurements obtained using Acoustic Doppler Velocimeter (ADV) and ducted impeller current meters. During the SANDYDUCK experiment, horizontal and vertical swash velocities approximately 5 cm above the bed were measured at a 2 Hz sampling rate at one location using a Sontek ADV [Figure 4]. Additionally, 4-Hz cross-shore current measurements at 4 and 8 cm above the beach surface were available from "Smith" ducted impeller sensors deployed during an experiment at Gleneden OR in 1994 (Puleo et al. submitted). Figure 5 shows an example of the comparison. In general, the results are similar. The timing of the uprushes measured by the in-situ gauges closely corresponds to that of the leading edge of the swash as it reaches the sensor location. Current meter velocities were also very small during time intervals where the video indicated the sensor was dry (u = 0 m/s). Peak uprush and backwash velocity magnitudes were often similar and the slopes of the temporal velocity gradients from each method were roughly equivalent. Since there was only a small amount of structure in the interval between the beginning of uprush and the end of backwash, the constant gradient assumption in the video method appears justified.

Figure 4: ADV instrumentation designed to monitor swash velocities as part of the SANDYDUCK experiment.

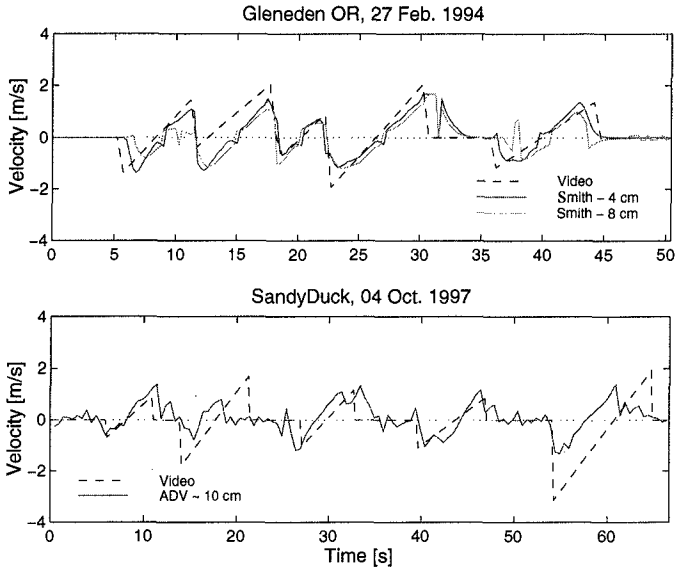

Figure 5: Time series showing cross-shore current estimates in swash zone obtained using video and in-situ instrumentation.

Table 1 shows the quantitative results of the comparison of 333 swash events. The means of the various parameters are comparable, although video-based uprush and backwash speeds and swash durations were on average of greater magnitude than the observations from the in-situ instrumentation. Estimates of higher moments of cross-shore currents (e.g. u^3) were quite variable, even between sensors of the same type. However, theses discrepancies are somewhat expected since the ADV and Smith meters sampled flows at higher elevations than that sensed by the video. For example, the minimum depth required for the in-situ gauges is on the order of 4 to 5 cm; and for optimal operation, the ADV sensor (positioned 5 cm above the sampling volume) must be fully immersed, thereby requiring depths of over 10 cm. The response times of the in-situ instrumentation appear to be somewhat slow, especially during uprush. Given that the in-situ instrumentation was out of the flow more often, coarsely sampled, and essentially excluded portions of the swash signal very near the bed, the video results, although simplified, appear sensible. One possible source of additional error is that obliquely incident swash motions will positively bias the cross-shore current estimates from the video. Measurements of the longshore trend of the swash edge suggest this error with respect to mean velocities was on the order of 10%. Longshore swash currents sampled with the ADV were less than 0.08 m/s.

	u_{up}	u_{down}	u^3	$u^3\|u\|$	*dur*	*m*
Gleneden (235)						
Video	-0.94	0.85	0.07	0.12	6.4	0.33
Smith (4 cm)	-0.69	0.71	0.13	0.06	3.6	0.42
Smith (8 cm)	-0.71	0.64	0.04	0.02	3.4	0.43
Sandyduck (98)						
Video	-1.73	1.61	-0.28	-0.15	7.1	0.46
ADV (5-10 cm)	-0.83	0.89	-0.03	-0.01	4.5	0.38

Table 1. Comparison of video-based and in-situ estimates of cross-shore swash velocity parameters. Symbols denote various swash moments, mean swash durations, and slope of the temporal velocity gradient.

Swash Velocity Characteristics

Unfortunately, no in-situ instrumentation was deployed during the Duck94 experiment, therefore, only video-based cross-shore current measurements were made. Over the approximately six-hour period of measurements, velocity magnitudes of up to 1.78 m/s were observed. The mean duration of a swash cycle at the approximate setup level was 3.9 s. Average initial uprush and final backwash speeds were essentially equivalent with magnitudes of 1.16 and 1.19 m/s respectively. However, shorter-term averages of the swash time series showed a tendency toward offshore-dominated flow prior to high tide and onshore-dominated flow during the falling tide. Also observed was an inequality between peak uprush and backwash velocities for individual swash events. Spatial gradients in the velocity structure tended to follow the trends in the mean velocities with positive gradients during the rising tide and negative gradients after high tide.

Foreshore Profile Change

Stereo-estimated foreshore surfaces on Oct 10 are shown in Figure 6. An optimal interpolation technique was used to fit the estimates to a constant grid surface, $h(x,y)$, with an even spacing of 40 cm between grid points. Temporal derivatives of the surfaces showed erosion rates of over 0.25 m^3/hr with a maximum of 60 cm of erosion occurring in the center of the study area. Figure 7 shows the alongshore-averaged profile change rate as a function of cross-shore distance and time. A fairly constant loss of sediment is apparent proceeding in the landward direction with the rising tide. Of particular interest was the fact that the offshore wave conditions throughout the run were approximately equivalent, yet morphologic response was dramatically different before and after high tide.

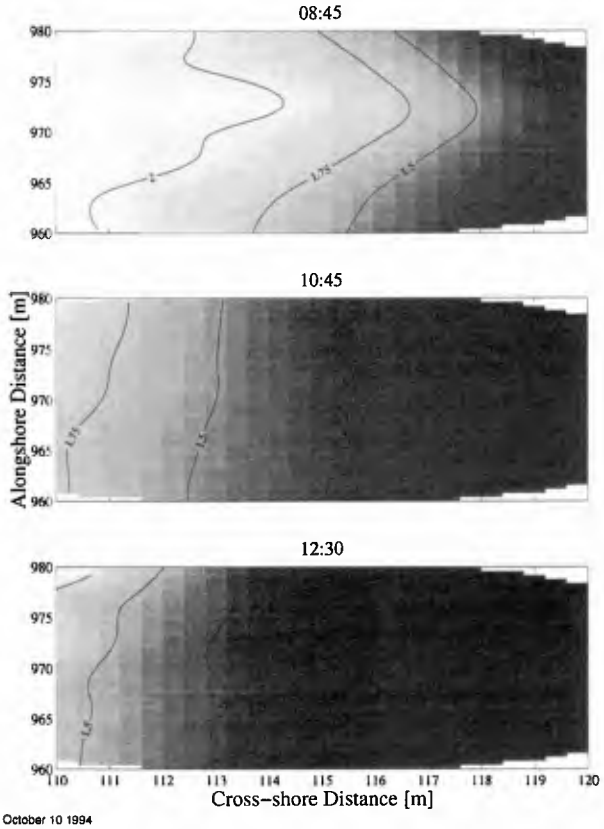

Figure 6: Stereo surfaces gridded and contoured following optimal interpolation analysis. The foreshore morphology changed from cuspate at 0845 hours to plane by 1045 with more than 60 cm of erosion measured over the entire four-hour period.

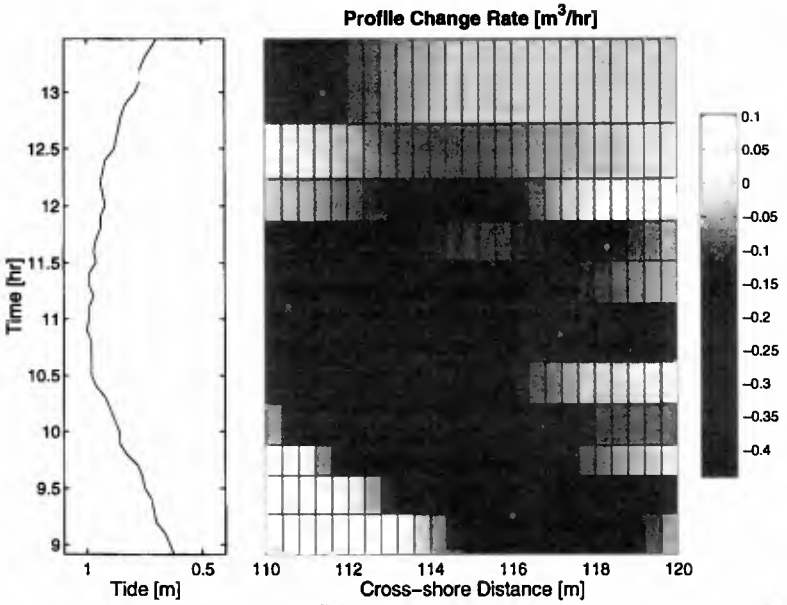

Figure 7: Alongshore-averaged profile change as a function of cross-shore distance and time.

Sediment Transport Model

A simple numerical model was developed and validated using the time histories of foreshore surface change in conjunction with video-based swash velocity measurements. Bagnold's (1963; 1966) energetics-based, depth-integrated volume transport equation was adopted as the description of sediment dynamics for these data since it directly relates transport rates to instantaneous shear stresses derived from the local velocity field, $u(x)$. The form of the equation is given by:

$$q_t = \frac{\rho_w c_f}{(\rho_s - \rho_w)g}\left(\left\{\frac{\varepsilon_s(1-\varepsilon_b)}{\left(w/\langle|u|\rangle\right) - \tan\beta}\right\} + \left\{\frac{\varepsilon_b}{\tan\phi - \tan\beta}\right\}\right)\langle u^3\rangle \qquad (1)$$

where q_t represents the time-averaged, cross-shore volumetric total sediment load transport per unit width per unit time, ρ = 1.025 g/m^3 is the seawater density, ρ_s = 2.65 g/m^3 is the sediment density, β is the beach gradient, ϕ is the friction angle of the sediment ($\tan(\phi)$ = 0.63), w is the sediment fall velocity (~ 6 cm/s assuming a mean grain diameter of 0.5 mm), and g is the gravitational acceleration. Angle brackets represent

time averaging and values for the friction, bedload, and suspended load efficiency factors, (c_f, ε_b, and ε_s, respectively) were defined following Bagnold (1966). This type of formulation has been previously applied to the swash zone (Hardisty et al. 1984; Hughes et al. 1997a; Masselink and Hughes in review) and serves as a good candidate model for these data using inputs of cross-shore current at a given cross-shore location and time varying beach slope.

Model results were compared to observations obtained using the stereo method by estimating profile change given spatial gradients in sediment transport predictions via the sediment continuity equation:

$$\frac{\partial h}{\partial t} = \frac{1}{1-\nu}\frac{\partial q_t}{\partial x} \tag{2}$$

This relation assumes that no alongshore gradients in sediment transport contribute to profile change and ignores advection of sediment from the surf zone into the swash zone. The results, shown in Figure 8, indicate that the model was successful at describing the qualitative trends in profile evolution, however the magnitudes and positioning of observed sediment fluxes did not match the transport model predictions. For example, the erosion of the foreshore surface was observed to occur earlier than predicted. Also, a period of accretion was predicted after high tide (approximately 1230), while the measured profile remained stable.

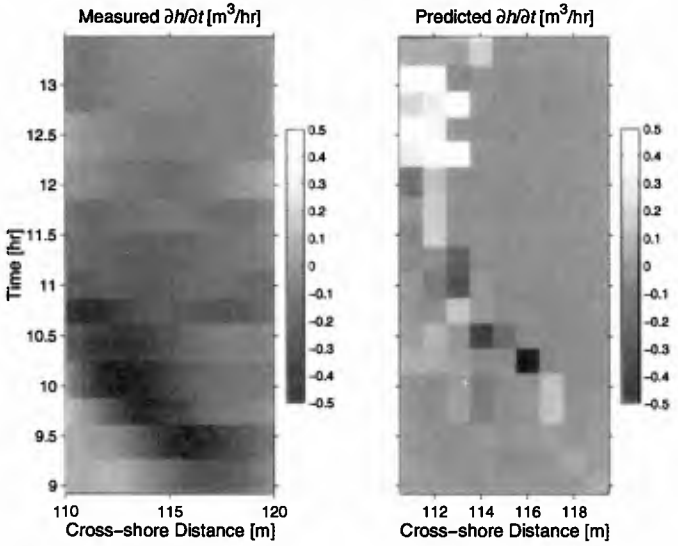

Figure 8: Measured (left panel) and predicted (right-panel) profile change as a function of cross-shore distance and time.

Discussion and Conclusions

Video-based methods were utilized to allow rapid and simultaneous measurement of swash zone hydrodynamic forcing and morphodynamic response. Although a small number of prior investigators have presented observations of swash zone sediment transport and cross-shore flow velocities, namely Hardisty et al. (1984), Hughes et al. (1997b), and Masselink and Hughes (in review), this study is distinguished by the large temporal and spatial coverage allowed by the video techniques. Another advantage of these methods is that velocity patterns associated with infragravity band wave motions are sampled. However, at present, alongshore currents cannot be directly estimated and extension of these methods to deeper surf zone flows is difficult.

An energetics-based sediment transport model (Bagnold 1963; Bagnold 1966) was validated using these data and was shown to be insufficient in predicting the magnitudes, and in some cases sign, of transport observed. Qualitative correlation between the model and observations during the first half of the measurement period suggests that swash flow velocity is an important parameter affecting foreshore sediment transport, however, the magnitude discrepancies indicate that other factors should be considered in future efforts. For example, the effects of water depth variations, infiltration, groundwater, and the influx of sediment from offshore, may well be responsible for a significant portion of the mismatch. One possibility for future adaptation of the model is through the use of variable efficiency coefficients during uprush and backwash as suggested by Masselink and Hughes (in review).

Acknowledgements

The authors thank the outstanding support personnel from the Scripps Institution of Oceanography and the US Army Corps of Engineers Field Research Facility for their assistance in the field data collections. We also appreciate the data contributions and insight of Mr. Jack Puleo and Dr. Reginald Beach. This work was funded by the Coastal Dynamics program at the Office of Naval Research, the US Geological Survey's Center for Coastal Geology, and from base program funding to the Naval Research Laboratory from ONR.

References

Bagnold, R. A. (1963). "Mechanics of marine sedimentation." The Sea, M. N. Hill, ed., Wiley-Interscience, New York, 507-528.

Bagnold, R. A. (1966). "An Approach to the Sediment Transport Problem from General Physics." 422-I, U.S. Geological Survey, 37.

Beach, R. A., and Sternberg, R. W. (1992). "Suspended sediment transport in the surf zone: Response to incident wave and longshore current interaction." Marine Geology, 108(3-4), 275-294.

Duncan, J. R. (1964). "The effects of water table and tide cycle on swash-backwash sediment distribution and beach profile development." Marine Geology, 2, 186-197.

Guza, R. T., and Thornton, E. B. (1982). "Swash oscillations on a natural beach." Journal of Geophysical Research, 87(C1), 483-491.

Hardisty, J., Collier, J., and Hamilton, D. (1984). "A calibration of the Bagnold beach equation." Marine Geology, 61(1), 95-101.

Holland, K. T., and Holman, R. A. (1993). "The statistical distribution of swash maxima on natural beaches." Journal of Geophysical Research, 98(C6), 10,271-10,278.

Holland, K. T., and Holman, R. A. (1997). "Video estimation of foreshore topography using trinocular stereo." Journal of Coastal Research, 13(1), 81-87.

Holland, K. T., Raubenheimer, B., Guza, R. T., and Holman, R. A. (1995). "Runup kinematics on a natural beach." Journal of Geophysical Research, 100(C3), 4985-4993.

Horn, D. P., and Mason, T. (1994). "Swash zone sediment transport modes." Marine Geology, 120(3-4), 309-325.

Howd, P. A., and Holman, R. A. (1987). "A simple model of beach foreshore response to long period waves." Marine Geology, 78(1-2), 11-22.

Hughes, M., Masselink, G., Hanslow, D., and Mitchell, D. (1997a). "Towards a better understanding of swash zone sediment transport." Coastal Dynamics, Plymouth, U.K., 804-823.

Hughes, M. G., Masselink, G., and Brander, R. W. (1997b). "Flow velocity and sediment transport in the swash zone of a steep beach." Marine Geology, 138(1-2), 91-103.

Masselink, G., and Hughes, M. (in review). "Field investigation of sediment transport in the swash zone." Continental Shelf Research.

Osborne, P. D., and Rooker, G. A. (1997). "Surf zone and swash zone sediment dynamics on high energy beaches: West Auckland, New Zealand." Coastal Dynamics, Plymouth, UK, 814-823.

Puleo, J. A., Beach, R. A., Holman, R. A., and Allen, J. S. (submitted). "Observations of swash zone sediment suspension and transport on a steep beach: Variations between the uprush and backwash and the importance of bore-generated turbulence." Journal of Geophysical Research.

Raubenheimer, B., Guza, R. T., Elgar, S., and Kobayashi, N. (1995). "Swash on a gently sloping beach." Journal of Geophysical Research, 100(C5), 8751-8760.

Sallenger, A. H., Jr., and Richmond, B. M. (1984). "High-frequency sediment-level oscillations in the swash zone." Marine Geology, 60, 155-164.

Waddell, E. (1976). "Swash-groundwater-beach profile interactions." Beach and Nearshore Sedimentation, R. A. Davis, Jr. and R. L. Ethington, eds., SEPM, Tulsa, OK, 115-125.

FIELD MEASUREMENTS OF SWASH INDUCED PRESSURES WITHIN A SANDY BEACH

D. P. Horn[1], T. E. Baldock[2], A. J. Baird[3] and T. E. Mason[2]

Abstract

This paper describes field measurements of near-surface hydraulic gradients within a sandy beach during individual swash cycles. We show several different types of behaviour which may have implications for swash zone sediment transport: (1) measurements of swash depth; (2) 'unloading' events with large upward-acting hydraulic gradients; (3) infiltration events with smaller downward-acting hydraulic gradients; (4) situations where the probes lower in the bed measure significantly lower heads than the probe at the surface, leading to strongly downward-acting hydraulic gradients; and (5) measurements in the capillary fringe. Large hydraulic gradients, which are more than sufficient to induce fluidisation, occur in the top 15 mm of the bed under swash and backwash. These large hydraulic gradients, which occur only in the very top section of the bed, may coincide with a significant depth of water (up to 40 mm), which suggests the potential for entrainment of the fluidised bed under backwash.

Introduction

Accretion and deposition on the foreshore is a function of the interaction of surface and subsurface flow regimes in the swash zone, and an understanding of the interaction between surface and groundwater flows is necessary to model swash zone sediment transport. Previous research has suggested that infiltration and exfiltration in the swash zone may be important mechanisms in beach profile changes, governing sediment deposition and erosion rates above mean sea level. Much of this work has focused on examining the link between tidally-induced groundwater flows and swash infiltration/exfiltration, with the assumption that changes in swash volume would alter swash/backwash flow asymmetry. However, Turner and Nielsen (1997) identified several other mechanisms by which vertical flow through a porous bed could affect swash zone sediment transport, including an alteration in the effective weight of the surface sediment due to vertical fluid drag and modified shear stresses exerted on the bed due to boundary layer thinning due to infiltration or thickening due to exfiltration.

1) Lecturer, Department of Geography, Birkbeck College, University of London, London, W1P 2LL, UK. Fax: 0171 631 6480, email: d.horn@geog.bbk.ac.uk
2) Research Associate, School of Civil and Structural Engineering, University of Plymouth, Plymouth PL1 2DE, UK
3) Lecturer, Department of Geography, University of Sheffield, Sheffield S10 2TN, UK

It has been suggested by a number of authors going back to Grant (1946, 1948) that groundwater outflow from a beach during the ebb tide may enhance the potential for fluidisation of sand, and thus the ease with which sand can be transported by swash flows. However, groundwater outflow from a beach in response to a falling tide is unlikely to be sufficient to induce fluidisation since hydraulic gradients under the sand surface will tend to be relatively small, generally of the order of the beach slope (1:100 to 1:10). Baird et al. (1996,1997,1998) suggested a different mechanism for the local fluidisation of the sediment bed due to the propagation and release of a pressure pulse into the seepage face during swash. They showed theoretically how hydraulic gradients in the saturated sediment beneath swash can exceed the threshold for fluidisation.

Despite recent measurements of pore water pressures under swash such as those of Turner and Nielsen (1997), there is still considerable uncertainty about the effects of hydraulic gradients on sediment transport mechanisms and rates (Oh and Dean, 1994; Baldock and Holmes, 1998, this volume), and it is important to determine the magnitude of the hydraulic gradients near the surface of the sediment bed in order to identify the nature of the seepage flow within the bed. This paper addresses this point and describes field measurements of the near-surface hydraulic gradients within a sandy beach during individual swash cycles.

Field site and methodology

Field measurements were made on a sandy beach at Canford Cliffs, Poole, England, a groyned beach with a mean slope of 3.2° ($\tan\beta = 0.055$) on the upper foreshore and a mean slope of 1.5° ($\tan\beta = 0.027$) on the lower foreshore. The sand is well-sorted and negatively skewed, with a mean sediment size of 0.24 mm. The mean hydraulic conductivity of the sediment was 0.00225 ms^{-1}, with a range from 0.00036 to 0.01179 ms^{-1}, and a coefficient of variation of 143%, which is typical for this parameter. The beach is backed by a concrete sea wall set in underlying poorly-permeable silts giving no-flow conditions on the inland and lower boundary. The tidal range at Canford Cliffs varies between 0.2 and 2.2 metres on neap and spring tides respectively. The field site is described in more detail in Baird et al. (1998).

Two deployments were undertaken, one in March 1997 and one in October 1997. The March 1997 deployment was conducted on a spring tide, with a tidal range of 1.3 metres. The wave conditions during the March deployment were atypical for this coastline, with long period swell ($T \approx 16$ s, $H_b \approx 0.8$ m) resulting in a swash zone in excess of 30 m width and with little interaction between sequential swash cycles. The October 1997 deployment was also conducted on a spring tide, with a tidal range of 2 metres. Wave parameters seaward of the swash zone were measured with a seabed-mounted pressure transducer located approximately 17.5 m seaward of the swash instruments. All instruments were logged at 4 Hz. The wave conditions in the October deployment were much more typical of this limited-fetch coastline. The significant wave height varied over the measurement period between 0.23 and 0.43 m, while H_{rms} varied between 0.16 and 0.3 m. The peak wave period varied between 3 and 4.7 seconds, and the width of the swash zone varied between 3 and 7 m. The value of the surf scaling parameter ($2\pi^2 H_b/gT^2\tan^2\beta$) varied between 9 and 16.9, indicating intermediate conditions. Low values of the surf scaling parameter (<2.5) indicate reflective conditions, whereas high values of the surf scaling parameter (>20) are associated with dissipative conditions.

Near-surface hydraulic gradients in the swash zone were measured by a technique developed by Baldock and Holmes (1996). This uses a series of 2 mm internal diameter probes, inserted into the sediment and connected to pressure transducers above the water surface (Figure 1). Pressure variation is transmitted into each probe through twelve 0.4 mm holes drilled into the tip. The probes cause negligible disturbance to the

swash flow or the sediment, and may be moved vertically within the bed to compensate for bed level changes over several swash cycles. The whole system may be easily moved to any location on the foreshore and therefore swash zone measurements can be made at different tidal stages. Four probes were deployed with a horizontal spacing of 1 cm (shore parallel) and with a range of vertical spacings (minimum 1 cm). Vertical hydraulic gradients could therefore be obtained within the upper 3 cm of the beach sediment at a single position in the beach.

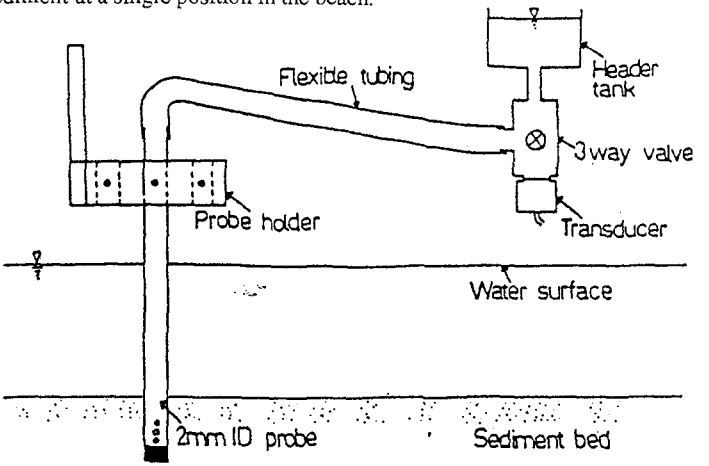

Figure 1. The pressure measurement system.

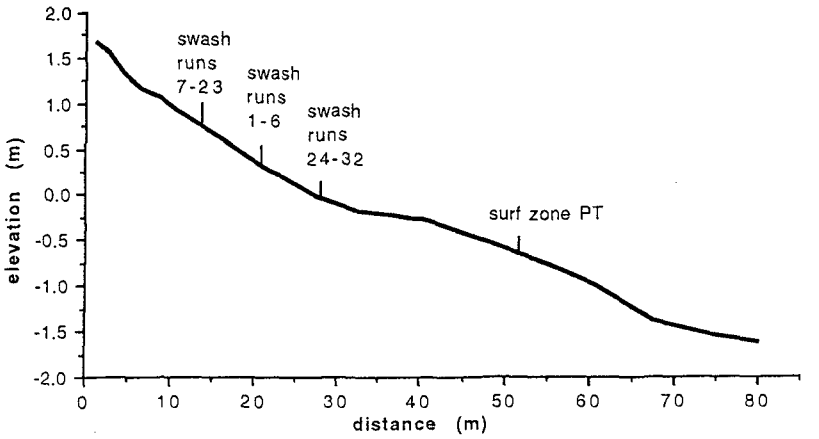

Figure 2. The beach profile and instrument locations on 19 October 1997.

In the October deployment, the spacing between the top probe and the second probe was 11 mm, the spacing between the second probe and the third probe was 11 mm, and the spacing between the third probe and the fourth probe was 10 mm. Measurements were taken with the array at a number of positions, the lowest of which was with the top probe at -65 mm and the bottom probe at -97 mm. However, the most common configuration was with the top probe 5 mm below the surface, and probe 2 at -16 mm, probe 3 at -27 mm and probe 4 at -37 mm. The position of the array was adjusted

constantly to ensure that the top probe remained at the surface as the bed level changed. Measurements were made at two positions on the flood tide and one position on the ebb tide (Figure 2); however, only data obtained on the rising tide are shown in this paper. Measurement was begun when the instruments were at the landward edge of the swash zone, and the swash zone moved past the measurement point as the tide rose. Twenty six data sets were collected in March 1997 and thirty-two data sets in October 1997. A selection of the results will be shown here, mainly from the October data. Some results of the March deployment were presented by Baird et al. (1997).

Results

All data are shown as either head (h) in mm or hydraulic gradient (dh/dz), which is expressed in head units and therefore dimensionless. All pressure readings from the probes were zeroed to hydrostatic pressure with the watertable at the sand surface. In effect, therefore, all probe readings can be converted to length units to give total head values with the surface acting as a datum. Thus, positive values mean that the water level is above the sand surface: in other words, swash or backwash. Negative head values mean the water level is below the sand surface. However, negative heads do not necessarily mean a real negative pressure (i.e. suction). Only if the head value is less than the probe elevation below the surface is there a suction. In the convention used here, a positive hydraulic gradient represents a downward-acting seepage force (infiltration) and a negative hydraulic gradient represents an upward-acting seepage force. The fluidisation criterion adopted here is based on Packwood and Peregrine (1980), who noted that for many sands and fine gravels, fluidisation occurs when the upward-acting dynamic hydraulic gradient is greater than (i.e. more negative than) about -0.6 to -0.7 (in the convention used here).

Figures 3 and 4 show time series of heads 5 mm below the bed surface (in effect the swash depth) for the March and October deployments, respectively. Small changes in the saturated bed level can be seen, indicated by deviations from zero head at the end of the backwash. Wave groups are evident in both diagrams, with little interaction between sequential swash cycles. Despite the difference in the wave conditions on the two deployments, grouping is evident in all of the swash records. Low-frequency swash motions will be directly induced by these wave groups and are probably dominant over standing long waves in this case (Baldock et al., 1997). However, here we are mainly concerned with short wave swash motion.

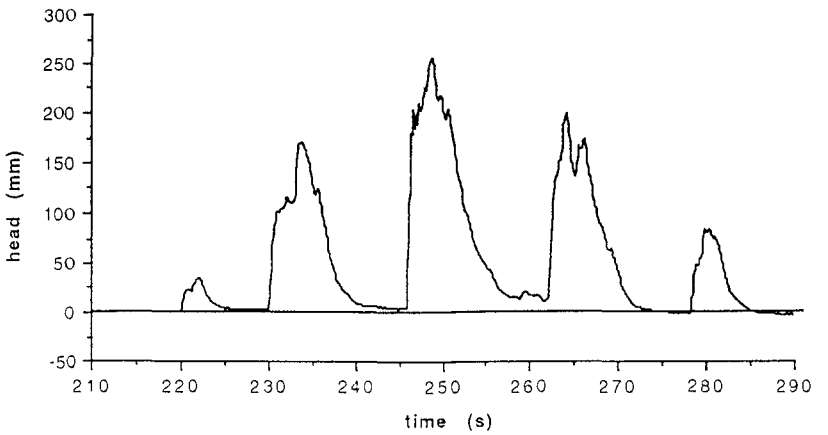

Figure 3. Swash-induced head 5 mm below the bed surface (run 1, 25 March 1997).

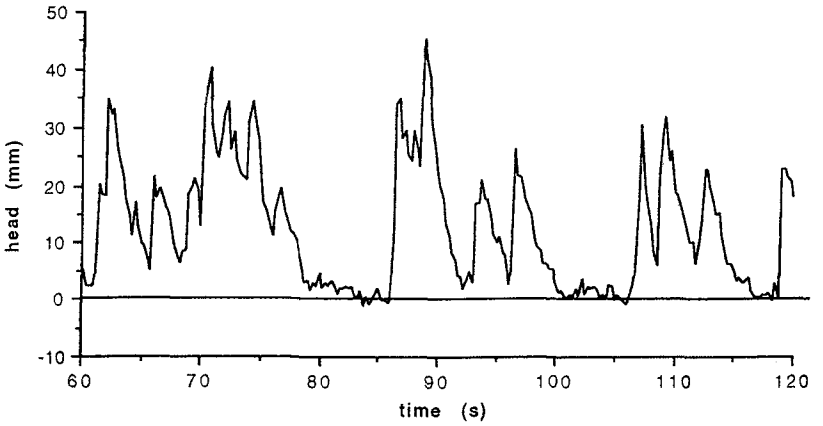

Figure 4. Swash-induced head 5 mm below the bed surface (run 2, 19 October 1997).

Figures 5 and 7 show heads immediately below the surface from the March and October deployments, respectively, while Figures 6 and 8 show the associated hydraulic gradients in the 15-16 mm immediately below the bed surface. Despite the difference in incident wave conditions, a similar phenomenon is observed in both cases (and in many others not shown here). All data were obtained on a rising tide. Similar effects were not observed on a falling tide, where positive hydraulic gradients appeared to dominate. Only very small positive hydraulic gradients (infiltration) were observed during the uprush, while large negative hydraulic gradients (upward flow) were observed at the end of the swash cycle. In both Figures 5 and 7, the head at the top probe (-5 mm) drops more rapidly than the head at the second probe (-15 or -16 mm). This is associated with large negative (upward-acting) hydraulic gradients, as illustrated in Figures 6 and 8. The maximum (i.e. most negative) hydraulic gradient associated with the first case (Figures 5 and 6) is -2.7 and the maximum (most negative) hydraulic gradient in the second case (Figures 7 and 8) is -2.3. In both cases, this is more than sufficient to fluidise the bed, as the fluidisation criterion is a hydraulic gradient of -0.7.

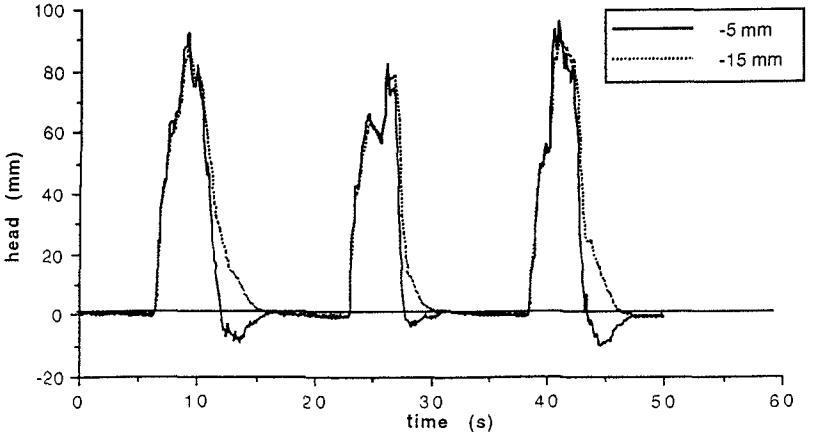

Figure 5. Swash-induced heads at -5 mm and -15 mm (run 12, 25 March 1997).

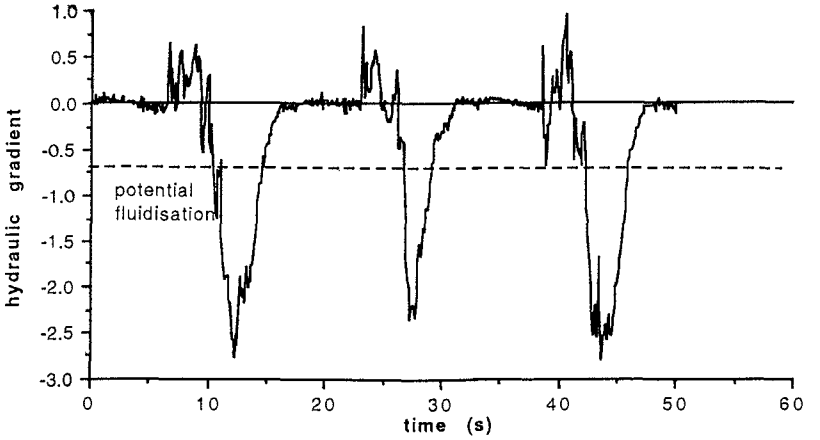

Figure 6. Hydraulic gradients under swash (run 12, 25 March 1997).

These large upward-acting hydraulic gradients appear to be the result of a rapid drop in the head in the upper 15-16 mm of the sediment, which occurs prior to the release of head/pressure deeper in the bed. Although this could indicate suction and hence partial drainage of the sediment, this effect may also be due to the rapid unloading experienced by the sediment as the swash retreats, as suggested by Baird et al. (1996). Suction without drainage could be produced if air trapped in the sediment comes under positive pressures during loading, whereas during unloading the air is no longer under pressure and suction forces develop around the sand grains. However, the unloading occurs on every swash event in the data set from 25 March, whereas it occurs only occasionally in the data from 19 October. The sediment in this region was loosely consolidated and probably had a small but significant air content. Observations on 25 March, when significant cliffing occurred on the beach face and ebullition from the bed was observed, suggested that the air content in the sediment was higher on that day than in October. Also, during the March deployment the longer swash cycles, with very little swash interaction, allowed more time for drainage of the beach between swashes.

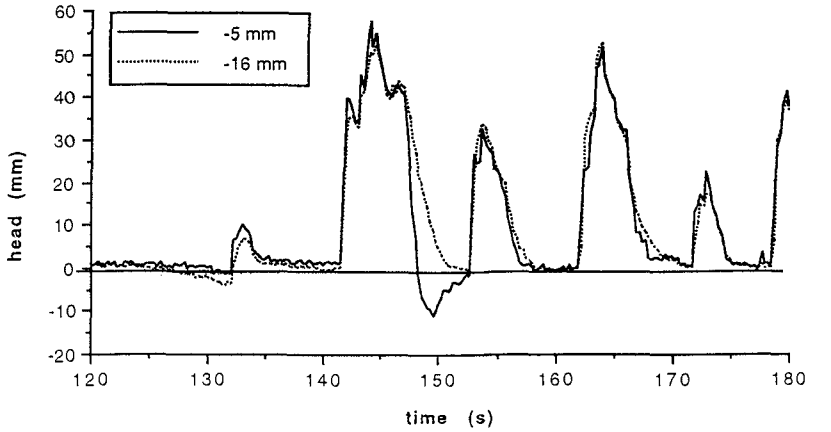

Figure 7. Swash-induced heads at -5 mm and -16 mm (run 11, 19 October 1997).

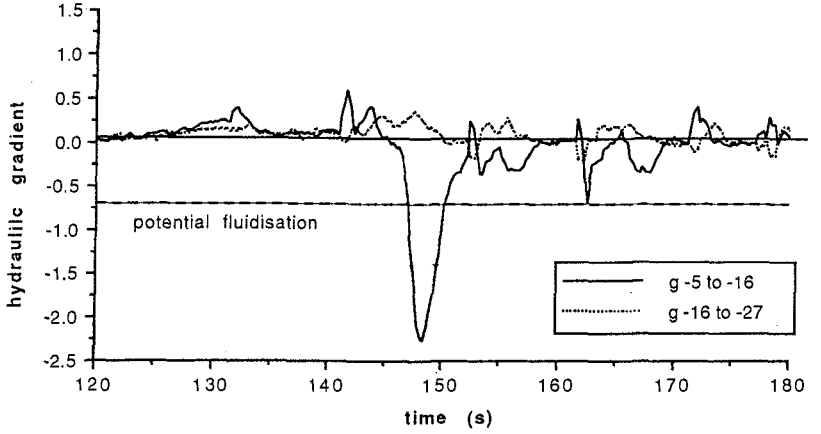

Figure 8. Hydraulic gradients under swash (run 11, 19 October 1997). The solid line is the hydraulic gradient between the probes at -5 and -16 mm. The dotted line is the hydraulic gradient between the probes at -16 and -27 mm.

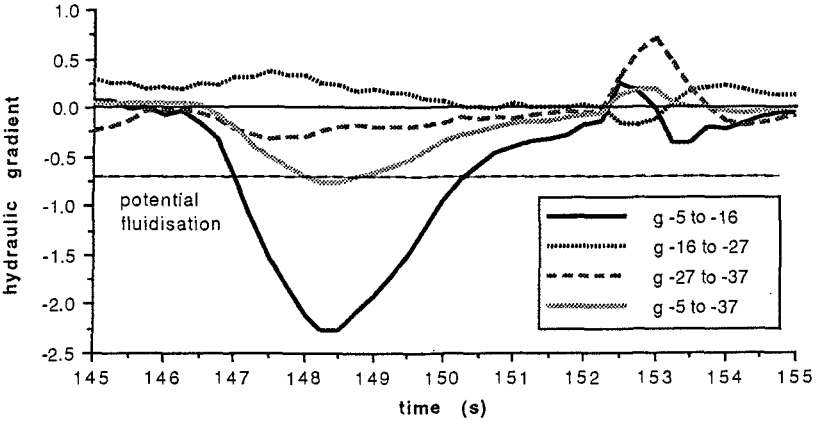

Figure 9. Hydraulic gradients in the top 37 mm of the bed for the 'unloading' event illustrated in Figures 5 and 6 (run 11, 19 October 1997).

Figure 9 illustrates the hydraulic gradients from the same data on 19 October, showing that the extremely large hydraulic gradient associated with the release of pressure as swash retreats occurs only in the top 16 mm of the bed. The hydraulic gradients lower in the bed are much smaller, and are generally not sufficient to fluidise the bed. At deeper depths (-27 to -37 mm) hydraulic gradients were in the range -0.3 to 0.5, which although less than the hydraulic gradients in the top 16 mm, are still considerably in excess of tidal groundwater hydraulic gradients (of order β). As reported by Baird et al. (1997), in some of the data, gradients in the sand bed were observed to be acting both downwards and upwards at the same time. For example, in the section of the record shown in Figure 9, the hydraulic gradient between -16 mm and -27 mm is positive (downward), whereas all of the others are negative. (The hydraulic gradient over the whole measurement area, between -5 mm and -37 mm, which is also

negative, is only included on Figure 9 to show that if the sensors had been further apart, a much smaller hydraulic gradient would have been measured and much useful information would have been lost.) There are a number of possible explanations for these apparently anomalous results. The beach sediment was probably not uniform with depth, in which case the hydraulic properties of the sediment, such as hydraulic conductivity, packing, or air content would also have varied. There may have been divergent flow because of lags in the system due to changes in specific storage. One of the probes may have had an air bubble, which would have distorted the results. This last reason is unlikely, however, as the phenomenon was observed on many occasions.

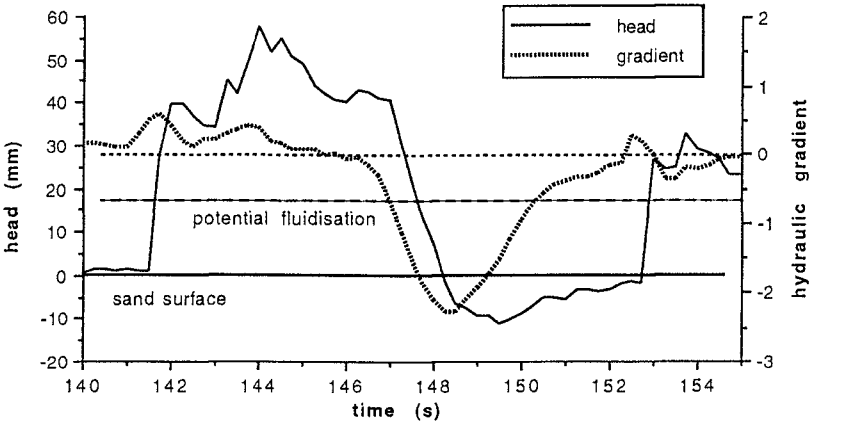

Figure 10. Head at top probe (-5 mm) and hydraulic gradient for the 'unloading' event illustrated in Figures 5,6 and 7 (run 11, 19 October 1997).

Figure 10 shows the swash depth (head at -5 mm) and the hydraulic gradient in the top 16 mm of the bed for the 'unloading' event which occurs between 145 and 155 seconds, which is also illustrated in Figures 7, 8 and 9. The fluidisation criterion is exceeded while a significant depth of swash exists (maximum 40 mm), and exceeds the fluidisation criteria for several seconds while still under swash/backwash. These data also appear to support the hypothesis of Baird et al. (1996,1997,1998), where the large upward hydraulic gradients, sufficient to induce fluidisation of the sediment at the surface, may occur during the latter stages of backwash, thus providing readily entrainable material that can be carried seaward by the backwash flow. Note that this does not necessarily conflict with the findings of Turner and Nielsen (1997). The hydraulic gradients reported here were measured in the top 16 mm of the bed, whereas Turner and Nielsen's top pressure measurement was at a depth of 40 mm. Our data showed strongly negative hydraulic gradients only in the top 1-2 cm of the bed.

Figure 11 shows another example of an 'unloading' event from earlier in the tide on 19 March. The first swash event begins at t≈7s, as the head and water depth rise rapidly. The hydraulic gradient before the swash arrives fluctuates around zero and is mainly just barely positive (and therefore downward-acting), indicating drainage after the previous swash. As the swash depth increases, the hydraulic gradient increases. The hydraulic gradient then begins to decrease as swash depth decreases. However, the hydraulic gradient remains positive throughout this swash event, suggesting infiltration is occurring under both swash and backwash. Between t≈12s and t≈32s, both the swash depth and the hydraulic gradient fluctuate around zero, suggesting conditions similar to those observed by Turner and Nielsen (1997), with the top of the capillary fringe at the sand surface and the phreatic surface fluctuating within this zone of tension

saturation. The hydraulic gradient begins to rise at about t≈32s, before the water level begins to drop. At t≈38 s, the hydraulic gradient reaches its maximum and the water level begins to drop rapidly. Between t≈39s and t≈49s, the hydraulic gradient is very slightly positive, while the water level decreases at a slower rate, suggesting less rapid drainage. In this section of the record, the water surface is below the probe, suggesting that it is measuring pressures/heads in the capillary fringe. The next swash arrives at t≈49 s and the water level rises almost instantaneously. The hydraulic gradient becomes negative for the first second of this swash event, and then rises until t≈53s, when it begins to fall. Just before t≈54s, the swash reaches its maximum depth and the hydraulic gradient becomes negative (upward-acting). Between t≈54s and t≈56s, the hydraulic gradient is less than (i.e. more negative than) -0.7 (sufficient to induce fluidisation of the bed), reaching the most negative value of -1.2 while there is still a significant depth of water in the backwash (30 mm). Throughout the time that the swash depth is decreasing, the hydraulic gradient remains negative, suggesting upward flow at the end of the swash/backwash cycle. However, as in the previous examples, the very large upward-acting hydraulic gradient is only measured in the top 16 mm of the bed. The upward-acting hydraulic gradients lower in the bed are much smaller, between -0.1 and -0.5. The swash depth reaches zero at t≈56s; at this time the hydraulic gradient is increasing, but still negative. The hydraulic gradient does not become positive again until t≈59s. Both the depth and the hydraulic gradient then fluctuate slightly around zero until the next swash arrives at t≈77s.

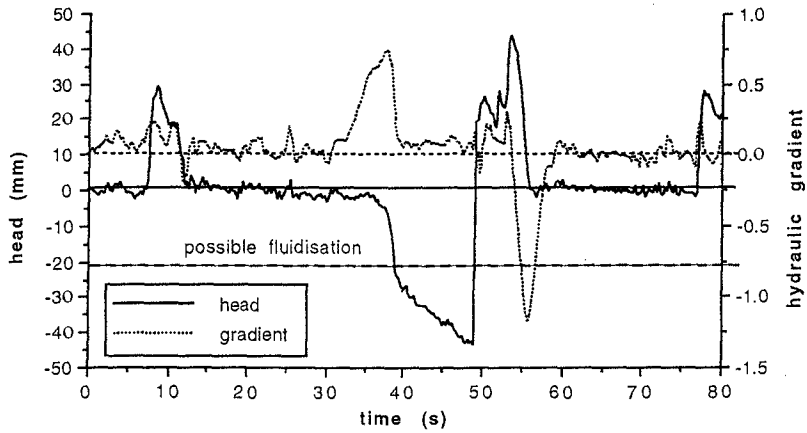

Figure 11. Head at top probe (-5 mm) and hydraulic gradient (run 8, 19 October 1997).

Another phenomenon can be seen in the portion of this data set where infiltration is occurring, between t≈32s and t≈49s, which is associated with a hydraulic gradient of 0.7. This is illustrated in Figure 12, which shows the head at the top probe (-5 mm) and the bottom probe (-37 mm). Although the head measured by the surface probe does not begin to drop until t≈38s, the head measured by the bottom probe begins to decrease several seconds earlier, at t≈32s. At t≈40s the two probes are again measuring the same head, which they continue to do for the rest of the infiltration event. The reason why the bottom probe drops off before the top one is not clear. There may be several explanations for this time lag between the pressure drop at the top and bottom probes. These data were collected when the saturated sand surface was moving back and forth past the measurement point. One possibility, based partly on our ideas and a suggestion from Nielsen (pers. comm.), who suggested that the formation and destruction of meniscuses between sediment particles could cause the pressure at the bottom probes to drop before the pressure at the top probe, is that there is a thin 'tongue' of fully saturated sediment (i.e. no meniscuses) propagating within the sediment. This thin

totally saturated zone, just below the bed surface, may influence the pore pressure within sediment that is not quite fully saturated (i.e. a capillary fringe where meniscuses are present). This tongue of full saturation may propagate in advance of swash or may be formed due to small amounts of swash infiltration. Below this saturated zone, the sediment is likely to be less than fully saturated due to drainage between sequential swashes. A second fully saturated zone is then reached at the tidally-induced watertable elevation. The observed head difference occurs between the top probe and the bottom three probes, over only a few centimetres of the beach material, which suggests that the subsurface layer of full saturation is quite thin.

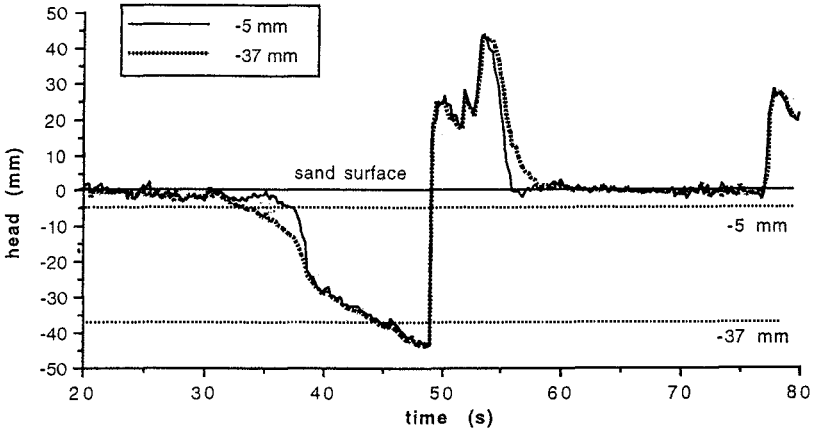

Figure 12. Head at top and bottom probes (run 8, 19 October 1997).

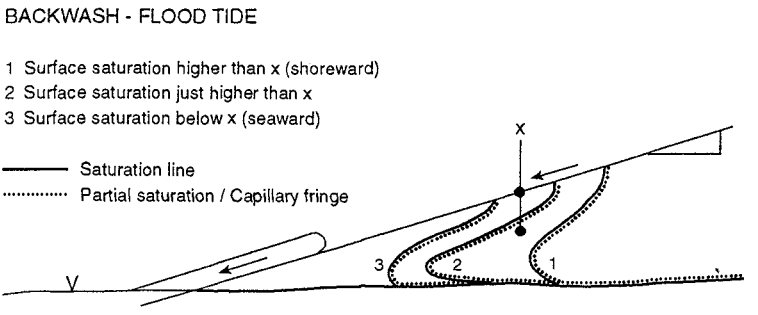

Figure 13. Possible configuration of subsurface water under backwash on a flood tide.

Figure 13 illustrates a possible configuration of this subsurface water under backwash on a flood tide. At time 1 (equivalent to the period before t≈32s on Figures 11 and 12), the position of the saturated surface is shoreward of the measurement point, and both probes are within the saturated tongue and measuring virtually the same head. At time 2 (t≈32s), the tongue has moved downslope. The bottom probe is no longer in the tongue, whereas the top probe is. Therefore the bottom probe measures a lower head than the top probe. At time 3 (before t≈40s) the tongue has moved further

downslope and neither probe is in it. After this, the head measured at both probes decreases at the same rate due to natural drainage of the beach. This continues until the next swash arrives (before t≈49s).

Figure 14 illustrates a situation similar to that described by Turner and Nielsen (1997), showing rapid groundwater response to swash, with a near instantaneous rise followed by a slower rate of decline. Large watertable fluctuations (>80mm) can be seen under relatively shallow swash flows (<20mm). In this data set, the top probe is at -15 mm and the bottom probe is at -47 mm. At the beginning of the record, the apparent water level is below the elevation of both probes and they are measuring 'real' negative pressures, suggesting both are in the capillary fringe. The uprush arrives at the measurement point at t≈286s and the head at both probes rises instantaneously, although the head measured by the bottom probe does not rise as much. Both probes are measuring positive pressures, but they are not measuring the same head of water. Between t≈287s and t≈298s, the head decreases at both probes, suggesting a falling local watertable. However, throughout this period the top probe continues to register a higher head than the bottom probe. The two probes measure the same head and decrease at the same rate for a brief time after t≈298s, until at t≈300s the next swash arrives and the same pattern recurs. The head rises instantaneously at both probes as the swash arrives, but the bottom probe again registers a lower head than the top probe. On this second uprush, however, the discrepancy between the heads measured at the top and bottom probes only lasts for about 2 seconds. From t≈301s both probes measure the same head again. The reason for the differences in head measured by the top and bottom probes is not totally clear, but could be due to downward vertical drainage, which would give lower heads at depth. After backwash, infiltrated water will tend to drain downwards and seawards, and even though such drainage may be minimal and short-lived, it should be sufficient to give rise to the differences in heads observed.

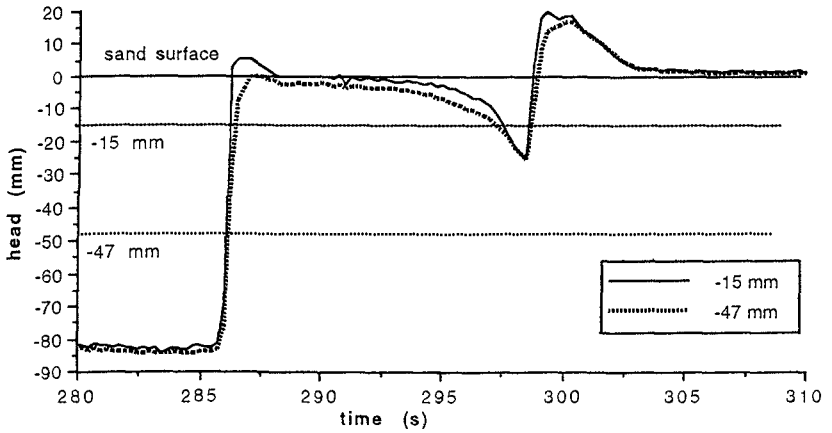

Figure 14. Head at top and bottom probes (run 20, 19 October 1997).

Figure 15 shows the head measured at the top probe and the hydraulic gradient between the top probe (-15mm) and the bottom probe (-47 mm) for the same event as Figure 14. The times when the top and bottom probes are measuring different heads are associated with large positive (downward-acting) hydraulic gradients, suggesting infiltration into the beach. However, it is also possible that the observations illustrated in Figure 14 could be explained by the thin sloping tongue of fully saturated sediment hypothesised earlier. Figure 16 illustrates a possible configuration of this tongue under uprush on a flood tide, which could correspond to the conditions shown in Figure 14.

At time 1 (corresponding to the period before t≈286s in Figure 14), the uprush has not reached the measurement point, and both probes are in the partially saturated zone or capillary fringe and measuring the same heads. At time 2 (t≈286s), the uprush has just reached the measurement point. The bottom probe is not yet in the fully saturated layer and therefore measures a lower head of water than the upper probe. At time 3 (t≈298s and t≈301s), the uprush and the fully saturated layer have moved past the measurement point and both probes measure the same head of water. After this, the head measured at both probes decreases during the backwash and then due to natural drainage of the beach. This continues until the next swash arrives.

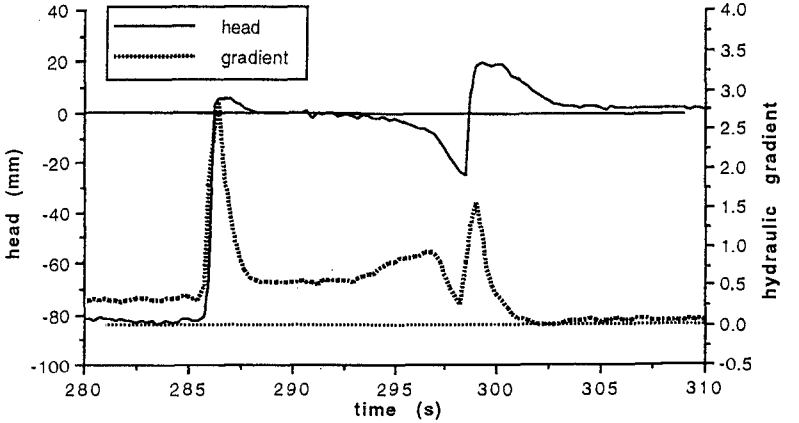

Figure 15. Head at top probe (-15 mm) and hydraulic gradient (run 20, 19 October 1997).

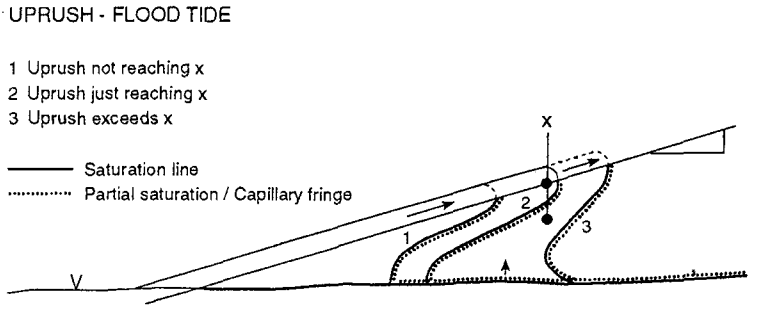

Figure 16. Possible configuration of subsurface water under uprush on a flood tide.

Figure 17 shows a longer time series of the same record (run 20, 19 October 1997). Even larger fluctuations can be seen than in Figure 14 (>90mm) under shallow swash (<20mm). On several occasions (starting at t≈110s and t≈236s), the uprush does not reach the measurement point; however, the head at the top and bottom probes rises, although suctions still persist at both probes. Although in these cases the probes are not measuring pressures under swash, they still appear to be measuring pressure changes related to swash motions. We interpret this as pressures in the not fully saturated zone

or capillary fringe being influenced by pressure changes around its boundaries as groundwater moves up the beach in response to swash. Again, Figure 16 illustrates the possible saturation levels but, in this instance, neither the swash or the total saturation line reach the measurement position. The pressure in a medium which is not fully saturated appears to respond in the same way as the watertable. In the event beginning at t≈110s, both probes are in the capillary fringe and are measuring real negative pressures (suction), as the water level is below the elevation of the probes. In the event beginning at t≈236, the top probe is measuring a real negative pressure and is thus in the capillary fringe. The water level is slightly above the elevation of the bottom probe, so the bottom probe is not in the capillary fringe. At other times (t≈75s, t≈187s, t≈202s, t≈286s and t≈299s), the uprush reaches or very nearly reaches the measurement point. In these cases, a situation similar to that shown in Figure 14 is observed, where the head rises instantaneously at both probes as the swash arrives. However, the bottom probe measures a lower head than the top probe, again suggesting that the sediment is not fully saturated. This situation occurs on each of these events and is associated with positive (downward-acting) hydraulic gradients of between 1.1 and 2.8. Note that the long time scale between individual swashes reaching the measurement point is due to wave grouping effects. This leads to large amplitude low-frequency fluctuations in the pressure just below the sand surface (which may also occur deeper in the bed). However, these pressure fluctuations are not due to long wave pressure pulses propagating through the beach material, but are simply due to the intermittent nature of the pressure forcing toward the landward limit of the swash zone.

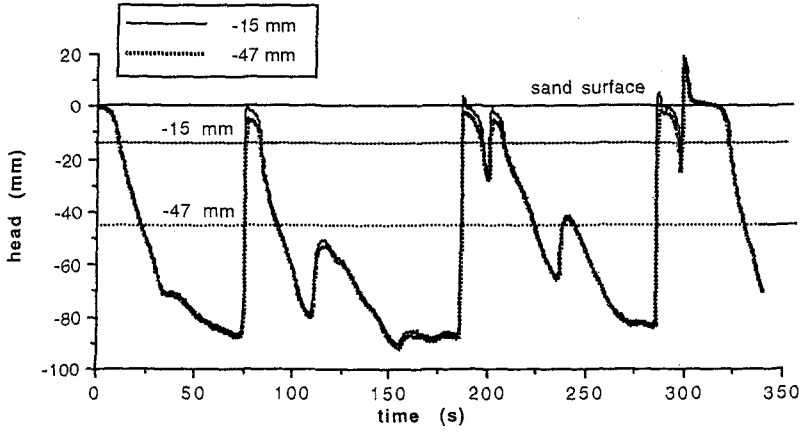

Figure 17. Head at top and bottom probes (run 20, 19 October 1997).

Conclusion

Field measurements of near-surface heads and hydraulic gradients within a sandy beach during individual swash cycles have been presented. The hydraulic gradients measured under swash are considerably larger than the hydraulic gradients produced by tidal groundwater motion. The data shown here demonstrate several different types of behaviour which may have implications for swash zone sediment transport: (1) measurements of swash depth; (2) 'unloading' events with large upward-acting hydraulic gradients: (3) infiltration events with smaller downward-acting hydraulic gradients; (4) situations where the probes lower in the bed measure significantly lower heads than the probe at the surface, leading to strongly downward-acting hydraulic gradients; and (5) measurements in the capillary fringe. Of particular note is the situation when large hydraulic gradients, which are more than sufficient to induce fluidisation, occur in the top 15 mm of the bed under swash and backwash. These large

hydraulic gradients may coincide with a significant depth of water (up to 40 mm), which suggests the potential for entrainment of the fluidised bed under backwash. The fact that these large upward-acting hydraulic gradients occur only in the very top section of the bed highlights the importance of measuring pressures very close to the sand surface. The results also indicate that regions which are fully and less fully saturated appear to develop below the sand surface, particularly a thin layer of totally saturated sediment which moves up and down the beach with the swash. This suggests that very small changes in the amount of water in the sediment can lead to large differences in heads, which highlights the importance of knowing more about the saturation characteristics of the bed.

Acknowledgements

We would like to thank Poole Borough Council, who kindly allowed us to use the Surf Lifesaving Club building at Canford Cliffs. We would also like to thank Emily Altham, Mike Bloys, Gerry Delbourgo, Matt Foote, Mark Lee and Pat Stephenson for assistance with the measurements in the two deployments. Funding for the design of the swash measurement technique was provided by an EPSRC grant (GRK20514) to Professor Patrick Holmes and Tom Baldock in the Department of Civil Engineering, Imperial College. Other instruments were provided from a Natural Environment Research Council grant (GR9/01726) awarded to Andrew Baird and Diane Horn. Funding for the field deployments was from a Royal Geographical Society HSBC Holdings research grant to Diane Horn. Finally, we would like to thank Peter Nielsen for useful discussions about the data.

References

Baird, A.J., Mason, T.E. and Horn, D.P. 1996. Mechanisms of beach groundwater and swash interaction. Proceedings of the 25th International Conference on Coastal Engineering. New York: American Society of Civil Engineers, 4120-4133.

Baird, A.J., Mason, T.E., Horn, D.P. and Baldock, T.E. 1997. Monitoring and modelling groundwater behaviour in sandy beaches as a basis for improved models of swash zone sediment transport. In Thornton, E.B. (ed) Coastal Dynamics 97. New York: American Society of Civil Engineers, 774-783.

Baird, A.J., Mason, T.E. and Horn, D.P. 1998. Validation of a Boussinesq model of beach ground water behaviour. Marine Geology 148: 55-69.

Baldock, T. E. and Holmes, P. 1996. Pressure gradients within sediment beds. Proceedings of the 25th International Conference on Coastal Engineering. New York: American Society of Civil Engineers, 4161-4173.

Baldock, T. E. and Holmes, P. 1998. Seepage effects on sediment transport by wave and currents. Proceedings of the 26th International Conference on Coastal Engineering. New York: American Society of Civil Engineers, this volume.

Baldock, T.E., Holmes, P. and Horn, D.P. 1997. Low frequency swash motion induced by wave grouping. Coastal Engineering 32(2/3): 197-222.

Grant, U.S. 1946. Effects of groundwater table on beach erosion. Geological Society American Bulletin 57: 1952. (abstract).

Grant, U.S. 1948. Influence of the water table on beach aggradation and degradation. Journal of Marine Research 7: 655-660.

Oh, T-M. and Dean, R.G. 1994. Effects of controlled water table on beach profile dynamics. Proceedings of the 24th International Conference on Coastal Engineering: 2449-2460.

Packwood, A.R. and Peregrine, D.H. 1980. The propagation of solitary waves and bores over a porous bed. Coastal Engineering 3: 221-242.

Turner, I. L. and Nielsen, P. 1997. Rapid watertable fluctuations within the beachface: implications for swash zone sediment mobility? Coastal Engineering 32: 45-59.

Flow Structures in Swash Zone

H. H. Hwung[1], K. S. Hwang[2]
W. S. Chiang[3], C. F. Lai[4]

Abstract

In order to understand the external and internal flow structures of broken waves on a sloping bottom, a special design of run-up gauge combined with LDV measuring system is used to detect the velocity fields of run-up and run-down in our experiments. According to the experimental results, it is found that the heights of run-up and run-down are mainly determined by incident wave steepness. The dimensionless heights of run-up, run-down and the related swash length for different wave breakers are also discussed respectively. In addition, the elaborate measurements of flow structures, turbulent intensity and Reynolds stress in swash zone are also analyzed in this paper.

Introduction

The internal and external flow fields of swash zones were investigated on plunging breakers and spilling breakers. To understand the transformation processes of broken waves is of great importance for predicting wave-induced currents and sediment transport in the swash zones. Many researches, such as Hunt (1959), Battjes (1974), Kemp and Plinston (1968) and Fuhrboter (1986), have reported on the external flow fields in the swash zones, of which the relations between the uprush lengths, backwash lengths and wave conditions were proposed. On the other hand, only few researches have paid attention on the internal flow fields. Miche (1944) assumed that the uprush and backwash is a symmetrical cycle and obtained a formula to evaluate the run-up velocity. Kemp and Plinston (1974) proposed a model to calcuate the velocities of surging breakers. Kato and

[1] Prof. Of Hydraulic and Ocean Engineering Department, Director of Tainan Hydraulics Laboratory, National Cheng Kung University, Tainan, Taiwan
[2] Associate Researcher of Tainan Hydraulics Laboratory, National Cheng Kung University, Tainan, Taiwan
[3] Assistant Research of Tainan Hydraulics Laboratory, National Cheng Kung University, Tainan, Taiwan
[4] Assistant Research of Tainan Hydraulics Laboratory, National Cheng Kung University, Tainan, Taiwan

Matsuno (1986) used a high-speed camera to obtain the velocity profiles of the first broken wave from the taken images of released hydrogen bubbles.

The objective of this paper is to investigate the flow structures of swash zones. The uprush lengths, the backwash lengths and the velocities of broken waves along a slopping bottom are detected by a special design of run-up gauge combined with LDV measuring system, and the comparison between our experiments and previous studies are made in this paper. Furthermore, the turbulent intensity and Reynolds stress induced by the different wave breakers are also discussed.

Experiments

The experiments were carried out in a wave flume of 950 cm in length, 70 cm in depth and 30 cm in width as shown in Fig. 1. Only one slope condition, 1/15, was conducted throughout the experiments. The wave body being very thin in swash zones, therefore, the velocities have to be measured by a 2-D laser Doppler velocimetry. Besides, a capacitance gauge leaning parallel with the sloping bottom was used to measure the uprush and backwash lengths. In order to avoid capillary effects, the gauge was carefully designed and installed on the sloping bottom until the recording signals were good performance.

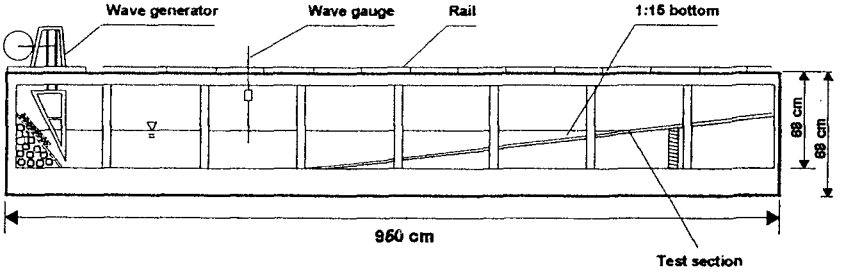

Fig. 1 The Sketch of Wave Flume

The processes of run-up and run-down are recorded by capacitance gauge, and the relating velocity measurements are detected simultaneously by LDV system in this experiment. The typical spilling and plunging breakers are generated in wave flume.

All the test conditions and the arrangements of measured points are shown in Fig. 2. The shoreline, where the still water surface and the slopping bottom intersected, is defined as the origin of X axis, and the origin of Z axis is defined at the local bottom boundary upward.

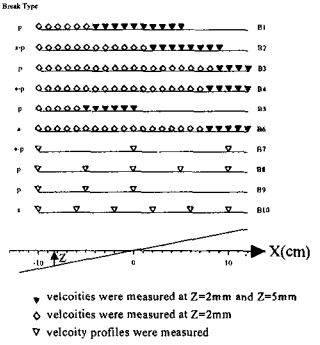

CASE	T(sec)	H(cm)	H_0/L_0
B1	1.62	4.4	0.010862
B2	0.88	4.6	0.040604
B3	1.45	8.5	0.027647
B4	1.21	7.9	0.037627
B5	1.20	3.6	0.014631
B6	0.91	8.3	0.063636
B7	1.04	6.4	0.042648
B8	1.33	4.7	0.018340
B9	1.60	4.3	0.011052
B10	1.10	10.4	0.059587

Fig. 2 Sketch of the arrangements of measured points

Based on the dimensional analysis, we obtained that the dimensionless run-up (Ru/H) and dimensionless run-down (Rd/H) are function of H/gT^2, H/L h/L, $v\sqrt{gH}$ and $\tan\theta$ respectively. Where, H is the incident wave height, T is wave period, L is wave length, h is water depth, v is water particle velocity and θ is the angle of sloping bottom. Therefore, three kinds of water depths and the appropriate wave conditions are made in the experiments.

Results

The flow fields of swash zone being so furious and chaotic that traditional analysis methods, such as the phase averaged method and the inverse fast Fourier transform method, are subject to overestimate or underestimate the turbulent components. It is consequent that a weight moving average method combined with modified phase average method is used to analyze the experimental data.

The results show that the uprush lengths are mainly associated with the incident wave steepness. For the both types of breakers, the dimensionless uprush height, R_u/H_o, decreases as the wave steepness increases, as plotted in Fig. 3. In addition, the dimensionless downrush height, Rd/H_0, decreases as wave steepness increases for $H_0/L_0>0.03$, however, for $H_0/L_0<0.03$, the dimensionless downrush height decreases

as wave steepness decreases. The comparison between the experiments and the previous studies are displayed in Fig. 4. From the above two figures, the relationship between dimensionless height difference of $(R_u - R_d)/H_o$ and wave steepness is plotted in Fig. 5. It shows that the experimental results are coincided with the empirical formula proposed by Battjes (1974) and Shuto (1984).

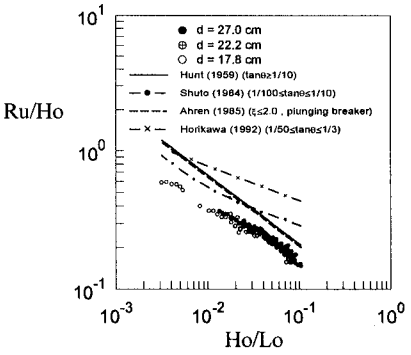

Fig. 3 The relationship between dimensionless uprush height and wave steepness

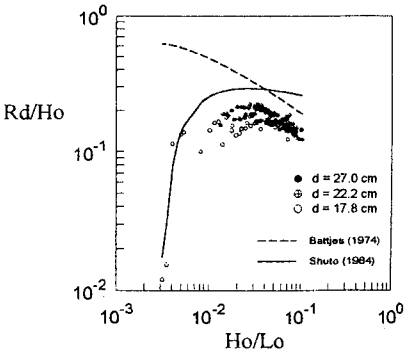

Fig. 4 The relationship between dimensionless downrush height and wave steepness

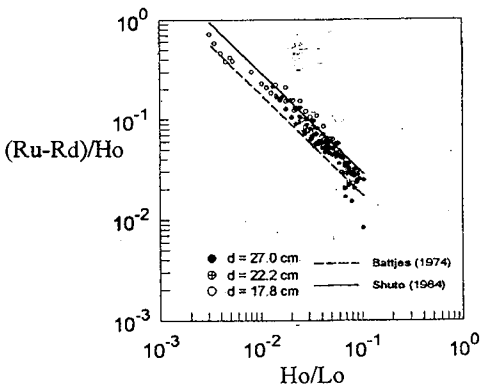

Fig. 5 The relationship between dimensionless height difference and wave steepness

Regarding the internal flow fields, Kemp and Plinston (1974) indicated that the whole water body moves, either shoreward or seaward, in the same direction in swash zone for surging breakers. While in our experiments of plunging breakers and spilling breakers, they show that both shoreward and seaward directions of flows are existent in swash zone simultaneously. The velocity profiles of different phases along the sloping bottom for plunging breakers are shown from Fig. 6(a) to 6(e). The different phases shown are referred to the locations of the wave tip where 6(a) is the phase of run-up beginning at t/T≒0.0, 6(b) is the phase of run-up moving at t/T≒0.18, 6(c) is the phase of approaching the highest run-up at t/T≒0.42, 6(d) is the phase of beginning backwash at t/T=0.6, and 6(e) is the phase of backwash at t/T=0.9. Furthermore, it is obvious that at $X/L_i = -0.05$ where is located in the initial run-up region, most of the velocity profiles are moving on-shore except around the phase of t/T=0.42. This is resulted from the set-up of wave breaking. At the location of $X/L_i = 0.00$, it has similar phenomena, while the velocity profile is moving offshore only between the phase of $t/T = 0.42$ and $t/T = 0.6$. However, at $X/L_i = +0.05$ where is located in the end of run-up region, most of the velocity profiles are moving offshore except from t/T=0.18 to t/T=0.42 are onshore.

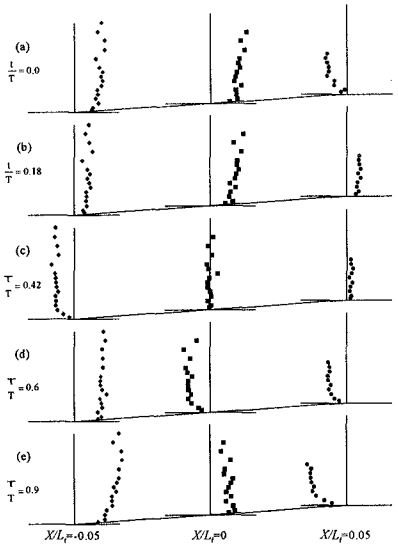

Fig.6 Velocity profiles at different phases (case B7)

In order to obtain the relevant flow structures in swash zone, the on-shore extreme velocity profiles, $\langle U \rangle^+$, offshore extreme velocity profiles $\langle U \rangle^-$, horizontal mean velocity prifiles, $\overline{U}$, and vertical mean velocity profiles, $\overline{W}$, of spilling and plunging breakers are plotted in Fig. 7 and Fig. 8 respectively. Herein, it is found that both of spilling and plunging breakers, the on-shore extreme velocities are larger than the offshore extreme velocities and the horizontal mean velocity profile is moving shoreward in the initial run-up region. However, the offshore extreme velocities are larger than on-shore extreme velocities and the horizontal mean velocity profile is moving seaward in the end of run-up region. Generally speaking, the uprush of the water body is mainly related to the onshore velocity and the phase celerity, while on the other hand, the offshore velocity and the gravity determine its backwash. The exchanges between kinetic energy and potential energy during the uprush and the backwash stages are of reason. Thus a retardation of velocities along the uprush process is expected, and vices versa. Fig. 9 shows that the mean velocities and the onshore extreme velocities decrease as x/L_i increases. An interesting result is that the offshore extreme velocities also decrease as x/L_i increases, which do not follow our intuition to exhibit an opposite tendency with the onshore ones. Yet the backwashing water body is evidently not only controlled by the gravity but the propelling of the subsequent uprush water body which must be also taken into account.

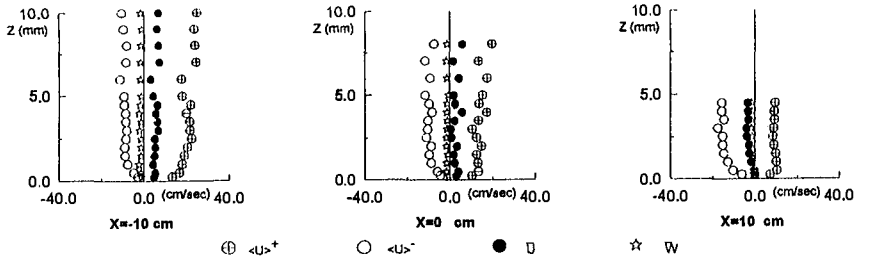

Fig. 7 Extreme velocity profiles and mean velocity profiles at different locations on sloping bottom (case B7, $H_0/L_0 = 0.042648$)

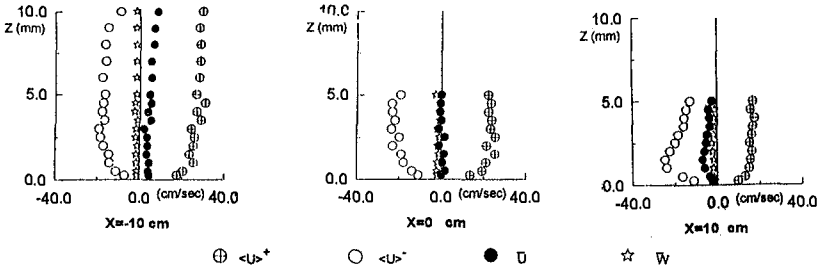

Fig. 8 Extreme velocity profiles and mean velocity profiles at different locations on sloping bottom (case B8, $H_0/L_0 = 0.018340$)

The turbulent flow in swash zone is created by wave breaking, bottom boundary and the mixing during the processes of uprush and backwash. According to LDV measurements, the Reynolds stress of plunging and spilling during the wave period are displayed in Fig. 10 and Fig. 11 respectively. It is evident that the maximum Reynolds stress almost occurs at the phase of backwash stage, and the Reynold stress of plunging breaker is bigger than that of spilling breaker.

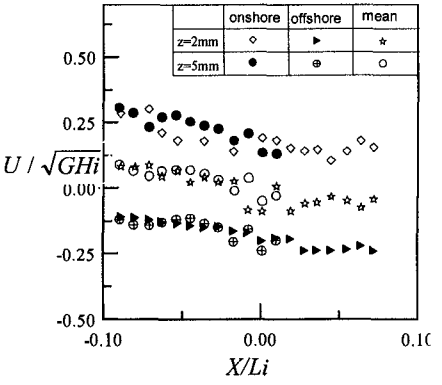

Fig. 9 The onshore, offshore extreme velocities and the mean velocities along the slopping bottom (case B2)

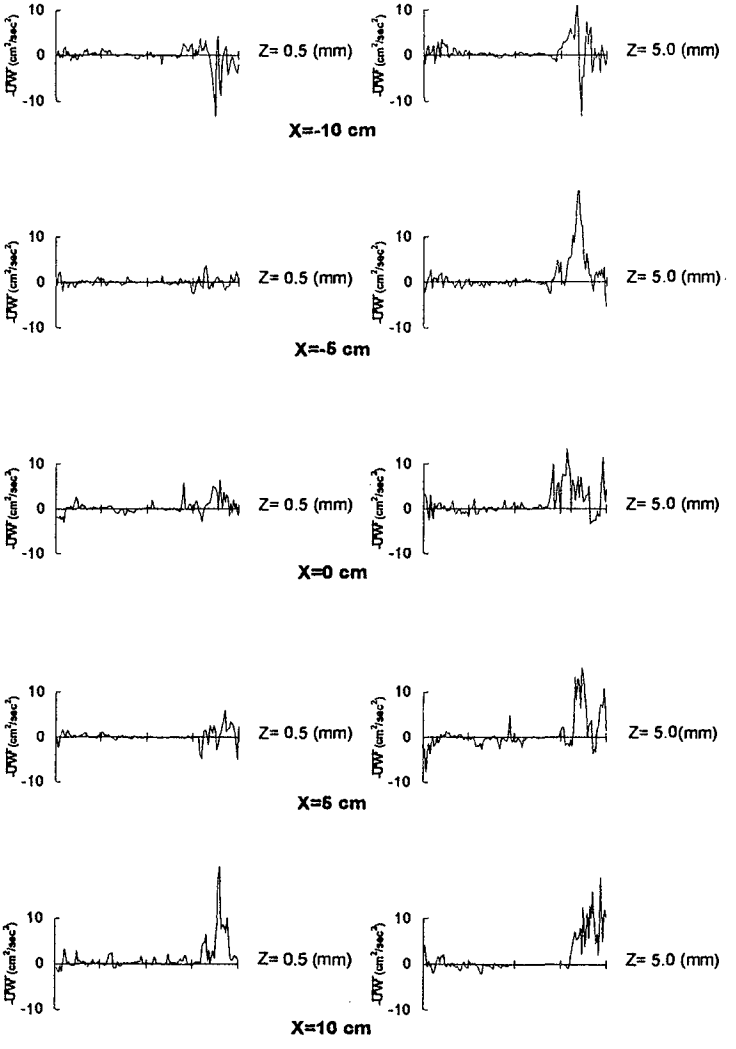

Fig. 10 The Reynolds stress during a wave period (plunging $H_0 / L_0 \fallingdotseq 0.01834$)

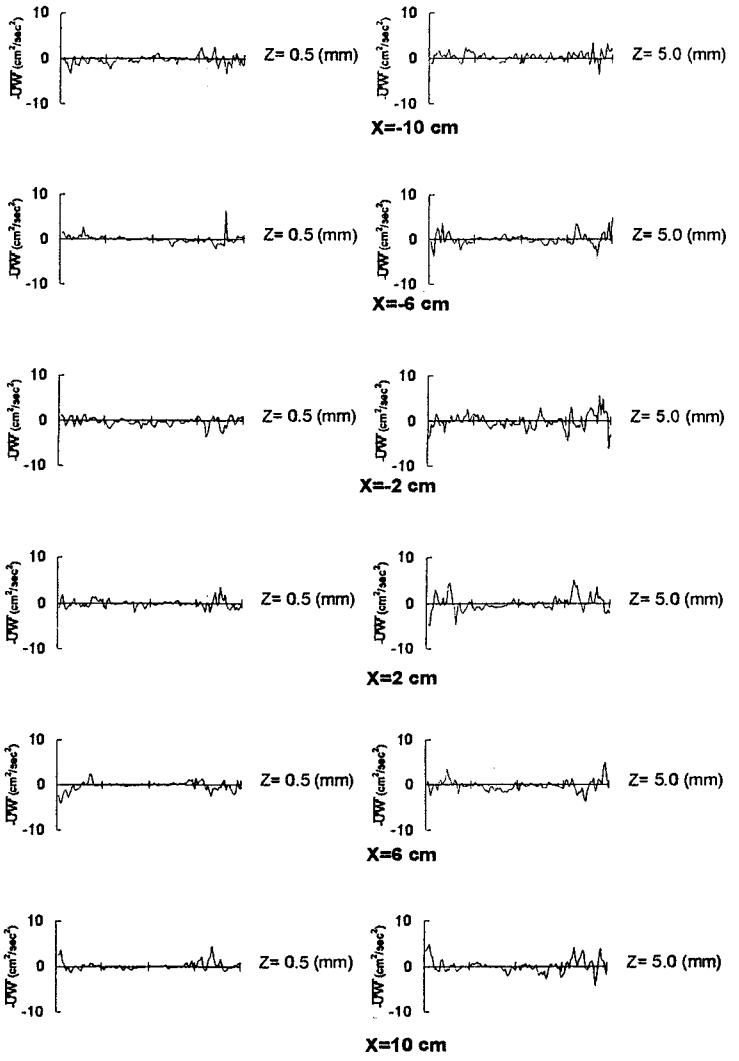

Fig. 11 The Reynolds stress during a wave period (spilling $H_0 / L_0 \fallingdotseq 0.05958$)

Conclusions

The swash height and the velocities of broken waves along a slopping bottom are recorded and analyzed. The remarkable conclusions are as follows:

1.The run-up heights decrease as the wave steepness increase for the both types of breakers.

2.The moving direction of the water body of a spilling-plunging breaker shows that both shoreward and seaward movements are existent simultaneously either in the uprush or backwash stages, which is not consistent with that of a surging breaker described by Kemp and Plinston(1974).

3.The mean velocities, the onshore extreme velocities and the offshore extreme velocities all decrease as x/L_i increases.

1. The maximum Reynolds stress almost occurs at the phase of backwash stage, and the Reynold stress of plunging breaker is bigger than that of spilling breaker.

References

1.Hunt, I. A. (1959), Design of seawalls and breakwaters, Proc. ASCE, 85, ww3, pp.123-152.

2.Battjes, J. A. (1974), Surf Similarity, Proc. 14th Coastal Engineering Conference, pp.466-479.

3.Kemp, P. H., Plinston, D. T. (1968), Beaches produced by waves of low phase difference, Proceeding of ASCE, Journal of Hydraulics Division, pp.1183-1195.

4. Fuhrboter, A. (1986), Model and prototype tests for wave impact and run-up on a uniform 1:4 slope, An Int. Journal for Coastal Harbor and Offshore Engineering, vol.10, pp.49-84.

2. Kemp, P.H., Plinston, D. T. (1974), Internal velocities in the uprush and backwash zone, Proc. 14th Coastal Eng. Conf., pp.575-585.

3. Kato K. and A. Mano, (1986), Velocity measurement in Wave Tip Running Up on a Dry Bed, Proc. of Coastal Engineering, JSCE, vol.33, pp.76-79.

7. Shuto, N. (1967): Run-up of long waves on a sloping beach, Coastal Engineering in Japan, Vol. 10 pp. 23-38.

8. Nadaoka, K., Kondoh, T. (1982): Laboratory measurements of velocity field structure in the surf zone by LDV, Coastal Engineering in Japan, Vol. 25 pp. 125-145.

MODELLING LARGE-SCALE DYNAMICS OF HEL PENINSULA, PL

Marek SZMYTKIEWICZ, Ryszard B. ZEIDLER, Grzegorz RÓŻYŃSKI & Marek SKAJA[1]

Abstract

Two-stage methodology of shoreline prediction for long coastal segments is presented in the study. About 30-km stretch of seaward coast of the Hel Peninsula was selected for the analysis. In 1st stage the shoreline evolution was assessed ignoring local effects of man-made structures. Those calculations allowed the identification of potentially eroding spots and the explanation of causes of erosion. In 2nd stage a 2-km eroding sub-segment of the Peninsula in the vicinity of existing harbour was thoroughly examined including local man-induced effects. The computations properly reproduced the shoreline evolution along this sub-segment over a long period between 1934 and 1997.

Introduction

The study presents the methodology of shoreline change analysis, which was developed for large scale modelling of shoreline evolution of potentially eroding coastal segments. Results of the study are intended to optimise shore protection activities. A case study of the Hel Peninsula (Fig. 1) is used to demonstrate the concepts of such an approach.

The observed shoreline changes are induced by a number of mutually correlated hydro-meteorological and lithodynamic factors. They can be roughly divided into two basic groups:

- external factors encompassing spatial and temporal distribution of wave energy, followed by similar distribution of longshore currents and sediment transport, coupled with bed topography and granular diversification of sediment;
- local factors attributed to the presence of man made constructions, such as groins, seawalls and harbour breakwaters, which intensify coastal processes in their vicinity.

Shoreline changes are modelled in two steps. The first step takes account of the whole coastal segment ignoring the existing constructions and hypothetically assuming that all variations of shoreline positions are caused solely by external factors. The

[1] Snr Res Assoc., Prof, Snr Res Assoc & Eng, resp., Polish Academy Sciences' Inst Hydro-Engng IBW PAN Gdańsk, Phone: (+48) 58 552 20 11, Fax: (+48) 58 552 42 11, E-mail: mareksz@ibwpan.gda.pl

calculations identify potentially eroding coastal sub-segments and explain main causes of erosion.

In the second step calculations are executed for shorter, eroding sub-segments, which must be protected for various reasons. These calculations include the effects of all local factors; the existing shore constructions in particular and the results from 1st step are utilised to determine boundary conditions of 2nd step.

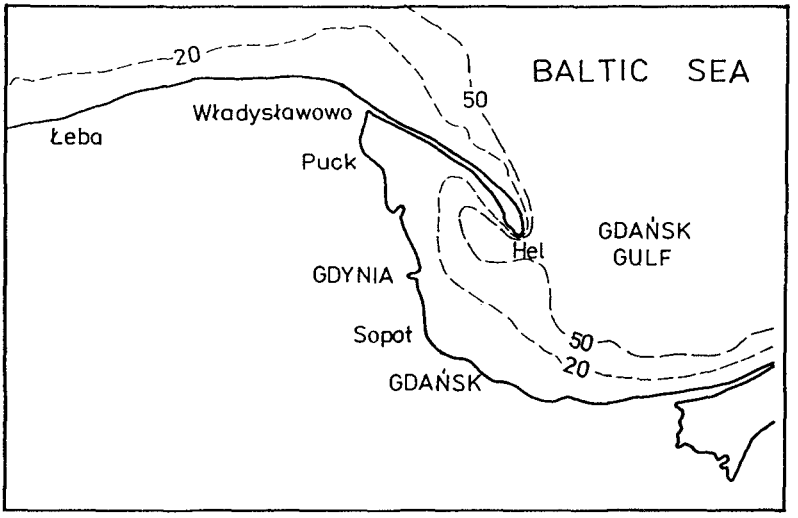

Figure 1. Layout of Hel Peninsula

For Hel Peninsula this procedure was applied in the following manner.

- For 1st step shoreline change computations for a 22-km seaward stretch of Peninsula's coastline were carried out. It was assumed that with exception of the harbour at Władysławowo, situated at the root of the Peninsula, the shore could be treated as a free segment without any artificial structures. A numerical model SAND94 was developed to analyse the possible diversification of wave energy, longshore currents and sediment transport rates. The computations allowed for identification of potentially eroding locations and were done for the period between 1991 and 1995. For that period detailed bed topography was used. Simultaneous comparative shoreline change computations were also obtained with the UNIBEST computer package.
- For 2nd step a 2-km long sub-segment lying in the vicinity of Peninsula's root, in the close proximity of the Władysławowo harbour was selected. The harbour was erected in the 30-ties and the computations were aimed at long-term shoreline evolution between 1934 and 1997. The evolution of this area has been controlled by local factors *i.e.* the construction of harbour breakwaters in 1936-37 followed by shore protection structures on the lee side of the harbour, which were built after 2nd world war. Shoreline change for step 2 was computed with four models: UNIBEST, GENESIS, LITPACK and SAND94. Currently, extensive artificial beach nourishment is conducted in this part of the Peninsula, so practical objective of the study was to predict the future shoreline evolution with proper reproduction of local effects, followed by optimisation of future beach fills.

Hel Peninsula and Władysławowo harbour

Being a fairly narrow, 35-km barrier separating the Gulf of Gdańsk from open waters of the Baltic Sea, the Hel Peninsula is an important segment of the Polish coast. Its area measures 32.4 km^2 and its width varies from 200 m to 3 km. The western part of the Peninsula is narrow and rather flat, with heights ranging from 1 to 2 m above mean sea level (MSL), higher dune crests up to 13 m above MSL. The south-eastern part is much wider (1-3 km) and higher (between 3 and 5 m above MSL). Hel Peninsula is a holiday place for thousands of people. There are two towns and three villages.

Władysławowo harbour construction was started in early 1936 and completed in late autumn of 1937. The length of the western breakwater is 763 m, while its eastern counterpart is only 320 m long. Immediately after construction they reached some 400-m offshore. In 1937, because of the anticipated shore erosion east of the harbour, the shore there was protected with a heavy seawall, which was 250 m long. The seawall is a massive, concrete wall, resting on wooden piles and a bulkhead. It was elongated by 300 m in 1952, to prevent scour east of tbe initial seawall.

The first group of groins at the root of the Peninsula, east of the harbour, was built after heavy storms in February and March 1946, which severely hurt the Peninsula on the first 3 kilometres of its stretch. The first groins were completed in August 1946 and until 1949 another group of 44 groins was built from km H 0.02 to km H 4.45 of Peninsula's chainage. They were made of wood in form of a single palisade, each 100-m long. The span between them was 90 m, doubled to 180 m between the last four. The groins were intended to be perfectly impermeable to sand, but in reality they exhibit cavities on some 20%÷30% of the length. The groins were being gradually destroyed, mainly by ice phenomena.

Protection work had been continued in the next years. Currently, there are 162 groins between Władysławowo and Kuźnica and 1500 m of sand dike with seaward slope jointly protected by rubble mound and concrete sleepers in the Kuźnica region.

The dredging, primarily at the harbour entrance, started in 1948, and in total 2.217 million m^3 was dredged until 1975. Artificial nourishment of the Peninsula was started at the end of 70-ties and was associated with the maintenance of the navigation channel of the Władysławowo harbour. Before that time, the sediment was deposited offshore. Later, it was being dumped closer to the shoreline, at depths of 3÷5 m. In 1984 the sediment was dumped at about km H 3.4÷3.5 in the surf zone at depths 2÷3m. Since 1989, the sediment has been dumped directly onto the beach.

Shoreline change during and after harbour construction

Before the harbour construction, the zone up to 300m offshore exhibited two longshore bars. The inner one was smaller and was usually situated some 150m offshore. The outer one was greater, the average distance to that bar was 200÷250m. The average depth over crest of the outer bar was 2m. The depth of trough between that bar and the shore reached some 3÷4m. Outside the outer bar the depths were increasing gently and steadily. Distinct bottom movements occurred at depths up to 7 m; the comparison of hydrographic maps implies that at greater depths the bed is either stable or its movements are insignificant.

During and after the harbour construction, bathymetric surveys were executed twice a year. They covered a stretch of some 1000-m west and east of the harbour. The construction of the harbour triggered bed movements, whose intensity was coupled

with increasing breakwater lengths. Figure 2 illustrates the early construction stage, where underwater part of breakwater body was nearly completed, and shows a developing shoal running west and far east of the future harbour. The shoals are very distinct and run along the whole surveyed area and further east. Outside western breakwater they formed a sand bank. Natural depths at the harbour entrance were 6 m.

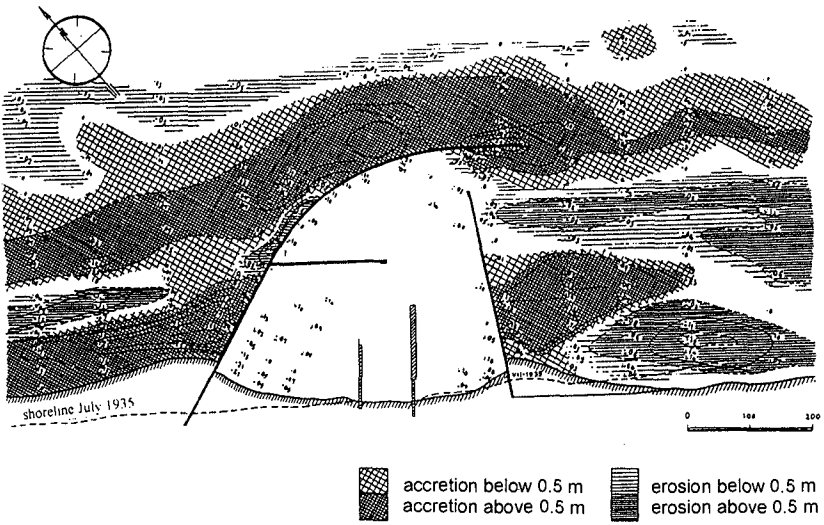

Figure 2. Depth changes at Władysławowo harbour from May 1936 to March 1938

The completion of the harbour at Władysławowo started the accretion of sand west of the western breakwater. This effect appeared rapidly (Adamski 1938), and the rate of deposition became the basis of longshore sediment transport assessments in the harbour area. The transport rate for the period between spring 1936 and spring 1938 was calculated at 70,000 m^3 per year, upon the assumption that no bypassing occurred during that period. Gradual beach accretion west of the harbour led to such bed configuration that the bar, which was cut by the breakwater, surrounded it and maintained the 2÷3 m depth over crest (Szopowski 1958). This fact gave a clue that the longshore sediment transport, which was initially interrupted by the breakwater, was restored at the time the bar appeared in front of it (Hueckel 1968, Mielczarski 1984, Szopowski 1958, Tubielewicz 1957). Restoration of longshore sediment transport due to beach accretion updrift of the breakwater was also reported in many other cases (Zenkowicz 1962). The appearance of the main bar in front of the breakwater led to gradual shallowing of the harbour channel. Therefore, dredging became indispensable as early as in 1948.

Upon the analysis of shoreline changes along the Hel Peninsula and along the whole Polish coast, it can be assumed that the existence of breakwaters has only a local influence on shoreline evolution, so the changes become insignificant 2 km west and east of the harbour (Basiński, Szmytkiewicz. 1990).

Description of forecast model SAND94

With a realistic evaluation of the factors controlling the decadal evolution of the Polish

coast, a single-line numerical model SLineR has been formulated with IBW's package SAND94.

The computer package SAND94 was developed at IBW PAN. SAND94 is the software package intended for computations of waves, wave-induced currents, sediment transport and shore evolution. Deep-water wind wave parameters for SAND94 are computed on the basis of wind speed, direction and fetch, stemming from Krylov's quasi-spectral forecast method, which involves semi-empirical equations of the following form:

$$\frac{g\overline{H}}{W^2} = f_1\left(\frac{g}{W^2}, \frac{gt}{W}\right) \qquad (1)$$

$$\frac{g\overline{T}}{W} = f_2\left(\frac{gX}{W^2}, \frac{gt}{W}\right) \qquad (2)$$

where:

g -gravity accerelation, $\overline{H}$ - mean wave height, W -wind speed, $\overline{T}$ -mean wave period, X - wind fetch and t -time of duration.

This approach takes account of the arbitrary shoreline layout and bathymetric variability along each directional spectral component. The directional energy distribution in terms of $\cos^2\alpha$ in the range $\pm\pi$ from wind direction is assumed, each directional sector comprises 22.5° while the radii in all directions are divided into the segments of constant depth maximum 40 Mm long. For each segment, the average depth is determined for the stripe 20 Mm wide. The compliance between measured and post-dicted deep-water wind wave parameters is good for the conditions of open sites, undisturbed by headlands, harbour breakwaters etc. The model yields wave parameters at the offshore deep-water boundary of a coastal zone.

Coastline evolution package is based on a standard one-line model. The single-line routine can be run either for sediment transport rates determined from wave input given in chronological order or for net sediment transport computed for the entire analysed period. In the first (full run) option the transport is computed at each time step and for each cross-shore profile, taking account of instantaneous wave-shoreline angle. In the second (simplified run) option the net transport rates for each transect, treated as the representative ones for all period, are computed and then are modified in all time steps as functions of changes of shoreline angles determined in the previous step. It should be noted that only longshore-related routines have been used in the SAND94 full run, to match the general objective of the project, dealing with coastal evolution due to longshore transport variability.

Hel Peninsula shoreline change modelling

As mentioned before, the 22-km seaward stretch between Władysławowo and Jastarnia was chosen for 1st step of the analysis. For simulation the period between 1991 and 1995 was selected, because detailed bed topography from 1991 and measurements of shoreline positions in 1991 and 1995 provided real data for model input and testing.

Distribution of wave energy, velocity of longshore currents and intensity of sediment transport along the Peninsula were computed with numerical model SAND94. The computations embraced spatial change of wave field including refraction-diffraction effects in a strip of 40 km from Rozewie (first mainland locality west of Władysławowo) to Hel town. The width of that strip varied between 9 km for Rozewie and 38 km for Hel town. Bed topography for those computations, recorded in 1991, is shown in Figure 3. It can be seen that the bed topography along the Peninsula is featured by two distinct troughs, surrounded by shallow waters in direct proximity of the coast. The first one is situated between Władysławowo and Chałupy (km H 4.0), the second one lies in the vicinity of Kuźnice (km H 12-13).

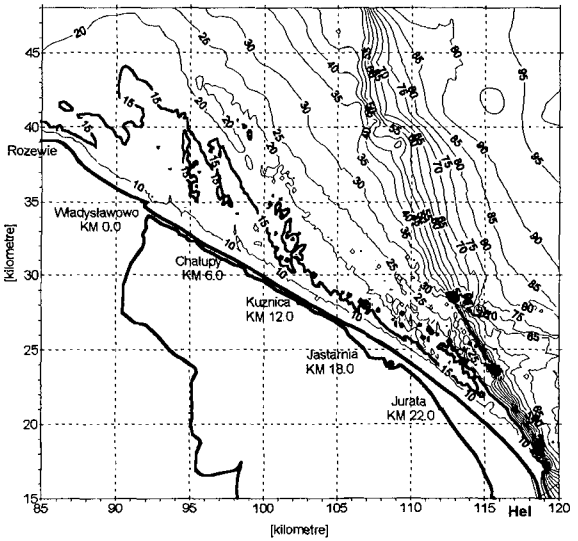

Figure 3 Bathymetry along Hel Peninsula

Assuming the computed wave climate parameters *i.e.* significant wave height H_S, wave period T_P and angle of wave incidence Θ as boundary conditions, dissipation of wave energy was calculated together with change of wave height along profiles approximately perpendicular to average shoreline configuration in the wave transformation zone and the surf zone. The spacing between consecutive profiles was set to 100 m.

On the basis of wave height change velocities of longshore currents were computed, which were used as the input for Bijker-type routine for longshore sediment transport calculations.

For long-term assessment of Peninsula's vulnerability to erosion, the conditions of average statistical year were chosen. In order to properly discretise the conditions of that year, the wind rose of all seaward winds from W to SE was thoroughly examined with the 22.5° resolution. Wind speed ranged between 1 and 20 m/s with 1m/s step. Exemplary fields of significant wave heights and azimuths of wave ray for 10 m/s of wind speed and the most frequent westerly winds are shown in Figs. 4a and 4b.

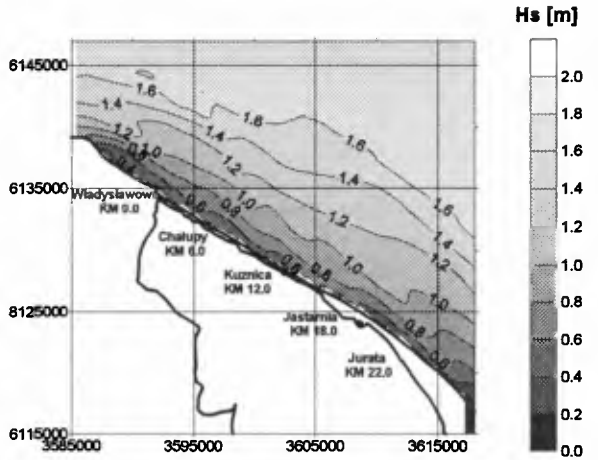

Figure 4a Distribution of wave significant height H_S along Hel Peninsula; wind direction W, speed 10 m/s

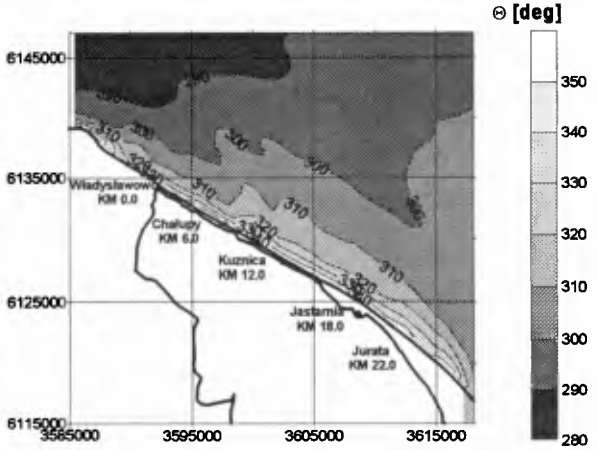

Figure 4b Distribution of wave approach Θ along Hel Peninsula; wind direction W, speed 10 m/s

Wave ray azimuth represents the direction of wave approach. For sake of computations the average azimuth of shoreline was assumed to equal 121.5° (equivalently 301.5°). The isolines of wave heights and wave ray azimuths indicate spots of intensive wave energy, reaching the vicinity of coastal zone. Upon thorough scrutiny of individual stormy situations, the following conclusions can be drawn:

- for westerly winds (W) the amount of wave energy reaching the shore is fairly evenly distributed along the Peninsula and the angle of wave incidence equals some 40° with respect to a shore normal direction, waves come from the western sector (Figure 4a and 4b);

- for north westerly winds (NW) high concentration of energy was identified on a short, 1 km long, sub-segment between Władysławowo and Chałupy and in the proximity of Kuźnica, the angle of wave incidence is 40° and is identical to the case of westerly winds;
- for northerly winds (N) spots with higher energy concentrations are scattered all over the Peninsula, the incidence angle is between 75° and 80° with regard to a shore-normal direction, winds come from the western sector;
- for north easterly winds (NE) energy concentrations were found in the vicinity of Kuźnica and locally close to the Władysławowo harbour, the incidence angle is equal to some 85° to a shore normal direction, waves arrive from the eastern sector;
- for easterly winds (E) the Chałupy region absorbs most of the energy, whose distribution then gradually declines heading east along the Peninsula, waves come from the eastern sector at 50° to the shore-normal line;
- for south easterly winds (SE) energy distribution is fairly uniform; it only gently grows east of Jurata, waves reach the shore from the eastern sector at 20° to the shore normal direction.

The computed, resultant sediment transport curves for average statistical year is plotted in Figure 5. It can be seen that the littoral drift is directed eastwards and is characterised by two distinct areas where it grows. The former is well pronounced and lies on first four kilometres of the Peninsula between Władysławowo and Chałupy. The latter, less conspicuous but still clearly visible, is situated between Kuźnica and Jastarnia. The sediment transport pattern thus has a positive gradient in those two areas, so it can be expected they are exposed to erosion. The computational results comply well with the observed spots of local erosion. They show that the most heavily eroded segments are 2 km stretch just east of Władysławowo harbour breakwaters, the zone at km H 4.0, the Chałupy region and the area between Kuźnica and Jastarnia.

Artificial beach nourishment between 1991 and 1995 was being executed at the following locations:

- 1991: KM H 0.0-0.8, 3.2-3.7, 10.3-13.6, 16.3-16.5, 18.2-19.2
- 1992: KM H 0.145-4.6, 10.0-10.9, 15.8-17.2, 22.1-22.5
- 1993: KM H 0.0-2.0, 4.1-4.56, 9.55-12.45, 14.45-17.15, 21.5-22.8
- 1994: KM H 0.2-2.75, 9.6-11.0, 16.3-17.2
- 1995: KM H0.1-0.5, 3.1-4.4, 10.0-10.7, 15.2-16.25,22.1-22.7

The amounts of sediment deposited on the beaches and nourishment periods were precisely quantified in SAND94 input files. The hindcast input wave data, was assumed constant in each 24-hour interval, being the computational time step for the whole simulation. The depth of closure was also constant and set to 7 m.

The mean grain size diameter used in the computations varied from 0.18 to 0.26 mm. The lower limit stems from extensive field studies of the Peninsula, carried out since 1983, the upper one – from the data collected recently. The latter data are distorted by artificial nourishment, which has been carried out eastwards of Władysławowo since 1990.

Results obtained by SAND94 were verified with UNIBEST, which requires only one cross-shore profile assumed to represent the entire modelled coastal zone. Upon detailed analysis of all transects from 1991 year the one of km H 10.0 was chosen.

The results of shoreline change computations along the Peninsula by SAND94 and UNIBEST for 1995 are jointly presented in Figure 6. The comparison shows that both models yield very similar results, which are fairly consistent with measurements done in 1995. Certain discrepancies can be attributed to local effects, which were deliberately ignored on this stage of the analysis.

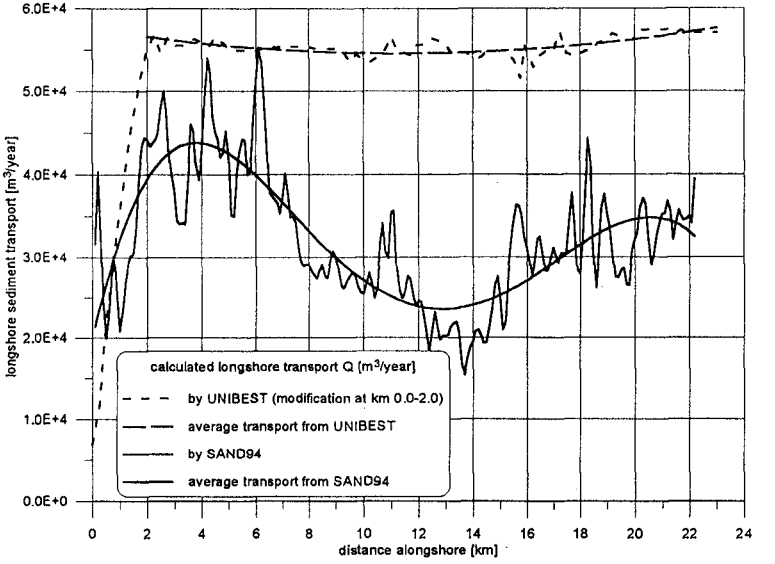

Figure 5 Net longshore sediment transport rates computed along Hel Peninsula by UNIBEST and SAND94 without beach fills

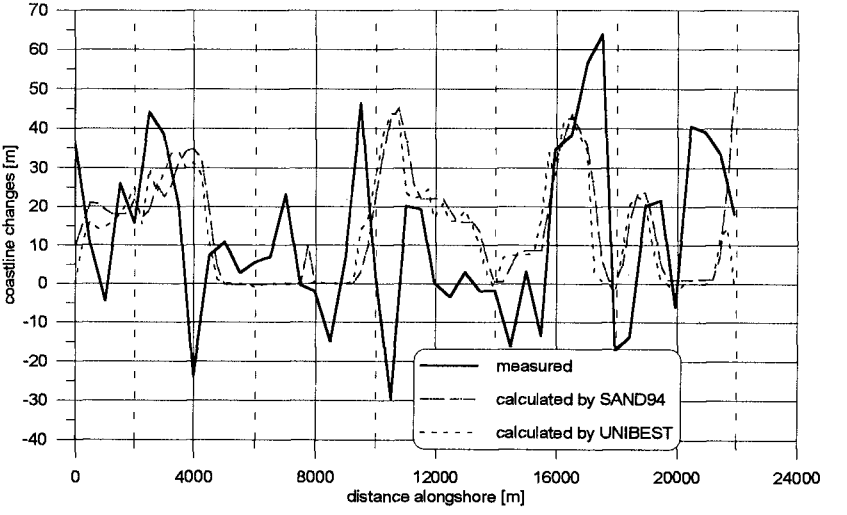

Figure 6 Computed and measured coastline changes along Hel Peninsula in 1991-1995; beach fills included

Modelling of the Władysławowo harbour effect

The 2nd step of shoreline change modelling takes into account local effects. Such modelling is aimed at detailed examination of local effects on small sub-segments of the area analysed in the 1st step. Man-made structures locally disturb natural processes, so special attention should be paid to properly reproduce the effects they cause. Hence, the vicinity of Władysławowo harbour, and the relative abundance of data acquired over decades, gives an excellent opportunity for analyses of coastal phenomena as well as extensive model testing.

Shoreline evolution in the proximity of the Władysławowo harbour was modelled by four models (GENESIS, LITPACK, SAND94 and UNIBEST) in the long-term time scale, for the shore segments stretching 2-km westwards and 2.3-km eastwards of the harbour. The initial conditions for computations were set to the year before the harbour construction (1934) and the simulation period covered more than 60 years until 1996/1997. The computations were designed to provide proper representation of the long-term shoreline migration in the close vicinity of the harbour on its both sides. The available model options were used to arrive at the most accurate reproduction of shoreline positions. The tests were carried out with wave input based on the representative meteorological annual chronology, retrieved for the period 1952-1990. The analysis of statistics of the meteorological data for each of those years revealed that the year 1970 was the most similar to the mean statistical year. The meteorological record of this year was then assumed as typical in determination of wave input for the modelled shoreline changes in 1934-1996/97. Hence, the offshore wave conditions were calculated from the actual wind measurements taken in 1970, with the time step of one day, and were assumed to be valid for the entire analysed period of 62 years. Wind parameters were assumed constant during each 24-hour interval. In all tested models the depth of closure in the single-line models was set to 7 m. Artificial beach fills on the lee side were included into consideration for the period in which detailed records of fills are available, i.e. 1991-1996.

Apart from LITPACK, the tested models assume the same sediment grain size in the entire region modelled; GENESIS uses a median grain size only. The median grain diameter used in the computations varied as in the 1st step from 0.18 to 0.26 mm. The sensitivity tests for all models except for LITPACK show a very weak response of the modelled shoreline to the variation of grain diameter.

Most groins east of Władysławowo are damaged and their influence on coastal processes was found to be negligibly small. The efficiency of these groins in the past is reported as very doubtful, so their existence in the modelling processes could be neglected. The simplified run option of SAND94 was used. The transport of 1934 was computed from the model of Bijker, yielding net value of 50000 m^3/year at average for the analysed shore segment. This transport was directed eastwards. The harbour was represented in the modelling procedure by two jetties closed by an offshore breakwater. The seawall was defined in its actual location, as well as beach fills in accordance with the actual records of nourishment.

In order to include the harbour impact, the longshore transport was modified and the blocking percentage was assumed, varying gradually from 20 % in 1936 (harbour appearance) to 1% in 1965-1997. The modified transport distributions for consecutive three sub-periods is shown in Figure 7. It can be seen that both spatial and temporal trends of sediment transport were reproduced satisfactorily. The sediment transport

variability has produced the reasonable shoreline evolution, which is presented in Figures 8. It can be seen from the plot that the model result for west side of the harbour is proper, while the erosion at the close east side is underestimated. The latter results from beach fills of 1991-1996, which apparently are not in model balance with erosive processes. Further eastwards of the harbour, the model shoreline changes are correct for the entire analysed period.

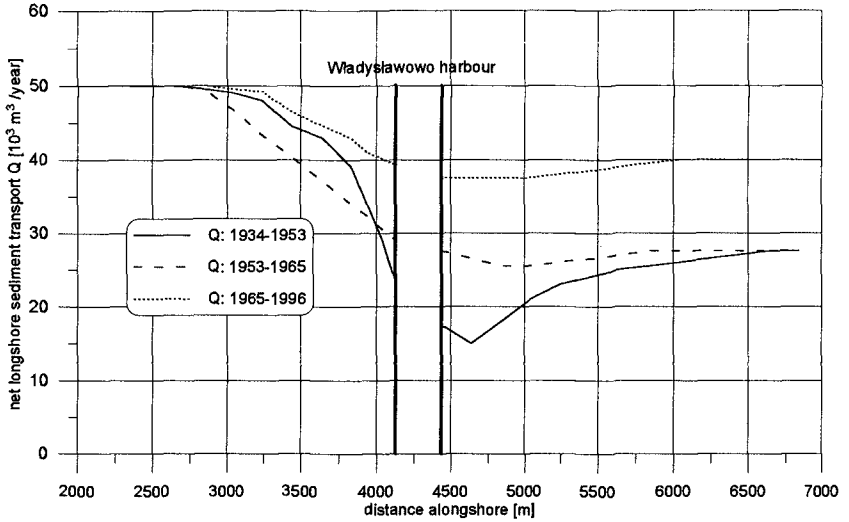

Figure 7 Net longshore sediment transport rates computed from SAND94 in 3 consecutive sub-periods

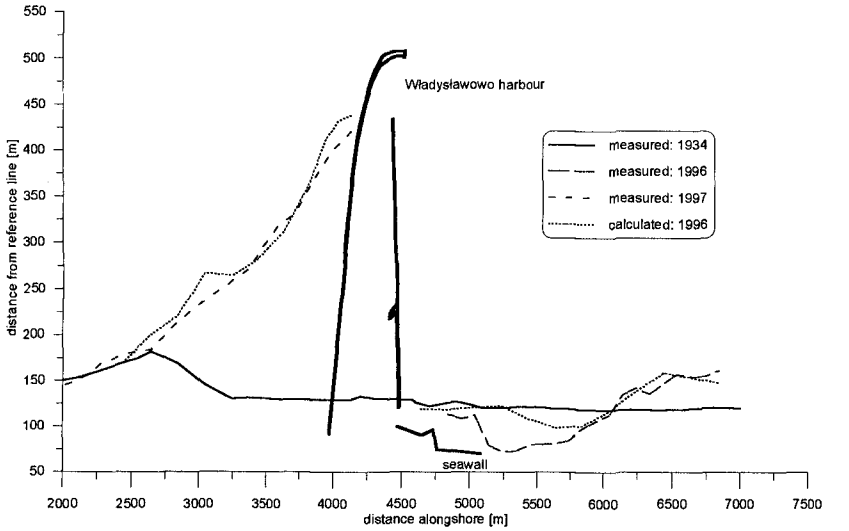

Figure 8 Shoreline positions nearby the harbour measured and computed from 1934-1996/97 from SAND94

The above results have been compared with the output provided by the other three models (GENESIS, LITPACK and UNIBEST). The comparison of final measured and computed shoreline positions is given in Figure 9. It can be seen that the long-term accretion westwards of the harbour are well represented. Almost the same accuracy of hindcast in the long time scale has been achieved at the lee-side of the harbour. It can be concluded that UNIBEST produced at least satisfactory shoreline positions in all sub-periods of the analysed period. The modelled transport rates also look very realistic.

In general it can be seen that all outputs are at least satisfactory. Westwards of the harbour, the outputs produced by all models are acceptable. The most accurate shoreline representations have been obtained from UNIBEST and LITPACK. Eastwards of the harbour, however, LITPACK clearly underestimates the lee-side erosion effects, while the shoreline retreats produced by GENESIS and UNIBEST are quite satisfactory.

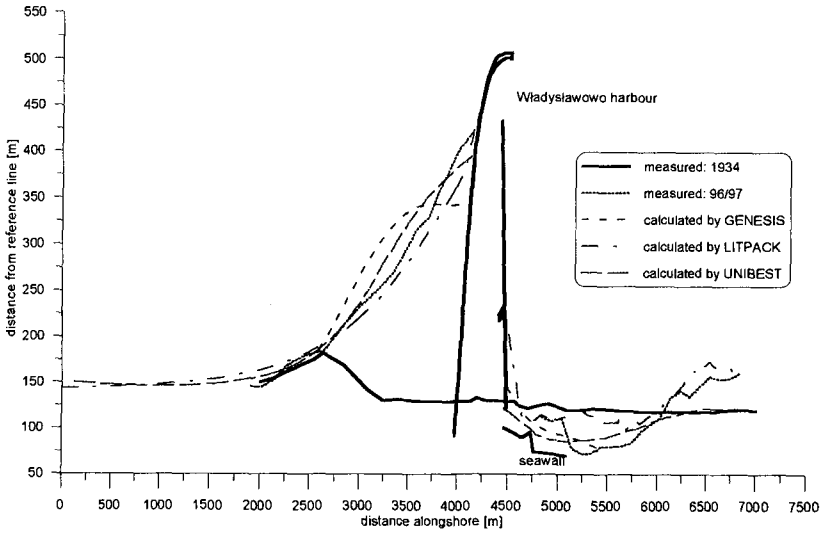

Figure 9 Shoreline positions nearby the harbour computed for 1934-1996/97 by GENESIS, LITPACK and UNIBEST

Conclusions

Two-step shoreline change modelling for the case study of the Hel Peninsula is presented in the study.

In the 1st step the large-scale calculations done for the vast portion of the Peninsula allowed for identification of potentially eroding spots and gave way to explain the causes of erosion.

In the 2nd step the vicinity of the Władysławowo harbour was thoroughly examined including local man-made effects. Long-term shoreline evolution was properly modelled and thus prediction of future evolution can easily be simulated. This in turn

modelled and thus prediction of future evolution can easily be simulated. This in turn facilitates and optimises future beach fills design and other shore protection activities in this region.

The following detailed conclusions for 1st step can be drawn:

- bed topography along the Peninsula, featured by two distinct troughs in the shallow water zone results in local concentrations of wave energy that reaches the shore in two regions adjacent to troughs;
- the 1st region of high energy concentration is situated between Władysławowo and Chałupy (km H 4.0), the 2nd one lies near Kuźnica (km H 12.0 – 13.0);
- analogously to wave energy, the calculated resultant longshore sediment transport is characterised by two zones of increasing intensity, one between Władysławowo and Chałupy and the other between Kuźnica and Jastarnia, such configuration implies that increasing transport rates are driven by high wave energy concentrations;
- energy concentrations occur mainly for north westerly winds, energy distributions for other winds is far more uniform;
- shoreline change computations comprising beach fills were done for the period between 1991 and 1995 by means of SAND94 and UNIBEST; the selection of that period guaranteed extensive background information in form of detailed bed topography and measurements of shoreline positions, a fairly good compliance with final shoreline configuration was achieved, certain discrepancies between computational results and measurements can be ascribed to local effects, which were ignored on this stage of analysis.

Results of computations in the 2nd step indicate that:

- thorough mapping of local conditions around Władysławowo harbour helped to properly model shoreline evolution history between 1934 and 1996/97;
- computations were executed with four models (GENESIS, LITPACK, UNIBEST and SAND94), the compliance with final shoreline positions is excellent for them all on the updrift (west) side of harbour breakwaters, good compliance on the lee side was achieved for GENESIS, LITPACK and SAND94, UNIBEST reached even better fit after tuning in with available user defined options;
- the results allow for accurate forecasting of future shoreline evolution and can be used for optimisation of artificial beach fills.

References

Adamski, Z. (1938). Fishery harbour of Wielka Wieś, in Port Władysławowo, Polish Academy of Sciences' Sea Research Committee, Studia i Materiały Oceanologiczne, No. 8, Wrocław-Warszawa-Kraków-Gdańsk, 5-35 (in Polish).

Basiński, T., A. Mielczarski & M. Szmytkiewicz (1990). Hel Peninsula protection concept. *Report*, Polish Academy of Sciences' Institute of Hydro-Engineering, Gdańsk (in Polish).

Coastal protection at Hel Peninsula (1974). Collective work edited by I. Semrau, Maritime Institute of Gdańsk, No. 1245 (in Polish).

GENESIS Manual (1991). GENESIS: Generalised model for simulating shoreline change, *Report 2, Workbook and system user's manual*, Technical Report CERC-89-19.

Hueckel, S. (1968). On the history of maritime civil engineering in Poland, Gdańsk, GTN (in Polish).

Kryłow, J. M., S. S. Striekałow & W. F. Cypluchin (1976). Wind waves and their influence on structures, Gidrometeoizdat, Leningrad (in Russian).

LITPACK Manual Release 2.0 (1994). User's guide and reference manuals for LITPACK, Danish Hydraulic Institute, Denmark.

Mielczarski, A. (1970). Accuracy of shoreline change measurements, *Rozprawy Hydrotechniczne, Zeszyt 27* (in Polish).

Mielczarski, A. (1984). Protection problems at Hel Peninsula, *Inżynieria Morska*, No. 3 (in Polish).

Semrau, L. (1985). Influence of maritime structures on morphodynamics and lithodynamics of Polish coastal zone, Maritime Institute of Gdańsk (in Polish).

Szopowski, Z. (1958). Bathymetric changes in the region of Władysławowo harbour in 1949-1956, *Rozprawy Hydrotechniczne*, Gdańsk, Vol. 4, 47-69 (in Polish).

Tubielewicz, W. (1957). Coastal changes at the root of Hel Peninsula, Historical Materials, *Rozprawy Hydrotechniczne*, Gdańsk, Vol. 2, 3-66 (in Polish).

UNIBEST Manuals (1993). A software suite for simulation of sediment transport processes and related morphodynamics of beach profiles and coastline evolution, Delft Hydraulics, Delft.

Zenkowicz W.P. (1962). Scientific bases for coastal evolution, Moscow, USSR Acad. Sc. (in Russian).

ACKNOWLEDGEMENTS

This study stems from research under the international EU programme PACE (MAST III; MAS3-CT95-0002) and Project DWW-1149 "Validation of Existing Coastal Dynamics Models".

MORPHODYNAMICS OF SHOREFACE–CONNECTED RIDGES

A. FALQUES[1] D. CALVETE[1] H. E. DE SWART[2] N. DODD[3]

Abstract

A morphodynamic model is developed and analyzed to gain fundamental understanding on the basic physical mechanisms responsible for the characteristics of shoreface-connected sand ridges observed in some coastal seas. These alongshore rhythmic bedforms have a horizontal length-scale of order 10 km. It is found that the positive feedback between the topographic disturbances of a sloping bottom and the subsequent deflection of the mean coastal current is the main cause of the ridges. To be effective, this mechanism needs an averaged sediment transport mainly due to wave stirring during storms and an averaged current driven by pressure gradients rather than surface stresses. Even in the presence of significant tidal currents, their origin — related to the mean current instead of tidal oscillation — is essentialy different from that of tidal sand banks.

1 Introduction

Shoreface-connected ridges are elongated sand banks found in the inner part of some continental shelves in horizontal patterns with a length-scale of order O(10 km). Such ridges are present, for example, near the Dutch coast (see e.g. Van de Meene, 1994, and figure 1), near the east coast of the United States of America (Swift *et al.* 1985), near the Argentinian coast (Parker, Lanfredi & Swift, 1982). They start at the offshore end of the shoreface and they extend seaward forming an angle of $20^o - 35^o$ with respect to the coastline. In contrast with the

[1]Departament de Física Aplicada, Universitat Politècnica de Catalunya. 08034 Barcelona, Spain

[2]Institute for Marine and Atmospheric Research, Utrecht University. 3584 CC Utrecht, The Netherlands

[3]Coastal Group, HR Wallingford. OX10 8BA Wallingford, United Kingdom

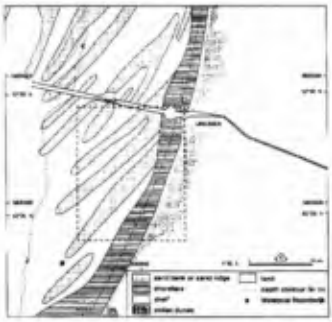

Figure 1: The dutch shoreface-connected sand ridges (Van de Meene, 1994).

more offshore tidal sand banks (see e.g. Hulscher, De Swart & De Vriend, 1993), their orientation is not cyclonically oriented with respect to the tidal current, but it is related to the alongshore mean coastal current, the seaward end of the ridge being shifted upstream with respect to its shoreface attachement. Hereafter we will refer to this as *upcurrent rotated* bars. The opposite orientation will be defined as *downcurrent rotated*.

The alongshore spacing between successive crests of shoreface-connected ridges ranges between 5 and 10 km. The length of individual crests is between 10 and 25 km. Their height is between 1 and 6 m in water depths between 4 and 20 m. The ridges slowly migrate in the direction of the dominant current with a celerity of a few $\mathrm{m\,yr^{-1}}$.

In general, sand banks are important, since they may form shallow areas which are hazardous for shipping traffic and may affect the stability of pipelines and oilrigs, due to lateral movements. They are also possible sources for sand mining. The shoreface-connected ridges, which form the seaward boundary of the nearshore zone, play a relevant role in the dynamics of the coastal system (Van de Meene, 1994).

There is geological evidence that the ridges are not relict features, that is, they are active under the present hydrodynamic conditions and their growth has taken place during the Holocene. For instance, on the Dutch inner shelf they started to form about 3400 years ago. Therefore, as it is the case for many sea bed patterns an explanation of the origin of the ridges as an inherent free instability of the coupled bottom-fluid system under the action of some current seems plausible. Given a small disturbance of a simple reference topography (e.g., a flat bottom) the response of the flow to this perturbation can result in a sediment transport pattern which reinforces the bottom undulation. Then a positive feedback is induced and both disturbances will grow in time.

According to Trowbridge (1995), storms are the main cause of the currents capable of generating shoreface-connected ridges. Indeed, storm driven currents can be of order $0.5 - 1\ \mathrm{m\,s^{-1}}$ in the areas where ridges are observed off the coast of Holland, Florida and Argentina. However, while tidal currents are rather weak on the American shelf, they are important near the Dutch coast ($0.7 - 1.1\ \mathrm{m\,s^{-1}}$, at the surface). Also, as we will see, an important contribution from alongshore gradients on the free surface elevation can occur on the mean current.

Trowbridge (1995) studied the morphologic stability properties of a storm-driven alongshore current, with a cross-shore gradient, on a shelf bounded by a straight coast and with a transverse slope. It was shown that the system is unstable and leeds to the growth of bedforms very similar to the observed ridges. It was suggested that the basic physical mechanism was the offshore deflection of the flow over the shoals and the related loss of sediment carrying capacity in the offshore direction due to the transverse slope. However, a severe assumption in this model is the condition of irrotational flow. This implies that the production of vorticity due to bottom frictional torques and Coriolis terms, which has been proven to be very important for tidal sand banks dynamics (see Zimmerman 1981; Hulscher *et al.* 1993) is neglected. In addition, a crude sediment transport parametrization is used, where the sediment flux is assumed to be linear in the mean flow velocity and the downslope effect on the transport direction is not accounted for. As a result his model does not predict any preferred spacing between ridge crests. Furthermore, the model deals with linearized evolution equations just allowing for the initial growth of small amplitude solutions.

In this paper we investigate a generalized and physically more realistic model for both the water and sediment motion. The fluid is described by the full 2D shallow water equations, which include bottom friction and Coriolis terms. The sediment flux is assumed to be proportional to some power m of the current so that the role of different choices for m can be explored. Finally, a nonlinear extension of the model is briefly described and some preliminary results of finite amplitude evolution is presented.

2 Model formulation

2.1 Equations of motion. Scaling

As shown in figure 2, the inner shelf is schematized as a sloping sea bed, bounded by a straight vertical wall which represents the seaward end of the shoreface. Further offshore, a horizontal flat bottom describes the outer shelf. An orthogonal coordinate system is taken with the x, y and z-axes pointing in the cross–shore, longshore direction and vertical direction, respectively. The still water level is represented by $z = 0$. Although the vertical structure of the currents can have an important role in the ridge area, in view of earlier studies on large scale bedforms it is worthwhile to investigate whether a 2D model can describe the main characteristics of the ridges. Therefore, the fluid motions are considered to be governed by the 2D shallow water equations, which consists of the depth–averaged momentum equation and mass conservation equation. The bottom evolution follows from the sediment conservation equation.

In order to make the equations of motion dimensionless we now introduce characteristic magnitudes L_H, L_V and U for the horizontal length, the depth and the current. L_H is the width of the inner shelf, L_V and U are typical values of the water depth and the mean current. For example, representative values for the Dutch inner shelf are $L_H \sim 12 \times 10^3$ m, $L_V \sim 15$ m and $U \sim 0.25\,\mathrm{m\,s^{-1}}$. The variables are made dimensionless as follows:

$$(x, y) \to L_H(x, y) \qquad z_b \to L_V z_b \qquad \boldsymbol{v} \to U\boldsymbol{v} \qquad t \to T_m t \qquad z_s \to \frac{U^2}{g} z_s \,. \tag{1}$$

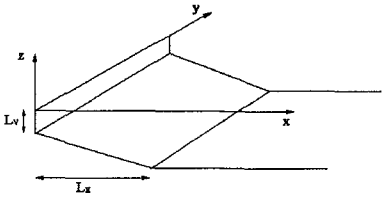

Figure 2: Sketch of the geometry and the coordinate system.

The scaled momentum and mass conservation equation read:

$$\epsilon\frac{\partial \boldsymbol{v}}{\partial t} + (\boldsymbol{v}\cdot\boldsymbol{\nabla})\boldsymbol{v} + \hat{\boldsymbol{f}}\times\boldsymbol{v} = -\boldsymbol{\nabla} z_s + \frac{\boldsymbol{\tau}}{D} \tag{2}$$

$$\epsilon\frac{\partial D}{\partial t} + \boldsymbol{\nabla}\cdot(D\boldsymbol{v}) = 0 \tag{3}$$

and the sediment conservation equation read:

$$\frac{\partial z_b}{\partial t} + \boldsymbol{\nabla}\cdot\boldsymbol{q} = 0\,. \tag{4}$$

Here $\boldsymbol{v}$ is the current vector, $\hat{\boldsymbol{f}}\times\boldsymbol{v}$ is the Coriolis acceleration, $\boldsymbol{\tau}$ represents the free surface and bottom stress terms ($\boldsymbol{\tau} = \boldsymbol{\tau}_s - \boldsymbol{\tau}_b$). The free surface, the bottom and the total height of the water column are given by $z = z_s$, $z = z_b$ and D, so that $D = F^2 z_s - z_b$. The nabla–operator is defined by $\boldsymbol{\nabla} = (\partial/\partial x, \partial/\partial y)$. The volumetric sediment flux per unit width is denoted by $\boldsymbol{q}$. It is important to note that, since the growth of the ridges takes place on very long time scales (O(10^3 yr)), all the quantities in the governing equations have to be considered as averages over a long time O(1 yr).

The boundary conditions imposed for this system are periodic conditions in the longshore direction. Furthermore, at $x = 0$ (the transition shoreface-inner shelf) and for $x \to \infty$ we assume that the cross-shore flow component vanishes and the bottom elevation is fixed to its reference value.

In order to close the model parametrizations for the bed shear stress $\boldsymbol{\tau}_b$ and the sediment flux $\boldsymbol{q}$ are required. We will consider a linear friction law and the volumetric sediment flux parametrized as

$$\boldsymbol{\tau}_b = r\boldsymbol{v} \qquad\qquad \boldsymbol{q} = |\boldsymbol{v}|^m\left(\frac{\boldsymbol{v}}{|\boldsymbol{v}|} - \hat{\gamma}\boldsymbol{\nabla} h\right)\,. \tag{5}$$

The coefficient $\hat{\gamma}$ is related to the angle of repose of the sediment, so the term $-\hat{\gamma}\boldsymbol{\nabla} h$ accounts for the tendency of sand to move downslope and m is an exponent which is usually between 1 and 6. Finally, h is the elevation of the bottom with respect to a specific equilibrium profile, to be discussed in the next subsection. Further details on sediment transport can be found in Van Rijn (1993) and Fredsoe & Deigaard (1993).

Two time scales appear which are defined as

$$T_h = \frac{L_H}{U} \qquad\qquad T_m = \frac{L_H L_V}{\nu U^m} \tag{6}$$

The hydrodynamic time scale T_h follows from scaling the three equations (2)–(3) and the morphodynamic time scale T_m results from scaling equation (4). Here ν is the coefficient that multiplies the right hand side in the dimensional version of the sediment flux parametrization (eq. (5)). For simplicity, it has been assumed to be constant. Other parameters in the model are

$$\epsilon = \frac{T_h}{T_m} \qquad F^2 = \frac{U^2}{gL_V} \qquad \hat{f} = f_c \frac{L_H}{U} = Ro^{-1} \qquad r = r_* \frac{L_H}{UL_V} \qquad \hat{\gamma} = \gamma \frac{L_V}{L_H} \tag{7}$$

The hydrodynamic timescale is assumed to be much smaller than the morphodynamic one. This allows for the adoption of the quasi-steady hypothesis, that is, the fluid instantaneously adjusts to the bathymetric changes. This permits to drop the time derivatives ($\epsilon \approx 0$) in the three differential equations (2)–(3). Using the scales of motion, it appears that the Froude number F is very small, $F \sim 0.02$. Consequently, in the forthcoming analysis the water column is assuumed to be equal to the bottom, $D = -z_b$.

2.2 Basic state

In this study we model the reference bottom profile as

$$H(x) = \begin{cases} 1 + \beta x & (0 \leq x < 1) \\ 1 + \beta & (x \geq 1) \end{cases} \tag{8}$$

Note that $H(x)$ and x are dimensionless, and that the depth at the seaward end of the shoreface has been chosed as vertical length-scale, L_V. In case of the Dutch inner shelf, $L_V \sim 15$ m, $L_H \sim 12 \times 10^3$ m and the water depth on the outer shelf is ~ 20 m , so that $\beta = 0.33$.

It is easily seen that a steady basic state of the form

$$\boldsymbol{v} = (0, V(x)) \qquad z_s = \delta\, y + \xi(x) \qquad z_b = -H(x) \tag{9}$$

where $\delta = g\, s\, L_H / U^2$ is the dimensionless parameter for the longshore gradient, s, is a solution of the governing equations (2), (3), (4) . The alongshore momentum balance between forces related to the longshore pressure gradient, windstress and bottom friction is achieved by

$$V = \frac{\tau_{sy} - \delta\, H}{r} \tag{10}$$

It has been demonstrated by Scott & Csanady (1976) and Van der Giessen, De Ruijter & Borst (1990) that the momentum balance using the linear friction law (5) yields a good description of mean currents in the coastal zone.

Analysis of current data obtained on the East American inner shelf (Scott & Csanady 1976; see also Chase 1979) indicate that the sea surface slope $s \sim 1 - 2 \times 10^{-7}$ and the friction coefficient $r_* \sim 5 \times 10^{-4}$ m s^{-1}. Similar values appear to apply to the Dutch inner shelf. The physical mechanism causing the longshore pressure gradient is discussed by Chase (1979). Based on the field data discussed above we choose $\tau_{sy} \simeq -0.1$ Nm^{-2} and $s \simeq 2 \times 10^{-7}$. This yields an estimate of the longshore velocity scale: $U \equiv V(x = 0) \simeq 0.25$ m s^{-1}. Both the longshore windstress and pressure gradient are comparable and force a flow in the same, negative, y-direction.

Combining equations (8) and (10) and including the new parameter $a = |\delta|/r$, the velocity profile for the basic state reads:

$$V(x) = \begin{cases} \pm(1 + a\beta x) & \text{if } 0 \leq x \leq 1 \\ \pm(1 + a\beta) & \text{if } x > 1 \end{cases} \tag{11}$$

and the sign of the flow is determined by the direction of the applied wind and longshore pressure gradient forces. The parameter a measures the relative effect of the longshore pressure gradient in maintaining the basic state velocity. By using the definition of velocity scale U it follows that a can vary between 0 (no pressure gradient) and 1 (wind stress negligible).

2.3 Linear stability analysis

The formation of rhythmic bedforms can then be investigated by studying the dynamics of small pertubations evolving on this steady state:

$$z_s = \zeta + \eta(x,y,t) \quad z_b = -H + h(x,y,t) \quad \boldsymbol{v} = (0,V) + (u(x,y,t), v(x,y,t)) \tag{12}$$

where $\zeta = \delta\, y + \xi(x)$. The scaled linearized momentum (2) and mass conservation equation (3) read:

$$V\frac{\partial u}{\partial y} - \hat{f}v = -\frac{\partial \eta}{\partial x} - \frac{r}{H}u \quad , \quad V\frac{\partial v}{\partial y} + \frac{\mathrm{d}V}{\mathrm{d}x}u + \hat{f}u = -\frac{\partial \eta}{\partial y} - \frac{r}{H}v + \delta\frac{h}{H} \tag{13}$$

$$\frac{\mathrm{d}H}{\mathrm{d}x}u + H\frac{\partial u}{\partial x} + H\frac{\partial v}{\partial y} - V\frac{\partial h}{\partial y} = 0 \tag{14}$$

and the sediment conservation equation (4) reads:

$$\frac{\partial h}{\partial t} = -|V|^{m-1}\left\{\frac{(m-1)}{V}\frac{\mathrm{d}V}{\mathrm{d}x}u + \frac{\partial u}{\partial x} + m\frac{\partial v}{\partial y} - \hat{\gamma}|V|\left(\frac{m}{V}\frac{\mathrm{d}V}{\mathrm{d}x}\frac{\partial h}{\partial x} + \frac{\partial^2 h}{\partial x^2} + \frac{\partial^2 h}{\partial y^2}\right)\right\} \tag{15}$$

The equations (13)-(15) allow for alongshore travelling and growing wave solutions of the form

$$(u, v, \eta, h) = \mathrm{Re}\{(\hat{u}(x), \hat{v}(x), \hat{\eta}(x), \hat{h}(x))e^{\mathrm{i}ky + \omega t}\} \tag{16}$$

Here k is the wavenumber and ω a complex frequency. The real part, $\mathrm{Re}(\omega)$, denotes the growth rate of the perturbation and $-\mathrm{Im}(\omega)$ the frequency. Instability occurs if $\mathrm{Re}(\omega)$ is positive: then the mode grows exponentially in time. The part which describes the bottom is called a topographic wave. As a result of (16), equations (13)-(15) can be written as an eigenvalue problem where ω is the eigenvalue and $h(x)$ the eigenfunction. The mathematical details and the solution procedure can be seen in Falqués *et al.* (1997), Falqués *et al.* (1998*b*).

3 Model Results

In this section the results obtained with the linear numerical model will be presented. In order to fit our model to the situation on the Dutch inner shelf, we choose values for the parameters L_V, L_H, U, r_*, and s as discussed in section 2.3. A value $\gamma = 0.08$ will be adopted for the Coulomb coefficient in the sediment flux. The Dutch coast is at a latitude of 51°N, thus the Coriolis parameter is $f_c = 1.12 \times 10^{-4}\,\mathrm{s}^{-1}$. Consequently, the default values of the non-dimensional parameters in our study are

$$\hat{f} = 5.35 \qquad r = 1.5 \qquad \hat{\gamma} = 1 \times 10^{-4} \qquad \beta = 0.33 \qquad a = 0.23$$

In this study we will focuss on the dynamics of bedforms in the case where the current has the coast to the right in the Northern Hemisphere ($\hat{f} > 0, V < 0$), which is the case of the Dutch and the North American coasts. On the Argentinian shelf the current is directed to the north ($V > 0$ in the present model) but then, $\hat{f} < 0$. However, the latter situation is equivalent to the former one because the system has a mirror symetry with respect to the $y = 0$ plane, so that there are only two independent situations, $\hat{f}V < 0$ and $\hat{f}V > 0$. Some results for the latter case will also be presented when discussing the effect of Coriolis force.

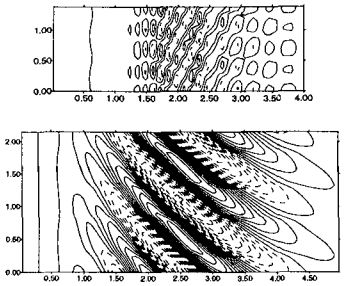

Figure 3: Bedforms for $m = 3$. See the text for explanation.

A sediment transport proportional to the current will be considered, i.e., $m = 1$. This choice is representative for situations where the wave-induced orbital velocity near the bed is much larger than the steady current. The sediment is then stirred by the waves and subsequently transported by the current. The effects of a sediment transport faster than linear, $m > 1$, have also been explored. In this case, the model gives bedforms different from the observed shoreface-connected ridges. These can be of two types: patches of alternate shoals and pools or cyclonically oriented ridges, see figure 3 up and down, respectively. The results in the case $m > 1$ can be seen in Falqués, Calvete & De Swart (1998*a*) and will be not further described here.

In figure 4 curves are presented of the growth rates of the first three eigenmodes for $a = 1$. In this case the basic state current is fully determined by the longshore pressure gradient. Note that the ratio V/H is constant, as was also studied by Trowbridge (1995). An important difference is that in the present model the preferred downslope movement of the sediment is accounted for. This causes the growth rate to have a maximum for $k \simeq 10$, which corresponds to a spacing

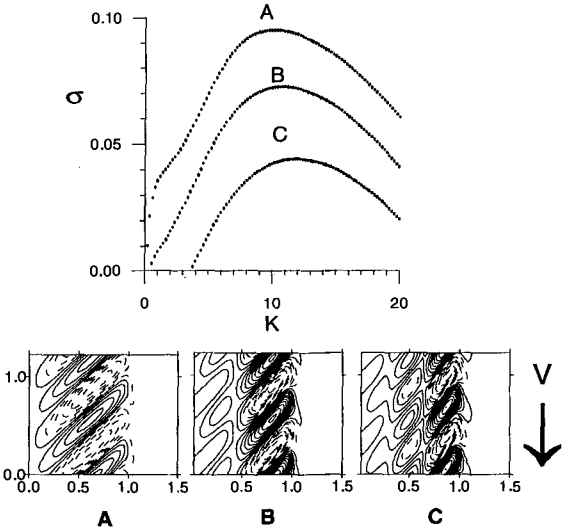

Figure 4: Nondimensional growth rate, $\sigma = \mathrm{Re}(\omega)$ as a function of the wavenumber, k, for the first three modes (upper part). Parameter values are $m = 1$, $a = 1$, $r = 1.5$, $\hat{f} = 5.35$, $\hat{\gamma} = 10^{-4}$, $\beta = 0.33$ and $V < 0$. The contour plots of the three bottom modes with the largest growth rate, are shown below. Crests and troughs are indicated by continuous and dashed lines, respectively. In each plot the y axis (vertical on the left) represents the shoreface and the $x > 0$ axis (horizontal on the bottom) the inner shelf. The direction of the basic current is shown by a big arrow. Note the upcurrent rotation of the ridges.

of about 7 km. This agrees with the observed spacings of shoreface-connected sand ridges on the Dutch inner shelf (Van de Meene, 1994). The corresponding phase speeds are $\simeq -1$ and this variable shows almost no dependence on k. This means that ridges behaves like topographic waves which migrate downcurrent with a celerity $V_{mi} \simeq L_H/T_m$. In view of the fact that the maximum growth rate is $\simeq 0.1$, the amplitude of the dominant bottom mode grows approximately 6% during the period that the pertubation travels one wave-length. An estimate of the characteristic growth time (e-folding time) can be obtained from the horizontal lengthscale, $L_H \sim 12$ km and a typical migration speed, $V_{mi} \sim 4\,\mathrm{m\,yr^{-1}}$, by means of $\tau = cL_H/V_{mi}\mathrm{Re}(\omega)$. This yields $\tau \sim 3 \times 10^4$ yr. The shape of the modelled ridges are shown in figure 4b. Clearly, the orientation of the dominant bedforms is such that they are upcurrent rotated: the seaward ends of the crests are shifted upstream with respect to their shoreface attachments. This agrees well with the observed orientation of the three ridge patches discussed in the introduction. Figure 5 shows the contour plot of mode 1 in figure 4 along with the corresponding perturbation on the current. The offshore deflection of the current over the crests and the onshore deflection over the troughs can be seen.

For $a < 1$, the longshore windstress contributes to the maintenance of the basic current profile and hence the ratio V/H is no longer constant. This leads to substantial differences compared with the case that $a = 1$. For a close to 1 the

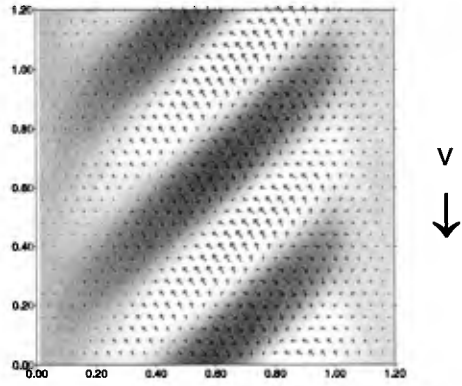

Figure 5: Contour plot of the first mode in figure 4 with the associated perturbation of the current indicated by arrows. Crests and troughs are indicated by dark and white colours, respectively. Note the offshore current deflection over the crests.

dominant wavenumber is close to 7, but with decreasing a this role is taken over by a much lower wavenumber, $k_m \sim 7$ for $a = 0.8$ and $k_m \sim 1$ for $a = 0.6$. Obviously, the predicted ridge spacings become much larger than those observed in the field. Besides, the growth rates decrease with decreasing a and hence the e-folding time scale of the bedforms becomes unrealistically large. Another interesting aspect is the competition between different modes with different spatial structures. The main differences are that some of them are attached to the shoreface while some are not. Sometimes they appear to be very elongated. Anyway, a striking overall characteristic of all modes is the upcurrent orientation of their crests.

The effect of earth rotation on the instability mechanism has been investigated by carrying out experiments with all parameters having their default values but for $a = 1$ and different values of the Coriolis parameter: $\hat{f} = 0, 7, -7$. The results, shown in figure 6, indicate that earth rotation hardly affects the topographic waves in the observed wavenumber range, $k \sim 10$. In this range, Coriolis force produces just an inshore shift of the ridges (C) in the Southern Hemisphere and an offshore shift in the Northern Hemisphere (A) along with a slight inhibition of the instability in the latter case. In contrast, earth rotation has a strong influence on long topographic waves, making the instability mechanism to be much more effective on the Southern Hemisphere. In this case, a sharp peak in the growth rate curve occurs for very long wave-lengths. The corresponding bedforms show a little obliquity with respect to the coast and differ substantially from the observed elongated ridges (D).

The sensitivity of the model results to the friction parameter has also been investigated. The general trend appears to be that growth rates increase with increasing r, in particular for relatively small wavenumbers ($k < 8$). However, for k around 10 or larger, the growth rates hardly depend on r. Furthermore, the wavenumber for which the instability mechanism is most effective become smaller if the friction parameter is increased. The shape of the preferred bottom modes do not change significantly.

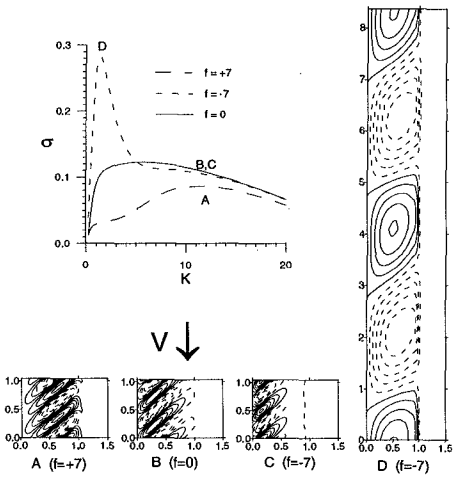

Figure 6: Growth rate curves of the first mode for different values of the Coriolis parameter $\hat{f}$. All other parameter values are $m = 1$, $a = 1$, $r = 1.5$, $\hat{\gamma} = 10^{-4}$, $\beta = 0.33$ and $V < 0$. The bottom contours are also shown, for $k = 12$ (A,B,C) and for the peak at $k = 1.5$ (D).

The bed slope β and the Coulomb coefficient $\hat{\gamma}$ have counteracting effects, the former de-stabilizing, the latter stabilizing. If $\hat{\gamma}$ becomes larger than about 8×10^{-4} instabilities do not longer exist.

4 Physical mechanisms

In this section the physical mechanisms which originate the formation of the ridges according to our model will be discussed. For this purpose it is useful to combine the continuity equation (14) and the bottom evolution equation (15) to obtain (in the quasi-steady limit $\epsilon \to 0$ and for small Froude number $F \to 0$)

$$\frac{\partial h}{\partial t} + \frac{m q_0}{H} \frac{V}{|V|} \frac{\partial h}{\partial y} - \frac{\partial}{\partial x}\left(\hat{\gamma} q_0 \frac{\partial h}{\partial x}\right) - \frac{\partial}{\partial y}\left(\hat{\gamma} q_0 \frac{\partial h}{\partial y}\right) = \frac{q_0}{|V|}\left(\frac{m}{H}\frac{\mathrm{d}H}{\mathrm{d}x} - \frac{(m-1)}{V}\frac{\mathrm{d}V}{\mathrm{d}x}\right) u + (m-1)\frac{q_0}{|V|}\frac{\partial u}{\partial x} \tag{17}$$

where $q_0 = |V|^m$. On the left-hand side an advective contribution and two diffusive terms appear. Thus, in absence of the right-hand side, this equation would describe just migrating and decaying bedforms. The principle sources for instability appear on the right-hand side. The first term only acts in case there is a transverse sloping reference bottom. The last two terms are only active in case $m > 1$ (i.e., a 'faster than linear' sediment transport parametrization).

Consider the first term on the right-hand side of equation (17). It shows that an offshore deflection over a bar ($u > 0$) on a transverse sloping reference bottom causes a growth of the bar ($\partial h/\partial t > 0$). This can be intuitively understood by considering a control volume at a crest (where $\partial/\partial y = 0$) with vertical sides

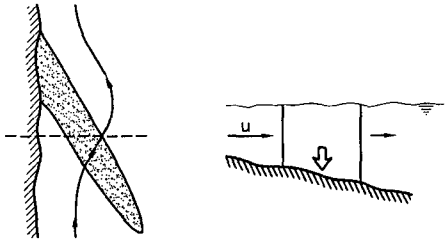

Figure 7: Schematic view of the transverse bottom slope mechanism. An upcurrent oriented ridge produces offshore deflection of the flow. Then, flow into deeper water must converge so that a sediment convergence occurs over the ridge.

parallel and perpendicular to the coast (see figure 7). In case of an offshore flow component ($u > 0$) the mass deficit caused by the movement of the column into deeper water must be compensated by a convergence of the flow. As the sediment flux, q, is proportional to a power of the velocity of the current, there will be convergence of sediment above the crests and thus the ridges will grow (see figure 7). Therefore, what we need now to explain the formation of the ridges is just a confirmation of the offshore deflection of the current over the crests. As a consequence of mass conservation in case of irrotational flow (Falqués *et al.*, 1998*a*) it can be seen that an upcurrent oriented ridge causes an offshore deflection and that an downcurrent oriented ridge causes an inshore deflection. This is also confirmed by numerical simulation of the flow (see figure 5). Therefore, this behaviour achieves a positive feedback between bedforms and flow disturbance which is responsible for the growth of upcurrent oriented ridges.

The numerical simulation described in section 3 shows that the mechanism just explained is quite robust and that coriolis and frictional forces have only a moderate effect on it. What has a strong influence on the effectiveness of the transverse slope mechanism are the exponent m of the sediment transport and parameter $a = \delta/r$. The mechanism is most efficient for $m = 1$ and $a = 1$. This seems related to the fact that in this case the local migration celerity of the topographic waves, mq_0/H (according to eq. (17)), is cross-shore uniform. Apparently, the cross-shore gradients on the migrational celerity inhibit the growth mechanism. The reason has not yet been fully understood.

In case of $m > 1$, and in conection with the last term in equation (17), two different instability mechanisms appear which are related to the production of vertical vorticity. The first one is caused by bottom frictional torques over an uneven sea bed and tends to produce patches of alternate shoals and pools (see figure 3). The second one comes from the stretching of planetary vorticity by an uneven sea bed and tends to originate elongated ridges which are cyclonically oriented (see figure 3). A detailed analysis of them can be seen in Falqués *et al.* (1998*a*).

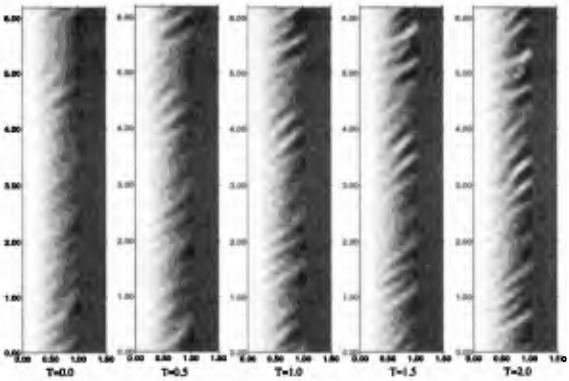

Figure 8: Nonlinear evolution. See explenations in the text.

5 Nonlinear model. Preliminary results

Nonlinear theory provides the tool for examining the long-term evolution of the shoreface-connected ridges into some form that is observable in the field. Following Schuttelaars (1997), the nonlinear solution is expanded in terms of the linear eigenfunctions. Time evolution equations are derived by inserting the expansion into the full nonlinear equations and then projecting the resulting equations onto the adjoint linear eigenfunctions. This Galerkin-type method has the considerable appeal of using actual linear solutions as a basis—rather than, say, some arbitrary polynomial—so that comparatively few terms are necessary to describe the nonlinear evolution accurately. Work regarding the nonlinear equations is in progress. Figure 8 is shown as an example of some preliminary results. The time evolution of bathymetric contours from $t = 0$ to $t = 2$ (morphological time units) can be seen for $m = 1$, $a = 1$, $r = 1.5$, $\hat{f} = 5.35$. A number of 30 long-shore modes have been used, ranging from $k = 1$ to $k = 30$.

6 Conclusions

It has been shown that shoreface-connecte sand ridges are formed due to a positive feedback between the water motion and the erodible bottom. However, the results of the model depend essentialy on the sediment transport parametrization through the exponent m. In case $m = 1$ (sediment transport proportional to the current) the dominant bedforms are trapped to the inner shelf and they are elongated and upcurrent rotated. The growth rate and longshore spacing are largely determined by the relative contribution of wind and the longshore pressure gradient in the maintenance of the background current. In case the latter effect dominates the model results show good agreement with field data, e.g. in case of the Dutch inner shelf a spacing of about 7 km is obtained (see figure 1). With increasing wind effects the growth rates become smaller and the wave-lengths increase. Coriolis and bottom friction also affect the instability mechanism, but they do not induce significant qualitative changes. Physically, the bedforms are due to the transverse sloping bottom mechanism and their formation is associated with an offshore

current deflection over the bars. The mechanism is effective only for $1 \leq m < 1.05$.

If a larger exponent m in the sediment flux is considered other types of bottom modes are obtained which donot resemble the observed shoreface-connected ridges. They are generated by the coupling between topography and flow through the vorticity production due to an uneven sea bed either by frictional torques or by planetary vortex stretching.

It appears that the best comparison between model results and observed shoreface-connected ridges is obtained in case $m = 1$. A further condition is that the ratio V/H is almost constant, where V is the background current and H the equilibrium bottom profile, which is realistic if the background flow is mainly controlled by a longshore pressure gradient and not by the windstress. Thus, the present modeling provides a valuable information on the regions where shoreface-connected ridges occur: apparently, the long term averaged sediment transport is mainly due to wave stirring plus advection by the mean current which is in turn controlled by pressure gradients.

It is important to realize that observed shoreface-connected ridges on the inner shelf are finite amplitude features while the linear analysis only yields information on their initial formation. This limitation can be overcome by the nonlinear model which has been set up. Prelimany results reported here have proven to be promissing.

An examination of the large-scale bedforms in the map of the Southern Bight of the North Sea presented in figure 1.1 of (Van de Meene, 1994), suggests that the Dutch shoreface-connected ridges could very well be tidal sand banks just distorted by the proximity of the coast. However, the present study shows that shoreface-connected ridges have an entirely different origin. Indeed, tidal sand banks are associated to a $m > 1$ power in the sediment transport and to bottom friction, and their orientation depends on earth rotation (Hulscher *et al.*, 1993). On the other hand, the observed orientation of the ridges is obtained only if $m \simeq 1$ and is not affected by Coriolis. Therefore, it is clear that the transverse slope mechanism is the main cause of the observed ridges and this has nothing to do with tidal oscillations. Nevertheless, it is conceivable that tidal currents affect the ridges in some way. To explore this possibility, an important extension of the present model consists in the assumption of a basic undisturbed current with a steady component plus an oscillatory one (tidal). This type of modelling is currently in progress and preliminary results are reported in Falqués *et al.* (1997).

Acknowledgements

This paper is based on work on the PACE-project, in the framework of the EU-sponsored Marine Science and Technology Programme (MAST3), under contract no. MAS3-CT95-0002. Part of the research has been done during a stay of Daniel Calvete and Albert Falqués in Utrecht, (IMAU). The visit of Albert Falqués was partially funded by RIKZ (National Institute of Coastal and Marine Management, The Netherlands).

References

CHASE, R. R. P. 1979 The coastal longshore pressure gradient: temporal variations and driving mechanisms. *J. Geophys. Res.* **84**, 4898–4904.

FALQUÉS, A., CALVETE, D. & DE SWART, H. E. 1997 Combined tidal and steady current model for shoreface-connected ridges. *Tech. Rep.* R97-4. IMAU, Utrecht Univ.

FALQUÉS, A., CALVETE, D. & DE SWART, H. E. 1998*a* Modelling the formation of shoreface-conected sand ridges: dynamic coupling between mean currents and topography. *J. Fluid Mech.* (submitted).

FALQUÉS, A., CALVETE, D. & MONTOTO, A. 1998*b* Bed-flow instabilities of coastal currents. In *Proc. 8th Biennal Conf. on Physics of Estuaries and Coastal Seas* (ed. J.Dronkers & M.Scheffers), pp. 417–424. A.A.Balkema. Rotterdam.

FREDSOE, J. & DEIGAARD, R. 1993 *Mechanics of coastal sediment transport.* World Scientific, Singapore.

HULSCHER, S. J. M. H., DE SWART, H. E. & DE VRIEND, H. J. 1993 The generation of offshore tidal sand banks and sand waves. *Cont. Shelf Res.* **13** (11), 1183–1204.

PARKER, G., LANFREDI, N. W. & SWIFT, D. J. P. 1982 Seafloor response to flow in a Southern Hemisphere sand-ridge field: Argentina inner shelf. *Sedimentary Geology* **33**, 195–216.

SCHUTTELAARS, H. M. 1997 Evolution and stability analysis of bottom patterns in tidal embayments. PhD thesis, Universiteit Utrech, Faculteit Wiskunde en Informatica.

SCOTT, J. T. & CSANADY, G. T. 1976 Nearshore currents off Long Island. *J. Geophys. Res.* **81**, 5401–5409.

SWIFT, D. J. P., NIEDORODA, A. W., VINCENT, C. E. & HOPKINS, T. S. 1985 Barrier island evolution, Middle Atlantic Shelf, U.S.A., part 1: shoreface dynamics. *Mar. Geol.* **63**, 331–361.

TROWBRIDGE, J. H. 1995 A mechanism for the formation and maintenance of shore-oblique sand ridges on storm-dominated shelves. *J. Geophys. Res.* **100** (C8), 16071–16086.

VAN DE MEENE, J. W. H. 1994 The shoreface connected ridges along the central Dutch coast. PhD thesis, Netherlands Geographical Studies, 174.

VAN DER GIESSEN, A., DE RUIJTER, W. P. M. & BORST, J. C. 1990 Three-dimensional current structure in the Dutch coastal zone. *Neth. J. Sea Res.* **25**, 45–55.

VAN RIJN, L. C. 1993 *Principles of sediment transport in rivers, estuaries and coastal seas.*. Aqua Publ., Amsterdam.

ZIMMERMAN, J. T. F. 1981 Dynamics, diffusion and geomorphological significance of tidal residual eddies. *Nature* **290**, 549–555.

THE SPATIAL VARIABILITY OF LARGE SCALE SAND BARS

C. R. Worley[1], T. C. Lippmann[1], J. W. Haines[2], A. H. Sallenger[2]

Abstract

In this work we describe preliminary results from a newly developed aerial video system which can be used to rapidly (2-4 hours) and accurately (5 m resolution) sample the horizontal scales of sand bar morphology over several hundred km's of coastline. Observations from, for example, the North Carolina coastline on the central eastern seaboard of the U. S., indicate marked changes in the alongshore morphological patterns, which can be cyclic with lengths scales of 5-10 km's along one stretch of coast but adjacently the bars can be absent altogether. Other observations from the lower sloping west coast beaches of the U. S. Pacific Northwest show highly complex sand bar morphology which also exhibit marked alongshore variability. Along this coast the beach systems are not continuous and are separated by large headlands, and the morphology at any particular beach behaves independently from the bar morphology in adjacent compartments.

Introduction

Nearshore morphology exhibits spatial variability spanning over 5 decades of scale. Morphologies ranging from wave- and mega-ripples (10-100's of centimeters) to large scale sand bars and shoreline features spanning 10-100's of kilometers reflect a variety of fluid-sediment interactions spanning comparable scales. The temporal response of these features is similarly broad (from 10's of seconds to years). This wide range of scales presents difficult sampling problems. Commonly used nearshore

[1]Center for Coastal Studies, Scripps Institution of Oceanography, University of California, San Diego, La Jolla, CA, 92093-0209, USA
[2]Center for Coastal Geology, U. S. Geological Survey, St. Petersburg, FL, 33701, USA

surveying techniques are limited in spatial and especially temporal resolution, require a large resource of manpower, and are generally only feasible in moderate wave conditions. Yet, for many applications it is of interest to sample the sometimes rapid, large changes in beach morphology that occur during single storm events, or over a series of several to many storm cycles.

One remote sensing technique which has successfully resolved rapid changes in large scale sand bar morphology is based on sub-aerial video of surf zone wave breaking (Lippmann and Holman, 1989; 1990). Time-averaged video images detect the horizontal scales of the average wave breaking patterns, and because waves preferentially break over shallow regions, the large scale morphologic features associated with bars are revealed. The video techniques are not limited by adverse wave conditions, and have thus proven useful in sampling long time series (up to 5 years and continuing today) of nearshore morphologic variability (Lippmann and Holman, 1990; Lippmann, *et al.*, 1993).

The most severe limitation of the video techniques is that the resolution of the images degrades rapidly as the distance from the camera increases, particularly for the highly oblique views typically used to study nearshore processes (*i.e.*, Holman, *et al.*, 1993). The useful spatial coverage of the land-based video techniques is determined by the pixel resolution of the image, which depends strongly on camera elevation above mean sea level and the distance to the target (Holland, *et al.*, 1997). For the Duck, NC, camera location, the useful ground coverage imaged in Lippmann and Holman (1990) and Lippmann, *et al.* (1993) spanned alongshore distances of about 400 m alongshore. Since the bar position was averaged over the entire view for the time-exposure data used in Lippmann, *et al.* (1993), any alongshore variability that may have been present at wavelengths greater than 400 m could not be addressed, nor the potential for alongshore migrating large-scale bar features which could also produce the transition sequence observed by either Lippmann, *et al.* (1993) or Birkemeier (1984).

Sand bars with large alongshore length scales of O(10 km) have been observed to migrate along the Dutch coast using 40 years of annual profile measurements spanning 350 km alongshore (Wijnberg, 1995). These large scale features dominate the variability over the 40 year time series, and show variability in time and length scales that is presently not understood. The Dutch JARKUS profile data is unique in

its breadth of temporal and spatial sampling. It is, however, a very difficult task to produce a single survey of 350 km of coast, often taking 6 months to complete one survey.

Aerial Video System

Recent advances in aerial videography have shown that rapid acquisition of the spatial patterns of large scale sand bar morphology is possible (Worley, *et al.*, 1997). The development of an aerial system was motivated by the need to measure larger length scale sand bars accurately and in a timely manner. The modular, low-cost system was configured so that it could be quickly deployed in easily accessible, inexpensive Cessna 172 or 182 aircraft at locations where forecasted weather predictions indicated the development of large storm systems, and thus the potentially large scale changes of the beach system to could also be quantified. The system utilizes a gyro-stabilized compass and inclinometer to maintain the camera in a vertically down-ward orientation within a walk-circle of 1 degree diameter. The azimuthal angle of the camera view and altitude (measured with a pressure sensor) is recorded on a lap-top PC and is synchronized with the video using timing obtained from a hand-held GPS receiver. The horizontal real-word UTM coordinates and vertical elevation of the aircraft are also measured using differential GPS systems with reliable positioning and high accuracy of order 0.05-0.5 m, depending on distance to the base station.

The precision and accuracy of the components of the aerial video system and image resolution and averaging times are summarized in Worley, *et al.* (1997). Assuming precise positioning, and for a typical deployment using a 2/3 inch format video camera with wide angle lens, the expected image resolution ranges between 1.1-5.9 (1.6-8.8) meters in the cross-shore (longshore) directions, depending on flight altitude ranging 457-2438 m (1500-8000 ft). With a typical aircraft ground speed of 80-100 knots (~50 m/sec) we expect sampling periods and averaging times in one flyby to be about 17-89 seconds for flight altitudes. The averaging time can be increased linearly by making several flyby's of the same ground area.

Field Data

We have conducted over-flights periodically for the past 13 months at several regions of the U. S. (Figure 1). Approximately bi-monthly flights have been

conducted from the Mexican border to Santa Barbara, spanning the entire Southern California Bight. Flights have been conducted also along the Central California coast from Monterey to Tomales Bay at the north end of Pt. Reyes, and along the northern Oregon-southwest Washington coast from Waldport, OR, to Pt. Grenville, WA. Finally, several flights have been conducted along the North Carolina coast from Cape Hatteras to the Virginia border, and span the period of the 1997 SandyDuck experiment.

Sand bar morphology is inferred from the location of average breaking patterns in time-exposure images created over the approximately 30-40 second duration (for aircraft altitude of 3000 ft) that ground features remain within the camera field of view, similar to the land-based methods (Lippmann and Holman, 1989; 1990). In the aerial techniques, the image transformation must be done on a frame-by-frame basis, and is accomplished by synchronous integration of the measured azimuthal orientation of the camera view and position of the aircraft with the VITC time-stamp on each video frame. Individual frames are rectified into the UTM ground coordinate system and digitally added in sequence using image processing, video, and computer hardware in our laboratory. Time-exposure images span the length of the flight-track which ranges about 75 km for some of the shorter southern California flights to about 300 km in the Pacific Northwest.

The data have shown remarkable alongshore variability in sand bar morphology, and have revealed, for example, alongshore regular patterns in sand bars along the North Carolina coastline with length scales of the order of 5-10 km that dominates the alongshore variability in bar position. An example 35 second aerial time-exposure spanning about 10 km alongshore, obtained about 20 km north of Duck, NC, on 27 September 1997, is shown in Figure 2. The resolution for this image is 5 m horizontally, and shows well defined sand bars emanating obliquely away from the shoreline, eventually fading away seaward behind adjacent, more shoreward bars further down the coast. Interestingly, several similar obliquely oriented bars were observed at approximately regular spacing along 36 km of the same stretch of coast (Figure 3), yet just to the south, the aerial time-exposure indicates the presence of only a single bar very close to shore (Figure 4).

The possible migration of the large scale bar features can be addressed from time series of aerial time-exposures. The behavior of the coast to changing wave

conditions in relation to the alongshore configuration of the bar system, and is the subject of ongoing research.

The morphologic variability can also be quite high at other beaches with different characteristics than North Carolina, where low-relief barrier islands span the length of coastline and the beaches are relatively steep. Along the U.S. Pacific Northwest coast, most beaches are backed by cliffs or high dunes and bounded laterally by many headlands, are generally more gently sloping, and are subjected to the more energetic Pacific swell for much of the year. Figure 5 shows an 11 km section of coast near Siletz Spit (shown in the center of the image) in the central Oregon coast obtained on 2 June 1998. The wave heights were over 2 m for this day and the surf zone spans about 400 m across-shore. The alongshore variability is quite complicated, without any particular regularity apparent. In contrast, about 90 km or so to the north the bar forms appear more regular in morphology, with sinuous bars extending alongshore continuously for several kilometers and sometimes attach to the shoreline (Figure 6).

Summary

Results from deployment of a recently developed aerial video system for measuring large scale sand bar morphology are briefly discussed. The system, based on inferring sand bar shapes and location from time-averaged breaking patterns, was deployed on both the west and east coasts of the U.S. Observations of sand bars, for example, offshore of North Carolina coast along the central eastern seaboard and along the Pacific Northwest coast, reveal substantial alongshore variability in sand bar patterns. Series of large scale oblique bars, emanating from the shoreline and diminishing down the coast behind other similar bars, were observed over 30-40 km of part of the North Carolina coast, yet observations of the 30-40 km just to the south revealed only a single bar located close to shore. In the Pacific Northwest, highly complex bar patterns were observed with no apparent connection between adjacent beach systems separated by headlands. The evolution of these large scale bar forms, from both the steeper east coast beaches and the more gently sloping, energetic west coast beach systems, are the subject of ongoing investigations utilizing data obtained from the aerial video system.

Acknowledgments

Expert piloting for the over-flights was done by Kimball Millikan, John Stanley, Chuck Rosenfeld, and Dean Morris, and we greatly appreciate their conscientious efforts. Several people generously helped with differential base station deployment and post-processing, particularly Jeff List, Amy Farris, Tom Reiss, Mark Hanson, Peter Ruggiero, Mike Leffler, and Jerry Sain. Funding was provided by the U. S. Geological Survey and the California Department of Boating and Waterways.

References

Birkemeier, W. A., 1984, Time scales of nearshore profile change, in *Pro. of the 19th Intern. Conf. Coastal Engineering*, ASCE, New York, 1507-1521.

Holland, K. T., R. A. Holman, J. Stanley, and N. Plant, 1997, Practical use of video imagery in nearshore oceanographic field studies, *IEEE J. of Ocean. Eng.*, 22(1), 81-92.

Lippmann, T. C., and R. A. Holman, 1989, Quantification of sand bar morphology: A video technique based on wave dissipation, *J. Geophys. Res.*, 94, 995-1,011.

Lippmann, T. C., and R. A. Holman, 1990, The spatial and temporal variability of sand bar morphology, *J. Geophys. Res.*, 95(C7), 11,575-11,590.

Lippmann, T. C., R. A. Holman, and K. K. Hathaway, 1993, Episodic, nonstationary behavior of a double bar system at Duck, NC, USA, 1986-1991, *J. Coast. Res.*, 15, 49-75.

Wijnberg, K. M., 1995, Morphologic behavior of a barred coast over a period of decades, *Ph.D. Thesis*, Universiteit Utrecht, pp. 245.

Worley, C. R., T. C. Lippmann, J. W. Haines, and A. H. Sallenger, 1997, An aerial video system for rapidly measuring the spatial variability of very large scale (10^1-10^3 km) sand bar morphology, *Proc. Coast. Dyn. '97*, ASCE, 346-354.

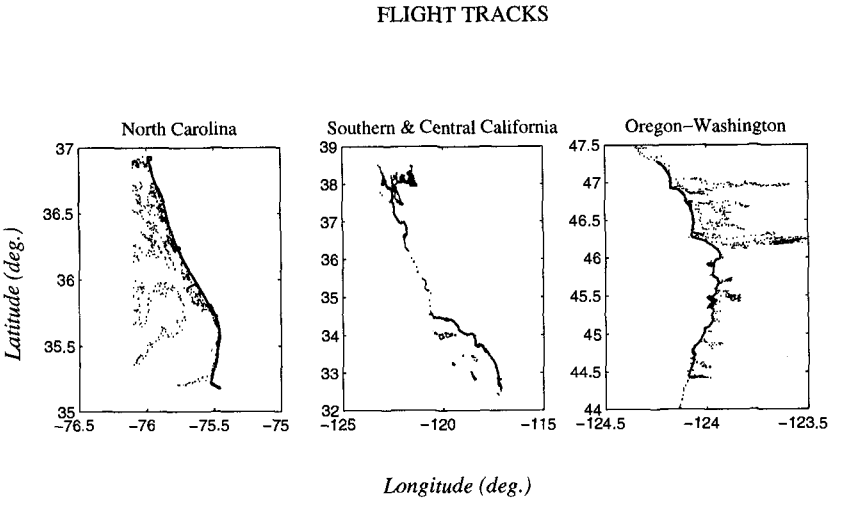

Figure 1. Maps of the coastline (dotted lines) and the flight tracks (solid lines) for the geographical regions studied with the aerial video system. The flight track in North Carolina (left panel) extends from Cape Hatteras to the Virginia border, in California (center panel) from the Mexican border to Santa Barbara and from Monterey to Pt. Reyes, and in northern Oregon and southwest Washington from Waldport, OR, to Pt. Grenville, WA.

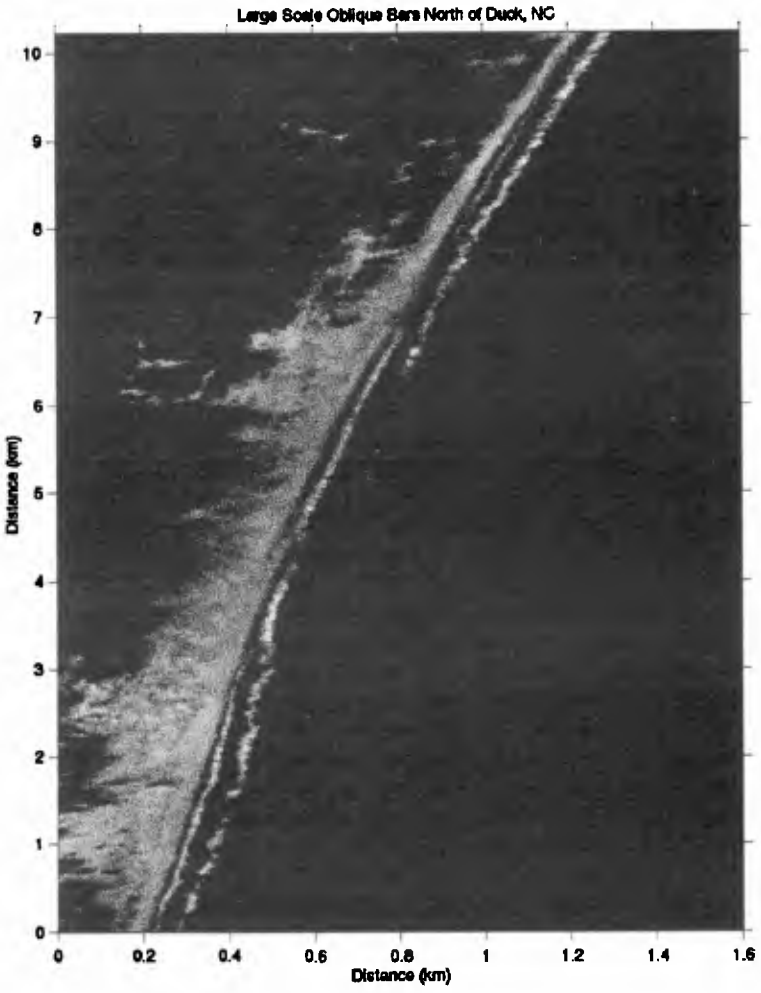

Figure 2. Example 35 second aerial time-exposure along 11 km of the North Carolina coast just north of Duck. The coordinate system (in km) has arbitrary origin with north towards the top and ocean (east) to the right in the image. The image resolution is 5 m in both the cross- and along-image axes. The location of large scale oblique sand bars are indicated by the white bands located 25-200 m offshore.

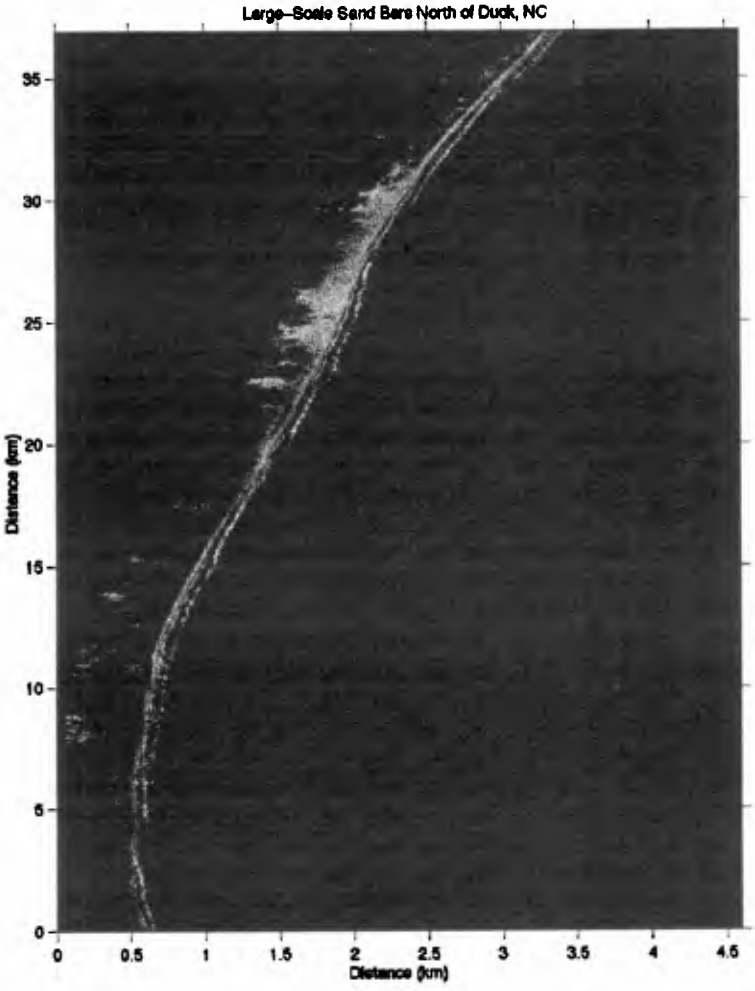

Figure 3. Example 35 second aerial time-exposure along 36 km of the North Carolina coast just north of Duck. The coordinate system (in km) has arbitrary origin with north towards the top and ocean (east) to the right in the image. The image resolution is 5 m in both the cross- and along-image axes. Several oblique sand bars emanating away from the coast are visible in the image as the white bands with 25-200 m of the shoreline.

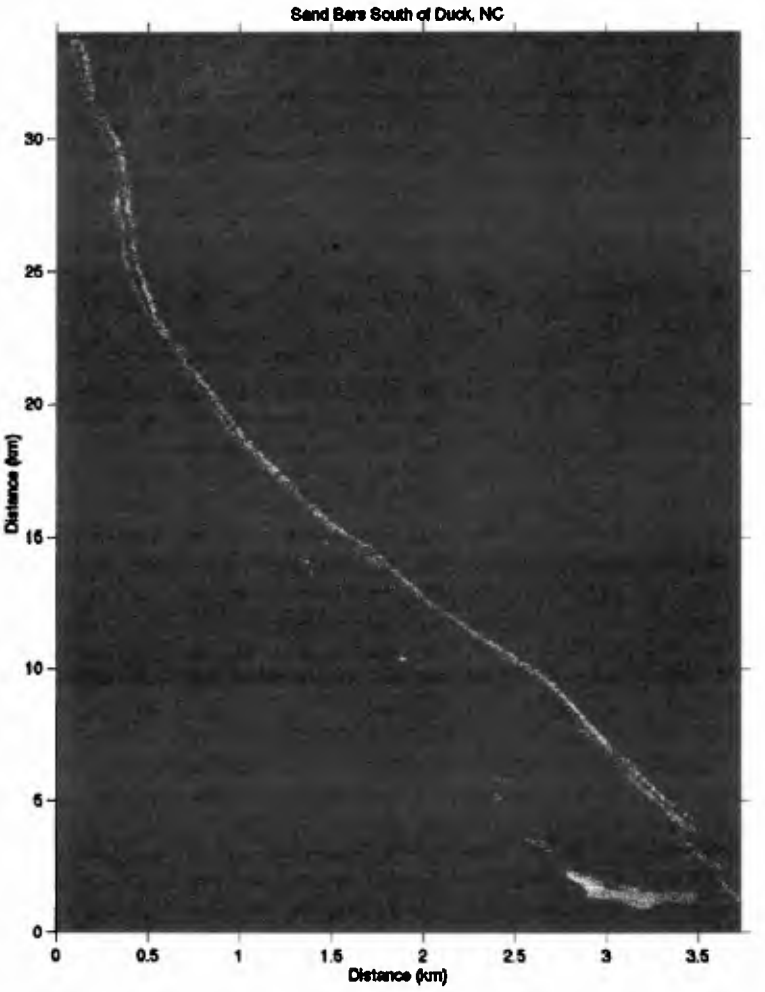

Figure 4. Example 35 second aerial time-exposure along 33 km of the North Carolina coast just south of Duck. The coordinate system (in km) has arbitrary origin with north towards the top and ocean (east) to the right in the image. The image resolution is 5 m in both the cross- and along-image axes. The sand bar is located very close to shore, with no discernible offshore breaking apparent seaward of about 80 m from the shoreline.

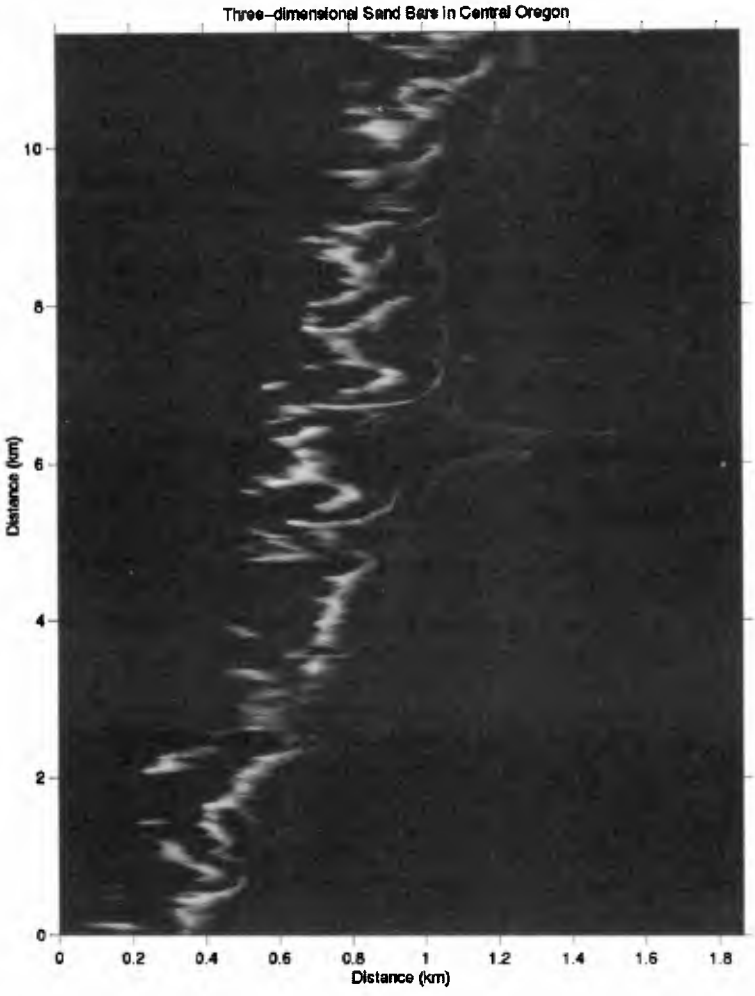

Figure 5. Example 35 second aerial time-exposure along 11 km of the central Oregon coast near Siletz Spit. The coordinate system (in km) has arbitrary origin with north towards the top and ocean (west) to the left in the image. The image resolution is 5 m in both the cross- and along-image axes. The large scale nearshore morphology is highly variable alongshore with no regularity apparent.

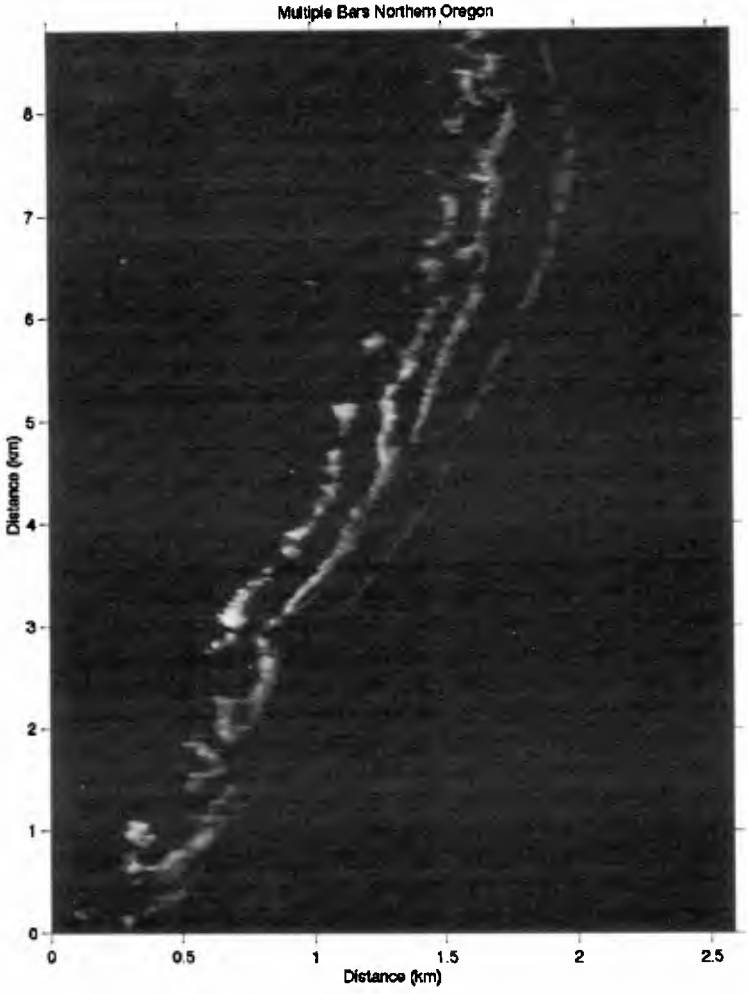

Figure 6. Example 35 second aerial time-exposure along 9 km of the northern Oregon coast near Tillamook Bay. The coordinate system (in km) has arbitrary origin with north towards the top and ocean (west) to the left in the image. The image resolution is 5 m in both the cross- and along-image axes. The large scale nearshore morphology shows long, sinuous bar features which sometimes attach to the shoreline.

MODELING THE DYNAMICS OF A BAR SYSTEM AT DUCK, NC, USA

B. Boczar-Karakiewicz[1], W. Romańczyk[1], J.L. Bona[2] and E.B. Thornton[3]

ABSTRACT

The temporal evolution of nearshore bar topography forced by incident, wind-generated waves is predicted by a two-dimensional (2D) model. Predictions are compared with observed bathymetry from Duck, North Carolina, USA, acquired by the Field Research Facility (FRF) of the US Corps of Engineers over a period of 17 years (1980 - 1997). The model simulations presented are seen to approximate well the formation of the most frequently-observed shore-parallel bars at Duck as well as dynamic changes in their pattern caused by storm waves and varying mean water level.

1. INTRODUCTION

The two-dimensional model applied in the present work describes the temporal evolution of nearshore bar systems forced by incident, wind-generated waves (Boczar-Karakiewicz *et al.* 1987 and 1995). In this model, surface waves are described by simplified Boussinesq equations. Nonlinear wave forcing is transmitted through a wave-induced boundary layer to the bed, which is characterized by small-scale bed roughness. The model allows a finite-amplitude beach response which, in turn, feeds back to modify the wave field. At present, we consider the temporal evolution of the bed when it is forced by incident monochromatic and regular wave trains at the observed wind-wave peak-frequency. The energy is exchanged among the evolving wave modes as the wave propagates into shallower water. In the simulations presented, wave breaking and related undertow are not considered, though their incorporation is currently under development. Such simplifications allow the application of

[1]INRS-Océanologie (Université du Québec), Rimouski, Québec, Canada
[2]University of Texas, Department of Mathematics and Texas Institute for Computational & Applied Mathematics, Austin, Texas, USA
[3]Oceanography Department, Naval Postgraduate School, Monterey, CA, USA

a model without free parameters. According to the model, distances between bar crests, the number of bars, their position and amplitude, at a given site, are scaled by naturally-occurring and site-specific units: the bar geometry is scaled by the incident wavelength, while the time of bar formation and their dynamics are scaled by the wave energy. These model predictions also explain changes in bar position in response to waves at high water levels induced by tides and storm surges.

Incident wave parameters and typically observed bed topographies are selected from field data in Section 2 and compared with model predictions in Section 3. General conclusions drawn from our work are set forth in Section 4.

2. FIELD DATA AND INITIAL MODEL PARAMETERS

In the present section, wave and bathymetry data from Duck, NC, spanning a period of 17 years (1980 - 1997) are analyzed. These data were acquired by the Field Research Facility (FRF) of the US Corps of Engineers in the following way: directional wave data were measured every 3 hours at a 10 m water depth, and bathymetry was carried out at least monthly.

In this report, a single line of cross-shore bathymetry is analyzed (#62 according to the FRF coordinates). This profile was chosen to represent the entire experimental area. It is located close to the northern extreme of the site to avoid the local topography effects of the piers. Measured data are scattered as shown in Figure 1 and no prevailing bar pattern is visible in the cloud of points. From this data, a featureless

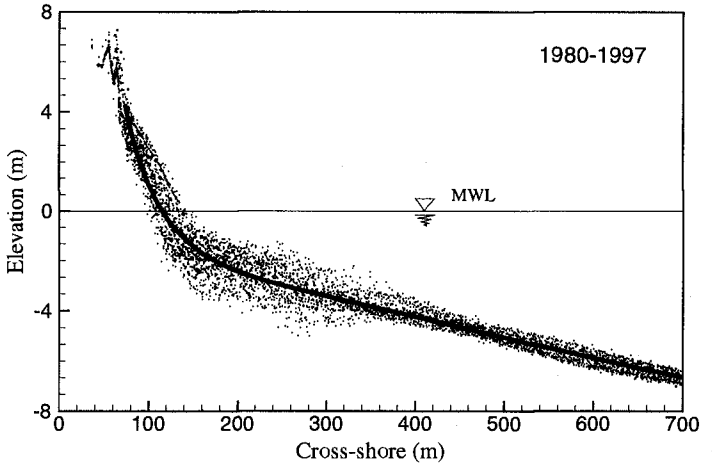

Figure 1: Foreshore morphology data at profile 62, Duck, NC, (1980-1997) and the featureless equilibrium profile

mean bed profile was determined (heavy line in Figure 1), by use of Dean's beach

equilibrium formula with an additional function fitting observations lying in the very nearshore and on the upper beach. This profile was selected as the topographical input to the model calculations simulating bar formation in Section 3.

A subsequent, more detailed analysis of the topography observations was conducted to understand better the dynamics of the bed. First, the temporal sequence of profiles measured in the period 1980-1997 was animated. This interesting exercise revealed considerable temporal variability, and, occasionally, rapidly-changing bed configurations. These data suggested that metastable states exists which result from a longer sequence of wave events and not just from a single storm preceding the measured bathymetry. We proceeded by selecting from the temporal sequence of profiles (1980-97) several groups of typical bed types. The segregation criteria were based on morphological similarity, including the position of bar crests and number of bars. One among the selected groups of bed profiles is shown in Figure 2. This result confirmed conclusions from earlier work (see, e.g., Birkemeier 1984, Lippmann et al. 1993): the most frequently-observed bed profile at Duck is a two-bar system with bar crests at about 200 and 400 m relative to the FRF coordinates and the mean shoreline position at 100 m.

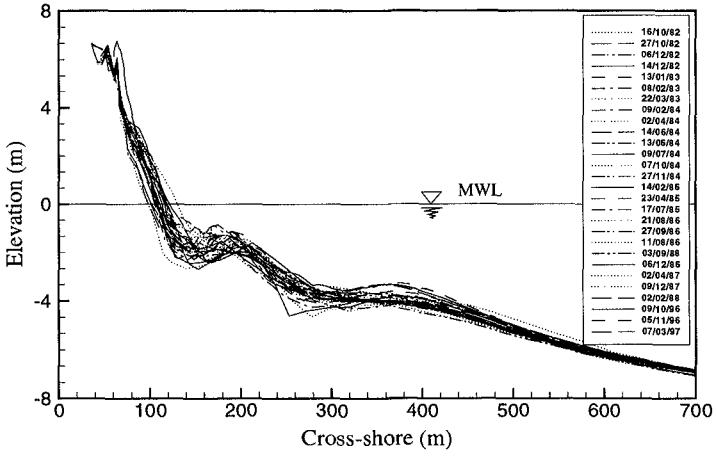

Figure 2: Typical two-bar system at Duck, NC, with indicated dates of data acquisition (based on measurements at cross-section 62)

However, during the period 1988-1995, a distinct one-bar topography (as shown later in Section 3) was predominant and the outer bar corresponding to the two-bar morphology seemed to be completely flattened out. Generally, in 17 years of measurements, the position of the nearshore bar crest varied over an interval of some 150 m, and the second offshore bar crest, when it existed, migrated about its mean 400 m position by $\pm$ 100 m.

Observations at Duck also show that every 8-9 years the previously mentioned "slow" changes in bar patterns are disturbed by episodic "anomalies" that occur at inter-seasonal cycles. During these anomalies, the bar crest positions change rapidly: for example, the inner bar may migrate 100 to 150 m in only a day or two (Birkemeier 1984, Holman and Sallenger 1993, Lippmann *et al.* 1993). These anomalous episodes are puzzling, especially in light of the metastability exhibited in Figure 2. In Section 3, we show a simulation of an anomalous event at Duck using our previously decribed model (see Section 1 and the references mentioned there). The observed wave environment pertaining to anomalies is now described.

In the predictions of the bar dynamics made in Section 3, the observed prevailing bar patterns, as seen in Figure 2, and the episodic change in the bar system are correlated with events in the local wave climate, in particular with single storms, or sequences of storms with and without a simultaneous water level change.

Input wave parameters, which are required by the model, are specified at the deep-water end of the nearshore zone by peak periods T_p, incident wave energy a^2 (where a denotes wave amplitude), and the mean water level. These data were obtained by analyzing the measured parameters of waves and waterlevels from 1980-1997 as presented in the format shown for the year 1990 in Figure 3.

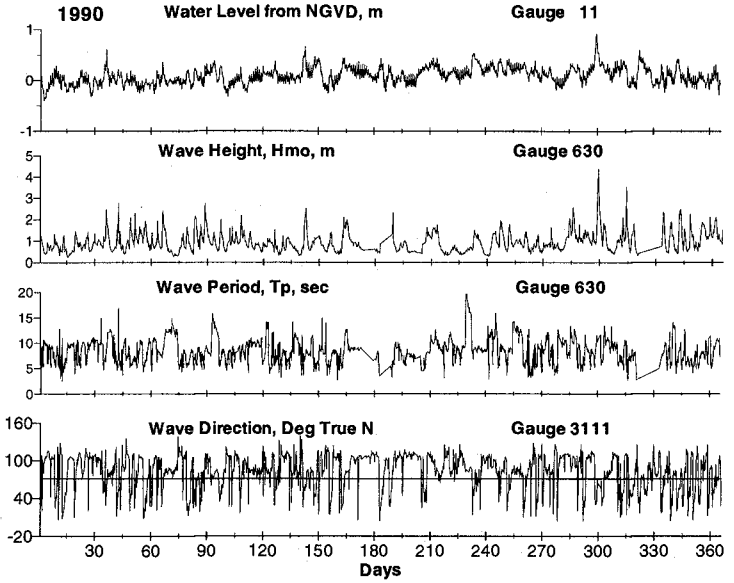

Figure 3: Observed wave and water level parameters at Duck, NC, in 1990

The analysis of data showed the wave climate at Duck to be, quite "noisy". Peak periods and related wave energy in incident waves vary irregularly during the year

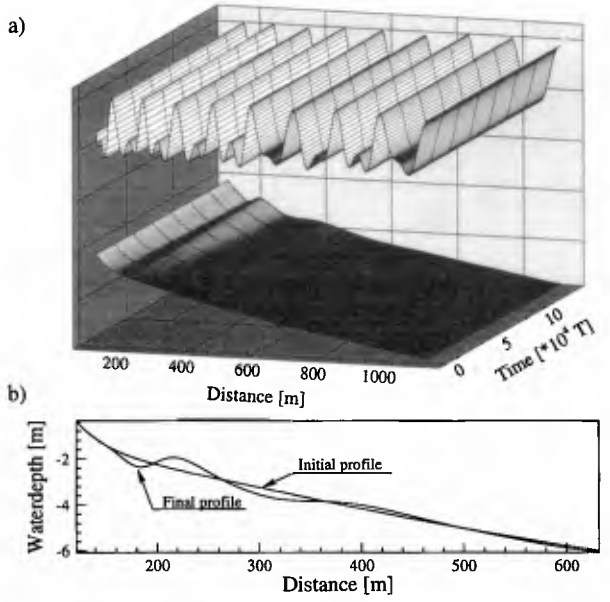

Figure 4: Prediction of the formation of the typical two-bar system by major storms (with T_p = 15s) at Duck, NC: (a) temporal evolution of the bar system from the featureless equilibrium profile, (b) initial and final profiles from (a).

with large differences between consecutive years. However, certain "seasonal" patterns could be discerned: extreme storm events and hurricanes occur predominantly in the autumn-winter season (with T_p from 12 s to 20 s); these stormy periods are followed by a summer season of moderate wave activity (T_p below 10 s). During the episodic anomalies mentioned above, there occur major storm events with water levels on the order of +1 m above the mean (see again Figure 3).

In the model predictions, the value T_p = 15 s was chosen to initiate simulations of major storm events both at mean and high water levels. Extreme storm events are represented by incident waves of period T_p = 17.5-s. On the other hand, summer waves are represented in the model by wave trains with T_p = 10 s.

3. PREDICTIONS AND COMPARISONS WITH OBSERVATIONS

Formation of the most frequently-observed two-bar system (Figure 2) by major storm events was simulated by the model with topographical input in the form of the mean featureless bed profile (heavy line in Figure 1) and deep-water incident wave parameters with peak period T = 15 s and wave amplitude a = 1.5 m. The temporal evolution of the seabed in the surveyed part of the nearshore is shown in Figure 4a

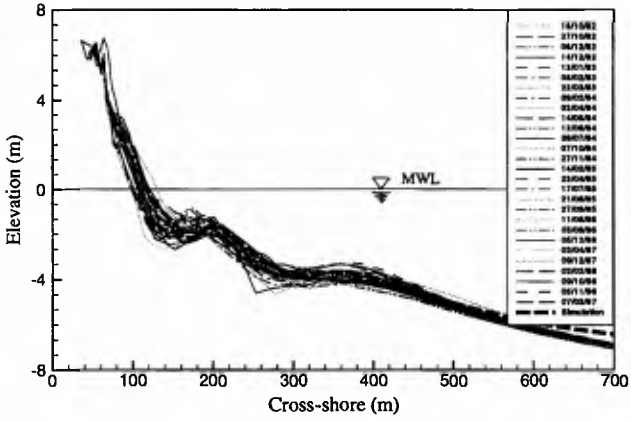

Figure 5: Comparison of predictions (heavy dashed line) and measurements of the most frequently-observed two-bar system at Duck, NC

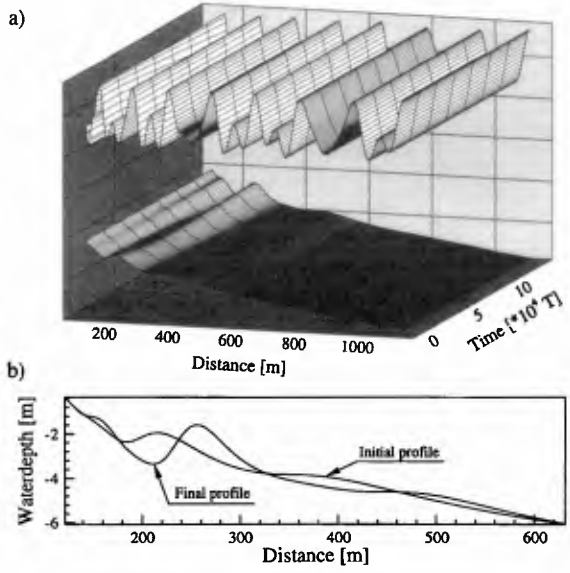

Figure 6: Prediction of changes from the typical two-bar system by extreme autumn-winter storms (with $T_p = 17.5$s): (a) temporal evolution of the new two-bar system from the original two-bar profile, (b) initial and final profiles from (a).

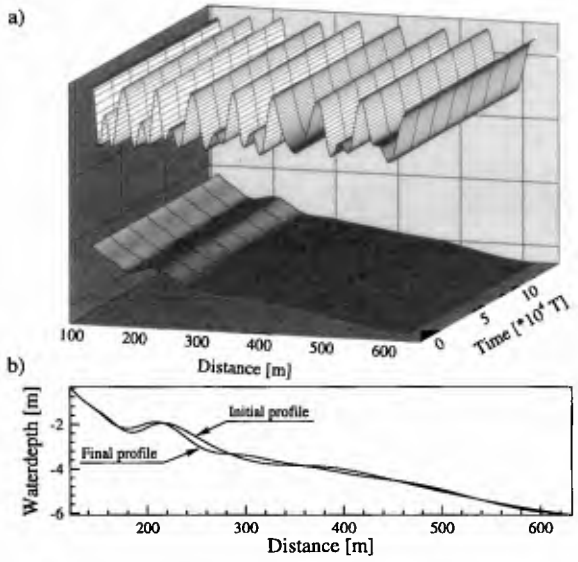

Figure 7: Prediction of changes from the typical two-bar system by moderate summer storms (with $T_p = 10$s): (a) temporal evolution to a one-bar system from the typical two-bar profile, (b) initial and final profiles from (a).

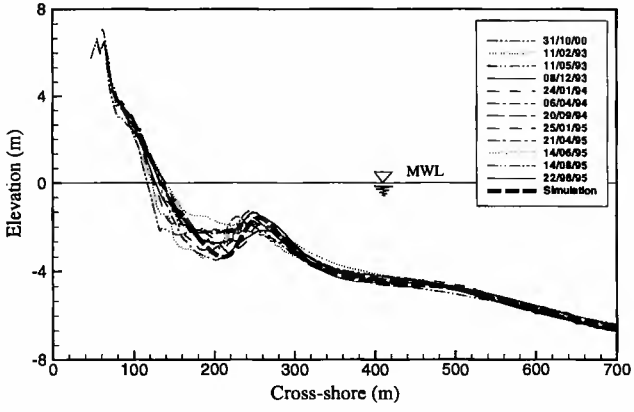

Figure 8: Comparison of predictions (heavy dashed line) and measurements of an observed two-bar system at Duck, NC (with bar crest positions at 250 m and 500 m).

and the initial and final profiles are depicted in Figure 4b.

In Figure 5, the heavy dashed line showing the predicted final bed configuration from Figure 4 is superimposed on observations from Figure 2. Comparisons of position, the number of predicted bars and their amplitudes are in quite good agreement with the 17 years of observations.

In the following simulations, the dynamics are initiated with the two-bar bed topography provided by the model, as depicted in Figures 4a and 4b. In the simulation shown in Figure 6a, the incident waves represent hurricane waves ($T_p = 17.5$ s). In a second calculation shown in Figure 7a, initiated with the same two-bar initial profile, the incident waves are moderate summer waves ($T_p = 10$ s).

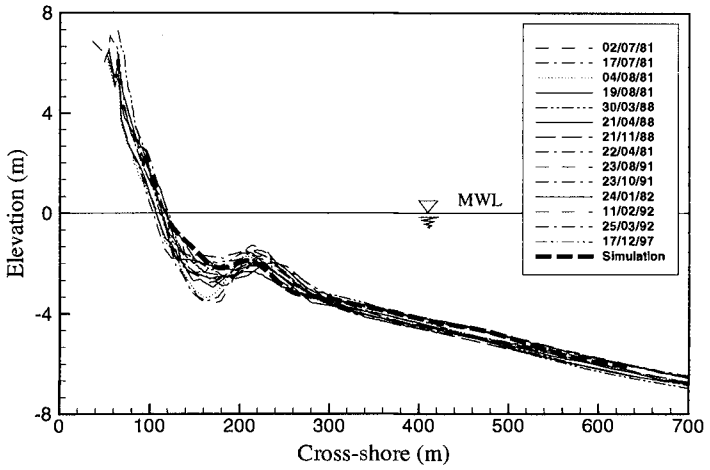

Figure 9: Comparison of predictions (heavy dashed line) and measurements of an observed one-bar system at Duck, NC (with the bar crest position at 220 m).

In both the cases shown in Figures 6 and 7, the model predicts the response of the frequently observed two-bar bathymetry to ambient hydrodynamic regimes representing simplified versions of winter ($T_p = 15$ s and 17.5 s) and summer ($T_p = 15$ s and 10 s) wave activity. In the winter season (Figure 6a), the model predicts a transformation of the primary two-bar system via the migration of bar crests to new locations: the inner bar shifts from its 200-m position to a 250-m location; the outer bar migrates offshore by some 100 m from its mean 400-m position. In the first stages of the summer calculation (see bed profile at time $t = (2 \times 10^4)T_p$ in Figure 7), the post-storm two-bar system is only slightly changed by moderate waves ($T_p = 10$ s). However, the model also shows that at later stages of the calculation (a long-lasting period of moderate waves in a non-stormy year), the two-bar system goes over into a single bar system (see the final profile in Figures 7a and 7b).

In Figures 8 and 9, the final bed configurations from Figures 7b and 8b are

superimposed on observations. Again, the comparison of predicted positions, number of bars and their amplitudes shows quite acceptable agreement.

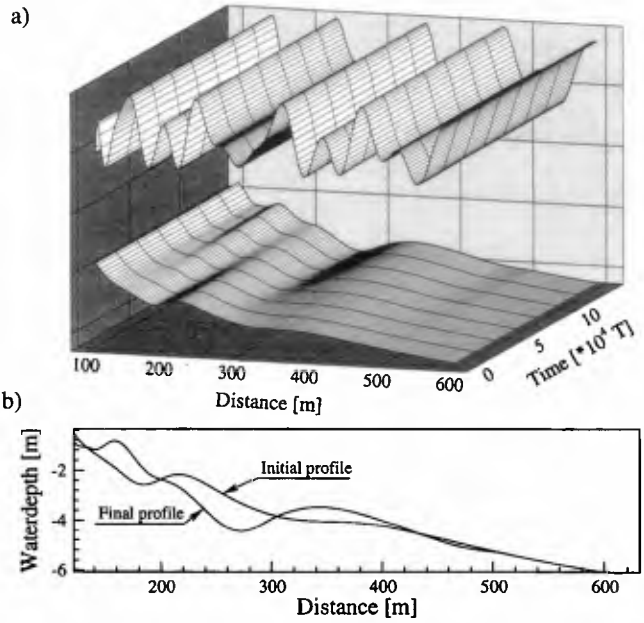

Figure 10: Prediction of an episodic change in the two-bar system at Duck, NC (a) migration of the post-storm profile under extreme waves (T_p = 15 s), accompanied by a 1.2-m surge above the mean water level, (b) initial and final bed profiles from (a).

The final simulation reported here was concerned with an "anomalous" situation wherein a storm with T_p = 15 s came on with a simultaneaos 1.2-m surge in the water level. As shown in Figure 10, the bottom response to extreme waves at this high water level was for the primary two-bar system to shift to a new position. In a period of two days, the outer and inner bar crests migrate some 100 m in the shoreward direction (compare the initial and final bed profiles in Figures 10a and 10b).

Comparisons of the predictions depicted in Figure 10 with observations are shown in Figure 11. During this episode, the calculation predicts a significant increase in the volume of the outer bar as measured at the site.

5. CONCLUSIONS

1. The model simulations presented here are aimed at approximating the temporal

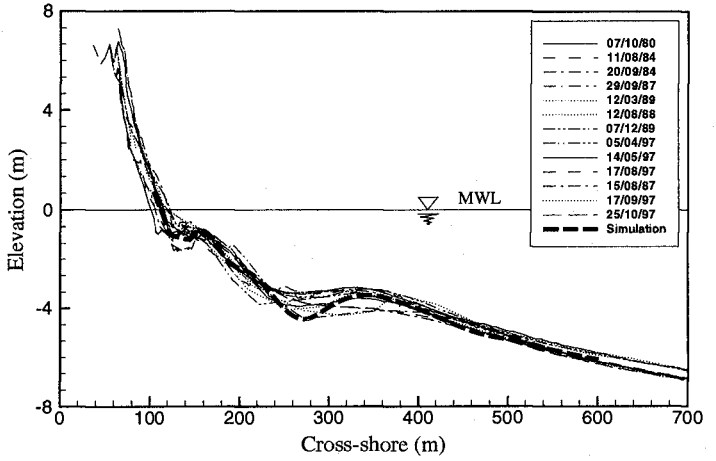

Figure 11: Prediction (heavy dashed line) and observations of episodic, nonstationary behavior of the two-bar system at Duck, NC.

evolution of the most frequently-observed shore-parallel bars at Duck and the dynamic changes in their pattern.

The following results were obtained.

- The predominant two-bar bed configuration is associated with forcing by large storms ($T_p = 15$ s) and the model approximates the observations, as shown in Figure 8.
- Predicted modifications of bar crest positions in the most frequently-observed two-bar system occur in the winter season during extreme storm events, as shown in Figure 7. The predicted bed configuration correlates well with observations (Figure 9).
- Predicted modifications from the most frequently-observed two-bar system to a single bar occur over several months of moderate storm activity, as seen at the site and illustrated in Figure 10.

2. The rapid and episodic response of the most frequently-observed two-bar system are predicted during extreme storm events accompanied by elevated mean water levels (Figure 10). Figure 11 illustrates the relation between model predictions and observed changes in bar morphology. These anomalous events occur on an abnormal cycle of several years duration. The one featured in our comparison was taken from 1989 data.

ACKNOWLEDGEMENTS

This work was sponsored by the Natural Sciences and Engineering Research Council of Canada and Almerco Inc. (University-Industry project 1996-2001) and supported by the North Atlantic Treaty Organization (Grant 960362, 1996-97).

REFERENCES

W.A. Birkemeier. 1984. Time scales of nearshore profile changes. *19th Proc.Int. Conf. Coast. Eng.*, ASCE, Houston, Texas, USA:1507-1521.

Boczar-Karakiewicz, B., J.L. Bona and D.L. Cohen. 1987. Interaction of shallow-water waves and bottom topography. *Dynamical problems in continuum physics, mathematics and its application*, J. L. Bona, C. Dafermos, J. Erickson & Kinderlehrer eds., Springer-Verlag, New York, NY, IMA Series in Mathematics and its Applications, **4**: 131-176.

Boczar-Karakiewicz, B., D.L. Forbes and G. Drapeau. 1995. Nearshore bar development in the Southern Gulf of St. Lawrence. *J. Waterways, Port, Coast. & Ocean Eng.*, ASCE, 129: 49–60.

Holman, R.A. and A.H. Sallenger. 1993. Sand bar generation: a discussion of the Duck experiment series. *Journal of Coastal Research*, SI(15): 76–92.

Lippmann, T.C., R.A. Holman and K.K. Hathaway. 1993. Episodic, nonstationary behavior of a double bar system at Duck, North Carolina, U.S.A., 1986-1991. *Journal of Coastal Research*, SI(15): 49–75.

DEPTH OF CLOSURE: IMPROVING UNDERSTANDING AND PREDICTION

Robert J. Nicholls[1], Magnus Larson[2], Michele Capobianco[3] and William A. Birkemeier[4]

ABSTRACT

The closure concept is a fundamental cross-shore boundary condition for morphodynamics and other applications such as beach nourishment and sediment budgets. This paper examines closure at a range of scales, particularly from events up to years. At these scales, closure is primarily a function of direct external forcing (cross-shore redistribution of sediment by waves), indirect external forcing (sediment loss/gain by littoral transport and the resulting profile translation) and internal system dynamics (bar dynamics). Therefore, simple wave-based models such as Hallermeier (1981) cannot be expected to predict the actual closure, although they can predict distributional properties such as the limit. A general approach to develop more user-orientated estimates of closure over a range of timescales is outlined based on equilibrium theory. This will include a user-defined depth change criterion as a function of timescale.

INTRODUCTION

Depth of closure is widely used within coastal engineering as an empirical measure of the seaward limit of *significant* cross-shore sediment transport on sandy beaches. More fundamentally, it is an important parameter which distinguishes two cross-shore zones with different levels of morphodynamic activity. The closure

1. Middlesex University, Enfield, London EN3 4SF, UK.
2. Dept. Water Resources Engineering, University of Lund, Box 118, SE-221 00 Lund, Sweden
3. R & D Division, Environment, Tecnomare SpA, San Marco 3584, IT-30124Venezia, Italy
4. US Army Engineers Waterways Experiment Station, Field Research Facility, 1261 Duck Road, Kitty Hawk, NC 27949, USA.

concept initially arose from the comparison of repetitive beach-nearshore profiles (henceforth beach profiles). Such profiles define an envelope of variation which declines with depth. The seaward limit of this envelope is generally interpreted as the "depth of closure". However, the precise location of closure is a matter of the depth change criterion used to define closure from a set of measurements: the larger the criterion the more deeper changes are ignored and the shallower the estimate of closure. In practical terms closure is often defined using the measurement accuracy.

Models to predict closure are limited. Using an argument based on the critical value of a sediment entrainment parameter, Hallermeier (1981) developed the only analytical approach to estimate an annual depth of closure on sandy beaches (d_ℓ). It is a function of extreme wave conditions and in a generalised time-dependent form is:

$$d_{\ell,t} = 2.28\, H_{e,t} - 68.5(H_{e,t}^2 / gT_{e,t}^2) \quad (1)$$

where $d_{\ell,t}$ is the predicted depth of closure over t years, referenced to Mean Low Water; $H_{e,t}$ is the non-breaking significant wave height that is exceeded 12 hours per t years; $T_{e,t}$ is the associated wave period; and g is the acceleration due to gravity. This method explicitly recognises that some sediment movement will occur seaward of d_ℓ.

Given that depth of closure is an important morphodynamic parameter common to all scales, it has been explored as part of the EU-funded MAST III PACE (Predicting Aggregated-Scale Coastal Evolution) project. This has included investigating its field characteristics, testing existing models and developing new models, which cover the range of engineering timescales ($\leq$ 50 years) (e.g., Nicholls et al., 1996; Capobianco et al., 1997). The datasets which have been examined are summarised in Table 1. It is important to distinguish the wide range of time (and space) scales considered in Table 1 and the following terminology is used: (1) *small scale* for events to seasons, (2) *medium scale* for one year to one decade, (3) *large scale* for decades to one century, and (4) *very large scale* for centuries to millennia (cf. Stive et al., 1990; Hinton and Nicholls, 1998). Collectively, these data covers the morphological response to individual storm events (small scale) up to the integrated effects of several decades of morphological evolution (large scale). All sites are wave-dominated, microtidal beaches, with the exception of Terschelling which is mesotidal.

The following generic results are apparent.

- Depth of closure is time and space-scale dependent, and generally increases with timescale (Capobianco et al., 1997).
- Depth of closure is a morphodynamic boundary, not a sediment transport boundary. Sediment transport should be expected to occur seaward of closure, especially during storms (Wright et al., 1991; Garcia et al., 1998). However, at the timescale defined by a closure measurement, the start of measurable morphological change is a good empirical indicator of an increasing capacity

for cross-shore sediment transport. At longer timescales, this may not be the case.

- At small scales, depth of closure is usually the product of bar migration due to surf zone processes (Nicholls and Birkemeier, 1997; Nicholls et al., 1998). As the scale increases, so beach-nearshore profile translation and ultimately shoreface processes come to control the location of closure (Hinton and Nicholls, 1998). At large scales on the Holland coast, it is possible to distinguish a "shoreward" closure due to breaking waves, reopening of the profile lower on the shoreface, and then a deeper middle/lower shoreface closure due to shoreface processes. Thus, the closure concept can define four distinct cross-shore zones at this scale.
- Equation 1 provides robust estimates of the *limit* to closure for individual erosional events up to the annual timescale (Nicholls et al., 1996; 1998; Garcia et al., 1998; Rozynski et al, 1998). At medium scales, it continues to act as a limit, but with an increasing tendency for overprediction. Equation 1 only considers cross-shore redistribution of sediment and excludes the effects of beach-nearshore profile translation (Nicholls and Birkemeier, 1997). In particular, it is invalid in areas which are accreting rapidly due to longshore supply of sand.
- Analysis of closure at a nourished site (Terschelling) finds that Equation 1 and pre-nourishment profiles provide a good estimate of the *limit* of post-fill closure (Marsh et al., 1998).

Therefore, the processes which control closure vary with scale. At small scales, closure is a product of episodic, short intense erosional events (and offshore transport), and/or more continuous accretional processes (and onshore transport) (Nicholls et al., 1998). Over days and weeks, we might associate closure with a specific process and cross-shore transport direction, but over seasons and longer, closure is the integrated result of onshore and offshore sediment transport. As the scale increases, so the number of processes which influence closure increases. At large scales, slow progressive morphological changes on the shoreface may become significant, moving closure to significantly greater depths than typically considered by engineers (Hinton and Nicholls, 1998). At very large scales, both models and geological evidence suggest that closure will lie at the base of the shoreface (cf. Stive and deVriend, 1995; Niedoroda et al., 1995; Cowell et al., 1995).

Based on these results, this paper reviews and refines our understanding of the methods available to predict closure for engineering application. Small and medium scales are considered using the Duck dataset (e.g., Lee and Birkemeier, 1993) for validation. Given that closure is user-defined, the concept can be generalised as a family of depth change contours, which define a number of cross-shore zones (Capobianco et al., 1997). This approach allows a user to select the most appropriate depth change criteria for their application.

Table 1. Summary of the datasets examined for depth of closure within the PACE project (see also Hamm, 1997)

Site	Period (yrs)	No of Profile Lines	Area Covered		Accuracy (cm)	Spring tidal range (m)	Typical extreme wave height (m)	Sources
			Long-shore (km)	Depth (m)				
Duck, USA	13	4	1	8	3	1.2	4 to 5	Nicholls et al. (1996; 1998), Nicholls and Birkemeier (1997), Capobianco et al. (1997)
Terschelling, the Netherlands	30	13	12	10	25	2.8	5 to 6	Marsh et al. (1998)
Holland Coast, the Netherlands	25	82	81	≤16	25	1.4 to 1.7	5	Hinton and Nicholls (1998)
Ebro Delta, Spain	4	36	40	15	10	<0.5		Garcia et al. (1998)
Lubiatowo, Poland	10	4	0.4	8	25	<0.5	2 to 2.5	Rozynski et al. (1998)

CONTROLS ON CLOSURE AT SMALL AND MEDIUM SCALES

When considering the prediction of closure, it is important to understand what forcings and internal dynamics influence this morphological response. Based on our present understanding, a conceptual model linking forcing to closure is shown in Figure 1. The primary forcing which produces closure under microtidal, wave-dominated situations appears to be wave action (Capobianco et al., 1997; Nicholls et al., 1998). The skill of Equation 1 in predicting the limit of closure for erosional events and annual timescales is one indicator of the importance of this forcing. Wave action may produce closure in two distinct ways: (1) *directly* by cross-shore redistribution of sediment; and (2) *indirectly* by net gains or losses of sediment due to longshore transport and the resulting profile translation (see Nicholls and Birkemeier, 1997). While the indirect effect of waves might be observed at small scales, it is more important at medium scales due to the cumulative effects of littoral transport.

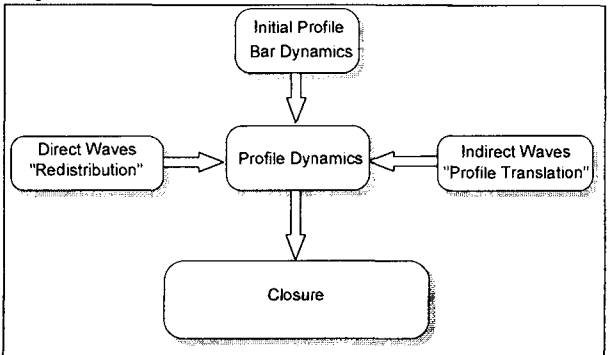

Figure 1. A simple conceptual model showing the major controls on closure at short and medium scales.

The response to this forcing is constrained by the internal dynamics of the morphological system. At small scales, the pre-event bar configuration influences closure during erosional events (Nicholls and Birkemeier, 1997; Nicholls et al., 1998). At medium/large scales, the shoreward closure along the Holland coast shows two distinct closure provinces in response to (broadly) the same wave climate (Hinton and Nicholls, 1998). However, these two provinces can be directly related to zones of distinct bar behaviour, showing that bar morphodynamics influence closure at these scales.

Therefore, closure is a response to the direct and indirect wave forcing, conditioned by the starting morphology and/or bar dynamics. In terms of prediction this has important implications. To predict closure both the forcings and the internal dynamics need to be described and this is not presently possible (see Capobianco et al., 1997). Models which only consider the forcing can only predict properties of the distribution of closure for that forcing (i.e., a minimum, or a maximum, or a mean). This limits our prediction capability, although just knowing the limit to closure is often useful to engineers (Nicholls et al., 1996; 1998).

CLOSURE AT SMALL SCALES

Nicholls et al. (1998) examined closure (defined with a 6-cm depth change criterion) at weekly to monthly intervals using data from Duck. Each closure event was defined as erosional if associated with consistent offshore bar movement, and accretional if associated with consistent onshore bar movement. The *limit* to closure is well-predicted by Equation 1 during erosional events (the closure response can normally be related to a specific storm). However, the scatter below Equation 1 is large and partly due to pre-event profile configuration: for the same wave forcing deeper closures occur when an outer bar is well-developed (Nicholls and Birkemeier, 1997). An empirical best fit shows that observations are 67% of predictions. Under accretional conditions, Equation 1 often underpredicted the observed closure. This is not a surprising result as Equation 1 is based on extreme waves, while accretion is a slow steady process which may have occurred near continuously between surveys.

To generalise closure at small scales for a range of depth changes, Capobianco et al. (1997) examined empirical relationships with the wave forcing, again using data from Duck. Closure was defined using an automatic algorithm for 5-cm, 10-cm and 20-cm depth change criteria. Empirical distribution functions were derived from the waves and the calculated depths. Assuming that there is a general relationship between waves and depth variation, the exceedance probabilities can be matched (i.e., the x% highest waves produce the x% largest depth changes). Note that accretional and erosional closures are not distinguished. The result is given in Figure 2.

An empirical fit which allows extrapolation to larger wave heights is also shown:

$$D_p = k.H^{0.67} \qquad (2)$$

where D_p is the predicted depth of closure, H is the *mean* wave height over the 12 hour exceedance (see Equation 1), and k is a constant of 2.1, 2.8 and 3.4 for 20-cm, 10-cm and 5-cm change, respectively. For the deeper closures, Equation 2 provides a good fit for 20-cm change. However, for the 5-cm and 10-cm change, there is significant underprediction for the deepest closures that one would most like to predict. However, this could represent spurious data generated by the automatic algorithm used to estimate closure and an independent check of these results is required.

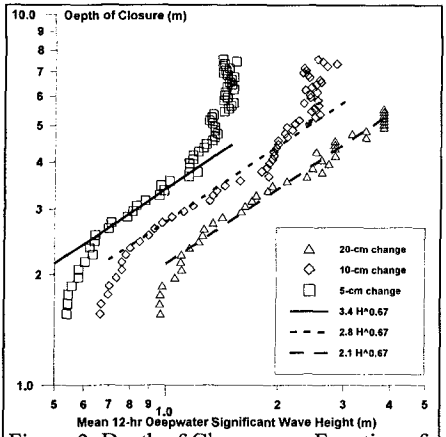

Figure 2. Depth of Closure as a Function of Mean 12-hr Significant Wave Height (from Capobianco et al., 1997)

The dataset of accretional and erosional cases from Duck developed by Nicholls et al. (1998) is suitable for such a check as it has been manually quality controlled to remove spurious values. It is compared with Equations 1 and 2 in Figure 3. The general form of Equation 2 is shown to provide a reasonable limit to the all the closure observations. For 5-cm change, the accretional and erosional cases occupy distinct areas, as discussed above. Equation 2 provides a limit to both the accretional and erosional cases, but Equation 1 provides a better limit for the deeper erosional cases. For 20-cm change, there is less distinction between the erosional and accretional cases, and Equation 2 still defines a reasonable upper limit to the entire dataset, although this can be improved with adjustment to k (Table 2). For the deep erosional cases, Equation 1 still provides a better limit than Equation 2 if an empirical adjustment is made (Table 2).

Table 2. Empirical coefficients to determine the limit to closure using Equations 1 and 2 based on the data in Figure 3.

Depth Change Criteria (cm)	Equation 1 Adjustment (for erosional cases only)	adjusted k for Equation 2 (all cases)
5/6	100%	3.4
10	90%	3.2
20	75%	2.4

The general applicability of Equation 2 to sites other than Duck is less certain, given its empirical basis. However, it provides useful guidance and shows the potential for the prediction of a limit to closure for a range of depth change criteria. Finally, these results reinforce the value of distinguishing erosional from accretional closures at small scales.

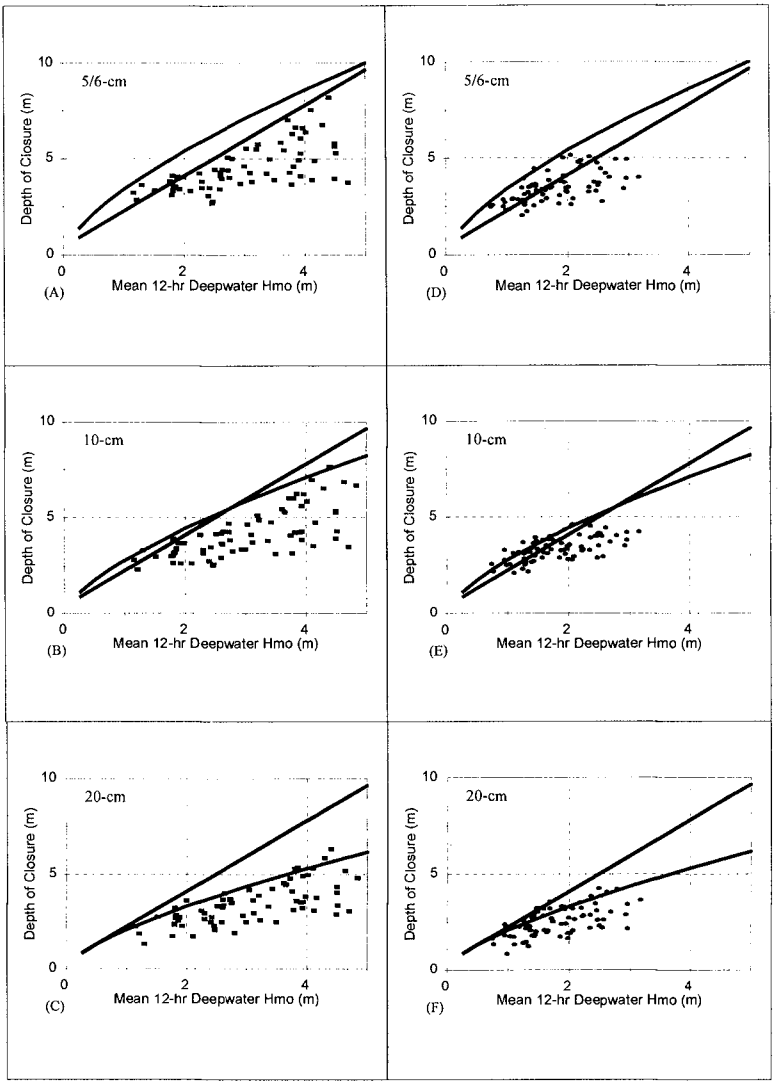

Figure 3. Depth of closure versus the mean extreme 12-hour deep-water wave height. Equation 1 (straight line) and Equation 2 (curved line) are shown together with data from Duck using a 5/6-cm, 10-cm and 20-cm depth change criteria. (A), (B) and (C) show erosional cases, and (D), (E) and (F) show accretional cases.

CLOSURE AT MEDIUM SCALES

Closure at medium scales is an integrated response to both erosional and accretional processes, including cross-shore redistribution of sediment and profile translation. At the annual timescale, Nicholls and Birkemeier (1997) showed that while Equation 1 acted as a limit to the closure data, volume change was an additional controlling factor. Profile retreat and volume loss reduces closure compared to a case with no translation, while it was inferred that volume gain and profile advance enhanced closure compared with no translation. The residual ($d_{\ell t}$ - observed closure) versus volume change is shown for annual, two-yearly and four-yearly time intervals in Figure 4. Linear regression explains 21% of the variance. However, net volumetric changes at Duck have been relatively minor over the period of observations. An analysis of more data on closure from other sites with large net volume changes is needed to better understand this factor.

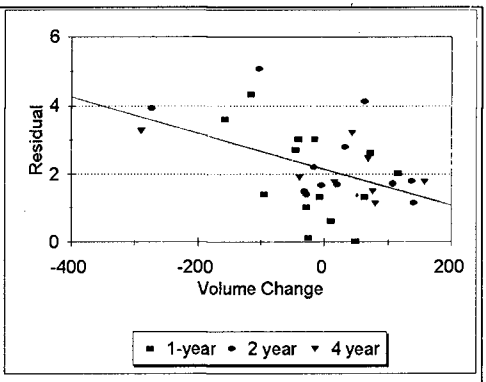

Figure 4. Residual (m) versus net volume change (m^3/m) at Duck for 1-year, 2-year and 4-year intervals and a 6-cm depth change criterion.

However, these results show that a better test of Equation 1 is under conditions of no volume change. In the subsequent analysis, only closures defined using a 6-cm criterion using profiles where the volume change is <50 m^3/m are considered. Table 3 summarises the data in terms of residuals, including erosional events for comparative purposes. While the sample size is small, the mean residual is smallest for the annual timescale, and then increases with timescale. Regression coefficients (forced through the origin) are also given in Table 3:

$$D_c = a\, d_{\ell t} \quad (3)$$

where D_c is the observed closure and a is the regression coefficient. The regression coefficient shows a similar pattern to the mean residuals and is closest to unity at the annual timescale. These results are all consistent with the results of Nicholls et al. (1996) that Equation 1 provides best agreement with observations at annual timescales.

Table 3. Mean residuals and regression coefficients as a function of timescale.(All regressions are more than . 95% significant)

Timescale (years)	Mean Residual (m)	Regression Coefficient (a)	Sample Size
Erosional Event	1.6	0.69	68
1	1.5	0.82	9
2	2.2	0.77	7

The slower growth of observed closure than predictions using Equation 1 at timescales above annual may be related to bar migration. Annual closure is strongly related to cross-shore bar movement. However, cross-shore bar migration is constrained to the shore and the crest of the outer bar at Duck rarely moves more than 300 m offshore (Lee et al., 1998). Therefore, as timescale increases the influence of bar movement at depth changes little and deeper closures are related other processes such larger-scale cross-shore sediment redistribution or profile translation.

MODELLING DEPTH OF CLOSURE USING EQUILIBRIUM PROFILE THEORY

The analysis above gives insight into the factors which control closure. However, it also shows that the prediction of closure as a function of both depth change criteria and timescale is quite difficult with the existing range of tools. This section outlines how a general predictive approach might be developed based on recent improvements to equilibrium profile (EP) theory (see also Capobianco et al., 1997).

In many cases it is possible to describe a beach profile through simple analytical expressions derived from EP theory (e.g., Dean 1977, Inman et al. 1993, Larson and Wise 1998). These expressions contain empirical parameters that depend on the beach and wave characteristics. Therefore, profile dynamics can be predicted as a function of wave climate. Although such an approach involves considerable simplifications, it may provide a basis for a generalised statistical definition of the depth of closure that is more easily adapted to engineering use than existing methods. Figure 5 outlines a proposed modelling approach based on EP theory which takes account of all the key variables, including wave statistics, slope and grain size and could provide useful estimates of closure at all engineering scales (small, medium and large scales).

A preliminary investigation on the possible timescale dependency of the equilibrium profile was undertaken using wave data from Duck. A 13-year long time series of waves measured every 6 hr was used. The approach of Larson and Wise (1998) for non-breaking conditions was adopted to evaluate the EP using the wave climate resulting from a period ranging from one month to 12 years using steps of one month. Clearly the significance of the statistics for one month is lower than that for

the statistics of twelve years; nevertheless we expect such an approach to give an indication of possible trends or of the possible changes of the EP. We expect such computations to be significant as the one month time-step is considered to be sufficient for the profile to respond to the most significant storms.

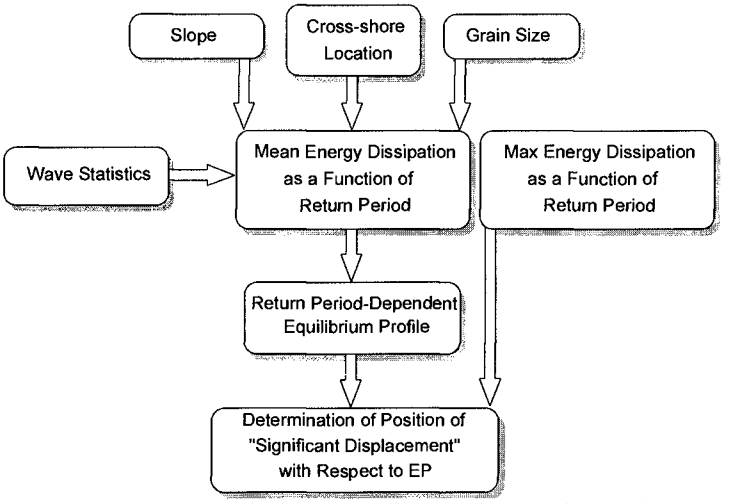

Figure 5. Proposed method to model depth of closure using EP theory

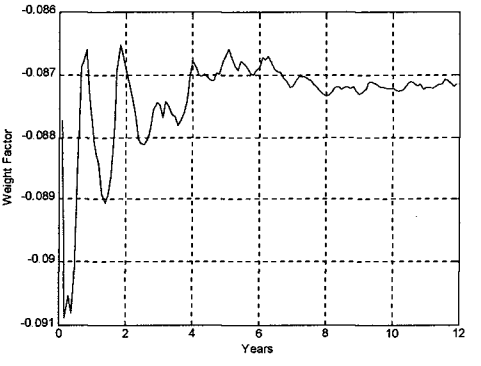

Figure 6. First Principal Component of EP estimated (for non-breaking conditions) as a function of a variable Time Window

The resulting EP data were analysed using Principal Component Analysis; in Figure 6 the behaviour of the First Principal Component is shown as a function of time. It is interesting to note that it stabilises after 4 years. While we must interpret such results with caution, from this simple analysis it appears reasonable to conclude that when the whole profile is considered an (engineering significant) EP requires several years to become established.

Larson and Wise

(1998) have derived a composite EP where the equilibrium shapes differ in the surf zone and offshore zone (compare Inman et al. 1993). The typical break point location separates the two zones; in the surf zone the Dean (1977) EP is employed, while in the offshore zone a lower exponent (0.3) is used. Two empirical shape parameters (A and B) define the composite EP: in the surf zone the shape parameter (A) depends primarily on grain size; and in the offshore zone shape parameter (B) depends mainly on the typical depth at breaking. Thus, if the characteristic wave conditions are known in the offshore, the break point may be calculated and the composite EP could be constructed from knowledge of the grain size. The composite EP includes one mobile bar related to the break point, and so captures some of the bar dynamics raised by Figure 1. For a series of offshore waves a corresponding series of EP may be computed from which statistical properties describing profile variability at different cross-shore locations can be derived.

In order to evaluate this method to compute profile variability, data from Duck was again employed. The time series of waves was used to compute the corresponding EPs for various values on the shape parameter B (A was set to 0.1, which approximately agrees with the grain size at the site -- 0.2 mm (see Larson, 1991)). The conditions at breaking were computed from the significant wave height and peak spectral period in the offshore using the formula given by Larson and Kraus (1989) and a ratio between wave height and water depth at breaking of 0.78. From the generated time series of EP the standard deviation was computed. Figure 7 displays this quantity for two different values of B and compares it with the standard deviation for profile lines 62 and 188 at Duck. While the qualitative form of the results is encouraging, they clearly illustrate that some aspects of the method need to be improved before reliable quantitative results can be obtained. For example, no attempt was made to translate the shoreline in response to changing wave conditions in the model leading to zero standard deviation at the shoreline in marked contrast to the data. Also, since the composite EP responds instantaneously to the wave conditions much more depth variation is predicted in deeper water than is observed. However, these two deficiencies in the model could be remedied by introducing a mobile shoreline (depending on the wave conditions) and a response function that takes into account the increasingly lagged response of the profile with depth. After the introduction of these features a simple EP based model may be used to theoretically determine the profile variability from which statistically defined depth of closures could be derived.

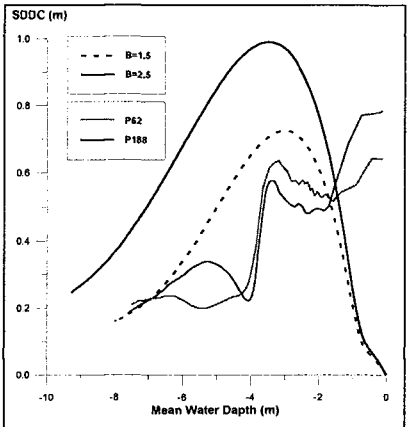

Figure 7. Standard deviation as a function of mean water depth for two values of the shape parameter B in the offshore equilibrium profile. Data from profile lines 62 and 188 at Duck are also shown.

CONCLUSIONS

Closure is a time- and space-scale dependent concept and hence, the controlling processes also vary with scale. Therefore, while closure is an empirically simple concept, its prediction remains difficult. For specific scales and circumstances, robust tools are already available. Equation 1 defines a limit to observations using a 6-cm depth change criterion for erosional events and at annual timescales, assuming limited net profile translation. As timescale increases above one year, so Equation 1 tends to increasingly overpredict the actual closure. This reflects a change in the processes that control closure from cross-shore bar migration to net gains and losses of sediment (and the resulting profile translation) and ultimately, shoreface processes. At sites with sufficient data, empirical methods to predict closure can also be developed as a function of different depth change criteria. These relationships may be applied at other sites with caution. They also illustrate the utility of treating depth change as a variable which can be of benefit to endusers.

Further analysis is required and this includes continued data analysis and preparation of calibration datasets (cf. Table 1). In addition, new robust modelling approaches are required which can generalise the different factors which influence closure over the range of engineering timescales. The equilibrium profile theory approach presented here is one promising method for quantifying profile variability over these scales.

Acknowledgements: This study represents a collaboration between the PACE-project in the framework of the EU-sponsored Marine Science and Technology (MAST-III) under contract no. MAS3-CT95-002 and the Field Research Facility Measurement and Analysis Work Units under the Coastal Research and Development Program of the US Army Corps of Engineers. Nicoletta Lo Turco assisted Michele Capobianco. Permission was granted by the Chief of Engineers to publish this information.

References

Capobianco, M., Larson, M., Nicholls, R.J. and Kraus, N.C., 1997. Depth of Closure: A Contribution to the Reconciliation of Theory, Practise and Evidence. *Proc. Coastal Dynamics '97*, Plymouth, ASCE, New York, pp. 506-515.

Cowell, P.J., Roy, P.S. and Jones, R.A., 1995. Simulation of LSCB using a morphological behaviour model. *Marine Geology*, 126, 450-461.

Dean, R.G., 1977. "Equilibrium Beach Profiles: U.S: Atlantic and Gulf Coasts." Department of Civil Engineering, Ocean Engineering Report No. 12, University of Delaware, Newark, DE.

Garcia, V., Jimenez, J.A., Sanchez-Arcilla, A., Guillen, J. and Planques, A., 1998. Short-term relatively deep sedimentation on the Ebro delta coast: Opening the closure depth. *Proc. 26th ICCE*, Copenhagen, ASCE, New York, *in press*.

Hamm, L., 1997. Prediction of Aggregated-Scale Coastal Evolution. Task Force on Datasets. Summary of Available Datasets. Sogreah Ingenierer, Grenoble, France.

Hallermeier, R.J., 1981. A profile zonation for seasonal sand beaches from wave climate, *Coastal Engineering*, 4, 253-277.

Hinton, C. and Nicholls, R.J., 1998. Spatial and temporal behaviour of depth of closure along the Holland coast. *Proc. 26th ICCE*, Copenhagen, ASCE, New York, *in press*.

Inman, D.L., Elwany, M.H.S., and Jenkins, S.A., 1993. Shorerise and Bar-Berm Profiles on Ocean Beaches. *Journal of Geophysical Research*, Vol 98, No. C10, pp 18,181-18,199.

Larson, M., 1991. Equilibrium profiles of a beach with varying grain size *Proc. Coastal Sediments 91*, ASCE, New York, pp.905-919.

Larson, M. and Kraus, N.C., 1989. SBEACH: Numerical Model for Simulating Storm-Induced Beach Change. Report 1. Empirical Foundation and Model Development. *Technical Report CERC-89-9*, Coastal Engineering Research Center, US Army Engineer Waterways Experiment Station, Vicksburg, MS.

Larson, M. and Wise, R.A., 1998. Simple Models for Equilibrium Profiles Under Breaking and Non-Breaking Waves. *Proc. 26th ICCE*, American Society of Civil Engineers, *in press*.

Lee, G. and Birkemeier, W.A., 1993. Beach and nearshore survey data: 1985-1991. CERC Field Research Facility. *Technical Report CERC-93-3*, CERC, US Army Corps of Engineers Waterways Experiment Station, Vicksburg, MS.

Lee, G., Nicholls, R. J. and Birkemeier, W.A., 1998. Storm-driven variability of the beach-nearshore profile at Duck, North Carolina., 1981-1991. *Marine Geology*, 148, 163-178.

Marsh, S., Nicholls, R.J., Kroon, A. and Hoekstra, P., 1998. Assessment of depth of closure on a nourished beach: Terschelling, the Netherlands. *Proc. 26th ICCE*, Copenhagen, ASCE, New York, *in press*.

Niedoroda, A.W., Reed, C.W., Swift, D.J.P., Arato, H. and Hoyanagi, K., 1995. Modeling shore-normal large scale coastal behaviour, *Marine Geology*, 126, 181-199.

Nicholls, R.J., Birkemeier, W.A. and Hallermeier, R.J., 1996. Application of the depth of closure concept. *Proc. 25th ICCE*, Orlando, FL, ASCE, New York, 3874-3887.

Nicholls, R.J. and Birkemeier, W.A. 1997. Morphological and sediment budget controls on depth of closure at Duck, NC. *Proc. Coastal Dynamics 97*, Plymouth, ASCE, New York, pp. 496-505.

Nicholls, R. J., Birkemeier, W. A. and Lee, G. 1998. Evaluation of depth of closure using data from Duck, NC, USA. *Marine Geology*, 148, 179-202.

Rozynski, G., Pruszak, Z., Okroj, T. and Zeidler, R., 1998. Depth of Closure and Seabed Variability Patterns. *Proc. 26th ICCE*, Copenhagen, ASCE, New York, *in press*.

Stive, M.J.F. and deVriend, H.J., 1995. Modelling shoreface profile evolution. *Marine Geology*, 126, 235-248.

Stive, M.J.F., Roelvink, J.A. and deVriend, H.J., 1990. Large scale coastal evolution concept. *Proc. 22nd ICCE*, Delft, ASCE, New York, pp. 1962-1974.

Wright, L.D., Boon, J.D., Kim, S.C. and List, J.H., 1991. Modes of Cross-shore Sediment Transport on the Shoreface of the Middle Atlantic Bight. *Marine Geology*, 96, 19-51.

Short-term relatively deep sedimentation on the Ebro delta coast. Opening the closure depth

Vicente Gracia[1], José A. Jiménez[1], Agustín Sánchez-Arcilla[1], Jorge Guillén[2] and Albert Palanques[2]

Abstract

Morphological changes at the shoreface of the Ebro delta have been analysed with emphasis on the Trabucador barrier, using two types of approximations: (i) an aggregated-scale approach, i.e. by evaluating the depth of closure from comparison of beach profiles from a data set of 4 years and, (ii) a process-oriented one, where changes are analysed in terms of driving factors and resulting sediment transport from a small scale experiment. Results from the depth of closure analysis show that acting processes are restricted down to an average depth of 6.5 m, with an important spatial variability. A year with high energy contents gives same results than using the whole data set. A sedimentation of about 7 cm was detected during the small scale experiment at 8.5 m and 12.5 m depth under the passage of several storms. The analysed velocity field and sediment flux showed that onshore transport close to the bottom and offshore transport in the upper part prevailed under storms. These forcing conditions were similar to the registered in previous analysis although no morphological changes were previously detected. Results show that the depth of closure analysis is a good starter point to define morphological activity in the nearshore profile, but it has to be complemented with other type of approaches such us the process-oriented one to accurately define the limits for morphological activity.

Introduction

The *closure depth* is a common concept, which is usually applied in coastal morphology studies. Basically it consists in the determination of a depth beyond that no significant changes can be detected in the bathymetry. Recently, some authors have introduced the effect of the temporal scale to permit its variation as the time scale increases and, as a consequence, the probability of occurrence of more energetic wave states (Nicholls *et al.* 1996).

[1] *Laboratori d'Enginyeria Marítima, UPC, c/Jordi Girona 1-3, Campus Nord, Ed. D-1, 08034 Barcelona, Spain*

[2] *Instituto de Ciencias del Mar, CSIC, Paseo Joan de Borbó s/n, 08039 Barcelona, Spain*

One of the intrinsic problems is that profiles used to estimate closure depth usually do not have a good temporal resolution or, its spatial coverage does not permit to measure the deepest part of the profile, which implies to make an initial assumption of negligible variation.

Recently, Gracia *et al.* (1998a) have estimated the averaged medium-term (at the scale of several years) closure depth along the Ebro delta coast to be about 7,5 -8 m. Their estimations were based in the analysis of beach profiles down to 15 m depth taken every 3-4 months during a period of 4 years. During that time span, several very energetic storms impacted the Ebro delta coast although no significant deep changes were observed in the surveyed profiles.

However, in a very recent experiment, in which two instrumented tripods were deployed on the Ebro delta shoreface at 8,5 m and 12 m depths (figure 1), an "unexpected" behaviour was observed (Jiménez *et al.* 1997a; Guillén *et al.* 1997), resulting in a sedimentation of about 7 cm at both places.

It is the aim of this paper to characterise the depth of closure at a medium term scale and to link it with the observed "deep" bottom changes. To do this, a process-oriented analysis of this sedimentation event is presented. The results are compared to estimates of the medium term depth of closure for the area.

Study Area

The Ebro delta is located on the Spanish Mediterranean coast, with a 50 km sandy shoreline with two spits at the north and southern part (see figure 1).

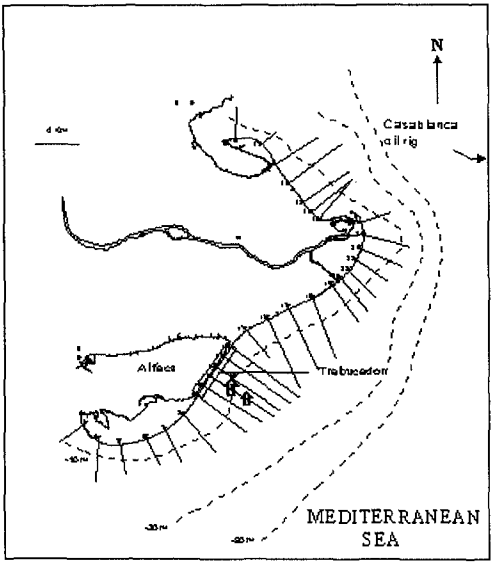

Figure 1. The Ebro delta. Arrows indicate Tripod deployment.

At present the delta is a micro-tidal wave dominated environment with an astronomical tidal range of about 0.25 m, being the average significant offshore wave height of about 0.7 m with an associated mean period of 4 s (Jiménez *et al.* 1997b).

Cross-shore distribution of sediment grain size (Guillén and Jiménez 1995) shows a finning trend offshore with medium sands (250 μm) at the shoreline to very fine sands (125 μm) at 12 m depth. At about 15 m depth there is a mud belt surrounding the delta and in consequence the system can be considered as close at the present evolutive state.

A typical cross-shore profile of the area shows up to 3 bar systems which have experienced in some sites an important longshore growth (Guillén and Palanques, 1993; Gracia et al. 1995).

The study is focussed in a barrier beach, the Trabucador bar, located at the southern part of the delta which has a length of about 5 km, a width between 150 m to 200 m and a height above the mean sea level of 1.5 m.

Medium term closure depth

The Medium term closure depth has been analysed by Gracia et al. (1998a) using a set of bathymetric profiles surveyed every 3 to 4 months from 1988 to 1992, which basically consists of 36 nearshore profiles spaced every 1-2 km reaching depths up to 15 m. Two techniques were used: a topographic survey for the inner part and a vessel with echo-sounder with a positioning system for the deeper one, giving a nominal accuracy of ± 5 cm, which defines a non significant change threshold value of 10 cm (the best case).

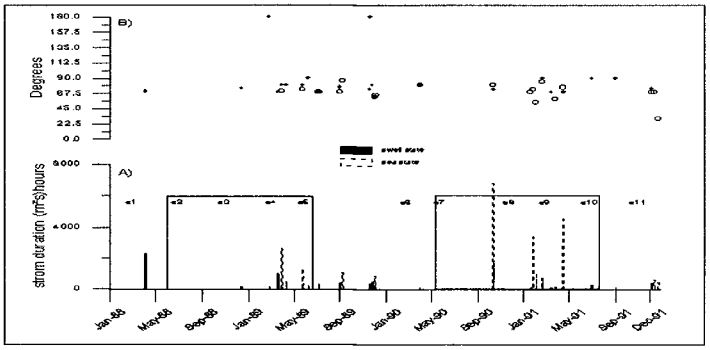

Figure 2. Wave energy events during the surveyed period and associated direction, from visual observations at Casablanca oil ridge.

The analysis has been done in three different time frames according to the wave energy conditions observed during the surveys (see figure 2). The first window corresponds to fair-weather year with a moderate wave energy content. The second is defined as a year of high energy conditions, with several eastern storms, where one of them impacted the coast producing the breach of the barrier (Sanchez-Arcilla and Jiménez, 1994). This high-energy event had a significant wave height of 4.5 m and peak period of 10 s, being the associated return period of 10 years. Finally, the depth of closure has been analysed using the overall data set, *i.e.* 4 years. Moreover within

these 3 time frames the Hallermeier formula was also tested. The equation was fed with the corresponding local significant wave height propagated from offshore to 10 m depth for each profile, in order to have a more realistic charaeterisation (in terms of nearshore waves) and to account spatial variability in wave conditions due to changes in bathymetry.

Among the different methods analysed by the authors by comparing cross-shore profiles the standard deviation of bottom depths is presented here for the entirety coast (see figure 3). This technique is usually applied when a relative large number of campaigns are available, although they must be well distributed on time to avoid "false" values. Moreover, the standard deviation is the most proper technique to retain short-term changes, *i.e.*, the highest variability (Gracia *et al.*, 1998a).

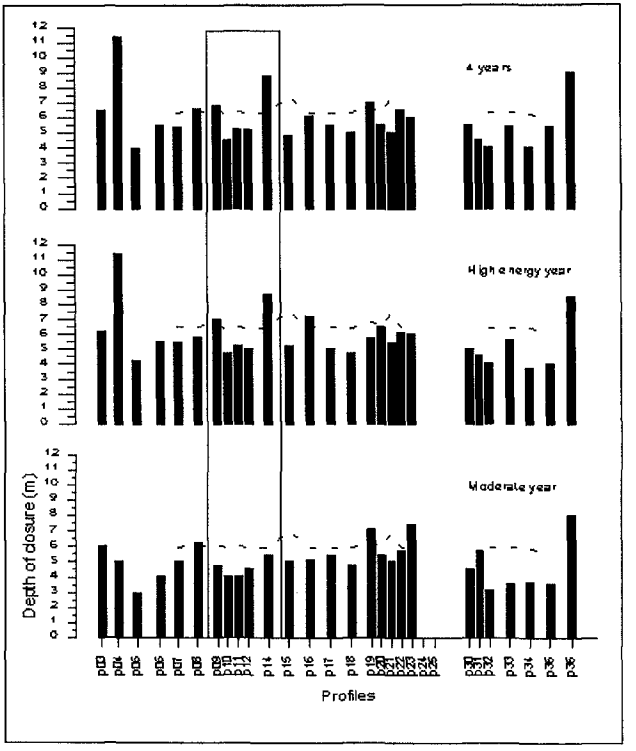

Figure 3. Depth of closure for the Ebro delta coast using the standard deviation method applied at tree different time frames (Trabucador bar indicated in a window).

As expected, the fair-weather year presents the lowest values being the average closure of about 4 m depth for the central part of the barrier with a maximum value of about 5.5 m. The resulting closure using the Hallermeier equation at this time windows was almost constant along all the barrier and about 6 m depth. For the stormy year an average depth of closure (d_c) of about 6 m was found whereas the predict d_c was about 6.5 m. Using the overall data set similar values of d_c were

obtained. In any case, the Hallermeier equation over predicts the values obtained by comparing profiles, and these differences are greater in the Trabucador bar.

Another aspect that must be pointed out is the high spatial variability in the estimated d_c. This is, the spits, and, in the area of interest at the Trabucador bar, which maintains a more or less constant value in the central part while at the ends of the barrier there is an important increase, with independence of the time span analysed.

As a summary, looking at the aggregated scale, *i. e.* morphological changes, most of the acting processes in the area of study are important (in terms of the observed changes) down to 6.5 m depth (as an average value), *i.e.*, the estimated medium-term depth of closure. However, since this d_c has been obtained from a discrete set of data, this result can not be generalised without including some "confidence band", since changes between surveys are not recorded unless they are reflected in a longer time scale. Moreover, it has to be stressed that d_c does not represent a limit for sediment movement and, in this sense, it can not be used as an indicator of sediment mobility.

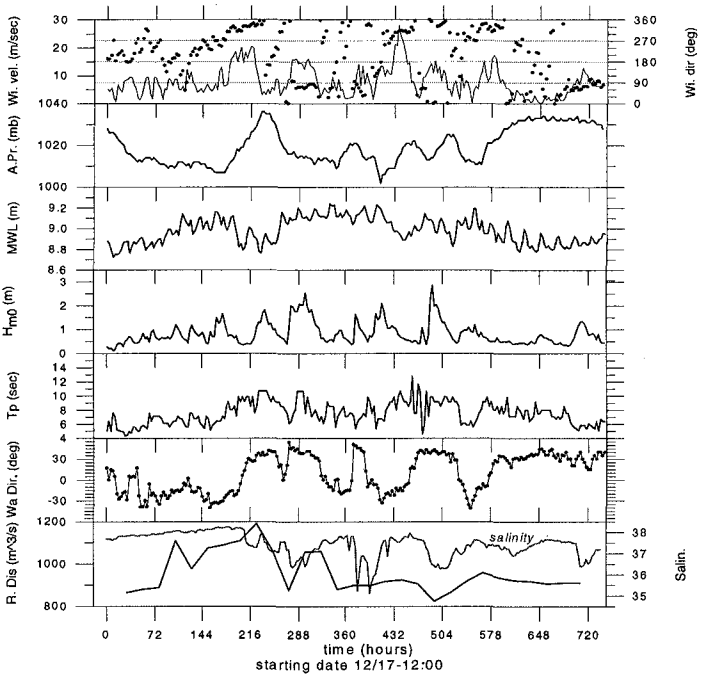

Figure 4. Forcing conditions during the inner shelf campaign at the shallowest position (8.5 m depth).

Inner shelf experiment

From December'96 till January'97 an inner shelf experiment was carried out in the surveyed area (Trabucador bar), which basically consisted in the deployment of two instrumented tripods at depths of 8.5 m and 12.5 m (see fig 1 for location). The basic configuration was, three bi-axial electromagnetic current meters (Delft

Hydraulics, 1993) and three optical backscatterance sensors (D & A Instruments, 1991), placed at 0.1 m, 0.5 m and 1 m above the bottom, an absolute pressure transducer (Druck PDCR-1830) and a compass (KV Industries C-100). The sampling interval selected during the experiment was 1 Hz obtaining data during 20 minutes every 3 hours (see Jiménez et al., 1998, for further details). Additionally, the outer tripod had a Doppler current meter with a nephelometer. Before deployment and after recovery, bottom surface sediment and core samples were taken.

The wave and atmospheric conditions are summarised in figure 4, up to six consecutive moderate storms can be identified with significant wave heights up to 3 m and associated peak periods from 4 s to 10 s. These storms mobilised large amounts of sediment, reaching near-bottom suspended sediment concentration up to 8 gr./l. The resulting morphological response was a sedimentation of about 7 cm at both locations.

The surface granulometric distribution obtained before and after deployment in the inner site shows a very small change in fine percentages of 1%, a slight increase in mean grain size (from 150 μm to 160 μm) and better classified sediments. On the other hand, in the deepest site (12 m depth) the fines percentage drastically increased (from 15% to 40%), the mean grain size decreased from 90 μm to 30 μm and the sediment was better sorted (decrease in deviation).

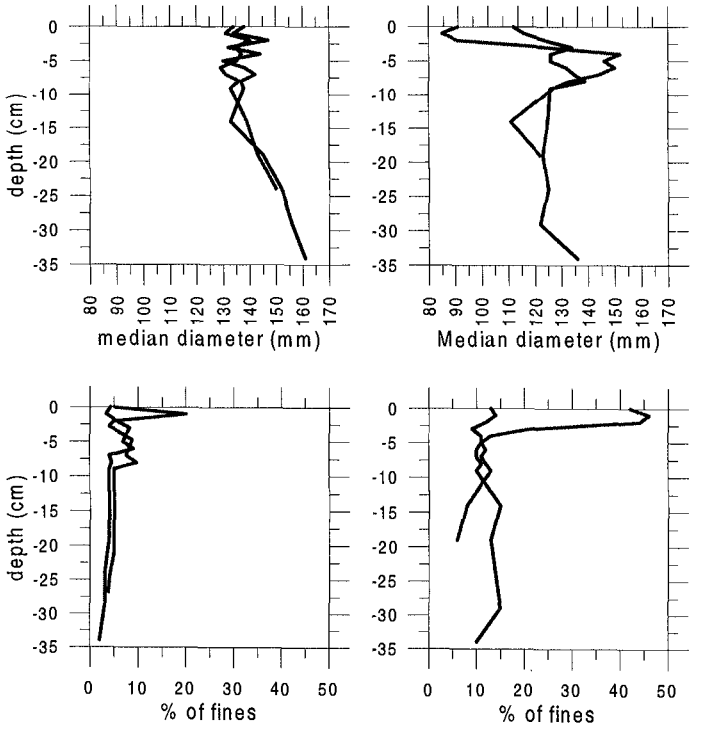

Figure 5. Vertical distribution of core samples before and after recovery. From left to right 8.5 m and 12.5 m depth deployment

Figure 5 shows the vertical distribution of fine percentages and median diameter at both locations before and after tripod recovery for the first 20 cm below the bottom. In the inner site, the median diameter is almost the same whereas the fine percentage increases in the upper part reflecting the changes observed in the surface samples. The highest variations are detected in the outer location, where, in the upper layer there is a significant decrease of the grain size diameter with an associated increment of fines of about the 40%.

Therefore, the resulting morphological response of the energetic conditions during the surveyed period was visible and, in principle, if it was "permanent" has to be detected in the previous analysis. However, wave conditions are not more energetic to those covered in the analysis of d_c for the stormy year.

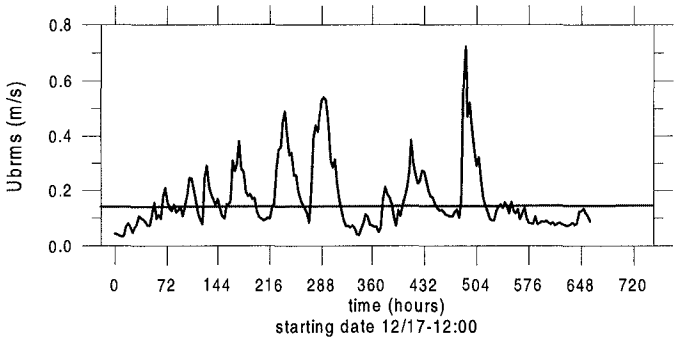

Figure 6. Near-bottom cross-shore velocity at 8.5 m depth and initiation of sediment movement according to Shields criteria.

To study the capacity of mobility of the monitored conditions, a detailed process-oriented analysis is done. The objective is to see if hydrodynamic conditions and resulting sediment transport were important enough to explain such sedimentation. Figure 6 shows the near bottom velocity (10 cm) at 8.5 m depth where the pass of the different storms are reflected. According to the sediment characteristics for the area it can bee seen that during most of the time the threshold value for initiation of movement (according to the Shields criteria) was exceeded in a significant manner, *i.e.* there was a high capacity of transport. Considering the third order velocity moment as an indicator of the transport capacity (figure 7) it can be seen that during the storms it was significantly different from zero and directed onshore (negative values in the figure).

Computing the mean and total cross-shore sediment flux directly from the measurements at 8.5 m depth (see figure 8), the impact of the different storms at all elevations can be identified, more evident at the lowest level. However a differential behaviour is detected in the water column: close to the bottom, most of the transport is directed onshore whereas in the upper part some reversals can be observed. These reversals were found to be related to the presence of seaward directed currents due to the presence of strong wind blowing offshore (Jiménez *et al.* 1998). Preliminary analysis of the vertical structure of the current showed that under certain conditions (just after storms), the mean current close to the bottom (0.1 m) was onshore whereas in the upper part of the water column was offshore (Gracia *et al.* 1998b).

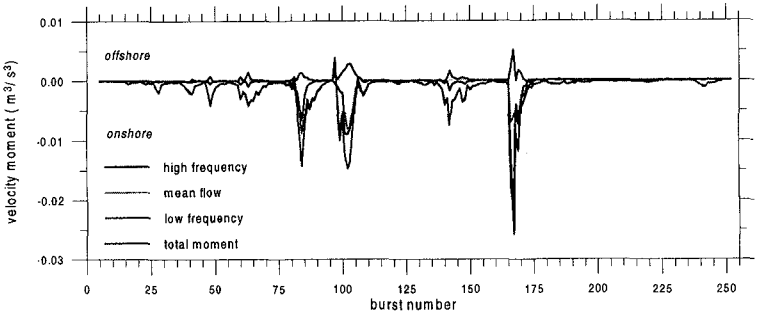

Figure 7. Third order velocity moment at 10 cm above the bottom for the 8.5 m depth deployment.

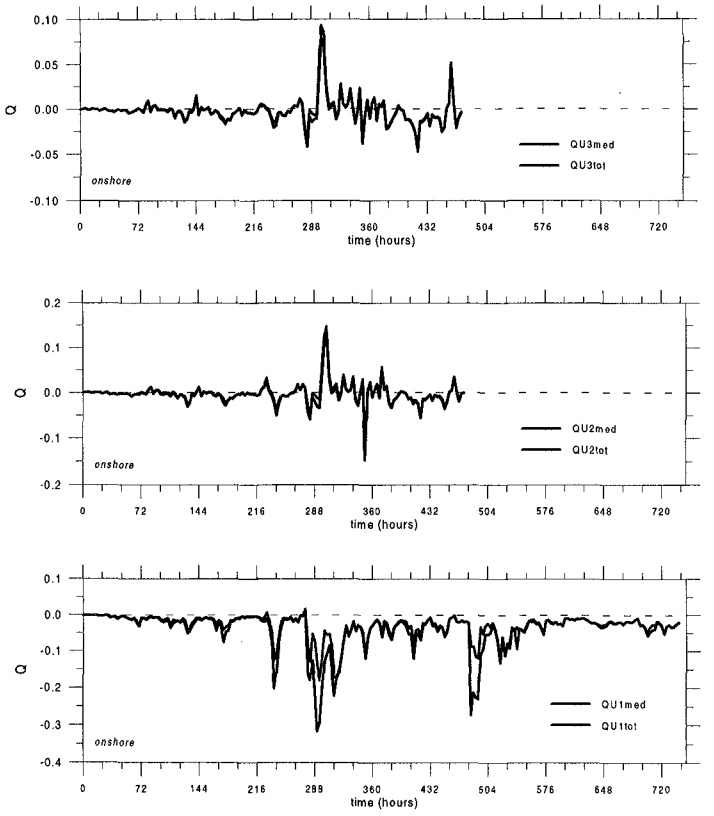

Figure 8. Cross-shore transport rates (gr./l·m/s) at 8.5 m depth. From top to bottom. 1 m, 0.5 m and 0.1 m above the bottom.

Mean current (assuming waves energetic enough to mobilise the sediment) mainly controls sediment flux but during storms the asymmetry of the wave-induced

velocity field increases and largely contribute to it. This can be clearly seen in figure 8, where the contribution of the mean current to the total transport increases towards the surface due to an increase in current speed whereas oscillatory velocity is almost the same.

The longshore component (see figure 9) shows a more or less similar pattern. It is mainly directed towards the north changing the direction during the pass of storm events.

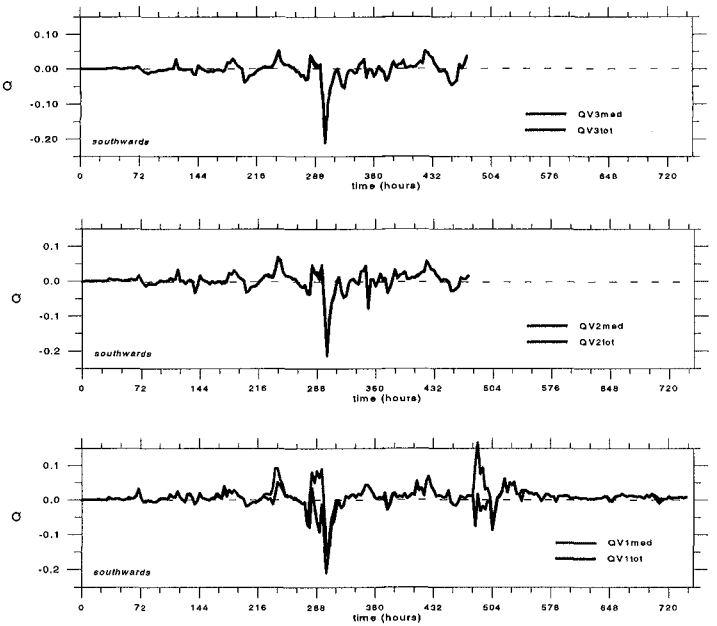

Figure 9. longshore transport rates (gr./l·m/s) at 8.5 m depth. From top to bottom. 1 m, 0.5 m and 0.1 m above the bottom.

Summary and discussion

Results of the depth of closure analysis show that at the aggregated-scale, morphological changes in the study area (Trabucador bar) are restricted down to an average depth of 6.5 m. However, in a yearly scale analysis, the deepest closure is obtained for high energetic periods, which fully control this depth when a longer time span is considered, i.e. the time window is not relevant per se but the energetic conditions during the considered time frame. Moreover, a high spatial variability in d_c was found, mainly at the spits and the area of interest (Trabucador Bar), the former presenting deepest values and the latter showing an important decrease. Thus, the Trabucador bar is usually overwashed during E storms (two to three times per year) which can "subtract" energy from the outer coast resulting in a decrease in the magnitude of the return flow in the upper shoreface. This could explain the shallower depth of closure values obtained in the central part of the barrier, in comparison with those observed at the barrier ends.

When a deterministic approach such as the Hallermeier's method is applied, an overprediction of the depth of closure is obtained. In this sense, it is a conservative choice for engineering purposes. However, it is not able to reproduce the actual spatial variability unless other factors such as the evolutive behaviour of each coastal stretch or alongshore variability in wave conditions are considered.

Thus, results following this approach seems to suggest that the maximum depth for morphological changes is restricted to 6.5 m. However, during an experiment at the inner shelf, a sedimentation event of about 7 cm was detected at 8.5 m and 12.5 m depth. This occurred under the action of several storms in one month, but the energetic content of the storms did not exceed the recorded in previous data (those included in the previous analysis). A detailed analysis of the velocity field and the sediment fluxes close to the bottom showed a strong sediment mobility, specially under the storms. In a general manner, onshore sediment transport close to the bottom and offshore transport in the upper part of the water column prevailed during storms. The high mobility as well as the magnitude of the sediment concentration measured during the experiment are able to explain the observed changes, including the variability of the sediment grain size distribution in the first cm of the bottom layer.

Since the forcing conditions during this small scale experiment are relatively frequent in the area (at least one per year), this type of "deep" changes should be relatively frequent, although they had not been detected at the aggregated scale analysis. The only way to do it, is by increasing the frequency of profile data acquisition (covering periods before and after storms) and reaching the deeper parts of the profile.

As a summary, although depth of closure is a good starter point to define morphological activity in a nearshore profile, the analysis has to complemented with other type of approaches, not only to define the limit of sediment transport (which in fact cannot be considered as included in the depth of closure analysis) but also to characterise the induced changes.

Acknowledgements

This work has been done in the framework of the *PACE* and *FANS* projects (EC MAST-III, MAS3-CT95-0002 and MAS3-CT95-0037 respectively) and TRASEDVE (MAR98-0691-C02-01). Second author thanks to DPTOP (Generalitat de Catalunya) for a grant given through the Faculty of Civil Engineering.

References

D & A Instrument Company, 1991. OBS-1 & 3. Suspended solids and turbidity monitor, Instruction manual. 41 pp.

Delft Hydraulics, 1993. P-EMS. Programmable electronic liquid velocity meter. User's manual.

Gracia, V., Jiménez, J.A. and Sánchez-Arcilla, A. 1995. Nearshore profiles along the Ebro delta coast. Implications for coastal processes. *Proc. 2nd International Conference on the Mediterranean Coastal Enviroment.*

Gracia, V., Jiménez, J.A. and Sánchez-Arcilla, A. 1998a. Variabilidad temporal y espacial de la profundidad de cierre. El caso del delta del Ebro. Revista Ingeniería del Agua, Spain. (accepted).

Gracia, V., Jiménez, J.A. and Sánchez-Arcilla, A. 1998b. Sediment fluxes in a tideless fetch-limited inner shelf. The Ebro delta. *2nd Fans Overall Meeting*, Bangor.

Guillén, J. and Jiménez, J.A. 1995. Process behind the longshore variation of the sediment grain size in the Ebro delta coast. *Journal of Coastal Research.*, 11: 205-218.

Guillén, J. and Palanques, A. 1993. Longshore bar and trough systems in a micro-tidal storm wave dominated coast: The Ebro delta (North-western Mediterranean). *Mar. Geol.*, 115:239-252.

Guillén, J., Palanques, A. and Puig, P. 1997. Tripod measurements on the Ebro delta shoreface. Winter'96, outer field site. *1st Fans Overall Meeting*, Barcelona.

Jiménez, J.A., Gracia, V. and Sánchez-Arcilla, A. 1997a. Tripod measurements on the Ebro delta shoreface. Winter'96, inner field site. *1st Fans Overall Meeting*, Barcelona.

Jiménez, J.A; Sánchez-Arcilla, A.; Valdemoro H.I.; Gracia, V. and Nieto F. 1997b. Processes reshaping the Ebro delta. *Mar. Geol.*, 144; 59-79.

Jiménez, J.A; Guillén, J., Gracia, V., Palanques, A., García M.A.; Sánchez-Arcilla, A., Puig, P.; Puigdefábregas J. and Rodríguez, G. 1998. Water and sediment fluxes on the Ebro delta shoreface. On the role of low frequency currents. *Mar. Geol.*(in press).

Nicholls, R., Birkemeier, W. and Hallermeier, R.J. 1996. Application of the depth of closure concept. *Proc. 25th ICCE*, ASCE, (in press).

Sánchez-Arcilla, A. and Jiménez J.A. 1994. Breaching in a wave dominated barrier spit: The Trabucador bar (North-eastern spanish coast). *Earth Surface Processes and Landforms*, 19:483-498.

Spatial and Temporal Behaviour of Depth of Closure along the Holland Coast

Claire Hinton* and Robert J. Nicholls*

Abstract

Depth of closure has been identified and its characteristics investigated over larger temporal ($\geq$ 25 years) and spatial (< 100 kilometres) scales than previous research. In addition to the 'normal' shoreward closure produced by breaking waves and cross-shore bar migration, at longer timescales ($\geq$10 years) shoreface morphodynamics also produce significant profile changes. The shoreward closure is primarily controlled by wave breaking with a secondary control of bar morphodynamics. Shoreface changes are slow and steady and as timescale increases, so more profiles exhibit re-opening in depths typically greater than 10 metres. This is then usually followed by the re-closure of the profile on the middle/lower shoreface. Such phenomena have not been observed in past studies of this type and result from the large temporal and spatial extent of the data set used here. Over long time scales ($\geq$ 10 years) such changes have a coastal engineering significance.

Introduction

The application and scope of coastal engineering schemes i.e. shore protection and land reclamation, is increasing. For example, the present Dutch coastal policy is to maintain its coastline at its 1991 position for the foreseeable future. In order to ensure the long-term reliability of such projects it is vital that coastal evolution over the same temporal scale is understood. So, with the advent of focused research within this field, many relevant concepts are being developed through both observation and predictive techniques.

*Flood Hazard Research Centre, Middlesex University, Queensway, Enfield, Middlesex, EN3 4SF. United Kingdom

A key concept in beach morphodynamics is depth of closure (Dc). Dc represents the 'seaward limit of '*significant*' depth change' (Nicholls *et al*, 1996); it does not, however, refer to an absolute depth beyond which there is no cross-shore sediment transport. Therefore, it is seen to act as a morphodynamic boundary separating a landward, morphodynamically active region from a more seaward inactive region, where vertical changes are less than the criterion chosen to define closure. (Figure 1.)

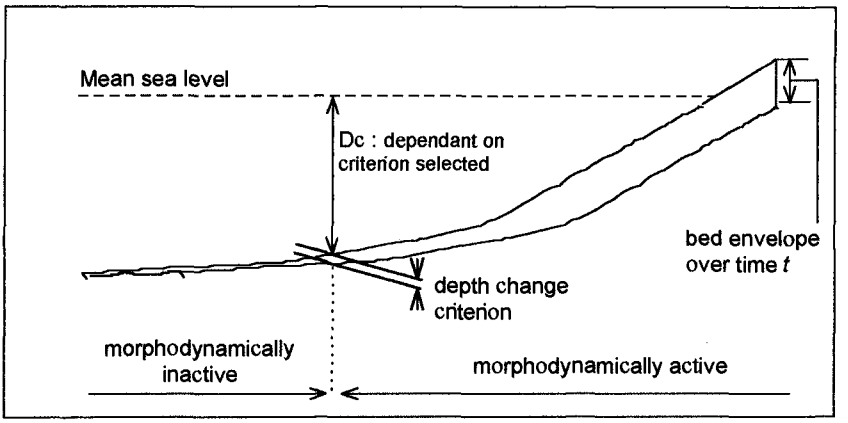

Figure 1. Zonation of a cross-shore profile over time *t* where Dc represents the seaward limit of significant depth change using the depth change criterion shown (adopted from Hallermeier, 1981).

Dc is of fundamental importance in coastal sediment budgets and associated applications such as beach and shoreface nourishment. Specific examples of its use are; i) as a boundary between active and inactive zones it allows for the correct placement of offshore mounds; location in the active region could provide material for onshore feed (Hands and Allison, 1991); and ii) as the limit of morphological change enabling the volume of beach fill material to be calculated (Davison *et al*, 1992).

In this paper the Large Scale Coastal Evolution concept of Stive *et al* (1990) is used to distinguish different scales of closure behaviour. The three scales are i) Large-Scale which has a morphodynamic length scale of 10 km and time scale of decades; ii) Medium-Scale with a morphodynamic length scale of 1 km and time scale of years; and iii) Small-Scale which has a morphodynamic length scale of 100 m and time scale of storms to seasons.

Closure has previously been investigated on the Medium-/Short-Scale (Garcia *et al*, 1997; Nicholls *et al*, 1996, 1998; Nicholls and Birkemeier, 1997). For example the Duck, North Carolina data has a 12 year time span and extends 1.2 km alongshore and 0.8 km cross-shore (Nicholls *et al*, 1996). These investigations have shown that Dc is time- and space-scale dependant (cf. Capiobianco *et al*, 1997). In particular, as the time interval increases then closure increases in depth.

The control of the extreme wave conditions upon closure is used in the analytical Hallermeier (1978) model to predict Dc. It has been adapted to a time-dependant form:

$$d_{l,t} = 2.28H_{e,t} - 68.5\left(\frac{H_{e,t}^{\ 2}}{gT_{e,t}^{\ 2}}\right) \quad (1)$$

where: $d_{l,t}$ = closure (Dc) (referenced to MLW);
$H_{e,t}$ = significant wave height exceeded 12 hours per t years;
$T_{e,t}$ = associated wave period; and
g = acceleration due to gravity.

Field validation of Equation 1 has shown that it provides a *limit* to the observed closure on micro-tidal, wave-dominated, sandy coasts during i) storms; and ii) annual periods (Nicholls *et al*, 1996, 1998). This suggests that spatially similar regions of closure will exist; a less energetic hydrodynamic environment will result in shallower closure values than those in a more energetic environment (cf. Marsh *et al*, 1998).

Most closure studies are limited to the surf zone and upper shoreface due to survey constraints (a maximum depth of 8m is reached at Duck, North Carolina; Lee *et al*, 1998). The JARKUS data set used here offers the opportunity to extend analysis to the Large-Scale; 100 km alongshore, 25 years (1965 to 1990) and 16 m depth. In addition this will allow the existence of '*significant* depth changes' on the shoreface at depths exceeding previous observations of closure to be investigated (as previously recognised by Stive *et al*, 1990).

Study Area

The study area is the Holland coast bound from Den Helder in the north to Hoek van Holland in the south. (Figure 2.) It is a closed coast uninterrupted by tidal inlets or barrier islands, allowing the determination of Dc characteristics in a wave-dominated, alongshore uniform environment. Anthropogenic interventions are mainly smaller-scale beach nourishment schemes, although the Petten sea dike (km 20 - 26) and Ijmuiden harbour moles (km 55/56) are present in the north and centre of the coast, respectively.

The study area is a micro-tidal, wave-dominated sandy coast with multiple bars. The bars extend to a maximum depth of approximately 8 m. The mean tidal range is 1.4 m in the north increasing to 1.7 m in the south. Peak tidal velocities generally do not exceed 1 ms^{-1}. The annual mean wave height is 1.2 m (associated wave period 5 sec); whilst the extreme annual wave height is 5.3m (associated wave period 7.7 sec) (Roskam, 1988). The wave climate is relatively similar along the length of the coast, deviations in wave height from north to south are in the order of 0.2 m.

Cross-shore bathymetric measurements have been measured by the Rijkswaterstaat since 1963 at regular, fixed locations alongshore. The measurements are held within the JARKUS data set. They have a vertical accuracy of 0.25 m which is the standard

deviation of the measurements, as determined within this study. An independent study, using both stochastic and systematic error sources, has also determined the accuracy of the data to be 0.25 m (Nanninga, 1985). Annual (short) profiles extend 0.8 km seaward, equivalent to a depth of approximately 6 m, with alongshore spacing of 0.25 km. In addition there are five-yearly long profiles ('doorlodingen') which extend to a minimum 2.5 km seaward, equivalent to approximately 15 to 16 m depth, and have an alongshore spacing of 1km. (Figure 3.) It is due to the greater cross- shore extent of the doorlodingen that it is analysed in this study; primary analysis indicates that Dc is not observed in the annual data even over a 1 year period. In addition, the most northern and southern profiles are rejected due to the tidal influence of the Marsdiep and the Europort inlets, respectively. The total study area therefore covers an alongshore distance of 81 km (km 16 to 97; Figure 2).

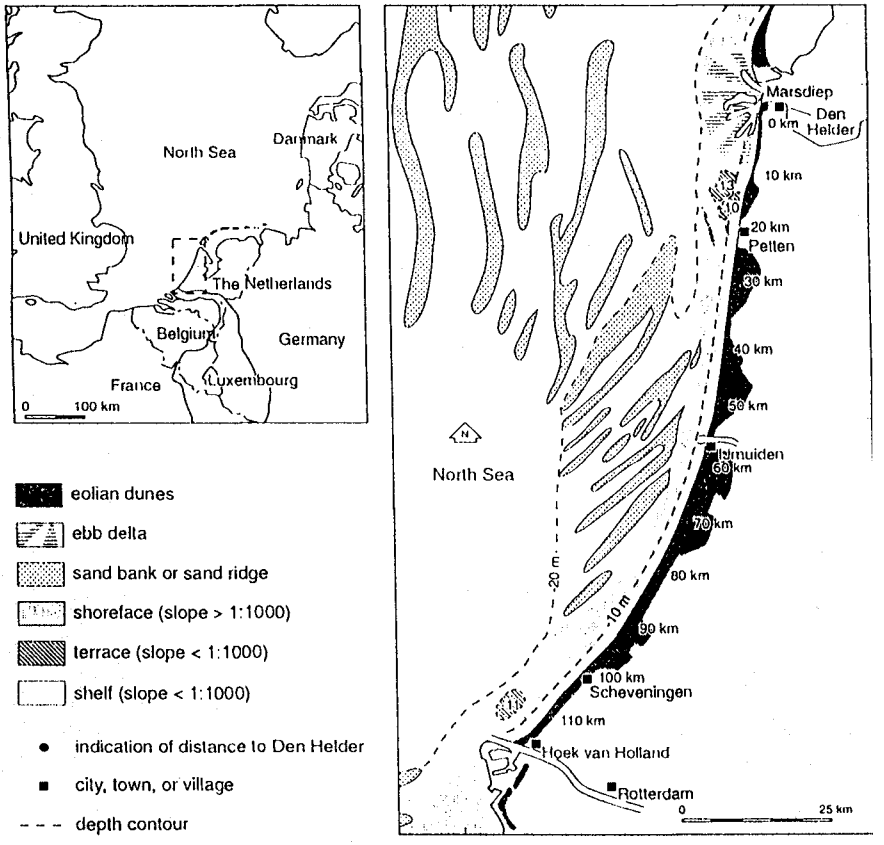

Figure 2. Location map showing the closed Holland coast. (Wijnberg, 1995)

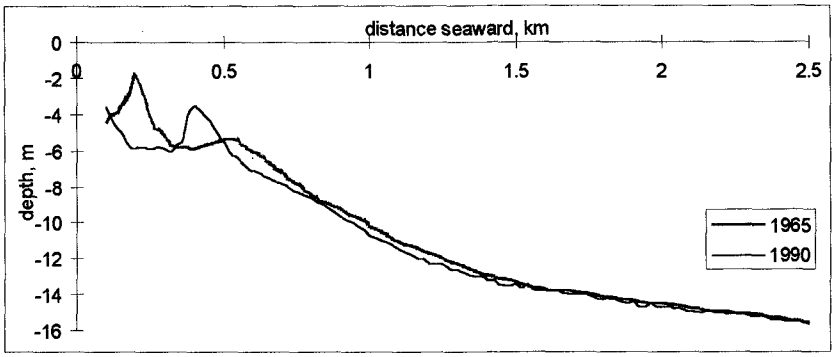

Figure 3. Example of the bathymetry along the closed coast using the doorlodingen from 1965 and 1990, located at km 31 (Noord-Holland).

Data Analysis

Values of Dc have been derived using two methods: i) the standard deviation of depth change (Kraus and Harikai, 1983) and ii) the fixed depth change (Nicholls *et al*, 1996). This analysis has been performed for all profiles over a range of temporal periods, 5, 10, 15, 20 and 25 years.

Standard deviation of depth change (sddc)

This is a simple method, effective in both dealing with large data sets and removing bias from outlying values. Variation in the standard deviation of elevation is shown as a function of the cross-shore distance for x number of profiles from the same alongshore location. Dc is then equated to that point at which the standard deviation reaches a constant, non-zero tail, which often has a value of about 0.25 m (the measurement accuracy). (Figure 4.)

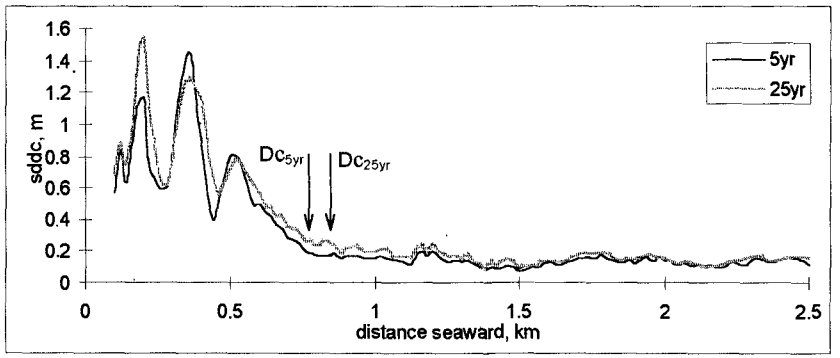

Figure 4. Sddc for km 31 which exhibits closure at a seaward distance of approximately 0.8 km for all time periods. ($Dc_{5yr} \approx 8$ m depth; $Dc_{20yr} \approx 9$ m depth)

Fixed depth change (fdc)

Dc can also be equated to that point at which, for 2 profiles from the same location, the depth variation is equal to, or less than, a pre-selected criteria. Here two criteria are selected: 0.25 m and 0.5 m. This means that there is 66% and 95% confidence that a real change in the bathymetry has occurred, respectively, assuming that the data measurement errors are normally distributed with a standard deviation of 0.25 m.

Results

General

Both methods produce similar results for all profiles along the Holland coast; the fdc criteria of 0.5 m generally gives the more landward value of closure as it allows the greatest depth variation.

Upon the examination of all results it became apparent that, in some instances, not only does the profile close at some distance x from the shore, but the profile re-opens and then usually re-closes towards its seaward limit. Such behaviour can be most clearly seen using the sddc plots. (Figure 5.) These phenomena are hereafter termed i) the shoreward closure (Dc_s); ii) the re-opening point (Ro) and associated re-opening zone; and iii) the middle/lower shoreface closure ($Dc_{m/l}$), respectively. Re-opening is only observed over the longer time scales (>10 years) and at distances offshore greater than 1.5 km (typically 12 m water depth). In addition, as the temporal period is increased the number of cases in which this behaviour occurs increases (18% of profiles re-open after 10 years increasing to 37% over 20 years).

Large-Scale Behaviour

All three 'modes' of behaviour only exist in temporal periods greater than one decade; therefore the observed behaviour during the 20 year period will be concentrated on here. The results from both methods show similar spatial behaviour. (Figure 6.) However, the sddc method does give a greater proportion of profiles which do not close; as sddc depends on a self-selecting non-zero tail, it was hard to extract exact values of the re-opening zone and middle/lower shoreface closure using this method. A fixed non-zero tail could overcome this problem and may be used in subsequent analysis.

Shoreward closure

It is apparent in Figure 6 (a) and (b), that two distinct alongshore regions exist. The first is in the north (Noord-Holland), and can be sub-divided into two; km 16 to 24 and 25 to 54 where Dc_s is quite deep ($\bar{x}$ = 8.5 m) and irratic. In the south (Zuid-Holland), km 55 to 97, a different regime is observed; Dc_s is shallow ($\bar{x}$ = 5.0 m) and relatively

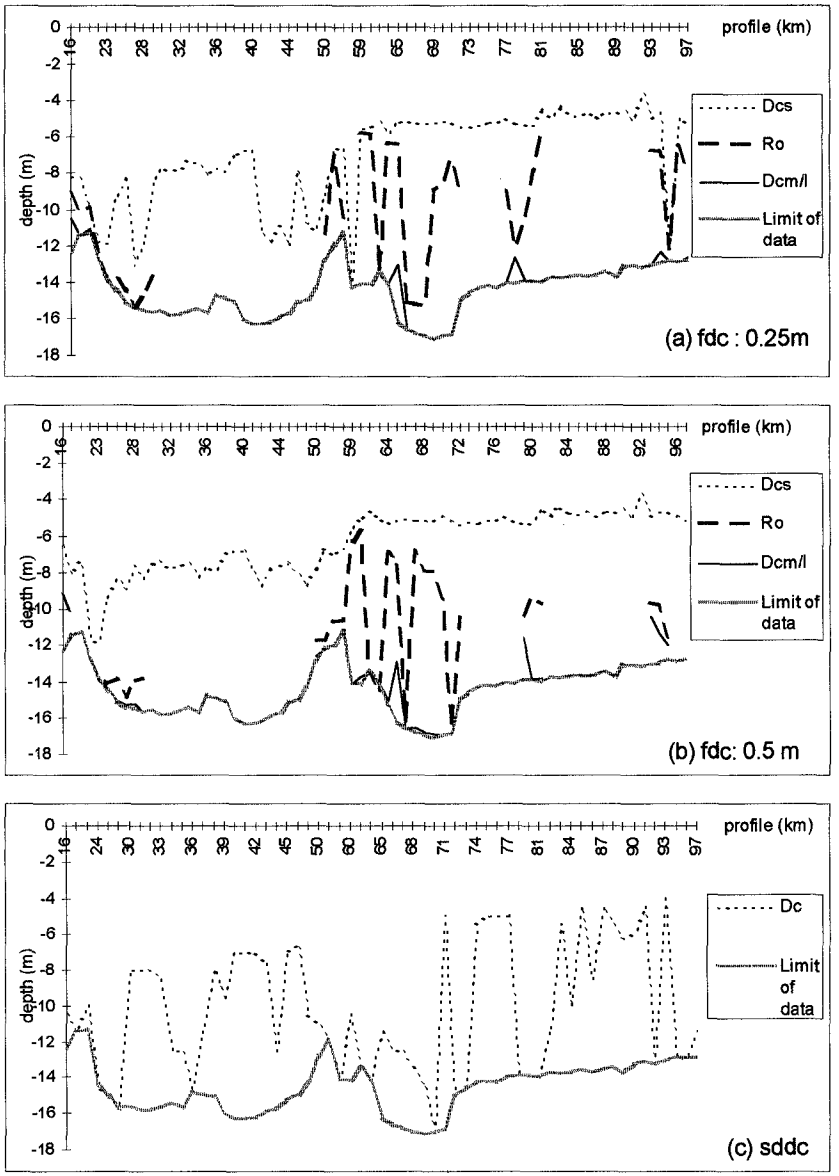

Figure 6. The spatial characteristics of the shoreward closure (Dc_s), re-opening point (Ro) and middle/lower shoreface closure ($Dc_{m/l}$) over 20 years using (a) fdc analysis (criteria 0.25 m); (b) fdc analysis (criteria 0.5 m), and (c) sddc analysis. The seaward limit of the data set is also shown.

constant in depth. (Table 1.) Interestingly, the regions observed here are bound by the two major anthropogenic influences on this coast; the Petten sea dike (km 20 - 26)and Ijmuiden harbour moles (km 55/56).

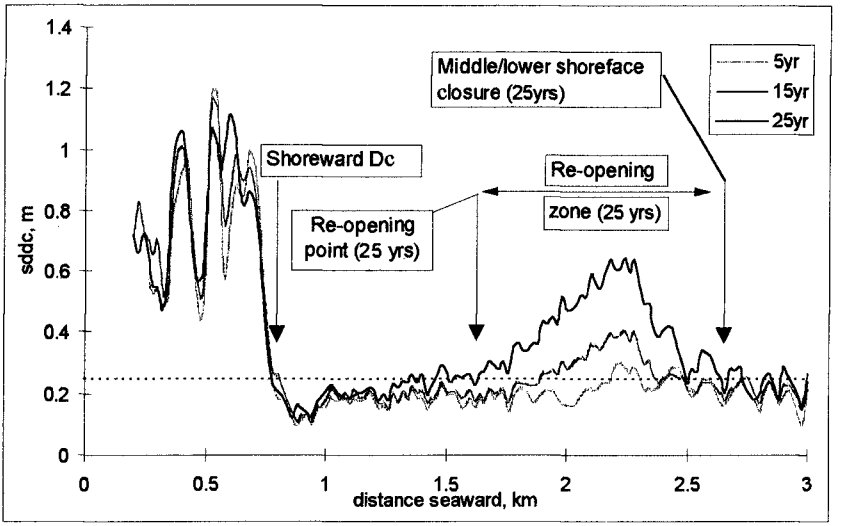

Figure 5. Sddc at km 69 which exhibits re-opening and subsequent closure for time periods of 15 and 25 years.

REGION	MEAN DEPTH (m)	STANDARD DEVIATION (m)
1) km 16 - 24	9.2	2.2
2) km 25 -54	7.7	0.6
3) km 55 - 97	5.0	0.3

Table 1. Characteristics of the shoreward closure over 20 years in the 3 regions, as given by the fdc criteria of 0.5 m.

Application of Hallermeier (1978)

The shoreward closure can be compared with a value calculated using Equation 1. The input data is a time series of wave heights and associated periods measured over a five year period at a station offshore from Ijmuiden, in 18 m water depth. Given the alongshore similarity of the wave climate this is a reasonable comparison for all observed Dc_s. The calculated value for this study is 9.2 m (relative to MLW) over a 5 year period (1980 to 1985). (Hydrodynamic data is insufficient at present to allow calculation over a 20 year period.) This predicted value is a limit to the observed value over the same period, and over 20 years (Table 1), and is consistent with the behaviour observed in earlier studies and Marsh *et al* (1998).

Re-opening and middle/lower shoreface closure

The re-opening zone represents a 'significant' depth change on the shoreface, as defined by the criteria selected. This behaviour is typically followed in the cross-shore by middle/lower shoreface closure. Those instances in which it does not re-close may result from data limitations. It is hypothesised that if the measurements were extended in the seaward direction then re-closure would be observed.

Re-opening does not occur along the whole of the Holland coast. (Figure 6.) It occurs in four alongshore zones defined in Table 2.

RE-OPENING ZONES	MEAN DEPTH (m)	STANDARD DEVIATION (m)
1) km 16 -29	13.0	1.9
2) km 47 - 72	10.3	3.4
3) km 77 - 81	9.8	0.5
4) km 91 - 92	10.0	1.1

Table 2. Characteristics of the re-opening point by longshore zone, over 20 years, as given by the fdc analysis (using a 0.5 m criterion).

Discussion

General

This data has shown a shoreward closure in 5 m to 8 m depth similar to that observed at other sites such as Duck, North Carolina (Nicholls *et al*, 1996, 1998). As the time scale increases it has also shown *significant* profile changes seaward of this shoreward closure.

Shoreward closure

Dc_s appears to be primarily a function of sediment movement under extreme breaking waves (cf. Nicholls *et al*, 1996). Comparison of closure predicted with Equation 1 and that observed on the Holland coast suggests that this is also true here. These preliminary calculations show that Hallermeier (1978) can be used as a predictive tool for the seaward *limit* of Dc_s along the Holland coast. Similar results have also been observed in past studies; at Terschelling, The Netherlands (Marsh *et al*, 1998) and Duck, North Carolina (Nicholls *et al*, 1996, 1998). Interestingly, Dc_s does not appear to increase with time scale as rapidly as Equation 1 would suggest.

Alongshore variation of closure defines two main regions; i) Noord-Holland, which can be further sub-divided into two, and has a mean closure of 8 m; and ii) Zuid-Holland which has a mean closure of 5 m. This indicates that processes, in addition to extreme waves, exist which play a role in the morphological behaviour of the active zone over time scales greater than 5 years. Other factors which have been shown to be of some importance in past studies are i) pre-event outer bar volume (at the Small-Scale); and ii) sediment budget (at the Middle-Scale) (Nicholls and Birkermeier, 1997).

Scale); and ii) sediment budget (at the Middle-Scale) (Nicholls and Birkermeier, 1997). Wijnberg (1995) classified the Holland coast using bar behaviour, defined using eigenfunction analysis which shows both i) the different time scales of active bar behaviour; and ii) the along- and cross-shore migratory behaviour. For the area studied here, three regions of similar behaviour were observed; 1) km 16 - 23; 2) km 24 - 55; and 3) km 57 - 97. These directly correlate with the three regions identified using Dc_s. (Figure 7).

The multiple bars in Holland migrate offshore at different rates and ultimately disappear; the morphological cycle repeats every 15 years in regions 1) and 2) (Noord-Holland) and every 4 years in Zuid-Holland. The degeneration of the outer bar in the Noord-Holland system occurs at a greater depth than in Zuid-Holland. This agrees with the greater closure depths observed in Noord-Holland as compared to Zuid-Holland. It is therefore concluded that shoreward closure is primarily controlled by extreme breaking wave conditions with the bar morphodynamics acting as an additional control, similar observations have been made on the meso-tidal barrier island of Terschelling, The Netherlands (Marsh *et al*, 1998).

Re-opening and middle/lower shoreface closure

This behaviour has not been systematically observed in previous studies. Activity on the shoreface has, however, been recognised in past studies (Stive *et al*, 1990), although the processes which control this behaviour are poorly understood. The occurrence and size of the re-opening zone is seen to be time-dependant; as the time period increases, the extent (both in the cross-shore distance and degree of depth variation) steadily increases. This suggests that this behaviour is due to slow, cumulative change, rather than fast, infrequent events. Indeed, the middle/lower shoreface behaviour has been indicated to be morphodynamically weakly varying (Stive *et al*, 1990). In most cases the re-opening is associated with a local shoreface steepening. Roelvink and Stive (1990) and Stive *et al* (1990) have shown that the significant depth change observed on the shoreface represents the effect of the onshore transport of material to the active zone. The specific location of this phenomena within four zones along the Holland coast may help towards the identification of the controlling processes; at present only tentative correlations between process and response have been made. It is expected that this behaviour will be related to hydrodynamic parameters, as with the shoreward closure. It is hypothesised that it is the asymmetry of shoaling waves which are the primary influence, with an additional forcing introduced by tidal and wind- induced currents, which become more significant in the offshore (Komar, 1976; Stive *et al*, 1990).

In addition the two major anthropogenic structures along the closed coast, the Petten sea dike (km 20 - 26) and Ijmuiden harbour moles (km 55/56), are located in the two largest re-opening zones, km 16 -29 and km 47 - 72 respectively. These can influence offshore behaviour. The Ijmuiden harbour moles, which are 2.5 km in length, have influenced tidal excursion and so accretionary/erosive behaviour for substantial distances, tens of kilometres, from the structure (Roelvink *et al*, 1998). Other morphodynamic controls should be considered. For example, shoreface-connected ridges are present from km 45 - 65 (Van de Meene, 1994); coinciding with the

occurrence of re-opening. These ridges are mapped to minimum depths of 14 m although they may occur further onshore.

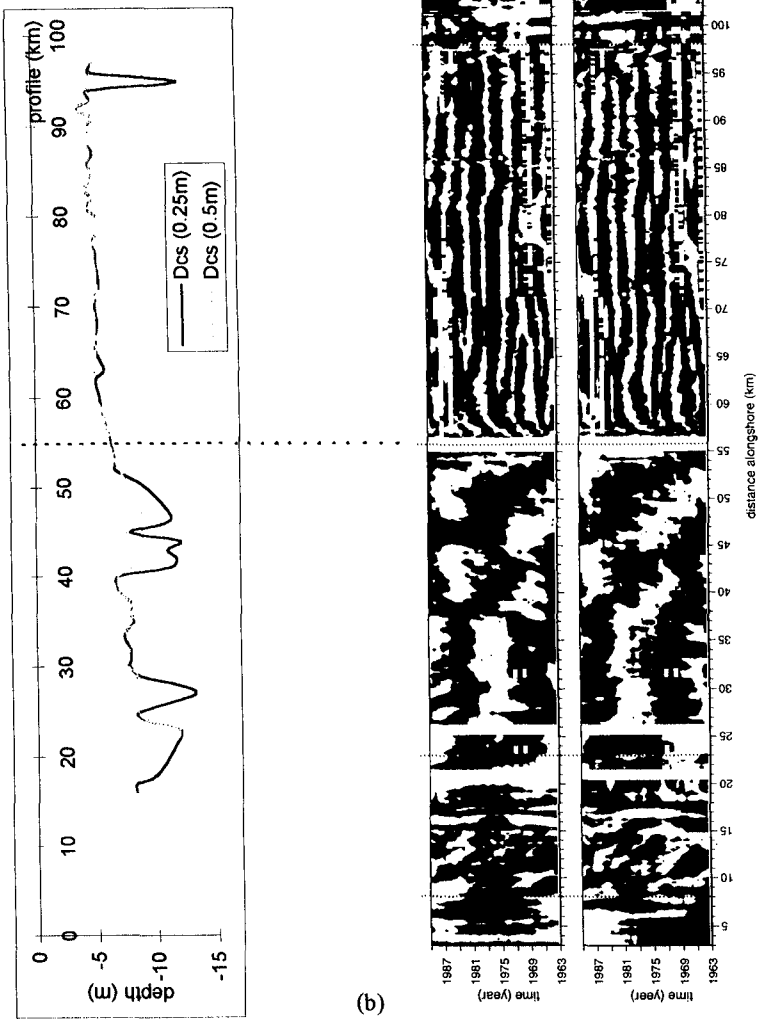

Figure 7. Alongshore correlation between the shoreward depth of closure (a) and bar behaviour (b) (as defined by eigenfunction analysis; Wijnberg, 1995).

Conclusion

The large temporal and spatial extent of the JARKUS data set has enabled Large-Scale closure behaviour to be determined. The profile closes at depths of 5 m to 8m (shoreward closure). In addition, as the time scale increases *significant* profile changes are observed in four alongshore zones seaward of the shoreward closure; re-opening of the profile occurs and is typically followed in the cross-shore by middle/lower shoreface closure. All of the observed characteristics are temporally dependant.

Shoreward closure shows alongshore variation with deeper values observed in the north. It is hypothesised that Dc_s is primarily under the control of wave breaking, as seen by the generalised value given by the Hallermeier (1977, 1981) formulation. An additional control is imposed by bar behaviour (Wijnberg, 1995). Profile re-opening and the subsequent middle/lower shoreface closure is identified in four distinct zones along the closed coast. The possible hydrodynamic, morphodynamic and anthropogenic controls are being investigated.

In addition to the obvious engineering applications of closure, e.g. for the calculation of beach fill volumes, the occurrence of the re-opening zone reminds users that *significant* depth changes can occur seaward of the shoreward closure. It is vital that this is taken into consideration by engineers, especially over decadal and longer time scales.

Acknowledgements

This work was carried out as part of the PACE project, within the EU sponsored Marine Science and Technology programme (MAST-III) under contract number MAS3-CT95-002. The JARKUS data set is collected by Rijkswaterstaat/RIKZ (the Dutch National Institute for Coastal and Marine Management) and made available within the PACE project. The authors would like to thank all those involved in its collection and processing.

References

Capiobianco, M., Larson, M., Nicholls, R.J., and Kraus, N.C., 1997. Depth of closure: A contribution to the reconciliation of theory and practise. Proc.Coastal Dynamics '97. ASCE, New York. pp. 506 - 515.

Davison, A.T., Nicholls, R.J., and Leatherman, S.P., 1992. Beach nourishment as a coastal management tool: An annotated bibliography on developments associated with the artificial nourishment of beaches. Journal of Coastal Research, 8(4), pp. 984-1022.

Garcia, V., Jimenez, J.A., and Sanchez-Arcilla, A., 1997. Temporal and spatial variability of the depth of closure in the Ebro delta. First Annual PACE Workshop, Abstracts-In-Depth, Abstract #1.4, 4pp.

Hallermeier, R.J., 1978. Uses for a calculated limit depth to beach erosion. Proc. 16th Coastal Engineering Conf., ASCE, New York. pp. 1493 - 1512.

Hallermeier, R.J., 1981. A profile zonation for seasonal sand beaches from wave climate. Coastal Engineering, 4, pp. 253-277.

Hands, E.B., and Allison, M.C., 1991. Mound migration in deeper water and methods of categorising active and stable depths. Proc. Coastal Sediments '91, ASCE, New York. pp 1985 - 1999.

Kraus, N.C., and Harikai, S., 1983. Numerical model of shoreline change at Orai beach. Coastal Engineering, 7, pp. 1-28.

Komar, P.D., 1976. Beach processes and sedimentation. Prentice-Hall, Englewood Cliffs, New Jersey, 429pp.

Lee, G., Nicholls, R.J., and Birkemeier, W.A., 1998. Storm-driven variability of the beach- nearshore profile at Duck, North Carolina, USA, 1981 - 1991. Marine Geology, 148, 163 - 177.

Marsh, S.W., Nicholls, R.J., Kroon, A., and Hoekstra, P., 1988. Assessment of depth of closure on a nourished beach: Terschelling, The Netherlands. These proceedings.

Nanninga, M., 1985. The accuracy of echo sounding - description in a mathematical model. Masters Thesis. Rijkswaterstaat, National Institute for Coastal and Marine Management/RIKZ.

Nicholls, R.J., Birkemeier, W.A., and Hallermeier, R.J., 1996. Application of the depth of closure concept. Proc. 25th ICCE, Orlando (USA), ASCE, New York pp. 3874-3887.

Nicholls, R.J., and Birkemeier, W.A., 1997. Morphological and sediment budget controls on depth of closure at Duck, NC. Proc. Coastal Dynamics 1997, ASCE, New York. pp. 496 - 505.

Nicholls, R.J., Birkemeier, W.A., and Lee, G., 1998. Evaluation of depth of closure using data from Duck, NC, USA. Marine Geology, 148, pp. 179-201.

Roelvink, J. A., and Stive, M. J. F., 1990. Sand transport on the shoreface of the Holland coast. Proc. 22nd Coastal Engineering Conf., ASCE, New York. pp. 1909 - 1921.

Roelvink, J.A., Boutmy, A.E.G., and Stam, J-M, T., 1998. A simple method to predict long-term morphological changes using complex model results. These proceedings.

Roskam, A.P., 1988. Golfklimaten voor de Nederlandse kust. Rijkswaterstaat, Nota GWAO-88.046, 21pp. + figures.

Stive, M.J.F., Roelvink, J.A., and De Vriend, H.J., 1990. Large-scale coastal evolution concept. Proc. 22nd Coastal Engineering Conf., ASCE, New York. pp. 1962 - 1974.

Van de Meene, J.W.H., 1994. The shoreface connected ridges along the central Dutch coast; The Netherlands. PhD Thesis, Utrecht University, Department of Geography, The Netherlands. 222pp.

Wijnberg, K.M., 1995. Morphologic behaviour of a barred coast over a period of decades. PhD Thesis; Utrecht University, The Netherlands. 250pp.

Depth of Closure and Seabed Variability Patterns

Grzegorz Różyński, Zbigniew Pruszak, Tomasz Okrój and Ryszard Zeidler[1]

Abstract

A method of analysis of depth of closure and bed variability is presented in the study. Statistical analysis of measurements showed standardized depths are gaussian random variables Repetitive measurements revealed peaked patterns of standard deviation of depth change and range between extreme measurements. They were approximated by a smooth functional type in form of a sum of exponential curves. The peaks were then associated with both the corresponding time scales and locations of bed features. The patterns can thus be used to identify segments of beach profiles controlled by events typical of given time scales The tail of the outermost peak was extrapolated to evaluate decadal depth of closure.

Introduction

Depth of closure (Dc) describes the seaward limit of significant depth change (Hallermeier, 1978, 1981), basing on repetitive records of beach profiles showing that their vertical variability declines with increasing depth. It is therefore a morphological boundary between an active and non-active part of the nearshore zone over the period determined by observations of the profile. For high-quality data Dc is assigned to a point where depth changes beyond that point become small. The position of Dc is a function of several factors. The closure criterion, and the associated time scale are usually regarded as the most important ones, because the former frequently depends on data accuracy, whilst the latter deeply affects Dc *per se;* a fixed closure criterion moves offshore for increasing time scales. Dc can be defined for (i) single events e.g. storms, where surveys before and after the event are examined (ii) time interval change, where bed evolution between two routinely done surveys is investigated, or (iii) time integrated (cumulative) change, where the history of bed evolution can be traced, providing very ample datasets are available. The processes controlling Dc in the current study are associated with quasi-seasonal, annual and decadal time scales, given 10 years of available observations. The site was usually sampled twice a year, which matched the concept of time interval Dc.

Nicholls et al. (1997) investigated Dc upon a high-quality dataset, consisting of 12 years of systematic surveys, taken twice a month and after extreme events, which were collected at Field Res. Facility at Duck, NC, USA. The variability of beach

[1] Snr Res Assoc., Assoc. Prof., Res Assoc. & Prof., resp., Polish Academy of Sciences' Institute of Hydro-Engng IBW PAN Gdańsk, Poland, ph: (+48) 58 552 2011, Fax: (+48) 58 552 4211, e-mail: grzegorz@ibwpan.gda.pl

profiles of that tidal shore (m = 1.5%, D_{50} = 0.2÷0.4 mm) revealed the existence of peaked bed variability patterns. The analysis of a steeper (m = 2%, D_{50}= 1 mm), non-tidal shore of Thyrrenian Sea at Cecina Mare I, cf. Różyński et al. (1998) also detected the existence of at least one peak. Too short records failed to undoubtedly establish the position of 2nd peak and Dc at that site. Since similar patterns were discovered for multibar, mildly sloping shore (m = 1÷1.5%, D_{50} = 0.22 mm) at Coastal Res. Facility (CRF) at Lubiatowo PL as well, the idea of generalized bed variability patterns is proposed in order to establish a universal concept of cross-shore variability.

The Lubiatowo Dataset

CRF Lubiatowo is a wave dominated, non-tidal sandy beach located on Polish coast of the Baltic Sea, some 80 km north-west of Gdańsk. It is a natural, mildly sloping, dune type unit, which usually exhibits 3÷4 longshore bars (Fig.1).

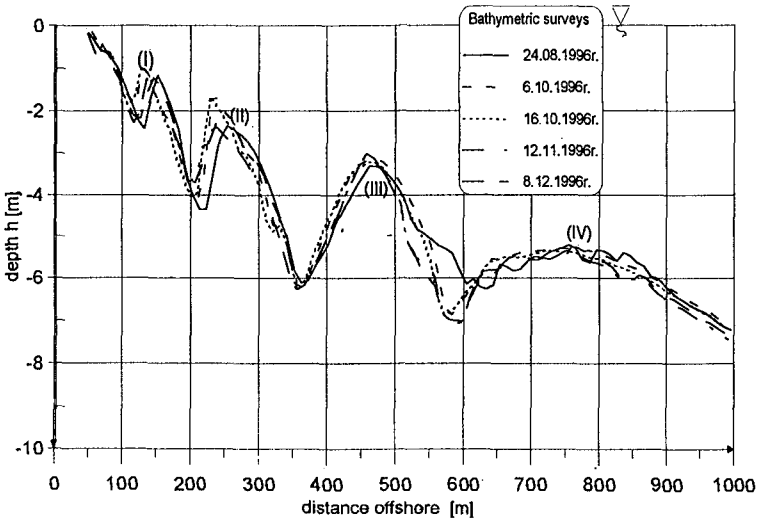

Fig.1 Typical beach profiles at CRF Lubiatowo

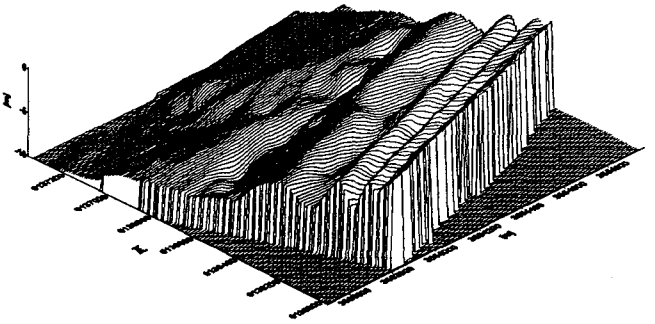

Fig.2 3-D picture of bar system at Lubiatowo in 1997

An ephemeral 5th innermost bar is sometimes observed, bars 1-3 are very stable, clear-cut features. They show little alongshore variability and perform some oscillations about their average positions (Pruszak et. al. 1997, Pruszak &Różyński 1998). The outermost bar is a transitional entity between a typical bar and deep water sediment deposit. It exhibits high alongshore irregularities on its offshore slope (Fig.2), so the determination of Dc needs long surveys, because the irregularities show unexpectedly large variations. For average storms the significant wave height outside the surf zone (h = 7 m) reaches Hs = 2÷2.5 m (3.5 m at the most) with the period T = 5÷7 s. During shoreward transformations the wave height is only 0.5÷1 m and T = 4÷5 s at depths 2÷3 m.

The bathymetric data applied in the analysis consists of surveys done along four neighbouring beach profiles between 1987 and 1996, spaced every 100 m and referred to as profile 4 (westernmost), 5, 6 and 7 (easternmost). All surveys are attached to a geodetic base in order to eliminate errors caused by a moving shoreline. The profiles were sampled with an echosounder, usually twice a year, more or less in the same time of spring and autumn, so quasi-seasonal and annual Dcs could be found. They all extend beyond the crest of the outermost bar, but few are long enough to capture the full, initially unexpected variability of its offshore slope. Only one survey was executed in 1991, 1994 and 1995, the 1991 records were too short for the Dc study and they were skipped. On the other hand, four surveys were done in 1987 and six in 1996, but only two of them for each of those years were selected for the Dc study (cf. Tab.1).

Table 1 Surveys employed in Dc investigations

Sampling date	remarks	Sampling date	remarks	Sampling date	remarks
16th May 1987	+	5th Jun. 1990	+	25th Oct.1995	++
14th Aug. 1987	not used	14th Aug. 1990	++	24th Aug.1996	+
22nd Sep. 1987	++	29th Oct. 1991	skipped	6th Oct.1996	++
15th Oct. 1987	not used	21st May 1992	+	16th Oct. 1996	not used
28th Apr. 1988	+	21st Oct. 1992	++	12th Nov. 1996	not used
5th Oct. 1988	++	20th Jul. 1993	+	26th Nov. 1996	not used
24th May 1989	+	30th Sep. 1993	++	8th Dec. 1996	not used
13th Sep. 1989	++	20th Jun. 1994	++		

(+) - quasi-seasonal time scale, (++) - annual time scale

Quasi-Seasonal and Annual DC

Various criteria yield various estimates of Dc. A standard deviation of depth change (*sddc*) is a widely used criterion, provided the number of surveys **n** sufficiently reduces the scatter of *sddc* value. Its value at closure is usually chosen between 0.06 and 0.15 m. However, equations (1) and (2) indicate the scatter of *sddc* declines very slowly, as the mean value is a random variable itself, and the *sddc* precision is proportional to squared number of observations:

$$\bar{h} = \frac{1}{n}\sum_{i=1}^{i=n} h_i \qquad (1)$$

$$\sigma_h = \sqrt{\frac{1}{n}\sum_{i=1}^{i=n}(h_i - \bar{h})^2} \quad (2)$$

Hence, it is better to apply a criterion which is less dependent on number of observations, such as the range of depth change (*rdc*), which quantifies the scatter between extreme measurements of given sample space. For Dc purposes this criterion was adapted in 'tight' and 'loose' variant i.e. 0.2 m and 0.3 m respectively. These values match well findings based on much more ample datasets (cf. Nicholls et al.,1997), where such *rdc* corresponded to *sddc* of 0.06 to 0.15 m.

Tab.2 presents quasi-seasonal Dcs between spring and autumn surveys (Fig.3). It shows that quasi-seasonal closures do not always occur, so even during summer period of a year the wave climate may be severe enough to produce quite substantial depth changes.

Table 2 Quasi-seasonal Dc [m.]

Year	profile 4		profile 5		profile 6		profile 7	
	0.2 m *rdc*	0.3 m *rdc*	0.2 m. *rdc*	0.3 m. *rdc*	0.2 m. *rdc*	0.3 m. *rdc*	0.2 m. *rdc*	0.3 m. *rdc*
1987	—	—	7.8	7.2	—	—	6.8	6.3
	5.8	5.7	4.7	4.6	5.7	5.7	—	5.5
1988								
1989	—	6.6	—	8.0	—	—	—	8.7
1990	—	8.0	6.3	6.3	5.0	5.0	5.0	5.0
1992	—	—	—	—	—	—	—	—
1993	—	5.7	—	7.3	5.2	5.2	—	—
1996	—	7.8	—	7.2	10.7	6.5	10.5	8.0

(—); non closing cases

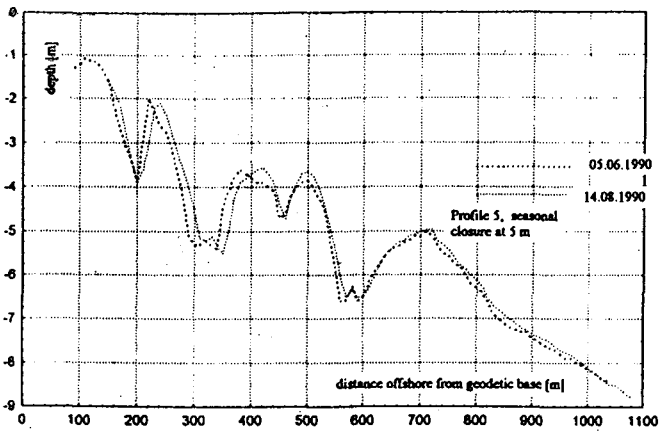

Fig.3 Exemplary quasi-seasonal closure

In most cases Dcs for loose criterion could be found on offshore slope of the outermost bar. However, their estimates for even neighbouring profiles vary to unexpected extent, e.g. profiles 4 and 5 in 1989 with Dc being equal to 6.6 m vs. 8.0 m respectively, or the same lines a year later, where Dc values are nearly ideally reversed (8.0 m vs. 6.3 m).

This indicates that local effects at offshore part of the outermost bar may play very important role in evolution of that part of the littoral zone even during apparently calm periods between late spring and early fall. This can be supported by routinely observed intermittent breaker patterns in the vicinity of 4th bar during stormy events, which profoundly influences local bed changes. For example the bed was so active in 1992 that no Dc could be found whatsoever. Consequently, high bed activity allowed for only few estimates of Dc for tight criterion. Tab.2 gives an overview of quasi-seasonal Dc as a random variable. It varies widely from 4.7 m to 10.7 m for tight, and from 4.6 m. to 8.7 m for loose criterion.

The only closing cases of annual Dc were obtained for autumn surveys of pairs 1989-90 (Fig.4) and 1995-96. These closures are rather shallow and valid for both tight and loose criteria, indicating rapid profile convergence. All this suggests a mild wave climate in winter seasons of those years.

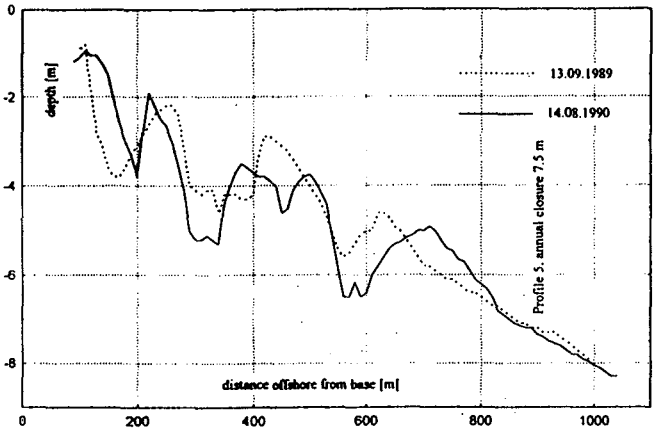

Fig.4 Exemplary annual closure

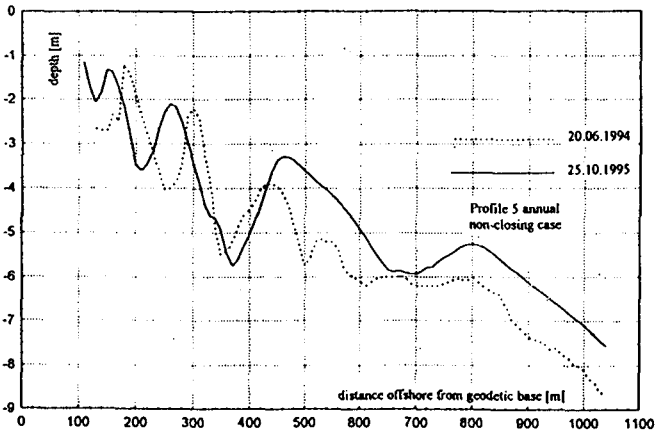

Fig.5 Exemplary annual non-closing case

By contrast, huge divergence of 1992-93, 1993-94 and 1994-95 (Fig.5) profiles over deeper portions of littoral zone proves high wave action intensity. The closing cases show much lower variability of Dc at various profiles i.e. for 1989-90 it is equal to **5.5 m** for profile 4 and **7 to 7.5 m** for the other three. The 1995-96 is even more stable and equals **6 m** for profiles 5,6,7 and **5.5 m** for profile 4. Such a result suggests that local effects, clearly visible in quasi-seasonal closures, were averaged to some extent over annual periods. The estimated values provide information on lower limit of annual Dc, which is greater than most annual Dcs Nicholls detected in Duck between 1982 and 1993. Therefore, greater average annual Dcs should be expected, which can be explained by extending further offshore, more complex multibar system at Lubiatowo, than basically 2 bar shore at Duck.

General Statistical Properties of Beach Profiles

The surveys employed in the study extend 1000 m offshore with some exceptions, where the depths were recorded up to 1400m. This prevents direct, empirical assessment of decadal Dc. However, it still can be evaluated, if the existing records of offshore slope of the outermost bar share the same general statistical properties. To verify this, depths corresponding to offshore distances of 800, 850, 900, 950, 1000, 1050 and 1100 m from geodetic base were lumped together ignoring individual profiles. This could be done, because the geodetic base forms a straight line and is parallel to the shoreline, so offshore distances are generally retained. A family of standardized probability distribution functions was then constructed and plotted together with a normal pdf, (Fig.6).

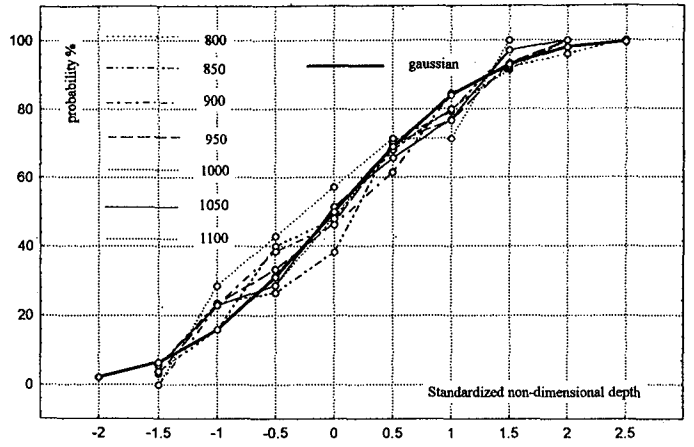

Fig. 6 Standardized empirical pdfs of depths 800-1100 m offshore vs gaussian

It can clearly be seen that the distributions do not depart much from normal pdf. What is more important those departures seem to be normal themselves, i.e. some of them are positive and other negative at a given point with respect to gaussian curve. Thus, no systematic behaviour of pdfs can be detected, so it may be assumed they are all gaussian and share the same general statistical properties, although mean depths and their standard deviations vary with distance offshore. This finding implies that depth changes are caused by independently acting factors, (wave height and direction, duration of a

given wave climate, storms, breaker locations, longshore and cross-shore currents, bed configuration at a given time, etc.) It may thus be inferred that similar general statistical characteristics are retained further offshore, so the seabed variability pattern(s) can be analytically extrapolated.

The same pdf analysis was carried out for less remote depths 300 - 600 m. offshore. It shows that also this part of beach profiles is generally gaussian (Fig.7). This finding is very interesting, because statistical normality of beach profiles allows for 2nd moment analysis with loss of no information. In other words mean depths and their covariance structure contain all probabilistic information on beach profile evolution.

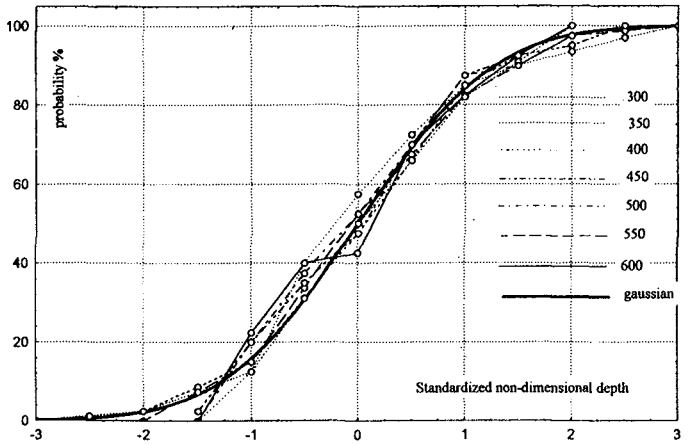

Fig.7 Standardized empirical pdfs of depths 300-600 m offshore vs. gaussian

Generalized Seabed Variability Patterns

As already mentioned, peaked patterns of cross-shore variability have been observed at several sites (Duck, Cecina Mare, Lubiatowo). Hence, a generalized bed variability pattern may be postulated, which can be adapted for different shores in analytical form of a smooth functional type to properly reproduce the peaks on the lines of standard deviations and/or ranges. Upon numerical experiments, the sum of exponentially decaying curves was selected, because this functional type fits best the line of standard deviations $\sigma(x)$ or ranges r(x):

$$\sigma(x) \text{ or } r(x) = \sum_i a_i \cdot \exp[-b_i((x-p_i)/p_i)^2] \qquad (3)$$

To illustrate the concept, the two peak *sddc* pattern for Lubiatowo was obtained for truncated surveys taken from 1964 until 1994. Even though these records are attached to a movable shoreline and lumped together, the pattern is still clearly visible (Fig.8).

In Eq.3 p_i denotes the position of *i*-th peak on the profile, read from the line of standard deviations or ranges, the coefficients a_i and b_i need to be least square fitted. The peak positions can be associated with phenomena that occur in different time scales, the greater p_i the longer the corresponding time scale. They may also be linked to characteristic profile features, such as bar crest, location of trough, etc. The bed

variability pattern can thus be used in order to identify segments of beach profiles controlled by events typical of given time scales, which can be done for each pair of a_i

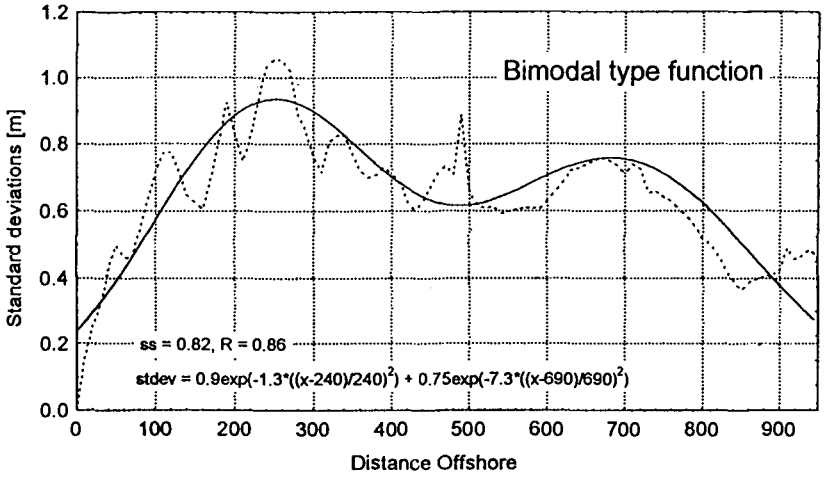

Fig.8 Peaked sddc pattern 1964-1994, lines attached to movable shoreline

and b_i. At locations sufficiently remote from the peak, the influence of that peak becomes negligible and it can be assumed the events associated with it no longer affect a beach profile at that location. Hence, such an analysis of the outermost available peak may determine the Dc associated with its time scale. In case when surveys do not reach the spot, where the tail of the outermost peak is sufficiently small, bearing in mind common general statistical properties of depths, the tail is extrapolated beyond the longest surveys and the bed equilibrium curve is employed:

$$h = A \cdot x^{2/3} \tag{4}$$

The average value of A for the 1987-1996 period is equal to 0.084. The peak line of *sddc* or *rdc* Eq.3 converges towards the bed equilibrium curve Eq.4 and Dc associated with the outermost peak can be evaluated. Fig.9 shows raw *rdc* lines of 4th, 5th, 6th and 7th profile together with the line of average *rdc*. Two clear-cut peaks, the greater one some 300 m and the smaller one at 580 m from geodetic base can be distinguished immediately. Interestingly, the inner one ideally corresponds to the position of 2nd bar crest, while the outer one perfectly matches the position of trough between 3rd and 4th bar (Figs.10a-d). They are both concentrated over small portions of beach profiles, which is a direct consequence of their link to very stable cross-shore locations of two morphological bed features. The 3rd peak is also visible, although it is very long and flat. It should not be surprising, because it matches the location of offshore slope of the outermost bar, which is very long and sometimes merges with sediment deposits further offshore. Since bed evolution of that part of the littoral zone is controlled by extreme storms, it should be expected that bed variability generating the outermost peak is spatially distributed. Its character is thus different from inner peaks, which are associated with firmly stable cross-shore bed features (crest of 2nd bar and trough between 3rd and 4th bar). Upon thorough scrutiny and the goodness of fit criterion, its

position was established at 1200 m from geodetic base, knowing that more long surveys will yield a better estimate.

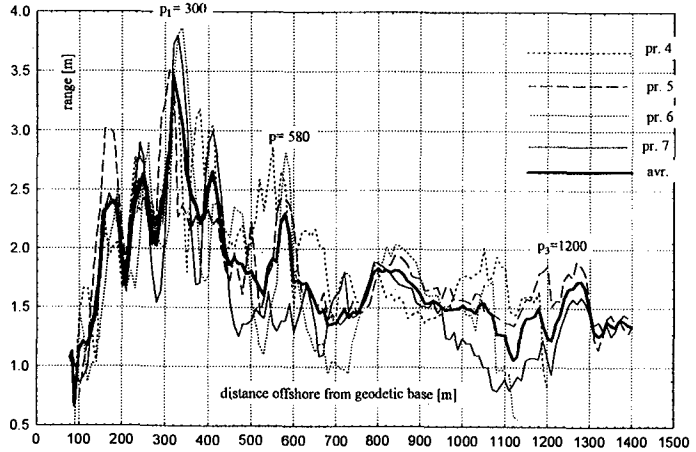

Fig.9 Rdc for profiles 4-7 with average rdc

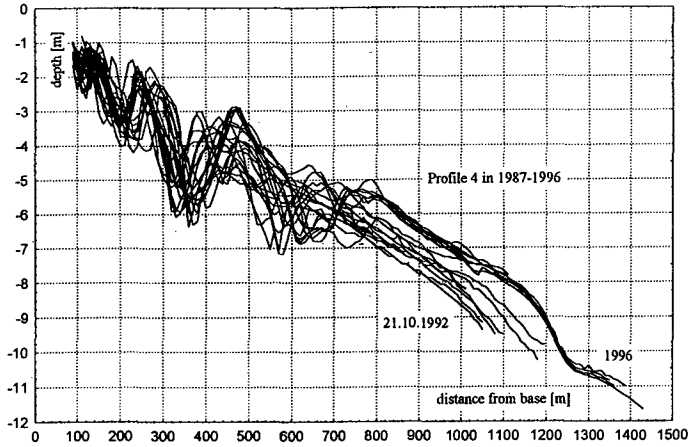

Fig.10a Collective chart of surveys for profile 4 between 1987-1996

The fit for mean ranges produced quite a peculiar result; a three peak model was assumed but the combination of 2nd and 3rd one resulted in a plateau between them (Fig.11). It slowly declines with distance offshore, so the decadal Dc can be evaluated by extrapolating the fitted line out of the existing surveys, cf. fitted functional type, Eq.5.

$$rdc(x) = 1.4 \cdot \exp[-1.8 \cdot (\tfrac{x-300}{300})^2] + 0.5 \cdot \exp[-1.4(\tfrac{x-580}{580})^2] + 1.3 \cdot \exp[-(\tfrac{x-1200}{1200})^2] \quad (5)$$

The fit of Eq.5 is very accurate, given $R = 0.85$ correlation between the model and data. Other attempts, aiming to retain the vivid 2nd peak produced results with worse goodness of fit, so they were skipped. Employing the bed equilibrium curve, a Dc could be found for both 'tight' and 'loose' *rdc* criteria. For a 'tight' variant it lies some **2800 m** offshore and equals **17 m** vs. **2600 m** offshore and **16 m** obtained for its 'loose' counterpart. This estimate appears to be realistic, given extreme ranges recorded 1300 m offshore for profile 7 and 1400 m for profile 5, where the greatest depth of **12.5 m** was recorded. By contrast, the longest survey, reaching 1500 m in 1988 for profile 7, revealed the depth of only **11m**. Knowing such high irregularities of offshore slope of 4th bar and the tendency to merge with sediment deposits further offshore, it can be believed that the decadal Dc should lie much further offshore, and be quite great itself, as the extrapolation of bed patterns indicates.

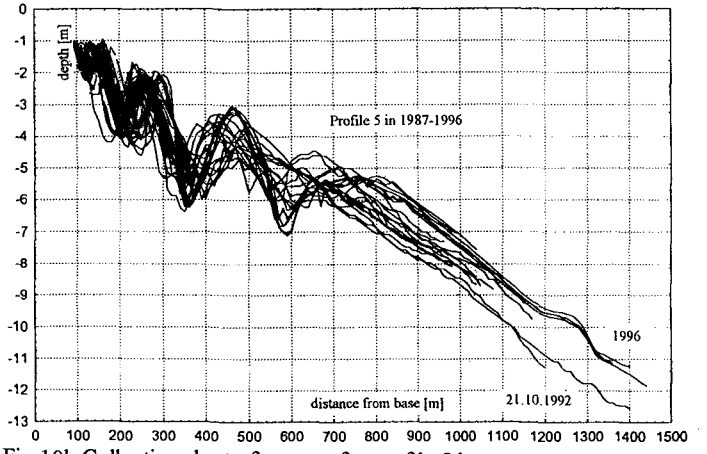

Fig.10b Collective chart of surveys for profile 5 between 1987-1996

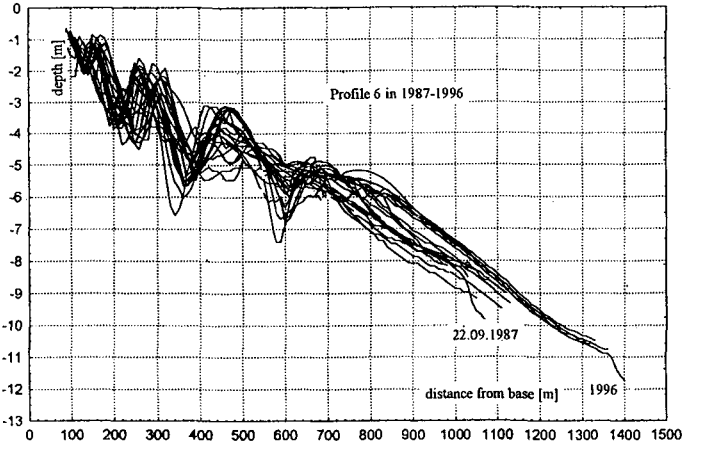

Fig.10c Collective chart of surveys for profile 6 between 1987-1996

evaluated, even though general statistical properties of depth between 300 and 600 m offshore are also gaussian. This however is not enough to assign a particular time scale to the innermost peak. The application of a tight *rdc* criterion shows that its tail practically disappears 600 m from geodetic base, corresponding to shallow Dc of 5.7 m. This value is equal to the most shallow quasi-seasonal Dc, which clearly indicates that the innermost peak is in general governed by a shorter time scale. It could only be detected if the bed was sampled more than twice a year.

Annual DC and Hallermeier Formula

Dc can also be calculated from extreme (deep water) wave conditions. Such computations can be done for different types of shores (tidal, non-tidal, one bar, multi-bar, etc.). In cases the Dc was established upon the analysis of bathymetric profiles, the approach basing on wave climate can be directly verified for a given shore type. Hallermeier, 1978, 1981 postulated that annual Dc can be assessed from the formula:

$$Dc = 2.28 \cdot H_s - 68.5 H_s^2 / g \cdot T^2 \qquad (6)$$

where H_s stands for significant, non-breaking wave height that is exceeded 12 hours in a year, T is the corresponding period and g is gravitational acceleration. The application of Hallermeier's formula needs long-term deep water wave measurements. In case they are not available, wave parameters can be hindcast from existing wind records. Wind measurements were carried out between 1960 and 1986 at Hel Harbour, situated some 50 km east of Lubiatowo and they are deemed representative for Lubiatowo. Only wave heights were hindcast, but knowing that the 2nd term in Eq.6 is usually close to unity, one may crudely assess annual Dc as $2.28 \cdot H_s - 1$. Wave height hindcasts were calculated upon wind samples, which were obtained every three hours as averages of 10 minutes time window, from 1st Jan. 1960 until 31st Dec. 1986. Bathymetric data and reconstructed wave heights do not overlap in time, so it is not possible to directly compare the results from the same years. Moreover, eight daily records appear to be too crude to extract wave heights lasting 12 hours a year. Therefore, annual Hallermeier Dc estimates could only be found for a small subset of years, cf. Tab.3.

Table 3 Hallermeier estimates of annual Dc

Year	H_12 [m.]	Dc [m.]
1960	3.88	8
1963	> 5.59	> 11.7
1968	< 5.59	< 11.7
1981	> 5.59	> 11.7
1984	3.5	7
1985	4.64	9.6

The value of 7 m for 1984 and equally shallow empirical annual Dcs for 1989-90 and 1995-96 show that shallow annual Dcs are not uncommon and may occur quite frequently. On the other hand, two cases where 12 hour wave could be identified (1963, 1968) indicate that more severe wave climate produces realistic, deeper Dc. Hence, Hallermeier's criterion seems to provide a reliable assessment of annual Dc for multibar shore at Lubiatowo, which a bit contradicts Nicholls'es view, based on Duck study, that it is biased towards conservative bound of annual closures. It may be justified by high

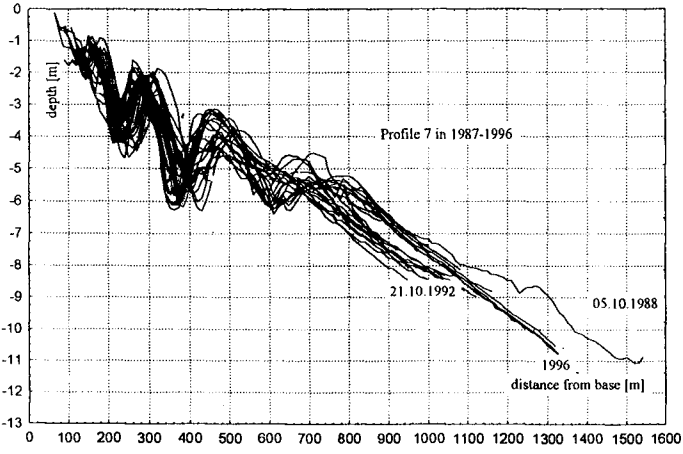

Fig.10d Collective chart of surveys for profile 7 between 1987-1996

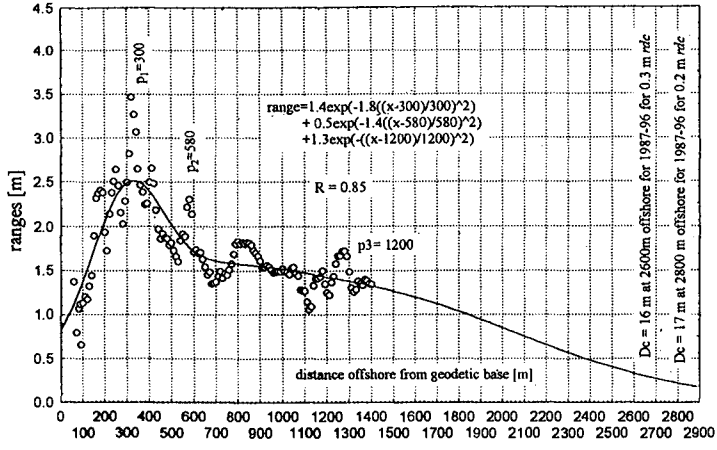

Fig.11 Generalized 3-peak seabed variability pattern for Lubiatowo

As mentioned before, each peak corresponds to a certain time scale and spatial distribution of the 3rd peak implies it accounts for longer periods, such as decades. The time scale of the 2nd peak can be found upon the following reasoning: if we skip the 3rd peak and apply either tight or loose *rdc* criterion, we arrive at h = 8.4 or 7.7 m respectively, calculated from Eq.4 for 1000 and 880 m offshore. General statistical properties of depths are the same, so it may be assumed that Dc associated with 2nd peak is equal to some **8 m**. This value defines a boundary for time scale, which in light of tab.2 corresponds to quasi-seasonal variability. Hence, the 2nd peak is generated by quasi-seasonal events. The time scale of the most conspicuous 1st peak cannot be

complexity of bar system at Lubiatowo with highly irregular offshore slope of the outermost bar vs. fairly regular, basically two bar shore at Duck.

Conclusions

1. The analysed beach profiles are gaussian all over their cross-shore range, so their covariance structure contains the whole statistical information. The profiles at other sites are likely to exhibit similar behaviour.
2. Repetitive measurements reveal the existence of peaked profiles of *rdc* and *sddc*. The peaks can be associated with relevant time scales generating them and can be analytically expressed by least square fitted sum of exponential functions. *Sddc* lines yield better description of profile variability, provided sufficient number of samples (50+) is available. *Rdc* lines need less samples to map profile variation, so they are handy in remote parts of beach profiles, where samples are usually scarce.
3. Statistical normality of beach profiles and their peak features permit to split beach profiles into segments associated with time scales of peaks.
4. Inner peaks correspond to locations of spatially concentrated bed features i.e. position of bar crest for the innermost peak and trough between two bars for the middle peak. The outermost peak corresponds to spatially distributed offshore slope of the outermost bar.
5. Temporal resolution of measurements prevents the evaluation of the time scale of the most conspicuous, innermost peak, so more frequent sampling would be needed to remedy this. The middle peak was identified as being driven by quasi-seasonal phenomena. The outermost peak is generated by much longer time scales of a decade or so, which is supported by its spatial distribution. Such distribution is characteristic for extreme events, where the whole profile, including its deeper parts, undergoes substantial evolution.
6. All detected Dcs that are situated outside the crest of the outermost bar, either on its offshore slope or on sediment deposits situated further offshore. Quasi-seasonal Dcs are equal to 5÷10 m and exhibit significant alongshore variation, which shows the importance of local effects in short time scales. Only few annual Dcs were found between 5.5 and 7 m, and they seem to represent upper bound of annual Dcs. Alongshore variation, although visible, is much less pronounced than for quasi-seasonal cases. It is not surprising, because longer time scales average local effects. Longer surveys up to 1500 m offshore are recommended to establish a set of empirically determined annual Dcs, if gentle nearshore slopes with multi-bar profiles, similar to CRF Lubiatowo are examined.
7. Very high bed irregularity outside the crest of the outermost bar results in high estimate of decadal Dc (16÷17 m), obtained from extrapolation of the outermost peak. The verification of this value would require very long surveys (3 km offshore) taken at least once a year over decades. Before this is done, an extrapolation based on the same general statistical profile properties, provides an unverified, yet based on realistic assumptions, assessment of decadal Dcs.
8. Hallermeier's formula for annual Dc seems to work well for the case of multibar shore with very irregular offshore slope of the most seaward bar.

References

Hallermeier R.J.,(1978) Uses for a calculated limit depth of beach erosion. *Proc. 16th Coastal Engineering Conference, ASCE, 1493-1512.*

Hallermeier R.J.,(1981) A profile zonation for seasonal sand beaches from wave climate. *Coastal Engineering, 4, 253-277.*

Nicholls R.J., Birkemeier W.A., Hallermeier R.J.,(1997) Application of the depth of closure concept. *Proc. 25th Coastal Engineering Conference, ASCE, 3874-3887.*

Pruszak Z., Różyński G., Zeidler R.B., (1997) Statistical properties of multiple bars, *Coastal Engineering 31, 263-280.*

Pruszak Z., Różyński G. (1998) *Variability of multibar profiles in terms of random sine functions. Journal of Waterway, Port, coastal and Ocean Engineering, ASCE, Vol.124, No.2, 48-56.*

Różyński G., Pruszak Z., Aminti P.,(1998) Dynamics of one bar and multibar beach profiles. *Proc 3rd Coastal Dynamics Conference, ASCE 325-336.*

Acknowledgements

This study has been based on work in the PACE project, in the framework of the EU-sponsored Marine Science and Technology Programme (MAST III), under contract MAS3-CT95-0002. The study was co-sponsored by the PAN Supported Programme IBW 2-1998

2DH NON-LINEAR DISPERSIVE WAVE MODELLING AND SEDIMENT TRANSPORT IN THE NEARSHORE ZONE

Theofanis V. Karambas[1]

Abstract

A 2D-horizontal sediment transport energetics model is developed in this work for the evaluation of the wave-induced sediment transport. The time dependent energy equation is incorporated into a nonlinear dispersive wave model in order to simulate breaking wave propagation in the surf zone. Total immersed weight transport is related, through an energetics approach, to the total dissipated fluid power. Both the dissipation due to bed friction and, inside the surf zone, due to the wave breaking are considered. The methodology is applied to predict the longshore transport rate and to simulate the coastline evolution in beach nourishment scenario assuming a trapezoidal beachfill.

Introduction

Long-shore and cross-shore sediment transport due to wave action play an important role in various engineering problems. One of the most important problems is the wave and the wave-induced sediment transport effects on coastal environment in terms of the bed morphology changes.

There exist two main approaches for the estimation of the sediment transport rate inside and outside surf zone: the deterministic and the energetics. The deterministic models are based on the description of both the wave induced mean flow and the concentration of suspended sediment, usually using quasi 3D models and linear wave theory (deVried and Stive 1987, Katopodi and Ribberink 1992, Briad and Kamphuis 1993). The energetics approach is based on the idea that the sediment transport is related to the rate of energy dissipation of the flow (Bailard 1981, Roelvink and Stive 1989). In the present work the second approach is adopted.

[1]Division of Hydraulics and Environmental Engineering, Department of Civil Engineering, Aristotle University of Thessaloniki, Thessaloniki, 54006, GREECE.
E-mail: karambas@civil.auth.gr

A 2DH non-linear breaking wave model is developed based on the numerical solution of the time dependent wave energy equation which is incorporated into a Boussinesq model. The main advantages of the use of the Boussinesq type of equations are outlined below:

- A unified model, without the assumption of progressive waves, is used for non- linear wave refraction, shoaling, diffraction, reflection (presence of structures), breaking, dissipation after breaking, run-up.
- The equations are easily extended in deeper waters
- The propagation of irregular waves is modelled including LFW and non-linear wave-wave interactions.
- Breaking wave induced current are automatically incorporated. Thus there is no need for additional current and sediment transport model (i.e. coupling of 3 models).
- 3D effects (inclusion of a 'mean' undertow) are present.
- The models can be extended for the simulation of sediment transport in swash zone.

For the evaluation of the sediment transport rate (i.e. bed load and suspended load) the Bailard (1981) theory is used as in the 1D version of the model (Karambas et al. 1995). Following the sediment transport calculations, the morphological changes of the sea bed are updated in the model according to the conservation equation of sediment mass.

2DH non-linear wave breaking wave model

Karambas (1996) incorporated the time dependent energy equation into a nonlinear wave model based on the Boussinesq equations in order to simulate breaking wave propagation in the surf zone. Extending the analysis in two dimensions the continuity and the momentum equations are written (Peregrine 1972, Madsen and Svendsen 1979):

$$\frac{\partial \zeta}{\partial t}+\frac{\partial (Uh)}{\partial x}+\frac{\partial (Vh)}{\partial y}=0$$

$$\frac{\partial (Uh)}{\partial t}+\frac{\partial \left(\int_{-d}^{\zeta} u^2 dz\right)}{\partial x}+\frac{\partial \left(\int_{-d}^{\zeta} uv dz\right)}{\partial y}+gh\frac{\partial \zeta}{\partial x}=\frac{d^2}{2}\frac{\partial^3 (Ud)}{\partial x^2 \partial t}-\frac{d^3}{6}\frac{\partial^3 U}{\partial x^2 \partial t}+$$
$$\frac{d^2}{2}\frac{\partial^3 (Vd)}{\partial x \partial y \partial t}-\frac{d^3}{6}\frac{\partial^3 V}{\partial x \partial y \partial t}+\frac{\partial}{\partial x}\left(\nu_\tau h\frac{\partial U}{\partial x}\right)+\frac{\partial}{\partial y}\left(\nu_\tau h\frac{\partial U}{\partial y}\right)-\frac{\tau_{bx}}{\rho}$$

$$\frac{\partial(Vh)}{\partial t}+\frac{\partial\left(\int_{-d}^{\zeta}uvdz\right)}{\partial x}+\frac{\partial\left(\int_{-d}^{\zeta}v^2dz\right)}{\partial y}+gh\frac{\partial\zeta}{\partial y}=\frac{d^2}{2}\frac{\partial^3(Vd)}{\partial y^2\partial t}-\frac{d^3}{6}\frac{\partial^3V}{\partial y^2\partial t}+$$
$$\frac{d^2}{2}\frac{\partial^3(Ud)}{\partial x\partial y\partial t}-\frac{d^3}{6}\frac{\partial^3U}{\partial x\partial y\partial t}+\frac{\partial}{\partial x}\left(\nu_\tau h\frac{\partial V}{\partial x}\right)+\frac{\partial}{\partial y}\left(\nu_\tau h\frac{\partial V}{\partial y}\right)-\frac{\tau_{by}}{\rho} \quad (1)$$

in which ζ is the surface elevation, d is the still water depth, h is the total depth, u and v are the horizontal velocity components in the x and y directions respectively, U and V are the depth integrated velocities, ν_τ is the eddy viscosity coefficient and τ_{bx}, τ_{by} are the bottom shear stresses.

The shear stresses are estimated from:

$$\frac{\tau_{bx}}{\rho}=\frac{f_w}{2}u_o\sqrt{u_o^2+v_o^2}$$

$$\frac{\tau_{by}}{\rho}=\frac{f_w}{2}v_o\sqrt{u_o^2+v_o^2} \quad (2)$$

where u_o, v_o are the components of the bottom velocity (adopting the velocity distribution given by Peregrine, 1972) and f_w a friction factor (Nairn and Southgate 1993):

$$f_w=\exp(5.2\,(r/\alpha)^{0.2}-6.0) \quad (3)$$

in which α is the orbital amplitude at the bed and r is the bottom roughness:

$$r=170\sqrt{\theta_{2.5}-0.05}\,D_{50} \quad (4)$$

where $\theta_{2.5}$ is the Shields parameter for $f_{2.5}=\exp(5.2\,(2.5D_{50}/\alpha)^{0.2}-6.0)$.

The equation of the conservation of the energy density E of the mean flow per unit horizontal area is written:

$$\frac{\partial E}{\partial t}+\frac{\partial E_{fx}}{\partial x}+\frac{\partial E_{fy}}{\partial y}=-D-u_o\tau_{bx}-v_o\tau_{by}+U\,BT+V\,BT \quad (5)$$

$$E_{fx}=\int_{-d}^{\zeta}\frac{1}{2}u^3dz+\int_{-d}^{\zeta}\frac{1}{2}uv^2dz+g\zeta Uh\,,$$

$$E_{fy}=\int_{-d}^{\zeta}\frac{1}{2}v^3dz+\int_{-d}^{\zeta}\frac{1}{2}u^2vdz+g\zeta Vh$$

in which D is the dissipation of the mean energy (equal to minus the production of turbulent energy) and BT are the Boussinesq dispersion terms of the momentum equations (1).

The dissipation of the wave energy D is given by (Karambas, 1996):

$$D = \Omega \ (c-u_{ot})^3 \tag{7}$$

in which c is the wave celerity, $u_{ot} = \sqrt{u_o^2 + v_o^2}$ is the bottom velocity in the direction of the wave propagation and Ω a constant, Ω=0.03.

The eddy viscosity coefficient v_τ is calculated from the solution of the turbulent kinetic energy equation (Nwogu, 1996):

$$\partial k/\partial t + \mathbf{U}\nabla k = v_\tau \nabla^2 k + B\, D - C_d k^{3/2}/ l_t \tag{8}$$

in which $\mathbf{U}$=(U,V), k is the turbulent kinetic energy, C_d=0.08, and l_t is the turbulent length scale, l_t=0.15 d.

In the 1D case (Karambas, 1996) the constant Ω is equal to 0.015. In the present work a greater value (Ω=0.03) is adopted. This value (according to Morfett, 1995) is claimed to give a good fit to measured longshore transport rate. To compensate the increase of the value of Ω, the turbulent length scale l_t is taken equal to l_t =0.15 d, instead of l_t =0.3 d which has been adopted in the 1D case.

The rate of production of turbulent kinetic energy is taken equal to the dissipation D of the wave energy (equation 7). The parameter B (Nwogu, 1996) is introduced to ensure that turbulence is produced only when horizontal velocity at the wave crest u_{st} exceeds the celerity c.

$$B = \begin{cases} 0 & \text{in the region where } u_{st} < c \\ 1 & \text{in the region where } u_{st} > c \end{cases}$$

where u_{st}, is the velocity at the wave crest, $u_{st} = \sqrt{u_s^2 + v_s^2}$, and u_s and v_s are its components from Boussinesq theory (Peregrine, 1972).

The eddy viscosity is given by:

$$v_\tau = k^{1/2} l_t \tag{9}$$

The two integrals in the equations (1) are estimated form (Karambas 1996):

$$\int_{-d}^{\zeta} \frac{1}{2} u^2 dz = E - \int_{-d}^{\zeta} \frac{1}{2} v^2 dz - \frac{1}{2} g\zeta^2$$

$$\int_{-d}^{\zeta}\frac{1}{2}v^2dz = E - \int_{-d}^{\zeta}\frac{1}{2}u^2dz - \frac{1}{2}g\zeta^2 \qquad (10)$$

The integrals in equations (1) and (6), containing the terms u^3, v^3, uv, u^2v, uv^2, are estimated numerically adopting the following horizontal velocity distribution in the turbulent region of a breaking wave (Karambas 1996):

$$u(z)=u_o+u_d\, f(\sigma)$$

$$v(z)=v_o+v_d\, f(\sigma) \qquad \text{for } \zeta-\delta<z<\zeta \qquad (11)$$

where δ is the depth of the turbulent region and

$$u_d = u_s - u_o\ , \quad v_d = v_s - v_o, \quad f(\sigma)=-A\sigma^3+(1+A)\sigma^2\ , \quad \sigma=(d+z)/h, \quad A=1.4$$

Using the definition of the mean velocity U and equation (11) the turbulent region depth δ can be estimated from (Karambas, 1996):

$$\delta = \frac{U - u_o}{u_d}\frac{h}{0.45} \qquad (12)$$

In the non-turbulent region, D=0, $E=0.5hU^2+0.5g\zeta^2$ and the system reduces to the classical Boussinesq equations.

An important result of the above model is the prediction of the nonlinear instantaneous bottom velocity which also includes the mean motion (mainly responsible for the sediment transport).

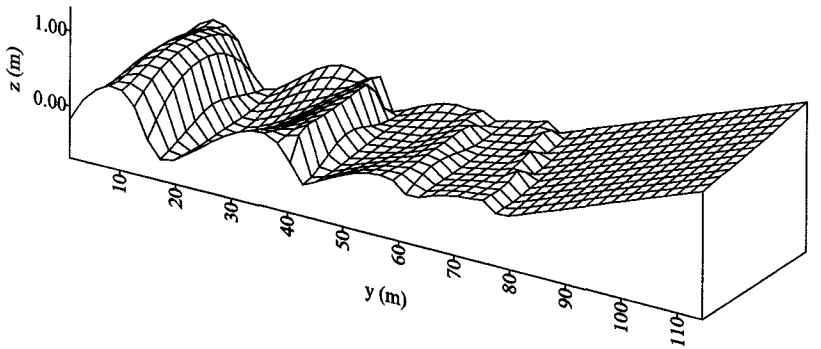

Figure 1. Perspective view of the wave field for oblique wave incidence. Wave height H=1m, period T=6 secs and slope 1:30.

Numerical solution

The system of equations (1) and (5) is simultaneously solved as in the 1-D model (Karambas, 1996) in the following way:

1. Calculation of U^{n+1} , V^{n+1} , ζ^{n+1} (at time level $(n+1)\Delta t$) from the solution of the Boussinesq equations (1).
2. Calculation of E^{n+1} *explicitly* from the energy equation (5) using exactly the same Finite Differences approximations (both new time step $(n+1)\Delta t$ and previous time step nÄt values of the variables are employed). The integrals containing the terms u^3, v^3, u^2v, uv^2, are estimated numerically (equation 6).
3. Calculation of the integral in the momentum Boussinesq equations (1) using equation (10). The integrals containing the terms uv are estimated numerically.
4. Next time step: replacement in the non linear terms of the momentum Boussinesq equations (1) the values of the integrals of step 3.

In this manner energy equation is numerically solved simultaneously with the Boussinesq equations and its effects are introduced explicitly in the momentum equation. The main advantage of the above procedure is that it can be easily introduced in the existing models without the need for changing their numerical scheme.

Waves propagating out of the domain are artificially absorbed using sponge layer technique. The Orlanski open boundary condition is also applied, since it is more efficient for the absorption of the generated currents and long waves.

The 'dry bed' boundary condition is used to simulate runup (Figure 1). Consider the one-dimensional case the condition is written:

$$\text{if } (d+\zeta)<0.00001 \quad \text{then} \quad z=-d \tag{13}$$

The above conditions has been successfully used in long wave runup modelling (Karambas et al., 1991).

The Finite Differences numerical scheme is described in Karambas et al. (1990).

An energetics sediment transport formula

The energetics approach is based on the Bagnold's original idea that the sediment transport load is proportional to the time averaging energy dissipation of the stream (Bailard 1981).

In an energetics approach the submerged weight transport rates, i_{xt} in the x direction and i_{yt} in the y direction, are given by Bailard:

$$< i_{xt} >=< \left[\frac{\varepsilon_b}{\tan\phi}\left(\frac{u_o}{u_{ot}}+\frac{d_x}{\tan\phi}\right)\omega_b + \varepsilon_s \frac{u_{ot}}{w}\left(\frac{u_o}{u_{ot}}+\varepsilon_s d_x \frac{u_{ot}}{w}\right)\omega_t \right] >$$

$$< i_{yt} >=< \left[\frac{\varepsilon_b}{\tan\varphi} \left(\frac{v_o}{u_{ot}} + \frac{d_y}{\tan\phi} \right) \omega_b + \varepsilon_s \frac{u_{ot}}{w} \left(\frac{v_o}{u_{ot}} + \varepsilon_s d_y \frac{u_{ot}}{w} \right) \omega_t \right] > \qquad (14)$$

where the angled brackets represent (numerical) time-averaging, w is the sediment fall velocity, φ is the angle of internal friction, ε_b and ε_s are the bed and suspended load efficiency factors respectively, ω_t is the local rate of energy dissipation given by:

$$\omega_t=\omega_b+C_d\, k_b^{3/2} / l_t\ h \qquad (15)$$

where k_b is the turbulent kinetic energy at the bottom and ω_b is the dissipation at the bottom:

$$\omega_b= f_w/2\ u_{ot}^3 \qquad (16)$$

The above sediment transport formula has been derived directly form the primitive equations (equation 7 of Bailard 1981 paper) without the assumption that the only dissipation mechanism is the bed friction. This is the most important limitation of the Bailard theory and precludes the use of the original formula within the surf zone, where the dissipation of energy associated with the process of wave breaking is largely dominant.

Since a Boussinesq model automatically includes the existence of the mean wave-induced current there is no need to separate the bottom velocities $u_o(t)$ and $v_o(t)$ into a mean and a oscillatory part as in most of the previous works which adopt only period-mean approaches. This is another significant advantage of the present model since the approach is based on the original energetics formula without the above simplification. In addition there is no need for the decomposition of the moments by assuming that the bottom wave velocity is larger than the mean current velocity. This assumption (Roelvink and Stive, 1989) is not always valid, especially in complicated wave fields near coastal structures (behind a detached breakwater there is a strong mean current without significant wave motions).Finally the present model includes a quasi 3D structure of the motion (mean and oscillatory) predicting in this way the undertow effects on the cross-shore sediment transport rate.

According to the original Bagnold estimations (from river data) the bed and suspended load efficiency factors ε_b and ε_s take the values ε_b=0.13 and ε_s=0.01.

Bailard (1981) first calibrated the energetics approach based on laboratory and field measurements. Least square estimates of ε_b and ε_s resulted in values 0.21 and 0.025 respectively. However, the Bailard's value of ε_s has to compensate for increased turbulence due to breaking in the surf zone. Since the breaking wave-induced dissipation has already been incorporated, the Bailard's value is not valid. Here the value ε_s=0.01 is used, considering the following exponential, over the depth, decay of the turbulence kinetic energy k (according to Roelvink and Stive 1989):

$$k_b=k[(\exp(d/H)-1]^{-1} \qquad (17)$$

in which H is the wave height.

For typical values of the ratio d/H inside surf zone the dissipation of k (i.e the term $C_d\, k_b^{3/2} / l_t\, h$) is finally multiplied by a factor 0.002, which is similar to the value proposed by Morfett (1995).

Morphology module

The morphological changes are calculated by solving the conservation of sediment transport equation:

$$\frac{\partial q_x}{\partial x} + \frac{\partial q_y}{\partial y} = \frac{\partial z_b}{\partial t} \tag{18}$$

where z_b is the bed elevation above arbitrary datum and q_x, q_y are the volumetric sediment transport rate related to the immerged weight sediment transport through:

$$q_{x,y} = \frac{i_{x,y}}{(\rho_s - \rho) g N} \tag{19}$$

in which N is the volume concentration of solids of the sediment (N= 0.6) and ρ_s and ρ are the sediment and fluid densities.

Applications

In two previous work of the author (Karambas et al, 1995, and Karambas et al., 1997) the 1D version of the model has been successfully used to predict cross-shore sediment transport and bed evolution. In the present model the simulation of the runup leads also to the prediction of the sediment transport in swash zone. In this work two applications are presented: the prediction of the longshore transport rate and the simulation of the coastline evolution in a beach nourishment scenario.

In the computations of the longshore transport rate it is assumed that the shoreline and depth-contour lines are straight and parallel to each other, the incident waves are regular and uniform in the alongshore direction and that the sediment grain size is spatially uniform. The following four parameters are varied in the numerical experiments: breaking wave height H_b, incident angle θ_b, beach slope tana and grain size D_{50}. Wave period T is assumed constant, T=9 secs. For certain values of the three of the above parameters and different values of the fourth, the longshore transport rate Q, from the swash zone across the surf zone to deep water, is calculated by the cross-shore integration of $q_y(y)$:

$$Q = \int_{Ru}^{\infty} q_y(y)\, dy \tag{20}$$

where Ru is the location of the run-up point.

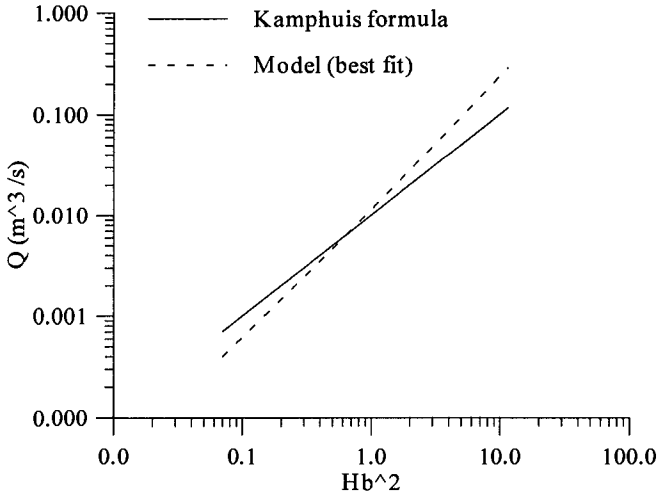

Figure 2. Comparison of longshore transport rate between Kamphuis formula and present model in different breaking wave heights H_b (T=9 secs, D_{50}=0.0003 m, θ_b=0.3 rad, slope=0.015).

The Kamphuis longshore transport formula is used for comparison with the present model. The improved Kamphuis formula (Schoones and Theron, 1996) is written as follows:

$$Q_{Kamphuis} = 63433 \frac{1}{(1-p)\rho_s} (\rho / T) L_o^{1.25} H_b^2 (\tan a)^{0.75} (1 / D_{50})^{0.25} (\sin 2\theta_b)^{0.6} \quad (m^3 / year) \qquad (21)$$

where p is the porosity, L_o is the deep-water wavelength, H_b is the wave height, θ_b is the incident angle, tana is the beach slope and D_{50} the grain size.

Model predictions are plotted against H_b^2, $(\sin 2\theta_b)^{0.6}$, $\tan a^{0.75}$ and $(1/D_{50})^{0.25}$ in Figures 2 to 5. The longshore transport rate Q which is predicted by the model is generally close to the values obtained by Kamphuis formula. In general a more strong dependence on breaking wave height, incident angle and grain size is predicted by the model. However, for the verification of the model, comparisons with experimental data and field measurements are required.

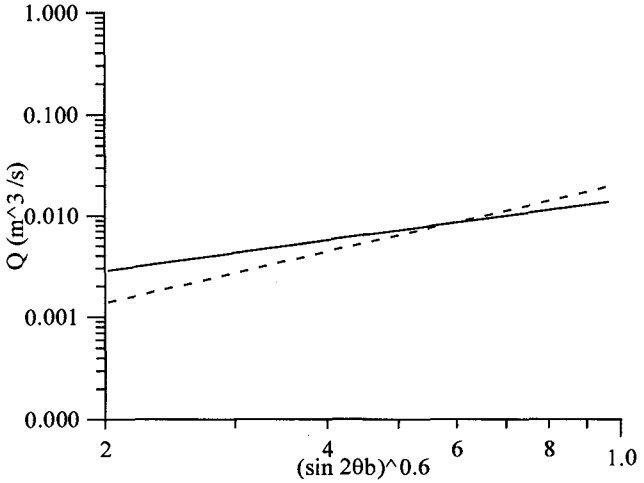

Figure 3. Comparison of longshore transport rate between Kamphuis formula (solid line) and present model (dashed line) in different wave directions θ_b (H_b=1.0 m, T=9 secs, D_{50}=0.0003 m, slope=0.015).

The model is also applied to simulate the coastline evolution in a beach nourishment scenario assuming normal wave incidence on a trapezoidal beachfill (Figure 6). In Figure 7 the predicted shoreline change after nondimensional time T=0.5 is compared with an analytical solution of the Pelnard-Considere equation (one-line model, Work and Rogers, 1997). The nondimensional time T is defined as: $T=4(Gt)^{0.5}/l_1$, where G is 'longshore diffusivity' parameter (Work and Rogers, 1997) and l_1 is the longshore length (l_1=20m in the present case). The depth at the toe of the beachfill is h_t=1.5m, the slope 1:15, the incident wave height H=1m, the period T=6 secs and the fall velocity w=0.03 m/s.

In an one-line model changes in shoreline position are assumed to be produced by spatial differences in the **longshore** sand transport rate. However present model is also able to simulate cross-shore transport (Karambas et al., 1995, Karambas et al., 1997). Thus the predicted shoreline change is expected to include the effects of the cross-shore (offshore or onshore) transport, i.e. erosion or accretion. In Figure 7 the difference between the present model and the analytical solution is the shoreline displacement due to offshore transport. Under the applied conditions (H=1m, T=6 secs and w=0.03 m/s) the nondimensional fall speed N=H/(wT)=5.55, also known as the Dean number, is greater than the critical value N_c=3.2 and consequently the direction for the cross-shore sediment transport is expected to be offshore (erosion).

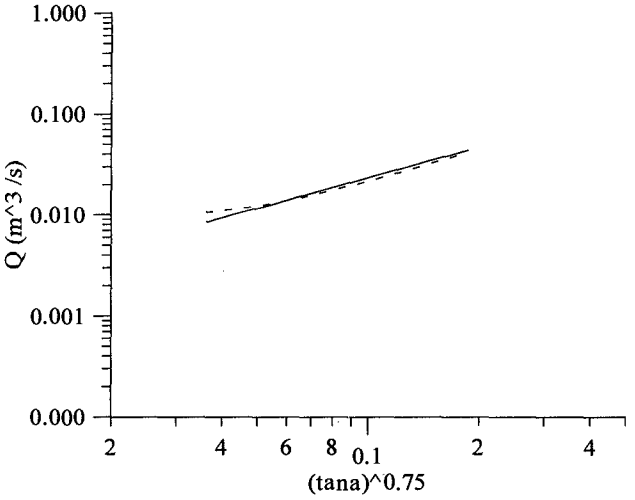

Figure 4. Comparison of longshore transport rate between Kamphuis formula (solid line) and present model (dashed line) in different slopes tana (H_b=1.0 m, T=9 secs, D_{50}=0.0003 m, θ_b=0.3 rad).

Conclusions

The 2DH energy and the Boussinesq equations are simultaneously solved for the simulation of breaking wave propagation in the surf zone. Model results are used in an energetics sediment transport model based on the Bailard formula.

The unified model is capable of predicting:

- 2DH breaking wave propagation
- Longshore transport rate from the swash zone to shoaling region
- Coastline evolution in a beach including cross-shore sediment transport

The comparison of longshore transport rates between present model and Kamphuis formula shows close agreement.

Coastline evolution is also predicted well in comparison with an analytical solution of the one-line equation.

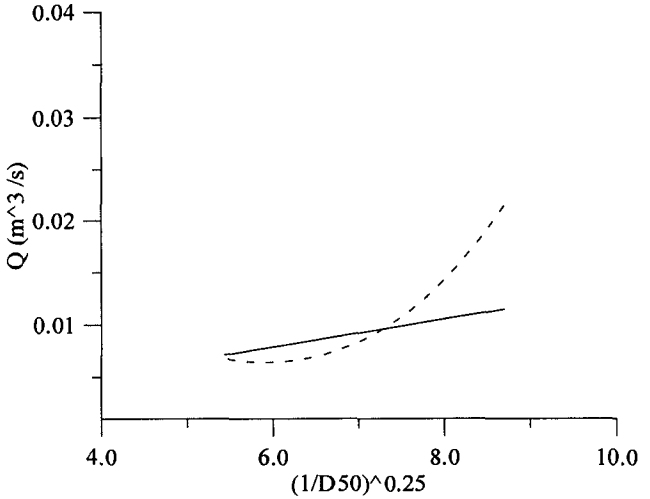

Figure 5. Comparison of longshore transport rate between Kamphuis formula (solid line) and present model (dashed line) in different median grain size D_{50} (H_b=1.0 m, T=9 secs, θ_b=0.3 rad, slope=0.015).

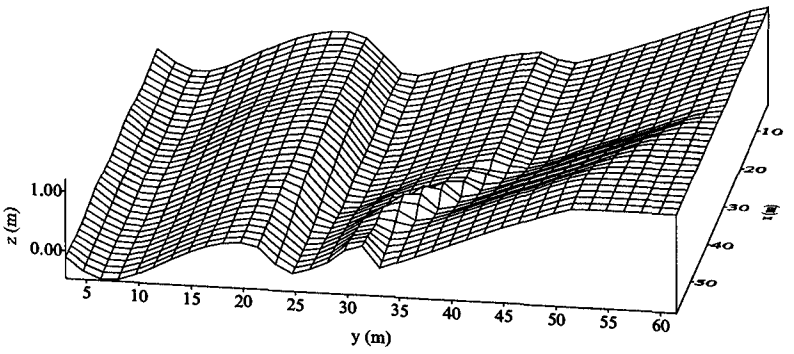

Figure 6. Perspective view of the wave field for normal wave incidence on a trapezoidal beachfill. Wave height H=1m, period T=6 secs, depth at toe h_t=1.5m and slope 1:15.

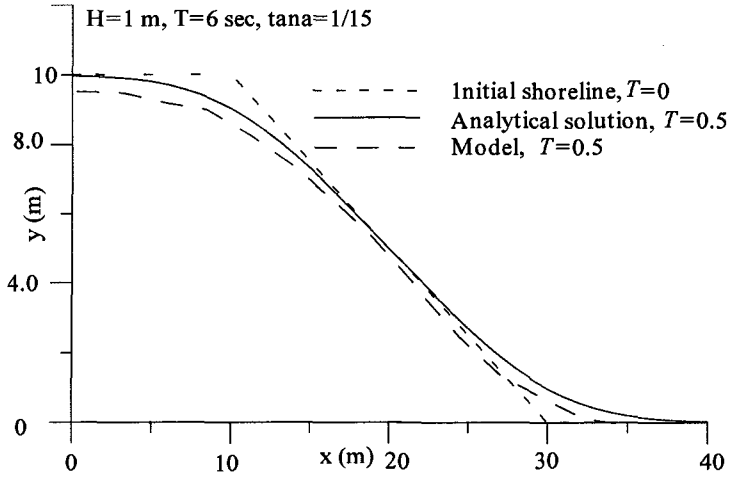

Figure 7. Shoreline change of a trapezoidal beachfill. Comparison between analytical solution (Work and Rogers, 1997) and numerical model.

Acknowledgements

The present work is part of the MAST3 SAFE research programme funded by the Commission of the European Communities, Directorate General for Science, Research and development, MAS3-CT95-0004.

References

Bailard J. A. 1981. An energetics total sediment transport model for a plane sloping beach. *J. of Geophysical Research* 86, No C11: 10938-10954.

Briad M-H. G. and J.W. Kamphuis 1993. Sediment transport in the surf zone: a quasi 3-D numerical model. *Coastal Engineering* 20:135-156.

Hamm L. and M. Mory 1995. Hydrodynamic Measurements around a Detached Breakwater in a 3-D Wave Basin. *SOGREAH and LEGI MAST G8 CM report.*

Karambas Th. V., Krestenitis Y. and Koutitas C., 1990. A numerical solution of Boussinesq equations in the inshore zone. *Hydrosoft*, Vol. 3, No 1: 34-37.

Karambas Th. V., Krestenitis Y. and Koutitas C., 1991. Numerical model on tsunami propagation. *The International Journal of the Tsunami Society*, Vol. 9, No 1: 63-71.

Karambas, Th. V., Southgate H. N. and Koutitas C. 1995. A Boussinesq model for inshore zone sediment transport using an energetics approach. In Dally and Zeidler (eds), *Coastal Dynamics '95*, ASCE: 841-849.

Karambas, Th. V. 1996. Nonlinear wave energy modelling in the surf zone. *Nonlinear Processes in Geophysics* 3: 127-134.

Karambas, Th. V., P. Prinos and K. K. Kriezi. 1997. Modelling of hydrodynamic and morphological effects of submerged breakwaters on the nearshore region. In E. B. Thornton (ed), *Coastal Dynamics '97*, ASCE: 764-773.

Katopodi, I. and J.S. Ribberink 1992. Quasi-3D modelling of suspended sediment transport by currents and waves. *Coastal Engineering* 18:83-110.

Madsen, P. A. and I.A. Svendsen 1979. On the form of the integrated conservation equations for waves in the surf zone. *Inst. of Hydrodynamics and Hydraulic Eng., Technical Univ. of Denmark., series paper 48.*

Morfett J. C. 1995. Computational modelling of sediment transport by breaking waves. *2nd Int. Conference on Computer Modelling of Seas and Coastal Regions*, Mexico, vol II, 241-248.

Nairn R. B. and H. N. Southgate 1993. Deterministic profile modelling of the nearshore processes. Part 2. Sediment transport and beach profile development. *Coastal Engineering* 19: 57-96.

Nwogu, O. G., 1996. Numerical prediction of breaking waves and currents with a Boussinesq model. *Proc. 25th Int. Conf. on Coastal Engineering*, ASCE: 4807-4820.

Peregrine, D. H. 1972. Equations for water waves and approximation behind them. In R. E. Meyer (ed), *Waves on Beaches*, Academic press.

Roelvink J. A. and M. J. F. Stive 1989, Bar-generating cross-shore flow mechanics on a beach. *Journal of Geophysical Research* 94, No C4: 4785-4800.

Schoones J. S. and A. K. Theron. 1996. Improvement of the most accurate longshore transport formula. *Proc. 25th Int. Conf. on Coastal Engineering*, ASCE: 3652-3665.

de Vried H. J. and Stive M. J. F. 1987. Quasi-3D modelling of nearshore currents. *Coastal Engineering* 11: 565-601.

Work P. A. and W. E. Rogers, 1997. Wave transformations for beach nourishment projects. *Coastal Engineering* 32: 1-18 .

Comparison of Storm Longshore Transport Rates to Predictions

Herman C. Miller[1], M ASCE

Abstract

Longshore sediment transport (LST) is of primary importance to long-term shoreline changes and must be accounted for in most coastal designs. Predicting LST has been hampered by the lack of direct measurements during storm conditions against which the models can be calibrated. The Sensor Insertion System (SIS) developed at the US Army Corps of Engineers (USACE) Field Research Facility provides a way to directly measure LST during storms. The SIS was operated during the growth, peak, and waning stages of three storms between April, 1997 and February, 1998 in which the waves reached a maximum individual height of 5.6m. In up to 14 cross-shore locations, concentration and velocity measurements were made throughout the water column. These measurements were compared to total transport models of USACE 1984, Kamphius 1991, Kraus, et al. 1988, Walton 1980, and the cross-shore distribution model of Bodge and Dean 1987. The results show the storm measurements had a consistent pattern; rapidly increasing to a peak rate, then gradually decreasing during the waning stages of each storm. Cross-shore distributions of longshore flux tended to peak over the offshore bar and at the beach where wave dissipation caused high suspended sediment concentrations. These peaks were not co-located with maximum longshore currents, which tended to peak at mid-surf. The comparisons show that the models would benefit from comparison to the storm measurements.

Introduction

Anticipating long-term shoreline changes; designing coastal structures and beach renourishment projects; determining funding allocations for the maintenance of our navigable waterways, inlets, and harbors are some of the reasons it is important to predict longshore sediment transport (LST). Accurate predictions of LST has been a goal of coastal

[1]US Army Engineer Waterways Experiment Station Coastal & Hydraulics Laboratory Field Research Facility, 1261 Duck Road, Kitty Hawk, NC 27949, USA

engineers for decades. While many models have been introduced, some very sophisticated, others simple and robust, few have attained wide use (see reviews, Bodge 1989, Sternberg et al. 1989, Komar 1990, Kraus and Horikowa 1990). Consequently, the need for improvement continues. Until new models, based on a better understanding of the transport mechanisms are developed, improving the modeling capability might best be achieved by comparing existing models to field measurements during storms. It is well known that storms, with waves generally higher than 2 m, are responsible for the largest changes in our coasts. Thus, the models need to work well under these conditions. The problem is there is a paucity of these data. A thorough review of the LST data by Schoonees and Theron (1993) concluded that almost all field data were for wave heights below 1.8 m. The consequence is that existing transport models are calibrated against rates measured during low to moderate wave conditions.

This study has produced a number of high quality storm data sets. LST rates and highly-resolved cross-shore distributions of longshore sediment flux during three storms are compared to five easy to use LST formulations. The results demonstrate how LST models could benefit from field measurements under storm conditions. The paper includes brief descriptions of the site characteristics, a new system for making direct measurements during storms, instrumentation, and data collection/analysis procedures. Then, examples of the measurements are given and comparisons are made to LST models.

Site Characteristics

This investigation was conducted in the United States (US) at the US Army Engineer Waterways Experiment Station, Coastal and Hydraulics Laboratory's Field Research Facility (FRF) located in Duck, North Carolina (NC), on the Atlantic Ocean (Figure 1). With an average of 20 storms per year, including the close passage of tropical storms and hurricanes, this site is ideal for studying sediment transport during storms.

The characteristics of the FRF have been well studied and the processes are summarized in the series of annual reports, (Leffler et al. 1998). Average annual significant wave height is near 1 m with a 9-sec period. Significant wave heights in excess of 4 m (in 8 m depth) are not uncommon. The tide is semi-diurnal tide with a spring range of 1.2 m and storm surges in excess of 1 m have been recorded. Wave information used in this study were collected from the FRF directional array located in 8 m depth (Long and Oltman-Shay 1991).

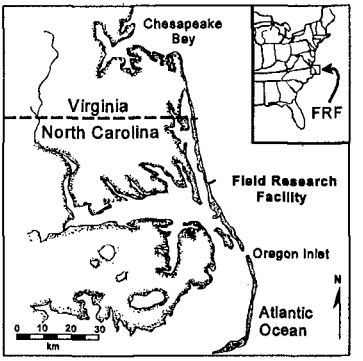

Figure 1. FRF Site

The beach, locally oriented NNW-SSE, is typical of the barrier island system along the mid-Atlantic coast of the US. The typical nearshore profile has two bars, but varies with season and longer time scales (Birkemeier 1984). The nearshore consists of 0.15 to

0.18 mm sand that grades toward 0.12 mm further offshore, with coarse sand and gravel from submerged river beds abundant at the beach (Stauble 1992, Schwartz et al. 1997).

Figure 2. SIS During October, 1997 Storm

Sensor Insertion System

There are many reasons for the lack of direct measurements of LST during storms, including the expense and logistics required to operate a monitoring program that can operate in severe wave conditions through many storms. To overcome this, the FRF has developed the Sensor Insertion System (SIS). The pier based SIS, Figure 2, is capable of measuring hydrodynamic processes and the resulting sediment transport anywhere across 500 m of the nearshore.

The SIS is a 70,000 kg crane with an array of instrumentation that is moved along the length of the research pier to measure sediment transport at different positions across the surf zone during storms. The SIS is designed to operate in up to 5.6-m individual wave heights. To minimize the influence of the pier, the SIS, with 20-m-long booms, can place instruments on the ocean bottom in 9 m depth as far as 22 m updrift of the pier centerline. This system provides an economical way to make these measurements. It does not require divers and can reposition the sensors as the profile evolves during a storm. A disadvantage of the SIS measurement system is that measurements across the shore are not simultaneous, but occur over a 3-hour period.

Instrumentation

Optical backscattering concentration sensors (OBS) in combination with electromagnetic current meters (EMCMs) have proven most reliable during storms for measuring sediment flux throughout the water column. Each concentration sensor is considered representative of a portion of the water column as shown in Figure 3. Many of

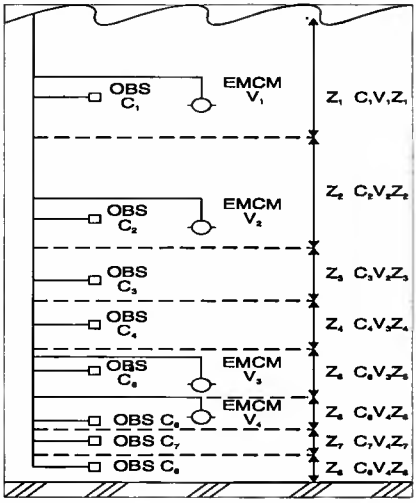

Figure 3. Schematic of SIS Flux Sensors

the sensors are positioned near the bottom since the measurements show that much of the sediment is transported within 1 m of the bed. The lowest concentration sensor is typically 3 to 5 cm above the bottom. Distance to the bottom is measured with a down-looking sonic altimeter.

The instruments are held updrift of the SIS on a frame as shown in Figure 4. This minimizes contamination of the measurements by any wake effect off the SIS. Since the instrumentation is parked on the pier deck between use, the instruments can be frequently inspected, rinsed with fresh water, are virtually unaffected by biological fouling, and thus tend to hold their calibrations well.

Figure 4. Sensors on SIS

Data Collection And Analysis

This single instrument array was used to directly measure sediment concentration and fluid velocity at a large number of cross-shore locations. From these measurements the cross-shore flux distribution can be determined and integrated to compute the LST rate. Starting about 1½ hrs before high or low tide, and operating for 3 hours, up to 14 cross-shore locations can be measured while the water level changes very little. This provides a quasi-synoptic "snap-shot" of the cross-shore distribution of the longshore sediment flux. At each location along the pier, 512-sec-long records were sampled at 16 Hz. The high sample frequency is required because sand resuspension events last for only a fraction of the wave cycle. All of the cross-shore measurement locations along the pier during one tide will be referred to as a "transect."

Instantaneous concentration and velocity values are used to compute the flux at each gauge location in the water column by multiplying the instantaneous concentration, $c(x,z,t_i)$, after accounting for the "turbidity" offset (Ludwig and Hanes 1990, Schoelhamer 1993), by the instantaneous longshore velocity, $v(x,z,t_i)$, and time-averaging the products.

$$F(x,z) = \frac{1}{N} \sum_{i=1}^{N} c(x,z,t_i) v(x,z,t_i) \qquad (1)$$

where N is the number of samples and F(x,z) is the longshore sediment flux, which is the rate per unit area in the x (cross-shore) and z (vertical) directions.

Cross-shore distribution of the longshore flux was obtained by summing the vertical contributions at each location along the transect

$$G(x)=\sum_{j=1}^{M} F(x,z_j)\delta z_j \quad (2)$$

where G(x) is the vertically integrated flux per unit cross-shore length and M is the number of concentration sensors.

Longshore transport rates were computed in a similar way by summing the across-shore contributions

$$I=\sum_{k=1}^{L} G(x_k)\delta x_k \quad (3)$$

where L is the number of measurement locations and I is the longshore sediment transport rate. These rates were converted to volume transport rates, Q (m^3/hr), assuming the density of quartz sand is 2,650 kg/m^3, the density of sea water is 1,025 kg/m^3, and the solid fraction is 0.6.

Results

Measured Transport Rates

Three storms were selected for analysis because the measurements included the growth, peak, and waning storm stages. The peak rates are compared in Table 1. With approximately the same peak wave directions and periods, the measured LST was observed to vary approximately linearly with wave energy up to a rate of 3,400 m^3/hr, the highest measured to date.

Table 1. Peak Transport Rates

Date	Wave Height, m	Wave Period, sec	Wave Angle From Normal, Deg	Longshore Transport Rate, cu m/hr
1 Apr 97	2.7	9	18	1,500
19 Oct 97	3.3	10	20	2,700
4 Feb 98	3.8	11	20	3,400

The LST rates for each transect during the growth, peak, and waning stages of the October, 1997 storm are shown in Figure 5. The rapid growth to a peak, followed by a

gradual waning of the LST is typical of the storm measurements at the FRF. On 19 October, a total volume of 33,200 m^3 of sediment was measured moving south.

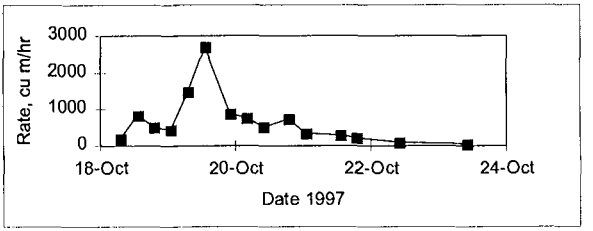

Figure 5. LST Rates During October, 1997 Storm

Cross-Shore Distribution

The unique capabilities of the SIS to rapidly reposition the sensors during a storm resulted in highly-resolved cross-shore distributions of longshore flux measurements. Cross-shore locations were selected to document both the peak and minimum values, so an accurate representation of the LST rate could be determined. From experience obtained during many prior storm tests, a minimum of 8 cross-shore positions are required across the barred profile. An example of a cross-shore distribution of the longshore sediment flux with 14 measurement positions is shown in Figure 6. The graph is for one transect on 20 October, 1997 during low tide when the waves were 2.4 m. This example was chosen because it is a typical storm distribution. The two curves represent the vertically integrated sediment flux per unit cross-shore length and water depth at the measurement locations. As can be seen, peak flux values are associated with the inner and outer bars along the profile.

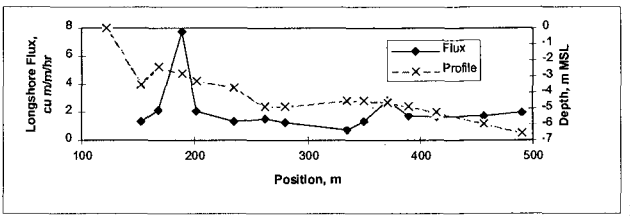

Figure 6. Flux Distribution, 20 Oct 97

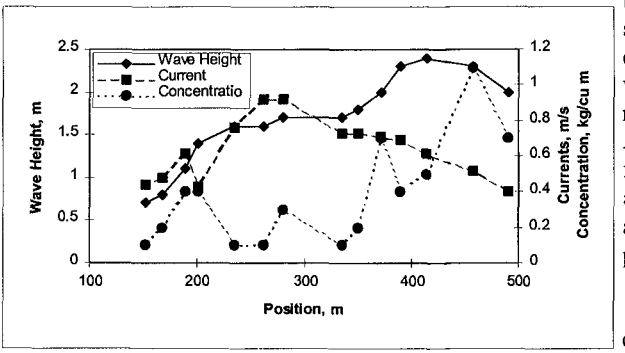

Figure 7. Processes Distribution, 20 October, 1997

It is interesting to compare the resulting flux values to the cross-shore distribution of the processes. In Figure 7, wave height, longshore current from the near surface EMCM, and near-bed sediment concentrations are displayed. Beginning offshore, the waves shoal and dissipate energy over the outer bar, remain consistent across the trough between the bars, before dissipating energy again at the inner bar and beach. The break point defining the surf

zone would be considered located near position 425 m where predominate breaking occurred; however, breaking of the highest waves was observed seaward of that location. The longshore current builds to a peak over the trough between the bars. This distribution is somewhat like the classic longshore current distribution of Longuet-Higgins (1970) and has been observed previously at the FRF (Smith et al. 1993). Sediment concentration peaks are associated with wave shoaling and wave energy dissipation.

Comparing Figure 6 to 7 shows that the longshore sediment flux and sediment concentration peak at the same locations, which do not coincide with the longshore current peaks. The importance of wave dissipation suspending sediment in the cross-shore distribution of longshore flux is well documented in all of the storms measured to date. That is not to say this is the only cross-shore distribution of longshore flux. In fact, many different distributions have been measured that reflect differences in profile features and wave energy levels. For example, during low wave conditions, a single peak near the inshore bar or beach occurs.

Comparison to LST Rate Models

Arguably, the most widely used LST model is that given in the Shore Protection Manual (SPM) (USACE 1984). This formulation equates, I , the immersed weight transport rate to a constant, K , times the longshore wave energy flux factor, P_{lb}

$$I = K\ P_{lb} \tag{4}$$

where K equals 0.39 when using significant wave height. This constant was determined primarily from long-term averaging of waves and sediment accumulation at coastal structures.

The longshore wave energy flux factor is given in terms of the wave conditions at breaking

$$P_{lb} = (EC_g)_b\ \sin\alpha_b\ \cos\alpha_b \tag{5}$$

where E is the wave energy, C_g is the wave group velocity, α is the wave crest angle relative to the beach, and "b" denotes breaking conditions.

For these predictions, the peak wave parameters measured at the FRF's directional array were shoaled conserving wave energy flux according to

$$E_{d.a.}\ C_{gd.a.}\ Cos\ \alpha_{d.a.} = E_b\ C_{gb}\ Cos\ \alpha_b \tag{6}$$

and the waves were refracted using Snell's Law:

$$\frac{Sin\ \alpha_{d.a.}}{L_{d.a.}} = \frac{Sin\ \alpha_b}{L_b} \tag{7}$$

where L is the wave length and "d.a." is at the directional array. A breaking criteria of H/d = 0.78 was used.

The SPM predictions were made every 3 hrs when the wave data were available. The LST measurements are only at times of high or low tide. Figure 8 compares the measured and predicted LST rates. In this case, the SPM somewhat overpredicted the lower rates and underpredicted the peak rate. However, in general, it compared reasonably well with the measurements. Note, after more storm measurements are obtained and an error analysis is performed, many of these differences may prove insignificant.

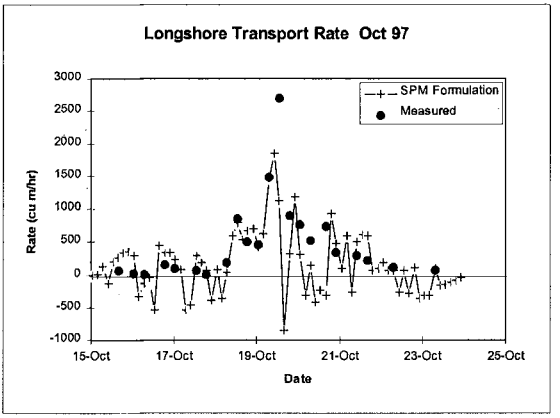

Figure 8. SPM Predictions and Measurements; Oct 97

The SPM predictions show a high degree of variability. This is in part because the SPM assumes all the wave energy is in a single wave train. Because the storms tend to move along the coast past the FRF, multiple peaked spectra frequently are measured. Small shifts in the energy level of similar spectral peaks can cause considerable variation from one prediction to the next.

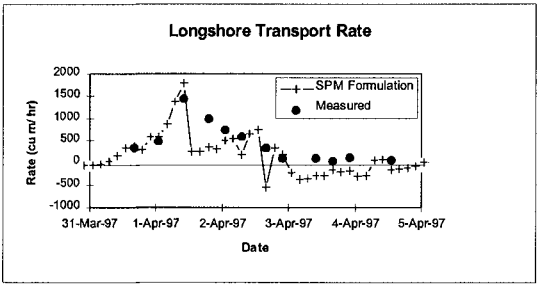

Figure 9. SPM Predictions and Measurements; Apr 97

Figure 9 shows a similar comparison between SPM predictions and measurements for the storm in April, 1997. Again there is reasonable agreement, particularly, during the growth and peak of the storm; although, in this case the peak was over predicted. The measured LST gradually decreased as is common during the waning stages of the storm.

Negative predictions indicate a direction reversal caused by the arrival of the southerly swell after the storm passed.

For the February, 1998 storm (Figure 10) the waves were from the south side of the pier and the transport was directed to the north as designated by the negative values. The SPM formulation over predicted the peak.

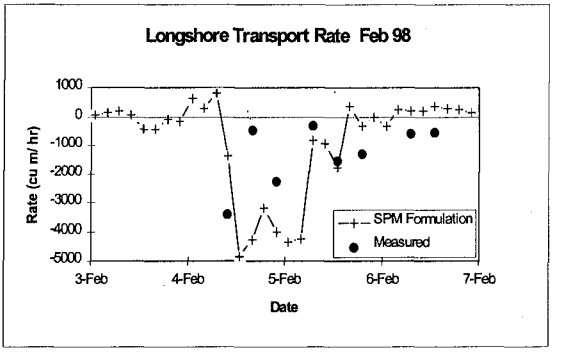

Figure 10. SPM Predictions and Measurements; Feb 98

The Kamphius 1991 model was attractive because it included bottom slope, sediment size, and wave period, in addition to the wave height and angle of approach.

$$Q = 7.3\ H_{sb}^{2}\ T_{p}^{1.5}\ m_{b}^{0.75}\ D_{50}^{-0.25}\ \sin^{0.6}(2\alpha_{b}) \qquad (8)$$

where H_{sb} is the significant wave height at breaking, T_p is the peak spectral wave period, m_b is the bottom slope, D_{50} is the sediment size, and α_b is the wave angle at breaking.

Using the transects near the peak of the April, 1997 storm, Figure 11, shows the model underpredicts the magnitude of the rates. The Kamphius coefficient was evaluated primarily with laboratory data. It appears the predictions are off by an order of magnitude. When the Kamphius coefficient is multiplied by a factor of 10, Figure 12, the predictions are improved.

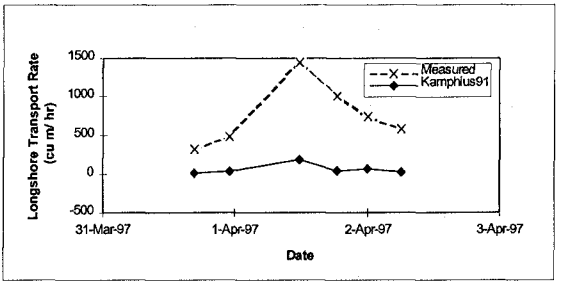

Figure 11. Kamphius Predictions, April, 1997 Storm

Kraus et al. (1988) proposed a LST rate model which included a water discharge parameter, R, which must exceed a critical discharge value they call R_c,

$$I = 2.7\ (R - R_c) \tag{9}$$

where the discharge parameter, R , is

$$R = V\ X_b\ H_{sb} \tag{10}$$

with V the longshore velocity, X_b the surf zone width, H_{sb} the significant wave height, and $R_c = 3.9\ m^3$ / sec.

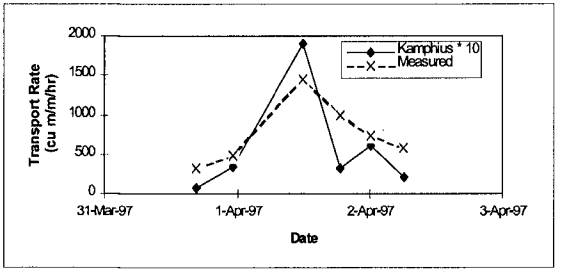

Figure 12. Modified Kamphius Predictions

This model, which was developed from field measurements under low to moderate wave conditions, is compared to three transects during the April, 1997 storm (Table 2). These transects were chosen because of the range of wave heights. The model underpredicts the measured values from 30 to 60 percent. Kraus et al. (1988) provide a velocity term correction based on the standard deviation of the velocity and another correction based on the wave height gradient, but these did not improve the results. This model, which is easily applied, may only lack the storm measurements to recalibrate the model coefficient.

Table 2. Kraus, Gingerich, and Rosati, 1988 Predictions for April, 1997 Storm

Transect	H_{sb}, m	V, m/s	X, m	Q_{pred}, m^3/hr	Q_{meas}, m^3/hr	Q_{pred} / Q_{meas}
2	1.6	0.49	220	170	480	0.4
6	2.5	1.18	198	610	740	0.8
4	3.0	1.21	300	1100	1500	0.7

The Walton (1980) model was intriguing because it included Longuet-Higgins cross-shore current distribution and a water discharge parameter that resembled that of Kraus et al. (1988).

$$P_{ls}=\rho g\frac{H_{sb}WVC_f}{\frac{5\pi}{2}(\frac{v}{v_o})_{LH}} \tag{11}$$

where W is the surf zone width, C_f is a friction coefficient and the Longuet-Higgins current distribution is given by

$$(\frac{V}{V_o})_{LH}=0.2(\frac{X}{W})-0.74(\frac{X}{W})\ln(\frac{X}{W}) \tag{12}$$

with X being the cross-shore position that the velocity was measured.

For the same three transects, the Walton model greatly overpredicts the LST rate (Table 3). However, there is some similarity in how the Walton and Kraus et al. models differed from the measurements. The prediction to measurement factor, Q_p/Q_m, for transects 4 and 6 are about twice that for transect 2 for both models. The similarity in how the models perform is probably because both models have a water discharge parameter. Recalibration with data from multiple storms should benefit these models.

Table 3. Walton, 1980 Predictions for April, 1997 Storm

Transect	H_{sb}, m	V, m/s	X, m	W, m	Q_{pred}, m^3/hr	Q_{meas}, m^3/hr	Q_{pred} / Q_{meas}
2	1.6	0.49	220	22	910	480	1.9
6	2.5	1.18	198	198	3100	740	4.2
4	3.0	1.21	300	300	8100	1500	5.4

Comparison to Cross-Shore Distribution Models

The new USACE Coastal Engineering Manual (CEM) (scheduled for publication and public release in 2000) presents the cross-shore distribution of longshore sediment flux proposed by Bodge & Dean (1987) as an example of the available models. This model is attractive because it includes wave energy dissipation and longshore velocity and therefore

can account for local wind effects and depth.

$$q_x(y) = \frac{k_q}{d} \frac{\delta}{\delta x}(E\ C_g)\ V_l \qquad (13)$$

The dimensional constant, k_q= 48 sec, was evaluated from laboratory experiments and low to moderate wave conditions in the field. As can be seen in Figure 13, the model re-creates the peaks over the bars for this transect near the peak of the storm. It is interesting to note that the strong dependence of the model on wave dissipation resulted in negative predictions, (that do not represent a direction reversal), at the seaward most locations where the waves were shoaling. Bodge & Dean (1987) indicate the model is only valid inside the surf zone where the wave energy is expected to dissipate. The magnitudes of the predictions appear to be much larger than the measured flux values. Bodge and Dean do provide a correction that is dependent on the bottom slope; however, that made the agreement worse. Since it appears from matching the first few values in Figure 13 that the predictions are approximately a factor of four larger than the measurements, k_q was reduced to 0.12 sec and replotted in Figure 14. The agreement, although not perfect, is better. The intent here is not a rigorous recalibration of the models, but simply a first attempt to demonstrate the utility of the measurements. After more measurements are obtained, model recalibrations will be performed. The goal of the SIS measurement program is to gather data during storms so models, such as this, can be calibrated under a range of storm wave conditions and improve our ability to predict LST. Two other distribution models (Briand and Kamphius 1993, Watanabe, et al. 1991) were considered, but proved difficult to apply.

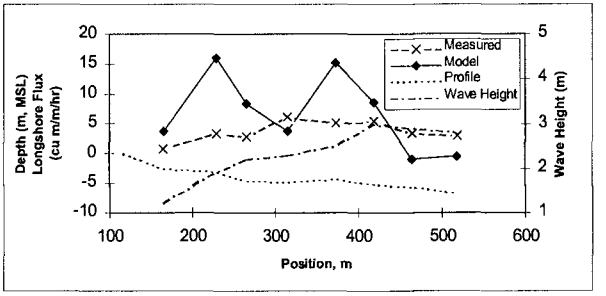

Figure 13. Bodge and Dean Predictions, 1 April, 1997

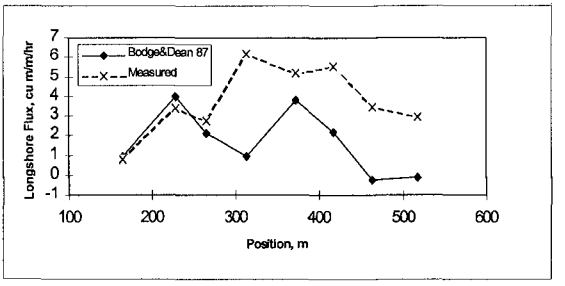

Figure 14. Modified Bodge and Dean Predictions

Conclusions

The SIS provides a powerful platform to measure LST during storms. Quasi-synoptic "snap shots" of highly-resolved cross-shore distributions of longshore flux have been obtained for storms with significant wave heights that reached 3.8 m. LST rates as high as 3,400 m^3 per hour were measured. For the three storms presented, the transport rate rapidly increased to a peak, then gradually decreased during the waning stages of the storms.

The cross-shore distribution of longshore sediment flux shows that, near the peak of a storm, maxima occur over the bars where the wave dissipation increases the suspended-sediment concentration. These, in general, are not co-located with the longshore current maxima which tends to peak over the trough between the bars.

The SPM formulation seemed to capture the trend of the measurements reasonably well. The SPM tends to over predict low wave conditions. The SPM shows considerable variability, even direction reversals, during the waning stages of a storm. This was due to the presence of sea and swell with comparable energy levels due to the rapidly moving storm systems which are common at the FRF. The Kraus et al. (1988) model underpredicted the LST rates. Walton (1980) over predicted the rates. These models would benefit from comparison to storm measurements.

The shape of the cross-shore distribution of longshore sediment flux was modeled reasonably well in the surf zone by Bodge and Dean (1987). Their wave energy dissipation model overpredicted the magnitude. Reducing their coefficient by a factor of four improved the agreement.

While this investigation is a start toward filling the need for storm measurements that can be used to calibrate existing models and develop improved formulations, additional measurements over a range of conditions are still needed and will be a future focus.

References

Birkemeier, W. A. (1984). "Time scales of nearshore profile changes," Proc. 19th Coastal Eng. Conf., Houston, Texas, ASCE, 1507-1521.

Bodge, K.R. (1989). "A literature review of the distribution of longshore sediment transport across the surf zone," J. Coastal Res., Vol 5, No 2, 307-328.

Bodge, K. R., and Dean, R. G. (1987). "Short-Term Impoundment of Longshore Sediment Transport," TR CERC-87-7, WES, Vicksburg, Miss.

Briand, M. G. and Kamphius, J.W. (1993). "Sediment transport in the surf zone: a quasi 3-D numerical model," Coastal Eng., Vol 20, 135-156.

Kamphuis, J.W. (1991). "Alongshore sediment transport rate," J. of Waterway, Port, Coastal, and Ocean Eng., ASCE, Vol. 117, No. 6, 624-640.

Komar, P.D. (1990). "Littoral sediment transport," In Handbook of Coastal and Ocean Engineering," Vol. II, J.B. Herbich, ed., Gulf Pub. Co., Houston, TX, Chap. 25.

Kraus, N.C., and Horikawa, K. (1990). "Nearshore sed. tran.," In "The Sea," Vol. 9,

Part B, B. Le Mehaute and D.M. Hanes, ed., John Wiley & Sons, Inc. NY, Chap. 22.
Kraus, N.C., Gingerich, K.J., and Rosati, J.D. (1988). "Towards an improved empirical formula for longshore sand transport," Proc. 21st Coastal Eng. Conf., Costa del Sol-Malaga, Spain, ASCE, 1182-1196.
Leffler, M., Baron, C., Scarborough, B., Hathaway, K., Hodges, P., and Townsend, C. (1998). "Ann. Data Sum. for 1995 CERC FRF," TR CERC-98-14, WES Vicksburg,MS.
Long, C.E. and Oltman-Shay, J. (1991). "Directional Characteristics of Waves in Shallow Water," TR CERC-91-1, WES Vicksburg, MS.
Longuet-Higgins, M. S. (1970). "Longshore Currents Generated by Obliquely Incident Sea Waves, I," J. Geophysical Res., Vol. 75, No. 33, 6788-6801.
Ludwig, K.A., and Hanes, D.M. (1990). "A lab. eval. of optical backscatterance suspended solids sensors exposed to sand-mud mixtures," Mar. Geol., Vol 94, 173-179.
Schoelhamer, D.H. (1993). "Biological interference of optical backscatterance sensors in Tampa Bay, Florida," Mar. Geol., Vol 110, 303-313.
Schoonees, J.S., and Theron, A.K. (1993). "Review of the field-data base for longshore sediment transport," Coastal Eng., Vol 19, 1-25.
Schwartz, R. K., Cooper, D. W., and Etheridge, P. H. (1997). "Sedimentologic Architecture of the Shoreface Prism, Relationship to Profile Dynamics, and Relevance to Engineering Concerns: Duck, North Carolina," TR CHL-97-19, WES, Vicksburg, MS.
Smith, J. M., Larson, M., and Kraus, N. C. (1993). "Longshore current on a barred beach: field measurements and calculations," J. Geophysical Res., 98(C12), 22,717-22,731.
Stauble, D.K. (1992). "Long-term profile and sediment morphodynamics: Field Research Facility case history," TR CERC-92-7, WES Vicksburg, MS.
Sternberg, R.W., Shi, N.C., and Downing, J.P. (1989). "Susp. sed. Meas.," In: Nearshore Sediment Transport, R.J. Seymour, ed., Plenum Press, NY, NY, Chap. 11.
USACE (1984). "Shore Protection Manual," Vol. I and II, WES, Vicksburg, MS.
Walton, T. L. (1980). "Computation of Longshore Energy Flux Using LEO Current Observation," CETA 80-3, CERC, WES Vicksburg, MS.
Watanabe, A. (1991). "Field Application of a Numerical Model of Beach Topography Change," In: Coastal Sediments '91, Ed. by Kraus, et al., ASCE, Seattle, WA.

Approvals

The author would like to acknowledge the tireless efforts of the STORM team who helped collect these unique data, including: Don Resio, Jarrell Smith, Jane Smith, Ed Hands, Joe Gailani, Dave King, Ernie Smith, Dave Hamilton, Pete Lozis, and others. Permission to publish this paper was granted by the Chief of Engineers.

Depth of Erosion Under Storm Conditions

John F.A. Sleath[1]

Abstract

A model is presented for the dynamics of the mobile layer of sediment on the sea bed under sheet flow conditions. The Karman-Polhausen method is used to determine the thickness of the mobile layer, the scaling for velocity phase and amplitude, and the phase lead of the velocity at the bottom of the mobile layer. The model does not make use of constitutive equations such as those suggested by Bagnold (1956). Agreement between the predictions of the model and existing laboratory measurements is good.

1. Introduction

When a pipeline is trenched into the seabed it is important to know how far below the surface of the bed the sediment may be disturbed by the action of extreme waves or currents. One element in a calculation of this disturbance depth is the thickness of the mobile layer of sediment.

In oscillatory flow, the thickness δ_s of the mobile layer depends on the relative importance of the bed shear stress and the force due to the pressure gradient. When the pressure gradient term is small δ_s is also small and is determined by the magnitude of the Shields parameter. However, when the pressure gradient is no longer negligible δ_s increases rapidly. It is this situation which is of most concern when considering the stability of structures on or in the seabed. Unfortunately, the experimental measurements (see, for example, Horikawa et al, 1982, Sawamoto and Yamashita, 1986, Dick and Sleath, 1991, Asano, 1992, Ribberink and Al-Salem, 1994, 1995, Li and Sawamoto, 1995a, and Zala Flores and Sleath, 1998) show considerable scatter under these conditions.

Several theoretical models have been proposed for the fluid/sediment motion in mobile layers in oscillatory flow (Bakker and Van Kesteren, 1986, Asano, 1990, Nadaoka and Yagi, 1990, Dibajnia and Watanabe, 1992, Li and Sawamoto, 1995b, Kaczmarek et al, 1995, Ono et al, 1996, Katori et al, 1996). Unfortunately, here too, there is significant disagreement between the predictions of the various models when

[1]Reader, Dept. of Engrg., Cambridge Univ., Trumpington Street, Cambridge, CB2 1PZ, UK. FAX: +44 1223 332662, e-mail: jfas@eng.cam.ac.uk

δ_s is large. Part of the problem is that some models assume quasi-steady relationships for sediment transport rate, etc, and are consequently most relevant to the situation where δ_s is small and pressure gradient and inertia terms may be neglected. Others, make use of constitutive equations, such as those of Bagnold (1956), whose reliability in oscillatory flow is uncertain.

The aim of the present paper is to re-examine this question using the well-known Karman-Polhausen method (see, for example, Schlichting, 1979). This method has been shown to give good results in a variety of applications. One of its advantages in the present case is that it allows us to choose a form of velocity profile which is known to be physically realistic when pressure gradient is significant and δ_s is large. Another advantage over the model presented by Sleath (1994) is that it is not necessary to make use of constitutive equations like those of Bagnold (1956).

Only oscillatory flow will be considered here. Also, since the main objective is to examine the mobile layer under extreme wave conditions, the discussion will be limited to flat beds, i.e. sheet flow.

2. The present model

A first step in the Karman-Polhausen method is to select a generalized velocity profile with sufficient disposable constants to ensure a good fit to the unknown real profile. For present purposes we take the horizontal component of velocity to be given by

for $K_1 y \le 1$

$$u = U_0 K_1 y \quad R\left\{e^{i(\omega t+\phi-K_2 y)}\right\}, \tag{1}$$

for $K_1 y > 1$

$$u = U_0 \; R\left\{e^{i\omega t}\right\} \tag{2}$$

where $R\{\ \}$ indicates the real part, U_0 is the amplitude of the fluid velocity in the free stream above the bed, ω is the angular frequency, K_1, K_2, ϕ are coefficients which remain to be determined and y is measured vertically up from the still bed level. This form of velocity profile was shown by Dick and Sleath (1991) to give good agreement with their measurements.

The Karman-Polhausen method involves integration of the momentum equation. In the present case we integrate between the still bed level (y=0) and the initial bed height ($y=\delta_S$) which we define as the level of the crests of the grains on the surface when the flow is stationary and all sediment has settled on the bed. Thus

$$\delta_s = \frac{1}{C_*}\int_0^\infty C\, dy \tag{3}$$

where C is the concentration of sediment at any height y and C_* is the limiting value of C for a stationary bed.

To start with we consider only the situation where $K_1\delta_s \le 1$. If we denote the amplitude of u at $y=\delta_S$ by U_m we have

$$K_1 = \frac{1}{\delta_s}\frac{U_m}{U_0}. \tag{4}$$

Also, if there is to be no discontinuity in phase at $K_1 y = 1$ we must have

$$K_2 = \frac{\phi}{\delta_s}\frac{U_m}{U_0} \tag{5}$$

We take the shear stress at $y=\delta_S$ to be

$$\tau = \tau_0 \; R\left\{e^{i(\omega t+\theta)}\right\}, \tag{6}$$

where τ_0 and θ are constants. At the lower boundary ($y=0$)

$$(\tau)_{y=0} = const\ \mu\left(\frac{\partial u}{\partial y}\right)_{y=0} \tag{7}$$

where μ is dynamic viscosity. The constant in this equation is intended to allow for the fact that the effective viscosity is a function of C/C_*. We assume that it is a constant because C/C_* must reach some limiting value as $y \to 0$ and so effective viscosity must tend to a limit also.

If Eq (7) holds it follows from Eq(1) that we may also write

$$(\tau)_{y=0} = \tau_b \; R\left\{e^{i(\omega t+\phi)}\right\}. \tag{8}$$

The momentum equation is

$$\rho_m \frac{\partial u}{\partial t} = -\frac{\partial p}{\partial x} + \frac{\partial \tau}{\partial y}, \tag{9}$$

where ρ_m is the density of the fluid/sediment mixture. Outside the boundary layer at the bed it follows from Eqns (9) and (2) that

$$\frac{\partial p}{\partial x} = \rho U_0\, \omega \sin \omega t \tag{10}$$

where ρ is fluid density. Substituting in Eq (9) and integrating from y=0 to $y=\delta_S$ we have

$$\tau_0 e^{i(\omega t+\theta)} - \tau_b e^{i(\omega t+\phi)} = \int_0^{\delta_s}\left(\rho_m \frac{\partial u}{\partial t} - i\rho U_0 \omega\, e^{i\omega t}\right)dy \tag{11}$$

$$= \frac{\rho_m U_0 \omega}{K_1}\left[B^2\left(i - \frac{U_m}{BU_0}\right)e^{i(\omega t+\phi(1-U_m/U_0)} - iB^2 e^{i(\omega t+\phi)} - \frac{iU_m}{U_0}\frac{\rho}{\rho_m}e^{i\omega t}\right]$$

where

$$B = \frac{K_1}{K_2} = \frac{1}{\phi}, \tag{12}$$

and we have assumed ρ_m to be constant throughout the mobile layer. Dividing through by $\exp(i(\omega t + \theta))$ and then equating real and imaginary parts of Eq (11) we find

$$\tan(\phi-\theta) = \frac{\cos(\phi-\theta) - \cos\gamma + \frac{U_m\phi}{U_0}\sin\gamma + \frac{U_m}{U_0}\frac{\rho}{\rho_m}\phi^2\cos\theta}{\frac{\tau_0 K_1\phi^2}{\rho_m U_0\omega} - \sin(\phi-\theta) + \sin\gamma + \frac{U_m\phi}{U_0}\cos\gamma + \frac{U_m}{U_0}\frac{\rho}{\rho_m}\phi^2\sin\theta} \tag{13}$$

and

$$\tau_b \sin(\phi-\theta) = \frac{\rho_m U_0\omega}{K_1\phi^2}\left[\cos(\phi-\theta) - \cos\gamma + \frac{U_m\phi}{U_0}\sin\gamma + \frac{U_m}{U_0}\frac{\rho}{\rho_m}\phi^2\cos\theta\right] \tag{14}$$

where

$$\gamma = \phi\left(1 - \frac{U_m}{U_0}\right) - \theta \tag{15}$$

As mentioned earlier, the flow may be treated as quasi-steady when the pressure gradient and inertia terms are negligible, i.e when the parameter

$$S = \frac{\rho U_0\omega}{(\rho_s - \rho)g} \tag{16}$$

is small. Here ρ_s is the density of the sediment. Under these conditions the normal stress due to grain/grain interactions supports the sediment above at each instant in the wave cycle. If the ratio of shear stress to normal stress at the bottom of the mobile layer is some constant K (as shown by Bagnold, 1954, Savage and McKeown, 1983, Hanes and Inman, 1985)

$$\tau_b = K(\rho_s - \rho)\, g\, C_*\, \delta_s \tag{17}$$

where δ_s is, under these conditions, the maximum thickness of the mobile layer during the course of a half cycle.

Dick and Sleath (1991) showed that δ_s remains nearly constant during the cycle at larger values of S. Under these circumstances we assume that it is the average value of the normal stress over a half cycle which supports the sediment above. Thus

$$\tau_b \frac{2}{\pi} = K(\rho_s - \rho)\, g\, C_* \,\delta_s \tag{18}$$

Substituting from Eq (14) into Eq (18)

$$\frac{\pi}{2}\sin(\phi-\theta)\, KC_* = \frac{\rho U_0 \omega}{(\rho_s-\rho)g}\frac{\rho_m}{\rho K_1 \delta_s \phi^2}\left[\cos(\phi-\theta) - \cos\gamma + \frac{U_m \phi}{U_0}\sin\gamma + \frac{U_m}{U_0}\frac{\rho}{\rho_m}\phi^2\cos\theta\right] \tag{19}$$

(This is the expression for high S. The expression for low S is the same with the leading $\pi/2$ deleted).

Finally, from Eqns (1), (7) and (18),

$$const\ \mu K_1 U_0 = \frac{\pi}{2} K(\rho_s - \rho)\, g\, C_* \,\delta_s . \tag{20}$$

Eqns (4), (13), (19) and (20) allow us to determine U_m/U_0, $\rho U_0 \omega \delta_s/\tau_0$ and ϕ for any value of $\rho U_0 \omega/(\rho_s-\rho)g$ provided we know the flow conditions, the sediment properties, and the value of the constant in Eqn (7).

So far, we have considered only the case where $K_1\delta_s \le 1$. This is the situation which applies at small to medium values of S. At large values of S we need to consider $K_1\delta_s > 1$. This involves extending the integration in Eq (11) into the region covered by Eq (2). The extension is straightforward and, consequently, will not be discussed further here.

3. Comparison with experiment at large S

The main aim of the present paper is to investigate trends at high values of S. Consequently, we will compare the computed curves with the measurements of Dick and Sleath (1991) and Zala Flores and Sleath (1998) for acrylic sediment of density 1141 kg/m^3 and median diameter 0.7 mm.

The best fit of the experimental data for mobile layer thickness to the computed curves gives a value for the constant in Eq (7):

$$const = 14860 \tag{21}$$

Assuming this value to be correct, we can calculate curves for the various quantities of interest for given values of the parameter V defined as

$$V = f_w \frac{U_0}{(\omega\nu)^{1/2}} \tag{22}$$

where

$$f_w = \frac{\tau_0}{\frac{1}{2}\rho U_0^2} \tag{23}$$

is the friction factor calculated from Jonsson's (1963) curve for flat beds.

Fig. 1 shows how the ratio of the scaling factors K_1 / K_2 varies with the parameter $S = \rho U_0 \omega / (\rho_s - \rho) g$. Both theory and experiment show that the ratio is close to unity over a wide range of S, although the theory predicts a rise in K_1 / K_2 as $S \to 0$. The theoretical value of K_1 / K_2 at large S shows little dependence on the value chosen for the various constants.

The way in which the phase lead ϕ of the velocity at the bottom of the mobile layer varies with S is shown in Fig. 2. The parameter S is a measure of the importance of the pressure gradient terms in the equations of motion. As $S \to 0$, the

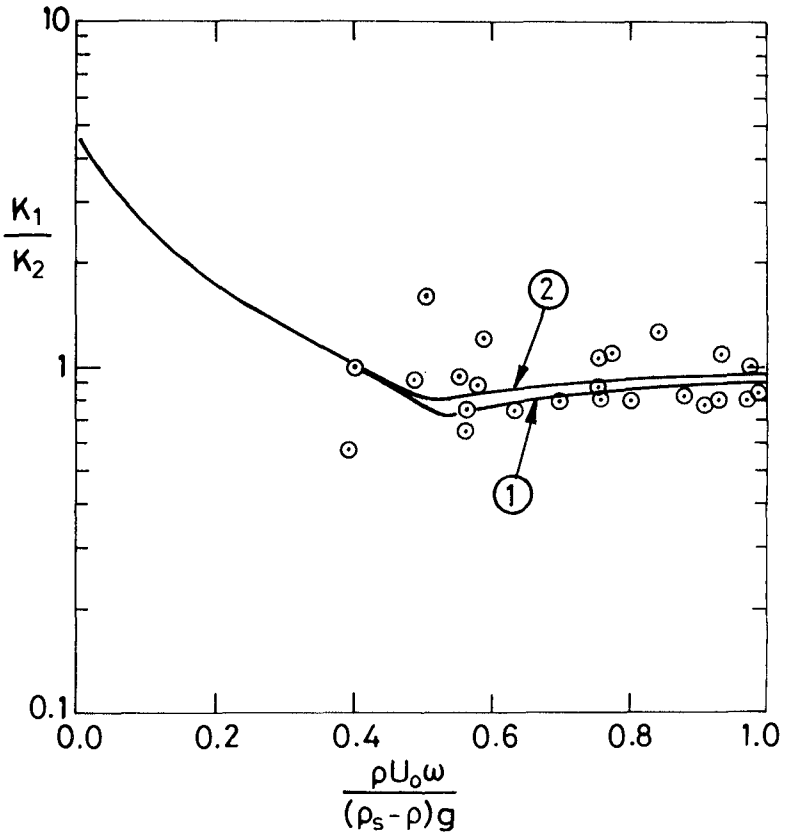

Fig.1 Variation of K_1 / K_2 with $\rho U_0 \omega / (\rho_s - \rho) g$ for the acrylic sediment of Dick and Sleath (1991). Curve 1, V=10; curve 2, V=25 (assuming $C_* K$=0.35, θ = 12.5°).

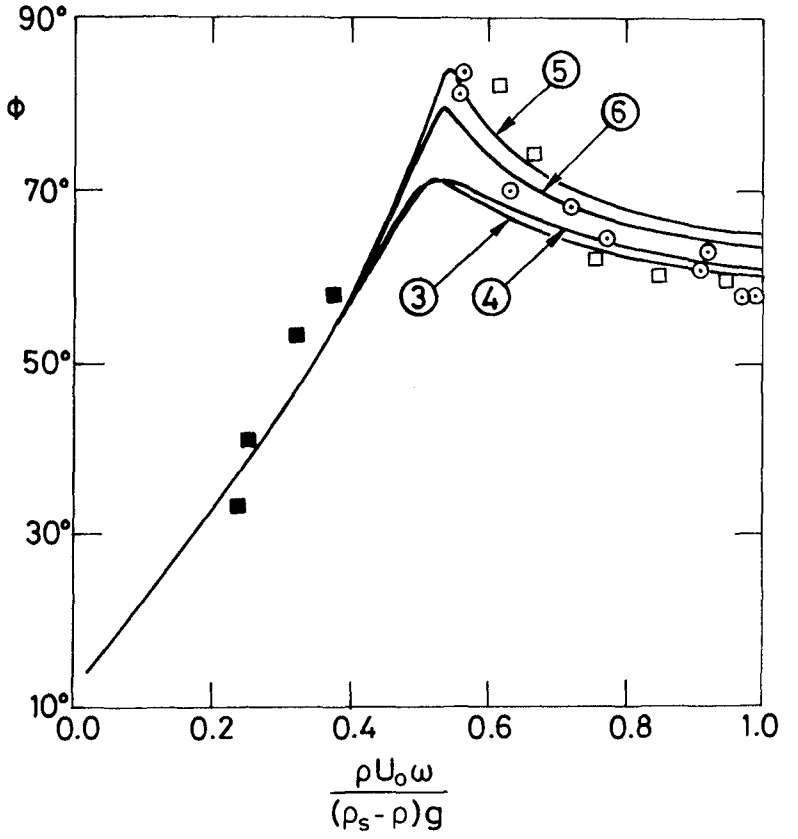

Fig.2 Variation of ϕ with $\rho U_0 \omega / (\rho_s - \rho) g$. Dick and Sleath (1991): o (acrylic). Zala Flores and Sleath (1998): □ (acrylic), ■ (PVC). Curve 3, V=25; curve 5, V=4; curve 6, V=10; curve 4, inertial boundary condition with I=0.8, (C_*K=0.35, $\theta = 12.5°$ in each case).

pressure gradient terms become negligible and the flow is dominated by the shear stress acting on the upper surface of the mobile layer. Consequently, in this limit $\phi \to \theta$. As S increases from zero, pressure gradient becomes more important and the phase ϕ moves closer towards that of the pressure gradient. However, when S exceeds C_*K the thickness of the mobile layer becomes much larger and consequently the inertia of the fluid/sediment mixture in the mobile layer becomes significant. This is why the value of ϕ falls at large S.

In Dick and Sleath's (1991) tests with acrylic sediment the values of V ranged from 6.8 at S=0.55 up to 18.5 at S=0.96. Consequently, the agreement between these tests and the computed curves in Fig. 2 is good. Zala Flores and Sleath's (1998) tests with acrylic sediment, which cover a similar range of values of S and V also show good agreement with the computed curves. This is more surprising since most of these

tests showed plug formation. It would appear that plug formation does not significantly modify the value of ϕ.

Fig. 2 also shows Zala Flores and Sleath's (1998) results for PVC granules. Once again there is good agreement with the trend of the computed curves even though we would expect the computations to be less reliable at small S.

In both Figs 1 and 2 the value of C_*K has been taken as 0.35. An increase in C_*K would move the computed curves bodily to the right and a decrease to the left. The value of 0.35 was chosen so that the maximum of the computed curves fell in approximately the right place in Fig. 2. The value of θ selected for the computations is typical of velocity measurements over rough beds. The computed curves were found to be relatively insensitive to the value chosen for θ.

It was suggested by Bagnold (1954) that under some conditions the component of shear stress due to grain/grain interactions is proportional to the square of the velocity gradient rather than directly proportional to it. He referred to this situation as the "inertial" regime. The interstitial component of shear stress at the bottom of the mobile layer would be relatively small in this situation and so Eq (7) would have to be replaced by an expression of the form

$$(\tau)_{y=0} = const\ \rho_s D^2 \left(\frac{\partial u}{\partial y}\right)^2_{y=0} \tag{24}$$

where D is median grain size. Fig. 2 shows, for purposes of comparison, a curve computed with this inertial boundary condition instead of Eq (7). For this curve, the constant in Eq (24) has been taken equal to 125 and the parameter

$$I = f_w \left[\frac{a}{D}\right]^{2/3} \tag{25}$$

is equal to 0.8. Clearly, the use of an inertial boundary condition does not significantly change the general trend of the computed curves.

A quantity of great interest from the engineering point of view is the thickness δ_s of the mobile layer. At low values of S pressure gradient terms are unimportant and consequently δ_s is a function only of $\tau_0/(\rho_s - \rho)g$. Sleath (1994) suggested, from comparison with experiment, that

$$\frac{\delta_s}{D} = 2.94 \frac{\tau_0}{(\rho_s - \rho)gD} \tag{26}$$

At high values of S it is the shear stress which is unimportant and, consequently, we expect the parameter $\beta\delta_s$ to be a function of S alone. Fig. 3 shows how the computed curves for $\beta\delta_s$ compare with the measurements of Dick and Sleath (1991) and Zala Flores and Sleath (1998) for acrylic sediment. We see that there are distinct curves for different values of V at low values of S but that at high values of S the various curves are almost identical. Dick and Sleath's (1991) results lie in the range $6.8<V<18.5$ so the agreement with the computed curves is good. The agreement with the experimental results of Zala Flores and Sleath (1998) is less good. This is probably because these tests showed plug formation. Under these conditions the assumption leading to Eq (18) is not correct.

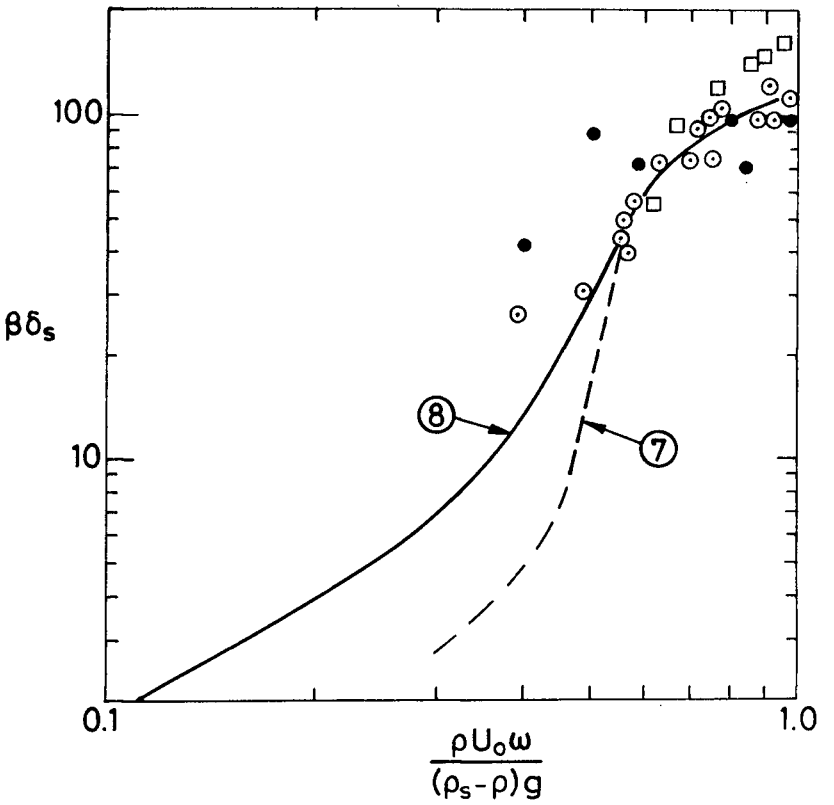

Fig.3 Variation of $\beta\delta_s$ with $\rho U_0\omega/(\rho_s-\rho)g$. Dick and Sleath (1991): ○ (acrylic), ● (nylon). Zala Flores and Sleath (1998): □ (acrylic). Curve 7, V=10; curve 8, V=25, (C_*K=0.35, θ = 12.5° in each case).

Fig. 3 also shows Dick and Sleath's (1991) measurements with Nylon pellets of density 1137 kg/m^3 and median diameter 4.0 mm. The agreement with the computed curves is less good than for the acrylic sediment, particularly at low values of S. The reason may be that curves 7 and 8 in Fig. 3 are upper bounds, as discussed in the next Section.

4. Upper bound and lower bound

So far, we have assumed that the thickness of the mobile layer varies little during the course of a wave cycle and, consequently, it is the average value of the dispersive stress which supports the weight of sediment above. The measurements of Dick and Sleath (1991) showed that this was the situation at very large values of S. At low values of S the sediment settles onto the bed as the flow slows down and then is

eroded again after flow reversal, so there is significant variation in mobile layer thickness during the course of the cycle. Under these circumstances we should use Eq (17) rather than Eq (18).

Most flows show variations in mobile layer thickness during the course of the wave cycle which are somewhere between the two extremes outlined above. Consequently, we should regard curves computed with the aid of Eq (18) as upper bounds and those computed with the aid of Eq (17) as lower bounds. Fig. 4 shows how these upper and lower bound curves compare with the measurements of Li and Sawamoto (1995a) and of Zala Flores and Sleath (1998) with PVC pellets. The upper bound curves are the same as those shown in Fig. 3. We see that the measurements lie between the upper and lower bound curves.

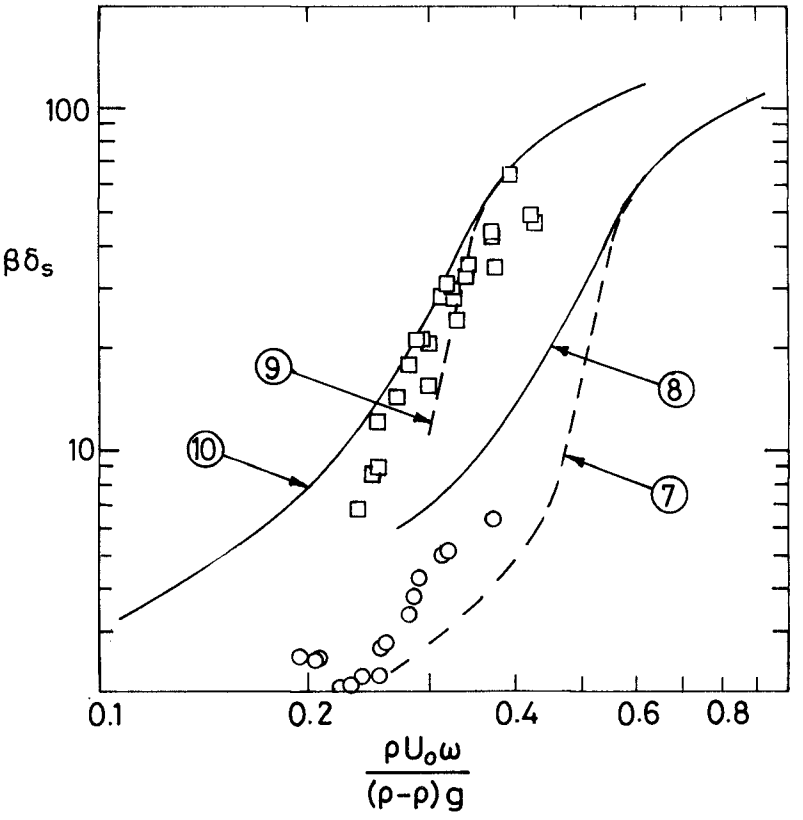

Fig.4 Variation of $\beta\delta_s$ with $\rho U_0\omega/(\rho_s-\rho)g$. Li and Sawamoto (1995a): ○. Zala Flores and Sleath (1998): □ (PVC). Upper bound, Eq (18): curve 7, V=10; curve 8, V=25. Lower bound, Eq (17): curve 9, V=10; curve 10, V=25. (C_*K=0.35, θ=12.5° in each case).

5. Maximum thickness of mobile layer

The experimental measurements in Figs 1,2,3,4 extend to much larger values of S than those likely to be encountered on site. For example, even under extreme conditions the value of S in the Leman Field in the Southern North Sea does not exceed about 0.2. Madsen's (1974) calculations suggest that a local value of S under the steep forward slope of a near-breaking wave might be as high as 0.36. But, even accepting this higher figure, it would seem from Figs 3 and 4 that the value of $\beta\delta_s$ for beds of sediment on site is unlikely to exceed about 100.

For the Southern North Sea a typical value of wave period for a 50-year storm might be about 13s. With $\beta\delta_s$=100 we obtain $\delta_s \approx 0.2$ m. This value is significantly less than that given by existing empirical formulae for depth of disturbance in the surf zone. For example, the results of King (1951) suggest a depth of disturbance of about 0.5 m for a 50-year storm in the Southern North Sea and Williams' (1971) results lead to even larger values. The most likely explanation for this difference is that the empirical formulae include effects such as the movement of the offshore bar or the migration of sand waves. Clearly, the experimental data and the computations discussed in this paper are for very restricted conditions. The existence of effects such as bed form migration needs to be borne in mind when extending the results to the real world.

6. Conclusions

(1) Use of the Karman-Polhausen technique makes it possible to calculate parameters of interest without having to assume constitutive equations such as those suggested by Bagnold (1954).

(2) The calculated curves show good agreement, at high values of S, with existing laboratory measurements of the mobile layer thickness, the phase lead of the velocity at the bottom of the mobile layer, and the ratio of the velocity amplitude and phase scales K_1 / K_2.

(3) It is suggested that curves based on the assumption that δ_s is constant during the course of a wave cycle provide an upper bound on the value of S for any given value of $\beta\delta_s$. A lower bound is provided by the assumption that maximum δ_s during the course of a cycle correlates with maximum dispersive stress.

(4) Although the calculated curves show good agreement with laboratory measurements, the estimates of mobile layer thickness are smaller than the values for depth of disturbance in the surf zone provided by existing empirical formulae. This may be because the present results are for flat beds and, consequently, do not include any allowance for the effects of bed form migration.

Appendix. References

Asano, T. (1992). Observations of granular-fluid mixture under an oscillatory sheet flow, *Proc. 23rd Conf. Coastal Eng.,* ASCE, Reston, Va., 1896-1909.

Bagnold, R.A. (1954). Experiments on a gravity-free dispersion of large solid spheres in a Newtonian fluid under shear, *Proc. R. Soc. London,* A, 225, 49-63.

Bagnold, R. A. (1956). The flow of cohesionless grains in fluids, *Phil. Trans. R. Soc. London,* A, 249, 235-297.

Bakker, W.T., and Van Kesteren, W.G.M. (1986). The dynamics of oscillating sheet flow. *Proc. 20th Conf. Coastal Eng.*, ASCE, Reston, Va., 940-954.

Dibajnia, M and Watanabe, A. (1992). Sheet flow under nonlinear waves and currents, *Proc. 23rd Conf. Coastal Eng.,* ASCE, Reston, Va., 2015-2028.

Dick, J.E., and Sleath, J.F.A. (1991). Velocities and concentrations in oscillatory flow over beds of sediment, *J. Fluid Mech.,* 233, 165-196.

Hanes, D. M., and Inman, D. L. (1985). Observations of rapidly flowing granular-fluid materials, *J. Fluid Mech.*, 150, 357-380.

Horikawa, K., Watanabe, A., and Katori, S. (1982). Sediment transport under sheet flow conditions, *Proc. 18th Conf. Coastal Eng.*, ASCE, Reston, Va., 1335-1352.

Jonsson, I.G. (1963). Measurements in the turbulent wave boundary layer, *J. Hydr. Res.,* 14(1), 45-60.

Kaczmarek, L.M., Ostrowski, R., and Zeidler, R.B. (1995). Boundary layer theory and field bedload, *Proc. Coastal Dynamics 95, Gdansk,* ASCE, Reston, Va., 664-675.

Katori, S., Mizuguchi, M., and Watanabe, A. (1996). A numerical model of sheet flow sediment transport, *Proc. 25th Conf. Coastal Eng.*, ASCE, Reston, Va., 3818-3829.

King, C.A.M. (1951). Depth of disturbance of sand on sea beaches by waves, *J. Sed. Petrol.,* 21, 131-140.

Li, L., and Sawamoto, M. (1995a). Experiments on sediment transport in sheet-flow regime under oscillatory flow, *Coastal Eng. Japan, 38,* 143-156.

Li, L., and Sawamoto, M. (1995b). Multi-phase model on sediment transport in sheet-flow regime under oscillatory flow. *Coastal Eng. Japan,* 38, 157-178.

Nadaoka, K., and Yagi, H. (1990). Single-phase fluid modelling sheet-flow toward the development of numerical mobile bed, *Proc. 22nd Conf. Coastal Eng.*, ASCE, Reston, Va., 2346-2359.

Ono, M., Deguchi, I., and Sawaragi, T. (1996). A numerical model of sheet flow sediment transport, *Proc. 25th Conf. Coastal Eng.*, ASCE, Reston, Va., 3888-3900.

Ribberink, J. S. and Al-Salem, A. A. (1994). Sediment transport in oscillatory boundary layers in cases of rippled beds and sheet flow. *J. Geophys. Res.,* 99, C6, 12 707-12 727.

Ribberink, J. S. and Al-Salem, A. A. (1995). Sheet flow and suspension of sand in oscillatory boundary layers, *Coastal Eng.*, 25, 205-225.

Savage, S.B. and McKeown, S. (1983). Shear stresses developed during rapid shear of concentrated suspensions of large spherical particles between concentric cylinders. *J. Fluid Mech*, 127, 453-472.

Sawamoto, M., and Yamashita, T. (1986). Sediment transport rate due to wave action, *J. Hydrosci. Hydraul. Eng.*, 4(1), 1-15.

Schichtling, H. (1979). *Boundary Layer Theory,* 7th ed., McGraw-Hill, New York.

Sleath, J.F.A. (1994). Sediment transport in oscillatory flow, *Sediment Transport Mechanisms in Coastal Environments and Rivers,* M. Belorgey, R.D. Rajaona, and J.F.A. Sleath, eds., World Scientific, Singapore.

Williams, A.T. (1971). An analysis of some factors involved in the depth of disturbance of beach sand by waves, *J. Mar. Geol.,* 11, 145-158.

Zala Flores, N., and Sleath, J.F.A. (1998). Mobile layer in oscillatory sheet flow. *J. Geophys. Res.*, 103, C6, 12 783-12 793.

Numerical Investigation of Sediment Transport for Combined Waves and Currents

Juan Savioli[1]

Abstract

This paper presents a numerical investigation of sediment transport under the combined effect of waves and current motion. Comparison of predictions to experimental measurements showed good agreement. The presence of a second peak over the decelerating and flow reversal was predicted by the numerical model due to the inclusion of an extended bed reference concentration and a turbulence model that is able to predict a sudden increase of the turbulent properties of the flow over this stage. Evidence suggests that the second peak is caused by an inflection point in the velocity profile leading to high diffusivities near the wall.

Introduction

Sediment transport in a coastal environment occurs under the action of a number of hydrodynamic processes. These cover flow situations ranging from waves to currents while passing though a variety of combined wave-current situations. In order to describe these complex mechanisms it is rather common to simplify them into ideal cases as pure waves or pure currents, but in most real situations we are confronted with rather complex situations, where waves and currents interact. The purpose of this work is to perform a numerical experiment of sediment transport under the combined effects of waves and currents

Model Description

The temporal description of the suspended sediment can be expressed as a transport equation where particles are advected by means of their own settling velocity and

[1] Coastal Engineer, Danish Hydraulic Institute, Agern Allé 5, DK-2970 Hørsholm, Denmark. Email: jcs@dhi.dk. International Institute for Infrastructural, Hydraulic and Environmental Engineering, (IHE), PO Box 3015, 2601 DA Delft, The Netherlands.

diffused by the natural turbulence of the flow. This, for the one-dimensional (in vertical) case, can be mathematically expressed as:

$$\frac{\partial c}{\partial t} = \frac{\partial (c w_s)}{\partial z} + \frac{\partial}{\partial z}\left(\varepsilon_s \frac{\partial c}{\partial z}\right) \tag{1}$$

where c is the concentration of sediment particles, w_s the settling velocity of the particles and M_s the turbulent diffusion of sediment particles.

This equation can be solved numerically if the value of the settling velocity, the turbulent diffusion of the sediment particles and an appropriate reference concentration or sediment flux are known. The description of the flow is carried out by solving the momentum equation in the x-direction

$$\frac{\partial u}{\partial t} = -\frac{1}{\rho}\frac{\partial p}{\partial x} + \frac{\partial}{\partial z}\left(\nu \frac{\partial u}{\partial z} - \overline{u'w'}\right) \tag{2}$$

where $\overline{u'w'}$ is the effective component of the Reynolds-stresses and Y is the kinematic viscosity.

Since the case to be simulated is associated with high Reynolds numbers the viscous stresses are negligible. The turbulent stresses, on the other hand, have to be expressed as function of the mean quantities. A turbulence model has to be applied then to express the correlation between the turbulent velocities as a function of the mean flow variables. Adopting the Boussinesq assumption, the effective shear stress, arising from the cross-correlation of fluctuating velocities, can be replaced by the product of the mean velocity gradient and a turbulent viscosity; the turbulent stresses can then be expressed for the one-dimensional case as:

$$\overline{u'w'} = \nu_t \frac{\partial u}{\partial z} \tag{3}$$

where Y_t, unlike the molecular viscosity T, is not a property of the fluid. Under this assumption, the Reynolds stresses are defined in terms of only one unknown quantity, the eddy viscosity, therefore it is necessary to express the value of the turbulent eddy viscosity in terms of the known mean-flow quantities therefore the *k*-M model was applied (Rodi, 1984).

This model is based on two transport equations, one for the turbulent kinetic energy *k* and a second one to compute the rate of turbulent energy dissipation M. These two equations are expressed for the one-dimensional case as:

$$\frac{\partial k}{\partial t} = \frac{\partial}{\partial z}\left(\frac{\nu_t}{\sigma_k}\frac{\partial k}{\partial z}\right) + \nu_t\left(\frac{\partial u}{\partial z}\right)^2 - \varepsilon \tag{4}$$

$$\frac{\partial \varepsilon}{\partial t} = \frac{\partial}{\partial z}\left(\frac{\nu_t}{\sigma_\varepsilon}\frac{\partial \varepsilon}{\partial z}\right) + c_\varepsilon \frac{\varepsilon}{k}\ \nu_t\left(\frac{\partial u}{\partial z}\right)^2 - c_{\varepsilon 2}\frac{\varepsilon^2}{k} \tag{5}$$

where the turbulent eddy viscosity is defined as:

$$\nu_t = c_1 \frac{k^2}{\varepsilon} \tag{6}$$

The value of the constants considered for this type of flow are expressed in Table 1

c_1	c_{M1}	c_{M2}	$[_k$	$[_M$
0.09	1.44	1.92	1.00	1.30

Table 1 *Values of the constants applied in the k-*M *model*

In the case of combined waves and current it can be assumed that the ambient pressure can be obtained as a combination of the oscillatory component added to the pressure gradient that drives the current, therefore the 'total' ambient pressure can be obtained as the sum of the individual components. In oscillatory boundary layers it is assumed that the ambient pressure penetrates the entire boundary layer undisturbed. The pressure gradient can be obtained by applying the momentum equation in the x-direction to an outer boundary layer where the turbulence-representing quantities are assumed to vanish and the velocity approaches the free stream velocity u_∞. In the case of a pure current the pressure gradient is then related to the slope of the energy line and the pressure gradient of both effects can be expressed as follows:

$$\frac{1}{\rho}\frac{\partial p}{\partial x} = -\frac{\partial u_\infty}{\partial t} - gHS \tag{7}$$

The resulting one-dimensional equation for the mean flow is then expressed as:

$$\frac{\partial u}{\partial t} = \frac{\partial u_\infty}{\partial t} - gHS - \frac{\partial}{\partial z}\left(\nu_t \frac{\partial u}{\partial z}\right) \tag{8}$$

Boundary conditions at the free boundary must be also introduced. Here the distribution of kinetic energy and the rate of dissipation of kinetic energy are defined as a symmetric condition.

$$\frac{\partial k}{\partial z} = 0 \qquad \frac{\partial \varepsilon}{\partial z} = 0 \tag{9}$$

On the wall, a non-slip condition applies, so that the velocity is considered to be zero

$$u = 0 \tag{10}$$

The behaviour of the wall can be considered hydraulically rough, so that the friction velocity can be obtained by assuming a logarithmic velocity distribution

$$u = \frac{u_f}{\kappa} \ln\left(\frac{z}{z_0}\right) \tag{11}$$

where u_f is the friction velocity, P is the von Karman constant and $z_o = k_n/30$, k_n being the Nikuradse equivalent roughness.

In this area close to the wall, the Reynolds stresses are nearly constant so that the convection and diffusion of turbulence can be considered negligible and local equilibrium prevails. Accordingly, the production and dissipation of kinetic energy balance out and applying the assumption of a logarithmic velocity distribution, the values of k and M at the wall boundary can be expressed as follows:

$$k = \frac{u_f^2}{\sqrt{c_1}} \qquad \varepsilon = \frac{u_f^3}{\kappa\, z_0} \tag{12}$$

The solution of the transport equation requires also the definition of the boundary conditions for the bed and the free surface. In the case of the free surface, no flux of sediments is possible; therefore:

$$w_s c + \varepsilon_s \frac{\partial c}{\partial z} = 0 \tag{13}$$

In the case of the bed the definition of the concentration of more complicated. In this case the ratio between the stabilizing and agitating forces, defined as Π', is related to the value of the concentration at the bottom, so that a relationship between a bed concentration and Π' can be established. Zyserman and Fredsøe (1994), proposed and empirical formulation which related the bed concentration at $z = 2\ d_{50}$ to the Shields parameter, Π'. This formulation, which will be applied in the present model, is expressed as follows:

$$c_b = \frac{A(\theta' - \theta_c)^m}{1 + A/c_m(\theta' - \theta_c)} \tag{14}$$

where $\Pi' > \Pi_c = 0.045$ and A=0.331, c_m=0.46 and m=1.75

Figure 1 shows a comparison of the bed reference concentration as obtained from this empirical equation with measured data.

In the case of a flow which is reduced from a value of Π' which is larger than the critical value to zero, the reference concentration drops to zero as soon as the value Π' is less or equal to the critical value, and this does not seem physical correct. For this reason Justesen et al. (1986) proposed a so-called flux boundary condition where the value of the bed concentration, c_b, is also a function of the settling velocity of the particles, expressed as:

$$c_b = \max\{c_b(\theta'), c(w_s)\} \tag{15}$$

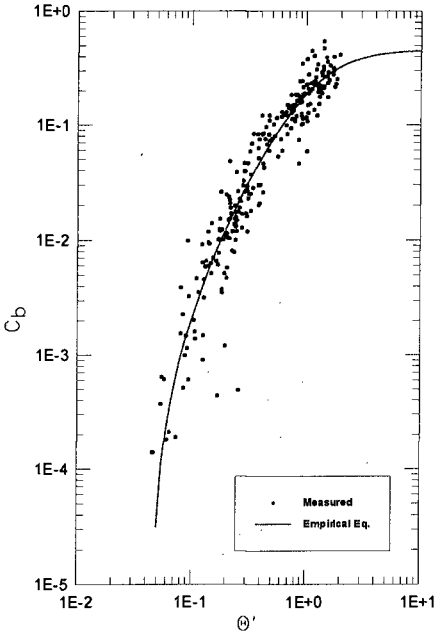

Figure 1. *Comparison of Zyserman and Fredsøe's empirical formulation with measured data*

This expresses that the concentration is obtained as the maximum value of the predicted concentration based on the instantaneous shear stresses or the one obtained by considering the sediment settling down by it falling velocity. This was further developed, as presented by Savioli and Justesen (1997), by including the effect of the turbulent

diffusion in the movement of the sediment particles. The boundary condition is then expressed as:

$$c_b = \{c_b(\theta'), c(w_s, \varepsilon_s)\} \tag{16}$$

In this case the bed concentration is obtained as the maximum value obtained for the concentration based on the instantaneous shear stresses, or by considering the sediment settling down and being also influenced by the turbulent diffusion generated by the flow. A detailed description of the implementation of this boundary condition is presented in Savioli and Justesen (1997). It should be remarked that this boundary condition has been applied in order to investigate the behaviour of sediment for waves and current but it is not readily applicable in practical engineering cases.

Comparison of Results and Discussion

In order to compare the model with measured data a test case was simulated. The test case has been obtained from the experimental work carried out by Katopodi et al. (1994). This was performed at the Large Oscillating Water Tunnel of Delft Hydraulics where waves, currents and wave-current flow can be simulated. Natural uniform sand was used for the tests where sediment concentrations were measured. The mean grain size of the sediment particles was d_{50}= 0.21 mm with a settling velocity of 2.6 cm/s. Test case E1 has been chosen for the comparison which is based on a sinusoidal wave combined to a current. Table 2 presents the values of the mean current velocity U_m, the wave amplitude velocity U_o and the period T for the test case.

Case	U_m *(m/s)*	U_o *(m/s)*	*T (s)*
E1	0.15	1.65	7.2

Table 2. *Characteristics of the flow for test case*

Figure 2 shows the time evolution of the measured and calculated sediment concentrations at different heights from the bed: z= 1.45 cm, 2.35 cm and 3.65 cm. At the top the undisturbed velocity is also presented.

Two major concentration peaks occur when the flow velocity is at its maximum, these are not equal in magnitude due to the combined effect of the wave and current motion. Very good agreement is obtained between the predicted and the measured data, especially close to the bed at z=1.45 cm. The model predictions show remarkable agreement in phase and value of the concentration, during the first peak. The second peak, on the other hand, is slightly underestimated. As we move up from the bed, to z= 2.35 cm and z= 3.65 the difference between the predicted and measured values of concentration becomes more significant.

It is also observed a peak in the sediment concentration at flow reversal in the measured data. This has been captured by the numerical model due to the inclusion of an extended formulation which makes sediment available at flow reversal when the flow velocity is nearly zero and therefore the Shield's parameter value is smaller than the critical value Π_c

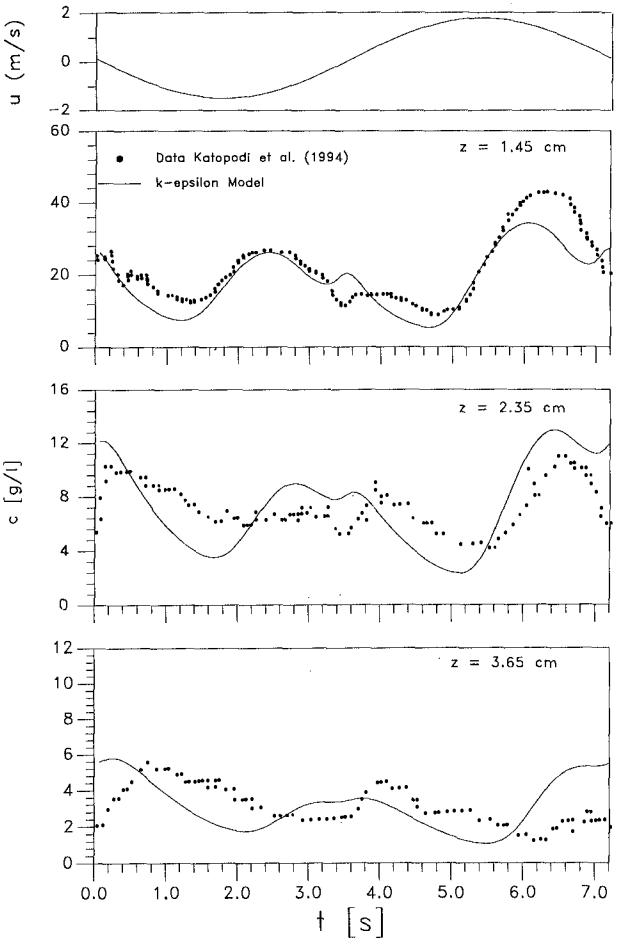

Figure 2 *Observed and predicted sediment concentrations during a whole wave period*

If the bed reference concentration would have been related only to the instantaneous bed shear stresses, $c_b = f(\theta')$, the concentration increase at flow reversal would not have been obtained since the value of the shear stresses over this period of

time is smaller than the critical value. In fact the inclusion of an extended bed reference concentration allowed this increase in the concentration at flow reversal to occur.

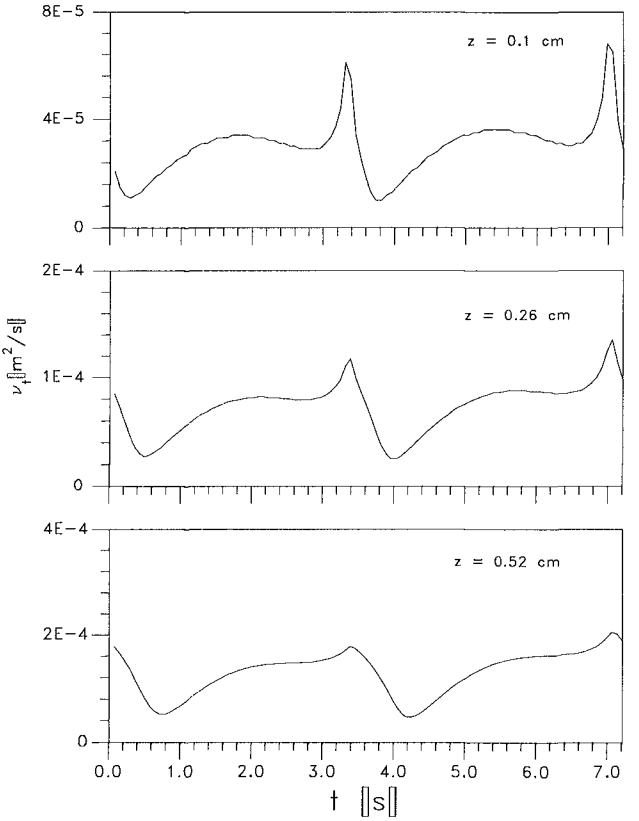

***Figure 3** Predicted value of the turbulent eddy viscosity at different distances from the bottom during a whole wave period*

In order to observe the behaviour of this extended boundary condition, the values of the turbulent eddy viscosity have been extracted at three different elevations above the bottom. Figure 3 shows the temporal variation of the turbulent eddy viscosity at z=0.1, 0.26 and 0.52 cm. It can be observed that the value of the turbulent eddy viscosity follows closely the flow velocity so that it is at its maximum when the velocity is also peaking. Nevertheless, at flow reversal, a sudden and large increase of the turbulent eddy viscosity occurs generating a period of high diffusivity that promotes the spreading of sediment particles if the sediment particles are available, as introduced in the extended boundary condition.

As it has already been introduced, the value of the turbulent eddy viscosity is dependent on the turbulent kinetic energy to the power 2 and the rate of dissipation of the turbulent kinetic energy. If we now follow the evolution of the instantaneous value of k^2 and M over a wave period, as presented in Figure 4, it is clear that the rate of growth of both of these during the acceleration stage is rather similar. O the other hand, over the deceleration phase, the rate of decay of M is much larger than and a singular point is observed at flow reversal. At this particular moment there is an inflexion point in the instantaneous velocity profile, the velocity gradient is at its maximum and there is a large production of turbulence (the production term in the k and M equations is dependent on the velocity gradient to the power 2).

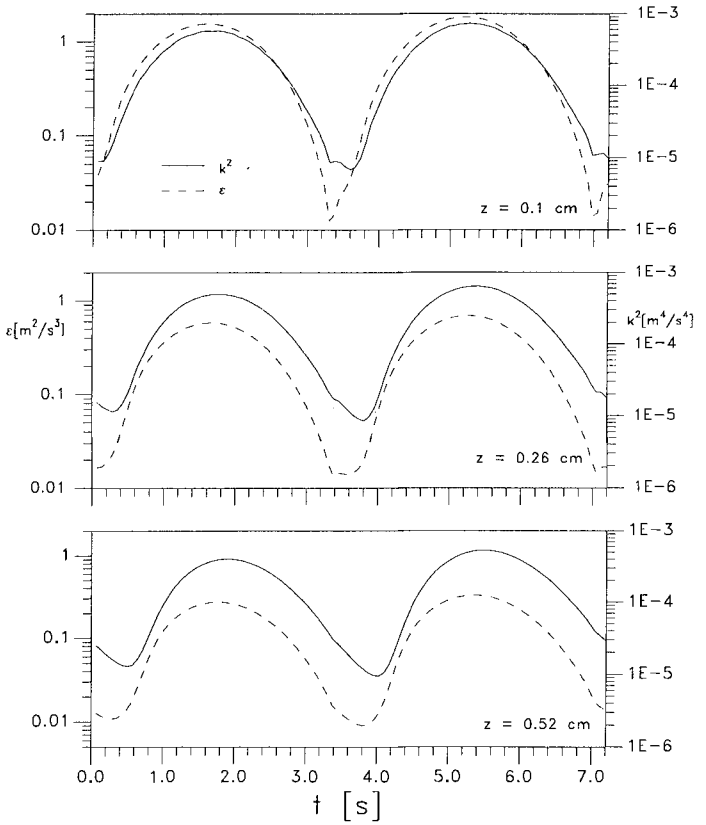

Figure 4 *Evolution of k^2 and* M *at different distances from the bottom during a whole wave period*

By analogy from the theory of gases the turbulent diffusion can be expressed as $\nu_t \propto u' l$ where u' is related to k and M to the mixing length l. What is visible from the results is that, at maximum velocity, u' is dominant while, at flow reversal, l predominates.

One of the explanations regarding this behaviour was presented by Smith in 1977 where it was expressed in the form that the non-slip condition at the bed causes the fluid close to the bed to have a smaller inertia. It will consequently respond more rapidly to the free stream pressure gradient prior to the fluid both in the upper part of the boundary layer and in the free stream. Thus, the boundary layer leads the free stream flow, resulting in an inflection point (see Figure 5) in the bottom boundary profile during flow deceleration, reversal and subsequent acceleration.

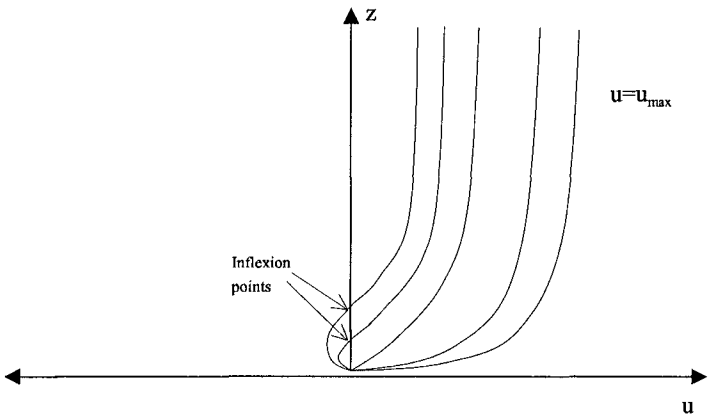

Figure 5. *Schematization of the flow velocity profiles during deceleration and flow reversal*

Foster, in 1984, presented a theoretical study that suggested that flow in the bottom leads that of the free stream, resulting in an inflection point (a necessary condition for an instability to occur) in the vertical profile of cross-shore velocity during flow deceleration and reversal. During this period small perturbations may grow exponentially to breaking, leading to increased levels of turbulence. The existence of shear instabilities during the period of flow reversal was modelled by a simple linear stability analysis on a time varying bottom boundary layer. Predicted growth rates were large enough to yield an order of magnitude increase in initial perturbation amplitudes.

Conclusions

A numerical investigation has been performed in order to predict sediment transport in a combined wave-current flow. The predictions showed good agreement with the experimental measurements. A second peak near flow reversal has been predicted due to the use of and extended boundary condition and a turbulence model that is able to predict a sudden increase of the turbulence over the deceleration stage and at flow reversal. The results suggest that there is an inflection point, a necessary condition for a shear instability. Nevertheless further analysis should be carried out to investigate the flow behaviour and the bed reference concentration in this type of flow. Soon the advance of computer technology will allow to carry out Direct Numerical Simulations which resolve all the flow features avoiding the use of turbulence models based on average quantities.

Acknowledgements

This work formed part of a doctoral degree of IHE of Juan Savioli, supervised by Prof. Michael Abbott. The author wishes to thank several of the staff of DHI and the Institute of Hydrodynamics and Hydraulic Engineering (ISVA) of the Technical University of Denmark for their support.

References

Foster, D. L., R. A. Holman and R. A. Beach (1994). Sediment events and shear instabilities in the boundary layer. In Coastal Dynamics'94, ASCE, Barcelona, Spain.

Fredsøe, J. (1984). Turbulent boundary layers in wave-current motion. J. Hyd. Eng., ASCE, 110(HY8):1103-1120.

Fredsøe, J. and R. Deigaard (1992). Mechanics of coastal sediment transport. Advanced Series of Ocean Engineering- Volume 3, World Scientific.

Justesen, P., J. Fredsøe. and R. Deigaard, (1986). The bottleneck problem for turbulence in relation to suspended sediment in the surf zone. In Proc. 20th Int. Conference of Coastal Eng., Taipei, Taiwan.

Katopodi I. et al. (1994). Intra-wave sediment transport in an oscillatory flow superimposed on a mean current. Report H-1684, Part III, Delft Hydraulics.

Li Zhihong and Alan G. Davies (1996). Towards predicting sediment transport in combined Wave-current flow. Journal of Waterway, Port, Coastal and Ocean Engineering, July/August 1996.

Savioli, J. and Justesen, P (1997). Sediment in oscillatory flows over a plane bed. Journal of Hydraulic Research IAHR, vol. 35, No 2.

Savioli J. and P. Justesen (1997) Dicussion of "Towards predicting sediment transport in combined Wave-current flow". Journal of Waterway, Port, Coastal and Ocean Engineering, November/December 1997.

Smith, J. D. (1977) Modelling of sediment transport on continental shelves, In The Sea, volume 6.

Zyserman, J. A. and Fredsøe, J. (1994). Data Analysis of bed concentration of suspended sediment. Journal of Hydraulic Engineering, ASCE, 120(9):1021-1042.

A Morphodynamic Model for River and Estuary Management

Volker Barthel* and Ulrich Zanke**
* Directorate North, Federal Administration of Waterways and Navigation, Kiel, Germany
** Technical University of Darmstadt, Germany

1. INTRODUCTION

The Elbe estuary as part of the German Bight of the North Sea provides the waters for the worlds most frequented waterway to the City and Port of Hamburg in Northern Germany (Fig.1). At semi-diurnal tides with a range of approx. 3.5 m, alternating tidal currents and sediments ranging from fine cohesive material such as clay or silt to fine and coarser sands signify the estuary. Maintenance of approximately 100 kilometers of navigational channel with widths ranging from 250 to 450 m and minimum depths of

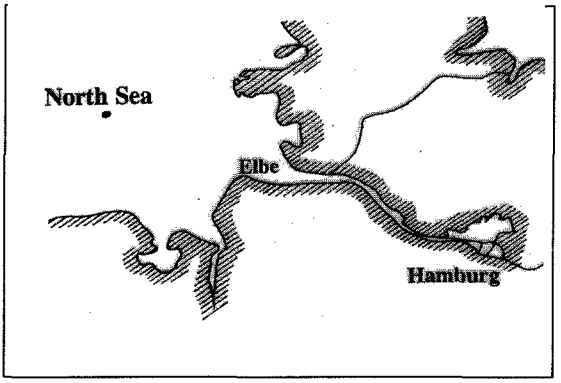

Fig.1 Elbe Estuary

13,5 m below chart datum is mostly done by dredging. Some stretches are holding natural depths of more than the required depth; in other parts the necessary flushing force of the current is achieved by concentration of flow through the arrangement of groynes and training walls.
Dredging quantities are dependent on the hydrological conditions and vary between

12 and 20 Mio. m^3 / year. In the early eighties, dredging strategies permitted material to be pumped directly ashore for deposition. However, decreasing space and increasing prices for dump sites required a change of strategy. Nowadays, most dredged spoils stay within the system. Consequently, it is dumped in deeper parts of the estuary and even of the naviagational channel. In either case, the sediment dynamics of the system will replace the dredged material and erode the dump sites and, therefore, lead to a continuous change between accumulation and erosion. Sediment which has been dredged at point A and deposited at point B can easily be transported back to A by tidal currents in no time. Therefore, the choice of dumpsites and the right time when to dump the material is of major importance.

The immediate effect of dredging operations and river training measures can easily be monitored through surveying and bathymetric comparisons. The complex nature of the estuary system and the multitude of factors of influence, however, prevent a direct correlation between bathymetric changes and the abiotic changes. This, and an effective prognosis can only be done by applying sophisticated engineering prognosis tools.

2. MORPHODYNAMIC MODELLING

The development of numerical models as engineering tools has made an enormous leap from simple 1-D-models for the simulation of hydrodynamic processes to 3D-models including the simulation of the most complicated turbulence structures in currents and waves, the transport of matter etc. Limitations are more or less set by the available computing power. While the 'real-time' inclusion of sediment transport in hydraulic modelling had found its way fairly early into physical models where scaled bed-material such as sand, coal, bakelite, ground walnut shells etc. was used to simulate the real world, the consideration of sediment transport in numerical models went through various steps of development. From a sole estimate of sediment transport on the basis of the computed hydrodynamic conditions various methods of computing sediment transport capacities were used. The hydrodynamic computation, however, was always based on a non-modified bathymetry. The step to the morphodynamic model has finally closed another gap in the suite of prediction tools by including in real time the bathymetric changes in a model (Fig.2).

The continuous calculation of the sediment transport and the sediment balance in a single grid point leads to upgrading the bathymetry at every time step. The immediate reaction of the bottom to waves and currents and, vice versa, the reaction of the hydrodynamic conditions to the changing bathymetry guarantees a much more realistic simulation of the processes than could be done with only a hydrodynamic model.

A very detailed study of morphodynamic modelling has been undertaken under the auspices of the MAST project of the European Community (Ref. Ref. To KÜSTE-paper in prep.). While the inclusion of the very details of the physical processes

involved in the transport of sediment under currents and waves can be included in the simulation process, the necessity to introduce filtering procedures [3] and/or

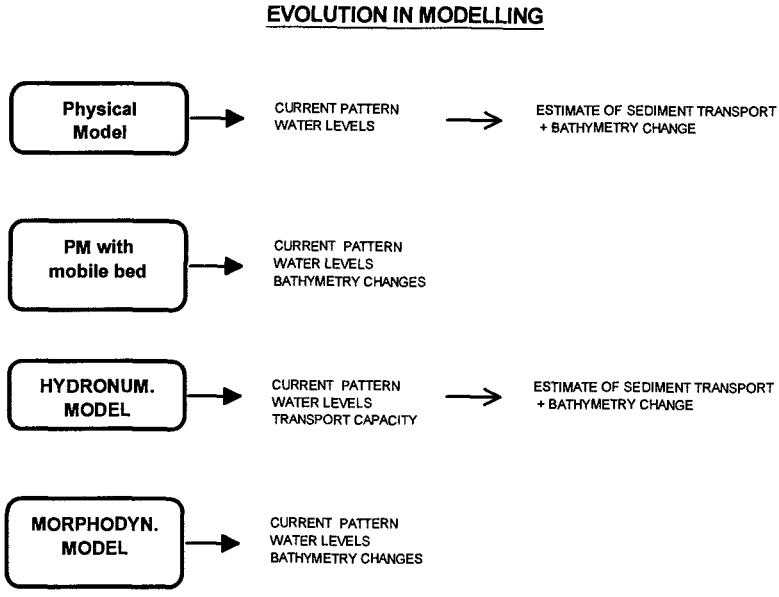

Fig. 2 Modelling Evolution

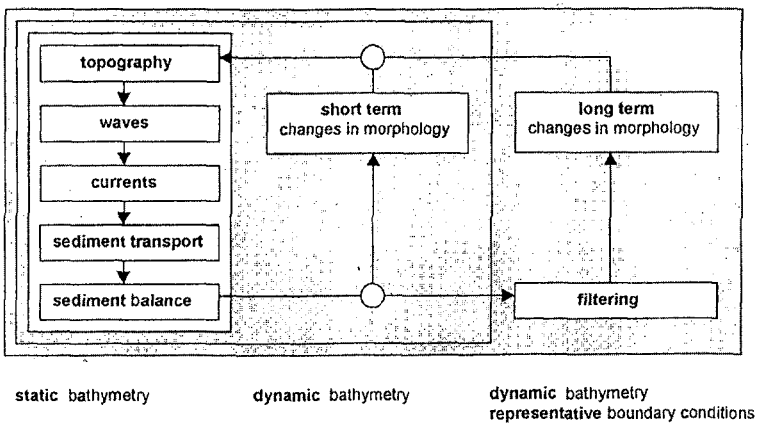

Fig . 3 Morphodynamic Modelling Concept

eliminate the influence parameters of lesser importance due to the enormous requirements of computational capacity became apparent from the beginning.

3. THE MODELLING CONCEPT

This paper describes the application of the well proven code TICAD [2] for the solution of the shallow water equations on the basis of a finite element system. The subsequently developed code TIMOR3 [7] includes the sediment transport. Basis of the morphodynamic processes is the evolution equation for the bottom:

$$\frac{\partial z}{\partial t} = \frac{\partial q_{tx}}{\partial x} + \frac{\partial q_{ty}}{\partial y} + E - S$$

with:
z = bottom elevation
q = transported quantity in x-direction
q = " " " y –direction
E = source term for erosion due to re-suspension
S = sink term for deposition

The equation is being solved numerically in time steps $\Delta t_S < \Delta t$ by an upwinding scheme. For the computation of the transported volume several sediment formulae were included in the model:

a) Integrated transport equation by Vollmers/Pernecker [8] , without transition between immobility and mobility:

$$G^* = 25 \cdot Fr^* - 1$$

with

G^* = dimensionless transport parameter
Fr^* = Froude number of the grain

Zanke [9] expands this equation by adding a likelihood function for the incipient motion:

$$G^* = 25 \cdot Fr^* \cdot R$$

with

R = risk of motion acc. to equ. 4 in Zanke [8]

$$R = (10 (Fr^* / Fr^*_{crit})^{-9} + 1)^{-1}$$

with

Fr^*_{crit} = Froude number of the grain at beginning of motion

The dimensionless transport parameter G* can be expressed in terms of the transported volume to be

$$G^* = \frac{q_{tx,ty}\,\rho' g}{u^{*3}}$$

with

qtx = transported sediment volume per unit of time and x-direction

qty = transported sediment volume per unit of time and y-direction
ρ' = relative density $(\rho_s - \rho_w) \setminus \rho_w$
ρs = sediment density
ρw = water density
g = acceleration of gravity
u* = shear stress velocity

This equation is set equal to the integrated transport equation to be solved for the transported volume per unit time and length:

$$q_{tx} = \frac{u_x^{*3}}{\rho' q}\,(25 \cdot Fr^* \cdot R)$$

$$q_{ty} = \frac{u_y^{*3}}{\rho' q}\,(25 \cdot Fr^* \cdot R)$$

with:

G^* = dimension less transport = $q_t \rho' g/u^{*3}$
q_t = transported sediment volume per unit of time and width relative density
ρ' = relative density = $(\rho_s-\rho_w)/\rho_w$
ρ_s = sediment density
ρ_w = density of water
g = acceleration of gravity
u* = shear stress velocity

In the case of the total load based equation E and S are implicitly included in the transport formula. The simulation of erosion, suspended transport and sedimentation

is solved in TIMOR3 by using entrainment-settlement-terms. The basic principle is demonstrated in Figs. 4 and 5 . Dependent on the net sediment flux of bed-load and suspended load in the bottom evolution equation the nodes of the topographic mesh change their level.

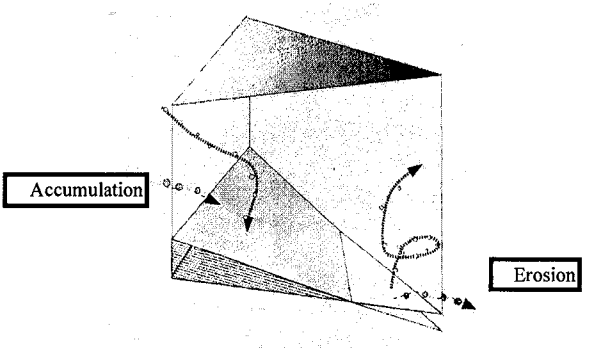

Fig. 4 Movable bed

This concept permits to continuously lift sediment from the bottom, carry it in the water column under concentration control and dump it depending on the hydrodynamic conditions. By doing this, the concentration of the suspension is not handled deterministically but simulates nature in a dynamic equilibrium. The entrainment rate for non-cohesive sediment can be taken from van Rijn [7], while the terms given by Partheniades [5] are best suited for cohesive material.

A major advantage of TIMOR3 against its predecessors is the ability to handle layered material where at every node in each layer an individual grain distribution can be defined. More than 1000 layers at each node and 10 grain size classes in each layers are possible dependent on computer capacity. Investigations with more than 100 layers have been carried out. These layers were static layers of constant thickness.

The thickness of the top layer, however, is related to the processes in the bed. As a mixing layer , which is dependent on the height of bottom ripples or dunes and follows the bed evolution, it can include one or more of the static layers. In case of accumulation active layers in the mixing zone switch from active to static one after the other. The main difference of this TIMOR3 concept to other mixing layer concepts , based only on two or three active layers [6] is the memory effect of the sediment distribution of the bottom in case of alternative and repeated accumulation and erosion. Fig. 5 demonstrates the multi-layer concept.

During the calculation the grain distribution within the active surface layers can change according to the hydrodynamic activity. As an example for the validation of the implemented sediment mixing procedure, all laboratory tests on armouring carried out by Günther [1], were re-run numerically. A main result was, that the resulting size distributions of the armour layer found by TIMOR3 were independent of the used transport formula. Only the computational time differed.

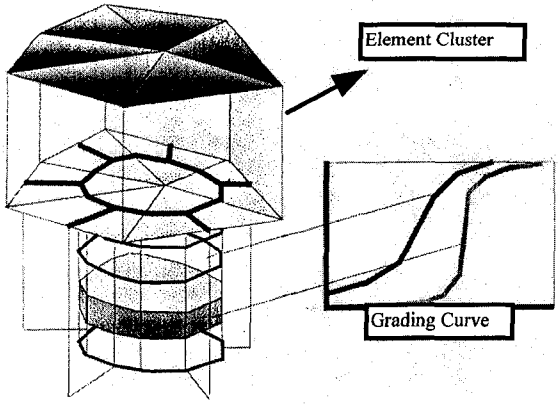

Fig. 5 The Multi-Layer Concept for an Element Cluster

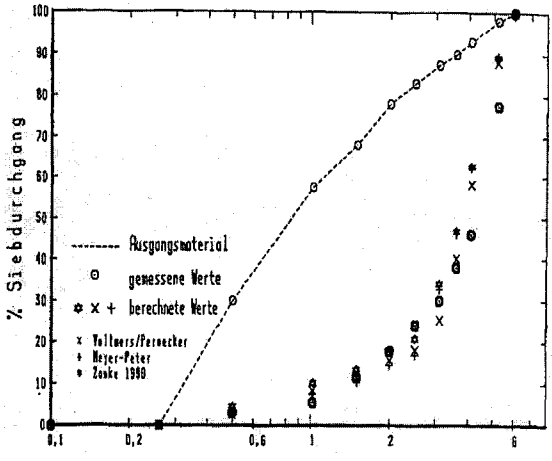

Fig. 6: Comparison between measured and calculated sediment transport
dashed line: initial cond. - o : measured values + x ✡ : calculated values

Considering the possibilities of the numerical code as mentioned before and the problems to be solved through the model application the steps in the various simulation runs, as indicated in Fig. 7 had to be followed.

The simulation of long term processes such as the evolution of an estuary under currents and waves considering the variability of the tide can be a time consuming operation. For short term simulations such a neap-spring cycle reproducing the actual tidal signal may be still feasible. However, if the development of the bathymetry and the long-term effect of construction measures is to be investigated the computational costs can become excessive. Therefore, methods needed to be developed which

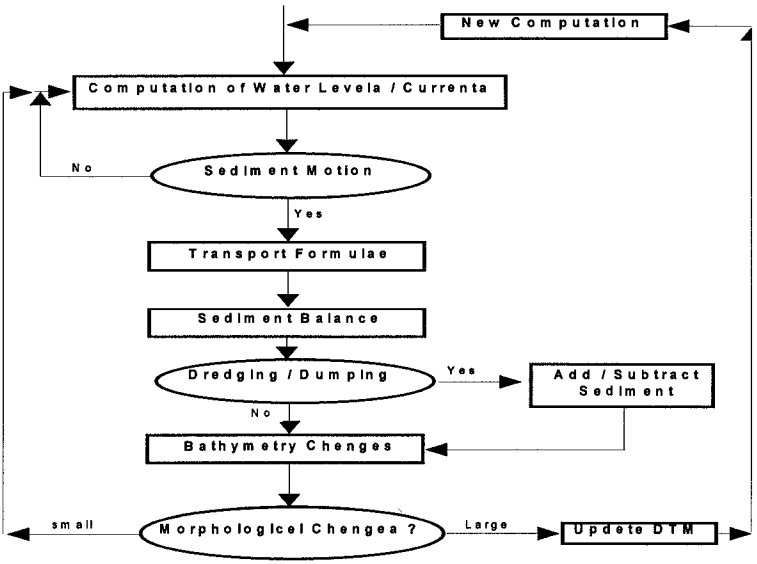

Fig. 7 Computational Steps for the Morphodynamic Model

reduce or simplify the number of events driving the model and increase the bathymetrical time step, i.e. reduce the number of updates of the bathymetry during the process.

Latteux [3] has described in detail the methods which can be applied to achieve this goal. For the simulation, e.g. of the tidal climate of one year, a limited set of natural events has to be found which forms the bathymetry as an actual set of tides would do. This could, e.g., be a weighed combination of mean and storm tides. The upgrade of the bathymetry is done at every 'tidal phase' where the definition of the "tidal phase' is not quite clear. Within this study we have achieved good results by integrating the sediment transport and bathymetric changes every x minutes with x ranging from 0.5 to 2 minutes. After extended research on the effect of mean and storm tides on the bed

of the Elbe a weighted combination of mean and storm tides was used to control the model.

4. THE STUDY

The investigation area had to be selected carefully on the basis of the availability of permanent recording stations for water levels and field investigations of currents in the area. Boundaries were also chosen such as not to cut across side branches and tributaries of the river. Moreover, the area was limited by economic considerations of available computer power. Thus, a 25 km stretch of the Elbe estuary which is prone to high sedimentation and/or sediment drift, was chosen. Included in this reach of the estuary is a shallow water region where tidal flats frame the access channel to a small craft harbour, a tidal barrage and a ferry terminal. The stability of this channel is very much threatened by continuous drift and deposition of silt and clay the removal of which approaches the limits of economical maintenance. The drift and deposition of very fine sands and silt at the southern tip of the island 'Rhinplatte' triggers frequent dredger deployment and has caused several navigational restrictions in the past. Quantities to be dredged in this area can amount to several million cubicmetres if the hydrodynamic conditions show low tides combined with a frequently low or average fresh water discharge. Fig. 8 shows a map of the Elbe estuary, the main navigation channel and the investigation area.

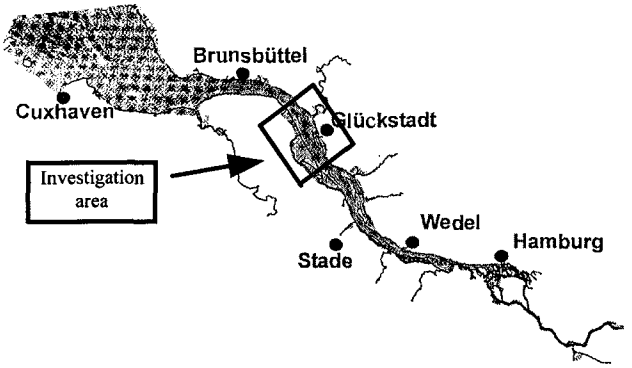

Fig. 8 Elbe Estuary With Investigation Area

Boundary conditions for the model for the calibration/ verification phase as well as for short term simulations were provided through tidal records at the lower boundary and by discharge at the upper boundary. The results of the calibration show that the match between computed and actual water elevations is not perfect. Considering, however, that prognostic runs to be carried out are based on a system comparison and 'artificial' tides are being used for model control the estuary is simulated with a satisfactory similitude. The same applies to the comparison of tidal currents as shown

in Fig. 9 .

The strongly structured bathymetry of the investigation area required a high resolution in various parts. Particularly well known deposition and erosion areas, more important small tidal gullies and side branches were to be overlaid by a finite element grid with element lengths down to 15 m. The diversity of the grid is demonstrated in Fig. 10.

Generally, this pilot study for the deployment of a morphodynamic model was initiated to determine its capability to simulate short-term and long-term sediment processes as a result of man-made changes to the system. This would include

- the effects of dredging operations on the channel
- the selection of dump sites for dredged spoil to prevent backdrift into the channel
- the design of access channels in areas of heavy sedimentation, and

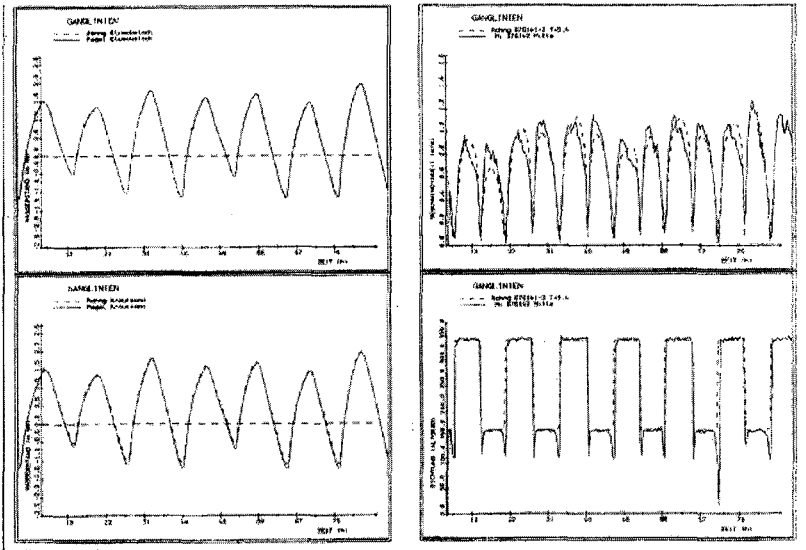

Wasserstände
Pegel Krautsand: Randlage: Einfluß Pagensand fehlt

Strömungsmessungen
ELBEX'92

Fig. 9 Water Levels and Current Velocities - Verification Runs

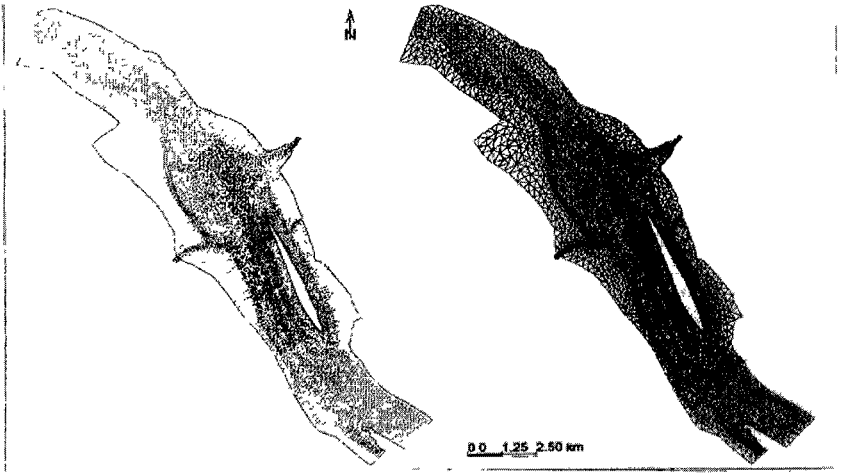

Fig. 10 FEM - Grid of 7,000 Grid Points and 14,000 Elements

- the design of river training measures for channel stability and economic maintenance

To achieve this, the evolution of the investigated stretch of the estuary was simulated for a period of **twelve and twentytwo** years with and without the usual maintenance by dredging In a pre-run and to generate an initial situation a period of two years was simulated to allow for the necessary morphodynamic adjustment of the bathymetry created from echo soundings Fig 11 shows the intial bathymetry and the changes after these two years without and with man-made changes (dredging) The difference after 12 years would give an indication of the trend in the natural development of the system. The difference after 22 years gives clues as to where the changes occur and at what order of magnitude they will occur Hence, the given time frames cannot be taken as absolute A more accurate information can be given only after intensive calibration of the model with historical developments or long-term morphological comparisons. The difficulties of obtaining continuous environmental data for the same period is well known Fig 12 finally shows the difference of 22 years of morphodynamic development with and without maintenance dredging.

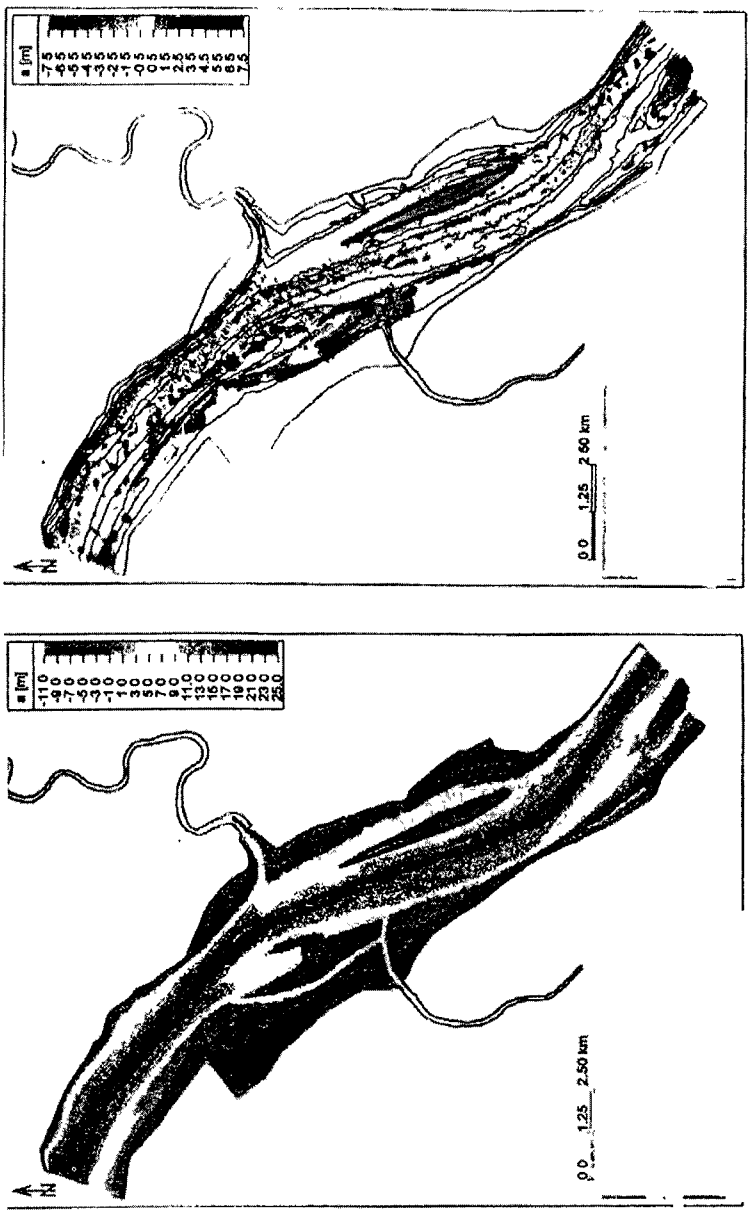

Fig. 11 Evolution of Bathymetry After 2 Years

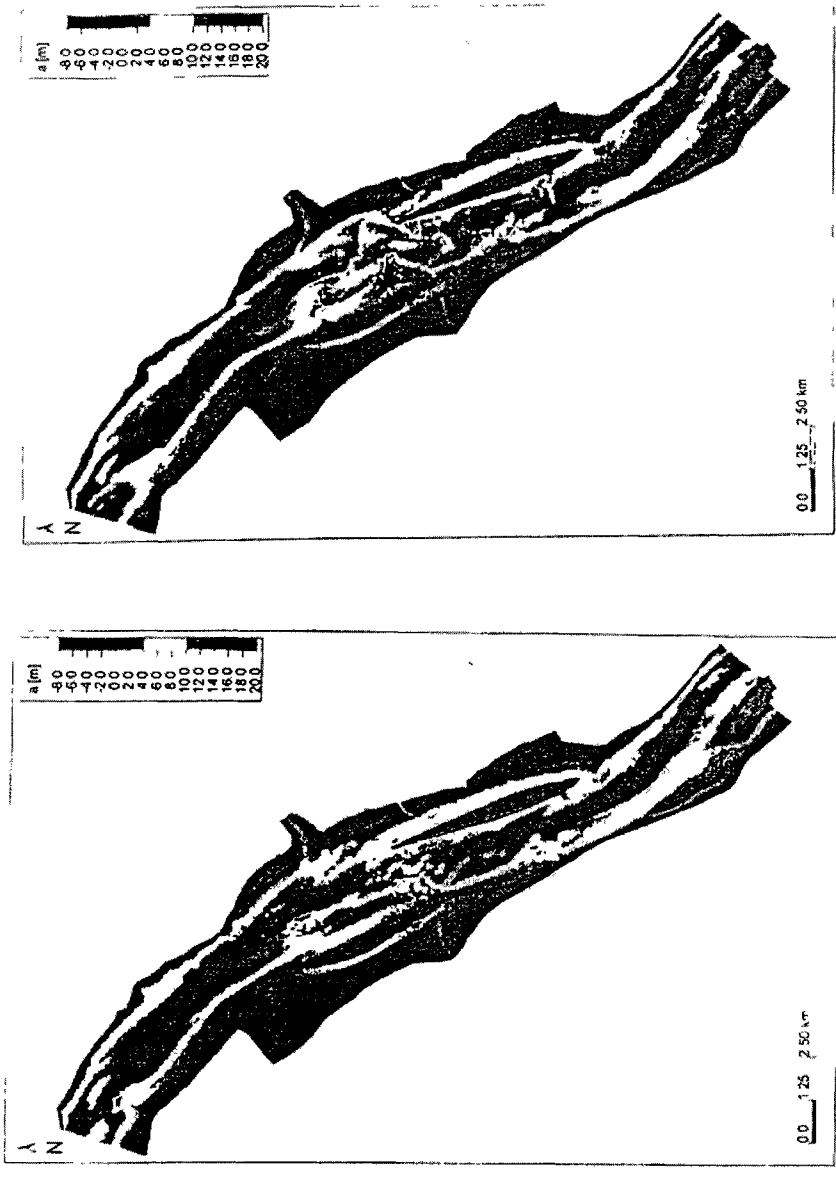

Fig. 12 Development of the Investigation Area in 22 Years Without (Top Graph) and With Maintenance Dredging

Even though the grey shading in the graph cannot well reproduce the differences between the two stages of development as the original coloured graph could the effect of maintenance can well be detected. Without going into detail here one can interpret the results of the
investigation in a way to show

- the effects of dredging activities for the channel and adjacent areas,
- the effect of dumping operations on the bathymetry,
- possibilities to change dredging strategies, and
- the imminent danger of meandering of the system if maintenance is not carried out on a regular basis.

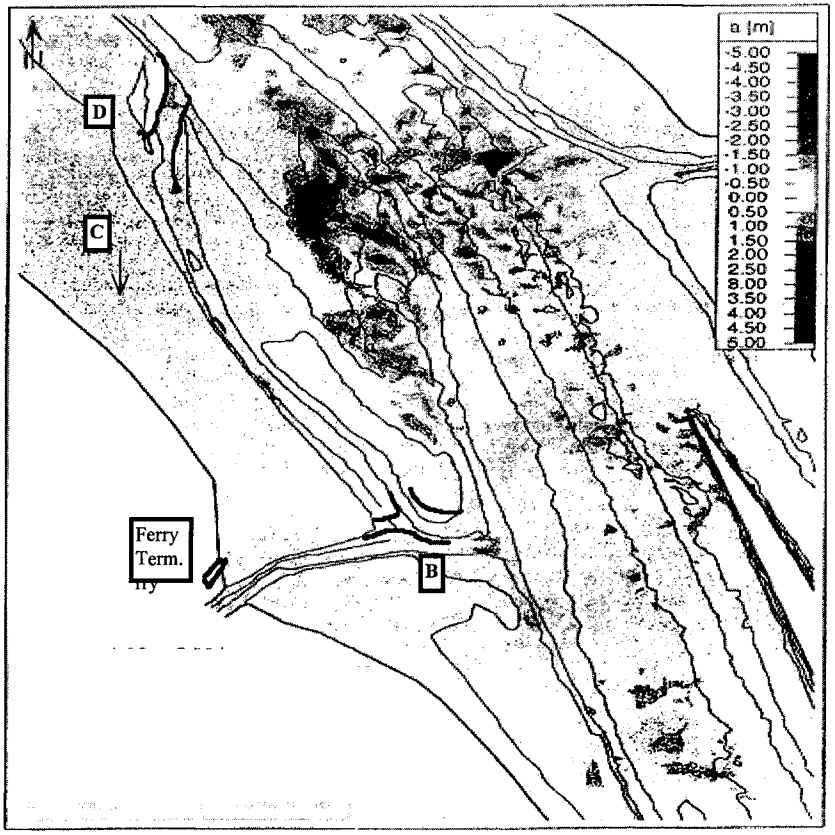

Fig. 13 Investigation Area of the Ferry Access Channel - Alternatives

In a more detailed analysis of short term changes for the ferry access channel a morphodynamic development period of one year was simulated. This included the existing situation and various alternatives which theoretically should improve the situation (Fig. 13).

The investigation showed clearly that none of the proposed alternatives would improve the existing set-up. This is demontsrated through the graph in Fig. 13 showing the quantities to be dredged annually according to the numerical simulation. These quantities are in accord with the acctually dredged material.

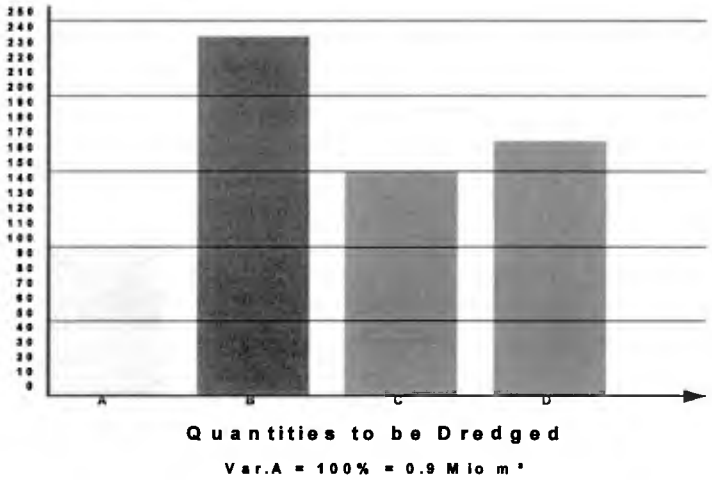

Fig. 14 Quantities of Dredged Spoil for Alternatives A - D

5. CONCLUSIONS

The investigations with a morphodynamic model set up to simulate the short-term and long-term sediment processes in an estuarine environment revealed that

- the model can be used as an economical engineering tool to plan and/or optimize dredging operations and river training measures,
- with a suitable hardware basis the calibrated model can even be deployed as a case-to-case- tool for maintenance dredging when changing tidal patterns required an immediate decision for dump sites,
- the comparison between the one-grain-model and the multi-layered system clearly

points towards the latter. However, for cheap and fast analysis, the simple model may be sufficient.

A major conclusion from this model study is, that the set-up, calibration, verification and running of a morphdynamic model requires the cooperation and functioning-as-a-team of experts from various disciplines. The interaction of these experts who seldom can be united at the same location is a major basis for the economic and successful conclusion of studies of larger extent. Therefore, a project has been intitiated which combines the expertise from various fields in a 'virtual institute'. Utilizing modern information and communication technology on the basis of the INTERNET these experts collaborate form various locations in the same project. Further information about the MORWIN-project and a copy of the first milestone report can be obtained through

hhtp://morwin.bauin.uni-hannover.de

6. REFERENCES

1) Günter, A.: Die kritische mittlere Sohlenschubspannung bei Geschiebemischungen unter Berücksichtigung der Deckschichtbildung und der turbulenzbedingten Sohlenschubspannungsschwankungen.
Mitt. der VAW, ETH Zürch, Nr. 3, 1971
2) Holz, K.-P.; Feist, M.; Nöthel, H.; Lehfeldt, R.; Plüß, A. u. Zanke, U.: The TICAD-Toolbox. Hydrosoft '90,
Proc. 3rd Int. Conf. of Hydr. Eng. Software, Massachusetts, USA, 1990
3) Latteux, B.: Techniques for long-term morphological simulation under tidal action.
Marine Geology 126, 1995
4) Meyer-Peter, E. u. Müller, R.: Eine Formel zur Berechnung des Geschiebetriebes.
Schweizer Bauzeitung, 67. Jg., Nr. 3, 1949
5) Partheniades, E.: Erosion and Deposition of Cohesive Soils., Proc. Am. Soc. Civ. Eng., Vol. 91, 1965
6) Ribberink, J.S.: Mathematical Modelling of One-Dimensional Morphological Changes in Rivers with Uniform Sediments . Comm. on Hydraulic and Geotechn. Eng., Fac. of Civ. Eng., TU Delft, The Netherlands, 1987
7) Rijn, v. L.: Sediment Pick-Up Function. ASCE, Journal of Hydraulic Engineering, Vol. 110, No. 10, Oct. 1984
8) Vollmers, H.J., Pernecker, L: Neue Betrachtungsmöglichkeiten des Feststofftransports in offenen Gerinnen., Die Wasserwirtschaft , 55, Jg, 1965
9) Zanke, U.: Der Beginn der Sedimentbewegung als Wahrscheinlichkeitsproblem, Wasser und Boden, 1, 1990
10) Zanke, U.: Sachstandsberichte I und II zur Entwicklung eines numerischen Modells mit beweglicher Sohle, HYDRO-CONSULT-HANNOVER, 1993/1995

RANDOM WAVE MODELLING APPROACH INCLUDED IN A BEACH DEFORMATION MODEL

Ioan Nistor[1] and Tomoya Shibayama[2]

Abstract

The paper presents the results of a study dealing with the inclusion of wave randomness into a beach deformation and a sand transport model developed for the regular wave input. The effect of wave irregularity is considered by employing the significant wave characteristics method and a joint distribution of wave heights and wave periods. The theoretical framework and the practical method for obtaining the joint distribution together with its application procedure are presented. The validity of the random wave approach modelling is verified by applying it for two different models: a time-averaged beach deformation model and a time-dependent sand transport model. The time-averaged model is capable of computing the beach deformation profiles while the time-dependent turbulent sand transport model is capable of computing the total sand transport rate over the entire surf zone. The simulation results for both numerical models are compared with laboratory data in order to verify, analyze and discuss the validity of the random wave approach as presented.

1. Introduction

Over the last years, numerous studies have been carried out for modeling beach profiles evolution under various wave conditions. Most of these efforts, whether physical or numerical, have been conducted for regular waves. Since the theoretical assumptions for many of the regular wave input models are reasonable and based on detailed physical and numerical assumptions, it is therefore necessary to try to extend the results of such models for the case of random waves. In natural conditions, the state of the sea is irregular. The present theoretical models, with a few exceptions, are considering the wave input as a regular one. Despite their usually good results, when compared to laboratory

[1]Doctoral Student, Dept. of Civil Engineering, Yokohama National University, 79-5 Tokiwadai, Hodogaya-ku, Yokohama 240-8501, JAPAN.
[2]Professor, ditto.

data dealing with regular waves, the practical purpose of such models is limited when it comes to practical applications since wave randomness, the true state of the ocean waves, is not included. The irregularity of the waves should be included in a theoretical model whose aim is – beyond its theoretical value - some level of practical application. Researchers opinioned that the relatively low level of understanding the sediment transport problems considerably slowed the introduction of the wave irregularity concept within sediment transport models. However, at this point, it is still difficult to incorporate a complicated random wave model coupled with the Navier-Stokes equations (even in their Reynolds averaged form) due to the very large computational effort required.

2. Random Wave Modelling

Random waves should be taken into account for a realistic modelling of the surf zone phenomena. For the practical application, Wu *et al.* (1994) discussed three basic approaches for the treatment of the random wave transformation in shoaling water and through the surf zone.

(1) Using a deepwater random wave time series as input and transforming each individual wave in the series as if it were a regular wave component with a distinct wave amplitude and period. The input deepwater time series could be generated from (a) real-time data series, (b) simulated from a given spectrum or (c) simulated from a given distribution function.

(2) Carrying out a spectral transformation, first from deepwater into shallow water. A time series is then created from the shallow water spectrum for further shoaling and surf zone transformation of each individual wave. The first step is equivalent to the transformation of Fourier components under the constraint of energy conservation. Some numerical models were used to accomplish this transformation.

(3) Conducting a "parametric" type transformation of deepwater random wave directly into the surf zone. The surf zone wave properties are then expressed as significant wave parameters and, sometimes, associated with distribution functions.

Each approach presented above can be considered as random wave input information. Approach (1) and (2) are conceptually the same. The third approach yields local wave information inside the surf zone but is difficult to reconstruct a continuous spatial variation of each wave which is required in some of the sand transport models. Many surf zone hydrodynamic or sand transport models focus on using individual wave analysis since this was proved to be more suitable for the surf zone. The probabilistic approach, which considers individual waves in the time domain, can be used to predict the distribution of wave heights and wave periods. In the surf zone, energy dissipation produces a strong coupling between components of the spectrum that is not well known. Therefore, a detailed description of the wave spectrum is not needed - in most of the practical cases - to compute wave-driven currents and sand transport. As a result, the researchers proposed simpler parametric approaches, which seek to reduce the computational effort - implicit in a fully discrete spectral model - by expressing the wave action balance in terms of a small number of characteristic parameters.

For the present case, a joint distribution of wave heights and wave periods is proposed. The method and theoretical framework for obtaining this distribution is further on presented.

Joint Distribution of Wave Heights and Wave Periods

In the last few years, few reliable experiments involving irregular wave action were performed in different laboratories around the world. In spite of the fact that not all-complete data parameters are available to public use (sometimes they are still being processed or incompletely reported), part of them can be used for the kind of analysis which the present work is dealing with.

The experiment involving irregular waves which is used for the present study is the Beach Deformation Research Project - BDRP – which was performed at the Central Research Institute for Electric Power Industry (CRIEPI), Japan in October 1995. All the cases involved in the BDRP experiment have several common features:

- were performed in Large Wave Flumes;
- all involved random waves action on a sloping sandy beach;
- all cases investigated the cross-shore hydrodynamics, sand transport and beach profile changes processes;

Two approaches were considered for including the irregularity of the input wave data (1) using significant wave parameters such as the significant wave height, $H_{1/3}$, and significant wave period, $T_{1/3}$, and (2) using a joint distribution of wave heights and wave periods.

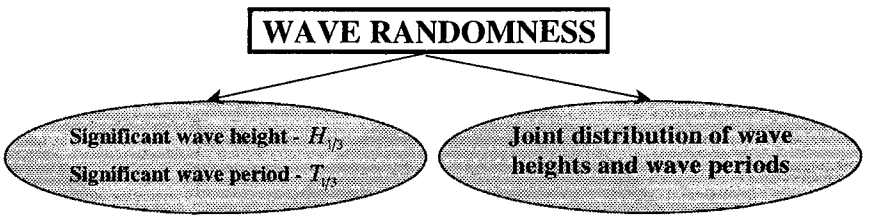

Fig. 1: Wave randomness input for the present study.

In order to obtain the above-mentioned elements, the time-history of water surface elevation was necessary. For the case of the BDRP, Japan, the time-history of water surface elevation was available, so that it was possible to calculate the joint distribution of wave heights and wave periods. The details of the experimental set-up are not described in detail in the present material. A full description of the experimental facility and of the three cases analyzed in the present paper can be found in the paper of Shimizu *et al.* (1996).

The time-history of the water surface elevation throughout the entire surf zone was available for the case of the present experiment as recorded by a number of wave gages. For this latter case, the zero-down crossing method was employed, obtaining thus the time series of waves which were generated for all the three cases performed during the

laboratory experiments. For all cases, the number of raw data from the time-history of water surface elevation was 16384 (approximately 13.6 minutes duration) while the sampling frequency was 20 Hz. A Fortran program was developed to smooth the raw water surface data by using a low passing filter with a cut frequency of 5 Hz. Then, the zero-down crossing method was employed. The final outputs of zero-down crossing method were the wave characteristics (wave heights and periods) for all the waves in the series. Figure 2 explains the procedure used to obtain the joint distribution of wave heights and wave periods.

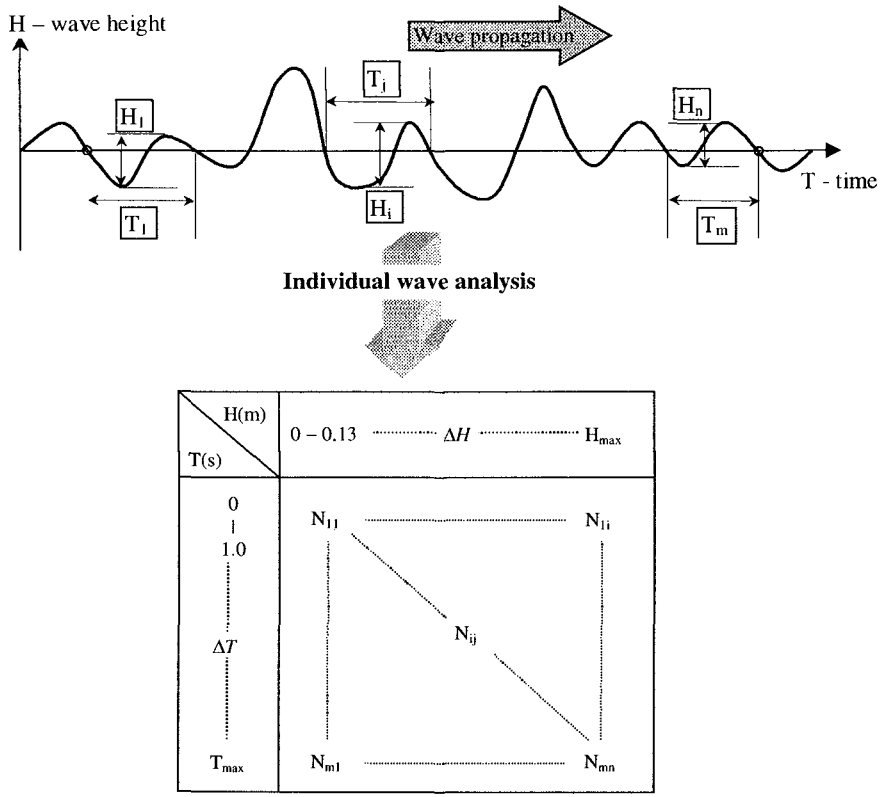

Fig. 2: Calculation of the joint distribution of wave heights and wave periods.

The columns represented equal wave period intervals ($\Delta T = 1.0$sec) while the rows represented wave height intervals ($\Delta H = 0.13cm$). The size of the intervals was defined in correlation with the maximum recorded wave height, H_{max}, and maximum recorded wave period, T_{max} Then, all waves in the three series were considered in order to

determine the number (or percentage of the total number of waves) of waves corresponded to each matrix location (e.g., what number (or percentage) of the total number of waves have the period in the interval between 5.0 and 6.0 seconds and the height in the interval between 0.40 and 0.53 m). All the waves in the time series were thus analyzed so that a particular distribution was obtained for all the three cases.

For these cases, 1a, 1b and 2 of the BRDP experiment, the wave series were analyzed and the results of the joint distribution are presented in Figs. 3, 4 and 5.

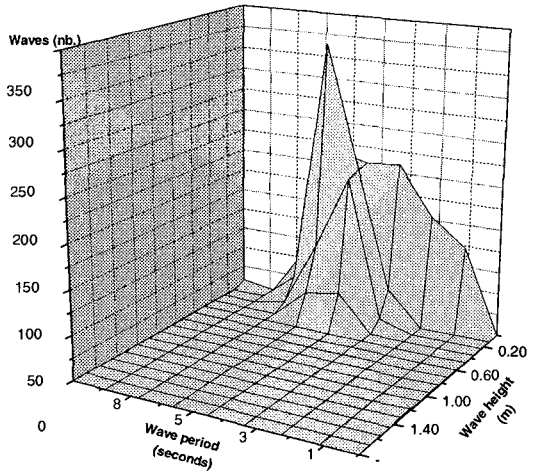

Fig. 3: Joint distribution of wave heights and wave periods for Case 1a (BDRP, Japan).

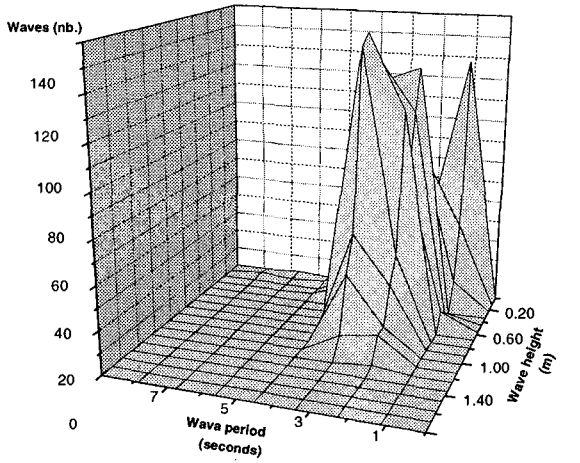

Fig. 4: Joint distribution of wave heights and wave periods for Case 1b (BDRP, Japan).

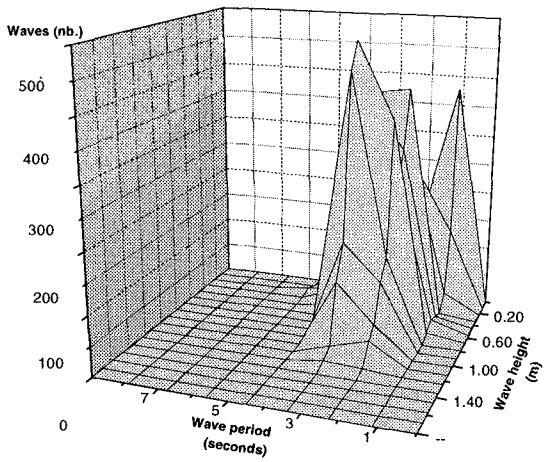

Fig. 5: Joint distribution of wave heights and wave periods for Case 2 (BDRP, Japan).

Basically, the irregularity of the wave series is reduced to a number of regular waves having their characteristics (heights and periods) comprised within certain selected intervals. As a result, it is possible to input the joint distribution output to any numerical model, which was developed for the regular wave input.

The values $N_{i,j}$ represented on the vertical axes of the Figs. 3, 4 and 5 are the numbers of waves having the wave height comprised between (H_i, H_{i+1}) and the wave period within the interval (T_j, T_{j+1}). For each matrix element, $N_{i,j}$, the mean value of wave height and wave period, $(\overline{H_i}, \overline{T_j})$ is calculated as

$$\overline{H_i} = \frac{H_{i+1} - H_i}{2} \tag{1}$$

$$\overline{T_j} = \frac{T_{j+1} - T_j}{2} \tag{2}$$

The pairs of wave characteristics, $(\overline{H_i}, \overline{T_j})$, are taken as input data for the beach deformation model. The total duration of action for each of the pairs was obtained as

$$\mathrm{T}_{ij} = N_{ij} \times \overline{T_j} \tag{3}$$

However, the input data for the duration of the simulation is the entire duration of the experiment, T_d. The corresponding weight for each of the matrix elements is then calculated as

$$p_{ij} = \frac{\mathrm{T}_{ij}}{\sum_{i=1}^{n}\sum_{j=1}^{m}\mathrm{T}_{ij}} = \frac{\mathrm{T}_{ij}}{\mathrm{T}_d} \tag{4}$$

The number of output data - i.e., final beach deformation profiles or sand transport rates – is thus equal to the number of matrix elements. The elements are characterized by each combination of wave heights and wave periods. Then, the values of water depth in each location, h_{ij}, (the vertical distance between the bottom and the mean water level which reflects the changes in the beach profile) are multiplied with the value of each weight, p_{ij}, obtaining thus the final beach profile. A Fortran program was developed to compute the final beach profile.

$$h = \sum_{i=1}^{n} \sum_{j=1}^{m} \left(h_{ij} p_{ij} \right) \tag{5}$$

The joint distribution is further verified using a numerical beach deformation model initially developed by Winyu and Shibayama (1996) and a turbulent sand transport model developed by the authors of the present paper. The beach deformation model is based on the time-averaged concept when computing the flow field and sediment concentration and the final output is represented by the beach profile change. The turbulent sand transport model is based on the time-dependent calculation of the hydrodynamic and sand concentration fields and its final result is the sand transport rate integrated over the entire water thickness and also, over one wave period. Further on, a brief description of the framework of the numerical models and their output as a result of applying the random wave approaches is presented.

3. Time-averaged Beach Deformation Model (Winyu and Shibayama, 1996)

The modified time-averaged beach deformation model of Winyu and Shibayama (1996) is composed of a sand transport model driven by a hydrodynamic model. The cross-shore change of local water depth, h, can be calculated by solving the equation of conservation of sediment mass.

Assuming a steady concentration above the bed within the control volume, conservation of sand mass can be expressed as

$$\frac{\delta h}{\partial t} = -\frac{1}{1-\lambda} \frac{\partial q_T}{\partial x} \tag{6}$$

where t: the time, x: the horizontal coordinate in cross-shore direction, λ: the sand porosity and q_T: the total sand transport rate per unit width. In order to estimate the water depth change, the sand transport rate has to be evaluated at each local point.

A two-layer sand transport model is considered. In the upper layer, the transport rate is computed as a product of time-averaged suspended sand concentrations and time-averaged particle velocities at respective elevations. Integrating the product over the upper layer one can obtain the suspended load. The transport rate in the bottom boundary layer (bedload) is calculated in the form of an empirical formula. Therefore, the total load at the local point of the cross-shore sand transport rate, q_T, is expressed as

$$q_T = q_S + q_B \tag{7}$$

where q_S: the suspended sand transport rate and q_B: the bedload transport rate. In order to compute the total sand transport rate, q_T, the sand concentration, fluid velocity and

bed load should be known first. Figure 6 shows the functional diagram of the 2-DV time-averaged beach deformation model.

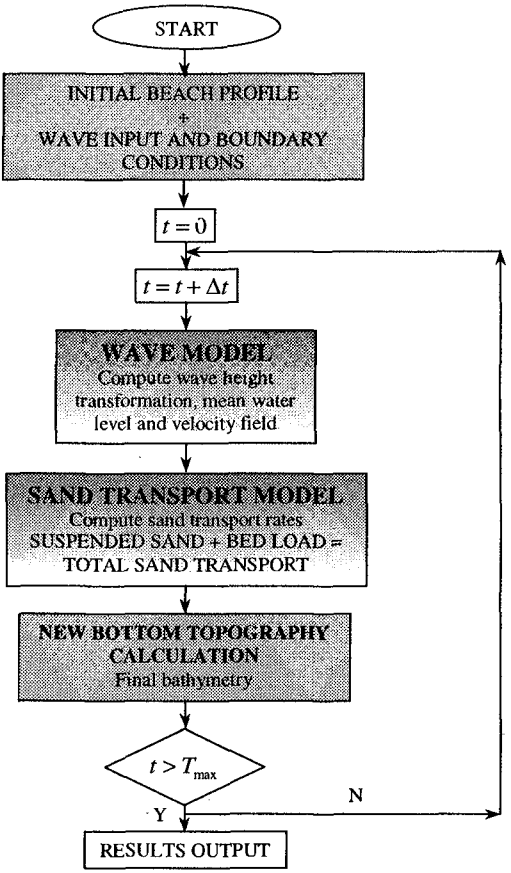

Fig. 6: Beach deformation model - functional diagram.

The Wave Model

In order to calculate the sand transport rate and beach profile change, wave height at each location must be computed. Wave height transformation in cross-shore direction is calculated using the energy flux conservation method in the form

$$\frac{\partial E c_g}{\partial x} = -D_B \tag{8}$$

where, E: the wave energy density, c_g: the wave group velocity and D_B: the energy dissipation rate which is zero outside of the surf zone. The energy dissipation rate is

calculated assuming its proportionality with the difference between the local energy flux and the stable energy flux.

$$D_B = \frac{K_d}{h}\left[Ec_g - \left(Ec_g\right)_s\right] \tag{9}$$

where all the variables are computed using linear wave theory, so that $E = \rho g H^2/8$: the wave energy, $K_d = 0.15$: a constant, h: the local water depth while subscript s means "stable". The advantage of this procedure is that it is able to reproduce the pause (or stop) in the wave breaking process at a finite wave height on a horizontal bed or in the recovery zone.

The Sand Model

A two-layer sand transport model is considered. The upper layer includes the suspended sand while the lower one defines the bedload. The transport mechanisms for the two layers are essentially different concerning all phases of sand transport: initial movement, displacement of sand particles and deposition.

For calculating the sand transport rate in the case of suspended load, the employed approach is the *time-averaged concept*. That is, calculating the time-averaged sand concentration and velocity profiles for each section of the beach in cross-shore direction, multiplying their values and integrating the product over the time and space. The time-averaged concentration profiles are calculated using the simplified diffusion equation, neglecting the horizontal convection and diffusion.

$$\bar{c} w_s + \varepsilon_s \frac{\partial c}{\partial z} = 0 \tag{10}$$

where $\bar{c}$: the time-averaged sand concentration, w_s: the falling velocity of the sand grain and ε_s: the diffusion coefficient. To solve the diffusion equation, the concentration at the reference level should be given as boundary condition and the distribution of the diffusion coefficient should also be known. The reference concentration is calculated for both the cases of breaking and non-breaking waves. The diffusion coefficient is calculated using a new empirical formula developed by Winyu and Shibayama (1996), based on a large number of laboratory data and is given as

$$\varepsilon_s = 0.21 u_* a_b \left(\frac{w_s}{u_*}\right)^2 \left(\frac{\eta}{d}\right) d_*^{-1.5} \tag{11}$$

where u_*: the maximum bed shear velocity, a_b: the orbital amplitude of fluid particle just above the bottom boundary layer, w_s: the falling velocity of the sand grain, η: the ripple height, d: the mean sand particle diameter and d_*: the dimensionless parameter of sand grain diameter.

The vertical distribution of time-averaged velocity profiles is calculated based on the assumption of the eddy viscosity model. By considering the time-averaged values, the eddy viscosity model can be expressed as

$$\bar{\tau} = \rho \nu_t \frac{\partial \bar{u}}{\partial z} \tag{12}$$

where $\overline{\tau}$: the time-averaged shear stress, ρ: the fluid density, ν_t: the eddy viscosity coefficient, $\overline{u}$: the time-averaged velocity and z: the upward coordinate from the bed. Finally, the suspended sand transport rate is

$$q_S = \frac{1}{T}\int_0^T \int_{z_m}^h \overline{c}(z)\overline{u_s}(z)dzdt \tag{13}$$

where $\overline{c}(z)$: the time-averaged vertical distribution of sand concentration, $\overline{u_s}(z)$: the time-averaged vertical distribution of sand grain velocity, T: the wave period, z_m: the level bellow which there is no movement of suspended sand particles, z: the vertical coordinate measured upward from the bed. The bedload is calculated using an empirical formula calibrated with a large set of experimental data.

4. Time-dependent Turbulent Sand Transport Model (Integrated Model)

The present numerical model is a 2-DV (two-dimensional vertical) model, named here as "Integrated Model", which is divided into two distinct parts: (1) the upper model comprising the description of the upper layer (suspended sediment) and (2) the lower model (sediment as bedload), concerned with the bottom boundary layer.

The structure of the numerical model ensures continuity in the final calculation of the sediment transport rate over the entire water depth. Also, the hydrodynamic field and the sand concentration values are also obtained as equi-phase mean values. At first, the upper hydrodynamic model of Shibayama and Duy (1994), which is based on the averaged form of the Navier-Stokes equations (Reynolds equations), is used to calculate the velocity field in the area above the boundary layer. At the same time, the free stream velocity at the upper edge of the bottom boundary layer is obtained. The model assumes a time-dependent eddy viscosity coefficient depending on the wave breaking characteristics. The time series of the horizontal and vertical velocity at the upper limit of the bottom boundary layer which represent the "forcing factor" driving the flow inside the area close to the bed are the output of the upper hydrodynamic model. These values are imposed to the next model, which is the hydrodynamic and sediment model for the bottom boundary layer. This model is also based on the averaged Navier-Stokes equations (computing the velocity vector) and on the two-dimensional convection-diffusion equation (computing sand concentration). The output of the model include the equi-phase mean values of the horizontal and vertical velocity, of the sediment concentration and the sediment transport rate integrated over one wave period and over the thickness of the bottom boundary layer is calculated. The last element of the "Integrated Model" is the suspended sediment model for the area above the bottom boundary layer. This is a modified version of the suspended sediment model of Duy and Shibayama (1997) based on the same mechanism of diffusion combined with convection. Unlike the original model, which included a time-dependent pick-up function as bottom boundary condition, the modified model uses the time series of the concentration at the upper edge of the bottom boundary layer as the lower boundary condition. Then, the sediment transport rate is calculated for the upper layer using the time series of velocities and the time series of suspended sand concentration. Finally, the total sediment transport rate averaged over the entire surf zone and over one wave period is the summation of the

sediment transport rate in the upper and lower layer. The diagram of the "Integrated Model" is presented in Fig. 7.

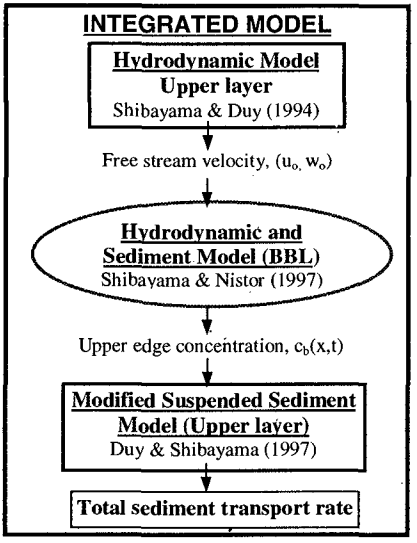

Fig. 7 Diagram of the Integrated Model

5. Comparison with Laboratory Data

Since the random wave input is the first step for the research processes of the present paper, it is necessary to evaluate the ideas proposed. The validity of the random wave input (as presented here) is evaluated by verifying it with laboratory data.

The Time-averaged Beach Deformation Model

The computed final beach profiles and the laboratory measured ones are shown in Fig. 8 (a, b and c). The calculated beach profile for all the three cases (Case 1a, 1b and 2) were determined using as input data both the significant wave characteristics and the joint distribution of wave heights and wave periods. As shown in the previously mentioned figures, each case involved different input data in terms of either the significant wave characteristics or the experiments duration. Using the joint distribution of wave heights and wave periods led to better results comparing to using the significant wave characteristics, both in terms of the horizontal location and vertical amplitude of beach profile deformations. For all the three cases shown in Fig. 8, using the significant wave height and wave period as wave input led to an overestimation of the beach deformation patterns. For a short duration of the experiment, using the joint distribution of wave heights and wave periods underestimates the laboratory data.

Concluding, the comparisons of the numerical and laboratory data seem to show a better performance when using the joint distribution compared to the use of the significant wave characteristics.

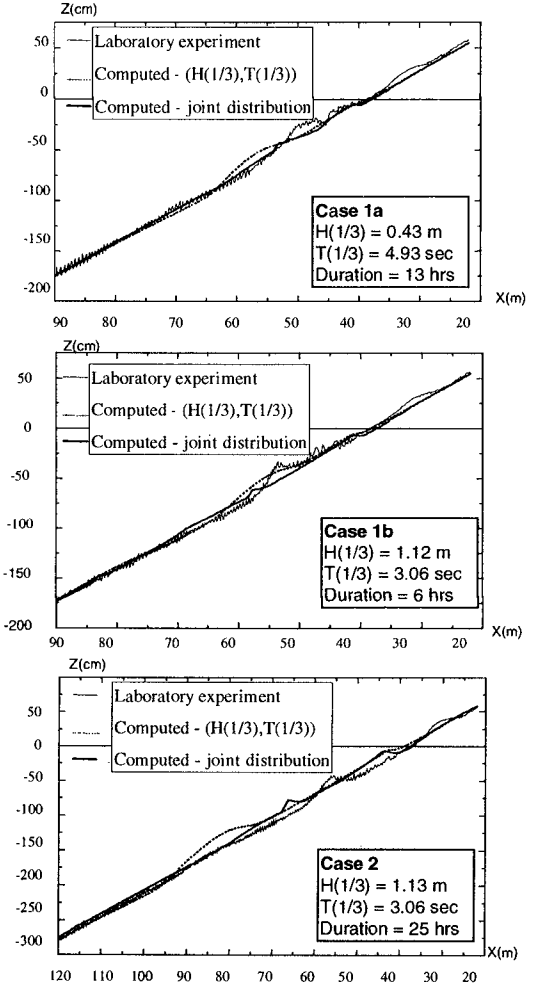

Fig. 5.25 Comparison of computed and laboratory data for Case 2.

Fig. 8: Comparison of computed and laboratory data for BDRP – Japan (1995).

More than that, the differences between laboratory data and the computation using the significant wave characteristics are increasing with the duration of the experiment. The differences between computation and laboratory data for the case of the joint distribution have an opposite trend and tend to get closer in terms of deformation pattern and location.

The Time-dependent Turbulent Sand Transport Model (Integrated Model)

The measured sand transport rates (calculated from the beach profile change) are compared with the sand transport rates as computed by the Integrated Model. For the case of the Integrated Model, the sand transport rate is computed after a relatively small number of waves (6-8 waves for stable computational conditions), *assuming a uniform beach profile without any small structure.* Therefore, the computed sand transport rate does not take into consideration any change of the beach profile and remains uniform for any duration of the wave action. At the same time, it does not include the slope effect on the transported sand.

In Fig. 9 (a, b and c), the total measured sand transport rates together with the computed ones for both irregular wave approaches are compared. For all the three cases, a general characteristic is that the total sand transport rate computed by using significant wave characteristics has similar magnitude and space location as the ones resulted from the application of the joint distribution of wave heights and wave periods.

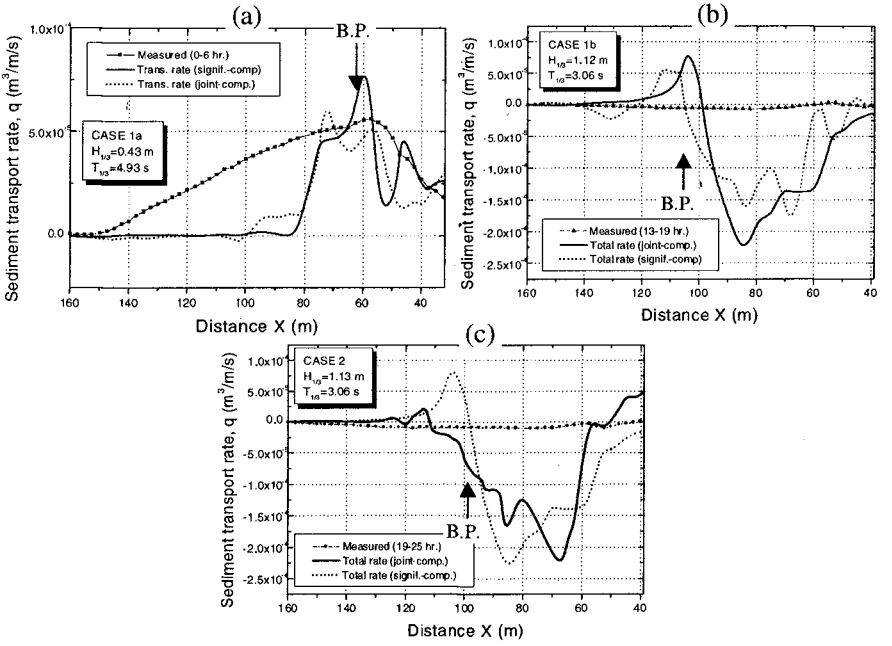

Fig. 9: Total sand transport rate for BDRP – Japan (using joint distribution of wave heights and wave periods and significant wave characteristics).

For Case 1a and Case 1b and to some extent for Case 2, the volume of sand transported as a result of applying the joint distribution of wave heights and wave periods appears to be smaller than the volume of sand computed by using the significant wave. The observation confirms previous conclusion of other studies, which suggested that, the

volume of sand transported under the effect of an irregular wave train, is smaller than the one transported by a regular wave train having the same significant dimensions (wave height and wave period) as the irregular wave train.

7. Concluding Remarks

The aim of the present study is to analyze the inclusion of wave irregularity through two approaches: (1) the significant wave characteristics and (2) the joint distribution of wave heights and wave periods. The two approaches were applied for two different models: (1) a time-averaged beach deformation model, based on the linear wave theory, which is capable of simulating the beach profile changes for the entire duration of wave action and (2) a time-dependent, high computationally demanding turbulent sand transport model, based on the Navier-Stokes equations and on the in turbulent convection-diffusion equation, which is capable of computing the sand transport rate for a relatively short duration of the wave action.

For both models, using the joint distribution of wave heights and wave periods led to better results than for the case of using the significant wave characteristics. For the case of the beach deformation model, the advantage of using the joint distribution becomes clearer with a longer duration of the irregular wave action. For the case of the turbulent sand transport model, the application of the joint distribution of wave heights and wave periods reflects into slightly reduced sediment transport rates than when employing the significant wave heights and periods. At the same time, the sand transport rate is more uniformly distributed over the surf zone area when applying the joint distribution.

Yet, the results found for the present stage are not evident enough to draw a clear-cut conclusion so that more experimental and numerical results should be analyzed before a well-endorsed and solid statement to be made.

References

Duy, N.T. and Shibayama, T., (1997): A convection-diffusion model for suspended sediment in the surf zone, *J. of Geophys. Res.*, AGU, Vol. 102, No. C10, pp. 23169-23186.

Shibayama, T. and Duy, N.T., (1994): A 2-D vertical model for wave and current in the surf zone based on the turbulent flow equations, *Coastal Eng. in Japan*, JSCE, Vol. 37, No. 1, pp. 41-65.

Winyu, R. and Shibayama, T., (1996): Cross-shore sediment transport and beach deformation model, *Proc. of the 25th Int. Conf. of Coastal Eng.*, ASCE, pp. 3062-3075.

Shimizu, T., Ikeno, M., Okayasu, A., Kuriyama, Y., Sato, S., Shimada, H., Takewaka, S., and Nishi, R., (1996): Simultaneous observations on irregular waves, current, suspended sediment concentration and beach profile changes with Large Wave Flume, *Proc. of Coastal Eng Conf.*, JSCE, Vol.43, pp. 491-495, (in Japanese).

Wu, Y., Dette, H., and Wang, H., (1994): Cross-shore modeling under random waves, *Proc. of the 24th Int. Conf. of Coastal Eng.*, ASCE, pp. 2843-2855.

Geomorphological Modelling in Coastal Waters

Morteza Kolahdoozan[1], Roger A. Falconer[2] (Fellow), Yiping Chen[3]

Abstract

Details are given herein of the development and application of a three dimensional layer integrated numerical model to predict geomorphological changes in estuarine and coastal waters. An Alternating Direction Implicit finite difference scheme has been used for solving the governing differential equations, which include the conservation of mass and momentum for flow, the transport equation for suspended sediment fluxes and mass conservation for bed level changes. Model predictions have been compared to predictions using other existing models and against laboratory measurements. A series of experiments have been carried out for a laboratory model harbour, with the model predictions being compared to laboratory measurements.

1. Introduction

Rivers, lakes, estuaries and coastal zones have been used as a means of navigation, disposal of waste, fishing and many commercial and economic activities for centuries. One of the most important phenomenon in these regions is the transport of sediments, which may cause erosion and deposition and produce problems for navigation and marine economic activities. In recent years there has been a growing interest in long term geomorphological processes in estuarine and coastal waters, which are related to the transport of sediment particles.

In modelling the geomorphological changes in coastal waters the main processes are the flow, sediment transport and bed level changes. These three independent processes also depend upon each other. The current structure causes sediment particles to erode from the bed and settle out through the water column, thereby causing bed level changes. The changed bed elevation can in-turn then effect the current structure and hence the sediment transport rate etc. Therefore, a complete numerical model to predict the geomorphological processes should contain a set of

[1] PhD Student, Department of Civil & Environmental Engineering, University of Bradford, UK
[2] Hyder Professor of Environmental Water Management, Cardiff School of Engineering, Cardiff University, UK
[3] Lecturer, Department of Civil & Environmental Engineering, University of Bradford, UK

coupled equations, solving for the flow and sediment transport processes and bed level changes in the region of interest.

Rivers, estuaries and coastal zones are continually undergoing geomorphological development, including sudden changes due to tectonic movement or human interference and gradual evolution as a natural process. In this study, geomorphological processes by means of gradual changes have been studied. Mathematical models now provide an efficient and relatively accurate method for studying many phenomena relating coastal and estuarine engineering problems, including geomorphological processes. Different models have been developed and used for predicting bed level changes. The theoretical aspects of one-dimensional geomorphological models were studied by de Vries, 1981. De Vriend (1986) worked on the theoretical basis of the behaviour of two-dimensional models. Van Rijn (1987) developed a two dimensional vertical model for predicting geomorphological changes in laboratory channels. Following a two-dimensional depth averaged asymptotic solution for the advective-diffusion equation, introduced by Galappatti and Vreugdenhil (1985), Wang (1989) developed a two-dimensional geomorphological model for tidal basins. Van Rijn (1987) used a two-dimensional depth integrated model, together with a logarithmic velocity profile in the vertical direction, to provide a quasi three-dimensional geomorphological model and applied it to steady state flows in straight channels.

In this paper details are given of the development and application of a three-dimensional layer integrated geomorphological model for coastal water studies, with the model predicting bed level changes as a result of both suspended and bed load transport. The hydrodynamic field has been modelled by using a combined layer integrated and depth integrated set of equations [see Falconer et al. (1991) and Lin and Falconer (1997a)]. The suspended sediment transport equation was solved using an operator splitting algorithm, as the ratio of the vertical to the horizontal length scale was generally very small in coastal waters [Lin and Falconer, 1996]. A depth integrated mass balance equation has been used for predicting bed and suspended load fluxes, and subsequently predictions in bed level changes. An Alternating Direction Implicit finite difference method has been used to solve the governing equation for bed level changes.

2. Mathematical Formulation

In order to simulate the geomorphological processes occurring in estuarine and coastal waters, the governing equations were divided into three categories, representing the hydrodynamic, sediment transport and bed level changes. The governing hydrodynamic equations include the continuity and momentum equations in three dimensions, together with a turbulence closure equation for the determination of the eddy viscosity and diffusivities. In the sediment transport model, the advective-diffusion equation for suspended sediment transport is solved. The bed load transport is determined using a box model originally developed by van Rijn (1984). With the velocity and sediment concentration fields predicted, and by using the mass balance equation for the bed material, then bed level changes can be determined accordingly.

Governing Hydrodynamic Equations

The governing equations used to describe the velocity distribution in estuarine and coastal waters are generally based on the 3-D Reynolds equations for incompressible, unsteady turbulent flows. Usually in 3-D tidal models the assumption of a vertical hydrostatic pressure distribution is assumed, as is the case in the current model. According to this assumption the vertical acceleration of the flow must be much smaller than gravitational acceleration. As the water can be assumed to be well mixed in many estuarine and coastal zones, the water density can often be assumed to be constant throughout the domain. In applying these approximations, the governing three dimensional differential equations of mass and momentum can be written in their conservative form as follows [Lin and Falconer, 1997a]:

$$\frac{\partial u}{\partial x}+\frac{\partial v}{\partial y}+\frac{\partial w}{\partial z}=0 \tag{1}$$

$$\frac{\partial u}{\partial t}+\frac{\partial uu}{\partial x}+\frac{\partial uv}{\partial y}+\frac{\partial uw}{\partial z}=fv-\frac{1}{\rho}\frac{\partial P}{\partial x}+\frac{1}{\rho}\left(\frac{\partial \sigma_{xx}}{\partial x}+\frac{\partial \tau_{xy}}{\partial y}+\frac{\partial \tau_{xz}}{\partial z}\right) \tag{2}$$

$$\frac{\partial v}{\partial t}+\frac{\partial vu}{\partial x}+\frac{\partial vv}{\partial y}+\frac{\partial vw}{\partial z}=-fu-\frac{1}{\rho}\frac{\partial P}{\partial y}+\frac{1}{\rho}\left(\frac{\partial \tau_{yx}}{\partial x}+\frac{\partial \sigma_{yy}}{\partial y}+\frac{\partial \tau_{yz}}{\partial z}\right) \tag{3}$$

$$\frac{\partial P}{\partial z}+\rho g=0 \tag{4}$$

where: t = time, x, y, z =Cartesian co-ordinates, u, v, w = components of velocity in x, y and z directions respectively, P = pressure, ρ = density of water, f = coriolis parameter, g= acceleration due to gravity and $\sigma_{xx}, \tau_{xy}, \tau_{xz}, \tau_{yx}, \sigma_{yy}, \tau_{yz}$ = components of stress tensor in x-z and y-z planes respectively.

Sediment Transport Equations

For the sediment transport sub-model both suspended load and bed load transport have been considered, with the sediment type depending upon the size and density of the bed material and the flow conditions. For predicting the suspended sediment concentration in estuarine and coastal waters, the advective-diffusion equation is usually used and which can be written as:

$$\frac{\partial s}{\partial t}+\frac{\partial}{\partial x}(us)+\frac{\partial}{\partial y}(vs)+\frac{\partial}{\partial z}\left((w-w_s)s\right)-\frac{\partial}{\partial x}\left(\varepsilon_x\frac{\partial s}{\partial x}\right)-\frac{\partial}{\partial y}\left(\varepsilon_y\frac{\partial s}{\partial y}\right)-\frac{\partial}{\partial z}\left(\varepsilon_z\frac{\partial s}{\partial z}\right)=0 \tag{5}$$

where: s = sediment concentration, w_s = particle settling velocity and $\varepsilon_x, \varepsilon_y, \varepsilon_z$ = sediment mixing coefficients in x, y and z directions respectively. For the case of bed load transport a box model, originally developed by van Rijn (1984), has been used giving:

$$q_b = 0.053\,T^{2.1}(\Delta g)D_{50}^{1.5}D_*^{-1} \tag{6}$$

where: T = transport stage parameter = $\frac{(u_*)^2 - (u_{*,cr})^2}{(u_{*,cr})^2}$, D_* = particle diameter = $D_{50}\left[\frac{(s-1)g}{\upsilon^2}\right]^{\frac{1}{3}}$, Δ = relative density and $u_{*,cr}$ = critical bed shear velocity = $(\theta_{cr}(s-1)gD_{50})^{\frac{1}{2}}$. For the critical mobility parameter (θ_{cr}), a novel unsteady criteria for the initiation of motion has been introduced and used in this study. Based on this hypothesis, the forces acting on a sediment particle can be divided into steady and unsteady flow forces. For unsteady flow effects, the significance of time dependency of the hydrodynamic parameters on the motion of sediment particles has been considered. Assuming a sediment particle rests on a horizontal bed as shown in Fig. (1), then the

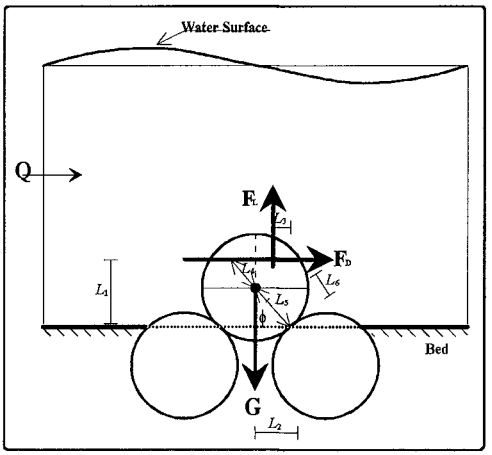

Fig. (1) Forces acting on the sediment particle

fluid forces acting on this particle are the pressure force and the skin friction. These forces can be divided into drag and lift forces, in the vertical and horizontal plane, and in the Cartesian co-ordinate system. For unsteady tidal flow the drag and lift forces consist of two components, i.e. steady state flow effects and time dependency effects of the fluid parameters. Therefore these drag and lift forces can be represented as follows:

$$F_D = F_{DST} + F_{DUST} \quad (7)$$

$$F_L = F_{LST} + F_{LUST} \quad (8)$$

where: F_{DST} = steady drag force effect, F_{LST} = steady lift force efffect, F_{DUST} = unsteady drag force effect and F_{LUST} = unsteady lift force effect. For steady state flows the drag and lift forces can be shown to be:

$$F_{DST} = \frac{1}{2} C_D A \rho u^2 \tag{9}$$

$$F_{LST} = \frac{1}{2} C_L A \rho u^2 \tag{10}$$

Similarly, for unsteady flows the force due to the time dependency of hydrodynamic parameters can be shown to be:

$$F_{UST} = m\left(-\frac{A_w}{\omega^2} Sin(\omega t + \varphi) + u \frac{\partial u}{\partial x} \right) \tag{11}$$

where: m = mass of sediment particle, A_w = amplitude of tidal wave, ω = angular velocity and φ = tidal phase. Combining equations (9), (10) and (11), the critical mobility parameter for unsteady tidal flows can be shown to be:

$$\theta_{cr} = \frac{4}{3} \frac{1}{C^2 (L_1 C_D + L_3 C_L)} \left\{ -\left[-\frac{A_w}{\omega^2} Sin(\omega t + \varphi) + u \frac{\partial u}{\partial x} \right] (Sin\psi + Cos\psi) + g L_2 \right\} \tag{12}$$

where the coefficients L_1, L_2 and L_3 are distances from the contact point of the particle, as shown in Fig. (1).

Bed Level Changes Equation

Bed level changes can be described mathematically using the mass balance equation for sediment fluxes. In the three dimensional computational domain a control volume is assumed in the vertical direction of the water column as shown in Fig. (2). The depth integrated mass balance equation for sediment in this case can be shown to be given as:

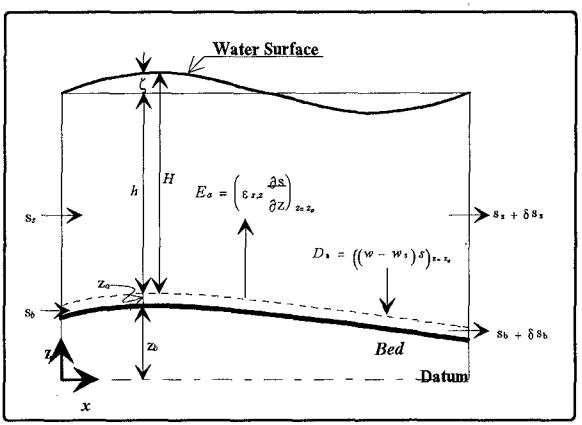

Fig. (2) A control volume in the water body

$$\frac{\partial z_b}{\partial t} + \frac{1}{1-p}\left\{\frac{\partial}{\partial t}(h\bar{s}) + \frac{\partial}{\partial x}(S_{t,x}) + \frac{\partial}{\partial y}(S_{t,y})\right\} = 0 \tag{13}$$

where: z_b = bed level above datum, $\bar{s}$ = depth averaged concentration, S_t = total transport = $s_s + s_b$ and s_s = depth integrated suspended load flux which given as:

$$s_{s,x} = \int_a^h \left(us - \varepsilon_{s,x}\frac{\partial s}{\partial x}\right)dz \tag{14}$$

$$s_{s,y} = \int_a^h \left(vs - \varepsilon_{s,y}\frac{\partial s}{\partial y}\right)dz \tag{15}$$

s_b = bed load transport.

3. Numerical Procedure

The 3-D layer integrated TRIVAST model, originally developed by Falconer et al., (1991) and refined by Lin and Falconer, (1997b), has been used for both the hydrodynamic and sediment transport part of the model. For the hydrodynamic model the depth integrated continuity and momentum equations are first solved to define the water elevations across the domain. Then the three dimensional continuity and momentum equations are solved for each layer giving the velocity components in three dimensions. In solving the to the above set of equations the Alternating Direction Implicit (ADI) finite difference method was used.

For the sediment transport sub-model an operator splitting algorithm was used to solve the advective-diffusion equation for suspended load transport. The basic principle of this method is to split the advective-diffusion equation into several smaller and simpler sub-equations, with each sub-equation being solved using the most efficient numerical algorithm (Lin and Falconer 1996). For more details about the solution procedure of this part of the model see Lin and Falconer, (1997b). As the accuracy of the sediment flux predictions is significant in the bed level change predictions, it is therefore important to use a highly accurate scheme for solving the sediment transport equation. Since the advection terms (of order Δx^{-1}) are likely to dominate over the diffusion terms (of order Δx^{-2}) in estuarine and coastal waters, then for this part of the equation it was particularly important that an accurate scheme was used to discretize the advective-diffusion equation. Based on a study carried out by Cahyono (1992), the ULTIMATE scheme, originally proposed by Leonard (1991), was particularly attractive since it was more general than the other schemes considered and easier to apply. Lin and Falconer (1996) in their 2-D depth integrated estuarine model, used both splitting and non-splitting methods for the third order QUICKEST scheme, combined with the ULTIMATE limiter, to produce solute and sediment flux predictions [see Lin and Falconer, 1997b]. In this study, the ULTIMATE QUICKEST scheme was used to represent the advective terms in the sediment transport sub-model given by equation (5).

For the bed level sub-model, the depth integrated mass balance equation was solved using an Alternating Direction Implicit finite difference method. It is assumed that in the three-dimensional computational domain the sediment flux is integrated over each layer and then over the whole water depth, to calculate the depth integrated suspended sediment flux. These three sets of equations have been solved together in an uncoupled model resulting in predictions of the geomorphological changes occurring in coastal waters.

4. Experimental Set-up

For the validation of the model a laboratory experimental programme was carried out in the tidal flume [Falconer and Chapman, 1996] at the University of Bradford. This model was first set-up to study the tidal currents and flushing characteristics within a rectangular harbour. The overall working area of the tidal basin was 5.34×3.68 m, with the square harbour being positioned on a level platform covering the full width of the tank and extending 3 m out from the rear wall of the basin, as illustrated in Fig. (3). The square harbour had a plan-area of 1.08×1.08 m with varying entrance widths being considered in this study. Tides were generated using a variable elevation waste weir driven by a computer and producing a sinusoidal wave for this study. The flat bed of the harbour was first covered with a uniform depth of non-cohesive bed material. After 24 repetitive model tides, the bed level changes inside the harbour were measured. These changes mainly occurred along the entrance

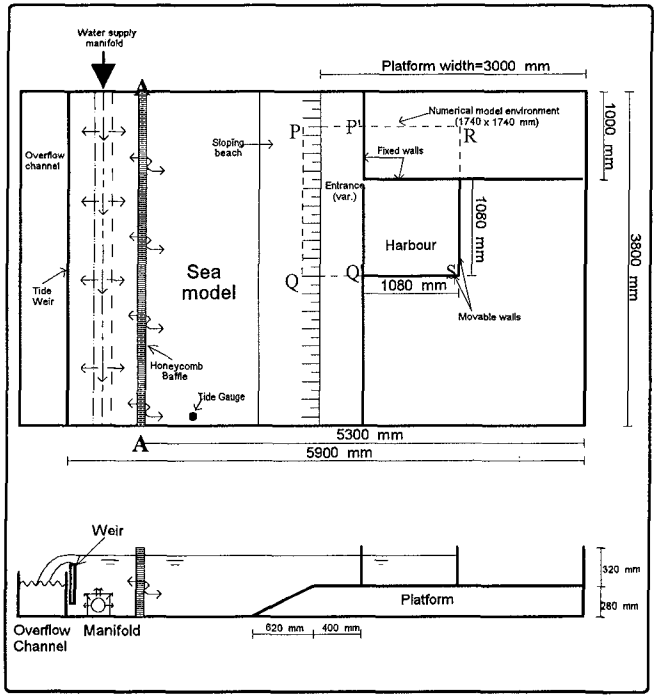

Fig. (3) Schematic illustration of the tidal basin

centreline of the harbour, where a strong jet-flow was produced due to the narrow harbour entrance. Measurements were taken for a number of parameters, including: the depth inside the harbour and the tidal range. A comparison of the results for different tidal ranges is shown in Fig. (4), with increased erosion occurring as the tidal range increased and the mean water depth decreased.

5. Model Application and Verification

In verifying the mathematical model for the case with suspended sediment transport, a straight channel, 3 km long and 1 km wide, under uni-directional and steady state flow conditions was chosen [van Rijn, 1987 and Wang, 1989]. A 400 m long headland was sited in the middle of the channel as illustrated in Fig. (5). The upstream and downstream boundary conditions were set to a constant discharge of 4000 cumecs and a flow depth of 6 m respectively. In the three-dimensional numerical model the water column was divided into 10 layers in the vertical. The predicted velocity and streamline fields are shown in Figs. (6) and (7) respectively. The predicted depth averaged

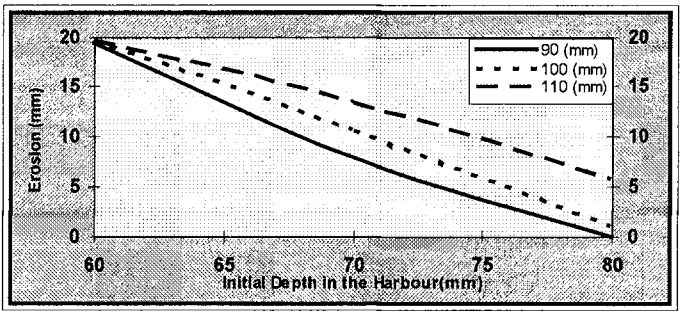

Fig. (4) Influence of depth and tidal range on erosion

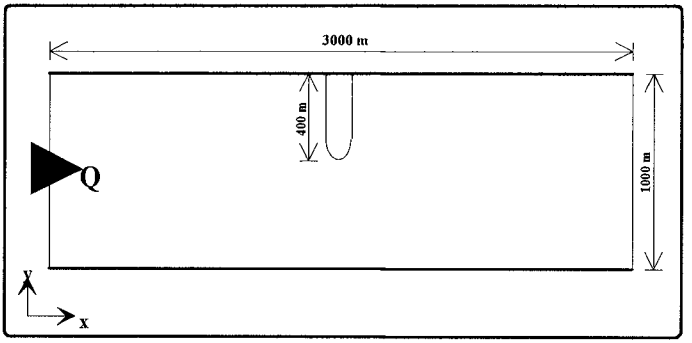

Fig. (5) Layout of channel and boundaries

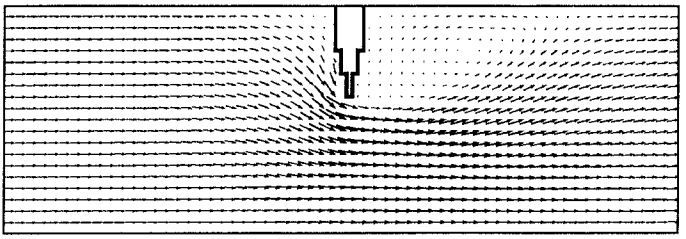

Fig. (6) Predicted depth averaged velocity field

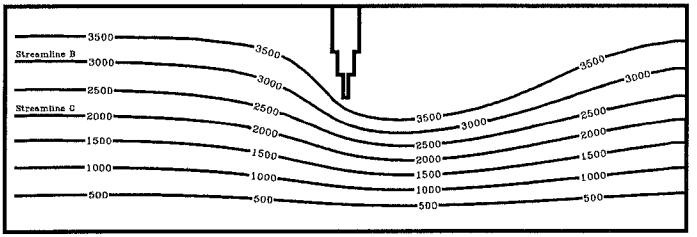

Fig. (7) predicted streamline pattern

velocity field has been compared with predictions from the SUTRENCH and ESMOR models, developed by Delft Hydraulics (van Rijn, 1987 and Wang, 1989). The results obtained from these two models were compared along streamlines B and C with the current model, with the comparisons being shown in Figs. (8) and (9) respectively. As can be seen from Figs. (8) and (9), the depth averaged velocity prediction obtained from the three-dimensional model were in good agreement with the Delft Hydraulic model predictions.

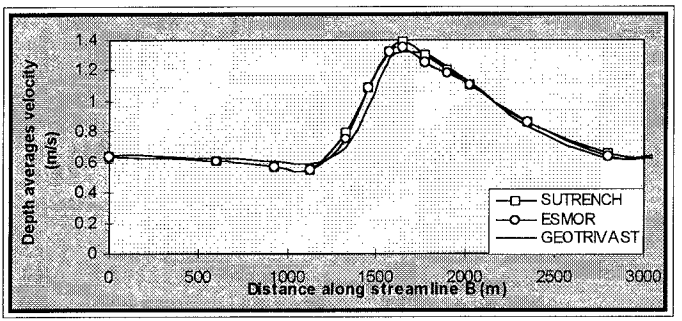

Fig. (8) Comparison of velocities along streamline "B"

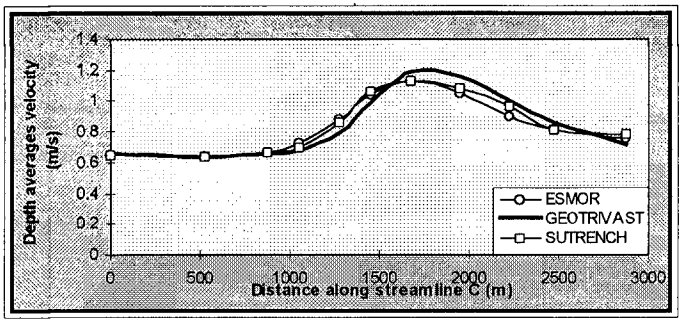

Fig. (9) Comparison of Velocities along streamline "C"

A comparison of the depth averaged suspended sediment fluxes for five different numerical model predictions are shown in Figs. (10) and (11) along streamlines B and C respectively. As can be seen from the results, the current model predictions are again in good agreement with the other models. Finally, the sediment concentration

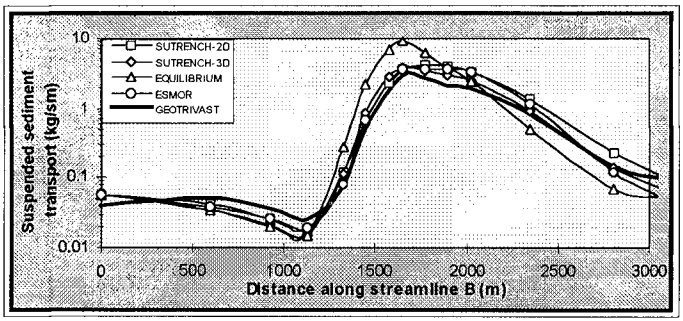

Fig. (10) Comparison of sediment fluxes along streamline "B"

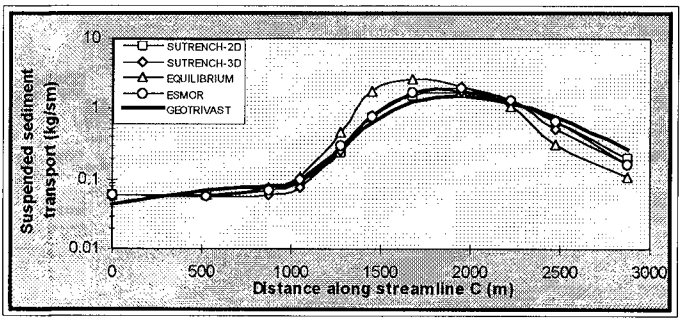

Fig. (11) Comparison of sediment fluxes along streamline "C"

patterns using this model are shown in Fig. (12), with the rate of bed level changes being predicted as shown in Fig. (13).

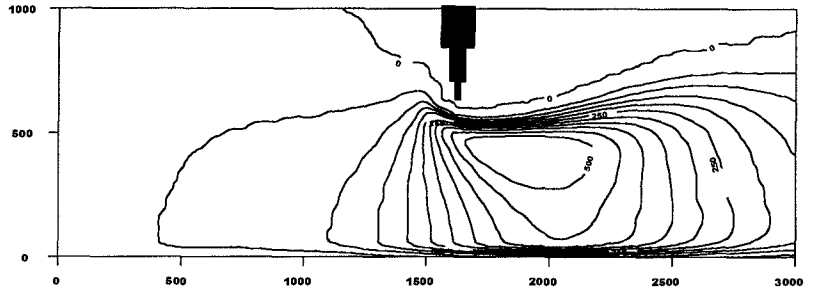

Fig. (12) Suspended sediment concentration in 10^{th} layer

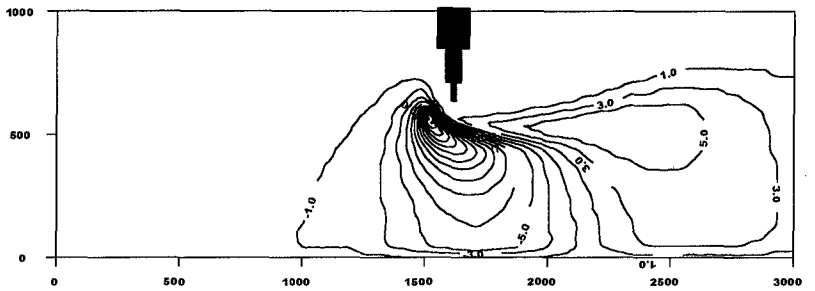

Fig. (13) Rate of bed level change using 3-D model (mm/hr)

The maximum erosion rate near the tip of the headland was predicted to be 44.6 mm/hr and the maximum deposition rate was 6.9 mm/hr. In contrast, the results using a 2-D model gave lower values for the erosion and deposition rates. The values reported by Wang and van Rijn for maximum erosion were 43 and 100 mm/hr respectively, and the maximum deposition rates were 10.5 and 25 mm/hr respectively. A comparison of the above results shows that the results using the current 3-D model were in close agreement with the results of Wang (1989).

In terms of bed load transport, the model was then set-up to predict the bed level changes in the laboratory model harbour. A tidal period of 300s, with a tidal range of 10cm and an entrance width of 60mm gave rise to the predicted depth averaged velocity distribution for different tidal phases and using a no-slip boundary condition as shown in Fig. (14).

By including the sediment transport part of the model in predicting the bed load transport in the tidal basin, it was found that the Shield's criterion for the initiation of motion-which is based on extrapolation of the bed shear stresses obtained from experimental measurements for steady state flow conditions in flumes - failed to predict any changes in the bed level for the laboratory model harbour. Therefore a new criterion for the initiation of motion under unsteady flow conditions had to be

developed and used in this model. Results from the refined model for the bed level changes along the harbour entrance centreline are shown in Fig. (15), together with the experimentally measured results. As can be seen from this comparison, the refined model was capable of accurately predicting the bed level changes in the laboratory model harbour.

6. Conclusion

A three-dimensional layer integrated geomorphological model has been developed to predict bed level changes in coastal and estuarine waters. As the accuracy of the bed level predictions highly depends upon the accuracy of the sediment transport predictions, an accurate finite difference scheme - named the ULTIMATE QUICKEST scheme - was used to predict the suspended sediment fluxes. For bed load transport, the criterion for the initiation of motion for steady and unsteady flow conditions has been investigated. A comparison between laboratory measurements and the predictions obtained from the numerical model, for both steady and unsteady initiation of motion, was undertaken. These comparisons showed that a new criterion for the initiation of motion, based on a tidal flow, was capable of predicting bed level changes accurately in comparison with the physical model measurements.

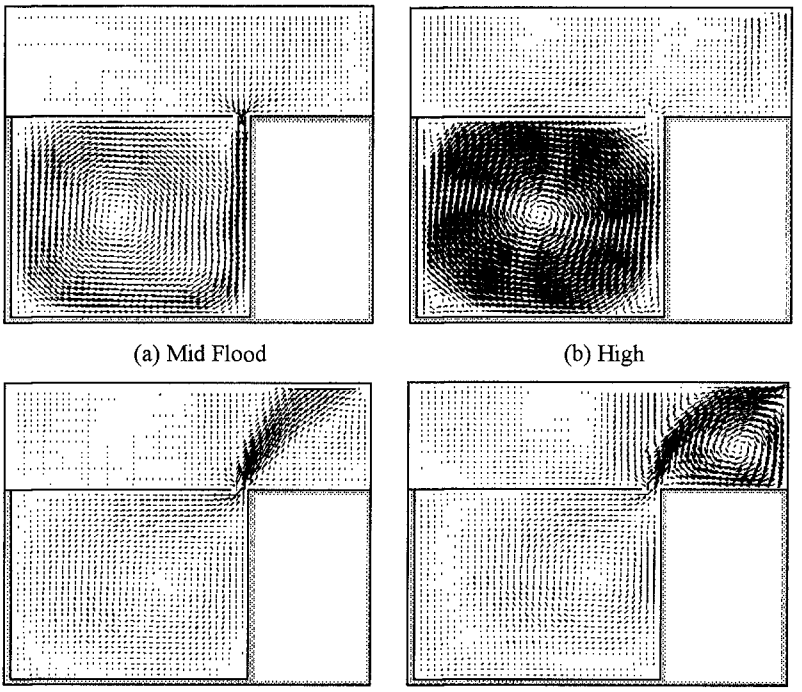

(a) Mid Flood (b) High

(c) Mid Ebb (d) Low

Fig. (14) Predicted velocity distribution for different tidal phases

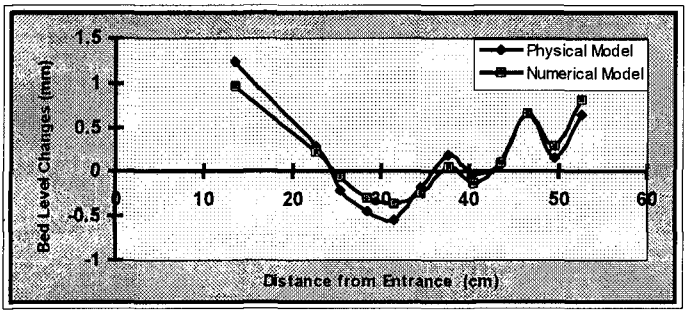

Fig. (15) Bed level changes along harbour entrance centreline

References

Cahyono, M., (1992), "Three Dimensional Numerical Modelling of Sediment Transport Processes in Non-stratified Estuarine and Coastal Waters", PhD Thesis, Department of Civil Engineering, University of Bradford, Bradford, UK.

de Vriend, H.J., (1986), "Two and Three Dimensional Mathematical Modelling of Coastal Morphology", Report No. H284-2, Delft Hydraulics Laboratory, Delft, The Netherlands.

Falconer, R.A. and Chapman, B.C., (1996), "Design and Operation of a Laboratory Tidal Basin for Model Harbour Studies", Dock and Harbour Authority, Vol. 746, No. 864, pp. 175-179.

Falconer, R.A., George, G.D. and Hall, P., (1991), "Three Dimensional Numerical Modelling of Wind Driven Circulation in a Shallow Homogeneous Lake", Journal of Hydrology, Vol. 124, pp. 59-79.

Galappatti, R. and Vreugdenhil, C.B. (1985), "A Depth Integrated Model for Suspended Sediment Transport", Journal of Hydraulic Research, Vol. 23, No. 4, pp. 359-377.

Leonard, B.P. (1991), "The ULTIMATE Conservative Difference Scheme Applied to Unsteady One-Dimensional Advection", Computer Methods in Applied Mechanics and Engineering, Vol. 88, pp. 17-74.

Lin, B. and Falconer, R.A., (1996), "Numerical Modelling of Three-Dimensional Suspended Sediment for Estuarine and Coastal Waters", Journal of Hydraulic Research, Vol. 34, pp. 435-456.

Lin, B. and Falconer, R.A., (1997a), "Three Dimensional Layer Integrated Modelling of Estuarine Flows with Flooding and Drying", Journal of Coastal and Shelf Research, Vol. 44, No. 6, pp 737-751.

Lin, B. and Falconer, R.A., (1997b), "Tidal Flow and Transport Modelling Using ULTIMATE QUICKEST Scheme",Journal of Hydraulic Engineering ASCE, Vol. 123, No. 4, pp. 303-314.

van Rijn, L.C., (1984), "Sediment Transport, Part I: Bed Load Transport", Journal of Hydraulic Engineering, ASCE, Vol. 110, No. 10, pp. 1431-1456.

van Rijn, L.C., (1984), "Mathematical Modelling of Morphological Processes in the Case of Suspended Sediment Transport", PhD Thesis, Delft University of Technology, Delft, The Netherlands.

Wang, Z.B., (1989), "Mathematical Modelling of Morphological Processes in Estuaries", PhD Thesis, Delft University of Technology, Delft, The Netherlands.

Beach Recharge Design and Bi-modal Wave Spectra

T T Coates[1] and P J Hawkes[1]

Abstract

Recent field and laboratory research indicates the potential importance of complex wave spectra (combining swell and wind sea) in the design of gravel beach recharge schemes. The paper discusses the research and introduces a swell wave atlas as an aid to understanding the occurrence probability of complex wave conditions around England and Wales.

Introduction

Gravel beaches are found on the shores of many parts of the world, and are of particular importance along stretches of the heavily populated south coast of England where they are known as shingle beaches. Fully developed shingle beaches provide an excellent barrier against erosion or flooding. Unfortunately they are becoming depleted due to a lack of natural sediment supply and modifications to natural processes caused by coastal works (harbour construction, dredging, beach control structures). Shoreline managers are increasingly using beach recharge as a method of improving beaches for coastal defence purposes.

Design of shingle beach recharge schemes in the UK over the past ten years has relied heavily on a parametric beach profile model developed at HR Wallingford (Powell, 1988). The model was developed from an extensive mobile bed wave flume study using waves defined by JONSWAP spectra; effects on wave height and period, water level, sediment size and underlying impermeable layers are all considered.

Results from three recent research projects indicate a possible weakness in the model, and in all other beach or structure response models that are driven by simple wave conditions, whether numerical or physical. These results provide evidence of the potential importance of complex wave conditions that combine wind sea and swell, forming a wide spectral distribution that can separate into two distinct peaks or a bi-modal spectrum. These conditions arise when locally generated storm seas occur in conjunction with longer period swell waves.

[1] Coastal Group, HR Wallingford, Howbery Park, Wallingford, Oxfordshire, UK. OX10 8BA (ttc@hrwallingford.co.uk, pjh@hrwallingford.co.uk)

The projects discussed in this paper include:

- Field work that recognised the occurrence and potential importance of bi-modal wave conditions.
- Development of a swell wave atlas for England and Wales that identifies the coastal areas likely to be affected by bi-modal conditions.
- A wave flume study that investigated the response of beaches under laboratory conditions.

The paper also touches briefly on further flume studies that looked at the impact of bi-modal waves overtopping seawalls and the stability of armour stone revetments.

The research projects were all funded by the UK Ministry of Agriculture, Fisheries and Food under their Flood and Coast Defence programme. Detailed descriptions of the work and the full results are presented in Coates *et al* (1998), whilst discussions and conclusions are presented in Hawkes *et al* (1998).

Field study

The response of shingle beaches to long period wave conditions has been noted and observed many times, but quantitative data regarding sea conditions and beach profiles are not generally available. An exception to this is the data set collected at a recharged beach at Highcliffe in Christchurch Bay on the UK south coast (Coates & Bona, 1997).

The Christchurch Bay field site is within an embayment and is partially protected from wave attack by headlands and an offshore reef. The steeply sloping upper beach is formed of shingle (5mm-50mm), while the lower beach comprises a wide sand platform. A three year study was commissioned to record the post-construction development of the recharged beach and to determine the effectiveness of the design process. Measurements were taken of beach profiles, sediment distribution, wave conditions and water levels.

Over the first two years the beach crest remained relatively stable, with variations of +/- 0.1m from the design elevation of 3.9mOD. This apparent equilibrium situation changed during a storm in late December 1994. The post-storm survey showed a distinct rise of the crest elevation to 4.3mOD. Initial analysis of the field data showed that the storm event was not unusual in terms of pre-storm beach profile, storm sequence and duration, peak water levels or maximum significant wave height. In most respects it was apparently similar to the previous storm in early December 1994, during which the beach crest had shown no increase in elevation. As there was no obvious reason for the difference in beach response a more detailed analysis of the wave record was undertaken.

The maximum recorded significant wave height was 3.17m for the 7-8 December and 3.14 for the 29-30 December. Plots of the wave spectra for these two events (Figure 1) show that the headline wave heights were misleading. The early December storm gave a typical wind sea spectra with a single peaked energy distribution (dashed line). The post-Christmas storm shows a distinctly different

distribution (solid line); the bi-modal shape comprises a less severe wind sea overlying a 15-20 second swell. The swell accounts for about 20% of the total energy and gives an estimated 1.15m wave height.

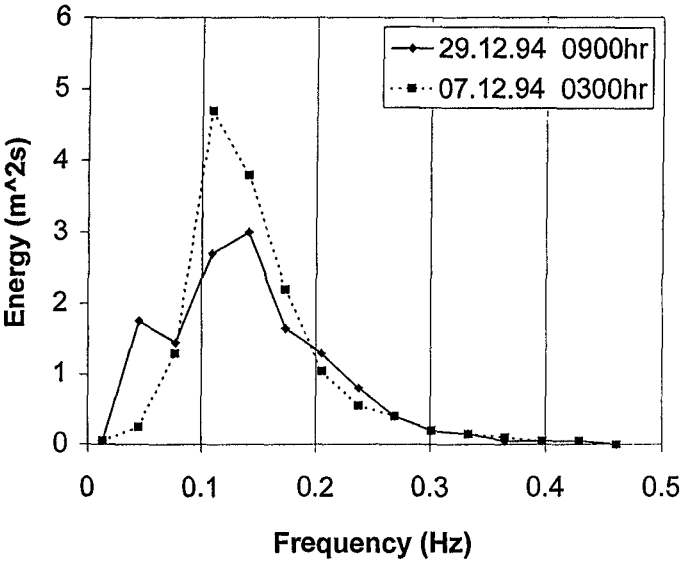

Figure 1 Storm wave spectra: 7-8 Dec and 29-30 Dec, 1994

Although these field records of beach response and wave spectra did not form conclusive evidence, they did suggest that bi-modal wave conditions could be important to beach recharge designs. Schemes designed using simple wave conditions could under estimate the equilibrium beach crest elevation and therefore the total volume of material required to provide coast protection. The field results were of sufficient interest to justify further work, first on the occurrence probability of complex wave conditions and second on a wave flume study to extend the beach response investigation under laboratory conditions.

Swell wave atlas

An atlas of offshore swell wave conditions around England and Wales has been developed (Hawkes *et al*, 1997), based on the UK Meteorological Office (UKMO) wave model for European waters. The UKMO model predicts both wind sea and swell waves at three hourly intervals for points on a 25-30k grid around Europe. Five years of data from the grid points around England and Wales were analysed to estimate extremes and were then presented as representative conditions for twenty five coastal areas. The atlas information is broken down by swell wave period and probability of occurrence. Figure 2 shows the distribution of UKMO grid points and the coastal areas. Figure 3 presents the swell wave distribution (H_s vs T_m) for the area of the field study over the five year analysis period.

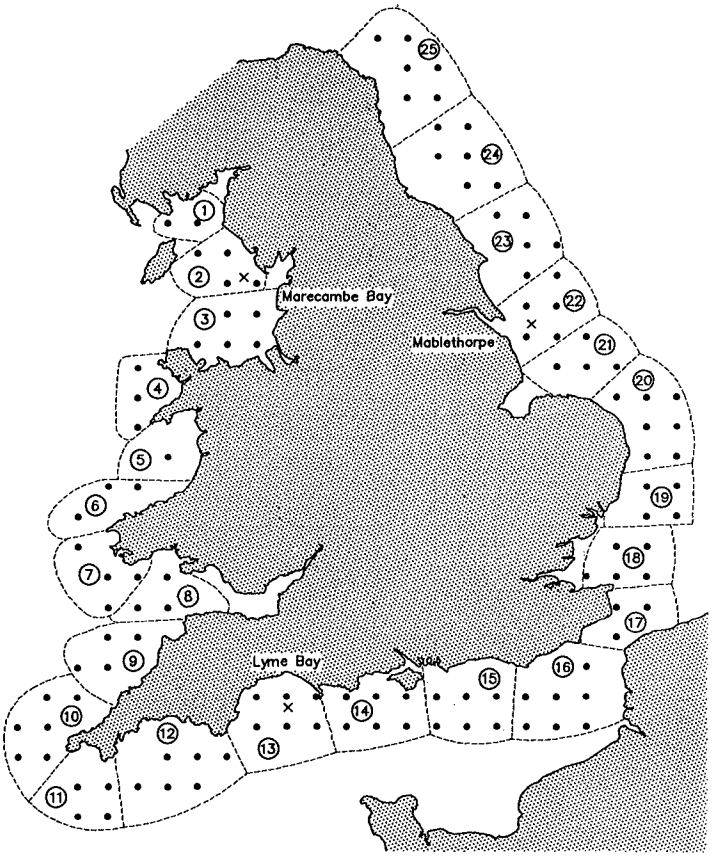

Figure 2 UKMO grid points and wave atlas areas

From the basis of this new swell wave information and an existing knowledge of wind sea climates the authors were able to consider their joint probability of occurrence. The interdependence of swell and wind sea were considered and correlation coefficients were proposed for each of the twenty five coastal areas. The results are presented as a series of tables of the range of wave combinations that have return periods from 1 to 100 years. In most locations the wave energy for a given return period is greatest for the wind sea only condition, while the swell wave only condition has the lowest energy; bi-modal conditions of combined wind sea and swell fit between these two limits. The shape of the energy curve for different wave combinations is critical in determining the potential importance of bi-modal conditions at any given site.

Figure 4 presents the energy distribution curve for Lyme Bay on a moderately exposed part of the south-west coast of England. The energy level drops away with increasing percentages of swell energy, but the rate is dependent on the swell wave period. Interestingly, for the same return period the total energy for wind sea only is approximately equal to wind sea plus a small percentage of swell; this observation is of importance in relation to the non-linear wave flume results presented below.

The shape of the energy curves is dependent on exposure to swell, exposure to storms and on local bathymetry. Further information on the development of the swell atlas is presented in Hawkes *et al* (1997).

Wave flume study

A physical model study was commissioned to investigate shingle beach response to varying combinations of swell and wind sea under laboratory conditions. The model was built in a 45m flume with a working water depth of 800mm. The required ranges of simple and bi-modal spectra were generated by an electro-hydraulic piston paddle to a notional scale of 1:20. Equipment included camera, video, automatic profiler and wave probes. The mobile beach simulated a typical UK shingle beach. It was formed of crushed and graded anthracite coal scaled according to well established and field validated principles that reproduce threshold of motion, fall velocity and beach permeability (Powell, 1988).

The test programme looked at beach response under six sequences of wave conditions. The five tests comprising each sequence had a constant total wave energy but varying proportions of swell and wind sea. The tests did not consider the probabilities of occurrence that can be derived from the swell atlas for specific sites.

Initial tests in each sequence used wind sea only. These were followed by three bi-modal spectra tests with an increasing percentage of swell energy relative to total energy. The final test used swell only. Figure 5 presents the spectra for one of the test sequences. Energy levels and peak swell periods for all of the sequences are presented in Table 1.

Table 1

Sequence	Equivalent wave height (H_s)	Swell period (T_p)
1	2.12m	11s
2	2.12m	19s
3	2.83m	11s
4	2.83m	14s
5	2.83m	19s
6	3.53	11s

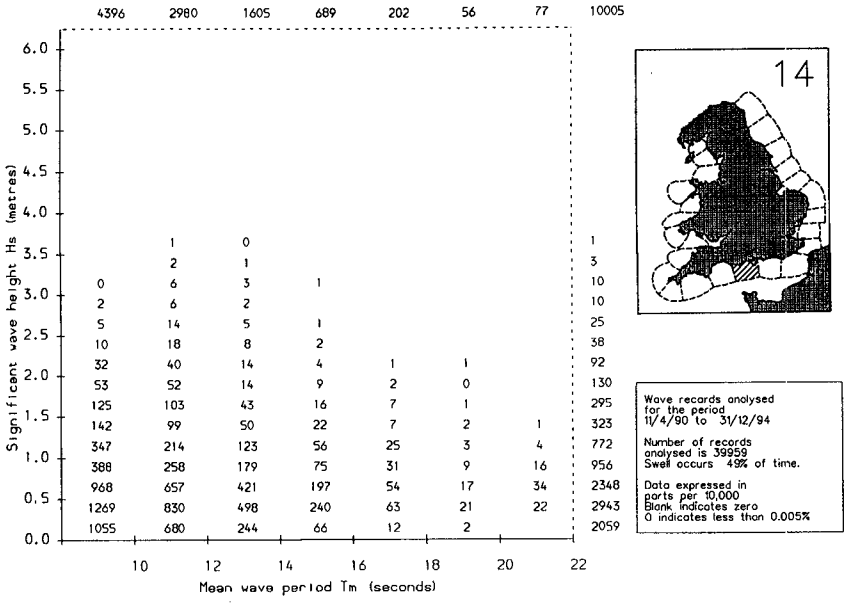

Figure 3 Sample swell wave distribution plot (central south coast of England)

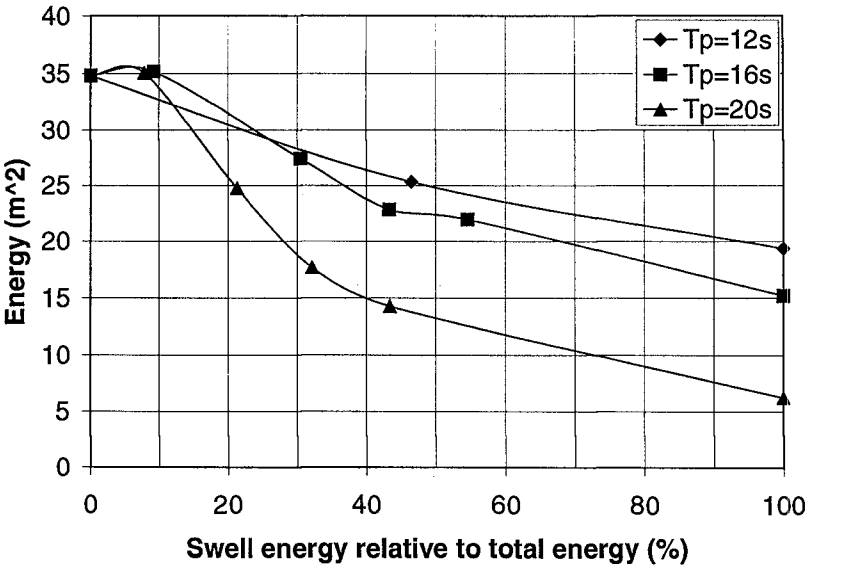

Figure 4 Wave energy curve for a range of swell/wind sea combinations with an equal return period (Lyme Bay)

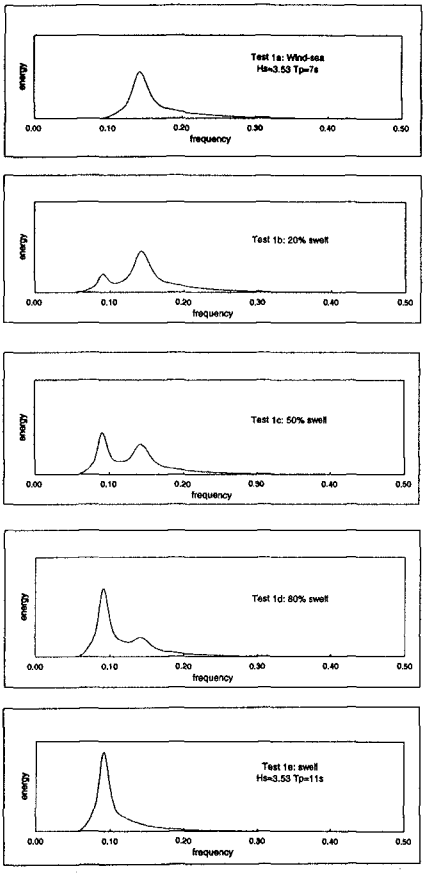

Figure 5 Typical wave energy spectra for test sequences

Complete cross-shore beach profiles were measured after each test using the automatic profiler. Analysis concentrated on the elevation and cross-shore location of the crest relative to the initial beach water line. These two parameters are considered critical indicators of shingle beach response under storm conditions and are important to beach nourishment design.

Figure 6 shows the variation in crest elevation with increasing percentages of swell at periods ranging from 11s to 19s. The wind sea only condition has an H_s of 2.83m and is taken as the reference against which the other conditions are compared. The crest elevations have been non-dimensionalised to a percentage increase relative to the wind sea only result.

The elevation response to increasing amounts of swell energy and swell period are non-linear. The rate of elevation change decreases when swell accounts for more than 50% of total energy and when swell period increases above 14s.

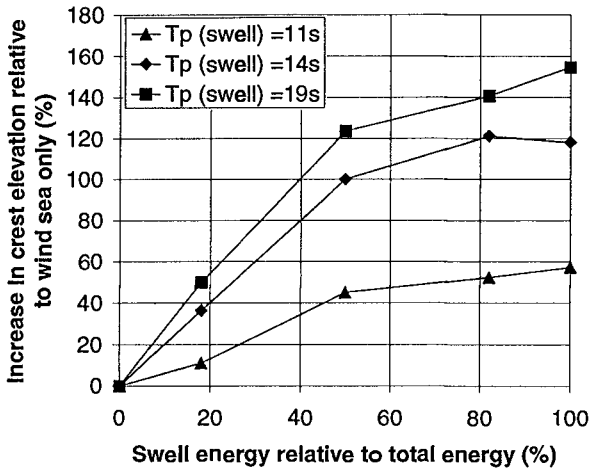

Figure 6 Relative shingle beach crest elevations under bi-modal sea conditions

Figure 7 shows a similar pattern of results for the change in crest cut back with percentage and period of swell energy. The non-linearity is much more pronounced for percentage swell with the greatest change occurring up to 20%. Change with period appears to increase significantly between 14s and 19s.

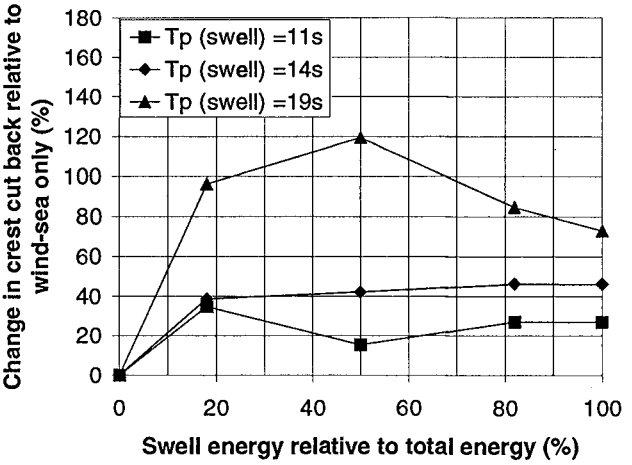

Figure 7 Relative shingle beach crest cut back under bi-modal sea conditions

These results confirm the field observation that relatively small levels of swell energy in combination with wind waves can cause greater beach response than an equal amount of energy in the wind sea only frequencies. This conclusion has importance in the design of shingle beach recharge schemes in those areas identified by the swell atlas as being subject to significant bi-modal wave conditions.

Other flume studies

A series of additional studies were undertaken in the wave flume to determine the importance of bi-modal wave conditions to structure design. Work concentrated on wave overtopping of simple sloping walls, but some tests of rock armour stability were also completed.

Overtopping tests considered seawall slopes of 1:2 and 1:4, foreshore slopes of 1:7, 1:10, 1:20 and 1:50, and crest freeboards of 2m and 4m. Wave conditions included those used for shingle beaches, plus some additional heights and periods to provide a larger data set for analysis.

Measured overtopping rates varied with each structural parameter and with wave conditions. Bi-modal and swell only waves were shown to be most significant for the 1:4 wall slope with a 4m freeboard. Foreshore slopes made little difference.

Figure 8 shows the results for a 1:50 approach slope. Unlike the beach response results discussed earlier, the overtopping curves tend to be linear, apart from an apparent steepening towards the 100% swell conditions.

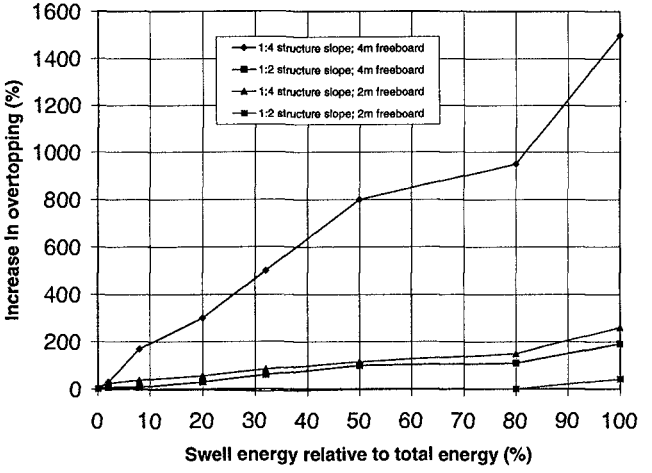

Figure 8 Relative change in overtopping rates under bi-modal sea conditions

The overtopping test programme showed conclusively that sloping seawall design should consider complex wave spectra in areas exposed to even moderate swell. Failure to do so could result in a significant underestimation of risks during storms.

A brief series of tests were run to determine the potential significance of bi-modal waves in determining armour rock stability. The damage results were inconclusive but suggested that complex sea states could be important to structural design.

Conclusions

The important influences of bi-modal wave conditions (combining wind sea with an underlying long period swell) have been observed in the field and in a large scale wave flume model. The probabilities of occurrence of these wave conditions around England and Wales have been estimated and published as part of a wave atlas (Hawkes, *et al*, 1997).

These conditions are believed to be important to the design of shingle beach recharge schemes and to some coastal structures. As yet little work has been done on defining the physical processes involved in the interaction between complex sea conditions and beaches. The results of this study can be used by coastal engineers to improve beach design, but no formal design tools have yet been developed.

Acknowledgements

The UK Ministry of Agriculture, Fisheries and Food provided the financial support for this work.

References

Coates, T. T. and Bona, P. F. D. (1997). Recharge beach development – a field study at Highcliffe Beach, Dorset, HR Wallingford Report SR 438.

Coates, T. T., Jones, R. J. and Bona, P. F. D. (1998). Wind/swell seas and steep approach slopes. Technical report on wave flume studies. HR Wallingford Report TR 24.

Dodd, N. (1998). Numerical model of wave run-up, overtopping and regeneration. Journal of Waterway, Port, Coastal and Ocean Engineering. March/April, 73-81.

Hawkes, P. J., Bagenholm, A. C., Gouldby, B. P. and Ewing, J. A. (1997). Swell and bi-modal wave climate around the coast of England and Wales. HR Wallingford Report SR 409.

Hawkes, P. J., Coates, T. T. and Jones, R. J. (1998). Impact of bi-modal seas on beaches and control structures. HR Wallingford Report SR 507.

Powell, K. A. (1988). The dynamic response of shingle beaches to random waves. Proceedings of the 21st International Conference on Coastal Engineering, ASCE, 1763-1773.

MANAGEMENT OF BEACH NOURISHMENT IN AN OPEN SAND SYSTEM

Hans H. Dette[1)]

Abstract

The nourishment of beaches is an environmentally friendly method of shore protection but the annual sand requirement may lead to substantial expenditure. Therefore the annual sand demand should be minimized. Factors which affect the sand demand along a sandy coastline in order retain the shoreline at a given position will be discussed. A wide normally dry beach on which waves can dissipate their energy at raised water levels without substantial reshaping of the underwater profile is desirable. Where such a beach cannot be created measures have to be taken to minimize sand losses from dunes during extreme events into the everyday surf zone. Furthermore the sand requirement for an open sand system, like the Island Sylt/North Sea, can be obtained by a reduction of the amount of sand from longshore transport which is carried over the ends of the island and is lost from the system.

Introduction

The west coast of Sylt (Fig. 1) is fully exposed to the North Sea waves from westerly directions and subjected to ca. 2 m high tides. Due to the geometry of the German Bight the coast is also affected by storm tides which lead to a rise in MHW level of up to 3.5 m. A maximum wave height H_{m0} = 6 m in 13 m depth of water (approx. 5 km off the coast) has been recorded so far.

The nearshore area is characterized by a longshore bar which is located approximately 300 m seaward of the shoreline. There high waves break as plunging breakers. During storm surges with a water level rise of more than 2 m the protective effect of the bar (crest height approx. MSL - 3 m) is lost and the waves pass over the bar without breaking (Fig. 2).

According to geological estimates the west coast of Sylt has been receding approximately 13 km over a period of 7,000 years (1.8 m per year). During all these

1) Academ. Dir., Leichtweiss-Institute, Technical University of Braunschweig, P.O. Box 3329, 38023 Braunschweig, Germany

years the underwater profile has been translated eastward, probably without much change in shape. The eroded material established spits to north and south of the core of the island. These are now curtailed by major tidal channels. The tidal currents carry the sand that arrives at the ends of the spits away from the island. Thus, Sylt is a typical example of an open sand system, because eroded material is not returned to the island.

Figure 1. Open sand system: Island Sylt/North Sea

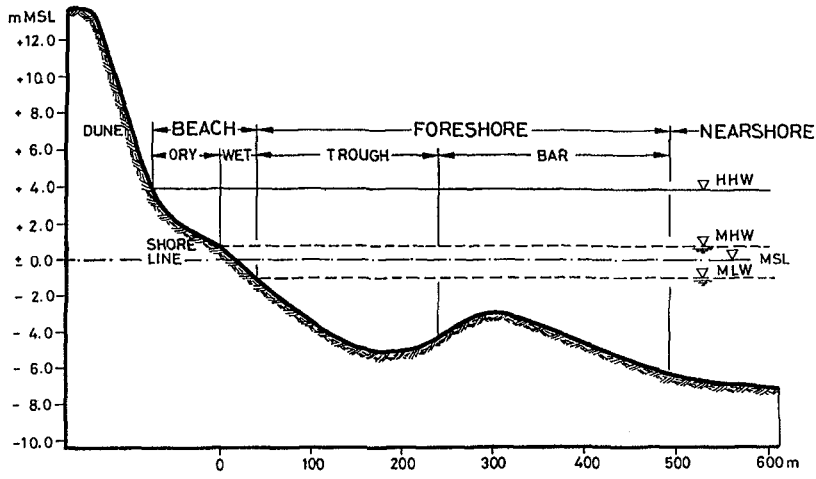

Figure 2. Typical beach, foreshore and nearshore profile of the Sylt west coast

The 36 km long west coast consists mainly of unprotected dunes and an up to 25 m high cliff (Fig. 1). Only 10 % of the coastline are protected by heavy coastal structures (city of Westerland). Since 1950 the mean yearly recession has increased from 0.9 m/year (1870 - 1950) to 1.5 m/year (1950 - 1985) due to an increased storm surge frequency (Dette, 1997). This is equivalent to an annual sand loss of 1.5×10^6 m^3 (1/3 to the south and 2/3 to the north). As a consequence of this accelerated recession a coastal protection concept for a period of 35 years (1985 - 2020) was initiated. This was done on the supposition that the increased storm surge frequency would continue and with it the erosion, which would endanger the island if no counter-measures were undertaken. The consideration of all possible alternatives of future coastal protection, their technical, economic and environmental aspects indicated that repeated beach replenishments appeared to be the most favourable solution. These repeated nourishments aim to replace the mean yearly loss of sand off the coast. A Sylt-specific masterplan based on the above considerations was introduced in 1985. It includes the task of monitoring, especially land and sea surveys before, during and after the individual nourishment schemes.

The first experiences gained from monitoring led to modifications of the the initial profile of the berm nourishment to a lower and broader shape in 1988 (Fig. 3). Fig. 4 shows that the initial fill geometry (1992) has been altered considerabely by a single storm surge within one year after the fill. The storm surge established an equilibrium profile for its raised water level (1993), which remained fairly stable even during a following storm surge of comparable strength (1994). Attempts to optimize the current design practice have been made since the beginning of the 90's.

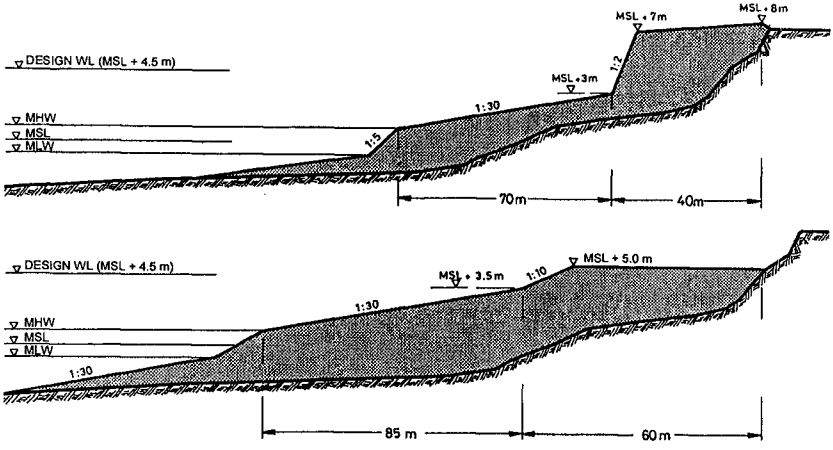

Figure 3. Change of intial berm nourishment profile (above) to a lower and broader shape (below)

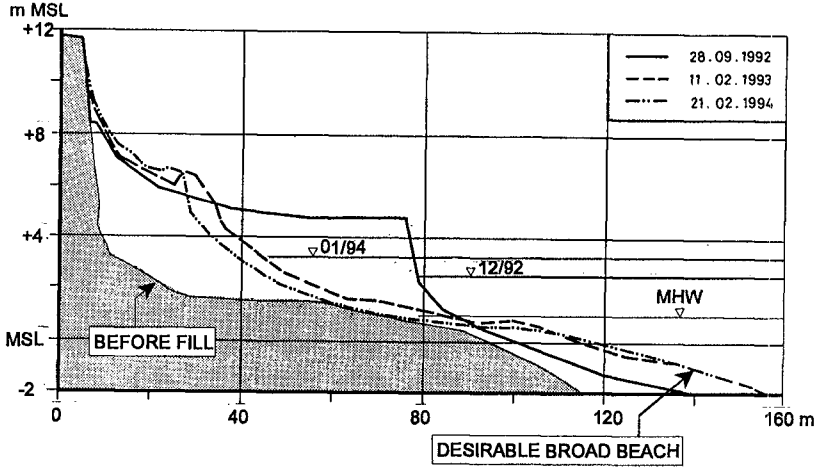

Figure 4. Changes of beach fill geometry (Sylt) during major storm surges in two consecutive years

Boundary Conditions on Nourishment Optimization

Having beautiful beaches and sea ambience Sylt developed into the primary recreational area in the North Sea since the middle of the last century. Any method of optimizing the coastal protection has to take into account the following boundary conditions:

- retention of the shoreline and the surf zone in its present form
- prevention of negative impacts on the near- and farfield coastline and islands
- minimization of any environmental impacts
- retention of a sandy beach
- acceptability for tourism

In addition protection has to meet the policy decision by the government that: "As a general principle hard structures should be avoided on sandy beaches."

These requirements basically predetermine beach nourishment as the best method of coastal protection. The normal longshore transport along the west coast of Sylt which is necessary to maintain the present appearance of the surf zone should not be influenced. The minimization of transport along the coast into the tidal channels can only be focussed on surplus sand masses exceeding the normal demand of sand in the surf zone. That is the uncontrolled transfer of sand from unprotected dunes or fills in front of dunes into the everyday surf zone at raised water level.

Under these premisses the following alternatives will be discussed:

- reduction of sand losses into the surf zone by design of nourishment techniques
- reduction of sand losses into the surf zone by measures that reduce the losses by storm surges
- reduction of sand losses from the island into the tidal channel by structural means

Protection by Exclusive Nourishment

Since 1972 repeated beach nourishments have been carried out for the protection of a seawall and revetment (length: 3 km) at Westerland (Fig. 1) against underscouring of the structures (Führböter, 1974 and Dette, 1977). On the basis of the masterplan the nourishments were extended to the so far unprotected dune and cliff sites (length: 33 km) in order to maintain the shoreline in its natural appearance. The nourishments are nowadays aimed at the retention of the 1992-position which was legally introduced as the reference. Up to 1996 the total volume of beach fills amounted to 25×10^6 m^3 of sand from offshore borrow areas (Fig.5). Practical experiences with the placement of beach fill, its effectiveness and life span have been gathered over a period of more than 25 years (Dette et al., 1994).

In the case of exclusive nourishment an optimization of the necessary amount of sand for the everyday surf zone is not possible because the longshore transport potential remains unaltered by an ordinary fill. As mentioned before in case of an exclusive nourishment, that is without any additional constructive measures, the supply of the surf zone from the high beach is uncontrolled (Newe and Dette, 1995).

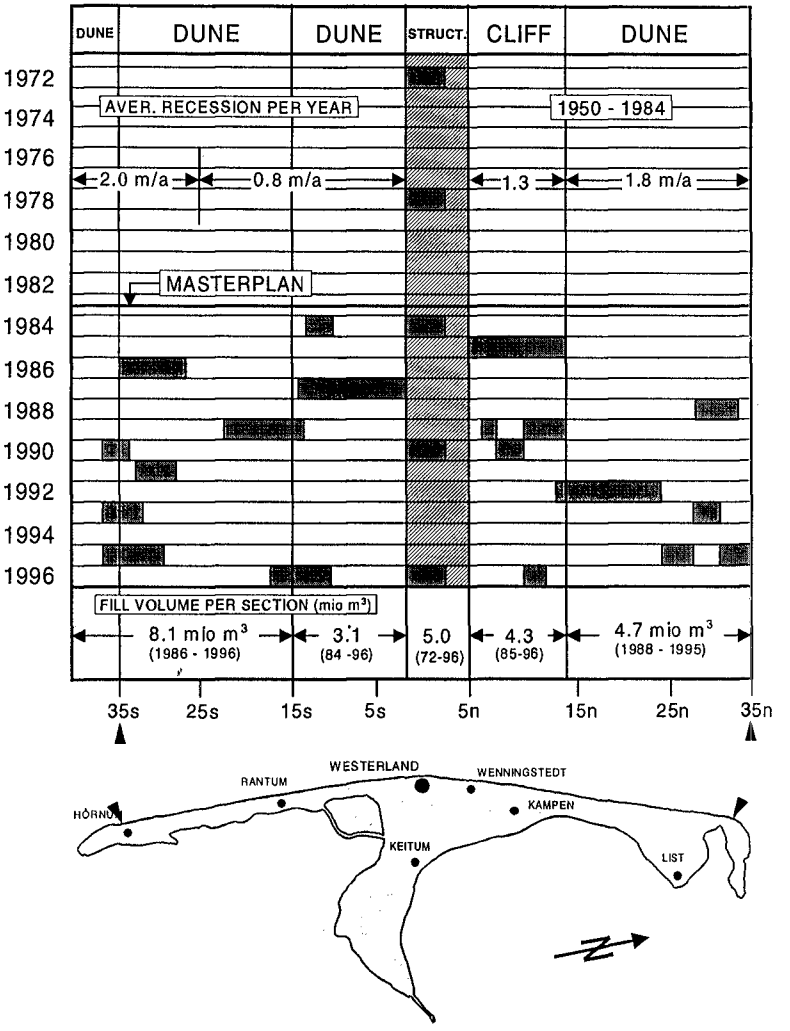

Figure. 5 Overview over beach fills at the west coast of Sylt in the Period 1972 to 1996

It depends on the occurence of storm tides. An optimization of sand requirement is restricted to the following alternatives:

- shaping of the fill geometry on the dry beach
- control of replenishment frequency

Shaping of Beach Fill Geometry

The day-to-day processes occur in the surf zone. The erosion during storm surges affects the normally dry beach and dune. The material is carried cross-shore into the everyday surf zone. On the basis of detailed profile surveys before and after a storm tide it was calculated that two major storm tides in 1990 caused a loss of 1.8×10^6 m^3 of sand from the 36 km long west coast of Sylt. This is equivalent to 60 m^3/m shoreline. This large volume of sand in the everyday surf zone leads to a profile which is out of equilibrium with the everyday wave conditions. During the following normal weather conditions waves start to reshape the profile left after the storm into an equilibrium profile. This is associated with an increased mobilization of sediment and an increased longshore transport. Consequently, increased sediment volumes are transported by superimposed wave and tide-induced currents to the ends of the island during the reestablishment of the equilibrium profile. That means increased losses of sand. Only a minor part of the sand dumped into the surf zone by the storm will be returned to the beach, because the wave climate off Sylt contains only a small portion of long and swell waves. However, at times appreciable accretion of the beach does occur, as illustrated in Fig. 6 (12/73 - 12/74).

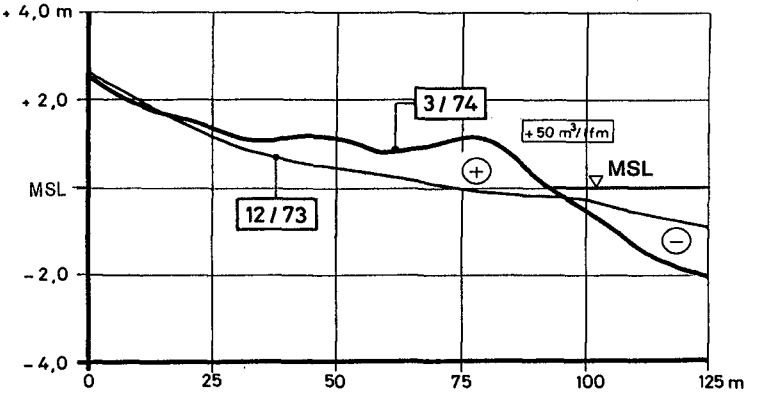

Figure 6. Appreciable accretion of the beach (Sylt) during occasional environmental conditions (seaward winds)

The shaping of beach fill geometry should be focussed on the creation of an as broad as possible dry beach with a flat slope which would suffer minimal sand losses during minor storm surges.

In case of raised water levels the flat slope of the usually dry beach (ca. 1:15) will lead to wave runup without creating an erosion escarpment. The amount of sand required for the reestablishment of an equilibrium profile, corresponding to the raised water level, is small (Fig. 7). The initial establishment of a broad beach along the west coast of Sylt would, however, requires a very substantial amount of sand (Fig. 4, similar to 2/93 profile).

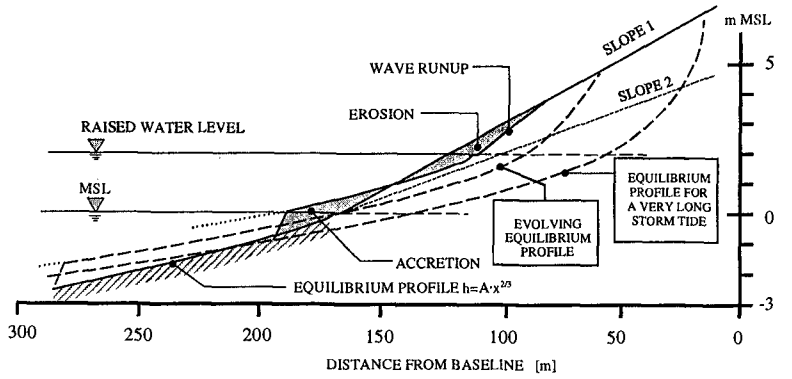

Figure 7. Development of a new equilibrium profile at raised water level (schematic)

Even with this solution losses from the fill geometry at all storm tides would occur, and by these means nourish the everyday surf zone. This process is an uncontrolled one and associated with occurence of storm surge tides.

Controlled Beach Nourishment

Controlled beach nourishment is considered under the aspect of the establishment of a flat and as broad a beach as possible without attempting to "relocate" the surf zone seaward. This can be achieved by protecting the dune with a built-in membrane (Fig. 8). The membrane limits the amount of sand lost from the dune during a storm tide to the volume of sand cover on the membrane, i.e. the membrane serves damage as limitation measure (Dette and Raudkivi, 1994). The membrane does not affect the appearance of the beach. If the membrane is exposed during a storm tide the sand cover has to be restored.

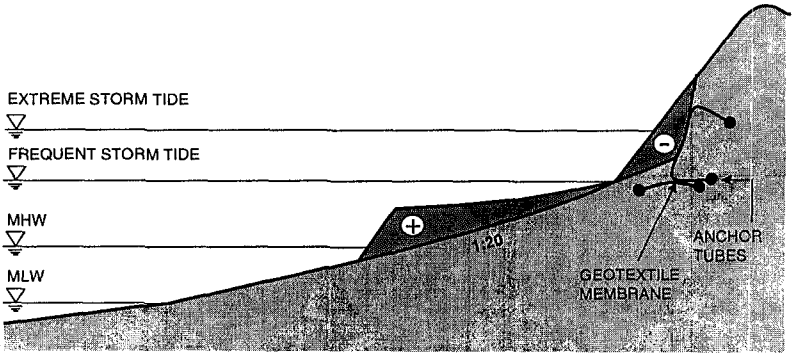

Figure 8. Barrier to limit dunes erosion by extreme storm tides (schematic) showing the erosion at extreme water level

If the dry beach is very narrow the frequency of the membrane being exposed can be reduced by installing a stone wall at its toe. It limits the frequency of storm tides which overtop the wall to ten or more year intervals (Fig.9). The maintenance of the surf zone by means of sufficient longshore transport in this case is from the beach which has to replenished at required intervals.

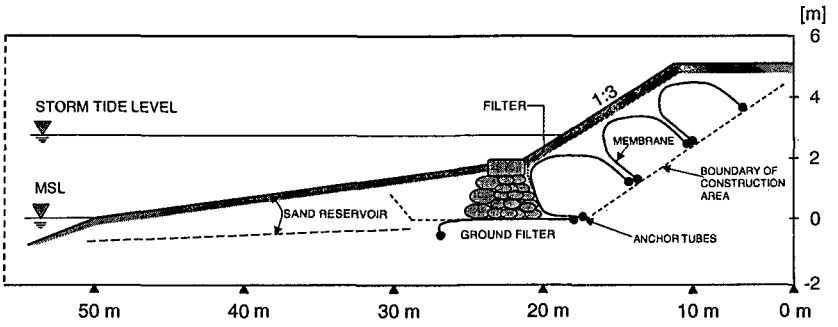

Figure 9. Dune and flood protection on a narrow beach (schematic)

Reduction of Sand Requirements

The sand requirement can only be reduced by reduction of the sand loss from the western shoreline. That is the reduction of the amount of sand carried into the main tidal channels at the ends of the island. The installation of underwater sills at the ends of the island will counteract the concentration of the longshore currents at the island's ends and the development of deep channels. The sills will spread and slow down the longshore current and lead to accretion of sand. This will reduce the slope of the underwater beach and induce it to assume more the plan shape of a half moon bay. The reduction of the slope leads to wave energy conversion over a broader surf zone and reduce the energy loading per unit area.

The non-erodible sills will reduce the sand loss into the main tidal channels but will not stop it. That means that a supply to the adjacent areas will continue. Such a sill existed as a natural ridge at the northern end some 50 years ago, linking the end of the island to the larger offshore sand bank. Today the ridge is been eroded down to a 6 m deep channel with concentrated high velocities. At the northern end the installation of the sill means restoration of the ridge which was there before. It is schematically shown in Fig. 10.

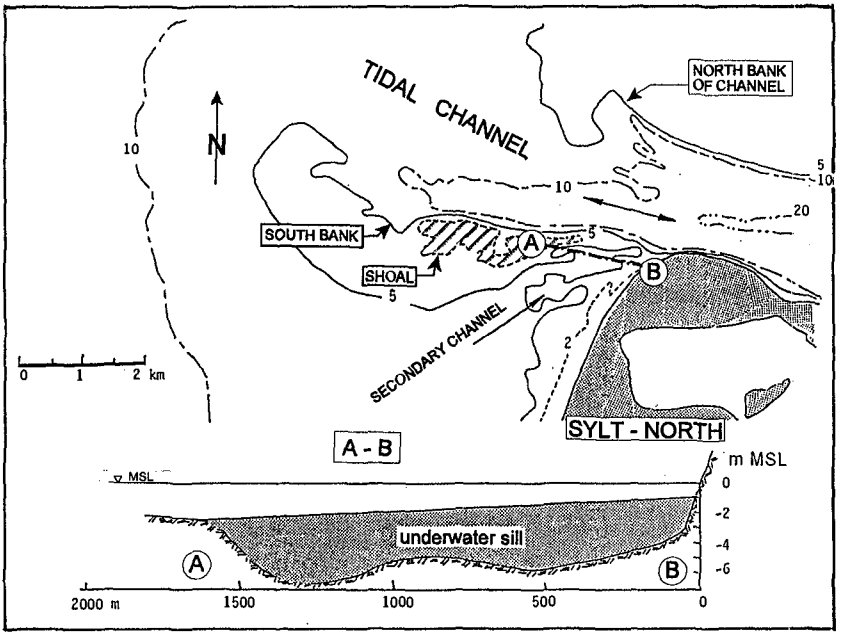

Figure 10. Layout of an underwater sill at the northern end of sylt to reduce longshore transport into the tidal channel (schematic)

At the southern end the installation of a sill involves a substantial effort. The dynamic equilibrium of the southern end of the island was disturbed by the construction of the large tetrapod groyne at Hörnum in the 70's. It deflected seaward the southerly longshore transport and it continued offshore to the main tidal channel (Fig. 11). The shoreline south of the groyne suffered by lee erosion and the southern end has retreated nearly 1 km. The ridge along the tidal channel to the offshore sand bar has increased in length from 800 m to 1750 m and the depth over it by 2 m (Fig. 12).

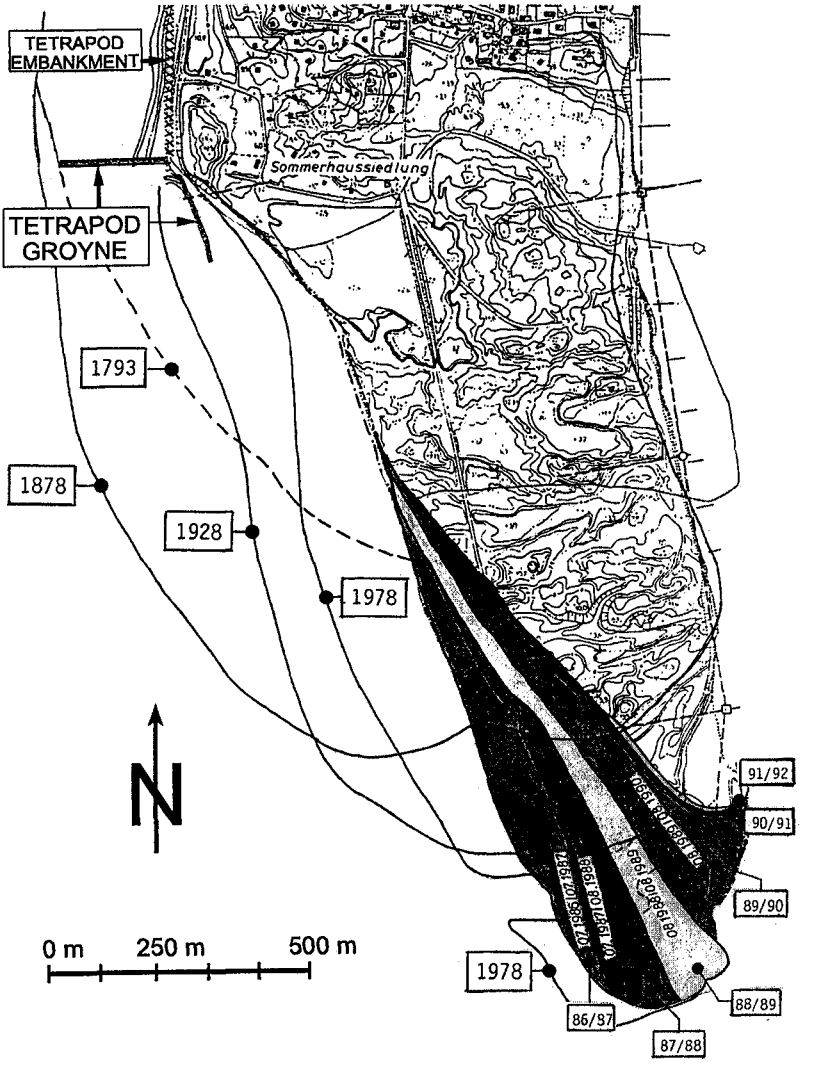

Figure 11. Acalerated shoreline recession after construction of a Tetrapod groyne in the 70-ties (ALR Husum)

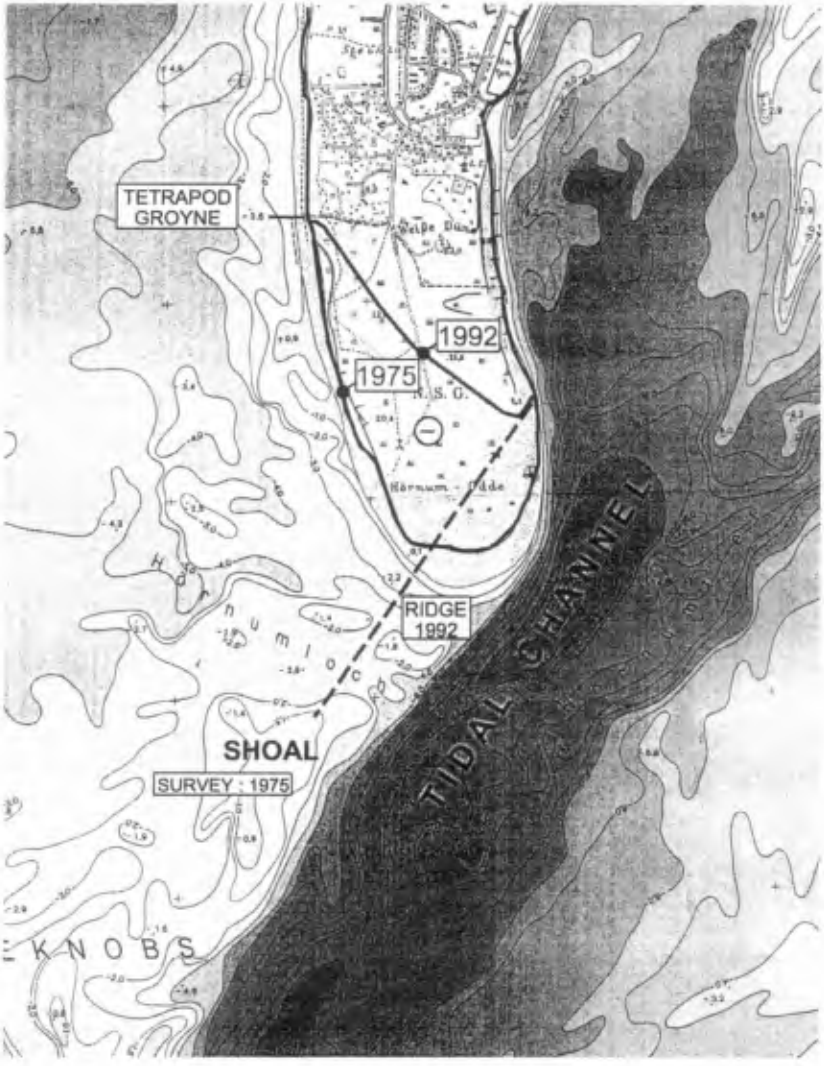

Figure 12. Extension of the ridge along the tidal channel from the shoreline to the offshore shoal and lowering of the depth contour by 2 m in the average

A sill at the southern end would stabilize that end. It would involve some "reconstruction" of the end and a sill as illustrated schematically in Fig. 13.

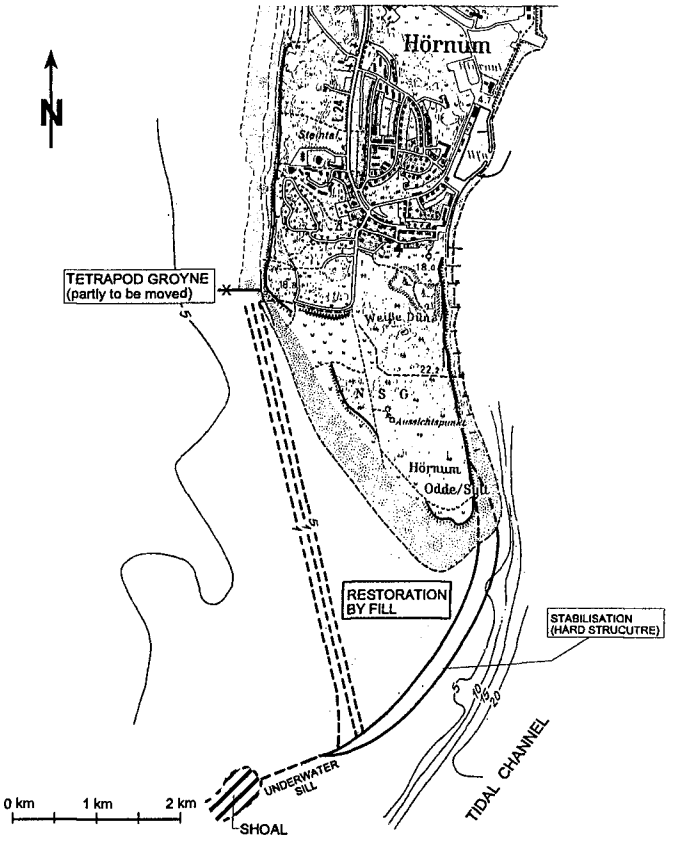

Figure 13. Restoration of former island's shape and its fixing at the southern end of Sylt (schematic)

Conclusions and Recommondations

In order to protect an open sand system the entire coastline should be considered as one single unit, i.e. it should not be splitted into sectors with different protection standards. The most favorable solution for the management of an open sand system like the westcoast of Sylt would be the minimization of the everyday longshore transport to that magnitude which just is necessary to preserve the present appearance of a wide beach and surf zone.

The required minimization of sand loss can be achieved by a barrier inside the dune or inside a berm nourishment profile that limits uncontrolled erosion by extreme storm tides. In case of a narrow beach the barrier, e.g. a geotextile membrane, can be protected by an additional stone wall at its toe. Sand deficits to the everyday longshore transport due to this measure could be compensated by additional sand supply (nourishment) to the beach in the middle of the island, from where the sand will be moved alongshore to the ends of the island.

Underwater sills at the ends of the island will reduce the concentrated longshore flux into the tidal channels and by these means extend the residence time of sand in the open system.

The realisation of such an overall solution, with the aspect of changing philosophy from shortterm, mostly remedial measures to a longterm preventive strategy, necessitates persuasive power and last not least the availability of substantial funds.

Acknowledgement

This work is undertaken as part of the MAST III - SAFE Project supported by the Commission of the European Communities, Directorate General for Science, Research and Development, under contract no. MAS-CT95-0004. The Coastal Authority in Husum ('Amt für Ländliche Räume') is gratefully acknowledged for their cooperation and supplying the Sylt data.

References

DETTE, H.H. (1977) Effectiveness of Beach Deposit Nourishment. Proceedings International Conference Coastal Sediments '77, Charleston, ASCE, pp. 71 - 86.

DETTE, H.H. (1997) Evaluation of Long-Term Dune Recession Data. Proceedings Coastal Dynamics '97, Plymouth, pp. 634 - 644.

DETTE, H.H.; RAUDKIVI, A.J. (1994) Beach Nourishment and Dune Protection. Proceedings of the 24th International Conference on Coastal Engineering, Kobe, ASCE, pp. 1934 - 1945.

DETTE, H.H.; FÜHRBÖTER, A.; RAUDKIVI, A.J. (1994) Interdependence of Beach Fill Volumes and Repetition Intervals. Journal of Waterway, Port, Coastal and Ocean Engineering, Vol. 120, No. 6, ASCE, pp. 580 - 593.

FÜHRBÖTER, A. (1974) A Refraction Groyne Built by Sand. Proceedings of the 14th International Conference on Coastal Engineering, Copenhagen, ASCE, pp. 1451 - 1469.

NEWE, J.; DETTE, H.H. (1995) Simulation of Dune and Nourished Berm Erosion during Storm Surges. Proceedings Coastal Dynamics '95, Gdansk, ASCE, pp. 850 - 861.

BEACH FILLS IN EUROPE - PROJECTS, PRACTICES, AND OBJECTIVES

L Hamm[1], H Hanson[2], M Capobianco[3], H H Dette[4], A Lechuga[5], and R Spanhoff[6]

ABSTRACT: *The beach fill situation in five European countries is highlighted and discussed with respect to the general situation, project type and objectives, design and evaluation procedures, legal framework, and financial aspects. As expected, significant differences were found between the investigated countries. In general, the study shows that it would be very profitable for south European countries to learn about the Dutch and German practices, particularly regarding the long-term coastal management and the regular monitoring of the coastal morphology. On the other hand, recent Dutch experience has shown that their legal system is a bit too rigid leading to automatic local renourishments that are unnecessary to reach the global objective.*

INTRODUCTION

The present study is a part of a project called SAFE (*Performance of Soft Beach Systems and Nourishment Measures for European Coasts*), sponsored by the European Commission. The overall objective of the SAFE project is to develop a sound and improved methodology to predict the medium and long-term performance of artificial nourishment schemes by introducing reliable and validated numerical modeling tools (Hamm 1998). As a part of this project, an inventory of and a comparison between the major nourishment countries involved in the SAFE project was performed.

The objective of this particular study is to compile, disseminate and exchange national information on a European level concerning beach fill operations for coastal protection, projects involved, and practices used. Below follows a tour through the participating countries in Europe, in no particular order, to reveal the present situation. For each country, the general situation is briefly discussed together with an overall description of

[1]Doctor, SOGREAH Ingénierie, 6 rue de Lorraine, 38130 Echirolles - France (Email: HAMM-L@sogreah.fr), [2]Associate Professor, Dept. of Water Res. Engrg., Univ. of Lund, Box 118, S-22100 Lund, Sweden, [3]Senior System Engineer & Project Manager, Tecnomare Spa, R & D Division Environment Area, San Marco No 3584, 30124 Venezia - Italy, [4] Academic Director, Leichtweiss Institut für Wasserbau, Technischen Universität Braunschweig, PO Box 3329 - D-38023, Braunschweig - Germany, [5]Centro de Estudios de Puertos y Costas, Antonio López 81, 28024 Madrid, Spain, [6]National Institute for Coastal and Marine Management/RIKZ, Ministry of Transport, Public Works, and Water Management, P.O. Box 20907, 2500 EX, The Hague, The Netherlands.

project types, objectives, design, and evaluation. In the concluding section at the end of this paper, a comparison between the different countries is presented, where common features as well as differences are discussed. This includes the more detailed design aspects - methods, considerations, constraints, and fill types, methodologies, and equipment.

BEACH FILLS IN GERMANY (DE)

Up until 1950, shore protection in Germany was mainly achieved through hard structures. The first fill in modern times was performed in 1951 on the Island of Norderney. Since then, there has been a gradual change from hard to soft protection measures in sandy coastal zones. After the first fill, more than 130 fills have been performed at 60 different sites (Figure 1) adding up to a total fill volume of about $50 \cdot 10^6$ m^3.

The mainland of the German North Sea coast is protected by seadikes. Beach fills are carried out at sandy beaches which are predominant on the Eastfrisian and Northfrisian Islands in the North Sea and along the coastline of the Baltic Sea. The islands have to be maintained, because their existence is considered as large scale-natural barriers which protect the mainland.

Project Types and Objectives

Because the federal states in Germany have different protection policies, the project objectives may vary depending on location: *1.* Soft protection of seawalls and revetments against local scour through toe nourishments. *2.* Strengthening of dunes and beaches in order to keep shorelines at their 1992 positions (Dette 1987). *3.* Preserve at all times a minimum natural dune width of 40-45 m. *4.* Erosion mitigation. *5.* Compensation of lee-erosion caused by coastal structures. These five types of projects are carried out in the framework of legal coastal protection by coastal authorities. In addition, local communities take initiatives to improve their beaches for recreational purposes.

Design and Evaluation

The design methods to meet the various objectives can all be classified into the category of generic templates. Refined design stage methods are at the very beginning of being considered as design tools. For the protection of the Westerland seawall on Sylt three unusual design types were developed (Dette and Gärtner 1987) including *1.* a successful spit-type fill which extended seawards more than 350 m from the seawall, *2.* a less successful, linear, 1.0-km long fill up to 3 m above MHW, and *3.* the combination of both previous designs called a "girland-type" fill with satisfying results.

In general, coastal protection in Germany is done within a well-developed longterm strategy for actions along the coast. For most projects the responsible authorities are implementing follow-up programs. However, serious overall performance evaluation programs are still not used to any extent, but only in some special cases.

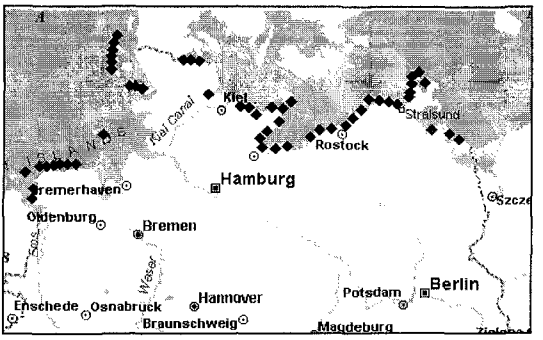

Figure 2. Documented beach nourishment sites in Germany. The ✦ denotes a beach fill site.

Legal and Financial Aspects

German coastal protection is regulated by the Constitutional Law in terms of a Conflicting Legislation Act. The national Government may apply this right, if a matter is not regulated effectively by federal law or if the legislation of one state interferes with the legislation of other states or that of the entire nation. The five coastal federal states have formulated special regulations for coastal protection in their federal legislation. Although these regulations differ in certain aspects, the national Government has not yet made any use of the Conflicting Legislation Act.

The national Government, being aware of its overall responsibility, financially supports the coastal protection works of the coastal federal states. This support is subsidiary, i. e., national funds are only granted if matched by funds from the concerned federal states.

In 1969, Article 91a was amended to the Constitutional Law of 1949. In this Article the co-operation between the national Government and the federal states was legally established by means of "Joint Tasks". Such tasks have to be classified as being of national importance and as being necessary for improving the standard of living. Coastal protection has been identified as such a Joint Task and, thus, included in article 91a. The national financial share in these tasks was fixed at 70 per cent.

The protection of sandy coastlines against storm surges and erosion by means of repeated beach fills and nourishments is handled individually by the coastal federal states in terms of "General Protection Guidelines" or site specific master plans. Since 1950 more than 95 % of all nourishment sites in Germany have been benefitting from those regulations. The rest, e.g. small fill projects for mostly recreational purposes, are financed by local authorities on the basis of their own interest. Within this legal scheme, the economy of coastal protection projects is not dealt with. Until this day economic justification of such projects is not obligatory.

BEACH FILLS IN ITALY (IT)

In Italy, modern beach fills have been practiced since 1969. During this period about 50 fills have been performed at 36 sites (Zaggia, 1998) adding up to a total fill volume of about $15 \cdot 10^6$ m^3 (Figure 2). A large majority of these fills are small-size interventions around 100 - $150 \cdot 10^3$ m^3. The exceptions are four large interventions at Cavallino and Pellestrina near Venice ($7.6 \cdot 10^6$ m^3), Ravenna in the Po river delta ($1.4 \cdot 10^6$ m^3), Ostia close to Rome ($1.4 \cdot 10^6$ m^3), and Bergeggi on the Italian Riviera ($2\ 10^6$ m^3).

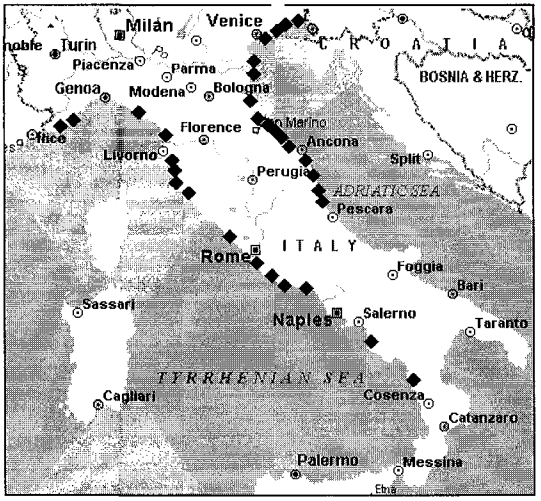

Figure 2. Documented beach nourishment sites in Italy.

Project Types and Objectives

Almost all projects comprise of a combination of sand nourishment and hard structures (Benassai *et al.* 1997). These different projects may be attributed to one of the following general objectives: *1.* Erosion mitigation at local scale. *2.* Enhanced recreation at very small scale. *3.* In southern Italy there is often the need to safeguard the coastal railway. These interventions may, almost generally, be regarded as remedial (counter-active) rather than preventive (pro-active) measures, i.e., emergency-type actions are taken as problems are identified along the coast without any long-term planning or overall strategy.

Design and Evaluation

Most projects are based on a generic design with a combination of hard and soft structures. Most minor projects are designed by simple scoping methods utilizing crude evaluations of shoreline retreat rate together with an evaluation of the equilibrium slope. In larger projects, somewhat more refined design methods are used, where a crude evaluation of the longshore sediment transport rate is combined with detailed computations of the volume budget. In addition, the Dutch CUR (1987) manual is consulted for determining longterm trends, renourishment intervals, *etc.*

Physical model tests are quite common in larger projects. However, numerical models are not used, with the exception of the Pellestrina and Cavallino projects where, to some extent, such models were used. These projects were, however, undertaken in the particular framework of the Special Law for the Safeguard of Venice. In general, monitoring is only limited or not done at all. Also, there is no established methodology for maintenance schemes and no actual performance evaluation is made for the projects.

Legal and Financial Aspects

In Italy, coastal waters and beaches are State owned. This means that initial costs have generally been attributed to the State, while the regional Governments are responsible for maintenance and associated costs, at least formally. Exceptions to the attribution of the maintenance costs are the rule, typically based on the occurrence of extreme events which require the support of emergency measures (with funds coming from the State). Revenues go to the Municipalities. In the past there were hardly any cost-benefit analyses of

projects. What is most evident is, thus, the discrepancy between who is paying and who is receiving the benefits. The situation is anticipated to change in the future.

The Law of 1907 distinguished between two types of coastal defenses, those to protect built-up areas and those to halt beach erosion. Concerning the former, the local planning authority is in charge and can obtain financial support from the Ministry of Public Works, once its operative sections have considered the works to be technically feasible. In the second case, both the Municipality and the Port Authority can apply for financial supports from the Ministry of Public Works in order to build up the defenses.

The Decree Law of 1985 restricted development to 300 m inland from the high water mark. The regions were requested to issue territorial and landscape plans aimed at regulating the uses of these areas and at ensuring their sustainable exploitation. Stabilization of the dunes in order to protect the hinterland is now being considered.

New legislative developments are expected by the application of the so-called "Coastal Plan", currently under preparation by the Ministry of the Environment. Other new legislative developments, that could eventually go in the direction of "Coastal Zone Management" are also expected following the possible adoption of the Strategic Environmental Assessment for the coastal zone and the transfer of competence from the State to the Regions (Law of 1997).

BEACH FILLS IN THE NETHERLANDS (NL)

In the Netherlands, modern beach fills have been practiced since 1970. During this period about 150 fills and refills have been performed at about 30 sites adding up to a total fill volume of about $110 \cdot 10^6$ m^3 (Figure 3). Since 1991 the average fill volume amounts to about $6 \cdot 10^6$ m^3 per year.

The Netherlands have struggled for many centuries to safeguard its territory from flooding. The western part of the country is below mean sea level. Large portions of the Dutch coast are receding since long. Historically, this recession has been stopped at some places with dikes, whereas at various other places no strict measures have been taken, or the recession has merely been slowed down with groins and fences. Thus, in general, the policy was previously one of selective retreat. The disastrous flooding in 1953 of large parts of the south-western part of the Netherlands led to a change of this policy. New legislation concerning minimal safety standards for the coast against flooding was adopted.

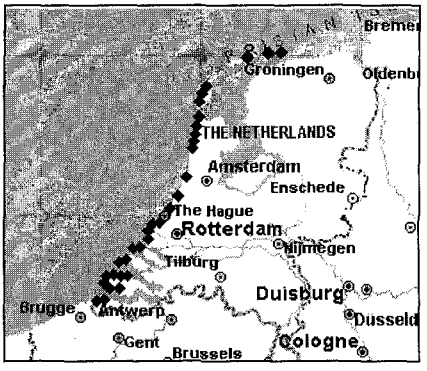

Figure 3. Documented beach nourishment sites in the Netherlands.

A further step in this direction was taken in 1990 when the policy of Dynamic Preservation was adopted. This was based on the presumption that it is technically and economically possible to compensate natural erosion of sandy coasts by nourishment. Prior to this policy, most nourishments were done for reinforcing dunes against breaching.

Project Types and Objectives

After adopting the Dynamic Preservation policy, the overall objective has been to preserve the 1990 coastline location though nourishments on a national scale. Thus, policy implies that the future coastline should nowhere be landward of the 1990 position. When required, sand is nourished to warrant the latter.

Design and Evaluation

The responsibility for coastal protection in the Netherlands is divided between national (Rijkswaterstaat which also have local offices) and regional authorities, so-called Water Boards. A local Rijkswaterstaat's body designs the nourishment and produces a blue print covering all aspects to be taken into account by a contractor, such as place of sand mining, shape of the nourished profile, i.e., how much sand has to be placed in each profile, in which time-frame the work should be performed, *etc.* Thus, the design is very strict and with little variation from site to site (CUR 1987).

The principal design parameters are nourishment volume, depending on the rate of autonomous erosion and the requested lifetime and the effectiveness factor of nourished sand. The latter is defined as the ratio of the autonomous erosion rate before to the actual erosion after implementation of the nourishment. Beach nourishments are designed to compensate for the natural loss of sand in a coastal stretch for a defined period of time to come. The amount of sand is, thus, calculated by multiplying the design lifetime with the annual loss derived with the regression over the previous 10 years. The amount is then corrected with a site-dependent effectiveness factor (10%-20%) to account for the possible slightly increased erosion rate after the nourishment, compared to the autonomous one.

The coastline is obtained from a measured sand volume rather than from an observed horizontal line such as the MLW. This volume is contained in a horizontal layer and is bounded by the profile and a fixed vertical reference line. For some places one has deliberately defined another position, more seaward, to ensure that the safety or a required beach width is automatically warranted as long as the coast line meets the 1990 criterion. In addition, the safety against flooding is checked every year, on the basis of the measured profiles. The evaluation of nourishments is based on annual surveys, performed along the entire Dutch coast since 1965, with cross-shore profiles 200 to 250 m apart. During the operations the treated sections of the nourishment site are surveyed before and soon after their treatment, in order to achieve proper nourishment volume values.

Legal and Financial Aspects

The Sea Defense Law of 1996 regulates the responsibility for maintaining the safety against flooding and the division of tasks between Government and regional authorities. Maintenance of the primary sea defenses is handled at a regional level, through the Water Boards who are supervised by the provinces. Because of the national interest of safety, the

Minister of Transport, Public Works, and Water Management has the overall supervision. For dune systems, a large part of the profile is considered to make up the primary defense, from the shoreface to the landward side of the first dune. The local Water Boards are in first instance responsible for the dunes while the Government has to maintain the coast line. This approach obviously requires close collaboration between the two levels, which takes place on a provincial level in the so-called Provincial Consultative Bodies (POK's), each consisting of representatives from the province Government, the local Water Board(s), and the Rijkswaterstaat. The provincial authorities chair the POK's to ensure that the coastal management is in line with the regional planning policy. According to the Sea Defense Law, the dune profiles are measured each year and whenever the standards are not met, measures will be taken with a high priority.

The local Rijkswaterstaat's authority is also responsible for numerous permits needed. They have to be granted by local municipalities, Water Boards, *etc.* They concern amongst other things permission to work in the areas, such as installing pipelines and pumping stations. There may be regional differences. For example, in one province the beach has remained under the jurisdiction of Rijkswaterstaat, for the specific reason of controlling the permits to work there, while in another it has become part of the Water Board's responsibility. Fortunately, with the present day experience, obtaining these permits is a routine operation.

In the policy of Dynamic Preservation the Minister of Transport, Public Works, and Water Management has to inform parliament every 5 years about the results of this policy. A first (interim) report was provided in 1993, a first full report in 1995, while the next one is foreseen for the year 2000. The policy will be continued for the time being. With the maintenance scheme built into the legal structure, little economic justification is necessary for individual projects.

BEACH FILLS IN FRANCE (FR)

In France coastal defense works are quite significant but nourishment is only a marginal technique adopted to control the erosion. A recent inventory (Hamm *et al.* 1998) showed that modern beach fills have been practiced since 1962. During this period about 115 fills and refills have been performed at 26 sites adding up to a total fill volume of about $12 \cdot 10^6$ m^3 (Figure 4). This very limited quantity reflects that most coastal defense works in France still comprise the construction of groins, seawalls and detached breakwaters.

Project Types and Objectives

The French approach of beach nourishment is traditionally to couple it with hard structures as supporting measures to minimize sand losses and maintenance. In addition, in the most important nourishment projects, the nourishment option was chosen on the basis of the desire to get rid of available sand dredged to maintain navigable depths in a nearby harbor. A slight change of policy may possibly be reflected in two recent projects representing a new approach with much less supporting measures and allowance of an annual loss of material (implying some periodic renourishment).

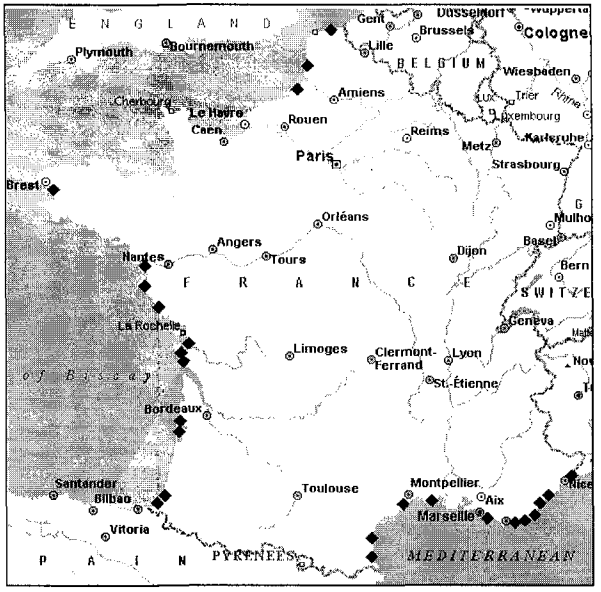

Figure 4. Documented beach nourishment sites in France.

Project motivations include the creation of recreational beaches, coastal defense, dune restoration, and, as mentioned above, the use of dredged sand from harbor extensions or maintenance. No difference is made in practice between protection against flooding and stabilization of the shoreline. In general - as in Italy - the measures may be classified as remedial rather than preventive.

Design and Evaluation

Design methods of coastal defense works are rather well developed in France. The survey of the completed projects has shown that detailed design studies have been performed for 15 cases. Typical design is based on classical coastal engineering concepts (SPM 1984) but includes also environmental considerations.

The movable bed scale model is the traditional tool in France to perform morphodynamic impact investigations since 1950's. Shoreline numerical models are also being used in recent years to study large-scale evolutions. In several cases, *in situ* tests have been performed to check the design. However, the monitoring after nourishment is in most cases not systematic. The monitoring program is not planned in advance and is often not comprehensive. Topographic surveys are quite frequent for dune and beach nourishments. However, they are typically not complemented by bathymetric surveys. The wave climate is seldom recorded but international databases (synopships, satellite data) as well as hindcast techniques are used.

Legal and Financial Aspects

The Law of 1807 specifies that the Ministry of Public Works shall certify the necessity of coastal defense works. All costs incurred for coastal defense works shall be borne by the protected landowners in proportion to their interests, except in cases where the Government decides that subsidies from public funds would be advisable or merited. In practice, such subsidies have usually been extremely small, owing to the limited financial resources generally devoted to coastal defense works. This law also sets out guidelines for the so-called "compulsory" associations that are responsible for having these works carried out and maintained. It has always been difficult to put these laws into effect, which has

given rise to the saying that "France has no coastal defense system, only expenses". (De Rouville, 1954).

Since 1970, the certification is now provided by the local representative of the Government with possible funding (10 to 30%) in cases of the defense of urbanized areas. Such funding is, however, exceptional. The Law of 1973 allows local communities to take initiatives in this area when common interests are threatened. In practice, local municipalities are nowadays in charge of coastal defense works with possible partial financial support of regional authorities. As a consequence, there is no national coastal management in France and no national standard for doing beach fill design and evaluation. Each project is managed according to prevailing and local conditions. On the other hand, mentalities are slowly changing and many regional funders are now becoming aware of the necessity to think regionally before funding locally.

The Law of 1977 was aiming at the protection of nature and institutes an environmental impact assessment study when the budget of works exceeds 1 million ECU. Further legal texts improved the accreditation procedure including public inquiries, concertation and administrative procedures when the works occupy a surface over 2,000m^2. In practice, the financial threshold is not reached and the surface area threshold is difficult to define. Thus, nourishment projects escape to this law. So, in practice, accreditation procedures are seldom in effect for nourishment operations in France.

The so-called Littoral Law of 1986 extends the concept of coastal defense works to natural sites with an accreditation procedure when the budget of works exceeds 0.15 million ECU. It also forbids new artificial beach developments and protects the natural state of the coastline. Furthermore, the coherence between the earlier laws and the new environmental laws needs improvements which are reported to be in progress.

BEACH FILLS IN SPAIN (ES)

Practically the entire Spanish Mediterranean coast is, a sandy coast (Lechuga 1994). The principal causes of erosion along this coast is the interruption of the sand transport by numerous harbor installations. Modern beach fills have been practiced only since 1983. During the last five years alone more than 600 fills and refills have been performed at about 400 sites adding up to a total fill volume of about $110 \cdot 10^6$ m^3 (Figure 5). The vast majority of the projects are along the Mediterranean coast.

Project Types & Objectives

Beach fills are usually done without any supporting structures. In some cases detached breakwaters are used. In quite a few cases existing detached breakwaters have been removed in connection with the nourishment project. Being a nation with a significant portion of its income based on tourism, the overall objective of these nourishments is connected to recreational space rather than the exact position of the shoreline or concerns about flooding. Thus, the objective may be stated as: "The dry beach width must exceed 60 m at all times for recreational reasons". As for the French and Italian cases the measures are mostly remedial rather than preventive.

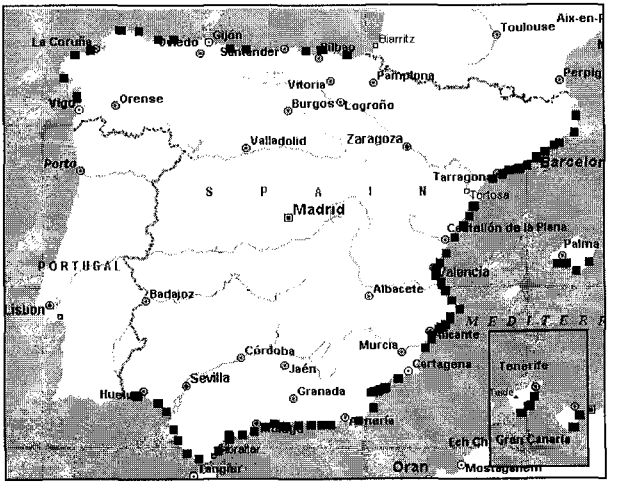

Figure 5. Documented beach nourishment sites in Spain.

Design and Evaluation

The overall Spanish design type may be classified as profile translation. Numerical or physical models have only been used in a few important projects. Similarly, follow-up studies, including annual bathymetry and grain size studies, are only performed for these major projects. In the design process, environmental concerns seem more important than engineering aspects.

Legal and Financial Aspects

The financial processes involved in beach nourishment are regulated by The Shores Act of 1989, according to which all beaches in Spain are State owned. This Act states that works within the jurisdictions of the central Government shall be financed by proper budgetary appropriations and, if applicable, with contributions from the regional Governments, local Governments, international organizations, and private parties. The Shores Act imposes severe restrictions to build and develop in a "protection zone" 100 to 200 m inland from the beach.

In practice, almost all nourishments are financed by the central Government, because, according to the Shores Act, the coastal defense is strictly its responsibility. In some projects, with a more infrastructural rather that pure protective character, such as beachfront promenades, regional and local Governments may contribute financially jointly with the central Government. In the near future, more of the coastal works are going to be considered as parts of an integrated coastal zone management process. A first example of this could be seen in the management of the Castellon coastal zone project.

COMPARATIVE RESULTS

Rates and Volumes

There are big differences in nourishment fill rates and volumes between the investigated countries. Table 1 shows number of fills, fill rates and volumes for the respective countries together with the year when beach modern nourishments were introduced on a more regular basis. As seen from the Table, Spain and the Netherlands are by far the biggest nourishing countries in Europe. The most distinguishing difference between the two is that the sand in the Netherlands is placed on a few locations, while in Spain the

sand is portioned out over a large number of smaller sites. Table 2 shows the present annual fill rates for the above countries together with estimations of the corresponding numbers for some other countries around the world.

Table 1. Beach fill numbers, rates, and volumes.

Country (start year)	Total volume (10^6 m^3)	No. of fills	No. of sites	Average volume/ fill (10^3 m^3)	Average volume/site (10^6 m^3)	Fills/site
FR (1962)	12	115	26	104	0.5	4.4
IT (1969)	15	36	36	420	0.4	1
DE (1951)	50	130	60	385	0.8	2.1
NL (1970)	110	150	30	733	3.7	5
ES (1985)	110	600	400	183	0.3	1.5

Table 2. Annual Fill Rates for Selected Countries.

Country	Annual fill (10^6 m^3)	Country	Annual fill (10^6 m^3)
FR	0.7	Denmark	3
IT	1	Great Britain	4
DE	3	Japan	0.5
NL	6	South Africa	0.5
ES	10	Australia	1
		USA	30

Thus, the total annual rate of the European countries adds up to about $28 \cdot 10^6$ m^3, which is about the same volume as that for the USA.

Design Parameters

The Tables below show a first attempt to classify the design parameters taken into account in the respective countries. Table 3 indicates which wave and sediment related conditions that are included in the design process where the parameters listed are: Storm = storm surge levels, Q_L = longshore sediment transport rates, Run-up = run-up levels, D_C = depth of closure, Waves = wave height (and direction), Sed. dist. = spatial distribution of sediment grain size, and Aeolian trp. = losses of sediment due to aeolian transport. Table 4 shows which fill properties and procedures that are explicitly taken into account in the nourishment design.

Table 3. Design Considerations for Coastline Maintenance in the Respective Countries

	FR	IT	DE	NL	ES
Storm	Y	Y	Y	N*	N
Q_L	Y	Y	Y	N	Y
Run-up	Y	N	N	N*	N
D_C	Y	N	N	N	Y
Waves	Y		Y	N*	Y
Sed. Dist.	Y		Y	N*	Y
Aeolian tpt.	N		Y	N	N

* considered for safety nourishment, not for coastline management.

Table 4. Design Elements in the Respective Countries

	FR	IT	DE	NL	ES
H_B	Y	Y	Y	Y	Y
W_B	Y	Y	Y		Y
Overfill	Y	Y	N	Y	N
Vol./m	Y	Y	Y	Y	
Transition	N	Y	Y	Y	
D_B/D_N	>1	1	>1	≥1	>1
Structures	Y	Y	N	N	Y/N
Ren. period (yr)	N	N	~5 - 7	~5	
Follow-up	N	N	Y	Y	Y/N
Perf. eval.	N	N	Y/N	Y	N

where H_B = berm height, W_B = berm width, Overfill = the use of overfills, Vol./m =volume of fill per m of beach, Transition = the use of transitions at the lateral ends, D_B/D_N = grain size of borrow material relative to the natural sediment grain size, Structures =the use of supporting structures, Ren. period =calculated renourishment period, Follow-up = the use of follow-up programs, and Perf. eval. = the use of performance evaluation programs.

OVERALL CONCLUSIONS

The Tables above are hard to evaluate as they still only present *which* parameters that are taken into account, not *how*. Countries, such as Italy, that consider more parameters may seem to perform a more thorough design than others. However, it could also indicate that these countries improvise more from cases to case than others, such as the Netherlands, that has a more consistent design. Also, the number of parameters *needed* to be taken into account certainly reflects the degree of varying conditions from site to site, which is of course smaller in the Netherlands than in Italy.

Beach Fill Practice

There are - as expected - significant differences between the investigated countries regarding *1.* Engineering methods and evaluation procedures, *2.* Overall coastal management strategies (which are very developed in some countries and virtually non-existing in others), and *3.* Legal and financial framework. The following more specific remarks can be made concerning the different national characteristics:

- NL is the only country that has a serious overall performance evaluation program integrated into their legal framework.
- NL and DE have developed a long-term strategy for actions along the coast and are implementing thorough follow-up programs.
- ES has a fairly well-developed organization and a long term philosophy for their actions, but anticipate to run into problems of finding suitable borrow areas in the near future.
- ES, IT and FR all apply a strategy of remedial rather than preventive measures and seem to suffer from a lack of overall long-term strategy, coastal management, regular monitoring of the coastline, as well as a comprehensive survey of available borrow areas.
- IT and FR suffer from a lack of financial support for regular renourishments.
- IT experiences unclear commitments and sharing of responsibilities between the Ministry of Environment and the Ministry of Public Works.
- All investigated countries foresee a continued transfer from hard to soft measures and regard beach nourishments a an effective means of coastline preservation.
- Nourishments are expected to continue over foreseeable future in all participating countries.

The SAFE project is contributing to disseminate the experience of each of the participating countries in Europe and to promote an integrated and large-scale approach of these problems. The present study shows that it would be very profitable for south European countries to learn about the Dutch and German practices, particularly regarding

the long-term coastal management and the regular monitoring of the coastal morphology. On the other hand, the recent Dutch experience has shown that their legal system is a bit too rigid leading to automatic local renourishments that are unnecessary to reach the global objective.

ACKNOWLEDGMENTS

This work is undertaken as part of the SAFE project partly funded by the European Commission/Directorate of Science, Research and Development (DG-XII), contract N° MAS3-CT95-0004 and by Ministère de l'Equipement, des Transports et du Logement/Direction de la Recherche et des Affaires Scientifiques et Techniques/Service Technique des Ports Maritimes et des Voies Navigables (France), subvention N° 97 M/3.

REFERENCES

Abbruzzese, L., Amatucci, F., and Piro, G. 1987. "A Railway Protection. Coastal Structures on Tyrrhenian Calabrian Coastline," *Proc. Coastal Zone '87*, ASCE.

Benassai, E., Gentilomo, M., Ragone, A., Setaro, F., and Tomassichio, U. 1997. "Littoral Restoration by means of Protected Beach Nourishment - Recent Italian Works," *PIANC Bulletin No. 94*, PIANC, 43-55.

CUR, 1987. "*Manual on Artificial Beach Nourishment*," Centre for Civil Research, Codes and Specifications, Recommandation 1, Rijkswaterstaat/Delft Hydraulics,The Netherlands.

De Rouville, A. (1954). "Remarques Générales sur les Mémoires Présentés pour la Défense des Côtes." *Proc. 5th Coastal Engrg. Conf.*, ASCE, 432-440.

Dette, H. H. 1977. "Effectiveness of Beach Deposit Nourishments," *Proc. Coastal Sediments '77*, ASCE, 211-227.

Dette, H. H. 1997. "Evaluation of Long-Term Dune Recession Data," *Proc. Coastal Dynamics '97*, ASCE, 634-643.

Hamm, L. 1998. "Performance of Soft Beach Systems and Nourishment Measures for European Coasts." *Proc. 3rd European Marine Science and Technology Conf.*, Synopses volume II, EUR 18220, European Communities Publications, Luxemburg, 931-944.

Hamm, L., Billard, N., Viguier, J., and l'Her, J. 1998. "Les rechargements de plage en France." *Internal report Sogreah Ingénierie n°518904R13*, Grenoble, France. (in prep.)

Lechuga, A. 1994. "Littoral Dynamics and shoreline Erosion: Selected Spanish Cases". U.S.-Spain Workshop on Natural Hazards.

SPM 1984. "*Shore Protection Manual*," 2nd ed., 2 Vols., U.S. Army Corps of Engineers, Coastal Engrg. Res. Cntr., US Govt. Printing Off., Washington, DC.

Zaggia R., 1998. Analisi Critica degli Interventi di Ripascimento in Italia, Degree Thesis, Università di Padova, Facoltà di Ingegneria, Dipartimento di Ingegneria Idraulica, Marittima e Geotecnica., pp. 160.

Evaluation of the Effect of 20 Years of Nourishment

Christian Laustrup[1] and Holger Toxvig Madsen[2]

Abstract

Since 1982, large-scale coastal protection works have taken place on the Danish North Sea coast. The subject of the first part of this paper is the coastal protection policy, the engineering approaches to erosion and flood control and the results achieved. An important tool for coastal protection has always been and still is nourishment. In the second part of the paper, the effect of the nourishment will be evaluated with focus on the positioning of the nourishment in the profile and on the use of coarse materials.

1. Introduction

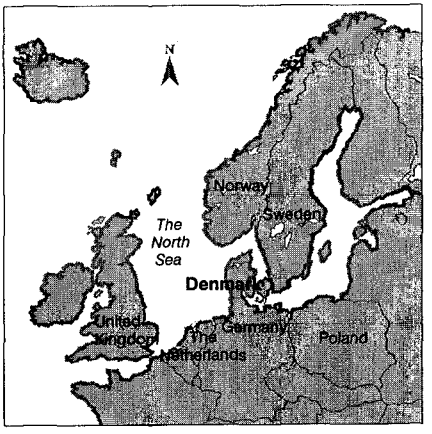

Figure 1. The North Sea countries

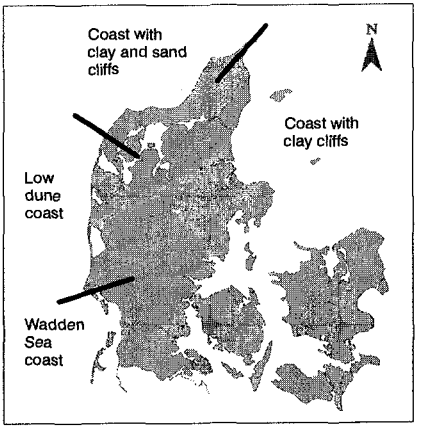

Figure 2. Classification of the Danish coasts

The Danish coastline is 7000 km long. Roughly speaking, there are four different types of coast:

1 Deputy Director
2 Senior Coastal Engineer
Danish Coastal Authority, Box 100, DK7620 Lemvig, Denmark, E-mail: ki@kyst.dk

- A tidal coast with a tidal range of 1.5 - 2 m where the low hinterland is protected against flooding by dikes.
- The southern part of the North Sea coast with sandy beaches where dunes protect the low hinterland against flooding.
- The northern part of the North Sea coast with sand and clay cliffs.
- The Baltic Sea coasts mainly with clay cliffs.

Figure 3 illustrates the different degrees of exposure.

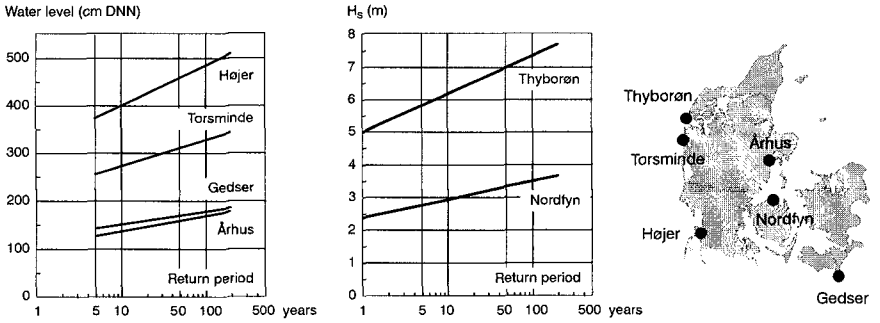

Figure 3. Water level and wave height statistics

2. The coastal protection policy

2.1 Regulations and funding

In Denmark, we do not have a basic coastline defined by law as it is the case in for example the Netherlands. For the two major dikes in the tidal region, the dike safety level was decided by the government to be a 200-year return period. Apart from that, there are no national rules for safety assessment of dikes or dunes. The actual policy for safety assessment and the erosion control policy are established as an agreement between local authorities and the government based on Danish Coastal Authority recommendations. There are probably a number of reasons for the lack of national regulations but the main reason is that apart from the land protected by the two main dikes, the danger to human life is small and "only" land is damaged by erosion and flooding.

The costs of coastal protection on the North Sea coast are shared between the government and the local authorities. The government typically pays 50 to 70 %. In some cases the government pays 100 %.

On the Baltic Sea coasts, coastal protection is regulated by an act passed in 1988. According to this act, the counties are responsible for the administration of coastal protection projects. Since the counties do not have any coastal engineering expertise, the Coastal Authority provides assistance at the planning stage and the consultants provide assistance at the project

stage. The general practise is that there is no public funding of coastal protection in the Baltic Sea area. Here the individual landowner has to bear all the costs.

2.2 The situation and strategy in 1982

The following chapters deal with the problems on the North Sea coast, especially on the southern part of the coast.

Figure 4 shows the coastline retreat rate before 1977 for the southern part of the North Sea coast. There are very high rates of leeside erosion caused by harbour breakwaters and large groyne groups. Besides the loss of valuable recreational areas, the high erosion rates had the effect of significantly reducing the protection against flooding provided by the dunes.

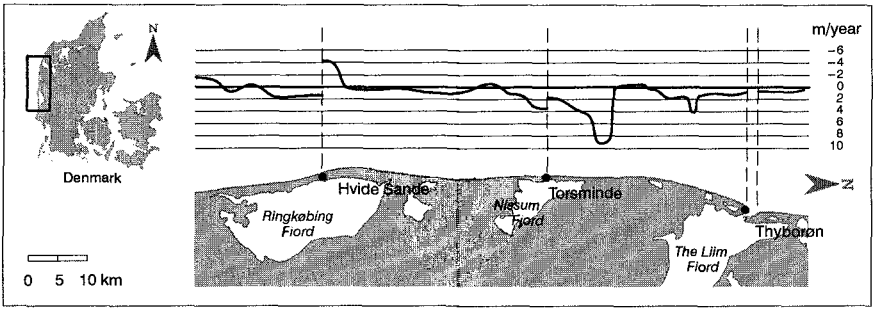

Figure 4. Retreat rates before 1977

About 100 years ago, the dunes were stabilized by marram grass planting. At the same time, harbours and groyne groups were built which resulted in serious downdrift erosion. The combined result of the stabilization of the dunes and the erosion was that in 1982, the dunes had disappeared or were weak along 50 km of the coast. So in 1982, it was decided to implement a coastal protection scheme.

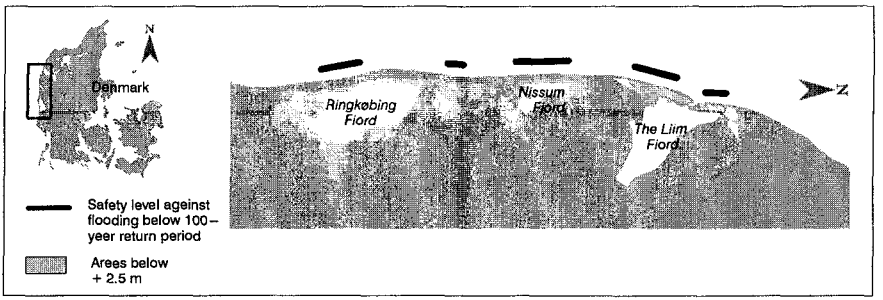

Figure 5. Low areas and critical safety levels

The headlines of this policy were:

- To re-establish a safety level against flooding to a 100-year return period minimum.
- To stop the erosion where towns were situated close to the beach.
- To reduce erosion on parts of the coast where erosion in the near future would reduce the safety against flooding to less than 100 years.

The dunes were reinforced and new dunes were built to re-establish the safety against flooding to a 100-year return period. However, in many cases it was not possible to reach the safety level required because there was not enough land between the beach and the houses or the road to build a sufficient dune volume. In this case, the dunes were protected by a revetment.

Placed concrete block revetment

To stop or slow down the general erosion of the coastal profile, the following approach was used:

- On highly exposed stretches where erosion should be stopped, low detached breakwaters were used in combination with nourishment. One reason for the use of breakwaters was that for historical reasons, local politicians trusted in hard structures like groynes and breakwaters. Another reason was the high price of the nourishment sand.
- Nourishment was applied but on a small scale. The main reason for this was that the principle of beach nourishment was new to the politicians. It was difficult to convince the politicians that "the erosion of the nourishment sand during storms is part of the plan". This meant that volumes were small and unit costs were high which was one reason for stabilizing the nourishment by means of breakwaters.

Detached breakwaters, beach nourishment and revetment

Rubble-mound breakwater

2.3 Important developments since 1982

Figure 6 shows the coastline retreat rate in 1998 for the southern part of the North Sea coast. The very high erosion rates are no longer a fact. We do not have an absolute zero erosion but the erosion has been stopped where it is important for the dune safety and on average, the coastal erosion rate is 0.1 m/year.

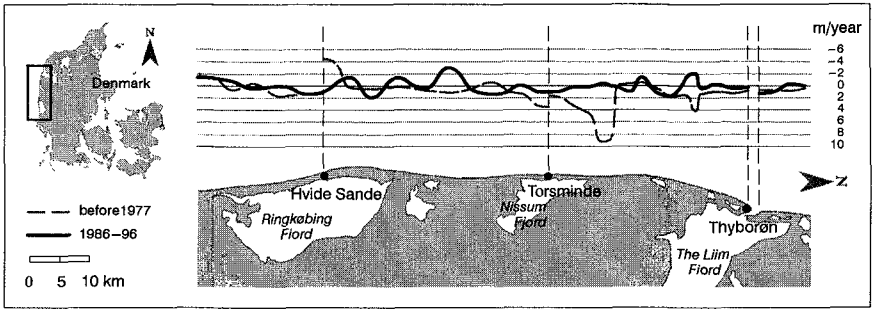

Figure 6. Retreat rates 1986 - 96

The safety level of the dunes has been re-established to a level of at least 100 years which was the goal in 1982.

Figure 7 shows the development in the use of structures and beach nourishment for the period, including costs.

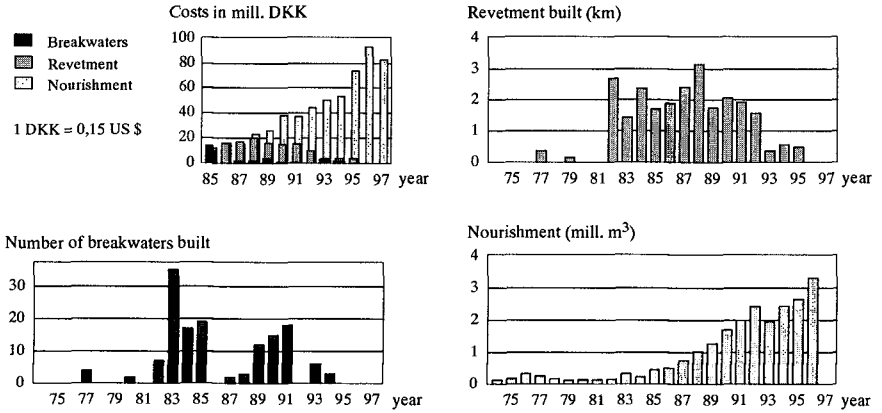

Figure 7. Development in the use of structures and nourishment

The effect of using low detached breakwaters has been studied (Laustrup and Toxvig Madsen, 1994). The results were based on 10 years of monitoring of a group of breakwaters. The purpose of the study was to confirm the design theory which had been used and which was based on theoretical computations. The paper confirmed that the use of breakwaters in this group had reduced the need for nourishment landward of the breakwaters by 50%.

Since 1982, the engineering solutions have changed from a hard to a soft approach. There is a number of reasons for this development of which the most important are:

- A growing awareness among the general public and among politicians of environmental issues.

- The problems which required hard solutions have been solved.
- The budgets have been raised dramatically rendering soft solutions more competitive.

Because of the small volumes and the lack of experience of the Danish contractors regarding pumping of sand directly on shore on the North Sea coast, the mobilization costs were quite high and consequently, the unit costs were high. With increasing volumes and experience, a better approach for nourishing the different parts of the profile has been developed. Today, three methods are used. The methods are pumping onshore through a submerged steel pipe, pumping over the bow and dumping from split barges.

3. Evaluation of the effect of the beach nourishment

Some effects of the nourishment have now been evaluated. In this chapter, some of the aspects concerning a steepening of the coastal profile, positioning of the nourishment sand in the profile and the effect of using coarse sand will be discussed.

3.1 Profile steepening

The retreat rates shown in figure 6 have been calculated for the profile section from -6 to +4 m. For nourishment we only use a volume equivalent to the erosion on this part of the profile. As it could be expected, this policy leads to a steepening of the profiles. Figure 8 shows a number of bars each representing a number of profiles on a part of the coast. The length of the bars represents the difference between erosion velocity of the profile seaward of -6 m and landward of -6 m. This difference represents the steepening of the profiles. Before 1986, the steepening took place on parts of the coast where groyne groups had been built (sections 3,4 and 5 in figure 8). After 1986, the steepening mainly took place where the nourishment projects were carried out (sections 1-5 in figure 8).

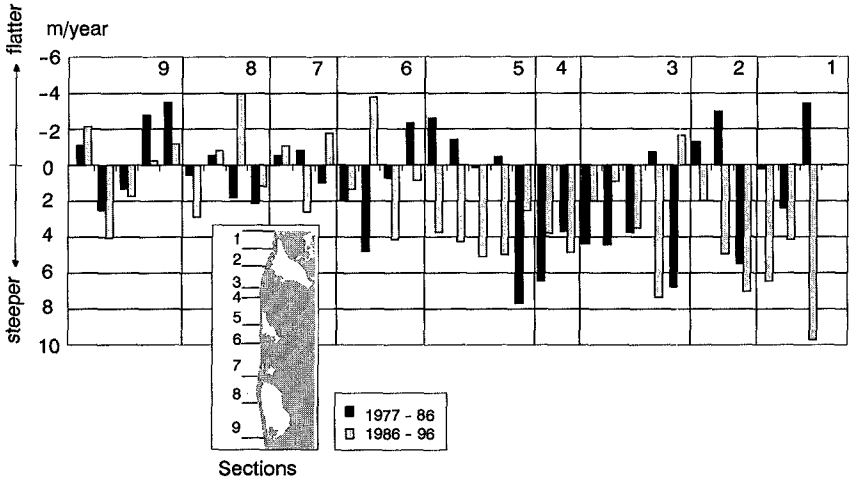

Figure 8. Difference between retreat rates seaward and landward of -6 m

3.2 Positioning the nourishment in the profile

In 1993 - 96, the European Union MAST project Nourtec was carried out with participation from the Netherlands, Germany and Denmark. In the Danish case, a nourishment project on the longshore bar and a project on the beach were studied (Laustrup and Madsen, 1996).

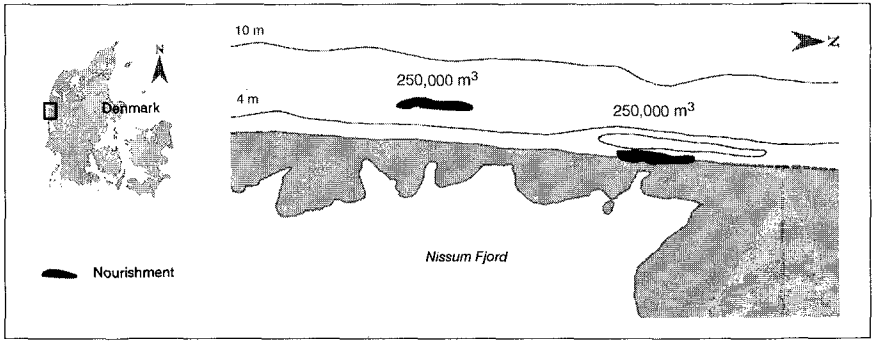

Figure 9. The Nourtec general location plan

The main results were:

- In the first year, the beach nourishment gives the better stabilization of the beach.
- At the end of the period, the shoreface nourishment is the better option for the stabilization of the beach.
- The shoreface nourishment is more stable than the beach nourishment. The main reason is that the shoreface nourishment sand was coarse, $D_{50} = 0.57$ mm. The effect of the beach nourishment is that of a feeder berm and the effect of the shoreface nourishment is that of a breaker berm. The effect of the shoreface nourishment on the outer part of the profile is that of a feeder berm.

The conclusion was that the profile from the bar and out should be nourisbed by dumping sand on the bar. This is also cheaper than placing the sand on the beach. There was nearly no migration of sand from the bar to the beacb so for tbe inner part of the profile it was recommended to place the sand on the beach. Figure 10 shows the principles of positioning tbe sand in the profile that we are going to implement in the future. Part of the nourishment on the beach is used as a buffer to prevent erosion of the dunes during storms.

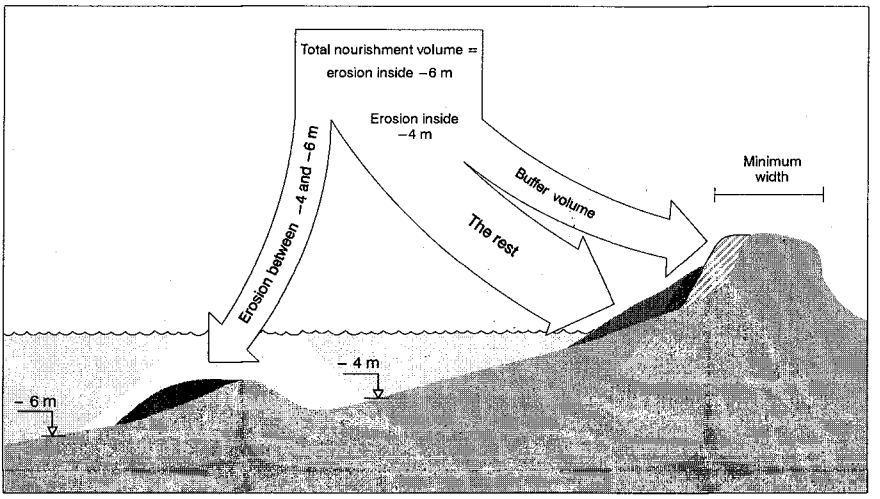

Figure 10. Principles of the positioning

3.3 The effectiveness of coarse sand

We are now studying the relationship between the D_{50} and the effectiveness of the sand. For that purpose, we have evaluated nine projects involving annual nourishment during the period 1986-96. The length of the project stretches are 3-5 km and the volume per metre is 10-50 m^3.

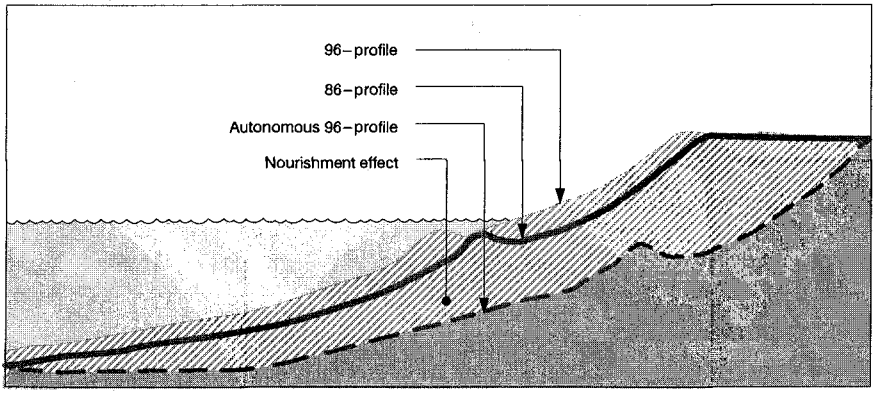

Figure 11. Principles of calculating the nourishment effect

The principle used for the study is shown in figure 11. We know the 1986 and the 1996 profile. However, the effect of the nourishment is the shaded area between the 1996 profile and

the autonomous 1996 profile (the profile without nourishment). Since we do not know the theoretical profile and since this profile is important for the result, we have estimated it in three different ways.

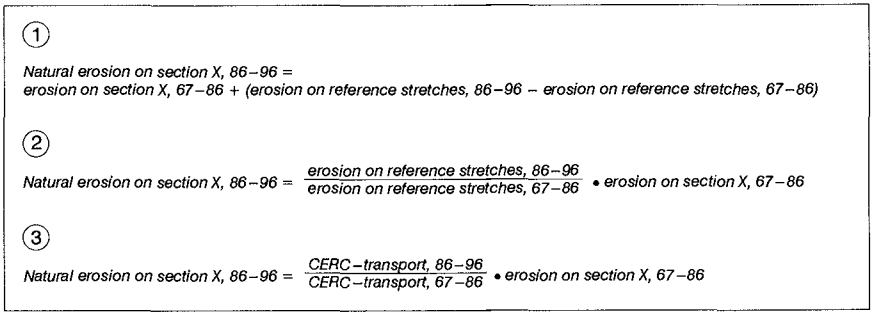

Figure 12. Methods for calculation of the natural erosion rates

Figure 12 illustrates the three methods used to estimate the natural erosion. We are looking for the natural erosion in the nourishment period 1986-96 on each of the nourished stretches.

Method 1 and 2 use the erosion on stretches of the coast which developed naturally and which have the same degree of exposure as the nourished stretches (reference stretches). In method 1, the difference between the period 1986-96 and 1967-86 is used. In method 2, the ratio between the erosion of the two periods is used. In method 3, the ratio between transport capacities calculated by use of the CERC formula in the two periods is used.

Profile erosion 1967–86		*79.4 m^3/m/year*
Difference 1967–86 to 1986–96		*–3.2 m^3/m/year*
Natural erosion 1986–96		*76.2 m^3/m/year*
Effect of breakwaters		*–10.1 m^3/m/year*
Anticipated erosion 1986–96 without the effect of nourishment included		*66.1 m^3/m/year*
Monitored erosion 1986–96		*6.2 m^3/m/year*
Effect of nourishment		*59.9 m^3/m/year*
Nourishment volume		*40.3 m^3/m/year*
Effectiveness of nourishment	*59.9/40.3*	*1.49*

Figure 13. Example of the calculation of the effectiveness

Figure 13 shows an example of a calculation of the effectiveness. The effect of the nourishment is the shaded area in figure 11. The nourishment volume is known so the effectiveness is the effect divided by the volume. In this case, it is greater than one. The effectiveness can also be defined as the ratio between erosion velocity in native and borrow material. Since the renourishment factor (James, 1975) is the ratio of erosion velocity in borrow material to native material, this is the inverse of the effectiveness.

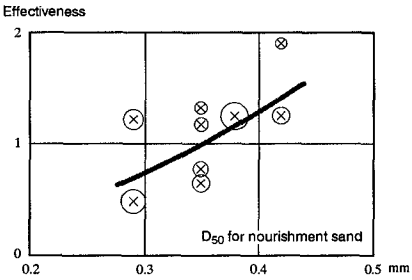

Figure 14. Results of the calculation of the effectiveness using method 1

Figure 14 shows the effectiveness as a function of the D_{50} for the nourishment sand, if we use method 1 to estimate the theoretical profile in 1996. The area of the individual dots is proportional to the nourishment volume. The total volume represented by the dots is 10 mill. m^3. The curve is a weighted best fit curve.

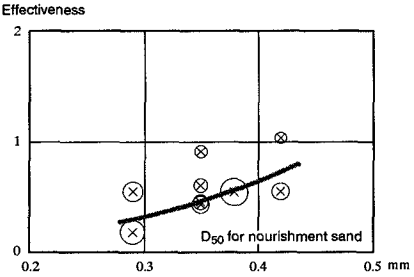

Figure 15. Results of the calculation of the effectiveness using method 2

Figure 15 shows the same relationship if we use the ratio between erosion on reference stretches in the two periods.

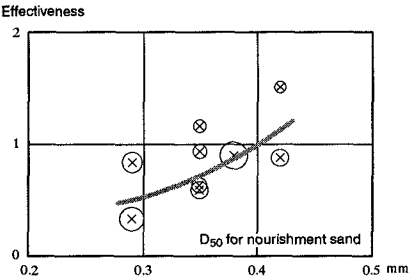

Figure 16. Results of the calculation of the effectiveness using method 3

Figure 16 shows the relationship if we use the ratio between CERC transport capacities for the two periods.

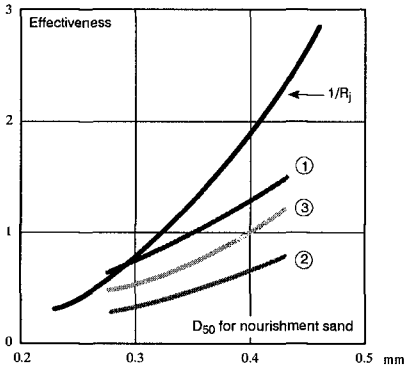

Figure 17. Comparison of the three methods and the renourishment factor

Figure 17 shows method 1, 2 and 3 and the inverse renourishment factor.

To improve the results we are going to work on getting better sediment characteristics and to improve the method to calculate the theoretical erosion. Besides, the comparison with the inverse renourishment factor is not correct if there has been some erosion in the native material in a project. We know that is the case at the beginning of the period 1986-96 because at that time, we did not have enough money to stop the erosion completely, so we are going to do some more work along that line.

4. Conclusions

Erosion control with a combination of nourishment and low detached breakwaters has reduced the retreat rate to average zero for the depth range from -6 m to +4 m. The policy of only nourishing this part of the profile has resulted in a steepening. The safety against flooding has been raised to a return period of more than 100 years by building new dunes and by protecting the dune foot with a revetment.

Based on monitoring of nine nourishment projects with a total volume of 10 mill. m^3 for a period of 11 years, guidelines for positioning of nourishment sand in the profile and for the use of coarse sand in nourishment projects have been developed. Better quality information about the native and borrow sand characteristics is needed.

References

James W. R. (1975). Techniques in evaluating suitability of borrow material for beach nourishment. Report TM60. US Army Corps of Engineers, Coastal Engineering Research Center, Vicksburg.

Laustrup C. and Madsen H.T. (1994). Design of Breakwaters and Beach Nourishment. Proceedings, ICCE 1994, pp. 1359 - 1372.

Laustrup C. and Madsen H. T. (1996). Comparison of Beach and Shoreface Nourishment, Torsminde Tange, Denmark. Proceedings, ICCE 1996, pp. 2927 - 2940.

ZURRIOLA BEACH EVOLUTION TWO YEARS AFTER NOURISHMENT

José C.Santas[1], José M.Medina[2], Alejandro Caballero[3], Adolfo Uriarte[4] and Vicente Esteban[5]

Abstract

First results about the behaviour of the nourishment done at Zurriola beach, Vasc Country, Spain, have been obtained, by means of the data acquired during 2 years monitoring. The general conclusion appoint to a good agreement with the previous physical model results: in spite of a small percentage of sand is lost, the beach is "self kept". A rough evaluation of losses has been done, helping us to predict the future maintenance to do. The topography and bathymetry of the beach do not help to a easy modelling by means of mathematical models.

Introduction: The Nourishment Project

Zurriola beach, located in Gros neighbourhood of San Sebastian, in the North of Spain, has been progressively disappearing along this century, mainly due to the advance of the city over the beach. Its reconstruction project, tested at 1992-93, was based on the construction of the prolongation of the embankment Urumea river breakwater and a nourishment of the beach, with an urban promenade of 1100m. on the interface with the city.

The project begun at 1993(1), and $1*10^6$ m^3 of sand were used, that was borrowed form a submarine area close the 15 Kms from the beach. The grain size was .33mm. and the final slope was 0.013.

It ended at March-95, with a total cost of $13.3*10^6$ECUS(1996). After this moment the evolution of this new beach is being studied. Directional waves, tide and currents data are recorded simultaneously with monthly bathymetry,

---

[1]*Marine Sc.Ph.D. and Physicist; Head of Field Adv. Measurements Prog.; CEDEX, Study and Research Centre for Public Works, Antonio Lopez 81, 28026-Madrid; Spain.*

[2]*Civil Eng.,Head of Division, Coastal Service; CEDEX*

[3]*Marine Sc., Agustin Bethencourt Institution; Civil Eng. School, Techn. University of Madrid*

[4]*Geology Ph. D.; AZTI; Satrustegui Ave.,8, 20008-SanSebastian; Spain*

[5]*Civil Eng, San Sebastian Coasts Department; Spanish Coasts Authority, Prim st.,10, 20006-San Sebastian; Spain.*

topography and grain size data acquisition surveys.

Figure 1: The layout of the beach before and after the nourishment.

Field data acquisition survey:

The information acquisition survey incorporated data of directional waves, tides, currents, bathymetry and topography for both submerged and emerged areas of the beach, completed by remote sensing of the dry beach. Since July-1995 the monitoring is being carried out. Four control profiles have been measured to obtain the beach evolution, employing DGPS. The closure depth for the noticeable sand movements was initially estimated at 15 metres depth but due to discrepancies between successive surveys, the number of control profiles and its final depth were modified adding other 4 with a total length prolonged till 25m. depth (May97)

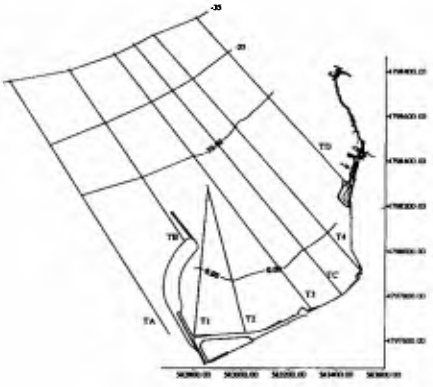

Figure 2: Final scheme of "control profiles": T1 to T4 (initial scheme) and Ta, Tb, Tc and Td control profiles added and prolonged at May97.

The sea weather conditions have been studied with 2 in situ systems:

1. First at all a S4DW EMCM that was deployed at a point located on the

T3 control profile, 1.5 metre over the bottom which is 11 metre deep.

2. At May-97 a Directional Waverider Buoy(DWB) has been deployed at 37 metres depth outside the Zurriola Bay.

Estimation of deep water storm conditions was done using the information provided by a Wavescan Ocean - Meteorological Directional Buoy (named EMOD-1) located at 600 metres depth, 40 miles north-west away.

Figure 3: A) Buoy locations at studied area. B)Detailed zone of San Sebastian with the S4 and Datawell buoy situations.

The characteristics of Wave data acquisition survey were as follows(2):

EMOD1: Time series of 2048 points, 0.5 seconds sampling period, every 3 hours. Spectral process with 32 freedom degrees, without overlapping.

DWB: Time series of 1536 points, 0.78 seconds sampling period, every 1 hour. Spectral process with 24 freedom degrees, without overlapping.

S4DW: Time series of 4096 data points, 0.5 seconds sampling period, every 3 hours. Spectral process with 64 freedom degrees, without overlapping

Equipment S4DW provides the tidal data, that have been used for the bathymetry data corrections, and the current data.

The coverage of data during all the monitoring duration that began at June-1995, reaches more that the 80%. Specially the amount of information of the DWB is done better that the 95% since its installation at 19th-June/1997.

Bathymetry and topography data surveys were initially scheduled as monthly but the rough sea conditions do not enable to be realised every month.

The chosen methodology that is based on measurements only along same previous selected control profiles to optimise the balance between cheaper total costs and better knowledge of the short term temporal evolution, has allowed us to reach a big total amount of data of the 81% (36 monthly surveys done over 37 possible) tacking into account the temporal coverage. This point allows us to get a good base to estimate the beach evolution.

The selection of the closure depth (CD) was obtained from the Harllemeier's criteria (CERC, Shore Protection Manual, 1984):

$$d_1=2.H_s(p=0.50).12.\sigma(H_s) \quad \text{and} \quad d_2=2.H_s(p=0.137) \qquad [1]$$

The data taken from the EMOD-1 Data Base allow us to propagated the selected sea conditions from deep waters to 30 metres depth, obtaining d_1=27.2 m and d_2=12 m. for the Zurriola Bay external border. Due to that a CD of 15 m. was initially taken, but the successive comparisons of volumes for summer conditions evidenced that it should be greater. At May-97 it was enhanced till CD=25 m.

By other way it was added 4 control profiles more in order minimise the errors produced by the interpolation between them. All the features are produced because the extreme roughness of the bottom as its mobility. As a test point it was observed visually that the depth for the installation point of the S4DW varies 1.2 metres on 1 month at the moment to be done the monthly maintenance operations.

The grain size surveys were done every 3 months and they also reflected the high mobility of the bottom, specially along the river moth area and the extreme of the breakwater due to the currents created by waves diffraction.

Finally the remote optically observation of dry beach by means of a PC controlled camera allow us to contrast the results obtained from topography surveys as estimate the greater effects done by storms on the sandy and promenade areas.

Physical and mathematical modelling

First at all the Zurriola Regeneration Project was previously studied by REF-DIF propagation numerical model (3) to evaluate the best solution. At 1993 It was modelled by means a movable bed physical model to study the best choice for the groin to be constructed (4). The input data for deep water conditions, obtained from EMOD-1 buoy was H_s=9.3 , T_p=16 s, γ=7 , s_{max}(Mitsuyasu)=20, Θ_m(Incoming)=NW.

Evolution of control profiles in their swash and surf zones shows appreciable variations as it is presented on the picture 4. The behaviour of the beach + groin system was enough satisfactory but appointed a lost of sand that would appear in the future.

The area is too difficult to be mathematically modelled in order to employ shoreline and cross shore evolution models. But it was studied the the local behaviour of the beach, appearing a very active zone with big rip-current effects after storms, corresponding with the T3 control profile.

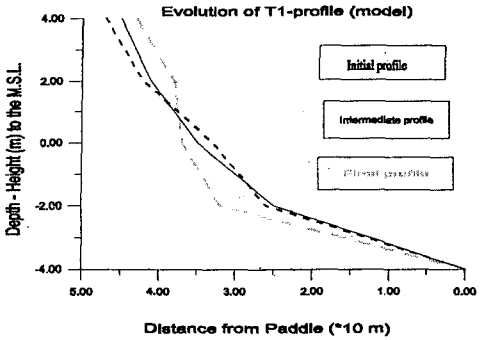

Figure 4: Experimented evolution of the T1 control profile by means the Physical model under storm conditions

Beach evolution: Shoreline position and width of dry beach

The shoreline evolution has been estimated taking into accunton data from the measured control profiles and its crossing point with zero level. The figure 5 shows the evolution along the monitoring period, from August-95 to February-98.

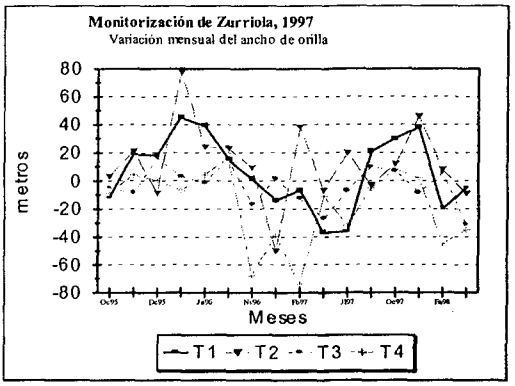

Figure 5: Monthly evolution of dry beach width (reference: August-95)

Maximum variations of 130 metres appear on T2 profile, while the minimum is on the T3 profile. The evolution along the year looks like the general rules, but it is dominated by other effects that masks it; the more important could be the movement of sand done by the local authorities focussed on the aesthetic aspect and leisure use purposes. This conclusion has been obtained doing the comparison with Monthly Averaged Waves, estimated at the no - surpassing levels of 50%, 84%, 97.7% and 99.87%, figure 6.

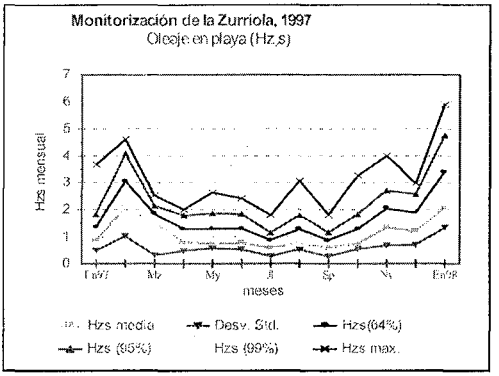

Figure 6: Time evolution during 1997 of Sea Wave conditions close to the beach. Data from S4DW equipment. Values corresponding to no - surpassing probability for Significant Wave Height Hzs , averaged along every month.

The more active zone, Profile T2, coincides with those that exhibit the rip currents effects after storms. This events fit well to the results from the numerical wave propagation model.

Beach evolution: Volumetric variation of wedge sand

Due to the two different used schemes of control profiles there are 2 zones to establish the evolution of the sand wedge (figure 7):

-Reduced area: comprised between the –15 metres bathymetric line, the breakwater and the cost line, that includes the zero depth contour line of the beach and the cliff of Ulia Mountain.

-Enhanced area: comprising from 25 metres depth contour line, the river mouth and the cost line.

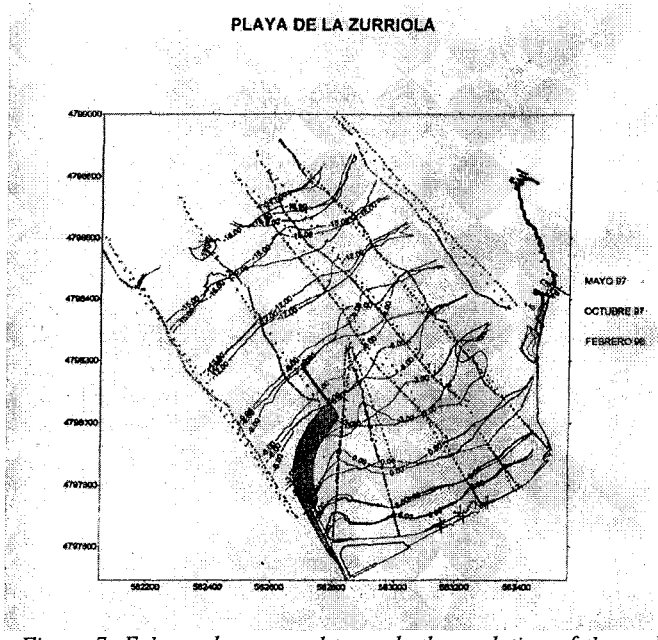

Figure 7: Enhanced area used to study the evolution of the wedge sand, after May-97. The reduced area is constraint to the inner part of the beach located between the breakwater, the 15 meters depth contour line and the coast line.

The evolution recorded along the 2-years monitoring is presented on the figure 8 for the period between Jnauary97 to February98.

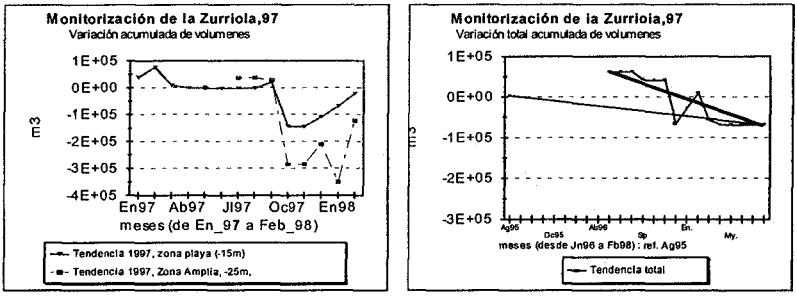

Figure 8: A) Relative evolution of Sand wedge, referenced to Reduced area (continuos line) and enhanced (dashed line).

B) Absolute variation from the beginning of monitoring(narrow line)corresponding to 2-years and for Ag96-Ag97 period.

Estimate of sand balance and tendencies

The evolution is not continuos during all the monitoring period. For the **reduced area**, where the information volume is greater, it was recorded an accretion of 46.000 m^3 during the period Ag95 to Ag96, while the lost of sand from Ag96 to Ag97 has been evaluated as 110.000 m^3. The general tendency could be assumed is about –60.000 m^3 for the 2-years period.

The **enhanced area** shows greater variations due to the inclusion of the river mouth. For the period between the beginning of working with this area, May97, to February98 the total amount of lost sand has been about 124.000 m^3 but the maximum sand losses, located between September and October 1997, has been about 312.000 m^3, while the maximum accretion is about 227.000 m^3 (dated between January to February 1998) after the biggest storm recorded since last 5 years (5).

These data show the high degree of mobility that the bottom has in this area. The factors that do that are:

1) The existence of the river mouth that acts as a sand reservoir. This fact is also proved because the relative high grain size that has been measured in this area:

Average: 2.6 mm , Sorting : 1.43 mm (October 97)

" : 0.14 mm , " : 0.4 mm (July-97).

2) The layout of this area that provides losses of sand from the studied area toward the east , outside of the Zurriola Bay.

Estimate of errors of the used control profiles schemes

The magnitude of figures before mentioned drive us to do an estimate of the errors that the methodology employed could have.

One of the source of errors to eliminate is the consideration of extrapolated areas, far of data. It produces extra data added by the working program, that have to be eliminated. These areas have been previously "blanked", as it can be appreciated on the picture 7, between the more external control profiles and the cost line.

First at all keeping in mind the wave data obtained by the buoys, we can assume that the movement of sediment during summer must be very short, specifically for the period from June to August, 1997. Due to that the variation recorded must be errors of the methodology. The evaluation of that are about 22.000 m^3 for the reduced area and about 45.000 m^3 for the enhanced one.

Secondly the gap between the control profiles can produce a source of

errors directly proportional to that gap. Due to that it have to be greater for the used scheme with 4 profiles (before May97) than the used after, but it must increase with the area size. After May 98 it has been done a big density survey, with separation between points less than 10 metres along tracks (perpendicular to the cost) and less than 20 metres laterally to the track. The 3-D surface obtained has been cut by the control profiles and the new surface has been compare to the previous one. The estimated errors are about the following figures:

-Reduced area scheme (with 200 metres gaps and CD=15m): 10.000 m^3

-Enhanced area scheme (with more profiles, 100 metres gap, CD=25m):16.500 m^3

It is clear to deduce that the figures obtained by the reduced scheme are not so good to obtained an accurate estimate of sand balance, although the tendency could be taken as a draft conclusion. In opposite the figures deduced by the enhanced area and its scheme are more accurate and show an more approximated reality of the evolution.

Conclusions

- The main objective of the nourishment done was to recover an open space for social and leisure uses that the citizens had lost. This objective has been achieved with this reconstruction and opens new possibilities to the city.
- The control profiles scheme previously used with gap close to 200 metres, is not enough dense and wide to produce good estimation because the rough conditions of the sea, the mobility of the bottom and the quality of abruptness of the bottom surface. In the opposite the second scheme is enough good to produce a draft estimation of nourishment evolution.
- The order of the errors on the evaluation are about 35.000 m^3. If all the volume of the wedge sand is taken in mind (13.000.000 m^3), it is about 3 $^0/_{00}$.
- The beach experiences a little tendency to loss sand as it was predicted by the physical model. The evaluation of this tendency is about 30.000 m^3 per year, but it is a primary draft estimation because of factors like the amplitude of time dependent variations, with very high excursion during the year, and the errors .
- There are zones with high tendency to loss sand in the middle of the beach , profile T3, where rip currents happen after storms. In the same way the area close to the end of breakwater shows high mobility due to diffraction effects.
- Because aesthetic questions the layout of the beach, and specially the coast line contour and the dry beach surface, is man-made modified in order to obtain a good aspect for citizen uses. This character must be kept into consideration for all the urban beaches, and this disables to employ these to

calibrate numerical models.

- The presence of a river mouth modifies the evolution, doing an "open" character to the ensemble.

Acknowledgements:

This study is being realised by the Harbours and Coast Research Centre of the CEDEX, (Study and Research Centre for Public Works) under the Annual Schedule of Collaboration between CEDEX and the Directorate General of Coasts of the Environment Ministry of Spain. The Local Coastal Service and the Technology Institute of Foods and Fisheries, AZTI, are collaborated with CEDEX.

Also it has been co-sponsored by the European Union, by means the MAST-III Program. It is included in the SAFE Project , under contract number Mast3-CT95-004-PL950057.

REFERENCES:

(1)Gomez-Pina, G, et alt.;1994;"Urban beach nourishment Project, La Zurriola Beach, San Sebastián, Spain", 25th Int. Conf. On Coastal Eng., Orlando, EEUU.

(2)Santás, Jose C.;1997,"First year of monitoring in Gros Beach", Workshop on "Performance of soft beach systems and nourishment measures for European coasts", Thessaloniki, Greek, 1997

(3)Medina-Villaverde, J.Mª.; 1992;"Litoral Dynamic and proposal for Regeneration of Gros Beach, San Sebastián, Guipuzcoa" (in Spanish), CEDEX technical report to Directorate General of Coasts.

(4)Medina-Villaverde, J.Mª.; 1993;"Study and Analysis of Gros Beach" (in Spanish), CEDEX technical report to Directorate General of Coasts.

(5)Santás, Jose C. and alt.;1997," Monitoring and Analysis of the Zurriola Beach, 1997 ", (in Spanish), CEDEX technical report to Directorate General of Coasts.

MODEL TESTS FOR EVALUATING BEACH NOURISHMENT PERFORMANCE

Massimo Tondello[1], Piero Ruol[2], Mauro Sclavo[3] and Michele Capobianco[4]

Abstract

After having shortly discussed about the nourishment fundamentals, focussing the attention on the benefits and on the factors promoting the beach fills, some specific questions on fill design, on related processes and on the temporal aspects of such beach-protecting intervention were addressed and tentatively answered.

In the second part, the physical-model tool, as a way for answering to the suggested questions is presented and three different case studies are discussed.

Introduction

In the last decades the use in coastal protection of soft intervention schemes such as beach nourishment has largely substituted the use of "hard" intervention approaches like seawalls and groins, because of economic reasons and mostly because of the lower impact on coastal resources and activities.

Nowadays the first task of a project manager is the quantification of the on-going beach erosion phenomenon. This involves the identification of the relevant morphological processes and the consideration of the aspects related to local interests such as safety, recreation, environment and economy.

Once the problem has been defined, the protective measures must be carefully

[1] Ph.D., University of Padova, Dipartimento di Ingegneria Idraulica, Marittima e Geotecnica, Via Ognissanti, 39 - 35129 Padova, Italy. e-mail: *tondello@geomar.ing.unipd.it.*

[2] Researcher, University of Padova, Dipartimento di Ingegneria Idraulica, Marittima e Geotecnica, Via Ognissanti, 39 - 35129 Padova, Italy. e-mail: *ruol@geomar.ing.unipd.it.*

[3] I.S.D.G.M.- CNR, S.Polo 1364, 30125 Venezia, Italy. e-mail: *sclavo@ocean.isdgm.ve.cnr.it*

[4] Tecnomare S.p.A., R&D, Environment, San Marco n. 3584, 30124 Venezia, Italy. *e-mail: capobianco.m@tecnomare.it*

selected. The increasing need of solutions at low environmental impact suggests the choice of soft intervention schemes, which may be integrated with some supporting hard structure. However, "soft" projects need some additional experience in order to derive consistent evaluation criteria for technical problems, economic matters and public policy issues. A beach nourishment project, in fact, includes design considerations on the following aspects: frequency and duration of the fills, pre- and post-fill erosion rates, post-fill profile equilibrium, project length, volumetric requirements, grain size compatibility, protective dunes, long-term sand resources, placement location, "hybrid" projects and downdrift impacts. Because of its relatively short design life, a beach nourishment project needs to be periodically refinanced for maintenance, rehabilitation and environmental permitting.

The first part of this work deals with the choice of the "most suitable" solution. A general framework for comparing the possible solutions is presented in terms of morphological impact and economic aspects that define a number of "objective evaluation criteria".

The determination of the design life is important because it gives the designer the chance of a long term management of the interventions. The long-term evaluation of beach nourishment performance can be obtained by means of numerical or physical modelling. We focus here on the physical modelling approach, which will be proven to be valuable when mutually interacting physical processes are to be taken into account.

The second part of the paper presents the results of three sets of model tests, performed referring to different beach nourishment projects in Italy.

Basic considerations on beach nourishment

For a number of reasons, not lastly historical and legislative, the coastal zone was seen as a "low cost" resource. The adoption of hard engineering practices, heavily based on concrete and steel structures, results in a completely artificial set of forcing factors and boundary conditions, further exacerbating the problem. This has led to the present tendency of developing "soft defence techniques" as a tool to be used in Integrated Coastal Zone Management (ICZM). Among these techniques, periodic artificial nourishment is widely regarded today as an environmentally acceptable method of beach and dune protection and restoration for short-term urgencies (viz. storm-induced erosion) as well as long-term issues (i.e. structural erosion and relative sea-level rise).

Beach nourishment or fill can generally be defined as the artificial addition of suitable (in terms of beach quality) sediment to a coastal area that has a sediment deficiency in order to rebuild and maintain that beach at a certain width and height which provides storm protection and/or a recreation area (CBNP, 1995; Delft Hydraulics, 1987). This definition encompasses restoration (an initial and major sediment contribution to widen the beach) and periodic renourishment (an additional, usually smaller, sediment contribution necessary for the preservation of project integrity). Frequently, nourishment projects include an artificial dune for additional protection against storm surge and waves.

The most important benefits of beach nourishment can be summarised as follows:

- reduction of erosion and flood damage;

- resetting of the long-term erosion trend;
- enhance of recreation and tourism;
- spreading of cost outlays over time;
- reduction of downdrift impact of coastal protections;
- increasing of sand budget for global coastal stability;
- project reversibility.

For these reasons, over the past several decades the beach nourishment has become a preferred coastal hazards management tool. In the future, this reliance is expected to increase mainly for the following reasons:

- increasing of coastal populations
- increasing use of beach for recreational purposes
- increasing public awareness of coastal hazards
- increasing concern about the impact of hard structures.

Technical issues in beach nourishment planning

The technical issues in nourishment planning have been in depth analysed in a previous paper of the authors (Ruol et al, 1997; Capobianco and Stive, 1997) which discusses the beach fill management, focussing on the requirements of fill-design, the correct definition of active processes and the planning of a beach-fill timing strategy. For the benefit of the further discussion, some results are summarised in tables 1-3.

TOPICS	SPECIFIC QUESTIONS ON FILL DESIGN
Design of beach fill	will the expected erosion phenomena be related to longshore transport, cross-shore transport or both?
Shape of planform	what will be the optimal shape of the nourished beach?
Along-shore position	what will be the best technique for placing sand into the beach? • direct placement; • stock-piling; • continuous nourishment
Volumetric requirements	what is the depth of closure and the post-placement profile?
Project length	Is there a minimum project length longshore? Will hard structures be necessary to protect the toe or the ends of the nourished beach?

Table 1

TOPICS	SPECIFIC QUESTIONS ON PROCESSES
Determination of erosion rates	How should future erosion rates be estimated?
Grain size compatibility	What will be the best choice for the grain size of the nourishing material?
Areas downdrift of projects	Should the downdrift benefit (if any) be considered while designing a beach fill?

Table 2

TOPICS	SPECIFIC QUESTIONS ON TEMPORAL ASPECTS
Design life	What is an appropriate (minimum/maximum) design life for a project?
Design frequency	Should design frequency be quantified? Should design imply a coupled analyses of storm probability and erosion processes?
Periodic maintenance requirements	Should design include a time schedule to optimise periodic nourishment cycles, with regard to beach requirements? Should a flexible approach be adopted?
Vulnerability	Should the designer carry out an analysis of risks, with regard maintenance schedule? Should alternative solutions for coastal protection be adopted?
Post-fill profile equilibration	When should projects be accredited (after fill placement or after fill equilibration)?

Table 3

Physical model tests as a tool for beach nourishment behaviour evaluation

Physical model tests represent a technique to answer to those questions in tables 1 to 3. This technique is used most appropriately when a decision problem under analysis is too complex to be solved by analytical models. Simulation through physi-cal models is a quantitative procedure that describes morphodynamics process by constructing a model and then observing how the model behaves in order to learn how the process itself might behave. As a general rule, physical simulation should be used only as a last resort and never as the first option. There may be theory or analytical techniques available to solve a problem. When there are, they should be used.

We should also not forget that "communication and involvement" increasingly play a fundamental role in environmental protection activities in general and nourishment interventions in particular. The adoption of physical model tests have a strong potential also because can be immediately understood (even if only partially) by a large audience. The advantages of physical model tests are:

- The effect of interaction between the different forcing agents can be taken into account;
- complex boundaries can be reproduced;
- wave conditions vary continuously according to seabed modifications;
- up to now, other modelling techniques are not as useful as physical models in morphological analysis where cross-shore and longshore sediment transport together must be taken into account,

while the limits of physical model tests are:

- they are expensive and time consuming;
- the analysis of different situations or the repetition of tests often implies a new setup of the model;
- scale effects are not always assessable.

As a general approach, fixed bed models are suitable for the study of:

- wave propagation;
- sediment transport patterns (particle tracks);
- armour stability;
- forces on structures,

while movable bed models are suitable for the study of:

- planform beach evolution;
- longshore sediment transport;
- beach profile evolution;
- cross-shore sediment transport;
- scour.

Where physical models are probably giving signs of their limits is in the context of long-term and large scale modelling. Such limitation is however still largely compensated by their intrinsic ability to handle complex situations.

In many practical situations, while waiting for the latest developments in the field of morphological modelling and particularly long term morphological modelling, the contribution that physical model tests can give is still of paramount importance, being implicitly integrative of all the (scaled and complex) processes that determine the evolution of the nourishment interventions. In particular they can when the validity of numerical models is limited by large uncertainty in the relevant input parameters which propagates to the model output.

Case studies

The following paragraphs describe how physical model tests have been applied for evaluating the performance of three beach nourishment projects.
The general purpose of physical modelling was to assess if the planned interventions were able to protect the infrastructures located on and behind the beaches and if the beach fill maintenance cost was acceptable.

The projects hereafter presented (fig.1) deal with two protected beach nourishments located close to Rome (Ostia) and in Northern Sicily (Capo d'Orlando), and with a "self nourishment" induced by a coastal protection intervention located in the Po river delta (Barbamarco).

Beach nourishment at Capo d'Orlando (Sicily)

The first application of physical modelling is a protected beach nourishment designed for a 1200 m long beach located close to Capo d'Orlando and facing the Southern Thyrrenian Sea.

The project area is today characterised by an increasing beach erosion caused by an unbalanced longshore sediment transport condition. This erosion is exposing the street and the buildings to the wave attacks; the picture in fig. 2 shows the present condition of the village and underlines the need of a quick intervention.

The design requirements for this project were mainly:

- safety of infrastructures behind the beach;
- availability of a larger beach area for recreational activities.

Figure 1. Project sites.

Figure 2. Capo d'Orlando beach.

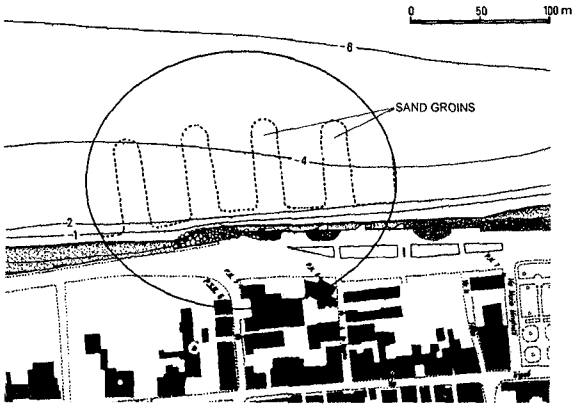

Figure 3. Beach fill technique at Capo d'Orlando

The design solution of the 1200 meters long protected beach nourishment prescribes a sand fill of about 205 m^3/m of sand operated by means of building 39 sand groins (fig. 3) followed by the placement of 6 quarry groins spaced about 200m.

The general interest was to evaluate whether the designed project was suitable to protect the urban area behind the beach and if the beach fill technique (sand groynes) was really effective. These questions have been answered using mobile bed physical models: a number of tests have been planned to study the two- and three-dimensional sand transport phenomena occurring on the beach.

The models have been designed according to the Froude critcrion, whereas the bed material has been scaled according to the Dean criterion (in the model and in the prototype a constant ratio between the wave height and the fall velocity times the wave period has been imposed).

The specific questions on the beach fill design for Capo d'Orlando project can be summarised as follows:

- which short term evolution of the Capo d'Orlando littoral without any additional beach protection is expected?
- is it the beach fill technique effective?
- does the designed construction sequence optimise the effectiveness of the beach fill?
- is it possible to define a construction schedule that does not interfere with the tourist activities?

The physical modelling program designed for the study of Capo d'Orlando beach erosion phenomena included:

- 2D model 1:25 (cross-shore profile)
- 3D model 1:25 (representative cell reproducing the beach delimited by two rubble mound groynes)
- 3D model 1:60 (whole project area);

The waves used for modelling the local climate have been selected from local wave hind-

casting by the UKMO (United Kingdom Meteorological Office). In particular, the waves to be reproduced in the 3D models were obtained respecting the energy flux criterion.

The study of the cross-shore profile (2D-model) started with the simulation of beach evolution from the present condition; the results clearly demonstrated that the surveyed profile are indeed in critical condition and can not be maintained without adding new sediments. The nourished profile and the erosion rate related to cross-shore sand transport have been studied through the simulation of the two nourishment phases planned in the project.

The first phase of the nourishment consisted in building-up a first series of sand groines and in placing a certain amount of sand directly on the beach (fig. 4).
A three-month long (all time data are referred to prototype units) wave attack (simulating an average wave climate) has been simulated on this artificial beach and a first nourished profile has been obtained; in the second phase, again sand groins have been built on the new cross-shore profile and a second 3 months long wave attack has been simulated.

In order to compare the final condition (fig. 5) with the surveyed starting profile (summer profile), a new 1.5 months long mild wave attack has been performed to simulate the summer wave conditions. The summer profile obtained after this test is shown in figure 6.

Figure 4. Beach nourishment 2D – Phase 1(sand groynes and beach fill)

Figure 5. Beach profile after beach nourishment and wave attacks

Figure 6. Final beach profile (summer profile)

The results of the 2D modelling can be summarised as follows:

- beach profile is indeed in critical condition: after having simulated 1.5 months of waves, the retreat of the shoreline (cross-shore transport) was about 8 m;
- after the nourishment a quasi-equilibrium profile was reached, with the shoreline moved about 12 m seaward;
- since the existing profile is far from an equilibrium condition, most of the sand supplied from the sand groins moved offshore, without significant contribution to shoreline advance.

Both the 3D models (the "cell-model", scaled 1:25 and the global one scaled 1:60) followed the wave schedule already used for the 2D model; the longshore energy flux has been analysed in order to obtain a set of 4 wave spectra reproducing the existing sand transport conditions. Figure 7 shows the experimental layout for the 3D "cell model".

In figg. 8 and 9 the final results obtained after the construction of the quarry groins built up after the reshaping of the beach operated by the wave attacks.

The results of the 3D-models can be summarised as follows:

- the three-month long simulation from the present condition (without additional protections) shows that the shoreline position reaches the seawall, endangering houses and infrastructures;

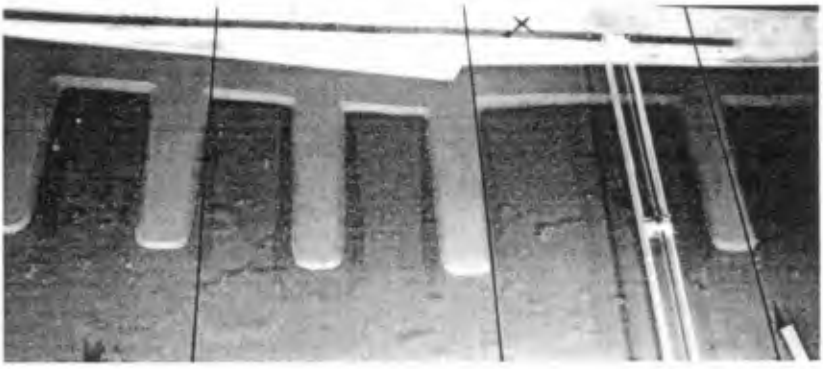

Figure 7. Beach nourishment 3D – Phase 1(sand groynes and beach fill)

- the beach fill forces the shoreline to move 15 m (average displacement) seaward, even if in critical points the shoreline advance appears negligible;
- the late construction of the rubble mound groins allows beach fill material to move downdrift before being protected;
- the model results show that the reshaping of the sand groins will occur in a very short time (e.g. 1 day, if a 2.5 m high wave is used). The beach fill does not need to be ended long time before summer. If operated in wintertime, it is very likely that the wave action will destroy the groins before the end of their construction.

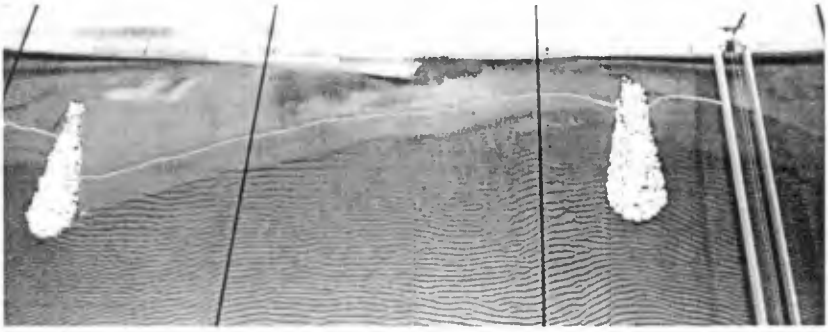

Figure 8. Final beach condition 3D

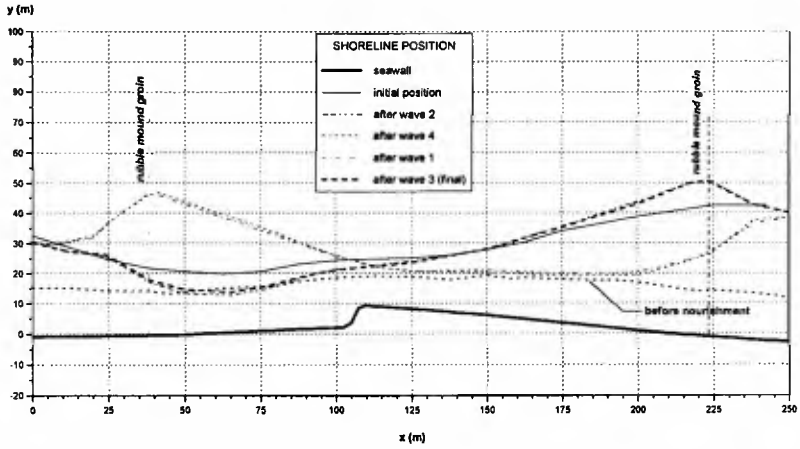

Figure 9. Shoreline beach evolution 3D – Phase 1(sand groynes and beach fill)

Beach nourishment at Ostia (Lazio)

The project consists of the build up of a submerged breakwater, distant some 80 m from the shoreline, located in a water depth of about 4 m, with the top at -0.5 m from m.w.l.; the area delimited by this parallel-to-the-shoreline structure and the shoreline is going to be filled with an amount of 250 m^3/m of sand (fig. 10, upper panel).

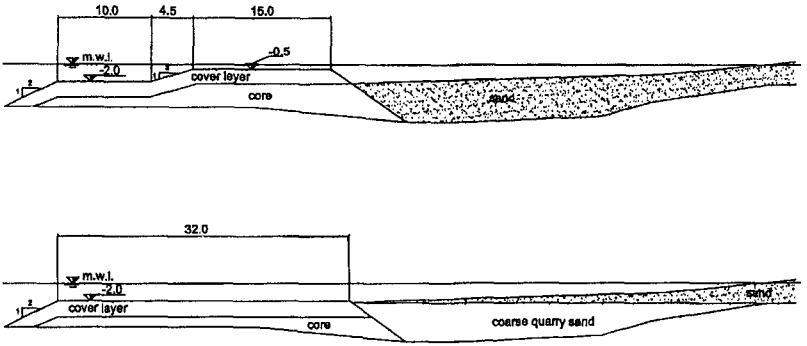

Figure 10. Beach fill technique at Ostia

The specific questions on the beach fill design tried to be answered by means of physical model tests were:

- is it the hard structure suitable for beach fill protection?
- is it the hard structure suitable for recreational purposes?
- are there any alternative solution that suits both beach protection and recreational purposes?
- which is the life expectancy of the beach fill (or the expected maintenance schedule)?

Based upon the waves recording of the site, it was possible to reproduce a morphological period corresponding to about 3 months in nature; the sequence of waves: summer, autumn, winter, spring was used.

The results obtained by mean of 2D-physical model tests can be outlined in the following list:

- the model tests demonstrated a good stability of the nourished beach (upper panel of fig. 10), with only small variations from the initial beach profile;
- a considerable increase of the water level in the region between the submerged breakwater and the shoreline (ranging between 13 to 43cm, referred to prototype) was measured and, as a consequence,
- very "dangerous" return currents have arisen over the top of the submerged structure (this behaviour seems not to be acceptable in the framework of a safe utilisation of the beach).

As a consequence of the described results, a different solution (fig. 10, lower panel), with the top of the structure protecting the "perched beach", placed at –2.0m from m.w.l.

was reproduced and studied in the 2D-model. In particular with the analysed solution the stability of the artificial nourishment was increased using a double layer fill (lower coarse-quarry-sand covered with fine sand, suitable for beach activities). The results of this second round of tests is outlined in the following:

- the model tests demonstrated a lower effectiveness of the structure in protecting the beach fill (fig. 11);
- the coarse-quarry-sand layer was not reshaped by the wave action;
- an initial sand loss of about 25 m^3/m was evaluated in a 3 months period, with a retreat of 10 m, but further simulations showed that the beach profile is close to equilibrium (expected retreat 5 m/year);
- return currents over the breakwater are much lower than in the previous case and seem to be acceptable in the framework of a safe utilisation of the beach;

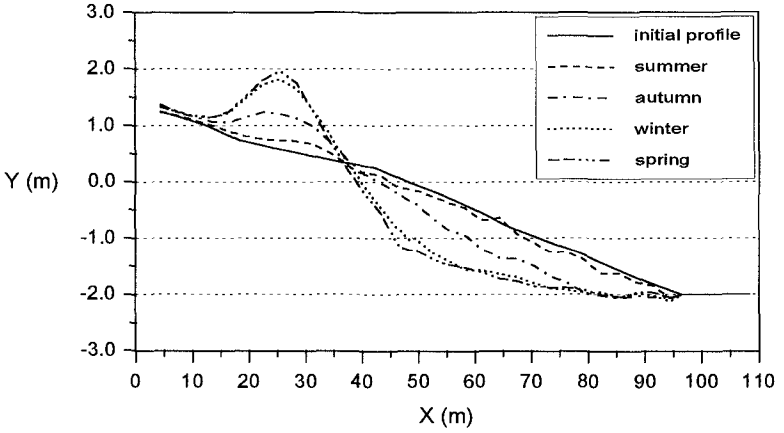

Figure 11. Beach profile evolution after the wave attacks

Beach reshaping and inlet stabilisation at Barbamarco (Po delta)

This project (located at Barbamarco, Northern Adriatic Sea) deals with the stabilisation and reshaping of a deltaic lagoon inlet. This stabilisation, obtained placing sand filled geosynthetic tubes for limiting the inlet fill up, induces the accretion of the updrift beach. The beaches adjacent to the inlet have also been nourished using the sand dredged from the channel, which has been dredged up to –3.0 m. The investigation area is sketched in fig. 12.

The specific questions on beach fill design to be answered using physical modelling were the following:

- is it the longshore sediment transport able to fill the area close to the geosynthetic tubes?
- how long will it take to reshape the beach?
- what will be the filling rate of the dredged channel?

The physical modelling programme designed to answer the previously mentioned questions implied the construction of a 3D model in a 1:100 scale, reproducing the whole project area. The 3D physical model tests designed to evaluate the performance and the time schedule of the project were carried out using light bed material (anionic resin CPN80-bayer®, see tab. 4 for a detailed characterisation). This bed material allows to reproduce the prototype sediments behaviour with respect to the Dean criterion also using very small scale models.

grain size class	D (mm)	w (m/s)	s
1	0.51	1.15	1.13
2	0.72	1.63	1.11
3	1.02	2.01	1.09

Table 4. CPN80-bayer® characteristics (w: fall velocity; s: specific weight)

The model has been calibrated using field data obtained by means of a successive bathymetric campaigns and allowed to determine a morphological model time scale.

The rate of sand bypassing the tubes and filling the dredged channel has been evaluated in the physical model using sand traps located within the channel; a value of about 2000 m^3/year was found.

The calibrated model has been used also for evaluating the beach accretion rate updrift the inlet; it was determined that, by the end of 1997, the coastline south of the inlet should have reached the edge of the tube groin (a recent inspection confirmed this forecast).

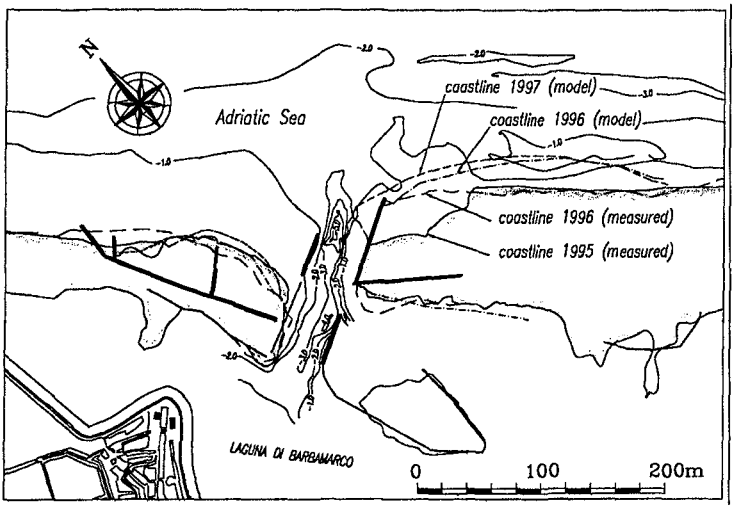

Figure 12. Barbamarco inlet (tubes are sketched with solid lines).

Final remarks

After a brief survey of the still open questions related to the beach nourishment performance evaluation, three cases studies has been presented and analysed by means of physical model tests. This methodology allowed to give satisfactory answers to some practical questions not easily manageable with numerical techniques.

The experimental study of the nourishment design of Capo d'Orlando allowed to point out some useful information concerning the temporal aspects of sand groins remodelling phenomenon induced by the wave attacks.

From the tests on the Ostia littoral nourishment, it was possible to obtain interesting results concerning both the most suitable design of the submerged detached breakwaters and the behaviour of a double-layer supply of material.

Finally, the Barbamarco study evidenced the effectiveness of light bed material in describing transport phenomena when using very small model scale.

As a final remark, it can be stressed that the contribution of physical model tests is still of paramount importance, being implicitly integrative of all the (scaled and complex) processes that determine the evolution of the nourishment interventions.

Acknowledgements

This paper was partially supported by the SAFE Research Projects, in the framework of the EU-sponsored Marine Science and Technology Programme (MAST-III), under contract no. MAS3-CT95-0004.

References

Capobianco M., Stive M.J.F., (1997). *Soft Protection Technologies as a Tool for Integrated Coastal Zone Management.* Proc. MEDCOAST '97, *Malta.*

CBNP (Committee on Beach Nourishment and Protection), 1995. Beach Nourishment and Protection. *National Research Council*, National Academy Press, Washington, D.C., 334 p.

Dalrymple R.A. (1989) Physical Modelling of Littoral Processes. *Recent Advances in Hydraulic Physical Modelling*, Kluwer Academic Publ., pp.567-588.

Dean R.G., Yoo C.H. (1992). Beach Nourishment Performance Predictions. *Journal Waterways, Port, Coastal and Ocean Eng.*, ASCE, v. 118, n. 6, pp. 567-586.

Dean, R.G. (1992). Beach Nourishment: Design Principles. *Proc. of the Short Course on Design and Reliability of Coastal Structures*, Venice Oct. 1-3, pp.285-348.

Delft Hydraulics, (1987). Manual on Artificial Beach Nourishment. *Centre for Civil Engineering research, codes and Specifications.* Rijkswaterstaat, Report 130, pp. 195.

Hugens S.A., (1993). Physical Models and Laboratory Techniques in Coastal Engineering, World Scientific Publishing Co. Pte. Ltd., Singapore, 568p.

Ruol P., Capobianco M., Tondello M. (1997). Physical Model Tests in the Framework of Beach Nourishment Performance Evaluation. *Proc. MEDCOAST '97*, Malta.

Assessment of Depth of Closure on a Nourished Beach: Terschelling, The Netherlands

S. W. Marsh*, R. J. Nicholls*, A. Kroon** and P. Hoekstra**

Abstract

Depth of closure is studied on a nourished beach in the light of its autonomous behaviour over long temporal and large spatial scales. Long term data show that depth of closure is variable alongshore, being shallower to the west and deeper to the east. Following placement of a shore nourishment along the middle section of the coast, the spatial variation of depth of closure changes. Initially the depth of closure is shallowest where the fill was placed. With time after the placement of the fill, this effect diminishes. Depth of closure observed in this study is influenced by bar behaviour. The fill material affects the observed depths of closure by reducing offshore bar migration. Maximum depths of closure for any particular timescale observed in this study are well predicted by the Hallermeier (1981) formulation for the depth limit to the active profile. In conclusion, pre-fill observations and Hallermeier (1981) provide a useful limit to the observed post-fill depth of closure. Similar analysis of other beach nourishment projects would be useful.

Introduction

Beach or shore nourishment is increasingly the preferred engineering solution when eroding coastlines require protection (Davison *et al*, 1992; Khabidov *et al*, 1996; Cooper, 1998). When designing a nourishment project it is important to have a detailed understanding of how the nourished coast will respond to the local hydrodynamic and morphodynamic regime. Furthermore it would also be useful to know whether placement of fill material will affect the local morphodynamic regime, even if the hydrodynamic conditions do not change. One fundamental aspect of the morphodynamic regime that has received increasing attention in recent years is depth of closure (Hallermeier, 1981; Nicholls *et al*, 1998).

* Flood Hazard Research Centre, Middlesex University, Queensway, Enfield, Middlesex, EN3 4SF, United Kingdom.

** Institute for Marine and Atmospheric Research Utrecht, Utrecht University, PO Box 80115, 3508 TC Utrecht, The Netherlands.

If a series of beach and nearshore profiles are collected at a given location, the profile will change through time. In any normal set of profiles, it will be clear that bed elevation is highly variable within the littoral zone. Moving offshore this variability decreases; consequently a plot showing several profiles collected over time will have a depth at which the profiles "close" within the accuracy of the data. In other words, the depth of closure represents the seaward limit of the profile envelope. Depth of closure is a morphodynamic boundary which separates a landward, morphodynamically active zone from a seaward, morphodynamically inactive zone over the period defined by the observations (Nicholls *et al*, 1996). Depth of closure does not represent a barrier to cross-shore sediment transport.

Depth of closure is a key design parameter in the design of beach or shore nourishments (Davison *et al*, 1992). Depth of closure allows coastal engineers to estimate how far offshore morphological change is likely to extend, and hence, calculate the volume of sediment required to nourish a section of coast. However it remains unclear if placing nourishment material influences depth of closure. To investigate this question, depth of closure on a nourished shoreline will be compared to depth of closure on the same shoreline prior to nourishment. Any changes that occur because of the placement of nourishment material can then be investigated. The study will also include an examination of the validity of the Hallermeier (1981) formulation for the depth limit to the active profile.

Study Area

This work focuses on data collected at the Dutch barrier island of Terschelling, figure 1. Two morphological data sets covering this site will be analysed; these are the JARKUS data set and the NOURTEC data set. The combined data sets cover a longshore distance of 12 km and span a time period of 30 years from 1965 to 1995.

The JARKUS data set is comprised of annual surveys along the whole of the Dutch coast. Data collection began in 1963 with annual surveys extending seaward 1200 m. Since 1965 there have been five-yearly surveys extending to 2500 m. Depth of closure tends to occur seaward of 1200 m, so in this study only the five yearly extended JARKUS data are used. The central section of Terschelling has suffered from severe shoreline erosion. In an attempt to overcome this problem, 2.1 million cubic metres of sand were placed in the nearshore zone, between the middle and outer bars of the triple barred system, figure 2. The nourishment sand was slightly coarser ($D_{50} = 200\mu m$) than the native sand ($D_{50} = 180\mu m$) at the point where the fill was placed. The sand grain size decreases across the profile from $220-260\mu m$ on the beach to $150-160\mu m$ on the lower shoreface, (Hoekstra *et al.*, 1994).

The nourishment was placed by RWS-RIKZ, the Dutch National Institute for Coastal and Marine Management and was monitored under the European Community Marine Science and Technology (MAST), Innovative Nourishment Techniques Evaluation (NOURTEC) programme. The length of the nourishment was 4.4 km (from 13.7 km to 18.1 km). Its placement depth ranged from -5 to -7 m NAP (NAP is Dutch Ordnance Datum; zero NAP is approximately mean sea level), Hoekstra *et al* (1996). Many previous nourishment projects have been criticised for failing to

monitor the fill response adequately after placement; see Davison *et al*, (1992). The Terschelling nourishment has been surveyed in considerable detail following its placement. Ten surveys were carried out with one in spring 1993, immediately prior to the fill placement and nine after placement of the fill between autumn 1993 and winter 1995. Dates of surveys and survey reference numbers are shown in table 1.

The survey area is approximately 25 km^2 , and surveys extend from the top of the dunes backing the beach to 2 km offshore, at a water depth of 9 to 10 metres. The spring tidal range is 2.8 m, and the average annual significant wave height is approximately 1.5 m (associated wave period 8 seconds). Severe winter storms can generate waves up to 6 m high (period 10 - 15 seconds); the highest waves are typically from the northwest.

Survey Date	Survey Number
19 May 1993	1
17 November 1993	2
11 January 1994	3
20 April 1994	4
14 June 1994	5
10 October 1994	6
2 December 1994	7
10 March 1995	8
7 September 1995	9
13 December 1995	10

Table 1: NOURTEC Survey dates and survey numbers.

Previous studies (Ruessink and Kroon, 1994; Ruessink, 1998) show that the bars normally migrate offshore and similar morphology recurs about every 12 to 15 years. Ruessink (1998) shows that ebb tidal shoals are present at the eastern and western ends of Terschelling and it is possible that tidal inlets influence the profiles at the eastern end of the study area.

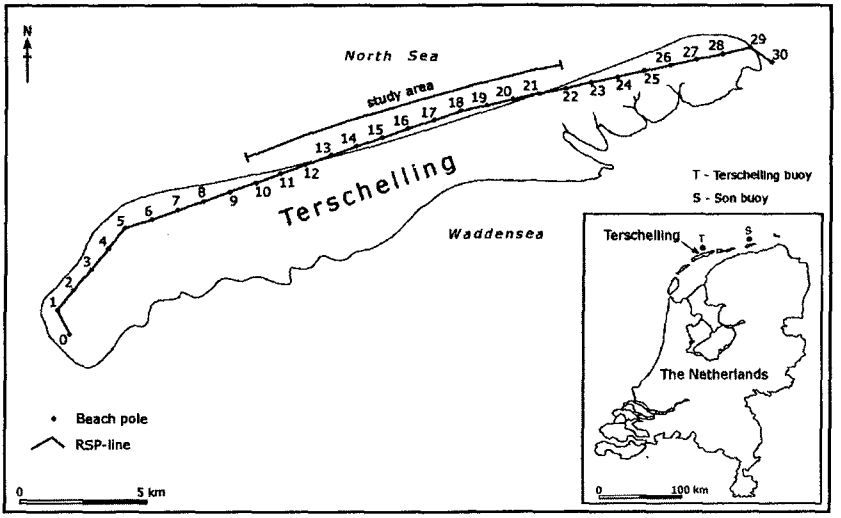

Figure 1. Location map showing the barrier island of Terschelling on the Northern Holland coast and the location of the study area.

The NOURTEC profiles were collected along the same transect lines as the JARKUS profiles. The combined use of JARKUS data and NOURTEC data means that depth of closure in an artificially forced situation can be compared with the autonomous behaviour of closure over the preceeding 25 years.

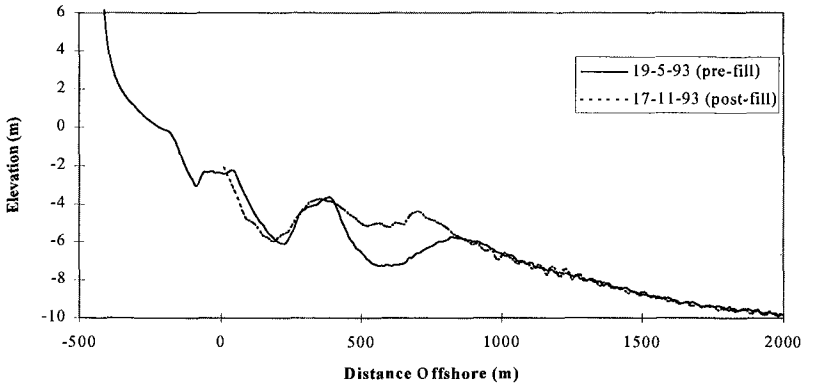

Figure 2. The fill material was placed between the middle and outer bars of a triple barred system.

Quantifying Depth of Closure

Closure occurs at a depth below which there is no measurable change in bed elevation, so measurement accuracy defines the criteria used to recognise closure in field data. In this study two techniques for determining depth of closure will be used; these are the standard deviation of depth change (SDDC) technique and a fixed criteria technique.

Standard Deviation of Depth Change (SDDC) Technique

For any given point that has been repetitively surveyed, it is possible to calculate the standard deviation of depth through time. When these standard deviation values are plotted along surveyed lines it is possible to discriminate between variability due to true changes in depth and variability that is due to measurement error (Kraus and Harikai, 1983). When the variability is due to measurement error alone, the profiles can be considered closed for the time period concerned. In the JARKUS data set, the standard deviation of depth typically falls to a non-zero tail with a value of approximately 0.25 m for profiles which exhibit closure. The mean depth at the beginning of the non-zero tail is defined as the depth of closure.

Fixed Criteria Technique

When two profiles are taken at the same location at different times it is possible to calculate the difference between the profiles along their length. When the difference falls below some value (determined by the accuracy of the data) then the profiles can be considered closed. We can assume that the JARKUS data

measurement errors are normally distributed, and as stated above, these errors have a standard deviation of about 0.25 m. This means that if we observe a depth change of 0.25 m and 0.50 m between two profiles, then we can be 66% and 95% confident that a real change has occured, respectively. In this study a fixed criteria of 0.50 m will be used when calculating fixed criteria depths of closure (*cf.* Nicholls *et al.*, 1998). The depth of closure is then calculated by moving up the profiles from the seaward end, with closure being the mean depth where the difference between the profiles exceeds 50 cm.

Results

Pre-Fill Behaviour

Firstly, depth of closure for the whole JARKUS period will be examined using SDDC and fixed criteria techniques. SDDC profiles were constructed for lines 10 to 22 using JARKUS data for 1965, 1970, 1975, 1980, 1985 and 1990. The alongshore variation in depth of closure is shown in figure 3.

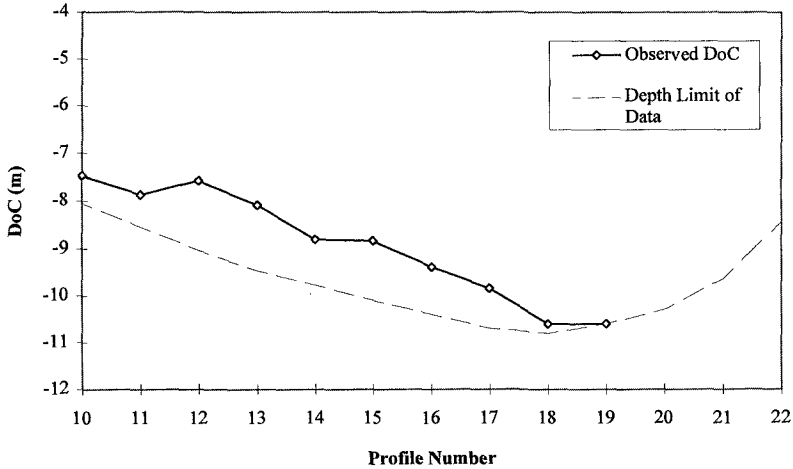

Figure 3. Observed longshore variation in depth of closure from 1965 to 1990, calculated using the SDDC method.

At the west of the island (lines 10, 11 and 12) the observed depth of closure is in the region of 7.5 to 8 m. This increases to the east as far as line 19, where the observed depth of closure is 10 to 10.5 m. Lines 20, 21 and 22 do not exhibit closure. This is attributed to the profiles ending before the depth of closure is reached. The depth limit of the profiles is indicated on figure 3, and we infer that if closure occurs it is deeper than the maximum depth of the profiles. A tidal channel is also present at the east of the island, and this is likely to extend into the study area. The migration of this tidal channel may affect depth of closure, and hence morphological change is occuring which is not simply wave driven.

Depths of closure using the fixed criteria technique were calculated for each five year interval between JARKUS surveys, for each line in the study area. These are shown in figure 4. Again there is a trend for depth of closure to become deeper to the east of the island. The trend is significant at the 95% level for three periods: 1965-1970, 1970-1975 and 1975-1980.

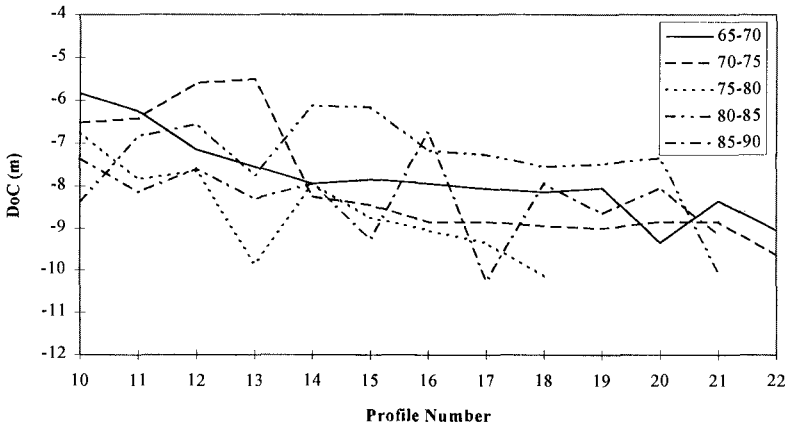

Figure 4. Observed depths of closure determined using a fixed criteria depth change criterion of 50 cm for five-year time intervals.

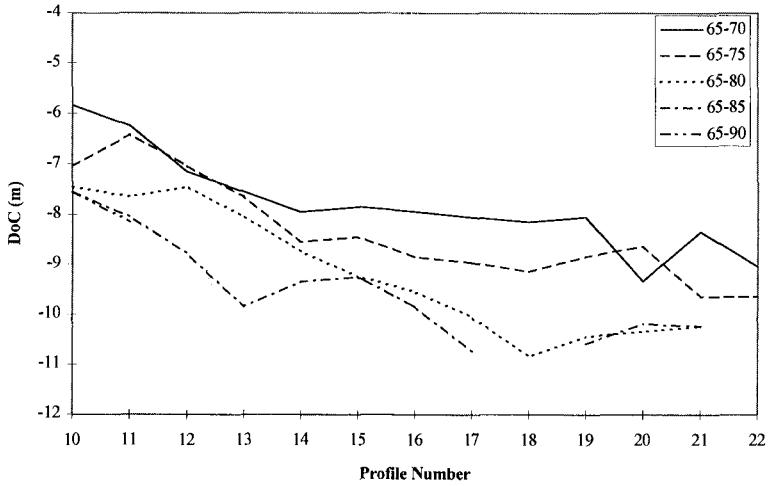

Figure 5. Observed depth of closure determined using a fixed criteria depth change criterion of 50 cm for an expanding time window for 5 to 25 years (relative to 1965).

If the timescale is increased the trend is similar, with deeper closure to the east. Figure 5 shows depth of closure for 5, 10, 15, 20 and 25 year time intervals using 1965 as the reference profile; the alongshore variation is significant at the 95% level for all of these time intervals. Depth of closure also tends to increase with timescale as has been observed at other sites, such as Duck, NC (Nicholls *et al,* 1998).

Post-Fill Behaviour

Using data collected as part of the NOURTEC project, post-fill depths of closure were calculated using the SDDC and fixed criteria techniques. The first pre-fill NOURTEC survey is excluded. Depths of closure calculated using the SDDC technique for the post-fill period are shown in figure 6.

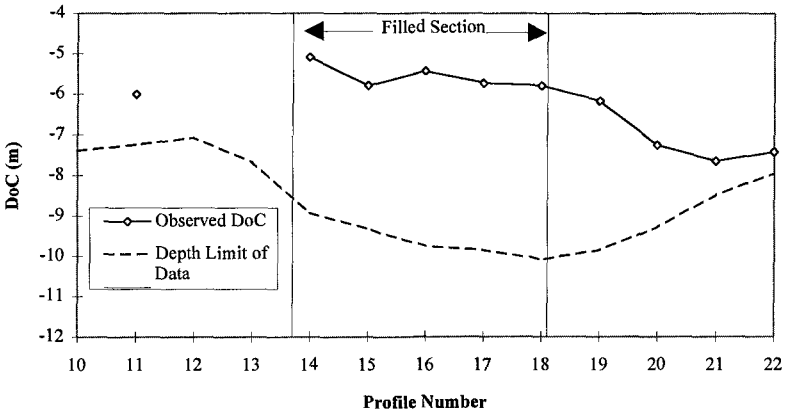

Figure 6. Observed longshore variation in depth of closure determined using the SDDC technique for the post-fill period (17th November 1993 to 13th December 1995).

The profiles for lines 10, 12 and 13 did not exhibit closure during the NOURTEC period. To give some representation of depth of closure at these locations, the depth limit of the profile data is shown. It is inferred that if closure does occur on these lines then it would be deeper than this depth. Interestingly the shallowest depth of closure occurs along the nourished section of the coast, which is quite different to the pre-fill behaviour (figure 3).

The depths of closure calculated using the fixed criteria method for each of the time intervals between NOURTEC surveys begin to explain the observed "average" behaviour shown using the SDDC method. Using the fixed criteria method, depth of closure still varies along the coast, but in general this variation does not show the systematic deepening to the east seen for the longer JARKUS periods which show shallow closure to the west and deeper closure to the east.

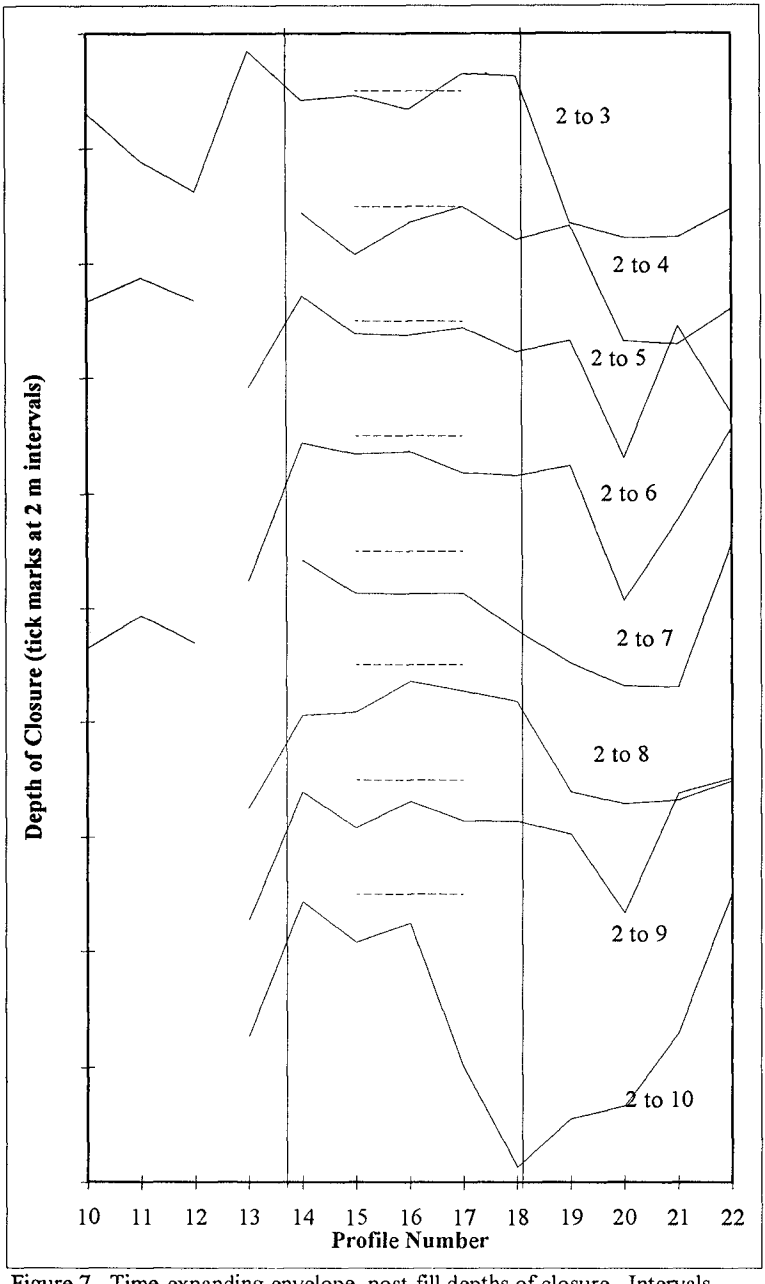

Figure 7. Time-expanding envelope, post-fill depths of closure. Intervals refer to survey numbers shown in Table 1. Each interval is offset by 2 m, and the dashed line indicates -5 m on each transect. The vertical lines mark the fill boundaries.

Depths of closure using a time-expanding envelope analysis were calculated to give a representation of the cumulative post-fill evolution of depth of closure. For these calculations the second NOURTEC survey (immediately after placement of the nourishment) was used as the reference.

The results of this analysis are shown in figure 7; the data are offset by 2 m for each survey to allow spatial patterns to be seen more clearly. Cases where no closure is observed are left blank. For most of the post fill period, there is a tendency for the shallowest depths of closure to occur in the nourished area, or just east of the nourished area. Westlake (1995) shows that sediment moved to the east following placement of the fill, and it is possible that this movement of sediment has an effect on the depths of closure observed.

Predicting the Depth Limit of the Active Profile

The depth limit to the active profile has been examined by Hallermeier (1981). Hallermeier proposed a predictive formula for the active depth limit which can be generalised to ($d_{\ell,t}$):

$$d_{\ell,t} = 2.28H_{e,t} - 68.5(H_{e,t}^2 / gT_{e,t}^2) \quad (1)$$

where $H_{e,t}$ is the significant wave height exceeded for 12 hours per t ycars and, $T_{e,t}$ is the associated wave period; g is acceleration due to gravity.

Evaluation of this method suggests that it provides a limit to actual closure during storms and for annual periods on wave-dominated, microtidal sandy coasts (Nicholls *et al*, 1996, 1998).

The wave data available in this study cover the end of the JARKUS monitoring period and the whole of the NOURTEC monitoring period. Wave data collection began at Schiermonnikoog (the Son buoy in figure 1) in 1979. The offshore buoy at this location is exposed to similar wave conditions to Terschelling (van Beek, 1995), and the wave data from Schiermonnikoog are used to calculate the depth limit predicted by equation 1 for the JARKUS data. The time intervals used for this calculation were 1980-1985, 1985-1990 and 1980 to 1990.

The depth limits predicted by Equation 1 for the NOURTEC data were calculated using wave data from the buoy located offshore of Terschelling (in 15 m water depth), and extend the analysis of Westlake (1995). The predicted depth limit, for each time interval between surveys, is compared with the observed depth of closure for each of the profile lines.

Figure 8a shows observed depths of closure plotted against the predicted depth limit for all data. The JARKUS data have a deeper predicted depth of closure than the NOURTEC data because they are based on a longer time interval. However, for both short and long timescales, the predicted depth limit based on a 12-hour exceedance wave height, acts as a good limit to the observed depths of closure. The range of

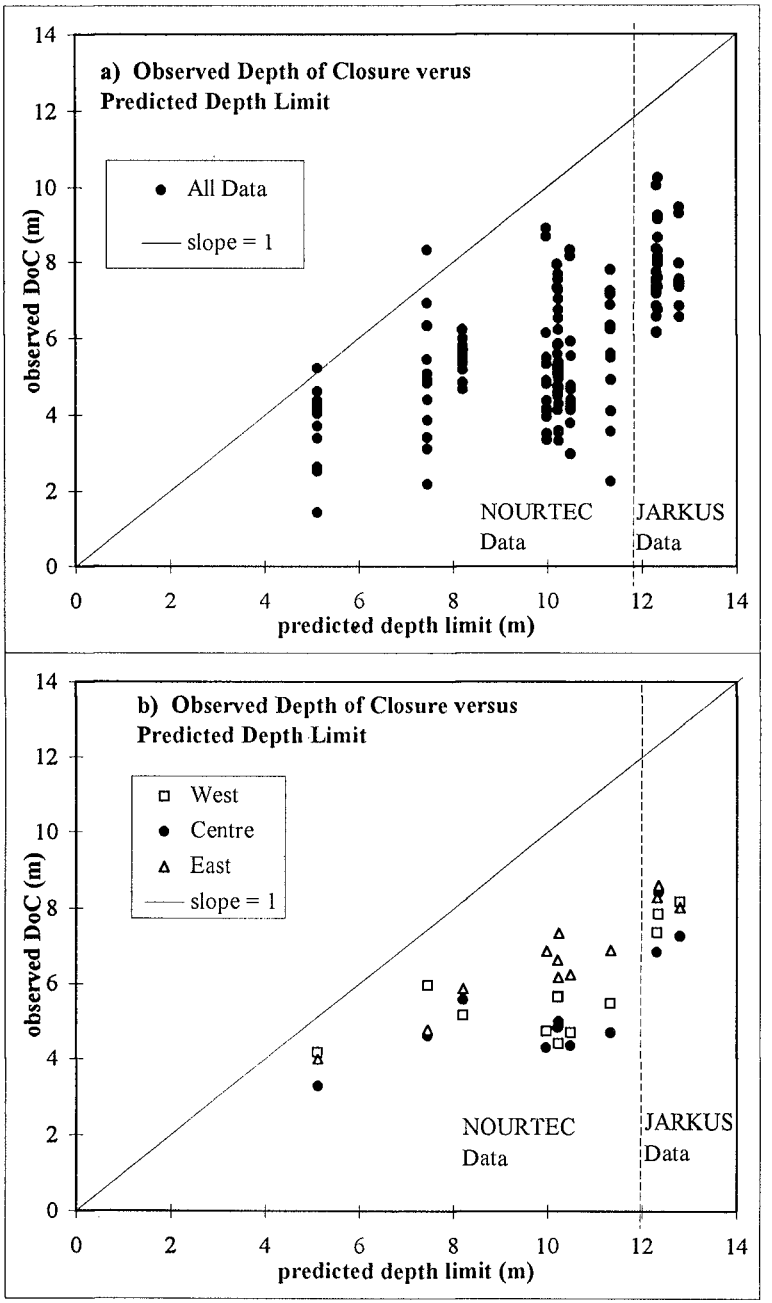

Figure 8. Observed depths of closure versus predicted depth limit of active profile. a) shows all data, b) shows average values for the western, central and eastern sections of the study area.

observed depths of closure for any measurement period is roughly constant at 4 metres. Hallermeier (1981) suggests that equation 1 approximates a yearly closeout of about 0.15 m using field data available in 1981. Nicholls *et al.* (1998) show that equation 1 is a limit to annual closure at Duck using a closure criteria of 6 cm. Therefore, using a 50 cm closure criteria, we would expect the observed depths of closure to be significantly shallower than equation 1 predicts (see figure 1, in Capobianco *et al*, 1997).

Figure 8b shows how the observed depths of closure vary in space, using the average observed depths of closure in the western, eastern and central sections of the study area (western is west of the fill boundary, the eastern section is to the east of the fill boundary; and the central section is the nourished section). It reinforces the observation of alongshore variation in the observed depths of closure.

Discussion

Equation 1 provides a limit to the closure observations which suggests that wave breaking is a fundamental control on the observed depth of closure (cf. Hallermeier, 1981; Nicholls *et al*, 1998). However it is also clear that depth of closure is variable alongshore. Assuming that the whole length of the shore is exposed to similar waves, then if the incident wave field were the only control over depth of closure we would expect depth of closure to be the similar along the whole coast. It is therefore likely that there are other controls on depth of closure along the Terschelling coast. In this study, the relatively large depth change criteria that has been used to define closure means that we may observe a depth of closure which is largely influenced by the outer bar position; it is the offshore migration of the outer bar that controls depth of closure. The depth change criteria of 50 cm used here would be expected to give shallower depths of closure than a 15-cm or 6-cm closure criteria, and we do not resolve some sub-50-cm morphodynamics in the profile that occurs deeper than our observed closures. However, using the data available gives us some understanding of how closure behaves over longer timescales than previous studies have investigated. This in turn allows more robust conclusions to be drawn regarding the influence that the nourishment has on the observed depth of closure.

Previous studies have shown that the migration of bars at Terschelling involves both longshore and cross-shore components of movement. The largest waves approach from the northwest and generate longshore currents to the east. Morphological studies (Ruessink and Kroon, 1994; Ruessink, 1998) show that bars propogate alongshore towards the east. There are ebb tidal shoals to the west of the island, and these are likely to protect the western section of the study area from the largest waves, hence the shallower depth of closure at the west of the island. In the centre of the island, the dominant process that is likely to affect the depths of closure observed in this study is cross-shore movement of the outer bar. Ruessink and Kroon (1994) show that the natural bar cycle involves a degeneration of the outer bar, and subsequent seaward migration of the middle bar. The return period of this cycle is approximately 12 to 15 years. An analysis of the furthest offshore position of the outer bar for the JARKUS data and the position of closure during the same time intervals shows that the position of closure is closely associated with the position of

the outer bar as illustrated in figure 9. The observation of deeper closure to the east of the study area may be attributed to the presence of tidal channels which extend from the tidal inlets at the eastern end of the island, and hence produce tidally driven morphological change.

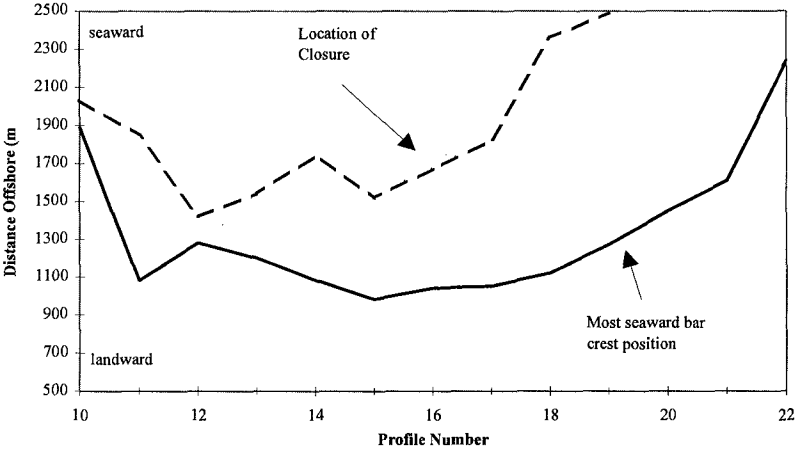

Figure 9. Location of closure (SDDC) in the JARKUS data and the most seaward bar crest position for the period 1965-1995. .

Given these observations, we are still faced with the question posed initially:

"What effect does the nourishment have on depth of closure?"

The long-term data suggest that depth of closure does vary alongshore, under natural conditions. However, the longshore variation of depth of closure is different in the post-fill period. In particular the mean behaviour, observed using the SDDC method, and the post-fill cumulative evolution of depth of closure, show that depth of closure is shallower than we would expect in the nourished area for the two year interval following placement of the fill. It appears that as the timescale considered increased, so the effect that the fill has on closure may diminish.

It has been suggested above that the closure we observe is influenced by bar migration. Assuming this is true, we then seek to explain how the fill has affected bar migration. The nourishment appears to have suppressed the offshore migration of the bar system, which might make the depth of closure we observe shallower than we might otherwise expect. Kroon *et al.* (1994) show that placement of the nourishment has decreased bar morphodynamics by making the middle bar stable in a position where it would have been expected to migrate offshore, based on observations before the fill.

Ruessink and Kroon (1994) argue that if the outer crest height is greater than about 5.5 m then on- and off-shore bar driving forces are balanced. Placing the fill between two crests effectively provided a much broader area to dissipate wave energy.

It also means that much more sediment had to be moved before cross-shore movement of bars could occur.

Westlake (1995) shows that after the nourishment sediment moved to the east and towards the land at the eastern end of the fill. Figure 7 shows that the section of coast with the shallowest closures migrates eastwards for much of the two-year period following fill placement. It is likely that the buffering effect that the fill has on bar migration also moves eastwards because of this *en masse* transport of material. However, the outer bar height is not diminished sufficiently for the middle bar to move offshore and take up the outer bar position in the time period for which we have observations.

The observation of shallower closure in the fill area in the short time period following placement of the fill is surprising. Based on first principles, the opposite behaviour would be expected because the fill would be expected to oversteepen the profile. In this case, the fill doesn't oversteepen the profile because it was placed in a trough between bars. On the basis of the observations of shallower closure in the nourished area, it is possible that placing the fill between the bars reduces the rate of loss of sediment from the nourishment site to the offshore zone in the period following placement of the fill. To assess the impact of the fill over long time periods, it will be necessary to examine data from the study area for at least one natural bar cycle period, approximately 12 years (Ruessink and Kroon, 1994).

Conclusions and Engineering Implications

Depth of closure is observed using SDDC and fixed criteria techniques over short and long time periods off the coast of Terschelling. Depth of closure observed in this study tends to vary systematically alongshore. Over long periods of time (5 years to 25 years), depth of closure is in the range 4 to 10 m, and is shallower to the west of the island, and deeper to the east.

Our ability to *predict* depth of closure remains relatively poor, but for both long and short time intervals, the depth *limit* to the active profile suggested by Hallermeier (1981) is a good upper limit to the observed depths of closure for both the nourished and un-nourished profiles. The terminology as used by Hallermeier (1981) is deliberate; formulations such as Equation 1 should be considered as a *limit* to the depth of closure, and not as a prediction of depth of closure. In this study, the autonomous variation below the limit predicted by Equation 1 is attributed to large scale morphological features.

This analysis shows that closure is influenced by beach nourishment but in this case, the closure depth was reduced by the placement of the fill. Therefore, the historical perspective of the extended JARKUS data, or Equation 1 are both useful to determine a limit to the actual closure. However, they do not allow prediction of the actual closure in the post-fill period. It will be interesting to continue to monitor the profile development at this site over a complete bar cycle (12 years), to see if the placement of the fill has a lasting effect on the bar behaviour and depth of closure.

This study gives some confidence in using the depth of closure concept as part of beach nourishment design. However, it represents one site and systematic monitoring of beach fills should be encouraged to extend our understanding of a wider range of situations (eg. Stauble and Grosskopf, 1993). As technology improves we look forward to more accurate vertical resolution, and the ability to resolve closure using smaller depth change criteria.

References

Capobianco, M., Larson, M., Nicholls, R.J., and Kraus, N.C., 1997. Depth of Closure: A Contribution to the Reconcilation of Theory and Practise. Proc. Coastal Dynamics '97.

Cooper, N.J., 1998. Assessment and prediction of Poole Bay (UK) sand replenishment schemes: application of data to Fürhböter and Verhagen models. Journal of Coastal Research, 14(1), pp. 353-359.

Davison, A.T., Nicholls, R.J., and Leatherman, S.P., 1992. Beach nourishment as a coastal management tool: An annotated bibliography on developments associated with the artificial nourishment of beaches. Journal of Coastal Research, 8(4), pp. 984-1022.

Hallermeier, R.J., 1981, A profile zonation for seasonal sand beaches from wave climate, Coastal Engineering,4, pp. 253-277.

Hoekstra, P., Houwman, K.T., Kroon, A., van Vessem, P., and Ruessink, B.G., 1994. The NOURTEC Experiment of Terschelling: Process-Oriented Monitoring of a Shoreface Nourishment (1993-1996). Proc. Coastal Dynamics '94.

Hoekstra, P., Houwman, K.T., Kroon, A., Ruessink, B.G., Roelvink, J.A. and Spanhoff, R., 1996. Morphological development of the Terschelling shoreface nourishment in response to hydrodynamic and sediment transport processes, Proc. 25th, Int. Conf. Coastal Eng., Orlando (USA), 1996, pp. 2897-2910.

Khabidov, A., Bazhenov, Y., Glodenis, M., Ivanova, N., Kaskevitch, L., Rybak, O., Savkin, V., Trizno, A., Zelensky, G., and Yedapin, V., 1996. Beach Nourishment versus shore protection structures. Proc. 25th, Int. Conf. Coastal Eng., Orlando (USA), 1996, pp. 2918-2926.

Kraus, N.C., and Harikai, S., 1983. Numerical model of shoreline change at Orai beach. Coastal Engineering, 7, pp. 1-28.

Kroon, A., Hoekstra, P., Houwman, K.T. and Ruessink, B.G., 1994. Morphological Monitoring of a Shoreface Nourishmnet NOURTEC Experiment at Terschelling, The Netherlands. Proc. 24th, Int. Conf. Coastal Eng., ASCE, New York, pp. 2222-2236.

Nicholls, R.J., Birkemeier, W.A., and Hallermeier, R.J., 1996. Application of the depth of closure concept. Proc. 25th, Int. Conf. Coastal Eng., Orlando (USA), 1996, pp. 3874-3887.

Nicholls, R.J., Birkemeier, W.A., and Lee, G., 1998, Evaluation of depth of closure using data from Duck, NC, USA, Marine Geology, 148, pp. 179-201.

Ruessink, B.G., 1998. Infragravity waves in a dissipative multiple bar system. PhD Thesis, University of Utrecht.

Ruessink, B.G and Kroon, A., 1994. The Behaviour of a Multiple Bar System in the Nearshore Zone of Terschelling, The Netherlands: 1965-1993. Marine Geology, 121, pp. 187-197.

Stauble, D.K. and Grosskopf, W.G., 1993. Monitoring Project Response to Storms: Ocean City, Maryland Beach Fill. Shore and Beach, 61(1), pp. 23-33.

van Beek, L.P.H, 1995. Wave climate of Terschelling: A statistical analysis ofr the NOURTEC project. Institute for Marine and Atmospheric Research Utrecht. Report R 95-10.

Westlake, S.J., 1995. Behaviour of a Shoreface Nourishment, Terschelling, The Netherlands. M.Sc. Thesis, International Institute for Infrastructural, Hydraulic and Environmental Engineering, Delft, The Netherlands.

Acknowledgements

This work was carried out as part of the PACE project, within the EU sponsored Marine Science and Technology programme (MAST-III) under contract number MAS3-CT95-002. Gerben Ruessink and Klaas Houwman provided valuable comments about the geomorphic and hydrodynamic setting of Terschelling.

POST-STABILIZATION MORPHOLOGY OF OREGON INLET, NC

Brian P. Joyner[1], Margery F. Overton[2], John S. Fisher[3]

Abstract

The behavior of Oregon Inlet, located north of Cape Hatteras, North Carolina, on the Pamlico Sound estuary, and its commercial, ecological, and recreational importance have been the subject of much study and controversy. The construction of a terminal groin on the southern shoulder of the inlet in 1990 served to heighten this interest. Both the U.S. Army Corps of Engineers (USACE) and the NC Department of Transportation (NCDOT) have maintained monitoring programs since that time to study the impact of the terminal groin on the morphology of the inlet and the adjacent shorelines. This paper utilizes data from the USACE and NCDOT programs to examine the relationship between the growth of the Bodie Island spit and the resulting bathymetric changes in the inlet. Data collected are compared with results from the literature.

The morphology of Oregon Inlet exhibited changes expected with the stabilization of a single shoulder of a tidal inlet. In contrast, the cross-sectional area of the channel at the minimum inlet width changed little. When analyzed in light of empirical equilibrium conditions reported in the literature, the results supported the conclusion that the inlet had achieved a new equilibrium configuration due to the presence of the terminal groin.

1. Introduction and Location of Study Area

Since the construction of a terminal groin at Oregon Inlet, NC, both the U.S. Army Corps of Engineers (USACE) and the NC Department of Transportation (NCDOT) have maintained programs to monitor the morphology of the inlet and the adjacent shorelines. This paper utilizes data from the USACE and NCDOT programs to examine changes in inlet width and orientation due to migration of the non-stabilized northern inlet shoulder (Bodie Island); also discussed are associated changes in the bathymetric configuration of the inlet. The results of the measurements are analyzed for consistency with empirical equilibrium indicators reported in previous studies of inlet behavior.

Oregon Inlet is located on the Outer Banks of North Carolina, just south of Nags Head and north of Cape Hatteras. It is the only inlet in the Outer Banks between Cape Hatteras and Cape Henry, VA, providing an exchange for Pamlico, Currituck, and Albemarle

[1] Dewberry & Davis, 8401 Arlington Boulevard, Fairfax, VA, USA 22031-4666.
[2] Associate Professor of Civil Engineering, North Carolina State University, Box 7908, Raleigb, NC, USA 27695-7908.
[3] Professor of Civil Engineering, North Carolina State University, Box 7908, Raleigh, NC, USA 27695-7908.

Sounds with the Atlantic Ocean. Figure 1 shows the location of the inlet in relation to the United States and, on a smaller scale, to the North Carolina coastline and coastal waters. The inlet is the site of the only bridge currently spanning a major inlet in North Carolina, the Herbert C. Bonner Bridge, completed in 1964.

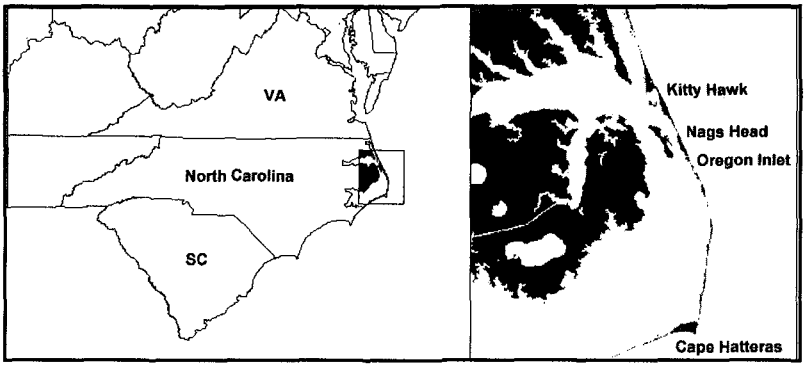

Figure 1. Location of study area, Oregon Inlet, NC.

The mean ocean tidal range at Oregon Inlet is 2.0 ft, with a spring range of 2.4 ft (Moffatt and Nichol, 1990). The average significant wave height at Oregon Inlet is approximately 3 ft, with an extreme height of approximately 10 ft (Moffatt and Nichol, 1990). Wind effects on tidal flow at Oregon Inlet may be very dramatic, especially in cases of rapid wind reversals over Pamlico Sound (Inman and Dolan, 1989). Winds from severe storms have caused differences in water levels in excess of 9 ft across the inlet (Moffatt and Nichol, 1990). Gross longshore sediment transport has been estimated to be 5.8×10^7 ft^3/yr in the vicinity of Oregon Inlet (Inman and Dolan, 1989). Hollyfield, et al. (Inman and Dolan, 1989) and Dennis (1997) have reported values for the tidal prism of Oregon Inlet of 3×10^9 ft^3 and 2.3×10^9 ft^3, respectively. The tidal prism values were both determined from pre-terminal groin measurements and will be used in later sections of this paper.

At Oregon Inlet, the net longshore sediment drift is in a southerly direction, resulting in a predominant southward inlet migration. Between 1846 and 1989, Oregon Inlet migrated approximately 2.2 miles southward and 2,070 feet landward. By the late 1980s, the southern approach to the Bonner Bridge had become endangered by inlet migration, and the NCDOT sponsored construction of a terminal groin to stabilize the southern (Pea Island) shoulder. Construction was begun in October 1989 and was completed early in 1991. The present study considered data gathered from October 1989 until April 1997.

2. Data and Methods

The purpose of the present research was to characterize the migration and equilibrium condition of Oregon Inlet since the terminal groin was constructed. The study was accomplished using time series of shoreline positions and bathymetric data taken between October 1989 to April 1997. Using these data, changes in inlet geometry were analyzed in light of empirical equilibrium indicators reported in the literature, specifically in studies by O'Brien (1931, 1969) and Jarrett (1976).

The primary sources of data for this study included a database of shoreline positions and hydrographic surveys of the inlet area. The shoreline database was generated as part of a shoreline erosion monitoring project conducted by the NCSU-Kenan Natural Hazards Mapping Program at North Carolina State University (Overton and Fisher, 1997), in conjunction with the NCDOT. The shoreline positions were digitized by the NCDOT from rectified aerial photographs, taken at a bimonthly frequency beginning in October 1989.

Morphological parameters observed from the shoreline database include minimum inlet width, planimetric accretion and erosion of the Bodie Island shoulder, and location and orientation of the minimum width section. The majority of definitions for this study are consistent with work done by Vincent and Corson on inlet geometry (1981); detailed definitions for the parameters follow this section.

The hydrographic surveys were obtained from the U.S. Army Corps of Engineers, Wilmington district (USACE, 1990a, 1990b, 1994, 1995, 1996, 1997). The dates of the surveys and the related shoreline positions are listed in Table 1. Three full-inlet, bank-to-bank surveys were available; the remaining surveys covered only the channel section through the inlet. The data were processed to create contours, grids, and profiles of the submerged inlet area from which subsequent measurements were made. Parameters measured included cross-sectional area, maximum channel depths, and ebb delta area.

Table 1. Summary of hydrographic surveys analyzed

Survey date	Related shoreline date	Extent of survey
Jan. 17, 1990	Feb. 14, 1990	Full inlet, bank-to-bank
Dec. 12, 1990	Dec. 6, 1990	Full inlet, bank-to-bank
Aug. 25, 1994	Aug. 9, 1994	Partial channel
Apr. 20, 1995	Apr. 5, 1995	Partial channel
Dec. 4, 1996	Jan. 3, 1997	Full inlet, bank-to-bank
Apr. 30, 1997	Apr. 8, 1997	Full channel

Data were collected from the shoreline positions and hydrographic data sets by the measurement of several geometric parameters of inlet configuration. All measurements were made using the MicroStation CADD software in conjunction with Intergraph's Terrain Analyst software for profile creation and contouring of the bathymetric data. The contours were used to determine channel position, which was digitized by following the deepest contiguous contours through the inlet. An example of channel delineation is

shown in Figure 2. Unless otherwise noted, all measurements of depth were taken from Mean Sea Level 1929 (referred to hereafter as "mean sea level"). The following is a list of the parameters and the working definitions:

1. Minimum inlet width (W) is defined as the narrowest point between the inlet shoulders, as shown by the shoreline data set. The location of the minimum width section was determined by constructing the minimum distance line between the digital shoreline shoulders using the CADD software. An example of width delineation is displayed in Figure 2. The section of minimum width may also be referred to as the gorge or throat section.

2. Maximum channel depth (d_m) is defined as the maximum depth occurring at the section of minimum inlet width. Maximum depth and all other bathymetric measurements were determined from computer-generated digital profile plots of the bathymetric data. Figure 3 graphically portrays gorge profile definitions.

3. Cross-sectional area (A_C) was taken at minimum width by digitally measuring the area bounded by the profile, the water surface at 0.0 ft on the plot (mean sea level), and the vertical axes of the plot. The vertical axes represent the locations of the Bodie and Pea Island shoulders of the inlet; see Figure 3.

4. Ebb tidal delta area (A_E) was defined, again following Vincent and Corson (1980), as the area of the region bounded by the inlet shoulders, the minimum width line, the contour of controlling depth, and a set of boundary lines marking the point on either side of the inlet where the controlling depth contour became approximately shore-parallel (Figure 2). The area was measured by an application of the CADD software.

3. Graphical Presentation of Data and Discussion of Results

This section documents the results of the analysis of the shoreline and bathymetric time series. The results are presented in three parts. First, the observed trends in planimetric inlet morphology are discussed, followed by a description of changes observed in the bathymetric configuration of the inlet. Finally, Table 2 summarizes the results of the measurements of inlet minimum width, maximum depth, cross-sectional area, and ebb tidal delta area.

Planimetric inlet morphology

While the construction of the terminal groin has effectively halted the migration of the southern (Pea Island) shoulder of the inlet, the northern (Bodie Island) shoulder exhibited both alongshore and cross-shore migration over the study period. Inlet migration has resulted in changes in inlet width and orientation.

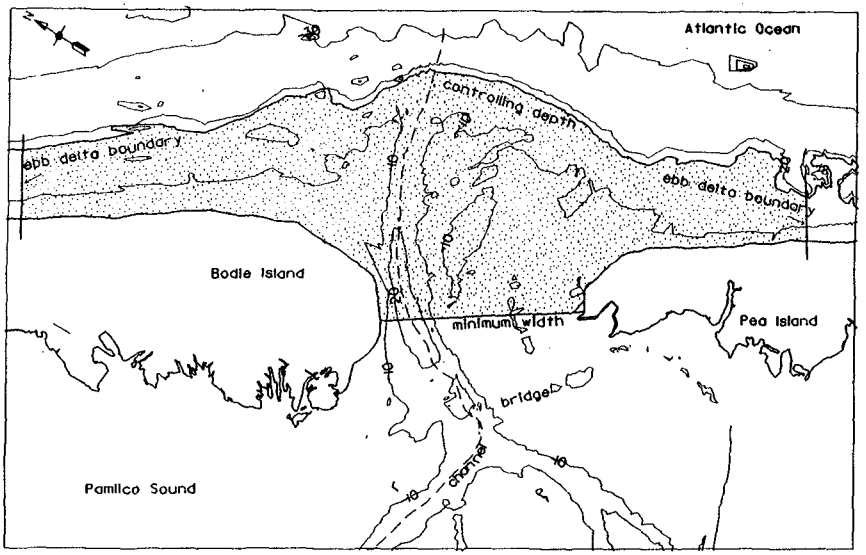

Figure 2. Parameter definition sketch, planimetric view.

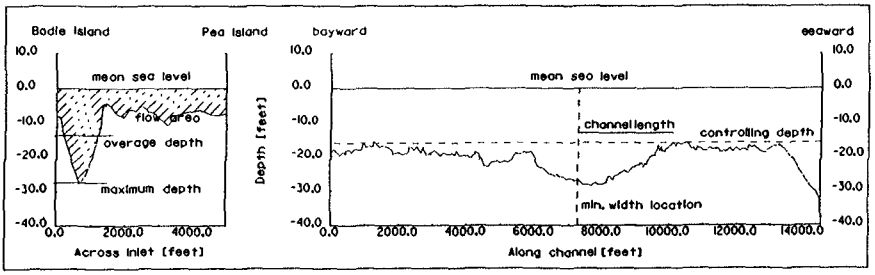

Figure 3. Parameter definition sketch, bathymetric view.

A progression of semi-annual shoreline positions is shown in Figure 4, beginning with April 1990 and ending with April 1997. The October 1989 position is included in each frame to provide a reference from which changes may be observed. In each frame, the dated shoreline position is marked by a dotted pattern fill. The solid lines crossing the inlet mark the gorge section for both the October 1989 and the designated positions; the most bayward solid line marks the location of the highway and bridge over the inlet.

The Bodie Island spit accreted bayward over the study period, reaching and crossing the location of the bridge. The beginning of this movement is noticeable from the figure as early as April 1991. This date marks the approximate completion of the terminal groin, which becomes a permanent reference point in the remaining frames. The spit continued to accrete bayward, with some migration into the inlet, until October 1993. At this point, the spit began to show more dramatic accretion toward Pea Island. From this date through the end of the study period, the spit continued to migrate toward Pea Island, with accretion taking place at the northern portion of the bridge as the end of the spit widened.

Trends in inlet width may be observed from Figure 5, a plot of minimum inlet width vs. time since construction of the terminal groin. The narrowing between the April 1990 and October 1990 positions was due primarily to the encroachment of the terminal groin into the inlet. After this date, the terminal groin stabilized and defined the location of the southern shoulder, and changes in width were due to the migration of the Bodie Island spit. Following the initial decrease in width, the inlet continued to show a slighter narrowing trend, with short-lived minor widenings observed. The inlet reached its narrowest width of the present study period, 2,732 ft, on February 11, 1996. Since that time, the data showed a relatively short but distinct trend toward widening, with the latest measured value at 3,017 ft in April 1997.

Accretion of the spit was also responsible for a change in location and orientation of the gorge section. The shifting of the gorge became most noticeable beginning in April 1995, which coincided with the beginning of significant widening of the spit at the bridge. The shift of the gorge bayward required a rotation of the section, since the terminal groin remained as the southern extent of the inlet. The gorge continued to move bayward and orient itself in a more northerly direction through the remainder of the study period.

Bathymetric inlet morphology

Changes in the inlet's bathymetric configuration were observed coincident with the changes in inlet width and orientation. Using data from the hydrographic surveys, profiles were created to measure changes in channel location and shape. The profiles, shown in Figure 6, were taken across the gorge section, using the minimum width line as a transect. The plots are aligned using the axis representing Pea Island as a reference point. This alignment was chosen because the terminal groin has stabilized this shoulder of the inlet, so that its position is constant. The plots show the bottom elevations, relative to mean sea level, of the gorge section from Bodie Island to Pea Island (left to right).

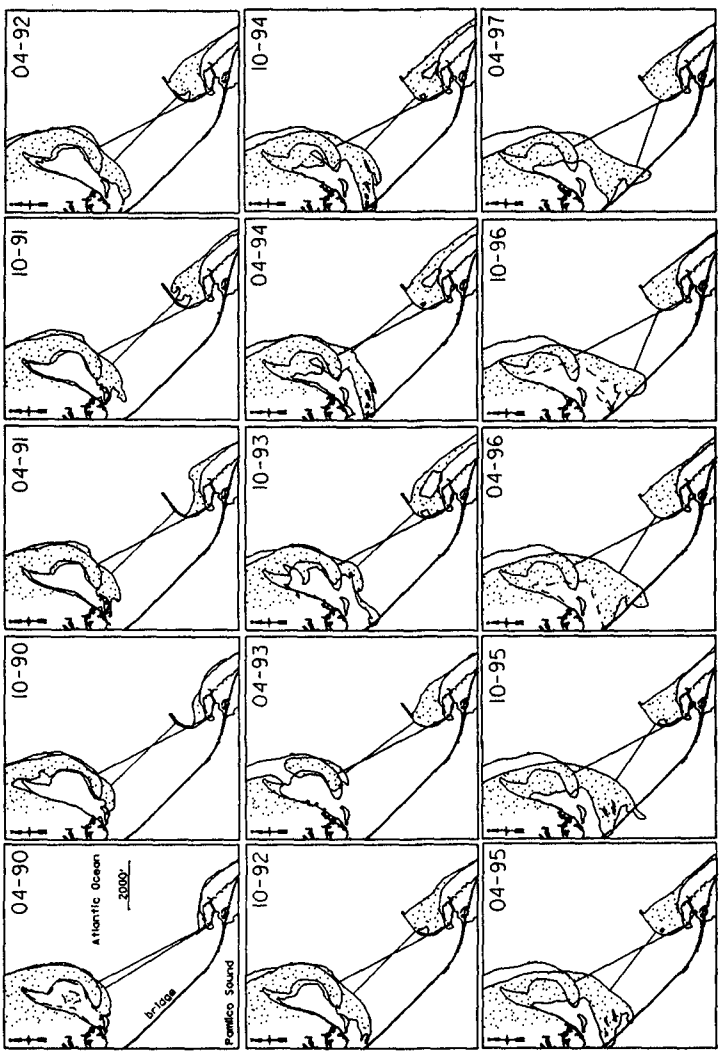

Figure 4. Inlet migration, October 1989 to April 1997.

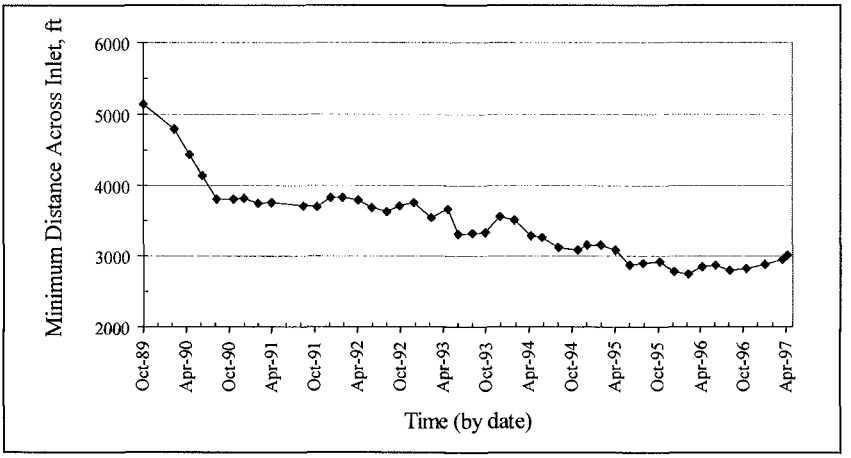

Figure 5. Oregon Inlet minimum width, October 1989 to April 1997.

The channel at the gorge section showed lateral migration toward the terminal groin (Pea Island). This is evident between the January 1990 and December 1990 profiles. A more visible migration was noticed between December 1990 and December 1996, as the channel shifted 2,160 ft toward Pea Island. In contrast, the position of the channel relative to the Bodie Island axis has remained relatively constant, at a distance of 700 to 900 ft.

Along with its lateral migration, the channel deepened, with maximum depths increasing from approximately 27 feet below mean sea level in January 1990 to 50 feet in December 1996, then slightly decreasing to 46 feet in April 1997. The deepening trend was dominant over the study period, except for the April 1995 survey, which showed a maximum channel depth of only 26 feet.

A second set of profiles was constructed along the lines marking the channel locations from bayward of the bridge to seaward of the ebb delta. The profiles are displayed in Figure 7, and show the bottom elevations along the channel from the sound toward the ocean entrance (left to right). The bridge location was chosen as an alignment reference point for these profiles; its position is marked on the figure by a solid vertical line. The dashed vertical lines mark the location of the minimum inlet width.

As the inlet width decreased through December 1996, the maximum depth of the channel at the gorge increased. While these changes took place, the cross-sectional area of the gorge remained relatively constant, hovering around 50,000 ft^2. A constant cross-sectional area suggests that a state of equilibrium exists, as do the changes in depth coincident with changes in width. From inspection of the profiles in Figure 6, the

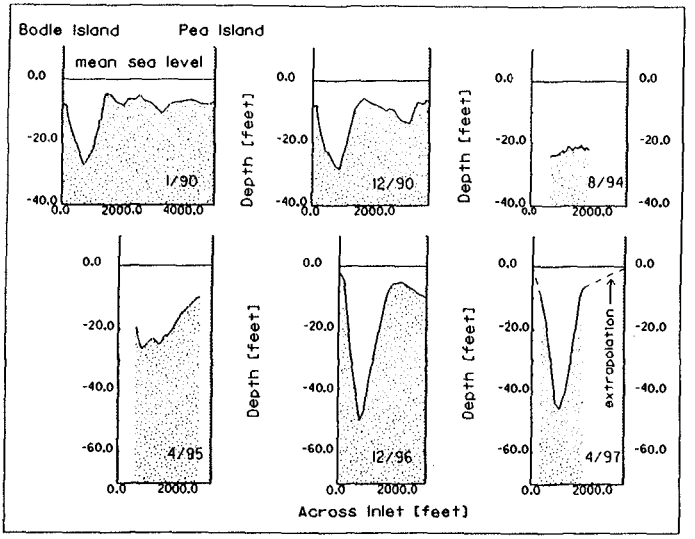

Figure 6. Gorge cross-section bathymetric profiles.

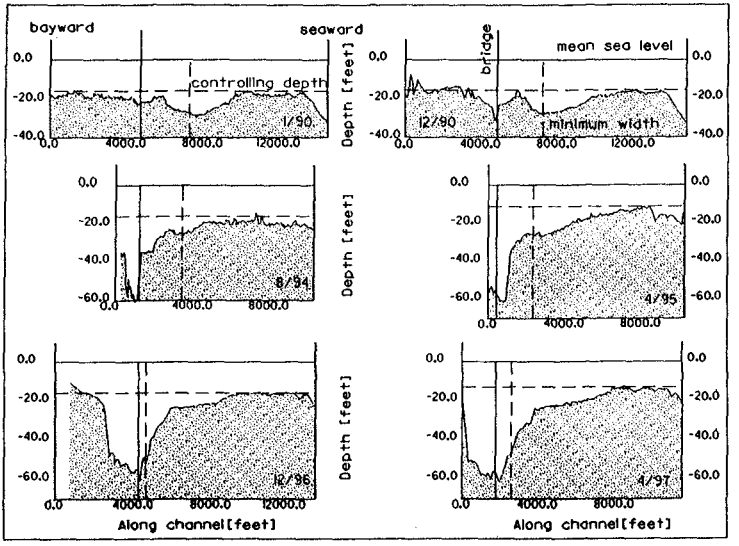

Figure 7. Channel lengthwise bathymetic profiles

channel itself became narrower as the inlet width decreased. In order to maintain a constant cross-sectional area, a narrowing inlet must become deeper to accommodate the same discharge volume, or tidal prism. The data show that this has been the case at Oregon Inlet since the terminal groin was constructed.

Summary of results

A summary of observed planimetric and bathymetric parameter measurements is displayed in Table 2. Measurements of bathymetric parameters were taken from the channel profile plots previously described. The three bank-to-bank surveys contained sufficient data for the measurement of all parameters under study; at least one parameter was not measurable for the remaining profiles, due to insufficient data. All vertical measurements were made relative to mean sea level.

Table 2. Summary of data measured from shoreline positions and hydrographic surveys.

Date	W, ft	A_C, ft^2	d_m, ft	A_E, mi^2
Jan. 17, 1990	4,968	50,235	-27.4	2.17
Dec. 12, 1990	3,819	48,687	-28.5	1.92
Aug. 25, 1994	3,122	I/D*	-23.0	I/D*
Apr. 20, 1995	3,081	I/D*	-25.0	I/D*
Dec. 4, 1996	2,878	51,192	-50.0	2.07
Apr. 30, 1997	3,017	46,335	-46.0	I/D*

*I/D denotes insufficient data for measurement.

A note should be made about the measurement of A_C for the April 1997 data. As can be seen from the profile in Figure 6, the survey did not span the entire inlet, so that the area could not be measured exactly as defined. However, it was judged that enough information was present to allow the reasonable measurement of cross-sectional area by extending the profile on either side of the channel to the vertical axes. It is believed that, though the measurement is not as exact as those for the bank-to-bank surveys, the area determined in this way is reasonably close to what would actually be measured from a full survey, if it existed. Any error in the measurement from the actual value should be an underestimate, since most of the profiles showed some deepening on either side of the channel banks which would not be accounted for in the profile extrapolation. This method of measuring cross-sectional area was considered for the August 1994 and April 1995 surveys, but it was judged that insufficient information existed for any reasonable extrapolation to the vertical axes of the plots.

A second aspect of the analysis that deserves comment is the fact that the shoreline position dates do not exactly coincide with the dates of the hydrographic surveys. Since inlet parameters may adjust themselves rapidly to existing wave and tidal current conditions, the difference in time between a hydrographic survey and its corresponding shoreline position may be a significant source of error. Unfortunately, it is a source of error that could not be quantified or known for certain. However, since most of the

survey/shoreline position sets were collected within two to three weeks of each other, it was assumed for the sake of the study that the shoreline data was representative of the actual shoreline position at the times of the surveys.

The changes in inlet width became smaller in magnitude, or "slower" in rate, as the study period progressed. Small changes from a certain state were described by van de Kreeke (1992) as an indication of inlet equilibrium. Though it was not clear whether the inlet would continue to widen or remain more constant in width, the data suggested that the hydraulic forcing factors at Oregon Inlet are currently sufficient to maintain an inlet width greater than 2,732 feet. The inlet has been narrower, at 2,100 feet in 1975 (Moffatt & Nichol, 1990), so that the narrowing was no indication in itself of progression toward inlet closure due to the presence of the terminal groin. Conversely, the combination of small changes in inlet width and small variance in cross-sectional area supported the hypothesis that the inlet had reached equilibrium since terminal groin construction. An analysis of the data using empirical results from previous researchers on equilibrium inlet geometry was conducted to further test the hypothesis; Section 4 of this paper describes the comparative analysis.

4. Comparison of results with reported empirical equations

The relationship between tidal prism and cross-sectional gorge area is a commonly studied and used empirical description of inlet equilibrium (Escoffier, 1940; van de Kreeke, 1992; O'Brien, 1931, 1969; Jarrett, 1976). Since the results of this study showed small variance in cross-sectional area, it was believed that the data would fit one of the classic tidal prism-flow area relationships. This section documents the results of a comparison of empirical equations from studies by O'Brien (1931, 1969) and Jarrett (1976) with the measured cross-sectional area data and reported tidal prism values for Oregon Inlet.

The empirical equations describing the equilibrium relationship between tidal prism and cross-sectional area take the form $A_C = C \, x \, P^n$, where A_C is cross-sectional area in ft^2 and P is tidal prism in ft^3, and C and n are empirically determined constants. Table 3 lists the specific equations of this form considered for the present study, along with the geographic locations and stabilization status of the inlets considered in the development of each equation.

Table 3. Tidal prism-flow area relationships.

Researcher and Date	Inlet Source Data Types	Equation
O'Brien (1931)	Mostly Pacific coast, with and without jetties	$A_C = 4.69x10^{-4} P^{0.85}$ (1)
O'Brien (1969)	Atlantic, Pacific, and Gulf coasts, without jetties	$A_C = 2.0x10^{-5} P$ (2)
Jarrett (1976)	Atlantic, Pacific, Gulf coasts, single or no jetty	$A_C = 1.04x10^{-5} P^{1.03}$ (3)
	Atlantic coast, all inlets	$A_C = 7.75x10^{-6} P^{1.05}$ (4)
	Atlantic coast, single or no jetty	$A_C = 5.37x10^{-6} P^{1.07}$ (5)
	Atlantic coast, two jetties	$A_C = 5.77x10^{-5} P^{0.95}$ (6)
	Pacific coast, two jetties	$A_C = 5.28x10^{-4} P^{0.85}$ (7)

The cross-sectional areas measured by this study were compared with calculated results from Equations (1) through (6). Equation (7) was not included in this analysis, because it was intended to describe Pacific coast, dual-jettied inlets, and it agrees closely with Equation (1) from O'Brien (1931). For the analysis, tidal prisms were calculated using Equations (1) through (6) with the measured values of A_C. The results are reported in Table 4. The calculated tidal prisms were compared with values reported for Oregon Inlet by Hollyfield, et al. (Inman and Dolan, 1989) and Dennis (1997), also included in Table 4. The reported values for Oregon Inlet's tidal prism fell within 95% confidence limits determined by Jarrett for reliability of his equations.

Table 4. Calculated values vs. reported values for tidal prism at Oregon Inlet.

Equation	Calculated tidal prism ($x10^9$ ft^3)				Reported tidal prism (ft^3)
	1/17/90	12/12/90	12/4/96	4/97	
(1)	0.939	0.882	0.904	0.752	Hollyfield, et al: 3×10^9
(2)	2.80	2.65	2.71	2.32	
(3)	3.43	3.25	3.32	2.85	
(4)	3.40	3.24	3.30	2.84	Dennis: 2.30×10^9
(5)	3.62	3.45	3.51	3.04	
(6)	2.00	1.90	1.94	1.64	

The best prediction of Oregon Inlet's tidal prism was obtained using Equation (2), O'Brien's 1969 result for inlets without jetties. Equation (1) consistently underestimated tidal prism values, as did Equation (6). Equations (3), (4), and (5) tended to overestimate. Since the reported tidal prisms fall within the confidence limits of Jarrett's data, it is reasonable to believe that Equations (3), (4), (5) and (6) may be used to generally

describe Oregon Inlet's behavior. From this analysis it appears that the relationship between post-groin cross-sectional gorge areas and tidal prism at Oregon Inlet is similar to those determined by O'Brien and Jarrett. This information supports the hypothesis that the inlet has exhibited an equilibrium condition over the study period.

The values reported for Oregon Inlet's tidal prism were calculated using pre-terminal groin data. To the author's knowledge, post-terminal groin data for calculation of the tidal prism were not available, though the data would be helpful in accurately understanding changes that have occurred since the construction of the terminal groin.

5. Conclusions

This report documented a study of morphological changes observed at Oregon Inlet, NC. The study period was from October 1989 to April 1997, the time since the construction of a terminal groin on the downdrift shoulder of the inlet. It was hypothesized that the hydraulic and sedimentary environment of the inlet had approached or reached a state of equilibrium since the construction of the terminal groin, and that the groin had not negatively affected the stability of the inlet. To test the hypothesis, shoreline position and bathymetric data were analyzed to examine changes in inlet geometry. The results of the analyses supported the hypothesis.

Further study of the morphology and hydraulic and sedimentary conditions of Oregon Inlet is necessary to more fully understand its behavior, particularly as it relates to future engineering works for transportation safety and reliability. Specifically, an accurate hydraulic model of the inlet and adjacent waters it affects would be helpful in determining a post-groin tidal prism as well as predicting effects of winds, waves, and engineering efforts on flows through the inlet. Furthermore, the application of a sediment transport model with a hydraulic model of the inlet would provide means for determining the effects of influencing factors on inlet morphology and stability.

6. References

Dennis, W.A., 1997. Personal communication. Tidal prism estimate for Oregon Inlet, US Army Corps of Engineers, Wilmington District, Wilmington, NC.

Escoffier, F.F., 1940. The stability of tidal inlets. *Shore and Beach*, 8(4): 114-115.

Fisher, J.S., Overton, M.F., 1994. Interpretation of shoreline position from aerial photographs. In Edge, B., ed., *International Conference on Coastal Engineering 1994 Conference Proceedings*, 1998-2003.

Inman, D. L., Dolan, R., 1989. The Outer Banks of North Carolina: Budget of sediment and inlet dynamics along a migrating barrier system. *Journal of Coastal Research*, 5(2): 193-237.

Jarrett, J.T., 1976. Tidal prism-inlet area relationships, *General Investigation of Tidal Inlets, Report 3*. US Army Corp of Engineers, Coastal Engineering Research Center, Vicksburg, 1976.

Joyner, B.P., 1997. Morphology and equilibrium of Oregon Inlet, NC since construction of the Pea Island terminal groin. Master's Thesis, North Carolina State University, Raleigh, NC.

Moffatt & Nichol, Engineers, 1990. Existing coastal conditions at Oregon Inlet, NC, prepared for Parsons, Brinckerhoff, Quade & Douglas, Inc., Raleigh, NC.

O'Brien, M.P., 1931. Estuary tidal prisms related to entrance areas. Trans. ASCE, 1(8): 738-739.

O'Brien, M.P., 1969. Equilibrium flow areas of inlets on sandy coasts. *Proceedings of the ASCE, Journal of Waterways, Harbors, and Coastal Engineering*, 15(WW1): 43-52.

Overton, M.F., Fisher, J.S., 1997. Shoreline monitoring at Oregon Inlet terminal groin, Report 13, prepared for NCDOT. Department of Civil Engineering, North Carolina State University, Raleigh, NC.

USACE, 1990a. Hydrographic survey of Oregon Inlet, January 1990. US Army Corps of Engineers, Wilmington District, Wilmington, NC.

USACE, 1990b. Hydrographic survey of Oregon Inlet, December 1990. US Army Corps of Engineers, Wilmington District, Wilmington, NC.

USACE, 1994. Hydrographic survey of Oregon Inlet, August 1994. US Army Corps of Engineers, Wilmington District, Wilmington, NC.

USACE, 1995. Hydrographic survey of Oregon Inlet, April 1995. US Army Corps of Engineers, Wilmington District, Wilmington, NC.

USACE, 1996. Hydrographic survey of Oregon Inlet, December 1996. US Army Corps of Engineers, Wilmington District, Wilmington, NC.

USACE, 1997. Hydrographic survey of Oregon Inlet, April 1997. US Army Corps of Engineers, Wilmington District, Wilmington, NC.

van de Kreeke, J., 1992. Stability of tidal inlets; Escoffier's analysis. *Shore and Beach*, 60(1): 9-12.

Vincent, C.L., Corson, W.D., 1981. Geometry of tidal inlets: Empirical equations. *Proceedings of the ASCE, Journal of the Waterway, Port, Coastal and Ocean Division*, 107(WW1): 1-9.

Vincent, C.L., Corson, W.D., 1980. The geometry of selected US Tidal Inlets. *General Investigation of Tidal Inlets Report 20*, United States Army Corp of Engineers Research Center, Fort Belvoir, VA., United States Army Waterways Experiment Station, Vicksburg, MS, May 1980, 161.

PREDICTIVE MODEL OF THREE-DIMENSIONAL DEVELOPMENT AND DEFORMATION OF A RIVER MOUTH DELTA BY APPLYING CONTOUR LINE CHANGE MODEL

Takaaki UDA[1], Hiroshi YAMAGATA[2], Ken-ichi KATOH[2] and Naohiro AKAMATSU[2]

Abstract

A predictive model of the three-dimensional development and deformation of a river mouth delta is developed. This model enables the prediction of not only the shoreline change but also the three-dimensional, long-term topographic changes around a river mouth, and offshore sand transport can be taken into account when the sea bottom slope exceeds a critical value given by the angle of repose of sand. Numerical simulation of three cases of initial beach slopes is carried out and compared. The calculated and actual beach changes measured around the Fuji and Tenryu River mouths are compared. It is concluded that calculated results can reproduce real phenomena measured around river mouths qualitatively.

I. INTRODUCTION

In order to evaluate the influence of the construction of a dam in a large river basin on coastlines, since the river supplies a large amount of sand to the surrounding coastline, the impact of a decrease in fluvial sand supply should be predicted quantitatively. In past studies, the shoreline change model has been widely used for this purpose (Hashimoto, 1975; Rafaat and Tsuchiya, 1991; Tsuchiya et al., 1995). This model is very simple and can be applied under any kind of practical conditions, but it cannot be used to predict profile changes caused by longshore sand transport and offshore discharge of sand. Recently, Uda and Kawano (1996) developed a new model called the "contour line change (CLC) model" which can be used to predict successive changes in each contour line position through numerical solution of the continuity equation of sand and longshore sand transport, with assumed values of depth change in the longshore sand transport rate. This model was applied to the prediction of the movement of a sand body on the Shizuoka coast in Japan, and it well reproduced this phenomenon quantitatively (Uda et al., 1997). This study is aimed at developing a new model to predict three-dimensional deformation of a river mouth delta.

1) Dr. Eng., Director, River Department, Public Works Res. Inst., Ministry of Construction, Asahi 1, Tsukuba, Ibaraki 305, Japan.
2) Nihon-kensetsu Consultant Co. Ltd., 5-2-4 Higashi-gotanda, Shinagawa-ku, Tokyo 141, Japan.

II. NUMERICAL MODEL OF DEVELOPMENT OF A RIVER MOUTH DELTA

2.1 Contour Line Change Model

Uda and Kawano (1996) and Uda et al. (1997) developed a model which enables the prediction of the spatial and temporal changes in contour line positions by assuming the depth distribution of the longshore sand transport rate. This model is designed for a coast with a steep slope near the shoreline, without bar/trough topography. It was originally developed as one of the applications of the analytical method in which temporal and spatial changes in offshore distance to some reference contours are investigated in place of simple comparison of sounding maps based on beach survey data collected on actual coasts. The fundamental idea of this model is as follows: on a steep coast without bar/trough topography the change in offshore distance to contours located between wave run-up height and the critical depth for beach changes is very closely related to the change in shoreline position if the beach changes are caused by longshore sand transport. This suggests predictability of subsequent locations of each contour due to longshore sand transport, if the relation between the changes in those contours can be determined. As schematically shown in Fig.1, this model can be used to predict the subsequent locations of contours $y_1, y_2 \cdots$, including the changes in longitudinal profile of the beach, by dividing the beach profile between h_R and $-h_C$ into thin layers and assuming the depth distribution of the longshore sand transport rate. Here, h_R and h_C are the wave run-up height and the critical depth for beach changes, respectively.

The introduction of a cross-shore distribution of longshore sand transport can be performed similar to the present model, but in this case, the cross-shore distribution must be transfered every time the shoreline changes its location, and in addition, even if the change in depth is calculated, complicated transformation is required to calculate the change in contours from the change in depth. For these reasons, in the present study we assume the depth distribution of longshore sand transport instead of the cross-shore distribution. In the CLC model the distribution of longshore sand transport

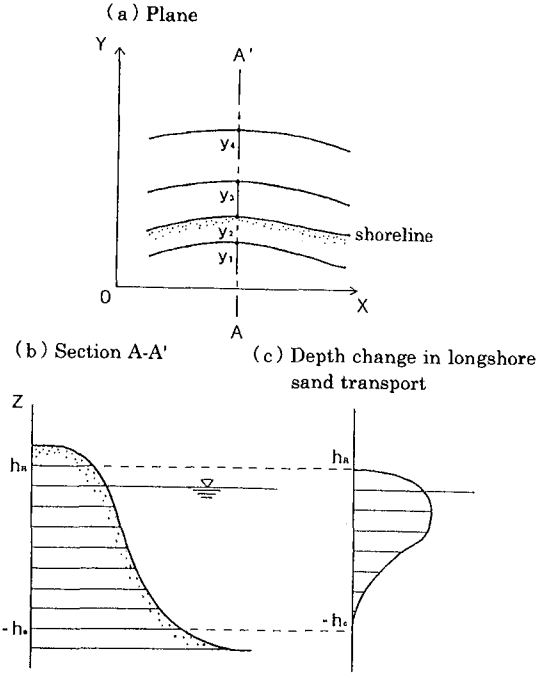

Fig.1 Schematic of the concept of the contour line change (CLC) model.

ranges between h_R and $-h_C$, as shown in Fig.1. Longshore change in wave height can easily be taken into account since h_C and h_R are assumed to be a function of breaker height H_b.

If the incident angle at the breaking point is assumed to be sufficiently small, Eq.(1) is satisfied using the Savage formula for longshore sand transport.

$$Q = F_0(\tan\alpha_0 - \frac{\partial y_s}{\partial x}) \tag{1}$$

where Q : littoral transport rate, F_0 : a coefficient depending on wave energy flux, α_0 : incident angle at breaking point, x : longshore distance, and y_s : shoreline position measured normal to x axis. Eq.(1) is satisfied only if the beach profile undergoes parallel movement in time and space, and the rate of longshore sand transport is determined by the relationship between the shoreline and the incident angle of waves.

Now, for a region divided by n contour lines, and if the longshore sand transport at a water depth corresponding to k = 1 ... n is assumed to be q_k and if it is also assumed that a similar relationship is established between the contour line distance y_k and q_k in analogy with Eq.(1), the following equation is obtained.

$$q_k = F_{0k}(\tan\alpha_0 - \frac{\partial y_k}{\partial x}) \tag{2}$$

where $F_{0k} = F_0 \cdot \mu_k$, $\Sigma \mu_k = 1$. Eq.(2) assumes that the longshore sand transport in each layer is governed by the relationship between the location of each contour line and incident wave direction. This model, therefore, does not require parallel movement, unlike the shoreline change model.

μ_k is a coefficient to give the longshore sand transport rate at each water depth and is calculated using Eq.(3) by giving the depth change of the longshore sand transport rate.

$$\mu_k = \int_{z_k}^{z_{k+1}} \xi(z)dz \Big/ \int_{-h_C}^{h_r} \xi(z)dz \tag{3}$$

z is the vertical distance with the still water level as the reference. The continuity equation of the longshore sand transport is given as

$$\frac{\partial q_k}{\partial x} + h_k \frac{\partial y_k}{\partial t} = 0, \quad k = 1 \cdots n \tag{4}$$

where h_k (k = 1 .. n) is the characteristic height of beach changes related to the topographic change represented by the contour lines, and is given by

$$h_k = z_k - z_{k-1} \tag{5}$$

If the functional form of $\xi(z)$ is given, μ_k is calculated using Eq. (3), and so the change in contour for each water depth is calculated by simultaneously solving Eqs.

(2) and (4). If the vertical distribution of the longshore sand transport rate is assumed to be between the wave run-up height on the foreshore and beach changes, the following relation can be assumed based on the field observation.

$$z^* = z / H_b, \quad h_c^* = h_c / H_b \tag{6}$$

When $-h_C < z < h_R$,

$$\xi(z)^* = 2 / h_c^{*3} (h_c^* / 2 - z^*)(z^* + h_c^*)^2 \tag{7}$$

When $z < -h_C$ and $z > h_R$,

$$\xi(z^*) = 0 \tag{8}$$

Uda and Kawano (1996) showed a correction method for the overhanging state of contours, namely, the state that the offshore distance to some reference contour becomes larger than that to a deeper contour. This induces offshore sand movement due to the gravity effect, and the sea bottom slope becomes more stable. Accordingly, the physical meaning of this correction is equivalent to the profile adjustment in order for the local sea bottom slope to maintain this critical value if the sea bottom slope exceeds a critical value, and eroded and accreted areas in the profile are always equivalent, while satisfying the continuity of sand volume per unit distance. Figure 2 shows a schematic of this process.

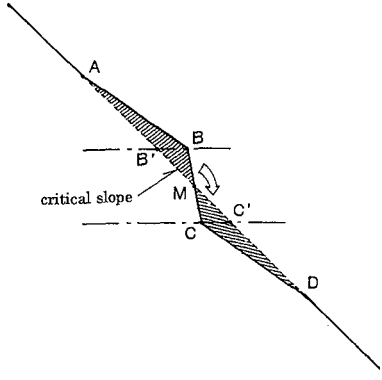

Fig.2 Schematic of stabilization mechanism of beach profile change due to Offshore sand movement.

Assuming that the local sea bottom with a slope exceeding the critical value is equivalent to the critical slope and the point of intersection between BC and B'C' is set to be M, a procedure for transformation from point B to B' and from C to C' is carried out so as to satisfy the equivalence of areas ABMB' and DCMC'. Since this mechanism is included in the model, sand movement to a far-offshore zone deeper than the critical depth for beach

Table 1 Conditions for calculation.

Case No	initial bottom slope	fluvial sand supply (m^3/yr) ($t \geqq 2yrs$)
①	1/ 5	0
②	1/10	0
③	1/20	0
④	1/ 5	2.5×10^5
⑤	1/10	2.5×10^5
⑥	1/20	2.5×10^5

changes is possible.

2.2 Conditions of Numerical Simulation

Six cases of numerical simulation of the development and deformation of a river mouth delta were investigated as shown in Table 1. The effect of the initial sea bottom slope on the formation of a foreset slope is investigated first for three different sea bottom slopes of 1/5, 1/10 and 1/20. The initial sea bottom slope is a key parameter because it influences the amount of accumulation space of fluvial sand supplied from the river mouth. Cases ①, ② and ③ aim at the investigation of this point. In each case a constant sand supply of $5.0 \times 10^5 m^3/yr$ from a river mouth is assumed from the initial stage up to two years, and thereafter, sand supply from the river is stopped completely (cases ①~③) and in another three cases, ④, ⑤ and ⑥, prediction is carried out for an additional 2 years after sand supply from the river was cut to half, in order to study the topographic changes around the river mouth due to the decrease in fluvial sand supply. Accordingly, the conditions in cases ①, ② and ③ are the same as those in ④, ⑤ and ⑥, except for the boundary condition at the river mouth after two years.

As a calculation domain, a 3km stretch, in the longshore direction, of uniform sandy beach is considered, and this domain is divided into 61 points at 0.05km intervals alongshore. A river is located at the center of this region and the open-boundary condition is set at both ends of the calculation domain. In the model, landward and offshore limits are given by the maximum run-up height, h_R and the critical depth for beach changes, h_C, respectively. Furthermore, the critical slopes of the beach on land and in the sea are assumed to be 1/1.7 and 1/2 , respectively. As the wave condition, a simple condition of a constant breaker height of 3m alongshore is selected as an example, and the wave direction is assumed to be perpendicular to the initial shoreline in order to facilitate the understanding of the mechanism of the development and deformation of a river mouth delta. Furthermore, h_R and h_C are set to be 4m and -7m, respectively. The calculation period is four years, which requires the total number of time steps of around 4.15×10^5, because one time step is set to be 300s.

Sand is supplied from three points located at the distance of $2\Delta x$ in the longshore direction and the amount of supplied sand per unit time is divided into three portions; $0.6Q_0$ at the central point and $0.2Q_0$ at a point on either side, where Q_0 is the amount of fluvial sand supply from the river per unit time. The supplied sand is assumed to be rapidly divided in each layer separated vertically in correspond to the depth change in longshore sand transport by wave action.

Ⅲ. RESULTS OF NUMERICAL SIMULATION

(1) Initial sea bottom slope of 1/5 (cases ① & ④)

Figures 3 (a), (b), (c) and (d) show the results of the calculations, for case ①, in which a river supplies sand at a rate of $Q_0=5.0 \times 10^5 m^3/yr$ to the surrounding sandy coast with the initial sea bottom slope of 1/5 and parallel contours. Under the condition of a constant sand supply, the development of a river mouth delta continues for two years. As the river mouth delta protrudes, the sea bottom slope gradually exceeds the critical slope given by the angle of repose of sand, leading to the discharge of sand into a deeper zone. As a result, the interval of contours in the deep

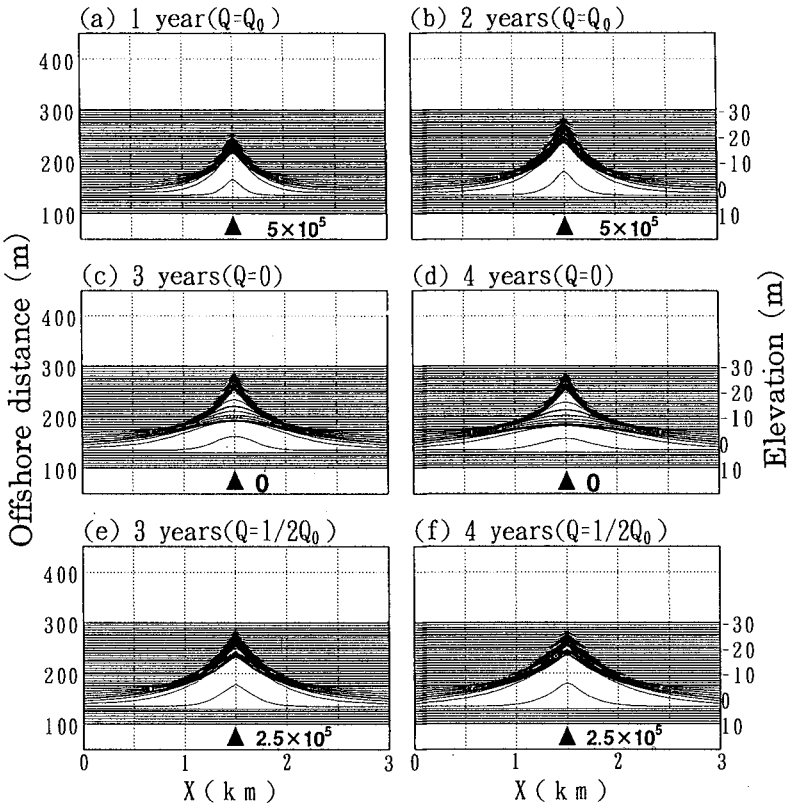

Fig.3 Results of calculation for development and deformation of a river mouth delta (initial beach slope 1/5: cases ① & ④).

zone is greatly narrowed. In the two years after sediment supply from the river is totally cut off, the protruding contours of a triangular shape in the zone shallower than $-h_C$ become milder. In this case the redistribution of sand due to longshore sand transport is impossible in the zone deeper than $-h_C$, and therefore a gentle slope is formed by erosion in the zone shallower than $-h_C$ with the formation of a mildly protruding shoreline. In case ④, as shown in Figs.3 (e) and (f), where sediment supply had been cut in half, sand further accumulates to build a river mouth delta while crutosis of the protruding contours in the vicinity of the center of the river mouth delta decreases gradually.

(2) Initial sea bottom slope of 1/10 (cases ② & ⑤)

Figure 4 shows the results of the calculation for cases ② and ⑤ with initial sea bottom slope of 1/10. The only difference between cases ① and ④, and cases ② and ⑤ is the initial sea bottom slope. Figures 4 (a)～ 4 (d) show that the aerial range, in which offshore sand movement is observed with the formation of a very

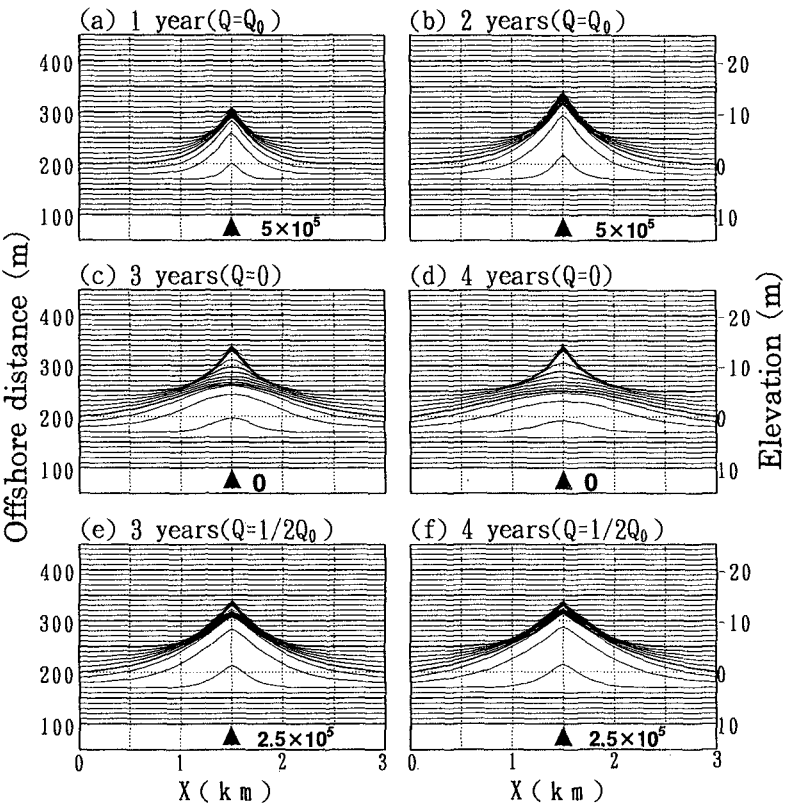

Fig.4 Results of calculation for development and deformation of a river mouth delta (initial beach slope 1/10: cases ② & ⑤).

steep angle of repose of sand, is narrowed, since the sea bottom slope in cases ② and ⑤ becomes gentler than that in cases ① and ④. Therefore the area expressed by dense contours in the offshore zone decreased. The rate of protrusion of the river mouth delta, however, is increased with a decrease in the average water depth of the accumulation zone of sand in cases ② and ⑤, as shown in Fig.4, compared with that in cases ① and ④, as shown in Fig.3. Furthermore, in case ④, in which sediment supply from the river is cut in half, as shown in Figs.4 (e) and (f), sand further accumulates to build a river mouth delta, while crutosis of the protruding contours in the vicinity of the center of the river mouth delta decreases gradually.

(3) Initial sea bottom slope of 1/20 (cases ③ & ⑥)

Figure 5 shows the results of the calculations for cases ③ and ⑥ with initial sea bottom slope of 1/20. The width of the region, where offshore sand movement is observed with the formation of a very steep angle of repose of sand, is greatly narrowed, since the sea bottom slope in cases ③ and ⑥ becomes much gentler

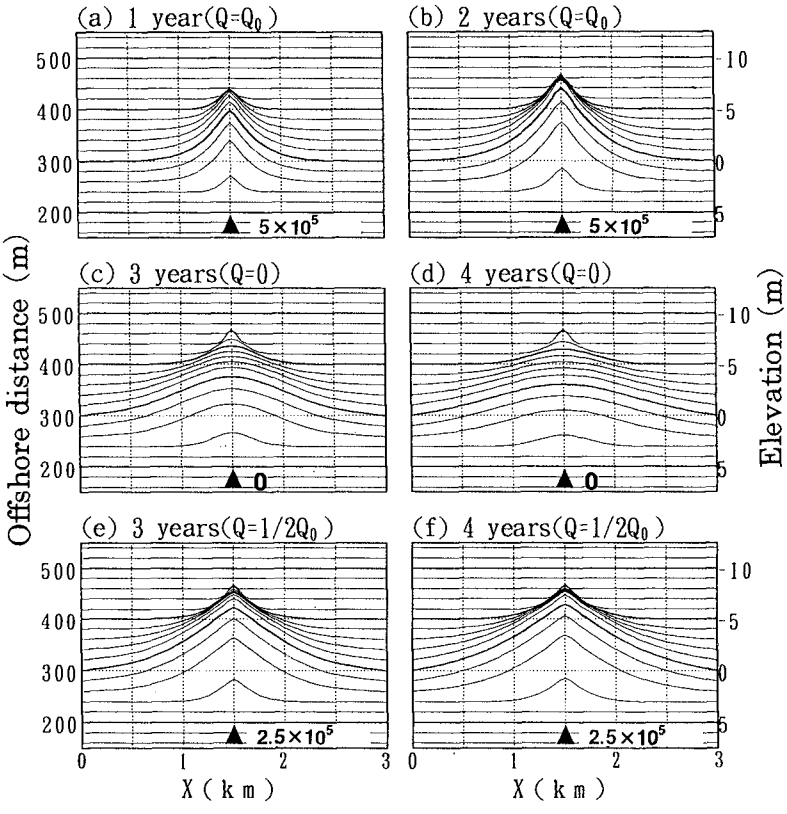

Fig.5 Results of calculation for development and deformation of a river mouth delta (initial beach slope 1/20: cases ③ & ⑥).

than that in cases ① and ④. For example, the foot depth of the foreset slope, which was formed by the successive deposition of fluvial sand, increases to 8m, 14m and 26m in cases ③, ② and ①, respectively, as shown in Figs.5 (b), 4 (b) and 3 (b).

Figure 6 shows the relation between the reciprocal of the initial beach slope and the foot depth of the foreset slope. The gentler the initial beach slope is, the shallower this foot depth becomes.

Here consider the case

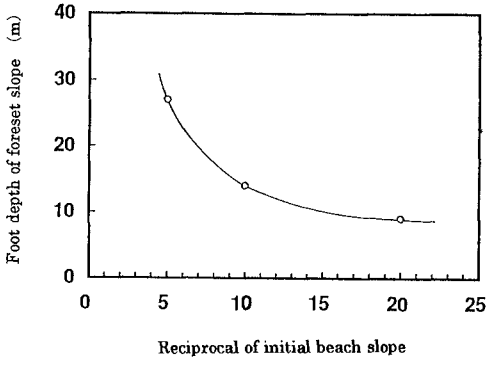

Fig.6 Relation between foot depth of foreset slope and initial beach slope.

where sand is supplied to a coast with a gentle initial slope, as in case ③ shown in Fig.5. After cut-off of the fluvial sand supply, deposited sand will be carried away by longshore sand transport, resulting in less protruding contours, since a large portion of the sand had been deposited in a zone shallower than the critical depth for beach changes. In contrast, in case ⑥, as shown in Figs.5(e) and (f), the development of a river mouth delta further continues, although crutosis of the river mouth contours are decreased.

(4) Comparison of beach profiles along the centerline of the river mouth delta

Figures 7 (a), (b) and (c) show the profile changes along the centerline of the river mouth delta. After the sand supply from the river was cut off 0, a gentle slope is formed in the zone shallower than $-h_C$ in each case. In the case of the slope of 1/5, as shown in Fig.7 (a), a large portion of the sand carried into the sea is deposited at a depth where sand movement is impossible due to wave action, so that the nourishment effect to the surrounding coastline of fluvial sand is minimum. In the case of the slope of 1/10, as shown in Fig.7 (b), a large portion of fluvial sand can be redistributed by longshore sand transport, since the water depth of the accumulation zone is sufficiently small. In the case of the slope of 1/20, as shown in Fig.7 (c), a large portion of the supplied sand is eroded due to wave action, since almost all the sand is deposited in the zone shallower than $-h_C$. It is concluded that if the initial sea bottom slope is sufficiently gentle, the protrusion of the river mouth delta, and therefore shoreline advance, will be large with a constant sand supply from the river. On the contrary the influence of a decrease in fluvial sand supply to the surrounding coastline becomes strong in terms of shoreline recession.

Figure 8 shows the temporal change in shoreline position along the centerline crossing the river mouth delta, where Figs.8 (a) and (b) are for cases in which sand supply from the river is totally cut off and reduced to half over two years, respectively.

The results in both cases are the same up to two years; the advancement rate of the shoreline position gradually decreases, though the change in shoreline position monotonically increases. This is because the water depth in the deposition zone of

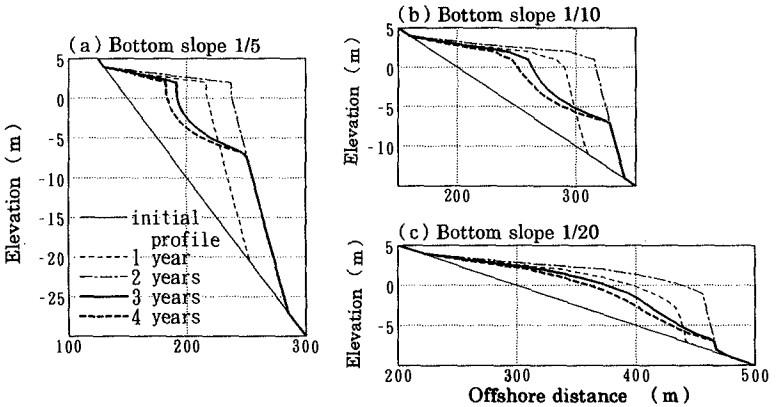

Fig.7 Temporal change in beach profile along centerline crossing the river Mouth delta.

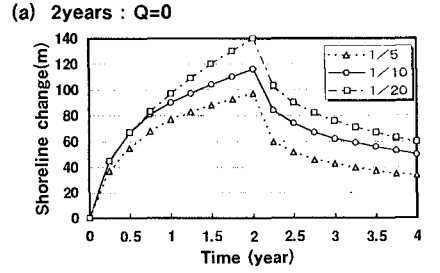

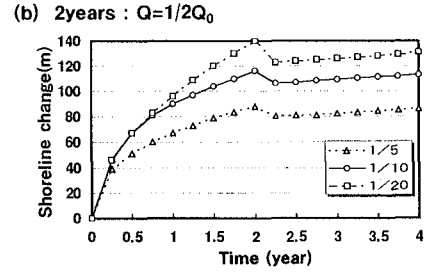

Fig.8 Temporal change in shoreline position at centerline crossing the river mouth delta.

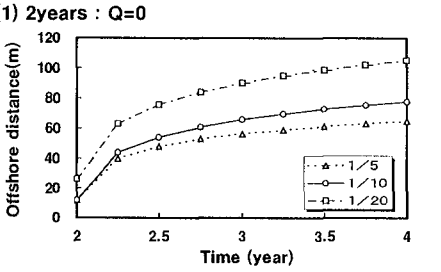

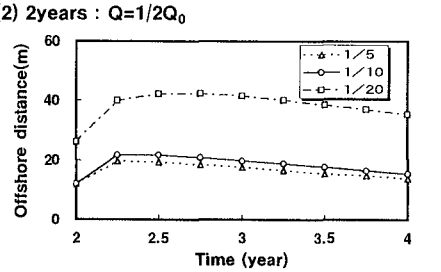

Fig.9 Temporal change of offshore distance between shoreline position and critical point for beach changes at the most protruding location of river mouth delta.

sand gradually increases with the seaward advance of the river mouth, and sand supplied from the river mouth is carried offshoreward and deposited in a deeper zone. In the case that the sand supply from the river is cut off over two years, shoreline recession starts immediately, and this response is expressed by an exponential curve. In contrast, in the case that the sand supply from the river is reduced to half, the shoreline initially retreats but later gradually advances.

Consider the case in which the river mouth delta being accretive for a long time is eroded due to a decrease in the fluvial sediment supply. In this case, a steep sea bottom slope formed by the successive deposition of sand is distinguished very well from the very gentle slope reformed by erosion upon a sudden change of slope, as shown in Fig.7. Figure 9 shows the offshore distance from the shoreline position to the location of the sudden change in slope at each time. This offshore distance gradually increases with time after the sand supply from the river is totally cut off over two years, whereas it increases immediately after the sand supply from the river is reduced to half but then changes to a gradual decrease with time. These findings indicate that the offshore distance from the shoreline position at each time to the location of sudden change of the slope is a useful index for expressing the elapsed period of erosion of the river mouth delta. This point shows the importance of fluvial sand supply to nourish the surrounding shoreline even if the sand supply rate has been decreased.

IV. DISCUSSION

In the present study, the topographic changes around a river mouth delta were

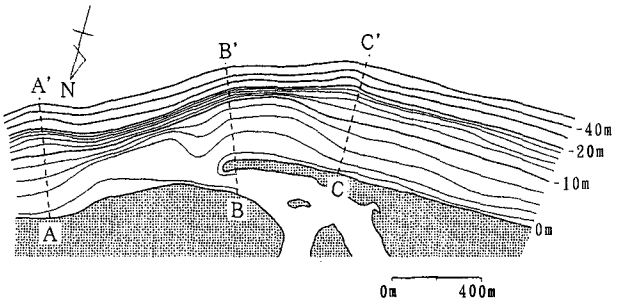

Fig.10 Sea bottom contours around Fuji River mouth measured in 1989.

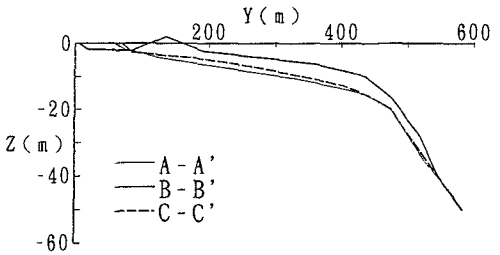

Fig.11 Comparison of beach profiles around Fuji River mouth.

predicted under the conditions that sand supply from a river is totally cut off and reduced to half over two years, after a constant supply of sand for two years. For actual rivers it is generally considered that a large amount of sand is supplied to the sea by infrequent, large floods through the river mouth and thereafter, sand supply to the sea decreases for a considerably long period. Taking this into account, it is considered that for an actual river mouth, a cyclic mode of topographic change is induced from the stage shown in Fig.3 (b) via the stage shown in Fig.3 (c) or Fig.3 (e), depending on the decrease rate of sand supply, back to the stage shown in Fig.3 (b), if a large amount of sand is supplied from the river mouth.

An example of a case ① river mouth is the Fuji River discharging at the Fuji coast in Suruga Bay facing the Pacific Ocean. The median diameter of river bed materials at the river mouth is around 75mm and the riverbed slope near the river mouth is very steep at 1/400. Figure 10 shows the beach topography around the Fuji River mouth measured in 1989. Close examination of contours between the shoreline and -20m depth reveals that the contour line intervals between the shoreline and -12m depth are very wide, whereas the contour intervals in the zone deeper than -12m are abruptly narrowed west of the mouth. Inversely, there is a very gentle slope near the depth of -4m east of the mouth, but beyond this gentle slope, the seabed slope becomes very steep. In short, contours around this river mouth show remarkable asymmetry between the east and west directions with respect to the centerline of the river mouth as well as the eastward extension of the river mouth barrier. All these findings indicate that over the long term, eastward longshore sand transport is

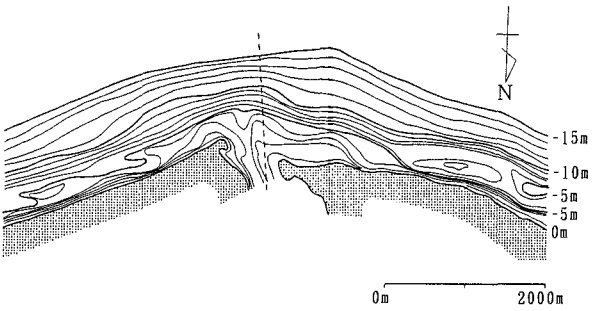

Fig.12 Sea bottom contours around Tenryu River mouth measured in 1984.

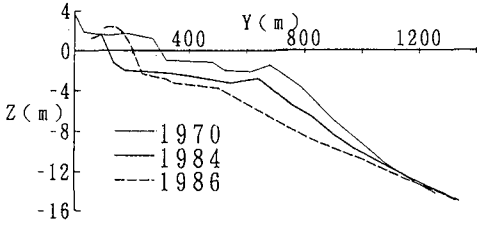

Fig.13 Comparison of deformation process of the terrace topography off Tenryu River mouth.

predominant at the Fuji River mouth with waves obliquely incident from the south. Profiles along the three crosssections shown in Fig.10 are shown in Fig.11 by superimposing crosssections off the critical depth for beach changes given at around -8m (Uda, 1997). There is a terrace with a gentle slope and a very steep seabed with a slope of 1/4 off this terrace. Profiles of the east and west crosssections of the river mouth are approximately the same, whereas the sea bottom elevation along the centerline crossing the mouth is higher than those along both sides, and the profile is upward convex, implying excess sand deposition from the river in front of the river mouth. These topographic characteristics are very similar to the results of the calculation for case ①, although temporal changes in profiles are not known in field data.

An example of a case ③ river mouth is the Tenryu River discharging at the Enshu coast facing the Pacific Ocean. The riverbed slope near the mouth of this river is 1/1,230, the median diameter of riverbed materials is around 13.9mm and the mean sea bed slope of this coast is 1/90.

Figure 12 shows river mouth topography around the Tenryu River measured in 1984. There is a flat terrace at -2m depth west of the river mouth. The contour of -10m shows that the western area is concave and the eastern area convex with respect to the centerline of the river mouth. This asymmetry of the contours in the two directions is the same as that observed at the Fuji River mouth, and implies the predominance of an oblique wave incidence from clockwise direction.

Figure 13 shows profile changes along the centerline of the river mouth. In

September 1970, the water depth at the flat river mouth terrace was about 2m and the terrace was as wide as around 400m from the shoreline. In July 1984, the offshore slope of the terrace retreated to a large extent compared with the one in September, 1970. In July 1986, the river mouth terrace was eroded and narrowed. These changes are considered to be caused by the imbalance between the longshore sand transport flowing away from the river mouth and sand supply from the Tenryu River which was decreased due to river bed excavation before 1967. These results agree well qualitatively with the topographic changes shown in Fig.5.

V. CONCLUSIONS

A predictive model of the three-dimensional development and deformation of a river mouth delta was developed. This model enables the prediction of not only the shoreline change but also the three-dimensional topographic changes around a river mouth. In this model, offshore sand movement is taken into account, with constant critical slope, when the sea bottom slope exceeds a critical slope given by the angle of repose. This has the advantage that the shoreline change, the progression rate of which gradually decreases with time can be simulated, since the depth of the sand deposition zone increases with the progression of the shoreline position.

References

Hashimoto H. (1975): Characteristics of shoreline change around a river mouth, Civil Eng. Jour., Vol.7, No.12, pp.32-37. (in Japanese)

Rafaat H.E.A.A. and Y. Tsuchiya (1991): Formation and Reduction Processes of River Deltas; Theory and Experiments, Bull. Disas. Prev. Inst., Kyoto Univ., Vol.41, pp.177-224.

Tsuchiya Y., T. Yamashita and T. Izumi (1995) : Large scale shore processes of Niigata coast and control of beach erosion, Proc. Japan. Coastal Eng., Vol.42, pp.681-685. (in Japanese)

Uda, T. (1997): Beach erosion in Japan, Sankaido Press, p.442. (in Japanese)

Uda, T. and S. Kawano (1996): Development of contour line change model for Prediction of beach changes, Proc. JSCE, No.539/ II -35, pp.121-139. (in Japanese)

Uda, T., Y. Yamamoto, N. Itabashi and K. Yamaji (1997): Field observation of movement of sand body due to waves and verification of its mechanism by numerical model, Proc. 25th ICCE, ASCE, pp.137-150.

Field Investigation on Sediment Transport into the Submarine Canyon in the Fuji Coast with the New Type Tracers

Shigenobu Tanaka[1], Koji Yamamoto[2], Hitoshi Ito[3], Toshiharu Arisawa[4], and Toshimitsu Takagi[5]

Abstract

The Fuji coast in Japan is one of the beach which is suffering from coastal erosion. One reason for erosion is seemed to be the offshore sedimcnt transport through the submarine canyon in front of eroded area. The present paper concerns the field investigation in order to confirm the sediment transport into the submarine canyon with two new type tracers. One tracer is the artificial sand and gravel made of the hard plastic. The other is the tracer with an ultrasonic transmitter. These tracers are very effective for tracking the sediment.

1. Introduction

The Fuji coast, facing on the Suruga bay in Japan which has the Suruga trough over 2,000 m depth, is known for one of the most beautiful coast where Mt. Fuji is seen behind (Figs.1 and 2). The coast is 19 km long between the estuary of Fuji River and Numazu harbor. The coast is made of sand and gravel and the sea bottom has a steep slope, close to 1/2 over 20m depth. In this coast, the longshore sand transport toward east is dominant, which amounts to almost 100,000 m^3/year. The western side of the coast has been suffering from erosion since 1970 as shown in Fig. 3. These reasons are partly reduction of discharged sediment from the Fuji river and stopping the longshore sediment transport by the breakwater of Tagonoura harbor. Since the coastal erosion

[1] Deputy Director, Japan Inst. of Constr. Eng., Tranomon 2-8-10, Minato-ku, Tokyo 105-0001, Japan.

[2] Researcher, River Department, PWRI, Min. of Constr., Asahi-1, Tsukuba, Ibaraki 305, Japan.

[3] Chubu Region Constr. Bureau, Min. of Constr., San-nomaru 2-5-1, Naka-ku, Nagoya, Aichi 460, Japan.

[4] Numazu Constr. Office, Chubu Regional Constr. Bureau, Min. of Constr., Shimokanuki 3244-2, Numazu, Shizuoka 410, Japan.

[5] Coastal Engineering Department, INA Corporation, Sekiguchi 1-44-10, Bunkyo-ku, Tokyo 112-8668, Japan

started, the wave dissipating breakwater has been constructed along the shore. Because of the effect, the backward movement of shoreline stopped. However, the erosion has been spread to the downdrift side of longshore sediment transport. The wave dispersion breakwater might cause the decrease of sediment transport. Recently the erosion occurs from the Outlet 1 to east where is the end of the wave dissipating concrete block. Therefore, the countermeasure is necessary for protection of the eroded beach. To make a plan for countermeasure, the mechanism of sediment movement must be clarified. In this coast the sand transport is dominant toward not only longshore but also offshore because the sediment budget is not maintained along the coast with 15 m or less in depth according to the analysis of topography maps. Particularly a large submarine canyon exists in front of the eroded beach, and its entrance (20m depth) is close to the shoreline (Fig.3). Therefore, there is a possibility of offshore sediment transport through this canyon. Thus, the field investigation on sediment transport was carried out around the submarine canyon with the two types of new tracers.

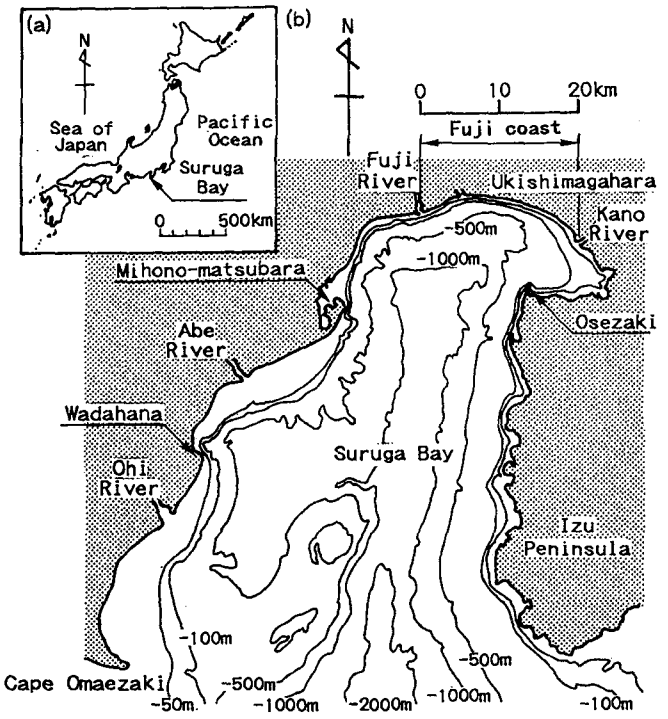

Figure 1 Location map of the Fuji Coast

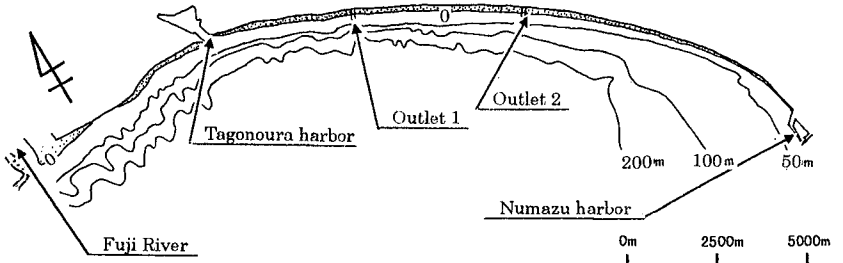

Figure 2 Map of the Fuji coast

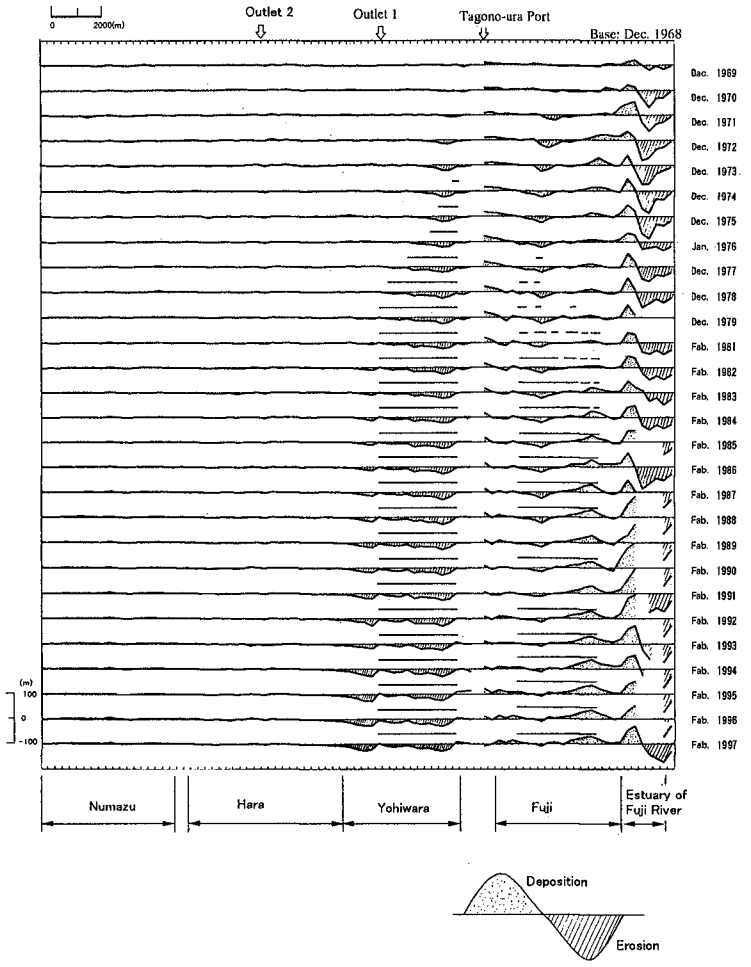

Figure 3 History of the shoreline change

2. Topography around the Submarine Canyon and Characteristics of Sediment

The study coast has very steep bottom, approximately 1/10 from the shore to 20m depth and approximately 1/2 offshore from 20m depth. Especially in front of the Outlet 1 the 20m contour is close to shoreline. These characteristics of topography of Fuji coast are found obviously from the variation of depth contours as shown in Fig.4. According to the topography analysis, the critical depth of topography change is about 14m depth (Fig. 5). The distribution of sediment grain size around the submarine canyon shows in Fig. 6. It is found that the variation of the grain distribution in 50m depth of the canyon from No.48 to 49 is much more than that out of the canyon. This fact shows the movement of sediment even in 50m depth of the canyon.

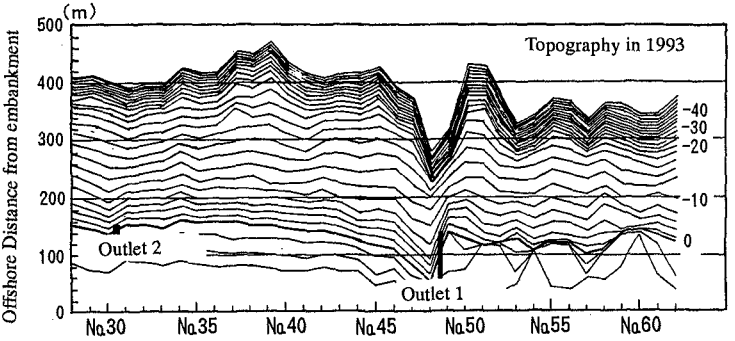

Figure 4. Distribution of topography

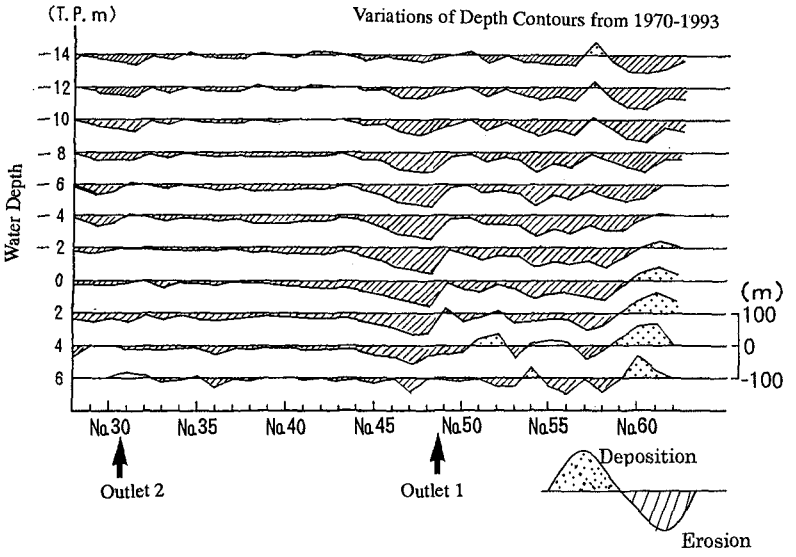

Figure 5. Variations of depth contours

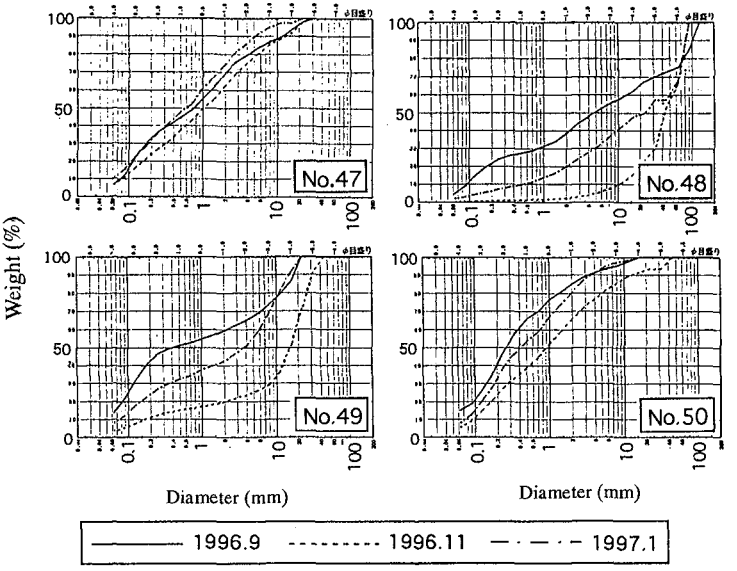

Figure 6. Grain size distribution at 50m depth nearby the submarine canyon

3. Field Investigation Using New Type Tracers

3.1 Artificial gravel tracer (Type A tracer)

The artificial sand and gravel, which are made of the hard plastic, colored pink, with approximately the same density and grain size distribution as the field, were put on the bottom in 16 m depth offshore No.49+125m(Fig.7). Three different sizes of gravel, 1 mm, 10 mm and 50 mm, which are taken as the representative sizes for the field sediment were made (Fig.8, Photo 1). The 100mm tracers as the maximum size in the field were also made. The tracers with 1mm and 10 mm mean diameters were made by crush of the hard plastic panels. The tracers with 50 and 100mm diameter were cast in cup-shaped mold. After mixing these tracers as almost same distribution of grain size as that in the field (Fig.8), three ton of these were put on the bottom in 16m depth offshore to No.49+125 m (Fig.7). On three times tracks including immediately after typhoon, divers collected the sediments of approximately five kilograms weight on the several places of the bottom around the injection place of tracers. The weight of tracers included in the collected sediment was measured in each grain size group.

3.2 Small ultrasonic transmitter(Type B tracer)

The other tracer is the artificial gravel with a small ultrasonic transmitter (Photo 2) that has approximately five months of life (Table 1 and Fig.9). The small ultrasonic transmitter is often used in trace of fish. Three pieces of tracers that have the different

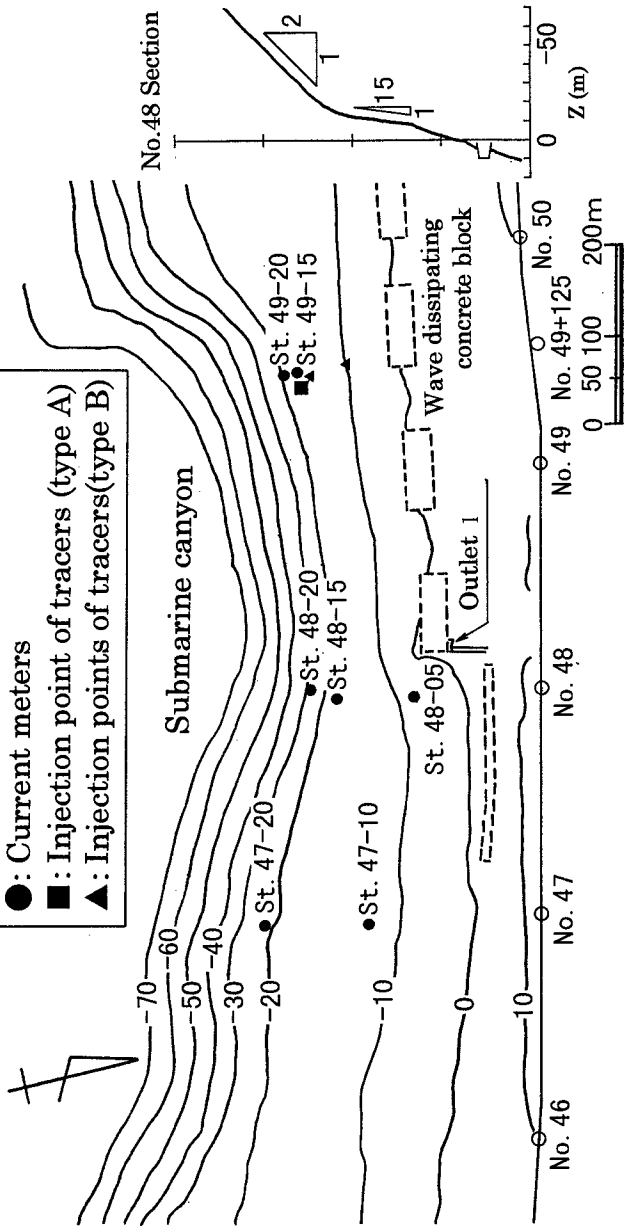

Figure 7 Topography nearby submarine canyon and position of survey equipment

Photo 1 Artificial sand and gravel for tracers

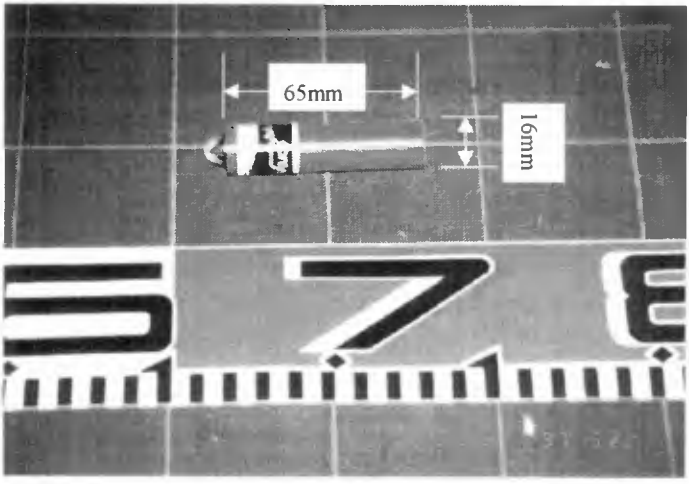

Photo 2 An ultrasonic transmitter

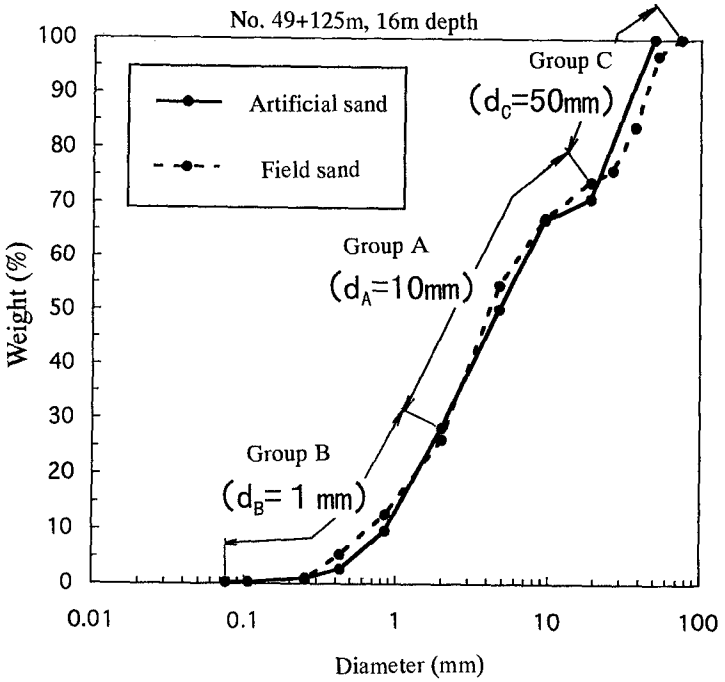

Figure 8 Distribution of artificial and field sands.

Table 1 Characteristics of Small Ultrasonic Transmitter

Parameters	Models
Length/Diameter (mm)	65/16
Weight in water (g)	10
Frequency (kHz)	50,54,60,65.5,69,76.8
Service life (day)	268 (approximately 9 months)
Output (dB)	147
Effective Range (m)	50-800

frequency transmitters were separately put on the bottom each in 10 m and 15 m depth (Fig. 7). By using an ultrasonic receiver fixed on a boat, the position of the tracer with the small ultrasonic transmitter can be searched

4. Tracking of Tracers and the Force of These Movements

4.1 *Wave and current climate*

The history of wave and current climate in St.49-15 from 10 Sept. 1996 to 10 Oct. 1996 is shown in Fig.10. Three typhoons, 9617, 9620, and 9621 attacked this coast on

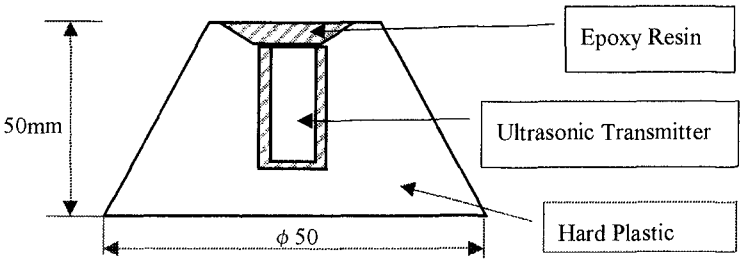

Figure 9 A tracer with ultrasonic transmitter

Table 2 High Wave during Observation by Tracers with Small Ultrasonic Transmitter

Period	$H_{1/3max}$ (m)	$T_{1/3max}$ (s)	Wave direction	Main causes
Nov. 12-13, 1996	3.13	17.6	SW	Typhoon 9624
Dec. 5-6, 1996	4.45	9.2	SSW	Low barometric pressure
Jan. 2-3, 1997	2.57	6.9	SSW	
Jan. 6-7, 1997	2.41	7.2	SSW	

the investigation. Especially the typhoon 9617 caused big waves, about 3.5m height of significant wave and a period of 15 second. Although the velocity of mean current was below 10 cm/s, the orbital velocity of wave was about 1.0 m/s in significant value and 2.0 m/s in maximum value when the maximum wave height 5.25m was recorded. During the tracking of the tracer, type B, the big waves attacked as shown in Table.2. According to the wave data, the wave was coming to the shore from SSW dominantly, which is about 5.0 degree clockwise from the normal direction of shoreline.

4.2 *Tracking results of artificial sand and gravel*

The artificial tracers of the type A were put on 12 Sept. and the tracking of them was carried out three times, 27 Sept. immediately after the typhoon 9617, 9 Oct. and 7 Nov.. The results of tracking of tracers are shown in Fig.11. After the typhoon 9617 the tracers moved toward south along the steepest bottom slope of the canyon. In particular, 100mm tracers were found even in the bottom of 40m depth. Although the sediment could not be collected in 50m depth, divers confirmed the existence of some tracers in it. In addition, any tracer was not found in onshore and longshore from the injection point. The movement of each grain size group of tracers is shown in Fig.12. According to this result, the different movement due to the grain size was not confirmed.

4.3 *Tracking result of tracer with an ultrasonic transmitter*

The tracers with ultrasonic transmitter (Type B) were put on 12 Oct. 1996. The tracking was carried out on 9 Nov. 1996 and 23 Jan. of the next year. The tracking result is shown in Fig.13. On the first tracking, the movement of them was not

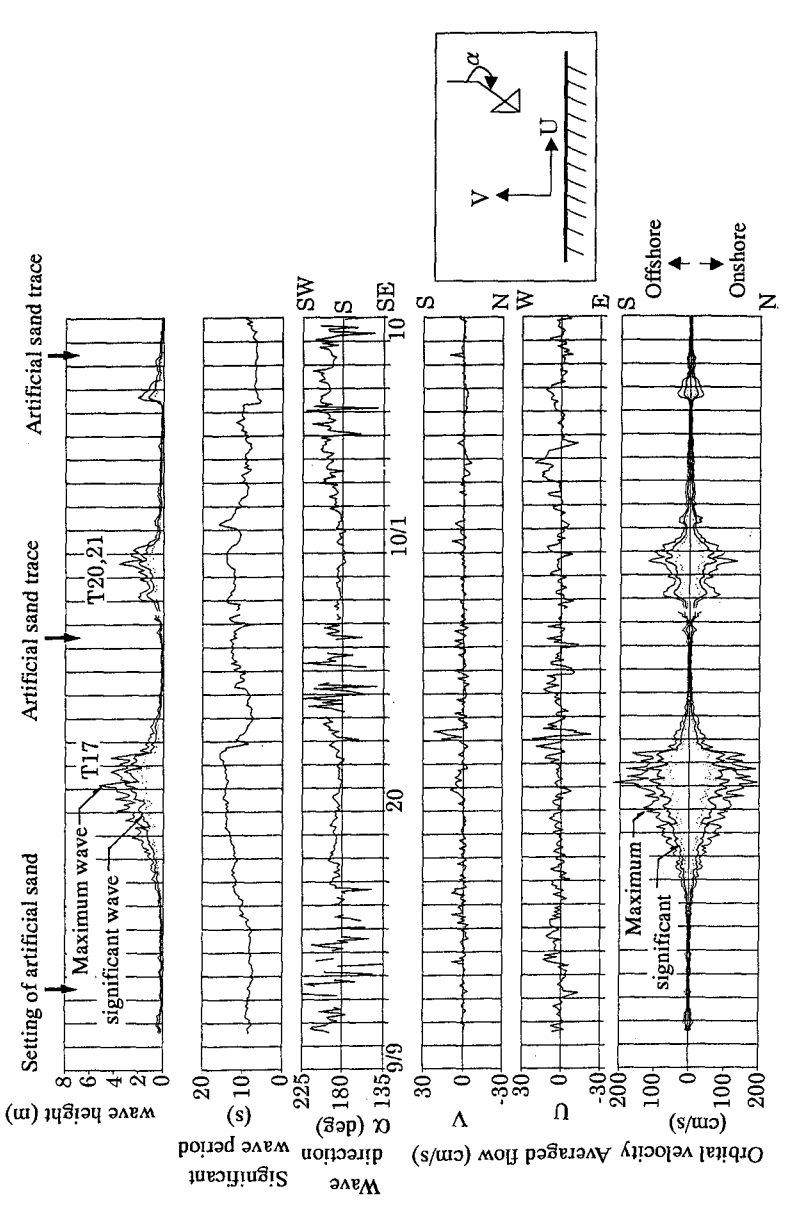

Figure 10 Wave and current at St. 49.5-15

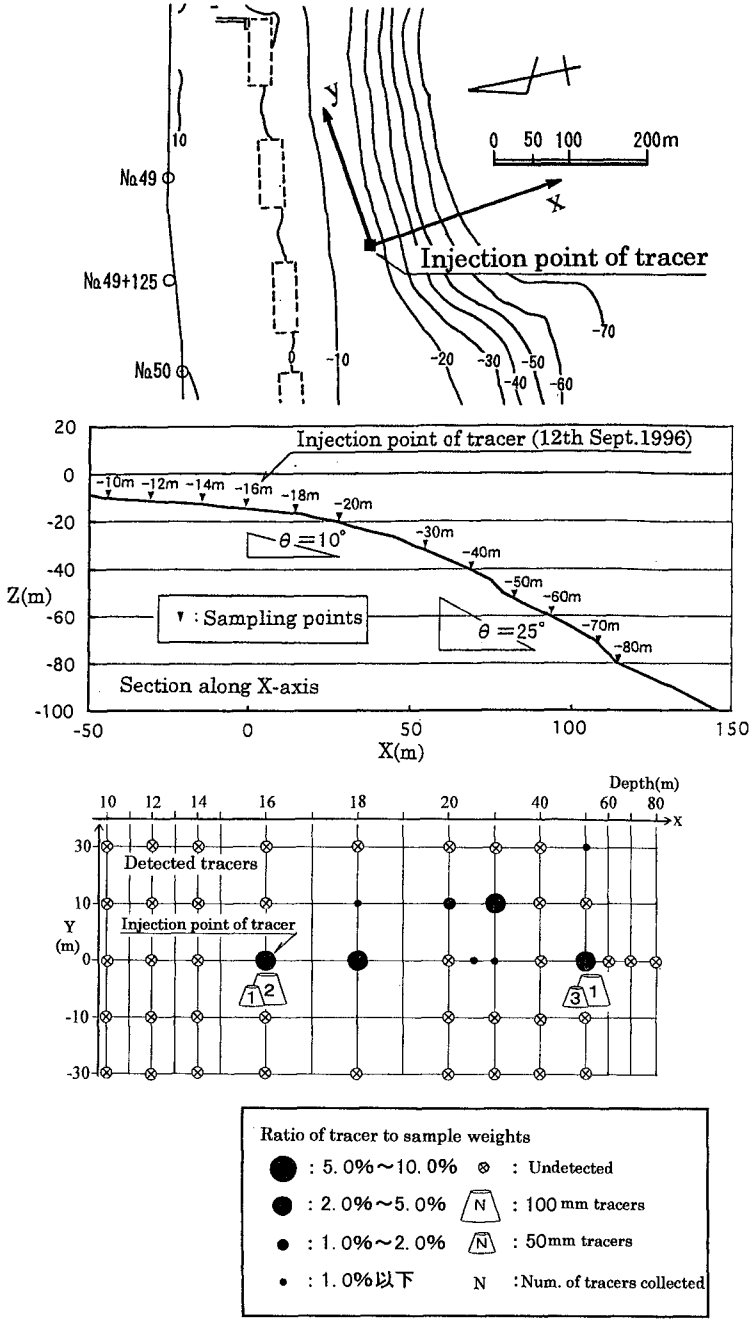

Figure 11 Detected the type A tracers after the typhoon 9617

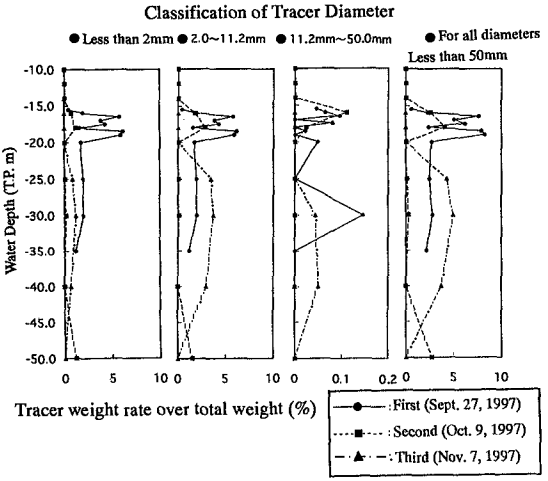

Figure 12 Detected tracer weight rate over total weight (%)

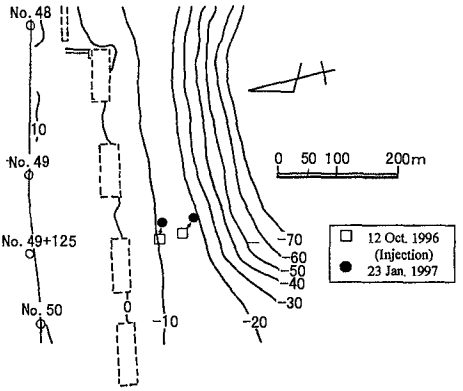

Figure 13 Track of the type B tracers

confirmed. However on the second time, the tracers put on the bottom in 15m depth moved toward offshore about 30m away, and those put on the bottom in 10m depth moved toward both longshore and offshore about 20m far away. The movements of tracers Type A and B injected on 15m depth were toward offshore. However, the movement of tracer type B injected on 10m depth had a longshore component more than that on 15m depth.

5. Mechanism of Sediment Movement on the Steep Bottom

According to the result of the field investigation, it was found that the sediment in 15 m depth where is the entrance of the submarine canyon, moved toward the offshore during the typhoon. The force of the sediment movement is seemed to be the orbital velocity due to wave and gravity because the mean current velocity is not domainant toward offshore. Then using the Shields parameter obtained by the orbital velocity, the stability of sediment was analyzed. On this analysis the critical Shields parameter was revised using Lane's equation (Lane, 1955),

$$K = \Psi_{cs} / \Psi_c = \cos\theta\sqrt{1-(\tan\theta/\tan\varphi)^2} \quad (1)$$

where Ψ_{cs} is the critical Shield parameter on a slope, Ψ_c is the critical Shield parameter on a flat bottom, θ is the angle of bottom slope, and φ is the stable angle of bottom slope. Fig. 14 shows the influence of the bottom slope to the critical Shields parameter with respect to the sediment grain sizes. From this figure, the sediment with 4mm on 1/2 slope starts moving by the half of the critical force at the flat bottom. Fig. 15 shows the histories of the Shields parameters during typhoon 9617 over a range of the grain sizes from 1mm to 100mm. In this case the critical Shields parameter on the flat bottom is 0.05 that is obtained by Madsen and Grant (1976). The bottom slope is 1/6 at the injection point of tracers (Type A). It is found that the sediment with grain size less than 100mm has the possibility of movement at the attack of typhoon. It can be estimated that due to the gravity, the direction of movement is inclined to the offshore with the steep bottom slope.

6. Conclusions

It is found in this investigation that the sediment transport around the 15m depth, partly made of the gravel with 100mm diameter, move toward the submarine canyon when the big waves generated by the typhoons attacked. The force of the sediment movement could be the wave orbital velocities up to 2.0 m/s in typhoon and gravity according to the Shields parameter analysis. By the fact that the averaged offshore velocities are weak, the steep bottom slope determines dominantly the direction of the sediment movement even deeper than 15m around the submarine canyon. Furthermore, the effect of the new type tracers was confirmed in this investigation.

Reference

Lane, E. W. (1955): Design of stable channels, Trans., ASCE, Vol. 120, pp.1234-1279.

Madsen, O.S. and Grant, W.D. (1976): Quantitative description of sediment transport, Proc. 15th Coastal Eng. Conf., ASCE, pp. 1093-1112.

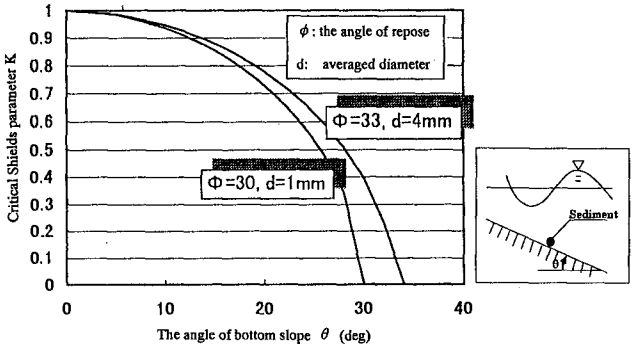

Figure 14 Critical Shields parameter on the slope

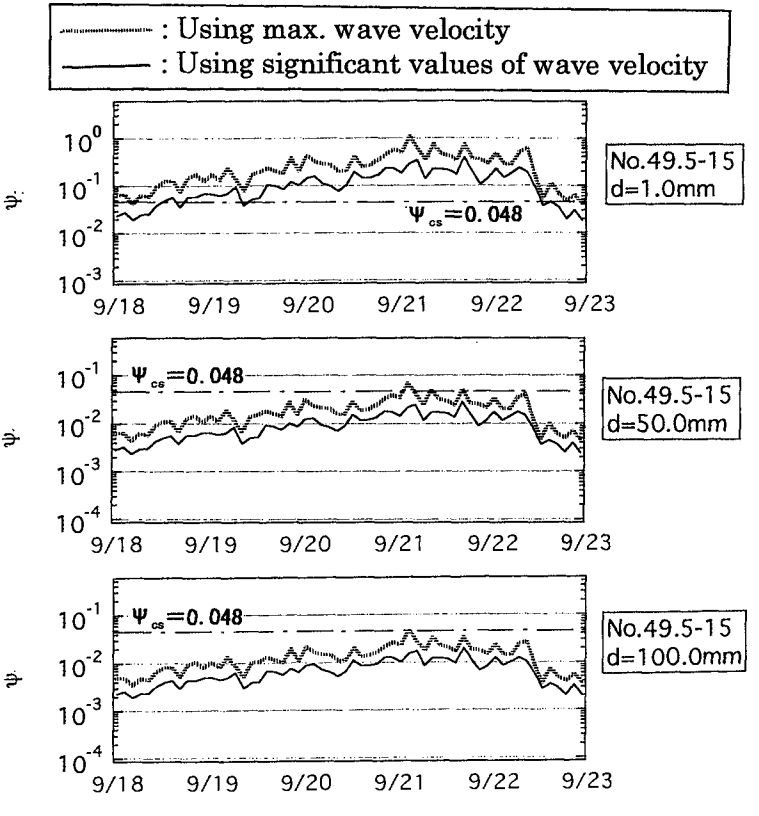

Figure 15 History of Shield parameters during the typhoon 9617

Sea Breeze Climatology and Nearshore Processes along the Perth Metropolitan coastline, Western Australia

G. Masselink[1] and C.B. Pattiaratchi[2]

Abstract

The Perth metropolitan coastline is characterised by one of the strongest and most consistent sea breeze systems in the world. In contrast to the 'classic' sea breeze system, characterised by sea breezes blowing in the onshore direction, the sea breeze in Perth blows in a predominantly alongshore direction. Each year, around 200 sea breezes are experienced with an average wind speed of 5.7 m/s. Sea breezes in summer are stronger and more persistent than in winter. The importance of the sea breeze is clearly indicated by wind spectra showing significant spectral peaks at the diurnal frequency. The sea breeze system directly forces the incident wave field and induces a diurnal cycle of nearshore change by causing: (1) an increase in wave height; (2) a decrease in wave period; (3) an intensification of the nearshore currents; and (4) an increase in suspended sediment levels and suspended sediment transport. In addition, the seasonal variation in sea breeze activity, with frequent and strong sea breezes in summer and infrequent and weaker sea breezes in winter, is responsible for a seasonal change in the littoral drift direction. In summer, longshore sediment transport is towards the north and causes beaches located south of structures or headlands to widen considerably. In winter, when littoral drift is towards the south due to northwesterly storms, beaches located north of structures or headlands will become wider. It is further demonstrated that strong sea breeze activity is common along the entire Western Australian coastline, implying that the results obtained for the Perth metropolitan coastline can be applied to some extent to the entire state.

[1] Research Fellow, Department of Environmental Engineering, Centre for Water Research, University of Western Australia, Nedlands, WA 6907, Australia.
[2] Head, Department of Environmental Engineering, Centre for Water Research, University of Western Australia, Nedlands, WA 6907, Australia.

Introduction

The Perth Metropolitan coastline experiences mixed, microtidal tides with a mean spring tidal range of 0.9 m (Department of Defence, 1996). Because of the relatively low range of the tide, it is frequently over-ridden by barometric pressure effects on sea level (storm surge and shelf waves), wind/wave set-up and seiching (Eliot and Clarke, 1986). The offshore wave climate is dominated by a low to moderate energy, deep water wave regime characterised by persistent south to southwest swell and an average significant wave height of 1.5–2.5 m (Lemm, 1996; Fig. 1). Closer to shore, the swell is refracted and diffracted by several offshore reef systems and greatly attenuated by shoaling across the inner continental shelf. As a result, the inshore wave height is about 40% of that outside the reef system (Steedman, 1993). A highly variable wind wave climate is superimposed on the swell regime, dominated by northwesterly to westerly storm waves during winter and by the wave field associated with strong south to southwesterly summer sea breezes.

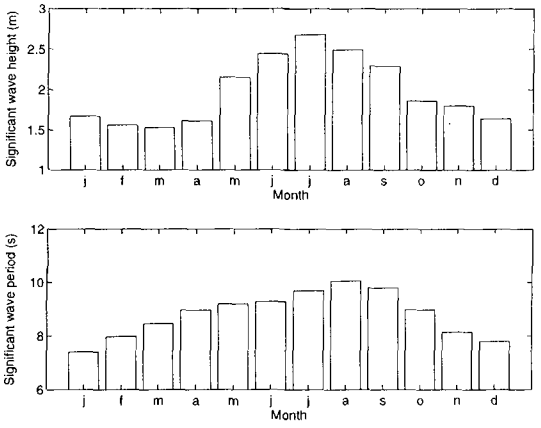

Fig. 1 - Offshore wave climate of Perth (data from Lemm, 1996).

The coastline of Perth is subject to one of the most energetic and consistent sea breeze systems in the world. A typical sea breeze cycle is characterised by offshore winds from an easterly direction (80–100°) in the morning, switching to shore-parallel southerly (180–200°) winds in the afternoon (Fig. 2). A significant feature of the sea breeze system along the Perth coast is that it blows parallel to the shoreline, in contrast to the "classic" onshore sea breeze. The shore-parallel sea breeze system in Perth, and in fact along most of Western Australian coastline, is attributed to the interaction between the sea breeze system and synoptic weather patterns (Pattiaratchi et al., 1997).

The impact of sea breeze activity on surf zone processes and morphology along the Perth metropolitan coastline has been extensively discussed by Masselink (1996), Pattiaratchi et al. (1997) and Masselink and Pattiaratchi (1998a, b). These studies indicate that the energy levels in the surf zone increase dramatically during the sea breeze, and suggest that the effect of a strong sea breeze on nearshore processes is similar to that of a small storm. The objective of this paper is put these previous

morphodynamic investigations in a wider perspective by characterising the Perth sea breeze climate using more than 50 years of wind data collected at Perth airport. The wind analysis is extended to nine other Western Australian coastal locations to demonstrate that strong sea breeze activity is common along the entire Western Australian coastline, implying that the results obtained for the Perth metropolitan coastline can be applied to some extent to the entire state.

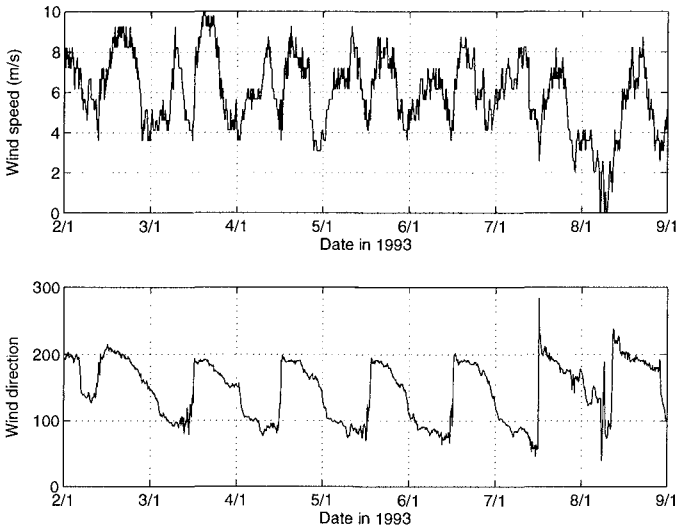

Fig. 2 - A typical 1-week time series of wind speed and direction collected at Ocean Reef, 2–9 January, 1993 (data from Pattiaratchi et al., 1997).

Time-Domain Analysis of Sea Breezes in Perth

Three-hourly wind data collected at Perth Airport from 1948–1997 were used to determine the sea breeze climate of Perth. The data were subjected to an algorithm that selected the days during which sea breezes occurred. A day was considered a "sea breeze day" if: (1) the wind direction in the afternoon (15:00 hrs) was from the sea breeze direction (190°–300°), but the wind in the morning (09:00 hrs) was not from that direction; or (2) The wind direction in the morning and afternoon were both from the sea breeze direction, but the afternoon wind speed was larger than during the morning. Using these selection criteria the number of sea breezes per month and the mean sea breeze speed and direction were determined.

A strong seasonal variation in sea breeze activity is apparent (Fig. 3). In the summer months, more than 20 sea breezes are experienced per month with speeds (at 15:00 hrs) of 6–7 m/s. In the winter, only 10–15 sea breezes occur per month with speeds of around 5 m/s. On average, each year 197 sea breezes are experienced with a mean wind speed of 5.7 m/s. The direction of the sea breeze is consistently from the WSW throughout the year. However, the summer sea breeze blows from a slightly more southerly direction (240°) than the winter sea breeze (250°).

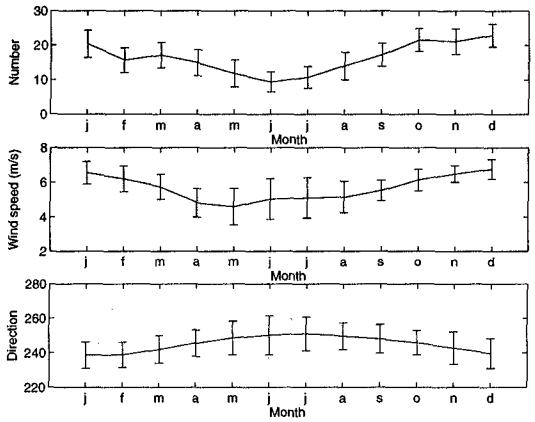

Fig. 3 - Seasonal variation in the number of sea breezes (upper panel) and the wind speed (middle panel) and direction during the sea breeze (lower panel) from three-hourly data collected at Perth Airport from 1948–1997. The vertical lines indicate the standard deviations associated with the averages.

Frequency-Domain Analysis of Sea Breezes in Perth

The Perth wind data was also subjected to spectral analysis. For each year, spectra were computed for the periods December–February (summer), March–May (autumn), June–August (winter) and September–November (spring). Subsequently, an average spectra was determined for each of the seasons (Fig. 4). All spectra show three main characteristics. Firstly, a large amount of energy is present at the low-frequency end of the spectrum (periods longer than 1.5 days). This corresponds to the time scale of synoptic weather patterns, such as storms. Secondly, a pronounced peak can be found at the diurnal frequency (period of one day). This peak represent sea breeze activity. Thirdly, complementary peaks occur at the first and second harmonics of the diurnal frequency (periods of 12 and 6 hours, respectively). These are primarily due to the non-linear (non-sinusoidal) nature of the sea breeze signal. However, the occurrence of strong land breezes during night may also have contributed to the first harmonic frequency (refer Fig. 2). The diurnal peak is present in all the seasonal spectra, but is widest in the summer spectrum and narrowest in the winter spectrum.

Using the same data set, monthly wind spectra were computed and an average spectra was determined for each month. The total spectral energy was then partitioned into a low-frequency band (period larger than 1.5 days; 'synoptic band') and a high-frequency band (period smaller than 1.5 days; 'sea breeze band') to allow investigation of the seasonal variation in the importance of these components (Fig. 5). The spectral energy of the synoptic band and the sea breeze band show an anti-phase relationship; the synoptic band reaches its maximum energy levels in June/July when storm activity is prevalent, whereas the sea breeze band dominates from November–January when sea breeze are at their strongest and most abundant. In the summer months, the sea breeze band accounts for 60–70% of the total variance in the wind record.

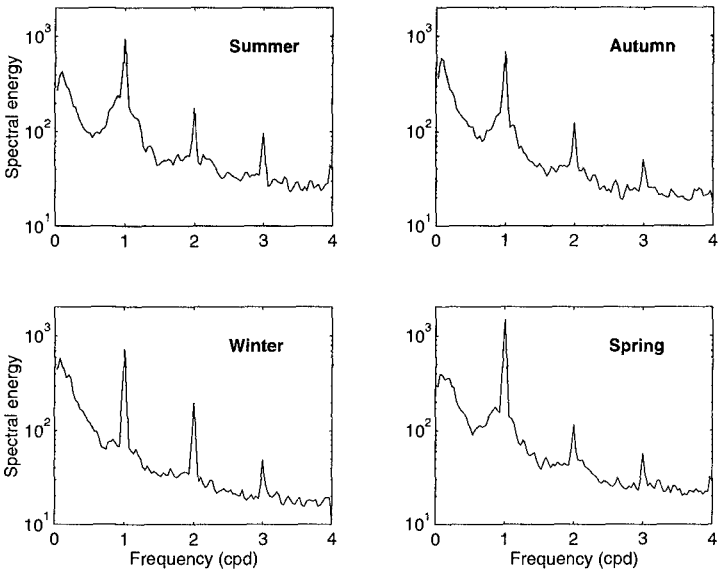

Fig. 4 - Average wind spectra for summer, autumn, winter and spring from three-hourly data collected at Perth Airport from 1948–1997.

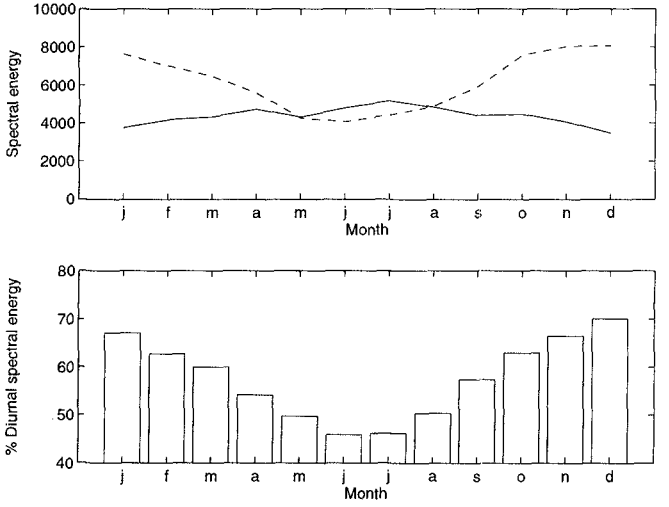

Fig. 5 - Monthly variation in spectral energy in the synoptic (solid line) and sea breeze (dashed line) frequency band (upper panel) and relative contribution of the sea breeze band to the total wind variance (lower panel). Based on three-hourly data collected at Perth Airport from 1948–1997.

Effect of Sea Breeze Activity on Nearshore Processes

Offshore wave conditions are significantly affected by the sea breeze and this is clearly illustrated by seasonal offshore wave spectra (Fig. 6). All spectra show a peak around the diurnal frequency, similar to that of the wind spectra (refer Fig. 4). However, in contrast to the wind spectra, the synoptic band in the wave spectra is of greater importance than the sea breeze band. This simply indicates that the variability in wave conditions due to storm activity is greater than that generated by sea breezes.

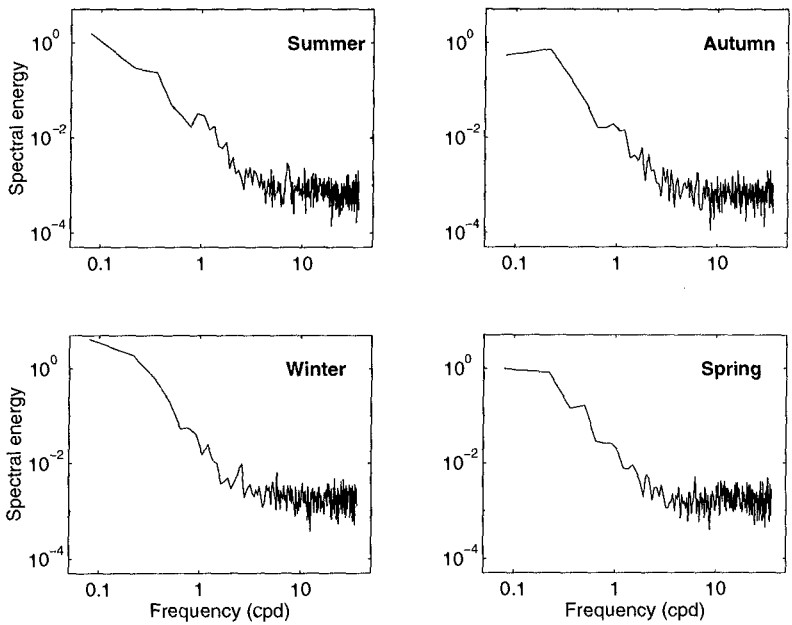

Fig. 6 - Wave spectra for summer (Jan–Feb 1995), autumn (Mar–Apr 1995), winter (Jun–Jul 1995) and spring (Sep–Oct 1995) from data collected off the coast of Perth in 48 m water depth. The spectra were computed from 20-min wave summary statistics.

Sea breeze activity has a pronounced effect on coastal processes. Pattiaratchi et al. (1997) and Masselink and Pattiaratchi (1998a) report on the results of a field experiment conducted on City Beach in Perth that monitored the effect of a strong sea breeze on the nearshore environment (Fig. 7). Prior to the onset of the sea breeze, offshore winds with speeds less than 5 m/s prevailed. During the sea breeze, alongshore winds with speeds higher than 10 m/s were experienced. The sea breeze induced pronounced changes to the nearshore morphodynamics which were similar to that of a storm event: (1) root mean square wave height increased from 0.3 to 0.5 m; (2) zero-upcrossing wave period decreased from 8 to 4 s; (3) mean cross-shore flows reached velocities of 0.2 m/s directed offshore; and (4) the longshore current increased in strength from 0.05 to 1.0 m/s. As a result of the increase in longshore current velocity and suspended sediment concentration during the sea breeze, the suspended

sediment flux increased by two order of magnitude. In addition, pronounced beach cusp morphology that was present on the beachface prior to the sea breeze, was completely destroyed during the sea breeze.

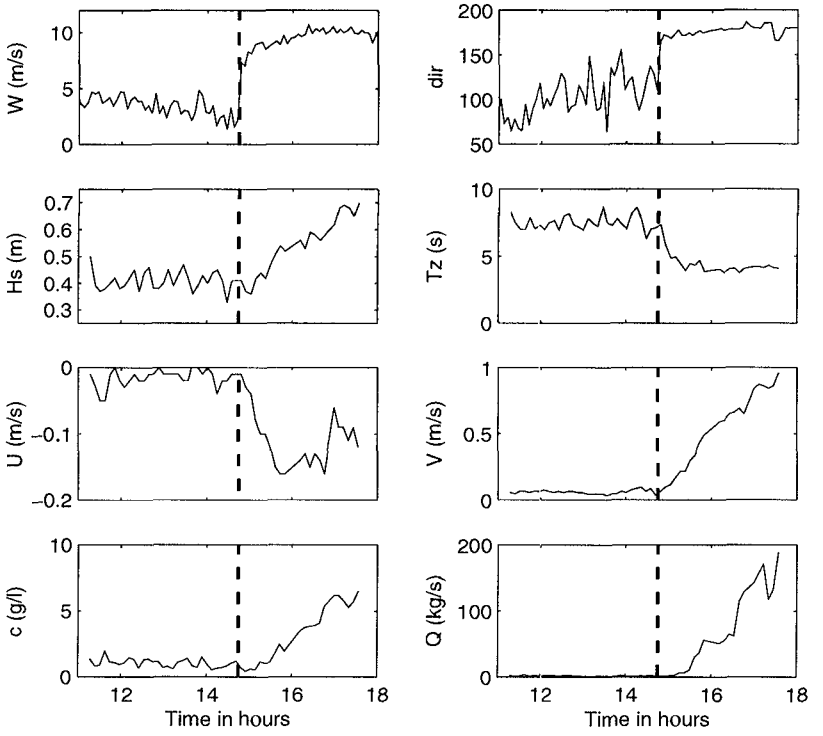

Fig. 7 - Wind speed (W), wind direction (dir), significant wave height (H_s), zero-crossing wave period (T_z), cross-shore current velocity (U), longshore current velocity (V), suspended sediment concentration measured 0.275 m above the bed (c) and longshore suspended sediment transport averaged across the surf zone (Q). The start of the sea breeze is indicated by the dotted line. The data were collected on City Beach, Perth on the 23rd of January 1992.

Masselink and Pattiaratchi (1998b) discuss the effect of weak sea breeze activity on nearshore processes. They demonstrate that even weak sea breezes with wind speeds of around 6 m/s induce pronounced changes to the surf zone hydrodynamics. A three-day time series of wind speed, direction, offshore wave height and nearshore current spectra illustrates clearly that the impact of sea breeze activity extends significantly longer than the duration of the sea breeze (Fig. 8). Over the three-day period, the narrow-banded swell peak remained at a constant frequency of around 0.085 Hz. Wind-wave energy starts appearing immediately after the onset of the sea breeze and remained present long after the cessation of the sea breeze. The presence of wind wave energy long after the sea breeze had ceased to blow is attributed to the alongshore component of the sea breeze (Masselink and Pattiaratchi (1998b).

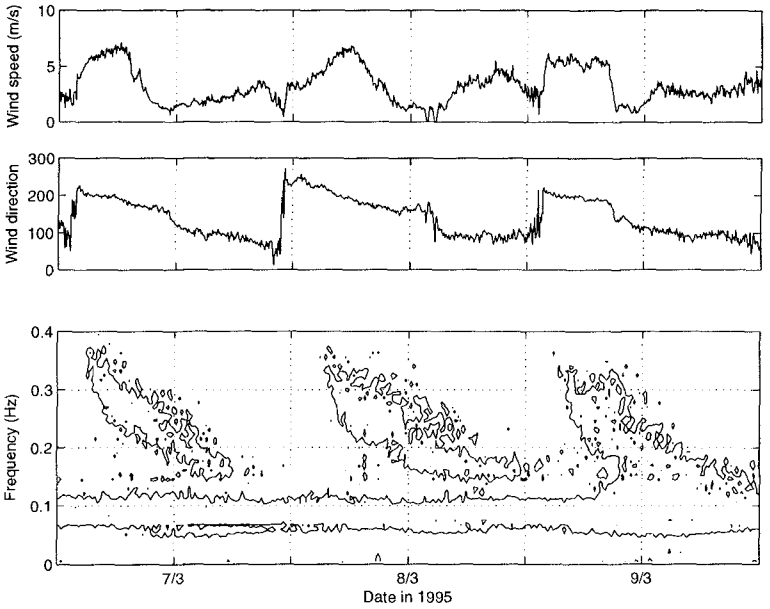

Fig. 8 - Three-day time series of wind speed (upper panel), wind direction (middle panel) and spectral shape of cross-shore current velocity data collected just outside the surf zone (lower panel). The contour lines represents an energy level of 0.25 m^2/s. All three sea breezes started at 14:45 hrs. The data were collected on City Beach (Perth) during three successive sea breeze cycles from the 6th to the 9th of March 1995.

Seasonal Variation in Beach Morphology

A number of Perth metropolitan beaches have been monitored weekly to two-weekly since November 1995. All display a strong seasonal variation in beach width (Fig. 9). Three of the beaches display a widening trend during summer (City, Brighton and Triggs Beaches), one becomes narrower over summer (Floreat Park) and one displays a hybrid behavior (Port Beach). These dissimilar trends are somewhat at odds with the strong seasonal variation in the incident wave conditions (refer Fig. 1) on the basis of which one would expect all beaches to behave in a similar manner. In addition, the amplitude of the beach width cycle varies substantially between the different beaches.

To explain the observed trends in beach width one needs to take into consideration the seasonal change in the direction of littoral drift. In the summer, when the southerly sea breeze prevails, longshore transport is towards the north. As a result, beaches that are located south of coastal structures (City Beach) or headlands (Triggs Beach) become wider during summer due to the accumulation of sediment against the structure/headland. These beaches will erode in winter when the longshore sediment transport is towards the south due to northwesterly storm waves. In contrast, beaches located to the north of coastal structures (Floreat Park) or headlands will become narrower during summer and wider during winter. Beaches located at

relatively "straight" coasts (Brighton Beach) will conform to the wave-induced seasonal cycle of beach change by widening during summer and narrowing during winter. The amplitude of the straight beach cycle, however, will be smaller than those beaches affected by the seasonal reversal in the littoral drift direction.

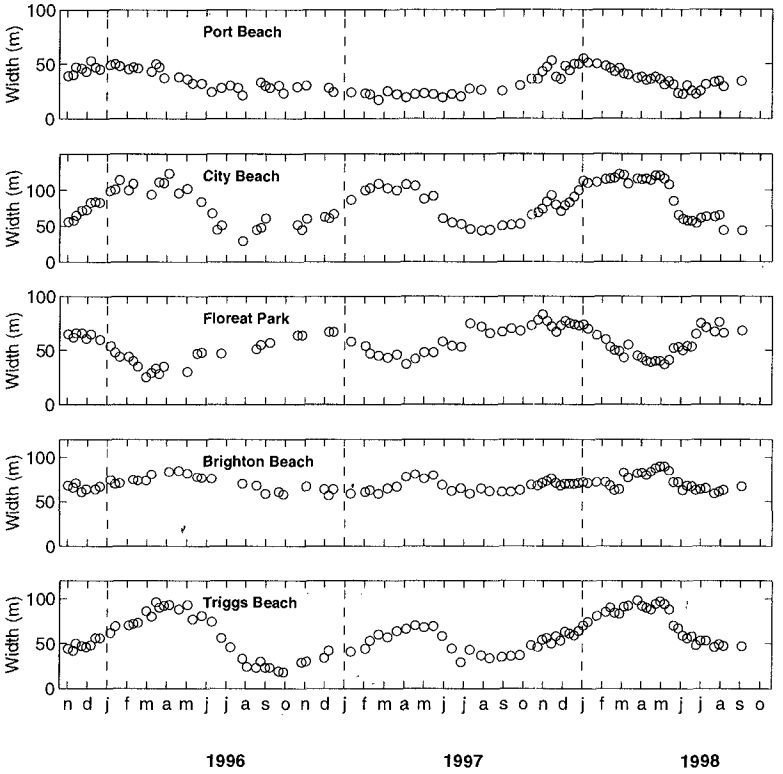

Fig. 9 - Temporal variation in beach width for five Perth metropolitan beaches for the period November 1995 to September 1998. The data were collected weekly or two-weekly.

The profile behavior of Port Beach is complicated and shows only two beach cycles in the 3-year monitoring period. During the first part of the time series, the beach width decreased in summer as well as in winter. From mid-1996 to mid-1997, the width of the beach remained constant. During the last part of the time series, Port Beach has been widening from mid-winter to early summer 1997, narrowing from mid-summer to early winter 1998 and widening again from mid-winter 1998. The complex behavior of Port Beach is attributed to anthropogenic influences (Masselink and Pattiaratchi, 1997). Prior to 1996, Port Beach was located about 500 m north of a small groyne. The beach behaved like a straight beach, attaining its maximum width just prior to the start of the winter storm season (cf., Brighton Beach). At the end of 1995, however, the groyne was significantly extended to accommodate for a marina development. As a result, Port Beach is now acting like a beach located north of a coastal structure, attaining its maximum width early-summer (cf., Floreat Park).

Analysis of Coastal Stations along Western Australian Coastline

The analysis of the wind data was extended to include nine additional coastal meteorological stations spread out along the coast of Western Australia (Fig. 10). Most of these stations were located some distance inland of the coastline at local airports, except for Ocean Reef and Cape Leeuwin which were directly located on the coast and Abrolhos, which was located on an island. One year of data (1995) were analyzed. Prior to analysis, all data were converted to hourly data for reasons of consistency.

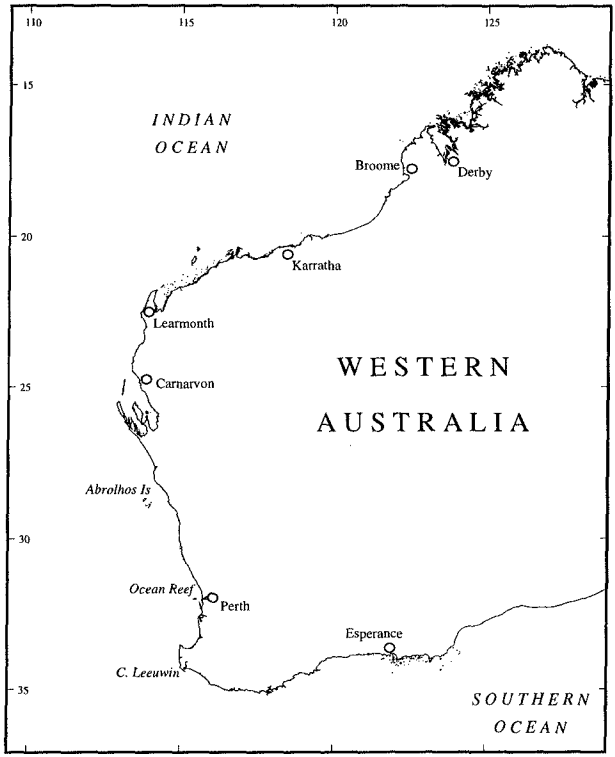

Fig. 10 - Map of Western Australia with ten coastal meteorological stations.

Table 1 summarises the time and frequency domain analysis of the ten Western Australian coastal weather stations. In the northern region (Derby, Broome, Karratha, Learmonth), the sea breeze mainly blows from an offshore and northwesterly direction. In the central region (Carnarvon, Abrolhos, Ocean Reef, Perth), alongshore and southeasterly sea breezes prevail. In the southern region (Cape Leeuwin and Esperance), the sea breeze blows from a predominantly onshore and southeasterly direction. The data were subjected to the same analysis as the long-term Perth wind data and the number of sea breezes and the mean sea breeze wind speed were determined. Excepting Cape Leeuwin, the mean annual wind speed for all coastal stations is significantly less than the wind speed associated with the sea

breeze. This indicates that at all locations, the sea breeze represents a condition that is more energetic than normal. The number of sea breezes that occurred in 1995 ranges from 137 (Cape Leeuwin) to 304 (Karratha).

Table 1 - Summary of time and frequency domain analysis of 1995 wind data collected at ten coastal meteorological station in Western Australia. W = mean annual wind speed; N = number of sea breezes; W_{sb} = mean wind speed during sea breeze at 15:00 hrs.

					% of variance in the sea breeze band (period smaller than 1.5 days)				
	Dominant sea breeze direction	W	N	W_{sb}	Sum.	Aut.	Win.	Spr.	Ann.
Derby	250-340°	4.3	191	5.8	72	73	61	71	69
Broome	230-330°	2.8	179	4.3	63	69	51	71	63
Karratha	260-90°	5.6	304	7.0	40	72	64	46	55
Learmonth	250-60°	5.4	164	6.0	40	63	53	47	51
Carnarvon	180-290°	6.1	266	7.3	48	61	55	41	51
Abrolhos	170-220°	7.1	174	7.1	31	34	22	23	28
Ocean Reef	170-230°	5.7	193	6.7	66	54	28	50	50
Perth	190-300°	4.5	190	5.6	63	59	40	61	56
Cape Leeuwin	120-210°	8.6	137	7.2	20	18	15	21	19
Esperance	120-260°	5.3	193	6.7	67	49	31	55	50

The importance of sea breeze activity is somewhat underestimated in Table 1 because most meteorological stations are located some distance landward of the coastline. A comparison between the characteristics of the sea breeze measured at Ocean Reef (on the coast) and Perth (about 20 km inland) indicates a reduction in the wind speed by about 20%. In addition, the direction of the sea breeze becomes more onshore with distance from the coastline. The number of sea breezes at Ocean Reef and Perth, however, are very similar.

Wind spectra were computed for all coastal stations and except Cape Leeuwin, all exhibit a pronounced diurnal peak with associated harmonics (Fig. 11). Partitioning the total spectral energy into the low-frequency synoptic band and the high-frequency sea breeze band (period smaller than 1.5 days; 'sea breeze band') further demonstrated the dominance of the sea breeze for most of the coastal stations. In general, more than 50% of the total variability in the wind record can be attributed to the sea breeze band. The only exceptions are Cape Leeuwin and the Abrolhos Islands. The former is one of the stormiest locations on the Western Australian coastline and winds at this site are expected to be dominated by storm activity. At the latter site, strong southerly winds prevail throughout the year, with the sea breeze only inducing a modest increase in the wind speed and a slight change in the direction.

Discussion and Conclusions

The diurnal sea breeze system in Perth, Western Australia, is a very important contributor to the overall wind climate. Around 200 sea breezes are experienced per year with an average wind velocity at 15:00 hrs of 5.7 m/s. In summer, more than 20 sea breezes occur on a monthly basis, whereas in winter between 10 and 15 sea breeze cycle are experienced each month. Throughout the year, more than half the variance in

the wind speed record can be attributed to the sea breeze frequency band (period less than 1.5 days). Analysis of wind data collected at nine other coastal meteorological stations in Western Australia indicated similar results, demonstrating that the sea breeze system is highly significant state-wide.

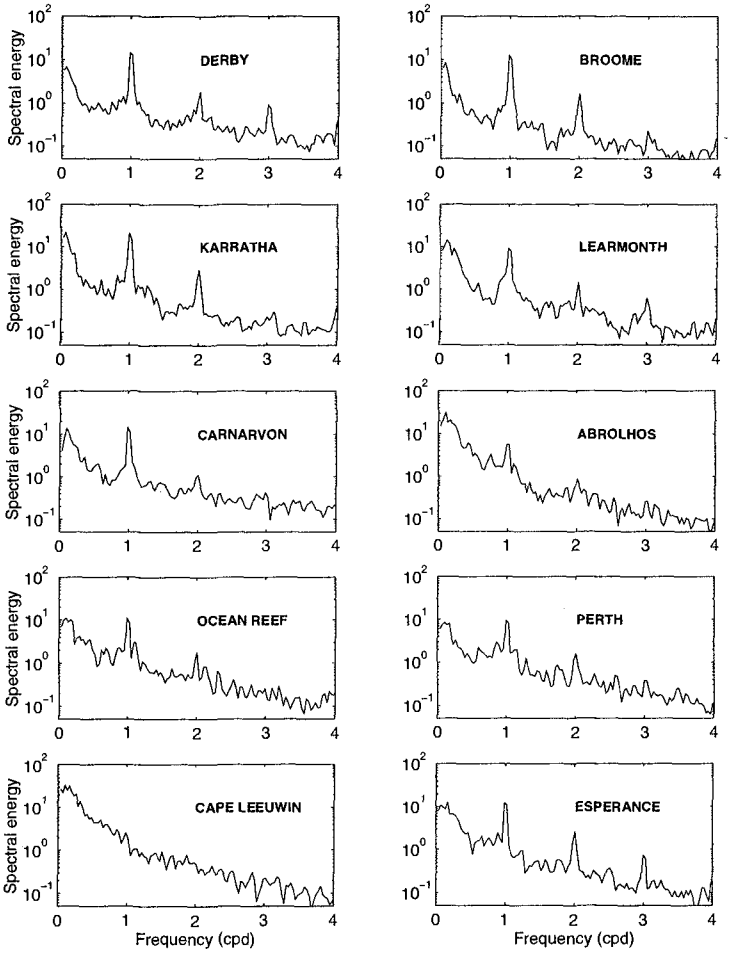

Fig. 11 - Wind spectra for ten Western Australian coastal stations. The data represent hourly data collected in 1995.

The strength and persistence of the sea breezes has important implications for the offshore wave climate and nearshore processes and morphology in the area. Spectral analysis of wave data collected off the coast of Perth revealed significant amounts of spectral energy present within the sea breeze band, in particular during summer when the sea breeze system is best developed. In the nearshore zone, the sea breeze generates energetic, obliquely-incident wind waves. In turn, theses waves generate strong longshore currents and sediment transport.

The wind climate along the Perth metropolitan coastline displays a pronounced seasonality characterised by strong and persistent southerly sea breezes in the summer and infrequent northwesterlies associated with the passage of mid-latitude storms. As a consequence, the dominant direction of the littoral drift is towards the north in the summer and towards the south in winter. In the vicinity of coastal structures or natural headlands, the seasonal variation in littoral drift direction induces a seasonal cycle of beach change that is different from the classic transition from summer to winter profile. During summer, a beach located south of an obstacle becomes progressively wider due to the piling up of sediment against the obstacle. At the same time, the beach located north of the obstacle becomes narrower. The opposite will occur during winter.

References

Department of Defence, 1996. Australian National Tide Tables 1996. Australian Hydrographic Publication 11, Canberra.

Eliot, I.G. and Clarke, D.J., 1986. Minor storm impact on the beachface of a sheltered beach in southwestern Australia. Marine Geology, 73, 61–83

Lemm, A. 1996. Offshore wave climate, Perth, Western Australia. Department of Environmental Engineering, University of Western Australia, Nedlands.

Masselink, G., 1996. The effect of the sea breeze on nearshore processes in Western Australia. Proceedings Royal Society of Western Australia, 79, 199–205.

Masselink, G. and Pattiaratchi, C.B., 1997. Review of "Port and Leighton Beaches Coastal Study (Report-E4352)". Centre for Water Research, University of Western Australia, WP 1275 GM, p. 30.

Masselink, G. and Pattiaratchi, C.B., 1998a. The effect of sea breeze on beach morphology, surf zone hydrodynamics and sediment resuspension. Marine Geology, 146, 115–135.

Masselink, G. and Pattiaratchi, C.B., 1998b. Morphodynamic impact of sea breeze activity on a beach with beach cusp morphology. Journal of Coastal Research, 14, 393–406.

Pattiaratchi, C.B., Hegge, B.J., Gould, J. and Eliot, I.G., 1997. Impact of sea breeze activity on nearshore and foreshore processes in southwestern Australia. Continental Shelf Research, 17, 1539–1560.

Steedman, R., 1993. Collection of wave data and the role of waves on nearshore circulation. Report prepared for the Water authority of Western Australia, Perth.

FIELD OBSERVATION OF EROSION AND ACCRETION WAVES ON SHIZUOKA AND SHIMIZU COASTS IN SURUGA BAY IN JAPAN

Itabashi, Naoki[1] and Takaaki Uda[2]

ABSTRACT

A distinct propagation of erosion and accretion waves was discovered along the Shizuoka and Shimizu coasts facing Suruga Bay in Japan. Their propagation velocities were 270m/yr and 250m/yr. "Hagoromo-no-matsu", a scenic beach famous in Japan, where, along the shoreline, people can see Mt. Fuji in the distance, sandy beaches and pine trees, will be eroded in two years, whereas it takes 30 years for longshore sand supply to reach this beach. Countermeasures must be taken, without relying on natural sand supply from the upcoast by longshore sand transport which will take for at least 30 years. Severe beach erosion began at the time of large-scale river bed excavation conducted before 1967 in the Abe River which is the source of littoral sand, and beach erosion has a propagation mode of erosion waves. Measures combining the construction of headlands to stabilize the natural sandy beach with beach nourishment should be taken immediately.

I. INTRODUCTION

In recent years, shoreline change of a wavy mode has been extensively studied. Such shoreline changes are classified into the longshore sand waves discussed by Thevenot and Kraus (1995) and a type in which the wavelike shoreline propagates alongshore while keeping its form. In addition, there are various names for the longshore sand waves. Sonu (1968) called them cusp-type sand waves, Bruun (1954) and Grove et al. (1987) migrating sand humps, Inman (1987) accretion and erosion waves, and Verhagen (1989) simply sand waves. In particular, the accretion and erosion waves reported by Inman (1987) are produced when a coastal structure such as a groin is installed or the sediment supply from a river or the source of littoral drift is sharply increased due to flooding, and they propagate along the coastline, accompanied by weak diffusion. Uda and Yamamoto (1994) and Uda et al. (1996) investigated this phenomenon of a longshore movement of a large mass of sediment (hereinafter called sand body), analogous to a soliton, along the Shizuoka coast in Japan and concluded that this sand body movement was triggered by the trapping effect of sand supplied from the Abe River by detached

1) Coastal and Environment Engineering Department, INA Corporation, Sekiguchi 1-44-10, Bunkyo-ku, Tokyo 112, Japan (tel +81-3-5261-5841, fax +81-3-3268-8256)

2) Dr. Eng., Director, River Department, Public Works Research Institute, Ministry of Construction, Asahi-1, Tsukuba, Ibaraki 305, Japan (tel +81-298-64-2830, fax +81- 298-64-1168, e-mail uda@pwri.go.jp).

breakwaters built along this coast, by using a contour line change model.

On the other hand, before the propagation of this positive wave along the Shizuoka coast, it was also found that an erosion wave with the phase velocity of 0.5-0.8km/yr propagated (Uda and Yamamoto, 1994). Presently, this erosion wave is approaching the northeastern end of the Shimizu coast, the famous viewpoint called "Hagoromo-no-matsu" where a sandy beach with pine trees and a backdrop of Mt. Fuji provides a scenic view. "Hagoromo-no-matsu" means a pine tree on which a young lady has draped her clothes. This study is aimed at investigating beach changes associated with the propagation of these erosion and accretion waves occurring along the Shizuoka and Shimizu coasts, with special attention paid to the preservation of this beach.

II. FIELD OBSERVATION OF EROSION AND ACCRETION WAVES ALONG SHIZUOKA AND SHIMIZU COASTS

(1) General

Figure 1 shows the location of the Shizuoka and Shimizu coasts situated on the outer margin of the Mihono-matsubara sand spit on the west shore of Suruga Bay. Suruga Bay opens south to the Pacific Ocean and rough waves are incident from the south. Since the coastline runs southwest to northeast, as shown in Fig.1,

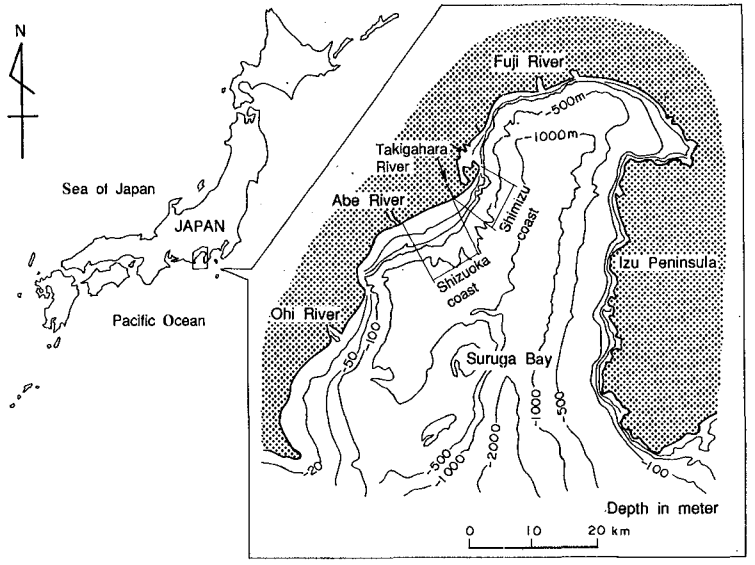

Fig.1 Location of the Shizuoka and Shimizu coasts in Suruga Bay facing the Pacific Ocean.

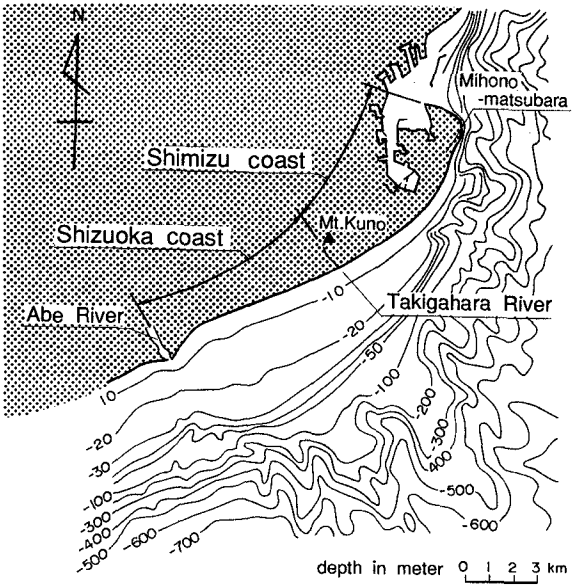

Fig.2 Sea bottom contours off Shizuoka and Shimizu coasts.

northeastward longshore sand transport prevails along these coasts. The Shizuoka coast extends 7.8km northeastward from the Abe River mouth to the mouth of the Takigahara River and the 9.8km coastline from this river mouth to the tip of the sand spit is called the Shimizu coast. Figure 2 shows the sea bottom contours off the Shizuoka and Shimizu coasts. Here, the beach slope near the shoreline is as steep as 1/10. A continental shelf of mild slope of 1/150 is spread along the offshore zone ranging from 10m to 30m in depth, but the sea bottom slope at the tip of the Mihono-matsubara sand spit is steep at about 1/5.

It is considered that during the Jomon Transgression of the sea level about 6,000 years ago, erosion of the side of Mt. Kuno, as shown in Fig.2, supplied sediment to the Mihono-matsubara sand spit, but at the present sea level, the only source of sediment to the sand spit is the Abe River. River bed excavation was carried out extensively before 1968 in the Abe River, causing a sharp decrease in fluvial sand supply from this river, and the dynamic balance of longshore sand transport was lost, giving rise to the northeastward extension of the eroded area from the river mouth. Uda and Yamamoto (1994) revealed that the erosion wave propagated at 0.8km/yr in the period between 1975 and 1983 and 0.5km/yr between 1983 and 1988 along the Shizuoka coast. At present, the most severely eroded portion of the beach is near the tip of the Mihono-matsubara sand spit at the northeastern end of the Shimizu coast. Most of the sediment transported by northeastward longshore sand transport discharges into the submarine canyon located at the northeastern end of the Shimizu coast.

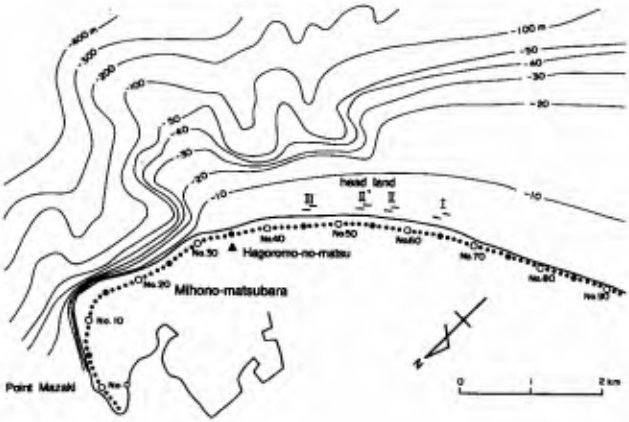

Fig.3 Detailed sea bottom contours off Shimizu coast and alignment of measuring lines.

Photo.1 Sandy beach, Mt. Fuji and pine trees at Hagoromo-no-matsu on February 10, 1995 taken at a point No.35.

Figure 3 shows the sea bottom topography around the tip of the Mihono-matsubara sand spit, as well as the alignment of measuring lines on the Shimizu coast. In this area, sea bottom surveys have been conducted once a year in March since 1988. The interval of measuring lines is 100m. The origin of the measuring lines is located at a point No.0 at Mazaki at the tip of the sand spit and measuring lines are set alongshore southwestward. In Fig.3 the turning point of the shoreline is located at a point No.12, and there exists a submarine canyon between points No.12 and No.30. The beach slope is very steep around this submarine canyon. Hagoromo-no-matsu, as shown in Photograph 1, is located at a point No.35. According to the sampling test of bottom materials conducted at nine points at 1km intervals alongshore from the Abe River mouth on February 20, 1989, the median diameter of beach materials near the shoreline of the Shizuoka coast is around 7.5mm.

(2) Changes in Shoreline Configuration and Sand Volume of Shizuoka and Shimizu Coasts

Figure 4 shows the shoreline change of the Shizuoka and Shimizu coasts with reference to the shoreline position in 1983 obtained from the sea bottom surveys. The Abe River mouth is located at the right end of the figure, and the left end is the tip of Mihono-matsubara sand spit called Masaki Point. The Shizuoka and Shimizu coasts are separated by the mouth of the Takigahara River. Along the Shizuoka coast, a sand body formed by sand accumulation moves northward (leftward in the figure) with time and its propagation velocity is around 250 m/yr, as shown in Fig.4. Uda et al. (1996) showed that the propagation velocity of the leading edge of this sand body between 1984 and 1993 was 233m/yr. The value obtained in the present study is slightly larger due to the selection of a longer comparison period.

The shoreline of the Shizuoka coast was totally covered by concrete armor units before the propagation of the sand body and there existed no sandy beaches, which means an absence of littoral sand to be transported alongshore. The sand body was considered to be moving northeastward, while sand was also covering the concrete armor units set along the shoreline, since a large amount of sediment was supplied from the mouth of the Abe River located at the southwestern boundary of the coast. Furthermore, Uda et al. (1996) revealed, by numerical simulation using "the contour line change model", that the movement of the sand body was triggered by

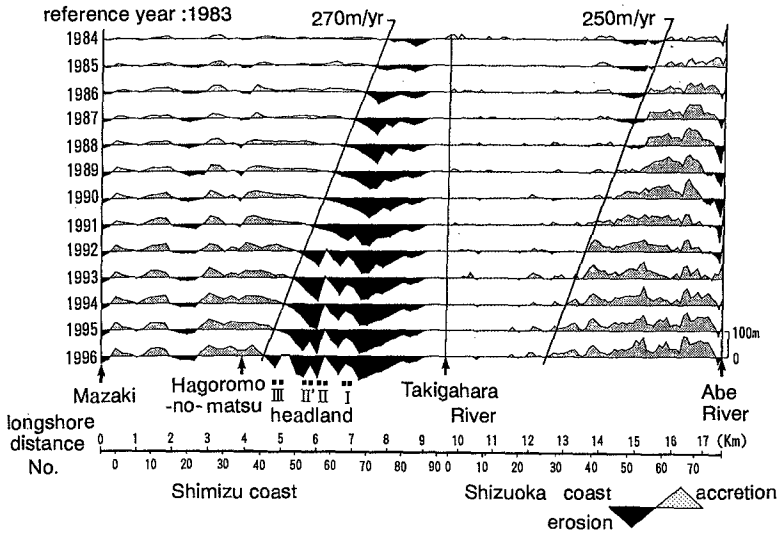

Fig.4 Shoreline changes along the Shizuoka and Shimizu coasts showing the propagation of erosion and accretion waves. The propagation velocities of erosion and accretion waves are around 270m/yr and 250m/yr, respectively.

Photo.2 Coastline totally covered by seawall and concrete armor units on the Shimizu coast. This picture was taken in July, 1995. The river flowing into the sea is the Takigahara River, which separates the Shizuoka and Shimizu coasts. These coastal structures were built to protect farmland just behind the seawall.

Photo.3 Coastline protected by a continuous seawall, concrete armor units and a number of detached breakwaters further north of the location shown in Photograph 2 on the Shimizu coast.

the blocking effect of longshore sand transport due to the presence of a number of detached breakwaters constructed off the coastline.

Along the coast between the location of longshore distance of around 12.5km, which the leading edge of the sand body reached in 1996, and the location around 0.5km north of the mouth of the Takigahara River, no shoreline change is observed because this area is totally covered by concrete armor units, as shown in Photographs 2 and 3.

Along the Shimizu coast, beach erosion has clearly occurred since 1983. Shoreline recession first began from the location of around 9km and extended northeastward with time, approaching Hagoromo-no-matsu in 1996. Beach erosion along the Shizuoka coast was originally triggered by a sharp decrease in fluvial sand supply from the Abe River due to large-scale river bed excavation to obtain construction materials in the period around 1970, and it propagated from the Shizuoka coast to the Shimizu coast (Uda and Yamamoto, 1994). Presently it is approaching the tip of the Mihono-matsubara sand spit. Shoreline change of a zigzag type have occurred after the construction of headlands using two sets of detached breakwaters built as a countermeasure against beach erosion, as shown in Photographs 4, 5 and 6. The eroded zone is monotonously extending northward and its propagation velocity is around 270 m/yr. This propagation velocity is comparable to the propagation velocity (250m/yr) of the sand body on the

Photo.4 The shoreline around detached breakwaters I. A couple of detached breakwaters were built alongshore. The offshore distance of the detached breakwater downcoast is close to the original shoreline. Large cuspate foreland was formed behind the upcoast detached breakwater.

Photo.5 The shoreline downcoast of detached breakwaters II'. Downcoast erosion was so severe that beach nourishment is being conducted, as shown in the photograph of the most severely eroded location.

Photo.6 The shoreline around detached breakwaters III. In this area, the foreshore is still fairly wide.

Shizuoka coast, but with an excess of about 8%. Since the distance between the tip of the eroded zone (No.40) and Hagoromo-no-matsu (No.35) was only 500m in 1996, only two years remain before severe beach erosion reaches Hagoromo-no-matsu, if the propagation velocity of the erosion zone remains unchanged. Uda et al. (1994) determined that the rate of extension of the erosion zone was about 271m/yr on an average in the period between March 1990 and March 1993; this means that the same propagation velocity of the erosive zone has been maintained thereafter.

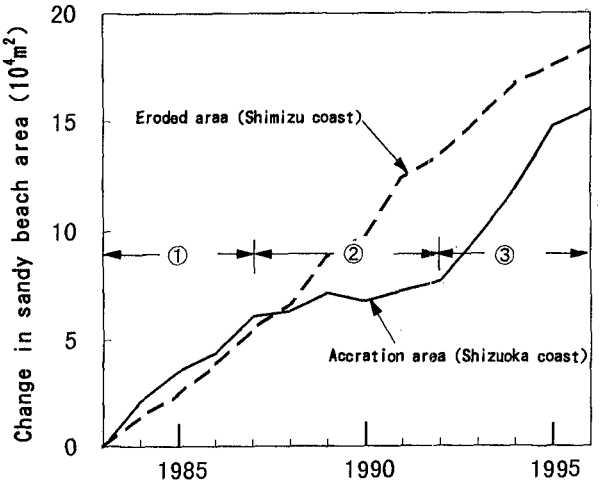

Fig.5 Change with time in eroded and accretion areas along Shizuoka and Shimizu coasts.

In addition, the north end of the erosive zone was located at a point No.46 in 1993.

The change in foreshore area in the accretion area of the Shizuoka coast and erosion area of the Shimizu coast compared to that in 1983 was calculated and is shown in Fig.5. Along the Shizuoka coast, the rates of increase of the accretion area during each of the three periods shown in Fig.5 differ; the rate of increase was $1.42 \times 10^3 m^2/yr$ in the first period between 1983 and 1987, which decreased by one order of magnitude to $0.44 \times 10^3 m^2/yr$ in the second period between 1987 and 1992, and in the last period between 1992 and 1995, the rate increased to $1.98 \times 10^3 m^2/yr$, larger than that in the first period. The only sand supply to the Shizuoka coast is from the Abe River. In addition, the shoreline north of the tip of the sand deposition zone is covered by a large number of concrete armor units and there are no sandy beaches. This means that this artificially protected coast suffers from a shortage of sand before the arrival of the tip of sand body. Accordingly the only reason for the accretion zone increase as shown in Fig.5 must be due to the sand supplied from the Abe River mouth. Table 1 shows the records of large floods since 1980 at location 4.7km upstream from the river mouth. Daily average flood discharges of $1{,}000 m^3/s$ or

Table 1 Flood discharge of Abe River.

year	month	day	average discharge (m^3/s)	maximum discharge (m^3/s)
1982	August	2	1,129	3,857
1982	August	3	1,466	
1982	September	12	1,723	
1983	August	2	1,731	2,981
1985	July	2	1,523	–
1990	August	10	1,005	–
1991	September	2	1,396	2,511

larger occurred seven times between 1980 and 1993, as shown in Table 1, and particularly, on September 12, 1982 the flood with the largest discharge of 3,857m^3/s occurred, but thereafter, large-scale floods have rarely occurred. This indicates that the variation in the rate of increase of the foreshore area in the accretion zone of the Shizuoka coast mainly corresponds to the occurrence of large floods that supply large amounts of sediment to the coast.

Along the Shimizu coast, the eroded area monotonously increased from 1983 to 1996 at the rate of 1.42x10^3m^2/yr, as shown in Fig.5. This rate is approximately equal to that in the first period along the Shizuoka coast. The long-term rate of increase of the foreshore area of the Shizuoka coast between 1983 and 1996 became 1.21x10^3m^2/yr, although there are short-term variations in this rate, as shown in Fig.5. This value is only 14% smaller than that obtained on the Shimizu coast. This indicates that the foreshore area exhibits a large variation along the Shizuoka coast in the area next to the river mouth depending on the variation in the amount of river sediment discharge, but along the Shimizu coast located far from the river mouth, such a variation is minimal and monotonous change is dominant, resulting in a smooth shoreline change.

Along the Shizuoka and Shimizu coasts, the shoreline change correlates well with the change in cross-sectional area of the beaches, and the regression coefficient between these parameters gives characteristic heights of beach changes of 7.7m and 7.2m on the Shizuoka and Shimizu coasts, respectively (Uda and Yamamoto, 1994). The changes in foreshore area were multiplied by the characteristic height of beach changes to calculate the change in sand volume due to erosion and accretion. Since the coast near the boundary between the Shizuoka and Shimizu coasts is totally covered by concrete armor units and there exists no sandy foreshore as shown in Photographs 3 and 4, longshore sand transport passing this location is assumed to be 0. Accordingly, calculated change in sand volume is approximately equal to the inflow or outflow rate of longshore sand transport to the examination zone from the continuity condition of sand mass. Table 2 is the results of the calculation in each period. Inflow rate of longshore sand transport to the Shizuoka coast has a considerably large variation and it varies from 3.4x10^4 m^3/yr to 15.2x10^4m^3/yr. Average rate of longshore sand transport is found to be 10.1x10^4m^3/yr. In contrast, the rate of longshore sand transport on the Shimizu coast has an approximately constant value of 10.2x10^4m^3/yr.

Figure 6 shows temporal change in sand volume calculated by multiplying the decrease of the foreshore area in the region between No.55 and No.85 by the characteristic height of beach changes of 7.2m. The reference year is taken in 1983 the same as that in Fig.5. In

Table 2 Longshore sand transport rates on Shizuoka and Shimizu coasts.

coast	duration	change in foreshore area ($\times10^4m^2$/yr)	characteristic height of beach changes (m)	longshore sand transport rate ($\times10^4m^3$/yr)
Shimizu	1983~1996	1.42	7.2	10.2
Shizuoka	1983~1987	1.53	7.7	11.8
	1987~1992	0.44		3.4
	1992~1995	1.98		15.2
	1983~1996	1.21		9.2

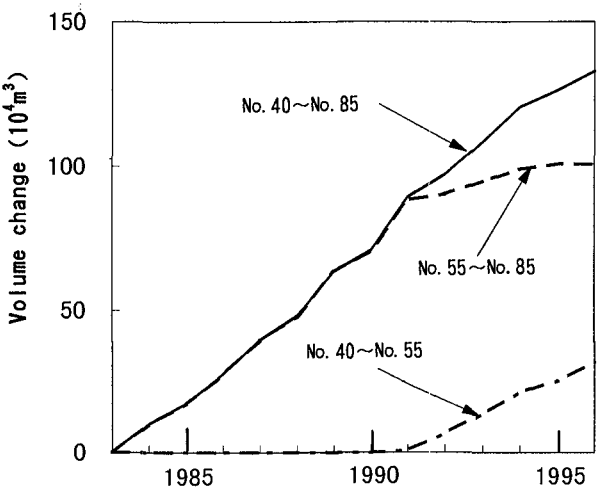

Fig.6 Change in sand volume with time in the regions between No.55 and No.85, and between No.44 and No.55 along the Shimizu coast.

Fig.5 it was clear that total volume of sand in the erosion zone on the Shimizu coast had increased monotonously since 1983. However, precise examination of the change in sand volume in each zone in Fig.6 gives another features. Eroded sand volume in the region between No.55 and No.85 attains to an equilibrium state after it increased up to 1991, whereas the eroded sand volume in the zone between No.40 and No.55 increased after 1991 at a rate of increase equal to the increase rate of the eroded area along the entire Shimizu coast. This means that the construction of a headland using a couple of detached breakwaters prevents further beach erosion at the site but instead, the erosion zone extends further downwards.

In short, accretion and erosion waves were triggered by the imbalance in these longshore sand transport rates. In Fig.4, Hagoromo-no-matsu was about 7.9km from the tip of the sand body (x=12.5km) in 1996 and therefore it should take 30 years for the tip of the sand body to reach the most severely eroded location of Hagoromo-no-matsu, if the movement of the sand body takes place in an unchanging manner. During this period, natural sand supply by longshore sand transport cannot be expected along the Shimizu coast and therefore, it is necessary to effectively utilize the sand existing along the coast. This period is a long time compared with that required for erosion waves to reach north tip of the Shimizu coast. During this period, measures to stabilize the shoreline must be taken without relying on sand supply from upcoast. Beach nourisbment is one of the possible measures, but the longshore sand transport along this coast is around $10x10^4m^3/yr$, with ultimate discharge into the deep ocean through the submarine canyon located at the tip of sand spit, implying that beach nourishment only is not a sufficient measure.

III. BEACH PROFILE CHANGES ALONG SHIMIZU COAST

Beach profile changes are investigated in detail along several measuring lines where large shoreline recession was observed in Fig.4. As typical measuring lines, four lines are selected: No.44 located north of the group of detached breakwaters III very close to Hagoromo-no-matsu, No.50 located between detached breakwaters II and II', No.55 located north of detached breakwaters II, and No.62 to the north of detached breakwaters I which was built the earliest.

Figure 7 shows the beach profile changes along No.44. The beach profile in 1985 is selected as a reference and beach profiles after this year are shifted along the vertical axis. At this location, accretion prevailed until 1995, corresponding to the shoreline advance in comparison with the beach profile in 1985, but beach erosion became dominant in 1996 in the zone shallower than -4m. At No.50 0.6km south of survey line No.44, intense beach erosion has taken place since 1992, as shown in Fig.8. In this case it should be noted that the beach profile change at around 1994, as shown in Fig.8, is very similar to that in 1996 in Fig.7, implying that recession of the beach extended gradually alongshore while maintaining almost the same profile.

Figure 9 shows the beach profile changes along No.55. As shown in Fig.4, the shoreline retreated considerably until 1994 in the vicinity of this measuring line (No.55) because detached breakwaters II' were constructed between detached breakwaters II and III. Depending on this shoreline change, the beach was eroded until 1994 but thereafter, sand accumulated again until 1996 and almost the same beach profile as in 1993 was recovered. Re-accretion occurred at No.55 due to the sand accumulation effect of the detached breakwaters constructed immediately downcoast.

Figure 10 shows the beach profile changes at No.62. Severe beach erosion can be observed in the profile after 1989, corresponding to the extensive shoreline recession shown in Fig.4. It is noted that the time when beach erosion became dominant at this location was 8 years before the initiation of beach erosion at No.44 located 1.8km north of No.62. In addition, it is found that an upward convex profile near the shoreline reduced to a concave profile, because the sea bed in the zone shallower than -6m was eroded as a result of beach erosion.

The beach profile changes mentioned above are similar to each other except in terms of the initiation time of beach erosion. As mentioned earlier, only two years remain before the shoreline recession zone reaches Hagoromo-no-matsu. After that, the shoreline profile is predicted to become steep, as shown in Figs.8, 9 and 10.

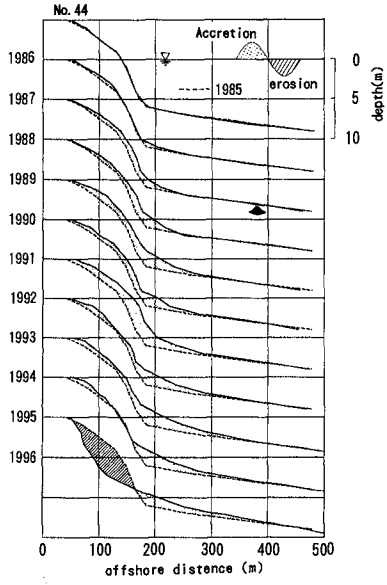

Fig.7 Profile changes along No.44.

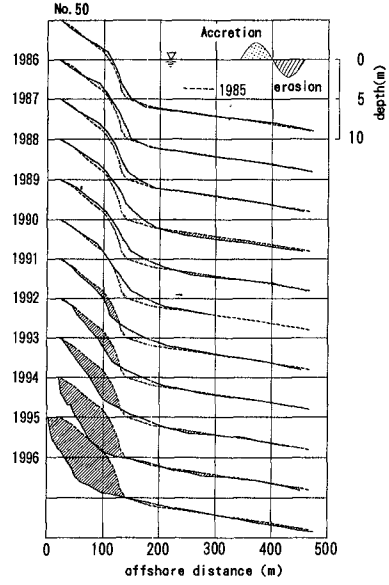

Fig.8 Profile changes along No.50.

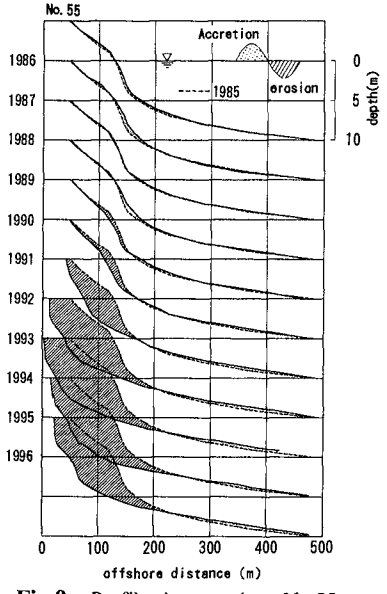

Fig.9 Profile changes along No.55.

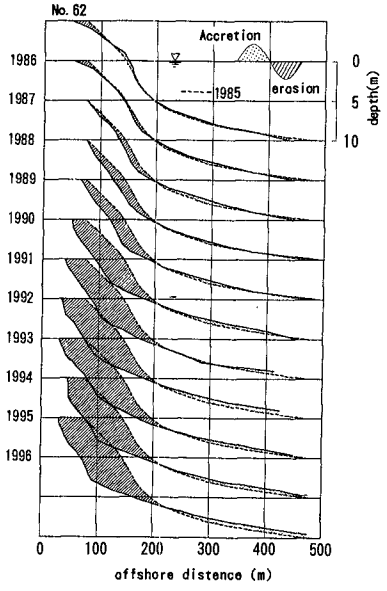

Fig.10 Profile changes along No.62.

IV. TOPOGRAPHIC CHANGES AROUND DETACHED BREAKWATERS

Since dominant beach changes along the Shimizu coast can be observed in the area between No.40 and No.60, as shown in Fig.4, beach changes in this area from March 1992 to March 1996 are invcstigated in detail through a comparison of bathymetric survey maps. Figure 11(a) shows the sea bottom topography in March 1992. At this time, northeastward longshore sand transport was partly blocked by detached breakwaters II located at around No.57 and No.58 and therefore, sea bottom contours shallower than -3m became concave at the northeast end of the detached breakwaters, whereas the contours far from this area were straight. In contrast, on the southwest side of the detached breakwaters, the shoreline connects smoothly to the detached breakwaters and offshore contours hetween -4m and -6m protrude off the detached breakwaters, implying that some longshore sand transport is discharged downdriftward while passing around the detached breakwaters, since longshore sand transport is blocked by the detached breakwaters.

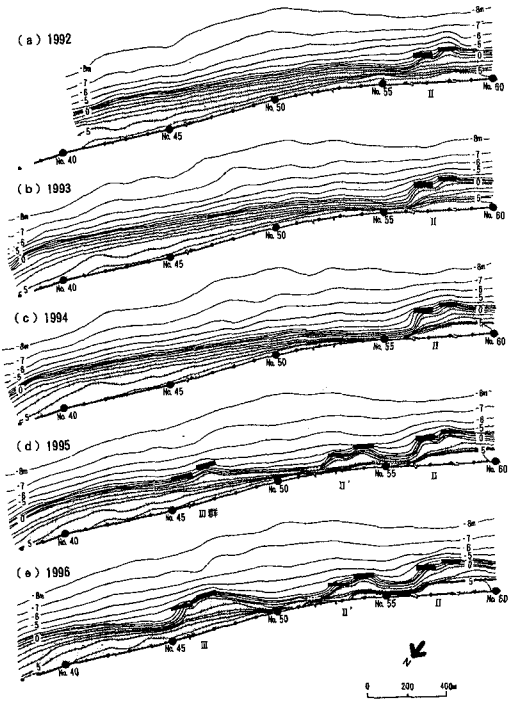

Fig.11 Sea bottom changes around the detached breakwaters between March 1992 and March 1996.

In March 1993, as shown in Fig.11(b), sea bottom contours in the vicinity of No.55 became further concave and the foot depth in front of the seawall considerably increased. In March 1994, as shown in Fig.11(c), according to the dense contours near the shoreline, the seawall was directly exposed to sea waves in the vicinity of No.55, and also, a steep scarp between No.55 and No.51 was formed. Beach erosion near No.55 was so severe as to cause the failure of the seawall such that not only the detached breakwaters III were set in the vicinity of No.46 but detached breakwaters II' were also constructed at No.53 to prevent further beach erosion. As a result, the foreshore was widened near No.53, as shown in Fig.11(d) and the seawall was protected against scouring. The shoreline north of detached breakwaters II' is considerably stable because the shoreline is fixed at detached

breakwaters III. By contrast, shoreline recession has begun northeast of detached breakwaters III.

Figure 11(e) shows the sea bottom topography in March 1996. A stepped shoreline was formed due to the construction of detached breakwaters. However, the contours northeast of detached breakwaters III are still unstable because of the open boundary condition and therefore, urgent measures to stabilize the shoreline in front of this area should be adopted by constructing a facility to stabilize the shoreline, such as a groin or detached breakwaters downcoast of this point. As shown in Photograph 1 taken at a point No.35, a snowcapped Mt. Fuji in the distance beyond the sandy beach and pine trees produce a beautiful scene, so that the disappearance of the sandy beach is considered to be a definite damage to this coast.

V. CONCLUSIONS

Distinct propagation of erosion and accretion waves was revealed along the Shizuoka and Shimizu coasts facing Suruga Bay. Their propagation velocities are 270m/yr and 250m/yr, respectively. It was found that the famous scenic beach called "Hagoromo-no-matsu", will be eroded in two years, whereas it takes 30 years for longshore sand supply to reach this beach. Therefore, countermeasures must be taken without relying on natural sand supply from upcoast by longshore sand transport for at least 30 years. Furthermore, taking into consideration that such severe beach erosion dates from the large-scale river bed excavation of the Abe River conducted before 1968 and that it has a propagation mode of an erosion wave, it can be said that beach erosion along the Shimizu coast is inevitable. Measures combining the construction of headlands to stabilize the natural sandy beach, with beach nourishment should be adopted immediately.

REFERENCES

Bruun, P. (1954): Migrating sand waves or sand humps, with special reference to investigations carried out on the Danish north coast sea, *Proc.5th Coastal Eng. Conf.*, ASCE, New York, pp.269-295.

Grove, R.S., Sonu, C.J. and Dykstra, D.H. (1987): Fate of massive sediment injection on a smooth shoreline at San Onofre, California, *Proc. Coastal Sediments '87*, ASCE, New York, pp.531-538.

Inman, D.L. (1987): Accretion and erosion waves on Beaches, *Shore & Beach*, Vol.55, No.3 and 4, pp.61-64.

Sonu, C.J. (1968): Collective movement of sediment in littoral environment, *Proc.11th Coastal Eng.* Conf., ASCE, New York, pp.378-398.

Thevenot, M.M. and N.C. Kraus (1995): Longshore sand waves at Southampton Beach, New York: observation and numerical simulation of their movement, *Mar. Geol.*, 126, pp.249-269.

Uda, T. and K. Yamamoto (1994): Beach erosion around a sand spit-an example of Mihono-matsubara Sand Spit-,*Proc.24th ICCE*, pp.2726-2740.

Uda, T., Y. Yamamoto, N. Itabashi and K. Yamaji (1996): Field observation of movement of sand body due to waves and verification of its mechanism by numerical model, *Proc. 25th ICCE*, ASCE, pp.137-150.

Verhagen, H.J. (1989): Sand waves along the Dutch coast, *Coastal Eng.*, 13, pp.129-147.

Coastal Erosion at Keta Lagoon, Ghana
- Large Scale Solution to a Large Scale Problem

R.B. Nairn[1], K.J. MacIntosh[1], M. O. Hayes[2], G. Nai[3], S.L. Anthonio[4] and W.S. Valley[5]

Abstract

This paper describes the development of a solution to a large scale, long term erosion process along the Atlantic coast of eastern Ghana in West Africa. The understanding of the erosion process was developed through a combination of geomorphic investigations and numerical and physical modeling of coastal processes. Key aspects of the investigations are described in this paper. The performance of the adopted sea defence system, consisting of rubblemound structures and beach nourishment, was evaluated using the GENESIS and COSMOS numerical models of shoreline change. The numerical models were also used to modify the sea defence system such that an acceptable level of downdrift impact was confined within the study area.

Introduction

This paper describes the development of a solution to address a large scale erosion problem along the Atlantic Coast of Ghana, West Africa. A background of the problem is presented followed by a summary of some of the more important design investigations. Finally, the various components of the sea defence system are described. The overall project also includes an 8.5 km causeway across Keta Lagoon for the coastal highway, a flood relief system to address lagoon flooding and land reclamation. The sea defence system is the focus of this paper.

1 - Baird & Associates, 627 Lyons Lane, Oakville, ON, Canada L6J 5Z7, www.baird.com
2 - Research Planning Inc., 1200 Park St., P.O. Box 328, Columbia, SC, USA 29202
3 - Ministry of Works and Housing, P.O. Box M43, Accra, Ghana
4 - Water Research Institute, P.O. Box M32, Accra, Ghana
5 - Great Lakes Dredge & Dock, 2122 York Rd, Oak Brook, IL, USA 60521

This paper presents a brief summary of some of the key aspects of the Keta Sea Defence Project. Full details are presented in the Final Report on the technical aspects of the Keta Sea Defence Project (Great Lakes Dredge & Dock and Baird & Associates, 1997).

Background

Keta Lagoon is located immediately east of the Volta River mouth along the east coast of Ghana in West Africa (refer to Figure 1). The Volta River historically carried large quantities of sediment, including coarse-grained sand, to the sea and this sediment was deposited at the river mouth, forming the modern (Holocene) delta. Several thousand years ago, at a lower sea level stage, and when the river mouth was located further to the east, another large delta lobe was formed. This old delta is now a large offshore shoal in depths of 10 to 20 m below sea level.

Figure 1 – Regional Study Area – The Volta Delta

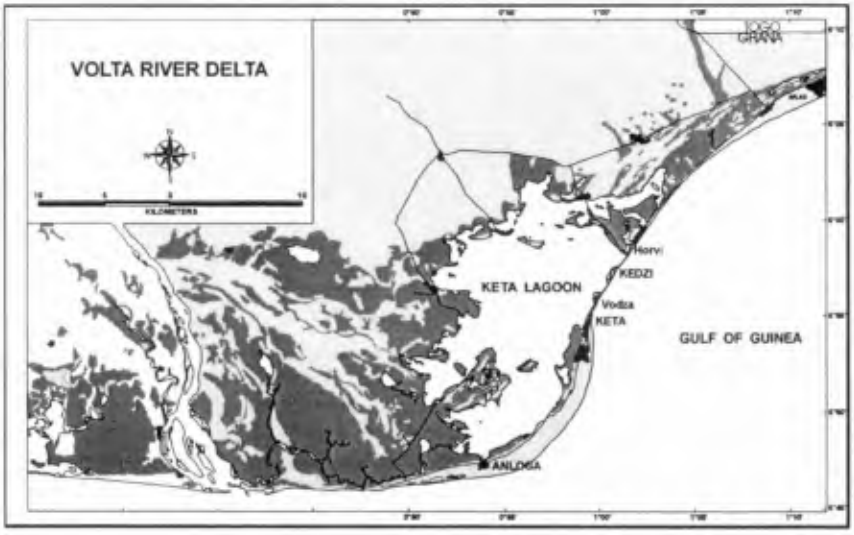

Wave action from the South Atlantic is incessant along this section of the West African coast and invariably originates from the south to southwest sectors resulting in continuous eastward directed sand transport with rates in the range of 500,000 to 1,500,000 m^3/yr at most locations. As a result, the shape of the existing delta and the older submerged delta are skewed towards the east. The present eastward migrating delta features a zone of rapid deposition near its eastern leading edge, which is now located immediately southwest of the town of Keta (see Figure 2). This zone is sheltered from wave action by a large depositional protuberance located 20 km east of the river mouth and by the older submerged delta located offshore. As a result, potential sediment transport rates are low.

An apparent repositioning of the river mouth to the west and a decrease in sediment supply, to the area east of Keta, have resulted in erosion and realignment of the delta front east of the present river mouth (see Figure 3). This realignment is thought to be at least partially responsible for the initiation of the depositional protuberance on the delta front.

Figure 2 – Project Area and Recession Rates

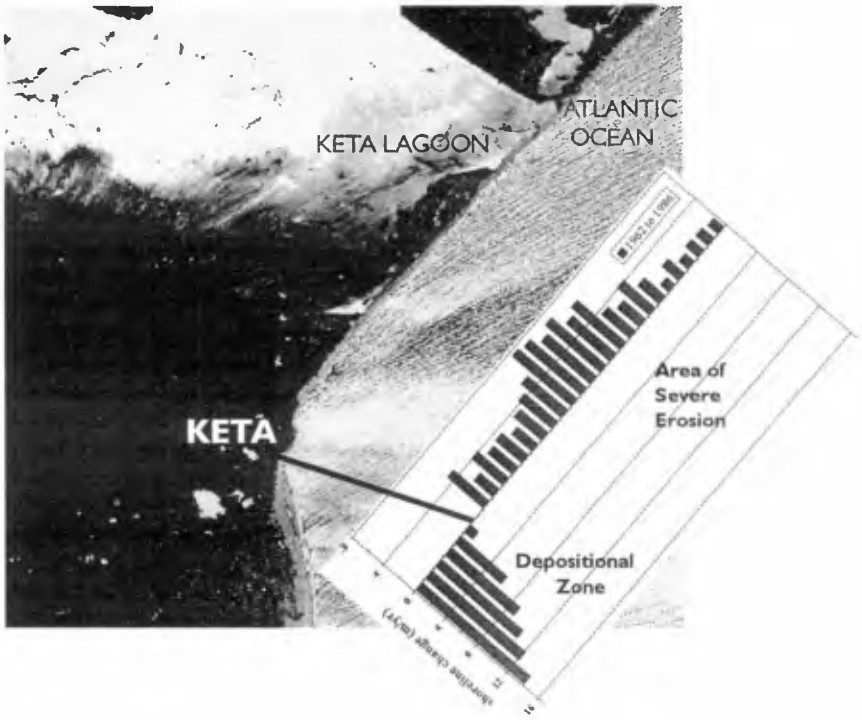

Figure 3 –Proposed changes of the Volta River Delta shoreline as a result of river mouth switching and shoreline realignment.

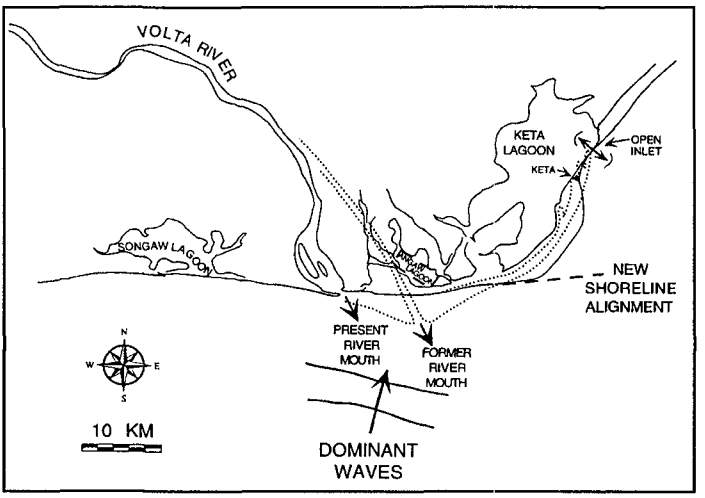

This large scale, long term process of sediment deposition on the deltaic protuberance is directly responsible for the shoreline recession in the study area, which is located immediately downdrift of the protuberance. The study area consists of a narrow 7 km long washover terrace separating Keta Lagoon from the sea (see Figures 4a and b). The terrace sits on lagoonal sediments, which are presently being transgressed. Annual average recession rates along the narrow section of beach range from 8 m/yr at the southwest end to less than 2 m/yr at the northeast end (refer to Figure 2). In addition, the coastline features migrating sand waves from 10 m long beach cusps to 300 m long tongues of sand. The migration of these features results in fluctuations in shoreline position of 50 m or more over a period of several weeks. These large sand waves appear to be generated by the creation and release of sand spits at beach bends along the leading edge of the delta front protuberance. Small changes in wave direction may initiate the break away of the spits to form migrating sand waves.

The erosion problem at Keta has been the focus of many investigations dating back to the first published engineering report by Coode (1929). This report concluded that the erosion problem had existed for at least 50 to 60 years prior to 1929 and relocation was proposed as the only practical solution. A series of reports by Batley between 1947 and 1950 suggested that the erosion problem at Keta was diminishing and that changes in erosion trends in the Keta area are related to dynamics of the Volta River mouth (including long term changes in the position of the mouth). Halcrow (1954) investigated the potential impact of the Akosombo Dam (which resulted in the creation of Lake Volta) on the coastal erosion at Keta. That study concluded that the regulated flow conditions

would result in a reduction of the rate of depostion in the vicinity of Cape St. Paul, and therefore, alleviation of the erosion problem at Keta. Freedman (1955) disagreed with Batley's conclusion that the erosion problem at Keta was coming to an end. Emphasis was placed on seepage from the lagoon through the beach face during low tide conditions as an important factor in the erosion process. Groynes were rejected as a viable solution while the construction of a continuous seawall was endorsed as a practical but costly solution, relocation was proposed for further consideration. In 1960 a recommendation in a report by the Hydrological Branch of the Public Works Department of Ghana resulted in the construction of 1600 m long steel sheet pile wall at Keta (the remains of this can be seen offshore of Keta in Figure 4a). Following construction of the wall serious erosion occurred at the northeast (downdrift) end of the wall. NEDECO (1964, 1976 and 1980) and Delft Hydraulics (1993) have prepared several reports on the flooding and erosion problem at Keta. These reports agree with the view that the erosion problem is slowly shifting northeastwards. In the 1980 report a series of groynes was proposed to protect the shoreline between Keta and Horvi. Most recently, Anthonio and Valentine (1995) developed a numerical nearshore wave transformation model to describe the variability in alongshore transport passing Keta depending on the direction of wave attack.

Figure 4a - A view of Keta and the delta protuberance looking southwest

Figure 4b - A view of the washover terrace looking northeast from above Keta at Vodza in the foreground and Kedzi in the background

Design Investigations

Geomorphic investigations consisted of air photo and satellite imagery analysis, mapping historic beach ridges; hydrographic surveys; subsurface investigations including vibracores, augers, boreholes, sediment sampling, seismic profiling and radiocarbon dating; and monitoring of 10 permanent beach profile stations (some of which have been monitored since the early 1970's). The key findings of these investigations are listed below:

- Earlier during the present Holocene high-stand of sea level, the mouth of the Volta River was located further to the east and the leading edge of the delta probably consisted of spits curving into an open bay which is now the enclosed Keta Lagoon (see Figure 3);
- The northeastward migration of the leading edge of the Volta River delta has been occuring in an episodic manner at the existing location for a period of centuries and will continue to do so (see Figure 5);
- The section of eroding shoreline is a washover terrace consisting of a wedge of sand migrating into the lagoon through overwash processes and through shoreface erosion of underlying lagoonal sediments (see Figure 6).

Figure 5 – Beach –ridge development. (A) Overlay tracing of the beach ridge margins seen on aerial photographs taken in October 1993. (B) Interpretation of episodes of beach-ridge growth (1=oldest; 6=youngest).

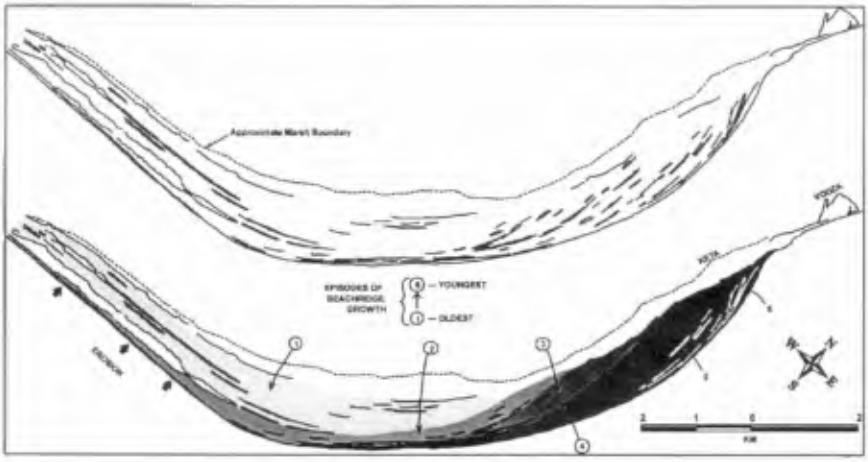

Figure 6 – Section of Washover Terrace

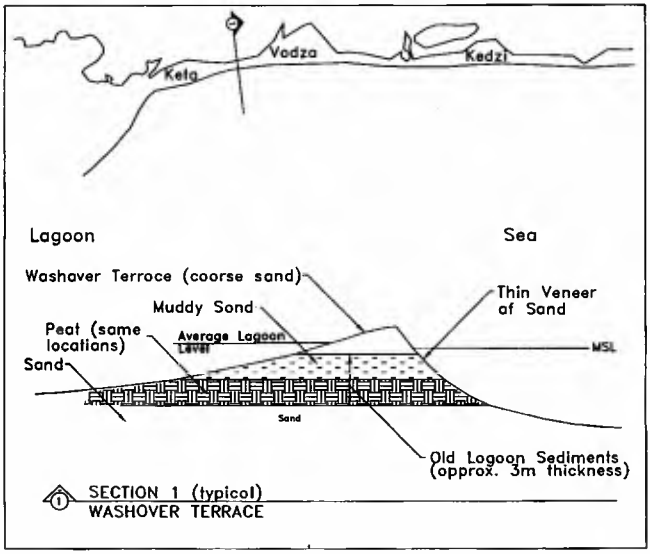

The findings of the geomorphic investigations were corroborated or refined based on the coastal engineering analyses described below.

Coastal process investigations included prediction of the deepwater wave conditions with the U.K Global Wave Model calibrated by satellite data by Oceanor (1997) and verified against wave measurements with pressure sensors deployed by Baird. Nearshore wave transformation was completed using the Nearshore Spectral Wave model of the MIKE21 package developed by DHI. The nearshore wave transformation results showed that the degree of sheltering at Keta varies significantly with only a small change in incident wave angle. For a typical 12 s wave period, the wave height in the vicinity of Keta is reduced to 20% of the incident wave height for SW incident wave attack, 50% for SSW wave attack and 70% for S wave attack.

An overtopping analysis was completed to simulate serious flooding events that occurred during the course of the design investigations. The findings of this analysis demonstrated the importance of washover in the retreat of the beach terrace. Samples of the underlying lagoonal sediment (peat and clay) were found to contain little or no beach sand. Therefore, once the underlying lagoonal sediment was exposed in the surfzone, it was readily and irreversibly eroded, with little or no contribution of sand to the littoral system.

Prediction of longshore and cross-shore currents and sand transport rates (including in the vicinity of the headlands) were completed using the COSMOS model (see Nairn and Southgate, 1993). There were two purposes of these estimates: 1) to quantify the geomorphic findings and specifically to develop a sediment budget to provide the basis for a solution; and 2) to assess the potential performance of the proposed solution.

In summary, the sediment budget found that between Cape St. Paul and just southwest of Keta, the net eastward transport rate decreases from nearly 1,000,000 m^3/year to less than 50,000 m^3/year. The result is deposition of sand and the migration of the leading edge of the delta. The rate of shoreline progradation is greatest at Keta where the depths of water are shallow (owing to the fact that this area was recently eroded). Northeast of Keta the potential sand transport rate increases from 50,000 to 200,000 m^3/year towards the east at the northeast end of the study area near Horvi. The deficit in the potential transport rate of approximately 150,000 m^3/year compares well to the estimated average annual loss of 164,000 m^3 of sand sized sediment from this reach of coastline (determined from historic recession rates and a consideration of the thickness of sand eroded - accounting for the fact that the washover terrace material is conserved and that the lagoonal muds do not produce sand sized material).

The GENESIS model (Hanson and Kraus, 1989) was used to assess the potential performance of large headlands in protecting the shoreline from erosion and regulating the rate of alongshore transport. Two key aspects of the GENESIS model that required calibration to address specific site and project conditions are: 1) the potential sand transport rate; and 2) the rate of bypassing at each headland (referred to as the permeability of the structure in the GENISIS input). The transport rate was established by the COSMOS model and the sediment budget findings discussed above. The rate of

bypassing, or groyne permeability, is a critical factor as it establishes the offset of the shoreline from the tip of the downdrift groin with a groin cell. This setback distance must be determined to assess the required groin or headland spacing to optimize the transport rate through the study area and to avoid flanking erosion on the downdrift side of the headlands. The setback distance was determined for a given alongshore transport rate (i.e. associated with a given shoreline orientation) by finding the position that resulted in equilibrium between alongshore and offshore transport just updrift of the headland (see Figure 7). It was determined that the shoreline must advance to within 50 m of the end of the headland before the offshore transport rate matches the alongshore transport rate of 150,000 m^3/year. However, for an alongshore transport rate of 50,000 m^3/year, the setback distance increases to 120 m. The prediction of setback distances was corroborated by a review of setback distances for many existing groin and headland structures.

Physical modelling was completed to examine the impact of the headlands on the beach orientation and the bypassing process as well as the stability and constructability of the rubblemound structures. One of the key findings of the mobile bed modelling was that the advantages of implementing T-head, L-head or angled groins or headlands at this location did not justify the additional cost compared to a straight, shore perpendicular headland. The finding that the T and L head layouts did not add significantly to the length of protected beach (and the required spacing between headlands) may be a function of the narrow window of wave attack at this site (i.e. all significant waves approach from the SW to SSE sectors). The model test results for beach planform compared well to empirical predictions from expressions developed by Hsu et al (1989).

Figure 7 – Estimating bypassing at the headlands

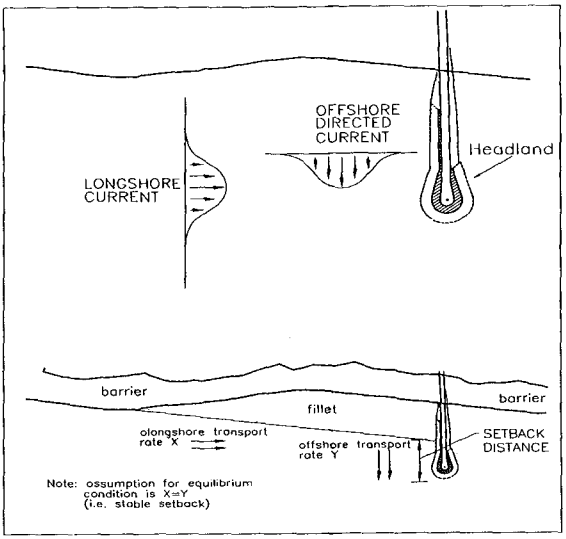

The Sea Defence System

The objectives of the sea defence system are:

- stabilize areas of existing and planned development;
- prevent flooding of the coastal communities;
- minimize disruption to human activities associated with the coastline, particularly seine netting and the launching of fishing canoes; and
- avoid transferring the erosion problem to developed areas downdrift and northeast of the study area.

In order to stabilize the study shoreline and meet the above objectives, it is necessary to address a deficit of approximately 150,000 m^3/yr of sand between the updrift and downdrift limits of the developed area (a distance of 5 km). It is also necessary to protect the erosion susceptible lagoonal sediments underlying the beach.

Prior to developing a solution to the erosion problem, the "do nothing" scenario was considered in detail. Based on the results of the geomorphic investigation, the coastal process modelling and the sediment budget analysis, projeetions of shoreline position for the next 75 years were made (see Figure 8). It is evident that perhaps within 25 years time, erosion will no longer be a threat to the community of Keta. However, the communities of Vodza and Kedzi will suffer severe erosion. Relocation of these communities was not an acceptable option as there are no remaining suitable locations for ocean seine netting – the primary occupation of the communities. In addition, it is possible that the erosion may result in the breach of the narrow washover terrace separating the lagoon from the sea. The introduction of seawater into fresh/brackish water of Keta Lagoon would have disastrous effects on local drinking water, lagoon fishing and irrigation of adjacent agricultural land. Therefore, the "do nothing" option was considered to be unacceptable.

The adopted large scale solution consists of constructing one breakwater and 7 rubblemound headlands, prefilled with 2.5 million cubic metres of sand dredged from the lagoon bed. The breakwater (not shown on Figure 8) will protect the town of Keta from erosion until this area is naturally protected by the migrating delta front. One of the reasons a breakwater was preferred to a headland at this location was to minimize the disruption to alongshore transport between the depositional area at the leading edge of the delta and the downdrift erosion area. On average, the headlands are approximately 200 m long and extend out to a depth of 5 m. The average spacing between the headlands is 750 m. The function of the headlands is to extend the longevity of the beach nourishment and to protect the underlying lagoonal sediments from erosion. The purpose of the beach nourishment is to act as a feeder beach to address the potential transport deficit within the study area. Figure 9 illustrates the solution in terms of its performance relative to the sediment budget. It is noted that Figure 9 shows eight headlands, the design was recently modified to eliminate the most northerly headland (reducing the total number to 7).

Figure 8 –Projections of future shoreline change under the 'Do Nothing' scenario

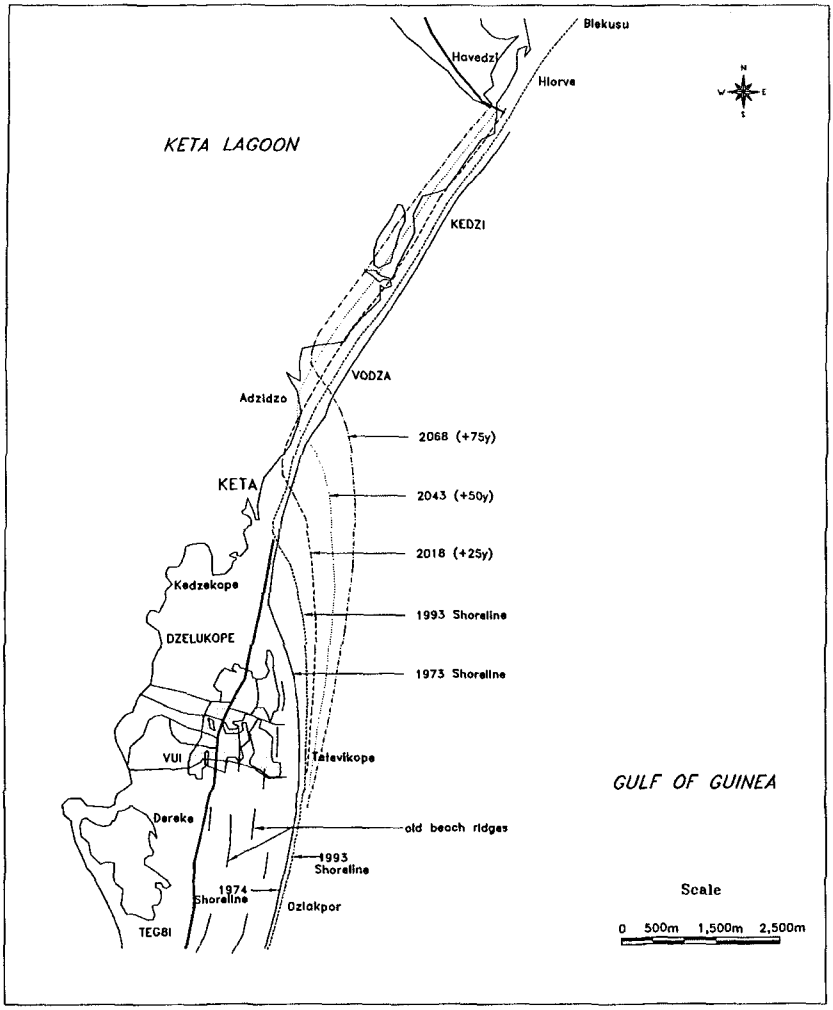

Figure 9 – Proposed Sea Defence Scheme

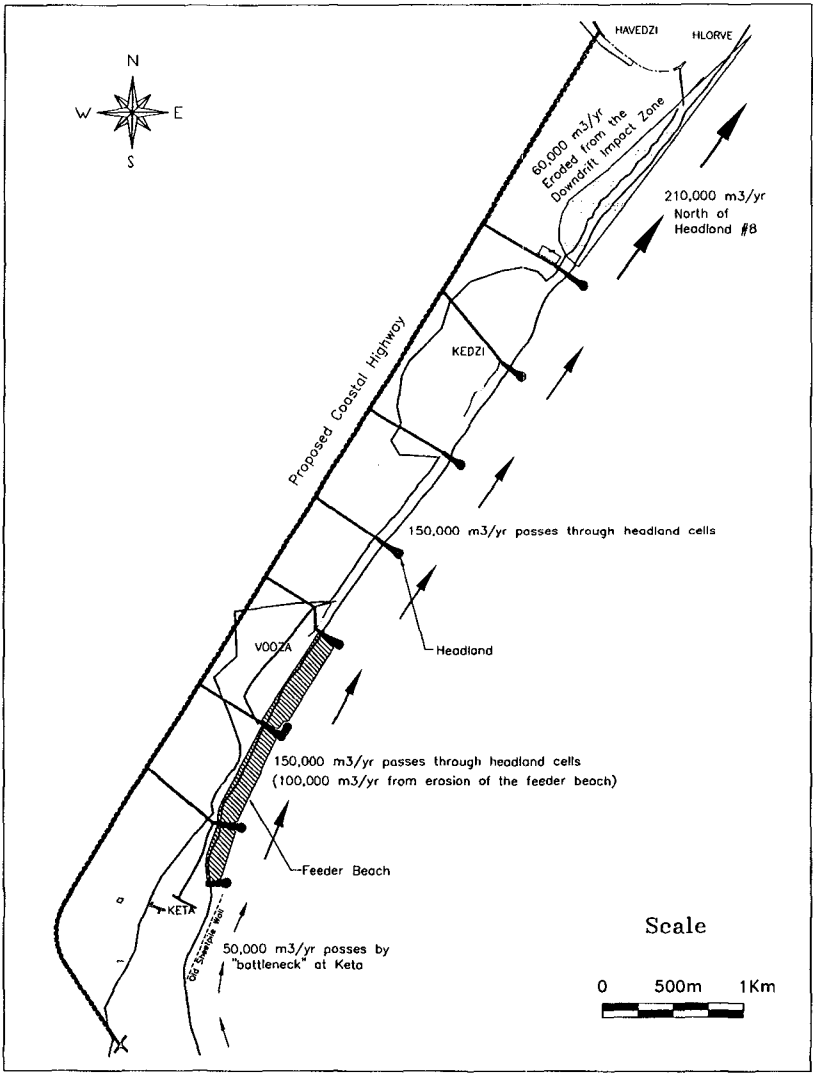

(Note: The proposed breakwater is located along the alignment of the old sheet pile wall and the most northerly headland has been removed from the latest design revision.)

Another important aspect of the sea defence system is the 2 km section of unprotected shoreline at the downdrift end of the project. This undeveloped area will erode to make up the remaining 60,000 m^3/yr deficit between the transport through the project area and the potential rate downdrift of the sea defence system.

Based on the COSMOS and GENESIS numerical modeling, it was determined that the feeder beach area will have to be renourished every 10 to 15 years. Model simulations showed that failure to renourish the feeder beach would result in flanking erosion at the base of the headlands and accelerated downdrift erosion, to the extent that downdrift communities may eventually be affected.

A range of other possible solutions was considered in detail. These included the use of rubblemound structures without beach nourishment, and beach nourishment without structures. In the former case it was determined that twelve headlands would be required and that five more headlands would have to be added every 10 to 15 years to address downdrift erosion. This solution would simply transfer the problem downdrift. One alternative that consisted exclusively of beachfill was a "sand bridge" extending from updrift of Keta to Vodza. The purpose of the sand bridge was to link updrift and downdrift locations with similar potential transport rates (eliminating some of the deposition updrift and alleviating the downdrift supply deficit). The net present value of this solution was similar to the adopted solution of the feeder beach and headlands, however, it was not selected owing to the higher risk associated with estimating the performance of the sand bridge.

Conclusions

The combined investigation of coastal processes, geology and geomorphology was utilized to develop an understanding of the coastal morphodynamics across a wide range of temporal and spatial scales. This understanding was used to predict future shoreline change in order to develop a coastal management solution to the ongoing impact of the shoreline recession on the coastal communities in the study area. The solution addresses the erosion problem within the limits of the study area and avoids the downdrift transfer of the problem.

Construction is planned to commence in early 1999. An extensive monitoring program through the four year construction period will assess the waves, shoreline change, scour and stability of structures in addition to environmental conditions as part of the environmental impact assessment requirements.

References

AESC (1976). Coastal erosion and proposed protection works at Keta. Tech. Rept. No. CE/2, Hyd. Div., Arch. and Eng. Services Corp., Accra, Ghana, 20 pp. plus appendices and illustrations.

Anthonio, S.L. and Valentine, E.M. (1995). Influence of Wave Climate on Coastal Erosion in Keta, South Eastern Ghana. Int. Conf. on Coastal and Port Engineering in Developing Countries. pp. 253-262.

Batley, W. (1950). Keta coastal erosion. Rept. Public Works Dept., Gold Coast, (Ghana), Accra, 13 pp.

Coode, A.T. (1929). Keta coast erosion - Rept. Messrs Coode, Wilson, Mitchell & Vaughan-Lee, Accra, 1929-30: 13 pp.

Delft Hydraulics Laboratory (1993). Keta-Kedzi Road Rehabilitation Project. Coastal Hydraulic Aspects. Prepared for Wayss & Freytag AG.

Freedman (1955). Referenced in AESC, 1976 Technical Rept. CE/2.

Great Lakes Dredge & Dock and Baird & Associates (1997). Keta Sea Defence Project - Detailed Engineering Design of the Works, Final Report. Volume 1. Prepared for the Ministry of Works and Housing, Republic of Ghana.

Halcrow. (1954). Volta River project. An investigation into the effect of the Volta River upon the coastal erosion at Keta and the industries of the Volta Delta. Sir William Halcrow & Partners, London, England.

Hanson, H. and Kraus, N.C., 1989, GENESIS: Generalized Model for Simulating Shoreline Change. Report 1. Technical Reference. Tech. Rept. CERC-89-19. Waterways Experiment Station, U.S. Army Corps of Engineers. 185 pp.

Hsu, J.R.C., Silvester, R. and Xia, Y.M., 1989, Generalties on Static Equilibrium Bays. Coastal Engineering, 12, pp. 353-369.

Hydrological Branch. (1960). Coastal Erosion, Sea Defences and Lagoon Flooding at Keta. Ghana Public Works Department.

Nairn, R.B. and Southgate, H.N. (1993). Deterministic Profile Modelling of Nearshore Processes. Part 2. Sediment Transport and Beach Profile Development. Coastal Eng. Vol. 19. p. 57-96.

NEDECO (1964). Flood relief and resettlement plan for Keta Town: Project Report.

NEDECO (1976). Ghana - Keta coast erosion - report of an identification mission: Project Report.

NEDECO (1980). Coastal Erosion and protective measures at Keta: Project Report.

Oceanor (1997). Directional Wave Timer Series for Deepwater Offshore Ghana (1986 to 1996). Report OCN R-97002 prepared for Baird & Associates.

Morphological vulnerability index: A simple way of determining beach behaviour

Óscar Ferreira[1], Rui Taborda[2] and J. Alveirinho Dias[1]

Abstract

A simple morphological based index to determine beach vulnerability is proposed in this paper. The presented morphological vulnerability index (I_V) relates maximum annual volumetric difference and average beach volume for each particular site. High index values are representative of coastlines vulnerable to erosion.

After the index application to 15 Portuguese sites it was possible to determine empirical threshold values, defining limits between beach stages. Based on these limits the beaches can be classified as: robust beaches, for $I_V < 0.35$; fragile beaches, for $0.35 < I_V \leq 0.9$; and extremely fragile beaches, for $I_V > 0.9$. The index validation tests against field observations and recent shoreline evolution gave good results, indicating that the I_V has a strong potential application to characterise medium to long-term beach evolution.

Introduction

A successful approach to characterise large-scale sediment transport, including cross-shore rates, must use information on the principles underlying key features of the larger scale morphology (Larson and Kraus, 1995). However, to our knowledge there are no simple morphological based indexes available in literature describing beach behaviour at macro and megascale timescales (year to decades).

The main goal of this study was to develop an index capable of determining the morphological vulnerability of a given beach or coastal stretch. For the purpose of this study a beach with high morphological vulnerability is defined as having a small ability to support high energy conditions without strong morphological changes. Thus, a

[1] UCTRA, Universidade do Algarve, Campus de Gambelas, 8000 Faro, Portugal.
[2] Departamento de Geologia, Faculdade de Ciências, Universidade de Lisboa, Campo Grande, 1700 Lisboa, Portugal.

beach with high vulnerability can also be referred as a fragile beach, due to the possibility of effective shoreline or dune retreat to occur. Conversely, a low vulnerability beach can also be referred as a robust one, meaning that even facing some erosion during high energy conditions the beach will not show effective shoreline or dune retreat. It is meant by effective shoreline or dune retreat the total remotion of the upper beach (foreshore and backshore) sedimentary stock with erosion of the dune or cliff.

In order to introduce an index of this kind studies were carried out on 15 Portuguese beaches. Two different coastal sectors were surveyed including; 10 sites from Aveiro - Cape Mondego (figure 1), Northwest of Portugal (surveys from September 1992 until June 1993) and 5 sites from Praia de Faro (figure 2), Algarve (surveys from May 1995 until May 1997). The 10 sites of the Northwest coast belong to a coastal stretch with about 50km length and include beaches updrift and downdrift of groins as well as beaches without human intervention. On the Algarve coast three of the surveyed beaches are backed by human occupation (sites A to C) and two of them by a dune ridge (sites D and E). The surveys were made during low spring tides, once a month in Praia de Faro and every two months at Aveiro - Cape Mondego. All these sites were intermediate to reflective Atlantic facing sandy beaches with moderate (Algarve) to high wave (Aveiro - Cape Mondego) energy. Both coastal areas are mesotidal with maximum tidal ranges reaching about 3.6m-3.8m.

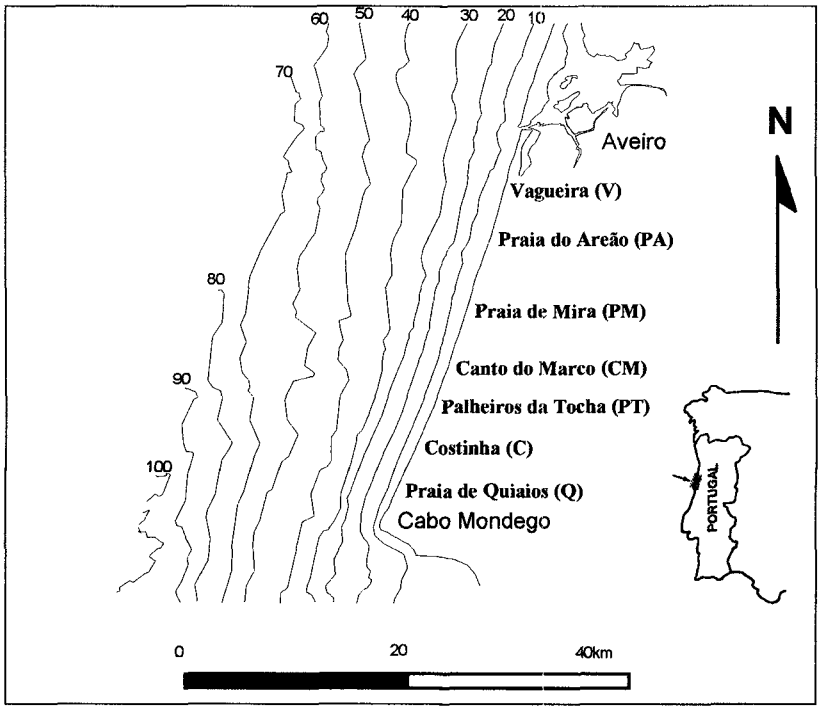

Figure 1. Location of the study sites from Aveiro - Cape Mondego coastal stretch.

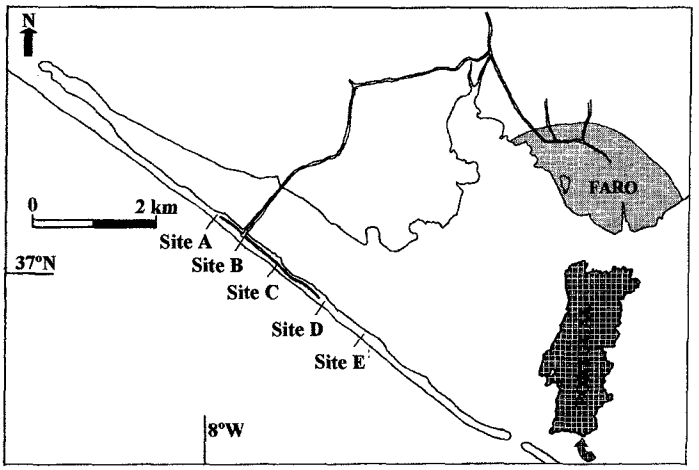

Figure 2. Location of the study sites at Praia de Faro coastal stretch.

Vulnerability index

Concepts

The main concept underlying the proposed vulnerability index is that the annual beach variability can be an indicator of its future evolution. The index application assumes that the beach variability is mainly dependent on cross-shore exchanges and that after an annual cycle the upper beach morphology becomes similar to the initial one, even if there was effective dune or shoreline retreat. Thus, this index can only be used in beaches where a seasonal behaviour exists.

To obtain the morphological vulnerability index (I_V) it was necessary to compute the beach volume above mean sea level for each obtained profile (figure 3). The landward limit for these calculations was taken to be the "non - mobility point" of the site (the inland point at which no sand movement due to wave action was observed). Using the obtained volumes, mean profile volumes (V_{mean}) were calculated for each beach and for the desired periods.

The morphological vulnerability index (I_V) is then given by the relationship,

$$I_V = (V_{max} - V_{min})/V_{mean} \quad (1)$$

where V_{max} and V_{min} are the maximum and the minimum volumes computed for the chosen survey period. A high index indicates a high range in beach volume (a dynamic site) and low mean values. Thus, high indexes will be indicative of coastlines vulnerable to erosion while low index values will be representative of shorelines without evident retreat.

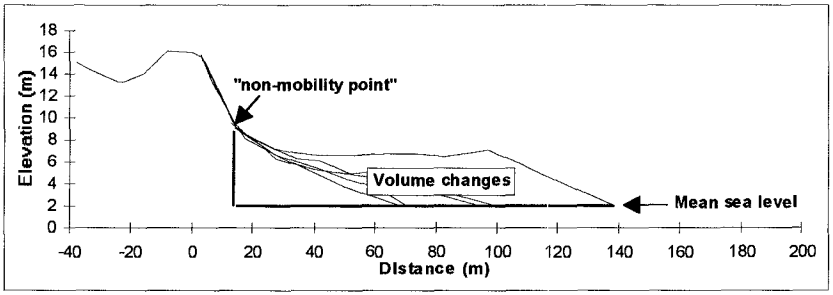

Figure 3. Schematic representation of the limits used for beach volume computation.

From the available data and after some application tests, it was found that the index only shows stable results if survey data is included for a full seasonal (Summer/Winter) cycle, with a period between successive surveys no longer than 2 months. Figure 4 illustrates the index evolution (I_{Vni}/I_{Vni-1}) with an increasing number of profiles (*ni*) used in the calculation of I_V. This figure shows that the index variation tends to be small or nule ($I_{Vni}/I_{Vni-1} \approx 1$) when the number of used profiles (*ni*) is higher than 12/13 (one year of monthly observations). On the basis of these results I_V is computed at each site using one full year of survey data, and thus indicating the beach behaviour of that period.

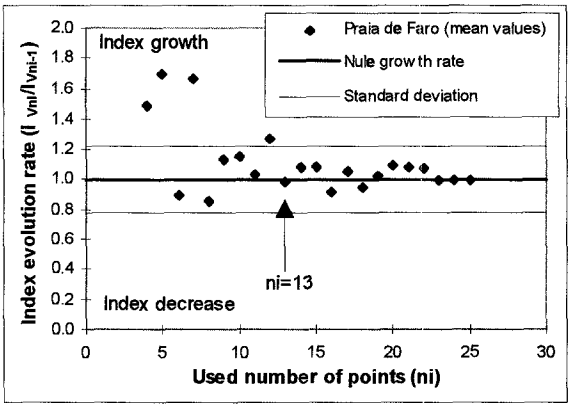

Figure 4. Index variation with the number of points used in the computation.

Application to Praia de Faro

By the application of equation (1) to the Praia de Faro data set 13 indexes were obtained for each site, from months 1-13 (first year of surveys) until months 13-25 (last year of surveys). The minimum, maximum and mean values, obtained to each site, are expressed in Table I. It is apparent from Table I that site B (parking place at Praia de Faro) is the most vulnerable to erosion or overwash. This is in agreement with field observations of frequent overwashes at this site. Dune erosion is impossible to occur at this site since the parking area was built over the former dunes, destroying them. From field observations it is also evident that sites A and C are less robust than

sites D and E, since the dune at site A and the seawall at site C have been eroded and damaged by the sea. Conversely, at sites D and E the dunes remained unaffected by the swash. The conclusions obtained by the analysis of Table I agree with those reached by previous studies at Praia de Faro (Martins *et al.*, 1996; Ferreira *et al.*, 1997), using different evaluation methods.

Table I - Computed I_V values for Praia de Faro.

I_V	Site A	Site B	Site C	Site D	Site E
Mean	0.38	0.62	0.36	0.29	0.27
Max	0.41	0.69	0.44	0.34	0.34
Min	0.34	0.54	0.23	0.22	0.17

Figure 5 shows the mean values and the index variability at sites B and E, for the observed period. The difference between sites is evident, with site B having a significantly higher vulnerability index than E. With the knowledge that the dunes at sites D and E did not experienced erosion or overwash, which occurred on sites A to C, it is possible to infer a robustness limit of approximately 0.35. Above this limit coastal erosion will be frequent. Figure 6 shows the relationship between the computed index values at the different sites together with this empirical limit.

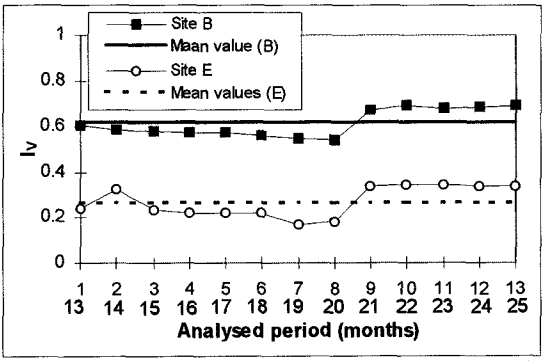

Figure 5. Index variation for sites B and E, along the surveyed period.

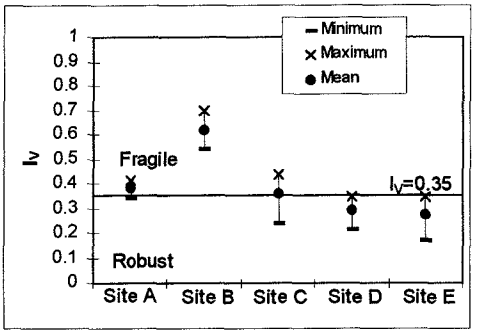

Figure 6. Determined index variability for the studied period, at each site, and its relation with the empirical limit.

Application to the Aveiro - Cape Mondego data

By the application of this index to the data resulting from the Aveiro - Cape Mondego monitoring program, it was only possible to obtain one set of I_V values, since the survey period was only 10 months in duration. From these observations two distinct groups of beaches were identified (figure 7). Three of the surveyed sites (white symbols) exhibited very high index values, and thus may be classified as extremely fragile (prone to overwash and erosion). These 3 sites (PMS, PA and VS) are placed downdrift of groins, facing strong dune retreat.

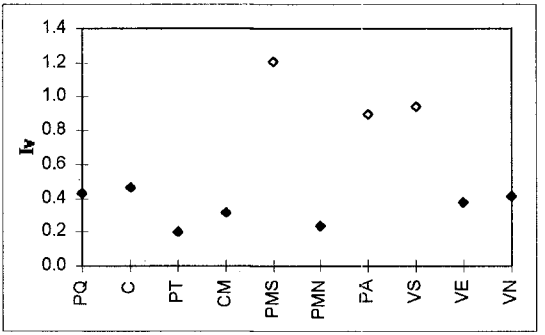

Figure 7. I_V values for the Aveiro - Cape Mondego coastal stretch.

In figure 8 the observed beach/dune retreat or accretion, for the 1980/90 period, was plotted against the computed I_V for each site. A strong correlation was observed between I_V and beach/dune evolution. These data indicate that I_V values greater than 0.9 denote extreme beach vulnerability (effective shoreline retreat higher than 2m/year).

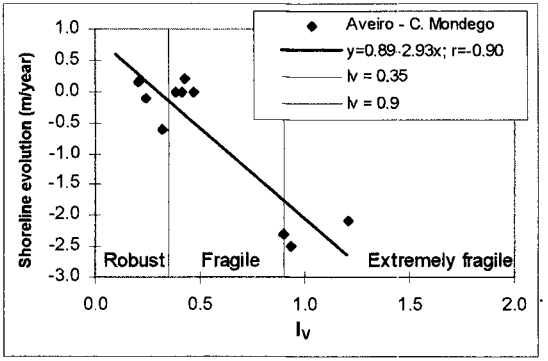

Figure 8. Relation between I_V and beach/dune evolution at Aveiro - Cape Mondego (negative values represent erosion).

Combining the results obtained by the analysis of the two coastal sectors, the following limits are proposed: $I_V < 0.35$, Robust beach; $0.35 \leq I_V < 0.9$ Fragile beach; $I_V \geq 0.9$ Extremely fragile beach.

The obtained limits are based on a restrict number of data, being necessary a future confirmation of the thresholds for other coastal areas with different wave energy and morphodynamic conditions.

Index validation

In order to confirm the results obtained by the application of the morphological vulnerability index, a validation test was performed. For this test nine beach profiles, obtained in April 1995 on the same sites of the 1992/93 surveys for the Aveiro - Cape Mondego coastal stretch, were used. The new profiles were compared with the previous ones, by measuring the observed dune retreat and computing the volumetric difference between each new profile and the corresponding average volume for the 1992/93 surveys. Table II shows the volumetric differences and the maximum observed dune retreat at each site.

Table II. Computed volumetric differences and maximum observed dune retreats between the average profiles of the 1992/93 surveys and the April 95 profiles.

Site	Volumetric difference (m^3/m)	Maximum dune retreat (m)
Praia de Quiaios (PQ)	+111.0	0
Palheiros da Tocha (PT)	+38.5	0
Canto do Marco (CM)	-38.3	0
Praia de Mira South (PMS)	-105.5	-5.1
Praia de Mira North (PMN)	-182.6	0
Praia do Areão (PA)	-141.6	-11.3
Vagueira South (VS)	-226.4	-1.6
Vagueira Central (VE)	-82.3	0
Vagueira North (VN)	-144.1	-4.1[a]

[a] Retreat due to seawall reconstruction.

A high volumetric difference occurred at most sites, showing a global erosional trend from 1992/93 to April 1995. However, an effective dune retreat only occurred at beaches where the I_V value was higher than 0.9 (PMS, PA and VS). At the other sites the dune was not reached by the sea, even if the volumetric difference was very high (e.g. PMN, where a volume change of -182.6 m^3/m was measured). This observation confirms that the robustness of a beach is not only given by the sedimentary volume exchange but mainly by the relationship between that volume and the available sand stock. Two examples of profiles from the same coastal stretch (Aveiro - Cape Mondego) showing high volumetric changes, with and without dune retreat, are presented in figure 9.

According with the obtained results, the index proved to give a good discrimination of the fragile sites, being able to point out the beaches where an effective retreat could occur.

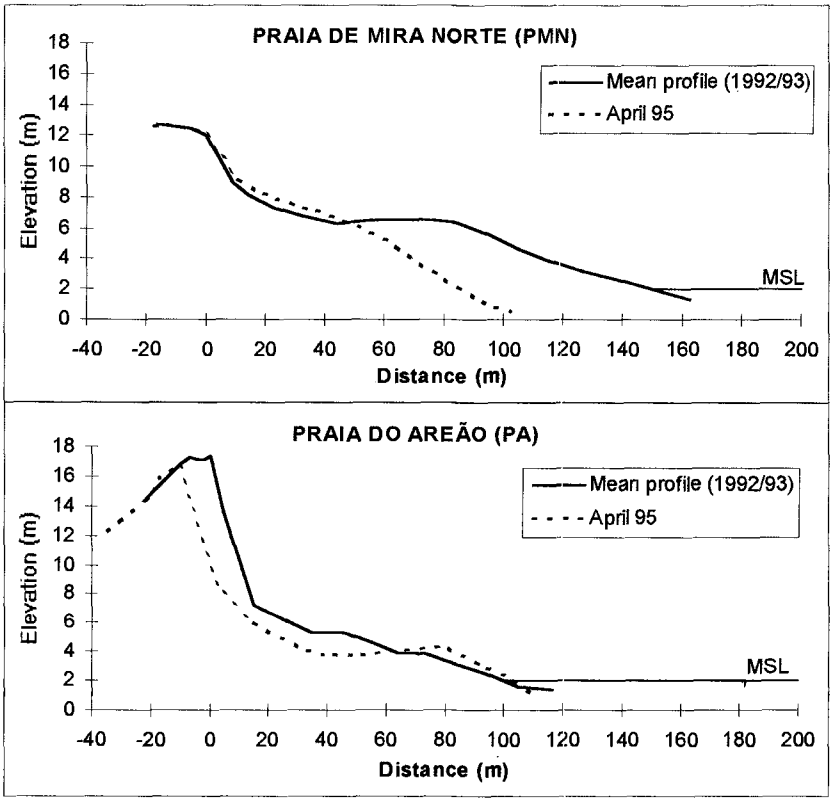

Figure 9. Comparison of behaviour between a robust (PMN) and an extremely fragile site (PA) for the same observation periods.

Conclusions

In this paper a new and simple index to determine morphological vulnerability of sandy beaches is proposed. This index was applied to 15 different Portuguese sites showing that it is possible to use simple morphological parameters to characterise the beach behaviour as well as the medium to large-scale beach evolution. For the available data sets three classes of beach behaviour are proposed: robust, fragile and extremely fragile. The morphological vulnerability index can be easily applied on beach monitoring programs, providing coastal managers a clear and simple indicator of beach stability. However, future work is required, namely in the determination of the I_V limits with larger data sets and testing the index validation to different beach types (dissipative and extremely dissipative beaches, pocket beaches, shingle beaches, etc.).

Acknowledgements

The authors wish to acknowledge João Martins for data processing and Mark Davidson for comments and revision of a previous version of this manuscript. This work is DISEPLA contribution n. A128 and was undertaken as a part of the following

research projects: INDIA (MAST Contract n° MAS3-CT97-0106) and RIMAR (PRAXIS XXI n.2/2.1/MAR/1743/95).

References

Ferreira, Ó., Martins, J. T. and Dias, J. A., 1997. Morfodinâmica e vulnerabilidade da Praia de Faro. In: *Seminário sobre a Zona Costeira do Algarve*, EUROCOAST Portugal, 67-76.

Larson, M. and Kraus, N. C., 1995. Prediction of cross-shore sediment transport at different spatial and temporal scales. *Marine Geology*, 126, 111-127.

Martins, J. T., Ferreira, Ó., Ciavola, P. and Dias, J. A.,1996. Monitoring of profile changes at Praia de Faro, Algarve: a tool to predict and solve problems. In: J. Taussik and J. Mitchell (eds.), *Partnership in Coastal Zone Management*, Samara Publishing, 615-622.

Homogeneity aspects in statistical analysis of coastal engineering data

P.H.A.J.M. van Gelder[1] and J.K. Vrijling[2]

Abstract

In this paper, the problem of (in)homogeneous data in coastal engineering applications is studied. Statistical analysis of coastal engineering data such as flood data, wind data, wave height data, etc., is essentially a problem of information scarcity. Records are usually too short to ensure reliable estimates of low-exceedance probability quantiles in many practical problems. Determination of quantiles is needed for the design, construction and operation of hydraulic structures, insurance studies and protection of populated areas. To perform a frequency analysis of data from coastal engineering practice, the data first has to be tested for homogeneity. Non-homogeneous data may lead to wrong quantiles. A homogeneity test must be able to separate data sets that do not come from the same distribution. In this paper statistical and physical-based homogeneity tests will be presented.

Introduction

Statistical analysis of coastal engineering data is a problem of information scarcity. Usually records are very short. Datasets with 100 years of water levels may seem much, but when one is interested in the 10^{-4} quantile, 100 years of data is very little. Apart from the data scarcity problem, there is also a data homogeneity (or rather data inhomogeneity) problem. A basic assumption is that data is coming from one and the same process. Or in mathematical terms: the data are realisations from one and the same probability distribution function. Statistical procedures are available to check the homogeneity of a dataset. A short overview of these procedures will be given in the paper. However their weakness will appear quickly, since these procedures are not very

[1] Delft University of Technology, Faculty of Civil Engineering, P.O. Box 5048, 2600 GA Delft, The Netherlands, E-mail: P.vanGelder@ct.tudelft.nl
[2] Delft University of Technology, Faculty of Civil Engineering, P.O. Box 5048, 2600 GA Delft, The Netherlands, E-mail: J.Vrijling@ct.tudelft.nl

powerful to reject inhomogeneous- or accept homogeneous data. A Monte Carlo experiment will illustrate this. A second method to judge the homogeneity of a dataset is more physically based. It will be shown that this way is more powerfull than the statistical procedures. A case study will be presented in order to show the physical based judgement of a coastal engineering dataset. Other physical based techniques will be reviewed in the paper. The paper will end with some conclusions and a list of references in the area of homogeneity analysis.

Homogeneity

Statistical distribution functions play an important role in coastal engineering. In the design of coastal structures they are used to determine the so-called p-quantiles. A p-quantile of a random variable is the value of that variable which is exceeded with a probability p. In coastal engineering p-quantiles in the order of 10^{-1} for small-scale defence structures to 10^{-4} for important coastal defence structures are commonly applied. In the Netherlands the seadikes for instance are designed with p-values of 10^{-4} and river dikes with p-values of $1.25\ 10^{-3}$. The reason for the difference is that a possible inundation from the rivers is not so disasterous as an inundation from the sea.

The importance to estimate the correct p-quantile is quite high. A too low estimate may lead to an unsafe structure, whereas a too high estimate may lead to a conservative overdesigned structures which costs unnecessarily too much. Lots of research has been carried out for finding the best p-quantile estimation method. Well known methods are for example Maximum Likelihood (ML), Method of Moments, Least Squares (LS), Weighted Least Squares (WLS), Method of L-Moments, Bayesian methods, and many more. Methods to select the optimal distribution function are also available. Various goodness-of-fit criteria such as χ^2 , Kolmogorov-Smirnov (KS), etc. can be used for that purpose. All these p-quantile estimation techniques and distribution selection methods have one important assumption in common, and that is that the data under consideration must be homogeneous. To verify the homogeneity assumption, statistical procedures have been developed.

Homogeneity analysis has been carried out a lot in the field of flood frequency analysis (FFA). FFA tries to combine data from other sites in order to improve the accuracy of the p-quantile estimate. However, combining data from different sites may only be done when the sites can be considered homogeneous. Therefore numerous papers have appeared dealing with this problem. We mention Dalrymple's test and the L-moment X10 test (Fill et.al., 1995). Homogeneity tests based on L-moment ratios have received quite some attention lately (Rao et.al., 1994, Zrinji et.al., 1996). Sample L-moments are less biased than traditional moment estimators.

Not only homogeneity tests have been developed in the field of FFA. Also literature is available from the behavioural sciences such as sociology and psychology. Well known statistical tests are for example the Mann-Whitney test, and the Wald Wolfowitz test (Harnett, 1970). The Mann-Whitney test is a non-parametric homogeneity test which can test the nul-hypothesis that two independent datasets are

coming from the same distribution. The performance of this test can be studied with help of Monte Carlo simulations. A dataset 1 with a given size can be simulated from a given distribution function. Also a dataset 2 can be generated and the two datasets can be compared with eachother from a homogeneity point of view. Under the nul-hypothesis that the datasets come from the same distribution, the test statistic should be normally distributed with mean 0 and standard deviation 1. If the Mann-Whitney test is analyzed in this way, it will appear that the test is not so powerfull for small sample sizes. Only for large sample sizes in the order of 100 or more, the test may reject or accept the nul-hypothesis with high reliability. Also the recently developed L-Moment techniques have difficulties to judge the homogeneity of a dataset. A Monte Carlo experiment was designed for that purpose. A sample of size 40 is generated from a certain extreme value distribution (Gumbel[10]). From this sample the ordinary moments and the L-moments are calculated. Another sample of size 40 is generated from a quite different extreme value distribution (Normal[10]) with the same mean and standard deviation however. Its ordinary and L-moments are calculated. The experiment is repeated 100 times and the moments and L-moments values of each sample are depicted in figure 1. Note that as well as the ordinary moments graphic as the L-moments graphic show a non-distinguishable behaviour between the Gumbel[10] and Normal[10] distribution. In other words: it is impossible to separate the two distribution functions with the traditional and newly developed L-moment techniques.

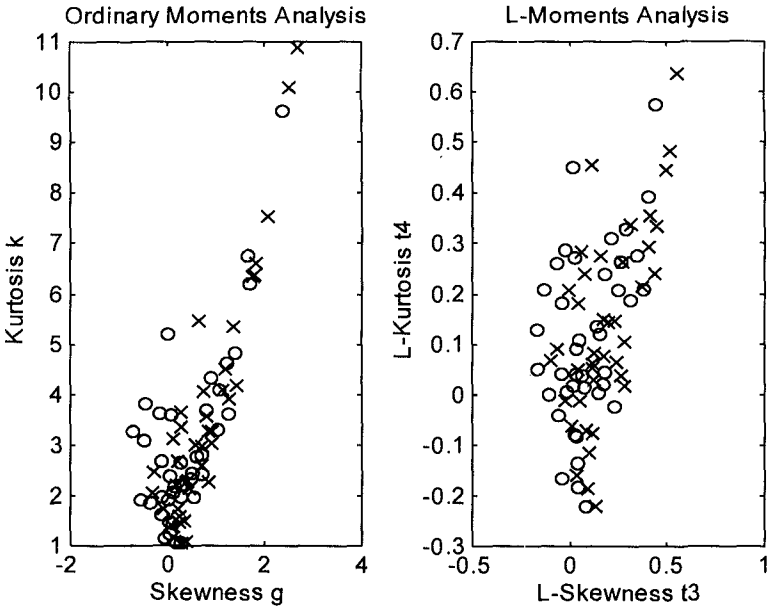

Figure 1. Homogeneity analysis with L-moments techniques.
Data from Gumbel[10] are indicated with x; data from Normal[10] with o.

The before mentioned homogeneity tests do not include any physical arguments to judge the data. In the following part we will propose procedures in order to examine the homogeneity of a data set on basis of physical arguments.

Physical based homogeneity analysis

Rather than a statistical analysis of the data, the data is examined on basis of its physical origin.

Physical arguments to judge the homogeneity of a data set are for instance:
1. Type of spectrum (swell, wind, single or double peaked wave height spectrum);
2. Season, calendar period of the data set (sea level data in the winter or summer);
3. Physical characteristics of the phenomena (breaking, non-breaking waves).

Combining statistical tests with physical arguments leads to more homogeneous data than only applying the statistical tests. This will be shown in a case of wave height and peak period data measured in the Bay of Bengal near the city of Madras.

Case study

In this case study registrations of the wave rider campaigns in the Bay of Bengal near the city of Madras during the south-west monsoon from mid-April to mid-August 1993 were used for analysis. A set of peaks over threshold values is available with significant wave heights. The set consists of 144 values and the threshold is given by 39cm. A statistical data analysis gives the following figure 2.

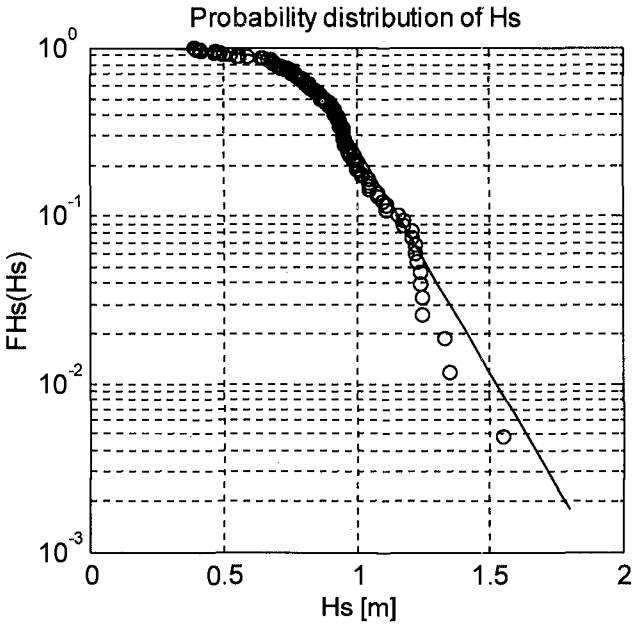

Figure 2. Wave height data with optimal fit (Normal).

A statistical homogeneity check on the data set with 144 values as described in the previous section does not lead to a rejection of the data set. Also a visual inspection of figure 2 does not suspect inhomogeneous data.

An investigation on the origins of wave generation in the Bay of Bengal however leads to:

1. Locally generated waves; these waves are generated in the Bay of Bengal either by the north-east or south-west monsoon or by hurricanes.
2. Swell; these waves are generated in the Roaring Forties, south of Cape Town. They reach the southern point of India from the south-west in approximately three days.

From the given data set with 144 significant wave heights, also the corresponding peak periods were available. A visual inspection of the data set with the peak periods immediately leads to the conclusion of inhomogeneity (figure 3). The waves can be separated into two classes. The first class contains waves with periods of about 5 sec. The second class contains waves of about 12 sec.

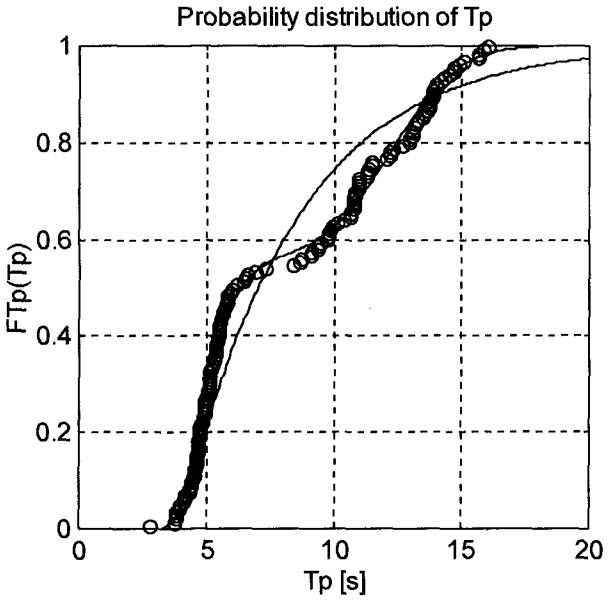

Figure 3. Peak periods data with Exponential inhomogeneous fit and Combined homogeneous fit.

Trying to model the probability distribution of the peak periods by one single distribution function leads to inacceptable deviations, as can be seen from figure 3. Therefore the inhomogeneous data set had to be split up into two sub sets. Each sub set is modeled by its own distribution and the probability model of the total data set is obtained by combining both sub models (figure 3).

Returning to the original goal: a probability distribution for the significant wave height, the following result is obtained (figure 4). The significant wave height with exceedance probability of 10^{-3} is 1.55m in stead of 1.90m; a difference of about 30%. This might have lead to an overdesigned coastal structure. However, the multivariate analysis of the data (including wave period in the analysis together with wave heights) had shown the inhomogeneous behaviour of the second tuple.

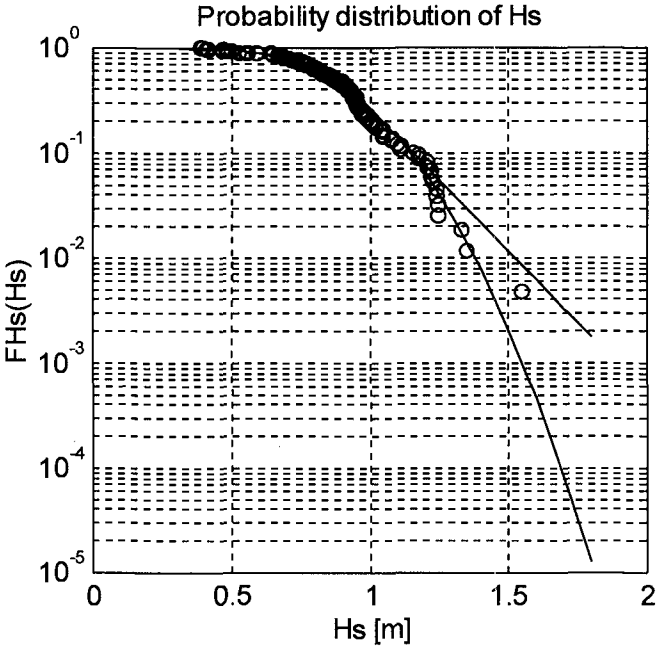

Figure 4. Comparison of in-/homogeneous fit.

North-European climate

Coastal engineering data from Northern European seas differ from the data presented above. Monsoons and hurricanes are not present in Northern Europe. However, strong winds can occur during the winter months November, December and January. These winds may yield extreme wave heights and water levels along the coasts. The analysis of such datasets also requires homogeneity studies. One of the first extensive homogeneity studies of the water levels along the Dutch coast was performed in 1960 by the Delta Committee. They homogenize the dataset of water levels by looking at the trajectory of the depression that caused the high water level. Extreme water levels can only occur when the depression follows a trajectory through a certain area. From the meteorological archive the area could be confined to:

At 10° W between 51° N and 62° N;
at 0° W between 52° N and 61° N;
at 7° E between 52° N and 61° N.

The cause of an extreme water level is found in the trajectory of the depression combined with the behaviour of the body of water in the North Sea basin. Therefore

the statistics of the water level data is confined to those water levels that were caused by the dangerous trajectories. Such a physically based homogeneity selection method can also be succesfully applied at other locations.

Multivariate analysis

What was seen in the case study was that the homogeneity of a univariate dataset can be judged by extending the univariate set to a multivariate dataset and analyzing the other tuples of the dataset. This principle can be applied to all kind of studies and appears to be very powerful. Consider for example the total yearly precipitation in the Netherlands (figure 5).

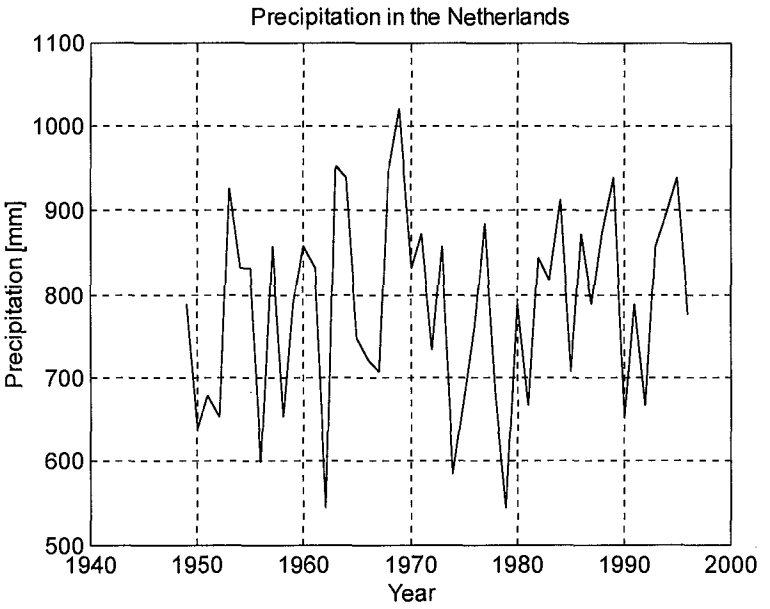

Figure 5. Total yearly precipitation with high variation coefficient.

Although the total yearly precipitation might be expected to be a stable quantity, a variation coefficient of 15% is observed. The univariate dataset of precipitation at each year can be extended to a multivariate dataset with (precipitation, dominant wind direction). Due to the geographic location of the Netherlands, winds from the west are very humid and bring a lot of rain; winds from the east however are very dry. Therefore two different processes can be distinguished and the precipitation dataset should be splitted into at least two subsets.

Conclusions

Homogeneity aspects in the statistical analysis of coastal engineering data have been discussed in this paper. Apart from statistical tests to judge the homogeneity of a data set, also physical arguments have to be included in the judgement. A case study of significant wave height data has been presented to illustrate the differences between the tails of distributions when the homogeneity aspects are left out of consideration.

References

Delta Committee, (1960) Considerations on storm surges and tidal waves (in Dutch), *Rapport Deltacommissie*, Deel 3, Staatsdrukkerij, Den Haag.

Fill, H.D., Stedinger, J.R., (1995) Homogeneity tests based upon Gumbel distribution and a critical appraisal of Dalrymple's test, *Journal of Hydrology*. v 166 p 81-105.

Harnett, Donald L., (1970) *Introduction to Statistical Methods*, Addison-Wesley, London.

Mutua, Francis M., (1994) The use of the Akaike Information Criterion in the identification of an optimum flood frequency model, *Hydrological Sciences Journal*, 39, 3, June 1994.

Rao, A Ramachandra. Hamed, Khaled H., (1994) Frequency analysis of Upper Cauvery flood data by L-momcnts, *Water Resources Management*. v 8 n 3 1994. p 183-201.

Zrinji, Zolt. Burn, Donald H., (1996) Regional flood frequency with hierarchical region of influence, *Journal of Water Resources Planning & Management*-ASCE. v 122 n 4 Jul-Aug 1996. p 245-252.

A simple method to predict long-term morphological changes

Dano Roelvink[1,2] , Alain Boutmy[2] and Jean-Marie Stam[3,4]

[1)] WL | Delft Hydraulics
[2)] Delft University of Technology
[3)] Netherlands Institute for Marine and Coastal Management (RIKZ)
[4)] Netherlands Centre for Coastal Research.

Abstract

A method is presented to obtain a first estimate of long-term bathymetric changes based on an initial transport field obtained from a 2DH process model. The results are compared with full morphodynamic simulations and measured bottom developments after extension of the harbour moles at IJmuiden, the Netherlands.

Introduction

Over the past decade, process-based morphodynamic models based on depth-averaged two-dimensional equations for wave action, flow, sediment transport and bed level change have been developed at several institutes and have now become generally available for application in practical model studies (for a review see De Vriend et al., 1993 ; Nicholson et al., 1993).

The strength of these models lies within their ability to represent the various processes simultaneously, and to evaluate the changes in these processes due to human interference in the form of structures, nourishments or dredging. The outcome of the model is often not very accurate and expertise is needed to calibrate it for a given situation. Even then, absolute predictions are often difficult to make, but a comparison of simulations with and without various scenarios of interference usually yields useful and objective results, based on which an overall advice can be given.

A major problem still lies in the fact that the time-scale of interest in many cases is in the order of decades, whereas the simulation period that can be feasibly covered is usually not much longer than some years. In this paper a simple method will be presented which reduces the computational effort by an order of magnitude, while maintaining an acceptable accuracy. This clears the way for simulations over periods in the order of decades. The simple method will be compared with the full morphodynamic method, and both will be tested against measured bathymetric changes after constructionof a large extension of the harbour of IJmuiden in the Netherlands.

'Standard' morphodynamic method

The 'standard' morphodynamic method applied by various institutes (e.g. de Vriend et al. (1993), Nicholson et al., 1997) involves a coupled simulation of waves, currents, transport and bottom changes. The Delft3D-MOR system, developed by WL | Delft Hydraulics, is one of the systems designed to apply this method in consulting practice. The details are outlined in Roelvink and Van Banning (1994) and Roelvink et al. (1994). Here we present the main features.

Figure 1 Delft3D model structure

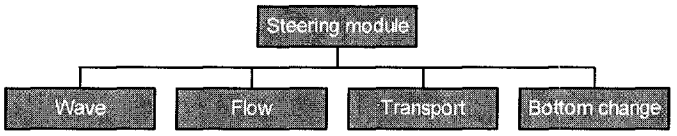

The model structure consists of a steering module and four computational modules, as outlined in Figure 1. The steering module calls the computational modules in any prescribed order, and arranges the time-progress of each module. It allows iterations between modules. The computational modules are:

- Wave module based on HISWA (Holthuijsen et al, 1989). Refraction and dissipation of directionally spread random waves. Several computations through a tidal cycle in one call.
- Flow module solves non-steady, 2DH or 3D shallow water equations on a curvilinear finite difference grid, using ADI scheme. Wave effects on flow through bottom friction and driving terms.
- Transport module solves quasi-3D advection-diffusion equation for sediment. Equilibrium concentrations in this study based on Bijker with wave effects. Recently added cross-shore transport terms using Bailard approach.
- Bottom update module solves sediment balance using explicit scheme of Lax-Wendroff type, with automatic timestep.

Figure 2 Process tree

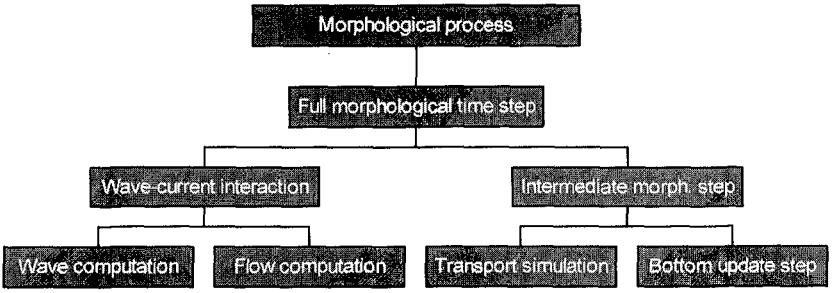

A simulation in Delft3D-MOR is built up like a hierarchical tree structure, a so-called process tree. In Figure 2 a typical tree is given. A morphological process is built up from morphological time steps, which consist of a simulation of wave-current interaction over a tidal cycle, followed by a number of intermediate steps where transport is computed and averaged over a tidal cycle, and the bottom is updated. The transport and bottom computations are repeated a number of times using "continuity correction" (see below), until bottom changes are so large that a full hydrodynamics computation is required.

Sediment balance

The sediment balance equation reads:

$$\frac{\partial z}{\partial t_{mor}} - \frac{\partial S_x}{\partial x} + \frac{\partial Sy}{\partial y} = 0 \tag{1}$$

Here, z is the bed level (positive downward), S_x and S_y the components of the tide-averaged sediment transport vector, and t_{mor} the time; the subscript refers to the fact that the time scale of bottom changes is generally much larger than the tidal period.

Continuity Correction

The sediment transport field is generally a function of the velocity field $\vec{u}$ and the orbital velocity u_{orb}:

$$\vec{S} = f(\vec{u}, u_{orb}) \tag{2}$$

When the bathymetry changes, the flow field and orbital velocity change, and have to be recomputed. The "continuity correction" is a frequently applied method to adjust

the flow field after small changes in the bathymetry. The flow pattern is assumed not to vary for small bottom changes:

$$\vec{q} \neq f(t_{mor}) \tag{3}$$

where $\vec{q} = h\vec{u}$ is the flow rate vector and h is the water depth. The same goes for wave pattern: wave height, period and direction are kept constant, and only the orbital velocity is adapted for the local water depth:

$$H_{rms} \neq f(t_{mor}) \tag{4}$$
$$T_p \neq f(t_{mor}) \tag{5}$$

Since $\vec{u} = \vec{q} / h$ and $u_{orb} = f(H_{rms}, T_p, h)$, adaptation of the sediment transport field is now simply a matter of adjusting the velocity and orbital velocity and recomputing the sediment transport using eq. (2).

In case of a tidal flow situation, a number of velocity and wave fields based on the original bathymetry are stored, and when the depth changes, the adapted transport field is computed for a number of time points in the tidal cycle and subsequently averaged. This averaged transport field is then used in the sediment balance (1).

The method still requires full transport computations through tidal cycle, which can be time-consuming when suspended-load transport is to be accounted for. The morphological time step is often dominated by some shallow points, which are usually not of interest. This means that typically after some 10-20 continuity correction steps, the full hydrodynamic model has to be run on the updated bathymetry.

Rapid Assessment of Morphology (Delft3D-RAM)

In practical consultancy projects there is often a need to interpret the outcome of initial transport computations without having to resort to full morphodynamic simulations. One way of doing this is looking at initial sedimentation/erosion rates, but this method is flawed in many respects. Initial disturbances of the bathymetry lead to a very scattered pattern, and, as De Vriend et al. (1993) point out, sedimentation/erosion patterns tend to migrate in the direction of transport, a behaviour which is not represented in the initial sedimentation/erosion patterns.

What we propose in this paper is a simple method which overcomes these disadvantages. In the previous section, we have seen that under the assumptions used in the "continuity correction", the tide-averaged transport rates are a function of flow and wave patterns which do not vary on the morphological time-scale, and the local depth, which does vary on this time-scale. In other words: given a certain set of

currents and waves, the transport at a given location is only a function of the water depth.

If we can now approximate this function by some simple expression with coefficients which vary from place to place, we end up with a very simple set of two equations: the sediment balance (1) which expresses bottom change in terms of sediment transport gradients, and :

$$\vec{S} = \frac{\vec{S}_{t=0}}{\left|\vec{S}_{t=0}\right|} f(z) \tag{6}$$

This equation describes the reaction of sediment transport to bottom changes. The form of the function f(z) can be estimated by considering that transport usually is proportional to the velocity to some power *b:*

$$\left|\vec{S}\right| \propto |u|^b \propto \left(\frac{|\vec{q}|}{h}\right)^b \propto |\vec{q}|^b h^{-b} \tag{7}$$

Since a similar relationship with the orbital velocity can be assumed, a suitable function is:

$$\left|\vec{S}\right| = A(x,y)h^{-b(x,y)} \tag{8}$$

where the water depth h is taken as $h=z+HW$, and HW is the high water level, which ensures that water depth is always positive.

As a further simplification b can be assumed constant throughout the field. In this case, the value of A in each point can be derived directly from the local water depth and the initial transport rate, which may be computed using a sophisticated transport model.

The combination of equations (1) and (8) can be solved using the same bottom update scheme as in the full morphodynamic model and requires very little computational effort (in the order of minutes on a PC).

In De Vriend et al. (1993), a steady-state version of this concept, aiming at a direct estimate of the equilibrium bathymetry, was presented for the case of a schematised river outflow. In this case, the solution is governed by the upstream boundary condition. In real life, such a condition cannot be found; by using a time-dependent approach as given here and choosing weak boundary conditions far from the area of interest, this problem is avoided.

Applications

RAM is applicable where the flow- and wave patterns are restricted by the geometry, so small bottom changes do not change the overall pattern. This is typically the case near river outflows, around harbour moles and near river training works. In these cases the behaviour simulated by RAM is similar to that using a full morphodynamic model. At the beginning of a simulation, the RAM simulation matches the full solution exactly: the simplified transport equation is made to fit the full model and the bottom update scheme is the same. As time progresses, the two models will deviate as the flow *pattern* starts to react to the bottom changes.

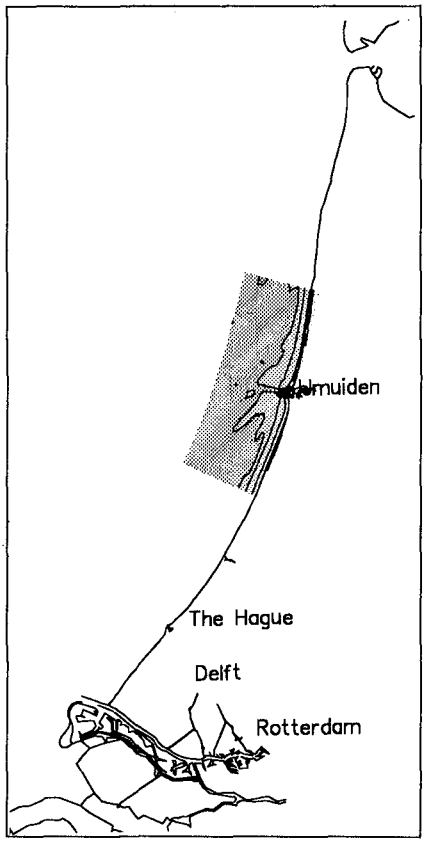

Figure 3. Location map

Test case: IJmuiden harbour

The harbour moles of IJmuiden, the sea port of Amsterdam (see Figure 3), were extended by approx. 2500 m in the period of 1962-1968. A large scour hole has since developed near the tip of the longest, southern harbour mole, and the coast line has accreted more than 500 m since then, especially on the southern side. Further away from the harbour, the coast has suffered erosion.

Regular surveys of the area have been performed and dredging data collected routinely, apart from the yearly sounding of coastal profiles which takes place along the whole of the Dutch coast. In the framework of this study, these data have been compiled, digitised where necessary and tailored for model validation. Data have been collected over a period of 28 years; in this paper we focus on the first 8 years of this period, from 1968 to 1976. Directional wave data are available from stations in approx. 20 m water depth.

The full data set and details of simulations are described in Boutmy (1998).

The tidal motion in the area is well documented and several operational models exist which can be used to generate boundary conditions for a detailed model of the vicinity of the harbour.

In Figure 3 the detailed model area is shown. A curvilinear grid was constructed with a good resolution near the harbour entrance and near the coast, but gradually coarsening towards the model boundaries, which were put some 10-15 km from the harbour. A single representative tide was chosen with an amplitude of 1.1 times the average amplitude. Simulations were carried out without waves, with waves perpendicular to the coast, and with two wave conditions representing south-westerly (245^0 N) and north-westerly (335^0 N) wave directions. This coarse schematisation was (for the time being) thought to be good enough to represent most of the important processes in this comparative study, and allows an insight into the importance of:

- tide only
- waves acting as stirring agent for sediment
- wave-driven currents and
- other wave-induced processes.

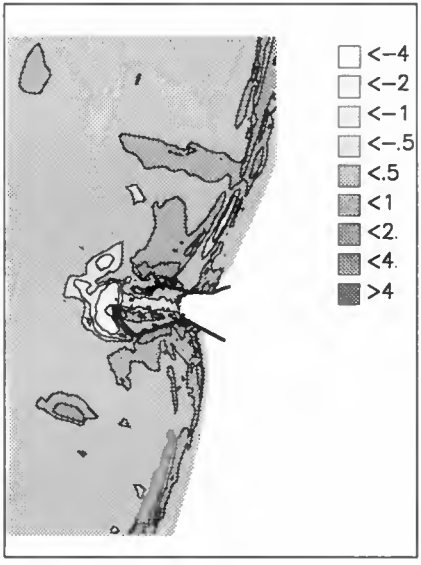

Figure 4. Measured bottom change 1968-1973

Tide only

In Figure 4, the measured sedimentation and erosion is shown for the period 1968-1973. Clearly a scour hole develops in front of the southern harbour mole. The coast southward of the moles accretes strongly, as does the foreshore to the north of the moles. In Figure 5, the same period is simulated with the full morphological model, but taking into account only the tidal flow. Due to contraction around the moles, a scour hole develops; the eroded sand is deposited on either side of the harbour, in deep water. Near the coast and in other areas, nothing happens at all.

In Figure 6, the results are shown for a simulation with RAM based on the first computed transport field. As could be expected for this situation where RAM is clearly applicable, the results are quite similar to the full model. Both runs simulate the development of the scour hole reasonably well.

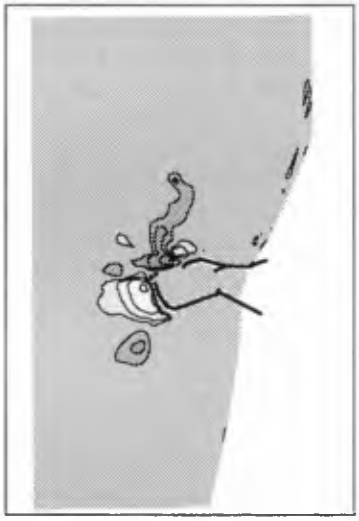

Figure 5. MOR computation '68-'73

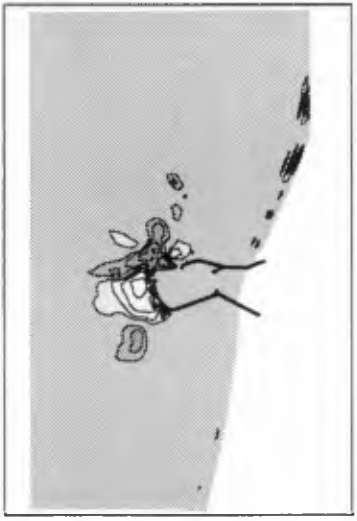

Figure 6. RAM computation '68-'73

Tide plus wave stirring

In the next simulations, waves incident perpendicular to the coast have been introduced in the sediment transport module. The effect of the waves is merely to stir up the sediment which is transported by the tidal current. A representative significant wave height of 1.68 m was derived from the available wave data.

The first simulation with standard settings revealed a rather surprising result (Figure 7): there was a small scour hole some distance from the southern mole, but the dominant feature is the accretion at the entrance. The area near the coast is now eroded, which can be attributed to the large eddies downstream of the moles which transport sand towards the harbour mole and outwards; there, the stirring by waves decreases and the sediment is dropped. This also explains the reduced scour hole in this simulation.

One way to reduce the somewhat exaggerated effect of waves on the stirring of sediment is to reduce the wave-related roughness applied in the Bijker formulation from 5 cm (standard run, Figure 7) to 1 cm. The results are shown in Figure 8. The development of the scour hole and the accretion areas near the harbour is much more

Figure 7. MOR with wave stirring, '68-'73, roughness 5 cm..

in line with the measurements, and the scour hole develops to much greater depth. The interesting conclusion here is, that *decreasing* the transport rates (by reducing the roughness) has the effect of *increasing* the scour.

In Figure 9, the results are shown for RAM, based on the same initial transport field as in Figure 8. The agreement is still quite good, albeit that the changes in RAM are sharper, since it lacks the smoothing effects of a free water surface and spatial lag in the suspended transport.

In none of these simulations the accretion of the shoreline is represented.

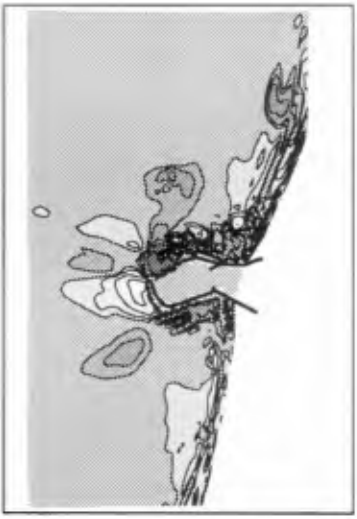

Figure 8. MOR with wave stirring

Figure 9. RAM with wave stirring 1968-1973, roughness 1 cm

The results so far show that for a case where the flow pattern is severly restricted by the geometry, the RAM model is able to reproduce the pattern of sedimentation and erosion over a number of years with reasonable accuracy. The computational cost of the RAM simulation is in the order of minutes on a PC. Obviously, the outcome is

very much determined by the quality of the initial sediment transport field provided by the Delft3D process model.

The nearshore area is dominated by wave-driven currents and cross-shore transport phenomena: the longshore current will deposit sand near both sides of the moles, which will be redistributed across the profile. As a result of this, the coastline moves in seaward direction, while the coastal profiles keep more or less the same shape.

In the final set of simulations, we will review the effect of processes not yet introduced in RAM, in order to see how much further a full process modelling approach will take us.

Tide plus waves

In the final scenarios the simulations were run with alternating wave directions; since we are only interested in the long-term evolution, the wave direction is switched each half year of simulation. Figure 10 shows a detail of the initial tide-averaged sediment transport field for southwesterly wave conditions.

Figure 10. Initial transport field, SW waves.

The northward longshore current is stopped and diverted seaward near the southern mole. At the tip of this mole we see an area with accelerating transports, responsible for the scour hole in that region. Near the tip of the northern mole, the eddy during northward tidal flow and the contraction of the southward ebb current combine to generate a southward nett transport in the direction of the harbour entrance, responsible for considerable accretion. North of the northern breakwater, the longshore current is first directed towards the harbour, due to shielding of the southern waves, but further northward the full transport capacity is restored.

These simulations have been carried out over a somewhat longer period, from 1968-1976. The measured depth changes are shown in Figure 11. In Figure 12, the simulated development is shown. There is now clearly accretion of the coast due to the effect of the longshore current. The developments near the tip of the breakwaters are quite similar to the simulations without wave-driven currents, so that we may conclude that the two systems can be looked ate seperately, at least for the first decade.

The accretion near the southern breakwater takes place about one kilometre from the coast; therefore the coastline itself does not move seaward at all.

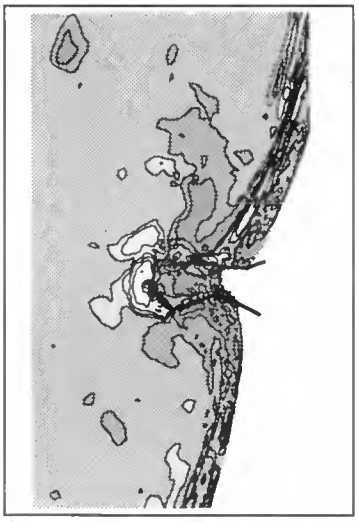

Figure 11. Measured depth changes

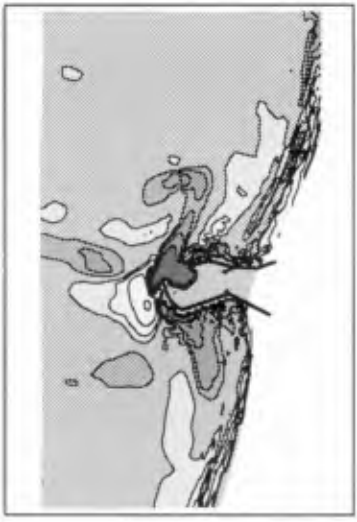

Figure 12. MOR with wave-driven currents
1968-1976, roughness 1 cm

This is due to the fact that in these simulations redistribution of sand across the profile by cross-shore transport is not taken into account. In a final simulation, this effect was investigated.

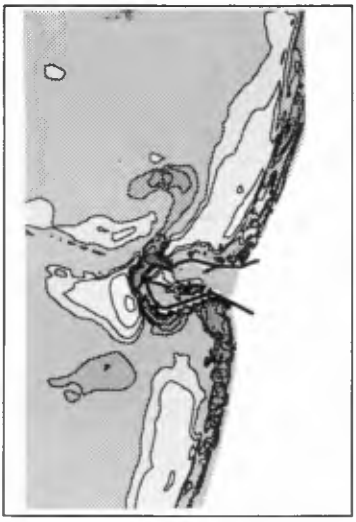

Figure 13. Depth changes '68-'76, simulation including cross-shore transport and dredging.

The Bailard formula (Bailard, 1981) was used to account for the effect of bed slope and wave asymmetry. The contributions of these terms to transport were simply added to the total transport during each morphological step. Calibration coefficients were applied to both terms in order to make the model produce reasonable equilibrium profiles and adaptation time scales. The results for a first test run are shown in Figure 13. Also in this run, a realistic dredging scenario was applied in the simulation, to avoid a build-up of sediment in the harbour entrance. The results appear to be more realistic, and show a clear accretion at the beach. The present settings of the cross-shore transport model are not ideal yet, and lead to profiles wich are somewhat too steep; this explains the erosion of the foreshore in areas outside the direct influence of the harbour.

Finally, the measured 1976 bathymetry is compared with the last simulation in Fig 14 and 15, respectively. This shows that the cross-shore transport module generates too steep profiles; on the other hand, it has the effect of shifting the coastal profiles in seaward direction in a more or less uniform way; this has important benefits in longer-term simulations. The overall shape of the coastal evolution is qualitatively in line with the observed shape.

All simulations shown so far underestimate the depth of the scour hole which develops in front of the harbour. A likely explanation for this is the lack of large-scale 2D turbulence generated near the breakwaters in the model. This is a point of further study at the moment.

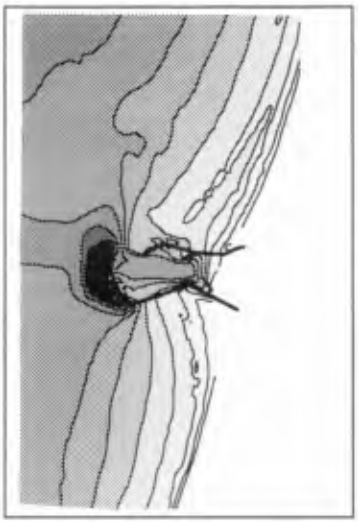

Figure 14. Measured 1976 bathymetry

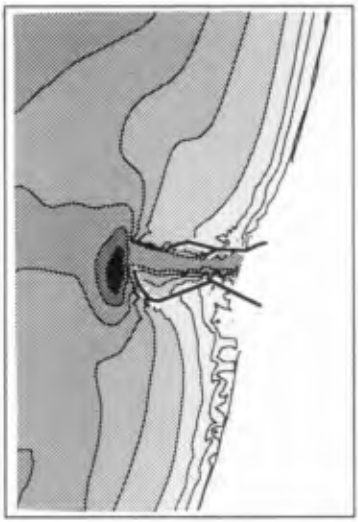

Figure 15 Computed 1976 bathymetry

Conclusions and recommendations

A method has been presented to estimate long-term bathymetric changes based on a single initial transport field. The results over a 5-year period show good agreement between the full morphodynamic MOR model and the simplified RAM approach.

For the present test case, the developments around the harbour entrance can be seen as separated from the coast, and can be modelled well using the RAM approach. This approach means a significant improvement over initial sedimentation/erosion models.

The quality of the initial transport field dominates the outcome; inaccurate modelling of the transport due to combined currents and waves can lead to completely wrong morphological developments. The large-scale 2D turbulence generated near the tips of the breakwaters is likely to be important and must be incorporated in the model.

The simulations with the full model taking into account more wave-related processes show much better predictions in the nearshore area. The processes active in this area cannot be represented in the RAM module for the moment. Further work should be done on implementing these processes in a simplified way.

Acknowledgements

The work presented in this paper was funded by Rijkswaterstaat, the Netherlands, as part of the research programme KUST*2000, order no RIKZ 22971187, and co-funded by the EU-sponsored MaST-3 project SASME, under contract no.MAS3-CT97-0081.

References

Bailard, J.A. (1981). An energetics total load sediment transport model for a plane sloping beach. J. Geophys. Res., Vol. 86, pp. 10,938-10,954.

Boutmy, A.E.G. (1998). Morphological impact of IJmuiden harbour. WL|Delft Hydraulics report Z 2321, August 1998.

De Vriend, H.J., J. Zyserman, J. Nicholson, J.A. Roelvink, P. Pechon and H.N. Southgate (1993). Medium-term 2DH coastal area modelling. Coastal Engineering, 21(1993), pp. 193-224.

Holthuijsen, L.H., N. Booij and T.H.C. Herbers (1989). A prediction model for stationary, short-crested waves in shallow water with ambient currents. Coastal Engineering, 13 (1989) pp. 23-54.

Nicholson, J., I. Brøker, J.A Roelvink, D. Price, J.M. Tanguy, L. Moreno (1997). Intercomparison of coastal area morphodynamic models. Coastal Engineering, 31(1997) pp.97-123

J.A. Roelvink and G.K.F.M. van Banning. Design and development of DELFT3D and application to coastal morphodynamics. Hydroinformatics '94, Verwey, Minns, Babovic & Maksimovic (eds), Balkema, Rotterdam, 1994, pp. 451-455.

J.A. Roelvink, D.J.R. Walstra and Z. Chen. Morphological modelling of Keta Lagoon case. Proc. 24th Int. Conf. on Coastal Engineering, ASCE, Kobe, Japan, pp. 3223-3236.

Coastal Morphologic Variability of High Energy Dissipative Beaches

Peter Ruggiero[1], George Kaminsky[1] and Nathaniel Plant[2]

Abstract

A beach morphology monitoring program was initiated in the Columbia River littoral cell along the coasts of Oregon and Washington, USA, during the summer of 1997. The field program is designed to document short- to medium-term morphologic variability of the high-energy dissipative beaches within the littoral cell over a variety of spatial scales. Following the installation of a dense network of geodetic control monuments, a nested sampling scheme of cross-shore beach profiling, 3-dimensional beach surface mapping and shoreline reference feature surveying was devised. Monitoring is being conducted using RTK DGPS survey methods that combine both high accuracy and speed of measurement. Sampling methods resolve alongshore length scales of O(100 m) to O(100 km) and cross-shore length scales of O(1 m) to O(1 km). Long-term beach profile evolution, estimated via a comparison with surveys collected in the 1940s, feature regional variability. Some beach profiles revealed remarkably little change over the last 50 years. Although this study is in its infancy, large signals in both forcing and response have yielded exciting results. During the 1997/1998 winter, the littoral cell was influenced by one of the most significant El Niño events on record. Steeper than typical southerly wave angles forced alongshore sediment transport gradients that were evident in seasonal morphology on a regional scale. The morphologic data from the monitoring program are being integrated with other geophysical data sets to develop a conceptual model of the region and to begin shoreline change modeling to predict coastal evolution at a management scale (*ie.*, decades and tens of kilometers). The magnitudes of both the environmental forcing and morphologic variability of the beaches along the Columbia River littoral cell are greater than the better understood, lower energy and more reflective beaches of, for example, Duck, North Carolina and the central Dutch coast (Holland). These differences in scale raise questions regarding the validity of directly applying morphologic change models developed from these coasts to the Columbia River littoral cell.

[1] Washington Department of Ecology, Coastal Monitoring & Analysis Program, P.O. Box 47600, Olympia, WA, 98504-7600, USA, tel 360.407.6230, fax 360.407.6535, prug461@ecy.wa.gov (Ruggiero); tel 360.407.6797, fax 360.407.6535, gkam461@ecy.wa.gov (Kaminsky).

[2] University of Twente (CT&M), PO box 217, 7500 AE Enschede, The Netherlands, tel (31).053.489.4753, fax (31).053.489.4040, N.G.Plant@sms.utwente.nl.

Introduction

A regional study of long-term coastal evolution and shoreline response has been initiated for a 160 km long littoral cell in the Pacific Northwest of the United States extending from Tillamook Head, Oregon to Point Grenville, Washington (Kaminsky *et al.*, 1997). The Columbia River littoral cell (CRLC) is characterized by wide dissipative beaches of fine sand, ranging between 0.13 and 0.23 mm in mean diameter, typically backed by broad dune fields or sea cliffs. Beaches in the region have 3-dimensional multiple bar systems with infragravity energy dominating the inner surf zone. Four sub-cells exist within the region separated by three large estuaries, the Columbia River, Willapa Bay and Grays Harbor. Although this region is well known for the severity of its wave climate, most of the littoral cell has historically been accretionary. Recently, however, episodes of severe erosion throughout the cell (Figure 1) have resulted in lost or damaged infrastructure, threatening local economies. To date, millions of Federal and State dollars have been spent on erosion mitigation efforts. In many areas the long-term accretion appears to have slowed or even reversed, indicating a regional trend of erosion. Both anthropogenic influence and variability in large-scale environmental forcing may be causing these changes in morphologic behaviour.

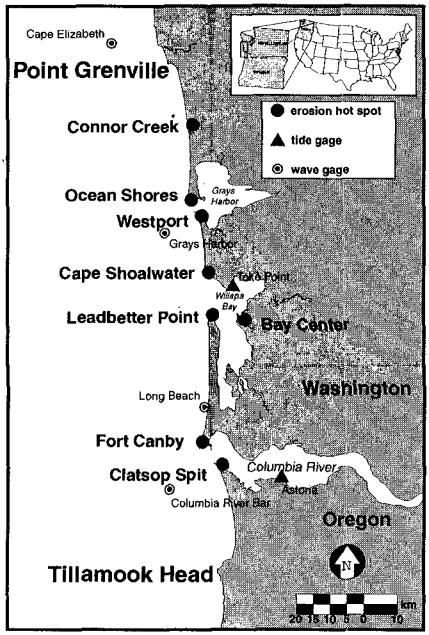

Figure 1. The Columbia River littoral cell with erosion hot spots and the locations of long-term wave and tide measurements.

This paper discusses the variety of survey techniques being applied to and the initial results from a regional beach morphology monitoring program designed to quantify morphologic variability within the CRLC at a variety of spatial and temporal scales. The objectives of the monitoring program include: the quantification of short- to medium-term (event-seasonal-interannual) morphologic variability; development of data sets for beach profile modeling; shoreline change and coastal flooding predictions; and the comparison of variability scales with other coastlines. These objectives are aligned with a primary goal of the Southwest Washington Coastal Erosion Study, predicting coastal behaviour of the CRLC at a management scale. Several existing long-term monitoring programs, specifically the beach profiling done at the US Army Corps of Engineers Field Research Facility (FRF) in Duck, North Carolina and the Jarkus data base of the Dutch Department of Public Works (Rijkswaterstaat), provide guidance for designing sampling schemes. Since 1981, bi-monthly beach surveys have been collected at the FRF over a 1 km alongshore reach with the Coastal Research Amphibious Buggy (CRAB). Utilizing this dense data set, many researchers have examined long-term beach profile evolution and sand bar migration patterns to develop valuable engineering models of coastal morphology (*eg.*, Larson and Kraus, 1994 and Plant, 1998). The Jarkus data set, which consists of 30 years of annual profiles spaced every 250 meters along the Dutch coast, has also led to advances in understanding temporal profile evolution and the spatial variability in morphologic behaviour. Components of these programs, particularly observations of meso- to large-scale fluctuations and alongshore inhomegenity, were considered in the design of the CRLC beach morphology monitoring program. The program has been established to acquire regional coverage of the littoral cell that is dense enough to resolve short-term change of kilometer scale evolution of the coastal planform. Results from this study are being used to develop a conceptual model of coastal morphologic variability on high-energy dissipative beaches.

Monitoring Program Components

Beach morphology monitoring is being conducted using Real Time Kinematic Differential Global Positioning System (RTK DGPS) surveying techniques, widely accepted as an accurate and efficient means to collect coastal morphology data (Morton *et al.*, 1993). The following sections describe the techniques associated with each component of the monitoring program.

Geodetic Control

In order to reference all monitoring program data to consistent horizontal and vertical datums, a dense network of 77 geodetic control monuments was established during the summer of 1997 (Figure 2a). After an inventory of existing monuments within the littoral cell, 13 additional monuments were installed to ensure consistent spacing of 3 to 4 km along the coast. A two-week field campaign was then conducted using 8 dual-frequency full-wavelength GPS receivers to establish a 2 cm-level vertical control network in accordance with the most recent guidelines provided by the National Geodetic Survey. The network has been referenced to the Washington State Plane (South) North American Datum of 1983 (NAD 83) and the land-based North American Vertical Datum of 1988 (NAVD 88).

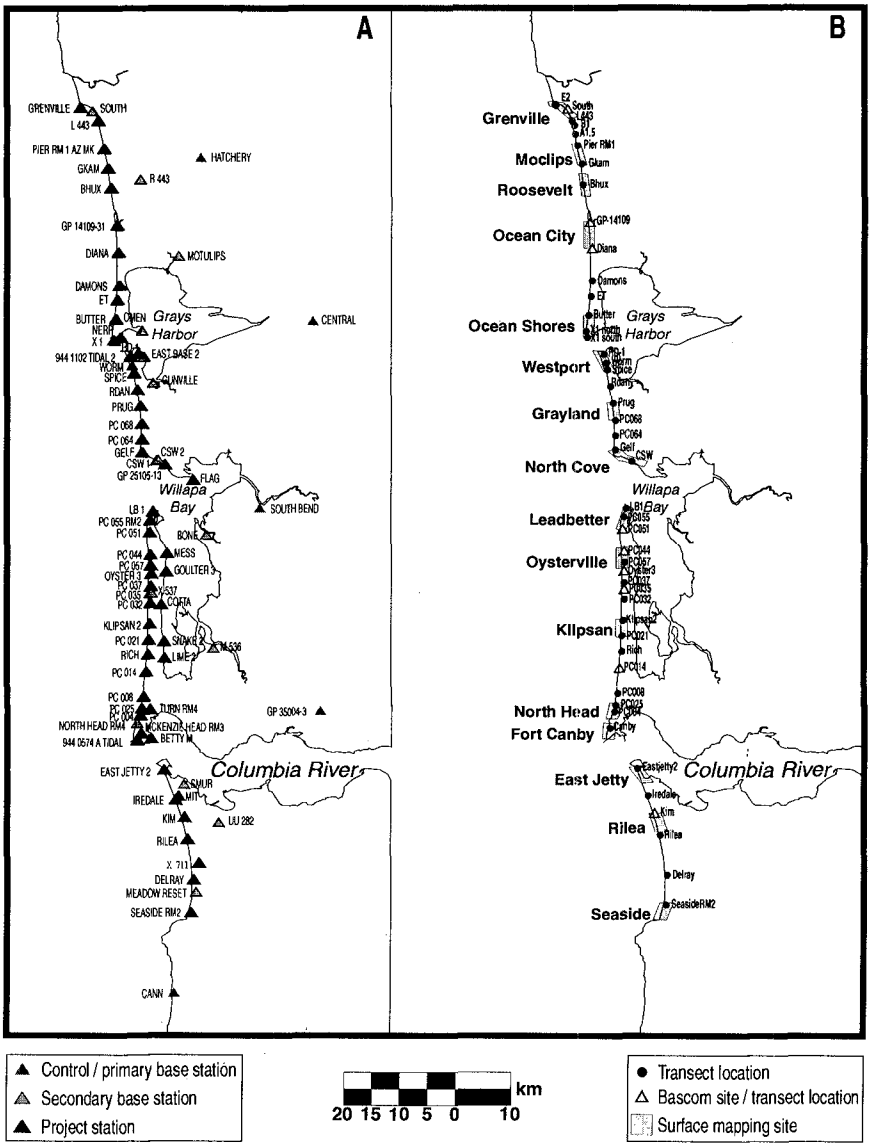

Figure 2. a) Locations of geodetic control monuments and b) locations of beach profiles and 3 dimensional surface maps.

Cross-shore beach profiles

The high-energy dissipative beaches of the Pacific Northwest have been studied less intensely than the lower energy, more reflective beaches typical of the US East Coast. Initial attempts at creating a regional database (Peterson *et al.*, 1994) and scattered work by resource management agencies, comprised the only beach morphology data for the Columbia River littoral cell before the onset of the Southwest Washington Coastal Erosion Study (Kaminsky *et al.*, 1997). The first comprehensive regional morphology monitoring program began in the summer of 1997. In an effort to quantify seasonal morphologic change, cross-shore beach profiles are being collected bi-annually at 47 locations, spaced approximately 3-4 km throughout the littoral cell (Figure 2b). Profile locations are typically coincident with the locations of control network survey monuments. The beach profiles are obtained by walking from the landward edge of the primary dune to wading depth at spring low tides with a GPS receiver and antenna mounted to a backpack. Although the manufacturer's reported 3-dimensional error of the RTK GPS receiver is less than 2 cm, the vertical RMS error of this technique compared to surveying with a leveled pole and bipod is typically 4 cm. While not as accurate as standard terrestrial surveying, this technique is justified by both the reduction in survey time and the large morphologic change signals observed on these beaches. A field experiment scheduled to begin in spring 1999 will begin to examine beach profile evolution on even shorter (processes) time scales via bi-weekly surveys at a number of locations.

Due to the difficulty of surveying in the Pacific Northwest's dissipative, yet energetic nearshore environment (mean annual significant wave height is 2.0 m), most beach profiles do not extend beyond the inner surf zone. Willard Bascom and associates, in conjunction with the Wave Project of the University of California at Berkeley, collected the only set of nearshore bathymetric surveys in the region prior to the onset of this study (Komar, 1978 and Kraus *et al*, 1996). In an attempt to document long-term morphologic change, these profiles are now being re-occupied utilizing a new technique, the Coastal Profiling System (CPS), developed at Oregon State University (Beach *et al.*, 1996, Cote *et al.*, in press). The system consists of a Yamaha Waverunner III equipped with an RTK GPS receiver, an echo sounder and onboard data storage capabilities. The system was extensively tested during the SandyDuck field experiment at the FRF in the fall of 1997 with results indicating an RMS error ranging from 10 to 20 cm. A reconnaissance level, nearshore bathymetric survey campaign was initiated in the CRLC in April 1998. Beach profiles, spaced at 150 m over 2-3 km long sections, from the beach to the 12 m depth contour, have been collected in the approximate center of each of the four sub-cells. These study sites were chosen to overlap with beach surface mapping sites (described in the next section) and include Ocean City, Grayland, Oysterville, Rilea, and Fort Canby (Figure 2b). A series of seasonal surveys in April, July, and October 1998 is underway at the northern most site, Ocean City, WA, in an attempt to document seasonal bar migration patterns.

Beach Surface Maps

Although analysis of beach profiles can reveal both cross-shore variability in beach elevation and volumetric change over an individual profile, little information about the

longshore component of morphologic change can be obtained. In lieu of multiple closely-spaced cross-shore transects, three-dimensional surface maps are being generated by mapping the beach surface with a GPS antenna mounted to a six-wheel drive amphibious all-terrain vehicle called the CLAMMER (CoastaL All-terrain Morphology Monitoring and Erosion Research vehicle). Alongshore reaches, approximately 4 km in length, are being mapped between the toe of the primary dune and the swash zone (typically 100's of meters in the cross-shore direction due to mild sloping beaches). To determine both the alongshore and cross-shore morphologic variability at a variety of spatial scales, 16 sites (Figure 2b), totaling more than 60 km of alongshore distance, are being surveyed bi-annually.

Individual measurements are densely spaced in the alongshore direction, O(5-10 m), to resolve relatively small-scale features such as beach cusps, and are over long enough distances to resolve larger scale, potentially migrating features such as mega-cusps, rip-current embayments, sand waves and regional gradients. The cross-shore distance between alongshore transects is typically 20 - 30 m but is determined in the field based on cross-shore breaks in beach slope such as at swash bar crests and troughs. The non-uniformly spaced raw data (typically 5,000 to 10,000 points) is mapped onto a surface via triangle-based, weighted linear interpolation. The model surface is then interpolated on a uniform 2-dimensional grid for comparing subsequent data sets. Although individual model elevations feature sub-decimeter accuracy, the RMS error of the interpolated surface compared to detailed surveying using a leveled pole is typically 5 cm. Surface maps are collected bi-annually at all 16 sites to determine seasonal fluctuations, however, in areas that are eroding rapidly, survey frequency has been increased in an attempt to determine shorter scale temporal changes, *eg.* mega-cusp migration.

Other Monitoring Components

Four surface sediment samples are collected at each beach profile location, within the dune, at the dune toe, at mid-beach and within the swash zone at low tide. Sand grain size distributions are being determined by using ASTM approved dry sieves at quarter phi intervals following current EPA protocols for sediment analysis in the state of Washington. Modern shorelines are being mapped on rapidly eroding beaches by walking erosion reference features, such as scarps or driftlines, with a GPS backpack. This shoreline position data is being used to complement the historical shoreline change analyses being conducted by digitizing historical NOS topographic sheets and aerial photography (Kaminsky *et al.*, in press, a). Shoreline change reference features also serve to expand the regional coverage between cross-shore profiles and provide a definite shoreline boundary to the beach surface maps. Several remote sensing techniques have also been applied within the CRLC as part of the Southwest Washington Coastal Erosion Study including airborne laser mapping and remote video technology. Lidar coverage, as part of a NASA/NOAA/USGS cooperative, will be used to create a high resolution Digital Elevation Model of the littoral cell. A video station (Argus camera) has been installed at Cape Shoalwater and a second station is scheduled for deployment at Ocean Shores in October 1998 for processes scale (*e.g.*, mega-cusp migration) studies.

Waves and Water Levels

Coupled with the beach monitoring program is the long-term analysis of environmental data, *eg.*, waves and water levels. The locations of long-term wave (both NOAA and CDIP gages) and tide measurements are shown in Figure 1. Mean annual significant wave height along the CRLC is approximately 2.0 m with a peak period of 10 s with winter storms generating waves greater than 8.0 m with 20 s periods (Ruggiero *et al.*, 1997). There is a distinct seasonality in wave height, period and direction with increased wave heights and periods propagating from the south in the winter and lower waves and periods arriving from the north in the summer. The littoral cell is meso-tidal with a 2.0 to 4.0 m range and winter water levels as much as 0.3 m higher than the summer water levels. Figure 3 illustrates the seasonality of both the water levels measured at Toke Point, WA, and the wave parameters taken from the Grays Harbor directional waverider buoy.

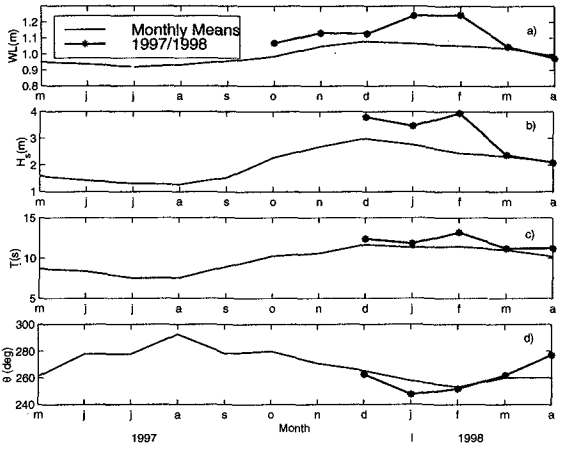

Figure 3. Monthly mean a) water levels, WL, for the Toke Point tide gage (NAVD 88), b) significant wave heights, H_s, c) periods, T, and d) direction, θ, from the Grays Harbor buoy. Values from the 1997/1998 El Niño event are shown with darker lines and asterisks.

1997/98 El Niño

The winter of 1997/1998, the first winter of the monitoring program, coincided with one of the largest El Niño events of the 20th century. In the Pacific Northwest, strong El Niños are decadal scale forcing anomalies featuring increased frequency of extreme waves from the south-southwest and higher than normal sea levels (Komar and Good, 1989). During the previous major El Niño, 1982/1983, large wave heights and acute wave angles forced excessive offshore and northerly sand transport, causing severe beach erosion and shoreline orientation change that persisted for several years (Peterson *et al.*, 1990). The 1997/1998 El Niño fit this pattern by generating some of the highest water levels on record in the Pacific Northwest (Figure 3a). Monthly mean water levels were

typically 10-15 cm higher than usual for much of 1997 with the main increase in elevation occurring in January and February 1998.

Wave conditions were also more intense than typical during the 1997/1998 winter. Figures 3b and 3c show the increase in monthly mean values for both significant wave height and period. The most intense month, February, featured wave heights on average of 1 m higher than normal with wave periods over 2 s greater than normal. During the months of January and February 1998 there were 13 storm events in which the significant wave height reached or exceeded 6 m, approximately the 1 year event (Ruggiero *et al.*, 1997). Figure 3c shows that in January 1998 waves approached the coast from a more acute southerly angle than typical, as derived from monthly mean calculations since 1993, when the gage became directional.

Initial Results

Like any long-term monitoring program, the data collected as part of this study will increase in value over time. Although limited to one year of data at the time of this publication, the monitoring program is beginning to reveal scales of morphologic change within the littoral cell for comparison with lower energy reflective beaches. Results from other monitoring components, *ie.* Argus remote sensing techniques and shoreline change analyses will be provided in subsequent publications.

Cross-Shore Beach Profiles

The 47 beach profiles in the monitoring program provide a regional inventory of the variability of beach slope, elevation and volume change during the seasonal exchange from summer (calm or berm profile) to winter (storm or barred profile). In order to extract comparable quantitative statistics from beach profiles ranging over the 160 km long littoral cell, standard methods need to be adopted. Many predictive runup models depend on foreshore beach slopes, (Ruggiero *et al.*, 1996). Therefore, slopes have been computed for each of the profiles between the 1.0 m and 3.0 m contour elevations. This definition of beach slope coincides with the Bascom (1951) definition of a "reference point" for comparison of profiles taken at a variety of locations, *i.e.*, the "part of the beach face subject to wave action at mid-tide elevation." The elevation of MSL varies along the length of the cell between approximately 0.9 and 1.4 m NAVD 88. Foreshore beach slopes vary between 1:100 and 1:10 while a mean slope for this dissipative cell is approximately 1:75.

Volume change between subsequent profiles has been calculated between the 1.0 m and 4.0 m contour elevations. Although many of the summer profiles extend to lower contours, the winter profiles were taken during periods of high wave conditions when both wave setup and swash limited the depth to which profiles could be safely obtained. The volume calculations have been further standardized, reducing the effect of beach slope variability, by normalizing by the cross-shore length between contours. Regional scale volume change is thus presented as an average vertical change across subsequent profiles between the 1.0 m and 4.0 m contours for each of the 47 profiles in Figure 4a. As anticipated, the southern ends of sub-cells, Ft. Canby, Cape Shoalwater and Ocean

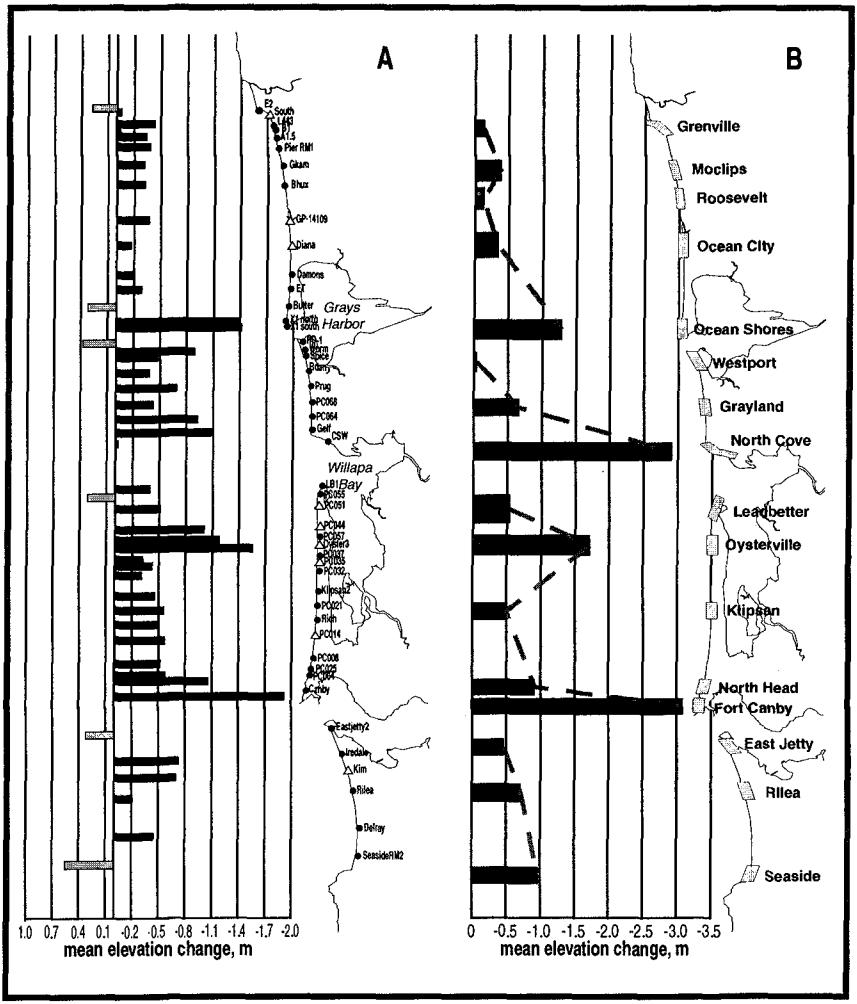

Figure 4. Beach elevation change calculated from a) beach profiles and b) surface maps.

Shores, experienced high levels of erosion during the El Niño winter of 1997/1998. The accretion at Tillamook Head (profile Seaside RM2) is associated with the northerly migration of a small creek, consistent with the expected pattern of El Niño influenced sediment transport. Remarkably, erosion hotspots at the northern ends of sub-cells, Clatsop Spit and Westport, showed net accretion during the winter. The three northern most sub-cells each reveal a trend of decreasing erosion from south to north, however erosion volumes are not balanced between erosion and accretion indicating substantial

offshore sediment transport. A detailed description of other El Niño related observations can be found in Kaminsky *et al.* (in press, b). Initial analyses of profile data from the summer of 1998 reveal a surprisingly rapid recovery of many of the beaches within the cell. More data will be necessary to identify anomalous morphologic change signals in response to this decadal scale forcing event.

The Coastal Profiling System was utilized to extend the cross-shore beach profiles and surface maps beyond the swash zone at 5 locations during summer 1998, including 3 of the 9 Bascom profiles. A simple Hallemeir-type calculation based on the 1-year return wave height and period gives an estimated profile closure depth of 12 m. It was not always possible to survey to this depth during the field campaign due to high waves and fog. Figure 5 provides sample profiles, Ocean City (a) and Oysterville (b), in which CLAMMER and CPS data have been merged and compared to Bascom's data collected in the 1940s. The large gap in the Ocean City profile (approximately 300 m) is due to the CPS not resolving the bathymetry in the surf zone under relatively high wave conditions (approximately 3 m in April 1998). The origin of the coordinate system has been set at the cross-shore position of the 4.0 m NAVD 88 contour in the 1945 profile. The Bascom data was originally collected and reported in MLLW and has been adjusted to the land based vertical datum. Corrections for the horizontal offset between subsequent profiles were determined via historical aerial photographs and shoreline change rates.

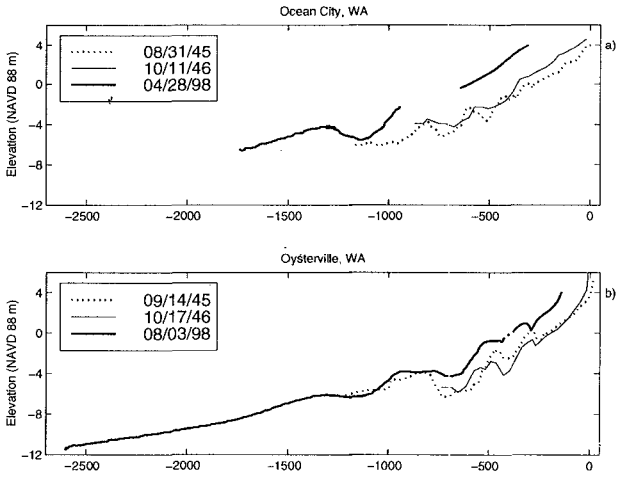

Figure 5. Beach profiles at a) Ocean City and b) Oysterville comparing data collected by Bascom and associates in the 1940s with modern profiles collected with the Coastal Profiling System and the CLAMMER.

The example profiles illustrated in Figure 5 suggest that recent beach slopes are similar to those of Bascom's profiles collected over a half century ago. However, dramatic shoreline change has occurred during this period, with approximately 2 m of beach

elevation gain along most of the profile. The earlier surveys show substantial short-term fluctuations of the upper beach profile associated with either seasonal variability or alongshore sediment transport gradients. The modern Ocean City profile is different than the Bascom data in that the sand bar is broader and contains more sediment volume. The Oysterville data is remarkable, as the form of the profiles, separated by over 50 years, is almost identical with 3 distinguishable bars of similar magnitudes in the same cross-shore position. All sites where nearshore bathymetry has been collected are characterized by multiple barred profiles with varying levels of 3-dimensionality. Two offshore sand bars can be identified at each survey site between the 2.0 m and 7.0 m depth contours with vertical relief O(2 m). An additional bar in the swash zone at the 0.0 m contour was resolved in some cross-shore profiles. Sand bar formation and migration patterns will be determined from the series of quarterly surveys at Ocean City, WA.

Beach Surface Maps

Surface maps have been collected at 16 sites throughout the littoral cell in order to resolve 3-dimensional morphologic features and changes and to eliminate the alongshore aliasing problem of single cross-shore beach profiles. Figure 6 shows the difference between surface maps collected at Ocean Shores, WA, on 18 August 1997 and 27 February 1998. The patterns of alternating accretion and erosion represent the migration of morphologic features such as megacusps and rip current embayments. A series of monthly surface maps has been collected at this site since summer 1997 generating a 1-year time series of morphodynamic change. Superimposed on the map are the 1.0 m, 2.0 m and 3.0 m contour elevations over the 4 km stretch of beach. The average horizontal retreat of these contours has been calculated for each of the 16 surface maps. Flatter beaches will experience greater contour recession than steeper beaches for a similar forcing. For inter-comparison, the horizontal retreat has been normalized by multiplying by the average beach slope along the length of the mapped region. This calculation gives a proxy for the average vertical change between the position of the elevation contours. Figure 4b illustrates this quantity for the 2.0 m contour between the summer 1997 and winter 1998 surface maps. These results show the regional gradient in erosion from south to north along each of the sub-cells. The southern boundaries at each sub-cell, Seaside, Fort Canby, North Cove and Ocean Shores, exhibited severe erosion, while the northern sub-cell boundaries all showed nearly the minimum elevation change for the sub-cell. Most of these areas are erosion hot spots, therefore it will be important for future monitoring to distinguish the El Niño signal from typical seasonal changes and long term trends.

Engineering Applications of Morphology Data

Beach morphology monitoring data is being directly applied to a variety of existing coastal processes models with the ultimate goal of predicting shoreline evolution. The Dutch model UNIBEST (Delft Hydraulics, 1995) is currently being applied to the northern sub-cell to model decadal scale shoreline evolution. Nearshore bathymetric surveys will be used in attempts to determine closure depths within the cell, a critical parameter in one-line shoreline change models such as UNIBEST. Engineering profiles such as the Dean equilibrium profile (Dean, 1977) and exponential profiles (Komar and McDougal, 1994) are being fitted to the measured cross-shore bathymetry for input into

these processes models. The tuning parameters for each model have been determined by minimizing the RMS error between the measured profile and the modeled profile in a least squares sense. The Dean profile typically has a slightly lower RMS error which better models the inner-surf zone, while the exponential profile performs better in deeper water.

Beach slopes and intersection elevations of the beach face and backing dune are being used in a probabilistic model (Ruggiero *et al.*, 1996), developed specifically for high-energy dissipative beaches. The model evaluates the relative susceptibility of coastal properties to flooding and erosion based on extreme water levels and wave conditions. Model results will be used to enable coastal planners to make informed, long-term coastal management decisions. Surface mapping data, coupled with nearshore bathymetric surveys, are being used to quantify seasonal and long-term adjustments of the entire nearshore planform. Following a spring 1999 experiment, event driven cross-shore beach profile response will be correlated with environmental forcing data in efforts to calibrate cross-shore beach and dune erosion models for Pacific Northwest beaches.

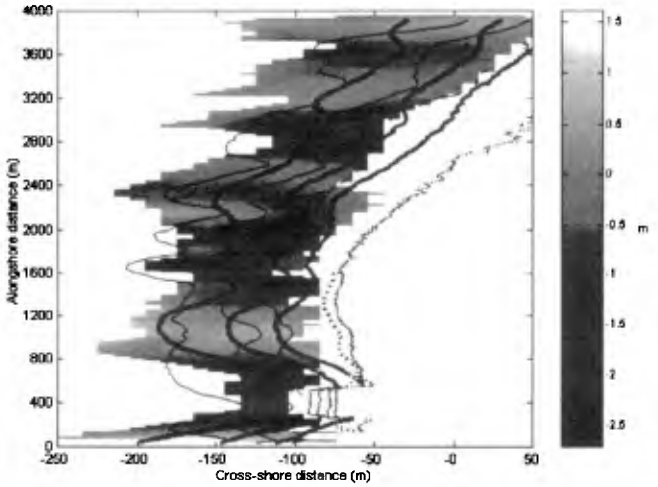

Figure 6. Surface difference map for Ocean Shores, WA from 18 August 1997 to 27 February 1998. The grayscale bar to the right of the figure represents the vertical change over the mapped area with darker shades indicating erosion and lighter shades indicating accretion. The 1.0 m, 2.0 m and 3.0 m contour positions are shown for both the summer 1997 data, light lines, and the winter 1998 data, darker lines. Also shown in the diagram is horizontal retreat of the erosion scarp backing this site, dashed to solid line, and the location of a rock revetment (solid lines show the stepped revetment at the 400 m alongshore distance) designed to slow this shoreline retreat at one location.

Conclusions

A morphology monitoring program has been initiated in the CRLC, consisting of 47 cross-shore beach profiles and over 60 km of beach surface topography, documenting short- to medium-term morphologic variability. This program is beginning to provide regional scale quantitative data on high-energy dissipative beaches for the first time in the Pacific Northwest. The 1997/1998 seasonal response was very large, in part due to a major El Niño event. Gradients in sediment transport are evident in the regional morphologic response to this decadal-scale forcing event.

High quality long-term data sets exist in other locations, with two of the most comprehensive collected at Duck, NC and the Dutch coast. Much has been learned about morphologic behaviour at these sites and many models have been formulated from the data. In order to determine the applicability of these morphodynamic models to the CRLC, the scales of environmental forcing and morphologic response need to be compared. Table 1 lists several parameters and gives ranges and mean values from the CRLC as well as typical values for Duck and the central Dutch coast (Plant, 1998; Wijnberg, 1995). The CRLC features higher energy than the other two coastlines and the morphology is more dissipative with finer sediment sizes and lower beach slopes, β, both on the foreshore and within the surf zone (from the +1 m contour to 750 m seaward). At least for the winter of 1997/1998, the seasonal morphologic variability (average change in elevation across a profile, ΔZ, and the average 2.0 m contour recession, ΔX) appears to be greater in the CRLC than at Duck or in Holland. Future work will include the collection of data to improve the temporal resolution of morphologic variability and existing models will continue to be tested, identifying modifications necessary for application to the CRLC.

Table 1. Scales of environmental forcing and morphologic change.

Parameter	Range (CRLC)	Mean (CRLC)	Duck, NC	Holland
H_s (m)	1.0 – 8.0+	2.0	1.1	1.2
T (s)	5.0 – 20.0	11.0	8.4	5.0
Tide (m)	2.0 – 4.0	3.0	1.5	1.6
β (foreshore)	0.01 – 0.095	0.02	0.10	0.03
β (surf zone)	0.0067 – 0.0095	0.008	0.01	0.0065 – 0.017
D_{50} (mm)	0.13 – 0.23	0.18	0.50	0.26
ξ_o (surf similarity)	0.10 – 0.75	0.19	0.5 – 2.5	0.20
Bar Height (m)	1.0 – 2.8	2.0	0.9	2.0
Δ Z (m)	-1.92 – 0.55	-0.45	-0.3 – -0.1	-0.3
Δ X (2.0 m)	-109.0 – -0.6	-33.0	-15.0 – -10.0	-15.0 – -10.0

Acknowledgements

The United States Geologic Survey and the Washington Department of Ecology are providing funding to support this work as part of the Southwest Washington Coastal Erosion Study. The authors would like to thank Brian Voigt for his inspiration and

creative figure development. We would also like to thank Jessica Cote, Diana McCandless, Josh Fisher and Emily Lindstrum for their substantial contributions to the field program.

References

Bascom, W.N., (1951). "The relationship between sand size and beach-face slope," *Transactions, American Geophysical Union*, 32, No. 6, pp. 866-874.

Beach, R.A., R.A. Holman, and J. Stanley, (1996). "Measuring nearshore bathymetry on high energy beaches." *Book of Abstracts, American Geophysical Union Fall Meeting*, p. F286.

Cote, J.M., R.A. Holman, and P. Ruggiero, (in press). "Nearshore bathymetry within the Columbia River littoral cell," *Book of Abstracts, American Geophysical Union Fall Meeting.*

Dean, R.G., (1977). "Equilibrium beach profiles: U.S. Atlantic and Gulf coasts," *Ocean Engineering Technical Report No. 12*, Department of Civil Engineering, Newark, University of Delaware.

Delft Hydraulics (1995). "Yearly averaged sediment transport along the Dutch shore; upgrading of UNIBEST-TC." Report H2129.

Kaminsky, G.M., P. Ruggiero, G. Gelfenbaum, and C. Peterson (1997). "Long term coastal evolution and regional dynamics of a US Pacific Northwest littoral cell," *Proceedings of Coastal Dynamics '97, the International Conference on Coastal Research through Large Scale Experiments*, pp. 614-623.

Kaminsky, G.M., R.C. Daniels, R. Huxford, D. McCandless, and P. Ruggiero (in press, a). "Mapping erosion hazard areas in Pacific County, Washington," *Journal of Coastal Research.*

Kaminsky, G.M., P. Ruggiero and G. Gelfenbaum (in press, b), "Monitoring coastal change in Southwest Washington and Northwest Oregon during the 1997/1998 El Niño," *Shore and Beach.*

Komar, P.D., (1978). "Beach profiles on the Oregon and Washington coasts obtained with an amphibious dukw," *Shore and Beach*, 46, No. 3, pp. 27-33.

Komar, P.D. and J.W. Good, (1989). "Long-term erosion impacts of the 1982-83 El Niño on the Oregon coast," *Proceedings of Coastal Zone '89*, pp. 3785-3794.

Komar, P.D. and W.G. McDougal, (1994). "The analysis of exponential beach profiles," *Journal of Coastal Research*, pp. 56-69.

Kraus, Nicholas C., R.L. Weigel, and W.N. Bascom, (1996). "Beach profile surveys along the U.S. Pacific Coast 1945-1947," *Proceedings of the 25th International Coastal Engineering Conference, ASCE*, pp. 3020-3033.

Larson, M. and N.C. Kraus, (1994). "Temporal and spatial scales of beach profile change, Duck, North Carolina," *Marine Geology*, 117, pp. 75-94.

Morton, R.A., M.P. Leach, J.G. Paine, and M.A. Cardoza, (1993). "Monitoring beach changes using GPS surveying techniques," *Journal of Coastal Research*, 9(3), pp. 702-720.

Peterson, C.D., P.L. Jackson, D.J. O'Neill, C.L. Rosenfeld, and A.J. Kimerling, (1990). "Littoral cell response to interannual climatic forcing 1983-1987 on the central Oregon coast, USA," *Journal of Coastal Research*, 6, No. 1, pp. 87-110.

Peterson, C.D., M.E. Darienzo, D.H. Hamilton, D.J. Pettit, and R.K. Yeager, (1994). "Cascadia beach-shoreline database, Pacific Northwest Region, USA," *State of Oregon Department of Geology and Mineral Resources, Open File Report 0-94-2.*

Plant, N.G., (1998). "The role of morphologic feedback in surf zone sand bar response," *Ph.D. Thesis, COAS, Oregon State University*, Corvallis, Oregon, 167 pp.

Ruggiero, P., P.D. Komar, W.G. McDougal, and R.A. Beach (1996). "Extreme water levels, wave runup and coastal erosion," *Proceeding 25th International Conference on Coastal Engineering, ASCE*, pp. 2793-2805.

Ruggiero, P., G.M. Kaminsky, P.D. Komar, and W.G. McDougal, (1997). "Extreme waves and coastal erosion in the Pacific Northwest," *Ocean Wave Measurement and Analysis, Proceedings of the 3rd International Symposium, Waves '97*, pp. 947-961.

Wijnberg, K.M., (1995). "Morphologic behaviour of a barred coast over a period of decades," *Ph.D. Thesis, University of Utrecht*, Utrecht, the Netherlands, 245 pp.

EFFECT RESONANCE ON MORPHOLOGY OF TIDAL CHANNELS

Willem T.Bakker [1]

Abstract

Tidal basins with a length of the order of 1/4 of a wave length of the dominant tide, susceptible to resonance, occur on many sites on the world. This paper will show, that these basins can become morphologically unstable. The most primitive schematization possible has been investigated: a prismatic channel, closed at one end. Under some circumstances (for which dimensionless criteria are given), small increments in depth intensify the vertical tidal amplitude at the landward side of the basin, which in turn triggers increased erosion of the basin. Knowledge on this subject can lead to redirect sand fluxes in the basin by taking small measures just in time. Starting from the assumption of a power-law sand transport formula, it is found, that for prismatic channels, morphodynamic instabilities occur when a small increment dh of depth generates a larger value[2] of Z_0/h, where Z_0 is the amplitude of the vertical tide at the landward end of the channel. This criterium can be translated in relative length of the basin and in bottom roughness (fig.2).

Method

Only the Eulerian resultant current and the first harmonic of the tidal motion have been taken into account. The morphological model consists of 3 parts: "hydraulics"; "accretion/erosion" and "morphodynamic stability".

a. hydraulic computation (the water motion in the channel):

- The first harmonic is calculated analytically with the harmonical method of LORENTZ et al. (1926). If friction would have been neglected, the incoming tidal wave and the corresponding reflected wave would have resulted in a standing wave. However, friction makes the reflected wave much weaker than the incoming wave. Thus, the character of the wave shifts from "propagating" at the entrance of the basin (vertical tide and velocity are nearly in phase) to

1 Delft University of Technology; P.O.Box 5048; 2600 GA DELFT; Netherlands tel.+31-15-2785476; fax +31-15-2783187; e-mail W.Bakker@ct.tudelft.nl

2 I.e.: the generated relative increase of Z_0 should be larger than the assumed relative increase of h

"standing" at the closed end (90° phase difference between vertical and horizontal tide). The analytical computations can be presented in a dimensionless way. Results depend on angle θ, indicating the rate of bottom friction: $\theta = 0°$ for zero- and $\theta = 45°$ for infinitely large friction.

- The tide-averaged Eulerian current below the LW-level is calculated in the following way. The harmonic Eulerian horizontal velocity in each point of the vertical cross-section above the LW-line is tide-averaged. During the part of the tide, when the level considered lies above the actual water level the velocity is taken equal to zero.
  Next, these values are integrated over the height (between the LW- and HW-line), thus giving a tide-averaged residual flow rate above the LW-level. The magnitude of this Eulerian residual strongly depends on phase difference between vertical and horizontal tide.
- At the (seaward) end of the channel, the tide-averaged flux of water above LW will be relatively large and landward-directed: velocities there are high anyway and the horizontal and vertical tides are approximately in phase. At the closed end, all velocities are zero. Continuity requests a seaward-directed tide-averaged velocity below LW, increasing towards the entrance. Hence, all along the channel there must be a tide-averaged flux from the upper to the lower level, down through the LW-line (fig.1).

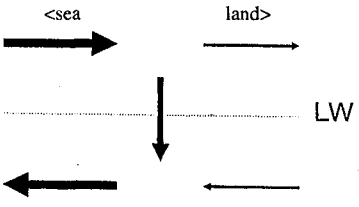

Fig 1. Rain in the drain

BAKKER & DE VRIEND (1995), consider a network instead of a single channel. They concentrate this flux in the nodes of the network and call it: "rain in the drain", because of the analogy with a drain system: water flushing in above the "pavement" (at LW-level) flushes out through the drain system, i.e. the tidal channels below LW. In the case presently considered, the "rain in the drain" is a continuous function of the horizontal co-ordinate x; its dimension is $[(m^3/s)/m^2]$. So it degenerates to a tide-averaged downward velocity (fig.1), called "w".

- the model has been checked (BAKKER & DE VRIEND (1995); fig.6) with the fully non-linear DUFLOW computer model (SPAANS et al.,1989).

b. calculation accretion/erosion rate:

- The sand transport rate is assumed proportional to the third power of the velocity, the latter being represented by its zeroth and first harmonic. Thus the tide-averaged gradient of the sand transport (=erosion/accretion rate) is calculated analytically as a function of those zero- and first harmonics and their gradients in x-direction. The gradients in the tide-averaged current are caused by the rain in the drain. Dimensionless presentation is possible again.

c. Morphodynamic stability analysis:

- The stability analysis reveals, how hydraulic conditions change, when the water depth changes and whether this can be a reason for enhanced erosion. Rate of change of depth dh/dt as function of depth h (cf.ad "b") renders a differential equation, resulting in depth as function of time. Thus (in)stability can be determined.

Results

For derivations refer to "Details". Morphodynamic stability depends on the ratio $L^* = L/L_0$, where L is the length of the channel and $L_0 = T\sqrt{gh}$ would be the tidal wave length, if friction would be neglected. Criterium for instability appears to be (cf.eqn. (9)) that a small increase of depth dh increases Z_0/h, whcre Z_0 is the amplitude of the vertical tide at the closed end of the channel. Relative growth of Z_0 should surpass the one of h. If friction is very low ($\theta = 7.5°$) instability would occur for values of $\frac{1}{4} < L^* < \frac{3}{8}$ and $\frac{3}{4} < L^* < \frac{7}{8}$ (standing-wave effects). If friction is higher, near the entrance no effect of reflection is found: here the tidal wave is a propagating, attenuating wave. After some initial deepening, reflection may reach the entrance: this will increase the tidal motion and trigger further deepening. This kind of instability occurs for $L^* > \frac{1}{2}$ ($\theta = 30°$) or $L^* > \frac{1}{4}$ ($\theta = 37.5°$).

Figure 2, Explanation:
The following criterion will be derived for instability of the channel (cf. eqn.(12)):

$$\left[\frac{d(\ln \hat{z}^*)}{dx^*}\right]_{x=L} > 2/L^* \qquad (1)$$

where x is the horizontal coordinate of the prismatic channel, starting at the closed end of the channel and pointing seaward; $\hat{z}$ is the local amplitude of the vertical tidal wave related to its value at the closed end.
The figure depicts the lefthand side of equation (1) as function of $x/T\sqrt{gh}$. Thus, for a given case, determined by L^* and friction factor θ the value of the lefthand side of (1) is determined by a point in the plot of the figure. If this point is in the gray area, the case is unstable.

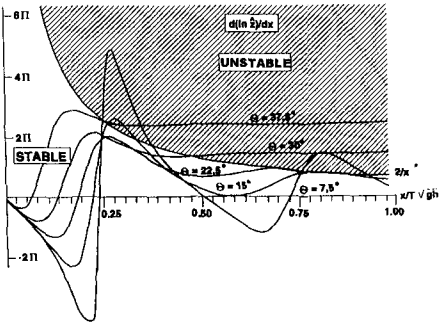

Relation to other investigations; discussion of assumptions

Classifying estuary models as empirical models, semi-empirical models and dynamical models, the present model should be earmarked as a one-dimensional analytical dynamical initial morphological model. Equilibrium conditions are not assumed a priori, contrarily to many morphological models, like BRUUN & GERRITSEN, 1960, which start from assumptions that a profile adjusts itself until a certain maximum shear stress is reached.
It is a core model with a large mathematical rigidity, aiming at the demonstration of easy to understand input-output relations. Where on one hand matters as (for instance) interaction between shoal-channel interaction remain (as yet) out of scope, on the other hand no further unknowns like diffusion coefficients are introduced.
The present model is "initial": difference between absolute instability and metastability is not made. The present investigation is a part of a joint Dutch effort to improve the insight in the morphodynamics of Wadden Sea and estuaries. This concerns as well the tidal basins itself as its interaction with the adjacent outer delta's.

BAKKER & DE VRIEND, 1995 report on the general approach of this problem. One of the constituents is: modeling the behaviour of the outer delta under the influence of a combination of sources and sinks (DE VRIEND et al.,1994). Source is the sand output of ebb-channels in the outer delta, a sink (for the outer delta) is the influx of sand in the tidal basin through a flood channel.
Another constituent (one of the other subjects of BAKKER & DE VRIEND, 1995) is the quantification of such a "source": an embouching ebb-channel as most seaward channel of a network of channels in the tidal basin. Furthermore, BAKKER & DE VRIEND (1995) treat the morphological behaviour of those tidal channels itself, using the results of the present paper.
The power-law transport formula presumes immediate adjustment of sand transport to bed shear; the transport rate equals the transport capacity.
In the present model all sediment is transported below LW. This excludes the effect of fines, which explains why near the closed end of the estuary hardly any bottom change is found; partly because of low velocities, partly because horizontal and vertical tide are 90° out of phase. In practice, those areas will silt up quickly. Possibly, combination of present theory with the theory of KROL (1990), (assuming a uniform sediment concentration over the depth) could shed any light on this matter. Water motion being investigated only up to first order of accuracy, effects of imported or internally generated higher harmonics are overlooked. In practice, those might lead to sedimentation of (short) basins (VAN DONGEREN & De VRIEND, 1994). On the other hand, V.D.KREEKE & ROBACZEWSKA (1993), investigating for the Ems estuary interactions of M_0..M_6, find the tide-averaged sediment transport dominated by interactions between M_0 and M_2. Thus, for longer channels the used schematization might be appropriate.
BLIEK points out (cf. BAKKER et al. (1998)) that also in well-mixed estuaries mostly a longitudinal salt gradient will counteract the rain in the drain. At a smaller space scale the horizontal tide-averaged circulation in ebb- and flood channels will interact with the "rain in the drain" effect.
The "closed" end of the channel does not have to be strictly "closed". An extensive underwater sill (artificial? sand? silt?) with (about) the same reflection coefficient for the tide as the closure dam could react morphodynamically about in the same way[3]. Refer furthermore to ch.7 ("Discussion") of BAKKER & de VRIEND (1995).

Details.

Hydraulic calculation

Concerning the first harmonic of the vertical and horizontal tidal motion, the relevant equations of the Lorentz method are summarized in Appendix A.
Let $\zeta(x,t)$ denote the elevation of the water surface (in reference to the still-water level) and $v(x,t)$ the horizontal motion, which is assumed uniform over the depth. The positive x-axis, originating at the closed end of the channel points seaward ; t denotes time. Given channel length and depth, amplitudes $\hat{\zeta}$ and $\hat{v}$ depend upon the bottom friction, in the Lorentz method determined by the friction angle θ.
In the following, dimensionless variables (cf."Method") will be indicated with a star.

3 This under the restriction of zero (or slightly seaward) tide-averaged drift at the site of the sill

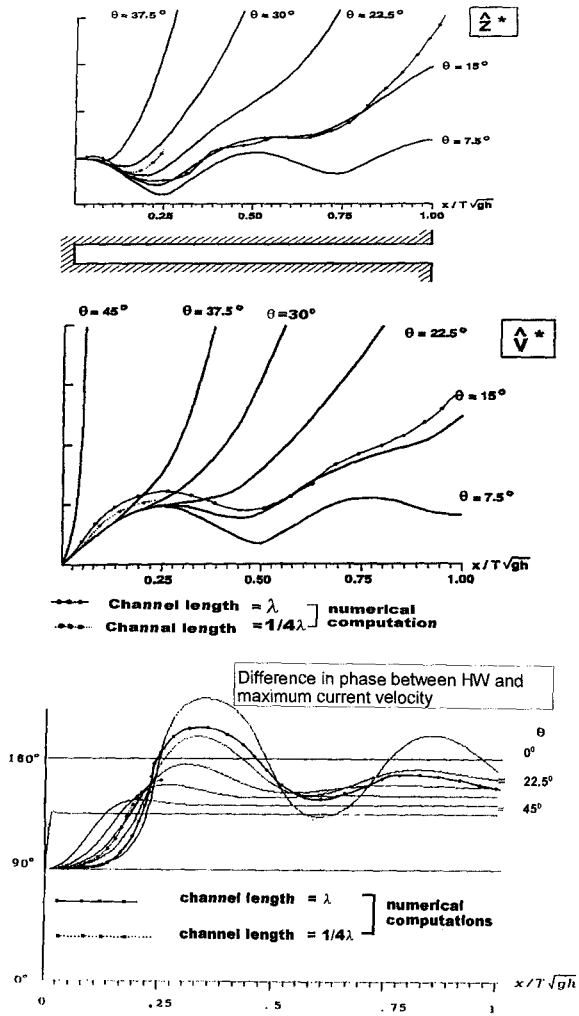

fig.3. Amplitude vertical tide and horizontal tide along the channel;
phase difference vertical tide and horizontal tide;
comparison numerical and analytical computation.
a: Vertical tide; b: plan view channel; c: horizontal tide; d: Phase difference

As elucidated in appendix A, fig.3a shows the dimensionless amplitude $\hat{z}^*$ of ζ as function of x^*. Curves are given for various values of θ. In the same way, fig. 3b shows the velocity amplitude $\hat{v}^*$. For zero friction, curves would have the shape of a | cos |- and a | sin |-function, respectively.

Important for the calculation of the tide-averaged resultant current is the phase difference of the first harmonic between ζ and v, called ϕ. Fig. 3c depicts the phase difference ϕ between ζ and v. Phase difference is about 180°-θ near the seaward end and is 90° at the landward end. This indicates, that the wave has the character of a propagating wave at the seaside (moving in negative x-direction) and of a standing wave at the closed side.

Checking the values with a non-linear computation is difficult, as - because of non-linear friction - a constant Chezy- friction value does not result in a constant θ-value over the channel. Furthermore, for friction values which are physically real the reflected wave under normal conditions of real estuaries practically always will be attenuated after half a wave length or less: values of θ of 7.5° or 15° are not very likely in practice.
In order to check the mathematics, some tests with physically unrealistic values of the Chezy -value have been performed. Two cases have been checked, in which the channel length was L_0 and $L_0/4$ respectively. The channel length in either case was equal (86.4 km), but the depth h was different: .408 m, resp. 16*.408=6.41 m. The tidal wave period T was taken: 12 hours. Chezy-values C_h were: 120, resp. 60 $\sqrt{m}/s$ and the amplitude $\hat{z}_s$ at the seaward boundary was takcn $h/10$.
When relating C_h to θ, the velocity amplitude $\hat{v}$ enters the formula (see (A3)). In the case of a channel with a closed end, neglecting friction, one finds a channel-averaged value of $\hat{v}$:

$$\hat{v} \approx \frac{2}{\pi} \cdot \frac{\hat{z}_0}{h} \cdot \sqrt{gh} \tag{2}$$

Here $\hat{z}_0$ denotes the vertical wave amplitude in the antinodes.
Then from (A3) the following relation between relation between C_h and θ can be derived:

$$\tan(2\theta) = \frac{8}{3\pi^3} \cdot \frac{\hat{z}_0}{h} \cdot \frac{L_0}{h} \cdot \frac{g}{C_h^2} \tag{3}$$

For the $L_0/4$-channel a value $\theta = 25,44°$ is found. For the L_0-channel, the fact that friction is neglected in the derivation of (2) gives some ambiguity: in fact $\hat{v}$ in the most landward node (at $x \approx L_0/4$) will be much less than the one in the most seaward node ($x \approx 3L_0/4$). If for $\hat{z}_0/h$ in (3) the seaward boundary value of .1 is taken,

the same value of θ results as for the L_0/4-channel as (3) shows[4]. However, if one takes for $\hat{z}_0/h$ the value at the landward side of the channel, which is .01377/.408, a value of 11.37° is found. Thus, for the L_0-channel θ should be in the range

$11.4° < \theta < 25.4°$

Fig.3[a,b,c] shows the correspondence between the given ranges of θ, for the amplitudes of the vertical and horizontal tide, as well as for the phase differences.

Calculation accretion/erosion rate

Let S_1 be (in magnitude) the transport (per unit of width), when the velocity is 1 m/s. Writing $S = S_1 v^3$, the appropriate unit for S_1 is [sec²/m], since the transport is expressed in m²/sec. The calculated transport rate is expressed in terms of deposited sediment volume. In order to obtain the solid volume, one should multiply by 1- the pore content of the bed.

Denoting tide-averaged values by <>, the third-power sand transport formula yields for the tide-averaged local erosion rate, $< \partial h/\partial t >$:

$$< \frac{\partial h}{\partial t} > = \frac{3}{2} \frac{S_1 \hat{v}^2}{h} (w + 2\delta\omega\hat{z} \sin\phi) \qquad (4)$$

This equation is derived in Appendix B. Here ω is the angular velocity of the dominant tidal constituant (mostly M_2) and δ and w are defined by:

$$\delta = < v > / \hat{v} \qquad w = h \frac{\partial < v >}{\partial x} \qquad (5a,b)$$

w being the rain in the drain. Starting from the definitions (5a,b) w can be expressed as:

$$w = h\left(\hat{v} \frac{d\delta}{dx} + \delta \frac{d\hat{v}}{dx} \right) \qquad (6)$$

The second term inside the brackets of (4) shows the effect on the erosion $< \partial h/\partial t >$ of the phase coupling between vertical tide ζ and horizontal tide v: $\sin\phi = 1$ for a standing wave, where ζ and v are out of phase and $\sin\phi = 0$ when ζ and v are in phase).

For the derivation of (4), it has been assumed, that δ is much smaller than 1.

Remembering that gS_1 is dimensionless one may write (4) in a dimensionless form, yielding:

$$\frac{\partial h^*}{\partial(\omega t)} = -\frac{g S_1}{(h^{*2})(h^* - 1)} \quad f(x^*, \theta) \qquad (7)$$

---

4 for the long channel $\hat{z}_0/h$ remains the same; L_0 is divided by 4 and h is divided by 16; C_h is multiplied by 2

Function $f(x^*, \theta)$ (of which the exact expression is derived in appendix C) follows from (4) to (7) and the harmonical tidal theory (LORENTZ et al. (1926); THIJSSE;(1965)). It is depicted in fig.4.

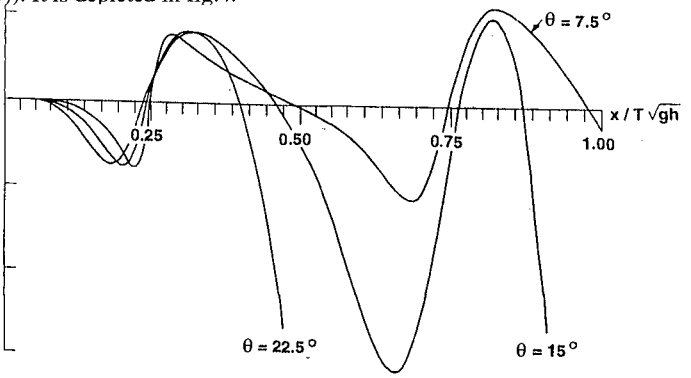

Fig.4. Dimensionless accretion/erosion as function $f(x^*, \theta)$ of site and bottom friction

Morphodynamic stability analysis

With the aid of (7), the morphological instability of a channel can be traced. Here instability will be defined as an acceleration of erosion ($\partial^2 h/\partial t^2 > 0$).
Mechanism will be: increased h gives increased tidal wave length, whence the ratio "channel length/ wave length" becomes less. When originally the channel was somewhat larger than 1/4 of a wave length, a subsequent decrease of the relative channel length enhances the wave amplitude Z_0 at the closed end of the channel. This may enhance the erosion process in the channel, etc.
In the following some simplifying assumptions will be made: the effect of changes in friction (in angle θ and thus in $f(x^*, \theta)$) will be neglected. As θ tends to decrease during the erosion process described, the probability of instability will be underestimated.
Let x_s^* be the dimensionless channel length and let $\bar{f}$ be the mean value of f between 0 and x_s^*.

The tide-averaged equivalent of eqn. (7) shows, that if x_s^* is such, that $\bar{f} > 0$ no instability has to be expected.
Investigate now the case: $\bar{f} < 0$. Considering eqn. (7) as a differential equation in a dimensionless depth and a dimensionless time, it seems logical[5] to incorporate the dimensionless $gS_1\bar{f}$ in the reference time scale, call t_0:

$$t_0 = -T/(2\pi \bar{f} g S_1) \qquad (8)$$

5 Thus switching from the hydraulic time scale to the morphological time scale,

Note that in the present case ($\bar{f} < 0$) t_0 will be larger than zero.

For convenience, the dependent variable h^* in (7), equal to h/Z_0, will be replaced by $h' = h/\hat{z}_s$, in which $\hat{z}_s$ is the amplitude at the seaward boundary, For h' only changes in time if h changes, where in h^* a change of h affects also the reference, i.e., the vertical tide Z_0 at the closed end of the channel. Denoting t/t_0 by t', and $\hat{z}_s/Z_0$ by $\hat{z}_s^*$, the non-dimensional depth-evolution equation becomes:

$$\frac{\partial h'}{\partial t'} = \left[(h'\hat{z}_s^*)^2 (h'\hat{z}_s^* - 1)\right]^{-1} \tag{9}$$

where $h'\hat{z}_s^*$, equal to h/Z_0 can be assumed much larger than 1. Instability occurs, if the righthand part of eqn.(9) increases with h'. This implies, that h/Z_0 should decrease as h' (or h) increases[6]. In other words: instability occurs when $\partial(h'\hat{z}_s^*)/\partial h'$ is negative. Thus the stability criterion is:

$$\hat{z}_s^* + h\frac{\partial \hat{z}_s^*}{\partial h} > 0 \quad \Rightarrow stable \tag{10a}$$

$$1 + h\frac{\partial(\ln \hat{z}_s^*)}{\partial h} > 0 \Rightarrow stable \tag{10b}$$

Here one finds $\partial(\ln \hat{z}_s^*)/\partial h$ as:

$$\frac{\partial(\ln \hat{z}_s^*)}{\partial h} = \frac{\partial(\ln \hat{z}_s^*)}{\partial x^*} \cdot \frac{\partial x^*}{\partial h} \tag{11}$$

Differentiation of $x^* = x/T\sqrt{gh}$ to h gives $-x^*/(2h)$ as result. Thus the stability criterion becomes:

$$\frac{\partial(\ln \hat{z}_s^*)}{\partial x^*} < \frac{2}{x^*} \quad \Rightarrow stable \tag{12}$$

Here x^* denotes the channel length, expressed in $T\sqrt{gh}$. In fig. 2, both $\partial(\ln \hat{z}_s^*)/\partial x^*$ and $2/x^*$ are plotted. All the points above the line $2/x^*$ (which corresponds with a certain dimensionless channel length and a certain friction angle θ) refer to potential unstable channels, provided that $\bar{f}$ (cf. fig 4) is negative.
When the channel length is less than about a quarter of a wave length, no instabilities are found. However, longer channels with a moderate bottom friction should theoretically become often unstable.

6 This was, mentioned in "Results"

Acknowledgements.

The author gratefully acknowledges the work done by Mr.G.Bult, in checking the analytical results with DUFLOW. The reviews of C.v.d.Kreeke, A.Langerak, K.Dyer, E.Bouwmeester and A.Baquerizo were stimulating.
Special thanks to prof.dr.ir H.J. de Vriend for his comments and support.

Appendix A. The Lorentz theory

The Lorentz theory starts from the linearized equation of motion and the continuity equation, viz.:

$$\frac{\partial v}{\partial t} + g\frac{\partial \zeta}{\partial s} + (\omega \tan 2\theta)v = 0 \qquad (A1)$$

$$\frac{\partial \zeta}{\partial t} + h\frac{\partial v}{\partial t} = 0 \qquad (A2)$$

Here, $\omega \tan 2\theta$ is a linearized friction coefficient, related to the Chezy coefficient C_h in the following way:

$$\omega \tan(2\theta) = \frac{8g}{3\pi C_h^2 h}\hat{v} \qquad (A3)$$

For the case of a prismatical channel, closed on one side, the following solution is found, which can be presented in a dimensionless way.

Define the complex function $Z(kx)$ in such a way, that

$$\zeta(x,t) = Z_0 Re\{Z(kx)e^{i\omega t}\} \qquad (A4)$$

and the complex function V such, that

$$v(x,t) = T\sqrt{g/h}\, Re\{V(kx)e^{i\omega t} \qquad (A5)$$

where the wave number k equals:

$$k = \frac{\omega}{c}(1 - i.\tan\theta) \qquad (A6)$$

and where the propagation velocity c of a wave component (incoming or reflected) equals:

$$c = \sqrt{gh(1 - \tan^2\theta)} \qquad (A7)$$

In the paper, the horizontal coordinate is dimensionless (x^*), where in (A4) and (A5) still the original coordinate "x" is used; however, kx is dimensionless and can be written as "k^*x^*", where k^* can be derived from (A6) and (A7).
For the given boundary conditions the solution of (A1) and (A2) is:

$$Z = \cos kx \qquad V = i\sqrt{\cos 2\theta}.\sin kx \qquad (A8)$$

$\hat{v}$ and $\hat{z}$ are found as the modulus of Z and V and are shown in fig 3[a] and 3[c].
The difference in argument between Z and V is depicted in fig.3[d].

Appendix B. Derivation of equation (4)

The local erosion according equation (4) can be derived from the transport equation. Splitting into means and harmonics gives (indicating first harmonics by a tilde):

$$\frac{\partial S}{\partial x} = 3S_1(\tilde{v} + < v >)^2\left(\frac{\partial \tilde{v}}{\partial x} + \frac{\partial < v >}{\partial x}\right) \qquad (B1)$$

Neglecting the effect of bottom changes, the equation for momentaneous continuity of water gives:

$$-h\frac{\partial \tilde{v}}{\partial x} = \frac{\partial \zeta}{\partial t} \qquad (B2)$$

According to (B2) $\partial\tilde{v}/\partial x$ is proportional to $\partial\zeta/\partial t$, of which the phase is 90° ahead with respect to ζ. Denoting the phase difference between $\tilde{v}$ and ζ by ϕ, the phase difference between $\tilde{v}$ and $\partial\tilde{v}/\partial x$ will be $90° - \phi$.

Choose $t = 0$ in this way, that $\tilde{v} = \hat{v}\sin\omega t$. Use of (B2), (5a) and sand continuity transfers (B1) into:

$$\frac{\partial h}{\partial t} = 3\frac{S_1\hat{v}^2}{h} < (\sin\omega t + \delta)^2\left\{\omega\hat{z}\sin\left(\omega t + \frac{\pi}{2} - \phi\right) + w\right\} > \qquad (B3)$$

Neglect of δ^2-terms leads to (4), as all odd powers of $\sin\omega t$ and combinations of $\sin\omega t$ and $\cos\omega t$ cancel during the time-averaging process.

Appendix C. THE FUNCTION $f(x^*, \theta)$

The function $f(x^*, \theta)$ has been derived from (4). The equation has been made dimensionless by dividing by $-\omega Z_0$; thus emerges the lefthand side of (7).

Call $\hat{z}^*$ the dimensionless local amplitude of ζ.

For the flux above the LW-line (calculated as described in "Method") is found: $(\hat{z}\hat{v}\cos\phi)/2$.

Because of continuity, this flux should pass (in opposite direction) as well between the LW-level and the bottom. It is assumed, that the latter flux is stationary and uniform over the depth. Approximating further this separation plane between seaward and landward flux as horizontal, i.e. everywhere equal to the LW-level at the closed end of the channel, one finds for δ:

$$\delta = \frac{(\hat{z}/Z_0)\cos\phi}{2\left(\frac{h}{Z_0} - 1\right)} \qquad (C1)$$

Here $\hat{z}$ indicates the local tidal amplitude and Z_0 the amplitude at the closed end of the channel.

Furthermore δ will be replaced in this Appendix by a more concise variable δ^*:

$$\delta^* = \frac{\hat{z}^*}{2}\cos\phi \qquad (C2)$$

and thus, according to (C1), $\delta = \delta^*/(h^* - 1)$. Thus (6) reads, in a dimensionless way:

$$\frac{w}{\omega Z_0} = \frac{1}{2\pi(h^* - 1)}\left(\hat{v}^*\frac{\partial\delta^*}{\partial x^*} + \delta^*\frac{\partial\hat{v}^*}{\partial x^*}\right) \qquad (C3)$$

Substitution of (C3) into (4) gives, in a dimensionless shape:

$$\frac{\partial h^*}{\omega t} = \frac{gS_1}{h^{*2}(h^*-1)} \cdot \frac{3}{2} \hat{v}^{*2} \cdot \left[\frac{1}{2\pi} \left(\hat{v}^* \frac{\partial \delta^*}{\partial x^*} + \delta^* \frac{\partial \hat{v}^*}{\partial x^*} \right) - 2\delta^* \hat{z}^* \sin\phi \right] \qquad (C4)$$

Using (7) and (C4), and after after substitution of (C2), one can express $f(x^*, \theta)$ in values, to be derived from the Lorentz theory (1926; app.A):

$$f(x^*, \theta) = \frac{3}{2} \hat{v}^{*2} \cdot \left[\frac{-1}{4\pi} \left(\hat{v}^* \hat{z}^* \sin\phi \frac{d\phi}{dx^*} + \hat{v}^* \cos\phi \frac{d\hat{z}^*}{dx^*} + \hat{z}^* \cos\phi \frac{d\hat{v}^*}{dx^*} \right) + \hat{z}^{*2} \cos\phi \sin\phi \right] \qquad (C5)$$

This function $f(x^*, \theta)$ has been depicted in fig.4. It is memorized, that in the Lorentz theory vertical and horizontal tide are found as the real part of the complex values z^* and v^* (made dimensionless according to (A1a,b) and to be multiplied with $\exp(i\omega t)$):

$$Z = \cos kx \qquad V = i\sqrt{\cos 2\theta} \cdot \sin kx \qquad (C6)$$

with:

$$k = \frac{\omega}{c}(1 - i \quad \tan\theta) \qquad c = \sqrt{gh(1 - \tan^2\theta)} \qquad (C7a,b)$$

The difference in argument between Z and V is depicted in fig.3[d]; $\hat{z}$ and $\hat{v}$ are found as the modules of Z and V.

References

Bakker, W.T & friends (1998), *Coastal Dynamics.* National Institute for Coastal and Marine Management/RIKZ

Bakker W.T. & H.J.de Vriend (1995) *Resonance and morphological stability of tidal basins.* Mar.Geol.126.

Bruun, P. & F.Gerritsen (1960) *Stability of coastal inlets.* North-Holland, Amsterdam, 123 pp.

De Vriend, H.J., W.T.Bakker & D.P.Bilse, (1994) *A morphological model for the outer delta of mixed-energy tidal inlets.* Coastal Engng. 23 pp. 305-327

Krol, M., (1990) *The method of averaging in partial differential equations.* Ph.D.Thesis, Univ. of Utrecht.

Lorentz, H.A. et al. (1926) *Report of the State Commission Zuiderzee.* Landsdrukkerij.

Spaans, W., N.Booy, N.Praagman, R.Noorman & J.Lander (1989) *DUFLOW* IHE-Delft, TU-Delft, Rijkswaterstaat-DGW

Thijsse, J.Th. (1965) *Theory of Tides* Int.Course Hydr.Engng (IHE)

Van Dongeren,A.R. & H.J. de Vriend, (1994) *A model of morphological behaviour of tidal basins.* Coastal Eng., 22 (3/4): 287-310

V.d.Kreeke, J. & K.Robaciewska, (1993) *Tide-induced transport of coarse sediment; application to the Ems estuary.* Neth, J. Sea Res. 31 (3):209-220

Symbols

c	propagation velocity of a sinusoidal wave
C_h	Chezy coefficient
f	local accretion in the channel, expressed in a dimensionless way
g	acceleration of gravity
h	water depth
i	$\sqrt{-1}$
k	wave number (cf.(A6))
h'	$h/\hat{z}_s$
h^*	h/Z_0
L_0	wave length (if friction could be neglected): $T\sqrt{gh}$
n	the sand transport is assumed to be proportional to the n-th power of the velocity. In the paper, $n = 3$ is assumed.
t	time
t'	t/t_0
t_0	reference time scale as given by (7)
T	tidal period
v	instantaneous water velocity in seaward direction in the channel
v^*	$v/(Z_0\sqrt{g/h})$
V	complex, dimensionless presentation of v (cf. (A5))
w	rain in the drain (cf."Method; hydraulics" and eqn. (4b)
x	horizontal coordinate; the origin is at the closed side of the channel
x^*	$x/(T\sqrt{gh})$
z	vertical coordinate (positive upward)
$\hat{z}$	amplitude of ζ
$\hat{z}^*$	$\hat{z}/Z_0$
$\hat{z}_s$	amplitude vertical tide at the seaward end of the channel
$\hat{z}_s^*$	$\hat{z}_s/Z_0$
Z	complex, dimensionless presentation of ζ (cf.(A4))
Z_0	amplitude vertical tide at the closed end of the channel
δ	$< v>/\hat{v}$
δ^*	$\delta(h^* - 1)$
θ	friction angle (cf.(A3))
ϕ	phase difference between horizontal tide v and vertical tide ζ
ζ	elevation of water surface (function of x and t
ω	$2\pi/T$

INLET CROSS-SECTIONAL AREA CALCULATED BY PROCESS-BASED MODEL

Nicholas C. Kraus[1]

ABSTRACT: This paper introduces a process-based model for calculating the equilibrium cross-sectional area of a tidal inlet and temporal behavior of small perturbations in channel area from equilibrium. The model accounts for the dynamic balance between inlet ebb-tidal transport and longshore sand transport at the inlet entrance. Expressed in terms of a water discharge through the inlet and the gross longshore sand transport rate, the formulation can account for tidal, river, and wind-driven flows. The resultant predictive equation recovers the form of the well-known empirical formula $A_E = CP^n$, where A_E is the equilibrium (minimum) cross-sectional area, P is the tidal prism, and C and n are empirical coeffieients. An explicit expression is obtained for C in terms of coastal sediment-transport processes, and the value of n derived is in the range found empirically. The process-based model qualitatively predicts the difference in trends in inlet cross-sectional area on wave-sheltered and fully-exposed coasts. In time-dependent mode, the model reproduces qualitative behavior of the departure of the cross-sectional area from equilibrium under perturbations in the driving forces of discharge and waves.

INTRODUCTION

A quantitative empirical relation between the equilibrium or minimum stable cross-sectional area A_E of an inlet and its tidal prism P has been known for almost a century (LeConte 1905). Based on data from a limited number of locations along the coast of California, LeConte arrived at the linear equation $A_E = CP$. The value of the empirical coefficient C was about 34 % larger for inner harbor entrances (restricted longshore sediment transport) than for unprotected entrances (unrestricted longshore transport). LeConte's observation indicates that the same tidal prism on a coast with restricted longshore transport can maintain a larger equilibrium channel area than on a coast with less restricted or greater longshore sediment transport.

The presently accepted empirical relation for the cross-sectional area of inlets on exposed coasts is still expressed in terms of the bulk properties of the hydrodynamics

1) U.S. Army Engineer Waterways Experiment Station, Coastal and Hydraulics Laboratory, 3909 Halls Ferry Road, Vicksburg, MS 39180-6199 USA. n.kraus@cerc.wes.army.mil.

(tidal prism). Following the work of O'Brien (1931, 1969), Johnson (1972), and others, Jarrett (1976) analyzed 108 inlets (yielding 162 data points) along the Atlantic, Gulf, and Pacific Ocean coasts of the United States. His objectives were to determine if inlets on all three coasts of the United States follow the same inlet area – tidal prism relation, and if inlet stabilization altered that relation. With relatively high correlation coefficients, all predictive relations were found to fit the form

$$A_E = CP^n \tag{1}$$

in which C and n are empirically determined. Jarrett found the exponent n to vary between 0.86 and 1.10 for inlets with no jetty or with a single jetty and between 0.85 and 0.95 for inlets with two jetties. For coasts fully exposed to wave action, n varied between 0.85 and 0.95.

Table 1 summarizes Jarrett's findings (converting his U.S. customary units to metric units). Among other observations, Jarrett (1976) noted that the smaller waves on the Gulf coast relative to those on the Pacific Coast and on (most of) the Atlantic Coast would produce smaller littoral drift.

Table 1. Inlet-area and tidal prism regression values found by Jarrett (1976) for $A_E = CP^n$ (area units of m^2; tidal inlets on U.S. coasts)

	All Inlets		Unjettied, Single-Jettied		Dual Jettied	
Location	C	n	C	n	C	n
All Inlets	1.576×10^{-4}	0.95	3.797×10^{-5}	1.03	7.490×10^{-4}	0.86
Atlantic Coast	3.039×10^{-5}	1.05	2.261×10^{-5}	1.07	1.584×10^{-4}	0.95
Gulf Coast	9.311×10^{-4}	0.84	6.992×10^{-4}	0.86	Insuff. Data	Insuff. data
Pacific Coast	2.833×10^{-4}	0.91	8.950×10^{-6}	1.10	1.015×10^{-3}	0.85

The concept that the equilibrium area of an inlet (tidal entrance or river mouth) is determined by a balance between the transporting capacity of the inlet flow and the littoral or longshore transport has appeared throughout the literature (e.g., LeConte 1905, O'Brien 1931, 1969, Bruun and Gerritsen 1960, Bruun 1968, Byrne et al. 1980, Riedel and Gourlay 1980, Hume and Herdendorf 1990). In particular, Byrne et al., Riedel and Gourlay, and Hume and Herdendorf studied inlet channel stability on sheltered coasts and demonstrated that larger values of the empirical coefficient C and smaller values of n apply to coasts with limited littoral transport. Quoting Riedel and Gourlay, "In contrast (to exposed coasts), for sheltered inlets the littoral drift rate is small and, consequently, a much smaller volume of material needs to be moved out of the entrance in each tidal cycle." The aforementioned three studies also indicate that the mean-maximum velocity (mean over the cross section of the maximum at spring tide; see Bruun (1978), p. 321) required to maintain stability of the inlet channel is less (reaching approximately one-third less) than the typical 1 m/s (Bruun and Gerritsen 1960, O'Brien 1969) required to maintain a channel on an exposed coast.

Changes in inlet cross-sectional channel in response to changes in hydrodynamic forcing (waves, tidal or river current, tidal range. storms) have been documented by Mason and Sorensen (1972), Byrne et al. (1974), Behrens et al. (1977), FitzGerald and FitzGerald (1977), Nummedal and Humphries (1978), Van de Kreeke and Haring (1980), and others. FitzGerald and FitzGerald also discuss inlet channel response to changes in neighboring beach morphology.

In this paper, a mathematical model is introduced that describes, in a rational and quantitative way, the two main concepts described above. First, the model produces an equilibrium or stable channel cross section under the balance of tidal (and river) transporting capacity and the longshore sediment transport at the inlet. Second, the model can describe variations of the cross-section about its equilibrium in response to small changes in sediment-transport forces. The time scale governing the response of a channel to perturbations is also obtained.

PROCESS-BASED APPROACH

In the following, a tidal-inlet entrance or river mouth is considered on an alluvial shore with no geologic controls such as a rock or clay substratum.

Referring to Fig. 1, we assume that an ebb shoal or entrance bar forms and is maintained by a balance between the transport capacities of the ebb-tidal (or river) current and the longshore current. The gross longshore transport rate Q_g is given by

$$Q_g = \varepsilon_L Q_L + \varepsilon_R Q_R \tag{2}$$

where ε_L and ε_R are efficiency factors associated with the longshore transport rates for sediment moving to the left (for an observer on land) at rate Q_L and to the right at rate Q_R. The cfficiency factors are, in general, functions of time and vary between the limits $0 \leq \varepsilon \leq 1$ to account for blocking at jetties, bar bypassing, sediment availability, and similar processes. In this paper, $\varepsilon = 1$.

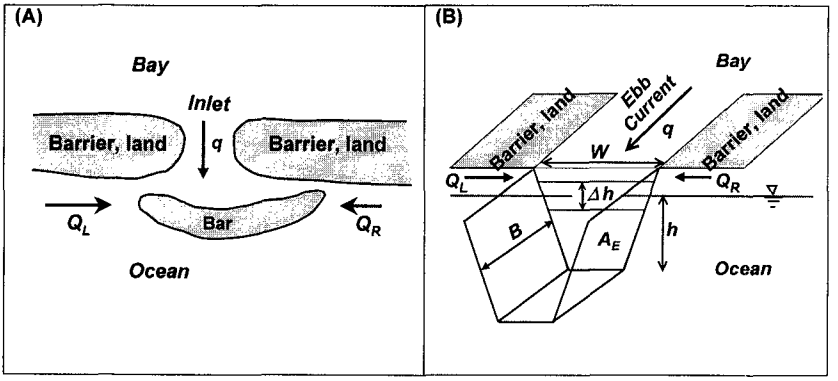

Fig. 1. Definition sketch for process model, (A) plan view, and (B) cross-section view.

The rate of sediment transport out of the inlet entrance is qW. Here q is the rate per unit width (m^3/s per meter across the inlet channel) as transported by the current (whether tidal-ebb, river-, or wind-generated current, or a combination), and W is the width of the inlet. We are interested in the channel equilibrium area, related to the water volume above the sea bottom. The time rate of change in bulk volume of sediment transported to the channel V_S and that of the volume of water V above the bed are related as $dV_S/dt = -dV/dt$, where t is time. Balance of the rates of sediment transported to the channel bar in Fig. 1 with the change in volume of water above the channel gives

$$\frac{dV}{dt} = qW - Q_g \tag{3}$$

If simple rectangular geometry for the entrance bar is assumed such that the $V = BWh$, where B and h are, respectively, the cross-shore width of and depth over the bar, and further assuming B is constant, then the channel area $A = Wh$, and Eq. 3 becomes

$$\frac{dA}{dt} = \frac{W}{B}q - \frac{1}{B}Q_g \tag{4}$$

The gross longshore sediment transport rate Q_g will be assumed to be known, as from the CERC formula or data. The transport rate q will be expressed as a Meyer-Peter and Muller (power law) in the form expressed by Watanabe et al. (1991) as

$$q = \alpha \frac{(\tau_m - \tau_c)}{\rho g} v_m \tag{5}$$

in which α is an empirical coefficient expected to be of order unity, τ_m is the bottom shear stress associated with the mean maximum velocity, τ_c is the critical shear stress for sediment transport, ρ is the fluid density, g is the acceleration of gravity, and v_m is the depth-averaged mean-maximum velocity along the channel. In the following, τ_c will be neglected. The critical shear could play a role at inlets where the hydrodynamic forces are weak or at inlets with coarse sediments.

The bottom shear stress under the maximum current is parameterized as

$$\tau_m = \rho c_f v_m^2 \tag{6}$$

where c_f is a bottom friction coefficient taken to be $c_f = gm^2/h^{1/3}$ where m^2 is the Mannings coefficient squared (units of $s^2/m^{2/3}$). Then Eq. 5 becomes,

$$q = \frac{\alpha m^2}{h^{1/3}} v_m^3 \tag{7}$$

and Eq. 4 becomes

$$\frac{dA}{dt} = \frac{\alpha m^2 W}{B h^{1/3}} \left(\frac{D_m}{A} \right)^3 - \frac{1}{P} Q_g \tag{8}$$

in which the velocity was replaced by $v_m = D_m/A$, where D_m is the maximum discharge, for example, the mean-maximum discharge at spring tide for the case of a tidal inlet without river flow or other non-tidal contribution to the discharge.

At equilibrium, $dA/dt = 0$, giving the equilibrium or minimum channel cross-sectional area A_E as

$$A_E = \Lambda_h D_m \tag{9}$$

where

$$\Lambda_h = \left(\frac{\alpha m^2 W_E}{h_E^{1/3} Q_g} \right)^{1/3} \tag{10}$$

in which h_E and W_E are the depth and width corresponding to the equilibrium area A_E. It is noted that a linear form as Eq. 9 will result for any transport rate formula for q that is a simple algebraic function of v_m or D_m.

Eq. 9 has the same form as the classical Eq. 1, but with the tidal prism P replaced by the discharge D. At equilibrium we have $h_E = A_E/W_E$, where W_E is the width of the channel at equilibrium. Replacing h_E in Eq. 10 by this relation results in

$$A_E = \Lambda D_m^{0.9} \tag{11}$$

where

$$\Lambda = \left(\frac{\alpha m^2 W_E^{4/3}}{Q_g} \right)^{0.3} \tag{12}$$

Eqs. 11 and 12 can be compared to Eq. 1 by assuming that the discharge is solely related to the tidal prism. Keulegan and Hall (1950) assumed a sinusoidal discharge so that the tidal prism P or volume of water ebbing in half a tidal period T is

$$P = \int_0^{T/2} D_m \sin\left(\frac{2\pi}{T} t \right) dt \tag{13}$$

They introduced a coefficient C_K such that $0.81 \leq C_K \leq 1$ to account for a more realistic non-sinusoidal tide, giving,

$$D_m = \frac{\pi C_k}{T} P \tag{14}$$

Then, Eq. 11 expressed in terms of the tidal prism becomes,

$$A_E = C_p P^{0.9} \tag{15}$$

in which the process-based coefficient C_p is given by

$$C_p = \left(\frac{\alpha \pi^3 C_K^3 m^2 W_E^{4/3}}{Q_g T^3} \right)^{0.3} \tag{16}$$

Eq. 15 is similar to the classical and well-verified Eq. 1 with the empirical coefficient C in Eq. 1 replaced by C_p. Eq. 16 shows that C_p depends on Q_g inversely as the 3/10 power, an inverse dependence in qualitative accord with observations for sheltered and unsheltered coasts. The inverse dependence on the tidal period as $T^{0.9}$ is testable if adequate data are available for coasts with a diurnal tide.

Bruun (1978), in his Table 5.35, lists data for 11 jettied and unjettied inlets that include the channel cross-section (assumed to be near equilibrium), maximum discharge, and the approximate total longshore sediment transport to the inlet. The data set contains estimates of annual Q_g ranging from 7×10^4 m^3 (with D_m of 0.87×10^3 m^3/s) for Mission Bay, California to 8×10^5 m^3 (with D_m of 36.4×10^3 m^3/s) for Grays Harbor Washington. In this limited data set, Grays Harbor falls along trend lines to be discussed, but is omitted because the discharge is an order of magnitude larger than any other. The next largest inlet is Thyboron, Denmark, with annual Q_g of 7×10^5 m^3 and D_m of 5.6×10^3 m^3/s.

Figure 2 plots the channel cross-sectional area against the mean-maximum discharge, indicating a close relation, as noted earlier by Bruun and Gerritsen (1968). Figure 3 plots A versus the functional relation $D_m^{0.9}/Q_g^{0.3}$. The scatter about the best-fit line is considerably greater than in Fig. 2 owing, in part, to the uneertainty in knowledge of Q_g. Although the data set is limited, the result is promising. The process-based approach appears capable of predicting the cross-sectional area without necessity of determining an empirical coefficient, while accounting for variations in sediment type (through α and m^2, longshore transport rate, and width of the inlet).

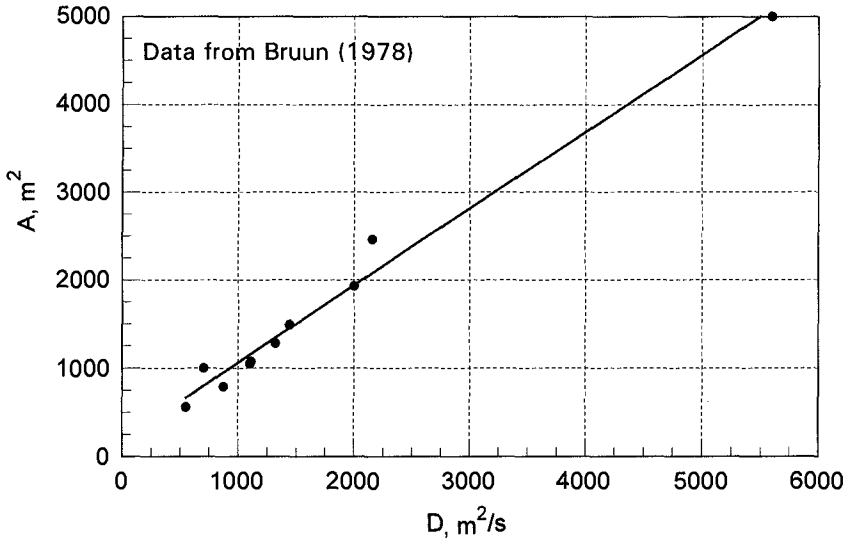

Fig. 2. Inlet cross-sectional area versus discharge.

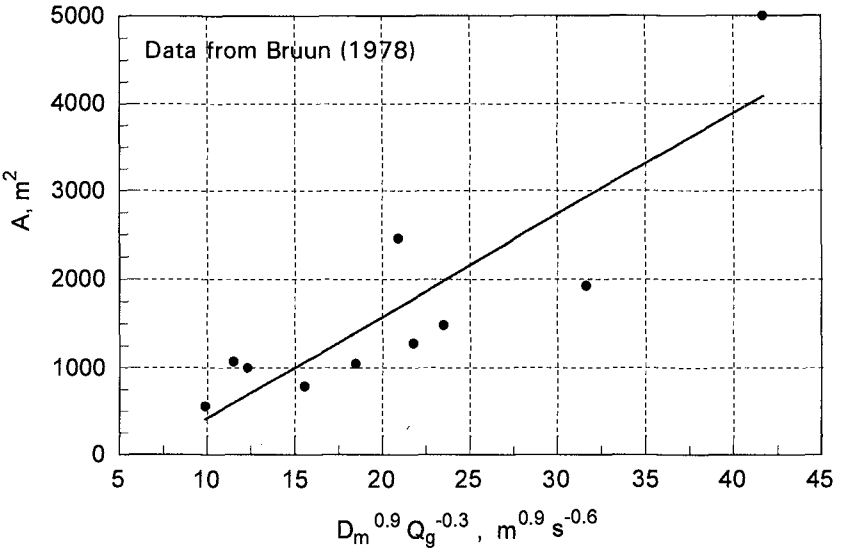

Fig. 3. Inlet cross-sectional area versus functional form of Eq. 11.

To examine the validity of the above formulation, the magnitude of C_p is estimated with representative values for the East Coast of the United States as follows: $\alpha = 1$; $C_K = 1$; $m^2 = (0.025)^2$ s^2/m$^{2/3}$; $W_E = 400$ m; $Q_g = 315{,}000$ m^3/year = 1×10^{-2} m^3/s; and $T = 44{,}712$ s for a semi-diurnal tide. With these values, one finds $C_p \cong 8.7\times10^{-4}$ m$^{-7/10}$. Because of the assumption of constant width of the inlet channel, comparison with C-values for dual-jettied inlets is most appropriate. From Table 1, Jarrett (1976) found $C = 7.5\times10^{-4}$ for all U.S. tidal inlets considered that had dual jetties, and with exponent $n = 0.86$. The close agreement of the estimated C_p and C, as well as the n-values (0.9 derived versus 0.86 empirical) is considered fortuitous, but achieving the correct order of magnitude is encouraging. The exponent 0.3 in Eq. 16 makes the magnitude of C_p relatively insensitive to reasonable changes in values comprising it. For example, changing the value of α from 1 to 0.1 reduces the value of C_p by one-half.

CHANNEL RESPONSE TO TIME-DEPENDENT FORCING

This section explores time dependencies of the change in channel cross-sectional area in the process-based approach.

Characteristic relaxation time

Eq. 8 is the time-dependent governing equation for the channel cross-sectional area $A(t)$. Noting from Eqs. 9 and 10 that

$$A_E^3 = \frac{\alpha\, m^2 W_E}{h_E^{1/3} Q_g} D_m^3 \tag{17}$$

then, assuming that $W_E/h_E^{1/3} = W/h^{1/3}$, Eq. 8 can be rewritten as

$$\frac{dA}{dt} = \frac{Q_g}{B}\left(\frac{A_E^3}{A^3} - 1\right) \tag{18}$$

If, instead, the assumption $W = W_E$ is made, the exponent 3 in Eq. 18 becomes 10/3.

Suppose that for some reason A is perturbed by a certain small amount a from equilibrium, that is, $A(t) = A_E + a(t)$, where $|a|/A_E << 1$, with the driving forces remaining constant. Then, by applying the binomial expansion to lowest order, Eq. 18 becomes

$$\frac{da}{dt} - \frac{1}{\tau_0} a = 0 \tag{19}$$

where $\tau_0 = BA_E/3Q_g$ is a characteristic relaxation time scale for the channel cross section to return to equilibrium according to the solution of Eq. 19, $a = a_0 \exp(-t/\tau_0)$, in which a_o is the magnitude of the initial perturbation. Order-of-magnitude estimates show τ_0 in the approximate range of 0.3 to 2 year.

Time-Varying Forcing

More generally, suppose that the discharge and gross longshore sediment transport rate are time varying, leading to a time variation in the channel cross-section. Let

$$\begin{aligned} A &= A_E + a(t) \\ D &= D_E + d(t) \\ Q_g &= Q_{gE} + Q(t) \end{aligned} \tag{20}$$

where a, d, and Q are small departures from their respective equilibrium values such that $|a|/A_E << 1$, $|d|/D_E << 1$, and $|Q|/Q_{gE} << 1$. Then Eq. 8 becomes

$$\frac{da(t)}{dt} + \frac{\beta}{A_E} a(t) = \frac{\beta}{D_E} d(t) + \frac{1}{B} Q(t) \tag{21}$$

where $\beta = 3Q_{gE}/B$, and

$$\frac{\beta}{A_E} = \frac{3Q_{gE}}{A_E} = \frac{1}{\tau_0} \equiv \sigma_0 \tag{22}$$

This equation is general, subject to the small-perturbation assumption, and can be solved once the functional dependencies of $d(t)$ and $Q(t)$ are known.

As an illustrative analytical solution of Eq. 21, we consider simple sinusoidal forcing, namely,

$$d(t) = d_o \sin(\sigma_1 t)$$
$$Q(t) = Q_o \sin(\sigma_2 t - \phi) \tag{23}$$

where d_o and Q_o are the magnitudes of the perturbations, σ_1 and σ_2 are angular frequencies for the respective perturbations or forcings, and ϕ expresses a possible phase shift between the forcings. For example, σ_1 might relate to a cycle of higher spring tides and corresponding change in the discharge, and σ_2 might relate to seasonal changes in waves. With the notation, $A_1 = \beta\, d_o / D_E$, and $A_2 = Q_o / B$, Eq. 21 becomes

$$\frac{da}{dt} + \sigma_0 a = R(t) \tag{24a}$$

where $R(t)$ is the known forcing,

$$R(t) = A_1 \sin(\sigma_1 t) + A_2 \sin(\sigma_2 t - \phi) \tag{24b}$$

The solution of Eq. 24a for the initial condition $a = 0$ at $t = 0$ is

$$\begin{aligned} a(t) = {} & \frac{\sigma_1 A_1}{\sigma_o^2 + \sigma_1^2}\left(\frac{\sigma_o}{\sigma_1}\sin(\sigma_1 t) - \cos(\sigma_1 t)\right) \\ & + \frac{\sigma_2 A_2}{\sigma_o^2 + \sigma_2^2}\left(\frac{\sigma_o}{\sigma_2}\sin(\sigma_2 t - \phi) - \cos(\sigma_2 t - \phi)\right) \\ & + \left[\frac{\sigma_1 A_1}{\sigma_o^2 + \sigma_1^2} + \frac{\sigma_2 A_2}{\sigma_o^2 + \sigma_2^2}\left(\frac{\sigma_o}{\sigma_2}\sin(\phi) - \cos(\phi)\right)\right]\exp(-\sigma_o t) \end{aligned} \tag{25}$$

Similarly, a numerical solution of Eq. 24a can be developed with the discretization scheme

$$\frac{a' - a}{\Delta t} + \frac{\sigma_0}{2}(a' + a) \approx R(t) \tag{26}$$

where the prime symbol denotes the next time step. Eq. 26 leads to the algorithm

$$a' = \frac{1 - \delta}{1 + \delta} a + \frac{\Delta t}{1 + \delta} R(t) \tag{27}$$

in which $\delta = \sigma_0 \Delta t / 2$. Solutions with Eq. 27 will be plotted for comparison with the analytic solution given by Eq. 25. Eq. 27, which is unconditionally stable, is a general numerical solution to Eq. 24 for any given forcing $R(t)$ and associated initial condition.

Eqs. 25 and 27 were calculated with the values given in Table 2. The parameter values correspond to a moderately-sized inlet on the east coast of the United States with $A_E \cong 10^3$ m^2, $Q_{gE} \cong 3\times10^5$ m^3/year, and $B \cong 3\times10^2$ m. The annual maximum of spring tides, hence greatest mean-maximum discharge, was assumed to have periodicity of a half-year, and the gross longshore sand transport rate was given an annual cycle to represent a characteristic winter-summer difference in wave conditions.

Table 2. Values of parameters for the sinusoidal forcing perturbation example.

A_1 m^2/year	A_2 m^2/year	$\lvert d_0\rvert/D_E$	$\lvert Q\rvert/Q_{gE}$	σ_0 day^{-1}	σ_1 day^{-1}	σ_2 day^{-1}
100	100	1/10	1/10	1/120	$2\pi/182.5$	$2\pi/365$

Calculations for an elapsed time of 3 years after initiation of the perturbative forcing are plotted in Figs. (4) and (5) for phase lags ϕ of 0 and π, respectively. Both the analytical and numerical solutions are shown in these figures. For the numerical solution, the forcing $R(t)$ was set to 0 after 1.5 years to show the decay of the perturbation (dashed line) according to the relaxation time τ_0. The time step for the calculation was Δt = 1 day. Even for this relatively large time step, the analytical and numerical solutions are almost indistinguishable (prior to setting of the forcing to zero).

The transient portion of the solution for this example damps after about one-half year. After that, the perturbation a varies periodically. Phasing between the two forcings of discharge and longshore transport rate can greatly alter the behavior of the solution at initiation of the forcing or for a change in forcing. In the present example, the two lags produced a difference in cross-sectional area of approximately 45 m^2 in the first half year (difference of +23 m^2 and -22 m^2).

As a final example, a calculation was made with parameters held as in Table 2, except that σ_1 was changed to an approximate fortnightly variation. Also, Δt was reduced to 0.5 day to allow the numerical solution to better capture the rapid variations in the inlet cross-sectional response, as shown in Fig. 6. The more rapid variation in the discharge, as compared to that shown in Figs. 4 and 5, produces considerably smaller changes in the cross-sectional area. The inertia of the inlet system does not allow rapid response of the cross-section, being scaled by the relaxation time τ_0. In addition, because one of the two forcings does not have sufficient time to fully develop, the magnitude of the total response is less than shown in the previous example, where the periods of the forcings were longer and comparable.

In summary, on the assumption that a channel cross section tends to be stable, Eq. 21 is capable of describing small changes in area about equilibrium in response to changes in the two major forcings that move sediment along or toward the channel. Such changes have been documented by Byrne et al. (1974), Behrens et al. (1977), FitzGerald and FitzGerald (1977), Nummedal and Humphries (1978), Van de Kreeke and Haring (1980), and others.

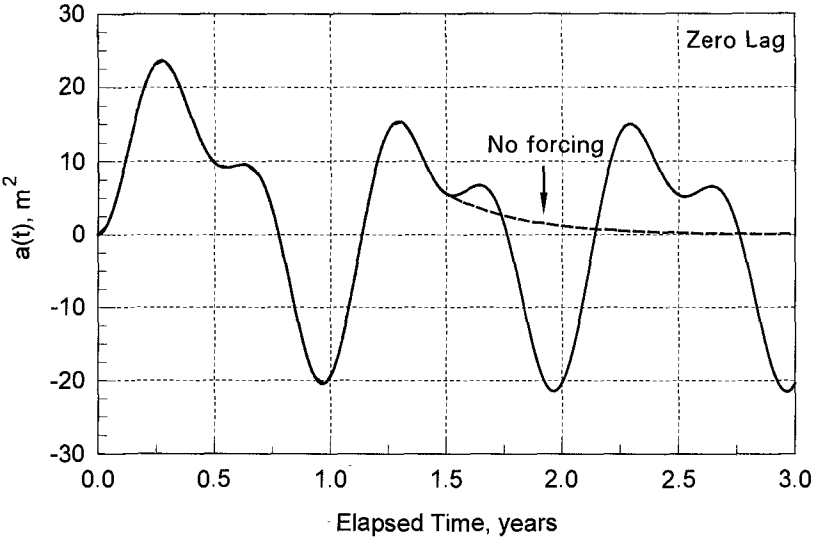

Fig. 4. Change in inlet area around equilibrium for forcing by sinusoidal discharge and sinusoidal longshore sediment transport rate, no lag between the forcings.

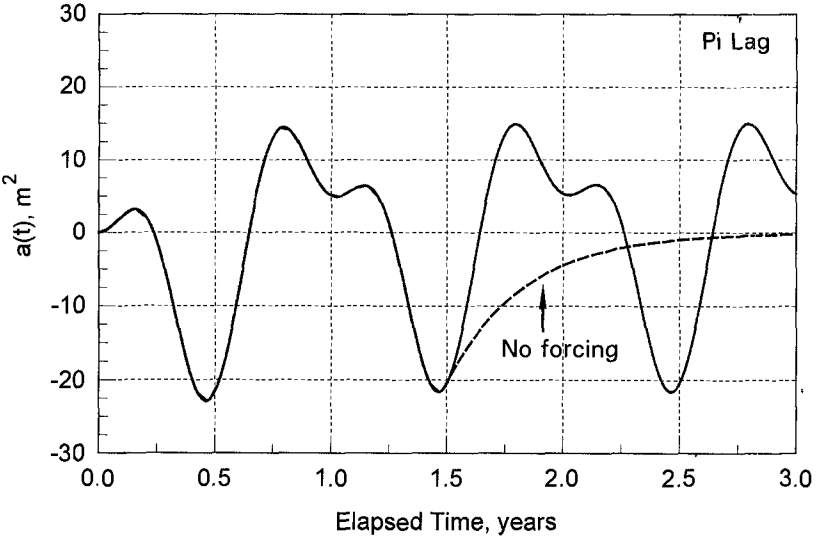

Fig. 5. Change in inlet area around equilibrium for forcing by sinusoidal discharge and sinusoidal longshore sediment transport rate, lag of 180 deg between the forcings.

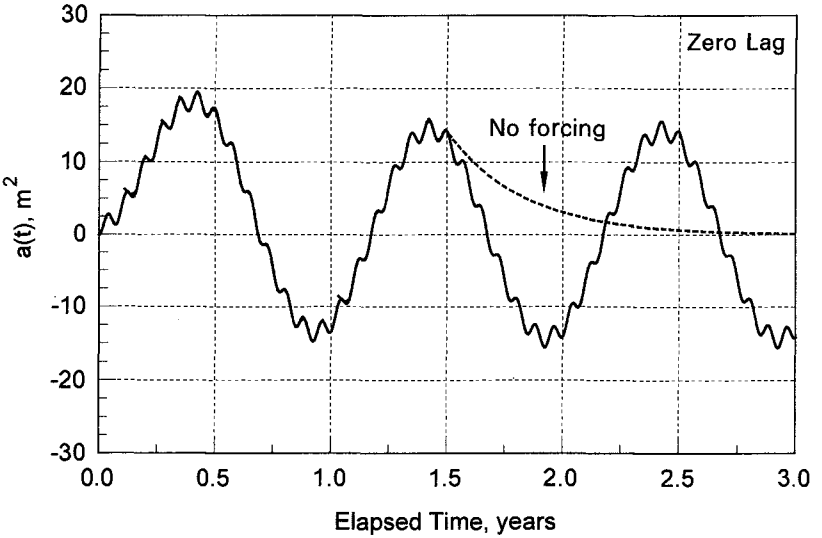

Fig. 6. Change in inlet area around equilibrium for forcing by sinusoidal discharge with rapid (bi-weekly change) and sinusoidal longshore sediment transport rate, no lag between the forcings.

CONCLUDING DISCUSSION

An equation relating the equilibrium or minimum cross-sectional area of an inlet channel was derived by balancing the input of longshore sediment transport with the transporting capacity of the inlet's discharge or tidal prism. The equation has the same functional form as previous empirical equations, but with the empirical coefficient expressed as a function of quantities related to the acting coastal processes. By expressing the inlet discharge in terms of the tidal prism, the derived coefficient C_p was found to have the same order of magnitude as accepted empirical values. The process-based expression qualitatively explains the long-recognized, greater inlet cross-sectional areas, for the same tidal prism, which are observed on more sheltered coasts where longshore sediment transport is less than on exposed coasts.

The time-dependent governing equation was perturbed from equilibrium to give a general linear differential equation describing variations in channel cross-section for small changes in the discharge and longshore sediment transport rate. The equation showed that longer-period perturbations (perturbations with periods comparable to or greater than the relaxation time of the inlet channel) tend to greatly alter the cross-sectional area of an inlet channel.

To arrive at the simple governing equation, three model-defining assumptions were made. First, the channel bar has idealized geometry, by which a simple form of the sediment continuity equation could be derived. Second, sediment exchange such as among the entrance bar, flood shoal, and beaches, is omitted. And third, it was assumed that the sediment-transport dynamics can be represented by relatively simple

expressions. In principle, these assumptions can be weakened or eliminated by extension of the process-based formulation that would be solved numerically. Because little is known about sediment pathways at inlets, a comprehensive process-based model would lend insight to the functioning of these pathways.

In summary, although the model introduced here has limitations, it represents rational incorporation of the main physical processes that have been identified by observations made at coastal tidal inlets by numerous authors. Extensions of the model can readily be accomplished, and the author expects to report some of these in future publications.

POSTSCRIPT

After presentation of this paper at the Twenty-Sixth International Coastal Engineering Conference, an attendee, Dr. Hitoshi Tanaka brought to my attention his work and that of his colleagues at Tohoku University, Japan. Their work concerns river mouth closure, and in it they have introduced a model similar to that of Eq. 4 concerning balance of river discharge and longshore sediment transport. Details can be found in Tanaka et al. (1996), which references an earlier work, Ogawa et al. (1984). Tanaka et al. examine the evolution of the width of an unstabilized river mouth, considering the time dependence of the variable W in the present work.

ACKNOWLEGEMENTS

I appreciate stimulating discussions with Mr. William Seabergh of the U.S. Army Engineer Waterways Experiment Station (WES), Coastal and Hydraulics Laboratory. Also, I would like to thank Dr. Hitoshi Tanaka for providing several articles on his studies related to modeling of river mouth closure that were not available to me. The work reported in this paper was conducted under the Inlet Channels and Adjacent Shorelines Work Unit of the Coastal Inlets Research Program conducted at WES. Permission was granted by Headquarters, U.S. Army Corps of Engineers, to publish this information.

REFERENCES

Behrens, E. W., Watson, R. L., and Mason, C. 1977. Hydraulics and Dynamies of New Corpus Christi Pass, Texas: A Case History, 1972-1973. GITI Report 8, U.S. Army Corps of Engineers, Waterways Experiment Station, Vicksburg, MS.

Bruun, P. 1968. *Tidal Inlets and Littoral Drift*. University Book Co., Oslo, 200 pp.

_____. 1978. *Stability of Tidal Inlets*. Elsevier, New York, 510 pp.

Bruun, P., and Gerritsen, F. 1960. *Stability of Coastal Inlets*. North Holland, Amsterdam, 140 pp.

Byrne, R.J., DeAlteris, J.T., and Bullock, P.S. 1974. Channel Stability in Tidal Inlets: A Case Study. *Proc. 14th Coastal Eng. Conf.*, ASCE Press, NY, 1585-1604.

Byrne, R.J., Gammisch, R.A., and Thomas, G.R. 1980. Tidal Prism-Inlet Area Relations for Small Tidal Inlets. *Proc. 17th Coastal Eng. Conf.*, ASCE Press, NY, 2517-2533.

FitzGerald, D. M. and FitzGerald, S. A. 1977. Factors Influencing Tidal Inlet Geometry. *Proc. Coastal Sediments '77*, ASCE Press, NY, 563-581.

Hume, T.M. and Herdendorf, C. E. 1990. Morphologic and Hydrologic Characteristics of Tidal Inlets on a Headland Dominated, Low Littoral Drift Coast, Northeastern New Zealand, *Proc. Skagen Symposium (2-5 Sep. 199), J. of Coastal Res. Special Issue 9*: 527-563.

Jarrett, J.T. 1976. Tidal Prism-Inlet Area Relationships. GITI. Report 3, U.S. Army Corps of Engineers, Waterways Experiment Station, Vicksburg, MS.

Johnson, J. W. 1972. Tidal Inlets on the California, Oregon, and Washington Coasts. Tech. Rep. HEL 24-12, Hydraulic Engineering Lab., U. of California at Berkeley, Berkeley, CA.

Keulegan, G. H. and Hall, J. V. 1950. A Formula for the Calculation of Tidal Discharge Through an Inlet. U.S. Army Corps of Engineer, Beach Erosion Board Bulletin, Vol. 4, 15-29.

LeConte, L.J. 1905. Discussion on River and Harbor Outlets, "Notes on the Improvement of River and Harbor Outlets in the United States," Paper No. 1009, by D. A. Watts, *Trans., ASCE* 55: 306-308.

Mason, C. and Sorenson, R. M. 1972. Character and Stability of a Natural Tidal Inlet. *Proc. 13th Coastal Eng. Conf.*, ASCE Press, NY, 781-800.

Nummedal, D. and Humphries, S. M. 1978. Hydraulics of North Inlet, South Carolina, 1975-1976. GITI Report 16, U.S. Army Corps of Engineers, Waterways Experiment Station, Vicksburg, MS.

O'Brien, M.P. 1931. Estuary and Tidal Prisms Related to Entrance Areas. *Civil Eng.* 1(8): 738-739.

O'Brien, M.P. 1969. Equilibrium Flow Areas of Inlets on Sandy Coasts. *Jour. Waterways and Harbors Division* 95(WW1): 43-52.

Ogawa, Y., Fujita, Y., and Shuto, N. 1984. Change in the Cross-Sectional Area and Topography of at River Mouth. *Coastal Eng. in Japan*, 27: 233-247.

Riedel, H.P., and Gourlay, M.R. 1980. Inlets/Estuaries Discharging into Sheltered Waters. *Proc. 17th Coastal Eng. Conf.*, ASCE Press, NY, 2550-2562.

Tanaka, H., Takahashi, R., and Takahashi, A. 1996. Complete Closure of the Nanakita River Mouth in 1994. *Proc. 26th Coastal Eng. Conf.*, ASCE Press, NY, 4545-4556.

Van de Kreeke, J. and Haring, J. 1980. Stability of Estuary Mouths in the Rhine-Meuse Delta. *Proc. 18th Coastal Eng. Conf.*, ASCE Press, NY, 2627-2639.

Watanabe, A., Shimuzu, T., and Kondo, K. 1991. Field Application of a Numerical Model of Beach Topography Response. *Proc. Coastal Sediments '91*, ASCE Press, NY, 1814-1928.

STABILISATION OF THE TIDAL ENTRANCE AT HORNAFJORDUR, ICELAND

Gisli Viggosson[1], Sigurdur Sigurdarson[1] and Bjorn Kristjansson[1]

Abstract

Hornafjordur is a tidal entrance on the south-east coast of Iceland, a shore with a heavy littoral drift. An extreme storm hit the coast in January 1990. It caused large shoaling to encroach upon the entrance channel from both sides, and a breakthrough occurred between the rock headland Hvanney and the South Barrier. The inlet was closed for several weeks.

A rubble mound shore protection was built on its west side in 1991 to restore the South Barrier. A curved breakwater of berm type was constructed during the summer 1995. Due to severe wave action and strong current a berm structure with toe protection was chosen.

The paper presents the experiences gained on the tidal inlet based on hydrodynamic and hydraulic models, both calibrated to the field data.

Introduction

The inlet is the entrance channel to the town of Hornafjordur, an active fishing harbour. The entrance has a rock headland on its west side and rock reefs which

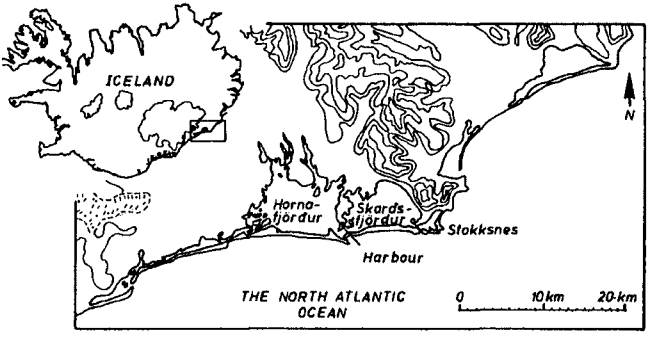

Figure 1. The location of Hornafjordur

[1] Icelandic Maritime Administration, Vesturvor 2, 200 Kopavogur, Iceland

shelter the entrance from southerly waves are located about 2 km south of it. Although the entrance has been stable in its present location for about 100 years, heavy shoaling has occurred in the entrance at 10-15 year intervals. The configuration of the coastline around Hornafjordur is controlled by two headlands, Skinneyjarhofdi 15 km in the west and Stokknes 7 km in the east as shown in Figure 1. The sea off Hornafjordur is very rough. While the total amount of drift along the shore may be of the order of millions of cubic meters of material, the net drift appears to be relatively small due to the headland configuration of the shore which made an entrance possible (Viggosson et al, 1994).

Southeast storms move material into the entrance to the shoal at the tip of the East Barrier and at high tides some material is flushed over the East Barrier into the navigation channel. At an interval of 10 to 15 years, shoaling has occurred in the navigation channel at the tip of the East Barrier as the ebb current is not able to flush material out to the shoal. Southwest and southeast storms move material into the entrance to the shoal at the tip of East Barrier and at high tides during storms some of the material may be flushed over the barrier into the navigation channel. During the summer when the wave activity is low the ebb current flushes material from the tip of East Barrier out to the shoal, so the tip may recede up to 100 meters. Usually in late August the entrance is considerably wider than in January when the wave activity is normally the highest. The diversion of currents due to shoaling and material being carried over the East Barrier cause the shore on the inlet side of the South Barrier to recede and the southeasterly waves cause the shore on the ocean side to receded due to the westward littoral drift. This leads to weakening of the barrier.

Figure 2. About 700,000 m^3 of material flushed into the navigation channel and a breakthrough through the South Barrier

On January 9, 1990, a severe south-west storm struck, with offshore wave heights exceeding 16.7 m. The storm was followed by unusually high wave activity and a breakthrough through the South Barrier occurred in March as shown on Figure 2. It is estimated that over 200,000 m^3 of material was flushed over the East Barrier into the navigation channel during this period and about 500,000 m^3 were flushed over South Barrier. As a result, the inlet was closed for coasters for several weeks.

Environmental parameters

An extensive field measurement program commenced during the summer of 1990 and continued to 1994. Included were several bathymetric surveys, water level measurements, bottom sampling, seismic refraction surveys, hydraulic measurements in the inlet and the channels into the west and east bays, aerial photography, offshore wave measurements, collection of weather data, geological assessments and research for quarry selection for the construction of rubble mounds.

Wave Climate

A Waverider buoy has since 1988 been located offshore off the south coast of Iceland close to Surtsey at 130 m water depth. The results of a statistical ana-lysis fitting the data with a three parameter Weibull distribution is shown in table 1.

Table 1

The long term wave statistics at Surtsey offshore and Hornafjordur buoy

% of time	Return period,year	Hs (m)	Tp (s)	Hs (m)	Tp (s)
60		2.3	10	3.4	10
90		4.1	11	5.8	12
99		6.5	15	9.2	15
	1	9.3	16	12.9	16
	10	10.7	18	15.2	18
	100	11.8	20	17.4	20

Waverider buoy has been located 4 km offshore the Hornafjordur entrance since February 1990, at a water depth of 32 m. The buoy is located just south of a cluster of reefs offshore from the entrance.

Tide Levels

Harmonic analysis of measured water levels in the entrance and harbour are shown in table 2.

Table 2

Tide levels in the entrance and the harbour of Hornafjordur

	Hornafjordur entrance (m)	Hornafjordur harbour (m)
Mean High Water Spring	2.11	1.81
Mean High Water Neap	1.53	1.54
Mean Sea Level	1.12	1.27
Mean Low Water Neap	0.71	1.01
Mean Low Water Spring	0.13	0.75

Measurements of currents and estimation of discharge in the Inlet

At the time when the measurements were performed, the inlet was still recovering form the shoaling that occurred the preceding winter and there were still two channels in the entrance (Snorrason et al, 1994). Current velocity measurements were made in cross section at the tidal entrance during August, 1990, twice during ebb tide and once during flood tide. The maximum recorded current velocity was 2.7 m/s and the maximum discharge during ebb tide was 3,125 m^3/s and 4,239 m^3/s during flood tide. Flow measurements were made in cross section to the Hornafjordur bay (west bay) , once during ebb tide and once during flood tide, Figure 3. The maximum recorded current velocity was 2.1 m/s, ebb tide discharge of 2,008 m^3/s and flood tide discharge of 1,920 m^3/s. The same measurements were repeated for cross section to Skardsfjordur bay (east bay), with the maximum recorded current velocity of 1.2 m/s, ebb tide discharge of 1,080 m^3/s and flood tide discharge of 1,130 m^3/s.

The fresh water influx to the inlet was estimated to be less than 5% of the tidal prism and is therefore of minor importance to the total water budget of the inlet.

For each set of measurements, the current velocity is measured in several locations distributed across the width of the cross section at different depths. The discharge is calculated from the current velocities and area of the cross section. The water level measurements at the three cross sections were made by pressure gauges from May, 1990 to January, 1991 with few brief interruptions.

The current measurements were made from July until September 1990 in cross sections to the west and east bay and outside the entrance to the harbour. Measured parameters were the current velocity, its direction, temperature of the water, the all-around pressure and the sea conductibility.

Seismic Refraction Measurements

In May 1993, a seismic profiling survey was carried out in the inlet area and the navigation channel up to the harbour. The survey indicated a basalt, generally occuring at a depth of 25 m or more, and is overlain by sediments of a variable provenance. In the channel outside the harbour entrance, for example, a thick sequence of cross-bedded sediments, dipping towards the north, may be precursors of the East Barrier.

Bottom Sampling

The material in the inlet is coarse. The main trends that can be noted are that it is primarily 3-5 mm material in the shoal off the East Barrier. The material in the channel is very coarse, d_{50} of 3-20 mm. Outside of Hvanney and west of Einholtsklettar, the material is generally fine, 0.2 mm, except in an isolated spot between Einholtsklettar and Hvanney with d_{50} of 10 mm. These samples were taken shortly after the closing of the gap between Hvanney and the South Barrier.

Hybrid Model

The goal of the study was to improve the stability and the navigational conditions in the tidal inlet of Hornafjordur. The plan for construction of shore protection and stabilisation of the inlet consists of three elements. Firstly, a rubble mound shore protection on top of the South Barrier was built to prevent overflowing of material. Secondly, a curved jetty was laid out from the tip of the East Barrier to stabilise the tip and the shoal in the entrance. The aim of the curved jetty was also to improve the current conditions, by deepening and channelling the entrance and thus

improving the navigational conditions. And thirdly, a groin has to be built at Thinganessker which is about 1.2 km east of the entrance to minimise sediment transport from the east.

For a very complex situation like the one at Hornafjordur only a hybrid model was possible. It composed of field data, properly interpreted, including sediment budget, numerical and hydraulic models, both calibrated to the field data. In 1994 and 1995 both numerical and physical models of the inlet hydraulics were run to obtain further data to improve the design of solutions for the navigation through the entrance and stabilisation of it.

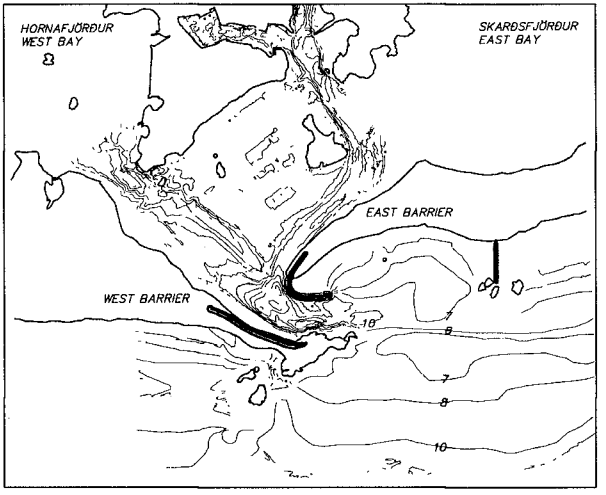

Figure 3. Stabilisation of the Hornafjordur tidal inlet. Layout of the shore protection on the South Barrier, the curved jetty on the East Barrier and the groin 1.2 km east of the entrance which will be constructed in 1999

Numerical Modelling

The AQUASEA mathematical modelling system, developed by Vatnaskil Consulting Engineers, was used to set up a numerical model of the hydrodynamics of the tidal inlet of Hornafjordur (Tomasson et al, 1994). The goal of this model applications was:

- to describe currents and discharge and to establish the relationship between the different types of field measurements carried out at different times and locations
- to describe currents and discharge in the tidal inlet for winter and summer conditions.
- to describe currents around the tip of East Barrier for different proposals for stabilising the barrier.
- to evaluate the influence of dredging the navigation channel and adding a landfill south of the harbour.
- to evaluate the influence of a proposed harbour inside the entrance.

- to evaluate the siltation of suspended load from the Hornafjordur rivers into the existing harbour and the proposed harbour.

The basis for calibration of the model was the field measurements conducted in August 1990 and a bathymetric survey from the same time. As the inlet was still recovering from the shoaling the preceding winter, bathymetric surveys performed in January 1991 and in June 1992 were chosen the basis in the model to describe typical winter and summer conditions respectively. The effects of drying of the two bays, Hornafjordur and Skardsfjordur are included in the model.

Evaluation of Data

Discharge and Tidal Prism

Table 3 summarises the discharges and tidal prism through the different cross sections at mean spring tide (Tomasson et al, 1994). The water levels are approximately the same at the start and the end of the tidal cycle.

Table 3

Results for flow and tidal prism (summer conditions, spring tide)

Cross section	Max. discharge (m^3/s)		Tidal prism (x m^6 m^3)	
	Ebb tide	Flood tide	Ebb tide	Flood tide
Tidal inlet	3440	4420	63.8	63.2
West bay	1750	2120	31.6	30.4
Harbour entrance	890	1180	18.5	16.5
East bay	730	1060	12.2	14.6

The high water in the harbour is reached over 2 hours later than the maximum discharge and velocity in the entrance. At low water in the harbour, the velocity and discharge in the entrance are very nearly zero. The maximum velocity is 2.7 m/s on the ebb and 2.0 m/s on the flood tides. The change in velocity is very rapid. As an example, it increases from 0.7 to 1.3 m/s over a period of 10 minutes.

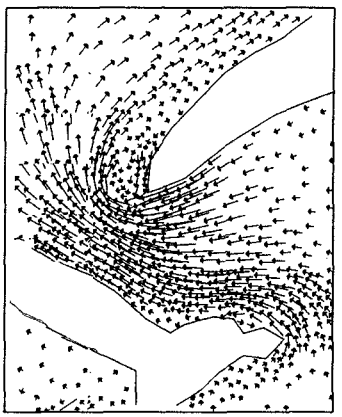

Figure 4. Maximum flood flow at spring tide at summer condition

It is interesting to note the eddy generated on the lee side of the East barrier as shown on Figure 4. A corresponding eddy, but much larger in extent forms on the other side of the east barrier at maximum flood tide.

Hydraulic Model Studies

In April 1994, a physical model study for Hornafjordur was prepared in the 20 x 40 m hydraulic model hall runned by the Icelandic Maritime Administration (Viggosson et al, 1994).

The goal of the model study was to provide design data and information for the improvements to navigation, maintenance and stability of the entrance.

The model was constructed to the scale 1:100, both in plan and vertically, covering the area from a water depth of 10 m up to the harbour area including the entrance and the inlets into the two bays, Hornafjordur and Skardsfjordur. Calibration of the model was done both by field measurements and by results from the numerical model. The model is constructed according to a 1992 bathymetric survey (summer conditions) which corresponds to the topographic information used in the numerical model. The model was built with a fixed bottom but the facility to reproduce a movable bottom in limited areas is featured. Random wave generators simulate south-west and south-east waves. Closed circuit water pump simulates a the currents by creating a steady state flow conditions through the inlets.

Stabilisation of the Entrance

In order to stabilise the entrance it has to be protected against rapid inflow of sediments to the navigation channel. Although the net drift is eastward, stability considerations following Bruun (1978) procedures, reveal that the quantity of westward drift towards the entrance may be of the order of 200,000 to 300,000 m^3 per

Figure 5. Construction of the shore protection on the South Barrier.
The alignment of the shore protection is set according to the maximum known scouring from the entrance

year causing large deposits in the outer entrance area, in the ocean and on the either side of the lava reef, Thinganessker, located about 1.2 km east of the entranee.

Improvements to the South Barrier

After the gap between Hvanney and South Barrier was closed, a southerly swell started to build up the barrier. In 1991, a 665 m long rubble mound shore protection was built along South Barrier. The alignment of the shore protection are shown in Figure 5. To prevent overflowing of material over the South Barrier a decision was made to accelerate this phase as it did not affect the hydraulics in the entrance.

Improvements to the East Barrier

To stop the transfer of material into the navigation channel it was necessary to build a curved jetty at the tip of the East Barrier. It served the dual purpose of putting a strong brake on the drift towards the channel from east at the same time working as a training wall for currents in the entrance. An accumulation capacity exceeding to 80,000 m^3 was sought. It could come during a couple of storms but as the updrift shoreline curves out the accumulation close to the jetty slows down and more material is deposited updrift. We were, therefore, facing a double-sided problem; (1) we wanted less sand from the east towards the entrance, (2) at the same time we wanted material enough to keep a stable shore between the entrance jetty and the Thinganessker tombolo.

During the evaluation of the improvement of the tip of the East Barrier a range of scenarios were developed with respect to bathymetry in the inlet, summer and winter flow conditions and different forms of the proposed jetty and the accumulation of material on the updrift side of the jetty.

Three different forms of a proposed jetty at the tip of the East Barrier, varying in the size, shape and location, were investigated. Considerable differences were found in the current field in the entrance depending on the form of the jetty, especially at flood tide where one form of the jetty was found to channel the current quite efficiently through the entrance and around the tip, while an eddy of considerable size formed on the leeward side of the two other jetties.

Comparison of flow separation at the tip of the East Barrier in the numerical versus hydraulical models reveals high degree of separation in the hydraulic model, especially after the curved jetty has been added. Therefore, careful recalibration of the models were carried out.

For each scenario, the numerical and hydraulic models were calibrated and tested. But the flow conditions at ebb and flood tide were not acceptable regarding eddies with the bathymetry from 1990 and 1992.

The bottom conditions in the spring 1994 had almost stabilised. The depth at the shoal at the tip of the East Barrier was about 4 m along the proposed jetty. By testing various forms of the jetty with material accumulated on the lee side and the bottom topography of 1994, minimum flow separation and turbulence was achieved, both in the hydrodynamic and the physical models when the depth along the jetty was increased from – 4 m by natural slope down to – 8 m. Figure 6 shows the currents at spring tide for the final proposal of the layout of the East Jetty.

To fulfil the criteria of natural slope down to – 8 m along the jetty some 60,000 m^3 of material had to be dredged. Based on these findings, dredging along the proposed jetty was planned a year or two after the construction of the east jetty. Due

to the curvature of the east jetty some maintenance dredging along the jetty can be expected in near future.

The methods of (van Rijn, 1993) for bed load transport were used to predict the bottom changes in various time steps from the building of the curved jetty, where both current and wave related transport was included. Coarse sand and gravel are transported primarily as bedload where larger gravel tend to armour the upper most layer.

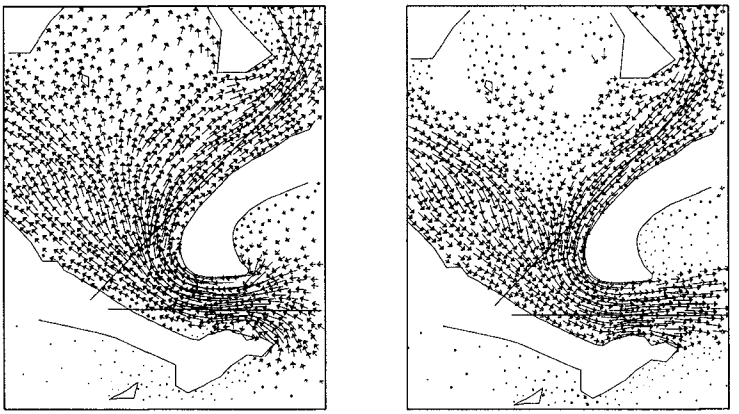

Figure 6. Currents at spring tide for the final proposal of the layout of the east jetty

To investigate the influence of expected increased depth along the proposed jetty, shear stress calculation were carried out. The Chezy bottom friction coefficient in the calibration process of the numerical model was found in the inlet C_h = 45 $m^{1/2}/s$. Comparisons were made between the shear stress at maximum flood and ebb tide with and without increased depth to – 8 m along the proposed jetty. At flood tide the maximum shear stress were calculated at the bottom in 1994, to maximum 80 N/m^2 in the curved of the jetty compared to 30 N/m^2 with increased depth. Nearby the entrance the maximum shear stress were 45 N/m^2 compared to 30 N/m^2 with increased depth. At maximum ebb tide, peak shear stress occurs at the tip at the jetty and along the straight leg of the jetty. In both areas the maximum shear stress decreases from 50 N/m^2 to 40 N/m^2 with increased depth.

The results for flow and tidal prism of the final proposal of the layout of the east jetty are shown in table 4.

Table 4

Results for flow and tidal prism (Summer conditions, spring tide)

Cross section		Max. discharge (m^3/s)		Tidal prism (x m^6 m^3)	
Entrance		Ebb tide	Flood tide	Ebb tide	Flood tide
Normal condition		3440	4420	63.8	63.2
Summer	1994	3435	4415	64.1	63.3
Proposed jetty	1994 (- 4 m)	3520	4435	64.6	63.8
Proposed jetty	1994 (- 8 m)	3940	4835	68.7	68.4

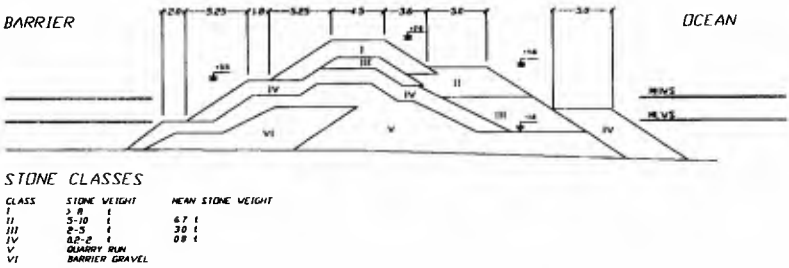

Figure 7. Typical cross section of the shore protection on the East Barrier.

A total of 99,700 m^3 were excavated from the quarry, of which 27,400 m^3 were over 2 tonne. Total project cost was 1.53 million USD, in comparison to the original cost estimate of 1.50 million USD, a difference of only 2%. (All prices include 24.5% VAT).

In the tender documents the contractor was asked to build a construction road between station 262 and 462 during the neap tide from June 3 to 10, but this could be postponed in case of a bad weather. The purpose to minimise the risk of erosion in front of the construction road and at the toe of the breakwater during the construction period. The contractor constructed a 6 m wide low road of quarry run and managed to complete the structure to station 500 within this period, Figure 8. At the same time the road was secured with 0.2 - 2 tonne rocks at the inlet side. Due to the fast progress of the work the erosion in front of the tip was limited, a maximum of 30 cm was observed. The outcome from the quarry was carefully monitored and a 100% utilisation of the quarried material was achieved.

Figure 8. During spring tide after the completion of the construction "road". Note the head difference of about 1 m.

Construction of the Rubble Mounds

The shore protection on the South Barrier

During the summer of 1991, in the early phase of field measurement and modelling, a 665 m long conventional rubble mound shore protection was constructed at the South Barrier (Sigurdarson et al, 1994). The rock in the main quarry for the South Barrier is an 8 m thick basalt lava situated about 30 km from the construction site. A total of 60,000 m^3 of material was needed from the quarry. Total contractor cost was 1.80 million USD, in comparison to the original cost estimate of 1.64 million USD, a difference of only 10 %. (All prices include 24.5% VAT).

The berm breakwater on the East Barrier

The jetty is 330 m long in addition to the 200 m long shore protection along the tip of the East Barrier was constructed during the summer 1995. The design condition of the wave height, current and erosion were evaluated by the numerical and the physical models(Sigurdarson et al, 1997).

Design conditions for the jetty were established as follows:

- The bottom material in the tidal entrance consists of coarse lava sand with particle size of 2-30 mm in diameter with some larger gravel.
- The barrier material is 1-5 mm with some gravel.
- The maximum current velocity was estimated 3.0 m/s at ebb tide and 3.5 m/s at flood tide.
- At spring tide the maximum discharge through the inlet during ebb tide was estimated 3,440 m^3/s and 4,420 m^3/s during flood tide.
- At spring tide the water level is about +2.1 m and the design water level is +3.5 m.
- The offshore significant wave height with 100 year return period is about 17 to 19 m with peak period 18 to 20 s.
- At 30 m water depth outside the entrance the 100 year significant wave height is about 12 m with peak period 18 to 20 s.
- During the design storm the significant wave height just outside the jetty is 3.8 m.

The design of the jetty had to take into account strong currents and moderate storms during the construction time. This led to a berm type breakwater of several stone classes with large toe protection as shown in Figure 7. Stone classes in the range of 2 tonne up to over 10 tonne were used. The berm consists of two classes of mean weight 6.7 and 3.0 tonne, the larger on top of the other, which corresponds to a stability numbers of 1.5 and 2.0. In front of the berm there is a toe protection of 0.2 - 2 tonne stones 20 m^3 per meter length of the structure. The predicted quarry yield over 2 tonne was 25 - 30 % which the design aimed to utilise completely to the advantage of the berm structure.

Monitoring of the tidal inlet and the breakwaters

Depth soundings in the entrance are performed regularly at an interval of 2 - 3 months and the breakwaters are visually inspected every two months. During the construction phase, bottom changes were in accordance with the predictions of the mathematical model (Viggosson et al, 1998). Figure 9 and 10 show an arial photos of the tidal entrance at Hornafjordur on the completion of the stabilisation.

Large volumes of sand and gravel were transported as shown on differential plan in Figure 11 between May 1995 and June 1998 which have not caused any problems for ships navigating the inlet.

Figure 9. Arial photo of the tidal entrance at Hornafjordur

Local accretion of sand of up to 2 meters started already near the strait part of the jetty during its construction. According to Figure 11 this accretion has eroded and the distance has decreased between the two erosion areas at the end of the jetty and near the curved jetty. The volume needed to be dredged along the jetty to fulfil the criteria of natural slope down to – 8 m are about 15,000 m^3 instead of 60,000 m^3 after the completion of the jetty.

Special attention is paid to the toe of the breakwater. The toe protection 0.2-2 tonne has been washed down and protects the eroded slope from further erosion. Figure 11 the differential plan between May 1995 to June 1998 shows an erosion up to – 7 m near the tip and - 11 m along the curved part of the jetty and accretion up to 5 m. The erosion along the curved jetty and at the tip started during the construction. The maximum erosion reaches temporary - 10 m at both places compare with 7–8 m today.

The accumulation of material at the updrift side of the jetty developed fast during the first winter. An accumulation of some 80,000 m^3 was observed after the first winter but since then the accumulation has slowed down. At present some 100,000 m^3 of material has been accumulated and more material is deposited updrift. With 10 to 15 years interval, storms from east and southeast with duration of up to 10

days have cause heavy littoral drift to the entrance. It is, therefore, planned to build a 250 m long groin next year, connecting the Thinganessker reef to the shore, some 1.2 km east of the entrance. The groin is expected to prevent littoral drift to the west and thereby stabilise the entrance.

Figure 10. Arial photo of the tidal entrance at Hornafjordur

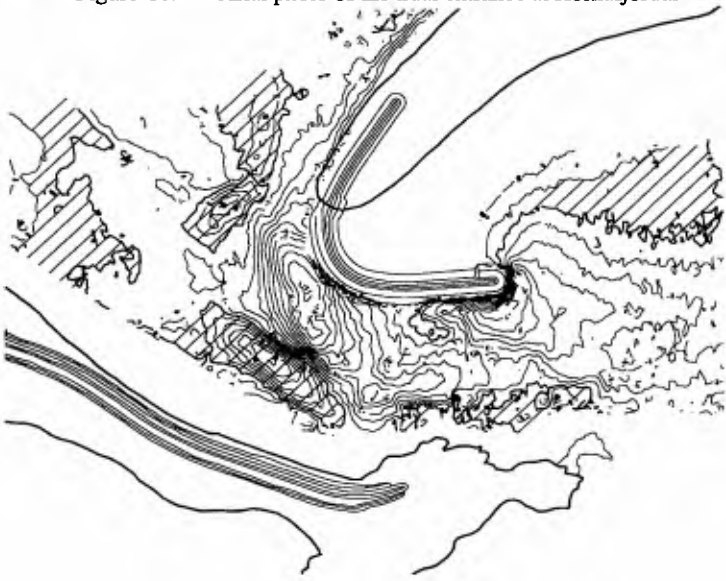

Figure 11. Differential plan between May 1995 to June 1998 showing erosion up to – 7 m near the tip and - 11 m along the curved part of the jetty and accretion up to 5 m. Dashed areas show accretion.

Conclusions

A natural inlet on a shore with heavy littoral drift, large wave forces, coarse material and strong current velocity. It was successfully stabilised with minimum inpact on the surrounding environment and navigational conditions were improved.

In 1991, a 665 m long rubble mound shore protection was built along South Barrier. To prevent overflowing of material over the South Barrier a decision was made to accelerate this phase as it did not affect the hydraulics in the entrance.

Large volumes of sand and gravel have been transported through the tidal inlet since the construction of the east jetty in 1995 and until now it has not caused any problems for ships navigating the inlet or for the berm breakwater.

Instead of a dynamic approach to berm breakwaters, as was the initial philosophy, a more stable approach has been adopted. This has lead to the "Icelandic berm" which is more economical and a more stable design than the original dynamic design approach. The toe protection and the berm breakwater have functioned as expected and the navigation conditions in the entrance are according to expectations.

According to the sounding of June 1998 it is necessary to dredge some 15.000 m^3 to fulfil the criteria of natural slope down to – 8 m along the jetty. Dredging is planned in the autumn of 1998.

There are plans to build a 250 m long groin next year, connecting the Thinganessker reef to the shore, some 1.2 km east of the entrance. The groin is expected to prevent littoral drift to the west and thereby stabilise the entrance. Due to the curvature of the east jetty some maintenance dredging along the jetty can be expected in near future

References

Bruun, P., 1978. Stability of Tidal Inlets. Elsevier, 500 p.

Sigurdarson, S,. Viggosson, G and Halldorsson, A. A. 1994. Rubble mound breakwaters and shore protection, *Proc. of the International Hornafjordur Int. Coastal Symposium*, Iceland

Sigurdarson, S., Einarsson, S., Smarason, O.B., Viggosson, G., 1997. Berm breakwaters in the tidal inlet of Hornafjördur, Iceland, *Proc. of Third International Conference on the Mediterranean Coastal Environment, Medcoast 97,* Malta.

Snorrason, Á., Zophoniasson, S. and Johannesson, T., 1994. Current Velocity and Flow Measurements in Hornafjordur Tidal Inlet During the Summer of 1990. *Proceedings of the Hornafjordur Coastal Symposium*, IMA, Kopavogur.

Van Rijn, L.C. 1993. Principles of sediment transport in rivers, estuaries and coastal seas. *Aqua Publications,* The Netherlands.

Viggosson, G., Sigurdarson, S. and Halldorsson, A. and Bruun, P 1994. Stabilisation of the tidal entrance at Hornafjordur, Iceland. *Proc. of the Hornafjordur international coastal symposium*, Iceland pp.681 - 688.

Viggosson, G., 1998. The Hornafjordur Tidal Inlet, Iceland. .Proceedings of the International Coastal Symposium, ICS 98. *Journal of Coastal Research.* Fort Lauderdale, Florida, 1998.

Tomasson, G.G., Holm, S.L., Kjaran, S.P., Viggosson, G. and Sigurdarson, S., 1994. Hydrodynamic Modelling of the Tidal Inlet of Hornafjordur. *Proceedings of the Hornafjordur Coastal Symposium*, IMA, Kopavogur.

APPLICATION OF A LONG-TERM EVOLUTION MODEL OF TIDAL INLETS TO THE DESIGN OF A NAVIGATION CHANNEL, THE NAVIA INLET CASE.

R. Medina[1], M. A. Losada[2], Member, ASCE, P. Lomónaco[1] and A. Baquerizo[3]

Abstract

The navigation channel of Navia is designed applying a long-term evolution model of tidal inlets. Navia is a port located on the North coast of Spain, and accessed by a narrow inlet, influenced by strong tidal currents, waves and a variable morphology. To define the design depth, the most important oceanographic processes are included in a probabilistic approach. The model allows comparing different scenarios, according to jetties length and maintenance dredging. In this way, optimum design represents a balance between capital costs and maintenance requirements. The long-term evolution model turns out to be an efficient tool for navigation channel design, and a must for optimum design.

Introduction

Tidal inlets are among the most active sedimentary units. Waves, tidal currents, river discharge, density currents and wind driven currents influence them. Sediments are continuously in motion, due to the strong hydrodynamics and the sediment size ranges from fine silt to pebbles. On the other hand, estuaries are generally used for port activities, since they provide naturally sheltered areas and allow inland navigation. The access to these ports is done through the estuary inlet.

The tidal inlet natural cross section is the result of a balance between sediment input, onset of motion and transport, tidal current patterns and tidal prism, among other factors. The result is a dynamically stable section, which tends to an equilibrium condition. Hence, a tidal inlet may be in equilibrium even though its morphology changes

[1] Ocean & Coastal Research Group, E. T. S. I. de Caminos, C. y P., University of Cantabria, Avda de los Castros s/n, 39012 Santander, Spain.
[2] Department of Civil Engineering, E. T. S. I. de Caminos, C. y P. University of Granada, Campus 'La Cartuja', Granada, Spain.
[3] Department of Hydraulic Engineering, Civil Engineering Faculty, Delft University of Technology, Stevinweg 1, 2628 CN Delft, The Netherlands.

continuously, since the latter is given by the current hydrodynamic conditions, but the mean condition is, in long-term, constant.

Therefore, two time scales are defined for the morphological variability of the inlet, the short-term variability (days, weeks), controlled by the time scale of waves, tides or river, and the long-term variability (months, years), controlled by the natural tendency towards equilibrium of the inlet. Several authors had proposed relationships between some estuary properties in equilibrium and the hydrodynamic conditions, e.g. tidal prism versus inlet cross section (O'Brien, 1930, Bruun, 1966), or tidal flats extension versus estuary area (Eysink, 1990). Any change in these properties will produce a different equilibrium condition, and the estuary morphology will tend towards a new stability state. Since the most active unit inside the estuary is the tidal inlet, one can find the strongest changes in it.

But the problem is that natural equilibrium conditions may not fulfil navigational requirements, at least during some time periods (at low tide or during storms). In most cases, it becomes very hard to achieve these requirements, particularly with respect to depths, and it is necessary to accept nature's conditions, or to pay a very high price in maintenance dredging.

As mentioned before, after dredging, the inlet will evolve and, after some time, will attain its equilibrium condition. In order to preserve the required depth, maintenance dredging must be performed and the time evolution of the inlet has to be assessed. A long-term evolution model can predict the inlet behaviour.

In this paper, a long-term evolution model will be applied to the Navia inlet, in the northern coast of Spain. The model is based on the work published already by several authors and will be presented here in detail. First, the physical environment within Navia will be shown and the navigation channel design principles will be defined. Then the long-term evolution model concepts and theory will be elucidated in order to apply it in the design of Navia's navigation channel and the maintenance works. With these results, an optimum balance between capital costs and maintenance dredging can be found for a particular channel geometry.

The Navia Inlet

The North coast of Spain consists of a series of pocket beaches and bays separated by pronounced rocky headlands. The coast in general faces North, towards the Cantabrian Sea, in the northern Atlantic Ocean. Depths here reach more than 4000 m far offshore and the continental shelf has an average width of 30 km. The mean tidal range is about 4 meters; spring tides reach ranges up to 5 meters and they are all semidiurnal.

Navia is a small inlet on this coast, in Figure 1 its location is indicated, and also can be seen the large fetch area to the Northwest, where strong extra-tropical cyclones generate wind and waves which make the Cantabrian Sea one of the roughest in the

world. Hence, waves arrive to Navia from the NNW and a typical winter storm has a significant wave height between 4-6 meters.

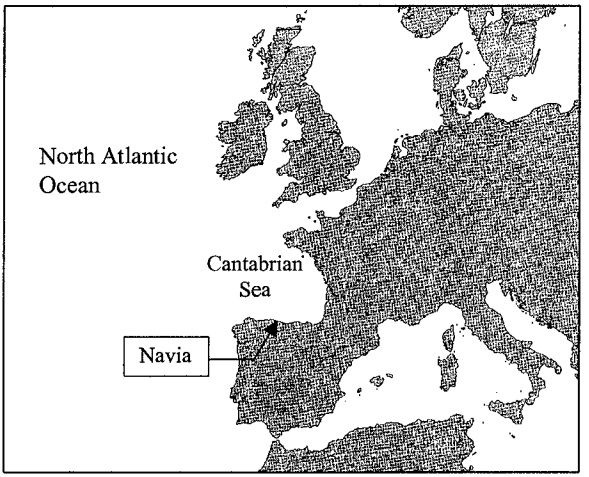

Figure 1. North Atlantic and the Cantabrian Sea. Navia inlet location.

Navia is an old port, meant for bulk cargo (iron ore) and fishing. In Figure 2 a 1786 chart is presented, where one can identify the original shape of the outer shoal, the river path and water depths. Comparing with recent charts, even though some differences are clear, it can be found that, in general, the shape and depth of the shoal are very similar. This means that the estuary is in equilibrium, and since the rocky headlands protrude quite offshore, the amount of sediment in the system is fixed and constant, no longshore transport occurs. Furthermore, several dams had been constructed along the river basin, stopping all sediment before it reaches the estuary and controlling the river discharge.

Nowadays, (Figure 3) Navia estuary presents a tidal prism of about $5*10^6$ m^3 and an offshore shoal that almost emerge in low tide. Human intervention in Navia's estuary starts at the end of the last century, with dredging, reclamation of tidal flats, shore protection along the river margins and the construction of two small jetties. Land reclamation was not very extensive, and the jetties become a lateral support for a beach east from the tidal inlet.

Recently, a new expansion project has to be made for the port, considering the possibility of maintenance dredging versus jetties enlargement. The outcome was a new approach for optimum design applying a long-term evolution model.

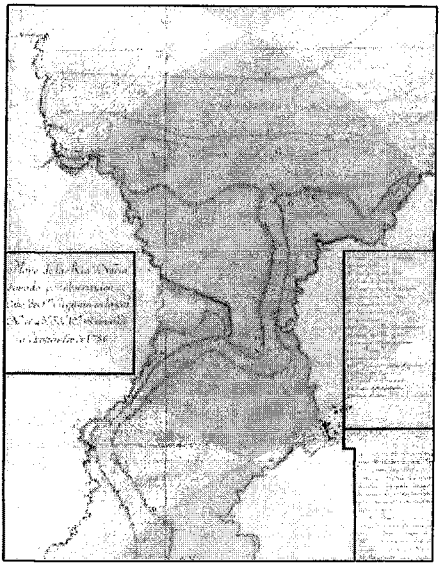

Figure 2. Navia inlet. Chart from 1786.

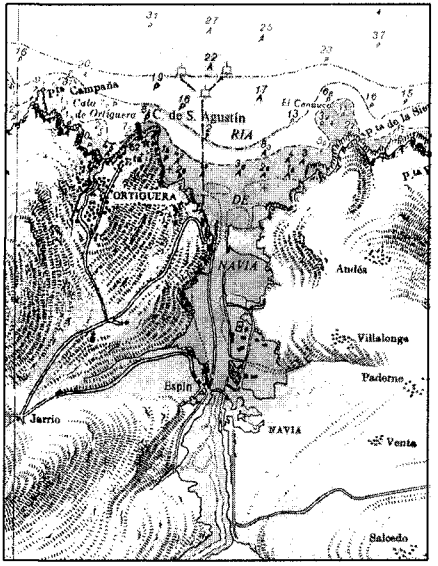

Figure 3. Navia inlet. Present day chart.

Navigation Channel Design Principles

Water depth at the inlet is one of the factors controlling the access to a port. On one hand there is a minimum channel depth required for a given ship to enter safely, this depth is the result of considering ship's draft, the under keel clearance corresponding to cargo's characteristics and bottom material, and ship's dynamical response to waves and displacement, i.e. squat and heave. On the other hand, the real water depth at a certain moment is the result of minimum depth, astronomical tides and storm surge (see Figure 4). As one can see, some of these factors varies with time and, furthermore, a few are purely stochastic parameters. Thus, for a given vessel, there is a percentage of time where the channel can be accessed, in other words, to be operational. A combination of all these factors gives a curve for different dredged channel scenarios and a plot of percentage of time versus channel depth can be constructed for each vessel (Figure 5). In this curve, the minimum design water depth can be obtained given a desired functionality and vice versa.

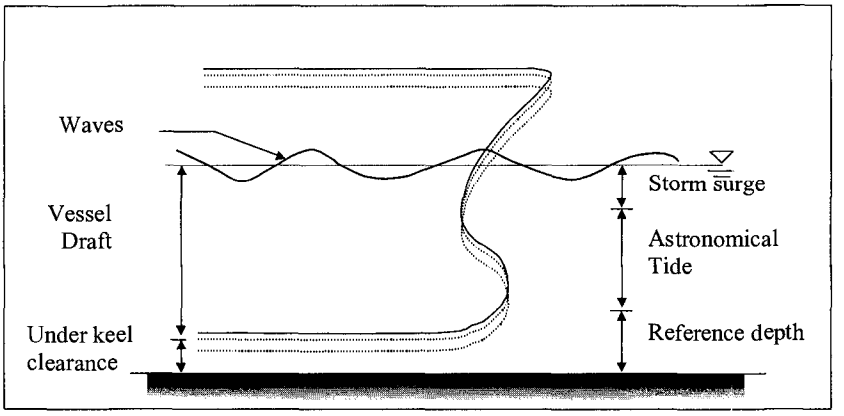

Figure 4. Real and required channel depth definition.

The obtained design depth corresponds to vessel requirements and has nothing to do with nature's equilibrium depth. Typically, both depths are different and the problem arises when the equilibrium depth is smaller than the required depth, thus the access channel is dredged. According to the preceding paragraphs, the inlet will try to recover the equilibrium immediately after changing its original condition, but this will take some time, depending on the strength of the hydrodynamic and morphologic processes, and sediment availability. Consequently, in order to warrantee the desired functionality, over dredging is commonly performed, as a sedimentation bulk capacity, delaying maintenance dredging. Thus, maintenance (m) should be done as soon as the inlet has evolved to the minimum depth, at least to fulfil the minimum requirement for functionality. Hence, three depths has been defined: the initial depth (i.e. over-dredged depth, h_o), the minimum depth for required functionality (design depth, h_L) and the final depth or equilibrium depth (h_f).

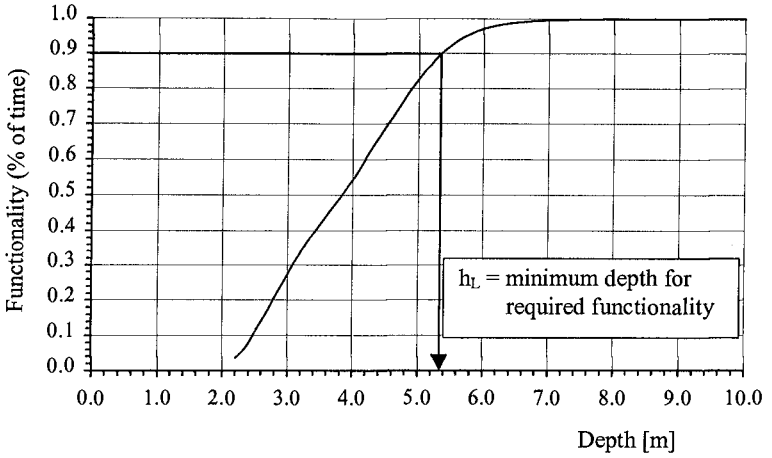

Figure 5. Functionality versus channel depth for the design vessel.

As a result, it is required to know the depth evolution time history at the inlet. A long-term evolution model will provide this information. Figure 6 shows an example of channel depth time evolution, indicating the initial, design and final depths and defining the maintenance interval. Here two approaches can be followed: to dredge and maintain the inlet or to modify the evolution trend by constructing jetties, or changing any of the main parameters that control the time evolution. In any case, the long-term evolution must be determined. The theory behind, concepts and how it was applied to Navia will be presented in the following paragraphs.

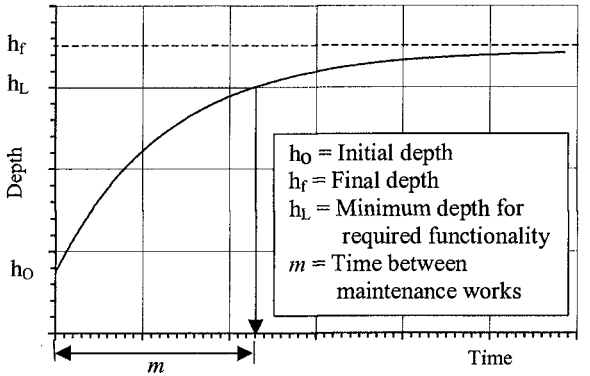

Figure 6. Time evolution example of channel depth.

Long-Term Evolution Model

As mentioned before, a long-term evolution model is based on the assumption that the estuary, and its elements, will tend to a known natural equilibrium condition. The dynamical stability, with a mean morphology, is a feature of tidal inlets measurable all over the world. Several researchers had studied these mean morphologies, and found empirical relationships between the morphology and some parameters representative of the estuary.

Hence, if any estuary parameter is modified, there will be a change in the morphology accordingly, or if the inlet cross section is altered, it will recover its original shape (van Dongeren, 1992).

The main approaches for modelling long-term inlet morphology are:

1. To use small scale physics and to integrate the results over larger time scales. This is known as aggregated scales and can only be used when the process modelled is dominated by a linear behaviour.
2. To use empirical relationships, i.e. those mentioned before which relate an estuary parameter with hydrodynamics.
3. To use a hybrid model (van der Kreeke, 1996).

In the present paper, a hybrid model has been developed to evaluate the long-term evolution of Navia inlet. Following de Vriend, *et al*, 1994, the proposed model is based on the assumption that the system, which consists of four interacting elements (the tidal basin, the outer shoal, the offshore shelf and the adjacent coast, see Figure 7), will try to attain the equilibrium after a human work (dredging and/or jetties).

The model describes the transition of the outer shoal from the initial disturbed position to the equilibrium. It uses physics as well as empirical relationships. In particular, the along-shore and cross-shore transport are calculated using physics based models. Tidal basin sediment transport and outer shoal equilibrium is calculated by means of empirical relationships.

Basically, the evolution model performs a sedimentary balance at the inlet, from the input and the output volume of material. It is assumed that the output volume is inversely proportional to the degree of instability of the inlet, in other words, the closer is the inlet to equilibrium, the more sand is exported to the adjacent morphologieal units.

In a long-term time step (months/years), the inlet organises the input volume in the shoal, thus some part will be under the waves and currents influence and will be transported back to the beach or inner estuary. The volume of sediment, which actually remains is, therefore, a fraction of the originally deposited (Losada, *et al*, 1997):

$$\Delta V_I = k_1 (Q_O + Q_R + Q_B) \Delta t \qquad (1)$$

Where V_I is the volume of the outer shoal, which includes the inlet, and is proportional to the inlet depth (Eysink, 1990). k_I is a constant and represents the fraction of sand volume, which remains at the inlet. The value of k_I is obtained from the wave incidence pattern (Hicks and Hume, 1996) and is also calibrated from adjacent inlets. The rest of parameters are defined below.

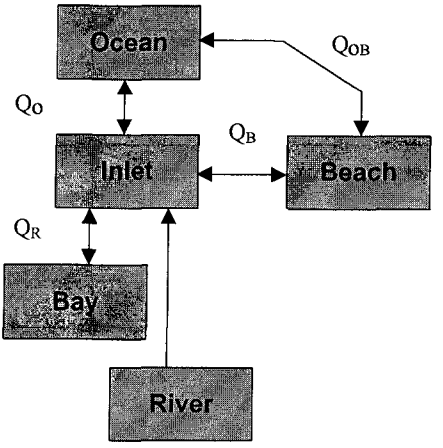

Figure 7. Morphological units of a tidal inlet.

In Figure 7 also the sediment transport flux between each unit is shown. Q_O is the cross-shore transport, mainly induced by waves. Q_R is the estuary sediment input and output due to tidal oscillatory currents and river discharge. Q_B is the longshore transport from the adjacent beach produced by oblique wave incidence, set-up and tidal currents, and Q_{OB} is the cross-shore transport from the outer shoal to the adjacent beach. Hence, two different processes has been defined, the process within units, based on empirical relationships and formulations, which is considered to be instantaneous, and the process among units, defined by the continuity of sediment flux between units.

Notice that in each time step, the value of the fluxes depends on the inlet condition, the farther the inlet is from its equilibrium condition, the larger is the sediment input. With this approach, each unit is modelled in a different way, according to its morphological response.

The estuary will contribute with sediment linearly according to the degree of instability of the inlet:

$$Q_R = k_2 (V_I - Ve) \quad (2)$$

Where: Q_R is the sediment flux from the estuary,
V_I is the volume of sediment in the inlet,

Ve is the tidal inlet equilibrium volume, and
k_2 is a constant based on empirical models (Eysink, 1990) and calibrated from adjacent inlets.

The river input is independent to the inlet condition; therefore its flux is assumed to be constant. The ocean unit can endow or receive sediment from the inlet. The ocean-inlet flux is an exponential function of inlet degree of instability:

$$Q_O = Q_{OE} \exp(-k_3(h-h_f)) \quad (3)$$

Where: Q_{OB} is the ocean-beach sediment flux,
Q_O is the ocean-inlet sediment flux,
Q_{OE} is the ocean-inlet sediment flux for equilibrium conditions,
h is the inlet water depth,
h_f is the inlet equilibrium water depth, and
k_3 is a constant based on empirical data and calibration.

Finally, the beach will supply sediment to the inlet according to the incident wave field. If there is no jetty, the wave will approach to the spit of the sand bar with an angle, which will create a longshore current and sand transport. If there is a jetty, the shoreline position, relative to the tip of the jetty, will indicate the percentage of sand flux from the beach to the inlet.

$$\begin{aligned} Q_B &= Q_{B(MAX)} && \text{if } D_L = 0 \\ Q_B &= k_4 D_L && \text{if } 0 < D_L < D_{L(MIN)} \\ Q_B &= 0 && \text{if } D_L > D_{L(MIN)} \end{aligned} \quad (4)$$

Where Q_B is the beach-inlet sediment flux,
$Q_{B(MAX)}$ is the long-shore sediment transport, computed with the overall incident wave climate,
D_L is the distance from the shoreline to the tip of the groin,
$D_{L(MIN)}$ is the surf zone width, where long-shore transport mainly occurs, and
k_4 is a constant based on equation (4) requisites.

The sand transport, $Q_{B(MAX)}$, is computed using one of the several formulae available from the literature, and the actual flux is computed using a multi-line model of the beach profile, which in turn depends on the total volume of sand at the beach.

The beach behaves as a special sedimentary unit in this case, since the total amount of sand in it will define the shoreline position. The actual volume of sand is a balance from the output flux towards the inlet and the input flux from the ocean (or any other source, e.g. sand by-passing, wind transport, nourishment, etc). The model assumes that the ocean-beach flux (Q_{OB}) will be exactly all the sand volume exported by the inlet during its sedimentary balance, thus:

$$Q_{OB}=(1-k_1)(Q_O+Q_R+Q_B) \quad (5)$$

The sand volume and distribution at the beach is based on accurate bathymetry and charts. The shoreline position and cross-shore profiles are based on empirical formulations and similar beaches formed on inlets along the North coast of Spain (e.g. Zumaya, Orio, Suances, among many others).

Each morphological process, for every sedimentary unit, has a stochastic character. Thus a probabilistic approach is used to include individual strong events, such as a storm or high runoff discharges. The first case, linked with high wave energy, will try to close the inlet, moving sediment from the outer shoal and the adjacent coast. The second case will wash off the sediment from the inlet, due to the related high velocities. Each situation will delay or shorten the evolution time.

Introducing for each process a mean value and its standard deviation, the procedure is repeated several times to assess the overall trend and confidence intervals (Montecarlo simulation). To attain the mean values and deviations, historical data is collected from Navia and adjacent inlets, similar in behaviour and configuration. Some of these inlets have been modified in the same way as planned for Navia, so detailed surveying of medium and long-term evolution has been undertaken to calibrate the model.

In this way, knowing the sediment flux for each unit, the sedimentary balance at the inlet is performed, as mentioned above. The relationship between the inlet sand volume and depth will provide its time evolution.

Next, the model will be applied to Navia's inlet and a relationship between percentage of operational levels, jetties length and mean maintenance requirements will be studied, leading to an optimum design procedure based on capital and maintenance costs.

Results

The long-term evolution model, combined with the percentage of operational time data, has been used to determine the maintenance requirements at Navia inlet for different scenarios of jetty construction. The optimum solution is somewhere in between two extremes:

1. No jetty construction and maintenance of functionality purely with dredging, and
2. Extremely long jetties, reaching a depth such as the inlet becomes independent of the adjacent sedimentary units. This includes an initial dredging of the whole inlet up to the closure depth.

In the first solution, continuous dredging has to be undertaken, and the solution is more sensitive to individual events like storms or high river discharges. The second solution is extremely expensive, and might have tremendous effects on the environment, not only the estuary under consideration, but also to the neighbouring coast.

Two different scenarios will be presented as possible solutions. One with two short parallel jetties (240 m) and an initial dredging depth h_O = -2 m, the other with two long parallel jetties (600 m) and dredging up to h_O = –6.5 m. All levels are referred to chart datum, which is at MLWS. The required data and computed parameters to apply the long-term model are given below.

Equilibrium depth at the inlet, h_f:	1.1 m
Equilibrium volume of the inlet, V_e:	420,000 m^3
Initial estuary and river sediment flux, Q_R:	5,000 m^3/yr
Ocean sediment flux for equilibrium conditions, Q_{OE}:	10,000 m^3/yr
Maximum long-shore transport, $Q_{B(MAX)}$:	15,000 m^3/yr
Surf zone width, $D_{L(MIN)}$:	680 m
Constant k_1:	0.5
Constant k_2:	$(h_O-h_f)/Q_R$
Constant k_3:	0.35
Constant k_4:	$-Q_{B(MAX)}/D_{L(MIN)}$

The equilibrium depth is obtained from O'Brien, 1930 and Bruun, 1966 formulations. Also this depth is compared with present and old data from charts (Figures 2 and 3). The equilibrium volume is computed following Hicks and Hume, 1996 and the estuary and river sediment flux are based on comparisons with similar inlets in the neighbourhood. The ocean-inlet flux for equilibrium conditions is also based on adjacent inlets and the maximum long-shore transport is computed as in the Shore Protection Manual, 1984. The surf-zone width was assumed to be the same as the active profile at the beach, measured and observed in several beaches along the Cantabrian Sea coast. The constant k_1 was proposed by a simple geometrical consideration, from the wave incidence pattern and the inlet characteristics. The constant k_3 was defined arbitrarily; in order to have half of the volume flux when the actual depth is the equilibrium depth plus 2 metres.

In Figure 8 the time mean evolution of the inlet is shown for the long groin scenario, as can be seen the fastest changes occurs at the beginning and the equilibrium is attained in less than, say, 40 years. Also, in Figure 9 the sediment fluxes between units are presented. Notice that these curves are not given formulations, but the output of the model for each time step according to inlet demands and morphological evolution.

Figure 10 presents the time evolution of the inlet for the short groin scenario; also the evolution sensitivity is presented as a function to process variability. In this case the inlet will attain the equilibrium in 4 – 6 years, depending on the environmental conditions present. The sensitivity analysis was not presented for the long groin scenario, since it becomes almost negligible, due to the relatively long equilibrium period.

As shown before, each scenario will present a different evolution pattern. Hence, fixing the minimum depth for a given required functionality (h_L), the maintenance interval (m) is obtained from the time evolution curves. Including all scenarios, a curve can be constructed with the groin length on one axis, and the maintenance interval, on the

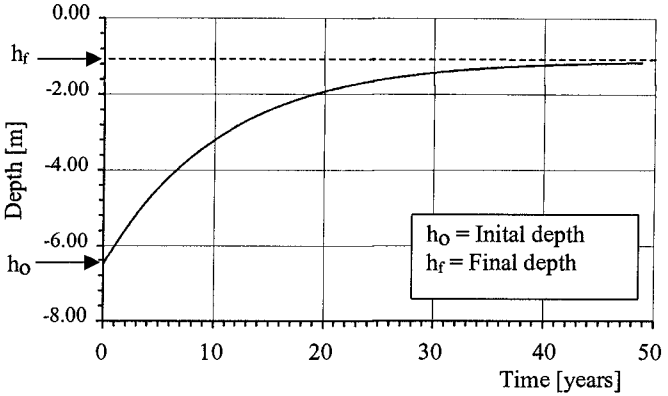

Figure 8. Time mean evolution for the long groin scenario (600 m).

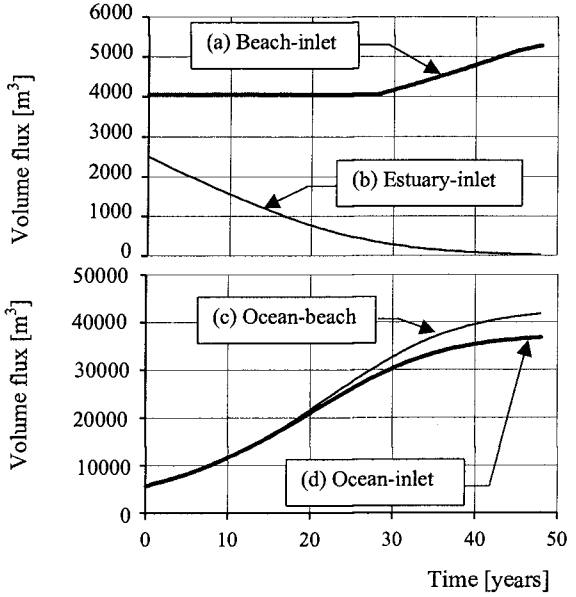

Figure 9. Sediment fluxes for the long groin scenario. Beach-inlet flux (a), estuary-inlet flux (b), ocean-beach flux (c) and ocean-inlet flux (d).

other, for a given functionality, as presented in Figure 11. Here, the short groin scenario implies maintenance dredging every 6 months and the long groin scenario a maintenance dredging every 5 years. Both scenarios presented are meant to allow the entrance to the port 90% of the time for the design vessel. Nowadays, Navia's inlet functionality is less than 30%.

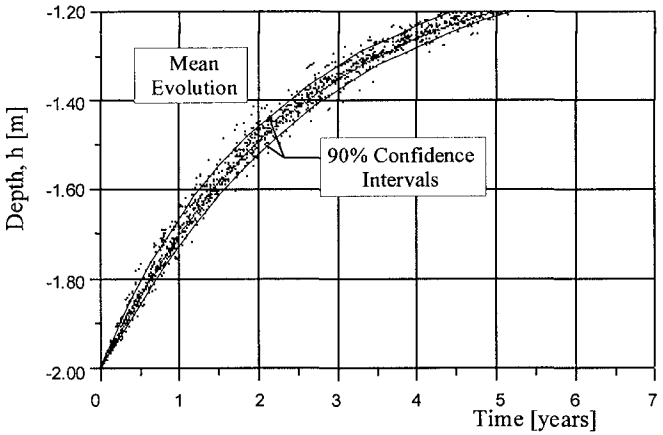

Figure 10. Time mean evolution for the short groin scenario (240 m) and 90% confidence intervals.

Translating these results to economical meaning is straightforward, and depending on each case and budget availability, one solution might be better than the other might be. The financial and environmental best solution was beyond the scope of this paper, but it was clear that, to give the port authority a better forecast for the investment, based on technical foundation was, for the first time, an improved approach for optimum design.

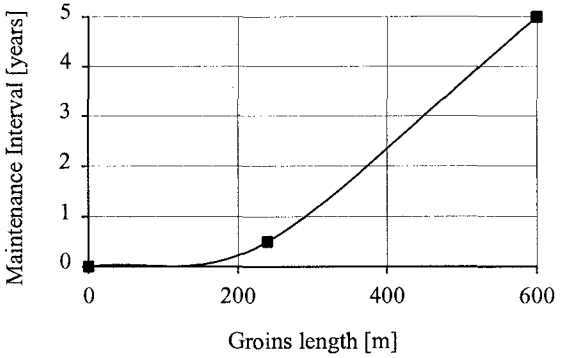

Figure 11. Groins length versus maintenance interval for Navia inlet (Functionality: 90%)

Conclusions

In order to attain an improved methodology for optimum design of Navia's navigation channel, a long-term evolution model of tidal inlets is applied. The special

features of Navia coast and oceanographic process are presented and the navigation channel design principles lead to require the knowledge of the long-term evolution in the inlet.

Thus, an aggregated scales model was implemented and used in Navia inlet, where the sedimentary units were modelled in a simplified way, employing historical data and surveying from adjacent inlets. The time evolution was found to be in the order of decades and the obtained information was not old enough to ensure the morphologic response. Therefore a sensitivity analysis was performed to study the variability of each process leading to a relatively more sensitive solution for shorter evolution periods.

The long-term evolution model was then applied for different scenarios and, by means of a minimum required functionality for the port, a maintenance period was obtained. As a result, a relationship between groin length and maintenance dredging was obtained. The economical impact is evident and a financial study for optimum groin length and periodic maintenance will provide, for the first time, a long-term evolution forecast and better budget planning.

Acknowledgements

This study was partially supported by the Spanish CICYT (Comisión Interministerial de Ciencia y Tecnología), as part of the projects MAR95-1845 and MAR95-1896.

References

- Bruun, P., 1966. Tidal inlets and littoral drift. Stability of tidal inlets, Vol. 2.
- de Vriend, H.J., Bakker, W.T., Bilse, D.P., 1994. A morphological behaviour model for the outer delta of mixed-energy tidal inlets. *Coastal Engineering, 23*, pp. 305-327.
- Eysink, W.D., 1990. Morphologic response of tidal basins to changes. *Proc. 22nd Coastal Eng. Conference, Vol. II,* pp. 1948-1961.
- Hicks, D.M. and Hume, T.M., 1996. Morphology and size of ebb tidal deltas at natural inlets on open-sea and pocket-bay coasts, North Island, New Zealand. *Journal of Coastal Research, 12(1),* pp. 47-63.
- Losada, M.A., Medina, Raul, Baquerizo, A., Lomonaco, P., 1997. Estudio de la Canal de Navegación de la Ría de Navia (in Spanish), *Fundación Leonardo Torres Quevedo*, Universidad de Cantabria, Spain.
- O'Brien, M.P., 1930. Estuarine tidal prism related to entrance areas. *Coastal Engineering 1,* pp. 738-739.
- Shore Protection Manual, 1984. Coastal Engineering Research Centre. U.S. Army Corps of Engineers.
- Van de Kreeke, J., 1996. Morphological changes on a decadal time scale in tidal inlets: Modelling approaches. *Journal of Coastal Research, 23*, pp. 73-81.
- Van Dongeren, 1992. A model of the morphological behaviour and stability of channels and flats in tidal basins. MSc Thesis. TU Delft, The Netherlands.

Change of mean tidal peaks and range due to estuarine waterway deepening

Hanz D. Niemeyer[1]

Abstract:

The deepening of estuarine waterways enforces essential changes of mean tidal water level peaks and range. Legal requirements ask for their determination by preservation of evidence. A method has been established to evaluate these effects quantitatively by statistical tools for each measure, even in the case of subsequent deepenings.

Intruction

Deepening of estuarine waterways enforce there changes of tidal water levels. They start immediately after deepening but continue after execution of dredging for a certain period of time being necessary for the development of a new dynamical equilibrium between estuarine geometry and tides. The order of magnitude of changes of mean tidal water levels is particularly of importance for water management and ecological zonation but is also regarded as a primary indication for changes of tidal currents, salinity and storm surge levels. Therefore the quantitative determination of changes of mean tidal

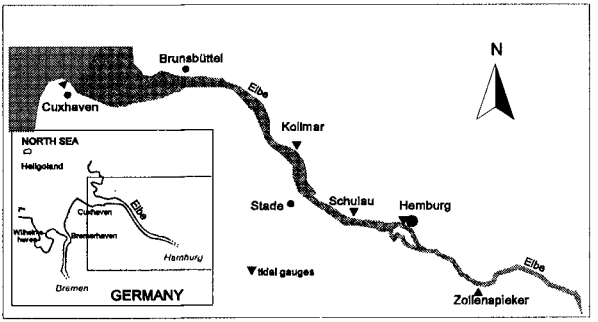

Fig.1: Elbe estuary, southern North Sea

[1] Coastal Research Station of the Lower Saxonian Central State Board for Ecology, P.O. Box 1221, 26534 Norderney/East Frisia, Germany

peaks and tidal range due to waterway deepening is given high priority in order to qualify its impacts. This is not only necessary for planning purposes but also for the environmental assessment studies and for the later preservation of evidence procedure due to legal requirements in Germany. Preservation of evidence gets increasingly difficult if subsequent deepenings have been carried out and their impacts are still continuing at the beginning of the successive one. An impressing example is the continuous increase of tidal range at the tidal gauge of Hamburg-St. Pauli since the beginning of this century whereas during the same period neither the tidal range at the island of Heligoland and in Cuxhaven at the estuarine mouth nor the fresh water discharge have experienced comparable changes (fig. 2).

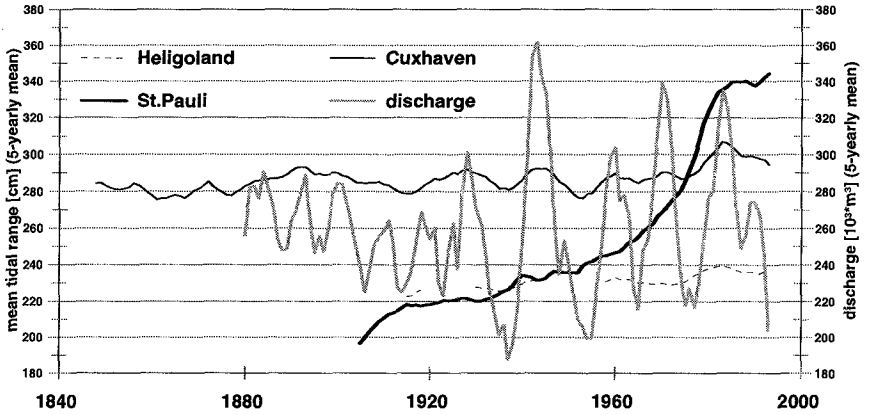

Fig. 2: Tidal range at the gauges Heligoland, Cuxhaven, Hamburg-St. Pauli and fresh water discharges of the Elbe river since 1843

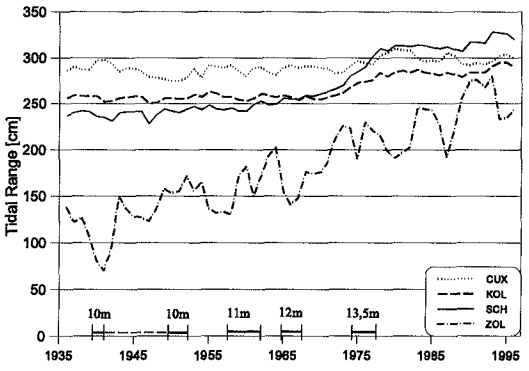

Fig. 3: Periods of sucessive waterway deepenings ↔ and time series of tidal range at estuarine tidal gauges Cuxhaven, Kollmar, Schulau and Zollenspieker (fig.1)

This paper deals with a method to quantify the changing of mean tidal water levels and range due to a waterway deepening in the Elbe estuary (fig. 1) for a navigational depth of 13,5 m below mean low spring tide water level (C.D.) during the years 1974 to 1976 being the fourth since 1949. The legal boundary conditions required a preservation of evidence procedure quantifying the singular effects occurring due to the specific deepening. The significant changes of mean tidal

water levels for the last sixty years are documented here explanatory for the tidal range at four estuarine tidal gauges connected with the periods of the coincidently executed successive deepenings in the Elbe estuary. (fig. 3). The tidal range has increased relatively the more the further upstream the tidal gauge is located. Due to that effect the relations of local tidal range in the estuary have changed: E. g. at the gauge Schulau located immediately downstream of Hamburg it does therefore nowadays exceed that one at the gauges Kollmar and Cuxhaven. Before the intensive deepenings during the last decades tidal range decreased continuously from the estuarine mouth upstream (fig. 3); but meanwhile the maximum tidal range occurs in the central part of the estuary. The relatively largest increase has occured upstream of Hamburg where no dredging has been carried out. The development of tidal ranges during that period highligths two major effects: the changes are not only correlated to the period of dredging itself and the changes increase the more the gauge is further upstream located.

Basic effects of waterway deepening on mean tidal peaks

The deepening of an estuarine waterway leads to an extension of cross-sections allowing the propagation of a higher amount of tidal energy further upstream. The increase of the range of the tidal wave is symmetrically distributed to high and low water level peaks (fig. 4).The lowering of the bottom -generally increasing in upstream direction- creates additionally a lowering of the mean water level (fig. 5).

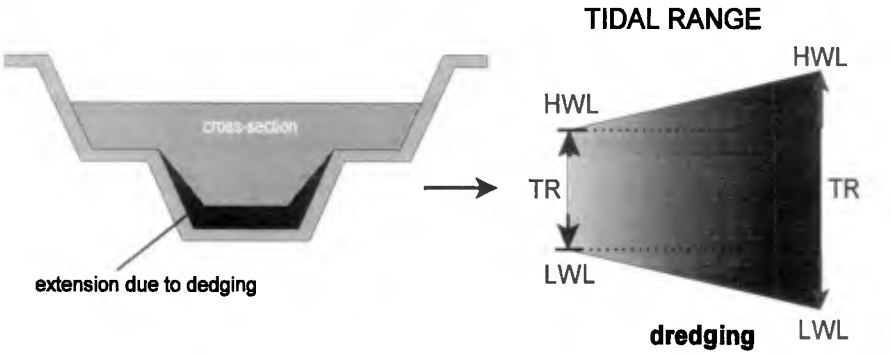

Fig. 4: Basic effect of cross-sectional extension on tidal range and peaks

The superimposition of both effects leads to a resulting relatively larger lowering of the tidal low peaks than heightening of the tidal high peaks (fig. 6). This phenomenon is well known from estuarine deepenings for the stretches of waterway deepening. Beyond there is only an increase of tidal range which is nearly evenly distributed to the high and low water level peaks.

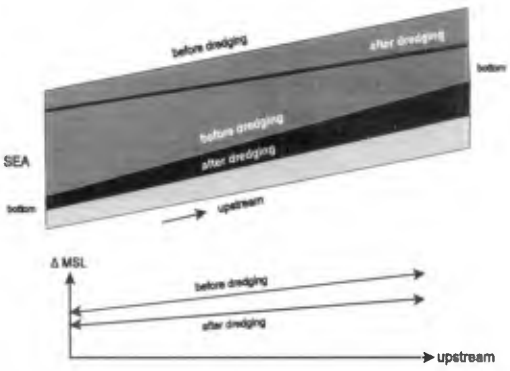

Fig. 5: Schematized lowering of estuarine mean water levels due the bottom lowering by estuarine deepening

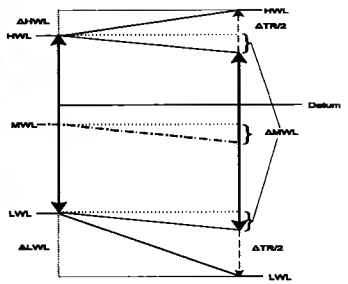

Fig. 6: Superimposed effects of cross-sectional extension and bottom lowering due to estuarine deepening on mean tidal water level peaks

Evaluation of suitable time series

In order to determine time series of mean tidal water levels which experienced only significant impacts due to the last deepening double-mass analysis [SEARCY & HARDYSON 1960] was applied to the time series as well of yearly mean high and mean low water levels as of mean tidal range in the downstream and central part of the estuary with respect to the same parameters at the offshore tidal gauge on the island of Heligoland (fig. 1) which was taken as base station representing the natural variation of tidal water levels in the southern North Sea. It is assumed that as far as offshore as the location of the island of Heligoland (fig. 1) no impacts of estuarine deepenings will occur. Further upstream the method has not been applied since ther the impacts of the fresh water discharge variations being not considered in the double-mass analysis would be to strong in order to allow a successful application of that method.

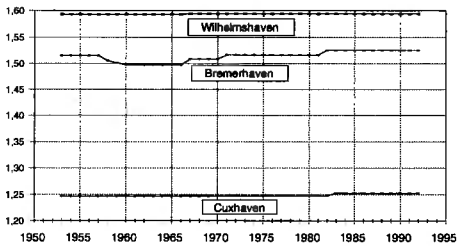

Fig. 7: Gradients of double-mass analysis for the tidal range at the gauges Wilhelmshaven (Jade), Bremerhaven (Weser) and Cuxhaven (Elbe) with correlation to that at the gauge on the island of Heligoland (fig. 1).

First a comparison was carried out for distinct tidal gauges at the German North Sea coast in order to check if there are general changes not related to impacts in the Elbe estuary itself in order to avoid any misinterpretation of effects being not specific for the Elbe estuary. The double-mass analysis of the tidal ranges at the gauges of Wilhelmshaven (Jade Bay), Bremerhaven (Weser estuary) and Cuxhaven (Elbe estuary) with respect to that one at the at the island of Heligoland makes evident that its variations differ locally at the German North Sea coast (fig. 7).

Exemplary for the analysis for the Elbe estuary here the results for the tidal range at the gauges Kollmar and Schulau are dicussed. In order to avoid the typical difficulties occuring by application of double-mass analysis no interpretation by visual observation of the double-mass curve itself has been carried out. The gradient of the double-mass curve was continuously computed and any change of more than 0,75 % is taken into consideration (fig. 7a + b). The results led to the conclusion to use the time series between 1970 and 1974 being representative for the situation before the deepening incorporating also the total effects of the previous deepening. The time series between 1977 and 1992 were used in order to determine the impacts of waterway deepening whereas 1975 and 1976 were regarded as a transition period between dredging and readaption .

Another check was carried out for the data of the tidal gauge Schulau (fig. 1): The gradient is changing for the whole period but with significant increase since about 1970 (fig. 8a). In order to gain results allowing a proper interpretation the tolerance for changes of the gradient of the double-mass curve was doubled to 1,5 %. The results of that analysis fit well with that carried out for the data of the tidal gauge Kollmar: during the period between 1970 and 1974 there is no change in the behavior of the tidal range at the gauge Schulau

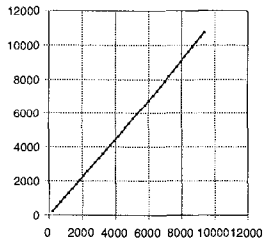

Fig. 7a: Double-mass curve for the tidal range at the tidal gauge Kollmar correlated to that at the gauge of Heligoland.

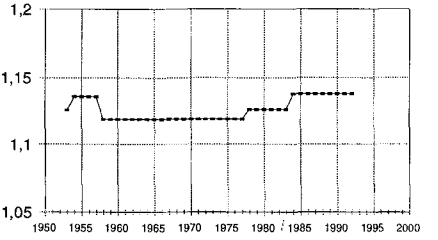

Fig. 7b: Gradient of the double-mass curve for the tidal range at the tidal gauge Kollmar correlated to that at the gauge of Heligoland (tolerance for change: 0,75 %).

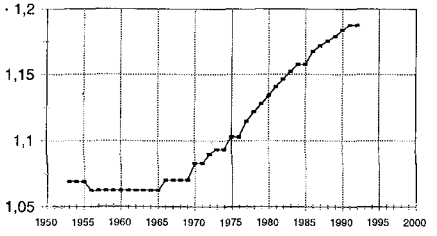

Fig. 8a: Gradient of the double-mass curve for the tidal range at the tidal gauge Schulau correlated to that at the gauge of Heligoland (sensivity for change: 0,75 %).

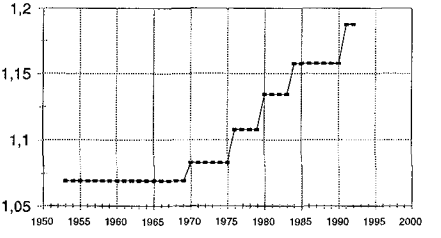

Fig. 8b: Gradient of the double-mass curve for the tidal range at the tidal gauge Schulau correlated to that at the gauge of Heligoland (sensivity for change:1,5 %).

with respect to that one at the gauge of Heligoland (fig. 8b). The higher tolerance for the data of the gauge Schulau is obviously necessary for getting proper results. The reason behind is that at this further upstream located gauge the impacts of freshwater discharge variations on tidal water levels are stronger than at Kollmar. The higher tolerance is explainable as a filtering technique for supressing these effects.

Determination of deepening effects

Estabilshed method

The local estuarine mean low and high water levels at each estuarine gauge (LWL_{EGi}, HWL_{EGi}) were approximated by use of multiple regression as a function of the corresponding parameters (LWL_{Hel}, HWL_{Hel}) and the mean tidal range(TR_{Hel}) at the offshore gauge Heligoland (fig.1), the latter one as a measure for the offshore energy input, and additionally the inland fresh water discharge (Q_f). Effects of estuarine waterway deepening on tidal water levels at the island of Heligoland (fig. 1) do not occur; they could therefore be used as well as an independent boundary condition as the inland fresh water discharge. Empirical optimizations led to the following functional equations for estuarine mean low and mean high water levels:

$$LWL_{EGi} = a_{1,i} \cdot LWL_{Hel} + a_{2,i} \cdot TR_{Hel} + a_{3,i} \cdot Q_f^{b1,i} \quad (1)$$

$$HWL_{EGi} = a_{4,i} \cdot HWL_{Hel} + a_{5,i} \cdot TR_{Hel} + a_{6,i} \cdot Q_f^{b2,i} \quad (2)$$

Regression analysis was initially carried out for the period immediately before the waterway deepening on the basis of the time series of monthly means of the period from 1970 to 1974 in order to determine the coefficients. A comparison of computed and measured data made evident the reliability of the approximation (fig. 9 - 11). Afterwards these coefficients were used to determine the estuarine mean tidal peaks on the basis of the boundary conditions for the offshore tidal parameters and the freshwater discharge for the period after the waterway deepening. The differences between measured and computed data are regarded as the deepening effects D_L and D_H (fig. 9 - 11).

Changes of mean tidal peaks and range

The changes of mean tidal peaks and range are rather small at the estuarine mouth but increase upstream. Exemplary the changes of mean high and low tide at the gauges Cuxhaven, Kollmar, Schulau and Zollenspieker (fig. 1) are compared: There is no change for mean high tide at the gauge Cuxhaven and the change in mean low water is only 4,5 cm (fig. 12). Further upstream at the tidal gauge Kollmar the changes are more pronounced: 6,0 cm for mean high tide (fig. 9a) and 8,9 cm for mean low tide (fig. 9b). Again for this gauge also the scatter is much lesser for mean low tide than for mean high water levels. The effects of waterway deepening on mean tidal peaks at the gauge Schulau is higher than downstream: Mean high tide has risen for 12,8 cm (fig. 10a) and the mean low water level has been lowered for 25,1 cm (fig. 10b). The scatter of the monthly mean peaks is of an acceptable

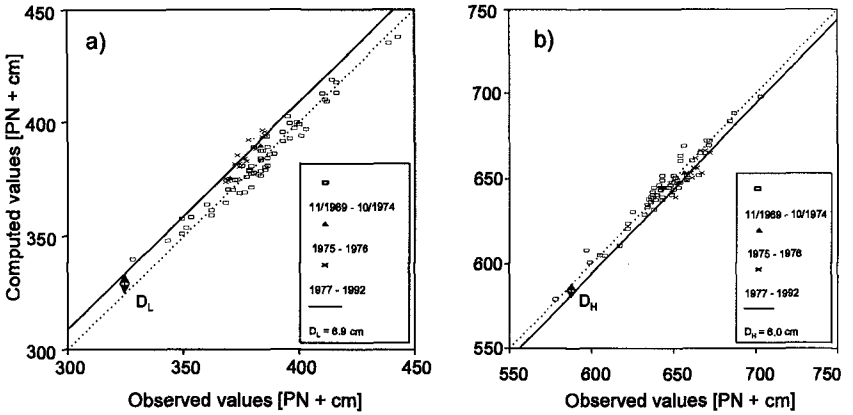

Fig. 9: Determination of mean low water level changes D_L (a) and mean high water level changes D_H (b) due to waterway deepening to C.D.-13,5 m (tidal gauge Kollmar)

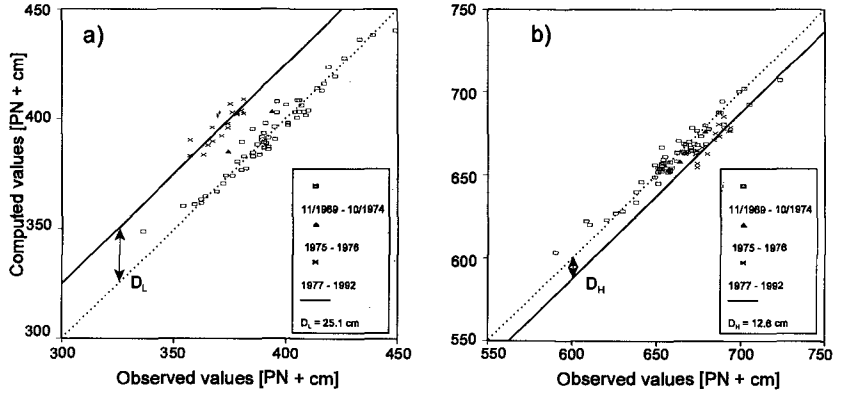

Fig. 10: Determination of mean low water level changes D_L (a) and mean high water level changes D_H (b) due to waterway deepening to C.D.-13,5 m (tidal gauge Schulau)

order of magnitude with respect to the objective of the analysis. The tidal gauge Zollenspieker is located upstream of the harbour of Hamburg; there has been no dregding in that part of the estuary. Nevertheless the deepening effects are also here significant: an increase of mean high tide of 17,3 cm (fig. 11a) and a lowering of the mean low water level of 18,3 cm (fig. 11b). Particularly for the mean low water levels the scattering of data is remarkably higher than for the time series of the gauges being located further downstream. This effect must be credited to the here stronger impact of the variations in freshwater discharges.

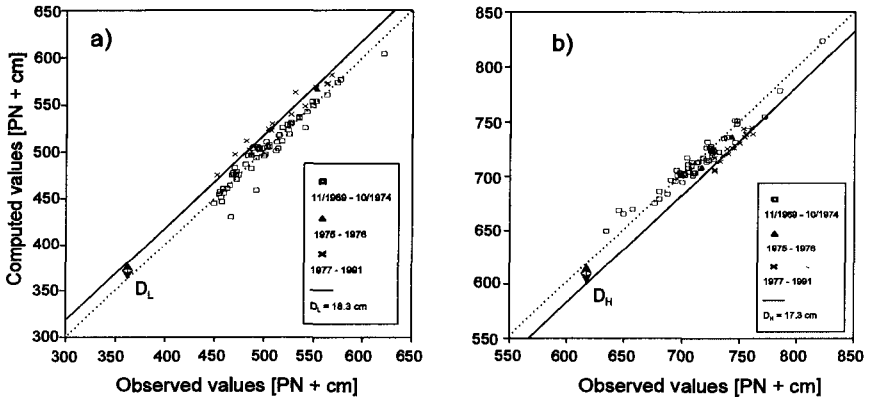

Fig. 11: Determination of mean low water level changes D_L (a) and mean high water level changes D_H (b) due to waterway deepening to C.D.-13,5 m (tidal gauge Zollenspieker)

The changes of the tidal peaks are mostly non-symmetrical with respect to that of the tidal range (fig. 12): In the estuarine stretch where the deepening has taken place the descendence of the LWL is larger than the rise of the HWL. Contradictory in the upstream area where no dredging has been carried out the changes in tidal range are symmetrically distrubuted on mean high and low tide. The deepening causes two superimposing effects: a

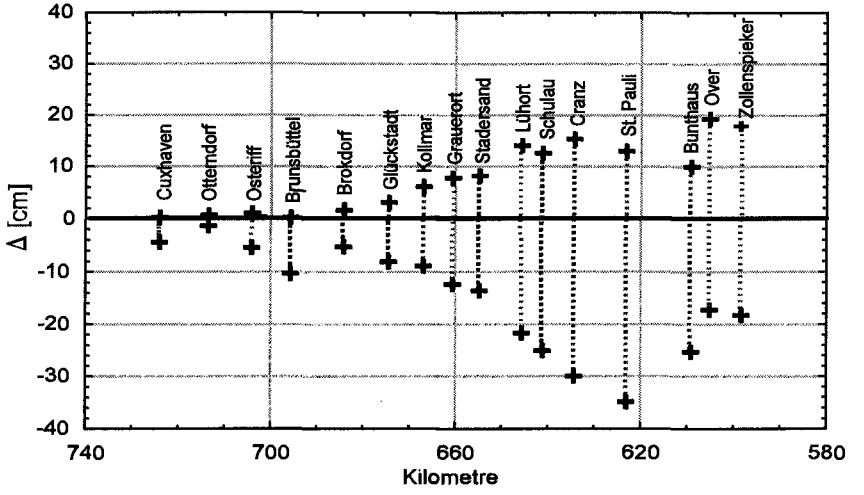

Fig.12: Changes of mean low an high water levels along the Elbe estuary due of waterway deepening to C.D.-13,5 m

lowering of mean sea level and an increase of tidal range resulting in a lower rise of high tide than fall of low tide. In the non-deepened stretches of the estuary the increase of tidal range due to the impact of higher tidal energy from the downstream deepened part of the estuary is dominant. Since there is no lowering of the mean water level the changes for high and low water peaks have a similar order of magnitude (fig. 12) which fits into the explanation of the deepening effects on tidal water levels given before (fig. 4 - 6).

Comparison with previous model tests

The effects of the Elbe waterway deepening have been investigated before execution by hydraulic model tests with both a movable and a non-movable bed [BAW 1974]. In comparison to the measured effects the forecasted changes are remarkably smaller (fig. 13). But the test results fit much better if compared with the changes occuring immediately after dredging in the transition period of the first two years (fig. 9 - 11) whereas the later changes of the mean peaks exceed the forecast significantly. This is due to a readaption of estuarine morphology to the changed tidal hydrodynamics occurring after deepening. This cross-sectional enlargement allows again an increase in tidal energy enforcing afterwards once more morphological changes. Generally the slopes of the estuarine navigation channel are

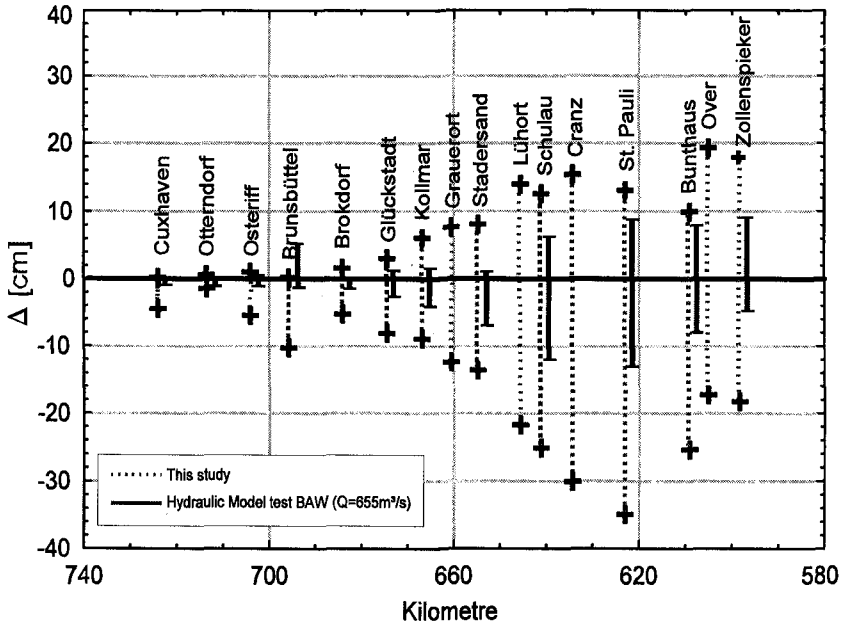

Fig. 13: Comparison of evaluated changes of mean tidal peaks and range with forecast by hydraulic model test

after deepening steeper than fitting to natural conditions. Furthermore both capital and maintainance dredging leads to lowering of the bottom beyond the required navigational depth. Consequently these effects in acting together with the increased tidal energy create a process of cross-sectional readaption continuing after capital dredging, until a new morphodynamical equilibrium is established (fig.14). This effect of a morphological phase-lag after estuarine deepenings has to be considered for forecasts in order to get proper and reliable results for the effects of anticipated estuarine deepenings with respect to tidal water levels.

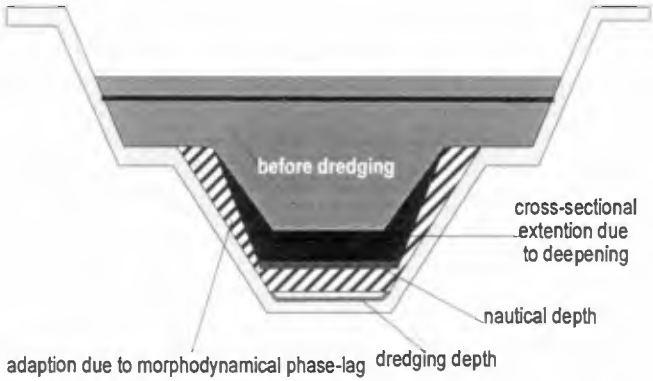

Fig. 14: Scheme of morphodynamical phase-lag after deepening of an estuarine navigation channel

Conclusions

Deepenings of estuarine waterways effect an increase in tidal range and a lowering of the mean water level. The superimposition of both leads to relatively larger lowering of the tidal low water peaks than heightening of the high water levels. Upstream of the dredged parts of the estuary only an increase of tidal range occures contributing evenly to the changes of the low and high water peaks.

It has been shown that even for successive deepenings of estuaries a separated quantification for singular measures is possible by combined application of double-mass and regression analysis. Double-mass analysis is a useful tool for the evaluation of coherent time series being suitable for event-related regression analysis. The implemantation of physically sound boundary conditions and parameters allows a proper quantification of deepening effects on tidal range and peaks.

The morphological phase-lag after the dredging itself allows a further significant change of tidal water levels afterwards. Its time scale is about years. Hydrodynamical modeling of deepening effects must take these effect into consideration for getting reliable results.

Acknowledgements

The basic work for this paper was carried out in the framework of a joint working group of the Federal Waterway Aministration and the Water Management authorities of the States of Lower Saxony and Schleswig-Holstein. The author is indebted to his colleagues in that team, particularly to its former chairman Dr. Heinz Wismer (Federal Diretorate North for Waterway Engineering) who provided both support and advice. Valuable advice was also delivered by Ralph Annutsch (German Hydrographic Service) and Werner Dietze (Federal Diretorate Northwest for Waterway Engineering). The author is also grateful for the support which he got from his colleagues Jochen Fleßner, Detlef Glaser, Thomas Hartkens and Ralf Kaiser from the Section of Coastal Hydrodynamics at the Coastal Research Station.

REFERENCES

BAW (1974): Deepening of the Elbe waterway from 12 to 13,5 m below C.D. (In German). Bundesanstalt für Wasserbau, Hamburg (unpubl.)

Niemeyer, H.D. (1995): Determination of changes of mean tidal peaks and range in the Elbe estuary due to the waterway deepening 13,5 m below chart datum (in German), Bund-Länder Arbeitsgruppe Beweissicherung zum KN -13,5m Ausbau von Außen- und Unterelbe, Kiel/Lüneburg, Juni 1995 (unpubl.)

Searcy, James K. & Hardison, Clayton, H. (1960): Double-mass curves. Man. Hydrology: Part 1. General Surface-Water Techniques, Geol. Survey Water-supply Paper 1541-B; U. S. Governm. Print. Office, Washington/D.C.

Weiss, L.L. & Wilson, W.T. (1953): Evaluation of significance of slope changes in double-mass curves, Trans. Am. Geophys. Un., Vol. 34, No 6

Inlet Dynamics from Semi-Annual Surveys

Owen W. Callard[1], William R. Dally[1], M.ASCE, and Kathy FitzPatrick[2]

1. Introduction

Field surveys, carefully conducted with state-of-the-art equipment, remain the best source of information for studying tidal inlets. Data from an ambitious hydrographic surveying program that is ongoing at Sebastian Inlet, Florida (see Figure 1), are being analyzed to examine the morphologic dynamics of the inlet, to maintain a sediment budget, and to identify any ongoing impacts of the inlet to the adjacent beaches.

Historically, the presence of Sebastian Inlet caused the formation of both ebb and flood shoals, and accretion and erosion along the beaches to the north and south, respectively. However, because 1) the inlet is relatively small, 2) its jetties were originally constructed in 1923-24, and 3) a sediment trap in the inlet's throat is periodically dredged and the material placed on the downdrift beaches, any persistent, long-term erosion/accretion trends have abated. Modern-day changes are limited to variation about a quasi-equilibrium state (Dally and FitzPatrick, 1997).

The predominant wave energy along the east central Florida coast during the winter months emanates from the north and northeast sectors due primarily to extratropical storms commonly referred to as 'northeasters'. It is thus expected during the winter months sand will accrete at the north side of the inlet, and erode from the south. During the summer months, the direction of predominant wave energy switches to the southeast quadrant. Low-energy 'recovery' swell is caused by persistent winds from an entrenched system of high pressure (Bermuda High) which dominates the summer weather in the central North Atlantic. Higher energy swell from this sector also occurs as a result of occasional hurricanes. Consequently during the summer, erosion of the north fillet is expected, with accretion on the south. The purpose of the study described below is to identify and quantify this seasonal behavior, and any other patterns or trends present.

[1] Ocean Engineering Program, Florida Institute of Technology, 150 W. University Blvd., Melbourne, FL 32901, U.S.A.

[2] Sebastian Inlet Tax District, 114 Sixth Avenue, Indialantic, FL 32903, U.S.A.

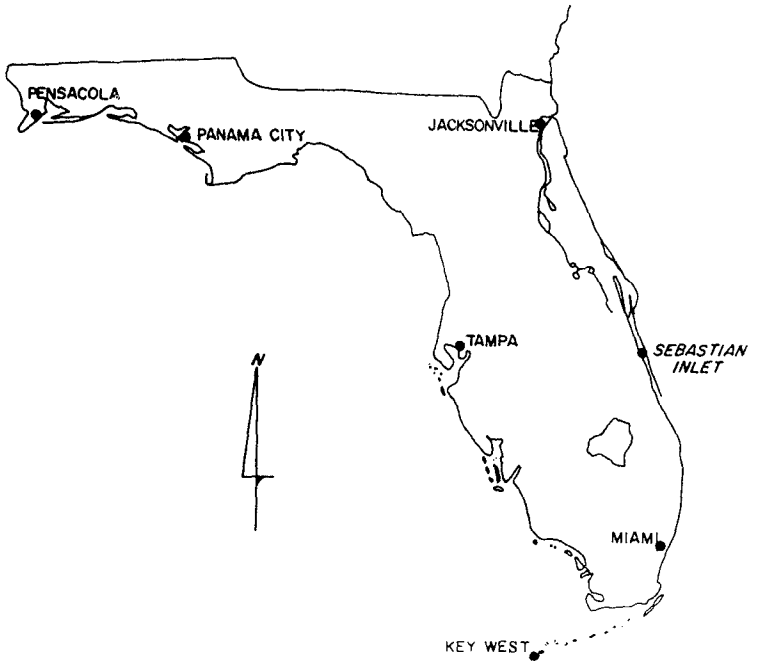

Figure 1 - Location of Sebastian Inlet, on Florida's central Atlantic coast.

2. The Survey Data Set

The data set used in this study consists of 15 surveys of the Sebastian Inlet system, which cover the flood shoal, navigation channel, sediment trap, inlet throat, ebb shoal, and north and south beaches. Figure 2 presents a plan view of the data coverage from a recent survey. Although an initial survey was conducted in August, 1989, surveys have been performed on a semi-annual basis since July, 1990, usually in February and July.

Although the equipment and techniques used in the surveying program are continually improved, in general, standard land surveying methods are used to wading depth, with boat/fathometer methods used in deeper water. Transect spacing in the ebb shoal, sand trap, and navigation channel is 100 ft, whereas the spacing in the inlet throat and flood shoal is 200 ft. Beach profiles are measured at 500 ft or 1000 ft intervals, and are based upon the system of monuments ('R-monuments') maintained by the Florida Department of Environmental Protection. The spatial coverage, resolution, and semi-annual basis of the surveys makes this a distinctive data set, from which seasonal changes at Sebastian Inlet can be determined.

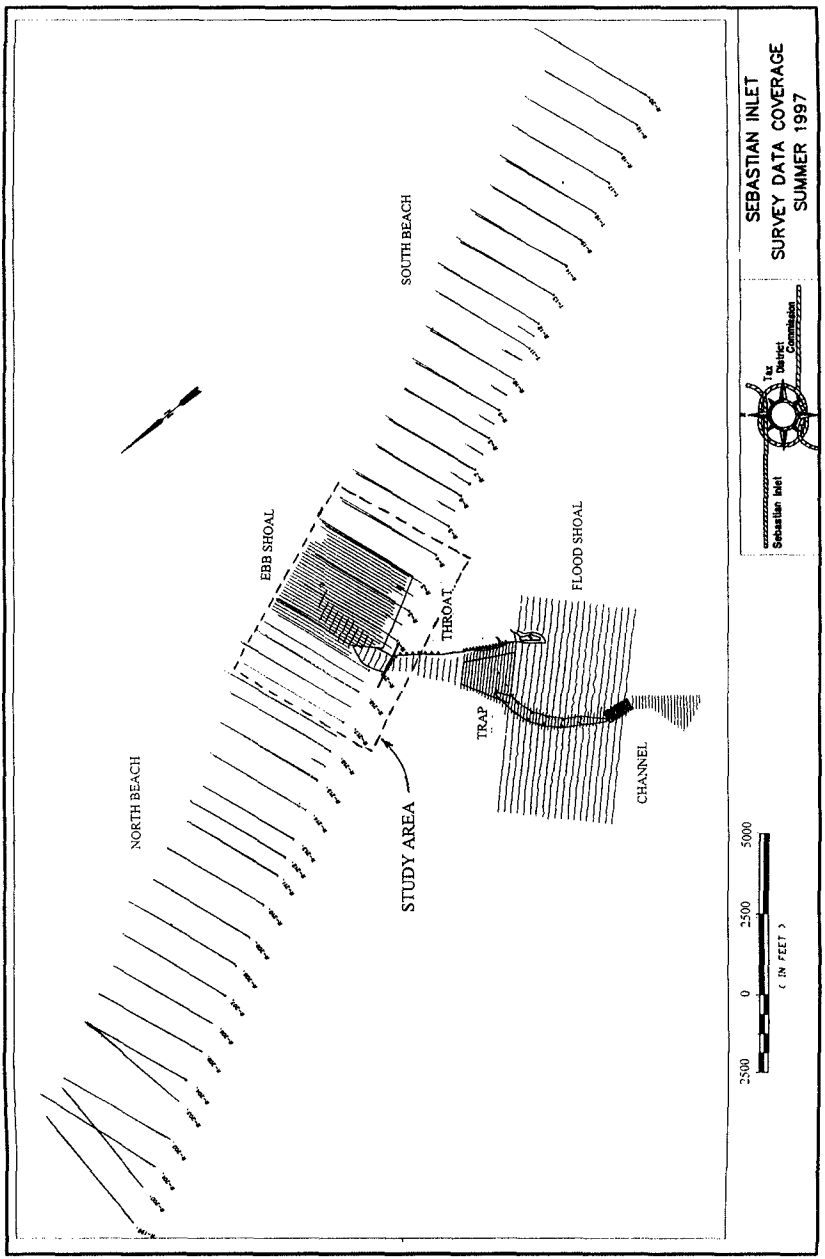

Figure 2 - Plan view of data from July 1997 survey of Sebastian Inlet, showing area used in studying fillets and ebb shoal.

3. Analysis Methods

For the purposes of studying morphodynamics in the immediate vicinity of the mouth of the inlet, herein the study domain was limited to 6000 ft (1830 m) in the longshore direction, from R-217 in Brevard County to R-004 in Indian River County. In the seaward direction, the domain extended roughly 5000 ft (1524 m) offshore, as is shown in Figure 2.

The survey data were analyzed using commercially available Digital Terrain Modeling software, specifically, the *Eagle Point* Civil Engineering Series (v. 13.2) that runs using AutoCAD (v. 13) as an operating platform. The *Eagle Point* Surface Modeling module was first used to create a three-dimensional representation of each survey by generating a Triangular Irregular Network (TIN), from which maps of bathymetric contours were created. The TINs created for each data set were then used to develop difference-contours, i.e contours of the changes in bathymetry that occurred between sequential surveys. Using maps of these difference contours, seasonal behavior of the inlet could be examined synoptically. Finally, the Site Design module of *Eagle Point* was used to make volumetric computations, in order to quantify seasonal changes to the inlet system.

4. Results and Discussion

4.1 Difference Contours

Difference contours were developed between consecutive seasonal surveys, beginning with 7/90 and concluding with 7/97, and allow one to examine the Sebastian Inlet region in a synoptic fashion. Two-foot contour intervals were used in order to identify areas where change was significant, and Figure 3 presents an example of typical results for a winter-to-summer comparison (2/94-7/94). The elevation contours of the earlier survey are also shown for reference. The area of the north fillet closest to the north jetty experienced up to 8 ft (2.4m) of erosion, with the amount of erosion decreasing northward. In contrast, the area of accretion in the south fillet extends over a larger area, between R-001 and R-003 (at which point the ebb shoal ties into the beach), but shows only up to 4 ft (1.2 m) of accretion. Although relatively inactive during this particular time period, the ebb shoal has a small spot of 2 ft (0.6 m) of accretion on its seaward flank, and a slightly larger spot of erosion on its landward side. An area of accretion is found directly off the end of the north jetty.

The 7/94-2/95 comparison shown in Figure 4 displays typical behavior for summer-to-winter changes. Extensive and significant accretion of up to 8 ft (2.4 m) is found on the north fillet whereas the south fillet experienced up to 6 ft (1.8 m) of erosion. As mentioned in the introduction, northeasters and other lesser storms cause sand to accrete as it becomes trapped against the north jetty, at the expense of the south fillet. In contrast to the previous season, the ebb shoal experienced significant (and reversed) change. A broad area of up to 6 ft (1.8 m) of accretion is seen on the landward side of the shoal, and erosion, but to a lesser degree is found on the seaward flank.

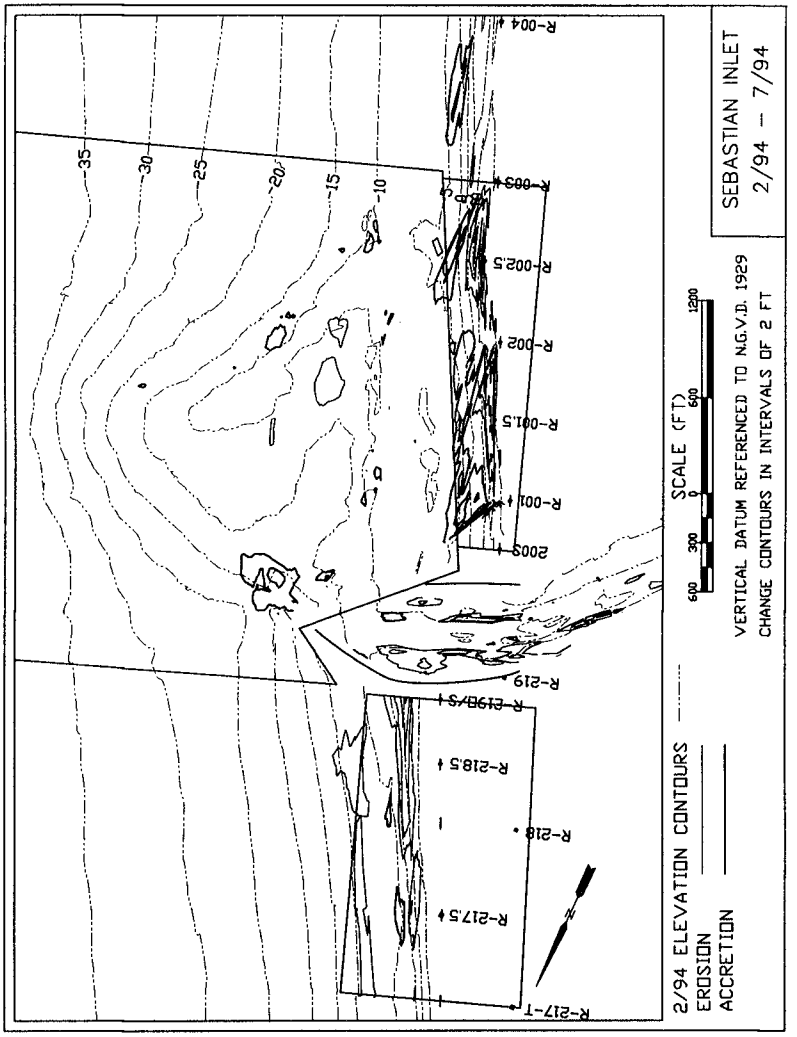

Figure 3 - Bathymetry and difference-contours for 2/94 - 7/94 surveys showing erosion of north fillet and accretion on south fillet, with only minor change to ebb shoal.

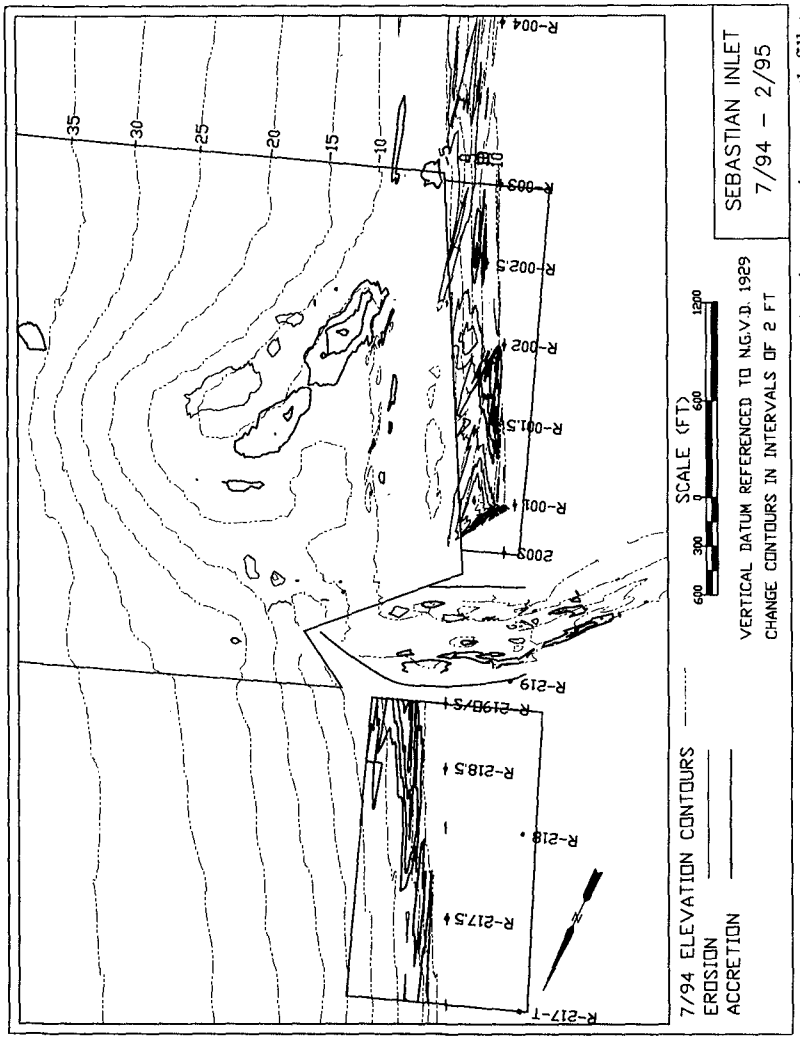

Figure 4 - Bathymetry and difference-contours for 7/94 - 2/95 surveys showing accretion on north fillet and erosion of south fillet, with moderate shift of material on ebb shoal.

The typical seasonal changes displayed by Sebastian Inlet in Figures 3 and 4 confirms expectations, given the usual seasonal shift in wave climate characteristic of the region. That is, high-energy, short-period, erosive waves from the northeast are typical during the late fall and winter, with low-energy, long-period, accretive swell from the south during the summer.

Although most seasonal changes experienced by Sebastian Inlet are qualitatively similar to those of Figures 3 and 4, the results from the 2/91-7/91 and 7/91-2/92 comparisons are significantly different. The difference-contours presented in Figure 5 show erosion as expected at the north fillet. Significant accretion is displayed by the south fillet region extending from the beachface to the -10 ft (-3 m) contour. The ebb shoal shows an area of mild accretion that is broader than would be considered normal, and little erosion is found on the leeward side of the shoal. It is noted that in 2/91, severe weather precluded boat/fathometer surveying of the north and south beaches, and reduced the coverage of the ebb shoal.

The 7/91-2/92 comparison of Figure 6 displays essentially a pattern reversed from the previous season but with even stronger change, especially on the ebb shoal. Uncharacteristically, erosion of the ebb shoal is widespread, typified by changes of 2 ft (0.6 m). Although these findings were originally viewed with skepticism, the field notes and reduced data were checked exhaustively, and the tide stage corrections for the boat survey verified. It is also noted that the large changes observed on the north and south fillets were documented using land surveying techniques, and were not subject to boat-survey errors. It is believed that the changes to the ebb shoal were real, and possibly caused by waves from the 'Halloween Storm' of late October, 1991. These waves were not only large ($H_{m0} \approx 2.5$m), but more importantly were atypically long for the region ($T_m \approx 20$s), and so were capable of mobilizing sand at even the 20 ft (6m) depth contour.

4.2 Volume-Change Computations

Volume changes were computed for the three specific domains examined above, in order to quantify their seasonal behavior. Indicated in Figures 3-6, the north fillet domain extended from R-217 to R-219 o/s - a distance of 1800 ft (549 m), and extended seaward to roughly -10 ft (-3 m) NGVD, a distance of 1000 ft (305 m). The south fillet domain extended from R200-S to R-003, which is 2250 ft (686 m) in the longshore direction. The south fillet domain was extended offshore to only -5 ft (-1.5 m) NGVD in order to capture changes in the south fillet while excluding the ebb shoal. The ebb shoal domain extended seaward 3275 ft (998 m), and 3248 ft (990 m) in the longshore direction, and its border cut diagonally across the jetty mouth.

In order to calculate volumes within the selected domains, the Site Design module in *Eagle Point* was used to superimpose the TINs in pairs sequentially, to determine raw cut and fill volumes within the area of interest. The computed cut and fill volumes were then used to obtain a net volume change within a domain for each season.

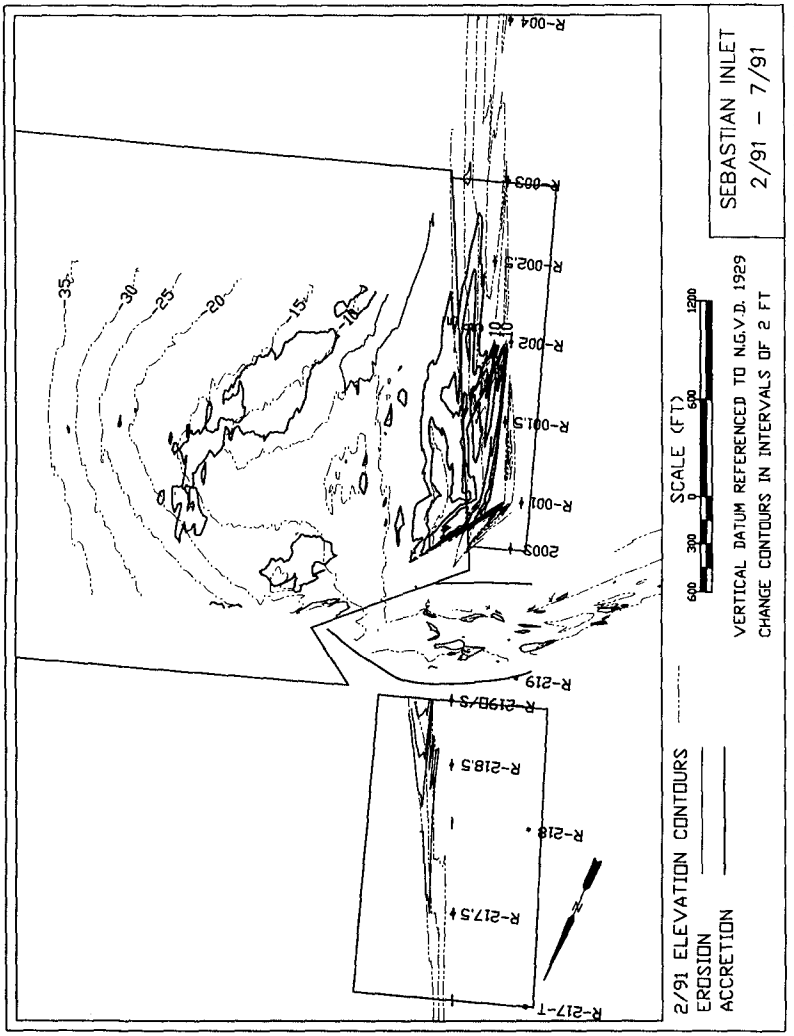

Figure 5 - Bathymetry and difference-contours for 2/91 - 7/91 surveys showing erosion of north fillet and major accretion on south fillet, with significant deposition on ebb shoal.

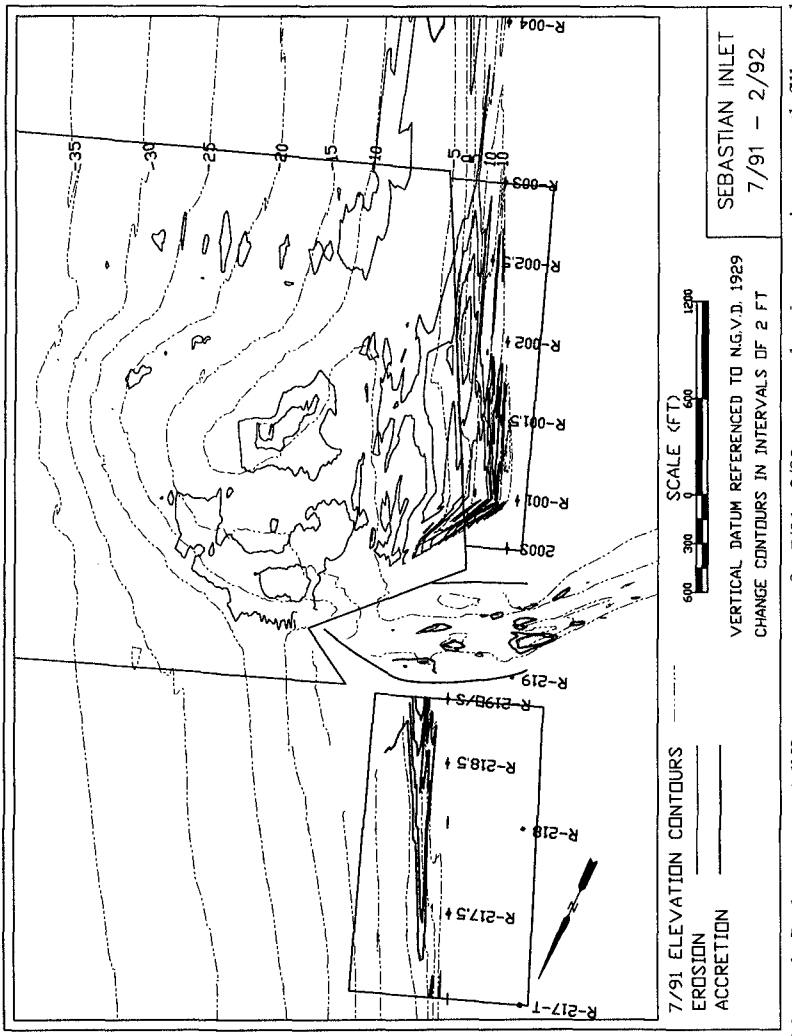

Figure 6 - Bathymetry and difference-contours for 7/91 - 2/92 surveys showing accretion on north fillet, and significant erosion of south fillet and ebb shoal attributed to long-period waves of the 'Halloween Storm'.

North Fillet

Results for the north fillet are presented in Table 1 and Figure 7. Of the fourteen seasonal comparisons made, eleven fit the expected pattern of accretion during the summer-to-winter transition and erosion in the winter-to-summer. Three comparisons displayed behavior not expected at the north fillet. The 7/90-2/91 comparison had a net

Season	North	Cumulative Volume (CY)
7/90-2/91	-10,856	-10,856
2/91-7/91	-20,525	-31,381
7/91-2/92	31,223	-158
2/92-7/92	22,225	22,067
7/92-2/93	11,542	33,609
2/93-7/93	2,636	36,245
7/93-2/94	36,056	72,301
2/94-7/94	-33,536	38,765
7/94-2/95	45,097	83,862
2/95-7/95	-20,408	63,454
7/95-2/96	640	64,094
2/96-7/96	-41,067	23,027
7/96-2/97	21,577	44,604
2/97-7/97	-992	**43,612**

Table 1. Volume Change Calculations for North Fillet.

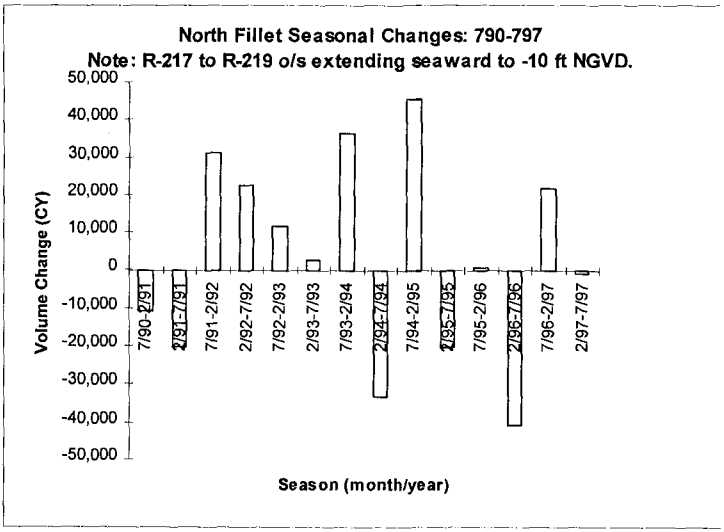

Figure 7. Volume Changes for North Fillet.

loss of 10,856 yd^3 (8,300 m^3) when a net accretion would have been expected. During the 2/92-7/92 season a net accretion of 22,225 yd^3 (16,992 m^3) was observed when erosion might be expected. Finally, there was a net accretion of 2,636 yd^3 (2015 m^3) for the 2/93-7/93 surveys, but this quantity is not significant. Noting the seasonal and annual variability, the net cumulative volume of 43,612 yd^3 (33,344 m^3) from 7/90 to 7/97 also is not wholly significant, and indicates that the north fillet was experiencing no net trend towards erosion or accretion during this time.

It is noted that the volume-change calculations were repeated for the north domain, but with the seaward boundary reduced to -5 ft (-1.5 m^3) NGVD to be consistent with the south fillet domain. The seasonal volume changes were identical in their pattern, but generally smaller in magnitude. A net cumulative volume of 13,306 yd^3 (10,173 m^3) was computed in this smaller domain.

South Fillet

In the south fillet domain, ten of the fourteen comparisons showed erosion in the summer-to-winter and accretion in winter-to-summer, as shown in Table 2 and Figure 8. Of the four comparisons that displayed reversed behavior for the south fillet, (i.e. 7/92-2/93, 2/94-7/94, 7/95-2/96, and 7/96-2/97), only 7/96-2/97 was significant (16,511 yd^3 accretion). The net cumulative volume of 50,039 yd^3 (38,258 m^3) found on the south fillet is significant in that it is accretion, and is larger than the net cumulative volume of 43,612 yd^3 (33,344 m^3) found on the north fillet for the same time period.

Season	Volume (CY)	Cumulative Volume (CY)
7/90-2/91	-3,200	-3,200
2/91-7/91	58,793	55,593
7/91-2/92	-60,787	-5,194
2/92-7/92	28,202	23,008
7/92-2/93	5,488	28,496
2/93-7/93	6,366	34,862
7/93-2/94	-33,666	1,196
2/94-7/94	-983	213
7/94-2/95	-19,995	-19,782
2/95-7/95	15,207	-4,575
7/95-2/96	2,675	-1,900
2/96-7/96	20,206	18,306
7/96-2/97	16,511	34,817
2/97-7/97	15,222	**50,039**

Table 2. Volume Change Calculations for South Fillet.

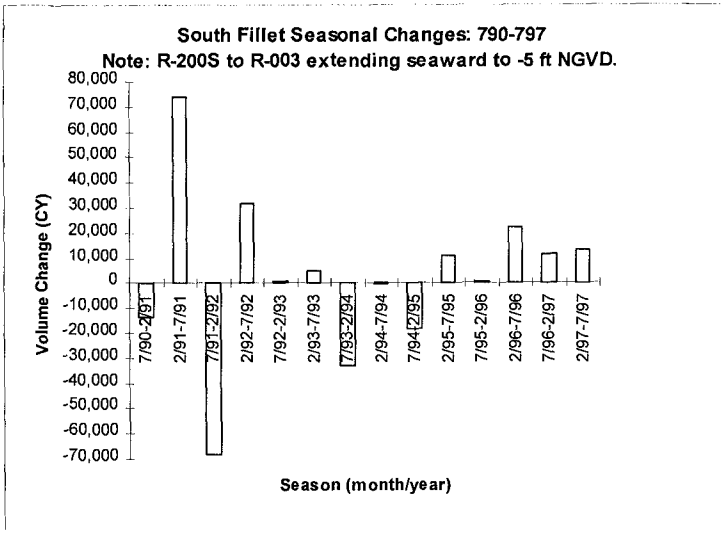

Figure 8. Volume Changes for South Fillet.

Ebb Shoal

It appears from the fourteen comparisons made for the ebb shoal domain, presented in Table 3 and Figure 9, that although half showed erosion and half accretion, no clear seasonal pattern exists. Overall, when accretion happens, it occurs at a fairly uniform rate, whereas erosion is much more variable. During the erosion episode in 7/91-2/92,

Season	Volume	Cumulative Volume (CY)
7/90-2/91	-47,507	-47,507
2/91-7/91	203,140	155,633
7/91-2/92	-444,574	-288,941
2/92-7/92	155,133	-133,808
7/92-2/93	107,755	-26,053
2/93-7/93	-33,847	-59,900
7/93-2/94	-53,565	-113,465
2/94-7/94	118,075	4,610
7/94-2/95	120,203	124,813
2/95-7/95	-143,411	-18,598
7/95-2/96	140,297	121,699
2/96-7/96	-13,647	108,052
7/96-2/97	-75,386	32,666
2/97-7/97	14,502	**47,168**

Table 3. Volume Change Calculations for Ebb Shoal.

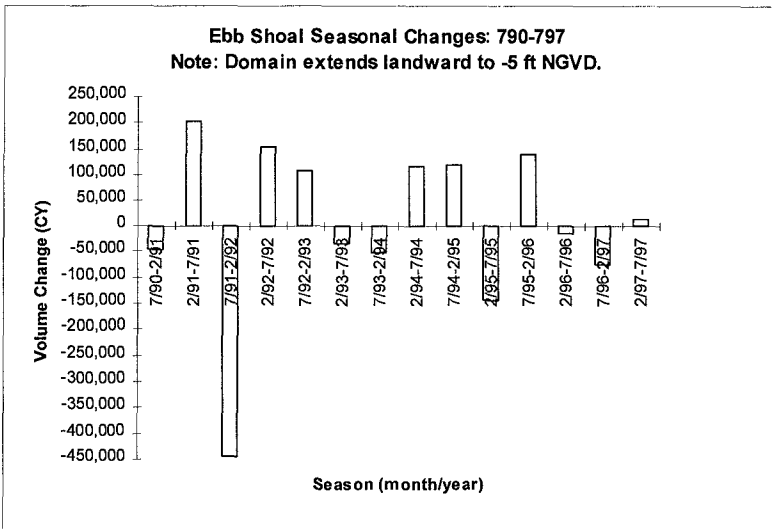

Figure 9. Volume Changes for Ebb Shoal.

more than 440,000 yd^3 (336,660 m^3) of sediment was lost from the shoal. The lack of seasonal pattern on the ebb shoal is attributed to the fact that, in addition to the wave climate, the hydrodynamics here are governed by the flood and ebb currents, which of course vary in the long-term according to general trends in ocean and lagoon water levels.

5. Conclusions

Clear patterns of seasonal behavior occur in the north and south fillet domains of Sebastian Inlet; however, the ebb shoal appears to experience gradual accretion and episodic erosion. All three domains show cumulative accretion for the seven-year time period, with that on the south fillet being the most significant as it is contrary to 'conventional wisdom' for the Atlantic coast of Florida. Further interpretation of these findings awaits detailed study of the long-term wave climate, meteorology, and water levels for the region.

6. References

Dally, William R., Ph.D., P.E. and FitzPatrick, Kathy, P.E. Survey-Based Sediment Budget Analysis For Sebastian Inlet, Sebastian Inlet Tax District Commission, Indialantic, Florida, 1997, 121 pp

NEARSHORE COASTAL PROCESSES ADJACENT TO A TIDAL INLET

Thomas O. Herrington[1], Associate Member, ASCE, Michael S. Bruno[2], Member, ASCE, Majid Yavary[3], Student Member, ASCE, and Kelly L. Rankin[1]

Abstract

Two tidal inlets with strikingly different physical characteristics have been investigated through an analysis of multi-year beach survey results and field investigations of the nearshore wave and current structure adjacent to the inlets. The survey results indicate that the downdrift shoreline adjacent to both inlets is dominated by persistent inlet directed currents, which run counter to the net sediment transport direction. The two wave and current studies differed in both their spatial and temporal resolution, requiring the use of separate analysis techniques to determine the forcing mechanisms responsible for the observed inlet directed currents. The two analysis techniques produced similar results which indicate that tidal-induced circulation generates the persistent nearshore current structure. Episodic wind-generated currents and nonlinear wave and current interactions were found to reach the same order of magnitude as the tide-induced currents, and could either enhance or reverse the observed nearshore current structure.

Introduction

It has been observed that in the vicinity of coastal inlets, complex interactions between tidally-driven currents and shoreward propagating waves produce unique wave transformation patterns that in turn give rise to sediment transport characteristics that differ greatly from adjacent shoreline areas. Shorelines adjacent to tidal inlets are subjected to a number of spatially- and temporally-varying forces, such as tidal motions, wind stress, wind waves, swell, freshwater inflow, density driven circulation, and variations in atmospheric pressure. Although much has been learned about the nature of these interactions, and their impact on sediment transport, there are very few comprehensive

[1] Res. Asst. Prof, Dept. of Civ.,Envir.,and Ocean Engrg., Stevens Inst. of Tech., Hoboken, NJ 07030
[2] Prof., Dept. of Civ.,Envir.,and Ocean Engrg., Stevens Inst. of Tech., Hoboken, NJ 07030
[3] Grad. Student, Dept. of Civ.,Envir.,and Ocean Engrg., Stevens Inst. of Tech., Hoboken, NJ 07030

measurements in dynamically-active regions such as tidal inlets that would allow one to examine the response of the shoreline to the multitude of forcing mechanisms.

Two recent multi-year shoreline monitoring studies in New Jersey have focused on the impact of tidal inlets on shoreline evolution. Each study included an analysis of long-term beach profile surveys and short-term wave and near-bottom current measurements. The initial study was conduced at Townsends Inlet in Avalon, New Jersey (Figure 1). Townsends Inlet is a relatively unimproved inlet approximately 500 m wide, stabilized by a 180 m long stone jetty located on the south side of the channel. Analysis of 10 years of beach profile data at the site indicate that the sediment transport pattern adjacent to the inlet is opposite the net southerly transport direction along this reach of coast (Farrell et. al., 1995). A second multi-year study was conducted 110 km north of Townsends Inlet at Manasquan Inlet, New Jersey (Figure 1). This improved inlet has a 122 m wide entrance channel protected by two 400 m long parallel stone jetties. Analysis of 3 years of beach profile data north of the inlet also indicates the presence of a localized reversal in the net northerly sediment transport direction.

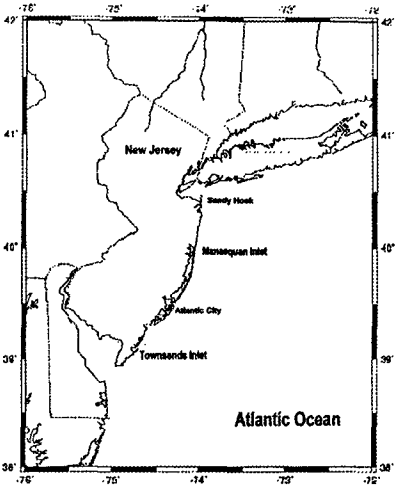

Figure 1. Location Map

Field Measurements and Analysis

Manasquan Inlet

Repetitive, high-resolution cross-shore beach profile measurements, obtained over a period of 3 years along the shoreline north of the Manasquan Inlet, indicated the presence of an area of localized erosion between 250 m and 750 m from the inlet. This erosion hot spot is characterized by a 38 m recession in the position of the mean low water line relative to the shoreline position 100 m to the north and south.

In an effort to identify the possible causes for the area of accelerated erosion, a comprehensive field study was conducted in and around Manasquan Inlet on 17 April 1996. Wave and near-bottom current measurements (1 m above the seabed) were obtained during the one day study by 3 bottom mounted InterOcean Systems S4 electromagnetic current meters fitted with high resolution pressure, temperature and conductivity sensors. Two of the bottom mounted gauges were located seaward of the inlet; S1 approximately 700 m offshore in a water depth of 13 m mean sea level (MSL), and S2 approximately 360 m offshore at a depth of 11 m MSL (Figure 2). The third gauge was located 385 m offshore of the erosion hot spot, 550 m north of the inlet, in 9.5 m of water MSL. All of the gauges were configured to sample continuously at 2 Hz and internally record the measured parameters over the duration of the study. In addition to the near-bottom point measurements, the spatial distribution of both the horizontal and vertical current structure was obtained through the use of a towed Acoustic Doppler Current Profiler (ADCP) (Bruno, et. al., 1998). The ADCP provided measurements of the top to bottom current profile along a series of transects that spanned the inlet throat, the adjacent shorelines to the north and south, and across the ebb shoal out to a water depth of 13.5 m MSL. The position of the ADCP during each transect was determined continuously using a shore-based surveying total station equipped with an Electronic Distance Meter (EDM), which obtained angle and distance measurements to a reflective prism mounted on the boat. Meteorological conditions (wind speed and direction) during the study were obtained by an anemometer located at the eastern tip of the southern inlet jetty, 10 m above the water surface.

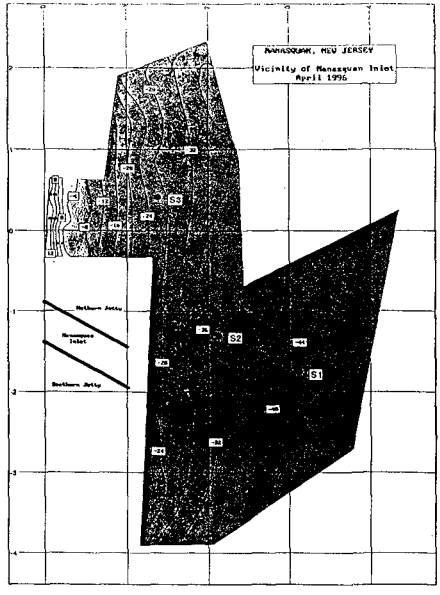

Figure 2. Location of bottom mounted S4 meters. Depth contours in feet, MSL

The high-resolution current study spanned both the ebb and flood portions of a spring tidal cycle with a predicted range of 1.5 m. The meteorological and oceanographic conditions over the duration of the study are presented in Table 1.

Table 1. Measured Physical Conditions, 17 April 1996

Time (GMT)	Wind Speed (m/s)	Wind Dir. (N)	Gauge	Water Depth (m)	Wave Height Hmo (m)	Wave Period Tp (s)	Wave Dir. (N)	Salinity (ppt)	Temp. (C)
1540	10	303	s1	13.29	0.94	9.5	55.7	31.2	5.0
(Ebb)			s2	11.45	1.00	9.0	50.0	31.5	5.0
			s3	9.64	0.91	9.1	82.0	31.6	5.5
1900	10	303	s1	13.12	0.95	9.1	60.5	31.5	5.0
(Slack)			s2	11.30	0.65	9.1	57.6	31.8	5.0
			s3	9.53	0.81	9.8	80.0	31.8	4.8
2040	10	303	s1	13.70	0.88	8.0	47.5	31.5	5.0
(Flood)			s2	11.89	0.74	9.3	59.0	31.8	5.0
			s3	10.11	0.90	10.2	81.0	32.5	4.5

Throughout the study period the wind was directed offshore toward the southeast at 10 m/s, significant wave heights ranged from 0.74 to 1.00 m propagating from the northeast with an average peak period of 9.2 s.

The high-resolution current survey spanned both the flood and ebb portions of the tidal cycle. Each round of transects was completed in approximately 30 minutes in order to provide a nearly synoptic measurement of the current pattern at various phases of the tide. Figure 3a illustrates the near-surface current distribution at peak ebb tide (1500 GMT). The measurements indicate a strong flow exiting the inlet, with near-surface currents exceeding 1 m/s. The near-bottom current structure exiting the inlet at peak ebb (Figure 3b) indicates a reduction in the current velocity to between 0.33 and 0.55 m/s. In contrast to the strong jet-like outflow on the surface, the weaker near-bottom currents are directed inshore toward the inlet. Interestingly, in both the surface and bottom currents there is evidence of inlet-directed return flows along the transects north and south of the inlet. This return flow is reflected in the near-bottom current measurements obtained by the three S4 gauges. Figure 4 illustrates the time history of the north-south component of the 9 minute average near-bottom velocity at each gauge (north is positive). Note that although the two gauges located seaward of the inlet , S1 and S2, recorded a reversal in current direction as the tide turned from flooding to ebbing, the nearshore gauge, S3, recorded a nearly constant southward directed near-bottom motion.

In an effort to gain some insight into the forcing mechanism responsible for the observed persistent inlet directed near-bottom flow seaward of the erosion hot spot, an order of magnitude comparison of the measured forcing mechanisms can be conducted. The physical forcings of interest include, wave-induced longshore transport, wind-generated currents, and inlet-induced circulation.

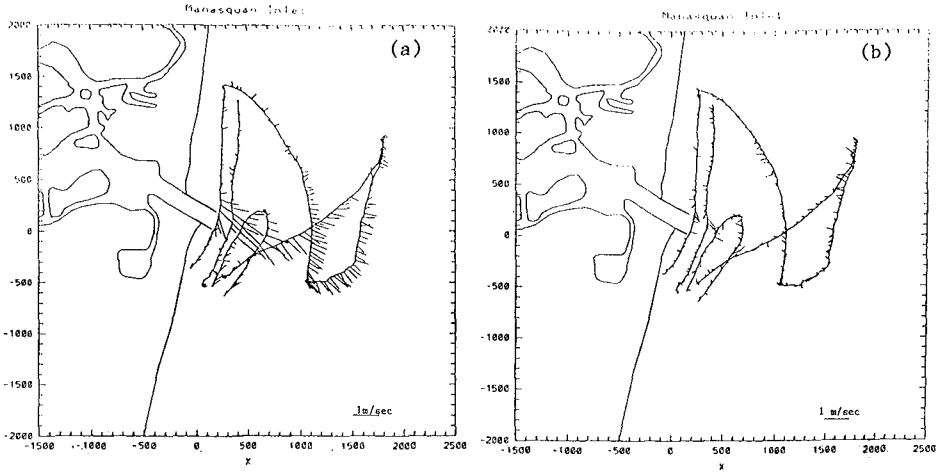

Figure 3. Spatial Current Distribution at 1500 GMT: (a) Near-Surface; (b) Near-Bottom

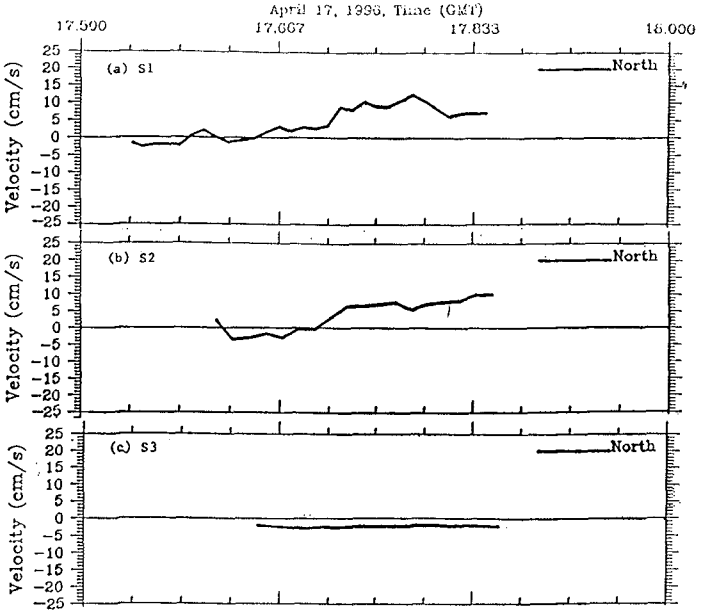

Figure 4. Average (9 min.) Near-Bottom Current: (a) S1; (b) S2; (c) S3

Utilizing the breaking criteria, $h_b = 1.28\ H_b$, where H_b, is the wave height at breaking and h_b, is the water depth at breaking, the location of the average location of the surfzone on 17 April, 1996 was in 1.1 m of water MSL, placing meter S3 approximately 305 m seaward of the surfzone. Based on Longuet-Higgins' (1970) formulation, the wave-induced longshore current 300 m seaward of the surfzone is negligible.

The wind-generated current at the surface of the water column can be estimated as 3 % of the wind speed 10 m above the water surface (U_{10}). In shallow water the wind-generated transport is essentially in the direction of the wind stress (Pond and Pickard, 1983). Assuming a logarithmic decay of the surface current with depth, the current generated by the wind stress 1 m above the bottom can be expressed as:

$$V_0 - V_1 = \frac{u_*}{\kappa} \ln\left(\frac{h}{z}\right) \tag{1}$$

where V_0 is the surface current ($= 0.03 U_{10}$), V_1 is the current speed 1 m above the bottom, u_* is the current shear velocity, κ is von Karman's constant ($\kappa = 0.4$), h is the water depth, and z is the distance of the current meter above the bed. The current shear velocity is calculated as:

$$u_* = \sqrt{\frac{\tau}{\rho}} \tag{2}$$

where the bottom shear stress, τ, is given as:

$$\tau = \frac{1}{2} \rho C_f V_0^{\,2} \tag{3}$$

In equation 3, ρ is the water density and C_f is the current friction factor. Substituting equations (2) and (3) into (1) and rearranging:

$$C_f = \left(\frac{2}{V_0}\right)\left(\frac{\kappa(V_0 - V_1)}{\ln(h/z)}\right)^2 \tag{4}$$

Utilizing the ADCP current profile data, equation 4 can be used to directly solve for the current friction factor, C_f. Table 2 lists the near-surface and near-bottom current velocities, and the calculated friction factor, C_f, measured within 300 m of gauge S3 at peak ebb (1500 GMT) on 17 April 1996.

Table 2. Measured Current Shear within 300 m of gauge S3 at 1500 GMT

Point	Wind Speed (m/s)	Wind Dir. (N)	Water Depth (m)	Surface Current (m/s)	Bottom Current (m/s)	Current Shear, u_* (m/s)	Shear Stress, τ (kg/ms^2)	Friction Factor C_f
1	10	303	9.64	0.20	0.05	0.026	0.72	0.04
2	10	303	9.64	0.11	0.02	0.016	0.26	0.04
3	10	303	9.64	0.09	0.00	0.016	0.26	0.06
4	10	303	9.64	0.05	0.00	0.009	0.08	0.06
5	10	303	9.64	0.21	0.00	0.037	1.41	0.06
6	10	303	9.64	0.27	0.11	0.028	0.82	0.02

Substituting the data obtained at peak ebb, $h = 9.64$ m, $U_{10} = 10$ m/s, $z = 1$ m, $\rho = 1026.9$ kg/m^3, and the average $C_f = 0.05$, into equations (1) through (3) and solving for V_1, yields a near-bottom wind-generated velocity of 3.1 cm/s directed 123° from North. Decomposing the current vector into north and east components gives an alongshore wind-generated current component of 1.7 cm/s to the south.

Joshi and Taylor (1983) analyzed the alongshore and cross-shore velocity components induced by the entrainment of water into nonbuoyant tidal jets issuing into water of constant depth with arbitrary bottom friction. The potential motion induced by an ebbing tidal jet is modeled as a series of sink singularities which constitute elementary solutions to Laplace's equation:

$$\nabla^2 \psi = 0 \tag{5}$$

where ψ is the two dimensional stream function $\psi(x,y)$. Analytic solutions for the jet-induced circulation are obtained by relating the sink strength to the inlet characteristics. These characteristics and the values for Manasquan Inlet include inlet half-width, b_0=61 m, mean channel depth, h_0=3.05 m, inlet throat cross-sectional area. A_c=366 m^2, average velocity over the throat area, u=1.0 m/s, length of inlet channel or jetties, a=400 m, the Darcy-Weisbach friction factor, f= 0.043 the Chezy coefficient, C=42.82 m$^{1/2}$/s, and Manning's n= 0.028.

A series of nondimensional solution curves are presented to determine V, the ratio of alongshore velocity to inlet velocity, based on ζ, the ratio of distance alongshore from the inlet to inlet half width. Solution curves are given for various combinations of dimensionless jetty length, $A = a/b_0$, and dimensionless friction parameter, $\mu = fb_0/8h_0$. For the Manasquan Inlet, $A = 6.5$ and $\mu = 0.107$. From the solution curves presented in Figure 12 (Joshi and Taylor, 1983), the predicted alongshore current 550 m north of the inlet, due to steady potential motion induced by the tidal jet alone, is 1.04 cm/s.

Townsends Inlet

A seven-day time series of wave and near-bottom current measurements were obtained 60 m inshore of the western edge of the main ebb channel of Townsends Inlet,

Avalon, New Jersey, in September, 1993 (Figure 5). The wave and current meter was mounted 1 m above the sea bed, 180 m south of the southern inlet jetty, in a mean water depth of 3.0 m MSL. In this configuration the meter was exposed to both nearshore wave and current action as well as strong tidal currents. The meter was initialized to provide measurements of the pressure and two orthogonal components of velocity at 2 Hz over 9 minute burst samples, at one hour intervals.

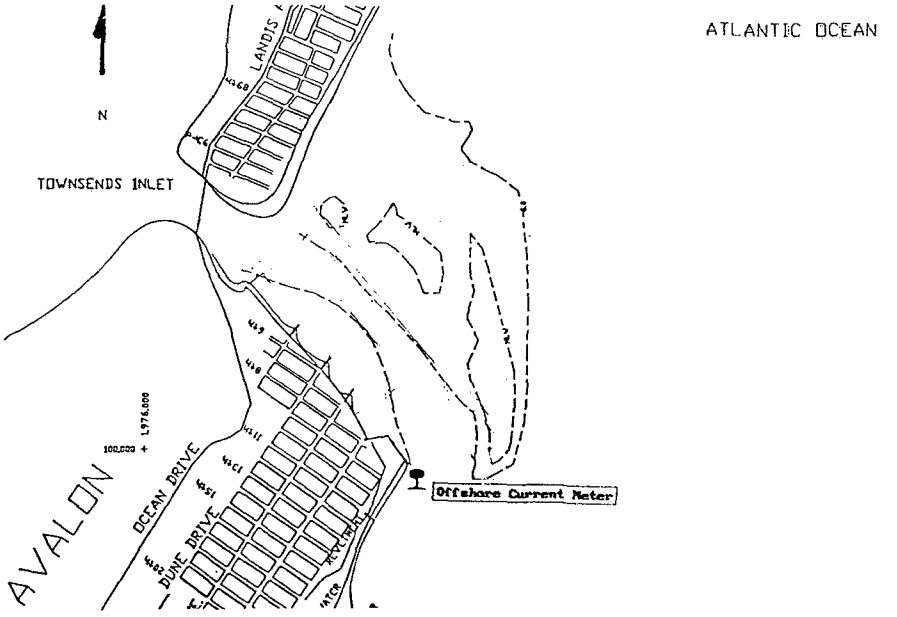

Figure 5. Townsends Inlet. Location of channel and shoals indicated by dashed line.

The measured time series is presented in Figure 6. The tidal elevation record is plotted in the upper panel, followed by the surface wind observations from Atlantic City, (located 45 km north of the inlet), the measured significant wave height ($H_s=4(m_0)^{1/2}$), the peak wave direction, and the 8.5 minute average current measured 1 m above the bottom.

All of the recorded vectors were decomposed into shore-parallel and cross-shore components. Since the axis of the ebb channel of the inlet lies on a bearing of 0° Magnetic North (MN), all of the recorded directions are reported relative to Magnetic North. Thus, shore-parallel components are parallel to the axis of the inlet channel and cross-shore components are perpendicular to the inlet channel. Positive values of the shore-parallel and cross-shore components are directed to magnetic north and east, respectively. Directions are given as the direction of propagation (i.e. a shore-parallel wind of -5 m/s is a wind directed from the north). The x-axis is scaled in tenths of days Eastern Daylight Savings Time (EDT) so that 20.5 would represent the 20th day of the month at 1200 hours.

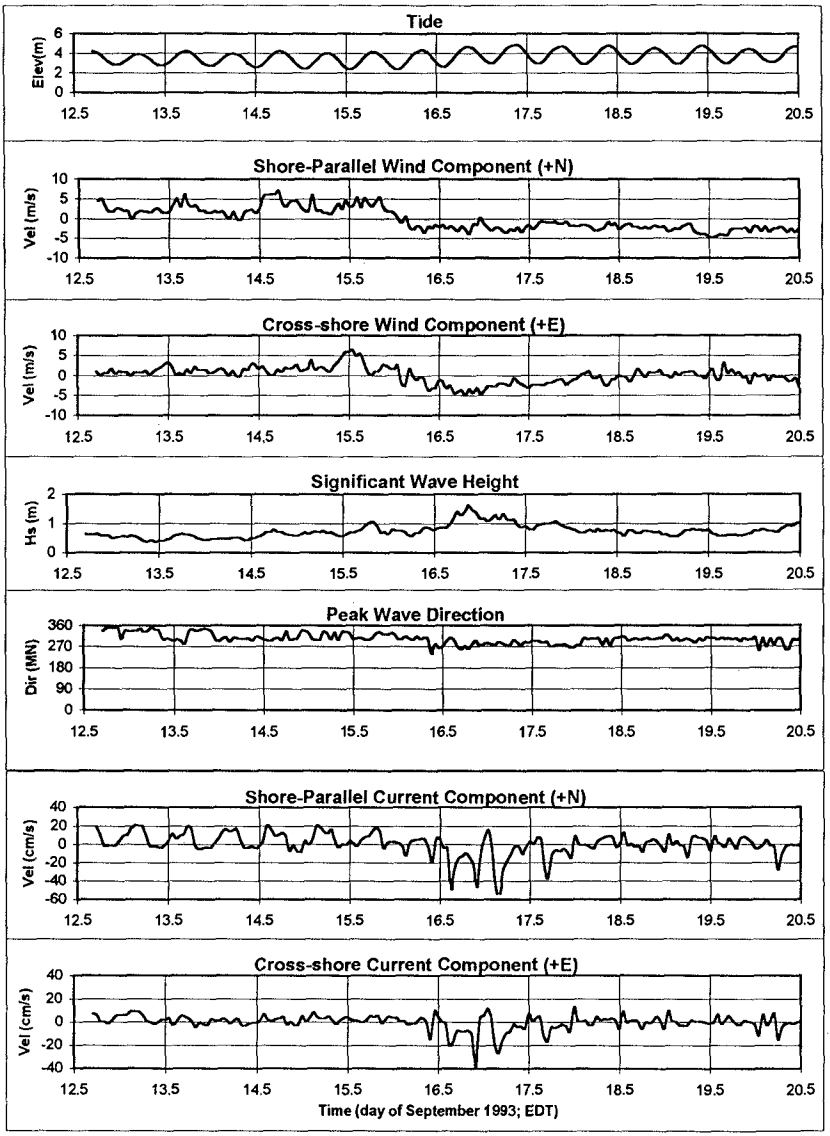

Figure 6. September, 1993 Observations at Townsends Inlet

The energy density spectra for the tidal elevation and shore-parallel component (U-Comp) of velocity is presented in Figure 7. Energy density spectra were calculated for the zero mean records of tidal elevation and the shore-parallel current component for the 7 day data set. The time series were divided into five 64 hour data segments and ensemble averaged with 50% overlap, providing spectral estimates with 10 degrees of freedom and a 95% confidence interval of 25 to 150 percent of the estimates. Examining Figure 7, two peaks are evident in the tidal elevation energy density, one centered at the semidiurnal frequency (0.08 cph) and one centered at a frequency of 0.02 cph. Three peaks in kinetic energy are present in the shore-parallel velocity component. Peaks of equal magnitude (0.175 $(m/s)^2s$) are centered at 0.02 cph and the semidiurnal tidal frequency and a lesser peak of 0.13 $(m/s)^2s$ is centered at a frequency of 0.16 cph.

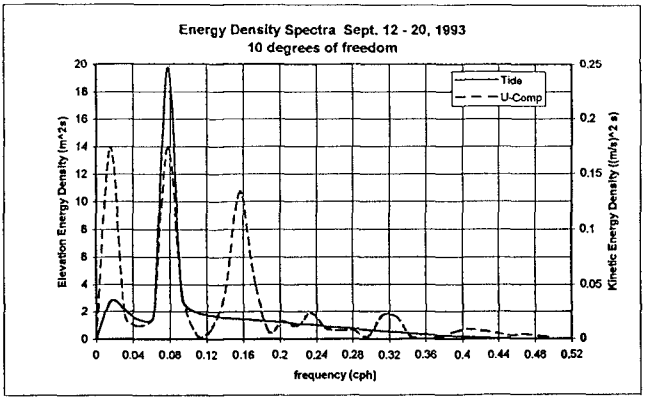

Figure 7. Elevation and Kinetic Energy Density

In an effort to determine the forcing mechanisms responsible for the observed energy density distributions, a multivariable polynomial autoregressive analysis with exogenous variables (PARX) model was utilized to produce empirical fits to the measured nearshore current data. The analysis technique decomposes the measured time series data into a multivariate data set which is utilized to predict one measured variable based on a polynomial function of the remaining variables (see Herrington and Bruno, 1998). Utilizing the six parameters measured, water elevation, h, wave amplitude, a, shore-parallel wave number, k_x, wave frequency, ω, shore-parallel wind speed, W, and the time rate of change of shore-parallel wind speed, dW/dt, a PARX model was developed to predict the measured shore-parallel current velocity. The empirical equation developed by the PARX model to predict the shore-parallel component of velocity, U_{SP}, is

$$U_{SP} = K_W + K_{dW} + K_{AH} + K_K \qquad (6)$$

where

$$K_W = [\, 0.015157(\omega^2 / W_{t-1}) - 0.0016022\, h^2_{t-2} W_{t-1} \,] + [\, 0.13338\, a^2 + 0.011704\, \omega_{t-1} + 0.00058704 / (k\, W^2)] \, W$$

$$K_{dW} = [0.0020512\, (\, dW/dt\,)/k - 0.0017450\, (\, dW/dt\,)_{t-1}/k_{t-1} - 0.0025645\, k_{t-1}/(dW/dt\,)_{t-2}]$$

$$K_{AH} = [0.010630\, (\, h^2 / a_{t-2}\,) - 0.010994(\, h^2_{t-1} / a_{t-2}\,)] + [53.695/h - 92.342/h_{t-1} + 40.090/h_{t-2} - 0.087996\, h^2_{t-2}\,]\, a^2_{t-1} + 0.10636\, a_{t-1}\, h_{t-2}$$

$$K_K = [\, -0.0000040479 / (k_{t-1}\, k_{t-2}\,)\,]$$

Figure 8 presents the measured (solid line), fit (dotted line) and predicted (dashed line) shore-parallel current component. The fitted nonlinear model, spanning the first 150 hours (day 12.75 to 19.0) of the time series, is able to resolve to a reasonable degree most of the peaks contained within the shore-parallel current record. The fit does quite well in resolving the strong southerly directed flow between day 16.5 and 17.5, only missing the magnitude of the initial strong spike in velocity. The predicted shore-parallel current over the final 36 hours (day 19.0 to 20.5) of the time series indicates that the model is able to predict the overall magnitude and direction of the current but loses some of the higher resolution peaks contained in the data.

A determination of the dominant terms in equation 6 can be obtained by comparing the contribution of each forcing term utilized to fit the shore-parallel current component. Figure 9 is a comparison plot of the contribution of each predictive term in equation 6 relative to one another. The four terms in the empirical equation are those terms which are a function of the wind velocity, K_W, rate of change of the wind velocity, K_{dW}, tidal elevation and wave amplitude, K_{AH}, and the wave number, K_K. Examining Figure 9a and 9c, it is apparent that the dominant tidal structure of the predicted current velocity during these periods is driven by K_{AH}, the terms containing both the change in water surface elevation, h, and the wave amplitude, a. Additionally, it is evident that the frequency of the forcing produced by the tidal elevation and wave amplitude terms increases during the time period of strong southerly-directed currents (Figure 9b). As Figure 10 indicates, the frequency distribution of the kinetic energy density associated only with the terms containing the variation of water depth, h, and the wave amplitude, a, verifies that the nonlinear interaction between the two parameters is responsible for the measured current variability at 0.16 cph. The relative contributions of the remaining terms in equation 6 (Figure 9) indicate that the predicted current is strongly modified by the magnitude and direction of the shore-parallel wind velocity term, which can be of equal or greater magnitude than the water depth and wave amplitude terms. The shore-parallel wind velocity and the water depth - wave amplitude terms combine to produce the strong southerly-directed currents observed during the period of increased wave height (see Figures 6 and 9b). These two predictive terms are slightly modified by the rate of change of the wind velocity and the wave number terms during the wave event.

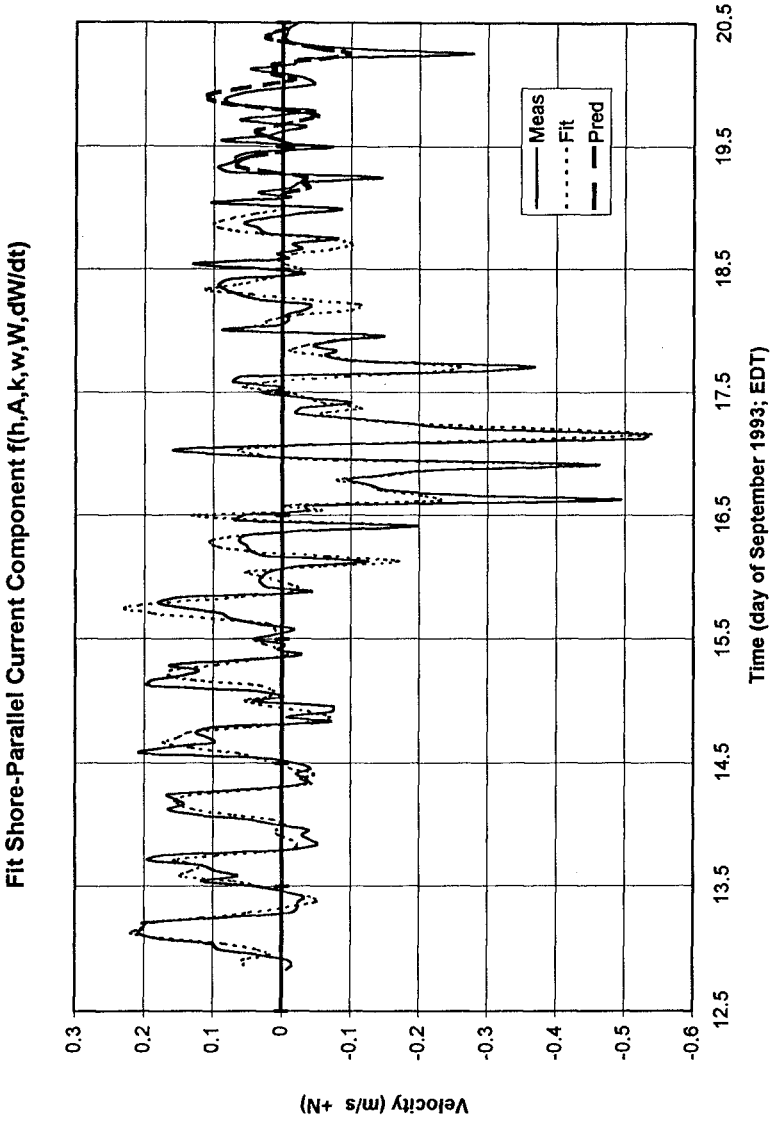

Figure 8. Empirical Fit of Measured Shore-Parallel Current

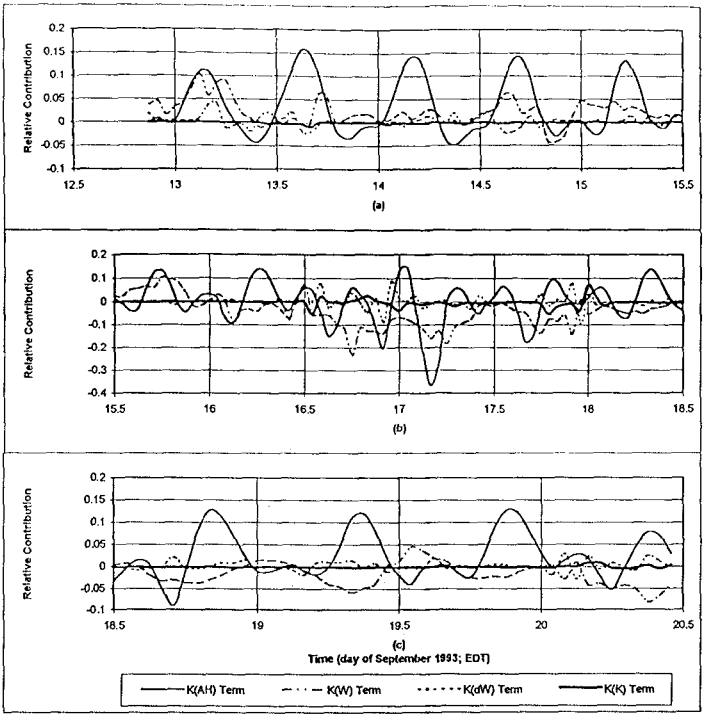

Figure 9. Relative Magnitude of Terms in Equation 6

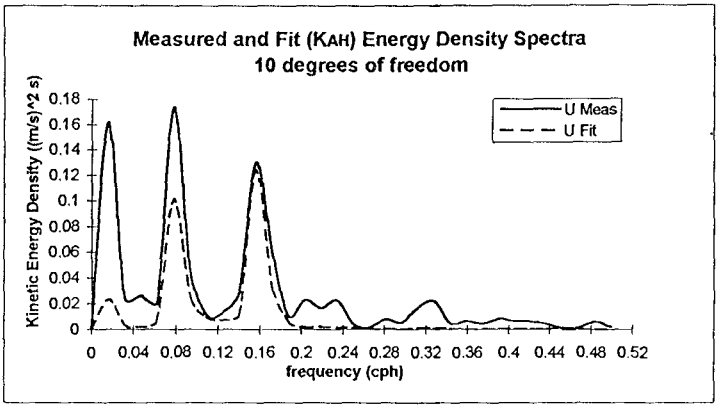

Figure 10. Influence of Water Depth and Wave Amplitude on Energy Distribution

Conclusions

Two tidal inlets with strikingly different physical characteristics have been investigated through an analysis of multi-year beach survey results and field investigations of the nearshore wave and current structure adjacent to the inlets. The downdrift shoreline adjacent to both inlets is dominated by persistent inlet directed currents, which run counter to the net sediment transport direction. The nearshore wave and current data obtained over a 8 day period at Townsends Inlet revealed that the nearshore current structure is dominated by inlet directed currents over both the flood and ebb tide. The empirical analysis of the measured data determined that an interaction between the wave climate and tide generate the observed inlet directed currents. However, strong episodic wind and wave events can reverse the observed current structure. The one day, high-resolution, wave and current study conducted at Manasquan inlet indicated a strong tidally-generated jet-like current exiting the inlet during ebb and persistent inlet-directed nearshore currents 550 m north of the inlet. A simplistic order of magnitude analysis of the measured data indicated that the potential motion induced by an ebbing tidal jet, and/or the wind-generated current contribute significantly to the observed current structure.

Although the characteristics of the two inlets differ, the hydrodynamic forcings are quite similar. Entrainment into the ebbing tidal jet leads to prolonged inlet directed nearshore currents updrift and downdrift of the inlet. The prolonged flood currents result in the reversal of the net alongshore current direction downdrift of the inlet, resulting in the formation of hot spots of erosion at the nodal points. The incident wind and wave forcing can be of equal magnitude to the potential flow generated by the tide, leading to episodic enhancement or reversal to the predominant flow characteristics.

Acknowledgements The authors wish to acknowledge the efforts of numerous individuals who assisted in the conduct of the field studies, including S. Glenn, R. Chant, and E. Creed from Rutgers University; and R. Hires and the numerous graduated students from Stevens Institute of Technology.

References

Bruno, M.S., Yavary, M. and Herrington, T.O. (1998). The influence of a stabilized inlet on adjacent shorelines: Manasquan, New Jersey, *Shore and Beach,* 66(2), 19-25.

Farrell, S.C., Sullivan, B. and Hafner, S. (1995). Annual report for 1994 to the borough of Avalon on the condition of municipal oceanfront and inlet beaches, 24pp., Coastal Research Center, Richard Stockton College of New Jersey.

Herrington, T.O. and Bruno, M.S. (1998). Empirical techniques for a priori parameter estimation, Estuarine and Coastal Modeling, Proceedings of the 5th International Conference, Alexandria, VA., Oct. 22-24, 1997, ASCE, 323-337.

Joshi, P.B. and Taylor, R.B. (1983). Circulation induced by tidal jets, *J. Wtrwy., Port, Coast., and Ocean Engrg.,* ASCE 109(4), 445-464.

Longuet-Higgins, M.S. (1970). Longshore currents generated by obliquely incident sea waves, 2, *J. Geophys. Res.,* 75(33), 6790-6801.

Pond, S. and Pickard, G.L. (1983). *Introductory Dynamical Oceanography, 2nd ed.* Pergamon Press, Inc., Maxwell House, Fairview Park, Elmsford, NY 10523.

Inlet Impacts on Local Coastal Processes

Rajesh Srinivas[1], Associate Member, and R. Bruce Taylor[1], Fellow

Abstract

St. Augustine Inlet, a trained, ebb-dominated inlet, acts as an efficient sediment trap by impounding sediments in ebb and, to a lesser extent, flood shoals. The ebb shoal, containing 23 million cy of sand by 1994, impounds 425,000 cy/yr of sand without signs of abatement. Inlet sand trapping causes chronic erosion of the south beach. The large inlet sand trapping capacity appears to be related to the large magnitudes of and the large mismatch between the ebb and flood discharge prisms. Spreading characteristics of the ebb jet are consistent with observed sedimentation patterns of the ebb shoal.

Introduction

St. Augustine Inlet, located in northeast Florida (a state in the Southeastern United States), connects the Tolomato River, flowing from the north, and the Matanzas River, flowing from the south, to the Atlantic Ocean (Figure 1). Vilano Beach and Conch Island lie to the north and south of the inlet, respectively. Salt Run, a 2.1-mile long embayment extending south from the inlet, is a relic of the old, pre-stabilization inlet.

The natural orientation of the inlet was northwest to southeast until about 1940. The U.S. Army Corps of Engineers (COE) cut a new, east-west oriented channel approximately 1,200 ft north of the natural inlet and constructed a 1,580-ft north jetty between 1940—1941. A 3,695-ft south jetty was later constructed by the COE in 1957.

This paper quantifies the inlet sand trapping effects by examining bathymetric and beach profile data, historical mechanical bypassing rates, and littoral drift in the inlet vicinity. An inlet hydrodynamic model and an ebb jet model are employed to relate the inlet sand trapping effects to inlet hydraulics.

Bathymetric and Beach Profile Data

A COE 1937 survey of St. Augustine Inlet, supplemented by aerial photographs and an old quadrangle, was used to characterize the pre-inlet stabilization bathymetry.

[1]Taylor Engineering, Inc., 9086 Cypress Green Drive, Jacksonville, FL 32256, U.S.A.

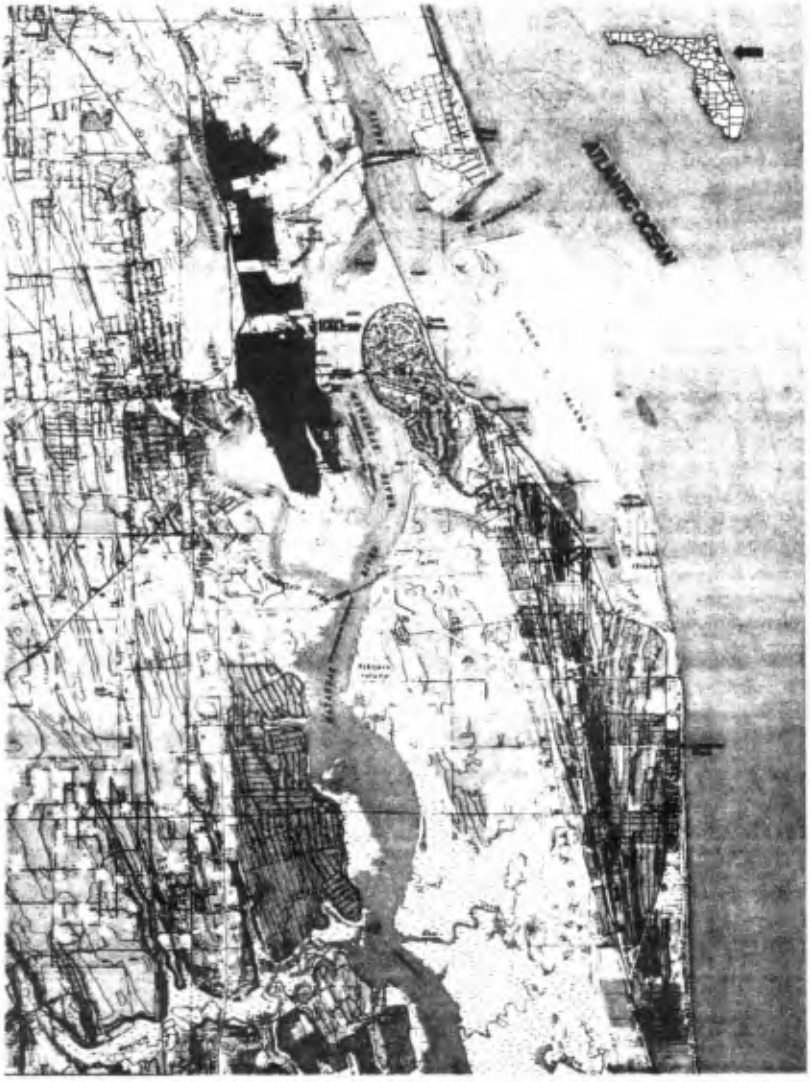

Figure 1 Location Map of the St. Augustine Inlet Vicinity

A 1974 survey of the Atlantic Ocean waters in the St. Augustine Inlet vicinity conducted by the National Ocean Survey (NOS) served as the primary bathymetric survey for this year. Another 1974 survey, performed by the COE, provided bathymetric information for the inlet throat and adjacent Atlantic Ocean waters. These surveys were supplemented as follows. Depths of inlet interior waters for 1974 were obtained from a National Oceanic and Atmospheric Administration hydrographic chart. Depths along a small region were obtained from a 1975 Florida Coastal Engineers (1976) survey of the nearshore north and south beaches. Additional subaerial elevations along some locations were obtained by adjusting 1972 and 1984 Florida Department of Environmental Protection (FDEP) survey data to 1974 conditions.

In October 1994, Taylor Engineering surveyed the interior waters of St. Augustine Inlet. The untoward occurrence of winter storms precluded survey of the inlet exterior waters that year. Taylor Engineering subsequently surveyed the inlet throat and nearby offshore waters in July 1995. The FDEP surveyed the subaerial beach system along the north and south beaches in September 1995. The combination of these three surveys served to define the inlet vicinity for 1995.

Region of Inlet Influence

The region of inlet influence is about 19,000 ft to the north and about 30,000 ft to the south of the inlet based upon shoreline and subaerial beach volume change analyses.

Bathymetric and Subaerial Beach Analysis

All the surveys were reduced to a common digitized format by representing the bottom elevations with respect to mean low water (MLW) at known horizontal locations. These discrete, digitized data were input to digital terrain modeling software. Using triangulation techniques, the software created continuous, three-dimensional surfaces of the inlet bathymetry for 1937, 1974, and 1995. Overlaid, these surfaces lent themselves to accurate computations of bathymetric change.

The 1937—1974 bathymetric comparison was used to estimate the beach and inlet short-term response to inlet relocation and structural improvements (Srinivas et al., 1996). The 1937 surface was also used to generate the bathymetric grid for the pre-inlet stabilization hydrodynamic model, described later. The 1974—1995 bathymetric comparison was used to estimate the present, long-term inlet impacts on the inlet-beach system. For this purpose, erosion-deposition volumes were computed in different submerged regions of the inlet vicinity, as presented in Table 1.

Though the north beach was erosive along almost its entire longshore length, this erosion was generally confined to the nearshore region close to the shoreline. The average total vertical change at any eroding location was generally of the order of 3 ft or less. The inner and outer ebb shoal areas experienced significant changes. Intensive accumulation of sand occurred in the outer ebb shoal region as the ebb shoal expanded eastward. Another notable feature, consistent with measured south beach shoreline

Table 1 Subaqueous Volume Change Rates (10^3 cy/yr)[1]

Interval	North Beach	Ebb Shoal	Inlet						South Beach
			Throat	Interior	North Channel	South Channel	Inner Salt Run	Outer Salt Run	
1974—1995	-198.4	405.7	-26.7	76.6	5.8	-14.5	94.6	42.6	-340

[1]- denotes erosion, + denotes accretion

advancement adjacent to the south jetty, was the accretion of the beaches immediately south of the inlet as the ebb shoal welded to the shore. The inlet throat experienced substantial changes as the natural channel migrated south. The north channel experienced net accretion whereas the south channel experienced net erosion. Salt Run was almost entirely accretionary. The south beach experienced considerable net erosion. Generally, most of the erosion occurred close to shore and the magnitude of erosion exhibited a slow decrease from north to south.

Also, between 1974—1995, the subaerial beach typically eroded modestly on the north beach while eroding chronically on the south beach; however, the subaerial beach accreted immediately north and south of the inlet due to ebb shoal sheltering effects.

Ebb Shoal Evolution

During the inlet stabilization period, the system of shoals close to the old inlet channel started to collapse, consolidate, and emerge. Finally, by 1957 and into the post-stabilization period, the shoals welded to the mainland to form a continuous beach south of the inlet.

The ebb shoal was defined according to the method outlined by Dean and Walton (1973). Calculated from this procedure, the ebb shoal volume was about 29 million cubic yards (cy) in 1937 (Table 2). After 1940, the ebb shoal migrated in both the northerly and westerly directions in response to inlet relocation. By 1974, the relocated ebb shoal had about 14 million cy of sand. With continued growth, the ebb shoal had accumulated about 23 million cy of sand by 1995.

Table 2 Ebb Shoal Volumes

Year	Volume ($\times 10^6$ cy)
1937	29
1974	14
1995	23

These ebb shoal volumes contrast sharply with the values reported about two decades ago. Upon investigating 44 inlets including St. Augustine Inlet, Walton and Adams (1976) developed a useful relationship between inlet tidal prisms and equilibrium

ebb shoal volumes. They estimated the 1957 ebb shoal volume for St. Augustine Inlet as 106 million cy. Given the northerly ebb shoal migration in response to inlet relocation in 1940 and the south jetty construction in 1957, together with the continuous accretion of the post-inlet stabilization ebb shoal, the 1957 ebb shoal volume is expected to be less than the 1974 ebb shoal volume. However, Walton and Adams' estimate for the 1957 ebb shoal volume is almost an order of magnitude greater than the 1974 ebb shoal volume estimate of the present study. Though the source of Walton and Adams' bathymetric data is not documented, NOS hydrographic and navigation charts (scales 1:10,000—1:40,000) were typically used in estimating ebb shoal volumes. The limited resolution of data obtained from such charts might contribute to some differences in estimates; however, the magnitude of the discrepancy is hard to explain. Walton and Adams also failed to document the planform area used in the volume computations. Given the relative higher resolution of the bathymetric data used in the present study, the current estimates are believed to be more reliable.

Finally, it is interesting to compare the present estimate of the St. Augustine Inlet ebb shoal volume with the equilibrium volume predicted by the functional relationship developed by Walton and Adams (1976) which relates equilibrium ebb shoal volumes, tidal prisms, and degree of beach exposure. In particular, they predict the relation

$$V_{shoal} = 10.5 \times 10^{-5} P^{1.23} \qquad (1)$$

for the vicinity of St. Augustine where V_{shoal} is the equilibrium ebb shoal volume in cubic yards while P is the tidal prism in cubic feet. According to their estimates, the tidal prism was 13.1×10^8 ft^3 in 1957; whence Equation 1 predicts an equilibrium ebb shoal volume of 17.2 million cy. Notably, this ebb shoal volume is of the same order of magnitude as the current estimate and substantially less than the Walton and Adams estimate. As computed later, the ebb tidal prism for current conditions is estimated to be about 13.6×10^8 ft^3. Applying Equation (1) yields a predicted equilibrium ebb shoal volume of 18 million cy. In contrast, the current ebb shoal volume is about 23 million cy and growing steadily with no evidence of abatement. In conclusion, the exact applicability of the Equation (1) relationship between equilibrium ebb shoal volumes and the tidal prism for St. Augustine Inlet is questionable.

Littoral Drift

The revised Wave Information Study (WIS) hindcast (Hubertz et al., 1993), believed to be the most reliable long-term wave climate information available, was chosen for estimating littoral drift in the area of interest. Twenty years of hindcast hourly wave data and the orientation of the local shoreline in the region of inlet influence were utilized to evaluate characteristic annual variations in longshore transport with the CERC (COE, 1984) littoral drift formula. Table 3 presents the results of the analysis for the region just north of the region of inlet influence. The average net drift is about 212,000 cy/yr from the north to the south. The magnitudes of the standard deviations indicate a fairly uniform yearly gross longshore transport rate; however, the northward, southward, and especially the net transport rates vary considerably from year to year. The analysis

Table 3 Littoral Drift for the North Beach Just Outside the Region of Inlet Influence

Longshore Transport Component	Average Magnitude cy/yr	Standard Deviation cy/yr
Northward	264,000	71,000
Southward	475,000	141,000
Net	212,000	175,000
Gross	739,000	139,000

revealed that the net transport rate is negligibly small for some years, and is actually reversed (south to north), albeit of small magnitude, for some other years.

Mechanical Bypassing

Over the period of interest (1974—1995) for sediment budget computations, about 480,600 cy of sand (a rate of 21,800 cy/yr) were dredged from locations east of the inlet entrance and placed in nearshore waters off the south beach (St. Augustine Beach).

Sediment Budget

A sediment budget is a comprehensive delineation of sediment transport pathways and magnitudes (Figure 2). Such a delineation, possible from results of the preceding analyses, is necessary to establish the sources and magnitude of sand being trapped by the ebb shoal and the inlet interior and to quantify sand loss rates from the south beach area.

About 212,000 cy/yr (the littoral drift) of sand enter the north beach from the north due to wave-driven littoral drift. About 5,500 cy/yr erode from the subaerial regions and about 198,400 cy/yr erode from the subaqueous regions of the north beach. Thus, about 415,900 cy/yr of sand move into the ebb shoal area from the north.

The ebb shoal vicinity gains sand at a substantial rate—about 405,700 cy/yr (after mechanical bypassing). The subaerial beach fronting the ebb shoal immediately north of the inlet accretes at a rate of 3,785 cy/yr whereas the subaerial beach fronting the ebb shoal immediately south of the inlet accretes at a rate of 14,900 cy/yr. Further, the inlet throat and the south channel erode at rates of 26,700 and 14,500 cy/yr while Outer Salt Run, the inlet interior, and the north channel accrete at rates of about 42,600, 76,600, and 5,800 cy/yr, respectively. Thus, about 83,800 cy/yr of sand deposit inside the inlet as flood shoals. About 21,800 cy/yr of sand is mechanically bypassed from the ebb shoal vicinity to the south beach vicinity. Balancing the influx of sand into the ebb shoal area from the north, losses to the inlet, efflux due to dredging, and accumulation shows that about 114,100 cy/yr of sand move into the ebb shoal area from the south beach vicinity.

The subaerial regions of the south beach erode about 59,400 cy/yr while the subaqueous regions of the south beach erode about 340,000 cy/yr. Thus, about 307,100 cy/yr move south out of the southern limits of the area of inlet influence. This value is

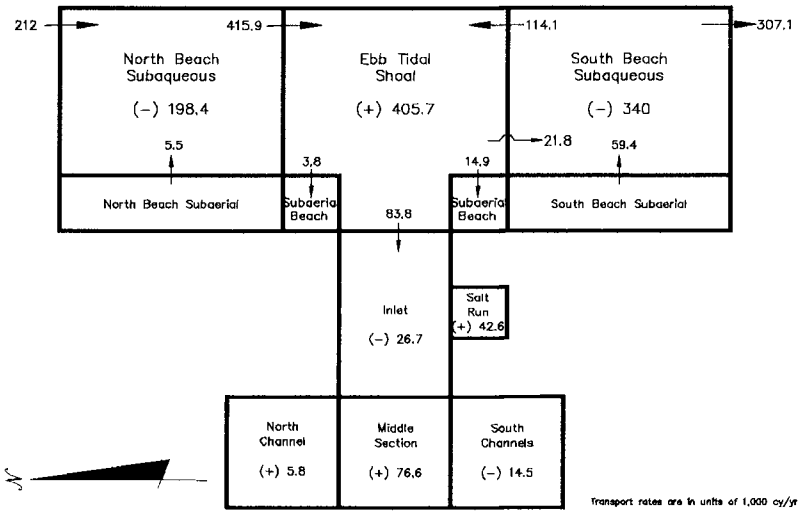

Figure 2 Sediment Budget (1974-1995) for the St. Augustine Inlet Vicinity

within 7% of the 330,000 cy/yr potential longshore transport rate computed by the independent analysis of spatial distributions of littoral drift. The potential longshore transport rate estimates should be reasonably accurate away from the region of inlet influence due to the diminished impacts of inlet hydraulics. Thus, given the preceding sediment balance, the supply of sand for beaches about 30,000 ft south of the inlet is sufficient to balance the sand requirement demanded by the local nearshore wave climate; this facet is consistent with observed beach behavior.

In summary, the ebb shoal draws sand from both the north and south beaches. Acting as a sink, the ebb shoal area accumulates sand at the rate of 427,500 cy/yr (after discounting the mechanical bypassing volume). The flood shoals gain sand at the rate of about 83,800 cy/yr. Consequently, sand does not naturally bypass the ebb shoal. The 330,000 cy/yr sand requirement of the region south of the zone of inlet influence, as predicted by the potential longshore transport capacity of waves, is approximately satisfied by sand supplied through aggravated erosion of the south beach.

Effects of Inlet Hydrodynamics

The constant recurrence of inlet-related tidal currents plays a key role in transporting sediments in the inlet vicinity. Waves transport sand into the inlet vicinity, primarily through longshore transport mechanisms. These sediments get entrained in the tidal currents which flow into the inlet during flood tide and out of the inlet during ebb tide and eventually get deposited as flood and ebb shoals. Thus, an understanding of inlet hydraulics is indispensable to understand the cause-effect relationships governing sediment interactions and exchanges in the St. Augustine Inlet vicinity. This was accomplished by the setup and application of numerical models of the St. Augustine Inlet vicinity for the post-stabilization (1994) and pre-stabilization (1937) conditions. Pre-stabilization model results are only briefly described in this paper, complete results for all conditions are presented in Srinivas et al. (1996). The modeling was used to define spatial and temporal distributions of currents in the vicinity of St. Augustine Inlet to develop an understanding of the hydraulic characteristics for the two stages of the inlet's existence. Further, using existing conditions as a baseline for comparison purposes, the inlet model is necessary to assess the unique impacts of proposed inlet modifications on these conditions to evaluate their relative merits (Srinivas et al., 1997).

The inlet model is the hydrodynamics portion of TRANQUAL, originally developed by Taylor and Dean (1972) and updated and refined by Taylor and Pagenkopf (1981). TRANQUAL, a vertically integrated, two-dimensional model, uses an implicit finite difference numerical scheme to solve the governing equations of fluid motion and conservation of mass. The formulation incorporates a full treatment of the nonlinear propagation of long waves in complex, shallow estuaries. The model domain extends 334,000 ft and 287,000 ft, centered about the inlet, in the approximate north-south and east-west directions, respectively. The grid scheme consists of 95,858 grid elements, each of dimensions 100 × 100 ft, arranged in a 287 × 334 matrix.

To provide model boundary conditions, Taylor Engineering collected synoptic tide data using bottom-mounted pressure sensing tide gages offshore and inshore the inlet. This data was used to provide the offshore tide forcing and for model calibration.

Figure 3 presents a snapshot of the ebb velocity vectors in the inlet vicinity at approximately the time of peak flow velocity through the inlet throat. The vectors are overlaid on an image of the inlet bathymetry. Most of the flow in the inlet interior occurs along the east banks of the Tolomato and Matanzas Rivers. The maximum velocities are generally about 1 ft/sec. The flow accelerates on approaching the inlet throat and velocities of about 2 ft/sec occur immediately west of the inlet throat. Flow velocities in Salt Run are minimal. The flows from the Tolomato River, the Matanzas River, and Salt Run converge just west of the inlet throat and accelerate to velocities of about 3.8 ft/s just north of the south jetty towards the western region of the throat. Thus, flow through the inlet concentrates towards the southern regions of the throat where greatest depths occur. Regions towards the north of the throat are almost stagnant with flow velocities less than 1 ft/sec. Though velocities of around 3 ft/sec occur in some regions of the throat further east, the bulk of the flow exits the inlet at about 2 ft/sec. The 2-ft/sec contour persists into the channel through the ebb shoal until about 3,000 ft east of the inlet entrance. Upon exiting the inlet, the flow immediately curves southeast. Velocities elsewhere in the ocean are of the order of 1 ft/sec or less. Interaction of the ebb flow with the north jetty is minimal. A north to south circulation exists further offshore. Thus, the majority of the conveyance through the inlet throat is through the deep water channel in the south.

Figure 4 presents a snapshot of the flood velocity vectors in the inlet vicinity at approximately the time of peak flow velocity through the inlet throat. The vectors are of the same scale as in Figure 3. The south to north circulation in the offshore is consistent with the higher water level to the south during flood flow. Velocities in the ocean are of the order of 1 ft/sec or less. Immediately east of the throat, flood flow patterns are more symmetrical compared to the ebb flow patterns in the same region. Upon entering the throat, the flow accelerates to about 3 ft/sec as it feels the effects of the north jetty. The shoal regions in the north of the throat, which were relatively stagnant during ebb, now experience velocities of the order of 1 to 2 ft/sec. Thus, the flow becomes relatively well distributed in the eastern regions of the throat. However, the flow skews towards the south (in the deep water channel) in the western regions of the throat. Velocities of the order of 2 to 3 ft/sec, with peaks of about 5 ft/sec, occur in these southern regions. The bulk of the flow decelerates and exits the throat at velocities of about 1 ft/sec; however, higher flow velocities, of the order of 2 to 3 ft/sec, occur immediately northwest of the throat. Upon exiting the throat, most flow is diverted into the Tolomato River with lesser flow entering the Matanzas River. Flow velocities are between 1 to 2 ft/sec in the Tolomato River while the velocities are generally 1 ft/sec or less in the Matanzas River. Flow velocities are less than 1 ft/sec in Salt Run. In summary, the flow is relatively better distributed in the inlet vicinity during flood as compared to the ebb conditions. Peak flood velocities are also higher than the peak ebb velocities.

Discharge time histories through various cross sections revealed that the peak ebb and flood discharges are very similar everywhere. However, the ebb phase lingers longer

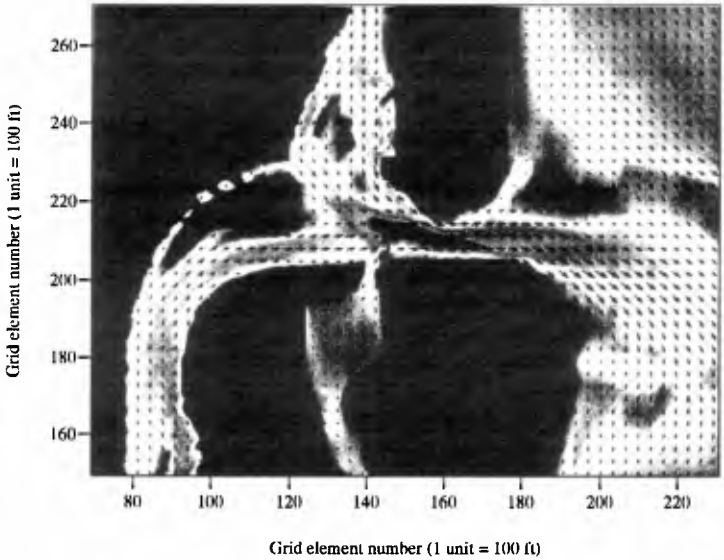

Figure 3 Ebb Velocity Vectors

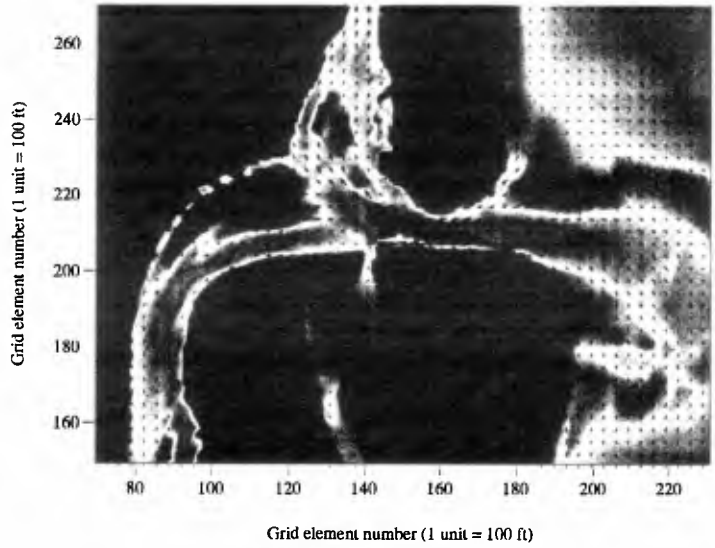

Figure 4 Flood Velocity Vectors

than the flood phase. Discharge magnitudes through the Matanzas and Tolomato Rivers are of comparable magnitudes; however, flow through Salt Run is very small.

Similar analyses were also conducted for the pre-inlet stabilization condition (Srinivas et al., 1996). Table 4 presents the comparison of the discharge prisms. For the 1994 conditions, as inferred earlier from the discharge time-histories, the ebb prism through the inlet entrance is substantially more than the flood prism. This mismatch was smaller in 1937. Though the ebb and flood prisms through the Tolomato River are better balanced for both the 1994 and the 1937 conditions, the ebb prism is slightly larger than the flood prism for both conditions. Further, the ebb and flood prisms for the 1994 conditions are slightly larger than the corresponding prisms for the 1937 conditions. The ebb and flood flow prisms in the Matanzas River are smaller than the corresponding prisms in the Tolomato River. The ebb prism is substantially larger than the flood prism for the 1994 conditions. For the 1937 conditions, the prism mismatch is smaller. Finally, the ebb and flood prisms through Salt Run are minimal for the 1994 inlet.

Table 4 Comparison of Ebb and Flood Prisms for 1994 and 1937 Inlets

Location	1994 conditions ($\times 10^8$ ft^3)		1937 conditions ($\times 10^8$ ft^3)	
	Flood prism	Ebb prism	Flood prism	Ebb prism
Inlet Entrance	8.75	13.62	7.66	10.00
Tolomato River	4.47	4.83	4.14	4.60
Matanzas River	2.86	4.58	2.71	3.76
Salt Run	0.29	0.70	n/a	n/a
Total Interior	7.62	10.11	6.85	8.36

The final analysis considered the residual (velocity) circulation over a full tidal cycle for the present (1994) and pre-stabilization (1937) inlets. Ebb flow dominance was evident almost everywhere for the 1994 inlet except by the eastern side of the inlet throat and by the shoal to the west of the inlet throat. In fact, the circulation patterns show the convergence of residual ebb and flood flows towards the deep gorge in the inlet throat. Residual ebb flows through the Tolomato and Matanzas Rivers are fairly large. The bulk of the residual flow exits the inlet in a southeasterly direction through the channel across the ebb tidal shoal. Similarly, ebb flow dominance is evident almost everywhere for the 1937 inlet. Residual flows through the Tolomato and Matanzas Rivers are fairly weak. The bulk of the flow moves in a southeasterly direction through the deepwater channel in the inlet. On exiting the inlet, the flow splits and moves both northeast and southeast. In summary, the patterns of residual circulation reinforce the concept of an ebb-dominant inlet for both the present (1994) and the pre-stabilization (1937) configurations.

The flow patterns, discharge prisms, and residual circulation patterns verify an ebb-dominated inlet. Many earlier studies (e.g., Dean and Walton, 1975; Walton and Adams, 1976) indicate that the imbalance between the flood and ebb prisms generally

dictates the locations and volumes of the primary shoals. Large ebb shoals generally form when the ebb prism is large and when the imbalance between the ebb and flood prisms is also large. As shown above, such conditions currently exist at St. Augustine Inlet. The results also suggest that improvements to the inlet should focus on reducing the ebb prism magnitude, concomitant with a reduction of the existing ebb-flood prism imbalance and a more southerly ebb jet redirection. Such inlet hydraulic behavior has the potential to reduce ebb shoal sand trapping, reduce the offshore penetration of the ebb jet (discussed next), move the ebb shoal closer to shore, and improve natural sand bypassing.

Effects of Inlet Ebb Jet

Strong ebb flows through the inlet set up a relatively large-scale circulation in the ocean which can result in sediment transport towards the inlet. The ebb flow on the seaward side of tidal inlets often occurs as unsteady turbulent flow with many properties similar to jet flow. The jet entrains lateral waters as it spreads and results in the transport of sand towards the inlet. The entrained sediments, together with portions of the wave-driven longshore transport in the vicinity, are often jetted and deposited offshore.

A simple numerical model of the ebb jet, based on the work by Özsoy and Ünlüata (1982), was used to characterize existing jet effects on ebb shoal location and growth since bathymetric analyses for the St. Augustine Inlet vicinity indicated that the ebb shoal is currently growing seaward. For model application, the velocity at the inlet mouth was assumed 3 ft/sec based on characteristic maximum ebb velocities inferred from the inlet hydrodynamic model. The input cross shore bathymetry was the average of shore-parallel depths over a distance spanning 1,200 ft either side of the centerline.

Figure 5 presents the velocity contours in the inlet offshore vicinity superimposed on an image of the inlet bathymetry. An implicit assumption of the present model is that the centerline path is straight and perpendicular to the general shoreline orientation, that is, the southeasterly offshore curvature of the natural channel is not accounted for. Ebb flow decelerates with minimal lateral spreading on exit from the inlet. The jet is fairly compact till it decelerates to 1.5 ft/sec, lateral spreading is accentuated beyond this velocity contour. Velocities of 0.5 ft/sec extend till the outer limits of the model grid—about 10,000 ft from the inlet mouth. Given the general bathymetric and sediment size characteristics offshore the inlet, a critical depth-averaged velocity of 1 ft/sec is necessary to initiate sediment motion. Thus, ebb velocities are sufficiently high to keep sediment in motion to a point about 5,000 ft offshore the inlet. This implies that depositional characteristics should dominate further offshore. Given the limitations of the present analysis, this facet is remarkably consistent with the patterns of recent long-term bathymetric changes where the ebb shoal area was seen to be accreting prominently starting about 5,000 ft offshore from the inlet.

Conclusions

St. Augustine Inlet is a very efficient sand sink which stores sand stored in ebb and flood shoals. The ebb shoal, estimated to contain about 23 million cy of sand by

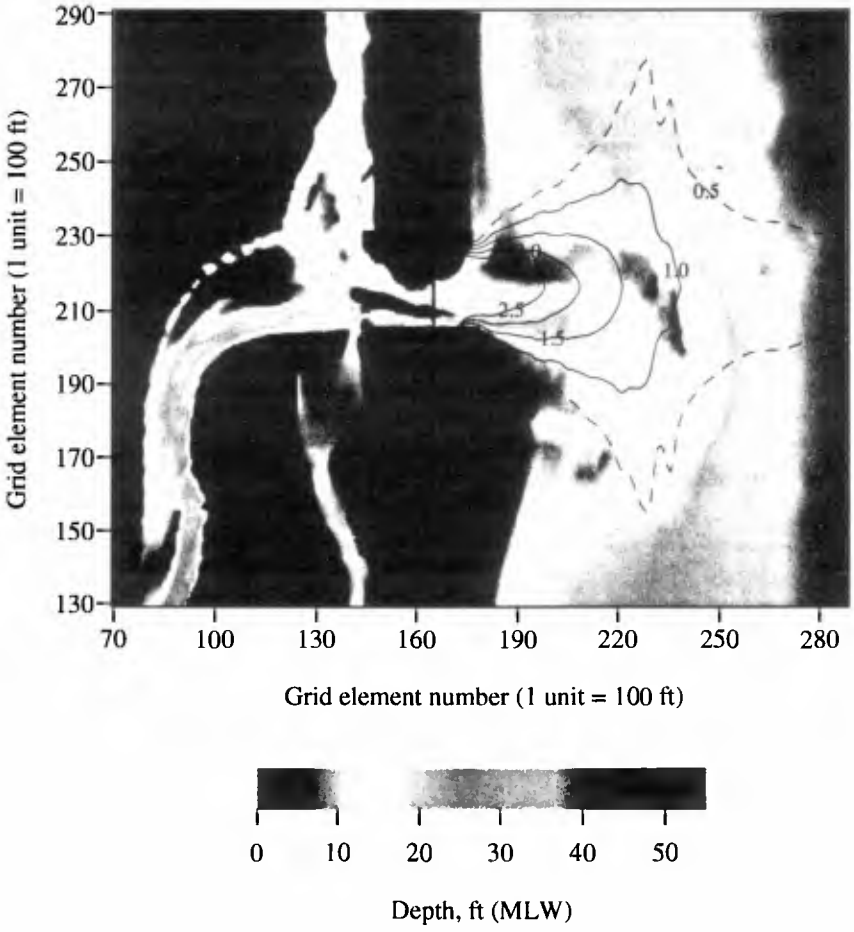

Figure 5 Ebb Jet Velocity Contours

1994, traps sand at the rate of about 425,000 cy/yr. Flood shoals trap sand at the rate of 84,000 cy/yr. This impoundment of sand deprives the south beaches of sand and causes chronic downdrift erosion. The sand trapping action of the inlet is attributable to the large magnitudes of and the large mismatch between the flood and ebb tidal prisms. The large offshore penetration of the ebb jet is responsible for the ongoing offshore growth of the ebb shoal. Substantial changes to the inlet jetties are possibly necessary to improve the natural bypassing characteristics of the inlet.

Appendix A References

Dean, R. G. and Walton, T. L. 1973. Sediment Transport Processes in the Vicinity of Inlets with Special Reference to Sand Trapping. *Proceedings, 2nd International Estuarine Research Conference*, 129—149.

Florida Coastal Engineers. 1976. *St. Johns County Beach Erosion Study*. Jacksonville, FL.

Hubertz, J. M., Brooks, R. M., Brandon, W. A., and Tracy, B. A. 1993. *Hindcast Wave Information for the U.S. Atlantic Coast.* U.S. Army Corps of Engineers, Waterways Experiment Station, Vicksburg, MS.

Srinivas, R., Schropp, S.J., and Taylor, R.B. 1996. *Inlet Baseline Conditions: Physical and Environmental Characteristics, St. Augustine Inlet Management Plan, Part 2.* Taylor Engineering, Inc., Jacksonville, FL.

Srinivas, R., Schropp, S.J., Trudnak, M.E., and Taylor, R.B. 1997. *Management Alternatives and Recommended Plan Elements, St. Augustine Inlet Management Plan, Part 3.* Taylor Engineering, Inc., Jacksonville, FL.

Taylor, R. B. and Dean, R. G. 1972. *Numerical Modeling of Hydromechanics of Biscayne Bay/Card Sound System Part II: Dispersive Characteristics.* University of Florida, Department of Coastal and Oceanographic Engineering, Gainesville, FL.

Taylor, R. B. and Pagenkopf, J. R. 1981. TRANQUAL: Two-Dimensional Modeling of Transport Water Quality Processes. *Proceedings, Stormwater and Water Quality Management Modeling Group Meeting,* U.S. Environmental Protection Agency, Niagara Falls, Canada.

U.S. Army Corps of Engineers. 1984. *Shore Protection Manual.* Waterways Experiment Station, Vicksburg, MS.

Walton, T. L. and Adams, W. D. 1976. Capacity of Inlet Outer Bars to Store Sand. *Proceedings, 15th Coastal Engineering Conference*, 1919—1937.

Appendix B Unit Conversions

English	SI
1 ft	0.3048 m
1 cy	0.7646 m^3
1 mi	1.6093 km

Long-term morphological development of the Accumer Ee tidal inlet and its impact on island beaches and engineering responses

U. Abels, H. Kunz, G. Ragutzki, H.-J. Stephan[1]

Abstract

At the East-Frisian coast (Germany) morphological changes of tidal inlets - anthropogenically or naturally caused - can have substantial effects on the sediment supply of adjacent beaches. Erosion periods of beach and dune areas occur, which necessitate engineering countermeasures to preserve the present shoreline. The East-Frisian barrier islands are integrated into the coastal protection strategy for the mainland as they reduce the impact of sea-forces on the flood defences. On the other hand, shoreline and foredunes have to be maintained to protect the urban and tourism infrastructures on the island itself. The maintenance by solid engineering works, like seawalls and groynes, is not favourable because it has drawbacks on the natural morphodynamic processes. Therefore, the technique of beach- and foreshore nourishment is implemented as an instrument of 'active coastal protection' whenever possible. The paper deals with an actual erosion problem on the island of Langeoog caused by morphological changes of its tidal inlet Accumer Ee. It discusses the long-term morphological development of the tidal inlet with its ebb delta shoals and of the adjacent shoreline. A coastal engineering solution for the coastal defence problem has been achieved by means of an integrative approach regarding the natural morphological processes, the ecological objectives, and the safety of the island population.

Introduction

The island of Langeoog is one of the seven East-Frisian barrier islands which extend along the North Sea at the western part of Germany (Fig.1). The sandy barrier islands are formed by the interaction of tides, currents, surf and wind-born accretion. The islands are separated from each other by tidal inlets which are connected with tidal flats located towards the mainland. The tides are semi-diurnal and propagate from west to east. The predominant wind direction is north-west. Tides and winds

[1] Coastal Research Station of the Lower Saxony State Agency for Ecology;
An der Mühle 5, D-26548 Norderney/Germany

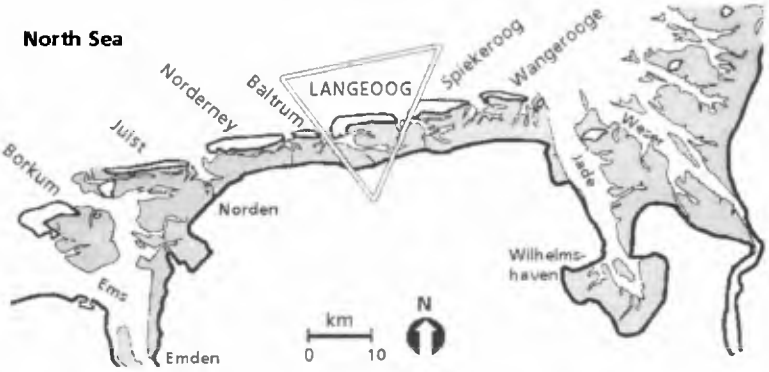

Fig.1: The East Frisian Islands - western German North Sea Coast

Fig. 2: Tidal inlet 'Accumer Ee' between Baltrum (left) and Langeoog (right)

generate a net littoral drift which is directed to the east. The tidal inlets exhibit a very high natural dynamic, which is characterized by morphological changes, both long-termed (structural) and comparatively short-termed. Most of the East-Frisian islands experience erosion of the western spit (Luck 1977). The protection of the barrier islands is part of the German coastal defence system. Consequently, erosion is counteracted by groynes, seawalls and artificial sand supply (Kunz 1996, 1997). The island of Langeoog is one of the two exceptions. Its western part has been subject to accretion as well as to erosion. The natural sand supply is related to the ebb delta shoal system (reef bow). It is created by interactions of tides, waves and littoral drift. The volume of the shoals as well as the movement-direction of the reef bow (downdrift foreshore bars) are essential for the sediment supply of the adjacent island beaches. A migration of the tidal inlet affects the configuration of the ebb delta bar system and therefore can cause a decrease in the sediment supply. The bars of the reef bow are only temporary accumulation areas as the sediment is permanently moved, resulting in a net sediment transport along the reef bow. The sediment bars of the reef bow can reach heights above low water level (Fig.2).

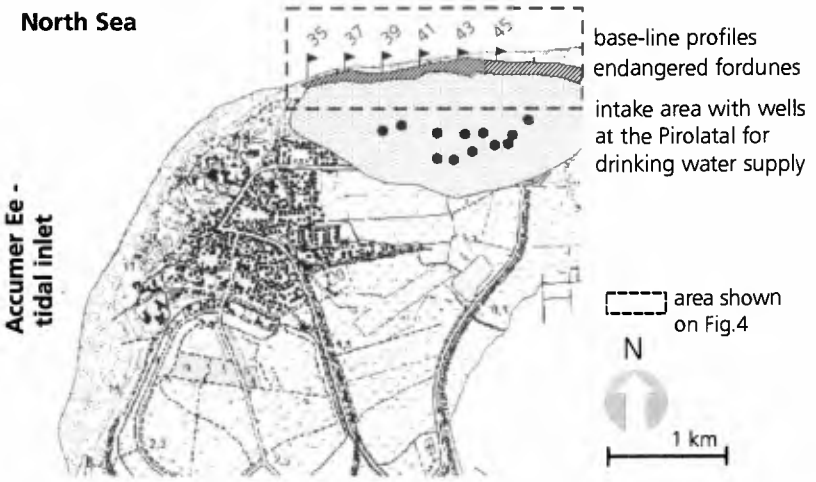

Fig. 3: Western part of Langeoog island with survey-profiles and infrastructures

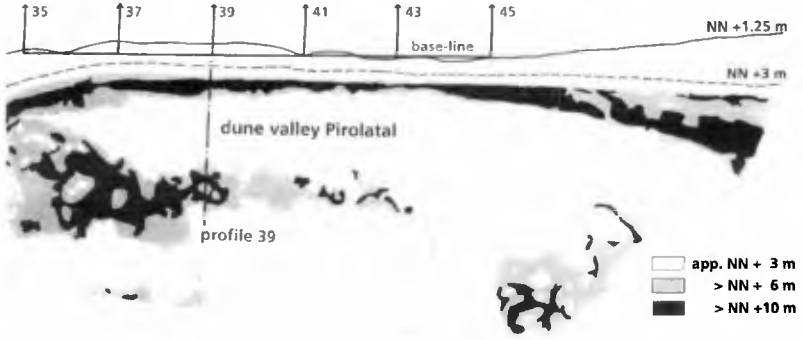

Fig. 4: Dune area Pirolatal (laserscan survey 1996)

The western part of Langeoog, especially the area of the Pirolatal (Fig.3), is endangered by erosion, which is caused by insufficient natural sand supply. The laserscan-survey of the year 1996 (Fig.4) clearly exhibits the weak condition of the foredunes. Especially the part between profile no.39 and no. 43 has the smallest dune widths and the lowest dune heights. The losses after a severe storm surge can be estimated as a retreat of 10 to 20 meters. Consequently, the endangered foredunes in the Pirolatal - with dune widths around 35 meters and very narrow beaches in front - are imminent to break through during a stormy winter season. The average height-level of the endangered dune valley Pirolatal amounts only to 3 meters, and a second closed dune ridge is not existing. A break through would endanger the village by flooding and would affect the drinking-water supply of the island (Fig.3) by intrusion of salt water into the fresh water lense. A further aspect is that the endemic vegetation is classified as a highly protected habitat according to the Lower Saxonian Nature Preservation Statute.

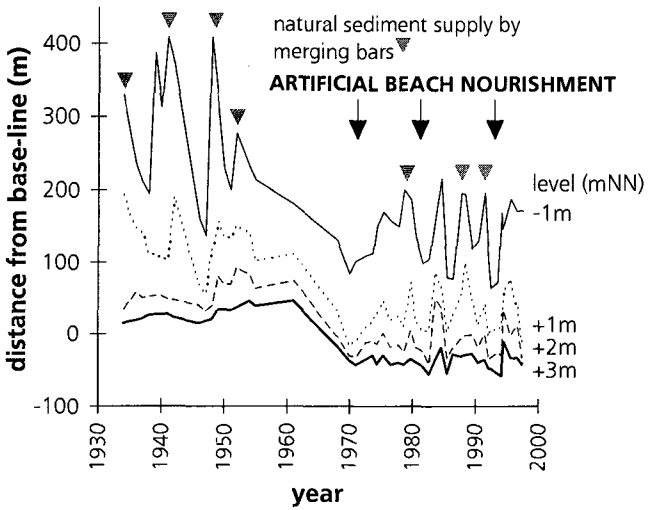

Fig. 5: Time distance diagram for different reference levels - profile 39 (see Fig.4)

Time-distance diagrams provide information about the beach and dune development, exemplary demonstrated by profile no. 39 (Fig.5). Regular surveys have been carried out since 1935. The development can be divided into three periods. First: between 1935 and 1960 a positive trend prevailed, and several "peaks" refer to natural sediment supplies by downdrift foreshore bars until 1950. Second: between 1960 and 1970 a drastic beach and dune decline occurred, retarded in the beginning as long as the beach was large enough to provide substantial aeolean sand transport. During this period the foredunes lost on an average 70 meters in width, considerably intensified by the hurricane storm surge from February 1962. Third: because of the large and lasting dune losses several beach nourishment projects have been carried out since 1972 (their implementation will be described later) partly compensating the beach decline. Furthermore, a renewed natural sand supply can be observed since the end of the seventies but the amount of it seems to be reduced.

Fig.6 demonstrates the extent of the dune losses: profile no. 39 shows a decline of 91m between the maximum in 1961 and the minimum in 1994 (reference level is NN +3m). In comparison with the erosion period (1960 to 1970) no considerable regeneration has occurred; decline and regeneration alternate with each other depending on whether natural or artificial supply take place or a shortage of sediment occurs. In general, no specific trend can be observed (see Fig.5: 1970 to 1996).

Long-term development of the tidal inlet and its ebb delta bar system

The discussed beach and dune development is determined by the processes within the tidal inlet. Temporal alterations of the tidal inlet configuration - with respect to the ebb delta bar system (reef bow) - can be linked to the processes within the downdrift area of the reef bow itself and thereby to the development of adjacent beach and dune areas.

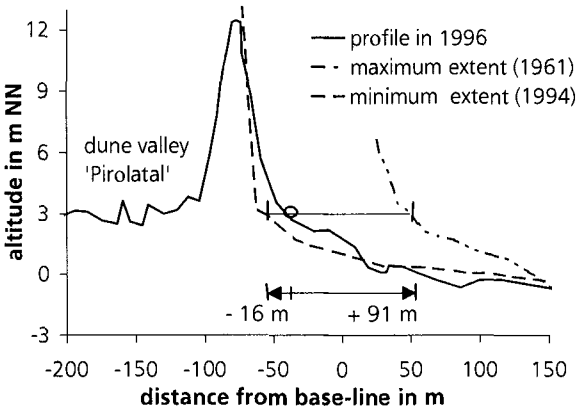

Fig. 6: Minimum and maximum dune extension between 1935 and 1996 - profile 39

The morphological development of the Accumer Ee tidal inlet and its ebb delta shoals is well documented over a period of more than 100 years (Homeier 1956; Homeier & Luck 1971). The large-scale and long-term morphological development was investigated by the evaluation of topographical maps (1866 to 1995). The maps of the last century are mere sea maps with only few information about depths (just enough for navigational purposes). Due to this restriction, only a few horizontal reference levels (SKN, SKN -1m and SKN -2m, where SKN is the low water level at spring tide) were chosen to investigate the sediment distribution within the reef bow (Fig.7). On a visual basis the ebb delta bar system shows over a long period a more or less compact shape; the single bars, as well as groups of shoals, are only separated by small channels. At the end of the investigation period, however, (around 1985) the channels started to expand and the map of 1995 already exhibits a large gap at the vertex area of the reef bow (see Fig.7, marked by an arrow in the map 1995). The solely visual interpretation already indicates that the sediment accumulation within the ebb delta bar system is decreasing.

To get a quantitative overview the morphological changes of the ebb delta bar system were estimated by the determination of the area covered by the bars referring to three distinguished horizontal reference levels (Fig.8). The calculated total area for the three reference levels are named as 'equipotential bar areas'. The development of the equipotential bar area values can be approximately transferred by constant factors to the corresponding changes of the sediment volume providing information on the predominant trends. Due to the limited number of available reference levels the calculation of volumes is not more effective than the applied method. The used German sea map reference level SKN is - in contrary to the fixed German datumn NN - a variable value. However, within the scope of the applied investigation methods these variations (up to 11cm for the entire investigation period) are irrelevant regarding the range of error connected with the small-scale of the maps and the limited accuracy of the survey, which exceeds this source of error to a great extent.

Results are shown in Fig.8. With reference to the entire investigation period, the equipotential bar areas of the reference level SKN -2m and SKN -1m have

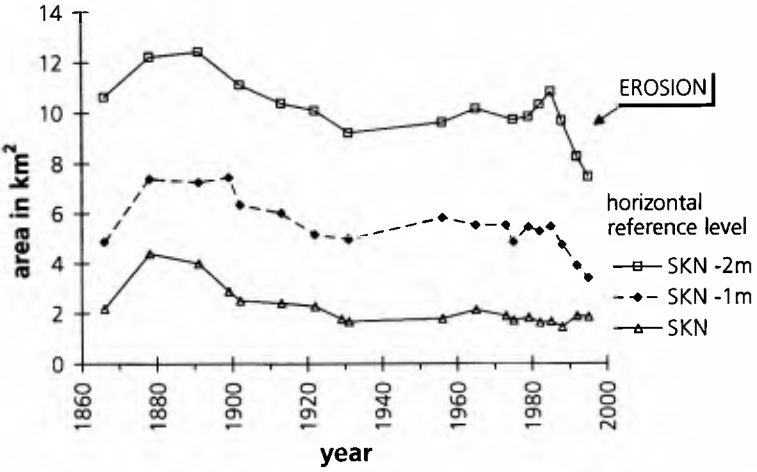

Fig. 8: Development of equipotential bar-areas for three different reference levels

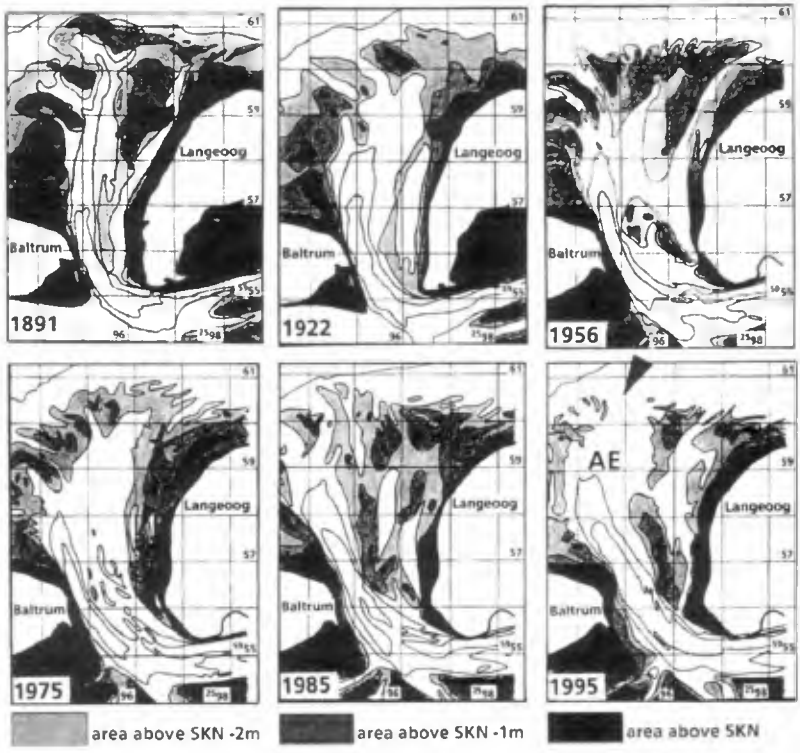

Fig. 7: Development of the ebb delta bar system of the Accumer Ee (AE) - tidal inlet between 1891 and 1995

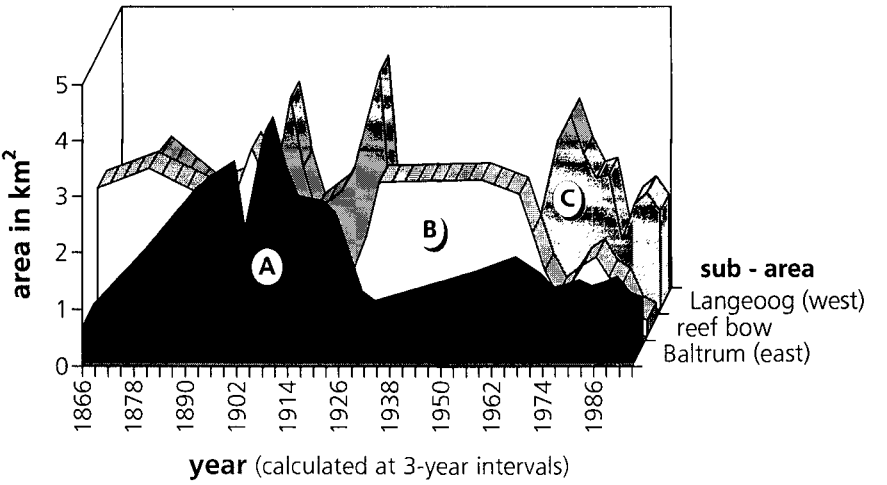

Fig. 9: Distribution of equipotential bar-areas for sub-areas (reference level SKN-1m)

decreased by about 30%; the area of the reference level SKN lost just around 15% of its former size. The decrease did not occur continuously. The ebb delta bar system shows its highest accumulation degree during the last quarter of the 19th century. At the end of the last century the equipotential areas of all reference levels gradually diminished. Between 1930 and 1980 their extent was more or less stable; afterwards the area for the reference levels SKN -2m and SKN -1m lost considerable size. Because of the more or less steady extent of the SKN reference level it is unlikely that the sediment has been transported and deposited in greater depths. Furthermore, the decrease took place rather quickly.

To allow a more detailed analysis the sediment distribution within different sub-areas of the ebb delta bar system - regarding the reference level SKN -1m - was examined. The distinguished 'sub areas' are: the east end of Baltrum, the bars of the reef bow, and the western part of Langeoog (Fig.9). Non available intermediate values have been calculated by linear interpolation (3-year intervals). The diagram does not show the shifting of single bars or groups of shoals but the shift of maximum sediment accumulations. Marked by A,B,C, the following becomes evident: in the beginning the sediment accumulated at the east-end of Baltrum leading to a rise with a maximum in this area between 1866 and 1908 (A); then the maximum moved into the reef bow area (B), where it reached a maximum between 1935 and 1960 (there is no distinct "peak" to be seen because no data were available for the period between 1931 and 1956; the values are exclusively based on calculation). At last, the maximum reached the western shore-line of Langeoog around 1975 (C). This shift of sediment covered a prolonged period. The extent of the subsequent sediment accumulation at the east of Baltrum is by around 40% to 60% smaller than the previous maximum. It accumulated around 1970, passed into the reef bow very quickly, and reached Langeoog around 1985. A further sediment supply is at the moment out of

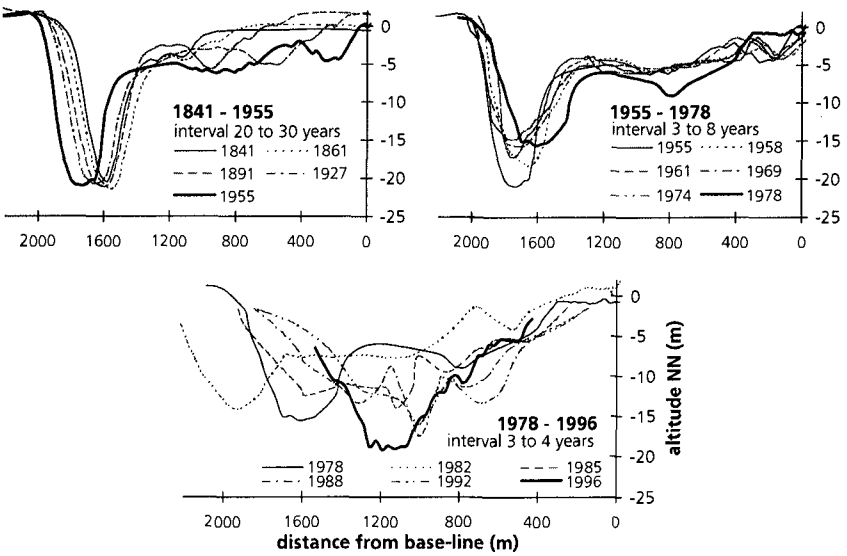

Fig. 10: Cross-sections of the tidal inlet Accumer Ee - profile no.6 (see Fig.2)

sight. Although the sediment accumulation at the east part of Baltrum is recently slightly growing the reef bow exhibits a so far unprecedented minimum. The actual reduced sediment transport indicates that fundamental morphological changes - probably concerning the littoral drift in general - are in progress.

The investigation so far does not explain why there is actually a sediment deficit, which leads to a beach and dune decline in front of the Pirolatal. According to Fig.8, sufficient sediment quantities have reached Langeoog since the seventies. This can be explained by the fact that the sediment supply not only depends on the quantity of sediment (equipotential bar area) but is also dependent on the position at which the downdrift foreshore bars merge with the island beaches. Therefore, the development of the main tidal channel of the tidal inlet Accumer Ee and its impact on the position of the ebb delta bar system were examined.

The morphological changes within an ebb delta bar system are - besides littoral drift and wave climate - mainly determined by the position of the main tidal channel and its residual ebb tide current. The main tidal channel of the Accumer Ee - in this investigation defined by the SKN -5m and SKN -10m contour line - is situated at the western part of the tidal inlet directly at the east-end of Baltrum. Therefore, the morphodynamic situation of Langeoog is favourable with respect to the conditions for a natural sediment supply of the beaches because the downdrift foreshore bars can reach Langeoog at its western part.

The development of the main tidal channel Accumer Ee is represented by a cross-section of the tidal inlet at the seaward boundary of the drainage basin (Fig.10). Over a long time of the entire investigation period (1841 to 1955) the main tidal channel exhibits a more or less steady position and constant depths, whereas the cross-section of the tidal inlet enlarged continuously. However, it has to be taken into account that the diagram for the first period (1841-1955) is based on survey-intervals

that amount to 20-30 years, i.e. intermediate short-termed developments are not visible. Afterwards (1955 to 1978) the depth of the main channel decreased, whereas the location within the tidal inlet remained unchanged. After 1978, during the last period (1978 to 1996), shifting tendencies of a larger extent occurred and the position of the main tidal channel became unsteady: at first it moved in a westward direction, finally the shifting process is directed eastwards, so that in the end the resultant new main tidal channel is located more eastward than it had been before. In the course of the last years a newly deepening of the channel can be observed.

The shifting tendencies of the former more or less steady main tidal channel indicate that the drainage basin might be subject to major morphological changes as the cross-section of a tidal inlet is closely connected with the volume of the tidal basin. Current investigations have shown that the volume of the tidal basin is actually increasing, possibly caused by structural erosion processes in the tidal flats (Schroeder et al. 1994).

In the eastern part of the ebb delta bar system there are three different approach directions to be distinguished by 'downdrift foreshore bar'-systems. Fig. 11 shows the average position of a median reef bow representing the ebb delta bars, which are characterized by a split of their alignment: the medium-grey coloured part is lined up eastwards; the dark-grey coloured part is directed southwards. The split is presumably determined by the predominant weather conditions (weather-influenced hydrodynamic factors like wave and current direction, surf etc.). Depending on the direction from which the main amount of sediment reaches Langeoog certain sectors of the beach obtain a sufficient sediment supply, whereas others suffer from a deficit. Fig.12 shows the size of the three downdrift foreshore bar-systems for the period from 1866 to 1995. The varying positions of the downdrift foreshore bars and their extent are obvious; the alternate maxima of the different directions are clearly visible.

The development of the beaches and dunes in front of the Pirolatal is dependent on the eastward directed sediment transport. The periods of supply and deficiency correspond with the development of the beaches and dunes (see Fig.5). During the distinct erosion period between 1960 and 1970 there was no major eastward directed sediment supply to this area, whereas since 1970 larger amounts of sediment have reached the Pirolatal-area again provided by the eastward directed approach of the shoals. The recent development of the downdrift area is characterized by an intermediate position of the downdrift foreshore bars located between the southern and eastern direction (light-grey colour). This development is caused by the north-west extension of the main tidal channel which leads to a more westward situated splitting point of the downdrift bars. A distinct shift of the reef bow in a solely northern direction - which would result in an eastward shift of the downdrift area - has not taken place so far. Consequently, the sediment supply is not affected adversely, and the downdrift foreshore bars reach Langeoog still in front of the western part of the island.

Coastline and dune management by artificial sand supply

The discussed results demonstrate that the beach and dune decline in the Pirolatal-area can be attributed to a temporal restricted lack of natural sediment supply. This deficit is caused by varying positions of the downdrift foreshore bars which lead to temporary periods of erosion. It was possible to compensate shortages of sand supply

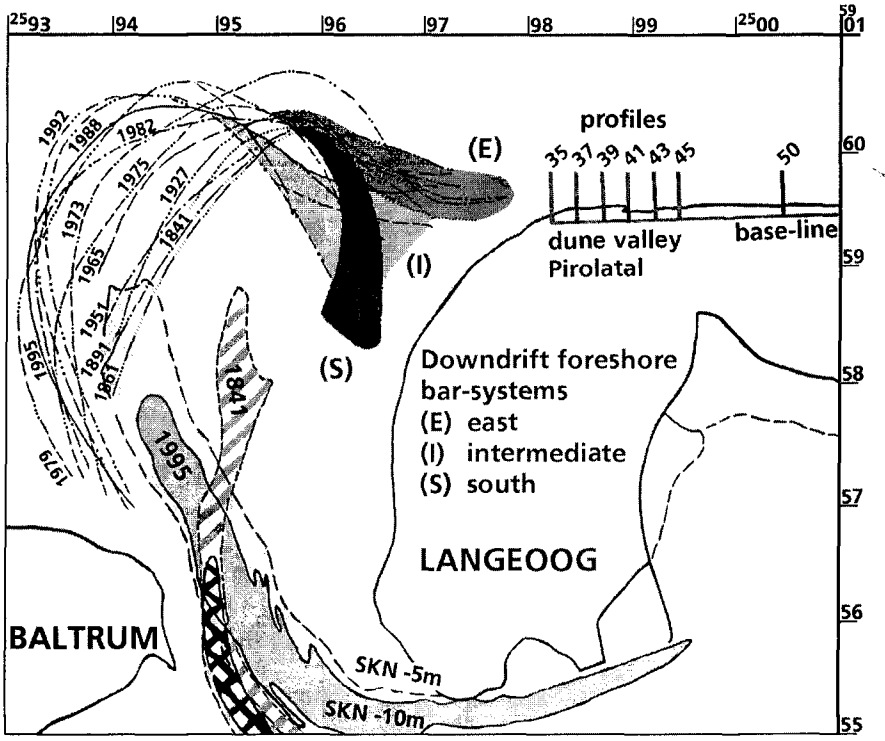

Fig. 11: Shifting of the main tidal channel Accumer Ee and its related ebb delta bar-system with three distinguished downdrift foreshore bar-systems (E), (I), (S)

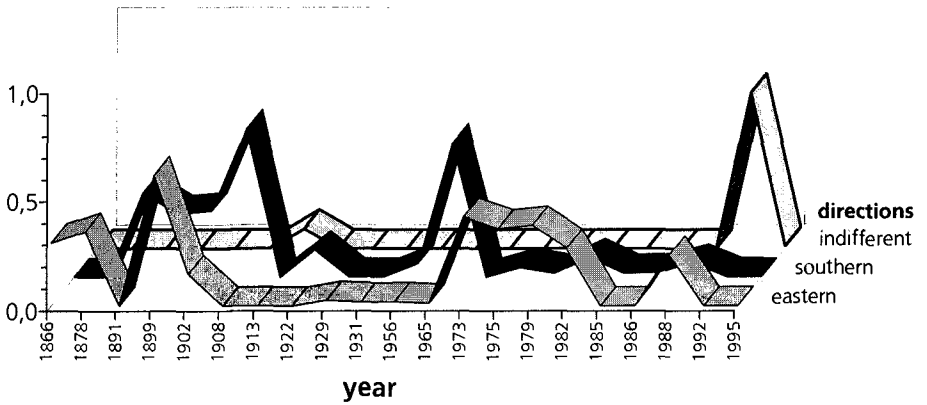

Fig. 12: Equipotential bar-area (reference level SKN) for merging downdrift foreshore bars with respect to different directions (see Fig.11)

year	profile area	nourishment volume (m^3)
1972	25 -45	550.000
1982	28 - 41	138.000 sand dam
1982	34 -34	126.000 dune fill
1982	37 - 37	7.300
1984	24 - 30	206.000 sand dam
1984	27 - 27	82.000
1987	22 - 32	560.000
1993	25 - 28	153.000
1993	41 - 41	91.000
1994	17 - 19	100.000
1994	23 - 37	460.000
1994	37 - 47	400.000

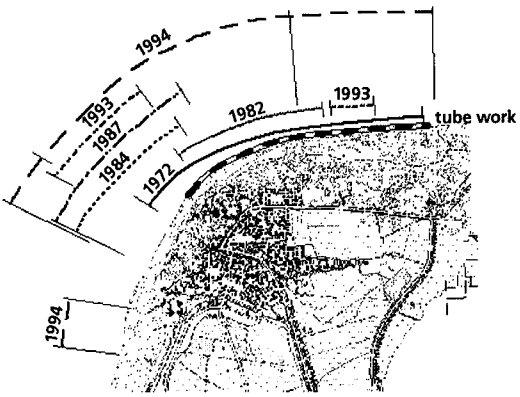

Fig. 13: Nourishment projects on Langeoog island
(Left: volumes. Right: year and location)

by 'soft' engineering means up to now because only limited periods of erosion have to be covered. Since the drastic beach and dune declines (Pirolatal from 1960 to 1970) several beach nourishment projects - functioning as sacrificial structures - have been implemented; Fig.13 shows the nourishment projects carried out on Langeoog up to now. As a further countermeasure against erosion an artificial reinforcement consisting of sandfilled plastic tubes was installed into the beach in 1972 to hold back and secure the artificially replenished sand. During distinct erosion periods the tubes become partly visible again, whereas during periods with sufficient sand supply they are covered. As an additional measure artificial sand dams were constructed in 1982 and 1984, which interrupted the current in a swash channel and thereby turned the merging downdrift bars onto the beach. Furthermore, a very endangered dune area (profile 37, see Fig.3) was reinforced by a dune-backfill in 1982 (Lüders et al. 1972, Erchinger 1986, Kunz 1987).

Barrier dunes are only expected to maintain themselves naturally in strong conditions, if the dry beach in front of them is wide enough to guarantee an aeolean sand transport for regenerational purposes. Concerning coastal defence, the fordunes must be maintained strong enough to withstand the impact of severe storm surges. Based on experience, Erchinger (1986) proposes that the distance between the NN 0m line and the mean high water line (MHWL) should be more than 90m or, alternatively, the distance from the NN 0m-line to the NN +3m-line should be more than 150m. Fig.14 applies these criteria to the time-distance-diagram of profile 39 (focusing on the period after 1960): during the erosion period between 1960 and 1970 the beach was smaller than the minimum according to the criteria. The implementation of the sand filled tubes and the beach restoration could stop the further decline of the foredunes. The several beach nourishments during periods of sediment deficiencies as well as the natural sediment supplies led to a more or less beach and dune stabilisation. Nonetheless, the periods in which the beach had a sufficient width were too short and the amount of natural sediment supply too small to initiate 'natural' dune and beach regeneration processes of a greater extent.

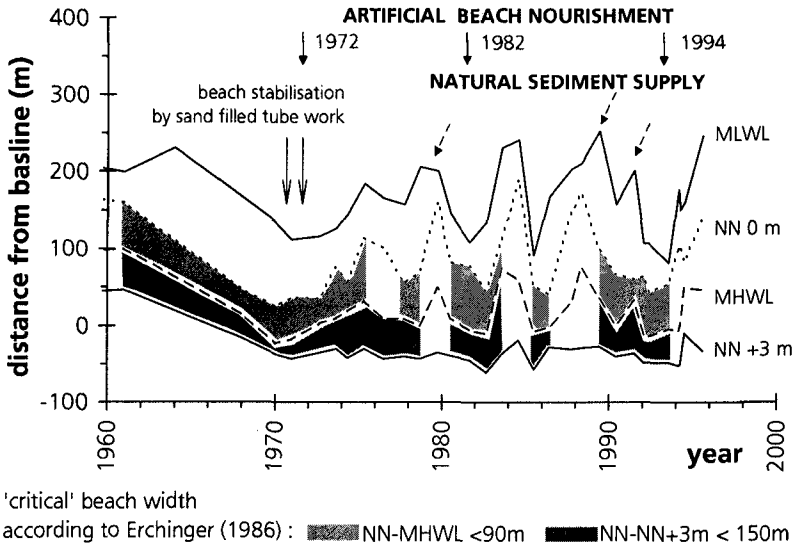

Fig. 14: Development of beach profile no.39 with nourishments and natural sand supply since the beginning of the dune erosion-period in 1960 (see also Fig.5)

Conclusions

The investigation has shown that the observed beach and dune decline in the Pirolatal-area on Langeoog island is not been caused by structural and therefore non-reversible morphological processes. The discussed development can be attributed to a temporal restricted lack of natural sediment supply caused by varying positions of the downdrift foreshore bars. However, a substantial and presumably structural morphological change revealed itself recently in the detected decrease of sediment accumulations within the ebb delta bar system. Further investigations are in progress to confirm, if there are structural changes developing within the littoral drift. If this assumption proved to be true, it is to be expected that extended beach areas of Langeoog are going to obtain comparatively smaller amounts of sand supply in the near future. Therefore, more beach nourishments will be inevitable, possibly accompanied by foreshore nourishments. A managed retreat of foredunes would provoke the opposition of the island population regarding losses of land. Furthermore, in some areas it would interfere with the existing drinking water supply out of the fresh water lense. As a preliminary answer to the problem, the most endangered parts of the foredunes were artificially reinforced at the landward side of the foredunes in 1997. By this means the capability of resistance at least for the next storm surges is guaranteed. A further beach nourishment is going to follow in 1998. The time gained by the two combined means (dune fill, beach restoration) allows further investigations of the tendencies of the natural developments and the elaboration of new concepts for engineering responses, which will include cost-benefit considerations. Up until now

the strategy for the classified protective fordunes on the German barrier islands is mainly based on the principle of 'hold the line'. Artificial beach nourishment is an effective technique but it has to be applied frequently. Also it has been proven as an effective tool to avoid conflicts with the island population concerned. In a long term perspective the possibilities of an accelerated rise of the relative sea level as well as a steepening of foreshore areas has to be taken into consideration. Concepts have to be proven and there is a need to discuss how we can proceed to more flexible responses creating a resilient shoreline by the process of an improved approach towards integrated coastal protection management.

Acknowledgement

The investigation was promoted by the regional government authority (Bezirksregierung Weser-Ems, Oldenburg) and has been carried out in close co-operation with the Lower Saxonian Local Board for Island and Coastal Protection (Staatliches Amt für Insel- und Küstenschutz, Norden) and the administration of the Authority for the National Park Wadden Sea of Lower Saxony, Wilhelmshaven.

References

Erchinger, H.F., (1986): Strandaufspülungen als aktiver Küstenschutz vor Schutzwerken und Dünen auf Norderney und Langeoog (Beach nourisments as means of active coastal protection in front of the coastal defence constructions and dunes on the islands of Norderney and Langeoog). Die Küste, vol.43, 181-205.

Homeier, H. (1956): Die Entwicklung des Westteils von Langeoog seit Beginn des 18. Jahrhunderts (The development of the western part of Langeoog island since the 18th century). Jahresber.Forschungsstelle Norderney (annual report CRS), 1955, vol.7, 38-69.

Homeier, H. & G. Luck (1971): Untersuchung morphologischer Gestaltungsvorgänge im Bereich der Accumer Ee als Grundlage für die Beurteilung der Strand- und Dünenentwicklung im Westen und Nordwesten Langeoogs (Investigation of morphological processes in the area of the tidal inlet Accumer Ee as a basis for the assessment of the beach- and dune development at the western and northwestern part of Langeoog island). Jahresber.Forschungsstelle Insel- und Küstenschutz Norderney (annual report CRS), 1970, vol. 22, 7-42.

Luck, G. (1977): Inlet changes of the East-Frisian islands. Proc. 15th Coast. Eng. Conf. (ICCE 76), Honolulu, ASCE, New York, 1938-1957.

Lüders, K., A. Führböter & W. Rodloff (1972): Neuartige Dünen- und Strandsicherung im Nordwesten der Insel Langeoog (New type of dune and beach protection at the northwestern part of Langeoog island). Die Küste, vol.23, 63-112.

Kunz, H. (1987): Shoreline protection of the East Frisian islands of Norderney and Langeoog. Proc. Fifth Symp. on Coastal a. Ocean Management (CZ '87), vol. 1, ASCE, New York, 1082-1086.

Kunz, H. (1996): Protection of the German barrier islands as part of the coastal defence system. 31st MAFF-Conference of River and Coastal Engineers, Keele, England, Proc.: 10.3.1 - 10.3.11.

Kunz, H. (1997): Groynes on the East Frisian islands: History and experiences. Proc. 25th Coastal Engin. Conf. (ICCE 96), Orlando, USA, vol. 2, ASCE. New York, 2128-2141.

Schroeder, E., R. Goldenbogen & H. Kunz (1994): Parametrization for conceptual morphodynamic models of Wadden Sea areas. Proc. 24th Coastal Engin. Conf. (ICCE 94), Kobe, Japan, vol. 3, ASCE, New York, 3251-3265.

Part V: Coastal, Estuarine, and Environmental Problems

Dredging and Reclamation Works for the Øresund Link

Installation of Environmental Monitoring Station, Øresund

INTEGRATED DESIGN OPTIMIZATION FOR A TROPICAL LAND RECLAMATION: BALI TURTLE ISLAND DEVELOPMENT

Andrew M. Driscoll[1], Tom Foster[1], Claus Pedersen[1], Palle Mikkelsen[2] and Yukimitsu Tateishi[3]

Abstract

Bali Turtle Island Development is a major tourism-related coastal development project situated in the SE corner of Bali, Indonesia. The project includes large-scale dredge-and-fill reclamation for the purpose of enlarging the existing natural island of Serangan by 3.7 km². The completed reclamation will include three artificial lagoons, four artificial pocket beaches, six artificial headlands and a causeway/bridge connection to the Balinese mainland.

This paper provides an overview of the development project as a whole, as well as describing the numerous coastal engineering and environmental investigations that have been applied in the optimization of the design. Due to the complex bathymetry and interrelated wave, flow, sedimentological and water quality mechanisms, an integrated approach for design optimization was required. The steps taken for the management of dredging operations in the vicinity of sensitive habitats are also discussed.

Site Description

The study area lies near the shallow Lombok Sill separating the Indian and Pacific Oceans (Fig. 1). Regional tidal forcing is strong and complex, with spring tidal flows in Lombok Strait exceeding 2m/s. Furthermore, net seasonal currents of ±1m/s may be present over the Lombok Sill (Murray and Arief, 1988).

The project site is the existing natural cay of Serangan (post-construction: Turtle Island). Intertidal reef flats extend seaward from Serangan, as well as from the developed beaches

[1] Coastal Engineer, Danish Hydraulic Institute, Agern Allé 5, DK-2970 Hørsholm, Denmark. Email: amd@dhi.dk.
[2] Chief Survey Engineer, Danish Hydraulic Institute, Agern Allé 5, DK-2970 Hørsholm, Denmark.
[3] Project Manager, Penta Ocean Construction Co. Ltd., Bali Project Office, Jl. Bypass Ngurah Rai No. 46XX, Denpasar, Bali, Indonesia.

of Sanur and Tg. Benoa, to the surrounding reef fringe. The reef flats feature a patchy coverage of vegetation, sand and hard material. The existing beach faces are steep (~1:10) and consist of medium to coarse coral sand. The project area has a spring tidal range of almost 3m, and is subjected to some degree of swell wave attack year-round. Coral reefs, seagrass beds and mangroves surround the project site and must not be seriously impacted by the development.

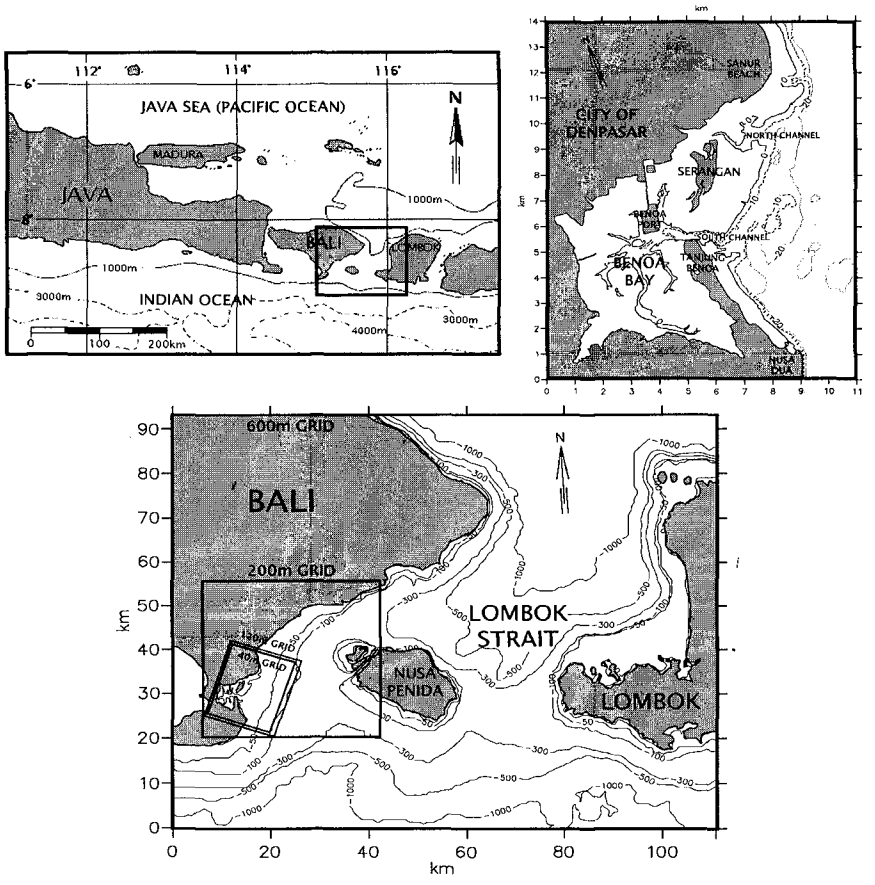

Fig. 1 *Geographical references for the study. Top left: The Indonesian Archipelago. Bottom: Bali, Lombok and the Lombok Strait. Top right: The pre-construction study area, the coverage shown is that of the local 40m model domain.*

The importance of these ecosystems is not purely aesthetic. The existing beach material consists entirely of eroded coral, and the degradation of the living corals due to increased pollution loading has resulted in a reduction in the natural production of beach material for the area. This fact, in combination with the mining of the reef crest for construction materials (thereby increasing wave exposure) has resulted in erosion problems for the beaches of the area (JICA, 1989). Furthermore, the living reef provides quality sport diving and is considered an essential recreational resource.

Project Description

With the exception of a village lying at the northern tip of the island, Serangan was undeveloped prior to 1996. The Bali Turtle Island Development project aims to establish an up-scale tourist enclave to complement those already existing at Nusa Dua and Sanur Beach. The completed project will include three artificial lagoons, four artificial pocket beaches, six artificial headlands and a causeway/bridge connection to the Balinese mainland (Fig. 2).

Both the dredging and reclamation areas lie within the intertidal zone. Dredging/reclamation activities were initiated in July 1996 and will continue into 1999. A large capacity (~20,000 m^3/day) cutter-suction dredger is being used for the work. The total reclamation area is 370ha, and the corresponding dredging volume is 20 million m^3. No significant levels of contamination have been found in the borrow material, which typically consists of 20% fine material below 63μm. All dredged material will be utilized for infilling.

The study described in this paper was divided into two phases. The first phase involved the evaluation of 8 proposed design layouts, and the making of recommendations toward the optimization of said layouts with respect to:

- Design conditions (wave, water level & current)
- Impact upon navigation
- Spreading of dredged material
- Water quality / eutrophication
- Revetment stability
- Flushing
- Sediment morphology
- Beach stability

The second phase of the study involved the management of dredging operations, such that the proposed construction activities could be performed without significantly impacting the surrounding ecosystems.

Field Campaign

An intensive survey campaign, including point measurements of water level, current, salinity, suspended and bottom sediments, and numerous water quality parameters was performed. The spatial variation of the wave- and tidally-generated flows was repeatedly

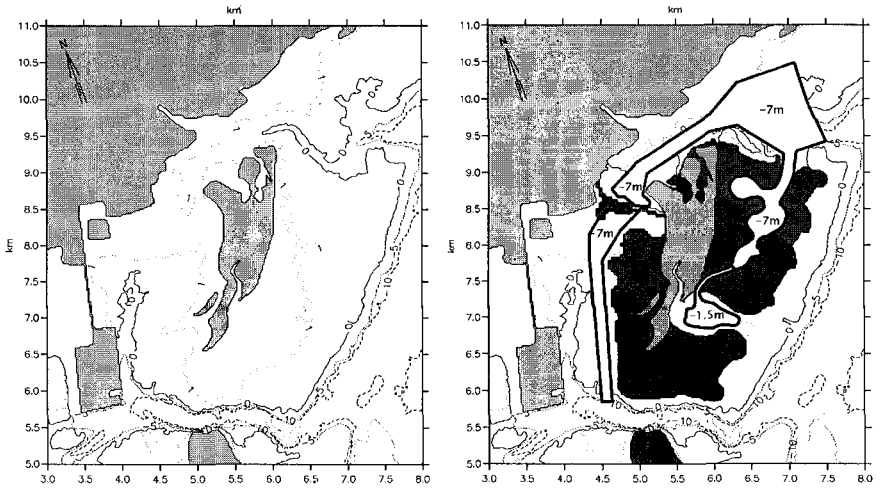

Fig. 2 *Detail of the area around Serangan / Turtle Island showing pre-construction (left) and post-construction (right) bathymetry. Reclamation areas are shaded; dredging areas outlined. Depth contours in meters to Port Datum (PD ~ LAT).*

measured in transects with a vessel-mounted ADCP. Fig. 3 shows the coverage of the ADCP transects, as well as the locations of CTD and suspended sediment profiling. The measurement locations for fresh water inflow / nutrient loadings are also shown.

Numerical Wave Modelling

Waves generated locally due to winds over Lombok Straits were determined using the simple hindcasting model PWAVE (after Hawkes, 1988). The offshore swell wave climate was determined from acquired global spectral ocean wave modelling data (Clancy et al., 1986), verified against satellite measurements, and then transformed to five locations just outside the reef using the parameterized wave action model MIKE21 NSW (after Holthuijsen et al., 1989). Detailed local wave simulations were performed using the same model. The wave transformations occurring on the reef slope and reef flats were tuned in the numerical model to be consistent with the physical modelling results discussed below, as well as with nearby field measurements (Sulaiman et al., 1994, see Fig. 3).

Physical Wave Modelling

An undistorted 1:40 scale 3D physical model was created for the purposes of (a) providing calibration data for numerical modelling of wave transformations across the reef slope, crest

and flats, (b) providing design wave data for the development frontage, and (c) optimizing revetment design with respect to overtopping and stability. This portion of the study is described in an accompanying ICCE '98 paper (Jensen et al., 1998).

Hydrodynamic Modelling

Regional and local high-resolution hydrodynamic modelling was performed in 2DH using the model system MIKE21 HD (Abbott et al., 1981; Warren and Bach, 1992). A regional tidal model, driven by tidal constituents and supported by predictions from a global tidal model (Eanes and Bettadpur, 1995), was established. The regional model, in which net seasonal flows were also present, included a dynamic nesting of two Cartesian model domains of 600m and 200m resolution (Fig. 1). An M_2 constituent co-amplitude plot from a tide-only regional model simulation is shown in Fig. 5. It is seen that there is a strong attenuation of the semidiurnal signal from south to north in the Lombok Straits.

The results of the regional tidal model were then used to provide boundary conditions to drive a local hydrodynamic model, which consists of a second pair of dynamically nested Cartesian grids with resolutions of 120m and 40m (Fig. 1). An excellent calibration was achieved through comparison with the ADCP transects and stationary profiles (Fig. 6).

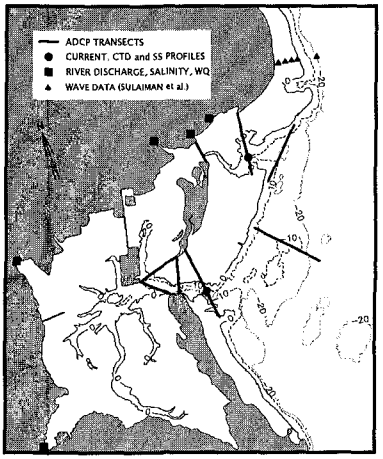

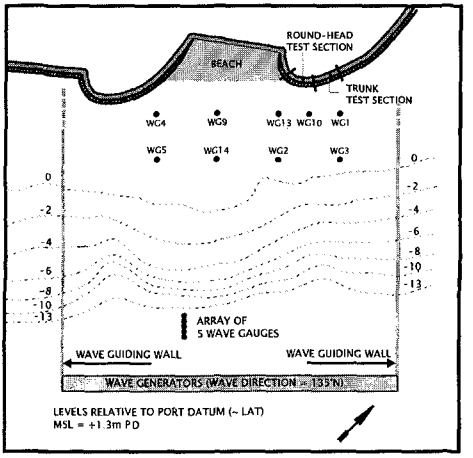

Fig. 3 (left) *Coverage of local field campaign. Extensive grab, suspended and water quality sampling omitted for brevity.*

Fig. 4 (right) *Setup of the 3D physical model, which covers a 1200m x 1200m section of the seaward face of the design.*

The water level gradients and strong tidal flow velocities in the Lombok Strait are seen to have a significant influence on the project area, even inshore of the reef crest. As a result of the strong attenuation of the tidal signal from south to north, at times which would normally be considered "high water slack" there exists a significant offshore forcing which drives a northward flow both on the reef flats and in the channel between Turtle Island and the Balinese mainland. A complimentary offshore gradient exists toward south during "low water slack". However, this southward forcing is inconsequential in the pre-construction layout as the area is largely dry at low water. The result is a tidally-forced net northward drift which, although small, has a large influence on the flushing response of the design layouts. This net drift is eliminated in the channel west of Turtle Island in the design layouts, as a deep channel will be present there even at LAT. However, net northward flows will still be present on the seaward side of the island and can be used to enhance the flushing response of the design. It can thus be concluded that a comprehensive regional modelling approach is essential for resolving the local flow conditions in this complex area.

Additional sensitivity tests performed with the local hydrodynamic model showed that wave-induced circulation was also significant on the reef flats. Waves effect the nearshore hydrodynamics by continuously pumping water shoreward over the reef crest due to the breaking and corresponding setup which occurs on the reef slope. The result is a net flow of water onto the reef flats from offshore, which in turn drives a return flow seaward through the North and South Channels. As this circulation is forced primarily by the cross-shore gradient in momentum transfer due to wave breaking, it is present even for waves of normal incidence. This mechanism, also observed during the field campaign, is clearly of great significance in the spreading of dredging spill during the construction phase.

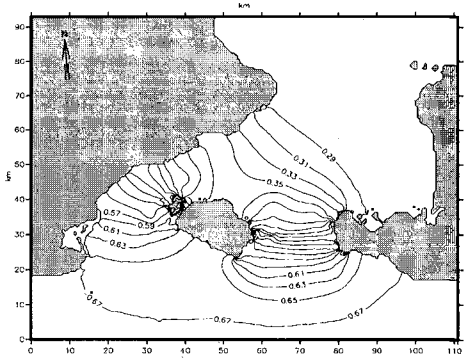

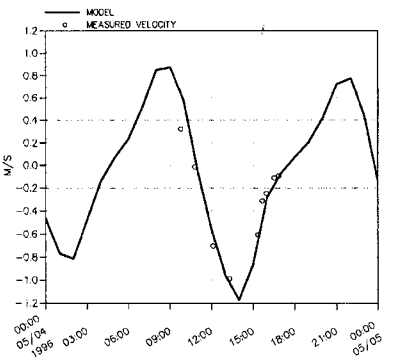

Fig. 5 (left) *Co-amplitude map extracted from the regional tidal model for the principle semidiurnal constituent M_2. Contours in meters.*

Fig. 6 (right) *Comparison of current speed from local hydrodynamic model vs. depth-average of measured current profiles in South Channel during spring tide.*

Flushing Modelling

The water quality in any semi-enclosed area is a function of the pollutant load and the time required for the resident water to be exchanged with unpolluted water from outside. For unchanged pollution loadings, the flushing response of a given layout relative to pre-construction provides a reliable indication of whether water quality problems are to be expected for the design. Two-dimensional advection-dispersion modelling was performed in the local nested 120m/40m model areas to evaluate the impact of various designs on the flushing regime. The model applied was MIKE21 AD (Ekebjærg and Justesen, 1991), which is coupled with the local hydrodynamic model discussed above. The dispersion coefficients applied in the model were verified by accurately reproducing the dynamic salinity distribution in Benoa Bay and the waters surrounding Serangan, balancing the measured fresh water inflow with the mixing processes occurring throughout the area.

The flushing simulations were performed by initializing the calibrated advection-dispersion model with a conservative "tracer" concentration of unity in all areas inshore of the reef fringe. The remaining offshore areas, as well as the offshore boundary conditions, were set to a concentration of zero. The time required for the tracer concentration to be reduced in a given area then gives an indication of the water residence time for a given layout. Fig. 7 shows the tracer concentration remaining after 3 days for

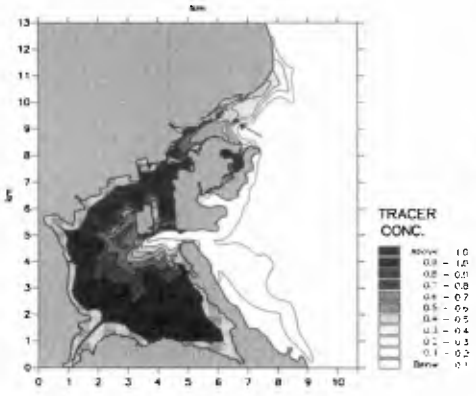

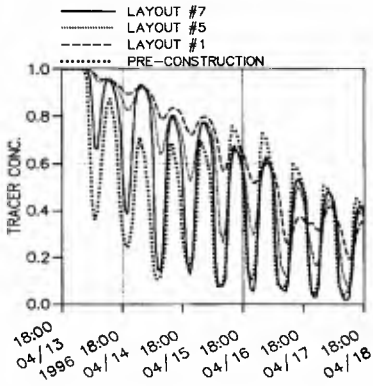

Fig. 7 (left) *Sample flushing results: map of tracer concentration at mean high water after 3 simulation days from advection-dispersion model. Darker areas imply longer retention times. Shaded edges of Benoa Bay denote dried water points.*

Fig. 8 (right) *Extracted time series of tracer concentrations from the same location (marked in Fig. 7) in the primary borrow area for 3 design layouts as well as pre-construction.*

the final layout. Fig. 8 shows extracted time series of tracer concentrations at a point in the primary borrow area, clearly indicating that at this location Layout #7 provides the best flushing, responding comparably to pre-construction.

Eutrophication Modelling

In addition to the flushing evaluation, a full 2D eutrophication model was established to gauge the effect of both the proposed development and increased loadings due to future population growth on the water quality around Turtle Island. The model applied was MIKE21 EU (Bach et al., 1990), which is also coupled with the previously established hydrodynamic model.

The eutrophication model describes the condition in the model area by using a number of state variables including carbon, nitrogen and phosphorus in phytoplankton, zooplankton, detritus and benthic vegetation and, with regard to nitrogen and phosphorus, also the dissolved form in the water. The model describes the seasonal and spatial variations of the interrelated state variables. The effect of dredging plumes was included by inputting construction-induced suspended sediment plumes calculated via the mud transport modelling described below.

Modelling of Littoral Processes

The longshore sediment budget for the study area was calculated using the process-based 1D model LITDRIFT (Deigaard et al., 1988), valid for arbitrary profile shapes. Wave transformations over the reef were calibrated versus the physical modelling results and field measurements (Sulaiman et al., 1994). Sediment recharge requirements were calculated for the pocket beaches fronting the development using the combined results of LITDRIFT, the 2D sediment transport model MIKE21 ST (Deigaard et al., 1986) and the 1D profile development model LITPROF (Hedegaard et al., 1991).

Not surprisingly, waves and water levels were found to be equally dominant factors in the longshore transport climate. Transport was found to be negligible for water levels below MSL (+1.3m PD). An excerpt of the four years' hindcast longshore transport rates is shown in Fig. 9, plotted along with the mean water level variation for the same period. The longshore transport as plotted is for the swell component of the wave climate only, which induces a drift which is almost exclusively northward. A separate transport calculation was made for the waves generated locally by winds over Lombok Strait, which contribute a smaller but significant net southerly drift.

The seaward reclamation limit of the completed project lies within 200m of the fringe of the surrounding reef, whereas the pre-construction beachface on Serangan was approximately 2km from the reef fringe. The reef flats act to dissipate wave energy through bed friction, enhanced by the locally irregular and vegetated bed. The post-construction beach face thus

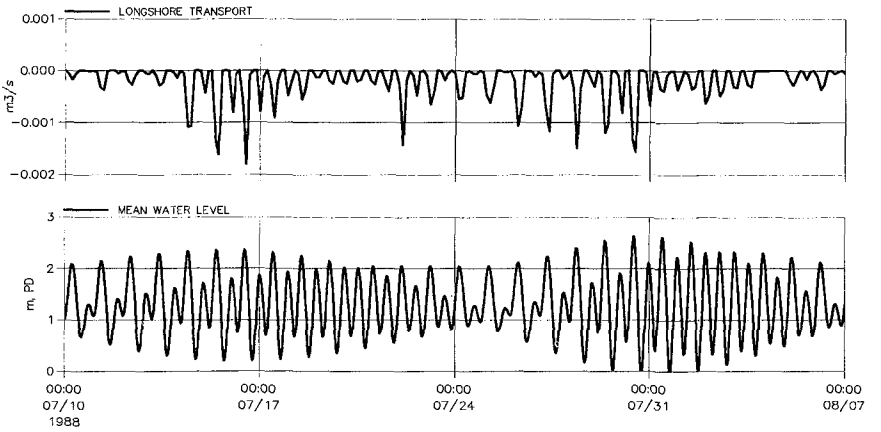

Fig. 9 *One-month excerpt from the 4 years' calculated longshore transport climate on the seaward face of Serangan (pre-construction, negative northward), along with the simultaneous mean water level.*

feels a significantly stronger local wave climate than was present on Serangan prior to construction. This is illustrated in Fig. 10, which compares the profiles, wave attenuation and net sediment transport calculated via LITDRIFT for pre- and post-construction profiles extracted across the seaward face of Serangan. This increase in net annual longshore drift demands both a rotation of the post-construction beaches and an increase in compartmentalization through the introduction of protective headlands in order to keep fill losses and seasonal beach rotations within acceptable limits.

Feedback Monitoring of Construction Activities

The scale of the dredging operations required for Turtle Island, in combination with the high content of fines in the borrow material and close proximity of sensitive habitats, dictates that the construction activities must be carefully managed to avoid serious environmental impact. Tools normally used for such a situation include (a) spill fate modelling performed prior to construction, or (b) biological monitoring of the status of the habitats during the construction process. The novel approach of *feedback monitoring* (Grey and Jensen, 1993; Bach et al., 1997) has been applied in the present study. On the simplest level, feedback monitoring can be described as an orchestrated joint application of spill fate modelling and biological monitoring. The strategy embraces four components:

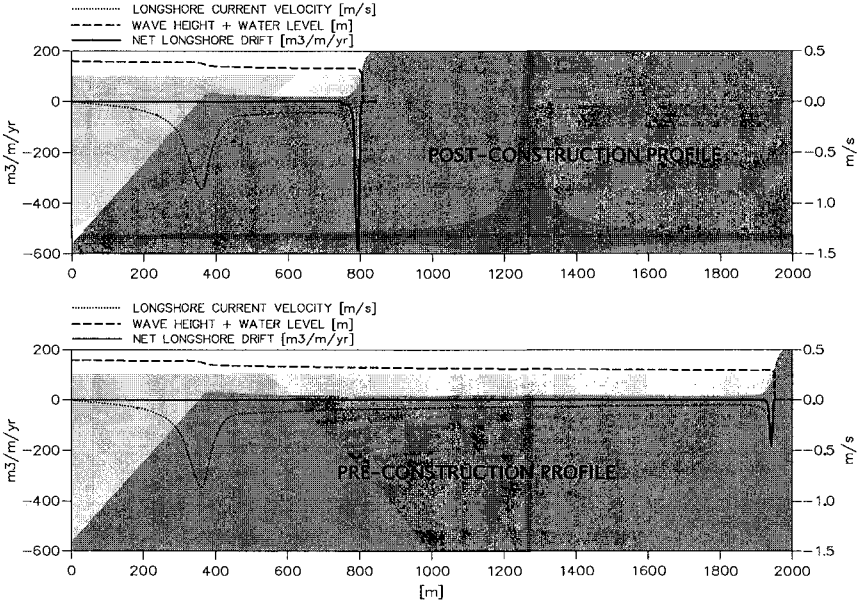

Fig. 10 *Comparison of pre-and post-construction profiles, wave attenuation and net longshore drift. Wave height and water level shown are instantaneous values (offshore: H_{rms} = 1.5m, T_z = 6s, dir = 145°, WL = +2.5m PD), whereas the net longshore drift shown is the annual rate. While the greatest transport potential is seen to lie just offshore of the reef crest, this portion of the profile has been rendered inactive in the model due to the lack of mobile sediment in these areas.*

1) Careful planning using numerical models to avoid unnecessary environmental damage by forecasting the effects of possible sediment spills. This is performed at the planning stage of the project.
2) Medium-term spill forecast modelling throughout the construction process, such that the potential environmental impact can be assessed on the basis of detailed dredging schedules for the forecast period. This allows the formulation and testing of mitigating actions if the predicted impact exceeds certain pre-defined limits.
3) On-site monitoring of selected key species and variables -- in the case of Turtle Island seagrasses, corals and mangroves -- to provide a direct indication of the impact upon the habitats and to provide feedback based on the impact criterion used in processing the results of the spill forecast modelling.

4) Updating the net environmental impact assessment by performing numerical model hindcasts on the basis of the *actual* achieved dredging schedule (as opposed to the predicted schedule assumed in 2 above) and the results of the biological monitoring of the selected species.

Feedback monitoring is in many ways a union stronger than the sum of its parts. Initial spill forecasting can be used to more efficiently design the scope of the biological monitoring so that energy can be focused on the areas of most likely impact. Furthermore, as numerical spill fate modelling greatly increases the understanding of the local sedimentation processes, the results of the spill hindcasting allow for a much more definitive interpretation of the results of the biological monitoring.

The application of feedback monitoring to Turtle Island is described in detail elsewhere (Driscoll et al., 1997), but is summarized here. A two-month repeat cycle was prescribed for the Turtle Island feedback monitoring. Thus, every two months the contractor provided a detailed plan of upcoming dredging operations (dredger locations and schedules, as well as outlet pipe locations and settling pond configurations). This information was combined with tidal predictions and typical seasonal values of wind, offshore net flows, and waves to produce a 2-month forecast of dredging spill to evaluate the impact of upcoming construction tasks. Parallel data was provided by the contractor documenting the actual realized dredging operations achieved in the prior two months. This historical information was merged with the available hydrographic data to construct a detailed 2 month hindcast of the most recent dredging operations. Two-monthly biological monitoring campaigns were then performed, with the hindcast results being utilized for the purpose of verifying causality in any observed impact to the habitats.

Spill fate modelling was performed using the Eulerian 2D model MIKE21 MT (Johnsen and Warren, 1993, with subsequent improvements) which describes cohesive sediment transport processes under combined current and waves. The spill model was coupled with the previously established local hydrodynamic and wave models, so that the effects of wave-generated currents and setup were included both with regard to physical forcing and sedimentation. The model was calibrated based upon daily measurements of suspended sediment concentrations at fixed stations throughout the area. Output consisted of time-varying maps of suspended concentration and net deposition/erosion. These outputs were then processed to provide maps of parameters useful for quantifying biological impacts, such as light attenuation at the seabed due to plume shading, daily exceedances of threshold deposition rates, etc. This approach allows for the proper consideration of environmentally positive steps such as timing high-spill activities during hours of darkness, when plume shading has no effect on light-sensitive organisms. A comparison of % light reduction at the bed is given in Fig. 11 for two spill hindcast periods, showing the improved environmental loading in the latter period.

The complimentary biological monitoring took the form of two-monthly surveys covering 5 to 6 stations each for coral, seagrass and mangroves. For each habitat, the focus was placed on the detailed monitoring of quantifiable variables rather than qualitative observations. For corals, variables included % coral coverage along fixed transects, recolonization rates, and measured growth rates of resident and transplanted specimens for the dominant species *Acropora sp.* Table 1 below shows the change in observed coral growth rates between two survey campaigns. These time periods may be compared directly to the spill hindcast periods shown in Fig. 11. A strong correlation is seen between modelled loading and observed impact. It should be noted that, while temporary reductions in growth rates were observed in the corals, the loadings were found to be sub-lethal.

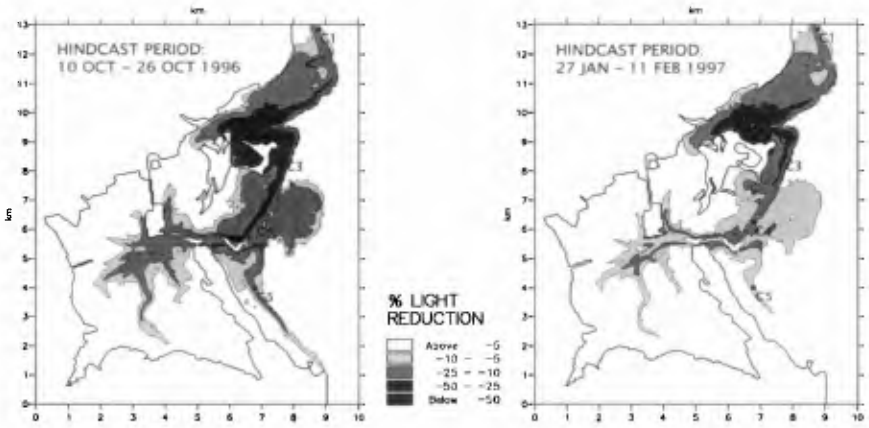

Fig. 11 *Results from two spill hindcast periods shown in terms of % light reduction at the bed. Depths > 20m are not plotted. Coral monitoring stations C1 through C5 also shown.*

Period	Max. growth rate of *Acropora sp.* (mm/month)*				
	station C1	station C3	station C4	Station C5	mean
Oct 96 - Dec 96	3.9	2.3	2.7	4.9	3.5
Dec 96 - Feb 97	5.5	7.6	8.5	8.7	7.6

Table 1 *Measured coral growth rates, based upon the results of the Oct. 1996, Dec. 1996 and Feb. 1997 biological monitoring surveys. (Station C2 omitted due to insufficient data coverage).*

Summary of Conclusions

The integrated hydraulic and environmental design evaluation for the Bali Turtle Island Development project resulted in (a) a detailed description of the complex physical and biological environment surrounding the site, (b) an accurate description of how the development will impact that environment, and (c) recommended modifications to improve the design in light of these findings. A summary of the conclusions is presented in the following:

The preliminary revetment design was found to be inadequate with respect to both the overtopping and stability criteria. Larger stone sizes and increases in revetment crest height and width were recommended.

The optimized development was shown to have a beneficial effect on navigation, slightly reducing the peak tidal current velocities in the South Channel. No areas of notable current intensification due to the development were found, with the exception of the channel beneath the causeway bridge which will see typical spring flows of 0.9m/s. Net tidal circulations were found to exist around Turtle Island. This tidal forcing has been utilized to optimize the flushing response of the design.

The flushing response around Turtle Island was optimized such that the final design shows either no change or a modest improvement in residence time for much of the area relative to pre-construction.

Due to the presence of the shallow reef flats between the reclamation and the reef crest, the wave climate and resulting littoral transport at the beach face was shown to be dominated by the water level. Waves attacking during water level below MSL produced negligible transport due to nearly complete attenuation over the reef crest and reef flat. Beach material losses for the optimized layout were within acceptable limits.

Feedback monitoring of the dredging operations was initiated to safeguard the habitats during the construction phase.

The results of the performed study have proven the benefits of integrating state of the art numerical modelling tools, supported by physical modelling and biological monitoring, for both the hydraulic / environmental optimization of the design and for feedback monitoring of the actual construction sequence.

Acknowledgement

This work was carried out under contract from Penta Ocean Construction Co. Ltd. on behalf of Pt. Bali Turtle Island Development (BTID).

References

Abbott, M.B., A. McCowan and I.R. Warren (1981). Numerical modelling of free surface flows that are two-dimensional in plan. *Transport Models for Inland and Coastal Waters*, Academic Press, pp-222-283.

Bach, H.K., K. Jensen and J.E. Lyngby (1997). Management of marine construction works using ecological modelling. *Estuarine, Coastal and Shelf Science*, Vol. 44, pp. 3-14.

Clancy, R.M., J.E. Kaital and L.F. Zambi (1986). The fleet numerical oceanography center global spectral ocean wave model. *Bulletin of the American Meteorological Society*, Vol. 67, No. 5.

Deigaard, R., J. Fredsøe and I.B. Hedegaard (1986). "Suspended sediment in the surf zone". *J. of Waterway, Port, Coast and Ocean Eng.*, ASCE, Vol. 112, No. 1, pp.115-128.

Deigaard, R., J. Fredsøe, I.B. Hedegaard, J. Zyserman and O.H. Andersen (1988). "Littoral drift model for natural environments". Proc. of 21st ICCE, Malaga.

Driscoll, A.M., T. Foster, P. Rand and Y. Tateishi (1997). Environmental modelling and management of marine construction works in a tropical environment. Proc. of 2nd Asian and Australasian Ports and Harbours Conference, Eastern Dredging Association.

Eanes, R. and S. Bettadpur (1995). The CSR 3.0 Global Tidal Ocean Tide Model. Center for Space Research Tech. Memorandum CSR-TM-95-06, Univ. of Texas.

Ekebjærg, L.C. and P. Justesen (1991). An explicit scheme for advection-diffusion modelling in two dimensions. *Computer Methods in Applied Mechanics and Engineering*, Vol. 88, No. 3.

Grey, J.S. and K. Jensen (1993). Feedback monitoring: A new way of protecting the environment. *Trends in Ecology and Evolution*, 8: 267-305.

Hawkes, P.J. (1988). A wave hindcasting model. *Advances in Underwater Technology; Ocean Science & Offshore Engineering*, Vol. 12.

Hedegaard, I.B., R. Deigaard and J. Fredsøe (1991). Onshore/offshore sediment transport and morphological modelling of coastal profiles. Proc. of Coastal Sediments '91, ASCE, Seattle, pp. 643-657.

Holthuijsen, L.H., N. Booij and T.H.C. Herbers (1989). A prediction model for stationary, short-crested waves in shallow water with ambient currents. *Coastal Engineering*, **13**, pp. 23-54.

Japan International Cooperation Agency (1989): The feasibility study on the urgent Bali beach conservation. Report for the Republic of Indonesia.

Jensen, T., P. Sloth and V. Jacobsen (1998). Wave dynamics and revetment design on a natural reef, Proc. of the 26th ICCE, Copenhagen.

Murray, S.P. and D. Arief (1988). "Throughflow into the Indian Ocean through the Lombok Strait, January 1985-January 1986". *Nature*, Vol. 333.

Sulaiman, D.M., S. Tsutsui, H. Yoshioka, T. Yamashita, S. Oshhiro and Y. Tsuchiya (1994). "Prediction of the maximum wave on the coral flat". Proc. of the 24th ICCE.

Warren, I.R. and H.K. Bach (1992). MIKE21: a modelling system for estuaries, coastal waters and seas. *Environmental Software*, **7**, pp. 229-240, Elsevier Publishers Ltd.

The influence of Marina Construction in Beach Stability: El Milagro Case Study

J. Galofré [1], F. J. Montoya [2] and R. Medina [3]

Abstract

The analysis of the behaviour of a beach, after the construction of a marina at one of its side, is made in this paper. El Milagro Beach, Tarragona, (Spain) is a 1.5 km long sandy beach. Two nourishment works were carried out along the beach, the first in 1986 and the second in 1993. Eleven surveys have been carried out since 1986. A marina was constructed in 1995. From the monitoring program, the shoreline evolution and profile changes have been determined before an after marina construction. It is concluded that the construction of the marina changed the beach stability.

Introduction

El Milagro Beach is located close to Tarragona, a city 100 km south of Barcelona, on the Catalonian coast, Spain. It is a 1.5 km long beach located between El Milagro Cape, on the east, and Tarragona Harbour breakwater, on the west. Figure 1 shows a location map. This paper analyses the nourishment projects carried out at the beach since 1986 by means of the morphologic data taken in two monitoring programs. The effect of a marina construction on the beach stability is also studied. Finally a set of conclusions will be made in order to understand beach behaviour and evolution.

[1]Coastal Civil Engineer. Tarragona Coastal Service. Environment Ministry. Pl.Imperial Tarraco 4-4ª. 43005 Tarragona, Spain.

[2]Coastal Civil Engineer. Head of Tarragona Coastal Service. Environment Ministry. Pl. Imperial Tarraco 4-4ª. 43005 Tarragona, Spain.

[3]Associated professor. Ocean & Coastal Research Group. Universidad de Cantabria. Avda. de los Castros s/n. Santander 39005. Spain.

Description

Morphology:

This is a half opened beach located between El Milagro cape, on the east, and Tarragona harbour breakwater, on the west, whose end reach more than 20 m depth. The native sand had a mean diameter D_{50} = 0.25 mm and the borrowed sand had D_{50} = 0.6 mm. The submerged bottom slope, from the shoreline to bathimetric -5.0 m, changes from 1.5% on the east, near the El Milagro cape, to 3.0% on the west, near the Harbour breakwater. The last feature has an important relevance on beach behaviour and affects beach stability. The value of bathymetric -5.0 is considered the profile closure depth.

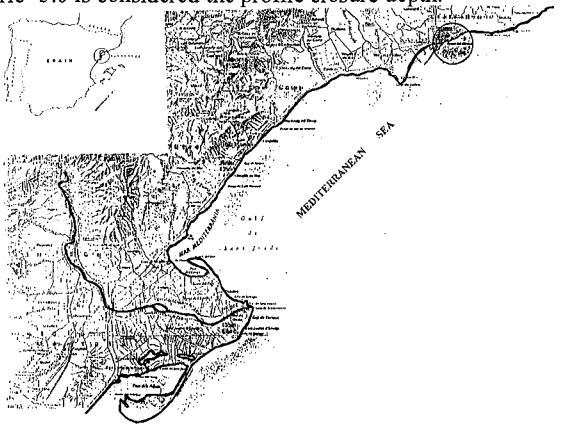

Figure 1.- Site location map.

Historical review

This beach has been noticed from Roman Times more than twenty centuries ago. This beach was graphed in several maps on the nineteen century. That means that the beach has been stable for a long time. The most recently changes are due to the human actuation from 1986 to now. On table 1 a resume of historical evolution and beach characteristics changes along the time is made

Beach nourishment projects

In 1986 a beach nourishment project was carried out with a 140.000 m^3 of borrowed sand. In 1993 a new nourishment work was carried out with a 165.000 m^3 of borrowed sand. The mean diameter of the sand was 0.6 mm. The

nourishment works were carried out because of the beach area reduction. This reduction is mainly due to the decrease of the sediment supply brought by the stream located in the middle of the beach. This has been theorised as a major factor in the erosion that has been witnesses in El Milagro beach.

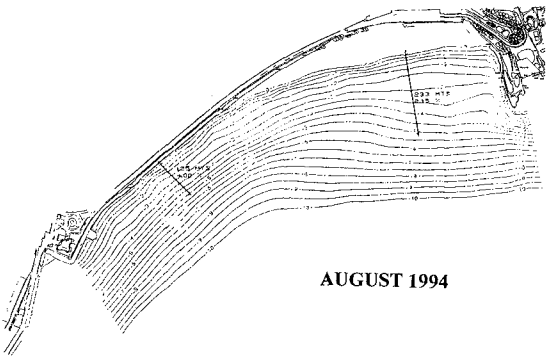

Figure 2.- Bathymetric map before marina construction.

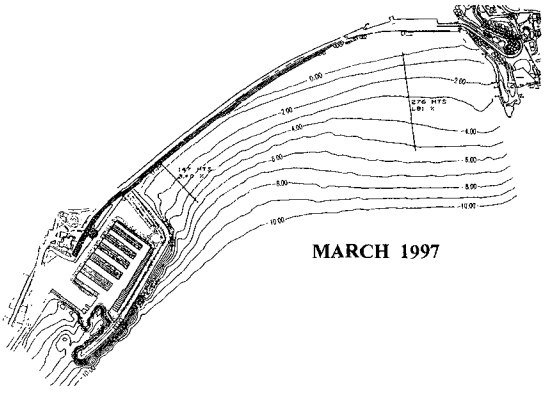

Figure 3.- Bathymetric map after marina construction.

Marina construction

In 1995 a marina was built in the West Side, near the harbour breakwater. Its breakwater reaches the bathymetric -10 m and it is a total barrier to the longshore transport. This marina changed the beach behaviour as it can be seen in

the next paragraphs. Figures 2 and 3 show the bathymetric maps before and after marina construction.

Monitoring program

Two monitoring programs were carried out, one from the first nourishment project to 1993, six bathymetric surveys were made: jun-86, mar-87, sep-87, oct-88, jan-88, nov-93. The other one from the second nourishment work to 1997, seven bathymetric surveys were made: aug-94, jun-95, feb-96, apr-96, oct-96, mar-97, nov-97. The data from the monitoring program can be used in order to evaluated the changes produced by the marina construction in 1995.

Wave climate

There are two predominant directions of wave approach: SW and E. More than three-quarter of deep-water waves approach El Milagro beach from those sectors. The annual average significant wave height is about 0.5 m with typical winter storm waves of H_s of about 3.0 m. Tides at El Milagro are negligible. In figure 4 a visual wave distribution is made and the affected area is show, wave limits are defined before and after marina construction. The north limit is the same in both cases but the south limit changes with the marina construction, and the energy resultant is different.

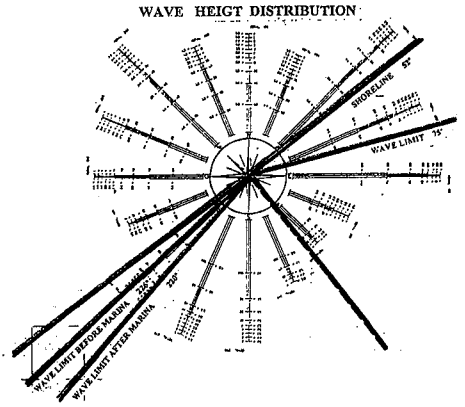

Figure 4.- Wave climatic

In order to understand beach behaviour qualitative and quantitative models have been run. Longshore currents have been obtained with different wave hypothesis, in order to analyse the influence of the marina in coastal dynamics, that are responsible of beach stability. Qualitative results have been obtained studying beach wave climatic and comparing with aerial pictures and topobathymetrics. Wave propagation and wave driven current models have been used considering pre and post marina construction behaviour. Different wave heights, periods and directions were used applying the REFDIF and COPLA programs computed by the parabolic wave propagation model that combines refraction and diffraction phenomena. Figures 5, 6, 7 and 8 shows the wave induced currents determined from the wave field, before and after marina construction considering different wave hypothesis, from the east and from the south-west approach deep water angles. The wave height considered was 1.0 m and the angle approach was +/- 45°. The object of these numerical models is to help to understand the beach behaviour from different hypothesis of wave climatic. It is not a real situation but it can be inferred from them the answer of the beach in these cases.

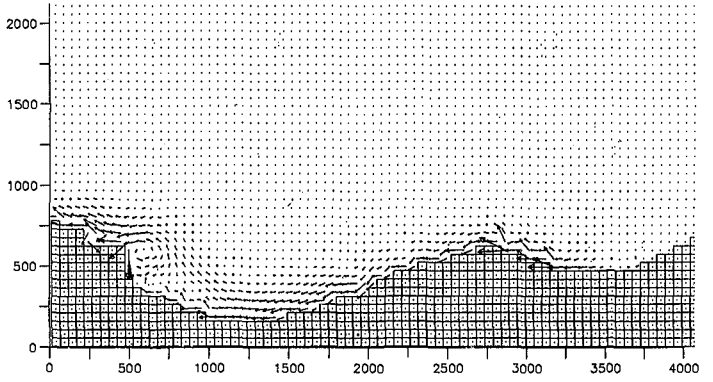

Figure 5.- Wave induced currents before marina construction, H =1.0 m, α = -45°, T = 10 s.

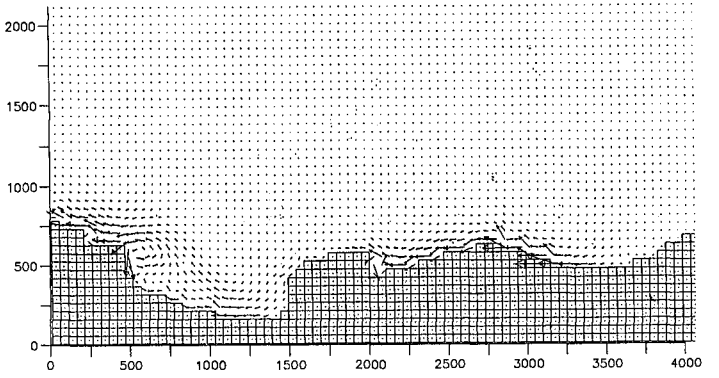

Figure 6.- Wave induced currents after marina construction, H =1.0 m, α = -45°, T = 10 s.

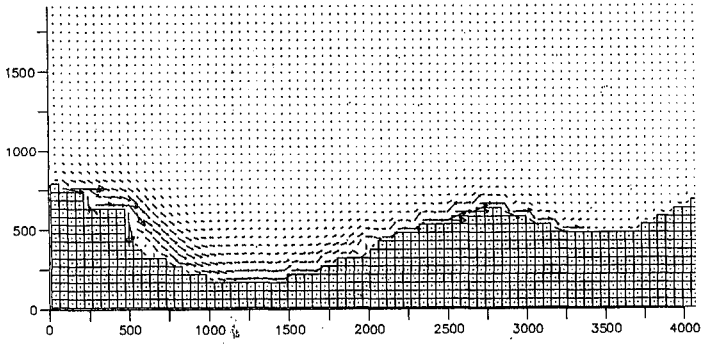

Figure 7.- Wave induced currents before marina construction, H =1.0 m, α = +45°, T = 10 s.

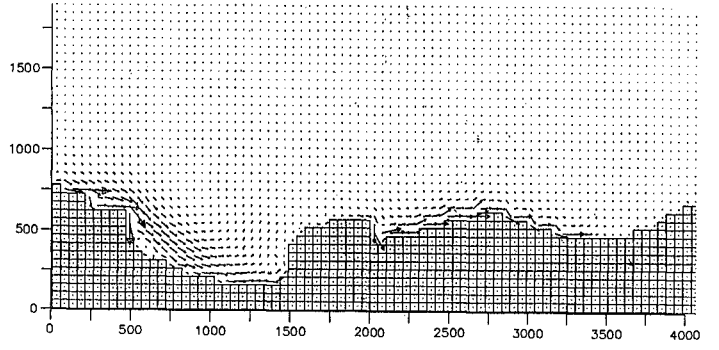

Figure 8.- Wave induced currents after marina construction, H =1.0 m, α = +45°, T = 10 s.

It can be seen that the breaking wave induced currents direction decrease in the boundary of marina. It means that the sand in the west part of the marina is retained and accumulates in this area. The storms from the Southeast transport the sand to this area and the storms from the Southwest part can not return the sand to the beach, the dynamics in the area change the behaviour of the beach. Figures 9 and 10 shows the qualitative behaviour of the beach before and after the marina construction deduced from the wave climate models.

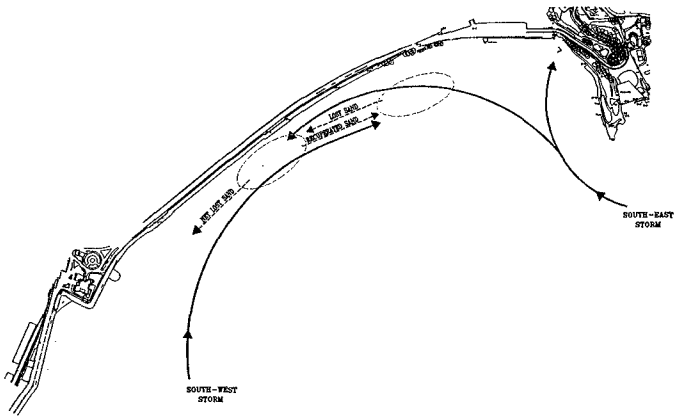

Figure 9.- Beach analysis before marina construction.

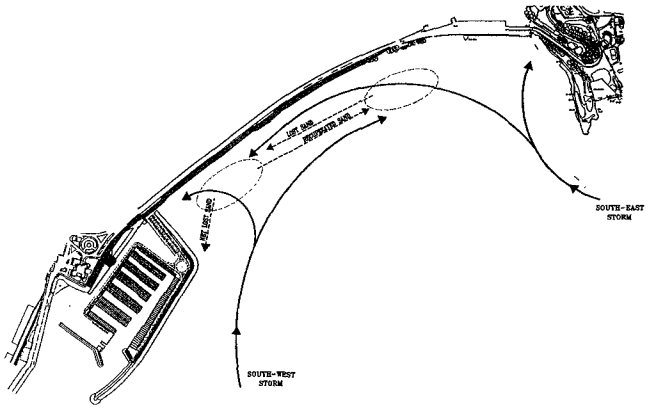

Figure 10.- Beach analysis after marina construction.

The recuperated sand, from the Southwest storms is minor after the marina construction than before, this sand is accumulated on the shadow area of the marina.

Morphodynamics

Topobathymetric data are a good information in order to analyse morphodynamic characteristics, to understand beach behaviour and to predict beach evolution. Shoreline evolution, planform analysis, longshore transport and profile analysis must be studied in this section.

Date	Beach Characteristic	Beach area (m^2)	A_i/A_1	Sand volume lost/win (m^3)	Transport ratio (m^3/year)	Grain size (mm)
jun-86	monitoring	15.069				0.2
nov-86	nourishment			+140.000		
jan-87	works			(5.8 m^3/m^2)		0.8
mar-87	monitoring	39.200	1.00			
sep-87	monitoring	33.085	0.84	-35.067	70.934	
oct-87	monitoring	27.170	0.69	-69.774	119.613	
jan-88	monitoring	31.299	0.80	-45.826	54.991	
nov-93	monitoring	23.596	0.60	-90.503	13.575	0.6-0.2
jan-94	nourishment			+165.000		
may-94	works			(6.8 m^3/m^2)		0.8
aug-94	monitoring	47.942	1.00			0.8-0.2
sep-94	marina					
may-95	construction					
jun-95	monitoring	45.784	0.95	-11.621	13.945	
feb-96	monitoring	45.952	0.96	-13.538	9.026	0.6-0.2
apr-96	monitoring	41.99	0.88	-40.412	24.247	0.6-0.2
oct-96	monitoring	40.113	0.84	-53.244	24.574	0.6-0.2
mar-97	monitoring	39.800	0.83	-55.366	21.432	0.6-0.2
nov-97	monitoring	36156	0.75	-80.145	24659	0.6-0.2

Table 1. Historical beach evolution

On Table 1 a summary of events that have incidence on beach performance is shown. The most representative dates of beach incidences can be found in it. That includes: beach characteristics (including beach monitoring surveys and beach nourishment works and marina construction); beach area evolution measuring beach surface from the shoreline to landward limits; sand volume lost/won (lost between monitoring surveys comparing the areas in each

monitoring with the first one after nourishment works and win from filling projects); longshore transport ratio deduced from the data obtained before and the grain size characteristic,

Figure 11 shows shoreline evolution taken from the most representative topobathymetric surveys, it is shown five shoreline position (jun-86, jan-88, nov-93, aug-94, mar-97) from the twelve it were taken. They represent the most significant date on beach behaviour the first one in before the first nourishment work, the second is after this works, the third is before the second nourishment works, the forth is after this works and before the marina construction and the fifth is after marina construction.

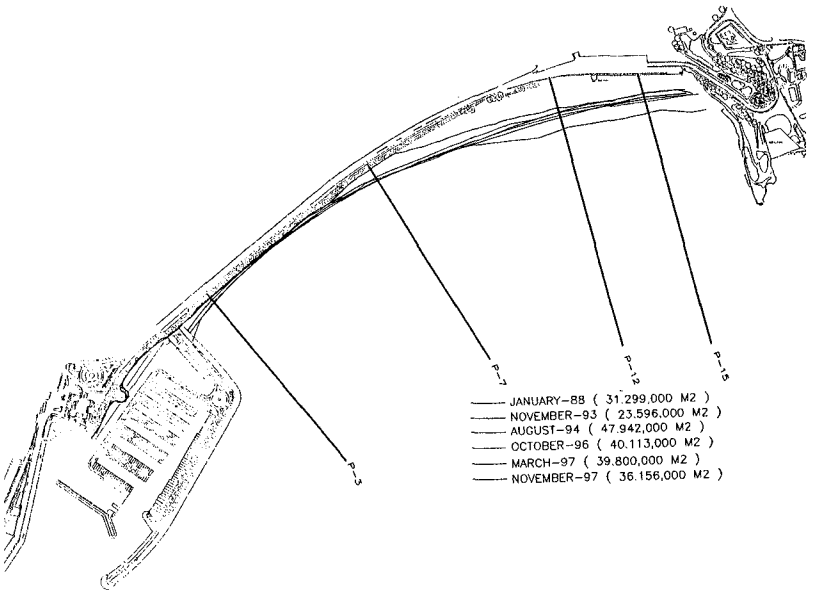

Figure 11.- Shoreline evolution from jun-86 to nov-97

In Figure 12 the analysis of beach area evolution is made. It is compared the relation between the relation Ai / A_1, where A_i is the area corresponding to the i topobathymetric survey and A_1 is the corresponding to the post nourishment work, to the time. The figure shows the evolution before and after marina

construction, A_1 in the first case correspond to march-87 and in the second case august-94. It can be inferred from this that comparing the graphic the medium slope is bigger after than before marina construction. It means that the erosion ratio, in El Milagro Beach, has been increasing since marina construction. A new beach appeared on the protected marina area, it is difficult to infer from the actual data about its stability, some consideration to profile slope must be considered in this analysis. The longshore transport calculated according with the field data surveys of the monitoring programs changes from 13.000 m^3 before marina construction to 24.000 m^3 after marina construction.

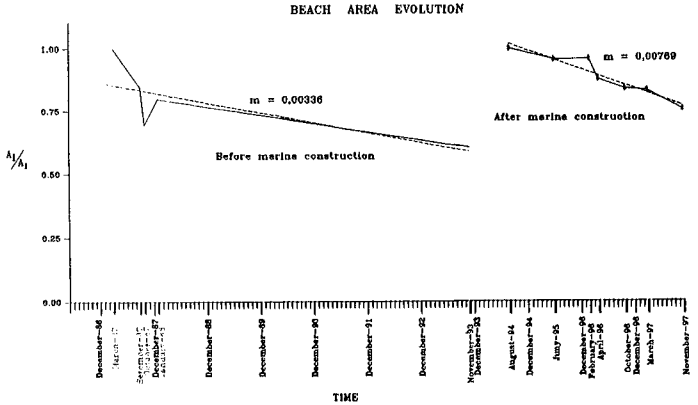

Figure 12.- Beach area evolution.

The analysis of beach profile can be made by comparing different profiles in the beach and each one in different topobathymetric surveys. The most interesting aspect in this case is how the natural bottom submerged slope change from the east to the west part. In the morphological description it can be seen how this slope change from the 2 % on the east to 4 % on the west. In Figure 13,14 15, 16 and 17 an overview of this changes is shown, four profiles have been selected for this analysis. Figure 13 give a location map of the situation of this profiles, the profiles are numerated from the west to the east the analysis will be made in the opposite order from profile P-15 to P-3, intermiddle profiles will be studied too. Profiles P-15 and P-12, Figure 14 and 15 have similar behaviour, profile changes has a range of variability from beach landward to bathymetric -5.0 m. The natural slope is around 2 % and beach nourishment works affect the slope of beach face and affect until bathymetric -2.5. Nourishment works were made from profile P-16 to P-7, it means that these profiles have the direct influence of the borrowed sand filling. The analysis of the three last bathymetries gives some information, after nourishment works a topobathymetric survey were made, august-94, in these

profiles the shoreline has an accretion compared with prenourishment shoreline, november-93, but the survey that was made in march-97 an erosion phenomena occurs in both in P-15 shoreline rise more than the situation in November-93 and in profile P-12 was in front of it. It means that the shoreline position is changing decreasing at the east part and accreting at the west.

The analysis of P-7 and P-3, Figure 16 and 17, show the sand accumulation that occurs in this area this phenomena is especially important on P-3. In this point sand accumulation is really significant, but the profile form with borrowed sand is not compatible with the natural bottom. It appears two peaks in the profile that broke the equilibrium profile, and the sand is lost on the foot of the profile.

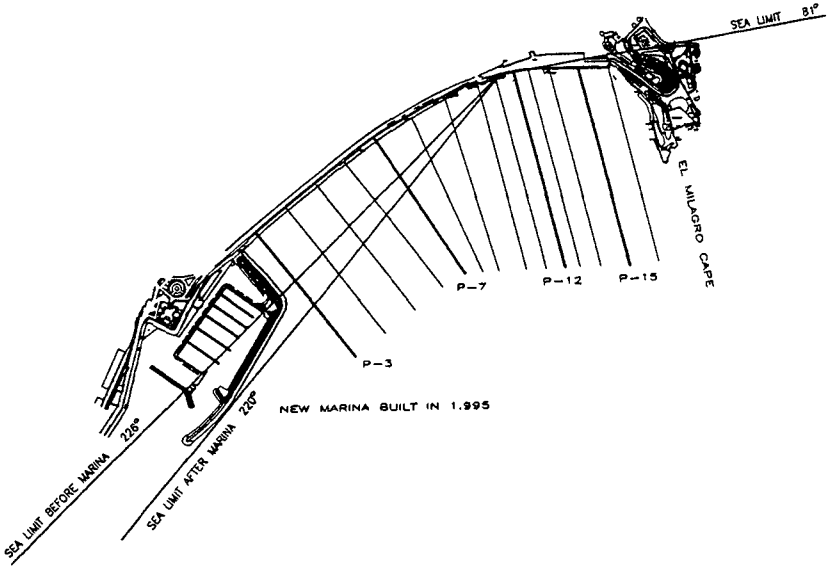

Figure 13.- Beach profile location map.

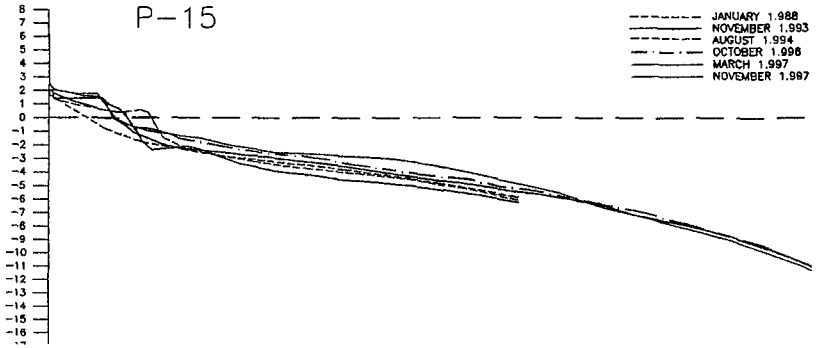

Figure 14.- Profile 15 evolution.

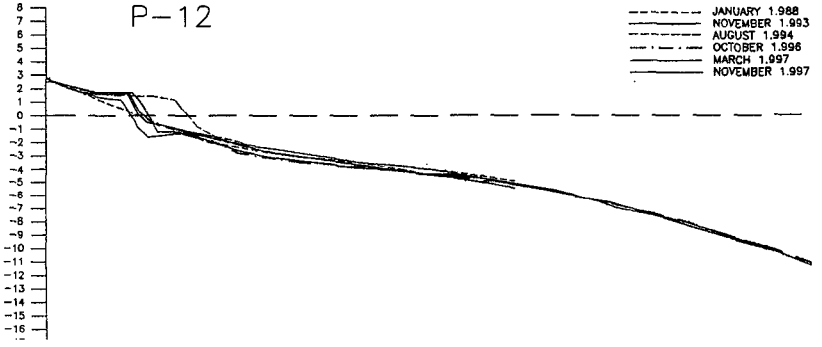

Figure 15.- Profile 12 evolution.

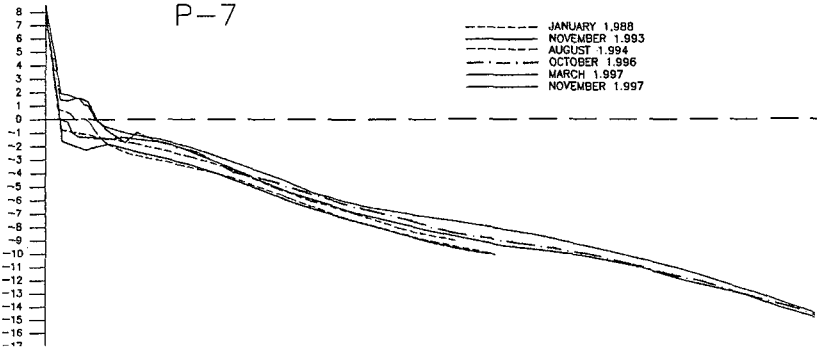

Figure 16.- Profile 7 evolution

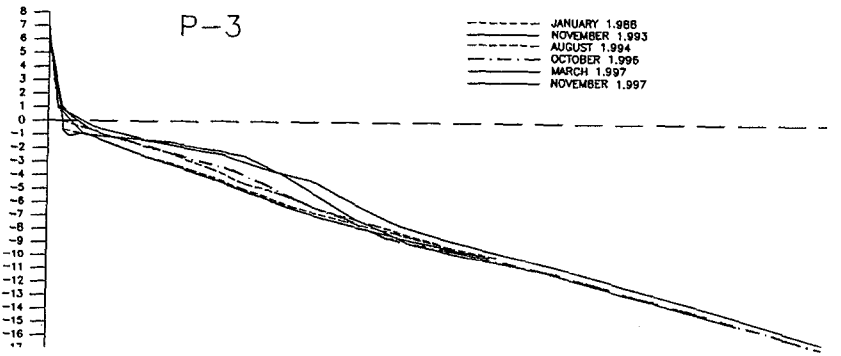

Figure 17.- Profile 3 evolution

Diagnosis

Marina construction has changed beach behaviour because fewer waves from the West Side arrive and some sand are retained in the protected area of the marina. Shoreline orientation changed due to the influence of marina on wave climatic.

The erosion ratio after marina construction is greater than before, 24.000 m^3/year and 13.000 m^3/year are the respectively values calculated with the field surveys data from the monitoring programs.

On the west part of the beach, close to the new marina, beach profile is milder than natural profile. In these area beach profile is not stable because of different bottom slope of natural beach and the profile formed by the borrowed sand. On the west part beach wide is decreasing.

Conclusion

-The analyses of the field surveys data from the monitoring program have been useful in order to understand beach evolution.

- From these data a beach behaviour have been obtained:

. The difference on beach slope, from 2% on the east side to 4% on the west side, has a lot of incidence on beach stability.

. The erosion ratio is greater after than before marina construction.

. The beach is not stable on the west side. Several alternatives must be studied in order to guarantee beach stability.

MAN MADE BEACHES BALANCING NATURE AND RECREATION

Ulf Anderskouv[1]
Hanne Bach[2]
Dan B. Hasløv[3]
Karsten Mangor[4]

ABSTRACT

Intensive mixed development of township, industry and tourism takes place in the coastal zone worldwide. This is often giving reason for conflicts between the commercial and industrial development, the need for recreational facilities and the interest for protection of the natural quality of the coastal zone and the environment.

Artificial beaches has been developed in Denmark at a high quality level with a successful balancing of the priorities of interest for the urban area population and for the natural and environmental content.

The paper describes with examples how the development of artificial beaches in great scale close to the City can be an efficient tool for the balanced development which combines solutions to known areas of conflict.

1. INTRODUCTION

Public beaches are often scarce in the close vicinity of densely built areas.

Artificial beaches will therefore strengthen the recreational value of the area when the beach is developed in balance with the interests of the commercial and industrial development.

[1]Portconsult, Consulting Engineers and Planners, Jagtvej 223, DK-2100 Copenhagen Ø, Denmark
[2]VKI, Agern Allé 11, DK-2970 Hørsholm, Denmark
[3]Hasløv & Kjærsgaard, Ny Østergade 32, DK-1101 Copenhagen K, Denmark
[4]DHI, Agern Allé 5, DK-2970 Hørsholm, Denmark

The environmental concerns for an artificial beach park are on the one hand the water quality at the new advanced sea beach and on the other hand the water quality in a created lagoon system. The water quality is usually related to hygienic water quality (bacterial and viral pollution) and eutrophication. The latter may be excessive growth of algae leading to accumulation of dead seaweed at the beaches or very turbid waters in the lagoon and potential problems with depression of the oxygen concentration in the water.

Many of these problems can be avoided when the proper methods for design are used including determination of the requirements for reduction of pollution load to the area, which may be conditional for turning the project into a success story.

The examples used in this presentation are from the two projects Køge Bugt Beach Park and Amager Beach Park, both located close to the center of Copenhagen and next to industrial areas and the densely populated township.

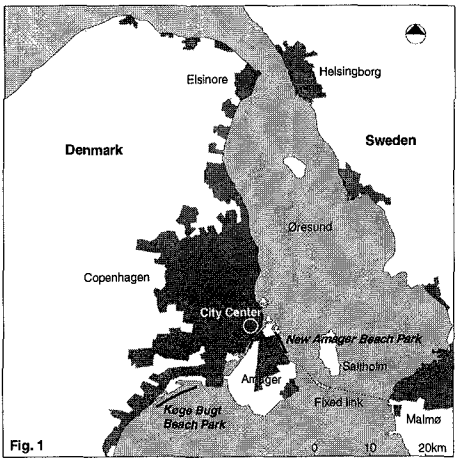

Figure 1, Location of Beach Parks near Copenhagen

2. BACKGROUND

The authors of this paper have through almost 25 years individually and in cooperation worked on a great number of projects in the coastal zone, in Denmark as well as internationally. They combine the wide experience from specialized scientists and practical planning, architecture and engineering and they have jointly been responsible for the technical preparation of conceptual design and model analysis of two alternatives for the new Amager Beach Park project. The design has been prepared for the Planning Section of the Danish Ministry of Traffic during 1995-1996.

Further the authors have, since their participation in the planning and construction in the seventies of the Køge Bugt Beach Park, followed and been involved in the monitoring and maintenance works for the beaches, dunes and dikes forming the waterfront of this beach park as well as in the functioning of the recreational facilities and the natural appearance developed by the artificially reclaimed areas.

3. AREAS OF CONFLICT

The Problem areas or Areas of Conflict which will be addressed through the examples in the paper are:

- **Recreational Values versus Densely built-up City Areas**
  Development of a sustainable connection between the high recreational value of the coastal zone and the densely built-up areas of the City with access for the public.

- **Recreational Coast versus Commercial Port**
  Combination of the recreational coastal zone and the continued development of the commercial port of Copenhagen as an important economic factor for the City.

- **Recreational Coast versus Industrial Development**
  Maintenance and renewal of the City's industrial areas and employment in balance with the recreational value of the coastal zone.

- **Public versus Private Financing and Maintenance**
  Balancing public and private interests in financing and maintenance of the project.

- **Stability against Wave Exposure**
  Coastal morphology and exposure to wave action balanced to a stable beach configuration.

- **Bathing Water Quality versus Waste Water Discharge**
  Attractive bathing water quality in the City's waste water environment.

- **Recreational activities creates increased pollution problems**

4. PREVIOUS PROJECTS

It has often been a tradition to develop densely built waterfronts with promenades and beaches based on the existing beaches with a well functioning coastal morphology.

The Køge Bugt Beach Park located south of Copenhagen, constructed in the late seventies, has previously been described at conferences as a new concept based on a qualitative development of the existing coastal zone with new beaches as a recre-

ational support to the developed township in the hinterland. The new beaches was developed on a system of shallow sand barrier islands located 500 to 1500 metres from the coastline. The shallow lagoon behind the barrier was developed as a combination of reclaimed land, dredged lagoons and for the marinas.

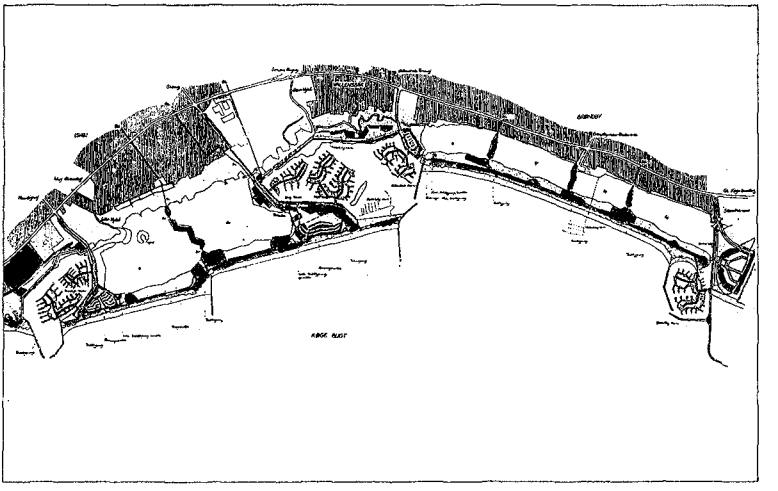

Figure 2, Køge Bugt Beach Park - Beaches and reclamation with lakes and marinas

The tools available at the time when the beach park in Køge Bugt was designed was very simple compared with today's numerical models. The alignment of the beaches and their stability was designed on basis of numerical refraction calculations and morphological indications provided by the existing barrier island formations.

The result was successful as the artificial beach line has practically stable during the following 20 years and there has not been any need for replacement of sand lost from the beaches.

The existence of algae and drifting seaweed has always been a problem in the bay and the project has not eliminated this problem. Algae and seaweed is still appearing along the shoreline during the bathing season as it is the case along most natural beaches in Denmark.

However, the quality of the bathing water at Køge Bugt Beach Park is so good - despite the existence of a next door large sewage treatment plant - that the beach park has been able continuosly to flag the attractive blue flag permitted only for recreational areas with a proven high quality of the bathing water. The project has thus proved that it is possible to retain a high recreational quality with a limited amount of maintenance resources in a highly developed area, however the precondition is that the society maintains a high standard with respect to the treatment of sewage.

5. NEW STEPS IN THE DEVELOPMENT

The New Amager Beach Park is an example of a new generation of artificial beaches. The location of the beach park, which is very close to the centre of Copenhagen and densely populated areas, has for generations been used for industrial development. The industry in the area is however undergoing a winding up process and a rehabilitation of the area to an attractive residential township is now being planned. The Port of Copenhagen is at the same time planning to merge all their bulk activities in the area in immediate vicinity of the beach park.

The area was previously burdened with some of the larger discharges of sewage from the city.

The coastal zone today is a narrow park with a beach of poor quality. The water quality is good following the implementation of one of Copenhagen's largest treatment plants some years ago, but still a number of storm water run-offs are existing.

The planned project will result in the development of a new advanced beach coast and lagoons.

Figure 3, Location of New Amager Beach Park

The new urban beach park will be a more intensive developed activity region for the city population, not only with beaches, but also with sports facilities and specialized centres of activity. The project is at the planning phase in which the government and the City of Copenhagen has cooperated in the preparation of a conceptual plan, for the development of the area. The possibilities for project financing is being analysed and negotiated at present.

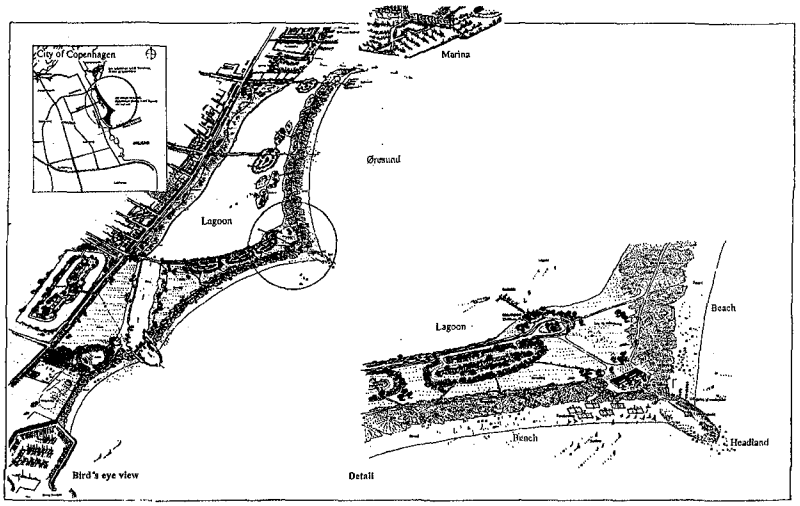

Figure 4, Amager Beach Park

The presentation will also describe how this type of project can be politically and economically integrated in the township development of the hinterland. The project is thus not based on a substantial reclamation to be sold in order to provide the economic background for the construction and maintenance of the public area as often practised in similar situations worldwide. It will be described how the concept used for the Amager Beach Park can be developed so that it is meeting the demand for actual town development as well.

6. COASTAL MORPHOLOGY AND HYDRODYNAMICS

The present Amager beach is located along the Sound approximately 5 km S of Copenhagen, as shown on Figure 1 and 3. Due to its location, the present Amager Beach Resort is not fully exposed to wave action. The island of Saltholm provides partly shelter for waves coming from Eastern directions. Consequently, waves from the direction intervals N-ENE and ESE-SSE are dominating along the frontage of the Amager Beach, refer Figure 5.

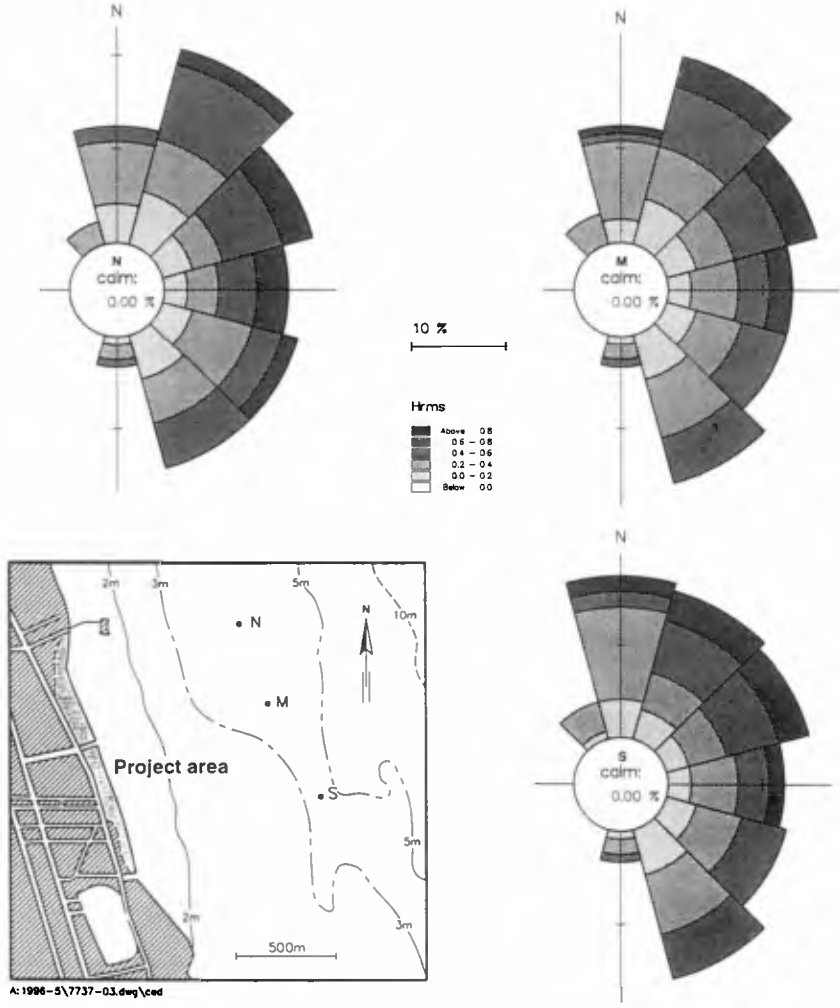

Figure 5, Wave roses for three locations along the Amager Beach according to numerical modelling by MIKE 21 NSW

Furthermore, the slope of the shoreface in front of Amager Beach is very mild. A large part of the wave energy is lost due to bottom friction.

In the layout of the new Amager Beach Resort, the quality of the beaches is improved considerably by increasing the exposure of the beaches to wave action by seaward shifting of the beach, thus eliminating the shallow shoreface.

The littoral transport distribution rose, Figure 6, right, for the area shows clearly the shadow effect from Saltholm Island and from the Port of Copenhagen.

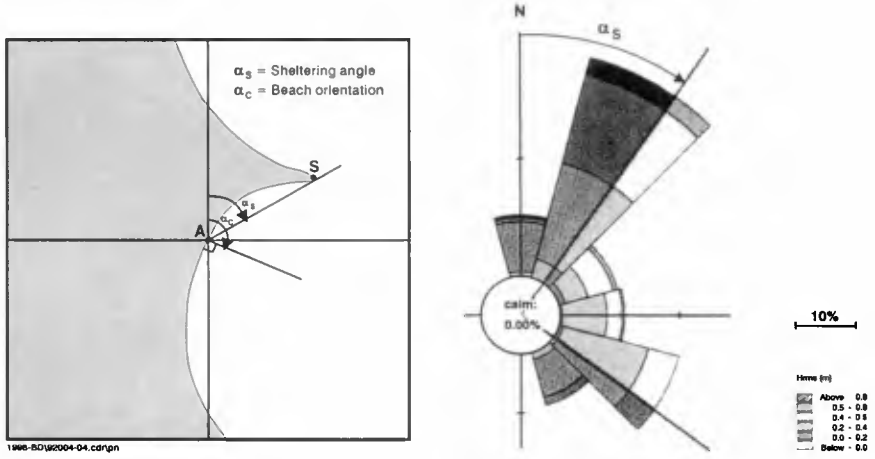

Figure 6, Definition of sheltering angle in relation the the artificial headlands (left) and the corresponding adjustment of the littoral transport distribution

Stable beach configurations were obtained by intersecting the beaches by artificial headlands. These stable beach planshapes have been computed by taking into account the sheltering effect of the headlands, as shown in Figure 6 (left and right), so that the orientation of all sections of the beaches corresponds to the equilibrium orientation. The design of the stable beach configurations were supported by detailed 2D modelling of waves, hydrodynamics and sediment transport.

The diagrammes in Figure 7 shows the longshore sediment transport profiles for the existing and the future beach configurations, respectively. It is noted that the present very wide distribution of the littoral transport is transferred to a narrow distribution concentrated on the foreshore of the future beach. This will provide a better beach quality.

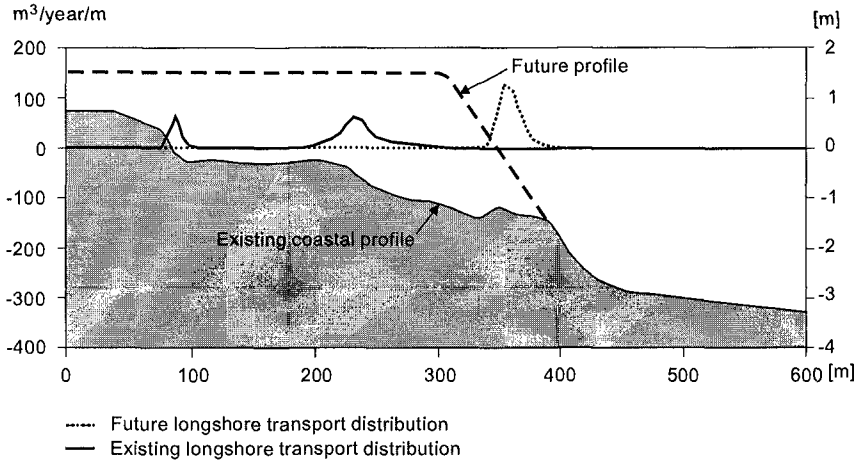

Figure 7, Distribution of the littoral transport in the coastal profile for the present and future coastal profiles as computed by LITPACK

7. WATER QUALITY

The firming water quality problem foreseen at Amager Beach park is the hygienic pollution due to the discharge of treated waste water from the two treatment plants for Copenhagen locatet not far away and storm water run-offs located along the existing beach as shown on Figure 8. The secondary problem is the potential excessive growth of algae in the lagoon and the accumulation of seaweed at the beaches in the lagoon area and at the seaside. Models describing the spreading and decay of bacteria and the eutrophication were established using MIKE21. Because of the large number of studies of water quality in the adjacent areas model calibration could be extracted very easily from previous works. Situations describing the year 2000 assuming the planned discharge and treatment of waste water and also some extra actions concerning diversion of storm water were investigated for two different beach layouts.

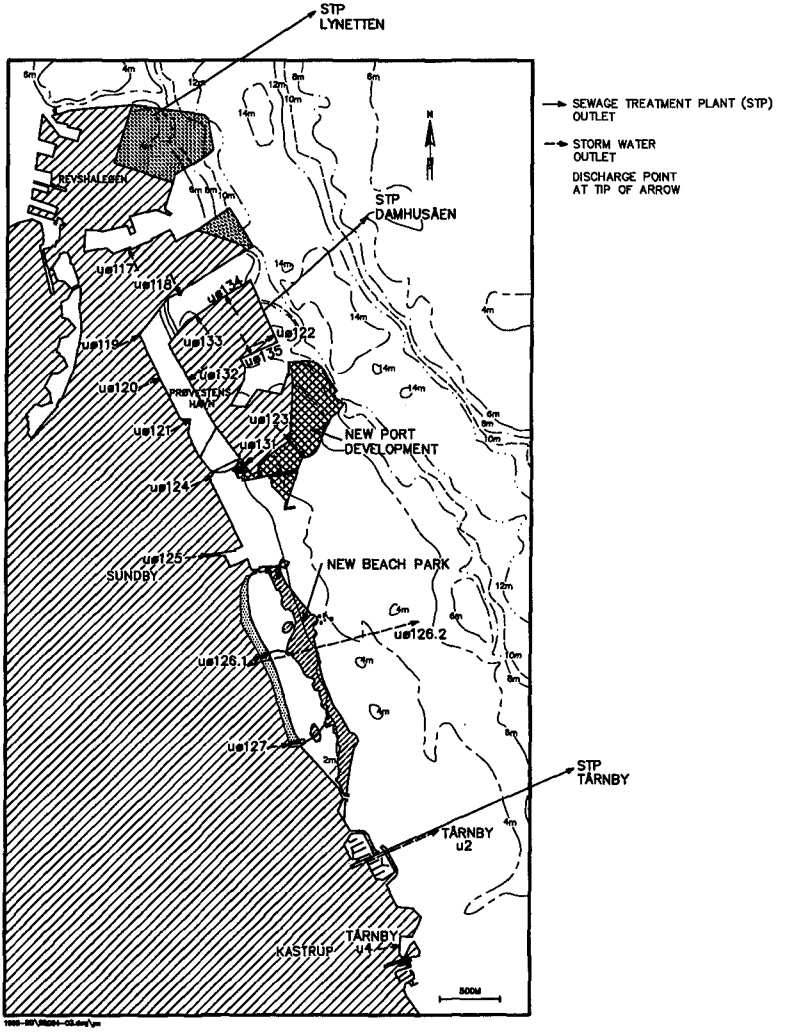

Figure 8, Overview of outlets from Sewage Treatment Plants and Storm Water outlets in the area near the New Amager Beach Park

The design and the natural conditions revealed a relatively high water exchange in the lagoon, which means that the fear of excessive algae blooming could be excluded. The primary production in the lagoon was predicted to be of the same order as in the adjacent areas, which means that some accumulation of seaweeds must be foreseen, similar to what can be observed at the beaches today. Due to the water depths in the lagoon, growth of eelgrass can not be expected. The bathing water criteria were achieved in the lagoon. The criteria were observed even under

At the seaside beach the water quality is expected to be better than at the present beach. The amount of accumulated seaweed is not expected to be larger than at similar beaches in the region. The bathing water quality (i.e. the hygienic water quality) is predicted to be even better than at the present beach due to avoidance of storm water run-offs at the new seaward shifted beach.

8. CONCLUSION

The development of artificial beaches which can support the demand for recreational outdoor life for the population in the urban areas and create the background for tourism development has proved to be an attractive concept for development. It is possible to create projects with a high quality level in which the prioritization of the urban against the natural content can be made according to the local interests and demand for development. The studies will underline that a preassump- tion for these projects is that they are viewed in their entirety and with a substantial and careful planning in order to ensure their environmental functionalism and viability.

9. REFERENCES

Jakobsen, P.R., Tougaard, N. and Larsen, K. (1987). "Copenhagen metropolitan region coast erosion management". Presented at Coastal Zone 87, Seattle, Washington.

Kaalund, P., Thougaard, N. and Hasløv, Dan Borgen. (1991). "Beach Resorts and Marinas in Denmark - Principles for Planning of Marinas". P.I.A.N.C. A.I.P.C.N.-BULLETIN 1991, No. 72.

Environmentally Friendly Coastal Protection
The ECOPRO Project

Brendan Dollard[1]

Abstract

In the battle to preserve land against the ravages of the sea man has created many inappropriate protection structures on the coast. Often the coastline which is being protected is, inherently, in dis-equilibrium with nature. When combined with the increased recreational usage of the coastal zone, the rise in sea level and the increased incidence of storms, accelerated erosion rates are often the result. The Environmentally Friendly Coastal Protection project, or ECOPRO for short, developed a coastal erosion assessment method for the non-specialist. It devised a system for optimising erosion monitoring and developed a guide to select of an appropriate coastal protection response. The project results are contained in the ECOPRO Code of Practice. This 320-page guide explains the steps involved in assessing and monitoring coastal erosion problems, planning protective actions and evaluating their environmental impact. Prepared by the Offshore & Coastal Engineering Unit of Enterprise Ireland, it is the result of four years of work which was supported under the EU LIFE Programme and drew on expertise from Ireland, Northern Ireland and Denmark. This paper presents details of the project and the development of the Code.

1. Introduction

In recent years it has become accepted that the coastline is a valuable natural resource which needs careful and sensitive management. This is especially so in the case of small island countries where the coastal zone has a direct and major influence on the economic welfare of the country. Coastal erosion has always been seen as one of the main threats to this resource and for centuries man has been fighting what was perceived as the ravages of the sea.

[1] **Senior Engineer, Offshore & Coastal Engineering Unit, Enterprise Ireland, Dublin 9, Ireland.**

In the Republic of Ireland, following destructive storms in the late 1980's which caused severe damage and accelerated erosion rates, there was a perceived need to seriously address the question of coastal erosion. A National Coastal Erosion Committee, formed under the auspices of the County and City Engineers Association, produced a report in 1992 which concluded that a Coastal Management policy rather than a purely Coastal Erosion policy was needed. This report also recommended that 'A code of practice for coastal protection should be drawn up to ensure the uniformity and appropriateness of all works'.

Following an initiative by Enterprise Ireland, the late Professor Bill Carter of the University of Ulster and The Department of the Marine, a proposal was developed for a coastal protection and management demonstration project and was successful in obtaining funding under the E.U. Life Programme. Managed by Enterprise Ireland, the project team consisted of the Department of the Marine and a number of local authorities in the Republic of Ireland, the Department of the Environment and the National Trust in Northern Ireland, Coastwatch Europe, and the Danish Coastal Authority (Kystinspektoratet). Inputs were also be sought from Universities in the Republic and Northern Ireland and from private firms with particular expertise in this field.

The project aims were to develop a method for the assessment of coastal erosion, to devise a system for monitoring erosion and to optimise the selection of an appropriate response. The project was titled Environmentally Friendly Coastal Protection and as this suggests the emphasis was on using environmentally friendly coastal protection techniques (i.e. soft engineering) wherever possible so as to mitigate the impact of coastal protection measures on the environment. These techniques, such as marram grass planting, dune ridge re-contouring, sand trap fencing, beach nourishment, etc., attempt to emulate the natural coastal processes rather than directly oppose them.

The final product of ECOPRO is the Code of Practice on environmentally friendly coastal protection. The principle behind the Code is the need to maintain as far as possible the protection afforded by the natural features of the coast. A beach is natures response to erosion and is extremely effective in dissipating the energy of the sea. Therefore the objective should be to keep beaches in place. The sand dunes backing beaches are an integral part of the system and must be allowed to fulfil their natural function of acting as a buffer zone between land and sea.

This Code of Practice should be of considerable use as a guide to current best practice on coastal protection and management. It is hoped that it will avoid the instant palliative response to storm damage and also ensure that those involved in coastal protection first look at the soft engineering techniques. It was not intended that the code would attempt to supplant the technical manuals on the subject of coastal protection as it is not aimed at the coastal engineer. It is instead, to be used by the non-expert and, it is hoped, will help them to avoid making mistakes in their response to coastal erosion. The code also attempts to make the non-expert more aware of the fragility of the coastal environment and how complex and interrelated is the problem of coastal erosion.

2. Project Objectives

The specific objectives of 'ECOPRO' were:

1. To develop coastline monitoring methods which will be adaptable to various types of coastline.

2. To develop a Sensitivity Index by which a coastline's susceptibility to erosion is graded.

3. To present an assessment of performance of shoreline protection/management methods.

4. To present a report on the design, construction and success of two types of protection methods at selected sites.

5. To present all of the above as a 'Code of Practice'.

These five objectives form the five main tasks of the project. Each is dealt with in the Code of Practice with the exception of the Sensitivity Index. While a lot of work was carried out on this, particularly by the University of Ulster, the Danish Coastal Authority and a private company Natural Environment Consultants Ltd., the conclusion was that at the present time it was not possible to develop a practical index which would be usable by non-experts. The work carried out in this area has been reported on separately (Dollard, B., *et al*, 1996).

The overall aim of the project was to promote the use of soft engineering coastal protection techniques by firstly promoting a methodology which will allow the non-expert to assess the erosion problem and identify the likely causes. Secondly, it aimed to provide information on suitable coastal protection and management solutions with particular emphasis on environmental impact. Finally, the project intended to supply reference information on coastal processes and identify useful environmental and historical data sources.

3. Project Management

The project organisational structure is shown in Fig. 1. Enterprise Ireland was the overall Project Manager and was responsible for the day to day running of the project. The project was directed by the Steering Committee which was chaired by the Department of the Marine. The Technical Group provides the Committee with technical analysis of its proposals and drew up specifications for project work. It also drafted the progress and interim reports of work in hand.

The collaboration between the Universities, Government and local authority personnel and public volunteers was excellent and the multi-disciplined mixture of scientists, engineers and environmentalists ensured that most viewpoints were aired. The international dimension between the North and South of Ireland and Denmark helped to broaden our perspective. A successful visit to Denmark by the ECOPRO members, where a number of soft engineering coastal protection methods were viewed, was also very beneficial.

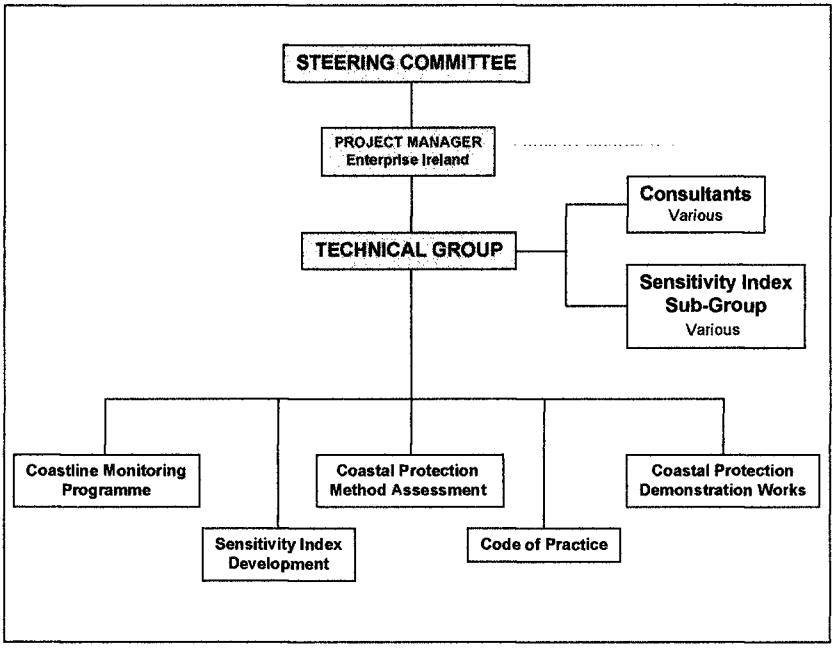

Fig. 1 Organisational structure of ECOPRO

4. Project Tasks Undertaken

4.1 Coastline monitoring

Project objective:

The objective of this work was to devise and test various coastline monitoring methods in order to optimise the time and money spent in obtaining data on coastline and beach level fluctuations. The resultant techniques were to be detailed in the ECOPRO Code of Practice.

Seven sites were chosen for detailed study and are shown in Fig.2. Each has a distinct soft coast and suffer from differing types of erosion. The extent of erosion also varies from place to place.

Coastline monitoring is a very important tool in assessing the sensitivity of the coast to erosion. There are two stages to monitoring the coast. Firstly, it was necessary to fix the present position of the coastline so that historical changes could be compared. This we termed the baseline survey. Secondly, regular monitoring of beach levels when compared with accurate environmental data gave an insight into the overall response of the beach to external forces. The results of these exercises were used in the assessment of the nature and cause(s) of the erosion problem.

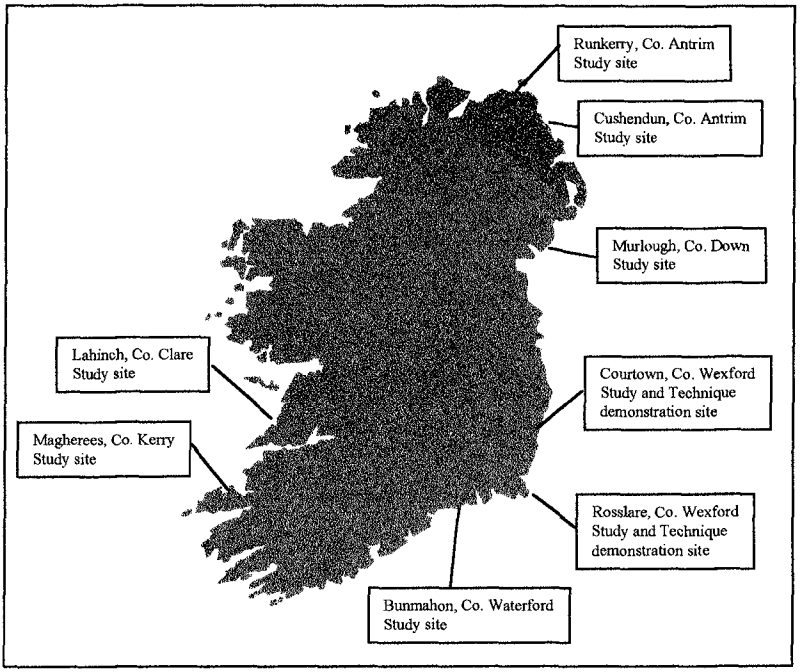

Fig. 2 - Location of ECOPRO study and technique demonstration sites

Baseline survey

This involved the association and comparing of the present day topography for the chosen embayment with the historical data. Under ECOPRO a number of methods were examined to try to fix the present position of the coastline at our seven sites as economically as possible. These were;

- Aerial video
- Aerial photography
- Satellite imagery
- Aerial digital CIR photography

ECOPRO commissioned an aerial video recording, of the entire coastline of the four ECOPRO counties in the Republic of Ireland and this was very useful as a source of information on land use and vegetation classification. Satellite imagery of the sites was also examined but the resolution from satellite imagery was not suitable for accurate erosion measurement.

Aerial photography was the most successful, although expensive. The colour, stereoscopic images, allowed the vegetation line to be easily identified and a height contour map, (0.5m contour interval) was prepared for one of the sites.

ECOPRO fixed the vegetation line for three of the ECOPRO study sites from commissioned aerial photographs. These were then compared with the position of the dune

toe line as given by the Ordnance Survey maps from 1841. A historical data search was conducted for four study sites and a list of sources along with practical information on the techniques are covered in the Code of Practice.

Aerial digital photography using an infrared filter was found to be the most economic technique for mapping large coastal areas. The imagery was easily stored on, and retrievable from, digital tapes or CD's and the infrared filters highlight the vegetation line and indicate the condition of the vegetation.

The methodologies involved in all of these methods are included in the Code of Practice

Beach level monitoring

Beach level monitoring is the measurement of vertical and horizontal erosion/accretion of beaches and nearshore bathymetry and the analysis of sediment. As with the baseline study, a number of different methods were employed to monitor the changes in beach levels. These were;

- Standard surveying techniques
- Cut-down monitors
- Measurements from fixed points (erosion questionnaire)
- Hydrographic surveys
- Sediment sampling

All seven study sites were monitored using either standard levelling or total station techniques and details are given in the Code of Practice. In order to facilitate the identification of which storm or event caused specific beach changes, ECOPRO initiated a programme of regular beach cut-down measurements. Measurements were taken every two weeks at each of the 16 monitor posts. This gave both the lowest beach level achieved and the amount of sand subsequently deposited on the beach. The Code of Practice includes details of this method and comments on its suitability.

Measurements from fixed points e.g. rocks, piers, etc. were also carried out at a number of sites as part of the Coastwatch Europe erosion questionnaire.

Hydrographic surveys

Hydrographic surveys were made at four sites. The bathymetry at a fifth site was measured on a regular basis to aid with the Sensitivity Index computer studies. Sediment sampling was carried out at the four Republic of Ireland sites. One of the Northern Ireland sites was regularly sampled, again as part of the Sensitivity Index work.

Data storage

ECOPRO opted for a custom built coastal data storage and display system SANDS (Shoreline and Nearshore Data System). Three packages were initially installed in the Department of the Marine, Enterprise Ireland and the Department of the Environment, Northern Ireland and later one copy was transferred to a Local authority, in order to determine its suitability for local data storage and analysis.

Wind and wave data

Offshore wind and wave data for 4 representative points around the island of Ireland was purchased from the UK Meteorological Office Wave Hindcast Model. This data covered a two year period. Storm data was obtained from the Irish weather service Met Éireann.

4.2 The Sensitivity Index

Project objective:

Gather together as much information on the factors that influence coastal erosion and 'weight' them accordingly. Based on these 'values' deduce the overall sensitivity of the coastline to erosion.

The background to this work was a paper written by V. Gornitz (Gornitz, V, 1990) who developed a simple scoring system which could be used to determine the vulnerability of coast to erosion. It was intended to be used on a large scale for isolated areas where it was not feasible or economical to collect accurate data. However, the ECOPRO group decided that for this method to be useful as an assessment tool and for its results to be used in the selection of protection methods it must be user friendly, accurate and on a scale that is practical. In addition the index should identify the causative factors of erosion as this will allow suitable protection to be prescribed. Fig. 3 lists the variables typically involved in coastal erosion.

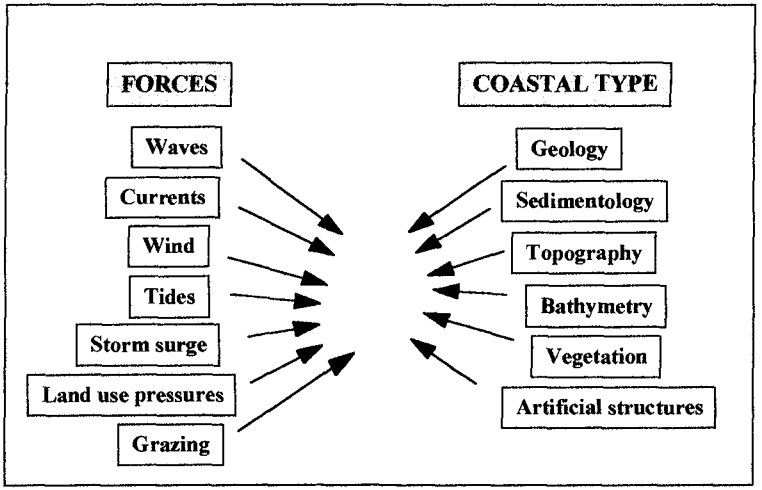

Fig. 3 Variables involved in coastal erosion

The ECOPRO group entrusted the Danish Coastal Authority (D.C.A.) (Kystinspektoratet) with the task of further developing Sensitivity Index method. The Environmental Studies Department of the University of Ulster was commissioned to examine the level of accuracy required of nearshore wave data for analysis of wave/sediment interaction. A private company, 'Natural Environment Consultants Ltd', who are specialists in coastal environment habitats, was also employed to carry out work on the dune vegetation condition aspect of the index. These three form a sub-group which reported on progress to the ECOPRO Technical group.

The ECOPRO group decided to tackle this work in two complementary stages. Firstly a method to calculate a general indicator of sensitivity needed to be devised. This was essentially an extension of the V. Gornitz work and would be useful as a first step assessment method by, for example, a local authority on the entire coast under its jurisdiction. The second stage was a refinement of the method based on the most accurate information available and on computed wave/sediment interaction data. This involved computer models, beach monitoring, vegetation classification, beach sediment analysis, wave and current measurement (or hindcasting). This method was used on short lengths of coast (typically 100m).

The prediction of sensitivity was correlated against historical and short term erosion trends and, thus, the index was fine tuned. Erosion rates usually vary across a coastal cell mainly due to the different levels of exposure of parts of the coastline to wave action. Modelling these processes using computers gives an indication of the sensitivity of the coast to erosion and when combined with other factors such as wind, geology and topography of the coastline, strength and regenerative ability of dune vegetation, beach sediment size, etc., an overall sensitivity grade was assigned. This was checked against historical records such as maps and aerial photographs and more recent beach level measurements.

Although the work on the index did not reach a stage where it was appropriate for inclusion in the Code of Practice, the exercise did provide some interesting results which could provide the basis for more extensive studies.

In order to satisfy the objective of this part of the project and to provide the users of the Code of Practice with an erosion assessment method it was decided to develop a technique using Field and Historical Survey decision support flowcharts. The result was a user friendly and practical approach to a complex problem and trials conducted by non-experts using the flowcharts have helped the ECOPRO team to refine the technique. Initial results are very encouraging but it is only when the method is more widely used will its full potential be realised.

4.3 Evaluation of coastal protection/management options

Project objective:

To examine current coastal protection measures being used and to evaluate their success. Each technique is to be summarised and included in the Code of Practice.

Once the nature of the erosion problem has been assessed, the method of protecting the coast needs to be decided. ECOPRO advocates the use of soft engineering options wherever possible. These attempts to work with the natural processes rather than oppose them. This approach often means that the shore zone is used as a buffer and must be wider than would be envisaged under conventional hard engineering schemes. An environmentally friendly scheme must often consider a certain amount of erosion as being beneficial, providing sediment interchange along the coast.

The ECOPRO Code of Practice identifies which type of erosion problems can be tackled with soft engineering and what particular method should be employed. 27 different coastal protection and management techniques are detailed in the Appendix of the Code.

In practice, the most commonly used protection methods are located in the lower and upper shore regions where most of the wave energy is absorbed. Lower shore techniques attempt to dissipate the incoming wave energy whereas upper shore techniques try to strengthen the existing natural structure. The supra shore or backshore and hinterland techniques assign land to act as a buffer against the sea. The most common form of these techniques is the use of set-back lines and this usually forms part of an overall Coastal Zone Management policy adopted by the relevant local authority. This involves the drawing of lines on maps by the local planning authority, seaward of which no new developments will be allowed and, more controversially, no attempt will be made to protect the existing land or buildings. This has two obvious advantages. Firstly, it almost eliminates the cost of coastal protection and secondly, it will reduce the demands for protection in the future. It does, however, raise the question of compensation to and also the longer term question of what to do when the buffer zone has been exhausted.

Many of these soft engineering techniques are not suited to exposed 'high energy' coastal areas where large waves impinge on the coast. Here, if protection is absolutely required, hard structures are necessary. General information on these and their likely impact on the environment is given in the Code of Practice.

The suitability of each technique is based on published literature and the results of a questionnaire survey of the Irish and Danish local authorities. Details of each technique are included in the Code of Practice and the experiences of the local authorities with the various methods is outlined.

4.4 Case histories of protection techniques

Project objective:

To give practical information on the design, implementation and monitoring of two different types of environmentally friendly coastal protection techniques.

One of the projects covered was a beach nourishment scheme in Rosslare Co. Wexford. Here 160,000m^3 of sand, dredged from offshore bars, was placed on the beach. This is the largest beach nourishment scheme carried out in Ireland to date.

The second was a small scale scheme involving the re-contouring of a sand dune ridge, marram grass planting and dune toe protection in Courtown Co. Wexford.

These two techniques are possibly the most popular soft engineering methods employed in Europe today. Practical information on both is included in the Code of Practice.

4.5 The ECOPRO Code of Practice

Project Objective:

To provide the non-expert with practical advice on how to identify the possible causes of marine erosion, select an appropriate response and how to evaluate its likely impact on the environment. Advice should also be given on coastal processes, data sources, monitoring techniques, legal implications and funding opportunities.

The layout of the code structure is shown in Fig. 4.

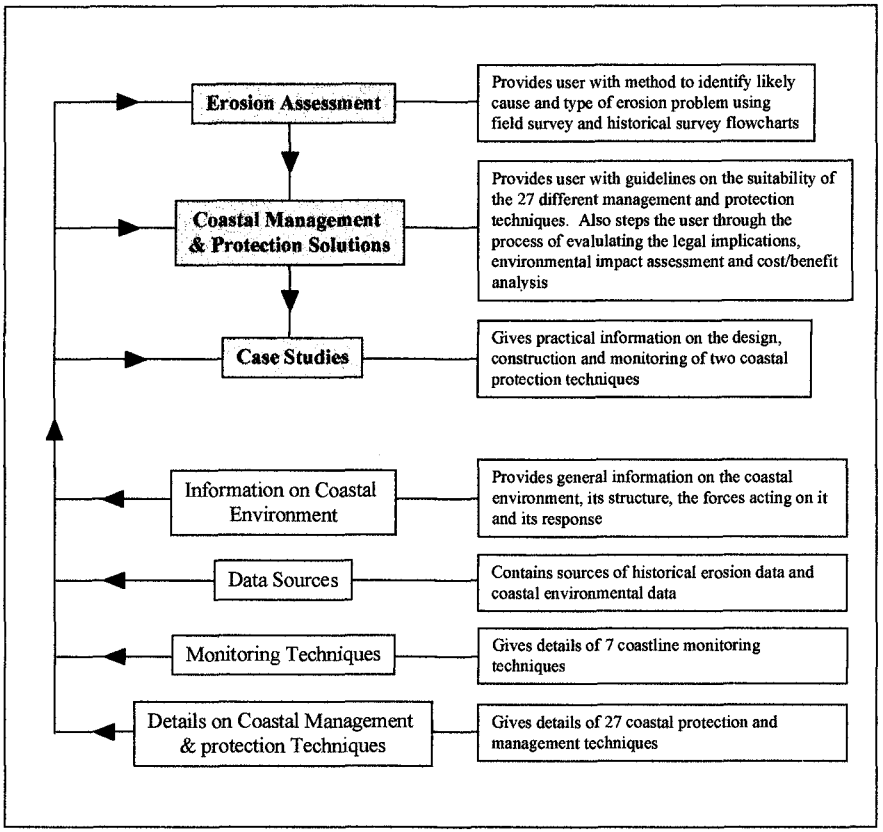

Fig. 4 - Code of Practice Layout

The Code of Practice deals firstly with the assessment of an erosion problem using field and historical erosion surveys. The aim is to try to determine the nature of the problem, whether it is continuous erosion or erosion caused by a single storm event or a sequence of storms. It also aims to identify the causes, whether natural or man induced. This section is structured around the use of decision support flowcharts which guide the user through a series of yes/no questions.

The next section of the Code uses these assessment results to identify suitable solutions. It gives information on the technical suitability of various coastal protection and management options. It also gives advice on assessing their legal and environmental impacts, and provides information on carrying out a cost/benefit analysis.

The following section is devoted to the two case studies. Practical information on their installation is supplied.

Appendix 1 of the Code gives general information on the coastal environment, its structure, the forces acting on it and its response. Appendix 2 contains sources of historical

and environmental data. Appendix 3 details coastline monitoring methods and Appendix 4 gives details of 27 different coastal protection and management options.

5. Project Results

Code of Practice

The Code of Practice is the final product of ECOPRO and whether it achieves its aims of increasing the awareness of the fragility of the coastal environment and preventing mistakes being made with coastal protection measures, will be the true result of the project. Initial indications in this respect are good. A workshop held in September in Cork was attended by engineers from most of the maritime counties in the Republic of Ireland and each were presented with copies of the Code of Practice. By general consent it was agreed that the code answered most of their queries on coastal erosion. Encouragingly the section on monitoring the coast was considered very useful. This bodes well for the future as once coastal monitoring begins, an awareness of the dynamic nature of the coastal zone is sure to follow.

The Code of Practice is essentially generic and can be used in all situations. The techniques are clearly and fully described using user friendly flowcharts wherever possible. The sections of the Code covering legislation and data sources are, through necessity, specific to the island of Ireland, but their format is such that they could be easily rewritten to suit other countries.

The Code of Practice follows a logical step-by-step path guiding the user through the assessment and solution of an erosion problem. General information on the coastal environment, contained in the appendix, is applicable, not only to North Atlantic coasts, but to most European Community waters. This section is also written in a clear style aimed at the non-expert. Formulae are only included where necessary and are usually backed up with graphic illustration.

The Sensitivity Index

The overall conclusion on the Sensitivity Index was that the use of such an index requires the availability of specialist knowledge and computer modelling capability. As such, it would not be of practical use to the target audience of the Code of Practice. Although an interesting formula to predict erosion rates from beach slope and wave statistics emerged from one study, it was considered that its application was only valid for micro-tidal, open coastlines. It was decided not to include it in the Code as it might be used inappropriately.

Coastline Monitoring

The data obtained from monitoring the seven pilot sites and the two case study locations have demonstrated the usefulness of the various techniques. The data collected covers:

- 8 sets of 70 beach profiles cross sections taken approximately every two months from October 1993 to March 1996
- 30 sets of 20 beach monitor post data taken approximately every month

- Wave hindcast data for 4 points offshore Ireland covering a two year period (3 hourly readings of wave height, period and direction for wind waves, swell waves and resultant waves)
- Four volumes of historical erosion data covering four of the study sites. Each contains all available maps and aerial photography along with reports from national and local sources
- Bathymetric survey data for four study sites
- Detailed digital ground survey data from commissioned aerial photography for one site
- Digital imagery (full spectrum and infrared) from aerial and video photography for 60 km of soft coast.

The survey methods advocated in the Code of Practice are devised with the premise that the user will have a limited amount of data available. In most European coastal areas there is a lack of coastal environmental data, especially nearshore wave data and water level measurements. Where economically justified, this difficulty can be overcome by specialist using computer models. However, these models are usually not available to the target users of the Code, the non specialist. The survey techniques should, therefore, be re-usable throughout the Community and the Code of Practice itself could provide the format for national guides to environmentally friendly coastal protection throughout Europe.

The analysis of the data collected has provided ECOPRO with the practical knowledge necessary to be able to optimise the choice of monitoring technique for a particular erosion problem. These recommendations are included in the Code of Practice and details of the techniques are given in the Code Appendix. The data was also used by the Sensitivity Group in their work on the Sensitivity Index.

The ECOPRO database has been used in a number of academic studies (to date four final year projects and two post graduate degree thesis). It has also been used to fine tune and validate two sediment transport computer modelling investigations carried out by coastal engineering specialist on behalf of a local authority and the owners of a golf course.

6. Dissemination of Project Results

Since the results of the project are contained in the ECOPRO Code of Practice, dissemination will be primarily through the distribution of the Code. The Code is available from;

Government Publications Sales Office, Molesworth Street, Dublin 2, Ireland.
Tel; +353 1 6613111 Fax; +353 1 4752760

The ECOPRO project promoted the cause of environmentally friendly coastal protection through public exhibitions. In 1994, as part of a exhibition on coastal environment matters in the ENFO centre, Dublin, ECOPRO provided a display stand promoting the projeet and its aims. The exhibition ran for two weeks and was attended by over 5,000 people. Under ECOPRO, Coastwatch Europe organised two national and a number of local workshops on dune dynamics, monitoring and coastal protection measures.

7. Recommendations on Future Work

One of the main findings of ECOPRO's work on the Sensitivity Index was the importance of accurate wave and water level data. This data is not available for the vast majority of European coastal sites. Obtaining this data for a particular site is very expensive and can only be justified where costly coastal protection schemes are being adopted to protect valuable property. In less developed areas this type of data collection is not viable. The alternative is to make decisions based on less accurate but more readily available information. ECOPRO attempts to help the user make these decisions based on best current practice. As technology advances and our knowledge of coastal processes improves, this best current practice will evolve and it is important that ECOPRO evolves alongside. The ECOPRO team have committed themselves to continuously update the Code of Practice and to conduct questionnaire surveys of selected users to ensure that it is achieving its aims.

The structure of the decision support flowcharts and the Code in general, is such that it would lend itself readily to being encoded as a computer program. This is currently being investigated by the ECOPRO team. If possible this would make the Code much more widely available especially if placed on the Internet.

The work on the Sensitivity Index could be progressed so that ultimately a more accurate technique on erosion sensitivity would be available. For this to be usable by non-experts much of the data required, i.e. nearshore wave statistics, water levels, etc., would need to be pre-processed and presented in atlas format for ease of use. Eventually it is envisaged that each local authority or coastal community could, without specialist knowledge, have a technique which would allow them to accurately assess each areas susceptibility to erosion and to identify the cause by using readily available information.

Acknowledgements
The author would like to express his gratitude to the European Commission, DGXI, for the financial assistance and encouragement given. My appreciation is also extended to the ECOPRO project team who worked tirelessly to make the project a success.

References

1. EOLAS, (1992). Coastal Management - A case for action. On behalf of the County and City Engineers Association. Eolas [Forbairt], Glasnevin, Dublin 9, Ireland.
2. Dollard, B. *et al*, 1996. Final Technical Report for ECOPRO - Environmentally Coastal Protection. Submitted to the European Commission DGXI - Life Programme.
3. Gornitz, V, 1990. Journal of Coastal Research, Special issue 9, 311-348

COASTAL RESTORATION CONSIDERATIONS

Karsten Mangor[1]

Abstract

The paper discusses the problems associated with the loss of coastal resources, which is often the result of applying traditional coast protection measures in densely developed areas. It is recommended to distinguish clearly between coast protection, as measures mainly securing the coastline, and shore protection, as measures protecting also the shore and the natural coastal resources. The planning concepts Shoreline Management Planning and Management Unit Master Planning have been discussed, in which connection the importance of obtaining broad consensus for a management strategy and for cost sharing has been highlighted. The importance of preserving the coastal resources by working with the nature has been illustrated and innovative shoreline protection principles have been proposed for different types of coastal classifications. New types of environmentally optimised coastal structures have been proposed and an overall comparison of various protection measures has been made.

Introduction

The paper discusses the important physical and management issues in the delicate balance between (a) the requirements of primary protection against coastal erosion and (b) protection of the coastal resource, which in this context is constituted mainly by the dynamic coastal landscape. Historically, protection measures have been reactive in nature and have concentrated on preventing loss of existing facilities and coast due to coastal erosion. This type of protection has at many locations resulted in loss of the shore (or beach) and it has seriously degraded the fascinating scenery of the dynamic coastal landscape. Such protection measures can consequently not be ealled "shore protection" as they result in loss of the shore, but should rather be called "coast protection", where the term coast is defined as the strip of land that extends inland from the coastline. For clarification, the definition of the generally used terms for the form elements in the coastal area is presented in Figure 1.

[1] Chief Engineer, Coastal Engineering and Environment, Danish Hydraulic Institute, Agern Allé 5, DK-2970 Hørsholm, Denmark, E-mail: *km@dhi.dk.*

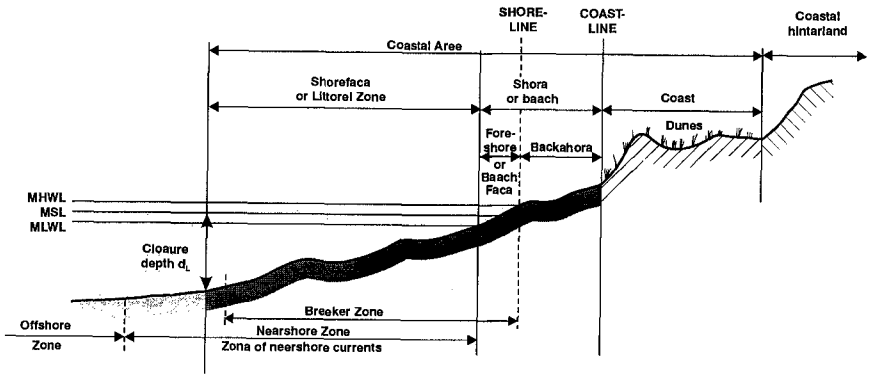

Figure 1. Definition of Coastal Terms, mainly from (Shore Protection Manual, 1984).

The most important terms are the following:

- COASTAL AREA: The land and sea areas bordering the shoreline.
- COAST: The strip of land that extends from the coastline inland to the first major change in terrain features.
- COASTLINE: Technically the line that forms the boundary between the COAST and the SHORE, i.e. the foot of the cliff. Commonly, the line that forms the boundary between the land and the water.
- SHORE or BEACH: The zone of unconsolidated material that extends from the low water line to the line of permanent vegetation (the effective limit of storm waves).
- SHORELINE: The intersection between the mean high water line and the shore.
- SHOREFACE: The active littoral zone off the low water line.
- CLOSURE DEPTH: The depth beyond which no significant longshore and cross-shore transports take place, and where no significant bed movements due to littoral transport processes take place. The closure depth can thus be defined as the depth at the seaward boundary of the littoral zone. (Hallemeyer, 1981)
- OFFSHORE ZONE: The offshore zone is not well defined. In relation to beach terminology, it is thus not clear if it starts from the littoral zone, from the breaking or from the nearshore zone or even from the shoal zone. In the present context, the offshore zone is defined as the zone off the nearshore zone.

There is, however, some confusion between the terms "shore" and "coast", as these terms in common perception are synonymous. Consequently the terms "shore protection" and "coast protection" are also synonymous in common perception and signal that the shore (or beach) is protected when such measures are introduced, which is not the case with traditional hard protection measures. Actually, traditional hard coast protection maintains the location of the coastline and protects the coast, according to above definition, but at the expense of the shore (or the beach); consequently it is proposed in the future to distinguish clearly between the two terms:

- COAST PROTECTION, as measures aiming at protecting against coastline retreat, thus protecting housing and infrastructure, the coast and the hinterland from erosion, however often at the expense of losing the beach and the dynamic coastal landscape;
- SHORE PROTECTION, as measures aiming at protecting, preserving or restoring the shore and the dynamic coastal landscape as well as protecting against coastline retreat to the extent possible.

Causes of Coastal Erosion

Most coastal erosion problems have their origin in deficit in the littoral budget for a specific area, such deficits can have many causes of which the most common are the following:

- Blocking, or reduction, of the littoral transport by some kind of protruding coastal structure, such as port structures, inlet regulation works, or coastal protection works.
- Reduction of the supply of littoral material to a section by river regulation works, sand mining or by protection of neighbouring coastlines.
- Loss of littoral material into tidal inlets.
- Loss of littoral material by dumping of maintenance dredging material offshore.
- Loss of sand inland by dune destruction.
- Blocking of part of the buffer zone on the shore by structures on the shore.

All these causes are well known, and in many cases their damaging effects have been eliminated, at least partly, by regulatory measures. However, many developed areas are characterised by a highly degraded coastal environment, brought on by a historic combination of the above mentioned causes and where sufficient mitigation of these is not realistic.

Problem Scoping and Overall Planning Concept

In modern legislation there are often requirements for sustainable development and preservation of natural resources, which has resulted in seeing shore protection in a new long-term perspective, which has led to the discipline of Integrated Coastal Zone Management (ICZM). The concept of ICZM may be defined as a structured co-ordination of the various activities and resource demands that occur in the coastal zone in order to achieve economically, environmentally and socially sustainable development in compliance with adopted relevant local, regional or international goals. ICZM is often expressed in the form of a Coastal Zone Management Plan (CZMP), which provides input to national or regional development plans. A CZMP thus provides an overall framework for a balanced development of the following main issues, which are normally exposing the coastal zone to competing pressures: (a) Coast protection and shore protection; (b) agriculture and fisheries; (c) habitation, infrastructure, industrial development, public utilities and navigation; (d) recreation, landscape and environmental preservation; and (e) raw material utilisation

The ICZM concept is best suited for planning in areas where there are still some options for the planning of the coastal hinterland. In areas prone to long term erosion and where the coastal development is already so advanced that comprehensive hard shore protection measures have been constructed years ago, the consequence is very often that

the shore has been heavily degraded or completely lost. Such highly developed areas, where the coastal resource has been degraded over many years, are numerous in most coastal countries. Typically, the population pressure on the sparse remaining coastal resources is very high, and the value of the development is correspondingly high. The present paper concentrates on management and technical methods for restoring such highly developed coastal areas.

Detailed Planning Concept

The modern management of shore protection and/or coastal restoration projects have their origin in the world-wide legal requirements for preservation and restoration of the natural resources through a sustainable holistic management. The challenge in this context is to combine the public shore protection/restoration interests with the private interests for coast protection. There are often inherent conflicting interests in such projects, both with respect to the objectives of the protection and with respect to cost sharing. Resolving these planning matters often proves to be equally challenging than to finding a suitable technical solution. Resolving planning matters is normally not the strong side of the coastal engineer, but it is important for the success of the entire planning and design process that the coastal engineer is aware of these conditions.

The level where coastal engineers are involved in the planning is normally not in the ICZM process, but at the more specific and project orientated level, where the planning concepts are Shoreline Management Planning and Management Unit Master Planning. A Shoreline Management Plan (SMP) is a strategic plan for shore protection or shore development covering a sediment cell or a sub sediment cell.
An SMP normally contains the following items:

- Basic data collection for the following types of data: Meteomarine conditions, coastal processes, coastline development and coastal structures, present and planned land use and environmental conditions.
- Programme for additional data collection.
- Overall description of coastal morphology and sediment budget.
- Identification of Management Units.
- Consultation with all interested parties with the purpose of obtaining consensus on the goal for a management strategy.
- Definition of the Management Strategy.

In Denmark the SMPs are prepared by the Counties. In other countries this may be the responsibility of other similar bodies. The SMP sets the strategy for shore protection projects in the various Management Units (MU). A Management Unit is a length of shoreline with basically similar characteristics in terms both of natural processes and land use. Different shore or coast protection measures may very well be used for neighbouring MUs, as the preferred measures are dependent on the land use and the ownership of the coastal land. However, the SMP has set out the general guidelines for applicable protection measures assuring that there will be no negative impact from one MU to the neighbouring units. The development of the protection options is often performed in the form of a Management Unit Master Plan (MUMP) or a Shoreline

Master Plan. In Denmark it is normally the landowners who take the initiative to request the County to prepare a MUMP. However, the County can also take the initiative by itself. The County is also responsible for the allocation of costs among the landowners and others, as found relevant in the specific cases. The general rule in Denmark is that the landowner must pay for the protection. The County will normally not prepare the MUMP itself, but it will establish a project organisation, which typically has the following composition:

Consulting team:	This should as a minimum include the following professionals: Coastal Morphologist, Coastal Design Engineer, Landscape Architect/Planner and Environmentalist.
Steering Committee:	County, Municipality, Coastal Authority and representatives from land owners and other involved groups (NGO's).

The preparation of a MUMP will normally involve the following activities:

- Establishment of consensus on local goals, especially with respect to the weighting between shore and coast protection objectives and on cost sharing.
- Performance of detailed data collection, field surveys and analysis.
- Detailed analysis of coastal morphology.
- Detailed analysis of land use and public access corridors.
- Preparation of conceptual design of alternative shore protection projects, including coastal and environmental impact assessment (by numerical modelling) and aesthetic optimisation.
- Preparation of costing for alternative projects and preparation of financing plan.
- Maintenance of contact to authorities responsible for approving alternative projects.
- Selection of preferred project.
- Preparation of plan for monitoring of project performance.
- Preparation of plan for maintenance organisation and follow-up.

The main output of a MUMP is thus a well documented conceptual design of a combined shore and coast protection scheme, which has been documented and balanced with respect to coastal impact, environmental impact and aesthetic considerations. Furthermore the cost sharing and the financing plan have been agreed and the project has been approved.

Based on this MUMP, the responsible body can now call for tenders for detailed design, including preparation of tender documents for construction.

Main Physical Principles in Shoreline Restoration

A precondition for establishing a successful shoreline restoration project is that all the involved parties have a minimum understanding of the coastal morphological processes, so that they can understand why the present situation has developed and why certain solutions are applicable and others are not.

The following perspectives should be considered in connection with shoreline restoration projects:

- Work with nature, for instance by re-establishing the coastal profile by nourishment and by utilising site specific features, for instance by strengthening of semi hard promontories.
- Manipulate littoral drift rate and gradient by use of a minimum of structures.
- Preserve sections of untouched dynamic landscape. Allow only protection measures if valuable buildings/infrastructure are threatened.
- Secure passage to and along the beach.
- Enhance aesthetic appearance, such as by minimising the use of structures thereby providing long uninterrupted sections of beach.
- Minimise maintenance requirements to a level, which is possible to manage by the concerned owner(s) of the scheme. A clean nourishment solution at an unstable section of coastline, which for many reasons may be the preferred one, will normally not be practical to handle by a group of land owners, as recharge will be required at short intervals.
- Secure good local water quality and minimise risk of trapping debris and seaweed.
- Secure safety for swimmers by avoiding structures generating dangerous rip currents.
- Be realistic and pragmatic, keeping in mind that the natural untouched coastline is an utopia in highly developed areas. Create small attractive locations at otherwise strongly protected stretches if this is the only realistic possibility.

Coastal classification

The general principles, which should be followed to develop a successful shoreline restoration project, were discussed above. However, in order to be able to arrive at the optimal shoreline restoration measure in an actual case, it is also important to take into account the actual coastal morphodynamic conditions of the site. A coastal classification has been established in the following in order to provide some guidelines as regards which measures are best suited for different types of coasts.

Only littoral coasts, which are characterised by the presence of non-cohesive sediments on the shoreface and on the beach, will be included in the following classification.

The littoral transport for a given coastal environment is mainly dependent on the wave climate in terms of wave height-direction distribution. A simplified classification of coastal areas based on wave exposure and the angle of incidence of the prevailing waves is presented in Figure 2.

The coastal classification is closely related to the variation in transport capacity as function of the angle of incidence and the magnitude of the waves, which has been expressed in form of exposed, moderately exposed and protected coastal areas. The possibility of artificially establishing a practically stable sandy shore is very much dependent on the angle of wave incidence of the prevailing waves and the magnitude of the transport deficit, which is closely related to the transport capacity.

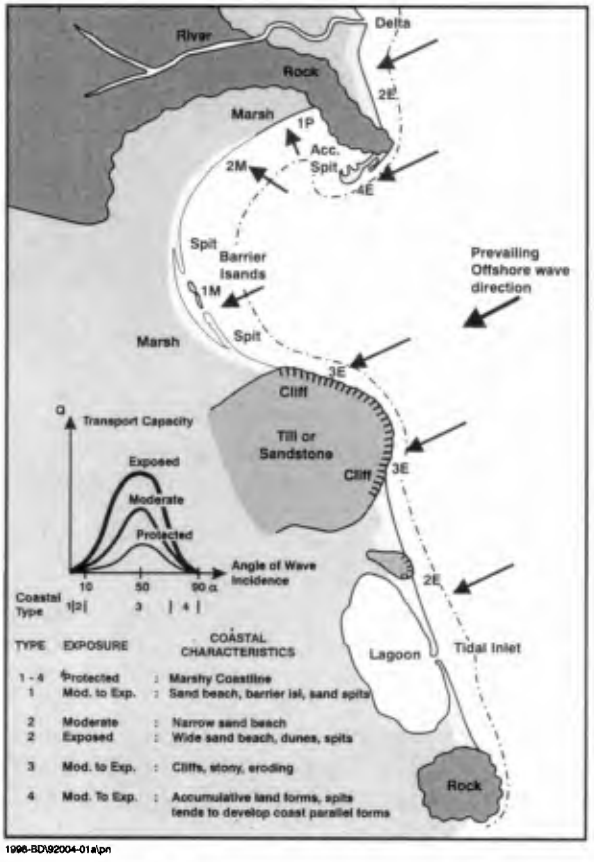

Figure 2 Coastline classification

It should be noted, that a prerequisite for obtaining an attractive sandy shore is that the location is exposed or moderately exposed, as it is the constant movement of the beach sand under these circumstances which generated the attractive clean sandy beach.

The coasts have been divided into four main types in relation to the angle of incidence of the prevailing waves and in subtypes in relation to the exposure. The resulting coastal characteristics are presented in Table 1.

It should be noted, that the above given classification is very simplified, and is in practice also dependent of many other parameters, such as the type of coast and sediment supply from the neighbouring areas, as well as seasonality in wave climate, tides and storm surges etc. Figure 2 also shows a schematised coastline, where different typical coastal types have been shown.

Coastal Type	Angle of Incidence (0° = shore normal)	Exposure	Coastal Characteristics
1P	< 3°	Protected	Marshy
1M		Moderate	Sandy beach, barrier isl., sand spits
1E		Exposed	Sandy beach, barrier isl., sand spits
2P	3 – 10°	Protected	Marshy
2M		Moderate	Narrow sandy beach, sand spits
2E		Exposed	Wide sandy beach, sand spits
3P	10 – 70°	Protected	Marshy
3M		Moderate	Mobile eroding beach with cliffs
3E		Exposed	Mobile eroding beach with cliffs
4P	70 – 90°	Protected	Marshy
4M		Moderate	Accumulative land forms, spits
4E		Exposed	Accumulative land forms, spits

Table 1 Coastal classification as function of angle of incidence and wave exposure for littoral coasts.

Discussion of Innovative Coastal Restoration Schemes

The discussion of the different types of suitable restoration schemes will be divided into the four main types of coastal areas, which reflects the angle of incidence of the prevailing waves, as the different types require different restoration measures.

Type 1P to 4P, Protected, all directions

These physical conditions result in a marshy coastline, where there will normally not be any problems related to coastal erosion, but where there may be some problems in relation to flooding. Furthermore, there may be a requirement for upgrading to a sandy shore. However, this is only possible if the reason for the protected status of the coastline is related to a very shallow shoreface. If this is the case, an attractive and more exposed coast can be constructed by moving the shoreline seawards by nourishment. The plan stability of the beach shall also be considered. This principle is shown in figure 3, left.

Type 1M and 1E, Perpendicular wave approach, moderate to exposed

These conditions will often result in a sandy beach. The perpendicular wave approach is characteristic for accumulative sand formations in bays, where the net littoral drift is close to zero. If the original bathymetry in such a bay is shallow, there will be a tendency towards formation of sand spits and barrier islands, which are separated from land by a shallow lagoon, refer Figure 2 and Figure 3, right. As these morphological features are characterised by accumulative processes, they will normally not be associated with erosion problems. However, there might be a requirement for upgrading of the entire coastal area towards a more attractive beach environment from a recreational point of view. This can be obtained in two principally different ways:

1. By filling the lagoon and moving the beach seawards, whereby a more exposed and attractive sandy beach is obtained with easy access, as the difficult access caused by the lagoon is eliminated.
2. By dredging the lagoon, whereby it can be upgraded to a recreational protected water area, in combination with seaward movement of the coastline.

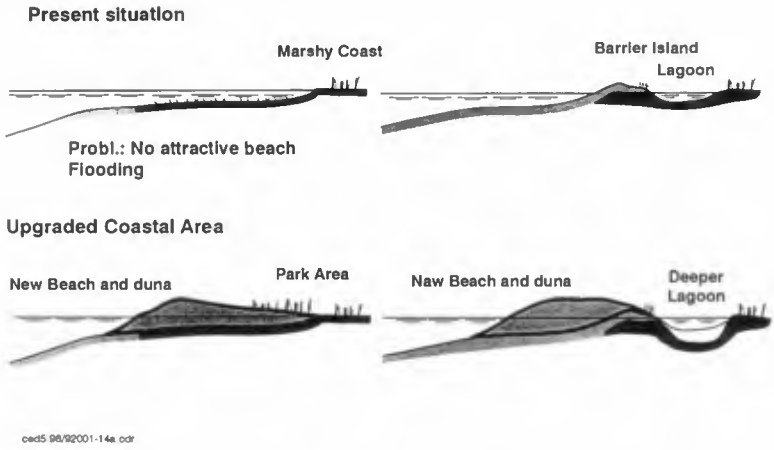

Figure 3 Upgrading of: (a) Protected coastal areas with all directions of wave approach, coastal types 1P – 4P and (b) Moderate/exposed beaches with perpendicular wave approach, coastal types 1M and 1E.

These two beach park rehabilitation solutions are shown in Figure 3, lower part. The Køge Bugt Beach Park, near Copenhagen, has been constructed according to this principle and the New Amager Beach is presently being planned also following these principles, Anderskouv et al. (1998).

Type 2M and 2E, Moderate/exposed beach with small angle of incidence

These types of wave conditions will often result in a narrow to wide sandy beach, however, also depending on tidal and storm surge conditions. These beaches are close to their equilibrium direction and normally subject to a moderate littoral drift; they are often seen in the form of crescentic beaches suspended between headlands or in connection with deltas or tidal inlets, see Figure 2. Their stability is dependent on a continuous supply of littoral material. If such supply does not occur or is interruped they will tend to rotate towards the direction of the new equilibrium. This will normally lead to shoreline setback.

Coastal protection of such beaches has traditionally been performed by revetments, groyne fields and coastal breakwaters. These traditional measures normally provide good protection of the coastline and, in the case of groynes and breakwaters, some short sections of beaches. However, they have also a series of negative effects on the beach quality as shown in Figure 4. These can be summarised as follows: (a) Revetments: Loss of the beach, erosion of down-drift beach, difficult passage and aesthetically undesirable, (b) Groyne field: Trapping of sand and debris, lee-side erosion, rip currents and offshore loss of sand, rips dangerous for bathers, difficult passage on beach and aesthetically undesirable, (c) Segmented breakwaters: Trapping of

sand and debris, poor water quality in narrow bays, lee-side erosion, rip currents and offshore loss of sand, rips dangerous for bathers, and obscured view to the sea.

An ideal rehabilitation of a coastal section, which has been protected by a combination of traditional coastal protection measures and thereby been degraded, will, from a physical point of view, be a beach nourishment programme. However, this has the disadvantage that is has to be maintained at regular intervals. This is not very attractive for most landowners. Normally, landowners have as one of the main objectives to a shoreline restoration project that the maintenance requirements shall be small. Therefore the coastal engineer has to find restoration solutions, which fulfil this objective. Such a rehabilitation solution is shown in the lower part of Figure 4. The philosophy behind this rehabilitation is to tidy up the old unplanned mixture of small structures, and to re-establish a wide stable sandy beach by the combined use of a few large structures and considerable initial nourishment, plus limited regular recharge.

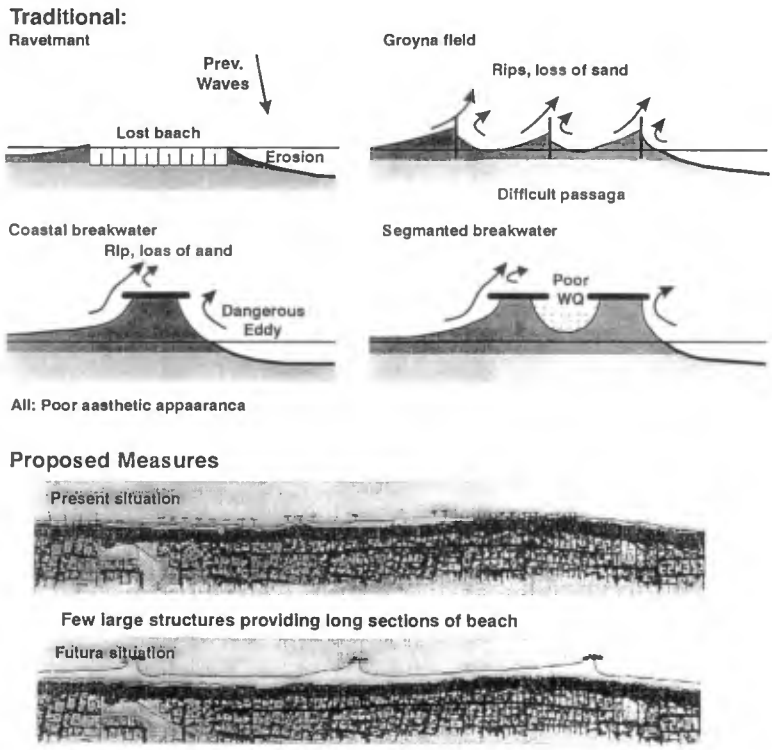

Figure 4 Performance of traditional coast protection measures and proposed upgrading to shore protection scheme for moderate/exposed coasts with small angle of incidence.

This concept is only applicable on coasts where the incidence angle of the prevailing waves is small, which means that a fairly long section of beach can be supported by each structure. The equilibrium angle of the new beach section is mainly dependent on the wave conditions and the supply of littoral material to the section from the updrift coastal section. The new beach concept can be characterised by the following qualities: (a) Long sections of natural looking sandy beaches, (b) Small maintenance, (c) Small downstream effects, (d) The protection against coast erosion is provided partly by the wide beach and partly by the structures. Identical safety towards coast erosion along the entire section may require the introduction of buried emergency revetments or the use of beach drains along the narrowest sections of the new beaches, and (e) The new large structures can be used as active elements in the landscaping, for instance to underline natural strong points in the original coastline.

The supporting structure has in Figure 4 been shown as a slightly curved coastal breakwater. However the layout of this structure can be optimised according to the principles shown in Figure 5.

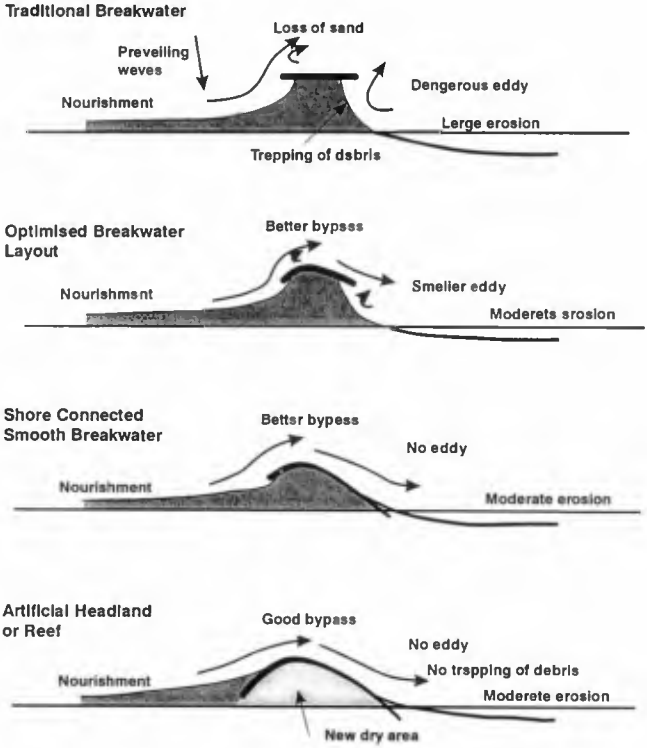

Figure 5 Optimisation of coastal breakwater to artificial headland, applicable for moderate/exposed coasts for small angles of incidence.

The philosophy in the optimisation of the breakwater in terms of a curved breakwater, a shore connected smooth breakwater or ultimately an artificial headland is to: (a) Improve the bypass, minimise the offshore loss and minimise the lee-side erosion, (b) To eliminate dangerous rip currents and to eliminate lee areas, thereby minimising the risk of trapping of debris, (c) To enhance the aesthetic appearance of the coastal structure and to gain some useful land.

Type 3M and 3E, Moderate/exposed beach with large angle of incidence

This type of coast has a large littoral transport potential, it is often eroding and will therefore in many cases already have been protected. Whereas a suitable coast protection measure for this type of coast is revetments, it is difficult to propose an optimal shore protection system. The protection principles counting on long sections of accumulated material upstream of protruding coastal structures cannot be used in this situation due to the very oblique wave attack. This type of coast is normally neither suitable for artificial nourishment as a stand alone measure, as this will result in large maintenance requirements, nor nourishment in connection with structures, as the structures can only hold a short beach section due to the oblique wave exposure.

A possible solution for an innovative upgrading of a small coastal section from being protected by a revetment into an attractive recreational environment is the construction of a small cove, as shown in Figure 6. The shape of the small cove will be fairly independent of the oblique wave attack due to its relatively narrow opening.

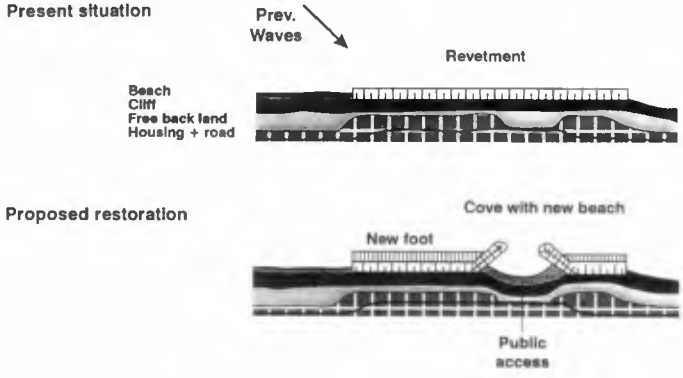

Figure 6 Innovative shore protection measure for a moderate/exposed coast with oblique wave attack.

Type 4M and 4E, moderate/exposed beach with nearly parallel wave attack

This type of coast is the downdrift section of a coastline of one of the other types; the littoral drift capacity is small due to the very large angle of wave incidence. This type of coastline is often accreting as the supply of littoral material is typically greater than the transport capacity. However, due to the very oblique wave attack, the coastline development is often unstable and shows a tendency to form coast-parallel land

forms some distance from the coastline, see Figure 7. A characteristic of this separated spit formation is that the coastline downstream of the spit has no supply of sediments, and consequently will be exposed to erosion.

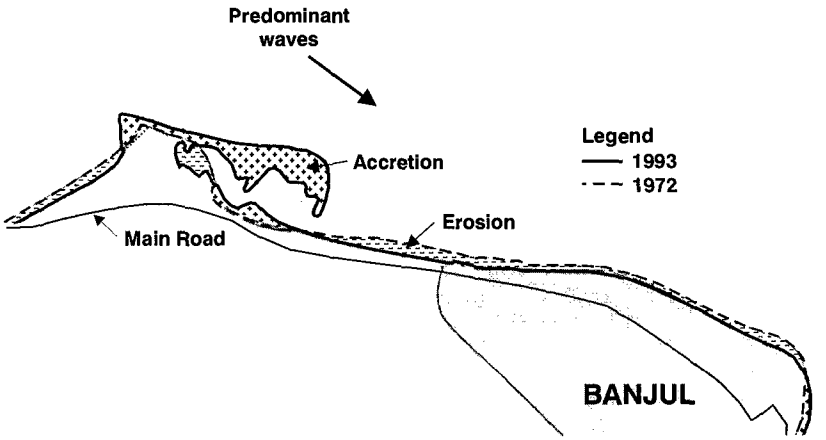

Figure 7 Special shoreline erosion problem at coastline with very oblique wave attack.

It is important to note that protruding coastal structures in such an environment can initiate the above-mentioned separation, for which reason such structures shall be avoided under these circumstances. The recommended shore protection measures at such a location are withdrawn emergency revetments in combination with artificial nourishment. The source for the nourishment could be the accumulated material in the spit, which is causing the local downstream erosion.

Final evaluation of coast protection and shore protection measures

Evaluations of the different kinds of coast protection and shore protection measures, which have been discussed in the paper, have been given in table 2. The protection and restoration measures have been divided in four categories:

- Structures
- Combined, which is combinations of nourishment and structures (beach parks)
- Soft, which is nourishment and beach drain
- Natural, which is management solutions without any structures or other physical measures

The evaluation of the different measures have been divided into four main categories:

- Protection, capability of protecting the coast and influence on adjacent stretches
- Recreation, divided into: capability of protecting the shore, safety for bathers and water quality
- Sustainability, divided into: aesthetics and preservation of coastal resource

- Management requirements, which is the associated efforts for obtaining consensus between stakeholders (not to be underestimated) and to the performance of shoreline management planning

Please note that the cost of the different measures has not been taken into account in the evaluation scheme.

Influence on Coastal Area / Protection and Restoration Measure		Protection		Recreation			Sustainability		Management Requirements	Score		
		Coast	Adjacent Coasts/ Beaches	Shore/ Beach	Safety for Bathers	Water Quality	Aesthetics	Preser-vation of Coastal Resource	Consensus, Shoreline Man. Planning	Pro-tec-tion	Rec. + Sust.	Total
Structures	Revetment (single)	1	0	-1	-1	0	-1	-2	0	1	-5	-4
	- (long stretch)	2	-1	-2	-1	0	-2	-2	-2	1	-7	-6
	Dyke (withdrawn)	2	0	0	0	0	-1	-1	-2	2	-2	0
	Groyne (single)	1	-1	1	-2	-1	-2	-2	-1	0	-6	-6
	Groyne Field	2	-2	1	-2	-1	-2	-2	-2	0	-6	-6
	Single Breakwater	1	-1	1	-2	-1	-1	-1	-1	0	-4	-4
	Segmented Breakw.	2	-2	1	-2	-2	-2	-2	-2	0	-7	-7
	Headland	2	0	2	0	0	1	0	-2	2	3	5
Combined	Beach Park	2	0	2	1	2	1	-1	-2	2	5	7
	Cove	1	0	1	0	0	0	-1	-2	1	0	1
Soft	Nourishment	1	1	1	0	0	0	0	-2	2	1	3
	Beach Drain	1	0	2	0	0	1	0	-1	1	3	4
Natural	Setback - Do nothing	-2	0	1	0	0	2	2	-2	-2	5	3
	Legend: +2	Good Protection		High rec. value			Enhances Sustainability		No demand			
	+1											
	0	Neutral		Neutral			Neutral		Moderate			
	-1											
	-2	Causes Erosion		Negative impact on Rec.			Non Sustainable		High demand			

Table 2 Evaluation of function and impact of coastal protection, shore protection and shoreline restoration measures.

It is of course difficult to make the scoring and some of the given scores can be discussed, however, the tendency is quite clear:

- Structures can provide coast protection, but most often at the expense of the coastal resources
- Combined solutions can be very attractive providing both protection and restoration
- Soft solutions can be attractive providing both protection and restoration
- Natural. Setback restrictions can normally not be used in already highly developed areas and do-nothing can only be used if continued coastal erosion can be accepted

References

Hallemeier, R.J. (1981): "A profile Zonation for Seasonal Sand Beaches from Wave Climate". Coastal Engineering, Vol. 4, 253-277.

Shore Protection Manual (1984), Coastal Engineering Research Center, Department of the Army, Waterways Experiment Station, Corps of Engineers, Vicksburg, Mississippi, USA, Appendix A. Glossary of Terms.

Anderskouv, U. et al. (1998): "Man Made Beaches Balancing Nature and Recreation". Proceedings ICCE 98.

General Experience from numerous DHI projects, which are not available in public domain.

Integrated approach on the safety of dikes along the Great Dutch Lakes

Jentsje W. van der Meer, M ASCE[1]
Harry de Looff[2]
Peter C.G. Glas[3]

Abstract

Two great lakes of approximately 1000 km^2 exist in the Netherlands surrounded by low lying land. Under extreme events storm surges of 2-3 m can be expected with significant wave heights up to 3 m. The question to answer was to what extent, under extreme conditions, the situations around the two lakes are comparable with situations along the sea coast. And whether or not the dikes along these lakes should give similar safety against flooding. An integrated approach was followed based on risk analysis. The study contained the following parts: hydraulic boundary conditions, probabilistic calculations on required dike heights, cost estimates on possible dike improvements, damage due to flooding and risk analysis on inundation. The main conclusion is that the two lakes have a similar behaviour with respect to risk of flooding which is also comparable with estuaries and other areas along the sea coast.

Introduction

Dikes protect the hinterland from flooding by storm surges from the sea or by high river discharges. Both situations are well known in low-lying countries and safety in the Netherlands relies heavily on reliable, strong dikes. On the basis of risk analysis, including both the probability of failure and the effects of flooding, it has been decided that such dikes in The Netherlands must be strong enough to withstand very extreme events with return periods up to 1/10,000 years. Compared to breakwaters, for example, this is two orders of magnitude higher and such events are difficult to imagine.

A sea such as the North Sea, can create high storm surges and high waves against coastal defences. But large lakes can also generate storm surges and waves, particularly in the case of the extreme events already mentioned.

[1] Projectmanager, Infram, Voorsterweg 28, 8316 PT, Marknesse, the Netherlands, email: jentsje.vandermeer@infram.nl
[2] Representing the Ministry of Transport, Publie Works and Management, P.O. Box 5044, 2600 GA, Delft, the Netherlands, email: a.p.dlooff@dww.rws.minvenw.nl
[3] Projectdirector, Delft Hydraulics, P.O. Box 177, 2600 MH, Delft, the Netherlands, email: peter.glas@wldelft.nl

Two great lakes exist in The Netherlands which both were part of the North Sea system before 1932. They were created at that time by closing the estuary with a dike (the Afsluit dike). Both lakes are only separated by a dam in between. The IJsselmeer ("meer" means lake) has a surface of about 1200 km^2 and the Markermeer about 750 km^2, see Figure 1.

Under extreme events, storm surges of 2-3 m can be expected with significant wave heights up to 3 m. Although not as severe as situations along the North Sea coast, it is comparable. Furthermore, some areas behind the dikes lie more than 4 m below the mean lake level. The differences between the two lakes are that a river flows into the IJsselmeer and that this lake can directly sluice water into the Norh Sea, which is not the case for the Markermeer.

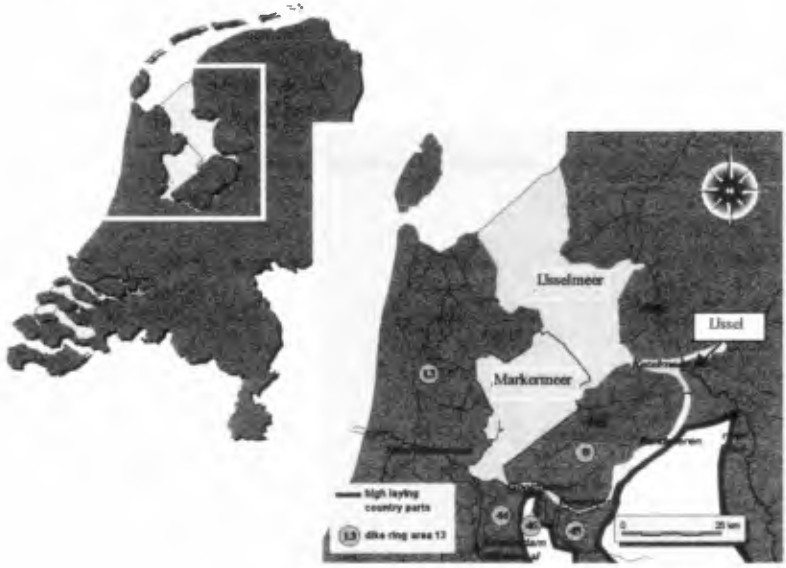

Figure 1. Study area

The question has arisen, both in Dutch Parliament and elsewhere, as to what extent the situations around the two great lakes under very extreme conditions are comparable with situations along the sea coast under similar conditions. And whether the dikes along these lakes should provide similar safety against flooding. An extensive study was performed by Delft Hydraulics, as an independent consultant, to give insight into the problem. An integrated approach was followed based on the concept of risk analysis. A full account of the study results is given in 15 reports by Delft Hydraulics, see the reference list. The study contained the following parts:

- hydraulic boundary conditions
- cost estimates on possible dike improvements
- damage due to flooding
- risk analysis on inundation
- integration of technical and legal aspects

Only the hydraulic boundary conditions with effects on safety and dike heights, the damage due to flooding and the risk analysis are treated in this paper. The problem in more detail can be defined as follows:

- are IJsselmeer and Markermeer comparable with respect to safety?
  - what will be the influence of a better control on the lake level of the Markermeer (the river IJssel flows into the IJsselmeer which gives less control)
  - what will be the difference in flood damage if the same areas are flooded by IJsselmeer or Markermeer
  - what will be the difference in risk of flooding
- is risk of flooding from the lakes comparable to sea coast areas?

Hydraulic boundary conditions: lake levels

A run-off model was first made of the entire lake system, calibrated using 20 years of measurements. The free parameters in the calibration were the control parameters of the sluices. Therefore, the calibration was carried out on management of the two lakes, because this determines the lake levels. A longer period of measurements for calibration than 20 years was not possible as the dike that separates the Markermeer and IJsselmeer was constructed in 1976. Data before 1976 was available, but then for one large and not separated IJsselmeer. Actually, data from the closure of the northern Afsluit dike in .1932 and onwards was available, resulting in more than 60 years of measurements.

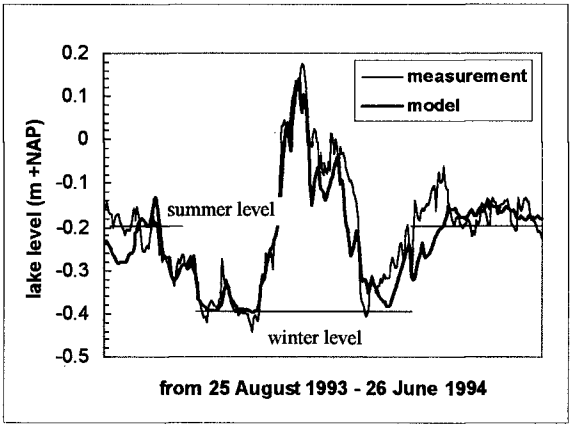

Figure 2. Example of calibration of the run-off model for the Markermeer for the winter of 1993-1994

A result of the calibration for the Markermeer is given in Figure 2 for the winter of 1993-1994. In that winter high lake levels occurred in December and January. The peak is fairly well predicted. In summer the lake level will be maintained at –0.2 m NAP and in winter the lake level is lowered to –0.4 m NAP. Here, NAP is a national level. It is, however, more difficult to control the level in

winter than in summer, which can also be concluded from Figure 2. This is caused by heavier rainfall, storms and higher discharges of the river IJssel in winter than in summer. The peak in December 1993 was the highest in the 20 years of measurements.

After calibration, data before 1976 was used to run the model and to predict lake levels for the two lakes. The maxima were then used to determine a statistical distribution based on 60 years. These distributions were then extrapolated to give predictions for events with return periods up to 1 in 10,000 years, by statistical methods which are also used to predict extreme river run-off.

Similar calculations were made for various scenarios like sea level rise or climate change, increase of pump or sluice capacity into the North Sea, partly reclaiming the Markermeer and a modified control of the sluices between IJsselmeer and Markermeer. Finally, all calculations resulted in three possible lake level statistics for each of the two lakes. These statistics are shown in Figures 3 and 4. The middle curves give the present situation and the highest curves include climate change. The lowest curves give the effect of double pump or sluice capacity into the North Sea.

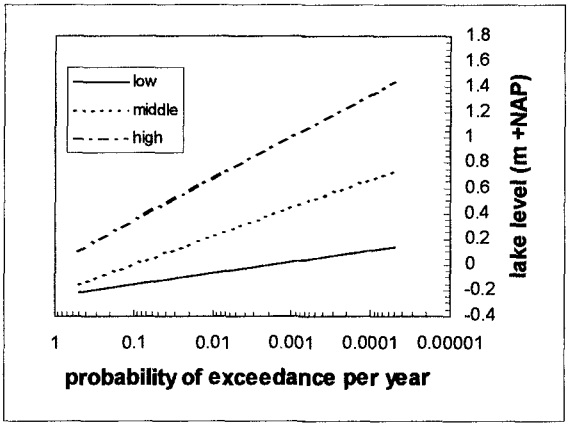

Figure 3. Three possible (extrapolated) lake level distributions for the Markermeer

A modified control of the sluices between IJsselmeer and Markermeer gives also the lowest line in Figure 3. This modified control means that, if due to the river IJssel the lake level in the IJsselmeer increases, the sluices to the Markermeer will be closed and that, therefore, the Markermeer will not be influenced by a high level in the IJsselmeer (which may increase the lake level in the IJsselmeer, however). The highest lines in Figures 3 and 4 are comparable. The lowest line in Figure 3 is much lower than the one in Figure 4.

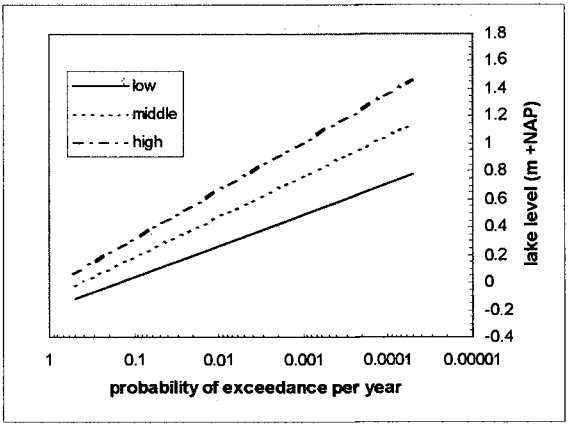

Figure 4. Three possible (extrapolated) lake level distributions for the IJsselmeer

Based on Figures 3 and 4 the following conclusions about extreme lake levels were derived:

- the river IJssel determines mainly the lake level of the IJsselmeer
- the sluice control between the IJsselmeer and Markermeer during high lake levels in the IJsselmeer determines the lake level in the Markermeer:
  - if the sluices stay open, the Markermeer level will follow the IJsselmeer level
  - if the sluices are closed, the Markermeer level will stay low

in principal the Markermeer level is better manageable than that of the IJsselmeer. But what will be the effect on safety of the dikes?

Hydraulic boundary conditions: extreme storms

Storms generate surges and waves and the dikes should withstand these conditions. Flow and wave height calculations were performed with DELFT-3D (in the 2DH mode), the integrated modelling system developed by Delft Hydraulics. These calculations result in storm surge levels and wave heights, periods and directions at more than 1000 locations along the lakes' dikes.

In total 216 calculations were performed covering the following conditions:

- lake levels of –0.4 m, +0.3 m and +1.3 m NAP
- 12 wind directions, each covering a sector of 30°
- 6 wind velocities, from 15 m/s up to 42 m/s

All data of the calculations and for the more than 1000 locations along the lakes' dikes was stored in a data management system and used for further analysis. Figure 5 gives an example of a calculation with DELFT-3D for the Markermeer. The condition given is a very extreme one: a lake level of +1.3 m NAP, combined with a wind velocity of 42 m/s from 330°. Figure 5 shows the storm surge levels. The highest levels occur in the south-east part where the levels may exceed +4 m NAP. The joint probability of this lake level and wind velocity is so small, however, that it

is not a realistic situation for the Markermeer. These conditions were the upper boundary of the set of conditions given above.

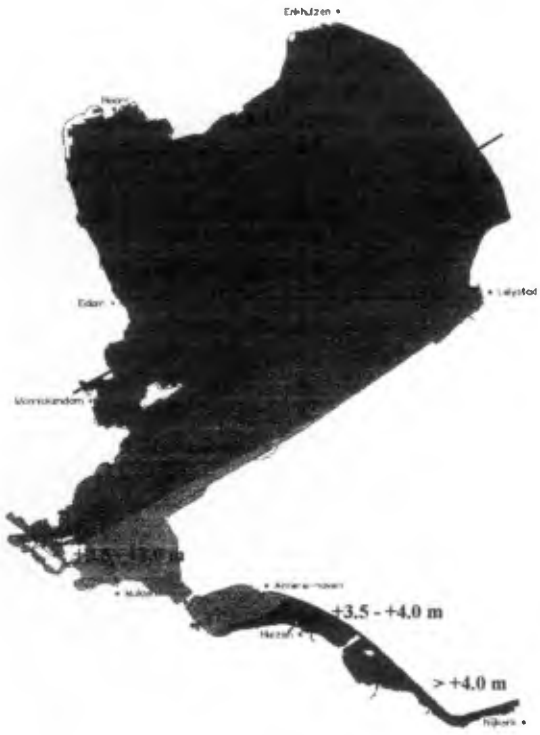

Figure 5. Calculation of storm surge levels in the Markermeer for a lake level +1.3 m NAP and a wind velocity of 42 m/s from 330°

Probabilistic calculations on required dike heights

The long-term statistics of the water levels (Figures 3 and 4) and the data management system on storm surge levels and waves were input for full probabilistic calculations of expected wave run-up or wave overtopping. The model includes also the long-term wind statistics (and through the data management system its effects in surges and waves).

The locations with the hydraulic boundary conditions from the data management system, however, were chosen about 400 m from the dike. Very often the foreshore leads to shallower water at the toe of the dike. And the wave conditions at this toe are required to make the right calculations on required dike height. If the water depth at the toe was different from the location from the data management system, calculations were performed to establish the required conditions.

With these boundary conditions, calculations on wave run-up or wave overtopping were performed according to Van der Meer and Janssen (1995). All these calculations were integrated in the full probabilistic model. With the long-term lake level and wind statistics, the conditions from the data management system, the geometry of the foreshore and the dike itself, a Riemann integration was performed to give the required dike height for a given safety level of say 1 in 10,000 years.

Comparison of the two lakes

Calculations with the full probabilistic model were performed to compare required and existing dike heights and to establish necessary improvements. Other calculations were made in order to compare the IJsselmeer with the Markermeer and to investigate possible essential differences. Figure 6 shows in each of the lakes 15 locations. Locations with the same numbers (for example M01 in the Markermeer and IJ01 in the IJsselmeer) have more or less a similar location in the lake and have also the same orientation of the dike.

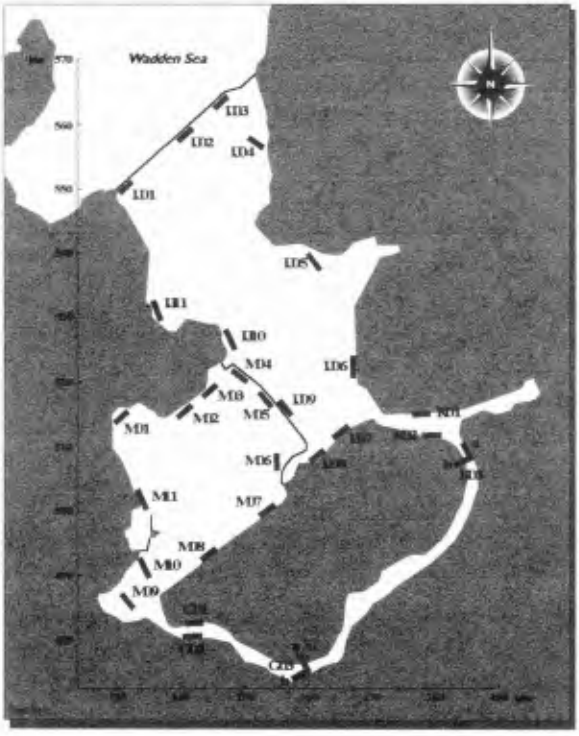

Figure 6. IJsselmeer and Markermeer with similar locations for comparison

Calculations were made for a "standard" dike with a smooth slope of 1:4 and without a foreshore. The required dike heights at all locations were determined for the 2%-wave run-up level as governing condition and for a safety level of 1 in 10,000 years. These calculations were performed for all three lake level statistics given in

Figures 3 and 4. The results are shown in Figures 7 and 8 for Markermeer and IJsselmeer, respectively. The low, middle and high points of the legend correspond with the curves in Figures 3 and 4.

The conclusion on the influence of the long-term lake level statistics on required dike heights becomes very clear from Figures 7 and 8. There is hardly any influence as most of the three lake level statistics give the same required dike height, except for a few, more sheltered, locations.

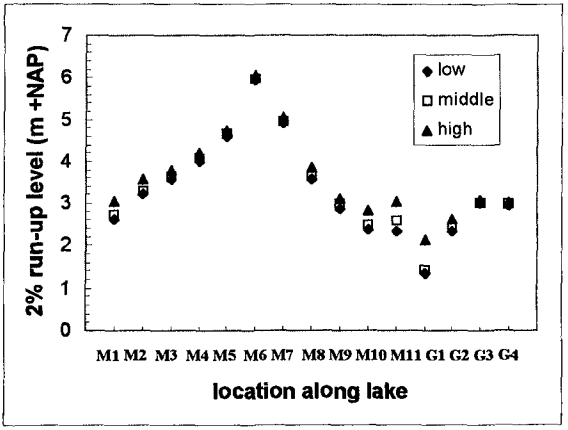

Figure 7. Required dike heights for locations in the Markermeer given in Figure 6 and for 3 long-term lake level statistics given in Figure 3

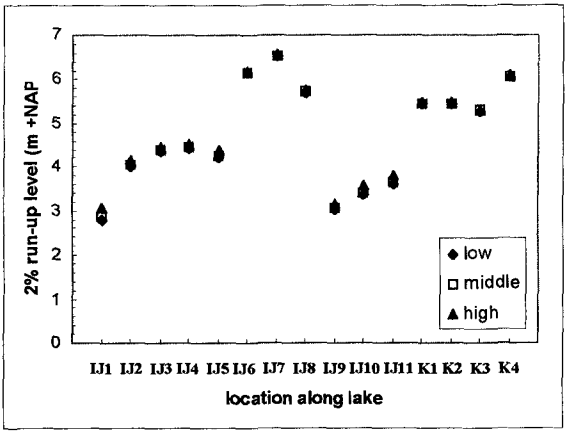

Figure 8. Required dike heights for locations in the IJselmeer given in Figure 6 and for 3 long-term lake level statistics given in Figure 4

The reason why the long-term lake level statistics have hardly influence on required dikes heights, is that extreme lake levels and extreme storms are independent events. A (very) strong wind with a level close to the winter level of –0.4 m NAP has a larger probability of occurrence, than a less strong wind with a much higher lake level to give the same required dike height. In fact very strong wind governs the required dike height and not the long-term lake level statistics. This means also that the lake level control of the Markermeer has no or only marginal influence on dike safety. From that point of view the Markermeer and IJsselmeer are comparable.

Possible damage due to flooding

There are two areas that can be flooded by both the IJsselmeer and the Markermeer, see Figure 9. One area is just north of the separating dike and the other just south. An in-depth study was made of the expected damage in the two areas. The main goal was to investigate the influence that the difference in lake size has on damage. The areas were divided in smaller areas with similar bottom levels. With a simple inundation model the maximum water depth after flooding was calculated for each of these areas.

Figure 9. Two areas that can be flooded by both lakes

A large number of damage categories were used to calculate the total damage. Each category had a given relationship between inundation depth and damage. A few of the damage categories were: agriculture, cattle breeding, horticulture, urban area, recreation, roads, houses, transport, etc. Also a category victims due to drowning was used. The expected damage and the expected number of victims for the southern area (Flevoland) is given in Table 1. Flevoland is one of the polders reclaimed from the lake and the depth is more or less equal to the old bottom of the IJsselmeer which is about –4 m NAP.

Flevoland	flooding from Markermeer	flooding from IJsselmeer	ratio IJM/MM
economic damage (billions guilders)	5.8	6.9	1.2
victims (number)	119	355	3.0

Table 1. Expected economic damage and number of victims by flooding of Flevoland

The damage by flooding from the IJsselmeer is a little larger than from the Markermeer. The reason is that the Markermeer in size is about 2/3 of the IJsselmeer, giving inundation depths that are approximately 0.5 m smaller. Inundation depths in average will be about 2.2 m to 3.3 m. Although the figures for the Markemeer are a little lower, the order of magnitude is the same. A similar conclusion was drawn for the northern area in Figure 9. This means that also from the point of view of damage due to flooding, both lakes are comparable.

Risk analysis on inundation

Dikes in the Netherlands are currently designed and examined on a prescribed load, given as an event with a certain return period (between 1/1,000 and 1/10,000 years). A dike must be capable of withstanding such an event. In future, rather than considering each dike section individually, a total area surrounded by dikes or other forms of protection must have a certain safety level. This should it make possible to describe the circumstances under which dikes really do breach and how a breach develops.

A further step will be to describe safety in terms of risk. Risk is then described as the combination of probability on flooding and the consequences in terms of loss of material (economic damage) and human lives (risk = probability * effect). It is currently not possible to perform a quantitative risk analysis in full detail as described above, but a first attempt was made in this study, using recent studies of the TAW (Technical Advisory Committee on Water Defences in the Netherlands).

In these studies existing dike ring areas were taken and all data on dikes and hydraulic boundary conditions were gathered. A probabilistic computer model was made that includes all possible failure mechanisms of a dike and that is able to calculate the probability of flooding by breaching of one of the dike sections. The description to the actual failure mechanism is still preliminary and needs more research in future (what overtopping discharge can a dike really withstand?).

Each dike section was designed for a prescribed load with a certain return period. The outcome of the probabilistic calculation was the probability of flooding of the whole dike ring area. In total six different dike ring areas were treated by the TAW. The main results are given in Figure 10.

A preliminary conclusion is that the probability of flooding of a dike ring area is similar to the probability of the prescribed load under which conditions the dike should be capable of withstanding this event. This conclusion needs further research for confirmation, but for the present study it was used for a complete risk analysis.

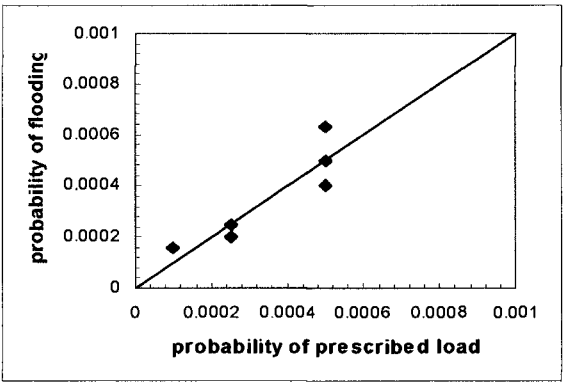

Figure 10. Relationship between a dike section designed for a prescribed load and the probability of flooding of the dike ring area, according to TAW-studies

The probabilities of occurrence of the prescribed loads of each of the dike sections around IJsselmeer and Markermeer have been given by law. These probabilities vary from 1/1,250 to 1/10,000 years. With above conclusion, the probability of flooding of each dike ring area was given the same value. The economic damage of two areas had already been calculated, see Figure 9 and Table 1. In a similar, but slightly simplified way, damage caused by flooding was calculated for all dike ring areas around the both lakes. Together with the probability of flooding it was then possible to calculate the risk of flooding for each dike ring area, by multiplying the probability of flooding with the economic damage.

The main question to consider, however, was the comparison of both lakes with each other and with areas situated along the sea coast. A lake or a sea is not a dike ring area, but a *threat* to the dikes. Therefore, the definition of risk is not applicable to the hydraulic system and a modified definition had to be established. The term *risk profile* was invented for these threats or hydraulic systems:

risk of flooding = probability of flooding of a dike ring area * damage due to flooding

risk profile = the cumulative flooding risks of all dike ring areas along the threat

In this way the risk profile of each hydraulic system like a lake, sea or estuary can be calculated and compared. Both risk and risk profiles are given in value per year, say in million Dutch guilders per year (one US dollar is about two guilder). Figure 11 gives the risk profiles of 5 hydraulic systems in the Netherlands. Two of them are of course the IJsselmeer and Markermeer. They have similar risk profiles of 4.5 and 4.2 million guilders per year.

Although the Markermeer gives lower inundation levels, and therefore lower damage compared to the IJsselmeer, the risk profile is the similar. The main reason for this is that more people live in the dike ring areas around the Markermeer than around the IJsselmeer (Amsterdam is situated on the Markermeer).

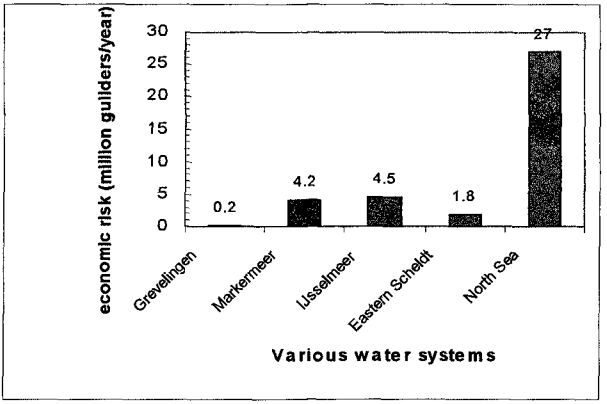

Figure 11. Risk profiles of various hydraulic systems in the Netherlands

The above system analysis leads to the first overall conclusion of the study:

- with respect to safety the two lakes do not show significant differences and should be treated in the same way.

Three other hydraulic systems are given in Figure 11. The Grevelingen is also a lake and after the Markermeer the largest in size in the country. There is more than an order of magnitude difference with the Markermeer and this lake should not be considered like the IJsselmeer or Markermeer or like estuaries or seas.

The last two hydraulic systems are the Eastern Scheldt and the North Sea which directly attacks the rest of the Netherlands. The Eastern Scheldt is an estuary which is closed by the well-known Eastern Scheldt barrier if the storm surge reaches a level of +3 m NAP. From that moment on the estuary becomes a closed lake. The risk profile for this estuary is smaller than for the IJsselmeer and Markermeer, but still comparable. The North Sea threats a large part of the Netherlands and gives of course the largest risk profile. There is, however, less than an order of magnitude difference with the two lakes. Comparing the two lakes with the two salt water systems gives the final conclusion:

- large lakes like the IJsselmeer and Markermeer give similar risk profiles as for areas along the sea coast and should, with respect to safety, be treated in the same way.

Conclusions

A system analysis of the threat that hydraulic systems, such as large lakes, estuaries and seas, can form for the safety of dike ring areas around these systems, gives a good insight into the physical aspects. Together with a risk analysis, finally leading to the description of the risk profiles of hydraulic systems, it makes it possible to compare the various hydraulic systems from the point of view of safety. To that

aspect the IJsselmeer and Markermeer should be treated in a similar way as estuaries and the North Sea.

Lake level control has hardly any influence on required dike heights, or safety, as the dike heights in most situations are determined by very strong wind, high storm surges and high waves. Flood damages from IJsselmeer and Markermeer are comparable, although the damage due to the Markermeer will be a little smaller as the lake is also smaller (the inundation depths, therefore, are a little smaller).

Acknowledgement

The authors wish to thank all those who have actively participated in the extensive technical, legal and managerial discussions, which have formed the basis for this study. During the 1½ year study representatives from the Netherlands' Ministry of Transport, Public Works and Watermanagement, several Provinces and Waterboards worked together with the research staff of Delft Hydraulics, the Technical University of Delft and the University of Utrecht. The outcome of this work underlines that a technical study, set in the context of a political and managerial debate, can indeed lead to consensus on the management steps to be taken and the legal changes that are necessary to make this happen.

References

Van der Meer, J.W. and J.P.F.M. Janssen (1995). *Wave run-up and wave overtopping at dikes.* In: Wave Forces on Inclined and Vertical Wall Structures. ASCE. Ed. N. Kobayashi and Z. Demirbilek. Ch. 1, p. 1-27

List of (Dutch) references of the independent investigation for the Markermeer, a Dutch inland lake

1 WL|DELFT HYDRAULICS, 1997. Projectplan for the independent investigation for the Markermeer, a technical study and integration (in Dutch). WL|DELFT HYDRAULICS, Report H3211, March, 1997

2 J.W. van der Meer, 1997. Inventory of the uncertainties in the projectplan for the 'independent investigation for the Markermeer' (in Dutch). WL|DELFT HYDRAULICS, Report H3176, March, 1997

3 P. Glasbergen, 1997. Administrative and legal investigation for the Markermeer, Phase report B1: The concept 'exterior waters' (in Dutch). WL|DELFT HYDRAULICS, Report T2145, May, 1997

4 P. Glasbergen, 1997. Administrative and legal investigation for the Markermeer, Phase report B2: 'Analysis of policy making networks and systemcomparisons' and B3: 'Administrative and legal consequences' (in Dutch). WL|DELFT HYDRAULICS, Report T2145, July, 1997

5 R.J. Fokkink, 1997. Independent investigation for the Markermeer, technically relevant and integrated study, subreport Phase 1A: 'Statistics of lake levels' (in Dutch). WL|DELFT HYDRAULICS, Report H3211, December, 1997

6 Y. van Haaren, 1997. Independent investigation for the Markermeer, technically relevant and integrated study, subreport Phase 1B-1: 'Bathymetry and geometry of the model' (in Dutch). WL|DELFT HYDRAULICS, Report H3211, August, 1997

7 Y. van Haaren and G.B.H. Spaan, 1997. Independent investigation for the Markermeer, technically relevant and integrated study, subreport Phase 1B-2: 'The set-up of the Delft-2D system' (in Dutch). WL|DELFT HYDRAULICS, Report H3211, December, 1997

8 Y. van Haaren, 1997. Independent investigation for the Markermeer, technically relevant and integrated study, subreport 1B-3: 'Stormprofile and windfields' (in Dutch). WL|DELFT HYDRAULICS, Report H3211, October, 1997

9 Y. van Haaren and G.B.H. Spaan, 1998. Independent investigation for the Markermeer, technically relevant and integrated study, subreport Phase 1B-4: 'Production runs and control' (in Dutch). WL|DELFT HYDRAULICS, Report H3211, January, 1998

10 Y. van Haaren and R.C. Ris, 1997. Independent investigation for the Markermeer, technically relevant and integrated study, subreport Phase 1C: 'Preparing HYDRA-M' (in Dutch). WL|DELFT HYDRAULICS, Report H3211, September, 1997

11 F. den Heijer and Y. van Haaren, 1998. Independent investigation for the Markermeer, technically relevant and integrated study, subreport Phase 2: 'The level of the high-water' (in Dutch). WL|DELFT HYDRAULICS, Report H3211, April, 1998

12 R.F. de Graaff, 1998. Independent investigation for the Markermeer, technically relevant and integrated study, subreport Phase 3: 'Measures and costs of dike-improvements, considering the Markermeer as exterior waters' (in Dutch). WL|DELFT HYDRAULICS, Report H3211, May, 1998

13 A.M. de Leeuw, F. den Heijer and J.J. de Jonge, 1998. Independent investigation for the Markermeer, technically relevant and integrated study, subreport Phase 4: Determination of damage accompanying inundation' (in Dutch). WL|DELFT HYDRAULICS, Report H3211, April, 1998

14 F. den Heijer, 1998. Independent investigation for the Markermeer, technically relevant and integrated study, subreport Phase 5: 'Inundation risks' (in Dutch). WL|DELFT HYDRAULICS, Report H3211, April, 1998

15 WL|DELFT HYDRAULICS, 1998. Independent investigation for the Markermeer, technically relevant and integrated study (in Dutch), final report. WL|DELFT HYDRAULICS, Report H3211, May, 1998

MAINTENANCE DREDGING REQUIRED AFTER PORT EXTENSIONS AT WALVIS BAY

R C Coppoolse[1] and J S Schoonees[2]

Abstract

Walvis Bay, the major port of Namibia, is earmarked for extensions. The extension of the entrance channel and the port can increase the maintenance dredging cost considerably, and if not correctly planned could impact negatively on the nearby Walvis Lagoon. An improved layout for the extended port is recommended, taking into account the sediment transport regime. The future maintenance dredging rate for the extended port is determined to be 720 000 m^3/year compared with the 200 000 m^3/year for the existing commercial and fishing harbours. The future general cargo quays could be located so as to minimise the influx of sediment into the Walvis Lagoon. It is shown that the water exchange to the lagoon will not be significantly affected.

1. Introduction

The Port of Walvis Bay is situated in a natural harbour along the central Namibian coastline (Figures 1 and 2). This harbour is formed by the Walvis Peninsula with Pelican Point located at its tip (Figure 1; see Schoonees *et al.*, 1998 for more details). The land surrounding Walvis Bay is low-lying and consists of desert sand. Traditionally the port has been operated as two entities, namely, the commercial and fishing harbours; however, at present the Namibian Ports Authority has jurisdiction of the full water area. The ecologically sensitive Walvis Lagoon (Figure 1) is located south of the town of Walvis Bay. This lagoon used to be the mouth of the Kuiseb River, which is a river that rarely reaches the sea except during large episodic floods.

As the only major deep-water port of Namibia and because of the short distance to the central heartland of Namibia (Windhoek) and the existing

[1]P O Box 4028, 7537 Old Oak, South Africa

[2] Research Engineer, CSIR, P O Box 320, 7599 Stellenbosch, South Africa

infrastructure, it can be expected that Walvis Bay will be the focal point of future commercial port development in Namibia and the adjacent landlocked regional countries. An extension and deepening of the entrance channel and the port is planned (Figure 3), which could increase the maintenance dredging cost considerably, as well as impacting negatively on the Walvis Lagoon.

A feasibility study (CSIR, 1994) was carried out to assess the viability of the proposed future extensions to the Port of Walvis Bay as shown in Figure 3. The aim of the feasibility study was to use existing information and to evaluate the environmental conditions (waves, current, winds and tides), assess the effect of the proposed port development (Figure 3) on the movement of sediment in the bay, comment on the present port capacity and the navigational aspects of the proposed berth and channel layout and carry out a preliminary ecological investigation into the effect of the development on the lagoon. This paper deals only with the sediment transport and dredging aspects such as the present sediment transport regime, the increased maintenance dredging requirements of the extended port and the effect of sediment transport on the Walvis Lagoon. The paper includes the prediction of mud infill rates and the minimisation of dredging costs without endangering the lagoon.

2. Environmental data

Seven sets of vertical *aerial photographs* are available from 1943 to 1980. These photographs show amongst other things, the development of the port and town, changes to the Walvis Lagoon and the growth of the Walvis Peninsula. The *bathymetry* of the whole Walvis Bay area is shown in Figure 2. From this figure it can be seen that the average water depth in the bay is about -10 m to chart datum (CD = 0.90 m below mean sea level). The main entrance channel to the port is dredged to -10 m to CD.

The *tide* is semi-diurnal with a spring tidal range of 1.44 m. From Waverider measurements obtained in 50 m depth of water outside the bay, it was found that the median significant *wave* height (H_s) is 1.1 m and the median peak wave period is 11.6 s. The 1-in-1 year deep-sea H_s is 3.6 m for Walvis Bay. Wave directions were obtained from voluntary observing ships. The dominant deep-sea wave directions are southerly to south-westerly (89% of the time). This means that Walvis Bay harbour is protected from the dominant waves. The port is, however, exposed to waves from the sectors between west and north which occur only 2% of the time.

Moored *current* buoys and drogues were mainly used in field studies to determine the current regime in Walvis Bay. A clockwise surface current circulation to an anticlockwise circulation occurs in the bay in the ratio 3:1. The velocities of these currents are low, generally of the order of a few cm/s. A diurnal reversal of current directions occurs as well, with clockwise (south-going along the eastern shore) currents in the morning followed by anticlockwise currents in the afternoon. This reversal is brought about by an associated change in wind direction. In the surf zone along the bay, especially along the eastern shore, wave-driven currents are

normally dominant. At both Dolfynstrand (Figure 1) and Langstrand (Figure 1), the surf-zone currents are usually northbound, while at the breakwater immediately to the north of the port (Figure 1), the current is southbound. This reversal in the surf-zone current direction is primarily due to diffraction effects. At the mouth of the Walvis Lagoon strong currents in and out of the mouth are found.

Generally speaking, the *material* found on the sea bottom in Walvis Bay consists of fine to medium shelly sand overlain by a soft marine mud layer. Mostly mud is dredged from the port in order to maintain the required depths. Sand is, however, found on the surface of the sea bottom along the shoreline. The present influence of the nearby *Kuiseb River* on the harbour is considered to be small and intermittent because a retaining wall diverts the infrequent major floods away from the bay and port.

3. Sediment transport regime

3.1 Growth of the Walvis Peninsula

The Walvis Peninsula is growing northwards at a rate of 22.6 m/year (Schoonees *et al.*, 1998) because of the northbound longshore transport along its western shoreline. The effect of this growth is primarily to decrease wave action at the harbour even further, since the dominant deep-sea waves are from the southerly to south-westerly sector. The secondary effect of this growth is that the sediment transport rates in the bay will also decrease in time as will be discussed below. However, because the circulation in the bay is wind-driven (and possibly tide-driven as well) this will most probably not reduce the sedimentation of the port significantly.

3.2 Longshore transport

In Schoonees *et al.* (1998) it was determined that the net *longshore transport* is about 860 000 m^3/year along the western shoreline of the Walvis Peninsula. Along the eastern shore of the peninsula a very low net longshore transport can be expected.

Inside the bay, at both Dolfynstrand and Langstrand, the net longshore transport is northbound. The respective potential net transport rates at these sites are about 150 000 m^3/year and 510 000 m^3/year (CSIR, 1985). Immediately to the north of the breakwater north of the port, accretion has taken place. The direction of the net longshore transport is therefore southbound at that location. This is due to a southerly current generated by a gradient in breaker wave height. This gradient is caused by wave diffraction around Pelican Point. Because of this reversal in the net longshore transport direction, an area subject to erosion has to exist between the breakwater and Langstrand. This is indeed the case: a rocky stretch of coastline is found around Dolfynstrand.

At the mouth of the lagoon there is a low net westbound longshore transport as evidenced by a spit on the eastern side of the mouth, which grows westwards, as can be seen on aerial photographs.

For the stretch of coastline between Dolfynstrand and Langstrand, 50 years

of growth of the peninsula results in a considerable reduction in the (still) northbound net longshore transport (CSIR, 1985).

3.3 Aeolian sand transport

Wind data collected from 1987 to 1993 south of the town of Walvis Bay have been used to compute seasonal and annual wind-blown sand transport rates. A median sand grain size of 0.29 mm was used.

The results show that, on an annual basis, the dominant aeolian transport is bound between the north-east and the north-west. Considering the position of the town of Walvis Bay and the lagoon (Figure 1), it is clear that the port and its proposed extensions are shielded from the dominant aeolian sand transport. It is only north of the breakwater at the shore connection of the future bulk cargo handling platform (Figure 3) where problems may occur. The influx of wind-blown sand there is estimated to be 15 m^3/year per m of westbound transport.

3.4 Cross-shore transport

Cross-shore transport is not a very important process causing sedimentation in the harbour, because the harbour is situated in a calm area and due to the extensive quays built all along the shoreline inside the port.

4. Dredging

4.1 Analysis of dredger records

Figure 2 shows the commercial and fishing parts of the port. The commercial harbour consists of the main entrance channel and the south-western side of the port while the fishing harbour is situated on the north-eastern side, including the secondary channel.

Dredging has been carried out fairly regularly in the commercial harbour. From 1965 to 1993, major maintenance dredging was performed about every five years. Dredging has also been done by means of a small grab-and-barge dredger on a continuous basis. Figure 4 shows the annual dredge volumes from minor and major maintenance dredging. The volumes given are not *in situ* volumes but hopper volumes; the bulking factor has been estimated to be 1.1. Also shown in Figure 4 is the running annual average rate (that is, the first point is the mean rate over one year, the second point is the mean rate of the first two years, etc.). The running average is about 130 000 m^3/year for the commercial harbour.

It is suggested that annual surveys be performed throughout the whole harbour. These surveys should be conducted before and after major maintenance dredging in order to determine the *in situ* quantities dredged (the so-called in-and-out surveys). At the same time, dredge data should be collected from the dredgers and volumes dredged should be determined as accurately as possible with a number of methods. It is further recommended that the harbour be divided into practical areas where maintenance dredging is to take place (Figure 11 shows these areas for the new proposed harbour layout) and to keep records of the quantities dredged in these areas.

4.2 Prediction of maintenance dredging requirements

Method

A number of techniques have been developed to predict dredging rates in harbours (O'Connor, 1985; Vicente and Uva, 1984; Schoonees, 1994). Most of these techniques are based on survey data being collected over a number of years (often from test pits). Plotting these data shows that in all cases there is an exponential or power law decrease in the depth (due to sedimentation) over time. This principle is used to predict the future dredging rates at the Port of Walvis Bay. The depth of the new channels and new basins is, however, far greater than the existing channels and basins. In theory each channel or basin with a certain relative depth (Ho; Figure 5) and its banks at a certain depth (do) have their own characteristic sedimentation curve in a certain environment. By using curves from similar areas with different depths, curves can be extrapolated to determine the sedimentation in deeper or shallower channels. The existing harbour (including the fishing harbour) has been subdivided into eight areas for this reason.

Surveys were conducted for the different areas on a number of occasions, but only subsequent surveys could be used when no major maintenance dredging had taken place in between. Data from two of the eight areas could not be used. This is because either the data covered only a short period of time and/or the sedimentation (decrease in water depth) was minimal during the particular period and thus within the accuracy of the survey method.

The sedimentation (Ho) and the sedimentation ratio (Ht/Ho; Figure 5) were plotted against time. Power law curves were fitted through the data points (exponential curves did not fit the data as well). The curves for the different areas were compared in order to evaluate the compatibility and to classify them according to the relative channel depth (Ho) and surrounding depth (do). Only the curves for the commercial harbour could be used for calibration purposes (as will be explained below) and eventually the calibrated curves could be extrapolated to obtain representative sedimentation curves for the new proposed layout.

Results

Figure 6 shows the sedimentation and the sedimentation ratio as a function of time for the south-turning circle area from November 1976 to February 1981. The goodness of fit is given by the coefficient of determination (R^2), which is 0.96 for the example in Figure 6.

In order to see if there are trends in the curves with regard to the relative depth (Ho) of the channels, the sedimentation ratio curves were plotted to indicate the relative channel depths (Figure 7). It is shown that the curves for the southern quays, south of the turning basin, the south channel (fishing harbour) and the northern quays all show similar curves while the inner channel of the commercial harbour and the tanker basin are the two extremes. No clear trends can be seen when comparing the relative channel depths. Comparing the depth of the surrounding areas in a similar way also showed that there is not a clear trend, although deepest depths show the highest sedimentation ratios.

Because no clear trends were detected when comparing the sedimentation ratios of the various areas, it was decided to use the average sedimentation ratio of the commercial and fishing harbours (Figure 8). The minimum and maximum curves were used to determine the extreme values (Figure 8).

Calibration

A twofold calibration of the method was carried out: (1) by fitting the power curves to the measured sedimentation of mud (Figure 6 shows an example); and (2), by comparing the computed sedimentation rates with the net average dredging rate in the commercial harbour. In the latter case, the computed sedimentation rate was determined for a specific area by multiplying the predicted vertical sedimentation of mud with the surface area of the specific area. By summing all these computed sedimentation rates for the different areas, the total predicted sedimentation rate was obtained for the particular period under consideration.

The calibration factor was defined as the computed sedimentation rate divided by the measured average dredging rate. Because of this calibration, the required maintenance dredging rates are given in terms of hopper (dredged) volumes. Figure 9 shows the calibration factor as a function of time. The apex of the curve is caused by the fact that the annual dredging rates, which are a linear function of time, are compared with the predicted dredging rates which change according to a power law over time. The average calibration factor is used for the whole harbour. The calibrated sedimentation curve is as follows:

$$Ht/Ho = 0.59\ (10^{0.0118\,t + 0.976})$$

where t = time (months)

Future dredging rates

The best estimate of the sedimentation volume for the total existing harbour is about 200 000 m^3/year (dredged volume), while for the new proposed layout (Figure 10) this value will be about 720 000 m^3/year with minimum and maximum values of about 165 000 m^3/year and 1 661 000 m^3/year respectively (also dredged volumes). The annual dredging rate will increase dramatically for the new proposed layout. This is mainly due to the increased surface area of the basins and channel, but also because of the increased channel depths. Adequate sediment (mostly mud) is available to cause the sedimentation.

4.3 Proposed port layout and influence of harbour extensions on the lagoon

With regard to sediment transport and the associated dredging considerations, it is logical to try and make entrance channels as short and berthing areas as small as possible. (Of course, navigational and other aspects also play a vital role in designing the size of berthing areas.) Applying this principle of minimising areas, the orientation of the main entrance channel should be north-west instead of north (Figure 2). This means that the channel will be about 500 m shorter

resulting in approximately 900 000 m^3 less to be dredged if the whole channel is to be dredged from scratch. Naturally an unnecessary cost would result if a completely new channel is dredged; it is much more feasible to use the existing channel and change its orientation when extending the channel. It is recommended that the new seaward portion of the channel should start at the extremity of the existing channel and head north-westwards (Figure 10 shows the new proposed port layout). In this way the channel will not only be 100 m shorter (and thus save on capital dredging), but it will be in a calmer (more protected) area and facing right into the waves requiring less maintenance dredging. In addition, the access to shipping will be easier because of reduced ship motions. For bigger ships the channel will lead straight to the future bulk cargo handling platform.

By further applying the principle to minimise channels and berthing areas, it is suggested that the turning circle in front of, and the access channel to the bulk cargo handling platform (Figure 3) be amalgamated with the main entrance channel as shown in Figure 10. This will not be a hindrance to shipping because at present fewer than one ship visits the port per day. Considering this access channel, only a short length of about 1.5 km of channel will be required. This will be about 2 million m^3 less to be dredged initially. Another saving is to discontinue using and maintaining the two entrance channels. This originally probably stemmed from the fact that the commercial and fishing ports were run by two different controlling bodies. It is recommended that the smaller entrance channel (to the fishing harbour) be left to fill up over time and that only the main channel be maintained. This also applies even if the port is not extended in the near future.

The harbour extensions will have the following effect on the Walvis Lagoon:

- Wave action and therefore wave-driven longshore sediment transport (which is southbound in this vicinity) will be drastically reduced.
- The quays will trap this longshore transport and will severely limit the influx of the finer sediment carried by the clockwise circulation to the mouth of the lagoon. In fact, the circulation pattern will be altered.

Less sediment will thus be available at the lagoon mouth to be transported into the lagoon. Historically the lagoon experienced siltation problems. Therefore the harbour extensions will in fact benefit the lagoon. Because the currents in and out through the mouth are tidally driven, the proposed port extensions will probably not affect the water exchange to the lagoon (which is an important ecological consideration) significantly.

5. Conclusions and recommendations

Presently about 200 000 m^3 of sediment (mainly mud; dredged volumes) is dredged annually from the navigable harbour areas.

Existing survey data have been used to verify that the depths of channels and basins decreased as a power function over time. The method was first

calibrated against the sedimentation rates, then calibrated against the required annual dredging rate for the commercial part of the port, and finally used to predict the future dredging rate for the enlarged harbour. A maintenance dredging rate of about 720 000 m^3/year was computed for the total future extended port as shown in Figure 10. All these volumes are dredged volumes; divide by the bulking factor of about 1.1 to obtain an estimate of *in situ* volumes. Adequate sediment (mostly mud) is available to cause this sedimentation.

The construction of the future general cargo quays on the south-western extremity of the port will most probably limit the influx of sediment into the Walvis Lagoon, thereby benefiting the lagoon. Because the currents in and out through the mouth are tidally driven, it is unlikely that the port extensions will significantly affect the water exchange of the lagoon.

Applying the principle of minimising channel lengths and berthing areas, the originally anticipated extensions (Figure 3) have been adapted to the layout shown in Figure 10. Considerable savings in both capital and maintenance dredging are the result.

Hydrographic surveys should be conducted before and after major maintenance dredging in order to determine the *in situ* quantities dredged as accurately as possible. At the same time, dredge data should be collected from the dredgers in order to determine the volumes dredged as accurately as possible. It is further recommended that the harbour be divided into practical areas where maintenance dredging is to take place and to keep records of the quantities dredged in these areas.

Acknowledgement

The permission granted by the Namibian Ports Authority to publish this paper is gratefully acknowledged.

References

CSIR (1985). Sediment transport and coastline changes at Walvis Bay. *CSIR Report* C/SEA 8544, Stellenbosch (in Afrikaans).

CSIR (1994). Feasibility of port extensions at Walvis Bay. *CSIR Report* EMAS-C 94031, Stellenbosch.

O'Connor, B A (1985). Siltation in navigation channels, dock entrances and marinas. *Three-day Short Course*: Dredging for waterways and harbours, Dept. Civil Eng., University of Liverpool, Liverpool.

Schoonees, J S (1994). Sedimentation of harbour entrance channels. *CSIR Research Report* 716, Stellenbosch.

Schoonees, J S, Lenhoff, L and Raw, A J (1998). Preventing natural breaching of the major sand spit protecting the Port of Walvis Bay. *26 Intern. Conf. on Coastal Eng.*, ASCE, Copenhagen (in press).

Vicente, C M and Uva, L P (1984). Sedimentation in dredged channels and basins. Prediction of shoaling rates. *19 Intern. Conf. on Coastal Eng.*, ASCE, Houston, Texas. Vol. 2: 1863 - 1878.

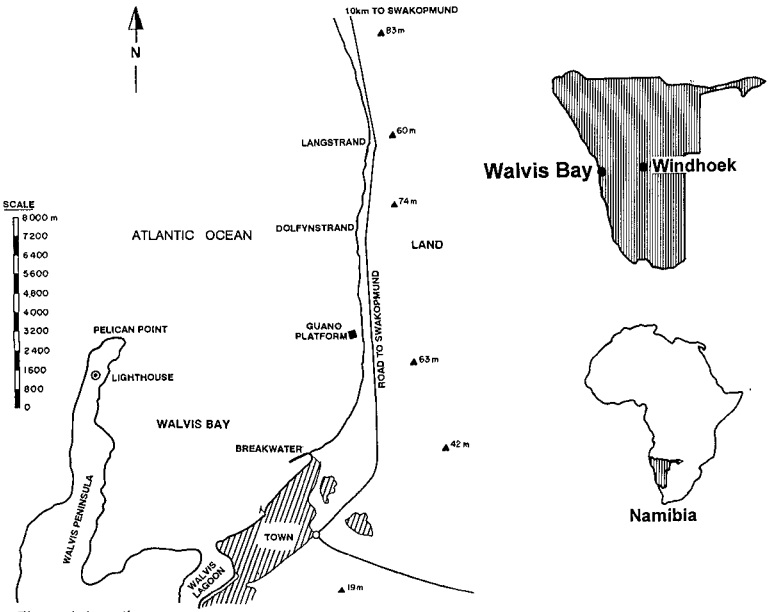

Figure 1: Location map

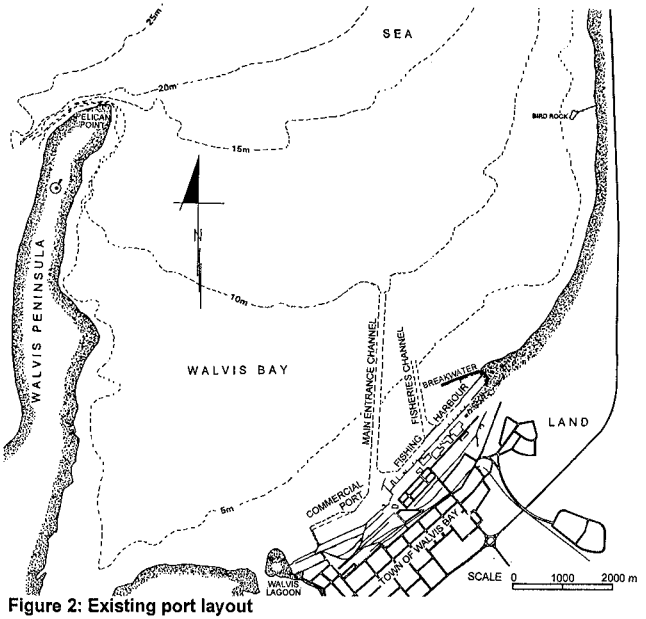

Figure 2: Existing port layout

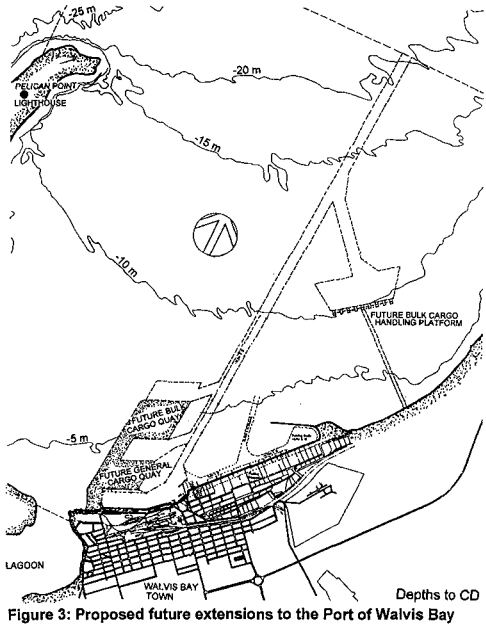

Figure 3: Proposed future extensions to the Port of Walvis Bay

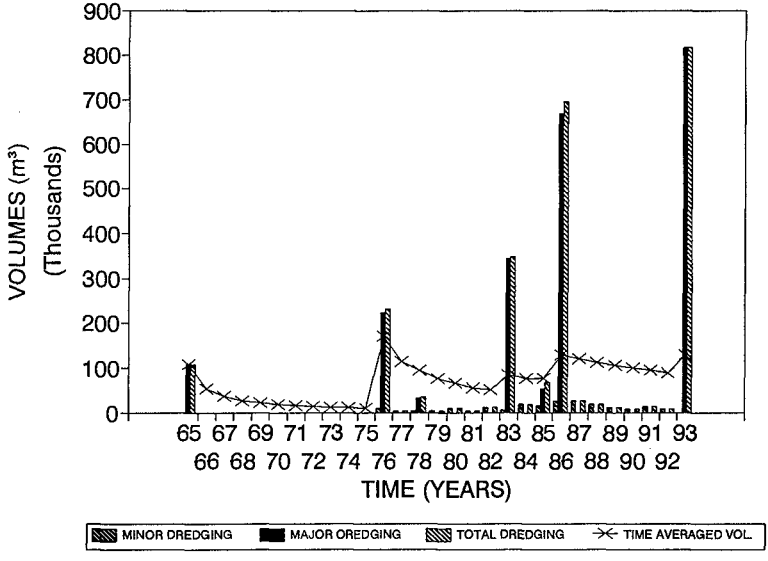

Figure 4: Annual dredge volumes from minor and major maintenance dredging (commercial port)

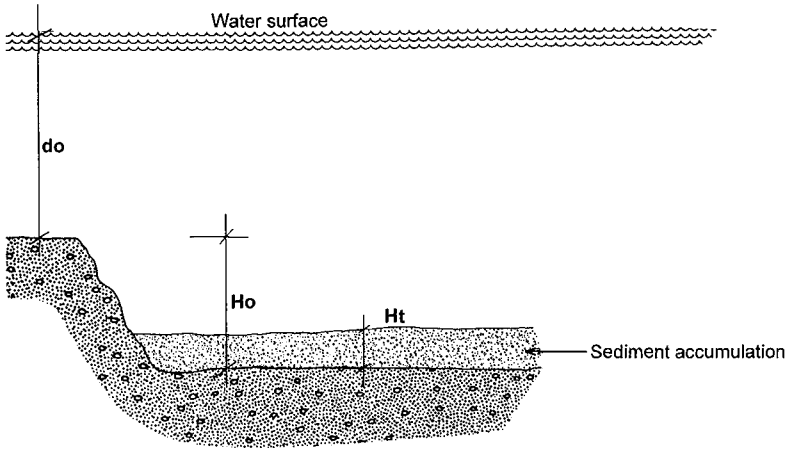

Figure 5: Definition sketch of the sedimentation of harbour basins

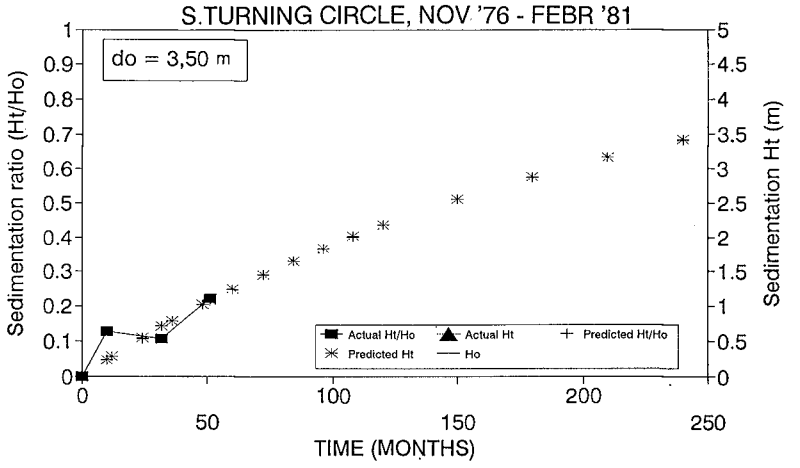

Figure 6: Sedimentation ratios and the sedimentation at the south turning circle (commercial harbour)

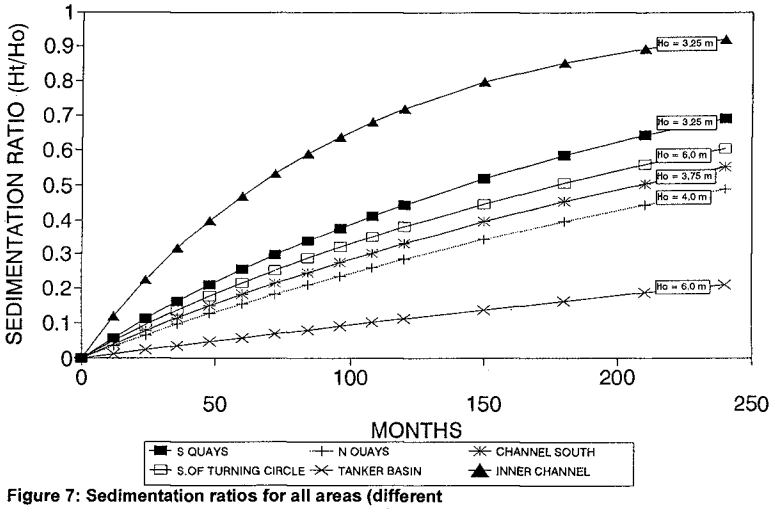

Figure 7: Sedimentation ratios for all areas (different initial channel depths indicated)

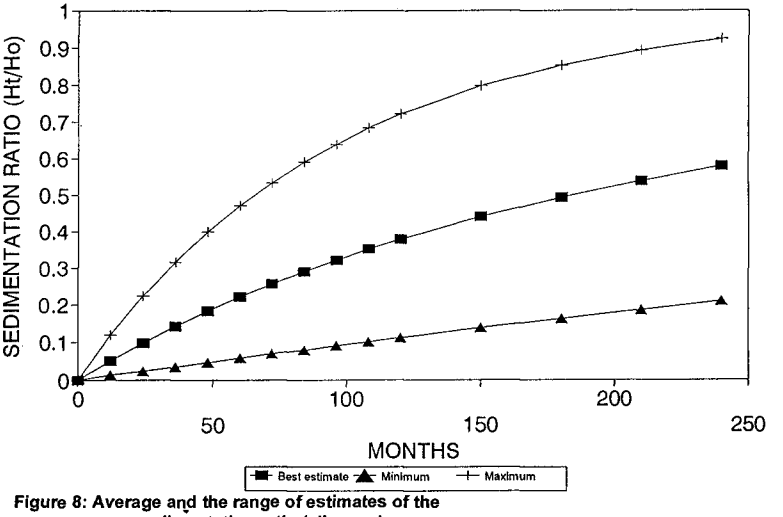

Figure 8: Average and the range of estimates of the sedimentation ratio (all areas)

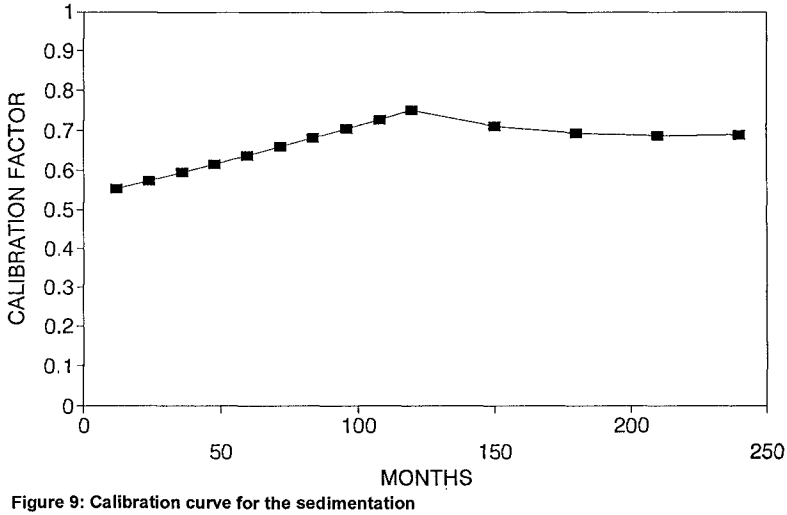

Figure 9: Calibration curve for the sedimentation

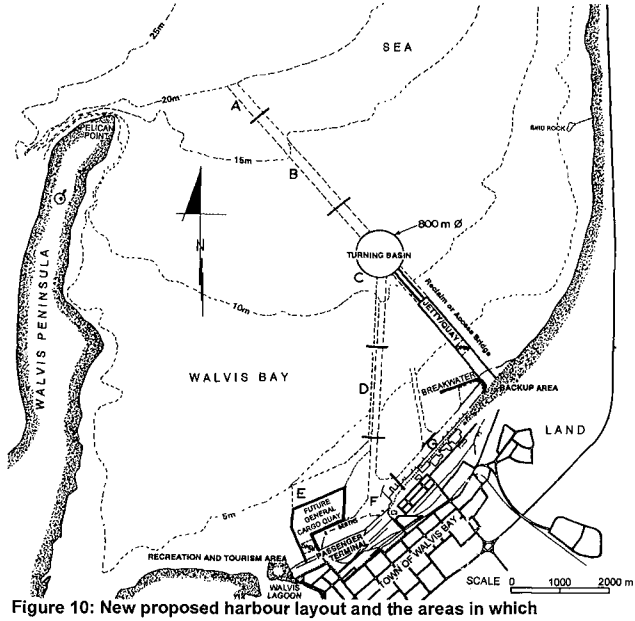

Figure 10: New proposed harbour layout and the areas in which the maintenance dredging rates should be recorded

Accuracy in Spill Monitoring
Turbidity Distribution and Conversion Factors

Klavs Høgh[1] (M.Sc.), Iris Buxbom[2] (M.Sc.) and Trine Borum Bojsen[2] (M.Sc.)

The present paper is based upon work carried out at the Spill Monitoring Department within Öresund Marine Joint Venture (ÖMJV)[3].

Abstract

In connection with the dredging and reclamation works at the Öresund Link Project between Denmark and Sweden carried out by the Contractor, Öresund Marine Joint Venture (ÖMJV), an intensive spill monitoring campaign has been performed in order to fulfil the environmental requirements set by the Danish and Swedish Authorities.

Spill in this context is defined as the overall amount of suspended sediment originating from dredging and reclamation activities leaving the working zone.

The maximum spill limit is set to 5% of the dredged material, which has to be monitored, analysed and calculated within 25% accuracy.

Velocity data are measured by means of a broad band ADCP and turbidity data by four OBS probes (output in FTU). The FTU's are converted into sediment content in mg/l by water samples.

The analyses carried out, results in high acceptance levels for the conversion to be implemented as a linear relation which can be forced through the origin.

Furthermore analyses verifies that the applied setup with a 4-point turbidity profile is a reasonable approximation to the true turbidity profile. Finally the maximum turbidity is on average located at a distance 30-40% from the seabed.

[1] Per Aarsleff A/S, Amager Strandvej 401, 2770 Kastrup, Denmark.
[2] Carl Bro a/s, Granskoven 8, 2600 Glostrup, Denmark.
[3] ÖMJV consists of: Per Aarsleff A/S, Denmark.
Great Lakes Dredge & Dock Company, USA.
Ballast Nedam Dredging, the Netherlands.

Nomenclature

P : production [T]
τ : turbidity [FTU], ([Formazin Turbidity Unit])
C : concentration [g/m^3]
V : current velocity [m/s]
I : flux intensity [$g/m^2/s$]
F : flux [g/s]
Q : discharge [m^3/s]
S : spill [g]

a_0 : conversion factor (with zero intercept) [$g/m^3/FTU$]
a_1 : conversion factor (free intercept) [$g/m^3/FTU$]
b_1 : conversion offset [g/m^3]

T : production period [s]
Γ : surface [m^2]
$\vec{\Gamma}$: surface normal unit vector
A : plane [m^2]

x : current perpendicular coordinate [m]
y : current parallel coordinate [m]
z : depth coordinate [m]
t : time coordinate [s]

μ : standard mean
σ : standard deviation
Δ : difference
d : distance from sea bed to maximum turbidity [m]
D : water depth [m]
∂ : normalised distance from sea bed to maximum turbidity

Area ID's:

TT : Tunnel Trench, sections A, B and C
CD : Compensation Dredging, sections 1 and 3
DCC : Drogden Construction Channel
FL : Flinte Channel, sections A, B2 and C1
EP : East Pylons
WP : West Pylons
LN : Lernacken
WB : Outlet from Sedimentation Basins

Introduction

In connection with the construction works at the Öresund Fixed Link Project connecting Denmark and Sweden, the potential environmental effects of the associated construction works were of great political interest.

For the dredging and reclamation works this meant strict environmental requirements regarding the allowable amount of spill caused by these activities. A large scale Spill Monitoring Programme as prescribed by the owner was put in action by the Contractor. The Spill Monitoring System was ship and land based, and monitoring of the spill causing activities was performed on a 24 hour basis as dredging was not permitted after 6 hours lack of spill monitoring.

In general the overall spill limit is set at 5% by weight of the design quantity to be dredged (some 7 million m^3) and has to be determined with a 25% accuracy with a 75% probability. Also seasonal variations in daily and weekly spill limits are to be followed in order to protect the biological life on a short term basis.

As spill monitoring in this intensive way with such strict specific requirements has never been carried out before, the system was (and still is) under continuous discussion and verification. The intention of this paper is to clarify some of the more serious discussions related to accuracy in spill monitoring that have been raised, based on the very large amount of data which are available after almost 3 years of spill monitoring.

Spill in this context is defined in the contract as the portion of dredged or excavated material brought into suspension during dredging, transport or filling and leaves the work zone or land reclamation areas as follows:

1. *Suspended and resuspended materials originating from the dredging activities leaving the work zone.*

2. *Suspended materials leaving the reclamation or backfilling areas.*

3. *Materials lost during transport from dredging to reclamation areas or from reclamation areas to backfilling areas.*

Spill at any time is the sum of 1. to 3. and is measured by dry weight of suspended material.

The work zone is defined as the area to be dredged plus a surrounding 200 metre zone.

Basic theory

The governing equations for the spill calculations are derived by considering a balance (continuity equation) of suspended material through an enclosed box as shown in Fig. 1.

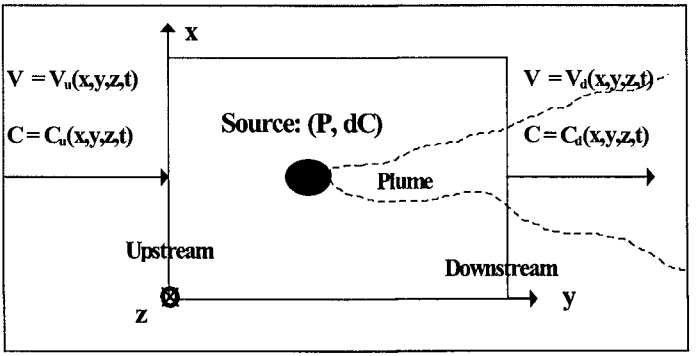

Figure 1. Spill Calculation Box.

The flux intensity of suspended material at a given coordinate in time is given by

$$\vec{I}(x,y,z,t) = C(x,y,z,t) \cdot \vec{V}(x,y,z,t) \tag{1}$$

and the net flux through the box at time (t) is calculated by integration along the vertical surface (Γ) of the box

$$F(t) = \int_{\Gamma} \vec{I}(x,y,z,t) d\vec{\Gamma} \tag{2}$$

This way the spill (S) related to the production (P) during a dredging period of duration (T) will equal

$$S = \int_{T} F(t) dt \tag{3}$$

which is the basic formula used for calculation of spill from dredges.

The most common situation is a one-directional current with a clear and well defined plume and in this case the spill calculation can be expressed as the difference between downstream and upstream values

$$S = \int_{T} (F_d(t) - F_u(t)) dt \tag{4}$$

Data Collection

Considering eq. (1)-(4) the necessary data needed for the spill calculations are current velocity and concentration of suspended material.

Current data are gathered by a broad band Acoustic Doppler Current Profiler (ADCP) mounted at the hull of the vessel. Data are hereby obtained from 0.7 m below the ves-

sel at intervals of 0.5 m (centre of each bin cell) until 1 m above sea bed. Output from the ADCP in [m/s].

Concentration data are gathered by four Optical Back Scatter (OBS) sensors with one mounted on a pole at a fixed depth and the remaining three mounted at 2 m intervals on a winch controlled streamer. Output from these sensors is Formazin Turbidity Unit [FTU] which is converted into sediment content by means of water samples.

Since the turbidity sensors work by light reflection, the magnitude of the output depends upon several material parameters such as colour, shape and grain size distribution. This means that water samples have to be gathered at regular intervals in order to reflect the geological changes in the dredged material. How the conversion process should be implemented will be discussed further in this paper.

Considering the gathered current and turbidity data approximated velocity and turbidity profiles are produced as described in the following. The velocity profile is constructed by vertical extrapolation of the top measurement to the water surface, straight line interpolation in between all points and a power fit from the lowest point towards sea bed. The turbidity profile is made by linear interpolation in between points and vertical extrapolation of top and bottom sensor registration. Examples of both profiles are shown in Fig. 2, and it is clear that the velocity profile is relatively well described due to the more measuring points. However the turbidity profile may stand as a weak part with its 4-point approximation when compared with the velocity profile. Furthermore the lowest measurement will always be located around 1-2 m away from the sea bed due to equipment safety.

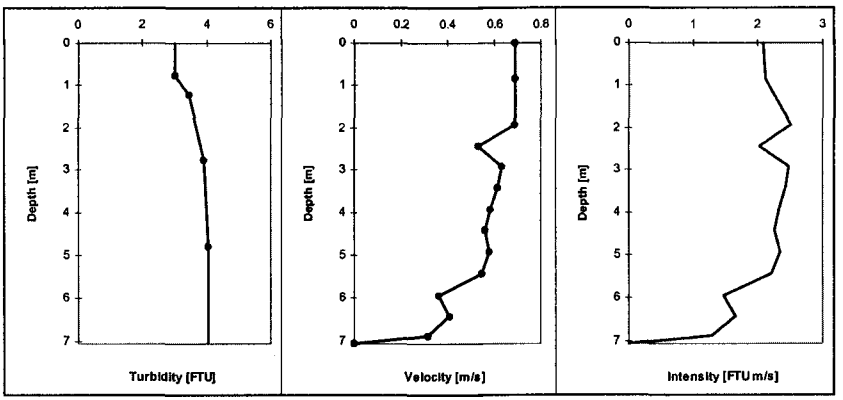

Figure 2. Approximated Profiles.

The turbidity intensity profile is obtained by multiplication of the two approximated profiles, and can be seen in Fig. 2. Current and turbidity data are logged continuously (10 per second) and average values are stored at regular intervals (e.g. every 6 s which corresponds to a registration at distances of average 10 m).

When enclosing a spill source with the survey vessel a discrete 3D picture of the intensity is derived and the net flux of suspended material through the box can be calcu-

lated numerically based upon eq. (2). Numerically integration in time is then obtained by sailing enclosed boxes continuously around the spill source and use of eq. (3).

Problems

The summary of the problems introduced in the previous section is:

I) What is the relation between turbidity and sediment content?

II) The 4-point approximated turbidity profile is coarse compared to the velocity profile. Does this lead to large deviations from the true turbidity profile?

III) Where is the maximum turbidity located? Does the lack of turbidity information close to the sea bed lead to any systematic error in the 4-point profile?

Conversion Factors - ad I)

An example of a water sample session can be seen in Fig. 3. It is important to cover as wide a turbidity range as possible during the water sampling process to obtain a satisfactory picture of the conversion relation. In Fig. 3 the best line fit is included and it seems evident that a linear relation exists.

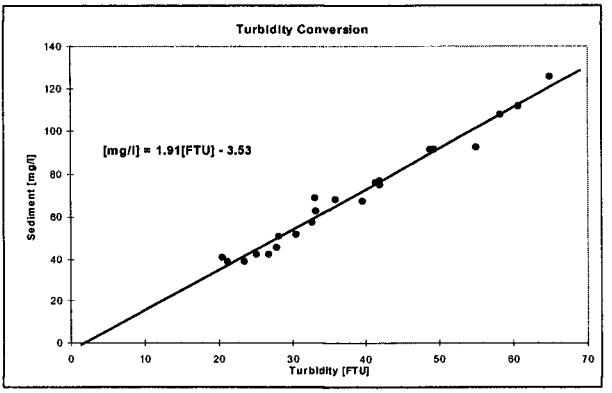

Figure 3. Ideal Water Sample Session Result.

When performing a water sample session it can be difficult to obtain a wide range of turbidity registrations due to the nature of the sediment plumes, which can lead to results as seen in Fig. 4. This water sample session does not indicate any linear relation. However a linear relation through the origin has proven to give reasonable values for the conversion factor when comparing with results obtained from more ideal water sample sessions.

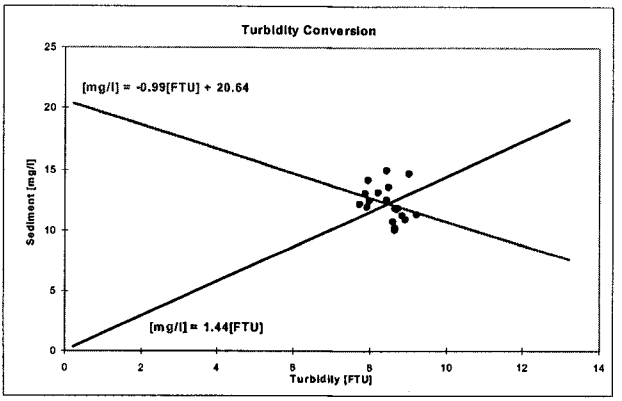

Figure 4. Forced and Non-Forced Line Fit.

In order to verify an existing linear relation a large amount of water samples have been analysed.

As mentioned previously the conversion factors are strongly dependent upon the type of suspended material. Therefore the dredging areas have been divided into subareas within each a high degree of geological homogeneity can be assumed. For each of these subareas all water samples have been plotted in one graph as shown in Fig. 5 and the linear relation becomes obvious.

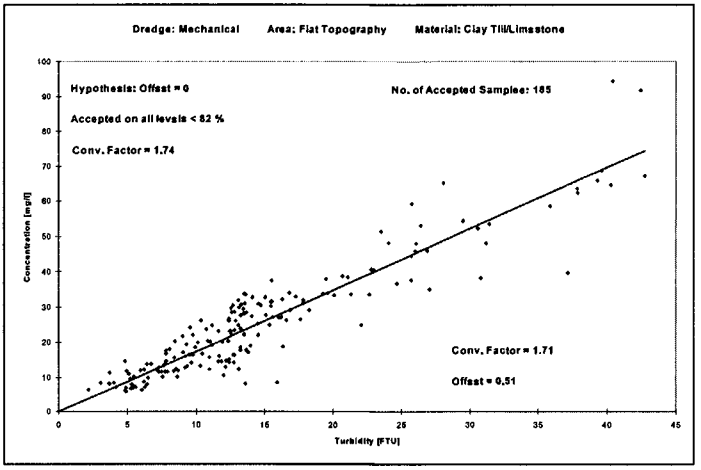

Figure 5. Conversion Graph for an Area of 50/50 Clay Till/Limestone.

In Fig. 5 all water samples for an area 900 metres long and 400 metres wide (FL A) are plotted in one graph. The dredged material is here a mix of approximately 50% Clay Till (or Moraine) and 50% Limestone.

Implementing the linear conversion

$$C(\tau) = a_1\tau + b_1, \text{ with } \tau = \tau(x,y,z,t) \tag{5}$$

in the spill equations (1)-(2) yields

$$F(t) = a_1 \int_{\Gamma} \tau(x,y,z,t)\vec{V}(x,y,z,t)d\vec{\Gamma} + b_1 Q_{net}(t) \tag{6}$$

and in the ideal case, that is if the time used to box in the source is small compared to the current velocity, the net discharge through the box will equal zero which reduces eq. (6) to

$$F(t) = a_1 \int_{\Gamma} \tau(x,y,z,t)\vec{V}(x,y,z,t)d\vec{\Gamma} \tag{7}$$

So in the case of a one directional current spill can be calculated as

$$S = a_1 \int_T \int_A (\tau_d V_d - \tau_u V_u)d\vec{A}dt \tag{8}$$

Eq. (8) shows that the spill calculation is independent upon the conversion offset (b_1) and depends upon the conversion factor (a_1) only.

With the result from Fig. 4 in mind and the fact that the origin is the natural zero (since clear water has zero turbidity) the conversion results are tested (T-test) for the hypothesis H_0: Offset = 0 against H_1: Offset $\neq$ 0 on a 95% significance level.

In the analysis related to Fig. 5 the best line fit has been determined with one (zero intercept) and two (free fit) degrees of freedom respectively by use of least squares method. With two degrees of freedom the conversion factor yields a_1 = 1.71 [g/m^3/FTU] with an offset b_1 = 0.51 [g/m^3]. The conversion factor with zero intercept becomes a_0 = 1.74 [g/m^3/FTU] corresponding to an increase Δa = 2% compared to the free fit. Finally the outcome of the T-test shows a minimum of 82% probability of rejecting a true hypothesis, if H_0 is rejected.

A summary of the results from all investigated sub areas can be seen in Table 1, where CS indicates a Cutter Suction dredge and M indicates a Mechanical dredge. The material is described by the relative amount of Clay Till (CT) and Lime Stone (LS).

In Table 1 the uppermost results originate from dredging activities whereas the last three results represent samples taken inside the pipelines used for pumping out of excess surface water from the reclamation basins. The suspended material inside these basins is very homogeneous and varies slowly with time. Only areas where more than hundred accepted samples were available have been included in the analyses.

Area ID	Dredge CS/M	Material CT/LS [%]	Number of Samples	a_1 [mg/l/FTU]	b_1 [mg/l]	a_0 [mg/l/FTU]	Δa [%]	Accept Level [%]
CD#3	CS	100/0	396	1.80	-1.81	1.76	-2	49
LN	M	90/10	644	1.61	-0.36	1.60	-1	84
FL A	M	50/50	185	1.71	0.51	1.74	2	82
EP	M	40/60	359	1.48	2.08	1.57	6	24
WP	M	40/60	442	1.63	-0.26	1.62	-1	87
TT A	CS	15/85	123	1.73	-0.28	1.72	-1	96
TT B	CS	15/85	622	1.69	-0.05	1.69	0	98
TT C	CS	15/85	688	1.71	0.18	1.71	0	93
DCC	CS	0/100	162	1.71	4.89	1.80	5	47
FL B2	M	0/100	510	1.92	-1.97	1.82	-5	18
FL C1	M	0/100	412	1.55	-0.13	1.54	-1	89
WB 1			*126*	*1.03*	*0.95*	*1.03*	*0*	*92*
WB 2			*124*	*1.17*	*-3.66*	*1.16*	*-1*	*87*
WB 3			*333*	*1.03*	*0.48*	*1.03*	*0*	*93*

Table 1. Water Sample Results for Subareas.

The areas named WP and EP consist of several small pits dredged over a long distance with an uncertain degree of homogeneity. This may explain the large offset and low acceptance level for EP.

From all these results it can be concluded that a linear relation exists between turbidity and sediment concentration. Furthermore the generally high acceptance levels imply that the conversion line can be forced through zero, indicating that a_0 can be assumed equal to a_1 (the difference Δa between a_0 and a_1 is within $\pm$ 5%).

Turbidity Profiles - ad II)-III)

Regarding the uncertainty that may be related to the turbidity profile a large series of spot checks have been carried out. A spot check was performed by logging the turbidity approximately each 4 cm from sea bed to water level. Hereby a very accurate turbidity profile was obtained, hereafter denoted "the true profile". In each of these spot checks the "would have been" survey positions of the four sensors are marked. The corresponding approximated 4-point turbidity profile can then be compared with the true profile, see Fig. 6 and Fig. 7.

As it can be expected that different dredging methods create different turbidity patterns, the analysis is divided into profiles originating from cutter suction, Fig. 6, and mechanical dredge, Fig. 7. Furthermore the cutter suction analysis has been subdivided based upon topography, as flat cut (data from two different areas available) or trench.

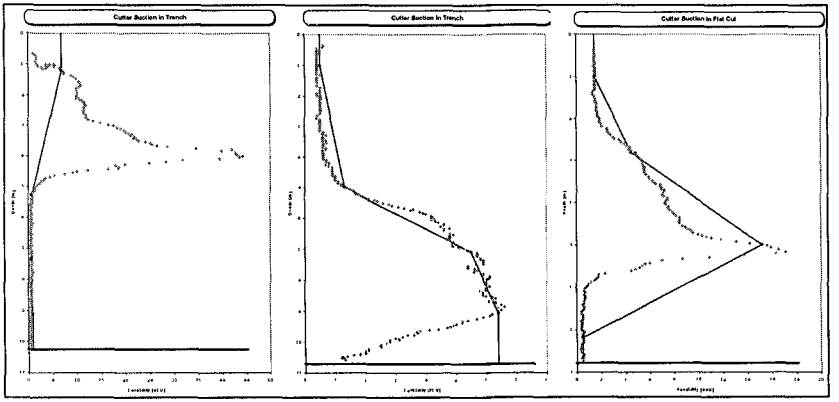

Figure 6. Examples of Turbidity Profiles for a Cutter Suction Dredge.

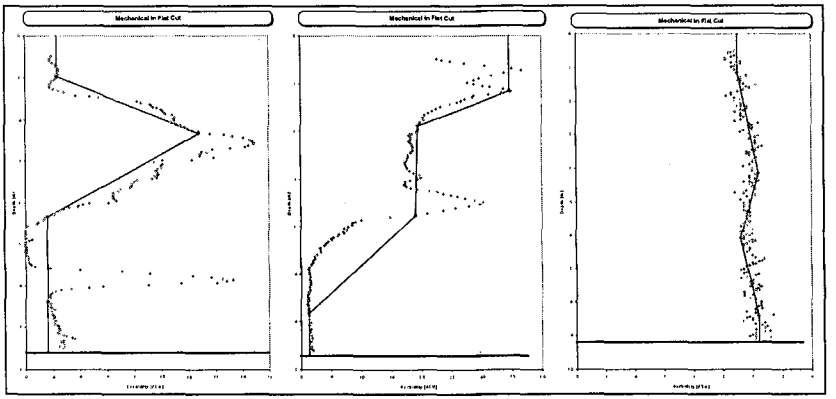

Figure 7. Examples of Turbidity Profiles for a Mechanical Dredge.

In order to compare the 4-point profile with the true profile, the depth averaged turbidity is calculated by

$$\mu(SC) = \frac{1}{2}\frac{1}{D}\sum_{i=1}^{5}(d_i - d_{i-1})(\tau_i - \tau_{i-1}) \tag{10}$$

$$\mu(WS) = \frac{1}{n}\sum_{j=1}^{n}\tau_j \tag{11}$$

SC indicating the 4-point approximation and WS indicating the true profile.

The depth averaged deviation from the true profile can then be directly calculated as

$$\Delta = \mu(SC) - \mu(WS) \tag{12}$$

Fig. 8 shows a frequency plot of Δ for 133 spot checks for a cutter suction dredge working on a flat topography.

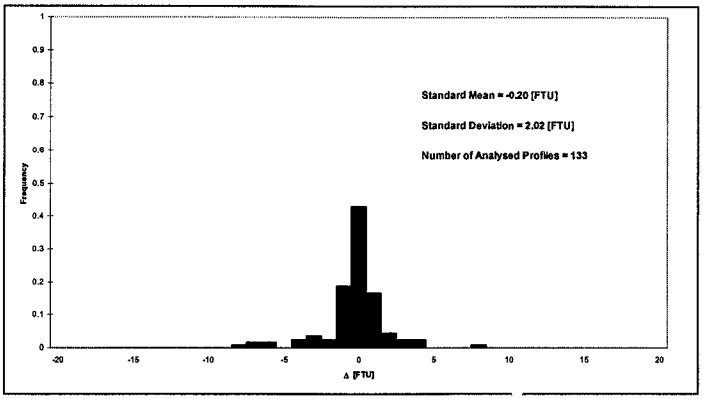

Figure 8. Frequency Plot of Δ.

The symmetrical shape of the frequency plot together with an average difference close to zero (which means that the error introduced because of the difference is nonbiased) is also recognised for the other analysed areas, se Table 2.

For all four areas an average value of Δ between ± 0.2 FTU has been found, thus indicating that the 4-point approximated profile on average describes the true profile satisfactory. The standard deviation on Δ seems to decrease with increasing number of spot checks.

Another important result from the spot checks is the distance, $d(\tau_{max})$, from the sea bed to the location of the maximum turbidity. This distance is normalised by the water depth.

$$\partial = \frac{d(\tau_{max})}{D} \tag{13}$$

Examples of frequency plots for ∂ are shown in Fig. 9 for a cutter suction dredge working respectively on a flat bed and in a trench, and for a mechanical dredge working on a flat bed.

Fig. 9 shows that the maximum turbidity most often occurs in the middle third of the water column for a cutter suction dredge working on a flat bed. This may be due to the rotation of the cutter head which whirls the sediment upwards. When the cutter suction is dredging in a trench the maximum turbidity most often is located in the lowest third of the water column, because the sediment has to be dragged over the edge of the trench. For the mechanical dredge on a flat cut the maximum turbidity occurs most often in the lowest third. Considering only the lowest 10% of the water column it

seems that the maximum turbidity occurs at a rate of respectively 15%, 30% and 30% in the three different situations.

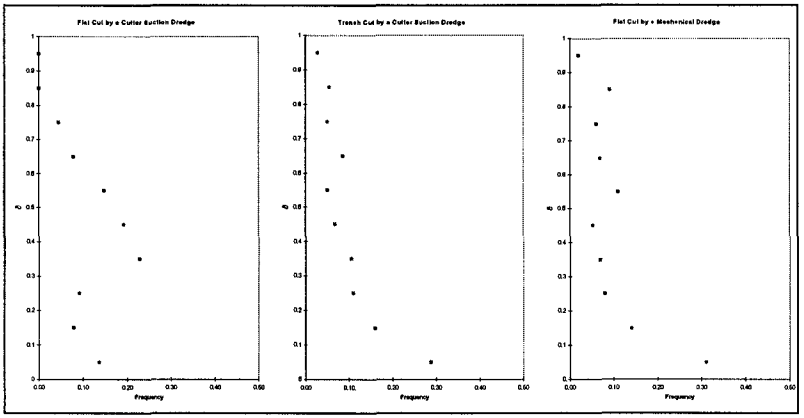

Figure 9. Frequency Plots for ∂.

Table 2 presents the average position of the maximum turbidity and related parameters.

Topography/ Area ID	Dredge CS/M	Spot Checks	$\mu(\Delta)$ [FTU]	$\sigma(\Delta)$ [FTU]	$\mu(\partial)$	$\mu(\tau_{min}/\tau_{max})$	$\mu(\tau_{mean}/\tau_{max})$
Flat/CD#1	CS	88	0.0	4.8	0.37	0.06	0.40
Flat/CD#3	CS	133	-0.2	2.0	0.29	0.36	0.63
Trench/TT	CS	167	0.1	2.9	0.32	0.29	0.57
Flat/FL	M	264	-0.1	0.9	0.35	0.29	0.54

Table 2. Results From Turbidity profile Spot Checks.

On average it has been found that the maximum turbidity is located 30% - 40% away from the sea bed for all areas. Based on this information it must be important to cover this depth region in order to avoid any systematic error in the turbidity measurements.

Furthermore the results indicate that the minimum turbidity amounts to some 30%-35% of the maximum turbidity and the mean turbidity is between 40%-60% of the maximum turbidity. This implies that the typical turbidity profile only varies over a limited turbidity range.

Conclusion

Based on the results from the analyses carried out on a large amount of data, the following can be concluded:

I) It has been validated that the conversion from turbidity into sediment concentration can be expressed by a linear relation. Furthermore the statistical T-test resulted in high acceptance levels for the offset = 0, implying that the conversion line can be forced through the origin.

II) The analysis of the applied 4-point approximation of the turbidity profile leads to results which on average comply with the true profile.

III) It is verified that the location of the maximum turbidity on average is located 30% - 40% away from the sea bed. Hence it can be concluded that the lack of turbidity information close to the sea bed does not lead to any systematic error in the 4-point profile.

References

Høgh, Klavs: Spill Monitoring at the Öresund Link Project, New Developments in Dredging Equipment and Technology, Proceedings of the Cede Dredging Days 1997.

DEFINING AN UNUSUAL LITTORAL REGIME TO OPTIMIZE DREDGING AT EAST LONDON

A K Theron[1] and J S Schoonees[1]

Abstract

Maintenance dredging at the Port of East London is a major annual expense. The aims of this investigation were to obtain relevant information on the sedimentary processes and to apply this information to reduce or optimize various facets of the required maintenance dredging. Information gleaned on various components of the sediment transport regime led to a holistic understanding of the sediment budget for the littoral sub cell at the port. The sedimentary regime is very interesting with a complex pattern of sediment movement around the harbour. In turn, this information could be applied practically in terms of: more efficient sandtraps, a new dump-site closer to the port, a spur which successfully protected the dolos armour units, and proposed extensions to the breakwater which potentially could significantly reduce maintenance dredging. Most of these applications have already led to significant savings on maintenance dredging costs for the port.

1. Introduction

Background

The Port of East London is situated on the south-eastern coast of South Africa on the Indian Ocean seaboard (Figure 1). It is one of the six largest ports in South Africa and maintenance dredging (ca. 600 000 m^3/annum) at this port also represents a major annual expense (ca. U$ 850 000). East London is exposed to fairly severe wave conditions (Figure 2) and is also renowned as the origin of the world renowned dolos breakwater armour unit. The port layout and local references are depicted in Figure 3.

Sedimentary regime

The sedimentary regime at East London is very interesting and quite unlike that of the other ports in South Africa. A major ocean current (the Agulhas) flows exceptionally close to the coastline in this area, thus significantly affecting nearshore sediment

[1]Research Engineers, CSIR, P O Box 320, Stellenbosch, 7599, South Africa
(fax: +27 21 888 2693, e-mail: atheron@csir.co.za)

movements. Of particular interest in this case, is that this strong deeper water current predominantly flows in the opposite direction of the longshore current in the surf zone (Figure 4). Furthermore, the Port of East London is the only riverine (the Buffalo River) harbour in South Africa; which all leads to a complex pattern of sediment movement around the harbour.

Aims

The aims of this investigation were to obtain relevant information on the sedimentary processes at East London and to apply this information to reduce or optimize various facets of the required maintenance dredging.

2. Environmental Data and Coastal Processes

General

The natural processes of sediment transport and deposition are the cause of sedimentation in ports, which necessitates routine maintenance dredging to maintain prescribed water depths. In order to reduce or optimize the required maintenance dredging at a specific port, it is therefore necessary to have a complete (as possible) understanding of the sedimentary processes at that port. To define the littoral regime at a specific site, certain environmental data and an understanding of the relevant coastal processes, are required (CSIR, 1994a, 1995, 1996).

Continental shelf sediment dynamics

The continental margin of the east coast of South Africa is characterised by an extremely narrow shelf. At East London the shelf is about 25 km wide and the shelf break is located at about the 100 m isobath. The south-westwardly (downcoast) flowing Agulhas Current reaches a peak surface velocity of over 2,5 m/s just beyond the shelf break off East London. The total downcoast sediment transport on the shelf along the East London coastline is estimated at about 24.10^6 m^3/annum.

In general it is possible to distinguish three more or less shore parallel physiographic seabed regimes, each reflecting specific wave and current characteristics (Martin and Flemming, 1986). The narrow nearshore zone is subjected to a high energy swell regime, and is covered by a thin wedge of sandy sediment. This wedge appears to have achieved dynamic equilibrium with the prevailing energy regime, and additional (terrigeneous) sediment is rapidly dispersed and fed into a sand stream, situated slightly further offshore on the broad continental shelf, where the Agulhas Current dominates sediment transport. Thus, the nearshore sediment wedge progrades seawards until it meets sufficient current strength for sand to be entrained. The sand is entrained and carried on the central shelf by the so-called "conveyor-belt process", driven by the Agulhas Current. This current-controlled part of the shelf can be further subdivided into two parallel zones: a broad central-shelf sand stream and a narrow outer-shelf gravel pavement. The current- scoured gravel pavement stretches along the outer margin of the shelf and probably extends onto the upper continental shelf slope. This lateral sequence clearly indicates a progressive increase in current velocity in the offshore direction - a phenomenon which is consistent with available current data.

The above description clearly indicates that vast amounts of sediment are transported along the shelf by the Agulhas Current. Furthermore, it appears that any excess sediment transported onto the current dominated zone of the shelf or deposited on the nearshore sediment wedge near the margin of the current dominated zone, would eventually be carried away by the south-westwardly flowing Agulhas current.

Tides

The mean spring tidal range at East London is 1,59 m, while the mean neap tidal range is 0,47 m.

Wind

The south-westerly wind is the dominant wind throughout the year, while strong north-easterlies may occur in all seasons. These directions are approximately parallel to the coast. The average recorded wind speed is about 4,5 m/s.

Waves

In this study, the incident wave climate was determined from deepsea VOS (Voluntary Observing Ships) data and nearshore Waverider recordings. The median significant wave height is 1,6 m and the 1% exceedance wave height is 3,4m. The median peak wave period is 11,2 s. The most common deepsea wave direction is south to south-west. To obtain more information on the nearshore wave climate, wave refraction modelling was also carried out. An example is shown in Figure 5, for a deep-water wave height of 3 m and a peak wave period of 13,5 s with a southerly deepsea wave direction. The weighted mean surf zone width along the seaward half of the main breakwater is about 150 m.

Currents

Currents were measured by means of Endeco and Aanderaa current profilers, drogue tracking, drifter buoys and dye tracking. Figure 6 shows information on some of the deeper water current measurements as well as the current patterns derived from this information. Thus, it was found (for example) that the offshore currents flow in a south-westerly direction for about two-thirds of the time and in the opposite (north-easterly) direction for about one quarter of the time.

Currents were also simulated by means of the Delft 3D mathematical model (WL|Delft Hydraulics, 1996). Figure 7 shows an example for the most common situation which is a south-westerly current of 0,3 m/s.

Surf zone (wave induced) currents were measured along the beach to the south-west of the port. These measurements were conducted by means of dye tracking tests (in conjunction with drogue measurements). The associated wave conditions were derived from Waverider recordings, while the waves directions were hindcasted.

Sediment

Sediment samples were collected over a wide area around the port. The sediment

characteristics were determined by analysing samples in a settling tube. The average median grain size is about 0,2 mm.

Aerial photographs

Analysis of aerial photographs provided additional information on nearshore wave directions, current patterns and shoreline changes. South of the harbour, the direction of the incident waves is such that in virtually all instances a current generally flowing towards the harbour would be generated near the shore. The wave attack on the seaward side of the main breakwater would mostly not generate very significant currents parallel to the breakwater. At the beach directly north of the port, no significant wave generated longshore currents are indicated. Past port developments initially caused the shorelines on both sides of the port to prograde significantly. More recently, the shoreline appears to have stabilised with smaller variations occurring.

Bathymetric surveys and dredging data

Analysis of subsequent bathymetric surveys proved to be a valuable tool in studying the changes in bottom topography, erosion and deposition areas and determining volume changes. Bottom topography changes, together with the dredging data, in terms of sediment volumes dredged over time in specific areas, provided an important part of the overall picture. Information on the dredging records for the main sandtrap is shown in Figure 8, while the annual dredging volumes for the other port areas are shown in Figure 9. The total volume of sediment dredged annually at the port, is about 600 000 m^3 to 650 000 m^3 on average.

3. Sediment transport regime/budget

3.1 Transport through/around main breakwater

A separate study was conducted to determine specifically the rate of sand deposition on the inside of the main breakwater and from where this sand originates. This basically entailed determining the volume of sand moved *through* the breakwater and the volume moved to the inside of the breakwater from *around* its head. A wide variety of different means were employed to determine this: long-term dredging records, repeated surveys of a specially dredged "test-pit", suspended sediment samples, a newly developed suction sampler, an electronic current profiler, drogue and dye tracking, drifter buoys and a theoretical determination of the suspended versus bedload ratio. Interesting comparisons of the results could thus be made. The results of a side-scan sonar survey of the area was also interpreted with regard to the study, as this information provided interesting circumstantial "evidence" completing a part of the sediment transport "puzzle". Thus, it was concluded that 60 000 - 80 000 m^3/annum of sediment moved through the breakwater, while 20 000 - 50 000 m^3/annum moved around the head of the main breakwater (The breakwater has since been made more impermeable and as such, the rate of sediment movement through the breakwater has been reduced.).

3.2 Longshore Transport

The longshore transport along the beach to the south-west of the main breakwater (300 000 - 500 000 m^3/annum) was estimated by means of the modified Kamphuis

method (Schoonees and Theron, 1996). The directional distribution of the longshore sediment transport was determined from the nearshore wave climate.

3.3 Transport in deeper water

The sediment transport in deeper water due to the combined effects of currents and waves was also estimated (by means of the Van Rijn (1989) method). Thus, the sediment carrying capacity of the currents was assessed, leading to estimates of the sediment transports at the dump-site and in the "bar" area (Figure 9). The strong deepwater current (the Agulhas) predominantly flows in the opposite direction of the longshore current in the surf zone.

3.4 Fluvial transport

Riverine sediment inputs were calculated from sediment production charts and the sediment trapping efficiency of dams in the river. The mean annual runoff of the Buffalo River is estimated to be about 41.10^6 m^3, with a sediment load of about 80 000 m^3/annum. However, the dams trap more than 90% of the sediment; thus, the sand transported into the port is estimated to be less than 10 000 m^3/annum.

3.5 Sediment balance/budget

Analysis and interpretation of all of the above lead to a relatively complicated sediment balance for the littoral sub cell at the Port of East London, as depicted in Figure 10 (CSIR, 1994a, 1995, 1996).

4. Applications

Having obtained a holistic understanding of sediment transport patterns, this enabled the use of this information to optimize maintenance dredging activities in the area (CSIR, 1994a, 1994b, 1995, 1996).

4.1 Sandtraps

The location and layout of a number of new sandtraps were determined so as to intercept the main sources of sediment deposition in the harbour and entrance channel. The old, newly dredged and proposed sandtraps are depicted in Figure 11. The optimum dimensions of these sandtraps were also determined in terms of theoretical sand trapping efficiency and practical aspects of the dredging.

4.2 Dump site

Based mainly on the current patterns and the carrying capacity of the offshore currents, the location of a new (closer) dredge-material dump site was determined, as depicted in the Figure 12. The risk of sediment moving back to the port is acceptably low and the much shorter dumping cycle represents a significant cost saving.

4.3 Spur

The location and layout of a spur on the main breakwater was determined conceptually. The main purpose of this spur is to traps stones, rocks and debris which damage the armour units and secondarily, to reduce sediment transport towards the

harbour. This spur was built (Figure 13) and functioned well in trapping rocks, etc, (but, as expected, was too small to significantly affect sediment transport).

4.4 Current deflecting structure

The practical and economical feasibility of reducing the amount of sediment transported towards the port by means of a "current deflecting" structure attached to the main breakwater was investigated conceptually. This investigation included limited hydrodynamic modelling of various alternative extensions to the main breakwater (eg. Figure 14). Such a structure could possibly significantly reduce the annual amount of maintenance dredging required with potential substantial direct cost savings. As an example, the estimated cost/benefit ratio of a 200 m extension to the main breakwater is shown in Figure 15. An additional major benefit of such as structure could be significant savings in maintenance costs of the present main breakwater. (More detailed investigations are being proposed at present.)

5. Final Conclusion

Information gleaned on various components of the sediment transport regime led to a holistic understanding of the sediment balance/budget. In turn, this information could be applied practically in terms of: more efficient sandtraps, and new dump-site closer to the port, a spur which successfully protected the dolos armour units, and proposed extensions to the breakwater which potentially could significantly reduce maintenance dredging. Most of these applications have already led to significant savings on maintenance dredging costs for the port.

References

CSIR (1994a). Oos-Londenhawe: Sedimentasie, sandvangput en storting. *CSIR Report* EMAS-C 94020, Stellenbosch.

CSIR (1994b). Oos-Londenhawe: Beplanning en invloed van golfbreker-uisteeksel. *CSIR Report* EMAS-C 94046, Stellenbosch.

CSIR (1995). Port of East London: Sedimentation on the inside of the southern breakwater. *CSIR Report* EMAS-C 95034, Stellenbosch.

CSIR (1996). Reduction of dredging costs by limiting sediment transport towards the Port of East London: Feasibility Study. *CSIR Report* EMAS-C 96018, Stellenbosch.

Martin A K and Flemming B W (1986). The Holocene shelf sediment wedge off the south and east coast of South Africa. Knight R J and McLean J R (Eds), Shelf Sands and Sandstones. *Canadian Society of Petroleum Geologists*, Memoir II, p 27-44.

Schoonees J S and Theron A K (1996). Improvement of the most accurate longshore transport formula. *25 Intern. Conf. on Coastal Eng.*, Orlando, Florida. ASCE, Volume 3, Chapter 282, page 3652 - 3665.

Van Rijn L C (1989). Sediment transport by currents and waves - Handbook. *Delft Hydraulics, Report* H461, Volume 2, page 10.15 - 10.21.

WLIDelft Hydraulics (1996). Delft3D-FLOW version 0.1, User Manual release 2.48, WLIDelft hydraulic, the Netherlands.

Acknowledgement

The above investigations were conducted by the CSIR under contract to Portnet who paid for the work. The CSIR gratefully acknowledge the help and assistance given by Mr Vonk Claassens (The Port Engineer) and his staff in conducting these investigations.

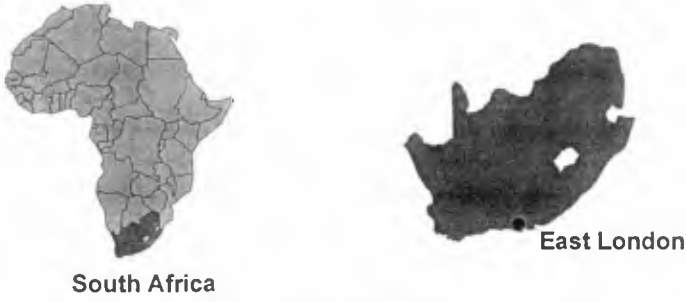

Figure 1: Site

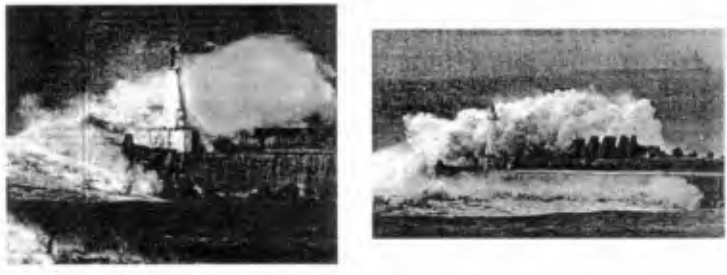

Figure 2: East London - Birthplace of the dolos

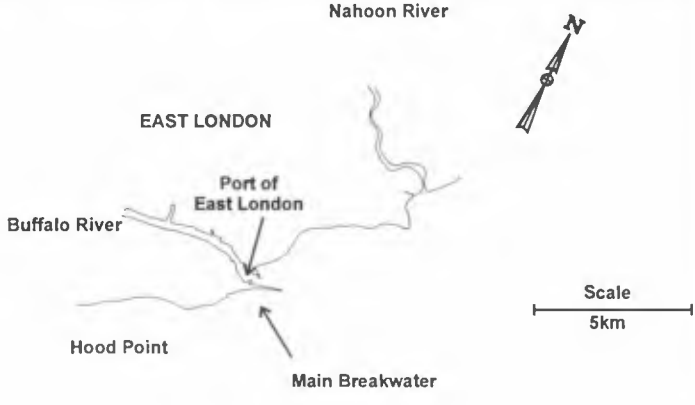

Figure 3: Location map

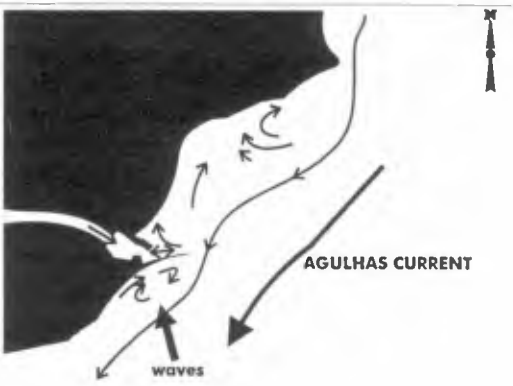

Figure 4: Complex current regime

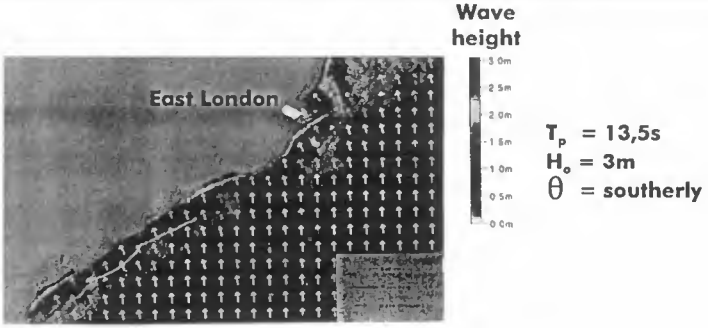

Figure 5: Wave refraction and bathymetry

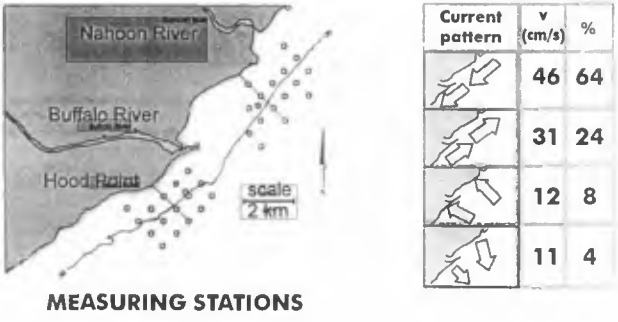

Figure 6: Current measurements

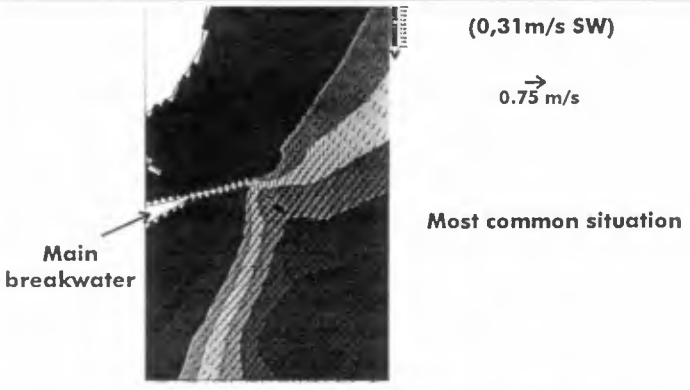

Figure 7: Current simulation

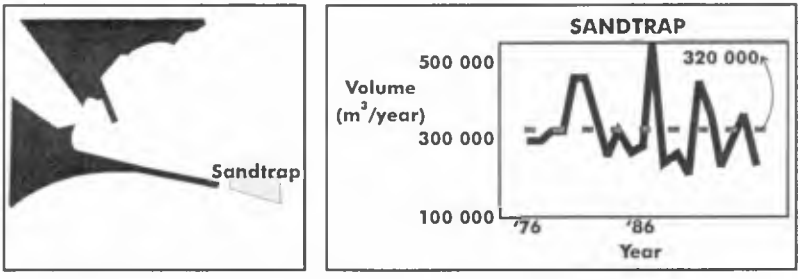

Figure 8: Sandtrap dredging records

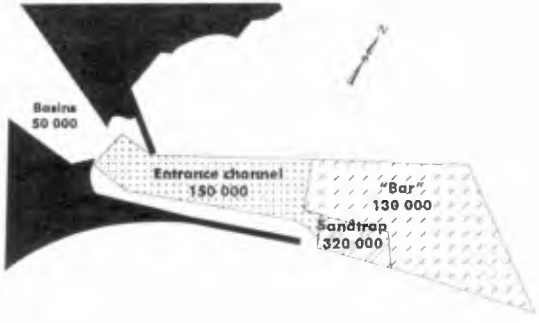

Figure 9: Annual dredging volumes (in m^3/a)

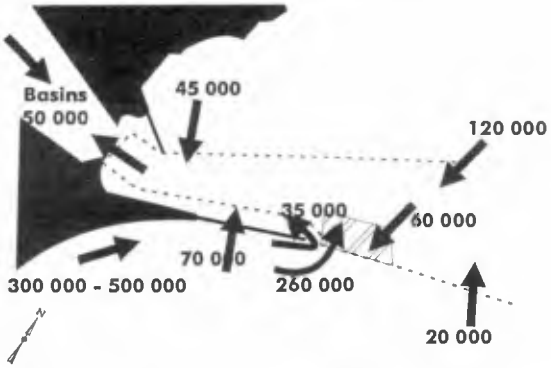

Figure 10: Sediment budget (m^3/year)

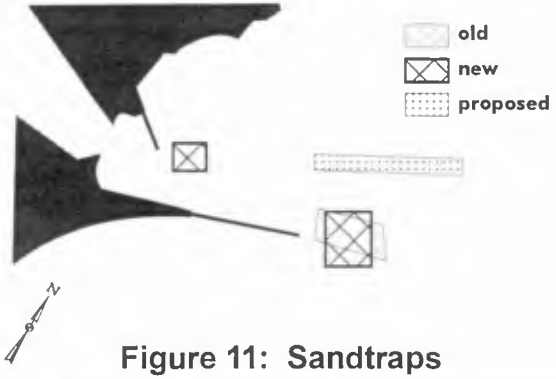

Figure 11: Sandtraps

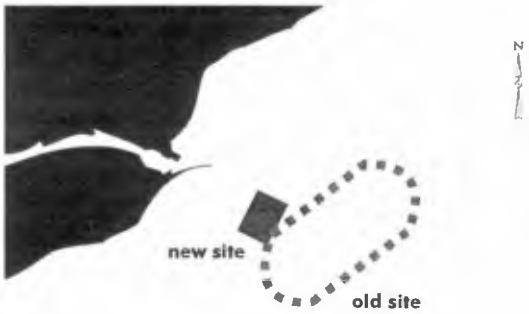

Figure 12: Dump sites

Figure 13: Rock Spur

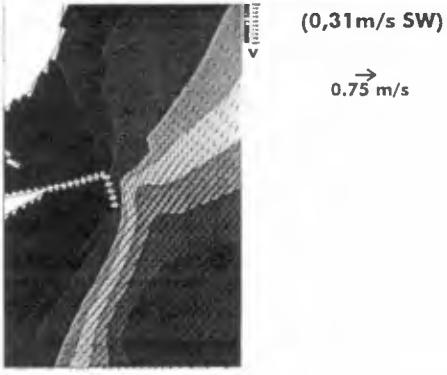

Figure 14: Currents around 300m extension

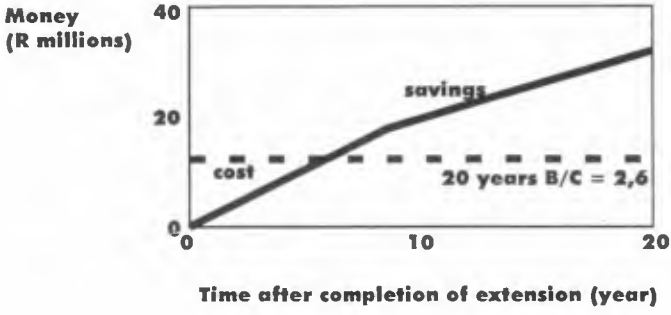

Figure 15: Cost/benefit of a 200m extension

The development of sand waves and the maintenance of navigation channels in the Bisanseto Sea

Kazumasa KATOH[1)], Hidetoshi KUME[2)],
Keiji KUROKI[3)] and Junzo HASEGAWA[3)]

Abstract

An Inosakinotsugai is a shoal located in the Bisanseto navigation channel, on which are formed sand waves of 100m wavelength. The heights of sand waves develop to be about 5 meters, which makes the water depth shallower than that required for navigation. Authors have analyzed the process of sand wave development by utilizing the sounding data obtained during a period from 1984 to 1996. As a result, it is shown that 1) the sand waves developed faster in the area where the speed of sand accumulation is faster, 2) the sand waves migrated from the both sides of the shoal toward the shoal ridge, and 3) the speed of migration is proportional to the horizontal distance from the ridge. In the maintenance dredging, the developing speed of sand waves must be taken into consideration.

1. Introduction

The Bisanseto navigation channel is the only trunk channel connecting the eastern and the western parts of the Seto Inland Sea and branches off to the southern and the northern channels in the offshore area of Kagawa Prefecture. The connection channel joins the southern and the northern channels near the juncture (Figure 1). As shown in Figure 2, a shoal (called Inosakinotsugai) extends from Mitsugo Island to the northwesterly direction at the depth of less than 20 m, and caldrons greater than the maximum depth of 85m are on the eastern and the western sides. In other words, the seabottom topography from the connecting channel to

1)Port & Harbour Res. Inst., Nagase 3-1-1, Yokosuka, Kanagawa, 239-0826, JAPAN
2)The Overseas Coastal Area Development Institute of Japan (OCDI),
Kazan Bldg., 3-2-4 Kasumigaseki, Chiyoda, Tokyo, 100-0013, JAPAN
3)ECOH co., Kitaueno 2-6-4, Taitou, Tokyo, 110-0014,JAPAN
E-mail:jhasegawa@ecoh.co.jp

the north channel resembles horseback. At the saddle are formed sand waves of about 5 m wave height and 100 m wavelength (Ozasa, 1975). There are several areas in Bisanseto where sand waves are formed at the saddle of the shoal. The problem here is that they are located inside the channel and the sand wave crests develop to the height which decreases the water depth below the required depth for a navigation channel (the northern channel; 19 m, the connection channel; 13 m).

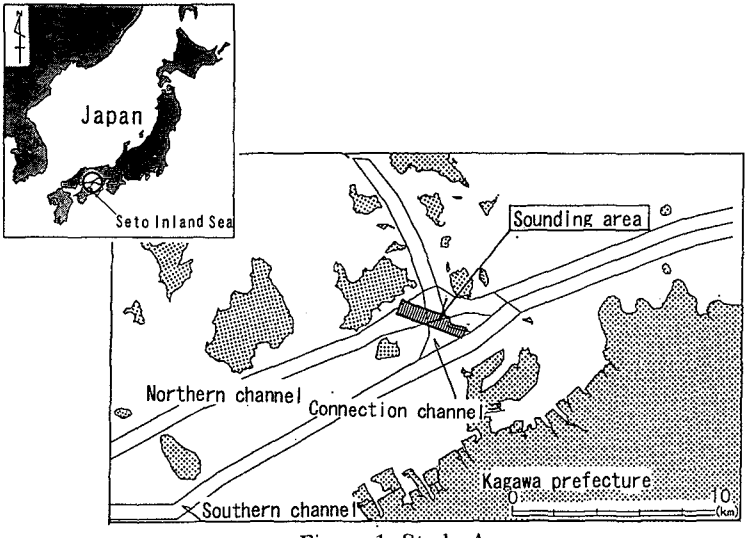

Figure 1. Study Area

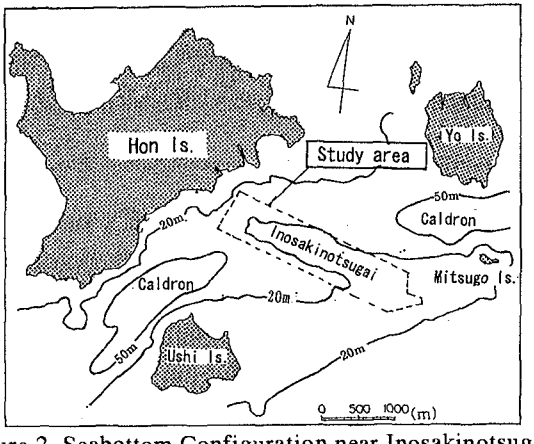

Figure 2. Seabottom Configuration near Inosakinotsugai

During the period between 1981 to 83, about 2.2 million m^3 dredging was performed to remove sand waves. Dredging to 22 m water depth in the north channel and 15 m in the connection channel was conducted by removing the convex portions of the sand waves. During 10 years following this period, sand waves were again formed and have developed to reduce the depth to less than the water depth that should be maintained.

Ozasa (1975) studied in detail the shapes and the mechanism of formation of sand waves at Inosakinotsugai. So, this paper discusses the maintenance of the navigation channels (water depth) in Inosakinotsugai area (Figure 2) and the future needs of maintenance dredging. We utilized the data obtained from the sounding surveys conducted once a year between 1984 (immediately following the dredging) and 1996, and conducted the analysis by converting the data to digital values in 10 m grids.

2. Outline of Sand Waves

Figure 3 shows deviations in the geological features of the seabottom observed in November, 1996 using the average profile of the entire study period as the standard, and shows the sand wave crests with deviations of +1 m and more than +2m. According to the figure, the crests occur successively in the direction from NNW to SSE. The reference lines of A to H are set in the direction perpendicular to the crests. The sand wave cross profiles along these lines are analyzed in Chapter 4.

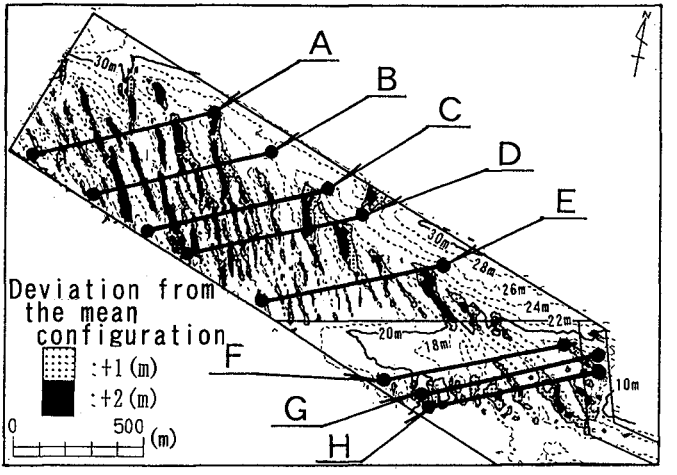

Figure 3. Sand Wave Formation

Ozasa (1975) conducted the sediment surveys, tidal current observations, and diving surveys in the area surrounding Inosakinotsugai. According to his surveys, the median grain size of sediments forming Inosakinotsugai falls within the range of 0.5 to 2.0 mm and tends to become smaller toward the tip (NNE direction) of Inosakinotsugai. The sorting coefficient was more than 2 at the base of Inosakinotsugai and becomes smaller toward the tip (or sorting becomes efficient). These results suggest that the net sand transportation occurs at "Mitsugo Island (the base of the shoal), passes over the shoal, and heads towards the tip of the shoal (see Figure 2)."

The currents are basically in the east-west directions. However, the velocity is different at the time of flood tide and the ebb tide; the flood current (the westerly current) predominates to the north of the shoal, and the ebb current (the easterly current) predominates to the south. Therefore, the crest line of sand waves is essentially normal to the direction of the predominant current.

According to the diver's visual observation, there are many ripples of a scale not sufficiently measurable by the sounding survey (the wavelength 50 to 100 cm, the wave height several cm).

3. Changes in the Depth of Navigation Channels

3.1 Definition of the Minimum Water Depth

Inosakinotsugai area was divided into eight segments as shown in Figure 4. The segments ① through ⑥ in the north channel are set by crossing the crest line of the sand waves at right angle. The areas of the

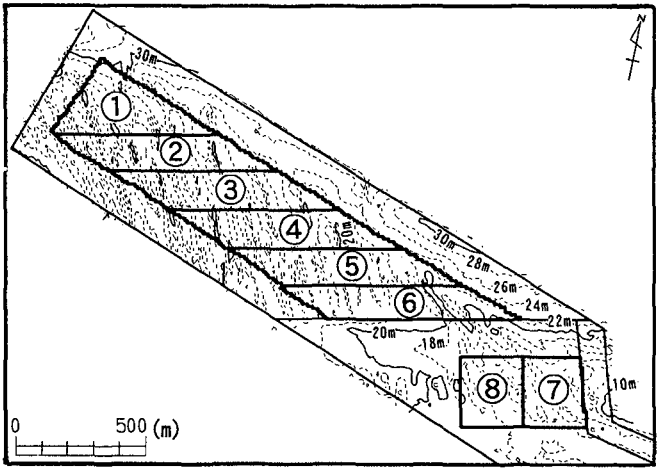

Figure 4. Segments for Water Depth Calculation

segments ① through ⑥ are substantially the same, but those of the segments ⑦ and ⑧ in the connecting channel are about 66% of the former.

The average depth in the segments is calculated for each sounding survey. The water depth above the sand wave crests (the minimum water depth) is important for maintaining the channel depth.

The segment ⑦ became shallower than the maintenance depth earlier than any other segments. The Maritime Safety Agency imposed navigation control in this area in December, 1992. Therefore the minimum water depth was defined based on of the conditions of the segment ⑦ prevailing at the time the control was initiated. Figure 5 shows the grid scores for each year of the water depth data in the segment ⑦ where the water depth is shallower than the maintenance depth of 13 meters. Increases in the grid scores can be approximated by parabolas shown by the dotted line in the figure, which is determined by the method of least squares of the data after 1988. Based on the approximated curve, the grid score of 8.89 for the month immediately preceding the month when the navigation control was imposed, November 1992, was obtained. Thus, the mean of the water depths for the top 9 grids from the shallower depth in the segment was defined as the minimum water depth. Since the area of segments ① through ⑥ is larger than that of ⑦, the number of grids to calculate the minimum water depth must be increased accordingly. However, the number of grids was set at 9 for all the segment in this paper.

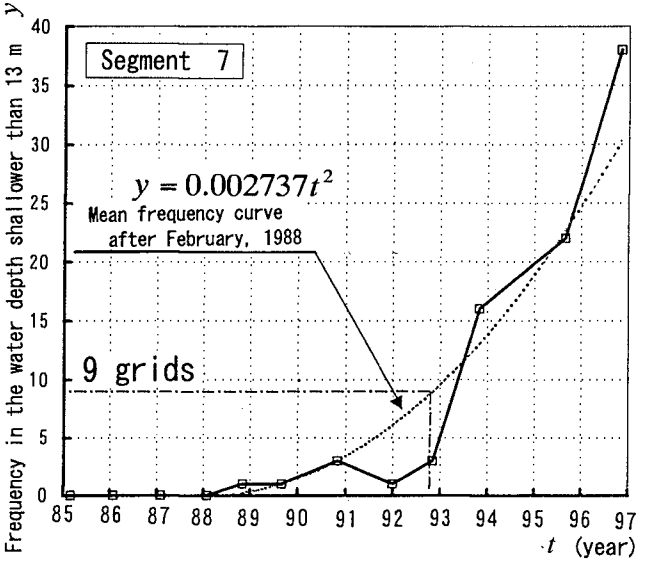

Figure 5. Grid Scores in the Water Shallower than 13 m

3.2 Chronological Changes in Mean and Minimum Water Depths

Figures 6-(1) and 6-(2) show chronological changes in the mean water depth, open circles, and the minimum water depth, solid circles, in the segment ④ on the side of the north channel and the segment ⑦ on the connecting channel side, respectively.

As the mean water depth becomes shallower at a substantially constant rate, the equation (1) is approximated;

$$h = a + bt \tag{1}$$

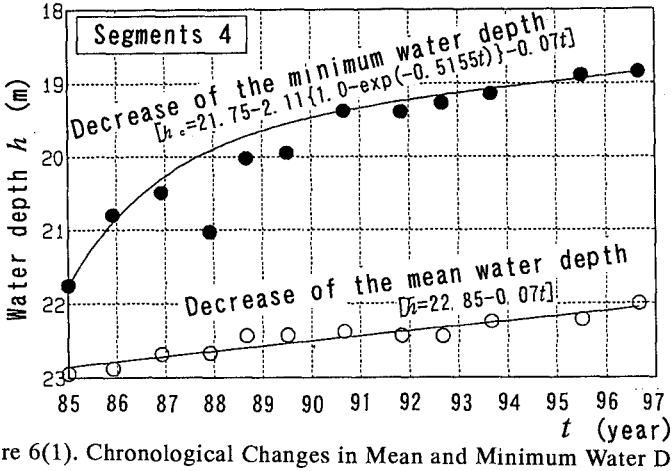

Figure 6(1). Chronological Changes in Mean and Minimum Water Depths (Segment 4)

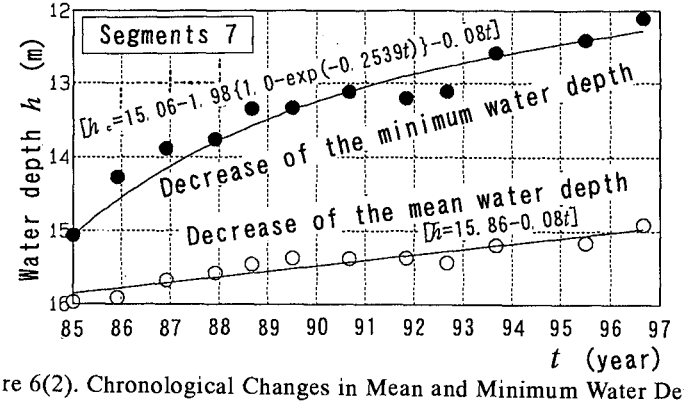

Figure 6(2). Chronological Changes in Mean and Minimum Water Depths (Segment 7)

where h is the mean water depth, t is the years after dredging, and a and b coefficients.

On the other hand, variations for the minimum water depth were large in the initial period and the amount of variation tended to decrease with time. This change can be interpreted that the sand waves were formed again after the artificial impact of dredging and developed toward equilibrium. This change can be approximated by exponential function. Provided, however, the change in the minimum water depth included that of the mean water depth, inflow of sand into the segment, the equation (2) is approximated;

$$hc = \alpha\{1 - \exp(\beta x)\} + \gamma + bt \qquad (2)$$

where hc is the minimum water depth, t is the elapsed years after dredging, α, β, γ are constants, α is corresponding to the half wave height of the sand wave which has reached the equilibrium, β is the speed with which the equilibrium is reached, and γ is the initial value of the minimum water depth.

Coefficients for the equations (1) and (2) are obtained by the method of least square. That is to say, the coefficient b in the equation (1) is obtained first, and the value b is substituted in the equation (2) to obtain remaining coefficients. Figure 6 shows the approximate straight line and curve using thus determined coefficients.

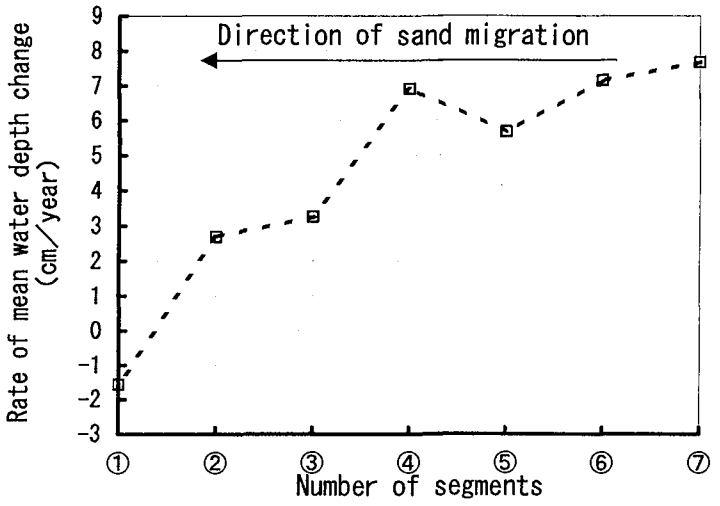

Figure 7. Changes in Mean Water Depth in Segments

Figure 7 shows the speed, the coefficient b in the equation (1), of changes in the mean water depth of the segments ① thorough ⑦. The rate of the mean water depth becoming shallower is faster in the segment ⑦ and becomes gradually slower towards the segment ①. In other words, the rate of accumulation heading from Mitsugo Island toward the tip of Inosakinotsugai decreases and the water depth toward the same direction tends to become larger, indicating that sands are being transported and accumulating in the same direction. This result coincides with the direction of sand transportation inferred by Ozasa (1975) from the plane distribution of the mean grain size and sorting coefficient of sediments. From the rate of accumulation (3 cm/year) in the segment ⑧ (not shown), it is presumed that the sand is being transported from the segment ⑦ toward the segment ⑧ even the quantity is small. Ozasa (1975) assumed similarly in respect of this brunch.

A relation between the rate of accumulation in each segment and the years of sand wave development is plotted in Figure 8. The years of development as used herein is the number of years required to reach 90% of the equilibrium value and is calculated using the coefficient β in the equation ②. The figure shows that the greater the amount of sand flowing into the segment is, the faster the sand waves develop.

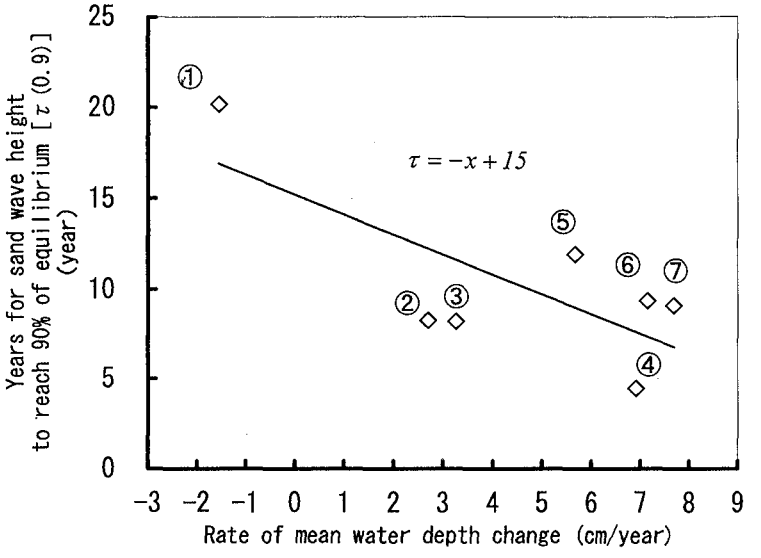

Figure 8. Relation between Accumulation Speed and Sand Wave Development Speed

4. Sand Wave Migration

Figures 9(1) and 9(2) show the transverse profiles of the reference lines A and F in the order of the years measured from the top to the bottom. Provided, however, the profiles are shown as deviations from the average profile during the period shown at the top.

Features of Figure 9 are also observed in respect of other reference lines not shown. The sand wave of 2 to 6 meters wave height and 80 to 180 meters wavelength exist, and when their crest positions, solid circles in the figure, are traced time-wise, they shift toward the top of the shoal as compared with the average profile at the top. The crest migration is approximated as in the solid lines and the rate of migration is calculated.

The migration rates for all the reference lines are plotted in Figure 10, where the horizontal axis is the crest position of sand waves in the median period during analysis as represented by distance from the shoal ridge with the positive direction toward east (to the right in Figure 9). According to this figure, the speed with which the sand wave approaches the shoal ridge is proportional to the horizontal distance, and holds the relation

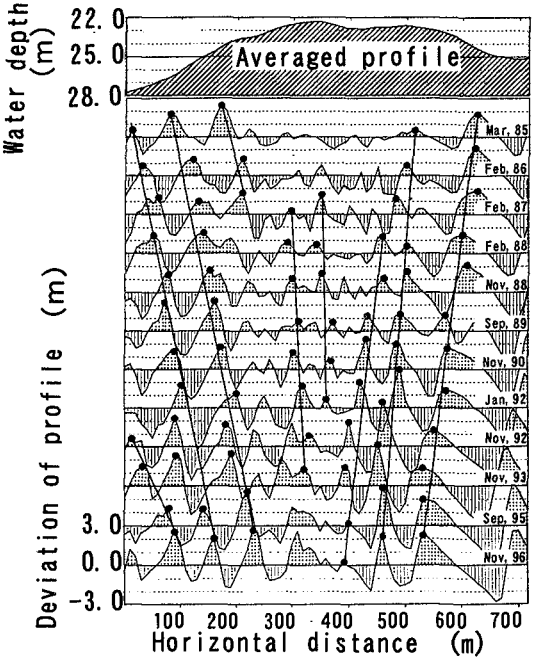

Figure 9(1). Changes in Average Profile and Sand Wave Forms (Measurement Line A)

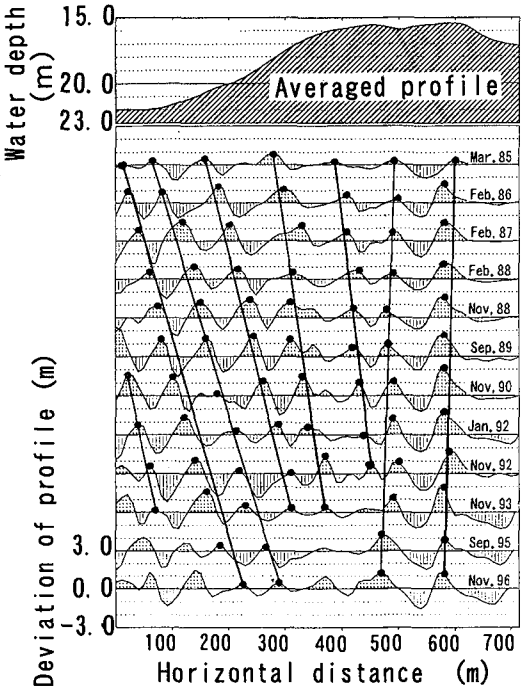

Figure 9(2). Changes in Average Profile and Sand Wave Forms (Measurement Line F)

of v = -0.04·x(m/year) up to 500 m on the horizontal axis. Here, x is in the relative position to the ridge. The data shown by solid circles where the horizontal distance is more than 500 meters are all inside the connection channel and are at the constant speed of 15 m/year.

There are many reports about sand waves migration (such as Harris, 1989). Mogi (1971) reported that the sand waves shift in the direction same as permanent current in long term. As, the westerly current prevails in the north side of Inosakinotsugai and the easterly current prevails in the south side, (Ozasa,1975) suggests that Mogi is correct also in respect of this point. The forms of sand wave observed by Harris (1989) are asymmetrical and sharp in gradient on its migrating side. Based on the above going, Figure 9 is re-examined and the forms of sand wave are recognized to have sloped sharply toward the direction of it's migration.

It is more reasonable to consider that the sand wave migration is not a mere phase shift but accompanies the sand transport in the same direction. The segment analyzed is therefore divided in the cross sectional direction to

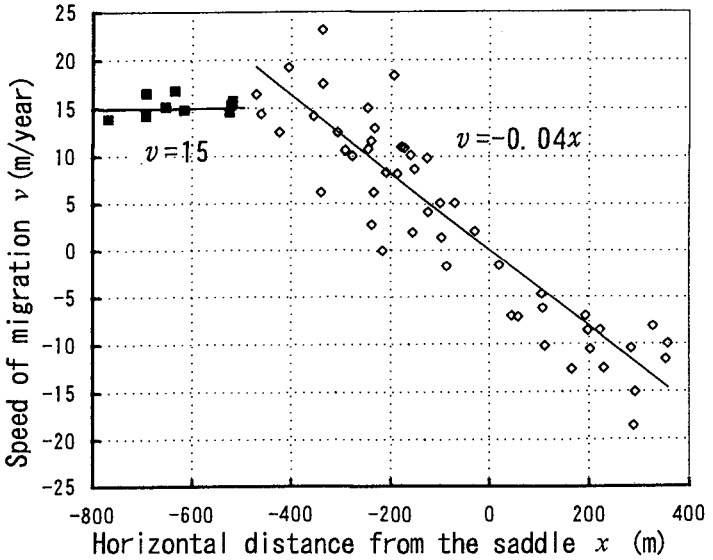

Figure 10. Speed of Migration to the Shoal Ridge

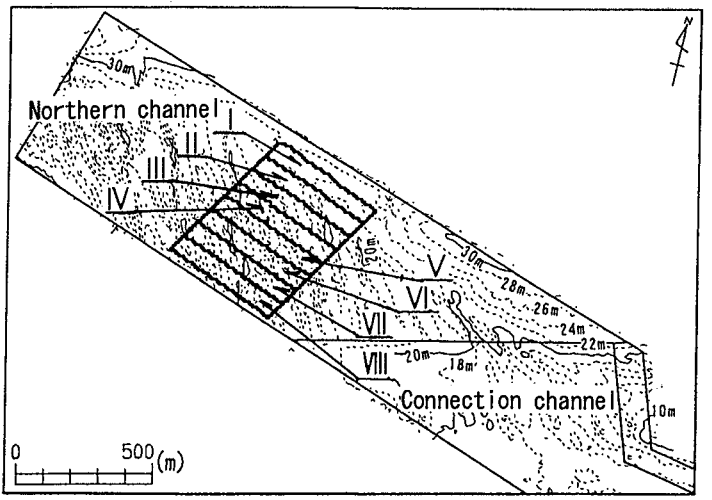

Figure 11. Segments for Calculation

extend the vertical direction of Inosakinotsugai (as shown in Figure 11). The volumes of sand accumulation during the analysis period in each

segment are shown in Figure 12. Figure 12 also shows the average profile in the south-north directions at the center of the segment, similarly to the average profile shown in the top of Figure 9. It is apparent that accumulations are greater toward the shoal ridge and decrease toward both sides. The result does not contradict the inference that sands are transported in the process of sand wave migration toward the shoal ridge.

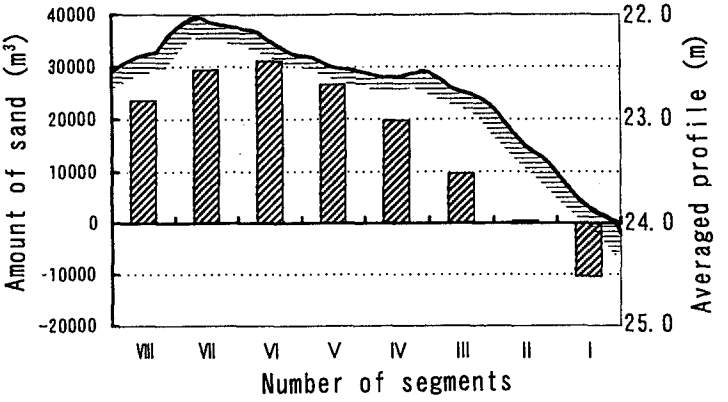

Figure 12. Sand Accumulation in Segments (Transverse Direction of the Shoal)

5. Discussion of Maintenance Dredging

It is observed that two different factors are overlapped, which basically make the navigation channel shallow. They are the decrease in the mean water depth caused by accumulation of sands which are transported from the direction of Mitsugo Island and development of sand waves. These two factors act in combination to decrease the minimum water depth. The next dredging project must take them into consideration.

Dredging performed during the period from 1981 to 1983 anticipated that the sand waves would reach equilibrium after dredging and removed the convex portions (Onodera, 1981), thereby addressing one of the two factors. In order to deal with another factor of the decrease in the mean water depth, overall dredging of the further depth or pocket dredging on the upstream side where the sands flow into the channel may be conducted to capture the sands. The former is considered to accompany great difficulties since the last dredging was performed up to 22 m, a substantially critical depth for dredging. The latter method entails hardly any problems in dredging as it is performed at a shallower depth.

Pocket dredging is expected not only to control the inflow of sands

into the channel but also to achieve secondly effects. As shown in Figure 8, the years required for sand wave development is shorter if the accumulation speed is faster. By referring to Figure 8, it is assumed that the time required for the sand waves to reach 90% equilibrium increases from 9 to 15 years if the rate of accumulation becomes 0 cm/year from 6 cm/year, thus delaying the decrease in the minimum water depth.

6. Conclusions

Following conclusions are obtained.

(1) Basically, two factors are overlapped for decrease of the navigation channel depth in Inosakinotsugai area; they are the decrease of the mean water depth due to accumulation of sand inflowing from the direction of Mitsugo Island, and development of sand waves.

(2) Sand waves develop faster in the segments where the rate of sand accumulation is faster.

(3) Sand waves formed after dredging migrated from both sides of the shoal toward the shoal ridge. The speed of migration is proportional to the horizontal distance from the ridge, and is 4 m/year if the distance is 100 meters. The direction of migration is the same as that of the permanent current.

(4) Maintenance dredging should be performed by considering development of sand waves and changes in the mean water depth. The former can be addressed by dredging in anticipation of sand waves developing to equilibrium as in the previous dredging project. The latter can be dealt with pocket dredging in the upstream side of the sand migration to decrease the sand inflow into the channel. This method may be effective to delay the sand wave development.

References

Harri, P.T.(1989): Sandwave movement under tidal and wind-driven currents in a shallow marine environment, Adolphus Channel, Northeastern Australia, Continental Shelf Research, Vol.9 No.11, pp.981-1002.

Mogi, A.(1971): Shoreline and breaker zone, Geology of Shallow Sea, Basic Lectures in Marine Studies 7, Tokai Univ. Press, pp.109-252. (in Japanese)

Onodera, S.(1981): Improvement of Seaways in the Seto Inand Sea for Large-sized Ships, PIANC, section 1, Vol.1, pp.89-111.

Ozasa, H.(1974): Field Investigation of Large Submarine Sand Waves, Coastal Engineering in Japan, Vol. 17, pp. 155-184.

Coastal Disaster Prevention Works in Japan

MOTONO Ichio and NARUSE Susumu[1]

Abstarct

In this paper, we will present the Japanese coastal disaster prevention policy for the 21st century. First of all, we will show the characteristics of Japan's geographic conditions and coastal disasters. The next, we will review the evolution of coastal disaster prevention policy in our country in the last 5 decades. The third, we will discuss some aspects that affect coastal disaster prevention policy in 1990's and explore a new policy in order to meet the new waves; such as an coastal engineering development, an emergence of environmental awareness, and needs for recreational use of shorelines.

Introduction

The total length of Japan's shoreline is approximately 36,000 kilometers including various peninsulas, bays and small islands; half of the country's economic and social activities is done in the coastal area. Where people and industries are concentrated along the coast, they have been suffered severe damages from coastal disasters. An appropriate coastal protection works that protect people and infrastructure from coastal disasters is urgently needed in those days. Japan organized a coastal protection by enacting Coastal Protection Act and allocating a central and local governments' roles. It also introduced long range fiscal plans to implement coastal protection works efficiently in 1970. These efforts made our land safety to some extent last fifty years. However people gradually valued a coastline as an environmental protection, recreational use as well as the economic activity. The purpose of the coastal protection is diversified by these new demands. We introduce environmentally and user-oriented coastal protection

[1] Ports and Harbors Bureau, Ministry of Transport, 2-1-3 Kasumigaseki, Chiyoda, Tokyo 100-8989, Japan

works as well as technically sound creditable coastal protection works to meet these new waves.

Natural and Geographic Condition of a Japan's Coastline

Japan is prone to several types of coastal disasters such as typhoons in the summer, wind waves in the winter and Tsunamis caused by earthquakes (Takayama,1997). **Figure 1** shows the major coastal disasters which run across our nation. High tides generated by the low pressure of a typhoon have caused floods in under sea level areas such as Tokyo Bay, Osaka Bay and Ise Bay. **Table 1** shows major high tide disasters and **Photograph 1** shows a high tide disaster at Yokosuka, Tokyo Bay 1996. The severe erosion caused by the wind waves is a significant problem in the coastal area that faces the Japan Sea. The disasters erode our national land by about 160 hectares each year.

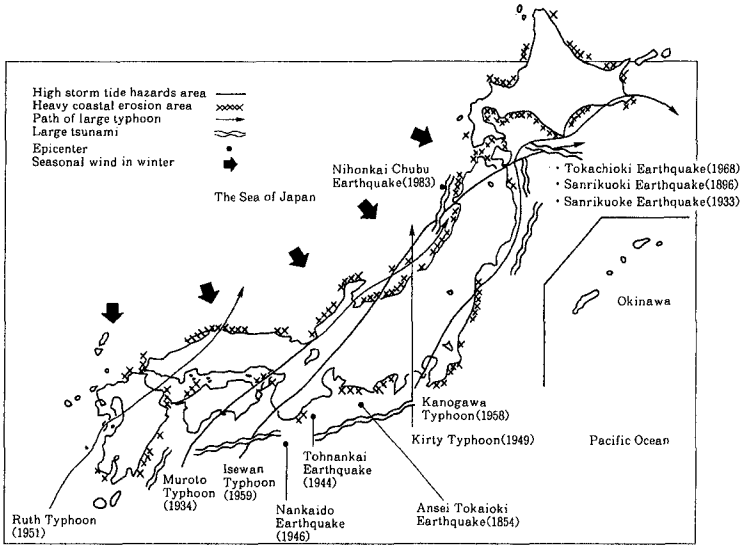

Figure 1 Characteristics of coastal disasters in Japan

Table 1 Major high tide disasters of the last 80 years

Year	Disaster region	High tide (m)	dead or missing	household missing	Typhoon
1917	Tokyo Bay	2.0	1,324	60,175	
1927	Ariake Bay	1.3	439	2,211	
1934	Osaka Bay	2.3	3,036	92,323	Muroto
1942	Suo Nada	1.7	1,158	102,374	
1945	South Kyushu	1.2	3,121	115,984	Makurazaki
1950	Osaka Bay	1.9	534	110,923	Jane
1951	South Kyushu	1.5	943	72,653	Ruth
1959	Ise Bay	2.6	5,098	156,676	Isewan
1961	Osaka Bay	2.2	200	54,782	2nd Muroto
1970	Tosa Bay	2.4	13	4,479	T 10
1985	Ariake Bay	0.8	3	589	T 13
1991	All Japan		62	170,447	T 19

Source: Nihon Kisho Saigai Nenpo (Meteorological Agency)

Photograph 1 A high tide disaster at Yokosuka 1996

Table 2 shows that Tsunamis are also a critical issue in the fjords such as Sanriku and Suruga Bay.

Table 2 Major Tsunami disasters of the last 100 years.

year	name of Tsunami	dead or missing	Residential building destroyed
1896	Meiji-Sanriku quake Tunami	27,123	10,617
1923	Kantou Daishinsai	142,807	702,495
1933	Sanriku quake Tunami	3,008	11,841
1944	Tounankai quake	998	76,139
1946	Nankai quake	1,443	68,006
1952	Tokachioki quake	32	2,230
1960	Chilean quake	139	22,693
1964	Niigata quake	26	92,012
1968	Tokachioki quake	52	19,695
1983	Nihonkai Chubu quake	104	6,359
1993	Hokkaidou Nanseioki	232	3,443

Source: Rika Nenpyou (1996)

Figure 2 indicates that the length of shoreline per land area of island nations such as Japan and the United Kingdom is relatively longer than that of peninsula nations (Korea and Italy) and continental nations (USA, France, Canada and the former USSR).

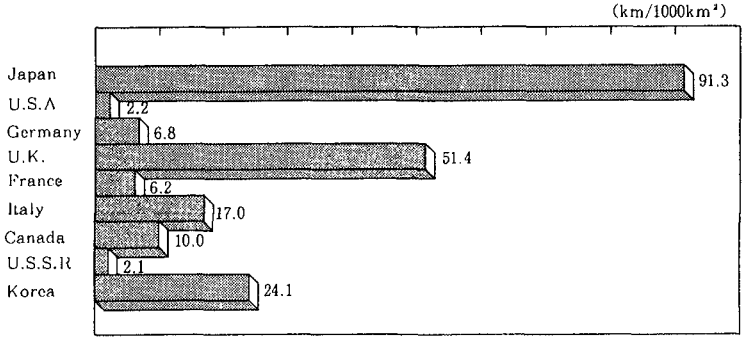

Figure 2 Comparison of coastal length per land area by nation

Figure 3 shows that population and industries are highly concentrated in the coastal municipalities. Nearly a half of nation's population and industries is found in coastal municipalities which occupy one third of the national land.

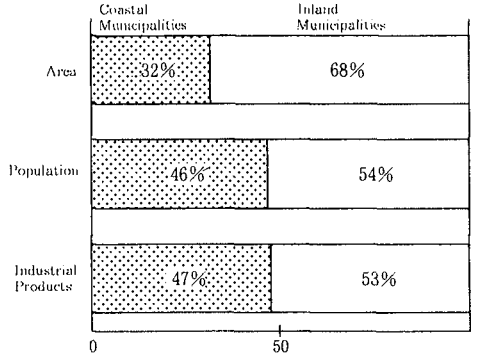

Figure 3 Comparison of coastal municipalities and inland municipalities by area, population and industrial products

The Coastal Protection Act

The protection of national land from the coastal disasters is defined to be a central government role under the Coastal Protection Act. The Act was established in 1956 to prevent coastal disasters which were very common after the W.W.II. Several coastal disasters such as those in the former chapter deteriorated our national land in those days. A coastal protection manager is responsible for coastal protection. Coastal protection is administrated by three competent Ministers depending on land use; Minister of Transport (MOT), Minister of Agriculture, Forestry and Fishery (MAFF), and Minister of Construction (MOC). MOT is in charge of sea ports and harbor areas. MAFF is in charge of agricultural areas and a fishery port areas. MOC is in charge of the rest of the coast. Under the Act, a governor can designate the coastal protection sea and land areas within 50 meters from seashore line by the due process of the law. In addition, a prefecture governor, a head of port authority or a fishery port manager manages a coast as a coastal protection manager. The manager's main task is to create a Coast Protection Facilities Plan and submit it to the Minister. He also has to register the coastal protection area and the coastal protection facilities and release this information to the public. Dredging, development or occupation of the area requires his permission. He collects a fee for all permitted activities. Those who violate the coastal protection ordinance will be fined by him. The central government supports the manager financially; up to half of investment when the manager constructs or renovates a coastal protection facility such as a dike, a jetty, a revetment or a sluice gate in the coast defense area. Each

Minister can construct or renovate the facility by himself when the coastal protection work is especially important for the national land protection when the work costs a lot, requires high technology and machinery power, or expands plural prefectures. The minister also has to show the design code of the coastal protection facility to the coastal protection managers in term of national land safety (Commission of Coastal Protection Facility Design Code ,1987). **Figure 4** shows a flow of construction or renovation of a coastal protection facility.

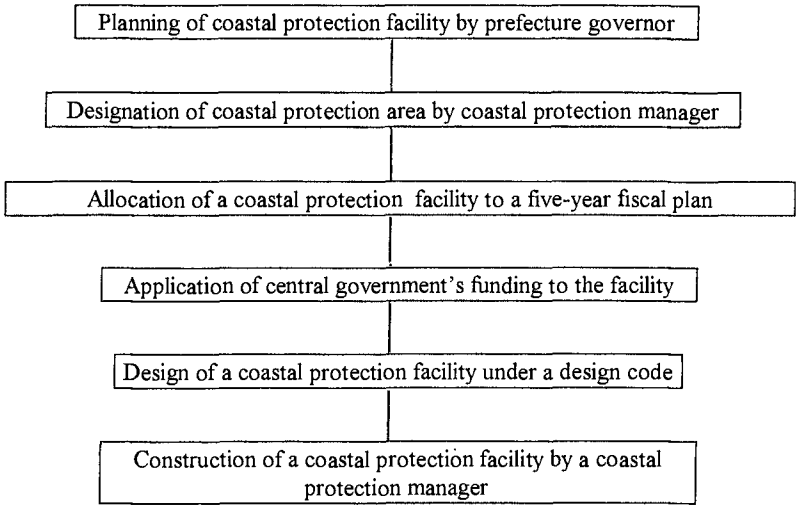

Figure 4 A flow of construction of a coastal protection facility

Evolution of Coastal Protection Work

The Ministers and coastal protection managers were previously not able to perform coastal protection work sufficiently due poor economic conditions. The construction of coastal protection facilities was urgently required in the 50's and the beginning of the 60's. For example, 4,700 people and 150,000 houses were lost by the Ise Bay Typhoon in 1959. The Congress requested the central government to allocate sufficient funds for coastal protection. Hence, the government introduced a long range fiscal plan to implement the annual investment efficiently and effectively in 1970. The aim of the plan is considered to be an administrative purpose to implement the investment efficiently and effectively, rather than legislative obligation of investment. **Table 3** shows a summery of the coastal protection work investment from 1970 to 2002.

Table 3 A Summary of the Coastal Protection Work Investment

Fiscal plan	1st		2nd	3rd	4th	5th	6th
Fiscal year	1970-74	75	76-80	81-85	86-90	91-95	96-02
Investment	260.4	73.0	561.3	673.8	822.6	1151.4	1340.0

(billions yen)

The Ministers and the managers quickly introduced low cost protection facilities and directed half of the budget to the densely populated and under water areas such as Tokyo bay, Osaka bay and Ise bay. **Figure 5** shows the coastal protection works at under sea level area in Osaka Bay.

Lock Facility on Amagasaki, Nishinomiya and Ashiya Port Coasts

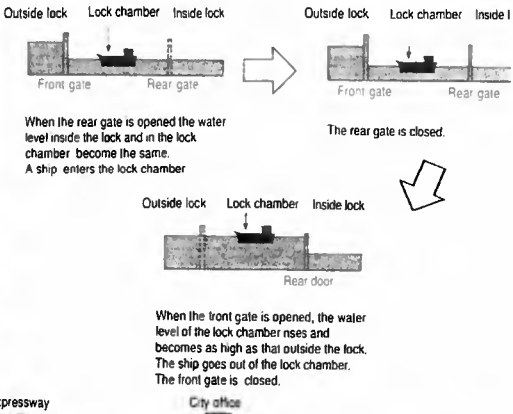

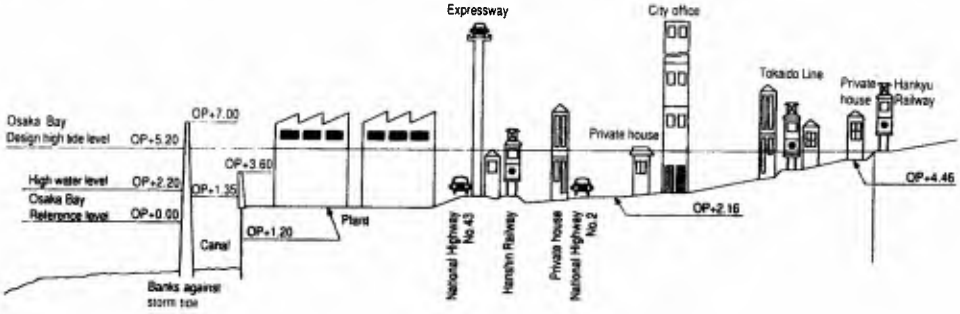

Figure 5 Coastal protection work under sea level area (Osaka Bay)

The damages inflicted by the coastal disasters might be mitigated to some extent with these rapid investments. However these facilities need high cost maintenance or even replacement since they deteriorated easily by tidal fluctuations and wave forces. The high crowns of the embankment and revetment have also prevented people from seeing water and accessing the beach, and the numbers of concrete blocks has messed up the seashore landscape. Furthermore, In the 70's environment protection movement became very popular. In the 80's people gradually conceived an especial value of the coastal zone such as recreational activities, richness of wildlife, amelioration of polluted water, and so on. The growing awareness of the importance of environment has influenced coastal protection policy (Coastal Protection Study Group,1995).

The 6th Seven-year Fiscal Plan For the 21st Century

The Cabinet established the 6th five-year fiscal plan with 1300 billion Yen (U.S. $10.8 billion when U.S. $1.00=120 Yen) in 1996. The coastal protection managers designated the 16,000 kilometer coastal protection area within the total 35,000 kilometer Japan's shoreline. According to a current study, 11 million people are living along the coastal protection area or behind it. However only 41% of the 16,000 kilometer coastal protection area is protected by the coastal protection facilities. More than 3.5 million people still live in fear of floods. **Table 4** shows that the range of protected area rate would be expected to increase to 48% in the 2000 years under the new fiscal plan.

Table 4 Coastal Protection Plan

	Present (1996)	**Seven-year plan (2002)**	**Final (2010)**
Defense Length (total 16,000 km)	**41 %**	**48%**	**70%**
Defense Population (total 11millions people)	**7.5 millions**	**8.8 millions**	**11 millions**
Defense Area (total 430 thousands ha)	**210,000 ha**	**260,000 ha**	**350,000 ha**
Erosion speed (present 160ha/year)	**160 ha/year**	**140 ha/year**	**+/- 0**
Length of Seismic Reinforcement (total 400km)	**-**	**200 km**	**400 km**
Integrated coastal protection configuration	**1,100 km**	**1,600 km**	**3,000 km**

The plan also has two goals; first, the ministries will speed up their coastal protection works and construct technically sound creditable coastal protection facilities. Next, the ministries will not only maintain the environmental standards but also promote the coastal wildlife preservation and user-oriented coast.

Technically Sound Creditable Coastal Protection Facilities

In order to produce a safe coast, the ministries are preparing three methods of defending the coast. The first method is to introduce an integrated coastal protection configuration consisting of offshore banks, beach fills, and gentle slope revetments. **Figure 6** shows that the configuration can weaken even the extraordinary strong wave forces with these serial facilities while an ordinary revetment is prone to suffer critical functional damage (Katoh,1994). Furthermore the configuration can expect town's local high amenity and the beach access.

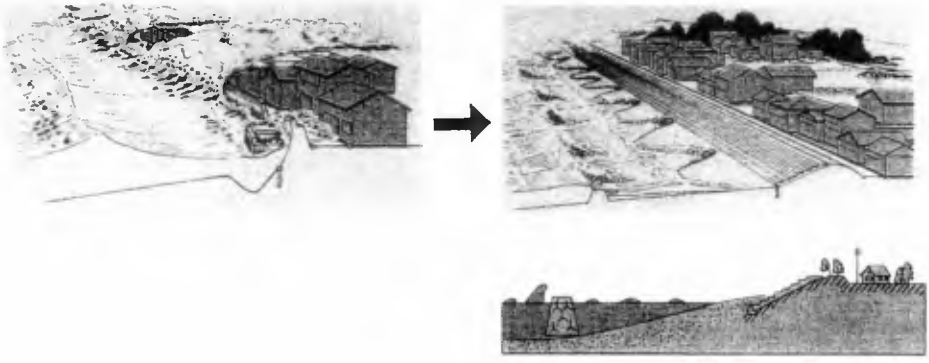

Figure 6 An integrated coastal protection configuration

The second method is to appropriate countermeasure against aearthquake. MOT checked all the facilities after Hanshin-Awaji earthquake which took place in January 1995. It found that some facilities constructed in the 60's had not been applied the seismic code properly. The code established in the 60's also needed to be revised. According to Ministers' investigation, at least 400 kilometer-length facility requires seismic reinforcement. Tsunamis also generated by earthquakes and caused severe damage on a densely populated fjord area. **Photograph 2** shows a breakwater would keep a harbor calm and break tsunami energy out. A coastal protection manager cooperates with a port authority to construct a breakwater in the fjord area.

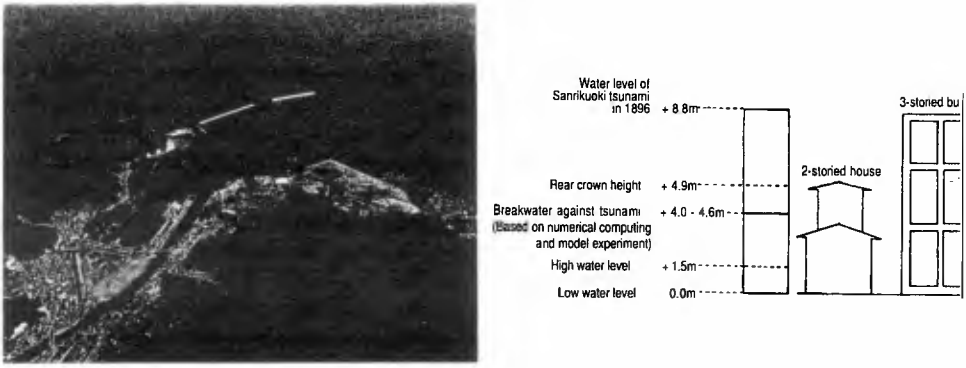

Photograph 2 A breakwater which has both function of defending a tsunami and of keeping the harbor calm (Kamaishi Port, Sanriku Region)

Finally, an automatic gate draw system and integrated disaster information system are introduced. There are many water/ land gate in a coastal protection area. It requires a huge labor and time to open/shut the gate. **Photographs 3** shows that the system network between an inland control room and gates. The control room monitors the area for earthquakes, tsunamis and high tide information 24 hours in a day and operates the gates by a remote control. The system enables a quick response to the unpredictable tsunamis and free from manual labor on operating a gate.

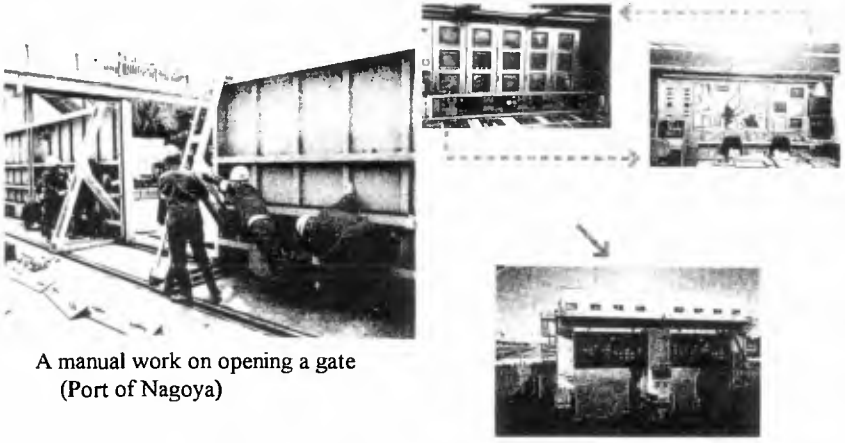

A manual work on opening a gate
(Port of Nagoya)

An automated gate draw system
(Port of Tokyo)

Photographs 3 An automated gate draw system and integrated information system

Environmentally Oriented and User Oriented Coastal Protection Works

The coastal protection manager is obliged to keeps his balance between coastal protection and coastal environment preservation owing to increase of environmental awareness. He is going to manage it by managing these conflicts rather than choosing either of them. A coast has rich but vulnerable wildlife resources. Environmentally oriented facilities such as an artificial reef, a tide pool, plantation and a beach should be considered when a coastal protection facility is designed and constructed on a coast. The facility has less impact to the coastal ecology than that we used to or ameliorate coastal environment. The artificial reef can cultivate sea weed and fish habitation. The tide pool also can keep water clean or bring rich oxygen into the water. The plantation can produce woods and supply a good atmosphere in the coast. The wild-life oriented beach can also become a sanctuary for endangered species such as red-turtles and

horseshoe crabs. **Photograph 4** shows that an artificial beach is also one of the best amenities to attract people to a coast. The purpose of beach replenishment is to defend a coast from disasters as well as to produce a recreational area where people can enjoy marine activities, bathing and sightseeing. The construction of pedestrian parkways, benches, trees as well as barrier-free facilities would enable elderly and handicapped persons to approach the coast easily.

Photograph 4 An artificial beach and bathing (Port of Utsumi, Ise Bay)

CONCLUSION

All the public work including coastal protection work is strictly required its efficiency and productivity in our country owing to the nation's fiscal deficit right now. We reviewed our coastal protection's institution and showed our policy for the next decade. We always question to ourselves; what the people expect on coastal protection work? is it worth to invest on an artificial beach instead of an reinforced concrete revetment under the tight budget condition? whether a central government or local government should have a responsibility on coastal protection? and who should fund coastal protection work ? . It will be great pleasure for us to exchange information on this matter over the world.

REFERENCES

Coastal Protection Study Group(1995): "Coastal Protection Vision - to promote and preserve our coast (in Japanese)"

Commission of Coastal Protection Facility Design Code(1987):" Coastal Protection Facility Design Code (in Japanese)"

Katoh,K.,et.al.(1994):Stabilization of beach in Integrated Shore Protection System, Proc. of HYDRO-PORT'94, PHRI, pp.1077-1096

Takayama,T(1997) Characteristics of Tsunami Disaster and Countermeasures against Tsunamis in Japan, The Fourth Japan-China(Taipei) Joint Seminar on Natural Hazard Mitigation.

BREACH EROSION IN SAND-DIKES

by

Paul J. Visser [1]

ABSTRACT

The process of breach erosion in sand-dikes is described. This process consists of five stages. For the final two stages three breach types are distinguished, depending on the erodibility of the base of the dike, the presence (or absence) of a solid toe construction on the outer slope and the presence and erodibility of a high foreland. A brief outline of a mathematical model based on the five-step breach growth process is presented. The validation of the model against the data of a field experiment shows good agreement.

1. INTRODUCTION

The Technical Advisory Committee on Water Defences (TAW) in the Netherlands has decided to substitute an inundation risk approach for the present design method for dikes based on an exceedance frequency of the water level. In this new method safety levels will be expressed in terms of risks. A risk-norm means that the inundation chance is combined with the consequences of flooding (deaths, loss of property and revenues, etc.), see Kraak et al. (1995). In order to determine the consequences of inundation, it is necessary to predict both the rate and speed of polder flooding. These are especially governed by the flow rate through the breach in the dike, which in its turn largely depends on the process of breach growth.

The aim of the investigation is a mathematical model that predicts the breach growth and the discharge through the breach in case of a dike-burst as function of relevant parameters as the cross-section of the dike (height, width, slope angles), the structure of the dike (dike material, revetments, foundation), polder area and the hydraulic conditions (water level against the dike, wave load). It is assumed that the dike was constructed with sand and that, after the formation of an initial breach at

[1] Delft University of Technology, Department of Civil Engineering, P.O. Box 5048, 2600 GA Delft, The Netherlands

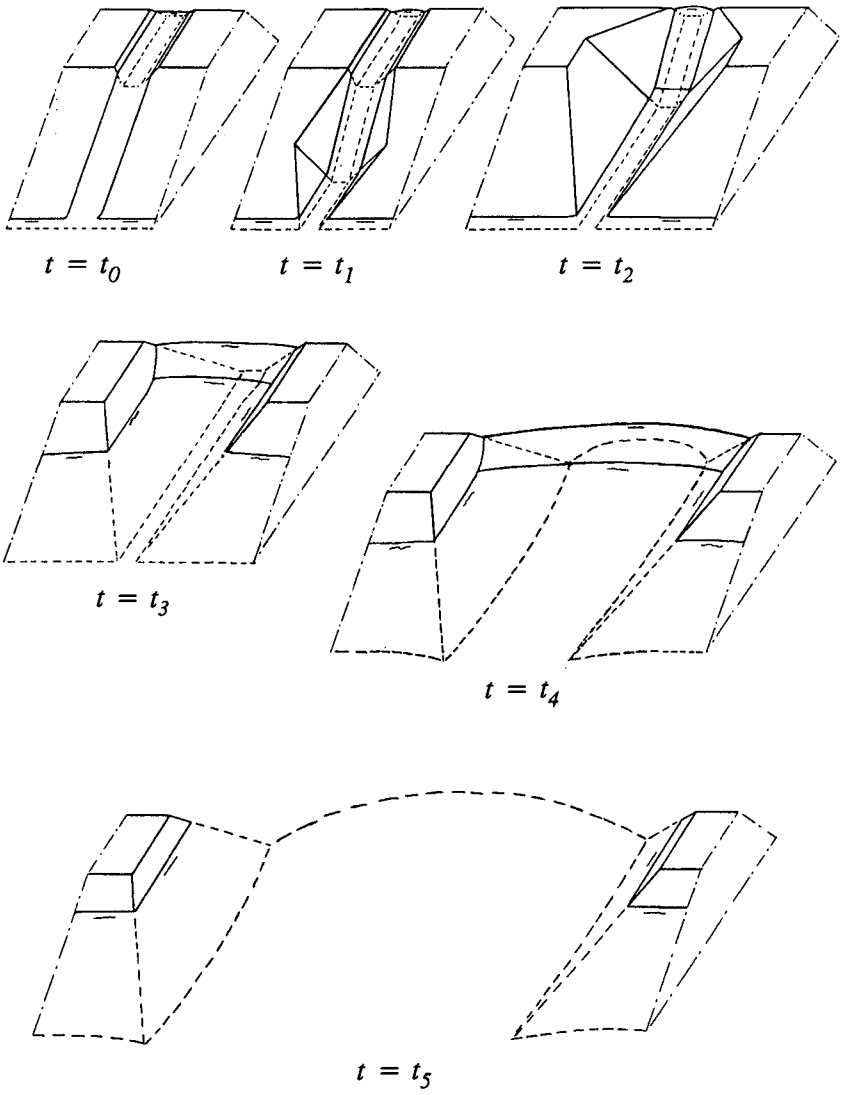

Figure 1 Schematic illustration of breach growth in a sand-dike.

the top of the dike, the clay-layers on the slopes do not decelerate the erosion process.

The first versions of the model (see Visser, 1995a) have been focused on the first three stages of the breach erosion process. The present model version includes also the final two stages of the dike breaching process. Also some improvements related to the physics of the erosion process have been implemented into the model.

2. BREACH EROSION PROCESS

It is assumed that the breach erosion starts (at $t = t_0$) with the flow of water through a small initial breach at the top of the sand-dike with a trapezoidal cross-section. Generally five stages can be distinguished in the process of breach erosion (see Figure 1). These five stages are:

- Stage I: steepening of the slope angle β of the channel in the inner dike slope from an initial value β_0 at $t = t_0$ up to a critical value β_1 at $t = t_1$.
- Stage II: retrograde erosion of the inner dike slope at constant angle β_1 for $t_1 < t \leq t_2$, yielding a decrease of the width of the crest of the dike in the breach; this stage ends at t_2 when the crest vanishes and the breach inflow starts to increase.
- Stage III: lowering of the top of the dike in the breach, with constant angle of the breach side-slopes and equal to the critical value γ_1, resulting in an increase of the width of the breach for $t_2 < t \leq t_3$. At $t = t_3$ the dike in the breach is completely washed out down to the base of the dike at polder level.
- Stage IV: critical flow stage, in which the breach flow is virtually critical throughout the breach for $t_3 < t \leq t_4$, and the breach continues to grow mainly laterally. The side-slope angles remain at the critical value γ_1. The breach growth in vertical direction depends in this stage on the erodibility of the base the dike. At t_4 the flow through the breach changes from critical ($Fr = 1$ in Stage IV to subcritical ($Fr < 1$ for $t > t_4$).
- Stage V: subcritical flow stage, in which the breach continues to grow, mainly laterally due to the subcritical flow in the breach for $t_4 < t \leq t_5$. The side-slope angles remain at the critical value γ_1. At t_5 the flow velocities in the breach become so small (incipient motion) that the breach erosion stops. The flow through the breach continues and stops when at t_6 the water level in the polder has equalled the outside water level.

In Stages I, II and III the initial breach cuts itself into the dike. Most of the discharge through the breach takes place in the Stages IV and V. At the end of Stage IV backwater starts to effect the flow through the breach. In case of a relatively tiny polder with a very small storage capacity, the downstream submergence may start earlier. In theory this may occur in each of the Stages I, II and III. In practice, however, it will take place in Stage III, since the total flow through the breach is too small in Stages I and II to allow downstream submergence. Hence, in case of a relatively tiny polder, Stage IV may be passed over.

3. DEVELOPMENT OF BREACH IN STAGES I, II AND III

Figure 2 shows the flow through the initial breach at $t = t_0^+$ shortly after the start of the breaching process at $t = t_0$. From a hydraulic point of view the slopes of dikes are very steep, i.e. $\sin\beta >> C_f$ (the slope angle β is defined here as the inclination of the inner slope of the dike in the breach in the flow direction with respect to a horizontal line, C_f is the bottom friction coefficient). This means that the water depth at the top of the inner slope at $x = 0$ (x is the coordinate along the inner slope) is equal to the critical depth d_c. The flow on the inner slope accelerates between $x = 0$ and $x = l_n$, and is virtually uniform for $x \geq l_n$. Consequently the capacity to transport sand also increases between $x = 0$ and $x = l_n$ and is nearly constant for $x \geq l_n$. This means that the rate of erosion increases along the stretch $0 < x < l_n$ and is nearly constant for $l_n \leq x \leq l_a$ (where l_a is the adaptation length of the suspended

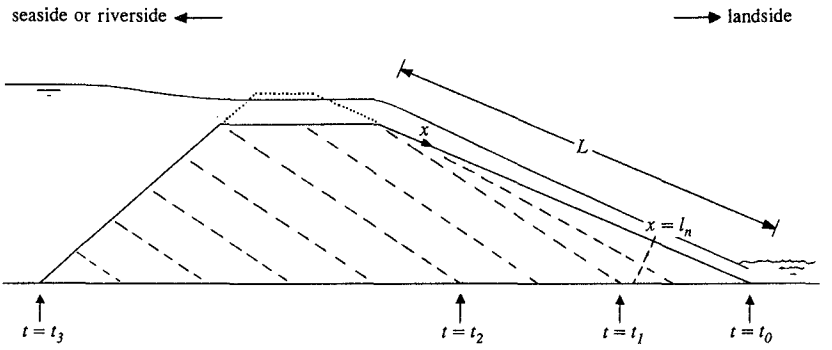

Figure 2 Flow over dike in the breach at $t = t_0^+$ shortly after the start of the breaching process (solid line) and development of inner slope of dike in the breach in Stages I, II and III (dashed lines).

sediment transport, similarly to l_n being the adaptation length of the flow). As a result of this the inner slope becomes steeper and steeper along the slope and in time along the stretch $0 < x < l_n$, and for $l_n \leq x \leq l_a$ the inclination of the inner slope remains constant. The slope angle along $0 < x < l_n$ will, however, not exceed a limit β_1 (say $\beta_1 \approx \phi$, where ϕ is the angle of internal friction). If this limit has been reached along the entire stretch $0 < x < l_n$ (at $t = t_1$), the rate of erosion becomes constant for $0 \leq x < l_n$ as indicated by the lines for $t \geq t_1$ in Figure 2, and Stage II starts.

In Stage II retrograde of the inner slope of the dike in the breach occurs at constant angle β_1, resulting in a decrease of the width of the dike-crest in the breach. Stage II ends when the width of the dike-crest has become zero (at $t = t_2$).

It can be concluded that for $t_0 < t \leq t_2$ the rate of erosion of the inner slope in the breach is controlled by the erosion at $x = l_n$ (or also the erosion along the stretch $l_n \leq x \leq l_a$). This means that only the rate of erosion at $x = l_n$ has to be known.

In Stage I the width of the channel (initial breach) in the crown of the dike remains at its initial value. The increase of the depth of the channel in the inner slope causes also an increase of the width of this channel in the slope (see Figure 1). At $t = t_1$ the width of the breach starts to grow at the downstream side of the dike-crown.

As long as the flow accelerates, its capacity to transport sediment increases. This means that the adaptation length for the sediment transport is always larger than the adaptation length for the flow, i.e. $l_a > l_n$. Visser (1998) has derived the following practical approximation for l_n:

$$\frac{l_n}{L} \approx 10 \frac{h}{H_D} \tag{1}$$

where h is the depth of the breach in the crest of the dike, H_D is the height of the dike above the polder level and L is the length of the inner slope.

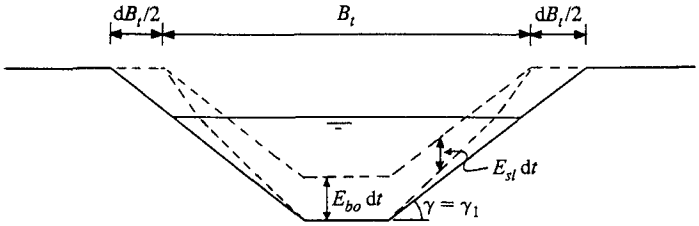

Figure 3 Increase dB_t in time dt of breach width B_t near the inflow in Stage III.

A relatively high dike in The Netherlands has a height $H_D \approx 10\,\text{m}$. If it is assumed that $h \approx 1\,\text{m}$ (i.e. the 1 m thick clay-layer at the crest of the dike has been washed out by the high water), then the ratio $l_n/L \approx 1$. Hence, the development of the inner slope in Stages I and II of the breach erosion process of such a typical dike will be as shown in Figure 2 for $x \leq l_n$.

Figure 2 shows also the triangular cross-section of the dike through the axis of the breach at $t = t_2$. Due to the proceeding erosion process, the top of the dike in the breach starts to drop. As a result, both the discharge per unit width q_{br} and the breach width increase in Stage III. It is assumed that also in this stage the angle of the inner slope remains at the critical value β_1. So again the rate of erosion is constant along the entire stretch $0 \leq x \leq l_n$, and also in the interval $t_2 < t < t_3$ it is entirely determined by the erosion at the toe of the slope.

At $t = t_2$ the width of the breach at the upstream side of the crown also starts to grow (see Figure 1). The rate of erosion at the breach bottom (E_{bo}) is larger than the erosion rate at the side-slopes (E_{sl}) due to the larger flow velocities (as a result of the larger water depths). For the same reason the erosion rate at the toe of the side-slopes is larger than higher on the slopes. This means that in Stage III the side-slope erosion is entirely controlled by the erosion at the bottom (i.e. the increase of the breach depth). Hence, the rate of increase of breach width is controlled by the rate of erosion at the breach bottom (see Figure 3):

$$\frac{dB_t}{dt} = \frac{2}{\tan\gamma_1} E_{bo} \tag{2}$$

In Stage III the breach growth accelerates drastically when deepening of the breach opening magnifies the inflow rate and the latter accelerates the erosion process. Consequently the flow and the sand transport through the breach change drastically in this stage: from a supercritical flow with a Froude number Fr much larger than 1 at $t = t_2$ to a supercritical flow with Fr slightly above 1 at $t = t_3$, from sheet flow transport with a Shields' mobility parameter θ of orders 10 and 100 at $t = t_2$ to sediment transport with θ of order 1 at $t = t_3$ (see Visser, 1998).

It is clear that the duration of the breach erosion process in Stages I, II and III depends largely on the dimensions of the initial breach. The larger these are, the shorter the total duration of these stages is, and consequently an accurate description of the breach erosion process in Stages I, II and III is then less important for the evaluation of the rate of flooding of the protected low-lying land.

4. BREACH DEVELOPMENT IN STAGES IV AND V

The continuation of the breach erosion process after the complete wash-out of the dike in the breach at t_3 depends on the following geometrical and material conditions of the dike:

- the resistance against further erosion of the base of the dike;
- the presence or absence of a berm and a toe construction on the outer slope and its ability to protect the outer slope against further erosion;
- the presence or absence of a relatively high foreland and its resistance against erosion.

Three types of breaches can be distinguished, dependent of these conditions. In a Type A breach the vertical erosion at the breach inflow is prevented by a solid clay foundation of the dike, or by a solid berm and a solid toe construction on the outer slope or by a solid, relatively high foreland (solid means here: with relatively high resistance against erosion). Dikes breach as Types B or C in the absence of a solid clay foundation, or a solid berm and a solid toe construction or a solid high foreland. If a relatively high (erodible) foreland is present then the dike breaches as Type B, otherwise as Type C. The Types A, B and C breaches are described further in next.

Type A breach

If the base of the dike consists of a solid clay-layer, then this layer will considerably slow down or prevent further vertical erosion, see Figure 4. This means that the breach continues to grow laterally in Stages IV and V, as shown in Figure 5. Since the erosion at the toe of the side-slopes is larger than higher on the slopes, the angle γ remains at its critical value γ_1. Hence, the erosion at the toe of each of the side-slopes (E_{sl} in Figure 5) determines the erosion of the overall side-slope, and consequently also the growth of the breach width. The discharge through the breach can be described simply by the formula for the flow over a broad-crested weir.

The lower parts of the outer slopes of sea dikes and river dikes in The Netherlands are protected against waves and currents by a (low water) berm and a toe construction. Less is known about the behaviour of these constructions in breaching dikes. It is, however, likely that these constructions may hinder or slow down further growth of the scour hole in upstream direction in cases where the foundation of the dike does not consist of solid clay. Downstream of the low water berm the breach continues to grow in vertical direction resulting in the formation of a scour hole, see Figure 9. The berm acts as a spillway (broad-crested or sharp-crested, which has only a secondary influence on the discharge coefficient of the spillway) controlling the breach inflow rate. Then the growth of the breach width is also determined at this upstream control section, resulting in an increase of the breach width as in the above situation of a solid base of the dike.

In cases where the dike has a relatively high foreland with a relatively large resistance against erosion, the development of the breach inflow and the breach growth is similar to that of a dike with a solid low water berm on the outer slope.

Types B and C breaches

If the base of the dike does not have much resistant against erosion and the dike does not have a solid berm and a solid toe construction on the outer slope, the breach continues to grow vertically (scour hole grows both with and against the flow, see Figures 9 and 11) and laterally (widening of the breach, see Figures 10 and 12).

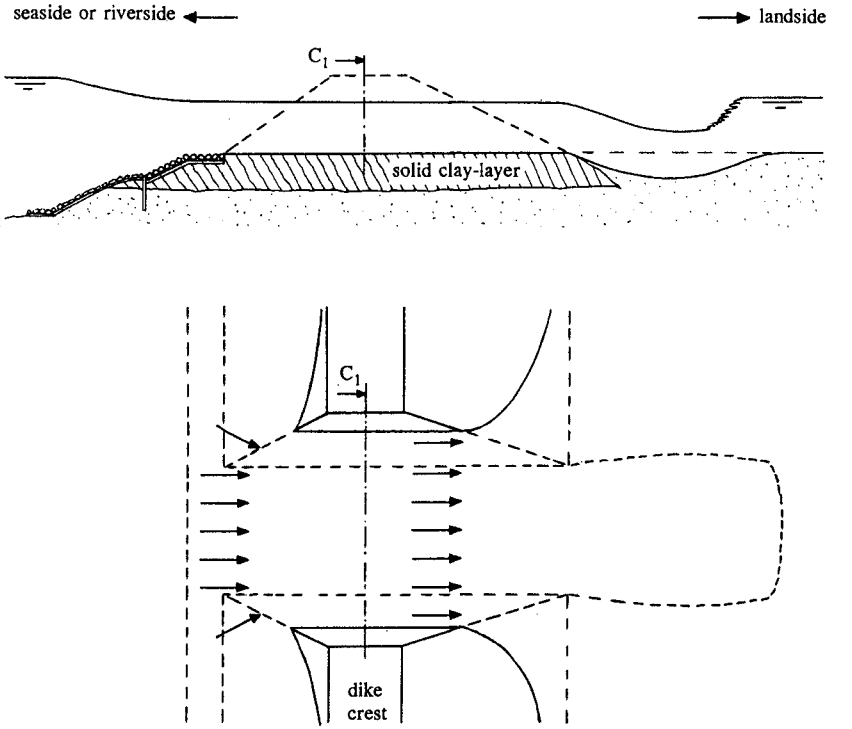

Figure 4 Cross-section and top view of flow in Stage IV through a breach in a dike constructed on a solid clay-layer (Type A breach).

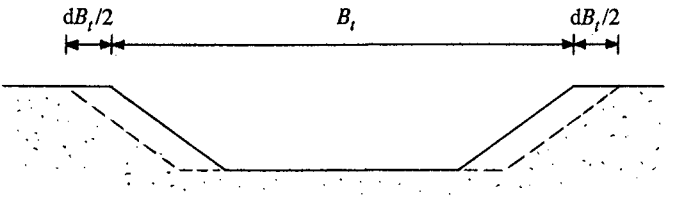

Figure 5 Cross-section C_1 (see Figure 4) of breach showing increase of breach width B_t in a Type A breach in Stages IV and V.

Upstream of the breach a spillway is formed which controls the breach inflow. The alignment of this spillway depends on the height of the foreland in front of the dike. The alignment of the overfall will be curved (elliptic or circular) in a Type B breach

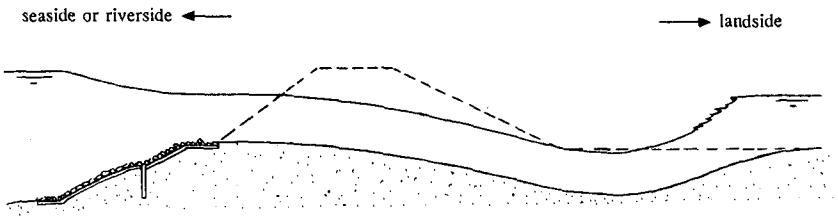

Figure 6 Flow in Stage IV through a breach when a toe construction protects the lower part of the outer slope against further erosion.

in a dike with a relatively high foreland (see Figure 7). In a situation where the outer slope abuts on the water course the shape of the spillway will be straight in the middle and curved near the side-slopes; this is called a Type C breach (see Figure 8).

As described in Chapter 3, the growth of the breach width in Stage III is controlled by the rate of erosion at the breach bottom (E_{bo}), and not by the erosion at the side-slopes (E_{sl}). In Stages IV and V, however, it is the erosion rate at the side-slopes (E_{sl}) that determines the increase of the breach width (see Figures 5, 8 and 10):

$$\frac{dB_t}{dt} = \frac{2}{\tan\gamma_1} E_{sl} \tag{3.3}$$

The argument behind this conclusion is simple. The order of magnitude of the widths of final-breaches is 100 m (see Visser, 1998), while the order of magnitude of their depths is 10 m. Hence, the widths of final breaches have always been much larger then their depths, so that:

$$E_{bo} << \frac{2}{\tan\gamma_1} E_{sl} \tag{3.4}$$

Visser (1998) argues that the side-slope erosion in Stages IV and V is governed by the flow at the upstream spillway, which simplifies the modelling of the breach growth process significantly.

In Stage V ($t_4 < t \leq t_5$) the breach continues to grow laterally. The continuous flow through the breach causes the water level in the polder to increase and the flow velocity in the breach to decrease, resulting in a deceleration of the breach growth.

At t_5 the flow velocities in the breach become so small (incipient motion) that the breach erosion stops. As far as the rate of flooding of the polder is concerned, Stages IV and V are the most important stages, since in these stages most of the water is discharged through the breach and the ultimate dimensions of the breach are determined.

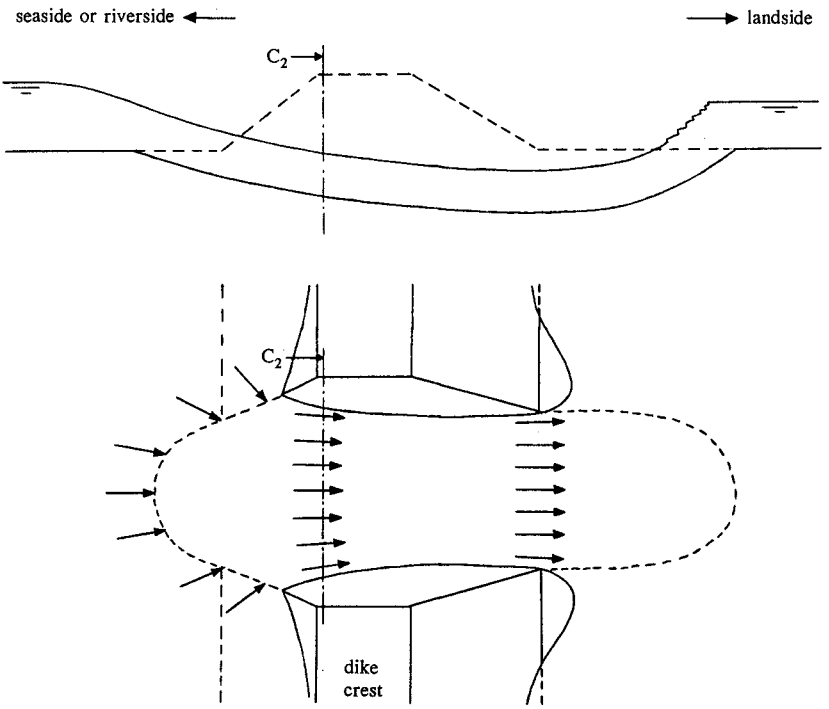

Figure 7 Cross-section and top view of flow in a Type B breach in Stage IV.

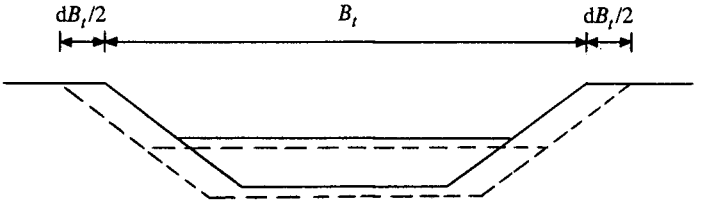

Figure 8 Cross-section C_2 (see Figure 7) showing growth of breach width B_t in a Type B breach in Stages IV and V.

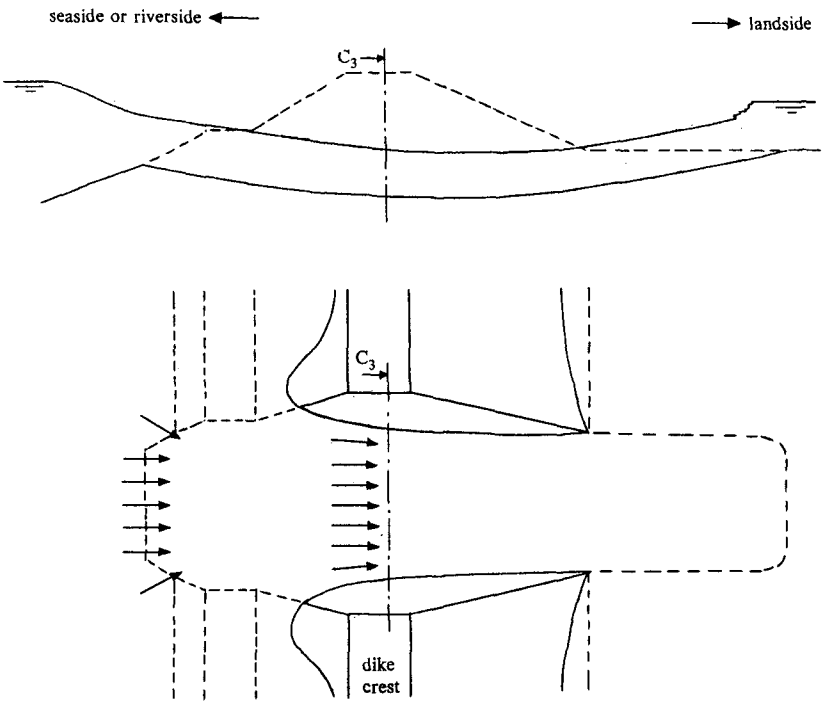

Figure 9 Cross-section and top view of flow in a Type C breach in Stage IV.

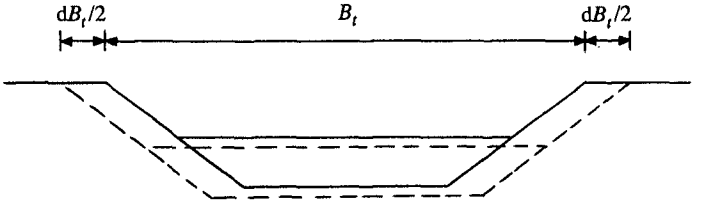

Figure 10 Cross-section C_3 (see Figure 9) showing growth of breach width B_t in a Type C breach in Stages IV and V.

5. MATHEMATICAL MODEL

Based on the five-step breach erosion process described above, a mathematical model for the growth of a breach in a sand-dike and the inflow rate through the breach has been developed. It is assumed that the dike was constructed with sand and that the clay-layers on the slopes do not decelerate the erosion process.

An essential part of a breach erosion model is the description of the entrainment of the sediment and its transport through the breach. In the mathematical model a simplified version of Galappatti's (1983) description for the entrainment of sediment is applied. This approach requires, however, a formulation for the equilibrium value of the sediment transport. None of the existing sediment transport formulae has been derived and tested for the relatively steep slopes in the initial stages and the large flow velocities throughout most of the breach erosion process. For application into the model, a number of existing sediment transport formulae has been tested to breach erosion tests (see Visser, 1995b), leaving only a few formulae with a reasonable performance. These transport formulae have been implemented into the model for the confrontation with experimental results and prototype data.

The numerical version of the model (BRES) has been written in C^{++} for use on a personal computer.

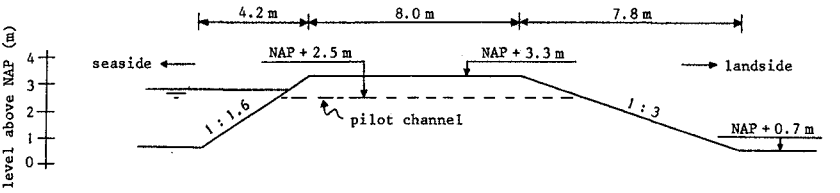

Figure 11 Cross-section of sand-dam in Zwin'94 experiment (NAP is reference level in The Netherlands at about mean sea level).

6. ZWIN'94 FIELD EXPERIMENT

The Zwin'94 experiment was performed in the Zwin Channel, a tidal inlet at the Dutch-Belgian border connecting the nature-reserve The Zwin with the North Sea (see Visser et al., 1996). The Zwin area measures about 1.5 km^2; the mean tidal prism is about 350000 m^3. The experiment was done in quiet autumn weather, with negligible wave heights against the sand-dam.

A sand-dam closing of the Zwin Channel (see Figure 11) was built with a height $H_D = 2.6$ m above the channel bottom, a width at the crest of 8 m and a length of about 200 m. The inclination of the outer slope was 1 : 1.6, that of the inner slope 1 : 3. A small trapezoidal pilot channel, 0.8 m deep and with a width of about 1 m at the breach bottom and about 3.6 m at the dike crest was made in the upper part of the dam to ensure breaching near the middle of the Zwin Channel.

The experiment started at $t = t_0 = 0$, about 20 minutes before high water, with the flow of water through the pilot channel. At 3 locations upstream and 3 locations

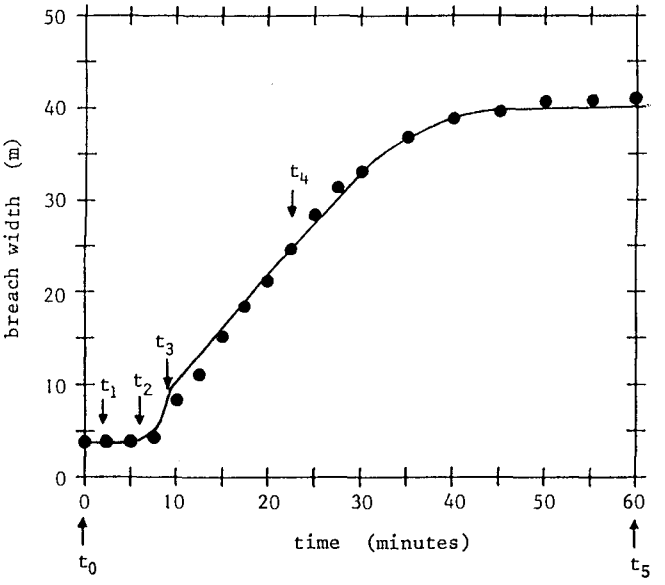

Figure 12 Comparison of model prediction (solid line) for width of the breach at the dike top (B_t) and observed B_t in Zwin'94 experiment (dotted line).

downstream from the breach, current velocity meters (Ott propeller type) and pressure probes measured continuously horizontal flow velocities and water elevations, respectively. The breach erosion process was both video-taped and photographed (marks put in the dike-top allowed the observation of the dimensions of the breach at different times from the video-images, slides and photos). A total number of 40 vibration probes, buried in the sandy bottom of the Zwin Channel, detected the development of the breach under water in Stages IV and V. Each probe acted as a burglar-alarm: by measuring its own rate of vibration it could detect when the erosion process had exposed it to the flowing water. The vibration probe system was tested and calibrated in a laboratory flume. The signals of all vibration probes were recorded on the hard disks of several personal computers. At $t = t_5 \approx 60$ min the flow velocities in the breach had become so small that the erosion process stopped. The Zwin'94 field experiment has clearly confirmed the five-step breach erosion mechanism as described above and shown in Figure 1. Figure 12 shows the result of the observations of the growth of the breach width B_t in time (observed at the top of the dike): B_t increased from $B \approx 3.6$ m at $t = t_0 = 0$ up to $B_t \approx 41$ m at $t = t_5 \approx 60$ min.

The data set of the Zwin'94 experiment is very useful for the validation of mathematical breach erosion models. Reference is made to Visser et al. (1996) and Visser (1998) for details about the data set resulting from this experiment.

7. COMPARISON OF MODEL PREDICTION WITH FIELD DATA

Figure 12 shows the comparison of the model prediction with the data of the Zwin' 94 experiment. It can be concluded that the agreement of the model prediction with the experimental data is good. This result has been obtained applying the Bagnold-Visser formula (see Visser, 1989) in Stages I, II and III and Van Rijn's (1984a,b) sand transport formulation in Stages IV and V.

Visser (1998) has applied the model also to a laboratory experiment and to a prototype dike failure of the 1953 flood in The Netherlands. For descriptions of both cases and details of these validations of the model reference is made to Visser (1998).

REFERENCES

Bagnold, R.A., 1963. Mechanics of marine sedimentation. In *'The Sea: Ideas and Observations', 3*, Interscience, New York, USA, pp. 507-528.

Galappatti, R., 1983. A depth-integrated model for suspended transport. *Comm. on Hydraulics, Rep. 83-7*, Dept. Civil Eng., Delft Univ. Techn., Delft, The Netherlands.

Kraak, A.W., Bakker, W.T, Graaff, J. van de, Steetzel, H.J. and Visser, P.J., 1995. Breach-growth research programme and its place in damage assessment for a polder. *Proc. 24th Int. Conf. Coastal Eng.*, Kobe, Japan, 1994, pp. 2197-2206.

Van Rijn, L.C., 1984a. Sediment transport. Part I: bed load transport. *J. Hydr. Eng., 110*, pp. 1431-1456.

Van Rijn, L.C., 1984b. Sediment transport. Part II: suspended load transport. *J. Hydr. Eng., 110*, pp. 1613-1641.

Visser, P.J., 1989. A model for breach growth in a dike-burst. *Proc. 21st Int. Conf. Coastal Eng.*, Malaga, Spain, pp. 1897-1910.

Visser, P.J., 1995a. A model for breach growth in sand-dikes. *Proc. 24th Int. Conf. Coastal Eng.*, Kobe, Japan, 1994, pp. 2755-2769.

Visser, P.J., 1995b. Application of sediment transport formulae for sand-dike breach erosion. *Comm. on Hydraulic and Geotechnical Eng., Rep. no. 94-7*, Dep. Civil Eng., Delft Univ. of Technology, Delft, The Netherlands.

Visser, P.J., 1998. Breach growth in sand-dikes. *Ph.D. thesis*, Fac. Civil Eng., Delft Univ. Techn., Delft, The Netherlands.

Visser, P.J., Kraak, A.W., Bakker, W.T, Steetzel, Smit, M.J., Snip, D.W., H.J. and Graaff, J. van de, 1996. A large-scale experiment on breaching in sand-dikes. *Proc. Coastal Dynamics'95*, Gdansk, Poland, 1995, pp. 583-594.

Bayesian Estimation of Quantiles for the Purpose of Flood Prevention

J.M. van Noortwijk[1] and P.H.A.J.M. van Gelder[2]

Abstract

In this paper, the problem of Bayesian estimation of flood quantiles is studied. Bayes estimators of the optimal dyke height under symmetric and asymmetric loss are investigated when the annual maximum sea water levels are exponentially distributed with unknown value of the mean. Three types of loss functions are considered: (i) linear loss, (ii) squared-error loss, and (iii) linex loss. In order to properly account for the statistical uncertainty in the mean, a modified linex loss function is to be preferred. This new modified linex loss function is derived from the economic dyke heigthening problem of Van Dantzig. Since the loss function is based on a benefit-cost analysis, its parameters have a clear economic significance.

Introduction

In statistical analysis of civil engineering data such as water levels, wave heights, soil parameters, etc., many attempts have been made to establish what kind of fitting method is preferable for the parameter estimation of a probability distribution in order to estimate the q-quantile, i.e. the value with a probability of exceedance equal to q (where q is usually very small, in the order of 10^{-3} to 10^{-5}). Recent research on this subject can be found in, for example, Yamaguchi (1997), Fortin et al. (1997), Burcharth and Liu (1994), and Van Gelder (1996). The main idea in their work is to generate random samples from a chosen probability distribution using Monte Carlo simulation, and to investigate the advantage of a certain parameter estimation method over the other method which is based on the viewpoint of bias and variance of the q-quantile. The estimation method with the

[1] HKV Consultants, P.O. Box 2120, 8203 AC Lelystad, The Netherland, and Delft University of Technology, Faculty of Mathematics and Computer Science, P.O. Box 5031, 2600 GA Delft, The Netherlands, E-mail: J.M.van.Noortwijk@hkv.nl.

[2] Delft University of Technology, Faculty of Civil Engineering, P.O. Box 5048, 2600 GA Delft, The Netherlands, E-mail: P.vanGelder@ct.tudelft.nl.

smallest bias and/or variance of the q-quantile is then considered to be the best parameter estimation method for that particular probability distribution. In this paper, a new concept is presented in which the parameter estimation method is defined as such that the bias of the estimated q-quantile is minimised within a Bayesian framework of asymmetric loss functions. The use of asymmetric loss functions gives us the possibility to differentiate between underestimation and overestimation of the q-quantile. In civil engineering applications, an underestimation error of the q-quantile generally leads to much higher losses than an overestimation error.

Although Fortin, Bobée and Bernier (1997) also use asymmetric loss functions for comparing statistical distributions and estimation methods, they do not apply these loss functions in a full Bayesian framework. The parameters of the probability distributions have been estimated by using three well-known methods from classical statistics: the method of maximum likelihood, the method of moments, and the method of probability-weighted moments. The Bayesian point of view only comes in when Fortin et al. (1997) use a nonparametric Bayesian simulation methodology, called Pólya resampling, instead of the classical bootstrap to draw observations with replacement from a reference sample.

Three loss functions have been studied: (i) the asymmetric linear loss function, (ii) the asymmetric squared-error loss function, and (iii) the linex loss function. For an overview of asymmetric loss functions, see Zellner (1986) and Thompson and Basu (1996). The linex loss function has been used in real estate assessment by Varian (1974). Basu and Ebrahimi (1991) determine an expression for the linex estimator of the survival function of a system having a Type II censored exponential lifetime. Using simulated data, Basu and Thompson (1992) and Thompson and Basu (1993) obtain linex estimates of the reliability of simple stress-strength systems. Pandey et al. (1994) study the problem of estimating the shape parameter of a Pareto distribution using a linex loss function.

The Bayes estimator of the q-quantile under asymmetric loss minimises the expected loss with respect to the probability distribution of an unknown parameter. In order to find the loss function that can best be applied to decision problems in civil engineering, we have studied the economic dyke-height optimisation problem of Van Dantzig (1956). He assumed the annual maximum sea water levels to be exponentially distributed. It appears that Van Dantzig's economic loss function differs slightly from the linex loss function. This modified linex loss function seems to be a promising candidate for solving quantile estimation problems in other civil engineering benefit-cost analyses.

The outline of the paper is as follows. First, an overview is given of the Bayesian estimation of quantiles by using the three above-mentioned loss functions. The economic optimisation of dyke heights is subsequently addressed. Next, we derive the relation between the economic optimisation and the loss function approach. This relation results in a modified linex loss function. The different methods are compared in a Dutch polder case study. Finally, conclusions are drawn.

Bayesian Estimation of Quantiles Using Loss Functions

Define the random quantity X_i to be the maximal sea water level in year i, $i=1,...,n$. We assume the random quantities $X_1,...,X_n$ to be mutually independent, identically distributed, random quantities with a cumulative distribution function $\Pr\{X_i \le x\} = F(x \mid \lambda)$ with parameter λ, $i=1,...,n$. As a function of λ, the q-quantile of the probability distribution of X is defined to be

$$y_q = g(\lambda) = F^{-1}(1-q \mid \lambda),$$

where $g'(\lambda) > 0$. Suppose the parameter λ is unknown with a prior probability density function $\pi(\lambda)$. After observing the data $\mathbf{x} = (x_1,...,x_n)$, this prior density can be updated to the posterior density using Bayes' theorem:

$$p(\lambda) = \pi(\lambda \mid \mathbf{x}) \propto l(\mathbf{x} \mid \lambda)\pi(\lambda) = \prod_{i=1}^{n} f(x_i \mid \lambda)\pi(\lambda),$$

where $l(\mathbf{x} \mid \lambda)$ is the likelihood function of the observations $\mathbf{x}$ when the value of λ is given.

For the purpose of flood prevention, we are interested in estimating the q-quantile of the probability distribution of the maximal sea water level X per year, denoted by $g(\lambda^*)$. In a Bayesian framework, this can be achieved by minimising the loss due to the simple estimation error $\Delta = g(\lambda^*) - g(\lambda)$. Since the loss due to flooding increases with overestimation error (i.e. the real q-quantile is less than its estimated value: $g(\lambda) < g(\lambda^*)$ or $\Delta > 0$) and, at a much faster rate, with underestimation error (i.e. the real q-quantile is greater than its estimated value: $g(\lambda) > g(\lambda^*)$ or $\Delta < 0$), we focus on asymmetric loss functions (see Thompson and Basu, 1996). Beside loss functions of the simple estimation error, loss functions of the relative estimation error can also be considered.

The three most well-known asymmetric loss functions are: (i) the asymmetric linear loss function, (ii) the asymmetric squared-error loss function, and (iii) the linex loss function.

Asymmetric Linear Loss

The asymmetric linear loss function is defined by

$$L(\Delta) = \begin{cases} a\Delta & \text{if} \quad \Delta \ge 0 \text{ or } \lambda \le \lambda^*, \\ -b\Delta & \text{if} \quad \Delta < 0 \text{ or } \lambda > \lambda^*, \end{cases} \tag{1}$$

where $a, b > 0$. This loss function is asymmetric for $a \ne b$. We can best choose the estimate λ^* for which the expected loss is minimal with respect to the probability

distribution of λ:

$$E(L(\Delta)) =$$
$$= \int_{-\infty}^{\lambda^*} a[g(\lambda^*) - g(\lambda)]p(\lambda)\,d\lambda + \int_{\lambda^*}^{\infty} b[g(\lambda) - g(\lambda^*)]p(\lambda)\,d\lambda =$$
$$= ag(\lambda^*)P(\lambda^*) - a\int_{-\infty}^{\lambda^*} g(\lambda)p(\lambda)\,d\lambda - bg(\lambda^*)[1 - P(\lambda^*)] + b\int_{\lambda^*}^{\infty} g(\lambda)p(\lambda)\,d\lambda,$$

where $P(\lambda)$ is the cumulative distribution function of λ. The Bayes estimator under asymmetric linear loss is the solution of the equation

$$\frac{dE(L(\Delta))}{d\lambda^*} = g'(\lambda^*)([a+b]P(\lambda^*) - b) = 0,$$

which results in $\lambda^* = P^{-1}(b/[a+b])$. Hence, the Bayes estimator λ^* equals the $b/[a+b]$-quantile of the posterior distribution of λ. When $a = b$, the linear loss function is symmetric and its Bayes estimator reduces to the posterior median $P^{-1}(0.5)$.

Asymmetric Squared-Error Loss

The asymmetric squared-error loss function is defined by

$$L(\Delta) = \begin{cases} a\Delta^2 & \text{if} \quad \Delta \geq 0 \text{ or } \lambda \leq \lambda^*, \\ b\Delta^2 & \text{if} \quad \Delta < 0 \text{ or } \lambda > \lambda^*, \end{cases} \tag{2}$$

where $a, b > 0$. This loss function is asymmetric for $a \neq b$ with expected value

$$E(L(\Delta)) = \int_{-\infty}^{\lambda^*} a[g(\lambda^*) - g(\lambda)]^2 p(\lambda)\,d\lambda + \int_{\lambda^*}^{\infty} b[g(\lambda) - g(\lambda^*)]^2 p(\lambda)\,d\lambda.$$

The Bayes estimator under asymmetric squared-error loss is the solution of the equation

$$\frac{dE(L(\Delta))}{d\lambda^*} = 2g(\lambda^*)g'(\lambda^*)\{[a-b]P(\lambda^*) + b\} -$$
$$-2g'(\lambda^*)\{[a-b]\int_{-\infty}^{\lambda^*} g(\lambda)p(\lambda)\,d\lambda + b\int_{-\infty}^{\infty} g(\lambda)p(\lambda)\,d\lambda\} = 0,$$

which must be solved for λ^* numerically. When $a = b$, the squared-error loss function is symmetric and the Bayes estimator $g(\lambda^*)$ reduces to the posterior mean of $g(\lambda)$.

Asymmetric Linex Loss

The asymmetric linex loss function is defined by

$$L(\Delta) = b[a\Delta + \exp\{-a\Delta\} - 1], \tag{3}$$

where $a, b > 0$. The expected loss can be written as

$$E(L(\Delta)) =$$
$$= b[\int_{-\infty}^{\infty} a[g(\lambda^*) - g(\lambda)]p(\lambda)\,d\lambda + \int_{-\infty}^{\infty} \exp\{-a[g(\lambda^*) - g(\lambda)]\}p(\lambda)\,d\lambda - 1].$$

The Bayes estimator under asymmetric linex loss, λ^*, is the solution of the equation

$$\frac{dE(L(\Delta))}{d\lambda^*} = ab\,g'(\lambda^*)[1 - \int_{-\infty}^{\infty} \exp\{-a[g(\lambda^*) - g(\lambda)]\}p(\lambda)\,d\lambda] = 0,$$

which results in

$$\lambda^* = g^{-1}\left(\frac{\ln(\int_{-\infty}^{\infty} \exp\{ag(\lambda)\}p(\lambda)\,d\lambda)}{a}\right).$$

Examples of Loss Functions

Examples of the three loss functions are displayed in Figure 1: (i) the asymmetric linear loss function with $a = 5.37\ 10^7$ and $b = 1.94\ 10^7$, (ii) the asymmetric squared-error loss function with $a = 1.07\ 10^8$ and $b = 3.88\ 10^7$, and (iii) the asymmetric linex loss function with $a = 3.03$ and $b = 1.32\ 10^7$. The parameters a and b have been chosen as such that the three loss functions are equal for $\Delta = \pm 0.5$.

Note that both linear loss and squared-error loss are special cases of what Thompson and Basu (1996) called monomial-splined loss, defined, for fixed $m = 1,2,3,...$, by

$$L(\Delta) = \begin{cases} a|\Delta|^m & \text{if} \quad \Delta \geq 0, \\ b|\Delta|^m & \text{if} \quad \Delta < 0, \end{cases}$$

where $a, b > 0$. Fortin, Bobée and Bernier (1997) applied monomial-splined loss for $m = 1,2,3$ within a framework of classical statistics.

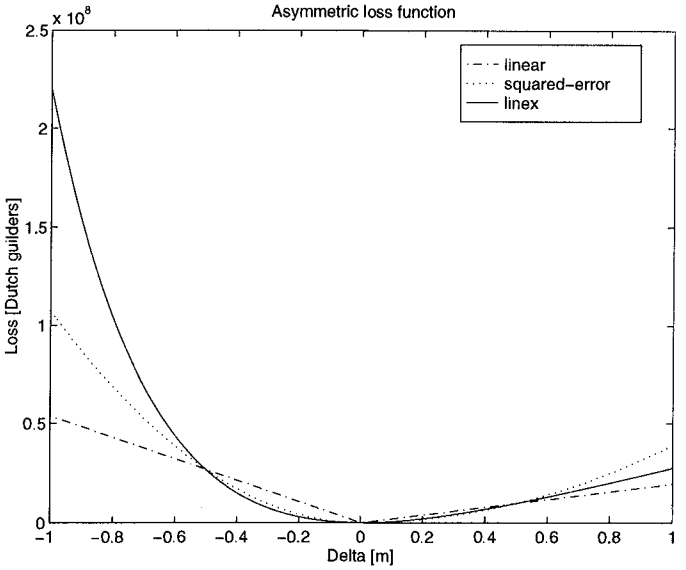

Figure 1. The linear, squared-error and linex loss function according to Eqs. (1-3).

Estimation of Optimal Dyke Height

Let us consider the benefit-cost analysis that is adapted from Van Dantzig (1956). Suppose we have to decide how high the dykes should be to prevent a polder from flooding. Let the height of the dyke h be the decision variable, and let $h_0 = 3.25$ metres be the initial height of the dyke at the moment the decision has to be taken. The only failure mechanism that we regard is overtopping, i.e. inundation of the polder will occur as soon as the sea water level exceeds the height of the dyke. To account for the stochastic nature of the sea water level, we assume the maximal sea levels per year X_i, $i = 1,...,n$, to be conditionally independent, exponentially distributed, random quantities with a known location parameter $x_0 = 1.96$ metres and an unknown scale parameter λ with expected value 0.33 metres. Hence, the likelihood function is

$$l(\mathbf{x} \mid \lambda) = \prod_{i=1}^{n} f(x_i \mid \lambda) = \prod_{i=1}^{n} \frac{1}{\lambda} \exp\left\{-\frac{x_i - x_0}{\lambda}\right\}.$$

Accordingly, the q-quantile of the probability distribution of X is

$$y_q = g(\lambda) = x_0 - \lambda \ln(q).$$

The costs of heightening the dykes with $h - h_0$ metres depend on the fixed cost $c_f = 1.1\ 10^8$ and the variable cost $c_v = 4.0\ 10^7$: i.e. $c_f + c_v[h - h_0]$. If the polder is inundated, an economic value of $c = 2.4\ 10^{10}$ Dutch guilders is lost. The discount factor is $\alpha = [1 + 0.015]^{-1}$, compounded annually, where $0 < \alpha < 1$. Since the probability of inundation of the polder is $\exp\{-(h - x_0)/\lambda\}$, the expected discounted costs due to inundation of the polder over an unbounded time-horizon can be written as

$$c(\lambda, h) = c_f + c_v[h - h_0] + \frac{\alpha}{1-\alpha} c \exp\left\{-\frac{h - x_0}{\lambda}\right\} \tag{4}$$

if the decision-maker chooses dyke height h and when the value of λ is given.

The decision with minimal expected costs, i.e. the dyke height for which the expected discounted costs due to inundation are minimal, is

$$h^* = x_0 - \lambda \ln\left(\lambda \cdot \frac{c_v}{c} \cdot \frac{1-\alpha}{\alpha}\right) \tag{5}$$

when the value of λ is given. Accordingly, the inundation probability that balances the cost of investment optimally against the cost of inundation is

$$q = \exp\left\{-\frac{h^* - x_0}{\lambda}\right\} = \lambda \cdot \frac{c_v}{c} \cdot \frac{1-\alpha}{\alpha}. \tag{6}$$

When the value of λ is given to be 0.33 metres, the optimal inundation probability is $q = 8.25\ 10^{-6}$.

To account for the statistical uncertainty in the mean of the maximal sea water level per year, the prior density of λ is assumed to be an inverted gamma distribution with scale parameter $\mu > 0$ and shape parameter $\nu > 0$:

$$\mathrm{Ig}(\lambda \mid \nu, \mu) = [\mu^\nu / \Gamma(\nu)] \lambda^{-(\nu+1)} \exp\{-\mu/\lambda\}$$

for $\lambda > 0$. The prior mean and variance are $E(\lambda) = \mu/(\nu - 1)$ and $\mathrm{Var}(\lambda) = E(\lambda)^2/(\nu - 2)$, respectively. Hence, the larger ν, the less uncertain λ. On the basis of this prior density, the expected discounted costs over an unbounded horizon transform into

$$\int_0^\infty c(\lambda,h)p(\lambda)\,\lambda = c_f + c_v[h-h_0] + \frac{\alpha}{1-\alpha}c\left[\frac{\mu}{\mu+h-x_0}\right]^\nu . \tag{7}$$

The dyke height with minimal expected costs, while taking the uncertainty in λ into account, is

$$h^* = x_0 - \mu + \left[\nu\mu^\nu \cdot \frac{c}{c_v}\cdot\frac{\alpha}{1-\alpha}\right]^{\frac{1}{\nu+1}} . \tag{8}$$

The inundation probability that balances the cost of investment optimally against the cost of inundation, while taking the uncertainty in λ into account, is

$$q^* = \left[\frac{\mu}{\mu+h^*-x_0}\right]^\nu = \left[\frac{\mu}{\nu}\cdot\frac{c_v}{c}\cdot\frac{1-\alpha}{\alpha}\right]^{\frac{\nu}{\nu+1}} .$$

When the expected value of λ is 0.33 metres, the optimal inundation probability under statistical uncertainty is $q^* = 1.02\ 10^{-5}$ for $\nu = 50$, $q^* = 9.17\ 10^{-6}$ for $\nu = 100$, and $q^* \to 8.25\ 10^{-6}$ as $\nu \to \infty$.

An advantage of the inverted gamma distribution as a prior density is that the posterior distribution of λ, when the observations $x_1,\ldots,x_n$ are given, is also an inverted gamma distribution with scale parameter $\mu + \sum_{i=1}^n (x_i - x_0)$ and shape parameter $\nu + n$. The inverted gamma distribution is said to be a conjugate family of distributions for observations from an exponential distribution with unknown mean (scale parameter). From now on, when we use the probability density function $p(\lambda)$, we refer to the posterior density. Note that (inverted) gamma priors have als been applied by Basu and Ebrahimi (1991), Basu and Thompson (1992), Thompson and Basu (1993), and Pandey et al. (1994).

Relation Between Economic Loss and Linex Loss

The question arises whether Van Dantzig's economic cost function and the Bayesian loss function are interrelated to each other. In this respect, we reformulate Van Dantzig's cost function in terms of Bayesian loss, i.e. we rewrite the loss function as

$$L(\Delta) = L(g(\lambda^*) - g(\lambda)) = c(\lambda, h^* + \Delta) - c(\lambda, h^*) =$$
$$= c_v\Delta + \frac{\alpha}{1-\alpha}c\exp\left\{-\frac{h^*-x_0}{\lambda}\right\}\left[\exp\left\{-\frac{\Delta}{\lambda}\right\} - 1\right].$$

There are now two possibilities for rewriting the probability of exceedence

$\exp\{-(h^* - x_0)/\lambda\}$: (i) as a constant and (ii) as a function of the unknown scale parameter λ.

First, we investigate the probability of exceedence $\exp\{-(h^* - x_0)/\lambda\}$ to be a constant, i.e. to be $q = 8.25\ 10^{-6}$:

$$L(\Delta) = c_v \Delta + \frac{\alpha}{1-\alpha} cq \left[\exp\left\{ -\frac{\Delta}{\lambda} \right\} - 1 \right], \tag{9}$$

where $\Delta = g(\lambda^*) - g(\lambda)$ and $g(\lambda) = x_0 - \lambda \ln(q)$. The Bayes estimator under asymmetric loss in terms of Eq. (9), λ^*, is the solution of the equation

$$\frac{dE(L(\Delta))}{d\lambda^*} = g'(\lambda^*) \left[c_v - \frac{\alpha}{1-\alpha} cq \int_0^\infty \frac{1}{\lambda} \exp\left\{ -\frac{g(\lambda^*) - g(\lambda)}{\lambda} \right\} p(\lambda)\, d\lambda \right] = 0,$$

which results in

$$g(\lambda^*) = x_0 - \lambda^* \ln(q) = x_0 - \mu + \left[\nu \mu^\nu \cdot \frac{c}{c_v} \cdot \frac{\alpha}{1-\alpha} \right]^{\frac{1}{\nu+1}} = h^*.$$

Second, we consider the probability of exceedence $\exp\{-(h^* - x_0)/\lambda\}$ to be a function of the unknown scale parameter λ, by substituting the optimal dyke height h^* according to Eq. (5):

$$L(\Delta) = c_v \left(\Delta + \lambda \left[\exp\left\{ -\frac{\Delta}{\lambda} \right\} - 1 \right] \right), \tag{10}$$

where $\Delta = g(\lambda^*) - g(\lambda)$ and

$$g(\lambda) = x_0 - \lambda \ln\left(\lambda \cdot \frac{c_v}{c} \cdot \frac{1-\alpha}{\alpha} \right).$$

The Bayes estimator under asymmetric loss in terms of Eq. (10), λ^*, is the solution of the equation

$$\frac{dE(L(\Delta))}{d\lambda^*} = c_v g'(\lambda^*) \left[1 - \int_0^\infty \exp\left\{ -\frac{g(\lambda^*) - g(\lambda)}{\lambda} \right\} p(\lambda)\, d\lambda \right] = 0,$$

which results in

$$g(\lambda^*) = x_0 - \lambda^* \ln\left(\lambda^* \cdot \frac{c_v}{c} \cdot \frac{1-\alpha}{\alpha}\right) = x_0 - \mu + \left[\nu\mu^{\nu} \cdot \frac{c}{c_v} \cdot \frac{\alpha}{1-\alpha}\right]^{\frac{1}{\nu+1}} = h^*.$$

Modified Linex Loss

We ought to notice that the two economic loss functions (9-10) differ slightly from the linex loss function (3). A difference is that both economic loss functions are not only a function of the simple estimation error Δ, but also of the relative estimation error Δ/λ. In terms of λ^* and λ, the loss function (9) can be written as

$$L(\Delta) = -c_v \ln(q) \cdot (\lambda^* - \lambda) + \frac{\alpha}{1-\alpha} cq\left[\exp\left\{\ln(q) \cdot \frac{\lambda^* - \lambda}{\lambda}\right\} - 1\right] = L(\Delta_1, \Delta_2), \qquad (11)$$

where $\Delta_1 = \lambda^* - \lambda$ is the simple estimation error of λ^* and $\Delta_2 = (\lambda^* - \lambda)/\lambda$ is the relative estimation error of λ^*. The general formulation of the modified linex loss function (11) is:

$$L(\Delta_1, \Delta_2) = b(a\Delta_1 + d[\exp\{-a\Delta_2\} - 1]),$$

where

$$a = -\ln(q), \quad b = c_v, \quad d = \frac{\alpha}{1-\alpha} \cdot \frac{c}{c_v} \cdot q.$$

Since the main aim of this paper is estimating the q-quantile of a probability distribution, the most appropriate loss functions seem to be the economic loss functions (9) and (11) (in terms of $g(\lambda)$ and λ, respectively). These economic loss functions are modified linex loss functions, for which the parameters have a clear economic significance. The parameters represent the cost of investment (dyke heightening) on the one hand, and the cost of flooding on the other hand. Since the modified linex loss functions are derived from estimating the mean of an exponential distribution, more research has to be undertaken to find out whether they can also be applied to estimate the statistical parameters of other probability distributions.

Comparative Results

On the basis of the dyke heightening problem, we have compared the linear, squared-error and linex loss function with the economic loss functions. The results are summarised in Tables 1-2. The coefficients a and b of the linear, squared-error and linex loss function have been assessed in the following way. As suggested by the economic loss functions (9-10), the coefficients of the linex loss function are assumed to be $a = [E(\lambda)]^{-1}$ and $b = c_v E(\lambda)$. Furthermore, asymmetric linear and squared-error loss

functions have been fitted to this linex loss function by, somewhat arbitrary, assuming the linear, squared-error and linex loss to be equal to each other for $\Delta = \pm 0.5$ (see Figure 1). Results are also presented for the symmetric linear and squared-error loss function.

Table 1: Bayes estimates of the scale parameter λ and the dyke height h for $\nu = 50$.

Estimation method for $\nu = 50$ observations	Eq.	a	b	λ^* [m]	h^* [m]
Van Dantzig without uncertainty	(5)	-	-	0.330	5.82
Van Dantzig with uncertainty	(8)	-	-	-	6.14
Bayes estimate symmetric linear loss	(1)	1	1	0.326	5.77
Bayes estimate symmetric squared-error loss	(2)	1	1	0.330	5.82
Bayes estimate asymmetric linear loss	(1)	$5.37\ 10^7$	$1.94\ 10^7$	0.356	6.13
Bayes estimate asymmetric squared-error loss	(2)	$1.07\ 10^8$	$3.88\ 10^7$	0.350	6.05
Bayes estimate linex loss	(3)	3.03	$1.32\ 10^7$	0.393	6.56
Bayes estimate modified linex loss	(9)	-	-	0.360	6.14
Bayes estimate modified linex loss	(10)	-	-	0.357	6.14

Table 2: Bayes estimates of the scale parameter λ and the dyke height h for $\nu = 100$.

Estimation method for $\nu = 100$ observations	Eq.	a	b	λ^* [m]	h^* [m]
Van Dantzig without uncertainty	(5)	-	-	0.330	5.82
Van Dantzig with uncertainty	(8)	-	-	-	5.98
Bayes estimate symmetric linear loss	(1)	1	1	0.328	5.80
Bayes estimate symmetric squared-error loss	(2)	1	1	0.330	5.82
Bayes estimate asymmetric linear loss	(1)	$5.37\ 10^7$	$1.94\ 10^7$	0.349	6.05
Bayes estimate asymmetric squared-error loss	(2)	$1.07\ 10^8$	$3.88\ 10^7$	0.344	5.98
Bayes estimate linex loss	(3)	3.03	$1.32\ 10^7$	0.354	6.10
Bayes estimate modified linex loss	(9)	-	-	0.345	5.98
Bayes estimate modified linex loss	(10)	-	-	0.343	5.98

From Tables 1-2, we can conclude the following. The cost-optimal dyke height without taking the statistical uncertainties involved into account is, due to Eq. (5), equal to 5.82 m. When asymmetric loss functions are applied, the optimal dyke height is higher while taking the statistical uncertainty in λ into account. The larger the uncertainty in the scale parameter λ, i.e. the smaller the number of observations ν, the higher the cost-optimal dyke height. On the other hand, a symmetric squared-error loss function results in the same height without uncertainty (5.82 m) and a symmetric linear loss function can result in even lower heights (5.77 m and 5.80 m, respectively). As expected, the optimal dyke height under uncertainty according to Eq. (8) equals the dyke height that follow from both economic loss functions (9-10). Recall that the main difference between Eq. (9) and Eq. (10) is that the former is regarded as a function of the optimal q-quantile, whereas the latter contains the substitution for q in terms of Eq. (6). Since the linex loss

function results in a dyke height much greater than the height in case of the economic loss functions, we recommend using the economic loss functions (modified linex loss functions) instead.

Conclusions

A Bayesian approach towards the estimation of flood quantiles has been suggested. Bayes estimators of the optimal dyke height under symmetric and asymmetric loss have been investigated when the annual maximum sea water levels are exponentially distributed with unknown mean. Three types of loss functions have been considered: (i) linear loss, (ii) squared-error loss, and (iii) linex loss. In order to properly account for the statistical uncertainty in the mean, a modified linex loss function can best be applied. This new modified linex loss function is derived from the economic dyke heigthening problem of Van Dantzig. The Bayes estimate of the dyke height under modified linex loss is equivalent to the optimal dyke height for which the economic loss is minimal. The modified linex loss function seems to be a promising candidate to solve quantile estimation problems in other civil engineering benefit-cost analyses. Moreover, unlike in most Bayesian literature, the parameters of the modified linex loss function have a clear economic significance. They represent the cost of investment (dyke heightening) on the one hand, and the cost of flooding on the other hand. The advantage of using a Bayesian loss function approach over a Van Dantzig approach is that the former approach is more closely related to the current design practice of hydraulic structures with fixed quantiles. The difference between under- and overdesign is more visible in the Bayesian loss function approach than in the Van Dantzig approach. The next step would be to repeat the type of work done in this paper on a larger scale in order to estimate the statistical parameters of other probability distributions.

References

Burcharth, H.F., and Liu, Z. (1994). On the extreme wave height analysis, In Port and Harbour Research Institute, Ministry of Transport, editor, *International Conference on Hydro-Technical Engineering for Port and Harbor Construction (Hydro-Port), Yokosuka, Japan, 1994*, pages 123-142, Yokosuka: Coastal Development Institute of Technology.

Basu, A.P., and Ebrahimi, N. (1991). Bayesian approach to life testing and reliability estimation using asymmetric loss function. *Journal of Statistical Planning and Inference*, 29, 21-31.

Basu, A.P., and Thompson, R.D. (1992). Life testing and reliability under asymmetric loss. In J.P. Klein, editor, *Survival Analysis - State of the Art*, pages 1-7, Dordrecht: Kluwer Academic Publishers.

Fortin, V., Bernier, J., and Bobée, B. (1997). Simulation, Bayes, and bootstrap in statistical hydrology. *Water Resources Research*, 33(3), 439-448.

Fortin, V., Bobée, B., and Bernier, J. (1997). Rational approach to comparison of flood distributions by simulation. *Journal of Hydrologic Engineering*, 2(3), 95-103.

Pandey, M., Singh, V.P., and Srivastava, C.P.L. (1994). A Bayesian estimation of reliability model using the linex loss function. *Microelectronics Reliability*, 34(9), 1519-1523.

Thompson, R.D., and Basu, A.P. (1993). Bayesian reliability of stress-strength systems. In A.P. Basu, editor, *Advances in Reliability*, pages 411-421, Amsterdam: Elsevier.

Thompson, R.D., and Basu, A.P. (1996). Asymmetric loss functions for estimating system reliability. In D.A. Berry, K.M. Chaloner, and J.K. Geweke, editors, *Bayesian Analysis in Statistics and Econometrics*, pages 471-482, New York: John Wiley & Sons.

Van Dantzig, D. (1956). Economic decision problems for flood prevention. *Econometrica*, 24, 276-287.

Van Gelder, P.H.A.J.M. (1996). How to deal with wave statistical and model uncertainties in the design of vertical breakwaters. In H.G. Voortman, editor, *Probabilistic Design Tools for Vertical Breakwaters; Proceedings Task 4 Meeting, Hannover, Germany, 1996 (MAST III/PROVERBS: MAS3-CT95-0041)*, pages 1-13.

Varian, H.R. (1974). A Bayesian approach to real estate assessment. In S.E. Fienberg and A. Zellner, editors, *Studies in Bayesian Econometrics and Statistics: In Honor of Leonard J. Savage*, pages 195-208, New York: North-Holland.

Yamaguchi, M. (1997). Intercomparison of parameter estimation methods in extremal wave analysis. In B.L. Edge, editor, *25th International Conference on Coastal Engineering, Orlando, Florida, U.S.A., 1996*, pages 900-913, New York: American Society of Civil Engineers (ASCE).

Zellner, A. (1986). Bayesian estimation and prediction using asymmetric loss functions. *Journal of the American Statistical Association*, 81(394), 446-451.

Flood Protection in the Danish Wadden Sea Area

Jens Otto Andersen

Abstract

In the Danish Wadden Sea area the main coastal problem is the risk of flooding while coast erosion only takes place in a few small localities and in larger measure at the peninsula of Skallingen. In the Danish Wadden Sea area some 100 km of dike protects the lowlying areas, the marsh areas, against flooding. Through the years the dike protection has been extended and reinforced.

Since the 1970s, the frequency of storm surges has been much higher than earlier in this century. These surges have worn the dikes and many reinforcements have been carried out, and two new dikes have been built protecting the towns Ribe and Højer.

The Danish dikes have always been green dikes, i.e. they are grass covered. They are rather easy to reinforce if necessary to withstand also a relative sea level rise caused by the green house effect, the continuing land subsidence in this area or possible more frequent and higher storm surges in the future.

Introduction

The Wadden Sea extends 500 km of the North Sea coast from den Helder in the Netherlands to the peninsula Skallingen in Denmark, the Danish part of the Wadden Sea being app. 70 km from the Danish-German border to Skallingen, fig. 1.

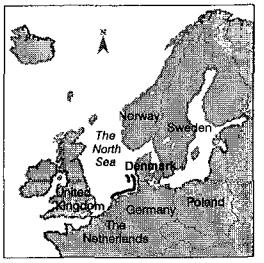

Figure 1. The Wadden Sea and the Danish part of the Wadden Sea.

Senior Coastal Engineer
Danish Coastal Authority, Box 100, DK7620 Lemvig, Denmark, E-mail: ki@kyst.dk

The Wadden Sea is dominated by the daily tide ranging from –0,7 m to + 0,7 m DNN (DNN is app. the same as the mean sea level, MSL) and by the strong in- and outgoing currents. At tidal low water app. 70% of the bottom of the Wadden Sea is dry.

Storm surges and floodings have influenced the landscape, the settlings as well as agriculture. In the Danish Wadden Sea, water levels above 3.5 m DNN are characterised as storm surges. In the last hundred years, the highest measured water levels during storm surges have been about 5 m DNN.

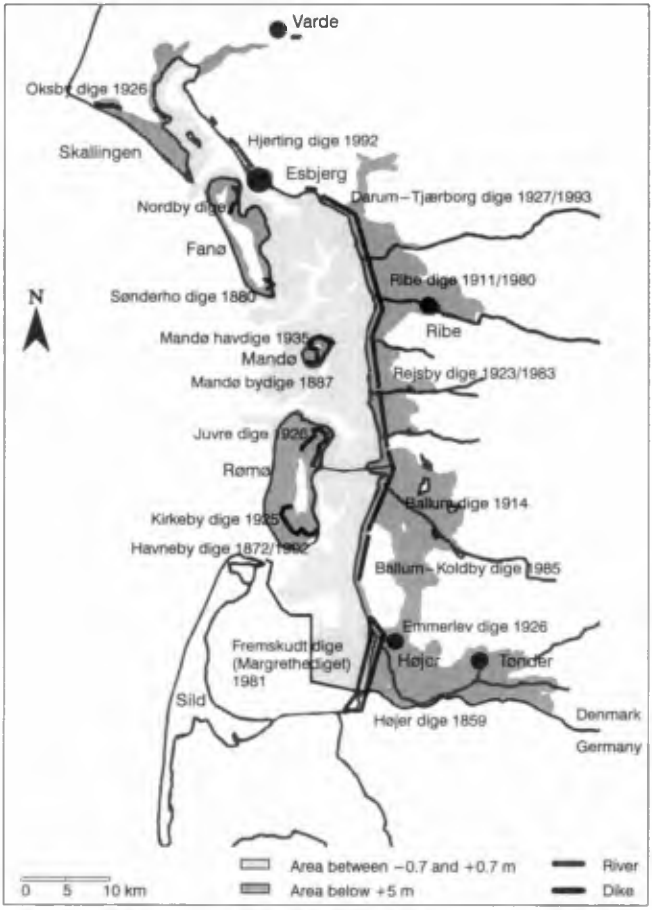

Figure 2. Upgrading of the dike system along the Danish Wadden Sea.

Large parts of the nearshore landscape are low lying and in risk of flooding if the dikes should breach, fig. 2. These low-lying areas are mainly 1 to 5 m above DNN, i.e. there are no areas below MSL. The areas are mainly used for agriculture but large parts of the two major towns Ribe and Tønder and also some villages are low-lying.

Severe Surges and Floodings

In 1362, the storm surge named "Grote Mandranke", i.e. "Great man-drowning" flooded the whole Wadden Sea area. Some sources mention up to 200,000 dead people, but this number has later been evaluated to be much too high. Still the flooding was indeed a disaster.

In 1634 another severe flooding caused 10,000 – 15,000 victims.

In Denmark, the last flooding where people drowned took place in 1923, where a storm surge unusually occurred in August. At this time, one of the dikes was being built and many of the workers were caught by the storm surge at the building site and drowned.

A severe flooding took place in 1953, app. 1,800 were killed in the Netherlands and 300 in England. In 1962 a storm flood killed 350 people in Germany. These two floodings did no harm in the Danish Wadden Sea area.

In 1976 and 1981, the two highest surges in this century occurred in Denmark, both with water level app. 5 m above DNN. These two surges are described below.

The 1964 Storm Flood Committee

After the disaster in the Netherlands and Germany in 1953 and 1962, a storm flood committee was appointed in 1964 in Denmark to evaluate the existing safety against flooding. As part of the work an extensive study concerning frequency and height of storm surges, hydraulic conditions, and safety problems was carried out. The first result of the work was the establishment of a warning and alert system. The work ended in 1975 resulting in an act of reinforcement of Ribe Dike to a safety level of 200 years and building of maintenance roads along most of the dikes. There was a difference of opinion whether Tønder Dike should be reinforced or a new forward dike should be built to achieve a safety level of 200 years against flooding of Tønder.

Ribe Dike and the Forward Dike at Tønder

A severe storm surge in 1976 ended the discussion. Denmark and Germany made an agreement on the building of a new dike in front of Tønder Dike continuing on the German side of the border also as a forward dike. The reinforcement of Ribe Dike was finished in 1980 and the new forward dike was finished in October 1981. Already in November 1981, a more severe storm surge than the one in 1976 struck the Wadden Sea. This only caused small local damages to these new dikes while large damages took place on the older dikes, one dike breached totally (fig. 9c). The profile of the two new dikes is shown in fig. 3.

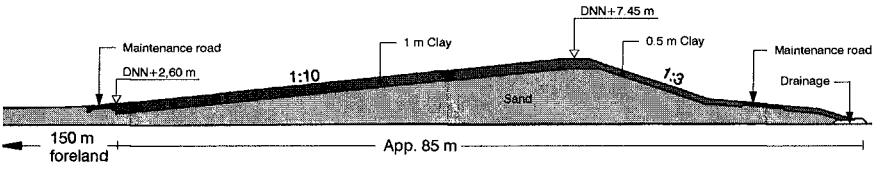

Figure 3. New dike design.

All the Danish dikes have always been green dikes i.e. covered by grass at the whole profile and no protection with stones, concrete, asphalt, etc.

The Dike Protection

Today, the dike length is app. 100 km.

The first dikes built some 500 years ago were only slight dikes functioning as so-called summer dikes, i.e. they protected the agricultural areas in the summer until the harvest was done. They would not protect against the more severe storms in the late autumn and winter. Most of the villages and sparse habitation were built either on natural higher areas or on artificially built rises.

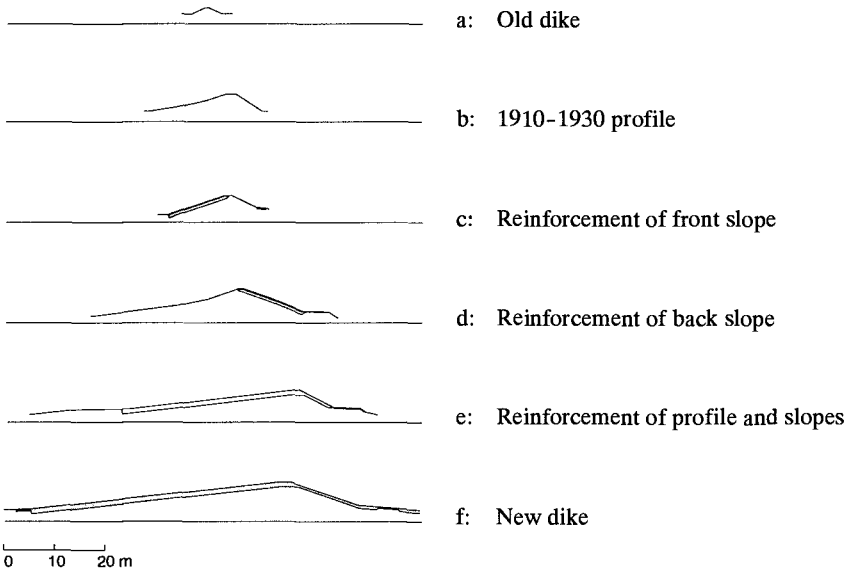

Figure 4. Evolution of dike profile

Fig. 4 shows the evolution in the dike profile since the first summer dikes, fig. 4a, to the newest dikes built some 15-20 years ago and shows the newer reinforcement of dikes.

The period 1910 – 1930 was very windy and some severe storm surges occurred. Because of this and the development in agriculture and habitation in the low-lying areas many new dikes were built, fig. 2 showing year of building and reinforcement, and fig. 4b showing the typical profile. The profile had a concave front slope with an average slope of 1:5 and a rather steep back slope 1:1.5 or 1:2. The strength against breaching has later been calculated to a safety level of 30-50 years.

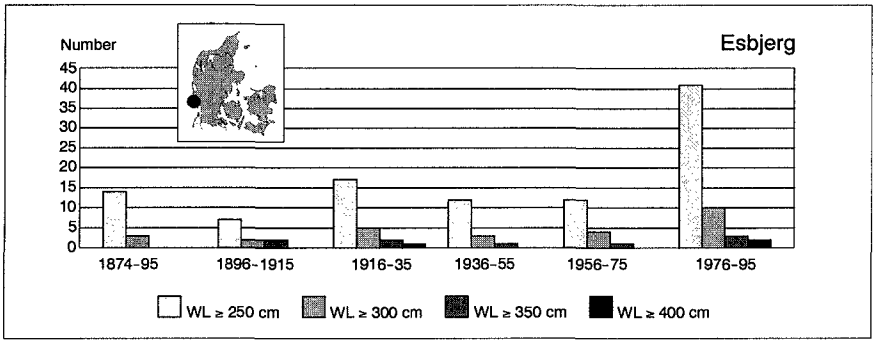

Figure 5 . Number of high water levels in 20 years periods.

The period from 1930 to the middle of the 1970s was rather calm. Since the middle of the 1970s there has been a "bad weather" period, fig. 5. Several storm surges have worn the dikes. It has been necessary to reinforce several of the dikes. These reinforcements have been made in different ways depending on the problem of the individual dike. Fig. 4c shows the reinforcement of the front slope with a clay cover to prevent erosion caused by wave attack. Fig. 4d shows a similar protection of the back slope but also a flattening of the back slope to prevent sliding and erosion caused by wave run over. Fig. 4e shows a reinforced dike profile with new flatter front and back slopes and reinforcements of the slopes with clay to protect against erosion from wave attack. Fig. 4f shows the profile of the new dikes in front of Ribe and Tønder.

Designing the Dikes

The principle of designing the height of the dikes is shown in fig. 6.

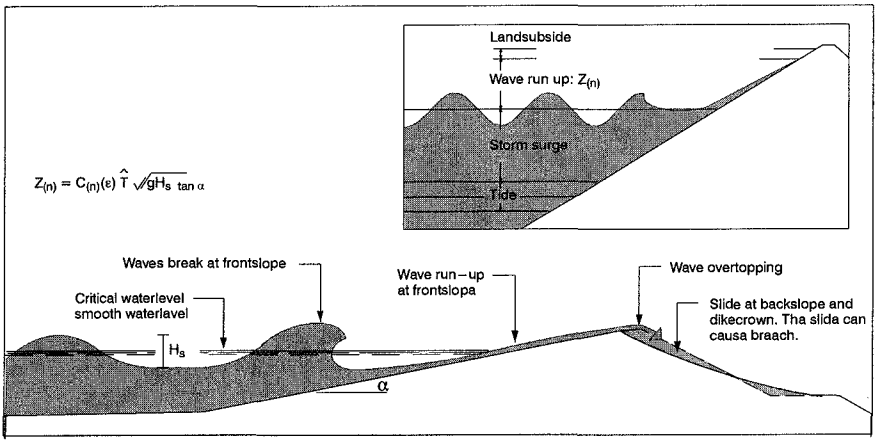

Figure 6. Design of dike height.

The design water level varies from a 50 year storm surge level to a 200 year level, depending on the areas protected.

Fig. 7 shows the frequency of extreme water levels at Højer in the southern part of the Wadden Sea in front of Tønder.

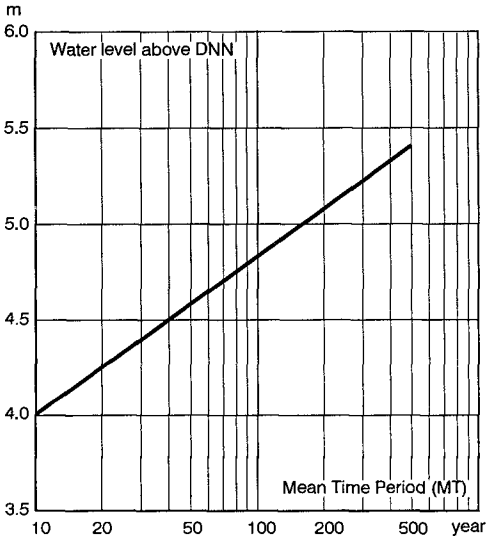

Figure 7 . Frequency of extreme water levels at Højer, 1920-1996.

The wave run up is added to the design water level. The run up depends on the gradient of the front slope, see fig. 6. The run up is app. proportional to tanα so the flatter front slope, the smaller wave run up. When reinforcing the dikes, the front slopes are built with a gradient of 1:7 to 1:10 to reduce wave run up but also because the erosion of the front slope by wave attack will be much reduced when the slope is flatter that 1:6.

By the reinforcements, the back slope is also flattened typically from 1:2 to 1:3, while this prevents sliding if wave run over should occur.

In this part of Denmark, the relative land depression is taken into account when designing the dike height. Fig. 8 shows why this has to be taken into account. During the Ice Age the ice covered the eastern and northern part of Denmark. In fact the whole Scandinavia except the south-western part of Denmark was ice-covered. The ice depressed the earth beneath. Since the melting of the ice Denmark has tilted, where the north-eastern part rises and the south-western part subsides. When designing the new dikes to a safety level of 200 years the dike height is added 20 – 30 cm to take this subsidence into account.

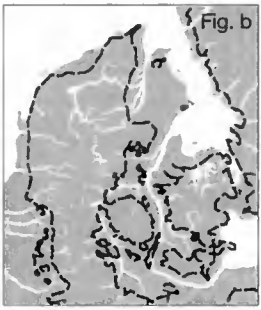

Fig. 8a Postglacial Period approx. 10,000 B.C.

Fig. 8b Continental Period approx. 8- 6,000 B.C.

Fig. 8c Littorina Sea Period approx. 5-2,000 B.C.

Fig. 8d Present situation

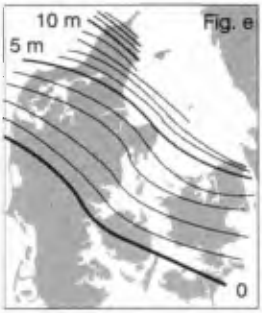

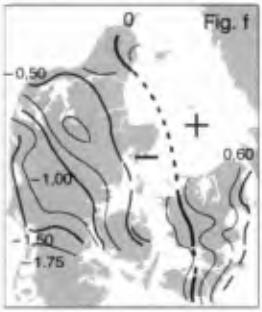

Fig. 8e Relative landrise for the Littorina Sea

Fig. 8f The present vertical Land movements in mm/year

The new dikes were designed in the late 1970s. Therefore the relative sea level rise caused by the green house effect has not been taken into account, but it will be rather easy to do this at coming reinforcements of the dikes when the relative sea level rise in the future may be well calculated. In fact the dikes just have to be heightened in the same way as when taking the land subsidence into account.

Fig. 9 shows photos of damages of dikes after a storm surge. Fig. 9a shows damages of the front slope, fig. 9b shows damages and sliding of the back slope, fig. 9c shows dike breach, and fig. 9d shows the situation of wave run over during a storm surge.

The damages and floodings caused by a storm surge depend not only on the surge level but also on the duration of the surge.

The two surges in 1976 and 1981 nearly reached the same maximum water level, app. 5 m above DNN, fig. 10. The rise in the water level happened very quickly (1 m/hour) in 1976 but the duration of water level above 3.5 m was only 4.5 hours while the surge in 1981 rised more slowly with 0.4 m/hours and had a duration of app. 7 hours with water level above 3.5 m DNN. These courses meant that in 1976 there was only short time to evacuate people, there were many damages on both dike front slopes and back slopes but because of the short dura-

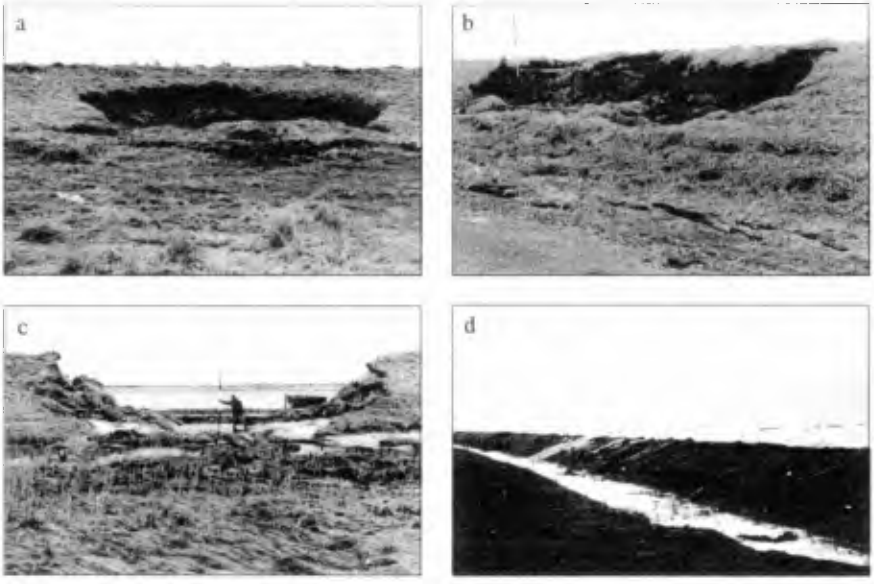

Figure 9. Examples of damages, breach, and wave run over.

tion no dike breach took place. In 1981 the storm surge was predicted very good and the evacuation of people happened without prohlems hut hecause of the long duration of the surge many and severe damages happened to the dikes and one of the dikes breached totally.

At the storm surge in 1976, the water level in the northern part of the Wadden Sea at Eshjerg was much lower than only 50 km more south at Højer, fig. 10. This example shows the great differences in the maximum storm surge level there can he in different localities in the Wadden Sea under the same storm. These differences depend on how the passage of the centre of the low air pressure takes place and the magnitude of the air pressure.

Flood Warning and Alert

As one of the results of the storm flood committee, a flood warning and alert system was established in 1975. The warning is based upon numerical models for the water levels. The water levels are monitored at five localities in the Wadden Sea and registered at once at the Danish Coastal Authority (DCA) and the Danish Meteorological Institute (DMI).

The models are run hy routine several times a day and if the predicted water levels exceed certain levels the relevant authorities and the press are informed. Depending on the predictions different levels of warning are introduced where the alarm situation is the most severe and implies evacuation of people from the flood threatened areas.

The overall system is managed by DCA, DMI, and the police in the county.

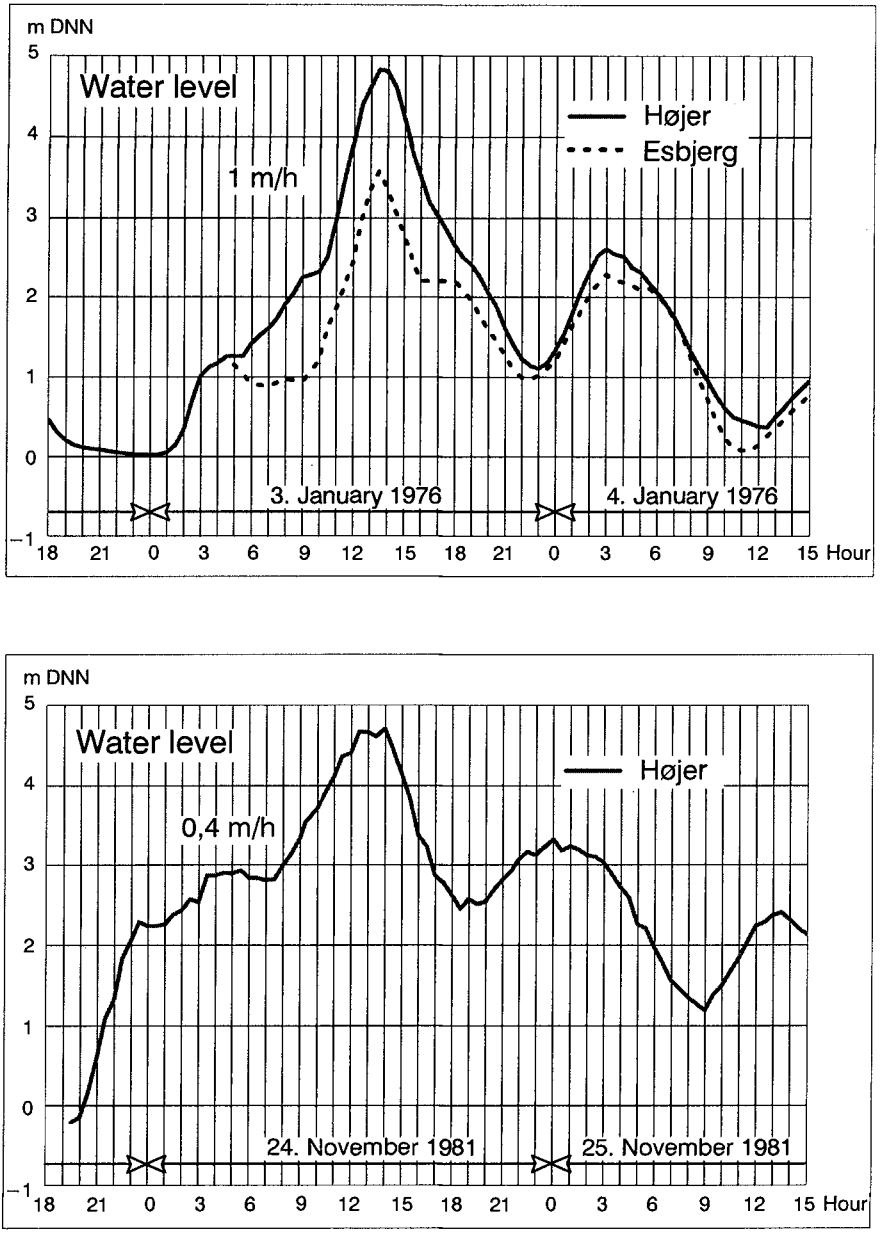

Figure 10. The courses of 1976 and 1981 storm surges.

Administration of the Dikes

Most of the dikes are funded by the State, others also with contribution from the local authorities. The maintenance is managed by local dike committees and one of the new dikes by the Regional Authority. Twice a year the dike committees and the Danish Coastal Authority inspect the dikes to point out possible damages or other aspects that can influence the safety of the dikes. Each dike committee then takes care of the repair.

Preservation of the Wadden Sea

Today, the Wadden Sea and the Wadden Sea coast are preserved and classified as a RAMSAR area. The preservation assumes that new dikes will not be built and reinforcements of the forelands in front of the dikes are not allowed, even though this would improve for the dike safety. In some localities where a narrow foreland is eroded this means that it can be necessary to protect against further erosion with solid constructions as stone revetments. Through the years sedimentation fields have created new foreland.

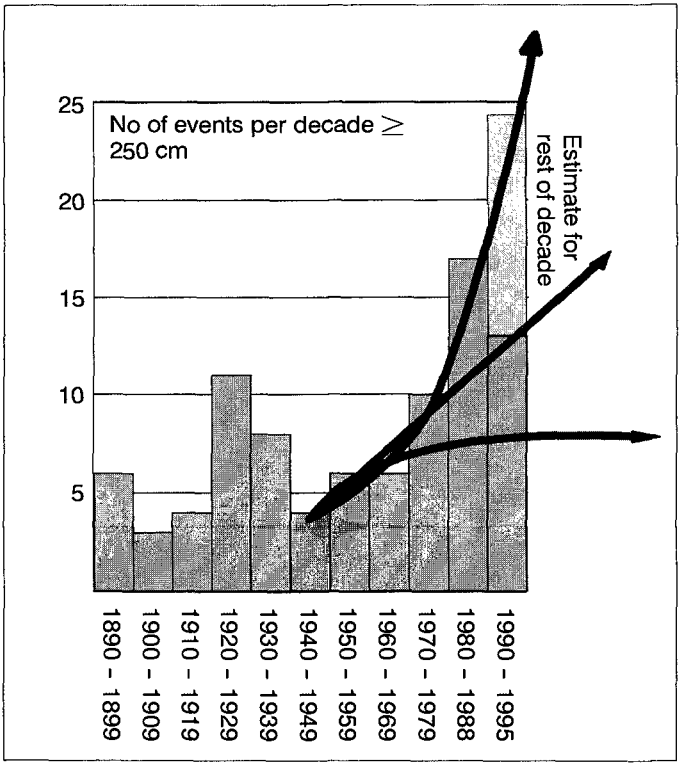

Figure 11. Future challenges.

The Future

The development in the Wadden Sea is observed carefully. Water levels are measured continuously at five localities and wave registration takes place at four localities. The Wadden Sea was surveyed in the 1960s. A similar surveying is carried out these years for calculation of changes in the bottom level of the Wadden Sea. The southern part of this surveying is carried out in co-operation with the German authorities. The dikes are surveyed every five years. A working group with participation of the Danish coastal Authority and the two counties in the Wadden Sea area evaluates the safety level of the dikes on the basis of settlement of the dikes/land, recalculation of the wave climate, update of storm surge statistics and co-ordination of results from a new national precision levelling.

By means of these continuing studies it will be possible to follow a possible sea level rise because of the green house effect and also if the Wadden Sea bottom should rise within the same or less time.

At this moment (1998) it seems that the bad weather period which began in the middle of the 1970s might have ended now, however, it is too early to state this on the basis of the last few calm years, so in fact we do not know the future challenges. They may be as sketched in fig. 11 where the future impact (number of surges) can be everything from the average impact of this century to a continuing of the bad weather period with addition of a general rise in the sea level because of the green house effect and of course the problem with the continuous land subsidence of this area.

Conclusions

The safety level against flooding of the lowlying areas varies from app. 40 years to 200 years based upon the statistics of storm surge levels since 1920. During the last 20 years there have been more frequent and higher storm surges than before, there may occur a general rise in the sea level caused by the green house effect and the relative land subsidence of the area will continue.

These parameters are studied carefully so it is possible to reinforce the dike protection as soon as it is necessary for maintaining the safety level against flooding.

References

Danmarks Natur (1979): Vol IV

Gram-Jensen, I. (1985): Sea Floods, climatological papers No. 13, Danish Meteorological Institute

Remmer, O. (1991): Kort- og Matrikelstyrelsen. Unpublished

Sørensen, T., Fredsøe, F., and Jakobsen, P.R. (1996): History of Coastal Engineering in Denmark. History and Heritage of Coastal Engineering. ASCE 103-141

Dispersion of Wave Action

James M. Buick[1] and Tariq S. Durrani[2]

Abstract

The dispersion of particles beneath a random sea, produced by the associated random variations in the Stokes drift is considered. In particular, a sea state described by a Pierson-Moskowitz spectrum is considered and the diffusion rate on and below the surface is examined. For such a random sea the diffusion rate at the surface can be related to the wind speed. This expression is extended to consider dispersion rates below the surface and to relates these to the wind speed. The theory is then applied to study the dispersion of particles denser than water as they fall through a random sea.

Introduction

An accurate prediction of the dispersion of pollutants in the sea is essential in the planning of contingency exercises and also in risk analysis. Computer models have been developed to simulate the spread of pollutants in the sea but these generally ignore the effects of wave action in dispersing the material which, on a scale of up to a few kilometers, can have a large role to play (Schott *et al.* 1978, Herterich and Hasselmann 1982). Recent oil spill disasters such as the sinking of the Braer off the Shetland Islands have highlighted the fact that the dispersion of pollutants is highly dependent on the prevailing wave climate. Discharges

[1]Research Fellow, Signal Processing Division, Department of Electronic and Electrical Engineering, University of Strathclyde, Glasgow G1 1XQ, UK. Present address: Department of Physics and Astronomy, The University of Edinburgh, J.C.M.B., Mayfield Road, Edinburgh EH9 3JZ, U.K, J.M.Buick@ed.ac.uk

[2]Professor,Signal Processing Division, Department of Electronic and Electrical Engineering, University of Strathclyde, Glasgow G1 1XQ, UK

from chemical and sewage works can also cause pollution. In such cases an understanding of the dispersion of the pollutants, on and below the sea surface, is clearly desirable. In this paper we consider the dispersion of such pollutants due to random wave motion described by a Pierson-Moskowitz (Pierson and Moskowitz 1964) surface spectrum. The Pierson-Moskowitz spectrum is a JONSWAP spectrum (Hasselmann *et al.* 1973) describing a fully developed sea and is given by

$$f(\omega) = \alpha g^2 \omega^{-5} \exp\left[-\frac{5}{4}\left(\frac{\omega_m}{\omega}\right)^4\right], \tag{1}$$

where ω_m is the peak frequency, g is the acceleration due to gravity, ω is the frequency and $\alpha = 0.0081$. Other processes related to dispersion include turbulence and ocean currents. These act on a larger scale than the wave dispersion considered here and are discussed elsewhere (Craig and Banner 1994, Sanderson and Pal 1990).

Diffusion at the Surface of a Random Sea

The diffusion of tracers at the sea surface due to wave action has been investigated by Herterich and Hasselmann (1982) who consider the random fluctuations in the Stokes drift velocity,

$$\langle \boldsymbol{u}_s \rangle = 2 \int F_\eta(\boldsymbol{k}) \omega \boldsymbol{k} e^{2kz} \mathrm{d}^2 k \tag{2}$$

where angle brackets denote ensemble averaging, ω is the frequency, z is the vertical distance, $\boldsymbol{k}$ is the wavenumber and the two-dimensional wave spectrum $F_\eta(\boldsymbol{k})$ is normalized to the mean-square surface displacement of the wave. Herterich and Hasselmann (1982) show that, provided the surface spectrum can by expressed as $F_\eta(\theta, \omega) = f_\eta(\omega) S(\theta)$ where $S(\theta)$ is a directional spreading function, the dispersion of particles is governed by a mean advection velocity and a diffusion tensor D_{ij} which is associated with the random wave-surface. The mean advection velocity is simply the means Stokes-drift velocity. For a single particle the diffusion tensor is given by

$$\begin{pmatrix} D_{xx} & D_{xy} \\ D_{yx} & D_{yy} \end{pmatrix} = \frac{\pi}{4g^2} \int_0^\infty \omega^6 f_\eta^2(\omega) \int_{-\pi}^{\pi} \int_{-\pi}^{\pi} S(\theta_1) S(\theta_2) [1 + cos(\theta_1 - \theta_2)]^2 M_{ij} \mathrm{d}\theta_1 \mathrm{d}\theta_2 \mathrm{d}\omega \tag{3}$$

where, provided $S(\theta)$ is symmetric about $\theta = 0$, we have $M_{xx} = (\cos\theta_1 + \cos\theta_2)^2$, $M_{yy} = (\sin\theta_1 + \sin\theta_2)^2$, $D_{xy} = 0$ and $D_{yx} = 0$.

Diffusion Below the Surface of a Random Sea

The derivation of equation (3) is not reliant on the particle being on the surface and can equally be applied at any depth provided the horizontal displacement spectrum is known. To find this spectrum we model the surface, η, of a random sea by

$$\eta(x,y,t) = \int_{-\infty}^{\infty}\int_{-\infty}^{\infty}\int_{-\infty}^{\infty} \mathrm{d}\Phi(k_x,k_y,\omega)e^{i(k_x x + k_y y - \omega t)} \tag{4}$$

where k_x and k_y are the x- and y-components of the two-dimensional wave number and $\{\mathrm{d}\Phi\}$ is a stochastic, typically complex, function representing an innovation process which incorporates all the random features of the sea surface. Assuming that the fluid is irrotational and so can be described in terms of a potential, ϕ, which is separable: $\phi(x,y,x,t) = a(z)b(x,y,t)$, then we can solve the Laplace equation for the surface, equation (4), to find the displacements $\xi_j(x,y,z,t)$. This is done in a manner analogous to the standard solution for a monotonic surface wave ($\eta = Ae^{i(kx-\omega t)}$) (Lighthill 1978) subject to the standard boundary conditions: no vertical motion at the bed; the vertical velocity at the surface is given by $\partial\eta/\partial t$; and the Bernoulli equation is satisfied at the surface. With these boundary conditions the displacements are found as

$$\xi_j(x,y,z,t) = \int_0^{\infty}\int_0^{2\pi}\int_{-\infty}^{\infty} \frac{a_j}{\sinh(kh)}\mathrm{d}\Phi(k,\theta,\omega)e^{i(kx\cos\theta + ky\sin\theta - \omega t)}, \tag{5}$$

where

$$\begin{aligned} a_x &= i\cos\theta\cosh[k(z+h)], \\ a_y &= i\sin\theta\cosh[k(z+h)], \\ a_z &= \sinh[k(z+h)], \end{aligned} \tag{6}$$

h is the mean water depth and $j = x,y,z$. Invoking the properties of $\{\mathrm{d}\Phi\}$ we can express

$$f_z(\omega;z) = \left(\frac{A_z}{\sinh(Kh)}\right)^2 f_\eta(\omega), \tag{7}$$

where f_z is the vertical displacement spectra and $A_z = a_z|_{k=K}$ where K is a solution of $\omega^2 = gK\tanh(Kh)$. Thus, replacing $f_\eta(\omega)$ with $f_z(\omega;z)$ in equation (3), we can calculate the diffusion tensor D_{ij} at any depth for any appropriate surface spectrum. We note here that the diffusion arises from considering the higher-order Stokes-drift term while the expression for $f_z(\omega;z)$ is only considered in the linear limit. This is a valid approach since higher-order terms will only have a small affect on the form of the displacement spectra below the surface and hence on the calculated diffusion terms.

For the Pierson-Moskowitz surface spectrum the diffusion tensor at the surface can be written $D_{ij} \propto \omega_m^{-3}\overline{D_{ij}}$ where $\overline{D_{ij}}$ is a non-dimensional function of $S(\theta)$. The peak frequency, ω_m, is given by $\omega_m = 0.280\pi g/U$ where U is the wind speed measured 19.5 m above the sea height. This means that once the surface diffusion coefficients have been calculated for one velocity, for a given S, they can be found for any other velocity using the scaling relationship $D_{ij}(U_1) = (U_2/U_1)^3 D_{ij}(U_2)$. In three dimensions the same surface relation

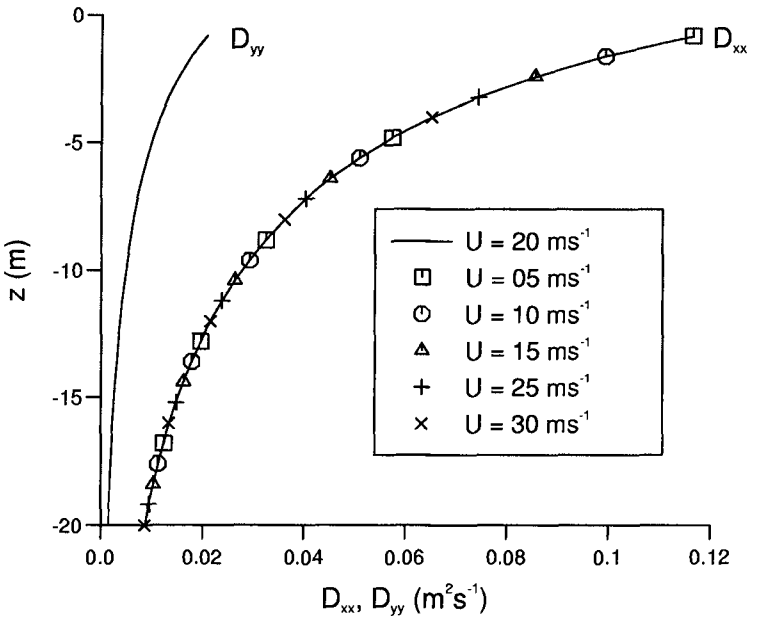

Figure 1: The value of D_{xx} and D_{yy} calculated for a Pierson-Meskowitz surface spectrum with $S(\theta) = 2\cos^2(\theta)/\pi$ for a wind speed $U = 20$ ms^{-1} and a water depth of 100 m. Also shown are results calculated for wind speeds $U = 25,15,10$ and 5 ms^{-1} after they have been scaled by equation (9) to align them with the results for $U = 20$ ms^{-1}.

must hold for $D(U, z = 0)$. Below the surface we note that the z-dependence appears only in the integral

$$\int_0^\infty \omega^6 f^2(\omega; z) \mathrm{d}\omega \tag{8}$$

as a product kz which in deep water can be expressed $\omega^2 z/g$. In this integral the function $f(\omega; z)$ is negligible except close to ω_m so we find, to a good approximation, the following scaling relation for different values of U:

$$D(U_2; z) = \left[\frac{U_2}{U_1}\right]^3 D\left(U_1; \left[\frac{U_1}{U_2}\right]^2 z\right). \tag{9}$$

This allows us to predict the value of D at different depths and different wind speeds from a knowledge of D for any U. Figure 1 shows D_{xx} and D_{yy} plotted against z for a wind speed $U = 20$ ms^{-1} in water of depth 100 m. Also shown are the values of D_{xx} calculated

for U = 5, 10, 15 and 25 ms^{-1} after they have been scaled according to equation (9) to align them with the $U = 20$ result. The good agreement validates the use of equation (9). Also shown in figure 1 is the difference between D_{xx} and D_{yy} for the spreading function $S(\theta) = 2\cos^2(\theta)/\pi$, where D_{xx} describes diffusion in the mean wind direction and D_{yy} in the direction perpendicular to the mean wind. As expected $D_{xx} > D_{yy}$ for all values of z. In fact, for any z the ratio D_{xx}/D_{yy} is a function of $S(\theta)$ and independent of z. Thus the good agreement of D_{xx} between the results for different wind speeds is also true for D_{yy}.

Diffusion of Particles Denser Than Water in a Random Sea

The above theory allows us to calculate diffusion rates for particles on the sea surface or at a fixed depth below the surface. We now wish to consider particles which do not remain at a fixed depth. To demonstrate how this can be done we consider, as an example, a particle denser than water falling through the sea under gravity. A particle with density $\rho > \rho_w$, the density of water, initially at the sea surface, will sink to the bottom. As it does so it will diffuse in the horizontal directions according to the diffusion tensor $D_{ij}(z(t))$ where $z(t)$ is the particle's vertical position as a function of time. Neglecting any vertical motion due to the wave action, since there is no vertical drift or diffusion (Herterich and Hasselmann 1982), the vertical velocity w of a spherical particle of radius a can be found by considering the forces acting on it. Gravity is acting with force $-4\pi a^3\rho g/3$, there is a buoyancy force $4\pi a^3\rho_w/3$ and there is a drag force $-6\pi\mu a w$, where μ is the fluid viscosity. This gives

$$w(t) = A\frac{\rho_w - \rho}{\rho}g\left(1 - e^{-t/A}\right) \tag{10}$$

where

$$A = \frac{2}{9}\frac{\rho a^2}{\mu}. \tag{11}$$

The vertical position of the particle is therefore given by

$$z(t) = A\frac{\rho_w - \rho}{\rho}gt + A^2\frac{\rho_w - \rho}{\rho}g\left(e^{-t/A} - 1\right) \tag{12}$$

for $t < t^*$ where $z(t^*) = -h$. Thus we can calculate the vertical position $z(t)$ and the ensemble average of the square of the difference between the components of the particles horizontal position at time t and it's ensemble position at time t, $\langle(x_i(t) - \langle x_i(t)\rangle)^2\rangle$ and $\langle(y_i(t) - \langle y_i(t)\rangle)^2\rangle$, which are given by

$$\begin{pmatrix} \langle(x(t) - \langle x(t)\rangle)^2\rangle \\ \langle(y(t) - \langle y(t)\rangle)^2\rangle \end{pmatrix} = \frac{\pi}{2g^2}\int_0^t \mathrm{d}t_1 \int_0^\infty \mathrm{d}\omega \int_{-\pi}^{\pi} \mathrm{d}\theta_1$$

$$\times \int_{-\pi}^{\pi} \mathrm{d}\theta_2 \omega^6 \left\{\frac{\sinh\{k[z(t_1) + d]\}}{\sinh(kd)}\right\}^4 f_\eta^2(\omega)S(\theta_1)S(\theta_2) \tag{13}$$

$$\times[1 + cos(\theta_1 - \theta_2)]^2 \begin{pmatrix} (\cos\theta_1 + \cos\theta_2)^2 \\ (\sin\theta_1 + \sin\theta_2)^2 \end{pmatrix}.$$

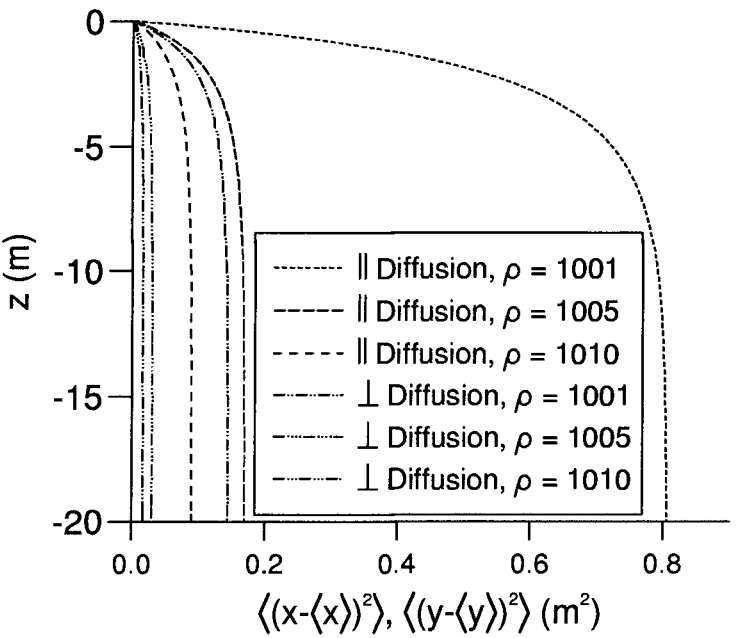

Figure 2: The value of $\langle (x_i(t) - \langle x_i(t) \rangle)^2 \rangle$ for diffusion parallel to the mean wind direction and $\langle (y_i(t) - \langle y_i(t) \rangle)^2 \rangle$ perpendicular to the mean wind direction for a single particle with radius $a = 1$ mm falling through the ocean plotted as a function of the vertical position for a random sea state described by a Pierson-Moskowitz spectrum with a wind speed $U = 10$ ms^{-1} and spreading function $S(\theta) = 2\cos^2(\theta)/\pi$. The particle densities considered were 1001, 1005 and 1010 kgm^{-3} and the density of the ocean was taken to be 1000 kgm^{-3}.

Figure 2 shows the value of $\langle (x(t) - \langle x(t) \rangle)^2 \rangle$ and $\langle (y(t) - \langle y(t) \rangle)^2 \rangle$ plotted against the vertical position of the particle for a particle with density 100.1%, 100.5% and 101% of the density of water and radius 1 mm. The surface spectrum is a Pierson-Moskowitz spectrum with $U = 10$ ms^{-1}, the spreading function used was $S(\theta) = 2\cos^2(\theta)/\pi$. The water depth is 100 m but only the top 20 m are shown since there is only negligible horizontal motion below this depth and the particle falls vertically to the ocean bed. The graph shows that the majority of the dispersion occurs in the top 10 m (for out choice of wind speed). This is to be expected since the horizontal wave velocities are maximum at the surface and decay exponentially below it. Clearly, the slower the particle falls through the top 10 m of the sea, the longer it is subject to the larger random velocities and so the larger its potential to be dispersed. Thus the closer the particle density is to the density of water, the slower it sinks and the larger its potential to be diffused by the wave motion.

Conclusion and Discussion

The dispersion of particles due to random wave motion have been studied. Consideration has been given to buoyant particles on the surface, neutrally buoyant particles suspended in the sea and particles moving through the fluid under the action of gravity. It has been seen that diffusion due to random waves can have a significant affect on the dispersion of particles or pollutants in the ocean. An approximate scaling relationship has been found which relates the diffusion tensor at different depths and different wind speeds. The validity of this relationship has been tested by calculating the diffusion tensor explicitly at different values of U and z and comparing them to the values obtained using the scaling relationship. Of the three cases considered, buoyant particles on the surface, neutrally buoyant particles suspended in the sea and particles dropping through the sea under gravity, particles on the sea surface were subject to the greatest dispersion. Particles suspended (at a constant depth) beneath the surface can also be dispersed by a significant amount if they are close to the surface (within the top 10 m for the values considered here). Particles falling through the ocean are only subject to significant dispersion, due to surface waves, during the time they are in the top 0-10 m of the ocean. Since they are only in this region for a limited time any dispersion is also limited. Below this region particles are virtually unaffected by the surface waves, however, other influences such as currents (Sanderson and Pal 1990) and internal waves (Sanderson and Okumbo 1988) may produce dispersion.

Acknowledgements

This work was supported by the Science and Engineering Research Council and the Marine Technology Directorate UK.

References

Craig, P. D. and Banner, M. L., 1994: Modelling wave-enhanced turbulence in the ocean surface layer, *J. Phys. Oceanogr.* **12**, 112–132.

Lighthill, J., 1978: *Waves In Fluids,* Cambridge University Press.

Pierson, W. J. and Moskowitz, L., 1964: A proposed spectral form for fully developed wind seas. *J. Geophys. Res.* **69**, 5181–5190.

Sanderson, B. G. and Okumbo, A., 1988: Diffusion by internal waves, *J. Geophys. Res.* **93**, 3570–3582.

Sanderson, B. G. and Pal, B. K., 1990: Patch diffusion computed from Lagrangian data, with application to the Atlantic equatorial undercurrent, *Atmosphere-Ocean* **28**, 444–465.

Schott, F., Ehlers, M., Hubrich, L. and Quadfasel, D., 1978: Small scale diffusion

experiments in the Baltic surface-mixed layer under different weather conditions, *Deutsch. Hydrogr. Z.* **31**, 195-215.

Hasselmann, K., Barnett, T. P., Bouws, E., Carlson, H., Cartwright, D. E., Ewing, J. A., Gienapp, H., Hasselmann, D. E., Kruseman, P., Meerburg, A., Müller, P., Olbers, D. J., Richter, K., Sell, W., and Walden, H., 1973: Measurements of wind wave growth and swell decay during the Joint North Sea Wave Project (JONSWAP), *Dtsch. Hydrogr. Z.* **8**, 1–95.

Herterich, K. and Hasselmann, K., 1982: The Horizontal Diffusion of Tracers by Surface Waves, *J. Phys. Oceanogr.* **12**, 704–711.

PREDICTING AND EVALUATING TURBIDITY CAUSED BY DREDGING IN THE ENVIRONMENTALLY SENSITIVE SALDANHA BAY

S A Luger[1], J S Schoonees[1], G P Mocke[1] and F Smit[1]

Abstract

Extension to the oil jetty at the Port of Saldanha will necessitate dredging of the entrance channel. This study was undertaken to determine the turbidity caused by the dredging and also the transport/dispersion of the dredging plumes. Hydrodynamic and water quality modelling were performed in order to determine the environmental impact of the dredging on the nearby mariculture activities, as well as to investigate possible deposition of mud in the Langebaan Lagoon. Turbidity levels due to storms and shipping were compared with the turbidity caused by the dredging. The environmental impact of the plumes is found to be within acceptable ecological limits and only insignificant sediment deposition is predicted in the Langebaan Lagoon.

1. Introduction

The environmental impact of dredging has recently come under increased public scrutiny within South Africa, especially when dredging is planned in an environmentally sensitive area like Saldanha Bay. The Port of Saldanha, situated 120 km north-west of Cape Town, was constructed mainly for the export of iron ore. Shelter from the swell conditions that occur there was obtained by building a sand (or spending beach) breakwater between the mainland and Marcus Island (Figure 1). A causeway and a jetty (extending 4 km offshore) were built in the lee of this breakwater for the loading of ore and loading/offloading of oil. This causeway divides Saldanha Bay into two: Small Bay and Big Bay (Figure 1). The adjacent Langebaan Lagoon, located some 9 km south of the oil and ore jetty of the Port of Saldanha, is a site of international (Ramsar) ecological significance. Mussel farming is practised within 1 km from the oil jetty, while commercial sea grass production areas are also in close proximity (Figure 1).

Plans to extend the oil jetty will entail dredging of up to 2.5 million m^3 of material in order to widen and deepen the entrance channel. Although the dredged material is to be disposed of in a confined disposal area, it is anticipated that "leakage" associated with the dredging will place a quantity of fine sediment into suspension. Transported by the ambient flow regime, the suspended material could conceivably

[1]Research engineers, CSIR, P. O. Box 320, 7599 Stellenbosch, South Africa

move throughout the bay in the form of turbid plumes and so impair water quality and the surrounding habitat. An assessment of turbidity phenomena as a result of the proposed dredging operations constituted a specialist study (Mocke *et al.*, 1996) as part of a comprehensive environmental impact assessment.

This paper describes how the anticipated turbidity loading due to the dredging was determined and how the associated suspended sediment concentrations compared with ecological thresholds and estimated turbidity levels due to storms and shipping. (The turbidity loading (in kg/s) is the rate at which sediment is released into the water during dredging.) Also described are the mathematical modelling of the water circulation, wave refraction-diffraction and the dispersion of plumes which were performed to predict the extent and fate of the dredging induced plumes. In general, conservative assumptions were made and conservative values were applied in the study. The rationale behind this approach is that, if the severest or most extreme scenario produces acceptable environmental impacts, then a less severe scenario will be even more acceptable.

2. Environmental Conditions

Saldanha falls in a semi-arid region with mild (air) temperatures. *Fog*, which may influence dredging operations, occurs between 88 and 111 days throughout the year. The *wind* regime is dominated by the south-westerly to south-easterly winds (about 57% in total) while the opposing north-easterly to north-westerly winds occur much less frequently (about 24% in total). Wind velocities are below 4 m/s for about 39% of the time and above 10 m/s for about 13% of the time.

A Waverider buoy is situated within Saldanha Bay across from Marcus Island next to the entrance channel. These nearshore measured data show that seasonal differences in *wave* heights are fairly small. The majority of H_{mo} measurements (89%) fall within the range 0.5 m to 2 m and the majority of T_p measurements (73%) within the range 10.7 s to 13.5 s. The wave heights measured in Saldanha Bay are significantly smaller than those measured offshore. Wave directions estimated by voluntary observations from ships in deep water, the so-called VOS data, showed that southerly to south-westerly wave directions are dominant. Wave directions inside Saldanha Bay do not vary as much as those outside the bay.

The *tidal range* at Saldanha Bay is relatively limited, with neap and spring tidal ranges of 0.5 m and 1.5 m respectively. There are no *river* inputs into Saldanha Bay.

Wind forcing is the dominant mechanism controlling *current* direction and magnitudes in both Small and Big Bay. Current speeds are generally low, with some 80% of surface currents less than 0.12 m/s. Current directions are found to be closely aligned with wind direction, except for surface flow in Small Bay, which is mainly clockwise.

Upwelling occurs from spring to autumn. Surface waters attain a maximum *temperature* of around 19 °C and the thermocline (at 13 °C) is generally found to be at a depth of between 3 m and 6 m below the surface.

Essentially three *sediment types* were found, namely, a greyish, medium sand (the most commonly occurring type), silty fine sand and calcrete (limestone). It was found that about 15.5% of the bottom material was fine gravel (between 2 mm and 4

mm) and 72% is relatively fine sand with an average median grain size of around 0.23 mm. The mean percentage of silt/clay (mud) in the bottom material is estimated to be 12.5%, with a median grain size of around 4 micron. The only hard material to contend with during the dredging is hardpan calcrete, which occurs in layers between 0.3 m and 3 m thick. The uniaxial compressive strengths (UCS) of the calcrete varied from 3 MPa to 42.8 MPa with a mean UCS of 18.1 MPa.

3. Conceptual Dredging Plan

3.1 General

A conceptual dredging plan was drawn up so that the turbidity loading caused by the dredging can be determined. This is relevant because the type of dredging and the operation influence the generation of turbidity.

3.2 Dredging Required

The entrance channel to the port needs to be widened and deepened in order to provide access to larger ships. Up to 2.5 million m^3 of material has to be dredged in order to deepen the channel between 0.8 m and 1.3 m (the depth of cut for the dredger varies between 0.8 m and 10 m).

3.3 Physical Conditions Affecting the Dredging

The sediment type has a profound influence on the performance of the dredger and is thus a key element in deciding what type(s) of dredger should be used. The bottom material consists mainly of medium to fine sand interspersed between "moderately strong" calcrete layers. It is important to note that the thickness of these layers is on average 1.5 m. This means that they will not be broken out easily.

Wave action mainly adversely affects the vertical movement of the dredger. This is a problem particularly when cutting hard material because vertical movement causes damage to the cutting device. A H_{mo} of 0.8 m will be exceeded between 10% (protected part of the channel) to 80 % (outer part of the channel). Currents make marine operations more awkward due to the difficulty of maneuvering and of obtaining good anchorage for the dredger. Normally the current velocities are between 0.10 m/s and 0.20 m/s. Weather conditions such as rain and temperature should not cause problems with the dredging. This is because Saldanha lies in the semi-arid region which does not experience extreme temperatures. Wind makes the manoeuvring of all vessels more difficult and it can cause the dragging of anchors. Wind speeds exceeding 10 m/s occur about 13% of the time. Fog could influence dredging operations because of the limited visibility for about 88 to 111 days per year. However, because of modern position fixing systems and radar, it is unlikely that dredging operations would have to be suspended due to fog.

3.4 Spoil Disposal

The bottom material, being mainly medium to fine sand and calcrete, is generally suitable as fill material. The dredger spoil is thus considered a valuable resource which should be stored for later use during port extensions. The disposal of the dredger spoil will most probably be a land-based operation. It has been assumed that

special precautions will be taken such as using stilling ponds. Therefore virtually no sediment-laden water will reach the sea. The marine environmental impact of plumes *from the disposal area* will therefore be negligible and will not be considered further.

3.5 Conceptual Dredging Plan

The conceptual dredging plan proposed is that a medium to large cutter suction dredger be used to dredge the medium to fine sand and the calcrete (blasting the calcrete will not be necessary). Dredging is expected to be done 24 h a day at a rate of about 1 100 m^3/h (a high production rate is required to limit the dredging period to 3 to 4 months). The down-time for a large cutter suction dredger was estimated to be between 10% and 80%, depending on where you dredge along the entrance channel. Disposal will take place by means of a pipeline to the reclamation site from where virtually no sediment-laden water will reach the sea. All the dredger spoil will be stored to be used as fill. The first section of pipe from the dredger will be a floating line to a large pontoon from where the rest of the pipeline will be submerged up to the causeway/ore jetty. From there the pipeline will run on land. A booster pump station will be necessary because of the distance between the dredger and the disposal site.

An alternative way of dredging could be by using a combination of a trailing suction hopper dredger and a cutter suction dredger. In this assessment only the most obvious dredging method, namely, of using a cutter suction dredger, has been analysed further.

4. Turbidity

4.1 General

The main purpose of this chapter is to determine the turbidity loading as caused by the dredging. The secondary purpose is to compare the turbidity caused by the dredging with the background turbidity and the estimated turbidity levels due to storms and shipping. It is believed that the background turbidity levels in Saldanha Bay are quite low (usually below 20 mg/l); however, this is based on very limited data which do not cover extreme conditions.

In order to determine the turbidity loading, it is necessary to know the settling velocities of the sediment fractions (Section 4.2) and the turbidity that will be generated at the dredger (Section 4.3) respectively. The turbidity loading is addressed in Section 4.4. Section 4.5 is a comparison of the turbidity caused by shipping and storms with turbidity due to dredging.

4.2 Settling Velocities

The settling velocity distributions of the *sand* were obtained in a standard settling tube. The average median settling velocity of the sand fraction was 0.023 m/s.

Laboratory tests were done to determine the settling velocity of the *mud* (silt and clay) fraction. These tests were done for a range of initial concentrations from 100 mg/l to 10 000 mg/l, with most of the tests done at 150 mg/l and at an average water temperature near the seabed of 13 °C. The 150 mg/l is the ecological threshold, determined from the level at which negligible effects on the mariculture will be found (Carter, 1995). All the tests were done in seawater taken from the site so as to ensure

the correct salinity and typical background turbidity (and thus typical organic material in the water). A pipette withdrawal tube was used to determine the distributions of the settling velocity. Because limited variation in the settling velocity distributions was found, it was decided to schematise the settling velocity of the mud into three parts:

Fraction of the mud	% of the mud	Mean settling velocity (mm/s)	Conservative settling velocity (mm/s)
Part 1	30	0.05	0.005
Part 2	40	0.50	0.19
Part 3	30	2.00	1.25
Weighted mean		0.80	0.45

These values correlate well with the typical range of values (0.01 mm/s to 10 mm/s) given by Berlamont *et al.* (1993) and the typical value (0.21 mm/s) for the Øresund link (Brøker *et al.*, 1994) given for chalk/limestone (supposedly similar to the Saldanha calcrete).

4.3 Turbidity at the Dredger

The turbidity at the dredger was determined in two different ways: (1) measurements of turbidities around cutter suction dredgers at other sites around the world were used and compared with the environment at Saldanha; and (2) a comparison with the turbidity caused by different types of dredgers was used. According to Van Wijck *et al.* (1991), a cutter suction dredger causes about twice the turbidity associated with bucket-ladder and trailing suction hopper dredgers. For a seabed grab the ratio is 2.7. In this way the measurements of turbidity caused by other types of dredgers could be used to estimate roughly the turbidity that could be found around a cutter suction dredger.

Van Raalte and Blokland (1988) and Pennekamp and Quaak (1990) defined a number of variables related to turbidity:

t = time for the turbidity to decline to the background levels after cessation of dredging

S = the amount of sediment which is lost by suspension from the immediate vicinity of the dredger (kg of dry material per m^3 dredged).

Typical values for these variables are discussed below.

Kirby and Land (1991) did a comprehensive study of the turbidity generated by different dredgers. For cutter suction dredgers they found that a maximum of 1 100 mg/l was measured immediately adjacent to the cutter head. The turbidity decreased rapidly from the dredger to only a few tens of mg/l (20 mg/l to 90 mg/l) at a distance of 50 m away from the dredger. The turbidity was not influenced by the size of the cutter suction dredger. For normal operations, S is about 6 kg/m^3 while it is approximately 3 kg/m^3 if the dredger works with reduced swing and rotation speeds. Huston (1976) found in a series of tests an increase in turbidity (which varied considerably) above background levels only in the immediate vicinity of the cutter head. Little turbidity reached the water surface, especially from depths of 12 m and more. Yagi *et al.* (1976) recorded turbidity of generally less than 210 mg/l with a depth-averaged value of approximately 70 mg/l.

If one applies the ratios of 2 and 2.7 for the respective dredgers by Van Wijck *et al.* (1991) and calculate the equivalent turbidities that can be expected for cutter suction dredgers, one obtains a mean turbidity of about 250 mg/l. This corresponds reasonably with the values derived from measurements for cutter suction dredgers.

Based on these findings and also on the measurements reported by Kuo *et al.* (1985) and Nichols *et al.* (1990), the turbidity and the initial diameter of the sediment plumes were estimated. The conditions of the sites at which the above-mentioned turbidities were measured were compared to the conditions at Saldanha Bay. For example, the currents of between 0.10 m/s and 0.20 m/s at these sites correspond well to the Saldanha case. The following table was compiled for Saldanha as input to the plume modelling:

Plume scenario	Mean concentration over height of the water column (mg/l)	Height of plume column* (m)	Initial plume diameter (m)	Remarks
1	100	10-15	50	best estimate; still somewhat extreme
2	300	15	100-250	best estimate of extreme turbidity duration

*The height of the plume column is the height above the sea bottom up to where the suspended sediment extends (which can be less than the water depth).

The turbidity caused by previous cutter suction dredging during two previous projects in Saldanha Bay has not been measured before. Photographs, however, show light coloured plumes which were mainly confined to the vicinity of the dredgers. These plumes were mainly caused by chalk particles being suspended in the water during the cutting of the calcrete layers.

Van Raalte and Blokland (1988) and Pennekamp and Quaak (1990) found that within about 0.5 h to 1 h after dredging (of mainly mud), the turbidity returned to the background levels. Aerial photographs and observations by the port pilots confirmed these values of t: within about 0.5 h to an absolute maximum of 2 h, the plumes caused by shipping in Saldanha Bay are no longer visible.

Using the S values of 3 kg/m^3 to 6 kg/m^3 given by Kirby and Land (1991) for cutter suction dredgers, the percentage leakage can be determined if the *in situ* density of the bottom material is known. Assuming typical densities between 1 600 kg/m^3 and 1 800 kg/m^3, leakages of 0.2% to 0.4% were obtained. Kuo and Hayes (1991) give leakage percentages for bucket-ladder dredgers of 0.11% to 3%. Nichols *et al.* (1990) recorded a value of 12% for a trailing suction hopper dredger. Brøker *et al.* (1994) quoted an upper limit value of 5% based on test dredging; this is a combined figure for the whole dredging operation (the type of dredging is not given). Based on these values the following leakage scenarios have been assumed for Saldanha: (1) 0.4% - 2% (best estimate, still somewhat conservative); and (2) 12.5% (best estimate of extreme turbidity generation, assumes that all fines will be lost).

4.4 Turbidity Loading

Four different approaches were used to determine the turbidity loading at the dredger, namely:

(1) A sediment balance (based on continuity considerations) was drawn up to calculate the loading required to achieve the turbidities obtained in the two plume scenarios given above. Essentially the method supposes that the sediment entering a cylindrical element of the water at the dredger is balanced by settling and transport of material out of the cylindrical zone of initial mixing. Lateral mixing is ignored, which is slightly conservative. It is also assumed that an equilibrium will be reached soon after the start of dredging.

(2) The percentages of leakage were combined with the possible production rate of the dredger to obtain the turbidity loading. Note that this method is independent of the turbidities that have been estimated to occur around the dredger.

(3) The behaviour of the turbidity plumes was considered in two dimensions and averaged over depth by using the advection-diffusion equation. This equation was solved with the modelling approach of Kuo and Hayes (1991) by assuming different loadings to obtain the required turbidity in the plume as given above as the plume scenarios (Section 4.3).

(4) The results acquired with the above-mentioned three approaches were correlated with turbidity loadings given in the literature. This was done to verify the results from other methods.

Two turbidity loadings were recommended for use in the plume modelling, namely: (1) 9 kg/s (best estimate loading, still somewhat conservative); and (2) 70 kg/s (best estimate of extreme loading). The 70 kg/s was determined by assuming pipeline failure (which is unlikely), the duration thereof and where it will occur. The turbidity loading was determined by assuming that all the fines (12.5% of the material) will stay in suspension whilst the sand and gravel will settle out. By using the production rate of 1 100 m^3/h, the turbidity loading of 70 kg/s quoted above was obtained. This value was checked by computing the pumping rate in the pipeline. Good agreement was found. Very conservatively, it was determined that the duration of the turbidity loading is 12 h. The place where pipeline failure would have the biggest impact is in the turning circle of the entrance channel because it is the closest to the mussel rafts. It was assumed in the modelling that the failure will occur in this most critical area.

4.5 Turbidity Caused by Shipping and Storms

Shipping

It is expected that, after the expansion of the oil transfer operations, about 297 ships will visit the port annually, that is, about one ship every 1.2 days.

Detailed turbidity measurements at Rotterdam during the normal passage of a bulk carrier (of similar size as the ships expected at Saldanha), revealed no increase in the turbidity (Pennekamp *et al.*, 1991). This is despite the fact that the bottom sediment is predominantly mud. Kirby and Land (1991) found, during the passage of a vessel in the Lower Rhine with a muddy bottom, that the disturbed sediment soon settled. This is in accordance with the results by Hochstein and Adams (1939) in St Mary's River in the

USA/Canada. The bottom material there was smaller than 0.075 mm and yet they found no noticeable degradation of water quality. This they attributed to the sediment settling within the 34 minutes before another ship passes. Recalling from above that for dredging, it took about 0.5 h to 1 h for the turbidity to decline to background levels. Compare these values to the 1.2 days between ships expected at the port. This means that most of the material in suspension will settle before the next ship arrives. It can therefore be concluded that normal sailing contributes very little to turbidity (Kirby and Land, 1991).

Because turbidity is mainly caused during manoeuvring such as turning and berthing, this aspect should be considered further. From the literature, measurements at 5 sites (including Saldanha) show that the increase in the turbidity due to shipping is typically between 100 mg/l and 210 mg/l (Pennekamp *et al.*,1991, Pennekamp and Quaak, 1990 and Kirby and Land, 1991). These values show that the increase in turbidity is not very large despite the fact that the bottom material is mud. The bottom material in the enlarged turning circle will be medium sand with some calcrete layers present. Comparing this material with the soft mud that was encountered during the above-mentioned measurements (except possibly Saldanha), it is clear that turbidities will generally be lower at Saldanha than the values quoted above. This is enhanced by the calcrete layers which armour the sea bottom and reduce the suspension of material.

It can therefore be concluded that it is unlikely that the turbidity caused by shipping, even during manoeuvring, will be significant at Saldanha during the operation of the extended oil jetty. Most of the time the turbidity caused by shipping in its immediate vicinity will be below the ecological threshold of 150 mg/l.

Storms

For a large number of *sites* from around the world, depth-averaged sand concentrations (turbidities) that were measured outside the surf zone ranged from 29 mg/l to 901 mg/l (Van Rijn, 1991). In a review Appleby and Scarratt (1989) found natural turbidity levels in estuaries of up to 1 200 mg/l. High turbidities therefore occur naturally. *Sand* concentrations were computed for 4 typical storms. Two different models were applied to calculate the sand concentration, namely, those of Van Rijn (1989) and Schoonees (1998). Most of the depth-averaged concentrations ranged between 8 mg/l and 80 mg/l. The two approaches yielded reasonably similar results although the Van Rijn (1989) formulation showed a wider range. Typical turbidities due to the suspension of the *fine fraction* were estimated by assuming that all the fines will be washed out of a layer of material on the sea bottom. These fines are then supposed to be redistributed in the water above the layers from where they originated. Typically the increase in turbidity due to the fines (mud) will range between approximately 10 mg/l and 60 mg/l.

In the study in the Thames River and the eastern Long Island Sound, Sosnowski (1984) found that the concentrations during storms are nearly an order of magnitude larger than those due to dredging. Dredging induced suspension was found to be a near-field or local phenomenon while storms have a regional impact. When comparing the dredging induced turbidity at the dredger at Saldanha with natural fluctuations during storms, it is clear that the concentrations are of the same order of magnitude. It can therefore be concluded that the turbidity that will be encountered during dredging

will be similar to that occurring naturally during storms.

5. Modelling of Wave and Current Regimes

5.1 Waves

Modelling of the wave refraction/diffraction was done for two reasons: (1) to determine what effect the deepening and widening of the entrance channel would have on wave conditions throughout Saldanha Bay and therefore if the coastline would be affected by the dredging; and (2) the wave regime inside the bay was required in order to be able to calculate bed shear stresses due to wave and current action. Because the effect of the dredging on the coastline does not form part of this paper, only results related to the second objective will be considered.

The scope of the study did not allow for a comprehensive numerical refraction/diffraction study of the total deep water wave climate. Instead a number of average and extreme wave conditions was modelled using both the present bathymetry and a post dredging bathymetry as input. Wave conditions were decided upon based on the wave data described in Chapter 2.

A widely used wave refraction model, Hiswa (Holthuijzen *et al.*, 1989), was used to transform the deep-water waves through nested grids up to the entrance of Saldanha Bay. As Hiswa allows only for wave refraction to be calculated and not wave diffraction, a wave refraction/diffraction model based on the mild slope equation was used to transform waves from the entrance into the bay.

Figure 2 contains a plot of wave heights for an average deep-water wave condition of H_{mo} = 2 m, T_p = 12 s and a deep-sea direction of south-west. From this figure it can be seen that wave heights along the south-eastern beaches of Big Bay are for the most part less than 1.2 m with the highest waves occurring opposite the entrance to the bay. Diffraction around the sand breakwater ensures that waves with heights in the order of 0.2 m to 0.4 m enter Small Bay.

5.2 Currents

The Delft3D-FLOW hydrodynamic model (WL|Delft hydraulics, 1996a) was used to simulate the three-dimensional flow regime in the semi-enclosed Saldanha Bay system. The processes included in the model were tidal forcing, wind forcing, Coriolis effects, baroclinic flows due to thermal stratification and the drying and flooding of tidal flats in the lagoon. The model uses constant eddy viscosity and diffusivity coefficients in the horizontal direction while a k-ε turbulence model is used in the vertical direction. An orthogonal curvilinear grid with cell sizes ranging from 200 m in the areas of interest to 1 000 m near the model boundary was used in the horizontal direction, with eight σ-coordinate layers used in the vertical.

The model was calibrated based on current and water temperature data measured at four locations in the bay for a 12 day period. Measured wind, water level and thermistor string data were used at the model boundaries. The following coefficients were found to give the best correlation to the measured data: Chezy coefficient for bottom friction = 65 $m^{0.5}/s$, horizontal eddy viscosity = 1 m^2/s, horizontal eddy diffusivity = 0.5 m^2/s, wind coefficient = $6.3 \times 10^{-4} + 6.6 \times 10^{-5} . U_{10}$ (Smith and Blanke, 1975) where U_{10} is the wind speed 10 m above the water surface. Figure 3

indicates a good comparison between the measured data and model currents. The water temperature is modelled less accurately since in this case the air-sea interaction module was not used and the thermal stratification is driven by the imposed open boundary conditions only.

Figure 4 depicts the predicted three-dimensional current structure at outgoing and incoming tides with a 10 m/s south-westerly wind under non-stratified conditions.

The predicted current magnitudes are generally below 0.5 m/s, except in the constriction at the entrance to Langebaan Lagoon where currents may exceed 1.0 m/s at spring tide. Under stratified conditions and the dominant southerly winds, the exchange between the bay and the adjacent shelf revealed cold water entering the bay near the seabed on the incoming tide and warmer water leaving the bay near the surface on the outgoing tide. This phenomenon will have a significant impact on the supply of nutrients to the primary producers and thus the mariculture activities in the bay as well as on the residence time of pollutants in the bay.

6. Turbid Plume Dispersion

The Delft3D-WAQ water quality model (WL|Delft hydraulics, 1995, 1996b) was used to simulate the advection, dispersion, settling and deposition of the turbid plumes arising from the dredging operations. This model solves the advection-diffusion equation in three dimensions including settling of particles and deposition or erosion based on specified critical shear stresses. The bed shear stress is computed as the sum of the stress due to currents and waves. The hydrodynamic database is obtained from the Delft3D-FLOW simulation via an offline coupling.

The silt/clay material (< 63 microns) was subdivided by mass into three fractions each with a characteristic settling velocity and a critical shear stress for deposition. Settling velocities of 0.05 mm/s, 0.5 mm/s and 2.0 mm/s (Section 4.2) and corresponding critical deposition shear stresses of 0.1 Pa, 0.2 Pa and 0.3 Pa were used in the simulations.

As discussed in Section 4.4, a best estimate loading of 9 kg/s for material less than 63 microns and an extreme loading of 70 kg/s due to a failure of the pipeline from the dredger were simulated. Based on occurrence statistics, a representative range of winds, tides and wave heights was selected. The model was used to obtain the following output: contour plots of the maximum turbidity for each scenario, maximum turbidity and exposure times at the ecologically-sensitive sites in the bay as well as contour plots of the deposition thickness throughout the bay upon completion of dredging. Figure 5 shows the predicted turbidity plume due to the extreme loading case of 70 kg/s.

The turbidity at the ecologically sensitive sites was predicted to be below 25 mg/l, which is within the range of the natural background turbidity. Wave-generated bottom shear stresses were found to have a significant influence on the results by inhibiting deposition of the finer mud fractions in the exposed areas of the bay and thus causing a pervasive spreading of these particles into the lagoon and also out to sea. The maximum deposition thickness in the lagoon, however, totalled less than 2 mm over the dredging duration of 4 months. Based on these results the ecological impact of the proposed dredging was predicted to be low.

7. Conclusions and Recommendations

The turbidity loading caused by the proposed dredging could be determined with reasonable accuracy. The circulation in Saldanha Bay was well modelled, with predicted currents generally below 0.5 m/s, except at the entrance to Langebaan Lagoon where currents may exceed 1 m/s under spring tidal conditions. The turbidity at the ecologically sensitive sites was predicted to be below 25 mg/l, which is within the range of the natural background turbidity and far below the ecological threshold of 150 mg/l. Wave action will inhibit deposition of the finer mud factions in the exposed areas of the bay, thus causing a pervasive spreading of these particles into the lagoon and also out to sea. The maximum deposition thickness in the lagoon will, however, be insignificant. These results showed that the environmental impact of the plumes will be within acceptable limits.

It was found that the turbidity caused by the dredging (having a local effect) will be of a similar order to that occurring naturally during storms (a widespread effect). The turbidity caused by shipping is short-lived and not significant.

It has been recommended that the background turbidity levels be monitored before commencement of the dredging, particularly under storm conditions. In addition, it is required to measure the turbidity levels in the vicinity of the dredging and in the ecologically sensitive areas while dredging is taking place.

References

Appleby, J A and Scarratt, D J (1989). Physical effects of suspended solids on marine and estuarine fish and shellfish, with special reference to ocean dumping: A literature review. *Canadian Technical Report of Fisheries and Aquatic Sciences,* No. 1681, 31 pp.

Berlamont, J, Ockenden, M, Toorman, E and Winterwerp, J (1993). The characterisation of cohesive sediment properties. *Coastal Eng.* 21: 105-128.

Brøker, I, Johnsen, J, Lintrup, M, Jensen, A, Steen Møller, J (1994). The spreading of dredging spoils during construction of the Denmark-Sweden link. *24 Intern. Conf. On Coastal Eng.*, ASCE, Kobe, Vol. 3: 2958-2971.

Carter, R A (1995). Specialist study on the effects of dredging on marine ecology and mariculture in Saldanha Bay. *CSIR Environmental Services*, Stellenbosch.

Hochstein, A B and Adams, C E (1989). Influence of vessel movements on stability of restricted channels. *J. Waterway, Port, Coastal and Ocean Eng.*, ASCE, Vol. 115(4): 444-465.

Holthuijzen, L H, Booij, N and Herbert, T H C (1989). A prediction model for stationary, short-crested waves in shallow water with ambient currents. *Coastal Engineering,* 13: 23-54.

Huston, J (1976). Techniques for reducing turbidity with present dredging procedures and operations. *7 WODCON*, San Pedro, California: 163-181.

Kirby, R and Land, J M (1991). Impact of dredging - A comparison of natural and man-made disturbances to cohesive sedimentary regimes. *CEDA-PIANC conference*: Accessible Harbours, Paper B3, Amsterdam.

Kuo, A Y and Hayes, D F (1991). Model for turbidity plume induced by bucket dredge. *J. Waterway, Port, Coastal and Ocean Eng.*, ASCE, Vol. 117 (6): 610-622.

Kuo, A Y, Welch, C S and Lukens, R J (1985). Dredge induced turbidity plume model. *J. Waterway, Port, Coastal and Ocean Eng.*, ASCE, Vol. 111(3): 476-494.

Mocke, G P, Luger, S A, Schoonees, J S, Smit, F and Theron, A K (1996). Effects of proposed dredging activities on turbidity levels and shoreline stability in Saldanha Bay. Specialist Study Report S3. In: EIA of proposed changes to oil transfer operations, Saldanha Bay. Vol. 2. Specialist studies report. CSIR Report EMAS-C96005D, Stellenbosch.

Nichols, M, Diaz, RJ and Schaffner, L C (1990). Effects of hopper dredging and sediment dispersion, Chesapeake Bay. *Environ. Geol. Water Sci.* 15(1): 31-43.

Pennekamp, J G S, Blokland, T and Vermeer, E A (1991). Turbidity by dredging compared to turbidity by navigation. *CEDA-PIANC Conf.* Accessible Harbours, Paper B2, Amsterdam.

Pennekamp, J G S and Quaak, M P (1990). Impact on the environment of turbidity caused by dredging. *Terra et Aqua*, Vol. 42: 10-20.

Schoonees, J S (1998). Longshore transport in terms of the applied wave power approach. *Ph.D thesis*, University of Stellenbosch, Stellenbosch (in preparation).

Sosnowski, R A (1984). Sediment resuspension due to dredging and storms: an analogous pair. Dredging and dredged material disposal: *Dredging'84*, ASCE, Clearwater Beach, Florida, Vol. 1: 609-618.

Smith, A and Blanke, E (1975). Variation of the sea surface drag coefficient with wind speed. *Quart. J. R. Met. Society*, No. 101: 665-673.

Van Raalte, G H and Blokland, T (1988). Determination of dredging induced turbidity. *CEDA Dredging Day Conf.*, Hamburg, Paper B1.

Van Rijn, L C (1989). Handbook. Sediment transport by currents and waves. *Report* H 461, Delft Hydraulics, Delft.

Van Rijn, L C (1991). Data base. Sand concentration profiles and sand transport for currents and/or waves. *Report* H 1148, Delft Hydraulics, Delft.

Van Wijck, J, Van Hoof, J, De Clercq, M, Jeuniaux, F and De Keyser, C (1991). Economic aspects of processing dredged material. *CATS Congress*. Antwerp: 4.71-4.82.

WL|Delft Hydraulics (1995). Delft3D-WAQ version 4.2, User Manual.

WL|Delft Hydraulics (1996a). Delft3D-FLOW version 0.1, User Manual release 2.48.

WL|Delft Hydraulics (1996b). DELWAQ version 4.2, Technical Reference Manual.

Yagi, T, Koiwa, T and Miyazaki, S (1976). Turbidity caused by dredging. *7 WODCON*, San Francisco, pp 1079-1109.

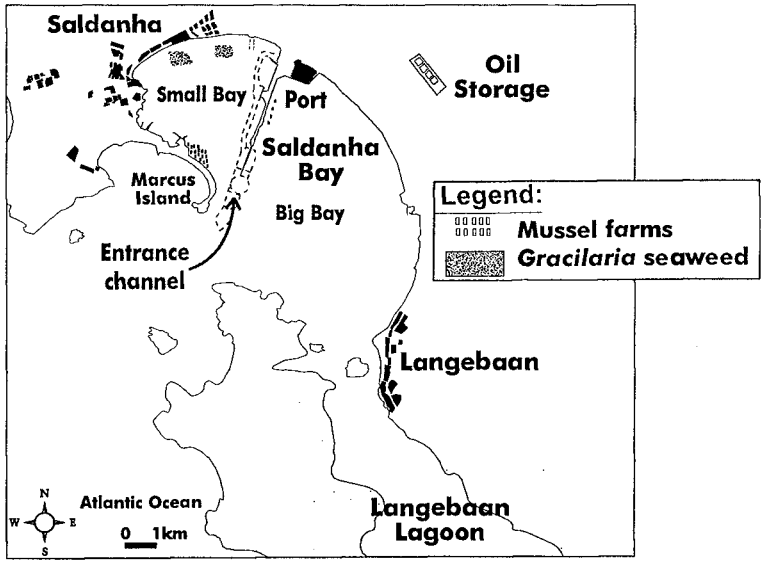

Figure 1: Location map

Figure 2: Modelled wave heights in Saldanha Bay

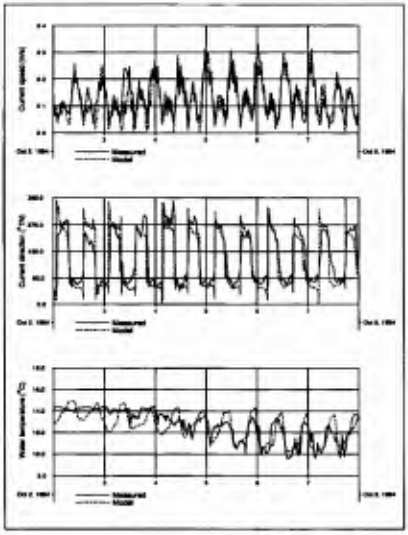

Figure 3: Comparison between measured data and model results in Saldanha Bay

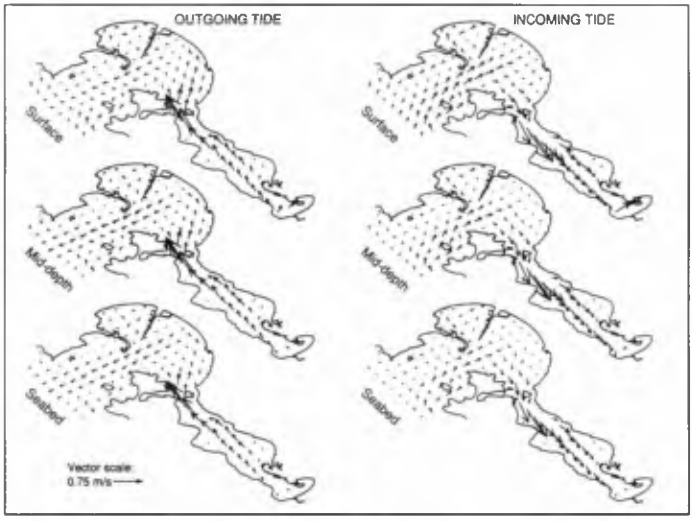

Figure 4: Modelled currents in Saldanha Bay at neap tide with a 10 m/s SW wind

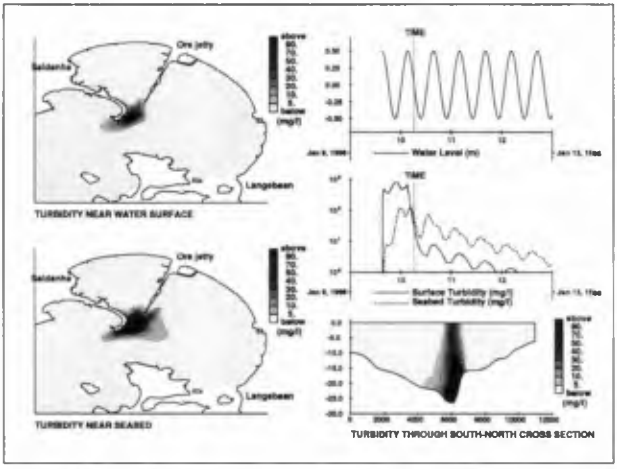

Figure 5: Predicted turbidity plume 3 hours after a simulated failure of the dredge line has been repaired

SIMULATION OF THE BEHAVIOR OF OXYGEN-DEFICIT WATER IN TOKYO BAY BY THREE-DIMENSIONAL WATER QUALITY MODEL

Nobuo Mimura[1], Member ASCE, Mitsuhiro Tsukada[2] and Masaharu Suzuki[3]

ABSTRACT

Semi-enclosed bays have been suffering from eutrophication in many countries. The present study deals with simulation of this problem focusing on Tokyo Bay, Japan. Tokyo Bay faces blue tides and fish death events caused by the oxygen-deficit water formed in the bottom layer during summer. To study the formation of the oxygen-deficit water, a model is developed to simultaneously simulate the flow, density stratification, and the material circulation in the ecosystem. The behavior of oxygen-deficit water, such as formation, growth, and stagnation, in Tokyo Bay is reproduced and examined by the model. The present model is effective in studying the temporal and spatial changes in water quality in a detailed manner. Moreover, countermeasures such as reduction of the land-based pollutant loads and sand capping on the polluted bottom mud are also examined.

1. Introduction

Semi-enclosed bay such as Tokyo Bay, Japan, have been suffering from water pollution. Tokyo Bay is about 65km and 25km long in the longitudinal and transverse directions, and 1,200km^2 in surface area. The inner part is occupied by shallow sea of less than 20m deep. The bay is surrounded by the Tokyo metropolitan area, where about 30 million people live, and major ports and industrial belts exist. Six major rivers flow into the bay, and the total fresh water inflow is about 325m^3/s including these rivers. From these settings, the organic nutrients loads to Tokyo Bay are extremely large(Fig.1).

[1] Professor and [2] Graduate Student, Center for Water Environment Studies, Ibaraki University, 4-12-1 Nakanarusawa, Hitachi, Ibaraki 316-8511, Japan

[3] Computer Technology Integrator Inc., 1-27-2 Meieki-Minami, Nakamura-ku, Nagoya, Aichi 450-0003, Japan

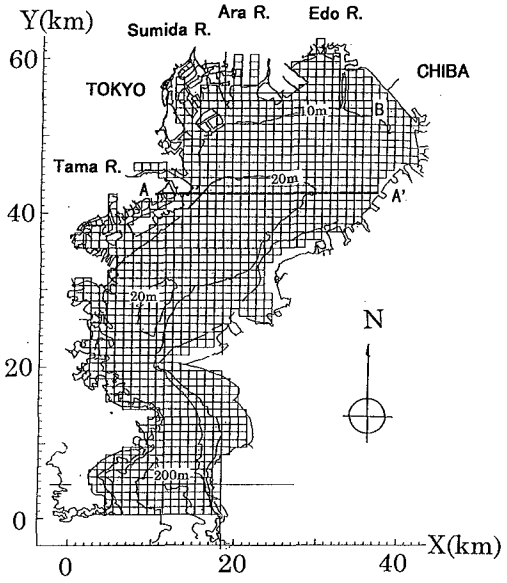

Figure 1 Tokyo Bay and computational grid

One of the major problems in Tokyo Bay is the formation of the oxygen-deficit water in the bottom layer during summer, which often causes blue tides and fish death by suffocation. The oxygen-deficit water is generated under specific combinations of the flow, density stratification, and the material circulation in the ecosystem. Therefore, a model with simultaneous equations for flows, density distribution, and ecosystem is needed to realistically calculate the processes related with water quality.

In this paper, a three-dimensional numerical model is developed to simulate the formation, growth, and stagnation of the oxygen-deficit water in Tokyo Bay. Then the spatial and temporal changes in water quality in 1993 are reproduced to trace the detailed behavior of the oxygen-deficit water mass.

2. Three-Dimensional Water Quality Model

The present model consists of three sub-models for flow field, density field, and material circulation in the ecosystem.

(1) Flow and density fields

The equations of continuity and momentum conservation are discretized by an FDM scheme on a three-dimensional grid system(Mimura et al., 1993; Kobayashi et al., 1995). Since the period of simulation often exceeds a year, an effective and stable method of computation is required. For this purpose, a special scheme to implicitly solve the terms of vertical turbulent transfer of momentum and pressure gradient is used(Sato et al., 1993). As boundary conditions, temporal records of tidal elevation at the bay mouth, wind stresses, and river discharges are given from field observations.

The density sub-model consists of the diffusion equations of heat and salinity. At the water surface, heat exchange by solar radiation, long-wave radiation, and sensible and latent heat transfer by evaporation are taken into consideration. Inflows of freshwater by rainfall and river discharge are also included. These terms are calculated by giving the time histories of the observed data for atmospheric temperature, solar radiation, wind etc as mentioned later.

(2) Material circulation in the ecosystem

In this sub-model, ecosystem is represented as a network of material flows among the components of phytoplankton, zooplankton, detritus, dissolved organic matter, phosphate, and inorganic nitrogen as shown in Fig.2. The key elements and nutrients, such as carbon, nitrogen and phosphorus, are stored in these components, and transported among them. As a result of such material flow, water quality changes. Chemical oxygen demand(COD) and dissolved oxygen(DO) are taken as the indices of water quality. The governing equations of the ecosystem sub-model are the diffusion equations with bio-chemical process terms.

$$\frac{\partial B}{\partial t} + U\frac{\partial B}{\partial x} + V\frac{\partial B}{\partial y} + W\frac{\partial B}{\partial z} = \frac{\partial}{\partial x}\left(K_x\frac{\partial B}{\partial x}\right) + \frac{\partial}{\partial y}\left(K_y\frac{\partial B}{\partial y}\right) + \frac{\partial}{\partial z}\left(K_z\frac{\partial B}{\partial z}\right) + \Delta B$$

where, U, V and W are velocity components, and K_i is diffusion coefficient in x, y, and z directions.

The bio-chemical process term, ΔB, expresses the temporal change in the concentration of each component. In the case of phytoplankton, this term includes photosynthesis, respiration, extracellular release, and grazing by zooplanktons. These processes are modeled by empirical and semi-theoretical relationships obtained in the existing studies. Equations to represent the relationships are shown in Fig.3 in a conceptual manner(Nakata, 1993). The factors controlling the rates of changes are given as empirical equations. Regarding the material flow, changes in carbon(C) flows are calculated first, then the contents of other nutrients, i.e. nitrogen(N) and phosphorus(P),

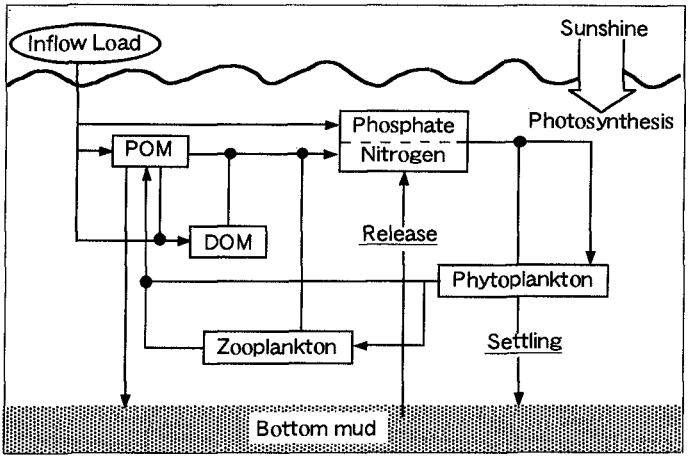

Figure 2 Material flow in the ecosystem

are determined based on the empirical ratios of N/C and P/C. The DO consumption of each bio-chemical reaction is calculated by the ratio between the theoretical oxygen demand and carbon content(TOD/C).

These equations include the terms for release of nutrients from bottom mud and consumption of DO in the bottom. It was pointed out that such exchange between bottom water and mud is very important, for the bottom mud play a role of significant nutrients' stock. These processes are controlled by the concentration difference of each component between bottom water and mud, water temperature and DO concentration. In this model, equations given by Matsunashi(1993) are used to represent these relationships.

3. Simulation for Tokyo Bay

(1) Grid system

Tokyo Bay is about 65 km long and 25 km wide, and the water depth decreases sharply from 200 m at the bay mouth to less than 20 m in the inner half of the bay. A three-dimensional grid was set in Tokyo Bay as shown in Fig.1. The horizontal grid is 1 km × 1 km, and water depth was divided into 20 layers with variable height. The layer height is 2 m each for the upper layers to reproduce the vertical density distributions precisely, while it is 30 m beyond the depth of 60 m. The time step of the calculation, Δt, is 4 minutes.

Phytoplankton (**Phy**)

$$\frac{\partial \mathbf{Phy}}{\partial t} = \text{Photosynthesis} - \text{Extracellular Release} - \text{Respiration} - \text{Grazing by Zoop.} - \text{Death} - \text{Settling}$$

Zooplankton (**Zoo**)

$$\frac{\partial \mathbf{Zoo}}{\partial t} = \text{Grazing of Phytop.} - \text{Egestion} - \text{Respiration} - \text{Death}$$

Detritus (**POM**)

$$\frac{\partial \mathbf{POM}}{\partial t} = \text{Death of Phytop.} + \text{Egestion of Zoop.} + \text{Death of Zoop.} - \text{Biodegradation} - \text{Settling}$$

Dissolved Organic Matter (**DOM**)

$$\frac{\partial \mathbf{DOM}}{\partial t} = \text{Extracellular Release of Phytop.} + \text{Biodegradation of POM} - \text{Oxidation}$$

Dissolved Inorganic Nitrogen (NH_4, NO_2, NO_3; **DIN**)

$$\frac{\partial \mathbf{DIN}}{\partial t} = -\text{Uptake by Phytop.} + \text{Respiration of Phytop.} + \text{Egestion of Zoop.} + \text{Decomposition of POM} + \text{Oxidation of DOM} + \text{Release from Mud}$$

Dissolved Inorganic Phosphorus (**DIP**)

$$\frac{\partial \mathbf{DIP}}{\partial t} = -\text{Uptake by Phytop.} + \text{Respiration of Phytop.} + \text{Egestion of Zoop.} + \text{Decomposition of POM} + \text{Oxidation of DOM} + \text{Release from Mud}$$

Dissolved Oxygen (**DO**)

$$\frac{\partial \mathbf{DO}}{\partial t} = \text{Photosynthesis} - \text{Respiration of Phytop.} - \text{Respiration of Zoop.} - \text{Oxidation of DOM} - \text{Oxidation of POM} - \text{Consumption by Mud} + \text{Reaeration}$$

Chemical Oxygen Demand (**COD**)

$$\frac{\partial \mathbf{COD}}{\partial t} = \text{Temporal changes in COD components of Phytop., Zoop., POM, and DOM}$$

Figure 3 Conceptual relationships of the bio-chemical processes

(2) Target year and field data

A serious problem which we faced during the study was lack of observed data. Though the present model can calculate the temporal and spatial changes very in detail, it is difficult to find data obtained in a similar manner for the calibration of the model. After gathering as much data as possible, the data set in 1993 was found to be relatively complete, then 1993 was chosen as the target for the calculation. In 1993, the oxygen-deficit water began to form in the middle of May, and seven blue tide events were recorded from June to September. Therefore, it was tried to hindcast the temporal change of water quality from April to September in 1993.

Initial and boundary conditions used for this calculation were as follows.

1) Water density: Salinity and water temperature were set as 34.3‰ and 14℃ respectively, uniform for all grid points.
2) Tide: Observed tidal elevation was given along the boundary of the bay mouth.
3) Climate: Rainfall, solar radiation, cloudiness, direction and speed of wind observed hourly in Tokyo were used.
4) River discharge: Daily records of the discharges were given for six major rivers (Edo R., Ex-Edo R., Ara R., Sumida R., Tama R., Tsurumi R.; Japan River Association, 1995). The salinity of the discharge was assumed 0 ‰, and the concentration of COD and other nutrients were set to be the yearly mean values, i.e. constant.
5) Bio-chemical terms: The bio-chemical components were set as the data observed on March 23, 1993.

4. Comparison of Simulation and Field Data

As mentioned above, there are no data set of water quality obtained continuously for a sufficiently long period of time. The longest record for salinity, water temperature, and DO was found for a month, from August 30 to September 28 in 1993. In order to verify the present model, the simulated results were compared with the observed data. The point of the comparison was Point B in Fig.1.

The comparisons are shown in Fig.4, 5 and 6 for salinity, water temperature, and DO, respectively. Overall agreements between the simulation and observed data are good, indicating that the present model could reproduce the real changes in water quality.

The observation of salinity and water temperature shows that strong density stratification formed in this period, while the difference of salinity and temperature between the surface and bottom layer disappeared on September 4, 13, 17, and 23. This indicates that strong vertical mixing took place during these days. This disruption of the

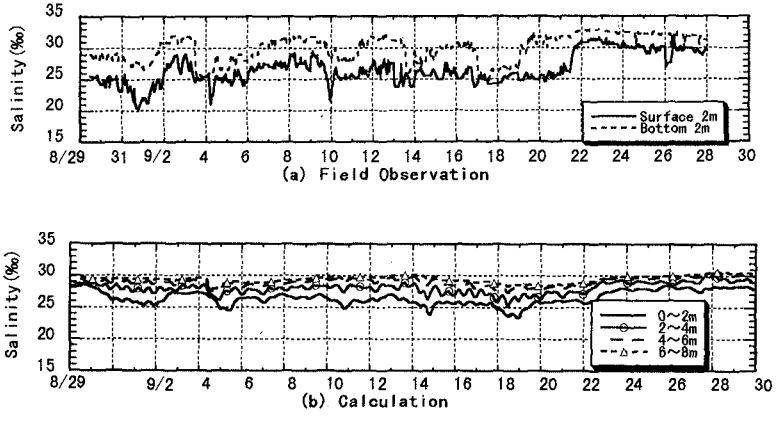

Figure 4 Comparison between observed and calculated results (Salinity)

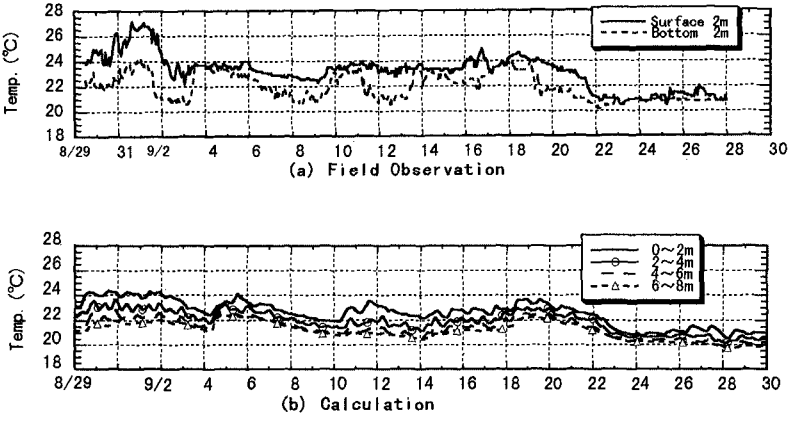

Figure 5 Comparison between observed and calculated results (Water temperature)

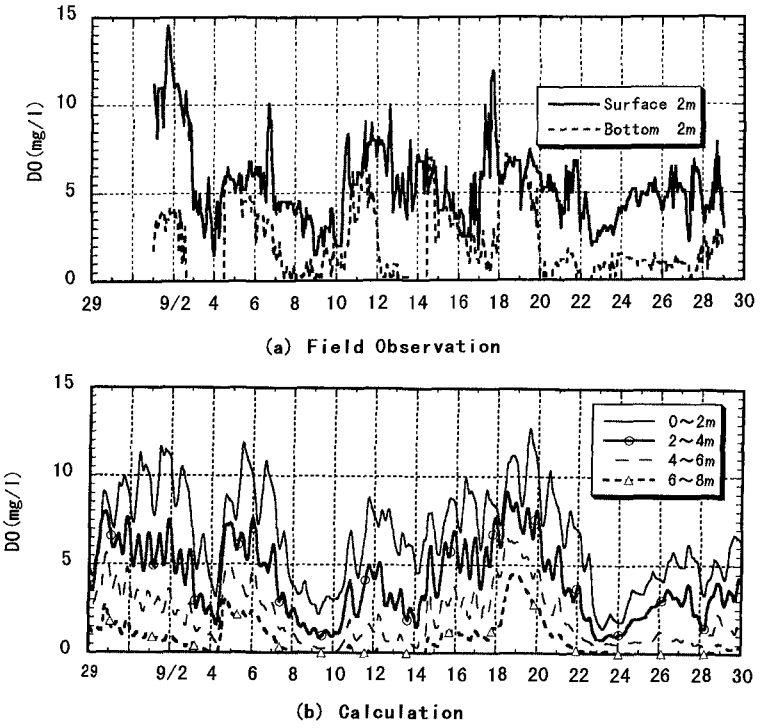

Figure 6 Comparison between observed and calculated results (Dissolved Oxygen)

density stratification corresponded to the wind condition; it occurred when the speed of southerly or south-westerly wind exceeded 5m/s. This means that such strong vertical mixing might be induced by the breaking of wind waves. On the other hand, the vertical mixing are relatively weak in the simulated results. In the model, the vertical mixing is expressed by the eddy viscosity and diffusivity, and the density effect is represented by a stratification function based on the Richardson Number. Therefore, the mixing term of the present model cannot represent the effect of turbulent mixing from water surface caused by wave breaking.

Regarding DO, the concentration over 10mg/l were observed on September 1, 6, 12, and 17. These events are considered to be supersaturation caused by the blooming of phytoplanktons. During the disruption of the density stratification on September 4, 14, and 18, DO also became uniform in the vertical direction. Though such vertical uniformity was not reproduced, the overall temporal change of DO shows good

agreement with the observed data. The blue tide occurrence corresponded to the upwelling of the oxygen-deficit water from the bottom layer to the shore along Chiba Coast.

5. Behavior of the Oxygen-Deficit Water

(1) Formation and expansion of oxygen-deficit water

From the simulation by the present model, the behavior of the oxygen-deficit water in Tokyo Bay can be examined. Figure 7 shows two different distributions of DO in Tokyo Bay; one is the planar distribution in the bottom layer and the other is the vertical distribution along the A-A' section indicated in Fig.3. The period is from early May to mid June. There have been several definitions of the oxygen-deficit water depending

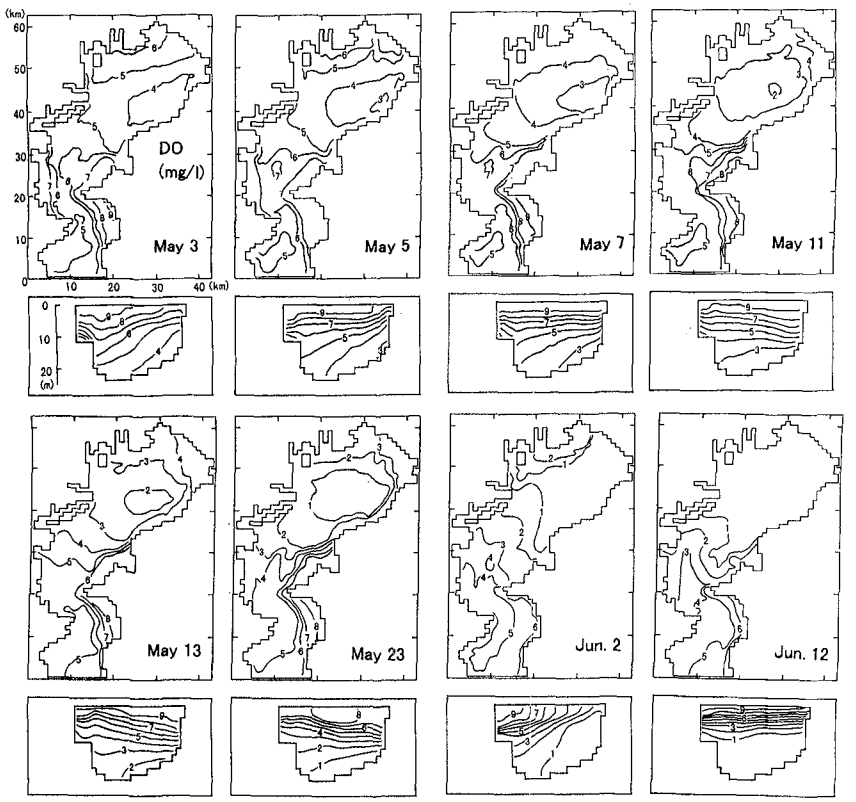

Figure 7 Formation and growth of the oxygen-deficit water

on the degree of harmfulness to the marine organisms. In the present study, DO of less than 3mg/l was taken as the criterion for the oxygen-deficit water.

On May 3, no significant oxygen-deficit water formed, though there was a water mass with 4mg/l of DO off Chiba Coast. Water mass with 3mg/l of DO appeared for the first time on May 5. It expanded on May 7, and the water mass with 4mg/l of DO covered a large portion of the inner bay surrounding the oxygen-deficit water. On May 11, the water mass with 3mg/l of DO expanded in the inner bay, and water mass with 2mg/l of DO appeared in the middle of it. Until June 12, such expansion of the oxygen-deficit water continued, and the bottom layer of the inner bay was finally covered by strong oxygen-deficit water with less than 1mg/l of DO. After this period, the oxygen-deficit water has been stagnant until September, the end of the computation.

The history of the vertical distribution also shows the formation and growth of the oxygen-deficit water very clearly. It was produced around the innermost place of 10 to 20m deep off Chiba Coast. The expansion of the oxygen deficit water was very quick. After May 5, the density stratification started to be intensified. This is due to the climatic conditions; the atmospheric temperature suddenly increased to 24℃ on May 11, and it kept above 20℃ during the daytime after then. This climatic condition is the major cause for the rapid formation and stagnation of the oxygen-deficit water in the inner part of Tokyo Bay.

Figure 8 shows the changes in the total volume of the oxygen deficit water mass for the complete period of the simulation. The volume of the oxygen deficit water mass was defined as the volume of water in which DO concentration is less than 3mg/l. The history of the atmospheric temperature for the same period is shown in Fig.9. From these figures, the history of the oxygen-deficit water formation can be understood again. As the water temperature increases in May, the oxygen-deficit water started to form. The volume reached its maximum in early July, then tended to decrease with fluctuation. Amazing thing is that the water mass still exist even at the end of September. These tendency is similar with the real situation qualitatively. However, more accurate quantitative verification needs more data densely measured both in time and space.

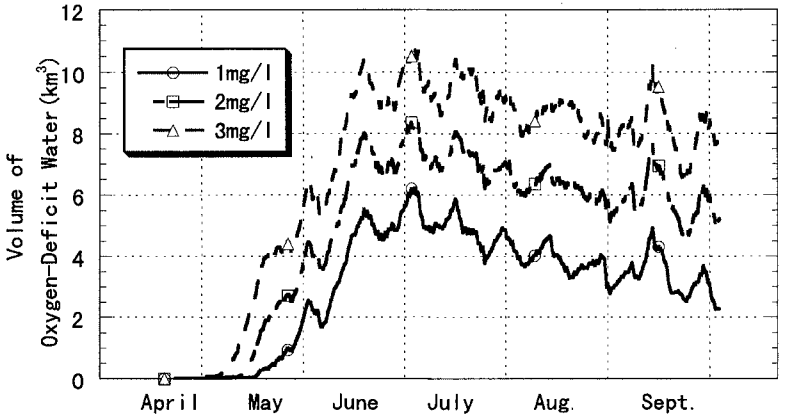

Figure 8 Changes in the total volume of the oxygen-deficit water (from April to September, 1993)

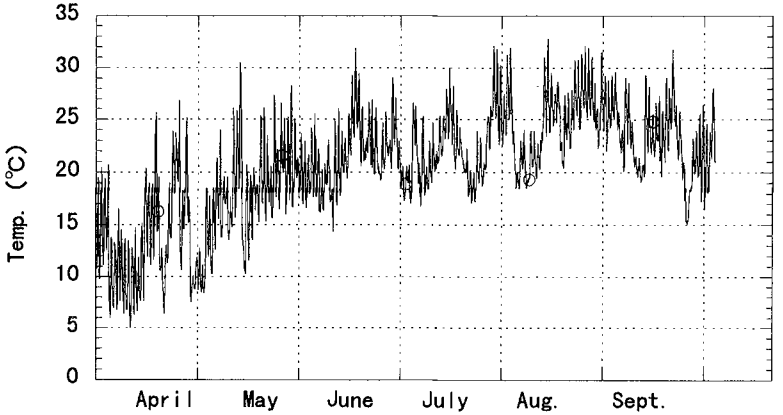

Figure 9 Changes in atmospheric temperature (from April to September, 1993)

(2) Up-welling of the bottom water and formation of blue tide

Figure 10 shows the temporal changes of the DO distribution in the surface and bottom layers during 22 to 30 in September. Throughout this period, the bottom layer of the inner bay was covered by strong oxygen-deficit water, while the appearance of the oxygen-deficit water in the surface layer was intermittent. Though DO was almost saturated on September 22, strong oxygen-deficit water suddenly appeared on the next

day, September 23. This is because wind changed to northerly on September 23, then up-welling was brought about by this wind in front of the north-east coast of Tokyo Bay. Actually blue tide occurred in the same area on September 23.

(3) Effect of countermeasures

The usefulness of such model is that it enables to examine the effects of countermeasures. The possible countermeasures for improving the water quality in Tokyo Bay are reduction of the inflow loads and sand capping over to depress oxygen consumption and nutrients release by bottom mud. In the present study, two trials were made for 50% reduction of the inflow lords and sand capping on the area shallower than 10m. Both countermeasures were not effective to improve the formation of oxygen-deficit water. However, they may be effective if the calculation is continued for several years. Since complete boundary conditions for climate, river discharge, tide, etc. are needed for longer simulation, such attempts are left for future studies.

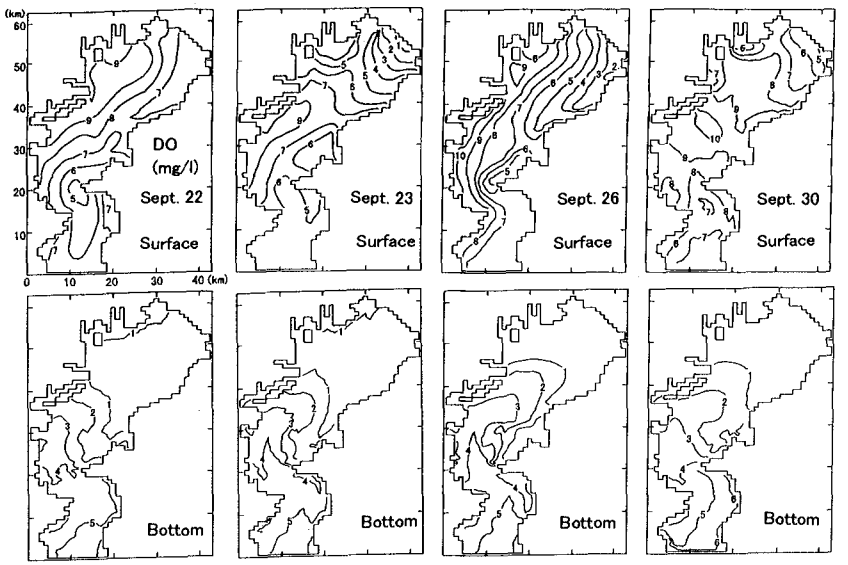

Figure 10 Up-welling of the oxygen-deficit water by wind

6. Conclusions

It is proved that the present model can reproduce the observed spatial and temporal changes in water temperature, salinity and DO rather well. The tendencies of the temporal changes in these parameters are quite similar between calculation and field data through the simulation period of 6 months.

In Tokyo Bay, oxygen-deficit water is generated even in early May in the bottom layer. Once a small mass of the oxygen-deficit water is generated, it expands very quickly to cover the wide area of the innermost part of the bay. During mid-summer, the bottom layer of a half of the bay is covered by strong oxygen-deficit water with DO concentration of less than 1 mg/l. Up-welling of such water occurs when north winds are strong, which in turn brings about blue tide along the north coasts of Tokyo Bay.

When the pollutants discharged from rivers is reduced by 50%, the concentration of nutrients such as phosphate and nitrogen decreases apparently, while the oxygen-deficit water continues to take place. Same tendency was observed, when the effects of sand capping work on the bottom mud was calculated. This indicates the difficulty to improve water quality in Tokyo Bay in a short time. For assessing the effects of such countermeasures, the present model is expected to be useful.

References

Kobayashi, T., N.Mimura and M.Tsukada (1995): Analysis of the tidal exchange in Tokyo Bay based on the three- dimensional tidal simulation, Proc. Japan Coastal Eng. Conf., Vol.42, pp.1071-1075.

Japan River Association(1995): River Discharge Tables 1993.

Matsunashi, S.(1993): A predictive model for nitrogen, phosphorus and dissolved oxygen in semi-enclosed bays, Proc. Japan Coastal Eng. Conf., Vol.40, pp.1076-1080.

Mimura, N., K.Yanai, T.Kobayashi and M.Tsukada (1993): Simulation of tidal currents in Tokyo Bay focusing on the density distribution, Proc. Japanese Coastal Eng. Conf., Vol.40, pp.1006-1010.

Nakata, K.(1993): Ecosystem model, Jour. Adv. Mar. Tech. Conf., Vol.8, pp.99-138.

Sato K., M.Matsuoka and K.Kobayashi(1993): Effective method of three-dimensional calculation for tide and its applicability, Proc. Japanese Coastal Eng. Conf., Vol.40, pp.221-225.

Watertable Fluctuations in a Sandy Ocean Beach

B. Raubenheimer [1], R.T. Guza[1], and Steve Elgar [2]

Abstract

Fluctuations of the watertable level within a fine-grained beach were observed for 2 months in Fall 1996. The magnitude of fluctuations at diurnal and semi-diurnal frequencies decayed rapidly inland, but fluctuations at spring-neap frequencies remained significant nearly 100 m inland of the mean shoreline location. During two storms that coincided with spring tides, overtopping and ponding of water behind the berm resulted in increased watertable levels that persisted for several days. Beach erosion during the second storm resulted in landward displacement of the shoreline location, and subsequent watertable fluctuations also extended farther inland. Numerical solutions of the nonlinear Boussinesq equation, with the seaward boundary condition given by the observed shoreline location, agree well with the observations. The landward attenuation and phase shifting of tidal watertable fluctuations are predicted well, as is the location of the seepage face.

Introduction

Beach watertable levels are believed to affect swash zone fluid motions (e.g., Packwood, 1983) and sediment transport (e.g., Grant, 1948; Duncan, 1964; Eliot and Clarke, 1988). Tidal watertable fluctuations in shallow (relative to the wavelength of the fluctuations) aquifers are often modeled with the nonlinear Boussinesq equation

$$\frac{\partial \eta}{\partial t} = \frac{K}{N}\frac{\partial}{\partial x}\left((D+\eta)\frac{\partial \eta}{\partial x}\right) \qquad (1)$$

where t is time, x is the cross-shore coordinate, η and D are, respectively, the deviation of the watertable elevation and the depth of the impermeable stratum relative to mean sea level, K is the hydraulic conductivity in the saturated beach, and N is the effective porosity. The observed asymmetry (the beach fills more rapidly than it drains) and

[1]Scripps Inst. Oceanography, 9500 Gilman Dr., La Jolla, CA, 92093-0209, britt@coast.ucsd.edu
[2]EECS 2752, Washington State University, Pullman, WA, 99164-2752

overheight (the mean inland watertable elevation is higher than mean sea-level) of tidal watertable fluctuations (e.g., Emery and Foster, 1948; Harrison et al., 1971; Waddell, 1976; Lanyon et al., 1982) that result from the moving intersection of the waterline with the sloping beach are predicted qualitatively by analytical solutions of (1) for small tidal excursions on a planar beach (Nielsen, 1991). However, the tidal overheight is underpredicted, possibly because the model neglects the effects of the seepage face, the decoupling of the watertable and offshore water level that occurs on fine-grained beaches near low tide (Turner, 1993). Comparisons of numerical solutions of (1) with watertable fluctuations observed over one or two tidal cycles suggest the seepage face and wave-driven setup at the shoreline are important to watertable fluctuations (Kang and Nielsen, 1996; Baird et al., 1998).

Here, watertable fluctuations observed along a densely instrumented cross-shore transect are used to extend the previous studies. The 2 months of observations span several spring-neap tidal cycles and include a storm that modified the beach profile. Comparisons of the observations with numerical solutions of (1) are used to identify processes important to watertable fluctuations and the seepage face location.

Observations

Waves, runup, tides, and watertable fluctuations were sampled nearly continuously at 2 Hz for two months during Fall 1996 at Torrey Pines Beach, CA (Figure 1). Surf zone waves and runup were measured with 16 pressure sensors located near the sand surface, and watertable fluctuations were measured with 22 buried pressure sensors. Runup and watertable sensors were stacked vertically to estimate vertical infiltration and to detect capillary effects. Beach profiles landward of about 2-m water depth were measured daily throughout September and October and approximately every other day during November. Other than erosion during a storm in late October (Figure 1), foreshore profile changes were small (< 10 cm). At the beginning, middle, and end of the experiment the profile was measured to about 5-m water depth. Offshore wave heights measured in 10-m water depth about 35 km north of the experiment site ranged from 40 to 330 cm and peak periods ranged from 5 to 20 s (Figure 2B). These offshore observations agreed well with measurements made at Torrey Pines Beach in about 3.5-m water depth at cross-shore distance 165 m (Figure 1), except during the storms when the shallower sensor was in the surf zone. Rainfall of 0.76 and 1.62 cm were recorded on Oct 26 and 30, respectively.

At fifteen locations between cross-shore distances 10 and 100 m, 8-m deep holes were drilled to collect sediment cores and to determine the beach stratigraphy. Sieve analysis was conducted on eleven cores to determine grain sizes, and five cores were used to determine porosity. Hydraulic conductivity was estimated from pumping tests (Bouwer and Rice, 1976) conducted at cross-shore distances 60 and 91 m. The beach is composed of approximately 2 to 4 m of uniform fine to medium sand with traces of silt ($d_{50} \approx 0.23$ mm, porosity $\approx 37\%$, and hydraulic conductivity ≈ 0.07 cm/s) overlying about 1 m of Scripps formation composed of dense, silty fine sand with traces of gravel ($d_{50} \approx 0.15$ mm, porosity $\approx 33\%$, and hydraulic conductivity ≈ 0.03 cm/s) on top of low permeability Ardath Shale ($d_{50} \approx 0.004$ mm, porosity $\approx 32\%$, and hydraulic conductivity ≈ 0.0005 cm/s). All pressure sensors were located above the Scripps formation and are identified by their distance (in m) inland from the mean shoreline location, defined as the intersection of the beach profile and mean

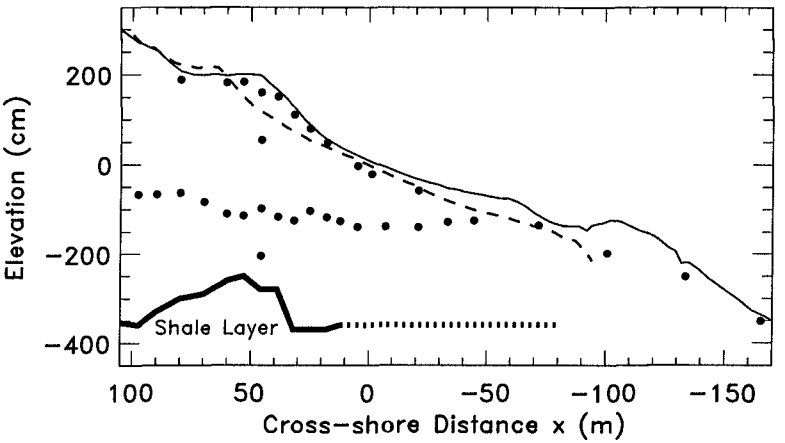

Figure 1: **Pressure sensor locations (solid circles) and beach profiles measured at Torrey Pines Beach before (thin solid curve) and after (thin dashed curve) a storm on Oct 25. The thick solid and dotted curves at the bottom of the figure represent the measured upper surface of the Ardath Shale and the (unmeasured) offshore shale position used in the numerical model, respectively.**

sea level (e.g., p098 is located at 98 m).

The observed mean watertable levels usually increased in the landward direction, suggesting that water usually flowed toward the ocean (Figure 2A). Tidal watertable and offshore fluctuations were dominated by waves with 25 and 12 hr periods (Figure 3). Similar to previous observations (e.g., Emery and Foster, 1948; Harrison et al., 1971; Waddell, 1976; Lanyon et al., 1982), tidal watertable fluctuations were asymmetrical in time (not shown), and decreased rapidly in magnitude in the landward direction (Figures 2 and 3). Offshore tidal amplitudes ranged from about 0.5 m during neap tides to 1 m during spring tides (Figure 2C), whereas watertable fluctuation amplitudes at cross-shore distance 60 m were usually less than about 10 cm (Figure 2A). At the most landward sensor, 98 m inland of the mean shoreline, diurnal and semi-diurnal tidal fluctuations were strongly damped, but fluctuations at the frequency of the spring-neap tidal cycle remained significant (Figure 2A). Spring-neap watertable fluctuations have not been observed previously, possibly because most observations spanned only a few days. For similar offshore tidal fluctuations and wave heights, watertable fluctuations near the berm were smaller in September than in November (Figure 2) because beach erosion (Figure 1) on Oct 26 reduced the distance from the berm to the mean shoreline.

Wind waves had a significant effect on the observed watertable fluctuations. During two storms (offshore wave heights greater than about 130 cm) that occurred during spring tides (Oct 15 and Oct 25 in Figure 2) runup overtopped the berm, resulting in large (up to 70 cm) increases in the berm watertable level. High watertable levels persisted for several days after each storm. However, tidal levels modulated the effect of storm waves on watertable fluctuations. For instance, although offshore wave heights exceeded 130 cm during the neap tides (Figure 2, Oct 20), berm overtopping did not occur and the berm watertable response was small.

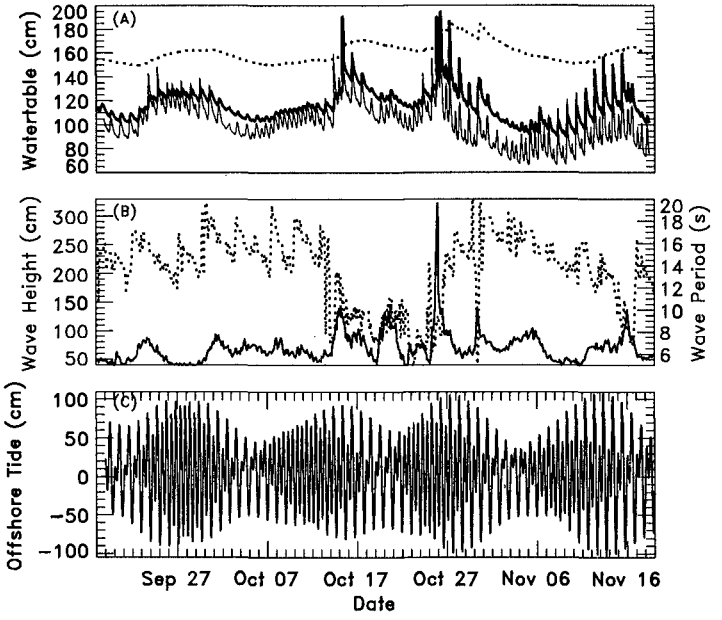

Figure 2: **Observed (A) 10-min averaged watertable levels at cross-shore locations 98 (dotted curve), 60 (thick solid curve), and 46 m (thin solid curve) inland of the mean shoreline, (B) offshore hourly significant wave heights (solid curve) and peak wave periods (dotted curve), and (C) 34-min averaged offshore sea-surface levels versus time.**

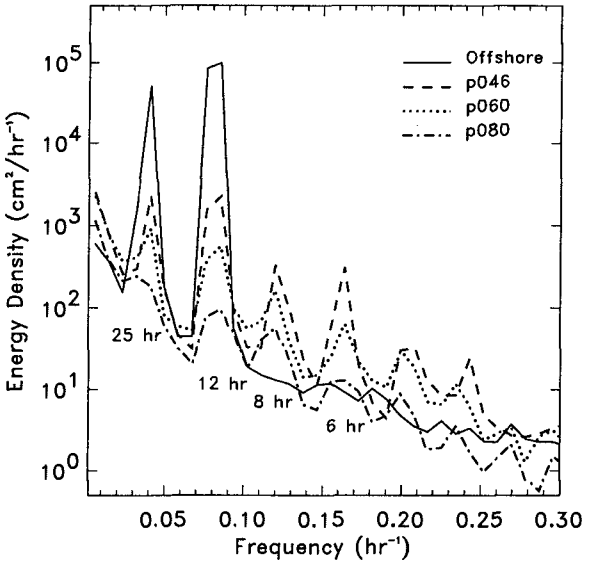

Figure 3: **Energy spectra (24 dof) of offshore water-level (solid curve) and watertable fluctuations at 46 (dashed curve), 60 (dotted curve), and 80 m (dash-dot curve) inland of the mean shoreline.**

Numerical Model

The observations are compared with numerical solutions of the nonlinear Boussinesq equation (1). A no flow bottom boundary condition is imposed at the top of the Ardath Shale (Figure 1), which is assumed to be horizontal both landward and seaward of the measured positions. Above the impermeable boundary, the beach material is assumed homogeneous and isotropic, with an average hydraulic conductivity K of 0.07 cm/s. The effective porosity N, determined using a least squares fit of the predictions to the observations, is 0.215. The model is initialized with the watertable level observed at the start of the experiment. Initial levels inland of the most landward sensor are estimated using a natural cubic spline extrapolation. The location of the inland boundary (250 m landward of the mean shoreline) was determined iteratively to ensure it was sufficiently far onshore that predicted watertable fluctuations were negligible. In the results presented below, a constant head (Dirichlet) condition is imposed at the inland boundary of the model domain. The model results are sensitive to the ratio K/N and to the aquifer thickness D, but are insensitive to the inland boundary condition.

The beach is assumed to be saturated at, and offshore of, the model seaward boundary, which is given by the shoreline location (e.g., the beach-ocean intersection). The moving locations of the shoreline and the watertable outcrop at the sand surface were estimated using water levels observed with the closely spaced foreshore sensors and measured beach profiles. The cross-shore structure of the mean water level was estimated by fitting a cubic spline to 10-min averaged observations at all sensors. Sand levels at each time step were determined by fitting a cubic spline to the measured beach profiles. The shoreline location was defined as the most seaward location where the water depth above the beach profile was less than a small number δ_s. The watertable outcrop location was estimated from the observations as the most landward position where the measured water level was less than δ_w below sand level. Owing to errors of a few cm in the measured mean pressure and beach profiles, nonzero values are used for δ_s and δ_w. The results shown below correspond to $\delta_s = \delta_w = 2$ cm and are not sensitive to values of δ_s and δ_w between 1 and 5 cm. Following van Gent (1994) and Baird et al. (1996), when the predicted watertable level exceeds the sand level within the model domain (landward of the shoreline), the watertable is reset to sand level and the excess water is assumed to be run-off.

The Boussinesq equation (1) is based on the assumption that horizontal flows u are much larger the vertical flows w. The flow through saturated sand was estimated using observed gradients of hydraulic head ($p_w/\rho g + z_R$, where p_w is measured pressure, z_R is the vertical sensor location relative to a fixed datum, ρ is water density, and g is gravitational acceleration) and Darcy's law for laminar flow,

$$u = +\frac{K}{N}\frac{\partial(p_w/\rho g - z_R)}{\partial x} \tag{2}$$

$$w = -\frac{K}{N}\frac{\partial(p_w/\rho g - z_R)}{\partial z} \tag{3}$$

where z is vertical distance positive upward. Consistent with the model assumptions horizontal velocities are on average about 10 times larger than the vertical velocities (Figure 4). Vertical and horizontal velocities had similar magnitudes only during spring high tides when wave runup ran onto the beach above the watertable sensors, resulting in relatively large downward (negative) velocities on the rising tides and relatively large upward velocities as the watertable drained on the falling tides (Figure 4, Sep 24 to 31). However, 10-min-averaged vertical velocities were smaller than horizontal velocities 95% of the time. The vertical velocities corresponding to individual wave uprushes will be considered elsewhere.

Model-Data Comparisons

The model, driven with the observed 10-min-averaged shoreline location, predicts the observed watertable levels, except during and immediately after the two October storms (Figure 5). The fluctuations at the spring-neap frequency and the increased watertable fluctuations near the berm following the beach erosion on Oct 26 (Figure 1) are modeled qualitatively well. Consistent with previous results (Baird et al., 1998), breaking-wave-driven setup is important to the watertable fluctuations. Driving the model with the observed offshore water level fluctuations rather than the shoreline location results in underprediction of both the mean watertable levels and

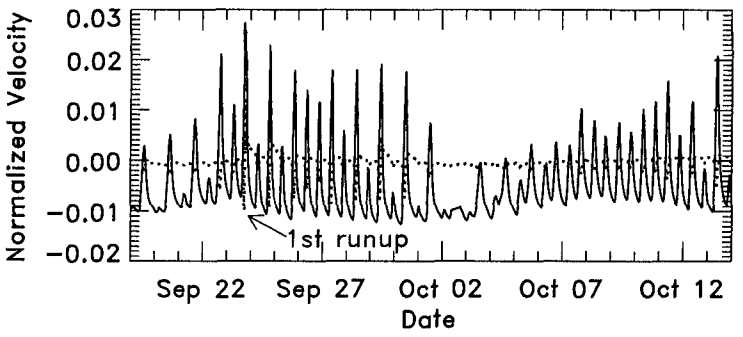

Figure 4: **Normalized horizontal (u/K, solid curve) and vertical (w/K, dotted curve) velocities versus time. Velocities were estimated from 10-min averaged hydraulic heads measured with horizontally separated sensors at 39 and 53 m and vertically separated sensors at 46 m and elevations 0.6 and -2.2 m, respectively.**

the fluctuation amplitudes, primarily because the shoreline is farther offshore when setup is not included (Figure 5).

The strong onshore decay and significant phase delays of diurnal, semi-diurnal, and higher frequency tidal watertable fluctuations are also predicted accurately (Figure 6). There is little energy at tidal harmonic frequencies in offshore tidal fluctuations (8 and 6 hr periods in Figure 3) and the increased energy in watertable fluctuations at these harmonics appears to be generated nonlinearly in the vicinity of the moving shoreline (Raubenheimer et al., in prep.). However, inland of the most onshore locations of the shoreline ($x \approx 35$ m), the watertable fluctuations are described well by solutions to the linearized Boussinesq equation, which have the form

$$\eta(x,t) = \eta_0 e^{-k_R x} \cos(\omega t - k_I x) \tag{4}$$

where η_0 is the shoreline fluctuation amplitude, ω is the frequency in radians, and k_R and k_I are the real and imaginary parts of the wavenumber, respectively, given by

$$k_R = k_I = \sqrt{\frac{N\omega}{2KD_{av}}} \tag{5}$$

where D_{av} is the average aquifer depth. Similar to observations, the linearized equation (4) predicts that the amplitudes decay exponentially, and the phase lags vary linearly with distance inland (Figure 6).

The Boussinesq model (1) does not predict the increase in the watertable elevation landward of the berm ($x > 50$ m) observed during the October storms

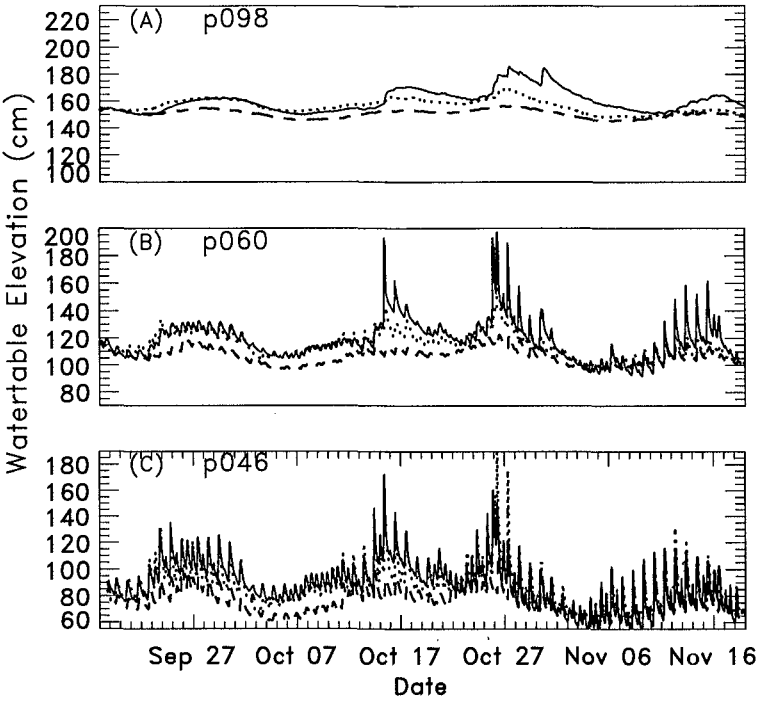

Figure 5: **Watertable fluctuations observed (solid curves) and predicted by the numerical model (1) driven with the observed shoreline location (dotted curves) and offshore water level (dashed curves) versus time. Cross-shore distances are (A) 98, (B) 60, and (C) 46 m.**

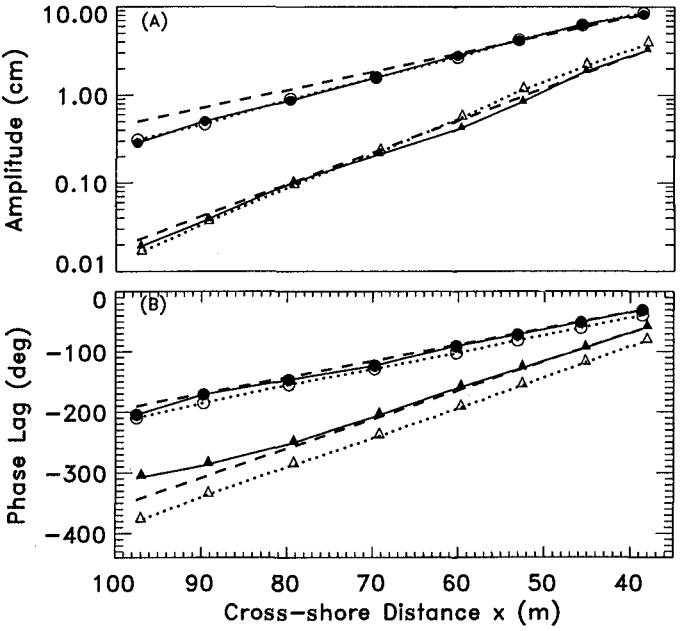

Figure 6: (A) Root-mean-square amplitudes and (B) phase lags relative to the shoreline for watertable fluctuations with periods of 25 (circles) and 8 hr (triangles) versus cross-shore distance inland from the mean shoreline location. Solid symbols with solid curves and open symbols with dotted curves are observed and predicted (with the nonlinear model) values, respectively, calculated from cross-spectra with 48 dof. Dashed lines represent linear theory predictions calculated using (4), (5), and observations at 39 m. Results for 6 and 12 hr periods are similar.

that coincided with spring tides (e.g., Figure 5, Oct 15 and 25). For the simplified case of no tides and monochromatic waves, the inland overheight of the watertable is independent of grain size and beach hydraulic conductivity (Kang et al., 1994). Using laboratory observations of watertable fluctuations owing to random breaking sea-swell waves, Kang et al. (1994) determined an empirical formula for $\bar{\eta}_w$, the time-averaged wave-driven overheight

$$\bar{\eta}_w = 0.62\sqrt{HL}\tan\beta_f \tag{6}$$

where H and L are the offshore significant wave height and wavelength, respectively, and β_f is the foreshore slope. The estimated (with (6)) wave-driven overheight ranges from 9 to 47 cm, but maxima of $\bar{\eta}_w$ do not coincide with the storm events during which offshore wave heights increased, but wavelengths ($L = gT^2/2\pi$) decreased (Figure 2B). Presumably, to predict the storm-induced watertable increases it is necessary to account for the effects of ponding water behind the berm (and the resulting infiltration) and the runup of (nonbreaking) infragravity waves. Differences between model predictions and observations may also result from neglecting the effects of the capillary fringe (e.g., Gillham, 1984; Li et al., 1997; Turner and Nielsen, 1997), trapped air within the watertable, and salinity (density) gradients (e.g., Nielsen, 1998). Despite the model simplifications and inaccuracies during the storms, model errors are small when the seaward boundary condition is given by the observed shoreline location (including setup). The 2 month average (and standard deviation) of differences between modeled and observed watertable levels are less than 6±7 cm for all sensors landward of the maximum shoreline.

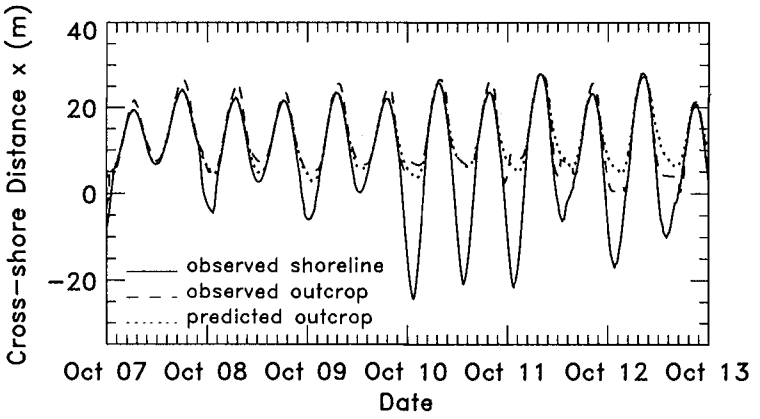

Figure 7: **Cross-shore position of the 10-min averaged observed shoreline (solid curve) and observed and predicted watertable outcrop (dashed and dotted curves, respectively) versus time. The seepage face is located between the shoreline and the watertable outcrop.**

When the tide falls more rapidly than the beach can drain, a seepage face forms between the watertable outcrop and the shoreline (Figure 7). The observed outcrop locations are predicted well by the nonlinear Boussinesq equation (1). Previous studies have suggested that the seepage face width on macrotidal beaches can be estimated assuming that the watertable outcrop position is independent of the pressure distribution within the beach, and depends only on the rate that the tide falls, the beach slope, and the value of K/N (Dracos, 1963; Turner, 1993). However reasonable agreement between the simple model of Dracos (1963) and the present outcrop observations is possible only if the ratio K/N is increased unrealistically (by a factor of 8) relative to that used in the numerical Boussinesq model.

Conclusions

Watertable levels observed for 2 months within a sandy beach depended on tidal levels, wind-waves and wave-driven setup, and the beach profile. Overtopping during spring high tides resulted in increased watertable levels for several days (Figure 2). Wind-waves of similar offshore height during neap tides had less effect on the watertable. Similar to previous observations, diurnal and semi-diurnal watertable fluctuations decreased inland (Figures 2, 3, 5, and 6). Although diurnal and semi-diurnal watertable fluctuations were damped almost completely 100 m inland of the mean shoreline location, fluctuations at spring-neap frequencies remained significant. Beach erosion during a storm resulted in larger tidal watertable fluctuations owing to the landward displacement of the shoreline. The observed horizontal flow in the watertable was usually much larger than the vertical flow (Figure 4), consistent with the assumptions in the nonlinear Boussinesq equation for watertable fluctuations in shallow aquifers.

The observed watertable levels (Figures 5 and 6) and seepage face width (Figure 7) are predicted accurately by a numerical model based on the nonlinear Boussinesq equation and driven with the observed 10-min averaged shoreline location (which includes wave-driven setup). When the model is driven with the offshore water levels (without setup), mean watertable levels and fluctuations are underpredicted. Watertable fluctuations (Figure 3) at harmonics of the tidal frequencies are nonlinearly generated near the moving shoreline location, but farther onshore the amplitudes and phases of watertable fluctuations are predicted well by solutions to the linearized Boussinesq equation (Figure 6).

Acknowledgements

This research was supported by the Office of Naval Research (Coastal Dynamics), the Naval Research Laboratory, the National Science Foundation, and the Mellon Foundation. Staff from the Center for Coastal Studies deployed and maintained the nearshore instruments. Offshore wave information was provided by the Coastal Data Information Program. The cooperation of the staff at Torrey Pines State Park is gratefully acknowledged.

References

Baird, A.J., T. Mason, and D.P. Horn, Validation of a Boussinesq model of beach ground water behavior, *Marine Geol.*, submitted, 1998.

Bouwer, H. and R.C. Rice, A slug test for determining hydraulic conductivity of unconfined aquifers with completely or partially penetrating wells, *Water Res. Res., 12,* 423-428, 1976.

Dracos, T., Ebene nichtstationare grundwasserabflusse mit freier oberflache, Swiss Federal Tech. Lab. Hydraul. Res. Soil Mech., Rep. 57, 114pp., 1963.

Duncan, J.R., The effects of watertable and tide cycle on swash-backwash sediment distribution and beach profile development, *Marine Geol., 2,* 186-197, 1964.

Eliot, I.G., and D.J. Clarke, Semi-diurnal variation in beachface aggradation and degradation, *Marine Geol., 79,* 1-22, 1988.

Emery, K.O., and J.F. Foster, Watertables in marine beaches, *J. Marine Res., 7,* 644-654, 1948.

Gillham, R.W., The capillary fringe and its effect on watertable response, *J. Hydrol., 67,* 307-324, 1984.

Grant, U.S., Influence of the watertable on beach aggradation and degradation, *J. Marine Res., 7,* 655-660, 1948.

Harrison, W., C.S. Fang, and S.N. Wang, Groundwater flow in a sandy tidal beach. 1. One dimensional finite element analysis, *Water Res. Res., 7,* 1313-1322, 1971.

Kang, H.-Y., P. Nielsen, and D.J. Hanslow, Watertable overheight due to wave runup on a sandy beach, *Proc. 24th Int. Conf. Coastal Eng.,* Kobe, Japan, 1994.

Kang, H.-Y., and P. Nielsen, Watertable dynamics in coastal areas, *Proc. 25th Int. Conf. Coastal Eng.,* Orlando, FL, 1996.

Lanyon, J.A., I.G. Eliot, and D.J. Clarke, Groundwater variation during semi-diurnal spring tidal cycles on a sandy beach, *Austr. J. Marine Fresh. Res., 33,* 377-400, 1982.

Li, L., D.A. Barry, and C.B. Pattiaratchi, Numerical modeling of tide-induced beach water table fluctuations, *Coastal Eng., 30,* 105-123, 1997a.

Li, L., D.A. Barry, J.-Y. Parlange, and C.B. Pattiaratchi, Beach watertable fluctuations due to wave run-up: Capillarity effects, *Water Res. Res., 35,* 935-945, 1997b.

Liu, P.L.-F., and J. Wen, Nonlinear diffusive surface waves in porous media, *J. Fluid Mech., 347,* 119-139, 1997.

Nielsen, P., Tidal dynamics of the water table in beaches, *Water Res. Res., 26,* 2127-2134, 1991.

Nielsen, P., R. Aseervatham, J.D. Fenton, and P. Perrochet, Groundwater waves in aquifers of intermediate depth, *Adv. Water Res., 20,* 37-43, 1996.

Packwood, A.R., The influence of beach porosity on wave uprush and backwash, *Coastal Eng., 7,* 29-40, 1983.

Raubenheimer, B., R.T. Guza, and S.L. Elgar, Tidal watertable fluctuations in a sandy ocean beach, in preparation, 1998.

Turner, I.L., Watertable outcropping on macrotidal beaches: a simulation model, *Marine Geol., 115,* 227-238, 1993.

Turner, I.L., and P. Nielsen, Rapid water table fluctuations within the beach face: Implications for swash zone sediment mobility?, *Coastal Eng., 32,* 45-59, 1997.

van Gent, M.R.A., The modeling of wave action on and in coastal structures, *Coastal Eng., 22,* 311-339, 1994.

Waddell, E., Swash-groundwater-beach profile interactions, *In:* Davis, R.A. and R.L. Ethington (eds.), *Beach and Nearshore Sedimentation,* SEPM No. 24, 115-125., 1976.

SEEPAGE EFFECTS ON SEDIMENT TRANSPORT BY WAVES AND CURRENTS.

T. E. Baldock [1] and P. Holmes [2]

Abstract

This paper considers the influence of seepage on the motion and transport of sediment. Under wave motion, steady upwards seepage (injection) increased erosion, while downwards seepage (suction) stabilised the bed. Conversely, seepage in the presence of a steady flow produced negligible changes in the sediment motion. A theoretical analysis examines the stability of the sediment particles and sediment bed under these conditions and provides an explanation for the different seepage effects. Seepage across the sediment/fluid interface also had a strong influence on the growth of sand ripples, even at pressure gradients of order 0.1. These results suggest that ripple dynamics in the nearshore may be affected by the watertable level and drainage within a beach.

1) Introduction

The stability of sediment particles under the influence of pressure gradients within the sediment bed is considered to be important with respect to the type and rate of sediment transport under both steady and oscillatory flows (Nielsen, 1992) However, previous work has provided conflicting results (Martin, 1970; Willets and Drossos, 1975; Oldenziel and Brink, 1974;Rao et al., 1994) and the effects of pressure gradients on sediment dynamics are not immediately obvious (Oh and Dean, 1994).

The rate and nature of sediment transport under steady flows and wave induced motions is generally considered to be dependent on the forces on the individual sediment particles. These include gravity forces, the surface drag force, pressure forces due to pressure gradients within the fluid, a lift force due to flow over the sediment particle and a seepage force due to flow across the fluid/sediment interface (Sleath, 1984). It may also be necessary to consider the stability of the sediment bed as a whole. In this instance the

[1] Research Fellow, School of Civil and Structural Engineering, University of Plymouth, PL1 2DE, UK.
[2] Professor, Department of Civil Engineering, Imperial College of Science, Technology and Medicine, London, SW7 2BU, UK.

effective stresses within the sediment may be increased, reduced or vanish completely (fluidisation) due to pressure gradients within the sediment. However, the effects of these pressure gradients on sediment transport are unclear and previous work has provided conflicting results. For example, in steady flows, Martin (1970), Watters and Rao (1971) and Willets and Drossos (1975) found that seepage did not affect sediment motion, while Oldenziel and Brink (1974) found the opposite to be true. The only experimental evidence under oscillatory flow in a water tunnel appears to be that from Kruijt (1976), who again found no significant effects. These results all pertain to steady vertical seepage, and as far as the authors are aware, no study has been carried out under oscillatory wave motion.

Surface gravity waves and bores will induce both vertical and horizontal transient pressure gradients within a sediment bed. The vertical pressure gradients induce flow into the bed under wave crests (suction) and upwards out of the bed under the wave troughs (injection). However, as noted by Packwood and Peregrine (1983), the vertical wave induced pressure gradients are approximately linearly proportional to the bed thickness. Consequently, scale modelling of sediment motion may be influenced by the relatively thin beds generally used in laboratory studies. Indeed, evidence to this effect was found by Conley and Inman (1992), who suggested that differences in bed ventilation might be responsible. Madsen (1974) showed experimentally that horizontal pressure gradients could be sufficient to fluidise a sediment bed under breaking waves while Yamamoto (1978) suggested that large steep waves and tsunamis transport huge amounts of sediment because the bed is fluidised by horizontal pressure gradients.

Previous work has also suggested that the pressure gradients and the seepage flow induced within beaches may be an important factor governing both long term beach morphology and short term (storm duration) beach evolution (Oh and Dean, 1994; Turner, 1995). In these instances, an unsaturated beach face appears to promote steepening of the profile, while a saturated beach face tends to result in a flattening of the beach profile. However, the mechanism by which the watertable influences the beach dynamics is not obvious. For example, Oh and Dean (1994) found that a raised water table increased shoreward transport, contrary to most previous studies (e.g. Emery and Foster, 1948; Waddell, 1976), while a lower water table appeared to result in increased stability and little profile change. Numerical calculations also suggested that the pressure gradients induced by the change in watertable were too small to influence the stability of the sediment.

2) Theory

The pressure distribution within sediments was first considered by Putnam (1949) and later expanded upon by Sleath (1970) and others. Sleath's (1970) solution was based on the assumption of an incompressible fluid, grain particles and grain skeleton. Flow velocities were then derived assuming Darcy's law for flow in a porous medium. A number of more exact solutions include the effects of fluid compressibility and the deformation of the grain skeleton (e.g. Yamamoto et al, 1978; Madsen, 1978). Darcy's law gives flow velocities in a porous medium as:

$$u = -ki_x, \quad v = -ki_y \tag{1}$$

An explanation for this anomaly may be found by comparing the fall velocity of the sediment particles with the velocity of the flow across the fluid/sediment interface. If Darcy flow applies, then the flow rate across the interface is given by equation (1). Prior to piping, the maximum possible flow velocity, V_s, out of a sand bed will therefore be approximately equal to the bed permeability, k, and of the order 0.25k for lightweight anthracite beds. This flow velocity is generally much smaller than the fall velocity of the sediment, w. For example, for a sand with $d_{50} \approx 0.2$mm, the permeability will be of order 10^{-4}m/s but the fall velocity is of order 10^{-2}m/s (van Rijn, 1989).

This difference of two orders of magnitude remains much the same for coarser sand. Consequently, once a sediment particle lifts out of its bed recess and the seepage force no longer acts, the fall velocity of the particle, w, will dominate over the vertical flow velocity V_s (figure 1). The effect of vertical seepage on a sediment particle rolling over the surface of the bed will therefore be minimal. The same argument applies in reverse in the case of downwards seepage and the fall velocity of the sediment particle again dominates the process. Note that the effect of boundary layer changes due to the seepage flow are not considered separately in this study. Consequently, the experimental results include both the effects of seepage and boundary layer changes together. Therefore, extrapolating the results from these flow conditions to radically different flow conditions or sediment sizes should be viewed with caution.

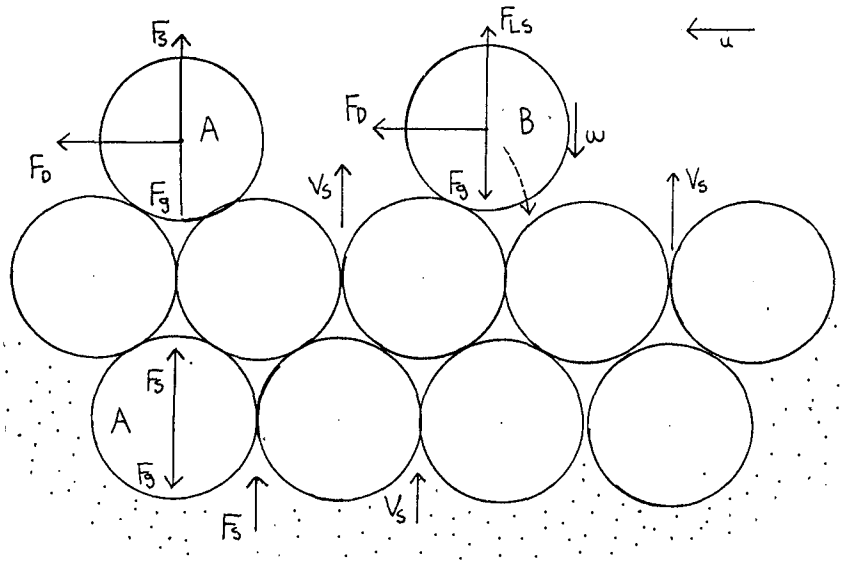

Figure 1. Forces and fluid velocities acting on particles on and just above a sediment bed at incipient fluidisation:
F_g - gravity force, F_s - seepage force, F_d - drag force, F_{LS} - lift force due to seepage velocity, u - free stream velocity, w - particle fall velocity, V_s - seepage velocity.
A: $F_s=F_g$, B: $F_g>>F_{LS}$, $w>>V_s$.

3) Experimental Method And Instrumentation.

The experiments were conducted in a 12m long combined wave-current flume in the Civil Engineering Department at Imperial College (figure 2). Waves can be absorbed at any position within the flume by a block of polyether foam and the reflection coefficient under these conditions was found to be less than 10%. In order to allow the thickness of the sediment bed to be varied whilst maintaining the same flow conditions in the flume, a raised bed was additionally installed. Vertical seepage was induced by means of a seepage box installed within the sediment bed, allowing a seepage flow over a length of 1m across the full width of the flume. The seepage box comprised a lower section 50mm deep, overlain by a baffle plate and 30mm of polyether foam. The foam was then covered with fine wire gauze to prevent the ingress of sediment. The seepage flow was induced through a pipe running under the raised bed. Upwards seepage was controlled through a tap and valve connected to a large constant head tank, while downwards seepage was induced by siphoning to a sump, the discharge in either case being proportional to the head across the sediment bed. During this phase of the investigation the depth of sediment above the box was kept constant at 70mm. For convenience, the origin of the horizontal co-ordinate in all figures is taken at the upstream end of the box.

Both the dynamic and steady pressure gradients were measured by a technique developed by Baldock and Holmes (1996). This uses probes connected to pressure transducers via semi-rigid flexible tubing to determine the pressure at any location quickly and easily, with minimal disturbance of either the fluid or sediment bed. When determining steady pressure gradients, the probe system requires no calibration and errors in the measurements are of order 5%. Baldock and Holmes (1996) also show the dynamic response of the probe system is good when measuring transient pressure gradients, with errors of order 10%-15%.

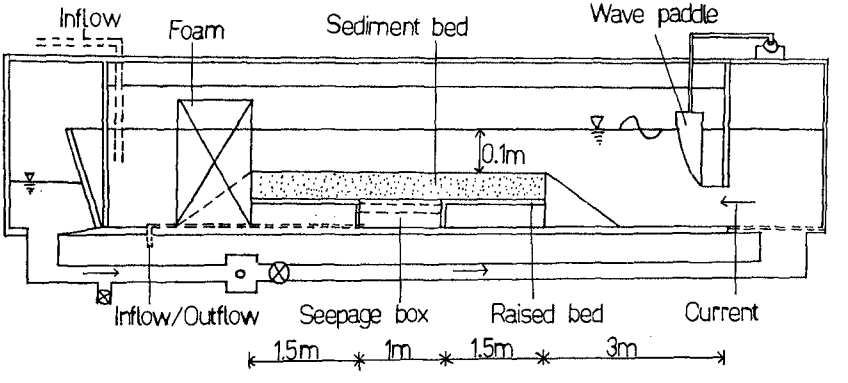

Figure 2. Wave and current flume.

where k is the coefficient of permeability, i_x and i_y are the dimensionless pressure gradients in the horizontal and vertical directions respectively, and u and v the corresponding flow velocities. Note that flow into the bed (suction) corresponds to a positive vertical pressure gradient. Fluidisation, or liquefaction, of the sediment bed occurs when the pressure gradient reduces the effective stress within the sediment to zero (e.g. Smith, 1968). For vertical seepage this occurs when the vertical pressure gradient exceeds the critical value i_{cy} given by:

$$i_{cy} = -(s-1)(1-n) \tag{2}$$

where s is the specific gravity of the sediment and n is the porosity, typically of order 0.4-0.6. For sand, this critical value is generally found to be approximately equal to 1, while for anthracite (s=1.4), the critical value is of order 0.2. The critical horizontal pressure gradient, i_{cx}, required for bed fluidisation is smaller than that needed with vertical seepage (Madsen, 1974):

$$i_{cx} = (s-1)(1-n)\ \tan\phi \tag{3}$$

where ϕ is the internal angle of friction. For typical values of ϕ of 35°, the critical horizontal pressure gradient is of order 0.5-0.6 for natural sand and 0.14 for anthracite. If both a vertical and horizontal pressure gradient act simultaneously, then failure of the bed material will occur earlier. In this instance the horizontal pressure gradient required for fluidisation of the bed will reduce to:

$$i_{cx} = (s-1)(1-n)\ \tan\phi\ (1-i_y/i_{cy}) \tag{4}$$

Hence, if a steady and critical vertical pressure exists ($i_y = i_{yc}$), then the sediment bed will be unable to resist any additional horizontal pressure gradients. Therefore, even the smallest degree of wave motion or turbulence will shear the sediment layers within the bed. If, however, the free fluid flow is steady (i.e. a current), there will be no significant additional horizontal pressure gradient and no horizontal shearing within the bed.

The stability of the interfacial particles is generally considered to be dominated by the drag force and is expressed in terms of the Shields parameter, θ. Considering flow conditions where the sediment bed is on the point of incipient fluidisation, then the particles within the bed are completely supported by the upwards seepage, although the interfacial particles might experience a smaller seepage force (e.g. Martin 1970). A modified Shields parameter could therefore be written in the form:

$$\theta' = \frac{\theta}{(1-i_y/i_{yc})} \tag{5}$$

As a result, the Shields parameter becomes large as the bed approaches fluidisation and we might expect the interfacial particles to become highly unstable. Indeed, Loveless (1994) suggests that the particles will be ejected into the flow. Incipient sediment motion should therefore occur at very much smaller flow velocities than normal, contrary to most of the previous experimental work discussed above

A series of preliminary measurements were made in order to determine the properties of the sediment bed and the flume set-up. The sediment bed was laid underwater and then repeatedly stirred in order to exclude as much air as possible, subsequently remaining submerged for the duration of each test. The bed permeability was measured in-situ at a number of locations with a falling head permeability test. The porosity of the bed material was also measured under conditions that approximated those within the flume. Sand ripple growth was promoted by introducing artificial disturbances. Ripple growth rates could therefore be measured under different seepage conditions. Both sand and lightweight anthracite particles were used in this study, the latter chosen to highlight seepage effects and aid visual and video observations. Table 1 shows the relevant sediment properties. Finally, as a check on the pressure measurement system and the method of laying the sediment bed, the pressures within a sand and anthracite bed were compared to the solution presented by Sleath (1970), with good agreement (figure 3).

Sediment	Specific gravity, s	d_{50} (mm)	Permeability, k (m/s)	Porosity, n
Sand	2.65	0.2	2×10^{-4}	0.6
Anthracite	1.4	3	1×10^{-2}	0.5

Table 1. Sediment properties.

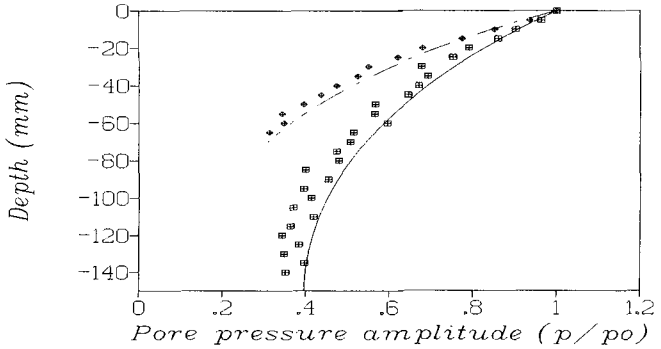

Figure 3. Pore pressure amplitude within a sediment bed under progressive waves. ■■■ Sand, T=0.7s, ——— Sleath (1970), ♦♦♦ anthracite, T=0.5s, — — Sleath (1970).

4) Experimental Results

Bed thickness

The influence of wave induced vertical pressure gradients was examined by comparing the conditions required for incipient motion of lightweight anthracite particles over a thin (10mm) and thick (150mm) sediment bed. Three different wave periods were selected and the tests were carried out by slowly increasing the wave height until incipient motion commenced. At incipient motion, the measured vertical pressure

gradients, i_y, just below the surface of the thick bed were about 0.08, approximately half those required for complete fluidisation of the anthracite, and negligible for the thin bed. Careful observation suggested that incipient motion of the anthracite particles commenced at the same wave height ($\theta \approx 0.06$), regardless of the bed thickness. Vertical wave induced pressure gradients therefore appear to have no significant effect on incipient sediment motion, and are also unlikely to effect sediment transport rates, at least prior to sheet flow conditions. This is consistent with the discussion in section 2, since at the time of maximum and minimum bed-stability wave induced horizontal pressure gradients are zero.

The effects of a steady vertical seepage across the fluid/sediment interface were examined under conditions of both suction and injection using the seepage box arrangement (figure 2). For the fine sand, a vertical pressure gradient, i_y, of 0.6 was used in both instances. The effective stress within the bed was therefore reduced to close to zero during injection and nearly doubled under suction. The vertical pressure gradients were reduced to 0.2 for the anthracite bed, approximating the same effective stress conditions within the bed. In each case the experimental conditions remained identical except for the seepage across the sediment/fluid interface.

With a steady seepage across the sediment bed, a current was introduced within the flume and then slowly increased until the threshold of sediment motion was reached. For both the sand and anthracite beds, incipient sediment motion started at Shields numbers of about 0.045, irrespective of the seepage direction. These results are again in agreement with the argument set out in section 2 and consistent with a number of previous studies (e.g. Martin, 1970; Willets and Drossos 1975; Kruijt 1976). However, in order to examine the effects of the seepage flow in more detail, a closer examination of the bed material during piping was carried out using the larger anthracite particles.

Initially, in the absence of a current, the seepage flow was slowly increased until piping first occurred over a small region of the bed. Under these conditions, sediment particles were not ejected into the body of the fluid but appeared very unstable within their bed recesses. In fact, close inspection suggested that the particles within the piped area appeared to vibrate. This is entirely consistent with transient nature of the seepage force as particles start to lift out of their bed recesses and then re-settle under their own weight. Furthermore, on the re-introduction of the steady current, incipient motion of the particles within the piped area occurred at the same flow velocity as previously and at the same time as incipient motion commenced at adjacent areas of the bed that were not piped. This therefore shows that as soon as a particle moves out of its bed recess, the gravity force completely dominates the lift force due to the small seepage velocity out of the bed. Consequently, steady seepage has very little effect on the stability of the interfacial particles.

Wave motion

Under wave motion, the sediment bed is subject to both vertical and horizontal pressure gradients, the latter being independent of the bed thickness. The effects of an additional steady seepage on the net sediment transport rate were now examined, initially using anthracite particles. Waves with a height of 38mm and wave period of 1s were selected for use in these and all subsequent tests, corresponding to a Shields number of about 0.12 and giving maximum measured horizontal pressure gradients, i_x, of 0.14, very

close to the conditions required for local fluidisation of the bed. Net sediment transport rates were inferred from bed level changes.

Figure 4a compares the bed level changes found without seepage with those obtained during injection. With no seepage, the net sediment transport was positive due to the shallow water wave conditions but tended to accumulate at the anti-nodes of the weak standing wave system within the flume, i.e. where the wave induced horizontal velocity was a minimum. The results obtained during injection show a significant change, with erosion occurring over the weakest area of the bed ($0<x<50$cm) and further upstream. The steady vertical seepage was found to have an effect at pressure gradients, i_y, as low as 0.05 and the net positive sediment transport rate increased fourfold when the bed was on the point of fluidisation (i_y=-0.2, figure 4c).

Close inspection of the bed using video analysis showed that the seepage had a clear effect on the sediment transport mechanism. The sediment within the bed tended to lift during the passage of a wave trough and the upper layers of the bed were then sheared by the horizontal pressure gradient and positive horizontal velocity induced by the approaching wave crest. Sediment was therefore transported in the direction of wave motion. The flow into the bed under the crest subsequently reduced the effect of the upwards seepage, stabilising the bed. However, although the wave induced horizontal pressure gradients were symmetric about the wave crest, a similar mechanism was not observed following the passage of a wave crest. This appears to confirm the results of Takahashi et al (1994), who suggested that the phase difference between the bed motion and wave motion is less than 180°.

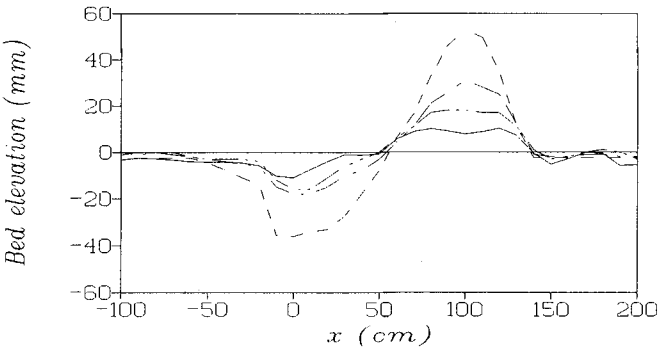

Figure 4a. Evolution of an anthracite bed under wave motion with steady vertical seepage (injection).
——— i_y=0, — — — i_y=-0.2, ——— — — i_y=-0.1, ——— — — ——— i_y=-0.05.

The behaviour of the sediment within a locally piped region was again closely observed. This also showed that even under wave motion the interfacial particles were largely unaffected by the seepage flow, with no relative movement between these particles and those within the bed. However, the sediment bed within the piped area behaved largely as a fluid, oscillating to a considerable depth under the smallest wave induced pressure gradients. Note that the piped bed had zero effective strength and, consequently, was unable to sustain a slope, leading to negligible net sediment transport.

The experiment was then repeated with suction applied across the fluid/sediment interface. In this instance the steady pressure gradients were in the range i_y=0-0.15, approximately doubling the effective strength of the bed. Suction was found to increase the stability of the sediment bed and consequently the shearing of the upper layers of the bed was prevented. The net positive sediment transport rate was therefore reduced (figures 4b&c). It is, however, very important to note that this reduction in the transport rate was not a result of an increase in the stability of the interfacial particles. The transport rate of these particles did not appear significantly affected by the applied suction, even when i_y=0.15. This is consistent with the data obtained previously under steady flows. In these instances the reduction in the transport rate compared to the case without seepage predominantly arose due to the reduced shearing of the upper layers of the sediment bed.

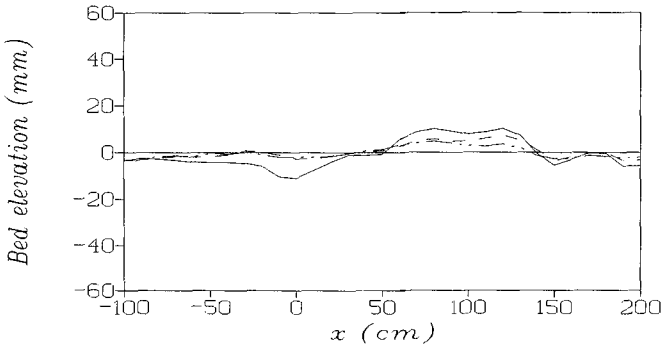

Figure 4b. Evolution of an anthracite bed under wave motion with steady vertical seepage (suction). ———— i_y=0, — — — i_y=0.1, —— — —— i_y=0.15.

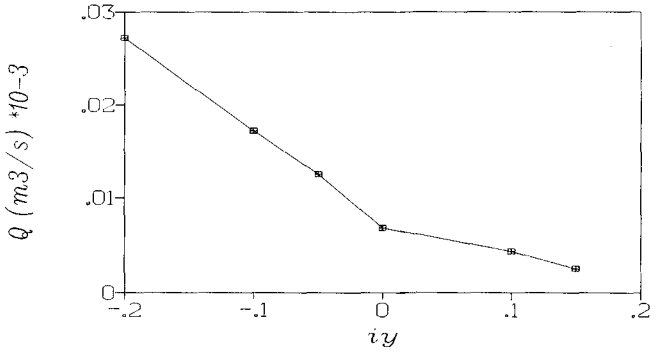

Figure 4c. Variations in the net positive sediment transport rate for anthracite under wave motion with steady vertical seepage.

Sand ripple dynamics

Seepage across the fluid/sediment interface was also found to have a significant effect on the formation and growth of sand ripples. For example, figure 5 shows the evolution of a fine sand bed after five hours of wave action. With no seepage, bed level

changes occurred due to the gradual formation of ripples, leading to suspended sediment transport and eventually the generation of larger scale features. Little change was observed when repeating the experiment with an upwards seepage flow (injection); however a considerable difference arose when suction was applied. In this instance, the sand bed over the seepage area (0<x<100cm) remained plane during five hours of wave action, with no ripple formation occurring, despite ripple formation either side of this region. It has been drawn to the authors' attention that Sakai and Gotoh (1996) found that the bed configuration and ripple regime could be changed by an oscillating pressure gradient across the bed.

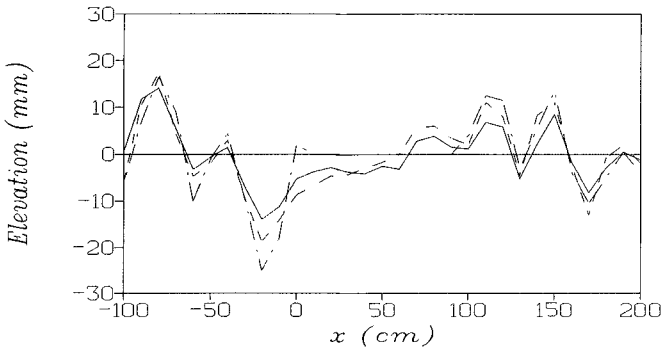

Figure 5. Evolution of sand bed after five hours of wave motion with steady seepage. ———— i_y=0, — — — i_y=-0.6 (injection), —— — —— i_y=0.6 (suction).

The growth rate of sand ripples on the fine sand bed with additional suction and injection was therefore compared to that over an adjacent region of the bed without seepage. Two discontinuities were introduced to promote ripple growth at specific positions on the bed. The first was at x=50cm, in the centre of the seepage area. The second, which acted as a control, was positioned at x=150cm, downstream from the seepage area.

Each discontinuity consisted of a hollow approximately 5mm wide and 1-2mm deep across the full width of the flume, formed by pushing a perspex wedge a fixed distance into the bed. After the onset of fluid motion, ripples started to grow from these discontinuities, spreading in both directions under wave motion and downstream in the presence of a steady current. The ripples could initially be classified as rolling grain ripples but subsequently grew to form vortex ripples. The effect of the seepage was then investigated by comparing the ripple growth rates at the two positions (the ripple growth rate at the two positions was the same when there was no seepage flow).

During injection, the upwards seepage started to have a significant effect at pressure gradients, i_y, as low as -0.2, with the ripple growth rate increasing nearly threefold as the bed approached conditions of local piping, i_y=-0.6, figure 6a. Close inspection of the bed showed that the ripple growth rate increased due to the increased instability of the bed surface as a whole, with small ridges of sediment forming across the flume. Indeed, at very high pressure gradients, the bed tended to ripple spontaneously all over the seepage area and not just at the position of the initial discontinuity. This is

consistent with the analysis outlined in section 2 and was due to the local shearing of the surface layers of the sediment bed by the additional wave induced pressure gradients. This shearing of the bed caused small distortions in the bed surface, prompting the formation of sand ripples.

In contrast, suction prevented the formation of ripples and took effect at steady pressure gradients as low as i_y=0.05 (figure 6b). Furthermore, at gradients in excess of 0.1, ripples did not grow at all, which confirmed the results obtained previously (figure 5). It is, however, important to note that the suction did not prevent the motion of the interfacial particles, the motion of which was similar at both the control section and over the seepage area. Seepage effects on ripple formation under steady flows appeared minimal, again due to the lack of additional wave induced pressure gradients and hence minimal shearing and deformation of the bed surface (figures 7a&b)..

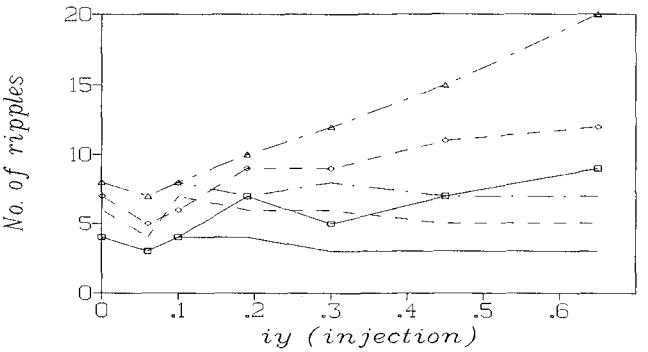

Figure 6a. Ripple growth rates under wave motion during injection.
———— control (t=5mins), ——■—— t=5mins, — — — control (t=10mins),
— ▾ — t=10mins, —— — —— control (t=15mins), —— —▲— —— t=15mins.

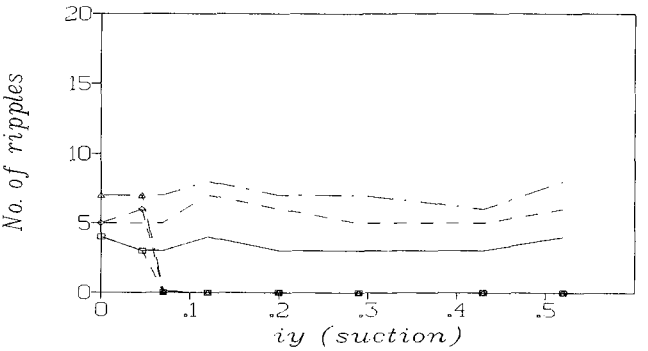

Figure 6b. Ripple growth rates under wave motion during suction.
———— control (t=5mins), ——■—— t=5mins, — — — control (t=10mins),
— ▾ — t=10mins, —— — —— control (t=15mins), —— —▲— —— t=15mins.

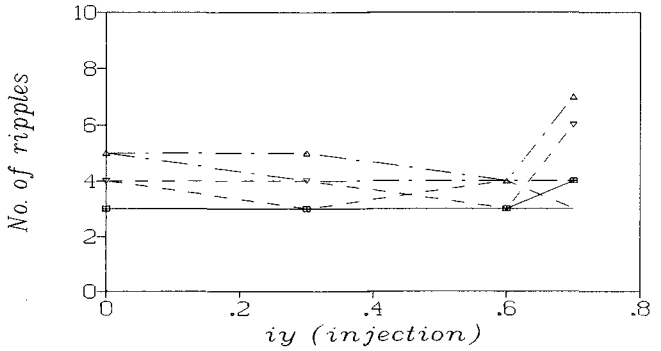

Figure 7a. Ripple growth rates under steady flow during injection.
———— control (t=5mins), ——■—— t=5mins, — — — control (t=10mins),
— ▾ — t=10mins, —— — — —— control (t=15mins), —— —▲— —— t=15mins.

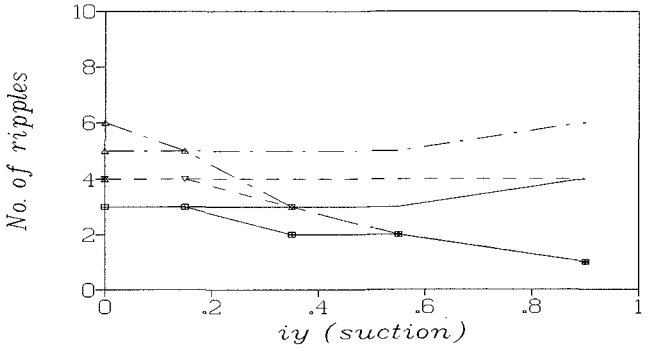

Figure 7b. Ripple growth rates under steady flow during suction.
———— control (t=5mins), ——■—— t=5mins, — — — control (t=10mins),
— ▾ — t=10mins, —— — — —— control (t=15mins), —— —▲— —— t=15mins.

The effect of suction on existing ripples (relic bedforms) was also examined. If the ripples were initially very small (i.e. rolling grain ripples) then they were slowly washed out by the wave motion and the bed tended to return to the initial plane state. If, however, the ratio of the ripple height to wavelength exceeded a value of about 0.1, then the ripples were not washed out, but neither did they continue to grow. These effects will, however, be dependent on the relative magnitude of the applied suction, the sediment grain size and the wave induced orbital velocity. Nevertheless, the results suggest that both the watertable level and/or the presence of a beach drain could influence the formation and growth of ripples within the nearshore region. This might then affect the quantity of both the bed load transport and the amount of sediment put into suspension.

6) Conclusions

On a plane sediment bed, vertical wave induced pressure gradients, i_y, were found to have no direct effect on the conditions required for incipient sediment motion. Steady vertical seepage across the sediment/fluid interface was also found to have no discernible effect on the threshold of motion of the sediment particles in the presence of a current, even when the sediment bed was locally fluidised. In contrast, steady vertical seepage in combination with wave motion had a significant effect on net sediment transport rates. Injection was found to promote erosion of the sediment, through shearing of the upper layers of the weakened bed by the additional wave induced horizontal pressure gradients. Conversely, suction stabilised the bed material, reducing wave induced shearing and reducing the net transport rate.

At low Shields numbers, seepage flow across the sediment/fluid interface appears to have very little effect on the threshold of motion or sediment transport rates. This is because the seepage force no longer acts on sediment particles rolling or saltating over the bed. Consequently, the vertical forces on moving sediment particles are little changed in the presence of a seepage flow. However, although sheet flow conditions could not be modelled in this study, the results do suggest that injection will enhance sediment transport by sheet flow, while suction will tend to reduce the occurrence of sheet flow conditions (neglecting boundary layer changes). In this instance, the sheet flow layer may act as a fluid/sediment matrix, within which a seepage force can exist. Seepage will therefore alter the effective weight of the sheet flow layer, enhancing or reducing mobility. In practical circumstances, such as in the swash zone, the experimental results therefore appear consistent with the suggestion that the sediment transport rate will differ over saturated and unsaturated beach faces. Further work is therefore required to identify if a modified Shields parameter will describe sediment transport rates under these conditions.

Vertical seepage greatly influenced the formation and growth rate of ripples on a sand bed at pressure gradients typically induced within beaches due to changes in watertable levels, infiltration/exfiltration and beach drainage. Therefore, since both bed load and suspended load sediment transport are influenced by the ripple regime, the effects of seepage on ripple dynamics may have important implications for net sediment transport rates in the nearshore. This, however, requires further work and should isolate the effects of turbulence and boundary layer changes (e.g. Turcotte, 1960).

Acknowledgements

The authors gratefully acknowledge the support of the UK Engineering and Physical Sciences Research Council.

References

Baldock, T.E. & Holmes, P.H., 1996. Pressure gradients within sediment beds. Proc. 25th ICCE, Orlando. ASCE, 4, 4161-4173..

Conley, D.C. & Inman, D.L. 1992. Field observations of the fluid granular boundary layer under near breaking waves. J. Geo. Res., 97 (C6), 9631-9643.

Emery, K. O. and Foster, J. F., 1948. Water tables in marine beaches. J. Marine Res., 7, 644-654.

Kruijt, J.A., 1976. On the influence of seepage on incipient motion and sand transport. Report no. STF60 A76046, Tech. Univ. Norway, Trondheim, 21p.
Loveless, J.H., 1994. Modelling toe scour at coastal structures. Proc. 2nd Int. Conf. on Hydraulic Modelling, Stratford, UK. BHR Group, 479-489.
Madsen, O.S., 1974. Stability of a sand bed under breaking waves. Proc. 14th ICCE, Copenhagen. ASCE, 2, 776-794.
Madsen, O.S., 1978. Wave induced pore pressures and effective stresses in a porous bed. Geotechnique, 28, (4), 377-393.
Martin, C.S., 1970. Effect of a porous sand bed on incipient sediment motion. Water Resources Research, 6, (4), 1162-1174
Nielsen, P., 1992. Coastal bottom boundary layers and sediment transport. World Scientific.
Oh, T. & Dean, R.G., 1994. Effects of controlled water table on beach profile dynamics. Proc. 24th ICCE, Kobe. ASCE, 3, 2449-2459.
Oldenziel, D. M. & Brink, W.E., 1974. Influence of suction and blowing on entrainment of sand particles. J. Hydraulics Div., ASCE, 100, 935-949.
Packwood, A.R. & Peregrine, D.H., 1980. The propagation of solitary waves and bores over a porous bed. Coastal Engineering, 3, 221-242.
Putnam, J.A., 1949. Loss of wave energy due to percolation in a permeable sea bottom. Transactions, AGU, 30, (3).
Rao, A.R., Subrahmanyam, V., Thayumanavan, S. & Namboodiripad, D., 1994. Seepage effects on sand bed channels. J. Irrigation and Drainage Engineering, ASCE, 120, 60-79.
Sakai, T and Gotoh, H, 1996. Effect of ave induced pressure on seabed configuration. Proc. 25th ICCE, Orlando, ASCE, 3, 3155-3168.
Sleath, J.F.A., 1970. Wave induced pressures in beds of sand. J. Hydraulics. Div., ASCE, 96, 367-378.
Sleath, J.F.A., 1984. Sea Bed Mechanics. Wiley Interscience.
Smith, G.N., 1968. Elements of Soil Mechanics. BSP Professional Books, London.
Takahashi, S., Yamamoto, S. & Miura, H., 1994. Fundamental characteristics of a new ave absorbing system using sand liquefaction. Proc. 24th ICCE, Kobe. ASCE, 3, 2698-2711.
Turcotte, D.L., 1960. A sub-layer theory for fluid injection into incompressible turbulent boundary layer. J. Aerosp. Sci. 27, (9), 675-678.
Turner, I.L. 1995. Simulating the influence of groundwater seepage on sediment transported by the sweep of the swash zone across micro-tidal beaches. Marine Geology, 125, 153-174.
van Rijn, L.C., 1989. Sediment transport by waves and currents. Report H461. Delft Hydraulics.
Waddell, E., 1976. Swash-groundwater beach profile interactions. In Beach and nearshore sedimentation, Davis, R A. and Etherington, R. L. (eds.), Soc. Econ. and Paleontological Mineralogists, SP 24, 115-125.
Watters, G.Z. & Rao, M., 1971. Hydrodynamic effects of seepage on bed particles. J. Hyd. Div., ASCE, 101, 421-439.
Willets, B.B. & Drossos, M.E., 1975. Local erosion caused by rapid infiltration. J. Hyd. Div., ASCE, 101, 1477-1488.
Yamamoto, T., 1978. Sea bed instability from waves. Proc. 10th OTC Conf., Houston. ASCE, Paper 3262.
Yamamoto, T., Koning, H.L., Sellmeijer, H. & van Hijum, E., 1978. On the response of a poro-elastic bed to water waves. J. Fluid Mech., 87, 193-206.

The Settlement, Hardness and Liquefaction of Sand Beds due to Fluctuating Water Pressure

Takaaki Minamimura[1], Masaki Niiyama[2], Takao Akutu[3],
Kenji Yano[4], Toshihiko Yamashita[2]

1. Abstract

The degree of sand beds compaction affects the accumulation and erosion of shorelines, and the popuration of creatures which live in sandy beach.The properties of the settlement, hardness and liquefaction of sand beds due to fluctuating water pressure were experimentally studied.The settlement of a sand bed was accelerated by liquefaction .The thickness of liquefaction layer which is estimated from the measured values of excess pore water pressure agreed well with one from the measured values of the rate of settlement.The hardness of sand bed was determined only by void ratio independent of liquefaction or non-liquefaction beds.

2. Introduction

Sand beds are repeatedly densified and sparsified due to wave action, and loose sand beds gradually settle and become compacted. Kraus et al.(1994) experimentally showed that the erosion of compacted sand on shorelines due to waves is less than that of loose sand, and Nishi et al. reported from the results of their field study that the degree of sand compaction affects the accumulation and erosion of sandhills and shorelines. Field studies have also been conducted on the effects of the degree of sand compaction on aquatic animals; Hodgin et al.(1992) showed that the degree of sand compaction affects the life of turtles, and Akutu et al.(1996) showed that, as it is difficult for bivalves to burrow into hard sand, the population of burrowing bivalves in compacted sand beds is less than that in loose sand beds.Although clarification of wave-induced settlement and compaction of sand beds is important from both engineering and biological points of view, there have been very few systematic studies of these

[1] Obayashi Corporation,3, 2-chome, Kanda Tsukasa-cho Chiyoda-ku,Tokyo 101-8533,Japan.
[2] Laboratory of Coastal and Offshore Engineering, Division of Environment and Resources Engineering, Hokkaido University, N-13 W-8,Kita-ku, Sapporo 060-8625, JAPAN
(Fax:+81-11-726-2296, E-mail: y-toshi@eng.hokudai.ac.jp)
[3] Hokkaido Development Bureau,N-8 W2,Kita-ku, Sapporo 060-8511,JAPAN
[4] Depertment of Marine science and Technology, Hokkaido Tokai University, 5-1,Minaminosawa,Mimami-ku,Sapporo 005,JAPAN

phenomena. On the other hand, it is known that the amount of settlement is greater if liquefaction of the sand bed occurs due to wave action(Zen et al,1987).

In this study, the characteristics of settlement, hardness and liquefaction of a sand bed due to fluctuating water pressure were experimentally investigated, and the interrelationships between settlement, hardness and liquefaction were quantitatively determined.

3. Experiments

Experiments were carried out using a fluctuating pressure-type liquefaction test apparatus (Fig. 1). A two-meter-high acrylic cylinder was made by joining together cylindrical rings of 40cm in diameter and 10, 20 and 40cm in height. The sand bed was a loose sand layer with a void ratio of 0.85 and a sand particle diameter of 0.15mm. Sand beds of four thicknesses were used in the experiments: L=0.7m, L=1.2m, L=1.5m, and L=1.8m. A sand container filled with water was set at a higher location than that of the experimental cylinder, and, using a hose, the cylinder was filled with water and sand by suction force generated due to the head gap between the container and the cylinder. The amount of air in a sand bed affects the properties of the sand bed, however, sand beds with same property containing very little air can be made by using this method. Table1 shows experimental conditions. In all cases, the period and average pressure of fluctuating water pressure were 5 sec and 10m, respectively. All experiments were first conducted at total head H=1.2m under conditions in which liquefaction does not occur, in order to determine the properties of a sand bed . For the theoretical analysis of pore water pressure, we used the theory of Zen et al.(1987). Underwater pressure and pore water pressure in the sand bed were measured at 11 points (see Fig. 1) and at sampling intervals of 0.01 sec, and the amount of settlement was determined by measuring the position of colored sand

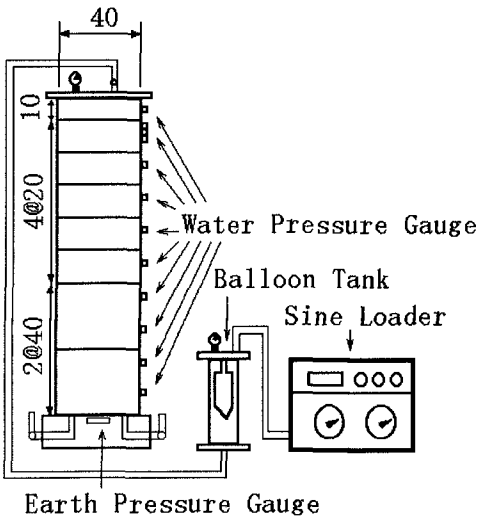

Fig 1. Experimental Device

Table 1. Experimental Conditions

Case	Sand bed thickness L(m)	Total head H(m)	Coefficient of transmission α	Coefficient of consolidation C(cm²/s)
1	0.7	1.2	1.15	0.35
2	0.7	6	1.15	0.35
3	1.2	1.2	1.15	0.35
4	1.2	6	1.15	0.35
5	1.2	1.2	1.2	0.35
6	1.2	6	1.2	0.35
7	1.5	1.2	1.15	0.35
8	1.5	4	1.15	0.35
9	1.5	6	1.15	0.35
10	1.5	1.2	1.25	0.35
11	1.5	6	1.25	0.35
12	1.8	1.2	1.3	0.35
13	1.8	6	1.3	0.35

(maker) at depth intervals of 10cm or 20cm. The surface hardness of the sand bed was determined by measurement of the depth penetration of a cone penetrometer (weighing 800g) that was dropped from the surface of the sand bed. The above three measurements were repeated 6 times under conditions of fluctuating water pressure of 3,000 waves.

4. Experimental Results and Discussion

4.1 Fluctuating pore water pressure

Fig.2(a) and (b) show the distributions of depth direction of phase delay $\Delta T/T$(= time difference between surface water pressure peak and pore water pressure peak ／ period) and the ratio of amplitude of pore water pressure to surface water pressure Pm/Po . Z is positive in a downward direction with the sand-bed surface as the origin. The theoretical values calculated according to the method of Zen et al. (1987) are shown in figures. In the case of the same period, the theoretical values are not affected by the amplitude of fluctuating pore water pressure. The parameters used for the theoretical calculation are the coefficient of transmission (α) and the coefficient of consolidation (C). The values of α =1.25 and C=0.35 were used for the theoretical calculation to coincide with the experimental results of pore water pressure under conditions in which liquefaction does not occur. The figure shows that the deeper the location of the pore water pressure gauge is, the smaller is the ratio of amplitude of pore water pressure to surface water pressure and the larger is the phase delay. Thus, the surface water pressure is transmitted throughout the sand bed accompanying attenuation and phase delay. Under conditions in which liquefaction of the sand bed does not occur (H=1.2m), the tendencies of the experimental values (i.e., decrease in Pm/Po and increase in $\Delta T/T$ with increases in Z) agreed well with the theory of Zen et al. On the other hand, under conditions in which liquefaction of the sand bed occur (H=6.0m), the decrease in Pm/Po and increase in $\Delta T/T$ with increases in Z were smaller than those of the theoretical values of Zen et al. This is thought to be due to the improvement in transmission properties of pore water pressure caused

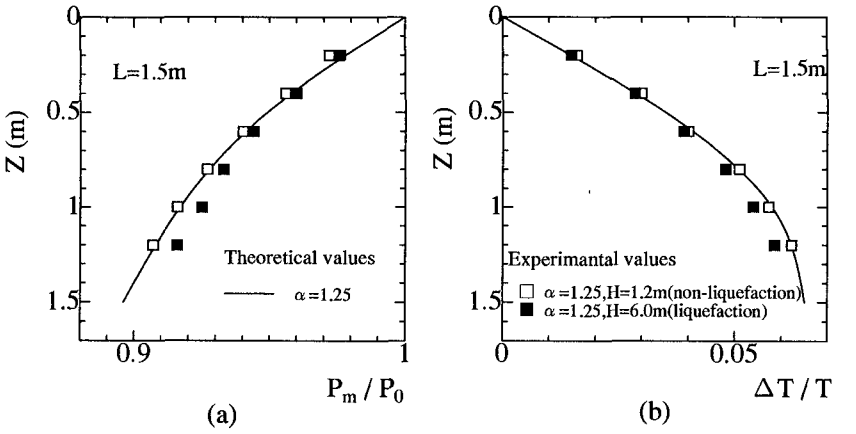

Fig 2. The ratio of ampulitude of pore water pressure to surface water pressure and the phase delay

by liquefaction.

In order to see the effect of thickness of the sand bed on transmission properties of pore water pressure, Fig. 3(a) and (b) show the distributions of depth direction of the ratio of amplitude of pore water pressure to surface water pressure and phase delay for each thickness of the sand bed under conditions in which liquefaction does not occur. The depth distribution of Pm/Po in Fig. 3(a) shows that the ratio of amplitude of pore water pressure to surface water pressure decreases with increases in the sand bed depth and sand bed thickness, which agrees with the properties of the theoretical values of Zen et al. In Fig. 3(b), the phase delay Δ T/T increases with increases in the sand bed depth and sand bed thickness, which also agrees with the properties of the theoretical values of Zen et al. In other words, the larger the sand bed thickness is, the greater is the effect on the transmission properties of pore water pressure.

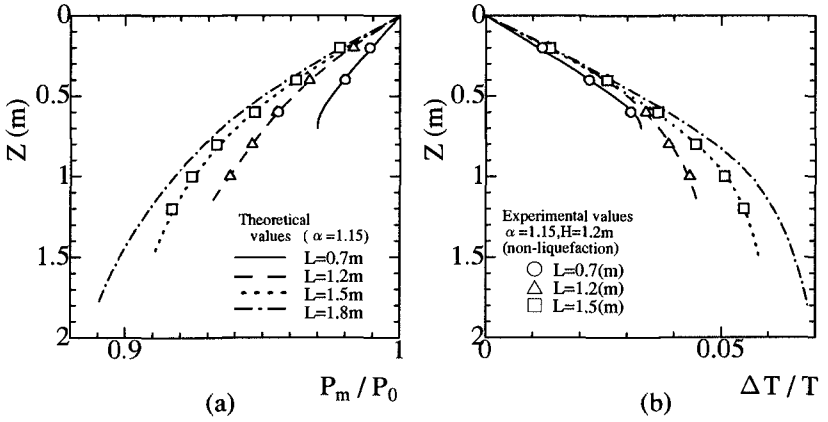

Fig 3. The ratio of ampulitude of pore water pressure to surface water pressure and the phase delay

4.2 Distribution of excess pore water pressure

Fig. 4(a) and (b) show examples of the distribution of excess pore water pressure Pe obtained by measurement and by the theoretical calculation of Zen et al. (solid line) in the case of a total head of 6.0 m. The phase where the fluctuating water pressure changes from negative to positive was made zero. The distributions of earth pressure (σ) are also shown in the figures. L=1.5m in both figures. In Fig.4(a), $\alpha = 1.15$ and the excess pore water pressure is smaller than the earth pressure, which are conditions under which liquefaction of the sand bed does not occur. Under these conditions, the measured values and theoretical values are very similar in all phases. It was found that in the phases $180^\circ \sim 270^\circ$, in which surface water pressure decreases from zero, positive excess pore water pressure increases, while in the phases $0^\circ \sim 90^\circ$, in which surface water pressure increases from zero, negative excess pore pressure increases. Maximum excess pore water pressure occurs at phase 225°. Also, excess pore water pressure increases with depth.

A comparison of the earth pressure and excess pore water pressure in Fig. 4(b) shows that the excess pore water pressure is greater than the earth pressure in the phases $180^\circ \sim 270^\circ$, which is the condition under which liquefaction of the sand bed occurs. In phases $0^\circ \sim$

90° , in which the measured values are very similar to the theoretical values, the density of the sand bed is higher due to the large negative excess pore water pressure. However, in the phases in which liquefaction occurs (225° and 270°), the measured values are smaller than the theoretical values. This is thought to be due to the improvement in transmission properties of pore water pressure caused by liquefaction. As can be seen in the figure, under this condition, liquefaction occurs down to a depth of 40cm at phases 225° and 270° .

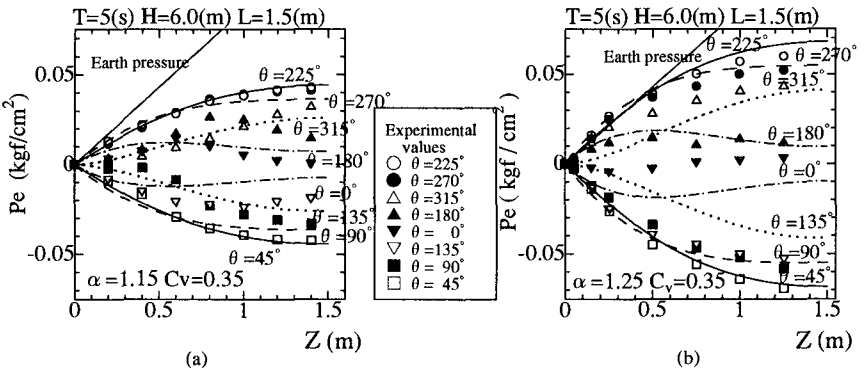

Fig 4. The distribution of depth direction of excess pore water pressure

4.3 Settlement properties

Fig.5 show the experimental results of amount of settlement Δ L at each depth of the sand bed in the case of fluctuating water pressure of 3,000 waves. Arrows in the figure show the depth of liquefaction obtained from experimental values of excess pore water pressure. Under conditions in which liquefaction of the sand bed does not occur (unshaded portion), the amount of settlement on the surface layer of the sand bed increases with increases in thickness of the sand bed, but the average rate of settlement Δ L/L (amount of settlement / thickness of sand bed) does not change regardless of the thickness of the sand bed. The similar degrees of settlement in every layer were thought to be due the good transmission of pressure throughout the sand bed because of the small value of α (1.15) and the fact that the ratio of amplitude of pore water pressure to surface water pressure was over 0.9 in every layer, as can be seen in Fig. 3. More detailed examination of the distribution of depth direction of the ratio of settlement Δ 1/1 (amount of settlement

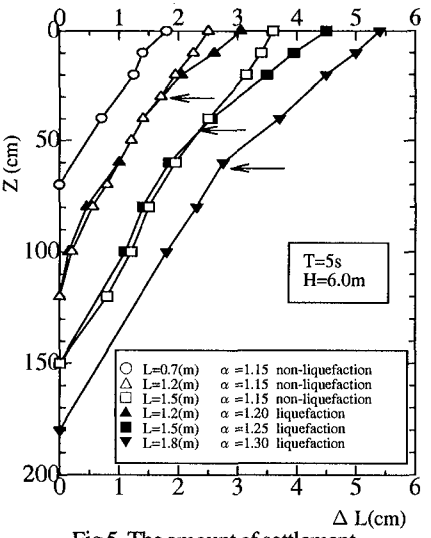

Fig 5. The amount of settlement

of each layer / thickness of each layer) shows that Z ≧ 40cm in the case of L=1.2m and Z ≧ 70cm in the case of L=1.5m, the ratio of settlement decreases slightly. These regions agree with the regions in which phase delay (Fig. 3) and an increase in excess pore pressure (for example, θ =225°) to depth direction (Fig. 4) become smaller. Next, a comparison of a liquefying sand bed (black-colored symbols) with a non-liquefying sand bed shows that the rate of settlement in the liquefying region of the sand bed (above the arrows) is about two-times greater than that in the non-liquefying region of the sand bed. This result suggests that the settlement of a sand bed is accelerated by liquefaction. The region with a higher rate of settlement coincides well with the the liquefying region calculated from excess pore pressure, indicating that the liquefying region can also be estimated from the distribution of depth direction of the rate of settlement. Moreover, in the non-liquefying region (under the arrows), the rates of settlement are very similar in both sand beds. This is thought to be because liquefaction of the surface of the sand bed at a thickness such as that in Fig. 2 or Fig. 4 has little effect on the transmission of pore water pressure to deeper layers.

Fig. 6 shows changes in the wave number N of the average rate of settlement in each thickness of sand bed in the case of a liquefying sand bed and non-liquefying sand bed. In the case of a liquefying sand bed, the average rate of settlement is that only in the liquefying region. As can be seen in the figure, in our experimental range of up to 1.8m in sand bed thickness, the average rate of settlement is not affected by the thickness of the sand bed in either the liquefying or non-liquefying sand bed,but the average rate of settlement in the liquefying sand bed is two-times greater than that in the non-liquefying sand bed. Also, the increase in the average rate of settlement in the liquefying sand bed is greater than that in the non-liquefying sand bed until about 100 waves; thus,settlement is accelerated by liquefaction of the sand bed, and the increase in the settlement rate later becomes smaller.

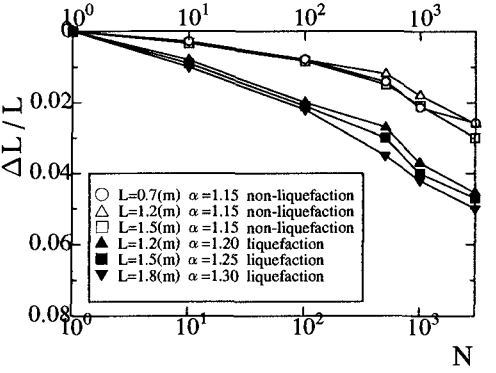

Fig 6. Changes in the wave number of the average rate of settlement

Fig. 7 shows the relationship between the average rate of settlement and the total head of fluctuating pressure of 1,000 waves for each sand bed thickness.As can be seen in this figure, in our experimental range of up to 1.8m in sand bed thickness, the average rate of settlement is almost the

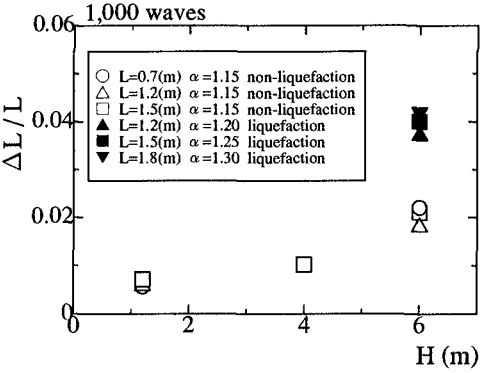

Fig 7. Relationship between the average rate of settlement and the total head

same in every thickness of sand bed that has the same total head regardless of whether the sand bed is liquefying or non-liquefying, indicating that the average rate of settlement is not affected by the thickness of the sand bed. In the non-liquefying sand bed, the average rate of settlement is almost proportional to H. Also, as stated before, the average rate of settlement in the liquefying region is two-times greater than that in the non-liquefying sand bed.

4.4 Effect of settlement on transmission properties of pore water pressure

In order to see the effect of settlement on the transmission properties of pore water pressure, examples of change in the wave number of the ratio of amplitude of pore water pressure to surface water pressure and phase delay are shown in Fig. 8(a) and (b). These examples are for the case in which liquefaction occurs in the sand bed and the surface layer of the sand bed has sunk by 4.5cm. The ratio of amplitude of pore water pressuire to surface water pressure and the phase delay remain almost constant regardless of the wave number, indicating that settlement has very little effect on the transmission properties of pore water pressure. This agrees with the results reported by Zen et al. (1987) and Yamashita et al. (1996).

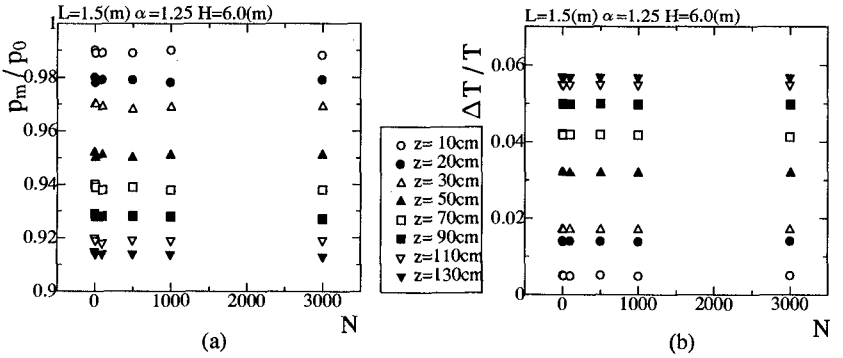

Fig 8. The change in the wave number of ratio of amplitude of pore water pressure tourface water pressure and phase delay

4.5 Liquefaction region

Fig. 9 shows the liquefaction depth obtained from measured values and theoretical values of excess pore pressure (see Fig. 4) and the depth of liquefaction obtained from the amount of settlement of the sand bed (see Fig. 5). In the case of α =1.15, liquefaction of a sand bed theoretically does not occur if the thickness of the sand bed is less than 1.8m. In this figure, it is quantitatively shown that the larger the thickness of the sand bed and the value of α are, the larger is the liquefaction depth obtained by theoretical values of excess pore water pressure. The liquefaction depths obtained by measured values of excess pore pressure and by the

amount of settlement are almost the same. The measured values and theoretical values of excess pore water pressure and the amount of settlement are very similar when the liquefaction depth is small, but when the liquefaction depth is large, (for example, the line and ▼ of L=1.8 in the figure), the measured values become smaller than theoretical values. This tendency for the measured values to be smaller than the theoretical values becomes larger as the liquefaction depth increases. This is thought to due to the improvement in transmission properties of pore water pressure as the liquefaction depth increases (and the phase of liquefaction becomes longer).

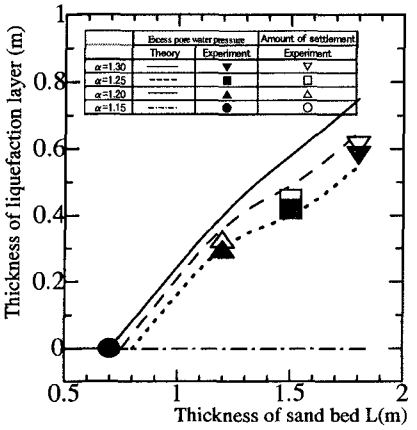

Fig 9. The liquefaction region

4.6 Hardness of the sand bed

Fig. 10 shows the relationship between void ratio e of the surface layer of the sand bed and the penetration depth Dp measured by a cone penetrometer in the case of a liquefying sand bed and non-liquefying sand bed. The void ratio e is obtained from the rate of settlement of the surface layer. As can be seen in the figure, the penetration depth is determined only by the void ratio e , and there is almost no difference in penetration depth of the liquefying and non-liquefying sand bed. In other words, it has been quantitatively shown that the penetration depth becomes smaller and the sand bed becomes harder with settlement of the sand bed.

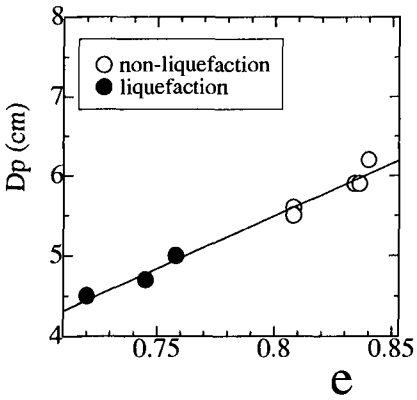

Fig 10. The hardness of sand bed

5. Conclusions

The following is a summary of the results obtained in this study:

① The values of pore water pressure in the sand bed subjected to fluctuating water pressure under conditions in which liquefaction does not occur agreed well with the theoretical values of Zen et al.(1987).

② Under conditions in which liquefaction occurs, in the phases in which the density of the sand bed is high (0° ~90°), the negative values of excess pore water pressure were similar to the

theoretical values of Zen et al. (1987), but in the phases in which liquefaction occurs (225° and 270°), the measured values of excess pore water pressure were smaller than the estimated values.

③ The rate of settlement in the liquefying region was about two-times greater than that in the non-liquefying region, indicating that settlement of a sand bed is accelerated by liquefaction.

④ In our experimental range of up to 1.8m in total thickness of the sand bed, the average rate of settlement was almost proportional to the total head of fluctuating water pressure in all thicknesses of the sand bed.

⑤ Settlement had very little effect on the transmission properties of pore water pressure.

⑥ It was quantitatively shown that the larger the thickness of sand bed and the value of α are, the larger is the liquefaction depth obtained by theoretical values of excess pore water pressure.

⑦ Liquefaction depths obtained from measured values of excess pore water pressure and from the amount of settlement were very similar.

⑧ In the case where the liquefaction region is small, the measured values of excess pore water pressure and amount of settlement agreed well with the theoretical values. However, the measured values became smaller than the theoretical values as the liquefaction region became larger.

⑨ The penetration depth measured by a cone penetrometer is determined only by the void ratio e regardless of whether the sand bed is liquefying or non-liquefying, and it was quantitaively clarified that the sand bed becomes harder with settlement of the sand bed.

6. References

Akutu T. , K. Yano and S. Akeda, (1996): Ground Environment of Short-necked Clam Fishing Grounds in Cold Regions, Proceedings of Civil Engineering in the Ocean, Vol.12, pp.473-478 (in Japanese).

Derek A. Hodgin, Clifford Truitt and Jerris Foote,(1992): Beach compactness regulatory criteria for nesting sea turtles on the Southwest Florida Shoreline, Proc. of 5th Annual National Conference On Beach Preservation Association Technology, pp.325-339.

Kraus, N. C.and J. BM. Smith, (1994): SUPERTANK laboratory data collection project, Technical Report CERC-94-3, US Army Corps of Engineers.

Nishi.R, S.Ohmi, M.Sato, T.Uda, N.C.Kraus (1996): Hardness of seashores and sand dunes, Proceedings of Coastal Engineering, JSCE, Vol.43, pp.681-685 (in Japanese).

Yamashita.T, M.Minamimura, S.Ito, K.Tno, S.Akeda (1996): Mechanism by which bivalves come up to the surface under fluctuating water pressure, Proceedings of Coastal Engineering, JSCE, Vol.43, pp.1076-1080 (in Japanese).

Zen K., H. Yamazaki and A. Watanabe, (1987): Wave-induced Liquefaction and Densification in Seabeds, Report of P.H.R.I., Vol.26, pp.125-180 (in Japanese).

A method for estimating the bed velocities produced by a ship's propeller wash influenced by a rudder.

G.A. Hamill [1], J. A. Mc Garvey [2], P.A.Mackinnon [3]

Introduction

When a ship manoeuvres within the confines of a harbour it does so with minimal bed clearance and at near to maximum power. The propeller produces thrust by drawing in water and accelerating it. This accelerated flow is discharged from the propeller in the form of a jet or wash. Under these circumstances the wash can impact on the bed with velocities in excess of 8 m/sec. These high velocities erode the seabed, and where this occurs near to quay structures serious damage may result. Bergh and Magnusson (1987) Chait (1987) and Johnston (1985) are among many who have given specific details of problems which have occurred world-wide.

In order that an engineer may provide adequate protection to the bed form the erosive power contained within the propeller wash a full understanding of the magnitude and distribution of the velocities within it must be known. Stewart (1983), Fuehrer (1977) and Berger (1981), among others, have studied the wash and have provided predictive equations for velocity calculations. However, they have not included the influence of the rudder on the formation and distribution of the wash.

Related Research

Robakiewicz (1966), Verhey (1983) and Fuehrer et al. (1987) carried out investigations which allowed for the presence of the rudder, and they presented methods by which the velocities on the sea bed could be calculated. These equations are limited in that a full velocity distribution cannot be calculated and they are related to an efflux velocity equation which has been found to be up to 20% in error.

1 Senior Lecturer, Department of Civil Engineering. The Queen's University Belfast, David Keir Bldg, Stranmillis Rd, Belfast . Ireland
2. Engineer, Mouchel Consulting Ltd. West Hall, Parvis Rd. West Byfleet, Surrey. England
3. Lecturer. Department of Civil Engineering. The Queen's University Belfast, David Keir Bldg, Stranmillis Rd, Belfast . Ireland

Hamill and McGarvey (1996) presented the initial findings from a study aimed at providing a method for designing for propeller action in harbours and this paper contains information which extends that already presented at ICCE'96.

Experimental set-up

A number of model propellers, operating at up to four speeds of rotation, have been tested in an experimental tank 7.5m x 4m x 1 m deep. Rudders were manufactured in accordance with the Ship Design Manual, and these were tested within the normal range of operation, at angles of up to 35 degrees on either side of the propeller axis. Velocity measurements, in both the axial and radial directions, were taken on a fine 3D grid within the wash using a twin component Laser Doppler Anemometer and an array of Pitot static tubes.

Rudder effect

Hamill and McGarvey (1996) discussed the influence of the rudder, on the propeller wash. The wash was found to split into two different jets, one directed towards the free surface the other directed towards the seabed, as shown in figure 1. It was found that there was an increase in the magnitude of the axial velocity by as much as 30% with the rudder present when compared to the jet without a rudder. A method by which the velocity distribution on the face of the propeller could be calculated was given. This has been shown to provide a more accurate value for the efflux velocity.

As the rudder turns into either the bottom jet, or surface jet, it changes the resulting velocity magnitudes and distributions which prevails within the wash. This can be seen in figure 2 which represents the same situations as figure 1 but with the rudder turned -15 degrees into the bottom jet. The bottom jet has now been moved in both the vertical 'y' and transverse 'z' plane when compared to the zero rudder location

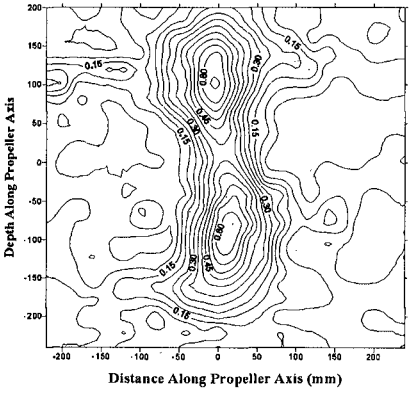

Figure 1 Isovels at zero rudder angle

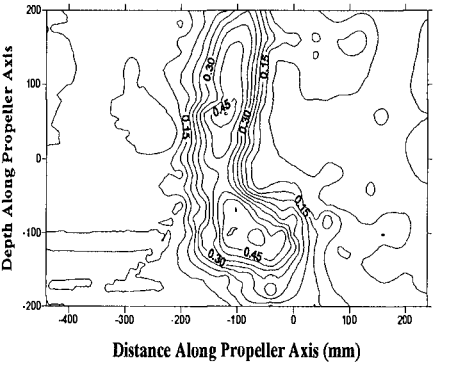

Figure 2 Isovels at –15 degree rudder angle

The equations presented by Hamill & McGarvey (1996) provide a method for calculating the position of the maximum velocity in the 'y' plane only. It is clear form figure 2 that transverse diffusion is also present within the wash.

The ability to locate the position of maximum velocity in the three dimensional space behind the propeller, along with a method for predicting its magnitude, allows the calculation of the velocity distribution around that value to be attempted. Previous distribution equations have been based on an axis-symmetrical approach. However, as the rudder angle changes it becomes clear that within the bottom stream a symmetric assumption would be invalid and as a consequence separate distribution equations have been developed which describe the velocities vertically and transversely within the jet, allowing for changes in rudder position.

Propeller wash characteristics

Having already established a relationship for the velocities on the 'y' (vertical) plane, Hamill and Mc Garvey (1996), the location of the maximum velocity along the 'z' plane was then observed. It was expected that this would be more influenced by altering the rudder angle due to the deflection of the jets by the rudder which provides directional control for a ship.

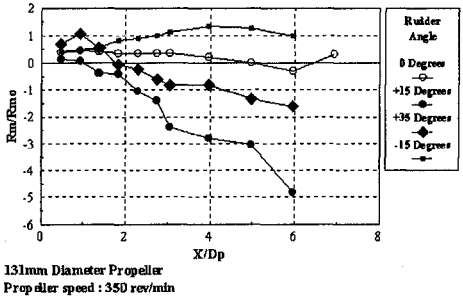

Figure 3 Location of Maximum Velocity on Z plane

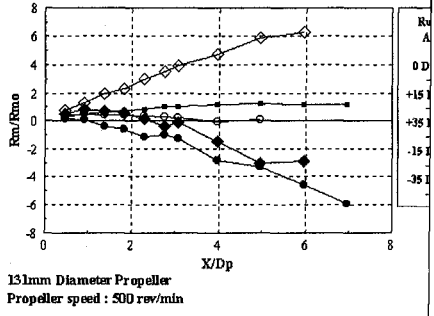

Figure 4 Location of Maximum Velocity on Z plane

The location of the maximum velocity within the bottom stream in the 'z' direction of the jet was tracked and plotted. It was found that the rudder had a significant effect in controlling the direction of the bottom stream. The location of the maximum velocity within the bottom stream of a typical wash is as shown in figure 3. The general trend of the surface stream showed that with a change in rudder position there was a corresponding change in the stream which tended in the general direction of the rudder, for all of the angles tested. Figure 3 shows however that this trend does not continue for the bottom stream. It can be seen that with an increase in the rudder angle from 15 to 35 degrees there is in fact a reduction of the diffusion angle of the bottom stream. Figure 4 shows the location of the maximum velocity in the bottom stream of another wash, for all of the angles tested. It can be seen that for the negative rudder angles the streams diffuse in the

direction of the rudder however once again it can be seen that there is a reduction of the horizontal diffusion angle as the rudder angle is increased from 15 to 35 degrees. The explanation for this ambiguous trend lies in the initial formation stages of the jet, and is the result of the direction of rotation of the propeller and increasing positive rudder angles.

Equation for location of maximum velocity on Z-plane

As was the case for the vertical plane, the location of the maximum velocity in the 'z'-direction is best described by a linear decay equation of the type;

$$\frac{R_{mz}}{R_{mo}} = Const.\left(\frac{X}{D_p}\right) \qquad 1$$

where R_{mz} is the location of maximum velocity in the 'z' plane at any axial distance 'X' from the propeller. Figure 4 showed the location of the maximum velocity in the Z-direction for a typical test propeller, for all of the rudder angles tested. It can be seen that for the zero rudder angle position the bottom stream moves towards and crosses the propeller centreline. It has been shown that the bottom stream tends in the direction of the rudder and as the rudder angle varies there is a corresponding variation in the direction of the bottom stream. There was a change in this trend observed for the +35 degree rudder angle in which there is a reduction of the jet deflection as the rudder is turned from +15 to +35 degrees.

With reference to figure 4 it is clear that the magnitude of the constant term in equation 1 is some function of the rudder angle. The magnitudes of these constants for each propeller, propeller speed of rotation and rudder angle combination was obtained by a simple regression analysis, and these are compared to the change in rudder angle in figure 5.

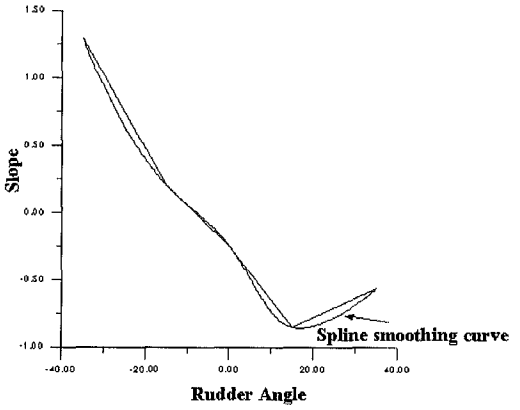

Figure 5 Measure slope for location of maximum velocity on Z plane at various ruder angles.

It can be seen that there is a gradual decrease in the slopes from the -35 degree rudder position to the +15 degree rudder angle and then as expected there is a reduction in the slope from +15 to +35 degrees. A spline curve was then fitted to determine if a mathematical relationship existed between the slopes and the rudder angle, and is plotted as shown in figure 5. It can be seen that the curve peaks at some position between +15 and +20 degrees and thereafter there is a reduction in slope and without further tests this rudder angle remains ambiguous. It was therefore decided to develop a relationship between the slope and rudder angle within the range of -35 and +15 degrees. It was found that the following linear relationship provided the best correlation for the data,

$$m_z = -0.27 - 0.04(\theta) \qquad 2$$

which achieved a correlation of 0.98 where θ is the rudder angle in radians. The location of the maximum velocity along the Z-plane may therefore be determined using the following equation, within the range -35<θ<+15 degrees,

$$\frac{R_{mz}}{R_{mo}} = 1 + m_z \left(\frac{X}{D_p} \right) \qquad 3$$

It would be recommended that further tests be carried to clear the ambiguity surrounding the location of the maximum velocity on the Z-plane when the rudder is located between +15 and +35 degrees. It appears that at some angle within this range the general trend changes where there is in fact a decrease in the rate of diffusion with increasing rudder angle.

This equation when used with those for the vertical plane position, R_{my}, reported in Hamill & McGarvey (1996), enable the location of the position of the maximum velocity in the 3D space behind the propeller to be determined.

The velocity distributions within the propeller jet.

A method has already been reported by which the magnitude of the maximum axial velocity, at any axial distance X within a propeller jet, can be determined, Hamill & McGarvey (1996). It is also necessary to predict accurately the velocity distributions around this maximum value so that adequate bed protection can be designed to protect quay structures.

The velocity distributions, within the zone of established flow, for a free expanding jet without a rudder present are symmetrical about the axis of the propeller. The velocity distributions at any point within the jet have been shown to follow the normal probability curve as proposed by Albertson (1950), and modified by Fuehrer and Romisch (1977). Their equation has been successfully used by several authors and was found to describe quite accurately the velocity distributions within a propeller jet without a rudder present.

Influence of rudder on velocity profiles

The rudder has been shown to split the flow into two high velocity streams, one directed towards the surface and the other directed towards the bottom. It was decided to investigate the velocity distributions within the bottom stream as this is the jet which induces bed velocities, and as a result, can lead to erosion of the bed. It has previously been shown that a variation in rudder angle significantly alters the diffusion characteristics of the bottom stream, with a confining and an elongation effect within the stream, resulting in a loss in the symmetry common to the free expanding wash.

Velocity distribution on vertical Y-plane.

The velocity profiles along the Y-plane through the jet axis, at increasing distance from the propeller, were plotted for the bottom stream. Figure 6 shows the axial velocity distributions for a typical jet with a zero rudder angle. It can be seen that with distance from the propeller there is a decay in magnitude of the velocity profiles and an increase in the distance to the location of the maximum velocity. It can be seen that they appear quite similar to the normal probability distributions suggested by previous authors. It can be seen that the distributions are approximately symmetrical through the stream axis, although the velocities are slightly greater along the profile above the stream axis that is due to the proximity of the surface stream close to the propeller. As the distance from the propeller increases, the distances between the streams also increase and the influence of the surface stream becomes less significant. This was found to be the general trend of all the results obtained for the zero rudder angle position.

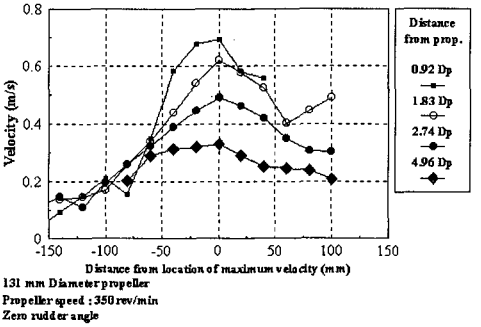

Figure 6 Axial velocity distributions on the Y plane measured from the location of maximum velocity within the bottom stream.

In order to describe the velocity distribution it is necessary to consider the normal probability curve proposed by Albertson to describe the velocity profiles,

$$\frac{V_{xr}}{V_{\max}} = EXP\left[-0.5\left(\frac{y}{\sigma}\right)\right]^2 \qquad 4$$

where V_{xr} is the velocity at the point under consideration and y is the distance from the propeller axis to the point. The term σ is the standard deviation of velocity and is the distance from the axis to the point at which the velocity has a value of 0.605 V_{max} and this term depicts the depth of the profile. It was therefore required to determine the location of the standard deviation of velocity so the velocity distributions within the propeller jet could be established.

The location of the maximum velocity, and the velocity distributions on the Y-plane within the propeller jet, were found to be dependent on rudder angle. Therefore, as the shape of the distribution profile depends on the standard deviation of velocity, it would be reasonable to assume that the standard deviation of velocity is dependent on the magnitude of rudder angle. The location of the maximum velocity on the Y-plane has been established in terms of the distance below the propeller axis. It was therefore decided to establish a point one standard deviation of velocity below the maximum as the distance below the propeller axis, $R_{\sigma y}$. It was observed that there was a gradual increase in the distance to this point with distance from the propeller and this can be observed when plotted as shown in figure 7. The location of the maximum velocity on the Y-plane is also plotted for comparison.

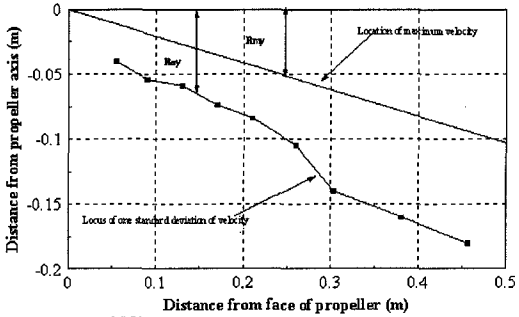

Figure 7 Location of standard deviation of velocity
On Y plane for a zero rudder angle

It was found that a linear regression provided the best relationship between the rudder angle and the locus of one standard deviation. Thus a point at one standard deviation of velocity can be located from the following equation,

$$R_{\sigma y}=-0.8R_{mo}-(-0.322+0.0012\theta)X \qquad 5$$

The velocity distribution can be established based on equation 4 proposed by Albertson where y is the distance from the location of the maximum velocity on the profile and is equal to $R_{my}-y_m$ in which y_m is the distance from the propeller axis to the point under consideration. Figure 8 shows a schematic view of the velocity profiles within the propeller jet to avoid confusion. The standard deviation of velocity, σ, as shown in figure 8 is equal

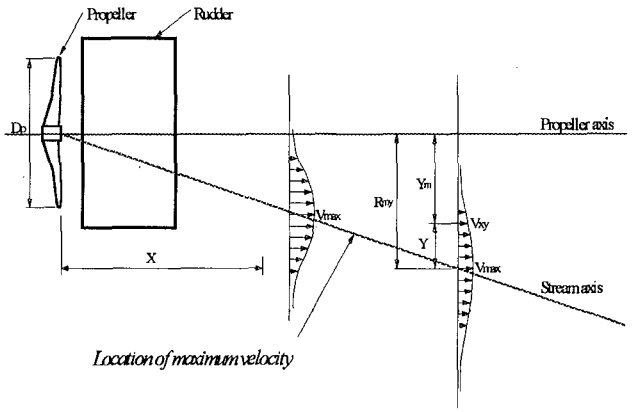

Figure 8 Velocity distribution schematic for Y plane

to $R_{\sigma y}$-R_{my}. The velocity distribution within the propeller jet can therefore be described as follows,

$$\frac{V_{xr}}{V_{\max}} = EXP\left[-0.5\left(\frac{R_{my}-y_m}{R_{\sigma y}-R_{my}}\right)^2\right] \qquad 6$$

where $R_{\sigma y}$ is calculated from equation 5.
This equation will predict quite accurately the velocity distributions within the propeller jet for a given rudder angle at distances up to 10 D_p.

Velocity distribution on the Z-plane

In a similar manner to that employed for the analysis of the locus of one standard deviation on the 'y' plane, a relationship for the 'z' plane was also established. Thus $R_{\sigma z}$ can be calculated from

$$R_{\sigma z}=0.2R_{mo}+(-0.141-0.014\theta)X \qquad 7$$

The velocity distribution along the Z-plane can now be established based on the normal probability equation where the distance along the profile, z, is equal to R_{mz}-z_m, in which z_m is the distance from the propeller axis to the point under consideration, and R_{mz} is the distance to the maximum velocity. For clarity this is shown in figure 9. The standard deviation of velocity, σ, is equal to $R_{\sigma z}$-R_{mz}, therefore the axial velocity distribution on the z axis may be expressed as follows,

$$\frac{V_{xz}}{V_{\max}} = EXP\left[-0.5\left(\frac{R_{mz}-z_m}{R_{\sigma z}-R_{mz}}\right)^2\right] \qquad 8$$

where $R\sigma z$ is calculated from equation 7.

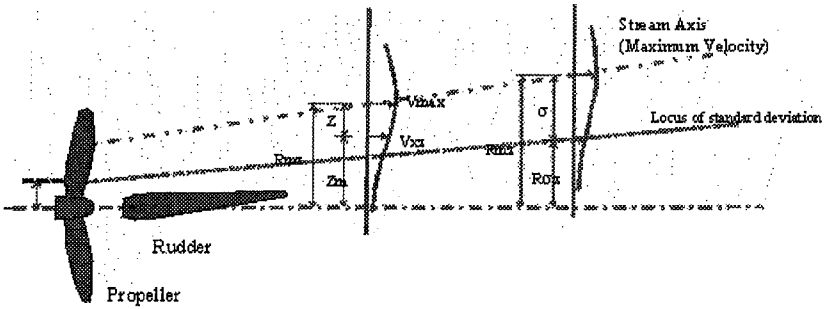

Figure 9 Velocity distribution schematic for Y plane

Concluding Comments

The present investigation has studied the influence of the rudder within a ship's propeller jet, and has confirmed the formation of two high velocity streams, one directed upwards to the surface and the other directed downwards towards the bottom.

The influence of the rudder on the maximum velocity at the face of the propeller i.e. the efflux velocity, was found to be insignificant, although at high propeller speeds and large rudder angles some confinement was observed with a variation of approximately 8% noticed.

It was found that there was an increase in magnitude of the axial velocities by as much as 30% with the rudder present when compared to the jet without a rudder.

The location of the maximum velocity within the propeller jet was on the axis of each stream which were established from the position of the rudder. The location of the maximum velocity within the jet was found to be independent of propeller speed however, there were significant changes in the location of the maximum velocity due to variations in rudder position. Equations are presented which locate the maximum velocity in the vertical and transverse directions allowing for changes in rudder position.

The velocity distributions were found to change dramatically when compared to the jet without a rudder. Investigations showed that the equations used to predict the velocity distributions within the jet without a rudder present cannot successfully be applied to the jet with a rudder. The rudder position significantly changed the diffusion characteristics of the propeller jet and as a consequence distribution equations were developed to describe the velocities vertically and transversely within the jet, allowing for changes in rudder position, based on the normal probability curve suggested by Albertson (1950).

The velocities at any point within the jet can be determined using the equations presented. They are first approximation equations and further work should consider a greater number of rudder positions. Having established knowledge of the velocities within the propeller jet, it is now possible to design adequate scour protection.

References

Albertson , M.L. (1950) "Diffusion of submerged jets" Transcript of the A.S.C.E. paper no. 2409 Vol. 115 , pp 639 - 697

Berger W., Felkel K., Hager M., Oebius H., Schale E., (1981) "Courant provoque par les bateaux. Protection des berges et solution pour eviter l'erosion du lit Haut Rhin". PIANC 25th Congress, Edinburgh, Section I-1

Bergh H., Magnusson N., (1987) "Propeller erosion and protection methods used in ferry terminals in the port of Stockholm". PIANC Bulletin No. 58, pp 112-120.

Chait S., "Undermining of quay walls at South African ports due to the use of bow thrusters and other propeller units". PIANC Bulletin No. 58, pp 107-110.

Fuehrer M., Romisch K., (1977) "Effects of modern ship traffic on islands and oceans waterways and their structures". PIANC 24th Congress, Leningrad Section I – 3

Fuehrer M., Pohl H., Romisch K., (1987) " Propeller jet erosion and stability criteria for bottom protection of various construction". P.I.A.N.C. Bulletin No. 58. 1987

Hamill G.A., McGarvey J.A., (1996) "Designing for propeller action in harbours" . 25th International Conference on Coastal Engineering. Orlando, Sept, 1996.

Johnston H.T., Elsawy E.M, Hamill G.A., and McKillen H.G. "A study of scour and deposition near a berth structure caused by the propulsion action of manoeuvring ships",. International Association for Hydraulic Research, 21st Congress, Melbourne, Australia, August 1985

Robakiewicz W., (1966) "The influence of the action of the jet behind the screw on the bottom. Example of model and field measurements with a trawler B-20". Rosprawy Hydrotechniczne, Vol. 19, pp 177-215.

Stewart D.P.J., (1992) "Characteristics of a ship's screw wash and the influence of quay wall proximity", Thesis submitted to the Queen's University of Belfast for the degree of Doctor of Philosophy.

Verhey H.J., (1983) "The stability of bottom and banks subjected to velocities in the propeller jet behind ships." Delft publication no. 303, April 1983, Delft Hydraulics Laboratory, Netherlands.

DESIGN OF SCOUR PROTECTION FOR THE BRIDGE PIERS OF THE ØRESUND LINK

Lars Kirkegaard[1], Mogens Hebsgaard[2] and Ole Juul Jensen[3]

Abstract

The Øresund Link between Denmark and Sweden consists of a cable stayed bridge, a man-made island and an immersed tunnel. The engineering design of the scour protection of the 45 approach bridge piers was made on the basis of numerical and physical modelling. The numerical studies included determination of the hydrographic design conditions and wave/current induced bed shear stresses along the bridge alignment, enabling the selection of the most exposed piers for each bridge segment and pier type. Physical model tests were then performed with the selected piers to investigate the necessary scour protection. This article describes the methods applied and the conclusions and resulting scour protection design.

Introduction

The 16 km long fixed link across the straight between Denmark and Sweden, the Øresund Link, will consist of three main elements: 1) an immersed tunnel, 2) a man-made island, and 3) a cable stayed high bridge. The immersed tunnel crosses the eastern channel between Kastrup on the Danish coast and the man-made island Peberholm just south of Saltholm. The cable stayed high bridge, including approach bridges, crosses the main shipping route in Øresund, Flinterenden, and reaches the Swedish coast at Lernacken. The location of the bridge is shown in Figure 1.

This article concerns the design of the scour protection for the approach bridge piers, which has been investigated through both numerical and physical model tests carried out by Danish Hydraulic Institute (DHI).

[1] Hydraulic Engineer, Ports, Waterways & Coastal Engineering Department, COWI Consulting Engineers and Planners AS, Parallelvej 15, DK-2800 Lyngby, Denmark. Email: lck@cowi.dk

[2] Chief Engineer, Ports & Hydraulic Structures Department, Danish Hydraulic Institute, Agern Allé 5, DK-2970 Hørsholm, Denmark. Email: mhe@dhi.dk

[3] Head of Department, Ports, Waterways & Coastal Engineering Department, COWI Consulting Engineers and Planners AS, Parallelvej 15, DK-2800 Lyngby, Denmark. Email: ojj@cowi.dk

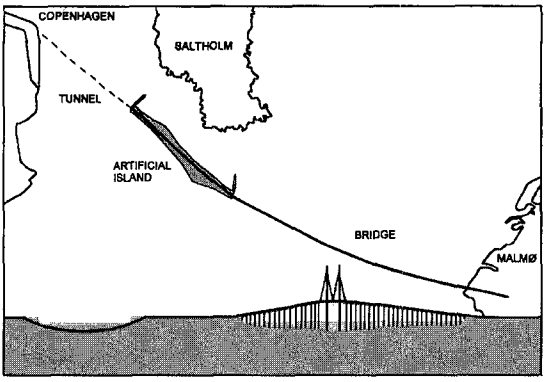

Figure 1 Alignment of the Øresund Link.

Bridge Design

The approach bridges are founded on 45 concrete piers at water depths less than 10 m. The cross-sections of the piers are prismatic with slightly streamlined up- and down-stream ends as shown in Figure 2.b. The dimensions of the pier shafts at seabed level are approximately 6 m x 18 m, and those of the supporting caissons 6 m x 18 to 22 m.

Due to a strict environmental requirement of zero blocking of the water exchange between the North Sea and the Baltic Sea, it was decided to place the pier caissons in excavated pits in the sea bed, see Figure 2.a. The zero blocking requirement further implied that only a few of the supporting caisson walls were allowed to protrude above the original sea bed level, and that the scour protection had to be placed flush with the sea bed.

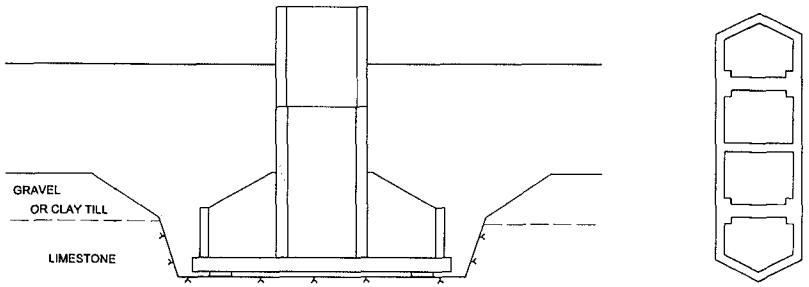

Figure 2 (a) Vertical cross-section of bridge pier placed in excavation
(b) Horizontal cross-section of streamlined pier shaft.

Placing the caissons in the excavated pits and founding them directly on the hard Copenhagen Limestone further enabled the bridge to withstand the large forces of ice

and design ship impacts, but also eliminated the risk of undermining of the caissons, which is usually the major risk of bridge scour.

To ensure the necessary geotechnical stability of the piers, backfilling of the excavated pits was required. The main purpose of the scour protection was thus to contain the backfill inside the excavation.

The geotechnical conditions vary along the bridge alignment, with a seabed consisting of hard non-erodible limestone covered by a layer of clay till or sand/gravel. The thickness of the erodible top layers varies between 0 and 4 m along the bridge alignment. Large differences are even found from one side of the excavation to the other at each pier location.

Numerical Studies

The hydrographic conditions in the region has been derived from intensive measuring campaigns and numerical model studies prior to the scour investigations and model testing, and these have been used to define the Design Requirements. From the previous studies and the specifications in the design requirements, the relevant design conditions for waves, currents and water levels along the bridge alignment have been established.

The wave conditions varies along the alignment and are relatively directional. The maximum significant design wave height, H_s, is up to 2.7 m for southerly wind directions. The wave heights are generally lower for the near-shore piers due to depth limited breaking of waves. The design wave heights for events with a 100 and 10,000 year return period (yrp) are shown in Table 1 (intervals).

Wave heights, Hs (m)	Northerly	Southerly
100 yrp	1.3-2.0 m	1.2-2.3 m
10,000 yrp	1.4-2.6 m	1.2-2.7 m

Table 1 Design Wave Heights.

The current conditions are nearly bi-directional, with the angle between the main current direction and pier orientation vaired between 10 and 20°. The maximum design current velocity was found to be 3.8 m/s close to the navigation channel for southward currents. The design currents velocities (intervals) are shown in Table 2.

Current velocities	Northward	Southward
100 yrp	1.1-1.8 m/s	1.2-2.7 m/s
10,000 yrp	1.4-2.4 m/s	1.7-3.8 m/s

Table 2 Design Current Velocities.

There is an inherent correlation between extreme wave and current events, as these events are primarily caused by the same meteorological conditions, and it was subsequently decided to use a straight forward combination of wave and current conditions in the design.

As the correlation between water levels and wind directions showed a rather large scatter and since the scour protection is most exposed at low water, assuming equal wave and current conditions, it was decided to adapt a conservative most probable low water level in the design. This level varied between -0.5 m and +0.5 m.

Based on the data described above, the bed shear stress distribution along the bridge alignment was computed using the numerical sediment transport programme STP, which is a part of LITPACK, DHI's deterministic modelling system for littoral processes. All relevant combinations of wave and current directions were calculated using a bed grain size of 0.2 mm. The resulting shear stresses are shown in Figure 3.

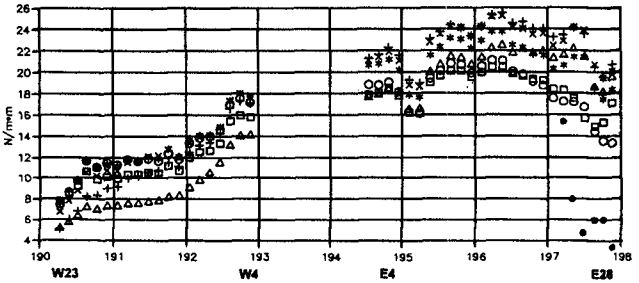

Figure 3 Bed shear stress along the bridge alignment.

The limited variation in the size of the maximum shear stress for the various wave directions indicate that the bed shear stress is largely dominated by the current. This is even more clear from the direction of the maximum shear stress, as the waves are only able to deflect the maximum shear stress direction approx. ±10-15° away from the main current direction. This fact was important for the selection of set-up of the physical model and definition of the test programme.

The shear stresscs shown in Figure 3 are not representative of the shear stresses actually experienced by the scour protection once the bridge piers and the protection have been placed, as the piers and the rocky protection themselves alter the flow pattern fundamentally by amplification and by generation of turbulence.

However, the figure enables the selection of the most exposed piers of each pier type to be tested in the hydraulic model along with the corresponding design conditions to be used in the model.

Three types of pier caissons exist, viz. Type A, B and C. These types are characterised by the number of supporting caisson walls and whether these protruded above sea bed/scour protection level. Type A (W11-W4 and E4-E11) have seven supporting walls terminated just below original sea bed level, Type B (W20-W12 and E12-E26) have

five supporting walls that protrude up to 1.0 m above original sea bed level, and Type C (W23-W21 and E27-E28) have seven walls that protrude up to 1.0 m above sea bed level.

The piers closest to the Swedish coast were placed in a 100 m wide excavated construction channel. The local bed levels were thus lower than those used for the computation of the bed shear stresses above. Using the actual bed levels significantly reduced the bed shear stresses, as indicated with • marks on Figure 3, and these piers could therefore be designed as the less exposed western piers.

Based on Figure 3, the following piers were selected for further investigation in the physical model:

- E11, representing all Type A piers
- E17, representing the eastern Type B piers
- W12, representing the western Type B piers

No tests were performed on Type C piers, as these were all relatively sheltered.

Physical Model Tests and Scour Protection Design

A physical 2D model was constructed to a linear scale of 1:40 in a 5.5 m wide flume in which unidirectional irregular waves and current could be generated simultaneously. The model set-up is shown in Figure 4.

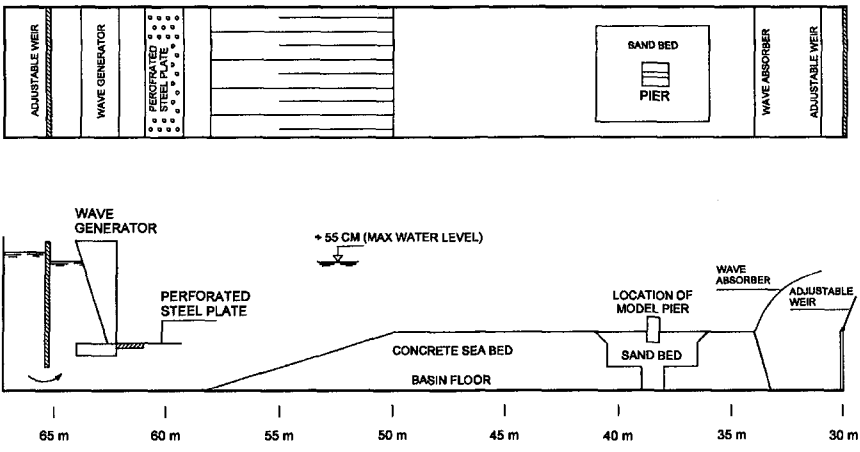

Figure 4 Two-dimensional model flume set-up.

The conditions created in the 2D model, combining extreme waves and currents from different directions into one single direction, is estimated to create more critical

conditions for the scour protection, as the amplification patterns of shear stresses from waves and currents coincide.

A total of fourteen test series were carried out on three different pier types in order to investigate the stability of the scour protection. Each test series included three standard tests: 1) 100 y waves and current, 2) 10,000 y waves and 100 y current, and 3) 10,000 y waves and current. Each test had a duration corresponding to four hours in nature.

Three different current (and wave) directions relative to the pier were studied. The first tests with current directions of 10° and 40° showed that the damage pattern is rather sensitive to the direction. The tests yielded *acceptable damage* and *collapse* respectively for otherwise identical situations. As the current was found to dominate the scour process outside the protection, it was concluded that a current direction of 20° relative to the pier should be applied in the design.

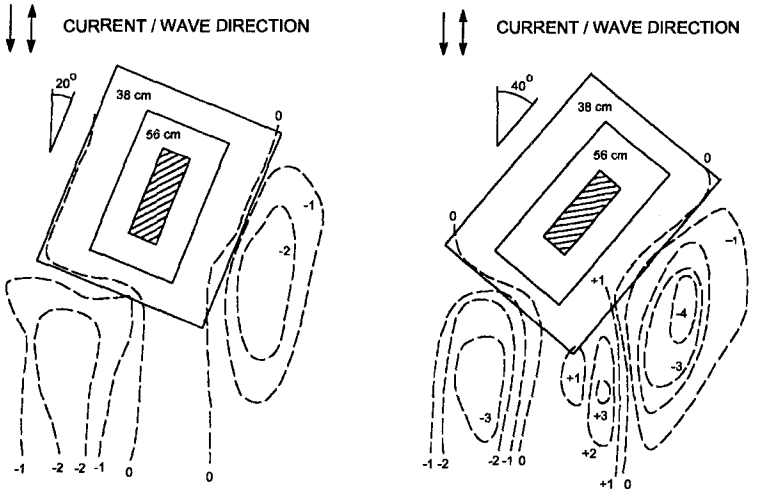

Figure 5 Typical damage pattern for 20° and 40° pier alignment.

Two types of damage were observed, viz. direct and indirect damage. Direct damage is caused by the direct action of waves and current on the surface of the protection, whereas indirect damage at the edges of the protection is a result of the scouring of the seabed just outside the protection resulting in stones being moved into the down-stream scour holes by wave action. Figure 5 shows some typical patterns of scour outside the protection and the resulting damage at the edges.

Indirect damage occurred along the downstream side and downstream end of the protection. The direct damage occurred in three areas: At the downstream side, the downstream end, and in the upstream cells (between the supporting walls) or all cells along the pier. Figure 6 shows the areas where damage occurred for a successful test.

To prevent any damage from impacting stones on the concrete, it was specified to use the largest stones of each fraction in the upstream cells and to place these with great caution. In the down stream area the stone size was slightly increased to reduce the number of stones being moved.

As a consequence of the results of the first test series showing larger damage than originally estimated, the test programme was currently changed and very often the layout of the scour protection in a test series was defined from the results of the previous test series in order to optimise the design.

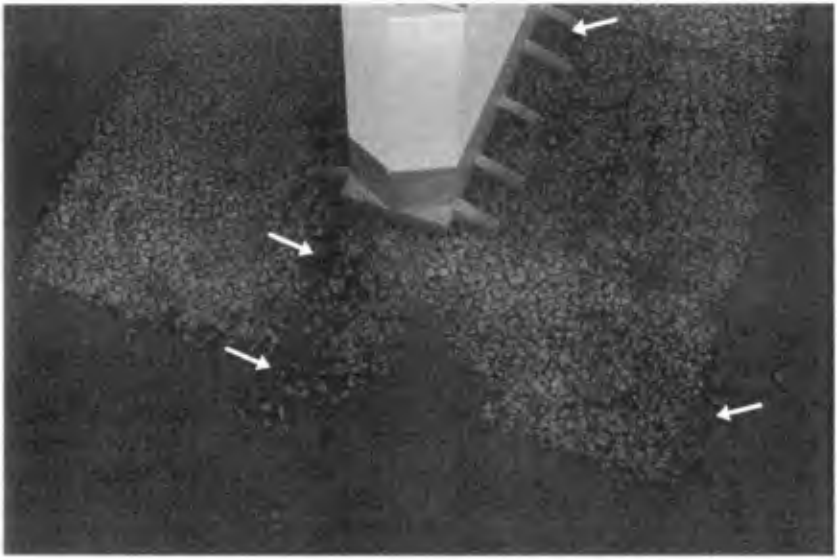

Figure 6 Typical damages observed in the physical model (looking upstream).

In addition to the traditional stability tests, it was decided to carry out a tests to investigate the effects of a thin layer of erodible material on top of the limestone. This test showed that the extent of the protection could be reduced significantly for piers placed in areas where the limestone is only covered by a thin layer of erodible soil. Figure 7 shows a photo taken after Test 3 (10,000 yrp). The dark areas is the limestone surface being exposed where the erodible material has been washed away.

Finally a test was carried out to investigate the time scale for the scouring in sand/gravel and clay till outside the protection. Analysis of the results indicated that the scour outside the protection would develop rapidly if the sea bed consisted of sand, whereas it would not exceed 1.0 m within an average 10 year period, if the sea bed consisted of 30 mm gravel. For clay till the scour was found to be in the order of 0.4 m for an average 10 year period, but this value could vary between 0.1 m and 3-4 m corresponding to fully developed scour holes. It is important to note that the values above are determined assuming homogeneous conditions. In reality the sea bed

consists of a mixture of sand, gravel, clay till and boulders. The sea bed will therefore to a certain extend tend to be self-armouring if erosion occurs.

The uncertainties of estimating the parameters for the clay till were considered too large to facilitate in the design, but indicated that it might be possible to include this in the design if more intensive studies and possibly a comparison of the results with available field observations were carried out.

Figure 7 Results of test with shallow limestone (looking upstream).

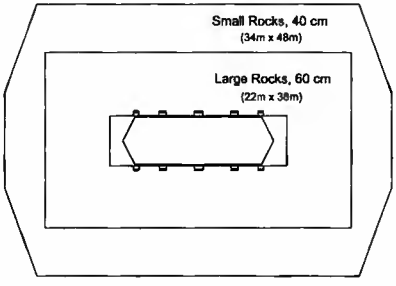

Figure 8 Plan layout of the largest scour protection (Pier Type A).

The final layouts of the scour protection were derived by comparing the damage patterns of each test series with the design requirements and taking the local soil conditions into consideration. An example of the protection layout is shown in Figure 8 and Figure 9.

It has further been specified in the design that the protection shall be adjusted according to the actual conditions found on site in the construction phase.

The most important change in the design concerned the back fill. It was originally foreseen that the caissons were to be back filled with the sound friction materials

recovered during excavation of the pits, and to place a filter layer between the back fill and the scour protection. However, the large difficulties experienced by the contractor keeping the back fill in place while placing the filter layer, caused him to substitute the native back fill with imported, coarse quarry run. This change in the original design has further increased the safety of the scour protection, and in case the protection is damaged, the maintenance costs will reduced significantly.

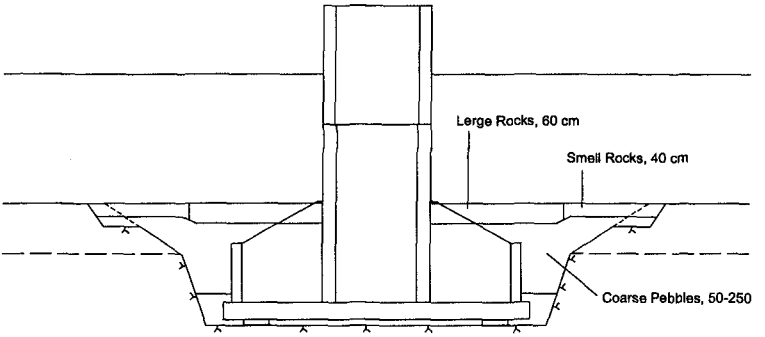

Figure 9 Cross-section of scour protection around Type A piers.

Conclusion

The detailed hydrographic design data were used in the design of the scour protection, including numerical calculations and hydraulic model tests. The test programme was continuously changed to optimise the design. This resulted in a differentiated design of the scour protection along the bridge alignment that fulfils the given requirements, taking both the pier specific hydrographic, geometrical and geotechnical conditions into account.

References

/1/ DHI/LIC Joint Venture (1993). The Øresund Link - Basic Information. Technical reports on waves, currents and water levels. Clients property.

/2/ DHI. Hebsgaard, M. et. al. (1997). Model tests with Scour Protection of Bridge Piers, Øresund Link. Clients property.

EXPERIMENTAL ANALYSIS OF WAVE-INDUCED LIQUEFACTION IN A FINE SANDBED

Kojiro Suzuki[1], Shigeo Takahashi[2] and Yoon-Koo Kang[1]

Abstract

A series of experiments were conducted to examine wave-induced liquefaction in a loosely packed fine sandbed, which was specifically used to ensure the presence of residual excess pore pressure. Also observed was the compaction of a liquefied sandbed in response to cyclic wave loading; a phenomenon thought to reduce the possibility of liquefaction. In addition, pore water was supplied from the bottom of the sandbed such that the effect of underground water pressure on liquefaction could be clarified.

1. INTRODUCTION

Wave actions are known to produce the phenomenon of sand liquefaction. One type of sand liquefaction is caused by seepage flow due to differences in water pressure, which typically occurs in the vicinity of a sheet pile (Figure 1), although it can also be caused by waves generating a pore pressure gradient in the sandbed. Such behavior is termed as "momentary wave liquefaction," and has been simulated by Zen *et al.* (1990) using a fluctuating pressure-type liquefaction test apparatus. Another type of liquefaction occurs during an earthquake (Figure 2), where in this case, pore pressure builds up due to shear stress in the sandbed such that the residual pore pressure produces liquefaction. Foda *et al.* (1991) simulated this behavior using a wave flume experiment, while Sekiguchi *et al.* (1995) did so using a centrifuge experiment.

Due to the unusual nature of sand boiling, which can cause devastating failure of coastal breakwaters, elucidating its mechanisms is a key task in breakwater design processes. This led to the present study that describes the results of experiments in which the following phenomena were observed: (1) liquefaction behavior of a loosely packed, fine sandbed due to residual excess pore pressure, (2)

[1] Research Engineer, Maritime Structures Lab., Port and Harbor Research Institute, MOT, Japan, 3-1-1 Nagase, Yokosuka, Kanagawa 239-0826, Japan.
[2] Chief, Maritime Structures Lab., Port and Harbor Research Institute.

compaction behavior of a fine sandbed due to cyclic wave loading, (3) the softening effect of a fine sandbed due to large standing waves, and (4) liquefaction behavior due to bottom-supplied feedwater.

2.EXPERIMENTAL SETUP

A large wave flume (105 m × 0.8 m)(Figure 3) was used to generate sand liquefaction. Water depth was changed from 0.35 to 1.0 m. The sandbed, which consisted of a mixture of silt and fine sand, was 6.0 m long and 1.0 m deep (Fig. 4). A feedwater system supplied water to the bottom of the sandbed, being used to produce an initially loose sandbed condition and to generate seepage flow liquefaction. The 50% sieve diameter of fine sand was 0.08 mm. We measured water surface displacement and pore pressure in the sandbed. Regular waves were mainly applied to sandbed without a structure, although a caisson was installed in order to investigate a standing wave condition.

The sandbed is equipped with a feedwater system to supply water from the bottom of the sandbed; a system used to produce an initially loose sandbed condition, and to generate seepage flow liquefaction.

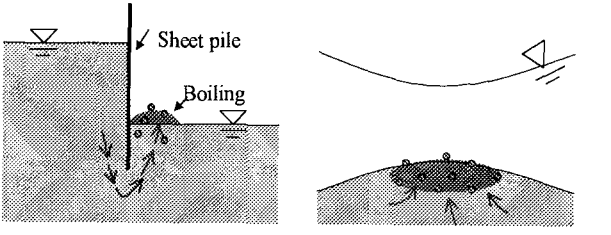

Figure 1 Diagrams showing causes of momentary wave liquefaction.

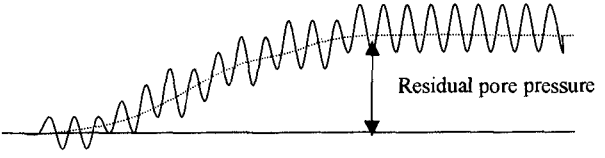

Figure 2 Liquefaction due to residual excess pore pressure.

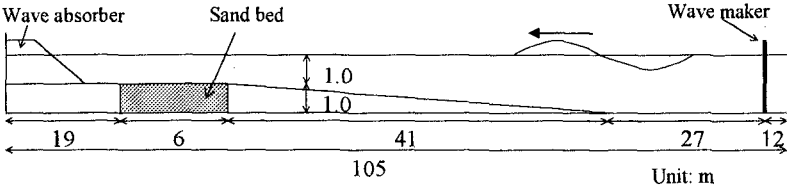

Figure 3 Cross sectional diagram of employed wave flume.

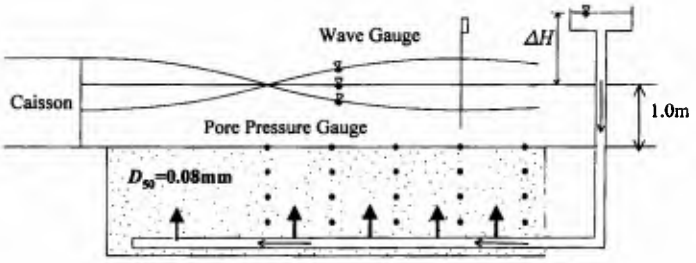

Figure 4 Sandbed model showing measurement locations.

3. EXPERIMENTAL RESULTS

Loose Sand under Progressive Waves

As can be seen in Photo 1, very loose sand behaves like a thick liquid. At the same time, the motion of the sand induces wave breaking and damping. Figure 5 shows typical pore pressures generated in the sandbed, where after just several waves the pore pressure oscillates and rapidly increases due to the wave-induced residual pore pressure. The magnitude of this pressure corresponds to the submerged weight of the sand.

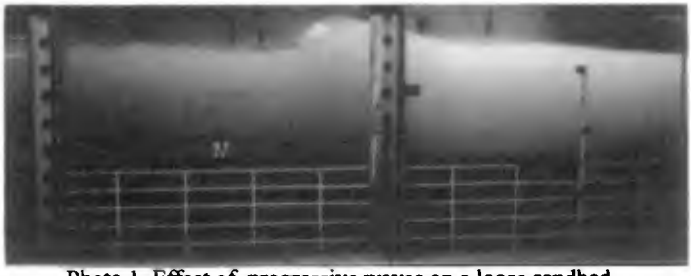

Photo 1 Effect of progressive waves on a loose sandbed.

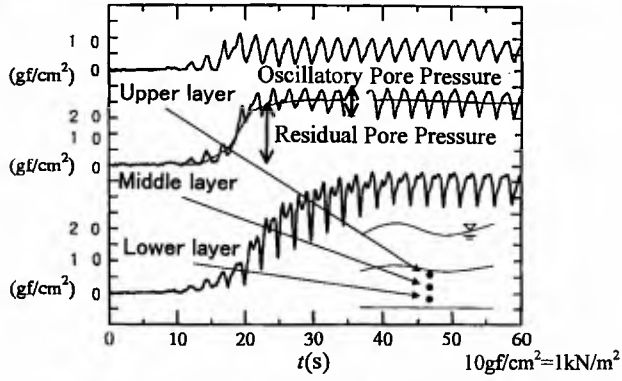

Figure 5 Pore pressure profile in a loose sandbed hit by progressive waves.

In the case of a loosely deposited sandbed (Fig. 6), the weight of sand is supported by both the pore water and the skeleton structure of the sandbed. Thus, when a wave acts on the bed, the sand skeleton structure breaks due to the shear stress such that only the pore water remains for supporting the sand's weight which corresponds to the increase in residual pressure.

It should be noted that this phenomenon only occurs when the permeability of the sand is low, *i.e.*, if permeability is high, such as in a coarse sandbed, the excess pore pressure easily escapes and the increase in residual pore pressure never occurs. Immediately after wave loading, sand boiling occurs (Photo 2) due to the excess pore water being squeezed out from the sandbed up to the sandbed surface. Such boiling is produced by residual pore pressure and lasts 2–3 min.

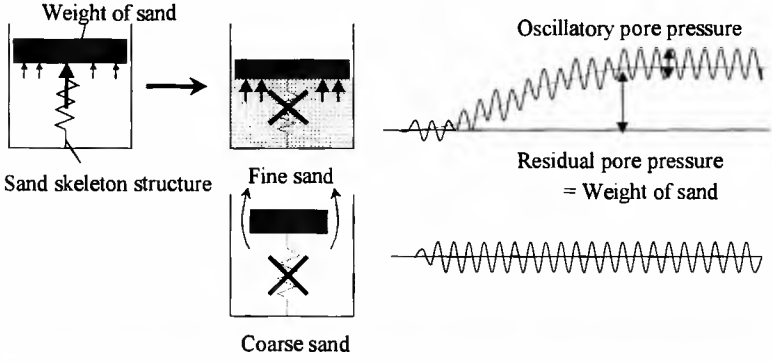

Figure 6 Diagram representing residual pore pressure

Photo 2 Sand boiling phenomenon.

Compaction Due To Cyclic Wave Loading

Because substantial settlement was observed in a fine sandbed, we investigated this compaction effect using series of cyclic loading tests in which a group of monochromatic waves was applied at 10-min intervals (figure 7). Wave period T was 2.08 s, wave height H was 48.8 cm, and each group consisted of 37 waves.

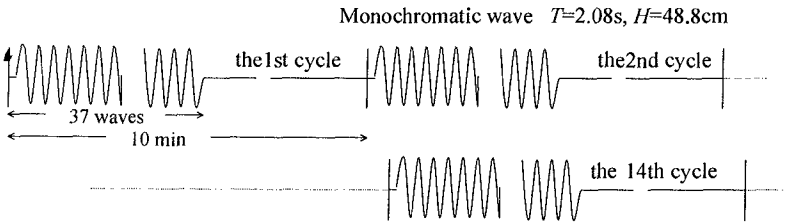

Figure 7 Applied cyclic loading scenario.

Figure 8(a) shows sandbed settlement after applying cyclic loading, where the effect of boiling forces the pore water out of the sandbed such that cyclic wave loading causes the bed to gradually settle. In fact, after the 14th loading, total settlement reaches about 13 cm; a substantial decrease in bed thickness.

Due to the presence of a loose sandbed during the 1st cyclic loading, sand particle motion is very large and vertical displacement is about 9 cm (Fig. 8(b)). However, the ensuing compaction effect with each loading subsequently reduces sand motion such that the 14th loading produces a displacement of only 0.3 mm, after which sand particle movement is not reduced by further loading, although sand ripples do appear such a compacted sandbed.

The compaction effect due to cyclic loading also leads to a reduction in residual pore pressure. Figure 8(b) shows the residual pore pressure P_r at different heights in the sandbed, where P_r gradually decreases such that after the 14th loading it vanishes.

Figure 9(a) shows the oscillatory component of pore pressure produced by 1st-loading water surface oscillations, where pore pressures have nearly the same amplitude and show no time lag. This result indicates that loose sand behaves like a thick liquid. At the 4th loading (Fig. 9(b)), however, a very sharp negative peak appears in the pore pressure, being is due to the "diletancy" effect which will be explained later. At the 14th loading (Fig. 9(c)), it is obvious that pore pressure decreases with respect to the depth of the sandbed, and that a significant time lag is present; an effect produced by compaction of the sandbed.

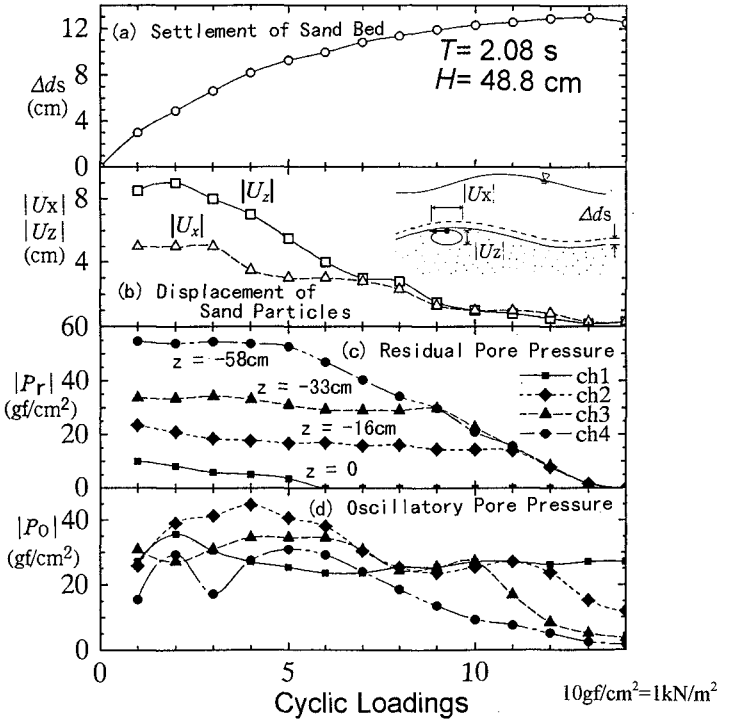

Figure 8 Compaction effect due to cyclic wave loading.

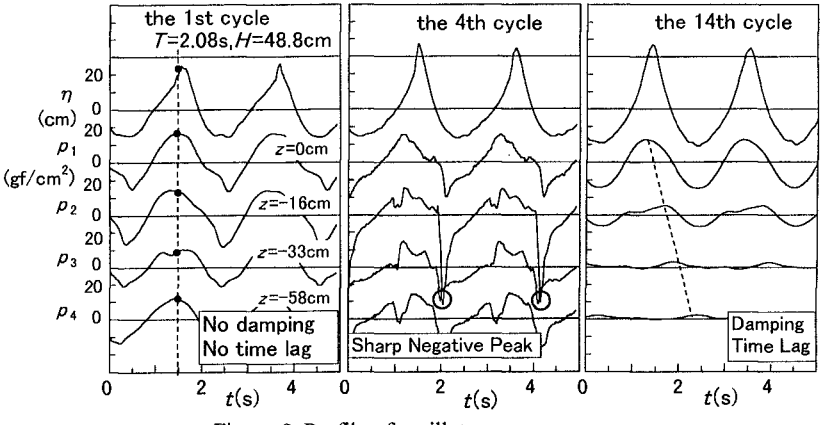

Figure 9 Profile of oscillatory pore pressure.

Sand Particle Motion after Compacted

Figure 10 shows the amplitude of sand particle motion after the sandbed is compacted, where only those waves larger than a certain height produce visible movement of the sand particles. In this case, large long-period waves acting on the sandbed increase sand particle motion and generate a large shear strain which in general results in the sand having small shear modulus. In other words, larger waves soften the sandbed.

When feedwater is applied from the bottom of the sandbed, the amplitude of the sand particle motion becomes much larger. That is, a 200-cm water head makes the sandbed boil and the amplitude of sand particle movement reaches 5 cm.

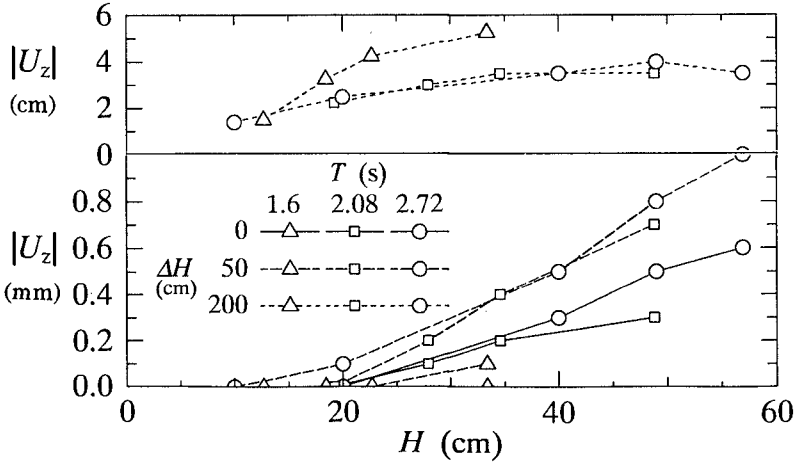

Figure 10 Sand particle movement after sandbed compaction.

Effect of Preceding Loading

Another interesting phenomena that occurred is re-liquefaction of the compacted sandbed. Figure 11 shows the change in residual pore pressure due to cyclic loading, where for smaller waves (T = 1.6 s, H = 12.7 cm) liquefaction does not occur until the 5th loading and residual pore pressure diminishes. However, after applying larger waves at the 11th loading, liquefaction reappears; a behavior we call "re-liquefaction."

Re-liquefaction probably occurs due to compaction by small waves being limited to near the sandbed surface, whereas the increase in shear stress produced by larger waves is sufficient to once again liquefy the bed. When larger waves were continually applied, the compaction expanded deep into the sandbed.

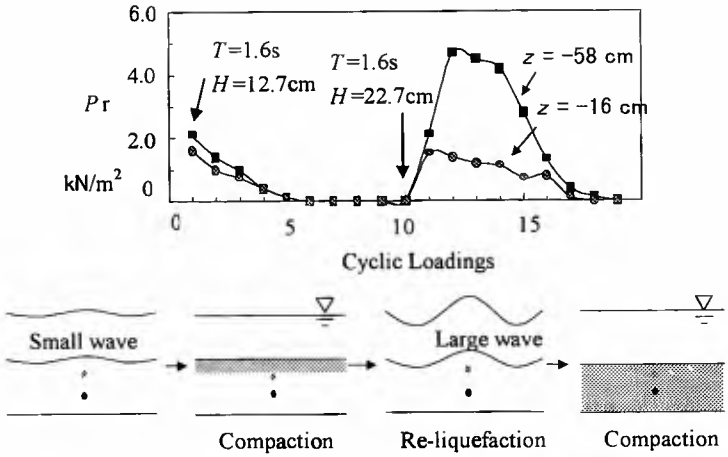

Figure 11 Effect of preceding loading (re-liquefaction).

Loose Sand under Standing Wave

Photo 3 shows a standing wave in front of a caisson model. When the sand bed is loose, it is easily liquefied due to the larger wave pressure compared to that by progressive waves. At the loop of standing wave, sand moves vertically in phase with the movement of surface water and at the node sand moves horizontally in phase with movement of water particles. On the other hand, for a compacted sandbed, its surface moves out of phase, that is lagging by 180 degrees.

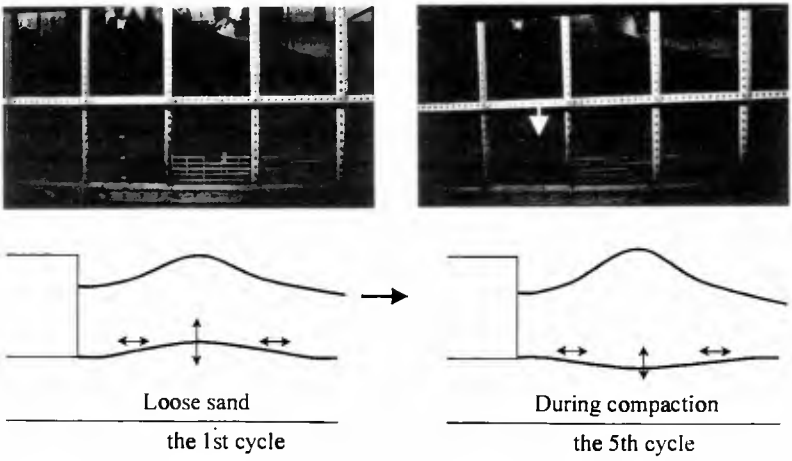

Photo 3 Applied standing wave.

Compaction due to Cyclic Wave Loading (Standing Wave Condition)

Figure 12 shows compaction of the sandbed under standing waves, where residual pore pressures are the same at the node and loop of the wave. On the other hand, oscillatory pore pressure is different. In particular, pore pressure at the node is quite large ($\approx 1.7 w_0 H$) from the 2nd–5th loading.

Figure 13 shows the oscillatory pore pressure profiles at the node of standing wave, where very sharp negative peaks appear. Since such peaks are not present at the loop of a standing wave, this indicates that they are caused by shear stress at the node of the wave. Such sharp negative pressure is surmised to be caused by the diletancy effect, *i.e.*, shear stress acting on the sand expands the volume of sand containing porous areas which in turn causes sharp negative peaks in pore pressure.

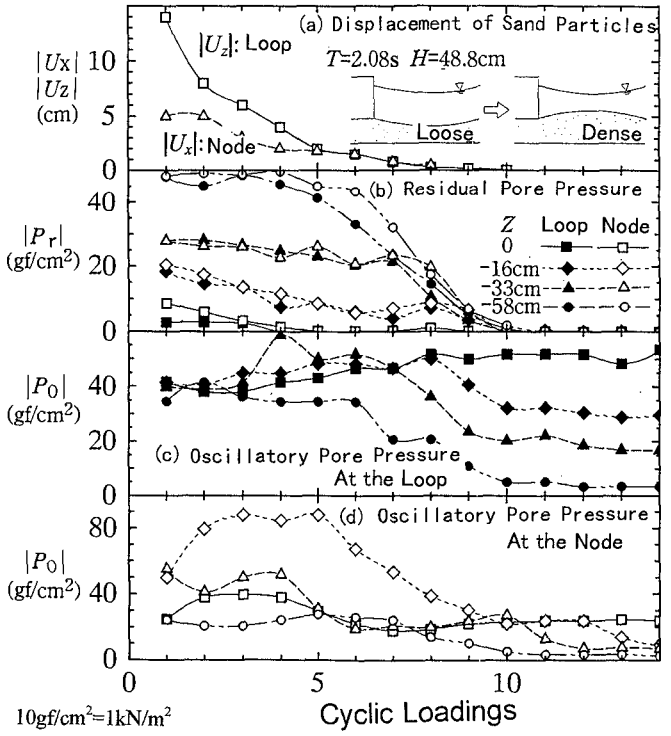

Figure 12 Compaction due to cyclic wave loading by standing waves.

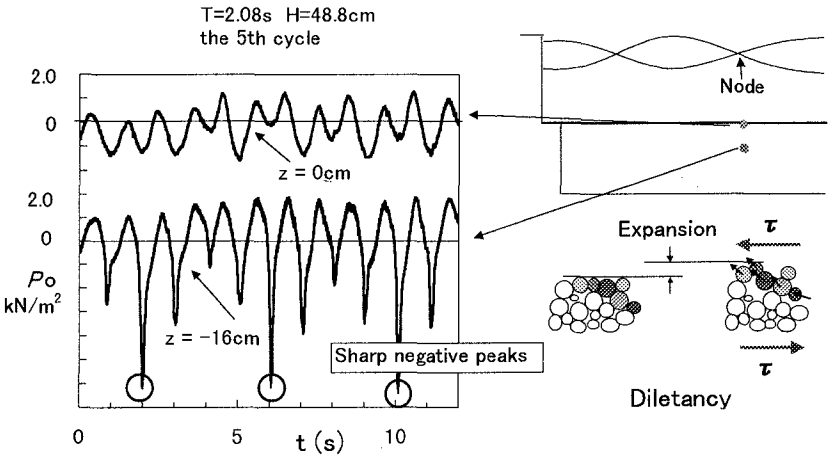

Figure 13 Pore pressure profiles at the node of standing wave at the 5th loading.

Softening Effect

Figure 14 (a)–(c) shows pore pressure profiles at the loop of a standing wave after it hits a fully compacted sandbed. For small waves (14(a)), the pore pressure lags out of phase and is damped out in the direction of sand bed depth; whereas for larger ones (Figure 14(b)), it penetrates deeper into the sand and is in phase. When feedwater is supplied (Figure 14(c)), this phenomena can be seen more clearly in that there is no lagging out of phase and no damping of pressure.

We call this phenomenon the "softening effect" because it exhibits the same characteristic as the shear modulus of soil. Namely, if the shear strain becomes large, the shear modulus of soil is reduced. Large shear strain is generated by strong wave pressure and amplified by upward seepage flow.

4. FEM SIMULATIONS

Using FEM in conjunction with Biot's equations (Park et al (1996)), pore pressure was numerically simulated for a standing wave ($T = 2.08$ s, $H = 48.8$ cm). Figure 15(a) shows results for compacted sand in which the strain is small with a large shear modulus G of 10000 kN/m^2, where in this case the oscillatory pore pressure lags out of phase and dampens out in the direction of sandbed depth. Figure 15(b) shows results for lower G = 1000 kN/m^2, a large wave, and feedwater being supplied, where due to the softening effect, pore water penetrates deeper into the sandbed and no time lag or damping occurs. Finally, Fig. 15(c) shows G = 10 kN/m^2 for loose sand, where it should be noted that such substantial lowering of G produces behavior similar to that observed in Fig. 15(b) with feedwater being supplied.

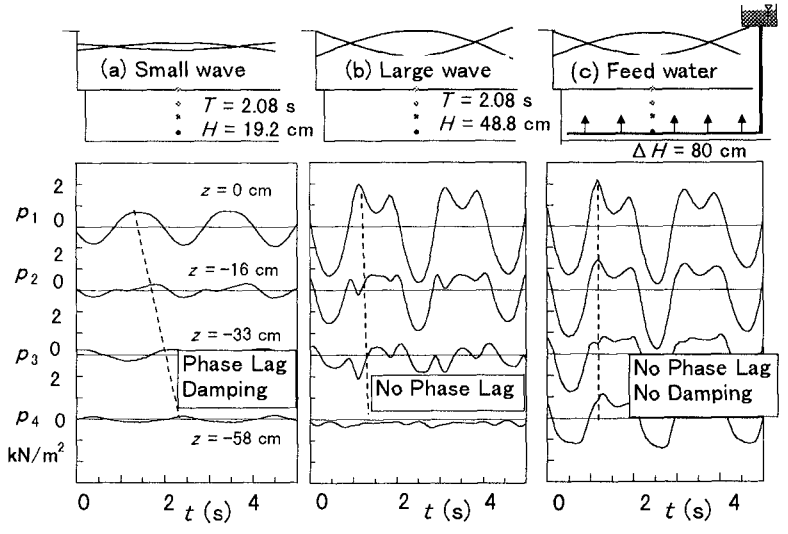

Figure 14 Pore pressure profile at the loop of a standing wave.

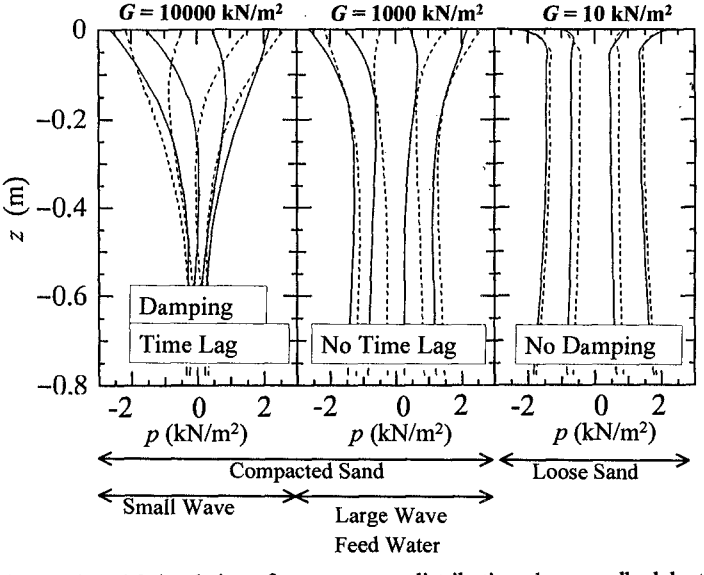

Figure 15 FEM simulation of pore pressure distribution along sandbed depth.

5. SUMMARY

Using model experiments, we observed the following phenomena:

1) When waves act on a loosely packed fine sandbed: (*i*) the skeleton structure of the sandbed easily breaks and it behaves like a thick liquid, and (*ii*) the internal pore pressure builds up within it, *i.e.*, sandbed liquefaction occurs due to the excess pore pressure.

2) Waves acting on a sandbed gradually squeeze out the excess pore pressure such that a compaction effects occurs.

3) For small waves, compaction is limited to near the sandbed surface. However, as the waves get larger, the sandbed is again liquefied and compaction substantially expands into deeper depths.

4) Once fully compacted, large waves produce large shear strain due to a corresponding decrease in the shear modulus, *i.e.*, a softening effect occurs allowing the pore pressure, which is in phase in the direction of sandbed depth, to penetrate deeper into the sandbed.

While it is important to gain experimental insights elucidating the effects of waves acting on a fine sandbed, our future work will be directed at developing methods to quantitatively evaluate the effects of such phenomena; as only in this manner can we assuredly prevent associated damage to coastal breakwaters.

REFERENCES

1) Foda, M. A., S. Y. Tzang and Y. Maeno (1991): Resonant soil liquefaction by water waves, GEO-COAST'91, Vol. 1, pp. 549–554.
2) Sekiguchi, H., K. Kita, and O. Okamoto (1995): Response of poro-elastoplastic beds to standing waves, Soils and Foundations, Vol. 35, 3, pp. 31–42.
3) Park, W. and Takahashi, S. (1996): FEM simulation of wave-soil-structure interaction problem, Proceeding of 3rd Asian Pacific Conference of Computation Mechanics
4) Zen, K. and Yamazaki, H. (1990): Mechanism of wave-induced liquefaction and densification in seabed, Soils and Foundations, Vol. 30, No. 4, pp. 90–104.

LONG-PERIOD OSCILLATIONS IN A HARBOUR WITH FLUID MUD BOTTOM

Wataru KIOKA[1], M. Akter HOSSAIN[2] and Kenji KASHIHARA[3]

ABSTRACT

Non-linear dynamic responses of fluid mud to the oscillating surface waves in a harbour basin and their consequential effects on the long-period harbour excitations are investigated. A set of Boussinesq-type equations based on the weakly nonlinear, dispersive and viscous wave theories is developed for coupled two-layer density stratified system, incorporating the boundary layer corrections for the interfacial shear and mud viscosity. Laboratory experiments are also conducted with fluid mud for different wave periods, and the generation, behavior and different propagation modes of the interfacial waves are examined. Both experimental and numerical results demonstrate that the amplification of water surface displacements is significantly reduced near the first peak of resonance oscillations in the harbour where the internal mode of the interfacial waves governs the surface mode in the motion of the interface. Near the second peak of resonance oscillations the surface mode of the interfacial waves dominates and the interface oscillates nearly in phase of surface waves. The amplification of water surface displacements at the second peak is also reduced to some extent.

1. INTRODUCTION

In many harbours with silty sediment bed, the stratified system of water waves overlying a fluid mud layer or suspended sediment layer frequently occurs. Such dense lower layer may have significant effects on the harbour excitations induced by

[1]Professor, [2]Graduate Student and [3]Research Associate: Department of Civil Engineering, Nagoya Institute of Technology, Gokiso-cho, Showa-ku, Nagoya 466-8555, Japan

long-period waves. Many studies have so far been conducted addressing the long-period excitations in harbours, but all the previous studies were based on the assumption that the bottom of the harbour is rigid and non-responsive to the surface waves. The behavior of soft mud bed in a harbour and its interaction with water surface waves are yet to be understood. In this study, the excitations induced by long-period waves in a harbour with soft mud bed are investigated. Generation of interfacial waves, their behaviors and different propagation modes are examined. Effects of bottom mud on the harbour excitations induced by the long-period waves are also analyzed.

For theoretical formulations, we adopted here a two-layer density stratified fluid system with lower layer as the fluid mud, and a set of Boussinesq-type equations based on the weakly nonlinear, dispersive and viscous wave theories is developed describing the nonlinear interaction of fluid mud with the propagating surface waves. The behavior of mud depends on the wave induced internal stresses, and the soft mud can behave elastically at very low strain, visco-elastically at intermediate strain and viscously at the high strain level (Foda et al., 1993). Since the resonant long-period oscillations may induce relatively high oscillatory strains in the mud, the present model assumes that the mud becomes fluidized and behaves like a viscous fluid (Dalrymple and Liu, 1978). For the verification of numerically predicted results from the adopted model, laboratory experiments are also conducted with fluid mud for different incident wave periods.

Long-period oscillations in a harbour are of concern because such oscillations are often responsible for disturbing the operations of ship terminals, for breaking the mooring of vessels and for flooding on the wharf. Countermeasure against such harbour excitations is however not yet established owing to the difficulty of controlling the incident long waves by means of conventional breakwaters. The present study is also aimed to investigate the behavior of fluidized mud inside the harbour, and thereby addresses the possible means of controlling the harbour excitations using fluidized mud. Since the wave heights inside the harbour are usually too small to liquefy the silty harbour bed, a fluidized sediment bed may be artificially generated by boiling (see Takahashi et al.,1994).

2. THEORETICAL FORMULATION

2.1 Governing Equations

A definition sketch of the two-layer fluid system adopted for the theoretical model is presented in Fig.1. The surface wave is propagating in water depth h over a dense mud layer of thickness d. Beneath the lower denser fluid mud, we assumed a rigid impermeable bed. In the analysis, the density-stratified fluid is confined to a harbour basin. The density and viscosity are respectively denoted by ρ and ν, and the subscripts 1 and 2 stand for upper and lower layers respectively. The governing equations for the fluid motion are the continuity and Navier-Stokes equations for an

incompressible fluid. For the simplicity, the mathematical formulations described hereinafter are only for the two-dimensional motion.

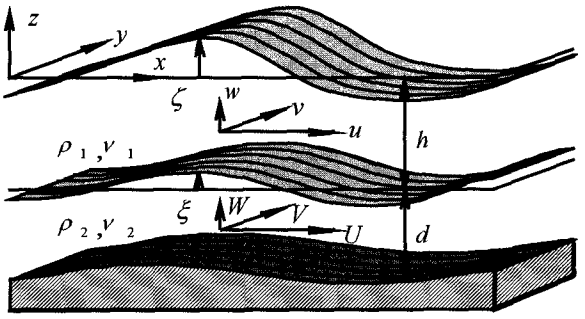

Fig.1. Definition sketch

The dynamic and kinematic boundary conditions at the free-surface are given by

$$p_1 = 0 \qquad (z = \zeta) \qquad (1)$$

$$w = \zeta_t + u\zeta_x \qquad (z = \zeta) \qquad (2)$$

where p_1 is the pressure, u and w are respectively the horizontal and vertical velocities in the upper layer, and ζ is the free-surface displacement. The subscripts x and t indicate the partial derivatives. At the water-mud interface, the following boundary conditions are imposed:

$$p_1 - 2\rho_1\nu_1 w_z = p_2 - 2\rho_2\nu_2(W + \hat{W})_z \qquad (z = -h + \xi) \qquad (3)$$

$$\{u - (U + \hat{U})\}\xi_x - \{w - (W + \hat{W})\} = 0 \qquad (z = -h + \xi) \qquad (4)$$

$$(U + \hat{U})_z + (W + \hat{W})_x = 0 \qquad (z = -h + \xi) \qquad (5)$$

$$u = U + \hat{U} \qquad (z = -h + \xi) \qquad (6)$$

where U and W are the horizontal and vertical velocities in the lower layer respectively, $\hat{U}$ and $\hat{W}$ are the horizontal and vertical rotational velocities at the interface for the lower layer respectively, ξ is the interfacial displacement, and p_2 is the pressure in the lower layer. The subscripts x and z indicate the partial derivatives. Eqs. (3), (4), (5) and (6) are respectively the condition for normal stress continuity, the usual kinematic condition, the condition for shear stress continuity and the continuity of horizontal velocity. The viscous effects of upper fluid are assumed very small, and the rotational velocities at the interface are disregarded in the upper layer. This assumption will be discussed in the following section.

The boundary condition on the fixed impermeable bottom of the lower layer is imposed as

$$W + Ud_x = 0 \qquad (z = -h - d) \qquad (7)$$

Based on the assumption of weak viscosity, the rotational velocities are neglected entirely near the bottom boundary.

2.2 Derivation of Boussinesq Equations

The continuity and Navier-Stockes equations for the two-layer density stratified system of flow of the incompressible fluids and the boundary conditions cited in the previous section provide a complete description of the present model. A perturbation from long wave theory to include the effects of frequency dispersion and viscosity, consistent with Boussinesq theory, is carried out to facilitate the approximate solutions to the above equations. As a first step of formulations, the following non-dimensional variables are introduced in terms of characteristic frequency ω, characteristic wave amplitude a_0, and characteristic water depth h_0:

$$x' = \frac{\omega x}{\sqrt{gh_0}}, y' = \frac{\omega y}{\sqrt{gh_0}}, z' = \frac{z}{h_0}, t' = \omega t, u' = \frac{h_0 u}{a_0\sqrt{gh_0}}, U' = \frac{h_0 U}{a_0\sqrt{gh_0}}$$

$$h' = \frac{h}{h_0}, d' = \frac{d}{h_0}, \zeta' = \frac{\zeta}{a_0}, \xi' = \frac{\xi}{a_0}, p_1' = \frac{p_1}{\rho_1 g a_0}, p_2' = \frac{p_2}{\rho_2 g a_0} \tag{8}$$

In addition, the following two length ratios are defined:

$$\varepsilon = a_0/h_0 \quad \mu = \omega^2 h_0/g \tag{9}$$

Introducing the potential ϕ for the upper layer and Φ for the lower layer, and substitution of these variables into the governing equations reduces to the following non-dimensional forms after some manipulations:

$$\mu^2\phi_{xx} + \phi_{zz} = 0 \qquad (-h + \varepsilon\xi \le z \le \varepsilon\zeta) \tag{10}$$

$$\mu^2\Phi_{xx} + \Phi_{zz} = 0 \qquad (-d - h \le z \le -h + \varepsilon\xi) \tag{11}$$

$$\varepsilon\phi_t + z + \frac{1}{2}\varepsilon\left[\phi_x^{\,2} + \frac{1}{\mu^2}\phi_z^{\,2}\right] = -p_1 \qquad (-h + \varepsilon\xi \le z \le \varepsilon\zeta) \tag{12}$$

$$\varepsilon\Phi_t + z + \frac{1}{2}\varepsilon\left[\Phi_x^{\,2} + \frac{1}{\mu^2}\Phi_z^{\,2}\right] = -p_2 \qquad (-d - h \le z \le -h + \varepsilon\xi) \tag{13}$$

$$p_1 = 0 \qquad (z = \varepsilon\zeta) \tag{14}$$

$$\varepsilon\zeta_t + \varepsilon\mu^2\zeta_x\phi_x - \phi_z = 0 \qquad (z = \varepsilon\zeta) \tag{15}$$

$$p_1 - \frac{2}{\mu^2}\rho_1\nu_1\phi_{zz} = p_2 - \frac{2}{\mu^2}\rho_2\nu_2\Phi_{zz} \qquad (z = -h + \varepsilon\xi) \tag{16}$$

$$\phi_{xz} + \Phi_{xz} = 0 \qquad (z = -h + \varepsilon\xi) \tag{17}$$

$$\mu^2 d_x\Phi_x + \Phi_z = 0 \qquad (z = -d - h) \tag{18}$$

For convenience the primes will be dropped from here on. The smallness parameters ε and μ are the measures of non-linearity and frequency dispersion respectively, and ε and μ^2 are assumed to be of the same order. This implies that the scales of water and mud depths are small compared to the horizontal scale, and that the free surface and interface displacements are also small compared to the depths of upper and lower layers respectively. The effect of viscosity is considered to be relatively weak in both layers and of the order of ε. The upper fluid is further assumed much less viscous than the lower mud such that the ratio of kinematic viscosity $\nu_1/\nu_2 = O(\varepsilon^2)$. This condition leads that the shear in the lower layer is entirely negligible at the interface (Hill and Foda, 1996). The vertical rotational velocity is zero to the leading order at the interface.

Integrating the continuity equations from the solid bottom to the interface, and from interface to the free surface, and applying the kinematic boundary conditions we get

$$\frac{\partial \zeta}{\partial t} + \frac{\partial}{\partial x}\int_{-h+\varepsilon\xi}^{\varepsilon\zeta} u\,dz + \frac{\partial}{\partial x}\int_{-h-d}^{-h+\varepsilon\xi} U\,dz = 0 \tag{19}$$

$$\frac{\partial \xi}{\partial t} + \frac{\partial}{\partial x}\int_{-h-d}^{-h+\varepsilon\xi} U\,dz = 0 \tag{20}$$

Similarly the momentum equations can be integrated over each fluid layer to give (see Mei,1983)

$$\frac{\partial}{\partial t}\int_{-h+\varepsilon\xi}^{\varepsilon\zeta} u\,dz + \varepsilon\frac{\partial}{\partial x}\int_{-h+\varepsilon\xi}^{\varepsilon\zeta} uu\,dz + \frac{\partial}{\partial x}\int_{-h+\varepsilon\xi}^{\varepsilon\zeta} p_1\,dz + p_1\Big|_{-h+\varepsilon\xi}\frac{\partial(\varepsilon\xi)}{\partial x} = 0 \tag{21}$$

$$\frac{\partial}{\partial t}\int_{z}^{\varepsilon\zeta} w\,dz + \varepsilon\frac{\partial}{\partial x}\int_{z}^{\varepsilon\zeta} uw\,dz - \frac{\varepsilon}{\mu^2}w^2 + g(\zeta - \frac{z}{\varepsilon}) - p_1 = 0 \tag{22}$$

$$\frac{\partial}{\partial t}\int_{-h-d}^{-h+\varepsilon\xi} U\,dz + \varepsilon\frac{\partial}{\partial x}\int_{-h-d}^{-h+\varepsilon\xi} UU\,dz + \frac{\partial}{\partial x}\int_{-h-d}^{-h+\varepsilon\zeta} p_2\,dz - p_2\Big|_{-h+\varepsilon\xi}\frac{\partial(\varepsilon\xi)}{\partial x} - p_2\Big|_{-h-d}\frac{\partial d}{\partial x} = 0 \tag{23}$$

$$\frac{\partial}{\partial t}\int_{z}^{-h+\varepsilon\xi} W\,dz + \varepsilon\frac{\partial}{\partial x}\int_{z}^{-h+\varepsilon\zeta} UW\,dz - \frac{\varepsilon}{\mu^2}W^2 + g(-\frac{h}{\varepsilon} + \xi - \frac{z}{\varepsilon}) + p_2\Big|_{-h+\varepsilon\xi} - p_2 = 0 \tag{24}$$

The horizontal velocities u and U may be expanded as Taylor series about the interface and the solid bottom respectively. The resultant horizontal velocities can be expressed in terms of layer-averaged velocities $\bar{u}$ and $\bar{U}$ for both layers as

$$u = \bar{u} - \mu^2\left[\left\{\frac{1}{2}(z+h)^2 - \frac{1}{6}h^2\right\}\frac{\partial^2\bar{u}}{\partial x^2}\right] + \mu^2\left[\left\{(z+h) - \frac{1}{2}h\right\}\frac{\partial^2(d\bar{U})}{\partial x^2}\right] + O(\mu^4) \tag{25}$$

$$U=\overline{U}-\mu^2\left[\left\{\frac{1}{2}(z+d+h)^2-\frac{1}{6}d^2\right\}\frac{\partial^2\overline{U}}{\partial x^2}\right]-\mu^2\left[\left\{(z+d+h)-\frac{1}{2}d\right\}\frac{\partial d}{\partial x}\frac{\partial\overline{U}}{\partial x}\right]$$

$$-\mu^2\left[\left\{(z+d+h)-\frac{1}{2}d\right\}\frac{\partial}{\partial x}(\frac{\partial d}{\partial x}\overline{U})\right]+O(\mu^4) \tag{26}$$

The horizontal velocities vary quadratically over each layer to this order. The corresponding expressions for vertical velocities are obtained from the continuity equation as

$$w=\frac{\partial\xi}{\partial t}-\mu^2(z+h)\frac{\partial\overline{u}}{\partial x}+O(\mu^4) \tag{27}$$

$$W=-\mu^2\left[(z+h+d)\frac{\partial\overline{U}}{\partial x}+\overline{U}\frac{\partial d}{\partial x}\right]+O(\mu^4) \tag{28}$$

Substituting Eq.(25) to Eq.(28) into the layer-integrated continuity and momentum equations (19)-(24) and retaining the terms up to $O(\varepsilon)$ and $O(\mu^2)$, a set of Boussinesq-type equations can be obtained for the adopted coupled two-layer density stratified system. This set of equations is given in terms of physical variables for the three-dimensional problem as

$$\zeta_t+\nabla\cdot[(h+\zeta-\xi)\overline{\boldsymbol{u}}]+\nabla\cdot[(d+\xi)\overline{\boldsymbol{U}}]=0 \tag{29}$$

$$\xi_t+\nabla\cdot[(d+\xi)\overline{\boldsymbol{U}}]=0 \tag{30}$$

$$\overline{\boldsymbol{u}}_t+(\overline{\boldsymbol{u}}\cdot\nabla)\overline{\boldsymbol{u}}+g\nabla\zeta-\left[\frac{1}{3}h^2\nabla(\nabla\cdot\overline{\boldsymbol{u}}_t)+\frac{1}{2}h\nabla(\nabla\cdot(d\overline{\boldsymbol{U}}_t))\right]=\mathbf{0} \tag{31}$$

$$\overline{\boldsymbol{U}}_t+(\overline{\boldsymbol{U}}\cdot\nabla)\overline{\boldsymbol{U}}+(1-\frac{1}{\gamma})g\nabla\xi+\frac{1}{\gamma}g\nabla\zeta+\left[\frac{1}{6}d^2\nabla(\nabla\cdot\overline{\boldsymbol{U}}_t)-\frac{1}{2}d\nabla(\nabla\cdot(d\overline{\boldsymbol{U}}_t))\right]$$

$$-\frac{1}{\gamma}\left[h\nabla(\nabla\cdot(d\overline{\boldsymbol{U}}_t))+\frac{1}{2}h^2\nabla(\nabla\cdot\overline{\boldsymbol{u}}_t)\right]-2(\nu_2-\frac{1}{\gamma}\nu_1)\nabla(\nabla\cdot\overline{\boldsymbol{U}})=\mathbf{0} \tag{32}$$

where γ is the density ratio defined as $\gamma=\rho_2/\rho_1$, and $\overline{\boldsymbol{u}}$ and $\overline{\boldsymbol{U}}$ are the velocity vectors in upper and lower layers respectively. The model equations (29)-(32) yield the standard Boussinesq equations if all the terms involving $\overline{\boldsymbol{U}}$ are omitted.

3. NUMERICAL SIMULATION

Eq.(29) to Eq.(32) are solved using a finite difference scheme. The spatial derivatives in one direction are approximated using a 5-grid-points centered differences with fourth-order accuracy, leading to a truncation error that is sufficiently small relative to all the terms retained in the equations. For the temporal integral, an iterative scheme based on Adams-Bashforth-Moulton method is employed. The free surface displacement ζ and interfacial displacement ξ are

computed explicitly from the continuity equations (29) and (30). The velocity components in x-direction are computed implicitly from the momentum equations (31) and (32), treating the derivatives of $\overline{u}$ and $\overline{U}$ in y-direction as explicit. Similarly, the computations of velocities in y-direction are done implicitly from momentum equations, treating the derivatives of $\overline{v}$ and $\overline{V}$ in x-direction as explicit.

At the incident boundary, both ζ and $\overline{u}$ are assumed to be given as input, and all the outgoing waves are absorbed applying radiation condition prescribed from the linear long wave theories. A harbour with fully reflective boundaries is treated as the solid walls and the velocity normal to the wall is taken as zero.

4. EXPERIMENTAL INVESTIGATION

Experiments were conducted to investigate the behavior of fluid mud in the harbour. The detailed experimental setup is shown in Fig.2. A laboratory wave flume of 26.0 m long, 0.60 m wide and 1.20 m high with glass walls throughout was used for the experiments. A model of rectangular harbour was installed on the horizontal bottom at 5.2 m apart from the step of the flume. A harbour basin, 50 cm long and 20 cm wide has straight breakwaters at both sides of its entrance. The experiments were also conducted for the rectangular harbour without breakwater. The harbour walls were made of acrylic fiber, so that the motions of the water surface and interface can be observed using a video camera through glass walls of the wave flume. A false bottom inside the harbour was lower than the horizontal bottom by 5cm. The hollow 5cm deep was filled up with mud.

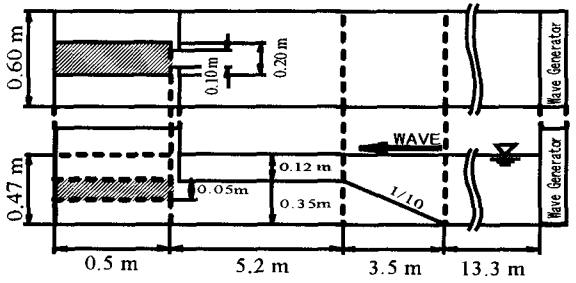

Fig.2. Experimental setup

The commercially available fine silts of mean diameter 50 μm were used to prepare the fluid mud for the experiments. Silts were mixed with water to make a well-mixed slurry of density about $\rho_2 = 1.2$ g/cm^3. The slurry was then gently poured into the harbour to fill the requisite depth of 5.0 cm. The harbour mouth was tightly fenced from the outside before filling up water to the required depth. After filling, the mud layer in the harbour was stirred again and allowed to settle half a day. The muddy water above the interface was removed before experiments. This procedure was repeated for each experimental run to keep the requisite depth of fluid mud. By taking samples through the mud layer, only the depth-averaged density ρ_2 is measured during the experiment.

The water depth over the fluid mud bed was kept at $h = 12$cm. A monochromatic wave with the wave height $H = 1.5$ cm was used as an incident wave for wave periods T ranging from 0.8 s to 2.0 s. Wave gauges were used to record the temporal surface wave profiles at several locations of the flume including the corner of the harbour. At the same time, the spatial profiles of the free surface and interfacial waves over the longer side of the harbour were recorded with a digital video camera through the glass walls. The interfacial displacements at the corner of the harbour were read out from the enlarged video pictures.

5. MOTION OF FLUID MUD

The observed responses of fluid mud in the harbour for various wave periods were compared with the numerical predictions for the purposes of model evaluation. In the numerical calculations the measured water surface profiles ζ were used as input data on the upwave control surface, and the corresponding horizontal velocities $\bar{u}$ were given from the linear long wave theory. The results were, however, essentially identical to the predictions based on sinusoidal profiles ζ as input. Viscosity measurements of fluid mud were not made in the laboratory experiments. Ting and Lemasson (1996) showed from rheological tests that the viscosity of fluid mud confined within a submerged rectangular trench was not significantly affected by shear rate and time of shearing in the low strain-rate region. Since the strain rates in fluid mud under the present wave conditions were still relatively small, the viscosity ν_2 was determined from their rheological tests using the asymptotic values at low shear rate as a function of mud density.

Fig.3 shows the snapshot of the computed free-surface and interfacial displacements in the harbour without breakwater. The line X=0 in the figure indicates the end of the

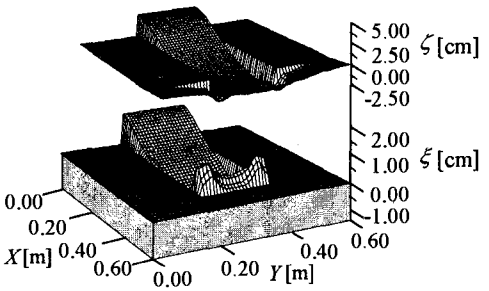

Fig.3. Snapshot of free surface and interfacial profiles
(T=0.8s, ρ_2=1.19 g/cm^3, ν_2=16.4 cm^2/s)

harbour. The figure is plotted for T=0.8s, which corresponds to the second peak of the resonant oscillations in the harbour. The oscillations of dense mud layer appear to be almost in phase of the free-surface profiles.

Fig.4 shows the comparison of spatial profiles of the free-surface and the interfacial displacements along the longer side of the harbour. Upper and lower figures show the

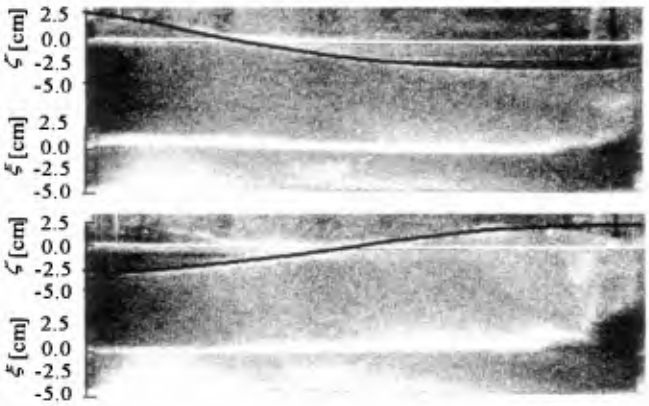

(a) Measured profiles

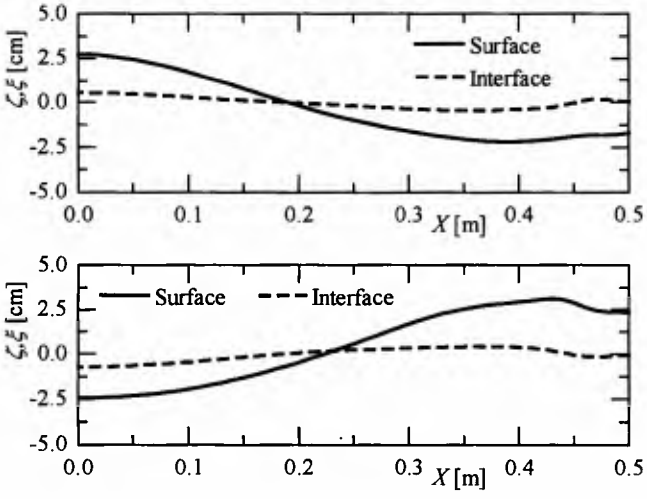

(b) Numerical profiles

Fig.4. Spatial profiles (T=0.8s, ρ_2=1.19 g/cm^3, ν_2=16.4 cm^2/s)

images respectively when the water surface displacements become maximum at the corner of the harbour and $T/2$ after that time. The surface mode of the interfacial waves governs the motion of the interface and the interface oscillates nearly in phase of surface waves. At the entrance of the harbour, small internal waves out of phase are observed both in the experimental and numerical results, but they quickly absorb their energy within a very short distance from the harbour mouth.

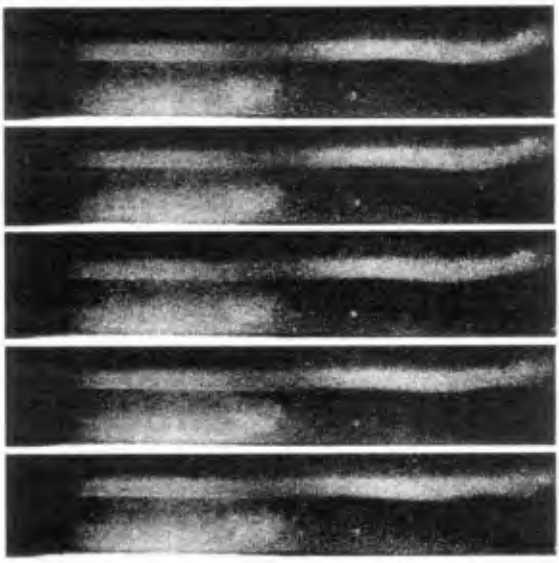

(a) Measured profiles

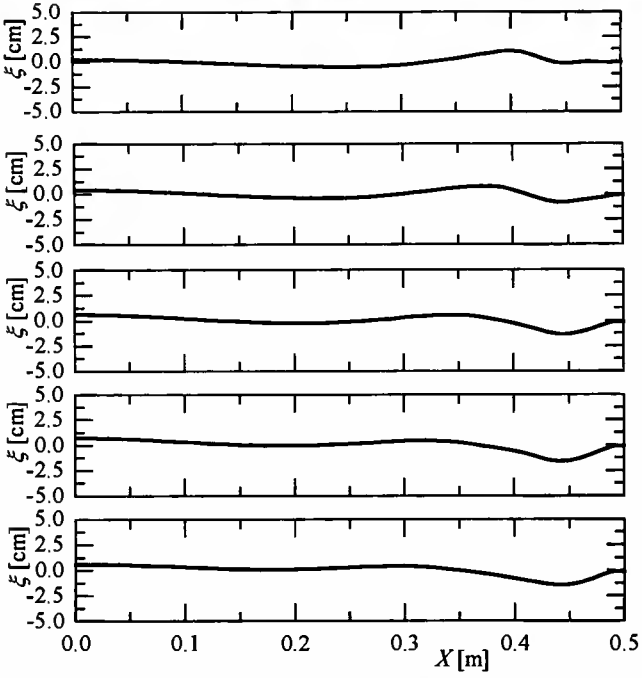

(b) Numerical profiles

Fig.5. Spatial profiles (T=1.2s, ρ_2=1.19 g/cm^3, ν_2=16.4 cm^2/s)

The sequence of pictures at intervals of 0.1s for the wave period of 1.2s is shown to demonstrate the motion of fluid mud inside the harbour in Fig.5. It is observed from both experimental and numerical profiles that the interfacial waves are first generated at the harbour mouth, and propagate at internal phase speed towards the harbour end. The amplitudes of the interfacial waves are substantially reduced in course of their propagation due to the energy dissipation. The phase of the numerically simulated profiles is slightly delayed from the experimental profiles.

Fig.6 shows the comparison of spatial profiles for T=1.6s which corresponds nearly to the first peak of resonant oscillations in the harbour without breakwater. Distinct

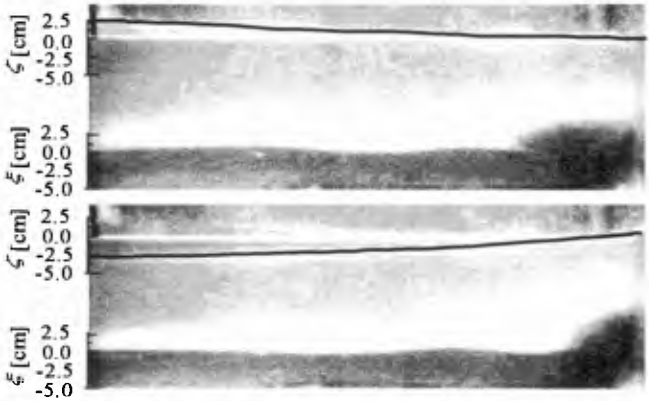

(a) Measured profiles

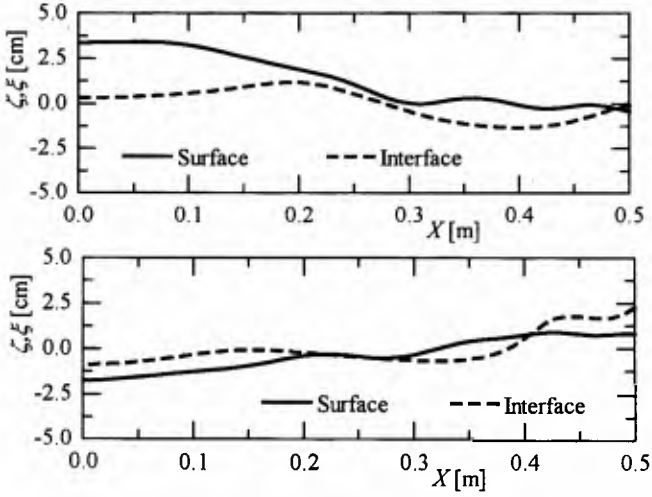

(b) Numerical profiles

Fig.6. Spatial profiles (T=1.6s, ρ_2=1.19 g/cm^3, ν_2=16.4 cm^2/s)

internal waves at the interface are observed in this case and the internal mode of the interfacial waves dominates the motion of the interface. Both the experimental and numerical results indicate that the internal wave generated at the harbour mouth propagates towards the harbour end without much dissipation. The amplification of the free-surface displacements inside the harbour is significantly reduced in this case. As shown in Fig.6 (a), the mud bed is strongly stirred up due to the vortex formed at the harbour mouth. The response of fluid mud to wave action may no longer be described by the two-layer model due to this suspended sediment. The present model must be modified for quantitative accuracy.

6. AMPLIFICATION FACTOR

The experimental and numerical results for the amplification factor of the water surface and interfacial displacements are shown in Fig.7 for the harbour without breakwater. The amplification factor is defined as the ratio of wave height H at the corner of the harbour to the incident surface wave height H_i and plotted as a function of the ratio of the harbour length l to the length of incident wave L, with L being determined from linear wave theory. The results for the harbour with breakwaters at

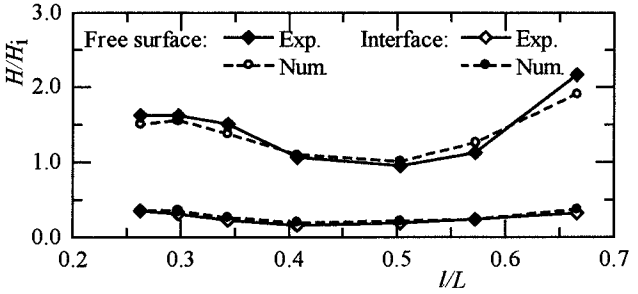

Fig.7. Amplification factors at the corner of harbour without breakwater

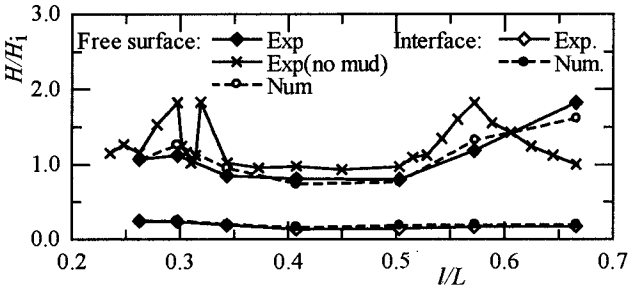

Fig.8. Amplification factors at the corner of harbour with breakwater

the entrance are shown in Fig.8. Two peaks observed near the first mode of the resonant oscillations without fluid mud bed is due to the effects of side walls of the wave flume. The amplifications of the water surface waves are significantly reduced

near the first peak of the resonant oscillations where the interfacial displacements governed by the internal mode increase to the maximum. At the secondary peak, the surface mode governs the motion of the interfacial waves, and thus the interface oscillates nearly in phase of the surface wave. In this case, the secondary peak for the water surface displacements shifts to the higher frequency with the apparent increase in water depth by the thickness of mud layer. The amplification factors decrease to a limited extent at the secondary peak.

7. CONCLUDING REMARKS

Behaviors of fluid mud in a harbour basin for various wave periods are investigated both experimentally and numerically. The study reveals that the amplification of water surface waves is significantly reduced near the fundamental peak of long-period oscillations, where the internal mode governs the motion of fluid mud. In the frequency range higher than secondary peak, the surface mode governs the motion of the interface, yielding an insignificant reduction in the amplification factor.

REFFRENCES

Dalrymple, R. A., and Liu, P. L. –F (1978). "Waves over soft muds: A two-layer fluid model", *J. Phys. Oceanogr.*, Vol.8, pp.1121-1131.

Foda, M. A., Hunt, J. R., and Chen, H. T. (1993). "A nonlinear model for the fluidization of marine mud by waves", *J. Geophys. Research.*, Vol.98, pp.7039-7047.

Hill, D. F., and Foda, M. A. (1996). "Subharmonic resonance of short internal standing waves by progressive surface waves", *J. Fluid Mech.*, Vol.321, pp.217-233.

Mei, C. C. (1983). "The applied dynamics of ocean surface waves", *John Wiley, New York*, 740p.

Takahashi, S., Shimosako, K., Yamamoto and Miura, H. (1994). "Small-scale experiments on a boiling sand bed and its wave absorbing effects", *Proc. of Coastal Eng., JSCE*, Vol.41, pp.611-615 (in Japanese).

Ting, F. C. K., and Lemasson, W. J. (1996). "Dynamic response of fluid mud in a submarine trench to water waves", *Coastal Engineering*, Vol.27, pp.97-121.

Non-Uniformity in the Wind Generated Gravity Waves Phase Distribution

Germán Rodríguez[1]
C. Guedes Soares[2]
E. Pérez Martell[1]
J. C. Nieto[3]

Abstract

Empirical results which show the existence of a relationship among the probabilistic behaviour of the sea surface elevation, the statistical properties of the phase spectral estimates and the sea surface bispectra are presented. Furthermore, some theoretical relations proposed to characterise the marginal density function of the waves phase for the linear and non-linear wave records are examined.

Introduction

The free sea surface elevation in deep waters is generally considered to be the result of the superposition of a large number of sinusoidal waves of different frequencies, amplitudes and phases. Besides, it is usually assumed that the phase angles are mutually independent and are uniformly distributed in the interval *(0, 2π]*. Hence, the free surface elevation at a given point can be represented as

$$\eta(t) = \sum_{n=1}^{\infty} a_n \cos(\omega_n t) + b_n \operatorname{sen}(\omega_n t) = \sum_{n=1}^{\infty} C_n \cos(\omega_n t + \varepsilon_n) \qquad (1)$$

where directionality of waves has not been considered. In Eq. (1), a_n and b_n are the Fourier coefficients, assumed normally distributed, $C_n = \left(a_n^2 + b_n^2\right)^{1/2}$ are the wave amplitudes, ω_n the frequencies, ranging from *0* to infinity and $\varepsilon_n = tan^{-1}\left(-b_n / a_n\right)$ the

[1] Universidad de Las Palmas de Gran Canaria, Departamento de Física, Las Palmas, Spain.
[2] Universidade Técnica de Lisboa, Instituto Superior Técnico, Lisboa, Portugal
[3]Clima Marítimo, Puertos del Estado, Madrid, Spain, (Present address: GKSS Institute, Geesthacht, Germany)

phases, uniformly random.

Under these assumptions it can be shown, by invoking the central limit theorem, that $\eta(t)$ posses a Gaussian distribution,

$$p(\eta)=\frac{1}{\sigma_\eta\sqrt{2\pi}}exp\left[-\frac{(\eta^2)}{\sigma_\eta^2}\right] \tag{2}$$

For waves of low steepness there is a reasonable agreement between this linear model and observations and the free surface is very nearly Gaussian. However, various authors (e.g. Huang and Long, 1980) have reported significant deviations from the Normal distribution for steeper waves, with the free surface displaying sharper peaks and shallower troughs. The observed deviations from Gaussianity can only be explained by the existence of nonlinear interactions among wave components. The first author dealing with this problem was Longuet-Higgins (1963), who suggested that the free surface elevations should be considered as a weakly non-linear process. In other words, surface elevations can be considered as a quasi-normal process. Given that wave-wave non-linear interactions are consequence of the existence of phase relationships, or phase coupling between wave components, deviations from the Gaussian distribution for $\eta(t)$ must be reflected on the probability distribution of phase angles. It can be shown that for a stationary process with a narrow spectral bandwidth the phase distribution can be uniform only if the probability density of the free surface elevations is strictly Gaussian (e.g. Bitner, 1980).

In this paper, the relations between the bispectrum and the statistical behaviour of the sea surface elevation and the phases of the wave components are analysed. Furthermore, the effects of the phase statistical properties on wave groupiness are investigated. Finally, some features of the probability density function of the wave phases are examined.

Probability distribution of wave envelope and phase

Upon the assumption of narrow band random function, the sea surface elevation can be expressed as

$$\eta(t)=A(t)cos\phi(t) \tag{3}$$

where $A(t)=\left(\eta^2+\hat{\eta}^2\right)^{1/2}$ is the wave envelope, $\phi(t)=tan^{-1}\left(\hat{\eta}/\eta\right)$ the phase and $\hat{\eta}$ is the Hilbert transform of $\eta(t)$. Then, introducing the normalised variable $\xi=A/A_{rms}$, where $A_{rms}=\sqrt{2}\eta_{rms}$ is the root mean square of the wave envelope amplitude, it can be shown (eg. Bitner, 1980, Tayfun, 1993) that the joint distribution of A and ϕ is given by the product of the corresponding marginal probability densities,

$$p(\xi,\phi)=p(\xi)p(\phi)=\left[2\xi exp\left(-\xi^2\right)\right]\left[1/2\pi\right] \tag{4}$$

This result reveals that for a linear narrow banded wave field both variables are statistically independent, with the amplitudes following a Rayleigh distribution and the phases uniformly distributed in $(0,2\pi]$.

From the above discussion it should be expected that, except for very low sea states, the probability density function of phase angles deviate from the uniformity, reflecting the existence of privileged phases. However, this fact is still controversial, with various authors presenting contradictory results.

On the other hand, the importance of phase information in the Fourier representation of wind generated waves have received very little attention because the phase spectrum contains no relevant information under the assumption of a Gaussian random process. However, phase information for non-Gaussian waves may result of vital importance in practical applications. Thus, for example, the presence of phase coupling among the various component wave frequencies results in a non-Gaussian signal which is capable of significantly alter the response of a system thought to be subject to a Gaussian input.

The present interest on the phase information has raised mainly in relation with the wave grouping phenomenon. Also, this subject is far from solved. Thus, while some authors consider that phase information is necessary for a good description of wave groups. (e.g. Johnson et al., 1978 and Burcharth, 1978), some other authors (e.g. Rye and Lervik 1981 and Goda, 1983) support that the phases of the spectral components for wind waves can be considered as independent and uniformly distributed on the interval $(0\text{-}2\pi]$.

Following the work by Longuet-Higgins (1963), Tayfun and Lo (1989, 1990) and Tayfun (1993, 1994) have examined the representation of second-order random waves in terms of the effect of second-order nonlinearities on the wave envelope and phase. These authors assumed that, in general, in deep water nonlinearities are relatively weak so that its statistical and spectral characteristics can be adequately described by a two-term perturbational solution to the governing nonlinear equations of motion.

Tayfun (1994), expressed the sea surface displacement from the mean level as the superposition of a first order solution η_1 , given by (1), and a second order solution η_2, which includes the nonlinear nonresonant components of frequencies $\omega_m + \omega_n$ and $\omega_m - \omega_n$ generated by any two components of η_1 with frequencies ω_m and ω_n. Thus, the sea surface elevation at a given point can be expressed as

$$\eta(t) = \eta_1 + \eta_2 = \eta_1 + \left(\eta_2^+ + \eta_2^-\right) \tag{5}$$

where,

$$\eta_2^{\pm} = \lim_{N\to\infty} \frac{1}{4} \sum_{m=1}^{N} \sum_{n=1}^{N} C_m C_n K_{m,n}^{\pm} \cos\left[\left(\omega_m \pm \omega_n\right) + \left(\varepsilon_m \pm \varepsilon_n\right)\right] \tag{6}$$

and

$$K_{m,n}^{\pm} = K^{\pm}\left(\vec{k}_m, \vec{k}_n\right) = K^{\pm}\left[k_m, k_n, \cos\left(\theta_m - \theta_n\right)\right] \tag{7}$$

with $\vec{k}_m, \vec{k}_n$ the horizontal wave-number vectors with moduli k_m and k_n; and directions θ_m, θ_n, measured positive counterclockwise from the x axis. $K^{\pm}$ represents the interaction coefficients (e.g., Longuet-Higgins, 1963, Tayfun, 1990).

In this context, the Gaussian law is not useful to characterise the probability distribution of $\eta(t)$. For this, some authors (e.g. Longuet-Higgins, 1963; Huang et al., 1983) have suggested alternative expressions for $p(\eta)$ by considering weak interactions among wave components. Besides, in this case, the wave envelope amplitude ξ and the phase ϕ are no more statistically independent (Tayfun, 1994). The marginal density function of ξ has the same expression as in (4) whereas the marginal density of ϕ is given by

$$p(\phi) = \frac{1}{2\pi}\left(1 - \frac{1}{6}\sqrt{\frac{\pi}{2}}\lambda_3 \cos\phi\right) \tag{8}$$

and the joint distribution function of these variables is given now by

$$p(\xi,\phi) = \frac{\xi}{\pi} exp\left(-\xi^2\right)\left[1 + \frac{\sqrt{2}}{3}\lambda_3\xi\left(\xi^2 - 2\right)\cos\phi\right] \tag{9}$$

where λ_3 is the coefficient of skewness. Under oceanic conditions this coefficient should be usually $\lambda_3 < 0.75$ (Srokosz and Longuet-Higgins, 1986). An asymptotic expression useful to estimate this parameter in terms of the zero m_0 and second order m_2 spectral moment is (Tayfun, 1990)

$$\lambda_3 = \frac{12\pi^2}{g}\left(\frac{m_2}{\sqrt{m_0}}\right) \tag{10}$$

From equation (4) it is easy to show (Tayfun, 1994) that in the linear case the mean value and variance of the wave phases are given by,

$$\langle\phi\rangle = \pi \quad ; \quad Var(\phi) = \frac{\pi^2}{3} \tag{11}$$

From Equation 8, in the nonlinear case the mean value of ϕ is equal to that in the linear one. However, the variance depends on the coefficient of skewness, and is given by,

$$Var(\phi) = \frac{\pi^2}{3} - \frac{1}{3}\sqrt{\frac{\pi}{2}}\lambda_3 \tag{12}$$

Measurements and Data analysis

The analysed wave records were measured, by using a Waverider buoy deployed at deep waters in the Stajfiord oil platform (Norway continental shelf). The sampling frequency was $2H_z$ and the total record length close to 20 minutes with 2048 digitised values. The overall period analysed covers from January to February 1989.

Since the pioneering paper by Hasselmann et al. (1963), bispectral analysis has been considered as a useful tool for investigating the nonlinear properties of random waves and to identify phase characteristics of non-Gaussian wind generated wave records. According to these authors, if the surface elevation $\eta(t)$ is a stationary zero mean valued random process, the spectra $S(\omega)$ and the bispectra $S(\omega_1,\omega_2)$ are defined respectively as

$$S(\omega)=\frac{1}{2\pi}\int_{-\infty}^{\infty}R(\tau)e^{-i\omega\tau}d\tau \tag{13}$$

$$S(\omega_1,\omega_2)=\frac{1}{(2\pi)^2}\int_{-\infty}^{\infty}\int_{-\infty}^{\infty}R(\tau_1,\tau_2)\,e^{-i(\omega_1\tau_1+\omega_2\tau_2)}d\tau_1 d\tau_2 \tag{14}$$

where

$$R(\tau)=E[\eta(t)+\eta(t+\tau)] \tag{15}$$

$$R(\tau_1,\tau_2)=E[\eta(t)+\eta(t+\tau_1)+\eta(t+\tau_2)] \tag{16}$$

and $E[\ ]$ denotes the mathematical expectation. The bispectra has been estimated by using the method suggested by Kim and Powers (1979). That is, by segmenting the wave records into N segments to obtain the following smoothed estimation of the bispectra,

$$B(k,l)=\frac{1}{N}\sum_{n=1}^{N}X_n(k)X_n(l)X_n(k+l) \tag{17}$$

where k and l are the frequencies of the interacting wave components and X are the complex Fourier coefficients, which can be computed efficiently by means of the Fast Fourier Transform (FFT) algorithm.

Assuming the linear wave theory, the sea surface elevation should be symmetric. Thus, the asymmetry of wave record profiles implies the existence of nonlinearities. Furthermore, the vertical asymmetry of the sea surface profile with respect to the mean water level can be characterised by the coefficient of skewness λ_3 of the sea surface elevation probability distribution. It can be shown (e.g., Kim et al., 1980) that for a stationary process with zero mean λ_3 and $S(\omega_1,\omega_2)$ are related through the following relationship

$$\lambda_3=\frac{1}{\left(E[\eta^2(t)]\right)^{3/2}}\int_{-\infty}^{\infty}\int_{-\infty}^{\infty}S(\omega_1,\omega_2)d\omega_1 d\omega_2 \tag{18}$$

Taking into account that λ_3 must be null for a Gaussian process and that it is proportional to the zero order moment of the bispectrum, a value different from zero for the bispectrum implies a non-zero value of the skewness and some deviation of the sea surface elevation probability function from the Gaussian distribution or equivalently asymmetries in the wave record. As a consequence, statistically significant deviations of $S(\omega_1,\omega_2)$ from zero can be interpreted as the existence on nonlinearities in the process being examined.

Results and Discussion

The sea surface displacement and the wave phase probability distributions have been obtained for each one of the wave time series recorded at the Stajfiord oil field. The phase spectrum was computed as a previous step to estimate the phase distributions. The Chi-square (with a significance level α=0.05) and Kolmogorov Smirnov tests were applied to examine the statistical significance of the possible deviations from the Gaussian and the uniform distributions.

From a total of 412 wave records analysed, the percentage of rejection of the hypothesis of the Gaussian distribution adequacy to describe the statistical structure of the sea surface elevation was of 64% and 59% for the χ^2 and the K-S tests, respectively. The goodness of fit of the uniform probability function to the wave phase distribution was rejected in a 60% of the cases for both tests. In addition, the probability distribution function given by equation (8) (Tayfun, 1994). Paradoxically, though this model depends on the coefficient of skewness, which represents a measure of nonlinearity, the percentage of rejection was of 66% and 62% for the χ^2 and the K-S tests, respectively. That is, greater than the obtained for the uniform distribution.

Figure 1 shows the sea surface elevation (1a) and wave phase (1b) distributions, and the bispectral density corresponding to a wave record with a very small value of skewness (-0.002) and kurtosis (fourth statistical moment) (-0.004), such as is revealed by the associated low bispectral density. In this case, the Gaussianity and the uniformity were accepted by the two statistical tests. Furthermore, the Tayfun's distribution, which tends to present a maximum at π and minima at 0 and 2π, was also accepted. In this example, the coefficient of skewnees computed by means of (10) is 0.133. Note the difference with that computed directly from the wave record which is slightly negative.

It should be remarked that, while the bispectra have been displayed in all the range of positive frequencies, it only needs to be represented between the origin, the line $f_i=f_k$ and the Nyquist frequency due to its symmetry properties, which can be easily observed in the figure.

In contrast with the low values observed for the bispectrum of the first example, the bispectral density represented in figure 2 presents a large peak revealing an important contribution of nonlinearities, mainly from the auto-interactions of the peak frequency. This effect is reflected in the deviations of the sea surface elevation from the Gaussian distribution, which was rejected by the two statistical goodness of fit tests applied. Such as expected, the probability distribution of wave phases deviate significantly from the uniformity, displaying a maximum at π and minima at 0 and 2π (the coefficient of skewness is 0.356). Hence, the goodness of fit is rejected for the uniform distribution and accepted for the Tayfun's model.

In various cases the wave phase distribution presents an inverse pattern to that expected. That is, the phase probability density presents a maximum at $\phi=0$ and another at $\phi=2\pi$ and a minimum near to $\phi=\pi$. An example of this kind of phase distribution is shown in figure 3. In this example, the Gaussian hypothesis was accepted but the goodness of fit of the wave phase distribution to the uniform distribution and to the Tayfun's model was rejected. In fact, the relatively large percentage of this kind of phase

distribution is the motive for the above mentioned large quantity of rejections for the Tayfun's model, greater than the obtained for the uniform distribution. In some of these cases, the deviation from uniformity is relatively small but the Tayfun's model tend to fit a distribution with an inverse structure to that displayed by the measurements and, as a consequence, it is rejected. Note that in this case the bispectrum presents a moderate amplitude and the coefficient of skewness is 0.356.

Wave phases distributions with a similar structure have been presented (but not discussed) by some authors (eg. Bitner, 1980; Mase et al., 1983). The properties of this wave records are being studied now in detail.

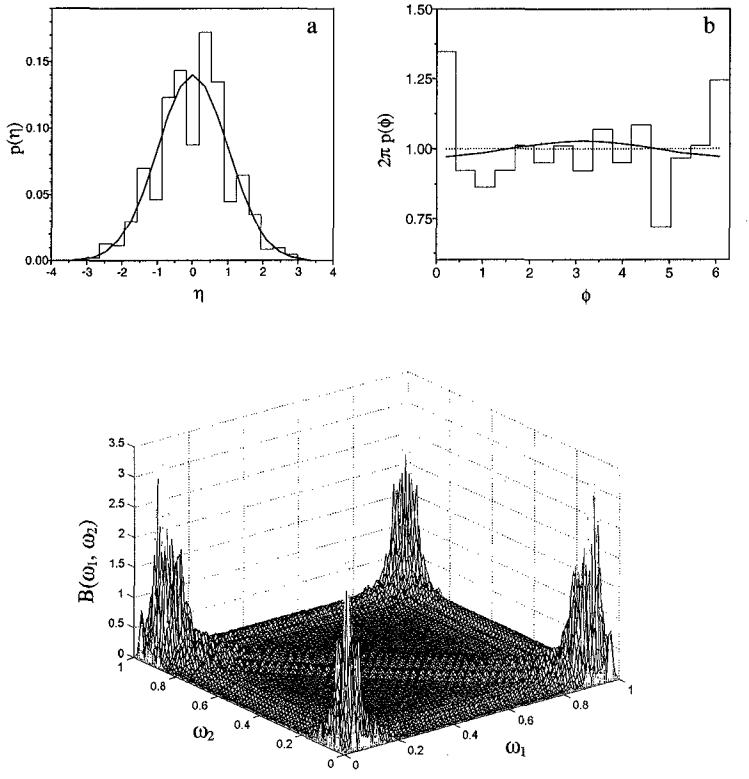

Figure 1. Sea surface elevation (a) and wave phase (b) probability distributions and bispectrum associated to a Gaussian and uniform wave phases distribution wave record.

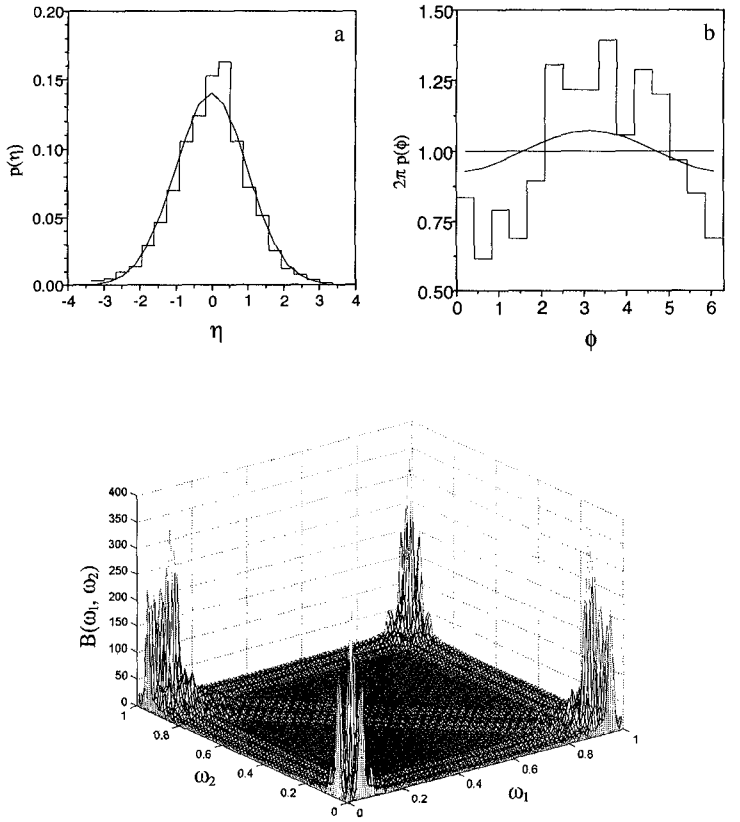

Figure 2. Sea surface elevation (a) and wave phase (b) probability distributions and bispectrum associated to a non-Gaussian and non-uniform wave phases distribution wave record.

In general, there is a trend of the coefficient of skewness to increase with the significant wave height (see Fig. 4a), such as expected according to the comments above and in agreement with results reported by various authors. On the other hand, according to Mase et al., (1983) if the groupiness factor GF, computed in terms of the SIWEH (smoothed instantaneous wave energy history) and proposed by Funke and Mansard (1980), is larger than 0.7, the phase distribution is not uniform, but the appearance frequency becomes large at the phases close to π. Similarly, Yuxiu and Manhai (1996) used a different groupiness parameter named group height factor (GFH) and expressed in terms of the standard deviation and the mean value of the wave envelope, which is estimated directly from the wave records with the Hilbert transform technique. These

authors analysed three sets of field wave data and observed that when GFH is large, the phase distribution is not uniform, but concentrated around π.

The values of the groupiness factor are represented versus the coefficient of skewness in Figure 4b. It can be observed that GF presents a large scatter and that there is not a clear trend of GF to increase with the coefficient of skewness. Thus, the observed results does not support the idea of an increase of the wave groupiness as the nonlinear interactions becomes more significant.

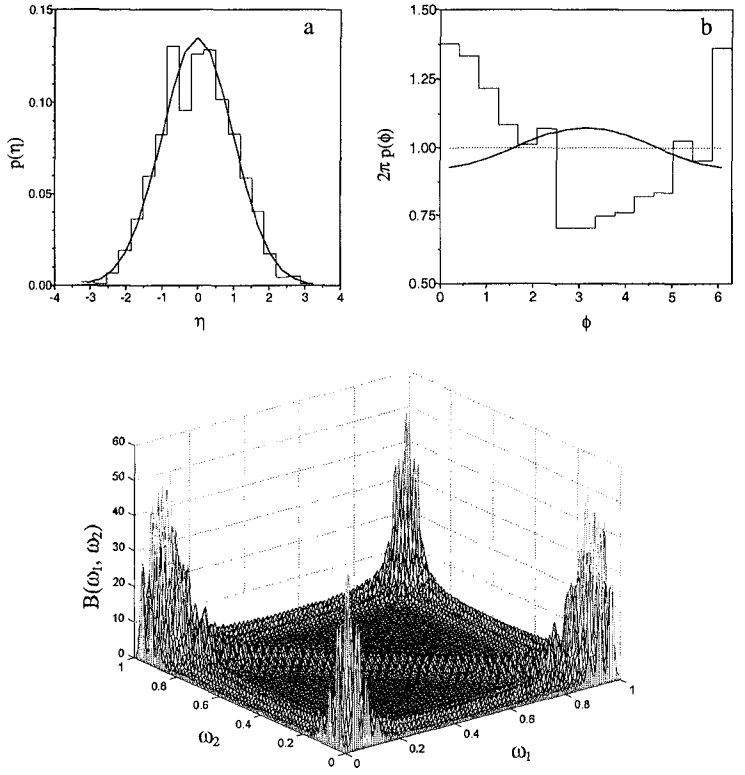

Figure 3. Sea surface elevation (a) and wave phase (b) probability distributions and bispectrum associated to a Gaussian and non-uniform wave phases distribution wave record.

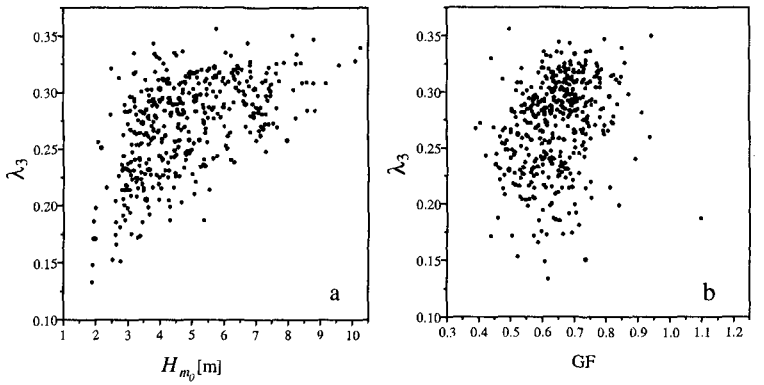

Figure 4. Coefficient of skewness computed by using Eq. 10 versus significant wave height (a) and the groupiness factor (Funke and Mansard, 1980), for the whole data set analysed.

In relation to the mean and variance of the wave phase distribution, Figure 5 displays the values of these parameters obtained for each one of the 412 wave records analysed. Figure 5a represents the observed values for the mean, together with the theoretical value , π, derived for the linear and nonlinear wave models. It can be observed that the theoretical mean value is coincident with that empirically observed only for very low values of the coefficient of skewness, but there is an increasing scatter as λ_3 increases. Similar results are observed for the variance of the wave phase distribution, which are represented together with the theoretical values predicted for the linear and the nonlinear wave model by Tayfun (1994).

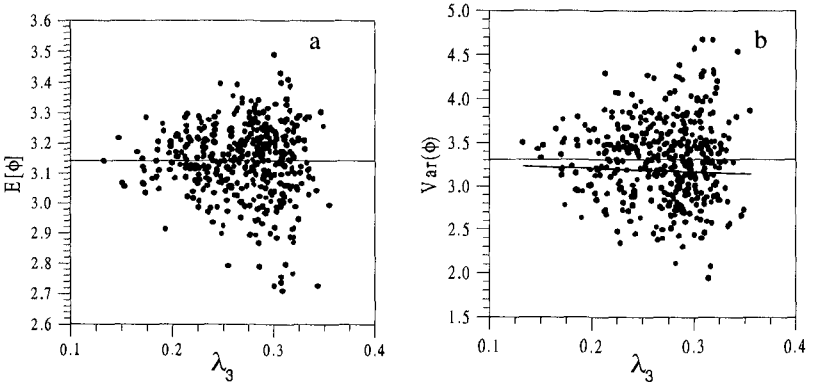

Figure 5. Variability of the wave phase mean value and variance with the coefficient of skewness for the whole data set analysed, and theoretical values for thc linear and nonlinear cases, according to Tayfun (1994).

Conclusions

Bispectral analysis of measured wave records has been used to detect the presence of phase coupling among the various component wave frequencies. It is shown that when bispectral density function is statistically insignificant, sea surface displacements are distributed according to the Gaussian law and the angle phases are uniformly distributed. On the another hand, a non zero bispectrum is related to non Gaussian sea surface displacements and non uniformly distributed phases.

It is observed that, in most cases, the phase distribution deviations from uniformity are characterised by a higher relative frequency of angles in the range from 0.5π to 1.5π. That is, it presents a maximum near $\phi=\pi$ and minima at $\phi=0$ and $\phi=2\pi$.

These results agree with those reported by Tayfun (1994) who analysed data from hurricane Camille and observed a similar behaviour in phase distributions. However, in same cases, our results display an inverse structure to that expected according to this author. In other words, phase probability density presents a maximum at $\phi=0$ and another at $\phi=2\pi$ and a minimum near to $\phi=\pi$.

There is not a clear trend of the wave groupiness to increase with the deviation of phase angles from uniformity, in contrast with the results previously reported by some authors.

The theoretical values of the mean and the variance of the wave phase distribution agree with the empirically observed values only for low values of the coefficient of skewness.

Acknowledgements

This work has been partially supported by the project HP, 1997-0009 " Stochastic characterization and digital simulation of random waves in deep and shallow waters" under the programe of the bilateral cooperation between Portugal and Spain. The authors would like to thank STATOIL for provision of field data.

References

Bitner, E.M., 1980: Non-linear effects of the statistical model of shallow-water wind waves, *Applied Ocean Res.*, 2(2), 63-73.

Burcharth, H.F.,1980: The effect of wave grouping on shore structures, *Proc. 17th Int. Conf. Coastal Eng.*, ASCE, 189-199.

Goda, Y., 1983: Analysis of wave grouping and spectra of long-travelled swell, *Rept. Port and Harbour Res. Inst.*, 22(1), 1-41.

Hasselmann, K., W. Munk and MacDonald, 1963: Bispectra of ocean waves, in *Time Series Analysis*, M. Rosenblatt (ed.), John Wiley, New York, 125-139.

Huang, N.E. and S.R. Long, 1980: An experimental study of the surface elevation probability distribution and statistics of wind-generated waves, *J. Fluid Mech.*, 101, 179-200.

Huang, N.E., S.R. Long, C.C. Tung, Y. Yuan and L. F. Bliven, 1983: A non-Gaussian statistical model for surface elevation of nonlinear random wave field, *J. Geophys. Res.*, 88, 7597-7606.

Johnson, R.R., E.P.D. Mansard and J. Ploeg, 1978: Effects of wave grouping on breakwater stability, *Proc. 16th Int. Conf. Coastal Eng.*, ASCE, 2228-2243.

Kim Y.C. and E.J. Powers, 1979: Digital bispectral analysis and its applications to nonlinear wave interactions, *IEEE Trans. Plasma Science*, 1(2), 120-131.

Kim Y.C., J.M., Beall, E.J. Powers and E.J. Powers, 1980: Bispectrum and nonlinear wave coupling, *Physics of Fluids*, 23, 250-263.

Longuet-Higgins, M.S., 1963: The effect of nonlinearities on statistical distributions in the theory of sea waves, *J. Fluid Mech.*, 17(3), 459-480.

Rye, H. and E. Lervik, 1981: Wave grouping studied by means of correlation techniques, *Norwegian Mar. Res.*, 4, 12-21.

Mase, H., Kita, N. And Iwagaki, Y., 1983: Random wave simulations considering wave groups, *Coastal Eng. Japan*, 26, 61-75.

Tayfun, M.A., 1993: Nonlinear effects on wave envelope and phase, *Proc. Int. Conf. Wave Measurement and Analysis*, ASCE, 775-768.

Tayfun, M.A., 1994: Distributions of envelope and phase in weakly nonlinear random waves, J. Eng. Mech., 120(4), 1009-1025.

Tayfun, M.A. and J.M. Lo, 1989: Envelope, phase and narrow-band models of sea waves, *J. Wtrwy., Port, Coast., and Ocean. Eng.*, ASCE, 115(5), 594-613.

Tayfun, M.A. and J.M. Lo, 1990: Nonlinear effects on wave envelope and phase, *J. Wtrwy., Port, Coast., and Ocean. Eng.*, ASCE, 116(1), 79-100.

Yuxiu, Y. and Manhai, G., 1996:, Groupiness of sea waves and their characteristic parameters, *China Ocean Eng.*, 10(1), 85-98.

Subject Index

Page number refers to the first page of paper

Accretion, 2382, 3178
Acoustic measurement, 787
Aerial photography, 2865
Aerial surveys, 1789
Africa, 3453
Algae, 537
Anemometers, 787
Approximation methods, 589
Aquatic habitats, 2166
Armor units, 1394, 1625, 1744, 1800, 1833, 1846, 1871, 1898, 1906, 1920, 2193, 2235
Artificial islands, 1576, 1679
Asymmetry, 161, 603, 2435, 2489
Australia, 3165

Barges, 1814
Barrier beaches, 230, 311, 603, 801, 1516
Barrier islands, 3110, 3359
Barriers, 2069, 2221
Bars, 1720, 2773, 2865, 2877, 3110, 3359
Bars, riverine, 297, 562, 801, 2409, 2495
Bathymetry, 551, 2395, 2773, 3124, 3224
Bayesian analysis, 3529
Bays, 3178, 3453, 3575
Beach erosion, 325, 1516, 1679, 2382, 2785, 2799, 3046, 3096, 3178, 3192, 3206, 3359, 3516, 3588
Beach nourishment, 45, 934, 1449, 1475, 1516, 1530, 1679, 1706, 2264, 2888, 2913, 3036, 3046, 3060, 3074, 3086, 3096, 3110, 3192, 3359, 3388, 3412
Beaches, 203, 1313, 1407, 2317, 2495, 2534, 2640, 2654, 2668, 2710, 2722, 2736, 2759, 2812, 2877, 2902, 2926, 3008, 3138, 3238, 3331, 3388, 3401, 3601
Bed load movement, 2559, 2968
Bed movements, 3624
Bed ripples, 2489, 2615, 2628
Bed roughness, 2628
Bedforms, 2851, 3624
Beds, 3615, 3643, 3655
Berms, 1394, 1407, 1421, 1435, 3279
Blocks, 1567, 1601, 1625, 1814
Boundary conditions, 72, 366, 892, 1323, 1638, 2028, 2888
Boundary element method, 551, 1613
Boundary layer, 443, 457
Boundary layer flow, 471, 484, 2449, 2615, 2628
Boundary value problems, 2166
Boussinesq equations, 126, 258, 272, 433, 617, 631, 3655
Brazil, 2353
Breaking, 1475, 2509
Breaking waves, 72, 86, 112, 126, 150, 258, 272, 297, 408, 457, 484, 745, 759, 787, 815, 853, 881, 892, 906, 1138, 1435, 1884, 1959, 1986, 2152, 2179, 2696, 2722, 2826, 2913, 2940

Breakwaters, 537, 617, 815, 843, 853, 867, 906, 1027, 1068, 1222, 1394, 1407, 1421, 1435, 1502, 1539, 1576, 1625, 1665, 1693, 1706, 1744, 1758, 1775, 1824, 1846, 1857, 1871, 1884, 1906, 1920, 1934, 1945, 1959, 1972, 1986, 2014, 2028, 2056, 2069, 2082, 2096, 2110, 2124, 2138, 2152, 2166, 2179, 2193, 2207, 2221, 2264, 2826, 3074, 3096, 3178
Bridges, cable-stayed, 3634
Bridges, piers, 3634

Caissons, 1539, 1824, 1934, 1945, 1959, 1972, 1986, 2056, 2096, 2138
Calibration, 2303, 2368, 2382
Cargo handling, 1337
Channel bends, 433
Channel morphology, 3252, 3265
Channels, waterways, 3490
Circulation, 853
Classification, 3206
Climatic changes, 2269
Climatology, 2269
Cnoidal waves, 471
Coastal engineering, 1, 15, 562, 920, 1461, 1516, 1601, 1814, 1934, 3215
Coastal environment, 1, 140, 297, 498, 706, 720, 787, 958, 1313
Coastal management, 15, 2759, 2837, 2992, 3046, 3074, 3151, 3401, 3412, 3425, 3503
Coastal morphology, 1693, 1706, 2264, 2269, 2281, 2368, 2495, 2548, 2640, 2668, 2710, 2773, 2799, 2851, 2865, 2888, 2902, 2913, 2926, 3046, 3124, 3206, 3224, 3238, 3252, 3293, 3318
Coastal processes, 1, 150, 325, 692, 985, 1679, 2294, 2303, 2317, 2331, 2344, 2353, 2382, 2463, 2475, 2489, 2548, 2696, 2877, 2888, 2902, 3022, 3165, 3178, 3192, 3206, 3331, 3345, 3359
Coastal structures, 408, 867, 906, 1027, 1039, 1053, 1461, 1502, 1553, 1601, 1720, 1730, 1744, 1758, 1920, 2000, 2014, 2042, 2056, 2082, 2179, 2207, 2221, 2409, 2837, 3215, 3425
Compaction, 3643
Comparative studies, 443
Composite structures, 867, 2193, 2207
Computation, 203, 366, 380, 422, 656, 843, 1665
Computer models, 1196, 2368
Concrete, 1846
Configuration, 2028
Construction, 1449, 1539, 1679, 1775, 1814, 3388, 3401
Construction costs, 1934
Container shipping, 1222
Control structures, 3046
Coriolis effect, 720, 1290
Cost analysis, 1407, 1934
Costs, 2124
Crossflow, 773
Currents, 338, 408, 692, 706, 732, 759, 815, 829, 945, 1290, 1720, 2368, 2435, 2654, 2799, 3331, 3601
Cyclones, 720
Cylinders, 1613, 2179

Damage, 1587
Damage assessment, 1884
Damping, 1124, 1489
Dams, 3516

Data analysis, 972, 985, 1124, 1364, 3086, 3215
Data collection, 985, 1013, 1378
Debris, 2520
Decision theory, 3529
Deep water, 1435, 3668
Deformation, 843, 853, 2317, 3008, 3138
Deltas, 934, 2264, 2668, 2902, 3138, 3192
Denmark, 1082, 1516, 1530, 3074, 3542
Density, 2463
Density functions, 3668
Depth, 2395, 2913, 2926, 3110
Design, 15, 45, 867, 1027, 1039, 1138, 1154, 1196, 1210, 1222, 1236, 1350, 1435, 1449, 1539, 1576, 1587, 1706, 1758, 1775, 1800, 1814, 1920, 1945, 2000, 2056, 2069, 2096, 2138, 2249, 3036, 3046, 3060, 3634
Design criteria, 1082
Design improvements, 1693
Design storms, 1871
Diffusion, 2573, 3553
Digital techniques, 1789
Dikes, 1567, 3439, 3503, 3516, 3529, 3542
Dimensional analysis, 1730
Disasters, 3503
Discharge, 2235
Dispersion, 98
Dolos, 1789, 1846
Doppler systems, 2607
Doppler tracking, 1898
Dredge spoil, 3466
Dredging, 1679, 2992, 3374, 3453, 3466, 3479, 3490, 3561
Dunes, 1449, 3359, 3412, 3516
Dynamic response, 1972, 1986
Dynamics, 1138, 2548, 2837, 2851, 3224, 3293, 3318

Economic analysis, 1449, 2124
Eddies, 86, 175, 745, 892
Eddy viscosity, 422, 484, 801, 2615
Edge effect, 244, 443
Eigenvalues, 2069
Energy, 2000
Energy dissipation, 112, 484, 537, 2152, 2166
Energy measurement, 2331
Environmental factors, 3479
Environmental impact statements, 3401
Environmental impacts, 3412
Equations of motion, 161
Equilibrium profile, 2722, 2736
Erosion, 1706, 1898, 2264, 2520, 2837, 2992, 3151, 3252, 3624
Estimating, 3624
Estimation, 682, 2249
Estuaries, 2992, 3022, 3124, 3307
Europe, 15, 3060
Eutrophication, 3575
Evaluation, 2423, 3425, 3561
Expansion, 1236
Experimentation, 471, 645, 692, 759, 1053, 1154, 1489, 1884, 1986, 2249, 2344, 2826, 2980

Failure modes, 2138
Failures, 1986, 2124, 3516
Field investigations, 297, 773, 2281, 2344, 2640, 3151
Field tests, 338, 1182, 1313, 1567, 1857, 1945, 2331, 2548, 2682, 2722, 2812, 2954, 3036
Financial analysis, 3060
Finite difference method, 394, 562, 631

Finite element method, 815, 1182, 1986, 2992
Fisheries, 1276
Flood control, 1601, 3503, 3529, 3542
Flooding, 3542
Floods, 720, 3215, 3345
Flow, 2826
Flow patterns, 773
Fluid flow, 2877, 2968
Flumes, 732, 1068, 1154, 1394, 1638, 1775, 1884, 2179, 2423, 2607, 2736
Forecasting, 1364, 1378
Foundation stability analysis, 2110
Foundations, 2124
Fractures, 2520
Free surfaces, 72, 189, 422, 892, 2785
Froude number, 325

Gabions, 1587
Geology, 1516
Geomorphology, 3022, 3192
Geotextiles, 1576
Germany, 3359
Ghana, 3192
Global positioning, 2640
Grain size, 2449, 2463
Gravel, 2654, 3036
Gravity waves, 203, 523, 3668
Greens function, 551, 1210
Groins, structures, 2264, 3124
Ground water, 3588

Harbors, 244, 394, 1182, 1196, 1210, 1236, 1250, 1263, 1276, 1290, 1350, 1530, 1789, 1871, 3224, 3624, 3655
Homogeneity, 3215
Horizontal flow, 2082
Hydraulic gradients, 2812
Hydraulic models, 1421, 1824, 2179, 3279
Hydraulic performance, 2207
Hydraulics, 1, 2353, 2509
Hydrodynamics, 945, 1276, 1378, 2014, 2269, 2423, 2463, 2968, 3561
Hydrographic surveys, 3318

Image analysis, 2395
Impact, 1489, 1502, 1959, 3345
Impact loads, 2056
Indonesia, 3374
Information, 15
Inlets, waterways, 934, 2281, 3124, 3265, 3279, 3293, 3307, 3318, 3331, 3345
Innovation, 2207
Instrumentation, 2423
Interactions, 706, 732, 759, 1613, 1638
International compacts, 498
Islands, 1758
Israel, 1236

Japan, 297, 3151, 3178, 3503, 3575
Jetties, 1744

Kalman filter, 1364, 1378
Kinematics, 380, 881, 1906
Korea, 1182, 1250

Laboratory tests, 457, 562, 656, 892, 1053, 1082, 1110, 1299, 1945, 2069, 2221, 2423, 2435, 2682, 2736, 2750, 3036
Lagoons, 2294, 3192
Lagrangian functions, 881
Lakes, 3439
Land reclamation, 2475, 3374
Large structures, 1613
Lasers, 1898

Layout, 1276
Legal factors, 3060
Legislation, 3503
Liquefaction, 2110, 3615, 3643
Littoral currents, 217, 230, 297, 352, 745, 787, 2710
Littoral deposits, 3479
Littoral drift, 1516, 1530, 2294, 2331, 2344, 2353, 2640, 2654, 2682, 2888, 2954, 3279
Loads, 867, 2110
Long waves, 244, 433, 720, 1138, 1154, 1210, 1222, 1299, 1337, 3655

Maintenance, 3453, 3479, 3490
Marinas, 2221, 3388
Mass transport, 443
Mathematical models, 934, 1276, 1502, 2682, 2722, 2877, 3516
Measurement, 338, 881, 1182, 1945, 1972, 2281, 2303, 2463, 2628, 2750, 2812, 2826
Methodology, 45, 72, 1013
Migration, 934
Mining, 2696
Mixing, 217
Model studies, 1871, 2000, 3086
Model tests, 1350, 1576, 1775, 1959, 2082, 2193, 2509, 3096
Modeling, 15, 86, 140, 189, 352, 433, 498, 576, 631, 732, 1378, 1693, 1775, 2269, 2344, 2353, 2368, 2395, 2559, 2736, 2837, 3008, 3238, 3561
Models, 112, 258, 311, 706, 759, 881, 972, 1053, 1553, 1814, 2331, 2382, 2409, 2449, 2495, 2548, 2573, 2615, 2640, 2773, 2785, 2799, 2851, 2954, 2992, 3224, 3265
Monitoring, 338, 1775, 1789, 1857, 2696, 2759, 3086, 3206, 3388, 3412
Mooring, 422, 1350
Moorings, 1758
Morphology, 2028
Movable bed models, 3096
Mud, 3655

Navier-Stokes equations, 843, 1650, 3008
Navigation, 3293, 3490
Navy, 1449
Nearshore circulation, 189, 217, 230, 272, 682, 773, 787, 801, 815, 829, 1124, 1323, 2409, 2587, 2607, 3165, 3331
Netherlands, 1567, 2281, 2913, 3110, 3224, 3439
Neural networks, 2096
New Jersey, 2668
Nile River, 2264, 2668
Nonlinear response, 126, 203, 272, 471, 576, 603, 617, 631, 670, 682, 1110, 1650
Nonlinear systems, 98, 189, 645
North Carolina, 2865
North Sea, 2759, 3307
Norway, 1800
Numerical analysis, 853
Numerical models, 150, 230, 366, 394, 408, 422, 484, 498, 523, 551, 562, 589, 617, 801, 815, 892, 1110, 1168, 1236, 1250, 1299, 1323, 1337, 1421, 1613, 1638, 1650, 1744, 2028, 2249, 2281, 2475, 2668, 2980, 3138, 3192, 3374, 3588, 3634

Ocean environments, 3151
Ocean waves, 972, 999, 1110, 3553
Oceans, 1013, 2294, 2395

Offshore engineering, 175
Offshore pipeline, 2968
Offshore structures, 1027
Optimal design, 2124, 3374
Optimization, 1276
Oscillations, 1182, 1972, 3655
Oscillatory flow, 471, 2449, 2559, 2573, 2628, 2968
Overtopping, 1039, 1068, 1138, 1276, 1394, 1553, 1576, 2235, 2249
Oxygen content, 3575

Parabolic bodies, 352
Parameters, 2382, 2520
Particle motion, 3553
Performance, 2179
Permeability, 1394, 1407, 2042
Perturbation, 656, 2710, 3265
Photographic analysis, 1857
Pipelines, 1650, 1730
Planning, 1196
Plates, 1489, 2166
Plumes, 2587, 3561
Polynomials, 589, 631
Pore pressure, 2110, 3643
Pore water pressure, 3615
Porous media, 537, 1720
Ports, 1222, 1236, 1337, 1475, 1539, 1857, 1871, 3293, 3453, 3479
Portugal, 985, 3206
Predictions, 45, 258, 311, 853, 999, 1053, 2409, 2595, 2785, 2837, 3022, 3138, 3561
Pressure distribution, 1553, 2042
Pressure measurement, 562, 1898
Probabilistic methods, 3668
Probabilistic models, 1920, 2750
Probability, 1027
Probability density functions, 958, 2096
Probability distribution, 958
Probability theory, 1461
Profiles, 2475, 2495, 2759, 2902, 2926, 3110, 3238
Programs, 15
Projects, 1461
Propellers, 3624
Prototypes, 1039, 1407, 1972

Quality assurance, 1567
Quarries, 1934

Radiation, 829
Random variables, 682
Random waves, 380, 706, 999, 1096, 2682, 3008, 3553
Reclamation, 1576, 3466
Recreational facilities, 3401
Reefs, 1138, 2152, 2166
Regression analysis, 3307
Regulations, 325
Rehabilitation, 3412
Reliability, 1945, 2096, 2138
Remote sensing, 2395, 2799
Repairing, 1775
Research, 15
Resonance, 1263
Resonance tests, 1196
Resonators, 1210
Restoration, 3425
Revetments, 1138, 1567, 1576, 1587, 1601, 3074
Reviews, 45
Rip currents, 230, 801, 2152
Ripple marks, 2489, 3601
Riprap, 1884
Risk, 1168
Risk analysis, 2124
Rivers, 720, 2992, 3138

Rocks, 1800, 2520
Rubble-mound breakwaters, 1638, 1665, 1720, 1730, 1789, 1800, 1814, 1833, 1846, 1857, 1906, 2000, 2235

Safety, 2138, 3074, 3439
Sand, 1475, 1530, 2409, 2573, 2812, 2851, 2865, 3046, 3074, 3086, 3453, 3516, 3601, 3615, 3643
Sand transport, 2435, 2449, 2495, 2509, 2534, 3008, 3265
Sand waves, 3490
Scale effect, 1068
Scale models, 1039, 1222, 1236, 1250, 1421, 3374, 3634
Scour, 1394, 3634
Sea cliffs, 2520
Sea floor, 906, 2968
Sea level, 1665, 2294, 3529, 3668
Sea state, 338, 1013, 1350
Sea walls, 906, 1502, 1553, 2056, 2249
Sea water, 1539, 3529
Sediment concentration, 2573, 2587, 2595
Sediment control, 2489
Sediment deposits, 3345, 3479
Sediment discharge, 2696
Sediment load, 3318
Sediment transport, 1, 1276, 1530, 1720, 2269, 2317, 2331, 2353, 2368, 2382, 2423, 2435, 2449, 2463, 2475, 2489, 2495, 2548, 2559, 2573, 2607, 2640, 2654, 2668, 2682, 2696, 2722, 2736, 2750, 2799, 2851, 2877, 2888, 2902, 2940, 2954, 2968, 2980, 3022, 3096, 3151, 3165, 3238, 3453, 3516, 3601
Sedimentary rock, 1
Sedimentation, 2344, 2902, 2992
Seepage, 3601, 3643
Sensitivity analysis, 945
Settlement analysis, 3615, 3643
Shallow water, 126, 140, 161, 244, 408, 422, 443, 498, 509, 523, 562, 603, 617, 745, 1154, 1299, 1435
Shear, 175, 311, 706, 1124
Shear stress, 457, 471, 1730, 2628
Shear waves, 203, 217, 230
Ship motion, 325, 1222, 1337
Ships, 1350, 3624
Shoaling, 98, 272, 457, 523, 603, 645, 670, 759, 3345
Shore protection, 1449, 1475, 1530, 1706, 1758, 1800, 2264, 3096, 3279, 3412, 3425
Shoreline changes, 2668, 2682, 2696, 2837, 2865, 2913, 2954, 3138, 3238, 3359, 3588
Simulation, 86, 150, 589, 670, 843, 892, 945, 1299, 1313, 1337, 1350, 2877
Simulation models, 2940, 3575
Skewness, 161
Slope stability, 2509
Soft soils, 3655
Sonar, 2607
South Africa, 1789, 1857
Spain, 920, 3086, 3388
Spatial data, 2913
Spectra, 682
Spills, 72, 3466
Spits, coastal, 1475, 3453
Stability, 1407, 1587, 1601, 1625, 1800, 1833, 1906, 1920, 2193, 3293, 3388
Stability analysis, 1435, 1730, 1824
Stabilization, 3279
Standing waves, 1489
State-of-the-art reviews, 1
Statistical analysis, 999, 1364, 2926, 3215

Statistical data, 3668
Statistical distributions, 1959, 2082
Statistics, 920, 972, 3529
Steady flow, 3601
Stochastic models, 126, 523, 3553
Stochastic processes, 161
Stones, 1394, 1421, 1587, 1744, 1906
Storm surges, 1378, 1553, 3439, 3542
Storms, 985, 1475, 2587, 2954, 3588
Stress, 829
Structural design, 906
Structural response, 1846
Structures, 1154
Submerged flow, 2000, 2014, 2028
Subsidence, 3542
Subsurface flow, 2812
Surf zone, 86, 217, 230, 258, 272, 286, 484, 745, 787, 829, 1124, 2317, 2409, 2785, 2799, 2940
Surface waves, 175, 523, 656
Surge, 945
Suspended sediments, 2303, 2317, 2344, 2559, 2587, 2595, 2980, 3165, 3466

Taiwan, 1263
Terminal facilities, 1222
Tests, 1601, 1625, 1693, 1824, 1846, 1884, 1972
Three-dimensional flow, 843
Three-dimensional models, 380, 670, 829, 1323, 1502, 3022
Tidal currents, 773, 2851, 3252
Tidal effects, 3345
Tidal waters, 720, 934, 945, 1168, 2281, 3124, 3252, 3265, 3279, 3293, 3307, 3318, 3331
Time dependence, 408
Time series analysis, 2587
Time studies, 2913
Toe aprons, 1720
Tracers, 2654, 3151
Tracking, 2654
Transformations, 150
Trap efficiency, 2534
Trenches, 2534
Tsunamis, 1168
Tunnels, 2435
Turbidity, 2303, 3466, 3561
Turbulence, 72, 86, 175, 457, 1898, 2303, 2607, 2980
Turbulent flow, 484, 732
Two-dimensional analysis, 1638
Two-dimensional flow, 2710
Two-dimensional models, 286, 1502, 2940
Typhoons, 1263

Uncertainty analysis, 1461
Undertow, 286, 297, 311, 815, 829, 2736, 2750
United Kingdom, 1461, 2759, 3479
United States, 1013

Variability, 999
Velocity, 98, 189, 380, 1290, 2595, 2607, 2826
Velocity distribution, 773
Velocity profile, 286, 576, 732, 2615
Vertical forces, 2110
Vibration, 1489
Videotape, 2773, 2865
Vortices, 175, 217, 258, 745, 1124, 2303

Wakes, 325
Walls, 1986, 2042, 2056, 2082
Water depth, 958
Water flow, 1290
Water levels, 3307
Water quality, 3575
Water table, 3588

Water waves, 72, 140, 150, 161, 189, 244, 286, 311, 443, 498, 509, 576, 589, 603, 631, 645, 732, 801, 843, 867, 985, 1138, 1313, 1489, 1625
Wave action, 3553, 3615, 3643
Wave attenuation, 1210
Wave climatology, 203, 338, 509, 934, 972, 985, 1013, 1364, 2235, 2294, 2331, 2344, 2353
Wave crest, 98, 1039, 1096, 1665, 2014
Wave damping, 537
Wave diffraction, 352, 366, 394, 551, 617, 1196, 1613
Wave dispersion, 140, 161, 576, 589, 631, 3553
Wave energy, 286, 1110, 2152, 2475
Wave forces, 682, 1263, 1489, 1539, 1587, 1638, 1650, 1945, 1959, 2056, 2069, 2082, 2096, 2193, 2221, 2317, 2423, 2573, 2595, 2654, 2710, 2888, 2940, 2980, 3178
Wave generation, 140, 325, 1082, 1096, 1110, 1168
Wave groups, 98, 645, 656, 881, 920, 1110, 1124, 1299, 1323
Wave height, 112, 258, 311, 352, 603, 906, 920, 958, 972, 999, 1027, 1096, 1154, 1182, 1313, 1364, 1833, 1884, 2014, 2235, 2750, 2785, 3165, 3215, 3439
Wave measurement, 509, 920, 1096, 1250, 3279
Wave pressure, 682, 867, 1824, 2042
Wave propagation, 112, 244, 338, 366, 394, 422, 433, 509, 523, 562, 670, 692, 1168, 1250, 1263, 3178
Wave reflection, 394, 433, 537, 1053, 1553, 1625, 1833, 2166, 2221
Wave refraction, 352, 366, 551, 617, 670, 692
Wave runup, 408, 1039, 1053, 1068, 1168, 1613, 1920, 2042, 2785, 2799, 2812, 2826
Wave spectra, 126, 706, 945, 1096, 3036
Wave tanks, 645, 656, 1082, 2628
Waves, 1364, 1502, 1693, 1744, 1906, 2000, 2249, 2368, 2395, 2435, 2607, 2615, 2954, 3601
Wind, 720, 3215
Wind forces, 509, 1068, 1290, 2534, 3165, 3668
Wind tunnel test, 1068
Wind waves, 945, 1313

Young's modulus, 2520

Author Index

Page number refers to the first page of paper

Aagaard, Troels, 2331
Aarninkhof, Stefan, 2409
Abecasis, Fernando, 985
Abels, U., 3359
Abeysirigunawardena, D. S., 1276
Abohadima, Samir, 617
Accetta, Domenico, 2353
Ahrens, John P., 2382
Akamatsu, Naohiro, 3138
Akeda, Sadamitsu, 1539
Akutu, Takao, 3615
Allsop, N. W. H., 906, 2056
Allsop, N. William H., 1758
Allsop, William, 2082
Andersen, Jens Otto, 3542
Anderskouv, Ulf, 3401
Anthonio, S. L., 3192
Araki, Susumu, 2654
Arisawa, Toshiharu, 3151
Arntsen, Ølivind A., 562
Atsumi, Youichi, 1290

Bach, Hanne, 3401
Baily, Brian, 2640
Baird, A. J., 2812
Bakker, Willem T., 3252
Baldock, T. E., 2812, 3601
Baquerizo, A., 3293
Baquerizo, Asunción, 1720
Bartels, A., 1775
Barthel, Volker, 2992
Basco, David R., P.E., 1449
Battjes, Jurjen A., 732, 1898
Becq, Françoise, 523
Beji, Serdar, 682
Bell, P., 2423
Benediktsson, Sigtryggur, 1407
Benoit, Michel, 523
Bergmann, Hendrik, 2042
Bettington, S. H., 2221
Bezuijen, Adam, 1567, 2509
Bird, C. C., 98
Birkemeier, William A., 2888
Blak-Nielsen, Jeppe, 1576
Bliek, Bram, 1706
Blockley, David I., 1461
Blondeaux, Paolo, 2710
Boczar-Karakiewicz, B., 2877
Bojsen, Trine Borum, 3466
Bokhove, O., 745
Bona, J. L., 2877
Bonmarin, Pierre, 881
Booij, N., 140
Booij, Robert, 1898
Bosboom, J., 2435
Bosboom, Judith, 2573
Boutmy, Alain, 3224
Bowen, A. J., 2587
Breteler, M. Klein, 1587
Breteler, Mark Klein, 1601
Brocchini, M., 72
Brøker, I., 1693
Brøker, Ida, 1516
Brorsen, Michael, 394
Bruno, Michael S., 2628, 3331
Büchmann, Bjarne, 1613
Buick, James M., 3553
Burcharth, H. F., 1959
Burcharth, Hans F., 1027, 2138
Buxbom, Iris, 3466

Caballero, Alejandro, 3086
Calabrese, M., 2056
Callard, Owen W., 3318

Calvete, D., 2851
Cañizares, Rafael, 1378
Capobianco, M., 3060
Capobianco, Michele, 2888, 3096
Cavaleri, L., 498
Chadwick, Andrew J., 2640
Chae, Jang-Won, 1250
Chang, Chien-Kee, 1263
Chang, Yeon-Sihk, 2344
Chatelus, Y., 2435
Chawla, Arun, 759
Chen, Qin, 2395
Chen, Yiping, 3022
Chiang, W. S., 2826
Chien, Chung-Ching, 1263
Chow, K. C. Ander, 1421
Cloin, B., 2435
Coates, L. E., 2423
Coates, T. T., 3036
Conner, Craig, 2344
Cooper, Nicholas J., 2759
Coppoolse, R. C., 3453
Cox, Daniel T., 311, 457, 1053
Cox, R. J., 2221

Dabees, Mohamed, 2668
Dally, William R., 3318
Dalrymple, Robert A., 175, 537, 1124, 2395
d'Angremond, K., 1934
Davies, A. E., 2423
Davis, John P., 1461
de Gerloni, M., 1945
de Groot, M. B., 2110
de Haas, Paul, 670
de Jong, J. C. M., 150
de Looff, Harry, 3439
de Meijer, R. J., 2463
de Ronde, John, 1039
de Rouck, Julien, 1039
De Rouck, Julien, 1638
De Swart, H. E., 2851
de Swart, Huib, 2710
de Vroeg, Hans, 1706, 2368
Dean, Robert G., 45
Debski, D., 1665
Deguchi, Ichiro, 2654
Dette, H. H., 3060
Dette, Hans H., 3046
Di Castro, F., 1236
Dias, J. Alveirinho, 3206
Dias, Wagner Santos Scisinio, 2353
Dingemans, Maarten, 670
Dodd, N., 2851
Dodd, Nicholas, 1313
Dohmen-Janssen, C. Marjolein, 2449
Dohmen-Janssen, M., 2435
Dollard, Brendan, 3412
Drennan, William M., 881
Driscoll, Andrew M., 3374
Durand, N., 906
Durrani, Tariq S., 3553
Duy, Nguyen The, 484

Edge, Billy L., 1053
Einarsson, Sigurdur, 1407
Eldeberky, Yasser, 161
Elfiky, Abdel-Fattah, 2264
Elfrink, Berry, 325, 2353
Elgar, Steve, 2799, 3588
Elsaeed, Gamal H., 2264
Endoh, Masao, 2166
Esteban, Vicente, 3086

Falconer, Roger A., 3022
Falques, A., 2851
Faure, T., 1350
Ferreira, Óscar, 3206
Fischer, M. P., 2179
Fisher, John S., 3124
FitzPatrick, Kathy, 3318
Fontijn, Harry L., 1898
Forget, Philippe, 523
Foster, D. L., 2587

Foster, Tom, 3374
Fournier, Charles P., 1421
Franco, L., 1945
Frigaard, P., 1959

Gal, J. H. Andorka, 150
Galofré, J., 3388
Gao, Q., 366
Gerken, William, 2069
Giménez, Marcos H., 920, 999
Gironella, X., 2014
Glas, Peter C. G., 3439
Gobbi, Maurício F., 631
Goda, Yoshimi, 2152
González, M., 1168
Govaere, Georges, 1920
Gracia, Vicente, 2902
Grasmeijer, Bart T., 2750
Gravesen, Helge, 1576
Greenwood, Brian, 2331
Grilli, Stéphan T., 603
Groeneweg, Jacco, 732
Grüne, Joachim, 338
Guillén, Jorge, 2902
Gunaratna, P. P., 1276
Guza, R. T., 3588

Haagsma, IJ. G., 140
Haas, K. A., 801
Haines, J. W., 2865
Hald, T., 1800
Hall, Jim W., 1461
Hall, K. R., 2179
Hall, Kevin R., 2000
Haller, M. C., 801
Haller, Merrick C., 1124
Hamill, G. A., 3624
Hamm, L., 2435, 3060
Hands, Edward B., 2382
Hanes, Daniel M., 2344
Hanslow, David, 720
Hanson, H., 3060
Hanson, Hans, 2682
Hanzawa, Minoru, 1625
Hardcastle, P. J., 2423
Hasegawa, Junzo, 3490
Hashimoto, Noriaki, 1364
Hasløv, Dan B., 3401
Hatada, Yoshio, 509
Hatanaka, Katsumori, 2534
Hawkes, P. J., 3036
Hay, A. E., 2587
Hay, Alex, 2607
Hayakawa, Norio, 843
Hayashi, Michifumi, 2193
Hayes, M. O., 3192
Headland, John R., P.E., 1337
Hebsgaard, Mogens, 2235, 3634
Hein, R., 2435
Helm-Petersen, Jacob, 394
Herbich, John B., 2264
Herrington, Thomas O., 3331
Hibbert, Kevin, 720
Hill, Alan A., 1758
Hinton, Claire, 2409, 2913
Hiraishi, Tetsuya, 1096, 2249
Hirayama, Katsuya, 1096
Hires, Richard I., 2628
Hoekstra, P., 3110
Hoekstra, Piet, 773
Høgh, Klavs, 3466
Holland, K. Todd, 2799
Holman, Rob A., 2773
Holmes, P., 3601
Holm-Karlsen, T., 1800
Holthuijsen, L. H., 140, 150, 498
Holtzhausen, A., 1857
Holtzhausen, Anton H., 1871
Horiguchi, Takahiro, 1679
Horikawa, Kiyoshi, 2534
Horn, D. P., 2812
Horton, P. R., 2221
Hoshi, Hideki, 1290
Hosoyamada, Tokuzo, 843

Hossain, M. Akter, 3655
Hotta, Shintaro, 2534
Hough, Gavin, 1789
Houwman, Klaas T., 773
Humphery, J. D., 2423
Huntley, David A., 286
Hurdle, D. P., 906
Hwang, K. S., 2826
Hwung, H. H., 2826

Ikeno, M., 2317
Irie, Isao, 2489
Isobe, Masahiko, 617
Itabashi, Naoki, 3178
Ito, Hitoshi, 3151
Ito, Masahiro, 1625
Iwagaki, Yuitch, 1625
Iwata, Koichiro, 853

Jacobsen, Vagner, 1138
Jakobsen, Per Roed, 1516
James, R. L., 706
Jayewardene, I. F. W., 1744
Jensen, Jesper Holt, 1516
Jensen, Ole Juul, 3634
Jensen, Thomas, 1138
Jeong, Weon Mu, 1182, 1250
Jiao, Haiying, 645
Jiménez, José A., 2595, 2902
Johannessen, T. B., 1110
Johanson, Hans, 1601
Johnson, Bradley D., 2785
Johnson, H. K., 1693
Johnson, Hakeem K., 352
Jørgensen, K., 1693
Jørgensen, Mads Peder, 1530
Joyner, Brian P., 3124
Juhl, Jørgen, 1394, 1530, 2235
Justesen, P., 1276

Kaczmarek, Leszek M., 2559
Kaiser, Ralf, 934
Kakuno, Shohachi, 2166
Kaminsky, George, 3238
Kamphuis, J. William, 1154, 2668
Kanayama, Susumu, 576
Kang, Yoon-Koo, 3643
Karambas, Theofanis V., 2940
Karjadi, Entin A., 408
Kashihara, Kenji, 3655
Kato, Hajime, 829
Kato, Shigeru, 787
Katoh, Kazumasa, 3490
Katoh, Ken-ichi, 3138
Katopodi, I., 2435
Kawasaki, Koji, 853
Kennedy, Andrew B., 589, 631, 2395
Kennedy, Douglas L., 311
Kieftenburg, A. T. M. M., 150
Kimura, Akira, 1906
Kimura, Katsutoshi, 1539, 2193
Kinoshita, Hiroya, 1290
Kioka, Wataru, 3655
Kirby, James T., 203, 217, 631, 759, 2395
Kirkegaard, Jens, 325
Kirkegaard, Lars, 3634
Kit, E., 645
Kjeldsen, Søren Peter, 881
Klopman, Gert, 2573
Kobayashi, N., 1884
Kobayashi, Nobuhisa, 189, 311, 408, 457, 1833, 2736, 2785
Kofoed, J. P., 1959
Kofoed-Hansen, Henrik, 126, 325
Kolahdoozan, Morteza, 3022
Koomans, R. L., 2463
Kortenhaus, Andreas, 867, 1553
Kos'yan, Ruben D., 2303
Kraus, Nicholas C., 3265
Kriebel, David, 2069
Kriebel, David L., 1613
Kristjansson, Bjorn, 3279
Kroon, A., 3110

Kruse, Gerard A. M., 1567
Kudaka, Masanobu, 1364
Kuijper, H. K. T., 2124
Kume, Hidetoshi, 3490
Kunitomi, Shoji, 1824
Kunz, H., 3359
Kuriyama, Yoshiaki, 297
Kuroiwa, Masamitsu, 815
Kuroki, Keiji, 3490
Kuznetsov, Sergey Yu., 2303
Kvalstad, T. J., 2110
Kwak, Moon-Su, 551

Lai, C. F., 2826
Lai, Ching-Piau, 1196
Lamberti, Alberto, 1972
Larson, Magnus, 2682, 2722, 2888
Laustrup, Christian, 3074
Lechuga, A., 3060
Lee, Jiin-Jen, 1196
Lee, Kil Seong, 1182
Lee, Mark, 2640
Leggett, Daniel J., 2759
Lenhoff, L., 1475
Li, Li, 175
Li, Yigong, 1196
Lippmann, T. C., 2865
Liu, Zhou, 1027
Lomónaco, P., 3293
López, Cristina, 1833
Lord, D. B., 1744
Losada, Íñigo J., 1730
Losada, Iñnigo J., 537
Losada, M. A., 537, 3293
Losada, Miguel, 2294
Losada, Miguel A., 1720, 1833
Loveless, J. H., 1665
Lowe, Jeremy P., 2759
Luger, S. A., 3561
Lykkeberg, Niels, 1576

Ma, P. F., 1421
MacDonald, Neil, 286
MacIntosh, K., 1350
MacIntosh, K. J., 3192
Maciver, Ruairi D., 692
Mackinnon, P. A., 3624
MacLeod, A. B., 1665
Madsen, Henrik, 1378
Madsen, Holger Toxvig, 3074
Madsen, Ole Secher, 2615
Madsen, Per A., 161, 272
Mangor, K., 1693
Mangor, Karsten, 1530, 3401, 3425
Mano, Akira, 2520
Mansard, E. P. D., 1350
Marsh, S. W., 3110
Martell, E. Pérez, 3668
Martin, Francisco, 1920
Martín, Francisco L., 1730
Martinelli, Luca, 1972
Maruyama, Haruhiro, 2249
Mase, Hajime, 1824
Mason, T. E., 2812
Masselink, G., 3165
Matsubara, Yuhei, 815
Matsumi, Yoshiharu, 1906
Matsutate, H., 1299
McDougal, William G., 1650
McGarvey, J. A., 3624
McKenna, Janice, 2082
Medina, José M., 3086
Medina, Josep R., 920, 1068
Medina, R., 1168, 3293, 3388
Melby, J., 1857
Melby, J. A., 1884
Melby, Jeffrey A., 1846
Méndez, Fernando J., 537
Mikkelsen, Palle, 3374
Miller, Herman C., 2954
Mimura, Nobuo, 829, 3575
Minamimura, Takaaki, 3615
Ming, Lu, 787

Mizuguchi, M., 1299
Mizuno, Yuzo, 2193
Mizutani, Norimi, 1650
Mocke, G. P., 2696, 3561
Mok, K. M., 443
Monbaliu, J., 945
Montaña, Juan, 2294
Montoya, F. J., 3388
Moores, S. P., 2423
Morfett, John, 2640
Mori, Nobuhito, 189
Morita, Satoshi, 1210
Mostafa, Ayman M., 1650
Motono, Ichio, 3503
Murakami, Hiroshi, 1625
Muttray, M., 2207

Nadaoka, Kazuo, 86, 682
Nagai, Toshihiko, 1364
Nai, G., 3192
Nairn, R. B., 3192
Nakamura, Satoshi, 1313
Nakamura, Takayuki, 1210
Naruse, Susumu, 3503
Nemoto, Kenji, 1625
Nicholls, R. J., 3110
Nicholls, Robert J., 2888, 2913
Nicholson, John, 286
Nielsen, Jørgen, 2331
Nielsen, Peter, 720
Niemeyer, Hanz D., 934, 3307
Nieto, J. C., 3668
Niiyama, Masaki, 3615
Nishi, Ryuichiro, 1679
Nishimura, Hitoshi, 551
Nistor, Ioan, 3008
Nobuoka, Hisamichi, 829
Noda, Hideaki, 815

Ochi, Michel K., 958
O'Connor, B. A., 2435
O'Connor, Brian A., 286
Oda, Kazuki, 2166
Ohno, Kenichi, 1906
Ohtani, Yasuro, 1679
Okada, Kozo, 972
Okayasu, Ako, 484
Okrój, Tomasz, 2926
Oltman-Shay, Joan, 217, 1124
Onderwater, Martijn, 2475
Ono, Masanobu, 2654
Ono, Nobuyuki, 2489
Ono, Osafumi, 86
Orloff, Leah S., 1013
Orzech, Mark D., 2736
Ostrowski, Rafal, 2559
Osuna, P., 945
Oumeraci, H., 2207
Oumeraci, Hocine, 867, 1553, 2042
Overton, Margery F., 3124
Özkan-Haller, H. Tuba, 203, 217

Palanques, Albert, 2902
Pan, Shunqi, 286
Park, Woo Sun, 1182
Partenscky, Hans-Werner, 15
Passoni, G., 1945
Pattiaratchi, C. B., 3165
Pedersen, Claus, 3374
Peregrine, D. H., 72, 98, 244, 745
Peregrine, D. Howell, 1502
Phelp, D., 1775, 1857
Phelp, David, 1789
Pilarczyk, K. W., 1587
Pillay, S., 1775
Pita, Carlos, 985
Plant, Nathaniel, 3238
Plant, Nathaniel G., 2773
Podymov, Igor S., 2303
Poon, Ying-Keung, 1222
Poon, Ying-Keung, P.E., 1337
Poulin, Sanne, 352, 1516
Pruszak, Zbigniew, 2926

Putrevu, U., 1323
Putrevu, Uday, 203, 217, 1124

Radder, A. C., 366
Radomir, M., 1236
Ragutzki, G., 3359
Raichlen, Frederic, 1222
Rakhorst, Dick, 2281
Rankin, Kelly L., 2628, 3331
Rasmussen, Jørgen H., 126
Rathbun, Joel R., 1053
Rattanapitikon, Winyu, 112
Raubenheimer, B., 3588
Raubenheimer, Britt, 2799
Raw, A. J., 1475
Reniers, Ad, 2573
Ribberink, J. S., 2435
Ribberink, Jan, 2281
Ribberink, Jan S., 2449
Rivero, F., 2014
Rodríguez, German, 2595
Rodríguez, Germán, 3668
Roelvink, Dano, 2281, 2475, 3224
Roelvink, J. A., 2028
Romańczyk, W., 2877
Różyński, Grzegorz, 2837, 2926
Ruggiero, Peter, 3238
Ruol, Piero, 3096

Sakamoto, Hirokazu, 2489
Sallenger, A. H., 2865
Sallenger, Asbury H., Jr., 2799
Salles, Paulo, 2615
Samothrakis, P., 2435
Sana, Ahmad, 471
Sánchez-Arcilla, A., 2014
Sánchez-Arcilla, Agustín, 2595, 2902
Sánchez-Carratalá, Carlos R., 920, 999
Sancho, F. E., 230
Santas, José C., 3086
Santos, João A., 244
Santoso, Eko, 720
Sato, Michio, 1679
Savioli, J. C., 2435
Savioli, Juan, 2980
Sawaragi, Toru, 2654
Sayers, Paul B., 1758
Schaap, J., 2028
Schäffer, Hemming A., 272, 1082
Scheffer, H-J., 1276
Schlütter, Flemming, 1039
Schoonees, J. S., 1475, 3453, 3479, 3561
Schüttrumpf, Holger, 1553
Sclavo, Mauro, 3096
Seabrook, Stuart R., 2000
Sekiguchi, Shin-ichiro, 1290
Shemer, L., 645
Shi, Aimin, 433
Shibayama, Tomoya, 112, 484, 3008
Shigematsu, Takaaki, 2166
Shimizu, T., 2317
Shimoda, Chikara, 787
Shimosako, K., 2207
Shimosako, Ken-ichiro, 1986
Shiu, W. Y., 1421
Shuto, Nobuo, 576
Sigurdarson, Sigurdur, 1407, 3279
Silva, Rodolfo, 1920
Simons, Richard R., 692
Skaarup, Peer, 1530
Skafel, Michael G., 881
Skaja, Marek, 2837
Skou, Ann, 1516
Skourup, Jesper, 603, 1613
Sleath, John F. A., 2968
Sloth, Peter, 1138, 1394, 2235
Smarason, Omar Bjarki, 1407
Smit, F., 3561
Smith, G. G., 2696
Soares, C. Guedes, 3668
Sobey, Rodney J., 1013
Sobierajski, Eugeniusz, 1489

Sollitt, Charles, 2069
Sørensen, John Dalsgaard, 2138
Sørensen, Ole R., 272
Sorensen, Torben, 1
Soulsby, R. L., 2548
Spanhoff, R., 3060
Srinivas, Rajesh, 3345
Stam, Jean-Marie, 2368, 3224
Stansby, P. K., 422
Steetzel, Henk, 1706
Steetzel, Henk J., 2368
Steijn, Rob, 2281
Stephan, H.-J., 3359
Stive, Marcel J. F., 2573
Stoutjesdijk, T., 1587
Stoutjesdijk, Theo, 1601
Suzuki, Kojiro, 1986, 3643
Suzuki, Masaharu, 3575
Suzuki, Shigenori, 2520
Suzuki, Yasushi, 972
Svendsen, I. A., 230, 801, 1323
Svendsen, Ib A., 258
Swan, C., 706, 1110
Szmidt, Kazimierz, 1489
Szmytkiewicz, Marek, 2837

Taborda, Rui, 3206
Takagi, Hiroshi, 2152
Takagi, Toshimitsu, 3151
Takahashi, S., 2207
Takahashi, Shigeo, 1986, 3643
Takayama, Tomotsuka, 1824
Takewaka, Satoshi, 2489
Tanaka, Hiroyoshi, 2534
Tanaka, Hitoshi, 471, 576
Tanaka, Shigenobu, 3151
Tanimoto, Katsutoshi, 892
Tateishi, Yukimitsu, 3374
Taylor, R. Bruce, 3345
Teixeira, Luis, 2294
Teng, Michelle H., 433
Theron, A. K., 3479
Thorne, P. D., 2423
Thornton, E. B., 2877
Thosteson, Eric D., 2344
Tomé, M., 2014
Tondello, Massimo, 3096
Torrini, L., 2028
Tørum, A., 1800
Tørum, Alf, 1435
Troch, Peter, 1039, 1638
Trouw, K., 2423
Tsuda, Muneo, 1986
Tsujimoto, Gozo, 843
Tsukada, Mitsuhiro, 3575
Turk, George F., 1846
Tutuarima, W. H., 1934
Tzeng, Hsiang-Maw, 1263

Uchida, Masahiro, 2489
Uda, Takaaki, 1679, 3138, 3178
Uijttewaal, Wim S. J., 1898
Umeyama, Motohiko, 656
Uriarte, Adolfo, 3086
Utsunomiya, Yoshihiro, 972

Valley, W. S., 3192
van Damme, Luc, 1039
van de Graaff, J., 2028
van de Graaff, Jan, 1706, 2475
van den Boogaard, Henk F. P., 2096
van der Biezen, S. C., 2028
van der Hout, Gizella, 2449
van der Meer, Jentsje W., 3439
van Dongeren, A. R., 1323
van Doorn, J. T. M., 1236
van Gelder, P. H. A. J. M., 3215, 3529
van Gent, Marcel R. A., 2096
van Hoven, A., 2110
van Noortwijk, J. M., 3529
van Oord, G., 1814
van Os, Patrick, 1898
van Overeem, Jan, 2281

van Rhee, Cees, 2509
van Rijn, L. C., 2423
van Rijn, Leo C., 2368, 2495, 2750
Van Wellen, Erik, 2640
Vargas, Berenice Motta, 2353
Veeramony, Jayaram, 258
Venema, L. B., 2463
Verdonck, Raf, 1039
Vergés, D., 2014
Vidal, César, 1730
Viggosson, Gisli, 1407, 3279
Vincent, Chris E., 2344
Visser, Paul J., 3516
Vittori, Giovanna, 2710
Voortman, H. G., 2124
Vrijling, J. K., 1814, 2124, 3215

Wakita. Masakazu, 1679
Walker, James (Kimo), 1222
Watanabe, Yoshihiro, 972
Weilbeer, H., 2269
Wijnberg, Kathelijne, 2409
Wilde, Piotr, 1489
Williams, J. J., 2423
Wise, Randall A., 2722
Wood, Deborah J., 1502
Worley, C. R., 2865
Wyllie, S. J., 1744

Yamagata, Hiroshi, 3138
Yamaguchi, Masataka, 509
Yamahita, Takao, 787
Yamaji, Hiroto, 471
Yamamoto, Koji, 3151
Yamamoto, Masato, 1625
Yamamoto, Yasushi, 1539
Yamashita, Toshihiko, 1290, 3615
Yano, Kenji, 1539, 3615
Yavary, Majid, 3331
Yeh, Harry, 443
Yoshida, Shigeru, 843
Yoshioka, Hiroshi, 787
Young, T., 1744
Yu, C. S., 945
Yu, Yu-xiu, 380

Zacconi, D., 1945
Zanke, Ulrich, 2992
Zedel, Len, 2607
Zeidler, Ryszard, 2926
Zeidler, Ryszard B., 2837
Zhang, Ning-chuan, 380
Zhao, Qun, 892
Zhong, Yiming, 2166
Zhou, J. G., 422
Zielke, W., 2269
Zwamborn, J. A., 1236
Zwanenburg, C., 2110
Zyserman, J. A., 1693